19-22 june, 2023,
Oslo, Norway

Timber for a Livable Future

World Conference on Timber Engineering

WCTE 2023

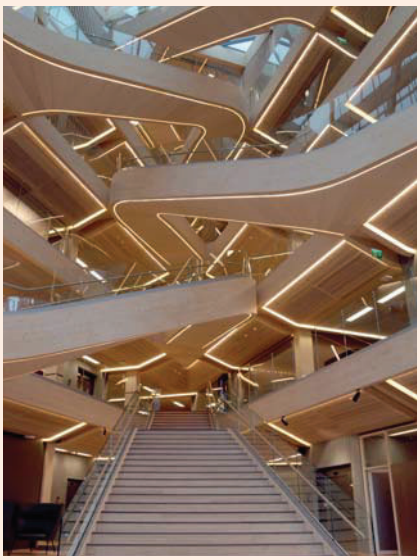

WCTE 2023
Proceedings

Proceedings from the 13th World Conference on Timber Engineering (2023)

Editors
Anders Q. Nyrud
The Faculty of Environmental Sciences and Natural Resource Management, NMBU Norwegian University of Life Sciences

Kjell Arne Malo
Department of Structural Engineering, NTNU Norwegian University of Science and Technology

Kristine Nore
Omtre

Co-editors
Knut Werner Lindeberg Alsén, Ingress
Saule Tulebekova, NTNU
Efthymia Ratsou Stæhr, NMBU
Gabrielle Bergh, NMBU
Wendy Wuyts, Omtre

All authors have submitted two-page extended abstracts, which were peer reviewed by the WCTE2023 International Scientific Committee. The full papers have not been further reviewed, but checked for conformity. Many of these papers represent ongoing research and it is expected that many of the papers will appear in a more comprehensive form in scientific journals in due course.

Design Concept
Uniform

Graphic Design
Knut Werner Lindeberg Alsén

Photo Cover
Nardo Skole / Eggen Arkitekter / Photo Synlig design og foto
Financial Park / Helen & Hard / SAAHA / Photo Jan Inge Haga
Astrup Fearnley Museum / Renzo Piano / NSW arkitektur / Photo Nic Lehoux, VisitOslo

The individual contributions in this publication and any liabilities arising from them, remain the responsibility of the authors. The designations employed and the presentation of material in this publication do not imply the expression of any opinion whatsoever on the part of the World Conference on Timber Engineering 2023, concerning the legal status of any country, territory, city or area or of its authorities, or concerning the delimitations of its frontiers or boundaries. The publisher is not responsible for possible damages, which could arise due to the content derived from this publication.

Copyright© (2023) WORLD CONFERENCE ON TIMBER ENGINEERING 2023 (WCTE 2023) All rights reserved.

ISBN: Print 9781713873297
ISBN: e-proceedings 9781713873273

Printed with permission by Curran Associates, Inc. (2023)
For permission requests, please contact WCTE2023 at the address below.
e-mail: WCTE2023@nmbu.no

Additional copies of this publication are available from:
Curran Associates, Inc. 57 Morehouse Lane Red Hook, NY 12571 USA
Phone: +1 845-758-0400, Fax: +1 845-758-2633, Email: curran@proceedings.com
www.proceedings.com

Proceedings from the 13th World Conference on Timber Engineering, Oslo, Norway 19-22 June 2023

The World Conference on Timber Engineering (WCTE) is the premier forum of the world for dissemination of the latest developments, technologies and innovations in wood materials and timber design, engineering and construction.

The scope covers research, education and practice topics from all over the globe. The conference has attracted wide international representation and attendance.

The name WCTE exists since 1998 when the world's timber engineering society decided to coordinate the former world events and to introduce biennial consecutive conferences in Europe, America, Asia & Pacific.

Conference Chairs WCTE2023
Kjell Arne Malo
Norwegian University of Science and Technology - NTNU

Anders Q. Nyrud
Norwegian University of Life Sciences - NMBU

Kristine Nore
Omtre

Executive Secretary WCTE2023
Knut Werner Lindeberg Alsén
Ingress

World Conference on Timber Engineering Oslo 2023

Timber for a Livable Future

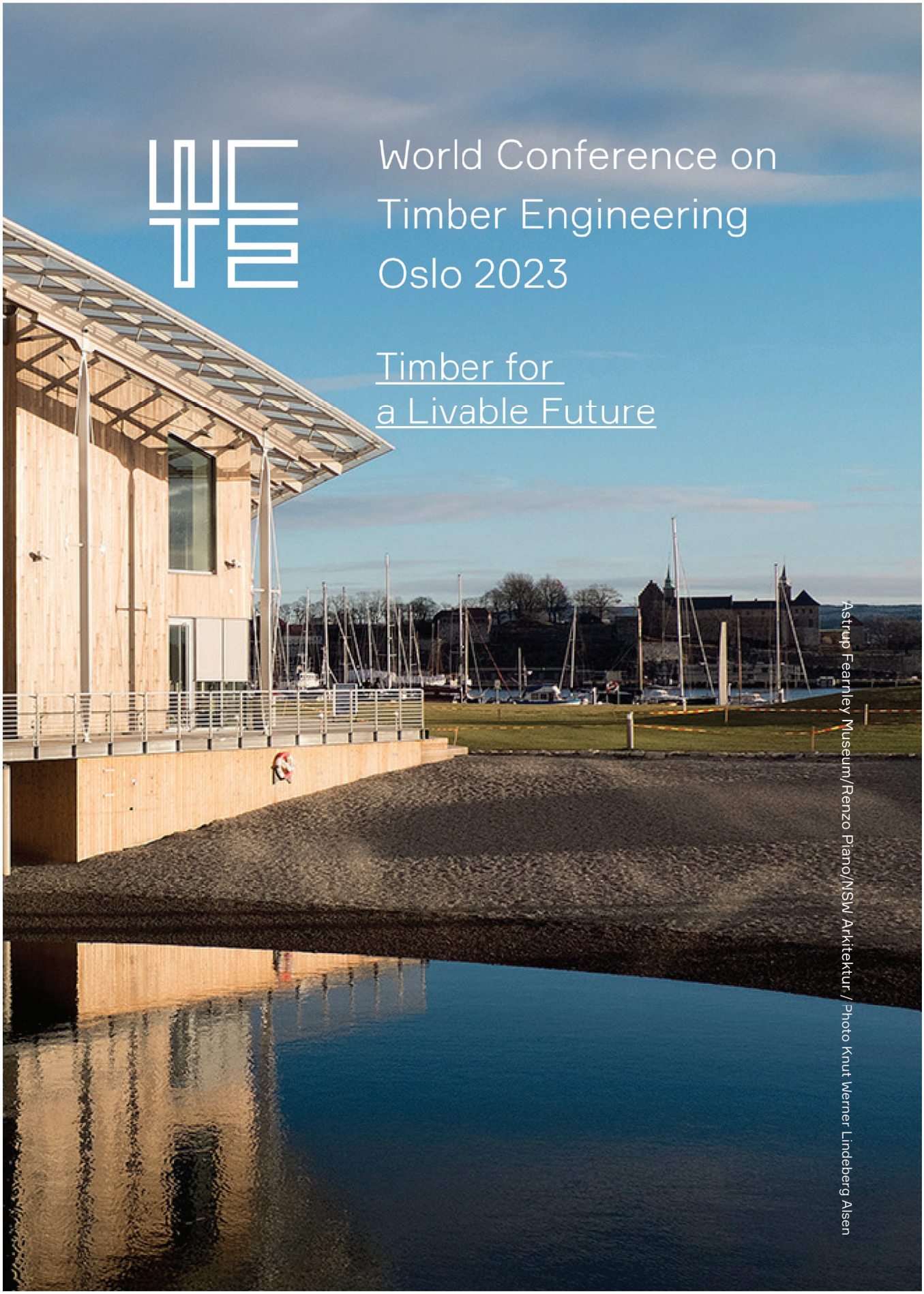

Astrup Fearnley Museum/Renzo Piano/NSW Arkitektur / Photo Knut Werner Lindeberg Alsen

About WCTE

History

The forerunner of WCTE dates back to May 1984, and the Pacific Timber Engineering Conference (PTEC) in Auckland, New Zealand. The first World Conference on Timber Engineering (WCTE) started in 1998 in Montreux, Switzerland, when the world's timber engineering society decided to coordinate the former world events and to introduce a biennial rhythm with consecutive conferences in Europe, America, Asia & Pacific.

Today WCTE is the world's premier scientific dissemination forum for presenting and discussing the latest technical and architectural developments and innovations in timber engineering and construction.The scope covers research, education and practice topics from all over the world. The conference has attracted wide international representation and attendance.

1984 PTEC Auckland, New Zealand
1988 ICTE Seattle, USA
1989 PTEC Auckland, New Zealand
1990 ITEC Tokyo, Japan
1991 ITEC London, UK
1994 PTEC Surfer's Paradise, Australia
1996 IWEC New Orleans, USA
1998 WCTE Montreux, Switzerland
2000 WCTE Whistler, Canada
2002 WCTE Shah Alam, Malaysia
2004 WCTE Lahti, Finland
2006 WCTE Portland, USA
2008 WCTE Miyazaki, Japan
2010 WCTE Trentino, Italy
2012 WCTE Auckland, New Zealand
2014 WCTE Quebec City, Canada
2016 WCTE Vienna, Austria
2018 WCTE Seoul, Rep. of Korea
2021 WCTE Santiago, Chile
2023 WCTE Oslo, Norway
2025 WCTE will be held in Brisbane, Australia

About WCTE

WCTE Coordinating Council 2023

Austria
Josef Eberhardsteiner
Wolfgang Winter

South Korea
Kugbo Shim
Jung-Kwon Oh

Chile
Juan José Ugarte
Sebastian Cárcamo
Carlito Calil

Norway
Kjell Arne Malo
Anders Q. Nyrud
Kristine Nore
Knut Werner Lindeberg Alsén

Germany
Jan Willem van de Kuilen
WCTE Coordinating Council Secretariat

National Organisers WCTE 2023

Main Organisers
Norwegian University of Life Sciences (NMBU)
Norwegian University of Science and Technology (NTNU)
The Oslo School of Architecture and Design (AHO)

Supporting Institutions
Oslo Metropolitan University (OsloMet)
SINTEF Building and Infrastructure
Bergen School of Architecture (BAS)
Norwegian Institute of Wood Technology (Treteknisk)
Norwegian Institute of Bioeconomy Research (NIBIO)
Oslo Municipality
Visit Oslo
Ingress
Uniform

Conference Chairs & Secretariat WCTE2023

Kjell Arne Malo, Professor, NTNU
Anders Q. Nyrud, Professor, NMBU
Kristine Nore, Omtre
Knut Werner Lindeberg Alsén, Executive Secretary - WCTE 2023, Ingress

International Scientific Committee

Eduardo Torrán	Argentina
Keith Crews	Australia
Jeff Morell	Australia
Gregory Nolan	Australia
Reinhard Brandner	Austria
Josef Fuessl	Austria
Herman Kaufmann	Austria
Markus Lukacevic	Austria
Gerhard Schickhofer	Austria
Thierry Descamps	Belgium
Carlito Calil Jr.	Brazil
Carlito Calil Neto	Brazil
Ghasan Doudak	Canada
Lin Hu	Canada
Geert Ravenshorst	Canada
Erol Karacabeyli	Canada
Frank Lam	Canada
Christiano Loss	Canada
Marjan Popovski	Canada
Alexander Salenikovich	Canada
Ian Smith	Canada
Thomas Tannert	Chile
Franck Schanack	China
Minjuan He	China
Shengdong Zhang	Colombia
Juan Francisco Correal	Czechia
Petr Kuklik	Denmark
Anders Bjørnfot	Denmark
Olga Larsen	Denmark
Jørgen Munch-Andersen	Finland
Gerhard Fink	Finland
Stefania Fortino	Finland
Mark Hughes	France
Rostand Moutou-Pitti	France
Stéphane Hameury	Germany
Simon Aicher	Germany
Hans Joachim Blass	Germany
Phillip Dietsch	Germany
Peer Haller	Germany
Ulrike Kuhlmann	Germany
Christopher Robeller	Germany
Carmen Sandhaas	Germany
Kay-Uwe Schober	Germany
Anette Harte	Italy
Marco Ballerini	Italy
Daniele Casagrande	Italy
Beatrice Faggiano	Italy
Massimo Fragiacomo	Italy
Maurizio Piazza	Italy
Andrea Polastri	Italy
Hiroshi Isoda	Japan
Kohei Komatsu	Japan
Adrian Leijten	Netherlands
Pierre Quenneville	New Zealand
Gary Raftery	New Zealand
Minghao Li	New Zealand
Pouyan Zarnani	New Zealand
Anders-Johan Almås	Norway
Ulrich Hundhausen	Norway
Dimitrios Kraniotis	Norway
Thomas Kringlebotn Thiis	Norway
Tore Kvande	Norway
Erik Larnøy	Norway
Kjell Arne Malo	Norway
Roja Modaresi	Norway
Petra Rüther	Norway
Haris Stamatopoulos	Norway
Roberto Tomasi	Norway
Audun Øvrum	Norway
Jochen Köhler	Norway
Jorge Branco	Portugal
Alredo Dias	Portugal
Igor Gavric	Slovenia
Francisco Arriaga	Spain
José Manuel Cabrero	Spain
Erik Serrano	Sweden
Henrik Danielson	Sweden
Eva Frühwald	Sweden
Robert Jockwer	Sweden
Marie Johansson	Sweden
Sigurdur Ormarsson	Sweden
Karin Sandberg	Sweden
Johan Vessby	Sweden
Andrea Frangi	Switzerland
Bettina Franke	Switzerland
Martin Lehmann	Switzerland
Christophe Sigrist	Switzerland
Rene Steiger	Switzerland
Callum Hill	United Kingdom
Vanessa Baño	Uruguay
Peggi Clouston	USA
Lech Muszynski	USA
Douglas Rammer	USA
James Wacker	USA
John Van de Lindt	USA

National Committee

Anders Homb	Martin Cepelka
Anna Ostrycharczyk	Morten Løvseth
Bård Sverre Solem	Niki Gaitani Nina Berre
Dag Pasquale Pasca	Olav A. Høibø
Ebenezer Ussher	Pasi Aalto
Efthymia Ratsou Staehr	Roberto Tomasi
Francisco Mirko Massaro	Rune Abrahamsen
Fredrik Shetelig	Saule Tulebekova
Gabrielle Bergh	Siv Helene Stangeland
Geir I. Vestøl	Solveig Sandness
Hauke Burkart	Sveinung Nesheim
Javad Darvishi	Themistoklis Tsalkatidis
Jonas Holme	Tor Håvard Ellingsen
Kolbein Bell	Ute Christina Groba
Kristian Dahl	Wendy Wuyts
Lone Ross	Åge Holmestad
Magne Bjertnæs	Aasmund Bunkholt
Mari Sand Austigard	
Martin Ebert	

Preface WCTE2023

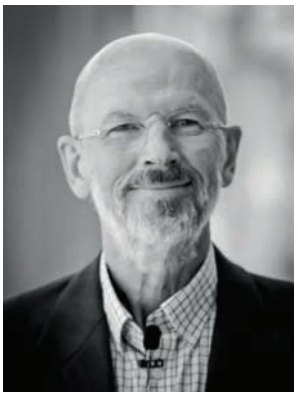

Kjell Arne Malo

Anders Q. Nyrud

Dear colleagues, Dear readers

Despite the exceptional COVID-pandemic situation experienced, we are now back on track with a physical gathering at the 13th World Conference on Timber Engineering (WCTE2023) in Oslo, Norway. Thanks to extensive effort by our Chilean colleagues, who organized the conference in 2021, WCTE could take place also during the COVID pandemic. We all do, however, appreciate to be back in the traditional physical conference context.

The slogan of the WCTE2023 is: Timber for a Livable Future. This is indeed a relevant slogan.

We are now experiencing increased interest in timber as a structural material as well as wood used for surface in architecture. Timber is in fact used in many different types of products and structures. It is a bio-based material, in which humanity has created shelters, tools and objects of art. Throughout history humans have adapted to timber. How do we take this wisdom into our modern timber structures?

Climate change is a driving force and pushes all of us to toward severe changes with more environmentally friendly, sustainable and circular materials in our built practice. Everyone with an interest in wood as a construction material in research, industry and education has a role for development of the field of timber engineering so that we can meet future demands and societal needs.

The forerunner of WCTE dates back to May 1984, at the Pacific Timber Engineering Conference (PTEC) in Auckland, New Zealand. The first World Conference on Timber Engineering (WCTE) took place in 1998 in Montreux, Switzerland. It was decided to consolidate the former world events and to introduce a biennial rhythm with consecutive conferences in Europe, America, Asia & Pacific. The conference has been hosted in the Nordic region only once before, in Lahti, Finland in 2004.

The conference has maintained its important position on the world scene with currently more than 600 papers accepted for presentation. WCTE2023 is the major event within the timber engineering society in 2023 and has attracted more than 800 attendants and more than 600 presentations. Participants have the opportunity to share ideas on nearly any subject related to timber engineering, from codes of practice, regulations and legislations, to innovations, new practices, and future trends of bio-based sustainable and circular building materials used in construction. WCTE2023 reflects the state-of-the-art in timber engineering.

This proceeding provides a collection of all the scientific contributions to the conference. The conference has attracted a wide range of academics, scientists, researchers, students, designers, policymakers, and other industrialists with a wide variety of backgrounds, including fields of engineering, materials, sustainable development, architecture, ecological technologies, biomaterials, materials sciences, environmental engineering, government agencies, end-users, and more.

The Organizing Committee of WCTE2023 would like to express our sincere gratitude to all contributors and participants for their carefully prepared, stimulating, and interesting manuscripts.

Kristine Nore

Knut Werner Lindeberg Alsén

Thanks are also extended to the members of the WCTE2023 International Scientific Committee for review of nearly one thousand submissions. Without their dedicated efforts, the conference and the proceedings would not have been realized in this way. The cooperation of the authors in accepting reviewers' suggestions and revising their manuscripts accordingly is greatly appreciated.

The organization of a conference of this scale was possible with the support and contributions from many organizations and individuals including financial support. We are grateful to Innovation Norway for supporting grants for conference preparation. We also would like to express our thanks to the Oslo Convention Bureau for their important support throughout the entire process, from application to implementation of WCTE 2023.

We would like to thank the Norwegian supporting organisations Oslo Metropolitan University (OsloMet), Norwegian Institute of Wood Technology (Treteknisk), Norwegian Institute of Bioeconomy Research (NIBIO), SINTEF and Bergen School of Architecture (BAS).

We would like to thank our platinum sponsors SWECO, Paper Province and Region Värmland, and the gold sponsors Moelven and Aanesland Treindustri, as well as sponsors on silver, bronze and supporting level.

We would like to thank PEFC Norge, Moelven, Hunton, Ny Struktur, Splitkon, County Governor of Vestland, Norwegian Wood Cluster, NTNU Wood, Wood Works Cluster, Norsk Folkemuseum, for participating in planning and preparations for the technical conference tours and other events.

A special thank you goes to AHO, SWECO, Aanesland Treindustrier, Bergene Holm, SirkTRE and Bymiljøetaten Oslo kommune, for making the WCTE-pavilion outside the conference venue such an exciting demonstration of timber engineering in real life.

We would also like to thank all those who have devoted their time and effort to the organization of the conference. We would like to thank the Coordinating Council of the WCTE for support and trust as well as our colleagues in WCTE2021 from Chile for sharing their expertise and experience with us.

Finally, we would like to thank the four hosting institutions, NMBU, NTNU, AHO and the City of Oslo, for cooperation and efforts in the process of planning and conducting the conference.

Oslo, 19 May 2023

Conference chairs
Kjell Arne Malo
Anders Q. Nyrud
Kristine Nore
Knut Werner Lindeberg Alsén

TABLE OF CONTENTS

1.1. STRUCTURAL PERFORMANCE OF MATERIALS

COMPARISON OF THE STRUCTURAL CAPACITY OF SHEAR WALLS SHEATHED WITH ORIENTED STRAND BOARD AND RECYCLED MATERIAL SUBJECTED TO CYCLIC LOADING 1
David Dinehart, Eric Musselman, Edward Bolte, Bridget Lasala

PENDULUM IMPACT HAMMER TESTS ON TIMBER BEAMS - EXPERIMENTAL SETUP 6
Alex Sixie Cao, Andrea Frangi

NUMERICAL AND EXPERIMENTAL EVALUATION OF WOOD NAILER OPEN WEB STEEL JOISTS 14
Sameer Fares, David Dinehart, Shawn Gross, Joseph Yost, Rebecca Hoffman

BEHAVIOR OF TIMBER BEAMS STRENGTHENED WITH CFRP 24
Zhang Shengdong, Blanche Blondel De Joigny, Jianrong Cui

MICROWAVE TECHNOLOGY AND ITS APPLICATIONS TO WOOD TREATMENT AND MODIFICATION 31
Fernando Mascarenhas, Alfredo Dias, André Christoforo, Rogério Simões

STRUCTURAL PERFORMANCE, AND FAILURE MECHANISM, OF HARDWOOD CROSS LAMINATED TIMBER CONCRETE COMPOSITE UNDER SHEAR LOAD 41
Aamir Khokhar, David Bell, Roshan Dhonju

SCALING STUDY ON VISCOUS DAMPING FOR GLULAM AND HYBRID GLULAM-FRP BEAMS 51
Tomas Bravo Tetlak, Joseph M. Gattas, Cristian Maluk

EXPERIMENTAL AND FINITE ELEMENT MODELLING (FEM) OF TIMBER-TIMBER COMPOSITE (TTC) UNDER HOGGING MOMENT 57
Mahmoud Wajdi Hammad, Hamid R Valipour

QUASI-STATIC OUT-OF-PLANE TESTING OF REINFORCED CROSS-LAMINATED TIMBER 65
Eric Kjolsing, Mark Weaver, Marco Lo Ricco, C. Adam Senalik, Jason Cattelino, Jim Henjum, Russell Edgar, Edwin Nagy

BALLISTIC TESTING OF CROSS-LAMINATED TIMBER LAYUPS TO FURTHER DEVELOP PROTECTIVE PANELS 75
Marco Lo Ricco, Mark Weaver, C. Adam Senalik, Jim Henjum, Jason Cattelino

PREDICTING MODULUS OF RUPTURE OF HEAT-TREATED WOODS BY ARTIFICIAL NEURAL NETWORK COMBINED WITH GENETIC ALGORITHM 84
Mehdi Nikoo, Reza Abbasi Malekabadi, Ghazanfarah Hafeez

TENSION LOADED CONNECTIONS WITH WOOD DOWELS 89
Matthias Brieden, Max Braun, Werner Seim

MECHANICAL PROPERTIES OF GLUE LAMINATED TIMBER BY SMALL SIZE TREE SPECIES (CASE STUDY OF OKINAWAN FOREST) 98
Juan Castro, Shogo Omi

EXPERIMENTAL INVESTIGATION ON IN-PLANE PERFORMANCE OF NAIL-LAMINATED TIMBER FLOORS 105
Zhaozhuo Gan, Minjuan He, Zheng Li, Xiaofeng Sun

AN EXPLORATORY STUDY ON MIXED-MODE FRACTURE AND STRAIN DISTRIBUTION NEAR A CRACK TIP OF ADHESIVELY-LAMINATED WOOD SPECIMENS USING THE MODIFIED ARCON FIXTURE AND DIGITAL IMAGE CORRELATION 112
Zizhen Gao, Meng Gong, Ling Li, Mohsen Mohammadi

GREEN OAK BUILDING WITH HIGH-TECH METHODS, PART 2: LOG BENDING TESTS FOR DETERMINATION OF STRENGTH AND STIFFNESS 119
Kay-Uwe Schober, Beate Hörnel-Metzger, Maximilian Leonhard Müller, Nicolas Hofmann, Franka Brüchert, Udo H. Sauter

EXPERIMENTAL STUDY ON IN-PLANE SHEAR PERFORMANCE OF CROSS-LAMINATED TIMBER 126
Kaito Yamagata, Ryo Inoue, Takuro Mori

SHEAR TESTS ON FULL-SCALE EUROPEAN ASH GLUED LAMINATED TIMBER BEAMS 132
Pedro Palma, René Steiger, Thomas Strahm, Ernst Gehri

STRUCTURAL USE OF CUT-OFFS FROM CLT-PRODUCTION – THREE EXAMPLES THAT UTILIZE THE UNIQUE PROPERTIES 139
Johan Vessby, Mikael Perstorper, Florian Demonte, Jacob Eriksson

EXPERIMENTAL STUDY ON CHARACTERISTIC VALUES OF PARTIAL COMPRESSION PERPENDICULAR TO THE GRAIN OF HARDWOOD WITH EDGE DISTANCE ORTHOGONAL TO THE LONGITUDINAL DIRECTION 147
Hiroto Suesada, Kohta Miyamoto

COMPARISON BETWEEN ACTUAL AND EQUIVALENT CRACK RESISTANCE R-CURVE FOR TIMBER AND TIMBER BOND UNDER MODE-II FRACTURE 153
Shaikh Atikur Rahman, Mahmud Ashraf, Mahbube Subhani

MODE I TESTS OF NORWAY SPRUCE USING SEN-TPB: DETAILED ANALYSIS OF THE CRACK LENGTH DETERMINED USING OPTICAL METHOD 162
Martin Hataj, Jirí Kunecký, Michal Kloiber

BAMBOO GRIDSHELL: FROM THE MATERIAL TO THE STRUCTURE 168
Esti Nurdiah, Tsung-Hsien Wang, Wen-Shao Chang

PRELIMINARY INVESTIGATION ON SAFETY PERFORMANCE OF CLT WALL PANELS UNDER IMPACT AND SUSPENSION TESTS 175
Gabriela Lotufo Oliveira, Fabiana Lopes De Oliveira

ENABLE THE USE OF MASS TIMBER PRODUCTS FOR NON-RESIDENTIAL BUILDINGS IN HIGH VELOCITY HURRICANE ZONES 182
Sovanroth Ou, Michael Stoner, Weichiang Pang

BENDING BEHAVIOR OF GLT-STEEL BEAM CONNECTED BY INCLINED SCREWS 188
Sung-Jun Pang, Kyung-Sun Ahn, Gwang-Ryul Lee, Min-Jeong Kim, Jae-Won Oh, Jung-Kwon Oh

THE PRODUCTION OF ADHESIVE FREE CROSS-LAMELLA TIMBER (CLT) PANEL USING PRODUCTS GENERATED BY THE SUSTAINABLE FOREST MANAGEMENT OF THE AMAZONIAN OLD GROWTH FOREST 196
Marcos Cesar Pereira, Adma M. D. Higuchi, Geraldo Lira, Antonio Alves Dias, Niro Higuchi

AN EXPERIMENTAL INVESTIGATION OF FAILURE MODES IN SHORT SPAN FRP REINFORCED GLULAM BEAMS 202
Catherine Shrimpton, Serena Siciliano, Herry Chen, Yannick Vetter, Daniel Lacroix

DAMAGE MODEL FOR A BIOSSOURCED HETEROGENEOUS MATERIAL: APPLICATION TO TIMBER 209
Amal Rebhi, Myriam Chaplain, Jean-Luc Coureau, Cedric Perez

NUMERICAL EXAMINATION OF THE BEHAVIOUR OF DOWEL LAMINATED TIMBER ELEMENTS UTILISING COMPRESSED WOOD DOWELS 216
Conan O'Ceallaigh, Annette M. Harte, Patrick J. McGetrick

BONDING OF FIRE-RETARDANT TREATED SPRUCE LAMELLAE FOR USE IN CROSS LAMINATED TIMBER (CLT) 225
Karl-Christian Mahnert, Stine Lønbro Bertelsen

EVALUATION OF TIMBER-CONCRETE SLAB CONNECTED WITH NOTCHED CONNECTION MADE OF KOREAN LARCH STRUCTURAL PLYWOOD 232
Kyung Sun Ahn, Sung-Jun Pang, Jiyong Kim, Jaewon Oh, Min-Jeong Kim, Gwang-Ryul Lee, Jung-Kwon Oh

MEASURING FIRE SAFETY PERFORMANCE: A COMPARATIVE EXPERIMENTAL STUDY ON DOVETAIL MASSIVE WOODEN BOARD ELEMENTS AND CROSS-LAMINATED TIMBER 238
Hüseyin Emre Ilgin, Markku Karjalainen, Mikko Malaska, Mika Alanen

LABORATORY INVESTIGATION OF CROSS-LAMINATED DECKS FOR BRIDGE APPLICATIONS 244
Justin M. Dahlberg, James P. Wacker, Douglas R. Rammer

COMPRESSIVE STIFFNESS PARALLEL TO GRAIN IN TIMBER 251
Marina Totsuka, Robert Jockwer, Kenji Aoki, Masahiro Inayama

COMPARISON OF THE DEGREE OF INFLUENCE OF VARIOUS CONDITIONS ON THE BEARING CAPACITY OF WOOD-BASED PANELS 259
Ryutaro Sudo, Kenji Aoki

REINFORCEMENT OF TIMBER STRUCTURES VERSUS CLIMATE IMPACT 268
Bettina Franke, Steffen Franke, Marcus Schiere

COMPONENT METHOD IN TIMBER CONNECTIONS: END-PLATE COMPRESSING TIMBER PARALLEL TO GRAIN COMPONENT STRENGTH 276
Arthur S. Rebouças, Jorge M. Branco, Paulo B. Lourenço, Hidelbrando J. F. Diógenes

COMPARISON BETWEEN EXPERIMENTAL RESULTS AND DESIGN EQUATIONS OF ARTIFICIALLY DEGRADED SINGLE STEP JOINTS 285
Daniel F. Lima, Jorge M. Branco, Lina Nunes

STUDY ON THE RELATIONSHIP BETWEEN INTERLAYER DEFORMATION ANGLE AND TORN WALLPAPER OF WOODEN HOUSES 292
Sora Sunakozawa, Kiyotaka Terui, Hideyuki Nasu

GLUED-LAMINATED TIMBER UNDER EXTREME COLD TEMPERATURES SUBJECTED TO IMPACT LOADING 299
Nicole Wight, Christian Viau, Patrick Heffernan

EXPERIMENTAL AND NUMERICAL ANALYSIS OF CLT FLOOR SUBASSEMBLIES UNDER CATENARY ACTION 307
Alicja Przystup, Thomas Tannert, Yong Lu, Thomas Reynolds

UNREINFORCED AND STEEL-REINFORCED COLUMNS MADE OF EUROPEAN BEECH GLUED-LAMINATED TIMBER 315
Katharina Sroka, Pedro Palma, René Steiger, Thomas Ehrhart, Andrea Frangi, Thomas Strahm, Ernst Gehri

MECHANICAL BEHAVIOUR OF COLUMN BASES FOR CLT ROCKING FRAMES 323
Akira Masuda, Chisato Inutsuka, Kazuhiro Matsuda

INVESTIGATION OF CROSS LAMINATED TIMBER'S LONG-TERM PERFORMANCE (CREEP) 333
Aaron Desantis, Michael Stoner, Weichiang Pang

LOW-TEMPERATURE BONDING OF TIMBER STRUCTURES 339
Morten Voss, Tobias Evers, Till Vallée

RAPID BONDING OF TIMBER STRUCTURES 345
Morten Voss, Jona Haupt, Till Vallée

EXPERIMENTAL RESEARCH ON POINT-SUPPORTED CLT PANELS: PHASE 1: ROLLING SHEAR STRENGTH 352
Md Shahnewaz, Carla Dickof, Houman Ganjali, Christian Slotboom, Mandy Tam, Robert Jackson, Marjan Popovski, Thomas Tannert

PRELIMINARY TEST RESULTS ON THE IN-PLANE STRENGTHENING OF TIMBER FLOORS WITH THE DOUBLE PLANKING TECHNIQUE 358
Giovanni Metelli, Alessandra Marini, Stefania Cominelli, Francesca Feroldi, Anna Maria Basso Bert, Ezio Giuriani

1.2. MATERIAL MODELLING

A NEW APPROACH TO DETERMINE AND EVALUATE THE POISSON´S RATIO OF WOOD 366
Klara Winter, Roland Maderebner, Philipp Dietsch

THEORETICAL AND EXPERIMENTAL INVESTIGATION ON PREDICTING LONGITUDINAL AND TANGENTIAL ELASTIC CONSTANTS AND RATIOS OF WOOD 376
Shaghayegh Kurzinski, Paul L. Crovella

PYTHON-BASED PLATE MODEL TO SIMULATE THE EFFECT OF KNOTTY AREAS ON SAWN TIMBER 383
Jorge Uribe Cisternas, Diego Valdivieso Cascante

SIMULATION OF WOOD FRACTURE MECHANICS USING THE PHASE FIELD METHOD FOR FRACTURE 391
Sebastian Pech, Markus Lukacevic, Josef Füssl

NUMERICAL SIMULATION OF MOISTURE INDUCED CRACKING IN INDOOR CLIMATE 398
Florian Brandstätter, Maximilian Autengruber, Markus Lukacevic, Josef Füssl

EXPERIMENTAL DETERMINATION OF R CURVES FOR EUROPEAN SPRUCE USING DCB TESTS 407
Marija Todorovic, Marko Pavlovic, Ivan Glišovic, Mathieu Koetsier

THE INFLUENCE OF WOOD COATINGS ON THE MOISTURE BUFFERING CAPACITY OF CLT AND THE INDOOR ENVIRONMENT 413
Ulrich Hundhausen, Robbe Heyvaerts, Sameer Ullah, Dimitrios Kraniotis

EVALUATION OF MODELS OF FIBRE ORIENTATION IN SAWN TIMBER USING SYNCHRONISED COMPUTED TOMOGRAPHY AND OPTICAL SCANNING DATA 421
Johannes Huber, Osama Abdeljaber, Johan Oja, Anders Olsson

MODELLING THE EFFECT OF THREE-DIMENSIONAL GRAIN ANGLE ON THE TENSION STRENGTH OF BIRCH WOOD 428
Steven Collins, Joonas Jaaranen, Gerhard Fink

HYGROTHERMAL PERFORMANCE OF SHEEP WOOL IN COLD AND HUMID CLIMATES ..... N/A
Yuchen Chen, Dehong Li, Bin Li, Denis Rodrigue, Xiaodong Alice Wang

EFFECTS OF THE CROSS-LINKING OF THE CELLULOSIC FIBRILLAR NETWORK ON THE EFFECTIVE MACROSCOPIC BEHAVIOUR OF WOOD 443
Nhat-Tung Phan, François Auslender, Joseph Gril, Rostand Moutou Pitti

A MULTI-PHASE HYGRO-THERMAL MODEL FOR WOODEN BRIDGE COMPONENTS EXPOSED TO SOLAR RADIATION 449
Stefania Fortino, Petr Hradil, Timo Avikainen, Keijo Koski, Ludovic Fülöp

NUMERICAL MULTI-SCALE HOMOGENIZATION OF MECHANICAL PROPERTIES OF PINUS PINASTER (AIT.) LAMELLAE CONSTITUTING GLUED LAMINATED TIMBER 455
Romain Chevalier, Bruno Vuillod, Mathilde Zani, Marco Montemurro, Régis Pommier, Anita Catapano

SIZE EFFECT OF LARGE GLUED LAMINATED TIMBER BEAMS – CONTRIBUTION TO THE ONGOING DISCUSSION 465
Christoffer Vida, Markus Lukacevic, Georg Hochreiner, Milena Stavric, Josef Füssl

MODE I FRACTURE ENERGY OF AUSTRALIAN NATIVE HARDWOOD SPOTTED GUM AT VARIOUS MOISTURE CONTENTS 474
Peiqing Lu, Benoit P. Gilbert, Chandan Kumar, Robbie L. McGavin, Hassan Karampour

FLEXURAL REINFORCMENT OF TIMBER ELEMENTS ON-SITE WITH PRF ADHESIVE AND WOOD-BASED PRODUCTS 482
Andreas Stenstad, Karl-Christian Mahnert, Kristine Vik

1.3. LONG-TERM BEHAVIOUR

WEAR RESISTANT PROTECTION OF WOODEN POLES IN ADVERSE ENVIRONMENTS 488
Thomas Lindblad, Knut Magnar Sandland, Andreas Treu

WOOD AND STEEL VISCOELASTIC DAMPERS: SHORT AND LONG-TERM PERFORMANCE 493
David W. Dinehart, Edward D. Bolte, David E. Lewicki

DURATION OF LOAD UNDER LONG-TERM BENDING LOAD OF LAMINATED VENEER LUMBER AND WOODEN I-BEAM 498
Ryuya Takanashi, Takahiro Tsuchimoto, Yoshinori Ohashi, Wataru Ishihara

DERIVATION FROM EN927 METHOD FOR EVALUATING OUTDOOR DURABILITY OF COATED FIRE-RETARDANT-TREATED WOOD 505
Ryo Takase, Atsuko Ishikawa, Daisuke Kamikawa

DIMENSIONAL VARIATIONS MONITORING OF RADIATA PINE CLT PANELS: A CASE STUDY IN CONCEPCIÓN, CHILE 512
Víctor Rosales, Fernanda Pascal, Franco Benedetti, Pedro Rebolledo, Alan Jara-Cisterna, Mauricio Vargas

EFFECTS OF PANEL DIRECTION, LOAD LEVEL AND AMBIENT HUMIDITY ON THE CREEP OF DOWNSCALED CROSS-LAMINATED TIMBER 521
Dawei Wang, Meizhen Chen, Meng Gong, Zhuo Cheng

SHEAR CREEP OF POLYSTYRENE CORES IN WOODBASED PANELS 529
André Jorissen, Johnny Van Rie, Jeff Modderman, Hèrm Hofmeyer

INTEGRATED APPROACH TO PREDICT DETERIORATION OF MECHANICAL PROPERTIES OF DECAYING WOOD 536
Petr Hradil, Stefania Fortino

CREEP TESTS ON NOTCHED BEAMS OF SILVER FIR WOOD (ABIES ALBA) 542
Arthur Bontemps, Gaël Godi, Rostand Moutou Pitti, Eric Fournely, Joseph Gril

SIMPLIFIED ENVIRONMENTAL ANALYSIS OF THE LONG-TERM PERFORMANCE OF WOOD CLADDING AND DECKING 549
Jonas Niklewski, Jakub Sandak, Philip Bester Van Niekerk, Christian Brischke, Richard Acquah, Anna Sandak

ON THE USE OF ARUCO MARKERS IN LONG TERM MONITORING OF TIMBER STRUCTURES 558
Jirí Kunecký

EXPERIMENTAL STUDY OF THE EFFECTS OF ACCELERATED AGING CYCLES ON THE FIRE REACTION PERFORMANCE OF FIVE WOOD SPECIES 564
María Pilar Giraldo, Alina Avellaneda, Laia Haurie, Marcel Vilches, Ana M. Lacasta

LONG TERM BEHAVIOR OF A TWO-WAY SPANNING TIMBER CONCRETE SLAB WITH STEEL TUBE CONNECTOR 571
Julian Brogli, Andrea Frangi

INVESTIGATING THE EFFECTS OF MOISTURE INGRESS ON THE PERFORMANCE AND SERVICE LIFE OF MASS TIMBER PANELS IN AUSTRALIAN CLIMATES-CHARACTERIZATION OUTCOMES 578
Maryam Shirmohammadi

EXPERIMENTAL INVESTIGATION ON LONG-TERM BEHAVIOR OF TIMBER-TO-TIMBER SHEAR CONNECTIONS MADE BY INCLINED SELF-TAPPING SCREWS 586
Alessandra Gubana, Massimo Melotto, Luca De Cillia, Alessandro Mazelli

PATINA AND ITS FORMATION ON A WOODEN CHURCH FLOOR – CASE PETÄJÄVESI OLD CHURCH AND VIIKKI CHURCH IN HELSINKI 593
Jonna Silvo

1.4. ENGINEERED TIMBER PRODUCTS AND PRODUCTION

ON THE UTILISATION OF THE WORKSPACE OF AN INDUSTRIAL ROBOT FOR MILLING STRUCTURAL TIMBER COMPONENTS – EXPERIMENTAL TRIALS WITH DIFFERENT ARM POSITIONS AND EVALUATION OF MACHINING QUALITY 599
Marc Pantscharowitsch, Finn Linzer, Hans-Berndt Neuner, Benjamin Kromoser

SHEAR THROUGH THE THICKNESS PROPERTY OF SCREW LAMINATED CROSS LAMINATED TIMBER 609
Shiro Nakajima

BIRCH FOR ENGINEERED TIMBER PRODUCTS: PART II 615
David Obernosterer, Georg Jeitler, Gerhard Schickhofer

INVESTIGATIONS ON MULTIFUNCTIONAL TIMBER ELEMENTS IMPREGNATED WITH PARAFFINIC PHASE CHANGE MATERIALS 621
Jens Hartig, Peer Haller

ADDITIVE MANUFACTURING OF WOOD COMPOSITE PARTS BY INDIVIDUAL LAYER FABRICATION – THE PRODUCTION PROCESS AND RESPECTIVE MACHINERY 629
Birger Buschmann, Daniel Talke, Klaudius Henke, Carsten Asshoff, Frauke Bunzel, Bettina Saile

ELASTOMECHANICAL PROPERTIES OF GLUED LAMINATED TIMBER MADE OF STRENGTH GRADED OIL PALM LUMBER 638
Katja Fruehwald-Koenig

FLEXURAL PROPERTIES OF OIL PALM WOOD BASED GLUE LAMINATED TIMBER USING FINITE ELEMENT METHOD 647
Martin Hackel

BENDING PROPERTIES OF 100 NARROW CLT-BASED BOARDS – STATIC AND DYNAMIC TESTS AND DIC ANALYSIS 657
Mikael Perstorper, Johan Vessby, Emil Lockner

DENSIFIED WOODEN NAIL FOR ADHESIVE- AND METAL- FREE TIMBER ASSEMBLES 666
Lei Han, Dusan Pauliny, Anna Sandak, Mariapaola Riggio, Andreja Kutnar, Dick Sandberg, Jakub Sandak

EXPERIMENTAL INVESTIGATION OF FINGER JOINTS UNDER TENSILE AND BENDING LOADS 671
Farid Vafadar, Steven Collins, Gerhard Fink

POTENTIAL OF REUSING SALVAGED WOODEN MATERIALS IN FABRICATING DOWEL LAMINATED STRUCTURAL ELEMENTS WITH WOODEN CONNECTORS 677
Mohammad Derikvand, Gerhard Fink

STRUCTURAL SAWN WOOD PRODUCTION IN THE CHILEAN SAWMILL INDUSTRY, DATA ANALYSIS FROM SURVEYS CARRIED OUT FOR 4 YEARS 683
Pamela Poblete, Janina Gysling, Carlos Kahler, Wilson Mejías, Daniel Soto, Verónica Álvarez, Evaristo Pardo

ROTATIONAL STIFFNESS OF NEWLY DEVELOPED LVL-BASED COLUMN-HEAD REINFORCEMENT FOR POINT-SUPPORTED SLAB-COLUMN BUILDING SYSTEMS 688
Cristóbal Tapia, Felix Amtsberg, Aaron Münzer, Simon Aicher, Achim Menges

MECHANICAL PROPERTIES TESTS OF DELIGNIFIED AND DENSIFIED WOOD 698
Jörg Wehsener, Martina Bremer, Peer Haller

DEVELOPMENT OF CONSTRUCTION METHODS WITH NATURALLY GROWN TIMBER AND BENDING-RESISTANT JOINTS 705
Kevin Moreno Gata, Alex Seiter, Denis Grizmann, Martin Trautz

1.5. QUALITY CONTROL OF TIMBER-BASED MATERIALS

GREEN OAK BUILDING WITH HIGH-TECH METHODS, PART 1: CHARACTERISATION OF THE RAW MATERIAL 711
Nicolas Hofmann, Franka Brüchert, Udo H. Sauter, Kay-Uwe Schober, Beate Hörnel-Metzger, Maximilian L. Müller

VARIATION IN MECHANICAL PROPERTIES WITHIN AND BETWEEN PLANTATION-GROWN GMELINA ARBOREA TREES 717
Stanley Emeka Iwuoha, Werner Seim

IN-GRADE CLT FROM UNGRADED PINUS RADIATA BOARDS 723
Paolo Lavisci, Marco Molinari, Michele Brunetti

COLLAGE QUALITY OF BRAZILIAN WOODS FOR USE IN GLUED LAMINATED TIMBER BEAMS 729
Julio Cesar Molina, Natália Andrade Bianchi, Felipe Dutra Lisboa, Nádia Barros Gomes

NON-PARAMETRIC LOWER CONFIDENCE BOUNDS FOR THE FIFTH PERCENTILE - EN 14358 IN COMPARISON TO A FULLY NON-PARAMETRIC APPROACH 735
Andreas Weidenhiller, Dan Ridley-Ellis, Andreas Neumüller

NEW CRITERIA FOR VISUAL STRENGTH GRADING OF SAWN TIMBER FROM BIRCH GROWN IN SWEDEN 740
Ulf Lemke, Marie Johansson, Rune Ziethén, Andreas Briggert

FIBRE-OPTIC MEASUREMENTS FOR MONITORING ADHESIVELY BONDED COMPOSITE BEAMS 750
Jens Frohnmüller, Werner Seim, Ann-Charlotte Spangenberg

ESTIMATION OF MOISTURE DISTRIBUTION IN SAWN TIMBER USING COMPUTED TOMOGRAPHY 759
Boris Poupet, José Couceiro, Sara Florisson, Lars Hansson, Dick Sandberg

PREDICTION OF DOUGLAS FIR SAWN TIMBER YIELD BASED ON LOG COMPUTED TOMOGRAPHY 766
Andreas Weidenhiller, Boris Sandor, Thomas Simlinger, Franka Brüchert, Johannes A. J. Huber

CONSIDERATIONS FOR GRADING SPECIES COMBINATIONS. THE EXAMPLE OF DOUGLAS FIR WITH LARCH IN IRELAND AND UK 773
David Gil-Moreno, Dan Ridley-Ellis, Annette M. Harte

CONSIDERATIONS FOR GRADING SPECIES COMBINATIONS. GENERAL REMARKS ON SCENARIOS AND REQUIREMENTS. 780
Dan Ridley-Ellis, David Gil-Moreno, Annette M. Harte

PREDICTION OF TIMBER TWISTING BASED ON MEASURED SPIRAL GRAIN OF SPRUCE TRUNKS AND LOGS 787
Michal Kloiber, Jirí Kunecký, Miroslav Kotmel

ULTRASONIC-BASED DEFECT IDENTIFICATION IN TIMBER USING UNIFORM MANIFOLD APPROXIMATION AND PROJECTION (UMAP) 794
Prashanth Gunasekaran, Mehrisadat Makki Alamdari, Hamid Valipour Goudarzi

2.1. SUSTAINABLE ENVIRONMENT AND USE OF WOOD

GLUED-IN HARDWOOD RODS USING BIO-SOURCED ADHESIVES — PART I: INVESTIGATIONS UNDER LABORATORY CONDITIONS 804
Jana Kolbe, Stephanie Koesling, Till Vallée, Nils Monard, Jona Haupt

GLUED-IN HARDWOOD RODS USING BIO-SOURCED ADHESIVES — PART II: INFLUENCE OF ENVIRONMENTAL CONDITIONS 812
Jona Haupt, Nils Monard, Till Vallée, Stephanie Koesling, Jana Kolbe

MATERIAL FLOW ANALYSIS AND CARBON FOOTPRINT OF FOREST RESOURCES IN JAPAN: A CASE STUDY ON BUILDING MATERIALS 819
Hongjun Wang, Atsushi Takano

GROUND IMPROVEMENT EFFECT OF TIMBER PILES BURIED IN SOFT CLAY GROUND 829
Tadashi Hara, Yoshitaka Kubojima, Hidao Kato, Satomi Sonoda

STUDY ON ENVIRONMENT DECOMPOSITION AND STRENGTH OF CLT WHEN TEMPORARILY USED ON CIVIL ENGINEERING 836
Naoya Iizawa, Kei-Ichi Imamoto, Chizuru Kiyohara, Hideyuki Nasu, Satoshi Onishi

DEVELOPMENT OF FUTURE-ORIENTED CONCEPTS FOR AGRICULTURAL CONSTRUCTION WITH WOOD 842
Carina Hartmann, Özlem Özdemir, Annette Hafner

BUILDING TOWARD ZERO EMBODIED CARBON 849
Richard Hough, Carsten Moeller

TRADE-OFFS IN EMBODIED CARBON AND ACOUSTIC INSULATION FOR MASS TIMBER FLOOR ASSEMBLIES 858
Samantha J. Leonard, Mohamad B. Eddin, Morgan K. Prichard, Jonathan M. Broyles, Nathan C. Brown, Sylvain Ménard

ECOLOGICAL PERFORMANCE AND RECYCLABILITY OF TIMBER-BASED CONSTRUCTIONS 868
Alireza Fadai, Daniel Stephan

EMBEDMENT STRENGTH OF RECOVERED SPRUCE AND OAK 875
Caitríona Uí Chúláin, David Gil-Moreno, Daniel F. Llana, Mitja Plos, Goran Turk, Paul Hogan, Annette M. Harte

PROPOSAL OF A METHOD FOR ESTIMATING THE RESIDUAL STRENGTH FROM THE DEPTH OF PILODYN PENETRATING FOR A CYLINDRICAL MEMBER 882
Makoto Imai, Hironobu Kobayashi, Tadashi Hara

BENDING CHARACTERISTICS OF CLT FROM RECOVERED SPRUCE 888
Caitríona Uí Chúláin, Daniel F. Llana, Paul Hogan, Patrick McGetrick, Annette M. Harte

COMPARISON OF ENERGY EFFICIENCY BETWEEN WOODEN-BASED HYBRID STRUCTURE SYSTEM AND RC STRUCTURE SYSTEM IN SUBTROPICAL AND TROPICAL AREA 895
Cheng-Chieh Hsu, Meng-Ting Tsai, Shao-Chi Wu

ENVIRONMENTAL PERFORMANCE OF NEXT-GENERATION TIMBER SCHOOLS FOR CLIMATE ACTION: A SIMULATION APPROACH 903
Ramit Debnath, Antiopi Koronaki, Dario Marino, Yiping Meng, Darshil U. Shah, Peter Hazzard, Simon Smith, Kirsten Haggart, Michael H. Ramage

DEVELOPMENT OF MATERIAL FOR CIVIL CONSTRUCTION WITH BABASSU PALM FIBERS 909
Antonio Da Silva, Francisco Lahr, Antonio Costa, Joaquim Costa

EXPLORING THE STRUCTURAL DESIGN, COST, AND DURABILITY OF MASS TIMBER NOISE BARRIER FOR HIGHWAY APPLICATIONS 914
Weichiang Pang, Michael Stoner, Harsh Bothra, Laura Redmond, Patricia Layton

CORROSION INHIBITOR POTENTIAL WITH BOLDO BRASILEIRO COMPARED TO COMMERCIAL INHIBITOR IN WOOD CONNECTIONS 920
Letícia Costa, Ana Farias, Antonio Da Silva, Francisco Lahr

2.2. SUSTAINABILITY AND LIFE CYCLE ASSESSMENT

REVIEW AND COMPARISON OF DIFFERENT TIMBER BUILDING PRODUCTS' EMBODIED EMISSIONS USING FREE DATABASES 927
Felipe Victorero, Daniela Mendez, Felipe Bascuñan, Waldo Bustamante

LIFE CYCLE ASSESSMENT ON DIFFERENT TIMBER BRIDGE TYPES: DECK BRIDGE, BLOCK GIRDER BRIDGE, TROUGH BRIDGE, PYLON BRIDGE..... 935
Özlem Özdemir, Annette Hafner

STRUCTURAL AND LIFE CYCLE ANALYSES FOR A TIMBER-CONCRETE HYBRID BUILDING..... 941
Xiaoyue Zhang, Wanru Huang, Mehdi Khajehpour, Mehrdad Asgari, Thomas Tannert

EVALUATION OF THE RECYCLABILITY OF WOODEN BEAM STRUCTURES 948
Zsofia Varga, Antonia Birkholz, Anna Wagner, Stefan Winter

SUSTAINABLE ASSESSMENT: A CONTRIBUTION TO IMPROVE THE RELIABILITY OF NDT ON OLD CHESTNUT PURLINS..... 957
Vittoria Borghese, Silvia Santini, Lorena Sguerri

COMPARATIVE LIFE CYCLE ASSESSMENT OF TIMBER-CONCRETE-COMPOSITE WALLS WITH CONCRETE AND CLT-WALL ELEMENTS 967
Anna Wagner, Klara Winter, Anna Nestmann, Stephan Ott, Stefan Winter, Oliver Fischer

GHGS EMISSIONS FROM SAWNWOOD PRODUCTS IN NORWAY– THE IMPORTANCE OF HARMONISED LCA METHODOLOGY IN ENVIRONMENTAL PRODUCT DECLARATIONS (EPDS) 976
Johann Kristian Næss, Ana Maria Santos Bouzada, Roja Modaresi

INFLUENCE OF DIFFERENT END-OF-LIFE CYCLE SCENARIOS ON THE ENVIRONMENTAL IMPACTS OF TIMBER-CONCRETE COMPOSITE FLOOR SYSTEMS 982
Hooman Eslami, Alireza Yaghma, Laddu Bhagya Jayasinghe, Daniele Waldmann

A STRUCTURAL-MEMBER LEVEL ASSESSMENT OF THE ENVIRONMENTAL IMPACT OF TIMBER, REINFORCED CONCRETE AND STEEL IN BUILDING CONSTRUCTION..... 989
Jae-Won Oh, Sung-Jun Pang, Kyung Sun Ahn, Jung-Kwon Oh

MEETING THE 2050 PARIS AGREEMENT TARGETS USING MASSIVE TIMBER IN SCHOOL BUILDINGS. 995
Efthymia R. Stæhr, Thomas K. Thiis, Arnkell J. Petersen, Leif D. Houck

HOLISTIC DESIGN OF TALLER TIMBER BUILDINGS – COST ACTION HELEN (CA20139) 1001
Gerhard Fink, Robert Jockwer, Iztok Šušteršic, Mislav Stepinac, Pedro Palma, Chiara Bedon, Daniele Casagrande, Steffen Franke, Giuseppe D'Arenzo, Daniel Brandon, Christian Viau

DESIGN AND CRADLE-TO-GRAVE LIFE-CYCLE ASSESSMENT: FULLSCALE SIX-STORY SHAKE-TABLE TEST BUILDING LATERAL SYSTEMS 1009
Steven Kontra, Andre R. Barbosa, Arijit Sinha, Gustavo A. Araujo Rodriguez, Patricio Uarac, Nathan C. Brown, Jace Furley, Tu X. Ho, Gustavo F. Orozco, Barbara G. Simpson, John W. Van De Lindt, Seyed Hossein Zargar

HYBRID STRUCTURES IN HIGH-RISE BUILDINGS: THE USE OF APPROPRIATE MATERIALS 1017
Guido Nieri, Carsten Hein, Stuart Smith

BENCHMARK LIFE-CYCLE AND CONSTRUCTABILITY ASSESSMENT OF COMPOSITE STEEL-TIMBER SYSTEMS 1027
Emma E. Rohde, David B. Roueche, Kadir C. Sener, Brian K. Via

2.3. ZERO EMISSION BUILDING TECHNOLOGIES

DEVELOPING AN APPLICATION FOR MASS PLYWOOD PANELS IN SEISMIC AND ENERGY WALL RETROFITS 1034
Mark Fretz, Jason Stenson, Gustavo Fernando O. Orozco, Payton Narancic, Flynn Casey, Dale Northcutt, Kevin Van Den Wymelenberg, Judith Sheine, Andre R. Barbosa

2.5. HUMAN PERCEPTION & HEALTH

EMISSION OF VOLATILE ORGANIC COMPOUNDS FROM WOOD MATERIALS AND IMPACT ON INDOOR AIR QUALITY 1044
Ingrid Bakke, Anders Nyrud, Roland Kallenborn, Lina Aarsbog

COMBINED EFFECTS OF VISUAL AND OLFACTORY STIMULATION BY INTRODUCING WOOD WHILE WORKING OR RESTING 1050
Takashi Shima, Katsuhiko Sakata, Motoki Yairi, Daisuke Fujii, Haruki Momose, Yuko Tsunetsugu

WOOD INTERIORS IN ARCHITECTURE: AN EYE-TRACKING STUDY 1056
Pasi Aalto, Martin Steinert

CROSS-LAMINATED PANELS WOOD PANELS IN A PATIENT ROOM AND STUDIES OF INTERIOR ENVIRONMENT 1062
Bror Sundkvist, Olena Myronycheva, Sarka Langer, Ingrid Liljelind, Bo Glas, Tomas Nord, Björn Nordin

CIRCULAR WOOD CONSTRUCTION – EXPECTATIONS, EXPERIENCES AND ACCEPTANCE AMONG USERS, ARCHITECTS AND INDUSTRY REPRESENTATIVES 1067
Kaja Heltorp, Ute Groba, Anders Q. Nyrud

2.7. BUILDING OPERATION & MAINTENANCE

FUNDAMENTAL STUDY ON REPAIR BY EPOXY RESIN MIXED WITH CELLULOSE FIBER TO RECOVER BENDING PERFORMANCE OF WOODEN PARTS 1075
Akiko Ohtsuka, Nozomi Satou, Naoyuko Itagaki, Run Minoura, Shinichi Terasaki

QUALITY ASSURANCE OF TIMBER STRUCTURES BY NEW MONITORING METHODS FOR THE MOISTURE CONTENT OF WOOD 1081
Bettina Franke, Steffen Franke, Marcus Schiere, Andreas Müller

CURRENT STATUS OF MAINTENANCE OF THATCHED ROOFS IN SHIKOKU 1088
Naoki Kakehashi, Miyako Kamatoko

3.1. CONNECTIONS

POSSIBILITIES TO PROMOTE CIRCULAR ECONOMY IN MID-RISE TIMBER CONSTRUCTION IN THE PROJECT PLANNING AND EARLY DESIGN PHASES 1095
Ninni Westerholm, Juha Franssila

EFFECT OF RESIN IMPREGNAITON INTO WOOD CELL ON LATERAL RESISTANCE OF SCREWED JOINT CONNECTING SOLID WOOD AND STEEL PLATE 1104
Keita Ogawa, Kenji Kobayashi, Satoshi Fukuta

STRUCTURAL PERFORMANCE OF GLULAM TIMBER-STEEL BRACE CONNECTIONS REINFORCED WITH SELF-TAPPING SCREWS.....1110
Thomas Breijinck, Joshua Woods, Colin Macdougall

PREDICTION OF WITHDRAWAL STIFFNESS OF SELF-TAPPING SCREWS 1117
Md Abdul Hamid Mirdad, Jan Niederwestberg, Arman Jucutan, Ying Hei Chui

RNN-BASED MONOTONIC LOADING BEHAVIOR PREDICTION OF CLT JOINTS.....1123
Yewei Ding, Haibei Xiong, Cheng Yuan, Lin Chen, Yurong Lu

CYCLIC BEHAVIOR OF MORTISE-TENON JOINTS REINFORCED BY SELF-TAPPING SCREW 1129
Tianxiao Yin, Chenyue Guo, Zhiqiang Wang, Wei Zheng, Jianhui Zhou, Meng Gong

SERVICEABILITY STIFFNESS OF TIMBER CONNECTIONS WITH DOWELS AND SLOTTED-IN STEEL PLATES.....1136
Kjell Arne Malo, Haris Stamatopoulos, Francesco Mirko Massaro, Saule Tulebekova

MOISTURE AND ASSEMBLY HISTORY EFFECTS ON EMBEDMENT PROPERTIES OF STEEL DOWELS IN SPRUCE AND BIRCH LOADED IN GRAIN DIRECTION 1146
Michael Schweigler, Romain Lemaître, Zijad Shehadeh, Thomas K. Bader

EXPERIMENTAL AND NUMERICAL ANALYSES OF A CONNECTION FOR CLT STRUCTURES 1154
Lars Blomqvist, Roberto Crocetti, August Claesson, Zakaria Ben Osmane, Rune Ziethén, Marie Johansson

ROBUSTNESS OF ADHESIVELY BONDED PANEL-TO-PANEL CONNECTIONS IN CLT FLOORS.....1160
Lei Zhang, Muster Marcel, Thomas Tannert, Hercend Mpidi Bita

EXPERIMENTAL INVESTIGATIONS ON THE STIFFNESS OF STEEL-TIMBER DOWEL-TYPE CONNECTIONS IN BEECH LVL 1168
Lea Buchholz, Ulrike Kuhlmann

SEISMIC PERFORMANCE OF BOLTED GLULAM TIMBER BRACE CONNECTIONS WITH INTERNAL STEEL PLATES 1176
Zoe Baird, Joshua Woods, Christian Viau, Ghasan Doudak

DEVELOPMENT OF A NOVEL JOINT SYSTEM FOR MID-TO-HIGHRISE CLT WALL BUILDINGS IN SEISMIC REGIONS 1183
Ahmad Ghazi Aljuhmani, Eito Atsuzawa, Arata Minegishi, Kazuki Tsuda, Yutaka Goto, Masaki Maeda

A NOVEL LIMITED-DAMAGE 3D-PRINTED INTERLOCKING INTERMODULE CONNECTION SYSTEM FOR CROSS LAMNINATED TIMBER (CLT) VOLUMETRIC STRUCTURES 1192
Zhengyao Li, Konstantinos Daniel Tsavdaridis

IMPACT OF MOISTURE CYCLING ON SCREW WITHDRAWAL CAPACITY OF TREATED AND UNTREATED RADIATA PINE 1200
Luis Yermán, Zidi Yan, Wen Feng, Lisa-Mareike Ottenhaus

ANALYSIS AND DESIGN ASPECTS OF MOMENT-RESISTING, BEAM-TO-COLUMN, TIMBER CONNECTIONS WITH INCLINED THREADED RODS: FROM FASTENER LEVEL TO CONSTRUCTION LEVEL 1206
Haris Stamatopoulos, Osama Abdelfattah Hegeir, Kjell Arne Malo

APPLICATION OF A TUBE CONNECTOR FOR CATENARY ACTION IN CLT FLOORS 1216
Johannes Huber, Yunbo Huang, Sivert Knutsen, Alicja Przystup, Thomas Tannert, Sven Berg

EXPERIMENTAL VALIDATION OF PROPOSED CAPACITY-BASED DESIGN APPROACHES FOR MULTI-PANEL CLT SHEARWALLS 1224
Mohammad Masroor, Ghasan Doudak, Daniele Casagrande

GLUED-IN ROD CLT CONNECTIONS WITH FLEXIBLE POLYMER ADHESIVE 1231
Boris Azinovic, Václav Sebera, Meta Kržan, Andreja Pondelak, Jaka Gašper Pecnik, Arkadiusz Kwiecien

EVALUATION OF BEARING STRENGTH PERFORMANCE OF STS CONNECTION ACCORDING TO BEARING SECTION ON LOADING DIRECTION 1238
Keonho Kim, In-Hwan Lee

INCLINED SCREW CONNECTIONS WITH INTERLAYERS: BEAM ON FOUNDATION NON-LINEAR MODELLING 1244
Yuri De Santis, Angelo Aloisio, Dag Pasquale Pasca, Igor Gavric, Iztok Šušteršic, Massimo Fragiacomo

A FRACTURE MECHANICAL AND ANISOTROPIC FEM MODEL OF THE “RECONWOOD JOINT” AND EXPERIMENTAL VERIFICATION 1252
Jesper Kierkegaard Hansen, Mads Friborg Nielsen, Søren Gustenhoff Hansen, Anja Kunic, Roberto Naboni

NUMERICAL AND EXPERIMENTAL STUDY OF GLULAM BEAMS JOINTED WITH SLOTTED-IN STEEL PLATE CONNECTION 1261
Sigurdur Ormarsson, Le Kuai, Musaab Ahmed Mahjoub, Simon Aicher

PERFORMANCE OF GLUED-IN RODS IN GLULAM AND MPP IN TENSION AND COMPRESSION 1269
Alexander Salenikovich, Étienne Lapointe, Bruno Zumbrunn-Maurer, Thomas Brotschi, Anthonie Kramer

QUASI-STATIC CYCLIC TESTS OF NOVEL HIGH-PERFORMANCE SHEAR-CONNECTORS FOR MASS-TIMBER PANELS 1275
Blériot Vincent Feujofack Kemda, Cristiano Loss

JOINT PERFORMANCE TESTING OF A CLAMPED JOINT FOR TIMBER STRUCTURES AND APPLICATION TO STRUCTURAL DESIGN 1283
Yoshisato Esaka, Tatsuki Ishizaki, Tsubasa Seguchi, Tokuma Azemi

EXPERIMENTAL STUDY ON CONTROL PARAMETERS FOR AUTOMATED APPLICATION AND IN-SITU PERFORMANCE ASSESSMENT OF JOINTS WITH SELF-TAPPING TIMBER SCREWS 1289
Alexandra Eckert, Reinhard Brandner, David Glasner

INFLUENCE OF LOW CURING TEMPERATURES ON THE STRENGTH DEVELOPMENT OF END-GRAIN BONDED TIMBER 1299
Dio Lins, Steffen Franke

EXPERIMENTAL CHARACTERIZATION OF THE MULTI-DIRECTIONAL BEHAVIOUR OF ANGLE BRACKETS AND HOLD-DOWNS 1305
Riccardo Fanti, Andrea Polastri, Daniele Casagrande, Ernesto Callegari, Alvise Ramazzini, Luca Sestigiani, Peter Lang

ASSESSMENT OF COMBINED EFFECTS OF AXIAL AND LATERAL LOADING OF GLUED-IN ROD CONNECTIONS IN LVL 1312
Daniel Fawcett, Eleni Toumpanaki

SOLUTIONS FOR EDGE CONNECTIONS TO BUILD TWO-WAY SPANNING CROSS LAMINATED TIMBER SLABS 1322
Thomas Stieb, Bernhard Maurer, Maximilian Bestler, Philipp Dietsch, Roland Maderebner

EXPERIMENTAL AND ANALYTICAL ANALYSIS OF TIMBER CONNECTIONS WITH INTERPOSED ACOUSTIC RESILIENT STRIP 1330
Luca Pozza, Giulia D'Amato, Paola Brugnara, Ernesto Callegari, Luca Sestigiani

ON-SITE GLUING AND WEATHER EFFECTS ON TALL WOODEN WIND TURBINE TOWERS 1336
Viktor Norbäck, Pierre Landel, Erik Dölerud, Anders Wickström

INFLUENCE OF DENSITY AND PREDRILL IN THE EMBEDMENT STRENGTH OF TWO HARDWOOD SPECIES 1342
Gonzalo Cabrera, Gonzalo Moltini, Vanesa Baño

STRUCTURAL PERFORMANCE OF HIGH CAPACITY GLULAM MOMENT CONNECTIONS 1350
Ryan Guay, Christopher Pitt, Reid B. Zimmerman, Ignace Mugabo, Peter Dusicka

THE IMPACTS OF SCREW TIP, INCLINATION ANGLES AND NUMBER OF PENETRATION LAYERS ON SCREW WITHDRAWAL CAPACITY IN AUSTRALIAN MACHINE GRADED PINE 1358
Zidi Yan, Lisa-Mareike Ottenhaus, Jingyuan Lin, Robert Jockwer, Andreas Ringhofer

DESIGNING AND TESTING OF A WOOD-ONLY TIMBER FRAME CONNECTION INSPIRED BY THE GROWTH FORMATION OF TREES' STEM-BRANCH JUNCTION 1365
Firas Hawasly, Naoyuki Matsumoto, Mikio Koshihara, Koji Adachi

EXPERIMENTAL STUDY OF A TYPICAL EXTERNAL WALL-FLOOR-WALL CONNECTION IN A CLT PLATFORM TYPE CONSTRUCTION 1375
Luka Vojnovic, Eleni Toumpanaki, James Norman

AN EXPERIMENTAL STUDY ON SHEAR PERFORMANCE OF CLT DOWEL JOINTS WITH SHEAR PLATES 1383
Tsuyoshi Akutagawa, Hiroya Hanaoka, Masamichi Sasatani

EXPERIMENTAL AND NUMERICAL INVESTIGATION OF CROSSLAMINATED TIMBER JOINTS WITH MULTIPLE GLUED-IN RODS 1389
Younes Shirmohammadli, Ashkan Hashemi, Reza Masoudnia, Pierre Quenneville

BEAM-ON-ELASTIC FOUNDATION MODEL OF MECHANICAL PROPERTIES OF RING NAILS AND HEAVY-DUTY SCREWS 1397
Petr Sejkot, Asif Iqbal

DUCTILITY OF WOOD CONNECTIONS WITH SDS SCREWS OR RING NAILS AND ANGLE BRACKETS 1403
Petr Sejkot, Asif Iqbal

EXPERIMENTAL INVESTIGATIONS ON TIMBER STEP JOINTS DETERMINING THE INFLUENCE OF INTENTIONALLY PLACED INACCURACIES ON THE LOAD-BEARING BEHAVIOUR 1409
Matthias Braun, Benjamin Kromoser

PREFABRICATED FOUNDATION SYSTEMS FOR TIMBER BUILDINGS 1416
Davide Canetti, Francesca Paoloni, Riccardo Fanti, Alessandro Setti, Andrea Polastri, Fabrizio Tamburini

UPPER AND LOWER RESISTANCE OF SMALL STEEL-TO-TIMBER CONNECTIONS AND COMPARAISION WITH REVISED EYM 1422
Jørgen Munch-Andersen

STRENGTH CHARACTERIZATION OF OVERLAPPED TIMBER SCREWS 1431
Luca Marchi, Davide Trutalli, Luca Pozza, Roberto Scotta

MEASUREMENT OF AXIAL FORCE OF SCREWS FOR SPLIT REINFORCEMENT AT TIMBER-STEEL-TIMBER DOWEL JOINT 1437
Kenji Kobayashi, Keita Ogawa

RIGID GLULAM JOINTS TO CONCRETE ABUTMENTS WITH GLUED-IN STEEL ROD 1443
Kai Simon, Simon Aicher

GLULAM FRAMES ADHESIVELY BONDED BY MEANS OF BIRCH PLYWOOD PLATES: PRELIMINARY INVESTIGATIONS 1453
Tianxiang Wang, Yue Wang, Roberto Crocetti, Magnus Wålinder, Pontus Persson, Patrik Hedlund

STRUCTURAL CHARACTERISTICS AND DEFORMATION BEHAVIOUR OF AN ADVANCED CARPENTRY CONNECTION IN TIMBER CONSTRUCTION 1462
Katrin Vögele, Moritz Tronnier, Yannick Plüss, Mike Sieder

REPAIR CONNECTION WITH WOODEN WEDGED DOWELS: AXIAL TENSILE AND SHEAR VERIFICATIONS 1472
Elena Perria, Mike Sieder, Svenja Siegert, Cordula Reulecke

PERFORMANCE VERIFICATION AND TRIAL DESIGN FOR HIGH-RISE TIMBER FRAME BUILDINGS WITH BUCKLING-RESTRAINED BRACES - PART.1 CONNECTION AND FRAME TESTING 1481
Kazuki Tachibana, Hiroki Nakashima, Taisuke Nagashima, Ryota Minami, Toshio Maegawa, Nobuhiko Akiyama, Yoshihiro Yamazaki, Takahiro Tsuchimoto

HASLETRE: NORWAY'S FIRST TIMBER OFFICE BUILDING DESIGNED FOR DISASSEMBLY AND REUSE 1491
Ona Flindall, Jørgen Tycho, Moritz Groba

TOWARDS ADAPTABILITY AND CIRCULARITY OF TIMBER BUILDINGS 1497
Robert Jockwer, Vera Öberg, Lisa-Mareike Ottenhaus, Paola Leardini, Yutaka Goto

INVESTIGATION OF STRUCTURAL BEHAVIOR OF WOODEN TRADITIONAL JOINTS VIA FINITE ELEMENT ANALYSIS 1506
Hafshah Salamah, Seung Heon Lee, Thomas Kang

BONDED-IN RODS IN BEECH GLULAM – EFFICIENCY OF A RECESS IN THE BONDLINE 1512
Steffen Franke, Bettina Franke, Alexander Salenikovich

3.2. FIRE ENGINEERING

USING X-RAY COMPUTED TOMOGRAPHY TO MEASURE FIRE DEGRADATION OF A TIMBER CONNECTION 1519
Quentin Rodrigues, Johannes Huber, Lars Hansson, Rhoda Afriyie Mensah, Rostand Moutou Pitti

ANALYTICAL MODELLING OF POST-TENSIONED TIMBER BEAM-COLUMN CONNECTIONS IN FIRE 1526
Paul D. Horne, Anthony K. Abu, Alessandro G. Palermo

MECHANICAL PERFORMANCE AT ELEVATED TEMPERATURES OF NON-METALLIC DOWELS FOR MASS TIMBER STRUCTURES 1536
Alexandra Boloux, Rafik Nizarali, Luke Bisby

FIRE PERFORMANCE OF PENETRATIONS IN GLULAM BEAMS: A PRELIMINARY STUDY 1545
Laura Hasburgh, Keith Bourne, David Barber

CALCULATION METHOD OF COLLAPSE TIME OF WOOD MEMBERS EXPOSED TO FIRE HEATING WITH HEAT AND WATER TRANSFER ANALYSIS: INFLUENCE OF INITIAL MOISTURE CONTENT ON CHARRING RATE AND MECHANICAL PROPERTIES OF REMAINING SECTION OF WOOD MEMBERS 1551
Tatsuro Suzuki, Yuji Hasemi

HEAT DELAMINATION IN CROSS LAMINATED TIMBER: INTERMEDIATE SCALE TEST BASED UPON THE NORTH AMERICAN STANDARDS 1559
Samuel L. Zelinka, Keith J. Bourne, Laura E. Hasburgh, Kara Yedinak

A NEW METHOD FOR MODELLING TEMPERATURE WITHIN STEEL BAR - TIMBER COMPOSITE BEAM USING DATA BY BURNING TEST 1566
Shizuka Matsushita, Shinichi Shioya

TRAVELLING FIRES IN COMPARTMENTS WITH EXPOSED CROSS-LAMINATED TIMBER SURFACES 1576
Andreas Sæter Bøe, Kathinka Leikanger Friquin

CHARACTERIZING THE FIRE PERFORMANCE OF ADHESIVES USED IN GLUED-IN RODS CONNECTIONS 1583
Diego Flores, Christian Dagenais, Pierre Blanchet

NUMERICAL MODELLING OF CONTEMPORARY MASS TIMBER CONNECTIONS IN FIRE 1592
Bronwyn Chorlton, Mathieu Létourneau-Gagnon, Christian Dagenais, Marc-André Langevin

BURNING TEST OF STEEL BAR - TIMBER COMPOSITE BEAM 1602
Shizuka Matsushita, Shinichi Shioya

ADVANCED FIRE MODELLING IN SUPPORT OF PERFORMANCE-BASED FIRE DESIGN OF TIMBER BUILDINGS 1610
Christian Dagenais, Zhiyong Chen

EFFECT OF THE SACRIFICIAL LAYER THICKNESS AND THE BARRIER LAYER TYPE ON SELF-EXTINGUISHING FOR WOODEN FIREPROOF-STRUCTURAL ELEMENTS..... 1620
Tomoyo Hokibara, Yuji Hasemi, Daisuke Kamikawa, Tsutomu Nagaoka

FIRE TESTING EXTERIOR CROSS-LAMINATED TIMBER WALLS TO NFPA 285 1627
David Barber, Hans-Erik Blomgren

FIRE SAFETY OF MID-RISE BUILDINGS WITH LIGHT TIMBER STRUCTURES – STUDIES OF THE FIRE RESISTANCE OF A NOVEL CONSTRUCTION SYSTEM..... 1637
Kathinka Leikanger Friquin, Johan Kr. Møller

EXPLORING THE INFLUENCE OF HEATING CONDITIONS IN THE CHARRING PROFILE OF BARE TIMBER AND TIMBER PROTECTED WITH A THIN INTUMESCENT COATING..... 1644
Stavros Spyridakis, Jeronimo Carrascal, Felix Wiesner, David Barber, Cristian Maluk

MEASUREMENT OF DIRECTIONAL CHARACTERISTICS OF MOISTURE TRANSPORTATION IN WOOD UNDER HEATING 1653
Hirokatsu Kimura, Tomoyo Hokibara, Yuji Hasemi, Soma Suzuki, Tatsuro Suzuki, Ryo Takase

FIRE SAFETY ENGINEERING OF BUILDINGS WITH VISIBLE TIMBER CONSTRUCTIONS..... 1660
Leif Tore Isaksen, Martin Hagen

OBSERVATIONS OF SMOULDERING FIRE IN A LARGE TIMBER COMPARTMENT..... 1667
Harry Mitchell, Rikesh Amin, Panagiotis Kotsovinos, Mohammad Heidari, Daniel Thomson, David Barber, Guillermo Rein

EXPERIMENTAL INVESTIGATION OF THE RELATIONSHIP BETWEEN TIMBER SPECIES AND SMOULDERING 1673
Wenxuan Wu, Luis Yermán, Juan P. Hidalgo, Jeffrey Morrell, Felix Wiesner

PREDICTING THE EFFECTIVE CHAR DEPTH IN TIMBER ELEMENTS EXPOSED TO NATURAL FIRES, INCLUDING THE COOLING PHASE..... 1681
Andrea Lucherini, Daniela Šejnová Pitelková, Vladimír Mózer

EXPERIMENTAL AND FINITE ELEMENT ANALYSIS OF IRISH SITKA SPRUCE CLT WALL PANELS UNDER EXPOSURE TO STANDARD FIRE CONDITIONS..... 1691
Muhammad Yasir, Conan O'Ceallaigh, Kieran Ruane, Andrew Macilwraith

A DESIGN APPROACH TO EXTERNAL FIRE SPREAD FROM BUILDINGS WITH EXPOSED MASS TIMBER 1701
Adam Glew, Rory Turnbull, Frederik Møller Poulsen, Eirik Christensen, Panagiotis Kotsovinos, Eoin O'Loughlin, David Barber, Judith Schulz

NUMERICAL ANALYSIS ON THE FLEXURAL PERFORMANCE OF COMPOSITE STEEL-TIMBER BEAMS UNDER FIRE CONDITIONS 1712
Zhiyuan Liu, Binsheng Zhang, Huijuan Jia, Tony Kilpatrick

FIRE-PROTECTED TIMBER ELEMENTS OF CONSTRUCTION – RESPONSE DURING FIRE DECAY AND COOLING PHASE 1721
Paul England, Boris Iskra

NUMERICAL SIMULATION OF FIRES WITH EXPOSED TIMBER 1728
Sabrina Spörri, Chamith Karannagodage, Joachim Schmid, Andrea Frangi

EXPLICIT FIRE SAFETY FOR MODERN MASS TIMBER STRUCTURES – FROM THEORY TO PRACTICE 1738
Laura Schmidt, Ryan Hilditch, Adam Ervine, Joshua Madden

FIRE CHARACTERISTICS OF A COMPARTMENT WITH EXPOSED CLT WALLS: AN EXPERIMENTAL INVESTIGATION USING THE STANDARD ISO 834 CURVE 1748
Andrianos E. Koklas, Dionysios Kolaitis, Maria A. Founti

FLAME SPREAD CHARACTERISTICS IN LARGE COMPARTMENTS WITH AN EXPOSED TIMBER CEILING 1758
Panagiotis Kotsovinos, Eirik G. Christensen, Harry Mitchell, Rikesh Amin, Mohammad Heidari, Guillermo Rein, David Barber, Judith Schulz

ACCOUNTING FOR POST-PEAK COMPARTMENT TEMPERATURE THERMAL DEGRADATION OF MASS TIMBER 1768
David Barber, Eirik Christensen, Panos Kotsovinos, Mohammad Heidari, Judith Schulz

PROTECTION AND THERMAL EXPOSURE OF CLT CEILING AND FLOOR SURFACES 1778
Eirik G. Christensen, Benjamin Khoo, Panagiotis Kotsovinos, David Barber, Judith Schulz

COMPARATIVE PERFORMANCE OF PROTECTIVE COATINGS FOR MASS TIMBER STRUCTURES 1788
Lorna Johnson, David Morrisset, Antonela Colic, Luke Bisby

FIRE DESIGN OF GLULAM CONNECTIONS WITH TIMBER-TO-TIMBER BEARING INTERFACES 1798
Hans-Erik Blomgren, David Barber, Graham Montgomery

FIRE RESISTANCE TESTING OF CLT-CONCRETE COMPOSITE FLOOR SLABS WITH STRIP NOTCH SHEAR CONNECTIONS 1807
Javad Tashakori, Sam Salem

FIRE RESISTANCE TESTING OF CLT-CONCRETE COMPOSITE FLOOR SLABS UTILIZING GLUED-IN STEEL PLATES AS SHEAR CONNECTORS 1814
Adam Petrycki, Sam Salem

FIRE RESISTANCE TESTING OF CLT-CONCRETE COMPOSITE FLOOR SLABS UTILIZING SELF-TAPPING SCREWS AS SHEAR CONNECTORS 1821
Sarah Barclay, Sam Salem

IMPLICATIONS OF A DOWN-STAND BEAM ON THE CEILING FLAME EXTENSION CHARACTERISTICS IN A LARGE-SCALE CLT ENCLOSURE FIRE EXPERIMENT 1831
Danny Hopkin, Michael Spearpoint, Renaud Blondeau, Tim Sleik, Harald Krenn, Gordian Stapf, Wojciech Wegrzynski

PERFORMANCE OF PASSIVE PROTECTION OF CROSS LAMINATED TIMBER DURING STANDARD FURNACE TESTS AND NATURAL FIRES 1839
Siyimane Mohaine, Antonela Colic, David Morrisset, Jean-Christophe Mindeguia, Jean-Marc Franssen, Jochen Zehfuss, Robert McNamee, Luke Bisby, Fabienne Robert

NATURAL FIRE TESTS ON GLT COLUMNS INCLUDING THE COOLING DOWN PHASE 1848
Fabienne Robert, Jean-Marc Franssen, Jochen Zehfuß, Sven Brunkhorst, Patrick Bamonte, Silvio Renard, Robert McNamee, Thomas Gernay

3.3. VIBRATIONS & ACOUSTICS

FULL SCALE VIBRATION TESTS ON A LONG SPAN TIMBER FLOOR 1855
Patricia Hamm, Valentin Knöpfle, Johannes Ruf, Philipp Bacher, Tobias Götz

ACOUSTIC SENSITIVITY ANALYSIS AND MODELING OF SOUND INSULATION PERFORMANCE OF LIGHTWEIGHT WOODEN FACADE STRUCTURES 1863
Mohamad Bader Eddin, Sylvain Menard, Delphine Bard, Jean-Luc Kouyoumji

DESIGN OF LONG-SPAN LIGHTWEIGHT TIMBER FLOORS SUBJECT TO WALKING EXCITATIONS: A CASE STUDY 1873
Hassan Karampour, Farid Piran, Adam Faircloth, Chandan Kumar, David Zhang, Benoit P. Gilbert, Hong Guan, Lin Hu, Ying Hei Chui, Wen-Shao Chang

EXPERIMENTAL STUDY ON THE VIBRATION CHARACTERISTICS OF A PREFABRICATED CROSS-LAMINATED TIMBER-STEEL COMPOSITE FLOOR 1880
David Owolabi, Cristiano Loss

EXPERIMENTAL INVESTIGATIONS ON VIBRATION PERFORMANCE OF TIMBER-CONCRETE COMPOSITE BEAMS USING LIGHTWEIGHT AGGREGATE CONCRETE 1888
Bo Wen, Benkai Shi, Haotian Tao, Huifeng Yang, Bowen Huang

DEVELOPMENT OF A STAND-ALONE VIBRATION MEASUREMENT SYSTEM FOR BRIDGE MONITORING 1894
Dio Lins, Steffen Franke, Roger Weber, Bettina Franke, Joel Karolin

ACTIVE MASS DAMPERS FOR TIMBER FLOORS 1900
Thomas Hillberger, Thomas Furtmüller, Philipp Dietsch, Roland Maderebner

FIELD MEASUREMENT OF VIBRATION LEVEL DIFFERENCE ACROSS VERTICAL JUNCTIONS IN A TIMBER FRAME BUILDING 1908
Simone Conta, Anders Homb

CHARACTERISATION OF RESILIENT INTERLAYERS 1914
Paola Brugnara, Alice Speranza, Luca Barbaresi, Luca Sestigiani

VIBRATION SERVICEABILITY PERFORMANCE OF MASS TIMBER FLOORS UNDER VARIOUS SUPPORT CONDITIONS 1921
Chenyue Guo, Jianhui Zhou

DYNAMIC CHARACTERISTICS AND DYNAMIC RESPONSE OF TIMBER FOOTBRIDGES TO DYNAMIC HUMAN ACTIVITIES 1930
Marek Pantak, Whokko Schirén, Carl Larsson, Michael Dorn

A COMPARATIVE STUDY OF DESIGN STANDARDS FOR ASSESSMENT OF LONG-SPAN STEEL-TIMBER COMPOSITE FLOORS UNDER HUMAN-INDUCED VIBRATION 1936
Sardar Malek, Najmeh Cheraghi-Shirazi, Keith Crews, Roger Parra, Ariel Creagh, Parham Khoshkbari

ASSESSING THE EFFECTS OF BOUNDARY CONDITIONS ON THE VIBRATIONAL COMFORT OF ON-SITE TIMBER-CONCRETE COMPOSITE FLOORS 1943
Francesca Lanata, Clement Boudaud

LOCAL DAMAGE ASSESSMENT STRATEGY OF A TWO-STORY CLT WALL THROUGH VIBRATION-BASED NON-DESTRUCTIVE TECHNIQUES 1953
Alexander Opazo-Vega, Franco Benedetti, Alan Jara-Cisterna, Peter Dechent

PREDICTION OF THE ACOUSTIC INSULATION OF A PREFABRICATED WOODEN-BASED SYSTEM FOR COLLECTIVE BUILDINGS 1960
Marina Tenório, Sandra M. Silva, Jorge M. Branco

IMPACT SOUND INSULATION PERFORMANCE OF RAISED DISCRETE FLOATING FLOOR ASSEMBLIES ON MASS TIMBER SLABS 1968
Jianhui Zhou, Zijian Zhao, Chenyue Guo

SOUND INSULATION IN CROSS LAMINATED TIMBER BUILDINGS AND THE EFFECT OF JUNCTIONS AND FASTENERS 1975
Eli Toftemo, Anders Løvstad

INFLUENCE OF MECHANICAL FASTENER SPACING ON ACOUSTIC PERFORMANCE IN TIMBER COMPOSITE PANELS 1983
Aedan Callaghan, Wilson Byrick

3.4. CYCLIC LOADING, EARTHQUAKES & FATIGUE

PLASTIC DEFORMATION CONTRIBUTIONS OF CLT AND LTF SHEAR WALLS: DEVELOPMENT OF AN ANALYTICAL CAPACITY MODEL 1988
Angelo Aloisio, Francesco Boggian, Massimo Fragiacomo, Roberto Tomasi

ASEISMIC DESIGN LEVEL USING RESPONSE SPECTRUM FOR WOODEN HOUSES 1994
Koji Yamada

MASS TIMBER BRACED FRAMES WITH MASS TIMBER BUCKLING RESTRAINED BRACES 2000
Emily Wiliamson, Chris Pantelides, Hans-Erik Blomgren, Douglas Rammer

EFFECT OF SMALL DEFORMATION DUE TO MODERATE EARTHQUAKES ON THE SHEAR PERFORMANCE OF SHEAR RESISTING WALL 2008
Ryo Inoue, Takuro Mori, Shinya Matsumoto

EXPERIMENTAL TESTING OF HIGH-CAPACITY SINGLE AND COUPLED CLT SHEAR WALL SYSTEMS 2014
Benjamin Moerman, Minghao Li

EXPERIMENTAL TESTING OF MIXED ANGLE SCREWED HOLD-DOWN CONNECTIONS FOR CLT SHEAR WALLS 2020
Thomas Wright, Minghao Li

DYNAMIC PERFORMANCE OF A FULL-SCALE WOOD FRAME SUBJECTED TO CYCLIC LOAD TESTING 2030
Félix Bouffard, Jean Proulx

EXPERIMENTAL PARAMETER STUDY ON CLT SHEAR WALLS WITH HIGH-PERFORMANCE SELF-TAPPING SCREW CONNECTIONS 2040
Yuxin Pan, Thomas Teflissi, Thomas Tannert

HORIZONTAL-LOADING TEST OF STEEL BAR-TIMBER COMPOSITE COLUMNS FOR LOW-RISE BUILDING 2046
Yuuto Shimoirisa, Takahiro Iju, Takao Ohta, Kazuya Mori, Shinichi Shioya

EVALUATION OF VIBRATION PROPERTY OF HIGH-DAMPING TWO-STORY TIMBER STRUCTURE BASED ON RESONANCE CURVE 2056
Yuji Miyazu

YIELD MECHANISM OF PERFORATED PLATE CONNECTIONS FOR MASS TIMBER SYSTEMS 2063
Hossein Daneshvar, Thomas Tannert, Ying Hei Chui, Carla Dickof

EXPERIMENTAL CHARACTERISATION OF GLULAM SHEAR WALLS UNDER LATERAL CYCLIC LOADING 2070
Giuseppe D'Arenzo, Werner Seim

CYCLIC LOAD TESTS AND NUMERICAL ANALYSIS OF CLT SHEAR WALLS WITH GIR JOINTS 2077
Shuhei Uesugi, Daisuke Kadono, Katsuhide Murakami, Masahide Murakami

FULL-SCALE 3-D SHAKE TABLE TEST OF A TEN-STORY MASS TIMBER BUILDING 2084
Shiling Pei, John W Van De Lindt, Jeffrey Berman, Keri Ryan, James D. Dolan, Steve Pryor, Sarah Wichman, Aleesha Busch, Reid Zimmerman

CONSTRUCTIVE REHABILITATION OF THE FLOOR STRUCTURES OF ZAGREB'S DOWNTOWN BUILT IN THE FIRST HALF OF THE 20TH CENTURY 2090
Dean Cizmar, Krunoslav Pavkovic, Marija Babic Toncic, Ivana Iljkic

EXPERIMENTAL RESEARCH ON THE SEISMIC PERFORMANCE OF WATTLE AND DAUB INFILLED CHUAN-DOU TYPE TIMBER FRAMES 2098
Rui Xu, Yunyang Qi, Hao Huang

EVALUATION OF SEISMIC PERFORMANCE OF WOODEN HOUSES WITH SLIDING BASE BY FULL-SCALE SHAKING TABLE TEST 2104
Ai Tomita, Yuji Miyazu, Takehiro Wakita, Takaki Tojo, Takashi Aoki, Masayuki Nagano

CYCLIC TESTS OF INTERLOCKING CROSS LAMINATED TIMBER SHEAR WALLS 2111
Wyatt Payne, Alex Winward, Johnn Judd

FATIGUE RESISTANCE OF ADHESIVE BONDED CONNECTIONS WITH AND WITHOUT INTERNAL STEEL PLATES IN LARGE TIMBER STRUCTURES 2118
Robert Jockwer, Pierre Landel, Viktor Norbäck, Rune Ziethén, Erik Dölerud, Leo Anderson Naveda, Carl-Johan Åkerström

TESTING OF STRONG MULTI-LAYERED WOOD FRAME SHEAR WALLS WITH NON-STRUCTURAL LAYERS 2125
Diego Valdivieso, Diego Lopez-Garcia, Jairo Montaño, Pablo Guindos

TESTING THE INFLUENCE OF 3D COUPLING EFFECTS ON THE LATERAL RESPONSE OF NON-PLANAR T-SHAPE WOOD FRAME SHEAR WALLS 2134
Diego Valdivieso, Diego Lopez-Garcia, José Luis Almazán, Jairo Montaño, Pablo Guindos

DATA-DRIVEN APPROACH FOR ASSESSMENT OF SEISMIC DAMAGE IN WOOD BUILDINGS 2143
Sifat Muin, Asif Iqbal, John W. Van De Lindt

EFFECT OF SMALL OPENINGS ON SHEAR CAPACITY OF PLYWOOD SHEATHED SHEAR WALLS 2150
Yuta Sakai, Kenji Aoki

CYCLIC TESTING AND NUMERICAL MODELING OF A THREE-STORY MASS-TIMBER BUILDING WITH A PIVOTING MASS PLY PANEL SPINE AND BUCKLING-RESTRAINED ENERGY DISSIPATORS 2156
Gustavo Adolfo Araujo Rodriguez, Barbara G. Simpson, Tu X. Ho, Gustavo F. Orozco O., Andre R. Barbosa, Arijit Sinha

HYSTERESIS - A PYTHON LIBRARY FOR ANALYSING STRUCTURAL DATA 2166
Christian Slotboom

MONOTONIC TESTS ON BEAM-TO-COLUMN JOINT WITH STEEL LINK FOR TIMBER SEISMIC RESISTANT STRUCTURES 2173
Giacomo Iovane, Leonardo Rodrigues, Jorge Branco, Beatrice Faggiano

MODELLING SEISMIC ISOLATION BEARING FOR WOOD BUILDINGS 2179
Asif Iqbal, Angelo Aloisio, Massimo Fragiacomo

EXPERIMENTAL MONOTONIC AND CYCLIC TESTING ON GLULAM BEAM-TO-COLUMN CONNECTIONS 2185
Erica Fischer, Haley Madland, Sujit Bhandari, Arijit Sinha

SEISMIC CONNECTIONS FOR CLT STRUCTURES WITH TUBULAR ELEMENTS AND UNCOUPLED TENSION-SHEAR INTERACTION 2194
Luca Marchi, Davide Trutalli, Luca Pozza, Roberto Scotta

VARIABILITY OF THE CROSS-LAMINATED TIMBER (CLT) SINGLE-PANEL SHEAR WALLS' RESPONSE UNDER IN-PLANE LATERAL LOADS 2200
Vincenzo Rinaldi, Igor Gavric, Massimo Fragiacomo

SHEAR PERFORMANCE ESTIMATION OF WOODEN LATHS AND PLASTER WALLS THROUGH EXPERIMENTS AND NUMERICAL ANALYSIS 2207
Naoyuki Matsumoto, Katsuhiko Yamawaki, Kaori Fujita

A SEISMIC RESPONSE ESTIMATION MODEL FOR CROSS-LAMINATED TIMBER WALLS USING MACHINE LEARNING 2214
Eknara Junda, Christian Malaga-Chuquitaype

ADAPTIVE COMPOSITE RUBBER BEARINGS FOR TIMBER STRUCTURE: A CASE STUDY FOR EARTHQUAKE-PRONE REGIONS 2221
Weichong Liao, Kin Sang Michael Wong

SEISMIC DESIGN OF A CLT MULTI-STOREY BUILDING IN DIFFERENT DUCTILITY CLASSES 2227
Giuseppe Cenci, Maurizio Follesa, Vincenzo Rinaldi, Daniele Casagrande, Massimo Fragiacomo

SEISMIC RESPONSE OF BALLOON TYPE CLT SHEAR WALLS 2234
Zhiyong Chen, Marjan Popovski

EFFECTS OF VARIABLE CLIMATE CONDITIONS ON THE BEHAVIOR OF POST-TENSIONED MASS TIMBER WALL PANELS 2244
Jacob Gesh, Esther Baas, Ryan Longman, Mariapaola Riggio, Andre R. Barbosa, Lech Muszynski, Gabriele Granello

OPTIMIZED CLT-RC FRAME CONNECTION FOR SEISMIC RETROFITTING 2253
Zabih Mehdipour, Jorge M. Branco, Elisa Poletti, Paulo B. Lourenço

3.5. STRUCTURAL MODELLING, ANALYSIS & DESIGN

LESSONS LEARNED FROM A DECADE OF RESEARCH ON WOOD ASSEMBLIES UNDER BLAST LOADING 2261
Ghasan Doudak, Christian Viau, Daniel Lacroix

A NONLINEAR DYNAMIC MODEL FOR COLLAPSE INVESTIGATIONS IN TALL TIMBER BUILDINGS – PRELIMINARY RESULTS 2268
Alex Sixie Cao, Lukas Esser, Ben Glarner, Andrea Frangi

RESEARCH AND DEVELOPMENT OF SMALL-SCALE TIMBER CONSTRUCTION SYSTEM “BI-TREE STRUCTURE” WITH SMALL-DIAMETER TIMBER 2278
Toko Kamata, Satoru Ito, Yuya Takaiwa

MODELLING OF TIMBER STRUCTURES 2288
Zhiyong Chen, Dorian Tung, Erol Karacabeyli

PREDICTIVE CAPABILITIES OF FINITE ELEMENT MODELLING FOR TIMBER MEMBERS SUBJECTED TO BLAST LOADS 2298
Damian Oliveira, Christian Viau, Ghasan Doudak

EXPERIMENTAL INVESTIGATIONS ON CLT PANELS WITH OPENINGS 2306
Xiaoyue Zhang, Lu Xuan, Weitian Li, Thomas Tannert

SEISMIC PERFORMANCE EVALUATION OF REINFORCED WOODEN TEMPLE BASED ON LONG TERM EARTHQUAKE OBSERVATIONS 2312
Toshiaki Sato, Yasuhiro Nambu, Yuji Miyazu, Masayuki Nagano

GLUED-LAMINATED TIMBER BEAMS WITH LARGE ROUND HOLES: AN EXPERIMENTAL AND NUMERICAL INVESTIGATION 2318
Francesco Mirko Massaro, Kjell Arne Malo

ASSESSMENT OF THE FUNDAMENTAL PERIOD OF MULTI-STOREY CROSS LAMINATED TIMBER BUILDINGS 2327
Ebenezer Ussher, Angelo Aloisio, Roberto Tomasi

NUMERICAL MODELLING OF LIGHT TIMBER FRAME WALLS – COMPARATIVE STUDY OF THREE FASTENER REPRESENTATIONS 2335
Lukas Rauber, Benno Hoffmeister

INCREMENTAL DYNAMIC ANALYSIS OF A FIVE STOREYS CLT BUILDING DESIGNED THROUGH FORCE-BASED METHODS 2342
Franco Benedetti, Tomás Valenzuela, Alan Jara-Cisterna, Alexander Opazo-Vega, Víctor Rosales

ESTIMATION METHOD OF DEGRADATION STATE FOR TIMBER BRIDGES USING VIBRATION ANALYSIS 2350
Daisuke Oikawa, Shuya Nemoto, Humihiko Gotou, Yukari Aoki

TECHNICAL DESGIN GUIDE FOR TIMBER-CONCRETE COMPOSITE FLOORS – A CANADIAN APPROACH 2356
Samuel Cuerrier Auclair, Christian Dagenais, Sylvain Gagnon

AN ENGINEERING MODEL FOR THE DESIGN OF CUT-BACKS IN RIBBED PANELS 2365
Medhanye Biedebrhan Tekleab, Manfred Augustin, Gerhard Schickhofer

LATERAL DEFORMATION AND KINEMATIC MODES OF MULTI-PANEL BALLOON-TYPE CLT SHEARWALL SYSTEM 2376
Dalu Xing, Ghasan Doudak, Daniele Casagrande

SEISMIC ASSESSMENT OF BALLOON-FRAMED CLT BUILDING WITH SELF-CENTERING HOLD-DOWN 2384
Yuxin Pan, Md Shahnewaz, Carla Dickof, Thomas Tannert

STUDY OF THE EFECT OF SEISMIC REINFORCEMENT USING CFRTP STRANDS ON WOODEN BUILDINGS 2390
Koji Kubo, Nobuji Sakurai, Yuya Takaiwa

SHEAR FAILURE MECHANISM III IN CROSS LAMINATED TIMBER – NUMERICAL INVESTIGATIONS OF FRACTURE BEHAVIOUR 2396
Henrik Danielsson, Erik Serrano

ANALYTICAL STUDY ON P-Δ EFFECT ON MEDIUM-RISE WOODEN BUILDINGS 2406
Shogo Aoki, Naohito Kawai, Takafumi Nakagawa

DETERMINATION OF THE EFFECTIVE WIDTH OF CROSS-LAMINATED TIMBER RIB PANELS USING DIGITAL IMAGE CORRELATION 2416
Miriam Kleinhenz, Martin Viertel, Thomas Demschner, Andrea Frangi

MODELLING OF OSB SANDWICH PANELS WITH ORIGAMI-INSPIRED CORE 2426
Jan Pelczynski, Kamila Martyniuk-Sienkiewicz, Anna Al Sabouni-Zawadzka

INNOCROSSLAM – ADDING KNOWLEDGE TOWARDS INCREASED USE OF CROSS LAMINATED TIMBER (CLT) 2432
Boris Azinovic, Erik Serrano, Henrik Danielsson, Josef Füssl, Markus Lukacevic, Philipp Dietsch, Matthias Arnold, Martin Schenk, Stefan Winter, Jose Manuel Cabrero, Pablo Gonzalez Serna, Tomaž Pazlar

REINFORCED NOTCHED CROSS-LAMINATED TIMBER PLATES: LOAD-BEARING CAPACITY AND METHODOLOGY FOR PREDICTING THE FORCE IN REINFORCEMENT 2442
Alen Malagic, Erik Serrano, Manfred Augustin, Gerhard Schickhofer

ANALYSIS OF DIFFERENT NUMERICAL MODELLING STRATEGIES OF MULTI-STOREY CLT SHEAR WALLS 2454
Elisabetta Maria Ruggeri, Giuseppe D'Arenzo, Marinella Fossetti, Werner Seim

IN-PLANE DEFLECTION OF CROSS-LAMINATED TIMBER DIAPHRAGMS 2464
Mahboobeh Fakhrzarei, Hossein Daneshvar, Ying Hei Chui

EVALUATION OF THE BEHAVIOUR FACTOR BY INCREMENTAL DYNAMIC ANALYSES FOR THE SEISMIC DESIGN OF LIGHT-FRAME TIMBER BUILDINGS 2471
Alessandra Gubana, Alessandro Mazelli

MODULE FOR ANALYSIS AND CAPACITY-BASED DESIGN OF BRACED TIMBER FRAMES 2479
Hossein Daneshvar, Brian Qi, Tahiat Goni, Md. Abdul Hamid Mirdad, Marjan Popovski, Zhiyong Chen, Ying Hei Chui

INVESTIGATING THE EFFECTS OF THE INTERACTIONS BETWEEN FLOOR DIAPHRAGMS AND SEGMENTED CROSS-LAMINATED TIMBER SHEAR WALLS 2489
Giuseppe D'Arenzo, Werner Seim

EXPERIMENTAL CHARACTERIZATION OF STIFF ALUMINIUM CONNECTORS FOR MULTI-PANEL CLT SHEAR-WALLS 2497
Pietro Rigo, Andrea Polastri, Daniele Casagrande, Ernesto Callegari, Alvise Ramazzini, Luca Sestigiani

REPRODUCTIVE ANALYSIS OF FULL-SCALE SHAKING TABLE TESTS OF WOODEN HOUSES USING QUALITY ENGINEERING 2504
Tokikatsu Namba, Takafumi Nakagawa, Yuji Kado, Atsuo Takino, Hiroshi Isoda

STIFFNESS OF WOODEN FLOORS FOR SEISMIC EVALUATION OF EXISTING MASONRY STRUCTURES IN NORWAY 2510
Joakim P. Munden, Francesco Graziotti, Guido Magenes, Roberto Tomasi

MODAL IDENTIFICATION AND MODEL UPDATING OF AN INNOVATIVE AUTOMATIC SELF-SUPPORTING TIMBER WAREHOUSE: THE CASE STUDY OF ROTHOBLAAS HEADQUARTERS EXPANSION 2517
Ernesto Callegari, Roberto Girardi, Luca Gottardi, Andrea Incerti, Claudio Mazzotti, Luca Pozza, Sebastian Rodemeier, Luca Sestigiani, Mirko Tommasini

EVALUATION OF THE STRUCTURAL PERFORMANCE OF SHEAR WALLS BUILT WITH MULTI-LAYER COMPOSITE LAMINATED PANELS 2523
Lin Zheng, Sigong Zhang, Meng Gong, Ying Hei Chui

TIMBER INTERACTIVE MODELLING AND POST-PROCESSING SOFTWARE (TIMPS) 2531
Manuel Sánchez-Solís, Màxim Lliso, Fernando Ibáñez

NUMERICAL AND EXPERIMENTAL INVESTIGATIONS ON THE STRESS STATE OF CLT-PLATES NEAR CONCENTRATED LOADS 2537
Heinz Wimmer, Christoph Huber, Robert Eder

ANALYTICAL STUDY ON SEISMIC BEHAVIOR OF NEWLY BUILT FIVE STORY PAGODA IN TENDO-CITY JAPAN 2548
Naohito Kawai, Mikio Koshihara, Iuko Tsuwa, Kohei Nakamichi

INNOVATIVE HIGH PERFORMANCE SEISMIC RESILIENT TIMBER WALL STRUCTURES WITH LOW DAMAGE FLOOR CONNECTIONS 2556
Soheil Assadi, Ashkan Hashemi, Pierre Quenneville

EVALUATION OF SEISMIC PERFORMANCE FACTORS AND FRAGILITY FUNCTIONS FOR POST-TENSIONED MASS PLY PANEL ROCKING WALLS 2562
Tu X. Ho, Patricio Uarac, Andre R. Barbosa, Arijit Sinha, Barbara Simpson, Gustavo A. Araújo, Gustavo F. Orozco

THE USE OF PARAMETRIC WORKFLOW ON TIMBER CONSTRUCTION AT SERVICE STATION TORGHATTEN 2570
Paul Hufnagel, Philipp Vehrenberg, Matthias Stracke

TIMBER PAVILION CONSTRUCTED IN COMBINATION WITH PARAMETRIC DESIGN AND THE ZOLLINGER CONNECTION SYSTEM 2577
Franziska Häuptle, Camilla By Kampenes, Matthias Stracke

DEVELOPMENT OF THE ANALYTICAL METHOD TO REPRODUCE SEISMIC BEHAVIOR OF CLT BUILDINGS AT LARGE DEFORMATION 2584
So Momose, Tatsuya Miyake, Hiroshi Isoda, Takafumi Nakagawa

RACKING RESISTANCE OF CLT PANELS MANUFACTURED FROM C16 GRADE TIMBER 2594
Conan O'Ceallaigh, Rimjhim Kashyap, Annette M. Harte, Patrick McGetrick

NUMERICAL ANALYSIS OF BIAXIAL HOLLOW TIMBER SLAB ELEMENTS 2600
Dominik Bissig, Marcel Muster, Andrea Frangi

EFFICIENT FINITE ELEMENT MODELS FOR ADHESIVE-FREE MULTI-LAYERED TIMBER STRUCTURES 2609
Jeanne Paroissien, Tuan-Anh Bui, Marcel Oudjene, Pascal Lardeur

STUDY ON THE STRUCTURAL PERFORMANCE OF PLYWOOD BEARING WALL WITH THE RUSTED NAIL AND DECAYED WOOD 2617
Yuki Ota, Hiroki Ishiyama, Shigefumi Okamoto

DEVELOPMENT OF A NUMERICAL MODEL TO CONSIDER THE FOUNDATION FLEXIBILITY EFFECTS IN CLT ROCKING WALLS 2627
Irshad Qureshi, Gustavo Acuña, Daniel Dolan

PRESCRIPTIVE SEISMIC DESIGN PROCEDURE FOR POST-TENSIONED MASS TIMBER ROCKING WALLS IN THE UNITED STATES 2633
Aleesha Busch, Reid B. Zimmerman, Shiling Pei, Erica McDonnell, Philip Line, Da Huang

EFFECT OF THE ASPECT RATIO ON THE SEISMIC PERFORMACE OF POST-TENSIONED CROSS-LAMINATED TIMBER ROCKING WALL SYSTEMS 2642
Gustavo Acuña Alegría, J. Daniel Dolan, Irshad Qureshi

THE ROLE OF INTERMODULAR CONNECTIONS IN THE GLOBAL BEHAVIOR OF HIGH-RISE MASS TIMBER BUILDINGS 2650
Juan Sebastian Zambrano Jaramillo, Erica C. Fischer

A COMPARISON OF PUNCHING SHEAR DESIGN APPROACHES FOR POINT SUPPORTED CLT PANELS 2660
Christian Slotboom, Carla Dickof, Robert Jackson

SEISMIC AND ENERGY RETROFIT OF MULTIFAMILY LIGHT-FRAME TIMBER RESIDENTIAL BUILDINGS USING MASS PLY PANEL (MPP) WALL FAÇADE SYSTEM 2669
Gustavo Orozco, Andre R. Barbosa, Mark Fretz, Judith Sheine, Jason Stenson, Kevin Van Den Wymelenberg, Payton Narancic, Flynn Casey

CROSS-LAMINATED TIMBER FLOORS WITH OPENINGS – SERVICEABILITY LIMIT STATE VERIFICATIONS 2678
Martin Schenk, Anja Husel, Philipp Dietsch, Pablo González-Serna, José Manuel Cabrero, Stefan Winter

TIMBER-FRAMED SHEAR WALLS WITH LARGE OPENINGS AS PART OF THE LATERAL FORCE-RESISTING SYSTEM - OPTIMIZATION OF THE SHEATHING-TO-FRAMING CONNECTION LAYOUT 2686
Nadja Manser, René Steiger, Martin Geiser, Lukas Kramer, Andrea Frangi

EXPERIMENTAL AND NUMERICAL INVESTIGATION ON THE EFFECT OF CIRCULAR HOLES ON GLULAM COMPOSITE BEAMS 2695
Dag Pasca, Yuri De Santis, Angelo Aloisio, Andreas Stenstad, Karl Christian Mahnert

EVALUATION OF HARDENING MODELS TO SIMULATE JOINTS IN TIMBER SHEAR WALLS 2709
Rajan Maharjan, Johan Vessby, Le Kuai

COLLAPSE FRAGILITY OF A 5-STORY CLT STRUCTURE UNDER CHILEAN SUBDUCTION EARTHQUAKE RECORDS 2717
Alberto Aravena, Alan Hellman, Joaquín Miranda, Franco Silva, Diego Valdivieso Cascante

FINITE ELEMENT ANALYSIS OF GLULAM BEAMS WITH TRANSVERSE AND LONGITUDINAL NOTCHES 2724
Sardar Malek, Azadeh Goodarzi, Roger Parra, Parham Khoshkbari

A STUDY ON THE SEISMIC PERFORMANCE OF SHEAR WALLS UNDER A DYNAMIC LOAD 2731
Tomoki Furuta, Masato Nakao

STRUCTURAL PERFORMANCE EVALUATION OF A TIMBER HOUSE USING NEW CONSTRUCTION SYSTEM WITH CLT HORIZONTAL DIAPHRAGM 2739
Masato Nakao, Tomoki Furuta

NUMERICAL ANALYSIS ON SEISMIC BEHAVIOUR OF TIMBER FRAME STRUCTURE WITH HYBRID SCREWED-IN ROD CONNECTIONS 2745
Jiwei Liu, Benkai Shi, Huifeng Yang

EXPERIMENTAL AND NUMERICAL ANALYSIS OF HIGH-CAPACITY SHEAR WALLS WITH MULTIPLE ROWS OF NAILS 2752
Ruite Qiang, Lina Zhou, Chun Ni

BUCKLING ANALYSES OF CROSS LAMINATED TIMBER PANELS 2761
Martina Sciomenta, Yuri De Santis, Chiara Bedon, Massimo Fragiacomo

CONNECTIONS TESTING AND RELIABILITY ASSESSMENT OF TIMBER CONNECTIONS WITH DOWEL-TYPE FASTENERS 2768
Ezequiel Moreno-Zapata, B. Iraola, R. Quinteros-Mayne, I. De Arteaga, P. Tanner, C. Lara, J. M. Cabrero

EFFECTS OF CONSTANT AND ELF STRENGTH PROFILES ON THE PERFORMANCE OF WOOD FRAME SHEAR WALL STRUCTURES 2776
Francisco Flores, Philip Line, Finley A. Charney

AN ANALYTICAL MODEL TO INVESTIGATE THE EFFECT OF DIAPHRAGMS ON THE ELASTIC BEHAVIOUR OF MULTI-STOREY COUPLED-PANEL CLT SHEARWALLS 2783
Damian Oliveira, Ali Mikael, Daniele Casagrande, Ghasan Doudak

DEFLECTION OF CANTILEVER CROSS-LAMINATED TIMBER DIAPHRAGMS UNDER IN-PLANE LOAD 2792
Bibek Bhardwaj, Weichiang Pang, Michael Stoner, Douglas Rammer, Steve Pryor

EXPERIMENTAL ANALYSIS OF THE INFLUENCE OF OPENINGS IN THE DEFLECTION OF CROSS-LAMINATED TIMBER PLATES LOADED OUT OF PLANE 2798
Pablo Gonzalez-Serna, Miguel Yurrita, José Manuel Cabrero

PHENOMENOLOGICAL MODEL FOR SEISMIC DESIGN OF MULTISTOREY CLT BUILDINGS: CALIBRATION OF INPUT PARAMETERS 2805
Luca Pozza, Stefano Pacchioli, Andrea Polastri, Valentino Nicolussi, Diego A. Talledo, Ian Smith

AN ACCURATE FINITE ELEMENT MODEL TO STUDY THE PROGRESSIVE COLLAPSE OF POST-AND-BEAM MASS TIMBER BUILDINGS.....2811
Chunhao Lyu, Benoit P. Gilbert, Hong Guan, Hassan Karampour, Shanmuganathan Gunalan, William Leggate

TIMBER STRUCTURES IN SUBTROPICAL CLIMATE ON DESIGN: BOIS DURAMHEN PROGRAMS FOR GUADELOUPE, MARTINIQUE AND GUYANE 2820
Paul Quistin, Eric Fournely, Joseph Gril, Gael Godi, Luc Cador, Thierry Lamadon, Laurence Romana, Jacques Beauchêne, Rostand Moutou Pitti

FRACTURE ANALYSIS OF CROSS LAMINATED TIMBER SHEAR-WALLS WITH OPENINGS 2826
Martina Sciomenta

EMBEDMENT STRENGTH AND STIFFNESS FOR LARGE DIAMETER MECHANICAL FASTENER 2834
Krunoslav Pavkovic, Dean Cizmar, Mislav Stepinac, Nina Pospiš

NUMERICAL MODELLING OF MASS TIMBER BEAM-COLUMN CONNECTIONS 2841
Labuwatte M. M. B. Jayasekara, Robert M. Foster

A NEW MULTI-SPRING ELEMENT TO SIMULATE CLT CONNECTIONS UNDER COMBINED LOADINGS 2851
Matías F. Chacón, Pablo Guindos, Jairo Montaño

EXPERIMENTAL AND NUMERICAL ASSESSMENTS OF LONG-SPAN MASS TIMBER FLOOR SYSTEMS SUBJECTED TO FOOT-FALL INDUCED VIBRATION..... 2861
Christian Slotboom, Carla Dickof, Tobias Fast

STRUCTURAL PERFORMANCE OF TWO-PANEL CLT SHEAR WALL WITH BOLTED CONNECTION 2870
Daiki Hinata, Jun Kubota, Takashi Shima, Shinji Takatani, Masanori Hisada, Naohiro Haneda

3.6. TALL TIMBER BUILDINGS

FORCED RESPONSE MEASUREMENTS ON A SEVEN STOREY TIMBER BUILDING IN SWEDEN 2877
Andreas Linderholt, Pierre Landel, Marie Johansson

SYSTEM IDENTIFICATION OF TALL MASS TIMBER STRUCTURES EMPLOYING AMBIENT VIBRATION TEST AND FE MODELLING..... 2885
Samira Mohammadyzadeh, Jianhui Zhou, Lin Hu, Fei Tong

ON FINITE ELEMENT MODELLING AND MODEL UPDATING OF MULTI-STOREY TIMBER BUILDINGS 2892
Blaž Kurent, Boštjan Brank, Wai Kei Ao, Aleksandar Pavic, Manuel Manthey

AMBIENT VIBRATION TESTS AND MODAL ANALYSIS OF A SIX-STORY LIGHTWEIGHT TIMBER FRAME BUILDING 2898
Carmen Amaddeo, Michael Dorn

DYNAMIC RESPONSE OF TALL TIMBER BUILDINGS UNDER SERVICE LOAD – RESULTS FROM THE DYNATTB RESEARCH PROGRAM 2907
Rune Abrahamsen, Magne A. Bjertnæs, Jacques Bouillot, Boštjan Brank, Roberto Crocetti, Olivier Flamand, Fabien Garains, Igor Gavric, Ludwig Hahusseau, Alan Jalil, Marie Johansson, Thomas Johansson, Wai Kei Ao, Blaž Kurent, Pierre Landel, Andreas Linderholt, Kjell Arne Malo, Manuel Manthey, Petter Nåvik, Alex Pavic, Fernando Perez, Anders Rönnquist, Iztok Šušteršic, Saule Tulebekova

QUANTIFYING ROBUSTNESS IN TALL (TIMBER) BUILDINGS: A CASE STUDY 2915
Konstantinos Voulpiotis, Styfen Schär, Andrea Frangi

LONG-TERM MONITORING OF TALL MASS TIMBER BUILDINGS – EVALUATION OF DYNAMICS PROPERTIES 2922
Samuel Cuerrier Auclair, Christian Dagenais, Girma Bitsuamlak

DIFFERENTIAL MATERIAL MOVEMENT IN TALL MASS TIMBER STRUCTURES 2930
Richard McLain, Josephine Racine, Bryce Lumpkin

SERVICEABILITY PERFORMANCE OF TIMBER DUAL FRAME-WALL STRUCTURAL SYSTEM UNDER WIND LOADING 2940
Osama Hegeir, Haris Stamatopoulos, Kjell Arne Malo

INVESTIGATION OF LONG-TERM MODAL PROPERTIES OF A TALL GLUE-LAMINATED TIMBER FRAME BUILDING UNDER ENVIRONMENTAL VARIATIONS 2950
Saule Tulebekova, Kjell Arne Malo, Anders Rønnquist, Petter Nåvik

INVESTIGATIONS ON SUITABLE LATERAL STIFFENING SYSTEMS FOR TALL TIMBER BUILDINGS 2958
Charles Binck, Andrea Frangi

PERFORMANCE VERIFICATION AND TRIAL DESIGN FOR HIGH-RISE TIMBER FRAME BUILDINGS WITH BUCKLING-RESTRAINED BRACE - PART 2: ANALYSIS OF THE TRIAL DESIGN BUILDING 2968
Ryota Minami, Toshio Maegawa, Taisuke Nagashima, Kazuki Tachibana, Hiroki Nakashima, Nobuhiko Akiyama, Yoshihiro Yamazaki, Takahiro Tsuchimoto

POINT-SUPPORT REINFORCEMENT FOR A HIGHLY EFFICIENT TIMBER HOLLOW CORE SLAB SYSTEM 2978
Cristóbal Tapia, Hans Jakob Wagner, Simon Treml, Achim Menges, Simon Aicher

R&D PROJECT FOR TECHNOLOGIES ABOUT MID- AND HIGH-RISE TIMBER CONSTRUCTION IN JAPAN 2987
Takahiro Tsuchimoto, Nobuhiko Akiyama, Yoshihiro Yamazaki

3.7. INTERNATIONAL CODES & TIMBER ENGINEERING

A PROPOSAL FOR THE MECHANICAL CLASSIFICATION OF BEAM-TO-COLUMN JOINTS FOR TIMBER STRUCTURES 2995
Giacomo Iovane, Raffaele Landolfo, Celeste Noviello, Federico M. Mazzolani, Beatrice Faggiano

SECOND GENERATION OF EUROCODE 5-2 ON TIMBER BRIDGES, AN OVERVIEW 3001
Matthias Gerold, Hauke Burkart

TALL WOOD BUILDINGS WITHIN THE 2020 NATIONAL BUILDING CODE OF CANADA 3007
Marc Alam, Rodney McPhee

BEARING SUPPORTS REINFORCED WITH SCREWS: EXPERIMENTAL INVESTIGATION AND DISCUSSION OF THE DESIGN MODELS IN EUROCODE 5 3015
Roberto Tomasi, Angelo Aloisio, Ebenezer Ussher, Kari Ryen Thunber, Eldbjørg Aaraas Hånde, Harald Liven

MODIFICATION OF PARTIAL SAFETY FACTORS FOR A SEMI-PROBABILISTIC EVALUATION OF EXISTING TIMBER STRUCTURES 3023
Maria Loebjinski, Wolfgang Rug, Hartmut Pasternak

REVIEW OF THE CODE DEVELOPMENT EFFORTS FOR TALL MASS TIMBER BUILDINGS IN THE US 3033
Lori Koch, Matthew Hunter, M. Omar Amini

IMPROVEMENT OF THE DURABILITY OF TIMBER BRIDGES BY INTELLIGENT DESIGN AND RESPONSIBLE MAINTENANCE 3041
Antje Simon, Markus Jahreis, Johannes Koch

WOOD DURABILITY BASED IN THE NEW BRAZILIAN TIMBER STRUCTURES CODE ABNT NBR 7190: 2022 3048
Leandro Dussarrat Brito, Everaldo Pletz, Carlito Calil Junior

UPDATING EUROCODE 5 – DESIGN GUIDANCE FOR INCREASING THE ROBUSTNESS OF TIMBER STRUCTURES 3054
Pedro Palma, Jørgen Munch-Andersen, Philipp Dietsch

THE NEW BRAZILIAN TIMBER STRUCTURES CODE NBR7190: 2022 3062
Carlito Calil Junior, Felipe Hideyoshi Icimoto, Leandro Dussarrat Brito

EVALUATION OF CLT SHEAR WALLS FOR INCREASED STRUCTURAL HEIGHT LIMIT AND FOR EFFECT OF VARYING PANEL ASPECT RATIO 3069
M. Omar Amini, Philip Line, John W. Van De Lindt, Doug Rammer, Francisco Flores

BEAVER: A PARAMETRIC DESIGN FRAMEWORK FOR TIMBER ENGINEERING 3076
Renan Prandini, João Tavares Pini, Márcio Sartorelli Venâncio De Souza

STRUCTURAL CHARACTERIZATION OF NATIVE SPECIES ACCORDING TO THE NEW BRAZILIAN STANDARD ABNT NBR 7190: 2022 – PART 4 3084
Fabiana Yukiko Moritani, Felipe Hideyoshi Icimoto, Rodrigo De Souza Nogueira, Carlito Calil Junior, Lorenzo Lube Dos Santos, Adriano Wagner Ballarin

3.8. MIXED, COMPOSITE & HYBRID STRUCTURES

PREFABRICATED TIMBER CONCRETE COMPOSITES 3091
Sam Winder, Daniel Chapman, Panayiotis Papastavrou, Simon Smith, Allan McRobie

NUMERICAL MODELLING OF A CROSS-LAMINATED TIMBER-TO-CONRETE DOWEL-TYPE CONNECTION USING THE BEAM-ON-FOUNDATION MODEL 3101
Joan W. Gikonyo, Eva Binder, Michael Schweigler, Thomas K. Bader

EXPERIMENTAL AND NUMERICAL STUDY OF MOULDED WOOD TECHNOLOGY WITH FIBRE-PLASTIC COMPOSITE NODE ELEMENTS 3111
Siavash Mahjourian Namari, Peer Haller

MECHANICAL BEHAVIOUR OF NOTCH CONNECTION FOR MARITIME PINE CLT-CONCRETE COMPOSITE 3121
Carlos Albino, Carlos Martins, Cláudio Ferreira, Renato Augusto, Alfredo Dias

EXPERIMENTAL INVESTIGATION OF AN INNOVATIVE BEAM-TO-COLUMN CONNECTION UNDER CYCLIC LOADING 3127
Ahmed Mowafy, Ali Imanpour, Ying Hei Chui, Hossein Daneshvar

AN EXPERIMENTAL STUDY ON THE SAFETY PERFORMANCE OF A WOOD MASONRY STRUCTURE 3134
Daiki Iwamoto, Joichi Nakakuki, Waikong Lam, Hiro Kawahara, Masamichi Sasatani

STRUCTURAL PERFORMANCE OF REINFORCED GLULAM BEAMS 3141
Laith Gharaibeh, Ghasan Doudak

BENDING TESTS ON TIMBER CONCRETE COMPOSITES WITH PERFOBOND CONNECTIONS 3148
Elif Appavuravther, Bram Vandoren, José Henriques

DESIGN OF ASYMMETRIC FRICTION CONNECTION FOR SESIMIC RETROFITTING OF RC FRAMES WITH CROSS-LAMINATED TIMBER PANELS 3154
Angelo Aloisio, Francesco Boggian, Roberto Tomasi

SHEAR TESTS ON PERFOBOND CONNECTIONS IN TIMBER CONCRETE COMPOSITES 3161
Elif Appavuravther, Bram Vandoren, José Henriques

DELTABEAM® WITH TIMBER FLOOR JOINTS – LOAD BEARING CAPACITY AT AMBIENT TEMPERATURE AND IN FIRE SITUATION 3167
Salla-Mari West, Elena Camnasio, Simo Peltonen

MECHANICAL BEHAVIOUR OF TIMBER-STEEL COMPOSITE CONNECTION SYSTEMS 3177
Alireza Shahin, Craig J. L. Cowled, Henri Bailleres, Sabrina Fawzia

FINITE ELEMENT MODELLING OF HYBRID WOOD/ALUMINIUM ASSEMBLY WITH WOOD-FILLED ALUMINIUM AND STEEL DOWELS 3184
Gotre Bi Djeli Bienvenu Boli, Marc Oudjene, Daniel Coutellier, Hakim Naceur

EXPERIMENT ON AXIAL CAPACTY-BENDING CAPACITY RELATIONSHIP OF STEEL BAR-TIMBER COMPOSITE COLUMN 3191
Keisuke Hayata, Motohiro Mukai, Shinichi Shioya

FINITE ELEMENT ANALYSIS OF BUCKLING BEHAVIOR OF TIMBER ENCASED STEEL COMPOSITE COLUMNS SUBJECTED TO AXIAL LOAD 3201
Ying Gao, Feiyang Xu, Minghao Geng, Qibin Hu, Xinmiao Meng

EFFECTS OF ELEVATED TEMPERATURE ON BENDING CAPACITY OF STEEL BAR-TIMBER COMPOSITE BEAM 3211
Tsukasa Ueno, Nao Matsuoka, Shinichi Shioya

THE ADHESIVE SHEAR CONNECTION OF TIMBER AND CONCRETE SLABS IN HUMID ENVIRONMENT 3221
Viktória Bajzecerová, Jan Kanócz, Viktor Karla, Miroslava Javoríková

CYCLIC TESTS ON AN INNOVATIVE FRICTION DISSIPATIVE DEVICE FOR SEISMIC RETROFIT WITH CLT PANELS 3229
Francesco Boggian, Angelo Aloisio, Roberto Tomasi

NAIL-LAMINATED TIMBER-CONCRETE COMPOSITE BEAMS WITH NOTCHED CONNECTIONS AND STEEL FIBRE REINFORCEMENT 3235
Hamidreza Chaboki, Lei Zhang, Thomas Tannert, Jianhui Zhou

PUSH-OUT TESTS OF WET-PROCESS ADHESIVE-BONDED BEECH TIMBER-CONCRETE AND TIMBER-POLYMER-CONCRETE COMPOSITE CONNECTIONS 3241
Matthias Füchslin, Philippe Grönquist, Sandro Stucki, Tim Mamie, Steffen Kelch, Ingo Burgert, Andrea Frangi

SEISMIC FRAGILITY OF A NEW MASS TIMBER-STEEL HYBRID BUILDING SYSTEM EQUIPPED WITH CLT FLOOR DIAPHRAGMS 3248
Chaoyue Zhang, Cristiano Loss

STRUCTURAL BEHAVIOR OF TIMBER-STEEL-JOINTS WITH EITHER DOWEL-TYPE FASTENERS OR CONTINUOUS JOINTS 3256
Simon Aurand, Jakob Boretzki, Peter Haase, Thomas Ummenhofer, Philipp Dietsch

SEMI-INTEGRAL FULL-SCALE STUTTGART TIMBER MODEL BRIDGE 3264
Simon Aicher, Kai Simon

LIMBERLOST PLACE: A 10-STOREY SLAB-BANDED STRUCTURE 3272
Md Shahnewaz, Robert Jackson

STRUCTURAL DESIGN OF HYBRID STRUCTURE WITH CLT SEISMIC PANELS AND STEEL FRAME 3281
Kouji Fukumoto, Marina Koda, Hiroshi Isoda

TECHNICAL CONCEPT AND FEASIBILITY OF STEEL SHEET REINFORCED SYNTHETIC WOOD BEAM 3290
Shogo Oda, Chikako Tabata, Yoshito Tomioka

TIMBER-CONCRETE-COMPOSITE BEAMS WITH DISCRETE PERFORATED STEEL PLATE SHEAR CONNECTORS 3296
Dolores Otero-Chans, Javier Estévez-Cimadevila, Emilio Martín-Gutiérrez, Félix Suárez-Riestra, José A. Vázquez-Rodríguez

A NEW BUILDING STRUCTURAL SYSTEM USING TIMBER-CONCRETE-COMPOSITE MEMBERS 3303
Javier Estévez-Cimadevila, Dolores Otero-Chans, Emilio Martín-Gutiérrez, Félix Suárez-Riestra, José A. Vázquez-Rodríguez

STUDY ON FAILURE MECHANISMS OF HYBRID STRUCTURE OF REINFORCED CONCRETE FRAME WITH CLT INFILL 3309
Hamood Alwashali, Ahmad Ghazi Aljuhmani

PRELIMINARY STUDY ON THE TENSION-ONLY BRACED SELF-CENTERING STEEL-TIMBER HYBRID FRAME 3318
Fei Chen, Minghao Li, Minjuan He, Zheng Li

DEVELOPMENT OF HYBRID RIGID FRAME STRUCTURE METHOD USING SEMI-RIGID TIMBER BEAMS 3325
Akihiko Miyake, Ryoma Murata

AN EXPERIMENTAL AND NUMERICAL INVESTIGATION ON A DOVETAIL NOTCHED CONNECTION FOR CROSS-LAMINATED-TIMBER-CONCRETE COMPOSITE SLABS 3333
Vanthet Ouch, Piseth Heng, Hugues Somja, Thierry Soquet

A 3D DUCTILE-NOTCHED CONNECTION FOR TIMBER-CONCRETE COMPOSITE BEAM : EXPERIMENTAL INVESTIGATION 3342
Adham Al Rahim, Piseth Heng, Clemence Lepourry, Hugues Somja, Franck Palas

HIGH CAPACITY SHEAR CONNECTORS AND APPLICATION FOR TIMBER-CONCRETE BRIDGES 3351
Raitis Lacis, Maris Karlsons

DEVELOPMENT OF LVL-CONCRETE COMPOSITE FLOOR SYSTEMS 3357
Alireza Fadai, Johann Scheibenreiter, Alex Müllner, Marie Theres Brunauer

ANALYTICAL AND EXPERIMENTAL STUDY ON REVERSIBLE STEEL-TIMBER COMPOSITE CONNECTION SYSTEMS 3364
Fabiana Yukiko Moritani, Pedro Santos, Luís Jorge, Alfredo Dias

EXPERIMENTAL AND NUMERICAL INVESTIGATIONS ON THE USAGE OF CLT PANELS TO FORM TIMBER-STEEL COMPOSITE FLOOR SYSTEMS 3373
Hugh Merryday, Megan Potuzak, David Roueche, Kadir Sener

EXPERIMENTAL TESTING OF SMALL-SCALE TIMBER-CONCRETE COMPOSITE BEAMS UTILIZING ADHESIVE SHEAR CONNECTIONS 3382
Adam Petrycki, Sam Salem, Matthew Leitch

3.9. WOOD-BASED BUILDING SYSTEMS

EFFECT OF DIFFERENT TESTING METHODS ON THE STRUCTURAL PERFORMANCE OF WOODEN SHEAR WALLS 3392
Yua Kosuge, Satoshi Onishi, Hideyuki Nasu

DEVELOPMENT OF HIGH STRENGTH BEARING WALLS FOR FRAMEWORK CONSTRUCTION METHOD USING 2X4 LUMBER AND PLYWOOD MADE OF JAPANESE TIMBER 3398
Hideyuki Nasu, Kenji Aoki, Hiro Kawahara

IMPACT OF EXTERIOR SIDING WALLS AND THE CONNECTING METHODS IN WOODEN HOUSES: COMPARATIVE VERIFICATION FOR STRUCTURAL PERFORMANCE WITH DIFFERENT CONNECTION METHODS OF WALL SIDINGS 3404
Kouta Matsumoto, Kiyotaka Terui, Hideyuki Nasu

STUDY ON THE EVALUATION OF THE RESTORING FORCE CHARACTERISTICS OF FLOOR OF TRADITIONAL WOODEN BUILDING IN KYOTO 3410
Rongji Fu, Mina Sugino, Yasuhiro Hayashi

INFLUENCE OF PLASTERBOARD ON THE STRUCTURAL PERFORMANCE OF TIMBER-FRAMED SHEAR WALLS 3417
Craig Cowled, Tom Slattery, Keith Crews, Harrison Brooke

EXPERIMENTAL CHARACTERIZATION OF CLT SHEAR WALLS CONNECTED TO PERPENDICULAR WALLS 3423
Elisabetta Maria Ruggeri, Giuseppe D'Arenzo, Denise Li Cavoli, Ignazio Casiraro, Marinella Fossetti

FULL-SCALE LATERAL TESTING AND MODELLING OF INDUSTRIALIZED TIMBER DIAPHRAGMS INCLUDING ONLY FRAMING AND NON-STRUCTURAL SHEATHING 3430
Fernando Véliz, Xavier Estrella, Pablo Guindos

FEASIBILITY STUDY ON LONG-SPAN CLT-GLULAM COMPOSITE FLOORING SYSTEM CONNECTED WITH BAMBOO-TENON SHEAR CONNECTORS 3439
Yue Diao, Cristiano Loss

STUDY ON FRAME DESIGN OF CONVENTIONAL WOODEN HOUSE 3449
Tomoya Sahata, Naohito Kawai, Hideyo Tsukazaki

EXPERIMENTAL ANALYSIS OF A SCREW-GLUED SHEAR CONNECTION FOR USE IN MASS TIMBER COMPOSITE PANELS 3455
Tyler Hull, Daniel Lacroix

LOADING TEST OF CLT-SHEAR WALL CONNECTED WITH STEEL BAR-TIMBER COMPOSITE COLUMN DISSIPATING HIGH-ENERGY 3465
Takumi Suyama, Riko Kawasaki, Atsuya Kawasoe, Tomokazu Yoshioka, Shinichi Shioya

TIMBER VAULTS FOR ULTRA-LOW-CARBON BUILDING STRUCTURES 3475
Shane Hossell, Will Hawkins, Antony Darby, Tim Ibell, Nicola Lines

SEGMENTED COMPOSITE SECTIONS WITH WOOD DOWELS 3485
Matthias Brieden, Max Braun, Werner Seim, Kristina Schramm, Philipp Eversmann

LIGHT-FRAME TIMBER SHEAR-WALLS WITH DIAGONAL BOARD SHEATHING: EXPERIMENTAL AND NUMERICAL INVESTIGATION 3492
Alessandro Setti, Daniele Casagrande, Andrea Polastri, Riccardo Fanti, Maurizio Follesa, Ezio Riggi

SEISMIC PERFORMANCE OF CLT SHEAR WALL INFILLED HYBRID STEEL MOMENT FRAME WITH CONCEALED STEEL PLATE AND DRIFT PINS CONNECTIONS 3499
Hiroshi Isoda, Richard Yip Je Too, Kazumi Kanazawa

INVESTIGATION OF A NOVEL TIMBER-MORTAR CONSTRUCTIVE SYSTEM 3507
Andrea Polastri, Riccardo Fanti, Pietro Rigo, Efrem Demarchi

SHEAR PERFORMANCE OF STRUCTURAL PARTICLEBOARD-SHEATHED LIGHT-FRAME WALL 3513
Chul-Ki Kim, Min Lee, Kugbo Shim

DEPLOYABLE WOOD STRUCTURES FOR DISASTER RELIEF AND MILITARY USE 3518
Jayson Leonard, Weichiang Pang, Michael Stoner, Dustin Albright

3.10. CIRCULAR DESIGN FOR SUSTAINABILITY, ALTERED USE, AND REUSE OF BUILDINGS & COMPONENTS

GLUED TIMBER TRUSSES 3526
Tuomo Poutanen, Markku Karjalainen, Valtteri Paananen, Jouko Tanskanen

3DP BIOWALL - CIRCULAR ECONOMY IN WOOD CONSTRUCTION THROUGH ADDITIVE MANUFACTURING OF FULLY RECYCABLE WALLS 3535
Benjamin Kromoser, Sara Reichenbach, Roman Myna, Raphaela Hellmayr, Bernhard Reinholz, Rupert Wimmer

SEISMIC ANALYSIS OF A MULTI-STORY TIMBER-CONCRETE BUILDING AND DESIGNING FOR REUSE 3542
Sivert Lie, Themistoklis Tsalkatidis

DEVELOPMENT OF TEMPORARY STRUCTURE USING CLT PANEL - INVENTION OF CONSTRUCTION AND VERIFICATION BY CONSTRUCTION EXPERIMENT 3551
Hiroaki Kubotera, Toshiaki Sato, Yohei Aioi, Kazuo Niikuma

HOW TIMBER BUILDINGS CAN BE DESIGNED FOR DECONSTRUCTION AND REUSE IN ACCORDANCE WITH ISO 20887 3558
Ylva Sandin, Marlene Cramer, Karin Sandberg

PUSH-OUT TESTS ON CONNECTIONS FOR DEMOUNTABLE AND REUSABLE STEEL-TIMBER COMPOSITE BEAM AND FLOORING SYSTEMS 3568
Alfredo Romero, Jie Yang, François Hanus, Hervé Degée, Christoph Odenbreit

STRUCTURAL PERFORMANCE OF TIMBER-CONCRETE COMPOSITE FLOOR ELEMENTS WITH DECONSTRUCTABLE CONNECTORS AND ITS POTENTIAL FOR REUSE 3575
Mohammad Derikvand, Gerhard Fink

ENVISIONING MASS TIMBER BUILDINGS FOR CIRCULARITY: LIFE CYCLE ASSESSMENT OF A MASS TIMBER BUILDING WITH DIFFERENT END-OF-LIFE (EOL) AND POST-EOL OPTIONS 3581
Namhyuck Ahn, Christina Bjarvin, Mariapaola Riggio, Lech Muszynski, Laurence Schimleck, Catarina Pestana, Ambrose Dodoo, Maureen Puettmann

A REUSE-READY TIMBER SLAB-AND-COLUMN SYSTEM FOR MODULAR BUILDING STRUCTURES 3588
Xavier Estrella, Alex Muresan, Dario Redealli, Jan Brütting, Jonas Warmuth, Corentin Fivet

ENGINEERED WOOD PRODUCTS MANUFACTURED FROM RECLAIMED HARDWOOD TIMBER 3594
Daniel Fernandez Llana, Violeta González-Alegre, María Portela, Justo García-Navarro, Guillermo Íñiguez-González

REUSE OF LOAD-BEARING TIMBER ELEMENTS – CASE STUDY OF A LOOKOUT TOWER IN LAUSANNE, SWITZERLAND 3600
Jonas Warmuth, Xavier Estrella, Benoît Kälin, Johannes Natterer, Corentin Fivet

VALUES OF RECLAIMED TIMBER 3608
Maxence Lebossé, Franck Besancon, Gilles Halin, Alain Fuchs

CHALLENGES IN THE DESIGN OF A MODULAR MULTI-STOREY CLT BUILDING USING IRISH TIMBER 3618
Hung Quang Phung, Conan O'Ceallaigh, Patrick McGetrick, Annette M. Harte, Rimjhim Kashyap

RE:SOURCE PAVILION – EXPLORING THE CIRCULAR USE OF WOODEN BUILDING MATERIALS 3625
Ute Groba, Samuel Blumer

ADAPTABILITY IN MULTI-STOREY TIMBER BUILDINGS – TOWARDS DIFFERENTIATED DURABILITY LAYERS IN ARCHITECTURE 3634
Esther Vandamme, Mario Rinke

PROPOSAL OF INTERACTIVE WORKFLOW FOR CIRCULAR TIMBER STRUCTURE DESIGN 3644
Marcin Luczkowski, Sverre M. Haakonsen, Artur Tomczak, Bunji Izumi

3.11. RILEM TC TPT

ENERGY DEMAND FOR THE DRIVING IN OF SELF-TAPPING TIMBER SCREWS AND ITS APPLICABILITY 3649
David Glasner, Andreas Ringhofer, Gerhard Hubmann, Werner Braun

INFLUENCE OF THE SPECIMEN PREPARATION ON THE EMBEDMENT STRENGTH OF SELF-TAPPING SCREWS 3660
Michael Gstettner, Andreas Ringhofer

INFLUENCE OF TEST METHODS ON THE PARALLEL TO GRAIN EMBEDMENT STRENGTH AND FOUNDATION MODULUS CHARACTERIZATION 3667
Caroline Dapieve Aquino, Leonardo G. Rodrigues, Meta Kržan, Michael Schweigler, Zheng Li, Jorge M. Branco

DEVELOPMENT OF COMPREHENSIVE TESTING PROCEDURES FOR HIGH-PERFORMANCE BONDED-IN RODS 3675
Robert Jockwer, Pedro Palma, Arthur S. Rebouças, Alexander Salenikovich

PROTOCOLS AND RESULTS ANALYSIS METHODS FOR CYCLIC TESTS OF TIMBER JOINTS. A DISCUSSION 3685
Meta Kržan, Caroline D. Aquino, Michael Schweigler, Zheng Li, Jorge M. Branco

4.1. ARCHITECTURAL POTENTIAL OF NEW WOODEN MATERIALS & TECHNOLOGIES

USAGE OF A BAMBOO HONEYCOMB STRUCTURE (COMBOO) IN TIMBER ARCHITECTURE 3694
Andreas Loth, Ralf Förster

BENDING OF CLT BY THE LATTICE HINGE METHOD 3701
Laurane Néron

STRATOCONCEPTION®, AN ADDITIVE MANUFACTURING PROCESS FOR TIMBER ARCHITECTURE: CHALLENGES AND OPPORTUNITIES 3708
Victor Fréchard, Laurent Bléron, Julien Meyer, Franck Besançon, Gilles Duchanois

HYPERBOLIC PARABOLOID SHELLS MADE OF DIAGONAL LAMINATED TIMBER ELEMENTS 3718
Matthias Arnold, Philipp Dietsch, Stefan Winter

MASS TIMBER PANELIZED WORKFORCE HOUSING IN OREGON, U.S. 3728
Judith Sheine, Mark Fretz, Simone O'Halloran, Mikhail Gershfeld, Jason Stenson

UTILIZING LOW-VALUE WOOD SPECIES FROM FOREST RESTORATION PROJECTS IN LOCAL CLT MANUFACTURE AND DESIGN 3738
Payton Narancic

AMAZONIAN MASS TIMBER IN THE NEW CIPEM'S HEADQUARTERS – MATO GROSSO, BRAZIL 3747
Roberto Lecomte, Sheila Beatriz

INTEGRATING TIMBER PANEL ELEMENTS INTO HISTORIC CHINESE TIMBER-FRAMED HOUSES TO ENHANCE MULTIPLE BUILDING PERFORMANCES 3753
Harrison Huang, Kapulanbayi Ailaitijiang, Zhan Hui

ARCHITECTURAL POTENTIAL OF NEW WOODEN MATERIALS & TECHNOLOGIES 3761
Ramona Schwertfeger, Markus Lager

SPECIAL SIZED TIMBER POLES AS MAIN STRUCTURAL MATERIAL IN TWO SPORTS GYMS AND A WINERY – BRAZIL 3769
Roberto Lecomte, Sheila Beatriz

MODULAR CONSTRUCTION WITH LOW-GRADE HARDWOOD CROSS-LAMINATED TIMBER 3775
Edward Becker

4.2. INTEGRATION OF PARAMETRIC ARCHITECTURAL DESIGN & CNC MANUFACTURING

MASS TIMBER, SMALL FORMAT: OPEN SOURCE FURNITURE PROTOTYPING FROM MASS TIMBER SCRAPS 3782
Cory Olsen, Linda Zimmer

CARPENTER AND ROBOT: HOW TO BENEFIT FROM THE KNOWLEDGE OF CRAFTSMEN AND THE STRENGTH OF ROBOTS 3788
Wolfgang Schwarzmann

A BIM-BASED MODULE DESIGN METHODOLOGY FOR THE ROOF PLANNING OF MODERNIZED KOREAN TRADITIONAL WOODEN BUILDINGS 3794
Dongwook Kim, Bonghee Jeon, Gee Heon Kim

STEPS TOWARDS A UNIVERSAL SCHEME FOR PARAMETRIC DETAILING OF COMPOUND TIMBER STRUCTURES 3801
John Haddal Mork, Sveinung Ørjan Nesheim

4.3. BUILDING PHYSICS & BUILDING SKINS

MOISTURE PREDICTION OF TIMBER FOR DURABILITY APPLICATIONS USING DATA-DRIVEN MODELLING 3808
Seyyed Hasan Hosseini, Jonas Niklewski, Philip Bester Van Niekerk

HYGRO-THERMAL EXPERIMENTAL ANALYSIS OF A FLAT ROOF STRUCTURE INTEGRATING A VARIABLE VAPOR-DIFFUSIVITY MEMBRANE 3816
Riccardo Pinotti, Paola Brugnara, Stefano Avesani

DEVELOPING SLIMMER TIMBER WINDOW FRAME 3823
Katarzyna Ostapska, Tore Myrland Jensen, Lars Gullbreken, Petra Ruther

OUTDOOR PANELS FROM NORWAY SPRUCE – THE EFFECT OF COATING COLOUR ON THE TEMPERATURE 3829
Sebastian Svensson Meulmann, Åsa Rydell Blom, Michael Dorn

HYGROTHERMAL PERFORMANCE OF NATURE-BASED INSULATION MATERIALS INTEGRATED IN TIMBER-BASED WALL-SYSTEMS 3835
Dimitrios Kraniotis, Samee Ullah, Stine Lønbro Bertelsen

ALCOHOLS AS A PHASE CHANGE MATERIAL WITH EXCELLENT THERMAL STORAGE PROPERTIES IN BUILDINGS ..... N/A
Dehong Li, Yuchen Chen, Bin Li, Alireza Kaboorani, Denis Rodrigue, Xiaodong Alice Wang

TIMBER CLADDING DISCOLOURATION IN TROPICAL MONSOON CLIMATES 3851
Shinya Okuda, Laurent Corpataux, Kua Harn Wei

4.4. SENSOR SYSTEMS FOR BUILDING PROCESS AND OPERATION

CREEP TESTING OF A TIMBER LATTICE FRAME USING IMAGE RECOGNITION 3860
Nicolas Giron, Hideyuki Nasu

A MOISTURE MANAGEMENT STRATEGY FOR CLT USING SENSOR TECHNOLOGY TO CREATE A ROBUST NORWEGIAN SCHOOL 3868
Laura Vestergaard Kellgren, Astrid Charlotte Seeberg, David Hagle, John Øvregård, Jeppe Rasmussen

PRINTED SENSORS FOR MONITORING WOOD MOISTURE CONTENT INSIDE TIMBER BUILDING ELEMENTS 3874
Boris Forsthuber, Michael Truskaller, Irene Spitaler, Pavel Kulha, Maximilian Scherf, Gabriel Partl, Albert Rössler, Gerhard Engelbrecht, Gerhard Grüll

MOISTURE AND TIGHTNESS MONITORING WITH DIFFERENT MEASURING SYSTEMS AND METHODS - EXAMPLE APARTMENT BUILDING 3880
Anton Kraler, Andreas Pomaroli

A PROMISING APPROACH OF LINEAR TIMBER STRUCTURAL HEALTH MONITORING 3888
Johannes Koch, Martin Ganß, Martin Kästner, Antje Simon

FEDERATED USE OF HYGROTHERMAL MONITORING DATA IN MASS TIMBER BUILDINGS: OPPORTUNITIES AND CHALLENGES 3896
Mariapaola Riggio, Jan Vcelak, Pekka Kaitaniemi, Andre R. Barbosa, Niki Hrovatin, Anna Sandak, Jakub Sandak, Michael Mrissa, Miklos Kresz, Anssi Yli-Jyrä, Ritva Toivonen, Laura Alakukku

4.5. NEW DESIGN PRACTICE AND BUILDING SYSTEMS

TOWARDS DESIGN FLEXIBILITY AND FREEDOM IN MULTI-STOREY TIMBER CONSTRUCTION: ARCHITECTURAL APPLICATIONS OF A NOVEL, ADAPTIVE HOLLOW SLAB BUILDING SYSTEM 3905
Hana Svatoš-Ražnjevic, Anna Krtschil, Luis Orozco, Gregor Neubauer, Jan Knippers, Achim Menges

RECIPROCAL FRAMES: AN ANCESTRAL STRUCTURAL PRINCIPLE TO USE NATIVE WOOD SPECIES IN CHILE 3917
Suzanne Segeur-Villanueva, Natalia Caicedo-Llano

DEVELOPMENT OF A NEW TYPE OF BUILDING IN TROPICAL REGIONS BASED ON THE ENERGETIC PERFORMANCE AND RECOVERY OF RECYCLED WOOD 3924
Horly Luzolo Nsumbu, Régis Pommier, Denis Bruneau, Alain Sempey

USING CO-DESIGN FOR DEVELOPING A NEW WOODEN FAÇADE SYSTEM 3931
Camilla Schlyter, Karin Sandberg

MULTI-CRITERIA ASSESSMENT FOR FLEXIBILITY IN MODULAR TIMBER SCHOOL PROJECT BASED ON AHP-TOPSIS 3937
Puxi Huang, Yiping Meng

MONO-MATERIAL TIMBER CONSTRUCTION RE-INVENTION OF PRESS-FIT TIMBER CONSTRUCTIONS 3944
Hans Drexler

A DESIGN FRAMEWORK FOR TIMBER BUILDING SYSTEMS 3954
Marius Nygaard, Kjetil Nordby

TAMANGO BUILDING: TYPOLOGICAL EXPLORATION FOR A 12-STOREY WOODEN APARTMENT BUILDING IN A SEISMIC AREA 3963
Gerardo Armanet, Juan José Ugarte G., Sebastián Cárcamo, Andrés Sierra, Diego Valdivieso, Juan José Ugarte Á.

MORPHOLOGIC STUDY OF HYBRID TALL BUILDING TOWARDS AN INTERDISCIPLINARY DESIGN 3973
Sebastian Carcamo, Diego Valdivieso

4.6. USE OF TIMBER IN TRANSPORT SECTOR (BRIDGES, AIRPORTS, HARBOURS)

AN INSIGHT INTO THE DEVELOPMENT OF TIMBER BRIDGES IN NORWAY AND SWEDEN 3979
Martin Cepelka, Per-Anders Fjellström, Ashish Aeran

NEBY BRU: ONE FOOTWAY, THREE WAYS OF SUSTAINABILITY 3989
Manuel Sánchez-Solís, Gaute Mo, Fernando Ibáñez

SKYTEBANEN BRIDGE – A TIMBER TRUSS BRIDGE WITH AN INTERMEDIATE SUSPENDED CONCRETE DECK 3995
Alfredo Skartveit, Kristian Mæland Rasmussen, Kristian B. Dahl

4.7. EXPLORATION & RESTORATION OF EXISTING STRUCTURES

METHODOLOGY OF REHABILITATION OF TIMBER STRUCTURES IN HISTORIC BUILDINGS 4001
José Amorim Faria

WEB-GIS-TOOL: ESTIMATION OF GREENHOUSE GAS SAVINGS DUE TIMBER USE IN THE URBAN BUILT ENVIRONMENT 4010
Caya Zernicke, Annette Hafner, Andreas Abecker, Harro Stolpe

IN-PLANE SHEAR TEST AND APPLICATION STUDY OF SEISMIC RETROFIT TIMBER FRAME WITH CFRTP STRANDS 4020
Hina Takizawa, Nobuji Sakurai, Yuya Takaiwa

POST-EARTHQUAKE ASSESSMENT AND DOCUMENTATION OF TIMBER ROOFS 4029
Mislav Stepinac, David Andic, Juraj Pojatina

EVALUATION OF VIBRATION CHARACTERISTICS OF EXISTING TIMBER ARCHITECTURE BY MICROTREMOR MEASUREMENT - EXAMINATION WHEN IT IS DIFFICULT TO INSTALL AN ACCELEROMETER IN THE ATTIC 4035
Hiroki Yoshinuma, Yuya Takaiwa

DEVELOPMENT OF SIMPLE REPAIRING HARDWARE FOR DAMAGED ENDS OF WOODEN BEARING WALLS 4043
Wataru Kambe

STUDY ON THE MECHANICAL PERFORMANCE OF MULTI-LAYERED BRACKET COMPLEX 4050
Kohei Komatsu

EXPERIMENTAL STUDY ON LATERAL PERFORMANCE OF A FRAME WITH DEEP BEAMS AND HANGING MUD WALLS IN TRADITIONAL JAPANESE RESIDENTIAL HOUSES 4058
Zherui Li, Hiroshi Isoda, Akihisa Kitamori, Takafumi Nakagawa, Yasuhiro Araki

ASSESSMENT OF NAILED CONNECTIONS IN EXISTING STRUCTURES 4064
Lars Völlmecke, Sascha Schwendner, Ai Phien Ho, Jens Fischer, Werner Seim

TESTING OF CONNECTIONS TAKEN FROM OLD NAILED ROOF TRUSSES 4071
Sascha Schwendner, Lars Völlmecke, Phien Ho, Jens Fischer, Werner Seim

INFLUENCE OF MOISTURE CONTENT ON THE ASSESSMENT OF DECAY LEVELS BY MICRO-DRILLING MEASUREMENTS IN WOODEN FOUNDATION PILES 4079
Michele Mirra, Giorgio Pagella, Wolfgang Gard, Geert Ravenshorst, Jan-Willem Van De Kuilen

A STUDY ON COORDINATED EXPRESSION OF THE SEISMIC DIAGNOSIS SCORE AND ITS APPLICATION TO RETROFIT REINFORCEMENT PROJECTS UNDER COST CONTROL FOR JAPANESE TIMBER HOUSES 4087
Daisuke Shimizu, Chikako Tabata, Yoshito Tomioka

SCALING UP ENGINEERED TIMBER FOR NEIGHBOURHOOD SCALE DEEP RENOVATION: FINDINGS FROM A STUDY IN COIMBRA, PT 4093
Nelson Brito, Thomas Thiis, Roberto Tomasi, Alice Airoldi, Andrea Penna

MODIFICATION OF ROOF STRUCTURE OF THE TRADITIONAL WOOD HOUSES IN THE URBAN AREA OF DAEGU, KOREA DURING MID TWENTIETH CENTURY 4102
Jaemo Cho

HYBRIDIZATION OF WESTERN TIMBER TRUSS AND TRADITIONAL KOREAN ROOF SHAPE IN THE EARLY 20TH CENTURY 4108
Jeonghyun Kim, Jihong Kim, Bonghee Jeon

SEISMIC PERFORMANCE EVALUATION OF A TRADITIONAL WOODEN TOWNHOUSE THAT DID NOT COLLAPSE IN THE 2016 KUMAMOTO EARTHQUAKE 4114
Yasuhiro Nambu, Toshihiko Ninakawa, Hiroki Tabata, Akio Kitahara

DEVELOPMENT OF TIMBER ROOF FRAMES IN KOREAN MODERN ARCHITECTURE 4122
Kangmin Lee, Don-Son Woo

COMBINATION OF NDT AND DESTRUCTIVE TESTS FOR GRADING THE STRENGTH CLASS OF TIMBER TO REHABILITATE STRUCTURES 4128
Marcel Vilches-Casals, Eduard Correal-Mòdol, Carles Labèrnia Badia, Giraldo M. P.

THE PRESENT STATE AND ISSUES ON RETROFITTING OF HISTORIC TIMBER-FRAMED BRICK CONSTRUCTION BUILDINGS IN JAPAN 4134
Manabu Fujimoto, Naoyuki Matsumoto, Mikio Koshihara

REUSE OF WOOD, LEARNING ABOUT THE BENEFITS AND CHALLENGES OF HIGH- AND LOW-TECH DIAGNOSTIC METHODS THROUGH ACTION RESEARCH IN NORWAY 4141
Wendy Wuyts, Artur Tomczak, Kristine Nore, Lizhen Huang, Thomas Haavi

FERROCEMENT WOODEN HOUSE: LEARNING FROM POST-DISASTER RECONSTRUCTION IN INDONESIA 4151
Andry Widyowijatnoko, Dibya Kusyala, Fajar Ikhwan Harnomo

HARVESTING THE URBAN FOREST: A CASE STUDY OF THE CIRCULAR BUILDING SEMINAR AT UHASSELT IN BELGIUM 4157
Rafael Novais Passarelli, Peggy Winkels, Ronald Rovers, Elke Knapen, Griet Verbeeck

5.1. BEST PRACTICE EXAMPLES

ADHESIVELY BONDED TIMBER-CONCRETE COMPOSITE CONSTRUCTION METHOD (ATCC) – PILOT APPLICATION IN A SCHOOL BUILDING IN GERMANY 4164
Jens Frohnmüller, Werner Seim, Christian Umbach, Johannes Hummel

APPLICATION OF A WOODEN PREFABRICATED SHELL EXOSKELETON FOR THE INTEGRATED AND SUSTAINABLE RETROFIT OF A RESIDENTIAL BUILDING 4173
Jacopo Zanni, Chiara Passoni, Alessandra Marini, Ezio Giuriani, Andrea Belleri, Simone Labò, Giovanni Brumana, Simone Castelli, Claudio Abrami, Stefano Santini, Giuliano Venturelli, Angelo L. Marchetti

BUILDING WITH WOOD STRUCTURES – SUCCESFULL DESIGN PROCESS 4182
Alain Bradette, Geir Glasø, Tor Øistein Andresen

CAN RISING DEMAND FOR TIMBER IN CONSTRUCTION ACCELERATE DEFORESTATION? 4190
Eduardo Rojas Briales, Simon Flinn

5.2. CASE STUDIES AND VISIONS

RIGID JOINTS ON GLUED-IN RODS OF BENDING AND COMPRESSION-BENDING ELEMENTS OF LARGE-SPAN LAMINATED TIMBER STRUCTURES 4201
Alexander Pogoreltsev, Stanislav Turkovsky, Vladimir Stoyanov

MJØSTÅRNET: THE WORLD'S TALLEST TIMBER BUILDING..... 4209
Harald Liven, Rune Abrahamsen

THE FIRST MASS TIMBER BUILDING IN BRAZIL..... 4215
Carlito Calil Neto, Alexander Takata, Vitor Afonso Neves Silva

SPOR X – 10-STOREY TIMBER OFFICE BUILDING, DRAMMEN, NORWAY 4222
Katie Overton, Gaute Mo, Ivana Katavic, Manuel Sánchez-Solís

CASE STUDY IN THE NEXT GENERATION OF POINT-SUPPORTED CLT STRUCTURES..... 4232
Jamie Pobre Sullivan, Carla Dickof, Christian Slotboom

TALLWOOD 1: LESSONS LEARNED ON COMPLETION OF CANADA'S FIRST 12 STOREY TIMBER-STEEL HYBRID BUILDING 4240
Ornagh Higgins, Ilana Danzig, Brendan Fitzgerald, Jackson Pelling, Mehrdad Jahangiri

SUITABILITY OF SLIM-FLOOR STEEL-TIMBER COMPOSITES AS INTERMEDIATE FLOOR CONSTRUCTIONS - CASE STUDY BASED ON PROJECTS IN FINLAND 4247
Aku Aspila, Lauri Lepikonmäki, Sami Pajunen

THE BV2020 SOLUTION – GOING BIG WITH LIGHT TIMBER STRUCTURES..... 4253
Knut Magnar Sandland, Julia Bosnes Tønne, Per Gunnar Nordløkken

THE BENEFITS AND CHALLENGES OF WOOD IN HIGH CORROSIVE SURROUNDINGS 4259
Sigurdur Gunnarsson, Tim Skotheimsvik

THE NEW CENTRE FOR ADVANCED TIMBER TECHNOLOGY: A LIVING LAB FOR DESIGNERS, INDUSTRY, AND EDUCATION..... 4265
Gabriele Tamagnone, Robert Hairstans

QUANTIFYING AND REDUCING EMBODIED CARBON IN THE ACOUSTIC DESIGN OF MASS TIMBER BUILDINGS..... 4273
James Bligh

NEW HQ COPENHAGEN A NEW STANDARD FOR SUSTAINABLE BUILDINGS IN AN INTERNATIONAL CORPORATION 4279
Elias Mohr Wilson, Dorthe Keis, Mai Marcussen Yoon

A WORKABILITY AND SUSTAINABILITY ASSESSMENT OF MULTI-STOREY EARTHQUAKE-RESISTANT TIMBER BUILDING..... 4286
Kazuki Tsuda, Ahmad Ghazi Aljuhmani, Arata Minegishi, Yutaka Goto, Masaki Maeda

COMPUTATIONAL DESIGN DEVELOPMENT OF A WOODEN FAÇADE SYSTEM..... 4295
Camilla Schlyter, Karin Sandberg

STUDY CASE: REFURBISHMENT OF THE GARE MARITIME IN BRUSSELS 4303
Charline Lefèvre

WIDE-SPAN LVL ROOF STRUCTURE FOR AN INDOOR SWIMMING POOL 4309
Laurent Giampellegrini, Samuel Blumer, Hendrik Pfeffinger

DESIGN OF A TALL MASS TIMBER TOWER FOR OCCUPANT COMFORT UNDER WIND-INDUCED ACCELERATIONS 4316
Laurent Giampellegrini, Anthony Rety, Guillaume Caussarieu, Tim Sleik, Lucia Theurer, Johannes Pohl, Tobias Wacker

BUILDING INFORMATION MODELING OF A TIMBER BRIDGE – A CASE STUDY 4325
Alvdis Hardeng

NLT DEVELOPMENT FOR BRAZILIAN MARKET – TESTS AND USE 4332
Carlito Calil Neto, Alexander Takata, Vitor Afonso Neves Silva

A SURVEY OF THE DESIGN OF TIMBER-CONCRETE HYBRID BUILDINGS IN SWEDEN 4338
Carl Larsson, Michael Dorn

CASE STUDY: A 10-STOREY TIMBER BRACED FRAME AND CLT STRUCTURE IN VANCOUVER, BC 4345
Carla Dickof, Robert Jackson, Jenna Kim, Ashkan Hashemi

HUT – INDOOR CLIMBING CENTRE, SKIEN, NORWAY 4353
Katie Overton, Gaute Mo, Fernando Ibañez, Sondre Dolsvåg

ECONOMIC COMPARISON OF MASS TIMBER AND CONCRETE CONSTRUCTION IN THE NORDIC REGION 4360
Julie Swartz Andersen, Yutaka Goto, Michael Englund, Henning Johansen, Ketil Armann Hansen, Alexander Hollberg, Daniela Grotenfelt

THE RELATIONS IN THE PLANAR AND SECTIONAL SCALES AND KAN COMPOSITION OF TRADITIONAL KOREAN ARCHITECTURE 4370
Sangyeon Park, Bonghee Jeon

COMPARATIVE RESEARCH OF SINGLE-FAMILY HOUSING CONSTRUCTION SYSTEMS BY CONSTRUCTION COST USING STRUCTURAL WOOD AND OTHER MATERIALITY 4377
Carlos Kahler, Janina Gysling, Daniel Soto, Wilson Mejías, Francisco Jiménez, Carolina Molina

CASE STUDY ON A LARGE-SCALE TIMBER ACADEMIC BUILDING DESIGNED TO ADDRESS CURRENT INDUSTRY CHALLENGES 4383
Javier Fierro, Herry Chen, Tyler Hull, Andrea Atkins, Daniel Lacroix

EUPHORBIA: MASS TIMBER STADIUM 4393
Alexandros Kitriniaris, Sotiris Monachogios, Zannis Konteas

PLASTIC DESIGN OF BESPOKE INTERLOCKING TIMBER-TO-TIMBER CONNECTIONS FOR ROBOTIC ASSEMBLY 4399
Davide Tanadini, Giulia Boller, Pok Yin Victor Leung, Pierluigi D'Acunto

CASE STUDY: TERMINUS – NEW FRONTIERS IN HYBRID MASS TIMBER SEISMIC DESIGN 4409
Brendan Fitzgerald, Ilana Danzig, Mehrdad Jahangiri, Ornagh Higgins, Jackson Pelling

HARDWOOD GLULAM IN COMPLEX STRUCTURES: DESIGN AND CONSTRUCTION OF THE MACA MUSEUM IN URUGUAY 4415
Vanesa Baño, Leandro Domenach, Carlos Mazzey, Thomas Vieillard, Jean-Bernard Journot

CASE STUDY – THE USE OF ROBOTICS IN THE CONSTRUCTION OF TIMBER STRUCTURES USING WESTERN AUSTRALIA'S LARGEST MASS ENGINEERED TIMBER BUILDING AS A TEST BED 4423
Ralph Belperio, Pratik Shrestha

VALIDATING MOISTURE-SAFE ENERGY EFFICIENT CLT ASSEMBLIES IN HOT AND HUMID CLIMATES USING EXPERIMENTAL TESTING 4429
Marcus Strang, Paola Leardini, Maryam Shirmohammadi

LOAD LEVELS AND CRITICAL DESIGN ISSUES IN A MULTI-STOREY RESIDENTIAL TIMBER BUILDING BUILT UP BY PREFABRICATED VOLUMETRIC ELEMENTS 4439
Johan Vessby, Tomas Forsberg, Marie Johansson, Rajan Maharjan

ARBORETUM, THE LARGEST EVER WOOD OFFICE CAMPUS IN EUROPE: TECHNICAL, ORGANIZATIONAL, AND SUSTAINABILITY CHALLENGES : AN EXAMPLE OF LOW CARBON PROJECT FAR BEYOND THE ALIGNMENT WITH THE EUROPEAN TAXONOMY 4447
Laurent Petit, Renaud Blondeau-Patissier

CLEAR THE STAGE FOR TIMBER CONSTRUCTIONS 4453
Jonas Schmidt

TRANSFORMATION OF RECLAIMED MATERIALS FROM BARN BUILDINGS – DESIGN OF A NEW TIMBER BUILDING FRAME..... 4460
Terje Planke, Kristine Nore, Victoria Rygh Nordhagen, André Bockelie, Dimitrios Kraniotis

5.3. PUBLIC INCENTIVES AND STRATEGIES

DESIGN OF THE ROADMAP FOR THE CONSTRUCTION OF WOODEN SOCIAL HOUSING IN URUGUAY 4465
Juan José Ugarte, Andres Sierra, Keren Codriansky, Marcia Croci, Carolina Pérez-Gomar, Virgina Campodónico

5.4. INDUSTRY STRATEGIES TO IMPROVE MODERN TIMBER USE IN CONSTRUCTIONS

USING ARIMA MODELS TO PROJECT SAWLOGS, AND SAWN WOOD PRICES IN THE CHILEAN CONSTRUCTION MATERIALS MARKET..... 4475
Wilson Mejías, Janina Gysling, Carlos Kahler, Daniel Soto, Evaristo Pardo

CHARACTERIZATION OF GLUED-LAMINATED TIMBER SUPPLY IN CHILE 4483
Janina Gysling, Carlos Kahler, Daniel Soto, Wilson Mejías, Pamela Poblete

ESTIMATING THE GLUED-LAMINATED TIMBER DEMAND IN THE NON-RESIDENTIAL BUILDINGS IN CHILE..... 4491
Daniel Soto, Janina Gysling, Carlos Kahler

DIGITAL TWIN FRAMEWORK FOR VISUAL EXPLORATION OF MATERIAL FLOWS AND CARBON IMPACTS OF ENGINEERED WOOD PRODUCT CHAINS FROM FOREST TO BUILDINGS 4496
Stephan Ott, Andreas Rudenå, Uwe Kies, Anna Wagner, Oliver Jancke

MATERIAL DISRUPTION: CROSS-LAMINATED TIMBER IN TEXAS 4505
Ulrich Dangel

ACCELERATION OF UNITED STATES MARKETS FOR WOOD 4513
Bill Parsons, Brian Brashaw

RECENT ADVANCEMENTS IN MASS TIMBER CONSTRUCTION TECHNOLOGIES IN CANADA 4518
Mohammad Mohammad, Julie Tourrilhes, Richard Coxford, Miranda Williamson

INVESTING IN MASS TIMBER CONSTRUCTION IN AUSTRALIA: THE CLEAN ENERGY FINANCE CORPORATION TIMBER BUILDING PROGRAM 4528
Christina Wijeratne, Paolo Lavisci

TOWARDS A BROADER USE OF WOODEN CONSTRUCTION MATERIALS: INTERMEDIARY ORGANISATIONS IN THE SUSTAINABILITY TRANSITION OF THE CONSTRUCTION SECTOR 4535
Antje Klitkou, Lina Ingeborgrud

STATUS QUO OF AUSTRIAN TIMBER CONSTRUCTION SECTOR 4545
Aida Santana Sosa, Martin Aichholzer, Elena Mitrenova, Iva Kovacic

THE ROLE OF BOARD INTERLOCKS IN INCREASING THE USE OF WOOD IN CONSTRUCTION 4555
Silje Marie Svartefoss

HARMONISATION OF THE ENVIRONMENTAL PRODUCT DECLARATIONS FOR WOOD PRODUCTS 4565
Lauri Linkosalmi, Harald Schwarzschachner, Tuovi Valtonen

5.5. EDUCATIONS AND FUTURE TRENDS

6X6X6: INTRODUCING THE CONCEPT OF REUSE OF TIMBER MATERIALS IN THE 1ST YEAR OF ARCHITECTURAL EDUCATION 4571
Colm O'Brien, Anna Røtnes, Mads Øiern, Petter Kveseth, Lone Sjøli, Sindre Wam, Katherina Putzer, Kristoffer Røgeberg

FINDINGS FROM THE 2022 NORTH AMERICAN MASS TIMBER RESEARCH NEEDS ASSESSMENT WORKSHOP 4576
Samuel L. Zelinka, Richard Bergman, Marco Lo Ricco, William A. Martin, Bill Parsons, Iain Macdonald, Jennifer Cover

HYBRIDTIM, DESIGN AND CONSTRUCTION OF ENVIRONMENTAL HIGH PERFORMANCE HYBRID ENGINEERED TIMBER BUILDINGS 4583
Kamyar Tavoussi, Alireza Fadai, Laia Haurie

HIBIWOOD – DIDACTIC APPROACHES FOR ACADEMIC EDUCATION ON MULTI-STOREY TIMBER BUILDINGS 4590
Elena Mitrenova, Martin Aichholzer, Aída Santana Sosa

HORIZONTAL AND VERTICAL KNOWLEDGE MANAGEMENT IN MULTIDISCIPLINARY RESEARCH AND DESIGN-BUILD TEACHING: A TIMBER-ONLY TRAIL 4597
Günther H. Filz, Gengmu Ruan

RESOURCE-EFFICIENT MATERIALIZATION | SUSTAINABILITY FUTURE TRENDS 4604
Alireza Fadai, Daniel Stephan

PROFESSIONAL WORKSHOP IN WOOD: STRUCTURAL EFFICIENCY INDEX, FOR ARCHITECTURE STUDENTS 4611
Martín Hurtado C., Andrés Sierra M.

THEORISING A NEW EDUCATIONAL AGENDA FOR SUSTAINABLE BUILT ENVIRONMENT PROFESSIONALS: TIMBER TECHNOLOGY, ENGINEERING, AND DESIGN PROGRAMME 4619
Aghlab Al-Attili, Robert Hairstans, Tim Belden, Gabriele Tamagnone, Sarah Hitts, Tabitha Binding, Joseph Walters

FIRE SAFE USE OF WOOD IN BUILDINGS - GLOBAL DESIGN GUIDE 4627
Christian Dagenais, Andy Buchanan, Birgit Östman, Michael Klippel, David Barber, Ed Claridge, Andrew Dunn, Paul England, Marc Janssens, Alar Just, Esko Mikkolo, Colleen Wade, Norman Werther

Author Index

HENT

Spor X / Dark Architects / Degree of Freedom / Photo Zinc - Thomas Mellbye

World Conference on Timber Engineering Oslo 2023

COMPARISON OF THE STRUCTURAL CAPACITY OF SHEAR WALLS SHEATHED WITH ORIENTED STRAND BOARD AND CELLULOSIC FIBER BOARD SUBJECTED TO CYCLIC LOADING

David W. Dinehart[1], Eric S. Musselman[2], Edward D. Bolte[3], Bridget LaSala[4]

ABSTRACT: Eight wood framed shear walls were subjected to the ASTM E2126-11 cyclic testing protocol at 0.5 Hz. Four 2.44 m x 3.66 m shear walls were sheathed with 12 mm (15/32") thick oriented strand board (OSB), oriented vertically and connected to the frame with 60 mm x 2.9 mm (2 3/8" x 0.113") nails spaced at 150 mm along all edges. Four walls were sheathed with 3.43 mm thick Cellulosic fiber board (CFB) sheathing connected to the frame with 16-gauge, 23.8 mm (15/16") crown staples spaced 75 mm on center along the perimeter and in the field. The TPB sheathing is comprised of 94% post-consumer recycled materials.

Hysteresis results show that both the OSB and CFB walls exhibited typical wood frame shear wall behavior, characterized by elliptical hysteresis with pinched behavior at low levels of displacement. For cycles 1 through 31 (displacements less than 25 mm), the percent difference in average load capacity from the CFB and OSB walls ranged from +10% to -1.2%. At large displacements (greater than 45 mm) the CFB walls exhibited less capacity than the CFB walls. The OSB average maximum load is 25.9 kN and occurs at a wall displacement of 61 mm (cycle 35), while the CFB average maximum load is 24.1 kN at a displacement of 43 mm (cycle 32).

KEYWORDS: wood shear wall, sustainable sheathing, recycled sheathing, load capacity, cyclic testing

1 INTRODUCTION

Plywood and oriented strand board (OSB) have traditionally been the most common and effective sheathing used on wood shear walls to provide strength against lateral loads. Drawbacks to utilizing traditional sheathing include construction time, moisture absorption, and in recent years, wildly fluctuating prices. Cellulosic fiber board (CFB) serves as an alternative to traditional sheathing. Construction utilizing CFB can be more efficient (time and effort); it can be moisture and mold resistant; and it is largely made from post-consumer material making its prices more stable. It is critical that the strength of these materials be understood for use in wood shear walls subjected to lateral loading.

2 BACKGROUND

Seismic and wind forces acting on wood structures are generally carried by wood framed shear walls. Until the mid 1980's shear walls were sheathed with plywood. At this time the use of oriented strand board gained in popularity and acceptance for lateral force resistance. [1] Research demonstrated that shear walls sheathed with comparable thicknesses of plywood and OSB performed similarly under static and cyclic lateral loading. Load capacity, walls stiffness, energy dissipation and failure modes were nearly identical. [2, 3]

While the construction industry continues to investigate sustainable, green, and recycled materials, CFB has not gained the same widespread acceptance as OSB. This may be in part due to the strength of CFB not being well understood. A review of the strength and stiffness of oriented wood and cellulose-fiber materials that indicates the strength potential inherent to biobased cellulosic materials has been conducted to ascertain their suitability for potential applications.[4] Each type of material was described in terms of structure and corresponding representative values for strength and modulus of elasticity in fiber direction.[4]

Structural sheathing products utilizing CFB can be made from recycled material, are much thinner than comparable OSB panels, and are connected to the wall framing via staples. Proprietary information regarding the strength of these products is shared with manufacturers; however,

[1] David W. Dinehart, Professor, Department of Civil and Environmental Engineering, Villanova University, USA, david.dinehart @villanova.edu,
[2] Eric S. Musselman, Associate Professor and Chair, Department of Civil and Environmental Engineering, Villanova University, United States, eric.musselman@villanova.edu
[3] Edward D. Bolte, Wiss Janey Elstner Associates, Inc., formerly undergraduate research assistant at Villanova University, USA, 2020-21, tbolte@wje.com
[4] Bridget LaSala, Villanova University, USA, undergraduate research assistant, 2020-21, blasala@villanova.edu

https://doi.org/10.52202/069179-0001

there has been little published data available. The structural sheathing utilized in this study is made from 94% post-consumer recycled materials and is marketed as Thermo-Ply®.[5]

3 SHEAR WALL TEST SPECIMENS

Eight, 2.44 m tall x 3.66 m long (8' x 12') shear walls were supplied by Ox Engineered Products, LLC. All studs and plates consisted of 2x4 SPF No. 2 lumber, with studs spaced at 406 mm (16") on center, continuous bottom and top plates, top plates fastened with 76.2 mm x 3.33 mm (3" x 0.131") nails at 610 mm (24") on center, staggered from each side. Studs were fastened to the plates with two 76.2 mm x 3.33 mm (3" x 0.131") toenails. Double end studs (each end) were fastened with 76.2 mm x 3.33 mm (3" x 0.131") nails at 609.6 mm (24") on center from each side.

Four walls were sheathed with OSB, oriented vertically, and connected to the frame with two 9.53 mm x 2.87 mm (3/8" x 0.113") nails spaced at 152 mm (6 inches) along all edges. Four walls were sheathed with CFB oriented vertically and connected to the frame with 16 gage, 23.81 mm (15/16") crown staples [minimum penetration of 25.4 mm (1") into the stud] with the crown parallel to the framing and spaced 76.2 mm (3") on center along the perimeter and in the field. The staple head was in contact with the CFB surface. The edge distance for all fasteners was 9.53 mm (3/8") and sheathing panel joints were butted. Figure 1 shows a completed CFB wall. The CFB used in this study was ThermoPly Blue.

Figure 1: *CFB Shear Wall Test Specimen*

4 EXPERIMENTAL TEST SETUP

4.1 TEST FRAME AND LOADING MECHANISM

The test frame consists of a frame base, actuator, load spreader device, and lateral restraints. An elevation of the framing plan is exhibited in Figure 2. Three W8x24 beams in series formed the frame base of the system. The beams were anchored to the concrete floor to ensure no slippage of the frame during the test. A 38.1 mm thick by 88.9 mm wide (1 ½" x 3 ½") plate was welded to the top flange of each beam, allowing for sheathing rotation and deformation without interference by the beam flange.

Threaded holes, 22.23 mm (⅞") in diameter, were drilled every 203 mm (8 inches) into the plate to accommodate the different anchorage patterns needed for the various wall configurations. Two 3.66 m 50.8 mm x 101.6 mm (12'-0" 2"x4") pieces of #2 Hem Fir were placed atop the welded plate, anchored to the beams using four 19.05 mm (¾") diameter hex bolts, and tightened down in countersunk holes to be flush with the wood surface. Two additional 19.05 mm (¾") holes were drilled, one at either end of the planks and in line with the existing holes of the welded plate, to accommodate the 15.88 mm (⅝") anchor bolts of the 10-gauge Simpson Strong-Tie HD5B hold-down anchors at the corners of the shear walls.

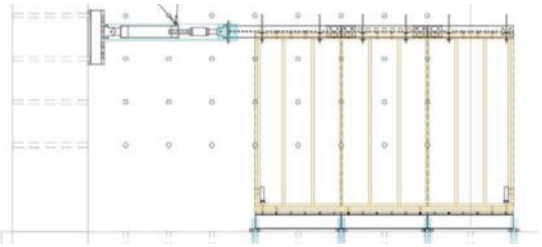

Figure 2: *Elevation view of experimental test setup*

The two 50.8 mm x 101.6 mm (2"x4") boards were incorporated to provide a realistic connection between the bottom plate and frame base. The single bottom plate of shear wall is nailed to the 50.8 mm x 101.6 mm (2"x4") plates using 76.2 mm x 3.33 mm (3"x0.131") nails at 152 mm (6") on center to resemble the connections used in practice and to lessen the influence of the support stiffness on the shear wall stiffness and ultimate capacity.

A hydraulic actuator was used to impart the lateral load during the testing sequence. Connected to the actuator, the load spreader acts as the mechanism imparting the horizontal force of the actuator to the wall specimen. The load spreader consisted of three W10x30 beams, situated such that the beam web rests on the top plate of the wall. The W10x30 beams were connected at each end using 12.7 mm (½") plates and 8 bolts on each side.

To connect the load spreader and the shear wall, 300 mm long, 19.05 mm diameter (1'-0", 3/4") rods were threaded through the beam web holes and corresponding holes in the shear wall double top plate. The rods were anchored to the shear wall top plate using a plate washer and nut on either end, such that the rod could not move, and the load spreader sits directly on the nut. A brass bushing was threaded through the hole in the beam web to ensure no slippage laterally between the rod and the load spreader. However, vertical movement was allowed as there was no restraint above the load spreader. The purpose of this connection was to prevent the stiffness of the load spreader from impacting the wall behavior.

https://doi.org/10.52202/069179-0001

To eliminate out-of-plane movement by the shear wall during testing, additional bracing was provided by roller bearings along the top of the framing system. As shown in Figure 3, roller supports were spaced every 1.22 m (4 feet) and positioned to be in contact with the flanges on both sides of the load spreader beam. A total of 6 rollers were mounted on columns anchored to the strong floor and cantilevers anchored to the strong wall.

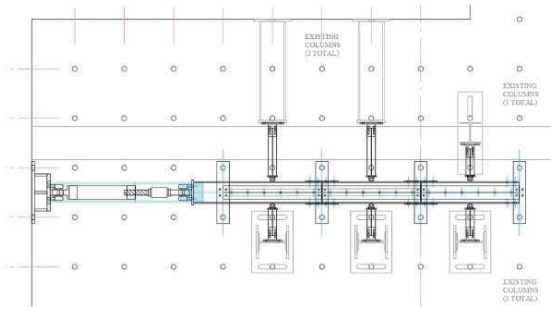

Figure 3: *Plan view of experimental test setup*

4.2 TESTING PROTOCOL

ASTM E2126-11, Test Method C, the CUREE Basic Loading Protocol was used for all tests. The basis for the loading sequence is a reference displacement founded on the maximum displacement, D, for which the specimen exhibits acceptable behavior when undergoing the given protocol. Alternatively, it can be described as a fraction of the reference displacement D_m, the displacement where the load of the primary cycle remains greater than 80% of the ultimate load on the degradation portion of the monotonically loaded curve. The reference displacement cannot exceed 1/40 the height of the wall, or 60.96 mm (2.40 in.) for the given specimen. For these tests, 60.96 mm was used. Figure 4 provides a graphical representation of the procedure.

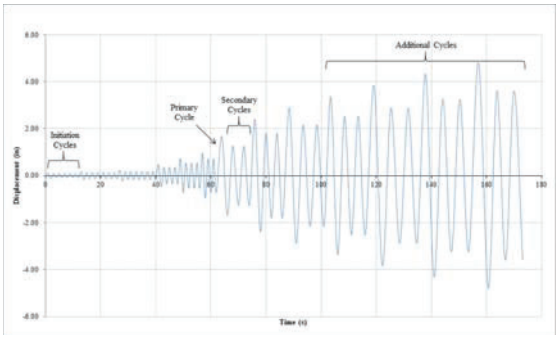

Figure 4: *ASTM E2126-11, CUREE Basic Loading Protocol*

To begin the loading sequence, six low amplitude initiation cycles are performed to allow equipment calibration. Following the first set, the remaining steps have a singular primary cycle amplitude a fraction of the established reference displacement, and several trailing secondary cycles of an amplitude 75% of the primary cycle. The amplitude and cycles for each set of cycles are provided by the standard, and the sequence is performed until failure occurs. Due to loading rate restrictions by the actuator, the frequency of the cycles decreased at higher amplitudes. The first 31 cycles of testing were rated at 0.50 Hz. The remaining cycles were measured as follows: Cycles 32 to 37 (0.25 Hz), and Cycles 38 to 43 (0.2 Hz).

5 EXPERIMENTAL RESULTS

5.1 OSB SHEAR WALL TEST RESULTS

Figure 5 presents the hysteresis plot for OSB shear wall specimen 3. This was typical of the four tests and is characterized by pinched behavior at small displacements with large loops for the primary cycles (1, 7, 14, 21, 25, 29, 32, 35, 38, 41).

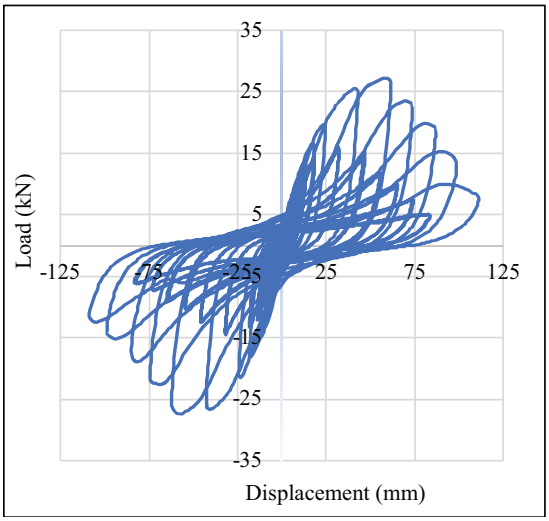

Figure 5: *Typical hysteresis plot for OSB walls (Test 3).*

Table 1 provides a summary for maximum load (P) at each primary step cycle for each shear wall tested, the average load, and the standard deviation. Maximum loads for each shear wall are shown in italic. A maximum average load capacity of 25.9 kN (5.8 k) was achieved during cycle 35 at a displacement of 61.0 mm (2.4 in). Tests were repeatable as evidenced by the standard deviations presented.

There were no visible signs of damage in the OSB walls at displacements below 25.4 mm (1 inch). As displacement levels increased nail pullout along the bottom and seams of OSB walls became evident. Beyond the maximum load, more significant nail deformation was seen, and the sheathing was separated from the frame along some seams and bottom edge. Some nails were broken.

https://doi.org/10.52202/069179-0001

Table 1: *Experimental OSB shear wall capacity*

Step	Cycle	Δ	Oriented Strand Board (OSB) Walls					
			1	2	3	4	AVG	STD
		[mm]	P [kN]	P [kN]	P [kN]	P [kN]	P [kN]	P [kN]
1	1	3.0	5.3	5.4	5.5	6.0	**5.5**	0.26
2	7	4.6	6.6	7.0	7.0	7.7	**7.1**	0.38
3	14	6.1	7.6	8.2	8.3	9.0	**8.3**	0.51
4	21	12.2	12.5	13.0	13.0	14.0	**13.1**	0.56
5	25	18.3	16.4	16.6	16.6	17.5	**16.8**	0.41
6	29	24.4	19.3	19.5	19.4	20.6	**19.7**	0.53
7	32	42.7	24.8	25.2	24.7	26.1	**25.2**	0.58
8	35	61.0	*25.1*	*25.4*	*25.9*	*27.3*	***25.9***	0.86
9	38	73.2	21.0	18.0	22.8	23.1	**21.2**	2.02
10	41	80.3	16.8	18.2	19.4	19.4	**18.5**	1.06

5.2 CFB SHEAR WALL TEST RESULTS

Figure 6 presents the hysteresis plot for CFB shear wall specimen 3. This was typical of the four tests and is characterized by pinched behavior at small displacements with larger loops for the primary cycles compared to the secondary cycles.

Table 2 provides a summary for maximum load (P) at each primary step cycle, the average load, and the standard deviation. Maximum loads for each shear wall are shown in italic. A maximum average load capacity of 24.1 kN (5.4 k) was achieved during cycle 32 at a displacement of 42.7 mm (1.68 in). Tests were repeatable as evidenced by the standard deviations.

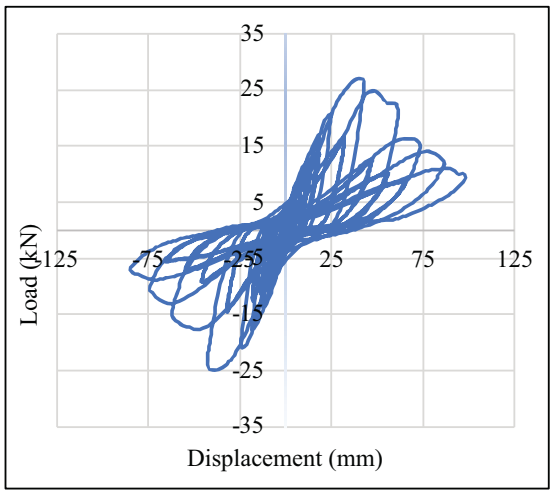

Figure 6: *Typical hysteresis plot for CFB walls (Test 3).*

Table 2: *Experimental CFB shear wall capacity*

Step	Cycle	Δ	Cellulosic Fiber Board (CFB) Walls					
			1	2	3	4	AVG	STD
		[mm]	P [kN]	P [kN]	P [kN]	P [kN]	P [kN]	P [kN]
1	1	3.0	5.0	6.6	5.6	6.3	**5.9**	0.62
2	7	4.6	6.5	8.0	7.1	8.0	**7.4**	0.62
3	14	6.1	7.9	9.0	8.7	9.3	**8.7**	0.54
4	21	12.2	12.7	12.9	13.2	13.0	**13.0**	0.18
5	25	18.3	16.4	16.5	17.3	16.3	**16.6**	0.40
6	29	24.4	20.0	19.1	20.8	18.9	**19.7**	0.76
7	32	42.7	*26.6*	*20.6*	*26.0*	*23.1*	***24.1***	2.42
8	35	61.0	26.0	19.4	21.3	19.0	**21.4**	2.80
9	38	73.2	15.1	14.9	14.7	15.1	**14.9**	0.16
10	41	80.3	11.7	10.6	11.4	11.4	**11.3**	0.42

There were no visible signs of damage in the CFB walls at displacements below 25.4 mm (1 inch). As displacements increased beyond 25.4 mm (1 inch), the CFB walls exhibited additional damage. Post ultimate load the CFB sheathing buckled between vertical framing studs. Following test completion, residual damage included highly deformed, unattached, and broken staples, as well as buckled sheathing.

5.3 COMPARISON OF OSB AND CFB LOADS

Table 3 presents a comparison of the average shear wall loads corresponding to the primary displacement cycles for both OSB and CFB walls. The percentage difference between the walls is also presented. For displacements below 12 mm (0.5 in) the CFB walls are slightly stiffer than the OSB walls. Between 12 mm (0.5 in) and 24 mm (1 in) the walls have the same load capacity.

The walls reached maximum capacity at different levels of displacement. At a displacement of 42.7 mm (0.47 in) the CFB reaches the maximum capacity of 24.1 kN (5.4 k), while the OSB reaches the maximum capacity of 25.9 kN (5.8 k) at a displacement of 61.0 mm (2.4 in)

Table 3: *Shear wall capacity and percent difference.*

Step	Cycle	Δ	OSB	CFB	Percent
			Avg Load	Avg Load	Difference
		[mm]	[kN]	[kN]	[%]
1	1	3.0	5.5	5.9	5.7
2	7	4.6	7.1	7.4	4.7
3	14	6.1	8.3	8.7	5.1
4	21	12.2	13.1	13.0	-1.2
5	25	18.3	16.8	16.6	-1.0
6	29	24.4	19.7	19.7	0.1
7	32	42.7	25.2	***24.1***	-4.5
8	35	61.0	***25.9***	21.4	-17.5
9	38	73.2	21.2	14.9	-29.6
10	41	80.3	18.5	11.3	-38.9

https://doi.org/10.52202/069179-0001

Figure 7 presents the data in Table 3 graphically. The load displacement response of the OSB and CFB shear walls is comparable up to a displacement of 42.7 mm (1.68 in). The drift limit used in wood shear wall design is generally far below this level of displacement. Beyond cycle 32 the CFB walls start to lose capacity while the OSB walls continue to carry addition load until cycle 35. Following maximum capacity both walls lose structural capacity; however, the CFB walls deteriorate at a far greater rate. This was verified visually by the damage patterns exhibited during testing as well.

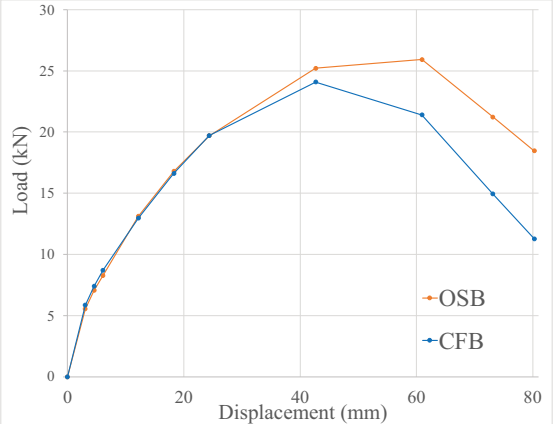

Figure 7: *Backbone plots for OSB and CFB shear walls.*

6 CONCLUSIONS

The four OSB and four CFB walls tested behaved as typical shear walls with repeatable results when subjected to ASTM E2126, Test Method C, CUREE Basic Loading Protocol. It is concluded that the OSB and CFB walls were structurally equivalent up to approximately 42.7 mm (1.68 in) of wall displacement.

The OSB average maximum load was 25.9 kN (5.8 k) at a wall displacement of 61 mm (2.4 in) (cycle 35), while the CFB average maximum load was 24.1 kN (5.4 k) at a displacement of 42.7 mm (1.68 in) (cycle 32). The CFB walls lost capacity at a faster rate than the OSB walls beyond the maximum load as the sheathing buckled.

Additional testing of shear walls sheathed with CFB is needed to verify comparable performance to OSB for other conditions, such as large window and door openings and/or alternative loading sequences.

ACKNOWLEDGEMENT

The authors thank Mulhern and Kulp, Inc. for financial support for this research. The guidance of Nicholas Martignetti and Richard Zabel is greatly appreciated. The authors are grateful for the laboratory assistance and support provided by Jeff Cook, Director of the Structural Engineering Teaching and Research Laboratory at Villanova University.

REFERENCES

[1] Rose, J. D., Preliminary Testing of Wood Structural Panel Shear Walls Under Cyclic (Reversed) Loading, Report 158, American Plywood Association, Technical Services Division, March, 1998.

[2] Dinehart, D. W. and Shenton III, H. W., "Comparison of the Static and Dynamic Response of Timber Shear Walls," *Journal of Structural Engineering*, Vol. 124, No. 6, 1998.

[3] Shenton III, H. W., Dinehart, D. W., and Elliott, T. E., "Stiffness and Energy Degradation of Wood Frame Shear Walls," *Canadian Journal of Civil Engineering*, Vol. 25, No. 3, 1998.

[4] Jakob, M., Mahendran, A. R., Gindl-Altmutter, W., Bliem, P., Konnerth, J., Muller, U., and Veigel, S., The strength and stiffness of oriented wood and cellulose-fibre materials: A review, *Progress in Materials Science*, Elsevier, 125, 2022.

[5] Ox Engineered Products, LCC, *Technical Evaluation Report, TER 1004-02, Thermo-Ply Blue & Thermo-Ply Blue AMG Structural Sheathing*, Revision Date, April 5, 2021.

[6] ASTM E2126-11, "Standard Test Methods for Cyclic (Reversed) Load Test for Shear Resistance of Vertical Elements of the Lateral Force Resisting Systems for Buildings".

https://doi.org/10.52202/069179-0001

World Conference on Timber Engineering Oslo 2023

PENDULUM IMPACT HAMMER TESTS ON TIMBER BEAMS – EXPERIMENTAL SETUP

Alex Sixie Cao[1], Andrea Frangi[2]

ABSTRACT: In this paper, a test setup for conducting impact testing of full-size timber beams is presented. The test setup comprises a pendulum impact hammer with an effective length of 4750 mm, mass of 3475 kg, and can be released from a near-horizontal position. On the impact hammer, 100g accelerometers and a shock-resistant high-speed camera with a capacity of up to 5700 pictures per second were installed. In addition, other cameras were installed, as well as an angular encoder to record the position of the pendulum impact hammer. The pendulum impact hammer was released using an electromechanical release system attached to a crane. The impact hammer was designed for impact tests on timber beam specimens with cross-sections ranging from 160x160 mm to 200x320 mm and lengths between 2700 and 4300 mm. The results include the energy release of the specimens upon failure, peak impact forces, time to failure, and high-speed imagery. With the test setup, similar knowledge can be gained for other engineered wood products.

KEYWORDS: Glued laminated timber, Impact loading, Pendulum impact hammer, Full-size tests

1 INTRODUCTION

In recent years, the popularity and use of timber as a structural material for tall buildings and bridges has increased [1,2] as the drive for sustainability continues. Because of the growing volume of structural timber in our built environment, structural robustness and disproportionate collapse prevention [3–7] is receiving renewed attention from timber engineers worldwide as timber buildings reach record heights with recent technological developments [3,8–15].

To assess the collapse behaviour and resistance of timber buildings, advanced numerical models are needed [4]. An important feature of the numerical models is the ability to simulate member failure and separation from rapid loading [3,14,15]. The rapid loading may stem from impact loading from vehicles, falling debris, projectiles, explosion debris, blast loading, and more.

Previous impact tests on wood or timber were conducted on 10 to 20 mm square small clearwood [16], 50 to 150 mm square lumber [17,18], and single boards [19–21] using either a small pendulum impact hammer or a drop test. However, the size effects in timber are considerable because of the natural growth imperfections in wood such as knots, distorted grains, and more [22,23]. In addition, the results from single boards cannot be generalised to glued assemblies, such as glued laminated timber (GLT) or laminated veneer lumber (LVL). Thus, it is necessary to conduct full-size impact tests on engineered wood products commonly used in practice.

Timber is known to be rate-dependent, which is reflected in the current set of design codes in Europe [24,25]. However, the shortest codified loading duration is in the order of seconds, which is not valid for impact loading, where the loading occurs within milliseconds [26].

To address these challenges, pendulum impact hammer tests were conducted on 86 full-size spruce GLT specimens without finger joints and nine full-size beech laminated veneer lumber specimens. The cross-sections were between 160×160 and 200×320 mm, and the lengths between 2700 and 4300 mm. The test setup was instrumented with accelerometers, angular encoders, and high-speed cameras. The effective length of the impact hammer was about 4750 mm, with a mass of 3450 kg.

In this paper, the conceptual framework and the most important aspects of the test setup are presented.

Data from the sensors are shown, as well as images from a high-speed camera. The full results of the experimental campaign are published in a test report [27]. The bespoke test setup was designed and built at ETH Zurich.

2 THEORETICAL FRAMEWORK

2.1 PENDULUM IMPACT HAMMER

A pendulum impact hammer setup was chosen because of the possibility of a direct measurement of the energy release E_r from the failure of a specimen. In such a setup, the energy balance can be written as:

$$m_p g h_0 = m_p g h_1 + E_r + E_c, \quad (1)$$

where m_p is the effective mass of the impact hammer, g=9.806 m/s^2 is the gravitational acceleration in Zurich, h_0 is the initial height of the impact hammer, h_1 is the post-impact height of the impact hammer, E_r is the energy release from the failure of the specimen, and E_c are other sources of energy loss, such as friction and drag. The

[1] Alex Sixie Cao, Institute of Structural Engineering, ETH Zurich, 8092 Zurich, Switzerland, cao@ibk.baug.ethz.ch
[2] Andrea Frangi, Institute of Structural Engineering, ETH Zurich, 8092 Zurich, Switzerland, frangi@ibk.baug.ethz.ch

https://doi.org/10.52202/069179-0002

concept of the pendulum impact hammer setup is shown in Figure 1, where L_{CM} is the length from the point of rotation to the centre of mass of the impact hammer, and θ_i are the initial and post-impact angles of the impact hammer. The energy release E_r can be used to find the peak dynamic impact force P_d and to quantify the toughness U_T of the tested material [28].

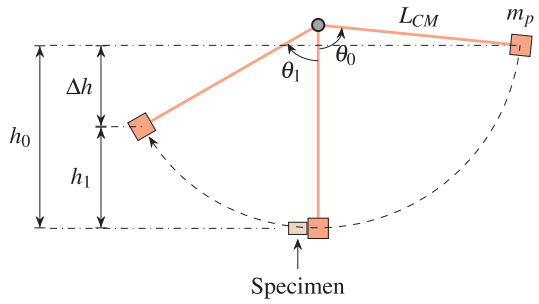

Figure 1: *Conceptual framework of the tests. The figure is reproduced from Cao et al.* [28].

2.2 PEAK IMPACT FORCE

To compare the energy release E_r in Equation (1) of different specimens or materials, it can be normalised with respect to the cross-sectional area A of the specimen:

$$U_T = \frac{E_r}{A}. \tag{2}$$

U_T in Equation (2) is defined as the toughness of the material. By assuming that the specimen can be idealised as an Euler-Bernoulli beam without shear deformations, and the load-displacement behaviour as linear-elastic perfectly brittle, the peak impact force P_d can be found by considering the equivalent single-degree-of-freedom system in Figure 3. In Figure 3, v_p is the impact velocity, U is the strain energy, U^* is the complementary strain energy, w is the mid-span deflection, and $k=48EI/L^3$ is the equivalent stiffness.

Since the load-displacement curve is linear-elastic perfectly brittle, the strain energy U is the same as the complementary strain energy U^*. The energy release E_r is the same as the strain energy U or the complementary strain energy U^*. Therefore, the peak impact force P_d can be found by considering the triangular area above the load-displacement curve:

$$E_r = \frac{1}{2}\frac{P_d^2}{k} \therefore P_d = \sqrt{2E_r k} = \sqrt{E_r \frac{96EI}{L^3}}, \tag{3}$$

where L is the length, E is the elastic modulus, and I is the second moment of area of the specimen. Equation (3) can also be found by following a strain energy approach.

If the collision between the impact hammer and the specimen is considered as perfectly inelastic until failure, the peak impact force P_d can be found by considering the deceleration a of the impact hammer. With Newton's second law, the peak impact force P_d can be expressed as:

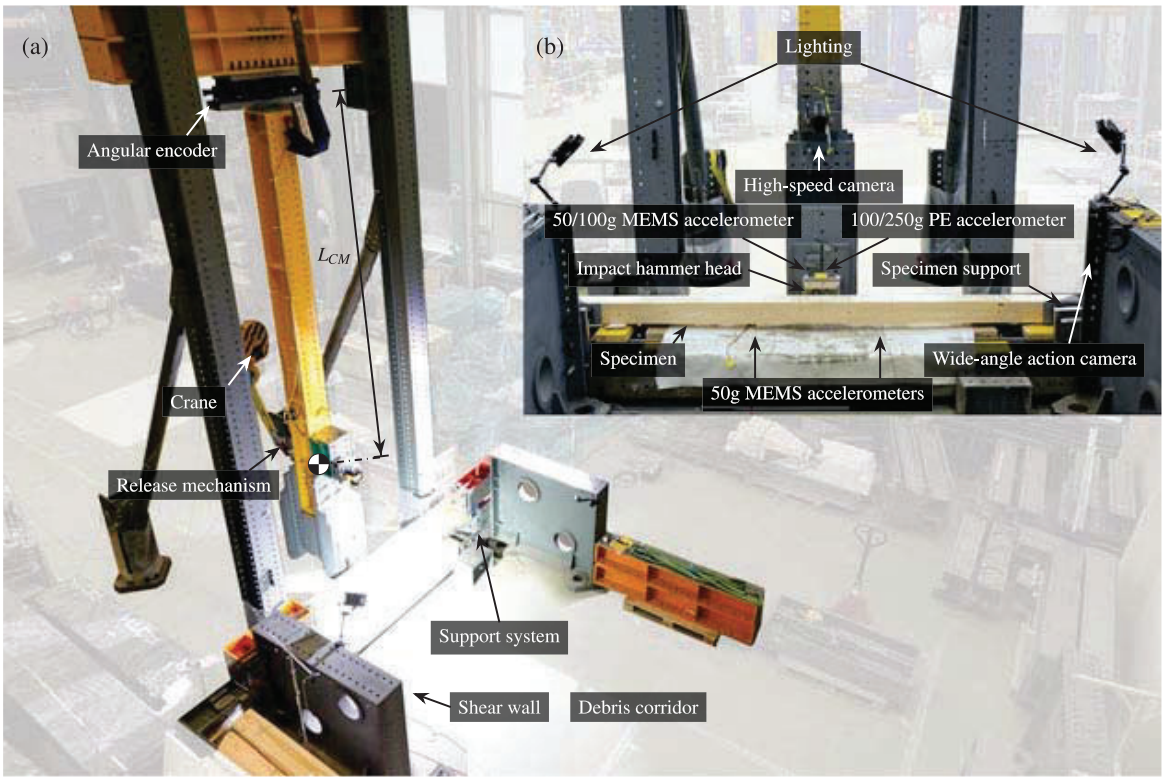

Figure 2: *Experimental setup, where PE denotes piezoelectric, and MEMS micro-electromechanical system. (a) Bird's-eye view; and (b) front view of the test setup. The figure is reproduced from Cao et al.* [28].

https://doi.org/10.52202/069179-0002

$$P_d = m_p a. \quad (4)$$

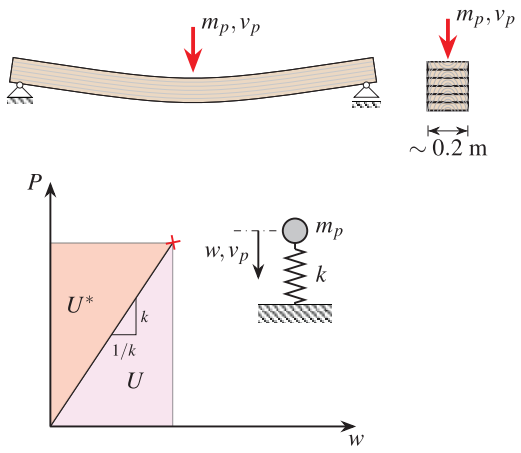

Figure 3: *Single-degree-of-freedom idealisation of a simply supported beam loaded at the mid-span. The figure is reproduced from Cao et al.* [28].

3 EXPERIMENTAL SETUP

3.1 PENDULUM IMPACT HAMMER

The test setup was designed using the computer-aided-design software Autodesk Inventor to accommodate simply supported specimens with and without axial restraints of dimensions between 160×160×2900 mm and 200×320×4300 mm. Because of the limited available information on the expected energy release E_r of the specimens, the energy capacity mgh_0 of the impact hammer setup was maximised. The length h_0 was constrained by the physically available space in the laboratory at ETH Zurich, and the mass m by the steel plates in the laboratory inventory. The effective length L_{CM} of the impact hammer became 4650 mm, and the mass was 3475 kg. The impact hammer could be raised to a maximum angle of about 87°, which results in a maximum potential energy mgh_0 of about 158 kJ.

To support the impact hammer, an S355 steel frame comprising two IPE 360×7040 mm columns and two stacked and bolted HEB 300×2050 mm beams was used, where the impact hammer was suspended from the HEB 300×2050 beams. To provide lateral stiffness to the frame in the pendulum's direction of motion, two ROR 159×25×4000 mm diagonal trusses were bolted to the IPE 360×7040 mm columns. The frame and the diagonal trusses were fixed to a strong floor using two M55 10.9 steel bolts for each steel footing, post-tensioned to 1000 kN. Most of the bolts were M24 8.8, with a few M16 8.8 bolts used in the shear pin. The experimental setup is shown in Figure 2.

3.1.1 SHEAR PIN & HINGE SYSTEM

The impact hammer was suspended from the two HEB 300×2050 mm beams via an elaborate hinge system. The hinge system comprised a Ø40×1210 mm 10.8 steel shear pin with a hardened surface, four double hinges, five single hinges, and various S355 adapter plates. In addition, steel tubes were attached at the ends of the shear pin to prevent the shear pin from sliding out of the hinges. This is shown in Figure 4.

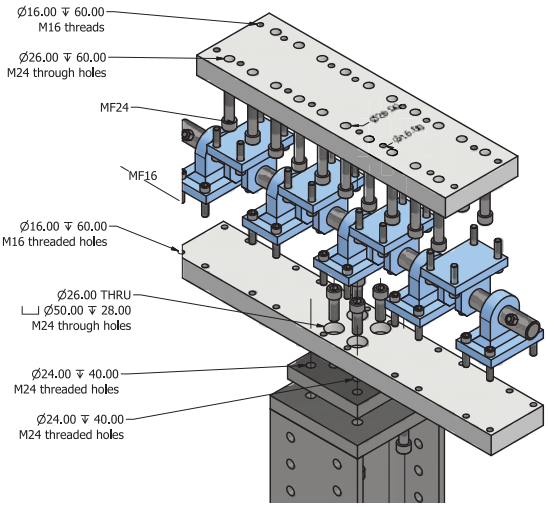

Figure 4: *Shear pin and hinge system, which connects the impact hammer to the pendulum frame. The figure is reproduced from Cao et al.* [27].

The shear pin was designed as a beam with a circular cross-section subjected to equidistant point loading on the characteristic material strength level. Since the hinges were standard inventory in the laboratory, the cross-section of the shear pin was fixed. Therefore, the design was focused on the necessary number of hinges to satisfy von Mises stresses on the characteristic level, as well as an L/400 maximum deflection criterion. The system was designed against a maximum shear force of 1000 kN, in combination with a 100 kN centrifugal force. The maximum allowable deflection was the governing design criterion. The thicknesses of the adapter plates were governed by the minimum thread length of the M24 bolts.

3.1.2 SPECIMEN SUPPORTS

The specimen ends were placed in steel brackets, which were bolted to rotation hinges. The hinges provided the simply supported support conditions. To enforce axial restraints, the specimens could be fixed to the steel brackets using glued-in or threaded rods. This is shown in Figure 5. In Figure 5a, the screws were mounted for transportation and were removed before testing.

To account for uncertainties in the specimen lengths and other parts of the setup, a sliding system with several centimetres of adjustability was designed. The sliding system comprised a steel plate with long holes, which was bolted to a shear wall. The reaction forces were transferred to the strong floor through the shear walls, which were connected to the pendulum frame via two connected HEB 300 mm beams. This is shown in Figure 6. To accommodate different specimen lengths, the shear walls could be moved with rough precision, and the steel plate with the long holes provided exact precision.

https://doi.org/10.52202/069179-0002

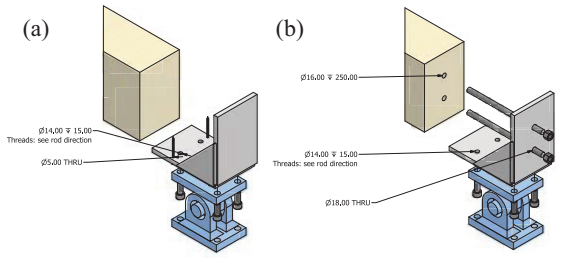

Figure 5: *Steel brackets with simply supported boundary conditions (a) without axial restraints, and (b) with axial restraints. The figure is reproduced from Cao et al.* [27].

For the axially unrestrained specimens, the halves of the specimens would fly out of the steel brackets in the direction of the impact hammer motion. However, this was not the case for the axially restrained specimens. Because of the axial restraints, the two halves were kept in the steel brackets by the glued-in rods. To prevent a reverse impact by the impact hammer on its return to the side of the initial release, a recoil control system was implemented for safety reasons. The recoil system comprised a pair of steel rods, which were released vertically after the first impact. This prevented the halves of the specimen from returning to its initial position, ensuring a gap that the impact hammer could return through. This is shown in Figure 7.

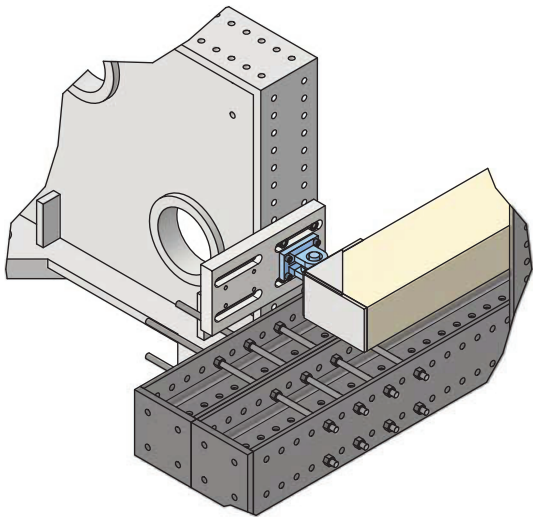

Figure 6: *Specimen support system. The figure is reproduced from Cao et al.* [27].

3.1.3 IMPACT HAMMER HEAD

The head of the impact hammer comprised steel plates of various dimensions to ensure a sufficient mass of the impact hammer. The steel plates were post-tensioned using M24 and M16 8.8 threaded rods. To provide a clean impact surface, a 300×350×70 mm S355 steel plate with rounded edges was machined and mounted at the tip of the impact hammer head. The effective contact surface between the impact hammer tip and the specimen was 250×200 mm. The total mass of the impact hammer head

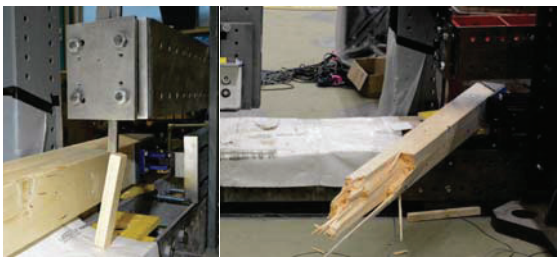

(a) Activated rods. (b) Rods post-release.

Figure 7: *Recoil system for the axially restrained specimens. The figure is adapted from Cao et al.* [27].

was about 2736 kg. The total mass of the impact hammer, including instrumentation, was approximately 3475 kg, with a centre of mass from the shear pin of 4649 mm. The impact hammer head is shown in Figure 2b, and the impact hammer tip in Figure 8.

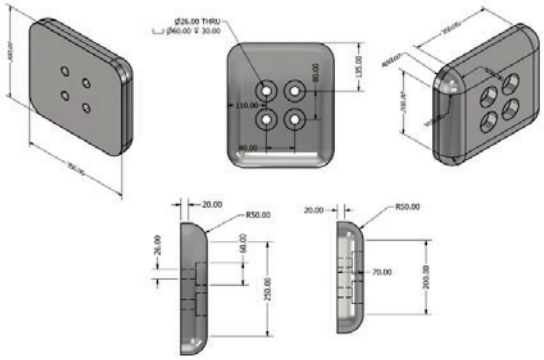

Figure 8: *Impact hammer tip. The figure is reproduced from Cao et al.* [27].

3.1.4 RELEASE SYSTEM

A crane was used to lift the impact hammer to its release height and an electromechanical release mechanism was used to release the impact hammer. This is shown in Figure 2a. Because the loading capacity of the electromechanical release mechanism was limited to 2500 kg, a load reduction system was necessary to reduce the weight $m_p g$ of the impact hammer on the electromechanical release mechanism.

The load reduction system comprised steel shackles, lifting slings, and a dynamic climbing rope. These parts were organised in a pulley system, such that the final load on the electromechanical release mechanism was reduced to $m_p g/6$. The load reduction system is illustrated in Figure 9. A dynamic climbing rope was preferred over steel cables or static ropes because of its ability to damp out vibrations and its flexibility and adjustability. The dynamic climbing ropes had a total length of approximately 1.6 m and were inspected after each test. Unless damage was detected during the visual inspection, they were used four to six times before being replaced. Figure of eight knots were tied at each end of the ropes, which is a standard knot used in sports climbing.

Once the release mechanism was triggered, the dynamic climbing rope would unloop itself from the shackles and remain on the crane. The induced energy loss from the

https://doi.org/10.52202/069179-0002

unlooping action was corrected for in the tests by comparing the energy loss between subsequent harmonic oscillations. This is described in Section 4.2.

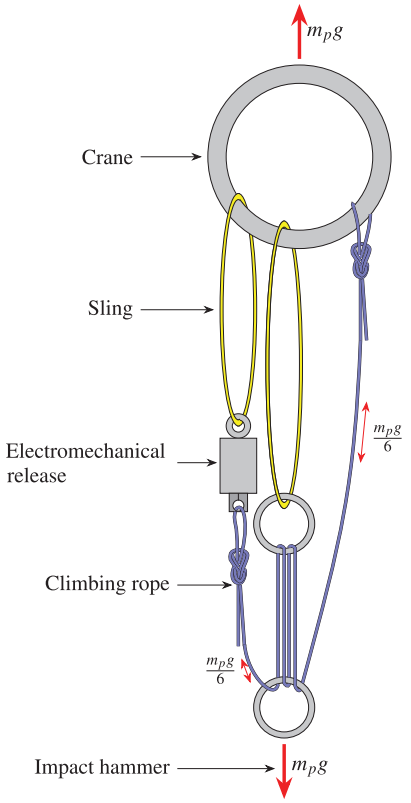

Figure 9: *Release and load reduction system of the impact hammer.*

3.2 CAMERAS AND SENSORS

To capture the impact and failure process of the specimen, several cameras were used. The main camera was an AOS M-VIT 4000 shock-resistant high-speed camera operating at 5700 pictures per second, which was mounted on the impact hammer facing the specimen. Because of the high frame rate and the sensor size of the camera, two GSVitec Multiled MT 50 000 lm lights were used with the camera. The AOS M-VIT 4000 camera was triggered to record for a minimum shock of 10g and had a memory capable of a few seconds of footage. Besides the AOS M-VIT 4000 camera, a GoPro Hero 10 action camera was mounted in the debris corridor to record the impact at 240 frames per second. The location of the AOS M-VIT 4000 and GoPro Hero 10 cameras can be seen in Figure 2b. A Nikon D7100 camera was placed at the end of the corridor and was also used to document the broken pieces of the specimen post-impact.

The primary measurement of the tests was the position of the pendulum, pre- and post-impact. This was recorded with an analog Baumer EIL580P angular encoder with a resolution of approximately 0.005°, which corresponds to a positional resolution at the centre of the impact tip of over 0.5 mm. The Baumer EIL580P was mounted at the shear pin, and its position can be seen in Figure 2a.

To measure the peak impact force P_d in Equation (4), accelerometers were mounted on the impact hammer beside the impact hammer tip in Figure 8. The positions of the accelerometers are shown in Figure 2b. Because of the difficulty in estimating the peak impact force P_d in the design phase, 10g micro-electromechanical (MEMS) accelerometers were initially used. In theory, the 10g MEMS sensors could measure impact forces of up to 700 kN. The estimated static strength for the shortest specimens with the largest cross-sections was in the order of 120 kN. After testing a few of the weakest specimens, it was apparent that the capacity of the 10g MEMS sensors was insufficient. Therefore, 50g and 100g MEMS sensors were ordered, with the same results. It was believed that piezoelectric accelerometers would give better results, which led to the use of 100g and 250g piezoelectric accelerometers. The capacities of these accelerometers were occasionally exceeded, which is equivalent to forces of over 6 900 and 13 800 kN, respectively. Upon post-processing of the accelerometer data and the high-speed imagery, this data was deemed unfit for determining the peak impact force P_d. This is discussed in Section 4.

10g MEMS accelerometers were used to measure the dynamic elastic modulus E_d of each specimen. Two 10g MEMS accelerometers were mounted ±500 mm from the mid-span of the specimens, and non-destructive impact hammer tests at the mid-span were used to induce vibrations in the specimens. The vibration data was then processed to find the natural period T_n. Together with the mass m of the specimen, the natural period T_n was used to compute the dynamic elastic modulus E_d.

A linear variable differential transformer (LVDT) was also used with a manual hand-crane and weights to conduct static three-point bending tests to find the static elastic modulus E_s. However, the displacements from the LVDT resulted in inconsistent static elastic moduli E_s. Therefore, the dynamic elastic modulus E_d from the vibration-based method was used for all further processing of the data. A complete list of the cameras and sensors can be found in Cao et al. [29].

4 RESULTS

4.1 HIGH-SPEED CAMERA IMAGERY

Images from the AOS M-VIT 4000 high-speed camera of a typical failure process are shown in Figure 10. Initially, the impact hammer made initial flat contact with the specimen at its centre. During the initial contact, momentum was transferred to the specimen via shock loading. This is shown in Figure 10a. After the initial impact, a gap formed between the impact hammer and the specimen. The first crack always appeared on the tension side of the specimen, and often in the outermost lamella close to a material imperfection. The first crack often developed when there was no physical contact between the impact hammer and the specimen. This is shown in Figure 10b. Eventually, the impact hammer made contact with the specimen again and pushed through the specimen. During this time, the failure propagated from the tension side towards the compression side of the specimen. This is shown in Figure 10c.

The high-speed imagery was used to describe the impact process qualitatively and uncovered a clear bouncing behaviour of the specimen on the impact hammer. The imagery enabled the classification of the failures into five different failure modes and the determination of the time to failure of each specimen [28,29].

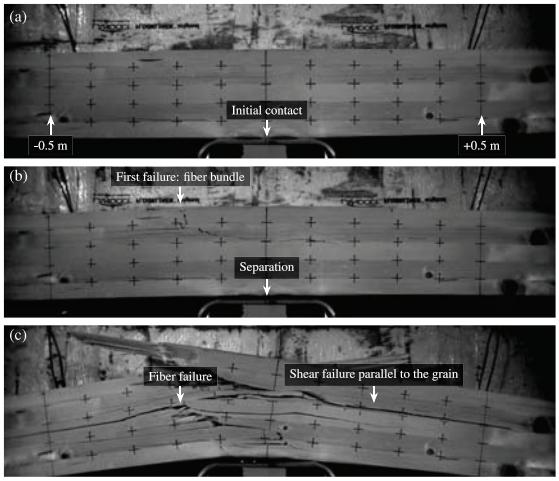

Figure 10: *Typical imagery and failure process from the AOS M-VIT 4000 high-speed camera with (a) initial contact between the impact hammer and the specimen at t=0 ms; (b) bouncing of the specimen with a gap forming between the impact hammer and the specimen at t=3.8 ms; and (c) full failure of the specimen with several failures at t=19.6 ms. The images are from tests on specimen 160×200×3600-F-4. The figure is reproduced from Cao et al.* [27,28]

4.2 SENSOR DATA

Data from an accelerometer mounted on the impact hammer is shown in Figure 11. If the 1 ms RMS-signal is interpreted, the peak impact force P_d based on Equation (4) was about 3500 kN. Compared with the mean value bending strength of GL24h [30], the peak impact force P_d was over 85 times higher with this method. It is obvious that this is not physically possible. This method of finding the peak impact force P_d can be further disowned by comparing the acceleration time history in Figure 11 with the high-speed imagery in Figure 10. Between t=3.0 ms and t=5.8 ms, there was no contact between the impact hammer and the specimen. The peak accelerations were measured at around t=3.3 ms. Therefore, there was no contact between the impact hammer and the specimen when the peak accelerations were measured. Moreover, the impact could not be characterised as perfectly inelastic based on imagery from the high-speed camera. Therefore, Newton's second law in Equation (4) cannot be used to compute the peak impact force P_d in such tests. The periodicity of the raw signal $|A|$ in Figure 11 corresponds to the natural period T_n of the impact hammer itself. The RMS accelerometer signal corresponded well to the observed bouncing of the specimen [26].

Figure 12 shows the data from the Baumer EIL580P angular encoder for specimen 160×200×3600-F-4. The release angle was 85.01°, which is equivalent to a potential energy mgh_0 of 146.7 kJ. The post-impact energy was measured after the pendulum impact hammer had completed a full cycle, coming back to the side of

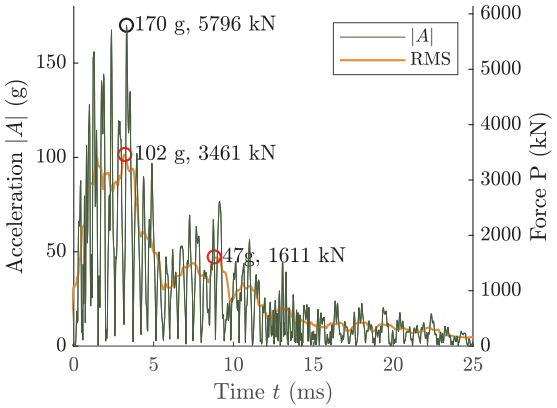

Figure 11: *Absolute values of the acceleration time history and the gliding 1 ms RMS signal for specimen 160×200×3600-F-4 from an accelerometer mounted on the impact hammer. The figure is adapted from Cao et al.* [27]

initial release. For the data shown in Figure 12, the post-impact angle was 80.32°, or 133.6 kJ. Because of the initial energy release from the electromechanical release system in Figure 9, the energy release during this cycle was corrected for by using data from free swing tests. By comparing the difference in potential energy mgh or the measured angles θ of the amplitudes following the impact hammer release for free swing conditions, the energy release E_r could be corrected for the release mechanism. Besides corrections for the release mechanism, corrections were also conducted for the intrinsic system damping by comparing free swing amplitudes with testing amplitudes, as well as the kinetic energy E_k from the propulsion of the broken halves of the specimens. This was done with the modal approximation technique [31].

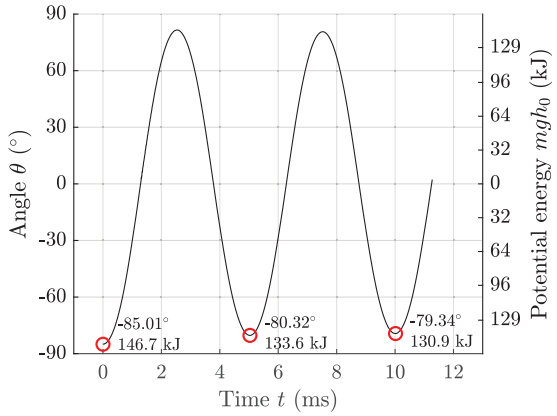

Figure 12: *Angular encoder data for specimen 160×200×3600-F-4.*

In Figure 12, the uncorrected difference between the initial and the first return peak was 4.69°, or 13.1 kJ. After corrections, the energy release E_r was $\Delta\theta$=3.22°, or E_r=8.99 kJ. The full results are presented in the test report [27]. By normalising the energy release E_r by the cross-sectional area, the toughness U_T can be found. For specimen 160×200×3600-F-4, the toughness U_T was 281 kJ/m^2.

https://doi.org/10.52202/069179-0002

5 CONCLUSION & OUTLOOK

In this paper, a pendulum impact hammer setup for impact testing of full-size timber beams was presented. The impact hammer was designed using computer-aided-design, and had a mass of 3450 kg, an effective length of 4750 mm, and could be released from a near-horizontal position. It was designed to accommodate simply supported timber beam specimens with and without axial restraints for cross-sections between 160×160 mm and 200×320 mm, and lengths between 2700 mm and 4300 mm. The main data from the tests was the energy release of the specimen throughout the impact, which was measured directly by the position of the impact hammer. The position of the impact hammer was recorded with an angular encoder. Besides the angular encoder, a shock-resistant high-speed camera operating at 5700 pictures per second was mounted on the impact hammer, and other cameras were also used to record the impact from several angles. Several accelerometers were also mounted on the impact hammer to measure the peak impact force. To date, 89 spruce glued laminated timber specimens without finger joints, nine beech laminated veneer lumber specimens, and four calibration specimens were tested.

Throughout the current experimental campaign, the test setup worked reliably at a high success-rate. Based on the current results, it is not recommended to measure the peak impact force by using accelerometers mounted at the impact hammer. For future tests, it is planned to measure the reaction forces at the supports directly via load cells. To extend the current knowledge on the behaviour of glued laminated timber subjected to impact loading, tests are also planned for specimens with finger joints. The pendulum impact hammer can also be used for impact tests of other materials with little or no modification.

ACKNOWLEDGEMENT

The authors would like to thank Roth Burgdorf AG and Pollmeier Massivholz GmbH & Co. KG for their contributions to the project. In addition, the authors remain thankful for the assistance and support provided by the Bauhalle team at ETH Zurich. This article is part of the project *Robustness of tall timber buildings* at ETH Zurich and is generously funded by the Albert-Lück Stiftung.

REFERENCES

[1] Ramage MH, Burridge H, Busse-Wicher M, Fereday G, Reynolds T, Shah DU, et al. The wood from the trees: The use of timber in construction. Renewable and Sustainable Energy Reviews 2017;68:333–59. https://doi.org/10.1016/j.rser.2016.09.107.

[2] Crews KI. Nonconventional timber construction. Nonconventional and Vernacular Construction Materials: Characterisation, Properties and Applications 2020:437–66. https://doi.org/10.1016/B978-0-08-102704-2.00016-0.

[3] Mpidi Bita H, Huber JAJ, Palma P, Tannert T. Prevention of Disproportionate Collapse for Multistory Mass Timber Buildings: Review of Current Practices and Recent Research. Journal of Structural Engineering 2022;148. https://doi.org/10.1061/(asce)st.1943-541x.0003377.

[4] Huber JAJ, Ekevad M, Girhammar UA, Berg S. Structural robustness and timber buildings–a review. Wood Mater Sci Eng 2019;14:107–28. https://doi.org/10.1080/17480272.2018.1446052.

[5] Voulpiotis K, Schär S, Frangi A. Quantifying robustness in tall timber buildings: A case study. Eng Struct 2022;265:114427. https://doi.org/10.1016/J.ENGSTRUCT.2022.114427.

[6] Cao AS, Grönquist P, Frangi A. Manuscript under peer review: Catenary action in strip-reinforced wood and timber beams. Constr Build Mater 2023.

[7] Cao AS, Palma P, Frangi A. Column removal analyses of timber structures - Framework to assess dynamic amplification factors for simplified structural design methods. World Conference on Timber Engineering 2021, WCTE 2021, Santiago, Chile: 2021, p. 1717–24.

[8] Svatoš-Ražnjević H, Orozco L, Menges A. Advanced Timber Construction Industry: A Review of 350 Multi-Storey Timber Projects from 2000–2021. Buildings 2022;12:404. https://doi.org/10.3390/buildings12040404.

[9] Binck C, Cao AS, Frangi A. Lateral stiffening systems for tall timber buildings–tube-in-tube systems. Wood Mater Sci Eng 2022. https://doi.org/10.1080/17480272.2022.2086066.

[10] Cao AS, Stamatopoulos H. A theoretical study of the dynamic response of planar timber frames with semi-rigid moment-resisting connections subjected to wind loads. Eng Struct 2021;240. https://doi.org/https://doi.org/10.1016/j.engstruct.2021.112367.

[11] Vilguts A, Malo KA, Stamatopoulos H. Moment resisting frames and connections using threaded rods in beam-to-column timber joints. WCTE 2018 - World Conference on Timber Engineering 2018:1–8.

[12] Johansson M, Linderholt A, Jarnerö K, Landel P. Tall timber buildings - A preliminary study of wind-induced vibrations of a 22-storey building. WCTE 2016 - World Conference on Timber Engineering 2016.

[13] Rebouças AS, Mehdipour Z, Branco JM, Lourenço PB. Ductile Moment-Resisting Timber Connections: A Review. Buildings 2022;12:240. https://doi.org/10.3390/buildings12020240.

[14] Cao AS, Frangi A. Mixed Element Method for Progressive Collapse Analysis: Method Description and Verification. In: di Trapani F, editor. Proceedings of Eurasian OpenSees Days 2022, Torino, Italy: Springer Nature; 2022.

[15] Adam JM, Parisi F, Sagaseta J, Lu X. Research and practice on progressive collapse and robustness of building structures in the 21st century. Eng Struct 2018;173:122–49. https://doi.org/10.1016/j.engstruct.2018.06.082.

[16] Baumann G, Brandner R, Müller U, Stadlmann A, Feist F. A Comparative Study on the Temperature Effect of Solid Birch Wood and Solid Beech Wood

under Impact Loading. Materials 2021;14. https://doi.org/10.3390/ma14247616.
[17]Pinto Moreira A, da Silveira E, Henrique de Almeida D, Hendrigo de Almeida T, Hallak Panzera T, Luís Christoforo A, et al. Toughness and Impact Strength in Dynamic Bending of Wood as a Function of the Modulus of Elasticity and the Strength in Compression to the Grain. International Journal of Materials Engineering 2017;7:61–7. https://doi.org/10.5923/j.ijme.20170704.01.
[18]Bučar DG, Merhar M. Impact and dynamic bending strength determination of Norway spruce by impact pendulum deceleration. Bioresources 2015;10:4740–50. https://doi.org/10.15376/biores.10.3.4740-4750.
[19]Widmann R, Steiger R. Impact loaded structural timber elements made from Swiss grown Norway spruce. In: Görlacher R, editor. CIB-W18 Meeting Forty-Two. International council for research and innovation in building and construction. Working commission W18 - timber structures., Dübendorf, Switzerland: Universität Karlsruhe; 2009, p. 1–11.
[20]Leijten AJM. Impact crash and simulation of timber beams. Transactions on Modelling and Simulation, vol. 30, Tallinn, Estonia: 2001, p. 859–68. https://doi.org/10.2495/CMEM010841.
[21]Jansson B. Impact Loading of Timber Beams. Master Thesis 1992. https://doi.org/10.14288/1.0050473.
[22]Blank L, Fink G, Jockwer R, Frangi A. Quasi-brittle fracture and size effect of glued laminated timber beams. European Journal of Wood and Wood Products 2017;75:667–81. https://doi.org/10.1007/s00107-017-1156-0.
[23]Madsen B, Buchanan AH. Size effects in timber explained by a modified weakest link theory. Canadian Journal of Civil Engineering 1985;13:218–32. https://doi.org/10.1139/l86-030.
[24]European Committee for Standardization. EN 1995-1-1:2004. Eurocode 5: Design of timber structures - Part 1-1: General - Common rules and rules for buildings. Brussels, Belgium: 2004.
[25]Schweizerische Ingenieur- und Architektverein. SIA 265. Zurich: 2021.
[26]Cao AS, Lolli M, Frangi A. Pendulum impact hammer tests on spruce GLT – Preliminary results. In: Topping BHV, Kruis J, editors. Proceedings of the Fourteenth International Conference on Computational Structures Technology, Edinburgh, UK: Civil-Comp Press; 2022, p. 1–8.
[27]Cao AS, Houen M, Lolli M, Frangi A. Pendulum impact hammer tests on glued laminated timber beams. Report 2022-01. Zurich, Switzerland: 2022. https://doi.org/10.3929/ethz-b-000585619.
[28]Cao AS, Houen M, Frangi A. Manuscript under peer review: Impact loading of glued laminated timber beams. Comput Struct 2023.
[29]Cao AS, Houen MT, Lolli M, Frangi A. Pendulum Impact Hammer Tests on Glued Laminated Timber Beams. Zurich: 2022. https://doi.org/10.3929/ethz-b-000585619.
[30]Schilling S, Palma P, Steiger R, Frangi A. Probabilistic description of the mechanical properties of glued laminated timber made from softwood. In: Görlacher R, editor. International Network on Timber Engineering Research, INTER: Proceedings, Meeting 54, 16-19 August 2021, Online, Timber Scientific Publishing, KIT Holzbau und Baukonstruktionen; 2021, p. 1–16.
[31]Martin JB, Symonds PS. Mode approximations for impulsively loaded rigid structures. 1965.

https://doi.org/10.52202/069179-0002

World Conference on Timber Engineering Oslo 2023

NUMERICAL AND EXPERIMENTAL EVALUATION OF WOOD-NAILER OPEN WEB STEEL JOISTS

Sameer Fares[1], David Dinehart[2], Shawn Gross[3], Joseph Yost[4], Rebecca Hoffman[5],

ABSTRACT: The wood-nailer open web steel joist is a steel truss intended for use with a wood roof or floor deck. The wood-nailer is attached via mechanical shear connectors (self-drilling screws) to the full width and length of the top chord of steel joist. Current engineering practice does not consider the contribution of the wood-nailer to the strength and stiffness of the steel and wood hybrid system. This paper investigates the composite behavior of wood-steel joist systems through full-scale experimental testing and comprehensive 3-D finite element (FE) modelling. The FE model was calibrated by comparing results to full-scale experimental results on the wood-nailer steel joist system. The validated FE model of the wood-nailer-steel joist system is then used to conduct parametric studies that investigate the influence of screw spacing and wood-nailer thickness on the structural performance of the wood-nailer joist. This information is critical for developing a comprehensive composite design procedure.

KEYWORDS: wood-nailer, finite element modelling, composite behavior, full-scale testing

1 INTRODUCTION

An open web steel joist is a standard steel truss that consists of three components: the top chord (TC), the bottom chord (BC), and the web members, which are connected to the top and bottom chord by welds [1]. Chord members are typically double angles, with a gap in between, while web members can be either angles, channels, or rods. The conventional wood-nailer open web steel joist (WNOWSJ) is a standard steel joist with a wood-nailer attached to the top chord, as shown in Figure 1.

Figure 1: Hybrid Wood-on-Steel Roof System

The wood-nailer (WN) acts as a filler to attach the wood deck to the steel joist using mechanical fasteners. It consists of several wood-nailer segments, butted but not joined, attached to the joist's top chord steel angles via mechanical shear connectors (self-drilling screws), as shown in Figure 2.

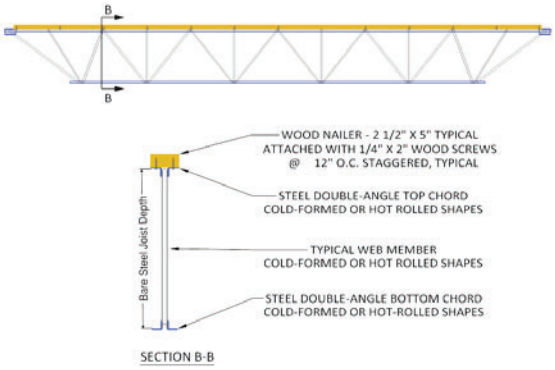

Figure 2: Wood-Nailer Steel Joist

Holes are punched in a staggered pattern into the horizontal legs of the top chord angles so self-drilling ¼-in (6.35 mm) diameter screws can be installed in pre-cut holes. The screw is then driven into the wood to attach the wood-nailer. A WNOWSJ is used in the panelized hybrid wood /steel roof system offering an attractive alternative to conventional timber joists. The conventional wood-nailer open web steel joist structural performance can be improved by making the wood-nailer structurally continuous and an integral component of the steel joist [2]. The structural continuity of the wood-nailer is achieved either through splicing the wood segments together along the length of the joist or by providing a

[1] Sameer Fares, Research and Development Structural Engineer, NMBS Building Systems, 3565 Hwy 32 North., Hope, AR 71801. Email: sam.fares@newmill.com
[2] David Dinehart, Ph.D., Professor of Civil Engineering, Villanova University, 800 Lancaster Avenue, Villanova, PA 19085. Email: david.dinehart@villanova.edu
[3] Shawn Gross, Ph.D., Associate Professor of Civil Engineering, Villanova University, 800 Lancaster Avenue, Villanova, PA 19085, Email: shawn.gross@villanova.edu
[4] Joseph Yost, Ph.D., P.E., Professor of Civil Engineering, Villanova University, 800 Lancaster Avenue, Villanova, PA 19085. Email: joseph.yost@villanova.edu
[5] Rebecca Hoffman, Ph.D., Principal Mechanical Engineer, Applied Mechanics Division, University of Dayton Research Institute. Email: Rebecca.Hoffman@udri.udayton.edu

https://doi.org/10.52202/069179-0003

single full-length wood member for each joist. As a structurally continuous wood-nailer, the strength of the wood-nailer can be incorporated in the steel joist design as either non-composite, partial composite, or fully composite with the joist steel top chord, depending on the shear connection behaviour. This paper investigates the composite behaviour of wood-steel joist systems through full-scale experimental testing conducted by Martignetti [4] and comprehensive 3-D non-linear finite element (FE) modelling. The FE model was validated by comparing the FE results to full-scale experimental data on the wood-nailer steel joist system. The validated FE model of the wood-nailer-steel joist system is then used to conduct a parametric study that investigates the influence of wood-nailer thickness and screw spacing on the structural performance of the wood-nailer joist.

2 EXPERIMENTAL

Martignetti et.al. [4] experimentally evaluated wood-nailer steel joist marks (J1) and bare steel joists (J3) performances. A total of four full-scale wood-nailer joist pair tests were conducted. Two full-scale joist pair tests involved a wood decking system, and the other two full-scale bare steel joist pair tests involved a steel decking system. The steel joists were 40 ft (12.19 m) long. Both joist marks J1 and J3 had a bare steel depth of 28-in (711 mm). J1 also had a 2 ½ in (64 mm) thick wood-nailer on the top chord for a total depth of 30.5 in (775 mm). The joist top and bottom chord angle sizes are described in

Table 1.

Table 1: Wood-nailer Steel Joist Dimensions

Joist Mark	J1
Steel Joist Type	Wood-Nailer
Deck Type	Plywood
WN Thickness in (mm)	2.5 (64)
WN Steel Joist Overall Depth in (mm)	30.5 (775)
Length ft (m)	40 (12.19)
Top Chord in (mm)	LL 2 x 3/16 (LL 51 x 5)
Bottom Chord in (mm)	LL 1.75 x 0.17 (LL 44 x 4)
Joist Mark	J3
Steel Joist Type	Steel Joist
Deck Type	Steel
Bare Steel Joist Depth in (mm)	28 (711)
Length ft (m)	40 (12.19)
Top Chord in (mm)	LL 2 x 3/16 (LL 51 x 5)
Bottom Chord in (mm)	LL 1.75 x 0.17 (LL 44 x 4)

All wood-nailer steel joists used in the experimental study had a wood-nailer 2.5-in (64-mm) thick x 5-in (127 mm) wide, attached to the top of the steel top chord angles with ¼-in (6.35 mm) diameter x 2-in (51 mm) long self-drilling screws staggered at 24-in (610 mm) on center. Figure 3 shows the attachment between the wood-nailer and the steel joist [2].

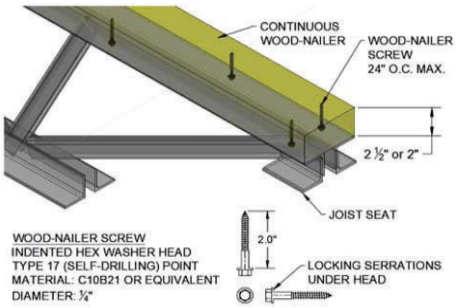

Figure 3: Wood-nailer Attachment to Steel Joist [2]

2.1 JOIST TEST SETUP

The wood-nailer steel joist pair was positioned 8 ft (2.44 m) apart to accurately simulate the joist's behaviour in a floor or roof system. Wood sub-purlins with nominal dimensions 2-in (51-mm) by 4-in (102-mm), and 24-in (610-mm) on center, are installed between the joists, and ½-in (13-mm) thick plywood sheathing is nailed to the sub purlins and joist wood-nailer by standard nailing techniques, creating a section of the roof. Figure 4 shows the wood-nailer joist (J1) specimen [4]. Steel joists (J3) were set up similarly to (J1). Figure 5 shows the steel joists (J3) and deck setup [3].

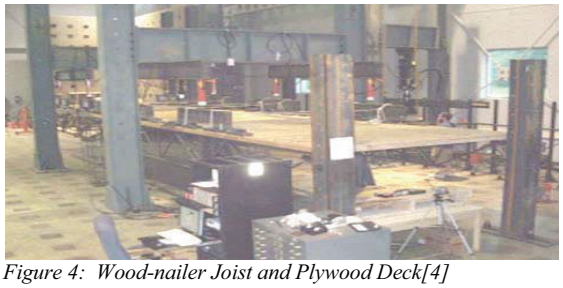

Figure 4: Wood-nailer Joist and Plywood Deck[4]

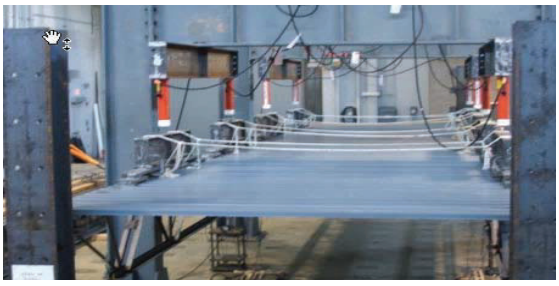

***Figure 5:** Steel Joist and Deck [4]*

2.2 LOADING

A loading pyramid was used to create a distributed load over the middle 32 ft (9.75-m) of the wood-nailer steel joist span. The load was applied to the wood deck directly above the top chord of the joists. Figure 6 illustrates the

https://doi.org/10.52202/069179-0003

distributed loading pattern. A 10,000-psi (69 MPa) manual hydraulic pump was used to apply a static load.

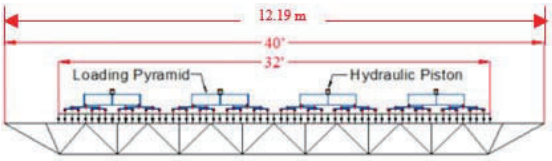

Figure 6: *Load Distribution Setup [4]*

2.3 DATA ACQUISITION

Linear variable displacement transducers (LVDTs) were used to measure the displacement near the mid-span of each joist. Eighteen strain gages were placed at the mid-span of each joist chord and wood-nailer to measure the strains and stresses in each component. Three Vishay Micro-Measurements scanners and the associated computer software recorded the signals from the load cells, LVDTs, and strain gages. Figure 7 shows strain gauge locations described in [4].

Figure 7: *Wood-Nailer Steel Joist Strain Gage Locations*

2.4 WOOD-NAILER MATERIAL TESTING

Martignetti [4][4] conducted a total of 28 tests per ASTM D4761 [5] to verify the modulus of elasticity of the Douglas-Fir wood-nailers. The statistical analysis of the test data shows that the median and the mean for the wood-nailer modulus of elasticity were both 1600 ksi (11000 MPa). The standard deviation was 314 ksi (2165 MPa)[4].

2.5 DETERMINATION OF STEEL PROPERTIES

Forty-eight steel coupons, one coupon per chord, were taken from all steel joists, then tested per ASTM E8-04 [6] for tensile testing. The statistical analysis of the test data shows that the median and the mean for the steel yield strength were both about 56 ksi (386 MPa), and the ultimate strength was about 81 ksi (559 MPa). The standard deviation for yield strength was 1.66 ksi (11.6 MPa), and for ultimate strength was 2.23 ksi (15.6 MPa)[4].

3 FINITE ELEMENT MODELLING

The finite element (FE) software package ANSYS [1][7] was used to develop a comprehensive 3-D non-linear finite element modelling (FEM) capable of replicating the experimental studies conducted on (J1) by Martignetti [4]. In addition, a bare steel joist (J3) was also simulated to serve as a reference structure against which the partial composite wood-nailer steel joist (J1) could be compared. The geometry, loads, and support conditions were applied to the numerical models. Steel joists were modelled as simply supported and subjected to a uniformly distributed load to simulate the experimental conditions.

3.1 MODELLING PROCEDURE

The following sections will describe the modelling procedure for material, geometry, shear connectors, boundary conditions, and mesh.

3.2 MATERIAL MODELLING

3.2.1 Hot-Rolled Steel

A simplified bi-linear stress-strain curve is used. The following mechanical properties were used:

Table 2: *Hot-Rolled Steel Mechanical Properties*

Property	Strength ksi (MPa)
Yield Strength	56 (386)
Modulus of Elasticity	29000 (199948)
Tangent Modulus	1450 (9997)

3.2.2 Shear Connector

The screw material is AISI-1021(C10B21). A simplified bi-linear stress-strain curve is used. Table 3 shows the mechanical properties that were used in the FE model.

Table 3: *Shear Connector Mechanical Properties*

Property	Strength ksi (MPa)
Yield Strength	57.3 (395)
Tensile Strength	68.2 (470)
Tangent Modulus	1450 (9997)

The AISI 1021 carbon steel is equivalent to ASTM 29.

3.2.3 Wood-Nailer

The variability of wood mechanical properties can significantly influence the structural performance of wood and steel-wood connections. Wood is an orthotropic material with unique and independent properties in different directions. However, since the primary strains and stresses are along the length of the joist, an isotropic material model using material properties for this direction are assumed. A simplified bi-linear stress-strain curve is used. Dowel bearing strength is used for the wood-nailer yield strength. Table 4 shows the Douglas-Fir wood's physical properties used in the FE model.

Table 4: *Douglas-Fir Wood-Nailer Mechanical Properties*

Property	Strength ksi (MPa)
Yield Strength	5 (34)
Modulus of Elasticity	1600 (11000)

https://doi.org/10.52202/069179-0003

Tangent Modulus	0.25 (1.73)

3.3 GEOMETRY

Symmetry constraints were used at the steel joist mid-length, as shown in Figure 8, to reduce the model size.

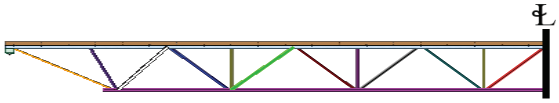

Figure 8: *One-Half FE Model of Wood-Nailer Steel Joist Span*

3.4 BOUNDARY CONDITIONS

Boundary Conditions in FEA are critical and significantly impact the outcomes. The wood-nailer steel joist has several components, and the contact types among the parts can significantly affect the results and require special consideration.

3.4.1 Support Conditions

Wood-nailer steel joists were modelled as simply supported at the ends of the span, as shown in Figure 9.

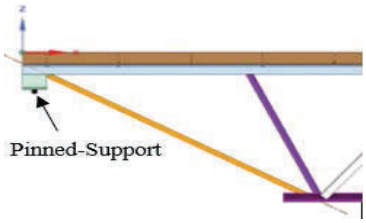

Figure 9: Pinned- Support

3.4.2 Shear Connector

The self-drilling screws acting as shear connectors between the steel joist and wood nailer were modelled as solid bodies, as shown in Figure 10.

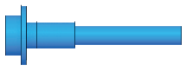

Figure 10: Screw Model

Threads on the shear connector were removed to reduce computational time and avoid convergence issues. Root diameter or the solid core of the screw was used. A pretension load of 150 lb (445 N) was applied to each shear connector.

3.4.3 Contact

ANSYS offers five different contact formulations [7]. In the FE model, bonded and frictional contacts were used. In bonded contact, separation, sliding, or penetration are not allowed. However, in frictional contact, the bodies in contact can slide relative to one another in the tangential direction and also can translate in the normal direction [8]. Bonded contacts were used to model the contact between the screw shank and the wood-nailer. In addition, frictional contact was used between screw shanks and the inner walls of the holes in the steel joist top chord. The fillet-welded connection between each web member end and the chord member was modelled with edge-bonded contacts.

3.4.4 Applied Load

A uniform load was applied directly over 16 ft (4.88 m) of the top surface area wood-nailer steel joist one-half FE model to replicate the applied distributed load, as shown in Figure 11.

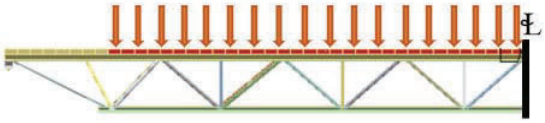

Figure 11: *Load Applied Directly to the Wood-Nailer*

3.4.5 Bracing

In the FE model, the wood-nailer was constrained laterally, in the perpendicular direction to the length of the steel joist, every 6 inches to simulate the lateral bracing provided by the wood deck to the steel joist top chord.

3.5 MESH

A rigorous mesh sensitivity analysis was conducted to determine the model discretization that provides the best cost-effectiveness and accuracy combination. The wood-nailer, top and bottom chords, and webs were meshed by quadratic hexahedral elements. For screw fasteners, axisymmetric hexahedra mesh with sweep method was used. Contact sizing was used to increase the number of elements to minimize mesh transitions. Figure 12 shows the FE mesh elements for different components.

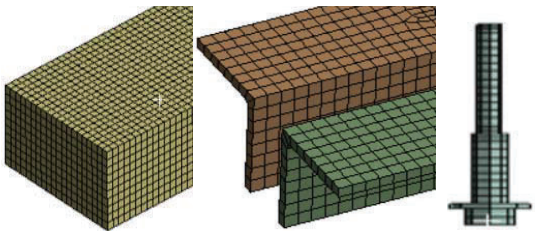

(a) *(b)* *(c)*

Figure 12: *FE mesh for (a) Wood-Nailer, (b) Top and Bottom Chords, (c) Screw*

3.6 VALIDATION OF THE DEVELOPED FINITE ELEMENT MODEL

3.6.1 (J1) Experimental and Numerical Deflection Results

Figure 13 shows the experimental load-deflection plots for the wood-nailer steel joists (J1) [4]

https://doi.org/10.52202/069179-0003

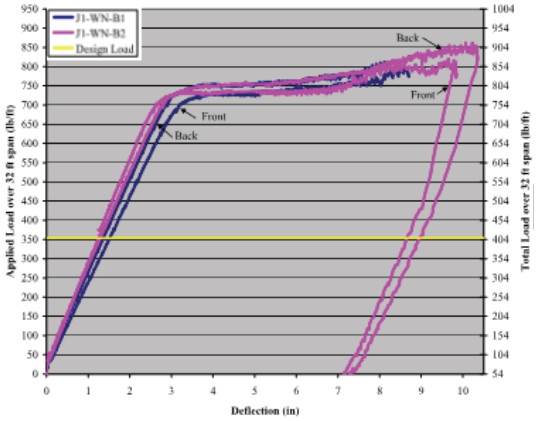

Figure 13: *(J1) Experimental Load (lb/ft) vs. Deflection [4]*

The experimental and finite element model mid-length deflection for wood-nailer steel joist (J1) mid-length is shown in Table 5.

Table 5: *J1 Experimental vs. FE Model Deflection*

Wood-nailer thickness- in (mm)	2.5 (64)
Screw Spacing- in (mm)	24 (610)
Uniform Load- lb/ft (kN/m)	700 (10.22)
Load Length- ft (m)	16 (4.88)

Wood-nailer Steel Joist Mid-Length Deflection		
Joist Mark	Experimental in (mm)	FE Model in (mm)
J1	2.61-3.15 (66-80)	2.71(69)

(J1) FE load-deflection plot is shown in Figure 14. At a point load of 11.2 kip (49.82 kN), the wood-nailer steel joist mid-length deflection is 2.71-in (69 mm).

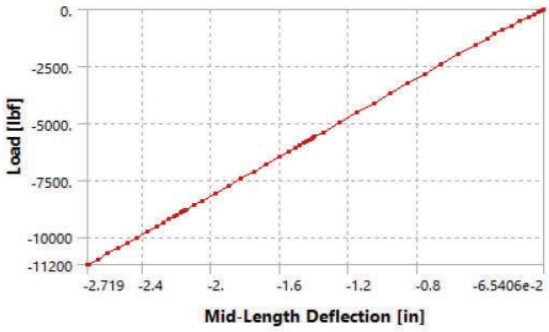

Figure 14: *(J1) FE Model Load(N) vs. Deflection*

As shown in Figure 15, (J1) FE model deflection prediction in the linear range shows a reasonably good agreement with the experimental data.

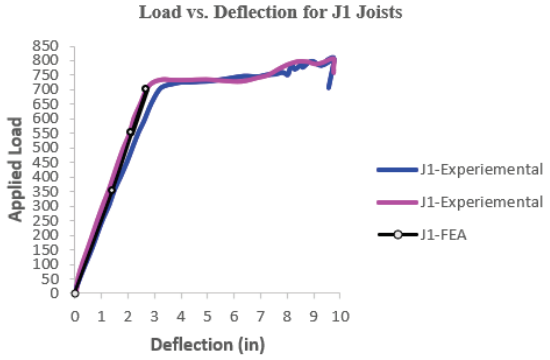

Figure 15: *(J1) Experimental vs. FE Load-Deflection Curves*

(J3) Experimental and Numerical Deflection Results

Figure 16 shows the experimental load-deflection plots for the bare steel joists (J3) [4].

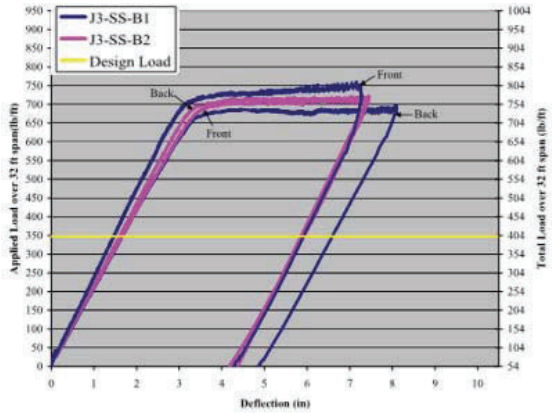

Figure 16: *(J3) Experimental Load (lb/ft) vs. Deflection [4]*

The experimental and finite element model mid-length deflection for bare steel joists (J3) is shown in Table 6.

Table 6: *J3 Experimental vs. FE Model Deflection*

Uniform Load- lb/ft (kN/m)	700 (10.22)
Load Length- ft (m)	16 (4.88)

Bare Steel Joist Mid-Length Deflection		
Joist Mark	Experimental in (mm)	FE Model in (mm)
J3	3.08-3.42 (78-87)	3.19 (81)

(J3) FE model load-deflection plot is shown in Figure 17. At a concentrated load of 11.2 kip (49.82 kN), the bare steel joist deflection at mid-length is 3.19-in (81 mm).

https://doi.org/10.52202/069179-0003

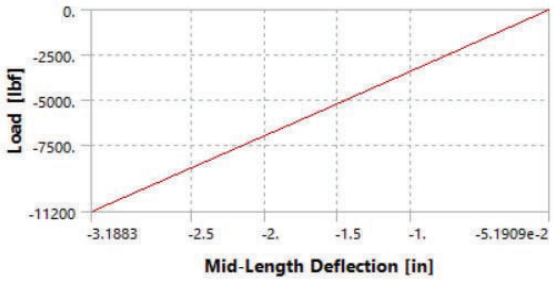

Figure 17: *(J3) FE Model Load-Deflection Plot*

Figure 18 depicts (J3) deflection at mid-length from the FE model.

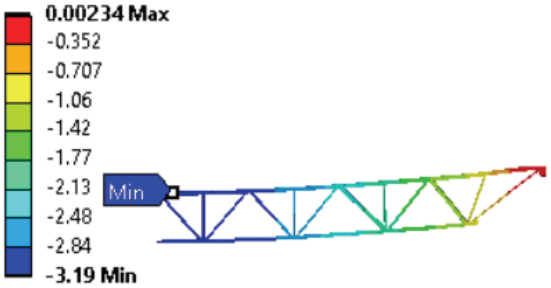

Figure 18: *(J3) FE Model Deflection in (in)*

As shown in Figure 19, (J3) FE model deflection prediction in the linear range shows a reasonably good agreement with the experimental data. Furthermore, as the FE model deflection data shows, the deflection of (J1) is less than (J3), indicating that the wood-nailer steel joist (J1) has a higher flexural stiffness than (J3). The higher flexural stiffness confirms that some level of partial composite action was attained in the wood-nailer steel joist.

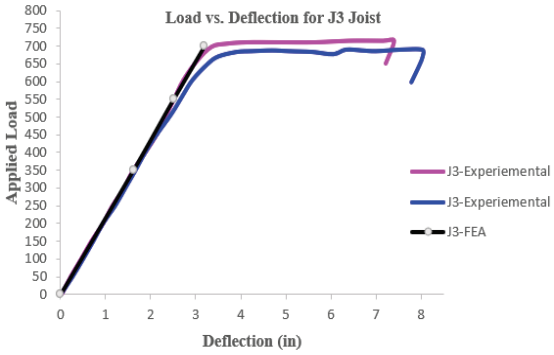

Figure 19: *(J3) Experimental vs. FE Load-Deflection Curves*

3.6.2 (J3) Experimental and Numerical Normal Strain Results

Figure 20 shows the applied-strain plots for the top chord of bare steel joist (J3) [3].

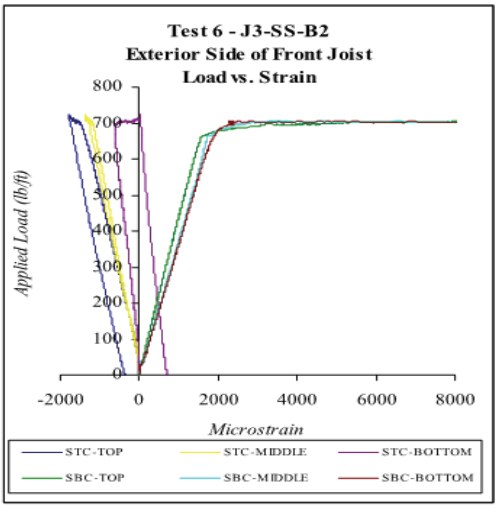

Figure 20: *(J3) Exterior Side of Front Joist Strain Plots. Experimental data from [4]*

Figure 21 shows (J3) normal strains in the top chord from the FE model.

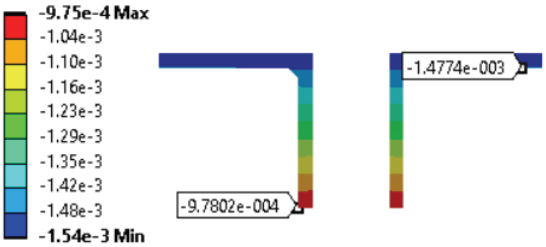

Figure 21: *(J3) Top Chord (TC) Normal Strains*

Table 7 shows the experimental vs. FE model normal strains at the top and bottom of (J3) top chord. The FE model analysis agrees well with the experimental strain results.

Table 7*: (J3) FE Model vs. Experimental Normal Strains*

Uniform Load- lb/ft (kN/m)		700 (10.22)
Load Length- ft (m)		16 (4.88)
WN Steel Joist Mid-Length Normal Strains		
Member	Strain Gauge Location	Experimental (microstrain)	FE Model (microstrain)
TC	Top	1400-1500	1480
	Bottom	600-700	978

3.7 (J1) WOOD-NAILER STEEL JOIST STRAINS

3.7.1 Experimental and Numerical Strain Results

Figure 22 shows the applied load-strain plots for the wood-nailer, top chord, and bottom chord at the locations described in Figure **7**.

https://doi.org/10.52202/069179-0003

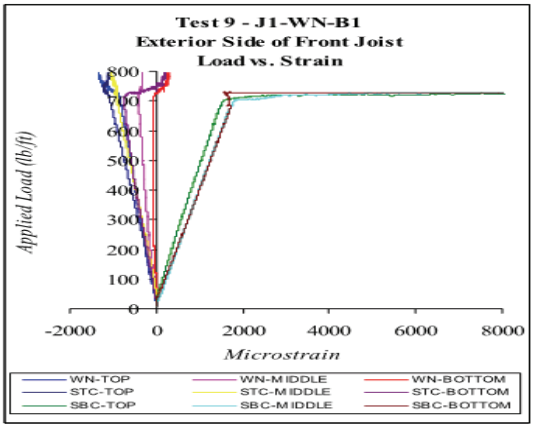

Figure 22: *J1-B1 Exterior Side of Front Joist Strain Plots. Experimental data from [4]*

3.7.2 (J1) Finite Element Model vs. Experimental Strains at the Top and Bottom of Each Member

Table 8 shows the experimental vs. FE model normal strains at the top and bottom of each component. The FE model analysis agrees well with the experimental strain results.

Table 8: *(J1) FE Model vs. Experimental Normal Strains*

Wood-nailer thickness- in (mm)	2.5 (64)
Screw Spacing- in (mm)	24 (610)
Uniform Load- lb/ft (kN/m)	700 (10.22)
Load Length- ft (m)	16 (4.88)

WN Steel Joist Mid-Length Normal Strains			
Member	Strain Gauge Location	Experimental (microstrain)	FE Model (microstrain)
WN	Top	600 - 000	980 - 1000
	Bottom	130-170	520-540
TC	Top	1080-1100	930
	Bottom	300-960	730-770
BC	Top	1500-1800	1700
	Bottom	1790-1820	1800

Figure 23 through **Figure 25** shows the normal strains in the wood-nailer, top chord, and bottom chord from the FE model.

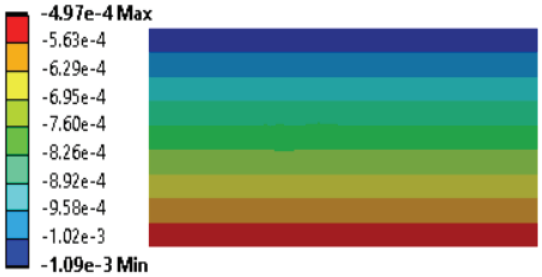

Figure 23: *(J1) Wood- Nailer (WN) Normal Strains*

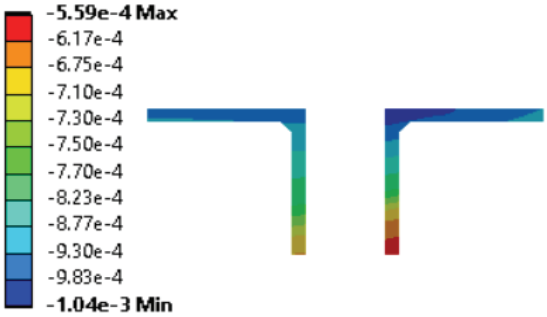

Figure 24: *(J1) Top Chord (TC) Normal Strains*

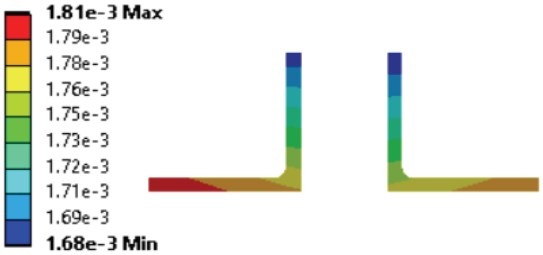

Figure 25: *(J1) Bottom Chord (BC) Normal Strains*

Table 7 and Table 8 show that the top chord combined normal strains in the wood-nailer steel joist (J1) are smaller than the bare steel joist (J3), which confirms that the wood nailer reduces the axial and bending stresses in the joist top chord through load-sharing under design loading.

3.7.3 Wood-Nailer Steel Joist (J1) And Steel Joist (J3) Component Axial Forces

Table 9 shows the FE model component axial forces for wood-nailer steel joist (J1) and steel joist (J3).

Table 9: J1 and J3 Component Forces

Wood-Nailer Thickness- in (mm)	2.5 (64)
Screw Spacing- in (mm)	24 (610)
Load- lb/ft (kN/m)	700 (10.22)
Load Length- ft (m)	16 (4.88)

FE Model Mid-Length Component Axial Forces			
Mark	WN kip (kN)	TC kip (kN)	BC kip (kN)
J1	19.9 (88.3)	37.5 (166.9)	57.8 (257.6)
J3	N/A	58.3 (259.5)	59.1(262.7)

The reduction in the bottom chord axial forces demonstrates that the wood-nailer steel joist's effective depth has increased. The increased joist effective depth with identical steel joist and added wood-nailer is evidence of the top chord elastic neutral axis moving upward due to composite behaviour between the steel top chord and the wood-nailer. The combined effect of the wood-nailer composite behaviour with the steel top chord,

https://doi.org/10.52202/069179-0003

the resulting change in the top chord neutral axis, and the resulting increased joist effective depth increase the overall joist moment capacity. Figure 26 shows the FE model axial load in the wood-nailer, top, and bottom chords.

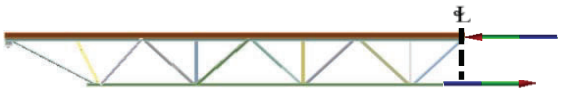

Figure 26: *Wood-Nailer, Top and Bottom Chord Axial Forces*

4 PARAMETRIC STUDIES

An essential part of a numerical study is conducting a parametric study. The validated FE model was used to conduct a parametric analysis to investigate the effect of screw spacing and wood-nailer thickness on the structural performance of the wood-nailer steel joist. First, for the standard screw spacing of 24-in, two alternative wood-nailer thicknesses, 2.25-in and 2-in, were modelled. Second, for a wood-nailer, 2.5-in thick, two alternative screw spacings, 20-in (508 mm) and 16-in (406 mm), were modelled.

4.1 WOOD-NAILER THICKNESS

The first parameter investigated was the effect of wood-nailer thickness on the joist component axial forces and the joist stiffness or deflection.

4.1.1 Wood-Nailer Steel Joist Deflection

FE model deflection results for two alternative wood-nailer thicknesses, 2.25-in and 2-in, are shown in Table 10. As expected, increasing the wood-nailer thickness resulted in a reduction in the wood-nailer steel joist deflection.

Table 10: (J1) FE Model Deflections

Screw Spacing- in (mm)	24 (610)
Load- lb/ft (kN/m)	700 (10.22)
Load Half Joist Length- ft (m)	16 (4.88)
FE Model Deflection at Joist's Mid-Length	
WN Thickness- in (mm)	Deflection- in (mm)
2.5 (64)	2.71 (69)
2.25 (57)	2.76 (70)
2.0 (51)	2.80 (71)

4.1.2 Wood-Nailer Steel Joist Component Axial Forces

Table 11 shows the FE model component axial forces for two alternative wood-nailer thicknesses, 2.25-in (57 mm) and 2-in (51 mm).

Table 11*: FE Model Component Axial Forces*

Screw Spacing- in (mm)		24 (610)	
Load- lb/ft (kN/m)		700 (10.22)	
Load Length- ft (m)		16 (4.88)	
FE Model Mid-Length Component Axial Forces			
WN Thickness in (mm)	WN kip (kN)	TC kip (kN)	BC kip (kN)
2.5 (64)	19.9 (88)	37.5 (167)	57.8 (257)
2.25 (57)	18.5 (82)	39.1 (174)	58.1 (258)
2.0 (51)	17.5 (78)	40.3 (179)	58.2 (259)

The FE model component axial force results shown in Table 11 demonstrate that increasing the wood-nailer thickness resulted in the following:

- An increase in the wood-nailer steel joist's effective depth decreases the axial force in the bottom chord.
- An increase in the axial force resisted by the wood-nailer and a decrease in the axial force resisted by the top chord. The shear strength of the screws limits the axial force transferred to the wood-nailer.

The FE analysis results demonstrate that there is a partial composite action in the wood-nailer steel joist system.

4.2 SCREW SPACING

The second parameter was to investigate the effect of screw spacing on the joist stiffness or deflection and component axial forces. Two alternative screw spacings, 20-in (508 mm) and 16-in (406 mm), were used, while the wood-nailer thickness is the standard 2.5-in (64-mm).

4.2.1 Wood-Nailer Steel Joist Deflection

Table 12 shows (J1) FE model deflections at mid-length using two alternative screw spacings, 20-in (508 mm) and 16-in (406 mm).

Table 12: *FE Model Wood-Nailed Steel Joist Deflection*

Wood-Nailer Thickness- in (mm)	2.5 (64)
Load- lb/ft (kN/m)	700 (10.22)
Load Half Joist Length- ft (m)	16 (4.88)
FE Model Mid-Length Deflection	
Screw Spacing- in (mm)	Deflection- in (mm)
24 (610)	2.71 (69)
20 (508)	2.64 (67)
16 (406)	2.55 (65)

Figure 27 and Figure 28 depict the FE model deflection when the screw fasteners are spaced at 16-in (406 mm) and 24-in (610 mm) on center, respectively.

https://doi.org/10.52202/069179-0003

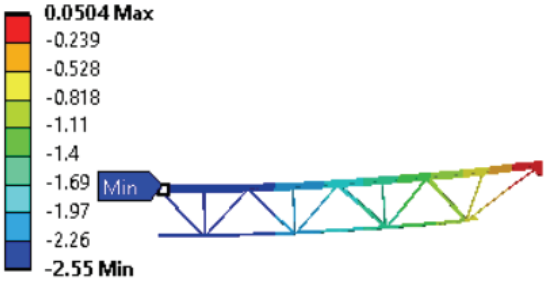

Figure 27: *FE Model Deflection (in) for screw spacing 16-in (406 mm)*

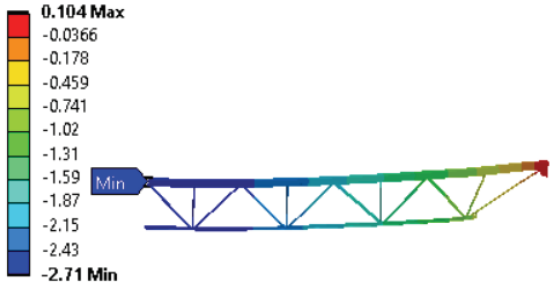

Figure 28: *FE Model Deflection (in) for screw spacing 24-in (610 mm)*

The FE model deflection results indicate that as the shear connector spacing decreases, the wood-nailer steel joist attains a higher level of composite action leading to 6% higher flexural stiffness.

4.2.2 Wood-Nailer Steel Joist Component Axial Forces

Table 13 shows the FE model component axial forces using two alternative screw spacings, 20-in (508 mm) and 16-in (406 mm).

Table 13: *FE Model Component Axial Forces for Screw Spacings 20-in(508-mm) and 16-in (406 mm)*

Wood-Nailer Thickness- in (mm)	2.5 (64)
Load- lb/ft (kN/m)	700 (10.22)
Load Length- ft (m)	32 (9.75)

FE Model Mid-Length Axial Forces			
Spacing in (mm)	WN Kip (kN)	TC Kip (kN)	BC kip (kN)
24 (604)	19.9 (88)	37.5 (167)	57.8 (257)
20 (508)	21.8 (97)	34.4 (153)	56.4 (251)
16 (406)	23.5 (105)	31.6 (141)	55.3 (246)

As expected, the FE model component axial force results indicate that a 33% reduction in the shear connector spacing results in an 18% increase in the axial force transferred to the wood-nailer. The axial force transferred to the wood-nailer is limited by the shear strength of the screws. In addition, the wood-nailer steel joist attains a higher level of composite action leading to an increase in the effective joist depth, which results in a larger moment capacity.

5 CONCLUSIONS

The structural performance of wood-nailer steel joists was numerically investigated. The non-linear finite element (FE) models were developed and analysed using Ansys software. The FE model developed was verified against available experimental data. The numerical predictions showed reasonably good agreement with the experimental data. Parametric analyses were conducted using the validated FE models, and the following conclusions can be drawn from the results of FE analyses.

- The wood-nailer acts partially compositely with the steel top chord and the transformed wood-nailer increases the effective depth of the steel joist.
- The continuous wood-nailer reduces bending stresses in the joist top chord through load-sharing under design loading.
- The combined effect of the wood-nailer composite behaviour with the steel top chord, the resulting change in the top chord neutral axis, and the resulting increased joist effective depth, increase the overall joist moment capacity and flexural stiffness.
- A higher level of composite action is achieved with a larger shear connector density.

6 FUTURE RESEARCH

There is a need to conduct push-out research to investigate the strength and ductility of the screw connection. The push-out tests would allow a direct data analysis of the connection itself, without the additional variables of truss load paths, composite behaviour, and relative stiffness of different materials. The load-slippage data collected from the push-out test will provide valuable connection strength and stiffness data to refine the current finite element model of the wood-nailer steel joist.

ACKNOWLEDGEMENT

The authors are grateful to New Millennium Building Systems for providing the financial support of this research and Joe Pote for his technical guidance.

7 REFERENCES

[1] Steel Joist Institute Standard Specifications, Load Tables, and Weight Tables for Steel Joists and Joist Girders Joist Girders. 45th Ed., Steel Joist Institute, Myrtle Beach, SC, 2020

[2] New Millennium Building Systems, Design Guide WN-Series Joists,2022

[3] M. J. Martignetti, S. P. Gross, S.S. Fares, D.W. Dinehart, J. R.Yost: Experimental Investigation Of Wood Nailer Top Chord Attachments For Open Web Steel Joists, In: World Conference on Timber Engineering, 2010.

[4] Martignetti, M.J, Strength and stiffness of open-web steel joists with and without wood-nailer attachments, Master of Science Thesis, Villanova University, Villanova, PA, 2008
[5] American Society for Testing and Materials (ASTM). 2005. Standard Test Methods for Mechanical Properties of Lumber and Wood-Base Structural Material. ASTM D4761, ASTM International, West Conshohocken, PA.
[6] American Society for Testing and Materials (ASTM). 2004. Standard Test Methods for Tension Testing of Metallic Materials. ASTM E8-04, ASTM International, West Conshohocken, PA.
[7] ANSYS, Inc. Theory Reference, ANSYS Release 2022R2 ANSYS, Inc. Southpointe 2600 ANSYS Drive Canonsburg, PA 15317.
[8] Ansys.net."A resource for Ansys users.".https://www.ansys.com/it-solutions/platform-support.

https://doi.org/10.52202/069179-0003

World Conference on Timber Engineering Oslo 2023

BEHAVIOR OF TIMBER BEAMS STRENGTHENED WITH CFRP

Shengdong Zhang[1], Blanche Blondel de Joigny[2], Jianrong Cui[3]

ABSTRACT: This paper shows a study on the flexural behavior of Larch and Douglas Fir beams strengthened with Carbon Fibre Reinforced Polymers (CFRP). 60 specimens are subjected to a three-point bending test; some are reinforced only on their lower face, and others on the lower and lateral faces (U-shape reinforcement). The maximum load and the mid-span deflection at rupture lead to the determination of the mechanical properties of timber elements. A finite element analysis is proposed to complete the experimental analysis of the flexural behavior of the beams. An elasto-plastic behavior is assumed for reinforced timber and interface elements are used to model the interaction between CFRP and timber. It is observed that the predicted FE results are in good agreement with the measured test data.

KEYWORDS: CFRP, Reinforced Timber Beams, Flexural Behavior, Three-point Bending Test, FE Analysis

1 INTRODUCTION

Wood is the only renewable and most environmentally friendly construction material in the world. It has been used for ages in construction and perform well. But properties of wood are easily degraded due to its natural defects (knots, etc.) and environmentally impacts (variation of humidity, fungi, insects, etc.) on it. Reinforcements on the degraded timber members are necessitated, especially for the existing timber structures with long service time. This paper focuses on the flexural behavior of structural timber strengthened with Carbon Fibre Reinforced Polymer (CFRP).

Usually, the ruptures of bending beams are located around the knots or the other defects of the wooden pieces, or around the butt-joints next to the tensile strength. This is why they need to be reinforced in those areas to improve the tensile resistance.

CFRP is a good solution to strengthen timber elements for its high tensile strength and durability. The efficiency of the strengthening is evaluated by comparing the timber mechanical properties of the different specimens including the Modulus of Elasticity (MOE), the stiffness and the ductility of the beam, the failure modes, the resistance under bending stresses, etc.

Fiorelli and Dias[1] realized a reinforcement of small samples with G(Glass)FRP and CFRP taped on lower face. They studied the mechanical behavior of the wood under compression, then under tensile strength and then under shear, and highlighted an increase in resistance and stiffness. The defects influence is diminished.

John and Lacroix[2] studied the effects on the length of CFRP taped on the lower face of timber beams under bending constraints. They noticed an increase of the resistance from 40% to 70% compared to the non-reinforced specimens. They also enhanced the importance of the length of the reinforcement or to implement the reinforcement in a U-shape.

Hernandez et al[3] investigated the bending resistance and the stiffness of glulam beams reinforced with GFRP. Three percent of the volume were added as a reinforcement, gluing two layers of GFRP on the stretched area. Some specimens were also reinforced on the top. It is noticed an increase of the resistance and the stiffness in tension: adding 3 percent of GFRP by volume increased bending stiffness by as much as 18 percent, and bending strength by as much as 26 percent. The improved efficiency of top and bottom reinforcement appears to be not significant enough to offset the added material and handling costs of two layers of GFRP, even if it enhances the beam bending strength.

Borri et al[4] taped CFRP in the stretched zone. Some of the beams were reinforced with a prestressed reinforcement. An increase of the maximum capacity and of the stiffness compared to the other beams that were not reinforced is respectively by 22.5% to 29.2%, and by 40% to 60%. The prestressed beams do not show significant improve compared to the non prestressed ones.

Ogawa[5] worked on the reinforcement of glulam beams made with Japanese cedar and limber pine with CFRP, around 0.08% and 1.3% of the wood volume. An epoxy resin was used to improve the shear capacity at the interface wood-carbon and the fire resistance. The bending capacity has highly increased, whatever the type of wood or the amount of CFRP used. The coefficient of the resistance variation dwindles to reach

[1] Shengdong Zhang, Department of Structural Engineering, Tongji University, 1239 Siping Road, Shanghai, 200092 China, zhangsh_d@tongji.edu.cn

[2] Blanche Blondel de Joigny, Department of Structural Engineering, Tongji University, 1239 Siping Road, Shanghai, 200092 China & Ecole Spéciale des Travaux Public ESTP, Civil Engineering School, Paris, France. blanche.dejoigny@hotmail.fr

[3] Jianrong Cui, Nantong Huarong Construction Group, 200 Chenggang Road, Nantong, Jiangsu, 226005 China, 1981290462@qq.com

https://doi.org/10.52202/069179-0004

6% to 8% compared to 10% to 25% for the non-reinforced wood.
The use of CFRP to reinforce wood structural elements is the object of more and more studies over the past decades. But we still lack a centralized data base with all the results of the literature. In this paper, the flexural behavior of Larch and Douglas Fir beams strengthened with CFRP only on their lower face, and on the lower and lateral faces (U-shape reinforcement) was experimentally and numerically studied.

2 MATERIALS AND METHODS

2.1 THE SAMPLES

60 specimens of Chinese North-eastern Larch (with mean moisture content 17.7% and density 595kg/m^3) and North American Douglas Fir (with mean moisture content 13.7% and density 527kg/m^3) were subjected to a three-point bending test. The size of the samples was decided according to the ASTM Standard D 143-14 "*Standard methods for Small Clear Specimens of Timber*" [6]. The specimens were as clear as possible, however few knots remained in some of them. The cross section is 50 mm by 50 mm, and the length is supposed to be 780 mm. The length of the beam between two supports is equal to 720 mm. This span was established in order to maintain a minimum span-to-depth ratio of 14. There are 30 specimens of each species, divided into 3 categories of 10 specimens each.

Type 1: Without any reinforcement (Figure 1-a). This group of timber specimens are the witness samples.
Type 2: With a reinforcement on the lower face of the timber beam (Figure 1-b), where wood fibers are the most solicited in bending.
Type 3: With a reinforcement on the lower face and on the two lateral faces (U shape) (Figure 1-c).

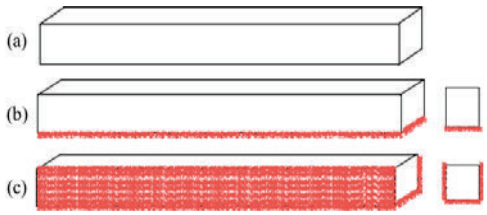

Figure 1 *a-Witness Specimen, b-Reinforcement on the lower face, c-U shape Reinforcement*

The carbon fibres used to reinforce the specimens have thickness 1.67mm, MOE 230000 MPa, tensile strength 3400 MPa, elongation percentage 1.7%. The taping of CFRP is parallel to the wood grain. The glue used is an epoxy resin mixed with a hardener at the ratio 1/2. A layer of 1 mm is applied 24 hours before the tapping of the CFRP sheets in order to let the resin impregnate the wooden fibers. Another layer of resin is applied just before the tapping, and a final layer above the CFRP sheet to ensure the fixing on the timber specimens.

Figure 2*. Cutting and gluing the Carbon Fibers on the specimens*

2.2 THE TESTING PROCEDURE

An electrohydraulic servo system was used for the destructive tests. The charge was thus applied continuously up to the specimens' failure, according to the pattern of Figure 3. The load was applied at mid-span with a speed of 5.0 mm/min. Termination of the test was at 80% of peak load of descendent stage. During the test the peak load and the load at rupture, the displacements at mid-span at the peak load and at the load of rupture were recorded for each specimen. The rupture mode was also carefully observed.

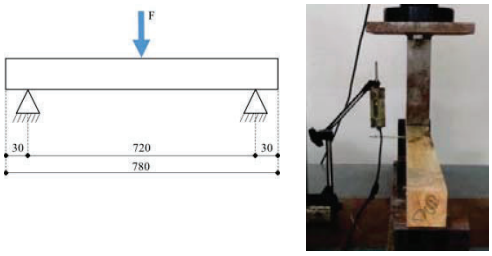

Figure 3. *Disposition of the specimen on the benchmark*

3 TEST RESULTS

3.1 FAILURE MODES

Larch specimens shows more flexible than Douglas Fir specimens (Figure 4) in this test.

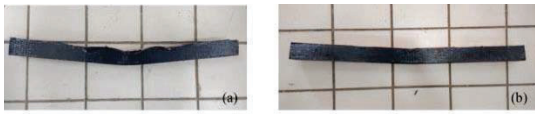

Figure 4*. Larch (a) and Douglas Fir (b) reinforced beams after the test*

With the same conditions of test (disposition on the benchmark, loading speed), the time before failure lasts on average 17% longer. This difference increases for the reinforced specimens, which means that the more flexible the timber is, the more efficient the CFRP strengthening is.
Except for the specimens having knots in their lower part, most of the failures occurr in tension or compression. As planned, all the witness specimens

https://doi.org/10.52202/069179-0004

break in tension. The specimens with one face reinforced have failure most of the time in both tension and compression, or tension only. And almost all the specimens reinforced on 3 faces have failures in compression. Some wrinkles are observed on the compressive side at the point of contact between the load and the wood (Figure 5). Those wrinkles are very tiny on the witness specimens and sometimes inexistent, but on the reinforced specimens they are more important which highlights the buckling from compression strengths.

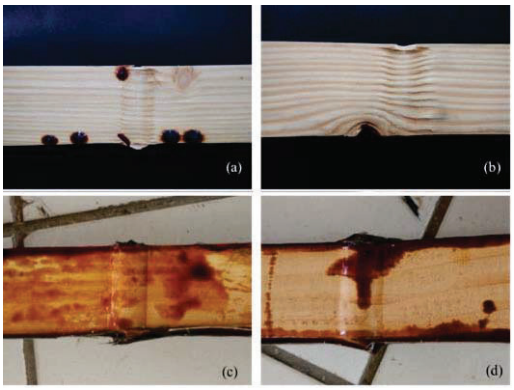

***Figure 5**. Buckling on compression side for the Larch specimens with one face reinforced (a, b) and for the Douglas Fir specimens with 3 faces reinforced (c, d)*

3.2 LOAD-DISPLACEMENT GRAPHS

The deflection of the beams at mid-span was recorded during the tests in order to sketch the load-displacement graphs. Figure 6-Figure 11 present the results for the 60 specimens.

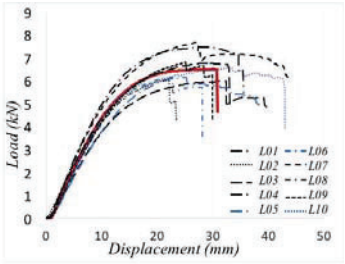

***Figure 6**. Load-displacement curves for Larch witness specimens*

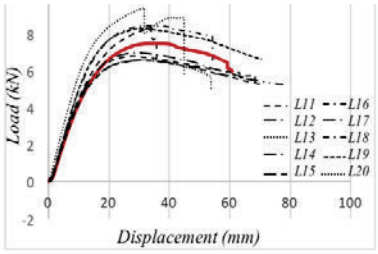

***Figure 7**. Load-displacement curves for Larch specimens with 1 face reinforced*

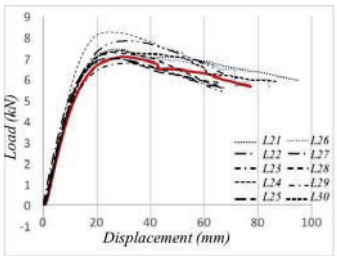

***Figure 8**. Load-displacement curves for Larch specimens with 3 faces reinforced*

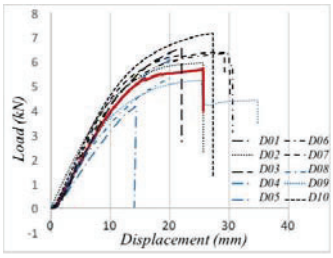

***Figure 9** Load-displacement curves for DF witness specimens*

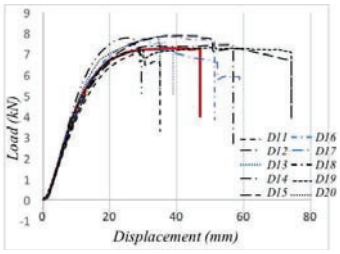

***Figure 10**. Load-displacement curves for DF specimens with 1 face reinforced*

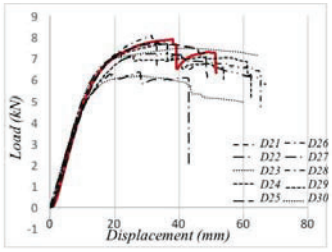

***Figure 11.** Load-displacement curves for Larch specimens with 3 faces reinforced*

In every figure, the curve in red represents the mean of all the others; the curves in blue represent the specimens that failed because of a knot. The mean curve has been sketched removing the knot failures cases because the tests are supposed to be conducted on clear specimens according to the Standards. The analysis of the curves leads to the determination of the evolution of the MOE, and the mode of rupture of the beams. In Figure 12 the curves for Larch highlight the mechanical behavior of a timber beam: an elastic part and a plastic part are observed.

The Elastic and linear part leads to the evaluation of the MOE[7]. Indeed, the graph equation in this first linear part is $F=k \cdot E \cdot u$ where u is the displacement, F the

measured load and ***k*** a constant. It is noticed that the slope increases significantly between the load-displacement curves of the reinforced specimens compared to the witness ones. Table 1 gives the average of all the recorded values during the tests. Those loads and displacement characteristics allow to explain the evolution of the mechanical behavior of the timber specimens. Both stiffness and ductility increase for the reinforced specimens compared to the witness ones.

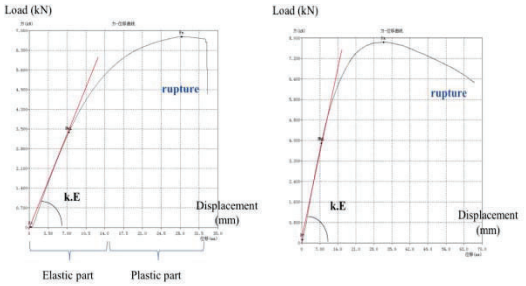

Figure 12. *Load-displacement curves of Larch witness sample – rupture in tension, and of Larch with 3 faces reinforced – rupture in compression*

Table 1. *Average experimental values for each specimen*

	Peak Load (kN)	Disp. at Peak Load (mm)	Load at Rupture (kN)	Disp.at Rupture (mm)
Witness DF	5,699	25,158	5,694	25,158
Witness Larch	6,548	27,874	5,855	34,559
1 CFRP DF	7,534	37,780	7,007	50,046
1 CFRP Larch	7,565	31,522	6,473	60,298
3 CFRP DF	7,356	33,325	6,286	63,819
3 CFRP Larch	7,287	27,816	6,046	74,267

3.3 LINEAR ANALYSIS OF THE MIXED SECTION

The MOE of the witness specimens was calculated with the equation of the second derivative of the deflection (Equation 1), and successive integrations gave the expression of the Modulus E_w (Equation 2).

$$E_w I_{Gz} y'' = M f_z(x) \quad (1)$$

$$E_w = -\frac{FL^3}{48 y_c I_{Gz}} \quad (2)$$

where y_c = the maximum deflection at mid-span (mm) , F = the peak load (kN), I_{Gz} = the section's moment of inertia (mm^4)
The computations lead to the following results:

$E_{w\ Douglas\ F}$ = 12 382 MPa

$E_{w\ Larch}$ = 11 925 MPa

The determination of the MOE of the mixed section (timber + epoxy resin + CFRP) is more complicated because the position of the center of gravity is modified as shown in Figure 13.

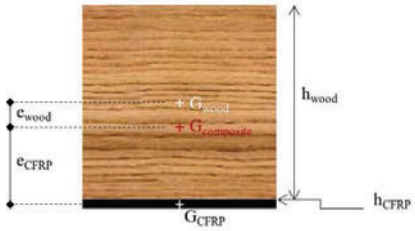

Figure 13. *Position of the new neutral axis within the reinforced specimens*

The bending stiffness is obtained with the theorem of Huygens (Equation 3); it will allow to be close to the reality and avoid the use of the glide factor γ pretending the bonding to be "perfect".

$$(EI)_{eff} = E_w I_w + E_w A_w e_w^2 + E_{CFRP} I_{CFRP} + E_{CFRP} A_{CFRP} e_{CFRP}^2 \quad (3)$$

The section of the CFRP is very low so the moment of inertia I_{CFRP} can be neglected faced to the wood moment of inertia I_w. The effective stiffness is easily calculated with the (Equation 3) and the modulus of elasticity shall be obtained by dividing this value by the effective moment of inertia of the section (Equation 4) when we neglect the proper moment of inertia of CFRP:

$$I_{eff} = I_w + A_w e_w^2 + A_{CFRP} e_{CFRP}^2 \quad (4)$$

The results are presented in Table 2. The comparison with the values of $E_{w\ Douglas\ F}$ and $E_{w\ Larch}$ obtained with the witness samples shows an increase of 47% of the MOE for both species.

Table 2*. Stiffness of the reinforced specimens*

	$(EI)_{eff}$ kN/mm2	I_{eff} mm4	$E_{w\ reinforced}$ MPa
DF	1.379E+7	7.536E+5	18 298
L	1.345E+7	7.635E+5	17 616

4 A NUMERICAL MODEL

4.1 Hypothesis

An elasto-plastic numerical model was introduced based on ABAQUS software.The dimensions used for the numerical modeling are 50×50×780 mm for the timber beam, and 50×1.5×780 mm for the CFRP reinforcement. C3D8R solid elements were used for the timber beam, and S4R shell elements for the reinforcement. The supports were fixed at 30 mm from the extremities of the samples, and the load applied at mid-span is located at 390 mm from each extremity. The wood plasticity model uses the Hill's stress

https://doi.org/10.52202/069179-0004

potential for anisotropic behavior[8]. (Equation 5) gives the Cauchy stress tensor used in this model:

$$\underline{\sigma} = \underline{\underline{\Lambda}} : \underline{\varepsilon}^{e} \quad (5)$$

This elastic law was used with the mechanical characteristics of Larch and Douglas Fir taken from the table 3[8]. The present model assumed that the behavior in the radial direction is equal to the one observed in the tangential direction. This is why the elasto-plastic model gets the following simplifications: $E_R = E_T$; $G_{RT} = G_{TR}$; $G_{LR} = G_{LT}$; $\nu_{RT} = \nu_{TR}$; $\nu_{LR} = \nu_{LT}$. The Hill's criterion was taken as yield criterion as follows, and also used as stress potential for anisotropic behaviour.

$$f(\underline{\sigma}) = \sqrt{H(\sigma_x - \sigma_y)^2 + G(\sigma_x - \sigma_z)^2 + F(\sigma_y - \sigma_z)^2 + 2N\tau_{xy}^2 + 2M\tau_{xz}^2 + 2L\tau_{yz}^2} - R - \sigma_{yield}$$

Table 3 *Material properties for wood*

Elasticity	E_L= 14.5 GPa E_R= 1.2 GPa E_T= 1.2 GPa	V_{LR} = 0.37 V_{LT} = 0.43 V_{RT} = 0.45	G_{LR} = 590 MPa G_{LT} = 590 MPa G_{RT} = 73 MPa
Plasticity	σ_{yield} = 40 MPa Q = 750 MPa b = 17	F = 0.35 G = 0.4 H = 0.6	L = 1.5 M = 1.5 N = 1.45

The CFRP material was considered as linear elastic orthotropic up to failure. E_L=110 (GPa), E_R = E_T=8.82 (GPa), V_{RT}=0.38, G_{LR} = G_{LT}=4.32GPa, G_{RT}=3.2GPa.
The surface-based cohesive behaviour was specified for modelling the adhesive interaction.
For the meshing of the timber beam and the CFRP sheet, 10 for the approximate global size for seed parts was taken.

4.2 Comparison with experiments

Figure 14-figure 17 show the displacements and stresses of the modelling witness sample and reinforced sample with lower face CFRP reinforcement.
The stresses modeled in the witness specimens confirm what was observed in the laboratory during the conduction of the experiments. The stretched fibers located in the lower part of the beam are the weakest and fail first. Besides, the modelling shows the location of the neutral axis: it has not been affected at all by the bending load. For the reinforced specimens, the distribution of stresses in the stretched area is much lower than in the witness beam. This explain the high number of specimens that failed in compression more than in tension. It is difficult to conclude on the modification of the displacements of the specimens, because if the load increases so does the maximum displacement. However, the displacement itself is limited because of the presence of the CFRP sheet which reinforce the wood. The experimental results highlight a global increase of the peak load and of the displacement at rupture for the reinforced specimens compared to the witness. A comparison of the load–deflection curves obtained from experiments and from FE analysis is made in Figure 18 for Larch specimens, and in Figure 19 for Douglas Fir specimens.

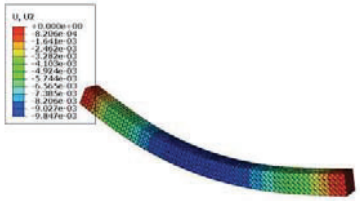

Figure 14*. Displacements obtained after the modelling of the witness sample*

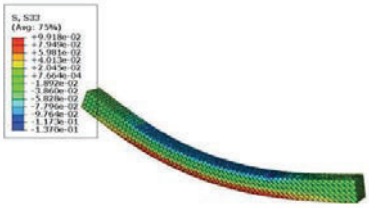

Figure 15. *Bending stresses obtained after the modelling of the witness sample*

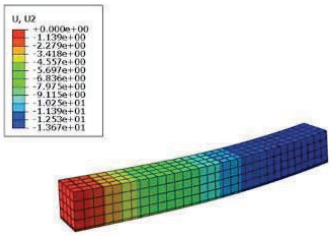

Figure 16*. Displacements obtained after the modelling of half a sample reinforced along its lower face*

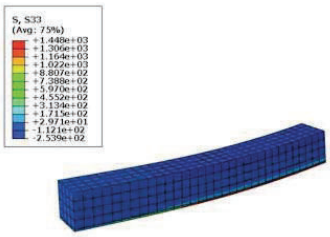

Figure 17*. Bending stresses obtained after the modelling of half a sample reinforced along its lower face*

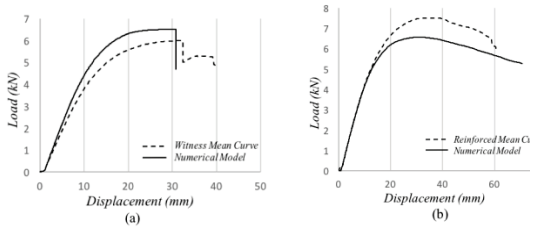

Figure 18*. Larch load–mid-span deflection curves: comparison between numerical and experimental data (a)-*

witness and (b)-reinforced specimens

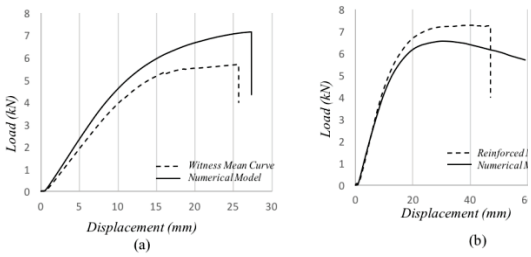

***Figure 19**. DF load–mid-span deflection curves: comparison between numerical and experimental data (a)-witness and (b)-reinforced specimens*

For the Larch's witness specimens, the behavior obtained with the FE analysis is linear up to a displacement of about 10 mm with a corresponding load that reached 4.5 kN, before entering in the plastic behavior. The witness mean curve has an elastic zone up to a displacement equal to 7.8 mm and a load of about 3.5 kN. Beyond those points the response became nonlinear and a discrepancy between predicted and experimental results was observed. The peak load is reached at rupture for the numerical model, and is about 6.5 kN for a maximum displacement of 30.4 mm. Whereas the experimental data lead to a peak load that does not correspond to the failure one, even if it is close to prediction of the FE model: 5.8 kN for a displacement of about 32 mm. However, the rupture occurs at the ultimate load of 5.3 kN with a displacement that reaches 39 mm. The comparison between the numerical and experimental data about reinforced specimens on the lower fibers also show similitudes in the elastic area and divergence in the plastic area. The behavior is linear up to a displacement of about 9.6 mm with a corresponding load of 4 kN. The plastic stage lasts longer in the FE simulation: ultimate displacement is equal to 73 mm for an ultimate load that reaches 5.3 kN. The experiments show a mean final displacement up to 58 mm with a corresponding load of 6.5 kN, and a rupture in both compression and tension (sudden drop of the load for constant displacement visible on the curve).

For the Douglas Fir's witness specimens, the FE analysis shows a linear behavior up to a displacement of about 9 mm with a corresponding load of 4.1 kN, before the plastic stage. The elastic zone of the mean curve goes up to a displacement of 10 mm with a load of about 3.8 kN. The rupture is similar between the experimental and the numerical results: it is sudden and typical of a tensile failure. The experimental rupture occurs for an ultimate load of about 5.4 kN and a maximum displacement of 25.5 mm, whereas the numerical model shows a rupture for a load equal to 7.2 kN and a displacement that reaches 27 mm. As for Larch specimens, the comparison between the numerical and experimental models shows similitude in the elastic area. The slopes of the curves are very close, and the behavior is linear up to a displacement of about 8 mm with a corresponding load of 3.2 kN. Once again, the plastic stage lasts longer for the FE simulation. The maximum displacement is about 60 mm and the ultimate load reaches 5.8 kN, whereas the plastic stage of the experimental results is shorter. The rupture mode is different because the curve shows a tensile rupture with a load that drops suddenly from 7 to 4 kN for a corresponding displacement of about 44 mm.

The comparison of the load-displacement curves of the reinforced specimens is surprising, because the peak load seams to decrease form the witness results to the reinforced scheme. This means that the numerical model is not close enough to the reality in the plastic area. The FE model shows an improvement of the ductility of the specimens because the final displacement increased a lot compared to the witness one. But the improvement of the specimens' stiffness is not obvious according to the numerical modelling. However, we can notice that the curves are close enough in the linear part to validate the numerical model as far as the elasticity of the wood is concerned.

5 CONCLUSIONS

The experiments conducted on the specimens of Larch and Douglas Fir and the numerical modelling allowed to reach the following conclusions:

(1) CFRP reinforcement increases the load carrying capacity of the specimens. The peak load of the Douglas Fir witness specimens is around 5.7 kN and reaches 7.5 kN for the reinforced specimens. For Larch witness specimens it is around 6.5 kN and reaches also 7.5 kN for the reinforced specimens. The MOE increased by 47 % for both Douglas Fir and Larch specimens with CFRP reinforcement.

(2) CFRP reinforcement improves the ductility of the timber specimens. The maximum displacement at rupture is much higher for the reinforced specimens than for the witness specimens.

(3) The U-shape reinforcement has no significant impact compared to the single one-layer reinforcement of the lower fibres as far as load carrying capacity is concerned, but significant impact compared to the single reinforcement of the lower fibres as far as ductility is concerned.

(4) The failure mode changes with reinforcement. Witness specimens fail in tension. Some specimens which had their 3 faces reinforced had their rupture in compression, others in compression coupled with tension, and few of them had their rupture at their defect's localization (knot).

(5) The Numerical model can be validated for the elastic behavior of the wood, but not for the plastic behavior. Even if the ductility is indeed improved, the maximal load carrying capacity decreases between the reinforced specimens and the witness which is the opposite observed during the experiments. The combination of the failure modes and the compressive failures both perpendicular and parallel to the grain can explain this difference.

https://doi.org/10.52202/069179-0004

6 DISSCUSION

Several improvements can be proposed in order to maximize the efficiency of the CFRP reinforcement.

(1) The experimental results showed that the U-wrapping of the beam with the Carbon fibers sheet delays the rupture by improving the ductility of the specimens, but does not improve the stiffness. Indeed, on the lateral faces only the wood fibers located below the neutral axis work in tension, the others are subjected to compression. For beams with bigger sections, the U-shape reinforcement could cover only half of the lateral face. This new reinforcement design would diminish the costs of the CFRP used for the reinforcement.
(2) The section of CFRP stayed constant during the whole experiment. An increase of the thickness of the carbon fibers sheets or the taping of several layers could improve the reinforcement. A study was led by Borri et al[4], where the efficiency of the reinforcements with one, two and three layers of CFRP were compared. Three sheets of CFRP resulted on a 60% increase of the flexural strength.
(3) The timber species has an impact on the testing results. Sometimes, CFRP reinforcements concern the renovation of old buildings built with oak or chestnuts. Those species have tyloses which can block pores. This feature allows the protection of wood against moisture so it can have an impact on the impregnation of the resin. Thus we obtain very thin adhesive film thicknesses, but it may not be quite adherent to the support. Besides for very thin film, the ambient humidity has an influence on the epoxy resin and may weaken it.

ACKNOWLEDGEMENT

The authors would like to thank the two companies who provided the materials for conducting the experiments Shanghai Yichang Carbon Fabric Materials Co., Ltd for the Carbon Fibers, and AONA Wood Structures for the timber specimens.

REFERENCES

[1] Fiorelli J. Dias AA. Analysis of the strenght and stiffness of timber beams reinforced with carbon fibre and glass fibre, *Material Research* 6, 193-202, 2003.
[2] John KC. Lacroix S. Composite reinforcement of timber in bending, *Canadian Journal of Civil Engineering*, 27, 899-906, 2000.
[3] Hernandez R. Davalos JF Sonti SS. et al. Strength and stiffness of reinforced yellow-poplar glued-laminated beams. US Department of Agriculture, Forest Service, Forest Product Laboratory, 1997.
[4] Borri A. Corradi M. and Grazini A. A method for flexural reinforcement of old wood beams with CFRP materials. *Composite: Part B – Engineering*; 36:143–53, 2005.
[5] Ogawa H. Architectural application of carbon fibers, development of new carbon fiber reinforced glulam. Carbon 38, 211-226, 2000
[6] American Society for Testing and Materials (ASTM). Standard methods for Small Clear Specimens of Timber, ASTM D 143-14. Annual book of ASTM standards. ASTM, West Conshohocken, Philadelphia, 1995.
[7] Tingley DA, The stress-strain relationships in wood and fiber-reinforced plastic laminate of reinforced glued-laminated wood beams, PhD Dissertation, Oregon State University, Corvallis, 1996.
[8] Khelifa M. et al. Finite Element analysis of flexural strengthening of timber beams with Carbon Fiber-Reinforced Polymers, Engineering Structures 101, 364–375, 2015.

World Conference on Timber Engineering Oslo 2023

MICROWAVE TECHNOLOGY AND ITS APPLICATIONS TO WOOD TREATMENT AND MODIFICATION

Fernando Mascarenhas[1], Alfredo Dias[2], André Christoforo[3], Rogério Simões[4]

ABSTRACT: Humanity has utilized wood, a renewable resource, for a long time. To capitalize on all of the wood's advantages as a building, structural, and furnishing material, the wood industries and academics have continuously sought innovative approaches that lead to better and larger usage of wood. Microwave (MW) treatment is a technology that has gained increased popularity in modifying wood properties. It has been applied to improve the drying quality, increase fluid permeability, and enhance the treatability and impregnability of wood specimens. Therefore, this paper aims to present a summarized state of the art about MW treatment for wood modification and study the application of MW energy to drying wood samples of the Portuguese *Pinus Pinaster*, investigating the changes in the water uptake and compressive strength parallel to the grain of the MW-treated and control specimens. Based on the results, it was identified that there was an average energy consumption of 1233 MJ/m^3 and an average energy application of 3038 MJ/m^3. In addition, the water uptake of MW-treated samples increased by four times, and their compressive strength parallel to the grain was reduced by 19 % compared to the control samples.

KEYWORDS: Microwave treatment, Literature review, *Pinus pinaster*, Water uptake, Compressive strength.

1 INTRODUCTION

Wood is a natural material that has been used for many centuries for different purposes. Nevertheless, certain wood species have low permeability, which causes problems throughout the lumber manufacturing process, such as lengthy drying durations, material losses after drying, expensive drying procedures [1], and even difficulties in impregnating wood elements with preservative agents [2].

Because of this, wood industries and researchers have increasingly sought technologies, procedures, and innovations that address the limitations that wood might have and improve the use of wood in several fields, such as civil construction. Hence, wood modifications, either chemical, impregnation, or thermal, are modern technologies that have been changing the wood industry and research. The goal is to increase the performance of wood or wood-based products, resulting in gains in dimensional stability, improvements in mechanical properties, decay, and weathering resistance [3]–[5].

The use of microwave (MW) energy to dry, treat or modify wood species has been a promising technology with several possibilities of application. MW energy was first created for communication purposes, and then it started to be used for food heating in 1945/1946 [3,4]. It has also been used to heat materials such as wood [2]. MW are electromagnetic energies that interact with the molecules of the materials at different frequencies [6–8]. Because water molecules have a strongly polar structure, they can absorb MW energy and convert it into heat [11], [12]. The water molecule's angular geometry produces a hydrogen and oxygen atom–based dipole at the angle's bisector. When exposed to an electric field, the dipole will alter its orientation. The positive end of the dipole experiences a torque in the positive field direction, whereas the negative pole aligns with the positive field direction. If the field is made to alternate, the molecule will oscillate as it seeks to align with the current field direction [11]. Thus, this movement generates heat.

The use of MW energy in wood elements effectively reduces the drying time, improves its quality, and enhances permeability, contributing to increasing the preservative uptake [5,8–10].

Data from the Portuguese National Forest Inventory shows that maritime pine (*Pinus pinaster*) is the most common softwood in Portugal, representing 22% of the total [15]. Pine trees have rapid development and strong adaptation to varied environmental circumstances, so they are key raw resources that may satisfy some present market needs [16]. Because it has been utilized in construction as a raw material for furniture, poles, and posts, it is one of the most significant wood species in Portugal from an economic standpoint [17], [18]. It is also important to mention that in the case of Portuguese woods, only wild maritime pine appears in the European

[1] Fernando J. R. Mascarenhas, University of Coimbra, ISISE, ARISE, Department of Civil Engineering, Coimbra, Portugal. SerQ—Forest Innovation and Competence Centre, Sertã, Portugal, fer.jr.resende@hotmail.com
[2] Alfredo M. P. G. Dias, University of Coimbra, ISISE, ARISE, Department of Civil Engineering, Coimbra, Portugal. SerQ—Forest Innovation and Competence Centre, Sertã, Portugal, alfgdias@dec.uc.pt
[3] André L. Christoforo, Department of Civil Engineering, Federal University of São Carlos, São Carlos, Brazil, christoforoal@yahoo.com.br
[4] Rogério M. S. Simões, Department of Chemistry, Unit of Fiber Materials and Environmental Technologies (FibEnTech-UBI) of Universidade da Beira Interior, Covilhã, Portugal, rmss@ubi.pt

https://doi.org/10.52202/069179-0005

standards with defined classification and testing procedures [19]. Hence, it is vital to comprehend all potential uses of this wood species for the wood sector, given the significance of this pine species in the economics and forestry of Portugal, as well as the rest of the Iberian Peninsula and other European areas, and the significance of forest sustainability [18], [20].

Given the importance of maritime pine for Portuguese construction and economy and the advantages that MW technology has for wood modification, this paper aims 1) to present the most relevant and recent studies regarding MW treatment for wood modification, pointing out the main usages and the scientific research possibilities, i.e., a brief literature review; 2) to analyze the improvement in water uptake (absorption) as an indirect way to analyze the improvement in the capability of being impregnated with preservative agents; and 3) to investigate the variations in the ultimate stress in compression parallel to the grain of wood samples with and without MW treatment of the Portuguese maritime pine.

2 MICROWAVE TREATMENT AND ITS MAIN APPLICATIONS – REVIEW

MW modification of wood is a new technology [5,11,12] with major applications for reducing wood drying time and improving fluid permeability [2]. When MW is applied, some parameters need to be adjusted to have different levels of MW wood modification: wood initial moisture content (IMC), MW power, frequency, energy supplied to the wood (intensity), and exposure time [5,8]. Wood industries have great concerns about the refractory species [21], which have low permeability and might show problems either during drying, impregnation, or retention of protective agents [10].

Conventional wood drying processes are time-consuming. Drying hardwood species might take long periods, and undesirable drying effects may emerge from it [10]. When MW wood drying is appropriately used, it can reduce the drying time and defects [2] and overcome the issue of hardwoods collapsing during drying [10].

In contrast to conventional wood drying, where heat is conducted from the outer layers towards the inner of the specimen through convection, conduction, and radiation, electromagnetic waves penetrate the entire volume of the sample in MW drying (treatment), promoting volumetric heat absorption by the wet wood [12], [23]. According to Sahin and Ay [23], energy is conveyed in the traditional drying heat process due to thermal gradients in the material; however, in microwave heating, electromagnetic energy is transformed into thermal energy rather than heat transmission. It produces rapid heating over the thickness of the material while also decreasing thermal gradients. Volumetric heating can also help to reduce drying times and conserve energy.

Wood is a biomaterial, so water plays an important role in it [21]. When MW energy hits the wood, the absorbed energy generates random vibrations of water molecules [13,14]. This motion raises the interior temperature of the wood, creating steam pressure that can quickly reach 600 kPa [10], [25], [26]. This increasing steam pressure damages the wood cell tissue to varied degrees [27]. Micro-structures that are prone to rupture include brittle ray cells, pit membranes in cell walls, and tyloses in arteries [28]. Variations in porosity and pore diameter distribution may result from changes in microstructure, opening up new channels for the easier passage of liquid. As a result, they affect crucial end-product qualities, such as permeability [28], [29] and absorption and retention of preservative agents [2].

The retention of acid copper chromate by MW-treated samples of *Eucalyptus tereticornis* increased by more than 375% after high-intensity MW treatment, from 2.03 kg/m^3 to 9.72 kg/m^3 [30]. Compared to wood samples without MW treatment, the absorption of Tanalith E in Spanish *Eucalyptus globulus* L. samples treated with MW increased by 148% [13].

After the MW treatment, Samani et al. [31] discovered a substantial improvement in the preservative retention and penetration of MW-treated wood specimens of Melia composita compared to the samples with no MW treatment. Compared to the control group, the retention capacity of *Pinus roxburghii* Sarg samples treated with MW was reported to be two times larger [32]. In addition, after submitting wood samples of Picea orientalis to an MW treatment with applied energy of 2158 MJ/m^3, Kol and Çayır [33] impregnated them with Tanalith E 8000. Their results showed that the retention rate increased by 61% compared to wood samples with MW treatment [33].

According to Wang et al. [34], MW treatment altered the chemical structures of cellulose, hemicellulose, and lignin, the three main constituents of wood. In contrast, lignin and cellulose were relatively stable. They only modified under limited circumstances, and hemicellulose sustained significant harm [34].

Both the physical and mechanical properties of wood are impacted by the microstructural changes that MW treatment causes to the wood cells. The damage in wood microstructure (and even macrostructure) increases when more MW energy is applied to the wood. Studies carried out by Weng et al. [27], [35], [36] using scanning electron microscopy (SEM) demonstrated that increased MW energy led to an increase in damage to wood microstructure. Numerous cavities were formed in the wood due to the high MW energies used, changing its porosity, permeability, strength, and flexibility [10]. The density of MW-treated samples tended to be lower than that of untreated samples, according to experimental research [10], [37], [38].

Several investigations have demonstrated that the values of modulus of rupture (MOR) and other strength parameters of MW-treated samples may decrease to varying degrees depending on the MW power and exposure period [10], [13], [21], [33], [38], [39]. According to Torgovnikov and Vinden [10], the degree of alteration that may be assigned to structural changes in wood following MW treatment – low, moderate, and high – depends on the MW treatment circumstances. The authors stated that there was no effect on the mechanical characteristics of wood and an increase in permeability of up to 1.5 times with low degrees of alteration. The moderate degree of alteration decreases the mechanical qualities of wood while increasing permeability 1,000 times. Finally, a high degree of modification greatly

increases permeability but greatly decreases mechanical properties [10].

Weng et al. [14] employed two MW powers, 15 and 20 kW, to treat wood samples of *Cunninghamia lanceolate* (Lamb.) Hook. The authors demonstrated that the damage to the wood microstructure was more severe under high MW treatment power (20 kW). For 20 kW, the produced macro-cracks were between 100 and 130 μm wide, while for 15 kW, they were between 1 and 25 μm wide. For 15 kW and 20 kW, the diameter of margo capillary holes in pit membranes increased by 23% and 55%, respectively. In addition, the results from the literature have demonstrated that the influence of the applied energy directly impacted the density and the mechanical properties of different wood species.

According to Torgovnikov and Vinden [10], samples with heartwood lost more strength than samples with only sapwood under the same MW applied energy, for example, to produce a modest degree of modification. This resulted in a slight change in the MOR. Mascarenhas et al. [40] also demonstrated a significant improvement in water uptake of small clear wood specimens of Portuguese maritime pine containing only heartwood compared to the samples containing only sapwood, demonstrating the necessity of providing the sapwood sample with more MW energy. This improvement in water uptake was demonstrated by drying wood samples with only sapwood and heartwood under the same MW parameters. In light of these results, it can be concluded that the density of the wood component was, in fact, a major parameter (that affects) the fluctuations in the MOR values following MW treatment.

According to Wang et al. [34], utilizing MW intensities (applied energy) ranging from 72 MJ/m^3 to 288 MJ/m^3, neither the cell architectures nor the cell wall morphology of any of the samples with an IMC of 40% changed substantially. On the other hand, the worst alterations to the cell wall structure were caused by MW treatments in wood samples with an IMC of 20% and applied energy of 288 MJ/m^3. As a result, the decline in the mechanical properties values of the wood samples treated with MW was closely related to the harm caused to the cell morphology.

He et al. [29] indicated that under the adopted MW treatment parameters, no significant influence was detected in the MOR values of wood samples with IMC over the fiber saturation point (FSP) (greater than 40%). Then, for these circumstances, the drop in mechanical characteristics during static bending tended to be less the greater the initial MC.

According to the results reported in the literature, the effects of MW treatment on strength and stiffness rely not only on the MW treatment parameters but also on the type of wood and IMC. Furthermore, it is challenging to impregnate wood with resins and preservatives. Wood components may be more easily impregnated with substances to boost biological and fire resistance because of their increased permeability due to MW treatment. They can even be used to create new wood-based products that are impregnated with polymers that have improved qualities [2], [10], [25].

3 MATERIALS AND METHODS

3.1 SAMPLE PREPARATION

Small clear heartwood specimens of the Portuguese maritime pine with 20 mm × 20 mm × 200 mm (radial × tangential × longitudinal) (Figure 1) from the Centre region of Portugal were obtained from commercial boards. The idea of using them is because they allow a safer comparison of results between different wood species [41], [42]. Small clear specimens also have better workability, are simple to obtain, economically attractive, rapid to condition, and straightforward in tests, for example, mechanical ones [43], [44].

In total, 24 specimens were used. They were divided into two groups, control (no MW-treated) and MW-treated, which were submitted to the MW treatment (MW drying). Table 1 shows the number of samples per group, their average initial moisture content (IMC), and standard deviation values.

Figure 1: *Small clear specimen of Maritime Pine*

Table 1: *Sample groups, their quantity, and IMC*

Group	Designation	Quantity of specimens	Average IMC (%)	Standard deviation (%)
HP_MW	Heartwood Pine – MW-treated	12	83.44	16.33
HP_Control	Heartwood Pine – Control	12	12.55	5.43

The wood samples submitted to the MW treatment were placed in a container of distilled water to preserve their "green" conditions so they would not lose water until the drying process began.

3.2 MICROWAVE TREATMENT

The MW treatment was carried out in a conventional MW device measuring 200 mm × 300 mm × 300 mm, at a frequency of 2.45 GHz, with a turntable that allowed a homogeneous distribution of the MW waves.

The wood samples were dried using full MW power of 800 W until they achieved an average final moisture content of 12 %. The MW treatment schedule is shown in Figure 2.

Figure 2: *MW treatment schedule*

https://doi.org/10.52202/069179-0005

As seen in Figure 3, four wood specimens were placed inside the MW oven during each MW drying cycle. The wood samples were exposed to continuous MW energy for 30 s, removed during a colling interval of 30 s to measure the samples' weight (and then to have the moisture content profile along the MW treatment process), and then placed again inside the MW oven.
The cooling intervals were necessary for measuring the weight of the specimens as well as for preventing overheating, which might seriously damage the wood. A similar approach was made by [11], [33], [45]. Oloyede and Groombridge [11] noticed that each succeeding MW exposure should have a larger penetration depth and that by cycling the drying process, the wood might be efficiently dried to any moisture content.

Figure 3: *Pine samples during the cooling interval*

The energy required to heat moist wood and vaporize the water in the wood, Q_w, was calculated according to equation (1) [46].

$$Q_w = \Delta T \cdot (c_1 \cdot m_1 + c_2 \cdot m_2) + \Delta m \cdot r \quad (1)$$

Where: Q_w is the energy required to heat moist wood and to vaporize the water in the wood, in kJ (kWs); ΔT is the temperature difference, in ºC; c_1 is the heat capacity of water, 4.18 kJ/kgºC; m_1 is the mass of water in the specimen, in kg; c_2 is the heat capacity of dry wood, 1.36 kJ/kgºC; m_1 is the mass of dry wood in the specimen, in kg; Δm is the mass of vaporized water, in kg; r is the heat of vaporization of water at 100ºC, 2250 kJ/kg.
The average effective power density consumed to dry the wood specimens is given by Equation (2) [46].

$$P_\delta = \frac{Q_w}{V.t} \quad (2)$$

Where: P_δ is the specific power density consumed to dry the wood specimens, in kW/m^3; V is the volume of wood specimen, in m^3; t is the drying time, in s.
The specific energy consumption during the process is given by Equation (3) [46].

$$E_{in} = \frac{P_\delta \cdot t}{1000} \quad (3)$$

Where:E_{in} is the specific energy consumption during the process, in MJ/m^3.

The specific energy supplied during the process is given by Equation (4) [33].

$$E_{out} = \frac{P \cdot t}{V \cdot 10^6} \quad (4)$$

Where:E_{out} is the specific energy supplied during the process, in MJ/m^3; P is the MW power supplied.
Finally, the overall MW efficiency, η, was calculated according to equation (5).

$$\eta = \frac{E_{in}}{E_{out}} \quad (5)$$

Once the MW treatment was completed, the mass percent loss (MPL) was calculated using equation (6):

$$MPL\ (\%) = \frac{M_f - M_i}{M_{od}} \times 100 \quad (6)$$

where MPL is the mass percentage loss, in %; M_f is the mass of the sample after the MW treatment, in grams; M_i is the mass of the samples before MW treatment, in grams; M_{od} is the oven-dry mass, in grams.

3.3 WATER UPTAKE

Both wood groups were impregnated with distilled water under constant pressure for 30 min. The water uptake (W) was measured using equation (7):

$$W\ (\%) = \frac{M_a - M_b}{M_{od}} \times 100 \quad (7)$$

where W is the water uptake, in %; M_a is the mass of the sample after the water impregnation at the instant in which it was measured, in g; M_b is the mass of the MW-treated samples before the impregnation, in g.

3.4 COMPRESSION STRENGTH PARALLEL TO THE GRAIN

The average ultimate stress in compression parallel to the grain at 12 % moisture content, $f_{c0,12\%}$, was evaluated according to ISO 13061-17 [47]. Wood specimens measuring 20 mm x 20 mm x 60 mm were used in this mechanical test. Before the compression tests, the wood samples were conditioned at a temperature of 20 °C ± 2 °C and 65 % ± 5 % of relative humidity for 14 days to achieve their equilibrium moisture content.

Figure 4: *Compression parallel to the grain test according to ISO 13061-17* [47]

3.5 STATISTICAL ANALYSIS

Pearson's correlation coefficient (r) measures the degree of linear correlation between two quantitative variables. This approach typically uses datasets with a normal distribution and an interval or continuous scale [48]. It can range from -1 to +1, presenting a low, moderate, or strong correlation, where a 0 value means that there is no correlation. It is calculated according to Equation 8:

$$r(X_i, Y_i) = \frac{cov(X_i, Y_i)}{\sqrt{var(X_i) \times var(Y_i)}} \quad (8)$$

Where: X_i and Y_i are the datasets of the MW-treated woods, $cov(X_i, Y_i)$ is the covariance, $var(\cdot)$ is the variance.

Simple linear regression models, which have one dependent variable (Y) and one independent variable (X), were used with Pearson's correlation coefficient to analyze the correlation between the $f_{c0,12\%}$ and the water uptake of the MW-treated wood samples. The general equation for a linear regression model is:

$$Y = b_0 + b_1 X \quad (9)$$

Where: Y is the dependent variable as output, X is the independent variable as input, b_1 is the regression coefficient, b_0 is the constant.

The analysis of variance (ANOVA), at a 5 % significance level, using Minitab Software (Version 18) [50], was applied to study the effectiveness of the MW treatment in improving the water uptake and the changes in the compressive strength of maritime pine wood samples. According to the ANOVA formulation, if p-values are smaller than the significance level (p-value ≤0,05), the samples (control group and MW-treated) can be considered different.

4 RESULTS AND DISCUSSION

4.1 MW DRYING

Once a total of 12 specimens were dried, and each treatment scheme was done with four specimens dried together, three rounds of drying were performed. Based on this, the average values of the MW drying (treatment) of the pine heartwood samples are shown in Table 2. The total time the wood samples were exposed to MW energy was, on average, 21 min, with a maximum of 27 min. The average effective power density, P_δ, to dry the wood specimens was 1005 kW/m^3, the average energy consumed, E_{in}, was 1233 MJ/m^3, and the average energy applied, E_{out}, was 3038 MJ/m^3, with an overall MW efficiency of 0.40 (average) and a maximum value of 0.46. According to [12], [46], the overall MW efficiency for MW ovens with industrial applications is approximately 0.50. Therefore, our results are in accordance with this value.

Table 2: *MW drying information*

Group	Average total MW exposure time (s)	P_δ (kW/m^3)	E_{in} (MJ/m^3)	E_{out} (MJ/m^3)	η
HP_MW	1260 (383)	1005 (131)	1233 (239)	3038 (958)	0.40 (0.05)

The values in brackets are the respective standard deviation.

In addition to this, Table 3 presents the average MPL and the amount of energy per MPL. The MPL average value was 67.17 %, ranging from 51.60 to 82.74 %. Based on these results, the consumed energy used to obtain 1 % of MPL was 17.78 MJ/m^3, i.e., it was consumed, on average, 17.78 MJ/m^3 to evaporate 1 % of the water from the wood samples. In addition, it was supplied 44.37 MJ/m^3, to have 1 % of MPL, which is in accordance with the previous results, such as the ones found by [33], [51], whose values ranged from 43.60 to 50.30 MJ/m^3.

Table 3: *Information about MPL after MW treatment*

Group	MPL (%)	$E_{in}/_{MPL}$ (MJ/m^3/%)	$E_{out}/_{MPL}$ (MJ/m^3/%)
HP_MW	67.17 (17.07)	17.78 (0.98)	44.37 (3.82)

The values in brackets are the respective standard deviation.

The average MW drying rate was 3.19 %/min, and the maximum was 6.31 %/min. Figure 5 shows the MW drying rates over the drying time. Drying small clear samples of another pine species, *Pinus banksiana*, applying an MW power of 800 W, Ouertani *et al*. [21] identified a maximum drying rate slightly higher than 6 %/min.

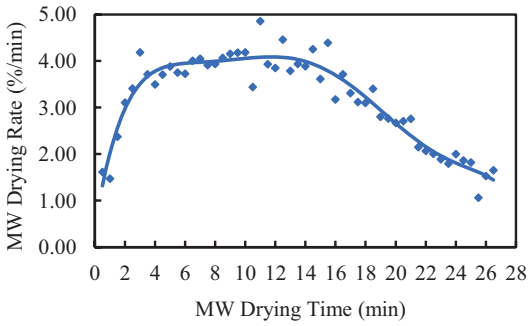

Figure 5: *MW drying rate*

Three stages can be seen in Figure 5. First, the drying rate increased, which may be interpreted as the time when a portion of the energy input was used to raise the temperature of both the water and the wood material from room temperature to around 100 ºC. After then, the drying rate remains relatively steady for the whole drying process. As the amount of free water in the wood approached zero, the drying rate decreased in the last stage.

https://doi.org/10.52202/069179-0005

4.2 WATER UPTAKE

The water absorption of the MW-treated and control wood specimens was measured through their water uptake, and the results can be seen in Figure 6. The average W of HP_MW was 42.57 % (stand. dev. of 16.69 %), and the average W of HP_Control was 10.32 % (stand. dev. of 3.63 %). Thus, the MW treatment significantly impacted the water uptake of MW-treated samples at a confidence level of 95%, i.e., it was almost six times higher.

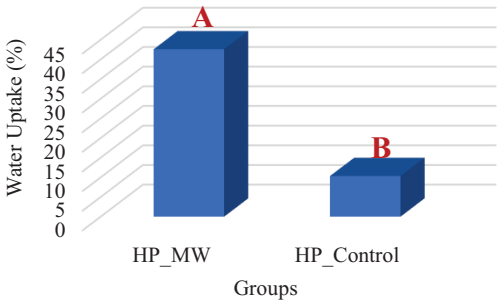

Figure 6: *Water uptake (W) of the wood samples (Values followed by the same letter do not differ significantly at α=0.05)*

According to EN 350 [52], the treatability, which is "the ease with which a wood can be penetrated by a liquid (for example, a wood preservative)" of maritime pine's heartwood, is considered extremely difficult to treat. This fact can be seen in the water uptake value of the wood control samples. Since the water uptake of the MW-treated samples increased, it might indicate that the permeability of the MW-treated sample enhanced, which may be beneficial for easier impregnating those heartwood pine samples with preservative chemicals.

4.3 COMPRESSION STRENGTH PARALLEL TO THE GRAIN

Compression is an important mechanical property in designing different elements, such as poles, trusses, and columns. The newest version of the Brazilian Timber Structures Code, ABNT NBR 7190-1 [53], uses compressive strength parallel to the grain to classify the batch strength.

The ultimate stress in compression parallel to the grain at 12 % moisture content, $f_{c0,12\%}$, of both wood groups is shown in Figure 7. The average $f_{c0,12\%}$ values for MW-treated and control groups were 61.94 MPa (minimum of 48.51 MPa, maximum of 78.41 MPa, and stand. dev. of 8.70 MPa) and 49.93 MPa (minimum of 36.82 MPa, maximum of 59.94 MPa, and stand. dev. of 7.68 MPa).

Studying the mechanical behavior of small clear samples of maritime pine, Santos [54] found that the average compressive strength of the specimens was 59 MPa.

Besides the compressive strength of studied MW-treated and control specimens being statistically different (at a confidence level of 95 %), the MW treatment of 3038 MJ/m^3 applied energy caused a decrease of approximately 19 % in the compressive strength of the specimens. Using an MW power of 925 W and applied energy of 2158 MJ/m^3, Kol and Çayır [33] identified a reduction of 4 % in $f_{c0,12\%}$ of MW-treated small clear sapwood samples of *Picea orientalis* (L). Link.

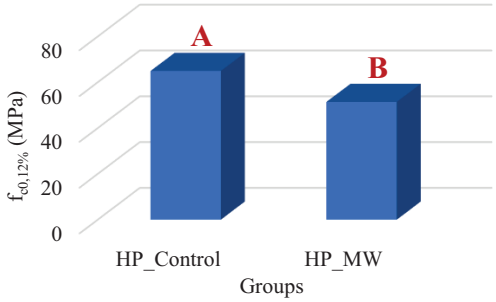

Figure 7: *Results of compression strength parallel to the grain, $f_{c0,12\%}$ (Values followed by the same letter do not differ significantly at α=0.05)*

Load-displacement curves in compression parallel to the grain of control and MW-treated samples are shown in Figure 8(a) and (b), respectively. Overall, both curves demonstrated an initial elastic domain almost up to the maximum applied force and, after that, a plastic behavior. As previously presented, the maximum average compressive stress of the MW-treated specimens is statistically lower than that of the control group specimens, which is also evident when analyzing Figure 8. The maximum average force of control samples was 26.2 kN with an average actuator displacement of 2.21 mm. On the other hand, the maximum average force of MW-treated samples was 21.1 kN with an average displacement of 1.65 mm.

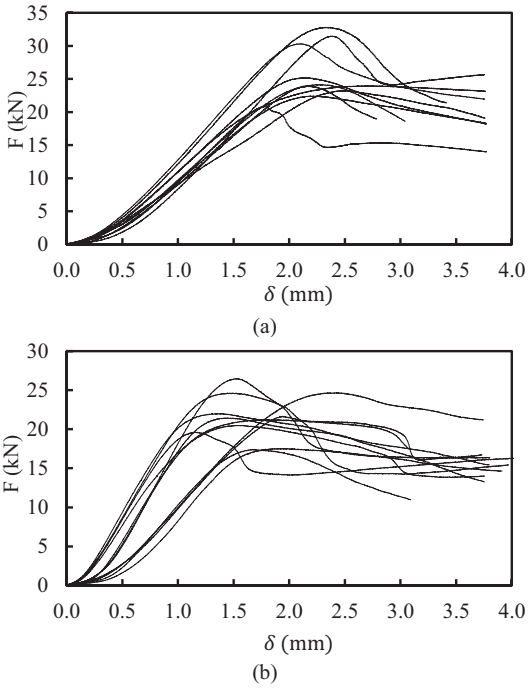

Figure 8: *Load-displacement curves of compression parallel to the grain of (a) control and (b) MW-treated groups (F=Force)*

Figure 7 shows four wood samples of maritime pine, (a) two with no MW treatment and (b) two MW-tread. The most common type of failure in control and MW-treated samples was crushing-shearing, which are normal types of failure according to ASTM D143 [55].

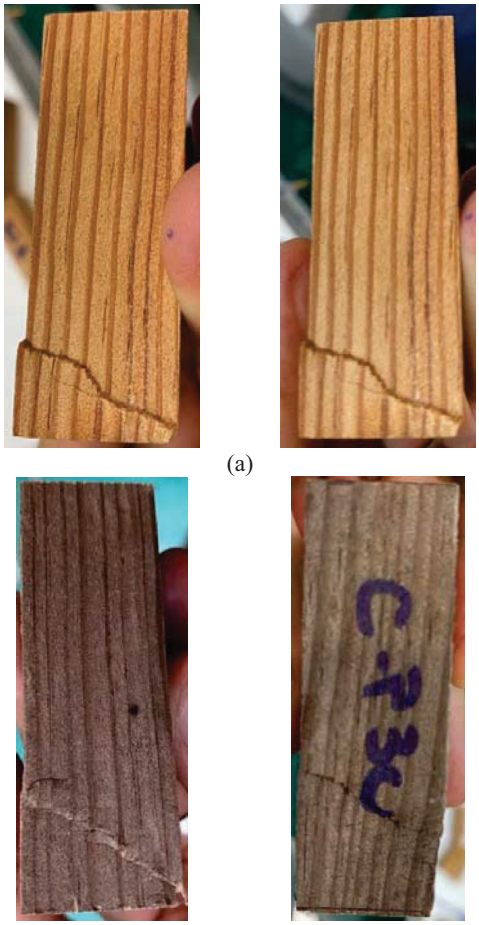

(a)

(b)

Figure 9: *Compression failure mode of (a) control and (b) MW-treated samples*

It is important to explain that the darker color of the MW-treated sample is not because of the MW treatment. As previously explained, the specimens were kept in water to preserve their "green" condition. Therefore, this period that they were immersed in water contributed to the change in their color.

According to Benabou [56], the compressive properties of wood play a crucial role in this behavior. Wood, in particular, exhibits a typical failure pattern known as kink banding when compression parallel to the grain. It is a shear-type failure that occurs in many aligned-fiber composites and wood materials. Benabou [56] also stated that under the kink banding mechanism, three main stages could be recognized (Figures 8 and 10). To begin, incipient kinking occurs in limited areas, beginning with ray cells of wood dispersed throughout the material and causing the stress-strain curve to become non-linear. Fibre shearing and buckling is the softest kind of deformation at this stage. The peak stress occurs shortly after the commencement of nonlinearity and indicates the conclusion of incipient kinking. After that, the transient kinking occurs when the stress decreases from its peak to a steady condition. During this phase, the tiny zones of incipient kinking get bigger and unite to produce a single dominant band with a specific direction across the specimen. The fibers within the band are compressed and rotated at the same time. Fiber rotation increases until the final lock-up position is reached. Due to volumetric preservation considerations, no more deformation inside the band is feasible at this lock-up angle. Third, steady-state kinking happens after fiber lock-up and is caused by continually applied tension, also known as steady-state stress. The band broadens laterally into the surrounding material throughout this period [56].

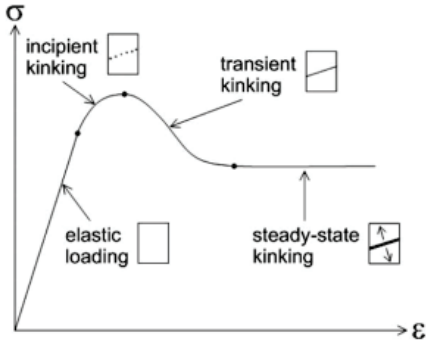

Figure 10: *Diagrammatic representation of the stress-strain crushing behavior of a wood specimen at various kinking stages (From Benabou* [56])

Figure 11 shows Pearson's correlation coefficient r and the p-values. First, the correlation between the ultimate stress in compression parallel to the grain at 12 % moisture content and the water absorption of the MW-treated specimens can be considered moderate to high and significant (p-value<0.05). It is a negative correlation, 0.639, which indicates that the higher the water uptake, the smaller the values of $f_{c0,12\%}$ were. This is easily understandable since a greater water retention capacity may indicate that more damage has occurred in the microstructure of the wood specimens, so this damage negatively affects the mechanical properties.

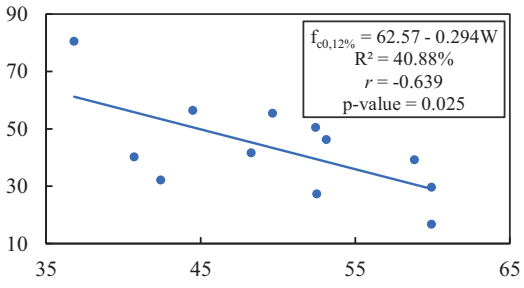

Figure 11: *Correlation analysis*

https://doi.org/10.52202/069179-0005

5 CONCLUSIONS

Microwave treatment or drying of wood is a modern technique with primary applications in wood drying and increasing the fluid permeability and the impregnation with preservative chemicals. When MW is used, the following main variables must be adjusted to achieve various degrees of MW wood modification and assure its efficiency: wood initial moisture content, MW power, frequency, applied energy (intensity), and exposure time.

Microwave treatments can expand the radius of pit membrane pores and even generate microscopic cracks inside the wood by altering the wood's microstructure (such as the pit and ray parenchyma cells). These effects may lead to increased permeability of wood, which is desirable for many wood species primarily to improve impregnability and retention of preservative chemicals and even to make novel wood-based composites.

Regarding the analysis impacts of the MW treatment on the samples of Portuguese maritime pine containing only heartwood, the following conclusions were drawn:

- With an average IMC of 83 %, there was an average energy consumption of 1233 MJ/m^3 and an average energy application of 3038 MJ/m^3. This gave an overall MW efficiency of 0.40 on average, with a maximum value of 0.46.
- The amount of consumed energy to dry 1 % water was around 18 %, and the amount of applied energy to dry 1 % water was approximately 44 %.
- The average MW drying rate was 3.19 %/min, and three stages were identified: a rapid increase of the drying rate after a constant period and then a decrease of the drying rate.
- An increase of about four times in the water uptake capability of the MW-treated samples compared to the control group was measured.
- A decrease of 19 % in the ultimate stress in compression parallel to the grain of the MW-treated specimens compared to the control group was identified.

Finally, based on the results of this study, MW treatment (drying) of Portuguese maritime pine presents interesting possibilities in increasing the absorption of preservative chemicals without causing significant reductions in the compressive strength parallel to the grain. Hence, fine adjustments in the MW treatment conditions might be made in order to maintain the improvement in the capability of absorbing fluids without causing severe reductions in the mechanical properties, which can be more extensively studied.

FUNDING

This work was financed by national funds through Foundation for Science and Technology – FCT, from Portugal, under grant agreement 2021.07636.BD, the FCT, the Ministry of Science, Technology and Higher Education (Portuguese: Ministério da Ciência, Tecnologia e Ensino Superior or MCTES), the Programa Operacional da Região Centro (CENTRO 2020), and the European Social Fund (Portuguese: Fundo Social Europeu or FSE).

ACKNOWLEDGEMENT

We are also thankful Institute for Sustainability and Innovation in Structural Engineering – ISISE Coimbra, the Department of Civil Engineering of the University of Coimbra, the Innovation and Competence Forest Centre – SerQ, and the Department of Chemistry, the Unit of Fiber Materials and Environmental Technologies (FibEnTech-UBI) of Universidade da Beira Interior, for all support provided in the development of this work.

REFERENCES

[1] N. Terziev, G. Daniel, G. Torgovnikov, and P. Vinden, “Effect of microwave treatment on the wood structure of norway spruce and radiata pine,” *Bioresources*, vol. 15, no. 3, pp. 5616–5626, 2020, doi: 10.15376/biores.15.3.5616-5626.

[2] F. J. R. Mascarenhas, A. M. P. G. Dias, and A. L. Christoforo, “State of the Art of Microwave Treatment of Wood : Literature Review,” *Forests*, vol. 12, no. 745, pp. 1–31, 2021, [Online]. Available: https://doi.org/10.3390/f12060745

[3] D. Jones and D. Sandberg, “A Review of Wood Modification Globally – Updated Findings from COST FP1407,” *Interdisciplinary Perspectives on the Built Environment*, vol. 1, pp. 1–31, 2020, doi: 10.37947/ipbe.2020.vol1.1.

[4] M. J. Spear, S. F. Curling, A. Dimitriou, and G. A. Ormondroyd, “Review of functional treatments for modified wood,” *Coatings*, vol. 11, no. 3, 2021, doi: 10.3390/coatings11030327.

[5] C. Aidan Stephen Hill FIAWS FIWSc, “Wood modification,” 2011.

[6] J. M. Osepchuk, “Microwave power applications,” *IEEE Trans Microw Theory Tech*, vol. 50, no. 3, pp. 975–985, 2002, doi: 10.1109/22.989980.

[7] D. E. Clark, D. C. Folz, and J. K. West, “Processing materials with microwave energy,” *Materials Science and Engineering A*, vol. 287, no. 2, pp. 153–158, 2000, doi: 10.1016/s0921-5093(00)00768-1.

[8] M. C. Ndukwu, L. Bennamoun, M. Simo-Tagne, M. I. Ibeh, U. C. Abada, and I. E. Ekop, “Influence of drying applications on wood, brick and concrete used as building materials: a review,” *Journal of Building Pathology and Rehabilitation*, vol. 6, no. 1, pp. 1–19, 2021, doi: 10.1007/s41024-021-00119-0.

[9] Q. Yin and H. H. Liu, “Drying stress and strain of wood: A review,” *Applied Sciences (Switzerland)*, vol. 11, no. 11, 2021, doi: 10.3390/app11115023.

[10] G. Torgovnikov and P. Vinden, “High-intensity microwave wood modification for increasing permeability,” *For Prod J*, vol. 59, no. 4, pp. 84–92, 2009.

[11] A. Oloyede and P. Groombridge, “The Influence of microwave heating on the mechanical properties of wood,” *J Mater Process Technol*,

vol. 100, no. 1, pp. 67–73, 2000, doi: 10.1016/S0924-0136(99)00454-9.

[12] A. C. Metaxas and R. J. Meredith, *Industrial Microwave Heating*, 3rd ed., vol. 24, no. 2. Short Run Press Ltd, Exeter, 2008. doi: 10.1080/08327823.1989.11688082.

[13] E. Hermoso and A. Vega, "Effect of microwave treatment on the impregnability and mechanical properties of eucalyptus globulus wood," *Maderas: Ciencia y Tecnologia*, vol. 18, no. 1, pp. 55–64, 2016, doi: 10.4067/S0718-221X2016005000006.

[14] X. Weng, Y. Zhou, Z. Fu, X. Gao, F. Zhou, and F. Fu, "Effects of microwave treatment on microstructure of Chinese fir," *Forests*, vol. 11, no. 7, 2020, doi: 10.3390/F11070772.

[15] Instituto da Conservação da Natureza e das Florestas (ICNF), "PORTUGAL PERFIL FLORESTAL," 2021. Accessed: Jan. 13, 2023. [Online]. Available: https://www.icnf.pt/api/file/doc/1f924a3c0e4f7372

[16] A. P. Acosta *et al.*, "Thermochemical and mechanical properties of pine wood treated by in situ polymerization of methyl methacrylate (MMA)," *Forests*, vol. 11, no. 7, pp. 1–10, 2020, doi: 10.3390/F11070768.

[17] J. Santos *et al.*, "Valorisation of non-timber by-products from maritime pine (Pinus pinaster, Ait) for particleboard production," *Ind Crops Prod*, vol. 168, no. April, 2021, doi: 10.1016/j.indcrop.2021.113581.

[18] C. Meredieu *et al.*, "Pinus pinaster in Europe: distribution, habitat, usage and threat," in *San-Miguel-Ayanz J, de Rigo D, Caudullo G, Houston Durrant T, Mauri A - European atlas of forest tree species*, 2016, pp. 128–129.

[19] A. das I. de M. e M. de P. AIMMP, *A riqueza das madeiras portuguesas. Propriedades e Fichas Técnicas*. Porto: AIMMP – Associação das Indústrias de Madeira e Mo- biliário de Portugal, 2015. [Online]. Available: https://issuu.com/aimmportugal/docs/a_riqueza_das_madeiras_portuguesas__8d753d0be8b6c4

[20] J. I. Alonso-Esteban, M. Carocho, D. Barros, M. V. Velho, S. Heleno, and L. Barros, *Chemical composition and industrial applications of Maritime pine (Pinus pinaster Ait.) bark and other non-wood parts*, no. 0123456789. Springer Netherlands, 2022. doi: 10.1007/s11157-022-09624-1.

[21] S. Ouertani, A. Koubaa, S. Azzouz, R. Bahar, L. Hassini, and A. Belghith, "Microwave drying kinetics of jack pine wood: determination of phytosanitary efficacy, energy consumption, and mechanical properties," *European Journal of Wood and Wood Products*, vol. 76, no. 4, pp. 1101–1111, 2018, doi: 10.1007/s00107-018-1316-x.

[22] H. Xiao, L. Lin, and F. Fu, "Temperature characteristics of wood during microwave treatments," *J For Res (Harbin)*, vol. 29, no. 6, pp. 1815–1820, 2018, doi: 10.1007/s11676-018-0599-4.

[23] H. Sahin and N. Ay, "Dielectric properties of hardwood species at microwave frequencies," *Journal of Wood Science*, vol. 50, no. 4, pp. 375–380, 2004, doi: 10.1007/s10086-003-0575-1.

[24] L. Hansson and A. L. Antti, "The effect of microwave drying on Norway spruce woods strength: A comparison with conventional drying," *J Mater Process Technol*, vol. 141, no. 1, pp. 41–50, 2003, doi: 10.1016/S0924-0136(02)01102-0.

[25] G. Torgovnikov and P. Vinden, "Microwave wood modification technology and its applications," *For Prod J*, vol. 60, no. 2, pp. 173–182, 2010, doi: 10.13073/0015-7473-60.2.173.

[26] J. Zemiar, I. Makoviny, M. Palko, and M. Gasparik, "Temperature and moisture profiles at microwave heating of wood," *Annals of Warsaw University of Life Sciences - SGGW. Forestry and Wood Technology*, vol. 67, no. 67, pp. 283–288, 2009.

[27] X. Weng, Y. Zhou, Z. Fu, X. Gao, F. Zhou, and J. Jiang, "Effects of microwave pretreatment on drying of 50 mm-thickness Chinese fir lumber," *Journal of Wood Science*, vol. 67, no. 1, 2021, doi: 10.1186/s10086-021-01942-2.

[28] S. He *et al.*, "Microwave Drying of Scots Pine Lumber: Structure Changes, Its Effect on Liquid Permeability," *J Renew Mater*, vol. 11, no. 1, pp. 321–331, 2023, doi: 10.32604/jrm.2023.022097.

[29] S. He, L. Lin, F. Fu, Y. Zhou, and M. Fan, "Microwave treatment for enhancing the liquid permeability of Chinese fir," *Bioresources*, vol. 9, no. 2, pp. 1914–1923, 2014, doi: 10.15376/biores.9.2.1924-1938.

[30] P. K. Poonia and S. Tripathi, "Effect of microwave heating on ph and durability of eucalyptus tereticornis wood," *Journal of Tropical Forest Science*, vol. 29, no. 3, pp. 389–394, 2017, doi: 10.26525/jtfs2017.29.3.389394.

[31] A. Samani, S. Ganguly, R. Kanyal, and S. Tripathi, "Effect of microwave pre-treatment on preservative retention and treatability of Melia composita wood," *J For Sci (Prague)*, vol. 65, no. 10, pp. 391–396, 2019, doi: 10.17221/39/2019-JFS.

[32] P. K. Poonia and S. Tripathi, "Effect of microwave heating on pH and termite resistance of Pinus roxburghii Wood," *Maderas: Ciencia y Tecnologia*, vol. 20, no. 3, pp. 499–504, 2018, doi: 10.4067/S0718-221X2018005031901.

[33] H. Ş. Kol and B. Çayır, "The effects of increasing preservative uptake by microwave pre-treatment on the microstructure and mechanical properties of Oriental spruce wood," *Wood Mater Sci Eng*, pp. 1–7, May 2022, doi: 10.1080/17480272.2022.2077656.

[34] Z. Wang, E. Xu, F. Fu, L. Lin, and S. Yi, "Characterization of wood cell walls treated by high-intensity microwaves : Effects on physicochemical structures and micromechanical

https://doi.org/10.52202/069179-0005

properties," *Ind Crops Prod*, vol. 187, no. PA, p. 115341, 2022, doi: 10.1016/j.indcrop.2022.115341.

[35] S. Ganguly, A. Balzano, M. Petriˇ, D. Kržišnik, and S. Tripathi, "Effects of Different Energy Intensities of Microwave Treatment on Heartwood and Sapwood Microstructures in Norway Spruce," *Forests*, vol. 12, pp. 1–16, 2021.

[36] Z. Fan, L. Peng, M. Liu, Y. Feng, J. He, and S. Wu, "Analysis of influencing factors on sound absorption capacity in microwave-treated Pinus radiata wood," *European Journal of Wood and Wood Products*, vol. 80, no. 4, pp. 985–995, Aug. 2022, doi: 10.1007/s00107-021-01774-3.

[37] G. Brodie, "MICROWAVE TREATMENT ACCELERATES SOLAR TIMBER DRYING," in *ASABE annual international meeting*, 2006, vol. 50, no. 2, pp. 389–396.

[38] B. M. Balboni, B. Ozarska, J. N. Garcia, and G. Torgovnikov, "Microwave treatment of Eucalyptus macrorhyncha timber for reducing drying defects and its impact on physical and mechanical wood properties," *European Journal of Wood and Wood Products*, vol. 76, no. 3, pp. 861–870, 2018, doi: 10.1007/s00107-017-1260-1.

[39] M. L. de Peres, R. de Ávila Delucis, D. A. Gatto, and R. Beltrame, "Mechanical behavior of wood species softened by microwave heating prior to bending," *European Journal of Wood and Wood Products*, vol. 74, no. 2, pp. 143–149, 2015, doi: 10.1007/s00107-015-0978-x.

[40] F. J. R. Mascarenhas, A. M. P. G. Dias, A. L. Christoforo, R. M. dos S. Simões, and A. E. P. Cunha, "EFFECT OF MICROWAVE TREATMENT ON DRYING AND WATER IMPREGNABILITY OF PINUS PINASTER AND EUCALYPTUS GLOBULUS," *Maderas-Cienc Tecnol 25(2023):6,* vol. 25, no. 6, pp. 1–21, 2023, doi: 10.4067/S0718-221X2023005XXXXXX.

[41] J. E. de Melo, M. R. de Souza, and A. F. da Costa, "Influência das dimensões dos corpos de prova e da velocidade de ensaio na resistência à flexão estática de três espécies de madeiras tropicais," *Ciencia Florestal*, vol. 25, no. 2, pp. 415–424, 2015, doi: 10.5902/1980509818461.

[42] J. Á. P. Lorenzo and G. R. Muñoz, "Inter-tree and intra-tree variation in the physical properties of wood of laurel (Laurus nobilis)," *Eur J For Res*, vol. 137, no. 4, pp. 507–515, 2018, doi: 10.1007/s10342-018-1119-y.

[43] L. Krajnc, N. Farrelly, and A. M. Harte, "Relationships between wood properties of small clear specimens and structural-sized boards in three softwood species," *Holzforschung*, no. June, 2019, doi: 10.1515/hf-2019-0039.

[44] C. Cunha, M. Tenório, D. F. Lima, A. Rebouças, L. C. Neves, and J. M. Branco, "Mechanical Characterization of Iroko Wood Using Small Specimens," *Buildings*, vol. 11, no. 116, pp. 1–16, 2021, doi: 10.3390/buildings11030116.

[45] F. J. R. Mascarenhas, A. M. P. G. Dias, A. L. Christoforo, R. M. dos S. Simões, and A. E. P. Cunha, "EFFECT OF MICROWAVE TREATMENT ON DRYING AND WATER IMPREGNABILITY OF Pinus pinaster AND Eucalyptus globulus," *Maderas: Ciencia y tecnología*, vol. 25, no. 6, pp. 1–14, 2023, doi: 10.4067/s0718-221x2023000100406.

[46] A. L. Antti, "Microwave drying of pine and spruce," *Holz als Roh- und Werkstoff*, vol. 53, no. 5, pp. 333–338, 1995, doi: 10.1007/s001070050102.

[47] ISO, "13061-17," *Physical and mechanical properties of wood — Test methods for small clear wood specimens —Part 17:Determination of ultimate stress in compression parallel to grain*, 2017, [Online]. Available: https://standards.iteh.ai/catalog/standards/sist/f061ba76-cdd8-4b3c-b717-www.iso.orgiTehSTANDARDPREVIEWhttps://standards.iteh.ai/catalog/standards/sist/f061ba76-cdd8-4b3c-b717-

[48] Z. Li, X. Gao, and D. Lu, "Correlation analysis and statistical assessment of early hydration characteristics and compressive strength for multi-composite cement paste," *Constr Build Mater*, vol. 310, no. August, p. 125260, 2021, doi: 10.1016/j.conbuildmat.2021.125260.

[49] J. Nowicki, J. Hebda-Sobkowicz, R. Zimroz, and A. Wyłomańska, "Dependency measures for the diagnosis of local faults in application to the heavy-tailed vibration signal," *Applied Acoustics*, vol. 178, 2021, doi: 10.1016/j.apacoust.2021.107974.

[50] Minitab, "Minitab," *Software Minitab 18*, 2018.

[51] H. Ş. Kol and B. Çayır, "Increasing the Impregnability of Oriental Spruce Wood via Microwave Pretreatment," *Bioresources*, vol. 16, no. 2, pp. 2513–2523, 2021.

[52] CEN, "EN 350," *Durability of wood and wood-based products - Testing and classification of the durability to biological agents of wood and wood-based materials Durabilité*, p. Brussels, 2016.

[53] ABNT - Associação Brasileira de Normas Técnicas, "ABNT NBR 7190-1 Projeto de estruturas de madeira Parte 1: Critérios de dimensionamento," 2022, [Online]. Available: www.abnt.org.br

[54] J. A. dos Santos, "Estudo de modelos e caracterização do comportamento mecânico da madeira," Universidade do Minho, Guimarães, 2007.

[55] ASTM, "ASTM D143," *Standard Test Methods for Small Clear Wooden Specimens*, p. United States of America, 2014.

[56] L. Benabou, "Predictions of compressive strength and kink band orientation for wood species," *Mechanics of Materials*, vol. 42, no. 3, pp. 335–343, 2010, doi: 10.1016/j.mechmat.2009.11.015.

World Conference on Timber Engineering Oslo 2023

STRUCTURAL PERFORMANCE, AND FAILURE MECHANISM, OF HARDWOOD CROSS LAMINATED TIMBER CONCRETE COMPOSITE UNDER SHEAR LOAD

Aamir Khokhar[1], David Bell[2], Roshan Dhonju[3]

ABSTRACT: The performance of Timber Concrete Composite(s) (TCC) is primarily governed by the type of connection used in connecting the constituent members together. This paper investigates the performance of various commonly used connections in a TCC. The main goal of this research is to identify which type of connection provides the optimal structural performance while also identifying the effects parameters such as inclination angle and penetration/notch depth have on the performance of connections. Shear tests on 40 hardwood CLT Concrete Composite specimens comprising of 5 connection configurations, utilising notched and screw connections were undertaken in accordance to BS EN 26891. The results showed that notched connections provided the most satisfactory structural performance in relation to load carrying capacity and stiffness, with the depth of the notch having a significant impact on the behaviour of the composite under load. In terms of timber screw connections, screws inclined at 45° yielded the best structural performance in relation to load carrying capacity and stiffness.

KEYWORDS: Hardwood, Cross laminated timber, Push-out test, Shear connectors, Slip modulus, Failure modes

1 INTRODUCTION

To date the study of Engineered Wood Products (EWP) such as CLT and Glulam has been widely undertaken. Such materials offer a means of building larger timber structures, due in part to their improved structural properties compared to sawn timber, yet much like traditional timber construction there is a boundary to their structural capabilities. As a result of this, an old building technology has seen a recent increase in academic and industrial research. Timber Concrete Composites (TCCs) are a composite material originally used to renovate old timber structures due to a global lack of steel [1]. Yet TCCs are currently being utilised as a material which can overcome the structural limitations of timber and indeed EWP construction. The benefits of TCCs are well documented, with improved structural, thermal and seismic performance compared to timber only construction [2,3], while also being faster to construct, and have a significantly lower global warming potential compared to conventional concrete and steel construction [4,5]. In recent years, there has been an increase in interest on the use of a TCC which uses an EWP as the timber member. The results from recent studies show that such composites can overcome the limitations associated with traditional mass timber construction [6]. Previous TCC research has shown that the most important element in such a system is the connection used, as using an ineffective connection can result in a large reduction in structural performance [7]. The limited research on EWP TCC has mainly been focused on the effectiveness of connections used in the composite [3,8]. These studies reported that the orientation of dowel, notched and glued connections can greatly influence the overall performance of the composite. Despite the benefits of TCCs, limitations to their widespread adoption exist and can be attributed to a lack of design and practical knowledge on the behaviour of connections [2,6]. Furthermore, guidance on the slip modulus for inclined screws and the behaviour of notched connections with various notch depths and screw inclinations has not yet been fully investigated [3,8,10].

Additionally, there has been no research investigating the suitability and performance of a hardwood CLT Concrete Composite, leaving a notable gap in the current published literature on Timber Concrete Composites. Using hardwood CLT can further increase the scope of timber construction while making TCCs even more competitive compared to traditional materials as a result of its improved structural properties. Therefore, the main objective of this work is to examine the structural performance of various types of connections used in a hardwood CLT Concrete Composite.

[1] Dr Aamir Khokhar, Lecturer, Edinburgh Napier University, UK, a.khokhar@napier.ac.uk
[2] Mr David Bell, Graduate Engineer, Arcadis, UK, David.bell@arcadis.com
[3] Dr Roshan Dhonju, Research technician, Edinburgh Napier University, UK, r.dhonju@napier.ac.uk

https://doi.org/10.52202/069179-0006

2. EXPERIMENTAL PROGRAMME

2.1 TESTING SUMMARY

A total of 40 specimens were tested, which comprised of two main connection categories, metal screw connections (S) and notched connections used in conjunction with screws (NS). Five different configurations of the (NS) and (S) connections commonly used in TCCs were adopted in this research. This included metal screw connections with various penetration depths (PD) and orientations (α) and notched connections cut to various PD coupled with screws at varying orientations. The PD for each of the (S) series specimens was based on the diameter of the screw, with d, being equal to the diameter (in this case d=5 mm). For the NS series the PD was measured as the depth from the top surface of the CLT as shown in Figure 1. Each (S) series specimen had a row of three (or six, if inclined screws were used) screws on each side of the CLT. Each (NS) series specimen had 2 notches and 2 screw (or 2 notches and 4 screws for the NS45 specimens) on either side of the CLT

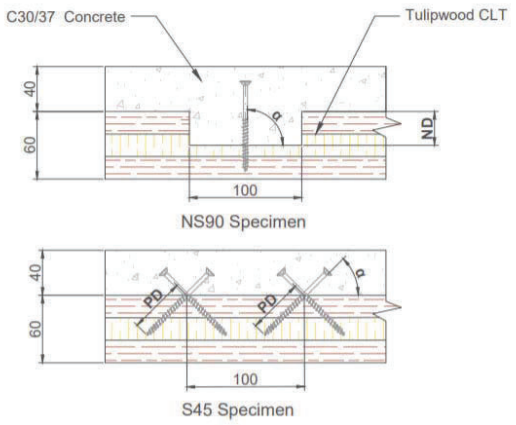

***Figure 1**: Type (NS) and (S) connection schematic*

Table 1 provides further details on the number of specimens and connection configurations. Each specimen consisted of a 60×140 mm CLT member with a height of 430 mm, connected to two 40×140 mm concrete members of the same height.

***Table 1:** Detail of test specimens*

Test code	Connection	Connection orientation (°)	Penetration depth/ Notch depth (mm)	Number of specimens
S90	screw	90		
			10d	2
			11d	2
S45	screw	45	9d	3
			10d	3
			11d	3
S30	screw	30	9d	3
			10d	3
			11d	3
NS90	Notched & screw	90	25	3
			30	3
			35	3
NS45	Notched & screw	45	25	3
			30	3
			35	3

2.2 MATERIAL PROPERTIES

The Tulipwood (*Liriodendron tulipifera*) CLT used in this research was supplied by the American Hardwood Export Council (AHEC). This CLT was chosen as it offers increased structural performance compared to conventional European softwood CLT. Additionally, as mentioned previously, no published work has been undertaken investigating the effects of using a hardwood EWP in a TCC. The high strength to weight ratio of Tulipwood CLT makes it a very suitable choice for TCC fabrication, where weight plays a vital role in the effectiveness of the composite. Additionally, the increased density of this hardwood is expected to improve the load carrying capacity of the connections and thus the performance of the overall composite. The properties of the CLT used in this research has been previously determined in work undertaken by [11] and is shown in Table 2.

Two possible manufacturing options for concrete used in TCC construction exist. These are offsite concrete casting and in-situ casting. This research is focused on TCCs that are cast in-situ and as a result, in-situ concrete casting was used. The strength of concrete used in this research has been based on what is currently used as an industry standard in TCC design, which comprises of C30/37 concrete. The quantities of the constituents used in the concrete was calculated using a Building Research Establishment (BRE) concrete mix design. The properties of the concrete used can be seen in table 2.

https://doi.org/10.52202/069179-0006

***Table 2**: Mechanical properties of CLT, concrete and screws*

Material	Properties	Values	Units
CLT	Density (ρ)	485.79	kN/m^3
	Modulus of elasticity (E)	11010	N/mm^2
	Shear modulus (G)	196.57	N/mm^2
Concrete	Compressive strength ($f_{c,k}$)	36	N/mm^2
	Mean target strength ($f_{c,k}$)	43	N/mm^2
Screw	Tensile strength ($f_{tens,k}$)	7900	N
	Yield moment ($M_{y,k}$)	5909	N.mm
	Characteristic yield strength ($f_{y,k}$)	1000	N/mm^2
	Length (L)	80	mm
	Threaded length (B)	45	mm
	Diameter (D)	5	mm

5 x 80 mm *Spax* Windrox screws were used in this research. They have been chosen for their quality, availability and cost which according to [12] are important criteria to consider when choosing a suitable connection for a TCC. The screws are also corrosion resistant, which is a further benefit for use in this application [13]. The screws are partially threaded which offers high withdrawal strength, while the lack of threading near the head of the screw reduces the potential for concrete cracking to occur. The properties (provided by [14]) of the screws can be found in Table 2.

An important consideration in the design of a TCC is the spacing of the connectors. The spacing of the screw connections adopted in this work was calculated in accordance to EN 1995-1-1. The spacing for the notched connections is based upon the recommendations provided by [3] in addition to the size restraints of the specimens.

2.3 TESTING PROCEDURE

Each specimen was simply supported at their base. The supports elevated the specimens 50 mm above the ground providing sufficient space for the specimens to deform vertically. Horizontal movement was restrained by the self-weight of the specimens. The vertical slip between the timber and concrete members was measured and recorded using two Linear Variable Displacement Transducers (LVDT) each with a 50 mm maximum displacement. The LVDTs were fitted on the front and back of the specimens as shown in Figure 2. The specimens were tested in accordance to BS EN 26891. A F_{est} (maximum load) was established for each connection type, by testing a sacrificial specimen for each connection configuration. The test specimens were then loaded following the loading profile set out in BS EN 26891 as show in Figure 3. The specimens were tested in a Schenck Trebel Instron 5500 testing machine fitted with a 100 kN load cell.

***Figure 2:** S-Series specimen (left) and NS-Series Specimen (right) in testing apparatus*

3 RESULTS AND DISCUSSION

3.1 LOAD-SLIP RESPONSE

A simple and effective way of determining the structural behaviour of a TCC and the performance of the connections used, is by analysing the load-slip response of the specimens under shear load. This allows for the determination of the relative stiffness and slip modulus of connections and helps classify the type of failure that occurred. The load-slip response of the specimens was obtained by testing the specimens in accordance to BS EN 26891-1991. Figures 4 and 5 provide the load-slip response for the (S) series of specimens.

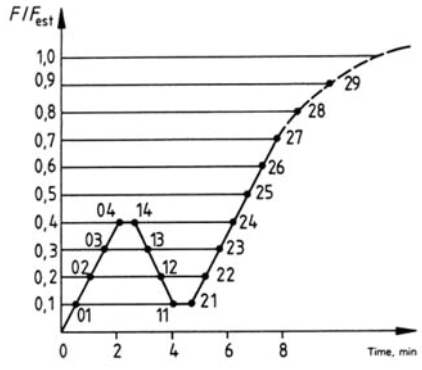

***Figure 3**: Loading procedure for slip modulus and maximum load, accordance of BS EN 26891-1991.*

https://doi.org/10.52202/069179-0006

3.1.1 Screw connections

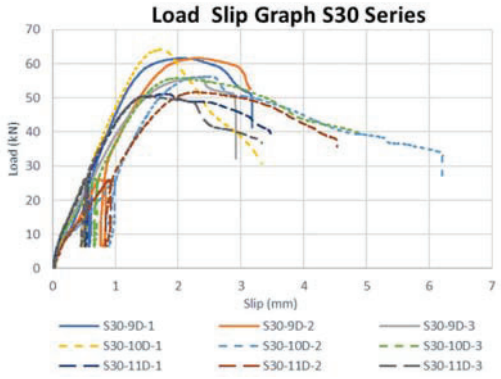

***Figure 4**: Load-slip Graph 30° screw orientation*

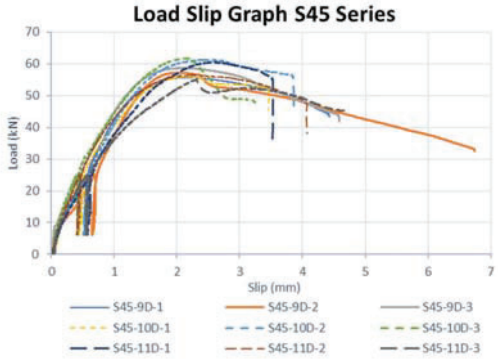

***Figure 5**: Load-slip Graph 45° screw orientation*

It can be observed in Figure 4 & 5, that the S30 and S45 specimens failed in a similar manner regardless of the screw orientation and penetration depth, with a plateau of load carrying capacity followed by the failure of the screws and sudden drop in load. Such failure is typical for screw connections in TCC [17]. In terms of structural performance, the S45 specimens showed a higher average maximum load than the S30 series. However, the S30 series displayed a greater initial stiffness as illustrated in Figure 4. As for penetration depths, 11D specimens, specifically for the S30 series, yielded the lowest load carrying capacity. This is as a result of the shallow orientation angle of the S30 screws and the thickness of concrete used in this research. The level arm produced by screws inserted at 30° provided less resistance to load, due to a reduced resistive contact surface compared to the S45 series. This is most evident when looking at the S30 11D specimens, which produced the lowest load carrying capacity out of the three penetration depths tested. The S30 11D specimens also failed at a lower Fmax and in a more brittle manner, compared to S45 inserted at a lower penetration depth. The resulting shallow angle of the screw in combination with the penetration depth did not allow for favourable deformation/settlement of the screw and as a result an increase brittle failure of the specimen was observed.

Specimens with perpendicular screws (S90) exhibited a more ductile behaviour and as a result a significantly lower Fmax than S30 and S45 specimens. This is shown when comparing Figure 6 to Figure 4 and 5. This outcome was expected, as previous work by [18] carried out on perpendicular connections in CLT Concrete Composites and TCCs has concluded the same findings. Similarly to the previous research carried out by [6], a penetration depth of 11D for S90 specimens resulted in a connection with increased stiffness and on average a greater load carrying capacity, in comparison to the other penetration depths tested. However, for both penetration depths tested, the large slip yielded from the S90 specimens under load showed that they exhibit the lowest levels of composite action, highlighting the structural limitations of this orientation of metal screw connections in CLT Concrete Composites.

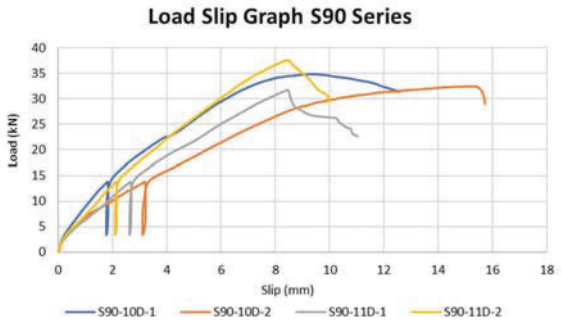

***Figure 6**: Load-slip Graph 90° screw orientation*

3.1.2 Notch connections

Similarly to the theory regarding penetration depth and connection stiffness for screw connections, an increase in notch depth is directly related to an increase in maximum load carrying capacity [8,10]. The main parameters which govern the behaviour of notched connections according to [3] are the geometry of the notch (primarily the notch depth) and whether or not a metal fastener is used in combination with the notch. However, according to [8,10] to date there has been little research investigating the effective number and orientations of screws used in combination with notched connections.

The results from this research show the effects a change in notch depth and orientation of screws used in tandem with notches have on the performance of notched connections in CLT Concrete Composites. NS specimens exhibited the greatest load carrying capacity and stiffness of out all specimen configurations tested, as shown in Table 3. For the NS45 specimens, a linear relationship

between Fmax and notch depth can be identified, with a clear increase in Fmax with an increase in notch depth. This ranges from a Fmax of 72.7 kN for a notch depth of 25 mm to a Fmax of 77.5 kN for a notch depth of 35 mm. Translating to an average increase of 3 percent in Fmax for every 5 mm increase in notch depth.

For the NS90 specimens, an increase in Fmax is noted between specimens NS90-25 and NS90-35 of 11.3 kN. However, unlike the NS45 specimens a further increase in notch depth to 35 mm does not result in an increase in maximum load. This difference in behaviour is likely a result of variance in the material used and not a result of the depth of the notch itself, as unlike screw connections, notched connections resist applied load through direct contact between the concrete and timber members. Thus, the performance of the composite is greatly dependant on the properties of said members. Additionally, the higher variance in results for the NS90, is also likely due to the manufacturing of the notch itself. As the notched specimens tested in this research were cut by hand, unlike the industry standard of using CNC machinery. Therefore, it is speculated that, despite the results shown in this research for the NS90 11D specimens, it is still believed that an increase of notch depth yields an increase in load carrying capacity. This interpretation is based on the results from the NS45 specimens and previous research by [3], [8] and [10] on notched connections in TCCs.

The depth of notched connections proved to have a significant influence on the performance of the connection, as an increase in notch depth provided greater ultimate load and lower slip modulus. This is shown in Figure 7 and 8. A similar relationship between notched depth and Fmax has also been recently reported by [10].

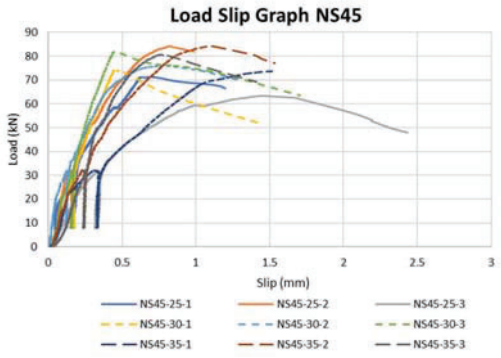

***Figure 7**: Load-slip graph NS45 specimens*

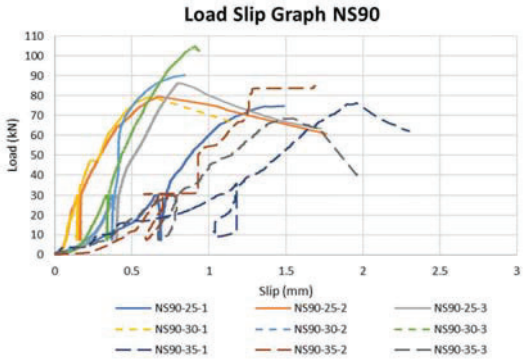

***Figure 8**: Load-slip graph NS90 specimens*

3.2 SLIP MODULUS

To calculate the slip modulus, displacements at 10, 40, 60 and 80 percent of the maximum load (F*est*) were obtained. Using these values, the initial slip modulus (Ki) and the Serviceability Slip modulus (Ks) were calculated according to BS EN 26891-1991.

***Table 3**: Maximum load and slip modulus results*

Connection type	Fmax	Slip at Fmax	Initial	Serviceability limit state
	(kN)	(mm)	Ki (kN/mm)	Ks Slip Modulus (kN/mm)
NS 45 25	72.9	0.99	151.0	161.5
NS 45 30	77.2	0.56	213.0	227.9
NS45 35	79.5	1.13	124.3	125.1
Average	76.6	0.9	162.7	171.5
NS 90 25	80.2	0.98	103.8	176.0
NS 90 30	91.5	0.79	127.2	200.5
NS 90 35	76.5	1.71	39.0	57.0
Average	82.7	1.2	90.0	144.5
S90 10D	33.7	12.33	6.0	5.1
S90 11D	34.7	8.47	5.9	5.1
Average	34.2	10.4	5.9	5.1
S45 9D	57.2	2.07	39.6	40.2
S45 10D	59.6	2.29	52.5	48.1
S45 11D	57.3	2.37	47.0	43.7
Average	58.0	2.2	46.4	44.0
S30 9D	59.0	2.20	42.3	39.3
S30 10D	58.7	2.07	38.7	34.9
S30 11D	51.1	1.89	43.1	34.3
Average	56.3	2.1	41.3	36.2

As shown in Table 3, the notched connections exhibited the greatest slip modulus compared to the other specimen configurations. This was expected as it was previously stated that notched connections offer the highest load resistance and lowest slip. In terms of comparing the slip modulus of the NS90 and NS45 connections, the slip modulus for NS45 specimens was 26.9 kN/mm higher on average than the NS90 specimens. This difference can be attributed to several factors ranging from material density, screw orientation and concrete properties. Therefore, in terms of notch connections, the NS45 specimen outperformed the NS90 specimens in terms of slip modulus, but further testing is required to validate this finding and establish which notch connection configuration yields the greatest structural performance.

https://doi.org/10.52202/069179-0006

For the S series connections both S30 and S45 specimens obtained a far greater slip modulus with up to 8 times the S90 values, ranging between 34.3 and 48.1 kN/mm respectively (as shown in Table 3). The low slip modulus of the S90 specimens shows good agreement with previous research on CLT Concrete Composites, as it was found that screws connected at 90° behave in a more ductile manner under load [2,5]. Furthermore, the slip modulus obtained for the S30 and S45 specimens also shows good agreement with the values obtained in previous research on CLT Glulam Concrete Composites which also tested the performance of inclined connections [2,5,18]. Additionally, similar results were found when correlating a relationship between the slip modulus and inclination of the connector. In the case of this research, S45 specimens showed a slightly higher slip moduli compared to S30 specimens, which is the opposite to what was found by [2]. However, it must be noted that [2] conducted tests on Glulam Concrete Composites and not CLT, which due to timber grain direction can potentially partially explain the discrepancies in results. Despite this, [5] tested screws with various inclinations inserted in CLT Concrete Composites and found that 30° specimens for any given penetration depth yields higher values of slip modulus than 45° specimens. Given the difference in slip modulus for inclined screws obtained in this research is low, the difference in findings between this paper and previous research can be associated with a large variance in the properties of the timber and connectors used. In spite of this, the results obtained from the BS EN 26891 testing shows good general agreement with previous research, whilst also highlighting key differences in slip modulus based on the type of connection, inclination and timber used.

3.2 FAILURE MODES

3.2.1 Johansen's failure modes

One way in which the load carrying capacity and failure of connections in timber structures can be predicted, is through a numerical approach known as the European Yield method or the Johansen's equations. This method is very effective for timber to timber connections, however, there has been no formal adaptation provided for connections in TCCs. Therefore, to classify the failure modes of TCCs, experimental work needs to be carried out. Previous research by [9, 6] has shown that only a handful of failure modes can occur in TCCs, this is due to the low possibility of connection embedment in the concrete member. The failure modes most likely to occur in TCCs are modes E and F.

3.2.2 S90 series

The S90 specimens deformed predictably, with the development of a plastic hinge associated with a mode E failure. The hinge occurred on the section of the screw located at the concrete-timber interface. Such deformation was also noted in previous research by [9] who tested screws oriented at 90° in CLT Concrete Composites. As clearly indicated from the slip modulus, Fmax and slip at Fmax, S90 series had the largest deformation out of all specimens tested. This resulted in large hinge development of the connector and embedment in the timber member. Differences in the magnitude of hinge development and timber embedment was noted for S90 specimens connected with varying penetration depths (as shown in Figure 9a). For S90-10D specimens a timber embedment of 13-15 mm was observed, compared to only 10–13 mm for S90-11D specimens. The difference in magnitude of failure is due to the connection performance in correlation to the connection's penetration depth, as shown in Table 3. The failure of the concrete members for all the S90 specimens showed typical and uniform failure. As recorded during testing, hairline fractures propagated at approximately 20 kN. These fractures occurred along the row of screws on the CLT member, which eventually fully developed and failed. This is shown below in Figure 9b. Such failure can be attributed to the deformation of the connector inside the concrete. It was found that penetration depth had little impact on whether cracking of the concrete member occurred. Rather the failure in the concrete member was related to the concrete thickness/cover adopted in the specimens.

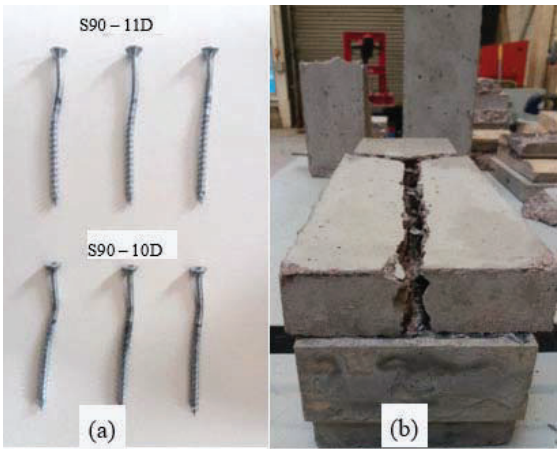

***Figure 9**: (a) S90 screw deformation (b) concrete failure S90 specimens*

3.2.3 S30 & S45 series

The deformation of screws for the S30 and S45 specimens differ to the deformation of the S90 specimens. This is due to their orientation, as when inclined, one screw is loaded in tension while the other is loaded in compression. As a result of the distribution of tensile and compressive forces, different yields can be identified, with the screws in tension showing very little deformation, while the screws in compression showing the development of a plastic hinge, as shown in Figures 10 and 11. According to [2] three failure modes of inclined screws should be examined in TCCs. These correspond to Johansen's failure modes A, E and F. From the examination of the inclined screws post testing, failure modes E and F were identified with two hinges being visible. It is important to note that the hinge development for the S30 specimens was not as visible compared to the S45 specimens at all

penetration depths. Evidently this provides insight into a reason for the lower S30 specimen loads, which was that the screws did not fully yield underload, thus loosing additional potential load bearing resistance.

A further area of interest with the failure of inclined screws is the concrete failure that occurred as a result of the applied load. For both S45 and S30 specimens the concrete members failed as a result of concrete punching failure (shown in Figure 10). This occurred just prior to and in most cases after the Fmax being reached. This type of failure was evident with almost all of the S45 specimens, regardless of their penetration depth. However, this concrete failure only occurred in S30 specimens with a penetration depth of 9D and 10D. It is believed that the lower inclination of the S30 specimens meant that they had increased concrete cover, thus requiring a far greater load to achieve the concrete punching failure. [2] Also noted a similar concrete failure in their research on inclined screws in Glulam Concrete Composites. [2] found that the failure is due to the displacement of screws inside the concrete member under load. It was found that the screws acting in tension, were responsible for this type of failure, as a result of the withdrawal of the screw while under load. Despite concrete punching failure only occurring at a force greater than Fmax, it would be recommended that either a minimum concrete thickness or a minimum penetration depth be adopted to mitigate this type of failure. In order to determine these values further testing on CLT Concrete Composites connected with inclined screws is advised.

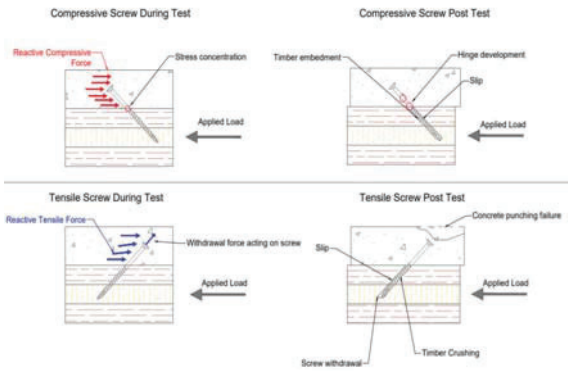

***Figure 10**: Failure process of S30/45 specimens*

***Figure 11**: Deformation of screws with 45° orientation*

3.2.4 NS45 & NS90 series

Unlike screw connections, the failure of notched connections cannot be classified using Johansen's equations. The failure mechanisms for notch connections are dependent on the strength of both the concrete and timber members, as the load is directly transferred from one material to another. It is therefore of critical importance that both members are sufficiently strong to ensure that premature failure of the section does not occur [19]. According to [8] and [16], the failure of notch connections can be caused by the following; (1) Failure of concrete in shear, (2) Crushing of concrete in compression in the notch, (3) Failure of the timber member in shear between two consecutive notches, (4) Failure of the timber member in crushing. From observations during the loading of the specimens both NS90 and NS45 specimens failed as a result of crack propagations originating at the concrete notches. After the development of the hairline cracks (1) at ≈ 40 kN (shown in Figure 12a), a loss of composite action was realised at ≈ 60 kN. After the failure of the concrete members, the load was then distributed to the CLT where the failure of the timber member between two notches (3) occurred (shown in Figure 12b) resulting in the sudden and brittle failure of the specimen. There were no obvious signs of timber crushing (4) on any of the specimens tested. This can be attributed to the high strength and density of the Tulipwood CLT and, additionally, to the grain direction of the CLT, as it varies, notches cut in CLT Concrete Composites can almost certainly be cut in the optimum grain orientation. According to [8] TCCs with notch connections made from Glulam exhibited large amounts of timber crushing and shearing (4) and (5) when they are cut in the transverse direction of the grain.

The difference in screw inclination proved to have little effect on the global failure, however, varying levels of uplift between the two types of notched connections was observed, with the NS45 specimens providing more restraint between the concrete and CLT members. Furthermore, the difference in screw deformation for the NS45 and NS90 specimens was negligible, with both specimens showing no sign of a plastic hinge. Therefore, it can be said that the effects of using inclined screws in tandem with notch connections has been seen to reduce the uplift between the concrete and timber members. To conclude the failure of the notched specimens tested in this research shows very good agreement with [8], [10] and [17]. This research also found that increasing the notch depth had no influence on the type of failure. Although it must be noted that in the case that hardwood CLT is used, and where a small timber section is adopted, a large notch depth > 35 mm could result in a significant loss of cross section, and thus in a reduction in overall strength. Therefore, further testing should be undertaken on inclined screws in TCC notched connections to determine the optimum notch depth.

https://doi.org/10.52202/069179-0006

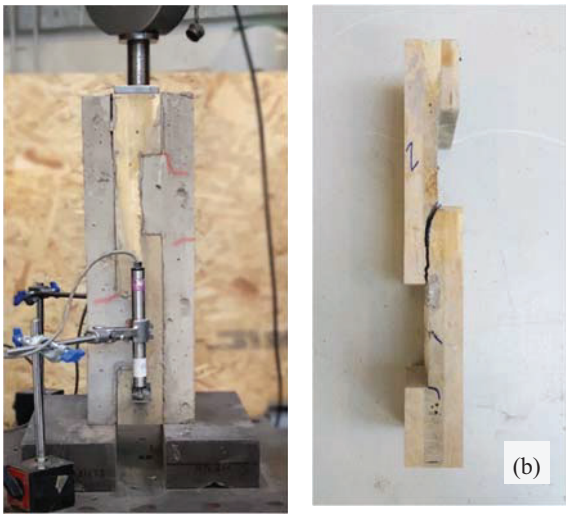

***Figure 12**: (a) Typical fracture in concrete (1), (b) failure in CLT for notched specimens (3)*

4 CONCLUSION

4.1 INFLUENCE OF PARAMETERS

4.1.1 Penetration depth

For the S90 series, a penetration depth of 11D was found to provide the greatest maximum load at 34.6 kN. From the post testing examination of the screws, it was found that screws inserted at 11D showed less deformation compared to the 10D specimens. Furthermore, the 11D specimens exhibited a lower slip on average at all stages of loading. These results concur with previous research on CLT Concrete Composite connections by [6] and [9].

In terms of the inclined screws, S45 specimen showed a linear increase in Fmax for penetrations 9D and 10D. 11D penetration depths for S45 specimens, resulted in a Fmax marginally lower than the 10D specimens. Additionally, the S30 specimens exhibited a decrease in Fmax with an increase in penetration depth, with a drop of 13.28 percent from 9D to 11D. This contradicts findings by [2] and [5] who have found that for both inclinations of 30° and 45° an increase in penetration depth results in an increase in both Fmax and slip modulus. However, the penetration depths studied by [5] was increased in increments of 20 mm for each penetration depth, while the penetration depth studied in this research increased in increments of 5 mm. Furthermore, [2] investigated TCCs which used Glulam Concrete Composites as opposed to CLT. These differences in scale of penetration increase and materials used, could be the result of the variation between findings. Therefore, further testing should be undertaken to support the current findings.

4.1.2 Notch depth

It was found that a linear increase in notch depth provides an increase in structural performance for both NS45 and NS90 specimens. These results show good agreement with research conducted by [10], who also investigated the influence of notch depth on CLT Concrete Composites. It was also found that the governing parameters of notched connections was the strength of the concrete and timber members, with hardwood CLT offering potential increases in structural performance for notched connections opposed to softwood CLT. Additionally, it was found that almost no timber embedment was evident in any of the specimens. This differs to what was found by [8], where timber embedment was clearly identifiable. The reason for the difference in specimen condition is that, CLT is orthogonally bound. [8] stated that notches cut in the longitudinal grain orientation are superior to notches cut in the transverse direction. Thus, notches cut in Hardwood CLT, due to the orthogonal nature of CLT and increased density of the hardwood, may be more suitable than notches cut in alternative softwood timber members. To validate this claim further testing should be undertaken.

4.1.3 Screw inclination

Out of the three screw orientations tested, an orientation of 45° proved to be the most effective, in both load carrying capacity and slip modulus. This result contradicts current findings, which state that decreasing the inclination angle of screw connections will increase their structural performance [5,21]. The reason for the difference in findings can be attributed to several factors ranging from the types of screws used, concrete thickness and spacing adopted. However, in the case of this research, and as mentioned previously the S30 provided a lower Fmax due to premature failure in the concrete member, and as a result of the connections reduced load resisting lever arm due to its shallow insertion angle.

The inclination of screws in notched connections, proved to have a minor influence on the load carrying capacity of the connection. The NS90 specimens showed increased values for Fmax, however, they also exhibited a greater slip at Fmax and a reduced slip modulus compared to the NS45 specimens. The orientation of the screws used in NS specimens did, however, have an impact on the failure of the specimen, with the NS45 specimens showing less signs of uplift between the concrete and timber members of the composite compared to the NS90 specimens. A reduction in uplift between the members shows that the timber and concrete members are achieving a greater level of composite action, which is evident as the NS45 yielded a greater slip modulus than the NS90 specimens. This provides an insight into which screw orientations provides the greatest structural performance in a notch connection. However, further research into the inclination of screws used in notched connections in TCCs should be carried

https://doi.org/10.52202/069179-0006

out to verify these findings and expand on current research.

4.1.4 Failure modes

After examining the screws taken from the specimen's post testing, two clear failure modes were identified. Mode E and F failures from Johansen failure modes were exhibited. This shows good agreement with previous research and highlights that only certain Johansen failure modes can occur in TCCs. It was also noted that the failure modes were governed by the penetration depth of the connection, with 11D specimens exhibiting less deformation compared to the 9D specimens for inclinations of 30° and 90°. It was also found that the failure of the concrete member was greatly governed by the penetration depth and inclination of the screws with failures such as concrete punching being observed for the inclined screw, which was also noted in research by [2]. The concrete failure for notched specimens identified in this testing showed good agreement with [8] and [10]. However, it must be noted that the failure mode of connections in CLT Concrete Composites cannot be calculated and can only be accurately obtained via laboratory testing. This is a result of a lack of guidance in the design standards. Therefore, the development of a new or even a modified equation based on the existing Johansen's equation is recommended.

4.1.5 Recommendations for future research

From the lack of guidance in the current design standards, there is a noticeable gap not only for an accurate equation to calculate the slip modulus, but for improved guidance on obtaining the load carrying capacity and failure modes of TCCs. Therefore, work addressing these issues is encouraged. Additionally, as the knowledge of connections under conventional loading is being increasingly covered, it is recommended that connections in TCCs be tested under dynamic loading, to gain a better understanding of the behaviour of various connections under such types of loads and how this will affect the overall structural performance of the composite

ACKNOWLEDGEMENTS

A thanks is reserved for the AHEC for providing the University with the CLT that was used in this research. Additionally, a thanks is reserved for the Centre for Offsite Construction + Innovative Structures (COCIS) at Edinburgh Napier University.

REFERENCES

[1] Wacker J. P., Dias A and Hosteng T. K.: Investigation of Early Timber-Concrete Composite Bridges in the United States. In: *International Conference on Timber Bridges*, 2017.

[2] Du H., Hu X., Xie Z and Wang H.: Study on shear behavior of inclined cross lag screws for glulam-concrete composite beams. *Construction and Building Materials*, vol. 224. pp. 132–143, 2019.

[3] Dias A. M. P. G., Kuhlmann U., Kudla k., Mönch S and Dias A. M. A.: Performance of dowel-type fasteners and notches for hybrid timber structures. *Eng. Struct.*, vol. 171, pp. 40–46, 2018.

[4] G. Churkina . Buildings as a global carbon sink. *Nat. Sustain.*, 2020.

[5] Mirdad M. A. H., Chui Y. H.: Load-slip performance of Mass Timber Panel-Concrete (MTPC) composite connection with Self-tapping screws and insulation layer. *Constr. Build. Mater.*, vol. 213, pp. 696–708, Jul. 2019.

[6] Mai K. Q., Park A., and Lee K.: Experimental and numerical performance of shear connections in CLT–concrete composite floor. *Mater. Struct. Constr.*, vol. 51, no. 4, pp. 1–13, 2018.

[7] Fragiacomo M., Lukaszewska E.: Time-dependent behaviour of timber-concrete composite floors with prefabricated concrete slabs. *Eng. Struct.*, vol. 52, pp. 687–696, 2013.

[8] Zhang L., Chui Y. H., and D. Tomlinson.: Experimental investigation on the shear properties of notched connections in mass timber panel-concrete composite floors. *Constr. Build. Mater.*, vol. 234, p. 117375, 2020.

[9] Bell D.: An Investigation into the Behaviour of Connections in Cross Laminated Timber – Concrete Composites Under Shear Load. Edinburgh Napier, 2019.

[10] Jiang Y., Crocetti R.: CLT-concrete composite floors with notched shear connectors. *Constr. Build. Mater.*, vol. 195, pp. 127–139, Jan. 2019.

[11] Plowas W., Hairstans R.: Preliminary Structural Assessment of Tulipwood CLT. Edinburgh, 2019.

[12] Lukaszewska E., Johnsson H and Fragiacomo M.: Performance of connections for prefabricated timber-concrete composite floors. *Mater. Struct. Constr.*, vol. 41, no. 9, pp. 1533–1550, 2008.

[13] Shi W., Angst U. M., Yilmaz D., Wenk K., and Frangi A.: Corrosion of Metallic Fasteners in Timber–Concrete Composite Structures. *Mater. Struct. Constr.*, vol. 52, no. 3, pp. 1–11, 2019.

[14] SPAX International GmbH.: European Technical Approval ETA-04/0101. Brussels, 2013.

[15] British Standards Institution.: BS EN 1995-1-1, 1995. Design of timber structures. London. British Standards Institution (1995).

[16] British Standards Institution.: BS EN 26891:1991, 1991. Timber structures - Joints made with mechanical fasteners - General Principles for the determination of strength and deformation characteristics. London. British Standards Institution (1991).

[17] Dias A. M. P. G., Jorge L. F. C.: The effect of ductile connectors on the behaviour of timber-concrete composite beams. *Eng. Struct.*, vol. 33, no. 11, pp. 3033–3042, 2011.

[18] Mai K., Park A., Nguyen K. T., and Lee K.: Full-scale static and dynamic experiments of hybrid CLT–concrete composite floor. *Constr. Build. Mater.*, vol. 170, pp. 55–65, 2018.

https://doi.org/10.52202/069179-0006

[19] Boccadoro L., Steiger R., Zweidler S., and Frangi A.: Analysis of shear transfer and gap opening in timber–concrete composite members with notched connections. *Mater. Struct. Constr.*, vol. 50, no. 5, pp. 1–15, 2017.

[20] Yeoh D., Fragiacomo M., De Franceschi M., and Buchanan A. H.: Experimental tests of notched and plate connectors for LVL-concrete composite beams. *J. Struct. Eng.*, vol. 137, no. 2, pp. 261–269, 2011.

[21] Berardinucci B., Di Nino S., Gregori A., and Fragiacomo M.: Mechanical behavior of timber–concrete connections with inclined screws. *Int. J. Comput. Methods Exp. Meas.*, vol. 5, no. 6, pp. 807–820, 2017.

World Conference on Timber Engineering Oslo 2023

SCALING STUDY ON VISCOUS DAMPING FOR GLULAM AND HYBRID GLULAM-FRP BEAMS

Tomas Bravo Tetlak[1], Joseph M. Gattas[2], Cristian Maluk[3]

ABSTRACT: Damping plays an important role in long-span, mass timber floors due to the relation it has to energy dissipation. Energy dissipation in these systems helps control how vibrations spread and whether its interaction with humans occupying the buildings causes discomfort or not. The present study focuses on the effect of scale on viscous damping in Glulam and fibre-reinforced Glulam beams. Twelve full-scale and thirteen small-scale equivalent Glulam beams (Australian Southern Pine) of two different depths were tested using the impact test method. Hybrid beams where manufactured with Fibre Reinforced Polymer (FRP) strips embedded at the interface between lamellas during manufacturing of test samples. Outcomes of this experimental study show that there is an effect of scale in viscous damping – small-scale beams experience a higher viscous damping when compared to equivalent full-scale beams, regardless of testing Glulam or Glulam-FRP beams.

KEYWORDS: Glulam, scale-effect, viscous damping, serviceability performance

1 INTRODUCTION

Timber has been a popular construction material for centuries, particularly for houses in lightweight frame structures. With the development of engineered wood products (EWPs) and adhesives, larger cross-sections, longer spans and improved structural properties have been made possible, allowing timber to compete with concrete and steel as a high-capacity building material [1]. During the last decade, mass timber buildings have rapidly gained prominence with projects all over the world, including Mjostartnet in Norway, HoHo Wien in Austria, T3 Minneapolis in the US, and Brock Commons in Canada. Australia has also contributed to the mass timber building industry with recent examples such as Daramu, International House, and 25 King St.

Timber-only floor and building systems are often limited by serviceability (static and dynamic) limitations. For taller buildings and longer spans, buildings have instead utilised hybrid-timber structural systems, such as timber concrete composites (TCC) or steel-timber composites (STC), by increasing mass and stiffness of the structural elements, as well as mechanical properties, Fibre reinforcement have also proven to be relevant in improving the timber elements properties [2].

The growing interest in studying EWPs and the surge of hybrid EWP elements to further improve their properties has led to many experimental studies to increase the knowledge of these novel systems. Most of these studies are focused on the mechanical properties of elements and structures, but for the serviceability checks required for long-span elements, variables such as natural frequencies, accelerations, damping, and stiffness are a key focus.

Many full-scale tests have been performed in long-span timber floors to study the dynamic behaviour of these systems, underlining the importance of the understanding of damping mechanisms in the context of long-span floors [3-8]. Although some standards, for example Eurocode 5 [9], indicate that vibration serviceability checks should focus on staying above the 8Hz threshold, studies indicate that increased damping can greatly improve the performance of a timber floor [4].

Testing for long-span floors and elements require large laboratory space, labour, and equipment to move and manipulate the specimens. This can be challenging when testing and can sometimes make full-scale testing difficult and cost prohibitive.

As an alternative evaluation method, down-scaled samples have been used to study and understand the equivalent full-scale performance of elements, particularly when full-scale testing is constrained by available space and budget [10]. Scaling factors are expected to make the small-scale and full-scale measurements and results related. Size effects in timber beams translate in a reduction of mechanical properties, such as strength [11]. It is known that shorter span elements present higher damping ratios [6], but no studies have been carried out to thoroughly investigate the effect of scale when determining the damping and serviceability performance of timber floors.

[1] Tomas Bravo Tetlak, School of Civil Engineering, The University of Queensland, Australia, t.bravo@uq.edu.au
[2] Joseph M. Gattas, School of Civil Engineering, The University of Queensland, Australia, j.gattas@uq.edu.au
[3] Cristian Maluk, School of Civil Engineering, The University of Queensland, Australia, and Semper, UK c.maluk@sempergrp.com

https://doi.org/10.52202/069179-0007

This work presents non-destructive testing of unreinforced and FRP-reinforced Glulam beams and scaled versions in a 1:2.14 ratio. Experimental data was analysed to obtain natural frequencies and compare material viscous damping scale factors obtained from small and large scales.

2 MATERIALS AND METHODS

2.1 SPECIMEN CONFIGURATION

Twelve full-scale and thirteen small-scale beams were tested for vibrations with cross sections and labels shown in **Error! Reference source not found.**. The full-scale beams consisted of five (G5, HG5) and seven lamella (G7, HG7) configurations with heights of 155mm and 217mm with a width of 86mm. HG5 samples had a positive reinforcement ratio of 1% and HG7 samples had both a negative and positive reinforcement ratio of 1.5%. Scaled samples were fabricated by scaling lamellas and reinforcement (scale was determined by the commercially available CFRP strip thicknesses).

Fabrication of beams included the lamination of timber beams in both scales and in-layer reinforcement as described by Bravo Tetlak, et al. [12], with the fabrication method developed by Zaben [13]. Table 1 shows the geometric properties of the full-scale and small-scale beams.

2.2 EXPERIMENTAL SETUP

Beams were tested in a free vibration setup. A schematic figure of the configuration is shown in Figure 2. The beams were instrumented with five accelerometers (Kistler 8630B5) placed evenly on the bottom face. The accelerometers were connected to a data acquisition system where accelerations were stored to be processed using modal analysis to estimate natural frequencies and damping, according to Hearmon [14] and Casiano [15], respectively. The beams were hit with a PCB 086B02 modal hammer also connected to the data acquisition system to measure force. The sampling rate was fixed to 2500Hz, allowing to identify frequencies of up to 1250Hz without accounting for Nyquist aliasing.

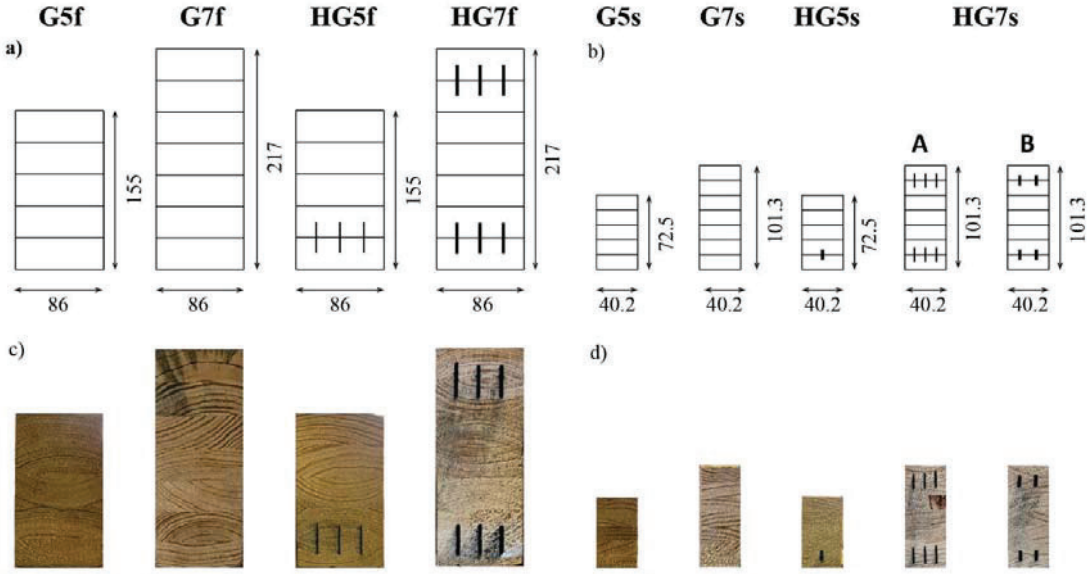

Figure 2. *Cross sections of unreinforced (G) and reinforced (HG) beams analysed. Adapted from: Bravo Tetlak, et al. [12].*

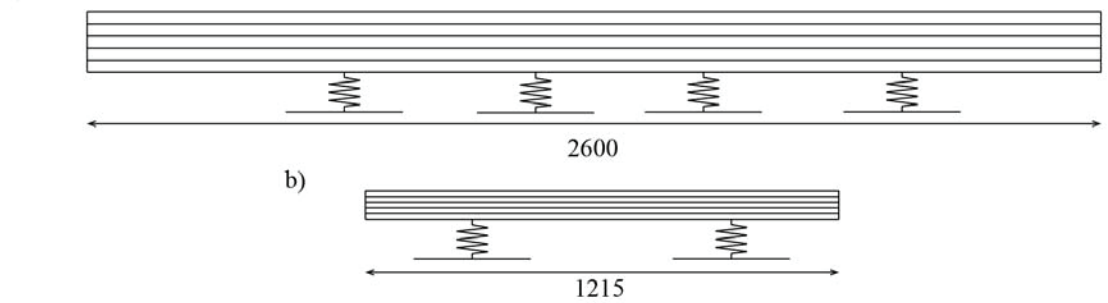

Figure 1. *Free vibration configuration and beam lengths, (top) Full-scale and (bottom) small-scale. Adapted from: Bravo Tetlak, et al. [12].*

https://doi.org/10.52202/069179-0007

Table 1. *Beam geometric properties.*

	Full-scale			Small-scale		
Beam ID	Width	Height	Length	Width	Height	Length
G5 # 1	85.4	155	2604	40.7	72.7	1215
G5 # 2	86.1	155	2605	40.6	72.8	1215
G5 # 3	87.0	155	2607	40.9	72.7	1215
Average G5	**86.2**	**155**	**2605**	**40.7**	**72.7**	**1215**
G7 # 1	86.1	216	2613	40.7	101.8	1215
G7 # 2	85.2	216	2603	40.4	101.3	1215
G7 # 3	85.6	216	2613	40.6	101.7	1215
Average G7	**85.6**	**216**	**2610**	**40.6**	**101.6**	**1215**
HG5 # 1	85.4	155	2607	40.6	72.7	1215
HG5 # 2	86.3	155	2620	40.4	72.5	1215
HG5 # 3	86.1	155	2620	40.3	72.5	1215
Average HG5	**85.9**	**155**	**2616**	**40.4**	**72.5**	**1215**
HG7 A # 1	86.8	216	2604	40.4	101.3	1215
HG7 A # 2	86.7	216	2601	40.3	101.2	1215
HG7 A # 3	86.7	216	2600	-	-	-
HG7 B # 1	-	-	-	40.4	101.4	1215
HG7 B # 2	-	-	-	40.4	101.3	1215
Average HG7	**86.7**	**216**	**2602**	**40.4**	**101.3**	**1215**

2.2 DAMPING COMPUTATION

According to Casiano [15] the half-power method can be used to estimate the damping values, where half of the amplitude of the power spectra at the peak (at $\frac{1}{\sqrt{2}}$ of the maximum amplitude, if using Fast-Fourier Transform FFT to obtain spectra), will yield f_u and f_l, the upper and lower frequencies at half-power. The ratio between the natural frequency of the mode, and the difference between f_u and f_l, yields the quality factor. Figure 3 shows a schematic explanation of the calculation of damping, for the case of an FFT-obtained spectrum.

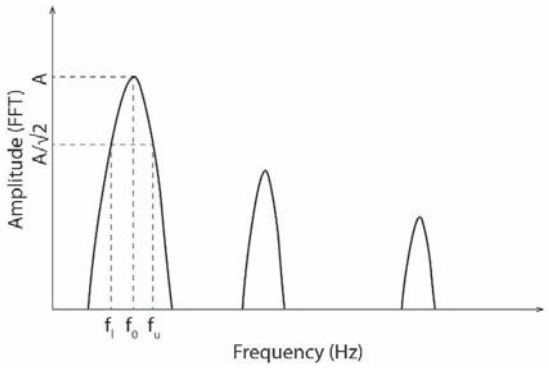

Figure 3. *Schematic representation of a frequency spectrum with the relevant parameters to estimate damping values.*

$$Q = \frac{f_0}{f_u - f_l} \quad (1)$$

If the damping values are expected to be less than 0.05 (5%), they can be estimated by [15]:

$$\xi = \frac{1}{2Q} = \frac{f_u - f_l}{2f_0} \quad (2)$$

2.3 SCALING OF SPECIMENS

According to Masaeli, et al. [16], it is assumed that, in static analysis, geometric properties and static parameters are proportional to the geometric scale. On the other hand, Carvalho [10] states that for scaled specimens, the scale factors should be derived depending on the force restoration mechanism. If the restoring forces are related to the elastic properties of the material only, scale factors should be deduced from geometric scaling and the Cauchy similitude (Equation (3)),

$$\text{Cauchy similitude: } Ca = \frac{\rho v^2}{E} \quad (3)$$

with equation parameters ρ, the specific mass, v the velocity and E, Modulus of Elasticity, as listed in Table 2.

If restoring forces are dependent on the material elastic properties and gravity loads, then the scaling factors must satisfy both the Cauchy similitude (Equation (3)) and Froud similitude (Equation (4)).

$$\text{Froude similitude: } Fr = \frac{v^2}{Lg} \quad (4)$$

with equation parameters v the velocity, L, length, and g, gravity, as listed in Table 2.

In this study, gravity loads do not play a significant role in the restoration loads, so only geometric parameters and Cauchy similitude are used to determine the theoretical scaling parameters, which are shown in Table 2.

Table 2. *Scale parameters derived from Cauchy similitude law. Adapted from [10, 17]*

Parameter	Symbol	Scale factor
Length	L	$L_p/L_m=\lambda=2.14$
Modulus of Elasticity	E	$E_p/E_m=1$
Specific Mass	ρ	$\rho_p/\rho_m=1$
Area	A	$A_p/A_m=\lambda^2=4.58$
Volume	V	$V_p/V_m=\lambda^3=9.80$
Mass	m	$m_p/m_m=\lambda^3=9.80$
Weight	W	$W_p/W_m=\lambda^3=9.80$
Frequency	f	$f_p/f_m=\lambda^{-1}=0.467$
Viscous damping	μ	$\mu_p/\mu_m=1$

3 RESULTS

3.1 GLULAM BEAMS

Natural frequencies up to the third mode are shown in Table 3 and acceleration spectra are presented in Figure 4, and were part of a broader study carried out by Bravo Tetlak, et al. [12].

https://doi.org/10.52202/069179-0007

Natural frequencies presented similar values between samples, with coefficients of variation of up to 2.4%. For each natural frequency, damping values were estimated using the half-power method. Values are presented in Table 4.

Damping values in Glulam were consistently in a range between 0.43% and 0.63% in every mode, except for outlier 0.86% in Mode 1 of small-scale G5 #2. It can be observed that the variability between samples and modes is 12.9%, by discarding the outlier, CoV reduces to 8.4%, with no specific trend regarding scale.

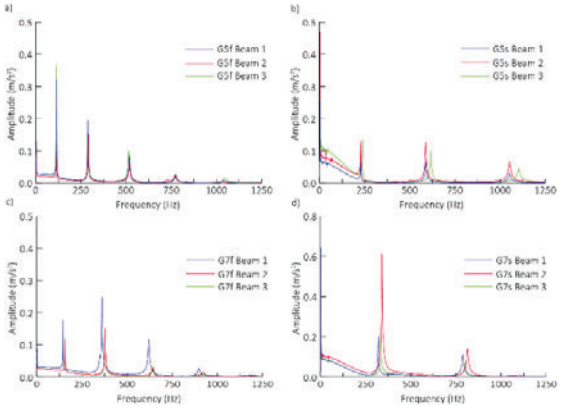

Figure 4 *Acceleration spectra for (a) G5f, (b) G5s, (c) G7f, and (d) G7s specimens. Adapted from: Bravo Tetlak, et al. [12].*

Table 3. *Natural frequencies of Glulam beams. Coefficient of variation in brackets. Source: Bravo Tetlak, et al. [12].*

	Full-scale			Small-scale		
Beam	**Mode 1**	**Mode 2**	**Mode 3**	**Mode 1**	**Mode 2**	**Mode 3**
G5 # 1	115.4	288.7	518.8	228.9	588.4	1053.0
G5 # 2	115.4	291.7	518.8	226.4	582.3	1053.0
G5 # 3	112.9	286.3	513.9	239.3	615.8	1102.0
Average G5	**114.6 (1.0%)**	**288.9 (0.8%)**	**517.2 (0.4%)**	**231.5 (2.4%)**	**595.5 (2.4%)**	**1069.3 (2.2%)**
G7 # 1	145.3	361.3	620.1	321.0	788.0	-
G7 # 2	157.5	378.4	645.1	340.6	814.2	-
G7 # 3	156.9	378.4	642.7	333.3	801.4	-
Average G7	**153.2 (3.7%)**	**372.7 (2.2%)**	**636.0 (1.8%)**	**331.6 (2.4%)**	**801.2 (1.3%)**	**-**

Table 4. *Damping values (in %) of unreinforced Glulam beams, G5 and G7. Coefficient of variation in brackets.*

	Full-scale			Small-scale		
Beam	**Mode 1**	**Mode 2**	**Mode 3**	**Mode 1**	**Mode 2**	**Mode 3**
G5 #1	0.54	0.51	0.63	0.54	0.54	0.53
G5 #2	0.48	0.51	0.61	0.86	0.58	0.57
G5 #3	0.54	0.50	0.60	0.48	0.51	0.57
Average G5	**0.52 (5.8%)**	**0.51 (0.5%)**	**0.61 (2.1%)**	**0.63 (26.1%)**	**0.54 (5.2%)**	**0.56 (3.2%)**
G7 #1	0.51	0.56	0.59	0.50	0.51	-
G7 #2	0.50	0.51	0.58	0.56	0.54	-
G7 #3	0.43	0.49	0.60	0.61	0.52	-
Average G7	**0.48 (6.9%)**	**0.52 (5.2%)**	**0.59 (0.8%)**	**0.56 (8.0%)**	**0.52 (2.1%)**	**-**

3.2 HYBRID FRP-GLULAM BEAMS

Natural frequencies up to the third mode are shown in Table 3 and acceleration spectra are presented in Figure 4, and were part of a broader study carried out by Bravo Tetlak, et al. [12].

Natural frequencies presented similar values between samples, with coefficients of variation of up to 1.6%. For each natural frequency, damping values were estimated using the half-power method. Values are presented in Table 4.

Damping values in Glulam were consistently in a range between 0.37% and 0.70% in every mode, except for outliers 0.94% in Mode 3 of small-scale HG5 #3. It can be observed that the variability between samples and modes is 18.9%, by discarding the outlier, CoV reduces to 13.8%, with no specific trend regarding scale.

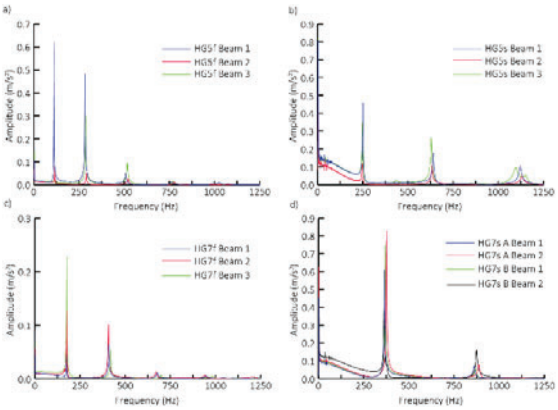

Figure 5 *Acceleration spectra for (a) HG5f, (b) HG5s, (c) HG7f, and (d) HG7s specimens, Adapted from: Bravo Tetlak, et al. [12].*

Table 5. *Natural frequencies of hybrid beams. Coefficients of variation in brackets. Coefficient of variation in brackets. Source: Bravo Tetlak, et al. [12].*

	Full-scale			Small-scale`		
Beam	**Mode 1**	**Mode 2**	**Mode 3**	**Mode 1**	**Mode 2**	**Mode 3**
HG5 # 1	111.7	283.2	507.2	252.1	640.3	1122.0
HG5 # 2	115.4	291.1	517.0	247.8	632.9	1132.0
HG5 # 3	114.1	286.9	521.2	248.4	629.9	1099.0
Average HG5	**113.7 (1.3%)**	**287.1 (1.1%)**	**515.1 (1.1%)**	**249.4 (0.8%)**	**634.4 (0.7%)**	**1117.7 (1.2%)**
HG7 A # 1	175.8	409.5	676.9	365.6	860.6	-
HG7 A # 2	176.4	407.7	672.0	376.6	887.5	-
HG7 A # 3	176.4	418.7	697.6	-	-	-
HG7 B # 1	-	-	-	369.3	871.6	-
HG7 B # 2	-	-	-	362.5	874.6	-
Average HG7	**176.2 (0.2%)**	**412.0 (1.2%)**	**682.2 (1.6%)**	**368.5 (1.4%)**	**873.6 (1.1%)**	-

Table 6. *Damping values (in %) of reinforced Glulam beams, HG5 and HG7. Coefficient of variation in brackets.*

	Full-scale			Small-scale		
Beam	**Mode 1**	**Mode 2**	**Mode 3**	**Mode 1**	**Mode 2**	**Mode 3**
HG5 #1	0.55	0.49	0.59	0.55	0.51	0.55
HG5 #2	0.57	0.52	0.56	0.59	0.51	0.56
HG5 #3	0.56	0.51	0.67	0.70	0.51	0.94
Average HG5	**0.56 (1.2%)**	**0.51 (2.4%)**	**0.61 (7.6%)**	**0.61 (10.1%)**	**0.51 (0.5%)**	**0.69 (26.2%)**
HG7 A #1	0.42	0.47	0.57	0.37	0.49	-
HG7 A #2	0.42	0.47	0.59	0.41	0.48	-

HG7 A #3	0.51	0.46	0.55	-	-	-
HG7 B #1	-	-	-	0.40	0.50	-
HG7 B #2	-	-	-	0.47	0.45	-
Average HG7	**0.45 (9.4%)**	**0.47 (1.3%)**	**0.57 (2.9%)**	**0.41 (8.7%)**	**0.48 (4.0%)**	**-**

4 DISCUSSION

4.1 SCALE TESTING EFFICACY IN GLULAM AND HYBRID-GLULAM BEAMS

Table 7 presents the experimental scaling factors of studied beams. While in most cases, a factor of less than 1.0 indicates small-scale samples presented a higher damping than their full-scale counterparts. HG7 for mode 1 and HG5 for mode 3 show higher average values for damping in full-scale. G7 and HG5 presented an average value of 1.0 for mode 2.

Table 7. *Average scale factors for damping of beams.*

Beam	Mode 1	Mode 2	Mode 3
G5 Average	0.83	0.93	1.09
G7 Average	0.86	1.00	-
HG5 Average	0.91	1.00	0.89
HG7 Average	1.09	0.95	-

Interestingly, if the outliers are removed from the analysis, the situation changes, as highlighted in Table 8. This indicates that more studies should be conducted to have higher statistical significance, and that there is no correlation observable between full-scale and small-scale tests that can be attributable to dynamic serviceability parameters, as consistent with that observed in Bravo Tetlak, et al. [12], and observed in Table 3 to Table 6.

Table 8. *Average scale factors for damping of beams without outliers (G5 small-scale, mode 1; HG5 small-scale, mode 3).*

Beam	Mode 1	Mode 2	Mode 3
G5 Average	1.02	0.93	1.09
G7 Average	0.86	1.00	-
HG5 Average	0.91	1.00	1.09
HG7 Average	1.09	0.95	-

4.2 GENERAL COMMENTS

Although the addition of CFRP increased the stiffness and natural frequencies of the beams, the damping parameters were not greatly affected, as observed in the studied set of beams.

The scattering of damping values for different modes in the studied beams shows no clear trend or correlation between scales, which can be a sign that scaled down elements can be studied under serviceability without accounting for size effect issues.

The ease testing of scaled down beams was greatly improved, when compared to full-scale testing, given the lighter and smaller sizes of the beams.

5 CONCLUSIONS

This work presented the damping characterisation of two sets of Glulam beams and two sets of carbon fibre reinforced hybrid-Glulam beams. Vibration tests were performed on full-scale and 1:2.14 scale beams and damping parameters were estimated from the accelerometers data acquired. The efficacy of scale testing was evaluated in the context of damping parameter calculations. The main findings can be summarised in the following:

- Downscaled versions of Glulam and hybrid-Glulam beams were significantly easier to test, compared to full-scale beams. This includes, use of laboratory space, freight, experimental set ups, and equipment demand.
- Damping of beams did not show a particular trend regarding scale, and values stayed in fairly determined boundaries, indicating no particular size effect in damping. Although more tests are required to determine if there is a statistical correlation.
- Small-scale samples presented two outlier cases in a Glulam beam, and a hybrid-Glulam beam at a higher mode. More tests should be carried out to understand if the phenomenon is common, or only a particular case in this analysis.

This study indicated that scaled down Glulam and hybrid-Glulam beams in terms of damping estimation is feasible, can yield similar results to full-scale beams and reduce the effort required for testing. In the context of long-span timber and hybrid-timber floor prototyping and testing, these results could lead to easier serviceability testing.

ACKNOWLEDGEMENTS

The authors gratefully acknowledge the financial support provided by the Australian Research Council Research Hub to Transform Future Tall Timber Buildings IH150100030. They are also grateful to Hyne Timber, for donation of material used in testing and prototyping.

The authors also wish to thank the technical staff at The University of Queensland for their valuable assistance, especially Stewart Matthews, Jason Van der Gevel, Chris Russ, and Van Thuan Nguyen. The help of the people at the Salisbury Research Facility of the Department of Agriculture and Fisheries (DAF), Andrew Outhwaite and Robert McGavin is gratefully acknowledged.

https://doi.org/10.52202/069179-0007

REFERENCES

[1] M. Bazli, M. Heitzmann, and H. Ashrafi, "Long-span timber flooring systems: A systematic review from structural performance and design considerations to constructability and sustainability aspects," *Journal of Building Engineering,* p. 103981, 2022.

[2] H. Yang, W. Liu, W. Lu, S. Zhu, and Q. Geng, "Flexural behavior of FRP and steel reinforced glulam beams: Experimental and theoretical evaluation," *Construction and Building Materials,* vol. 106, pp. 550-563, 2016-03-01 2016, doi: 10.1016/j.conbuildmat.2015.12.135.

[3] B. M. Basaglia, "Dynamic Behaviour of Long-Span Timber Ribbed-Deck Floors," 2019.

[4] A. Opazo-Vega, F. Muñoz-Valdebenito, and C. Oyarzo-Vera, "Damping Assessment of Lightweight Timber Floors Under Human Walking Excitations," *Applied Sciences,* vol. 9, no. 18, p. 3759, 2019-09-09 2019, doi: 10.3390/app9183759.

[5] K. Lewis, B. Basaglia, R. Shrestha, and K. Crews, "The use of cross laminated timber for Long span flooring in commercial buildings," in *WCTE 2016-World Conference on Timber Engineering*, 2016.

[6] N. Labonnote, A. Rønnquist, and K. A. Malo, "Experimental evaluations of material damping in timber beams of structural dimensions," *Wood science and technology,* vol. 47, no. 5, pp. 1033-1050, 2013.

[7] P. Hamm, A. Richter, and S. Winter, "Floor vibrations–new results," in *Proceedings of 11th World Conference on Timber Engineerig (WCTE2010), Riva del Garda*, 2010.

[8] K. Jarnerö, A. Brandt, and A. Olsson, "Vibration properties of a timber floor assessed in laboratory and during construction," *Engineering Structures,* vol. 82, pp. 44-54, 2015-01-01 2015, doi: 10.1016/j.engstruct.2014.10.019.

[9] *BS EN 1995-1-1. Eurocode 5: Design of timber structures. General. Common rules and rules for buildings*, B. S. Institution, London, 2004.

[10] E. Carvalho, "Seismic testing of structures," in *11th European Conference on Earthquake Engineering*, 1998, pp. 53-64.

[11] B. Madsen and A. H. Buchanan, "Size effects in timber explained by a modified weakest link theory," *Canadian Journal of Civil Engineering,* vol. 13, no. 2, pp. 218-232, 1986, doi: 10.1139/l86-030.

[12] T. Bravo Tetlak, J. M. Gattas, and C. Maluk, "Experimental study on the effects of scale on the static and dynamic behaviour of Glulam and hybrid-Glulam beams," *Construction and Building Materials,* vol. 369, p. 130563, 2023, doi: https://doi.org/10.1016/j.conbuildmat.2023.130563.

[13] A. Zaben, "Hybrid Glulam-FRP beam with improved fire performance (Under review)," Doctor of Philosophy, School of Civil Engineering, The University of Queensland, 2023.

[14] R. Hearmon, "The influence of shear and rotatory inertia on the free flexural vibration of wooden beams," *British Journal of Applied Physics,* vol. 9, no. 10, p. 381, 1958, doi: 10.1088/0508-3443/9/10/301.

[15] M. Casiano, "Extracting damping ratio from dynamic data and numerical solutions," 2016.

[16] M. Masaeli, B. P. Gilbert, H. Karampour, I. D. Underhill, C. H. Lyu, and S. Gunalan, "Scaling effect on the moment and shear responses of three types of beam-to-column connectors used in mass timber buildings," *Engineering Structures,* vol. 208, p. 110329, 2020-04-01 2020, doi: 10.1016/j.engstruct.2020.110329.

[17] E. Coelho, A. C. Costa, P. Candeias, M. F. Silva, and L. Mendes, "Shake table tests of a 3-storey irregular RC structure designed for gravity loads," in *INTERNATIONAL WORKSHOP*, 2005, p. 123.

World Conference on Timber Engineering Oslo 2023

EXPERIMENTAL AND FINITE ELEMENT MODELLING (FEM) OF TIMBER-TIMBER COMPOSITE (TTC) UNDER HOGGING MOMENT

Mahmoud Wajdi Hammad[1], Hamid R ValiPour[2]

ABSTRACT: This study aims to investigate the structural behaviour of timber-timber composite (TTC) systems subject to hogging moment. A total of thirty-one TTC and six bare timber beam-to-column subassemblies (including fourteen replicates) were fabricated and tested to failure under hogging moment. The TTC beams were fabricated by connecting a cross laminated timber (CLT) slab to the top edge of a pair of laminated veneer lumber (LVL) or glued laminated timber (GLT) beams/joists. The effect of the CLT slab thickness, width, and orientation (i.e., loaded lengthwise or crosswise), column penetration in the CLT slab, bending moment to shear force ratio (span length), degree of shear interaction between the slabs and beams (controlled by the size of the shear connectors), and type of beams (LVL or GLT) on the structural performance of the TTC subassemblies were investigated experimentally. In addition, an analytical model was adopted for composite Timoshenko beams and modified to predict the stiffness and load carrying capacity of the TTC beams under hogging moment. Furthermore, 3-Dimentional Finite Element Models (FEM) have been developed and analysed for TTC structures subjected to hogging bending moments using ABAQUS.

KEYWORDS: Hogging moment, Timber-timber composite (TTC), Finite Element Modelling (FEM).

1 INTRODUCTION

Since sustainability in construction has become a major headline, the popularity of timber structures has grown significantly. The advancement in the manufacturing and treatment of large engineered wood panels (EWPs) such as cross laminated timber (CLT), glued laminated timber (GLT) and laminated veneer lumber (LVL) with improved durability, dimensional stability and resistance to variable environmental conditions has made it conceivable to plan and construct massive timber structures with performance on par with conventional steel and concrete structures, but with less detrimental impact on the environment [2, 3].

The application of lightweight TTC (i.e., LVL-CLT or GLT-CLT) floors, which are easy to assemble and conducive to prefabrication, seems to be a promising solution for the development of hybrid frames with continuous timber beams/slabs that can cover long spans with fewer columns or load bearing walls. Structural behaviour of timer composite floors (e.g., TTC and TCC) subjected to hogging bending moment remains largely unexplored. Preserving the continuity of CLT slabs and LVL/GLT beams across the columns can reduce the mid-span deflection, which is a major governing factor in designing the long-span TTC floors under service conditions. However, benchmark experimental data required for the accurate evaluation of the failure modes, stiffness, ductility, and load carrying capacity of continuous TTC beams (to column connection) under hogging moment are not available in the literature.

Thus, experiments were conducted to comprehensively study the structural behaviour of CLT-LVL and CLT-GLT composite beams subjected to hogging (negative) moment over the beam-to-column connection zone. In total, thirty-seven TTC and bare timber beam-to-column subassemblies were fabricated and tested under hogging moments.

Furthermore, in the 3-Dimentional Finite Element Models developed, nonlinear behaviour of the Engineered Wood Products (EWPs) such as Cross Laminated Timber (CLT), Laminated Veneer Lumber (LVL) and Glued Laminated Timber (GLT) were defined in a UMAT code using continuum damage mechanics modified by Gharib et al [4]. CLT was modelled using the layer wise approach, assigning parallel and perpendicular to the grain, which will be further discussed in this chapter. Meanwhile, the veneers and the lumber in the LVL and GLT were ignored respectively in ABAQUS, having LVL and GLT

[1] University of New South Wales (UNSW) Sydney, School of Civil and Environmental Engineering, mahmoud.hammad@unsw.edu.au
[2] University of New South Wales (UNSW) Sydney, School of Civil and Environmental Engineering

https://doi.org/10.52202/069179-0008

modelled as a single piece of timber. Steel was modelled using the standard user materials defined in ABAQUS.

The EC5 model is only applicable for timber composite beams/floors under sagging moments and hence there is a need for simple analytical model (like gamma-method) that can be used for stiffness and strength evaluation of timber composite subjected to hogging.

2 MATERIAL TESTING

2.1 ENGINEERED WOOD PRODUCTS (EWP)

The characteristic strength and mean elastic modulus values for C24(CLT), GLT(GL17) and LVL were taken from AS1720.1 [5] and the manufacturer's catalogue, respectively. Moreover, 4-point bending tests on 60 mm and 100 mm thick CLT panels (five identical strips of each thickness) were performed according to BS EN408 [6] to determine the mean global elastic modulus $E_{m,g}$ and bending strength f_b of the CLT panels. The mean global elastic moduli of the 60 mm and 100 mm thick CLT panels (lengthwise) were $E_{m,g}$= 11.3 GPa (CoV = 7.7%) and 9.7 GPa (CoV = 7.6%), respectively. The mean bending strength of the 60 mm and 100 mm thick CLT panels (lengthwise) were f_b = 37.5 MPa (CoV = 13.4%) and 31.9 MPa (CoV = 8.8%), respectively. The glulam (GL13) and LVL beams were manufactured from Radiata Pine in accordance with AS/NZS1328.1 [7] and AS4357.0 [8] requirements, respectively. The characteristic strength and mean elastic modulus of the GL13 and LVL respectively taken from AS1720.1 [5] and the manufacturer's catalogue are given in Table 3 1. The moisture content (MC) of the LVL and GL13 beams were measured by oven-dry method of AS/NZS 1080.1 [9]. The mean MC (obtained from five samples) of the LVL and GL13 are provided in **Table 1** and
Table 2. Bending tests were performed on three 85×336 mm GLT beams and the mean bending strength of GLT beams from the tests was $f_{b,mean}$= 49 MPa (CoV= 9%). The mean bending strength of the GL13 closely correlate with the mean bending strength of 45 MPa obtained from the samples taken from six Australian manufacturers of the glulam [10].

The mean bending strength of 200 mm deep LVL beams was $f_{b,mean}$= 66.5 MPa and it was obtained from the bending tests performed on two pairs of 3.0 m long bare LVL (200 mm deep) beam subassemblies. A size effect strength reduction factor of was considered according to the manufacturer's catalogue and the bending strength of 400 mm deep LVL beams was estimated to be $f_{b,mean}$= 59.7 MPa.

Table 1: *mean elastic modulus of C24 timber (used in manufacturing CLT panels), GLT and LVL beams.*

Timber type	Compressive strength (MPa)		Elastic moduli ‖ (GPa)	Shear moduli (GPa)	Moisture content (%)
	‖ to grain	⊥ to grain			
C24	21	2.5	11.0	0.69	11.6
GLT (GL17)	33	---	16.7	1.11	13.1
LVL	42	12	13.2	0.66	8.6

Table 2: *Characteristic strength (# Flexural strength for 200 mm deep LVL joists)*

Timber type	Bending strength (MPa)	Tensile strength ‖ (MPa)	Shear strength (MPa)
C24	24	14	4.0
GLT (GL17)	40	20	4.2
LVL	45#	30	4.6

2.2 DIGITAL IMAGE CORRELATION (DIC)

A digital image correlation (DIC) system was used during the bending tests on LVL (200 mm) beams to capture the strain field over the depth of the beams and accordingly establish the flexural strength and its corresponding strain. The contours of longitudinal strains ε_{xx} and the ε_{xx} strains at three points (i.e., farthest bottom, and top fibre and mid height of LVL) captured by the DIC are shown in Figure 3 1. At the peak load, the max. tensile strain (averaged at the farthest bottom fibre point P1) of the LVL was ε_{xx}=((0.00574+0.0058))/2=0.00577 (**Figure 1**). If a linear elastic behaviour for LVL is assumed, the tensile strength of the 200 mm deep LVL can be estimated from σ_{xx} = 0.00577×E = 0.00577×13200 = 76.2 MPa that confirms the bending strength of LVL.

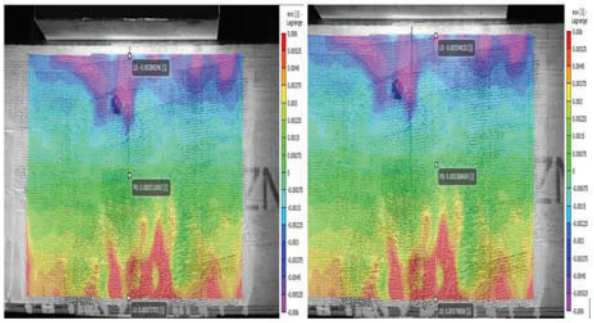

Figure 1: *Contours of ε_{xx} strains (DIC) at failure load of a bare LVL (200 mm) subassembly.*

https://doi.org/10.52202/069179-0008

2.3 SCREWS AND EPOXY (ADHESIVE)

Coach screws (KOP) 8 mm or 12 mm in nominal diameters with hexagonal heads manufactured in accordance with EN 14592 [11] were used as shear connectors in the TTC specimens. The KOP 8 mm screws were 160-200 mm, and the 12 mm screws were 160-220 mm in length **Figure 2**a [12]. The yield bending moment M y of 8 mm and 12 mm coach screws (i.e., KOP8 and KOP12) were obtained from 3-point bending tests in accordance with AS/NZS ISO 10984.1 [13], known as Method B. In total, five screws of each size were tested under 3-point bending with the screws spanning over 132 mm distance between the supports (**Figure 2**a) that satisfies the minimum span requirement of 11d and a minimum overhang of 2d as per AS/NZS ISO 10984.1 [13]. The sample load vs mid-span displacement obtained from the 3-point bending tests on KOP8 screws are plotted in **Figure 2**b. The intersection between the straight line offset 0.05d from the linear part of the graphs and the load-mid span displacement diagram is taken as the yield load F_y. The yield bending moment My of the coach screws was obtained from $My = F_y\, l / 4$, with l = 132 mm being the span length (**Figure 2**a). The mean yield bending moment of the KOP8 and KOP12 screws were My = 15.2 kNm (CoV = 10.6%) and 79.8 kNm (CoV = 9.5%), respectively. The yield strength σ_y of the screws was back calculated from the yield bending moment My, using $\sigma_y = M_y/S$, where S is the plastic section modulus. The plastic section modulus was calculated from $S = (1.1d_{in})3/6$, where d_{in} is diameter of the screw's cross-section excluding the threads and for KOP8 and KOP12 taken as 5.6 mm and 9 mm, respectively. The estimated mean yield strength of the KOP8 and KOP12 screws was σ_y = 442 MPa.

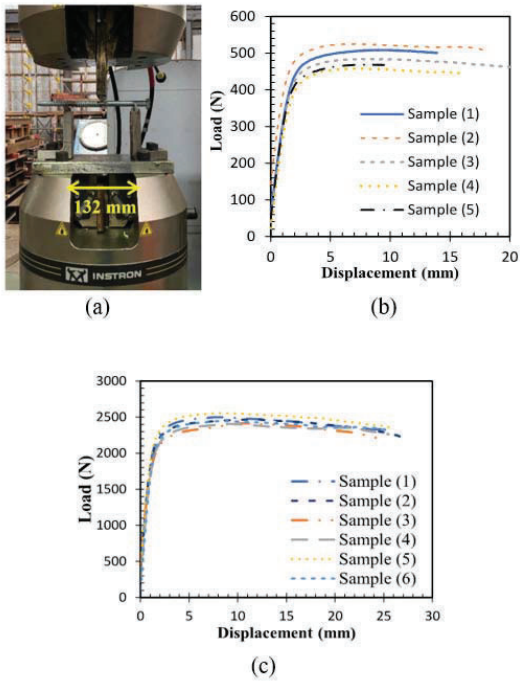

Figure 2: *(a) 3-point bending test of lag screws, and load vs mid span displacement of (b) KOP8, (c) KOP12 from 3-point bending.*

3 TTC SUBJECTED TO HOGGING MOMENT [1]

3.1 LOADING PROCEDURES

All the tests were performed according to the EN 26891 [14] loading protocol. All the specimens were loaded up to $0.4F_{est}$ over 2 minutes, then the load was kept constant for 30 seconds before the specimens were unloaded to $0.1F_{est}$ over 1.5 minutes (Figure 3a). At the end of the unloading stage, the load was kept at $0.1F_{est}$ for 30 seconds, before the specimen was reloaded to failure. The loading-unloading-reloading protocol of EN 26891 [14] was followed to eliminate (or minimise) the possible effects of internal friction between the CLT slab and LVL/GLT or test setup looseness on the structural behaviour of the specimens. The test was stopped once the applied (displacement-controlled) load dropped to 70% of the peak load (F_{max}), and accordingly the failure load was taken as the post-peak load corresponding to $0.7F_{max}$.

https://doi.org/10.52202/069179-0008

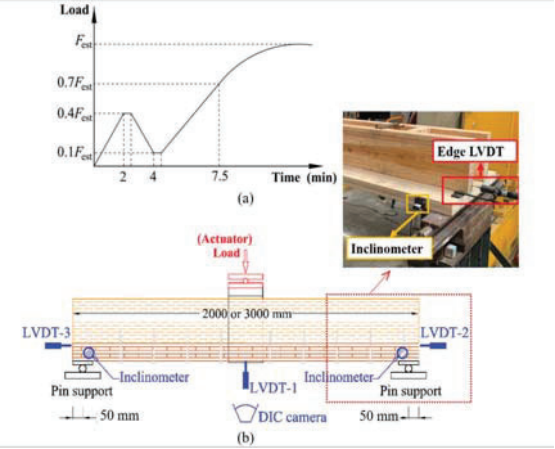

Figure 3: *(a) Loading procedure as per EN26891 [14] (b) loading and instrumentation of TTC subassembly.*

3.2 TTC subassemblies outline

Thirty-one TTC and six bare LVL or GLT beams representing the end span regions of a continuous timber/TTC floor (**Figure 4**) were fabricated and tested under hogging moment. The TTC and bare timber beams were either 2.0 m or 3.0 m long, which represent continuous TTC floors with span length in the range of L = 8-10 m, based on the assumption that the points of contraflexure are approximately located at cross-sections 0.125-0.15L away from the supporting columns. The TTC composites were benchmarked against the subassemblies with bare timber beams to determine contribution of the CLT slabs to the hogging moment and stiffness of the TTC beams/floors continuous across the columns.

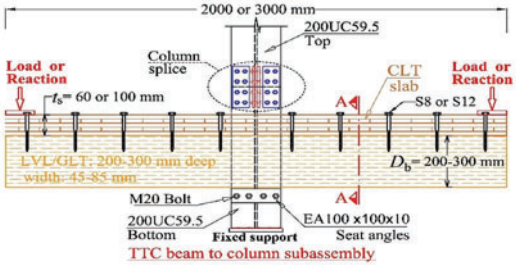

Figure 4: *TTC subassembly layout.*

Table 3: *Details of TTC specimen*

No.	Joists		Screw/Shear connector	Slab width (mm)	CLT Thickness (mm)	CLT orientation	Hole
	Size (mm)	Type/ Grade					
2 m long - Short span or group S							
S1 (No. 1)	200×65	LVL	KOP8	800	100	L	N
S1 (No. 2)	200×65	LVL	KOP8	800	100	L	N
S2	200×65	LVL	KOP12	800	100	L	N
S3	200×65	LVL	KOP12	800	60	L	N
S4 (No. 1)	300×45	LVL	KOP8	800	60	L	N
S4 (No. 2)	300×45	LVL	KOP8	800	60	L	N
S5	300×45	LVL	KOP8 + Glue	800	60	L	N
S6	295×85	GLT	KOP12	800	100	L	N
S7	295×85	GLT	KOP12	1000	100	L	N
S8 (No. 1)	200×65	LVL	KOP12	800	60	L	Y
S8 (No. 2)	200×65	LVL	KOP12	800	60	L	Y
S9 (No. 1)	300×45	LVL	KOP8	800	60	L	Y
S9 (No. 2)	300×45	LVL	KOP8	800	60	L	Y
S10 (No. 1)	295×85	GLT	KOP12	1000	100	L	Y
S10 (No. 2)	295×85	GLT	KOP12	1000	100	L	Y
S11	295×85	GLT	KOP12	800	100	L	Y
S12 (No. 1)	200×65	LVL	KOP12	800	60	C	Y
S12 (No. 2)	200×65	LVL	KOP12	800	60	C	Y
S13	295×85	GLT	KOP12	800	100	C	Y
3 m long - Long span or group L							
L1	295×85	GLT	KOP12	800	60	L	N
L2	295×85	GLT	KOP12	800	60	C	N
L3 (No. 1)	300×45	LVL	KOP8	800	60	L	Y
L3 (No. 2)	300×45	LVL	KOP8	800	60	L	Y
L4 (No. 1)	300×45	LVL	KOP8	800	60	C	Y
L4 (No. 2)	300×45	LVL	KOP8	800	60	C	Y
L5 (No. 1)	300×45	LVL	KOP8 + Glue	800	60	L	Y
L5 (No. 2)	300×45	LVL	KOP8 + Glue	800	60	L	Y
L6 (No. 1)	200×75	LVL	KOP8	800	100	C	Y
L6 (No. 2)	200×75	LVL	KOP8	800	100	C	Y
L7 (No. 1)	200×75	LVL	KOP12	800	100	C	Y
L7 (No. 2)	200×75	LVL	KOP12	800	100	C	Y

3.3 MODES OF FAILURE

In total, seven distinctive failure modes, i.e., I to VII, including six primary (I-VI) and one secondary (VII) were observed in the tested specimens. Failure mode I was associated with the onset of tensile flexural cracks (fracture) in the outermost lamella of the CLT panels. Failure modes II and III were observed in TTC beams with CLT panels loaded crosswise (i.e., perpendicular to the outer lamellae of the CLT). In mode II, fracture of the lamella along the edge of the glue line and in mode III, tensile fracture (perpendicular to the grain) took place. Failure mode IV was observed in CLT slabs loaded lengthwise and it was associated with rolling shear failure in the second lamella, which was loaded perpendicular to the grain.

Failure mode V was associated with the fracture of the epoxy line at the interface between the CLT and LVL beam when the composite action between the slab and the beam was developed by the combination of the screw and epoxy. Mode VI was associated with the onset of tensile flexural cracks in the LVL/GLT beams, and in mode VII shear cracks developed along the LVL/GLT beams and reached the end of the beam well into the post-peak (softening) stage. Mode VI predominantly took place in conjunction with Modes I-III while mode VII was mostly observed in 2 m long TTC beams. In all specimens (except for S6, S7 and S10), failure mode VII was a secondary mode that occurred after the onset of a primary mode and during the post-peak stage of the behaviour. In specimens S6, S7 and S10, mode VII was the dominant (primary)

https://doi.org/10.52202/069179-0008

failure mode that took place before others. The longitudinal shear cracks (in mode VII) mostly propagated along the glue line of the GLT beams and the shear cracks were at the height where the screw tips were located. This resulted in the tip of the screw to slightly bend.

Table 4: *Peak load, bending moment capacity, service stiffness and failure modes of the TTC specimens.*

No.	Peak load F_{peak} (kN)	Mean values			Failure modes
		Bending capacity M_{peak} (kNm)	Stiffness $K_{s,0.4}$ (kN/mm)	Peak load F_{peak} (kN)	
2 m long - Short span or group S					
S1 (No. 1)	211.7	100.1 [89.1][1]	11.3	210.9 (0.6%)[2]	I, IV, VI
S1 (No. 2)	210.0				
S2	252	119.7 [106.5]	13.3	252	
S3	170.6	81.1 [72.1]	9.5	170.6	
S4 (No. 1)	198.4	96.3 [85.7]	15.7	202.7 (3.0%)	I, VI & VII
S4 (No. 2)	206.9				
S5	206.5	98.1 [87.3]	21.0	206.5	I, IV, V, VI, VII
S6	397.1	188.6 [167.8]	32.9	397.1	I, IV, VI, VII
S7	428.4	203.5 [181]	34.3	428.4	
S8 (No. 1)	159.0	74.6 [66.4]	8.7	157.1 (1.7%)	I, IV, VI
S8 (No. 2)	155.2				
S9 (No. 1)	202.7	94.4 [83.9]	14.7	198.6 (2.9%)	I, IV, VI
S9 (No. 2)	194.6				
S10 (No. 1)	386.0	197.3 [175.5]	34.0	415.4 (10%)	I, IV, VI, VII
S10 (No. 2)	444.7				
S11	384.8	182.8 [162.6]	33.7	384.8	
S12 (No. 1)	143.7	67.1 [59.7]	8.2	141.2 (2.5%)	II & VI
S12 (No. 2)	138.7				
S13	370.3	175.9 [156.5]	28.1	370.3	II, III, VI, VII
3 m long - Long span or group L					
L1	282.8	205.0 [190.2]	11.3	282.8	I & VI
L2	239.8	173.9 [161.3]	10.1	239.8	II, III, VI
L3 (No. 1)	138.5	108.1 [100.2]	5.8	149.1 (10%)	I, IV, VI
L3 (No. 2)	159.6				
L4 (No. 1)	126.9	90.1 [83.6]	5.0	124.3 (3%)	II, III, VI
L4 (No. 2)	121.7				
L5 (No. 1)	176.2	136.7 [126.8]	10.4	188.6 (9.3%)	I, IV, V & VI
L5 (No. 2)	201.1				
L6 (No. 1)	99.5	73.7 [68.3]	3.1	101.7 (3.1%)	II, III, IV & VI
L6 (No. 2)	103.8				
L7 (No. 1)	130.9	90.8 [84.2]	3.4	125.2 (6.4%)	II, III, IV & VI
L7 (No. 2)	119.5				

The load versus deflection evolution for specimens with 2 m and 3 m long TTC beams are plotted in Figure 5 and Figure 6, respectively. The mean peak load F_{peak} and the serviceability stiffness $K_{s,0.4}$ of the TTC specimens obtained from the load versus deflection results are summarised in Table 4. The service stiffness was taken as the slope of the line between the two points corresponding to $0.1F_{peak}$ and $0.4F_{peak}$ [14] on the load-deflection diagram.

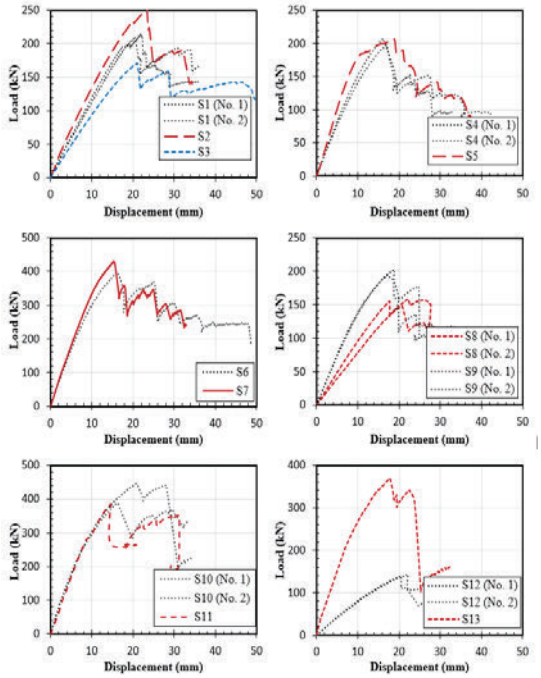

Figure 5 *Load versus deflection of the TTC subassemblies (group S, 2 m long TTC beams)*

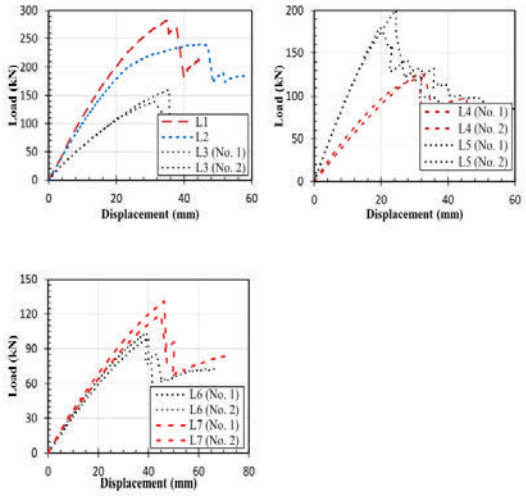

Figure 6 *Load versus deflection of the TTC subassemblies (group L, 3 m long TTC beams).*

3.4 EFFECT OF VARIOUS PARAMETERS

The width of the CLT slab and column penetration in the slab (resulting in the reduction of the slab area of up to 20%) had minor (less than 9%) influence on the stiffness and peak load. However, the CLT slab thickness (in the range of 60-100 mm) had a major (up to 48%) influence on the peak load and stiffness of the TTC beam subject to hogging moment. The size of shear connectors (degree of shear connection provided by 8-12 mm screws) and

https://doi.org/10.52202/069179-0008

orientation of the CLT slab had a moderate (max. 18-23%) influence on the load carrying capacity and stiffness of the samples. In the tested specimens, the stiffness and peak load of TTC specimens with lengthwise loaded CLT were up to 20% higher than the ones with CLT loaded crosswise.

3.5 ANALYTICAL RESULTS

The analytical model obtained from the solution to the Timoshenko composite beam was slightly more accurate than the *g*-method, especially for TTC beams with smaller shear span over cross-section depth ratio. But the *g*-method (EN 1995-1-1 [15]) is simpler, and more efficient and usable than the Timoshenko composite beam model. The comparison bar chart is shown in Figure 7.

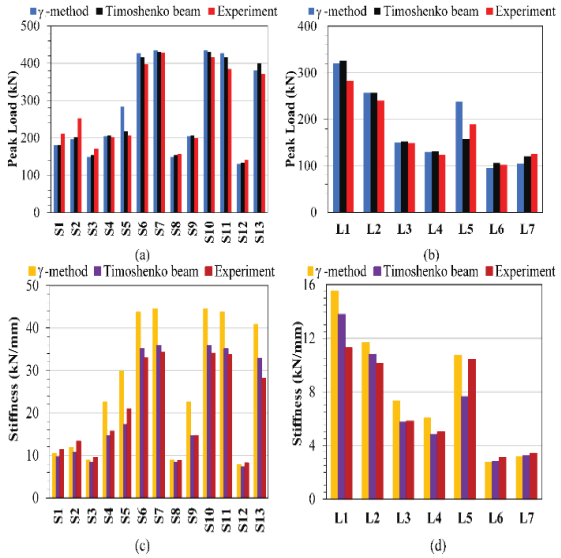

***Figure** 7 Comparison of (a-b) peak loads and (c-d) service stiffness values obtained from two analytical models and experimental results.*

For all specimens (except S5 and L5 with glued shear connections), the peak load analytically predicted by γ-method and Timoshenko beam model had close correlation with the experimental results. In the case of specimens S5 and L5, the gamma-method overestimated the peak load by 37.1% and 26.1%, respectively. The maximum difference between the peak load predicted by the Timoshenko beam model and the experimental peak load was less than 19.5% (observed in specimen S2). The service stiffness of the specimens (specially the S group with large cross-section depth over shear span ratio) predicted by the Timoshenko beam model was more accurate than the stiffness obtained from the γ-method as evident from the bar charts shown in Figure 7c-d.

4 FINITE ELEMENT MODELLING (FEM)

4.1 OVERVIEW

In the FE models, CLT panels were modelled using the layer-wise approach with mechanical properties assigned to parallel and perpendicular to the grain lamellae. However, the veneers and the lumbers in the LVL and GLT were not explicitly modelled, and LVL and GLT were treated as a single piece of timber. To enhance the computational efficiency and avoid numerical convergence/instability issues associated with stress concentration and fine meshes around the screw shear connectors, the shear connectors were modelled using nonlinear springs defined at the interface between slab and timber joists/beams. Apart from nonlinearities of steel, timber and concrete/grout, the geometrical non-linearity was also considered in the FE simulation, though effect of geometrical nonlinearity was deemed to be negligible.

The configuration and details of loading, boundary conditions and geometric outline of the TTC and TCC specimens modelled in ABAQUS are provided in Figure 8. To simplify the structure and increase speed of analyses without comprising the accuracy of the results, the steel column of the subassemblies was not modelled in the FE simulations. The load was applied to a stiff loading plate with a displacement rate consistent with the experiments. The supports of the timber composite beams were treated as an ideal pin and only the displacements in x, y, and z direction were fixed along the bottom centreline of the support plates accordingly (Figure 8). To prevent localised crushing and excessive deformation of the timber joists (loaded perpendicular to the grain), timber stiffeners were modelled underneath the loading plates (Figure 8). The stiffeners were assumed to be linear elastic materials with mechanical properties identical to timber joists/beams.

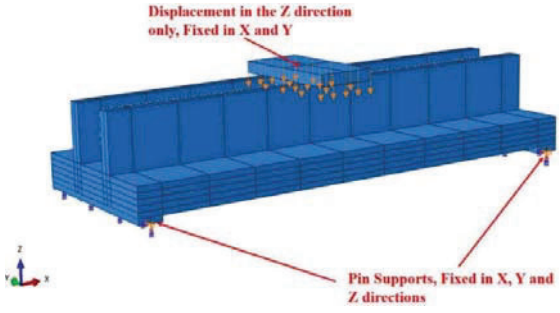

***Figure 8** Outline of the geometry, loading and support conditions considered in the FE model of TTC and TCC beams.*

4.2 MESH SIZE

The element used for modelling LVL, GLT, CLT, concrete slab, steel loading plate and support plates was a standard linear Hexagonal C3D8R (an 8-node linear brick) element with reduced integration and enhanced hour-glass control. The screws were modelled using a wedge 8-node linear brick (C3D8) element with full integration. The size and configuration of the FE mesh for the timber beams/slabs and screws are depicted in Figure 9 and the element size for each component is given in Table 5.

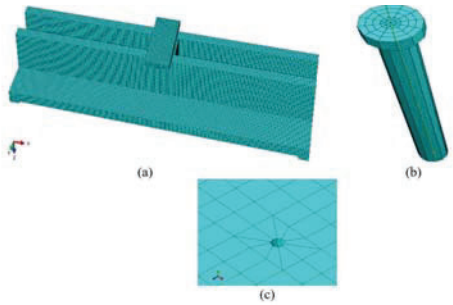

Figure 9 *FE mesh (a) entire TTC/TCC domain, (b) dowel and (c) domain around the hole.*

Table 5 *Mesh type and size for each respective element used in the TTC model.*

Structural component	Mesh type	Mesh size
CLT Slab	C3D8R	15
LVL	C3D8R	15
GLT	C3D8R	15
Stiffeners	C3D8R	15
Steel Load Plate	C3D8R	15
Steel Support plates	C3D8R	15
Dowel (KOP8 and KOP12 screws)	C3D8R	2

4.3 COMPARISON AND DISCREPANCIES

The FEM was adequately able to capture the results within close proximity. There was a slight discrepancy between the experimental GLT members and the FEM GLT. This can be attributed to rolling shear failure and stress localisation. Furthermore, some specimen was modelled with screws instead of line connectors. The results are summarised in Figure 10.

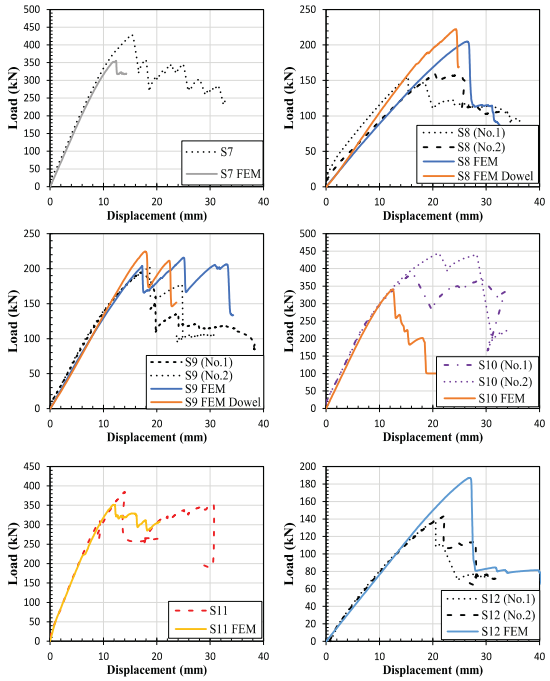

Figure 10 *experimental vs analytical Load vs displacement with line connectors and dowels.*

5 CONCLUSIONS

The purpose of this project was to investigate the structural performance of TTC and TCC systems through full scale laboratory experimentation, advanced numerical simulation, and development of analytical models. Emphasis was placed on structural behaviour of the TTC and TCC floors subjected to hogging moment.

- The dominant failure mode of TTC beams under hogging moment was brittle and it was associated with tensile flexural failure in the outermost lamellae of the CLT slabs combined with tensile flexural failure in the LVL/GLT joists. These modes were followed by rolling shear in the CLT slab, or shear failure of the LVL/GLT joists specially during the post-peak stage of the behaviour.
- The orientation of CLT slabs had some effect on the stiffness and load carrying capacity. In the tested specimens, the stiffness and peak load of TTC specimens with lengthwise loaded CLT were up to 20% higher than the ones with CLT loaded crosswise.
- Despite a 20% reduction in the cross-sectional area of the CLT slabs, because of the column penetration, the reduction in the stiffness and load carrying capacity was less than 9%.
- The size of screw shear connectors (8 and 12 mm) had a moderate (up to 18%) influence on the peak load and stiffness of the TTC under hogging moment. However, using the epoxy glue in conjunction with screws considerably increased stiffness of the TTC specimens. The joists glued to the CLT slabs with opening also prevented the crack initiation and propagation from

https://doi.org/10.52202/069179-0008

the corner of the penetration/opening and increased the peak load of the TTC accordingly.

- The analytical model obtained from the solution to the Timoshenko composite beam was slightly more accurate than the γ-method, especially for TTC beams with smaller shear span over cross-section depth ratio. But the γ-method is simpler, and more efficient and usable than the Timoshenko composite beam model.
- The nonlinear 3D FE models were able to capture the complex (combination of shear, tension parallel and perpendicular to the grain) failure modes of TTC and TCC beam to column subassemblies. Small difference was found between the results of two modelling strategies, i.e., explicit modelling of the screw shear connectors and implicit modelling of the she connectors with nonlinear springs/links.

ACKNOWLEDGEMENT

The Authors would like to thank UNSW Heavy Structure Lab (HSL) team for their efforts during the fabrication process of project.

REFERENCES

[1] Hammad, M., H. Valipour, and M. Bradford, *Timber-timber composite (TTC) beams subjected to hogging moment.* Construction and Building Materials, 2021. **321**.

[2] Woodard, A.C. and H.R. Milner, *Sustainability of timber and wood in construction*, in *Sustainability of Construction Materials*. 2016. p. 129-157.

[3] Milner, H.R. and A.C. Woodard, *Sustainability of engineered wood products*, in *Sustainability of Construction Materials*. 2016. p. 159-180.

[4] Gharib, M., et al., *Three-dimensional constitutive modelling of arbitrarily orientated timber based on continuum damage mechanics.* Finite Elements in Analysis and Design, 2017. 135: p. 79-90.

[5] *Standards Australia Limited, AS 1720.1-2010 Timber structures - Design methods*. 2010.

[6] British Standard, I., *BS EN 408:2010+A1:2012: Timber structures - Structural timber and glued laminated timber - Determination of some physical and mechanical properties.* BSI Standards Publication, 2012.

[7] *AS/NZ1328 (1998), Glued laminated structural timber Part 1: Performance requirements and minimum production requirements.* 1998.

[8] Zealand, S.A.o.A.a.S.N., *AS_NZS 4357.0_2005 Structural laminated veneer lumber - Specifications*. 2005.

[9] *Standards Association of Australia and Standards New Zealand, AS NZS 1080.1 2012 Timber Methods of test - Moisture content*. 2012.

[10] Milner, H.R., *Design Values for Australian Glulam*, F.W.P.R.D. Corporation, Editor. 2004: Australia.

[11] Standard, I., *EN 14592 Timber structures-Dowel-type fasteners-Requirements*. 2012.

[12] Blass, H.J. and C. Sandhaas, *Timber Engineering Principles for Design*. 2017, KIT Scientific Publishing.

[13] *AS/NZS 10984.1 Timber structures — Dowel-type fasteners Part 1 : Determination of yield moment.* 2015.

[14] *EN 26891:1991- Timber Structures - Joints made with mechanical fasteners - General principles for The determination of strength and deformation characteristics*. 2001. 43-43.

[15] Standards, B., *Eurocode 5 (EC 5), Design of timber structures- Part 1-1: General- Common rules and rules for buildings. BS EN 1995-1-1*. 2004, British Standards.

World Conference on Timber Engineering Oslo 2023

QUASI-STATIC OUT-OF-PLANE TESTING OF REINFORCED CROSS-LAMINATED TIMBER

Eric Kjolsing[1], Mark Weaver[2], Marco Lo Ricco[3], Adam Senalik[4], Jason Cattelino[5], Jim Henjum[6], Russell Edgar[7], Edwin Nagy[8]

ABSTRACT:

There is an increasing desire to use wood products, which are environmentally sustainable, in protective design. Although cross-laminated timber (CLT) panels can be designed to mitigate blast threats, softwood CLT needs some form of reinforcement to defeat typical design basis ballistic threats. The inclusion of thin steel plates within a CLT panel's layup, which has previously been shown to be feasible from both a cost and ballistic performance perspective at small scale, could conceivably be used to transform CLT into both a blast and ballistic resistant panel. To evaluate the response of such a reinforced CLT (RCLT) panel at full scale, an analytical methodology was developed to predict the performance of RCLT panels to out-of-plane loading. The methodology was used to develop three unique RCLT layups that varied both the lumber grade and ply orientation to achieve targeted failure mechanisms. Twelve RCLT panels were fabricated and subjected to quasi-static four-point bending. Tested specimens showed high levels of ductility, excellent wood-to-steel adhesion, and significant post-peak load carrying capacity. Dynamic analyses indicate that the 7-ply RCLT panels perform better than unreinforced 7-ply and 9-ply CLT panels.

KEYWORDS: Cross-Laminated Timber, CLT, Reinforced CLT, RCLT, Enhanced CLT, Protective Design, Blast

1 INTRODUCTION

Buildings used by the U.S. Department of State (DOS) and U.S. Department of Defense (DOD) often must meet blast, ballistic resistance, and forced entry (FE) design requirements to mitigate the hazardous effects associated with terrorism [1]. Historically, DOS and DOD buildings exposed to these threats have been constructed using concrete and steel. A significant amount of testing has been performed to demonstrate the ability of these building materials to resist blast, ballistic, and FE threats. A relatively smaller number of tests have been performed on wood construction for similar threats. At least part of this stems from the relative difficulty of designing light-frame wood construction to resist these threats efficiently and economically. However, the emergence of mass timber construction, particularly cross-laminated timber (CLT), presents a sustainable, modular, and cost-effective alternative building material for high-security infrastructure. Recent blast testing of cross-laminated timber [2] has informed the development of design guidance in the United States [3]. Additional ballistic testing has shown the feasibility of incorporating thin steel plates within a CLT panel's layup to defeat typical design basis ballistic threats [4]. It is hypothesized that by detailing the ballistic reinforcing layers to act compositely with the wooden CLT panel, this reinforced CLT (RCLT) panel may also demonstrate improved blast performance.

2 OBJECTIVE

An analytical method was developed to estimate the resistance function (i.e., the out-of-plane (flatwise) load versus displacement relationship) of RCLT panels with arbitrary (user defined) layups. This methodology was used to select three distinct RCLT layups that were fabricated by SmartLam North America and subsequently tested under quasi-static out-of-plane loading at the University of Maine. The objectives of this effort were to (a) develop a viable methodology to predict the performance of RCLT panels to out-of-plane loading, (b) generate test data to validate the methodology, and (c) demonstrate the post-peak behavior of RCLT panels.

[1] Eric Kjolsing, Karagozian & Case, USA, kjolsing@kcse.com
[2] Mark Weaver, Karagozian & Case, USA, weaver@kcse.com
[3] Marco Lo Ricco, USDA Forest Products Laboratory, USA, marco.loricco@usda.gov
[4] Adam Senalik, USDA Forest Products Laboratory, USA, christopher.a.senalik@usda.gov
[5] Jason Cattelino, Rotho Blaas, USA, jason.cattelino@rothoblaas.com
[6] Jim Henjum, SmartLam North America, USA, jim.henjum@smartlam.com
[7] Russell Edgar, University of Maine, USA, russell.edgar@maine.edu
[8] Edwin Nagy, University of Maine, USA, edwin.nagy@maine.edu

https://doi.org/10.52202/069179-0009

3 ANALYTICAL METHOD

An analysis methodology was developed to predict the out-of-plane bending resistance of RCLT panel designs. The methodology is similar to the shear analogy method used for standard CLT panels [3],[5],[6], but the relevant equations are modified to permit the inclusion of non-wood (e.g., steel) laminations. As a verification effort, the methodology was used to estimate the ASD design values for several standard CLT panels [7]. The comparison showed good agreement for most of the design values, with the methodology predicting an approximately 9% higher shear strength than published values. This difference was found to stem from different shear capacity equations used in the methodology [6] and by ANSI/APA PRG-320 [8]. The PRG-320 shear equation implicitly assumes a uniform wood cross section, resulting in the well-known equation for peak shear stress in a rectangular section, shown in Equation (1):

$$\tau = 1.5\frac{V}{A} \tag{1}$$

In contrast, the developed methodology based on the shear analogy method uses a shear flow calculation to estimate the shear capacity of the CLT/RCLT panels. Due to the alternating, orthogonal wood layers the shear stress through the panel thickness is non-parabolic, contrary to that assumed by Equation (1). The effect is that the shear flow calculation estimates a slightly lower peak shear stress demand in the panel for an applied unit shear, resulting in a larger estimate of the panel's shear force capacity. An analogy to the design of steel W-shapes is appropriate. The flanges in a steel W-shape drive the shear stress distribution in the web to be nearly uniform. Similarly, although to a lesser degree, the strongly oriented outer wood layers (in a CLT panel) and steel inserts (in an RCLT panel) result in a more uniform shear stress distribution through the panel thickness (relative to the parabolic shear stress distribution assumed in PRG-320), leading to a lower peak shear stress in the panel, and a larger shear force capacity of the panel.

4 TEST SPECIMENS

4.1 LAYUP SELECTION

The analysis methodology was used to select RCLT panel layups for quasi-static testing. Several dozen wood species and layups were considered. In each case the steel layers were placed near the exterior of the panel to maximize their contribution to bending strength and their effect on redistributing the shear stress through the panel. The steel layers were ASTM A1011 sheets with a specified minimum yield strength of 250 MPa. Based on the calculated capacity estimates and economy of material, three wood species/grades were selected: Spruce-Pine-Fir South (SPF-S) No.2, Southern Pine (SP) No.2, and 2400F-2.0E Southern Pine MSR (SP MSR). These three wood grades were oriented in three specific layups to target desired failure limit states.

Layup number 1 (Table 1) utilized SPF-S No.2 in each wood layer and acted as a baseline case (note that using SPF-S No.2 in an unreinforced CLT panel is a standard 'V4' grade CLT panel). SPF-S No.2 has a relatively low density, hardness, and toughness when compared to other wood species and thus served as a reasonable estimate for the lower bound case. The analysis methodology predicted layup number 1 would fail in rolling shear.

Layup number 2 (Table 2) utilized SP No.2 in each 0-degree layer (the major strength direction) and SP MSR in each 90-degree layer (the minor strength direction). SP provides a higher rolling shear capacity then SPF-S, which increases the overall shear capacity of the panel. The analysis methodology predicted the steel layers would yield nearly simultaneously with rupture of the outer wood layers.

Layup number 3 (Table 3) is similar to layup number 2, except the outer wood layers (wood plies 1 and 7) are oriented in the 90-degree (minor) direction. Changing the orientation of the outer layers only slightly changes the shear capacity of the panel but greatly reduces the panel's flexural capacity. Thus, the intent was a panel in which the steel plates would yield prior to either a wood flexural rupture or rolling shear failure. The analysis methodology predicted the steel layers would yield first, followed by rupture of the inner wood core.

Analogous unreinforced CLT panels (i.e., baseline cases) were not tested due to cost considerations.

4.2 SPECIMEN FABRICATION

For each of the three layups, four replicate specimens were fabricated by SmartLam North America (twelve specimens total). The fabrication process started by sandblasting the steel plates to remove oils and mill scale. The lumber was acclimated and processed according to normal CLT operations and PRG-320 requirements. Steel plates were placed by hand during the pressing operation to facilitate correct alignment. Adhesive, similar to that used for normal CLT production, was used. All specimens were approximately 1.22 m wide x 4.27 m long x 250 mm thick. Figure 1 shows the installation of the steel plates during the layup process. Figure 2 shows some of the finished panels.

https://doi.org/10.52202/069179-0009

Table 1: *Layup number 1*

Grade	Orientation	Thickness [mm]
SPF-S No.2	0-deg	35
A1011 Gr.36 Steel	-	3.4
SPF-S No.2	90-deg	35
SPF-S No.2	0-deg	35
SPF-S No.2	90-deg	35
SPF-S No.2	0-deg	35
SPF-S No.2	90-deg	35
A1011 Gr.36 Steel	-	3.4
SPF-S No.2	0-deg	35

25.4mm = 1 inch

Table 2: *Layup number 2*

Grade	Orientation	Thickness [mm]
SP No.2	0-deg	35
A1011 Gr.36 Steel	-	3.4
2400F-2.0 SP MSR	90-deg	35
SP No.2	0-deg	35
2400F-2.0 SP MSR	90-deg	35
SP No.2	0-deg	35
2400F-2.0 SP MSR	90-deg	35
A1011 Gr.36 Steel	-	3.4
SP No.2	0-deg	35

25.4mm = 1 inch

Table 3: *Layup number 3*

Grade	Orientation	Thickness [mm]
SP No.2	90-deg	35
A1011 Gr.36 Steel	-	3.4
2400F-2.0 SP MSR	90-deg	35
SP No.2	0-deg	35
2400F-2.0 SP MSR	90-deg	35
SP No.2	0-deg	35
2400F-2.0 SP MSR	90-deg	35
A1011 Gr.36 Steel	-	3.4
SP No.2	90-deg	35

25.4mm = 1 inch

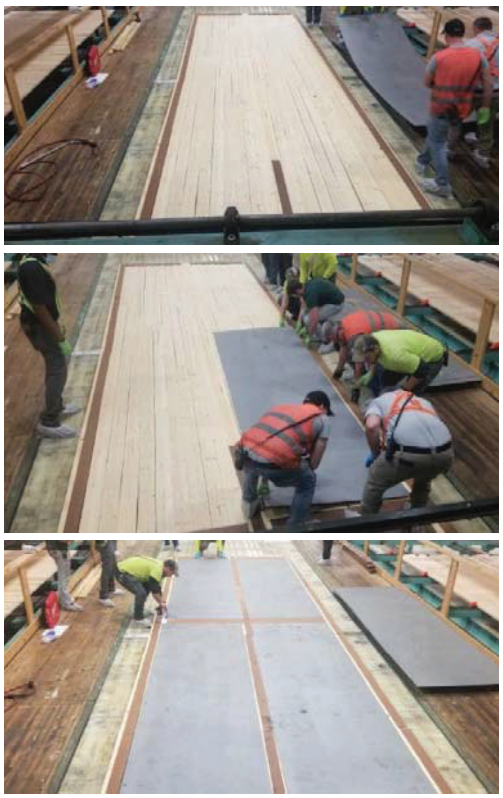

Figure 1: *RCLT steel plate installation*

Figure 2: *Finished RCLT panels*

https://doi.org/10.52202/069179-0009

5 TEST CONFIGURATION

The twelve RCLT specimens were tested at the University of Maine under quasi-static four-point bending. A schematic of the test setup is shown in Figure 3 with Figure 4 showing a corresponding isometric view of the actual test setup. For each test, a 1300-kN actuator loaded a steel spreader/cross I-beam which then loaded two steel W-shapes running orthogonal to the span length. The cross beam-to-W-shape connection was detailed to allow rotation of the W-shapes. The RCLT panels were supported on hollow structural sections (HSS) across the full width of the panels. The HSS sections were supported on concrete supports and were permitted to rotate. Between the W-shape-to-RCLT panel and RCLT panel-to-HSS section were lubricated sheets of high-density polyethylene (HDPE) to reduce frictional constraint of the RCLT panel. The test span length was 3.66 m. Three displacement gages recorded the midspan displacement while four video cameras oriented at the four panel corners (i.e., North-West, North-East, South-West, South-East) recorded the testing. The applied load was recorded via a calibrated load cell at the actuator. Testing was performed well beyond the maximum load carrying capacity of the panel.

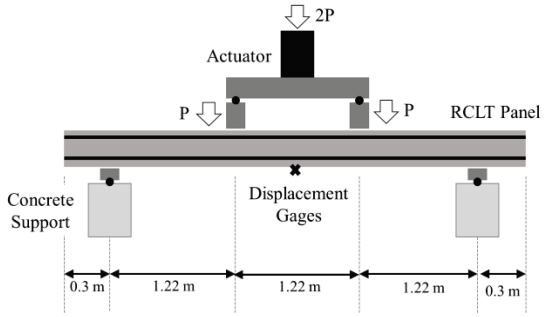

Figure 3: *Schematic test configuration (elevation)*

Figure 4: *Test configuration*

6 TEST RESULTS

6.1 LAYUP NUMBER 1

Figure 5 shows the force-displacement curves of the four specimens. On average, the layup displayed a rolling shear failure near 465 kN with a corresponding deflection of 25 mm. There is a sharp drop in load carrying capacity after the rolling shear failure, but a significant residual capacity remains. This residual capacity is attributed to the two steel plates, each acting compositely with the immediately adjacent (intact) wood layers, and quasi-compositely with the other steel plate. This adds ductility to the system, even after a rolling shear failure has occurred. Figure 6 shows specimen 1 under various levels of loading. The images correspond to (A) the specimen just after a rolling shear failure, (B) midspan flexural (tension) rupture of the wood, and (C) the post-test state of the panel.

6.2 LAYUP NUMBER 2

Figure 7 shows the force-displacement curves of the four specimens. On average, the layup first displayed a flexural wood rupture near 750 kN with a corresponding deflection of 35 mm, and later, a rolling shear failure near 76 mm of displacement. Figure 8 shows specimen 1 under various levels of loading. The images correspond to (A) the onset of wood flexural rupture, (B) a rolling shear failure, and (C) the post-test state of the panel.

As seen in Figure 7, specimen 2 displayed significant load carrying capacity through 250 mm of displacement. Unlike the other three specimens, specimen 2 did not display a rolling shear failure. Instead, after the outer wood ply on the underside of the panel ruptured, the core of the panel displayed an adhesive bond failure between the tension steel and wood core, as well as a flexural rupture of the wood core layers near midspan. The significant drop in load carrying capacity (around 250 mm) is due to this bond failure eventually propagating to the support. The force-displacement curve for specimen 2 is an ideal outcome for blast design as the area under the curve represents significant energy dissipation potential. Figure 9 shows the failure sequence from the specimen 2 test.

https://doi.org/10.52202/069179-0009

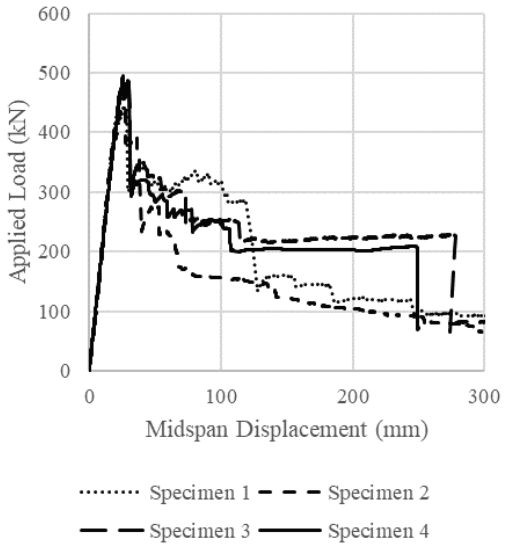

Figure 5: *Layup number 1 force-displacement curves*

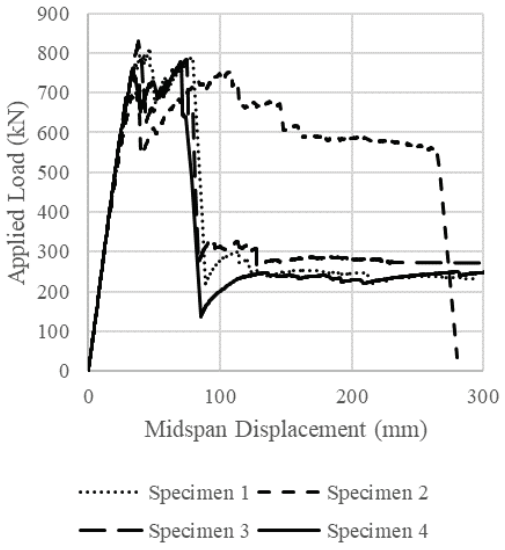

Figure 7: *Layup number 2 force-displacement curves*

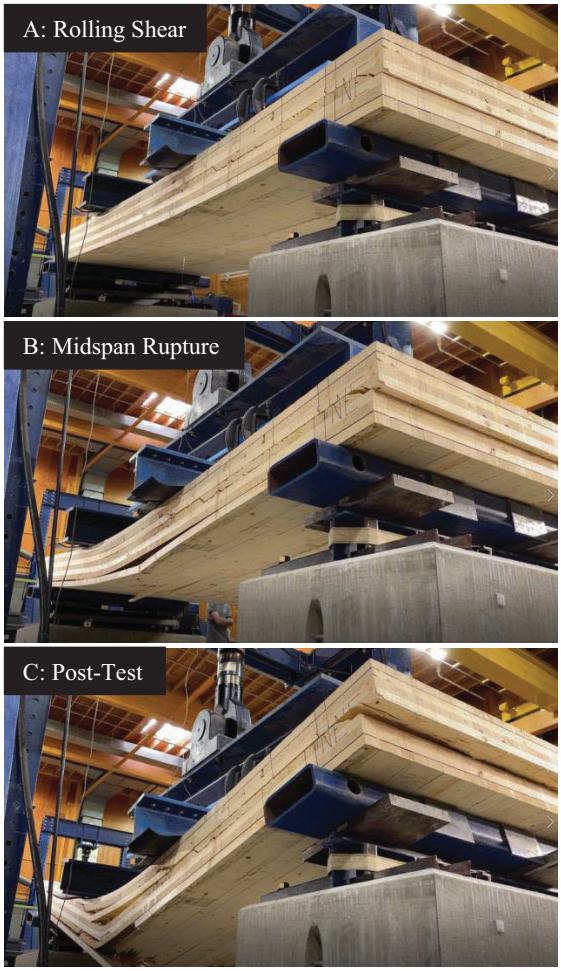

Figure 6: *Layup number 1, specimen 1, under loading*

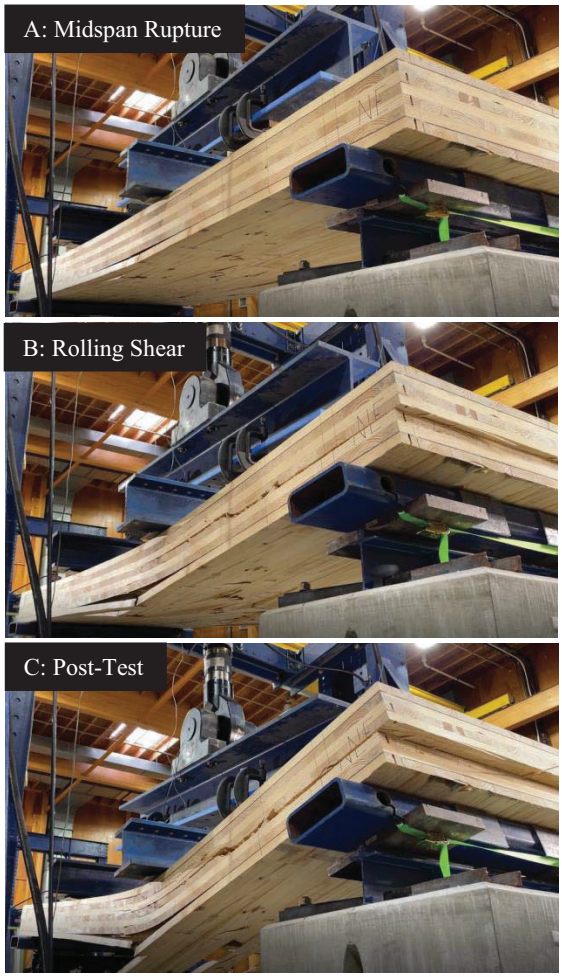

Figure 8: *Layup number 2, specimen 1, under loading*

https://doi.org/10.52202/069179-0009

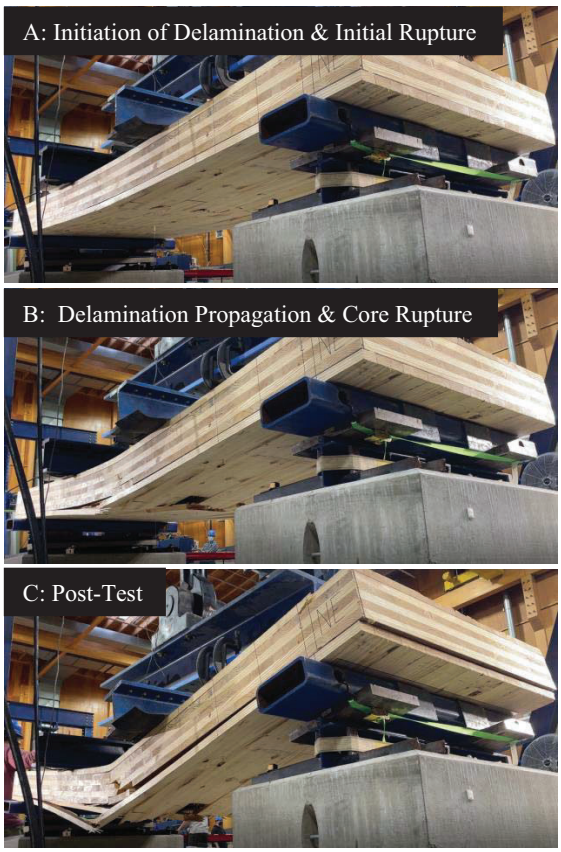

Figure 9: *Layup number 2, specimen 2, under loading*

6.3 LAYUP NUMBER 3

Figure 10 shows the force-displacement curves of the four specimens. On average, the layup displayed steel yielding behavior near 320 kN (23 mm corresponding displacement) and a rolling shear failure near 560 kN and 94 mm of displacement. Figure 11 shows specimen 1 under various levels of loading. The images correspond to (A) the specimen just before a rolling shear failure, (B) a rolling shear failure, and (C) the post-test state of the panel.

6.4 COMPARISON TO PRE-TEST ESTIMATES

Figure 12 compares pre-test estimates with average load-displacement curves obtained from testing. In all cases the pre-test initial stiffness underestimated the actual stiffness. The pre-test prediction for layup 1 was a rolling shear failure, which was observed in the actual test. The pre-test prediction for layup 2 was steel yielding followed by flexural rupture of the outer wood ply. The pre-test calculation erroneously assumed failure of the outer wood ply was an ultimate limit state, thus leading to the relatively brittle nature of the predicted force-displacement curve. In the actual test the outer ply ruptured, but significant ductility was observed before the final rolling shear failure was observed (the embedded steel plates carry considerable flexural load). The pre-test prediction for layup 3 was steel yielding followed by flexural rupture of the inner wood core. While the pre-test estimate accurately predicted the steel yielding, the ultimate strength and final limit state were inaccurately predicted. It is noted that the pre-test calculated shear strength was ~590 kN, which agrees with the observed peak shear strength of the panel.

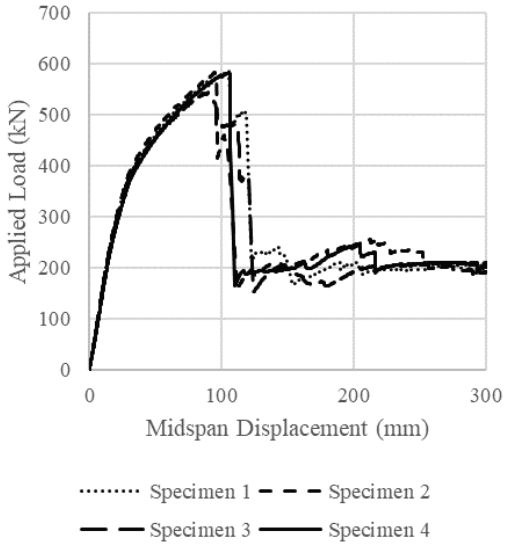

Figure 10: *Layup number 3 force-displacement curves*

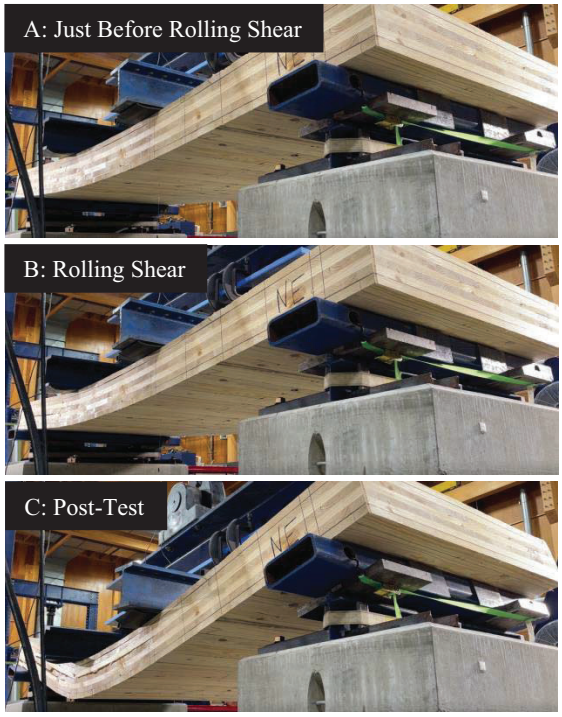

Figure 11: *Layup number 3, specimen 1, under loading*

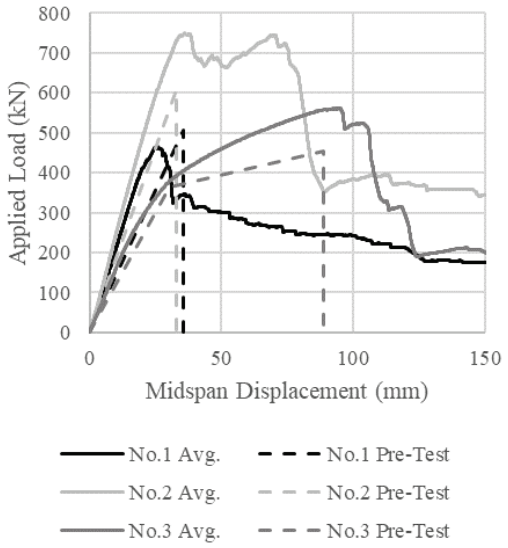

Figure 12: *Average force-displacement curves and pre-test predictions for the three layups*

6.5 POST-TEST ESTIMATES

Following the four-point RCLT panel bending tests, material tensile testing was performed on samples of the steel plates to improve the material properties used in the predictive analysis model. In addition, the analysis methodology was updated to include an incremental calculation approach, which accounts for damaged plies in the flexural calculations. Although still being developed, this updated methodology seems to better capture the evolution of flexural failures as degradation of load carrying capacity due to wood flexural rupture is now being captured, as shown in Figure 13.

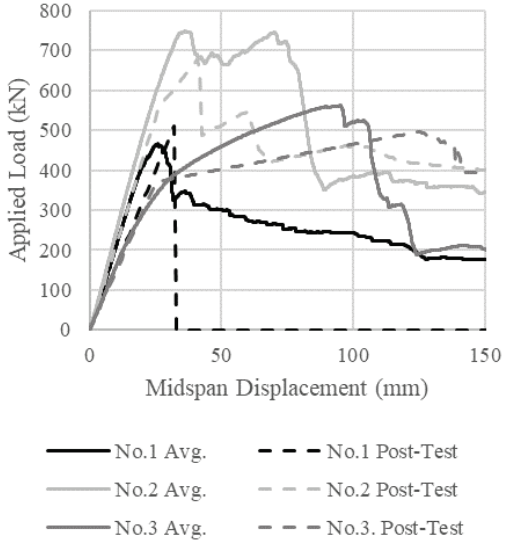

Figure 13: *Average force-displacement curves and updated methodology (post-test) predictions for the three layups*

7 DYNAMIC ANALYSIS

Following the test, calculations were performed to investigate the relative performance of these RCLT layups against unreinforced CLT layups under blast loading. Resistance curves were calculated for standard (unreinforced) CLT panels utilizing SP No.2 in 7-ply and 9-ply layups assuming a 3.66 m simply supported clear span. The layups assumed alternating 0 deg (strong) and 90 deg (weak) layers, with the exterior layers oriented in the 0 deg direction. Resistance functions for the three RCLT panels (layups 1, 2, and 3) were calculated with the updated methodology described in Section 6.5, using high-strain rate dynamic increase factors and assuming a uniform load distribution. The calculated resistance functions for all five panels are shown in Figure 14. The resistance function calculations predict: the two unreinforced CLT panels will display flexural failures near 105 kPa and 155 kPa; layup 1 will fail in shear near 165 kPa; layup 2 will demonstrate steel yielding near 180 kPa, followed by a shear failure near 215 kPa; layup 3 will demonstrate steel yielding near 130 kPa, and rupture of the wood core near 180 kPa. In all five cases the resistance function was set to perfectly plastic at the calculated ultimate resistance, generally following the approach in PDC-TR 18-02 [3].

Pressure-Impulse (P-I) diagrams were generated to compare the relative performance of the five panels. For each panel, a single-degree-of-freedom (SDOF) solver was used to determine the pressure-impulse combination that resulted in a specified ductility demand (i.e., μ = {maximum displacement / yield displacement} = 1, 2, 3, 4). The results are plotted in Figure 15 though Figure 18; note that the scales vary across the four figures. For each P-I curve, P-I combinations to the left or below the curve result in a smaller ductility demand while P-I combinations to the right or above the curve result in a greater ductility demand. Using Figure 15 as an example, the three RCLT panels are expected to sustain larger loads then the 7-ply CLT panel in the elastic range, while layup 2 is expected to sustain larger loads than both the 7-ply and 9-ply panels in the elastic range.

Although useful for comparison purposes, the P-I diagrams fail to account for the ductility capacity of the various panels. PDC-TR 18-02 defines ductility response limits for unreinforced CLT panels where, currently, ductility demands greater than 2 (i.e., $\mu \geq 2$) are expected to result in a 'Blowout' failure of unreinforced panels. On the other hand, Figure 13 indicates a ductility capacity for layup 3 of $\mu \sim 4$. Thus, if we compare the P-I diagrams of these three panels closer to their estimated limits of performance (see Figure 19), we see that layup 3 is expected to outperform both the 7-ply and 9-ply unreinforced CLT panels.

https://doi.org/10.52202/069179-0009

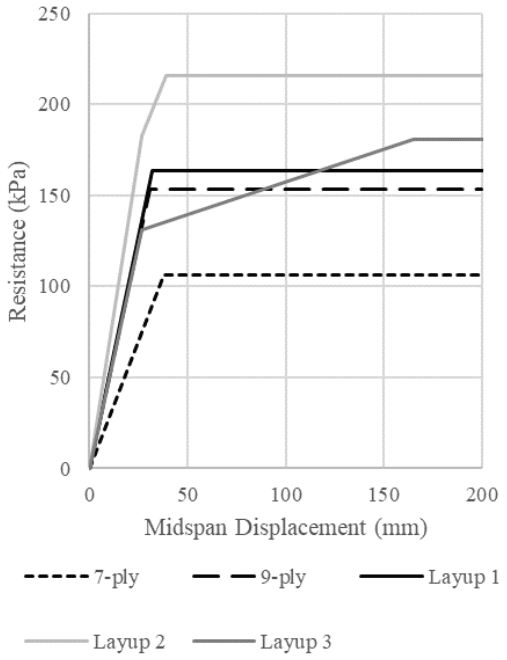

Figure 14: *Resistance functions for dynamic analysis*

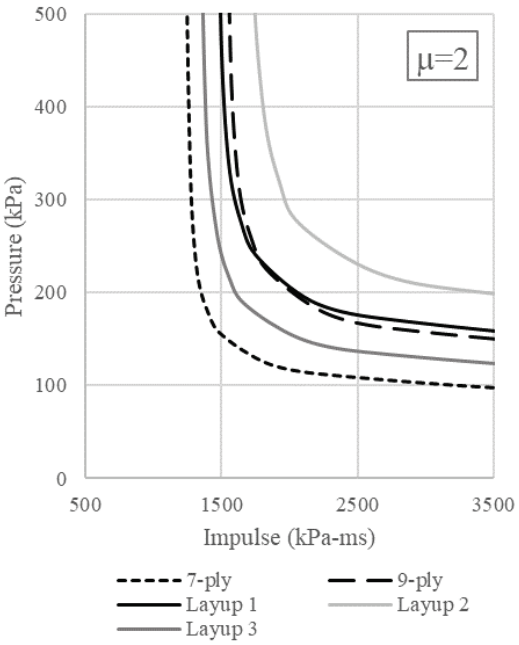

Figure 16: *Pressure-impulse diagram for μ = 2*

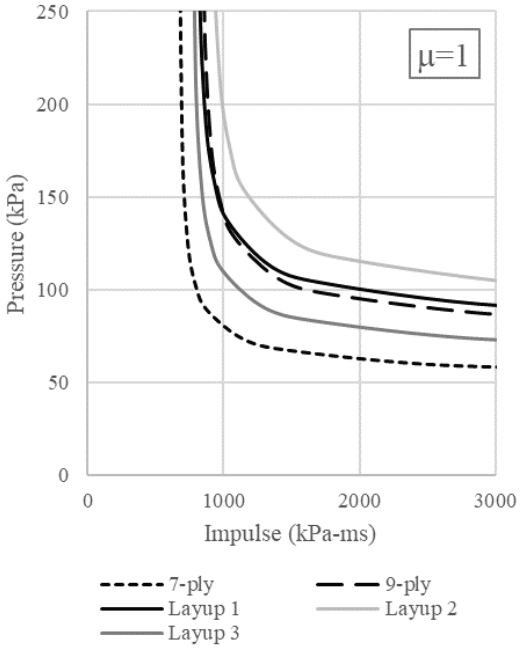

Figure 15: *Pressure-impulse diagram for μ = 1*

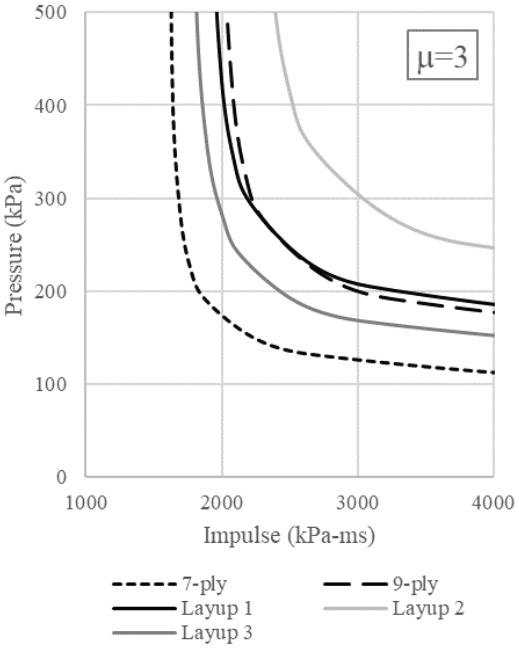

Figure 17: *Pressure-impulse diagram for μ = 3*

https://doi.org/10.52202/069179-0009

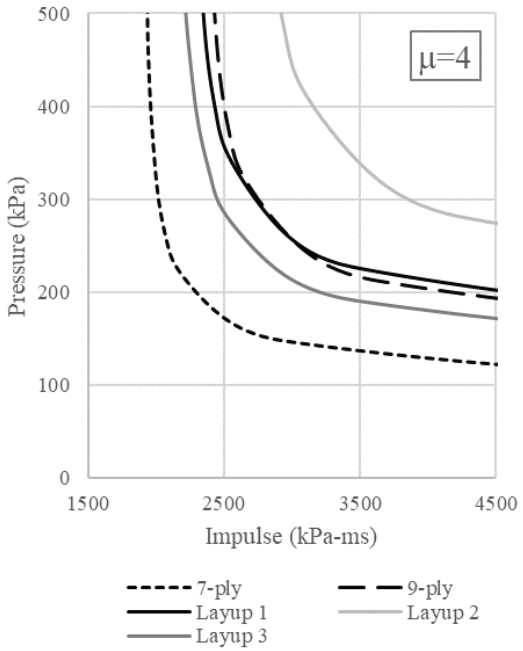

Figure 18: *Pressure-impulse diagram for μ = 4*

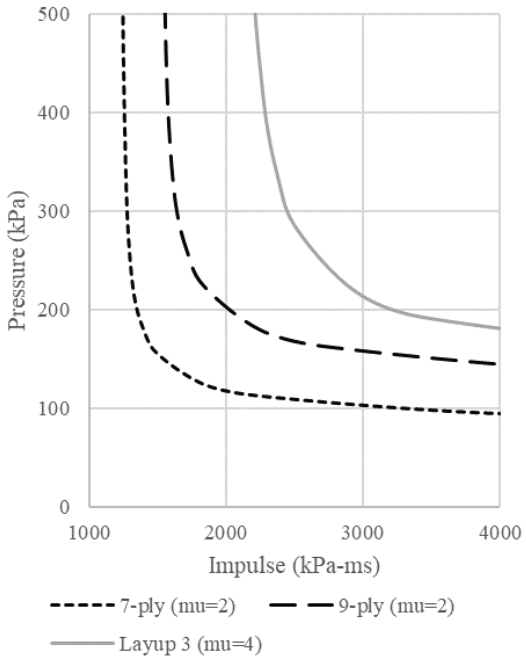

Figure 19: *Pressure-impulse diagram comparison for unreinforced CLT and layup 3 near limits of performance*

8 FUTURE EFFORTS

Several efforts are planned or ongoing to continue advancing the use of RCLT in protective design:

- Methodology Improvement (Ongoing). The methodology developed and utilized in this effort is being improved by implementing an incremental approach to calculating stiffness, flexural and shear capacities accounting for various damage mechanisms. The current version of the revised methodology provides better agreement with the test results presented herein (i.e., compare Figure 12 and Figure 13) and is planned to be included in a stand-alone software which calculates both CLT and RCLT resistance functions, as well as perform SDOF analyses.
- Weathering Study (Ongoing). Preliminary tests have shown the wood-to-steel adhesive bond not to be a limiting failure mechanism in RCLT panels. Both small-scale and large-scale weathering tests are ongoing to evaluate if temperature and moisture cycling degrades the adhesive bond and reduces the capacity of RCLT panels.
- Arena Blast Testing (Planned). Three RCLT layups will be subjected to arena blast testing. Two specimens will be fabricated for each layup, with one specimen subjected to six months of outdoor weathering prior to blast loading. Testing is scheduled for 2023.

9 CONCLUSIONS

This paper describes the development of a methodology to predict the performance of reinforced CLT (RCLT) panels, the manufacturing of full-scale RCLT panels, and quasi-static bending tests on those panels. The following general conclusions can be made from this work:

- The performance of RCLT panels can be well predicted. The methodology developed within this effort reasonably predicted the behavior of the RCLT panels selected. Future efforts include improving the methodology based on available test data.
- Full scale RCLT panels can be manufactured at an active CLT manufacturing facility. The cost to fabricate the RCLT panels is competitive with other protective solutions and would reasonably be expected to come down with wide-spread adoption of RCLT (e.g., automated vs. manual placement of the steel).
- Adhesive bond failure between the wood and steel layers was not typically observed, indicating that premature delamination failures at the embedded steel/lumber interface is not likely to compromise the out-of-plane resistance. Accelerated laboratory and short-term field weathering studies are currently ongoing to further evaluate the wood-to-steel adhesive bond.

https://doi.org/10.52202/069179-0009

- Rolling shear or delamination are the likely ultimate limit states for RCLT, although delamination was not typically observed. Because of the continuity, ductility, and capacity of the embedded steel plates, wood flexural rupture does not appear to cause a catastrophic panel failure. Further, even after a rolling shear failure RCLT demonstrates significant residual load carrying capacity.

ACKNOWLEDGEMENT

The work upon which this project was based was funded in part through a grant awarded by the U.S. Forest Service, Wood Innovations Grant (U.S. Federal Grant No. 21-DG-11052021-242). Additionally, the work was made possible with contributing funds provided by the Softwood Lumber Board and SmartLam. WoodWorks led the previous testing efforts to develop blast design guidance for mass timber construction. Testing was performed at the Advanced Structures & Composites Center at the University of Maine.

REFERENCES

[1] U.S. Department of Defence. UFC 4-010-01: DoD Minimum Antiterrorism Standards for Buildings, Change 2. Whole Building Design Guide, Washington, DC, July 2022.

[2] M. Weaver, C. Newberry, L. Podesto, and C. O'Laughlin. Blast loading of loaded cross-laminated timber structures. In: *Structures Congress 2018*, pages 400-411, 2018.

[3] USACE Protective Design Center. PDC-TR 18-02: Analysis Guidance for Cross-Laminated Timber Construction Exposed to Airblast Loading. USACE PDC, Omaha, NE, September 2018.

[4] M. Weaver, M. Lo Ricco, A. Senalik, J. Cattelino, R. Tudhope, P. van der Meulen. TR-19-41.1 Development of a Cost-Effective CLT Panel Capable of Resisting DOS/DOD Design Basis Threats. WIG No. 2021-DG-11052021-242, July 2020.

[5] The American Wood Council. National Design Specification for Wood Construction. American Wood Council, Leesburg, VA, 2018.

[6] FP Innovations and Binational Softwood Lumber Council. CLT Handbook: Cross-Laminated Timber. US Department of Agriculture, Forest Service, Forest Products Laboratory, Binational Softwood Lumber Council, Pointe-Claire, QC, 2013.

[7] ICC Evaluation Service: ESR-4733 Joint Evaluation Report: SmartLam Cross-Laminated Timber (CLT). ICC Evaluation Service, LLC, December 2021.

[8] American National Standards Institute (ANSI) and the Engineered Wood Association (APA). ANSI/APA PRG 320: Standard for Performance-Rated Cross-Laminated Timber. The Engineered Wood Association, Tacoma, WA, 2019.

World Conference on Timber Engineering Oslo 2023

BALLISTIC TESTING OF CROSS-LAMINATED TIMBER LAYUPS TO FURTHER DEVELOP PROTECTIVE PANELS

Marco T. Lo Ricco[1], Mark K. Weaver[2], C. Adam Senalik[3], Jim Henjum[4], Jason Cattelino[5]

ABSTRACT: Though ballistic projectile penetration of wood has been studied for centuries, standard models overestimate the thickness of wood required to stop projectiles, often by a large margin. Adhesive lamination via contemporary manufacturing methods can produce mass timber panels of unprecedented thickness, yet industry standard layups of softwood cross-laminated timber (CLT) cannot stop projectiles traveling at velocities specified by current protective design requirements. To develop mass timber panels that comprehensively mitigate blast, ballistic, and forced entry threats, seven reinforced or hardened CLT layups were manufactured to compare their ballistic performance with that of a baseline 7-ply softwood CLT layup. Three calibers of ammunition were fired at each panel specimen, and entry and exit velocities were recorded with high-speed cameras. For projectiles that did not fully perforate the panel, the depth of penetration was determined by radiography. Four of the eight tested layups stopped all projectiles. Among the successful layups, three included embedded steel reinforcements. The other successful layup was made entirely of hardwood laminations. Steel-plate-reinforced softwood CLT proved the most cost-effective option.

KEY WORDS: cross-laminated timber, ballistic penetration, protective structures, reinforced CLT, hardwood CLT

1 INTRODUCTION

Blast and ballistic threats are two primary concerns in protective design. Past testing has demonstrated that mass timber can resist blast threats [1]. Although the ballistic performance of wood has been studied over the course of three centuries [2, 3], satisfactory resistance to ballistic threats remains unresolved. Approximately two decades ago, Smrž et al. [4] tested 55 mm (2-⅛ in.) thick wood plates under ballistic impacts from 7.62-mm bullet, spherical, and simulated fragment projectiles. The model developed from these experiments, however, is limited to 100 mm (3-⅞ in.) of thickness and adapted a unified theory of penetration that has proven accurate for metal alloys [5]. Whether this unified theory of penetration simulates perforation of wood materials as well remains an open question.

Two classic models of ballistic penetration, the Robins-Euler and Poncelet equations, originated during the eighteenth century when wood materials were common targets, and remain relevant in the mechanics of terminal ballistics [6]. Koene and Broekhius [7] applied these classic models to the penetration of 9-mm ammunition into solid wood blocks of various species and showed that the models reasonably fit the penetration depth data for metal-tipped bullets. The models, however, did not apply to polyethylene tipped bullets used in the tests. To ensure that bullets would be stopped by the wood blocks, impact velocities were limited, so whether the models need parameters for projectiles hitting the targets at much higher velocities remains unknown.

Protective design of U.S. government facilities commonly uses an empirically based model that correlates hardness, density, and thickness of wood to calculate the dimension required to stop a bullet or the residual velocity of a perforating bullet. According to equations and tabulated data in UFC 4-023-07 [8], an unrealistic 4.55 m (179 in.) thick panel of pine or 1.5 m (59 in.) thick panel of hickory would be required to stop a NATO M80 round fired at a velocity of 853 m/s (2800 ft/s). However, test programs that form the basis of these UFC 4-23-07 estimates predate innovations like cross-laminated timber (CLT).

Sanborn et al. [9] conducted one of the first published ballistics tests on CLT targets and found that UFC equations, among other models, overpredicted both (a) the thickness required to prevent perforation and (b) the exit velocities of spherical projectiles. Although the tested specimens outperformed conventional ballistic model estimates, Sanborn [10] anticipated that softwood CLT would need reinforcement to stop more realistic ballistic threats and tested several enhanced “eCLT” layups using steel, fiberglass, aramid, and ultra-high molecular weight polyethylene reinforcement layers. While several reinforcing options reduced penetration depth of spherical projectiles, mild steel was the least costly reinforcement.

[1] Marco T. Lo Ricco, USDA Forest Products Laboratory, USA, marco.loricco@usda.gov
[2] Mark K. Weaver, Karagozian & Case, Inc., USA, weaver@kcse.com
[3] C. Adam Senalik, USDA Forest Products Laboratory, USA, christopher.a.senalik@usda.gov
[4] Jim Henjum, SmartLam North America, USA, jim.henjum@smartlam.com
[5] Jason Cattelino, Rotho Blaas USA, Inc. jason.cattelino@rothoblaas.com

https://doi.org/10.52202/069179-0010

2 OBJECTIVE

Wood's ballistic performance must be proven before governmental agencies and other institutions implementing protective design requirements can realize the sustainable and architectural benefits of mass timber construction. A feasibility study, therefore, was undertaken to investigate whether a CLT layup measuring 254 mm (10 in.) or less in thickness could stop ogive-nose bullets. To increase the ballistic resistance of softwood CLT layups and avoid the cost of exotic armoring materials, conventional steel sheets were incorporated into several layups. Other layups incorporated dense hardwoods, instead of steel reinforcement, to determine if wood panels without metal reinforcement could prevent ballistic perforation. The objective of the study was to demonstrate that CLT could meet ballistic protection requirements at a layup thickness and cost comparable to conventional reinforced concrete and steel protective options.

3 TESTING

3.1 SPECIMENS

The layups assessed in this study are schematically shown in Figure 1. All eight layups utilize seven layers of wood, with some layups utilizing up to four additional layers of embedded steel reinforcement. The layups are comprised of: (a) all softwood [to represent the control], (b) all hardwood, (c) alternating hardwood and softwood, (d) alternating interlocked grain hardwood and softwood, (e) thin steel plate reinforcement, (f) fine steel mesh reinforcement, (g) coarse steel mesh reinforcement, and (h) thick steel plate reinforcement.

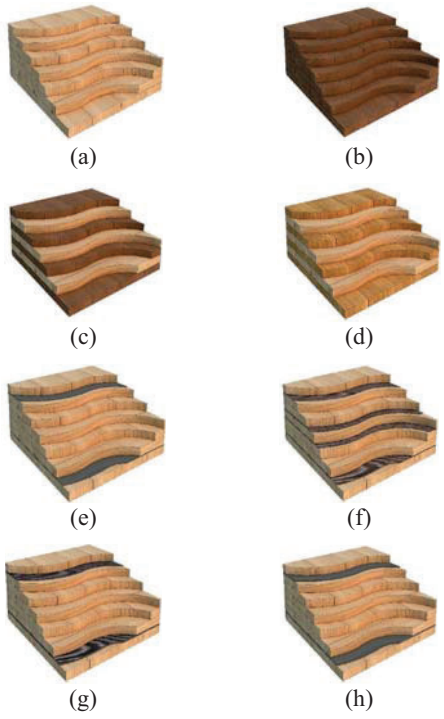

Figure 1: *Renderings of specimen layups.*

Layup (a) utilized Spruce-Pine-Fir, South (SPF-s), No. 2 Grade laminations of 35 mm (1.375 in.) nominal thickness, conforming to North American standards [11]. As the only standard CLT layup, this panel acted as a control that is representative of the ballistic resistance of unreinforced softwood CLT. Because Layup (a) had no hardwoods nor steel reinforcement, all other layups were compared and expected to outperform this control.

Layup (b) utilized laminations of shagbark hickory (Carya ovata) in select and better grades of 32 mm (1.250 in.) thickness. Shagbark hickory is selected as it is among the hardest and densest North American species, which is theorized to provide increased ballistic resistance when compared to softer and less-dense alternatives.

Layup (c) alternated hardwood (hickory) and softwood (SPF-s) layers, of respective 32- and 35-mm thickness, to assess whether contrasting combinations of hardness and density might outperform layups composed of a single species classification.

Layup (d) was similar to Layup (c) but substituted hickory with American sycamore (platanus occidentalis) to assess whether a hardwood with an interlocked grain microstructure might provide additional resistance. Previous tests indicated that sycamore has relatively high ballistic resistance relative to other woods [12].

Steel reinforcement is utilized in the four remaining layups, along with No. 2 SPF-s wood layers of 35-mm thickness. It was hypothesized that the hardness, density, and ductility of steel may sufficiently reinforce softwoods to prevent ballistic perforation. Past testing has shown that mild, low-carbon steel plates of 12.5 mm (0.5 in.) thickness are adequate in stopping the ammunition used in this study [13], so Layups (e) through (h) were limited to an embedded steel content equivalent to this thickness of steel plate or less. Two of the four layups utilize woven steel wire cloth while the other two layups utilize solid steel plates. Steel plates conform to ASTM A36 [14] with a minimum specified yield strength of 250 MPa (36 ksi), while the woven steel wire cloth conforms to ASTM E2016 [15]. The cold-drawn steel wires used in the woven steel cloth are uncoated and conform to the 1042 grade designation.

Layup (e) utilized steel plates of 3 mm (1/8 in.) thickness at the bond lines of the panel face laminations.

Layup (f) utilized finely woven steel wire cloth, with 47% open area and 1.6 mm (1/16 in.) wire diameter, at all bond-line interfaces except two. Although solid steel plates offer continuous coverage throughout the panel, woven steel cloth provides openings for adhesive contact between wood laminations, which may provide improved bond characteristics.

Layup (g) utilizes a coarsely woven steel wire cloth, with 27% open area and 3 mm (1/8 in.) wire diameter, at the bond lines of the panel face laminations.

Layup (h) utilizes 6 mm (1/4 in.) steel plates at the bond lines of the panel face laminations.

https://doi.org/10.52202/069179-0010

The thicknesses of the eight layups are similar but are all slightly different. Because softwoods and hardwoods are typically milled to different dimensions, Layup (b) made entirely of hardwoods results in the thinnest panel. The embedment of steel elements thickens Layups (e) through (h). While the eight layup thicknesses could have been held constant, practical considerations of lamella thickness are more representative of what the CLT industry would eventually produce. For each of the eight layups, a panel measuring approximately 915 mm (36 inches) square was pressed and subsequently cut into four 457 mm (18 in.) tiles. For the steel-reinforced panels, hardboard spacers are placed along the edges of embedded steel plates to make a path for saws to cut only through wood-based materials.

Of the four tiles produced from each panel layup, only three tiles were used as specimens for ballistics testing, so Table 1 provides panel thickness for each of the eight layups and three tiles used in ballistics tests. The resulting range of thickness is minus 22 mm (0.866 in.) and plus 14 mm (0.551 in.) relative to the baseline Layup (a) of 248 mm (9.75 in.) tile thickness.

Table 1: Panel thickness in mm

	Tile			
Layup	**1**	**2**	**3**	**Average**
(a)	248	248	248	248
(b)	227	225	225	226
(c)	235	235	233	234
(d)	232	232	232	232
(e)	252	251	254	252
(f)	259	259	260	259
(g)	262	262	262	262
(h)	257	257	257	257

25.4 mm = 1 inch.

Figure 2 plots the measured densities of the layups. Layup (b), the thinnest panel of Table 1 and made of shagbark hickory with a specific gravity reported as 0.72 [16], ranks as the densest panel. At the opposite end of the range, softwood Layup (a), made with a SPF-s of reported specific gravity of 0.36 [17], ranks as least dense.

Figure 3 plots the measured areal densities of the layups, calculated as the mass of each tile divided by the surface area. By this measure, Layup (h) has the highest areal density, while Layup (a) remains least dense. In other words, Layup (h) is the heaviest wall component among the tested layups because it has highest mass per square meter of exterior wall area. From a ballistics perspective, areal density provides the more useful measure, so both effective and areal density are reported here to highlight the distinction.

3.2 PROJECTILES

The test ammunition of Table 2 lists specified properties of the three NATO cartridges used is this ballistic study. A complete *round of ammunition* or *cartridge*, according to ballistics terminology [18], includes a bullet and cartridge case containing propellant and primer for ignition. The *bullet* is the only portion of the cartridge that is the *projectile* and has mass specified in units of *grains*. For enhanced aerodynamics and penetration of the projectile, the front end of bullets was ogive shaped. While levels of protection may vary for different facilities, the standard [13] used to evaluate this test program requires zero perforation for the projectiles impacting targets within the range of velocities specified in Table 2.

***Table 2:** Test Ammunition*

	Velocity (m/s)	
Cartridge	**Min.**	**Max.**
7.62 mm, M80, ball 147 gr.	823	853
5.56 mm, M193, ball, 55 gr.	955	986
5.56 mm, M855, ball, 63 gr.	899	930

1 m ≈ 3.28 ft; 1 grain ≈ 0.0647989 gram ≈ 0.00228571 oz.

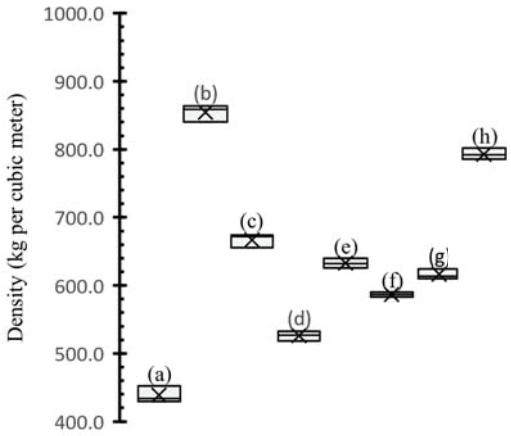

***Figure 2:** Effective density of layups used in ballistic testing.*
1kg ≈ 2.2 pounds mass; 1 m ≈ 3.28 ft.

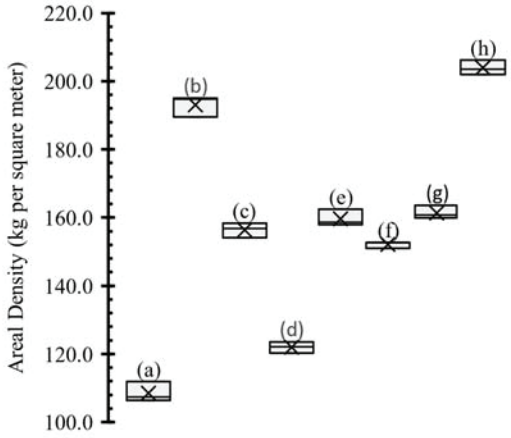

***Figure 3:** Areal density of layups used in ballistic testing.*
1kg ≈ 2.2 pounds; 1 m ≈ 3.28 ft.

https://doi.org/10.52202/069179-0010

Based on previous softwood CLT tests which utilized spherical projectiles [9], it was expected that a softwood 7-ply CLT layup will not be able to stop ogive-nosed cartridges fired at standard rifle speeds as the ogive-nose typically penetrates materials more efficiently than spherical projectiles, because of simultaneous driving and drilling actions.

3.3 PROCEDURE

Of the four tiles produced for each layup, one tile underwent bond integrity testing while three underwent ballistic testing. The tiles undergoing bond integrity assessments were subjected to AITC T110 cyclic delamination tests [19] and physical prying with a weighted hammer and crowbar to qualitatively assess bond integrity. Ballistic resistance testing was conducted by a qualified laboratory (H.P. White Laboratory, Inc., Street, MD) during the spring of 2020 [20]. The cartridges listed in Table 2 were fired into each tile from a muzzle 6.1 m (20 ft) away from the strike face of the tile target. The shots were oriented in a triangular pattern to minimize the influence of previous shots. Velocity screens positioned relative to the muzzle at distances of 1.52 m (5 ft) and 4.57 m (15 ft) recorded the times projectiles passed, so that an initial velocity could be estimated at a position of 3.05 m (10 ft) along the trajectory. Impact velocities were determined from the velocity screen data and high-speed cameras recording video of impact with the target within the fixture pictured in Figure 4.

For projectiles that fully perforated the tiles, residual velocities were determined by high-speed video cameras tracking projectiles exiting the back face of the target from both top and side views, as shown in the example of Figure 5. For projectiles stopped within the tiles, their position was measured from the back (non-strike) face of the target by a qualified laboratory (MCQ Labs, Inc., Aberdeen, MD) using radiography, as shown in the example of Figure 6. The penetration depths shown in Figure 6 include both calculated (C) and measured (M) values given in the computed radiography report.

Figure 4: *CLT tile mounted in steel frame for ballistic testing viewed from back, non-strike face (foreground) and looking toward velocity screen (background).*

Figure 5: *Residual velocity video-recorded upon projectile exit.*

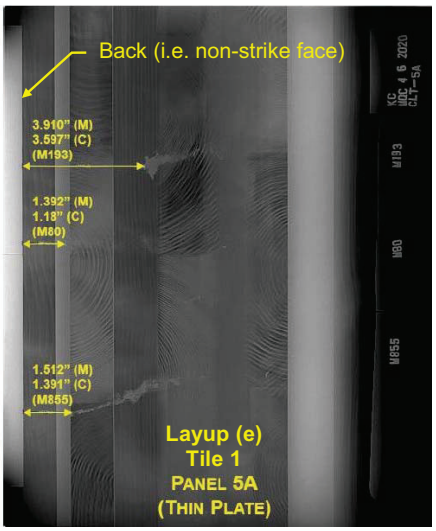

Figure 6: *Projectiles stopped from reaching exit face (datum).* 1 inch or 1.0" = 25.4 mm.

4 RESULTS

All nine projectiles fired at the Layup (a) tiles passed through the tiles (full perforation), while Layups (b), (e), (g) and (h), successfully stopped all projectiles from exiting the tiles (no perforations). Layups (c), (d) and (f) had multiple tiles perforated by M80 projectiles. Both Layups (c) and (f) stopped all shots of the M193 and M855 projectiles. Layup (d) failed to stop one of the M193 projectiles and all three shots of the M855 projectiles. Table 3 summarizes these results in terms of a binary pass-fail criterion. If panels stopped all the projectiles of a given cartridge type, it was deemed to pass. If at least one bullet passed through a panel and exited the back, non-strike face, the layup was deemed to fail. Regardless of the pass-fail determination, all targets were evaluated in more detail to estimate the energy absorbed by the CLT panels when shot with projectiles from each cartridge type.

https://doi.org/10.52202/069179-0010

Table 3: *Pass-fail results of ballistic perforation test.*

Layup	M80	M855	M193
(a)	FAIL	FAIL	FAIL
(b)	PASS	PASS	PASS
(c)	FAIL	PASS	PASS
(d)	FAIL	FAIL	FAIL
(e)	PASS	PASS	PASS
(f)	FAIL	PASS	PASS
(g)	PASS	PASS	PASS
(h)	PASS	PASS	PASS

PASS: Panel captured all bullets.

FAIL**:** One or more bullets exited the back face of panel.

Shaded: Layup failed to stop at least one bullet.

4.1 Perforated Targets

Figure 7 plots the striking velocity versus the residual velocity for projectiles associated with full penetration, where the M80 projectiles generally displayed the largest residual velocities. One residual velocity for the M80 round that breached Layup (c) could not be measured, though all three M80 projectiles exited the tiles. Since protective design is typically concerned with energy and a protective element's ability to dissipate energy, the recorded velocities of Figure 7 were converted to kinetic energy using the fundamental equation of one-half mass times velocity squared. For this calculation the mass of the bullet was assumed constant; (although this assumption cannot typically be made for ballistics traveling through hard or ductile materials, it is justified by video observations of the tests). Figure 8 plots the kinetic energy upon impact versus the residual kinetic energy for the projectiles associated with full penetration. The larger mass of the M80 projectiles results in a much larger striking kinetic energy then the M193 and M855 projectiles and, because the capacity of target tiles to absorb energy is finite, generally leads to a much larger residual kinetic energy.

To quantify the kinetic energy absorbed by each layup, the residual kinetic energy is subtracted from the striking kinetic energy. Figures 9, 10, and 11 show the differentiated kinetic energies for the M80, M193, and M855 projectiles, respectively. The total height of each bar chart represents the average striking kinetic energy on a specific layup. The light grey portion of the bar chart represents the energy absorbed by the impacted tile. The black portion of the bar chart represents the kinetic energy of the projectile after exiting the back of the tile.

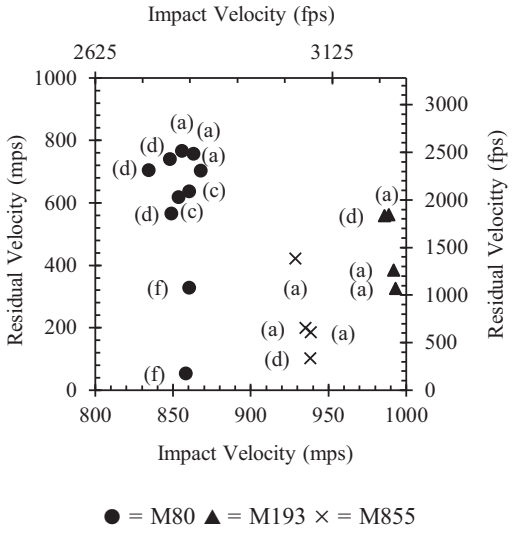

Figure 7: *Impact and residual velocities of projectiles breaching full thickness of panels.*

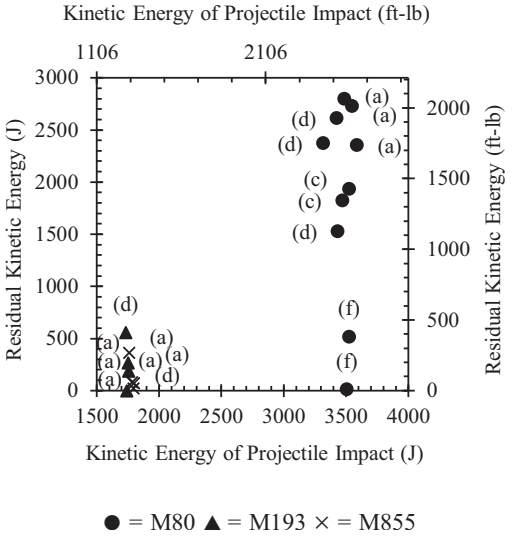

Figure 8: *Impact and residual kinetic energies of projectiles breaching full thickness of panels.*

Figure 9 shows that Layups (a), (c), and (d) absorbed less than half the kinetic energy of the striking M80 projectiles, in contrast to Layup (d) which absorbed nearly all projectile kinetic energy. Figures 10 and 11, plotted to the same y-axis scale as Figure 9, show that the M193 and M855 projectiles strike the tiles with approximately half the kinetic energy of the M80 projectiles. Though the full thickness of Layups (a) and (d) were breached by the M193 and M855 projectiles, Figures 10 and 11 show that nearly all the kinetic energy was absorbed by the tiles.

https://doi.org/10.52202/069179-0010

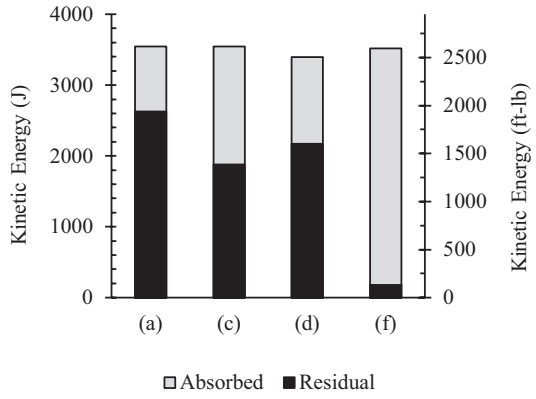

Figure 9: *Comparison of average striking and exiting kinetic energies of M80 projectiles.*

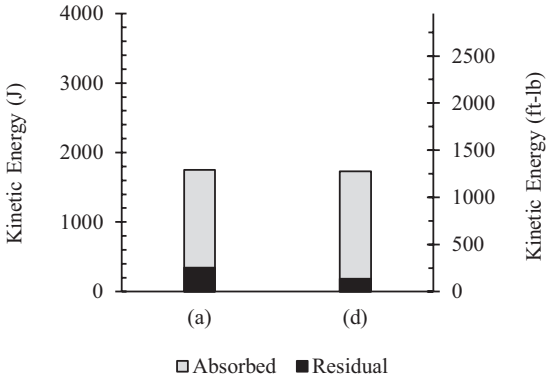

Figure 10: *Comparison of average striking and exiting kinetic energies of M193 projectiles.*

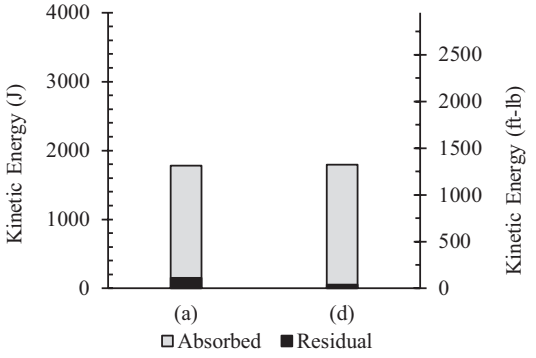

Figure 11: *Comparison of average striking and exiting kinetic energies of M855 projectiles.*

4.2 Embedded Projectiles

Table 4 provides the position of projectiles found within panel specimens, labelled as tiles, which were calculated using computed radiography. Blank entries of Table 4 indicate that no projectile of that ammunition type was found, supporting the penetration of full panel thickness observed during tests. The third M80 projectile into Layup (b) did not exit the panel but reached the back face and therefore was assigned a position of zero, to indicate near perforation.

Penetration depths of each projectile were calculated by subtracting position from total panel thickness, *t*. Because all shots were fired directly, with no oblique angles, the assume length of penetration of breached panels is the full thickness. Figure 12 shows the average depths projectile penetration alongside plots of average panel thickness for each layup. Projectile depths equal to panel thickness, *t*, indicate breaches. In panels that stopped bullets, the depth of penetration was generally proportional to the kinetic energy of the ammunition. Layup (h) reinforced with thick steel plates, however, presented an exception where the average depth of penetration of the M855 round exceeded the average penetration of the M80.

Table 4*: Positions of embedded projectiles measured from back face of panel.*

		Position from exit face		
		M80	**M193**	**M855**
Layup	**Tile**	**(mm)**	**(mm)**	**(mm)**
(a)	1	-	-	-
	2	-	-	-
	3	-	-	-
(b)	1	39	115	106
	2	40	148	111
	3	0	138	118
(c)	1	-	61	70
	2	-	95	94
	3	-	107	70
(d)	1	-	51	-
	2	-	22	-
	3	-	-	-
(e)	1	30	91	35
	2	44	85	61
	3	42	101	68
(f)	1	41	130	92
	2	-	127	96
	3	-	136	140
(g)	1	40	96	107
	2	45	108	89
	3	42	121	83
(h)	1	107	152	69
	2	100	143	75
	3	95	142	70

https://doi.org/10.52202/069179-0010

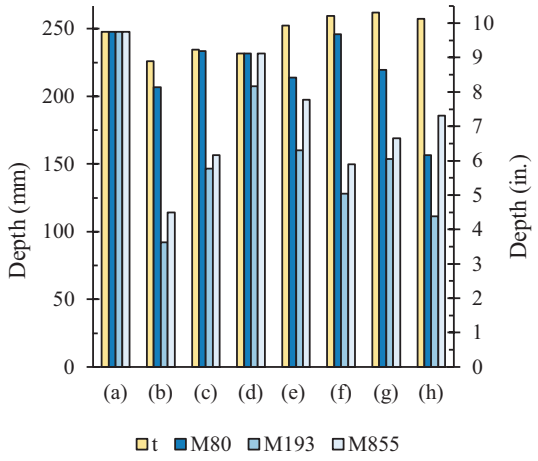

Figure 12: *Thickness and penetration depths of projectiles.*

4.3 Variation

Because all test ammunition was fired according to Table 2 specifications, with consistent velocities and mass, there was little variation in the striking kinetic energy. The coefficient of variation for the average striking kinetic energy of each tested layup given by Table 5 shows less than 2% variation in any given set of test ammunition. Variation of mass from the grain size specifications in Table 2 was neglected in the variation reported in Table 5, so the calculated variation is entirely attributable to the squared magnitude of velocity measured during testing.

Table 5: *Coefficients of variation for average kinetic energies of impact.*

Layup	M80 (%)	M193 (%)	M855 (%)
(a)	1.2	0.4	0.9
(b)	0.1	0.1	1.2
(c)	0.7	1.5	1.0
(d)	1.6	0.1	0.3
(e)	0.9	1.4	0.8
(f)	0.2	0.8	1.5
(g)	0.2	1.1	0.4
(h)	0.3	1.0	1.4

The coefficients of variation for averages of residual kinetic energy and penetration depth are respectively provided in Tables 5 and 6. Several factors account for the relatively high variation observed in the residual kinetic energy averages. First, the averages are based on a limited data set of three samples. In at least one instance, firing the M80 round into a Layup (c) panel, residual velocity could not be recorded, so results from two samples were averaged. In Layup (f), two M80 projectiles breached panels but one did not, which led to high variation in the average. With more tests, the effects of a limited number of samples would decrease. Second, woods have historically exhibited coefficients of variation greater than 20% for some mechanical properties [21]. The Spruce-Pine-Fir (South) commercial grouping further introduces variation by including 10 species [17]. Third, moisture content introduces additional variability that may affect results. In this study, ambient temperature and humidity readings were recorded and samples retained to verify that moisture content was typically 12% or less for each of the samples.

Table 5: *Coefficients of variation for average residual kinetic energies of breached layups.*

Layup	M80 (%)	M193 (%)	M855 (%)
(a)	7.4	47.6	78.9
(b)	-	-	-
(c)	2.9	-	-
(d)	21.4	141.4	48.2
(e)	-	-	-
(f)	135.9	-	-
(g)	-	-	-
(h)	-	-	-

The coefficients of variation for average depth of penetration listed in Table 6 range from approximately one to fifteen percent. For Layups (e) through (h) reinforced with steel, the variation is generally less than those of wood. For Layups (a), (c) and (d), the coefficients of variation are not reported for penetration values, because it is obvious that projectiles penetrated the full panel thickness. In these cases, the change in kinetic energy should be based on residual velocities with the variation reported in Table 5.

Table 6: *Coefficients of variation for average depth of penetration for layups with embedded projectiles.*

Layup	M80 (%)	M193 (%)	M855 (%)
(a)	-	-	-
(b)	14.0	15.5	4.7
(c)	-	13.8	7.2
(d)	-	10.0	-
(e)	3.1	3.3	7.0
(f)	7.9	2.7	14.0
(g)	1.1	6.7	6.1
(h)	3.3	4.2	1.5

4.4 Engineering model

Though variation poses challenges, it is possible to begin developing an engineering model from this limited data set. Ballistic modeling for wood has typically tried to correlate performance to fundamental properties of density, or specific gravity, and Janka hardness. Framing the problem in the context of energy is useful for the objective of stopping bullets. Although shape of the projectile is a factor in depth of penetration, the problem of armoring is largely dominated by kinetic energy delivered to an extremely localized scale. The challenge

https://doi.org/10.52202/069179-0010

lies in determining how much energy absorption wood may offer via breakage, friction, and other means of damping. The introduction of steel undoubtedly adds hardness, density, and ductility that enhances energy absorption of the panels.

For this data set, some additional steps may be taken to extract information that may be useful for engineering modeling. Resistance drilling studies [22] have developed models for distinguishing driving force, torque, and friction in correlation to density and Janka hardness. Via resistance drilling of retained samples, there may be a practical method to predict the ballistic performance based on the driving forces, torque, and friction measured near the ballistic perforations. Such studies have shown that numerous samples must be taken to develop statistical confidence in the models and obtain reasonable fit.

4.5 Costs and additional considerations

Among the four layups that stopped all test shots, the cost ranked in order from least to greatest is:

1. Layup (e), thin steel plates,
2. Layup (h), thick steel plates,
3. Layup (g), welded wire fabric
4. Layup (b), select shagbark hickory hardwood.

This ranking primarily factors the cost of raw materials and additional labor to produce the layups. Steel embedment requires preplanning of cuts and fastening zones, so that tools do not have to pass through wood and steel simultaneously. Despite this added fabrication planning, steel reinforcement facilitates use of economical and abundant softwoods in protective applications. Because protective panels must also resist blast effects and forced entry, the added ductility offered by the steel armoring enhances overall ductility and energy dissipation. Therefore, considering costs and enhancements to local and global ductility of panels, steel-reinforced softwood layups appear to be the most viable solution to develop and include in engineering models.

5 CONCLUSIONS

With either embedded steel reinforcement or an all hardwood CLT panel, it is possible to prevent ballistic perforation within a 254 mm (10 in.) panel thickness. One of the four successful CLT layups, however, stood out, because softwoods and thin steel plates are the most economical material options among those considered. Steel reinforcement, furthermore, provides ductility that may enhance the performance of panels in response to other hazards, such as blast, considered in protective design. For additional details of the ballistic tests described in this paper and other related testing, see the project report [20].

ACKNOWLEDGEMENT

This work was funded by the USDA, Forest Service, Wood Innovations Grant No. 2019-DG-11052021-226. SmartLam North America manufactured the CLT. H.P. White Laboratory performed the ballistic resistance tests.

REFERENCES

[1] Weaver MK, Newberry CM, Podesto L, O'Laughlin C.: Blast testing of loaded cross-laminated timber structures. In: Structures Congress 2018, Blast, Impact Loading, and Response; Research and Education, American Society of Civil Engineers Reston, VA, USA, pages 400-411, 2018.

[2] Hutton C. III. The force of gun-powder, and the initial velocities of cannon balls, determined by experiments; from which is also deduced the relation of the initial velocity to the weight of the shot and the quantity of powder. Philosophical Transactions of the Royal Society of London, 50-85, 1778.

[3] W. Johnson. Mostly on oak targets and 19th century naval gunnery. International Journal of Impact Engineering, 4:175-83, 1986.

[4] Smrž J., Havlíček M., Buchar J.: The behaviour of wood plates under ballistic impact. Acta Universitatis Agriculturae et Silviculturae Mendelianae Brunensis, Czech Republic, 2002.

[5] J. Dehn. A unified theory of penetration. International Journal of Impact Engineering, 5:239-248, 1987.

[6] Rosenberg Z., Dekel E.: Terminal Ballistics. Springer, Singapore, 2016.

[7] Koene L., Broekhuis F.: Bullet penetration into wooden targets. In: Proceedings of the 30th International Symposium on Ballistics, pages 1905-1916, 2017.

[8] U.S. Department of Defense. Unified Facilities Criteria, Design to Resist Direct Fire Weapons Effects (UFC 4-023-07). U.S. Department of Defense, Washington D.C., 2008 with 2017 update.

[9] Sanborn K.P., Gentry T.R., Koch Z., Valkenburg A., Conley C., Stewart L.K.: Ballistic performance of Cross-laminated Timber (CLT). International Journal of Impact Engineering, 128:11-23, 2019.

[10] Sanborn K.P. Exploring cross-laminated timber use for temporary military structures: ballistic considerations: Georgia Institute of Technology, Atlanta, GA, USA, 2018.

[11] ANSI/APA PRG 320. Standard for Performance-Rated Cross-Laminated Timber. APA—The Engineered Wood Association, Tacoma, WA, USA, 2018.

[12] Chinn S, Randow C.: Ballistic Performance of Bio-Based Materials. In *US Military Academy Technical Symposium* of DEVCOM Army Research Laboratory, West Point, NY, USA, 2019.

[13] Bureau of Diplomatic Security. SD-STD-01.01, Revision H, Certification Standard Forced Entry and Ballistics Resistance of Building Systems. U.S. Department of State, Washington D.C., 2018.

[14] ASTM A36/A36M-19.: Standard Specification for Carbon Structural Steel. ASTM International, West Conshohocken, PA, USA, 2019.

[15] ASTM E2016-22. Standard Specification for Industrial Woven Wire Cloth. ASTM International, West Conshohocken, PA, USA, 2022.

[16] Senalik C.A., Farber B. Mechanical properties of wood. Chapter 5 in R.J. Ross, editor, *Wood Handbook: Wood as an engineering material,* FPL-

GTR-282, pages 5.1-5.46. USDA, Forest Service, Forest Products, Laboratory, Madison, WI, USA, 2021.
[17] AWC. NDS Supplement: National Design Specification Design Values for Wood Construction. American Wood Council, Leesburg, VA, USA, 2018.
[18] Parker S, Wilson M. Part I. In: Inowlocki T, editor. A Guide to the UN Small Arms Process. third ed., pages 13-24, Small Arms Survey, Geneva, Switzerland, 2016.
[19] AITC. Test Methods for Structural Glued Laminated Timber. American Institute of Timber Construction, Centennial, CO, USA, 2007.
[20] Weaver M.K., Lo Ricco M.T., Senalik C.A., Cattelino J., Tudhope R., van der Muelen P.W.: Development of a Cost-Effective CLT Panel Capable of Resisting DOS/DOD Design Basis Threats. Karagozian & Case, Inc., Glendale, CA, USA, 2020.
[21] Wood L.W. Variation of strength properties in woods used for structural purposes. 1960.
[22] Sharapov E., Wang X., Smirnova E.: Drill bit friction and its effect on resistance drilling measurements in logs. In: *Proceedings of the 20th International Nondestructive Testing and Evaluation of Wood Symposium*, FPL-GTR-249, pages 413-423, USDA, Forest Service, Forest Products Laboratory, Madison, WI, USA, 2017.

https://doi.org/10.52202/069179-0010

World Conference on Timber Engineering Oslo 2023

PREDICTING MODULUS OF RUPTURE OF HEAT-TREATED WOODS BY ARTIFICIAL NEURAL NETWORK COMBINED GENETIC ALGORITHM

Mehdi Nikoo[1], Reza Abbasi Malekabadi[2], Ghazanfarah Hafeez [3]

ABSTRACT: A total of 104 spruce and Larix gmelinii wood samples were employed to generate a reliable ANN-based model for estimating the Moment of Rupture (MOR) of heat-treated woods. Seventy percent of the samples were used for training, while the remaining thirty percent were used for testing phases of the data set. The Feed Forward network with five topologies was used, including heat treatment at various temperatures, durations, and relative humidity as input parameters. The weights of the artificial neural network are optimized by employing a genetic algorithm. The model's accuracy is assessed by comparing results with the particle swarm optimization-based neural network model. The study concluded that the genetic algorithm-based ANN model performed better by yielding results with reduced error.

KEYWORDS: Modulus of Rupture (MOR), Heat-Treated Woods, Artificial Neural Networks, Genetic Algorithm, Particle Swarm Optimization

1 INTRODUCTION

While timber is a distinctive, renewable, and sustainable construction material, it is biodegradable, mainly in open-air applications. Modifying timber's physical and mechanical properties improves its durability, preventing degrading agents. Wood modification methods are an evolving fashion and an eco-friendly substitute of chemicals for wood preservation procedures. During heat treatment processes, the wood is heated and modified in various atmospheres [1]. The material's structural performance and durability depend on numerous properties of heat-treated wood. Heat treatment dramatically lowers the wood's water absorption, equilibrium moisture content, and wettability, increasing its dimensional stability and biological endurance. Additionally, changes in the various characteristics of heat-treated wood affect the wood's performance in its application area.

Fernandez et al. (2012) determined the MOR and MOE of structural plywood using an artificial neural network and verified the results through the Multiple Linear Regression (MLR) model. The study considered thickness, moisture content, and density as the input variables for determining MOR and MOE. The results showed that the ANN model with three hidden layers has higher accuracy than the MLR model [2].

Yapıcı et al. (2012) employed Fuzzy Logic Classifier to determine the MOR and MOE of the heat-treated chestnut woods. The authors found that the developed model can calculate the MOR and MOE parameters of the test specimens with an accuracy of 92.64% and 90.35%, respectively, emphasizing its implementation in the wood industry manufacturing stages [3].

Yang et al. (2015) modified wood at high temperatures and under steam pressure. They created an ANN model to determine the mechanical properties of wood, considering temperature, time, and relative humidity as input parameters. The proposed ANN-based model yielded MOR and MOE values with reasonable accuracy [4].

Jiang et al. (2021) performed non-destructive testing of bamboo-based wood. The authors considered a duo Artificial Neural Network (ANN) and support vector machine (SVM) models to determine the MOR and MOE parameters. The outcomes of the study demonstrated that the SVM model with correlation coefficients of 0.90, 0.93, and 0.95 in the training, validation, and testing stages possesses higher accuracy than the ANN model [5].

The current study investigates the MOR of heat-treated woods employing Feed-Forward networks on the selected dataset. A genetic algorithm is used to optimize the weights of ANNs, followed by selecting the best-performed model among all samples of the same type. The proposed model is compared with the Particle Swarm Optimization (PSO) algorithm to evaluate its accuracy.

2 BACKGROUND

2.1 ARTIFICIAL NEURAL NETWORKS (ANN)

An artificial neural network (ANN) is a data model that can be taught from past experiences while implementing the outcomes to new data [6,7]. ANN is fabricated with neurons that work simultaneously to resolve a problem locally. Neural networks learn through typical computations describing the intrinsic mechanisms of the dataset in a reduced human brain-like manner. This study uses the Feed-Forward model comprising more than three layers, including input, hidden and output.

[1] Department of Building, Civil and Environmental Engineering, Concordia University, Montréal, Canada, mehdi.nikoo@mail.concordia.ca

[2] Department of Building, Civil and Environmental Engineering, Concordia University, Montréal, Canada, reza.abbasimalekabadi@mail.concordia.ca

[3] Department of Building, Civil and Environmental Engineering, Concordia University, Montréal, Canada, ghazanfarah.hafeez@concordia.ca

https://doi.org/10.52202/069179-0011

Each layer carries a set of nodes known as neurons connected to the layer above it. Weights, biases, and an activation function that can be continuous, linear, or nonlinear frame the neurons in the hidden and output layers. Once the structure is framed for Feed-Forward training, several procedures will be implemented to optimize the weight and bias levels. The study employs, The Levenberg Marquardt technique for distributing the error to yield the best fit with the least error [8,9].

2.2 GENETIC ALGORITHM (GA)

GA is thoroughly described considering biological concepts, including genetics and evolution. An individual is a candidate solution (typically a parameter vector), and a gene is a component of an individual, while a population is a collection of candidate solutions. An algorithm iteration is generally referred to as a generation, as such, a candidate solution or parent is modified in some way to generate a new candidate solution or child, followed by the algorithm's execution [10]. The standard GA algorithm comprises three genetic operators, including selection, crossover, and mutation. The selection operator is used to pick parents during each generation. The individuals with higher fitness levels have a greater chance of selecting the operator, followed by producing additional individuals or children [10].

3 METHODS AND MATERIALS

3.1 DATASET

In this study, the required data set is extracted from past studies [4,11]. In all, 104 samples of heat-treated woods were studied. The Feed-Forward network, considering temperature, time, and relative humidity as input parameters, was implemented on the dataset to determine the MOR of heat-treated wood. The statistical properties of the input and output parameters are shown in Table 1. While Figures 1 and 2 illustrate the box normal plot and histogram of the MOR parameter, indicating the cluster of MOR values between 60 to 70 MPa.

Table 1:*Input and output parameters in heat-treated wood* [4,11]

Num	Parameter	Unit	Type	MIN	MAX
1	Temperature	°C	Input	120	210
2	Time	hrs	Input	0.5	9
3	Relative Humidity	%	Input	0	100
4	Modulus of Rupture	MPa	Output	45.1	78.2

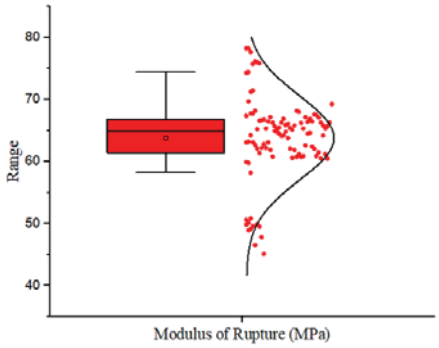

Figure 1: *Box normal plot of experimental data for MOR*

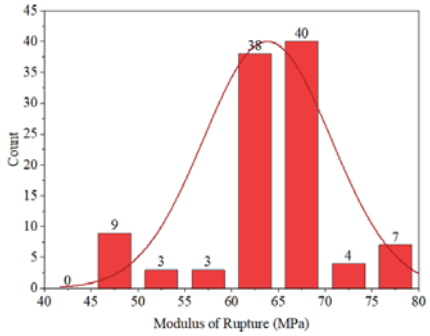

Figure 2: *MOR plot for experimental data histogram*

3.2 ANN MODEL COMBINED WITH GENETIC ALGORITHM

Of 104, 73 samples (70%) were used for training, and the remaining 31 (30%) contributed to testing the data. Two-layer neural networks with different transfer functions suggested the various topologies, as presented in Table 2. The weights and biases of the models were reduced by employing a genetic algorithm. Table 3 displays various properties of the genetic algorithm.

Table 2: *Different topologies used in ANNs*

No	Topology	Hidden and Output Activations
1	3-4-3-1	PURELIN-PURELIN-PURELIN
2	3-4-2-1	POSLIN-POSLIN-PURELIN
3	3-3-4-1	LOGSIG-LOGSIG-PURELIN
4	3-3-3-1	POSLIN-POSLIN-PURELIN
5	3-3-2-1	TANSIG-TANSIG-PURELIN

Table 3: *Genetic algorithm (GA) parameters* [12]

Parameter	Value	Parameter	Value
Crossover (%)	50	Max generations	150
Crossover method	single point	Recombination (%)	15
Lower bound	-1	Selection Mode	1
Upper bound	+1	Population Size	150

Table 4 presents the output of five GA based models, GA-ANN, created to determine the MOR of the heat-treated wood samples. Five different topologies, as illustrated in

https://doi.org/10.52202/069179-0011

Figure 3, were evaluated on the measures of Variance Account Factor (VAF) and Root Mean Squared Error (RMSE) values. The results indicated that the network with the GA-ANN 2L topology (3-4) design achieved the lowest RMSE error rates and the highest VAF percent when estimating the output parameters.

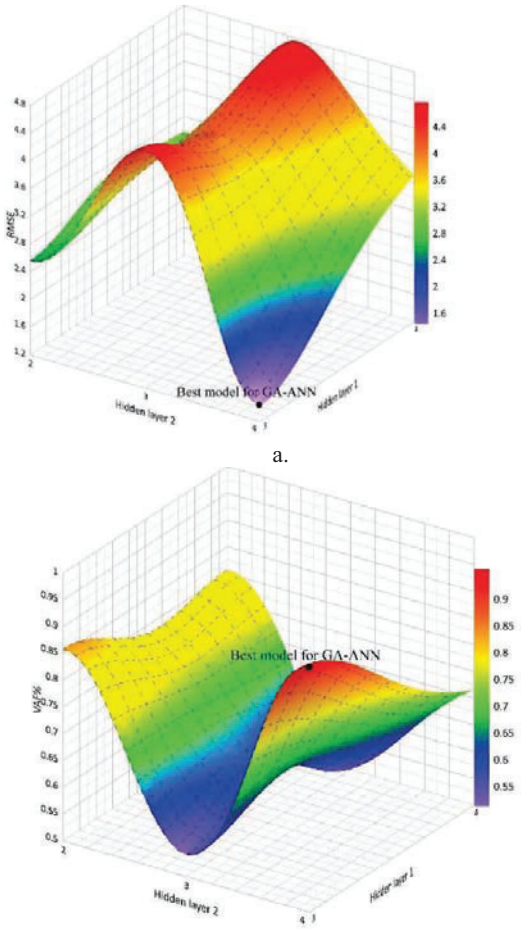

a.

b.

Figure 3: *Statistical values for the proposed topologies in all data: a) RMSE, b) VAF%*

Further, as presented in Table 4, the Feed-Forward network with a GA-ANN 2L topology (3-4) has the lowest value of the RMSE index in the training (1.28) and testing (1.75) phases. Additionally, the model with the same topology maintained the highest VAF value in the training (96%) and the testing (94%) phases indicating the least error among other topologies of the same algorithm. The GA-ANN 2L network topology (3-4) is shown in Figure 4.

Table 4: *Statistics of ANNs combined with the genetic algorithm (GA) for the MOR parameter*

Model Name	Hidden layer 1	Hidden layer 2	Train		Test		All	
			RMSE	VAF%	RMSE	VAF%	RMSE	VAF%
GA-ANN 2L(4-3)	4	3	4.59	51	5.15	46	4.76	51
GA-ANN 2L(4-2)	4	2	2.95	80	3.04	81	2.98	81
GA-ANN 2L(3-4)	3	4	1.28	96	1.75	94	1.43	96
GA-ANN 2L(3-3)	3	3	4.37	56	5.18	47	4.63	54
GA-ANN 2L(3-2)	3	2	2.78	82	1.95	92	2.56	86

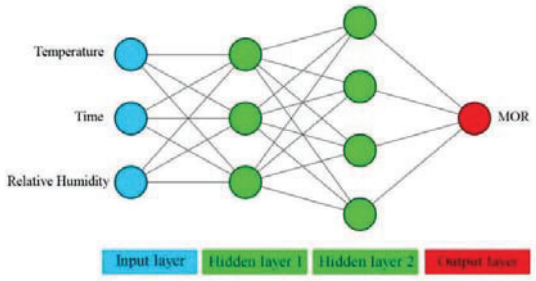

Figure 4: *The architecture of the ANN with the 3-3-4-1 topology*

Figure 5 illustrates the best performance of GA-ANN 2L (3-4), as depicted in the calculated values versus their experimental counterparts in the testing and training phases. The model's projected values fall in the vicinity of the line *(y=x)*, indicating the model's accuracy. Further, the R^2 value for the training and testing phases are found as 0.96 and 0.94, respectively, demonstrating the accuracy of the proposed model.

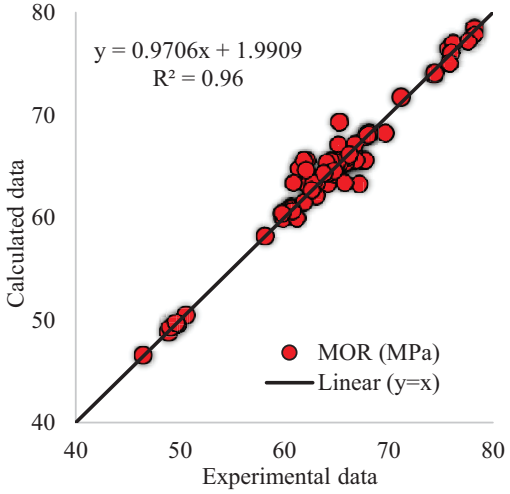

a.

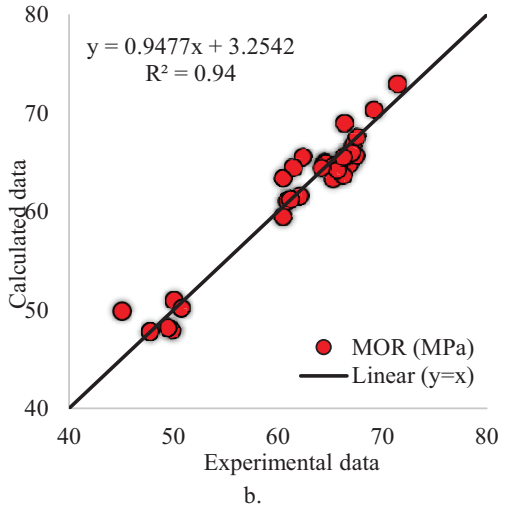

b.

Figure 5: *Experimental vs. predicted values of MOR for the GA-ANN 2L(3-4) model: a) training, b) testing*

3.3 ANN MODEL COMBINED WITH PARTICLE SWARM OPTIMIZATION

The study employs a PSO-optimized ANN to calculate the MOR variable. Similar to GA based models, five topologies presented in Table 2 were used, creating various models for estimating the output parameters.

The models with PSO-ANN 2L(4-2) topology best calculated the required parameter (MOR), as indicated in Table 5 and Figure 6. The testing and training outputs for VAF and RMSE indicators confirm the lowest error rate of the model compared to the experimental data. Also, as indicated in the figure, the R^2 values of the training and testing phases are found to be 0.73 and 0.86, respectively, indicating the model's appropriate accuracy.

Table 5: *Statistics of ANNs combined with the Particle Swarm Optimization algorithm for the MOR parameter*

Topology	Hidden layer 1	Hidden layer 2	Train		Test		All	
			RMSE	VAF%	RMSE	VAF%	RMSE	VAF%
PSO-ANN 2L(4-2)	4	2	3.43	73	2.79	85	3.25	77

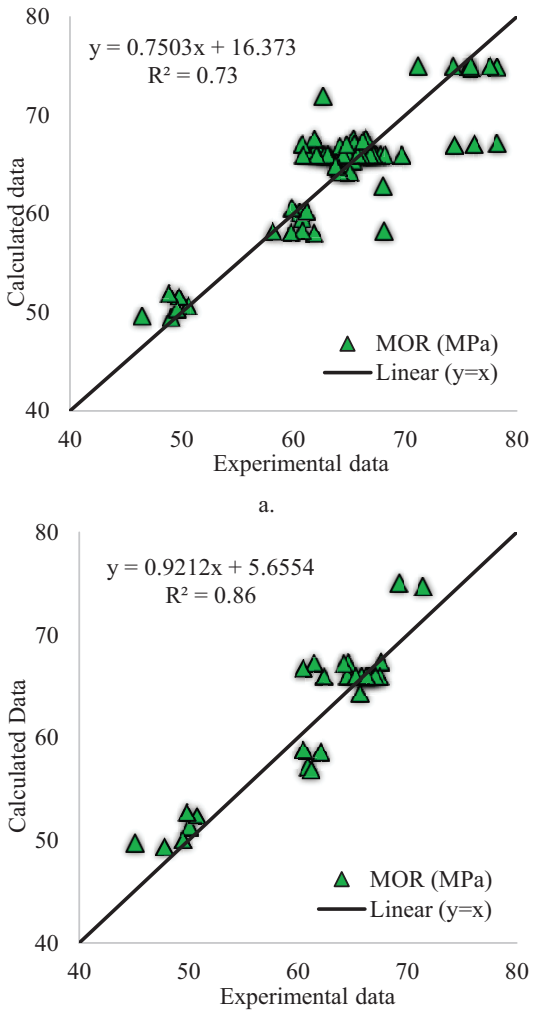

a.

b.

Figure 6: *Experimental vs. predicted values of MOR for the PSO-ANN 2L(4-2) model: a) training, b) testing*

3.4 SELECTION OF THE BEST MODEL

Finally, the best-performed GA-ANN and PSO-ANN models are compared on equal measures for all the datasets. Figure 7 illustrates the comparative normal distribution of the best-performed models with their experimental counterparts. As displayed in the figure, the normal distribution of GA-ANN is closer to the experimental data than the PSO-ANN model indicating the higher accuracy of the GA-ANN model. The comparison of the two models, illustrated in Figure 8, confirms the relatively higher accuracy of the GA-ANN model over the PSO-ANN model.

https://doi.org/10.52202/069179-0011

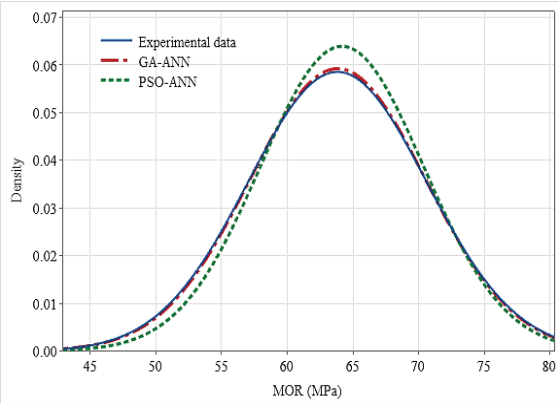

Figure 7: *Normal distribution of experimental data and GA-ANN and PSO-ANN models*

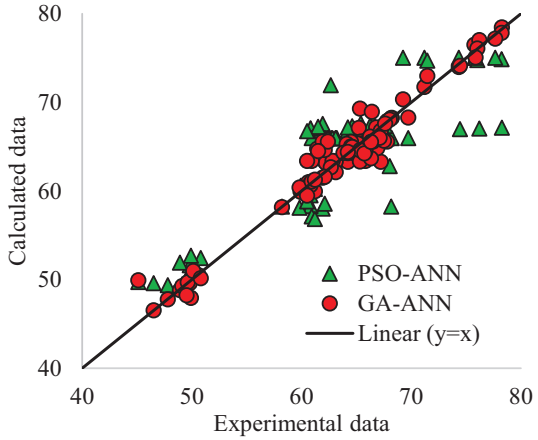

Figure 8: *Experimental vs. predicted values of MOR for different models*

4 CONCLUSION

A total of 104 experimental results obtained from spruce and Larix gmelinii woods were used to determine the MOR of the heat-treated woods. Artificial neural networks were optimized by employing genetic algorithms and particle swarm optimization to analyze the considered dataset. The analyses of the results suggested the better performance of GA-ANN over PSO-ANN for determining the modulus of rupture of the heat-treated woods.

ACKNOWLEDGEMENT

This research received no specific support from public, commercial, or not-for-profit funding organizations.

CONFLICT OF INTERESTS

The authors declare that they have no conflicting interests concerning the publication of this article.

REFERENCES

[1] A.R. Haftkhani, F. Abdoli, A. Sepehr, B. Mohebby, Regression and ANN models for predicting MOR and MOE of heat-treated fir wood, J. Build. Eng. 42 (2021) 102788.

[2] F.G. Fernández, P. de Palacios, L.G. Esteban, A. Garcia-Iruela, B.G. Rodrigo, E. Menasalvas, Prediction of MOR and MOE of structural plywood board using an artificial neural network and comparison with a multivariate regression model, Compos. Part B Eng. 43 (2012) 3528–3533.

[3] F. Yaplcl, D. Ulucan, Prediction of Modulus of Rupture and Modulus of Elasticity of Heat Treated Anatolian Chestnut (Castanea Sativa) Wood by Fuzzy Logic Classifier, Mater. Sci. 63 (2012). https://doi.org/10.5552/drind.2012.1135.

[4] H. Yang, W. Cheng, G. Han, Wood Modification at High Temperature and Pressurized Steam: a Relational Model of Mechanical Properties Based on a Neural Network, Bioresources. 10 (2015) 5758–5776. https://doi.org/10.15376/biores.10.3.5758-5776.

[5] Z. Jiang, Y. Liang, Z. Su, A. Chen, J. Sun, Nondestructive Testing of Mechanical Properties of Bamboo–Wood Composite Container Floor by Image Processing, Forests. 12 (2021).

[6] H. Adeli, Neural Networks in Civil Engineering: 1989–2000, Comput. Civ. Infrastruct. Eng. 16 (2001) 126–142. https://doi.org/10.1111/0885-9507.00219.

[7] F. Ian, K. Nabil, Neural Networks in Civil Engineering. I: Principles and Understanding, J. Comput. Civ. Eng. 8 (1994) 131–148. https://doi.org/10.1061/(ASCE)0887-3801(1994)8:2(131).

[8] S. Haykin, Neural Networks and Learning Machines, 2008. https://doi.org/978-0131471399.

[9] C. Bishop, Pattern Recognition and Machine Learning, Springer-Verlag New York, 2006. https://www.springer.com/gp/book/9780387310732.

[10] M.M. Nikoo, M. Hadzima-Nyarko, E.K. Nyarko, M.M. Nikoo, E. Karlo Nyarko, M.M. Nikoo, Determining the Natural Frequency of Cantilever Beams Using ANN and Heuristic Search, Appl. Artif. Intell. 32 (2018) 309–334. https://doi.org/10.1080/08839514.2018.1448003.

[11] S. Tiryaki, C. Hamzaçebi, Predicting modulus of rupture (MOR) and modulus of elasticity (MOE) of heat treated woods by artificial neural networks, Measurement. 49 (2014) 266–274. https://doi.org/10.1016/j.measurement.2013.12.004.

[12] N. Aalimahmoody, C. Bedon, N. Hasanzadeh-Inanlou, A. Hasanzade-Inallu, M. Nikoo, BAT Algorithm-Based ANN to Predict the Compressive Strength of Concrete—A Comparative Study, Infrastructures. 6 (2021) 80. https://doi.org/10.3390/infrastructures6060080.

World Conference on Timber Engineering Oslo 2023

TENSION-LOADED CONNECTIONS WITH WOOD DOWELS

Matthias Brieden[1]; Max Braun[2], Werner Seim[3]

ABSTRACT: Wood dowels carry tremendous opportunities concerning their application as fasteners and connection elements. Aspects such as sustainability and homogeneous recyclability can be addressed very well by using them to an increasing degree. Although they have been quite common for carpenters for hundreds of years, several characteristics need to be clarified systematically from an engineering point of view.
In this context, results and further investigations are presented within this paper. The load-bearing behaviour of beech dowels under tension force is subject to pull-out and shear testing. Both the inclination angle and the penetration length as major parameters are varied. The interrelation between the inclination, failure loading and ductility of wood dowels is not linear. This finding should be considered when designing and dimensioning new segmented cross-sections.

KEYWORDS: wood dowel, fastener, pull-out test, shear test, inclined connection

1 INTRODUCTION

1.1 HISTORIC AND CURRENT APPLICATIONS

Connections with wooden fasteners are one of the oldest techniques for connecting load-bearing elements. This type of pin-shaped fastener has often been found in historical structures. There, they serve to secure the position of carpenter's joints and transfer connection forces. In this application, the dowel connection is subjected to shear and tension forces [1] [2].
After having been replaced by steel fasteners in recent decades, wood dowels are now back in focus, even outside the rehabilitation of cultural heritage [3] [4]. Wood dowels could be a viable alternative, especially where the use of steel fasteners is critical. Their usage in salt silos, where metal fasteners would be exposed to chemical attack or the amount of electrically conductive material is to be reduced, offers several advantages. In addition, wood dowels have the same favourable properties in case of fire as structural timber. [5]

1.2 FUTURE PROSPECTS

A new aspect is the increasing potential of digital manufacturing methods. Complicated joint geometries are no longer a challenge, which means that, together with the geometry, the performance of wood dowels can be optimally utilised. In this context, the use of robotically manufactured composite components with wood dowels is being researched at the University of Kassel.
It has become clear through the planning and production on a prototype basis that questions regarding the load-bearing behaviour of wood dowels cannot be completely clarified by the relevant literature. The combination especially of tension and shear load has not been studied previously.

2 TEST SERIES 1

2.1 GENERAL INFORMATION

The main focus of the experimental investigations within the first test series is on evaluating the influence of the inclination angle of the fasteners. Therefore, pull-out and shear tests are conducted for different set-ups.
In order to get some statistical background for the research, each single test is repeated five times. Two different material combinations are additionally considered for the pull-out testing. Together with the four angles selected – α = 0°, 15°, 30° or 45° – this leads to 40 pull-out and 20 shear tests.
Both the diameter ($d_{fastener}$ = 10 mm) and the length ($\ell_{fastener}$ = 70 mm) of the wooden dowels are constant for test series 1. The penetration lengths $t_{h,1} = t_1$ and $t_{h,2} = t_e$ correspond to each particular set-up and are dependent on the specific test.
Regarding the style of presenting the experimental results, the single test results are marked as "X", the coloured columns represent the bandwidths and range, and the dotted lines show the mean values as well as the 5 % quantile in the following diagrams.
In the case where single values are identified as outliers, they are displayed as "X", and are not considered for the columns.
Outliers are identified according to the following rules. Results lower than 50 % of the mean value of the three medium results and higher than 150 % of the mean value of the three medium results are treated as outliers and, therefore, neglected.
As an example, the steps of this methodical approach are described for the results Series 1 – Pull-out test – max Force – LVL/LVL – α = 0° (see Figure 5). The single test results are given in Table 1.

[1] Matthias Brieden, Timber Structures and Building Rehabilitation, University of Kassel, Germany; mbrieden@uni-kassel.de
[2] Max Braun, Timber Structures and Building Rehabilitation, University of Kassel, Germany
[3] Werner Seim, Timber Structures and Building Rehabilitation, University of Kassel, Germany

https://doi.org/10.52202/069179-0012

Table 1: *Pull-out test – exemplary results for laminated veneer lumber (LVL)/LVL – α = 0°*

	test number				
	1	2	3	4	5
F_{max} [N]	268	677	466	347	357

As the data in Table 1 show, the minimal and maximal failure load measured occur for test $n = 1$ and $n = 2$. Neglecting these two results, the mean value of the remaining three tests produces ${F_{outlier}}^{mean} = 0.390$ kN, see (1).

$$ {F_{outlier}}^{mean} = (466 + 347 + 357)/3 = 390\ N \quad (1) $$

The upper and the lower limit can be calculated as ${F_{outlier}}^{upp} = 0.585$ kN and ${F_{outlier}}^{low} = 0.195$ kN, see (2) and (3).

$$ {F_{outlier}}^{upp} = 1{,}5 \cdot 390 = 585\ N \quad (2) $$

$$ {F_{outlier}}^{low} = 0{,}5 \cdot 390 = 195\ N \quad (3) $$

Comparing these values with the experimental results, test $n = 2$ ($F_{max} = 0.677$ kN) exceeds the bandwidth and is, therefore, identified as an outlier.

Out of the remaining four results, the mean value, the variance and the coefficient of variation (COV) can be determined as ${F_{max}}^{mean} = 0.359$ kN, $\sigma = 81.40$ and COV = 0.23, respectively, see (4) to (6).

$$ {F_{max}}^{mean} = (268 + 466 + 347 + 357)/4 = 359\ N \quad (4) $$

$$ \sigma^2 = 1/3 \cdot [(268 - 359)^2 + (466 - 359)^2 + (347 - 359)^2 + (357 - 359)^2] \quad (5) $$

$$ \sigma = 81.40 $$

$$ COV = \sigma / {F_{max}}^{mean} = 81{,}40/359 = 0.23 \quad (6) $$

Moreover the 5 % quantile can be calculated as ${F_{max}}^{5\%} = 0.280$ kN, see (7).

$$ 1 + (n-1) \cdot p = 1 + (4-1) \cdot 0.05 = 1.15 $$

quantile is between the smallest (268 N) and second smallest (347 N) result

$$ {F_{max}}^{5\%} = 268 + (347 - 268) \cdot (1.15 - 1.00) = 280\ N \quad (7) $$

2.2 PULL-OUT TESTS

2.2.1 Set-up

In order to study the load-bearing behaviour of connections with beech dowels under tension forces, a modified pull-out test for fasteners has been applied, which enables one to assess the tension resistance of different arrangements of fasteners.

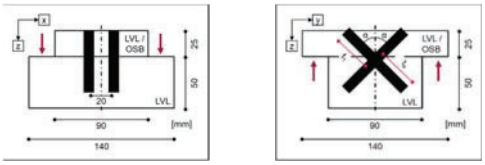

Figure 1: *Pull-out test – Test set-up*

Each pull-out test contains two wooden specimens that are connected by a pair of dowels in various geometric positions. The set-up can be seen in Figure 1.

The load protocol is chosen according to EN 26891 [6]: firstly, an estimated failure loading needs to be selected. The initial loading level is set at 40 % of this estimated failure loading – the strain is increased until this level and then kept constant for 30 seconds. After that, the strain is released to 10 % of the estimated failure loading and then again kept constant at this level. Finally, the strain is increased until the specimen fails – the failure loading has been reached.

2.2.2 Parameters

Forty pull-out tests were conducted with laminated veneer lumber (LVL) and oriented strand board (OSB) to be connected with four different inclinations of the dowels.

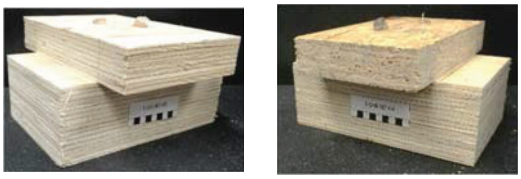

Figure 2: *Pull-out test – Specimen, wood dowels, inclination 30°, left LVL/LVL, right OSB/LVL*

An LVL specimen with wood dowels arranged with an angle of $\alpha = 30°$ can be seen in Figure 2. Figure 3 shows the situation during manufacturing for $\alpha = 30°$.

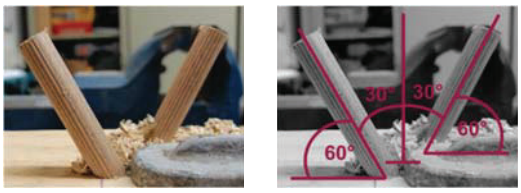

Figure 3: *Pull-out test – Detail, wood dowels, inclination 30° (pretesting)*

Variations considered

The test setting with vertically oriented dowels represents the most inappropriate case, where methodically, no forces straight orthogonally to the specimen surface can be transmitted. The pull-out resistance results because of friction between the specimen and the cylindrical surface of the dowels.

The second limit case considered occurs by tilting the dowels for $\alpha = 45°$. In this constellation, both vertical and horizonal forces are transmitted in addition to friction; moreover, tension and bending within dowels occur.

Intermediate tests with $\alpha = 15°$ and 30° were conducted to evaluate the influence of different angles.

Material and geometrical specifications

The bottom part of the specimens has a thickness of 50 mm and is always made of LVL. By contrast, the material of the upper layer is varied between LVL and

https://doi.org/10.52202/069179-0012

OSB, both with a thickness of 25 mm. Additional data concerning the dimensions of the specimen can be found in Figure 1.
The fasteners are made of beech and have a corrugated cylindrical surface. The diameter is 10 mm, and the dowel holes are predrilled with a diameter of 9.5 mm. The penetration lengths can be calculated for the individual situation.

2.2.3 Results

The F-t diagram and the corresponding F-u diagram are illustrated for one particular variation – OSB/LVL, inclination 15° – in Figure 4. These curves are exemplary for the whole pull-out testing campaign.

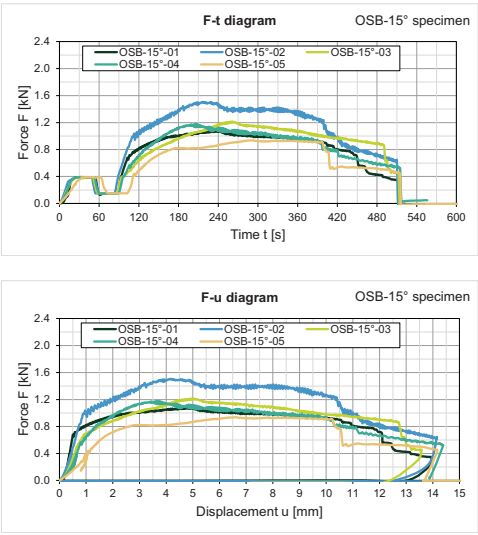

Figure 4: *Pull-out test – Exemplary test date*

All results which are presented in the following refer to "Two Fasteners in One Shear Plane with a Crossed ('X') Arrangement". This note can be found in the upper right-hand corner of the diagrams.

Failure loading and failure mode

Results of the pull-out tests are displayed in Figure 5 and Figure 6. The diagrams show the maximal tension force as a function of the installation angle.

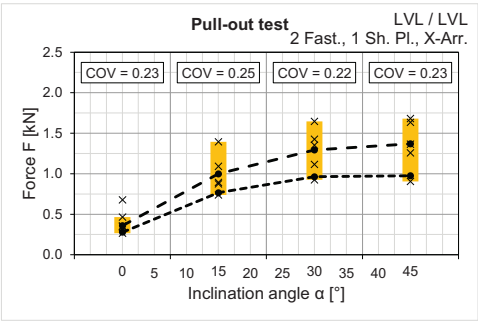

Figure 5: *Series 1 – Pull-out test – max Force – LVL/LVL*

One "0° test" is neglected in Figure 5, because of a faulty load protocol. Figure 6 shows that the maximal tension force fell below significantly for two of the five "0° tests". They are also neglected.

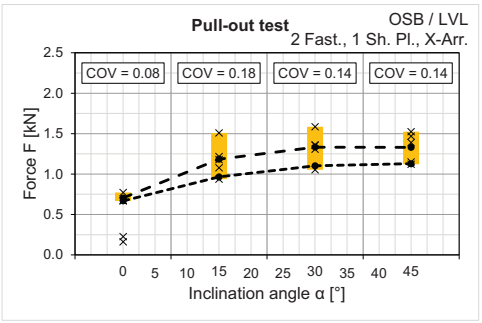

Figure 6: *Series 1 – Pull-out test – max Force – OSB/LVL*

The tension resistance rises considerably in relation to the vertical arrangement if the fasteners are tilted only about $\alpha = 15°$. Additional tilting improves the tension resistance in the following, but the increase is no longer as significant.
Both combinations considered – LVL/LVL and OSB/LVL – reach a similar level of failure loadings.

Slip modulus

In addition, the stiffnesses are also determined. Two different slip moduli (K_{init} and K_{re}) are determined corresponding to the specifications of the load protocol (initial load to 40 % of the estimated failure loading; relief to 10 % of the estimated failure loading; reload until the failure loading is reached). The gradient between 5 % and 35 % of the estimated failure loading is calculated for the initial slip modulus. The gradient in the force-displacement curve is determined between 10 % and 50 % of the failure loading to get the slip modulus of the reloading section.

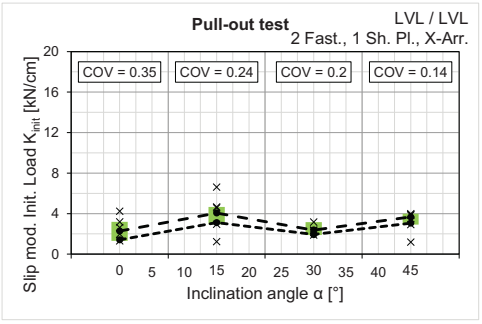

Figure 7: *Series 1 – Pull-out test – Slip modulus init. loading – LVL/LVL*

The results in Figure 7 to Figure 10 illustrate the particular slip moduli again as a function of the inclination angle. The style of the diagrams matches the ones already presented. Once more, the outliers are displayed as mentioned earlier, but are not considered for the further course of the discussion.

https://doi.org/10.52202/069179-0012

As seen in Figure 7 and Figure 8, no clear correlation between the slip modulus and inclination angle can be found. While K_{init} can be recognised as constant for the LVL/LVL specimen, a nearly linear increasing graph can be found for the OSB/LVL tests.
Concerning the different material combinations, it can be assumed that the OSB variation leads to higher slip moduli in contrast to the LVL variation.

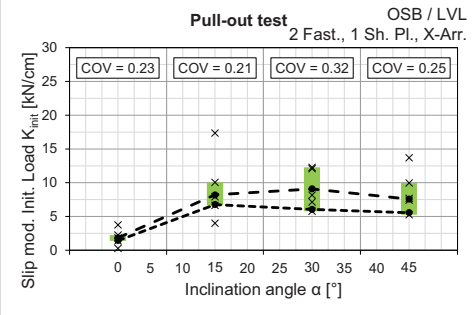

Figure 8: *Series 1 – Pull-out test – Slip modulus init. loading – OSB/LVL*

Figure 9 and Figure 10 show the slip moduli for the reloading section of the test series conducted. In this case, it can be seen even more clearly that no straight dependence occurs. The OSB/LVL tests in Figure 10 differ significantly due to the inclination angle.

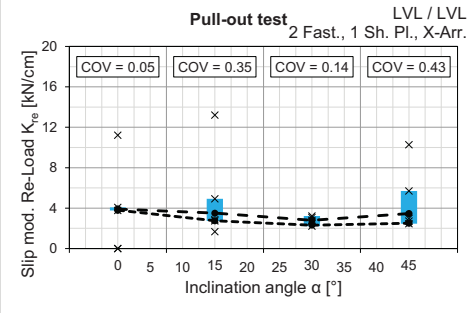

Figure 9: *Series 1 – Pull-out test – Slip modulus reloading – LVL/LVL*

Comparing the LVL and the OSB tests, higher slip moduli can again be determined for the latter.

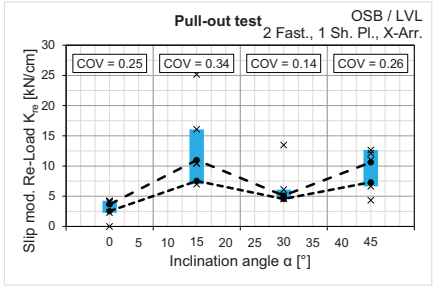

Figure 10: *Series 1 – Pull-out test – Slip modulus reloading – OSB/LVL*

2.3 SHEAR TESTS

2.3.1 Set-up

In order to evaluate the performance of the beech dowels under shear loading, several experimental tests were conducted. The test set-up is shown in Figure 11.

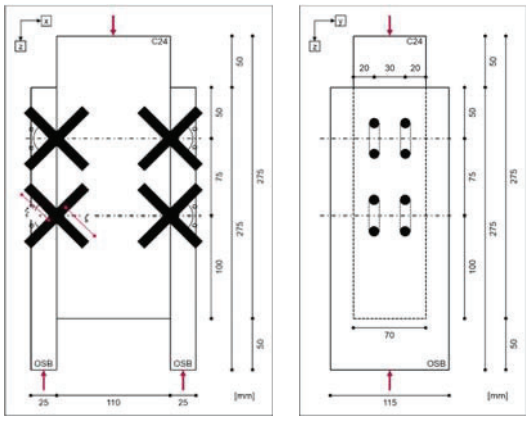

Figure 11: *Shear test – Test set-up*

Specimens with OSB elements and one C24 element are constructed for the investigations. The connection between the OSB panels and the C24 part is realised with eight wooden dowels. The fasteners are inclined with different angles, similar to those applied for the pull-out tests.
The middle parts have dimensions of 110 x 70 x 275 mm, while the panels are 25 x115 x 275 mm.
The load protocol is again chosen according to EN 26891 [6]. For more information, see 2.2.1.

2.3.2 Parameters

There are a total number of 20 shear tests in series 1. In terms of material specifications, only the combination of OSB panels with a C24 beam is considered. Again, four different angles are investigated.

Figure 12: *Shear test – Specimen and test set-up*

https://doi.org/10.52202/069179-0012

Figure 12 and Figure 13 show a specimen, the test set-up and some selected details.
Five tests are performed for each of the four different angles – α = 0°, 15° 30° and 45°.

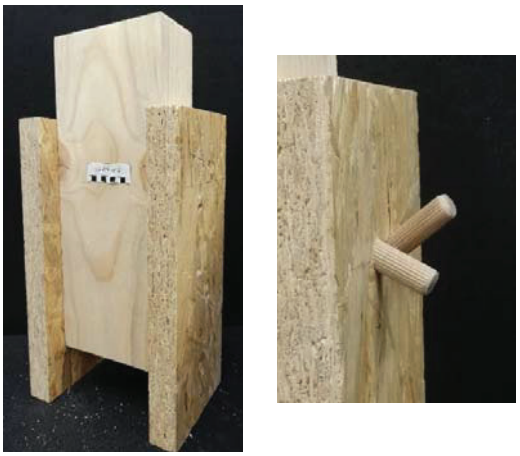

Figure 13: *Shear test – Specimen, detail, wood dowels, inclination 45°*

The diameter of the fasteners is again set at 10 mm, and the dowel holes are predrilled with a diameter of 9.5 mm. The penetration lengths correspond with the length of the fasteners of 70 mm and the particular set-up.
Details concerning the dimensions of the specimen can be found in 2.3.1.

2.3.3 Results

Figure 14 shows an example of the set-up with α = 15°; the values measured compiled as both an F-t and a F-u diagram. The current curves are valid for two fasteners with one shear plane.

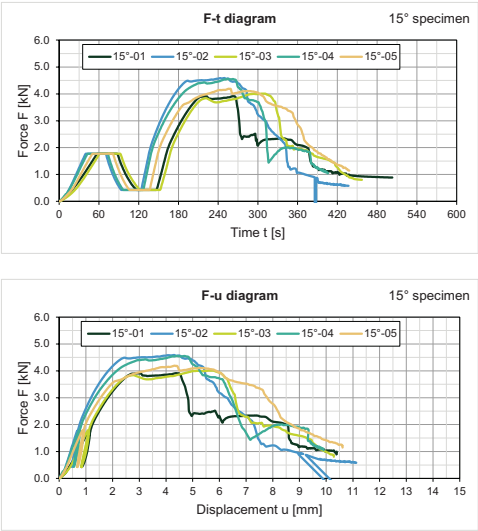

Figure 14: *Series 1 – Shear test – Exemplary test results*

All results presented in the further course refer to “Four Fasteners in Two Shear Planes with a Crossed (‘X’) Arrangement”. This note can be found in the upper right-hand corner of the diagrams.
See 2.2.3 for the style and layout of the results.

Failure loading and failure mode

The maximal loads as a function of the inclination angle can be seen in Figure 15. A rather clear correlation can be found. The maximum force decreases as the angle increases.

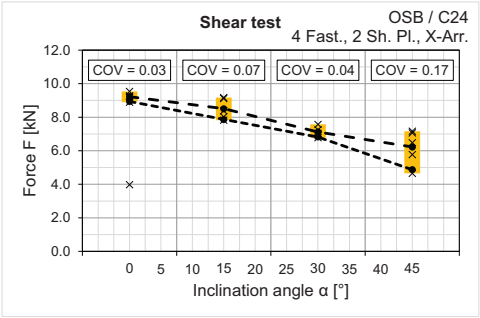

Figure 15: *Series 1 – Shear test – max Force – OSB/C24*

In this case, the cross-wise arrangement of the dowels – see detail in Figure 13 – indicates the course of the test results. Regarding α = 0°, each dowel is loaded in the same way, while for other angles, only one out of two dowels contribute to the load-bearing capacity.

Slip modulus

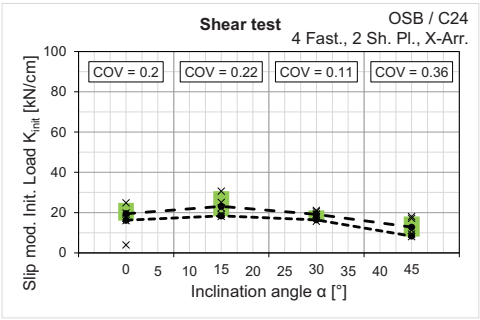

Figure 16: *Series 1 – Shear test – Slip modulus init. loading – OSB/C24*

In addition to the failure loadings, the slip moduli are also determined. The results – firstly, for the initial loading section, secondly, for the reloading section – can be found in the diagrams in Figure 16 and Figure 17.

https://doi.org/10.52202/069179-0012

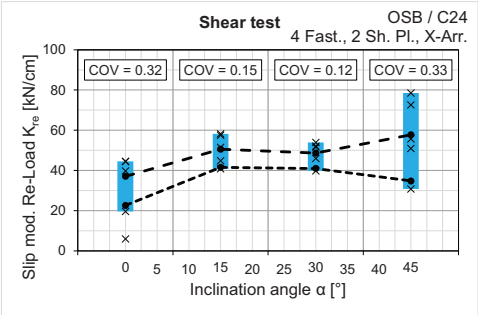

Figure 17: *Series 1 – Shear test – Slip modulus reloading – OSB/C24*

As the experimental results indicate, both slip moduli are more or less independent of the inclination angle. This may be due to the ambiguous effect of the different arrangements of the fasteners – on the one hand, tilting the dowels improves the load-bearing capacity, but, on the other hand, the pairwise opposing orientation reduces the load-bearing capacity.

While K_{init} slightly decreases with an increasing angle (Figure 16), K_{re} tends to increase in this course (Figure 17). The initial slip modulus is generally less than half of the slip modulus for the reloading.

3 TEST SERIES 2

3.1 GENERAL INFORMATION

The main focus in the second test series is on evaluating the influence of different penetration lengths of the dowels. As has already been conducted within test series 1, pull-out and shearing test are performed. This time, as a secondary parameter, the inclination angle is varied for only two values – pull-out tests are done for α = 15° and 30°, whereas shearing tests are conducted for α = 0° and 30°.

Five specimens were tested for each parameter combination. The material specifications are point, with OSB and C24 as materials for all investigations. A total of 30 pull-out and 30 shear tests were conducted.

The diameter ($d_{fastener}$ = 10 mm) of the wooden dowels constant, while the particular length for test series 2 corresponds with the penetration length of each set-up.

3.2 PULL-OUT TESTS

3.2.1 Set-up

The set-up for the pull-out test in the second test series complies with that in series 1. Details can be found in 2.2.1.

Similar to the first test series, the dimensions of the specimens are 90 x 140 x 50 mm for the lower element (C24) and 140 x 90 x 25 mm for the upper element (OSB).

3.2.2 Parameters

The penetration length in the lower timber element (C24) is given in relation to the thickness of the upper timber element (OSB). With t_1 = 25 mm and t_e / t_1 = 1.0, 1.5 and 2.0, the particular values are t_e = 25.0, 37.5 and 50.0 mm. The total length of the fasteners are $\ell_{fastener}$ = 50.0, 62.5 and 75.0 mm.

3.2.3 Results

Due to the corresponding testing conditions, the remarks given in 2.2.3 hold as well.

Failure loading and failure mode

The results of the experimental tests are illustrated in Figure 18. Here, the diagrams show the maximum force over the penetration length.

It can be seen that the penetration length has no significant influence on the failure loading. A clear effect cannot be found because of the statistical deviation. As a trend, it can be assumed that the rising penetration length leads to a higher failure loading.

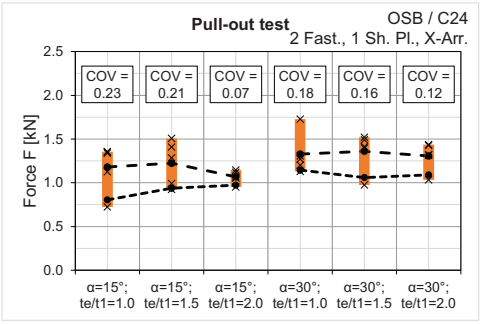

Figure 18: *Series 2 – Pull-out test – max Force – OSB/C24*

Slip modulus

In addition, the two slip moduli discussed already are also determined. Figure 19 and Figure 20 show the corresponding results.

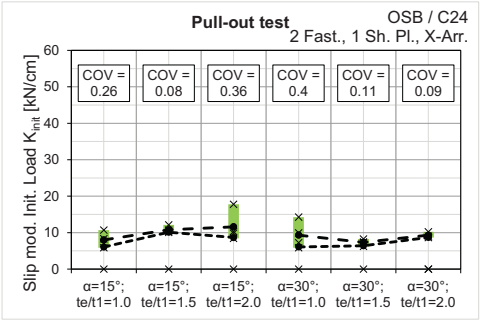

Figure 19: *Series 2 – Pull-out test – Slip modulus init. loading – OSB/C24*

Regarding the initial load section, the slip modulus is almost constant and, thus, not influenced by the penetration length (see Figure 19).

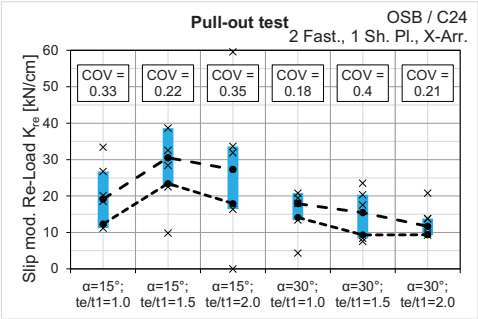

Figure 20: *Series 2 – Pull-out test – Slip modulus reloading – OSB/C24*

By contrast, although the slip modulus for the reloading section (see Figure 20) is obviously affected by the penetration length, a direct correlation cannot be found.

3.3 SHEAR TESTS

3.3.1 Set-up

The test set-up for the shear tests of the second test series is the same as test series 1. Further information can be found in 2.3.1.

3.3.2 Parameters

The main focus of the pull-out tests presented previously is on the influence of different penetration lengths. The particular lengths investigated are t_e = 25.0, 37.5 and 50.0 mm. Moreover, two inclination angles are considered: α = 0° and 30°.

3.3.3 Results

See 2.3.3 for the layout and more details about the following diagrams.

Failure loading and failure mode

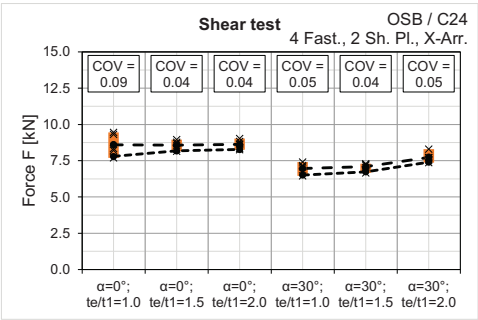

Figure 21: *Series 2 – Shear test – max Force – OSB/C24*

Figure 21 contains the maximal failure loadings determined experimentally for the different set-ups considered. It can be seen that there is only a slight effect of the penetration length. Regarding the inclination angle, the results presented show a decreasing trend when increasing the tilting.

Slip modulus

Figure 22 and Figure 23 show the slip moduli which are determined for the initial and the reloading section. The results indicate that at least K_{init} is not significantly influenced by the penetration lengths. No clear trend is obvious.

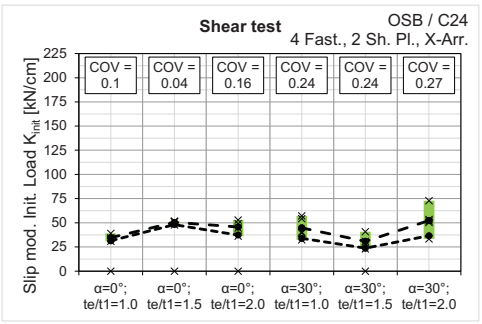

Figure 22: *Series 2 – Shear test – Slip modulus init. loading – OSB/C24*

Concerning K_{re}, on the one hand, there seems to be a corresponding correlation for α = 0°, however, on the other hand, no clear effect can be proved for α = 30°.

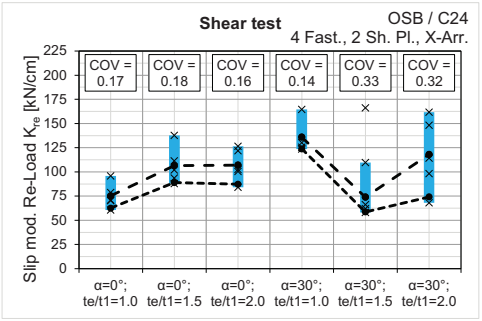

Figure 23: *Series 2 – Shear test – Slip modulus reloading – OSB/C24*

4 DISCUSSION AND INTERPRETATION

4.1 PULL-OUT TESTS

The results of the pull-out tests are summarised in Table 2, Table 3 and Table 4; the tables contain the mean value and the 5 % quantile of each particular configuration. Normal distribution was assumed and the quantiles have been calculated as given in (7).

Table 2: *Pull-out test – max Force*

Configuration			*n [-]*	*F [kN]* mean value	*F [kN]* 5 % quantile
Series 1	LVL/LVL	α=0°	4	0.359	0.280
		α=15°	5	0.999	0.765
		α=30°	5	1.294	0.964
		α=45°	5	1.370	0.976

https://doi.org/10.52202/069179-0012

	OSB/LVL			α=0°	3	0.705	0.669
				α=15°	5	1.184	0.966
				α=30°	5	1.333	1.104
				α=45°	5	1.332	1.128
Series 2	OSB/C24	t_e/t_1	1.0	α=15°	5	1.180	0.805
				α=30°	5	1.227	1.141
			1.5	α=15°	5	1.224	0.937
				α=30°	5	1.360	1.060
			2.0	α=15°	5	1.068	0.973
				α=30°	5	1.306	1.090

Comparing the results of both test series, it can be outlined that the failure loadings in series 2 fit in well to the ones of series 1. The increase of the inclination angle leads to a higher load-bearing capacity, whereby the effect flattens with increasing angles. Table 2 indicates that a clear effect of the different material combinations cannot be found. Thereby, the failure of the specimen seems to be caused by the fasteners themselves.

Table 3: *Pull-out test – Slip modulus init. loading*

Configuration					*n [-]*	*K_{init} [kN/cm]* mean value	5 % quantile
Series 1	LVL/LVL			α=0°	4	2.28	1.42
				α=15°	3	4.02	3.12
				α=30°	5	2.38	1.94
				α=45°	4	3.68	3.06
	OSB/LVL			α=0°	3	1.84	1.45
				α=15°	4	8.21	6.78
				α=30°	5	9.10	6.07
				α=45°	4	7.59	5.58
Series 2	OSB/C24	t_e/t_1	1.0	α=15°	4	7.98	6.04
				α=30°	4	9.32	6.07
			1.5	α=15°	4	10.78	10.11
				α=30°	4	7.31	6.39
			2.0	α=15°	4	11.58	8.64
				α=30°	3	9.29	8.66

By contrast, it can be detected that the two slip moduli and, with it, the deformation of the specimen, are influenced by the different materials. Table 3 and Table 4 show that the slip moduli of the LVL tests are lower than the other ones for most configurations. The results of series 2 especially indicate that the material combination has a large impact on the performance.

Table 4: *Pull-out test – Slip modulus reloading*

Configuration					*n [-]*	*K_{re} [kN/cm]* mean value	5 % quantile
Series 1	LVL/LVL			α=0°	2	3.92	3.79
				α=15°	3	3.51	2.76
				α=30°	5	2.80	2.32
				α=45°	4	3.47	2.51
	OSB/LVL			α=0°	4	3.66	2.53
				α=15°	4	11.01	7.53
				α=30°	4	5.12	4.58
				α=45°	4	10.62	7.62
Series 2	OSB/C24	t_e/t_1	1.0	α=15°	4	19.17	12.31
				α=30°	4	17.92	14.10
			1.5	α=15°	4	30.53	23.41
				α=30°	3	15.45	9.32
			2.0	α=15°	3	27.30	17.94
				α=30°	4	11.68	9.37

4.2 SHEAR TESTS

Table 5, Table 6 and Table 7 summarise the results of the shear tests of both series. The mean values determined and the corresponding quantiles are given for each configuration.

Table 5: *Shear test – max Force*

Configuration					*n [-]*	*F [kN]* mean value	5 % quantile
Series 1	OSB/C24			α=0°	4	9.232	8.942
				α=15°	5	8.504	7.864
				α=30°	5	7.119	6.819
				α=45°	5	6.227	4.877
Series 2	OSB/C24	t_e/t_1	1.0	α=0°	5	8.600	7.796
				α=30°	5	6.964	6.508
			1.5	α=0°	5	8.574	8.177
				α=30°	5	7.083	6.733
			2.0	α=0°	5	8.618	8.269
				α=30°	5	7.729	7.396

On the one hand, it can be seen that the results of both test series for the failure loadings (Table 5) are very close.

Table 6: *Shear test – Slip modulus init. loading*

Configuration					*n [-]*	*K_{init} [kN/cm]* mean value	5 % quantile
Series 1	OSB/C24			α=0°	4	19.50	16.21
				α=15°	5	23.11	18.38
				α=30°	5	19.15	16.41
				α=45°	5	12.81	8.36
Series 2	OSB/C24	t_e/t_1	1.0	α=0°	4	34.52	31.40

		α=30°	5	44.74	33.83
	1.5	α=0°	4	50.37	48.18
		α=30°	4	30.74	23.74
	2.0	α=0°	4	45.65	37.40
		α=30°	5	52.33	36.63

Table 7: *Shear test – Slip modulus reloading*

Configuration				*n [-]*	*K_{re} [kN/cm]* mean value	5 % quantile
Series 1	OSB/C24		α=0°	4	37.09	22.62
			α=15°	5	50.57	41.57
			α=30°	5	48.69	41.00
			α=45°	5	57.73	34.82
Series 2	OSB/C24	t_e/t_l 1.0	α=0°	5	75.26	62.58
			α=30°	4	135.96	123.90
		1.5	α=0°	5	106.54	89.03
			α=30°	4	74.00	58.62
		2.0	α=0°	5	107.06	87.33
			α=30°	5	118.16	74.16

Due to the slip moduli, on the other hand, the results indicate a significant deviation between the two test series. In this context, it has to be emphasised that the evaluation of the data is of great importance. The particular way of determining the gradients (initial and reloading section) of the load-displacement curves must be considered.
In addition, the effect of the different penetration lengths shows no clear tendency. More testing with other specifications is necessary in order to evaluate this effect.

5 CONCLUSIONS AND OUTLOOK

The results presented lead to a better understanding of connections with wood dowels under tension and shear. Wood dowels are easy to use, flexible, sustainable and represent a promising alternative not only in the restoration sector but also for new constructions.
More investigations concerning doweled connections under shear and tension will be carried out to understand the load-bearing behaviour of these fasteners and, thus, to expand the application area.
As an additional approach, other geometrical and material specifications – different diameters, wider range of penetration lengths, alternative arrangements of the fasteners – will be investigated.
As a consequence of the research approach, further application areas for wooden dowels and similar fasteners should be found. This will lead to a more sustainable and appropriate use of wooden construction elements.

ACKNOWLEDGEMENT

The results presented were achieved within the DFG research project “Additive robotic assembly techniques for timber construction – Computational design and integrated structural joining methods”. This project is funded by “Deutsche Forschungsgemeinschaft”. The work would not have been possible without this support.
The authors would like to thank the funding agencies, the colleagues named in the bibliography and the representatives of the companies involved in the project as well as the associated project committees for their contributions.

REFERENCES

[1] Meisel, A.: Historische Dachtragwerke; Graz: Verlag der Technischen Universität Graz, 2015.
[2] Görlacher, R.: Historische Holztragwerke – Untersuchen, Berechnen und Instandsetzen; F. Wenzel und J. Kleinmanns, eds., Karlsruhe: Universität Karlsruhe, 1999.
[3] O’Loinsigh, C.; Oudjene, M.; Ait-Aider, H.; Fanning, P.; Pizzi, A.; Shotton, E.; Meghlat, E.-M.: Experimental study of timber-to-timber composite beam using welded-through wood dowels. Construction and Building Materials, Vol. 36, November 2012.
[4] O’Ceallaigh, C.; Conway, M.; Mehra, S.; Harte, A.: Numerical investigation of reinforcement of timber elements in compression perpendicular to the grain using densified wood dowels. Construction and Building Materials, Vol. 288, June 2021.
[5] Blass, H.-J.; Ernst, H.; Werner, H.: Verbindungen mit Holzstiften – Untersuchungen über die Tragfähigkeit. Bauen mit Holz, October 1999.
[6] EN 26891: Timber structures – Joints made with mechanical fasteners – General principles for the determination of strength and deformation characteristics. Berlin. July 1991.

https://doi.org/10.52202/069179-0012

World Conference on Timber Engineering Oslo 2023

MECHANICAL PROPERTIES OF GLUE LAMINATED TIMBER BY SMALL SIZE TREE SPECIES (CASE STUDY OF OKINAWAN FOREST)

Juan Jose Castro[1], Shogo Omi[2]

ABSTRACT: Local islanders have used Okinawan forest products for construction since ancient times. However, the present state is that the local forest trees have only a tiny diameter of 30 to 40 cm and 4 to 5 m in length on average. Because of that limited size, the timbers do not meet the size requirements for building construction, thus, they have been used only for low added value products. Therefore, to utilize those local timbers more valued products, the authors have proposed the glue laminated timber technique, which enables larger sections of structural elements to be used for building construction. This study selected four types of local timber to elaborate solid type and glue laminated timber type specimens to examine their applicability. The test consists of bending and fiber longitudinal compression tests to assess the mechanical properties of the Okinawan timbers. The results showed that the mechanical properties, such as strength and modulus of elasticity of solid and glue laminated timber, were equal to or stronger than solid timber. In addition, the mechanical properties of those timbers tested in this study were even stronger compared to extensively used timbers in Japan, such as Cedar and Japanese Cypress.

KEYWORDS: small size timber, glue laminated timber, bending strength, compression strength, modulus of elasticity

1 INTRODUCTION

With a sub-tropical climate, Okinawa Prefecture is home to many tree species not found elsewhere on Japanese islands. Several of these species have long been used for local large scale public buildings such as Shuri Castle and traditional private houses, shipbuilding, etc. However, the social and political shift to present modern Japan in the late 19th century caused the destruction of local forests. Due to this change, people started to consume timbers intensively, but the implant project of wood had not been executed properly. This poor forest preservation has continued over the years. Consequently, Okinawan sub-tropical woods recently have limited resources of trees, such as a tiny diameter of 30 to 40 cm and 4 to 5 m in length on average. Thus, it is known that the size of Okinawan solid wood is limited and too small for structural building materials, as shown in Figure 1[1].

Figure 1: *Lumber in Okinawan Islands*

Since the market of Okinawan timber is small as explained above, most local timbers are utilized for small products.

Among the total lumber processed, as shown in Figure 2, 35% is for chips for livestock bedding, 35% is for fuel wood, and the remaining 30% is used for lumber elements. Among the last item, the main products processed are furniture, accessories, and other elements with small demand for timber volume.

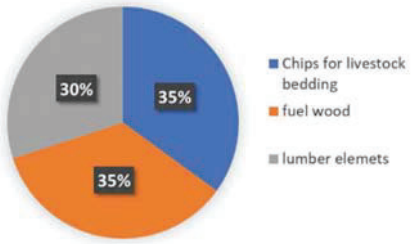

Figure 2: *Use of the Okinawan lumber*

The characteristic of the lumber produced in Okinawan islands such as Ryukyumatsu (Pinus luchuensis), Itajii (Castanopsis sieboldii), Iju (Schima wallichii) and Inumaki (Podocarpus macrophyllus) is that they have in average a density of 0.6 gr/cm^3[1]. This density is higher than the Cedar (0.34 gr/cm^3) and Japanese Cypress (0.42 gr/cm^3), which are more prevalent lumber in the Japanese timber industry. However, since Okinawan timber's mechanical properties are not standardized as the other

[1] Juan Jose Castro, Faculty of Engineering, University of the Ryukyus, 1 Senbaru, Nishihara, Okinawa, 903-02313, Japan, castro@tec.u-ryukyu.ac.jp

[2] Shogo Omi, Faculty of Engineering, University of the Ryukyus, Okinawa, Japan, omi@tec.u-ryukyu.ac.jp

https://doi.org/10.52202/069179-0013

species, they can not be used as structural elements for building construction due to the lack of technical information.

In this study, we would like to consider using this timber as a higher value-added structural material for construction. Therefore, we have proposed using small-sized Okinawan lumber for glue laminated timber (GLT), enabling high-quality structural elements with large sections with fewer defects.

The research focuses on whether the mechanical properties of the Okinawan timber can be improved by using GLT and comparing them with the Cedar and Japanese Cypress values. Also, this paper proposes a reference strength value to be used in the structural design.

In this paper, full-scale specimens of solid wood and glued laminated timber from Okinawa Prefecture were prepared and tested in bending and compression to assess their mechanical properties.

2 METHOD

2.1 MATERIAL AND SPECIMENS

Four tree species were selected for this study, Ryukyumatsu (Pinus luchuensis), Itajii (Castanopsis sieboldii), Iju (Schima wallichii), and Inumaki (Podocarpus macrophyllus). The timber was obtained from the Kunigami-village, Okinawa Prefecture's forestry cooperative, and was used to make solid and glue laminated timber specimens.

The specimens were manufactured following the Japan Housing and Wood Technology Center (HOWTEC) regulations[2]. Figure 3 shows the dimension of the specimens. Three solid and six GLT specimens were tested from each tree species, as shown in Table 1.

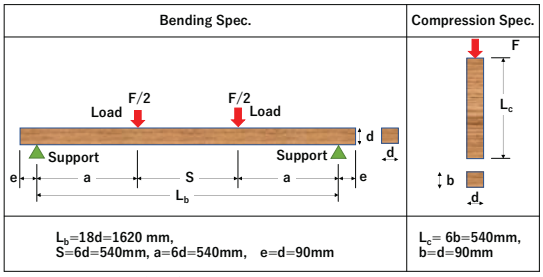

Figure 3: *Details of specimens*

Table 1: Specimens List

Test	Timber Type	Solid		GLT	
		Size (mm)	No. of Spec.	Size (mm)	No. of Spec.
Bending Spec.	Ryukyumatsu	90x90x1800	3	90x90x1800	6
	Itajii	90x90x1800	3	90x90x1800	6
	Iju	90x90x1800	3	90x90x1800	6
	Inumaki	90x90x1800	1	80x80x1600	1
Comp. Spec.	Ryukyumatsu	90x90x540	3	90x90x540	6
	Itajii	90x90x540	3	90x90x540	6
	Iju	90x90x540	3	90x90x540	6
	Inumaki	90x90x540	1	80x80x480	1

The glued laminated wood specimens were made of four layers of lamina boards, which were finger-jointed and glued together with water based polymer isocyanate adhesive, as shown in Figure 4. Also, Figure 5 shows the details of the finger joints.

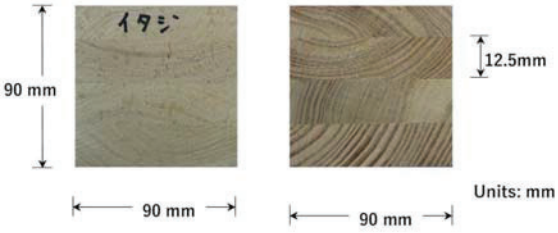

(a) Solid *(b) GLT*

Figure 4: *Section of specimens*

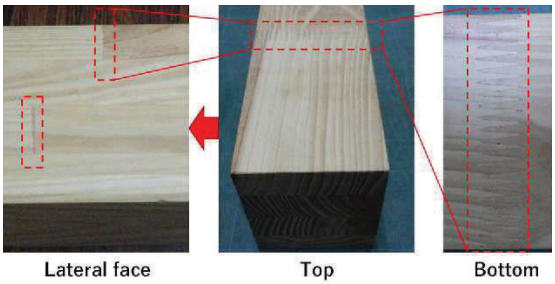

Figure 5: *Detail of the finger joint*

2.2 EXPERIMENTAL METHODOLOGY

In this test, bending and longitudinal compression tests were conducted on solid and glued laminated timbers following the Manual for Strength Testing of Structural Timbers[1]. The testing machine was a universal testing machine (Shimadzu Corporation, UH-FC, maximum capacity 2000 kN) at the experimental testing laboratory of the Faculty of Engineering, University of the Ryukyus. The loading rate was constant displacement so that the time to reach maximum load was at least one minute. The density and moisture content of all specimens were determined before testing. For moisture contents calculations, pieces cut from each specimen were placed in an oven from 101°C to 105°C until the quasi constant weight was obtained.

1) Bending Test

The loading system for the bending test is shown in Figure 6. This test determines the bending strength MOR_b and the bending modulus of elasticity MOE_b. The bending test was performed using the four points load method to have pure bending between the applied loads.

The load cell attached to the testing machine and the displacement transducer installed on the specimen were used to record the bending loads and deflections at the center of the span. A jig was attached to the neutral axis at the center of the specimen to measure the deflection.

https://doi.org/10.52202/069179-0013

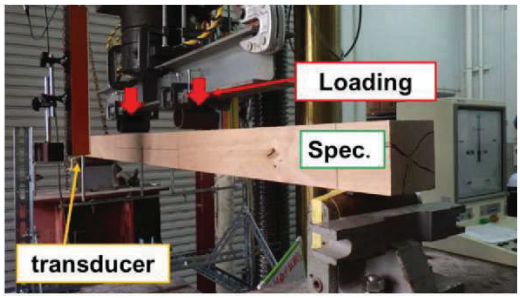

Figure 6: *Bending Test*

The displacements on both sides were measured with a displacement transducer (SDP-3000), and the average value was taken. Using the values measured in the test, MOR_b and MOE_b were calculated from the following equations (1) and (2) [2].

$$MOR_b = \frac{aP_m}{2Z} \quad (1)$$

$$MOE_b = \frac{a(3L^3 - 4a^2)(F_2 - F_1)}{48(w_2 - w_1)} \quad (2)$$

Where MOR_b=bending strength (N/mm^2), MOE_b= modulus of elasticity (N/mm^2), a = distance between the two supports (mm), P_m=maximum load, a=distance between loading points and support, Z= section modulus (mm^3), ΔP= increment of load at the elastic range (N), I=moment of inertia (mm^4), F_1-F_2= Incremental load on the straight line portion of the load-deformation curve F_1=Pm /10 、 F_2=4P_m/10 [N], w_2-w_1= Incremental deformation corresponding to F_2-F_1 (mm).

2) Compression test

The loading system for the longitudinal compression test is shown in Figure 7. This test determines the longitudinal compressive strength MOR_c and the longitudinal compressive modulus of elasticity MOE_c.

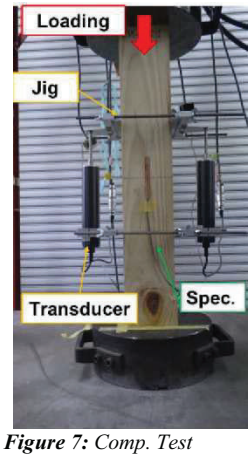

Figure 7: *Comp. Test*

The specimens were loaded using a universal testing machine with a spherically seated load head, allowing the application of uniform compressive load without creating bending stresses. The compression strains were measured by placing a jig located at the center of the specimen (l = 200 [mm]) with a displacement transducer (CDP-50). This jig was located 170 mm from both ends of the specimens. Using the values measured in the test, MOR_c and MOE_c were calculated from the following equations (3) and (4).

$$MOR_c = \frac{P_c}{A} \quad (3)$$

$$MOE_c = \frac{l(F_2 - F_1)}{A(w_2 - w_1)} \quad (4)$$

Where MOR_c=compression strength (N/mm^2), MOE_c= modulus of elasticity (N/mm^2), A = section of the specimen (mm), P_c=maximum load, l = test length (200mm), F1-F2= Incremental load on the straight line portion of the load-deformation curve F_1=Pm /10, F_2=4P_m/10 [N], w_2-w_1=Incremental deformation corresponding to F_2-F_1 (mm).

3 RESULTS

3.1 BENDING TEST

The strength-deflection curves for bending specimens are shown in Figure 8. The maximum strength value of the GLT specimens tended to be higher than that of the solid timber. In this study, the solid specimens showed a bigger deflection capacity before the failure than GLT ones. For example, solid specimens RM-S-B2 and RM-S-B3 showed deflection values greater than 50 mm, while GLT specimens showed deflection values around 35 mm.

The GLT specimens of Ryukyumatsu showed quite a similar trend in bending tests.

Specimens of Itaji and Iju showed similar bending behavior. The solid ones presented more significant deflections before failure than the GLT specimens.

In the case of Inumaki, there were no differences between solid and GLT specimens because of the limited number of samples.

Table 2 summarizes the bending test results. As the table shows, the bending strength values of GLT specimens were about 1.0 to 1.4 times higher than solid ones. The bending modulus of elasticity of GLT specimens was approximately 1.1 to 1.5 times higher than solid ones.

The measured water contents varied from 10 to 25 % depending on the period that passed since the tree was cut off. The difference between the solid and GLT specimens within the same kind of timber ranged ±5%, and then it was assumed to be no influence on the bending strength results.

Concerning the failure patterns, three types were observed. In some specimens, the failure occurs at the bottom face of specimens, as shown in Figure 9 (a), where the higher bending stresses occur.

https://doi.org/10.52202/069179-0013

In other cases, the failure starts from knots located at the lateral face, as shown in Figure 9 (b). In this particular case, several lateral face knots influenced the failure.
On the other hand, the failure of GLT specimens tended to occur from the finger joints, as shown in Figure 9 (c), especially those located at the bottom face between load points where the maximum bending stresses occur.

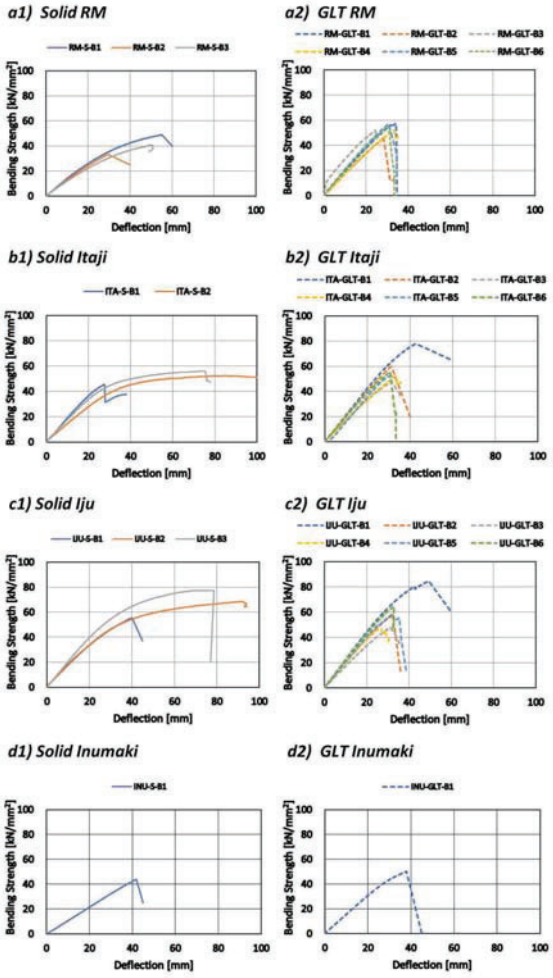

Figure 8: *Bending strength vs. deflection*

Table 2: *Bending Test Results*

Timber	Type	No of Spec.	Density (kg/m³)	WC (%)	Max Load (kN)	Bending Strength (N/ mm²)	Bending Elastic Modulus (kN/ mm²)
Ryukyumatsu	Solid	3	571.1 (24.9)	16.6 (1.3)	18.4 (2.9)	41.0 (6.4)	7.8 (0.6)
	GLT	6	681.5 (9.9)	20.8 (0.6)	24.2 (1.7)	53.8 (3.8)	11.6 (0.7)
Itajii	Solid	3	818.7 (57.7)	24.1 (2.3)	23.1 (2.0)	51.3 (4.3)	10.4 (1.3)
	GLT	6	732.3 (11.3)	18.2 (1.1)	26.4 (4.4)	58.7 (9.9)	12.1 (1.3)
Iju	Solid	3	643.1 (23.4)	10.7 (0.3)	30.2 (4.4)	67.1 (8.9)	11.3 (1.0)
	GLT	4	639.8 (10.8)	16.5 (1.1)	31.1 (5.2)	69.1 (9.7)	13.1 (0.6)
Inumaki	Solid	1	485.9 (-)	21.2 (-)	15.7 (-)	34.9 (-)	5.3 (-)
	GLT	1	559.0 (-)	25.2 (-)	17.7 (-)	49.8 (-)	7.6 (-)

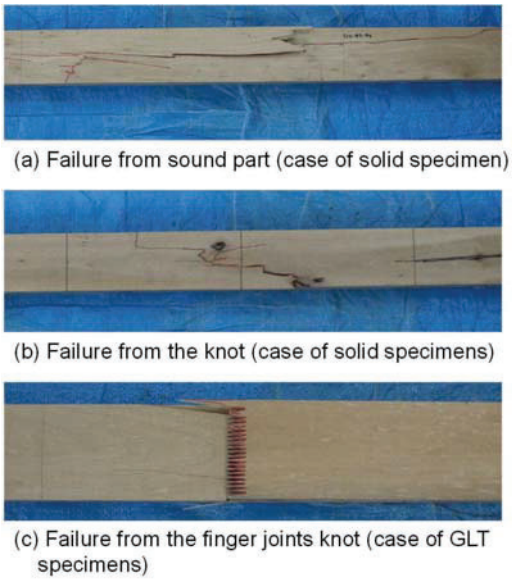
(a) Failure from sound part (case of solid specimen)

(b) Failure from the knot (case of solid specimens)

(c) Failure from the finger joints knot (case of GLT specimens)

Figure 9: *Failure Pattern*

Even though the failure of the GLT specimens occurred at the bottom due to the finger joints, all these specimens showed higher bending strength than their solid specimens counterparts. Therefore it is possible to infer that the finger joints do not influence the maximum strength values.

3.2 COMPRESSION TEST

The results of the longitudinal compression test are shown in Figure 10. The maximum compression strength value of GLT specimens was higher than that of the solid timber except for Inumaki specimens.
The solid and GLT specimens of Ryukyumatsu showed strength strain curves behavior proportionally. In both cases, some specimens showed bigger deformation capacity while others failed shortly after reaching the maximum strength. Also, the GLT specimens of Ryukyumatsu showed similar behavior in the initial stage at the elastic range.
It seems reasonable to suppose that a bigger strain means a larger deformation capacity without collapse. The solid specimens of Itaji showed more deformation capacity than the specimens of Iju. However, this group presented bigger compressive strengths.
The GLT specimens of Itaji and Iju have similar strength and deformation capacity trends. In this sense, solid and GLT specimens of Inumaki showed quite similar behaviors.
Table 3 summarizes the compression test results. As the table shows, the compression strength values of GLT specimens were about 2.2 times higher than solid ones.
The compression bending modulus of elasticity of GLT specimens was approximately 1.6 times higher than solid ones.
The specimen water contents were measured just after the experiment and varied from 10 to 22 % depending on the period since the tree was cut off. The difference between the solid and GLT specimens within the same kind of

https://doi.org/10.52202/069179-0013

timber ranged ±5%, and then it was assumed to be no influence on the bending strength results.

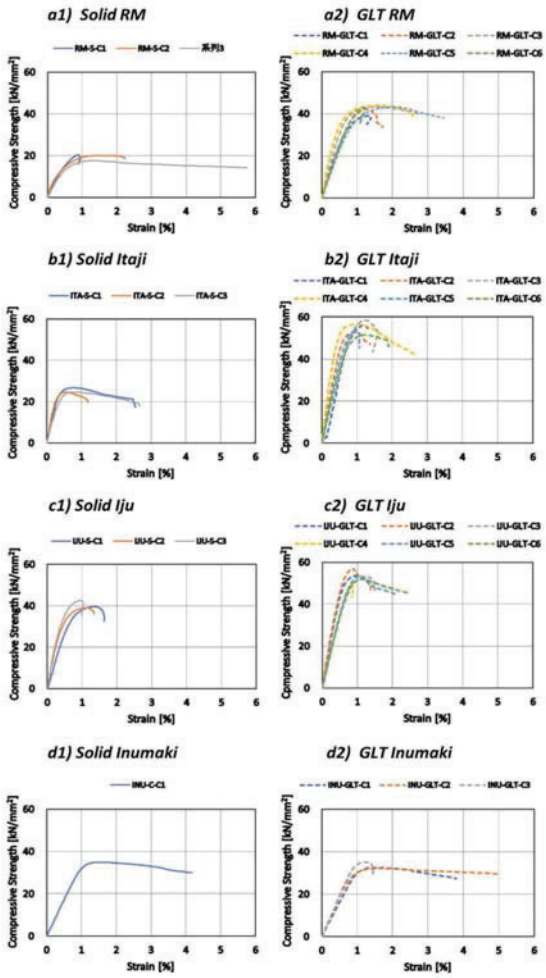

Figure 10: *Compression strength vs strain*

Table 3: *Compression Test Results*

Timber	Type	No of Spec.	Density (kg/m³)	WC (%)	Max Load (kN)	Comp. Strength (N/ mm²)	Comp. Elastic Modulus (kN/ mm²)
Ryukyumatsu	Solid	3	548.7 (13.1)	14.8 (0.4)	155.3 (10.9)	19.2 (1.3)	7.3 (0.9)
	GLT	6	665.7 (20.8)	14.0 (2.2)	343.3 (12.9)	42.4 (1.6)	11.6 (2.7)
Itajii	Solid	3	870.3 (20.5)	14.1 (2.3)	198.0 (16.0)	24.4 (2.0)	14.0 (0.8)
	GLT	6	731.6 (16.5)	22.4 (4.3)	442.9 (20.3)	54.7 (2.5)	18.1 (4.4)
Iju	Solid	3	711.8 (7.5)	10.7 (0.3)	327.0 (12.9)	40.4 (1.6)	16.0 (3.1)
	GLT	6	653.1 (12.4)	19.5 (0.4)	430.5 (16.9)	53.1 (2.1)	16.0 (2.8)
Inumaki	Solid	1	541.8 (-)	21.2 (-)	282.6 (-)	34.9 (-)	7.0 (-)
	GLT	3	571.8 (3.1)	19.5 (0.4)	212.8 (8.3)	33.3 (1.3)	7.2 (0.5)

Each value indicates the mean value, the numbers in parentheses indicate the standard deviation, and the symbol (-) are not calculable.

Concerning the failure patterns of GLT, two types were observed. In some specimens, the failure occurs at the finger joint, as shown in Figure 11 (a). In another case, the failure occurs in the specimens' middle part with no influence of finger joints, as shown in Figure 11 (b).

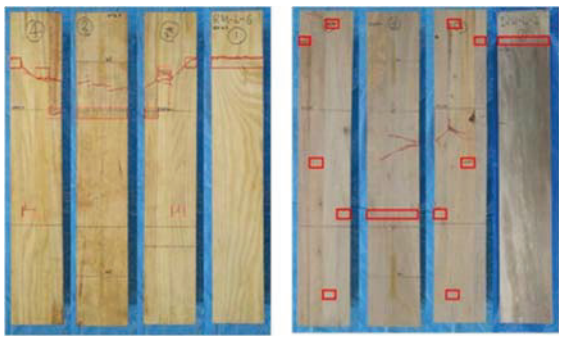

(a) Failure on finger joint (b) Failure on the middle part

Figure 11: *Failure pattern of compression specimens*

4 STANDARD MATERIAL STRENGTH

Cedar and Japanese Cypress are extensively used for building construction in Japan. Those timbers have authorized standards, so the authors compared the mechanical properties of Okinawan timbers with them. The test results proved clearly that Okinawan timbers are strong enough to be applied to structural building elements.

The reference strength F can be obtained from Equations (5) and (6). The coefficient K for obtaining the 5% lower limit at the 75% confidence level is the value shown in Tables 4 and 5, depending on the number of specimens. Based on this, the reference strength in bending of glued laminated wood in this study was calculated and compared with the reference strength of ungraded timber described by the Architectural Institute of Japan[5].

$$ {}_0F = \bar{x} - K \times s.d. \qquad (5) $$

$$ F = Kt \times {}_0F \qquad (6) $$

Where:

${}_0F$: is the Reference Strength Characteristic Value

$\bar{x}$: average value (average experimental value)

K: Value based on the number of specimens (coefficient for obtaining the lower 5% limit at the 75% confidence level)

$s.d.$: Standard deviation

Kt: Deterioration Effect Factor (In this case, it is considered the timber has no deterioration, therefore Kt is taken a 1)

Table 4: *Bending standard material strength*

Timber	Type	Bending Strength (N/ mm²) MOR	S.D.	Bending Standard Strength F_b
Ryukyumatsu	Solid	41.0	6.4	20.9
	GLT	53.8	3.8	44.9
Itajii	Solid	51.3	4.3	37.6
	GLT	58.7	9.9	35.6
Iju	Solid	67.1	8.9	39.0
	GLT	63.6	11.7	36.3
Inumaki	Solid	34.9	-	34.9
	GLT	49.8	-	49.8

https://doi.org/10.52202/069179-0013

Table 5: *Compression standard material strength*

Timber	Type	Comp. Strength MOR (N/ mm²)	S.D.	Comp. Standard Strength F_c (N/ mm²)
Ryukyumatsu	Solid	19.2	1.3	14.9
	GLT	42.4	1.6	38.7
Itajii	Solid	24.4	2.0	18.2
	GLT	54.7	2.5	49.8
Iju	Solid	40.4	1.6	35.3
	GLT	53.1	2.1	48.3
Inumaki	Solid	33.3	1.3	29.2
	GLT	19.2	1.3	14.9

Table 6: *Compression standard material strength*[5]

Tree Species			Standard Strength (N/mm²)	
			Bending	Comp.
Conifer	Category I	Pine	28.2	22.2
	Category II	Larch, Cypress	26.7	20.7
	Category III	Hemlock	25.2	19.2
	Category IV	Fir, Cedar	22.2	17.7
Hardwood	Category I	oak	38.4	27.0
	Category II	Chestnut, Zelkova	29.4	21.0

Although a small number of timber specimens for all four Okinawan timbers ranged from three to six specimens each except Inumaki, the result of the GLT bending test showed 1.4 times stronger than the standard bending strength of Cedar on average. Compared with another standard value of Japanese Cypress, the GLT performed even 1.7 times higher on average. On the other hand, concerning a longitudinal compression test, the GLT showed twice as strong as Cedar and Japanese Cypress. All those results encourage using the Okinawan GLT for building structural elements, as shown in Table 6. However, the number of specimens was limited, as mentioned above. More importantly, the data was dispersed for Itajii and Ijyu, which authors cannot find a particular reason to explain within this study.

In addition, in comparing solid timbers and the GLT, the GLT appeared to be higher figures in the bending and longitudinal compression tests, with a few exceptions.

5 DISCUSSIONS AND CONCLUSIONS

The results showed that the GLT of four kinds of Okinawan timbers, Ryukyumatsu, Itajii, Ijyu, and Inumaki, were stronger regarding the mechanical properties for both bending and compression tests compared to the same kinds of solid timbers. The material difference between GLT and solid timbers is noticeable because, naturally, the solid ones have knots and defects on the surface of timbers, whereas GLT does not. Therefore, it seems reasonable to suppose that this higher strength is due to the absence of knots and defects in timbers(GLT) when they are glue-laminated.

Here is one concern about the use of GLT for building construction. Using glue, some people are concerned about the strength of the adhesive and the part of the joints. However, our test results proved enough strength of timbers in bending and compression with finger joints. There is considerable validity to the test results, though it should not be pushed too far. For instance, further research should be included the deterioration of glue in the long term and /or to consider some different types of finger joints.

Historically Okinawan timbers had been limited and highly valued for building construction; however, recently, they have not been used for other reasons. One reason is that there is no technical endorsement of mechanical properties, and another is the small size in length and diameter. Thus, the Okinawan timber industry has shrunk over the years. If the GLT method is introduced as effective timber utilization, the Okinawan timbers can be used for structural building elements in this situation. Consequently, local industry and the economy can be boosted simultaneously.

From the viewpoint of industry activation, it should be considered in several aspects carefully. One is the production systems, and another is the market, in other words, the balance of demand and supply in the local economy and society. Additionally, since the growth rate of overall Okinawan timbers is low, the availability tends to be naturally limited.

In terms of GLT production in Okinawa, as explained before, the material supply itself is limited, so lucrative market sales cannot be expected in straight forward. For this reason, these Okinawan timbers, Ryukyumatsu, Itajii, Iju, and Inumaki, should be treated as least valued timbers so that the GLT processing system should not be prepared for a massive production system. Instead, after using solid Okinawan timbers for public historical and traditional wooden buildings, denominated as important cultural properties, the rest of the timber should be processed for the GLT production system for better-respected utilization. There is a general agreement that GLT production would work supportively instead of mainly in the timber industry. GLT production works even in a small but feasible industry in the local economy and society.

From the contrary viewpoint of industrialization, the authors considered the GLT production system might expand the effective timber use. Eventually, the system helps the sustainable circle of forest conservation, plantation, and utilization. It is expected that the loss of small timbers will be reduced remarkably because those timbers used to be assumed as residuals would convert into even stronger timber products by the GLT technique. At the same time, the consumption of timbers and the surplus of timbers would be managed under more controlled conditions because timber stock can be integrated as GLT products.

In conclusion, GLT of Okinawan timbers can be reliable for building structural elements.

https://doi.org/10.52202/069179-0013

REFERENCES

[1] Mechanical properties of structural elements for traditional wooden building in Okinawa Prefecture, Omi S., Castro J.J., et al., Architectural Institute of Japan, Summaries of Technical Annual Meeting (Chugoku), pp. 75-76, 2017.8(in Japanese).

[2] Manual for testing of wood material, Japan Housing and Wood Technology Center (Howtec), 2013.3 (in Japanese).

[3] Standardization of Testing and Evaluation Method for Full-size Structural Timber Strength in Japan, Yasuo Iijima, Journal of the Japan Wood Research Society, Vol.53, No.2, pp.63-71, 2007 (in Japanese).

[4] Research on the use of Okinawa forest products as structural elements, Miyasato T., Castro J.J., et al., Architectural Institute of Japan Kyushu Chapter, Summaries of Technical Annual Meeting, pp. 665-668, 2020.3 (in Japanese).

[5] Standard for Structural Design of Timber Structures, Architectural Institute of Japan, 2006.

https://doi.org/10.52202/069179-0013

World Conference on Timber Engineering Oslo 2023

EXPERIMENTAL INVESTIGATION ON THE IN-PLANE PERFORMANCE OF NAIL-LAMINATED TIMBER FLOORS

Zhaozhuo Gan[1], Minjuan He[2], Zheng Li[3], Xiaofeng Sun[4]

ABSTRACT: Nail-laminated timber (NLT) can be used as structural floors to transfer lateral force. However, the research on the in-plane performance of NLT floors is still insufficient. This paper presents the results of an experimental investigation on the in-plane performance of NLT floors. Three NLT floor configurations, a total of nine specimens, considering different sheathing nail spacings and orient strand board (OSB) sheathing fibre orientations, were subjected to fully reversed cyclic loading. Sheathing nail and lamina nail failure were observed as main failure mode during the cyclic loading. Sheathing orientation was noticed to have impact on the NLT floor deformation pattern. Equivalent energy elastic-plastic curves were obtained from each specimen group, from which the elastic shear stiffness, yielding load and displacement, ductility ratio, and shear strength were calculated. Secant stiffness and dissipated energy were also extracted from hysteresis loops. The comparison indicates that arranging OSB fibre perpendicular to lamina axis could significantly increase the elastic shear stiffness and ductility ratio of NLT floor, and a tightened sheathing nail spacing (i.e., 75 and 150 mm at the edge and centre, respectively) could provide higher elastic shear stiffness, shear strength, ductility, and improve energy dissipation capacity.

KEYWORDS: Timber structure, Nail-laminated timber, Timber floor, In-plane performance

1 INTRODUCTION

With its architectural aesthetics and structural reliability, timber structure has been increasingly accepted by both architects and structural engineers, and widely applied in recent years. Nail-laminated timber (NLT) is one of the mass timber products, which is constructed by nailing laminas side-by-side. NLT has been applied in timber decks and floors [1]. The existing research on NLT mostly focus on its bending performance. Derikvand et al. [2] investigated the modulus of elastic (MOE) of NLT constructed by fast grown eucalypt. The result shows that the overall MOE is higher than the MOE of most individual laminas, proving its ability to make good use of low-grade timber when properly arranged. Herberg [3] indicated that NLT could reach a similar MOE and flexural strength as solid timber, but with a relatively lower manufacturing cost. Other relevant research includes the nail connection in-between the laminas [4], push-out performance [5] and bending performance [6,7] of NLT-concrete composite floor. Moreover, a novel nail-cross-laminated timber (NCLT) was brought up to combine the advantages of both NLT and cross-laminated timber (CLT) [8,9].

Nevertheless, floor system not only transfers vertical loads using its bending performance, but also transfers lateral forces using its in-plane stiffness and bearing capacity. Tena-Colunga and Abrams [10] analysed the influence of timber floor on unreinforced masonry (URM) buildings. Results point out that the maximum horizontal acceleration of floors and walls increases as the in-plane stiffness of timber floor decreases. Similarly, Tamagnone et al. [11] analysed the influence of floor stiffness on the rocking behaviour of a CLT wall. Results show that the out-of-plane flexural stiffness of the floor is negligible to the CLT wall rocking behaviour, while the in-plane stiffness has a significant impact. Furtherly, Mendes [12] performed shaking table test on two URM buildings, one of which had the connection between timber floors and structure strengthened. Test results show that the damage index, which is defined as a function of natural frequency, of the strengthened URM building is 54% lower than the one of the original URM building. Moreover, the maximum horizontal displacement and maximum inter-storey displacement of the strengthened one is 20% and 31% lower than the original one, respectively. These test and/or analysis results indicate that the in-plane performance of floor system could play a critical role at seismic performance of the over-all structure.

Therefore, research on the in-plane performance of various timber floors have been widely investigated. Mirra et al. [13] studied the in-plane response of the traditional and retrofitted timber floor in Dutch, which is similar to those used in light-frame structure. Results show that the loading direction plays an important role on the in-plane response of a traditional flexible floor. An

[1] Zhaozhuo Gan, Tongji University, China, ganzhaozhuo@tongji.edu.cn
[2] Minjuan He, Tongji University, China, hemj@tongji.edu.cn
[3] Zheng Li, Tongji University, China, zhengli@tongji.edu.cn
[4] Xiaofeng Sun, Tongji University, China, 21310006@tongji.edu.cn

https://doi.org/10.52202/069179-0014

additional plywood sheathing panel can achieve a significant improvement in strength, stiffness, and energy dissipation. The deformation pattern was also observed to transform from mainly flexural to shear-related after retrofit. D'Arenzo et al. [14] developed a simplified equivalent frame model to predict the in-plane flexibility of CLT floor and validated using a planar finite element model. The model novelty included the effect of the floor-to-wall connection. Results show that connection to the supporting walls redistributes the bending moment but does not significantly affect the shear deformations between panels. Li et al. [15] studied the in-plane behaviour of timber-steel hybrid floor experimentally and numerically. Results indicate that shear deformation contributed up to 90% of the total in-plane deformation of the hybrid floor. The overall behaviour of the floor showed an obvious nonlinearity due to the screwed wood-steel connections. A numerical model was also developed to predict the behaviour of this hybrid floor. Newcombe et al. [16] conducted an in-plane experimental test of a timber-concrete composite floor. Results indicate that composite floor shows a high elastic stiffness compared to the connection between the floor and structure, and the composite floor can be modelled as single-degree-of-freedom in structural analysis.

To summarize the existing literatures, the in-plane performance of structural timber floors is critical to the seismic response of the overall structure. Research on the in-plane performance of various timber floors have been widely investigated. However, despite that there have been some applications of NLT floors, the research on its in-plane performance is still insufficient. This paper presents an experimental investigation on the in-plane performance of NLT floors. An in-plane shearing test of NLT floors is designed and carried out. Different sheathing nail spacings and orient strand board (OSB) sheathing fibre orientations were considered. Failure modes were observed. Equivalent energy elastic-plastic based in-plane performance characteristics, as well as energy dissipation capacity were extracted from the test.

2 TEST SET-UP

2.1 SPECIMEN DESIGN

A total of nine specimens at three different configurations, three specimen per configuration, were fabricated and tested. Comparing to control group, different sheathing nail spacings and OSB fibre orientations were considered in the remaining groups, respectively. The number of specimens was determined based on previous research considering the material deviation of timber, which also satisfied the requirement of American standard ASTM E2126-19. The three tested configurations are listed in Table 1, and detailed dimensions of specimens in the first group are shown in Figure 1. All tested specimens have an area of 2440 mm × 2440 mm and a thickness of 152 mm. Each specimen was constructed with a 140 mm thick NLT panel and a 12 mm thick OSB sheathing panel. The NLT panel was constructed by nailing roughly 61 pieces of 2440 mm long laminas side-by-side using nail gun. The nailing pattern of nail connections in-between the laminas followed the one described by Derikvand et al. [2], which is a staggered pattern with a nominal nail spacing of 135 mm per row, and a row spacing of 100 mm.

Table 1: *Overview of tested configurations*

Group	OSB nail spacing*	OSB fibre orientation**	Number of specimens
A-V	Spacing A	Vertical	3
B-V	Spacing B	Vertical	3
A-H	Spacing A	Horizontal	3

*: For OSB nail spacing, spacing A refers to an edge spacing of 150 mm and a centre spacing of 300 mm; spacing B refers to an edge spacing of 75 mm and a centre spacing of 150 mm.
**: For OSB fibre orientation, the horizontal is defined to be aligned with the direction of the lamina axial in NLT.

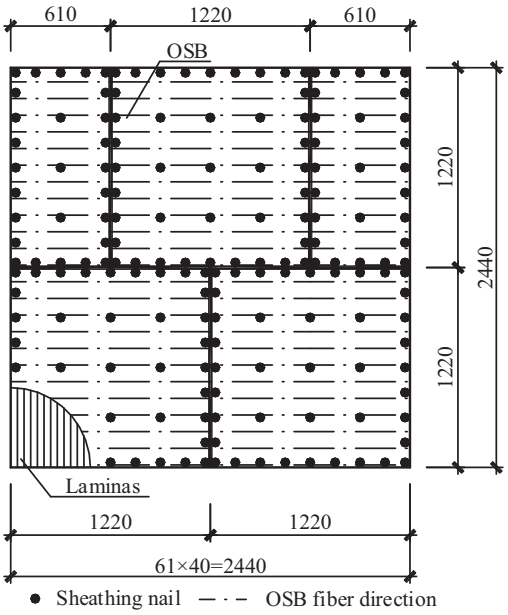

Figure 1: *Dimensions (in mm) of tested group A-V.*

2.2 MATERIAL

The materials used in the tests are listed as follows:

(1) Spruce-pine-fir (SPF) lamina, with a cross section of 40 mm × 140 mm (nominal 2″ × 6″), No. 2 and better grade according to Canadian National Lumber Grades Authority (NLGA) were used to construct NLT panels. Moisture content of each NLT specimen was measured using a moistures meter before testing, and the average value was 9.5%, with a coefficient of variation (CoV) of 10.6%. The density of SPF was evaluated after the test according to American code ASTM D143-22, and the average value was 462 kg/m^3, with a CoV of 5.4%.

(2) OSB with a thickness of 12 mm (APA rated 15/32) were used as sheathing material above the NLT.

(3) 3.3 mm × 83 mm smooth shank strip nails were used to construct NLT and to fasten OSB sheathing to the NLT panel. The tested yield strength according to American standard ASTM F1575-21 is 851 MPa with a CoV of 4.6%.

https://doi.org/10.52202/069179-0014

2.3 TEST SETUP AND LOADING PROTOCAL

Figure 2 illustrated the test set-up. In a practical application, both ends of NLT floor is usually connected to the supporting steel or timber beam using self-tapping screws (STSs). In this test, to represent its real-life boundary condition, the NLT floor specimens was securely connected to the top-and-bottom steel beams using STSs. A load distribution beam was used to apply loading force to the trisection point of specimen. The load distribution beam was then connected to a hydraulic actuator with 300 kN capacity and a stroke length of ±250 mm.

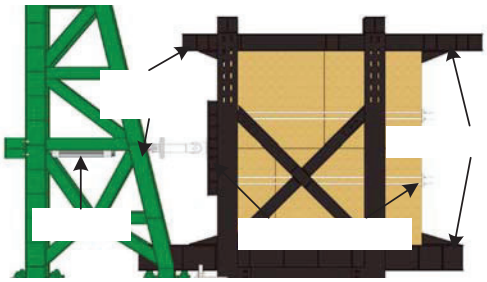

Figure 2: *Test set-up*

The cyclic loading protocol was established according to the CUREE method described in American standard ASTM E2126-19. The reference deformation Δ is determined as 70 mm by conducting a preliminary numerical analysis. The cyclic loading pattern is shown in Figure 3.

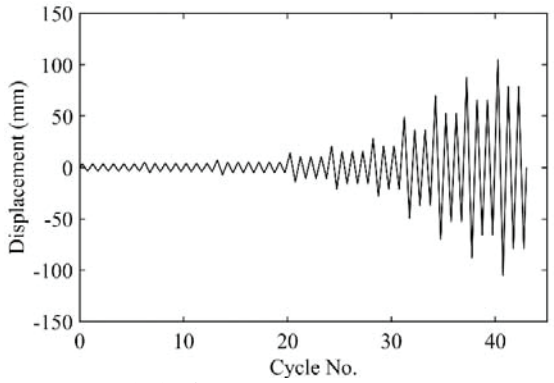

Figure 3: *Cyclic loading pattern.*

A total of 22 linear variable differential transformers (LVDTs) were attached to the specimen to acquire necessary displacement. As shown in Figure 4, LVDT 1-14 were evenly placed at the loading edges to acquire lateral deformation, LVDT 15-18 were placed at the trisection point of a loading edge to acquire shear deformation, and LVDT 19-22 were placed at the corners to acquire rotational deformation.

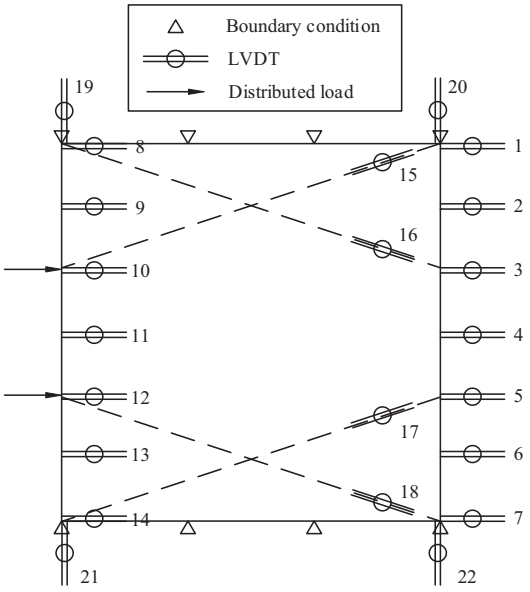

Figure 4: *Layout of LVDTs.*

3 RESULTS AND DISCUSSIONS

3.1 LOADING CURVES

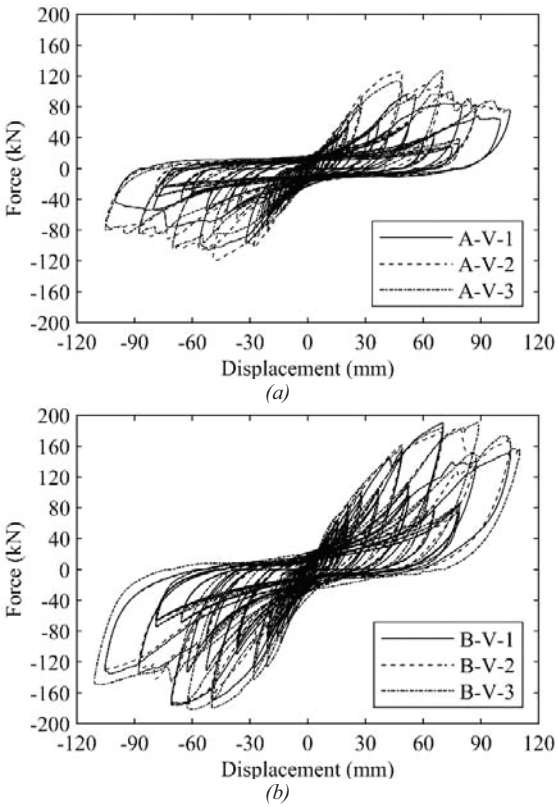

https://doi.org/10.52202/069179-0014

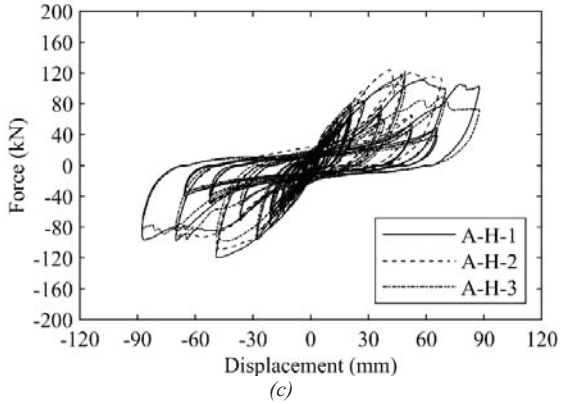

(c)

Figure 5: *Hysteresis loops of (a) group A-H, (b) group B-V, and (c) group A-V.*

Using the applied force from actuator as the force, and the average value of midspan displacement (LVDT 4/11) as the displacement, the force-displacement curves of tested specimens are shown in Figure 5. From the hysteresis loops, all specimens showed similar strength/stiffness degradation and pinching effect, due to the damage accumulation of nail connections, both in-between laminas and between lamina and OSB.

3.2 FAILURE MODES

The main failure modes observed were similar in all groups of specimens. During the loading process, sheathing nail embedment failure at the corners of sheathing panel (Figure 6(a)) was first noticed around cycle No. 20. Dislocation of adjacent sheathing panel (Figure 6(b)) was also observed at the peak of each cycle thereafter. As the loading displacement increases, beginning from roughly cycle No. 32, most sheathing nails were either embedded or withdrawn (Figure 6(c)). Finally, at around cycle No. 40, the failure of nail connection in-between laminas occurred (Figure 6(d)) and the floor lost its most capacity.

It's worth to mention that though all specimens showed the similar failure pattern, the difference of sheathing nail spacing did have impact on the deformation pattern of the floor. For the relatively larger nail spacing, which is an edge spacing of 150 mm and a centre spacing of 300 mm, the floor exhibited mostly shear deformation, as shown in Figure 6(e). While for the relatively smaller nail spacing, which is an edge spacing of 75 mm and a centre spacing of 150 mm, the floor exhibited a shear and flexural combined deformation, as shown in Figure 6(f). This difference is mainly due to that the tighten sheathing nail spacing enables the sheathing to coordinate the deformation of laminas. This thereafter led to the floor deformation pattern transform from shear controlled to shear and flexural combined.

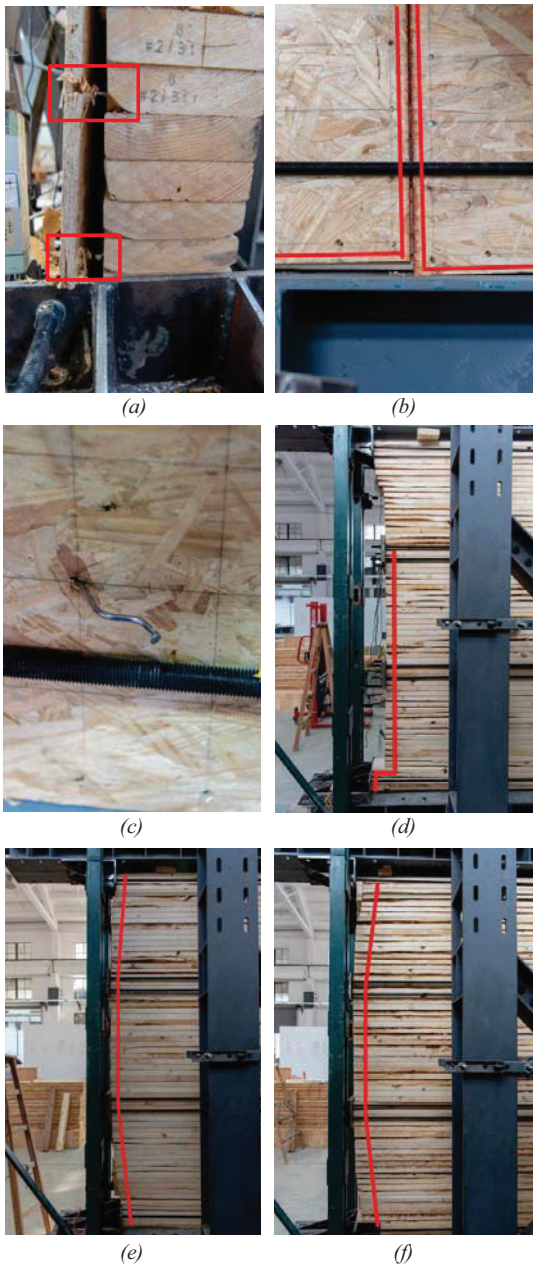

(a) (b) (c) (d) (e) (f)

Figure 6: *Failure modes of (a) sheathing nail embedment, (b) sheathing dislocation, (c) sheathing nail withdraw, (d) lamina nail failure, (e) floor shear and flexural combined deformation of relatively larger sheathing nail spacing (group A-V), and (f) floor shear deformation of relatively smaller sheathing nail spacing (group B-V).*

3.3 PERFORMANCE CHARACTERISTICS

Based on the averaged envelope curve of each group obtained from the test, equivalent energy elastic-plastic (EEEP) curve was calculated according to American standard ASTM E2126-19. The following performance characteristics were extracted from EEEP curve:

(1) Elastic shear stiffness $k_e=0.4P_{peak}/\Delta_e$, where P_{peak} is the maximum load in the envelope curve, and Δ_e is the displacement at $0.4P_{peak}$.

https://doi.org/10.52202/069179-0014

(2) Yielding load P_{yield} and yielding displacement Δ_{yield}, in which the enclosure area under EEEP curve equals to the one under envelope curve.
(3) Ductility ratio $D=\Delta_u/\Delta_{yield}$, where Δ_u is the displacement at ultimate load.
(4) Shear strength $R_d=P_{yield}/2B$, where B is the width of the floor.

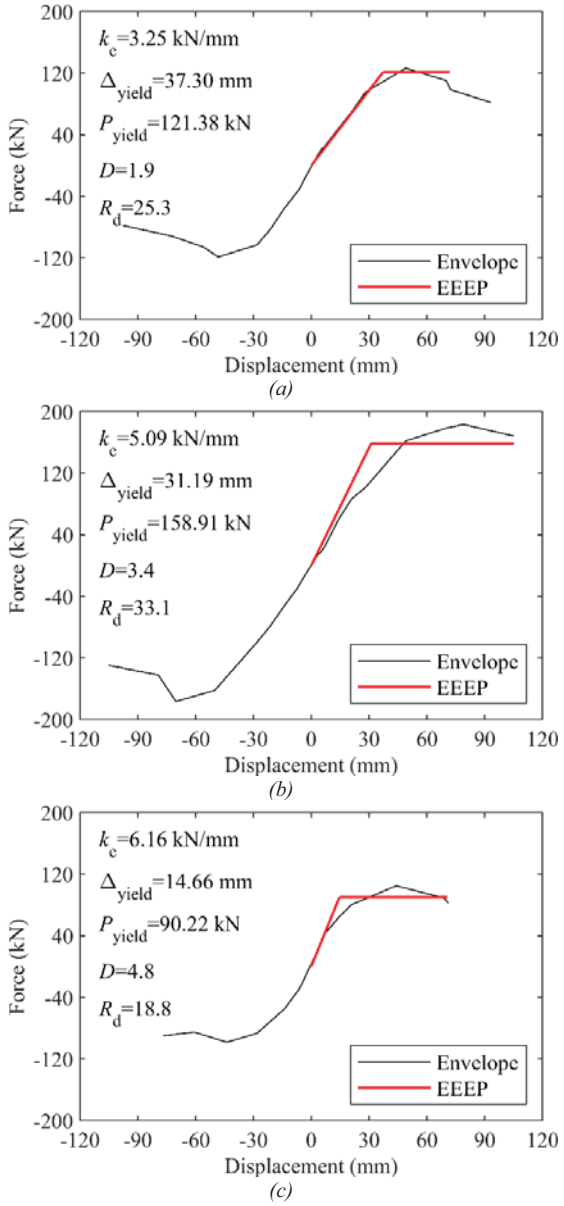

Figure 7: *EEEP analysis result of (a) group A-V, (b) group B-V, and (c) group A-H.*

Figure 7 shows the EEEP results of the three tested groups. In-between the tested groups, the EEEP analysis results indicate that reducing sheathing nail spacing by 50% could increase elastic shear stiffness, ductility ratio, and shear strength of the NLT floor by 56.6%, 78.9% and 30.8%, respectively. And by switching the OSB fibre orientation from aligning lamina axis to perpendicular, the elastic shear stiffness and ductility ratio increased by 89.5% and 152.6%, respectively, with no significant change on shear strength.

Similar to the discussion on the different floor deformation pattern, the EEEP analysis result also confirmed that the tighten sheathing nail spacing brought significant higher elastic shear stiffness, thereafter, led to a shear and flexural combined deformation patter.

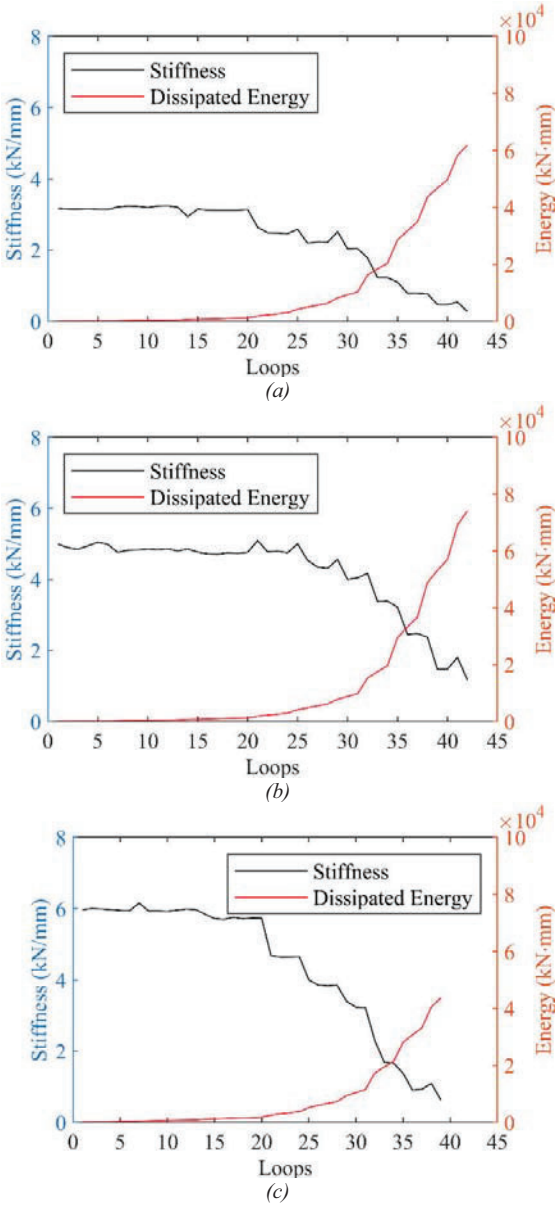

Figure 8: *Secant stiffness and cumulative dissipated energy per hysteresis loop of (a) group A-V, (b) group B-V, and (c) group A-H.*

Furthermore, the secant stiffness, calculated according to Chinese standard JGJ/T 101-2015, and cumulative dissipated energy was extracted from each hysteresis loop and shown in Figure 8. It can be noticed that the floors are basically linear elastic before cycle No. 20. Both reducing sheathing nail spacing and arranging OSB fibre

https://doi.org/10.52202/069179-0014

perpendicular to lamina axis can increase initial elastic shear stiffness significantly. Moreover, the energy dissipation capacity is mainly controlled by sheathing nail spacing, or rather the quantity of nail connections, since the energy dissipation is mostly contributed by the embedment and/or the withdrawn of nail connections, both in-between laminas and between lamina and OSB sheathing.

4 CONCLUSIONS

This paper presents an experimental investigation on the in-plane performance of NLT floor. Failure modes were observed, and performance characteristics were obtained.

(1) For failure modes, sheathing nail spacing and OSB fibre orientation didn't change the failure pattern, which is from the failure of sheathing nail connections to the failure of lamina nail connections.
(2) The sheathing nail spacing did have impact on the floor deformation pattern. That is, tightening sheathing nail spacing transforms the deformation pattern of NLT floor from shear controlled to shear and flexural combined.
(3) Placing OSB fibre perpendicular to lamina axis could induce a stiffness and ductility increasement of 89.5% and 152.6%, respectively, compared to parallel to lamina axis. Elastic shear stiffness could also be further improved by reducing sheathing nail spacing.
(4) The energy dissipation capacity is mainly controlled by the sheathing nail spacing, or rather the quantity of nail connections.

In conclusion, in design of a NLT floor, in order to obtain an optimal performance, the results indicate that the sheathing nail spacing and sheathing material orientation should be carefully decided. Nevertheless, a more detailed and parametrical numerical analysis could be carried out to determine an optimal sheathing nail arrangement, and to provide a detailed design method.

ACKNOWLEDGEMENT

The authors are grateful to the financial support by the National Natural Science Foundation of China (Grant NO. 52078371).

REFERENCES

[1] M. Mongiardini, S.K. Rosenbaugh, R.K. Faller, J.D. Reid, R.W. Bielenberg, D.L. Sicking, Design and Testing of Two Bridge Railings for Transverse Nail-Laminated Timber Deck Bridges, Transp. Res. Rec. J. Transp. Res. Board. 2262 (2011) 119–130. https://doi.org/10.3141/2262-12.

[2] M. Derikvand, H. Jiao, N. Kotlarewski, M. Lee, A. Chan, G. Nolan, Bending performance of nail-laminated timber constructed of fast-grown plantation eucalypt, Eur. J. Wood Wood Prod. 77 (2019) 421–437. https://doi.org/10.1007/s00107-019-01408-9.

[3] E.L. Herberg, Flexural Performance of Nail-Laminated Timber Crane Mats, University of Minnesota, 2018. https://hdl.handle.net/11299/202089.

[4] R. Widmann, Screw-laminated timber deck plates, in: IABSE Conf. Lahti 2001 Innov. Wooden Struct. Bridg., International Association for Bridge and Structural Engineering (IABSE), Lahti, Finland, 2001: pp. 223–228. https://doi.org/10.2749/222137801796348548.

[5] Z. Gan, Y. Sun, X. Sun, L. Zhou, M. He, Push-out performance of inclined screw shear connectors used in nail-laminated timber-concrete composite, Constr. Build. Mater. 366 (2023) 130175. https://doi.org/10.1016/j.conbuildmat.2022.130175.

[6] K.E.M. Hong, Structural Performance of Nail-Laminated Timber-Concrete Composite Floors, University of Waterloo, 2014. https://dx.doi.org/10.14288/1.0354482.

[7] M. Derikvand, N. Kotlarewski, M. Lee, H. Jiao, A. Chan, G. Nolan, Short-term and long-term bending properties of nail-laminated timber constructed of fast-grown plantation eucalypt, Constr. Build. Mater. 211 (2019) 952–964. https://doi.org/10.1016/j.conbuildmat.2019.03.305.

[8] Y. Zhang, M.L. Nehdi, X. Gao, L.V. Zhang, Flexural Performance of Novel Nail-Cross-Laminated Timber Composite Panels, Appl. Sci. 10 (2020) 5983. https://doi.org/10.3390/app10175983.

[9] S. Hosseinzadeh, B. Mohebby, M. Elyasi, Bending performances and rolling shear strength of nail-cross-laminated timber, Wood Mater. Sci. Eng. 17 (2022) 113–120. https://doi.org/10.1080/17480272.2020.1800089.

[10] A. Tena-Colunga, D.P. Abrams, Seismic Behavior of Structures with Flexible Diaphragms, J. Struct. Eng. 122 (1996) 439–445. https://doi.org/10.1061/(ASCE)0733-9445(1996)122:4(439).

[11] G. Tamagnone, G. Rinaldin, M. Fragiacomo, Influence of the Floor Diaphragm on the Rocking Behavior of CLT Walls, J. Struct. Eng. 146 (2020) 04020010. https://doi.org/10.1061/(ASCE)ST.1943-541X.0002546.

[12] N.A.L. Mendes, Seismic assessment of ancient masonry buildings: shaking table tests and numerical analysis, University of Minho, 2012.

[13] M. Mirra, G. Ravenshorst, J.-W. van de Kuilen, Experimental and analytical evaluation of the in-plane behaviour of as-built and strengthened traditional wooden floors, Eng. Struct. 211 (2020) 110432. https://doi.org/10.1016/j.engstruct.2020.110432.

[14] G. D'Arenzo, D. Casagrande, T. Reynolds, M. Fossetti, In-plane elastic flexibility of cross laminated timber floor diaphragms, Constr. Build. Mater. 209 (2019) 709–724. https://doi.org/10.1016/j.conbuildmat.2019.03.060.

[15] Z. Li, M. He, Z. Ma, K. Wang, R. Ma, In-Plane Behavior of Timber-Steel Hybrid Floor Diaphragms: Experimental Testing and Numerical Simulation, J. Struct. Eng. 142 (2016) 04016119. https://doi.org/10.1061/(ASCE)ST.1943-541X.0001601.

[16] M.P. Newcombe, W.A. van Beerschoten, D. Carradine, S. Pampanin, A.H. Buchanan, In-Plane

Experimental Testing of Timber-Concrete Composite Floor Diaphragms, J. Struct. Eng. 136 (2010) 1461–1468. https://doi.org/10.1061/(ASCE)ST.1943-541X.0000239.

https://doi.org/10.52202/069179-0014

World Conference on Timber Engineering Oslo 2023

AN EXPLORATORY STUDY ON MIXED-MODE FRACTURE AND STRAIN DISTRIBUTION NEAR A CRACK TIP OF ADHESIVELY-LAMINATED WOOD SPECIMENS USING THE MODIFIED ARCON FIXTURE AND DIGITAL IMAGE CORRELATION

Zizhen Gao[1], Meng Gong[2], Ling Li[3], Mohsen Mohammadi[4]

ABSTRACT: Glue-laminated lumber-based mass timber products, such as glue-laminated timber (GLT), have been widely used in construction. This study was aimed at understanding the mixed mode fracture behaviour of a bond-line of GLT using the modified Arcon fixture and digital image correlation (DIC) technique. The laminated wood specimens used were made of white spruce (*Picea glauca*), as the laminations, and structural adhesives, say emulsion polymer isocyanates (EPI) and polyurethanes (PUR). The modified Arcan fixture was employed to implement mixed mode stress conditions at different angles. The effects of adhesive type on the mixed mode fracture behaviour of a bond-line of laminated wood specimens were examined. In addition, the strain distribution near the crack tip of a bond-line was illustrated using the DIC system. The results showed that the critical mode I and mode II stress intensity factors, K_{Ic} and K_{IIc}, were 0.48 MPa√m and 0.72 MPa√m for the specimens made of white spruce and EPI, respectively, while those were 0.73 MPa√m and 0.90 MPa√m for the specimens made of white spruce and PUR, respectively. In addition, the mixed mode fracture criteria for the EPI and PUR bond-lines were proposed, resulting in a good correlation with the experimental data.

KEYWORDS: Glue-laminated specimen, Bond-line, Mixed mode fracture, Arcan test, Digital image correlation

1 INTRODUCTION

Adhesively bonding represents the most common joining technique in modern engineered wood products (EWPs). Lumber-based mass timber products are commonly made with an adhesive(s), such as glue-laminated timber (GLT) and cross-laminated timber (CLT), which have been widely used in construction [1, 2]. In these adhesively laminated products, the mechanical performance of a bond-line(s) plays a critical role in the structural behaviour of a wood product, and furthermore governs the safety and durability of a timber structure. Therefore, understanding of the mechanical performance of a bond-line(s) is of great importance in use of these mass timber products. Fracture characterized as the formation of new surfaces in wood is one of the most important properties mass timber products. It should be emphasized that the bond joints usually are subjected to mixed-mode loading [3]. Therefore, a deep understanding of the fracture behaviour of an adhesively bonded joint under a given load, in particularly under mixed-mode loading conditions, is no doubt required.

There are many studies in the measurement of mixed mode fracture toughness of EWPs. *Mall* et al. investigated the mixed mode fracture toughness of eastern red spruce (*Pieca rubens*) using the single edge notch and centre crack specimens, in a nominal equilibrium moisture content of 12% (±1%), with various crack inclinations in the tangential-longitudinal (TL) plane of wood [4]. Their results indicated that there was a definite interaction between two failure stress intensity factors (K_I and K_{II}) during the mixed mode fracture in wood [4]. *Jernkvist* tested the mixed mode fracture performance of Norway spruce (*Picea abies*), with moisture content of 12.2%, in the radial-longitudinal (RL) plane of wood and derived a criterion for predicting the mixed mode fracture toughness of wood [5, 6]. Their results showed that onset of mixed mode fracture could be predicted with a simple fracture criterion in the crack system [5, 6]. *Moura* et al. obtained a mixed mode fracture criterion for the maritime pine (*Pinus pinaster*), for the moisture content of 12.3%, based on the critical fracture energy from a modified mixed mode bending test [7]. The mixed mode fracture toughness (K_c) of a bond-line of phenol resorcinol formaldehyde (PRF) resin and a one-component polyurethane (PUR) adhesive with European beech (*Fagus sylvatica*) wood adherends at the relative humidities (RH) of 50%, 65%, and 95% of the surrounding air were examined by *Ammann* et al. [8]. Their results indicated that K_c of the specimens made of either adhesive increased with increasing shear stresses, and the PUR bond-line generally showed a lower K_c than the PRF one in dry climate [8]. It is well known that the fracture energy under mode-II loading is different from that under mode-I loading in adhesively bonded joints [9].

[1] Zizhen Gao, University of New Brunswick, Canada, zz.gao@unb.ca
[2] Meng Gong, University of New Brunswick, Canada, mgong@unb.ca
[3] Ling Li, University of Maine, USA, ling.li@maine.edu
[4] Mohsen Mohammadi, University of New Brunswick, Canada, mohsen.mohammadi@unb.ca

https://doi.org/10.52202/069179-0015

For the situation under the mixed-mode loading, there is an interaction between the two fracture modes, requiring to find a relationship between mode-I and mode-II stress intensity factors [4-6, 9].

The Arcan test was first proposed by *Arcan* et al. [10] with an attempt to produce uniform plane stress state in the test section of a specimen. The Arcan testing configuration has been proved very successful for testing and evaluating mixed mode fracture performance of different materials, including wood, plastic, composites and mental [8, 9, 11, 12]. One of the advantages of the Arcan test is that it allows mode I, mode II, and almost any combination of mode-I and mode-II loading to be tested with the same test specimen configuration [9].

Digital image correlation (DIC) technique is a popular non-contact method for measuring the distribution of displacement and strain on the surface of a specimen under loading [13]. As the development of DIC method and computer technology, researchers have widely employed it to evaluate the fracture performance of a material [14, 15].

This study was aimed at understanding the mixed mode fracture behaviour of a bond-line of laminated solid wood products with help of a modified Arcan testing setup and a DIC system.

2 FRACTURE MECHANICS

There are three types of cracks, termed Modes I, II, and III as illustrated in Fig. 1 [16]. The Linear Elastic Fracture Mechanics (LEFM) is deemed to be a useful tool for investigating the cracks in wood and wood products. The strain energy release rate (G) and stress intensity factor (K) are two main indexes for evaluating the fracture behavior of a material [16].

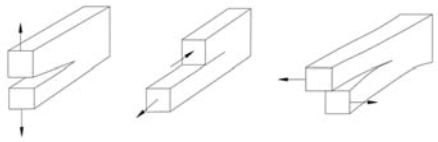

Figure 1: *Three fracture modes: (a) Mode I – Tension; (b) Mode II – In-plane shear; (c) Mode III – Out-of-plane shear.*

K_I and K_{II} for through the thickness edge crack in a finite body subjected to uniform stress at edges are given in Eqs. 1 and 2 [17]:

$$K_I = \sigma\sqrt{\pi a} f_1\left(\frac{a}{w}\right) \quad (1)$$

$$K_{II} = \sigma\sqrt{\pi a} f_2\left(\frac{a}{w}\right) \quad (2)$$

K_I and K_{II} for such stress condition in a Arcan specimen can be calculated using Eqs. 3 and 4 [11, 12]:

$$K_I = f_I\left(\frac{a}{w}\right)\frac{P}{wt}\sqrt{\pi a} \quad (3)$$

$$K_{II} = f_{II}\left(\frac{a}{w}\right)\frac{P}{wt}\sqrt{\pi a} \quad (4)$$

Where, P is the critical load on the specimen for crack propagation; t is the thickness; w is the width, and a is the initial crack length.

3 MATERIALS AND METHOD

3.1 MATERIALS

White spruce (*Picea glauca*) lumber of a thickness of 38mm was obtained from a sawmill in New Brunswick, Canada, which were stored in a conditioning chamber with a relative humidity (RH) of 65% and a temperature of 20 C° for two months. The physical properties of the lumber used after conditioning were tested in a separate study by the authors, which are given in Table 1. Two types of adhesives were used, two-component emulsion polymer isocyanates (EPI) and one-component polyurethanes (PUR), which were obtained from Ashland Inc. and Lepage Inc. respectively.

Table 1: *Elasticity and physical properties of lumbers*

Property	Mean (COV)
Density (g/cm^3)	0.38 (5.24%)
MC (%)	13.73 (1.13%)
E_L (MPa)	9932 (9.10%)
E_R (MPa)	517 (14.67%)
E_T (MPa)	221 (12.14%)
v_{LR}	0.41 (16.7%)
v_{LT}	0.51 (10.52%)

3.2 SPECIMENS

The EPI and PUR specimens were made using EPI and PUR as the adhesives with a spread rate of 220 g/m^2, respectively, while white spruce lumber was used as the adherend for both EPI and PUR specimens. The specimens used were processed to have a butterfly shape, Figure 2, to fit the modified Arcan fixture. An initial crack with a length of 10 mm was carefully made by placing a 0.1-mm-thick Teflon sheet between laminations after spreading adhesives. A speckle pattern with high contrast was applied to the surface of the specimens for DIC analysis, and the speckle size was 0.2 mm.

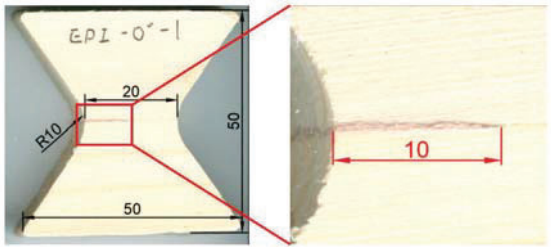

Figure 2: *The specimen used for Arcan test*

https://doi.org/10.52202/069179-0015

3.3 TESTING METHOD

The mixed mode fracture criteria of a bond-line were determined using the butterfly-shape specimens. To achieve this, seven angles were used in the modified Arcan fixture to generate the mixed mode stress conditions, Figure 3, ranging from 0 (Mode I) to 90 (Mode II) degrees with an interval of 15 degrees.

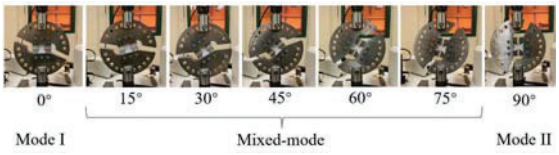

Figure 3: *Experimental setups of the Arcan fixture at seven angles.*

Two cameras were set up in the front of a specimen to capture the images from the DIC system, Figure 4. The image logging frequency of two cameras was set at 2Hz (2 images per second), which was the same as the data logging frequency of the mechanical testing machine. The load was applied at a rate of 0.5mm/min and the fracture loads were recorded. All the tests were carried out using an Instron testing machine (Model: 3367). A 3D-DIC system and software by the Correlated Solutions was used to analyse the images and calculate the strain distribution.

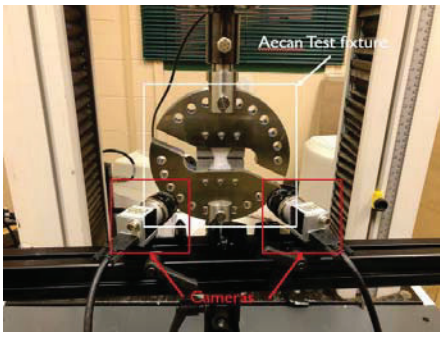

Figure 4: *Testing setup mounted with a DIC system.*

4 RESULTS AND DISCUSSION

Figure 5 gives the critical load (P_c) of EPI and PUR specimens loaded at different angles. It can be found that the P_c of PUR specimens are overall higher than those of EPI ones. For both EPI and PUR specimens, with the loading angle increasing, the P_c increases. The P_c under pure shear stress has the highest value. It is worth to note that, as airdry wood can be approximately treated as an elastic material, the process of crack propagation is usually instantaneous. Therefore, the peak load was recorded as the P_c in this study.

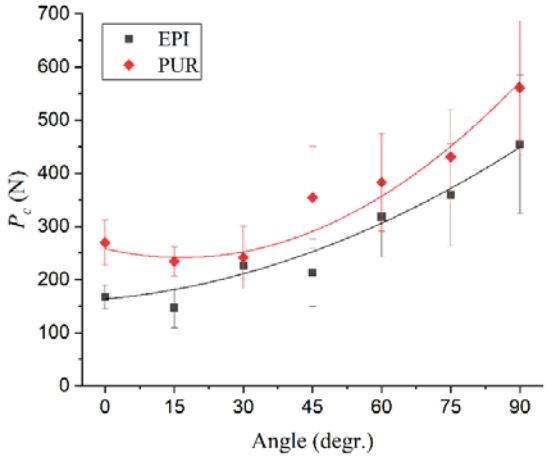

Figure 5: *Critical Loads at different angles.*

The critical strain distribution along a bond line means the strain distribution at the point at which a crack starts propagating. The critical strain distributions of EPI and PUR specimens are plotted in Figures 6 and 7, respectively. The results showed that the average tensile strain (ε_c) of both EPI and PUR specimens decreased with the loading angle increasing, while the average shear strain (γ_c) increased. In addition, for both EPI and PUR specimens, tensile strain is more concentrated at the crack tip than shear strain. Figure 8 gives the relationship between the critical tensile strain and critical shear strain at crack tips. It can be found that both critical tensile strain and shear strain of PUR specimens are overall larger than those of EPI specimens, which reflects the difference in P_c between these two types of specimens. Moreover, Figure 8 shows that with increasing the loading angle, the changes in tensile strain and shear strain are not linear, suggesting that the mixed mode facture criterion of a bond-line is a critical index for predicting the fracture of an adhesively-laminated wood product subjected to a mixed loading condition. In addition, under the pure tension or shear loading, both ε_c and γ_c of PUR specimens are about 42% higher than that of EPI specimens.

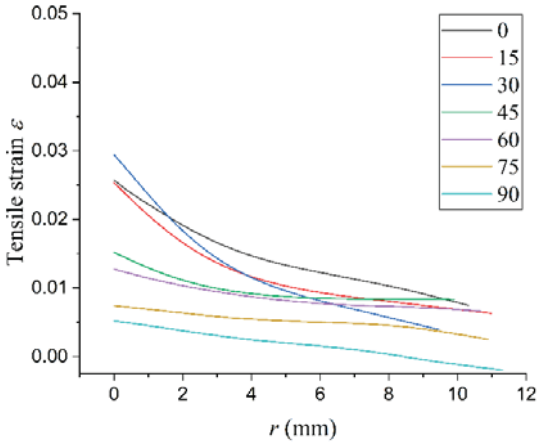

(a) Average tensile strain distribution

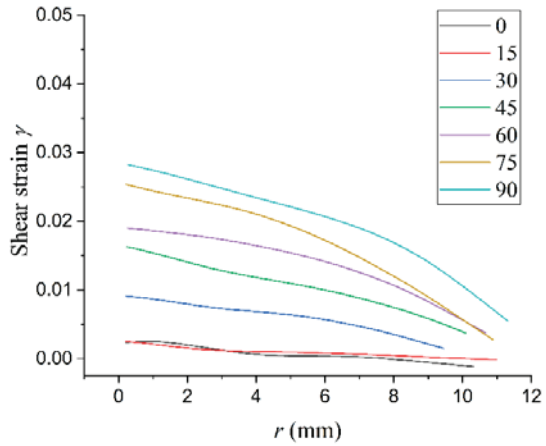

(b) Average shear strain distribution

Figure 6: *Average critical strain distributions along the bond-lines of EPI specimens under the criterial load.*

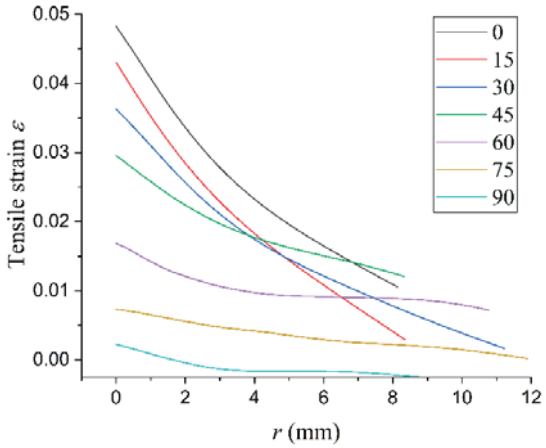

(a) Average tensile strain distributions

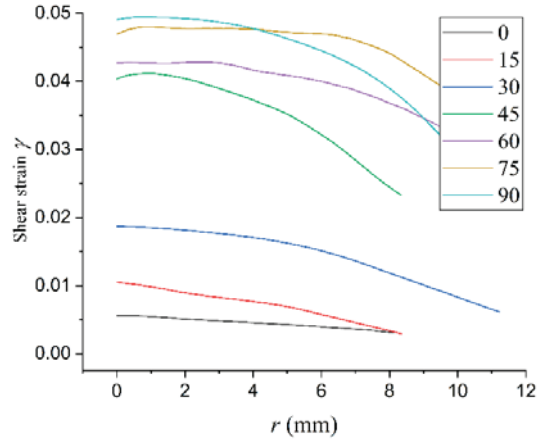

(b) Average shear strain distributions

Figure 7: *Average strain distributions along the bond-lines of PUR specimens under criterial load.*

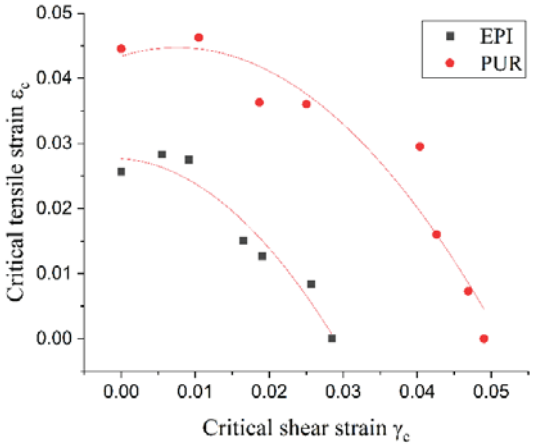

Figure 8: *Relationship between the critical tensile strain and shear strain at the crack tips of two-type specimens.*

According to Equations (3) and (4), the K_I and K_{II} represent the strength of the stress singularity that occurs at a sharp crack tip. The K_I or K_{II} is a function of the specimen geometry, applied load and crack length. The nondimensional stress intensity factors (e.g., geometrical factors, *f(a/w)*) of the modified Arcan specimens for mode I and mode II can be obtained by the finite element analysis (FEA) [18, 19], Figure 9. The geometrical factor functions for Mode I and Mode II fracture were determined in this study by using the least square fitting method, which are given in Equation (5) and (6).

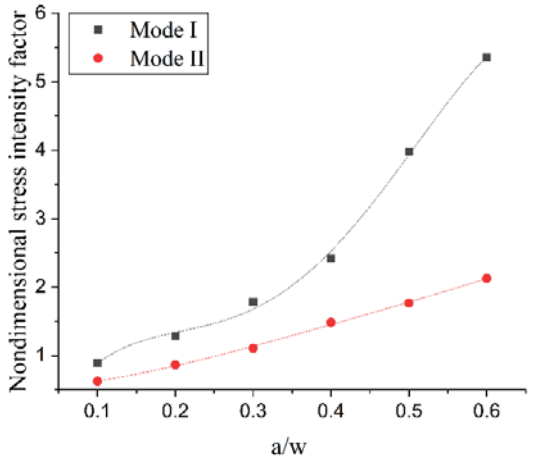

Figure 9: *Non-dimensional stress intensity factors for Mode I and Mode II fracture of the specimens tested using the modified Arcan fixture.*

$$f_I\left(\frac{a}{w}\right) = -237.04\left(\frac{a}{w}\right)^4 + 339.84\left(\frac{a}{w}\right)^3 - 150.15\left(\frac{a}{w}\right)^2 + 29.33\left(\frac{a}{w}\right) - 0.863 \quad (5)$$

$$f_{II}\left(\frac{a}{w}\right) = 7.42\left(\frac{a}{w}\right)^4 - 13.17\left(\frac{a}{w}\right)^3 + 9.26\left(\frac{a}{w}\right)^2 + 0.25\left(\frac{a}{w}\right) + 0.5223 \quad (6)$$

https://doi.org/10.52202/069179-0015

Tables 2 and 3 summarize the results of failure stress intensity factors K_I and K_{II}, obtained from all specimens at different loading angles. The critical mode I and mode II stress intensity factors, K_{Ic} and K_{IIc}, for EPI specimens are 0.48 MPa√m and 0.72 MPa√m, respectively, while those for specimens are 0.73 MPa√m and 0.90 MPa√m. The fracture mechanics parameters of the bond-lines of both EPI and PUR specimens made with white spruce have not yet been reported. However, the K_{Ic} and K_{IIc} in this study are comparable with the results from *Ammann's* study, in which the K_{Ic} and K_{IIc} of the bond-lines of the specimens made of PUR adhesive and European beech wood were 0.75 MPa√m and 1.85 MPa√m, respectively [8]. In addition, K_{Ic} and KI_{Ic} of the specimens made of solid Norway spruce wood, which were reported by *Jernkvist* [6], were 0.58 MPa√m and 1.52 MPa√m, respectively.

Table 2: *Failure stress intensity factors K_I and K_{II} of EPI.*

Angle	K_I (MPa√m)		K_{II} (MPa√m)	
	Mean	COV	Mean	COV
0	0.48	0.14	0.00	0.00
15	0.42	0.19	0.06	0.22
30	0.50	0.11	0.16	0.11
45	0.43	0.23	0.23	0.25
60	0.42	0.24	0.40	0.23
75	0.27	0.27	0.53	0.27
90	0.00	0.00	0.72	0.31

Table 3: *Failure stress intensity factors KI and KII of PUR.*

Angle	K_I (MPa√m)		K_{II} (MPa√m)	
	Mean	COV	Mean	COV
0	0.73	0.11	0.00	0.00
15	0.67	0.19	0.09	0.16
30	0.62	0.28	0.19	0.26
45	0.64	0.26	0.36	0.26
60	0.53	0.21	0.49	0.22
75	0.32	0.15	0.64	0.17
90	0.00	0.00	0.90	0.17

To examine the interaction between K_I and K_{II} of EPI and PUR specimens under different loading angles, all the data are plotted in Figure 10. This figure indicates that the trend of relationship between K_I and K_{II}, which defines the tensile stress and shear stress distributions near a crack tip, is similar to that between ε_c and γ_c.

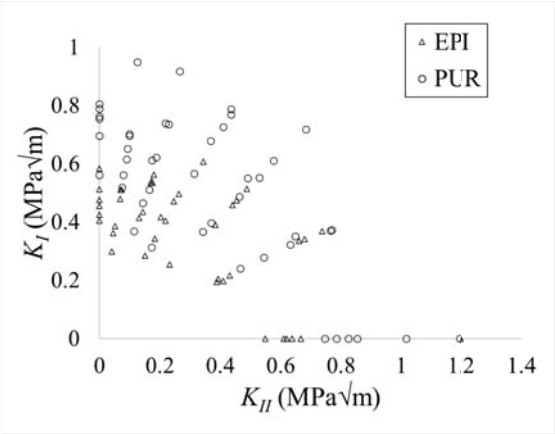

Figure 10: *Relationship between K_I and K_{II}.*

For the situation under a mixed-mode loading, there is an interaction between the two fracture modes, calling for investigating the relationship between K_I and K_{II} [20]. The mixed fracture criterion is generally proposed in Equation (7) [6]:

$$\frac{K_I}{K_{Ic}} + \left|\frac{K_{II}}{K_{IIc}}\right|^n = 1 \quad (7)$$

The subject of the mixed mode fracture in wood-based materials was first studied by *Wu* [21], who found that Equation (7) could well describe the interaction between K_I and K_{II} of balsa wood (*Ochroma pyranidale*) when n=2. *Mall* et al. [4] compared several mixed mode fracture criteria and discovered that *Wu*'s criterion was also applicable to eastern red spruce (*Pieca rubens*). *Jernkvist* found, using the least square fitting method based on their experimental data, that Equation (7) could be used as the fracture criterion of Norway spruce when n=2.2 [6]. The values of n in Equation (7) for the fracture of EPI bond line and PUR bond line could be obtained using the least square fitting method according to the data in Tables 2 and 3, and Figure 11. The fitting parameters are given in Table 4. The n values of the mixed mode fracture criterion for EPI and PUR are found to be 1.89 and 2.93, respectively, suggesting that the mixed mode fracture criterion of EPI bond line is similar to the clear softwood specimens such as red eastern spruce and Norway spruce [4, 6].

https://doi.org/10.52202/069179-0015

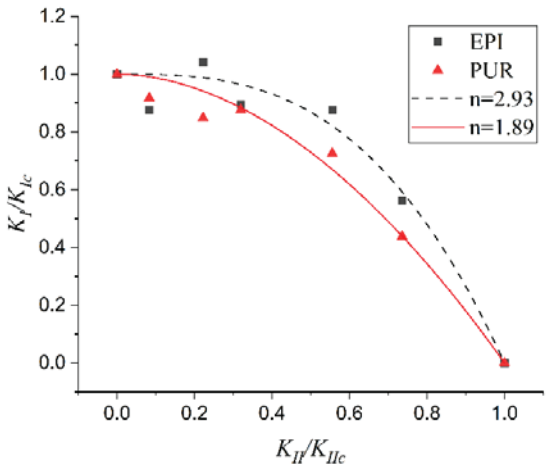

Figure 11: *Relationships between K_I/K_{Ic} and K_{II}/K_{IIc}.*

Table 4: *Fitting parameters of the relationship between K_I/K_{Ic} and K_{II}/K_{IIc}.*

	EPI specimen	PUR specimens
n	2.93	1.89
R-square	0.966	0.977
p-value	<0.0001	<0.0001

Figures 12 and 13 show the typical failure modes of EPI and PUR specimens. It was found that the crack propagation paths were similar between specimens, i.e., the crack propagation started from a crack tip and grew along the fibre direction of wood near a bond-line. Despite the crack propagation started from the glue-line, the crack path was totally along the clear wood, which means that, for both EPI and PUR specimens, the wood failure percentage were 100%.

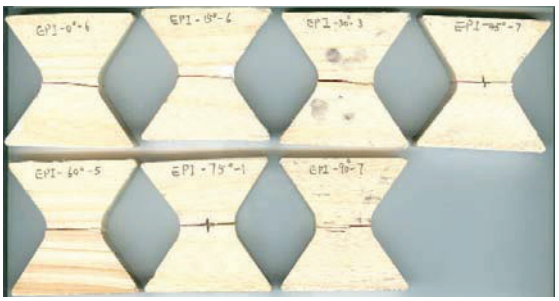

Figure 12: *Failure mode of EPI sample specimens.*

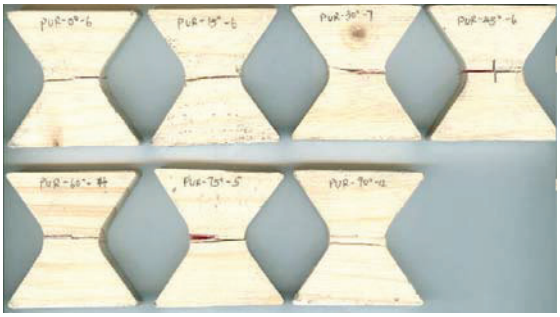

Figure 13: *Failure mode of sample PUR specimens.*

5 CONCLUSIONS

In this study, a modified Arcan testing setup equipped with a 3D-DIC system were employed to examine the mixed fracture properties of a bond-line of the wood products bonded with EPI and PUR adhesives. The strain distributions and critical strains of each specimen were obtained using the DIC system. Based on experimental observations, data analysis and above discussion, the conclusions could be drawn as follows:

(1) Under the pure tension or shear loading, both ε_c and γ_c of PUR specimens were 42% higher than those of EPI ones, and tensile strain was more concentrated at the crack tip than shear strain.

(2) The K_{Ic} and K_{IIc} of the bond-line of EPI specimens were 0.48 MPa√m and 0.72 MPa√m, respectively, while those for PUR specimens were 0.73 MPa√m and 0.90 MPa√m, respectively.

(3) The n of the mixed mode fracture criterion for EPI and PUR specimens were 1.89 and 2.93, respectively.

ACKNOWLEDGEMENTS

The authors would like to acknowledge the financial support from the Discovery Grant by Natural Sciences and Engineering Research Council of Canada (RGPIN 2017-03994), the New Brunswick Innovation Research Chair Initiative Program by the New Brunswick Innovation Foundation (Canada), and Doctoral Student Scholarship from the University of New Brunswick (Canada).

REFERENCES

[1] R. Ross. Wood handbook: Wood as an engineering material. Madison, Wis.: U.S. Dept. of Agriculture, Forest Service, Forest Products Laboratory, 2021.

[2] M. Gong. Lumber-based mass timber products in construction. In Timber buildings and sustainability. IntechOpen, 2019.

[3] I. Vintilescu, and J. Spelt. Mixed mode I, II, and III fracture characterization of adhesive joints. Journal of Composites, Technology and Research, 20(2): 129-139, 1998.

[4] S. Mall, f. Joseph M. Murphy, and E. Shottafer. Criterion for mixed mode fracture in wood. Journal of Engineering Mechanics, 109(3): 680-690, 1983.

https://doi.org/10.52202/069179-0015

[5] L. O. Jernkvist. Fracture of wood under mixed mode loading: I. Derivation of fracture criteria. Engineering Fracture Mechanics, 68(5): 549-563, 2001.
[6] L. O. Jernkvist. Fracture of wood under mixed mode loading: II. Experimental investigation of Picea abies. Engineering Fracture Mechanics, 68(5): 565-576,2001.
[7] M. De Moura, J. Oliveira, J. Morais and J. Xavier. Mixed-mode I/II wood fracture characterization using the mixed-mode bending test. Engineering Fracture Mechanics, 77(1): 144-152,2010.
[8] S. Ammann and P. Niemz. Mixed-mode fracture toughness of bond lines of PRF and PUR adhesives in European beech wood. Holzforschung, 69(4): 415-420, 2015
[9] N. Choupani. Mixed-mode cohesive fracture of adhesive joints: Experimental and numerical studies. Engineering fracture mechanics, 75(15): 4363-4382, 2008.
[10] M. Arcan. Z. Hashin and A. Voloshin. A method to produce uniform plane-stress states with applications to fiber-reinforced materials: a specially designed specimen yields material properties under pure shear or uniform plane-stress conditions. Experimental mechanics, 18: 141-146, 1978
[11] L. Banks-Sills, M. Arcan, and Y. Bortman. "A mixed mode fracture specimen for mode II dominant deformation." Engineering Fracture Mechanics, 20(1): 145-157, 1984.
[12] A. Braham, F. Ni, and S. Yang. "An introduction of the Arcan testing configuration for mixed-mode cracking in asphalt concrete." In: *The 11th international conference on asphalt pavements (ISAP)*, Nagoya Aichi, Japan, vol. 2,2010.
[13] G. Gonzáles, J. Castro, and J. Freire. A J-integral approach using digital image correlation for evaluating stress intensity factors in fatigue cracks with closure effects. Theoretical and Applied Fracture Mechanics, 90: 14-21, 2017.
[14] G. Han, M. Sutton and Y. Chao. A study of stationary crack-tip deformation fields in thin sheets by computer vision. Experimental Mechanics, 34(2): 125-140. 1994.
[15] G. Catalanotti, P. Camanho, J. Xavier, C. Dávila and A. Marques. Measurement of resistance curves in the longitudinal failure of composites using digital image correlation. Composites Science and Technology, 70(13): 1986-1993, 2010.
[16] N. Perez. Fracture mechanics, 79-130. Springer-Verlag Berlin Heidelberg New York, 2017.
[17] I. Smith, E. Landis, and M. Gong. Fracture and fatigue in wood. John Wiley & Sons, Chichester, UK, 2003.
[18] P. Gurubaran, M. Afendi, N. KanasaN, I. Haftirman, M. Tasyrif, and K. Basaruddin. Mixed mode loading fracture toughness of arcan adhesive joint: Effect of surface roughness. In: AIP Conference Proceedings. 1 (1775): 300-308, 2016.
[19] F. Alizadeh, and C.G. Soares. Experimental and numerical investigation of the fracture toughness of Glass/Vinylester composite laminates. European Journal of Mechanics-A/Solids, 73: 204-211, 2019.
[20] M. Nikbakht and N. Choupani. Experimental investigation of mixed-mode fracture behaviour of woven laminated composite. Journal of Materials Science, 44: 3428-3437, 2009.
[21] Wu, Edward M. "Application of fracture mechanics to anisotropic plates." (1967): 967-974, 1967.

World Conference on
Timber Engineering
Oslo 2023

GREEN OAK BUILDING WITH HIGH-TECH METHODS, PART 2: LOG BENDING TESTS FOR DETERMINATION OF STRENGTH AND STIFFNESS

**Kay-Uwe Schober[1], Beate Hörnel-Metzger[2], Maximilian Leonhard Müller[3]
Nicolas Hofmann[4], Franka Brüchert[5], Udo H. Sauter[6]**

ABSTRACT: The green oak building research project deals with small-diameter oak logs as sustainable construction material for timber truss structures. The basis for structural use and design are the specific mechanical properties and the knowledge of performance influencing factors like wood defects, moisture content and density distribution. In a first step, the characterisation of the raw material itself has been done by quality assessment, followed by the determination of strength and stiffness parameters as input for the parametric design process and a prototype building as proof of concept. This paper summarises the experimental investigations on strength and stiffness of naturally dried green oak logs. The laboratory tests were supplemented by non-destructive data acquisition of the geometry, moisture, and density distribution along the full length and over the entire surface. The results show that strength and stiffness properties are affected by growth conditions, especially the moisture content and drying behaviour of green oak. The obtained results were in line with similar tests on softwood logs and other studies comparing destructive and non-destructive mechanical characterisation methods for roundwood. The preliminary results of the green oak research project indicate that small-diameter oak logs (≤ 250 mm) appear suitable for load-bearing timber structures.

KEYWORDS: small-diameter logs, roundwood, bending strength, visual grading, oak, *Quercus petraea* (Matt.) Liebl.

1 INTRODUCTION

In Germany, only half of the annual increment of oak wood from forests is used. Especially small-diameter oaks (≤ 250 mm) are currently either not used or only used as firewood. But they also sequester carbon dioxide and this much longer compared to firewood which is an added benefit for the forest owner. To exploit these opportunities, the green oak building research project aims on making small-diameter oak logs available as sustainable construction material, e.g., for columns and frameworks and in agricultural buildings, like barns. For this purpose, the mechanical properties of the logs need to be determined, due to insufficient knowledge and investigations, especially for small-diameter oak logs as natural resource in the building sector. This requires exploring the characteristics and factors influencing the structural performance and serviceability of green oak logs, like wood defects, moisture content (MC), density distribution and others, which are part of the subsequent presented investigations.

Part one of the Green Oak Building project deals with the characterisation of the raw material [1]. This topic was the main task of the forestry research partner FVA, located in Freiburg on the edge of the Black Forest, while the determination of strength and stiffness has been done in Mainz, Rhineland-Palatinate. The research results of both interdependent investigations on small-diameter oak logs (*Quercus petraea*) shall serve to upgrade the potential of this currently in Germany unemployed forestry resource as a local source building material for rural areas.

Based on the findings carried out in Freiburg and Mainz an approach was specified to derive the most suitable log as a structural member in wooden buildings dependent on its specific dimensions, actions, load scenarios, structural behaviour and design requirements. The buildings itself will be formed by the “perfect log” for its specified position in the structure by parametric analysis and design subject to the raw material database and the structural member database. Drawbacks of the idea to use the yet unpopular assortment of green small-diameter oak logs are their high moisture content, the low drying rate and the high distortion along the centreline, making any sort of standardized grading impossible. Additionally, the high moisture content is affecting the mechanical properties negative and can lead to additional crack development. It is questionable whether the visual grading and property assignment system for round timbers adequately assesses the potential quality of these logs for structural use.

[1] Kay-Uwe Schober, Mainz University of Applied Sciences, Timber and Plastics Research Group, Mainz, Germany, kay-uwe.schober@hs-mainz.de
[2] Beate Hörnel-Metzger, Timber and Plastics Research Group, Mainz, Germany, beate.hoernel-metzger@hs-mainz.de
[3] Maximilian Leonhard Müller, Timber and Plastics Research Group, Mainz, Germany, maximilian.mueller@hs-mainz.de
[4] Nicolas Hofmann, FVA Forest Research Institute of Baden-Württemberg, Germany, nicolas.hofmann@forst.bwl.de
[5] Franka Brüchert, FVA Forest Research Institute of Baden-Württemberg, Germany, franka.bruechert@forst.bwl.de
[6] Udo H. Sauter, FVA Forest Research Institute of Baden-Württemberg, Germany, udo.sauter@forst.bwl.de

https://doi.org/10.52202/069179-0016

2 BACKGROUND

Nowadays, logs used as round and sawn round timber beams are graded by visual examination with properties assigned by testing procedures defined in standards, e.g. [2]-[6] in the Americas or [7] in the European Union. Allowable properties for round timber beams and struts are derived using strength ratios for limiting defects as specified in grading rules and clear wood strength values. And the visual quality evaluation sort into categories for assignment of design properties. The characteristics of green oak (*Quercus petraea*) logs or in general unsawn hard woods prevented the further development of grading standards and industrial applications for round wood.

A major European study by RANTA-MAUNUS investigated the application of round wood in the building sector with experimental studies on round and sawn timber to compare both cross-section types with each other [8]. 1400 specimens, composed of different softwood species, such as Scots pine (*Pinus sylvestris)* and Norway spruce (*Picea abies)*, were tested in this study at an average MC of 16% to determine bending, compression and tension strength properties parallel to grain. The bending tests were conducted with the logs simply supported and loaded symmetrically at the 1/3-point of the span and tested at a span-to-depth ratio of 18:1. The modulus of elasticity (MOE) values were calculated using the average diameter of the log and the modulus of rupture (MOR) values were calculated using the diameter near failure. Furthermore, short column compression tests were conducted using an unsupported free span of six times the log diameter, with the compression MOE calculated using deformation measured over a span of four times the diameter. The research results have shown higher strength values for round wood compared to sawn timber made from the same logs. The bending strengths for roundwood have been observed with even double the value of sawn timber. Similar studies have been carried out and published in the following years mostly by American and European researchers, e.g. [9], [10], [11], [12] and others.

The studies confirmed the potential of round wood as building material while grading and design rules for round wood elements are still missing. In contrast to the above outlined research to determine material properties by testing under usual moisture conditions around 15% MC or to grade logs for design purposes, the impact of a much higher moisture content near or above fibre saturation in green and naturally dried logs along with a much lower drying rate played a significant role in this joint research.

Figure 1: *Debarked small-diameter oak logs for testing.*

3 MATERIAL AND METHODS

210 oak logs (*Quercus petraea* (Matt.) Liebl.) with a length of five meters and an average mid diameter of about 25 cm were cut from one 90 years old stand in Rhineland-Palatinate. The trees have developed from stump sprouts. The logs were divided into three subsamples ($n = 70$, each) to facilitate the measuring process. Subsample 1 (cut 1) and subsample 2 (cut 2) underwent the complete measurement programme in non-destructive and destructive testing for material characterisation [1]. From these subsamples, 80 logs were debarked (Figure 1), 30 logs were edged on two sides and 30 logs were edged on four sides. Debarking was executed for faster drying and edging for a simplified construction geometry. The remaining logs were assigned for construction of the demonstration hall and excluded from this characterization due to a shorter test program without destructive measurements.

At the test facility, each log was weighed and measured, and the slope of grain was recorded. The logs were oriented with the round side down for the sawn round logs and the load was applied to the flattened surface as they would typically occur. A similar handling has been implemented for the unsawn round wood (Figure 2). The experimental program consisted of 4-point-bending tests following DIN EN 14251 [7], which specifies the requirements to obtain mechanical properties of round timber from laboratory tests under controlled air conditions (20°C, 65% rH). Table 1 gives an overview of selected specimen dimensions. Due to different shape and diameters at tip and butt and distortions, special support devices for this test series have been custom made to address the irregular and for each specimen different geometries and shapes of the log sections.

Figure 2: *Natural and load-induced distortion of test specimen.*

To investigate the influence of wood defects, such as knots (Figure 3), different parameters have been investigated and recorded for each specimen: i) The position of the knot along the longitudinal axis of the log (x-axis), ii) the position of the knot along the height in loading direction (y-axis), defined in cylindrical coordinates by the radial distance and the azimuthal angle. To simplify the observation and speed up the lab test documentation, the azimuthal angle was recorded as knot position clockwise, defining ninety degrees or a quarter section to three hours like on a clock-face (Table 1) with later-on conversion in the cylindrical coordinate system.

https://doi.org/10.52202/069179-0016

iii) The knot radius (size), iv) the knot diving angle (inclination), and if possible, v) the knot length. The largest knot in the log (max knot) had some influence on both strength and stiffness prediction, but it was less correlated with these properties than was the sum of the knots in each cross section (knot sum). The correlation of the sum of the knots divided by the diameter of the cross section was like the correlation of the knot sum alone.

Table 1. *Exemplary summary of specimen span and sections.*

Log No.	vertical diameter d_v [cm] butt	mid-span	tip	knot position clockwise [h]	span [cm]
803	18.58	17.69	17.40	5:00	334.80
805	19.10	18.20	17.40	4:00	344.25
809	21.50	19.30	17.90	6:00	378.00
820	17.92	17.55	16.67	6:00	349.20
828	22.80	22.50	22.20	7:00	411.75
832	18.20	16.30	16.90	6:00	354.15
839	21.10	19.38	20.23	5:00	365.40
840	17.88	16.54	18.35	4:00	334.80
843	20.00	18.37	17.83	7:00	350.00
845	15.10	14.20	14.00	6:00	264.00
846	27.30	24.20	22.70	5:00	411.75
858	30.00	28.20	27.20	6:00	460.00

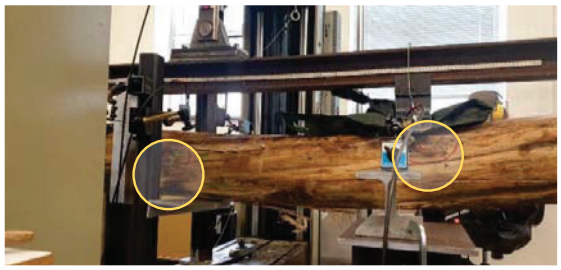

Figure 3: *Wood defects were recorded before flexural testing.*

Depending on the nominal diameter d_{nom}, the span was set-up as defined by the test standard [7] to (18 ± 1) d_{nom}, including loading and measuring points (Figure 4), while d_{nom} has been calculated as an average value of the vertical and for bending tests more influencing diameter. The different values have been measured in vertical and horizontal direction separate for each log at the two supports (tip and butt side), near loading at (6.5 ± 1) d_{nom} from the specimen support and additional in the middle of the span. The 4-point-bending tests were derived by application of hysteresis with peaks of deflections at around 30% of the calculated average maximum stress level.

All tests were carried out by continuous measurements of time, deflections, and forces. First, non-destructive evaluation measurement was taken on each log while it was simply supported at the ends. The specimen (diameters vary from 20 cm to 30 cm, Table 1) were loaded up to a third of the failure load according to a preliminary design, then unloaded and the MOE was determined from measuring the incremental deformation 60 s after the first load level was applied. The deflections at midspan, near loading and at the supports were obtained with a linear variable displacement transducer (LVDT) to the nearest 0.0025 mm and the highest deflections in 100 mm to 200 mm range were recorded by laser sensors with different measuring ranges. The load-deflection plots were obtained for each specimen to calculate the MOR and static MOE depending on the wood defects, the species and overall quality.

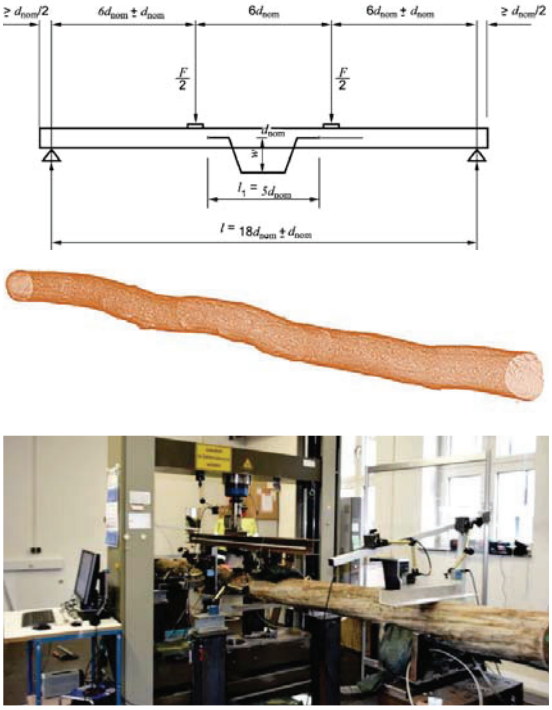

Figure 4: *Standard test arrangement with span-to-depth ratio 18:1 [7]; DiShape surface model of log no. 862 and lab view on log no. 862 waiting for action.*

After testing, a 50 mm thick section of each specimen has been removed from an area close to the location of failure to determine moisture content and the specific gravity (SG), as well as destructive investigations of geometry, oven-dry kiln density and moisture content in the defined section (failure location), [1]. The MC was measured in 2 cm and 4 cm depth at 0°/90°/180°/270° location (GANN Hydromette® CH 17). Then, the surface envelope of each log has been digital recorded from the images to calculate the cross-section data, e.g., diameter, section area, circumference, moment of inertia, etc. (Figure 5).

The lab tests were supplemented by non-destructive data acquisition of the geometry and raw wood density distribution along the full log length by MiCROTEC CT Log and DiShape, see Figure 4 middle and ref. [1]. The computed tomography scans and reconstructs the internal features of the log digitally and allow the assessment of the material in real time where size and position of internal wood defects can be accurately described in all three dimensions. The further use of the test outcome for design processes and material strength classification highly benefits from this technology and the accompanying research results and investigations.

https://doi.org/10.52202/069179-0016

Moment of inertia X: 292,666,326 mm⁴ *Area: 59,384.48 mm²*
Moment of inertia Y: 272,328,664 mm⁴ *Circumference: 883.73 mm*

Figure 5: *Section view of log no. 862 with special support construction (left) and digitalized cross-section (right) with corresponding section data.*

The MOR was calculated according to the round log testing standard [7], eq. (1), using the horizontal and vertical diameter (d_h ; d_v) at the point of failure, the maximum load (F_{max}), and the distance between the load head and nearest support (a).

$$\mathrm{MOR} = f_{m,0} = \frac{16\, F_{\max}\, a}{\pi\, d_h\, d_v^{\,2}} \tag{1}$$

The MOE was determined from measuring the incremental deformation and applied load linear regression, eq. (2), in a specific load range (F_1 ; F_2) corresponding to the elastic range of structural response (0.1 F_{max} ; 0.4 F_{max}) and the corresponding deflections (w_1 ; w_2). The coefficient of determination was greater than 0.99 for all series. The moment of inertia I_{cal} has been calculated from the digital sections as described before (see also Figure 5) and the span ℓ is defined by the distance of the supports.

$$\mathrm{MOE} = E_{m,0} = \frac{a\left(3\,\ell^2 - 4\,a^2\right)}{48\, I_{cal}} \cdot \frac{(F_2 - F_1)}{(\mathrm{w}_2 - w_1)} \tag{2}$$

The green oaks had an average moisture content of ca. 70% after felling, drying within 20 months to 35% at the time of testing, which is still above the FSP of approximately 25% MC for oak wood [13]. The moisture content at the time of destructive testing has been determined from the 50 mm sawn-collected section where failure occurred by regular weighing and measurement of the dry mass. For better comparison of the different specimen and considered that the findings of this research shall serve for green oak log building application guidelines, the elastic properties were standardized by moisture for indoor climate.

Normative indoor climate in the Eurocode 5 service class system is characterized by a material moisture content corresponding to a temperature of 20°C and a relative humidity of 65% in the surrounding air exceeding it only a few weeks per year. The design code itself and the assumptions serve in general for timber buildings in softwood, where in service class 1 (SC 1) the average moisture content of 12% is reached quite fast and will be not exceeded in most cases. This process takes much longer for hardwoods, such as naturally dried oak. All test results have been evaluated, considering the moisture content at time of testing is above or near fibre saturation. The slow drying process is not affecting the material properties, respectively the MOE, until the FSP is reached. The changing behaviour and moisture dependency of the MOE below FSP until SC 1 conditions $T = 20°C$, rH = 65%, $u = 12\%$, have been taken into account according to related research, e.g. [14], and eq. (3) with $u_1 \le u_2 \le$ FSP.

$$E_2 = E_1\left[1 - 0.016\left(u_2 - u_1\right)\right] \tag{3}$$

The test series of subsample 1 (cut 1) and subsample 2 (cut 2) have been evaluated statistically and design values have been derived for material properties, respective MOE, and MOR, to complete the characterisation of the raw material [1] done the forestry research partner FVA in Freiburg, Germany. The evaluation was following the "Design assisted by testing" guidelines of Eurocode – Basis of structural design, DIN EN 1990:2021-10 Annex D [15] with X_d as the design value of the specific property, s_x^2 the variance and V_x as the COV of X.

$$X_d = \eta_d / \gamma_m \cdot m_x \cdot \left(1 - k_n \cdot V_x\right) \tag{D.1}$$

$$s_x^2 = \frac{1}{n-1}\sum\nolimits_1^n \left(x_i - m_x\right)^2 \tag{D.2}$$

$$V_x = s_x / m_x \tag{D.3}$$

4 RESULTS AND DISCUSSION

The deflection of the log specimens was measured at mid-span and the positions of the loading rollers with two sensors under path-controlled loading. Figure 6 show the typical load-deflection behaviour including the observed local failure as small stepwise decreases in load before ultimate failure occurs.

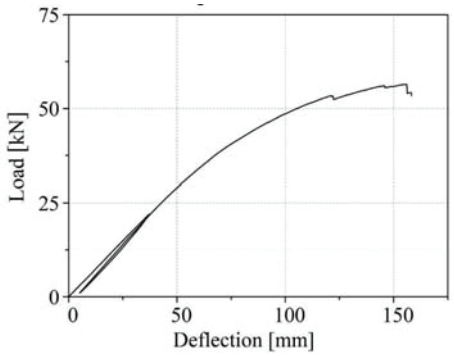

Figure 6: *Typical load-deflection relationship (hysteresis)*

The statistical evaluation has been done for cut 1 and cut 2 separately for the unsawn roundwood specimen, excluding the sawn roundwood in this stage of data interpretation. Table 2 show the results for all unsawn logs (cut 1 and 2) derived from testing as mean values of MOR and MOE, the characteristic and 5%-quantile values calculated from the statistical distribution over all samples and the influence of the moisture content when shifting the MC to normative indoor climate conditions.

https://doi.org/10.52202/069179-0016

The calculated MOE from testing ranged from 4,360 MPa to 32,956 MPa with an average of 11,026 MPa by scattering results and a coefficient of variation of 48.4%. The calculated MOR show a much better distribution in the range of 27.40 MPa to 103.77 MPa with an average value of 60.10 MPa, COV = 22.4% (Table 2).

Table 2. *Statistical evaluation of n = 71 log tests.*

	MOR (u_{test})		MOE (u_{test})	MOE (u_{12})
	[MPa]		[MPa]	[MPa]
mean	60.1	mean	11,026	13,500
char.	36.8	5%-Q	1,799	3,289

MOR(u_{test})	$f_{m,0,mean}$	MOR mean value at time of testing
	$f_{m,0,k}$	MOR characteristic value
MOE(u_{test})	$E_{m,0,mean}$	MOE mean value at time of testing
	$E_{m12,0}$	MOE mean value at calc. 12% MC
MOE(u_{12})	$E_{m,0,05}$	MOE 5%-Quantile from test series
	$E_{m12,0,05}$	MOE 5%-Quantile at calc. 12% MC

The statistical evaluation of all samples and subsamples shows that both, modulus of elasticity and modulus of rupture are normal distributed over the number of all samples. Figure 7 show the distribution of the MOR per example. The variation of around 22% for the fibre parallel bending strength is line with similar tests executed on softwood logs, [11], [12].

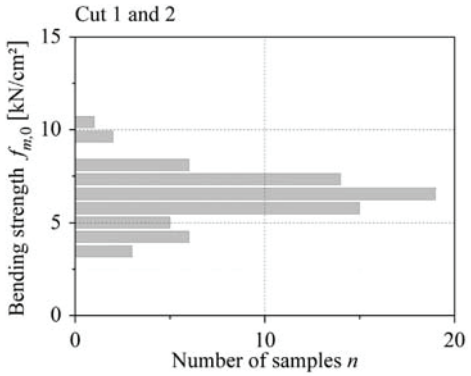

Figure 7: *Distribution of MOR for all samples.*

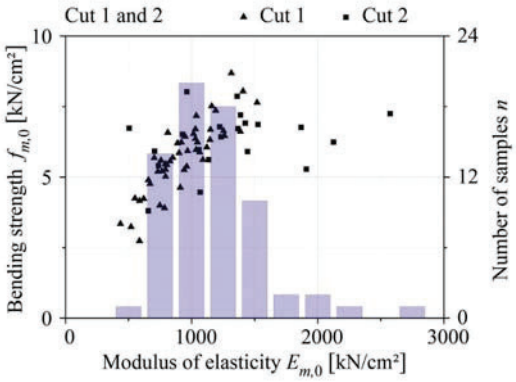

Figure 8. *Relation between MOE and MOR for all samples.*

Including the MOE in the evaluation, a linear regression dependency can be observed. Some specimens from cut 2 contribute a much higher MOE by medium strength in contrast to the rest of specimen (Figure 8). The mean MOE obtained by destructive tests appears 18% lower than the dynamic MOE measurement done in Freiburg [1]. This is also described in other research reports on comparison of destructive and non-destructive characterisation of material properties of wood.

Further investigations have been done relating the wood density and the moisture content to the mechanical properties tested. Fresh sawn or wet oak has a density of around 1,200 kg/m³ and a MC around 70%. To be in line with the test standards, the moisture content has been decreased over 18 months from the time of felling (December 2019 for cut 1) by natural drying. At the time of testing the MC was still over the FSP. To investigate further dependencies the MC have been reduced to 10-12% equilibrium humidity in service class 1 with the corresponding density ρ_{12} around 720 kg/m³. The kiln-dry density to the MOR relationship (Figure 9) and the kiln-dry density to the MOE relationship (Figure 10) could be confirmed as linear. The moisture content of the logs showed a good correlation with the modulus of elasticity and the bending strength. For further investigations, the relevant material properties have been also calculated for SC 1 conditions (u = 12%), as the MC at the time of testing was above FSP for all specimens.

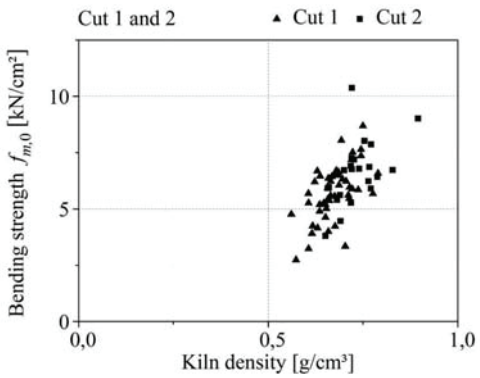

Figure 9. *Relation between MOR and kiln-dry density.*

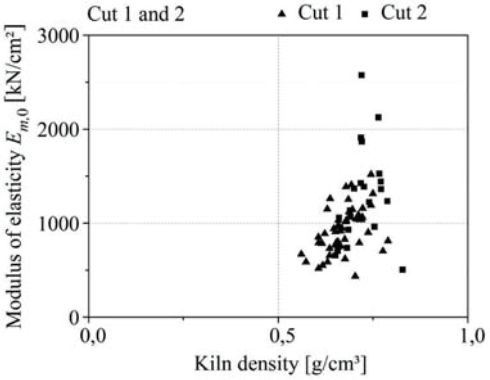

Figure 10. *Relation between MOE and kiln-dry density.*

https://doi.org/10.52202/069179-0016

5 CONCLUSIONS

The results of the research done show that small-diameter oak logs appear suitable for load-bearing structures. This could be a significant addition to the existing range of application, since those logs have no further use due to curvature, knot distribution or diameter. The work done is a first step towards sustainable applications of small-diameter oak as structural timber, using modern classification methods within the framework of forest management. The results are not perfect, but promising to go the next steps in roundwood classification to ensure a long-lasting and high-quality raw material for construction and the necessary increase in stocks of climate-resilient hardwood assortments in the coming decades.

A good correlation between flexural strength and stiffness could be observed in the first test series, basis for developing a grading system for round timbers. In the second batch only a few specimen delivered high stiffness values resulting in a high COV and scattering results. A follow-up study is needed in which logs of at least two nearby sites are sorted and then tested to confirm the flexural properties. Additional information is also needed on the compressive strength of lower diameter logs to quantify the relationship between compressive and bending material strength. These investigations have been started with destructive testing recently and will be expanded by studies of the effects of changing moisture content in logs on strength and stiffness as an aid for further classification and quality control issues.

The investigations done in Freiburg and Mainz have shown, that the more efficient team work and the use of digital and modern destructive and non-destructive applications and methods are beneficial to predict the material properties of irregular-shaped individual logs. Apart from shape and properties distribution along the trunk, the influence of knots is known and investigations on the sample assortment of this study have started already. Innovative machine learning procedures applied to computed tomography scans can help to reconstruct knots and other internal wood defects and shall serve for a better strength prediction of small-diameter hardwoods in the future.

ACKNOWLEDGEMENT

The project receives funding via the Waldklimafonds (WKF) funded by the German Federal Ministry of Food and Agriculture (BMEL) and Federal Ministry for the Environment, Nature Conservation, Nuclear Safety and Consumer Protection (BMUV) administrated by the Agency for Renewable Resources (FNR) under grant agreement No. 2218WK18D3. The authors would like to thank all employees of the National Material Testing Authority (MPA) in Mainz, going the extra mile for this project during the corona pandemic and Maximilian Leonhard Müller for his engagement and support in evaluating the experimental results.

REFERENCES

[1] Hofmann, N., Brüchert, F., Sauter, U.H., Schober, K.U., Hörnel-Metzger, B., and Müller, M.L. Green oak building with high-tech methods, Part 1: Characterisation of the raw material. *17th World Conference on Timber Engineering (WCTE 2023)*, Oslo, Norway, 2023.

[2] American Society for Testing and Materials (ASTM). Standard methods of static tests of lumber in structural sizes, D 198-02. *Annual Book of Standards*, Volume 04.10. Wood. ASTM, West Conshohocken, PA, USA, 2003.

[3] American Society for Testing and Materials (ASTM). Standard practices for establishing structural grades and related allowable properties for visually graded lumber, D 245-00. *Annual Book of Standards*, Volume 04.10. Wood. ASTM, West Conshohocken, PA, USA, 2003.

[4] American Society for Testing and Materials (ASTM). Standard test methods for establishing clear wood strength values, D 2555-98; Standard practice for establishing design stresses for round timber piles, D 2899-99. *Annual Book of Standards*, Volume 04.10. Wood. ASTM, West Conshohocken, PA, USA, 2003.

[5] American Society for Testing and Materials (ASTM). Standard practice for establishing stress grades for structural members used in log homes, D 3957-90. *Annual Book of Standards*, Volume 04.10. Wood. ASTM, West Conshohocken, PA, USA, 2003.

[6] American Society for Testing and Materials (ASTM). Standard practice for assigning allowable properties for mechanically graded lumber, D 6570-00. *Annual Book of Standards*, Volume 04.10. Wood. ASTM, West Conshohocken, PA, USA, 2003.

[7] DIN EN 14251:2004-04. Structural round timber - Test methods. German Version EN 14251:2003. DIN, Berlin, Germany.

[8] Ranta-Maunus, A. Round small-diameter timber for construction. *Final report of project FAIR CT 95-0091*, VTT Publication 383, Finnland, 1999.

[9] Kretschmann, D. E., and Green, D. W. Mechanical Grading of Oak Timbers. *Journal of Materials in Civil Engineering.* 11(2):91-97, 1999.

[10] Green, D. W., Gorman, T. M., Evans, J. W., and Murphy, J. F. Mechanical Grading of Round Timber Beams. *Journal of Materials in Civil Engineering.* 18(1):1-10, 2006.

[11] Zangiacomo, A.L. et *al.* Avaliação do módulo de elasticidade de peças estruturais roliças e de corpos-de-prova de Pinus elliottii (MOE evaluation for round timber and small wood specimens of Pinus elliottii). *Scientia Forestalis*, Piracicaba 41 (98): 283-291, 2013. (in Portuguese)

[12] Krajnc, L., Farrelly, N., and Harte, A. Mechanical characterization of green Sitka spruce logs. *Paper presented at Civil Engineering Research in Ireland 2016 (CERI2016)*, NUI Galway, 29-30 August, 2016.

[13] Krpan, J.: Untersuchungen über den Fasersättigungspunkt des Buchen-, Eichen-, Tannen- und Fichtenholzes. *Holz als Roh- und Werkstoff* 12 (3): 84-91, 1954.
[14] Hartnack, R. Langzeittragverhalten von druckbeanspruchten Bauteilen aus Holz (Long-time load-bearing performance of compressed wooden members), Doctoral Thesis, Bauhaus-Universität Weimar, Weimar, 2004. (in German)
[15] DIN EN 1990:2021-10. Eurocode: Basis of structural design; German version EN 1990:2002 + A1:2005 + A1:2005/AC:2010, DIN, Berlin, Germany.

https://doi.org/10.52202/069179-0016

World Conference on Timber Engineering Oslo 2023

EXPERIMENTAL STUDY ON IN-PLANE SHEAR PERFORMANCE OF CROSS-LAMINATED TIMBER

Kaito Yamagata[1], Ryo Inoue[2], Takuro Mori[3]

ABSTRACT: The in-plane shear performance of CLT using the asymmetric four-point bending test method was conducted to examine the test conditions. The parameters of specimens were the span, the height, the layups and the loading direction. As a result, it was found that the bending failure occurred when the span ratio was 1.25 times. This suggests that shear failure may occur reliably below the span ratio was 1.0 times. The shear strength was increased when loaded with the same lamina at the span ratio of less than 0.5 times. Therefore, it is recommended that the span ratio was 0.5 to 1.0 times to adapt for CLT in-plane shear testing method. The shear strength and the percentage of perpendicular layers were positively correlated, suggesting that shear strength may be estimated in a simplified manner. The diagonal measurement of shear modulus is considered to be the easier way to calculate the shear modulus, as it does not require any concern for the grain direction. The shear modulus values ranged from half to four times higher than the design values in Japan. A comparison of the shear strength and shear modulus between values in the reference using other testing methods and the experimental values in this study shows a tendency to show different values. This may be due to the different shear section areas of the specimens depending on the test method and the different restraint conditions.

KEYWORDS: Shear performance, Cross-laminated timber, Asymmetric four-point bending test

1 INTRODUCTION

Currently, the utilization of wood is promoted around the world since the environmental problem became serious. To increase the utilization of timber in buildings, the tall and large-scale wooden buildings are getting important. CLT is attracting attention because it has high shear performance and the usage ability of a large amount of wood. Therefore, CLT is used at walls and floors in wooden large structures. If CLT is used as earthquake-proof walls, the horizontal force applies at the in-plane direction of CLT panel. As the structure becomes larger, the in-plane shear force increase. Therefore, it is important to understand the in-plane shear performance of CLT.

However, the method for evaluating the in-plane shear performance of CLT is not established. We focused on the asymmetric four-point bending test method as shown in Figure 1 from among multiple test methods[1)-4)], because the method has the advantage that the stress control of bending and shear is easy. The span of the method for lumber and glulam is set by Japan Housing and Wood Technology Center (HOWTEC)[5)]. There are also existing studies using this test method for lumber[6),7)], glulam[8)] and MDF[9)], but there are almost no studies using it for CLT have been found[10)]. Therefore, it is not established about CLT, so it needs to investigate to adapt on CLT. Particularly with regard to the in-plane direction of CLT, appropriate test methods are difficult to implement, as bending and embedment failures may occur.

In this study, it was investigated the in-plane shear performance of CLT; the parameters of the targets are the loading span, loading direction and specimen's height. In addition, shear deformation is measured using three different measurement methods, and the simplest and most suitable measurement method is investigated. This study aims to propose the test method and measurement method of in-plane shear for CLT.

2 OUTLINE OF EXPERIMENT

Table 1 shows the specifications of the specimens. As shown in Figure 2, specimen's layups were set to 3 layers 3 plies, 4 layers 4 plies, 5 layers 5 plies. 4 layers 4 plies CLT is not standard used layups, but was used to study the differences in deformation under the same stress, as the front and back sides have different the grain directions. All specimens were made of *Japanese Cedar* (*Sugi*). The 3 layers 3 plies and 5 layers 5 plies have two load directions which are in major axis and minor axis against in-plane bending.

As shown in Figure 1, the testing method was the asymmetric four-point bending test method, the supporting and loading spans were 1 to 2 times as specimen's height. And the span of between supporting and loading span minus loading plate width (S-w_p), divided by specimen's height(d) is called span ratio. Here, it was named the major and the minor axis as shown in

[1] Kaito Yamagata, Hiroshima University, Japan, m213639@hiroshima-u.ac.jp
Ryo Inoue, Hiroshima University, Japan, d204777@hiroshima-u.ac.jp
Takuro Mori, Hiroshima University, Japan, moritaku@hiroshima-u.ac.jp

https://doi.org/10.52202/069179-0017

Table 1: *List of specimens*

Layups	width×height (mm)	{Span(S) – Width of plate(w_p)} / height(d) ratio	Loading direction	Density (kg/m^3)	Moisture (%)	Number of specimens
3 layers 3 plies	90×240	0.5	Major	410±50	11.9±1.1	Each 6 Total 12
		0.75	Minor			
4 layers 4 plies	120×240	0.5・0.75・1.0		438±36	11.6±0.7	Each 6 Total 18
5 layers 5 plies	150×120 150×360	0.25・0.5・0.75・1.0・1.25	Major	463±24	10.1±0.6	Each 3 Total 60
		0.5・0.75・1.0・1.25・1.5	Minor			

Figure 3. The major axis outer laminae are grain perpendicular to the loading direction, and the minor axis outer laminae are grain parallel to the loading direction. The width of the loading and supporting plate were set to 3/4 of the specimen's height for the major axis, and 1/2 for minor axis and 4 layers 4 plies in consideration of the compression stress. The loading rate was 1 mm/min and the load was applied until the load dropped to 0.8 P_{max} after the maximum load was reached.

The 4 layers 4 plies have different grain directions on the front and back side. Here, they were named the pe side and pa side as shown in Figure 4. The sides were determined in the loading direction and grain direction. As shown in Figure 5, the shear strain was measured by three ways. The shear modulus values calculated by each measurement methods are called as G_h, G_v and G_d respectively.

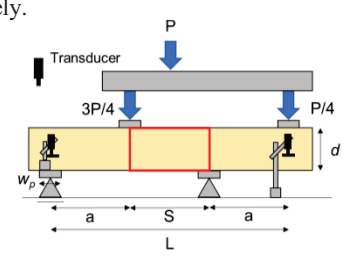

Figure 1: *Test method and measurement*

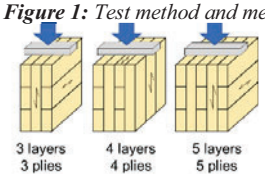

Figure 2: *Layups*

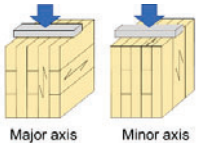

Figure 3: *Loading direction*

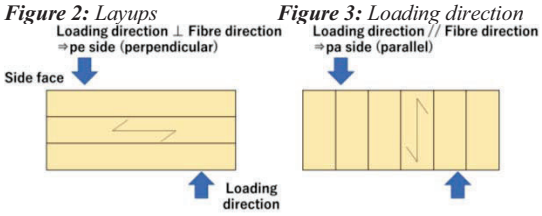

Figure 4: *Loading side of 4 layers 4 plies*

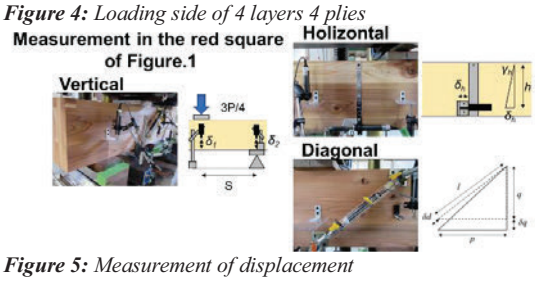

Figure 5: *Measurement of displacement*

3 RESULTS AND DISCUSSIONS

3.1 FAILURE MODES

The mainly failure phenomenon are shown in Figures 6 to 8. As shown in Figure 6, bending failure occurred in a part of the span ratio 1.25*d* and 1.5*d*. Shear failure occurred in the parallel layer as shown in Figures 7 and 8. Mode I failures were common on the major axis and pe side, while Mode III failures were common on the minor side and pa side as shown in Figure 9[11]. In the shear failure specimens, there was no difference in the failure phenomenon depending on the span ratio. Bending failure may occur if the span ratio is 1.25*d* or more, therefore the span ratio must be set to less than 1.0*d*.

Figure 6: *Bending failure*
(*Left: Major axis on 1.25d, Right: Minor axis on 1.5d*)

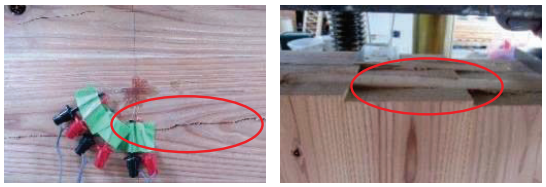

Figure 7: *Shear failure*
(*Left: Mode I, Major axis, Right: Mode III Minor axis*)

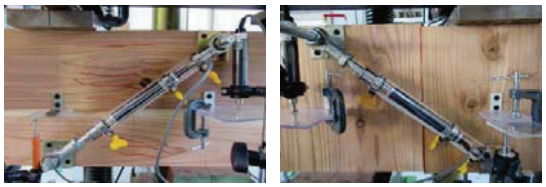

Figure 8: *Shear failure of 4 layers 4 plies*
(*Left: Mode I, pe side, Right: Mode III, pa side*)

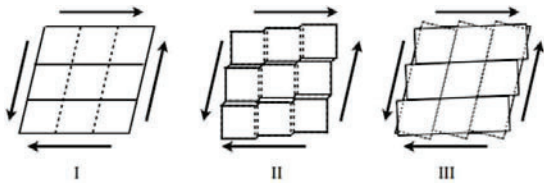

Figure 9: *Definition of shear deformation* [11]

https://doi.org/10.52202/069179-0017

3.2 SHEAR STRENGTH

The relationship between the span ratio and shear strength is shown in Figure 10. The reference value, which is the CLT Construction Manual in Japan (CLT-Manual-J)[12], is also shown in Figure 10. The value of the major axis was higher than that of the minor axis regardless of the span. In addition, the effect of specimen's height was small and the shear strength showed almost the same value in the minor axis of 120mm and 360mm. The experimental value was approximately 1.09 to 3.01 times that of the reference value. In the 120mm specimens, some high values were shown in a small span ratio. In this case, the specimen's height is small, the shear area is also short and there had only one vertical lamina in the shear area as shown in Figure 11. Therefore, the loads were applied to each end of one lamina, and the high struts occurred on one lamina as the vertical compression. Thus, it is necessary to consider the test conditions so that the lamina boundary is within the shear section. For larger heights, a size of 240mm is considered appropriate as the increased volume makes testing more difficult. A span ratio of 0.5 to 1.0d is considered a desirable span ratio, where bending failure does not occur and the same lamina is less likely to be loaded. In terms of layups, the major axis was higher than the minor axis in 3 layers 3 plies and 5 layers 5 plies. The factor was considered to be the proportion of perpendicular layers in the total layer thickness.

The relationship between the percentage of perpendicular layers and shear strength is shown in Figure 12. Mode I to III indicate the shear strength of each mode as determined by the shear reference strength calculation formula in the CLT Manual J[12].The calculation formulas for Mode I～III are shown in Equation(1).

$$F_s = min\left\{\begin{array}{c} f_{v,lam} \\ f_{v,lam90}\cdot\dfrac{t_{net}}{t_{gross}} \\ \dfrac{b\cdot n_{ca}}{2t_{gross}}\cdot\dfrac{1}{\dfrac{1}{f_{v,tor}}\cdot\left(1-\dfrac{1}{m^2}\right)+\dfrac{2}{f_R}\cdot\left(\dfrac{1}{m}-\dfrac{1}{m^2}\right)} \end{array}\right. \quad (1)$$

$f_{v,lam}$:Shear strength of parallel to the grain
$f_{v,lam90}$:Shear strength of perpendicular to the grain
t_{net} :Thickness of perpendicular to the grain
t_{gross} :Thickness of the CLT
b :Width of lamina
n_{ca} :Number of perpendicular bonded layers of CLT
$f_{v,tor}$:Torsional shear strength of the intersecting surfaces of two perpendicular bonded lamina
m :Lowest value out of the number of lamina in each layer in the width direction
f_R :Rolling shear strength

Figure 12 shows that the percentage of perpendicular layers and the experimental values are positively correlated, with a transition close to mode II. The approximate equation y=10x for the proportion of perpendicular layers x, suggesting the possibility of a simple shear strength estimate. Mode II is a failure caused by shear deformation the perpendicular lamina at the edge, but the failure was observed in this study. The calculation formula, experimental values and failure properties show different fracture mode tendencies. The factor is considered to be influenced by the test method and is an issue for further study. The range of perpendicular layer percentages in this study includes the Japanese Agricultural Standard (JAS)[13] for CLTs other than 5 layers 7plies. Further studies should be conducted on 3 layers 4 plies, where the proportion of perpendicular layers is 50% the same as with 4 layers 4 plies. In addition, 5 layers 7 plies should also be considered in the further studies. Figure 14 shows the relationship between shear strength and air-dry density, and Figure 15 shows the relationship between shear strength and moisture content calculated by the oven-dry testing. The approximate straight line, approximate equation and coefficient of determination are shown respectively. Neither showed much correlation and the results were almost unchanged. The slope of the approximate line and the value of the coefficient of determination also indicate that there is no correlation between density and moisture content and shear strength in the results of this study.

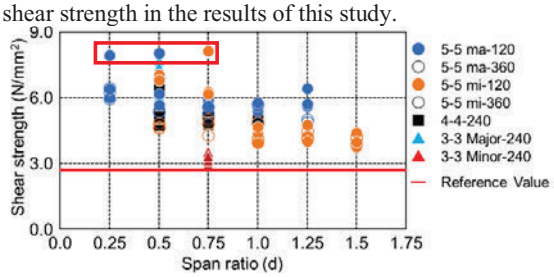

Figure 10: *Relationship between span and shear strength*

Example of notation

5 layers 5 plies, major axis, height is 120mm ⇒ 5-5ma-120

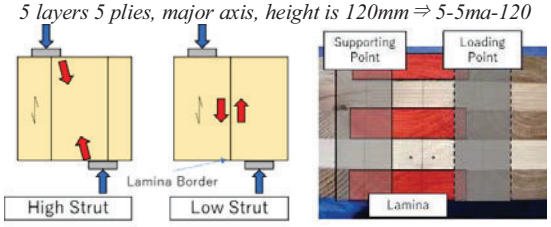

Figure 11: *Loading point and struts*

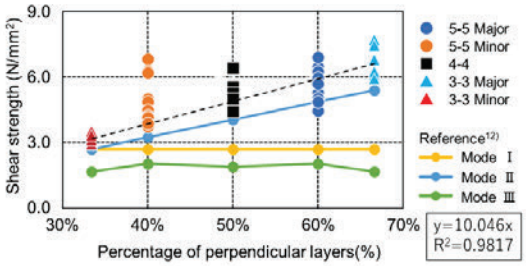

Figure 12: *Relationship between percentage of perpendicular layers and shear strength*

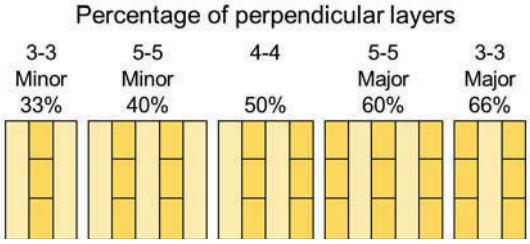

Figure 13: *Image of percentage of perpendicular layers*

https://doi.org/10.52202/069179-0017

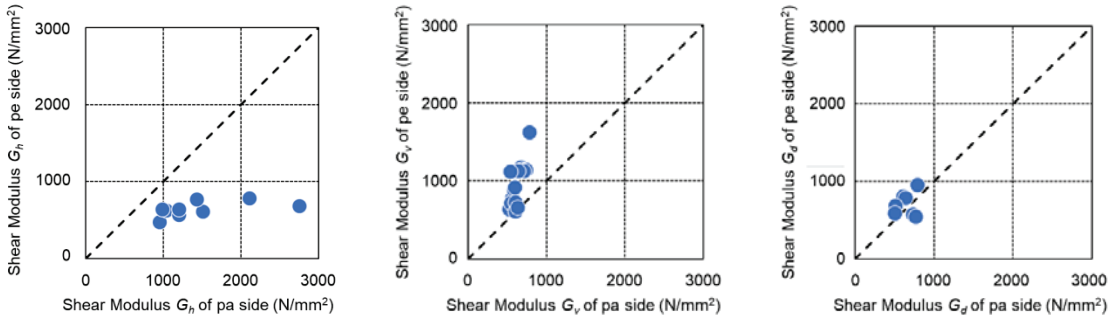

Figure 16: *Relationship between pa side and pe side of shear modulus*

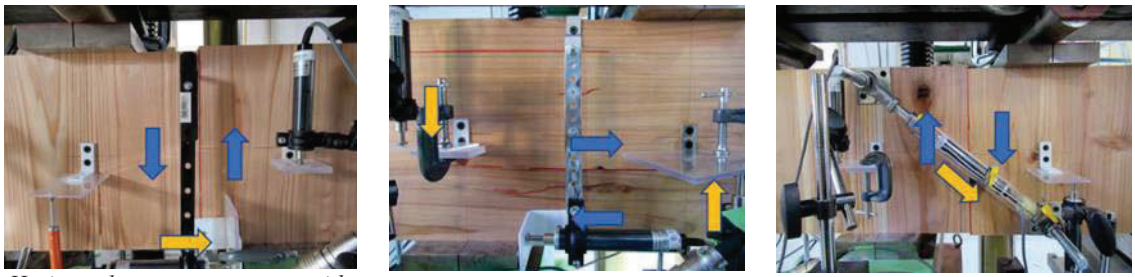

Horizontal measurement on pa side *Vertical measurement on pe side* *Diagonal measurement on pa side*

Blue arrow: grain direction (transformation) Yellow arrow: measurement direction

Figure 17: *Measurement direction of each side*

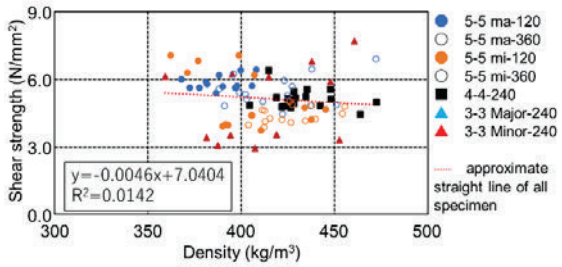

Figure 14: *Relationship between density and shear strength*

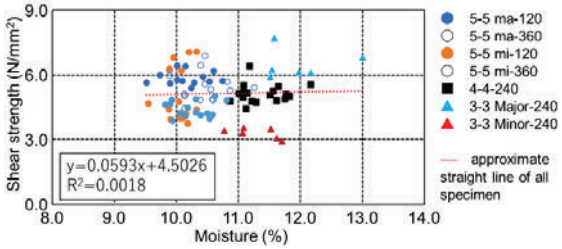

Figure 15: *Relationship between moisture and shear strength*

3.3 DIRECTIONS OF SHEAR MODULUS

Figure 16 shows the shear modulus for the pa side and pe side of 4 layers 4 plies for each measurement method. As the 4 layers 4 plies has different grain directions on the front and back, it was thought possible to study the differences in deformation due to the grain direction under the same stress.

The vertical and horizontal axes are the pe side and pa side, respectively. In G_h shown on the left, the pa side showed higher values than the pa side. In contrast, the pe side showed higher values for G_v shown on the middle. On the side with high values, the measurement direction was perpendicular to the grain direction on each surface as shown in Figure 17. Therefore, the horizontal and vertical measurement should be measured parallel to the grain. In G_d shown on the right, the shear modulus showed 500-1000N/mm^2 with small differences in each side. This is due to the fact that the diagonal measurement has a wider measurement range and can measure deformations in any direction. Therefore, diagonal measurement is less affected by the grain direction and is considered to be an easier measurement method. It is also considered a simple measurement method, as it does not require any concern for the direction of the grain.

3.4 SHEAR MODULUS

The relationships between the span ratio and shear modulus by each measurement methods in Figures 18-20. The legend is the same as in Figure 10. The values indicated in the CLT-Manual-J[12] are called reference values and are compared. The horizontal and vertical measurement methods in the previous section showed high values for the values measured in perpendicular to the grain direction. Therefore, for G_h and G_v in the 4 layers 4 plies, the values measured on the side parallel to the grain direction were used. For G_d, the difference between the values of the two sides was small, so the average value of the two sides was used. Figures 18-20 show that the values for the 4 layers 4 plies were higher than the reference values, ranging from 500-1000 N/mm^2 for all measurement methods. The horizontal measurement method showed a wide range of values, with a particularly large variation in the minor axis. Specimen height had no effect on the shear modulus. For span ratio, a negative correlation is observed for G_v and G_d, suggesting that bending deformation is affected. However, G_v and G_d are

https://doi.org/10.52202/069179-0017

considered to be suitable measurement method for shear deformation, as they show a smaller range of values than G_h. And they are closer to be reference value. In particular, G_d is considered to be a more suitable measurement method because its highest value is around 1000 N/mm^2 and it is easy to measure as mentioned above. A reason for the different variation in values is the difference in the measurement range. G_h is measured at the center of the specimen, whereas G_v and G_d are measured at over a wider area (including more lamina boundaries in parallel and perpendicular layers) between the inner supporting and loading points. Therefore, it is considered that the inclusion of the deformation of the entire CLT is a factor. These results suggest that the shear modulus is negatively correlated with the span ratio, that over test conditions have little influence. And that the diagonal measurement method is close to the reference value and stable because it is measured over a wide range.

3.5 COMPARE WITH OTHER TESTING

Figures 21 and 22 show a comparison with experimental values and reference values for full-scale horizontal loading testing[14)-15)], which are often used as in-plane shear testing for CLT. Only data from the same tree species used in this study were used in the reference. The shear modulus is based on values of diagonal measurement.

In the relationship between shear strength and the percentage of perpendicular layers shown in Figure 21, the values in the reference show a sideways trend that differs from the values in this study. The results of the 3 layers 3 plies (33%) in this study and the reference are also close. However, for the other layups, the divergence of the values according to the test method is greater, with an average difference of approximately 2.3 times the value for the percentage of perpendicular layers of 66%.

In the relationship between shear modulus and the percentage of perpendicular layers shown in Figure 22, the reference values show a slightly negative correlation, whereas the values of this study show a positive correlation. Specimens with 50% of perpendicular layers showed close values regardless of the test method and layups.

Thus, a comparison of the shear strength and shear modulus between values in the reference values using other test methods and the experimental values in this study shows a tendency to show different values. This may be due to the different shear section areas of the specimens depending on the test method and the different restraint conditions. The differences in performance between test methods are a subject for further study.

4 CONCLUSIONS

The asymmetric four-point bending test was conducted on CLT to investigate the effects of layups, span ratio, height and loading direction on shear strength and shear modulus. For shear strength, it was found that the height and span ratio did not have a significant effect. The results for the 4 layers 4 plies showed values around the major and minor axis of 5 layers 5 plies. The difference in between 3 layers 3 plies depending on the loading direction suggests that

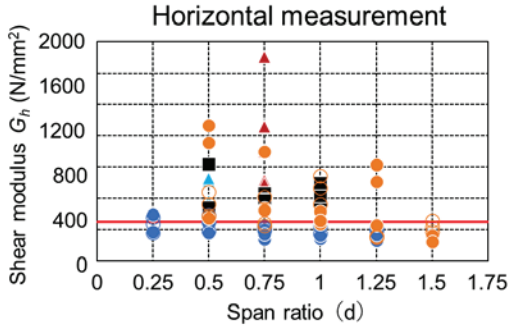

Figure 18: *Relationship between span and shear modulus G_h*

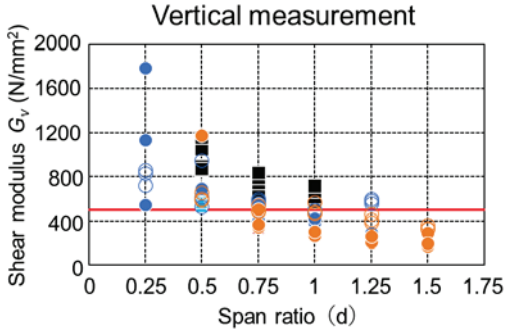

Figure 19: *Relationship between span and shear modulus G_v*

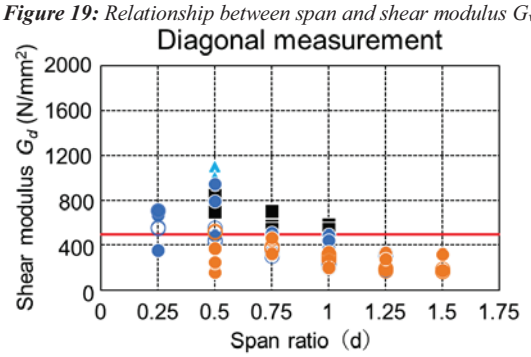

Figure 20: *Relationship between span and shear modulus G_d*

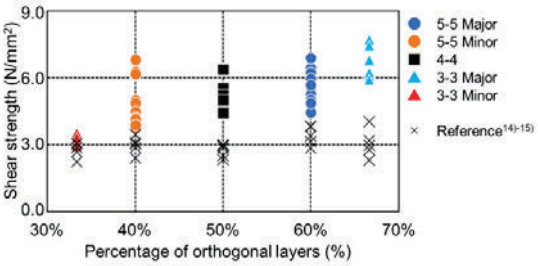

Figure 21: *Comparison with experimental values and reference values of shear strength*

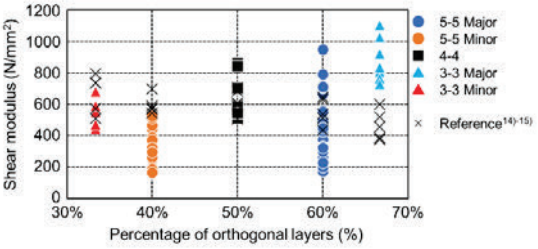

Figure 22: *Comparison with experimental values and reference values of shear modulus*

the percentage of perpendicular layers in the overall thickness may have an effect on shear strength. For shear modulus, the measurement in the diagonal direction (Gd) showed the least variation. In addition, it showed values close to those in the CLT-Manual-J[12] and is considered to be less affected by the grain direction. Based on these results, the method is considered to be an appropriate method for measuring deformation.
Based on the above results, it is considered that the appropriate test conditions are;

- The specimen's height should be 240 mm or more (two or more lamina in the direction of height)
- The span ratio should be in the range of 0.5-1.0*d*, avoiding bending failure and loading with the same lamina
- The layups are influenced by the percentage of perpendicular layers
- The shear strength is positively correlated with the percentage of perpendicular layers, suggesting that shear strength could be estimated in a simplified manner
- The measurement method is recommended because it is easier to measure in the diagonal direction.

Future research should include experiments on specimens with different proportions of perpendicular layers to investigate the relationship with shear strength and failure modes.

ACKNOWLEDGEMENT

We would like to thank all the students in the laboratory for their cooperation in conducting the experiment. Part of this study was based on the Architectural Institute of Japan Chugoku Branch Incentive Research Grants 2022. We would like to express our gratitude for all support.

REFERENCES

[1] Mehsam Tanzim Khan, Ying Hei Chui and Dongsheng Huang: A Review of the Methods for Predicting the Effective In-Plane Shear Modulus of Cross-Laminated Timber (CLT), Hindawi, Advances in Civil Engineering, Article ID 6616559, 2021
[2] Hiroshi Yoshihara: Characterization of Shear Properties of Wood and Wood-Based Materials, Journal of the Society og Materials Science, Japan, Vol.55, No.4, pp.349-355, 2006, in Japanese.
[3] Hirofumi Ido, Hirofumi Nagao and Hideo Kato: Evaluation of the Shear Strength of Lumber by Different Test Method, Mokuzai Gakkaishi, Vol.52, No.5, pp.293-302, 2006, in Japanese.
[4] Yasuo Iijima: Standarization of Testing and Evaluation Method for Full-size Structural Timber Strength in Japan, Mokuzai Gakkaishi, Vol.53, No.2, pp.63-71, 2007, in Japanese.
[5] Japan housing and wood technology center. Strength Test Manual for Structural Lumber. Tokyo (2011) , in Japanese.
[6] Hiroshi Yoshihara and Yoshitaka Kubojima: Measurement of the shear modulus of wood by asymmetric four-point bending tests, J Wood Sci, No.48, pp.14-19, 2002
[7] Hiroshi Yoshihara and Toshifumi Furushima, Shear strengths of wood measured by various short beam shear test methods, Wood Sci Technol, No.37, pp.189-197, 2003
[8] Hidekatsu Ohno, Yuusaku Kameyama, Yasuhiro Ando, Jun Tanabe, Kazuya Iizuka, Shinso Yokota and Nobuo Yoshizawa: Properties of Bending, Shearing and Partial Compression of Laminated Lumbers Composed of Sugi and Hinoki Wood with Elements or Laminae of Varying Thickness, Journal of the Society of Materials Science, Japan, Vol.60, No.10, pp.913-917, 2011
[9] Hiroshi Yoshihara, Shungo Suzuki and Masahiro Yoshinobu: In-plane shear properties of medium-density fibreboard measured by asymmetric four-point bending of a notched specimen, Wood Sci Technol, No.50, pp.475-187, 2016
[10] Seiichiro Ukyo, Atsushi Miyatake, Kenta Shindo and Yasushi Hiramatsu: Shear strength properties of hybrid (hinoki cypress and Japanese cedar) cross-laminated timber, J Wood Sci, Vol.67, No.23, 2021
[11] M.Flaig, H. J. Blaβ: Shear Strength and shear stiffness of CLT-beams loaded in plane, proceedings of CIB-W18, Vancouver, Canada, 2013
[12] Japan housing and wood technology center. 2016 CLT-based building design and construction manual. Tokyo (2016) , in Japanese.
[13] Ministry of Agriculture, Forestry and Fisheries: Japanese Agricultural Stundard Cross Laminated Timber, JAS3079, 2019
[14] Shoichi Nakashima, Yasuhiro Araki, Yoshinori Ohashi, Shiro Nakajima and Atsushi Miyatake: Evaluation of in-plane shear strength of CLT based on the real size horizontal loading shear test, J. Struct. Constr. Eng., AIJ, Vol.84, No.760, pp.843-849, 2019, in Japanese.
[15] Shoichi Nakashima, Yasuhiro Araki, Tsuyoshi Haramiishi, Shiro Nakajima and Atsushi Miyatake: Effects of layups and grades of laminations on shear strength of CLT under in-plane loading, Summaries of Technical Papers of Annual Meeting, Architectural Institute of Japan, pp.93-94, 2020, in Japanese.

https://doi.org/10.52202/069179-0017

World Conference on Timber Engineering Oslo 2023

SHEAR TESTS ON FULL-SCALE EUROPEAN ASH GLUED LAMINATED TIMBER BEAMS

Pedro Palma [1] , René Steiger [2] , Thomas Strahm [3] , and Ernst Gehri [4]

ABSTRACT: The influence of volume effects on the shear strength and stiffness of glued-laminated timber (GLT) made from European ash (*Fraxinus excelsior* L.) was assessed based on a comprehensive experimental campaign. The experiments were performed on full-scale GLT beams with rectangular cross sections $b \times h$ = 120 × 480 - 800 mm^2, shear lengths L_v = 720 - 1500 mm, and shear length/height ratios $\alpha = L_v/h$ = 1.2 - 2.5. The influence of the test configuration (3-point bending and asymmetric 4-point bending) was also assessed. The obtained shear strengths of European ash GLT had mean values $f_{v,mean}$ = 10.2 (CoV_{fv} = 14%) and 12.2 N·mm^{-2} (CoV_{fv} = 15%), for the 3-point and asymmetric 4-point bending test configurations. The shear strength showed some size dependency, with k = 0.2-0.4 for a strength modification factor $(h/600)^{-k}$ as a function of the beam height h.

KEYWORDS: shear strength, shear modulus, glued laminated timber, hardwood, experimental research, size effect

1 INTRODUCTION

1.1 BACKGROUND

The determination of shear properties, namely shear modulus G and shear strength f_v, is a decade-long discussion [1–8]. In the ongoing revision of EN 1995-1-1:2004 *Eurocode 5* [9], the determination of shear strength has also been under active discussion, namely regarding conversion factors required to convert results from small-scale tests into values that represent the behaviour of the material in a structure. As pointed out, e.g., by Ehrhart et al. [10], the main issues in the determination of the shear strength parallel to the grain are the: i) influence of perpendicular-to-the-grain stresses; ii) influence of volume- and geometry related parameters and; iii) the incidence of unrelated failure modes.

Regarding the influence of perpendicular-to-the-grain stresses, the presence of tensile perpendicular-to-the-grain tensile stresses reduces the shear strength, whereas the presence of low perpendicular-to-the-grain compressive stresses increases (or at least it does not decrease) the shear strength [11,12]. Most of these tests, however, were carried out on small clear specimens [13]. The incidence of unrelated failure modes, namely in bending and compression perpendicular-to-the-grain arises mostly in tests on large-scale specimens and is due to the test and load-application configurations. Finally, the influence of volume-related parameters arises from shear being a brittle failure mode and, therefore, dependent on the theoretical higher probability of a strength-reducing feature occurring in a larger stressed volume [8].

1.2 FULL-SCALE BEAM TESTS

Previous studies have concluded that realistic values of shear strength cannot be based on tests on small-scale specimens, such as those prescribed by EN 408:2010 [14], but should instead be based on full-scale beam tests [5,15–18]. Shear failures are brittle and, therefore, the shear strength depends on the stressed volume. In this cases, it is common to relate the strength to a reference volume V_{ref} (or dimension) in the form of a power law $(V/V_{ref})^{-k}$. Stress states of pure shear are difficult to materialise experimentally and hardly occur in real structures, therefore the test configurations should mostly aim to represent the conditions to which the material is subjected in reality. As already mentioned, an issue with using bending tests to determine the shear strength has been the high number of bending failures that tend to occur. To overcome this, beams with I-shaped cross sections have been used and at a certain point they were even included in the draft amendment to EN 408:2007/prA1:2007 [19], even though they were finally not adopted. The main shortcomings of these beams are the bigger preparation effort, a more complicated calculation of shear stresses and shear modulus, and stress concentrations in the web-flange transition.

Gehri [17] proposed the test configuration in Figure 1. This configuration comprises a simple three-point bending test and a beam with rectangular cross-section, allowing for an easy determination of shear strength and shear modulus. To ensure that the shear stresses are as constant as possible over the entire shear field, without significant perpendicular-to-the-grain stresses, the applied forces are introduced using glued-in rods (GiRs),

[1] Pedro Palma, Empa, Structural Engineering Research Lab, Switzerland, pedro.palma@empa.ch.
[2] René Steiger, Empa, Structural Engineering Research Lab, Switzerland.
[3] Thomas Strahm, neue Holzbau AG, Lungern, Switzerland.
[4] Ernst Gehri, Prof. emeritus ETH Zürich, Dr. h. c., Switzerland.

https://doi.org/10.52202/069179-0018

namely the GSA® system developed by *neue Holzbau* AG, and not through "conventional" compressive perpendicular-to-the-grain stresses [7]. Since the shear strength of hardwood is higher than that of softwood glued laminated timber (GLT), the requirements for the load-transfer system are also higher, otherwise the shear strength of hardwood could not be captured experimentally. The shear fields proposed by Gehri [17] have a ratio $\alpha = L_v/h = 1.75$, avoiding the

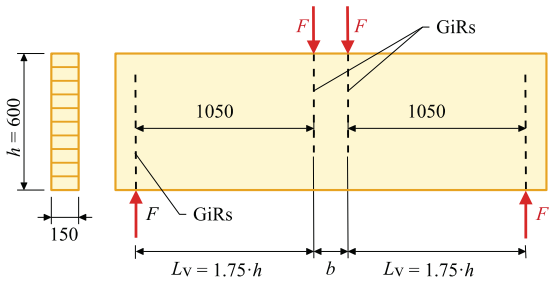

Figure 1: *Three point bending tests configuration proposed by Gehri [17] (dimensions in mm, drawing not to scale).*

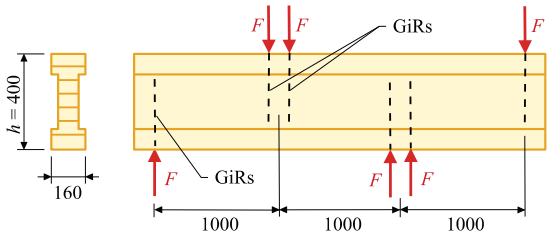

Figure 2: *Asymmetric four point bending tests performed by Ehrhart et al. [10] for the determination of shear properties (dimensions in mm, drawing not to scale).*

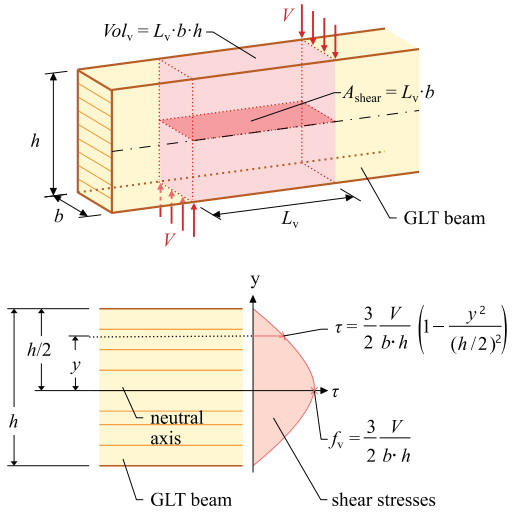

Figure 3: *Geometric parameters and distribution of shear stresses.*

bending failures that come with high values of α and still remaining within the classical beam theory with $\alpha > 1.5$. Ehrhart et al. [10] performed shear tests on beams with an I-shaped cross section under an asymmetric four-point bending configuration, based on a test configuration developed by Basler et al. [20], (Figure 2). In comparison with 3-point bending tests, this configuration allows for longer shear fields for the same beam height and bending moment, which gives the possibility to study the influence of the various geometric parameters over broader ranges. For structural engineering practice, the values of shear strength must be adjusted for the actual climatic and loading conditions and geometry of the structural member. It is therefore of interest to study the influence of geometric parameters on the shear strength (Figure 3), namely those that are easily available to the designer, since the shear strength of GLT is not correlated (or slightly negatively correlated) to the strength classes (EN 14080:2013) [21]. The most straightforward parameter is the beam height h, since the volume under the higher shear stresses around the neutral axis is correlated to the beam height. The shear length L_v is also a parameter of interest, since it is proportional to the shear crack area (Figure 3). In addition, the volume of the shear field Vol_v is a relevant parameter (Figure 3), but it is not always easy to determine, since it depends on the loading configuration and might be disturbed by perpendicular-to-the-grain stresses. Therefore, test configurations should ensure that shear stresses are as constant as possible over the entire shear field, without significant perpendicular-to-the-grain stresses. This is possible if the applied forces are introduced using GiRs, as mentioned above and described in detail by Steiger and Gehri [7].

1.3 OBJECTIVES AND SCOPE

The objectives of the study presented in this paper were to:

- obtain knowledge on the influence of the member size (geometrical parameters) and of the test configuration on the shear strength of hardwood (European ash) GLT and of a small sample of softwood (Norway spruce);
- develop tests methods for the experimental determination of the shear stiffness and strength parallel to the grain of GLT beams for research (where it is important to obtain only shear failures and it is possible to implement more complicated test set-ups) and for GLT production (where simple test set-ups are required);
- define the reference dimensions for cross-sections that meet the requirements for the two abovementioned fields of application;
- propose simple relationships to account for size effects in design standards (SIA 265:2021 and EN 1995-1-1:2004).

The experimental research presented in this paper was conducted on full-scale glued laminated timber (GLT) beams made of European ash (*Fraxinus excelsior* L.). For comparison purposes, tests were also performed on GLT made of Norway spruce (*Picea abies* (L.) H. Karst.).

https://doi.org/10.52202/069179-0018

2 EXPERIMENTAL RESEARCH

2.1 THREE-POINT BENDING TESTS ON ASH GLT

2.1.1 Materials and methods

The 3-point bending tests on European ash (*Fraxinus excelsior* L.) GLT beams (Figure 4 and Table 1) were performed at the Structural Engineering Research Lab of Empa (Switzerland). The test specimens were made from European ash GLT of strength class GL48c "special", with T33 laminations and three T50 outer laminations, without finger joints, in the tension zone. The mean density of the test specimens was $\rho_{mean} = 640$ kg·m^{-3} (coefficient of variation $CoV_\rho = 3\%$) at an average moisture content $\omega_{mean} = 10\%$. The load-application zones were reinforced with GiRs (GSA® system).

The tests were performed under force control. The shear modulus G was determined based on the shear field method, with square measurement fields with side lengths $h/2$. The shear strength f_v was calculated as $f_v = 3/2 \cdot F/(b \cdot h)$.

2.1.2 Results

The results of the 3-point bending tests on European ash GLT are presented in Table 2 and Figure 5. The mean shear modulus was $G_{mean} = 1162$ N·mm^{-2} ($CoV_G = 6\%$) and showed no size dependency. The global mean shear strength was $f_{v,mean} = 10.2$ N·mm^{-2} ($CoV_{fv} = 14\%$). Some size-dependency of the shear strength can be observed at the mean-value level, but the scatter of the results makes it less clear than for the equivalent Norway spruce GLT beams. The shear strength can be described as a function of the beam height h by

$$f_v = 34 \cdot h^{-0.19} = 10.2 \left(\frac{600}{h}\right)^{0.19}. \quad (1)$$

The position of the longitudinal shear cracks in the beam height was above the neutral axis in approximately 70% of the tests and below the neutral axis in approximately 30% of the tests [22].

For beam heights $h = 480$ and 600 mm, the shear cracks occurred within 25% of the beam height above the neutral axis (i.e. in the zone under longitudinal compressive stresses), which corresponds to shear stresses higher than $0.75 \cdot \tau_{max}$, with $\tau_{max} = 1.5 \cdot V/(b \cdot h)$. For the three beams with height $h = 800$ mm, the shear cracks occurred within 15 and 20% of the beam height above and below the neutral

Table 1: *Three point bending tests on European ash GLT: geometry of test specimens and test configuration.*

Test configuration		Cross-section Width b [mm]	Height h [mm]	Length L_v [mm]	Shear field Ratio $\alpha = L_v/h$ [ ]	Area A_{shear} [mm^2]	Vol. Vol_v [m^3]
ES-1.1	(n=3)	120	480	768	1.6	92160	0.044
ES-2.1	(n=3)	120	600	960	1.6	115200	0.069
ES-3.1	(n=3)	120	800	1280	1.6	153600	0.123

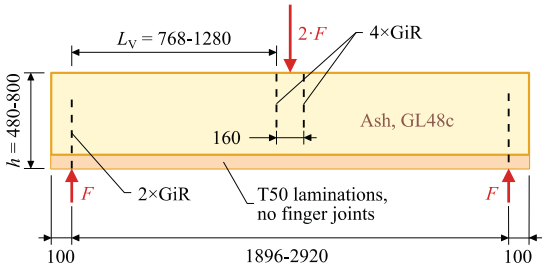

Figure 4: *Three-point bending tests on European ash GLT: geometry of test specimens and test configuration (dimensions in mm, drawing not to scale).*

Table 2: *Three point bending tests on European ash GLT: geometry of test specimens and test configuration.*

Test configuration		Shear modulus G_{mean} [N·mm 2]	CoV [ ]	Shear strength $f_{v,mean}$ [N·mm 2]	CoV [ ]
ES-1.1	(n=3)	1228	19%	10.7	18%
ES-2.1	(n=3)	1117	15%	10.4	16%
ES-3.1	(n=3)	1132	8%	9.6	10%
All	(n=12)	1162	15%	10.2	14%

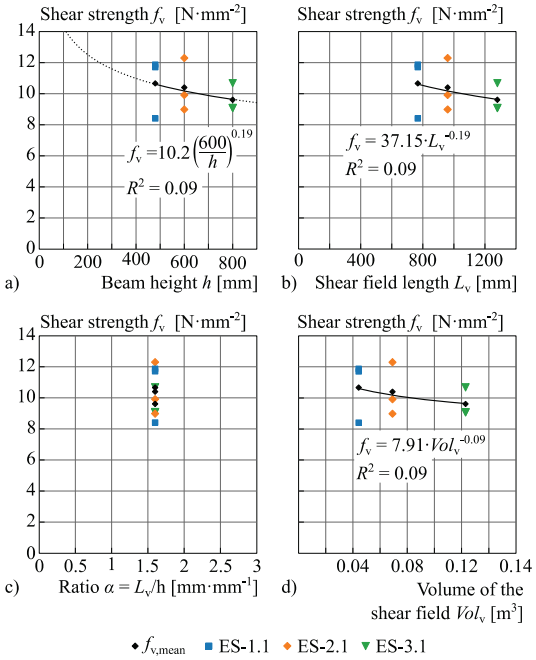

Figure 5: *Results of the 3-point bending tests on Norway spruce GLT – shear strength f_v as a function of the: a) beam height h; b) length of the shear field L_v; c) ratio $\alpha = L_v/h$; and d) volume of the shear field Vol_v.*

https://doi.org/10.52202/069179-0018

axis, respectively, which corresponds to shear stresses higher than $0.84 \cdot \tau_{max}$, with $\tau_{max} = 1.5 \cdot V/(b \cdot h)$. The mean maximum bending stresses reached when the shear failures occurred were $\sigma_{m,max,mean} = 70.9$ N·mm^{-2} ($CoV_{\sigma max} = 15\%$) and no bending failures happened.

2.2 ASYMETRIC 4-POINT BENDING TESTS ON EUROPEAN ASH GLT

2.2.1 Materials and methods

The asymmetric 4-point bending tests on European ash (*Fraxinus excelsior* L.) GLT beams were also performed at the Structural Engineering Research Lab of Empa. The test specimens (Figure 6 and Table 3) were made from ash GLT of strength class GL40c, except test specimens ES-2.5, which were made from ash GLT of strength class GL48c "special", with T33 inner laminations and three T50 outer laminations, without finger joints, in the tension zones. The mean density of the test specimens was $\rho_{mean} = 664$ kg·m^{-3} ($CoV_{\rho} = 3\%$) at an average moisture content $\omega_{mean} = 10\%$. The load-application zones were reinforced with GiRs (GSA® system).

The tests were performed under force control. This test configuration was more difficult to implement, namely because both reaction forces (supports 1 and 2) had to be measured and vertical displacements of both load-application points had to be the same, to ensure symmetry of applied loads and support reactions. The shear modulus G was determined based on the shear field method, with square measurement fields with side lengths $h/2$. The shear strength f_v was calculated as $f_v = 3/2 \cdot (F_1\text{-}F_2)/(b \cdot h)$ (see Figure 6).

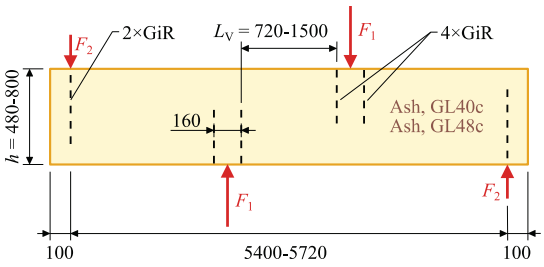

Figure 6: *Asymmetric 4-point bending tests on European ash GLT: geometry of test specimens and test configuration (dimensions in mm, drawing not to scale).*

Table 3: *Three point bending tests on European ash GLT: geometry of test specimens and test configuration.*

Test configuration	Cross-section			Shear field		
	Width	Height	Length	Ratio $\alpha = L_v/h$	Area	Vol.
	b	h	L_v	α	A_{shear}	Vol_v
	[mm]	[mm]	[mm]	[ ]	[mm^2]	[m^3]
ES-1.3 (n=3)	120	480	768	1.6	92160	0.044
ES-1.4 (n=3)	120	480	960	2.0	115200	0.055
ES-2.2 (n=3)	120	600	720	1.2	86400	0.052
ES-2.3 (n=5)	120	600	960	1.6	115200	0.069
ES-2.4 (n=3)	120	600	1200	2.0	144000	0.086
ES-2.5 (n=3)	120	600	1500	2.5	180000	0.108
ES-3.2 (n=3)	120	800	960	1.2	115200	0.092
ES-3.3 (n=3)	120	800	1280	1.6	153600	0.123

2.2.2 Results

The results of the asymmetric 4-point bending tests on European ash GLT are presented in Table 4 and Figure 7. The mean shear modulus was $G_{mean} = 1120$ N·mm^{-2} ($CoV_G = 6\%$) and showed no size dependency. The global mean shear strength was $f_{v,mean} = 12.2$ N·mm^{-2} ($CoV_{fv} = 15\%$). Some size-dependency of the shear strength can be observed at the mean-value level, but the scatter of the results makes it less clear than for the equivalent Norway spruce GLT beams. The shear strength can be described as a function of the beam height h by

$$f_v = 34 \cdot h^{-0.37} = 12.2 \left(\frac{600}{h}\right)^{0.37}. \quad (2)$$

The position of the longitudinal shear cracks in the beam height was above the neutral axis in approximately 60% of the tests and below the neutral axis in approximately 40% of the tests [22]. All but one shear crack occurred within ±20% of the beam height from the neutral axis, which corresponds to shear stresses higher than $0.84 \cdot \tau_{max}$, with $\tau_{max} = 1.5 \cdot V/(b \cdot h)$

The mean maximum bending stresses reached when the shear failures occurred were $\sigma_{m,max,mean} = 47.3$ N·mm^{-2} ($CoV_{\sigma max} = 29\%$) and no bending failures happened.

3 DISCUSSION AND CONCLUSIONS

3.1 TEST CONFIGURATIONS

From a production quality-control point of view, e.g. to check if a specified or declared material property (which in effect means a system value linked to a controlled procedure) is met, the simpler 3-point bending test configuration is adequate. The asymmetric 4-point bending test allows for a broader range of geometric parameters, namely higher $\alpha = L_v/h$ ratios, given the higher shear forces for the same bending moment. It is better suited to study the shear behaviour of timber beams but it is also significantly more complicated to perform. Reinforcement with GiRs is necessary to ensure a uniform shear field and to apply the required forces perpendicular to the grain, in particular for hardwood GLT.

3.2 Reference size of test specimens

The test results showed that it is possible to test beams with cross-sectional dimensions of up to 160×800 mm^2 for Norway spruce GLT and 120×800 mm^2 for European ash GLT, but the applied forces are quite high (up to 550 and 1150 kN, respectively). Since the bending properties

https://doi.org/10.52202/069179-0018

Table 4: *Asymmetric 4-point bending tests on European ash GLT: geometry of test specimens and test configuration.*

Test configuration		Shear modulus G_{mean} [N·mm^{-2}]	Shear modulus *CoV* [ ]	Shear strength $f_{v,mean}$ [N·mm^{-2}]	Shear strength *CoV* [ ]
ES-1.3	(n=3)	1097	5%	11.5	13%
ES-1.4	(n=3)	1108	4%	12.3	12%
ES-2.2	(n=3)	1105	4%	13.9	10%
ES-2.3	(n=5)	1124	12%	13.9	12%
ES-2.4	(n=3)	1124	4%	12.6	10%
ES-2.5	(n=3)	1092	3%	12.5	4%
ES-3.2	(n=3)	1172	6%	9.8	3%
ES-3.3	(n=3)	1134	5%	10.3	11%
All	(n=26)	1120	6%	12.2	15%

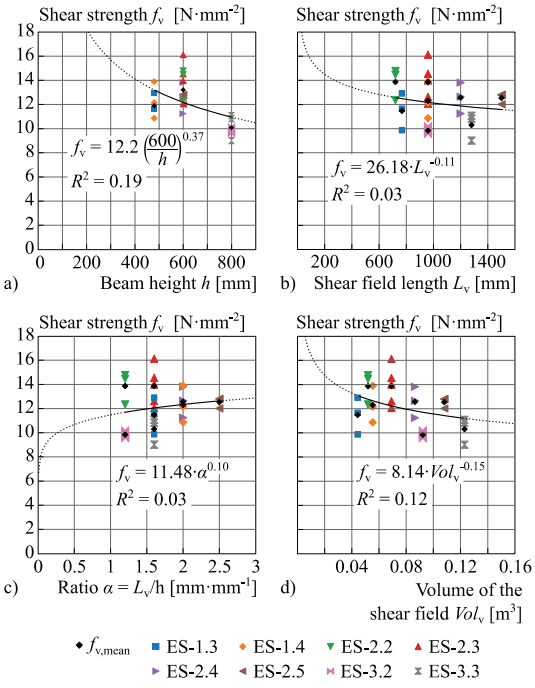

Figure 7: *Results of the asymmetric 4-point bending tests on European ash GLT – shear strength f_v as a function of the: a) beam height h; b) length of the shear field L_v; c) ratio $\alpha=L_v/h$; and d) volume of the shear field Vol_v.*

Table 5: *Shear strengths in the 3-point bending tests on Norway spruce GLT, 3-point bending tests on European ash GLT, and asymmetric 4-point bending tests on ash GLT.*

Test config.	Mean value $f_{v,mean}$ [N·mm^{-2}]	Coef. of variation $CoV(f_v)$ [ ]	5%-percentile $f_{v,mean}$ [N·mm^{-2}]	$f_{v,mean}$ [N·mm^{-2}]	$f_{v,mean}$ [N·mm^{-2}]
FI-3P	4.0	19%	3.2	2.6	2.9
ES-3P	10.2	14%	8.6	7.6	8.0
ES-4P	12.2	15%	9.6	8.8	9.5

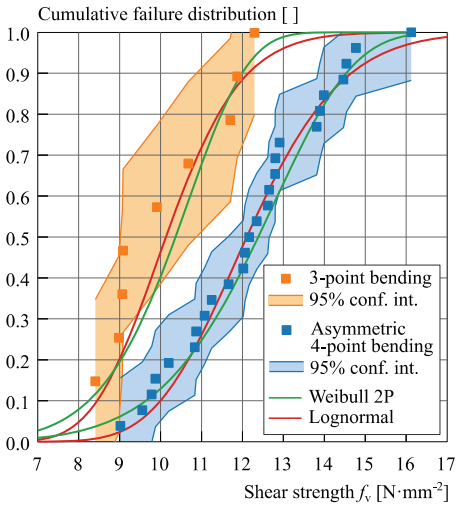

Figure 8: *Cumulative failure distributions of the shear strength in the 3-point bending tests on Norway spruce GLT, 3-point bending tests on European ash GLT, and asymmetric 4-point bending tests on ash GLT.*

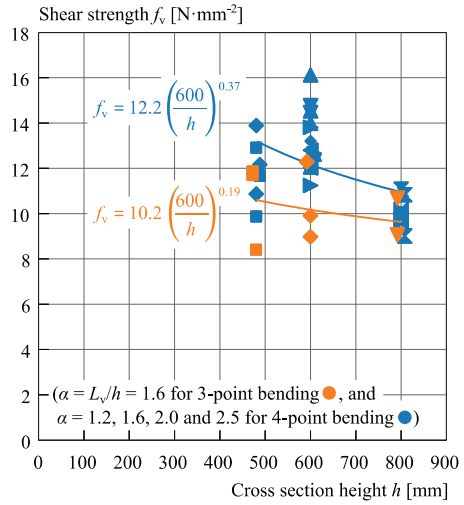

Figure 9: *Shear strength as a function of the beam height h of the cross section for the 3-point bending tests on Norway spruce GLT, 3-point bending tests on European ash GLT, and 4-point bending tests on ash GLT.*

https://doi.org/10.52202/069179-0018

are given for a reference beam height $h = 600$ mm (e.g. EN 14080:2013 [21], SIA 265:2021 [23]), it makes sense to adopt this dimension as the reference height, i.e. $h_{ref} = 600$ mm, also for the shear properties.

3.3 Shear modulus *G*

The shear modulus showed no size dependency. The stiffness of the tension and compression diagonals in the shear fields showed, however, some dependency on the ratio $\alpha = L_v/h$. The obtained mean values were $G_{mean} = 1162$ (CoV 6%) and 1120 N·mm^{-2} (CoV 6%), for the 3-point and asymmetric 4-point bending tests, respectively. This is in good agreement with the value $G_{mean} = 1000$ N·mm^{-2} specified in the publication Lignatec 33/2021 [24], which had been issued recently in Switzerland, to disseminate results from research projects on the use of hardwood in design practice.

3.4 Shear strength f_v

The obtained shear strengths of European ash GLT had mean values $f_{v,mean} = 10.2$ (CoV 14%) and 12.2 N·mm^{-2} (CoV 15%), for the 3-point and asymmetric 4-point bending tests, respectively (Figure 8 and Table 5). For Norway spruce, the corresponding value determined in 3-point bending tests was $f_{v,mean} = 4.0$ N·mm^{-2} ($CoV_{fv} = 19\%$) [22]. The test configuration showed a marked influence on the shear strength and on the position of the failures cracks. Failure cracks in the 4-point bending tests were evenly distributed within $\pm 0.2 \cdot h$ from the neutral axis, whereas in the 3-point bending tests the failure cracks occurred mostly within $0.25 \cdot h$ above the neutral axis.

The shear strength also showed some size dependency (obtained strength modification factors are presented in Figure 9), even though not as evident as in the preliminary tests on Norway spruce GLT. The exponent k of the strength modification factor $(h/600)^{-k}$ for the 3- and asymmetric 4-point bending tests is $k = 0.19$ and 0.37, respectively. The latter is close to the value $k = 0.4$ proposed by Ehrhart et. al. [10] for European beech (*Fagus sylvatica*) GLT, but that was based on 3-point bending tests on beams with I-shaped cross sections and $h_{web} < 240$ mm. The publication Lignatec 33/2021 [24] specifies a value of $k = 0.25$ for beech and ash GLT, which is approximately the average of the k values determined in the 3– and asymmetric 4-point bending tests. The same publication, for European beech and European ash, also specifies a conservative reference design shear strength $f_{v,d} = 3.2$ N·mm^{-2} for $h = 600$ mm and all strength classes.

3.5 Size effects in design standards

In Eurocode 5 (EN 1995-1-1:2004 [9]), the design shear strength is based on the characteristic 5th-percentile values derived from tests according to EN 408:2010 [14] and prescribed, e.g. for softwood GLT, in EN 14080:2013 [21] as $f_{v,g,k} = 3.5$ N·mm^{-2} for all strength classes. As already mentioned, the strength values derived from EN 408:2010 [14] are not adequate for typical structural applications and hence, a strength modification factor k_{cr} was introduced already in the first Amendment to Eurocode 5 (EN 1995-1-1:2004/A1:2008) [25]. This modification factor was supposed to account for the negative influence of "cracks" and the recommended value was $k_{cr} = 0.67$. Since it was a "nationally determined parameter", countries were able to set their own values of k_{cr}, which led to widely varying approaches. During the systematic reviews of EN 1995-1-1 *Eurocode 5*, there were many comments and requests regarding clarification and harmonisation of k_{cr}, namely to discretise it into more well-defined factors accounting for the influence of specific parameters on the shear strength. A revision of the verification of shear strength is ongoing within Working Group 3 of CEN/TC 250/SC 5 *Eurocode 5: Design of timber structures*. The latest draft of the revised verifications [26] includes a modification factor $k_{h,v}$ to account for the effect of size on the shear strength of softwood GLT that is a function of $(600/h)^{-0.2}$, i.e. sets $k_{h,v} = 0.2$ as proposed by Brandner et. al. [8] (based on 3-point bending tests on spruce beams with I-shaped cross sections and $h_{web} < 300$ mm). That value is in good agreement with the value $k = 0.19$ determined in the 3-point bending tests on ash GLT. In the latest draft of prEN 1995-1-1 [26], the influence of cracks on the shear strength may still be accounted for by means of a specific factor k_{var}.

ACKNOWLEDGEMENT

The authors gratefully acknowledge the financial support from the *Wald- und Holzforschungsförderung Schweiz* (WHFF-CH) of the Swiss *Federal Office for the Environment* (FOEN) and of the Swiss Cantons.

REFERENCES

[1] R. Foschi, J. Barrett, Consideration of size effects and longitudinal shear strength for uncracked beams, in: Proc. CIB-W18 Meet. 13, Otaniemi, Finland, 1980: pp. 13-6–2, 9 p.

[2] B. Madsen, Shear strength of Douglas Fir timbers, in: Proc. CIB-W18 Meet. 28, Copenhagen, Denmark, 1995: pp. 28-6–2, 37 p.

[3] F. Lam, H. Yee, J.D. Barrett, Shear strength of Canadian softwood structural lumber, Can. J. Civ. Eng. 24 (1997) 419–430. https://doi.org/10.1139/l96-119.

[4] D. Riyanto, R. Gupta, A comparison of test methods for evaluating shear strength of structural lumber, For. Prod. J. 48 (1998) 83–90.

[5] B. Yeh, T. Williamson, Evaluation of glulam shear strength using a full-size four-point test method, in: Proc. CIB-W18 Meet. 34, Venice, Italy, 2001: pp. 34-12–2, 13 p.

[6] R. Brandner, E. Gehri, T. Bogensperger, G. Schickhofer, Determination of modulus of shear and elasticity of glued laminated timber and related

https://doi.org/10.52202/069179-0018

examinations, in: Proc. CIB-W18 Meet. 40, Bled, Slovenia, 2007.
[7] R. Steiger, E. Gehri, Interaction of shear stresses and stresses perpendicular to the grain, in: Proc. CIB-W18 Meet. 44, Alghero, Italy, 2011: pp. 44-6–2, 14 p.
[8] R. Brandner, W. Gatternig, G. Schickhofer, Determination of shear strength of structural and glued laminated timber, in: Proc. CIB-W18 Meet. 45, CIB, Växjö, Sweden, 2012: pp. 45-12–2, 16 p.
[9] EN 1995-1-1:2004. Eurocode 5: Design of timber structures – Part 1-1: General – Common rules and rules for buildings, European Committee for Standardization (CEN), Brussels, 2004.
[10] T. Ehrhart, R. Steiger, M. Lehmann, A. Frangi, European beech (Fagus sylvatica L.) glued laminated timber: Lamination strength grading, production and mechanical properties, Eur. J. Wood Wood Prod. 78 (2020) 971–984. https://doi.org/10.1007/s00107-020-01545-6.
[11] H.-L. Mistler, Die Tragfähigkeit des am Endauflager unten rechtwinklig ausgeklinkten Brettschichtträgers, Technische Hochschule Karlsruhe, Karlsruhe, Germany, 1979.
[12] R. Spengler, Festigkeitsverhalten von Brettschichtholz unter zweiachsiger Beanspruchung - Teil 1 - Ermittlung des Festigkeitsverhaltens von Brettelementen aus Fichte durch Versuche, 1982.
[13] C. Sandhaas, Mechanical behaviour of timber joints with slotted-in steel plates, Doctoral thesis, Delft University of Technology (TU Delft), 2012.
[14] EN 408:2010+A1:2012. Timber structures. Structural timber and glued laminated timber. Determination of some physical and mechanical properties, European Committee for Standardization (CEN), Brussels, 2012.
[15] G. Schickhofer, Evaluation of glulam shear strength using a full-size four-point test method, in: Proc. CIB-W18 Meet. 34, Venice, Italy, 2001: pp. 34-12–6, 383–409.
[16] W. Klöck, Statistical analysis of the shear strength of glued laminated timber based on full-size flexure tests, Otto-Graf-J. 16 (2005) 225–244.
[17] E. Gehri, Shear problems in timber engineering – Analysis and solutions, in: Proc. 11th World Conf. Timber Eng. WCTE2010, Trentino, Italy, 2010: p. 6.
[18] S. Aicher, D. Ohnesorge, Shear strength of glued laminated timber made from European beech timber, Eur. J. Wood Wood Prod. 69 (2011) 143–154. https://doi.org/10.1007/s00107-009-0399-9.
[19] EN 408:2007/prA1:2007. Timber structures. Structural timber and glued laminated timber. Determination of some physical and mechanical properties, European Committee for Standardization (CEN), Brussels, 2007.
[20] K. Basler, B.-T. Yen, J.A. Mueller, B. Thürlimann, Web buckling tests on welded plate girders., Fritz Engineering Laboratory, Lehigh University, 1960.
[21] EN 14080:2013. Timber structures – Glued laminated timber and glued solid timber – Requirements, European Committee for Standardization (CEN), Brussels, 2013.
[22] P. Palma, R. Steiger, T. Strahm, E. Gehri, Shear stiffness and strength of European ash glued laminated timber, in: Int. Netw. Timber Eng. Res. INTER – Meet. Fifty-Five, Timber Scientific Publishing, Bad Aibling, Germany, 2022: pp. 225–241.
[23] SIA 265:2021. Holzbau, Schweizerischer Ingenieur- und Architektenverein (SIA), Zürich, 2021.
[24] Lignatec 33/2021. Verklebte Laubholzprodukte für den statischen Einsatz, Lignum, Holzwirtschaft Schweiz, Zürich, Schweiz, 2021.
[25] EN 1995-1-1:2004/A1:2008. Eurocode 5: Design of timber structures – Part 1-1: General – Common rules and rules for buildings, European Committee for Standardization (CEN), Brussels, 2008.
[26] F. Kupferle, CEN/TC 250/SC 5/WG 3 N 388. Revised INF ENQ Draft clauses: Verification of shear strength., (2022).

World Conference on Timber Engineering Oslo 2023

STRUCTURAL USE OF CUT-OFFS FROM CLT-PRODUCTION – THREE EXAMPLES THAT UTILIZE THE UNIQUE PROPERTIES

Johan Vessby[1], Mikael Perstorper[2], Florian DeMonte[3], Jacob Eriksson[4]

ABSTRACT: Production of CLT-panels typically results in 5-10% cut-offs due to window and door openings. CLT-boards can be made by slicing these cut-offs and finger-jointing them. It is worthwhile from economic and climatic aspects to find applications for such boards as building products with long service life. It is preferred to find uses where the premium transverse properties are utilized. This paper present three novel ideas for re-use of cut-offs from CLT. (a) The re-use as REX laminations in CLT production is a smart concept that minimize waste in an economical way. (b) By using finger-jointed CLT-boards as horizontal rails in timber frame buildings, the problems with over-load and deformations in multi-storey houses are minimized. (c) The capacity of glulam beams to carry concentrated loads is greatly enhanced by integrating CLT-boards as laminations.

KEYWORDS: CLT, REX lamination, perpendicular to grain, re-use, rails, glulam, concentrated load

1. INTRODUCTION

The background to this study is the urge to find smart use for cut-offs from CLT-production, see Figure 1. Due to window and door openings and waste due to non-rectangular shapes of the CLT-panels, 5-10% of all produced CLT material is typically chipped to become biofuel. The idea here is to slice these cut-offs and finger-joint them to CLT-boards with arbitrary length so that these boards have every second layer oriented with the longitudinal direction along the length direction of the board and the other, referred to as "cross-layer", perpendicular to that direction. The cross-layers gives the CLT-boards superior stiffness and strength properties when loaded perpendicular to their length direction since every second layer is then loaded in parallel to the fiber direction, see Figure 1.

It is worthwhile from economic and climatic aspects to find applications for such boards as building products with long service life. It is also favorable to find uses where the premium transverse properties are desired, beneficial and fully utilized.

In this paper, three concepts of re-use of cut-offs are presented and discussed, see Figure 1 (b-d):

a) Re-use as REX lamination in CLT made by Stora Enso
b) CLT-boards as rails in timber frame structures
c) CLT-boards as integrated glulam laminations to enhance capacity for concentrated load

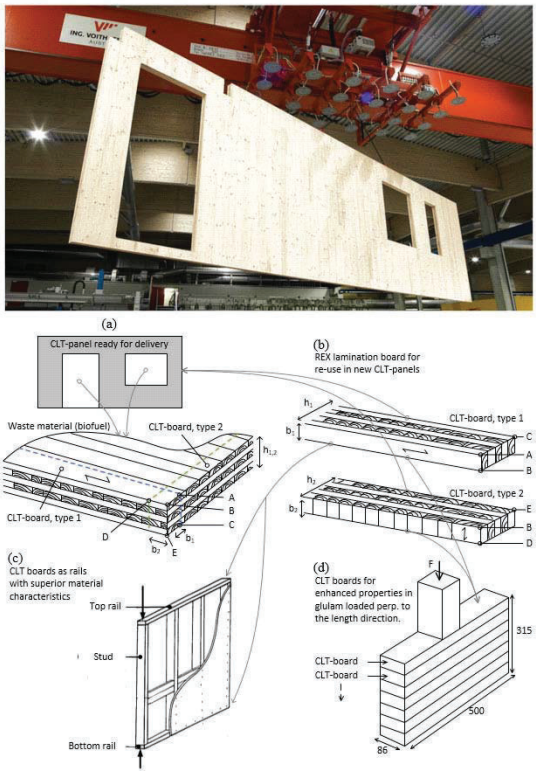

Figure 1: *(a) Waste material from CLT-panels sliced into CLT-boards and used for b) re-use in new CLT-panels c) rails in timber structures and d) to enhance performance locally in glulam beams.*

[1] Johan Vessby, Karlstad University, Sweden, johan.vessby@kau.se
[2] Mikael Perstorper, Karlstad University and Dynalyse AB, Sweden, mikael.perstorper@kau.se
[3] Florian DeMonte, Stora Enso, Austria, florian.demonte@storaenso.com
[4] Jacob Eriksson, Stora Enso, Austria, Jacob.eriksson@storaenso.com

https://doi.org/10.52202/069179-0019

2. RE-USE OF CUT-OFFS AS REX LAMINATION IN CLT

Stora Enso has developed the idea to finger joint slices of the cut-offs and reuse them as transverse layers of floor and roof slabs in CLT production. The properties of this so-called REX laminations are defined in a European Technical Approval (ETA-14/0349) [1], see Figure 2 (a). The effective E-modulus of the REX lamination depends on the proportion of end-grain, which varies between 20-40 %. However, the E-modulus has been set conservatively to E_{REX} = 6 800 MPa for all laminations type REX.

The properties of the longitudinal layers remain unchanged, which means that the difference in mechanical properties between standard CLT slabs and CLT slabs with REX transverse layers is limited. CLT panels with transverse layers made of REX lamination can significantly limit the carbon footprint by reducing the need for virgin material for producing a panel. CLT with transverse layers of REX lamella have on several occasions been produced in a production line at one of Stora Ensos pulps and used successfully in projects. A stack of five CLT-panels with REX lamellas are shown in Figure 2 (b).

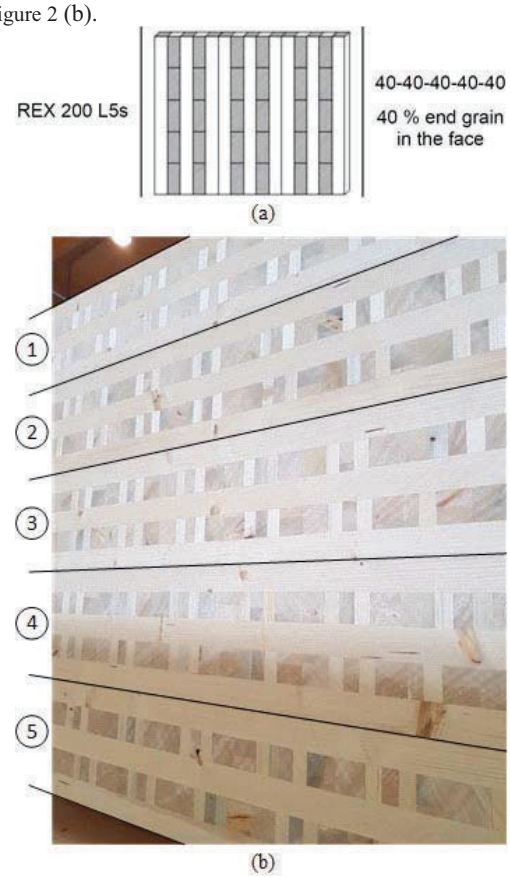

Figure 2: *a) Example of a REX lamination layer from a 5-ply CLT panel, from ETA-14/0349 [1] and b) photo of a stack of five CLT-panels with REX lamellas.*

3. CLT-BOARDS AS SUPERIOR RAILS IN TIMBER FRAME STRUCTURES

In multi-storey timber frame buildings the horizontal rails are often a weak point and the accumulated vertical deformations occasionally become problematic. Extra wall studs are at times needed to distribute the load onto a larger area on the rail and thus decrease the stress. By using CLT-boards as rails this problem is minimized thanks to the superior transverse properties. Since every other layer in a CLT-board has the fiber direction in the direction perpendicular to the length direction of the rail and in parallel to the stud, it can carry a much higher perpendicular load compared to structural timber.

Tests of the transverse properties were carried out on 50+50 CLT-boards cut from 5-ply (5·20 mm) CLT wall panels from the Stora Enso mill in Gruvön, Sweden, and on 15 specimens with similar dimensions using structural timber of quality C24. The boards were planed to the standard size 45·95 mm^2 and blocks were cut for the test following EN 408 [2]. In Figure 3 (a) and (b) the cross section of one of the tested specimens is shown together with the setup used for loading. The setup was designed

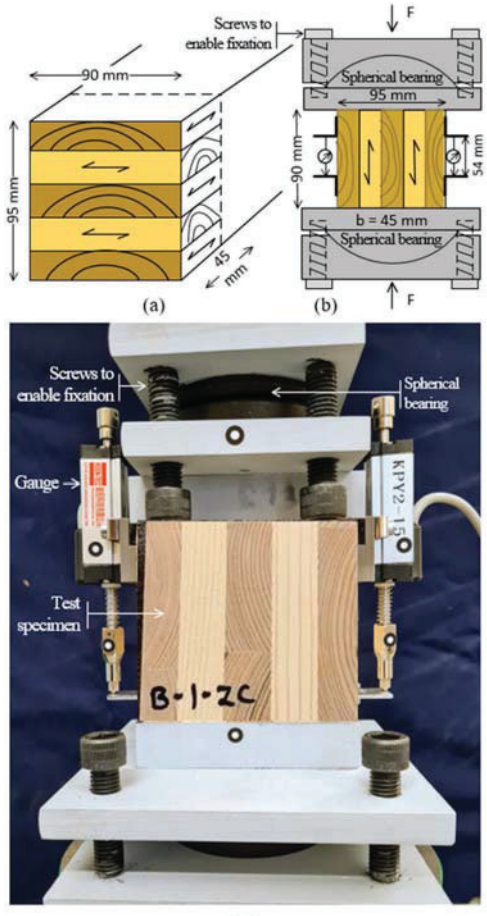

Figure 3: *Test specimen and setup used for testing the stiffness and strength.*

https://doi.org/10.52202/069179-0019

so that a spherical bearing was placed between two steel plates on top of the specimen and below the specimen respectively. Once a pre-load, being 0.2 kN, was applied any further rotation was prevented by means of four screws between the two steel plates fixing the configuration in desired position. The load was thereafter applied under displacement control at a constant displacement of 3 mm/min until a total of at least 2.5 mm. The vertical relative displacement was measured by means of two gauges placed centrically with respect to the height, one on each side of the specimen, measuring the variation in length between the two attachment points on each side being originally 54 mm apart. The data collected was used for calculating the stiffness and the strength of the material tested.

According to the EN 408 [2] the stiffness of the material is to be calculated as

$$E_{c.90} = \frac{(F_{40} - F_{10})h_0}{(w_{40} - w_{10})bl} \quad (1)$$

where F_{10} and F_{40} are the loads at 10 and 40 % of the compressive strength $F_{c.90.max}$ respectively, h_0 is thevertical distance between the measuring points w_{10} and w_{40} the deformation corresponding to the 10 and 40 % load levels and finally b and l the cross-section dimensions of the specimen. The strength of the test specimens was calculated as

$$f_{c.90} = \frac{F_{c.90.max}}{bl} \quad (2)$$

with obvious similar notations. A selection of results from the performed test series are presented in Table 1. Within parenthesis are the variation expressed as a percentage of the average. Since the moisture content was different in the specimens the result presented is compensated in line with the standard [2] to match M.C. = 12 %.

Table 1: *Table showing average values for performed material tests.*

	Structural timber, C24	Two layers par.	Three layers par.
n	15	50	50
Dens. [kg/m^3,%]	465 (6.8)	481 (2.9)	472 (4.0)
M.C. [%,%]	10.73 (2.9)	9.41 (2.4)	9.03 (3.3)
$E_{c.90}$ [MPa,%]	357 (14.7)	5552 (33.8)	7094 (55.7)
$f_{c.90}$ [MPa,%]	3.48 (9.2)	20.16 (8.2)	29.24 (12.1)
$f_{c.90,.05}$ [MPa,%]	- (-)	17.16 (-)	24.37 (-)

Table 2: *Stiffness values used for the simulation of orthotropic material.*

E_l = 12 GPa	E_r = 1.1 GPa	E_t = 800 MPa
G_{lr} = 750 MPa	G_{lt} = 750 MPa	G_{rt} = 50 MPa
ν_{lr} = 0.05	ν_{lr} = 0.05	ν_{lr} = 0.4

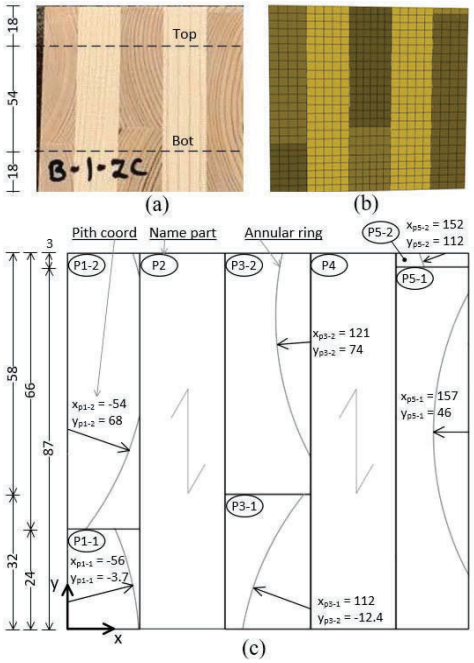

Figure 4: *Pith location for the boards in a selected specimen analysed by use of FEM.*

This way of evaluating the stiffness and the strength for material loaded perpendicular to the grain has been used successfully under long time, but as it turns out it is quite challenging to use for analysis of the CLT-boards due to their variable stiffness in various parts of the material. This will be addressed and exemplified by use of three selected specimens, one of each type tested, in the following. Such analysis is made possible due to the use of a Digital Image Correlation (DIC) system utilized for some of the specimens tested as a complement to the gauges previously described.

One of the tested specimens, of the sort with two layers with fibres in parallel to the loading direction, were analysed by means of the finite element method. The elastic analysis was performed so that the orthotropic material used followed the cylindrical coordinate system defined by the pith of each of the annular rings (assumed circular) in the visible cross sections of the boards, see Figure 4 (a) and (c). The mesh, with second order elements with reduced integration, used to analyse the

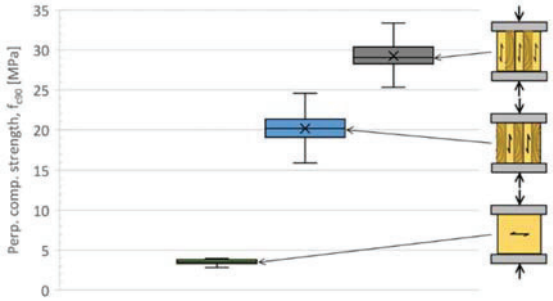

Figure 5: *Perpendicular compression strength f_{c90} of 5-ply CLT-boards compared with standard C24-timber.*

https://doi.org/10.52202/069179-0019

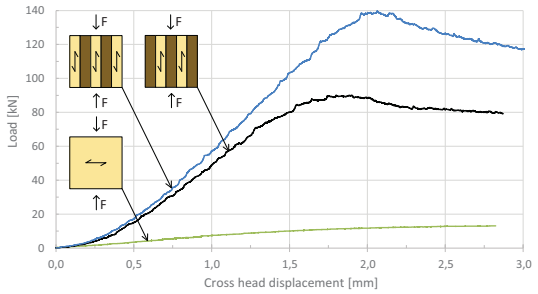

Figure 6: *Load displacement curves for three typical test specimens, one of each type tested, i.e. three parallel layers, two parallel layers and structural timber.*

loading of the specimen is illustrated in Figure 4 (b), each of the parts defined coded with a specific nuance of the brownish colour.

The tests of the perpendicular compression strength showed that a CLT-board had a capacity of 5-8 times the capacity of a standard C24 timber, depending on the proportion of transverse cross layers, see Figure 5. For the case with three layers in parallel with the load direction, corresponding to 57.4 % of the cross-section area, the average of the 50 specimens was calculated to $f_{c90.3par}$ = 29 MPa, see Figure 5. For the other case with two layers in parallel with the stud length direction, corresponding to 42.6 % of the cross-section area, the average strength was calculated to $f_{c90.2par}$ = 20 MPa. Finally, for the tested specimens of structural timber, quality C24, the strength was calculated to $f_{c90.C24}$ = 3.5 MPa on average. The results indicate the considerable potential for making use of the products in loading situations where timber is loaded perpendicular to the length direction of the board, e.g. in rails in prefabricated planar of module building elements.

Yet another property worth pointing out is the post peak behaviour. The load displacement curves for one representative test specimen of each type is shown in Figure 6. For the two CLT-boards the post peak load is falling, but there is no sudden considerable loss in load bearing capacity representing a fatal collapse. Rather, a plateau is reached and the material exhibit plastic behaviour at a load corresponding to the peak load reduced by 10-15 %.

Finally, the curves in the figure indicates a considerably higher stiffness in the CLT-boards compared to the structural timber. At this stage however it should be noted that the horizontal scale in the graph represents the cross head movement rather than the individual or average values of the two gauges installed on each side of the specimen. This means that any boundary effect along the top or bottom loading surfaces

Table 3: *Stiffness's and strength values for three specimens, one of each type tested.*

	Structural timber, C24	Two layers par.	Three layers par.
$E_{c.90}$	160 MPa	1.49 GPa	1.86 GPa
$f_{c.90}$	3.11 MPa	21.1 MPa	32.7 MPa

respectively will be included in the curves. Accepting this the stiffnesses equated by use of (1) can be calculated to values presented in Table 3.

The explanation to why the cross head displacement is used rather than values from the gauges is revealed by the results from the DIC. In Figure 7 (a) the test specimen with two layers having their longitudinal direction in parallel to the loading direction (and with the partitioning and annular rings according to Figure 4) is shown at peak load ($F_{c.90.max}$ = 89.6 kN) and with an overlay of strains in vertical direction at that given load level. It is evident from the strain concentrations at some specific localizations that local properties such as variations in stiffness, inclined fibres or a glue line between two layers of boards, will affect the properties of the specimen. To further investigate this the vertical displacement is plotted at the peak load along two lines, referred to as "top" and "bot" in Figure 7 (a). The result is presented in subfigure (c) and the relative distances between the two ("top" and "bot") lines is in turn shown in subfigure (d).

Not only are these results shown for the specimen described, but also for two other specimens, one from structural timber and one with three layers oriented with their fibres parallel to the loading directions. These results are shown in the two same graphs. Finally, subfigure (e) and (f) show the same thing but at 30 % load level compared to the peak load. The relative difference in vertical displacement between the "top" and the "bot" lines clearly indicates the challenges associated with the measuring technic often utilized to perform measurements used to calculate the stiffness $E_{c.90}$. The subfigures (d) and (f) show that in particular for the CLT boards, the relative length between the two lines is varying considerably over the section. This applies for peak load (c) and (d) as well as within the typical range used to calculate the stiffness, e.g. 30 % of the peak load, see subfigures (e) and (f). Based on this it is recommended simply to use the cross head displacement for the calculation of the stiffness values in case of CLT-boards. This will give conservative stiffness values in general.

At last Figure 7(b) shows results from the FE-simulation performed for the selected and previously discussed specimen with two layers with their fibres in parallel to the loading direction. Displacements are magnified by a factor 5 and maximum stresses $\sigma_{yy} \approx 58$ MPa are obtained in the two layers oriented with their fibres in the y direction.

4. CLT-BOARDS AS INTEGRATED GLULAM LAMINATIONS

When designing glulam beams with long spans there are occasionally critical design issues related to stress levels perpendicular to the fibers involved. According to the Eurocode [3] the design compressive stress in the contact area perpendicular to the grain $\sigma_{c,90,d}$ for a single supported or continuous beam should be less than the design compressive strength perpendicular to the grain, $f_{c,90,d}$, multiplied by a correction factor $k_{c,90}$ so that

https://doi.org/10.52202/069179-0019

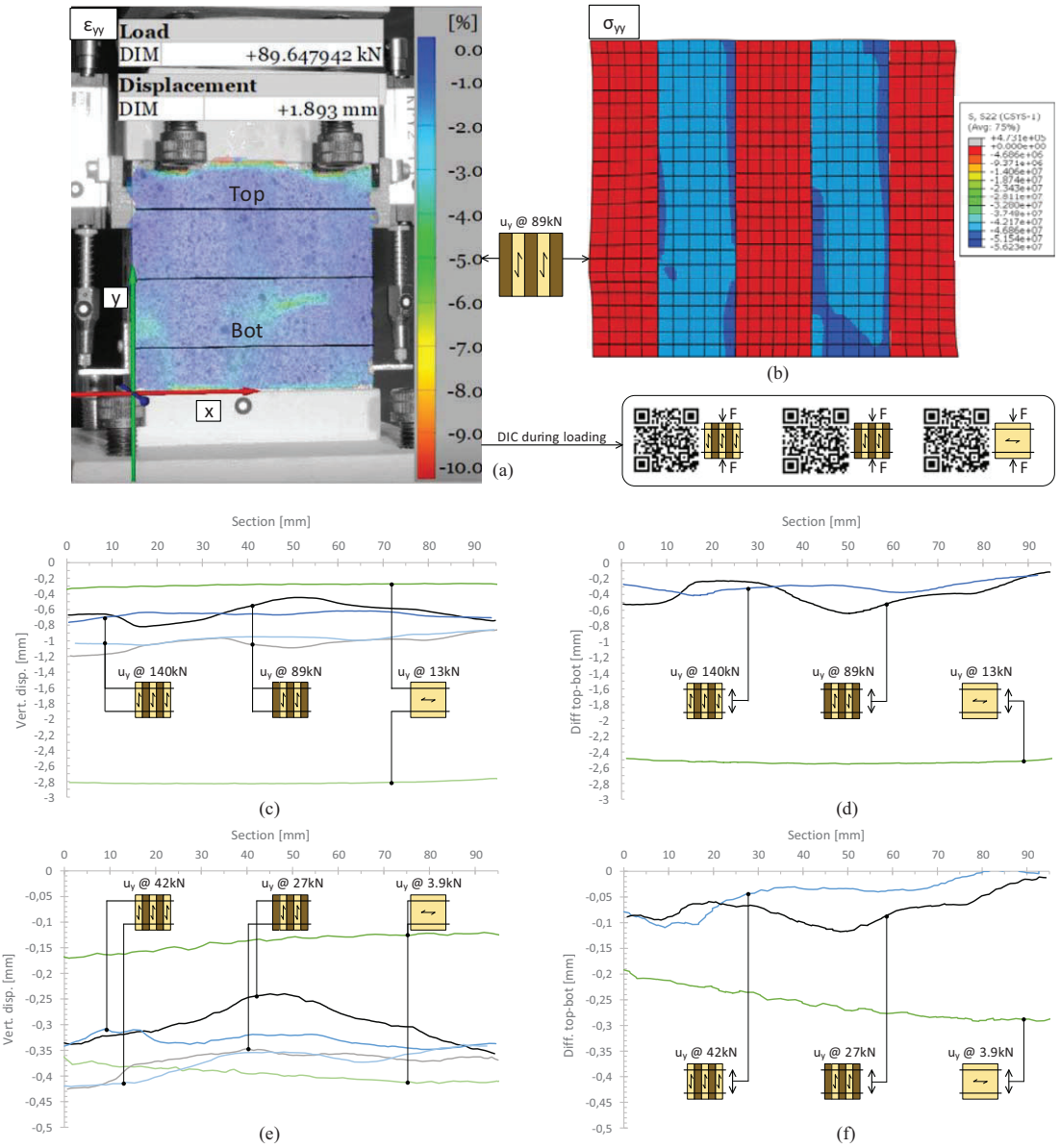

Figure 7: *Results from a) DIC during loading of specimen with two layers with longitudinal direction in parallel to the loading direction and b) results from stress component σ_{yy} from FEM-simulations of the same specimen and vertical displacement of reference lines at c) and d) peak load and e) and f) at 30 % of peak load.*

$$\frac{F_{c,90,d}}{A} = \sigma_{c,90,d} \leq k_{c,90} \cdot f_{c,90,d} \qquad (3)$$

For a beam with a depth $h > 2{,}5\ b$ resting on a support closer than $h/3$ to the beam end or on internal supports respectively the factor k_{90} is obtained as

$$k_{c,90} = (2.38 - \frac{l}{250})(1 + \frac{h}{12l}) \qquad (4)$$

$$k_{c,90} = (2.38 - \frac{l}{250})(1 + \frac{h}{6l}) \qquad (5)$$

where l is the contact length between column and beam. For a reference continuous beam 86 · 315 mm in cross-section being supported internally by a column with full beam width and l = 90 mm the design load can be calculated to $F_{c,90,d}$ = 47 kN (γ_M = 1.25, k_{mod} = 0.8).

The phenomenon with high stresses perpendicular to the fibers in the vicinity of supports has been the subject for several research studies [4, 5] and various suggestions have been made how to address the issue. These suggestions include to increase the contact length l (and thus the contact area) e.g. by placing a stiff and strong steel plate between the beam and the column, see Figure 8(b), to fasten long self-tapping screws into the beam so

https://doi.org/10.52202/069179-0019

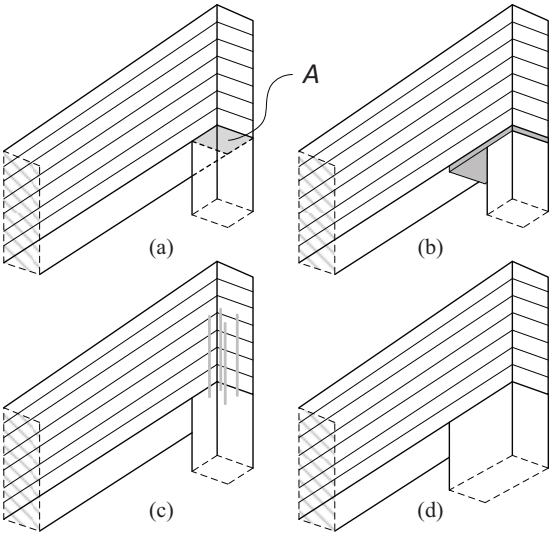

Figure 8: *a) Area loaded perpendicular to grain b) example of steel plate in the contact area between column and beam c) screws for distribution of the load and d) increased column area.*

that the forces are distributed into the beam [6], Figure 8(c), or to simply by increased dimensions of the column, see Figure 8(d).

In the current study another method is suggested to increase the stiffness and strength for a glulam beam loaded perpendicular to the grain in the support area. 1, 2 or 3 of the lamellas in the glulam beam located closest to the column are substituted by CLT-boards from a five layer CLT-panel. These are of type 1, see Figure 1, so that two of their layers are oriented with their longitudinal fiber direction in parallel to the length direction of the column. The CLT-boards were glued to the GLT beam by use of a polyurethane glue and cured for 4 hours under a constant pressure corresponding to 0.5 MPa. An example of an end support and an internal support for a glulam beam when 1 lamella is exchanged locally to a CLT-board is illustrated in Figure 9. Note that the CLT-board is finger jointed to the conventional lamella and that it might also include a finger joint itself.

Modified glulam beams with the dimensions according to Figure 1d were loaded under displacement control to a 15 mm piston displacement. In addition to the beams enhanced by 1, 2 or 3 CLT-lamellas, a reference glulam beam (GLT) without CLT-lamellas was included in the test series as well as a GLT-beam with a 12 mm thick steel plate being 86 · 200 mm in dimensions placed centrally in between the column and the GLT-beam. For each of the five types of setups, A-E, five specimens were tested. An illustration of the setup for the experimental test is shown in Figure 10, see also [7].

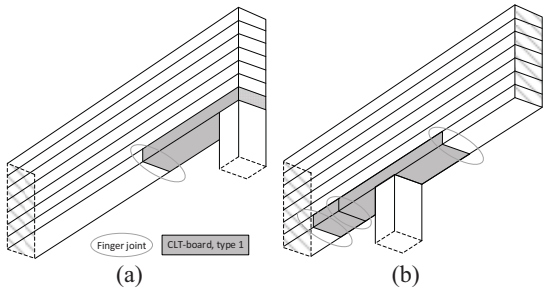

Figure 9: *Illustration of the concept for obtaining increased stiffness and load bearing capacity in a GLT beam for a) end support and b) internal support.*

The average load-displacement curves for the five specimens per setup, shown in Figure 11, indicates a surprisingly high increase in stiffness and strength when 1, 2 or 3 CLT laminations are built into the glulam compared to the reference conventional GLT-beam. It can be noted that the maximum applied load was slightly higher for the case with a distributing steel plate compared to that with a setup including one lamella made out of a CLT-board. However that load-level was obtain at substantial displacements, e.g. larger than 8 mm.

In Table 4 the stiffness, k, and the maximum applied force, F_{max}, is showed as an average of the five tested specimens in each setup. The stiffness is obtained as

$$k = \frac{0.4F_{max} - 0.2F_{max}}{u_{0.4Fmax} - u_{0.2Fmax}} \qquad (6)$$

were F_{max} is the maximum applied load and u_x is the displacement at 40 and 20 % of that load respectively. In addition to the stiffness and maximum load the table shows each of the two normalized against the reference GLT beam E, i.e. the quota k_x/k_E and $F_{max.X}/F_{max.E}$. It is striking that by use of three CLT-lamellas the stiffness can be increased by 98 % and the maximum applied load may be 132 % higher compared to the reference beam E.

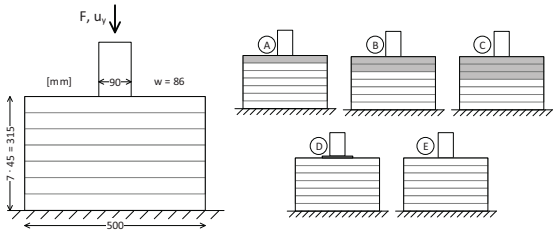

Figure 10: *Geometry and load cases for each setup and illustration of the five different setups, A-C with included CLT-boards, D with a steel plate and E with a pure GLT-beam as a reference.*

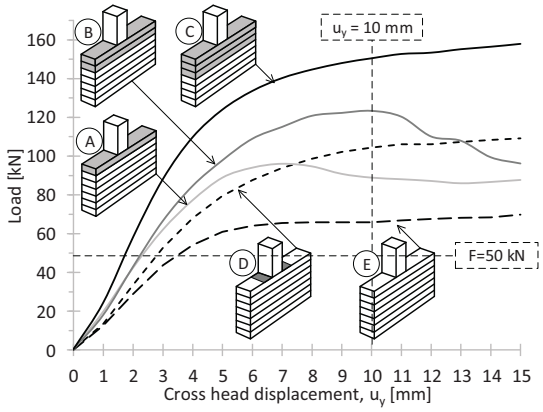

Figure 11: *Average load-displacement curves from experimental tests of 1, 2 and 3 CLT laminations in the beam and GLT beam with and without steel plate.*

Finally the piston displacement u_y at the design load $F_{c.90.d}$= 47 kN is given in the table. The displacement of the reference beam E is almost double that of the beam with three CLT-boards at that load.

For at least one of the specimens in each setup digital image correlation (DIC) was used for taking stereoscopic pictures during the loading event. In Figure 12 strains in vertical direction (ε_y) are shown at a load F = 50 kN and at a piston displacement u_y = 10 mm respectively. The black horizontal lines in the photos of the GLT indicates the centre of each lamella. Note that the scale for the strains are the same in all subfigures. Red colour indicates larger strains and blue is representing small strains and the total span for the scale is $0 \leq \varepsilon_y \leq 0.01$. For each setup a 20 sec film sequence showing the whole load event can be found if the qr-code at the right is followed and there a scale with the strains is included. One result worth noting is the relatively small strains in the CLT-boards. From the photos in the figure this is particularly clear for setup B and C. This is explained by the high stiffness in the CLT-boards achieved by the lamellas oriented in parallel to the load direction.

Table 4: *Stiffness and maximum applied force for the tested setups.*

Setup	k [kN/mm]	F_{max} [kN]	k/k_E	$F_{max}/F_{max.E}$	u_y@ $F_{c.90.d}$ [mm]
A	23.1	96.8	1.35	1.39	2.22
B	24.8	122.6	1.44	1.77	2.20
C	34.0	161.0	1.98	2.32	1.67
D	20.5	109.2	1.19	1.57	2.69
E	17.2	69.4	1.00	1.00	3.27

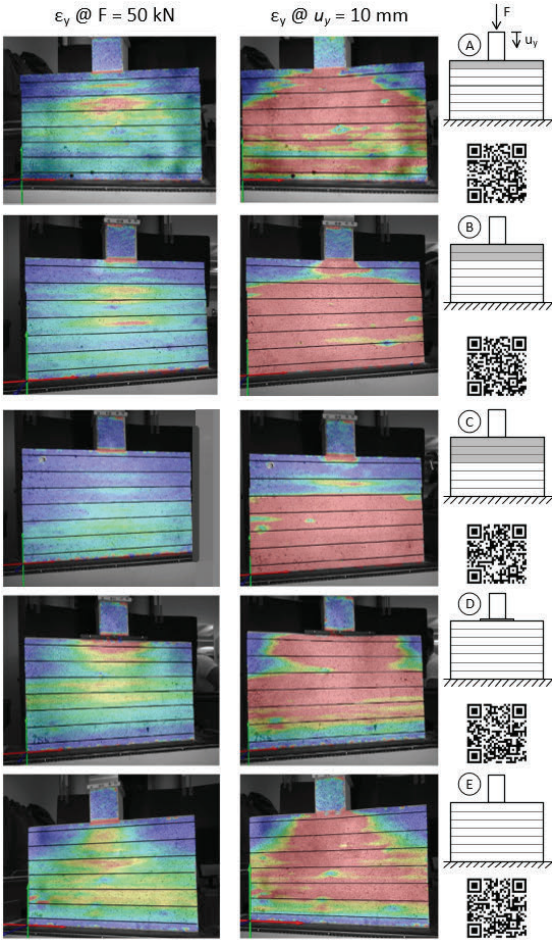

Figure 12: *Photos from DIC with strains in vertical direction (ε_y) for the load F = 50 kN and at a piston displacement u_y = 10 mm.*

5. CONCLUSIONS

In this paper, three concepts of re-use of cut-offs from CLT are presented.

a) The re-use of cut-offs as REX laminations in CLT production is a smart concept that minimize waste in an economical way.
b) By using finger-jointed CLT-boards as horizontal rails in timber frame buildings, the problems with high local compression perpendicular to the grains and large vertical deformations in multi-storey houses are minimized.
c) The capacity of glulam beams to carry concentrated loads is greatly enhanced by locally integrating CLT-boards as laminations.

ACKNOWLEDGEMENT

The support from several wood construction companies in Sweden, Stora Enso, the innovation program Bioinnovation/Vinnova, Paper Province and the Knowledge Foundation is gratefully acknowledged.

https://doi.org/10.52202/069179-0019

REFERENCES

[1] ETA-14/0349 (2020): European Technical Approval for Cross Laminated Timber. Stora Enso Wood Products.

[2] EN 408:2010+A1:2012 - Determination of some physical and mechanical properties.

[3] CEN, EN 1995-1-1. Eurocode 5: Design of timber structures - Part 1-1: General - Common rules and rules for buildings, Comité Européen de Normalisation, Brussels, Belgium, 2005.

[4] Leijten, A. J. M., Larsen, H. J., & Van der Put, T. A. C. M. (2010). Structural design for compression strength perpendicular to the grain of timber beams. Construction and Building Materials, 24(3), 252-257.

[5] Hoffmeyer, P., Damkilde, L., & Pedersen, T. N. (2000). Structural timber and glulam in compression perpendicular to grain. Holz als Roh-und Werkstoff, 58(1), 73-80.

[6] Bejtka, I., & Blaß, H. J. (2006). Self-tapping screws as reinforcements in beam supports. *CIB-W18, Florence*.

[7] Stenberg, F., & Hagberg, C. (2021). Korslimmat trä som förstärkningsåtgärd i limträbalk vid zoner där pelare möter balk (In Swedish). Retrieved from http://urn.kb.se/resolve?urn=urn:nbn:se:kau:diva-85613

World Conference on Timber Engineering Oslo 2023

EXPERIMENTAL STUDY ON CHARACTERISTIC VALUES OF PARTIAL COMPRESSION PERPENDICULAR TO THE GRAIN OF HARDWOOD WITH EDGE DISTANCE ORTHOGONAL TO THE LONGITUDINAL DIRECTION

Hiroto Suesada[1], Kohta Miyamoto[2]

ABSTRACT: The use of hardwoods for wooden joints is advantageous because of their higher density and superior structural performance compared to softwoods, which are generally used as construction materials in buildings. However, the effects of the dimensions of the hardwood specimens and wood species on the partial compression performance perpendicular to the grain are unclear. In this study, we conducted partial compression tests perpendicular to the grain of hardwoods clarify the effect of edge distance that is orthogonal to the longitudinal direction and wood species on the characteristic values. The tendencies of the relationships between the partial compression performance perpendicular to the grain and the edge distance perpendicular to the grain of hardwoods were found to be similar to those of softwoods. The effect of wood species on characteristic values needs to be examined in more detail.

KEYWORDS: Hardwood, Partial compression perpendicular to the grain, Edge distance in two directions

1 INTRODUCTION

The compression performance of wood perpendicular to the grain was considerably lower than that of wood parallel to the grain. Partial compressive deformation perpendicular to the grain is one of the primary causes of deformation of wooden joints.

In Japan, most planted forests are in the mature and utilisation stages [1]. In addition, the environmental advantages of wooden buildings have led to an increase in the number of mid-rise and large-scale non-residential wooden buildings. These buildings require higher structural performance than low-rise buildings.

Some hardwood species have a higher density and superior compression performance perpendicular to the grain compared with softwoods, which are generally used as construction materials in buildings. Therefore, it is advantageous to utilise such hardwoods in wooden joints. The estimation of the performance of hardwoods is essential for their utilisation as structural materials but not yet for the partial compression performance of hardwoods perpendicular to the grain. Furthermore, the effects of the dimensions of the hardwood specimens and wood species on the partial compression performance perpendicular to the grain is unclear.

Previously, the relationships between the partial compression performance perpendicular to the grain and the edge distance in the longitudinal direction were determined [2]. In this study, partial compression tests perpendicular to the grain were conducted to clarify the effect of the edge distance orthogonal to the longitudinal direction and wood species on the characteristic values.

2 MATERIALS AND METHODS

2.1 TEST SPECIMENS

Table 1 presents the specifications of the test specimens. Eight hardwood species were used as test specimens. Itayakaede (IT, *Acer mono Maxim.*), Udaikamba (UD, *Betula maximowicziana*), and Buna (BN, *Fagus crenata*) are diffuse-porous woods. Shirakashi (SR, *Quercus myrsinifolia*) is radial-porous wood. Kuri (KR, *Castanea crenata*), Keyaki (KY, *Zelkova serrata*), Yachidamo (YC, *Fraxinus mandshurica*), and Mizunara (MZ, *Quercus crispula Blume*) are ring-porous woods.

The height of each sample was fixed at 40 mm. Specimens with three different widths (w) (40, 60 and 80 mm) and two different lengths (l) (40 and 120 mm) were

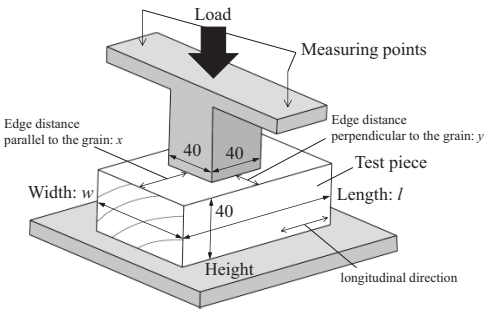

***Figure 1**: Schematic of partial compression test perpendicular to the grain (dimensions in mm)*

[1] Hiroto Suesada, Shinshu univ., Japan, suesada@shinshu-u.ac.jp
[2] Kohta Miyamoto, Forestry and Forest Products Research Institute, Japan, mkohta@ffpri.affrc.go.jp

https://doi.org/10.52202/069179-0020

***Table 1**: Specification of the test specimens*

wood species	length (mm)	width (mm)	n [a)]	ρ [b, c)] (kg/m^3)	MC [c, d)] (%)
Itayakaede (IT, *Acer mono Maxim.*)	40 / 120	40 / 60 / 80	6	734 ± 32.8	10.9 ± 0.89
Shirakashi (SR, *Quercus myrsinifolia*)	40 / 120	40 / 60 / 80	3	890 ± 59.5	12.6 ± 0.20
Udaikamba (UD, *Betula maximowicziana*)	40 / 120	40 / 60 / 80	4	707 ± 71.9	12.1 ± 0.72
Kuri (KR, *Castanea crenata*)	40 / 120	40 / 60 / 80	6	575 ± 73.7	13.9 ± 0.88
Keyaki (KY, *Zelkova serrata*)	40 / 120	40 / 60 / 80	6	747 ± 67.7	12.2 ± 1.93
Yachidamo (YC, *Fraxinus mandshurica*)	40 / 120	40 / 60 / 80	6	571 ± 80.4	13.3 ± 0.48
Mizunara (MZ, *Quercus crispula Blume*)	40 / 120	40 / 60 / 80	6	732 ± 59.7	12.4 ± 0.91
Buna (BN, *Fagus crenata*)	40 / 120	40 / 60 / 80	6	687 ± 17.8	12.9 ± 0.31

Notes: a) Number of specimens, b) Density, c) The values mean Average ± Standard variation, d) Moisture content

made. Thus, each wood specimen had 6 dimensional specifications, which are indicated by a four-digit number. For example, 4040 represents a width of 40 mm and a length of 40 mm, whereas 6120 represents a width of 60 mm and a length of 120 mm. For each species, six specimens of different widths and lengths were obtained from a single piece of wood in the longitudinal direction.

2.2 COMPRESSION TEST PERPENDICULAR TO THE GRAIN

Figure 1 shows a schematic of the partial compression test perpendicular to the grain. The tests were conducted according to Japanese Industrial Standards (JIS) Z 2101 [3]. Figure 1 shows that the centre of the specimen was loaded with a metal bearing plate with a length and width of 40 mm. Therefore, the edge distances parallel (x) and perpendicular (y) to the grain were represented by $(l-40)/2$ and $(w-40)/2$, respectively. Accordingly, x is 0 mm (4040, 6040, 8040) and 40 mm (4120, 6120, 8120), and y is 0 mm (4040, 4120), 10 mm (6040, 6120) and 20 mm (8040, 8120). When both x and y were 0 mm (4040), the tests were full-area compression tests perpendicular to the grain tests.

A tensile and compression testing machine (MAEKAWA MFG. CO., LTD. A-300-B4) was used for loading.

Vertical displacements of the bearing metal plate were measured at two points using displacement transducers (Tokyo Measuring Instruments Laboratory Co., Ltd., CDP-25), and the average value was considered as the test displacement. The ratio of the displacement to height was considered as the test strain. The load was measured using a testing machine. The load divided by the loading area (1,600 mm^2) was considered as the test stress.

The method of calculating the characteristic values was the same as that used in a previous study [2]. The elastic stiffness (E_e), plastic stiffness (E_p), yield stress (σ_y), and yield strain (ε_y) were calculated from the stress–strain curves. E_e was calculated following Inayama's study [4] and E_p, σ_y and ε_y were calculated following Fujita's study [5].

3 RESULTS AND DISCUSSION

3.1 DIFFERENCE IN STRESS-STRAIN CURVE DUE TO POROUS STRUCTURES

Figure 2 shows examples of stress-strain curves of the compression test perpendicular to the grain for diffuse-porous wood (Itayakaede) and ring-porous wood (Keyaki), each taken from the same piece, for each dimensional specification. In diffuse-porous wood, the stiffness gradually decreases after the yield point. The stiffness decreased more clearly in ring-porous wood than in diffuse-porous wood at the yield point. In the specification without the edge distance (4040), the load increased and decreased repeatedly after the yield point. This behaviour may be due to the sequential failure of vessels in the pore zone of ring-porous wood. The load increase/decrease behaviours were milder for the specifications with edge distance than for those without edge distance. Such behaviour was less apparent for the specifications with an edge distance parallel to the grain (4120, 6120, and 8120). The edge distance is considered to constrain the fracture of the vessels in the pore zone. For the edge distance perpendicular to the grain, shear failure occurred at the edge of the loading area, which may have weakened this effect compared with the edge distance parallel to the grain. The other diffuse-porous and radial-porous wood specimens showed similar trends to the example of diffuse-porous wood, and the other ring-porous wood specimens showed trends similar to those of ring-porous wood.

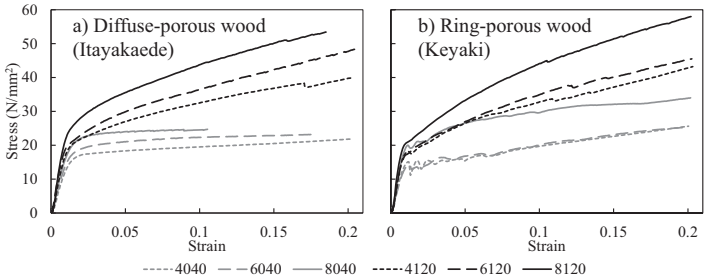

***Figure 2**: Example of stress-strain curves of compression test perpendicular to the grain for each porous structure.*

https://doi.org/10.52202/069179-0020

***Table 2**: Summary of results of partial compression test perpendicular to the grain*

	size	E_e [a, b] (kN/mm²)	E_p [b, c] (kN/mm²)	σ_y [b, d] (N/mm²)	ε_y [b, e] (%)		size	E_e [a, b] (kN/mm²)	E_p [b, c] (kN/mm²)	σ_y [b, d] (N/mm²)	ε_y [b, e] (%)
IT	4040	1.52 (0.146)	0.088 (0.016)	14.3 (1.79)	1.07 (0.071)	KY	4040	1.44 (0.267)	0.073 (0.034)	12.0 (1.25)	0.98 (0.135)
	6040	1.82 (0.277)	0.137 (0.028)	17.3 (2.93)	1.04 (0.069)		6040	1.67 (0.192)	0.116 (0.052)	14.5 (2.15)	0.98 (0.092)
	8040	1.88 (0.214)	0.167 (0.019)	17.3 (1.29)	1.01 (0.081)		8040	1.85 (0.387)	0.153 (0.045)	15.7 (2.96)	1.00 (0.146)
	4120	2.27 (0.209)	0.215 (0.025)	18.9 (2.18)	0.92 (0.065)		4120	1.89 (0.278)	0.200 (0.040)	17.0 (2.09)	1.04 (0.188)
	6120	2.64 (0.284)	0.267 (0.034)	20.7 (2.54)	0.85 (0.039)		6120	2.39 (0.342)	0.263 (0.053)	17.3 (2.12)	0.83 (0.036)
	8120	2.69 (0.273)	0.288 (0.041)	21.2 (1.89)	0.91 (0.099)		8120	2.50 (0.466)	0.294 (0.062)	18.4 (3.92)	0.87 (0.077)
SR	4040	1.29 (0.194)	0.138 (0.006)	13.3 (1.57)	1.12 (0.032)	YC	4040	0.95 (0.172)	0.004 (0.010)	5.86 (0.84)	0.71 (0.035)
	6040	1.75 (0.231)	0.214 (0.006)	16.9 (1.70)	1.12 (0.107)		6040	1.04 (0.236)	0.025 (0.017)	6.66 (0.93)	0.72 (0.062)
	8040	1.76 (0.031)	0.252 (0.024)	17.1 (0.36)	1.11 (0.027)		8040	1.08 (0.208)	0.032 (0.015)	6.73 (0.51)	0.74 (0.078)
	4120	1.94 (0.284)	0.283 (0.038)	18.9 (1.95)	1.06 (0.069)		4120	1.32 (0.239)	0.068 (0.032)	7.30 (0.82)	0.67 (0.041)
	6120	2.61 (0.212)	0.386 (0.045)	21.3 (2.20)	0.92 (0.125)		6120	1.53 (0.243)	0.093 (0.040)	7.38 (0.76)	0.58 (0.037)
	8120	2.41 (0.012)	0.403 (0.031)	22.7 (2.17)	1.05 (0.103)		8120	1.54 (0.212)	0.101 (0.030)	7.85 (1.01)	0.63 (0.052)
UD	4040	1.00 (0.284)	0.057 (0.011)	10.4 (1.98)	1.15 (0.098)	MZ	4040	1.02 (0.294)	0.040 (0.013)	8.67 (1.93)	0.95 (0.084)
	6040	1.40 (0.079)	0.078 (0.003)	13.0 (0.74)	1.01 (0.078)		6040	1.29 (0.418)	0.064 (0.012)	10.6 (3.27)	0.92 (0.075)
	8040	1.25 (0.051)	0.120 (0.022)	12.6 (0.27)	1.11 (0.065)		8040	1.26 (0.373)	0.096 (0.017)	11.4 (3.59)	0.99 (0.057)
	4120	1.52 (0.376)	0.164 (0.017)	13.7 (2.32)	1.04 (0.047)		4120	1.52 (0.357)	0.152 (0.050)	11.4 (2.81)	0.85 (0.052)
	6120	2.11 (0.081)	0.198 (0.024)	15.9 (0.72)	0.84 (0.041)		6120	1.89 (0.537)	0.193 (0.051)	12.4 (3.85)	0.75 (0.063)
	8120	2.02 (0.163)	0.229 (0.024)	16.3 (0.94)	0.90 (0.050)		8120	1.92 (0.463)	0.228 (0.060)	13.4 (3.87)	0.81 (0.047)
KR	4040	0.88 (0.480)	0.024 (0.011)	5.15 (1.62)	0.72 (0.211)	BN	4040	0.79 (0.069)	0.072 (0.013)	6.77 (0.52)	0.95 (0.079)
	6040	1.04 (0.517)	0.036 (0.025)	6.26 (2.20)	0.76 (0.197)		6040	0.97 (0.138)	0.097 (0.012)	8.43 (0.26)	0.99 (0.181)
	8040	1.04 (0.349)	0.040 (0.028)	6.46 (1.55)	0.77 (0.106)		8040	1.04 (0.129)	0.124 (0.014)	8.70 (0.61)	0.98 (0.071)
	4120	1.24 (0.411)	0.085 (0.026)	6.91 (1.47)	0.65 (0.109)		4120	1.20 (0.124)	0.143 (0.007)	9.92 (0.76)	0.94 (0.128)
	6120	1.49 (0.522)	0.113 (0.041)	7.15 (1.90)	0.57 (0.081)		6120	1.43 (0.240)	0.190 (0.012)	10.6 (0.46)	0.86 (0.144)
	8120	1.47 (0.479)	0.127 (0.030)	7.63 (1.72)	0.66 (0.109)		8120	1.43 (0.235)	0.192 (0.013)	10.9 (1.00)	0.90 (0.072)

Notes: a) Elastic stiffness, b) The values mean Average (Standard deviation), c) Plastic stiffness, d) Yield stress, e) Yield strain, size shows dimensional specifications

3.2 RESULTS OF COMPRESSION TESTS

Table 2 shows the mean values and standard deviations of E_e, E_p, σ_y and ε_y. The mean values of E_e, E_p and σ_y were higher for partial compression than for full-area compression for all the species. For the edge distance perpendicular to the grain, the values tended to be higher with increasing edge distance; however, little differences were noted between 6120 and 8120. The mean values of ε_y were higher for specimens without an edge distance parallel to the grain than for those with an edge distance parallel to the grain.

The coefficients of variation for E_e and E_p were 0.49–54.8% and 2.77–245% respectively. E_e for Kuri and Mizunara were particularly high. E_p for Kuri and Yachidamo were particularly high. Ring-porous wood tended to show a higher variation than diffuse- and radial-porous wood. Ring-porous wood is considered more affected by the annual ring angle than diffuse- and radial-porous wood because of the fracture of vessels in the pore zone. There is also the possibility of the influence of an increase/decrease in the load on the stress-strain curve after the yield point.

3.3 RELATIONSHIP BETWEEN THE CHARACTERISTIC VALUES AND DENSITY

Figure 3 shows the relationship between E_e and the density of each specimen. Figure 4 shows the relationship between σ_y and density for each dimensional specification. Figures 3 and 4 represent the regression line calculated for

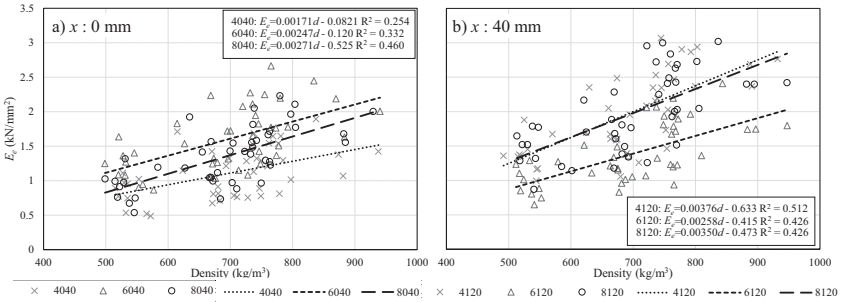

***Figure 3**: Relationship between E_e and density (d) of each specimen.*

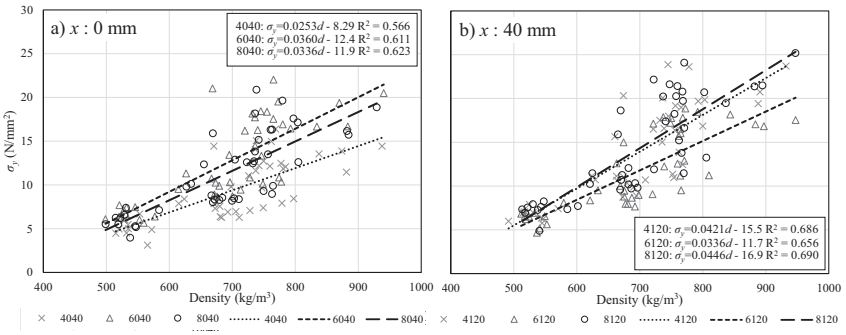

***Figure 4**: Relationship between σ_y and density (d) of each specimen.*

https://doi.org/10.52202/069179-0020

each dimensional specification for the relationships between E_e and density and σ_y and density.

For E_e and σ_y, a significant positive correlation was observed ($p < 0.01$) with density for all dimensional specifications. In both cases, the correlation was stronger in the specifications with edge distance than in those without it. A possible explanation for this is that the effect of factors other than density, such as the annual ring angle, was less affected by the partial compression specifications because the deformation was constrained by the edge distance. For σ_y, the correlation was stronger than that for E_e for all dimensional specifications. The effect of density may have been greater for σ_y than for E_e, while the effects of other factors may have been relatively less.

3.4 EFFECT OF EDGE DISTANCE ON INCREASE RATIOS OF CHARACTERISTIC VALUES

Figure 5 shows the relationship between the increase ratios of E_e and σ_y and the edge distance perpendicular to the grains. The increase ratios of E_e and σ_y are defined as the average of the ratio of the characteristic value of a specimen to that of the full compression specimen without both edge distances being prepared from the same material.

As shown in Figure 5, the increase ratios of E_e and σ_y were higher for the partial compression specimens than for the full compression specimens. Irrespective of the edge distance parallel to the grain (0 mm or 40 mm), the increase ratios of E_e and σ_y tended to increase with increase in the edge distance perpendicular to the grain. In contrast, at an edge distance perpendicular to the grain longer than 10 mm, the increase ratios of E_e and σ_y increased only slightly or remained constant depending on the wood species. It is suggested that the effect of the edge distance parallel to the grain on the improvement in the characteristic values converged. These trends agree with a previous study on softwood reported by Inayama [4].

3.5 DIFFERENCES IN INCREASE RATIONS BY WOOD SPECIESE

As shown in Figure 5, the increase ratios of E_e and σ_y tended to be higher for Shirakashi and Udaikamba and lower for Yachidamo compared to other species. These results suggest that there are differences among the wood species. However, further studies are needed to clarify the effects of the annual ring angles and other factors.

3.6 RELATIONSHIPS BETWEEN CHARACTERISTIC VALUES

Figures 6 and 7 show the relationships between E_e and E_p and σ_y and ε_y, respectively, and indicate that both relationships are significantly positively correlated. However, the relationships between σ_y and ε_y had a smaller correlation coefficient than E_e and E_p and were not strongly correlated. Figure 7 shows that the plots for each tree species fell within certain ranges, and the all ranges appeared to be different from the regression line for all specimens. Therefore, although a positive correlation was observed for all specimens, the relationship may be different for each tree species.

Table 3 summarizes the linear regression equations calculated for each tree species, the dimensional specifications for the relationships between E_e and E_p, σ_y and ε_y, and their coefficients of determination. For the relationship between E_e and E_p, significant positive correlations were found for all tree species and dimensional specifications. Therefore, there is a positive

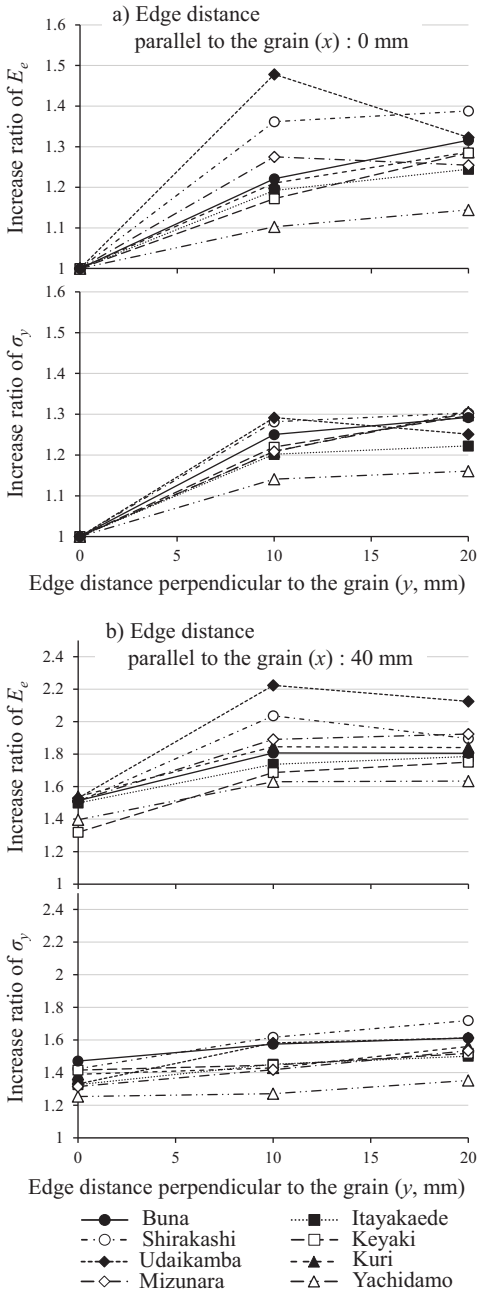

***Figure 5**: Relationships between the increase ratio of E_e and σ_y and edge distance perpendicular to the grain*

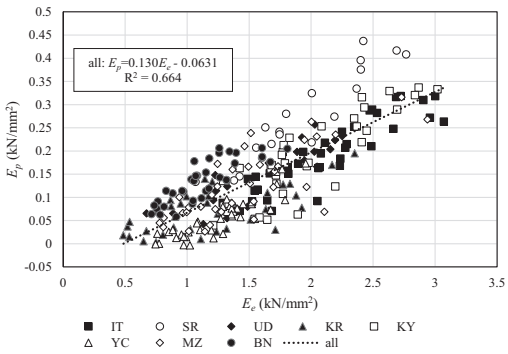

***Figure 6**: Relationship between E_e and E_p.*

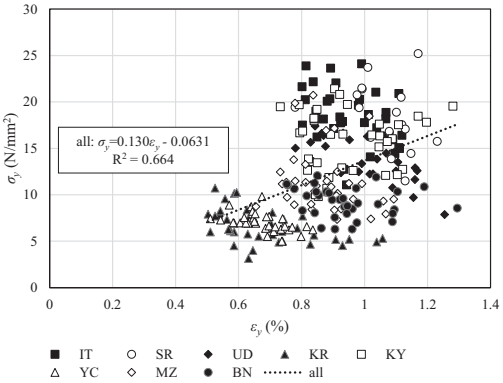

***Figure 7**: Relationship between σ_y and ε_y.*

***Table 3**: Results of correlation analysis for each specification in the relationship between characteristic values.*

	Relationship between E_e and E_p		Relationship between σ_y and ε_y	
	The linear regression equation	R^2	The linear regression equation	R^2
IT	E_p = 0.139E_e - 0.103	0.806**	σ_y = -12.2ε_y + 30.0	0.165*
SR	E_p = 0.193E_e - 0.0981	0.875**	σ_y = -10.7ε_y + 29.7	0.0948**
UD	E_p = 0.123E_e - 0.0493	0.701**	σ_y = -14.7ε_y + 28.5	0.606**
KR	E_p = 0.0658E_e - 0.00741	0.451**	σ_y = -5.84ε_y + 10.6	0.234**
KY	E_p = 0.160E_e - 0.130	0.747**	σ_y = 1.61ε_y + 14.3	0.00464
YC	E_p = 0.125E_e - 0.101	0.791**	σ_y = -6.65ε_y + 11.5	0.253**
MZ	E_p = 0.119E_e - 0.0472	0.604**	σ_y = -5.56ε_y + 16.2	0.0285
BN	E_p = 0.134E_e - 0.0175	0.681**	σ_y = -2.72ε_y + 11.8	0.0437
4040	E_p = 0.0404E_e + 0.0124	0.141*	σ_y = 11.9ε_y - 1.89	0.373**
4120	E_p = 0.110E_e - 0.0202	0.551**	σ_y = 18.9ε_y - 3.99	0.465**
6040	E_p = 0.0812E_e - 0.0206	0.380**	σ_y = 15.8ε_y - 3.31	0.339**
6120	E_p = 0.123E_e - 0.0404	0.646**	σ_y = 26.3ε_y - 6.55	0.465**
8040	E_p = 0.106E_e - 0.0317	0.492**	σ_y = 18.0ε_y - 5.43	0.356**
8120	E_p = 0.128E_e - 0.0314	0.641**	σ_y = 27.3ε_y - 8.34	0.458**

Notes: R^2 shows coefficient of determination, ** significant at $p<0.01$, * significant at $p<0.05$

correlation between elastic stiffness and plastic stiffness in the compression strength of wood perpendicular to the grain, regardless of the wood species and dimensional specifications. For the dimensional specifications, the slope and coefficient of determination of the linear regression equation were the smallest for the full-area compression specification (4040), and each value increased with an increasing edge distance perpendicular to the grain. In addition, they tended to be even larger for specifications with the edge distance parallel to the grain. The slope is because the plastic stiffness is close to zero for the full-area compression specification (4040) and the stiffness increases with increasing the edge distance. The coefficient of determination is due to the constraining effect of the edge distance on the deformation and fracture of the specimens, which reduces the variation between the elastic and plastic stiffnesses. In the relationship between σ_y and ε_y, significant positive correlations were found for each dimensional specification; however, significant negative correlations were found for many wood species. Previous studies on softwoods [4] and hardwoods [2] have shown that for the same species, loading area dimensions and specimen height, relationships between σ_y and ε_y are inversely related. This may also be true for the results of this study, as the relationship is not clear but is close to inversely proportional when the same wood species, loading area dimensions, and specimen height are held constant. However, the relationship between σ_y and ε_y was significantly positively correlated for each dimensional specification. Although the coefficient of determination was smaller than that in the relationship between E_e and E_p, the slope and coefficient of determination in the relationship between σ_y and ε_y were similar to those in the relationship between E_e and E_p. These results suggest that there is a positive correlation between σ_y and ε_y for dimensional specifications regardless of the species.

4 CONCLUSIONS

The aim of this study was to investigate the effect of edge distance orthogonal to the longitudinal direction and wood species on the compression performance of hardwoods perpendicular to the grain.

The results of this study are as follows.

(1) The behaviour of the stress-strain curve after the yield point might differ depending on the porous structure.

(2) With respect to the edge distance parallel to the grain, the variation in the elastic stiffness and yield stress can be

https://doi.org/10.52202/069179-0020

reduced by constraining the deformation and fracture with the edge distance perpendicular to the grain.
(3) The elastic stiffness and yield stress are significantly correlated with density, and specifications with an edge distance perpendicular, parallel, or both to the grain have a stronger correlation than those without it.
(4) The effect of the edge distance perpendicular to the grain on the increase ratio of elastic stiffness and yield stress tends to be similar to that of softwood [4] and may vary between wood species.
(5) The relationships between elastic stiffness and plastic stiffness, yield stress and yield strain tend to be similar to those for softwood.
These results support the conclusions of a previous study in which hardwoods were able to estimate the same degree of denting performance as softwoods [4]. However, some species showed greater variability in their characteristic values, particularly in ring-porous wood. More detailed studies are needed on the effects of different species, especially on the porous structure, and on the effects of the annual ring inclination angle.

ACKNOWLEDGEMENT

This work was supported by JSPS KAKENHI Grant Number JP20K15572

REFERENCES

[1] Forest Agency, Japan, Annual Report on Forest and Forestry in Japan Fiscal Year 2021 (Summary), 2022.
[2] H. Suesada, K. Miyamoto, T. Shibusawa, K. Aoki, M. Inayama. Experimental study on characteristic values of partial compression of hardwood perpendicular to grain. World Conference on Timber Engineering 2021, WPC0313, 2021.
[3] Japanese Industrial Standards Committee: JIS Z 2101 Methods of test for woods: Japanese industrial standard, 2009
[4] M. Inayama: Wooden embedment theory and its application (in Japanese): Dissertation, The University of Tokyo, 1991
[5] K. Fujita, M. Inayama, N. Ando: Embedding performance of four kinds of domestic hard wood used as wooden dowels (in Japanese). Mokuzai Gakkaishi 58(4):181–192, 2012

World Conference on Timber Engineering Oslo 2023

COMPARISON BETWEEN ACTUAL AND EQUIVALENT CRACK RESISTANCE R-CURVES FOR TIMBER AND TIMBER BOND UNDER MODE-II FRACTURE

Shaikh Atikur Rahman[1], Mahmud Ashraf[2] Mahbube Subhani[3]

ABSTRACT: This paper focuses on Mode-II fracture behaviour of solid timber and timber adhesive bond using end notched flexure (ENF) test. Mode-II strain energy release rates are obtained using three different data reduction methods known as compliance calibration (CC), direct beam theory (DBT) and corrected beam theory (CBT) that require actual crack length monitoring. At the same time, the compliance-based beam method (CBBM) is evaluated without the need for actual crack length measurements by considering an equivalent crack length. In both cases, the Mode-II strain energy release rates (G_{II}) obtained for the timber adhesive bond interface was found to be approximately 20% higher compared to timber fracture. The strain energy release rates calculated from actual crack and equivalent crack length values show similar trends in resistance curves. However, initial strain energy release rate (G_{II0}) and critical strain energy rate (G_{IIC}) for Mode-II significantly varies in actual crack methods than the equivalent crack method.

KEYWORDS: End Notched Flexure (ENF), Fracture energy, Glue delamination of timber joint, Crack resistance R-curve

1 INTRODUCTION

Currently, all design guidelines for timber and engineered timber products (ETPs) are based on the maximum elastic stress and stiffness criteria for strength analysis. However, it fails to attain the material's post-elastic plastic behaviour and localised failure owing to defects like cracks or delamination [1]. In the stress/stiffness method, the structural component is considered as a continuous homogenous material, which is not relevant to naturally grown materials such as timber. Those defects are often considered using a strength reduction factor in a conventional stress/stiffness design technique, which is very conservative for real-life structure.

To overcome such limitations, fracture mechanics-based design approach in timber structure could be a rational alternative. Fracture mechanics is often utilised in material testing on samples with well-defined characteristics [2]. It is, however, rarely employed in engineering design with structural elements of arbitrary shape. Fracture characterisation of softwood timber is essential, especially for the design of various timber joints, notches, holes, and connections. Timber failure can cause catastrophe as they lead to highly brittle failure produced by tension and shear acting perpendicular to grain direction of timber [1, 3, 4].

Material fracture characterisation is therefore vital in giving accurate fracture characteristics such as the critical strain energy release rate, $G_{I/IIc}$, which is defined as the material's resistance to crack propagation. Furthermore, using experimental $G_{I/IIc}$, the current design approach for brittle splitting failure prediction of connections loaded perpendicular to the grain (critical failure mode in timber structures) defined in Eurocode 5 (EC5). A new fracture based design approach is currently used in a few design standards only for certain connection designs [3]. To ensure safe and effective application of timber and ETPs, a comprehensive fracture-based design approach is necessary. Comprehensive knowledge of the fracture properties of solid timber and timber adhesive bond is a prerequisite to develop fracture-based design approach. Fracture behaviour of timber has recently gained momentum and fracture mechanics based numerical models has been shown to provide a superior mechanical rupture description than traditional strength-based techniques. The ability to consider the material non-linearity beyond the fracture tip, the limited stress capacity, and the material's non-linear stress-deformation performance at the crack tip can be address by non-liner fracture mechanics (NLFM) [3]. This may be accomplished by a variety of methods, the most straightforward of which is to characterise the material's fracture behaviour using

[1] Shaikh Atikur Rahman, Deakin University, Australia, sarahman@deakin.edu.au
[2]Mahmud Ashraf, Deakin University, Australia, mahmud.ashraf@deakin.edu.au
[3]Mahbube Subhani, Deakin University, Australia, mahbube.subhani@deakin.edu.au

https://doi.org/10.52202/069179-0021

crack resistance R-curve or stress deformation relation that incorporates material softening, generally referred to as σ-w curve. Continuum damage mechanics (CDM) or cohesive zone (CZM) based material modelling in finite element (FE) simulation have been shown to capture fracture behaviour of timber [5].

Two methods are typically used to identify the material fracture resistance, i.e., the stress intensity factor approach and the strain energy-based approach. The energy-based technique is used in this study since it is more suited to orthotropic materials like timber, and the derivation of the main equation is less dependent on sample geometry [3]. Timber is strong if load is applied in parallel to grain direction while very weak against perpendicular to grain loading. Timber parallel longitudinal fibre is strong and acts like reinforcement against any displacement. Thus, Parallel loading to the grain direction normally involves with longitudinal fibre breaking in LR and LT fracture plane which has significantly higher crack resistance than any other plane of timber. On the other hand, fibre has lots of gaps, faults and has less crack resistance while crack propagating along longitudinal direction in RL and TL plane. Therefore, crack plane RL and TL is one of the weakest crack planes of timber and widely seen in end notch, circular, rectangular holes and various timber connections [6]. Additionally, adhesives are used in most of the engineered timber products (ETPs) and timber connections. Failure of timber adhesive bond can be highly brittle and catastrophic like timber fracture due to perpendicular loading. Due to the softness of timber material, timber bond delamination shows combination of bond fracture and timber splitting along the longitudinal direction. Therefore, it is important to identify pure bond delamination resistance and timber resistance along the bond interface, which is usually the longitudinal direction of timber.

This paper presents Mode-II fracture behaviour of timber and timber adhesive bond using end notched flexure (ENF) test. In the last decades, methods to evaluate fracture energies (strain energy release rates in Mode-II (G_{II})) have been developed using simple analytical methods as well as complex compliance-based beam methods (CBBM) [1]. Crack resistance curves, commonly known as R-curves, are generated from the evolution of fracture energy release rate in relation to the crack length. Due to the complexities of monitoring actual crack length, an equivalent crack method is widely used for different modes of fracture tests. It is worth noting that fracture theories were mostly developed for fibre reinforced composites and there are significant gaps in their application for natural bio composite materials such as timber and ETP. Lack of specific guidelines and standards on timber fracture tests, R-curves generated only from the load-displacement behaviour may sometime lead to wrong projection of strain energy release rate due to inconsistent specimen size and testing procedure. Equivalent crack method has advantage for ENF test, but it also requires proper validation from actual crack length monitoring during test. Using digital image corelation (DIC) system in crack detection and crack length measurement will remove complexities of traditional crack identification techniques and increase the accuracy and robustness of actual crack method. This study presents a detailed comparison between actual and equivalent crack resistance R-curves to highlight the potential as well as the challenges associated with the equivalent crack method. This study also compare the Mode-II fracture behaviour of solid timber and timber adhesive bond.

2 MATERIALS AND METHODS

Samples required for ENF testing were produced from the Australian softwood timber species Radiata pine. The prepared timber specimens were maintained in a chamber at 20°C and 65% relative humidity until the moisture content reached equilibrium. Before the test, the density of each specimen was tested, and the average density was determined to be 580(±44) kg/m3. The average moisture content for all samples was 10.8(±0.94) percent. Figure 1 depicts a schematic of an ENF sample for solid timber. ENF timber samples have cross-sections of 20 mm×20 mm, and 500 mm long. The span length was kept at 460 mm to ensure smooth and steady fracture propagation, as previously reported by De Moura, et al. [7]. Carlsson, et al. [8] proposed that the initial fracture length (a_0) should be more than 0.7L to enable steady crack propagation. The first crack length (a_0) was taken as 162 mm long, greater than 0.7L, where L is half the specimen span length (= 230 mm). It is difficult to maintain smooth straight initial crack line using handheld saw blade and table saw machine does not have blades thinner than 0.80 mm. Therefore, to keep the initial notch width as small as feasible, a 162 mm notch was cut using a 0.80 mm blade of a table saw machine. The following notch was then cut using a handheld saw blade, and the width of the last 20 mm notch was kept 0.50 mm. Timber adhesive bond samples were made by bonding two different timber boards with 20 mm width and 10 mm height to ensure the same cross section (20 mm×20 mm) as solid timber samples. Glue specifications were used to maintain the bond curing time, moisture content, and relative humidity.

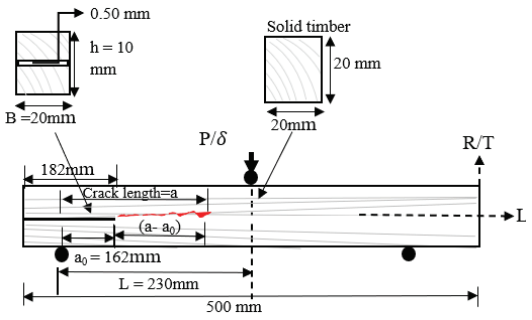

Figure 1: *Geometric dimensions and set-up of ENF solid timber specimen.*

Polyurethane based adhesive HB S309 PURBOND was used for timber adhesive bond. A schematic overview

https://doi.org/10.52202/069179-0021

and test set-up of the ENF test is shown in Figure 2. The timber adhesive bond specimen has same dimension as solid timber of 500 (l) × 20 (b) ×20 (t) mm. A thin plastic tape with a thickness of 0.1 mm was placed between two timber beam joints along 182 mm length to make an initial notch. This thin plastic produced a 0.1 mm gap at the initial notch, and remaining length of the sample were bonded properly. This method was implemented to protect timber fibres from damaging due to mechanical cutting.

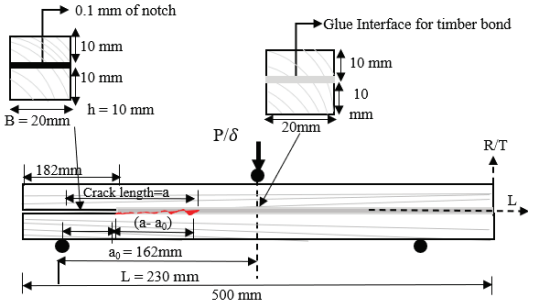

Figure 2: *Schematic overview and set-up of ENF timber adhesive bond test*

The test was conducted using a 10 KN Instron load frame with a displacement control of 5 mm/min. All the test was captured by the digital image corelation (DIC) to identify the crack and monitor the crack propagation length. DIC was calibrated and verified prior to test commencement with known displacement from Instron load frame. The Instron load frame and DIC system were ensured to have the same frequency so that both data can merge. The displacement (δ) was measured at the load application point and a continuous crack growth length (a) was measured by DIC. The testing set-up was identical in timber and timber bond fracture tests.

2.1 DATA REDUCTION METHODS

A bending load (p) is applied at the mid span for ENF test, causing Mode-II fracture propagation over the length of the test (L-a_0). Instron load frame was used to determine the applied load (p) and displacement (δ) at the loading point while continuous crack propagation length (a-a_0) is obtained by DIC. The basic formula to calculate strain energy release rate was introduce by Irwin-Kies [2]. The formula is based on compliance C, which is determined from load and displacement, as shown in Eq. (1)

$$G_{II} = \frac{P^2}{2B}\frac{dC}{da} \qquad (1)$$

Several data reduction schemes exist to calculate the evolution of Mode-II strain energy release rates [9]. Mode-II data reduction techniques are classified into two types: actual crack identification methods and equivalent crack methods. ASTM-D7905 [10] (Standard test method for fibre-reinforced polymer) suggested to use compliance calibration (CC), direct beam theory (DBT) and corrected beam theory (CBT) method based on actual crack monitoring. The accuracy and robustness of those methods largely depend on precision in monitoring actual crack length. Several investigations were carried out in the absence of a rigors technique for measuring crack length, resulting in a broad range of timber fracture energy[8, 11]. With the help of DIC system crack identification and monitoring can be more appealing than conventional methods. According to the compliance calibration (CC) method, strain energy release rate is determined using Eq (2).

$$G_{IIc} = \frac{3ma^2P^2}{2B} \qquad (2)$$

where m is the coefficient of CC obtained from the slope of compliance (C) verses crack length cube (a^3); B is the specimen width. Therefore, CC is not only dependent on load and crack length but also rely on experimental calibration by compliance. A simplified beam theory known as direct beam theory (DBT) evaluates Mode-II fracture energy directly from load, displacement and other constant geometric values. However, DBT does not implement any experimental data reduction scheme. The load head displacement from ENF test is comparatively higher than other testing method like compact shear test (CS) and tapered end notched flexure TENF [7]. Due to those issues DBT may overestimate the fracture energy than other method. DBT is also based on actual crack monitoring. DBT method can be expressed as shown in Eq (3):

$$G_{IIc} = \frac{9a^2P\delta}{2B(2L^3 + 3a^3)} \qquad (3)$$

To address the limitation of DBT, a correction factor of introducing flexural modulus is added to the fracture energy calculation. This corrected method is known as corrected beam theory (CBT) also a classical method based on actual crack monitoring [9]. In CBT, G_{IIC} is determined from Eq 4.

$$G_{IIc} = \frac{9a^2P^2}{2B^2h^3E_f} \qquad (4)$$

where E_f is calculated using Eq (5) and initial compliance (C_0) determined from the ratio of displacement and load.

$$E_f = \frac{L^3}{4Bh^3C_0} \qquad (5)$$

All aforementioned methods (CC, DBT, CBT) depend on accurate measurement of the actual crack length during test. The compliance-based beam method (CBBM) [12], which is based on Timoshenko beam theory, can predict G_{II} using the load-displacement data [9] without actual crack measurements. CBBM determines G_{II} following Eq (6) to (10).

$$G_{IIc} = \frac{9P^2{a_{eq}}^2}{16B^2h^3E_f} \qquad (6)$$

$$C = \frac{3a^3 + 2L^3}{8Bh^3E_{f(CBBM)}} + \frac{3L}{10BhG_{LR}} \qquad (7)$$

where $E_{f(CBBM)}$ is the flexural modulus; $I = 8Bh3$ /12 is the second moment of area and G_{LR} is the shear modulus in longitudinal-radial plane. Initial elastic compliance C_0 and initial crack length a_0 are used to calculate corrected

https://doi.org/10.52202/069179-0021

flexure modulus $E_{f(CBBM)}$ using Equation (8)

$$E_{f(CBBM)} = \frac{3a_0^3 + 2L^3}{12I}\left(C_0 - \frac{3L}{5G_{LR}A}\right)^{-1} \quad (8)$$

To get an equivalent crack length at each point, the experimental compliance C should be replaced by a corrected compliance C_C. An equivalent crack length a_{eq} and the corrected compliance C_C can be determined using Equation (9):

$$a_{eq} = \left[\frac{C_C}{C_{0C}}a_0^3 + \frac{2}{3}\left(\frac{C_C}{C_{0C}} - 1\right)L^3\right]^{1/3} \quad (9)$$

Where $C_C = C - \frac{3L}{5AG_{LR}}$ and $C_{0C} = C_0 - \frac{3L}{5AG_{LR}}$

Once a_{eq} is determined, equation (9) can be modified as G_{II} using Equation (10)

$$G_{II} = \frac{9P^2}{16B^2h^3E_f}\left[\frac{C_C}{C_{0C}}a_0^3 + \frac{2}{3}\left(\frac{C_C}{C_{0C}} - 1\right)L^3\right]^{2/3} \quad (10)$$

CBBM also depends on of the shear modulus in the longitudinal-radial plane G_{LR} but its effect in G_{II} calculation has been reported to be insignificant [13].

3 RESULTS AND DISCUSSION

Figures 3 and 4 illustrate the load versus displacement curves of ENF Mode-II fracture tests on solid timber and timber adhesive bond. The elastic part of the load-displacement curve is linear and has a constant initial slope prior to development of fracture. However, immediately after fracture initiation, the load curve drops to a lower magnitude for both solid timber and timber adhesive bond.

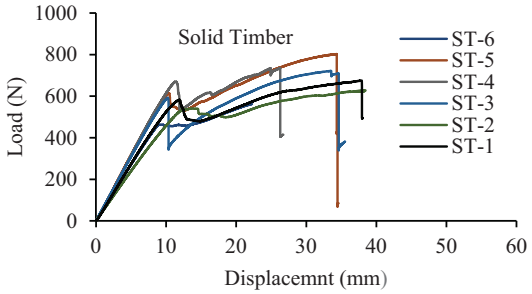

Figure 3: *Load vs Displacement from ENF test on sawn timber*

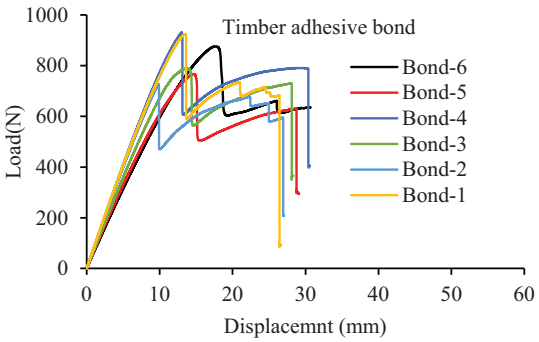

Figure 4: *Load vs Displacement from ENF on timber adhesive bond*

The post-elastic component of the load-displacement response was highly non-linear and showed variations between samples. Most critically, the post elastic section of the load-displacement curve did not follow linear elastic fracture mechanics (LEFM). To address the Mode-II fracture behaviour of solid timber and timber adhesive bond, advanced nonlinear fracture mechanics-based FEM analysis techniques such as cohesive zone model (CZM) or continuum damaged mechanics (CDM) would be required. It is also obvious from the load-displacement response that, after crack initiation, the timber and timber adhesive bond displayed strain hardening response, which finally led to ductile failure showing better structural response when compared with Mode-I fractures observed in timber [14]. The in-plane shear fracture in RL and TL plane showed slightly ductile failure than tensile fracture. In contrast to solid timber, timber adhesive bond fracture demonstrated higher stiffness and strength.

Crack propagation due to Mode-II loading is typically known as in-plane shear crack. Pure Mode-II shear crack developed due to horizontal movement of two cracked surfaces is characterised by a very thin crack line, which is extremely difficult to visualise using naked eye. The current study, hence, used DIC to identify and monitor exact crack length. Mode-II ENF sample of both solid timber and timber-adhesive bond developed ultra-thin cracks as shown in Figure 5. It is worth noting that unlike Mode-I fracture due to direct tension, the timber and timber adhesive fracture process and crack growth in Mode II was more gradual and consistent.

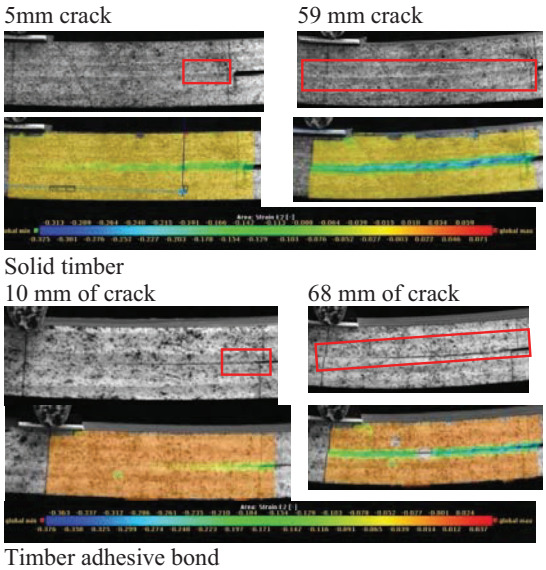

Figure 5: *Illustration of crack development in solid timber and timber adhesive bond*

3.1 CRACK RESISTANCE R-CURVE

The development of the strain energy release rate (G_{II}) as a function of the crack length is commonly known as R-curve. The area immediately around the crack tip, where

https://doi.org/10.52202/069179-0021

different toughening and softening processes due to many microcracks, cracks-branching, and fibre-bridging, occur, is known as the fracture process zone (FPZ). These non-linear events should be included in R-curve as they have obvious impact on how crack propagates through timber and timber adhesive bond. Since the critical fracture energy (G_c) is determined by the plateau value of these curves, the R-curve is a valuable tool for quantifying the critical fracture energy in the effect of the FPZ. Shape and pattern of R-curve depends on the material's crack resisatnce property. Material crack resistance can have three different shapes as rising R-curve, flat R-curve and falling R-curve [11]. For example Mode-I crack resistance R-curve for timber in RL plane show falling R-curve [14]. A simplified scematic of those three type of R-curves are illustrated in Figure 6. The shape and pattern of R-curve is a important material behaviour to catagorise the type of structural failure due to fracture. The material having falling R-curve (where fracture energy gradually or suddenly decrease with the increase of crack length) causes more catstropic and brittle failure of the structure. With a rising R cuve, material's crack resistance increases after the crack initiation or propagation to a point when G_c is greater than G_0. The specific plane of a maerial with rising R-curve will offer more ductile fracture behaviour than the plane with a falling R-curve.

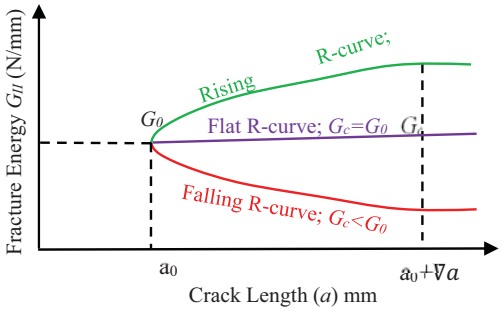

Figure 6: *Schematic of different R- curve patterns*

To develop crack resistance R-curve for solid timber and timber adhesive bond, all data reduction methods including actual crack method and equivalent crack method were applied. A typical comparison among all data reduction methods for solid timber and timber adhesive bond are shown in Figure 7 and Figure 8. The shape of the R-curve for both solid timber and timber adhesive bond are rising, i.e. crack resistance increase as the crack length propagates showing ductile failure. The governing equation of fracture energy (G_{II}) clearly depends on load, displacement, and corresponding crack length, and hence, hardening or softening responses of load-displacement curve are directly reflected in the corresponding R-curve.

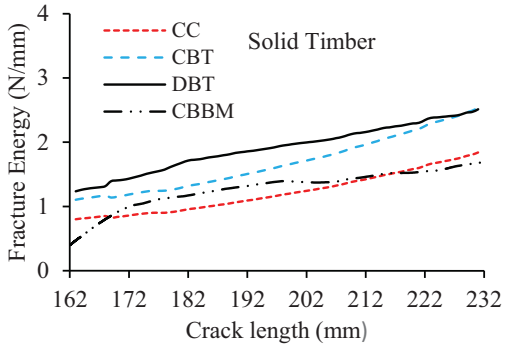

Figure 7: *R-curve for solid timber*

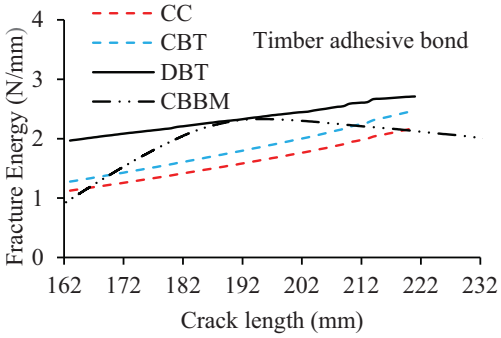

Figure 8: *R-curve for timber adhesive bond*

3.2 COMPARISON BETWEEN ACTUAL AND EQUIVALENT R-CURVE

R-curves were developed following actual crack methods as CC, CBT and DBT, and all three methods showed similar trends as shown in Figure 7 and Figure 8. However, DBT overestimate the fracture energy than other methods. DBT was simplified beam theory directly formed from load and load head displacement. It is also important to note that DBT does not implement any data reduction scheme which cause wrong prediction of fracture energy. Compliance calibration (CC) and corrected beam theory (CBT) showed well prediction of Mode-II fracture energy, although CBT prediction is higher than CC. In contrast, the fracture energy at crack initiation from CBBM is much lower than those obtained from CC, DBT and CBT. This raises a fundamental issue of identifying crack initiation point for the equivalent crack method. It is worth noting that in Figure 8, the actual crack length from (CC, DBT and CBT) culminated at 222 mm, but the equivalent crack from CBBM goes to the full length of 232 mm as the equivalent crack method cannot differentiate whether the crack was developed due to fracture or specimen damaged due to other material issues such as natural defects, and faulty notch width. In equivalent crack method, fracture energy release rate (G_{II}) is only calculated from load and displacement values, and hence validation with actual crack length measurement is essential. Despite some limitations and shortcomings,

https://doi.org/10.52202/069179-0021

CBBM remarkably produced consistent and stable R-curve after the crack initiation. CBBM produced excellent plateau shape in R-curve which signifies the stable energy release rate, known as critical strain energy release rate. The advantages of using CBBM are obvious as the technique does not require any sophisticated equipment such as travelling microscope and DIC system. The critical fracture energy determined using CBBM technique may be used in advanced structural analysis once the fundamental behaviour of the material is validated against classical techniques, i.e., CC/CBT. A comparison of G_{II} obtained from three different data reduction methods for solid timber and timber adhesive bond are summarised in Table 1 and Table 2. Considering the results obtained from six identical solid timber samples, the average fracture energy (G_{II}) from CC, CBT and CBBM are 1.32 N/mm, 1.41 N/mm, and 1.20 N/mm respectively. CBT produce 6.81% higher fracture energy than CC and 17.5% higher than CBBM.

Table 1: *ENF test result on Solid timber (ST)*

Test	Max Load (*N*)	Actual crack monitoring		Equivalent crack method
		CC (*N/mm*) (G_{IIc})	CBT (*N/mm*) (G_{IIc})	CBBM (*N/mm*) (G_{IIc})
ST-1	594.90	1.26	1.34	1.28
ST-2	539.84	1.21	1.30	1.32
ST-3	588.23	1.24	1.34	1.20
ST-4	528.62	1.18	1.27	1.04
ST-5	669.31	1.54	1.63	1.27
ST-6	608.90	1.50	1.59	1.07
Mean	**588.3**	**1.32**	**1.41**	**1.20**
COV%	8	11	11	9

The average Mode-II fracture energy for timber adhesive bond using CC, CBT and CBBM are 1.56N/mm, 1.69N/mm and 1.72N/mm individually. For timber adhesive bond equivalent crack method (CBBM) produced higher fracture energy than CC and CBT. During the crack development process, timber-adhesive bonded specimens experienced higher load than those for solid timber samples (as shown in Figure 3 and Figure 4) resulting in higher compliance (C_0 and C), which eventually contribute to flexural modulus (E_f) and fracture energy (G_{II}) (see the Eq(7-(10).

Table 2: *ENF test results on Timber adhesive bond*

Test	Max Load (*N*)	Actual crack monitoring		Equivalent crack method
		CC (*N/mm*) (G_{IIc})	CBT (*N/mm*) (G_{IIc})	CBBM (*N/mm*) (G_{IIc})
Bond-1	922.01	1.50	1.54	1.83
Bond-2	719.62	1.50	1.69	1.05
Bond-3	787.82	1.68	1.79	1.80
Bond-4	926.34	1.91	2.00	2.00
Bond-5	762.09	1.26	1.38	1.56
Bond-6	875.21	1.56	1.79	2.12
Mean	**832.1**	**1.56**	**1.69**	**1.72**
CV%	10	13	12	22

3.3 COMPARISON BETWEEN SOLID TIMBER AND TIMBER ADHESIVE BOND CRACK RESISTANCE

Results shown in Table 1 and Table 2 indicates that timber-adhesive bond would require more energy to fracture when compared to an equivalent sawn timber. With the same testing configurations, average crack initiation load was almost 42% high in timber bond than that for solid timber, and fracture energy from CC method was 18% high in timber bond than solid timber. An overall response of R-curve for all timber and timber-adhesive bond specimens obtained from CC (as a representative classical method) and CBBM are shown in Figure 9-Figure 12. Crack resistance R-curves for solid timber and timber adhesive bond followed rising R-curve. However, CBBM method for timber adhesive bond showed slightly flat curve after a significant length of crack propagation.

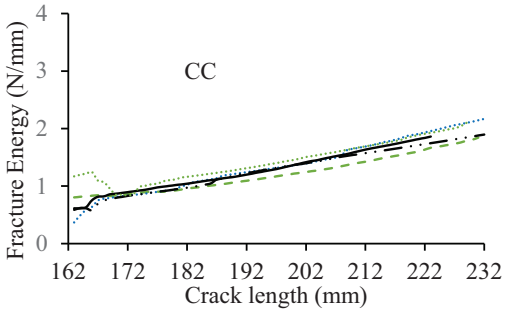

Figure 9*: R-curve for Solid timber using CC.*

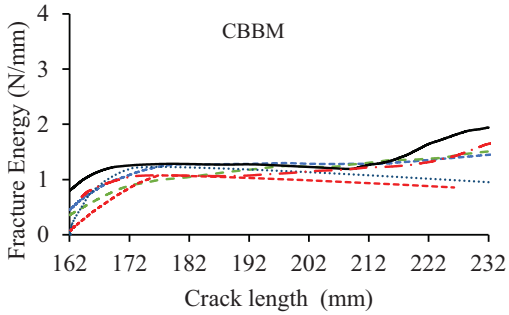

Figure 10*: R-curve for Solid timber using CBBM.*

https://doi.org/10.52202/069179-0021

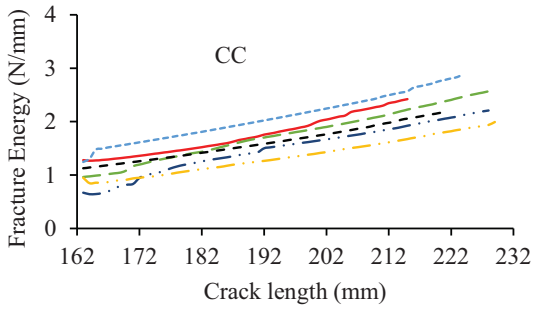

***Figure 11**: R-curve for timber adhesive bond using CC.*

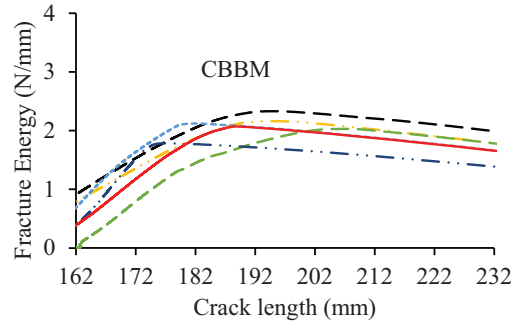

***Figure 12:** R-curve for timber adhesive bond using CBBM.*

4 DISCUSSION

This paper put emphasis on quantifying crack resistance of solid timber and timber adhesive bond under Mode-II fracture using two different techniques, i.e., actual crack method and equivalent crack method. A comparison shown in Table 3 were conducted between Mode-I and Mode-II fracture energy values for various timber species (results in bold are taken from the current study). Mode-II fracture energy for radiata pine was found to be 1.32 N/mm, which is consistent with other Mode II energy levels published in the literature.

Mode-I fracture energy values [5, 12-14] for radiata pine and other species are also shown in Table 3, which shows that Mode-II fracture energy of radiata pine is almost three time higher than its Mode-I fracture energy. This implies that that in case of mixed mode loading, timber structure will be vulnerable to Mode-I cracking. However, in cases where in-plane shear is dominant such as various holes in timber beams for service lines and in various joints, Mode II failure will trigger eventually splitting failure. Since that Mode II fracture in timber and timber adhesive bonding is more ductile than Mode I failure, a combined failure would be structurally preferable to the more catastrophic Mode I failure alone. A typical comparison between Mode-I and Mode-II R-curves is shown in Figure 13, in which R-curve for Mode-I is taken from [14]. Figure 13 clearly demonstrates the distinct difference in R-curves between Mode II and Mode I, with the former gradually rising in contrast to the latter showing a plateau as crack propagates.

This comparison reiterates the fact that Mode II timber failure shows resistance to cracking and is more ductile than Mode I failure. Additionally, timber fracture energy is compared with those of carbon fiber/epoxy composite laminates in Table 3. It is interesting to see that despite being a natural fibre, timber's resistance to fracture in Mode II is only 35% less than that of carbon fiber/epoxy composite [15].

***Table 3:** Comparison of energy with different material and different timber species*

Mode-I Fracture Species	G_{Ic} (N/mm)	Mode-II Fracture Species	G_{IIc}(N/mm)
Radiata pine[14]	0.48	**Radiata pine**	**1.20-1.41**
Timber adhesive bond[16]	0.48	**Timber adhesive bond**	**1.56-1.72**
spruce[6]	0.30	Eucalyptus globulus[17]	1.54
European beech[6]	0.46	Radiata pine[18]	1.27
CF/EP composite[15]	0.68	CF/EP composite [15]	1.92

This study also examined the difference in fracture behaviour between timber fracture and glue delamination. A thin plastic tape with 0.1 mm thickness was used in ENF bond samples which produced pure bond delamination along the glue line. Although solid timber and timber adhesive bond indicated similar behaviour, timber adhesive bond showed higher stiffness, strength but was less ductile and less stable than solid timber; this clearly highlights the importance of recognition of glue lamination in engineered timber structures.

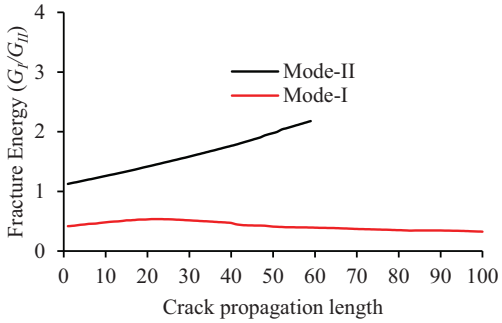

***Figure 13**: R-curves of timber in Mode-I and Mode-II*

https://doi.org/10.52202/069179-0021

In practice, however, glue delamination in softwood timber-adhesive joints is often ignored in both numerical and theoretical analysis of timber structures. Ignoring the glue delamination behaviour in engineered timber products may result in an incorrect prediction of resistance. Fracture properties presented in the current study should be useful in developing reliable numerical models for timber and ETPs such as cross-laminated timber (CLT), glue laminated timber (GLT), glulam etc.

5 CONCLUSION

The current research presents Mode II fracture behaviour of solid timber and timber adhesive bond utilising different data reduction strategies that are based on actual as well as equivalent crack length. In terms of Mode-II crack resistance R-curves, there were notable variations between the real crack method and the equivalent crack method.

Compliance calibration (CC) and corrected beam theory (CBT) methods produced reliable results for Mode-II fracture energy. While DBT fails to offer superior outcomes on Mode-II fracture energy. The equivalent crack method CBBM method showed outstanding response of crack resistance R-curve after crack initiation. However, CBBM suffered to identify the reliable fracture energy at crack initiation point.

A realistic comparison of Mode-II fracture properties between timber and timber adhesive bond were executed. Comparison result shows timber adhesive bond require greater fracture energy to initiate crack in bond line than solid timber. A new technique of creating initial notch without cutting or damaging timber fibre were introduce which produce pure glue delamination and guaranteed stable crack propagation across the glue line.

Digital image correlation (DIC) has been utilised effectively in timber fracture identification and crack length monitoring. Outputs from DIC could be important for cohesive zone modelling and continuum damaged based material modelling to evaluate timber and timber adhesive bond fracture. Finite element models, in conjunction with experimental findings, will give a strong solution for a wide range of difficult circumstances in wood joints and connections.

REFERENCES

[1] M. Yurrita and J. M. Cabrero, "On the need of distinguishing ductile and brittle failure modes in timber connections with dowel-type fasteners," *Engineering Structures,* vol. 242, p. 112496, 2021/09/01/ 2021, doi: https://doi.org/10.1016/j.engstruct.2021.112496.

[2] M. F. Kanninen, C. H. Popelar, and A. J. McEvily, "Advanced Fracture Mechanics," *Journal of Engineering Materials and Technology,* vol. 108, no. 2, pp. 199-199, 1986, doi: 10.1115/1.3225862.

[3] P. Zarnani and P. Quenneville, "Strength of timber connections under potential failure modes: An improved design procedure," *Construction and Building Materials,* vol. 60, pp. 81-90, 2014/06/16/ 2014, doi: https://doi.org/10.1016/j.conbuildmat.2014.02.049.

[4] N. Dourado, F. G. A. Silva, and M. F. S. F. de Moura, "Fracture behavior of wood-steel dowel joints under quasi-static loading," *Construction and Building Materials,* vol. 176, pp. 14-23, 2018/07/10/ 2018, doi: https://doi.org/10.1016/j.conbuildmat.2018.04.230.

[5] S. A. Rahman, M. Ashraf, M. Subhani, and J. Reiner, "Comparison of continuum damage models for nonlinear finite element analysis of timber under tension in parallel and perpendicular to grain directions," *European Journal of Wood and Wood Products,* vol. 80, no. 4, pp. 771-790, 2022/08/01 2022, doi: 10.1007/s00107-022-01820-8.

[6] N. Dourado, M. de Moura, S. Morel, and J. Morais, "Wood fracture characterization under mode I loading using the three-point-bending test. Experimental investigation of Picea abies L," *International Journal of Fracture,* vol. 194, no. 1, pp. 1-9, 2015, doi: https://doi.org/10.1007/s10704-015-0029-y.

[7] M. F. S. F. De Moura, M. A. L. Silva, A. B. de Morais, and J. J. L. Morais, "Equivalent crack based mode II fracture characterization of wood," *Engineering Fracture Mechanics,* vol. 73, no. 8, pp. 978-993, 2006/05/01/ 2006, doi: https://doi.org/10.1016/j.engfracmech.2006.01.004.

[8] L. A. Carlsson, J. W. Gillespie, and R. B. Pipes, "On the Analysis and Design of the End Notched Flexure (ENF) Specimen for Mode II Testing," *Journal of Composite Materials,* vol. 20, no. 6, pp. 594-604, 1986/11/01 1986, doi: 10.1177/002199838602000606.

[9] A. Gliszczynski and N. Wiącek, "Experimental and numerical benchmark study of mode II interlaminar fracture toughness of unidirectional GFRP laminates under shear loading using the end-notched flexure (ENF) test," *Composite Structures,* vol. 258, p. 113190, 2021/02/15/ 2021, doi: https://doi.org/10.1016/j.compstruct.2020.113190.

[10] ASTM, " D7905/D7905M–19e1," *Standard Test Method for Determination of the Mode II Interlaminar Fracture Toughness of Unidirectional Fiber-Reinforced Polymer Matrix Composites,* p. 20, 2019.

[11] J. Tiu, R. Belli, and U. Lohbauer, "Rising R-curves in particulate/fiber-reinforced resin composite layered systems," *Journal of the Mechanical Behavior of Biomedical Materials,* vol. 103, p. 103537, 2020/03/01/ 2020, doi: https://doi.org/10.1016/j.jmbbm.2019.103537.

[12] M. De Moura and A. De Morais, "Equivalent crack based analyses of ENF and ELS tests," *Engineering Fracture Mechanics,* vol. 75, no. 9, pp. 2584-2596, 2008.

[13] M. F. S. F. d. Moura, M. A. L. Silva, J. J. L. Morais, A. B. d. Morais, and J. J. L. Lousada, "Data reduction scheme for measuring GIIc of wood in end-notched flexure (ENF) tests," vol. 63, no. 1, pp. 99-106, 2009, doi: doi:10.1515/HF.2009.022.

[14] S. Rahman, M. Ashraf, M. Subhani, and J. Reiner, "Influence of initial crack width in Mode I fracture tests on timber and adhesive timber bonds," in *Current Perspectives and New Directions in Mechanics, Modelling and Design of Structural Systems*: CRC Press, 2022, pp. 1675-1680.

[15] C. Cheng *et al.*, "Simultaneously improving mode I and mode II fracture toughness of the carbon fiber/epoxy composite laminates via interleaved with uniformly aligned PES fiber webs," *Composites Part A: Applied Science and Manufacturing,* vol. 129, p. 105696, 2020/02/01/ 2020, doi: https://doi.org/10.1016/j.compositesa.2019.105696.

[16] J. M. Gagliano and C. E. Frazier, "Improvements in the fracture cleavage testing of adhesively-bonded wood," *Wood and Fiber Science,* pp. 377-385, 2001.

[17] J. Xavier, M. Oliveira, P. Monteiro, J. J. L. Morais, and M. F. S. F. de Moura, "Direct Evaluation of Cohesive Law in Mode I of Pinus pinaster by Digital Image Correlation," *Experimental Mechanics,* vol. 54, no. 5, pp. 829-840, 2014/06/01 2014, doi: 10.1007/s11340-013-9838-y.

[18] B. Franke and P. Quenneville, "Analysis of the fracture behavior of Radiata Pine timber and Laminated Veneer Lumber," *Engineering Fracture Mechanics,* vol. 116, pp. 1-12, 2014/01/01/ 2014, doi: https://doi.org/10.1016/j.engfracmech.2013.12.004.

https://doi.org/10.52202/069179-0021

World Conference on Timber Engineering Oslo 2023

MODE I TESTS OF NORWAY SPRUCE USING SEN-TPB: DETAILED ANALYSIS OF THE CRACK LENGTH DETERMINED USING OPTICAL METHOD

Martin Hataj[1], Jiří Kunecký[2], Michal Kloiber[3]

ABSTRACT: The paper deals with characterization of fracture properties of Norway spruce using SEN-TPB test. Although the matter is not new, methods of processing the results are relatively recent. The article focuses on determination of crack length using DIC, however, the core of the work is the algorithm which determines the crack length based on the correlated point data. Results of optical measurement are compared to compliance-based analytical formulas. Altogether 18 experiments in radial orientation have been made. Samples used for determination of the strain energy release rate were 60 mm in width and 120 mm in height. Wider specimens have been used to employ the orientation of anatomical directions of the tested timber. Two cameras were used to track cracks on both sides. The algorithm works well, although interesting questions arise, especially when we look at the crack length determination algorithm and its failure criteria.

KEYWORDS: SEN-TPB, Norway spruce, digital image correlation, strain energy release rate, crack length

1 INTRODUCTION

Energy-based methods, especially cohesive zone modelling or LEFM provide us with solutions for problems, which are problematic to solve using standard stress-based approaches. Such methods are crucially dependent on proper material properties characterization, especially strain energy release rate [1]. This quantity is, however, highly dependent on mode (or combination of modes) under which the material is loaded. This article deals with mode I, as it is the most common and easiest one to perform. There is a lot of literature about mode I testing and Norway spruce (as a typical softwood) which is also an advantage, since one can easily compare the results to the previously published values. In all quasi-brittle materials, including timber, there exists some kind of size effect [2], which has to be taken into account. That is also the reason why authors did not choose narrow and rather low sample size used in the previously published works [3,4]. Of course, for proper size effect description there is a need of many more experiments and configurations, nevertheless, just repetition of what has been done was not preferred. Also, it is clear that the orientation of anatomical directions of wood is important. The article shows result of radial direction of timber.

Digital image correlation is a method, which is highly suitable to study timber engineering problems, since relatively low values of stiffness of wood allows for good precision of results. Its drawbacks are, of course, that the abundant number of data have to be understood and reinterpreted. This was the most important part of the work, how to get the crack length using experimental data only. Although in the literature there exists a plethora of algorithms [7-9], there is missing an easy criterion to recognize the presence of a crack. Since we see in optical solution relative distance or deformation of two points, it is relatively tricky to say the threshold value to be used to evaluate the crack length properly.

The strain energy release rate is a quantity, which is usually computed using one of the compliance-based methods. Its advantage is that is does not require complicated tracking of crack length. In the literature e.g. Dourado et al. [1,3], the processing of the data is based on compliance change of the whole specimen, which looks robust, however, it has to be taken into account, that the procedure itself is not purely experimental, since it incorporates also an analytical model, which needs material properties to be inserted and which are only assessed using the initial compliance, which is often tricky due to nonlinearities present in the beginning of the experiment. Another question arises, that the algorithm uses complicated computation of equivalent crack length, which one is complicated to understand and which has to be solved numerically. Last, there is a coefficient k representing the influence of SRR width, which is based on a separate numerical model, thus producing values, which are not directly related to the measured values. Although all criticisms are possible, still it is very robust method.

[1] Martin Hataj, Czech Technical University in Prague, University Centre for Energy Efficient Building, Czech Republic, martin.hataj@cvut.cz
[2] Jiří Kunecký, Institute of Theoretical and Applied Mechanics, Czech Academy of Sciences, Czech Republic, kunecky@itam.cas.cz
[3] Michal Kloiber, Institute of Theoretical and Applied Mechanics, Czech Academy of Sciences, Czech Republic, kloiber@itam.cas.cz

https://doi.org/10.52202/069179-0022

During processing the data and the results the authors have noticed, that the processing of the data is not just a research task, but that it can be educational not only for the authors themselves, but that it is a nice example to help understand the complicated nature of fracture mechanics and eqLEFM especially [2, 6]. Such an approach, where all nonlinear behavior is directly related to a virtual equivalent crack is the simplification, which allows to construct a R-curve and makes understandable the complicated phenomena appearing near crack tip, mainly micro-cracking and fiber-bridging, but also plasticity etc. All the nonlinearities are present in the optical measurement.

2 METHODS

2.1 Samples

The work followed the methods well described in [3], called SEN-TPB, which is basically a three-point bending with glued-in (PVA based dispersions of one-component adhesive) middle part (see Figure 1), where the orientation of grain is rotated 90° to the original one. Dimensions of the samples were chosen 60 mm width and 120 mm height, length 840 mm. In this scale we have already the problem of annual rings, which have slightly rounded shape. This problem can add additional noise to the data. The studied timber was dried using a special protocol in order to simulate conditions present in construction timber: the green wood dried for three months in the forest after harvest and later dried artificially for 14 days to reach the final MC of 12% abs. This could be the way how to let the internal stresses induced by drying at a level commonly found in standard structural timber. The density of the specimens was measured in the range between 429 and 529 kg/m^3 with an average value of 477 kg/m^3.

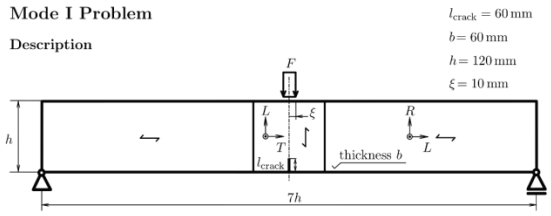

Figure 1: *Description of SEN-TPB test used in the article*

2.2 Loading

The force application was made using a steel plate to spread the loading and avoid shear loading due to misalignment; the supports were made using steel plates and valves to assure free move and omit embedment. When testing a component, usually in the first loading stage one experiences few peaks due to loading all the possible interfaces which are present. This actually happened also here and that was the reason to use curve fitting to the measured force. The test was driven using displacement control, this is important to understand the R-curve. The loading speed was chosen to cause damage in 8-10 minutes.

During the load test, the universal testing machine Galdabini Quasar 100 was used, equipped with a load cell with a range of 10 kN. The outputs from the test machine were processed by the Labtest test software. Furthermore, the DEWE2602 measuring center was used, which is designed to measure the static and dynamic behavior of monitored objects. The microcomputer built into the central unit automatically balances the connected sensors, calibrates the amplifier, and operates the individual measured points in the measurement mode. For each sensor, its constant K is entered, so that the measured values are then directly reported in the exact physical units of the monitored quantities. During the described test, the control panel was controlled by a computer and the DeweSoft program. For all samples, the load value of the joint and the corresponding deflection and path during the initiation and opening of the crack were monitored. Deflection and path during crack initiation and opening were measured by inductive LVDT sensors Micro-epsilon, type DTA-5G-CA throughout the duration of the load test, located on both sides of the test specimen. The average value of these LVDT sensors was used to evaluate the data.

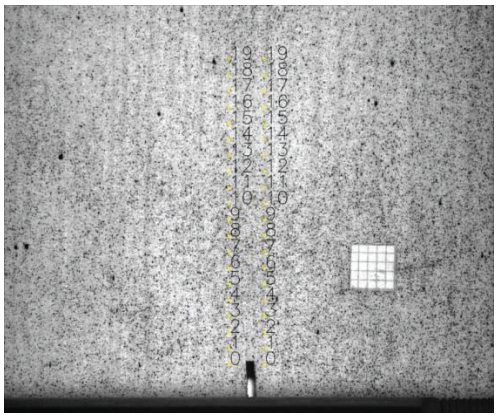

Figure 2: *20 points whose relative displacement was used as an input to the algorithm*

2.3 Compliance-based evaluation

Results were evaluated according to Dourado et al. [3]:

$$E_{Tf} = \left(\frac{L_2^3 - L_1^3}{bH^3} + \frac{L^3 - L_2^3}{b(H - ka_0)^3}\right)\left(\frac{C_0}{2} - \frac{L_1^3}{E_L bH^3}\right)^{-1} \quad (1)$$

where E_{Tf} = corrected value of the flexural modulus, L_1 = lateral arm length (distance between support and nearest glued surface, L_2 = distance between middle of span and support minus side of rectangular SRR – stress relief region (ka), L = distance between middle of span and support, C_0 = initial value of corresponding measured specimen compliance; b = specimen width, H = specimen hight, k = non-dimensional parameter (authors used k = 0,86), a_0 = initial value of the crack length, E_L = the Young's modulus on the longitudinal direction.

https://doi.org/10.52202/069179-0022

$$a_e = \frac{1}{k}\left\{H - \left[\left(\frac{C}{2} - \frac{L_1^3}{E_L b H^3} - \frac{L_2^3 - L_1^3}{E_{Tf} b H^3}\right)^{-1} \frac{L^3 - L_2^3}{E_{Tf} b}\right]^{1/3}\right\} \quad (2)$$

Where a_e = the equivalent crack length, C = specimen compliance (C = δ/P), δ = Castigliano theorem, P = load.

Fracture energy can be obtained by means of the Irwin–Kies equation:

$$G_I = \frac{P^2}{2b}\frac{dC}{da} \quad (3)$$

Equation of the specimen compliance:

$$C = 2\left(\frac{L_1^3}{E_L b H^3} + \frac{L_2^3 - L_1^3}{E_T b H^3} + \frac{L^3 - L_2^3}{E_T b (H - ka)^3}\right) \quad (4)$$

Where E_T = the Young modulus on the transverse direction.

applied to Eq. (3), which leads to:

$$G_I = \frac{3P^2}{b^2}\frac{(L^3 - L_2^3)k}{E_{Tf}(H - ka_e)^4} \quad (5)$$

The initial compliance was set usually between 0.15 and 0.35 times F_{max}. To avoid peaks the curves (force, displacement) were smoothed using moving average filter.

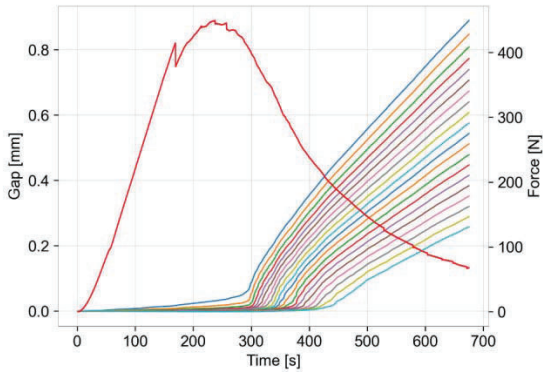

Figure 4: *20 pairs of points (0-9) and their relative displacement show the nonlinear behaviour; measured force in red*

2.4 Optical measurement

The whole test has been recorded with two Basler acA2440-20gm cameras from both sides with a frame rate at 1 Hz and a telecentric lens having 55 mm focal length. The cameras were synchronized using IP protocol and triggered using software trigger from the computer. The camera region of interest was set to not only the crack itself, but also a relatively long path has been recorded using the cameras (see Fig. 2). To ensure we know the ratio (size) of a pixel in distance units, a millimeter scale was glued onto the sample. Synchronization between the optical measurement and loading was made using minimization of error afterwards between the curves of optical displacement in y-direction and displacement measured. Pattern was applied using acryl black and white colors and an airbrush (Revell Masterclass), to meet the standard criterion (3-4 pixels/speckle).

The DIC part consisted of a) tracking several pairs of points (see Figure 2 and 3) using DICe correlation engine [10] and b) based on the data we introduced an algorithm to get the crack length distance.

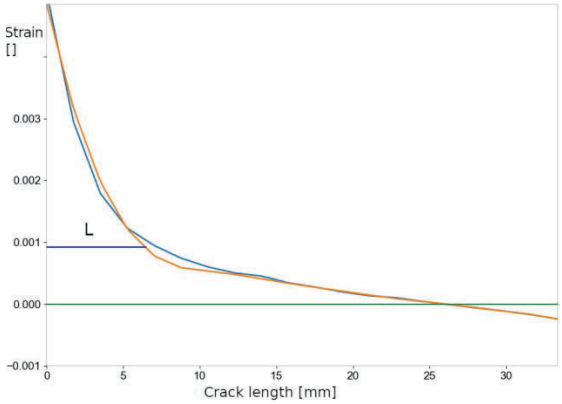

Figure 5: *Crack length determination, crack axis is now the horizontal one. L is the length determined when strain is equal 0.925e-3. Blue is the original data, orange curve is interpolated using polynomial.*

2.4.1 Crack length algorithm

The basic idea of eqLEFM: if there is some nonlinearity (change of compliance) present in the force-displacement curve, it means some length of virtual or equivalent crack is produced; we do not know exactly what happens in the region, however, we look at solution of equation:

$$U = 2\left[\int_0^{L_1} \frac{M_f^2}{2E_L I} dx + \int_{L_1}^{L_2} \frac{M_f^2}{2E_T I} dx + \int_{L_2}^{L} \frac{M_f^2}{2E_T I_{ST}} dx\right] \quad (6)$$

Where U = strain energy due to bending, M_f = the bending moment ($M_f = Px/2$), I = the second moment of area of the entire section (height H), I_{ST} = the second moment of area of the effective section in the SRR (height of H - ka).

$$I = \frac{bH^3}{12} \quad (7)$$

$$I_{ST} = \frac{b(H - ka)^3}{12} \quad (8)$$

Using Castigliano theorem:

$$\delta = \frac{\partial U}{\partial P} \quad (9)$$

We can evaluate compliance (4) and using (3) also G_I. This solution means in fact, that every change in the whole system will lead to change of equivalent crack length,

although it is not still apparent or visible. This is, however, not possible in direct experimental way – the FPZ region and nonlinearity at the crack tip do not allow for this. The biggest disadvantage is, that the most important parameter we want to assess, the resistance to crack growth at the ultimate load (G_c) is in this nonlinear region, not in the one, where the crack is already visible by naked eye, where the curve of loading already turns down.
The algorithm used for evaluation of the optical measurement cannot follow the same approach, however, it can try to do similar technology – recognize the crack as a threshold value of linear behavior between a pair of correlated points. In steps:

1. In each moment (time) we can plot the point difference divided by their original distance (see Fig. 2 and 5)
2. Stabilize the curve (in each step the curve is moving a bit) - smooth it using a curve (here we used piecewise cubic Hermite interpolating polynomial)
3. Threshold strain value can be computed according to EN 338-2016 [11] using ratio between $E_{m,90,mean}/f_{t,90,k}$ yielding 0.925e-3
4. Interpolate the point on the curve and read the actual crack length (here another criterion is added, that it happens after the first onset of nonlinear region).
5. Compute this on both sides and average the result – $a_{eopt}=a_{eoptL}+a_{eoptR}$

All the above-mentioned steps were programmed using Numpy/Scipy Python libraries.
Now when the length of crack in time is ascertained, we can do the final assessment of the optical measurement using the classic Irwin-Kies equation shown in Eq. (3). Numerically it yields:

$$G_I = \frac{P^2}{2b}\frac{\Delta C}{\Delta a_{eopt}} = \frac{P^2}{2b}\frac{\Delta \frac{u}{P}}{\Delta a_{eopt}} \qquad (10)$$

where u is the measured deflection of the sample under load P, b is the sample width and a_{eopt} is the optically measured length of crack. Note the presence of derivatives which always leads to scattered results. That is why the quantities are first smoothed using splines.

3 RESULTS

The results are summarized in Tab. 1. The values show the ones assessed using compliance-based methods (first two columns) and its graphical interpretation can be seen in Fig. 6. In the table also 5% percentile is computed, taking into account normal distribution of the results (which is in fact not absolutely ensured).
The energy denoted G_C (in some literature denoted G_{IC}, or $G_{I(PU)}$) is the resistance to crack growth at the limit load. In contrast, the critical energy release rate G_f, which takes on higher values.
A comparison of the results of compliance-based evaluation and optical measurement can be seen in Tab. 1. The authors state the value of the resistance to crack growth at the limit load in the case of optical measurement G_{copt}. The results of these two methods show good agreement for some specimens. However, the optical method generally shows higher energy values. In some cases, the difference between the results of these two methods is up to twofold.
Quantile values of energy obtained from compliance-based evaluation in comparison optical measurement show good agreement.

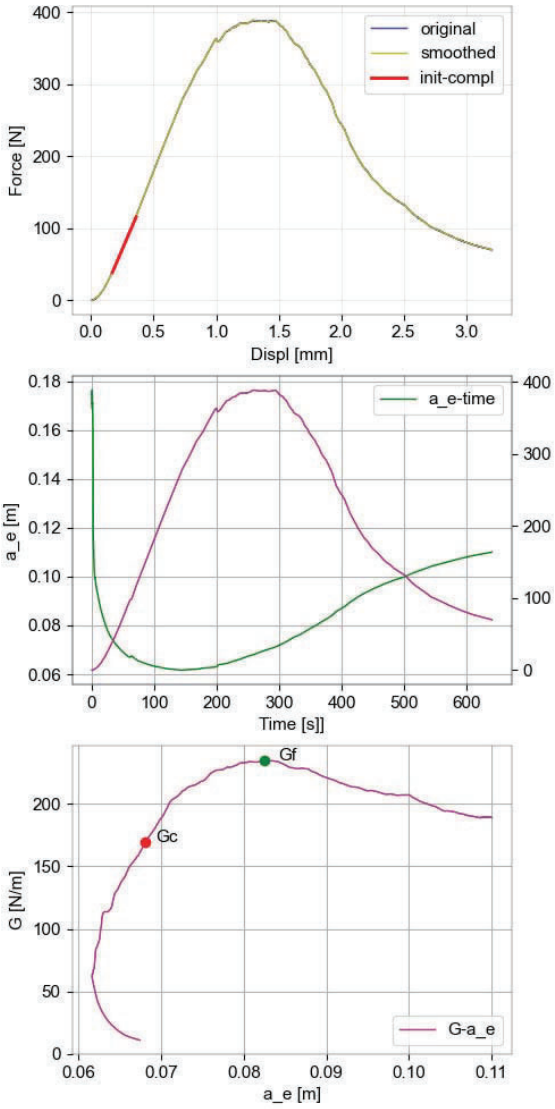

Figure 6: *Compliance-based method result of one sample: force-displacement curve with initial compliance shown in red (top), assessment of a_e (middle) and results in the form of a graph (bottom)*

It is also possible to compare the presented results with those already published, e.g., Dourado et al. [12]. It should be mentioned that the article presents the energy values of the specimens, which were calculated using the triangular stress relief region. Such a computation, to our best

https://doi.org/10.52202/069179-0022

knowledge and experience, shows similar results. The wood used to produce test specimens is the same - *Picea abies* L. The cross sections of the specimens are different (40/140 and 60/210 mm). Dourado reports a lower average wood density of 417 kg/m3 and average value of resistances to crack growth at the limit load G_c are 118 N/m for profile 40/140 mm and 106 N/m for 60/210 mm. The critical energy release rates G_f are 152 N/m (40/140 mm) and 156 N/m (60/210 mm). The published results are lower than the results in Tab. 1, more consistent with quantile values.

Table 1: *Results of the analysis*

Specimen	G_c [N/m]	G_f [N/m]	$G_c$opt [N/m]
R_007	172	238	169
R_008	184	300	264
R_009	215	258	240
R_010	171	227	270
R_011	130	211	278
R_012	170	235	185
R_013	174	229	162
R_014	167	245	219
R_015	148	217	222
R_016	144	180	211
R_017	175	241	301
R_018	156	221	288
$G_{I,mean}$	**167,2**	**233,5**	**234,1**
stdev	21,6	28,8	47,0
var.coef	0,13	0,12	0,20
$G_{I,k}$	**124,0**	**176,0**	**140,1**

It is good to discuss and mention some of the drawbacks of the method. First, of course, the threshold criterion plays an important role in the whole process. Here the authors used tabular data. Nevertheless, the nonlinear region (see Fig. 5) in the curve changes well with this criterion and looks like a reasonable one. Optical measurement is dependent on the way of smoothing the experimental data curves. The authors found that the experimental measurement does not provide a smooth flow of data. The final energy values are very sensitive precisely to the method of data smoothing.

On the other hand, the advantage of optical measurement is complete independence from other material characteristics (E_L and E_T) and also from the theory. To be exact, in compliance-based method the measured values are inserted into a very complicated model that nobody can understand directly. This is not the problem when considering the optical measurement, where the physics of the problem is clear.

Another problem is the crack length determination from two cameras. To date most SEN-TPB tests have been done without optical measurement or rather on narrower samples using DIC from one side. This is a nice contribution of the article. Actually, the difference in crack lengths on both sides was very often very high. The relatively higher values can be also attributed to the influence of this feature.

Last it should be pointed out that Dourado et al. [12] showed much lower density of timber tested, and here the authors see the biggest influence. However, the effect of different geometry of the sample could be also an important parameter.

4 CONCLUSIONS

The article summarizes the comparison of two different methods for obtaining resistance to crack growth at the maximum load. Specifically, it is a comparison of the results of compliance-based evaluation and optical measurement. The experimental work followed the methods SEN-TPB, which is basically a three-point bending with glued-in middle part, where the orientation of grain is rotated 90° to the original one.

The presented results were compared with those already published. The published results are lower than the results in this paper and are more like quantile values. It should be mentioned that the shape of the stress relief region (SRR) used in the calculation is different, but influence is not big. The cross-sections and average wood density of the samples are also different.

The quality of optical measurement results is very sensitive to the method of smoothing the experimental data curves. On the other hand, the advantage of optical measurement is complete independence from other material characteristics.

ACKNOWLEDGEMENT

This paper was created with a financial support from grant project of Grant Agency of the Czech Republic GACR No. 21-29389S “Experimental and numerical assessment of the bearing capacity of notches in timber beams at arbitrary locations using LEFM”.

REFERENCES

[1] de Moura M.F.S.F., Dourado, N.: Wood Fracture Characterization. ISBN 9780815364719, CRC Press 2018.

[2] Bažant, Z.P., Le, J.L., Salviato, M., Quasibrittle Fracture Mechanics and Size Effect: A First Course. OUP Oxford, 2021.

[3] Dourado, N., de Moura M.F.S.F., Morais, J. A numerical study on the SEN-TPB test applied to mode I wood fracture characterization, International Journal of Solids and Structures, Volume 48, Issue 2, 2011, Pages 234-242, ISSN 0020-7683.

[4] Gustafsson, P.J., A study of strength of notched beams, CIB-W18A/21-10-1.

[5] Ostapska, K., Malo, K.A., Crack path tracking using DIC and XFEM modelling of mixed-mode fracture in wood, Theoretical and Applied Fracture Mechanics, Volume 112, 2021, ISSN 0167-8442, https://doi.org/10.1016/j.tafmec.2021.102896.

[6] Coureau, Jean-Luc et al. “Cohesive zone model and quasibrittle failure of wood: a new light on the adapted specimen geometries for fracture tests.” Engineering Fracture Mechanics 109 (2013): 328-340.

[7] Oliveira, J.; Xavier, J.; Pereira, F.; Morais, J.; de Moura, M. Direct Evaluation of Mixed Mode I+II Cohesive Laws of Wood by Coupling MMB Test with DIC. *Materials* 2021, *14*, 374.
[8] Yu, Y.; Zeng, W.; Liu, W.; Zhang, H.; Wang, X. Crack Propagation and Fracture Process Zone (FPZ) of Wood in the Longitudinal Direction Determined Using Digital Image Correlation (DIC) Technique. *Remote Sens.* 2019, *11*, 1562.
[9] Xavier, J., Oliveira, M., Monteiro, P. *et al.* Direct Evaluation of Cohesive Law in Mode I of *Pinus pinaster* by Digital Image Correlation. *Exp Mech* 54, 829–840 (2014).
[10] Turner, D.Z. Digital Image Correlation Engine (DICe) Reference Manual, Sandia Report, SAND2015-10606 O, 2015.
[11] EN 338-2016 Structural timber - Strength classes, CEN Brussels, 2016.
[12] Dourado, N., de Moura M.F.S.F., Morel S., Morais, J. Wood fracture characterization under mode I loading using the three-point-bending test. Experimental investigation of Picea abies L., International Journal of Fracture, 194, 1–9, 2015.

https://doi.org/10.52202/069179-0022

World Conference on Timber Engineering Oslo 2023

BAMBOO GRIDSHELL: FROM THE MATERIAL TO THE STRUCTURE

Esti Nurdiah[1], Tsung-Hsien Wang[2], Wen-Shao Chang[3]

ABSTRACT: The majority of gridshell structures are built using timber lath and steel. only few are made from bamboo. Constructing a gridshell structure using bamboo is challenging because the anatomy, physical and mechanical properties affect the ability of bamboo culm to be bent. This paper aims to investigate the utilisation of bamboo for gridshell structures by examining bamboo as the material, the elements, and the whole gridshell structure. The experiments were conducted in three stages: testing material properties, examining bending capacity, and constructing a full-scale model of gridshell structure. The bamboo species used in the experiments was *Gigantochloa apus*, a species that is commonly found in Indonesia. The experiments showed that full-culm bamboo had a limitation on the depth of curvature, which then affected the height of gridshell, the form, and the structure.

KEYWORDS: bamboo, bamboo gridshell, material properties, bending capacity, form, structure.

1 INTRODUCTION

The construction sector has contributed significantly to global carbon dioxide (CO_2) emissions, and the use of environmentally friendly materials is highly promoted to maintain the sustainability of our planet [1]. Bamboo is one of the building materials widely known as a sustainable material. The sustainability aspect of bamboo has been researched, and findings have shown the capability of bamboo in sequestering carbon, reducing CO_2 emission, contributing to carbon storage, conserving water, controlling erosion and conserving energy, making a significant contribution to controlling climate change issues [2]–[4]. Moreover, bamboo is a fast-growing plant that can be harvested in 3 to 5 years, which makes bamboo an important replacement material for wood in terms of supply and demand [5]. Regarding workability, bamboo provides flexible and uncomplicated methods to work with, whether utilised as structures, such as portal frames, trusses and building envelopes, or as non-structural elements, such as walls and floors[6].

Gridshell structure is considered an efficient structure because it needs fewer materials than a solid surface shell structure, and is capable of enveloping a large span space [7]. Gridshell structure can be defined as a double-curvature shell built of grids instead of the usual solid surface [8]. In terms of construction methods, strained gridshell produce form by assembling the initial flat grid consisting of continuous members, which is lifted until the designated form is achieved. The curve is shaped by actively bending members; thus, the structural elements can be called active bending [9]. Gridshell built through this method also can be called 'elastic gridshell' which refers to the materiality and construction process [10].

Choosing a suitable material for elastic gridshell requires considering two important aspects. First, the material should have a sufficiently low modulus of elasticity (MOE) to minimise bending moments resulting during the shaping process. However, high MOE is needed to provide adequate global buckling stiffness. Second, materials with higher ultimate stresses can resist significant bending moments and adopt a lower radius of curvature; thus, they are suitable for achieving a strong curvature shape [11]. Bamboo has high flexibility and strength, making it capable of being employed as an active bending structure [12]–[14]. However, there is limited information about the degree to which the bamboo can be bent, especially for the utilisation in gridshell structures.

Literature on the construction and erection methods of bamboo gridshell is limited compared to timber gridshell. Rockwood's research [14] investigated the form finding and construction of bamboo gridshell. The form-finding process was through physical models, and the construction used very small-diameter bamboo. The experiments found that buckling and splitting were significant challenges in achieving desirable curvature, and some bamboo poles snap and break during the bending process. It also showed that despite bamboo being flexible, bending the material is challenging. Meanwhile, the ZBC pavilion designed by CUHK team showed the process of realising a bamboo gridshell designed through computational form-finding and modelling. During the construction, amendments were performed in response to the natural behaviour of bending bamboo which showed the discrepancy between the simulated model and the real material [15].

Therefore, some challenging questions need to be answered, such as the bending capacity of bamboo and

[1] Esti Nurdiah, PGR student, School of Architecture, The University of Sheffield, Sheffield, United Kingdom; Department of Architecture, Petra Christian University, Surabaya, Indonesia, eanurdiah1@sheffield.ac,uk, estian@petra.ac.id

[2] Tsung-Hsien Wang, School of Architecture, The University of Sheffield, Sheffield, United Kingdom, hsien.wang@sheffield.ac.uk

[3] Wen-Shao Chang, School of Architecture, The University of Sheffield, Sheffield, United Kingdom, w.chang@sheffield.ac.uk

https://doi.org/10.52202/069179-0023

bending methods that influence the depth of curvature and, hence, affect the maximum height of gridshell. Regarding the construction, there are some gridshell construction issues; whether the erection methods for timber gridshell are suitable for bamboo gridshell; whether gridshell as-design can be directly realised as-built.

This paper aims to investigate the utilisation of bamboo for gridshell structures from the material to the structure system. The paper discusses bamboo as the material by testing the material properties, as an element of the structure by investigating the bending capacity, and the whole structure system by erecting a full-scale model of bamboo gridshell.

2 MATERIAL AND METHODS

2.1 MATERIAL SELECTION

The experiment used the bamboo species *Gigantochloa apus* from Indonesia, known by the local name *bambu tali*. *Bambu tali* is readily available in most areas and cultivated in lowlands and highlands. It is known by local people for its flexibility and has been used for building construction. The features have a relatively small diameter with medium wall thickness (Figure 1). Thinner wall bamboo with a larger diameter would break easily during the bending process, while big diameter and thick wall bamboo would be hard to bend. Meanwhile, a very small-diameter bamboo was not selected because this research aimed to utilise bamboo for large-span gridshell. Bamboo with a very small diameter certainly has more flexibility, but its strength is questionable. Thus, *G. apus* was selected in consideration of its dimensions and wall thickness, and when the structure would need more than one layer, multiple layers of *G. apus* might not create a thick surface for the gridshell.

The experiment used full-culm bamboo aged 3-4 years and 5-7 cm in diameter. The age was considered the optimum age for bamboo for construction purposes. The bamboo was brought from a supplier in Magelang, Central Java province in Indonesia.

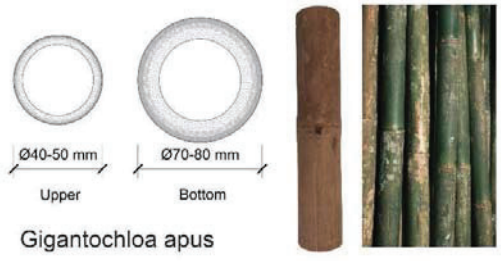

Figure 1: *Bamboo species Gigantochloa apus for the experiments.*

2.2 MATERIAL TEST

The material tests were carried out in accordance with BS ISO 22157:2019 tensile parallel to the fibres [16]. The specimens were taken from 20 bamboo culms with a length of six meters and extracted from three parts within the culm: upper, middle, and bottom. In total, 60 specimens were tested. For the tensile test, the bamboo had been treated by soaking in the boric borax solution for two weeks, then aired-dried and stored for at least six months before the testing.

The mechanical tests were carried out using JTM Universal Testing Machine with a maximum capacity of 30 Ton. The ultimate load at failure (F_{ult}) and displacement (Δ) were recorded, and the cross-section of the specimens (A) was measured from the specimen width (b) and wall thickness (δ) to calculate the strength. The formula used to determine the tensile strength was as follows:

$$\sigma_t = \frac{F_{ult}}{A} \quad (1)$$

2.3 TEST ON THE DEPTH OF CURVATURE

To design a bamboo gridshell, it is crucial to identify the maximum depth of curvature that can be reached by a bamboo culm. Whilst bamboo can be bent, due to its anatomy, there was a limitation in actively bending the bamboo. The bending capability and capacity of bamboo would determine the final geometry, apex height, and could be a consideration in determining the suitable erection method. To determine the depth of curvature, the tests were carried out in the laboratory through a bending test, and at the construction site by bending the bamboo on-site.

The first test on bending parallel to the fibres was conducted in accordance with BS ISO 22157:2019 [16]. The load was given continuously using Enerpac hydraulic jack, and a load cell was installed to record the load (F) and ultimate load (F_{ult}). To measure the displacement (Δ), three laser meters were positioned at the centre, left and right sides (Figure 2). The measurement taken for calculation were clear span (L), shear span (a), outside diameter of bamboo (D), and wall thickness (δ). Seven bamboo poles with a clear span of 3.60 meters were tested.

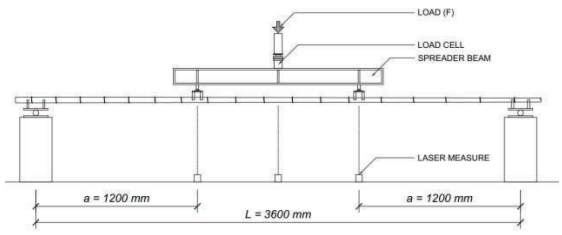

Figure 2: *Bending test set-up*

The formula used to calculate the bending moment (M_{ult}), bending strength parallel to the fibres (f_m) and tangent bending stiffness ($E_m.I_B$) were as follows:

$$M_{ult} = \frac{F_{ult} \times a}{2} \quad (2)$$

https://doi.org/10.52202/069179-0023

$$f_{m,0} = \frac{M_{ult} \times D}{2 \times I_B} \quad (3)$$

$$E_m \cdot I_B = \frac{(F_{60} - F_{20})a(3L^2 - 4a^2)}{48(\Delta_{60} - \Delta_{20})} \quad (4)$$

The apparent modulus of elasticity (E_m) was determined by dividing the tangent bending stiffnees (E_m I_B) by the second moment of area (I_B)

$$E_m = \frac{4(F_{60} - F_{20}) \cdot a(3L^2 - 4a^2)}{3\pi(\Delta_{60} - \Delta_{20}) \cdot [D^4 - (D - 2\delta)^4]} \quad (5)$$

The second test on the depth of curvature was done on the construction site by setting up bamboo poles with scaffolding and bending the bamboo manually. A set of bamboo poles was laid on two sets of scaffolding, a rope was tied at the middle of the poles, and two ropes were tied at the left and side parts. The ropes were knotted in a certain way that made them capable of being shortened by twisting a short blade installed in the middle. Alternatively, ratchet straps can also be used as a replacement for the ropes (Figure 3). The heat from a gas torch was applied to soften the bamboo's fibres in attempt to make the bamboo culm more flexible and add depth of curvature. Water was continuously applied to prevent the culm from overheating and getting burnt.

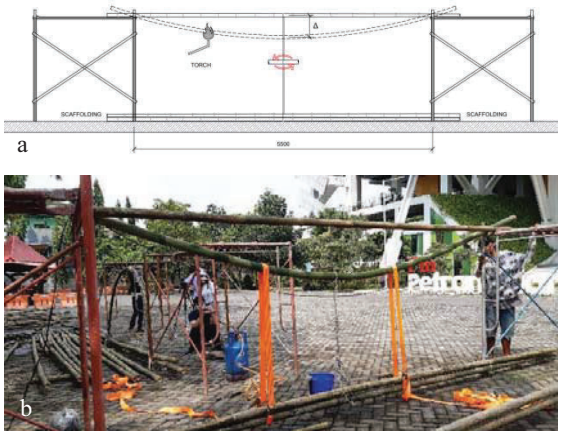

Figure 3: *Setting up of bending test on the construction site*

2.4 CONSTRUCTION METHOD

The full-scale model was built inside the campus area of Petra Christian University in Surabaya, Indonesia. Construction was carried out by building a full-scale model made from bamboo culms with a span dimension 10.80 m x 10.80 m. The entire process needed six days to complete a full-scale bamboo gridshell. The construction was done by hiring five construction workers with experience constructing bamboo buildings. However, even though they had long experience with bamboo, it was their first time constructing a bamboo gridshell.
Adjustments were made to the gridshell design and the erection method following the findings from the tests on the depth of curvature. The initial plan was to move the anchor inward and pull up the lattice. However, during several pre-construction testing events, it was hard to bend the whole culm of *bambu tali* by pushing the two tips inward. The bamboo tended to swing and return to its original shape, which would be dangerous for the workers; they could get hurt and thrown if the bamboo swung back to its original shape. Therefore, it was decided to lay the members one by one using scaffolding, then slowly pull down the members and tie them to the other members and boundary (Figure 4).

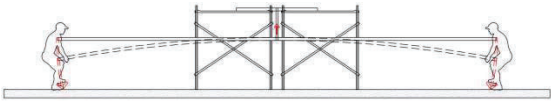

Figure 4: *Illustration of bending method to erect the bamboo gridshell*

The gridshell structure was erected by bending each member and utilising scaffolding. The two main arches at the centre were assembled and erected first, followed by other members. The connections were tied using ropes to allow rotation during the erection process. Later, the connections to the boundary were fixed using nuts and bolts.

3 DISCUSSION

3.1 TENSILE STRENGTH OF BAMBOO

A summary of the tensile test results can be seen in Table 1. The tensile strength of bamboo was particularly high but not evenly distributed within the culm, and the variation within the upper, middle, and bottom was quite significant. From the test, the highest strength was found in the upper section, with an average of 301.67 N/mm^2. Meanwhile, the middle section had an average of 289.61 N/mm^2, and the bottom section was 255.69N/mm^2.

Table 1. Summary of tensile test result

Specimens		δ (mm)	A (mm^2)	F_{ult} (kN)	σ_t (N/mm^2)
Bottom	Max	11.90	40.10	9.89	327.40
	Min	6.30	15.75	3.77	176.38
	Ave	8.42	26.23	6.52	255.69
	Stdev	1.50	7.23	1.45	40.95
Middle	Max	9.14	23.31	6.18	367.44
	Min	5.40	14.50	3.51	205.14
	Ave	6.66	17.26	4.96	289.61
	Stdev	0.85	2.20	0.78	48.24
Upper	Max	6.07	16.39	5.54	345.34
	Min	4.70	12.69	3.10	215.13
	Ave	5.30	14.05	4.32	307.67
	Stdev	0.36	0.94	0.56	31.87

The results showed good performance of bamboo in tensile, especially at the upper part. The difference between the upper and bottom sections was significantly high at 51.98 N/mm^2. The tensile test results showed that an increase in wall thickness resulted in a decrease in

tensile strength, which caused by the composition of fibres and lignin within the culm wall.

3.2 BENDING TEST OF BAMBOO

Results from the bending test are summarised in Table 2. The average bending strength parallels to the fibre (f_m) was 71.02 N/mm2, with the minimum being 41.04 N/mm2 and the maximum reaching 100.80 N/mm^2. The results were not significantly different from the previous research for *G. apus* [17], which found the modulus of rupture (MOR) of *G. apus* ranged between 376.5 kg/cm^2 (36.92 N/mm^2) and 965.6 kg/cm^2 (94.69 N/mm^2) with an average of 686.7 kg/cm^2 (67.34 N/mm^2). While the modulus of elasticity (E_m) from the experiment was found as 22,277 N/mm^2 on average. The specimens with an average culm diameter between 68.21 mm to 83.38 mm had variation in flexural rigidity with an average of 2.56E+10 Nmm^2.

Table 2. Summary of bending test result

Speci-mens	D (mm)	Δ_{max} (mm)	f_m (N/mm^2)	E_m (N/mm^2)	$E_m.I_B$ (Nmm^2)
AP 1	81.44	119.00	69.25	21,832.31	3.23E+10
AP 2	78.70	138.00	61.11	21,981.45	2.55E+10
AP 3	76.38	134.00	86.85	29,194.56	3.08E+10
AP 4	81.53	125.00	68.18	20,511.05	2.60E+10
AP 5	83.38	151.00	63.92	16,275.87	2.68E+10
AP 6	78.00	77.00	47.04	17,519.89	1.98E+10
AP 7	68.21	161.00	100.80	28,623.84	1.82E+10
Ave	78.23	129.29	71.02	22,277.00	2.56E+10
Min	68.21	77.00	47.04	16,275.87	1.82E+10
Max	83.38	161.00	100.80	29,194.56	3.23E+10
STdev	5.03	27.18	17.67	5,003.04	5.21E+9

The characteristics of failure observed during the bending test were due to compression and buckling (Figure 5), which can be seen from the crushing and splitting in the compression area. While from all specimens, no damage was found in the tension area. Previous research [17] on the flexural properties of *G. apus* showed the failure were shear and compression, and similarly, no failure in tension area and mode were found. Hence, the result presented the compression strength of the bamboo, which was significantly smaller than the tensile strength shown in Tabel 1. The failure characteristics also showed buckling in the compression area, in which the fibres were wrinkling at the top. The failure also happened due to load concentration at the saddle. The stress concentrated at one point, which caused the breaking located at the saddle.

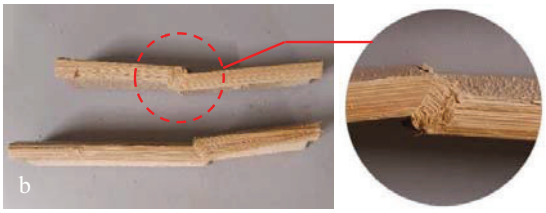

Figure 5: *Failures due to bending*

Similar failure characteristics were obtained through the bending test on the construction site using bamboo six metres in length. Failure modes recorded during the experiments were identified as splitting and fibres crushing within the uppermost area of the culm, which was the compression area. Buckling also occurred and caused sudden collapse during the bending process (Figure 6. a).

The application of heat by torching the bamboo added flexibility to the fibres and allowed the culm to reach deeper curvature. However, the heating process did not eliminate the limitation, and there was a maximum depth of curvature that the culms could reach. In the experiments, the bamboo culms were able to reach deeper curvature compared to the culms without heating; but when the culms were cooled down, they suddenly broke without any loads applied (Figure 6. c). It showed that the fibres returned to the original length and stiffness after removing the heat and showed buckling characteristics. Thus, applying heat to add the depth of curvature did not significantly help in reaching deeper curvature. Actively bending bamboo culms can only produce narrow curvature.

Figure 6: *Failures due to bending test on the construction site*

The tests on the depth of curvature resulted in a major revision to the initial design of the full-scale model. The initial design of gridshell form was based on the basic form of a simple gridshell structure (Figure 7). The form had been used by Labonnote [18] and Dyvik [19] and was based on form-finding from Pone [20]. The form finding

https://doi.org/10.52202/069179-0023

was done in Rhinoceros using plug-ins Grasshopper and Kangaroo. The initial construction plan was to build gridshell form by constructing a flat lattice and moving the anchor inward to create maximum curvature and form the gridshell surface.

Based on the experiments, the initial plan could not be realised. It was not possible to bend a whole culm bamboo into the expected depth of curvature based on the initial design. As can be seen in Figure 7, middle members had narrow curvature, but members near the boundary had deeper curvature. The depth cannot be formed and certainly would result in buckling and breaking. Therefore, the initial design was revised, and several adjustments were added concerning the bending capacity of bamboo.

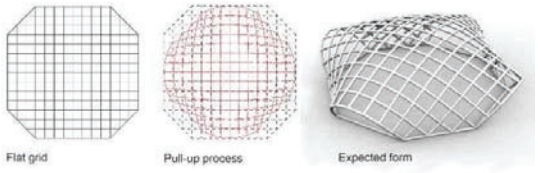

Figure 7: *Initial design of bamboo gridshell*

The adjustments involved lowering the apex height and increasing the span from 8.40 m x 8.40 m to 10.80 m x 10.80 m (Figure 8) to gain higher curvature. Following the result of bending tests, the maximum curvature a bamboo culm or pole could achieve was limited. Thus, by increasing the span, it was expected that the depth of curvature would also be increased, and the maximum apex height could be determined.

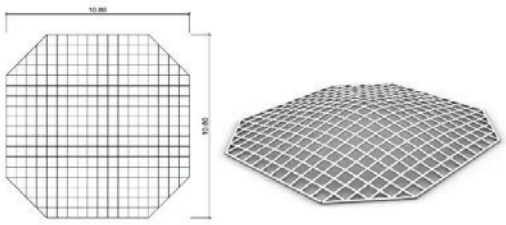

Figure 8: *Final design of bamboo gridshell for the experiment.*

3.3 CONSTRUCTION PROCESS OF BAMBOO GRIDSHELL

Methods of bending the bamboo to reach the maximum possible curvature and form a lattice structure became a crucial part of this construction stage. Based on their experience and craftsmanship, the workers preferred to employ slicing methods to create bamboo arches. Slicing methods provided a quick and easy technique; however, only small strips of the culm were left to bear the loads. The strength would be greatly reduced, and the deeper the curvature, the more slicing would be needed. Therefore, in this research, it was decided to actively bend the bamboo culm and use the heating method to help raise the curvature's depth

The span dimension of the full-scale model was 10.80 m x 10.80 m, and the mesh grids were 0.60 m x 0.60 m. Eight bamboo poles were assembled to form the boundary structure, which had an octagon shape. Around 120 bamboo culms, including those used for the depth of curvature test, were prepared for the construction. The model consisted of 34 long members to construct the surface. As the shortest members for the surface was 7.2 meters, two bamboo culms were joined into one long pole and cut according to the length. No joinery to lengthen the poles were needed for the boundary since the members' length did not exceed 6 meters.

The construction process began with the erecting of the first arch as the centre arch, which played a significant role in defining the maximum height of curvature or the apex of gridshell. Two sets of scaffolding were assembled, and a bamboo pole was strung across the centre to form the first arch (Figure 4 and Figure 9). Two workers held the tips of the bamboo pole and carefully pulled down the tips until they reached the ground. The bamboo was raised to its greatest possible height without snapping. After six poles were tested, it was determined to lift the arch to a height of 1.20 m, which could potentially break the bamboo poles. The height was considered narrow compared to the potential reach of timber gridshells. Afterwards, the arch was tied to a horisontal beam to hold the curvature (Figure 9).

Figure 9: *Erection process of the centre arch*

The second arch was erected perpendicular to the first arch by constructing another two sets of scaffolding, tying the centre of the second pole to the first arch, then carefully lowering the tips to the ground and tying the arch to straight poles, following a similar procedure as the previous arch (Figure 10). After constructing two major arches, the boundary was created. Then, other members were set one by one on top of the major arches and then carefully lowered and tied to the boundary. Throughout the assembly process, short poles were installed under the connectors as supports to maintain the curvature. To ensure that the connection could rotate during assembly, each connection was secured using ropes that permit rotation (Figure 11).

https://doi.org/10.52202/069179-0023

Figure 10: *Assembly process*

Figure 11: *The connections and the temporary supports*

After the members had assembled, the bamboo was heated by torching the culms. Water was regularly applied during heating to prevent the bamboo culms from overheating and cracking (Figure 12.b). The structure was then raised using a chain block. However, the outcome of attempts to increase the height of the apex was insignificant. The apex only raised around 3-5 cm during the process. In the last stage, nuts and bolts were used to secure the connection between the lattice and the boundary. Then, all supports were removed, resulting in the lattice independently forming the whole curvature of the gridshell.

Figure 12: *Heating and pulling the gridshell using chain block to add height*

Once all supports were removed, the gridshell structure quickly lost a certain height, and the final apex height only reached 1.12 m. It was recorded that when the supports were removed, the lattice members pressed against the boundary beams. The bamboo culm showed a tendency to swing back to its original shape, and the boundaries were crucial in holding the form.

During the construction, many bamboo culms failed and broke. Several causes of the failures were buckling and splitting, and some failures occurred at the connections. Buckling happened during the bending process, which has been discussed in section 3.2. However, when the curvatures were getting narrow near the boundary, the occurrence of buckling was not found. The critical failure resulting from bending was at the highest curvature area. Splitting was recorded to occur mainly at the boundary. The pressure from lattice members to the boundary increased the stress, and the beams started to split (Figure 13.a). The pressure also affected the connections between lattice members and boundary. One connection was heavily damaged and broke (Figure 13.b). The connection had been fixed using nuts and bolts, and thus, it no longer could move. On the other hand, fixing the connections was necessary to hold the curvature when the supports were removed. Otherwise, the gridshell would lose its height, and the bamboo would swing back to its original shape.

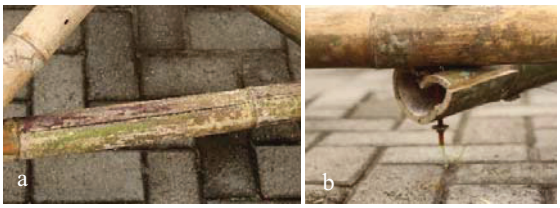

Figure 13: *Failures in the construction: a. due to splitting; b. due to breaking*

4 CONCLUSION

The experiments showed that the choice of bamboo as material influenced the final gridshell design and the construction method. As a material, bamboo has high tensile strength. However, limitation in bending significantly impacted its flexibility. Majority of failures in bending, both during the depth of curvature test and construction, was caused by fibres wrinkling in compression area, splitting, and buckling.

The bending limitation affected the depth of curvature of bamboo arches and the apex height of bamboo gridshell. The apex height produced by the full-culm bamboo was narrow, especially compared to the apex height that a timber gridshell can reach. The maximum depth of curvature or apex height in this study was compared to the span at a ratio of 1:9.64. Hence, designing a bamboo gridshell should take into account the maximum depth of curvature, and the curvature would have to be narrow if the gridshell were entirely made of full-culm bamboo.

The boundaries structure was crucial in keeping the curvature shape, particularly in holding the bamboo culm from returning to its original shape. Therefore, the connection between the lattice members and the boundaries should be considered to prevent breaking, in which, can cause the collapse to the whole structure system. Further analysis of stress distribution in boundaries and alternatives of suitable connections will surely be necessary for future research.

https://doi.org/10.52202/069179-0023

ACKNOWLEDGEMENT

The first author is supported by Indonesia Endowment Fund for Education (LPDP) from the Ministry of Finance, The Republic of Indonesia. The first author also would like to thank Petra Christian University for providing two laboratories: Concrete Laboratory and Building Structures Laboratory, to carry out the experiments.

REFERENCES

[1] Y. Goh, S. P. Yap, and T. Y. Tong, 'Bamboo: The Emerging Renewable Material for Sustainable Construction', in *Encyclopedia of Renewable and Sustainable Materials*, Elsevier, 2020, pp. 365–376. doi: 10.1016/B978-0-12-803581-8.10748-9.

[2] F.-C. Chang, K.-S. Chen, P.-Y. Yang, and C.-H. Ko, 'Environmental benefit of utilising bamboo material based on life cycle assessment', *Journal of Cleaner Production*, vol. 204, pp. 60–69, Dec. 2018, doi: 10.1016/j.jclepro.2018.08.248.

[3] P. van der Lugt, A. A. J. F. van den Dobbelsteen, and J. J. A. Janssen, 'An environmental, economic and practical assessment of bamboo as a building material for supporting structures', *Construction and Building Materials*, vol. 20, no. 9, pp. 648–656, Nov. 2006, doi: 10.1016/j.conbuildmat.2005.02.023.

[4] E. Zea Escamilla, G. Habert, and E. Wohlmuth, 'When CO2 counts: Sustainability assessment of industrialised bamboo as an alternative for social housing programs in the Philippines', *Building and Environment*, vol. 103, pp. 44–53, Jul. 2016, doi: 10.1016/j.buildenv.2016.04.003.

[5] J. Li, Y. Yuan, and X. Guan, 'Assessing the Environmental Impacts of Glued-Laminated Bamboo Based on a Life Cycle Assessment', *BioResources*, vol. 11, no. 1, Art. no. 1, Jan. 2016.

[6] A. Widyowijatnoko, M. Trautz, and B. Baier, *Traditional and innovative joints in bamboo construction*, 1. Aufl. Aachen: Mainz, 2012.

[7] C. Douthe, O. Baverel, and J. F. Caron, 'Form-Finding of a Gridshell in Composite Materials', *JOURNAL OF THE INTERNATIONAL ASSOCIATION FOR SHELL AND SPATIAL STRUCTURES*, vol. 47, no. 150, p. 10, 2006.

[8] D. Naicu, R. Harris, and C. Williams, 'Timber Gridshells: World Conference on Timber Engineering (WCTE) 2014', Aug. 2014. Accessed: Dec. 16, 2022. [Online]. Available: http://www.wcte2014.ca/

[9] S. Adriaenssens, P. Block, D. Veenendaal, and C. Williams, Eds., *Shell structures for architecture: form finding and optimisation*. London ; New York: Routledge/ Taylor & Francis Group, 2014.

[10] E. L. Hernández, O. Baverel, and C. Gengnagel, 'On the Design and Construction of Elastic Gridshells with Irregular Meshes', *International Journal of Space Structures*, vol. 28, no. 3–4, pp. 161–174, Sep. 2013, doi: 10.1260/0266-3511.28.3-4.161.

[11] E. L. Hernández, C. Gengnagel, S. Sechelmann, and T. Rörig, 'On the Materiality and Structural Behaviour of Highly-Elastic Gridshell Structures', in *Computational Design Modelling*, C. Gengnagel, A. Kilian, N. Palz, and F. Scheurer, Eds. Berlin, Heidelberg: Springer Berlin Heidelberg, 2011, pp. 123–135. doi: 10.1007/978-3-642-23435-4_15.

[12] K. Crolla, 'Bending Bamboo Rules: Beyond Century-Old Typologies', *Journal of Architectural Education*, vol. 72, no. 1, pp. 135–145, Jan. 2018, doi: 10.1080/10464883.2018.1410669.

[13] M. Seixas, J. Bina, P. Stoffel, J. L. Ripper, L. E. Moreira, and K. Ghavami, 'Active Bending and Tensile Pantographic Bamboo Hybrid Amphitheater Structure', *Journal of the International Association for Shell and Spatial Structures*, vol. 58, no. 3, pp. 239–252, Sep. 2017, doi: 10.20898/j.iass.2017.193.872.

[14] D. Rockwood, *Bamboo gridshells*. London ; New York: Routledge, Taylor & Francis Group, 2015.

[15] K. Crolla, 'Building indeterminacy modelling – the "ZCB Bamboo Pavilion" as a case study on nonstandard construction from natural materials', *Vis. in Eng.*, vol. 5, no. 1, p. 15, Dec. 2017, doi: 10.1186/s40327-017-0051-4.

[16] 'ISO 22157:2019(en), Bamboo structures — Determination of physical and mechanical properties of bamboo culms — Test methods'. https://www.iso.org/obp/ui/#iso:std:iso:22157:ed-1:v1:en

[17] Nurmadina, N. Nugroho, and E. T. Bahtiar, 'Structural grading of Gigantochloa apus bamboo based on its flexural properties', *Construction and Building Materials*, vol. 157, pp. 1173–1189, Dec. 2017, doi: 10.1016/j.conbuildmat.2017.09.170.

[18] N. Labonnote, J. H. Mork, S. H. Dyvik, M. Nilsen, A. Rønnquist, and B. Manum, 'Experimental and numerical study of the structural performance of a timber gridhsell', presented at the WCTE 2016, Vienna, Aug. 2016.

[19] S. H. Dyvik, J. H. Mork, M. Nilsen, and M. Luczkowski, 'Modular kinematic timber gridshell; a simple scheme for constructing advanced shapes', *Proceedings of IASS Annual Symposia*, vol. 2016, no. 19, pp. 1–10, Sep. 2016.

[20] S. Pone, S. Colabella, B. D'Amico, A. Fiore, D. Lancia, and B. Parenti, 'Timber Post-formed Gridshell: Digital Form-finding / drawing and building tool', 2013.

World Conference on Timber Engineering Oslo 2023

PRELIMINARY INVESTIGATION ON SAFETY PERFORMANCE OF CLT WALL PANELS UNDER IMPACT AND SUSPENSION TESTS

Gabriela Lotufo Oliveira[1], Fabiana Lopes de Oliveira[2]

ABSTRACT: Cross-Laminated Timber (CLT) panels are a relatively new construction element of the international construction industry. In Brazil, the manufacture of this technology started about ten years ago. The use of this innovative construction element in the country is still limited. For this reason, many of those who are first introduced to the material express several doubts regarding its applicability. Thus, this paper sought to analyse this type of panel in terms of safety performance, as this is the fundamental requirement of any building and one of the essential premises to guarantee its stability, as well as the safety of the user. The proposed verification was carried out according to the Brazilian technical standard ABNT NBR 15575:2013 – Residential Buildings – Performance. For this, the following laboratory tests were carried out in one specimen of CLT wall panel: soft body impact, hard body impact and determination of the resistance of the panel to the demands of suspended parts. At the end, it was found that the panels tested met the minimum requirements and criteria established by the studied standard.

KEYWORDS: Cross-Laminated Timber (CLT), safety performance, wooden structure, prefabricated structure, engineered wood.

1 INTRODUCTION

CLT panels are prefabricated structural timber panels, that can be used as floor or roof slabs, and internal or external walls, with or without structural function. As the name describes (Cross-Laminated Timber), they are composed of layers of solid wood glued perpendicularly to each other. Initially developed in the 1990s in Europe, they started to be manufactured in Brazil about ten years ago by a national manufacturer located in São Paulo state. The first Brazilian CLT structure was fabricated and assembled in 2012. Between this first example and 2018, as pointed by [1], more than 30 constructions were built in the country, most of them being single-family homes.

The use of this innovative construction element in Brazil is still limited. For this reason, many of those who are first introduced to the material express several doubts regarding its applicability. Thus, the study of the panels' performance is imperative. Additionally, considering the predominant residential use of CLT in Brazil, it is essential that the requirements established by the technical standard "ABNT NBR 15575:2013 – Residential Buildings – Performance" [2] are properly met by this new technology.

Therefore, this paper aims to analyse CLT wall panels in terms of safety performance, which is considered the fundamental requirement of any building as well as one of the essential premises to guarantee its stability and the safety of the user.

The basis for this study was the standard "ABNT NBR 15575: 2013 Part 2: Requirements" for structural systems, which presents the requirements that must be met by the construction to guarantee minimum building performance. Most of those presented requirements can be verified through the project's analysis, which varies according to each building. One of them, however, can be checked through laboratory tests, which is item 7.4 – Soft and hard body impacts.

In addition, since CLT panels may be applicable for structural walls, one must also verify its conformity with "ABNT NBR 15575:2013 Part 4: Requirements for internal and external vertical sealing systems – VVIE". In this part of the standard the item which can be verified through laboratory test was item 7.3 – Load requests from suspended parts acting on internal and external sealing systems.

Hence, for the proper determination of the safety performance of CLT buildings, the tests were carried out between September and October 2017 in one specimen of CLT wall panel. The results obtained were compared to the performance requirements established by the ABNT NBR 15575:2013, which are classified as minimum (M), intermediate (I) or superior (S).

[1] Gabriela Lotufo Oliveira, Faculdade de Arquitetura e Urbanismo da Universidade de São Paulo, Brasil, gabriela.lotuffo.oliveira@usp.br

[2] Fabiana Lopes de Oliveira, Faculdade de Arquitetura e Urbanismo da Universidade de São Paulo, Brasil, floliveira@usp.br

https://doi.org/10.52202/069179-0024

2 CONTEXT

As seen previously, CLT panels are of European origin. According to [3], this technology started to be developed in Switzerland, in the cities of Zurich and Lausanne, during the early 1990s. However, CLT, as it is currently known, is the result of a research that started in 1990 in Austria and involved a partnership between a wood-based systems' manufacturer and Graz University.

Since its development, the use of CLT panels has increased significantly, including the growth in the number of tall buildings that incorporate this innovative building technology along with other mass timber products, such as Glued-Laminated Timber (Glulam). As pointed by [4], almost 200 mass timber buildings with five storeys or more were developed between 2004 and 2019 around the globe. Over 80% of those are located in Europe. In North America, the implementation of CLT panels is still recent, although this is the region that concentrates most of mass timber tall buildings, after Europe [4] [5].

In Europe, the first standard that regulates CLT panels, EN 16351, was published in 2015. It addresses performance features, in addition to establishing minimum requirements for the manufacture of panels, whether straight or curved. It applies to panels made with at least three orthogonal layers, which can also have up to three successive layers glued in parallel, in the case of panels with at least four layers [6].

The American standard ANSI/APA PRG 320, which establishes rules for the manufacture and characterization of the CLT produced in the United States and Canada defines Cross-Laminated Timber as a prefabricated engineered wood product consisting of at least three layers of solid sawn wood or Structural Composite Lumber (SCL), glued with structural adhesive. The thickness of each layer must be a minimum of 16 mm and a maximum of 51 mm, resulting in panels up to 508 mm thick [7].

As indicated by [4], the cross configuration of the layers enables the distribution of loads in a bidirectional way, allowing to achieve high strength and stiffness capacities. Thus, the main innovation is the production of panel elements, which function as self-supporting walls or slabs.

The sizes of CLT panels vary according to the manufacturer, reaching dimensions of up to 2.95 m x 24.00 m [3]. Transport regulations, however, can also impose dimensional limitations on these construction elements. As highlighted by [8], the common dimensions are lengths of up to 18.00 m, reaching 30.00 m, and maximum widths of 3.00 m, reaching up to 4.80 m, with maximum thicknesses between 300 and 400 mm.

In national production, according to [1], the panels are manufactured with maximum dimensions of 12.00 x 3.00 m, with thicknesses varying between 60 mm and 250 mm. The author also mentions that the Brazilian construction process can be divided into three parts: raw material, manufacture of panels and assembly of the building. Each has its own internal phases. The raw material, after extraction, may or may not receive preservative treatment to prevent the attack of deteriorating organisms, such as fungi or insects. The manufacture, in turn, begins with visual screening of the lamellas, passing through the splicing of these, the assembly and pressing of the panel and the cutting and machining of the pressed panel. The assembly of the building includes logistics, that is, the transportation of the construction elements to the construction site, as well as the movement and connection of the parts, the execution of the building installation and facade [1].

Regarding the assembly of CLT buildings in Brazil, [1] reports that the panels are fixed together, or in other building systems, such as concrete slabs, metal beams, among others, by means of self-tapping screws or metal connectors. In the joints formed between two CLT elements, being parallel or perpendicular to each other, a line of weather-resistant silicone sealant is applied. The screws used in Brazil are manufactured by an Italian company specialized in connectors for wooden structures, the Rothoblaas®. They are used both in simple connections, as well as in more complex ones, that is, when the fixation occurs by means of metallic connectors.

In Brazil, as beforementioned, the production of CLT panels is even more recent than in North America, dating back to 2012. There are no multi storey buildings in the country yet.

However, the use of CLT panels is expected to increase soon. One of the reasons for that is the recent publication of the reviewed national standard for timber structures, that occurred in the second semester of 2022. This document, which regulates wood structures in Brazil, was going through a revision process since 2002. Among many important changes that were incorporated in its latest version was the mention of CLT panels and the introduction of five tests methods for panels that are produced in the country [9].

Even though, as any other construction technology, when used for residential purposes, CLT panels must also meet the criteria established by the technical standard "ABNT NBR 15575:2013 – Residential Buildings – Performance", which is also known by the denomination of "Performance Standard".

3 MATERIALS AND METHODS

To verify the safety performance of a CLT wall panel produced by the first Brazilian Manufacturer, the following laboratory tests were carried out: Soft body impacts, Hard body impacts, and Load requests from suspended parts acting on internal and external sealing systems.

For the three tests mentioned, a single sample was used, which was 80 mm thick (three layers panel, with 20 mm thick external layers and 40 mm thick internal layer), 4000 mm wide and 2700 mm height. It consisted of two CLT panels: the first one measuring 3000 mm wide and the second one 1000 mm wide (Figure 1). Such thickness is the most commonly used in CLT panels to build walls in Brazil.

https://doi.org/10.52202/069179-0024

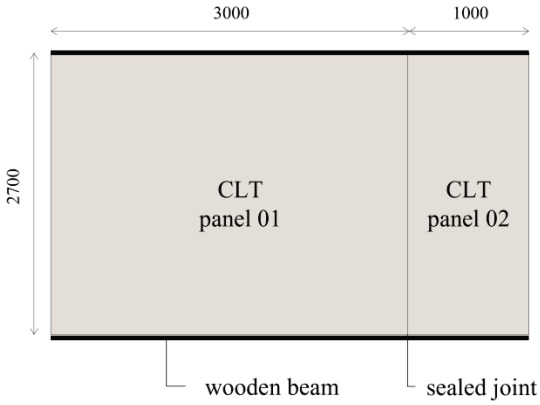

Figure 1: *Design of the specimen carried out to verify the safety performance of the CLT panel. Measures in millimetres (without scale)*

The panels were produced using a vacuum press, with lamellas of *Pinus taeda* wood that were glued with polyurethane structural adhesive. The grade and strength class of each layer was not provided. For more information about the production process of this manufacturer see [1], that describes the production process in detail.

In order to verify the performance of the system also at the point of attachment between the two panels, a joint in the panel was made. The fixation between the two panels occurred through Rothoblaas® VGZ7140 screws fastened with an angle of 45º in relation to the faces of the panels. The joint between the two panels received an application of silicone sealant weather resistant.

The specimen was fixed at its lower and upper edges in a pre-existing porch, composed of two metal beams filled with concrete (Figure 2). For this fixation, in order to replicate a real connection between CLT elements and concrete foundations, a wooden beam was adopted, which was fixed to the concrete sleeper by means of anchor bolts. An EPDM tape was positioned above the beam. The panels were fixed to the beam using Rothoblaas® VGZ7140 screws fastened with an angle of 45º in relation to the faces of the panels.

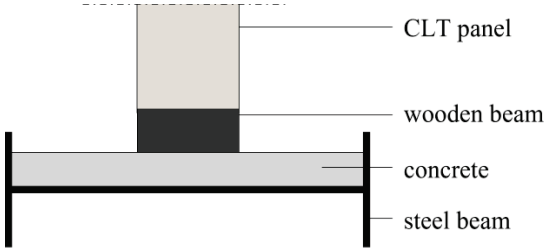

Figure 2: *Schematic detail of the lower fixation of the specimen carried out to verify the safety performance of the CLT panel. Measures in millimetres (without scale)*

3.1 SUSPENDED PARTS TEST

The first test carried out was the requirement Load requests from suspended parts acting on internal and external sealing systems. The method adopted for this test is set out in Annex A of the ABNT NBR 15575:2013 Part 4 [2]. The purpose of this test is to analyse the resistance of CLT panels to the demands caused by fixing suspended parts, such as cabinets, shelves, washbasins, hydrants, pictures and others. The application of the load on the panel, to verify its resistance, is carried out by means of a standardized shelving bracket.

Two tests of this type were performed, each one using different screws for fixing the shelving bracket. In the first, Rothoblaas® HBS 660 screws and, in the second, conventional screws for MDF in size 4.5 x 60 mm were used. The first screw is not produced in Brazil and, therefore, it is more difficult and expensive to acquire. That was the reason for conducting this test with a second screw, which is considerably more common and can be found in all regions of the country.

The load was applied to the shelving bracket at 50 N levels and without blows, according to the standard, with an interval of 3 minutes between the positioning of each level (Figure 3). The maximum load considered in the test had to be maintained after a period of 24 hours.

Figure 3: *Suspended parts test in progress*

3.2 HARD BODY IMPACT TEST

For the second test, which consisted of verifying the resistance of wall panels to hard body impacts, the method adopted is set out in Annex B of the ABNT NBR 15575:2013 Part 4 [2]. In this test, structural components under hard body impacts must not be broken or pierced under any impact energy, but the occurrence of cracks, chipping and other damages (impacts of use) can be tolerated. The test was carried out with the pendular release, at rest, of a body of known mass, at a specified height. The body consisted of steel balls of two types: a small hard body of 0.5 kg and a big hard body of 1 kg.

These bodies were suspended by a cable and released in a pendular motion, generating impact energies that are

https://doi.org/10.52202/069179-0024

indicated in the standard, until reaching the specimen (Figure 4). The impacts were applied at different random points, that is, each impact had to occur at a different point, without repeating. The standard in question establishes as impact energy 10 J and 20 J, for the big body, and 2.5 J and 3.75 J for the small body. To mark the point of impact on the panel, a carbon paper was used and fixed with self-adhesive tape on the specimen.

Figure 4: *Hard body impact test in progress. The picture shows the moment before the hard body is abandoned.*

3.3 SOFT BODY IMPACT TEST

The last test consisted of measuring the resistance of the panels to soft body impacts, according to the test method which is indicated in the ABNT NBR 11675:2016 Modulated internal light partitions – Verification of resistance to impacts [10]. For this purpose, a cylindrical leather bag was used as a soft body. It measured approximately 350 mm in diameter and 900 mm high and contained dry sand and sawdust inside, with a total weight of (400 ± 4) N (equivalent to about 40 kg). In addition, the measurement of the horizontal displacement of the panel was carried out by means of a depth calliper with a resolution equal to or less than 0.1 mm.

As the standard describes, the test begins with the suspension of the leather bag, through a steel wire, so that the projection of its centre of mass on the surface of the specimen coincides with the point where the impact must be applied. The device for the graphic record of the displacements of the panel must be installed in a position coincident with the centre of mass of the leather bag, on the face of the specimen opposite to that which will suffer the direct impact. The cylindrical leather bag is then abandoned in a pendular motion and must reach the specimen with the energies that are specified in the standard: 120 J, 180 J, 240 J, 360 J, 480 J, 720 J and 960 J (Figure 5).

After each impact, the specimen undergoes visual inspection. The instantaneous horizontal displacement (dh) and the residual horizontal displacement (dhr) of the panel are determined for each impact using the depth calliper. Five minutes after the application of each impact, one can register the residual displacement of the panel and, then, the device's graph paper is moved to record the displacements graphically in order to apply the following impact [10].

Figure 5: *Soft body impact test in progress. The picture shows the moment after the leather bag is abandoned.*

The test performed on the CLT panels followed the procedures described above and provided for the mentioned standard. Two points were determined where the impact was applied, the first being in the centre of the CLT Panel 01, with a width of 3000 mm and the second located at the joint between the two panels. For each point, an impact was made for every energy specified in the standard, registering the horizontal displacement by means of the depth calliper (Figure 6).

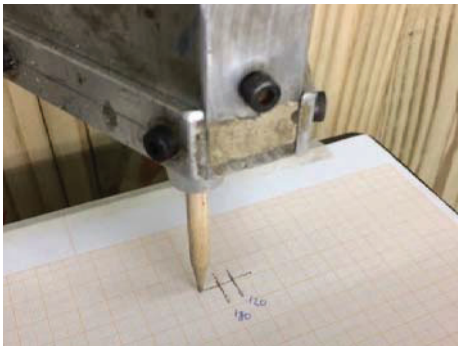

Figure 6: *Soft body impact test in progress. The picture shows the measurement of the instantaneous horizontal displacement (dh) and the residual horizontal displacement (dhr) of the panel by the depth calliper.*

4 RESULTS

4.1 SUSPENDED PARTS TEST

The first test aimed to verify the resistance of the panel to load requests from suspended parts acting on internal and external sealing systems. As a result, loads of 80 kgf and 100 kgf were kept in the shelving bracket for 24 hours, for both screws that were tested, without any kind of damage or instantaneous or residual horizontal displacements in the panel.

4.2 HARD BODY IMPACT TEST

When verifying the resistance of the wall panel to hard body impacts, the panel was tested only with energy of 3.75 J, for the small body, and 20 J, for the big body. It

was decided not to test the lowest energies, for, since the panel did not suffer damage with the highest energies, neither would it suffer with lower energies. Due to the impacts made, dents with small depths were observed. However, there was no rupture, piercing, and occurrence of cracks, chipping or other damages. The dents' depths verified in each impact are shown in Table 1.

Table 1: *Depth of the dents verified in each hard body impact.*

Impact nº.	Depth of dent (mm)	
	Impact of 3.75 J	Impact of 20 J
1	0.6	1.3
2	0.6	1.7
3	1.0	1.1
4	0.7	1.6
5	0.2	1.2
6	0.3	2.5
7	0.7	2.1
8	1.4	1.6
9	0.6	0.8
10	0.2	0.6

4.3 SOFT BODY IMPACT TEST

In the last test (soft body impacts) at the two points of impact and for all energies tested, there was no occurrence of ruin and piercing or surface flaws, such as dents, cracks, chipping, detachments and breakdowns. However, there was a small instantaneous horizontal displacement in the panels, which was recorded by the depth calliper. This displacement, for each point and impact energy, is shown in Table 2.

Table 2: *Displacements verified in each soft body impact.*

Energy (J)	Impact on the joint		Impact at the center of the specimen	
	Instantaneous displacement – dh (mm)	Residual displacement – dhr (mm)	Instantaneous displacement – dh (mm)	Residual displacement – dhr (mm)
120	8	0	6	0
180	9	0	7	0
240	11	0	9	0
360	13	0	12	0
480	14	1	13	1
720	18	0	16	0
960	22	1	18	1

5 DISCUSSION

5.1 SUSPENDED PARTS TEST

Regarding load requests from suspended parts acting on the CLT panel, the test was paused when the tested screws reached the load limit established by the ABNT NBR 15575:2013 for intermediate performance level (Annex F of the ABNT NBR 15575-4:2013) [2], that is 1.0 kN (equivalent to 100 kgf). In both cases, no cracks, detachments or instantaneous or residual horizontal displacements were identified. However, it is possible that the screws could withstand a load even greater than the value reached. Thus, it is not possible to say whether they would achieve intermediate or higher performance in this regard.

5.2 HARD BODY IMPACT TEST

In order to verify the wall panel's resistance to hard body impacts, as established by the ABNT NBR 15575:2013 [2], the minimum performance level for energies of 2.5 J and 10 J requires no failure in the structural element, although dents with any depth are allowed. For energies of 3.75 J and 20 J, surface flaws such as dents, cracks, chipping and disintegration are allowed. Ruins and piercing cannot occur. For 3.75 J energy, to reach the intermediate or higher performance level, the standard determines as the maximum depth allowed for the dent 5 mm and 2 mm, respectively.

In this test, as mentioned above, there was no rupture, piercing, cracking, chipping or other damage in any of the cases. While for dents, as seen in Table 1, the maximum depth obtained in the energy impact of 3.75 J was 1.4 mm. Consequently, regarding the panel's resistance to hard body impacts the higher performance level was reached, according to the criteria established in the ABNT NBR 15575: 2013 [2].

5.3 SOFT BODY IMPACT TEST

The analysis of the results obtained with soft body tests applied the performance criteria presented in Annex F of the ABNT NBR 15575:2013 Part 4 [2] for all CLT possible uses, which are: internal walls with and without structural function, external walls (facades) of single-story houses with structural function and external walls of single-story houses without structural function. In the last case, only the criteria for light seals were analysed, that is, with a density less than 60 kg/m², considering that the tested panel (80 mm thick and an average density of 550 kg/m³), by having a mass of approximately 44 kg/m², falls into this category.

Whereas the absence of ruins, piercing or any other failure, it is necessary to check the horizontal displacements caused by the impacts. The method that must be used to calculate the displacements, as presented by the mentioned criteria, are presented in Table 3.

Thus, it was calculated the maximum instantaneous and residual displacements that were allowed in each situation. These displacements were compared to the maximum values established by the Performance Standard, which determines three performance levels: minimum (M), intermediate (I) and superior (S).

Table 4 shows the calculated values and the actual values that were measured during the test for each impact point. It can be seen from the results presented in Table 4, that practically all the actual displacements measured, whether

https://doi.org/10.52202/069179-0024

instantaneous or residual, were lower than the values that were calculated with the equations presented by the ABNT NBR 15575-4:2013 [2] and in Table 3.

It is also interesting to analyse the use of "external walls of single-story houses with a structural function – external impact (external public access)". For this use and for the impact energy of the soft body of 240 J, the instantaneous displacement limit must be less than or equal to h/250. As mentioned, the specimen was 2700 mm high and, therefore, according to the equation, the dh limit is 10.8 mm. In this case, the 11 mm value measured for the instantaneous displacement would be higher than the calculated limit of 10.8 mm. However, considering the accuracy of the 1 mm depth calliper, and not 0.1 mm, as provided by the standard, it is not possible to say, for sure, that the actual displacement was, in fact, below the established limit. Thus, it was considered that the measured value would be equivalent to the one calculated, rounding the limit from 10.8 mm to 11 mm, by proximity.

Thereafter, it is possible to verify that, if used as an internal wall with or without structural function, CLT panels similar to the specimen from this study could reach the level of higher performance according to the resistance to soft body impacts. Also, as external structural walls of single-story houses, the level of performance that was achieved in this analysed requirement is also higher. Finally, CLT panels just like the one tested, when working as walls of a single-story house, without structural function, would also achieve the level of higher performance.

Table 3: *Compilation of the limitation of horizontal displacements presented in Annex F of the ABNT NBR 15575:2013 Part 4 for all possibilities of uses for CLT elements.*

Vertical seal type	**Impact energy (J)**	**Limitation of horizontal displacements**	**Performance Level**		
			M	**I**	**S**
Internal with structural function	**120**	d_h <= h/250; d_{hr} <= h/1250	X		
Internal without structural function	**120**	d_h <= h/125; d_{hr} <= h/625		X	X
	60	d_h <= h/125; d_{hr} <= h/625	X		
External of single-story houses, with structural function – External impact	**240**	d_h <= h/250; d_{hr} <= h/1250	X	X	X
External of single-story houses, with structural function – Internal impact	**120**	d_h <= h/250; d_{hr} <= h/1250	X	X	X
External of single-story houses, without structural function – External impact	**120**	d_h <= h/62.5; d_{hr} <= h/312.5	X		

Table 4: *Compilation of the results found for the horizontal displacements of the tested panel.*

Vertical seal type	**Impact energy (J)**	**Calculate displacement (mm)**	**Actual displacement (mm)**	
			Ponto A	**Ponto B**
Internal with structural function	**120**	d_h <= 10.8; d_{hr} <= 2.16	d_h = 8; d_{hr} = 0	d_h = 6; d_{hr} = 0
Internal without structural function	**120**	d_h <= 21.6; d_{hr} <= 4.32	d_h = 8; d_{hr} = 0	d_h = 6; d_{hr} = 0
	60	d_h <= 21.6; d_{hr} <= 4.32	- -	- -
External of single-story houses, with structural function – External impact	**240**	d_h <= 10.8; d_{hr} <= 2.16	d_h = 11; d_{hr} = 0	d_h = 9; d_{hr} = 0
External of single-story houses, with structural function – Internal impact	**120**	d_h <= 10.8; d_{hr} <= 2.16	d_h = 8; d_{hr} = 0	d_h = 6; d_{hr} = 0
External of single-story houses, without structural function – External impact	**120**	d_h <= 43.2; d_{hr} <= 8.64	d_h = 8; d_{hr} = 0	d_h = 6; d_{hr} = 0

6 CONCLUSIONS

The present work sought to verify the safety performance of CLT panels manufactured in Brazil according to the criteria established by the Performance Standard, ABNT NBR 15575:2013. To this end, the following laboratory tests were carried out: Hard body impacts and Load requests from suspended parts acting on internal and external sealing systems. The tests' results were compared with the minimum requirements and criteria established in the ABNT NBR 15575:2013, in order to verify their compliance.

The authors are aware that the study tested only one specimen of one producer. Therefore, the results cannot ensure that all Brazilian CLT panels have adequate performance according to national standards. There are a great number of other standards in Brazil and, also, other requirements in ABNT NBR 15575:2013 that must be achieved by this technology. It must be highlighted, further, that the performance analysis of the element in question should encompass other requirements not included by this study, such as thermal or acoustic comfort.

Moreover, since the latest publication of the reviewed Brazilian standard for timber structures and the introduction of tests methods for CLT panels that are produced in the country, it is also expected for the national production of CLT panels to meet those recent requirements. Therefore, it was not intended, in this work, to exhaust the studies on the use of CLT panels in Brazil.

Finally, it appears that CLT panels present themselves as an extremely promising option for the global and Brazilian construction industry. Certainly, as the demand to CLT panels in the national construction business increases, just like it has occurred in other countries, new challenges, and therefore new solutions, will be faced, and shall be overcome. Thus, the present study aims to be one unassuming step towards the actual and permanent implementation of this technology nationally.

REFERENCES

[1] G. L. Oliveira. Cross Laminated Timber (CLT) no Brasil: processo construtivo e desempenho – Recomendações para o processo de projeto arquitetônico. São Paulo: FAUUSP, 2018.

[2] Associação Brasileira De Normas Técnicas – ABNT. NBR 15575 – Edificações Habitacionais — Desempenho. Rio de Janeiro, 2013.

[3] P. Crespell; S. Gagnon. Cross Laminated Timber: a Primer. Pointe-Claire: FPInnovations, 2010.

[4] V. Salvadori. Multi-storey Timber-Based Buildings: an international survey of case-studies with five or more storeys over the last twenty years. Wien: Technische Universität Wien, 2021.

[5] I. Kuzmanovska; E. Gasparri; D. T. Monne; M. Aitchison. Tall Timber Buildings: Emerging trends and typologies. WCTE 2018 World Conference on Timber Engineering. Seoul, 2018.

[6] EN 16351. Timber structures — Cross laminated timber —Requirements. British Standards Institution. European Committee for Standardization, 2015.

[7] ANSI/APA– The Engineered Wood Association. Standard for Performance Rated Cross-Laminated Timber PGR 320-2018. ANSI/APA. Tacoma, WA, 2018.

[8] R. Brandner; G. Flatscher; A. Ringhofer; G. Schickhofer; A. Thiel. Cross Laminated Timber (CLT): overview and development. European Journal of Wood and Wood Products, v. 74, n. 3, 2016, p. 331–351.

[9] Associação Brasileira De Normas Técnicas – ABNT. NBR 7190 – Projeto de estruturas de madeira. Rio de Janeiro, 2022.

[10] Associação Brasileira De Normas Técnicas – ABNT. NBR 11675 – Divisórias leves internas moduladas — Verificação da resistência aos impactos. Rio de Janeiro, 2016.

https://doi.org/10.52202/069179-0024

World Conference on Timber Engineering Oslo 2023

ENABLE THE USE OF MASS TIMBER PRODUCTS FOR NON-RESIDENTIAL BUILDINGS IN HIGH VELOCITY HURRICANE ZONES

Sovanroth Ou[1], Michael Stoner[2], Weichiang Pang[3]

ABSTRACT: The wind design requirements for all regions designated as wind-borne debris regions are governed by the International Building Code (IBC). In Florida, stricter requirements apply to regions with high hurricane wind speeds, referred to as High Velocity Hurricane Zones (HVHZ). For non-residential buildings, the building products for the entire building envelope must be evaluated and meet the requirements of Section 1626 in the Florida Building Code (FBC). While there are construction assemblies deemed to comply with these requirements. Cross-Laminated Timber (CLT) is yet proven to be qualified. The goal of this project is to enable the use of CLT in HVHZ through experimental testing including windborne debris impact and cyclic pressure testing. The experimental results show that 3-ply CLT with a thickness of approximately 105 mm (4.125 in) satisfactorily passed all tests conducted with very little damage indicating that CLT is suitable for applications in HVHZ.

KEYWORDS: Cross-Laminated Timber, High Velocity Hurricane Zones, Debris Impact Test, Cyclic Wind Pressure Loading Test

1 INTRODUCTION

After Hurricane Andrew ripped through Florida in 1992, it exposed shortcomings of the current building codes. In September 1992, the Federal Emergency Management Agency's (FEMA) Federal Insurance Administration (FIA) assessed buildings' damages caused by Hurricane Andrew (FIA, 1992). It was observed that the damages differ significantly between neighbourhoods of proximity which were mainly due to the construction details and building products for the building envelope, shown in Figure 1.1. As a result, the FBC published the first version of enhanced wind provisions in 2001. Additionally, it was further enhanced following the damages due by Hurricanes Charley, Frances, Jeanne, Katrina, and Wilma in 2004 and 2005. Similar to Hurricane Andrew, FEMA's Mitigation Assessment Team's (MAT) building damage assessment caused by Hurricane Katrina showed excessive building envelope damage which was due to inadequate wind resistance and damage from windborne debris impact (FEMA, 2006). "In part, the building envelope failure problem is due to lack of high-wind design guides for envelope assemblies and various types of rooftop equipment.", says MAT. The most recent FBC requires the entire building envelope to be impact resistant in HVHZ. Studies, conducted by Bridwell et al. in 2013 and Falk et al. in 2015, show the ability of 5-ply CLT to resist a 6.8 kg (15 lb) 2x4 lumber missile with a velocity of approximately 44.7 m/s (100 mph) with minimal damage. In 2020, the capacity of 3-ply CLT to resist debris impact loads was investigated at Clemson University and showed that there is a 26% probability of failure for missiles expected in an EF-2 tornado (50 m/s – 60 m/s) and a 54% probability of failure in an EF-5 tornado (89+ m/s) (Stoner, 2020). In addition, recent experiments conducted at the Forest Products Laboratory (FPL) have shown that a 4-ply CLT wall, a 3-ply CLT roof, and a 4-ply CLT door can meet the requirements of ICC-500, the standard for the design and construction of storm shelters published jointly by the International Code Council (ICC) and the National Storm Shelter Association (NSSA) (Falk et al., 2019). While the ICC-500 and the HVHZ standard share some similarities, the specifications for the two necessary experiments, debris impact and cyclic wind pressure loading tests, are different for HVHZ.

[1] Sovanroth Ou, Clemson University, sovanr@clemson.edu
[2] Michael Stoner, Clemson University, mwstone@clemson.edu
[3] Weichiang Pang, Clemson University, wpang@clemson.edu

https://doi.org/10.52202/069179-0025

Figure 1.1: *Building performance difference between manufactured homes (outlined in the center) and conventional residential buildings (lower left) (FIA, 1992).*

There are several construction assemblies listed in Section 1626.4 of FBC, which have been proven to meet HVHZ requirements, including exterior concrete masonry walls, exterior wood-frame walls, and exterior reinforced concrete elements. This project presents the experimental test results, explaining the performance of CLT under HVHZ testing criteria. The main objective of this project is to qualify PRG-320 compliance CLT panels for HVHZ standards.

2 EXPERIMENTAL TESTING

To qualify CLT for HVHZ, debris impact test and cyclic wind pressure loading test must be conducted in compliance with Section 1626 of FBC, Testing Application Standard (TAS) 201-94, and TAS 203-94. CLT panels will be deemed to comply with HVHZ standards if three test specimens reject missile impacts without penetration and resist the cyclic pressure loading with no crack forming longer than 127 mm (5 in) and 1.6 mm (1/16 in) wide through which air can pass during cyclic wind pressure loading test.

2.1 DEBRIS IMPACT TEST

A total of three CLT test specimens will be tested in compliance with Section 1626 of FBC and TAS 201-94. In accordance with FBC's Section 1626, the test specimens must undergo large missile and small missile impact tests. However, it is specified in TAS 201-94 that any specimen that passes the large missile impact test with no opening that a 4.8 mm (3/16 in) sphere can pass through need not be tested for the small missile impact test. From preliminary testing, it was observed that CLT can resist the large missile without opening, therefore it is concluded that the small missile impact test is not necessary for this project. Figure 2.1 shows the test setup for the large missile tests while Figure 2.2.a shows a high-speed camera used to calibrate the missile velocity at a frame rate of 2000 fps. The description of the large missile impact test is summarized in Table 2.1. The missile is propelled using a 33-gallon compressed air tank, shown in Figure 2.2.b.

Table 2.1: *A summary description of a large missile impact test*

Missile	2" x 4" #2 surface dry Southern Pine 4 kg (9 lb)
Missile Velocity	24.4 m/s (80 ft/s or 54.5 mph)
Target	Within a 127 mm (5 in) radius circle having its center on the midpoint of the test specimen Within a 127 mm (5 in) radius circle in a corner having its center at 152.4 mm (6 in) away from supporting members
Test Specimen	1.2 m x 2.4 m (4-ft x 8-ft) PRG-320 compliance CLT panel
Fail Criterion	Openings ≥ 4.8 mm (3/16 in) (Exemption for small missile test)

Figure 2.1: *Test setup for large missile impact test*

https://doi.org/10.52202/069179-0025

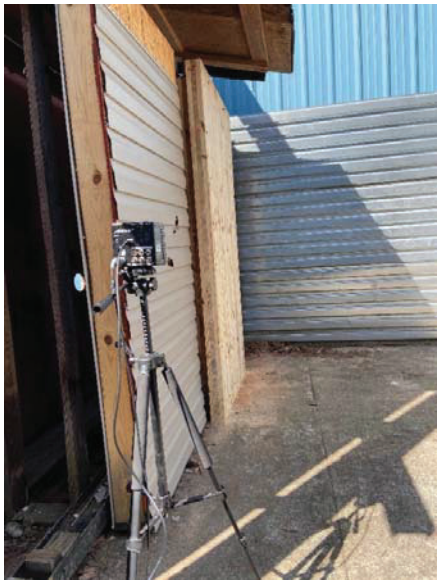

Figure 2.2.a: *Missile speed calibration with a high-speed camera*

Figure 2.2.b: *33-gallon compressed air tank used to propel missiles*

2.2 CYCLIC WIND PRESSURE LOADING TEST

Following the debris impact test, the CLT specimens go through the cyclic wind pressure loading test in conformity with Section 1626 of FBC and TAS 203-94. The assumptions for wind loads are determined using the Directional Procedure in ASCE 7-22, shown in Table 2.2. Additionally, the loading schedule for the cyclic test is shown in Table 2.3. Figure 2.3 shows the test setup for the cyclic pressure loading test.

Table 2.2: *Assumptions for wind loads*

Exposure Category	C
Building Height, H, m (ft)	18.3 (60)
Design Wind Speed, V, m/s (mph)	89.4 (200)
Directionality Factor, K_d	0.85
Exposure Coefficient, K_z	1.13
Topographic Factor, K_{zt}	1.00
Ground Elevation Factor, K_e	1.00
Gust Factor, G	0.85
Ultimate Design Load, P, kPa (psf)	5.79 (121)
Max. Cyclic Pressure, $P_{max,}$ kPa (psf)	3.5 (73)

Table 2.3: *Loading schedule for cyclic test*

Number of Cycles	Minimum Pressure kPa (psf)	Maximum Pressure kPa (psf)
600	0 (0)	1.77 (37)
70	0 (0)	2.11 (44)
1	0 (0)	4.55 (95)

Figure 2.3: *Test setup for cyclic pressure loading test*

The cyclic pressure protocol was achieved using a large fan which was connected to a bi-polar valve shown in Figure 2.4. The location and control of the valve allowed for air to be forced into the chamber (positive pressure) or taken out of the chamber (negative pressure). For all tests in this study, negative pressures were achieved through the calibration of the pressure to the location of the bi-polar valve. Positive pressures were avoided to test the

https://doi.org/10.52202/069179-0025

panel independent of the connection between the panel and the supporting elements. Prior to each test, calibration of the relationship between the location of the bi-polar valve and the pressure was performed. An example of this calibration is shown in Figure 2.5 and was dependent on the seal between the CLT panel and the pressure chamber.

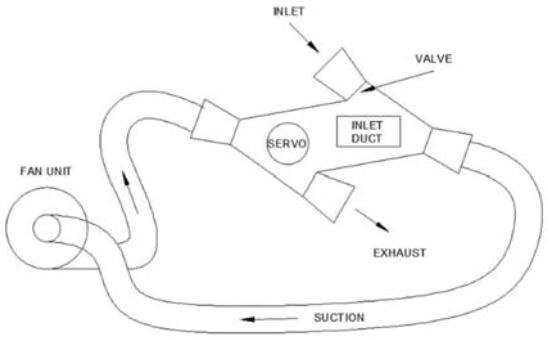

Figure 2.4: *Pressure controlled with a bi-polar valve*

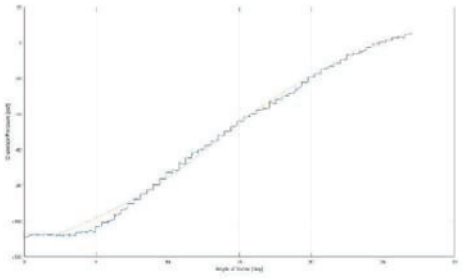

Figure 2.5: *Calibration curve, shown in yellow*

3 TEST RESULT

3.1 LARGE MISSILE IMPACT TEST

A CLT panel specimen was tested for the large missile. It received two impacts at the center and corner 152.4 mm (6 in) away from supporting members, shown in Figure 2.4. Table 2.4 shows the summary result of missile indentation for the test while Figure 2.4 shows their corresponding pictures. There were indentations of 6.35 mm (0.25 in) and 12.7 mm (0.5 in) at the center and corner, respectively. This corresponds to 6% and 12% of the CLT panel thickness (105 mm or 4.125 in), respectively which are minimal damages to the panel.

Table 2.4: *A summary result for missile indentation*

Impact Location	Missile Weight kg (lb)	Missile Length m (in)	Missile Speed m/s (mph)	Indentation Depth mm (in)
Center	4 (9)	2.17 (85.25)	29.5 (66)	6.35 (0.25)
Corner	4 (9)	2.17 (85.25)	31.7 (71)	12.7 (0.50)

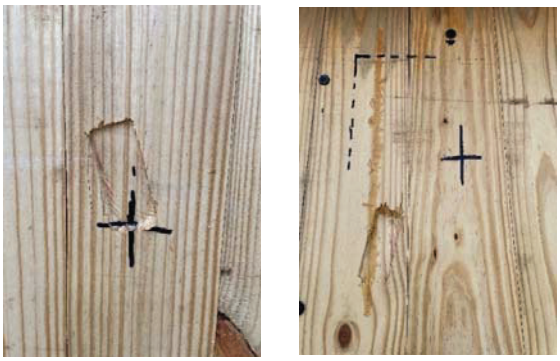

(a) Center (b) Corner

Figure 2.4: *Missile penetration depth of large missile test*

3.2 CYCLIC WIND PRESSURE TEST

A specimen was tested for cyclic wind pressure loading test with the loading schedule, shown in Table 2.3. The maximum deflection was measured to be 2.845 mm (0.112 in) throughout all three loading cycles with a permanent deformation of 0.686 mm (0.027 in). No crack or opening formed during or after the experimental test. Figures 3.1, 3.2, and 3.3 show the pressure loads and deflection for several cycles of the three loading cycles respectively (Table 2.3). The CLT specimen remains elastic during the cyclic test, as shown in Figure 3.4.

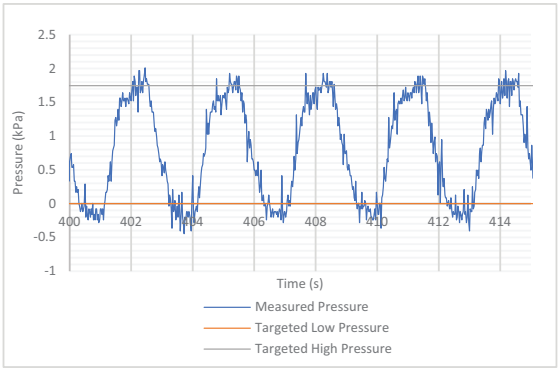

Figure 3.1.a: *Measured pressure for 5 cycles of 0-1.77 kPa*

https://doi.org/10.52202/069179-0025

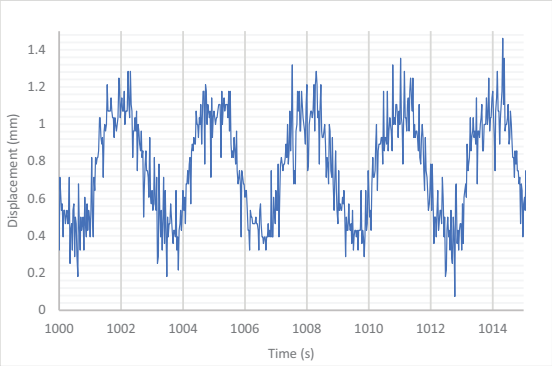

Figure 3.1.b: *Measured deflection for 5 cycles of 0-1.77 kPa*

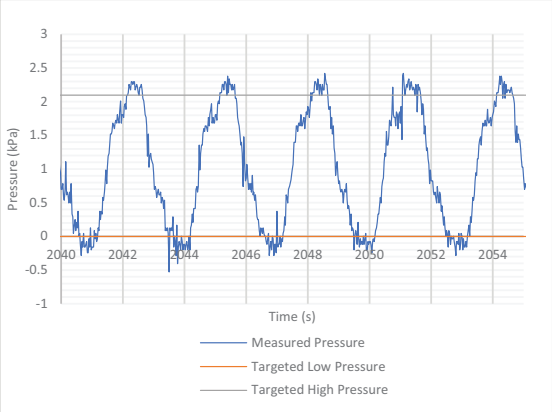

Figure 3.2.a: *Measured pressure for 5 cycles of 0-2.11 kPa*

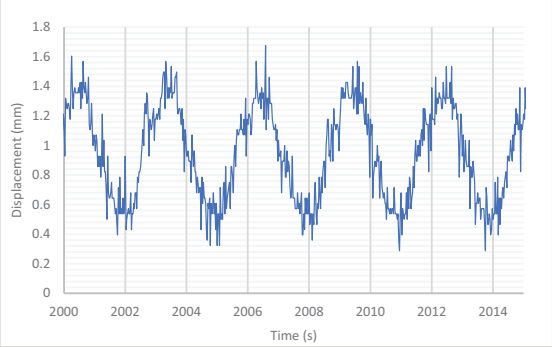

Figure 3.2.b: *Measured displacement for 5 cycles of 0-2.11 kPa*

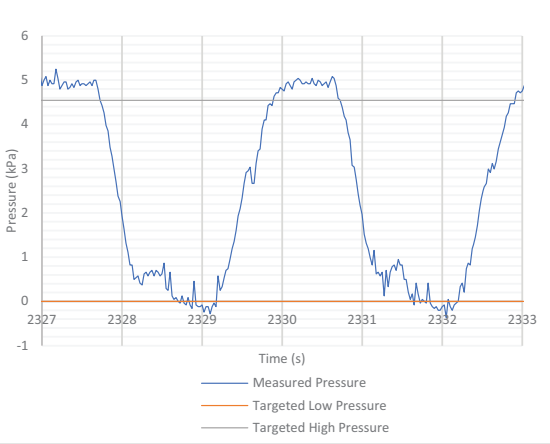

Figure 3.3.a: *Measured pressure for 5 cycles of 0-4.55 kPa*

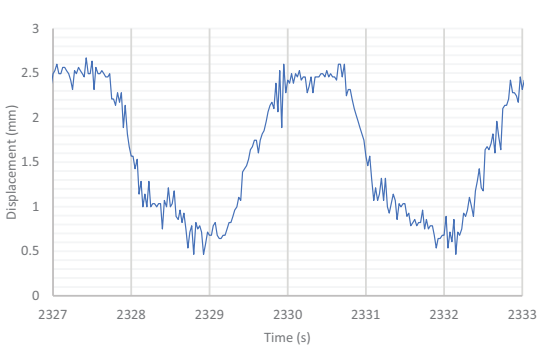

Figure 3.3.b: *Measured displacement for 5 cycles of 0-4.55 kPa*

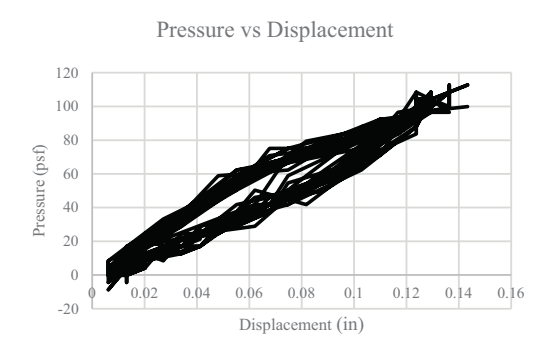

Figure 3.4: *Result from the preliminary test*

The measured pressures in the chamber were consistent with the targets outlined in Table 2.3. Deviation of the pressures from the target value was limited to 11% for the testing shown. Such deviation was the result of the pressure cycles which approached 0 Pa as they had the potential to interrupt the seal. Efforts were made to minimize deviation through the testing protocol such as

https://doi.org/10.52202/069179-0025

placing a plastic film over the panel and using clamps around the panel edges to ensure that if a positive pressure was experienced by the panel, it would not cause the panel to lift off the test chamber.

Overall, the results of the experimental testing indicate little damage to the CLT panel from the debris impact and cyclic pressure. Additional testing could be performed to determine the point at which 3-ply CLT panels would begin to experience more significant damage from such events.

4 CONCLUSIONS AND FUTURE WORK

As part of this study, the 3-ply CLT test specimen underwent debris impact and cyclic wind pressure loading test in accordance with FBC requirements. The results of the two tests indicate that 3-ply CLT can withstand such impacts and pressure testing with little to no permanent damage. It is recommended that CLT be included as a qualified construction assembly listed in FBC 1626.4. Moving forward, two additional CLT specimens will be tested, and a test report will be drafted, describing the performance of CLT under the HVHZ condition. This report will aim to serve as support for engineers and contractors seeking to implement CLT as a construction material in HVHZ.

ACKNOWLEDGEMENT

The experiments and analyses presented herein are supported by the Clemson Civil Engineering Department and the U.S. Department of Agriculture (USDA) Forest Service. Any opinions, findings, and conclusions presented in this paper are those of the authors and do not necessarily reflect the Clemson Civil Engineering Department and USDA Forest Service's views.

REFERENCES

[1] ASCE 7: Minimum Design Loads and Associated Criteria for Buildings and Other Structures. American Society of Civil Engineers, Virginia, 2017.
[2] FEMA 548: Summary Report on Building Performance Hurricane Katrina 2005. FEMA, 2006.
[3] FIA. Building Performance: Hurricane Andrew in Florida. FEMA, 1992.
[4] Florida Building Code, Building, 7th Edition. International Code Council, Illinois, 2020.
[5] Florida Test Protocols for High-Velocity Hurricane Zones, 7th Edition. International Code Council, Illinois, 2020.
[6] ICC/NSSA Standard for the Design and Construction of Storm Shelters. International Code Council, Illinois, 2020.
[7] J. J. Bridwell, R. J. Ross, Z. Cai, and D. E. Kretschmann. USDA Forest Products Laboratory's Debris Launcher. 2013.
[8] M. W. Stoner. Performance of Cross-Laminated Timber as a Residential Building Material Subject to Tornado Events. Clemson University, 2020.
[9] R. H. Falk, J. J. Bridwell, and J. Hermanson. Tornado Safe Rooms from Commodity Wood Products: Wall Development and Impact Testing. Res. Paper FPL-RP-681 U.S. Department of Agriculture, Forest Service, Forest Products Laboratory, 2015.
[10] R. H. Falk, J. J. Bridwell, T. Williamson, and T. Black. Development of a ready-to-assemble tornado shelter from cross-laminated timber (CLT): impact and wind pressure testing. FPL, Wisconsin, 2019.

https://doi.org/10.52202/069179-0025

World Conference on Timber Engineering Oslo 2023

BENDING BEHAVIOUR OF GLT-STEEL BEAM CONNECTED BY INCLINED SCREWS

Sung-Jun Pang[1], Kyung-Sun Ahn[2], Gwang-Ryul Lee[3], Min-Jeong Kim[4], Jae-Won Oh[5], Jung-Kwon Oh[6]

ABSTRACT: In this study, a glued-laminated timber (GLT) was reinforced with a steel plate and inclined screws, and its bending performance was analyzed. In a total of 8 GLTs, 3 GLTs were not reinforced (control group) and 5 GLTs were reinforced with steel plates (comparison group). The size of GLT was 80 mm (width) × 120 mm (thickness) × 2400 mm (length). The GLT in the comparison group, a steel plate (SPHC-P, yield strength: 227 MPa, modulus of elasticity 166.33 GPa) was installed with screws (Ø9x160mm, 45°). The deflection and load of specimens were measured by a third-point bending test to derive their bending stiffness and load-carrying capacities. As a result of the experiment, all specimens in the control group showed brittle tensile failure, but all specimens of the comparison group showed ductile behavior and maintained a load-bearing capacity of about 30 kN. After the compression failure of the GLT, there was no damage to the screw connection while the steel plate was extended. Therefore, the screw connection sufficiently supported the shear force generated between GLT and steel plate, and the steel plate reinforcement completely changed the GLT behavior.

KEYWORDS: Glued-laminated timber (GLT), Steel, Screw, Beam, Bending behavior

1 INTRODUCTION

Glued-laminated timber (GLT) and steel are structural building materials used in dry construction and recyclable. Both materials are cut or drilled in the factory using CNC cutting machines, so the machining precision is high and the machining error is small.

Several hybrid beams have been developed with GLT and steels. When the GLT are reinforced by steel, the bending performance of the GLT beam is improved and the deviation is reduced (André, Alan, 2006). Generally, the two meterals are glued with an adhesive, but it is not easy to maintain the adhesive performance enough to resist a large external force.

In this study, a new GLT and steel composite beam was designed which were mechanically joined using screws instead of bonding. The bending performance and failure modes of the mechanically connected GLT and steel beams were analyzed.

2 MATERIALS AND METHODS

2.1 SPECIMENS

Figure 1 shows the cross section of GLT and the combination of lamina. One lamina grade (E9) was used, and the modulus of elasticity (MOE) of that grade was greater than 9 GPa. The size of GLT was 80 mm (width) × 120 mm (thickness) × 2400 mm (length).
For GLT-steel beam specimens, a steel plate (SPHC-P, yield strength: 227 MPa, modulus of elasticity 166.33 GPa) was installed with screws (Ø9x160mm, 45°).

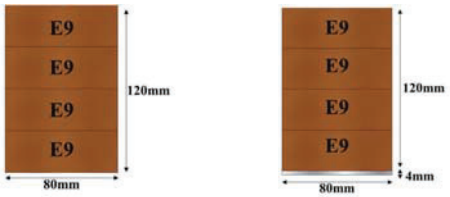

(a) GLT (b) GLT-steel

Figure 1: *Cross section of GLT and GLT-steel specimen*

[1] Department of Agriculture, Forestry and Bioresources, Seoul National University, Republic of Korea, pangsungjun@snu.ac.kr
[2] Department of Agriculture, Forestry and Bioresources, Seoul National University, Republic of Korea, rudtjs6339@snu.ac.kr
[3] Department of Agriculture, Forestry and Bioresources, Seoul National University, Republic of Korea, qweqweqwer@snu.ac.kr
[4] Department of Agriculture, Forestry and Bioresources, Seoul National University, Republic of Korea, minjeong.kim@snu.ac.kr
[5] Department of Agriculture, Forestry and Bioresources, Seoul National University, Republic of Korea, redhurse@snu.ac.kr
[6] Department of Agriculture, Forestry and Bioresources, Seoul National University, Republic of Korea, jungoh@snu.ac.kr

https://doi.org/10.52202/069179-0026

2.2 BENDING TEST

The deflection and load resistance of specimens were measured by a third-point bending test to derive their bending stiffness and load-carrying capacities (Figure 2).

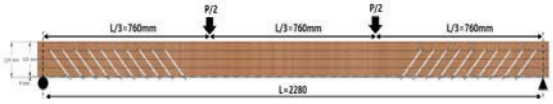

Figure 2: *Cross section of GLT and GLT-steel specimen*

Figure 3 shows the total thickness, neutral axis, and maximum load resistance of the specimen according to the thickness of the steel plate reinforcing the GLT. When GLT was reinforced with a steel thickness of 3 mm or less, the maximum load of the beam was governed by the tensile failure of the steel plate. However, when GLT was reinforced with a steel thickness of 4 mm or more, the maximum load of the beam was governed by compression failure of wood. Thus, in this study, when GLT was reinforced with a 4mm thick steel plate, it was checked whether or not compression failure of wood occurred.

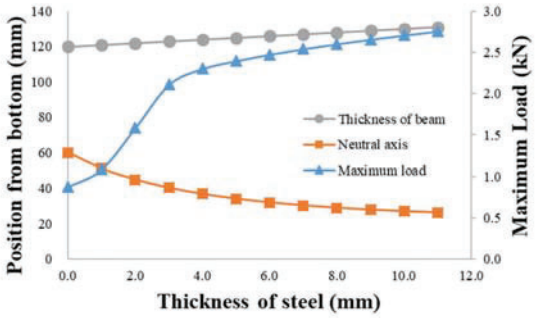

Figure 3: *Thickness of beam, neutral axis, and maximum load resistance by steel plate thickness*

3 RESULTS AND DISCUSSION

Figure 4 shows the failure mode of the non-reinforced GLT specimen. All specimens were broken around the knot in the tensile zone. At the time of failure, the load resistance dropped sharply as shown in Fig. 5. This brittle failure is a typical failure mode of GLT or wood in bending tests.

In the case of non-reinforced GLT, the bending stiffness was about 0.16×10^{12} N/mm^2 and the maximum load was 28.2 kN, which was determined by brittle failure.

Figure 4: *Failure mode of the non-reinforced GLT specimens*

https://doi.org/10.52202/069179-0026

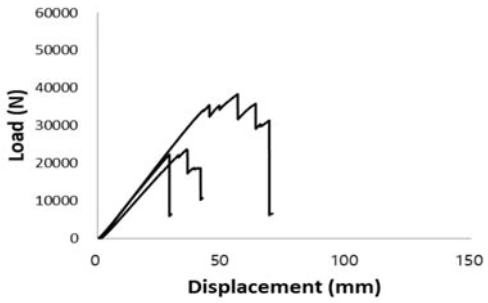

Figure 5: *Load-displacement curve of the non-reinforced GLT specimens (three specimens)*

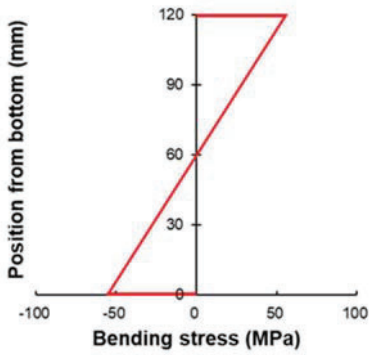

Figure 6: *Bending stress distribution of non-reinforced GLT specimens at the maximum bending moment*

Figures 7 through 9 show the failure mechanism of the reinforced GLT specimens. In two of the five specimens, tensile failure occurred first at the finger joint (Fig. 7a) or knot (Fig. 8a) of GLT. The finger-joint and knots are the main factors causing the strength reduction (Pang et al. 2011, 2018, 2021; Pang and Jeong 2019). Unlike the non-reinforced GLT, compression failure occurred at the top of the GLT (Fig. 7b and Fig. 8b) and large deformation occurred (Fig. 7c and Fig. 8c).

In three of the five specimens, compressive failure occurred first at the top of the GLT (Fig. 9a). After that, tensile failure occurred at the knot, but the tensile failure of the specimens did not lead to rapid brittle failure. The specimens showed ductile behavior due to the elongation of the steel plate. The elongation of the steel plate shows that the screw connection sufficiently supported the shear force between GLT and the steel plate.

(a) Tensile failure at finger joint of GLT

(b) Compression failure on top of GLT

(c) Tensile Large deformation

Figure 7: *Fracture mechanism of reinforced GLT in which tension failure (finger joint) of GLT occurs firs*

(a) Tensile failure at knot of GLT

(b) Compression failure on top of GLT

(c) Large deformation

Figure 8: *Fracture mechanism of reinforced GLT in which tension failure (knot) of GLT occurs first*

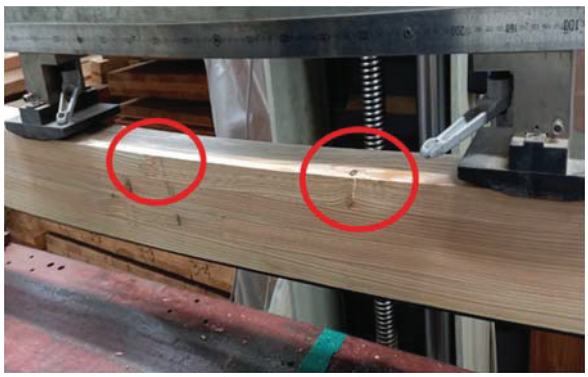

(a) Compression failure on top of GLT

(b) Tension failure on bottom of GLT

(c) Large deformation

Figure 9: *Fracture mechanism of reinforced GLT in which compression failure of GLT occurs first*

Figure 10 shows the load-displacement curve of the reinforced GLT specimens. Unlike the non-reinforced GLT, the reinforced GLT did not lose its load-carrying capacity significantly after the initial failure and maintained a load-carrying capacity of approximately 30 kN. The maximum load-carrying capacity was higher in the case where the compression failure occurred first (48 kN to 51 kN) than in the case where the tensile failure occurred first (32 to 38 kN). This shows that the tensile part (bottom of GLT) contributes to the load-carrying capacity of the reinforced GLT until the tensile failure occurred. The bending stiffness was also improved by about 64% from 0.161 to 0.265 $\times 10^{12}$ N/mm^2 by the reinforcement, and the coefficient of variation decreased from 0.056 to 0.03.

There was no screw damage while the steel was extending. This means that the screw connection supported the shear force generated between the wood and the steel plate.

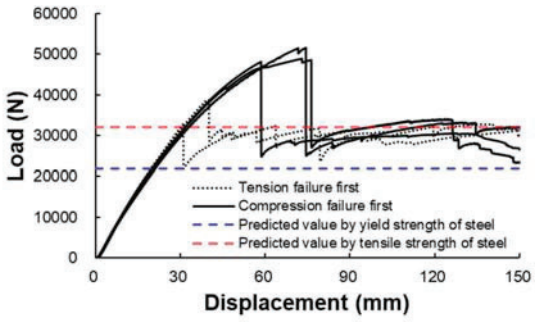

Figure 10: *Load-displacement curve of the GLT specimens reinforced with a 4mm thick steel plate (five specimens)*

https://doi.org/10.52202/069179-0026

As mentioned above, the reinforced GLT beam continuously supported a load of about 30 kN while undergoing large deformation. Figure 11 shows the bending stress distribution of reinforced GLT by elastic analysis (Eq. 1). The maximum bending stress acting on the steel plate (466.3 MPa, Fig. 11(a)) exceeds the yield strength of the used steel plate (227 MPa). This means that the steel plate was in a plastic state, and plastic analysis is required.

$$\sigma_{bending} = E_i \cdot \varepsilon_i \quad (1)$$

where $\sigma_{bending}$ is the bending stress in the elastic analysis (MPa), E_i is the elastic modulus of *i* material (MPa), and ε_i is the strain of *i* material.

Figure 11(b) shows the bending stress distribution of reinforced GLT considering the plasticity of the GLT and steel. The maximum bending moment of the reinforced GLT can be predicted by Eq. 2. Equation 2 consists of three terms. The first term is the plastic bending moment in GLT, the second term is the elastic bending moment in GLT, and the third term is the plastic bending moment of the steel plate. In the compression test of wood, the load-displacement curve shows a ductile behavior in which the strength decreases slowly as the wood wrinkles after the maximum load (Pang and Jeong 2018). For plastic analysis of reinforced GLT, the load-displacement curve of GLT in compressive stress was idealized as an elastic-plastic curve. Among the reported experimental data (Pang and Jeong 2018; Park *et al*. 2010), the compressive strength (58.8 MPa) of wood with similar elastic modulus in the same species was regarded as the yield strength of GLT,

$$M_{max} = \int_{c_1-h_{c,GLT}}^{c_1} \sigma_{c,GLT} \cdot y \, dA + \int_{c_2-t_{steel}}^{c_1-h_{c,GLT}} E_{GLT} \cdot \varepsilon_{GLT} \cdot y \, dA + \int_{c_2-t_{steel}}^{c_2} f_y \cdot y \, dA \quad (2)$$

where M_{max} is the maximum bending moment (kN·m), c_1 is the distance between the top surface and the neutral axis of the composite section (mm), $h_{c,GLT}$ is the height of the compressive zone in GLT (mm), $\sigma_{c,GLT}$ is the compressive strength of GLT (MPa), y is the distance from the neutral axis of the composite section (mm), c_2 is the distance between the bottom surface and the neutral axis of the composite section (mm), t_{steel} is the thickness of steel plate (MPa), E_{GLT} is the elastic modulus of GLT (MPa), ε_{GLT} is the strain of GLT, and f_y is the yield strength of steel plate (MPa).

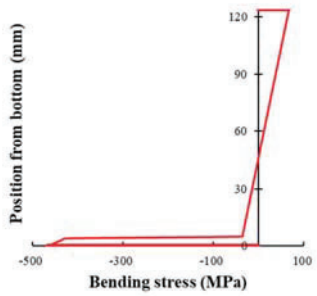

(a) Elastic analysis (bending stress exceeds the yield strength (227 MPa) of the steel)

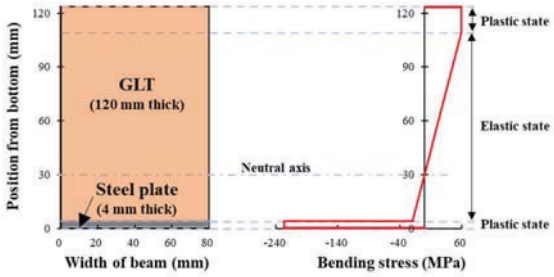

(b) Elastic-plastic analysis

Figure 11: *Bending stress distribution of the reinforced GLT specimen at the maximum bending moment*

Figure 12 shows the bending stress distribution of the reinforced GLT when the steel and timber in compressive zone reach plastic state. The compressive force acting on the upper part of the GLT and the tensile force by the steel plate are equal. Thus, the height of the compressive zone in the reinforced GLT can be calculated by Eq. 3. Figures 12 (a) and (b) show when the maximum stress of steel reached the yield strength (227 MPa) and the tensile strength (345 MPa) of the steel plate, respectively. When the maximum stress of the steel from yield strength to maximum tensile strength increased the height of the compressive zone in the reinforced GLT also increased.

The bending moment and the load-carrying capacity of the reinforced GLT can be predicted by Eq. 4, and Eq. 5, respectively. The predicted load-carrying capacity of reinforced GLT was 21,845 N by applying yield strength of steel (227 MPa) and 32,035 N by applying yield strength of steel (345 MPa). Figure 10 shows the load-carrying capacity predicted by Eq. 5 together with the experimentally measured load-displacement curve. The load capacity predicted by the tensile strength of the steel was similar to the maximum load capacities at the plastic condition of the test specimens. This indicates that the steel plate almost reached its maximum tensile strength. In addition, all of the load capacities of the test specimens were higher than the load predicted by the yield strength of steel. Therefore, the bending moment of GLT reinforced by steel plate can be safely designed with the yield strength of steel.

https://doi.org/10.52202/069179-0026

$$h_{c,GLT} = \frac{f_y \cdot t_{steel}}{\sigma_{c,GLT}} \quad (3)$$

$h_{c,GLT}$ is the the height of the compressive zone in GLT (mm), f_y is the yield or tensile strength of steel plate (MPa), t_{steel} is the thickness of steel plate (MPa), and $\sigma_{c,GLT}$ is the compressive strength of GLT (MPa).

$$M_{predict} = f_y \cdot w \cdot t_{steel} \cdot (h - \frac{t_{steel}}{2} - \frac{h_{c,GLT}}{2}) \quad (4)$$

where $M_{predict}$ is the predicted bending moment (kN·m), f_y is the yield or tensile strength of steel plate (MPa), w is the width of steel plate (mm), t_{steel} is the thickness of steel plate (mm), h is the height of reinforced GLT (mm), and $h_{c,GLT}$ is the height of compressive zone in GLT (mm).

$$P_{predict} = \frac{M_{predict}}{L_e} \cdot 2 \quad (5)$$

where $P_{predict}$ is the predicted load-carrying capacity of reinforecd GLT (kN), $M_{predict}$ is the predicted bending moment (kN·m), and L_e is the the distance between the load position and support position (mm).

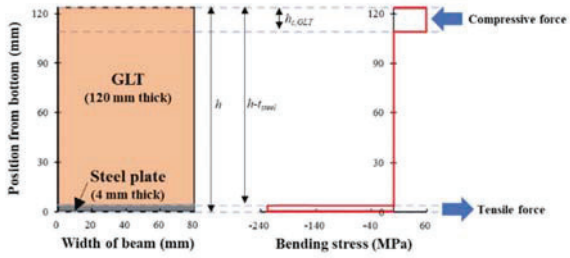

(a) Bending stress distribution at the yield strength (227 MPa) of the steel plate

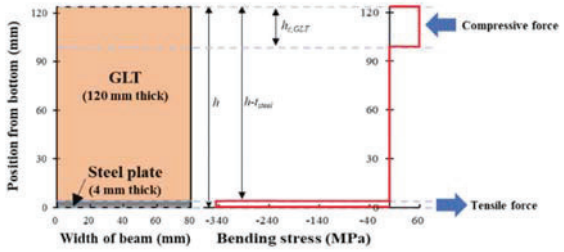

(a) Bending stress distribution at the tensile strength (345 MPa) of the steel plate

Figure 12: *Bending stress distribution of the reinforced GLT specimens at the plastic state*

4 CONCLUSIONS

1. The load resistance of non-reinforced GLT decreased to zero after brittle failure in the tensile side of the GLT. However, the reinforced GLT specimen showed ductile behavior even after GLT failure and maintained a load resistance of about 30 kN during large deformation. The bending stiffness was also improved by about 64% from 0.161 to 0.265 by the reinforcement.
2. The prediction model for the load-carrying capacity of the reinforced GLT was developed based on the compressive strength of wood and the yield strength of steel. The experimentally measured load capacity of the beam was higher than the load predicted load capacity. Therefore, the load and bending moment of the reinforced GLT can be designed with the compressive strength of wood and yield strength of steel.
3. The GLT and steel plate were mechanically connected using only inclined screws without the use of any adhesives. The resistance of the screw sufficiently supported the shear forces so that the steel plate can perform plastic behavior after yielding. This study shows the possibility of non-adhesive composite beam, and additional research to optimize the mechanical connection is needed.

ACKNOWLEDGEMENT

This research was supported by Basic Science Research Program through the National Research Foundation of Korea (NRF) funded by the Ministry of Education (No. NRF-2021R1I1A1A01045628).

REFERENCES

André, A. (2006). "Fibres for Strengthening of Timber Structures," *Master Thesis, Luleå tekniska universitet, Civil and Environmental Engineering, Structural Engineering*.

ASTM D198-15 (2010). "Standard test methods of static tests of lumber in structural sizes," ASTM International, West Conshohosken, PA, USA .

BS EN 408:2010+A1:2012 (2012). "Timber structures - Structural timber and glued laminated timber - Determination of some physical and mechanical properties," British Standards Institution, London.

Chang-Min, S., and Hyun-Chul, J. (2009). "Structural analysis of S-cam brake shoe for commercial vehicle by FEM," *J. Ocean Eng. Technol.* 23(4), 69-77.

Dietsch, P., and Brandner, R. (2015). "Self-tapping screws and threaded rods as reinforcement for structural timber elements - A state-of-the-art report," *Construction and Building Materials* 97, 78-89. DOI: 10.1016/j.conbuildmat.2015.04.028

ETA-11/0030. (2019). "European technical assessment. Screws for use in timber construction. ETA-Denmark, Nordhavn," ETA-11/0030. (2019). European technical assessment. Screws for use in timber construction. ETA-Denmark, Nordhavn.

Gerilla, G. P., Teknomo, K., and Hokao, K. (2007). "An environmental assessment of wood and steel reinforced concrete housing construction," *Building and Environment*, 42(7), 2778-2784. DOI: 10.1016/j.buildenv.2006.07.021

Hafner, A., and Schäfer, S. (2018). "Environmental

https://doi.org/10.52202/069179-0026

aspects of material efficiency versus carbon storage in timber buildings," *European Journal of Wood and Wood Products*, 76(3), 1045-1059. DOI: 10.1007/s00107-017-1273-9

KS D3501 (2018). "Hot-rolled mild steel plates, sheets and strip," Korean Standards Association, Yeoksamdong, South Korea.

KS F3021 (2013). "Structural glued laminated timber," Korean Standards Association, Yeoksamdong, South Korea.

Li, J., Rismanchi, B., and Ngo, T. (2019). "Feasibility study to estimate the environmental benefits of utilising timber to construct high-rise buildings in Australia," *Building and Environment* 147, 108-120. DOI: 10.1016/j.buildenv.2018.09.052

Loss, C., Piazza, M., and Zandonini, R. (2016a). "Connections for steel-timber hybrid prefabricated buildings. Part I: Experimental tests," *Construction and Building Materials* 122, 781-795. DOI: 10.1016/j.conbuildmat.2015.12.002

Loss, C., Piazza, M., and Zandonini, R. (2016b). "Connections for steel-timber hybrid prefabricated buildings. Part II: Innovative modular structures," *Construction and Building Materials* 122, 796-808. DOI: 10.1016/j.conbuildmat.2015.12.001

Metelli, G., Preti, M., and Giuriani, E. (2016). "On the delamination phenomenon in the repair of timber beams with steel plates," *Construction and Building Materials* 102, 1018-1028. DOI: 10.1016/j.conbuildmat.2015.09.038

Pang, S.-J., Ahn, K.-S., Jeong, S., Lee, G.-C., Kim, H. S., and Oh, J.-K. (2022). "Prediction of bending performance for a separable CLT-concrete composite slab connected by notch connectors," *Journal of Building Engineering* 49, 103900. DOI: 10.1016/j.jobe.2021.103900

Pang, S.-J., and Jeong, G. Y. (2018). "Load sharing and weakest lamina effects on the compressive resistance of cross-laminated timber under in-plane loading," *Journal of Wood Science* 64(5), 538-550. DOI: 10.1007/s10086-018-1741-9

Pang, S.-J., Lee, H.-J., Ahn, K.-S., and Oh, J.-K. (2020). "Sensitivity of censored data analysis to determine the characteristic value of structural timber," *Journal of Wood Science* 66(1), 39. DOI: 10.1186/s10086-020-01885-0

Pang, S.-J., Lee, H.-J., Yang, S. M., Kang, S. G., and Oh, J.-K. (2019). "Moment and shear capacity of Ply-lam composed with plywood and structural timber under out-of-plane bending," *Journal of Wood Science* 65(1), 68. DOI: 10.1186/s10086-019-1847-8

Pang, S.-J., Lee, J.-J., and Oh, J.-K. (2013). "Evaluation of allowable bending stress of dimension lumber; Confidence levels and size-adjustment," *Journal of the Korean Wood Science and Technology* 41(5), 432-439. DOI: 10.5658/WOOD.2013.41.5.432

Pang, S.-J., Oh, J.-K., Hong, J.-P., Lee, S.-J., and Lee, J.-J. (2018). "Stochastic model for predicting the bending strength of glued-laminated timber based on the knot area ratio and localized MOE in lamina," *Journal of Wood Science* 64(2), 126-137. DOI: 10.1007/s10086-017-1682-8

Pang, S.-J., Park, J.-S., Hwang, K.-H., Jeong, G.-Y., Park, M.-J., and Lee, J.-J. (2011). "Bending strength of Korean softwood species for 120×180 mm structural members," *Journal of the Korean Wood Science and Technology* 39(5), 444-450. DOI: 10.5658/WOOD.2011.39.5.444

Pang, S.-J., Shim, K.-B., and Kim, K.-H. (2021). "Effects of knot area ratio on the bending properties of cross-laminated timber made from Korean pine," *Wood Science and Technology* 55(2), 489-503. DOI: 10.1007/s00226-020-01255-5

Pang, S. J., and Jeong, G. Y. (2019). "Effects of combinations of lamina grade and thickness, and span-to-depth ratios on bending properties of cross-laminated timber (CLT) floor," *Construction and Building Materials* 222, 142-151. DOI: 10.1016/J.CONBUILDMAT.2019.06.012

Park, C.-Y., Pang, S.-J., Park, J.-S., Kim, K.-M., Park, M.-J., and Lee, J.-J. (2010). "Study of the distribution properties and LRFD code conversion in Japanese larch," *Journal of the Korean Wood Science and Technology* 38(2), 94-100. DOI: 10.5658/WOOD.2010.38.2.94

Petersen Raymer, A. K. (2006). "A comparison of avoided greenhouse gas emissions when using different kinds of wood energy," *Biomass and Bioenergy* 30(7), 605-617. DOI: 10.1016/j.biombioe.2006.01.009

Resch, E., Andresen, I., Cherubini, F., and Brattebø, H. (2021). "Estimating dynamic climate change effects of material use in buildings—Timing, uncertainty, and emission sources," *Building and Environment* 187. DOI: 10.1016/j.buildenv.2020.107399

Riola-Parada, F. (2016). *Timber-Steel Hybrid Beams for Multi-Storey Buildings*, Ph. D. Dissertation, Technische Universität Wien, Vienna, Austria. DOI: 10.34726/hss.2016.23820

Röck, M., Saade, M. R. M., Balouktsi, M., Rasmussen, F. N., Birgisdottir, H., Frischknecht, R., Habert, G., Lützkendorf, T., and Passer, A. (2020). "Embodied GHG emissions of buildings - The hidden challenge for effective climate change mitigation," *Applied Energy* 258. DOI: 10.1016/j.apenergy.2019.114107

Sandanayake, M., Lokuge, W., Zhang, G., Setunge, S., and Thushar, Q. (2018). "Greenhouse gas emissions during timber and concrete building construction — A scenario based comparative case study," *Sustainable Cities and Society* 38, 91-97. DOI: 10.1016/j.scs.2017.12.017

Schober, K.-U., Harte, A. M., Kliger, R., Jockwer, R., Xu, Q., and Chen, J.-F. (2015). "FRP reinforcement of timber structures," *Construction and Building Materials* 97, 106-118. DOI: 10.1016/j.conbuildmat.2015.06.020

Tomasi, R., Parisi, M. A., and Piazza, M. (2009). "Ductile design of glued-laminated timber beams," *Practice Periodical on Structural Design and Construction* 14(3), 113-122. DOI: 10.1061/(ASCE)1084-

0680(2009)14:3(113)
Tsai, M.-T., and Le, T. (2018). "Determination of initial stiffness of timber-steel composite (TSC) beams based on experiment and simulation modeling," *Sustainability* 10(4), 1220. DOI: 10.3390/su10041220
Wang, T., Wang, Y., Crocetti, R., Franco, L., Schweigler, M., and Wålinder, M. (2021). "An innovative timber-steel hybrid beam consisting of glulam mechanically reinforced by means of steel rod: Analytical and preliminary numerical investigations," *Journal of Building Engineering* 43, 102549. DOI: 10.1016/j.jobe.2021.102549
Yan, H., Shen, Q., Fan, L. C. H., Wang, Y., and Zhang, L. (2010). "Greenhouse gas emissions in building construction: A case study of One Peking in Hong Kong," *Building and Environment* 45(4), 949-955. DOI: 10.1016/j.buildenv.2009.09.014

https://doi.org/10.52202/069179-0026

World Conference on Timber Engineering Oslo 2023

THE PRODUCTION OF ADHESIVE-FREE CROSS-LAMINATED TIMBER (CLT) PANEL USING PRODUCTS GENERATED BY THE SUSTAINABLE FOREST MANAGEMENT OF THE AMAZONIAN OLD GROWTH FOREST

Marcos Cesar M. Pereira[1], Adma M. D. Higuchi[2], Geraldo Lira[3], Yago P. Souza[4], Estevão V. C. M. Paula[5], Antonio A. Dias[6], Niro Higuchi[7]

ABSTRACT: The dowel cross-lamella timber (DCLT) is a type of adhesive free construction system which uses wooden dowels as connectors between the lamella layers. The use of wood in construction is environmentally friendly because it is the only building material of renewable origin. This is true only if the wood comes from sustainable forest management plans. In this sense, This work aims to study physical and mechanical characteristics of four species in the Amazon Forest of sustained forest management, use these species for the production of dowels and to determine the rigidity of the connection. The species was Pau Rainha (*Brosimum Rubescens*), Matá Matá Amarelo (*Eschweilera Wachenheimi*), Cardeiro (*Scleronema micranthum)* and Breu Vermelho (*Protium altsonii*). Tests of compressive strength, shear, and density were performed according to the Brazilian Standard of Wooden Structures parameters and slip modulus was obtained by a test developed specifically for this purpose. Among the four wood species studied for use as a connecting element (dowel), only the Pau Rainha wood (*B. Rubescens*) and Matá Matá Amarelo (*E. Wachenheimi*) obtained good results. Mata Mata Amarelo did not get the best results, but in the criterion of abundance, that is, number of tree individuals per m² in the rain forest, it has advantages over the Pau Rainha. Thus, it is possible to apply the concept of sustainable forest management and rationally use this tree species.

KEYWORDS: Dowels, DCLT, Amazon Wood, Mass Timber, Hard Wood

1 INTRODUCTION

1.1 DCLT PANEL

Engineered wood market is expected to gain a market value of USD 4,9 million by 2030[1]. CLT panels are engineered timber products that have been standing out in the construction market mainly on the European continent, where they have been developed. However, for its production structural weather-resistant adhesives and a large hydraulic press are required to glue the panel layers together, which entails a high-cost production and makes recycling very difficult. The DCLT, on the other hand, uses dowels as a bonding agent to the lamellas disposed at 90° between themselves (Figure 1) and do not require neither the use of adhesive nor the press, reducing the process' costs and improving the environmental performance of the product [2]. The efficiency of the bonding is ensured by the moisture content variation between the oven dried dowels (48h at 100°C) and the lamellas [3].

In this process, it loses water impregnated in the wood cells, and consequently reduces its volume, facilitating the dowel insertion into the hole. After being placed in the hole, the dowel regains moisture from the environment, making its volume return to its original size, so that the dowel locks within the hole, providing a more efficient connection when compared to a dowel inserted without this drying process.

[1] Marcos Cesar M. Pereira, National Institute of Amazonian Research (INPA), Manaus, Brazil, marcoscesar@sc.usp.br
[2] Adma M. D. Higuchi, National Institute of Amazonian Research (INPA), Manaus, Brazil, adma.higuchi@posgrad.inpa.gov.br
[3] Geraldo Lira, National Institute of Amazonian Research (INPA), Manaus, Brazil, geraldolira05@gmail.com
[4] Yago P. Souza, National Institute of Amazonian Research (INPA), Manaus, Brazil, 92ysouza@gmail.com
[5] Estevão V. C M. Paula, Superior School of Technology, State University of Amazonas (UEA), Manaus, Brazil, estevaompaula@gmail.com
[6] Antonio Alves Dias, LaMEM, Department of Structural Engineering (SET), São Paulo University (EESC/USP), São Carlos, SP, Brazil. dias@sc.usp.br
[7] Niro Higuchi, National Institute of Amazonian Research (INPA), Manaus, Brazil, higuchi.niro@gmail.com

https://doi.org/10.52202/069179-0027

Figure 1: *a) Dowels fabrication; b) Panel lay-up; c) Edges compressions; d) Drilling of holes; e) Dowel hammering; f) Final panels.*

Similar panels were developed in United Kingdom using densified wood by a hot-pressing process to give greater densities dowels. The results were promising inclusive with the fabrication and assembly of a prototype of a construction [4].
In Brazil there are hundreds of high-density tree species (> 1000 kg / m³) that can be used to produce dowels without the need for densification process. Many of these have no commercial value and, as a result, are little or no exploited. Thus, selective logging is concentrated on a few specific species [5, 6].
European experience shows that it is possible to manage forest resources (timber) to fabricate structural elements from small to large civil works, without degrading or destroying forests and the environment (sustainably). The implementation of sustainable forest management (SFM) is the best alternative to sustainably assure supply of hardwood in Tropical forests.
Typically, SFM in rainforest, such as the Amazon, is based on selective logging of specific species. Specifically, maintain a sustained income regime, whilst conduction natural regeneration of the forest, over a certain period, without compromising his natural structure and its initial capital [7].

1.2 STIFFNESS OF CONNECTIONS

In the DCLT panel the connection's stiffness is given by the mechanical connection between the dowel and the wood layers.
The deformation between two or more members that are connected results from elastic and non-elastic deformation in the connecting members and the fasteners. To describe this behaviour that Eurocode 5 calls a slip module, which refers to of Slope of the Load-Deformation Curve [8].

2 OBJECTIVE

In this work were studied physical and mechanical characteristics of four Amazonian hard wood tree species to determine its suitability to compose a DCLT panel.

3 MATERIALS AND METHODS

3.1 MATERIALS

Some species of trees with higher incidences in the Amazon Forest per unit area were chosen for the dowel tests.
Pequiarana wood (*Caryocar glabrum)* was chosen as lamellas for all specimens tested, while dowels were made of *Eschweilera wachenheimii* (Matá Matá Amarelo), *Scleronema micranthum* (Cardeiro), *Brosimum rubescens* (Pau-Rainha) and *Protium altsonii* (Breu Vermelho).

In this study no characterization tests of Pequiarana wood (*Caryocar glabrum*) were performed. However, data from the literature present the following physical and mechanical characteristics [9, 10]:

- Density = 690 kg/m³;
- Parallel compression stiffness ($f_{c0,m}$) = 59,8 MPa;
- Shear Stiffness ($f_{v0,m}$) = 14,42 MPa
- Bending stiffness ($f_{b0,m}$) = 103 MPa

The trees were obtained from the Tropical Silviculture Experimental Station (EEST) under the management of the Forest Management Laboratory (LMF) of the National Institute of Amazon Research (INPA) of Manaus, Brazil. Figure 2 presents its location.

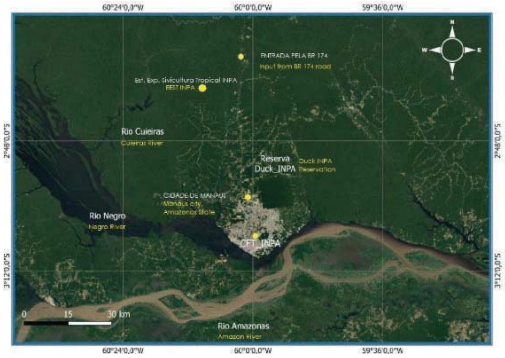

Figure 2: *Location map of Experimental Station of Tropical Silviculture (EEST), from INPA .*

3.2 METHODS

Tests to determine compressive strength resistance, shear and density parameters were performed according to the Brazilian Standard of Wooden Structures NBR 7190 part 3 - Test Methods for characterization of defect-free specimens for timber of native forests [11]. The connection slip modulus (Kser) was obtained by the test proposed by Pereira *et.al*. [3] (Fig. 3).

https://doi.org/10.52202/069179-0027

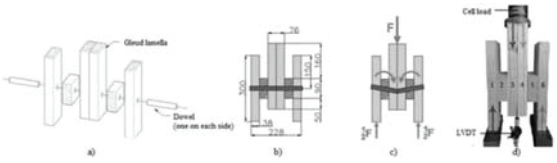

Figure 3: *a) Assembly scheme; b) Specimen measurements (mm); c) Static layout and d) Real model during the test.*

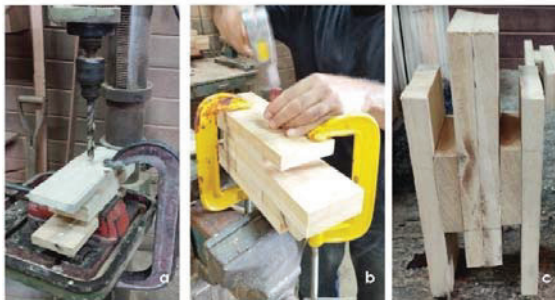

Figure 4: *a) Positioning of the lamellas and drilling; b) Placement of dowels in the holes; c) Test Specimen*

The slip modulus determination test has been proposed simulating the forces applied to the dowels during the use of the panel in bi-supported bending, as shown in Figure 5. In this purpose, the dowel bonding is submitted to a compressive force parallel to the lamellas and perpendicular to the dowel.

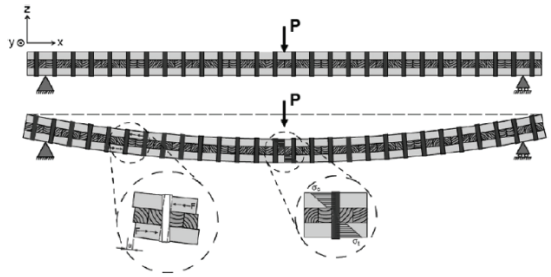

Figure 5: *Y-axis bending of the 3-layer slab, highlighting of the shear and bending forces in the panel.*

The calculations for obeying the value of the slip module were made using the methods described in the European Norm EN 26891:1991, ISO 10984/2009 and in Brazilian standard ABNT 7190-7/2022. The methodology of ISO and EN are equal. European norms and the Brazilian norm have methodology similar but the calculation method is different, as shown in figure 06 and equations 1 and 2.

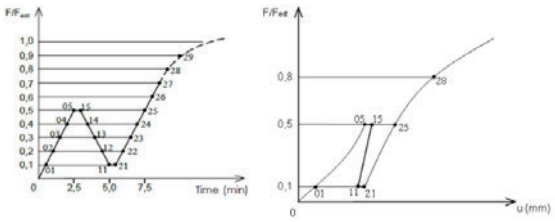

Figure 6*: Form of loading application during testing (left); Force diagram versus connection slip (right).*

For the Brazilian norm, k_{ser} is calculated for equation 1.

$$K_{ser} = \frac{0{,}5 \cdot F_{est}}{\frac{5}{4}(u_{05} - u_{01})} \quad (1)$$

Where F_{est} is a force estimated for rupture, u_{05} is displacement for 50% of force, and u_{01} is displacement for 10% of force.

For European Norm EN 26891and ISO 10984, k_{ser} is calculated for equation 2.

$$K_{ser} = \frac{F_{04}}{\frac{4}{3}(u_{04} - u_{01})} \quad (2)$$

Where F_{04} is the force of 40% of rupture force, u_{04} is displacement for 40% of force, and u_{01} is displacement for 10% of force.

4 RESULTS

The results obtained for the tests performed are presented in the following items.

4.1 COMPRESSIVE STRENGTH TEST

The results of compressive strength test parallel to the fibres and the Modulus of Elasticity in Compression of the analysed woods are presented in Table 1.

Table 1: *Compression and MOE in Compression parallel to the fibres*

Popular name	Matá Matá Amarelo	Breu Vermelho	Pau-Rainha	Cardeiro
Scientific Name	*Eschweilera wachenheimii*	*Protium altsonii*	*Brosimum rubescens*	*Scleronema micranthum*
$f_{c0,med}$ *(MPa)*	56.23	51.78	109.65	37.12
$f_{c0,k}$ *(MPa)*	58.95	48.16	120.0	38.76
St. Desv.	2.32	5.38	1.50	0.91
$E_{c0,med}$ *(MPa)*	12661	-	16243.74	6785
$E_{c0,k}$ *(MPa)*	14578	-	16523.44	5729
St. Desv.	1275	-	1653.25	7425

4.2 SHEAR TESTS

The results of shear tests of the analysed woods are presented in Table 2.

Table 2: *Shear stiffness results for the species*

Popular name	Matá Matá Amarelo	Breu Vermelho	Pau-Rainha	Cardeiro
Scientific Name	*Eschweilera wachenheimii*	*Protium altsonii*	*Brosimum rubescens*	*Scleronema micranthum*
$f_{v0,med}$ *(MPa)*	18.81	12.4	27.4	8.97
$f_{v0,k}$ *(MPa)*	14.30	11.3	31.41	7.91
St. Desv.	7.09	3.1	2.29	1.04

4.3 DENSITY TESTS

The results of density tests of the analysed woods are presented in Table 3.

Table 3: *Density results for the species*

Popular name	Matá Matá Amarelo	Breu Vermelho	Pau-Rainha	Cardeiro
Scientific Name	*Eschweilera wachenheimii*	*Protium altsonii*	*Brosimum rubescens*	*Scleronema micranthum*
Density med. (kg/m³)	810	605	910	590
St. Desv.	2.1	2.51	3.12	0.54

4.4 CONNECTION SLIP MODULUS TESTS

Figure 7 illustrates the *Pequiarana* wood specimen connected with *Pau rainha* dowel's during a binding test to determine the slip module. It is possible to observe that the cross layer was breaking by shear. This behaviour is similar to rolling shear in the ordinary CLT.

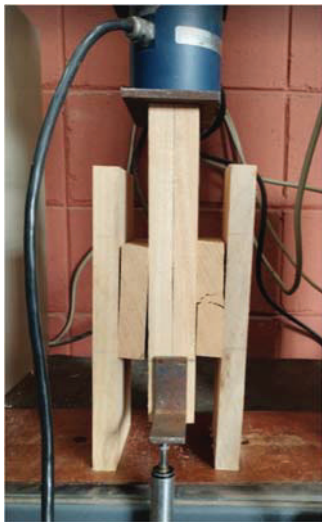

Figure 7: *Cross -sectional layer broke through shear*

Figures 8, 9 and 10 show the results of the connection sliding tests, of which the values used to calculate the K_{SER} were obtained, according to the European Standard and the Brazilian Standard of Wood Structures.

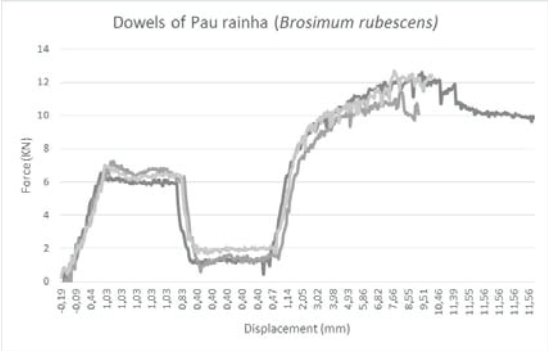

Figure 8: *Chart illustrating the force versus displacement during testing of the specimens using Pau rainha Dowel's.*

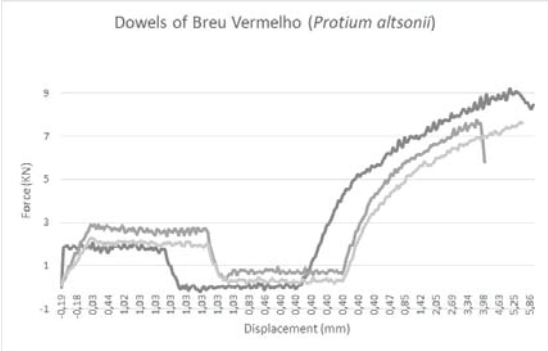

Figure 9: *Chart illustrating the force versus displacement during testing of the specimens using Breu vermelho Dowel's.*

https://doi.org/10.52202/069179-0027

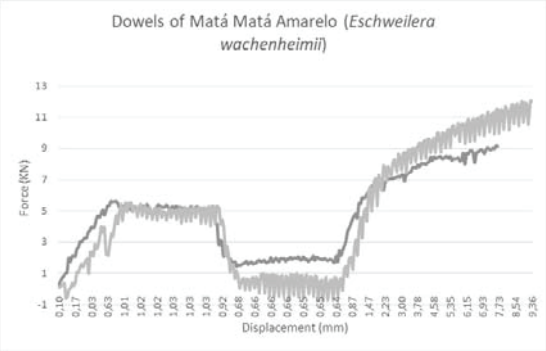

Figure 10: *Chart illustrating the force versus displacement during testing of the specimens using Matá Matá Amarelo Dowel's.*

The table 4 presents the values of the k_{ser} obtained using the calculations described in European and ISO standards and the Brazilian norm, for the tests performed.

Table 4: *Kser values for Brazilian and European Norms*

Wood of dowel (Ø16 mm)		$K_{ser,med}$ [N/mm]	
Popular Name	Scientific name	ABNT 7190-7/2022	ISO 10984 & EN 26891
Pau Rainha	*B. rubescens*	2061	3133
Breu Vermelho	*P. Altsonii*	1607	1216
Matá Matá Amarelo	*E. wachenheimii*	1754	807

The figure 11 presents some dowels after the test to determine the connection slip module.

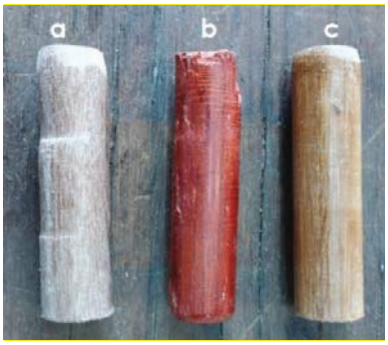

Figure 11: *Some dowels after slip test. a) Breu Vermelho; b) Pau rainha; c) Matá Matá Amarelo*

4.5 ANALYTIC CALCULUS

The analytical calculation of Slip Modulus was performed in accordance with the method described in the European Standard of wood structures - Eurocode 5, and in the current version of the Brazilian Standard of wood structures (NBR 7190/2022), which are equivalent [12, 13].

Equation 3 presents the analytical calculation to estimate the connection slip modulus. According to the standards, if the characteristic density of the joint members is different ($\rho_{k,1}$ and $\rho_{k,2}$), then calculating the stiffness may be taken as presented in equation 4.

$$K_{ser} = \rho_{med}{}^{1,5} \cdot \frac{d}{23} \quad (3)$$

Where ρ_{med} is the average specific density in kg/m³, given by multiplication of the apparent density characteristic by the value 1.20; d is the effective diameter of the dowel, expressed in millimetres (mm).

$$\rho_{med} = \sqrt{\rho_{k1} \cdot \rho_{k2}} \quad (4)$$

Where ρ_{k1} and ρ_{k2} are the density values of woods 1 e 2.

The Table 4 presented results for analytical values for the species studied.

Wood	Density ρ_k (Kg/m³)	Density ρ_{med} (Kg/m³)	Kser (N/mm)
Pequiarana	*690*	-	-
Breu vermelho	605	646	11425
Pau rainha	910	792	15517
Mata Mata Amarelo	810	748	14220
Cardeiro	590	638	11212

5 DISCUSSION

5.1 PHYSICAL AND MECHANICAL PROPERTIES OF WOOD

Through the characterization tests it was possible to conclude that the Pau Rainha (*B. rubescens)* obtained the highest values of the physical and mechanical properties, reaching a 120 MPa in parallel compression ($f_{c0,k}$). The Matá Matá Amarelo (*E. wachenheimii*) species also obtained good values for use in dowels, because the Brazilian standard recommends use of wood from class D60 for dowels. The value obtained for parallel compression ($f_{c0,k}$) by Matá Matá Amarelo did not exceed 60 MPa but was very close. The other two species, Breu Vermelho (*P. Altsonii*) and Cardeiro (*Scleronema micranthum*) obtained the lowest values, with parallel compression ($f_{c0,k}$) 48 and 38 MPa, responsively.

The Cardeiro species was excluded from the tests as a connection element because besides low mechanical resistance, it has traumatic channels, an anatomical feature that increases wood fending during machining.

Differences in perpendicular and parallel resistances the fibres of the three species studied can be seen in the image of the dowels after the test to determine the slip module, (Figure 11). It is clear that the Breu Vermelho scare has been compressed perpendicular to fibres while those of

Matá Matá Amarelo and Pau Rainha this compression was not evident.

5.2 SLIP MODULE TEST

The results of the rigidity tests of the connection according to the parameters of the Brazilian standard showed that Pau Rainha (*B. Rubescens*) obtained the highest value of k_{ser}, followed by Matá Matá Amarelo (*E. Wachenheimi*) and finally the Breu Vermelho wood (*P. Altsonii*). These results are aligned with the values of the physical and mechanical properties presented in tables 1, 2 and 3, where the Pau Rainha (*B. Rubescens*) presents the highest values of resistance and rigidity to compression parallel to fibres, resistance to shear and density, followed by Matá Matá Amarelo (*E. Wachenheimi*) and finally the Breu Vermelho wood (*P. Altsonii*).

The results of binding rigidity tests according to the parameters of EN26891 and ISO 10984 did not show the same behaviour. In the comparison between the values obtained by the method of calculating the Brazilian standard and the EN26891 and ISO 10984, the values range from 30 to 200%.

5.3 ANALYTIC CALCULUS RESULTS

The results of the analytical calculation indicated in Eurocode 5 and the Brazilian Standard of Wood Structures did not converge for the values obtained for the connection slip test. Other authors estimate k_{ser} using other relationships that also take into account the density of the wood and the dowel diameter, but with different equation [2]. New calculations using these other equations will be performed to obtain an analytical equation more consistent with the use of the dowelled connection in cross -lamella panels.

6 CONCLUSION

Among the four wood species studied for use as a connecting element (dowel), only the Pau Rainha wood (*B. Rubescens*) and Matá Matá Amarelo (*E. Wachenheimi*) obtained good results. Mata Mata Amarelo did not get the best results, but in the criterion of abundance, that is, number of tree individuals per m² in the rain forest, it has advantages over the Pau Rainha. Thus, it is possible to apply the concept of sustainable forest management and rationally use this tree species.

The preparation of cross-lamelas wood panels using high density wood caves from the Amazon rainforest presents itself as an alternative for the use of little-known species and great abundance in the forest. New studies are being conducted to validate these results, varying the diameter of the dowels and the lamellas woods.

ACKNOWLEDGEMENT

CNPq (Conselho Nacional de Desenvolvimento Científico e Tecnológico), Capes (Coordenação de Aperfeiçoamento de Pessoal de Nível Superior); FAPEAM (Fundação Amparo à Pesquisa do Estado do Amazonas); INCT Madeiras da Amazônia (Instituto Nacional de Ciência e Tecnologia Madeiras da Amazônia).

REFERENCES

[1] Market Research Future. *Global engineered wood market research report.* (2022).

[2] Sohier, L.A.P., Development of a new mass timber slab: the dowelled cross-laminated timber Analytical design methods and experimental validation, Master Thesi's, Faculté Polytechnique, UMONS, Belgium.

[3] Pereira M.C.M., Sohier L.A.P., Descamps T., Calil Junior C.: Doweled cross laminated timber: Experimental and analytical study, Construction and Building Materials, Volume 273, 2021,

[4] Guan Z. et al.: Development of Adhesive Free Engineered Wood Products –Towards Adhesive Free Timber Buildings. In: *World Conference in Timber Engineering*. Seul, 2018.

[5] ASNER, G. P. et al. Selective logging and its relation to deforestation. Geophysical Monograph Series, v. 186, p. 25–41, 2009.

[6] HIGUCHI, F. G. Dinâmica de volume e biomassa da floresta de terra firme do Amazonas. Thesis. Federal University of Paraná, 2015.

[7] Higuchi, N.: Utilização e manejo dos recursos madeireiros das florestas tropicais úmidas. *Acta Amazonica*, [S.L.], v. 24, n. 3-4, p. 275-288, 1994. http://dx.doi.org/10.1590/1809-43921994243288.

[8] Sandhaas, C., Munch-Andersen, J., Dietsch, P. (eds.), Design of Connections in Timber Structures: A state-of-the-art report by COST Action FP1402 / WG3, Shaker Verlag Aachen, 2018Pereira M.C.M., Sohier L.A.P., Descamps T., Calil Junior C.: Doweled cross laminated timber: Experimental and analytical study, *Construction and Building Materials*, Volume 273, 2021,

[9] Brasilian Woods, Forest Products Laboratory (LPF), Brasilia, DF, Brazil. 2022. Available in: https://lpf.florestal.gov.br/pt. Acess in 13/01/2023.

[10] Wood informations, Technology Research Institute (IPT – Instituto de Pesquisas Tecnológicas), São Paulo, SP, Brazil. Available in: https://www.ipt.br/informacoes_madeiras3.php. Acess in 13/01/2023.

[11] Associação Brasileira de Normas Técnicas. NBR 7190. Timber Structures Part 3: Test Methods for Characterization of defect-free specimens for timber of native forests, Rio de Janeiro, 2022.

[12] Associação Brasileira de Normas Técnicas. NBR 7190. Timber Structures Part 1: Design Criteria, Rio de Janeiro, 2022.

[13] EN 1995-1-1:2004 (Eurocode 5) Design of timber structures – Part 1-1: General – Common rules and rules for buildings. CEN, Brussels.

https://doi.org/10.52202/069179-0027

World Conference on Timber Engineering Oslo 2023

AN EXPERIMENTAL INVESTIGATION OF FAILURE MODES IN SHORT SPAN FRP REINFORCED GLULAM BEAMS

Catherine Shrimpton[1], Serena Siciliano[2], Herry Chen[3], Yannick Vetter[4], Daniel Lacroix[5]

ABSTRACT: Although the Canadian bridge code has provisions for fibre-reinforced polymer (FRP) timber stringers, the lack of tools and limited understanding of the structural behaviour prevents widespread adoption, specifically for glulam beams. Thus, an experimental investigation examining the effects of FRP reinforcement configurations on short span glulam beams was undertaken. A total of fourteen glulam beams were tested to failure under four-point bending with five of them being unreinforced and the remaining nine reinforced with two or four layers of simple tension and U-shaped tension FRP reinforcement. In comparison to the unreinforced beams, FRP reinforced beams were observed to have an increase in maximum load with a lower maximum displacement. Although the addition of FRP reinforcement contributed to an increase in strength and stiffness, the primary failure mode changed from pure flexure, as found in the unreinforced beams, to longitudinal shear, tension perpendicular-to-grain or a combination of brittle failure modes. The brittle failure modes can be attributed to insufficient development lengths, the low shear span to depth ratio, and the inherent low shear strength of the tested glulam. These factors need to be considered in future models to accurately predict the structural behaviour of short span glulam beams in flexure.

KEYWORDS: fibre-reinforced polymers, glulam, timber, shear failure, flexural failure

1 INTRODUCTION

1.1 BACKGROUND

The resurgence of timber within the construction industry has been heavily influenced by the development and commercialization of mass timber products, such as glued-laminated timber (glulam) and cross-laminated timber (CLT). Significant research efforts have thus been undertaken in Canada and internationally to investigate the performance of different mass timber products. As a result, significant updates to the newest editions of the National Building Code of Canada [1] and International Building Code [2] have been implemented allowing for the construction of encapsulated mass timber buildings up to 12- and 18-storeys, respectively.

Despite the significant progress towards the development of design provisions and guides, one area that has not been fully investigated is the behaviour of glulam beams reinforced with fibre-reinforced polymers (FRPs). To this date, there are no design guidelines in the CSA O86 "Engineering Design in Wood" [3] nor the CSA S6 "Canadian Highway Bridge Design Code" [4] for glulam beams reinforced with FRPs. Although there are design provisions in the CSA S6 for timber stringers reinforced with FRP fabric and bars, the increased strength is tied to a minimum reinforcement ratio being met, thereby resulting in an increased strength of one grade category (e.g., from No.1/No.2 to Select Structural).

The overarching aim of the current research program at the University of Waterloo is to provide designers with guidance in the detailing of FRP-reinforced wood members in addition to providing tools to understand and predict their structural behaviour. Within the scope of the current paper, traditional FRP reinforcement methods on the performance of short span glulam beams are investigated and discussed.

1.2 PREVIOUS RESEARCH

Several types of FRPs exist and can be applied to wood (e.g., sawn timber, glulam) to strengthen deficient structural members, retrofit against extreme hazards (e.g., earthquakes, blast loading), or to use as a hybrid product in a new design. Common FRP types include glass FRP (GFRP), carbon FRP (CFRP), aramid FRP (AFRP), or basalt FRP (BFRP). These types can be installed through external bonding of FRP sheets [e.g., 5–7] or insertion of FRP bars or plates into the members [e.g., 8,9].

In general, whether in the form of sheets or bars, FRP generally contributes to an overall increase in stiffness

[1] Catherine Shrimpton, MASc. Candidate, University of Waterloo, Waterloo, Canada, ceshrimpton@uwaterloo.ca
[2] Serena Siciliano, Undergraduate in Architectural Eng., University of Waterloo, Waterloo, Canada, serena.siciliano@uwaterloo.ca
[3] Herry Chen, Undergraduate in Architectural Eng., University of Waterloo, Waterloo, Canada, herry.chen@uwaterloo.ca
[4] Yannick Vetter, MASc., University of Waterloo, Waterloo, Canada, yvetter@uwaterloo.ca
[5] Daniel Lacroix, Assistant Professor, University of Waterloo, Waterloo, Canada, Daniel.lacroix@uwaterloo.ca

https://doi.org/10.52202/069179-0028

and strength with an upper limit of 3% of reinforcement to wood area. Vetter et al. [10] conducted an analytical study on the effects of the material wood properties on the flexural behaviour of FRP-reinforced glulam. In the study, three different cross-section sizes, two reinforcement schemes (i.e., simple tension, and U-shaped up to mid-depth), six different number of FRP layers provided (i.e., 0, 1, 2, 3, 5, 7), and three different ratios of tension-to-compression moduli (i.e., 2:1, 1:1, 0.5:1) were investigated for a total of 99 simulations. The tensile-to-compressive wood strength ratio was observed to significantly affect the increases in moment resistance when the wood in tension is significantly weaker than in compression (i.e., 0.5:1), with increases in moment resistance of 1.95. In comparison, for the case where the wood in tension is significantly stronger than that in compression (i.e., 2:1), a maximum moment resistance increase of 1.19 was observed. This observation is in line with the literature that the contribution of the FRP is most evident for weaker specimens [6].

Although the previous research provides a good insight on the behaviour of FRP-reinforced glulam beams, the material model used in Vetter et al. [10] assumed a flexural response and an infinitely rigid bond between the FRP and omitted FRP delamination and longitudinal shear failure in the wood.

1.3 OBJECTIVES

The primary aim of the research is to investigate the behaviour of both unreinforced and FRP reinforced glulam beams, in order to understand the limitations of reinforcement configurations on the flexural behaviour of glulam beams. This paper presents the findings of the research program, specifically the effects that FRP reinforcement has on the failure modes of short span glulam beams.

2 EXPERIMENTAL PROGRAM

2.1 DESCRIPTION OF SPECIMANS AND MATERIALS

The experimental program investigated the behaviour of fourteen unreinforced and FRP-reinforced 69 mm x 100 mm x 1355 mm 20f-EX glulam beams under four-point bending. Upon receipt of the glulam, it was observed that the specimens had minor deformities (e.g., uneven edges, inconsistent laminate widths, splits) which were removed by use of a planer and jointer to a final 69 mm x 100 mm cross-section. The specimen lengths, and clear span, were determined in accordance with ASTM D198 “Standard Test Methods of Static Tests of Lumber in Structural Sizes” [11]. According to the standard, a minimum shear span to depth ratio (a/d) of 4 allows for the evaluation of flexural properties. Therefore, shear and clear spans of 400 mm and 1,200 mm were chosen with beams having a total length of 1,355 mm. Prior to testing, the specimens were conditioned to an average moisture content of 11.4% (CoV 0.11). using a humidity chamber. The average density of the beams was determined to be 442 kg/m3 with a coefficient of variation of 0.06.

Of the fourteen specimens, five were unreinforced and nine were reinforced with glass FRP (GFRP). Five beams were reinforced with simple tension reinforcement and four with U-shaped reinforcement extending to mid-depth (Figure 1).

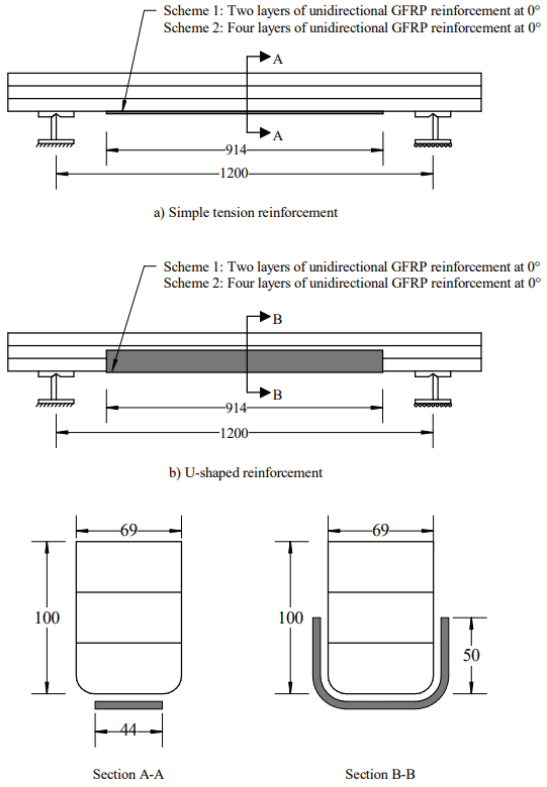

Figure 1: *Reinforcement Configurations*

All reinforced specimens were provided with either two or four layers of unidirectional GRFP reinforcement at 0°.The glulam tension laminate corners were routed using a corner round over bit (12.7 mm radius) prior to the application of the GFRP to prevent stress concentrations in the FRP extending beyond the bottom face. The application face(s) of the beams were wire brushed using a grinder to roughen the surface, providing an ideal interface for the bond between the FRP fabric and the glulam. The glulam FRP application face(s) were then coated with a layer of the epoxy resin mixture. The GFRP fabric was initially saturated with the epoxy resin followed by placing the FRP sheets onto the epoxy coated glulam beam surfaces. A summary of the test matrix is shown in Table 1.

https://doi.org/10.52202/069179-0028

Table 1: *Test Matrix Summary*

Specimen Number	Specimen Type	Reinforcement Configuration
G-1 - G-5	Unreinforced	-
GS_2-1 – GS_2-3	Reinforced	Simple Tension, 2 Layers
GS_4-1 – GS_4-2	Reinforced	Simple Tension, 4 Layers
GU_2-1 – GU_2 -2	Reinforced	U-Shaped, 2 Layers
GU_4-1 – GU_4 -2	Reinforced	U-Shaped, 4 Layers

2.2 DESCRIPTION OF TEST SETUP

A total of fourteen glulam beams were tested under static four-point bending, in accordance with ASTM D198-21a "Standard Test Methods of Static Tests of Lumber in Structural Sizes" [11]. Simply supported boundary conditions were provided through the use of an anchored pin and roller system.

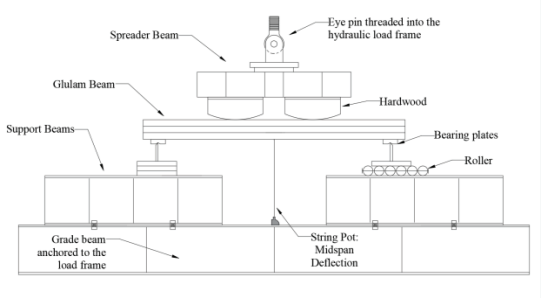

Figure 2: *Flexural Test Set Up*

A 500 kN hydraulic load frame with a load cell connected to the actuator was used to load all bending tests. The unreinforced and reinforced beams were loaded in displacement control until failure, with loading protocols ranging from 3.5 mm/min to 10 mm/min to ensure ultimate failure within five to ten minutes [11]. During the tests, a data acquisition system recorded the data. The applied load and midspan deflection were measured using the load cell in the test frame and a wire (i.e., string pot) respectively. Furthermore, the strains of the wood and FRP were recorded at midspan using strain gauges. Before testing the weights, moisture readings and visual observation of the specimens were recorded.

3 EXPERIMENTAL RESULTS

3.1 FAILURE MODES

A total of five unreinforced and nine FRP-reinforced glulam beams were tested to failure. The observed failure modes in the unreinforced glulam beams consisted of simple tension and splintering (Figures 3a and 3b), as well as cross-grain tension in one specimen (Figure 3c).

For the simple tension reinforcement configuration with two layers and four layers, the failure mode changed from a flexure failure to one that is dominated by longitudinal shear and stress concentrations. Figure 4 shows a representative failure progression where a longitudinal shear failure first occurred followed by a failure of the wood where the simple tension reinforcement ended (GS_2-2, GS_2-3, GS_4-1). For all three beams, FRP debonding on the tension face or tensile failure of the FRP were not observed. This observation conflicts with other studies that reported debonding of the FRP caused by a flexural failure of the wood material on the tension side pushing on the FRP laminations [12–15].

(a) G-1: Tension Failure

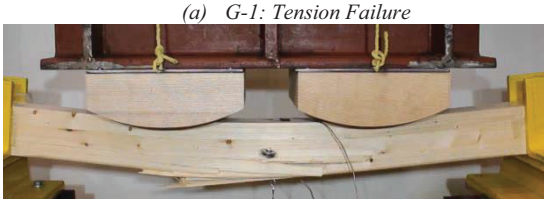

(b) G-3: Splintering Failure

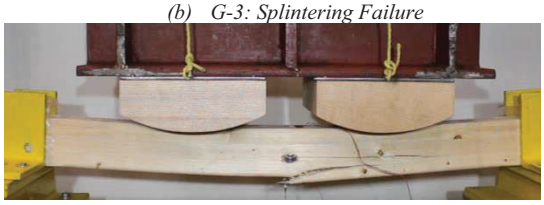

(c) G-4: Cross-grain Failure

Figure 3: *Failure Modes of Unreinforced Specimens*

(a) Before Failure

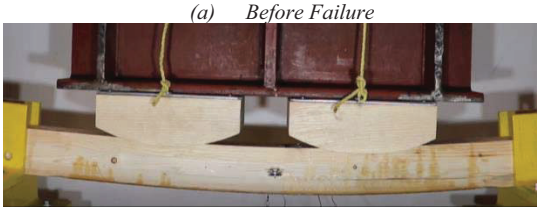

(b) At Failure

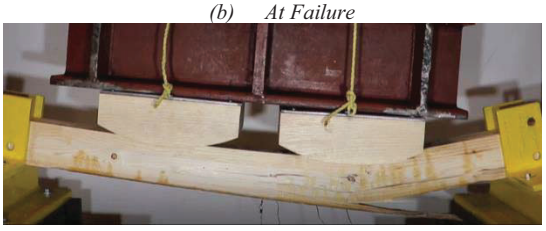

(c) After Failure

Figure 4: *Representative failure of longitudinal shear dominated failure modes in simple tension reinforcement (GS_2-2)*

https://doi.org/10.52202/069179-0028

A second failure mode was observed for specimens reinforced with simple tension reinforcement where failure was observed to occur at the ends of the simple tension GFRP strips causing horizontal shear and tension perpendicular to grain stresses (GS_2-1, GS_4-2). The bond between the reinforcement and the wood remained intact, followed by the propagation of the failure throughout the wood.

(a) Before Failure

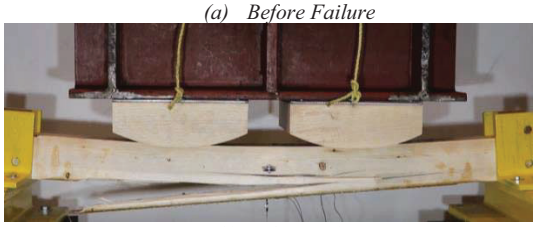

(b) After Failure

Figure 5: *Representative Failure of Tension Perpendicular-To-Grain Dominated Failure for Specimens with Simple Tension Reinforcement (GS_4-2)*

The conflicting failures modes observed for the configuration of simple tension reinforcement glulam beams can be attributed to a combination of factors including: 1. Insufficient development length of the reinforcement, 2. Lower bound shear span to depth ratio (a/d), and 3. Shear strength of glulam. The simple tension reinforcement configuration appears to have provided insufficient development length causing stress concentrations between the supports and end of FRP reinforcement, ultimately leading to an initial failure mode dominated by tension perpendicular-to-grain. In comparison to Lacroix and Doudak [12] for which the FRP reinforcement ended 82.5mm from the centre of the supports, the FRP reinforcement in the current study was terminated 143mm from the centre of supports. Furthermore, while the shear span to depth ratio (a/d) was within the recommended range in the standard [11] with a value of 4:1, it was at the lower end, thus even providing minimum reinforcement shifted the failure mode from flexure to one that is predominantly dominated by longitudinal shear. This can also be attributed to the fact that the glulam in the current study had a lower shear strength, thus only minimal reinforcement was required to alter the primary failure mechanism as Lacroix and Doudak had an a/d ratio of 3.85:1 [12], but did not observe the failure modes reported herein.

For all but one specimen, the U-shaped tension reinforcement eliminated the horizontal longitudinal shear failure as shown in Figure 6. All three specimens (GU_2-1, GU_2-2, GU_4-2) failed due to stress concentration at the end of the FRP reinforcement resulting in debonding of the FRP. Nonetheless, shear stresses are clearly evident as indicated by the splitting of the FRP. This failure mode in the FRP is to be expected due to the use of unidirectional FRP, thus there are no FRP fibres aligned with the depth of the beam. The addition of the reinforcement resulted in a primary failure mode of sudden brash failure at the end of the FRP reinforcement combined with horizontal shear failure of both the wood and FRP reinforcement on the side faces, rather than flexural failure as observed in the unreinforced specimens (Figure 6c). The change in failure mode was expected since the additional reinforcement provided some shear reinforcement.

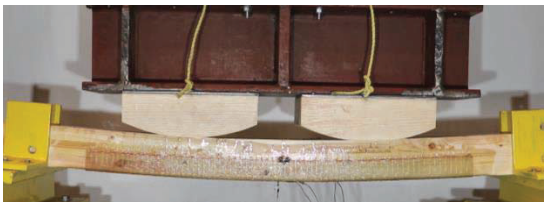

(a) Before Failure

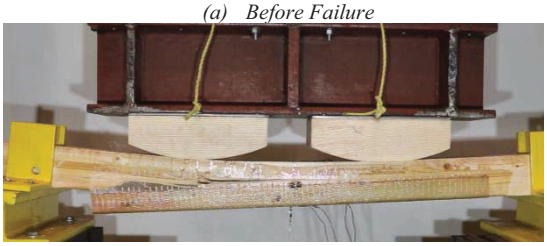

(b) At Failure

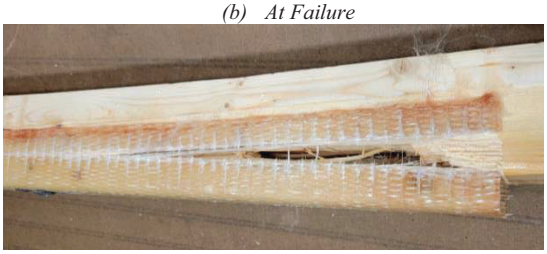

(c) Close Up of Back-Side Failure

Figure 6: *Representative Failure of Tension Perpendicular-To-Grain Dominated Failure for Specimens with U-Shaped Tension Reinforcement (GU_2-1)*

The second failure mode observed for the specimens reinforced with U-shaped tension reinforcement is one that is dominated by a longitudinal shear failure as shown in Figure 7. GU_4-1 failed in horizontal shear at the support with the failure propagating throughout the beam, accompanied with splitting of the FRP reinforcement. Debonding of the FRP was not observed even at large displacement (Fig. 7c).

In general, the failure modes of the unreinforced and reinforced specimens were observed to be different. For all unreinforced specimens, wood tension-dominated failures were observed. This failure mode was not the primary failure mode observed in reinforced specimens as the increase in the woods tensile strength provided by a minimum 2% reinforcement ratio proved to be significant enough to cause the failure mode to change from flexure

https://doi.org/10.52202/069179-0028

to shear for simple tension and U-shaped reinforced specimens.

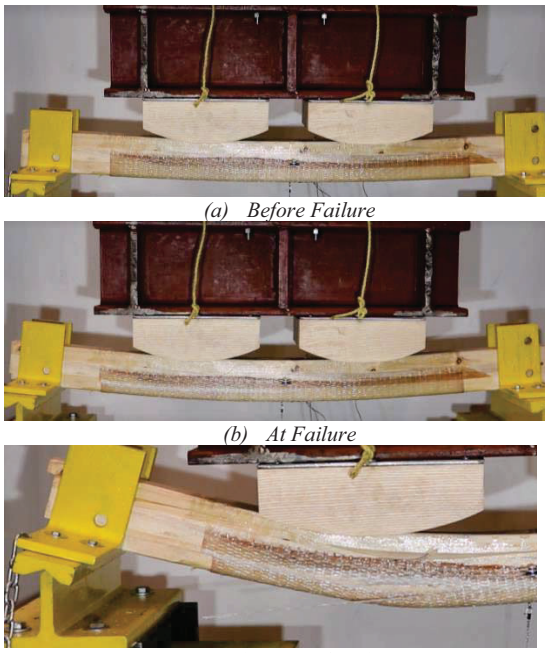

(a) Before Failure

(b) At Failure

(c) Close Up of Failure

Figure 7: *Representative Failure of Longitudinal Shear Dominated Failure Mode for U-Shaped Tension Reinforcement (GU_4-1)*

3.2 ANALYSIS OF EXPERIMENTAL RESULTS

In this section, key parameters describing the behaviour of the unreinforced and FRP-reinforced specimens are presented, including: the maximum applied load (P_{max}), displacement at the maximum applied load (Δ_{Pmax}), and the initial stiffness defined as the slope from 10 to 40% of load-displacement curve. The results are summarized in Table 2-3 and Figures 8-10. The flexural response of the unreinforced beams is summarized in Table 2 whereas the individual load-displacement curves as well as the average curve are presented in Figure 8.

Table 2: *Unreinforced Beam Flexural Test Results*

Specimen Number	P_{max} (kN)	Δ_{Pmax} (mm)	K (N/mm)
G-1	27.9	26.4	1620
G-2	30.8	29.3	1541
G-3	36.8	24.3	1731
G-4	36.8	23.3	2107
G-5	31.9	29.8	1510
Average	32.8	26.6	1702
Std. Dev.	3.5	2.6	216
CoV	0.11	0.10	0.13

The load-displacement curve of the unreinforced beams is observed to behave in a linear fashion with some level of softening caused by compression yielding prior to the wood tensile failure. Since glulam beams consist of different laminates glue-pressed together, the variability and location of naturally occurring defects often leads to wood tensile failures occurring prior to reaching the maximum compression resistance of the laminates.

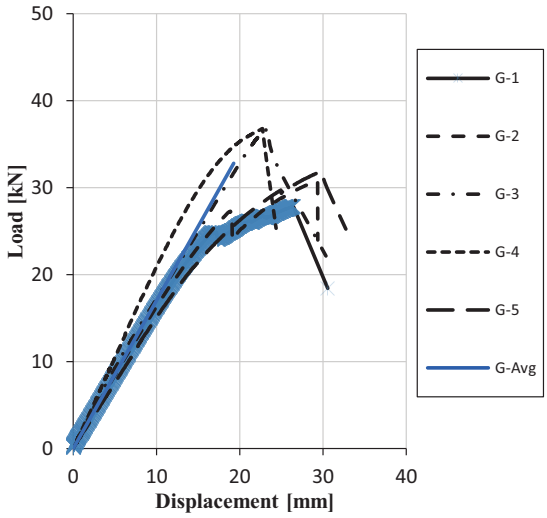

Figure 8: *Load – Displacement Curves of G-Specimens*

The flexural performance of the reinforced beams is summarized in Table 3. The majority of the reinforced specimens showed an increase in the maximum load (P_{max}) and stiffness (K). The provided FRP reinforcement contributed to stiffening of the beams, allowing for greater loads to be sustained. Therefore, leading to a combination of horizontal shear failures and tension perpendicular-to-grain as opposed to that of flexure for the unreinforced beams. As all reinforced beams failed in either shear, delamination, or a combination of alternative failure modes, rather than tensile flexural (e.g., splintering, cross-grain) this is an indication that an increase in tensile strength from the FRP reinforcement schemes can lead to an alternate failure mode. The reinforcement prevented failure of wood tensile fibres observed during the unreinforced beam tests, ultimately increasing the shear stresses in the specimens. This resulted in alterative brittle failures beyond tensile flexural failures observed in the unreinforced beams.

Table 3: *Reinforced Beam Flexural Test Results*

Specimen Number	P max (kN)	Δ_{Pmax} (mm)	K (N/mm)
GS_2-1	32.1	12.8	2544
GS_2-2	35.2	24.1	1783
GS_2-3	36.8	19.5	2082
Average	34.7	18.8	2137
GS_4-1	44.4	27.4	2459
GS_4-2	50.0	25.8	2499
Average	47.2	26.6	2479
GU_2-1	42.9	21.5	2277
GU_2-2	39.6	29.1	1976
Average	41.2	25.3	2126
GU_4-1	46.8	35.1	2259
GU_4-2	46.9	19.5	2844
Average	46.8	27.3	2552

https://doi.org/10.52202/069179-0028

3.2.1 GS Specimens

The addition of two unidirectional GFRP sheets applied longitudinally (GS) increased the capacity and stiffness of the beams on average by a factor of 1.06 and 1.26, respectively. With four unidirectional GFRP sheets, the capacity and stiffness increased by an average factor of 1.44 and 1.46, respectively. However, on average the GS_2 beams failed at a maximum displacement of 0.72 times less than that achieved in the unreinforced beam tests, whereas the GS_4 beams showed an increase of 1.02 times the displacement of unreinforced beams. Relative to the unreinforced beams, the displacement at maximum loads did not increase proportionally (Figure 9).

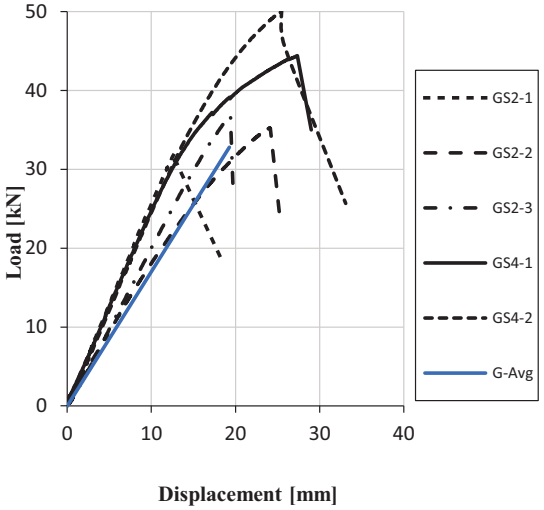

Figure 9: *Load – Displacement Curves GS Specimens*

The significant difference in the change of resistance versus the change of maximum displacement observed in GS can be attributed to a change in failure mode. The addition of simple tension reinforcement altered the failure mode from a wood tension failure in flexure to a horizontal shear failure or stress concentration failure located where the simple tension FRP reinforcement sheets were terminated. The FRP was shown to effectively increase the bending stiffness and reinforced the wood fibres, allowing for the specimens to support greater loads at smaller displacements. The reinforcement provided did not allow for further increase in the beams' bending performance by causing it to fail in a brittle manner (i.e., shear, tension perpendicular-to-grain).

3.2.2 GU Specimens

For beams reinforced with two layers of U-shaped reinforcement (GU), the average resistance and stiffness increased by 1.26 and 1.25 respectively, when compared to the unreinforced beams. For four layers, the average resistance and stiffness increased by 1.43 and 1.50, respectively. Similar to the GS beams, the increases in maximum load and maximum displacement were not proportional. When compared to the unreinforced beams, a decrease of 0.03 times the displacement was observed for the GU_2 beams, whereas a slight increase of 1.05 was observed for the GU_4 beams.

When comparing the effect of U-shaped reinforcement (GU) to the simple tension configuration (GS), the overall flexural behaviour of the specimens is similar. The specimens reinforced with 2 and 4 layers of U-shaped reinforcement (GU) were observed to have an increase in maximum resistance by an average of 1.26 and 1.43, respectively relative to the unreinforced beams.

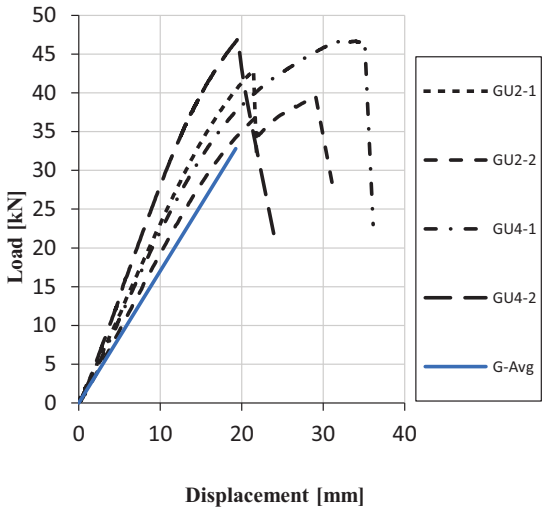

Figure 10: *Load – Displacement Curves GU Specimens*

4 CONCLUSIONS

The current research program investigated the effects of simple tension and U-shaped tension FRP reinforcement on the performance of short span glulam beams. It was observed that while the addition of FRP reinforcement to glulam beams contributed to an increased strength and stiffness when compared to the unreinforced glulam beams; that alternate failure modes consisting of longitudinal shear, tension perpendicular to grain, or a combination of rather than flexure were observed. The alternate brittle failure modes can be attributed to insufficient development lengths, the low shear span to depth ratio, and the inherent low shear strength of the tested glulam. The conflicting failure modes reported herein when compared with the literature [12] indicate that further investigation into the development length of the FRP reinforcement and the corresponding shear concentration at the start and end of FRP reinforcement should be undertaken for the development of future models.

Overall, specimens with two layers of FRP reinforcement increased in capacity by 1.06 to 1.26 for simple and U-shaped configurations respectively. For specimens with four layers of reinforcement, the capacity increased by 1.26 to 1.43, respectively. Similarly, the beams had an observed stiffness increase of 1.25 to 1.26 for two layered configurations, and 1.46 to 1.50 for four layered

https://doi.org/10.52202/069179-0028

configurations. Additionally, the increase in the resistance at a lower maximum displacement of the GS and GU specimens relative to the unreinforced beams indicate benefits attributed to specific FRP reinforcement schemes. While the main objective of the reinforcement is to increase the ultimate capacity of the beam at locations of large bending stresses, to remain effective, the reinforcement is required to be adequately anchored or bonded, to allow the transfer of stresses.

REFERENCES

[1] NRC. National Building Code of Canada 2015.

[2] 2021 International Building Code (IBC) | ICC Digital Codes.

[3] Canadian Standards Association. Engineering Design in Wood. CSA-O86 2019.

[4] CSA. Canadian highway bridge design code. CSA S6 2014.

[5] Buell TW, Saadatmanesh H. Strengthening timber bridge beams using carbon fiber. Journal of Structural Engineering 2005;131:173–87.

[6] Johns KC, Lacroix S. Composite reinforcement of timber in bending. Canadian Journal of Civil Engineering 2000;27:899–906.

[7] Lacroix D, Doudak G. Towards enhancing the post-peak performance of glued-laminated timber beams using multi-directional fibre reinforced polymers. Eng Struct 2020;215:110680.

[8] Rajczyk M, Jończyk D. Behavior of glulam beams strengthened with BFRP bars n.d. https://doi.org/10.1088/1757-899X/603/4/042004.

[9] Gentile C, Svecova D, Rizkalla H. S. Timber beams strengthened with GFRP bars: Development and applications. Journal of Composites for Construction 2002;6:10.

[10] Vetter Y, Stakheiko M, Chen H, Siciliano S, Lacroix D. Analytical Investigation of Wood Material Properties on the Flexural Behaviour of FRP Reinforced Glulam. CSCE 2021 Annual Conference, 2021, p. 10.

[11] ASTM. Static Tests of Lumber in Structural Sizes. ASTM D198 2014:26.

[12] Lacroix DN, Doudak G. Experimental and Analytical Investigation of FRP Retrofitted Glued-Laminated Beams Subjected to Simulated Blast Loading. Journal of Structural Engineering 2018;144:04018089.

[13] Dorey AB, Cheng JJR. The behavior of GFRP glued laminated timber beams. Adv Comp Mat in Bridges and Struct II 1996:787–94.

[14] Sonti SS, GangaRao HVS, Superfesky MC. Rehabilitation and strengthening of glulam stringers for bridge superstructures. First International Conference on Composites in Infrastructures 1996.

[15] Hernandez R, Davalos F. J, Sonti SS, Kim Y, Moody C. R. Strength and stiffness of reinforced yellow-poplar glued laminated beams. Madison, WI: U.S. Department of Agriculture, Forest Service, Forest Products Laboratory; 1997.

World Conference on Timber Engineering Oslo 2023

DAMAGE MODEL FOR A BIOSSOURCED HETEROGENEOUS MATERIAL: APPLICATION TO TIMBER

Amal Rebhi[1], **Myriam Chaplain**[2], **Jean-Luc Coureau**[3], **Cedric Perez** [4]

ABSTRACT: The purpose of this study is to investigate the damage mechanisms of timber, by developing a numerical model based on the concept of damage mechanics. The first stage of this work is to study the existing damage models used for quasi-brittle materials and then propose a fitting to timber. Then a new model is proposed which allows to take into account the orthotropy of timber, the local variation of the mechanical properties due to heterogeneity induced by the defects of timber and the behaviour of timber according to the mode of loading in relation to the longitudinal axis of the grain. Finally, the model calibration is carried out through different experimental tests: fracture characterisation tests in mode I and II and bending tests integrating the heterogeneity of timber.

Keywords: Numerical model, damage mechanics, fracture, timber, quasi-brittle, ductility.

1 INTRODUCTION

To achieve the goals of sustainable development, the use of renewable materials is a response to the climate change. Timber has many advantages allowing it to be more attractive than materials used mainly in the field of construction (steel and concrete). Indeed, it is the only one totally renewable, natural and biological building material. Due to its advantages, research is focusing on improving its mechanical characterization. This means that researchers are focused on better understanding the mechanical properties of wood and finding ways to optimize its performance in terms of strength, stiffness and durability.

The design of wood structures is carried out according to the Eurocode 5 standard to guarantee their durability. It essentially implies a macroscopic characterization of the timber which is regarded as a homogenous material integrating the intrinsic its variability by semi-probabilistic analyses. In fact, wood is a highly anisotropic material, its properties are highly variable and are sensitive to loading types and environmental conditions in relation with the moisture content of the material.

Its mechanical behaviour is strongly influenced by the singularities (like knots) and also by the mode of solicitation with respect to the orthotropy directions. In fact, the bending failure tests show that the fracture is due, in more than 90% of the cases, to the presence of knots and the corresponding deviation of the grain slope. The influence of these defects has been the subject of several studies [1, 4, 6, 7, 10, 11] which show that most of the mechanical properties are lower in sections with knots than free defect wood. Longitudinal tension strength is the most affected property, followed by bending strength, compressive strength parallel to the grain and elasticity modulus. This reduction is due to a stress concentration caused by the presence of knots and the change in the orientation of the local frame along the fibres, thus changing the complacency matrix as a function of the grain slope. In view of this material complexity due to the variation of its mechanical properties, the development of mathematical laws presents an interesting challenge to establish reliable predictive models.

In order to improve the mechanical grading of timber and to limit qualification tests. New numerical approaches need to be developed to study its mechanical behaviour at failure, considering the anisotropy and the influence of its heterogeneities induced mainly by knots.

The majority of existing approaches are based on failure criteria associated with elastic behaviour [1, 3, 9...]. they used elastic failure criteria such as the Tsai-Hill criterion and the Tsai-WU criteria. The load that corresponds to the initiation of damage is determined, but these models are not able to correctly predict the strength and describe the shape of the post-peak portion of the load-displacement curve.

The simulation of timber behaviour requires a model that takes into account the defects of wood, the variation of the grain slope and that integrates the damage of the quasi-brittle anisotropic material to predict the initiation and the progressive damage up to the failure. This work is part of this framework, we propose a new non-linear approach based on the Mechanics of Continuous Damage (MCD) to predict the mechanical behaviour of timber.

MCD is a non-linear elastic approach that was developed in 1958 by Rabotnov and Kachanov [8] to study creep rupture and was subsequently used by several researchers to describe metal damage and failure. This

[1]Amal Rebhi, Mechanics and Ingeniering Institute (I2M), University of Bordeaux, France, amal.rebhi@u-bordeaux.fr

[2]Myriam Chaplain, I2M, myriam.chaplain@u-bordeaux.fr

[3]Jean-Luc Coureau, I2M, jean-luc.coureau@u-bordeaux.fr

[4] Cedric Perez, University Laval, cedric.perez.bdx@gmail.com

https://doi.org/10.52202/069179-0029

concept is part of the thermodynamics of irreversible processes [9]. It has become a promising tool for describing material degradation. The damage is presented by scalar or tensorial variables depending on the objective to be achieved during the modelling. In our case, the damage is anisotropic and several variables are defined according to each type of stress (tension, compression or shear). The MCD is based on the concept of effective constraints which consists in associating to the damaged real space a fictional space for which the material is healthy (Figure 1). New quantities are defined in this space which must be related to the real quantities according to the principle of equivalence used (principle of equivalence in strain, principle of equivalence in stress or principle of equivalence in energy) [13].
Stress increments are calculated as a function of strain increments via an effective stiffness matrix determined as a function of the initial stiffness matrix and damage variables.
Validation of the approach is carried out in two stages. The purpose of the initial modelling is to verify the model parameters by applying it to mode I and II fracture tests on Maritime Pine wooden (free defects) specimens. Then the model is applying to study the bending behaviour of timber beams, integrating the local variation of mechanical properties due to defects.

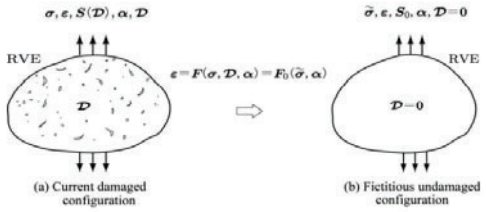

Figure 1: *Assumption of mechanical equivalence and effective stress [13]*

2 DEVELOPMENT OF THE BEHAVIOUR LAW

Before introducing the model, it is necessary to define some indices used for the wood material. Because of its mode of growth, the wood is characterized according to its three natural directions: longitudinal (L, axis of the tree), radial (R) and tangential (T) and its three planes: radial (LR), tangential (LT) and transverse (RT) (Figure 2)

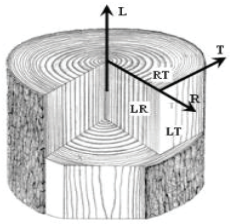

Figure 2: *orthotropy of wood [12]*

In the elastic field, the behaviour is determined by the generalized Hooke's law (Equation (1)), which shows the symmetrical elastic flexibility matrix, the components of this matrix are modified during loading according to the evolution of the damage variables.

$$\begin{bmatrix}\varepsilon_{RR}\\ \varepsilon_{TT}\\ \varepsilon_{LL}\\ \tau_{TL}\\ \tau_{LR}\\ \tau_{RT}\end{bmatrix} = \begin{bmatrix} \frac{1}{E_R} & \frac{-\vartheta_{RT}}{E_T} & \frac{-\vartheta_{RL}}{E_L} & 0 & 0 & 0\\ \frac{-\vartheta_{TR}}{E_T} & \frac{1}{E_T} & \frac{-\vartheta_{TL}}{E_L} & 0 & 0 & 0\\ \frac{-\vartheta_{LR}}{E_R} & \frac{-\vartheta_{LT}}{E_T} & \frac{1}{E_L} & 0 & 0 & 0\\ 0 & 0 & 0 & \frac{1}{G_{TL}} & 0 & 0\\ 0 & 0 & 0 & 0 & \frac{1}{G_{RL}} & 0\\ 0 & 0 & 0 & 0 & 0 & \frac{1}{G_{RT}} \end{bmatrix} \cdot \begin{bmatrix}\sigma_{RR}\\ \sigma_{TT}\\ \sigma_{LL}\\ \sigma_{TL}\\ \sigma_{LR}\\ \sigma_{RT}\end{bmatrix} \quad (1)$$

2.1 Initiation and evolution of damage

Existing damage laws developed for isotropic materials are generally applied even if the damage is anisotropic.
The proposed method to implement a damage model for an orthotropic material is based on laws often used for quasi-brittle isotropic materials [5]. These are adapted according to the mechanical and geometric characteristics of wood. In addition, the model must have a ductile behaviour relative to the compressive stresses.
For a complete description of timber as an orthotropic material, different strain and stress-based failure criteria have been defined in tension and compression (Figure 3).
Wood has a quasi-brittle behaviour in tension and shear and a ductile behaviour in compression.

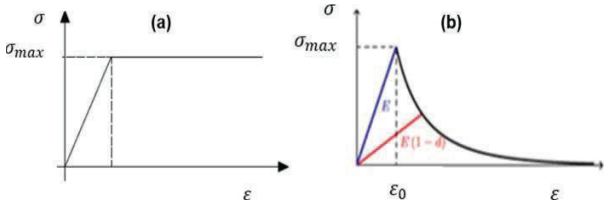

Figure 3: *Stress-strain: (a) ductile behaviour curve in compression, (b) softening behaviour in tension*

2.1.1 Tension behaviour

In tension parallel to the grain direction ($\sigma_L > 0$), damage initiation is governed by strain in the longitudinal direction ($\varepsilon_{t,L}$) and the elastic limit of tensile strain ($\varepsilon_{dt,L}$), the damage criterion ($F_{t,L}$) is given by the Equation (1):

$$F_{t,L} = \frac{\varepsilon_{t,L}}{\varepsilon_{dt,L}} - 1 \quad (2)$$

In tension perpendicular to the grain direction (σ_n>0) (n=R or T), damage is caused by tensile stresses (σ_n) and/or shear stresses (σ_{Ln} and σ_{RT}), the damage criterion in both directions perpendicular ($F_{t,n}$) is given by the Equation (2):

$$F_{t,n} = \frac{{\sigma_n}^2}{{f_{t,R/T}}^2} + \frac{{\sigma_{Ln}}^2}{{f_{Ln}}^2} + \frac{{\sigma_{RT}}^2}{{f_{RT}}^2} - 1 \qquad (3)$$

with $f_{t,n}$, f_{Ln}, f_{RT} are respectively the elastic limit of tensile stress in n direction (n=R or T), the maximum shear stresses in Ln plane and the maximum shear stresses in RT plane.

In order to take into account, the quasi-brittle behaviour of wood in tension as well as the parameters relating to failure, we are interested in existing laws on the damage of isotropic materials such as the Fichant and Mazars law. These laws use fracture energy and strains as the main parameters for predicting material behaviour.
In this quasi-brittle case, damage variables ($d_{t,n}$) have an exponential shape determined through the following relationship based on the Fichant law [5]:

$$\begin{cases} d_{t,n} = 1 - \frac{\varepsilon_{dt,n}}{\varepsilon_{t,n}} \exp\left(B_n\left(\varepsilon_{dt,n} - \varepsilon_{t,n}\right)\right) & if\ F_{t,n} > 0 \\ d_{t,n} = 0 & if\ F_{t,n} \le 0 \\ 0 \le d_{t,n} \le 1 \end{cases} \qquad (4)$$

with $F_{t,n}$ is the damage initialisation criterion, $\varepsilon_{dt,n}$ is the elastic limit in tension in the direction n (n=L, R, T), $\varepsilon_{t,n}$ is the tensile strain in the direction n at the current time increment and B_n is a damage parameters depending on the elastic modulus, strain limit, cracking energy in n direction ($G_{f,n}$) and finite element size (h) by the following relation :

$$B_n = \frac{hE_n\varepsilon_{dt,n}}{G_{f,n} - \frac{1}{2}hE_n(\varepsilon_{dt,n})^2} \qquad (5)$$

2.1.2 Compressive behaviour

For compressive strains parallel or perpendicular to the grain direction, timber has a ductile behaviour, in this case the damage is controlled by the compression deformations, the damage criterion ($F_{c,n}$) is given by the Equation (4):

$$F_{c,n} = \left|\frac{\varepsilon_{c,n}}{\varepsilon_{dc,n}}\right| - 1 \qquad (6)$$

with $\varepsilon_{dc,n}$ is the compression threshold deformation in the direction n and $\varepsilon_{c,n}$ is the deformation at time t.
The evolution of the damage variable ($d_{c,n}$) is determined from the following relationship:

$$\begin{cases} d_{c,n} = 1 - \frac{1}{F_{c,n}} & if\ F_{t,n} > 0 \\ d_{c,n} = 0 & if\ F_{t,n} \le 0 \\ 0 \le d_{c,n} \le 1 \end{cases} \qquad (7)$$

Wood has a quasi-brittle shear behaviour, which is in the proposed approach, related to its tensile and compressive behaviour. For example, a failure parallel to the LR plane can be caused by a tension perpendicular to the mode I, a shear (mode II) or a combination of both. Therefore, it is not possible to define separate failure modes for each direction of stress, a coupling is proposed. Therefore, shear damage is determined by the tensile and compression damage.
Finally, there are six damage variables, three in tension ($d_{t,n}$) and three in compression ($d_{c,n}$) (n=R, T or L).
Using Macaulay's mathematical operator to differentiate damage variables that are activated by the same stress component, but are sensitive to the sign of the component, i.e. tensile or compressive stresses.
So in each direction of orthotropy the damage variable is given by the following relation:

$$D_n = d_{t,n}\frac{\langle\sigma_n\rangle}{|\sigma_n|} + d_{c,n}\frac{\langle-\sigma_n\rangle}{|\sigma_n|};\ \text{with}\ \langle a\rangle = \frac{a+|a|}{2} \qquad (8)$$

We can define the diagonal tensor which represents the orthotropic damage due to the reduction of the effective bearing surface:

$$D = \begin{bmatrix} D_R & 0 & 0 \\ 0 & D_T & 0 \\ 0 & 0 & D_L \end{bmatrix} \qquad (9)$$

3 NUMERICAL SIMULATION OF FAULTLESS WOOD MECHANICAL BEHAVIOUR

In order to carry out the validation of the developed model, the experimental results of Perez [15] in mode I and II on perfect Maritime pine specimens are compared to the numerical results. The geometry of the specimen and the proposed limit conditions for the three experimental configurations (mode I and II) are shown in Figure 4. First, we used the mean experimental elastic and mechanical properties and mean experimental cracking energies.

Table 1: *Elastic and mechanical model parameters*

Parameter	Value
E_L (MPa)	10900
E_T(MPa)	1050
ϑ_{LT}	0.43
ϑ_{TR}	0.39
ϑ_{LR}	0.32
G_{LT} (MPa)	1030
$f_{t,L}$(MPa)	68
$f_{t,T}$(MPa)	3
$f_{c,L}$(MPa)	38
$f_{c,T}$(MPa)	4
$G_{f,I}$(J/m²) (Mode I cracking energy)	550
$G_{f,II}$(J/m²) (Mode I cracking energy)	1739

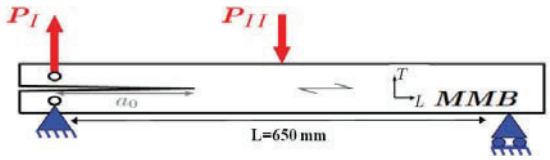

Figure 4: *Mode I DCB test (for* $\boldsymbol{P_{II} = 0}$*) and Mode II test (for* $\boldsymbol{P_I = 0}$*) (same specimen size for all tow failure modes)*

https://doi.org/10.52202/069179-0029

The numerical results are compared with the experimental ones by analysing the load-displacement curves and the corresponding resistance curves to verify the cracking energies declared in the model. The resistance curves (R-curve) are determined from the load-displacement curves and on the basis of the equivalent elastic fracture mechanics (MLER*eq*). They provide an estimate of the fracture properties and also information on the extent of the fracture development zone. Bazant and Kazemi [2] introduced the notion of equivalent elastic crack length (a_{eq}) in their expression of MLER*eq*. This approach defines the equivalent elastic crack length to that which, in a perfect elastic model, produces the same complacency as the actual crack with its development zone. Furthermore, the increase in complacency depends only on the extent of the potential fracture zone (FPZ) or the progression of the macro-crack with its development zone. On this basis, the crack propagation resistance can be estimated using the following equation proposed by Morel et al. (2005) [14].

$$G_R(a) = \frac{P^2}{2b}\frac{d\lambda(a)}{da} \qquad (10)$$

with λ(a) is the compliance such that λ(a) = δ(a)/P(a) with δ(a) and P(a) are the displacement and load for an equivalent elastic crack length a The equivalent elastic crack length is numerically determined from a linear elastic finite element model.

The R-curve for a quasi-brittle material can be divided into two zones. The first regime corresponds to the expansion of the elaboration zone until it reaches its critical size. The second regime is the plateau, which occurs when the macro-crack propagates in auto-similarity with its zone of development. The plateau value of the R-curve supplies the critical resistance to crack propagation, which is the cracking energy declared in the model to describe the mechanical behaviour of the material.

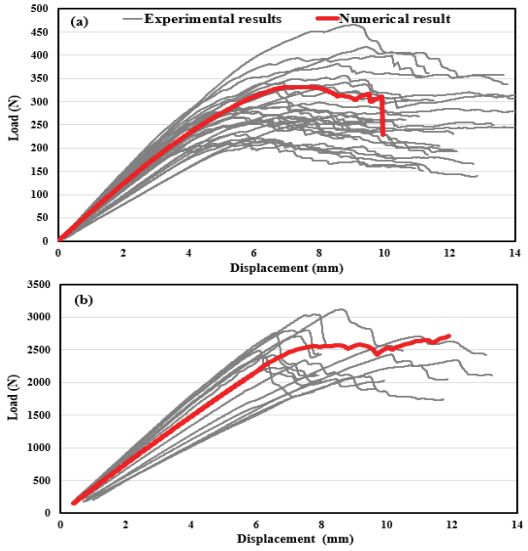

Figure 5: *Load -displacement curves: (a) mode I; (b) mode II; (c) mixed mode*

Using the average elastic and fracture properties of Perez, we observe a good agreement of the model in mode I and II (Figures 5 and 7).

Then, to verify each test, we performed a curve-to-curve comparison using the failure properties of each test (test 1: G_{fI}=400 J/m² ; test 2 : G_{fI}=520 J/m² ; test 3: G_{fI}=690 J/m²). The Figure 6 shows a comparison between experimental and numerical results for three tests performed in mode I.

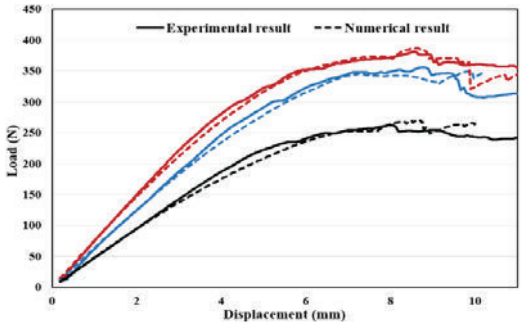

Figure 6: *Curve to curve comparison between numerical and experimental result (Mode I Mode II Mixed Mode colours)*

The numerical and experimental results are close and agree significantly, the numerical methods are reliable and can be used to predict the experimental results with some accuracy.

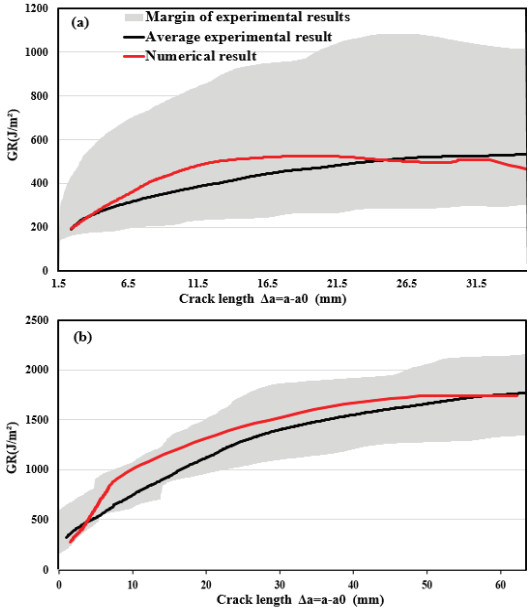

Figure 7: *Resistance curves: (a) mode I; (b) mode*

4 NUMERICAL SIMULATION OF THE MECHANICAL BEHAVIOUR OF HETEROGENEOUS WOOD

The model is then tested on heterogeneous wood by under bending tests. Eleven beams were tested in three-

point bending of 1200 mm length and a section of 100×50 mm².
Before the test, the variation of the grain slope and the geometric parameters of the knots is obtained experimentally and is taken into account in the modelling to determine the local elastic and fracture properties of the wood. The measurement of the grain slope is performed by a device named Xyloprofile. It is based on the projection of a line of laser points perpendicular to the longitudinal axes of the wood and by moving the beam longitudinally, it is possible to measure the fibre angle every 5 mm (Figure 8).

Figure 8: *Xyloprofile wood scan and measurement of the wire slope variation*

The modelling of the grain slope is performed from a numerical procedure that is able to read the experimental data of the slope as a function of the coordinates of each point of the beam and interpolate it in the mesh to build the field of variation of the slope. Then, the local elastic and mechanical parameters are determined by pass matrices calculated as a function of the slope value in each mesh element (Figure 9).

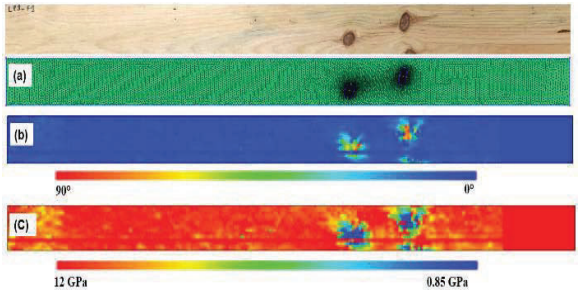

Figure 9: *Numerical modelling of grain slope: (a) mesh by EF, (b) variation of the grain angle in each point of the mesh, (b) variation of the longitudinal modulus of elasticity as a function of the grain slope*

Once we have all the necessary information on the variation of fibre inclination in the surfaces of each beam, on the position of knots and their geometry, the beams are then tested in three-point bending to determine their actual behaviour in the event of failure (Figure 10).

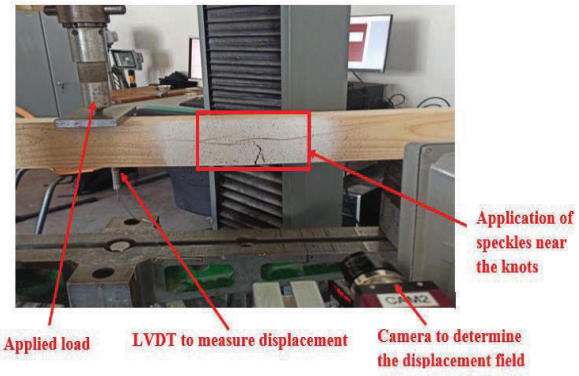

Figure 10: *three-point bending test*

Numerical modelling (2D) of these beams is performed using the average mechanical properties of perfect wood and experimental data of the slope variation. Then the failure stress is determined by taking the average of the numerical results found for the two load of the beam. The figure (Figure 11) shows the load-displacement curves found experimentally and by numerical simulation, as well as the cracking pattern at the fracture time of the three-points bending beams.

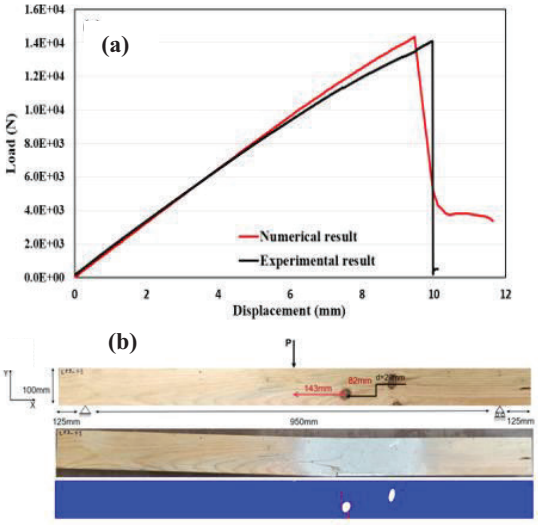

Figure 11: *Comparison between numerical and experimental results for a heterogeneous wood beam subjected to bending loading: (a) prediction of breaking load, (b) fracture facies.*

With the data of the variation of the grain slopes and the average mechanical properties of the perfect wood, we found a good correlation between the numerical and experimental results of the breaking load and displacement which corresponds to the breaking stress (Figure12).

https://doi.org/10.52202/069179-0029

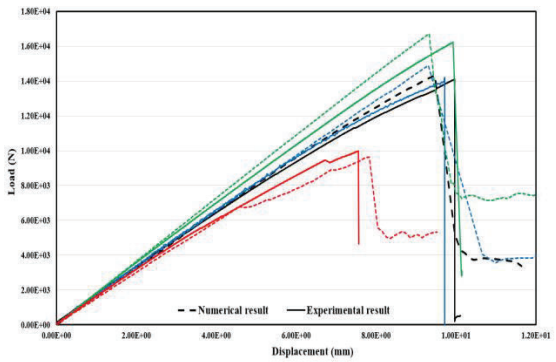

Figure 12: *Comparison between experimentally and numerically obtained fracture loads for four test cases*

In order to determine the displacement and strain fields that occur near the knots, a non-contact measurement method based on digital image correlation (2D) is used. This method allows for local observation of the material behaviour on the pre-nodal surface during the test. This can be very useful in understanding how the wood reacts to applied load and how the knots affect the stability of the structure in general. The results are then used to validate the developed numerical model by comparing the experimental and numerical deformation field values for the same loading times.

The Figure 13 shows the displacement fields (ε_{xx}) obtained from numerical modelling and by image correlation for the same imposed displacement. Comparing the two methods, it can be seen that the strain distribution is very similar around the knots. Furthermore, the strain values obtained from both methods are close in scale.

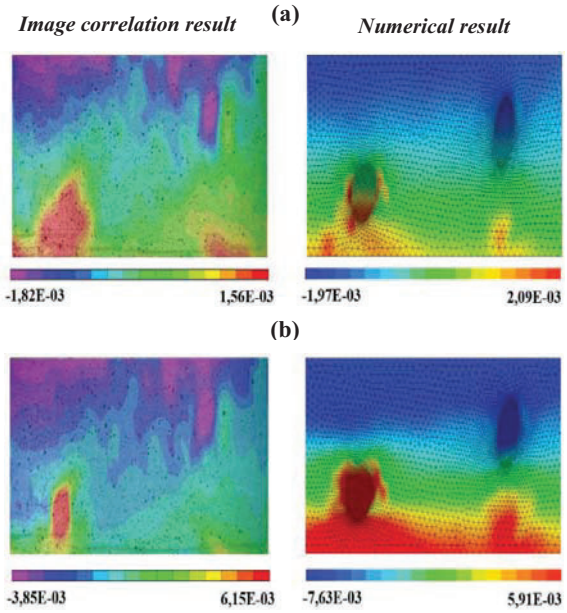

Figure 13: *Comparison between the displacement field obtained by numerical modelling and by image correlation: (a) ID= 3 mm; (b) ID = 6 mm (ID= imposed displacement)*

5 CONCLUSIONS

In this work, an anisotropic damage model for wood has been developed. The proposed model is able to model the fracture behaviour of wood with its heterogeneities, by implementing the damage criteria of wood according to the loading mode: a softening behaviour of wood in tension and shear and a ductile behaviour in compression. The satisfactory agreement obtained between the simulation results and the experimental results confirms the validity of the approach and the damage model proposed for the experimental conditions considered in this work. The integration of this mechanical model is a way of improvement. The next work consists in studying different timber species.

REFERENCES

[1] Baño, V., Arriaga Soilán, F., Soilán, A., and Guaita, M.: Prediction of Bending Load Capacity of Timber Beams Using a Finite Element Method Simulation ofKnots and Grain Deviation. Elsevier, 2011.

[2] Bazant, Z.P., and Kazemi, M.T.: Size Effect in Fracture of Ceramics and Its Use to Determine Fracture Energy and Effective Process Zone Length. Journal of the American Ceramic Society 73, 1841–1853, 1990.

[3] Cordebois, J., and Sidoroff , F.: Damage Induced Elastic Anisotropy. Materials Science, 1982

[4] Grazide, C., Coureau, J.-L., Cointe, A., and Stéphane, M.: Mechanical Performance Curves for the Strength Grading of Maritime Pine. Springer, 2018.

[5] Fichant, S., La Borderie, C., and Pijaudier-Cabot, G.: Isotropic and anisotropic descriptions of damage in concrete structures. Elsevier, 1999.

[6] Guindos, P., and Guaita, M.: A three-dimensional wood material model to simulate the behavior of wood with any type of knot at the macro-scale. Springer-Verlag Berlin Heidelberg, 2021.

[7] Khaloian Sarnaghi, A., and van de Kuilen, J.W.G.: Strength prediction of timber boards using 3D FE-analysis. Department of Wood Technology,

[8] Kachanov, LM.: Time of the rupture process under creep conditions. In Izv. Akad. Nauk. SSR. Otd. Tekh. Nauk, 1958.

[9] Lemaitre, J.: Tensorial nature of damage measuring internal variables. In Hult, J. Lemaitre, J. L. (eds.). Proceedings of IUTAM Symposium on Physical Nonlinearities in Structural Analysis, Springer, Senlis, France, 1981.

[10] Lukacevic, M., and Fussl, J.: Numerical simulation tool for wooden boards with a physically based approach to identify structural failure. Springer-Verlag Berlin Heidelberg, 2014.

[11] Li, M., Füssl, J., Lukacevic, M., Eberhardsteiner, J., and M. Martin, C.: Strength predictions of clear wood at multiple scales using numerical limit analysis approaches. Sciences direct, 2018.

[12] M, Moutee.: Modélisation du comportement

mécanique du bois au cours du séchage. PhD Thesis, Univ. Laval, Québec, 2006.

[13] Murakami, S.: Mechanical modeling of material damage. J. App. Mech, 55 :280–286, 1988.

[14] Morel, S., Dourado, N., and Valentin, G.: Wood: a quasi brittle material R-curve behavior and peak load evaluation. International Journal of Fracture 131, 385–400, 2005.

[15] Perez, C. : Fissuration en mode mixte I+II du boisà différentes teneurs en eau: expérimentation et proposition d'un modèle de courbe-R. Université de Bordeaux, 2021.

https://doi.org/10.52202/069179-0029

World Conference on Timber Engineering Oslo 2023

NUMERICAL EXAMINATION OF THE BEHAVIOUR OF DOWEL LAMINATED TIMBER ELEMENTS UTILISING COMPRESSED WOOD DOWELS

Conan O'Ceallaigh[1], Annette M. Harte[2], Patrick J. McGetrick[3]

ABSTRACT: This study examines the use of finite element software to model the failure behaviour of a dowel laminated timber (DLT) beam which is connected with the use of modified or compressed wood dowels. The numerical model is validated against experimental results and a parametric study is carried out to further examine the influence of dowel diameter and dowel spacing on the load-displacement behaviour of the DLT beams. The numerical model is shown to accurately simulate the ultimate failure load and the stiffness of the DLT beams. The influence of dowel diameter and dowel spacing are presented. The results demonstrate that DLT technology can be used to further improve the environmental performance of timber construction by replacing the use of adhesive which is commonly used when manufacturing laminated engineered wood products.

KEYWORDS: Compressed wood dowels; Dowel Laminated Timber (DLT); Engineered Wood Products (EWPs); Foundation zone, Numerical modelling; Parametric study

1 INTRODUCTION

In recent years, there has been an increased focus on the environmental impacts of construction and a movement towards more sustainable construction products. Dowel Laminated Timber (DLT) products are one such Engineered Wood Product (EWP) that can carry significant structural loads with a limited carbon footprint. The DLT process typically involves the use of hardwood dowels positioned within drilled holes to form a tight fit connection between adjacent laminations as shown in Figure 1. The use of such technology has been successfully utilised to form DLT panels and beams using a variety of different timber species [1–3]. This technology ultimately reduces the use of adhesives in EWPs and further improves the environmental credentials. The efficiency of the connection is reduced when compared to adhesively bonded EWPs and as such, it is important to understand the parameters that affect the strength and stiffness of such connections and the ultimate strength and stiffness of the developed DLT product.

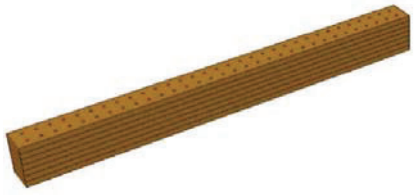

Figure 1: *Typical dowel laminated timber (DLT) beam connected with hardwood timber dowels.*

In this study, the use of compressed timber dowels is explored as a potential alternative to hardwood dowels. Compressed wood (CW) dowels are made from softwoods, which are compressed under heat and pressure which enhances their structural properties, and have been shown to have excellent properties when used in timber connections [4,5]. DLT members are manufactured and tested in accordance with EN 408 [6] to determine their ultimate failure behaviour and stiffness. The experimental results are utilised to validate a numerical model, which is then used in a parametric study to examine the influence of dowel diameter and dowel spacing on the structural response of the DLT members.

2 DOWEL LAMINATED TIMBER

2.1 INTRODUCTION

The use of dowel laminated technology has been the subject of a number of studies in recent years as an alternative to glued laminating technology to further improve the environmental performance of EWPs [1–3,7–12]. There have been significant advances in this technology and a number of commercial products are available and in use in several large timber structures across the world [1,13]. The DLT members utilised in this study were manufactured in the Timber Engineering Research Group (TERG) laboratory at the University of Galway. The timber substrate used is Sitka spruce, grown in Ireland, which is characterised as a fast-grown timber with a C16 structural grade. The CW dowels are

[1] Conan O'Ceallaigh, Timber Engineering Research Group, University of Galway, conan.oceallaigh@universityofgalway.ie
[2] Annette M. Harte, Timber Engineering Research Group, University of Galway, annette.harte@universityofgalway.ie
[3] Patrick J. McGetrick, Timber Engineering Research Group, University of Galway, patrick.mcgetrick@universityofgalway.ie

https://doi.org/10.52202/069179-0030

manufactured from Sitka spruce which has undergone a process known as thermo-mechanical compression which reduces the void space within the lumen between the cell walls increasing the density significantly and improving many structural properties of the timber. These are dicussed further in the following sections.

2.2 TIMBER & COMPRESSED WOOD DOWELS

For the purpose of this study, Sitka spruce, grown in Ireland, is the primary material under investigation. From a structural point of view, this species commonly achieves a structural grade of C16 due to the climatic conditions in which it grows. The standard EN 338 [17] provides a mean value of 8000 MPa for the elastic modulus of C16 timber in the longitudinal direction which is used as the primary substrate for the DLT members in this study. Typically, hardwood dowels have been used in the manufacture of DLT products, however, in this study, CW dowels are used. CW is a type of modified wood material that has been shown to have superior structural properties to natural timber and has proved to be an environmentally friendly alternative to metallic fasteners in timber connections [4,19–22]. The CW used in this study was produced by a process of thermo-mechanical compression of sitka spruce softwood timber to increase its density, strength, stiffness, hardness and to reduce its porosity [23,24].

CW in the form of dowels has demonstrated good properties when tested in shear and when compared with other standard hardwood dowels [24]. The modification process requires the application of pressure at a specific temperature. As the temperature of the timber increases, it may be easily compressed reducing the void space between the cell walls, increasing the density significantly and improving many structural properties of the timber. As the density of the timber is increased, a proportional improvement in stiffness, yield load and maximum load is expected. However, in contrast, the plastic modulus has been shown to decrease in some species [25]. The CW, with enhanced structural properties compared to standard hardwood dowel, also has a spring-back or shape-recovery property that means it will expand over time resulting in a tight fit connection that may be a beneficial characteristic in many structural timber engineering applications, particularly DLT beams and panels [26].

2.3 BEAM GEOMETRY

The beam geometry under investigation in this study is presented in Figure 2. The beam comprises three Sitka spruce timber laminations measuring 1140 mm in length and a cross-section of 20 mm x 60 mm. The three timber laminations are combined to form a final cross-section of 60 mm x 60 mm and a length of 1140 mm. The specimen geometry was chosen based on the criteria for the bending test specified in EN 408 [6]. The manufactured DLT members in Figure 2 are manufactured using CW dowels with a diameter of 10 mm and the dowel spacing of 100 mm. A total of 3 DLT members were manufactured with the same dimensions, dowel diameter and dowel spacing.

Figure 2: *Manufactured DLT members utilising 10mm diameter dowels and the dowel spacing of 100mm.*

3 EXPERIMENTAL TESTING

The DLT timber specimens were subjected to experimental testing under four-point bending in accordance with EN 408 [6]. This test standard specifies four-point bending over a test span of 18 times the specimen depth. As a result, the test specimen is supported over a test span of 1080 mm with point loads at 360 mm from each support. Steel plates (60 mm x 30 mm x 10 mm) are positioned at the support points and load points as specified by EN 408 [6]. As seen in Figure 3, the midspan of each beam is represented by a red dotted line and it is at this location that the global vertical displacement of the beam is determined for a given load until failure occurs. This is also the line of symmetry used when modelling the DLT member using finite element software discussed later.

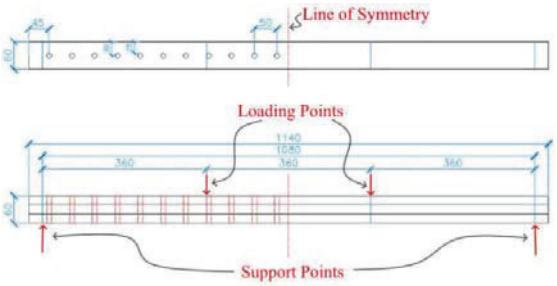

Figure 3: *DLT geometry for the 10mm diameter dowels and the dowel spacing of 50mm (DLT-D10-S50). Dimensions in mm.*

The load-displacement behaviour of each DLT member can be seen in Figure 4. It can be seen that the load-displacement behaviour of each DLT member is relatively similar and is characterised as linear elastic until brittle failure occurs. There are a series of small instances of failure whereby the load drops and is recovered until the ultimate failure occurs. In Figure 4, a line indicated as 'Glulam' represents the theoretical stiffness of a glued laminated beam with an elastic modulus of 9200 N/mm^2 to allow for comparison with the stiffness of the DLT members. It is clear that the stiffness of the DLT members is much less than that of the glued laminated member.

https://doi.org/10.52202/069179-0030

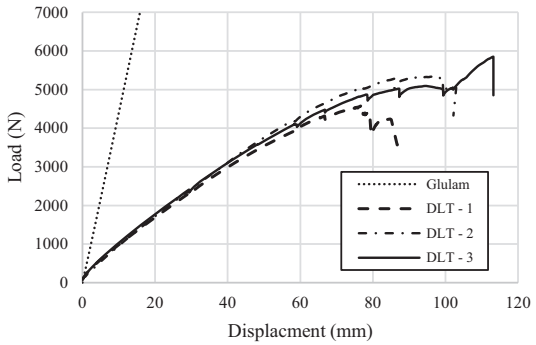

Figure 4: *Load-displacement behaviour of the DLT members*

A summary of the results is presented in Table 1. The results show that significant loads can be achieved for such DLT members connected solely with CW dowels. The maximum load (F_{max}) ranged from 4.57 – 5.85 kN with a mean value of 5.26 kN and a standard deviation of 0.6 kN. The corresponding ultimate displacement ranged from 76.6 - 113.2 mm with a mean value of 94.5 mm and a standard deviation of 18.3 mm. This magnitude of deflection indicates that the stiffness of the DLT members is relatively low. This is clear from the load-displacement curves presented in Figure 4 where the DLT members can be compared to an equivalent glued laminated member of similar dimensions. The only difference is the efficiency of the connection between the laminations of the elements. The adhesive used in glued laminated beams is quite efficient at transferring load between laminations and results in a fully composite beam. The dowels in the DLT are less efficient at transferring this load and as a result, reduced stiffness is observed.

The stiffness results from the tests are presented in Table 1. The stiffness ranges from 1520 – 1588 N/mm^2 with a mean value of 1548 N/mm^2 and a standard deviation of 35.3 N/mm^2. It should be noted that these results are also dependent on the dowel diameter and spacing used and there is a significant opportunity to optimise the dowel configuration to improve the strength and stiffness.

Table 1: *Experimental results of testing on DLT members*

Member	F_{max} (kN)	U_{max} (mm)	Stiffness (N/mm^2)
DLT-1	4.57	76.6	1520
DLT-2	5.34	93.8	1588
DLT-3	5.85	113.2	1537
Mean	5.26	94.5	1548
Std. Dev.	0.6	18.3	35.3

The typical failure behaviour of the DLT beams is shown in Figure 5. The most significant failure behaviour observed was a brittle failure of the timber along the bottom tensile laminate of the DLT beams. This occurred under the load point between the shear-free region of the beam. It is also clear from Figure 5 that significant interlaminar slip occurred in each beam between the load points and the support points. This can be seen at the end of the beam where a stepped profile can be observed.

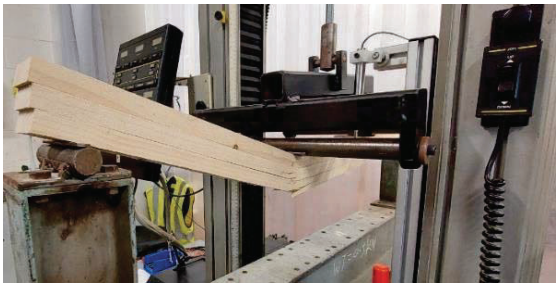

Figure 5: *Failure behaviour of DLT member (DLT - 2)*

To further examine this interlaminar slip, each specimen was split along the middle of the beam through the axis of the dowels to observe the behaviour at the dowel-timber interaction post-failure. An example of this can be seen in Figure 6. It is clear that significant dowel-timber embedment has occurred, particularly in the high-shear areas of each beam.

Figure 6: *Interlaminar slip, stepped profile and dowel-timber embedment.*

4 FINITE ELEMENT MODEL

4.1 MODEL DEVELOPMENT

A three-dimensional finite element model is developed, incorporating a UMAT subroutine to determine the total strain and associated damage experienced in DLT timber members when subjected to a structural load. The model is validated based on the results of the experimental test. As seen in Figure 7, the model utilises half symmetry to reduce the number of elements and computational time to solve the model. A symmetry boundary condition at the midspan is used to achieve this.

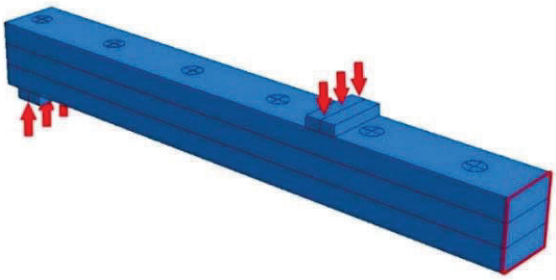

Figure 7: *Numerical model geometry subjected to four-point bending utilising half symmetry (DLT-D20-S100).*

4.2 FINITE ELEMENT FORMULATION

In this section, the constitutive model used to simulate the failure behaviour of Sitka spruce DLT members fastened with CW dowels is presented. As part of the development of the three-dimensional model, a UMAT subroutine has

https://doi.org/10.52202/069179-0030

been developed to simulate the damage experienced in timber elements when subjected to stress under loading. The elastic component of the timber, CW dowels and steel plates follows the generalised Hooke's law. The material behaviour of the timber and CW dowels are assumed to be orthotropic with a stronger and stiffer response along the fibre direction and reduced properties perpendicular to the grain. The material properties for both the timber and CW are presented in Table 2. For simplicity, the radial and tangential directions of the timber are considered equal in this model. The subscript '*L*' and '*T*' represent the longitudinal and transverse materials directions for timber. E_L and E_T represent the elastic modulus in the longitudinal or parallel to the grain direction and the transverse or perpendicular to the grain direction, respectively. G_{LT} and G_{TT} are the shear moduli and v_{LT} and v_{TT} are the Poisson's ratios.

Similar to the elastic properties, the strength characteristics are also assumed to be directionally dependent. The values are presented in Table 2 with superscripts '*t*' and '*c*' which refer to the tension and compression, respectively. For example, $\sigma_L{}^t$ represents the value of the longitudinal failure stress when loaded in tension. The shear failure stress, τ_{LT} is also presented.

$$f_L = \sqrt{\frac{\varepsilon_{11}^t}{\varepsilon_{11}^c}(\varepsilon_{11})^2 + \left(\varepsilon_{11}^t - \frac{(\varepsilon_{11}^t)^2}{\varepsilon_{11}^c}\right)\varepsilon_{11}} > \varepsilon_{11}^t \qquad (1)$$

where

$$\varepsilon_{11}^t = \sigma_L^t/_{C_{11}};\ \varepsilon_{11}^c = \sigma_L^c/_{C_{11}} \qquad (2)$$

where *Cij* are the components of the elastic matrix in the undamaged state. When Eq. (1) is satisfied, the damage variable d_L is determined according to Eq. (3).

$$d_L = 1 - \frac{\varepsilon_{11}^t}{f_L} e^{(-C_{11}\varepsilon_{11}^t(f_L - \varepsilon_{11}^t)L_c/G_L)} \qquad (3)$$

where L_C and G_L are the characteristic element length and the fracture energy, respectively.

The corresponding equations for the perpendicular to the grain direction are produced similarly in Eqs. (4), (5) and (6),

$$f_T = \sqrt{\frac{\varepsilon_{22}^t}{\varepsilon_{22}^c}(\varepsilon_{22})^2 + \left(\varepsilon_{22}^t - \frac{(\varepsilon_{22}^t)^2}{\varepsilon_{22}^c}\right)\varepsilon_{22} + \left(\frac{\varepsilon_{22}^t}{\varepsilon_{12}^\tau}\right)^2(\varepsilon_{12})^2} > \varepsilon_{22}^t \qquad (4)$$

where

$$\varepsilon_{22}^t = \sigma_T^t/_{C_{22}};\quad \varepsilon_{22}^c = \sigma_T^c/_{C_{22}};\quad \varepsilon_{12}^\tau = \tau_{LT}^t/_{C_{44}} \qquad (5)$$

When Eq. (4) is satisfied, the damage variable d_T is determined according to Eq. (6).

$$d_T = 1 - \frac{\varepsilon_{22}^t}{f_T} e^{(-C_{22}\varepsilon_{22}^t(f_T - \varepsilon_{22}^t)L_c/G_T)} \qquad (6)$$

The occurrence of damage is established when the elastic matrix is updated to form an effective elasticity matrix (C_d) which has terms reduced by including the two damage variables d_L and d_T as shown in Eq. (7).

$$C_d = \begin{bmatrix} (1-d_L)C_{11} & (1-d_L)(1-d_T)C_{12} & (1-d_L)C_{13} & 0 & 0 & 0 \\ & (1-d_T)C_{22} & (1-d_T)C_{23} & 0 & 0 & 0 \\ & & C_{33} & 0 & 0 & 0 \\ & Symmetric & & (1-d_L)(1-d_T)C_{44} & 0 & 0 \\ & & & & C55 & 0 \\ & & & & & C66 \end{bmatrix} \qquad (7)$$

G_T and G_L represent the fracture energies in the transverse and longitudinal directions, respectively and to improve convergence, a viscosity parameter, η is utilised in the user subroutine to regularise the damage variables and control the rate of damage.

The damage initiation criteria utilised in this model are based on the Hashin damage model which has been utilised in a series of studies to determine the failure behaviour of timber elements [27–31]. The damage initiation criteria are expressed in terms of strains and are treated differently for tension and compression strains however, one affects the other and if the strains are significant and cause partial or full damage (damage variable greater than zero) both tensile and compressive responses are affected. For example, damage in the longitudinal direction is initiated when the following criterion is achieved.

In the user subroutine, the stresses are then updated according to Eq. (8)

$$\sigma = C_d : \varepsilon \qquad (8)$$

The differentiation of the above equation is used to determine the Jacobian matrix as presented in Eq. (9).

$$\frac{\partial\sigma}{\delta\varepsilon} = C_d + \frac{\delta C_d}{\delta\varepsilon} : \varepsilon = C_d + \left(\frac{\delta C_d}{\delta d_T} : \varepsilon\right)\left(\frac{\delta d_T}{\delta f_T}\frac{\delta f_T}{\delta\varepsilon}\right) + \left(\frac{\delta C_d}{\delta d_L} : \varepsilon\right)\left(\frac{\delta d_L}{\delta f_L}\frac{\delta f_L}{\delta\varepsilon}\right) \qquad (9)$$

Furthermore, to improve the convergence, a viscosity parameter, η is utilised in the user subroutine to regularise the damage variables and control the rate of damage using the following Eqs (10) and (11).

$$\dot{d}_L^r = \frac{1}{\eta}(d_L - d_L^r) \qquad (10)$$

$$\dot{d}_T^r = \frac{1}{\eta}(d_T - d_T^r) \qquad (11)$$

where all parameters are as presented before but the superscript '*r*' indicates regularised and the accent '˙' indicates rate. The regularised damage variable is updated for each time step in the analysis.

https://doi.org/10.52202/069179-0030

4.3 MATERIAL DATA

The material data used in this model for the timber and the CW dowels are presented in Table 2. The steel plates are modelled as linear elastic material with an elastic modulus of 210 GPa and a Poisson's ratio of 0.3. The timber material is modelled as an orthotropic elastic material in Abaqus FEA software. The Sitka spruce material tested experimentally by O'Ceallaigh et al. [14–16] was graded to strength class C16. The standard EN 338 [17] provides a mean value of 8000 MPa for the elastic modulus of C16 timber in the longitudinal direction. The tangential elastic moduli (radial and tangential) directions were not measured experimentally; however, Bodig & Jayne [18] expressed a general relationship between the elastic modulus, E and shear modulus, G in the three material directions. Although these ratios are not without their inaccuracies, they are widely accepted for modelling the orthotropic properties of timber. The CW material properties presented in Table 2 are based on findings by O'Ceallaigh et al. [5,23]. Furthermore, a foundation zone was implemented within a 5 mm area surrounding each dowel home which accounts for reduced properties in this area. This approach is based on the foundation model proposed by Hong [32] which aims to account for the imperfect contact between the hole and fastener and also the reduction in strength due to the damage due to drilling to accommodate the CW dowels. Similar to Hong [32], both stiffness and yield properties are reduced. In this study, both stiffness and yield properties of timber are reduced to 20% [23].

Table 2: *FEM UMAT Material properties*

Property	Timber	CW Dowels	Unit
E_L	8000	13440	MPa
E_T	663	1075	MPa
G_{LT}	659	960	MPa
G_{TT}	66	96	MPa
ν_{LT}	0.038	0.48	-
ν_{TT}	0.558	0.35	-
σ_L^t	36	110.5	MPa
σ_L^c	40	110.5	MPa
σ_T^t	6	68	MPa
σ_T^c	9.6	68	MPa
τ_{LT}	6.9	5.9	MPa
G_T	10	30	N/mm
G_L	12	60	N/mm
η	0.0001	0.0001	-

The definition of the symbols and the notation has been presented in Section 0.

4.4 PARAMETRIC STUDY

In this study, Sitka spruce timber grown in Ireland is used as the primary structural material and the influence of a series of design parameters, namely, dowel diameter and dowel spacing, on the structural behaviour of a DLT beam is investigated. As part of the parametric study, three dowel diameters, 10 mm, 15 mm and 20 mm and three dowel spacing distances of 50 mm, 75 mm and 100 mm will be examined using a numerical model, once validated, to determine the structural behaviour. The naming convention of each specimen is presented in **Error! Reference source not found.**.

Table 3: *Numerical models and design parameters*

Numerical model Specimen	Dowel Diameter (mm)	Dowel Spacing (mm)
DLT-D10-S50	10	50
DLT-D15-S50	15	50
DLT-D20-S50	20	50
DLT-D10-S75	10	75
DLT-D15-S75	15	75
DLT-D20-S75	20	75
DLT-D10-S100	10	100
DLT-D15-S100	15	100
DLT-D20-S100	20	100

5 NUMERICAL RESULTS

The numerical model has been developed to simulate the load-displacement response with failure modes comprising a combination of dowel bending, dowel-timber embedment and tensile fracture of the bottom tensile laminate. This section presents the validation of the developed model against experimental results presented in Section 3 and then presents the parameter study investigating the influence of dowel diameter and spacing.

5.1 MODEL VALIDATION

The results of the numerical model are presented and compared to the experimental results in Figure 8. It can be seen that the numerically determined stiffness of the DLT beam matches that of the experimentally tested specimens. Typically, the simulated load-displacement behaviour of the DLT is in agreement with that observed experimentally, with linear elastic behaviour followed by a significant drop in the load-carrying capacity of the element.

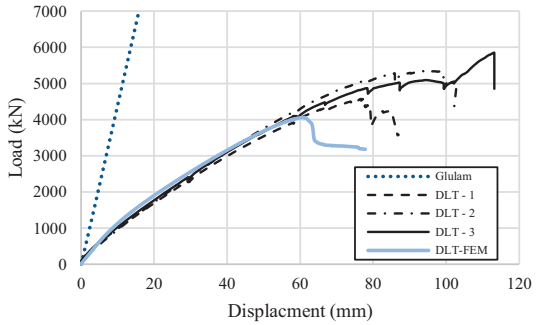

Figure 8. *Load-displacement behaviour of the 10 mm diameter dowel series*

Table 4: *Experimental results vs numerical model*

Member	F_{max} (kN)	U_{max} (mm)	Stiffness (N/mm^2)
DLT-1	4.57	76.6	1520
DLT-2	5.34	93.8	1588
DLT-3	5.85	113.2	1537
Mean	5.26	94.5	1548
DLT-FEM	4.06	61.03	1814.71
Perc. Diff.	26%	43%	16%

https://doi.org/10.52202/069179-0030

The maximum load, maximum displacement and stiffness of each beam are compared to the numerically simulated results in Table 4. The results show that the results are that conservative predictions are given for the maximum load and maximum displacement with percentage differences of 26% and 43%, respectively. In the case of stiffness, the numerically simulated results over-predict the stiffness that was observed experimentally. It is noted that the model does not provide a brittle rupture of the beam as was observed experimentally, and instead, the material that was damaged reduces in stiffness which mimics the failure of the material. This occurred experimentally in the tensile face of the DLT and was predicted in the zone in the numerical model. Furthermore, the damage observed in the dowels (Figure 6) and the stepped profile numerical model (Figure 9) were accurately captured by the model.

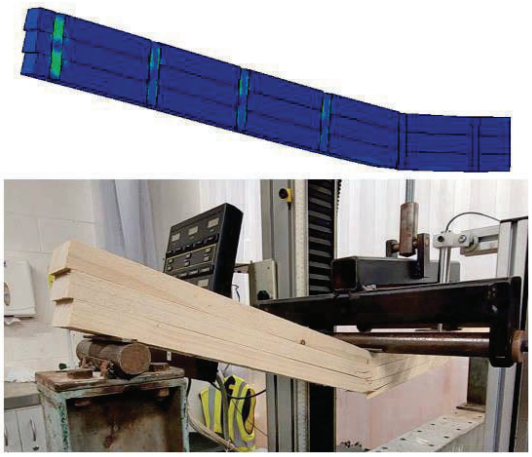

Figure 9: *FE vs experimental, tensile failure of bottom tensile laminate, and stepped profile from interlaminar slip.*

The model has demonstrated the ability to examine the local failure behaviour of the dowel/timber interaction with dowel bending and embedment at the dowel-timber interface and the load-displacement behaviour is in agreement with the experimental results.

5.2 PARAMETRIC STUDY RESULTS

In this section, the results of the numerical parametric study of the DLT specimens are presented. The load-displacement behaviour simulated by the numerical model is presented along with the maximum load (F_{max}) from each model, the displacement at maximum load (U_{max}) and the stiffness. The stiffness is determined on the linear proportion of the graph between 10% and 40% of the maximum load. These results are presented in Table 5 and the corresponding load-displacement graphs and presented in Figure 10, Figure 11, and Figure 12. In all cases, the numerically simulated curves are characterised by linear elastic behaviour until failure which comprised a combination of dowel bending, dowel-timber embedment and tensile fracture of the bottom tensile laminate.

Table 5: *Numerical model results*

Numerical Model Specimen	F_{max} (N)	U_{max} (mm)	Stiffness (N/mm^2)
DLT-D10-S50	4752	65.8	2292
DLT-D15-S50	4770	44.2	2913
DLT-D20-S50	3830	43.7	2503
DLT-D10-S75	4494	68.2	1984
DLT-D15-S75	4503	48.4	2731
DLT-D20-S75	3537	48.5	2395
DLT-D10-S100	4057	61.0	1815
DLT-D15-S100	4163	39.9	2705
DLT-D20-S100	3250	47.6	2338

The results presented in Figure 10, Figure 11, and Figure 12 are associated with DLT members with dowel diameters of 10 mm, 15 mm and 20 mm dowels, respectively. In each figure, a line indicated as 'Glulam' represents the theoretical stiffness of a glued beam with an elastic modulus of 9200 N/mm^2 to allow for comparison with the stiffness of the DLT members. In Figure 10, the influence of spacing on DLT members with a diameter of 10 mm can be observed and it is clear that decreasing the spacing between the 10 mm dowels has a positive impact on strength and stiffness. Reducing the spacing from 100 mm to 50 mm results in an increase in strength and stiffness of 17% and 26%, respectively.

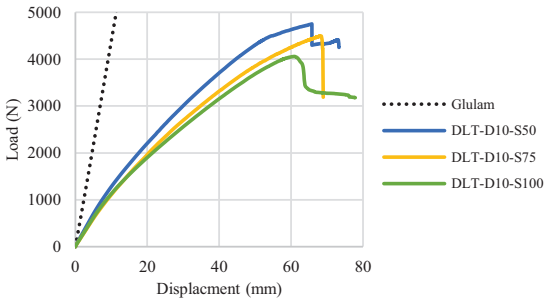

Figure 10. *Numerical load-displacement curves for specimens with 10 mm diameter dowels (D-10 Series).*

When the dowel diameter is increased to 15 mm, as seen in Figure 11, an improvement in strength and stiffness was observed for each dowel spacing studied. The influence of dowel spacing was not as significant as was observed for the 10 mm dowels with increases of 14% and 7% in strength and stiffness, respectively.

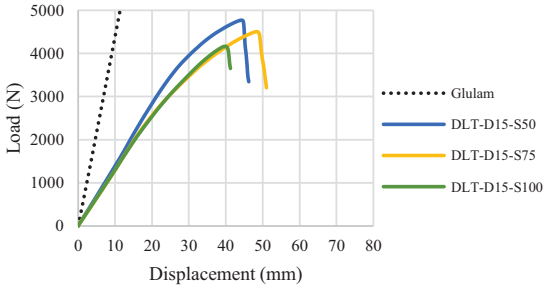

Figure 11. *Numerical load-displacement curves for specimens with 15 mm diameter dowels (D-15 Series).*

https://doi.org/10.52202/069179-0030

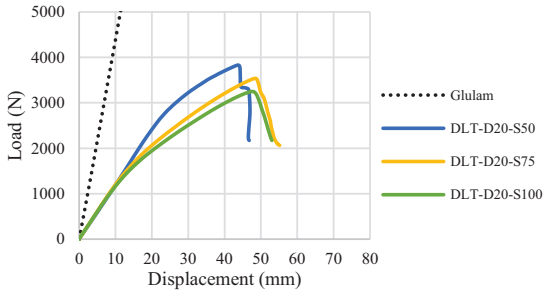

Figure 12. *Numerical simulated load-displacement curves for specimens with 20 mm diameter dowels (D-20 Series).*

Finally, for the 20 mm dowels, presented in Figure 12, contrasting load-displacement behaviour was observed. Increasing the dowel diameter to 20 mm has a negative influence on strength and stiffness. The results indicate that load-displacement behaviour is governed by the timber substrate with limited dowel/timber interaction and further studies should examine the effect for larger cross-sections.

The influence of dowel spacing for all specimens studied can be seen in Figure 13 and Figure 14. In Figure 13, it can be seen that the 50 mm spacing provided the highest loads for the 10 mm and 15 mm dowel diameters but this was not the case for the 20 mm dowels. This may be an issue with reduced edge distances and may not be the case for larger cross-sections.

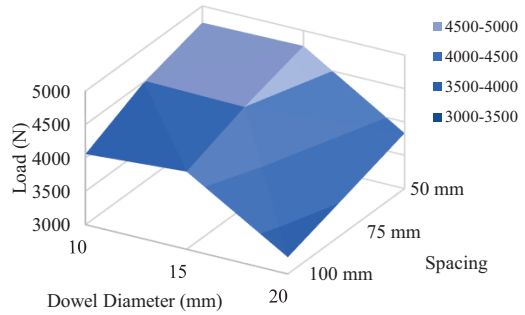

Figure 13. *The influence of dowel diameter and dowel spacing on maximum load (F_{max}).*

In Figure 14, the influence of dowel diameter and spacing on the observed stiffness for all specimens studied can be seen. It is clear that as the dowel diameter is increased from 10 mm to 15 mm, there was a positive influence on the stiffness of the DLT beam. The maximum stiffness was observed for the 15 mm CW dowels with a spacing of 50 mm. The stiffness of the 20 mm dowels did not perform as expected. While there was a positive increase in stiffness when increasing the dowel diameter from 10 mm to 15 mm, reduced stiffness was observed for dowel diameters of 20 mm, regardless of dowel spacing. The results of the numerical model indicated that the timber substrate was subjected to relatively high stress concentration adjacent to the dowel holes in the tension zone of the DLT members. This would indicate that the edge spacing criterion needs to be further examined.

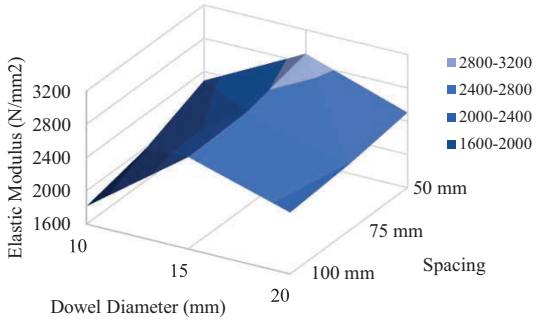

Figure 14. *The influence of dowel diameter and dowel spacing on elastic modulus.*

6 CONCLUSIONS

The feasibility of manufacturing DLT elements from Irish-grown Sitka spruce connected with CW dowels has been examined through experimental testing. A series of experimental tests have demonstrated relatively similar load-displacement behaviour in all specimens for the given dowel diameter (10 mm) and spacing (100 mm). The results have demonstrated that significant loads can be achieved through dowel laminating technology using Irish-grown timber which creates a value-added product with improved environmental credentials compared to adhesively bonded wood products. It is noted that the use of dowels instead of adhesive results in reduced capacity and stiffness for equivalent section sizes but this work has contributed to a better understanding of the behaviour for safe design in the future. There is also a significant opportunity to further refine the design and optimise this for increased structural capacity and stiffness.

A numerical model is presented and has been validated against the experimental results. The results show that the numerical model shows good agreement with the experimental results and the failure modes have also been adequately simulated by the numerical model. A parametric study has been carried out and the numerical results of DLT members connected using CW dowels have been presented for dowel diameters of 10 mm, 15 mm, and 20 mm with spacings arrangements of 50 mm, 75 mm and 100 mm. Typically, increasing the dowel diameter and reducing the dowel spacing have a positive influence on the strength and stiffness of the DLT members. This was not the case for the 20 mm dowels examined in this study and is believed to be due to edge spacing criteria which required further attention.

ACKNOWLEDGEMENT

The authors would like to express their gratitude for the support and funding of the Department of Agriculture, Food and the Marine's Competitive Research Funding Programmes, Project Ref: 2019R471 (MODCONS).

REFERENCES

[1] StructureCraft, Dowel Laminated Timber (DLT) - Design and Profile Guide, StructureCraft, USA, 2019.

[2] A. Thoma, D. Jenny, M. Helmreich, A. Gandia, F.

Gramazio, M. Kohler, Cooperative Robotic Fabrication of Timber Dowel Assemblies, in: Res. Cult. Archit., Birkhäuser, Berlin, Boston, 2019: pp. 77–88. doi:10.1515/9783035620238-008.

[3] I. El-Houjeyri, V.D. Thi, M. Oudjene, M. Khelifa, Y. Rogaume, A. Sotayo, Z. Guan, Experimental investigations on adhesive free laminated oak timber beams and timber-to-timber joints assembled using thermo-mechanically compressed wood dowels, Constr. Build. Mater. 222 (2019) 288–299.

[4] S. Mehra, C. O'Ceallaigh, A. Sotayo, Z. Guan, A.M. Harte, Experimental investigation of the moment-rotation behaviour of beam-column connections produced using compressed wood connectors, Constr. Build. Mater. 331 (2022) 127327. doi:10.1016/j.conbuildmat.2022.127327.

[5] C. O'Ceallaigh, P. McGetrick, A.M. Harte, The Structural Behaviour of Compressed Wood Manufactured using Fast-grown Sitka Spruce, in: WCTE 2021 - World Conf. Timber Eng., Santiago, Chile, 2021.

[6] CEN, EN 408. Timber structures - Structural timber and glued laminated timber - Determination of some physical and mechanical properties, Comité Européen de Normalisation, Brussels, Belgium, 2012.

[7] W. Plowas, T. Bell, R. Hairstans, J.B. Williamson, Understanding the compatibility of UK resource for dowel laminated timber construction, TH Build. Constr. (2015) 1–12.

[8] C. O'Loinsigh, M. Oudjene, E. Shotton, A. Pizzi, P. Fanning, Mechanical behaviour and 3D stress analysis of multi-layered wooden beams made with welded-through wood dowels, Compos. Struct. 94 (2012) 313–321. doi:10.1016/j.compstruct.2011.08.029.

[9] C. O'Loinsigh, M. Oudjene, H. Ait-Aider, P. Fanning, A. Pizzi, E. Shotton, E.M. Meghlat, Experimental study of timber-to-timber composite beam using welded-through wood dowels, Constr. Build. Mater. 36 (2012) 245–250. doi:10.1016/j.conbuildmat.2012.04.118.

[10] A. Sotayo, D. Bradley, M. Bather, P. Sareh, M. Oudjene, I. El-Houjeyri, A.M. Harte, S. Mehra, C. O'Ceallaigh, P. Haller, S. Namari, A. Makradi, S. Belouettar, L. Bouhala, F. Deneufbourg, Z. Guan, Review of state of the art of dowel laminated timber members and densified wood materials as sustainable engineered wood products for construction and building applications, Dev. Built Environ. 1 (2020) 100004. doi:10.1016/j.dibe.2019.100004.

[11] M. Oudjene, M. Khelifa, C. Segovia, A. Pizzi, Application of numerical modelling to dowel-welded wood joints, J. Adhes. Sci. Technol. 24 (2010) 359–370. doi:10.1163/016942409X12541266699473.

[12] Z. Guan, A. Sotayo, M. Oudjene, I. El Houjeyri, A. Harte, S. Mehra, P. Haller, S. Namari, S. Belouettar, F. Deneufbourg, Development of Adhesive Free Engineered Wood Products – Towards Adhesive Free Timber Buildings, in: Proc. WCTE 2018 World Conf. Timber Eng. Seoul, Rep. Korea, August 20-23, 2018, 2018.

[13] ETA-13/0785, European Technical Approval. Solid wood slab element - element of dowel jointed timber boards to be used as a structural elements in buildings, ETA-Denmark, Nordhavn, Denmark, 2013.

[14] C. O'Ceallaigh, K. Sikora, D. McPolin, A.M. Harte, An investigation of the viscoelastic creep behaviour of basalt fibre reinforced timber elements, Constr. Build. Mater. 187 (2018) 220–230. doi:10.1016/j.conbuildmat.2018.07.193.

[15] C. O'Ceallaigh, K. Sikora, D. McPolin, A.M. Harte, Modelling the hygro-mechanical creep behaviour of FRP reinforced timber elements, Constr. Build. Mater. 259 (2020). doi:10.1016/j.conbuildmat.2020.119899.

[16] C. O'Ceallaigh, An Investigation of the Viscoelastic and Mechano-sorptive Creep Behaviour of Reinforced Timber Elements, PhD Thesis, National University of Ireland Galway, 2016.

[17] CEN, EN 338. Structural timber - Strength classes, Comité Européen de Normalisation, Brussels, Belgium, 2016.

[18] J. Bodig, B.A. Jayne, Mechanics of Wood Composites. Reprinted edition, Kreiger Publishing Company. USA, 1993.

[19] M. Conway, C. O'Ceallaigh, S. Mehra, A.M. Harte, Reinforcement of Timber Elements in Compression Perpendicular to the Grain using Compressed Wood Dowels, in: Civ. Eng. Res. Ireland, CERI 2020. Cork Inst. Technol. 27-28 August, 2020: pp. 319–324. doi:https://doi.org/10.13025/sbeg-3p91.

[20] S. Mehra, I. Mohseni, C. O'Ceallaigh, Z. Guan, A. Sotayo, A.M. Harte, Moment-rotation behaviour of beam-column connections fastened using compressed wood connectors, in: SWST 62 Nd Int. Conv. Renew. Mater. Wood-Based Bioeconomy, 2019: p. 2019.

[21] C. O'Ceallaigh, M. Conway, S. Mehra, A.M. Harte, Numerical Investigation of Reinforcement of Timber Elements in Compression Perpendicular to the Grain using Densified Wood Dowels, Constr. Build. Mater. 288 (2021). doi:10.1016/j.conbuildmat.2021.122990.

[22] M. Conway, A.M. Harte, S. Mehra, C. O'Ceallaigh, Densified Wood Dowel Reinforcement of Timber Perpendicular to the Grain: A Pilot Study, J. Struct. Integr. Maint. 6 (2021) 177–186. doi:10.1080/24705314.2021.1906090.

[23] C. O'Ceallaigh, I. Mohseni, S. Mehra, A.M. Harte, Numerical Investigation of the Structural Behaviour of Adhesive Free Connections Utilising Modified Wood, in: WCTE 2021-World Conf. Timber Eng., Chile, 2021.

[24] S. Namari, L. Drosky, B. Pudlitz, P. Haller, A.

https://doi.org/10.52202/069179-0030

Sotayo, D. Bradley, S. Mehra, C. O'Ceallaigh, A.M. Harte, I. El-houjeyri, M. Oudjene, Z. Guan, Mechanical properties of compressed wood, Constr. Build. Mater. 301 (2021). doi:10.1016/j.conbuildmat.2021.124269.

[25] K. Jung, A. Kitamori, K. Komatsu, Evaluation on structural performance of compressed wood as shear dowel, Holzforschung. 62 (2008) 461–467. doi:10.1515/HF.2008.073.

[26] S. Mehra, A.M. Harte, A. Sotayo, Z. Guan, C. O'Ceallaigh, Experimental investigation on the effect of accelerated ageing conditions on the pull-out capacity of compressed wood and hardwood dowel type fasteners, Holzforschung. (2021).

[27] H. Valipour, N. Khorsandnia, K. Crews, A. Palermo, Numerical modelling of timber/timber-concrete composite frames with ductile jointed connection, Adv. Struct. Eng. (2016). doi:10.1177/1369433215624600.

[28] B. Kawecki, J. Podgórski, Numerical analysis and its laboratory verification in bending test of glue laminated timber pre-cracked beam, Materials (Basel). 16 (2019) 1–15. doi:10.3390/ma12060955.

[29] F. Portioli, R. Marmo, C. Ceraldi, R. Landolfo, Numerical modeling of connections with timber pegs, in: 11th World Conf. Timber Eng. 2010, WCTE 2010, 2010: pp. 1881–1886.

[30] N. Khorsandnia, H.R. Valipour, K. Crews, Nonlinear finite element analysis of timber beams and joints using the layered approach and hypoelastic constitutive law, Eng. Struct. 46 (2013) 606–614. doi:10.1016/j.engstruct.2012.08.017.

[31] M. Chybiński, Ł. Polus, Experimental and numerical investigations of aluminium-timber composite beams with bolted connections, Structures. 34 (2021) 1942–1960. doi:10.1016/j.istruc.2021.08.111.

[32] J.-P. Hong, Three-Dimensional Nonlinear Finite Element Model for Single and Multiple Dowel-type Wood Connections, PhD Thesis, The University of British Columbia, 2007.

World Conference on Timber Engineering Oslo 2023

BONDING OF FIRE-RETARDANT TREATED SPRUCE LAMELLAE FOR USE IN CROSS LAMINATED TIMBER (CLT)

Karl-Christian Mahnert[1], Stine Lønbro Bertelsen[2]

ABSTRACT: This paper presents results from bond line testing to investigate the influence of fire-retardant (FR) treatment on the bondability of spruce, tested in glued laminated timber (GLT) specimens as requested by standards for testing of the actual adhesive systems, and specimens of cross-laminated timber (CLT) produced under laboratory conditions to investigate a product bonded with the adhesives. One MUF- and two PUR adhesives were chosen for the investigations, selected on the basis of their use in CLT-production today as this product was the main focus. They were tested in five different material combinations: lamellae with high uptake of fire-retardant against lamellae with high uptake of fire-retardant, high uptake against untreated lamellae, low uptake against low uptake, low uptake against untreated lamellae and untreated against untreated lamellae.
All 22 GLT specimens fulfilled the requirements for resistance to delamination according to EN 302-2:2017/EN 301:2017. The requirements for compressive shear strength according to EN 14080:2013 were fulfilled by all 24 specimens cut from the GLT samples.
73 of 75 CLT specimens fulfilled the requirements for resistance to delamination according to EN 16351:2021.
The results do not show any influence of the FR treatment on the bondability of the FR treated spruce lamellae. Potential explanations for this might be that a) the adhesives are fully compatible with the FR, or b) the FR-treated wood was removed by the slight planing of the lamellae prior to bonding, leaving untreated but insufficiently planed surfaces for bonding.

KEYWORDS: Fire-retardant, fire-retardant impregnated spruce, B-s1,d0, CLT, shear strength, delamination

1 INTRODUCTION

The objective of this work is to look into the possibility of using commercially available fire retardant (FR) treated wood in the outer layers of Cross Laminated Timber (CLT) panels for interior use in order to achieve reaction-to-fire class B-s1,d0.

CLT is often used in walls, often covered in gypsum boards to achieve the necessary reaction-to-fire classification. Alternatively, the wooden surface can be treated with a FR after installing the element in the building to maintain the wooden surface. But this is found to be time consuming, and the possibility of receiving the element with the right properties from the factory would be more efficient.
CLT produced in Norway consists exclusively of spruce wood, the outer lamellae usually fulfil the requirements of strength class C24 [1]. Therefore, this raw material has been used in this study.

1.1 APPROACH

Several types of fire retardants and their application processes were screened to select the most suitable one for application in CLT-production. The aim is to make the treated layer a part of the panel and avoid adding extra thickness, maintaining the same properties of the panel except for the improved fire properties.
The different types of fire retardants – paint/varnish and impregnation – and some of the challenges by using each type in different processes, were identified and discussed, focusing on those adding the treatment before leaving the production facility.
The different processes were mainly divided into "before-" and "after pressing" of the panel. Discussions about the various challenges led to one process chosen for further investigations – to add FR impregnated spruce lamellae to the production line of CLT before pressing of the panels. A such panel would consist of untreated wood in the middle layers and only FR impregnation in the surface layer(s), as reaction-to-fire is mainly affected by the surface properties of the panel.

A potential reduction of mechanical properties of the FR treated lamellae and issues linked to the hygroscopicity of the FR were ignored in this initial study, as well as the challenge about maintaining the fire properties after transportation and construction, where possible damage to the surface can be expected to have an impact on the reaction-to-fire properties.

[1] Karl-Christian Mahnert, Norwegian Institute of Wood Technology (NTI), Norway, kcm@treteknisk.no
[2] Stine Lønbro Bertelsen, Danish Technological Institute (DTI), Denmark, slbe@teknologisk.dk

https://doi.org/10.52202/069179-0031

Two questions were raised to the chosen solution: 1) Is it possible to FR impregnate C24 spruce and obtain a B-s1,d0 classification? 2) Is it possible to bond FR impregnated spruce and ensure adequate attachment of treated lamellae? These two questions were investigated, and the results are presented in this paper.

1.2 STATE OF THE ART

1.2.1 Fire-retardant impregnation of spruce

Spruce is difficult to impregnate due to the blockage of the fluid pathways in the wood due to aspiration (irreversible closure) of up to 75 % of the bordered latewood pits during drying of the wood [3], relatively small ray size and high percentage of heartwood which is impermeable to impregnation [4]. Biotechnological attempts to increase the permeability of spruce have been developed on laboratory scale [5, 6], but are not yet commercialised.

As a consequence, a pressure impregnation will only penetrate the outer millimetres of spruce, an area prone to be removed during machining. Therefore, the surface of the treated lamellae cannot be machined [7], if necessary, only lightly sanded to maintain the improved reaction-to-fire classification.

Screening the market for FR treated wood showed that spruce lamellae treated with 5.7% (arto/arto, weight percent gain calculated based on dry matter) FirePRO® and coated fulfilled the required classification [2]. The purpose for coating of the wood is to protect the surface of the wood from high relative humidity which is known to cause migration of the hygroscopic components of the FR which often results in discoloration and loss of FR over time. This aspect was neglected in this study because the interior surface of the CLT-panels is usually not exposed to relative humidity exceeding 60% (Service class 1). Following recommendations by the treater, desired uptake in this case is set to 6.5%.
With this, the first of the two questions was answered.

1.2.2 Bonding of fire-retardant treated wood

Bonding of fire-retardant treated wood, mostly veneers for plywood, has been done on at commercial scale since 1954 [8]. [9] investigated the influence of monoammonium phosphate, diammonium phosphate, ammonium sulphate, ammonium sulfamate, borax and boric acid on adhesives urea-formaldehyde (UF) and phenol-formaldehyde (PF) adhesives used in plywood production. Impregnation of veneers with borax and boric acid gave severe embrittlement rendering the use of a mechanic glue spreader not feasible. Black reports that it was these two treatments which caused most of the problems in achieving good bonds. He ascribes the difficulties to the low pH of borax and the high pH of boric acid. However, all fire-retardant treatments reduced the water resistance of the adhesives. [9] states that it is difficult to qualify the influence of the fire-retardant treatments on the performance of PF due to the variability of their chemical composition and complexity of their curing reaction.
[8] summarizes results from trials including veneers impregnated with monoammonium phosphate, diammonium phosphate, ammonium sulphate, borax, boric acid, zinc chloride and chromated zinc chlorate bonded with various glues and adhesives. The author recommends phenol, resorcinol and combinations of these two resin types for all treatments. Melamine, fortified urea and urea adhesives are recommended for a treatment combining boric acid and borax. [10] conducted bonding trials with solid wood from Douglas fir and Western Hemlock impregnated with a mixture of ammonium sulfate, zinc chloride, boric acid and sodium dichromate. The surfaces were slightly planed before bonding of the members with a resorcinol resin (PRF) and a paraformaldehyde hardener (type A) and a resorcinol adhesive and a hardener with 54% formaldehyde content (type B). The shear strength of the bond lines of all samples made from treated wood were lower than the shear strength of the samples made from untreated wood. Schaeffer identified chemical interaction between the fire-retardant salts and the adhesives as reasons for the reduced bond strength: Ammonium sulphate, zinc chloride and sodium dichromate showed increased rate of gelation, boric acid was found to slightly retard the rate of gelation of a resorcinol-resin adhesive. However, also changes in the wood surface affect the adhesion properties of wood. [11] investigated the influence of natural weathering on the tensile shear strength of Desmodur-vinyl trie ketonol acetate bond lines between pieces of Scots pine and Oriental beech that had been dip-treated with borax and boric acid. Without natural weathering, the reduction of tensile shear strength was higher for boric acid compared to borax for both wood species. After four years of outdoor exposure, the Oriental beech samples treated with fire retardant showed higher tensile shear strength than the untreated controls, the values for the borax-treated samples were higher than those for the samples treated with boric acid. In case of the Scots pine samples, the borax treated samples showed lower tensile shear strength compared to the controls and the samples treated with boric acid.
[12] investigated the influence of diammonium phosphate and sodium silicate on the adhesion properties of impregnated birch veneer. The former increased the glue bond strength measure by ABES, the latter showed unchanged or slightly reduced glue bond strength for 15% and 30% concentration in the impregnation solution. [13] consider using lamellae impregnated with a fire-retardant for CLT-production problematic because of the reduced bondability of fire-retardant treated wood and issues linked to the disposal of planer shavings from fire-retardant treated wood. Investigations of potential alternatives to planing, hot pressure treatment, chemical treatment with a confidential substance and plasma treatment showed that planing provided bond lines with highest shear strength and wood failure percentage. The adhesive systems used were PRF and polyurethane (PUR).

2 MATERIAL AND METHODS

2.1 PRODUCTION OF TEST SAMPLES

Lamellae and fire-retardant treatment

Lamellae of spruce (*Picea abies* L.) graded C24 were fire-retardant treated with FirePRO®, a fire-retardant containing Borax and boric acid, in a commercial treatment process.

The uptake of FR for each lamella was compared to the desired uptake to ensure reaction to fire-class B-s1,d0 according to product certificate of constancy of performance [2] (Figure 1, Figure 2). The lamellae with a deviation of -10% to +35% from the desired uptake were sorted out for other tests. The rest of the lamellae were divided into two groups; High uptake (H) (40–62.5 kg dry fire retardant/m^3 wood) and low uptake (L) (17.5–26.8 kg dry fire retardant/m^3 wood) and were used for preparation of the samples for bondability testing. Machining of the impregnated surfaces was kept to a minimum to remove as little fire retardant as possible from the face of the lamellae intended for bonding, but still provide favourable surfaces for bonding.

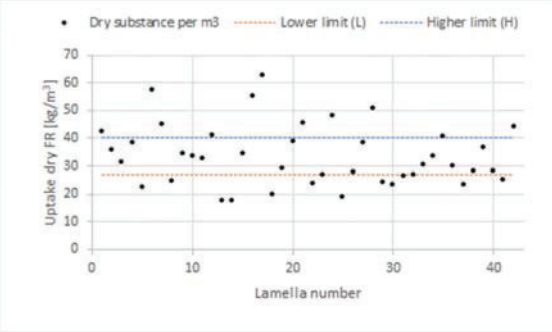

***Figure 1**: Distribution of impregnation liquid uptake in the lamellae (lamella no. 1-43).*

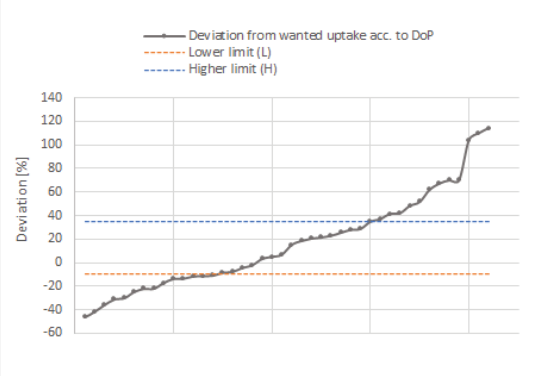

***Figure 2:** Distribution of dry substance uptake in the impregnated lamellae in relation to the desired uptake. 0% deviation marks the desired uptake, corresponding to 6,5% dry substance of the total weight after impregnation.*

Samples for testing of bondability

Glued laminated timber (GLT) samples were produced as described in EN 14080 [15] with the following combinations of treatments: L-U, H-U, L-L (L) and H-H (H) (illustration in Figure 3). With regard to CLT-testing, samples with the following combinations of treatments were assembled: L-U and H-U (illustration in Figure 4). For both GLT and CLT, reference samples of untreated lamellae (U) were assembled. Three different state-of-the-art adhesive systems for use in CLT were used: a 2-component MUF-system and two different 1-component PUR-systems.

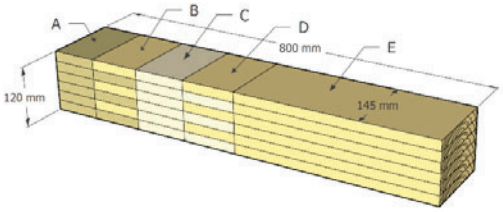

***Figure 3.** Illustration of the beams produced for adhesive testing. Each combination is partly shown, A (H) – B (HU) – C (L) – D (LU) – E (U).*

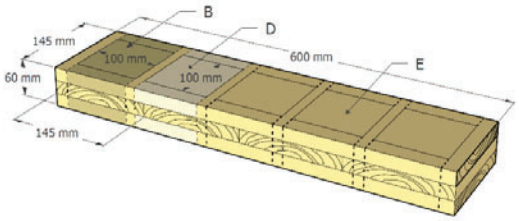

***Figure 4.** Illustration of the beams produced for product testing of small CLT specimens. Two beams were produced per combination B (HU), D (LU) and E (U) with the different adhesive systems. The marked areas illustrate the five specimens that are cut from each beam for testing of resistance to delamination, measuring 100 x 100 x 60 mm^3.*

2.2 TESTING BONDABILITY

The investigations of the material's bondability was divided into adhesive- and product testing. Adhesive testing covers testing of resistance to delamination of glulam samples according to EN 302-2 [14] and testing of compressive shear strength according to EN 14080 Annex D [15] on GLT as requested for testing of the actual adhesive systems.

Delamination was tested on two specimens per combination of treatment and adhesive with five bond lines per specimen (Figure 3). Compressive shear strength (CSS) was tested on two specimens per combination with five bond lines per specimen (Figure 3).

As the focus of the study is on CLT, product testing on CLT samples was conducted according to EN 16351 Annex A [16]. The standard requires maximum 40%

https://doi.org/10.52202/069179-0031

opening per individual bond line and an average of 10% opening of the sum of all bond lines. If a specimen exceeds these requirements, the bond areas are to be opened to quantify the wood failure percentage which may not be less than 50% for the individual bond area and not less than 70% for the total bond area per specimen.
In this study we evaluate the conformity of the bondings with the requirements defined in EN 16351. Additionally, we use the average opening of the bond lines in each specimen for further analyses.
The test was performed on five specimens per CLT-element, each specimen contained two bond lines (Figure 4).

3 RESULTS AND DISCUSSION

3.1 RESISTANCE TO DELAMINATION

The requirements for resistance to delamination of GLT according to EN 301 [17] were fulfilled by 22 of 24 specimens (Table 1). The evenly one-sided distribution of the delaminated areas on the samples produced from GLT.9 (6.2 and 6.4% delamination) (Figure 5) indicates deviation in thickness as reason for the failure of the specimens rather than the fire-retardant treatment. The results are therefore rejected.

***Table 1**: Delamination in GLT-specimens according to EN 302-2 in % of total bond line length, requirement: ≤ 5 % (Spec.= specimen).*

Sample	Adhesive and treatment	Delamination [%]	
		Spec. 1	Spec.2
GLT.1	1/MUF H	0.0	1.1
GLT.2	1/MUF HU	0.8	1.8
GLT.3	1/MUF L	0.6	1.4
GLT.4	1/MUF LU	0.0	0.4
GLT.R1	1/MUF U	3.8	0.7
GLT.5	2/PUR HU	1.7	3.3
GLT.R2	2/PUR U	0.0	0.4
GLT.6	3/PUR H	2.0	1.4
GLT.7	3/PUR HU	2.6	1.0
GLT.8	3/PUR L	4.8	2.2
GLT.9	3/PUR LU	N*	N*
GLT.R3	3/PUR U	0.7	1.9

N* Results rejected due to planing error

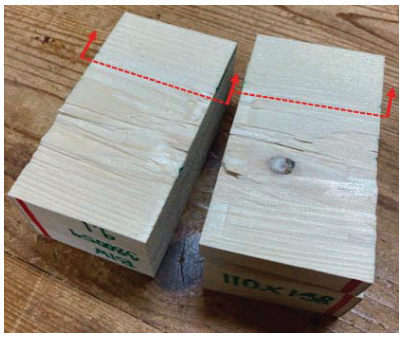

***Figure 5:** Evenly one-sided delamination on specimen GLT.9.1*

The average delamination of the visible bond line length per CLT element is compiled in Table 2. The specimens that did not fulfil the requirement were opened for further investigation of wood failure percentage in the glue line surface (results are found in Table 3).
Five specimens (Table 3) were rejected due to knots or resin pockets in the bond area and are therefore not included in all further analyses. Besides from these, two specimens did not fulfil the requirements given in EN 16351 (CLT3.1 and CLT10.1). The delamination of all remaining specimens was below the requirement of max. 30% of the bond area.

The delamination of the CLT-specimen was significantly higher than the delamination of the GLT-specimen (Figure 6). This is due to the higher stress on the bond line between cross-laminated lamellae in CLT compared to parallel laminated lamellae in GLT.

***Table 2.** Average ($\bar{x}$) and standard deviation (σ_x) of delamination according to EN 16351 Annex A in % of total bond line length, requirement: ≤ 10 %.*

Sample	Adhesive and treatment	Delamination [%]		Opened*
		$\bar{x}$	σ_x	
CLT1	1/MUF HU	7.0	3.4	1/5
CLT2		4.7	4.2	0/5
CLT3	1/MUF LU	21.8	6.1	5/5
CLT4		26.3	19.7	4/5
CLT.R1	1/MUF U	10.0	6.6	3/5
CLT.R2		9.6	6.6	4/5
CLT5	2/PUR HU	10.9	9.2	2/5
CLT6		5.2	2.4	0/5
CLT.R3	2/PUR U	9.9	8.2	3/5
CLT.R4		6.4	3.1	3/5
CLT7	3/PUR HU	12.0	7.7	3/5
CLT8		9.1	6.6	2/5
CLT9	3/PUR LU	13.0	3.4	4/5
CLT10		9.8	6.0	4/5
CLT.R5	3/PUR U	5.7	4.7	1/5
CLT.R.6		1.3	2.0	0/5

*Number of specimens that did not fulfil the requirement of total bond line length opening and therefore were opened for further investigation of wood failure percentage in bond area (Table 3).

***Table 3.** Average ($\bar{x}$) wood failure in the bond area of opened specimens in %, according to EN 16351 Annex A. Requirement: ≥ 70%.*

Sample	Adhesive and treatment	$\bar{x}$ wood failure of opened specimens [%]
		Specimen 1 – 2 – 3 – 4 – 5
CLT1	1/MUF HU	X – X – 98 – X – X
CLT2		X – X – X – X – X
CLT3	1/MUF LU	65^{N} – 70 – 83 – 98 – 78
CLT4		50^{N*} – 83 – 80 – X – 80
CLT.R1	1/MUF U	X – X – 88 – 85 – 88

https://doi.org/10.52202/069179-0031

CLT.R2		83 – 88 – 78 – X – 90
CLT5	2/PUR HU	80 – X – 55^{N*} – X – X
CLT6		X – X – X – X – X
CLT.R3	2/PUR U	88 – 88 – 70 – X – X
CLT.R4		X – 60^{N*} – 80 – X – 83
CLT7	3/PUR HU	X – 83 – 70 – X – 80
CLT8		X – X – 88 – 80* – X
CLT9	3/PUR LU	70* – 85* – X – 97 – 68^{N*}
CLT10		40^{N} – 80 – 90 – X – 75^{N*}
CLT.R5	3/PUR U	X – X – X – 100 – X
CLT.R6		X – X – X – X – X

*One opened bond line only.
^{N} Delamination does not fulfil the requirement.
^{N*} The specimens had knots or resin pockets in the bond line area and are therefore excluded from further analyses.

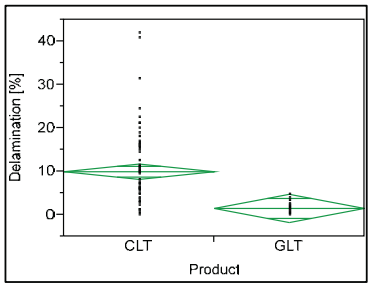

Figure 6: *Delamination in bond line of CLT and GLT specimens investigated according to EN 16351 and EN 302-2, respectively.*

3.2 COMPRESSIVE SHEAR STRENGTH

The compressive shear strength (CSS) of all 24 specimens fulfilled the requirements for shear strength according to EN 14080:2013 Annex D, the average results are shown in Table 4. The specimens showed wood failure only. Results from specimens with knots in the shear area are excluded from further analyses.

Table 4. *Average ($\bar{x}$) and standard deviation (σ_x) of compressive shear strength (CSS) according to EN 14080 Annex D. The requirement was ≥ 4.0 % for individual and ≥ 4.9 % for average values.*

Sample	Adhesive and treatment	CSS [N/mm²] $\bar{x}$	σ_x
GLT.1	1/MUF H	8.3	0.9
GLT.2	1/MUF HU	8.1	1.4
GLT.3	1/MUF L	9.8	0.9
GLT.4	1/MUF LU	9.3	1.0
GLT.R1	1/MUF U	9.5	0.9
GLT.5	2/PUR HU	7.5	0.7
GLT.R2	2/PUR U	9.0	0.9
GLT.6	3/PUR H	9.2	1.0
GLT.7	3/PUR HU	8.9	0.9
GLT.8	3/PUR L	8.7	1.2
GLT.9	3/PUR LU	8.3	0.8
GLT.R3	3/PUR U	8.3	0.7

3.3 INFLUENCE OF FIRE-RETARDANT TREATMENT ON OVERALL BONDABILITY

The delamination results of both GLT and CLT samples do not indicate any influence of the treatment intensity on the delamination of the respective specimen (Figure 7), only the delamination of treatment LU was significantly different from the remaining treatments. This difference can be ascribed to the CLT specimens 4.2 (40.9% delamination of bond line) and 4.3 (42.0 % delamination of bond line). Both specimens, however, fulfil the requirement of ≥70% wood failure in bond area according to EN 16351 (Table 3).
The latter are decisive for the significant difference between the delamination results for CLT-specimen from treatment LU and UU (Figure 8). The delamination results for the GLT-specimen from the different treatments do not differ significantly (Figure 9).

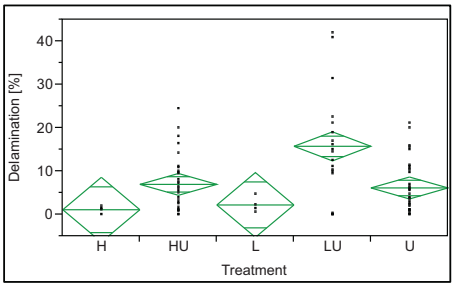

Figure 7: *Influence of treatment on the bond line delamination [%] of GLT and CLT samples.*

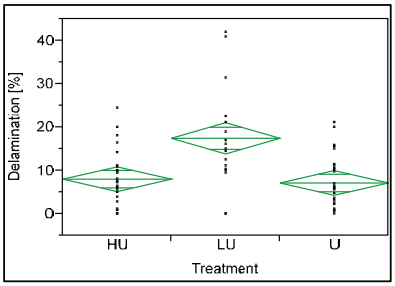

Figure 8: *Delamination of bond line of CLT samples based on the treatment.*

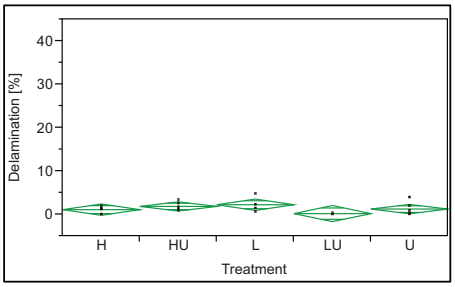

https://doi.org/10.52202/069179-0031

Figure 9: *Delamination of GLT samples based on the treatments.*

The compressive shear strength (CSS) of the GLT samples (Figure 10) did not differ significantly between the treatments. Thus, an influence of the treatment on the bondability was not found here either.

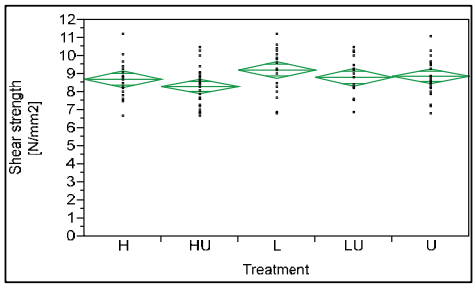

Figure 10: *Compressive shear strength of the bond lines in the GLT samples based on their treatments.*

3.4 INFLUENCE OF ADHESIVE

No significant differences between adhesives were found for the

- overall delamination (Figure 11),
- overall delamination as function of the treatment,
- delamination of CLT and GLT and
- delamination as function of the treatment within the specimens from CLT and GLT.

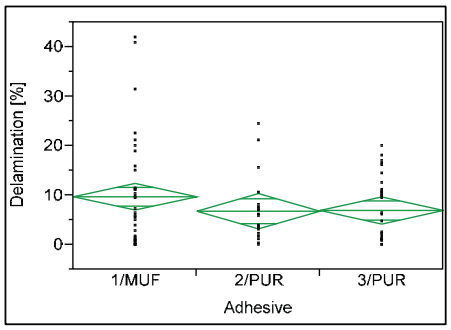

Figure 11*: Delamination in bond lines found in GLT and CLT samples as function of the adhesive.*

The compressive shear strength (CSS) of the bond lines of 1/MUF was significantly higher than the CCS of bond lines with 2/PUR (Figure 12), the same was observed for all treatments.
This is surprising as the delamination in the bond lines bonded with the different adhesives did not differ significantly. Additionally, bonding with 3/PUR yielded higher CSS than bonding with 2/PUR. Thus, the authors assume a combination of locally uneven uptake of FR or uneven planing with resulting local deviations in bond quality as explanation because incompatibility between PUR-adhesives and the FR can be excluded.

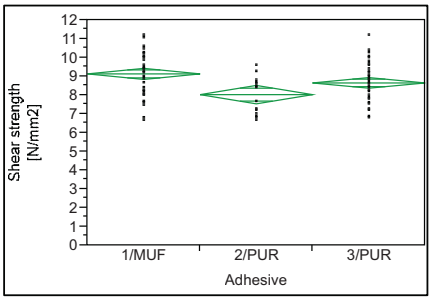

Figure 12*: Compressive shear strength as function of the adhesive*

4 CONCLUSIONS

The study did not show any influence of the fire-retardant treatment on the bondability of the spruce lamellae. This might be due to two reasons: Either the adhesives applied are fully compatible with the fire-retardant, or the fire-retardant has been removed from surfaces to be bonded during sample preparation.
The manufacturer of the impregnated material used in this study, as well as literature, advises against machining of fire-retardant treated wood as this will remove some of the impregnated surface [18, 19]. This is valid for all fire-retardant treated wood, but especially for refractory wood species such as spruce. Before this background, planing was limited to an absolute minimum, leading to wood surfaces of lower quality than usually accepted for bonding activities.
The combination of these two factors leads to the conclusion that the results from the current study do not represent the full bonding potential of the investigated adhesives and the fire-retardant treated wood.
Further investigations should be conducted where the planed surfaces are carefully re-treated with FR prior to bonding.

5 ACKNOWLEDGEMENTS

The work described in this paper was conducted as part of the H2020-project Build-in-Wood (grant agreement No 862820).

REFERENCES

[1] SINTEF Byggforsk, Etasjeskillere i massivtre, Byggdetaljer 522.891, 2009.
[2] RISE Research Institutes of Sweden AB, Intyg om kontinietet av byggproduktens prestanda 0402-CPR-SC0243-09, version 7, dated 2020-07-29.

[3] Liese, W. and J. Bauch. On the closure of bordered pits in conifers. Wood Science and Technology 1(1): 1-13, 1967.
[4] Flynn, K. A. A review of the permeability, fluid flow, and anatomy of spruce (Picea spp.), Wood and Fibre Science 27(3): 278-284, 1995.
[5] Militz, H. and Homan, W.J. Vorbehandlung von Fichtenholz mit Chemikalien mit dem Ziel der Verbesserung der Imprägnierbarkeit. Holz als Woh- und WErkstoff (51(1), 14-20, 1993.
[6] Lehringer, C. Permeability improvement of Norway spruce wood with the white rot fungus Physisporinus vitreus. Ph.D. Thesis, Georg-August-University, Göttingen, 2011.
[7] Koppers (2023), FIRE RETARDANTS – Koppers FirePRO, Exterior Fire-X and PROTIM Fireguard, https://www.kopperspc.eu/pdfs/fire-retardant-brochure.pdf, visited 28.02.2023
[8] Selbo, M. L.. Summary of information on gluing of treated wood. Report 1789, Forest Products Laboratory, United States Department of agriculture, 1965
[9] Black, J. M.. The effect of fire-retardant chemicals on glues used in plywood manufacture. Report 1427, Forest Products Laboratory, United States Department of Agriculture Report, 1958
[10] Schaeffer, R. E.: Gluing Fire-retardant Douglas-fir and Western Hemlock. Report FPL-0160, Forest Products Laboratory, United States Department of agriculture, 1968
[11] Özçıfçı, A. Effects of Outdoor Exposures and Boron Compounds on Bonding Strength of Desmodur-VTKA Adhesive, Journal of Adhesion Science and Technology, 24:2, 281-289, 2010
[12] Hautamäki, S., Altgen, M., Altgen, D., Larnøy, E., Hänninen, T. and Rautkari, L. The effect of diammonium phosphate and sodium silicate on the adhesion and fire properties of birch veneer. Holzforschung 74:4, 372-381, 2020
[13] Gangbo, H., Feng, M. and Roussiere, F.. Development of CLT-products with improved fire performance. Project number 301013602, FPInnovation, 2020.
[14] Comité Européen De Normalisation (CEN): EN 302-2: Adhesives for load-bearing timber structures – Test methids – Part 2: Determination of resistance to delamination, 2017.
[15] Comité Européen De Normalisation (CEN): EN 14080 Timber structures – Glued laminated timber and glued solid timber – Requirements, 2013.
[16] Comité Européen De Normalisation (CEN): EN 16351: Timber structures – Cross laminated timber – Requirements, 2021.
[17] Comité Européen De Normalisation (CEN): EN 301 Adhesives, phenolic and aminoplastic, for load-bearing timber structures - Classification and performance requirements, 2017.
[18] Wood Protection Association: Flame Retardant Specification Manual, Industrial flame retardant treatment of wood and wood-based panel products. 3rd Edition, 2016.
[19] BM Trada: Wood Information Sheet 2/3-3: Flame-retardant treatments for timber products, 2013.

https://doi.org/10.52202/069179-0031

EVALUATION OF TIMBER-CONCRETE SLAB CONNECTED WITH NOTCHED CONNECTION MADE OF KOREAN LARCH STRUCTURAL PLYWOOD

Kyung sun Ahn[1], Sung-jun Pang[2], Jiyong Kim[3], Jaewon Oh[4], Min-Jeong Kim[5], Gwang Ryul Lee[6], Jung-Kwon Oh[7]

ABSTRACT: In this study, a novel notched connection has been developed made of Korean Larch structural plywood for timber-concrete composite (TCC) slabs to improve their bending performance in non-residential buildings. The use of TCC for non-residential buildings has become increasingly popular as horizontal members such as beams and slabs in such structures have been designed to have longer spans to create more space. Because the TCC system can provide greater stiffness to horizontal members, TCC slabs or beams have advantages for application in non-residential building members. The notched connection design in this study divided a sheet of structural plywood into several units and fastened them with timber flanges using nails. Insulations were inserted between connections to create an even concrete layer, and concrete was cast. The bending performance of TCC specimens was then evaluated through tests, with the results compared to the performance of other slabs estimated with the gamma method. The study found that the new notched connection significantly improved the effective bending stiffness of TCC slabs, which could lead to the wider adoption of TCC in non-residential building design.

KEYWORDS: Timber-concrete composite, TPC slab, Notch connection, Plywood segment, Double shear test, Full-scale bending test

1 INTRODUCTION

According to statistical data from The Ministry of Land, Infrastructure, and Transport in South Korea, most buildings have been constructed in recent years for commercial, industrial, or public purposes called non-residential buildings. In general, Horizontal members (beam and slab) in non-residential buildings are designed to have long spans to make more space. Timber-concrete composite (TCC) is a suitable material to apply to non-residential buildings since its effective bending stiffness (EI_{eff}) is high because of concrete topping. EI_{eff} of TCC is decided by not only material properties; but the performance of the shear connection between timber and concrete. The composite efficiency is decided with connection efficiency derived from the stiffness of the shear connection. Numerous types of shear connections have been investigated by past research [1]. Among these, a notched connection which is made by grooving in timber showed higher stiffness than metal connections [2]. However, the notched connection is difficult to process. Also, the loss of cross-section in timber can reduce bending capacity, so the increase of stiffness by lengthening or grooving deeper can be limited [3]. Therefore, the performance of TCC with traditional notched connections can be improved by increasing the amount of timber or concrete, but it is thought to be inefficient from the engineering point of view. In this study, a notched connection made of Korean Larch structural plywood was designed. A sheet of structural plywood was divided into several units and they are fastened with timber flanges using nails. After insulations are inserted between connections to make the concrete layer level even, concrete is cast. With this processing, TCC specimens were prepared to evaluate the bending performance. Test results were compared with the performance of other slabs which is estimated with the γ-method.

Figure 1: *Notched connection made of plywood segments*

[1] Kyung-Sun Ahn, Seoul National University, South Korea, rudtjs6339@snu.ac.kr
[2] Sung-Jun Pang, Seoul National University, South Korea, pangsungjun@snu.ac.kr
[3] Jiyong Kim, Seoul National University, South Korea, led_zep@snu.ac.kr
[4] Jaewon Oh, Seoul National University, South Korea, redhurse@snu.ac.kr
[5] Min-Jeong Kim, Seoul National University, South Korea, minjeong.kim@snu.ac.kr
[6] Gwang Ryul Lee, Seoul National University, South Korea, qweqweqwer@snu.ac.kr
[7] Jung-Kwon Oh, Seoul National University, South Korea, jungoh@snu.ac.kr

https://doi.org/10.52202/069179-0032

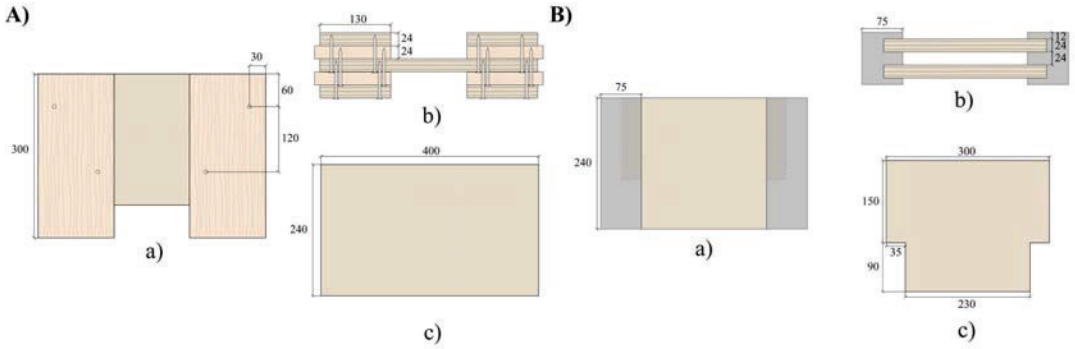

Figure 2: *Test specimen to evaluate the slip modulus value of A) nails, B) notches – a) front view, b) top view, c) plywood dimension*

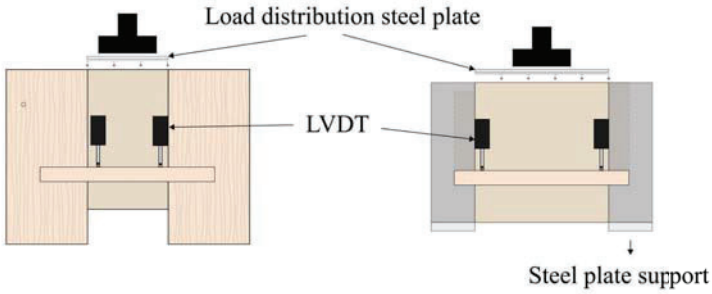

Figure 3: *Double shear test set up*

2 Materials and Method

2.1 CONSTITUENT ELEMENTS

TPC slab has three main components: Finger-jointed lumber, normal concrete and plywood segments.
Considering the properties of wood in South Korea, it is possible to achieve a depth of up to 140 mm. In a longitudinal direction, 6,210 mm length was obtained by finger-joint (24 mm × 140 mm × 6,210 mm - width × depth × length). The thickness of the concrete layer was set at 75 mm to satisfy the minimum cover thickness of the reinforcing bars if reinforcement is required by arranging reinforcing bars in the concrete layer, depending on the requirements. The mechanical properties of elements are specified in Table 1,2,3 and it was used to estimate the structural performance of TPC composite slab with the γ-method.

Table 1: *Mechanical properties of concrete*

Elements	F_c (MPa)	E (MPa)
Ready-mixed concrete	27	26,701

Table 2: *Mechanical properties of finger-jointed lumber*

Elements	F_t (MPa)	E (MPa)
Korean Larch lumber	13.5	10,000

2.2 DESCRIPTION OF THE COMPOSITE SYSTEM

Since wood fastened with plywood segments by nails (Figure 1). The spacing, edge and end distance of nails followed Nail-laminated timber design & construction guide and Eurocode 5 [4], [5]. In the compressive zone, ready-mixed concrete was topped on the timber-plywood panel and it was connected mechanically by notches, and the plywood segments were aligned in a line with 240 mm spacing.

2.3 DOUBLE SHEAR TEST

The slip modulus value is one of the main parameters in the γ-method estimation. It can be derived from by push-out test, and the test procedure has followed EN 26891 in most research [6]. To derive the slip modulus value, the double shear test was conducted as shown in Figure 3. The two types of test specimens were prepared to evaluate the slip modulus value of notches in the concrete layer and nails in the timber layer. Using LVDT, the relative slip of plywood segments between concrete and timber was measured. The slip modulus value can be derived from the load-slip curve. It can be used to calculate the connection efficiency factor (γ), and EI_{eff}. In the load-slip curve, the slip modulus values of the serviceability limit state (K_{SLS}) and the ultimate limit state (K_{ULS}) can be classified with the load level. K_{SLS} refers to the secant modulus of the load-slip curve between two specific points, namely 10% and 40% of F_{max} and K_{ULS}. K_{SLS} is utilized in determining the connection efficiency factor and EI_{eff} at the

https://doi.org/10.52202/069179-0032

serviceability limit state, while K_{ULS} is used to predict the load-carrying capacity of TCC

$$K_{SLS} = \frac{0.4F_{max} - 0.1F_{max}}{0.4v_{max} - 0.1v_{max}} \quad (1)$$

$$K_{ULS} = \frac{0.8F_{max} - 0.1F_{max}}{0.8v_{max} - 0.1v_{max}} \quad (2)$$

Where, K_{SLS} = the slip modulus value in the serviceability limit state, K_{ULT} = the slip modulus value in the ultimate limit state, F_{max} = The maximum load observed in the load-slip curve during double shear tests, v_{max} = The slip value corresponding to the point of maximum load.

2.4 FULL-SCALE BENDING TEST

The bending performance, including moment resistance (M) and EI_{eff} of TPC slabs, were measured through experiments with 10 specimens. The dimensions of the slab components are illustrated in the figure below, with a length of 6,210 mm and a span of 6,000 mm. In the longitudinal direction, the plywood segments are aligned. Figure 4C illustrates that plywood segments (b) function as shear connectors between layers. The plywood segments located at the midpoint of the span were aligned to ensure equal spacing of connections. the dimension of plywood was specified. Using a universal test machine, the load was applied to one-third of the TPC slab at a rate of 10 mm/min. Moment resistance was determined by the load at which failure occurred, while EI_{eff} was calculated by measuring the deformation at the centre of the span using a wire displacement sensor. The loading rate was 10 mm/min.

$$M = \frac{P_{max}a}{2} \quad (3)$$

Where, M = moment resistance, P = maximum load, a = the distance from support to the loading point.

$$EI_{eff} = \frac{a}{24}\frac{\Delta P}{\Delta v}(3l^2 - 4a^2) \quad (4)$$

Where, EI_{eff} = experimental effective bending stiffness, a = the distance from support to the loading point, ΔP = load increment, Δv = vertical deformation increment, l = length of the specimen.

2.5 GAMMA METHOD PREDICTION

The design of TPC was validated by comparing the bending performance of the TPC slab, as measured experimentally, with the predicted bending performance calculated using the equations specified in Eurocode 5. The slip modulus value used in the prediction equation was obtained from the value measured during a double shear test. It should be noted that the physical properties of plywood were not reflected in the equations since the plywood segments were not connected with each other.

$$EI_{eff,est} = E_1I_1 + \gamma_1E_1A_1{a_1}^2 + E_3I_3 + \gamma_3E_3A_3{a_3}^2 \quad (5)$$

Where, $EI_{eff,est}$ = estimated EI_{eff} of a specimen, E_i = elastic modulus, I_i = the moment of inertia, γ_i = connection efficiency factor, A_i = the cross-section of elements, a_i = the distance from neutral axis to centroid of elements, i = the number of elements (1- concrete, 3-timber)

$$M_{i,est} = \frac{f_i}{\gamma_iE_ia_i + 0.5E_ih_i} \times EI_{eff,est} \quad (6)$$

Where, $M_{i,est}$ = estimated moment resistance of elements, E_i = elastic modulus, h_i = the depth of elements,

The moment resistance of the TPC slab was determined based on the minimum moment resistance of its constituent elements, namely the compressive strength of concrete and the tensile strength of finger-jointed lumber.

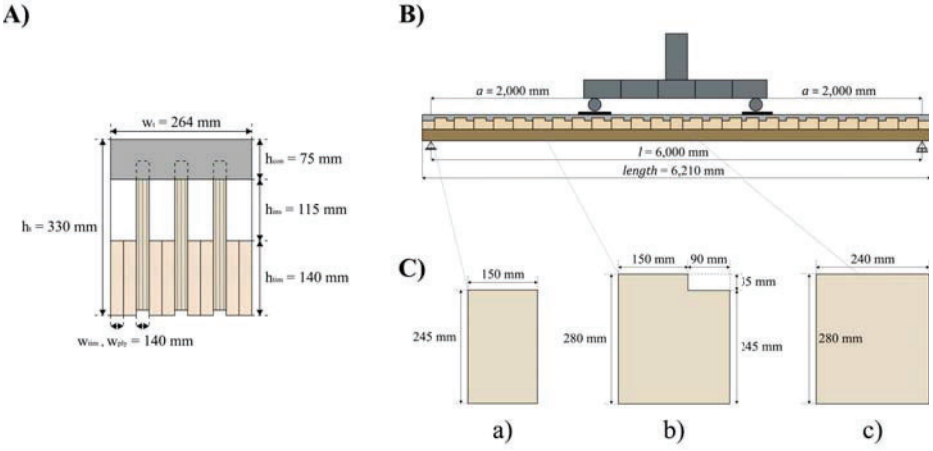

Figure 4: *A) the cross section of TPC slab specimen, B) 4-point bending test set up, C) detail of plywood segments*

https://doi.org/10.52202/069179-0032

3 RESULT & DISCUSSION

3.1 RESULT

3.1.1 DOUBLE SHEAR TEST

The slip modulus values for the nails and notches were determined experimentally by double shear tests, and these data were subsequently used to predict the bending performance of TPC slabs which have similar geometry to specimens in full-scale bending tests.

3.1.2 FULL-SCALE BENDING TEST

Based on the full-scale bending test, the primary failure mode of the TPC slab was identified as the tensile failure of the finger-jointed lumber. Additionally, some shear cracks were observed in the concrete layer; however, they were not considered critical to the load-carrying capacity of the TPC slab. A 2-parameter Weibull distribution was estimated using 10 datasets (Full data fitting), from which the 5% lower percentile value of the TPC slab's load-carrying capacity was calculated. The EI_{eff} was determined as the mean value of 10 datasets. (Figure 5).

Table 3: *Double shear test results*

Connection	$K_{0.4}$ (kN/mm)	$K_{0.8}$ (kN/mm)	v_{max} (mm)	F_{est}* (kN)
Notch in concrete	35.93	22.03	1.53	66.21
Nail in timber	15.28	3.66	8.09	20.00

*Measured by preliminary test to determine the loading rate.

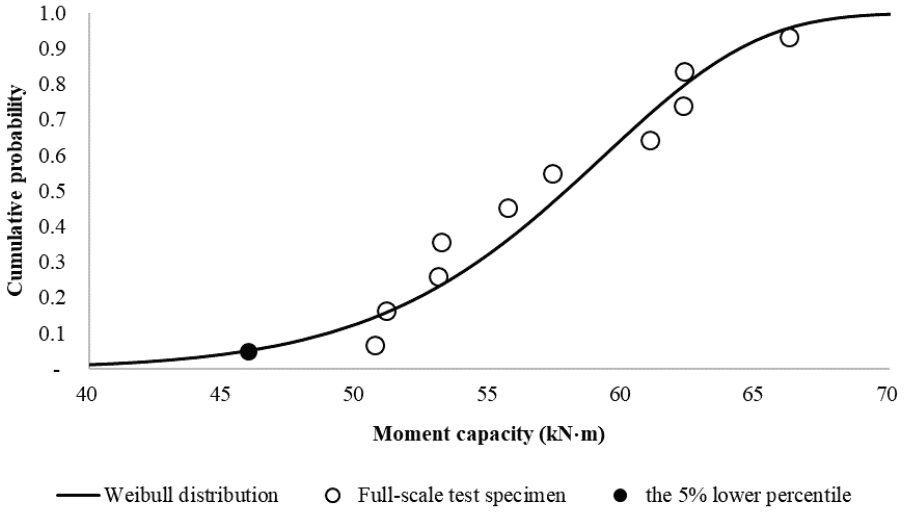

Figure 5: *Distribution of full-scale test specimen*

3.2 DISCUSSION

3.2.1 COMPARISON OF EXPERIMENTAL VALUE WITH PREDICTION

To assess the feasibility of the connection system, the bending performance of the TPC slabs measured experimental test was compared with the predicted values using the γ-method. The comparison showed that a conservative design of the TPC slab using the system is possible (Table 4). It was considered that plywood segments just serve as connections, but the observed error in comparison was attributed to the partial compression of the upper part caused by the rotation of the plywood during the experiment. This will be investigated in future research to enhance design efficiency.

Table 4: *Comparison measurement with estimation*

Test specimen	M (kN·m)	EI_{eff} (kN·m²)
Full-scale test	45.935	16,514
γ-method prediction	27.458	10,231

3.2.2 COMPARISON OF TPC SLAB WITH OTHER TCC SLABS

In order to evaluate the structural benefits of the TPC slab, a comparison was made with the structural performance of the TCC slab using other joints as proposed in the existing literature. However, it should be noted that objective comparison of different TCC slabs is challenging as they differ in not only the slip modulus of the joint used, but also the slab dimensions, physical

https://doi.org/10.52202/069179-0032

properties of the components, and longitudinal and width directions of the joint arrangement. To address this challenge, the bending performance of TCC slabs was calculated according to the following criteria. Firstly, assuming that the slab introduced in each paper was designed and optimized, the mechanical properties of elements and joint arrangement of the slab specimen were maintained. Secondly, the structural performance of each slab was compared using MOE and MOR values. The MOR and MOE values were calculated assuming a rectangular cross-section of the slab made up of a single material. As shown in Table 5, the load-bearing capacity of the TPC slab was lower than other TCC slabs. The reason why the MOR value is lower in this particular TCC slab is due to the arrangement of plywood segments instead of using timber laminae that resist tensile force. As a result, the tensile layer in the cross-section of the slab was lost to the same extent as the area where the plywood was placed, leading to a decrease in the load-bearing capacity. On the other hand, the EI_{eff} stiffness was found to be superior to that of other slabs. Through γ-method prediction, it is expected that the design of spans ranging from 8 m to 11 m can be possible with 1.2 m width, achieving the project's objective to apply the slab with long spans to buildings for using as non-residential purposes.

4 CONCLUSIONS

While the application of TCC systems has advantages in response to the increasing demand for non-residential construction in the market, various shear connections that connect timber and concrete have been developed, considering their performance and workability. This paper presents the development of a notch connection using structural plywood made of Korean larch species and an evaluation of the structural performance of the TCC slab. Also, the investigation was carried out to measure the actual bending performance and predict it using the gamma method on specimens of the same geometry. It was observed that the actual measured value exceeded the predicted value, confirming the possibility of the connection design through the gamma method. A comparison of the developed slab with other shear connections revealed that the effective bending stiffness of the former was superior to that of other TCC slabs. Considering that the structural capacity of building member with long span is determined by deflection, it is believed that this will confer structural advantages. However, future research is needed to evaluate the structural behavior of TPC slabs, including the improvement of load-bearing capacity and the efficiency of the prediction model.

ACKNOWLEDGEMENT

This study was conducted with the support of the 'R&D Program for Forest Science Technology (Project No. 2020224B10-2222-AC02)' provided by the Korea Forest Service.

Table 5: Bending performance comparison between each TCC slabs

Connection	Geometry			Bending performance				Reference
	Width (m)	Height (m)	Span (m)	M (kN·m)	EI_{eff} (kN·m^2)	MOR (kN/m^2)	MOE (10^3 kN/m^2)	
Inclined screw	0.4	0.3	5.1	105.9	5,440	24272.5	11353.9	[7]
Notch	0.6	0.2	6.0	112.2	5,642	25613.8	11442.5	[8]
Notch with inclined screw	0.6	0.2	6.0	118.4	5,686	24422.1	9842.3	[8]
Nail and notch in plywood segments	0.3	0.3	6.0	45.9	16,514	9586.5	20887.5	In this study

REFERENCES

[1] A. Ceccotti. Timber Engineering-STEP 2:Timber-concrete composite structures, Ed. by H. J. Blass, P. Aune, B. S. Choo, R. Görlacher, D. R. Griffiths, B. O. Hilson et al. Centrum Hout, The Netherlands, E13/1-12, 1995.

[2] A.M.P.G. Dias. Mechanical behaviour of timber-concrete joints. Doctoral thesis. University of Coimbra, 2005.

[3] L. Zhang, Y.H. Chui, and D. Tomlinson. Experimental investigation on the shear properties of notched connections in mass timber panel-concrete composite floors, Construction and Building Materials, 234, 117375, 2020.

[4] Binational Softwood Lumber Council. Nail-Laminated Timber U.S. Design and Construction Guide v1.0., Surrey, BC. 2017.

[5] Eurocode 5, Design of timber structures – Part 1-1: General rules and rules for buildings. the European Committe for Standardization, Brussels, Belgium, 2004.

[6] EN 26891, Timber Structures – Joints made with Mechanical Fasteners – General Principles for the Determination of Strength and Deformation Characteristics, the European Committe for Standardization, Brussels, Belgium, 1991.

[7] Y. Bao, W. Lu., K. Yue, H. Zhou, B. Lu, and Z. Chen. Structural performance of cross-laminated timber-concrete composite floors with inclined self-tapping screws bearing unidirectional tension-shear loads. Journal of Building Engineering, 55, 104653, 2022.

[8] L. Zhang, J. Zhou, Y.H. Chui, and D. Tomlinson. Experimental Investigation on the Structural Performance of Mass Timber Panel-Concrete Composite Floors with Notched Connections. Journal of Structural Engineering 148(2), 04021249, 2022.

https://doi.org/10.52202/069179-0032

World Conference on Timber Engineering Oslo 2023

MEASURING FIRE SAFETY PERFORMANCE: A COMPARATIVE EXPERIMENTAL STUDY ON DOVETAIL MASSIVE WOODEN BOARD ELEMENTS AND CROSS-LAMINATED TIMBER

Hüseyin Emre Ilgın[1], Markku Karjalainen[2], Mikko Malaska[3], Mika Alanen[4]

ABSTRACT: Adhesives and metal connectors play a critical role in the content of engineered wood products (EWPs). Though, the usage of adhesives can create challenges in terms of sustainability and recyclability because of toxic gas emissions. Metal fasteners are also critical to EWPs, but adversely affect end-of-life disposal, reusability, and recyclability. There is an alternative that is entirely pure wood, dovetail massive wooden board elements (DMWBEs) without adhesive and metal fasteners. In this paper, an experimental comparative fire-resistance study with cross-laminated timber (CLT) was conducted. Model scale test samples of 200 mm thickness, 950 mm width, and 950 mm length for CLT and DMWBE were tested in vertical position according to EN 1363-1. The charring performance of the DMWBE was found to be very similar to solid timber the charring rate being only slightly higher than that of solid timber. The char front was located in the third of the five lamella layers, but no flames or hot gases were observed on the unexposed side. With the tested lamella thickness, dovetail detail was able to effectively prevent the char fall-off. CLT specimens had a clear increase in the charring rate value due to the char fall-off of the first lamellae layer.

KEYWORDS: dovetail massive wooden board elements, CLT, fire safety, char depth, charring rate

1 INTRODUCTION

Owing to its numerous technical benefits e.g., uniform strength, stiffness, dimensional stability, and ecological properties, EWPs have been gradually used in the building sector as a construction material since the 1990s. They are getting more and more competitive in tall building construction [1] as in the 87-meter-high Ascent in Milwaukee (Figure 1) and the 85-meter-high Mjøstårnet in Brumunddal (Figure 2).

***Figure 1**: Ascent*
(Photo courtesy of Thornton Tomasetti)

***Figure 2**: Mjøstårnet*

Adhesives and metal connectors, with the regulation of the building sector, are frequently utilized as a connection in EWPs for modern wooden structures substituting traditional timber-to-timber assemblies. In this sense, adhesive bonding is among the essential parameters, and adhesives play a crucial role in EWPs, particularly by assisting to preserve the timber, enabling the building to be robust and light, and preventing shrinkage and expansion by natural humidity. But the usage of adhesives can create problems in terms of sustainability, recyclability, and broader ecological effect because of toxic gas emissions including VOC and formaldehyde during their lifetime [2]. Furthermore, in spite of

[1] Hüseyin Emre Ilgın, Tampere University, Finland, emre.ilgin@tuni.fi
[2] Markku Karjalainen, Tampere University, Finland, markku.karjalainen@tuni.fi
[3] Mikko Malaska, Tampere University, Finland, mikko.malaska@tuni.fi
[4] Mika Alanen, Tampere University, Finland, mika.alanen@tuni.fi

https://doi.org/10.52202/069179-0033

continuing developments in this study field, important questions remain about environmentally friendly bio-based adhesives. Metal fasteners are also critical to EWPs, but adversely affect end-of-life disposal, reusability, and recyclability [3].

There is an alternative that is entirely pure wood, dovetail massive wooden board elements without adhesive and metal fasteners (Figure 3). To date, many types of research have been conducted on the technical characteristics of timber with numerous construction solutions based on the usage of EWPs in the literature. However, there is limited research on DMWBEs, and the literature about DMWBE is based on quite a few structural analyses of connection details rather than even assessing the performance of load-bearing elements such as floor slabs [4,5]. This precludes our understanding of the potential of DMWBE, particularly in terms of environmental effects and recyclability [6].

Figure 3*: Dovetail wall connection*

This study examines dovetail massive wood board elements. They are made of wood lamellae connected using one of the oldest joint techniques. This manufacturing technology offers an adhesive- and metal-connector-free solution from which no harmful chemicals are released [7]. As this is a new solution, very limited information is available on the technical and structural performance and more research is needed in some areas e.g., dimensional stability [8,9]. Within the scope of the DoMWoB project *(Dovetailed Massive Wood Board Elements for Multi-Story Buildings)* (see Acknowledgment), technical performance tests (fire resistance, structural performance, moisture transfer resistance, airtightness, and sound insulation tests) were planned to develop DMWBE for the international market as a replacement for traditional EWPs.

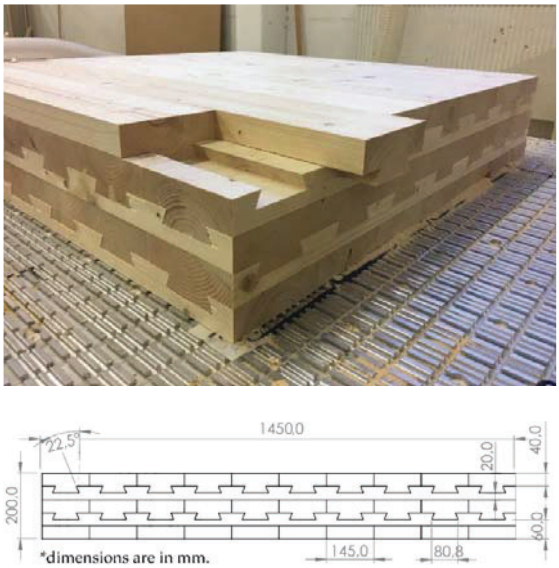

Figure 4*: DMWBE prototype as fire resistance test specimen*

An ongoing research project at Tampere University is aiming to investigate the performance of DMWBE structures at normal temperatures and when exposed to standard fire conditions. In this paper, an experimental comparative fire-resistance study with CLT was conducted as one of the important stages of evaluation of DMWBE's technical performance within the scope of the DoMWoB project. Model scale test samples of 200 mm thickness, 950 mm width, and 950 mm length for CLT and DMWBE (Figure 4) were tested according to EN 1363-1 [10] in vertical position.

The basic charring rate of a solid timber member made of pine or spruce is typically defined as 0,65 mm/min [11]. For CLT structures the charring rate values depend on many different parameters. The rate values are typically higher than that of solid wood as all the adhesives used are not able to prevent heat delamination and char layer fall-off when the char depth passes the bond lines between laminations. In DMWBE structure no adhesive is used and dovetail detail is used to prevent premature char fall-off.

In this research two fire tests have been conducted on DMWBE and CLT specimens with similar lamellae thicknesses. The study aimed to investigate if the dovetail detail can prevent the delamination of the DMWBE structure during a fire and how well the DMWBE structure maintains integrity and prevents the passage of flames and hot gasses through during the test. Also, charring rate estimates based on the temperatures measured inside the specimens were determined. The results and observations were compared with the results of the CLT specimens manufactured using a polyurethane adhesive. These experimental tests and the main conclusions were introduced in this paper.

https://doi.org/10.52202/069179-0033

2 FIRE TESTS

This section describes the fire test performed on DMWBE and CLT panels at the Fire Laboratory of Tampere University, considering char depth and charring rate.

2.1 TEST SPECIMENS

2.1.1 Dovetail test specimens

DMWBEs were produced at Vocational College Lapland (Ammattiopisto Lappia), Kemi, Finland [12]. A 5-axis CNC machine (Figure 5) with NUM operating system and compatible SOLIDWORKS computer application was used to manufacture the two test specimens. CNC post-processor methodology was employed, creating a unique integrated environment for the individual steps of finishing, toolpath optimization, and G-code simulation for manufacturing [13]. The moisture content of dovetail boards at the time of manufacture was between 10-12%. On the other hand, the relatively long production time due to the lack of a mass production line and the need for different types of tools such as blades and the removal of dust were the main challenges encountered during production.

***Figure 5**: 5-axis CNC machine used in DMWBE manufacturing at Vocational College Lapland (Kemi, Finland)*

To explore the fire resistance of DMWBE, two separate boards were manufactured. Each board was produced 200 mm thick, 1015 mm wide, and 1450 mm long (Figure 6), then cut into dimensions 200 mm thick, 950 mm wide, and 950 mm long. The boards were manufactured from Norway Spruce with C24 PS strength class. The moisture content of the test specimens at the time of the test was 10,3 %.

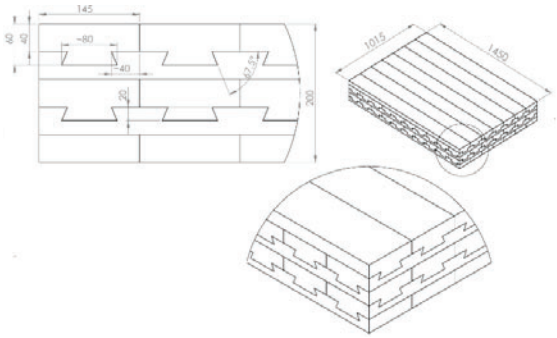

***Figure 6**: DMWBE test sample production drawings*

2.1.2 CLT test specimens

CLT panels were manufactured at CLT Plant Oy in Finland [14] for comparison with DMWBE. To explore the fire resistance of CLT, two separate panels were tested, and each test was performed on a panel 200 mm thick, 950 mm wide, and 950 mm long (Figure 7) as in DMWBE. The dimensions of a lamella were 145 mm by 40 mm. The adhesive used in CLT panels was M1 class polyurethane adhesive and lamellas supplied by Kiilto Oy (Tampere, Finland), where the adhesive was applied to all four faces of a lamella. The boards were manufactured from Norway Spruce with C24 PS strength class.

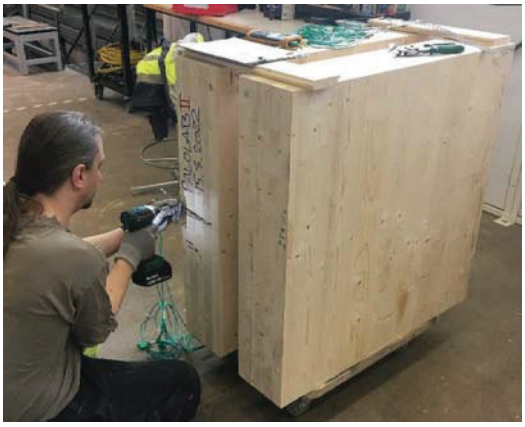

***Figure 7**: Preparation of CLT specimens for fire resistance test at Tampere University Fire Laboratory (Tampere, Finland)*

3 TEST SET-UP

In each test, two specimens of similar construction were mounted to supporting construction, made of aerated concrete blocks, in vertical position, as shown in Figure 8. The specimens were installed with their outer lamella layers in vertical direction.

https://doi.org/10.52202/069179-0033

***Figure 8**: Specimens mounted to supporting construction made of aerated concrete blocks. (Unexposed side)*

The tests were conducted according to EN 1363-1 (2020). During the test, furnace temperature, specimen temperatures, oxygen content within the furnace, and pressure differences between the furnace and test hall were monitored. The pressure was set to 20 Pa at the level of the specimen's top edge. The oxygen concentration in the middle of the furnace chamber was measured using a Dräger EM200-E multi-gas detector.

The char depth and charring rate assessments were based on temperatures measured inside the specimens during the test. Since the main aim of these tests was to observe the performance of the new non-adhesive construction in fire conditions and to investigate if the dovetail detail can restrict the delamination of the panels, it was considered that temperature measurements at main lamella interfaces only provide sufficient information. In a specimen, five thermocouples were used to monitor temperatures on one interface between two lamella layers. Schematic diagrams of the placement of the thermocouples in DMWBE and CLT elements are shown in Figure 9. In the vertical section of the slab, these thermocouples overlapped with the other thermocouples at different lamella interfaces. Shielded 3 mm diameter Type-K thermocouples were installed into 3,5 mm diameter holes drilled from the side face of the specimen and 150 mm along the interface between the layers.

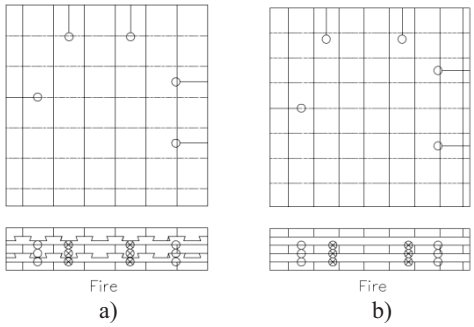

***Figure 9**: Elevation and cross-section of the CLT specimens and positions of the in-depth thermocouples: a) DMWBE and b) CLT panels.*

4 TEST RESULTS

Both tests were terminated, and the burners were shut off 140 min after the commencement of the test. The furnace temperature followed the standard temperature-time curve [10]. In both tests, the oxygen content in the furnace chamber was around 5 % during the first 60 minutes as seen in Figure 10. This is when the first lamella layer had charred through. In the case of DMWBE, the oxygen content decreases steadily thereafter, being approximately 2,5 % at 120 minutes. In the case of CLT, the oxygen content drops down to zero very rapidly at 65 minutes and remains for 15 minutes at this low level. Visual observations through the furnace camera showed that at the same time, large areas of the first lamellae layer fell off. After this, the content quickly increased again to 4 % and remained at this level until 117 minutes, after which the concentration decreased again to zero. This corresponded well with the visual observations of the falling off the second lamella layer.

The observations showed that both of the panel products were able to prevent the passage of flames and hot gases through the structures. In all the specimens, the char front was located in the third lamella layer at the end of the test, i.e. at 140 minutes.

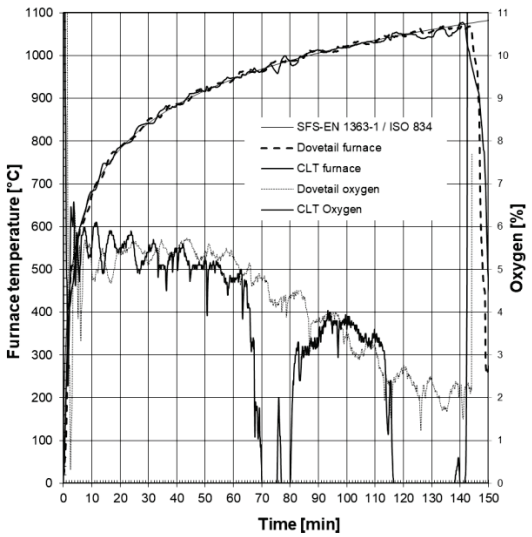

***Figure 10**: Furnace temperatures and oxygen concentrations measured during the fire tests.*

The char depths of the panel product were based on temperatures measured inside the specimen during the test; the charring temperature of the wood is considered to be 300 °C. Figure 11 illustrates the mean charring depths interpreted for the DMWBE and CLT panels. Also, the charring depth development based on the design charring rate of 0,65 mm/min for solid timber is shown in Figure 11. The results showed that the charring performance of the DMWBE panels corresponds well to the charring performance of solid wood, while the charring rate of the CLT panels starts to increase due to the char fall-off of the first lamella layer at 60 minutes. As the tests were terminated before the char front had reached 120 mm at

https://doi.org/10.52202/069179-0033

any thermocouple location, the mean charring depths can be determined only up to the point, when the temperature of a thermocouple at 80 mm first exceeds 300 °C. This is why the curve representing the mean charring depth for the CLT panel stops at 86 minutes.

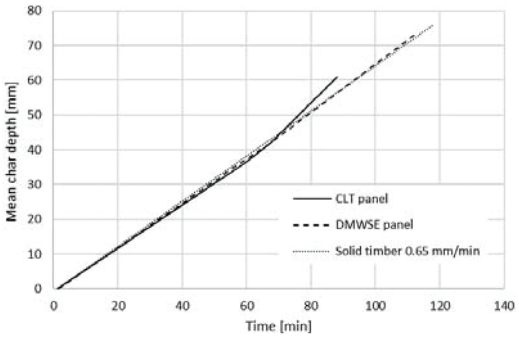

***Figure 11**: Mean charing depths for DMWBE and CLT panels. For comparison, charring depth development based on the design charring rate of 0,65 mm/min for solid timber is shown.*

Based on the test results the dovetail structure was able to limit the delamination of the unloaded DMWBE panel during the fire exposure. The estimated average charring rates determined between the exposed face and 40 mm and between 40 mm and 80 mm were 0,65 mm/min and 0,70 mm/min, respectively. The rate values were only slightly higher than that of solid timber. In the first layer, charring rates ranged from 0,57 mm/min to 0,70 mm/min, and in the second layer from 0,52 mm/min to 0,83 mm/min. Figure 12 shows the charred dovetail geometry after the test. In the structure tested, the panels were made of 60 mm thick lamellae. The charring performance can be very different and the charring rates are higher if thinner lamellae are used. In the case of the CLT panel, the charring rate of the first lamella layer was 0,62 mm/min, but when the charring progressed into the second lamella layer, the rate increased to 0,93 mm/min due to the char fall-off. This can be seen in Figure 11, as the curve representing CLT starts to deviate at this point from the curves of solid timber and DMWSE. In the CLT panel, charring rates for the first layer ranged from 0,57 mm/min to 0,69 mm/min, and in the second layer from 0,78 mm/min to 1,36 mm/min.

Uncertainties related to the accuracy of the position of the thermocouples and the thermal disturbance errors induced by shielded thermocouples were not analyzed in this research.

***Figure 12**: Remaining lamella layers and the dovetail structure of DMWBE at the end of the test.*

5 CONCLUSIONS

Two fire tests were conducted on DMWBE and CLT specimens with similar lamellae thicknesses to investigate the integrity and thermal insulation properties and charring of the adhesive-free DMWBE structure during a fire. The results and observations were compared with the results of a CLT panel of similar lamellae thickness manufactured using a polyurethane adhesive. The charring performance of the dovetail construction was found to be very similar to solid timber the charring rate being only slightly higher than that of solid timber. At the end of the test, the char front was located in the third of the five lamella layers but no flames or hot gases were observed on the unexposed side. With the tested lamella thickness, dovetail detail was able to effectively prevent the char fall-off. CLT specimens had a clear increase in the charring rate value due to the char fall-off of the first lamellae layer.

ACKNOWLEDGEMENT

This project has received funding from the European Union's Horizon 2020 research and innovation programme under the Marie Skłodowska-Curie grant agreement No [101024593].

Marjatta ja Eino Kollin SÄÄTIÖ
Lisää mahdollisuuksia

This project has also received funding (60,000 EUR) from the Marjatta and Eino Kolli Foundation for the technical performance tests including fire safety, structural, moisture transfer resistance & airtightness, and sound insulation.

REFERENCES

[1] Stepinac M., Šušteršič I., Gavrić I., Rajčić V.: Seismic Design of Timber Buildings: Highlighted Challenges and Future Trends, Applied Sciences, 10(4):1380, 2020.

[2] Kozicki M., Guzik K.: Comparison of VOC Emissions Produced by Different Types of Adhesives Based on Test Chambers. Materials, 14:1924, 2021.

[3] Sotayo A., Bradley D., Bather M., Sareh, P., Oudjene M., El-Houjeyri I., Harte A., Mehra S., O'Ceallaigh C., Haller P. et al.: Review of state of the art of dowel laminated timber members and densified wood materials as sustainable engineered wood products for construction and building applications. Dev. Built Environ. 1:1–11, 2020.

[4] Sha B., Wang H., Li A.: The Influence of the Damage of Mortise-Tenon Joint on the Cyclic Performance of the Traditional Chinese Timber Frame. Appl. Sci. 9:3429, 2019.

[5] Xie Q., Zhang B., Zhang L., Guo L., Wu Y.: Normal contact performance of mortise and tenon joint: Theoretical analysis and numerical simulation. J. Wood Sci., 67:31, 2021.

[6] Ilgın H.E., Karjalainen M.: Preliminary Design Proposals for Dovetail Wood Board Elements in

Multi-Story Building Construction. Architecture, 1(1):56-68, 2021.
[7] Ilgın H.E., Karjalainen M., Koponen O.: Various Geometric Configuration Proposals for Dovetail Wooden Horizontal Structural Members in Multistory Building Construction; IntechOpen: London, UK, 2022.
[8] Ilgın H.E., Karjalainen M., Koponen O.: Review of the Current State-of-the-Art of Dovetail Massive Wood Elements; IntechOpen: London, UK, 2021.
[9] Ilgın, H.E., Karjalainen, M., Koponen, O., Soikkeli, A.: A Study on Contractors' Perception of Using Wood for Construction; IntechOpen: London, UK, 2022.
[10] EN 1995-1-2:2004, Eurocode 5: Design of timber structures – Part 1-2: General – Structural fire design, Brussel, European committee for standardization.
[11] EN 1363-1:2020. Fire resistance tests. Part 1: General requirements. Brussel. European committee for standardization.
[12] Vocational College Lapland (Ammattiopisto Lappia), https://www.lappia.fi/, (accessed February 14, 2023).
[13] Rodriguez, E. Alvares, A.: A STEP-NC implementation approach for additive manufacturing. Procedia Manufacturing, 38, 9–16, 2019.
[14] CLT Plant Oy, Available at: https://www.cltplant.com/ (accessed February 14, 2023).

https://doi.org/10.52202/069179-0033

World Conference on Timber Engineering Oslo 2023

LABORATORY INVESTIGATION OF CROSS-LAMINATED DECKS FOR BRIDGE APPLICATIONS

Justin M. Dahlberg[1], James P. Wacker[2], Douglas R. Rammer[3]

ABSTRACT: The use of cross-laminated timber (CLT) has gained popularity during the past decade in North America, with many advances stemming from completed research and construction projects located in other countries. In particular, CLT has been utilized in vertical construction projects where many of its inherent features have been maximized. Despite these advances, the use of CLT in bridge structures has been limited and CLT has not been adopted into governing bridge design codes.

This paper reports the results and conclusions of the laboratory investigation of the feasibility of CLT as a primary structural material for highway bridge deck applications. Two common timber bridge superstructure systems are used in the United States: (1) longitudinal deck panels spanning the bridge abutments, and (2) transverse deck panels across the bridge width supported by longitudinal girders. The subject of this paper is the longitudinal CLT bridge deck system, which was tested under service loading to determine the structural behavior under static loading.

KEYWORDS: Cross-Laminated Timber, Bridge, Laboratory Investigation, Longitudinal Deck

1 INTRODUCTION

The use of cross-laminated timber (CLT) has gained popularity during the past decade, with many advances stemming from completed research and construction projects located in Europe. In particular, CLT has been utilized in vertical construction projects where many of its inherent features have been maximized. To name a few, CLT is prefabricated, relatively lightweight, dimensionally stable, and environmentally sustainable. North American design resources and standards have been developed for CLT in the form of PRG 320 [1], CLT Handbook [2], and the National Design Specification (NDS) [3] but these effectively limit the use of CLT to indoor applications where the moisture content can be maintained below 16%. The use of CLT in bridge structures has been limited and the adoption of CLT into governing bridge design codes has been slow-going.

CLT shows promise as a complementary or alternative construction material in bridge decks, and additional research evaluating the structural performance of these decks would further guide the appropriate use in bridge projects. This paper provides a summary of research conducted to characterize the structural characteristics of CLT bridge decks subjected to typical traffic loads.

CLT was first introduced in Europe in the 1990s to provide a potential alternative to more commonly used building materials such as concrete, masonry, and steel. Since that time, CLT and its production and distribution have vastly improved allowing for rapid growth and use. The building industry, in particular, has seen hundreds of projects completed using CLT, with mid-rise and high-rise buildings constituting the bulk of these projects.

The use of CLT for bridge projects has been very limited with very few in North America and none in the United States. In fact, there have been only a few notable bridge projects to incorporate CLT including the Mistissini Bridge located in Quebec, Canada, constructed in 2014 [4] and the Maicasagi Bridge located north of Quebec constructed in 2011 [5]. Both were long span bridges and the CLT was composite with other materials. Regardless, in each case, CLT was selected for its locally sourced material and shorter lead time compared with more commonly used materials. Both of these projects were considered a success and provide an example of CLT capabilities. Despite this fact, CLT is rarely considered for use in bridge applications, even with several inherent advantages. Additional research and proof of concept is

[1] Justin M. Dahlberg, Research Engineer, Iowa State University Bridge Engineering Center, Ames, IA, USA, dahlberg@iastate.edu
[2] James P. Wacker, Research Engineer, USDA Forest Products Laboratory, Madison, WI, USA, james.p.wacker@usda.gov
[3] Douglas R. Rammer, Research Engineer, USDA Forest Products Laboratory, Madison, WI, USA, douglas.r. rammer@usda.gov

https://doi.org/10.52202/069179-0034

required to help make CLT a viable bridge construction material to be used by designers and engineers.

CLT is not currently recognized in the American Association of State Highway and Transportation Officials (AASHTO) load and resistance factor design (LRFD) bridge design specifications (BDS) [6]. Glue-laminated timber has been recognized by AASHTO for use in treated bridge structures for several decades. The inherent similarities between each bridge type along with continued proof-of-concept research should provide supporting data for CLT viability and acceptance by AASHTO in the bridge industry.

2 RESEARCH METHODS

2.1 PRE-TEST INVESTIGATION

The research team conducted a literature review of bridge designs using CLT in the United States, Canada, and European countries where CLT technology has been more quickly advanced and implemented. A review of deck materials, including species, size, and layup, was conducted. Additionally, the viability of CLT with respect to economics, strength, and serviceability was reviewed. Existing details for CLT from any available bridge plans and vertical construction were reviewed for viability and adoption to bridge structure use. CLT manufacturers were surveyed to identify the capabilities of pressure treatment facilities and assess the size limits of CLT panels that can be singly pressure treated.

CLT panels consist of an odd number of layers of flatwise lumber boards or structural composite boards stacked crosswise (typically at 90 degrees) and glued together under pressure. Modern CLT initially resulted from industry–academia joint research efforts in Austria in the middle 1990s. The use of CLT increased significantly in Europe in the early 2000s, partially driven by the green building movement and better efficiencies, product approvals, and improved marketing and distribution channels.

While this product is well established in Europe, the work toward the implementation of CLT products and systems has only recently begun in the United States and Canada. The U.S. edition of the CLT Handbook [2] and first CLT performance standard, PRG 320 [1] were published in 2013 with the intent to assist the U.S. building design and construction industry. The CLT Handbook [2] describes only glued CLT; nonglued CLT products are outside the scope of the publication. In 2015, CLT design procedures were introduced in the National Design Specification for Wood Construction, and in 2021, the International Building Code (IBC) [7] incorporated a new class of wood building materials, mass timber, which included CLT. The IBC also limited the construction of mass timber structures to 18 stories high

A cross section of a CLT element has at least three glued layers of boards placed orthogonally, each layer in an alternating orientation to the neighboring layers. Thickness of individual lumber pieces varies from 16 to 51 mm, and the minimum width is 1.75 times the thickness in the major strength direction and 3.5 times the thickness in the minor strength direction. Lumber laminations are visually graded or machine stress rated and dried to 12% moisture content. Panel sizes vary by manufacturer, and typical widths are 0.6, 1.2, 2.4, and 3 m while length can be up to 18 m and thickness can be up to 508 mm [1].

CLT provides relatively high in-plane and out-of-plane strength and stiffness properties, giving it two-way action capabilities similar to a reinforced concrete slab. The 'reinforcement' effect provided by the cross-lamination in CLT also considerably increases the splitting resistance of CLT for certain types of connection systems. Likewise, for floor and roof systems, the outer layers run parallel to the major span direction to maximize the flexural load capacity.

In North America, CLT design values are developed in accordance with the ANSI/APA PRG 320 [1] standard and qualified by an approved agency in accordance with the qualification and mechanical test requirements specified in the standard. PRG-320 Annex A contains seven layups to give the manufacture a means to validate calculations but these are not required layups. Rather, they are representative of what could be manufactured. Each manufacturer is free to develop and certify their own layup configuration.

2.2 PRESSURE TREATMENT

Similar to other timber bridge types, protection of CLT panels for exterior use is essential for long-term serviceability. The ability to pressure-treat full panels is limited by current manufacturer capabilities. Common chamber sizes in the United States would effectively limit the panel sizes to no wider than 2.1 m. Furthermore, pressure treating individual members to be used in a final CLT configuration is disadvantaged by the overall cost. The researchers understand that CLT panel protection measures are critical to their overall acceptance. Further research is recommended to identify best options to protect CLT panels from outdoor elements.

2.3 LABORATORY TESTING

At the Iowa State University structures laboratory, the project team conducted load tests using CLT panels in two configurations. The first configuration was a longitudinal deck panel superstructure system. It used two 314-mm-deep x 2.48-m-wide, 9-lam-layup (Figure 1), single-span panels, which spanned 7.62 m longitudinally between two deck concrete blocks serving as abutments (Figure 2). The second configuration was a transverse deck panel superstructure system. It used three 175-mm-deep x 2.49-m-wide, 5-lam-layup panels spanning transversely across longitudinal steel simply supported W-shape girders. For both bridge configurations tested, untreated Douglas-fir (*Pseudotsuga menziesii*) lumber was utilized for all layers in the CLT bridge deck panels. In the direction of the

https://doi.org/10.52202/069179-0034

primary span, select-structural graded lumber was used. For the corresponding orthogonal layers, lumber was graded for #2 and better. For brevity, this paper will focus on the 9-lam, longitudinal deck panel configuration, testing, and results.

Figure 1 *CLT Panel for Load Testing*

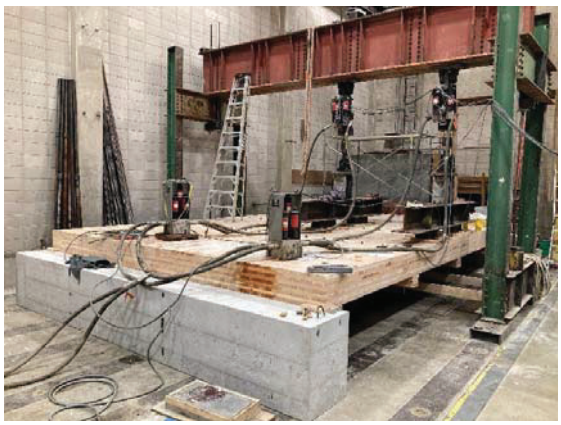

Figure 2 *Longitudinal Panel Test Configuration*

The configuration of the laboratory test setup included two equal-width panels set side-by-side spanning longitudinally as shown in Figure 3. The total width of the CLT deck was 4.88 m. This width constitutes approximately half of an actual in-service bridge. Three built-up spreader beams made up of five 38-mm x 191-mm boards connected with screws and measuring 191 x 216 mm in total were connected to the underside of the deck using 19-mm threaded thru-rods spaced at 305 mm on center, which is consistent with current AASHTO specifications.

Each of the panels were joined along their edge using a shiplap joint, which is a commonly fabricated joint used in the vertical construction industry and in nail-laminated timber bridge deck panels (Figure 4). The overlap width measured 76 mm, and the joint was stitched together using screws in the configuration shown in Figure 5. The vertical screws used were ASSY VG CYL 8 x 300 mm, and the inclined screws used were ASSY VG CSK 10 x 400 mm. This screw configuration was used because inclined screws tend to produce a stiffer connection with higher load capacities.

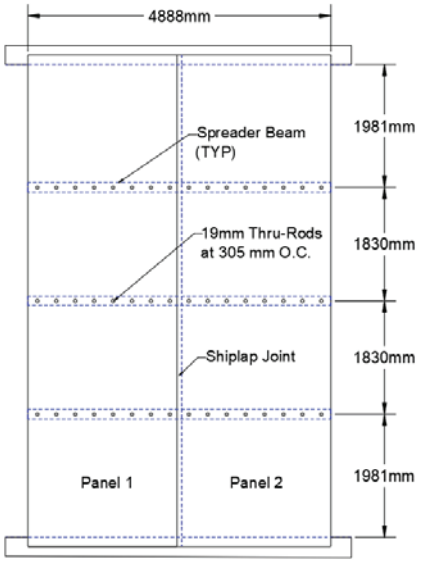

Figure 3 *Plan View of Longitudinal Deck Panel Configuration*

Figure 4 *Shiplap Connection used for Longitudinal Panel Deck*

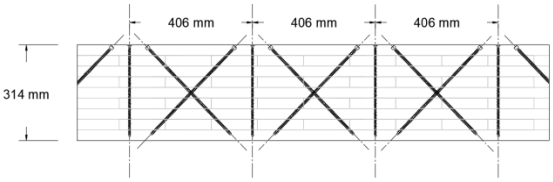

Figure 5 *Screw Pattern along Longitudinal Panel Shiplap Joint*

The tests were completed using typical highway service loads to simulate highway vehicle traffic. The panels were subjected to four load cases (LC), which simulated the rear tandem axle of a dump truck by placing loads at four specific locations as shown in Figure 6. The load, axle configuration, and tire spacing are consistent with the HL-93 AASHTO vehicular live loading design tandem. The locations were selected to maximize the shear and bending reactions within the panels and to determine how the applied force was distributed transversely across the panels, with a specific interest in how the longitudinal joint affected load distribution. The maximum applied load was 111 kN per axle, or 56 kN per tire location.

https://doi.org/10.52202/069179-0034

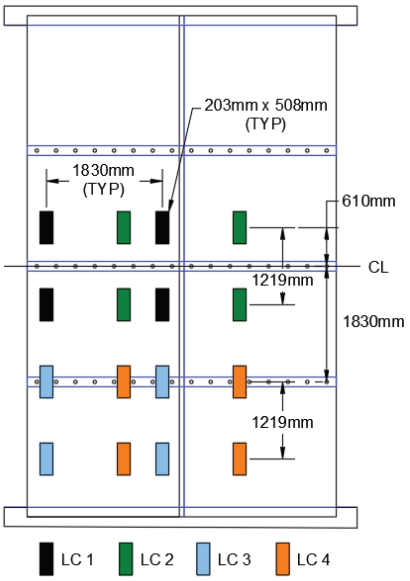

Figure 6 *Location of Rear-Axle Tandems for each Load Case*

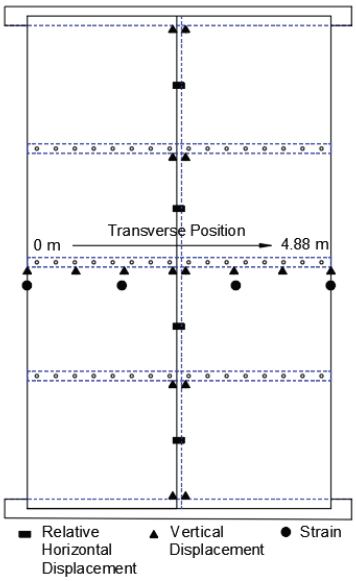

Figure 7 *Deflection and Strain Gage Placement*

2.4 DATA ACQUISITION

Strain and deflection gages were used to gather data for the purposes of structural characterization and comparison.

A series of deflection gages were placed transversely at midspan and along the longitudinal joint to capture the vertical deflection. Additional deflection gages were placed horizontally along the longitudinal joint to capture any relative movement or joint opening between the two panels.

Strain gages were placed at the top and bottom of the panel edges. During the manufacturing process, because of the overall panel width specifications, the outermost longitudinal boards were only 10 mm wide. This portion of the uppermost and lowest laminations was removed to allow the strain gage to engage the first full-width board. Top and bottom strain gages were also placed at approximately 1500 mm from each panel edge. The gage locations are shown in Figure 7.

At one of the panel edges (0-m transverse position), additional strain gages were placed on each of the longitudinal laminations. These gages were intended to determine the strain profile of the panel when loaded.

One horizontal displacement gage was placed at the lowermost transverse lamination to determine if any gapping occurs between individual members. The gages on the edge of panel are shown in Figure 8 and Figure 9.

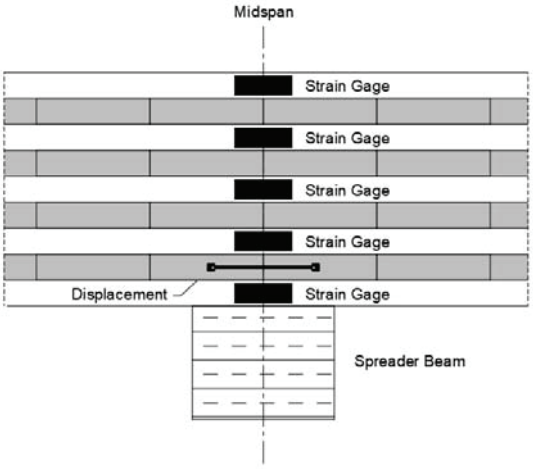

Figure 8 *Schematic of Strain Gages at Panel Edge*

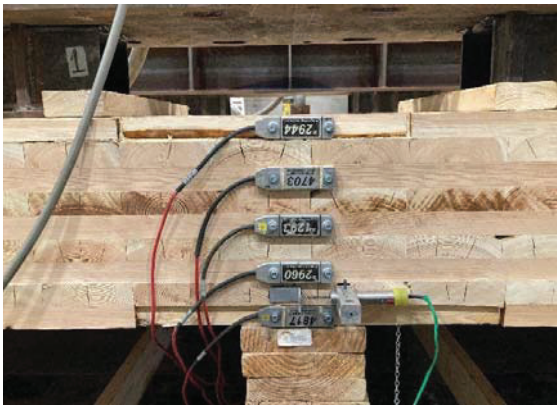

Figure 9 *Strain Gages at Panel Edge*

https://doi.org/10.52202/069179-0034

3 CLT PANEL EVALUTION

3.1 STRUCTURAL CHARACTERIZATION

Photographs of the reaction frame and load position for each load case location are shown in Figure 10 through Figure 13. Plots of the corresponding strain and deflection behaviour at midspan at the time of maximum load for each of the four load cases are represented in Figure 14 through Figure 17.

For Load Case 1, Figure 15 indicates that when the entirety of the load was placed on Panel 1, the deflection was greatest at the panel edge with approximately 39 mm of deflection. This corresponds to a span-to-deflection ratio (L/D) of 197. The deflection values linearly decreased relative to the transverse position until the minimum value of 1.3 mm was measured at the opposing panel edge. The strain values ranged between 545 and 572 microstrain in compression and tension, respectively, at the panel edge with a relatively linear strain profile through the depth of the panel as indicated by the five strain gages positioned on the longitudinal laminations at the zero position (Figure 9). The strain profile at the panel edge was linear throughout the full load range. The peak strain value of 648 microstrain was measured in compression at the top of the panel at the first interior position. Assuming a modulus of elasticity of 11.7 GPa for select structural Douglas-fir, the corresponding maximum stress is 7.6 MPa.

For Load Case 2, when the load was equally positioned on each panel, Figure 15 indicates fairly symmetric behaviour of the panels under peak load. The deflection was greatest at the longitudinal joint with a measured value of 21.7 mm. This corresponds to an L/D value of 351. The deflection values uniformly decreased from the longitudinal joint to the panel edges but did not significantly decrease overall. A similar behaviour was observed in the strain values. Peak strain values of 401 and 392 microstrain were measured at the interior positions at the top of the panels corresponding to stress values of 4.7 and 4.6 MPa, respectively. The strain values decreased slightly at the panel edges similar to the behaviour observed in the deflection data. As with Load Case 1, the strain profile as indicated by the strain gage series at the panel edge was fairly linear indicating linear strain behaviour.

For Load Case 3, the load was positioned in the same transverse position as Load Case 1 entirely on Panel 1 but near the endspan. The results presented in Figure 16 indicate many similarities in the overall deflection and strain trends among each of these load cases. The deflection was greatest at the panel edge (20.5 mm) with linearly decreasing values corresponding to the transverse position. The deflection on the opposing panel edge was nearly 0 mm. The strain values at midspan are understandably less than the measured values when the load was positioned at midspan. However, it should be noted that the pattern of relative strain magnitudes when comparing adjacent strain locations is similar between Load Cases 1 and 3. The peak strain value is observed at the first interior strain position. The strain profile observed at the panel edge grouping of strain gages further indicates linear behaviour.

For Load Case 4, the load was positioned symmetrically on each panel as with Load Case 2 but near the endspan. The results presented in Figure 17 indicate very similar deflection and strain behaviour as that in Load Case 2, albeit smaller magnitudes due to the longitudinal load position. The deflection was greatest at the longitudinal joint (11.5 mm) and gradually and minimally decreased with distance from the joint toward the panel edge (9.1 to 9.5 mm). Strain magnitudes were also nearly symmetric with respect to the longitudinal joint. Furthermore, the strain profile at the panel edge indicated linear behaviour.

3.2 EQUIVALENT STRIP WIDTH

Load distribution characteristics for each load case can be quantified by calculating the equivalent strip width (ESW). Calculation of the ESW using measured data is typically achieved by 1) numerically integrating the area under the moment distribution curve, and 2) dividing the summation by the estimated maximum moment. However, when assuming uniform stiffness of the panels, deflection data can be used instead (Equation 1).

$$ESW = \frac{\sum_{i=1}^{n}(deflection_i \times d_i)}{deflection_{max}} \quad (1)$$

where, n is the total number of deflection sensors, $deflection_i$ is the deflection reading of the i-th sensor, $deflection_{max}$ is the maximum deflection measured by the sensors, and d_i is the spacing of adjacent deflection gages. The ESW results for each load case are listed in Table 1.

Table 1: *Equivalent Strip Width*

Load Case	ESW (m)
1	2.48
2	4.30
3	2.50
4	4.40

It is evident that when the load is positioned on both panels rather than on one panel only, the ESW is approximately 70% greater indicating that a greater width of the bridge is engaged in the load resistance. The transverse load distribution is significantly less when the load is entirely on one panel despite the uniformity of the deflection trend. A stiffer spreader beam may aid the transverse load distribution characteristics. As a means of comparison, ESW values calculated using deflection data from recently completed load tests of in-service, longitudinal nail-laminated bridge decks range from 1.8 to 4.2 m [8]. It can be observed that the ESW values calculated from the CLT tests and nail-laminated bridge decks, which traditionally have one-way action, are similar.

https://doi.org/10.52202/069179-0034

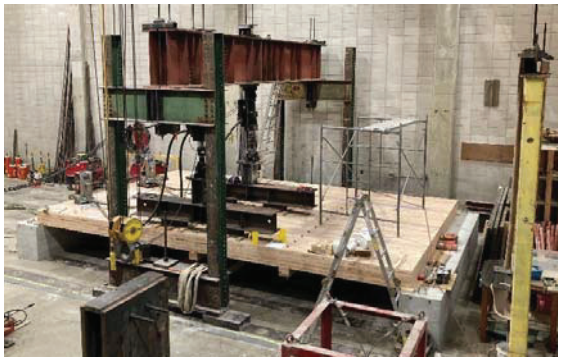

Figure 10 *Load Case 1*

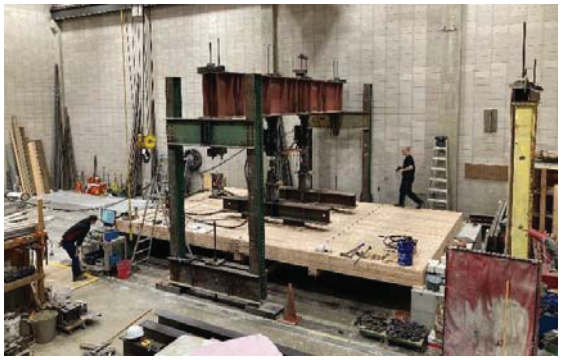

Figure 11 *Load Case 2*

Figure 12 *Load Case 3*

Figure 13 *Load Case 4*

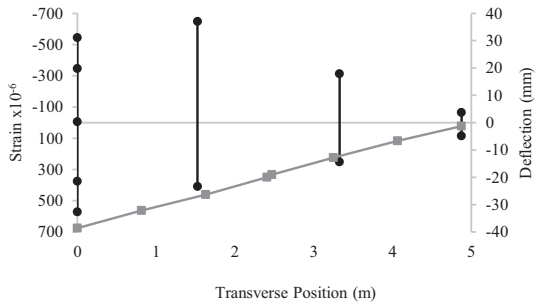

Figure 14 *Strain and Deflection at Max Load for Load Case 1*

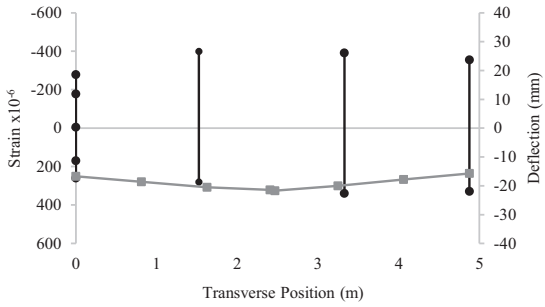

Figure 15 *Strain and Deflection at Max Load for Load Case 2*

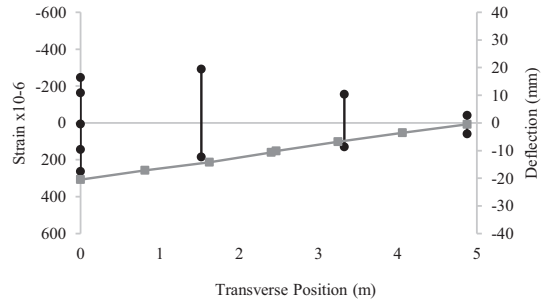

Figure 16 *Strain and Deflection at Max Load for Load Case 3*

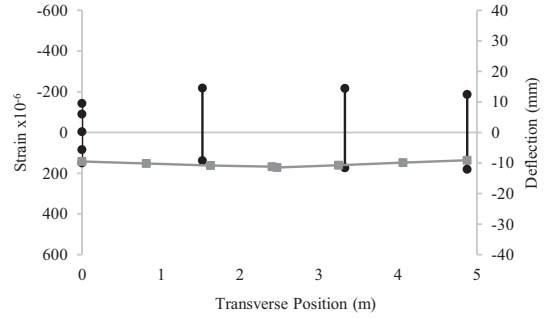

Figure 17 *Strain and Deflection at Max Load for Load Case 4*

https://doi.org/10.52202/069179-0034

4 SUMMARY AND CONCLUSIONS

Cross-laminated timber panels have gained popularity in recent history and have been widely used in the vertical construction industry. Despite this fact, there have been few instances where CLT panels have been used for bridge deck applications in North America. The impediments to using them are not dissimilar to the use of other timber structures in exterior environments. The ability to pressure-treat full panels is limited by current manufacturer capabilities. Furthermore, pressure-treating individual members to be used in a final CLT configuration is disadvantaged by the overall cost. Further research is recommended to identify best options to protect CLT panels from outdoor elements.

CLT has been used in ways that maximize many of its inherent features. CLT is prefabricated, relatively lightweight, dimensionally stable, and environmentally sustainable. North American design resources and standards have been developed for CLT in the form of PRG 320 [1], CLT Handbook [2], and the National Design Specification (NDS) [3], but these effectively limit the use of CLT to indoor applications where the moisture content can be maintained below 16%. The use of CLT in bridge structures has been limited, and the adoption of CLT into governing design codes has been slow-going.

During this study, two nontreated, longitudinal CLT panels were subjected to highway-type service loads to characterize their structural performance and behaviour. The panels were made up of two grades of Douglas-fir, select structural for longitudinal layers and No. 2 for transverse layers, and were connected together using a shiplap joint, screws, and spreader beams. The simply supported, single-span panels were equipped with deflection and strain gages placed at various locations on the structure to quantify the performance under load. Four load cases were used to place the loads at distinctive locations at midspan and near the end span. In two cases, the entirety of the load was applied to only one panel, whereas in the other two cases the load was equally applied to both panels.

The equivalent strip width (ESW) was calculated for each load case. It was observed that when a single panel was loaded (Load Cases 1 and 3), the ESW decreased by about 40% when compared with the ESW when both panels were simultaneously loaded (Load Cases 2 and 4). This phenomenon is similar to the ESWs observed during in-service, slab-type timber bridge tests previously completed by this research team. Improvements to the transverse load distribution characteristics of longitudinal CLT panel bridges decks would benefit the design and rating of these bridges.

Because of their structural characteristics, CLT panels lend themselves well to being used for highway bridge structures. The data prove their performance to be uniform and predictable. Strain profiles through the depth of the panel indicate the panel remains linear through the full load range. The data also prove the performance to be within the prescribed guidance by the AASHTO Load and Resistance Factor Design [6] for timber bridge structures with the exception of the recommended deflection limits of L/425. This recommended limit is to aid the bridge deck serviceability, not to set limits for structural adequacy. The performance of overlay wearing surfaces are most sensitive to higher deflection magnitudes, which can result in maintenance costs for the bridge owner. An increase in the panel depth, improved transverse load distribution, or shorter span lengths can simply reduce the panel deflection.

ACKNOWLEDGEMENTS

Partial funding for this laboratory project was provided by the U.S. Department of Agriculture, Forest Service, Forest Products Laboratory. The CLT panels used in the project were manufactured by SmartLam North America. Threaded fasteners along the longitudinal joint were from MTC solutions.

REFERENCES

[1] ANSI/APA PRG 320-2019, S*tandard for Performance-rated Cross-laminated Timber*, American National Standard Institute, USAPRG

[2] Karacabeyli, E. B. Douglas, eds. 2013. *CLT Handbook: Cross-laminated timber.* U.S. ed. Special Publication SP-529E. U.S. Department of Agriculture, Forest Service, Forest Products Laboratory, Binational Softwood Lumber Council.

[3] American Wood Council (AWC). 2018. *National Design Specification (NDS) for wood construction.* 2018 ed. ANSI/AWC NDS-2018. Leesburg, VA: AWC.

[4] Lefebvre D., Richard G.: Design and construction of a 160-Metre-Long Wood Bridge in Mistissini, Quebec, Internationales Holzbau-Forum, 2014.

[5] Egorov V., Poirier L., Levesque M.: Conception et construction d'un pont a Chibougamau, 2011.

[6] AASHTO 2020. *AASHTO Load and Resistance Factor Design (LRFD) Bridge Design Specifications*. Ninth Edition, LRFD BDS-9 American Association of State Highway and Transportation Officials, Washington, DC.

[7] International Code Council. International Building Code. Falls Church, VA. International Code Council, 2021.

[8] Dahlberg, J., Liu, Z., Phares, B., Wacker, J., *Analytical and Testing Methods for Rating Longitudinal Laminated Timber Slab Bridges.,* WisDOT ID no. 0092-20-01, 2021.

World Conference on Timber Engineering Oslo 2023

COMPRESSIVE STIFFNESS PARALLEL TO GRAIN IN TIMBER

Marina Totsuka[1], Robert Jockwer[2], Kenji Aoki[3], Masahiro Inayama[4]

ABSTRACT: This paper describes results and analysis of experiments of compressive stiffness parallel to grain of glulam, with the focus on the damage zones near loading plates and joints. To investigate the influence factors of physical properties and the mechanism of the damage zone near the loading plates or the joints, compression tests on 90 specimens were performed. As a result, it was observed that damage zones exist near the loading plates and the joints. The Young's modulus of the damage zone was approximately 2% of that of a common longitudinal modulus of elasticity. The lengths of the damage zone of wood-wood joints are larger than that of wood-steel joints. The length of the damage zone and its scatter increase as the width of the cross-section increases. In the specimens, the lengths of the damage zone were 0.7~4.7mm. Therefore, the length of the damage zone has a size effect of the cross-sectional area and depends on the processing accuracy on the contact surface. The size effect was evaluated by the strongest link model and the evaluation method of the compressive stiffness parallel to the grain was proposed.

KEYWORDS: Glulam, Damage zone, Compression parallel to grain, Joints, Connections, Timber

1 INTRODUCTION

In connections of timber buildings, the deformations under compression parallel to the grain are often ignored since the deformations under compression perpendicular to the grain are bigger than the deformations under compression parallel to the grain due to the anisotropy of wood. However, in high-rise timber buildings, we may need to consider the deformation under compression parallel to the grain as well [1].

The heterogeneity of the strains in members loaded in compression parallel to the grain of clear specimens was reported in papers [2, 3] (Choi et al. and Dahl and Malo). In compression parallel to the grain, it is observed that the largest strains are allocated near the loading plates [4] (Zink et al.), which create a zone often called the "damage zone" as shown in Fig. 1. The zone between these damage zones is referred to as the "middle zone". Xavier et al. [5] and Brabec et al. [6] investigated the behaviour of the damage zones, e.g. the length and the modulus of elasticity, in small clear specimens. In addition, Totsuka et al. [7] reported the heterogeneity of the strains of large-sawn-timber specimens and showed the possibility that the length of the damage zone increases with increasing widths of the loaded area and the length of the damage zone does not change when the full height of the specimens increases. However, there is no evaluation method of the damage zone and the behaviour of the damage zones in glulam specimens remains unsolved so far.

In this present work, the compressive stiffness parallel to the grain of glulam was investigated. The aims of this work are as follows:

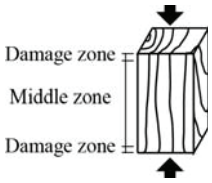

Figure 1: *Explanation of damage zone and middle zone*

(1) to clarify the influence factors of physical properties in the damage zone.
(2) to propose an evaluation method of compressive stiffness parallel to the grain.

2 EXPERIMENTAL WORK [8]

2.1 SPECIMENS AND TEST METHODS

Table 1 shows an overview of the test series of glulam specimens. The specimens were made from glulam of Norway Spruce (*Picea abies*) of quality GL30h according to SS-EN 14080:2013 [9], and Japanese cedar (*Cryptomeria japonica*) of quality E65-F255 and Japanese cypress (*Chamaecyparis obtusa*) of quality E95-F315 according to JAS (Japanese Agricultural Standards) [10]. The thickness of the glulam laminae was 42 mm for Norway Spruce and 30 mm for Japanese cedar and Japanese cypress. The width of the glulam laminae was the same as the specimen width. A total of 90 specimens were prepared by manufacturing 6 or 4 specimens per series. The test parameters are the size of the specimens and the type of joints (Fig.2). The specimens of series 20-3sSp had a 9mm steel plate. The specimens had typical wood characteristics, adhesive layers, and finger joints, however, the specimens of series 2.5-1Sp, 2.5-1Ce, and

[1] Marina Totsuka, Chiba University, Japan, mtotsuka@chiba-u.jp
[2] Robert Jockwer, Chalmers University of Technology, Sweden, robert.jockwer@chalmers.se
[3] Kenji Aoki, The University of Tokyo, Japan, aoken@g.ecc.u-tokyo.ac.jp
[4] Masahiro Inayama, The University of Tokyo, Japan, ainayama@g.ecc.u-tokyo.ac.jp

https://doi.org/10.52202/069179-0035

2.5-1Cy did not exhibit visual defects (knots and cracks) and did not have adhesive layers and finger joints.
The compression tests of the specimens were carried out with an in-line 3000 kN load cell and a spherically seated loading-head, an in-line displacement transducer under displacement control at a rate of 1 mm/min. The deformations and local strains were measured by the digital image correlation (DIC) system [11].

2.2 TEST RESULTS AND DISCUSSION

2.2.1 Compressive stiffness parallel to the grain

According to the equilibrium and linear elastic constitutive equations, the following closed-form solution can be obtained for the identification of the longitudinal modulus of elasticity:

Table 1: *Test series.*

Series	Species	#	Specimen size [mm]		Joint type
			A	*H*	
2.5-1Sp	Norway spruce	6	25×25	100	-
10-1Sp			100×100	100	-
20-1Sp			200×200	100	-
20-05Sp			200×200	50	-
20-3Sp			200×200	300	-
20-3bSp		4	200×200	300	Butt(Parallel)
20-3bxSp			200×200	300	Butt(Cross)
20-3sSp			200×200	300	Steel plate
2.5-1Ce	Japanese cedar	6	25×25	100	-
10-1Ce			100×100	100	-
20-1Ce			200×200	100	-
20-2Ce			200×200	200	-
2.5-1Cy	Japanese cypress	6	25×25	100	-
10-1Cy			100×100	100	-
20-1Cy			200×200	100	-
20-2Cy			200×200	200	-

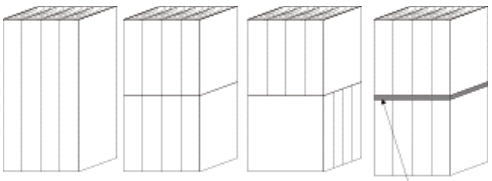

Table 2: *Mean statistics of specimens*

	Longitudinal modulus of elasticity in full height $E_{L,f}$ [N/mm^2]							
Mean	4383	4432	5349	6649	6823	6284	8242	10091
CV [%]	19	5	4	1	20	6	5	4
	Longitudinal modulus of elasticity in middle zone $E_{L,m}$ [N/mm^2]							
Mean	7549	8807	14318	9722	14966	15247	22575	14847
CV [%]	12	14	34	8	11	15	18	8

	Longitudinal modulus of elasticity in full height $E_{L,f}$ [N/mm^2]							
Mean	5327	4920	2507	1601	5510	2558	2381	2670
CV [%]	9	11	3	7	4	3	6	2
	Longitudinal modulus of elasticity in middle zone $E_{L,m}$ [N/mm^2]							
Mean	13155	12440	13950	13414	11865	13240	12500	14064
CV [%]	13	9	16	18	5	9	10	11

Note: CV is coefficient of variation.

$$E_{\mathrm{L}} = \frac{P}{A\varepsilon_1} \quad (1)$$

Where P is the applied compression load, A is the cross-sectional area (the loaded area), and ε_1 is the linear strain, from $0.2P_{\max}$ to $0.4\ P_{\max}$, along the longitudinal direction. In this study, two types of the E_L were calculated:
(1) the longitudinal modulus of elasticity in full height ($E_{L,f}$) using the ε_1 by the displacement transducers,
(2) the longitudinal modulus of elasticity in the middle zone ($E_{L,m}$) using the ε_1 in the middle zone measured by the DIC.
Table 2 shows the statistics of the specimens. The values of $E_{L,m,}$ were independent of the dimensions (height and width) of the specimens and the joint types. The mean values of $E_{L,m}$ were close to the literature values (7350 N/mm^2 for cedar and 11700 N/mm^2 for spruce[12], but no literature value for cypress) and considered to be equivalent to Young's modulus measured with a strain gauge or displacement meter attached to the middle of the test specimen. The mean values of $E_{L,m}$ of series 20-1Ce and 20-1Cy were bigger than those of the other series. The reason for this is unknown and further consideration will be needed to yield any findings about it.
Fig. 3 presents the influence of the heights and the widths of the loaded area on the values of $E_{L,f}$. The test results of solid timber of cedar [7] are also shown in Fig. 3 These values indicate mean values of the specimens with a cross-sectional area of 200×200 mm and 30×30 - 90×90 mm [7] for the influence of the heights and with a height of 100 mm and 30 - 90 mm [7] for the influence of the widths of the loaded area. The $E_{L,f}$ had an increasing trend as the height increased. This can be explained by the fact that the lengths of the damage zone do not change when the full height of the specimens increases. The $E_{L,f}$ had an increasing trend as the width of the loaded area decreased in the spruce-specimens and solid timber. This can be explained by the increasing lengths of the damage zone with the increase of the widths of the loaded area. However, the $E_{L,f}$ did not have an increasing trend in the cedar- and cypress-specimens. To clarify the mechanism of the damage zone, the damage zones were analysed in the following.

2.2.2 Strain field characterization and length of the damage zone

Fig. 4 shows an example of the deformation field of the longitudinal strain at 20% and 40% of the maximum load (P_{max}) of the series 10-1Sp by DIC. A damage zone near the loading plates or the joints and the middle zone can be recognized. The strain in the damage zone had a gradual distribution along with the height and exponentially increase as the distance from the loading plate or the joint

decreased. The phenomenon of the damage zone near the loading plates is in agreement with the observations made by Brabec [6]. The maximum strain is dependent on the load, but the length of the damage zone at 20% of the P_{max} was almost the same as that at 40% of the P_{max}.

Fig. 5 shows the longitudinal strain curves at 20% of the P_{max} of the specimens by DIC. The length of the damage zone seemed to be independent of the height, but the length of the damage zone increases as the loaded area increases. A detailed discussion of the length of the damage zone is provided in Fig.6-8. Fig. 5 (f)(g)(h) shows the longitudinal strain curves of wood-wood joints and wood-steel joints. The damage zones were also observed near the wood-wood joints and wood-steel joints, as well as near the loading plates.

Where the damage zone was defined at a strain ε_1 of -0.2% and less at 20% of P_{max}, the average lengths of the damage zone were 0.9 mm in 2.5-1Ce, 0.7 mm in 2.5-1Cy, 1.1 mm in 2.5-1Sp, 0.7 mm in 10-1Ce, 0.9 mm in 10-1Cy, 2.3 mm in 10-1Sp, 1.3 mm of the cedar- specimens with 200 mm, 1.0 mm of the cypress-specimens with 200 mm, and 4.7 mm of the spruce specimens with 200 mm width. Positive correlations were suggested between the length of damage zone and the width of the cross-section with correlation coefficients of +0.52 for the cedar-specimens, +0.41 for the cypress-specimens and +0.81 for the spruce-specimens. The length of the damage zone and its scatter increase as the width of the cross-section increases. This trend was especially remarkable in the spruce specimens. It was probably because the spruce specimens were processed on a different machine and the processing of the spruce specimens was rougher than that of the cedar- and cypress-specimens. The cedar- and cypress-specimens were processed on the same machine. The surface roughness of the contacted area is likely to increase as the cross-sectional area of the specimens increase. In other words, the length of the damage zone may depend on the accuracy of the processing machine. On the other hand, lower or negligible correlations between the length of the damage zone and the height of the specimen were indicated with correlation coefficients of +0.24 for the cedar-specimens, +0.46 for the cypress-specimens and +0.17 for the spruce-specimens in Fig.7. The length of the

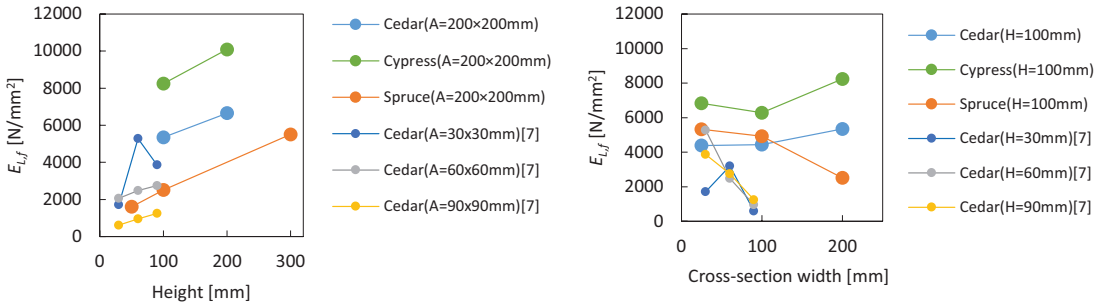

(a)Height vs. $E_{L,f}$ (b)Cross-section width vs. $E_{L,f}$

Figure 3: *Influence of heights and widths of cross-sectional area on values of EL,f .*

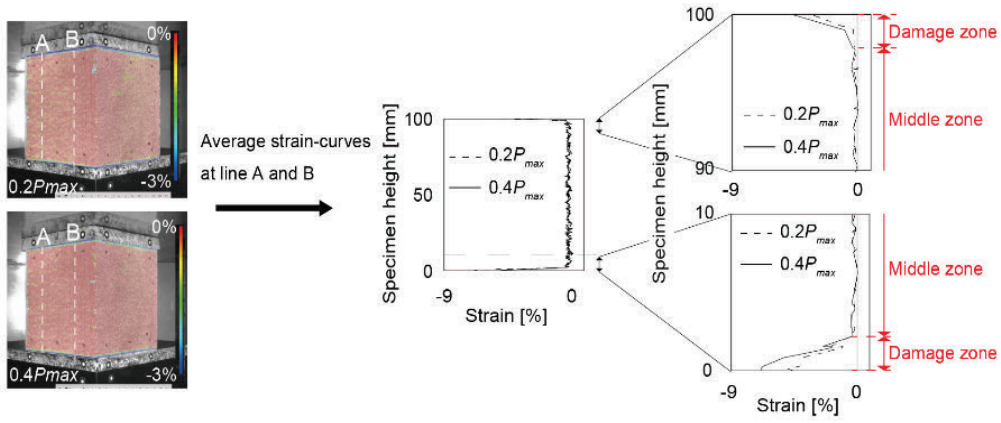

(a) Deformation fields of longitudinal strain (b) Average of the line A and B of 0.2 and 0.4 P_{max}

Figure 4*: Longitudinal strains of specimen 10-1Ce at 0.2 and 0.4 Pmax by DIC*

https://doi.org/10.52202/069179-0035

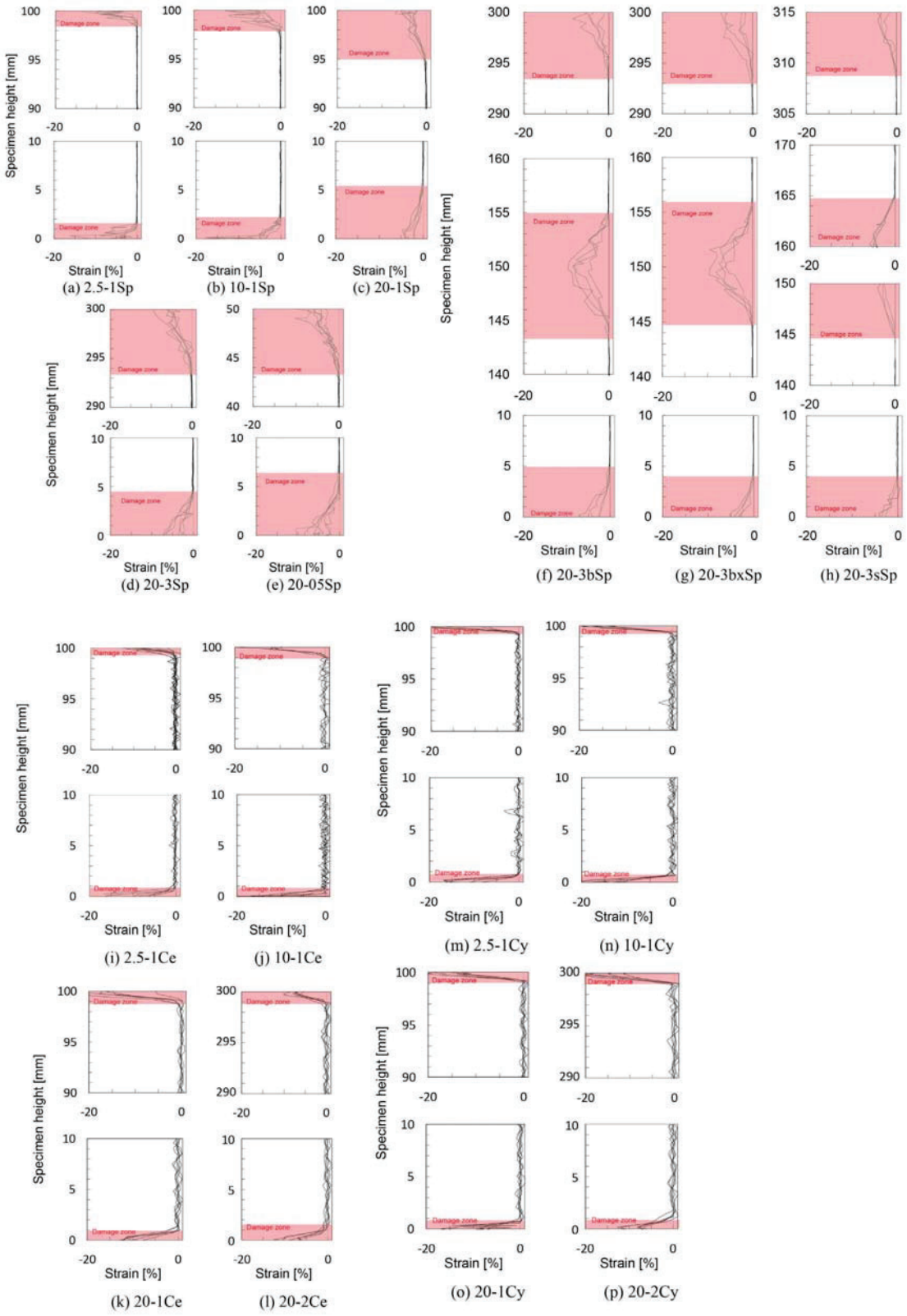

Figure 5: *Longitudinal strains distribution of specimens near loading plates in 0.2 Pmax*

https://doi.org/10.52202/069179-0035

damage zone did not change when the height of the specimen changed.

Fig.8 shows the length of the damage zone near wood-wood joints and wood-steel joints. It was considered that the lengths of the damage zone of wood-wood joints are larger than that of wood-steel joints.

3 EVALUATION METHOD OF COMPRESSIVE STIFFNESS

3.1 MODEL OF DEFORMATION DUE TO COMPRESSION PARALLEL TO GRAIN

A simple analytical spring model is used to evaluate the deformation of a specimen compressed parallel to the grain as shown in Fig. 9. If the Young's modulus is assumed to be constant in the damage zone, the specimen is modelled by two types of springs, and the stiffness at full height, K_f, is expressed by the following equations:

$$K_f = \frac{1}{\frac{2}{K_d} + \frac{1}{K_m}} = \frac{1}{\frac{2x}{0.02E_{L,m}A} + \frac{H-2x}{E_{L,m}A}} \quad (2)$$

where $E_{L.m}$ is the Young's modulus in the middle zone; A is the loaded area; H is the full height of the specimen; and x is the damage zone length.

In the previous study, Totsuka et al. [7] indicated that spreading effects in the compression parallel to the grain are small enough to be ignored for compressive stiffness. Therefore, the stiffness of specimens of partial compression are evaluated as the stiffness of specimens without margins.

3.2 DAMAGE ZONE LENGTH

The damage zone was considered to occur on the cut RT surface as shown in Fig. 10. The strongest link model was used to evaluate that the damage zone length and its scatter increased as the loaded area increased. The strongest link model [13] is the opposite of the weakest link model [14], in which a certain property (in this study, the damage zone length) is determined by the strongest (longest) element, as shown in Fig. 11. The probability $\boldsymbol{F_x}(x)$ that the length y of an element in a unit area is less than or equal to the length x is assumed to be a two-parameter Weibull distribution with the following equation:

$$\boldsymbol{F_x}(x) = 1 - e^{-\left(\frac{x}{x_0}\right)^m}, \quad (3)$$

where x_0 and m are the material parameters that define the magnitude and scatter in strength. In the model shown in Fig. 11, if all element lengths y are less than or equal to length x, the damage zone length is x. Therefore, when there are n elements, the probability $\boldsymbol{F_x}(x)$ that all element lengths y are less than or equal to x is expressed by the cumulative distribution function, given by the following equation:

$$\boldsymbol{F_x}(x) = \left(1 - e^{-\left(\frac{x}{x_0}\right)^m}\right)^n \quad (4)$$

For a specimen of a loaded area A, n can be replaced by A. Therefore, the probability $\boldsymbol{F_x}(x)$ is expressed by the following equation:

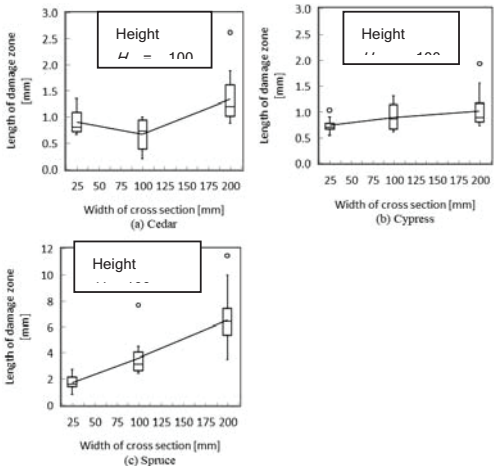

Figure 6: *Length of damage zone of specimens of varying widths of cross-section*

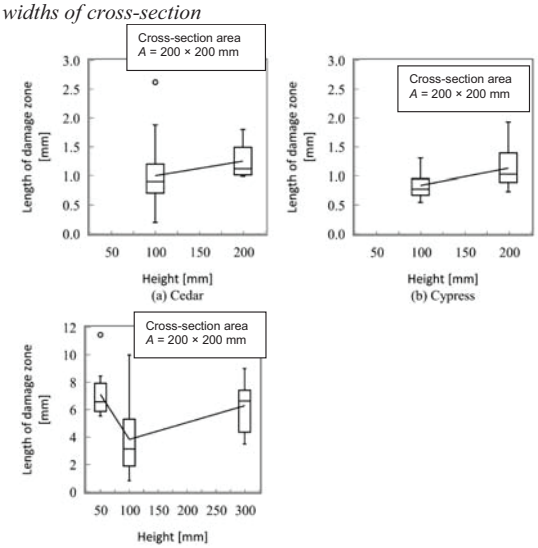

Figure 7: *Length of damage zone of specimens of varying heights*

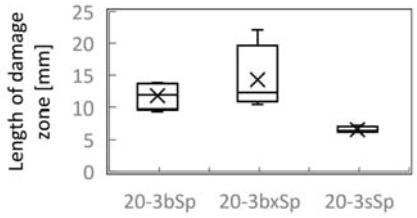

Figure 8: *Length of damage zone of specimens with wood-wood joints and wood-steel joints.*

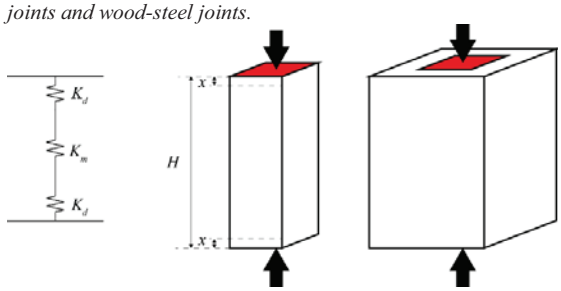

Figure 9: *Spring model of specimen compressed parallel to grain.*

https://doi.org/10.52202/069179-0035

$$\boldsymbol{F_x}(x) = \left(1 - e^{-\left(\frac{x}{x_0}\right)^m}\right)^A \quad (5)$$

Fig. 12 shows the cumulative probability distribution of the damage zone length obtained from the experiments and Eq. 5 with the material parameters, which are close to the experimental value. The solid line in the figure represents the experimental value, and the dashed line represents Eq. 5. The cumulative probability distributions of the experimental results can be successfully represented by the distributions of the strongest link model in Eq. 5, although the agreement was not perfect owing to the small number of specimens. Therefore, the size effect on the damage zone length can be explained by the strongest link model using the Weibull distribution.

In the strongest link model, the relationship between the damage zone lengths with loaded areas A_1 and A_2 can be as follows:

$$\boldsymbol{F_x}(x)^{\frac{1}{A}} = 1 - e^{-\left(\frac{x}{x_0}\right)^m} \quad (6)$$

$$1 - \boldsymbol{F_x}(x)^{\frac{1}{A}} = e^{-\left(\frac{x}{x_0}\right)^m} \quad (7)$$

$$\ln\left(1 - \boldsymbol{F_x}(x)^{\frac{1}{A}}\right) = -\left(\frac{x}{x_0}\right)^m \quad (8)$$

$$\left(-\ln\left(1 - \boldsymbol{F_x}(x)^{\frac{1}{A}}\right)\right)^{\frac{1}{m}} = \frac{x}{x_0} \quad (9)$$

If m, x_0, and $\boldsymbol{F_x}(x)$ are equal in the loaded areas A_1 and A_2, the relationship between the damage zone lengths x_1 and x_2 of the specimen with loaded areas A_1 and A_2 is as follows:

$$\frac{x_1}{x_2} = \left(\frac{\ln\left(1 - \boldsymbol{F_x}(x)^{\frac{1}{A_1}}\right)}{\ln\left(1 - \boldsymbol{F_x}(x)^{\frac{1}{A_2}}\right)}\right)^{\frac{1}{m}} = \left(\frac{\ln\left(1 - \boldsymbol{F_x}(x)^{\frac{1}{A_1}}\right)}{\ln\left(1 - \boldsymbol{F_x}(x)^{\frac{1}{A_2}}\right)}\right)^{k} \quad (10)$$

Where k is the size effect parameter. Fig. 13 shows the experimental results and approximate curves for Eq. 10 with the test of a 25 mm square section as the benchmark specimen (x_2 and A_2) when the cumulative probability is 50%. The size effect parameter k was 0.62 for cedar, 0.42 for cypress, and 3.12 for spruce specimens. The size effect parameter k of the strongest link model was similar to that of the weakest link model, indicating that the larger the parameter k, the larger the size effect.

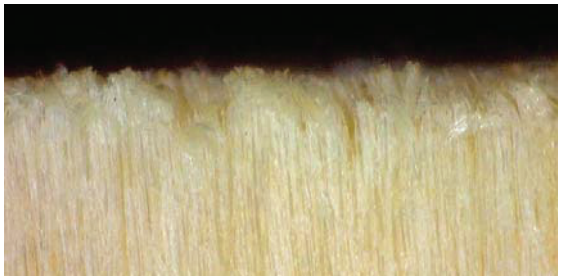

Figure 10: *Photo of cut RT surface.*

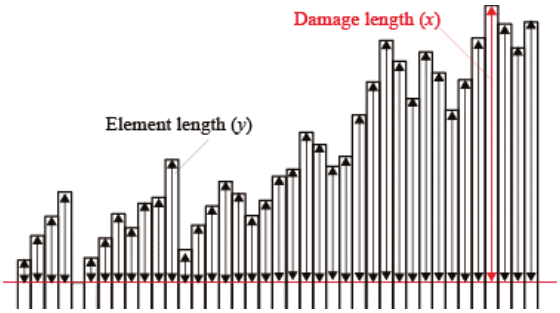

Figure 11: *Strongest link model of length of damage zone.*

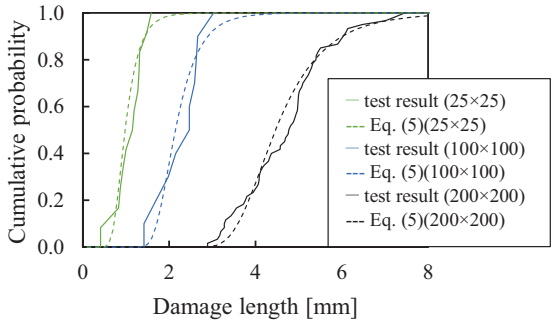

(a) Cumulative probability distribution of the damage zone length (Spruce)

Cross-sectional area [mm²]	25×25	100×100	200×200
A	625.00	10000	40000
x_0	0.05	0.05	0.05
m	0.479	0.601	0.645

(b) Material parameters (Spruce).

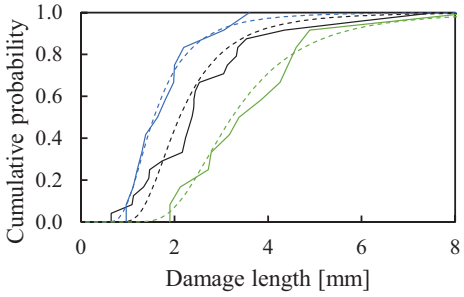

(c) Cumulative probability distribution of the damage zone length (Cedar)

Cross-sectional area [mm²]	25×25	100×100	200×200
A	625.00	10000	40000
x_0	0.0005	0.001	0.05
m	0.287	0.307	0.460

(d) material parameters (Cedar)

https://doi.org/10.52202/069179-0035

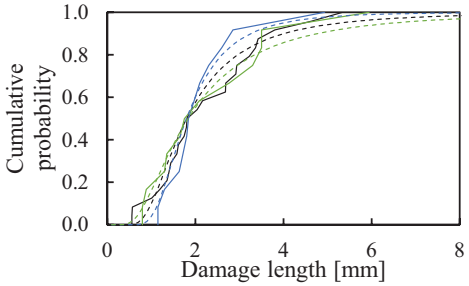

(e) Cumulative probability distribution of the damage zone length (Cypress)

Cross-sectional area [mm²]	25×25	100×100	200×200
A	625.00	10000	40000
x_0	0.001	0.001	0.00001
m	0.255	0.301	0.198

(f) material parameters (Cypress)

Figure 12: *Comparison of cumulative probability distribution of experimental result and Eq. 5.*

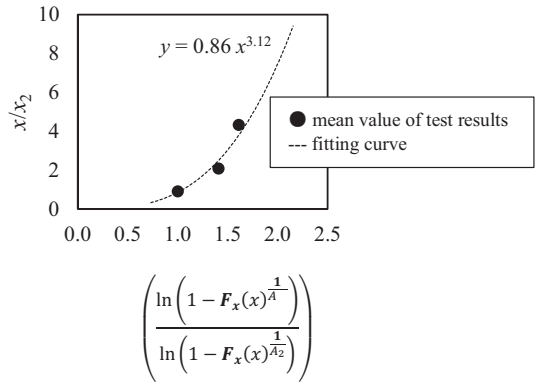

(a) Spruce specimens

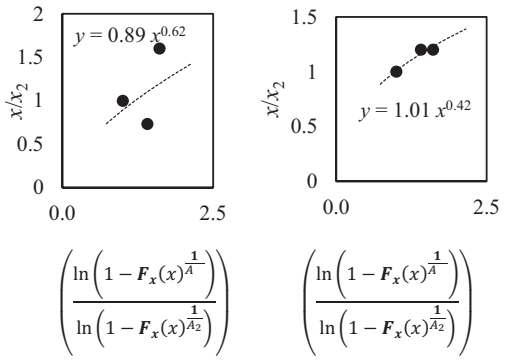

(b) Cedar specimens (c) Cypress specimens

Figure 13: *Experimental results and approximate curves for Eq. 10 when the cumulative probability is 50%.*

3.3 YOUNG'S MODULUS OF DAMAGE ZONE

The experimental value of the Young's modulus of the damage zone in Table 3 was calculated using Eq. 2 with the experimental data (mean value) in Table 2. The Young's modulus of the damage zone was 128-464 N/mm² for the spruce, 61-574 N/mm² for the cedar, and 98-491 N/mm² for the cypress specimens. The Young's modulus of the damage zone was higher for Japanese cypress than for cedar, even though the two specimens were processed by the same machine. Fig. 14 shows the ratio of the Young's modulus of the damage zone to the Young's modulus of the middle zone. No correlation was found between this ratio and wood species or dimensions of the specimen. The mean values of the Young's modulus ratios were 2.1% for the spruce, 2.4% for the cedar, and 1.5% for the cypress specimens, respectively. Therefore, the Young's modulus of the damage zone is considered to be approximately 2% of the Young's modulus of the middle zone.

Table 3: *Young's modulus of the damage zone*

Series [8]	Mean [N/mm²]	CV [%]
2.5-1Sp	197	19.0
10-1Sp	350	14.0
20-1Sp	293	8.33
20-05Sp	349	19.0
20-3Sp	304	16.2
20-3bSp	186	15.7
20-3bxSp	185	10.7
20-3sSp	196	13.0
2.5-1Ce	208	39.9
10-1Ce	118	38.3
20-1Ce	290	48.5
20-2Ce	270	27.4
2.5-1Cy	193	37.1
10-1Cy	192	22.9
20-1Cy	236	17.0
20-2Cy	359	21.2

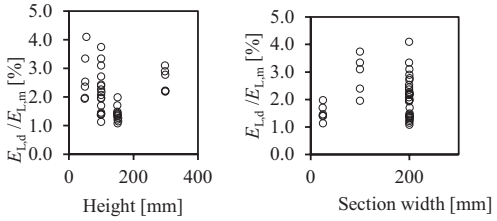

(a) Spruce specimens

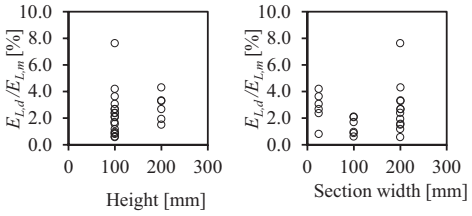

(b) Cedar specimens

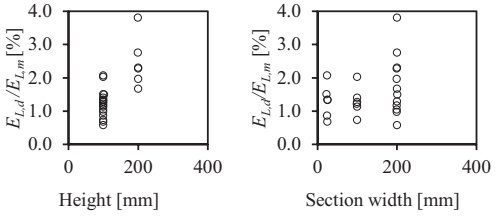

(c) Cypress specimens

Figure 14: Ratio of Young's modulus of damage zone to Young's modulus of the middle zone.

https://doi.org/10.52202/069179-0035

3.4 EXPERIMENTAL RESULTS AND CALCULATED RESULTS

The stiffness of the compression parallel to the grain can be evaluated using the following equations:

$$K_f = \frac{1}{\frac{2}{K_d} + \frac{1}{K_m}} = \frac{1}{\frac{2x}{0.02E_{L,m}A} + \frac{H-2x}{E_{L,m}A}} \quad (11)$$

$$x = \left(\frac{\ln\left(1 - \boldsymbol{F_x}(x)^{\frac{1}{A}}\right)}{\ln\left(1 - \boldsymbol{F_x}(x)^{\frac{1}{A_s}}\right)} \right)^{k} x_s \quad (12)$$

To shorten x, the size effect parameter should be small, and machining that does not increase the surface roughness significantly is recommended. Since a specimen with a smaller loaded area is less susceptible to the effects of machining accuracy, it is recommended that the benchmark specimen have a loaded area as small as possible (in this study, an ASTM 143 specimen, R25×T25×L100 mm, was used). The cumulative probability should be set to 50%, considering that the mean value is typically used as the stiffness of the joint in timber buildings. If the loaded area of the benchmark specimen is 25 mm square and the cumulative probability is 50%, Eq. 12 becomes:

$$x = \left(\frac{\ln\left(1 - 0.5^{\frac{1}{A}}\right)}{-6.8} \right)^{k} x_s \quad (13)$$

Fig. 15 shows the value calculated using Eq. 11 and 13 along with the experimental values of the stiffness K_f. The parameters k and x_s inserted in Eq. 13 were 3.12 and 0.86 for spruce specimens, 0.62 and 0.89 for cedar specimens, and 0.42 and 1.01 for cypress specimens, as shown in Fig. 13. The calculated values are considered to be satisfactorily close to the experimental values.

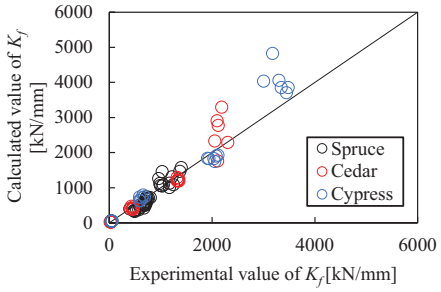

Figure 15: *Calculated value and experimental value of compressive stiffness parallel to the grain*

4 CONCLUSIONS

The properties of the damage zone of timber compressed parallel to the grain were studied using experimental results and computational models. The damage zone length and its scatter increased as the loaded area increased. No correlation was found between the ratio of the Young's modulus of the damage zone to the Young's modulus of the middle zone and the wood species or dimensions. The Young's modulus of the damage zone was approximately 2% of that of the middle zone. In addition, an evaluation method for the damage zone length is proposed using the strongest link model to consider the size effect of the damage zone length. The Young's modulus and damage zone length evaluation methods obtained above were used to evaluate the stiffness of the specimens compressed parallel to the grain. The proposed method could evaluate the experimental values reasonably well.

In the future, the proposed method for the damage zone can be applied to a variety of timber connections.

ACKNOWLEDGEMENT

This work was supported by a Grant-in-Aid for JSPS Research Fellows Number JP19J13253 and Grant-in-Aid for Young Scientists(Start-up) 21K204583.

REFERENCES

[1] M. Totsuka, J. Hayakawa, K. Aoki, M. Inayama (2022) Evaluation of stiffness parallel to grain of wood based on strongest link model, Journal of Structural and Construction Engineering (Transactions of AIJ),87(798): 770-779, doi.org/10.3130/aijs.87.770.

[2] Choi D, Thorpe JL, Hanna RB (1991) Image analysis to measure strain in wood and paper. Wood Sci Technol 25:251–262. doi. org/ 10. 1007/BF002 25465

[3] Dahl KB, Malo KA (2009) Planar strain measurements on wood specimens. Exp Mech 49:575–586. doi. org/ 10. 1007/ s11340-008- 9162-0

[4] A.G. Zink, R.W. Davidson, R.B. Hanna (1995) Strain measurement in wood using a digital image correlation technique, *Wood Fiber Sci.* 27 346–359.

[5] J. Xavier, A.M.P. de Jesus, J.J.L. Morais, J.M.T. Pinto (2012) Stereovision measurements on evaluating the modulus of elasticity of wood by compression tests parallel to the grain, *Constr. Build. Mater.* 26 207–215.doi.org:10.1016/j.conbuildmat.2011.06.012.

[6] M. Brabec, J. Tippner, V. Sebera, J. Milch, P. Rademacher, Standard and non-standard deformation behavior of European beech and Norway spruce during compression, *Holzforschung.* 69 1107–1116,2015. doi.org:10.1515/hf-2014-0231.

[7] M. Totsuka, R. Jockwer, K. Aoki, M. Inayama, Experimental study on partial compression parallel to grain of solid timber, *J. Wood Sci.* 67 2021. doi.org:10.1186/s10086-021-01972-w.

[8] Totsuka M, Jockwer R, Kawahara H, Aoki K, Inayama M (2022) Experimental study of compressive properties parallel to grain of glulam. J Wood Sci., 68:33. doi.org/10.1186/s10086-022-02040-7.

[9] SS-EN 14080 (2013) Timber structures—Glued laminated timber and glued solid timber—requirements. Swedish Institute for Standards. Stockholm.

[10] Japanese agricultural standards notice no. 1587 (2012) Glulam. Ministry of Agriculture. Forestry and Fisheries. Tokyo (In Japanese)

[11] GOM Correlate (GOM GmbH, Germany).

[12] Ringyo-shikenjo, (ed) (1958) Mokuzai kogyo handbook. Maruzen, Tokyo

[13] Gustafsson PJ, Jockwer R, Serrano E, Steiger R.(2015) A strongest link model applied to fracture propagating along grain. Proceedings of meeting 48. International network on timber engineering research. Timber Press Scientific, p. 351–66.

[14] Weibull W. (1939) A statistical theory of the strength of materials, R. Swedish Inst. J Eng Res. 151:1–45.

World Conference on Timber Engineering Oslo 2023

COMPARISON OF THE DEGREE OF INFLUENCE OF VARIOUS CONDITIONS ON THE BEARING CAPACITY OF WOOD-BASED PANELS

Ryutaro Sudo[1], Kenji Aoki[1],

ABSTRACT: Bearing property is important for the design of the connection. There are few studies about the bearing property of the wood-based panels. First, the tensile bearing test of the wood-based panels: Plywood and OSB of strong and weak axial specification, was conducted based on the comprehensive parameters. Test parameters were set as dowel insertion position, size of pilot hole and dowel diameter. The correlation between parameters and the mechanical characteristics: failure behavior, ductility, yield stress and maximum stress, was verified. To verify how much each parameter effect on maximum stress, standardized multiple regression analysis was conducted. These results provide insights into the failure behavior and stress distribution, supporting certain assumptions: (1) PW and OSB is deformed dominantly in-plane and out-of-plane respectively; (2) the relative stress spread range is decreased with the larger diameter of the dowel; (3) the stress spread range is widened by load step; and (4) the bearing stress is spread vertically and horizontally in strong and weak specification respectively, also verified in this section. A detailed investigation was performed using DIC and CT scanning techniques to shed light on the stress distribution and fracture processes. Three load steps were configured and subjected to cyclic loading. Verification and comparison were carried out for each specification, layer, and step, providing a clearer understanding of the stress distribution and fracture processes. These results are consistent with the conclusions drawn from the comprehensive testing.

KEYWORDS: Bearing, Wood-based panel, Plywood, OSB, Standardized multiple regression analysis, DIC, CT scan

1 INTRODUCTION

The structural properties of wood structures are greatly affected by the property of joints. Their behavior depends on the characteristics when the circular joints are embedding into the material, the bearing properties. There have been many studies on the bearing properties of timber[1)2)]. On the other hand, though studies on the bearing capacity of wood-based panels include Sekino et al.'s study on particle board[3)] and Ogawa et al.'s study on the bearing capacity of plywood[4)], there are only a few studies that have comprehensively examined the parameters and considered how the various conditions affect the bearing properties and how the degree of influence varies depending on the type of panels. The underlying mechanism of fracture remains elusive, which represents a crucial foundation for the development of theoretical equations for determining characteristic values.

The primary objective of this report is to systematically investigate the degree to which various conditions exert an influence on mechanical properties under the bearing stress of plywood (PW) and oriented strand board (OSB) through comprehensive testing. Additionally, the process of stress spread, and fracture was clarified by utilizing digital image correlation (DIC) and computed tomography (CT) scanning techniques.

2 STUDY BASED ON EXHAUSTIVE PARAMETERS

2.1 Material and method

The panels to be tested were 5-ply cedar PW[5)] and OSB[6)] for structural use. Since PW and OSB were orthotropy material, the test was conducted in both strong and weak axes. In addition, a trailing "-s" (e.g., PW-s) indicates a strong axial specification, whereas a trailing "-w" (e.g., PW-w) indicates a weak axial specification. Their thickness was 9mm. The detail properties of the panels are shown in Table 1. Other parameters were set as dowel diameter *d* (5.2 and 12mm), position (A~G), as shown in Figure

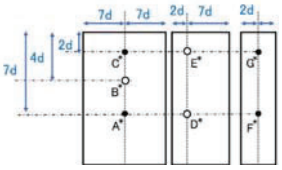

Figure 1: *Parameters of bearing tests. * Name of Position. Tests of 4 kinds of ph were conducted at place of black circle. Tests of 2 kinds of ph (0, 1d) were conducted at place of white circle.*

[1] Ryutaro Sudo, Japan.Department of Biomaterials Sciences, Graduate School of Agricultural and Life Sciences, The University of Tokyo, 1-1-1
sudo-ryutaro282@g.ecc.u-tokyo.ac.jp

Kenji Aoki, The University of Tokyo, Japan.
aoken@g.ecc.u-tokyo.ac.jp

https://doi.org/10.52202/069179-0036

1, the size of the pilot hole *ph* (0, 1/3, 2/3 and 1 time to the diameter). Figure 1 also shows the combination of the position and *ph*. As a dowel (*d*=5.2mm), N150 nail (defined by JIS[7]) was used and, as the other dowel (*d*=12mm), a custom-made dowel was used, as shown in Figure 2. Number of the specimen were six per a specification.

Figure 2: *Schematic of 12mm pin.*

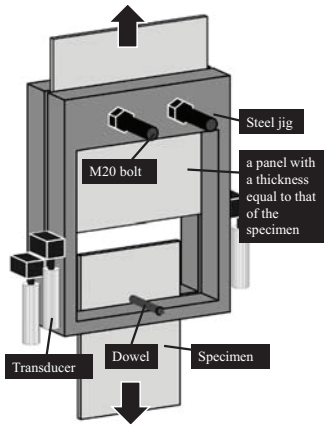

Figure 3: *Setting of bearing test.*

Bearing test was conducted as shown in Figure 3, applying shear force by sandwiching with a pair of steel plates with a rectangular hole. This jig was designed to enable to observe of the failure process and to eliminate depth clearance. The monotonical tensile load was applied to the specimen at 3~4mm/min (*d*=5.2mm) or at 6~7mm/min (*d*=12mm.). After the test, bending deformation of the dowel was not observed.

2.2 RESULT AND DISCUSSION

2.2.1 Failure mode

Two failure modes were observed as follows. One was shear failure at the area above dowel, as shown in Figure 4. It was named as "ESF (end shear failure)". The Other was tensile failure at the area next to the dowel, as shown in Figure 5. It was named as "STF (Side tension failure)". ESF was ductile failure, whereas STF was brittle failure. STF occurred only when the dowel position was D~G. The STF resembled a simple tensile failure, and it did not differ significantly among the panel types. Meanwhile, the ESF showed some differences among the panel types. Figure 6 shows a summary of the fracture progression during the test and the failure appearance of each panel after the test. In this figure, all parameters except the panel type are standardized uniformed (dowel position: A, *d*: 12 mm, *ph*: 1).

Figure 4: *The photo of ESF.*

Figure 5: *The photo of STF.*

Table 1: *Fundamental properties of wood-based structural panels.*

		Density (kg/m³)	MC (%)	In-plane Strength (MPa)	In-plane Elastic modulus (GPa)	Internal board Strength (MPa)	Internal board Elastic modulus (GPa)	In-plane Strength (MPa)	In-plane Elastic modulus (GPa)	Other information
PW	Ave.	416	11.1	13.5	5.28	0.930	0.0151	4.72	0.619	wood species; Cryptomeria japonica (Japanese cedar) Number of layers; 5, class; 2nd, use; for structural use [5].
	S. D.	20	1.2	4.0	1.56	0.245	0.0089	0.14	0.095	
OSB	Ave.	635	7.7	16.3	6.85	0.477	0.0098	9.97	1.838	Number of layers; 3, class; 4th [6].
	S. D.	42	0.7	4.1	0.96	0.147	0.0063	1.25	0.433	

Note: *Ave. means average, and S. D. means standard deviation. Three mechanical tests were conducted according to ASTM D 1037 [8].*

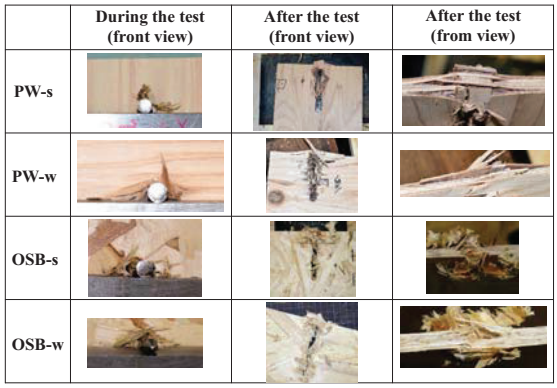

Figure 6: *Comparison of ESF behavior among panel types.*

The ESF mode exhibited two types of failure behavior: a crack on the surface of the panel generated by in-plane tensile or shear stress, termed "in-plane failure," and a peeled surface divided into several layers. The peeled surface failure is generated by the Poisson effect of the compressive stress immediately above the dowel and is termed "out-of-plane failure."

Although these two types of failure behavior generally occurred simultaneously, it was possible to identify the dominant failure behavior for each panel type.

After the test was completed, vertical and horizontal crack lines were observed in PW-s and PW-w, respectively. Although the layers of the specimens were separated after the test, they were only slightly peeled off. This separation of layers was caused by the difference in failure mode in the fiber direction of the veneer, not by the Poisson effect. Compared with the PW, the OSB did not show a clear clack line. Additionally, the surface layer of the OSB was peeled off more significantly than that of the PW. Therefore, based on a comparison between the PW and OSB, in-plane failure and out-of-plane failure were dominant in the PW and OSB, respectively.

To correlate these failure behaviors with the material property, the "in-to-out plane strength," which is defined by the tensile strength divided by the internal bond strength, was introduced. The in-to-out plane strengths of the PW and OSB were 14.6 and 34.6 respectively. A comparison of the in-to-out plane strength of panels shows that a panel with a higher in-to-out plane strength is dominated by the out-to-plane failure. The fracture mechanism is shown in Figure 7. These results suggests that the in-to-out plane strength is related to the failure behavior under the bearing pressure.

Number of specimens where STF occurred at D~G is shown in Table 2. About all of panels, STF more likely

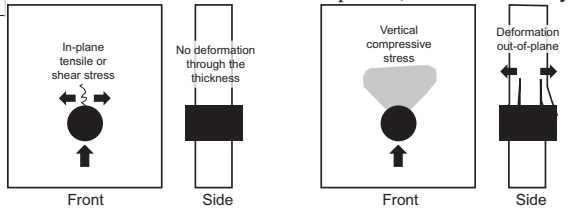

Figure 7: *Two fracture processes of ESF.*

https://doi.org/10.52202/069179-0036

Table 2: *Number of specimens where STF occurred.*

The dowel position	*ph*	PW-s		PW-w		OSB-s		OSB-w	
		d=5.2	*d*=12	*d*=5.2	*d*=12	*d*=5.2	*d*=12	*d*=5.2	*d*=12
D	0	3	2	5	3	3	2	5	4
	1	4	1	5	2	5	1	6	5
E	0	3	3	5	4	1	1	4	3
	1	4	0	5	4	1	2	2	3
F	0	3	3	6	0	6	4	6	5
	1/3	4	2	6	5	6	3	6	6
	2/3	5	2	6	4	4	3	6	6
	1	4	0	6	5	6	5	6	6
G	0	3	4	5	4	6	2	5	5
	1/3	3	2	5	4	5	3	5	6
	2/3	1	1	5	4	5	2	6	5
	1	2	0	3	3	6	0	6	4

occurred at the position of D and F than of E and G respectively. It is considered to be because ESF occurred earlier than STF when edge distance was short. This Table also indicates that STF more likely occurred when *d* was 5.2mm than when 12mm. According to some previous studies about embedment of timber[9)], stress spreading range is absolute range: not depending on the pressure area. Configurating the length of edge distance based on the diameter in this test, stress spreading range was wider relatively with d = 5.2mm than d = 12mm. Assuming that STF occurred when strong stress reached to the edge of specimen, this difference of the range is considered to result in the difference of the number of specimen where STF occurred. STF also more likely occurred loading in weak axis than in strong axis. This result suggests that horizontal stress spread range of weak axial specification was wider than that of strong one. Compared in the two kinds of panels, STF occurred more likely in OSB.

2.2.2 Evaluation method of characteristic value

Stress was calculated by dividing the load by the projection area of the dowel, after which the stress–displacement curves were obtained. Based on these displacement curves, the maximum stress σ_{max} (MPa), yield stress σ_y (MPa), and ultimate displacement u (mm) were derived using the method presented next.

A simple illustration of the method is shown in Figure 8. u was defined as the displacement at 80% of the maximum stress of the entire stress–displacement curve. σ_y was derived via the 5%-offset method using a linear elastic line in the linear range (i.e., offset the length to equal to 5% of the dowel diameter). Additionally, based on the cases where STF occurred, STF was shown to be

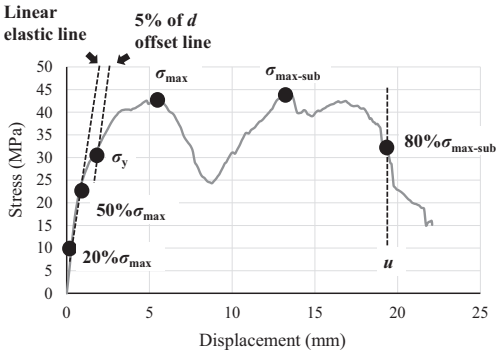

Figure 8: *Evaluation of characteristic values based on stress–displacement curve.*
Note: *The parameters of the specimen were as follows: panel type, PW-s; d, 5.2 mm; ph, 0; dowel position, A.*

a brittle failure, and the intersection between its curve and the offset line typically occurred after σ_{max}. In this case, σ_{max} was regarded as σ_y.

2.2.3 Comparison of ductility

The ultimate displacement is typically used to compare ductility. However, as the ultimate displacement measured in this study was significantly affected by the original end distance, it was not regarded as an appropriate indicator of ductility. Additionally, the original end distance was set based on d, and u is also affected by d. Hence, the remaining distance (*RD*) was introduced, which is derived by dividing the difference between u and the length of the original end distance by d. Figure 9 shows a comparison of the *RD* values. The shorter the *RD*, the higher is the ductility.

The trends observed in all the panel types were as follows: (1) The *RD* of A and B was similar, (2) the *RD* at D or F and their standard deviations were higher than those at any other dowel positions, and (3) the *RD* for d = 5.2 mm was typically higher than that for d = 12 mm.

First, the *RD* of A and B was similar, i.e., from 2 to 4. For the bearing of timber, if the ratio of the thickness to d is low and dowel bending is not observed, then brittle splitting will typically occur. For the bearing of wood-based panels, when the edge distance was sufficient, the failure mode was ductile, and the load did not decrease until the remaining end distance reached a certain value. This implies that the prevalent belief for timber is not valid for wood-based structural panels. This mechanism is independent of the original end distance.

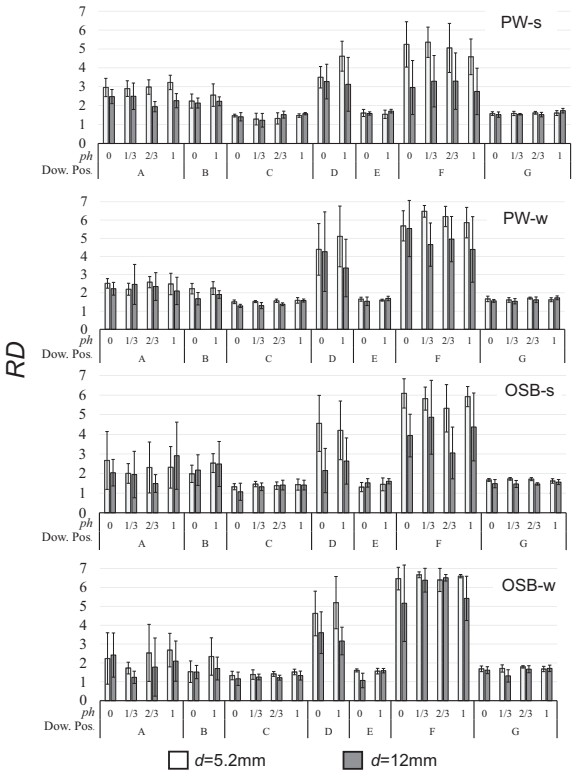

Figure 9: *Comparison of RD values.*
Note: *Dow. Pos. means dowel position. Error bars indicate standard deviation.*

https://doi.org/10.52202/069179-0036

Second, the values of *RD* at D or F and their standard deviations were higher than those at any other dowel positions. As described previously, the failure mode at dowel position D or F was STF in some cases and brittle. Consequently, the values of *RD* at D and F were high. In addition, a mixture of failures involving both ESF and STF occurred in the same specification, which resulted in a significant variation in the *RD*.

Third, the *RD* for d = 5.2 mm was higher than that for d = 12 mm. As described above, the spreading range of the horizontal stress was assumed to be larger when d = 5.2 mm in comparison with d = 12 mm. Therefore, the results at positions D–G, where STF is likely, can be theorized as in the previous section. Although ESF occurred at dowel positions A–C, the same justification can be used to explain these results, assuming the spreading range of the longitudinal relative stress was also larger when d = 5.2 mm. Therefore, this suggests that the relative stress spreading range was larger both horizontally and vertically when d = 5.2 mm in comparison with d = 12 mm.

A comparison of the *RD* values based on calculated "strong axial specification - weak axial specification" values for the PW and OSB are shown in Figure 10.

The values were positive at positions A–C and negative at positions D and F for both the PW and OSB. In the weak axial specification, STF occurred more frequently, and the *RD* was higher, as described above. Therefore, the values were negative at positions D and F. To account for the results at positions A–C, it is necessary to assume that the vertical stress spreading range is important for the *RD* when ESF occurs and that the vertical stress spreading range is larger in the strong axial specification. This makes it easier for stress to reach the top end and causes earlier fracture of the strong axial specification. These results suggest that the stress spreading range of the strong axial specification was larger vertically and smaller horizontally than that of the weak axial specification.

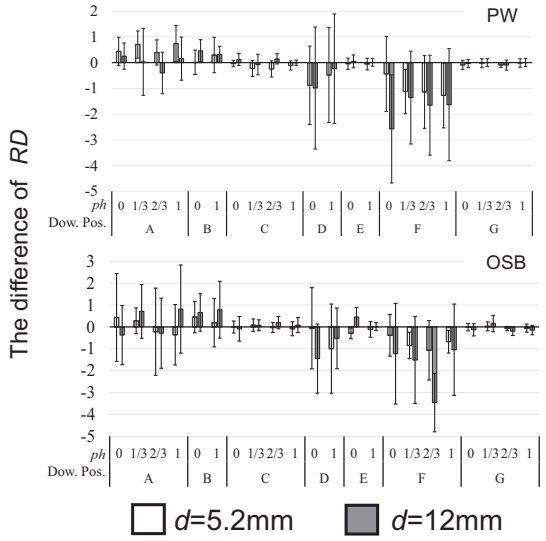

Figure 10: *Comparison of RD differences between strong and weak axial specifications.*
Note: *Values of "strong axial specification - weak axial specification" are presented.*
Error bars indicate standard deviation.

2.2.4 Standardized multiple regression analysis of characteristic values

To quantitatively verify how much each parameter had an influence on each characteristic value, SMRA was conducted.

The characteristic values with five explanatory variables are expressed in Eq. 1.

$$y = \sum_{i=1}^{5} a_i x_i + \epsilon\,, \tag{1}$$

where y is the objective variable, x_i is the explanatory variable, a_i is its partial regression coefficient, and ε is the error.

Five explanatory variables were set as follows: dowel diameter d (mm), ratio of the pilot hole *ph*, ratio of the end distance to the diameter *e*, variable *side2* that equals to 1 when the dowel position was D or E and 0 otherwise, and variable *side3* that equals to 1 when the dowel position was F or G and 0 otherwise. Additionally, σ_{max} and σ_y were set as the objective variables. Each variable was standardized to have a mean of 0 and standard deviation of 1 using Eq. 2 before analysis.

$$\bar{p} = \frac{p - \mu}{\sigma}\,, \tag{2}$$

where p is the original value, $\bar{p}$ is the standardized value, μ is the average value, and σ is the standard deviation.

Supposing that the variable with the upper line indicates they have been standardized, Eq. 1 can be rewritten as in Eq. 3.

$$\bar{y} = \sum_{i=1}^{5} a_i \bar{x_i} + \epsilon \tag{3}$$

The partial regression coefficients are representative of the influence degree of the parameter on the characteristic value. Therefore, this value can reveal the dominant influencing factor.

A comparison of the values of the partial regression coefficient is shown in Figure 11.

As shown in Figure 11, the overall results of σ_y and σ_{max} are roughly the same, but the degree of how the value is spread varies. Figure 11 indicates that *ph* had a stronger influence on σ_y than on σ_{max}. It also indicates that *e*, *side2*, and *side3* had a stronger influence on σ_{max} than on σ_y. These results are consistent where the stress redistribution increased the stress spreading range at σ_{max}. Based on this assumption, the nailed damaged area was not small enough to ignore at σ_y, the stress spreading range widened at σ_{max} and the damaged area narrowed relatively. Similarly, even when the end or edge distance was narrow, it had no effect on σ_y because the stress spreading range at σ_y was also small. However, when the stress spreading range widened to some extent at σ_{max}, the range reached the edge and affected the strength. Consequently, the coefficients for σ_y and σ_{max} would differ. However, this cannot be confirmed only by these results.

An analysis of the $a_{\bar{e}}$ of σ_{max} suggests that *e* exerted the strongest influence on the σ_{max} of the PW and a stronger

influence on the σ_{max} of the strong axial specifications than on their weak axial specifications. As described previously regarding the *RD*, the strong axial specification indicated a lower ductility than the weak axial specification when ESF occurred. This is assumedly attributable to the larger spread range of vertical stress in the strong axial specification. Based on this assumption, the σ_{max} of the strong specification will certainly be affected by *e*.

Based on a comparison between $a_{\overline{side2}}$ and $a_{\overline{side3}}$, the overall trends were similar and the absolute value of $a_{\overline{side3}}$ was larger than that of $a_{\overline{side2}}$. Additionally, the values of $a_{\overline{side2}}$and $a_{\overline{side3}}$ of σ_{max} were strongly negative for PW-w and OSB-w. In general, a large stress spreads horizontally when a compressive stress is applied in the direction perpendicular to the grain, and the spreading of this stress contributes to the strength [8]. Therefore, it is natural that the weak axial specification was highly influenced by the edge distance.

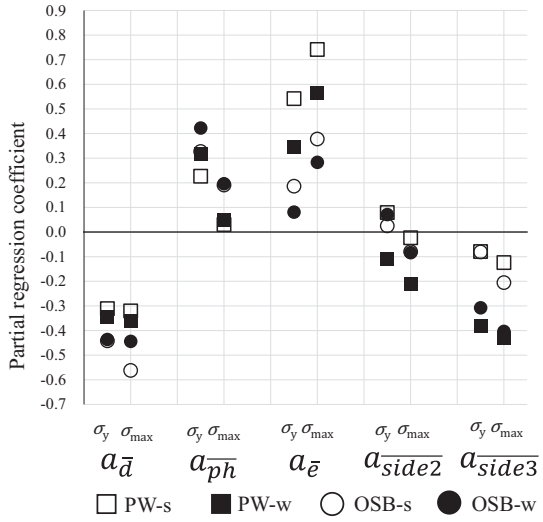

Figure 11: *Comparison of partial regression coefficients.*

3 STUDY BASED ON DETALED OBSEVATION

3.1 MATERIAL AND METHOD

In this section, the process of stress spread, and fracture was clarified by utilizing DIC and CT scanning. Additionally, the assumptions suggested in the previous section: (1) PW and OSB is deformed dominantly in-plane and out-of-plane respectively; (2) the relative stress spread range is decreased with the larger diameter of the dowel; (3) the stress spread range is widened by load step; and (4) the bearing stress is spread vertically and horizontally in strong and weak specification respectively, also verified in this section.

Parameter was *d* (5.2 and 12mm) and material (PW-s,w and OSB-s,w). *ph* was configurated as 1. Number of the specimen were two per a specification. The test setup was the same as in the previous section. Three test steps were set as shown in Figure 12 (1st step: 50% of the maximum load, 2nd step: maximum load, 3rd step: displacement equal to the diameter of the joint), and the force was applied and removed each time. DIC was conducted during load process and CT scanning was conducted after unloaded. In the 1st step, the average value of the maximum load in the previous section was used as the predicted value, and when the load reached 50% of this value, the test was stopped, and the specimen was unloaded. In the 2nd step, when the load dropped 0.01 kN, the specimen was considered to have reached a certain maximum load and was unloaded. The test speed was 0.5mm/min for *d*=5.2mm and 1mm/min for *d*=12mm in the first and second step. In the third step, the test speed was twice.

For DIC procedure, random black dots on a white surface was painted on the face of the specimen. The surface image was captured at frequency of 0.2 Hz in the loading process.

In the CT scanning, specimens were scanned at 200 kV/200 μA source output level, with no filters, scanning distance 962.5 mm to the specimen and 1400mm to the dictator, with 2000 angular projections (0.18 deg increments) and 0.75 second of exposure time per projection. The definition was 250 μ m/pixel.

3.2 RESULTS OF DIC TEST

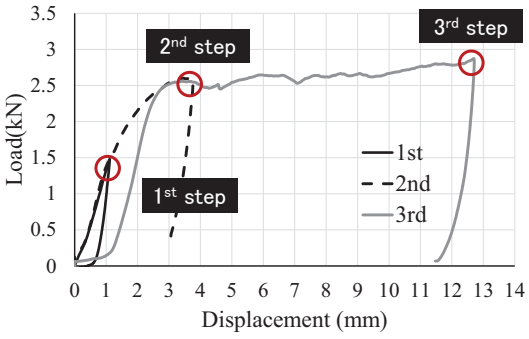

Figure 12: *Schematic of three steps.*

As shown in Figure 13, the *x*, *y* and shear strain distributions were obtained for five cross sections (load direction was regarded as *y* axis).

Figure 14 shows an example of the obtained strain distribution, which indicates that the strain is stronger in the central area than in other areas, and that some areas are not measured due to failure. We considered this area to be the local strain and fracture spread due to the bearing stress and measured the length of these areas by the following method. First, as shown in Figure 15, the mean μ and standard deviation σ of the

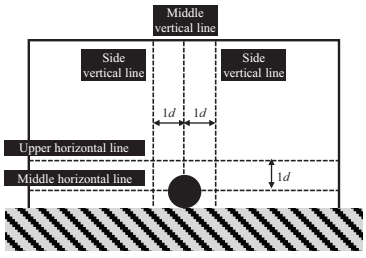

Figure 13: *Measurement line of DIC.*

https://doi.org/10.52202/069179-0036

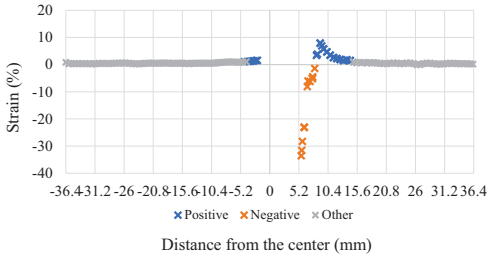

Figure 14: *Example of strain distribution.*
Note: *material; PW-w, cross section; Middle horizontal line, diameter; 5.2mm, step; 3rd, strain; y.*

strain in the range of 1~2 *d* from the left and right edges of the central horizontal section and the top of the central vertical section were calculated based on the strain. Then, we calculated the range of strain that was not measurable due to fracture over the entire cross-section: failure, the range of strain higher than $\mu+3\sigma$: positive, and the range of strain lower than $\mu-3\sigma$: negative. This process

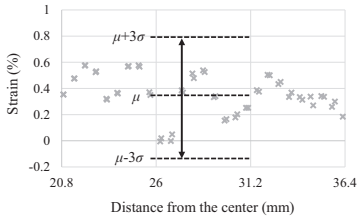

Figure 15: *Variation of the values of strain near the edge of specimen.*

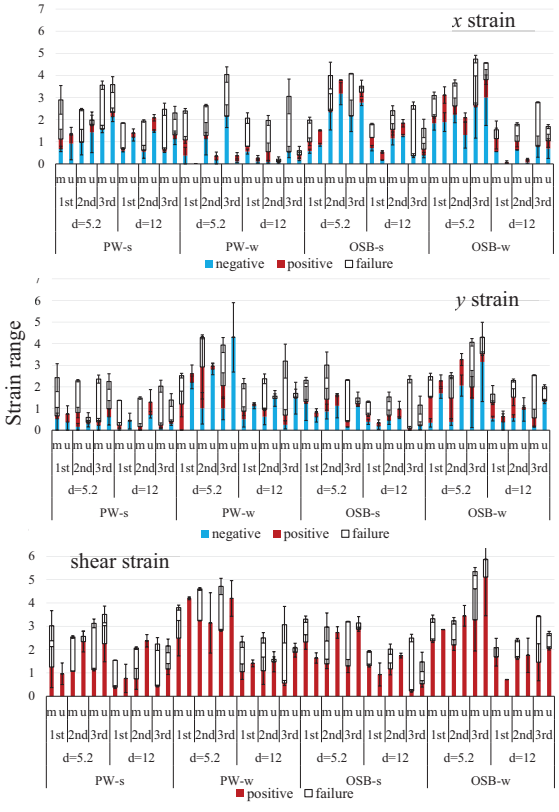

Figure 16: *Comparison of strain range of horizontal cross section.*
Note: *"1st", "2nd" and "3rd" indicate the test steps. "m" and "u" mean middle and upper horizontal cross section respectively.*

was conducted for each strain direction, specimen, and step. The value obtained was divided by *d*, and the standardized value was defined as "strain range".

Figure 16,17 shows comparison of strain ranges in the horizontal and vertical section respectively. The overall trend exhibited three distinct characteristics: I, the strain range was widened during each loading phase, particularly in the horizontal section; II, the relative strain range diminished with an increase in diameter; III, the strain range spread vertically and horizontally in the strong and weak axial specification respectively. The difference between strong and weak axial specification was more pronounced in PW. These results support the assumption referred in the previous section.

In PW-s, the range of vertical x-strain in the central and side sections exhibits positive and negative values, respectively. This outcome implies that the fiber was ruptured just above the dowel and concentrated on the lateral aspect of the dowel. This mechanism resulted in the compressive stress in the side section. The difference by *d* was smaller in PW-s than in any other panel type. The strain range was widened both horizontally and vertically during each loading phase.

The salient feature of the strain distribution in PW-w is that the y-strain spreads horizontally and extensively, akin to a stress distribution when timber is embedded laterally. The variation in *d* was substantial, which is likely attributed to the fact that the extent of spread is a fixed

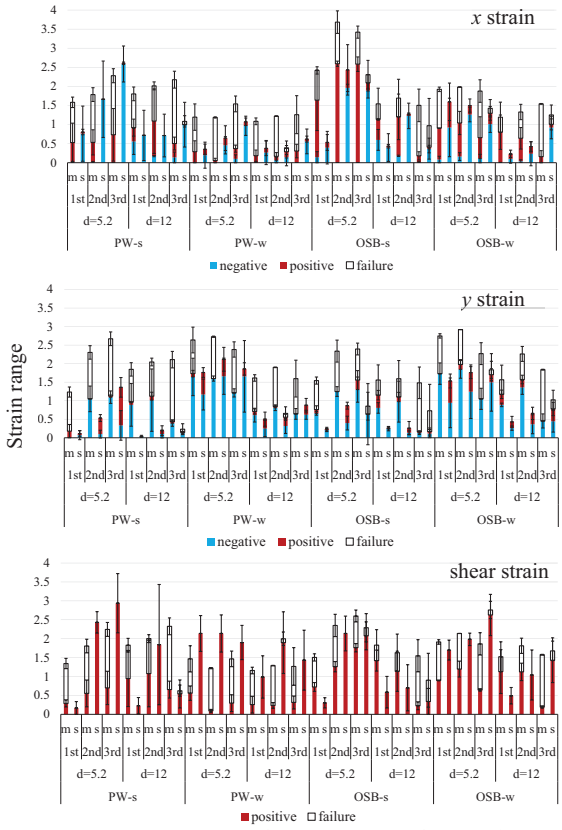

Figure 17: *Comparison of strain range of vertical cross section.*
Note: *"1st", "2nd" and "3rd" indicate the test steps. "m" and "s" mean middle and side vertical cross section respectively.*

range, regardless of the pressure area, and in alignment

with prior research[9]. Although the strain range was broadened horizontally during each loading phase, this was not the case for the vertical angle, suggesting that the embedding depth remained unchanged by the step.

The difference between strong and weak axial specification was pronounced more slightly in OSB than in PW. The variation in *d* was substantial. The strain range was broadened significantly only horizontally during each loading phase.

The shear strain in the horizontal section exhibited minimal expansion during each loading phase except horizontal section in OSB-s. Furthermore, the shear strain in the central vertical section was less pronounced than that in the peripheral section. As depicted in Figure 18, a graph of *y* strain and shear strain are superimposed in the upper horizontal section. The peak of shear strain was coincident with the base of the *y* strain peak. Thus, the range of shear strain can be considered to be situated at the periphery of the *y* strain range, and the length of this boundary did not expand, even as the range of *y* strain widened.

3.3 RESULTS OF CT SCANNING TEST

Internal cross-sectional images of five plywood layers and three OSB layers were acquired via CT scanning at the locations depicted in Figure 18. The brightness and contrast of each step were harmonized using the procedure illustrated in Figure 19, and differences in brightness were utilized to determine regions void or densified due to bearing pressure. The difference images were obtained for the "1st step-2nd step (plasticity difference (PD))" and "2nd step-3rd step (ultimate difference (UD))" for each specimen and each cross-section.

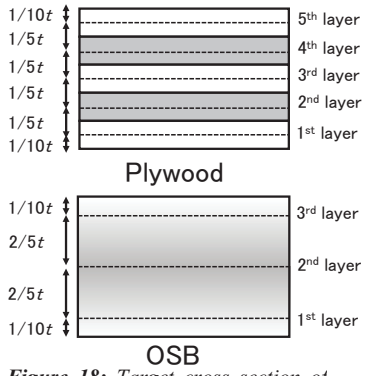

Figure 18: *Target cross section of analysis.*

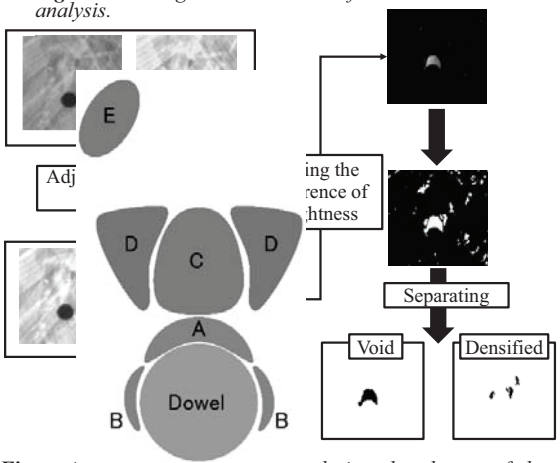

Figure 19: *Overall method of analysing the change of the density.* ***Figure 20:*** *Classification of void or densified area.*

For the derived difference images, the void and densified regions were categorized as A (immediately above to the dowel), B (left and right of the dowel), C (above the dowel), D (diagonally above the dowel), and E (otherwise), as depicted in Figure 20, to ascertain the location of the alteration for each specification, each layer, and each step. Based on this identification of fracture location, it was established whether the layer of varying specifications manifested identical forms of fracture or not. The concrete procedure is as follows.

Initially, an assessment was conducted to determine if the mode of failure varied contingent on the location of the target layer, either on the surface or inner layer. In this regard, the first and fifth layers of plywood, and the first and third layers of OSB were deemed as surface layers, while the third layer of plywood and the second layer of OSB were deemed as inner layers. The likelihood of density changes occurring under each condition was evaluated, and a comparison list was generated and presented in Table 3. Subsequently, a regression analysis was performed on this list, yielding a graph as depicted in Figure 21, with the R^2 value serving as an indicator of similarity in fracture form between surface and inner layers when other conditions were matched. This analysis was separately conducted for plywood and OSB, and for PD and UD, resulting in four distinct R^2 values. A similar method was utilized to establish whether the failure modes differed between strong-axis and weak-axis layers.

Table 4: *Comparison of R^2 values.*

Comparison	Material	Step	R^2 value
Inner vs Outer	PW	PD	0.85
		UD	0.66
	OSB	PD	0.66
		UD	0.38
Strong vs Weak	PW	PD	0.61
		UD	0.24
	OSB	PD	0.55
		UD	0.53

Table 3: *Schematic of list for comparison of failure behavior between outer and inner layer.*

Direction	Diamter (mm)	Void or densified	Probability of change in density at ...	Outer	Inner
			A	1	1
			B	0.5	0.5
		void	C	0.5	1
	5.2		D	0	0
			E	0	0
Strong		densified	A	1	1
		…	…		
		void	A		
		…			
	12	densified	…	…	…
		…			
Weak	5.2	void	A		
…	…	…	…		

The findings, presented in Table 4, demonstrate that for plywood, the impact of the layer's position on failure mode is negligible, whereas the variation in fiber direction accounts for the discrepancy in failure mode. Conversely, for OSB, the results indicate that the layer's position

https://doi.org/10.52202/069179-0036

significantly influenced the failure mode, particularly in the UD direction, and that the variance in fiber direction had no impact on the variation in failure mode. These results demonstrate the assumption referred in the previous section.

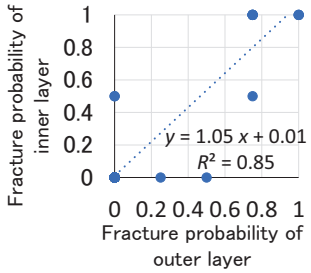

Figure 21: *Examples of regression analysis of fracture probability.*

Moreover, the orientation of the fibers in the odd-numbered veneer layers in PW-s and the even-numbered veneer layers in PW-w (and vice versa) are identical. Consequently, a common method was employed to ascertain if the disparity in fracture form was due to the disparity between the odd- and even-numbered layers. The R^2 value was 0.82 for PD and 0.80 for UD, demonstrating that the mode of plywood failure is predicated on the direction of the veneer fibers, independent of the layer's arrangement.

Table 5 illustrates the probability of density fluctuation occurring in each specification. The occurrence of densification at position B was commonplace in the case of strong axial veneers in plywood, which may be attributed to the convergence of fibers on both sides of the dowel brought about by fiber dissociation in the center. At location C in the UD, void and densification also occurred, likely as a result of the upward propagation of cracks during large deformation. The weak axial veneer experienced void and densification at locations C and D in the UD, whereby the veneer was altered by bearing stress and undergoes plasticization and fracture above and to the right and left of the dowel, with the deformation failing to recover even upon unloading. The surface layer of OSB displays a plethora of void areas (B, C, D and E), presumably resulting from surface delamination. Only the inner layer of OSB experienced densification, with void and densification occurring frequently at location C. The fracture location of the inner layer can be characterized as intermediate between a strong-axis veneer and a weak-axis veneer. These findings suggest that out-of-plane delamination is predominant in the surface layer, while in-plane compressive deformation is predominant in the inner layer.

The area of the difference image is divided by the area of the dowel and standardized for comparison in Figure 22. In PW, the weak axial veneer has a larger densified and void area than the strong axial veneer, and the difference in densification area is larger. This is because the covergence to the left and right due to fiber dessociation was an indirect deformation caused by a stress perpendicular to the direction of the applied force, while the embedment into the weak axial veneer is a direct deformation occurring parallel to the direction of the applied force. The densifi ed area decreased with increasing diameter, but the void area did not change significantly with diameter. As mentioned above, it can be concluded that OSB causes delamination in the surface layer and compressive deformation in the inner layer. In addition, the standardized void area of the surface layer shows differences depending on the diameter, although the standard deviation is significant. In other words, the absolute value of the delamination area does not seem to vary with diameter.

4 CONCLUSIONS

The comprehensive testing of wood-based panels was performed to assess their bearing capacity. A systematic examination was carried out to discern the correlation between failure mode and parameters. By incorporating the remained distance, the interdependence between ductility and parameters was validated. Standardized multiple regression analysis of the characteristic values was also executed, yielding an understanding of the influence of various conditions on the values. These results provide insights into the failure behavior and stress distribution, supporting certain hypotheses.

A detailed investigation was performed using DIC and CT scanning techniques to shed light on the stress distribution and fracture processes. Three load steps were configured and subjected to cyclic loading. Verification and comparison were carried out for each specification, layer, and step, providing a clearer understanding of the stress distribution and fracture processes. These results are

Table 5: *Comparison of probability of change in density at each area.*

layer	*d* (mm)	step	Change in density	A	B	C	D	E
Strong	5.2	PD	Void	**0.9**	0.2	0	0	0
			Densified	**0.9**	**0.6**	0	0	0
		UD	Void	**1**	0.4	**0.8**	0	0
			Densified	**1**	**0.9**	**0.6**	0	0
	12	PD	Void	**1**	0	0	0	0.1
			Densified	**1**	0.1	0	0	0
		UD	Void	**1**	0.4	**0.7**	0.2	0.3
			Densified	**1**	**0.5**	**0.5**	0.1	0.1
Weak	5.2	PD	Void	**0.8**	0.3	0.2	0.2	0
			Densified	**0.9**	0	0	0	0
		UD	Void	**1**	0.3	**1**	**0.9**	0.3
			Densified	**0.9**	0.2	**1**	**0.7**	0.1
	12	PD	Void	**1**	0	0	0	0
			Densified	**0.9**	0.1	0	0	0
		UD	Void	**1**	0.1	**1**	**0.5**	0.3
			Densified	**1**	**0.6**	**0.8**	**0.5**	0.1

layer	*d* (mm)	step	Change in density	A	B	C	D	E
outer	5.2	PD	Void	**1**	0.125	0.375	0.25	0.125
			Densified	**0.5**	0.25	0	0.25	0.125
		UD	Void	**1**	**0.625**	**0.875**	**0.625**	**0.75**
			Densified	**0.5**	0.125	0.125	0.25	0.25
	12	PD	Void	**1**	0	0	0	0.125
			Densified	0.375	0	0	0	0
		UD	Void	**1**	0.25	**1**	**0.75**	**0.75**
			Densified	0.125	0	0	0	0.25
inner	5.2	PD	Void	**1**	0.25	**0.5**	0.25	0.25
			Densified	**0.75**	0	0.25	0.25	0
		UD	Void	**1**	**0.5**	**0.75**	0.25	0.25
			Densified	**0.75**	0	**0.5**	**0.75**	0
	12	PD	Void	**1**	0	0.25	0.25	0
			Densified	**1**	0	0	0	0
		UD	Void	**0.75**	0	**0.75**	**0.5**	0
			Densified	**0.75**	0	**0.5**	0.25	0

Note: *left and right table shows results of plywood and OSB respectively.*

https://doi.org/10.52202/069179-0036

consistent with the conclusions drawn from the comprehensive testing.

ACKNOWLEDGEMENT

Plywood was provided by SEIHOKU CORPORATION. I would like to thank you all those involved. This study was also supported by Grant-in-Aid for JSPS Research Fellow (no. 20J20611).

REFERENCES

[1] K. Sawata, and M. Yasumura. Determination of embedding strength of wood for dowel-type fasteners. *J. Wood Sci.*, 48:138-146, (2002).

[2] C. Sandaas, ans A. K. Sarnaghi, and J. van de Kuilen. Numerical modelling of timber and timber joints: computational aspects. *Wood Sci. and Technol*.,54: 31-61, 2020.

[3] N. Sekino, S. Morisaki. The Effects of Board Density and Board-Edge Distance of Nails on Lateral Nail-Resistance of Low-Density Particleboards. *Mokuzagakkaishi*, 33(9):694-701(1987).

[4] K. Ogawa, M. Harada, T. Shibusawa, and K. Miyamoto. Method for measuring the resistances produced on parallel and perpendicular veneers in plywood under nail embedment loading. *J. Wood Sci.*, 65(1) (2019).

[5] Japanese Agricultural Standard (2003) JAS for plywood. Japanese Agricultural Standards Association, Tokyo.

[6] Japanese Agricultural Standard (2013) JAS for OSB. Japanese Agricultural Standards Association, Tokyo.

[7] JIS A 5508, “nails,” Japanese standard association, 2009.

[8] ASTM D1037-12 (2017) Standard test method for evaluating properties wood-based fiber and particle panel materials. ASTM International, West Conshohocken, PA.

[9] A. J. M. Leijten. The bearing strength capacity perpendicular to grain norway spruce- Evaluation of three structural timber design models, *Const. and Buid. Mater.*, 105(15):528-525(2016).

https://doi.org/10.52202/069179-0036

World Conference on Timber Engineering Oslo 2023

REINFORCEMENT OF TIMBER STRUCTURES VERSUS CLIMATE IMPACT

Bettina Franke[1], Steffen Franke[2], Marcus Schiere[3]

ABSTRACT: Wood is a hygroscopic material. The moisture content of wood changes due to ambient climate variations. The moisture content changes first on the surface and a moisture gradient develops over the cross section and results in moisture induced stresses (MIS). MIS occur in addition to normal stresses for the load-bearing resistance and can affect mechanical reinforcements. The paper shows results from experimental test series on the load, moisture, and deformation investigation of structural glulam members reinforced with internal mechanical fasteners. Stepwise climate scenarios were applied and considered climates experienced by the structural timber member before or after reinforcement. For the estimation of the swelling and shrinkage behaviour, effective hygro-expansion coefficients have been determined. The coefficients are significantly lower than previously assumed in the standards. This enables engineers to estimate more realistic wood deformations and the impact on reinforcements which is not neglectable and reduces damage in a wide range of applications. The research results promote the use of wood by ensuring quality, performance, and aesthetics in timber constructions.

KEYWORDS: Wood, reinforcement, self-tapping screws, moisture induced stress, hygro-expansion coefficients

1 INTRODUCTION

The performance of structural timber members can be enhanced by mechanical reinforcements e.g., in the form of bonded in rods, self-drilling fully threaded screws or threaded rods. Reinforcements of connections or timber members become necessary by restricted cross-sectional geometry or if e.g., curved, notched, or members with holes are used, as shown among others in [1], [2], [3], [4], [5], [6].

Wood as a hygroscopic capillary porous material adsorb or release water from the ambient air. Directly on the wood surface, an equilibrium moisture content develops, which depends on the relative humidity and temperature. The moisture transport over the cross-section takes place by diffusion and is very prolonged, [7]. Therefore, a moisture profile is formed over the cross-section which leads to moisture induced stresses (MIS) due to the non-uniform shrinkage and swelling of the wood cross section, [8]. In addition, the internal reinforcements not only improve the performance of timber structures but also change/restrict the free deformation behaviour of the cross-section which also leads to MIS. The two aspects, MIS and internal reinforcement, occur together in the life cycle of timber structures. The research done by Danzer et al. [9] shows that the load-carrying capacity of reinforced members with notches can even be reduced compared to unreinforced ones.

The objective is to provide answers to the load-bearing behaviour of reinforced timber constructions exposed to climate changes. The focus is on systematically defined experimental investigations on glulam beams of practical relevance with different reinforcement ratios. The research work focuses on findings on effective hygro-expansion coefficients for internal reinforced glulam members under drying and wetting climate exposure which can be used to estimate shrinkage and swelling deformations as well as additional stresses within the reinforcements.

2 STATE OF THE ART

2.1 CLIMATE IMPACT

Structural damage related to moisture was quantified by a study in which existing buildings in southern Germany were assessed. Moisture accounted for half of the observed structural damage: too wet, too dry, or varying moisture conditions [10]. The latter accounted for approximately one sixth of the damage in need of repair [11]. About 90% of the encountered damage was found in glued laminated timber. The damage not related to moisture content concerned wrong assumption of loads or errors in calculation of load-bearing capacities for instance.

Varying climatic stresses occur not only in exterior components but also in interior components in non-air-conditioned structures or through specific user profiles, [13], [14]. The analyses of monitoring data show that in heated not climatized structures (generally service class 1 according to EN 1995-1-1:2004 [15]), relative humidity in winter is lower than in summer. In buildings that are not heated but ventilated (generally service class 2 according to EN 1995-1-1:2004), the relative humidity is low in summer whereas it increases towards autumn/winter.

[1] Bettina Franke, Bern University of Applied Sciences, Switzerland, bettina.franke@bfh.ch
[2] Steffen Franke, Bern University of Applied Sciences, Switzerland, steffen.franke@bfh.ch
[3] Marcus J. Schiere, Wijma Kampen B.V., Kampen, Netherland, mjs@hupkeswijma.com

https://doi.org/10.52202/069179-0037

2.2 REINFORCEMENTS IN TIMBER STRUCTURES UNDER CLIMATE EXPOSURE

Reinforcements improve in general the load-bearing behaviour, but the full utilization level cannot be applied. The EN 1995-1-1:2004 [15] does not contain information on this reduced load carrying behaviour. Some national annexes or standards provide information for the calculation of the design value of the tensile force acting on the reinforcement, structural information is given on the distances between each other, from the edge of the notch or opening and on the insertion length for curved or pitched roof beams. Guidance on the calculation of the deformation behaviour or the consideration of additional moisture-induced stresses due to single or varying climate changes is not given in standards. It is known that the hygro-expansion coefficient is not fully effective due to viscoelastic behaviour, but only minor information is given, [16].

Research on mechanical internal reinforcements like bonded in rods, self-drilling fully threaded screws or threaded rod, was mainly done for the static short term load-bearing behaviour in constant climate, e.g. [17], [18]. There are first experiences available for reinforced beams under varying dynamic climate, [9], [6], [19], [20]. Sjödin [20] confirms an indeed reduced load-bearing capacity of steel-timber dowel joints loaded parallel to the grain under initial drying exposure. Wallner [19] only investigated processes during restricted shrinkage. There are no studies on restricted swelling, where tensile stresses in the screw can overlap with tensile stresses from external loads, and under varying climates. Likewise, the increasing influence of end-grain moisture transport was not considered. Trautz [6] measured the deformations of self-tapping screws as connectors and reinforcements on rigid frame corners in exterior climatic to evaluate the creep of the screws and the connections. The results for the specimens with a high degree of utilization also show a decrease of load-bearing capacity after an exterior exposure of 2 years.

The fact that damage can occur even in reinforced curved and pitched roof beams, support areas, notches and holes is well known, [21], [22]. Relaxations of 50% are realistic according to SIA 265/1, [16], [23] and would theoretically double the allowable moisture change. Dietsch [24] also states that a moisture reduction of 1% already cancels out the effect of the reinforcement measure. This was calculated for a curved beam and 50% relaxation.

3 MATERIAL AND METHOD

3.1 MATERIAL

Glulam produced from softwood is still one of the most important building materials in modern timber construction industry and most research focused on softwood members. Hence, GL24h from Spruce was used for the experimental test program. The glulam members were reinforced with 16 mm SFS WB-T threaded screws/rods.

Widths of glulam beams in modern timber engineering range between 160 mm and 240 mm, [13]. In discussions with practical engineers, the heights of glulam beams range from 600 mm to 2000 mm and rarely over 2000 mm. Therefore, the experimental test series comprises unreinforced and reinforced specimens with a standard beam width of 160 mm and heights of 600 mm and 1000 mm. The element lengths were either 160 mm or 320 mm, in line with work performed by Wallner [19]. The size of the elements and reinforcement ratio were chosen such that the reinforcement would have approximately the same stiffness as the glulam member, or twice the stiffness of the glulam member, cf. equation (6).

3.2 CLIMATE SCENARIOS

The ambient climate at structural members depends on the building occupation, their use, the meteorological conditions, local topography or environment, and altitude and varies throughout the year. The annual variations can easily be simplified using a sinus shape model, [14]. For further simplification, three stepwise climate changes A, B, and C were used for the experimental test programme considering sudden climate changes experienced by the wood before or after reinforcing (Figure 1). In each case the elements of the test programme were climatized in climate chambers. The start of the three step-climate changes is always related to the moisture content of 12 M% from the production phase.

- In climate scenario A, the climate change represents the reinforcement of the timber member during production directly going into service as in sports hall with a drying/desorption process.
- The climate scenario B also represents a reinforcement of the timber member during production but going into a construction period of 38 days with wetting/adsorption

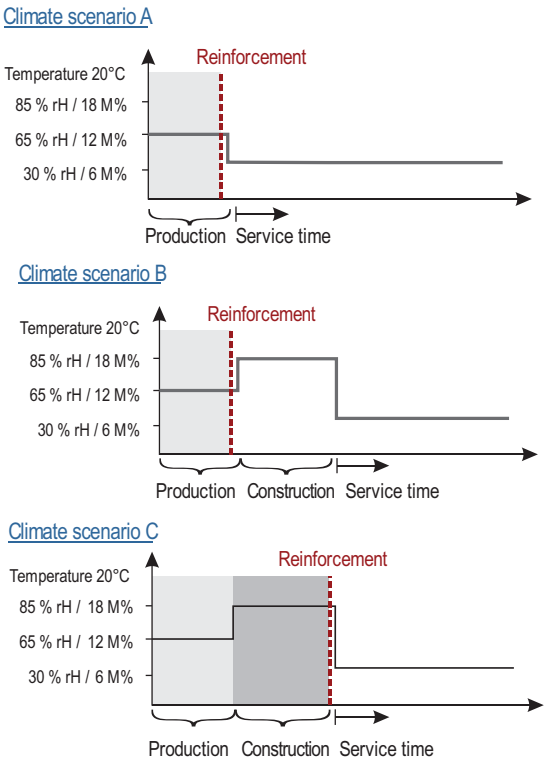

Figure 1: *Illustration of the three stepwise climate scenarios applied within the experimental test programme.*

https://doi.org/10.52202/069179-0037

process before starting service time with a drying/desorption process.

- In climate scenario C, the reinforcement is installed on-site at the end of the construction period of 38 days followed by service with a drying process. This results in a higher moisture load after reinforcing.

3.3 EXPERIMENTAL PROGRAMME AND CLIMATE CONDITIONING

The total of 28 test specimens was divided into the three defined climate scenarios A, B, C. Figure 2 shows an overview of the samples used, geometries, reinforcements, and climate loads. The end grains of most of the glulam beams were sealed to represent a continuous beam, only few end-grains were not sealed to represent reinforcements being located close to end grains, as at notches, holes or supports. The end grain sealing was done with aluminium tape.

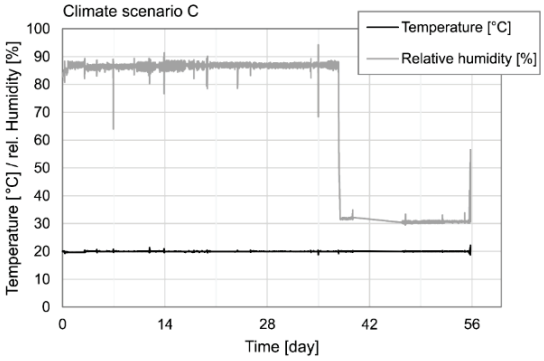

Figure 3: *Recorded climate data for climate scenario C, starting with 85% relative humidity and 20 °C to achieve a moisture content of 18 M%, followed with 30% relative humidity and 20 °C to achieve a moisture content of 6 M%*

To reach the moisture content steps of about 12, 18, and 6 M%, climates of 65, 85, and 30% relative humidity have been used respectively. The temperature was constant at 20 °C. Figure 3 shows representative the climate data for the drying process of climate scenario C. The measurement of climate was performed with calibrated Elprolog TH1 sensors and logged every 10 minutes.

4 MEASURING METHODS

4.1 MOISTURE CONTENT VARIATIONS/DISTRIBUTIONS

Moisture content variations within the glulam beams were measured using the electrical resistance method. Pairs of partially insulated GANN electrodes of 15 mm, 25 mm, and 40 mm lengths were inserted in predrilled holes at the corresponding measuring depths. The measurements of the electrical resistance were done and logged with the equipment of Scanntronik Mugrauer GmbH. Temperature sensors were installed too for temperature compensation within the conversion process from electrical resistance to the moisture content, [25]. The accuracy of this method lies between 1 M% to 2 M%, [25]. The moisture content at the surface was taken as equilibrium moisture content calculated from the surrounding climate using the Simpson equation, [26]. The measurement frequency was 1 hour.

Each measurement point was named according to the element number, the type of measurement, the location, and the length of the electrode:

- Px, specimen name/number
- HF, moisture content
- MI for middle (lengthwise) and SH for end grain
- 15, 25 or 40, measuring depth/length of electrode pair in millimetres

The name P3-HF-MI-15 represents the moisture content measurement, midsection at 15 mm depth of the test specimen P3.

Climate scenario	unreinforced unsealed	unreinforced unsealed	unreinforced sealed	reinforced unsealed	reinforced unsealed	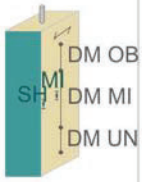 reinforced sealed	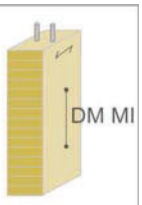 reinforced unsealed
[mm]	160/160/600	160/320/600	160/320/600	160/160/600	160/320/600	160/320/600	160/320/600
A	# P9	# P10	# P23	# P1	# P2[1)]	# P3[1)], P11[1)], P12	# P4
B			# P25	-	-	# P15[2)], P16	-
C			# P27	# P5	# P6[1)]	# P7[1)], P19[1)], P20	# P8

[1)] Measurment of moisture content in depths of 15 and 40 mm
[2)] Measurment of moisture content in depths of 15, 25, and 40 mm

Figure 2: *Overview of all experimental test series considering the climate scenarios and individual configuration*

https://doi.org/10.52202/069179-0037

4.2 DEFORMATION OF THE REINFORCEMENT

For the estimation of the deformation behaviour of the reinforcement, a measuring frame with gauge was used. The deformations of the reinforcement within a 600 mm high beam were estimated to be around 2 mm ($E_{t,90,m}$ = 300 N/mm^2 and α_{90} = 0.25%/M%) when reaching the tension strength perpendicular to the grain of $f_{t,90}$ = 0.5 N/mm^2 (EN 14080:2013). Therefore, a measuring frame/rig was constructed and equipped with a dial gauge of 10 mm measuring range and 0.01 mm measuring resolution, Figure 4. To reduce measurement uncertainties due to thermal expansion, a reference bar from the same material was measured together with the glulam beams and elongations were corrected. The errors lie within the measurement resolution of the gauge but remain small (order of 1/100th of a millimetre). Right after the start or the change of the climate, the deformations were measured more often than close to the end of the tests.

4.3 DEFORMATION OF THE GLULAM BEAM

For the deformation of the timber elements at the surface, a deformeter with measuring range of 100 mm and 200 mm was used. Before each measurement, the deformeter was calibrated using fixed reference bars.

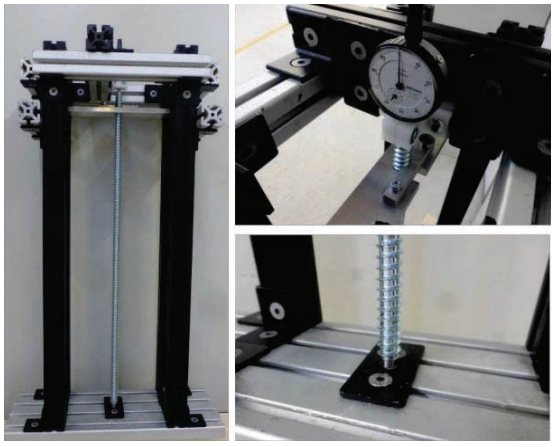

Figure 4: *Picture of the constructed frame (left) to measure 600 mm high beam with a gauge at the top (top right) and a nut (bottom right) to fit the screw into on the bottom*

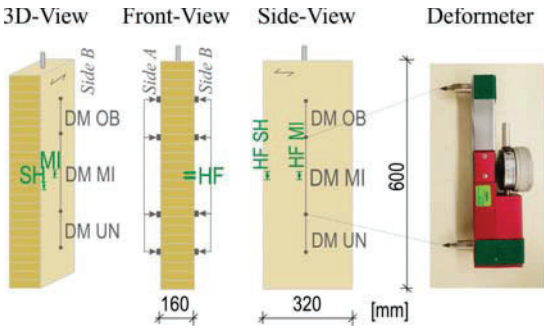

Figure 5: *Illustration of the positions and naming of the measurement of deformations on the wood surface of glulam beams as 3D-, front- and side view using the deformeter (right)*

Measurements were made on both sides of the beams and averaged, see Figure 5. Because an eccentricity in loading of 10% (width b and height h) lead to a measurement error of 60% if strains are measured on one side only. Averaging these two strains results in a representative strain.

$$\varepsilon_{\pm h/2} = \frac{F}{AE} \pm \frac{My}{IE} = \frac{F}{AE} \pm \frac{0.1hF0.5h}{IE}$$
$$\varepsilon_{\pm h/2} = \frac{F}{E}\left(\frac{1}{bh} \pm \frac{12h^2}{20h^3b}\right) = \frac{F}{Ebh}(1 \pm 0.6) \quad (1)$$

5 EXPERIMENTAL RESULTS

5.1 MOISTURE CONTENT MEASUREMENTS

The moisture content measurements are plotted in Figure 8. Since not all specimens could be equipped with moisture measurement sensors, the measured values are applied to all specimens of the same climate/group for further analyses.

The intended pre-climatization of the elements to a moisture content of 12 M% and 18 M% was not fully achieved for climate scenario A and C respectively.

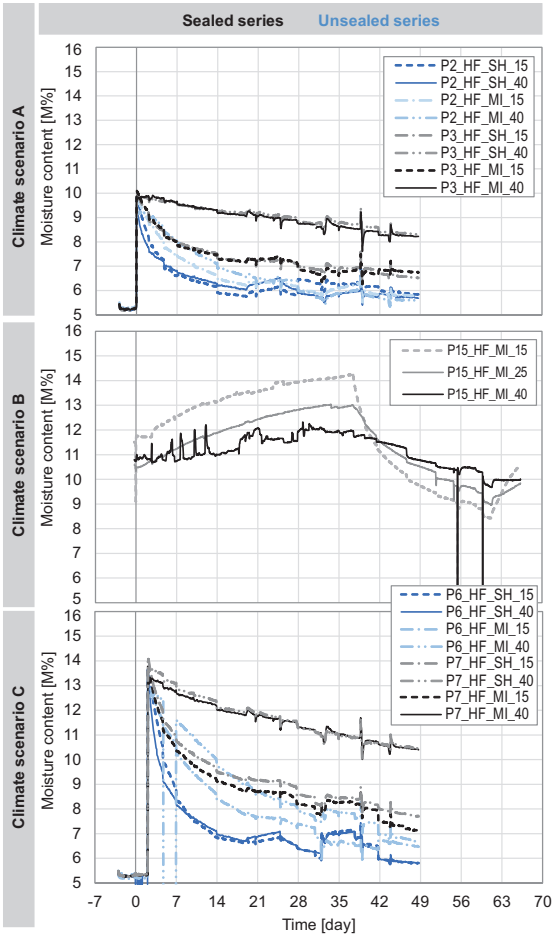

Figure 6: *Moisture content development of the three different climate scenarios, shown for the test specimen per series over the different depths observed*

https://doi.org/10.52202/069179-0037

Instead, moisture content levels of 10 M% and 14 M% were achieved because of too low relative humidity set up and conditioning time estimated. The climatization of the second series (P11 to P27) was adapted accordingly. To achieve the moisture content of 18 M%, the elements were stored in a climate chamber with a relative humidity of 85%. Instead of maintaining the temperature at 20 °C, like was done in the first series, a higher temperature of nearly 40 °C was maintained. In addition, the elements were artificially wetted by spraying water onto the end grains of the elements to accelerate the climatization. In the second series, the achieved moisture content at the start of the tests was around 13 M% and 18 M%.

The function of sealing can clearly be seen; the moisture transport in general is reduced. Once the end grain is not sealed like in P2 and P6, the moisture content on the cross section reduces more rapidly and equilibrium is reached after about 20 days. There is not only a moisture gradient along the width of the element but also along the length of the element. Whereas equilibrium is not reached for the sealed ones within 50 days (P3 and P7) and there is almost no difference between the measuring points in the centre (MI) and near the end grain surface (SH).

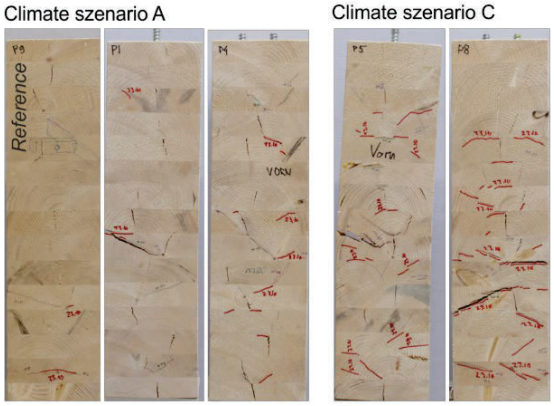

Figure 7: *Cracking pattern of the end grains for reference specimen P9 and specimens with double reinforcement stiffness P1, P4, P5, and P8 (l.t.r.)*

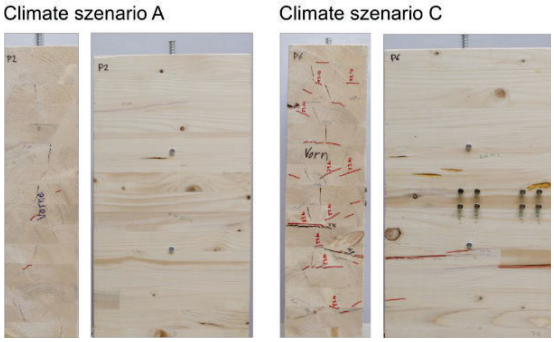

Figure 8: *Cracking pattern of the end grains for reference specimen P9 and specimens with double reinforcement stiffness P1, P4, P5, and P8 (l.t.r.)*

5.2 CRACK GROWTH BEHAVIOUR

Cracking was recorded for all specimens as e.g., shown in Figure 7 and Figure 8. For the higher moisture load of about $\Delta = 12$ M% (climate scenario C) more cracks developed at the end grain and even cracks on the side are visible. Almost no cracks are visible at the side for the lower moisture load with $\Delta = 6$ M% (climate scenario A). Specimen with single reinforcement show pronounced larger cracks on one side together with quite large bending deformations compared to the specimen with double reinforcements.

The relation between moisture content change and crack growth is illustrated in Figure 9. The cracked specimens show in average slightly smaller moisture content changes at time of failure compared to the uncracked specimens. P19 was perhaps prone to cracking, as a crack was visible already before the test starts.

5.3 DEFORMATION AND STRAIN

The measured deformations at the reinforcement and at the timber surface are shown as strains for each climate scenario and configuration in Figure 10. It can be seen that:

- Small moisture content changes (elements P1 to P4) have high deformation; medium moisture content changes (P5 to P8 and P11 to P14) lead to small deformation.
- An effect of the double reinforcement on 600 mm high elements is observed (P4/P2 ≈ 0.8 and P8/P6 ≈ 0.5)

6 EVALUATION OF THE EFFECTIVE HYGRO-EXPANSION COEFFICIENT

Based on the measured change of moisture content, the dependency of the strain of the reinforcement on moisture content change can be calculated too. This is like a hygro-expansion coefficient with the unit as %/M%. The effective hygro-expansion coefficient is calculated by Equation (5). This is based on a model for composite structures consisting of two different materials 1 and 2 with assuming equal strain in the materials, as shown in Figure 11 and expressed by following equations (2) to (6):

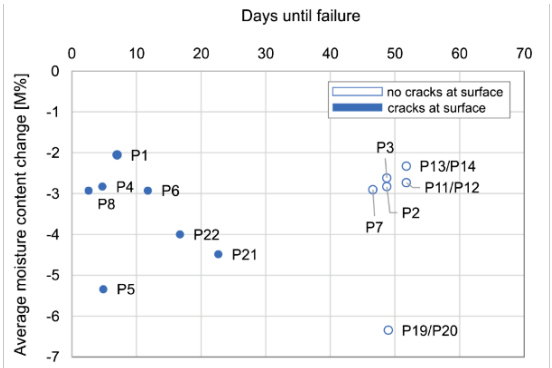

Figure 9: *Relation between days until failure and changed moisture content at time of failure*

https://doi.org/10.52202/069179-0037

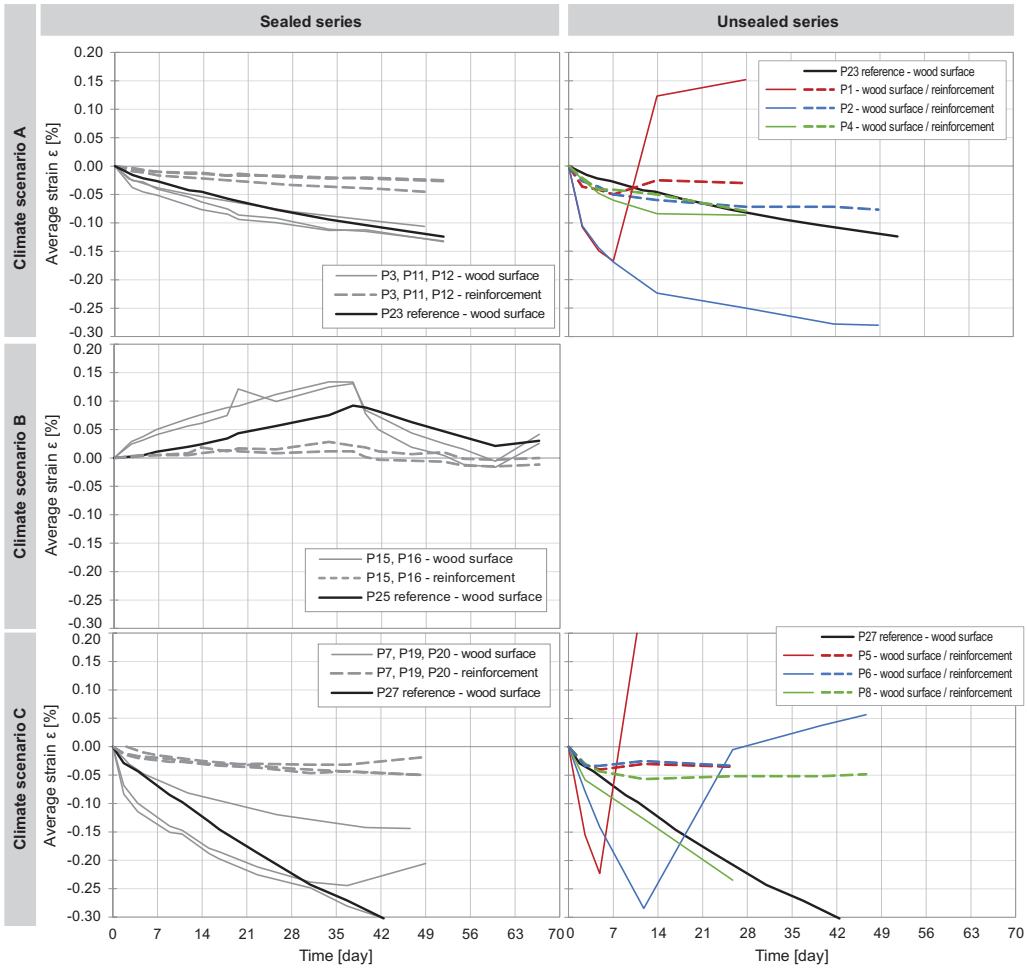

Figure 10: *Strain development in the reinforcement and on the surface separated for the sealed and unsealed specimens*

$$\Delta\varepsilon = \Delta\sigma / E + \alpha\Delta u \tag{2}$$

$$\Delta\varepsilon_0 = \left(F_e + \alpha_1 \Delta u_1 A_1 E_1\right) / \left(A_1 E_1 + A_2 E_2\right) \tag{3}$$

$$\begin{aligned} \Delta\sigma_1 &= \left(\left(F_e + \alpha_1 \Delta u_1 A_1 E_1\right) / \left(A_1 E_1 + A_2 E_2\right) - \alpha_1 \Delta u_1\right) E_1 \\ \Delta\sigma_2 &= \left(F_e + \alpha_1 \Delta u_1 A_1 E_1\right) / \left(A_1 E_1 + A_2 E_2\right) E_2 \end{aligned} \tag{4}$$

$$\begin{aligned} \Delta\sigma_1 &= \alpha_1 \Delta u_1 \left(\gamma - 1\right) E_1 \\ \Delta\sigma_2 &= \alpha_1 \Delta u_1 \gamma E_2 \end{aligned} \tag{5}$$

with γ as the ratio of stiffness between the timber cross section and the total cross-section, a value between 0 and 1:

$$\gamma = \frac{A_1 E_1}{A_1 E_1 + A_2 E_2} \tag{6}$$

The stress in the reinforcement is calculated from the strain corrected with the S-factor of 1.42 for 600 mm high beams considering the non-uniform strain distribution over the depth of the beam, cp. Figure 11. Furthermore, a correction on height of the specimen is also done to obtain the stresses in an infinitely high specimen. Therefore, investigation with different depths can directly be compared. The stresses in the reinforcement from the 600 mm high specimens are therefore corrected by a coefficient of 0.68. All strains and wood moisture content are taken from the last measurement before fracture was observed or at the end of the climatization.

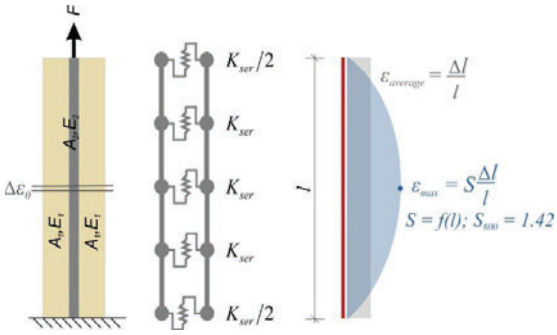

Figure 11: *A composite structure consisting of two different materials 1 and 2*

https://doi.org/10.52202/069179-0037

Figure 12 shows the calculated values as a function of time for the test specimens of climate scenario A. The hygro-expansion coefficient ends up between 0.05 and 0.10%/M% for this specimen series. Only specimen P1 shows much higher values just at the beginning of the climate change. This was also the time when fracture occurred.

The calculated effective hygro-expansion coefficients before failure are plotted in relation of the final moisture content changes the elements experienced just before the failure, see Figure 13. The value from specimen P1 can be excluded due to the early failure and the unsafe value. In average, an effective hygro-expansion coefficient of 0.055%/M% are calculated. No difference in the hygro-expansion coefficient between elements with or without end grain sealing or drying and wetting processes are observed. Generally, the expansion of the reinforcement is therefore about 1/5th of the hygro-expansion coefficient of wood perpendicular to the grain (0.24 %/M%, SIA 265).

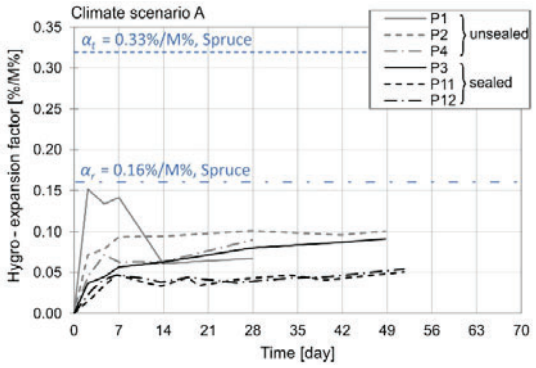

Figure 12: *Calculated hygro-expansion coefficients development for climate scenario A over time*

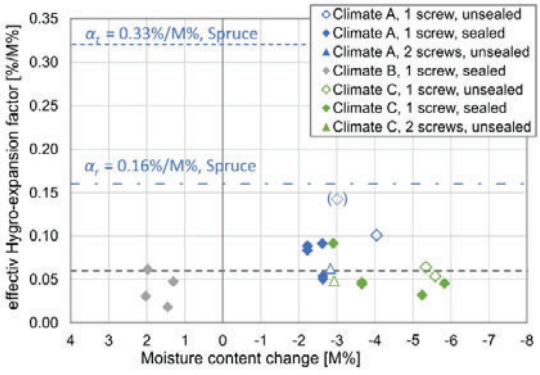

Figure 13: *Derivation of the effective hygro-expansion coefficient of the glulam cross-section according to the composite structure theory*

7 CONCLUSIONS

The calculated effective hygro-expansion coefficients for all specimens and climate scenarios presented show a quite constant reduced coefficient compared to the hygro-expansion coefficients for free swelling and shrinkage or even the half value for restricted shrinkage as specified in [16].

Using a simplified model, effective hygro-expansion coefficients could be calculated. In these calculations, theoretical design values for E-moduli (300 N/mm ^{2}) had to be used. An important conclusion is that whereas theoretical hygro-expansion values of wood perpendicular to the grain lie around 0.24%/M% (SIA 265, 2012), these might lie close to a fifth of this value in reality. This explains why larger moisture content values are possible without cracking and reflect reality more. To what extend this value is valid for other cross section ratios need to be proved.

Using a value of 0.055%/M% in combination with a correction for a height effect, allows estimation of realistic moisture induced strain changes of reinforced glulam cross-sections. The 0.055%/M% does not reflect the real hygro-expansion coefficient but is expected to be more of an 'effective' value that includes effects of mechano-sorptive relaxation and time-dependent creep too under the presence of reinforcements. To calculate the possible generated additional stress in a cross section due to moisture content changes, Equations (5) can be used where a hygro-expansion coefficient of 0.05%/M% is recommended.

ACKNOWLEDGEMENT

The research work was funded by Swiss Federal Office of Environmental under the Grant WHFF 2018.14. Thank you too to the research partners, experts and companies who supported the work.

REFERENCES

[1] H.J. Blass, I. Bejtka, T. Uibel. Tragfähigkeit von Verbindungen mit selbstbohrenden Holzschrauben mit Vollgewinde, *Universitätsverlag Karlsruhe*, 2006.

[2] H.J. Blass, O. Krüger Schubverstärkung von Holz mit Holzschrauben und Gewindestangen, *Karlsruher Berichte zum Ingenieurholzbau*, Band 15, 2010.

[3] H.J. Blass. Selbstbohrende Schrauben und Systemverbinder - Stand der Technik und Herausforderungen, *23. Internationales Holzbau-Forum*, Garmisch-Partenkirchen, 2017.

[4] P. Dietsch. Einsatz und Berechnung von Schubverstärkungen für Brettschichtholzbauteile. *Phd-Thesis*. Technical University Munich, 2012.

[5] P. Dietsch. Effect of reinforcement on shrinkage stresses in timber members. *Construction and Building Materials*, 150, 903-915, 2017.

[6] M. Trautz, C. Koj. Mit Schrauben fügen und bewehren - Langzeitversuche an biegesteifen Rahmenecken im Außenklima, *Bautechnik* 91 (1), 38-45, 2008.

[7] H. Kopfer. Wassertransport durch Diffusion in Feststoffen. *Bauverlag GmbH*, Wiesbaden, Germany, 1974.
[8] Jönsson, J. and Svensson, S. (2004) A contact free measurement method to measure internal stress states in glulam. Holzforschung, 58, 148–153.
[9] M. Danzer, P. Dietsch, S. Winter. Effect of shrinkage on cracking and structural behaviour of reinforced glulam members, *Construction and Building Materials*, 327, 1-14, 2022.
[10] M. Frese, H.J. Blass Statistics of damages to timber structures in Germany, Engineering Structures, 33 (11), 2969–2977. 2011
[11] Dietsch, P., Winter, S., 2018. Structural failure in large-span timber structures: A comprehensive analysis of 230 cases. Journal of Structural Safety, 71, 41-46.
[12] P. Dietsch. Reinforcement of timber structures – A new section for Eurocode 5, World Conference on Timber Engineering, Vienna, 2016.
[13] A. Gamper, P. Dietsch, M. Merk. Gebäudeklima - Langzeitmessung zur Bestimmung der Auswirkungen auf Feuchtegradienten in Holzbauteilen. *Research Report*, TU Munich, Germany, 2012.
[14] B. Franke, S. Franke, M. Schiere, A. Müller. Quality assurance of timber structures. *Research report*, Bern University of Applied Sciences, Switzerland, 2019.
[15] EN 1995-1-1, Eurocode 5. Design of Timber Structures – Part 1-1: General – Common Rules and Rules for Buildings, European Committee for Standardization, Brussels, Belgium, 2004
[16] H.J. Blaß, J. Ehlbeck, H. Kreuzinger, G. Steck. *Erläuterungen zu DIN 1052:2004-08 Entwurf, Berechnung und Bemessung von Holzbauwerken*, DGfH Innovations und Service GmbH München, 2004.
[17] H. Danielsson. *Perpendicular to grain fracture analysis of wooded structural elements - models and applications.* PhD Thesis, Lund University, Sweden, 2013.
[18] R. Jockwer. *Structural behaviour of glued laminated timber beams with unreinforced and reinforced notches.* Ph Thesis. ETH-Zurich, 2014.
[19] B. Wallner. *Versuchstechnische Evaluierung feuchteinduzierter Kräfte in Brettschichtholz verursacht durch das Einbringen von Schraubstangen*. Msc Thesis. TU Graz, 2012.
[20] Sjödin, J. (2008) *Strength and moisture aspects of steel-timber dowel joints in glulam structures - an experimental and numerical study*, Thesis (PhD). Växjö University.
[21] P. Dietsch, R. Brandner. Reinforcement with self-tapping screws and threaded rods in Reinforcement of timber structures: a state-of-the-art report. *Construction and Building Materials*, 97, 78–89, 2015.
[22] Franke, S., Franke, B., Harte, A.M., 2015. Failure Modes and reinforcement techniques for timber beams – State of the Art, Construction and Building Materials, 97, 2-13.
[23] S. Aicher, G. Dill-Langer. Climate induced stresses perpendicular to the grain in glulam, *Otto-Graf Journal,* 8, 209-231, 1997.
[24] P. Dietsch. Effect of reinforcement on shrinkage stresses in timber members, *Construction and Building Materials 150*, pp. 903-915, 2017.
[25] Forsén, H., Tarvainen, V., 2000. Accuracy and functionality of hand-held wood moisture content meters, VTT Publications 420, Technical Research Centre of Finland, Finland.
[26] Simpson W. (1973), Predicting equilibrium moisture content of wood by mathematical models, Wood and Fiber, 5 (1), p. 41-49
[27] M. Danzer, P. Dietsch, S. Winter. Shrinkage behavior of reinforced glulam members, *INTER Conference proceedings*, Karlsruhe, 2020.
[28] SIA 265:2012, Holzbau. Schweizerischer Ingenieur- und Architektenverein, Zürich

https://doi.org/10.52202/069179-0037

World Conference on Timber Engineering Oslo 2023

COMPONENT METHOD IN TIMBER CONNECTIONS: END-PLATE COMPRESSING TIMBER PARALLEL TO GRAIN COMPONENT STRENGTH

Arthur S. Rebouças[1], Jorge M. Branco[2], Paulo B. Lourenço[3], Hidelbrando J. F. Diógenes[4]

ABSTRACT: The component method considers the whole joint as a set of individual basic components, dividing them into zones of tension, compression, and shear. The strength of end-plate and timber parallel to grain in compression may influence total resistance and failure mode of the joint. The objective of this work is to characterize the strength of the component corresponding to a glulam beam under compression by an end-plate in bending within an application in moment-resisting timber connections. For this, an experimental campaign was conducted through compression tests on 25 specimens composed of steel T-stubs with five different flange thicknesses and glulam GL24h. The results were compared to reference compression tests using a rigid plate. A decrease in the component resistance was observed with the reduction in the flange thickness. The failure of the component was governed by the T-stub, due to flange yielding, while the timber did not show characteristic failure. Based on the Eurocode 3 equivalent plate concept, an approach with variable stress distribution was proposed, it proved to be coherent with the experimental behavior of the component and with a possible application in design since the analytical values maintain an acceptable safety margin in relation to the experimental ones.

KEYWORDS: Timber connections, Component method, Glulam beam in compression, End-plate in bending.

1 COMPONENT METHOD

One of the current design practices to predict the rotational behavior of steel joints adopted by EN 1993-1-8 [1] is based on the component method, an analytical method that considers the whole joint as a set of individual basic components, dividing them into zones of tension, compression and shear. It allows to obtain the design moment resistance, rotation capacity, initial and post-peak stiffness and built a moment-rotation curve using these data [2]. The application of component method provides a tri-linear moment-rotation curve to characterize a connection and requires the following steps:

I. Identification of the active/relevant components in the joint being considered;
II. Evaluation of the stiffness and/or resistance characteristics for each individual basic component (specific characteristics – initial stiffness, design resistance, … – or whole deformability curve);
III. Assembly of all the constituent components and evaluation of the stiffness and/or resistance characteristics of the whole joint (specific characteristics – initial stiffness, design resistance, … – or whole deformability curve).

The relevant components are the ones that transfer significant internal forces based on the joint behavior. Each of these basic components possesses its own strength and stiffness either in tension, compression or shear. The coexistence of several components within the same joint element can obviously lead to stress interactions that are likely to decrease the resistance of the individual basic components.

A large amount of research in the field of steel structures was conducted applying the component method to mechanical analysis of steel joints, since Zoetemeijer [3] and Jaspart [4] until more recent studies for cyclic loading [5] and other geometries [6]. From the recognition of the reliability and relevance of the component method to characterize steel joints, some research was conducted in several types of timber connections: historical [7], slotted-in steel plates [8], glued-in rods [9,10] and glued-in steel plates [11]. On the other hand, despite a considerable part of the timber joints using steel components, the effectiveness of the component method in the analysis of timber joints has not been fully assessed.

Therefore, the objective of this work is to characterize the strength of the component corresponding to a glulam beam under compression by an end-plate in bending within an application in moment-resisting timber connections.

[1] Arthur S. Rebouças, Federal Institute of Education, Science and Technology of Rio Grande do Norte, IFRN, Brazil & Department of Civil Engineering, University of Minho, ISISE, Portugal, arthur.reboucas@ifrn.edu.br
[2] Jorge M. Branco, Department of Civil Engineering, University of Minho, ISISE, Portugal, jbranco@civil.uminho.pt
[3] Paulo B. Lourenço, Department of Civil Engineering, University of Minho, ISISE, Portugal, pbl@civil.uminho.pt
[4] Hidelbrando J. F. Diógenes, Federal University of Paraíba, PPGECAM, Brazil, hjfd@academico.ufpb.br

https://doi.org/10.52202/069179-0038

2 GLULAM BEAM IN COMPRESSION AND END-PLATE IN BENDING

Tomasi et al. [12] and Andreolli et al. [9] modelled the glulam beam and the end-plate/steel profile flange in compression as equivalent T-stub in compression. In the connection studied by them (Figure 1), there is a direct contact between the end-plate and the glulam along the total joint depth. In this approach, the effective area of compression plays an important role, as it is directly related to the compressive resistance and stiffness of the component. In these studies, the compressive area was proposed according to EN 1993-1-8 [1], considering that the compression stress is uniformly distributed over a rectangular area measuring by an effective length ($l_{eff,c}$) and width ($b_{eff,c}$), as shown in Figure 2. These dimensions can be taken by the additional bearing width (c_t), which was also calculated based on the EN 1993-1-[1] with some adaptations (Equation 1). The glulam beam compression strength was determined by Equation 2.

$$c_t = t_{ep}\sqrt{\frac{f_y}{3 \cdot f_{c,0} \cdot \gamma_{M0}}} \quad (1)$$

$$F_{R,gb,c} = f_{c,0,d} \cdot b_{eff,c} \cdot l_{eff,c} \quad (2)$$

Where, t_{ep} [mm] is the thickness of end-plate, f_y [N/mm²] is the yield strength of steel, $f_{c,0}$ [N/mm²] is the compression strength parallel to grain of the glulam beam, and γ_{M0} [unitless] is the coefficient equal to 1.

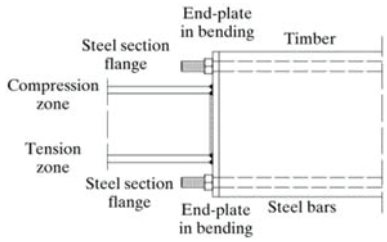

Figure 1. *Connection studied by Tomasi et al. [12] and Andreolli et al. [9].*

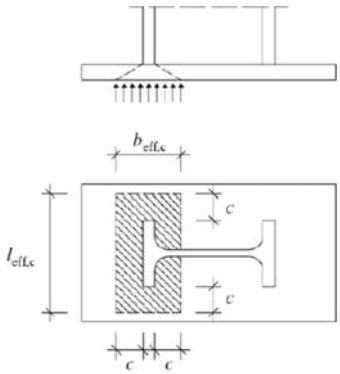

Figure 2. *Compressive area defined in Tomasi et al. [12] and Andreolli et al. [9].*

Yang et al. [10] and Tao et al. [11] applied the procedure proposed by [9] to calculate the resistance of glulam beam in compression parallel to the grain. In these studies, the timber beam is under compression by a steel plate which structural behavior can be modelled as an equivalent T-stub. In the connection studied by Yang et al. [10] (Figure 3), there is a contact area between the steel box and timber beam, where both are under compression. As the steel box width is equal to the glulam beam width, the effective compression area of glulam beam was defined as shown in Figure 4. The effective width was defined as equal to the glulam width (b_b) and the effective bearing length was taken as $0.5 \cdot h_{srt}$. However, no additional explanation was given on how to obtain these values. The glulam beam compression resistance was determined by Equation 3.

$$F_{R,gb,c} = f_{c,0} \cdot b_b \cdot 0.5 \cdot h_{srt} \quad (3)$$

Where b_b [mm] is the width of glulam beam and h_{srt} [mm] is the cross-sectional depth of the steel box.

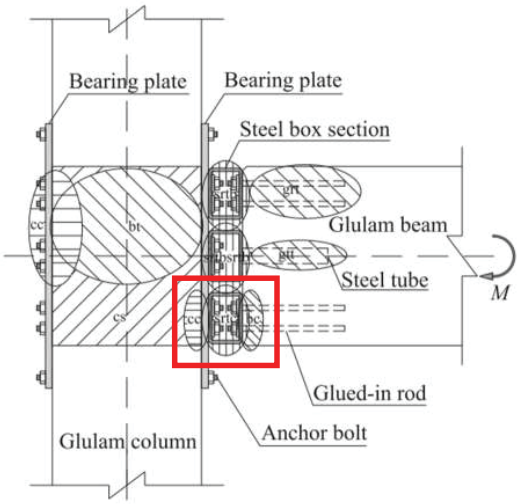

Figure 3. *Compression sub-region in the bottom of connection Adapted from [10].*

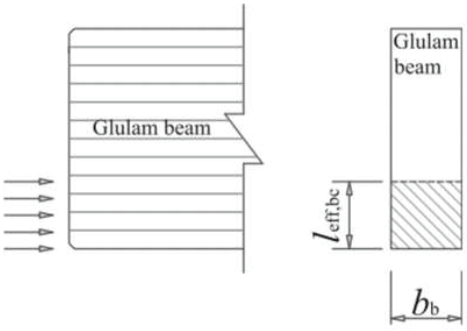

Figure 4. *Effective compression area of glulam beam. Adapted from [10].*

Nevertheless, the c_t and $F_{R,gb,c}$ mentioned above were determined from an adaptation of [1] for the component called "base plate and concrete block in compression". According to Steenhius et al. [13] this component is a base

https://doi.org/10.52202/069179-0038

plate, assumed to be flexible in bending and modelled as a T-stub in compression, supported by a concrete block in compression, with stresses concentrated around the footprint of the column section under the plate. Stockwell [14], Murray [15] and Steenhuis and Bijlaard [16] introduced the concept of replacing a flexible plate with a non-uniform stress distribution by an equivalent rigid plate with a uniform stress distribution, later added to Eurocode 3 (Figure 5).

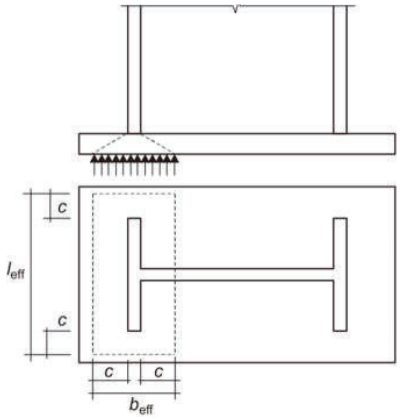

Figure 5. *Effective area of T-stub in compression [1]*

The resistance of the component is determined by two parameters: the bearing strength of the concrete and the dimensions of the equivalent rigid plate. The design compression resistance of the component $F_{C,Rd}$ and the maximum additional bearing width c is defined in the EN 1993-1-8 [1], section 6.2.5, as shown in Equations 4 and 5, respectively.

$$F_{C,Rd} = f_{jd} \cdot b_{eff} \cdot l_{eff} \quad (4)$$

$$c = t\sqrt{\frac{f_y}{3 \cdot f_{jd} \cdot \gamma_{M0}}} \quad (5)$$

Where b_{eff} [mm] is the effective width of the T-stub flange; l_{eff} [mm] is the effective length of the T-stub flange; t [mm] is the thickness of the T-stub flange; f_y [N/mm²] is the yield strength of the T-stub flange and f_{jd} [N/mm²] is the design bearing strength of the joint. It should be determined from Equation 6.

$$f_{jd} = \frac{\beta_j \cdot F_{Rdu}}{b_{eff} \cdot l_{eff}} \quad (6)$$

Where β_j [unitless] is the foundation joint material coefficient, which may be taken as 2/3 provided that the characteristic strength of the grout is not less than 0.2 times the characteristic strength of the concrete foundation and the thickness of the grout is not greater than 0.2 times the smallest width of the steel base plate. In cases where the thickness of the grout is more than 50 mm, the characteristic strength of the grout should be at least the same as that of the concrete foundation; F_{Rdu} [N/mm²] is the concentrated design resistance force given in EN 1992-1-1 (2014), here in Equation 7.

$$F_{Rdu} = A_{c0} \cdot f_{cd} \quad (7)$$

Where A_{c0} [mm²] is the loaded area, here equal to $b_{eff} \cdot l_{eff}$.

Therefore, it is possible to identify, by comparing the Equations 4, 5 and 7 with 1, 2 and 3 ones, that the formulation used by [9] and [12] is very close to the one used to concrete block in compression. For the resistance and the additional bearing width, it differs only by the strength of the material used.

It is believed that this approach needs some adaptations, since the deformation of a glulam beam under compression by a steel plate (equivalent T-stub) can be much pronounced than that seen in a concrete block. It also directly influences the computation of effective area in the equivalent rigid plate.

3 EXPERIMENTAL CAMPAIGN

An experimental campaign was conducted through compression tests on 25 specimens composed of steel T-stubs, with five different flange thicknesses (6, 8, 10, 15 and 20mm), connected to glued laminated timber specimens. The results were compared to reference compression tests using a rigid plate with thickness equal to 40mm, these specimens are regular plates, not T-stubs. Five tests were made for each group.

3.1 SPECIMENS

As timber elements, glulam made of spruce (*Picea abies*) from strength class GL24h, according to EN 14080:2013 [17], were used. As steel elements, T-stub specimens of steel S235, with yield strength equal to 235N/mm² and ultimate tensile strength of 360N/mm², according to the EN 1993-1-1:2010 [18] were applied. The timber specimens had the same dimensions for all test series, 120×240×240mm³. T-stubs geometry are similar (Figure 6), only the thickness varies, as presented in Table 1. The name of each series was defined as "T' plus its corresponding thickness and the reference one was called "REF". The front face of each specimen was painted to be adequate to DIC measurements, the detailed information about the whole configuration is presented in Figure 7. A summary of T-stub and timber specimens tested can be found in Table 1.

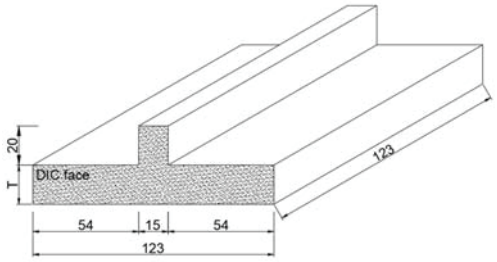

Figure 6. *T-stub specimens dimensions (mm)*

https://doi.org/10.52202/069179-0038

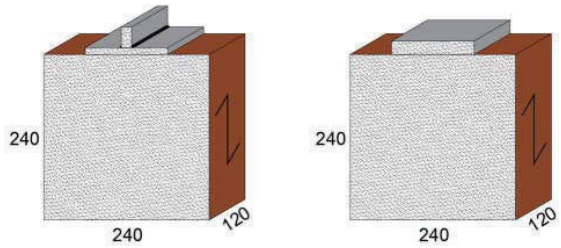

Figure 7. *Detailed geometry of the specimens, including T-stub and glulam, the DIC painted front face and positions of (a) T-stub specimens and (b) Reference specimens. Dimensions in mm.*

Table 1: *Summary of the steel and timber specimens tested, including the reference group (each series comprehends 5 specimens).*

Series	Steel specimens		Timber specimens	
	T-stub flange thickness [mm]	Plate thickness [mm]	Geometry [mm]	
			Cross section	Height
REF	-	40	120×240	240
T20	20	-	120×240	240
T15	15	-	120×240	240
T10	10	-	120×240	240
T8	8	-	120×240	240
T6	6	-	120×240	240

3.2 TEST METHOD

The compression tests of the specimens were carried out on a hydraulic jack with a load cell of 1500 kN under displacement control at a rate of 3 mm/min. The load was applied along the center part of T-stub. The tests were finished when the force reached 80% of the maximum force or when the central displacement reached 2,5% of the specimen total height. The vertical displacements were monitorized by three LVDTs positioned according to the Figure 8, as follows: the central one measured the total displacement of glulam specimen; the left and right ones measured the displacement from each T-stub edge to the glulam specimen. The 3D displacements, deformations, and local strains on the surface between the two materials were determined by the Digital Image Correlation (DIC). In the scope of this work, INSTRA 4D V4.4.7 x64 software was used along with two cameras (Master and Slave) of 2.0 megapixels positioned 100 cm between each other. The acquisition frequency to obtain the frames was 1 Hz.

Figure 7. *Positions of displacement transducers. The right and left ones were named based on the front face of the specimen (painted face).*

3.3 RESULTS

The average maximum experimental stress of the "REF" series was 33.35 MPa, 38.95% higher than the 24 MPa guaranteed by the manufacturer. For the other series, measuring the experimental stress applied by the T-stub flange on timber is complex, due to the lifting of the T-stub flange edges, there is a gradual reduction in the contact area between the two materials. Therefore, the resistance of the component can be better characterized in terms of force.

The Figure 9 shows the force-displacement curves, measured from the center transducer data for tests with average response in each thickness range. In the results of the series "REF" the force decreased gradually after maximum point, whereas for all other series, the force stayed on a plateau with a large increase in displacement. In general, a decrease in the maximum force was observed with the reduction in the thickness of the flange.

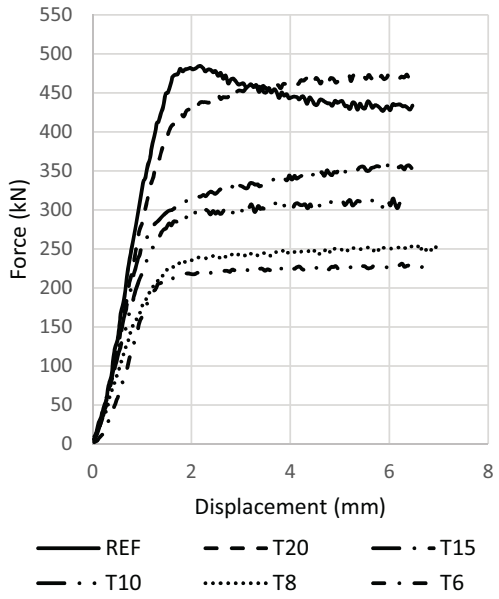

Figure 9: *Force-displacements curves for all different T-stub flange thicknesses.*

https://doi.org/10.52202/069179-0038

In all series, there was a greater displacement of the center of the T-stub flange in relation to the ends, from the beginning of the test. For example, this bending can be seen in the Figure 10, that shows the deformed shape of the T15 specimen when the maximum force was achieved.

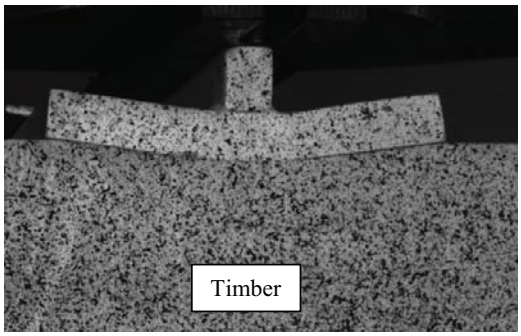

Figure 10: *Deformed shape of specimen T15-E4 at maximum force.*

The smaller the thickness of the flange, the greater was this difference in displacement between center and edges. For thicknesses of 10, 8 and 6 mm, a negative displacement was observed (the position of the end of the plate was smaller than its position at the beginning of the test), an example is shown in Figure 11.

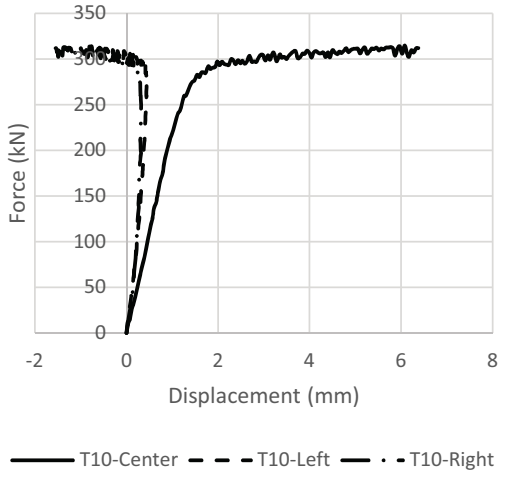

Figure 11: *Force-displacements curve for T10-E4.*

In all tests, the failure of the component was governed by the T-stub, due to the excessive displacement of its edges, without rupture (T-stub flange yielding), while the timber did not show characteristic failure (Figure 12). Except for "REF" series, which the timber presented local failure due to compression under the loading plate (Figure 13).

Figure 12: *Failure of specimen T6-E3 due to T-stub flange yielding.*

Thus, the component experimental behavior is based on identifying whether the stress applied by the T-stub to the timber is sufficient to reach the compressive strength parallel to the grain before reaching the plastic resistant moment of its flange. In all cases studied, although the elastic limit of timber has been clearly reached (see Figures 9 and 11), the compressive strength of the timber was not achieved, therefore, all T-stub flanges can be considered flexible.

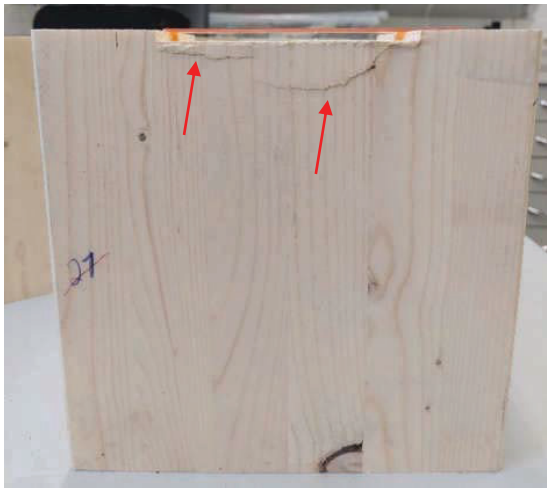

Figure 13: *Deformed shape of specimen T15-E4 at maximum force.*

The component strength based on the formulation proposed by Andreolli et al. [9] was assessed, considering the elastic moment resistance of the T-stub flange and the average maximum experimental stress of the "REF" series (33.35 MPa), as timber strength. It was identified,

from the DIC measurements, that the T-stub flanges are still below the steel yield strain limit for all tested series. The displacements in timber and steel when the force applied was equal to the component strength found by [9] proposition are shown in Figure 14. The strain values were obtained from the vertical displacement and the applied force.

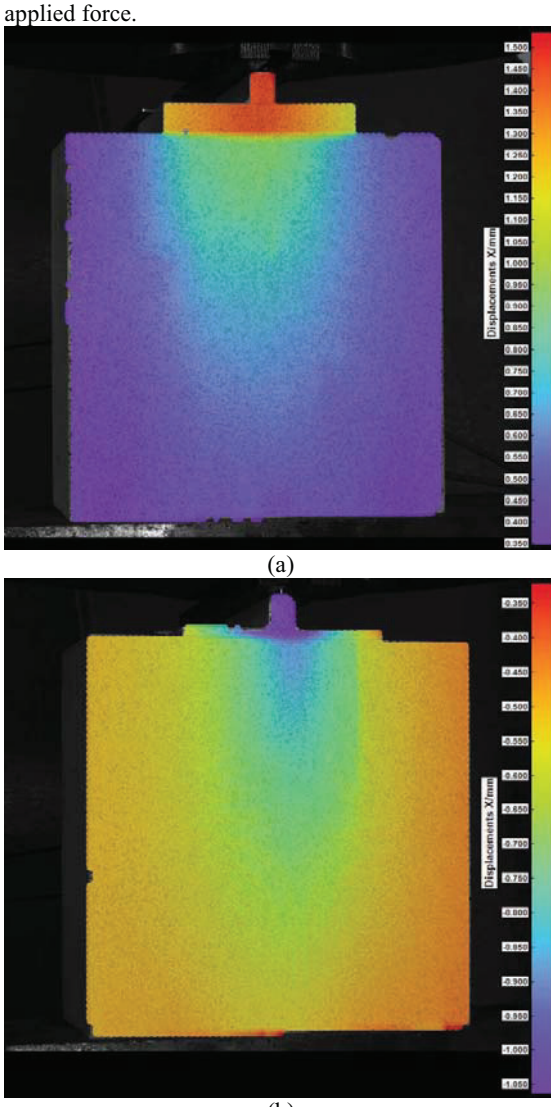

(a)

(b)

Figure 14: *Displacements registered through Digital Image Correlation for (a) T20 (b)T6.*

4 COMPONENT RESISTANCE PROPOSALS

4.1 PLASTIC RESISTANCE OF STEEL

The plastic bending moment resistance of the base plate per unit length should be taken as presented in Equation 8.

$$M_{pl} = \frac{1}{4} t_{ep} \cdot f_y \qquad (8)$$

Each side of T-stub was modeled as a cantilever beam and a uniform stress distribution in the contact between the plate and the timber was considered (Figure 15). According to the equivalent plate theory, equaling the plastic bending moment resistance of the base plate to a bending moment on the plate, Equation 9 is obtained to determine the equivalent bearing width. The resistance of the component can be obtained from the equivalent area, but in this case using the plastic additional bearing width (c_{tp}).

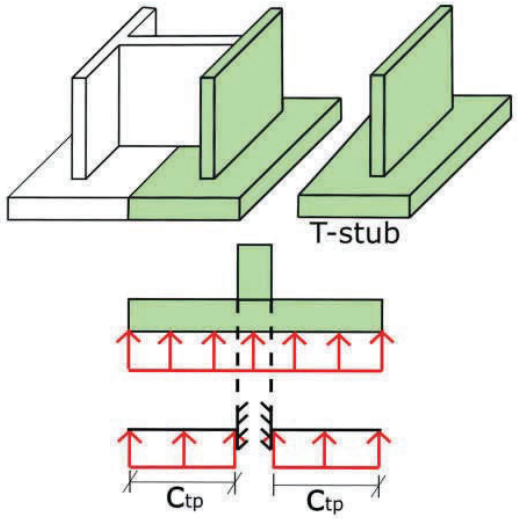

Figure 15. *Structural idealization of the component corresponding to the steel T-stub applying compression parallel to grain in timber member.*

$$c_{tp} = t_{ep} \sqrt{\frac{f_y}{2 \cdot f_{c,0} \cdot \gamma_{M0}}} \qquad (9)$$

4.2 VARIABLE STRESS DISTRIBUTION

From the DIC measurements, it was observed that, as expected, there is a non-uniform distribution of displacements in the contact between the steel plate and the timber. As shown in Figure 16(a), the displacements around the central part of the T-stub are greater, reducing towards the edges. This was repeated in all test types and for all plate thicknesses, since the beginning of the compression application. Based on those observations, a new approach is proposed for determining the equivalent bearing width, considering a variable distribution of stresses in contact between both materials, as shown in Figure 16(b).

https://doi.org/10.52202/069179-0038

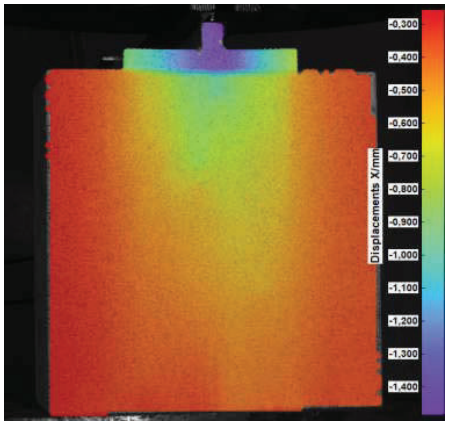

(a)

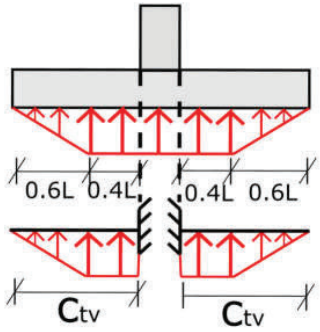

(b)

Figure 16. *(a) General displacements distribution from DIC tests. (b) Structural idealization for T-stub and timber in compression component with variable stress distribution.*

Considering this new stress distribution, the maximum moment acting on the T-stub becomes equal to $0.26 \cdot q \cdot L^2$ and, assuming the plate in elastic range, the Equation 10 can be formulated to calculate the c_{tv}. The component strength can be obtained from the equivalent area using variable distribution additional bearing width (c_{tv}).

$$c_{tv} = t_{ep}\sqrt{\frac{f_y}{1.56 \cdot f_{c,0} \cdot \gamma_{M0}}} \qquad (10)$$

5 RESULTS AND DISCUSSION

For simplicity in discussion of the results, the following nomenclatures were given for the propositions: Andreolli's one was called uniform distribution in elastic range (UD-ER), the plastic bending preposition was uniform distribution in plastic range (UD-PR) and the variable stress distribution was VD-ER. The analytical values of the component strength were calculated computing the $f_{c,0}$ equal to 24 MPa.

In Figure 17, it is possible to observe the curves of the relative displacements between the center and the edges of the T-stub flanges of two tests and in Table 2 the average strains for all the tests carried out. It appears that even considering the plastic limit of steel (UD-PR) or the variable stress distribution (VD-ER), the T-stub seems to be in a safe region from the design point of view, since the highest analytically determined strength is approximately 70% for specimen T20 and 55% for specimen T6 in relation to the experimental component strength.

As it is the T-stub that governs the structural behavior of the component, the strength reserve and ductility of steel can be exploited.

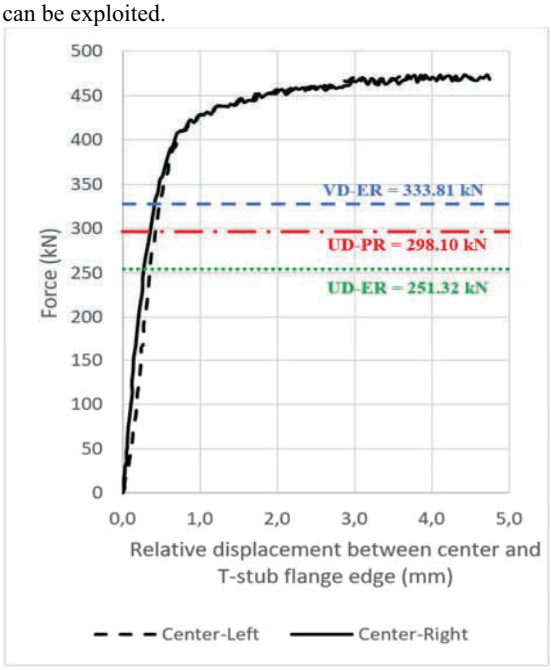

(a)

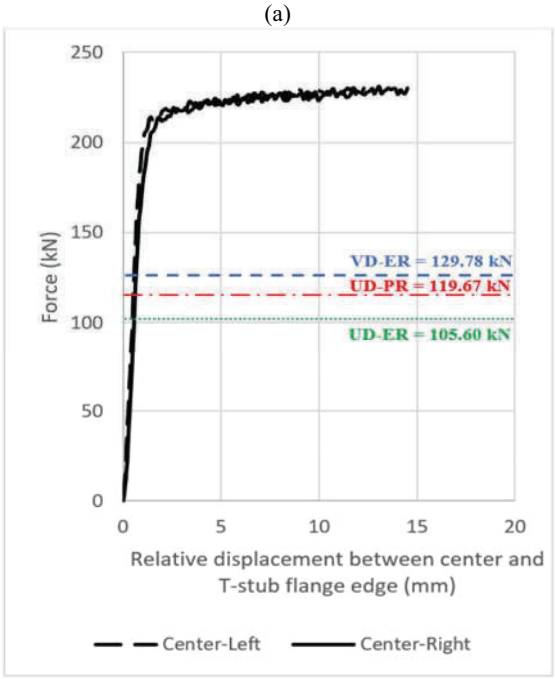

(b)

Figure 17: *Force-relative displacements curves for (a) T20 GT2 (b) T6 GT2.*

Table 2: *Summary of the steel and timber specimens tested, including the reference group.*

		UD-ER	UD-PR	VD-ER
T20	Force (kN)	251,32	298,10	331,81
	Relative Displac. (mm)	0,36	0,45	0,53
	Strain	0,0025%	0,0039%	0,0053%
T15	Force (kN)	199,29	234,37	259,66
	Relative Displac. (mm)	0,38	0,50	0,62
	Strain	0,0027%	0,0046%	0,0072%
T10	Force (kN)	147,26	170,65	187,51
	Relative Displac. (mm)	0,47	0,55	0,62
	Strain	0,0042%	0,0056%	0,0073%
T8	Force (kN)	126,45	145,16	158,65
	Relative Displac. (mm)	0,62	0,75	0,87
	Strain	0,0073%	0,0107%	0,0144%
T6	Force (kN)	105,60	119,67	129,78
	Relative Displac. (mm)	0,60	0,67	0,75
	Strain	0,0074%	0,0088%	0,0111%

The Figure 18 shows the maximum experimental component resistances and the theoretical values obtained by the three presented approaches: UD-ER, UD-PR and VD-ER. The proposals are coherent compared to the experimental tests. The bearing capacity of test specimens at T-stub failure is in the range from 1.36 (T20) to 1.88 (T6) times the capacity calculated according to variable distribution proposal, considering the average of experimental component strength. An improvement in the accuracy of the results was identified, since for UD-ER approach, the values were 1.80 (T20) and 2.31 (T6). In addition, the use of a variable distribution in elastic range (VD-ER), with greater displacements in the central region of the T-stub, is more consistent with the experimental behavior of the component.

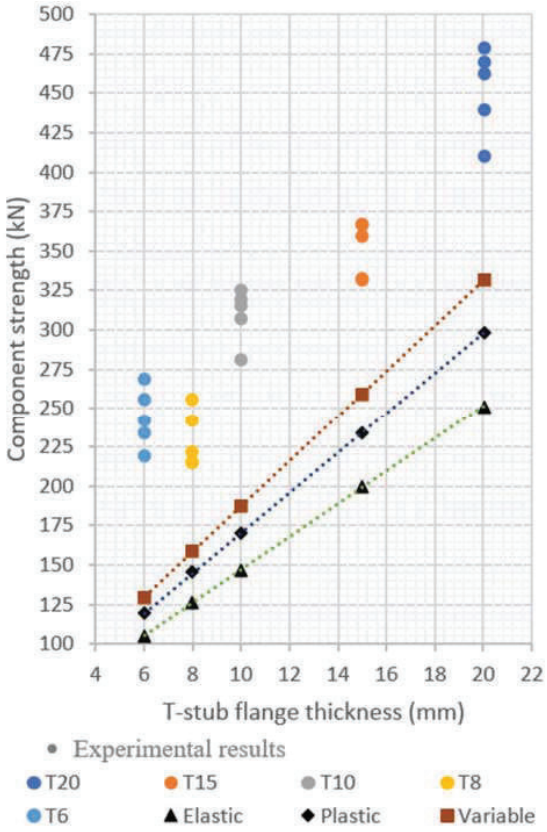

Figure 18: *Maximum component experimental resistances and theoretical values for the three different proposals.*

6 CONCLUSIONS

The structural behavior of the end-plate compressing timber parallel to grain component is governed by the yielding of the T-stub flange, for thicknesses usually used in design. In all compression tests, the timber did not show a clear and well-characterized failure, as occurred in the reference tests with a rigid plate.

As the stresses transmission is carried out by the contact between the two materials and according to the T-stub stiffness, the component strength is proportional to the thickness of the plate, that is, the greater the thickness of the plate, the greater the component strength.

From the beginning of each test, there is a difference in displacements between the central part and the edges of the T-stub flange, which indicates the occurrence of a non-uniform stress distribution between the T-stub flange and the timber. To analytically evaluate and predict the component strength, the concept of equivalent rigid plate was used, but in three different approaches.

The proposition of the equivalent plate with variable stress distribution proved to be coherent with the experimental behavior of the component and with a possible application in design, since the analytical values maintain an acceptable safety margin in relation to the experimental ones.

https://doi.org/10.52202/069179-0038

ACKNOWLEDGEMENT

Thanks to the Fundação para a Ciência e Tecnologia (FCT) for supporting this research under grant number BD/06301/2021. The work is part of RILEM TC TPT "Tests methods for a reliable characterization of resistance, stiffness and deformation properties of timber joints".

REFERENCES

[1] EN 1993-1-8 Eurocode 3: Design of steel structures - Part 1-8: Design of joints, European Committee for Standardisation, 2012

[2] J.-P. Jaspart, K. Weynand, Design of Joints in Steel and Composite Structures, ECCS Press/Ersnest & Sohn, 2016.

[3] P. Zoetemeijer, A design method for the tension side of statically loaded, bolted beam-to-column connections, HERON 20, 1974.

[4] J.-P. Jaspart, General report: session on connections, J. Constr. Steel Res. 55, 2000.

[5] Oliveira S., Costa R., Shahbazian A., Rebelo C., Harada Y., Simões da Silva L.: Component-based method for quasi-static cyclic behaviour ofsteel joints. Journal of Constructional Steel Research, 181, 2021.

[6] Wan W., Yan S., Zhang H, Rasmussen K.J.R.: A generalised component method for bolted angle connections. Journal of Constructional Steel Research, 2022.

[7] Wald F., Mares J., Sokol Z.: Component method for historical timber joints. The Paramount Role of Joints into the Reliable Response of Structures, 417-424, 2000.

[8] Postupka J., Kuhlmann U., Brühl F.: Ductile behaviour of dowl connections – application of the component method in timber construction. WCTE 2016

[9] Andreolli, M., Piazza, M., Tomasi, R., & Zandonini, R.: Ductile moment-resistant steel-timber connections. Proceedings of the Institution of Civil Engineers: Structures and Buildings, 164(2), 65–78, 2011.

[10] Yang, H., Liu, W., & Ren, X.: A component method for moment-resistant glulam beam-column connections with glued-in steel rods. Engineering Structures, 115, 42–54, 2016.

[11] Tao, H., Mao, M., Yang, H., & Liu, W.: Theoretical and experimental behaviour of a hybrid semi-rigid glulam beam-to-column connection with top and seat angles. Advances in Structural Engineering, 23(10), 2057–2069, 2020.

[12] Tomasi, R., Zandonini, R., Piazza, M., & Andreolli, M.: Ductile end connections for glulam beams. Structural Engineering International: Journal of the International Association for Bridge and Structural Engineering (IABSE), 18(3), 290–296, 2008.

[13] Steenhuis, M., Wald, F., Sokol, Z., Stark, J.: Concrete in compression and base plate in bending HERON Vol. 53, No ½, 2008.

[14] Stockwell, F.W. Jr. Preliminary Base Plate Selection, Engineering Journal AISC, Vol. 21, No.3, 1975, pp. 92-99.

[15] Murray T.M. Design of Lightly Loaded Steel Column Base Plates, Engineering Journal AISC, Vol. 20, 1983, pp. 143-152.

[16] Steenhuis, C.M., Bijlaard F. S. K. Tests On Column Bases in Compression, Published in the Commemorative Publication for Prof. Dr. F. Tschemmemegg, ed. by G. Huber, Institute for Steel, Timber and Mixed Building Technology, Innsbruck 1999.

[17] EN 14080: Timber structures - Glued laminated timber and glued solid timber - Requirements, European Committee for Standardisation, 2013.

[18] EN 1993-1-1 Eurocode 3: Eurocode 3: Design of steel structures - Part 1-1: General rules and rules for buildings, 2012.

World Conference on Timber Engineering Oslo 2023

COMPARISON BETWEEN EXPERIMENTAL RESULTS AND DESIGN EQUATIONS OF ARTIFICIALLY DEGRADED SINGLE STEP JOINTS

Daniel F. Lima[1], Jorge M. Branco[2], Lina Nunes[3]

ABSTRACT: In the case of interventions in existing buildings, the assessment of timber elements and joints, such as the Single Step Joint, is a challenge for engineers, especially when timber presents signs of biological degradation. In this context, many roof structures are subject to unnecessary substitutions due to the lack of knowledge about the behaviour of these types of joints, and specially the consequences of eventual biological attacks. This study aims to evaluate the residual shear strength of Single Step Joints artificially degraded by wood boring insects from the Anobiidae family (e.g. *Anobium punctatum)*. To achieve the established objectives, destructive tests were carried out on undamaged (reference level) and artificially degraded Single Step Joint specimens, varying the level of degradation. The results were analysed in terms of degradation level and compared with the results obtained with design equations for this type of joint found in the literature. From the analysis of the results, it was possible to observe the tendency of reduction of the shear strength with the increase of the degradation level.

KEYWORDS: Single Step Joint, Traditional carpentry connections, Biological degradation, *Anobium punctatum*

1 INTRODUCTION

Applying wood as a building material requires special attention, especially when it is used for structural functions. Despite its high complexity, when applied correctly with adequate protection and maintenance, wood is one of the most efficient building materials.

Like other natural organic materials, wood is subject to biological degradation, where the main agents are fungi and insects. Despite its recognized tradition and presence in the built heritage, knowledge about the biological degradation process of wooden structures, as well as its impacts on the service life of buildings, remains, to a certain extent, unknown.

Concerning degradation caused by insects, in countries with temperate climates, subterranean termites and woodboring beetles stand out, due to their ability to cause severe damage to structural elements with a consequent reduction in the service life of the structure [1]. On the other hand, anobiids (like the common furniture beetle or woodworm) represent a considerable challenge since the quantification of their impact on the mechanical strength of structural elements still raises many questions.

Typically, woodboring insects' infestation is assessed by the visual inspection of the element. In this case, the intensity of infestation is quantified by the density of apparent exit holes on the element surface. However, the diffuse attack of this insect makes the assessment of damage intensity more difficult [2]. In fact, despite being the most recurrent, this evaluation method presents too many uncertainties, since the number of internal galleries drilled by the insects is greater than the surface exit holes, which can lead to an underestimation of the level of degradation [3,4].

Regarding the reduction of the mechanical capacity caused by the anobiid infestation, in general, it is considered in the structural verification of old structural elements either by the reduction of the cross-section of the element (considering that the degraded zone does not present any strength) or assuming reduced mechanical properties for that element [5,6]. However, there is a clear lack of studies that can serve as a basis for engineers to adopt the appropriate reduction factors.

The lack of knowledge, combined with the difficulty in assessing the extent and severity of damage, is responsible for many unnecessary replacements of structures that could be subjected to curative treatments and/or reinforcements. In this context, timber roofs represent a great challenge, being common to find elements and joints degraded by insects and fungi due to their constant contact with the supporting masonry [7].

The present paper aims to discuss the impact of anobiids on the shear strength of Single Step Joints. Previously, Single Step Joint design equations were studied by [8] and will be used as reference to identify the need of introducing a safety factor for woodworm degraded elements.

2 Traditional Carpentry Joints

Carpentry connections are usually composed of notched joints and are traditionally used to connect the rafter and

[1] Daniel F. Lima, ISISE, University of Minho, Portugal, daniel.asmf.lima@gmail.com
[2] Jorge M. Branco, ISISE, University of Minho, Portugal, jbranco@civil.uminho.pt
[3] Lina Nunes, National Laboratory for Civil Engineering (LNEC), Portugal, linanunes@lnec.pt

https://doi.org/10.52202/069179-0039

the tie beam in timber trusses, where the stresses are transferred between the elements by axial compression and/or friction [9,10]. Over time, geometric variants of this type of connection have been developed, standing out the Single Step Joint and the Double Step Joint, being the former the most common due to their simplicity and easier manufacturing process.

Among Single Step Joints, exist three main families: the Geometrical Configuration Ideal Design (GCID), the Geometrical Configuration Perpendicular to the Rafter (GCPR), and the Geometrical Configuration Perpendicular to the Tie Beam (GCPTB) [11]. The difference between the three families relies on the inclination of the front notch (α) in relation to the rafter skew angle (β), where the GCID has α equivalent to β/2, the GCPR has α equivalent to β and the GCPTB has α=0º (figure 2.1).

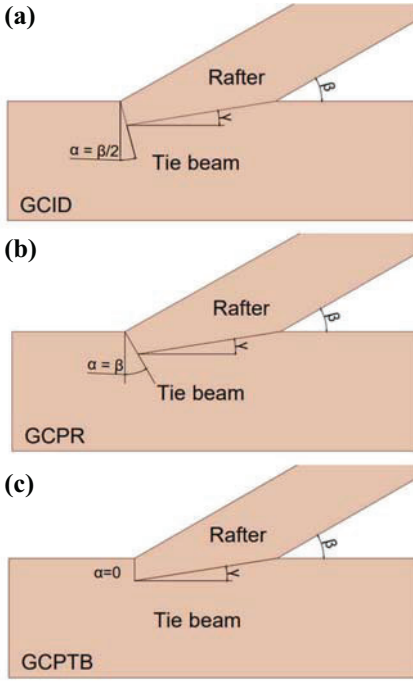

Figure 2.1: *Main SSJ geometrical variations. (a) Geometrical Configuration Ideal Design (GCID); (b) Geometrical Configuration Perpendicular to the Rafter (GCPR); (c) Geometrical Configuration Perpendicular to the Tie Beam (GCPTB)*

With the development of new precise technologies (for example CNC) and because it is considered the most efficient, the GCID is the recommended. However, due to the lack of accurate carpenter tools in the past, the other two configurations are commonly found in older constructions with low quality (in terms of carpenters' skills) [8].

Two possible failure modes are considered for the SSJ: shear parallel to the fibres at heel depth and crushing parallel to the fibres at the front notch [7]. However, Verbist et al. [8] questioned the consideration of crushing at the front notch as a failure mode for the SSJ, since the crushing will only cause the densification of the wood fibres and consequent deformations at the joint, being shear the final failure mode.

In recent decades, several studies have addressed the mechanical behaviour of Single Step Joint, for example, Verbist et al. [8], Branco et al. [7], Munafò et al. [12], Palma et al. [13], among others. Despite being traditional and commonly found in constructions, both in new and older constructions, the SSJ continue to present knowledge gaps to be explored.

3 Materials and methods

3.1 SSJ specimens

The Single Step Joints specimens with structural dimensions used on this study were made of scots pine (*Pinus sylvestris* L.), acquired in Northern Spain, followed the Geometrical Configuration Perpendicular to the Tie Beam (GCPTB), consequently, the front notch perpendicular to the tie beam grain (α=0°). Additionally, a skew angle between the tie beam and the rafter of 30° ($\beta = 30°$), a heel depth of 30mm ($h_V = 30mm$), a width of 100mm ($b = 100mm$), and a heel length of 100mm ($l_V = 100mm$) were adopted (figure 3.1). The geometry of the specimens was defined based on the results obtained by [8], with the aim to induce failure by shear at the heel depth.

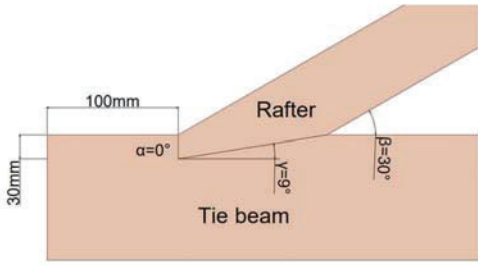

Figure 3.1: *Geometry adopted for the SSJ specimen*

Before carrying out the procedures of the experimental campaign, the specimens were stored in a climatic chamber at a constant temperature of 20 ± 1°C and a relative humidity of 60 ± 5% until mass stabilization (i.e., difference ≤ 0.1% between consecutive measurements, EN 13183 [14]]). Under these climatic conditions, the equilibrium moisture content of the wood should be approximately 12% [15]. Additionally, density ($\rho_{12\%}$) was determined following the procedures of NP 616 [16].

3.2 Visual grading

To ensure a control quality of the wood and to confirm the strength class in accordance with EN 338 [17], a visual grading of the specimens was carried out, based on a photographic survey followed by the application of the procedure described by UNE 56544 [18]. Therefore, all the defects and singularities referred to in the applied standard were duly identified and measured, namely: knots, resin pockets, fissures, wane, biological damage,

distortions, and width of the annual rings, among others. For visual inspections on structural elements with a rectangular cross-section width greater than 70mm, UNE 56544 [18] defines only one quality class named MEG (*Madera Estructural de Gruesa escuadría*). The quality class is correlated with the strength class (EN 338 [17]) using EN 1912 [19], which establishes that the scots pine classified as MEG quality, with origin in Spain, fits within strength class C22.

3.3 Shear test parallel to grain performed on small specimens

Additionally, the shear strength parallel to grain of the wood used in the SSJ tests was obtained out based on shear tests on small specimens. The test method was adopted according to the recommendations of the American standard ASTM D143 [20]. The test was performed on 50 by 50 by 63mm defect-free specimens to obtain failure in the 50 by 50mm section, as shown in figure 3.2.
The test was carried out with a load application controlled by the displacement of the actuator at a constant rate of 0.6 mm/min until failure.

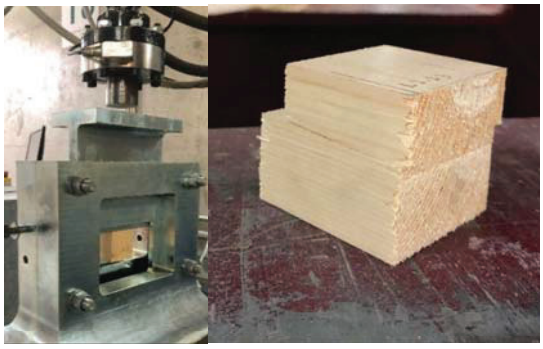

Figure 3.2: *Shear tests parallel to the grain performed on small specimens*

The shear strength was calculated using the Equation (1).

$$f_{v,SP} = \frac{N}{A_v} \quad (1)$$

Where $f_{v,SP}$ is the shear strength (MPa), N is the maximum load recorded by the load cell (N), and A_v is the shear-resistant area (mm^2) measured for each specimen after the test.
In total, 88 specimens were tested, and the value of the 5th percentile was adopted as the characteristic shear strength. All specimens used in those tests were stored in a climatic chamber at a constant temperature of 20 ± 1°C and a relative humidity of 60 ± 5% until mass stabilization and density ($\rho_{12\%}$) was determined following the procedures of NP 616 [16].

3.4 Simulation of the degradation

The degradation by anobiids was simulated by manual drilling in the direction parallel to the grain on the tie beam-end element [21]. The dimensions of the perforated galleries were approximately 2 mm in diameter and 100 mm in length, since the furniture beetle normally makes circular galleries of 1 to 3 mm in diameter [15], and the length of the tie beam-end is 100 mm.
Three different levels of degradation were adopted (DL-I, DL-II, and DL-III) varying the density of perforated galleries (1.67 holes/cm², 3.33 holes/cm², and 4.00 holes/cm²), seeking to achieve realistic degradation levels.

3.5 SSJ Tie beam-end shear test

The destructive test consists of applying an increasing normal load (N_{rafter}) on the rafter, controlled by the actuator displacement with a constant rate of 0.01 mm/s (figure 3.3). The normal load (N_{rafter}) results in compressive stresses on the surfaces of the SSJ (compression parallel to the grain on the Front Notch and perpendicular to the grain on the Bottom Notch) and shear stresses on the tie beam-end.
The expected failure mode of the specimen is the shear failure at the tie beam-end, induced by the low skew angle (β=30°) and reduced ratio between the heel depth and the shear length (lv/tv≤6) (section 3.1) [8].

Figure 3.3: *SSJ Tie beam-end shear test*

Forty specimens were tested: 4 undamaged specimens (i.e., reference) and 12 specimens for each of the three levels of degradation (section 3.4).

3.6 Design rafter load-bearing capacity ($N_{rafter,Rd}$)

In this study, Equation (2) [8] will be used to verify the design rafter load-bearing capacity ($N_{rafter,Rd}$).

https://doi.org/10.52202/069179-0039

$$N_{rafter,Rd} \leq k_{v,red} \cdot f_{v,k} \frac{k_{mod}}{\gamma_M} \cdot \frac{b \cdot k_{cr} \cdot l_{v,eff}}{cos\beta} \quad (2)$$

Where, $k_{v,red}$ is the reduction factor considering the non-uniform shear stress distribution, $f_{v,k}$ is the characteristic shear resistance, k_{mod} is the modification factor considering duration of load and moisture content, γ_M is the partial factor for wood properties, b is the width, k_{cr} is reducer factor considering the eeccentricity between the joint and the support of the tie beam, $l_{v,eff}$ is the effective shear length, and β is the skew angle between the rafter and tie beam.

4 RESULTS AND DISCUSSION

4.1 Visual grading

From the visual grading, it was possible to identify a series of natural defects inherent to the sawn wood. The most frequent defects were knots and drying fissures. However, all specimens submitted to the tests comply with the verifications established in UNE 56544 [18] and fall within the MEG quality class. Thus, applying the correlation from EN 1912 [19], the timber tested in this study was classified as C22. Moreover, EN 338 [17] establishes that the characteristic shear resistance of softwood classified as C22 is 3.8 MPa.

4.2 Shear test parallel to grain performed on small specimens

The results of the shear tests on small specimens and quantification of density, are presented in table 4.1.
The shear strength values varied between 5.42 MPa and 8.01 MPa, with an average of 6.59 MPa and a coefficient of variation of 8.88%. The characteristic shear strength parallel to the grain obtained on these tests is 5.66 MPa (5th percentile).
Regarding the density of the specimens, the values vary between 405.0 kg/m^3 and 566.3 kg/m^3, with an average of 501.6 kg/m^3. The EN 384 [22] standard considers the value of the 5th percentile of the sample as the characteristic density of wood (ρ_k). In the case of the present study, 419.9 kg/m^3.

***Table 4.1**: Shear tests parallel to the grain and density results for the 88 tested specimens*

	Shear strength ($f_{v,SP}$)	**Density ($\rho_{12\%}$)**
Max. Value	8.01 MPa	566.3 kg/m^3
Min. Value	5.42 MPa	405.0 kg/m^3
Average	6.59 MPa	501.6 kg/m^3
Stand. dev.	0.58 MPa	38.6 kg/m^3
C.V.	8.88%	7.69%
5th percentile	5.66 MPa	419.9 kg/m^3

4.3 Design rafter load-bearing capacity ($N_{rafter,Rd}$)

In this study, two different theoretical SSJ shear strength will be considered. The first, is considering the characteristic shear resistance as the value obtained through the visual grading, while the second considers the shear test on small specimens' 5th percentile value. Thus, the two characteristics shear strength adopted to apply on Equation (2) are 3.8 MPa and 5.42 MPa, respectively.
Regarding the other inputs for Equation (2), table 4.2 presents the values adopted and the references used to adopt it.

***Table 4.2:** Input values and references adopted for Equation (2)*

	Value	**References**
$k_{v,red}$	0.96	[8,23]
k_{mod}	0.9	[24]
γ_M	1.3	[24]
k_{cr}	1	[8]
$l_{v,eff}$	$\min(l_v; 8h_v) = 100mm$	Section 3.1,
b	100mm	Section 3.1
β	30°	Section 3.1

Therefore, the two values for the design rafter load-bearing capacity ($N_{rafter,Rd}$) obtained are 27.7 kN (for $f_{v,k}$=3.8 MPa) and 39.5 kN (for $f_{v,k}$=5.42 MPa).

4.4 SSJ Tie beam-end shear test

Table 4.3 presents the results obtained in the SSJ tie beam-end shear tests and the quantification of density.

***Table 4.3:** Summary of the results obtained from the quantification of the density and the SSJ tie beam-end shear tests*

Group		REF	DL-I	DL-II	DL-III
Nº		4	12	12	12
$\boldsymbol{\rho_{12}}$ [kg/m³]	$\bar{X}$	529	514	511	493
	σ	26	50	41	52
	C.V.	4.9%	9.8%	7.9%	10.6%
$\boldsymbol{N_{rafter,SSJ}}$ [kN]	$\bar{X}$	43.4	45.3	39.6	38.6
	σ	2.3	8.2	3.4	5.2
	C.V.	5.2%	18.2%	8.7%	13.5%

$\bar{\boldsymbol{X}}$ – Average; $\boldsymbol{\sigma}$ – Standard Deviation; C.V. – Coefficient of variation; $\boldsymbol{\rho_{12}}$ – Density corrected to a 12% moisture content; $\boldsymbol{N_{rafter,SSJ}}$ – Experimental rafter load-bearing capacity

As expected, all 40 specimens presented shear failure without crushing parallel to the grain at the front notch or perpendicular to the grain at the bottom notch (figure 4.1).

Figure 4.1: *Characteristic shear failure on the tie beam-end observed in the 40 SSJ specimens tested.*

Regarding the rafter load-bearing capacity, firstly, it was verified that the distribution of the results fit the normal distribution through the Shapiro-Wilk test (p-value = 0.14).

As previously mentioned, drilling densities equivalent to 1.66 holes/cm², 3.33 holes/cm², and 4.00 holes/cm² were adopted, corresponding to groups DL-I, DL-II, and DL-III, respectively. Figure 4.2 shows the bar chart that graphically represents the shear strength mean values and the respective standard deviations of the degradation groups.

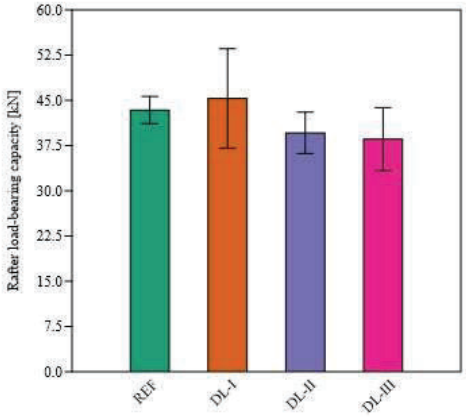

Figure 4.2: *Bar chart of the results of the tie beam-end shear tests*

Through the analysis of table 4.3 and figure 4.2, it is possible to observe that the group with the lowest level of degradation (DL-I) presented superior results (+4%, on average) compared to the reference group (REF). Therefore, it is possible to conclude that, at this level, the degradation was not enough to cause significant damage to the specimen and, in this group, other properties such as density and wood natural variability, were more determinant in the shear strength parallel to the grain. On the other hand, the higher two levels of degradation showed lower tests results than the reference group (-10% and -11%, on average), demonstrating the influence of the drilled galleries.

4.5 Comparison between experimental results and design equations

Table 4.3 presents the comparison between the theoretical rafter load-bearing capacity, calculated from Equation (2), and the average results of the SSJ tie beam-end shear tests. The comparison is made in terms of the relative variation $\Delta_{rel,rafter}$ (%). In table 4.4, $N_{rafter,Rd1}$ represents the design rafter load-bearing capacity considering the results of the visual grading, while $N_{rafter,Rd2}$ considers the results of the shear test on small specimens.

Table 4.4: *Experimental results divided by drilling density, design equation results, and relative variation between the experimental and theoretical results.*

	N_{rafter} [kN]	$\Delta_{rel,rafter1}$	$\Delta_{rel,rafter2}$
$N_{rafter,Rd1}$	27.7	-	-
$N_{rafter,Rd2}$	39.5	-	-
$N_{rafter,SSJ,REF}$	43.4	56.6%	9.8%
$N_{rafter,SSJ,DL-I}$	45.3	63.6%	14.7%
$N_{rafter,SSJ,DL-II}$	39.6	43.0%	0.2%
$N_{rafter,SSJ,DL-III}$	38.6	39.2%	-2.4%

From table 4.4, it is possible to observe the reliability of the design equation when considering the shear test on small specimens performed on this study ($\Delta_{rel,rafter2}$ between 14.7% and -2.4%), while the C22 grading shows theoretical results much lower than the experimental results ($\Delta_{rel,rafter}$ between 63.6% and 39.2%).
The results are exposed in figure 4.3 in a scatter plot, where the blue line represents the $N_{rafter,Rd1}$ and the red line $N_{rafter,Rd2}$.

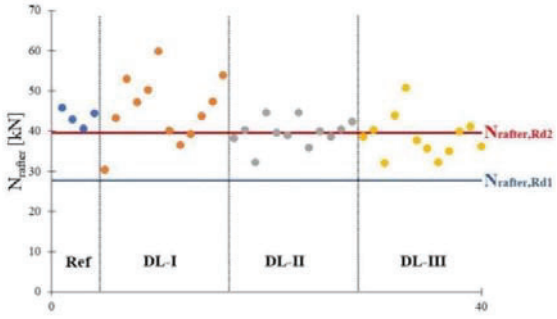

Figure 4.3: *Tests results separated by level of degradation and comparison with design values.*

Analysing the graph exposed in figure 4.3, it is possible to infer that, when considering the strength class C22 proposed by EN 1912 ($N_{rafter,Rd1}$), all 40 specimens presented higher values, discarding the need to consider a reduction factor due to degradation by anobiids. On the other hand, when considering the value of the characteristic resistance obtained by shear test on small specimens ($N_{rafter,Rd2}$), it is possible to notice that all the reference specimens (without degradation) presented

https://doi.org/10.52202/069179-0039

values slightly higher than those obtained by applying the equation (2) and that the number of tests with values below the $N_{rafter,Rd2}$ line increase with increasing of the level of degradation (3 tests for the DL-I, 5 for the DL-II and 7 for the DL-III level).

Therefore, based on the analysis of table 4.4 and figure 4.5, it can be concluded that although the shear test on small specimens more accurately represents the value of the wood's characteristic shear strength ($f_{v,k}$), it indicates the need to assign a reduction factor due to biological degradation to Equation (2) for the correct determination of the design rafter load-bearing capacity of SSJ degraded by anobiids.

5 CONCLUSIONS

From the results of the experimental campaign and the application of the design equation, it is possible to infer that, when considering the strength grading C22 for scots pine, the degradation achieved in this study is not enough to reduce the load-carrying capacity to the point that element replacement is required, confirming the theory that many replacements are unnecessary [3]. On the other hand, shear test on small specimens presented a more precise characteristic shear strength, and, in this case, it is clear the tendency of reducing the shear strength with the increase of the level of degradation and the necessity to impose a reduction factor to the design equation due to biological degradation. Thus, for future developments, it is intended to establish a correlation between the level of degradation by anobiids and the residual shear strength of SSJ, with the aim to propose values for that reduction factor.

ACKNOWLEDGEMENT

This work is supported by national funds through FCT – Fundação para a Ciência e a Tecnologia within a Ph.D. scholarship within MIT Portugal Program (PRT/BD/152833/2021).

REFERENCES

[1] Eaton RA, Hale MDC. Wood: decay, pests, and protection. 1st ed. London: Chapman & Hall; 1993.

[2] Reinprecht L. Wood deterioration, protection and maintenance. Chichester: John Wiley & Sons Ltd; 2016.

[3] Parracha JL, Pereira MFC, Maurício A, Machado JS, Faria P, Nunes L. A semi-destructive assessment method to estimate the residual strength of maritime pine structural elements degraded by anobiids. Materials and Structures/Materiaux et Constructions 2019;52. https://doi.org/10.1617/s11527-019-1354-9.

[4] Parracha J, Pereira M, Maurício A, Faria P, Lima DF, Tenório M, et al. Assessment of the density loss in anobiid infested pine using x-ray micro-computed tomography. Buildings 2021;11. https://doi.org/10.3390/buildings11040173.

[5] Cruz H, Yeomans D, Tsakanika E, Macchioni N, Jorissen A, Touza M, et al. Guidelines for on-site assessment of historic timber structures. International Journal of Architectural Heritage 2015;9:277–89. https://doi.org/10.1080/15583058.2013.774070.

[6] UNI 11119. Cultural heritage – Wooden artefacts – Load bearing structures of buildings – On site inspection for the diagnosis of timber members. Milan, UNI; 2004.

[7] Branco JM, Verbist M, Descamps T. Design of three Step Joint typologies: Review of European standardized approaches. Eng Struct 2018;174:573–85. https://doi.org/10.1016/j.engstruct.2018.06.073.

[8] Verbist M, Branco JM, Poletti E, Descamps T, Lourenço PB. Single Step Joint: overview of European standardized approaches and experimentations. Materials and Structures/Materiaux et Constructions 2017;50. https://doi.org/10.1617/s11527-017-1028-4.

[9] Branco JM. Influence of the joints stiffness in the monotonic and cyclic behaviour of traditional timber trusses. Assessment of the efficacy of different strengthening techniques. Doctoral Thesis. University of Minho, 2008.

[10] Yeomans D. The repair of historic timber structures. Thomas Telford Ltd; 2003.

[11] Oslet G. Encyclopédie théorique & pratique des connaissances civiles & militaires - Traité de charpente en bois. Paris: 1890.

[12] Munafò P, Stazi F, Tassi C, Davì F. Experimentation on historic timber trusses to identify repair techniques compliant with the original structural–constructive conception. Constr Build Mater 2015; 87:54–66. https://doi.org/10.1016/j.conbuildmat.2015.03.086.

[13] Palma P, Ferreira J, Cruz H. Monotonic tests of structural carpentry joints. WCTE2010 - World conference on timber engineering, Trento: 2010.

[14] EN 13183. Moisture content of a piece of sawn timber. Brussels, Belgium: European Committee for Standardization CEN; 2012.

[15] Cruz H, Jones D, Nunes L. Wood. Materials for Construction and Civil Engineering, Cham: Springer International Publishing; 2015, p. 557–83. https://doi.org/10.1007/978-3-319-08236-3_12.

[16] NP 616. Madeiras. Definição da massa volúmica. IGPAI, Lisbon; 1973.

[17] EN 338. Structural timber - Strength classes. Brussels, Belgium: European Committee for Standardization CEN; 2016.

[18] UNE 56544. Clasificación visual de la madera aserrada para uso estructural - Madera de coníferas. AENOR, Madrid; 2011.

[19] EN 1912. Structural timber. Strength classes. Assignment of visual grades and species. Brussels, Belgium: European Committee for Standardization CEN; 2012.

[20] ASTM D143. Standard Methods of Testing Small Clear Specimens of Timber. ASTM Annual Book of Standards, West Conshohocken; 2021.

[21] Lima DF. Estruturas antigas de casquinha. Avaliação do impacto do caruncho pequeno por

simulação da degradação. Master thesis. University of Minho, 2022.
[22] EN 384. Structural timber - Determination of characteristic values of mechanical properties and density. Brussels, Belgium: European Committee for Standardization CEN; 2016.
[23] Verbist M, Branco JM, Descamps T. Cohesive zone models of single step joint damaged due to the shear crack. 6th European Conference on Computational Mechanics (ECCM 6), Glasgow: 2018, p. 1257–68.
[24] EN 1995-1-1. Eurocode 5 – Design of timber structures – Part 1.1: General – Common rules and rules for buildings. Brussels, Belgium: European Committee for Standardization CEN; 2004.

https://doi.org/10.52202/069179-0039

World Conference on Timber Engineering Oslo 2023

STUDY ON THE RELATIONSHIP BETWEEN INTERLAYER DEFORMATION ANGLE AND TORN WALLPAPER OF WOODEN HOUSES

Sora Sunakozawa[1], Kiyotaka Terui[2], Hideyuki Nasu[3]

ABSTRACT: The purpose of this study is to clarify the elongation rate of wallpaper required to prevent wallpaper from breaking in wooden houses due to medium earthquakes. For this purpose, it is necessary to clarify the relationship between the elongation rate of wallpaper and the interlaminar deformation angle at which the wallpaper breaks. However, there is no defined method to measure the elongation rate of wallpaper. Therefore, this study first aimed to establish a method to measure the elongation rate of wallpaper and conducted three types of tensile tests. In addition, a shear test was conducted to reproduce the original tearing of the wallpaper, and the results were compared with those of the tensile test to verify which tensile test results are valid as a measurement method.

KEYWORDS: Wooden Houses, Interlayer deformation angle, Wallpaper, Plasterboard

1 INTRODUCTION

There is a problem of wallpaper tearing in houses due to earthquakes and other events. This is because horizontal forces acting on the house cause interlaminar deformation, which rotates the plasterboard, the base of the interior, and causes misalignments and openings between adjacent boards. According to the Japanese Building Standard Law, the angle of interstory deformation generated by a moderate earthquake should be kept within 1/120 rad. if no part of the house is damaged due to deformation of structural members. The interlaminar deformation angle at this point is generally called the damage limit. According to this definition, it can be interpreted that the house can be used continuously without repair if it is within the damage limit. However, previous studies have shown that wallpaper breaks even at interlaminar deformation angles smaller than the damage limit. Therefore, the objective of this study was to estimate the target elongation rate of wallpaper necessary to prevent the wallpaper from tearing within the damage limit.

2 SUMMARY OF RESEARCH

To estimate the target value, the relationship between the elongation rate of wallpaper and the interlaminar deformation angle at which breakage occurs is investigated. Since there is no established method for measuring the elongation rate of wallpaper, tensile tests of wallpaper were conducted to establish a measurement method. However, since the tensile test alone does not reproduce the original wallpaper breakage, a shear test of the wallpaper was conducted and compared with the results of the tensile test to confirm the correlation.

3 STANDARD TENSILE TESTS

3.1 SPECIMEN SPECIFICATIONS

The test specimens were made by cutting wallpaper into strips 15 mm wide and 280 mm long (Fig.1,2). The gripping position was set at 50 mm from both ends, and the center 180 mm was set as the elongation allowance. Six types of vinyl wallpaper, which are frequently used in Japan, were used for the test specimens. Six types of vinyl wallpaper with different surface shapes, foam amounts, and elasticity were used (Table 1). The first letter of the test specimen name is derived from the surface shape, and the second letter from a word indicating the characteristics of each specimen. A total of 36 specimens, six of each specification, were used.

Table 1 List of specimen specifications

Specimen name	Surface form	Thickness [mm]	Feature
SN	Stone	0.42	Normal vinyl cloth
SF	Stone	0.60	Foamed to increase thickness
SF’	Stone	0.55	Foamed to increase thickness
SS	Stone	0.58	Stretch performance
FF	Fabric	0.60	Foamed to increase thickness
FL	Fabric	0.72	Used for a long time

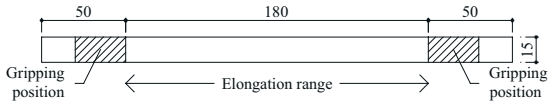

Figure 1. *Tensile specimen dimensions*

[1]Sora Sunakozawa, Graduate School, Nippon Institute of Technology, JAPAN, sora.sunakozawa@gmail.com
[2]Kiyotaka Terui, Head of Structural G, POLUS R&D Center of Life-Style Co., Ltd, JAPAN, 01452terui-sz@polus.co.jp
[3]Hideyuki Nasu, Prof., PhD. in Eng., Nippon Institute of Technology, JAPAN, hideyuki.nasu@nit.ac.jp

https://doi.org/10.52202/069179-0040

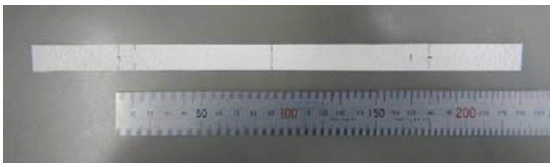

Figure 2. *Tensile specimen shape*

3.2 SUMMARY OF EXPERIMENTS

Tensile tests were conducted to measure the elongation rate of wallpaper. For the test, tensile force was applied to the specimen using a 1 kN universal testing machine at the Nippon Institute of Technology (Fig. 3). The test was applied at a rate of 20 mm/min until the wallpaper broke. Rupture was determined when the load dropped from the maximum load to half of the maximum load. Elongation was determined by dividing the displacement at break by the elongation threshold and expressed as a percentage.
If the wallpaper broke due to the tightening force when the testing machine gripped the specimen, the correct elongation rate of the wallpaper could not be measured. Therefore, if the specimen broke within 10 mm from the gripping position, the result was considered invalid (Fig. 4, 5).

Figure 3. *Testing machine*

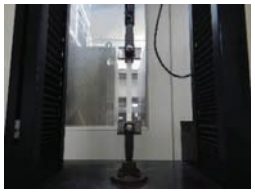

Figure 4. *Specimen installed*

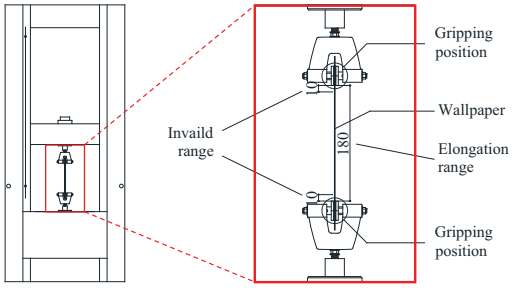

Figure 5. *Specimen installation state and invaild range*

3.3 EXPERIMENTAL RESULT

The test results from the standard tensile test are shown in Table 2 and Fig. 6. Slight differences in elongation rate and maximum proof stress were observed among the wallpaper types. The highest elongation value was obtained with SF, which has a stony surface and a large amount of foam, while SS, which has a stretch performance, showed the third highest elongation value. Fracture behavior was similar for all specifications, with the wallpaper breaking instantaneously at maximum load. One reason for the lack of difference was the shape of the vinyl wallpaper. Vinyl wallpaper is manufactured by coating vinyl chloride resin onto backing paper. Although the backing paper has higher resistance than the vinyl resin, it is not elastic and is therefore prone to rupture. When the backing paper breaks, the vinyl resin also breaks, and it is thought that it was difficult to obtain a difference in results.
However, when vinyl wallpaper is applied, a large amount of water is used to dilute the glue, which may reduce the resistance of the backing paper. Therefore, in the next test, the resistance of the backing paper will be reduced by adding moisture to the wallpaper, and the elongation rate will be measured with the effect reduced.

Table 2 *Standard tensile tests results*

Specimen name	Elongation rate [%]	Pmax [N]
SN (Stone Normal)	1.58	49.82
SF (Stone Foamed)	2.22	66.04
SF' (Stone Foamed)	1.86	70.05
SS (Stone Stretch)	1.89	71.07
FF (Fabric Foamed)	1.60	50.69
FL (Fabric Long)	2.11	62.91

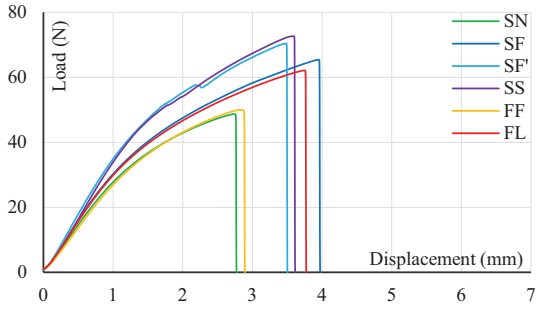

Figure 6. *Std. tensile tests graph*

4 WET TENSILE TESTS

4.1 SPECIMEN SPECIFICATIONS

The shape of the specimen was the same as in the standard tensile test. The same six types of vinyl wallpaper were used as in the standard tensile test. The test specimens were six of each specification, for a total of 36 specimens. The condition of the specimens was also changed to reduce the influence of the backing paper. In order to reproduce the decrease in resistance due to moisture in the glue when applying vinyl wallpaper, the specimens were impregnated with water for 5 minutes, and the excess water droplets were wiped off using tissue paper (Fig. 7,8).

Fig. 7 *Impregnating wallpaper*

Fig. 8 *Wiping off excess moisture*

4.2 SUMMARY OF EXPERIMENTS

In order to measure the elongation rate of wallpaper with the influence of the backing paper reduced, tensile tests were conducted with the specimens wet. For the test,

https://doi.org/10.52202/069179-0040

tensile force was applied to the specimens using a 1 kN universal testing machine at the Nippon Institute of Technology. After impregnating the specimen for 5 minutes before applying the force, water droplets on the surface were wiped off and the force was applied immediately. The test was applied at a rate of 20 mm/min until the wallpaper ruptured. Rupture was determined when the load dropped from the maximum load to half of the maximum load. Elongation was calculated by dividing the displacement at break by the elongation threshold and expressed as a percentage.
If the wallpaper broke due to the clamping force when the testing machine gripped the specimen, the correct elongation rate of the wallpaper could not be measured. Therefore, if the specimen broke within 10 mm from the gripping position, the result was considered invalid.

4.3 EXPERIMENTAL RESULT

The test results of the wet tensile test are shown in Table 3 and Fig. 9. As a result of the moisture content in the wallpaper, there were large differences in the maximum proof stress and elongation rate. In addition, the wallpapers exhibited two types of fracture behavior: integrally fractured and plastically deformed. The one-body break type (Fig. 10) is a rupture behavior in which the vinyl resin and the backing paper rupture at the same time, and was observed in SF, SF', FF, and FL, which have large amounts of foam. The plastic deformation type (Fig. 11) is a failure behavior in which the vinyl resin and backing peel off at the maximum proof stress (Fig. 12), and only the backing breaks, causing plastic deformation of the vinyl, and was observed in standard SN and SS with stretch performance. The stretch performance of SS was particularly clear, showing an elongation rate of 8.06 %, more than 60 % higher than the elongation rate of other specifications, which was around 5 %.
We believe that the wet tensile test was able to measure the performance of the vinyl resin itself by wetting the wallpaper and reducing the effect of the backing paper. However, the wallpaper is actually wet only when it is installed, and the glue is considered to have already dried when the earthquake occurs. Therefore, in the next tensile test, we decided to reproduce the wallpaper after it had dried and apply force.

Table 3 *Wet tensile tests results*

Specimen name	Elongation rate [%]	Pmax [N]
SN (Stone Normal)	5.43	16.04
SF (Stone Foamed)	5.24	32.32
SF' (Stone Foamed)	4.95	30.01
SS (Stone Stretch)	8.06	18.93
FF (Fabric Foamed)	5.23	15.23
FL (Fabric Long)	4.83	14.89

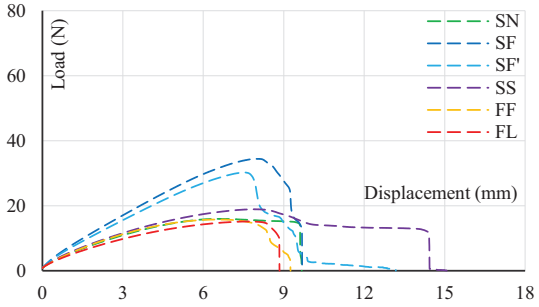

Figure 9. *Wet tensile tests graph*

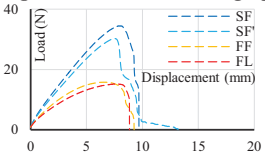

Fig. 10 *One-body break type*

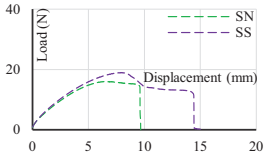

Fig. 11 *Plastic deformation type*

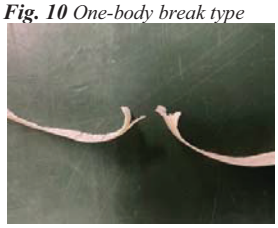

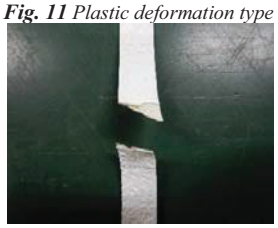

Figure 12. *Peeling of vinyl resin and backing paper*

Fig. 13 *Break point of SS*

5 DRY TENSILE TESTS

5.1 SPECIMEN SPECIFICATIONS

The shape of the test specimen was the same as in the standard and wet tensile tests. In this test, three types of vinyl wallpaper (SN, SF, and SS) were tested for verification purposes. A total of 18 specimens were tested, six for each.
After impregnating the specimens under the same conditions as in the wet tensile test, the specimens were allowed to dry for three days (Fig. 14, 15). This reproduced the condition of the wallpaper after drying at the time of the earthquake.

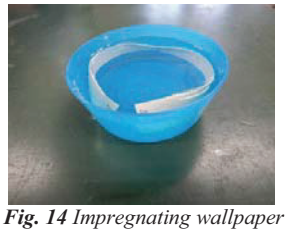

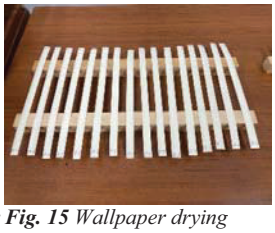

Fig. 14 *Impregnating wallpaper* ***Fig. 15*** *Wallpaper drying*

5.2 SUMMARY OF EXPERIMENTS

In order to reproduce the condition after the glue dried and measure the elongation rate of the wallpaper, a tensile test was performed by wetting the specimen and then drying it. For the test, tensile force was applied to the specimens using a 1kN universal testing machine at the Nippon Institute of Technology. After impregnating the specimens for 5 minutes, the force was applied to the specimens that had dried for 3 days. The test was applied at a rate of 20 mm/min until the wallpaper ruptured.

Rupture was determined when the load dropped from the maximum load to half of the maximum load. Elongation was calculated by dividing the displacement at break by the elongation threshold and expressed as a percentage. If the wallpaper broke due to the tightening force when the testing machine gripped the specimen, the correct elongation rate of the wallpaper could not be measured. Therefore, if the specimen broke within 10 mm from the gripping position, the result was considered invalid.

5.3 EXPERIMENTAL RESULT

The test results of the dry tensile test are shown in Table 4 and Fig. 16. Reproducing the results after the glue dried, the difference in elongation rate caused by the different types of wallpaper was minimal. The highest elongation value was observed for SF, which has the highest amount of foam, followed by SS, which has the highest stretch performance, and standard SN, which had the lowest elongation. The reason for the lack of difference could be due to the effect of the backing paper, as in the standard tensile test. We believe that the moisture absorbed during the impregnation process was dried, and the backing paper's resistance was restored.

Table 4 *Dry tensile tests results*

Specimen name	Elongation rate [%]	Pmax [N]
SN (Stone Normal)	1.66	48.95
SF (Stone Foamed)	2.51	71.37
SS (Stone Stretch)	2.29	71.40

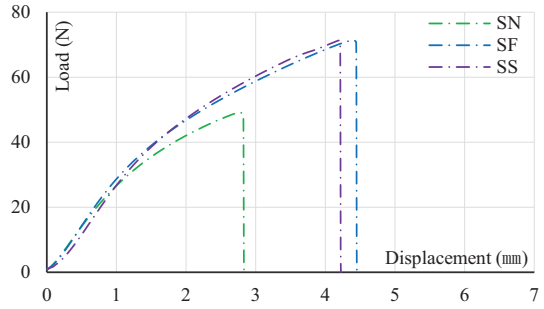

Fig. 16 *Dry tensile tests graph*

6 TENSILE TESTS COMPARISON

The elongation and Pmax obtained for all tensile tests are shown in Table 5.

Table 5 *Tensile tests results*

Specimen name	Tests type	Elongation rate [%]	Pmax [N]
SN (Normal)	Standard	1.58	49.82
	Wet	5.43	16.04
	Dry	1.66	48.95
SF (Foamed)	Standard	2.22	66.04
	Wet	5.24	32.32
	Dry	2.51	71.37
SF' (Foamed)	Standard	1.86	70.05
	Wet	4.95	30.01
SS (Stretch)	Standard	1.89	71.07
	Wet	8.06	18.93
	Dry	2.29	71.40
FF (Foamed)	Standard	1.60	50.69
	Wet	5.23	15.23
FL (Long)	Standard	2.11	62.91
	Wet	4.83	14.89

6.1 STANDARD-WET COMPARISON

A graph comparing standard tensile testing to wet tensile testing is shown in Fig. 17. Wetted wallpaper reduced Pmax by more than half for all specifications, but increased elongation by more than twice. In addition, all exhibited similar fracture behavior in the standard tensile test due to the influence of the backing paper, but differences in fracture behavior were observed when the backing paper was wetted and its bearing capacity was reduced. Based on the above, it can be considered that the standard tensile test almost always measures the performance of the backing paper, while the wet tensile test can measure the performance of the vinyl resin.

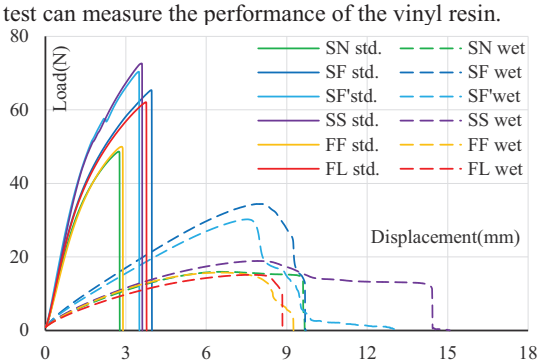

Figure 17. *Std.-Wet tensile tests comparison graph*

6.2 STANDARD-DRY COMPARISON

A graph comparing standard tensile testing to dry tensile testing is shown in Fig. 18. Compared to the standard wallpaper, the wallpaper that was dried after being moistened showed comparable values for both maximum proof stress and elongation. This is thought to be due to the fact that the backing paper, although once moistened, dried and returned to its original strength. Therefore, it was found that the dried tensile test showed equivalent test results to the standard tensile test.

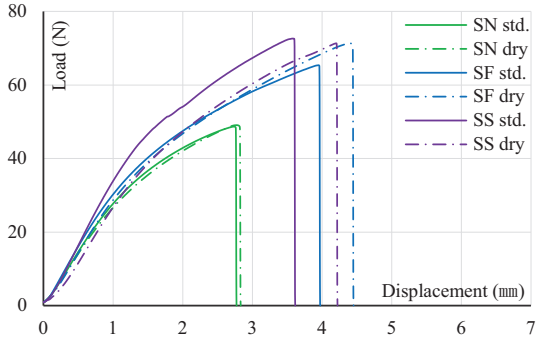

Fig. 18 *Std.-Dry tensile tests comparison graph*

6.3 TENSILE TEST CONCLUSIONS

We have conducted three tensile tests so far, and it is clear that vinyl wallpaper has a higher resistance than backing

https://doi.org/10.52202/069179-0040

paper, and that no difference can be seen due to the influence of the backing paper when tested in its original state. It is also clear that the effect of the backing paper can be reduced by adding moisture, and the difference in performance of the vinyl resin can be confirmed.
However, the actual cause of wallpaper breakage is the displacement or opening of the plasterboard, not pure tensile fracture. Therefore, we decided to conduct shear tests on wallpaper that reproduced the displacement of the plasterboard to confirm the displacement that causes rupture. The results of the shear test were compared with the results of the respective tensile tests to verify which elongation rate in the tensile test was a reasonable value for evaluating the rupture.

7 SHEAR TESTS

7.1 SPECIMEN SPECIFICATIONS

Since it is difficult to apply shear force to a single piece of wallpaper, we decided to reproduce the original house interior. 3 sheets of plasterboard (70 x 200 mm at both ends and 140 x 230 mm in the center) were lined up and the wallpaper was attached (Fig. 19). The gluing was done in such a way as to straddle all the plasterboards. A curing period of one week was allowed for the glue to dry.
Wooden frames (Fig. 20) were also made to hold the specimens in place. Only the plasterboards at both ends were fastened to the frame with screws; the center board was not fastened (Fig. 21). The frames were secured using a testing machine and bolts.
The wallpapers used were four types of wallpaper with stone surface geometry.

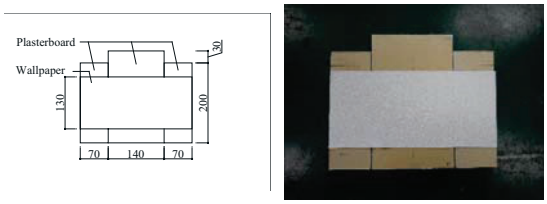

Figure 19. *Wallpaper placement of specimen*

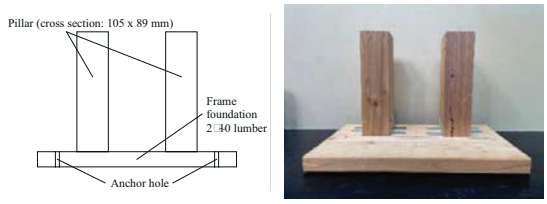

Figure 20. *Frame for specimen fixation*

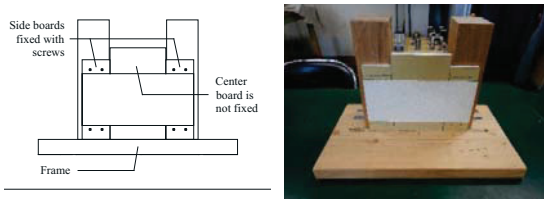

Figure 21. *Specimen fixed to the frame*

7.2 SUMMARY OF EXPERIMENTS

A wallpaper shear test is performed to measure the relative displacement between plasterboards when wallpaper breaks. A 50 kN universal testing machine from the Nippon Institute of Technology was used for the test. After the frame to which the specimen was fastened was fixed to the testing machine, the plasterboard in the center, which was not fastened, was grabbed by the upper jig of the testing machine (Fig. 22, 23), and the displacement of the boards was reproduced by raising only the center board. The force was applied at a rate of 2 mm/min until the wallpaper completely ruptured. Since it was difficult to determine rupture by the decrease in bearing capacity, damage was checked every 0.5 mm of displacement, and rupture was determined when more than half of the wallpaper was ruptured at the top of the joints.

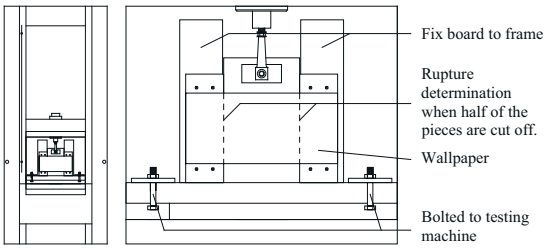

Figure 22. *Specimen installation state and invaild range*

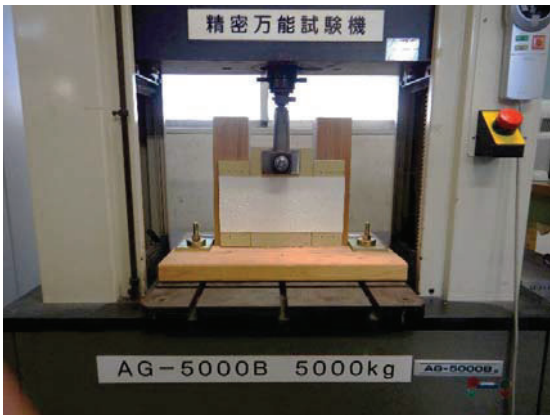

Figure 23. *Specimen installation state*

7.3 EXPERIMENTAL RESULT

The results of the shear test are shown in Table 6. The standard wallpaper, SN, and the wallpapers with high foam content, SF and SF', broke when the displacement was around 3.4 mm. On the other hand, SS, which has a stretch function, failed at a displacement of 4.5 mm at rupture compared to the other specifications (Fig.24). From the above results, it is considered that the stretch function is effective against shear failure.
Assuming that the plasterboard rotates at the same angle as the interlaminar deformation angle, the interlaminar deformation angle can be estimated from the board-to-board misalignment. 4.5mm corresponds to approximately 1/200 rad. However, this is only the case when there is no resistance to rotation of the faceplate, and is not an accurate estimate. It is necessary to actually test

https://doi.org/10.52202/069179-0040

the gypsum board bearing walls and measure the relative displacement between boards and the interlaminar deformation angle, and then re-evaluate the results. In addition, the chamfered edges of the gypsum board and the putty used to fill them were not reproduced in this study, so actual reproduction is also necessary.

Table 6 *Shear tests results*

Specimen name	Board displacement at break [mm]	Estimated interlayer deformation angle at break [rad.]
SN (Normal)	3.18	1/286
SF (Foamed)	3.67	1/247
SF' (Foamed)	3.34	1/272
SF (Foamed)	4.51	1/201

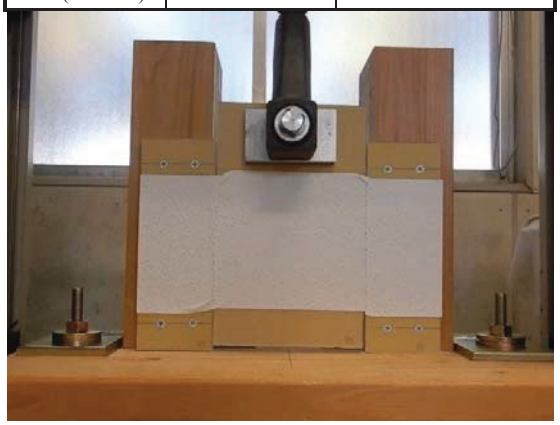

Figure 24. *Wallpaper at break judgment (SS)*

8 COMPARISON

The relationship between the increase in elongation in the standard tensile test and the rupture displacement in the shear test is shown in Fig. 25, and the relationship between the increase in elongation in the wet tensile test and the rupture displacement in the shear test is shown in Fig. 26. The trend of increasing elongation in the standard tensile test appears to be generally consistent with the trend of increasing rupture displacement in the shear test. However, the SS rupture displacement with stretching performance in the shear test is large and deviates from the trend. The trend of the rupture displacement in the shear test was generally consistent with the trend of the elongation ratio in the wet tensile test. In particular, the values of SS in both tests were very high compared to the other three specifications, which were similar. Therefore, it can be seen that there is a strong relationship between the rupture displacement in the shear test and the elongation rate in the wet tensile test.

Figure 25. *Tensile(std.)-shear tests result comparison*

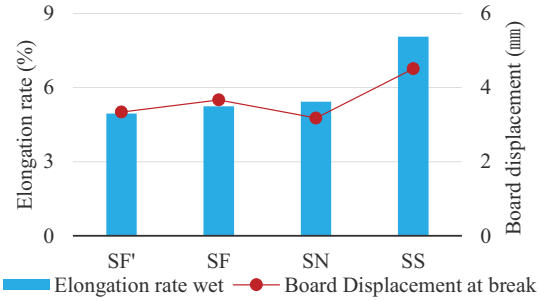

Figure 26. *Tensile(wet)-shear tests result comparison*

9 CONCLUSIONS

By moistening the wallpaper, the influence of the backing paper was reduced, and the elongation rate could be measured while the performance of the vinyl resin itself was brought out. The fact that the elongation rate in the wet tensile test is strongly related to the breaking displacement in the shear test indicates that there is a relationship between the interlaminar deformation angle at which the wallpaper breaks and the results of the wet tensile test. In the future, we plan to conduct static force tests on full-scale walls actually covered with wallpaper to measure the interlaminar deformation angle at which the wallpaper breaks, and to clarify the relationship with the results of partial tests.

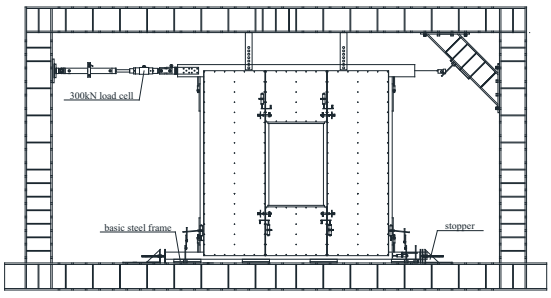

Figure 27. *Plan for in-plane shear static force test*

ACKNOWLEDGEMENT

The test specimens used in this study were provided by POLUS R&D Center of Life-Style Co., Ltd. I would like to thank all those involved.

https://doi.org/10.52202/069179-0040

REFERENCES

[1] Inoue R., Mori T., Tanaka K., Taki Y., Isoda H.; COMPARISON BETWEEN FINISH DAMAGE LEVEL AND STORY DEFORMATION OF WOODEN HOUSE AFTER EARTHQUAKE AIJ J Technol. Des. Vol.26, No.64, 917-922, Oct., 2020

[2] Japan Housing and Wood Technology Center : Allowable Stress Design of Wood Frame Construction Homes, 2017 ed.

[3] Japan 2 × 4 HOME BUILDERS ASSOCIATION : Guidelines for calculating the structure of framed wall construction methods, 2018

https://doi.org/10.52202/069179-0040

World Conference on Timber Engineering Oslo 2023

GLUED-LAMINATED TIMBER UNDER EXTREME COLD TEMPERATURES SUBJECTED TO IMPACT LOADING

Nicole Wight[1], Christian Viau[2], Patrick Heffernan[3]

ABSTRACT: With the increasing turbulence in the global security environment, comes the requirement for an increasing presence in the Canadian Arctic to respond to regional challenges and provide security. Such presence requires temporary and permanent installations, which must inherently carry with it some considerations for extreme load events, such as blast and impacts. In tandem with this is the expanding need to build more environmentally sustainable buildings, for which wood has been identified in recent years. However, questions remain on how wood responds to blast and impact loads when exposed to cold temperatures, typical of the arctic region. To respond to this gap in research, an experimental program was carried out to investigate the flexural behaviour of glued-laminated timber (glulam) subjected to impact loading under ambient and winter arctic temperatures. Dynamic testing was conducted using a drop weight impact hammer. For strain rates between 1.13 to 1.38 s^{-1}, an average dynamic increase factor of 1.23 on the maximum resistance at ambient temperatures was observed. The cold temperature beams were seen to experience a 13% increase in strength beyond their normal temperature counterparts under dynamic effects. Increases in stiffness due to cold temperature were also observed under static and dynamic loading.

KEYWORDS: Impact, Glulam, Arctic, Strain Rate, Cold Temperature, Dynamic Increase Factor

1 INTRODUCTION

In recent decades, there has been an upward trend in infrastructure and buildings being exposed to blast and impact loading, as well as an increased use of wood as a construction material for mid- and high-rise timber and timber-hybrid structures. However, despite wood being mentioned in blast design standards [1, 2], current provisions are lacking in quantity and extent, due to them being based on limited early research on light-frame wood shelters [3]. The exposure of structural materials to high strain rates typically leads to increases in strength and, in some cases, stiffness, generally quantified using a dynamic increase factor (DIF). Shock tube testing, which simulates the effects of far-field blast explosions, has been used to determine DIF values for various wood elements under normal temperature, most notably glued-laminated timber (glulam) and cross-laminated timber (CLT), where DIFs of 1.14 and 1.28, respectively, have been reported [4, 5]. Other studies investigating the behaviour of light-frame wood systems [6-9] and timber connections under high strain-rates [10-12] have also been conducted.

Various countries, including Canada and allies, have a vested interest in asserting sovereignty in their Northern regions, and the need to have an active and visible presence in these cold environments has become incredibly prevalent with the current global security environment [13]. Canadian Forces Station (CFS) Alert, located 817 km from the geographic North Pole, represents not only the most northerly permanently inhabited place in Canada, but also in the world, where during the winter months the average daily temperature is -40 °C [14]. As such, materials capable of withstanding these temperatures without adverse effects on their mechanical properties and durability are critical to expanding infrastructure in Northern Regions of Canada. Already, large infrastructure constructed with engineered wood products are being developed for use in colder regions of Canada. For example, the Macaisagi Bridge in northern Quebec, Canada, built in 2011 out of CLT and glulam with a 1,790 kN capacity, spans 68 m and experiences temperatures as low as -45 °C [15]. Understanding how extreme cold temperatures affect a material's mechanical properties is required to provide users with safe, durable, and effective designs. Despite its application in cold weather regions, little research has been conducted on the performance of glulam under arctic conditions, none of which examined static or dynamic bending strength [15-17].

Beirnes et al. investigated the impact resistance of thin ultra-high performance fibre reinforced concrete (UHPFRC) panels under extreme cold temperatures. An increase in the static strength and an increase in the panel residual strength under impact loading of the cold panels compared to their ambient temperature counterparts was observed [18]. No additional studies investigating the effects of cold temperature on the impact or blast resistance of structures could be found.

[1] Nicole Wight, Force Protection Engineer Officer, 1 Engineer Support Unit, Canadian Armed Forces, Canada, nicole.wight@forces.gc.ca

[2] Christian Viau, Assistant Professor, Department of Civil and Environmental Engineering, Carleton University, Canada, christian.viau@carleton.ca

[3] Patrick Heffernan, Professor, Department of Civil Engineering, Royal Military College of Canada, Canada, Pat.Heffernan@rmc.ca

https://doi.org/10.52202/069179-0041

Canada's Blast Design Standard, CSA S850, currently provides a DIF value for glulam of 1.4 under flexural loading [1], a value which has been reported to be nonconservative by recent studies on glulam [4, 19]. In addition, current blast design standards do not account for the cold weather behaviour of materials under blast loading [1, 2]. To address this gap in research, the below experimental program investigated the effect of extreme cold temperature on the mechanical strength properties of glulam under both quasi-static and high-strain rates for the purpose of expanding glulam's use in structures under extreme cold temperatures.

2 EXPERIMENTAL PROGRAM

2.1 DESCRIPTION OF TEST SPECIMENS

A total of fifteen 137 mm x 178 mm x 1650 mm NordicLam+ 24F-ES grade glulam beams were tested under quasi-static and dynamic loading, at both ambient and extreme cold temperatures, to document high strain-rate effects and their behaviour under impact loading conditions. As previous research has indicated that finger joints may affect the failure of beams under high strain rates, beams of multilaminate widths were chosen to minimise this effect [4]. For all specimens presented in this paper, the prefix "S" refers to a specimen that was tested quasi-statically, while the prefix "D" refers to a specimen that was tested dynamically. Similarly, this was followed by the letter "A" or "C", indicating that the specimen was tested at ambient temperature or cold temperature, respectively.

2.2 TEMPERATURE MONITORING

All cold specimens were placed into a cold temperature freezer at -70 °C for a minimum of seven days prior to testing. All beams were equipped with a Type T thermocouple adhered to their side approximately 8 cm from the centreline in order to record the beam's surface temperature. In order to assess internal temperatures of the specimens, a test beam was placed in the cold temperature freezer with thermocouples installed at depths of 63 mm, 42 mm, 21 mm, and on the surface. The readings obtained from the test beam were then used to develop a relationship between the surface and internal temperatures. Using this information to develop a correlative relationship, the time to required for the beams to reach an internal temperature of -70 °C and the beams' internal temperatures at the time of testing could be determined.

2.3 STATIC TESTING

Quasi-static four point bending flexural tests were conducted on seven of the fifteen specimens to serve as a baseline with which to compare the dynamic results. The quasi-static test setup can be seen in Figure 1. These tests, adapted from ASTM D198 [20], resulted in the quasi-static flexural strength values that were normalised to a standardized 1-minute load duration, as outlined in Section 3.2. A linear variable differential transformer (LVDT) connected at the beam's midspan recorded the beam's displacement, while two strain gauges positioned on the tension side of the beam and two on the compression side of the beam at midspan measured the specimens' strain deformations. A load cell within the hydraulic head measured the applied force, and applied a load at a displacement-controlled rate of 1 mm/min. This resulted in an average time to failure of 15.2 mins for the small normal temperature beams and 13.4 mins for the cold temperature beams. Simply supported boundary conditions were provided using the same rollers and load transfer bar used for the dynamic tests. A clear span of 1,479 mm was used throughout testing, with the load being applied at the beam third points. This allowed for an area of constant moment and zero shear force in the central third of the beam. To avoid crushing, 150 mm long plates at the load-application points and beam ends were used.

Figure 1: *Static test setup*

2.4 DYNAMIC TESTING

Dynamic testing was conducted using the newly established drop weight impact testing facility at the Royal Military College of Canada (Kingston, ON Canada), capable of imparting up to 23 kJ of energy onto small- to full-scale structural elements. The impact hammer consists of a weighted box that travels along six-meter-tall rails using six pillow block ball bearings to guide the box. All ambient temperature dynamic beams were subject to an 1800 mm drop with a weight of 141.7 kg and all cold temperature beams were subject to a 2000 mm drop with a weight of 141.7 kg. The dynamic test set-up can be seen in Figure 2. A data acquisition system capable of recording up to 500 kHz was used. An electromagnet was used to raise the box to the required

https://doi.org/10.52202/069179-0041

drop height, which was determined using a linear encoder attached to the drop weight. The linear encoder also permitted for the box kinematics at impact to be determined.

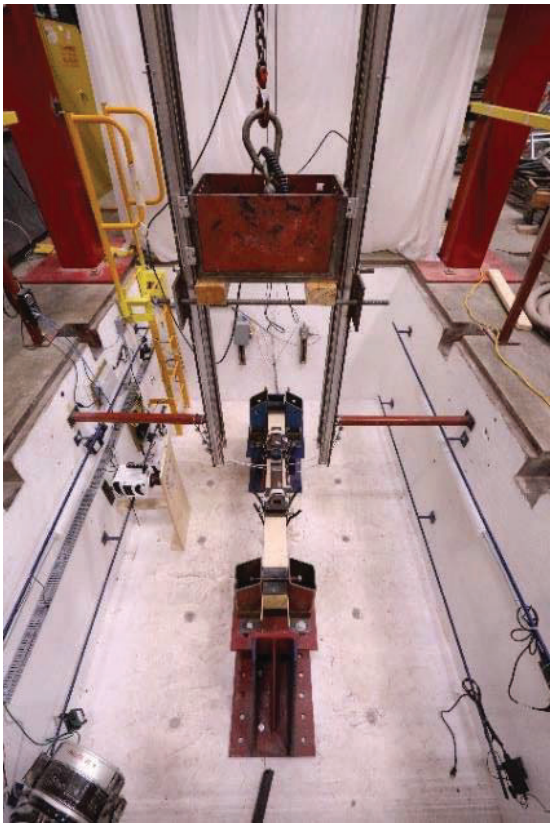

Figure 2: *Dynamic test setup*

Support rollers identical to those in the static test setup were utilized, facilitating the comparison between both sets of tests. Lateral supports were provided at the beam ends to minimize the likelihood of lateral beam instability during response. Additionally, brace plates were placed on top of the beam at each end to prevent upward motion of the beam after initial impact. A load transfer beam was used to distribute the impact load across the central third of the beam in order to create an area of constant moment and zero shear force. The beams were instrumented with piezoelectric force sensors under each support and under the load application points in order to determine the support reactions and the applied load. The beam's displacement-time history was recorded using both a laser and a string potentiometer, while two strain gauges positioned on the tension side of the beam and two on the compression side of the beam at midspan measured the specimens' strains. Three high speed cameras, capturing images at 10,000 fps, 1,000 fps and 500 fps, were used to record the beam's behaviour and potential failure locations.

3 EXPERIMENTAL RESULTS

3.1 TEMPERATURE MONITORING

Specimen SC3 was prepared in the manner outlined in Section 2.2. Upon conditioning, SC3 was removed from the freezer and the change in internal temperature was monitored over time. The output of this test allowed for the temperature time curves to be used to relate the internal temperatures to those of the various tests. The average rate of warming in the beam across the four thermocouple depths was 0.72 °C/min. The surface thermocouple temperatures recorded during the tests were also compared to the values obtained by the test beam and good agreement was observed. As a result, the average internal temperature for all static beams was -46.8 °C at the midpoint of testing and -43.5 °C at failure. Due to the short duration of testing, the average internal temperature for all dynamic beams was -47.1 °C at failure. In all cases, these temperatures are within the range of temperatures experienced in the Arctic.

3.2 STATIC TESTING RESULTS

Failure was established to be the point during testing where the specimen experienced a sudden drop in load and could no longer support additional load. The stiffness was taken as the slope of the resistance displacement curve from 40% to 90% of the beam's ultimate capacity. The failure load for each beam was normalized to a 100% strength value corresponding to a testing time of 1 minute in order to normalise all static results using Equation (1) [21].

$$SL = 100.0 - 3.5Log_{10}T_r \quad (1)$$

where SL = stress level factor in the beam and T_r = time to failure in minutes.

The results from the normal and cold temperature static tests are summarized in Table 1, including the static maximum resistance ($R_{s,max}$), stiffness (K), strain rate ($\dot{\epsilon}$), the time-to-failure and whether the beam failed in flexure, shear, or combined flexure and shear.

The average peak resistance for the normalized static normal temperature tests was 185.6 kN with a coefficient of variation (COV) of 0.12. From the results, it can be observed that some of the beams failed in flexure, while others failed in shear. Before testing, the beams' capacities were checked for governing failure mode, and the shear failure capacity of the beams was determined to not govern the design of the specimens. When only the beams that failed purely in bending were considered, the peak resistance was 166.3 kN with a COV of 0.02. The average stiffness for the normalized static normal temperature tests was 11,900 kN/m with a COV of 0.02. As would be expected, when only the bending failures are considered, the stiffness does not change dramatically, with the average stiffness being 11,670 kN/m with a COV of 0.01. The average surface temperature of the normal temperature beams was 19.7 °C during testing.

https://doi.org/10.52202/069179-0041

Table 1: *Static test results*

Sample	$R_{s,max}$	K	$\dot{\varepsilon}$ (x10^{-6})	Time to Failure	Failure Mode
	kN	kN/m	s^{-1}	mins	
Normal Temperature Beams					
SN1	163.4	11,490	5.48	13.3	Flexure
SN2	190.0	12,250	4.74	13.6	Shear
SN3	169.3	11,840	4.98	14.6	Flexure
SN4	219.6	12,020	5.08	19.3	Shear
Avg	185.6	11,900	5.07	15.2	
Std Dev	22.0	275	2.64	2.4	
COV	0.12	0.02	0.05	0.16	
Cold Temperature Beams					
SC1	182.9	13,760	6.44	13.0	Flexure
SC2	189.8	13,800	4.95	13.4	Shear
SC3	155.0	13,950	4.99	10.9	Flexure
Avg	175.9	13,840	5.46	12.4	
Std Dev	15.1	79	0.70	1.1	
COV	0.09	0.01	0.13	0.09	

The average peak resistance for all normalized static cold temperature tests was 175.9 kN with a COV of 0.09. When only the beams that failed purely in bending were considered, the peak resistance was 168.9 kN with a COV of 0.08. The average stiffness for all normalized static cold temperature tests was 13,840 kN/m with a COV of 0.01. As would be expected, when only the bending failures are considered, the stiffness does not change dramatically, with the average stiffness being 13,850 kN/m with a COV of 0.01. The average internal temperature of the cold temperature beams at failure was -43.5 °C and the average surface temperature at failure was -39.9 °C.

3.3 DYNAMIC TESTING

Dynamic failure of the beam specimens was determined to occur at the peak resistance, consistently followed by a sudden drop in resistance. Unlike static loading, the dynamic resistance of a beam cannot be obtained by the simple summation of the reactions as this will not give an accurate reflection of the beam's response. This is due to the dynamic resistance being dependant not only on the dynamic reactions, but also the boundary conditions, whether the element response is elastic or inelastic, and the applied load [22]. The dynamic resistance was obtained using Equations (2) and (3), where the latter was used in order to account for the distributed mass of the beam and the point loads of the load transfer beam. Further information on the derivation of these expressions can be found in [22, 23].

$$R(t) = \frac{6}{L}[V(t) \times x_{eq} + 0.5 \times \left(\frac{L}{3} - x_{eq}\right) \times F(t)] \qquad (2)$$

$$x_{eq} = \frac{0.102\bar{m} \times L^2 + 0.290m_c \times L}{0.319\bar{m} \times L + 0.870m_c} \qquad (3)$$

where $R(t)$ = beam dynamic resistance, $V(t)$ = dynamic reaction, $F(t)$ = applied force, L = beam clear span, x_{eq} = distance from the support to the point of application of the equivalent inertia force, $\bar{m}$ = the distributed mass of the beam and m_c = half of the mass of the load transfer beam lumped at the load application points.

Similar to the static tests, the initial beam stiffness was taken as the slope of the resistance displacement curve from 40% to 90% of the beam's ultimate capacity. The results from the dynamic tests for normal and cold temperature beams can be seen in Table 2, including the dynamic maximum resistance ($R_{d,max}$), stiffness (K), strain rate ($\dot{\epsilon}$), duration of load and whether the beam failed in flexure, or shear.

Table 2: *Dynamic test results*

Sample	$R_{d,max}$	K	$\dot{\varepsilon}$	Durat-ion of Load	Failure Mode
	kN	kN/m	s^{-1}	ms	
Normal Temperature Beams					
DN1	210.7	12,890	1.36	9.5	Flexure
DN2	207.7	16,140	1.13	10.0	Flexure
DN3	190.3	14,340	1.38	9.6	Flexure
DN4	208.9	15,410	1.33	9.4	Flexure
Avg	204.4	14,700	1.30	9.6	
Std Dev	8.2	1,220	0.10	0.2	
COV	0.04	0.08	0.08	0.02	
Cold Temperature Beams					
DC1	226.8	16,500	1.25	8.9	Shear
DC2	226.0	17,640	1.28	9.1	Flexure
DC3	229.2	16,700	1.14	10.0	Flexure
DC4	239.4	17,360	1.31	10.3	Flexure
Avg	230.3	17,050	1.25	9.6	
Std Dev	5.4	465	0.06	0.6	
COV	0.02	0.03	0.05	0.06	

For strain rates between 1.13 to 1.38 s^{-1}, the average dynamic peak resistance for the normal temperature beams was 204.4 kN with a COV of 0.04. The average stiffness for the normal temperature beams was 14,700 kN/m with a COV of 0.08.

All but one dynamic cold temperature beam failed in flexure, with specimen DC1 failing in shear. For strain rates between 1.14 to 1.31 s^{-1}, the average dynamic failure resistance for the cold temperature beams was 230.3 kN with a COV of 0.02. The average stiffness for the cold temperature beams was 17,050 kN/m with a COV of 0.03. If only the flexural failures are considered, the average dynamic failure resistance for the cold temperature beams was 231.5 kN with a coefficient of variation (COV) of 0.02. The average stiffness for the cold temperature beams was 17,236 kN/m with a COV of 0.02. As can be seen from these values, the beam that failed in shear, had very

similar failure values to the other beams and as such the results do not differ greatly when this beam's data is omitted.

3.4 FAILURE MODES

All specimens behaved in a linear elastic manner and failed in a brittle manner via tensile failure initiated at a knot or natural defect. Some specimens failed in shear or combined flexural and shear. One potential cause is the presence, or lack, of defects in the central third of the beam, where the bending moment is constant and at its maximum. In all cases of flexural failure, this was identified as having been initiated at a knot or natural defect in the beam. However, in all specimens that failed in shear, no visible natural defects, or knots on the tensile outer edge of the beams within the central third could be identified. This caused a shift in governing failure mode to a shear dominated failure mode, rather than flexural as initiated on the bottom tension-side fibres. While specimens without defects were not specifically chosen for this study, the beams were limited in size due to the geometrical constraints of the cold temperature freezer, whereas beams used in construction would likely be significantly greater in size, largely guaranteeing that defects would always be present.

Static normal temperature specimens consistently had more prominent crack dimensions than their cold temperature counterparts. Images of a representative failure of a specimen under static loading is shown in Figure 3. The failure in both the normal temperature and cold temperature beams, occurred at a knot or natural defect, and both exhibited a similar crack pattern.

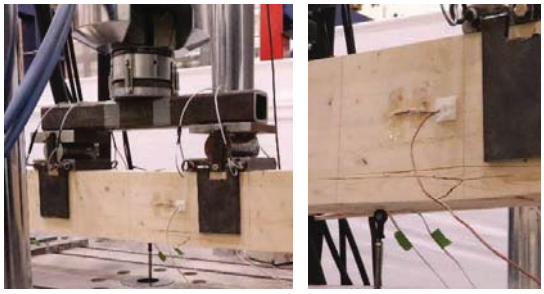

***(a)** Global view* ***(b)** Close-up view*

***Figure 3:** Failure of static normal temperature specimen SN3*

Figure 4 and Figure 5 show still images taken from one of the high-speed cameras of specimens DN4 and DC4, respectively, immediately following failure. It can be seen that the crack pattern in the normal temperature beam is more apparent that the crack pattern in the cold temperature beam. Both dynamic specimens, when viewing the beams after testing, had similar crack propagation patterns to the statically tested specimens.

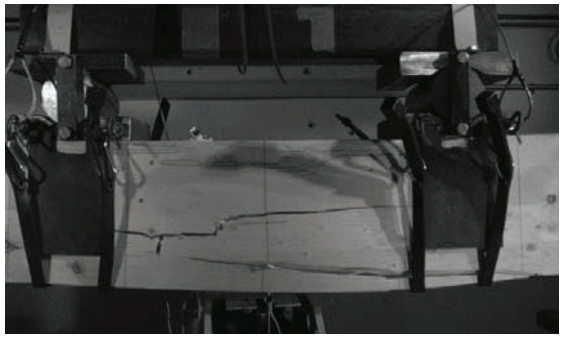

***Figure 4:** Failure of dynamic normal temperature specimen DN4*

***Figure 5:** Failure of dynamic cold temperature specimen DC4*

4 HIGH STRAIN RATE AND COLD EFFECTS

For the analysis presented below, inferences regarding the experimental test results must be limited to specimens with identical failure modes. It is for this reason that all specimens which failed in shear were not considered when determining the DIF for the resistance and stiffness. Representative resistance curves from the static and dynamic testing can be seen in Figure 6. In each resistance curve, the point at which failure occurred, based on the maximum resistance, is denoted with an 'x'. Here the trends in the data can be visually observed.

No increase in strength between the normal and cold temperature static tests is observed; however, it can be seen that the cold temperature specimens seem to experience an increase in stiffness.

The dynamic resistance curves can be seen to have more fluctuation, likely caused by dynamics of the system, or more specifically the vibrations that occur within a dynamic system, which is to be expected under impact loading. Earlier it was mentioned that 40-90% of the resistance curves were used in order to calculate the stiffness of the beams. The reasoning behind this is apparent when the curves are viewed. All dynamically tested beams exhibited a higher initial stiffness as the system settled, which was not representative of the remainder of the resistance curve. There is then a relatively constant second slope which was taken to be the beams actual response to the impact loading up until near failure. When looking at the dynamic resistance curves, it

https://doi.org/10.52202/069179-0041

can be seen that the dynamic specimens exhibited higher capacity and stiffness than their static counterparts, indicating the increase in strength and stiffness experienced by the glulam at high strain rates.

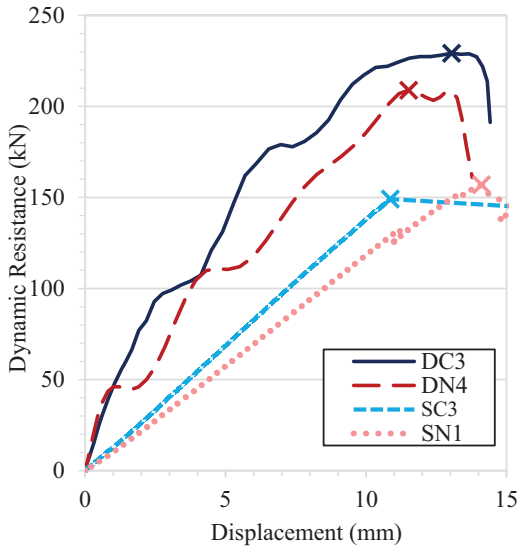

Figure 6: *Representative resistance curves*

The use of identical spans, boundary conditions, and loading conditions allowed for a direct comparison between the static and dynamic test results for the purpose of quantifying high strain-rate effects on the glulam specimens. The DIF on the peak resistance was calculated using Equation (4).

$$DIF = \frac{R_{d,max}}{R_{s,nor}} \quad (4)$$

where $R_{d,max}$ = maximum dynamic resistance and $R_{s,nor}$ = maximum static resistance normalized to a 100% strength value corresponding to a testing time of 1 minute based on Karacabeyli and Barrett [21].

The dynamic testing results, for strain rates in the range of 1.13 to 1.38 s^{-1}, revealed an increase in strength for both the ambient and cold temperature beams. For the normal temperature specimens, an average DIF of 1.23 on the normal temperature beam's peak resistance was determined when compared to the average static peak resistance. Looking at the current Canadian Blast Design Standard [1], a value of 1.4 is given, which is much higher than the value determined under normal temperature testing. For the cold temperature specimens, an average DIF of 1.37 was determined when compared to the average static cold temperature peak resistance. It is clear that high strain-rate effects are present within the cold specimens, and the preliminary results indicate that a higher DIF is attributable to cold temperature effects. A further number of tests are required to fully substantiate these effects. There is currently no stipulation for the performance of structures under cold temperatures in the current Canadian Blast Design Standard [1]. The observed DIFs can be visually seen in Figure 7, which summarises the obtained dynamic increase factors.

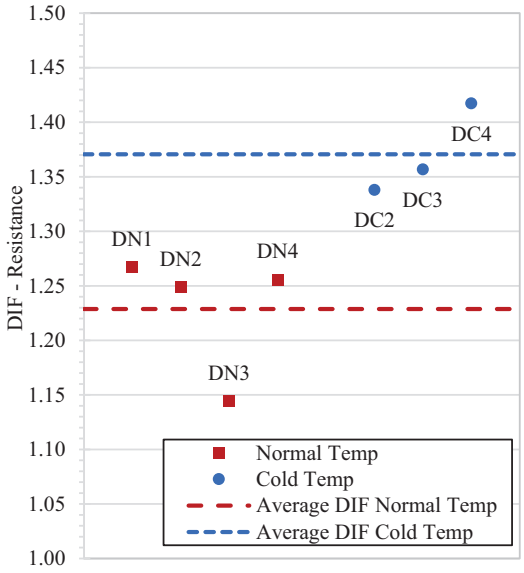

Figure 7: *Summary of observed DIFs*

Statistical analysis was done on each of these observations. It was found that the normal temperature beams dynamic to static resistance values were supported by statistical analysis using a T-Test with a 95% confidence interval. However, when looking at the cold temperature data the confidence interval that the results were statistically significant was only supported by a confidence interval of 85%. This was due to the smaller sample size, due to the omission of the specimens having failed in shear in the analysis. As such, it is recommended that further testing be done regarding the effects of cold under impact loading to further reinforce the observation that cold temperature beams under high strain rates exhibit an apparent increase in resistance when compared to their static cold temperature counterparts.

An increase in stiffness was observed when comparing the dynamic tests to their normal temperature counterparts. An average DIF on the modulus of elasticity of 1.26 and 1.24 on the beam's stiffness was determined for the normal and cold temperature specimens, respectively, when compared to their respective static tests. These observations were supported by statistical analyses by using a T-Test, with a confidence interval of 95%.

Cold temperature effects are summarized in Table 3 where cold temperature effects on the mechanical properties of glulam under static and dynamic loading were quantified.

In all cases, the normal and cold temperature values were juxtaposed against one another by comparing the static-to-static tests and dynamic-to-dynamic tests. These observations were supported by statistical analyses via T-Tests, with a confidence interval of 95%. Specifically, no cold temperature effects could be identified for the static resistance. Considering the dynamic tests, the cold temperature beams experience a 13% increase in strength compared to their normal temperature counterparts.

https://doi.org/10.52202/069179-0041

Table 3: *Effect of cold on strength and stiffness*

Comparison	Avg. Normal Temp. Value	Avg. Cold Temp. Value	Cold Factor
Static normal to cold temperature resistance (kN)	166.3	168.9	1.02
Static normal to cold temperature stiffness (kN/m)	11,670	13,850	1.19
Dynamic normal to cold temperature resistance (kN)	204.4	231.5	1.13
Dynamic normal to cold temperature stiffness (kN/m)	14,700	17,240	1.17

Previous research on clear wood found an 18% increase in bending strength at 4% moisture content on clear wood at -50 °C compared to 20 °C [24]. However, this testing was not on glulam but involved clear wood, which is void of defects and finger joints. As outlined in the above test results, the presence of defects highly influences the failure load of specimens. As such, the effects of cold temperature on the overall lignin matrix in the wood may be insignificant when compared to the effects of defects. No studies on the flexural behaviour of glulam under similar temperatures could be found.

One possible cause of this discrepancy between static and dynamic strengths amongst the cold temperature specimen is the effect of ice between the wood fibres. The ice content in the specimens from the inherent moisture content of the wood may alleviate and delay the initial growth of microcracks, resulting in a higher strength under short duration loading. When looking at the static tests, since the loading occurs under a much longer duration, microcrack growth is able to develop and not affect the beam strength over the significantly longer load duration. Additionally, the tested beams had a relatively low moisture content (on average 8.9%), which would have reduced the ice content, thereby reducing the effect that the water molecules would have on the behaviour of the glulam specimens.

In terms of initial stiffness, an apparent increase in stiffness observed in the cold temperature specimens under both static and dynamic testing when compared to their normal temperature counterparts could be observed. This observation is corroborated by previous studies, which studied different forms and types of wood at lower temperatures [16, 24-26]. This is likely due to the freezing of the water content within the beams and potentially the stiffening of the adhesive used. When looking at the static tests there was a 19% increase in stiffness observed. When looking at the dynamic tests, there was a 17% increase in stiffness observed. Both values are very close to one another, indicating a uniform increase in stiffness due to cold, regardless of the type of loading.

From a design perspective, cold temperature effects appear to improve the dynamic performance of glulam at cold temperatures. As such, if the structure is expected to remain at cold temperature for the duration of it's use and occupancy, then these potential strength increases could be considered. However, if the structure is expected to experience a wider range of temperatures, then cold temperature effects can conservatively be omitted for design purposes.

5 CONCLUSIONS

For a dynamic strain-rate range of 1.13 to 1.38 s^{-1}, a DIF of 1.23 on the maximum resistance at ambient temperatures was observed. An increase in strength of 13% in the cold temperature beams under dynamic loading was observed. The cold did not appear to influence the static resistance of the beams. Dynamic effects caused an increase in the stiffness, resulting in an average DIF on the stiffness of 1.25 for both the normal and cold temperatures beams. The cold resulted in an average stiffness increase of 18% under both static and dynamic conditions.

Further studies need to be completed to conclusively determine the effects of cold temperatures on glulam's stiffness under high strain-rate effects. Additional samples are required to confirm the results presented above. Additionally, tests at a wide variety of temperatures and cyclic temperatures should be considered. Lastly, considering specimens of other dimensions could improve the dataset and reliability of the effects reported in this study.

REFERENCES

[1] CSA. Design and assessment of buildings subjected to blast loads S850-12. CSA, Mississauga, ON, 2012.

[2] ASCE. Blast Protection of Buildings: ASCE/SEI 59-11 (Blast Protection of Buildings). 2011.

[3] K. A. Marchand. BAIT, BASS & RODS Testing Results. Applied Research Associates, Prepared for the USAF Force Protection Battlelab, 2002.

[4] D. Lacroix and G. Doudak. Determining the dynamic increase factor for glued-laminated timber beams. *Journal of Structural Engineering*, 144(9): 04018160-1 to 04018160-12, 2018.

[5] M. Poulin, C. Viau, D. N. Lacroix, and G. Doudak. Experimental and analytical investigation of cross-laminated timber panels subjected to out-of-plane blast loads. *Journal of Structural Engineering*, 144(2): 04017197-1 to 04017197-11, 2018.

[6] C. Viau and G. Doudak. Behaviour and retrofit options for light-frame wood stud walls subjected to blast loads. In: *Proceedings of the 11th International Conference on Shock and Impact Loads on Structures*, 2015.

[7] E. Jacques, A. Lloyd, A. Braimah, M. Saatcioglu, G. Doudak, and O. Abdelalim. Influence of high strain-rates on the dynamic flexural material properties of spruce–pine–fir wood studs. *Canadian Journal of Civil Engineering*, 41(1): 56-64, 2014.

[8] N. J. Parlin, W. G. Davids, E. Nagy, and T. Cummins. Dynamic response of lightweight wood-based

https://doi.org/10.52202/069179-0041

flexible wall panels to blast and impulse loading. *Construction and Building Materials*, 50: 237-245, 2014.
[9] D. Lacroix and G. Doudak. Investigation of Dynamic Increase Factors in Light-Frame Wood Stud Walls Subjected to Out-of-Plane Blast Loading. *Journal of Structural Engineering*, 141: 04014159-1 to 04014159-10, 2014.
[10] C. Viau. Investigation and Optimization of Connections in Timber Assemblies Subjected to Blast Loading. Doctor of Philosophy, Civil Engineering, Université d'Ottawa/University of Ottawa, 2020.
[11] C. Viau and G. Doudak. Energy-Absorbing Connection for Heavy-Timber Assemblies Subjected to Blast Loads–Concept Development and Application. *Journal of Structural Engineering*, 147(4): 04021027-1 to 04021027-13, 2021.
[12] A. McGrath and G. Doudak. Investigating the response of bolted timber connections subjected to blast loads. *Engineering Structures*, 236: 112112-1 to 112112-12, 2021.
[13] O. Stefanovich. Canada looks to reinforce Arctic sovereignty through diplomacy, military, says minister. In: CBC News, 2022.
[14] Government of Canada. Canadian Forces Station Alert. http://www.rcaf-arc.forces.gc.ca/en/alert.page (accessed 30 June 2021), 2021.
[15] X. Wang, J. Björnberg, O. Hagman, S. A. Ahmed, H. Wan, and P. Niemz. Effect of low temperatures on the block shear strength of norway spruce glulam joints. *BioResources*, 11(4): 9638-9648, 2016.
[16] G. Drake, M. Berry, and D. Schroeder. Effect of cold temperatures on the shear behavior of glued laminated beams. *Cold Regions Science and Technology*, 112: 45-50, 2015.
[17] R. Yang et al. Effects of Freeze-Thaw Cycles on Physical and Mechanical Properties of Glulam Exposed to Outdoor Environment. *Journal of Renewable Materials*, 9(7): 1293-1307, 2021.
[18] M. Beirnes, M.-A. Dagenais, and G. Wight. Cold temperature effects on the impact resistance of thin, lightweight UHPFRC panels. *International Journal of Impact Engineering*, 127: 110-121, 2019.
[19] N. Wight, C. Viau, and P. Heffernan. Behaviour and Resistance of Glued-Laminated Timber Subjected to Impact Loading. In: *Canadian Society for Civil Engineering Annual Conference*, Structural 149-1 to 149-10, 2022.
[20] ASTM International. Standard Test Methods of Static Tests of Lumber in Structural Sizes: D198 − 21a. ASTM International, Pennsylvania, United States, 2021.
[21] E. Karacabeyli and J. Barrett. Rate of loading effects on strength of lumber. *Forest Products Journal*, 43(5): 28-41, 1993.
[22] J. Biggs. Introduction to structural dynamics. McGraw-Hill College, 1964.
[23] D. N. Lacroix. Investigating the behaviour of glulam beams and columns subjected to simulated blast loading. Doctor of Philosophy, Civil Engineering, Université d'Ottawa/University of Ottawa, 2017.
[24] C. C. Gerhards. Effect of moisture content and temperature on the mechanical properties of wood: an analysis of immediate effects. *Wood and Fiber Science*, 14(1): 4-36, 1982.
[25] R. Schmidt and J. Pomeroy. Bending of a conifer branch at subfreezing temperatures: implications for snow interception. *Canadian Journal of Forest Research*, 20(8): 1251-1253, 1990.
[26] D. W. Green and J. W. Evans. The immediate effect of temperature on the modulus of elasticity of green and dry lumber. *Wood and Fiber Science*, 40(3): 374-383, 2008.

World Conference on Timber Engineering Oslo 2023

EXPERIMENTAL AND NUMERICAL ANALYSIS OF CLT FLOOR SUBASSEMBLIES UNDER CATENARY ACTION

Alicja C. Przystup[1], Thomas Tannert[2], Yong Lu[3], Thomas Reynolds[4]

ABSTRACT: Behaviour under combined axial tension and out-of-plane bending, typically observed in catenary action after loss of a support, was investigated on Cross Laminated Timber (CLT) floors. Uni-axial tension tests as well as combined tension and bending tests on CLT component and floor subassembly levels with screw butt joints and varying boundary conditions were performed. Bending moment capacity was shown to decrease with increasing of horizontal tension on the connection. Combined loading failure envelope was developed to observe a correlation between the test results of different scale, showing the potential of using component tests as predictors of the behaviour of more complex subassemblies.

KEYWORDS: Robustness, disproportionate collapse, progressive collapse, catenary action, combined loading

1 INTRODUCTION

1.1 Background

Robustness of large-scale mass timber buildings has become an important design consideration with their rise in scale and popularity [1]. The current tallest timber building is over 86m in height [2], and timber is increasingly widespread in multi-storey buildings. Ensuring that localised accidental damage will not result in disproportionate and progressive collapse is a vital design step that could save lives [3]. Eurocode robustness [4] design guidance is material independent. Since this objective-based approach is based on research conducted before mass timber was a commonly used construction material, research is required to provide design parameters and to ensure that the Eurocode framework can be reliably applied to mass timber. This need for more research and new comprehensive design guidance has been recognised by researchers and industry alike [5,6].

1.2 Catenary action in mass timber

One of the primary load resistance mechanisms after the loss of a load-bearing member is catenary action, which allows for redistribution of load in the structure [7] as visualised in Figure 1. It is also the main load redistribution mechanism allowed for in Eurocode 1 [4], which provides formulas for horizontal and vertical tie forces required for catenary to form. Under catenary action, the floors are subjected to combined bending and tension and therefore understanding of the effect of such combined loading on mass timber connections is instrumental for effective modelling and performance-based design. To date some early experimental work has been performed at a substructure level [8,9], but empirical data is lacking on the behaviour of variety of connections and types of engineered wood products used in practice.

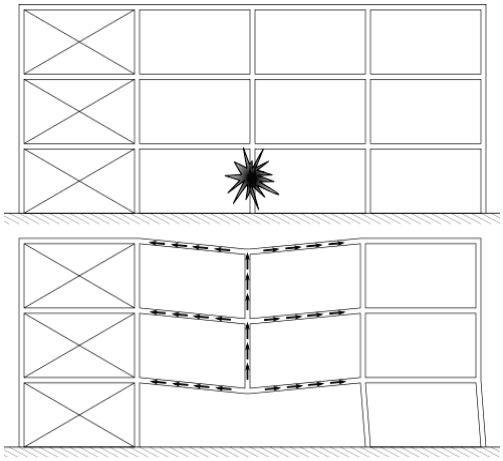

Figure 1: *Catenary action after compressive element loss*

1.3 Objective

The goal of the project presented in this paper was to apply a combined axial load and bending test method on substructures and components of mass timber floor systems that produces data to model the redistribution of forces in various substructure configurations. This correlation observed between the different scales of test results show that there is possibility for the component tests to be good predictors of the behaviour of the more complex subassemblies.

[1] Alicja Przystup, University of Edinburgh, Edinburgh, Scotland, a.c.przystup@sms.ed.ac.uk
[2] Thomas Tannert, University of Northern British Columbia, Prince George, BC, Canada, thomas.tannert@unbc.ca
[3] Yong Lu, University of Edinburgh, Edinburgh, Scotland, Yong.Lu@ed.ac.uk
[4] Thomas Reynolds, University of Edinburgh, Edinburgh, Scotland, T.Reynolds@ed.ac.uk

https://doi.org/10.52202/069179-0042

2 MATERIALS AND METHODS

2.1 Combined loading

The experiments were designed to investigate the influence of the applied tensile force on rotational stiffness, ultimate strength, and maximum angle of rotation of the floor panel-to-panel connection. A test method adequate for this purpose is one that can be replicated for multiple types of connections; therefore, it ought to be easily repeatable and cost effective. Since full-span set-ups might not be necessary to isolate the connection behaviour, a component test was proposed alongside full-span floor tests to investigate influence of specimen size. The free body diagram shown in Figure 2 allowed for conversion of the pushdown force P, applied tension at supports T, and displacement u data into moment M (Equation 1) and rotation θ. This allowed for direct comparison of the connection behaviour independently of scale.

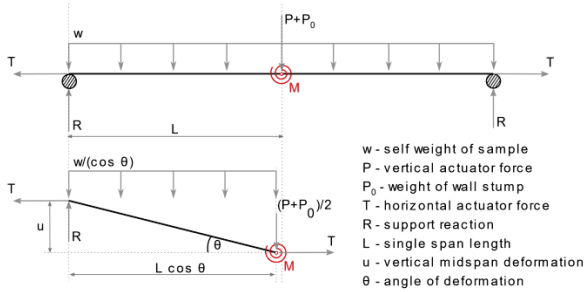

Figure 2 *Free body diagram of the tests*

$$M = \frac{P \cdot L\cos\theta}{2} + \frac{P_0 \cdot L\cos\theta}{2} + \frac{\omega \cdot L^2 \cos\theta}{2} - T \cdot u \qquad (1)$$

This calculated bending moment resistance of the connection in case of a butt joint will come from the moment couple forming between the compressive force forming at the top face and tension in the screws (Figure 3), which can be calculated as per Equation 2.

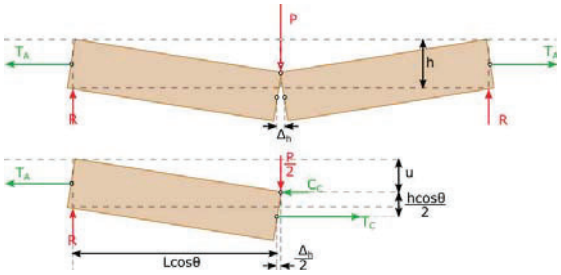

Figure 3: *Free body diagram showing the resultant connection forces dependant on component geometry*

$$T_c = P \cdot \frac{L}{h} + T_A \cdot \left(1 - \frac{2u}{h}\right) \qquad (2)$$

2.2 Materials

The CLT panels used were 5-ply 100 mm thick Binderholz BBS 125 of 20-20-20-20-20 mm layer thickness and 10% moisture content. SWG fully threaded self-tapping screws (STS) ϕ8 mm x 140 mm installed at 45° angle were used to make a butt connection, as shown in Figure 4. The full-scale test specimens had a width d = 600 mm and either 4 or 6 screws with spacings of a = 130 mm, b = 260 mm and c = 110 mm; the tension as well as component specimens had the width of d = 400 mm and spacings a = 110 mm, b = 100 mm and c = 90 mm.

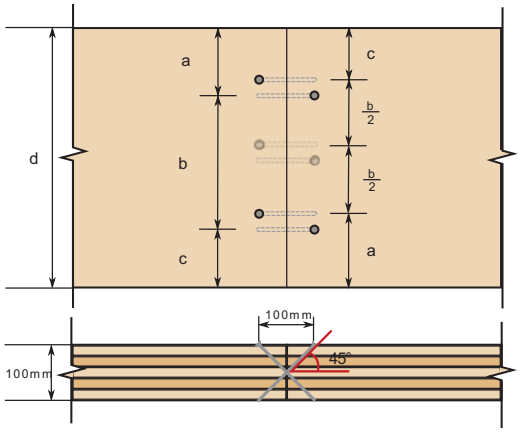

Figure 4: *Butt-joint connection design*

2.3 Axial tension tests

The horizontal force and stiffness of the connection is instrumental in dictating the force-displacement behaviour, the ultimate strength and deformation of the catenary substructure. It is therefore necessary to measure the mechanical behaviour of the connection under pure axial loading. To eliminate any bending effects of gravity loading, an upright configuration was chosen (Figure 5). The samples were attached with 6 tight-fit 15 mm diameter steel dowels on each side to minimise the slack in the system. Displacement was measured by two potentiometers installed on either side of the connection. The connections design was the same as in the component tests and therefore tension test results were also used as the equivalent of the combined test loads under maximum utilisation of tension (100% T).

Figure 5 *Axial tension test experimental setup*

https://doi.org/10.52202/069179-0042

2.4 Component tests

The component tests (Figure 6) were performed on the same test set-up as the full-span tests (Figure 7), but with the wall supports moved inwards to create the desired shorter span. The aim of the component tests was to gather information on the influence of tension level on the moment rotation behaviour and ultimate limit state values; therefore, the test series were designed in even increments of tension utilisation from 0%-75% (Table 2). These utilisation ratios were based on the average ultimate strength obtained from the axial tension tests. Together with the axial tension tests this allows for investigating of the changes in mechanical bending properties depending on the tensile utilisation ratio.

Figure 6: *Component test experimental setup*

Table 1: *Connection utilisation ratios in component tests*

Series	Tension utilisation	Tension (kN)	#STS
C1-B-0	0%	0.00	4
C1-B-25	25%	7.96	4
C1-B-50	50%	15.91	4
C1-B-75	75%	23.87	4

2.5 Full-span tests

The full-span pushdown tests were performed in 3-point bending on two butt-jointed panels with an effective length (midspan to support) of 3000 mm, see Figure 6. Four vertical string pots on either side were placed at 1 m increments and two additional string pots at the underside of the connection to monitor the joint opening.

The first full-span floor specimens were tested in a simply supported arrangement. This was used to verify whether moment rotation behaviour of the connection remained the same in such larger subassemblies as the component tests. Later specimens were tested using a variety of wall details and support conditions.

The problem with comparing tests of different spans while section size and connection design remain unchanged is the increase in relevance of the compressive arching, as it is directly proportional to the section depth to span ratio. To mitigate that issue, the tension was applied utilising chains rather than fixing the support to another member or directly to the strong wall, while the sample rested above steel rollers. That way, there was no horizontal compressive reaction possible aside from friction from the rollers which can be assumed to be negligible. Therefore, in this setup compressive arching was largely eliminated. The load was applied by two actuators, one vertically at midspan for pushdown and one installed horizontally on one end of the assembly for axial load application.

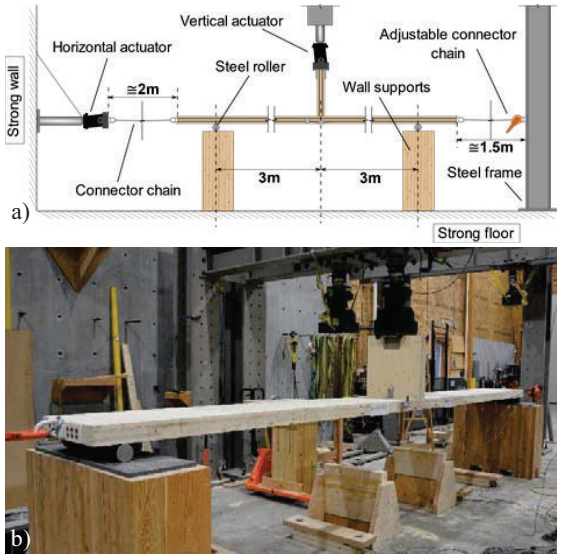

Figure 7 *Full-span test setup: a) schematic, b) photo*

Five variables were changed across the test series, summarised in Table 2. The first is the point of load application through the wall stump which either done by placing the wall loosely on top (*loose)* or attaching the load with one pair of Simpson ABR105 CLT angle bracket angle brackets installed on both sides close to the centre (*anchored)*. The second parameter was the support condition which was either simple *pin* or simulated double continuous span behaviour through restraining the overhang (*restrained)*. The tests had either 6, 4 or no screws (*#STS*). The series with no screws relied solely on the angle brackets (S5-N-P-L-15) and was performed as a control of the remainder of the tests using that connection alongside the butt joint.

Table 2: *Test series overview in full-span tests*

Series	Load	Support	T (kN)	STS
S1-B-P-L-15	Loose	Pin	15	6
S1-B2-P-L-15	Loose	Pin	15	4
S2-B-P-L-30	Loose	Pin	30	6
S2-B2-P-L-30	Loose	Pin	30	4
S3-B-P-A-15	Anchored	Pin	15	4
S4-B-P-A-F	Anchored	Pin	Fixed	4
S5-N-P-L-15	Anchored	Pin	15	0
S6-B-P-L-F	Loose	Pin	Fixed	4
S7-B-R-L-30	Loose	Restrained	15	4

https://doi.org/10.52202/069179-0042

3 RESULTS AND DISCUSSION

3.1 Axial tension tests

The axial tension test results are shown in Figure 8. An initial high-stiffness elastic region is followed by a peak and a softening branch. The mean value of the maximum force is 31.8 kN from the four tests. After around 6 mm displacement, the load reached a plateau, in most cases, at approximately 15 kN, until failure.

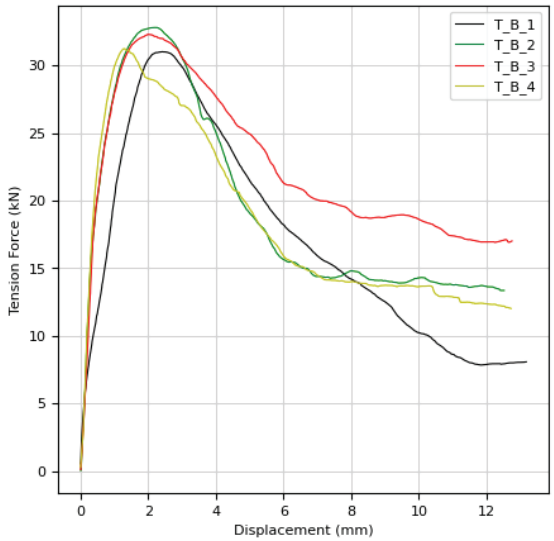

Figure 8: *Axial force displacement curves*

The initial stiffness k_0, maximum tension force T_{max}, and its corresponding deformation U_{Tmax} as well as the deformation at 50% load drop-off U_{T50} are summarised in Table 3. The latter is presented to investigate the extreme deformation behaviour which was relatively plastic. The long plateau of plastic behaviour after the initial drop-off past peak value could potentially allow for sufficient deformation to decrease tensile demand. However, the rapid loss of stiffness would lead to accelerations in the system and further release of kinetic energy. This would likely negate the initial benefits from this type of deformation and still result in connection failure.

Table 3 *Axial force test results summary*

Specimen	k_0 (kN/mm)	T_{max} (kN)	U_{Tmax} (mm)	U_{T50} (mm)
T-B-1	8.367	31.00	4.67	10.80
T-B-2	9.290	32.80	4.78	9.27
T-B-3	9.195	32.28	4.55	18.33
T-B-4	9.138	31.22	3.85	9.98
mean	8.998	31.83	4.46	12.09
CoV	4%	2%	9%	34%

3.2 Component tests

The maximum force, displacement, moment and rotation of the component-level tests are summarized in Table 4. In Figure 9, the force displacement behaviour of one specimen from each series is plotted to illustrate the main variabilities. The maximum vertical force resistance as well as maximum rotation initially increase between series C1-B-0 and C1-B-25, with one of the latter samples not failing fully after reaching the maximum actuator stroke (Figure 11a). This demonstrates activation of the catenary action. The benefit of the tensile force to the overall strength in comparison to the bending only series is also clearly visible in the C1-B-50, however with a relatively lower deformation capacity from C-B-25. The last test series with 75% tension utilisation ratio had vertical force resistance comparable to the bending only samples, but with a much higher variability.

Table 4: *Component test results summary*

Series	P_{max} (kN)	U_{max} (mm)	M_{max} (kNmm)	θ_{max} (rad)	Fracture (y/n)
C1-B-0	4.10	55.2	1668	0.028	y
	4.10	62.3	1668	0.026	y
	4.03	95.2	1640	0.028	y
	3.58	249.6	1461	0.026	y
C1-B-25	10.90	476.0	1779	0.442	n
	5.91	241.4	1336	0.035	y
	3.71	133.7	1349	0.036	y
	6.29	253.1	1278	0.035	y
C1-B-50	4.39	84.9	910	0.049	y
	4.24	91.1	894	0.042	y
	7.57	155.3	1068	0.188	y
	3.77	73.3	898	0.035	y
C1-B-75	5.78	65.8	1101	0.055	y
	0.11	16.0	71	0.003	y
	3.96	76.2	692	0.056	y
	5.41	270.7	960	0.074	y

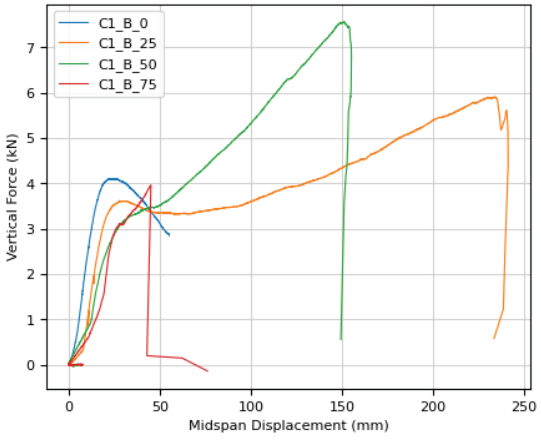

Figure 9: *Component test force displacement curves*

The maximum moment capacity of the connection, which can be observed as the peak values in Figure 10, drops proportionally to the level of tension applied to the connection. It can also be observed that the specimens loaded to the middle range of force between 25-50% performed best both in maximum deformation and

maximum force. However, all the tests reached their maximum moment at the same rotation of approximately 0.04 rad. Any further increase in vertical force resistance for the C1-B-25 and C1-B-50 samples occur directly from catenary action activation, which is only possible through the post-failure plastic plateau.

Failure of the screws in the component tests was observed in two different modes. Screws failed in withdrawal, with some having punched through the material from the headed side of the screw (Figure 11b). In either scenario material in the traverse layers of the panels was pulled due to the tension perpendicular to the grain. Some of that failure was shown to split all the way to the edge of the sample, indicating that a higher edge spacing and therefore more material to distribute the localised stresses could have a positive impact on the overall strength of that connection.

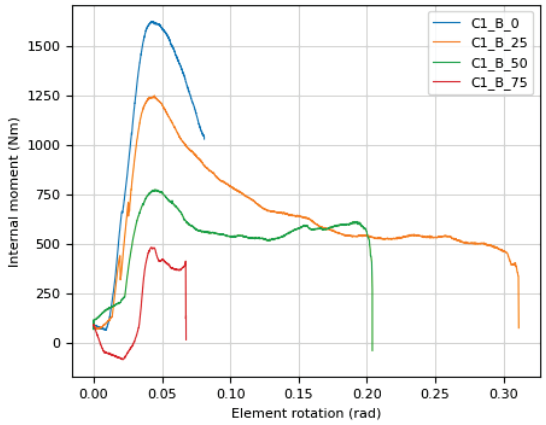

Figure 10: *Component test moment rotation curves*

Figure 11: *Butt joint component tested to maximum stroke (a) and to failure (b)*

3.3 Full span tests

Maximum force, displacement, moment, and rotation values recorded for each test are summarized in Table 5. One of the challenges of full-span testing was the relatively low vertical stroke to span ratio, which led to some of the samples not failing throughout the duration of the test (greyed out fields), meaning that their maximum values will likely be larger than the tabulated data shown.

Table 5: *Full span test results summary*

Series	P_{max} (kN)	U_{max} (mm)	M_{max} (kNmm)	θ_{max} (rad)	Fracture (y/n)
S1-B-P-L-15	5.53	498.1	2120	0.167	n
	5.81	487.9	2739	0.163	n
	5.57	434.2	2059	0.145	y
	5.68	522.3	2031	0.175	n
S1-B2-P-L-15	5.30	497.7	1814	0.167	n
	2.29	262.7	1284	0.088	y
	2.44	287.1	1233	0.096	y
	2.07	252.6	1233	0.084	y
	3.36	338.8	1438	0.113	y
	5.17	499.8	1563	0.167	n
S2-B-P-L-30	3.05	144.7	1757	0.048	y
	2.46	128.7	1348	0.043	y
	8.31	401.7	1794	0.134	y
	4.26	230.1	1303	0.077	y
S2-B2-P-L-30	1.90	117.8	1227	0.039	y
	0.02	45.6	1307	0.015	y
	2.06	121.7	1287	0.041	y
	0.43	65.5	1227	0.022	y
S3-B-P-A-15	5.12	437.9	2464	0.146	y
	4.25	375.2	2438	0.125	y
	5.20	454.9	2587	0.152	y
	5.34	495.8	2765	0.166	y
S4-B-P-A-F	3.39	489.6	1186	0.164	n
	3.72	486.4	1149	0.163	n
	3.68	449.4	1260	0.150	y
	2.99	391.3	1273	0.131	y
S5-N-P-L-15	0.54	2.5	2243	0.001	y
	0.55	101.0	1433	0.034	y
	0.24	31.9	1705	0.011	y
S6-B-P-L-F	2.86	230.2	1248	0.077	y
	2.26	264.6	1160	0.088	y
	1.96	227.6	1242	0.076	y
	1.73	215.6	1196	0.072	y
S7-B-R-L-15	16.49	155.9	1144	0.052	y
	15.25	140.3	879	0.047	y
	14.09	127.6	690	0.043	y
	18.31	162.2	1239	0.054	y

The shape of the load displacement curve is strongly influenced by the way in which the axial tension is applied, which confirms that the catenary action is the primary load resistance mechanism. For instance, in the test series where tension was increasing along with pushdown through fixed horizontal displacement (S4 and S6), the support stiffness of the system increased

https://doi.org/10.52202/069179-0042

throughout the test (Figure 12). The maximum tension values at supports for these test series are shown in **Error! Not a valid bookmark self-reference.**. The presence of angle brackets connecting the wall stub to the floor panels did not have a great influence on the maximum tension capacity; however, it did allow for a greater deformation which positively affects the overall force capacity presented in Figure 12.

Table 6: *Maximum tension in the fixed horizontal displacement tests*

	T_{max}	U_{Tmax}
S6-B-P-L-F	19.5	152.9
	16.5	120.6
	16.3	155.9
	15.2	113.8
mean	**16.9**	**135.8**
CoV	11%	16%
S4-B-P-A-F	14.0	243.5
	19.4	227.8
	15.0	167.6
	15.7	185.6
mean	**16.0**	**206.1**
CoV	15%	17%

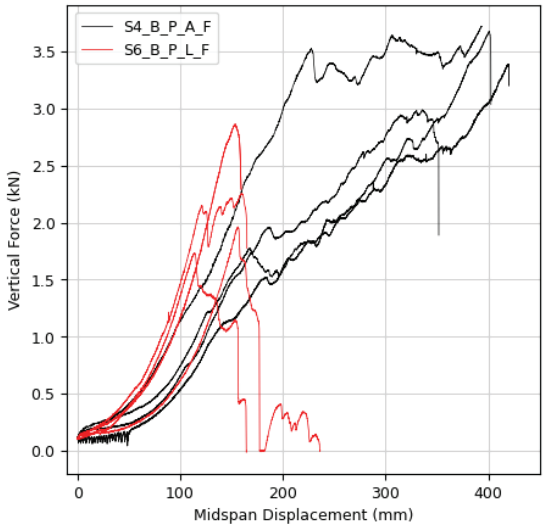

Figure 12: *Fixed displacement tests force displacement curves*

The effect of the additional brackets in samples S3-B-P-A in the load hold is less apparent, showing almost exactly the same behaviour as their S1 counterparts under the same 15 kN loading, see Figure 13. This is because due to the load control nature of the loading even a small drop-off in tensile force will lead to the actuator rapidly increasing the rate of displacement and therefore causing immediate failure. The caveat of such tests is if the connection does in fact have some remaining strength after that initial peak, but reduced stiffness, this will allow for greater deformation and therefore decreased tension demand, allowing to potentially achieve load equilibrium once again. However, the majority of timber connections being relatively brittle do not in fact have a large enough residual strength to be able to accommodate the resulting kinetic effect. Moreover, with the large variability of timber, especially in the region close to failure, it would not be safe to rely on this behaviour past the peak strength as a robustness design feature.

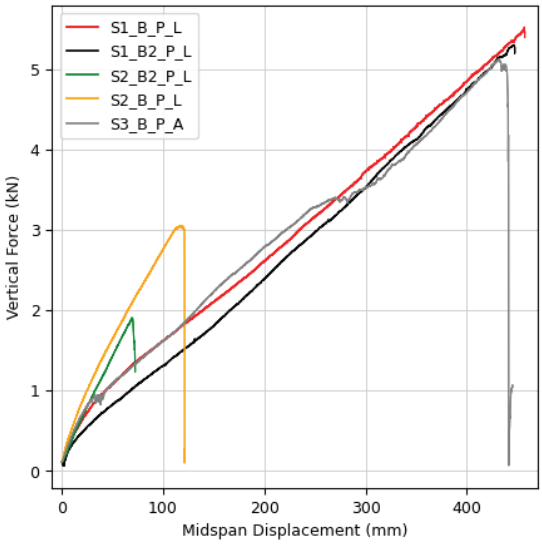

Figure 13: *Selected axial load hold tests force displacement curves*

Results of the test series which were tested over roller supports and in the horizontal tension load hold are presented in Figure 14. The stiffness of the system is again largely governed here by the tension and therefore the test series S2_B and S2_B2 which are under 30 kN horizontal load hold are visibly stiffer in comparison to the S1_B, S1_B2 and S3_B which were loaded with 15 kN. Notably, the number of screws (S1_B and S2_B with 6 screws total and S1_B2 and S2_B2 with 4 screws total) nor the presence of the wall bracket connection did not visibly affect the stiffness. Both the wall brackets and the extra pair of screw did have a positive effect on the ultimate load and moment capacity and maximum deformation/rotation as seen in Table 5.

The samples that have been tested to full failure, just as in the component tests, were observed to have failed in screw withdrawal, see Figure 14a. Most of them did not however have the layer split travel to the edge of the sample, which could be due to the extra 20 mm edge spacing. Connections in both full-scale and component tests were designed well within the minimum spacing, therefore when designing for large deformations, the guidance made for connections for the elastic limit might not apply in the same way.

Samples with the continuous span have produced the highest vertical force resistance of 14-18 kN, with more than 3x higher resistance than the catenary action. The failure mode of these samples was initially rolling shear in the traverse layers and eventually tensile splitting of the uppermost layer (Figure 14b). The test was stopped after this first load drop off due to the panel failure and before the ultimate failure of the connection due to safety concerns. The maximum moment exhibited by the

connection was on average lower than but approaching the values in series S1-B2 of the equivalent connection properties and magnitude of tension applied. This explains lack of connection failure but also implies that it was imminent, and the overall force capacity of the system was unlikely to rise back up above the initial peak.

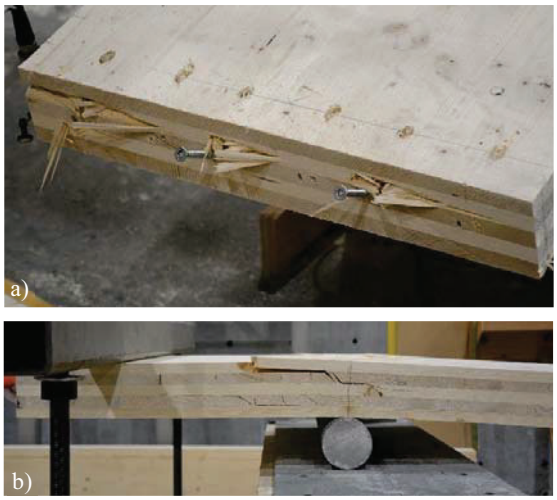

Figure 14: *Failure of the connection in test series S1 (a) and over the support in test series S6 (b)*

3.4 Combined analysis

Internal connection tension forces in selected component tests derived from equilibrium of forces as per Eq.2 are shown in Figure 15. In essence the tension present in the connection is a combination of the moment couple present from the opening of the joint and the tension resultant from catenary forces.

Although this was similarly visible in the component tests, several differences can be observed between tension displacement behaviour when comparing to the uniaxially loaded specimen illustrated in Figure 9. This was due to the slight changes in the failure modes, as the bent screws redistributed internal loads differently based on the angle of deformation. The ultimate strength however remained consistent across all samples, which means that despite different bi-axial load combinations this can be the reliable parameter for failure checks.

Results of the pin-support tests under constant tension have been summarised as a failure envelope for combined tension and bending in Figure 16. Each datapoint represents the maximum moment experienced by the sample and the corresponding tension utilisation value based on the axial load tests. An extreme value distribution analysis was performed on the results from 4 specimen in each of the component test series and linear regression lines were fitted through the corresponding median values and the upper and lower bounds of the 95% confidence interval.

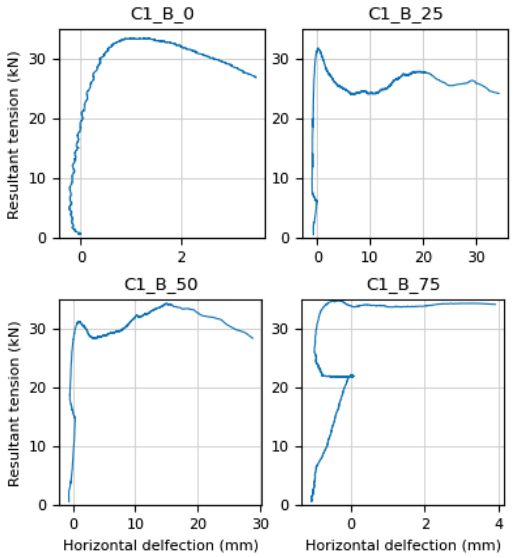

Figure 15: *Internal tension forces in component test results*

The moment capacity of both component and full span tests drops proportionally to the increased tensile utilisation. Horizontal withdrawal of the screw is the governing failure mode and both increased system tension as well as bending of the connection increase the tension resultant at the screw, therefore this relationship is numerically justified. As shown in Figure 15, the total of those two resultants reaching tensile capacity of the connection is the cause of connection failure.

The values of the full-span tests when compared to the component test data fit does fall on the higher side of the data distribution. This could be due to a multitude of factors such as data errors and the active changes in the effective span due to the horizontal travel distance of steel rollers, small changes in screw spacing and proportionally large variability of timber properties. However, they do still largely follow the same trend and are a deemed a good predictor of the large-scale behaviours.

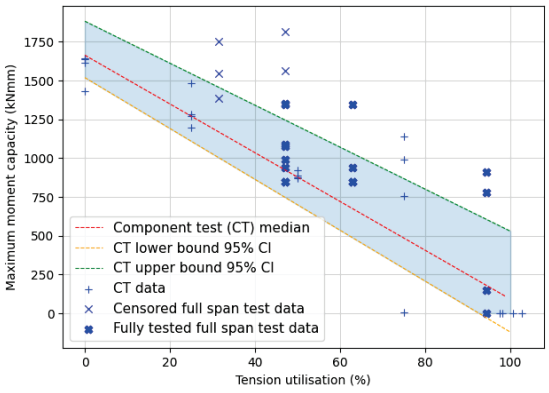

Figure 16: *Combined loading failure envelope*

https://doi.org/10.52202/069179-0042

4 CONCLUSIONS

The presented tests provide much-needed insight into the possibilities of smaller scale experiments as a base for empirical-based robustness analysis of mass timber floor systems. This correlation observed between the different scales of test results show that there is possibility for the component tests to be good predictors of the behaviour of the more complex subassemblies.

The analysis has shown that the tension increase in the system has both beneficial and compromising effects on the total force capacity on the system – the tension allows for the load redistribution to form, consequently lessening the bending capacity demand on the system, but at the same time decreases the bending capacity itself. In the tested samples the region where these two were balanced was between 25-50% of tension utilisation. However, the maximum moment capacity is consistently being reached at minimal deformations and the subsequent catenary activation occurs on a sample effectively past its failure load. Moreover, the variability of results increases drastically at the higher end of the utilisation scale meaning that relying on that behaviour is not advised.

The paper presents testing that can form the basis of future performance-based design frameworks. Still, a significant amount of research is needed to develop comprehensive, functional design guidance. Aiming for standardisation of test, modelling and design methods is essential for continuous growth of the industry and use of timber as modern construction material for years to come.

ACKNOWLEDGEMENTS

The authors acknowledge the financial support received by the Royal Society of Edinburgh Lessels Travel Scholarship. The experimental work was funded by the government of Canada through a Canada Research Chair. The support by the UNBC technicians Michael Billups, James Andal, and Ryan Stern is greatly appreciated.

REFERENCES

[1] Mpidi Bita H, Tannert T. Tie-force procedure for disproportionate collapse prevention of CLT platform-type construction. *Engineering Structures* 189(2):195–205, 2019.

[2] Abrahamsen R. Mjøstårnet: Construction of an 81 m tall timber building. 23. In: Internationales Holzbau-Forum IHF 2017, 1–13. 2017.

[3] Starossek U, Haberland M. Robustness of structures. *Int J Lifecycle Performance Engineering*. 1(1):3–21. 2012.

[4] European Committee for Standardization. Eurocode 1 - Actions on structures - Part 1-7: General actions - Accidental actions BS EN 1991-1-7:2006.

[5] COST Association AISBL. Memorandum of Understanding for the implementation of the COST Action “Holistic design of taller timber buildings” (HELEN) CA20139. Brussels; 2021.

[6] Voulpiotis K, Köhler J, Jockwer R, Frangi A. A holistic framework for designing for structural robustness in tall timber buildings. *Engineering Structures*. 227:111432, 2021.

[7] Kiakojouri F, de Biagi V, Chiaia B, Sheidaii MR. Progressive collapse of framed building structures: Current knowledge and future prospects. *Engineering Structures.* 206:110061, 2020.

[8] Mpidi Bita H, Tannert T. Experimental Study of Disproportionate Collapse Prevention Mechanisms for Mass-Timber Floor Systems. *ASCE Journal of Structural Engineering.* 146(2):04019199, 2020.

[9] Lyu CH, Gilbert BP, Guan H, Underhill ID, Gunalan S, Karampour H, et al. Experimental collapse response of post-and-beam mass timber frames under a quasi-static column removal scenario. *Engineering Structures* 213:110562, 2020.

World Conference on Timber Engineering Oslo 2023

UNREINFORCED AND STEEL-REINFORCED COLUMNS MADE OF EUROPEAN BEECH GLUED-LAMINATED TIMBER

Katharina Sroka [1], Pedro Palma [2], René Steiger [3], Thomas Ehrhart [4], Andrea Frangi [5], Thomas Strahm [6], Ernst Gehri [7]

ABSTRACT: With the aim of promoting the use of glued-laminated timber (GLT) made from European beech (*Fagus sylvatica* L.), experimental and numerical studies were conducted on high-strength columns for residential, office, and industrial applications. The experimental research comprised compression tests on stocky and slender unreinforced and steel-reinforced beech GLT columns of strength classes GL40h, GL48h, and GL55h. A finite element model was developed to perform parametric studies on geometrical and mechanical properties and to evaluate the load-carrying capacity across different slenderness ratios. The investigations revealed that the columns can be designed using the *effective length method*, however with adapted critical relative slenderness $\lambda_{rel,0}$ and straightness factor β_c. Corner steel reinforcement of grades ST900/1100 and ST950/1050 leads to a marked increase in the load-carrying capacity of stocky as well as slender GLT columns.

KEYWORDS: hardwood, GLT, column, buckling, compressive strength, steel-timber hybrid member

1 INTRODUCTION

Growing interest in timber high-rise buildings is creating demand for high-strength timber columns. In high-rise or industrial buildings, the required cross-sections of timber columns can become excessively large, critically limiting the available floor space or even the structural feasibility, and obstructing window views. Compared to softwood, European beech (*Fagus sylvatica* L.) glued-laminated timber (GLT) offers a high compressive strength parallel to the grain. Beech wood is widely available in Central European forests, but it is barely used for structural purposes [1] and beech GLT is not integrated in the European standards.

With the aim of using beech GLT for high-strength columns in residential, office, and industrial applications, the company *neue Holzbau AG* developed hybrid beech GLT columns reinforced with steel bars. The steel reinforcement substantially improves the load-carrying capacity and helps to overcome the buckling issues that limit the utilisation of the higher compressive strength, often making slender columns uneconomical. The steel reinforcement offers additional advantages by enabling an increased ductility of the columns, stiff connections to other elements, a ductile failure mode governed by the connections, reduced differential settlements to concrete elements in hybrid structures, and better resistance to impact loading. The glued-in steel bars can also be used to increase structural robustness by allowing floor-to-column and column-to-column connections to carry tensile forces and hold the floor below in case a column fails [2]. A similar strategy was implemented using glued-in steel rods as vertical ties in the HoHo building in Vienna [3].

Full-scale experiments and numerical simulations were conducted to investigate the axial load-carrying capacity of unreinforced and steel-reinforced columns with different slenderness ratios. Key factors influencing the load-carrying capacity were identified from parametric studies. A design model that can be easily adopted in engineering practice was developed.

The objective was to enhance the understanding of the buckling behaviour of these high-strength columns and to demonstrate their application potential.

[1] Katharina Sroka, Empa – Swiss Federal Laboratories for Materials Science and Technology, Structural Engineering Research Lab, Switzerland, katharina.sroka@empa.ch
[2] Pedro Palma, Empa – Swiss Federal Laboratories for Materials Science and Technology, Structural Engineering Research Lab, Switzerland, pedro.palma@empa.ch
[3] René Steiger, Empa – Swiss Federal Laboratories for Materials Science and Technology, Structural Engineering Research Lab, Switzerland, rene.steiger@empa.ch
[4] Thomas Ehrhart, Schnetzer Puskas Ingenieure, Switzerland, t.ehrhart@schnetzerpuskas.com
[5] Andrea Frangi, ETH Zürich – Swiss Federal Institute of Technology, Institute of Structural Engineering, Switzerland, frangi@ibk.baug.ethz.ch
[6] Thomas Strahm, neue Holzbau AG, Switzerland, thomas.strahm@neueholzbau.ch
[7] Ernst Gehri, Prof. emeritus ETH Zürich, Dr. h.c., Switzerland, gehri@emeritus.ethz.ch

https://doi.org/10.52202/069179-0043

2 EXPERIMENTS

2.1 MATERIALS

2.1.1 Hardwood GLT

Swiss-grown European beech boards were used for the production of the GLT columns. The boards were strength graded into tensile strength classes T33 (for GL40h), T42 (for GL48h), and T50 (for GL55h), applying the strength grading rules described by Ehrhart et al. [4]. The laminations were bonded using a 1-comp. PU adhesive and a primer [5]. The lamination thickness was 25 mm and the wood moisture content was $\omega = 8 \pm 2\%$ representing the climatic conditions of indoor use.

2.1.2 Reinforcement

The steel reinforcement bars placed either in the centre or in the four corners of the cross-section (Figure 1) were profiled Swiss-GEWI bars of grade ST900/1100 for diameters below 29 mm, and of grade ST950/1050 for diameters greater than 29 mm. The steel grades were chosen from products available on the market. To avoid preliminary yielding of the reinforcement, the yield strength of steel was chosen based on Formula (1).

$$\frac{f_y}{E_s} > \frac{f_{c,0,05}}{E_{c,0,05}} \therefore f_y > \frac{62.5 \cdot 210\,000}{15\,400} \approx 850 \text{ MPa} \qquad (1)$$

where f_y = yield strength of steel, E_s = modulus of elasticity of steel, $f_{c,0,05}$ = 5th percentile value of the compressive strength parallel to the grain for GL48h made of beech, and $E_{c,0,05}$ = 5th percentile value of the compressive modulus of elasticity parallel to the grain for GL48h made of beech. 5th percentile values for GL48h columns with a square cross-section and side length of 200 mm were reported by Ehrhart et al. [6, 7].

To insert the steel reinforcement, the GLT specimens were cut lengthwise at the designated position of each steel bar. Lengthwise notches for the steel bars were milled into the GLT pieces which were then block glued under pressure, using a 1-comp. PU adhesive with primer. Finally, the steel bars were inserted into the notches which were filled using an epoxy adhesive.

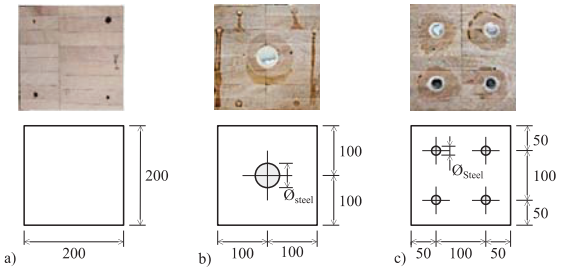

***Figure 1**: Unreinforced (a) and reinforced cross-sections using one central rebar (b) or four corner rebars (c).*

2.2 COMPRESSION TESTS ON STOCKY COLUMNS

2.2.1 Test configurations

Compression tests on 1200 mm long stocky columns were carried out to evaluate the axial compressive strength of unreinforced and steel-reinforced European beech GLT (Table 1). Due to the support conditions prescribed by EN 408 [8] (loading heads locked against rotation during the test), the effective length was $L_{eff} \approx 0.6\ L$ [9]. The tests on unreinforced beech GLT columns were performed by Ehrhart et al. [6, 7]. For the steel-reinforced columns, different arrangements (diameter $Ø_{steel}$ and number of bars n_{rebars}) and degrees (ρ) of steel reinforcement were investigated to optimise the axial load-carrying and deformation capacities, while considering the increase in production effort.

***Table 1:** Compression test specimens (square side length a = 200 mm, L_{eff} = 720 mm).*

Strength class [-]	$Ø_{steel}$ [mm]	n_{rebars} [#]	ρ [%]	$n_{specimens}$ [#]
GL40h	-	-	-	7
GL48h	-	-	-	7
GL55h	-	-	-	7
GL55h	30	1	1.77	3
	40	1	3.14	3
	15	4	1.77	3
	20	4	3.14	3

2.2.2 Test results

During the compression tests on the stocky columns, no horizontal displacement was observed before failure. Crushing of the fibres initially occurred close to local imperfections (i.e. knots, finger joints, deviations in the direction of wood fibres) and finally progressed over the whole cross-section, followed by splitting. Sample force-displacement curves of individual specimens are shown in Figure 2.

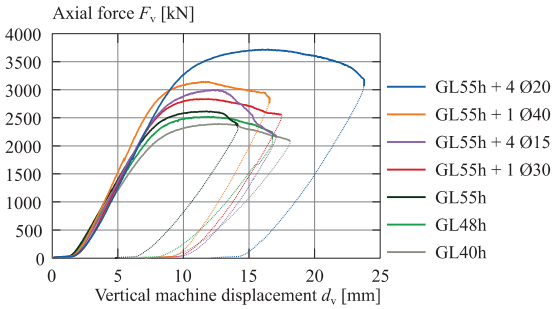

***Figure 2**: Sample axial force-displacement curves obtained for individual specimens in the compression tests on stocky columns.*

The steel reinforcement bars increased the compressive strength and the modulus of elasticity parallel to the grain of the beech GLT columns (Table 2). The corner reinforcement with 20 mm diameter (ρ = 3.14%) led to a particularly pronounced increase in the axial load-carrying capacity of around 40% compared to the unreinforced specimens. An equal amount of central reinforcement only led to a 20% increase, likely due to a less favourable distribution of the applied axial load into the cross-section.

In the tests on unreinforced columns, very similar mean values of compressive strength parallel to the grain $f_{c,0,mean}$ were obtained for all tested strength classes, with an increase of only 3% from GL48h to GL55h (Table 2). The stocky steel-reinforced specimens (Section 2.2) were of

https://doi.org/10.52202/069179-0043

strength class GL55h, whereas the slender steel-reinforced columns (Section 2.3) were of strength class GL48h. The results of both test series can be analysed together given the very small difference in compressive strength between GL48h and GL55h, which indicates that the strength class (GL48h or GL55h) has little influence on the axial load-carrying capacity in compression.

Table 2: *Mean experimental axial load-carrying capacity $R_{c,0,mean}$, compressive strength $f_{c,0,mean}$, and modulus of elasticity $E_{c,0,mean}$ parallel to the grain.*

Strength class [-]	$n_{specimens}$ [#]	$R_{c,0,mean}$ [kN]	$f_{c,0,mean}$ [MPa]	$E_{c,0,mean}$ [GPa]
GL40h	7	2393	60.4	15.1
GL48h	7	2526	63.8	16.0
GL55h	7	2607	65.8	17.0
GL55h + 1 Ø30	3	2851	71.3	20.1
GL55h + 1 Ø40	3	3104	77.6	22.2
GL55h + 4 Ø15	3	2985	74.6	19.0
GL55h + 4 Ø20	3	3585	89.6	23.3

2.3 BUCKLING TESTS ON SLENDER COLUMNS

2.3.1 Test configurations

Slender columns of strength class GL48h and with effective lengths of 2400 mm and 3600 mm were subjected to buckling tests. These effective lengths were chosen to represent the typical heights of columns in high-rise and industrial buildings. The planned initial eccentricity was $e_0 = L_{eff}/500$ but deviations occurred due to manufacturing inaccuracies. The tested configurations are listed in Table 3, the test setup is depicted in Figure 3. The tests on unreinforced beech GLT columns were performed by Ehrhart et al [6, 7].

Table 3: *Buckling test specimens (a = 200 mm, GL48h).*

L_{eff} [mm]	$Ø_{steel}$ [mm]	n_{rebars} [#]	$n_{specimens}$ [#]	$L_{eff}/e_{0,mean}$ [-]
2400	-	-	5	382
3600	-	-	5	590
2400	40	1	3	436
3600	40	1	3	554
2400	20	4	3	415
3600	20	4	3	618

2.3.2 Test results

The buckling tests on slender columns focused on the reinforcement layouts with higher reinforcement ratio (1× Ø40, 4× Ø20), since these demonstrated the maximum gain in mechanical properties during the compression tests on stocky columns.

The test results are presented in Figure 4, sample load-displacement curves are shown in Figure 8. For GL48h, the central reinforcement of 40 mm diameter led to a 20% gain in the axial load-carrying capacity in columns of low to medium effective length (≤2400 mm) and to a 10% gain for long columns (3600 mm). The corner reinforcement with four rebars of 20 mm diameter and an edge distance of 50 mm led to a 40% increase in the load-carrying capacity across the investigated buckling lengths because it increases the bending stiffness of the columns.

Figure 3*: Buckling test of slender column at Empa.*

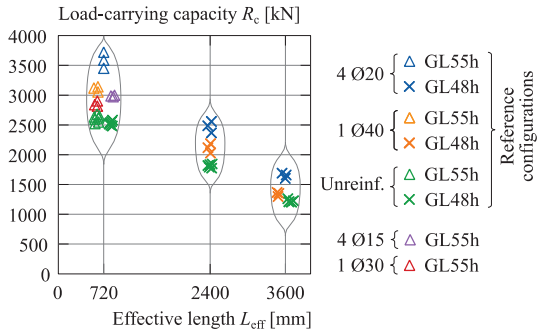

Figure 4*: Experimentally-determined axial load-carrying capacity of unreinforced and steel-reinforced European beech GLT columns.*

3 NUMERICAL SIMULATIONS

3.1 FINITE ELEMENT MODEL

A framework to model unreinforced and steel-reinforced GLT columns under compressive axial loads was developed using OpenSeesPy [10], which is a Python [11] library for the OpenSees finite element framework [12]. The model considered geometric and material nonlinearity. The initial deformed shape of the discretised column followed a sinusoidal curve with user-defined initial mid-span eccentricity. Boundary conditions were defined as depicted in Figure 5. An external vertical compression force (or displacement, as chosen by the user) was applied at the upper node.

The cross-section of the column elements was modelled as a fibre section using different patches for the timber laminations and the steel reinforcement (Figure 6). The fibres in these patches were associated with the uniaxial stress-strain relationship of the corresponding material. A bilinear material without hardening was adopted for the steel fibres, while the timber fibres were assigned the nonlinear material model for European beech defined by Glos [13].

Beech GLT material properties were based on the mean experimental results for unreinforced GL48h columns

https://doi.org/10.52202/069179-0043

with a section size of 200 mm ($f_{c,0,mean}$ = 63.8 MPa; $E_{c,0,mean}$ = 16.0 GPa). The quasi-static structural analyses were performed under load control, since the aim of the simulations was to determine the load-carrying capacity of the columns.

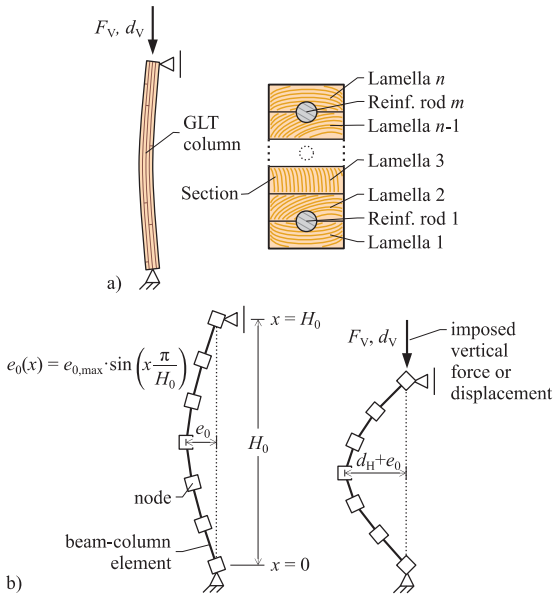

***Figure 5**: Numerical model of the GLT column: a) idealisation of the column and cross-section; b) FE model, including initial deformed shape.*

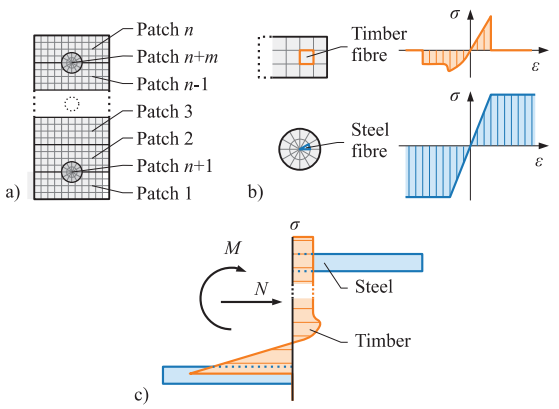

***Figure 6**: Modelling of the cross-sectional behaviour: a) fibre patches; b) uniaxial material models for timber and steel; c) stresses and internal forces in the cross-section.*

3.2 MODEL VALIDATION

The model was validated using the experimental results. A comparison between simulated and experimental load-carrying capacities is presented in Figure 7, showing a very good agreement. A small deviation occurred for the unreinforced specimens with effective length of 3600 mm. In contrast to the experimental results, the simulated load-carrying capacity of the unreinforced column was higher than that of the centrally reinforced column at high slenderness (see the orange and green data points in Figure 7 with load-carrying capacities between 1000 and 1500 kN). Since the buckling curves of unreinforced and centrally reinforced GLT columns converge for high slenderness, the impact of this deviation is negligible.

The load-displacement curves obtained from the simulations also agree well with the experimental results, as shown in Figure 8 for three exemplary specimens with effective length of 2400 mm. Since the simulations were carried out under load control, the post-peak behaviour is not captured by the numerical results.

The validation shows that the model was able to simulate the buckling behaviour of the columns and estimate the mean load-carrying capacity with adequate accuracy.

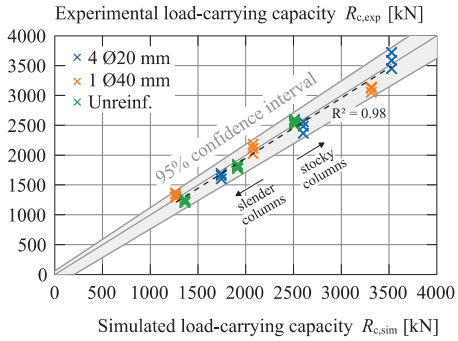

***Figure 7**: Validation of the numerical results: comparison with the experimental mean axial load-carrying capacity for each reference configuration (GL48h unreinforced, GL48h with 1× Ø40, GL48h with 4× Ø20).*

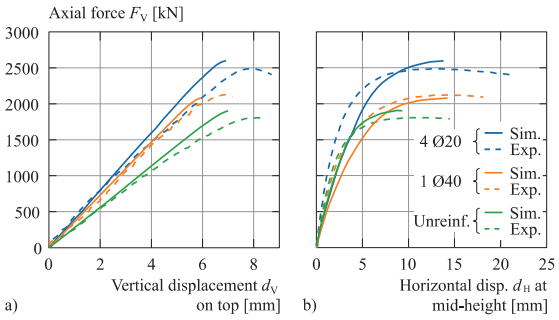

***Figure 8**: Comparison of simulated and experimental load-displacement curves for GL48h columns with L_{eff} = 2400 mm: a) vertical displacement at the top of the column; b) horizontal displacement at mid-height of the column.*

3.3 PARAMETRIC STUDIES

The objective of the numerical framework was to gain further insights into the buckling behaviour of the composite columns. First, buckling curves were generated by simulating columns of varying effective lengths around the experimental range (Figure 9). Second, parametric studies were conducted on the most important parameters identified in the experimental campaign: i) initial eccentricity ($e_0 = L_{eff}/300$, $L_{eff}/500$, and $L_{eff}/1000$); ii) diameter of the central and corner steel bars (1× Ø30, 1× Ø40, 4× Ø15, 4× Ø20, 4× Ø25); iii) size of the cross-section (a = 200, 250, and 300 mm); iv) timber strength class (GL40h, GL48h, and GL55h). Benchmarking values were $e_0 = L_{eff}/500$, a = 200 mm, and GL48h.

https://doi.org/10.52202/069179-0043

Maximum reductions in the load-carrying capacity of 13 to 17% were observed when increasing the initial eccentricity from L_{eff}/1000 to L_{eff}/300 (Figure 10). Decreasing the diameter of the central steel rod from 40 to 30 mm led to reductions of 15% for stocky columns and of less than 5% for slender columns (Figure 11). The load-carrying capacity for all investigated slenderness ratios reduced by more than 20% when changing the diameter of the four corner steel bars from 25 to 15 mm (Figure 12). The size of the cross-section has a pronounced impact on the load-carrying capacity for column lengths relevant for structural applications (Figure 13). The edge distance of 50 mm was kept constant when varying the section size of corner-reinforced columns. Figure 14 confirms that the influence of the GLT strength class is very limited.

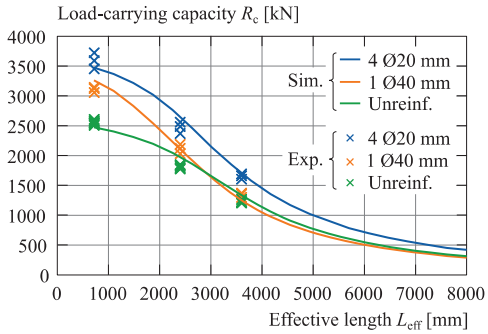

***Figure 9**: Simulated buckling curves for the three reference configurations, compared with the experimental results.*

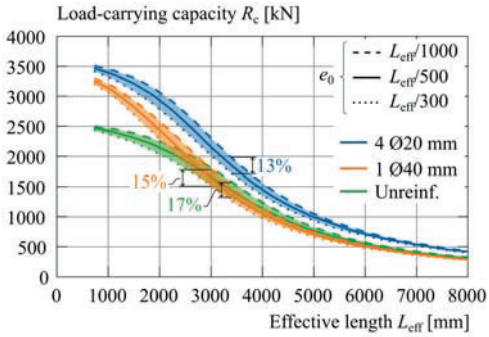

***Figure 10**: Parametric study on the impact of the initial eccentricity e_0 on the load-carrying capacity of the column.*

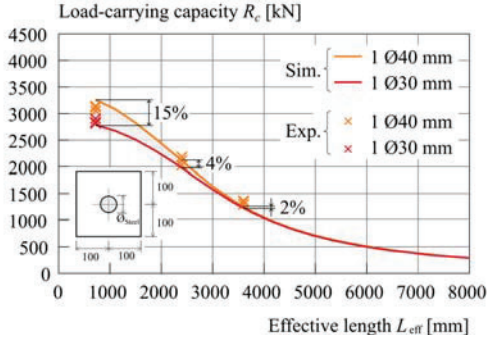

***Figure 11**: Parametric study on columns with different diameter of a single central reinforcement bar.*

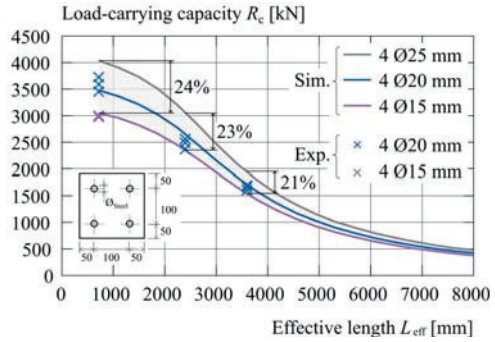

***Figure 12**: Parametric study on columns with different diameters of the four corner reinforcement bars.*

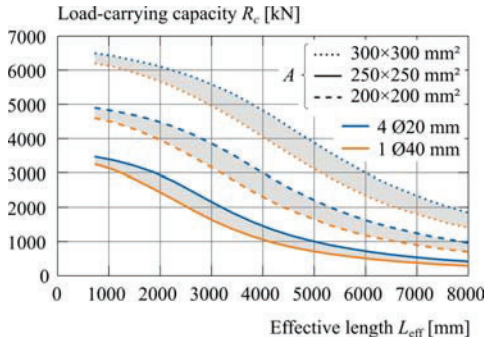

***Figure 13**: Parametric study on the impact of the cross-section size on the axial load-carrying capacity of the column.*

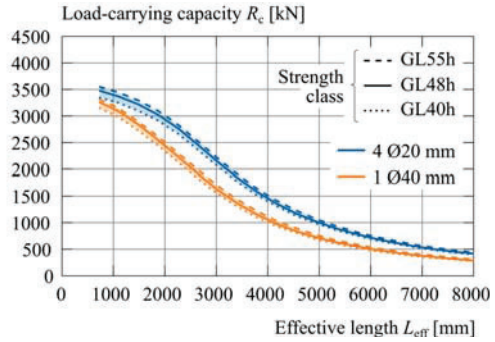

***Figure 14**: Parametric study on the impact of the GLT strength class.*

All parametric studies were carried out for effective lengths of up to 8000 mm to approximately match the range of slenderness ratios covered by buckling curves in current design standards, even though such long columns are not relevant in typical structural applications. Simulated results for these lengths were not verified by experiments and should thus be regarded with caution.

4 DESIGN MODEL

4.1 UNREINFORCED COLUMNS

The design rules in EN 1995-1-1:2004 (Eurocode 5) [14] for verifying the stability of columns subjected to axial compression are based on the *effective length method*, see Formulae (2)-(5).

https://doi.org/10.52202/069179-0043

$$R_{c,0} = k_c \cdot f_{c,0} \cdot A \tag{2}$$

$$k_c = \frac{1}{k + \sqrt{k^2 - \lambda_{rel}^2}} \tag{3}$$

$$\lambda_{rel} = \frac{L_{eff}}{\pi \sqrt{\frac{I}{A}}} \sqrt{\frac{f_{c,0,k}}{E_{0,05}}} \tag{4}$$

$$k = 0.5 \left(1 + \beta_c \left(\lambda_{rel} - \lambda_{rel,0}\right) + \lambda_{rel}^2\right) \tag{5}$$

where k_c = buckling factor, A = cross-sectional area, λ_{rel} = relative slenderness ratio, I = second moment of area, $f_{c,0,k}$ = characteristic value of the compressive strength parallel to the grain, $E_{0,05}$ = 5th percentile value of the modulus of elasticity parallel to the grain, β_c = straightness factor or imperfection coefficient, and $\lambda_{rel,0}$ = critical relative slenderness ratio. Both β_c and $\lambda_{rel,0}$ are material-dependent. The straightness factor β_c describes the steepness of the buckling curve while the critical relative slenderness $\lambda_{rel,0}$ defines the threshold relative slenderness above which buckling should be taken into account.

The experiments on unreinforced slender columns [6, 7], accompanied by the numerical investigations showed that the design parameters $\lambda_{rel,0} = 0.30$ and $\beta_c = 0.10$ currently specified for softwood GLT in Eurocode 5 [14] lead to an overestimation of the axial load-carrying capacity of up to 18% (L_{eff} = 2400 mm) in the case of unreinforced beech GLT columns. This deviation arises because the ratio between the compressive strength and modulus of elasticity parallel to the grain is higher for beech (1/250) [15, 16] than for softwood (1/370 to 1/420) GLT [17].

Ehrhart et al. [7] found a low scatter in compressive strength and modulus of elasticity parallel to the grain, based on tests on stocky columns according to EN 408 [8]. Values on a similar level were also reported by Westermayr et al. [16].

The calibration of buckling curves was conducted on the mean level of the material properties, including only results from test specimens of strength class GL48h. Mean values $f_{c,0,mean}$ = 60.6 MPa and $E_{c,0,mean}$ = 15.7 GPa were used, based on a more comprehensive set of test specimens with varying cross-section sizes [7]. The critical relative slenderness $\lambda_{rel,0}$ was determined based on the effective length of the stocky specimens. The straightness factor β_c was calibrated to the experimental data. A critical relative slenderness ratio of $\lambda_{rel,0} = 0.25$ and a straightness factor of $\beta_c = 0.25$ are proposed to ensure that the *effective length method* can be applied to verify the stability of beech GLT columns of strength classes GL40h, GL48h, and GL55h [7].

Figure 15 shows the load-carrying capacity as a function of the effective length according to the current and proposed buckling curves, along with the experimental and numerical results for unreinforced beech GLT of strength class GL48h.

4.2 STEEL-REINFORCED COLUMNS

At the same reinforcement ratio, corner reinforcement was shown to be much more effective in improving the mechanical properties of GLT columns than a single central rebar. Despite the more complex manufacturing process, four steel bars placed in the corners of the section are preferable for an economic design in demanding applications. A design approach was thus developed only for the corner reinforcement with four rebars of 20 mm diameter and 50 mm edge distance.

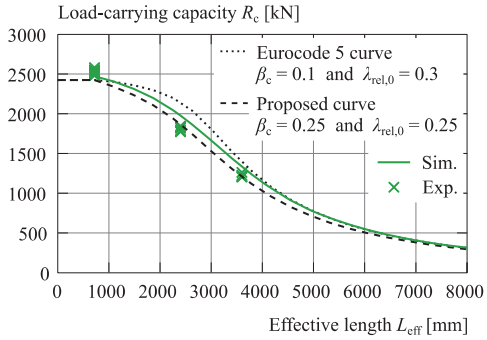

***Figure 15**: Comparison of current Eurocode 5 and proposed buckling curves for unreinforced European beech GLT columns of strength class GL48h, along with the experimental and numerical results [7].*

The *effective length method* cannot be applied directly to composite sections because the load is distributed across the materials in proportion to their stiffness. An equivalent unreinforced GLT section can be determined using Formulae (6)-(8). The method is valid for rigid (i.e. glued) composite sections and assumes direct load transfer to the cross-section at the supports without any load redistribution within the section. The steel has a reinforcing function and should not yield before the timber fails.

$$n = \frac{E_s}{E_{c,0,mean}} \tag{6}$$

$$A_c = A_{GLT} + (n - 1) \cdot A_s \tag{7}$$

$$I_c = I_{GLT} + (n - 1) \cdot I_s \tag{8}$$

where n = scaling factor to account for stiffness variation, A_c = cross-sectional area of an equivalent timber section, A_{GLT} = gross cross-sectional area of the timber (including the holes for the steel bars), A_s = cross-sectional area of the steel, I_c = second moment of area of an equivalent timber section, I_{GLT} = gross second moment of area of the timber (including the holes for the steel bars), and I_s = second moment of area of the steel cross-section.

The *effective length method* (Formulae (2)-(5)) can be adapted for composite sections as given in Formulae (9)-(10). As for unreinforced beech GLT, the buckling curve was calibrated based on the mean experimental results for GL48h, i.e. $f_{c,0,mean}$ = 60.6 MPa and $E_{c,0,mean}$ = 15.7 GPa [7].

$$\lambda_{rel} = \frac{L_{eff}}{\pi \sqrt{\frac{I_c}{A_c}}} \sqrt{\frac{f_{c,0,mean}}{E_{c,0,mean}}} \tag{9}$$

$$R_{c,0} = k_c \cdot f_{c,0,mean} \cdot A_c \tag{10}$$

https://doi.org/10.52202/069179-0043

A design based on the parameters currently specified by Eurocode 5 leads to an overestimation of the experimental buckling resistance by up to 20% (L_{eff} = 2400 mm) in the case of the corner-reinforced beech GLT columns, as shown in Figure 16. The same figure shows the buckling curve fitted for corner-reinforced European beech of strength class GL48h with four ST900/1100 rebars of 20 mm diameter and 50 mm edge distance. A least squares fitting to the experimental data points resulted in a straightness factor $\beta_c = 0.255$ and a critical relative slenderness ratio $\lambda_{rel,0} = 0.261$. Since the deviation from the buckling curve proposed for unreinforced European beech GLT is small, the same curve ($\beta_c = 0.25$ and $\lambda_{rel,0} = 0.25$) is proposed for corner-reinforced beech GLT. The resulting curve of the proposed buckling factor k_c is given in Figure 17.

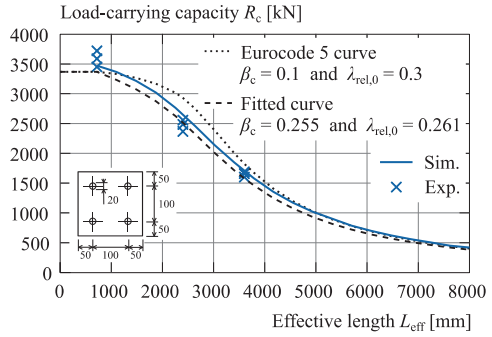

***Figure 16**: Comparison of current Eurocode 5 and fitted buckling curves for corner-reinforced beech GLT columns of strength class GL48h, along with the experimental and numerical results.*

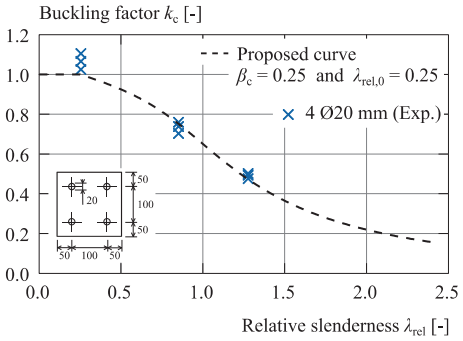

***Figure 17**: Proposed buckling curve for corner-reinforced beech GLT columns of 200×200 mm² and strength class GL48h with four ST900/1100 rebars of 20 mm diameter and 50 mm edge distance, along with the experimental results.*

5 CONCLUSIONS

The full-scale experiments on unreinforced and steel-reinforced European beech GLT columns revealed their immense potential for application in highly demanding residential, office, and industrial projects.

Material properties of European beech GLT were identified from the experiments on unreinforced columns. Different layouts of steel reinforcement were investigated in compression and buckling tests. A finite-element model was developed and shown to reliably predict the buckling behaviour of these high-strength columns and parametric studies were performed to investigate the main factors influencing their load-carrying capacity. The ultimate failure load was found to be mainly dependent on the column slenderness, the arrangement and diameter of the steel bars, the section size, and the initial deformed shape (eccentricity e_0). The strength class (GL40h, GL48h, or GL55h) was found to have very little impact.

The steel reinforcement using profiled Swiss-GEWI bars of grades ST900/1100 and ST950/1050 led to an increase of both the compressive strength and the modulus of elasticity parallel to the grain of European beech GLT. A central ST950/1050 rebar of 40 mm diameter was found to increase the load-carrying capacity of beech GLT columns by 20% for low ($\lambda_{rel} < 0.5$) to medium ($\lambda_{rel} \approx 1.0$) slenderness and by 10% for slender columns ($\lambda_{rel} \approx 1.5$).

At the same reinforcement ratio, corner reinforcement (four bars of 20 mm diameter, 50 mm edge distance, and grade ST900/1100) offers a much more pronounced gain of about 40% in the load-carrying capacity across all slenderness ratios relevant in structural applications. This is because the eccentric arrangement contributes to the bending stiffness of the column. Though requiring more manufacturing steps, corner reinforcement thus enables highly demanding structures such as high-rise buildings to be built using timber columns while avoiding excessively large cross-section sizes that reduce available floor space and obstruct window views. Sufficient timber cover must be provided for all steel bars to ensure fire safety and prevent buckling of the steel bars.

Current Eurocode 5 [14] design parameters were found to overestimate the load-carrying capacity of both unreinforced and reinforced beech GLT columns. Based on the experimental and numerical results, the *effective length method* as applied by Eurocode 5 was adapted for beech GLT. Proposed design parameters are $\lambda_{rel,0} = 0.25$ and $\beta_c = 0.25$ for both unreinforced and corner-reinforced European beech GLT columns. The buckling curve for corner-reinforced beech GLT was developed for square cross-sections of 200 mm width and strength class GL48h, reinforced with four ST900/1100 bars of 20 mm diameter, which were placed in the corners of the section with an edge distance of 50 mm.

Further experimental investigations and numerical simulations with probabilistic material modelling should be carried out to verify the presented findings while taking into account the variability of the mechanical properties. Research into the manufacturing process of corner-reinforced GLT could reduce its complexity and increase the economic viability of reinforced GLT columns, which offer a huge potential regarding moment resisting and tension connections, thereby enabling a reduction of the effective length and the use of columns to transfer tensile forces in alternative loads paths following element-removal scenarios.

ACKNOWLEDGEMENT

The investigations on the unreinforced specimens were supported by the *Swiss Federal Office for the Environment FOEN* within the framework of the *Aktionsplan Holz*, Project no. REF-1011-04200.

https://doi.org/10.52202/069179-0043

REFERENCES

[1] FOEN: Jahrbuch Wald und Holz. Swiss Federal Office for the Environment, Bern, Switzerland, 2019.

[2] Mpidi Bita H., Huber J., Palma P., Tannert T.: Prevention of disproportionate collapse for multi-story mass timber buildings: review of current practices and recent research. *Journal of Structural Engineering*, 148(7):04022079, 2022.

[3] Woschitz R., Zotter J.: Holzhochhaus HoHo Wien – Das Tragwerkskonzept (High-rise timber building HoHo Vienna – the structural concept). *Österreichische Ingenieur- und Architekten-Zeitschrift*, 162(1-12):69-73, 2017.

[4] Ehrhart T., Fink G., Steiger R., Frangi A.: Strength grading of European beech lamellas for the production of GLT and CLT. In *Proceedings of INTER-Meeting 49*, paper 49-5-1, 2015.

[5] Lehmann M., Clerc G., Lehringer C., Strahm T., Volkmer T.: Investigation of the bond quality and the finger joint strength of beech glulam. In *Proceedings of World Conference on Timber Engineering*, 2018.

[6] Ehrhart T., Steiger R., Lehmann M., Frangi A.: European beech (*Fagus sylvatica* L.) glued laminated timber: lamination strength grading, production and mechanical properties. *European Journal of Wood and Wood Products,* 78(5):971-984, 2020.

[7] Ehrhart T., Steiger R., Palma P., Gehri E., Frangi A.: Glulam columns made of European beech timber: compressive strength and stiffness parallel to the grain, buckling resistance and adaptation of the effective-length method according to Eurocode 5. *Materials and Structures,* 53(4):91, 2020.

[8] EN 408:2012. Timber structures – Structural timber and glued laminated timber – Determination of some physical and mechanical properties. CEN European Committee for Standardization, Brussels.

[9] von Tetmajer L.: Zur Frage der Knickfestigkeit der Bauhölzer. *Schweizerische Bauzeitung,* 17(11/12):110-113, 1888.

[10] Zhu M. J., McKenna F., Scott M. H.: OpenSeesPy: Python library for the OpenSees finite element framework. *Softwarex,* 7:6-11, 2018.

[11] Python (version 3.9), 2020. Python Software Foundation.

[12] McKenna F., Scott M. H., Fenves G. L.: Nonlinear Finite-Element Analysis Software Architecture Using Object Composition. *Journal of Computing in Civil Engineering,* 24(1):95-107, 2010.

[13] Glos P., Denzler J. K., Linsenmann P. W.: Strength and stiffness behaviour of beech laminations for high strength glulam. In *Proceedings of CIB-W18 Meeting 37*, paper 37-6-3, 2004.

[14] EN 1995-1-1:2004. Design of timber structures–part 1-1: General – Common rules and rules for buildings. CEN European Committee for Standardization, Brussels.

[15] Ehrhart T., Steiger R., Palma P., Frangi A.: Mechanical properties of European beech (*Fagus sylvatica* L.) glued laminated timber. In *Proceedings of INTER-Meeting 51*, paper 51-12-4, 2018.

[16] Westermayr M., Stapel P., Van de Kuilen J.-W. G.: Tensile and compression strength of small cross section beech glulam members. In *Proceedings of INTER-Meeting 51*, paper 51-12-2, 2018.

[17] Blaß H. J.: Tragfähigkeit von Druckstäben aus Brettschichtholz unter Berücksichtigung streuender Einflussgrössen. Dissertation, University Fridericiana Karlsruhe, Germany, 1987.

World Conference on Timber Engineering Oslo 2023

MECHANICAL BEHAVIOUR OF COLUMN BASES FOR CLT ROCKING FRAMES

Akira Masuda[1], Chisato Inutsuka[2], Kazuhiro Matsuda[3]

ABSTRACT: Although Cross Laminated Timber (CLT) mid-to-high-scale buildings have been realised worldwide, the technology for controlling damage in these buildings, which could minimise damage and facilitate continued use of buildings after a significant earthquake, is still in the developmental stage. In this study, a static horizontal loading experiment was conducted on CLT wall columns with origin return characteristics by introducing prestress, and the mechanical behaviour of the CLT wall columns was investigated. We determined the difference in the origin return characteristics and damage of wall columns when the prestress introduced to the wall columns and the diameter of the PC bar were varied. We also propose a method to evaluate the relationship between the bending moment and rotation angle of the column base. The evaluation method applies calculations that are commonly used for joints in large wooden buildings. In this case, it was necessary to evaluate the uplift of the column base in advance, and we created a spring model to evaluate the uplift. Although this evaluation method has some limitations, it is believed that the experimental results can be accurately replicated.

KEYWORDS: CLT, Rocking Wall-Column, Prestress, Embedding Stiffness, Anchorage Plate

1 INTRODUCTION

1.1 BACKGROUND

Due to the social imperative of sustainable and healthy forestry development and environmental CO_2 reduction, there is increasing demand for mid-to-high-rise wooden buildings, leading to the proliferation of Cross Laminated Timber (CLT). In general, CLT buildings use CLT panels as walls and floors (e.g. in Japan, CLT panel buildings [1]). However, because the restoring force characteristics exhibit slip behaviour [2, 3], it may be difficult to maintain the function after a large earthquake. Thus, developing damage control technology for CLT buildings to minimise damage and enable continued use after large earthquakes is crucial.

Matsuda et al. [4] conducted an experiment on a passively controlled CLT structure, utilising both a rocking wall column and a damper, resulting in a structure with reduced residual deformation and high energy absorption performance. While the behaviour of the frame was analysed, the behaviour of the wall column was not comprehensively identified.

Pei et al. [5], Sarti et al. [6], and Iqbal et al. [7] conducted research on damage control structures for mid-to high-scale wooden buildings. Pei et al. introduced prestressing by placing PC bar at the centre of the CLT wall column. This wall column was deformed by uplift while rotating the column base. Because the slip is reduced by prestress, the wall column is a structural system with high-origin return characteristics.

Isoda et al. [8] examined the implementation of Japanese specifications by referring to CLT rocking columns overseas. Harada et al. [9], Komoriya et al. [10], and Tanaka et al. [11] proposed CLT shear walls with a PC bar inserted at each edge of the wall column. In addition, Nagashima et al. [12] conducted an experiment on a laminated wood wall column in which prestress was introduced with a PC bar and proposed an evaluation method with high reproducibility in the elastic region.

1.2 PURPOSE AND STRUCTURE

In this study, a static horizontal loading experiment was conducted on CLT wall columns with origin return characteristics by introducing prestress to investigate the mechanical behaviour of the CLT wall column. We proposed a method for evaluating the relationship between the bending moment and rotation angle of the column base.

Figure 1 shows an image of the mid-to high-scale wooden buildings proposed in this study. By introducing a passively controlled CLT structure into a part of a general CLT building, such as a CLT panel building [1], we realise a mid-to-high-scale wooden building with excellent performance maintenance after an earthquake. The PC bar, which introduces prestress, is anchored to the column capital and the column base of the passively controlled frame with an anchorage plate. Steel dowels were used as the shear resistance for the column base. By creating steel dowel details that do not resist pulling

[1] Akira Masuda, Grad. Student, Meijo University of Sci. and Eng., Mr. Eng., Japan, 223443503@ccalumni.meijo-u.ac.jp
[2] Chisato Inutsuka, Grad. Student, Meijo University of Sci. and Eng., Japan, 213435002 @ccalumni.meijo-u.ac.jp
[3] Kazuhiro Matsuda, Associate Prof., Dept. of Architecture, Meijo University, Dr. Eng., japan, matsuda@meijo-u.ac.jp

https://doi.org/10.52202/069179-0044

out, that details actively causes rotation and rocking of the column base. Steel dowels were installed at the column-beam joint, and a tensile bolt was installed at the centre of the beam to actively cause rotational deformation at the column-beam joint of the passively controlled frame. However, a damper is installed in the passively controlled CLT frame because the prestressed wall column alone does not have sufficient seismic energy-absorbing performance. In addition, because the effect of creep cannot be neglected when the stress level increases, we assume that the detail of the passively controlled frame minimises the burden of long-term axial force on the wall columns. Section 2 describes the outline and results of the static experiment. Chapter 3 proposes an evaluation procedure for the relationship between the bending moment and the rotation angle of the column base.

2 STATIC EXPERIMENT WITH CLT ROCKING WALL COLUMNS

2.1 EXPERIMENT OUTLINE

Figure 2 shows the shapes of the specimens. The five specimens were RW0, RW30, RW50, RW30φS, and RW30φL, and CLT rocking wall columns with a width of 1,000 mm and a height of 2,970 mm. The CLT was composed of five layers and six plies of cedar (the thickness of one lamina was 25 mm), the strength grade was S60, and the cross-sectional dimensions were 150 mm × 1000 mm. A 30 mm × 30 mm through-hole was made at the centre of the cross-section of the CLT to insert the PC bar. A groove of 15 mm × 30 mm was made in the centre of three layers and three plies of CLT, and the through-hole was made by secondarily adhering the two CLTs with the grooves facing each other. The PC bar was anchored by the anchorage plate provided on the column capital and jig for fixing. The anchorage plate on the column was a 500 mm × 150 mm × 32 mm SS400 steel plate with a φ30 mm hole in the centre. The anchorage plate of the fixing jig was made of SS400 with a thickness of 60 mm, which is sufficiently stronger than that of the column capital. Two φ50 steel dowels were provided on the column base as shear resistance.

Table 1 lists the prestress applied to each specimen and the diameter of the PC-bar used for each specimen. The introduced prestresses were 0%, 30%, and 50% of the long-term allowable compressive strength, corresponding to the numbers in the names of the specimens. The long-term allowable compressive strength is the standard strength [1] multiplied by 1.1/3, and the cross-sectional area. The PC bars used were B2-type (manufactured by Neturen), with diameters of φ17, φ23, and φ32. ϕS in the name of the specimen corresponds to φ17, φL to φ32, and no dose to φ23.

Figure 3 shows the setup of the experimental specimen. The steel dowels and anchorage plate of the foundation were firmly fixed to the fixing jig using bolts. After the two points of the column capital were constrained out of the plane with the pantograph, a 200kN oil jack was connected at a height of 2,400 mm from the column base, and positive and negative alternating loads were applied. The positive force direction is shown on the right in Figure 3. As for the loading schedule, positive and negative deformations up to 1/450, 1/300, 1/200(1), 1/150, 1/100(1), 1/200(2), 1/75, 1/50, 1/100(2), 1/ 30 and 1/20 rad were repeated three times, and then pulled off in the positive direction. In addition, because the anchorage plate was significantly deformed just before 1/20 rad, RW-30φL was pulled without applying 1/20 rad.

Figure 4 shows the measurement items. The absolute horizontal displacement of the column capital was measured using a wire displacement meter (DP-500G, manufactured by Tokyo Sokki), and the absolute

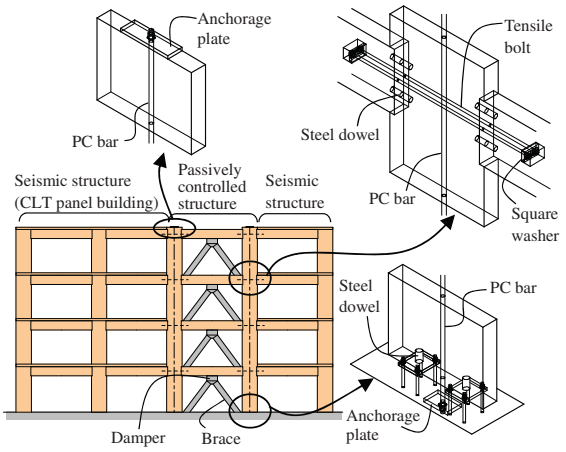

***Figure 1**: The building proposed in this study*

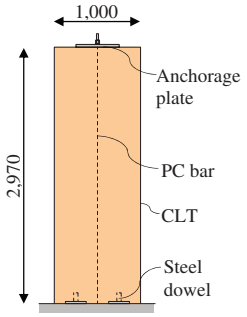

***Table 1**: Specimen list*

Specimen list		
Name	Prestress	PC-bar size
RW0	0%	φ23
RW30	30%	φ23
RW50	50%	φ23
RW30φS	30%	φ17
RW30φL	30%	φ32
Member parameters		
CLT	5 layers 6 plies of cedar	
PC bar	B2-type	
Anchorage plate	SS400 (500*150*32)	
Steel dowel	SS400 (φ50)	

***Figure 2**: Specimens*

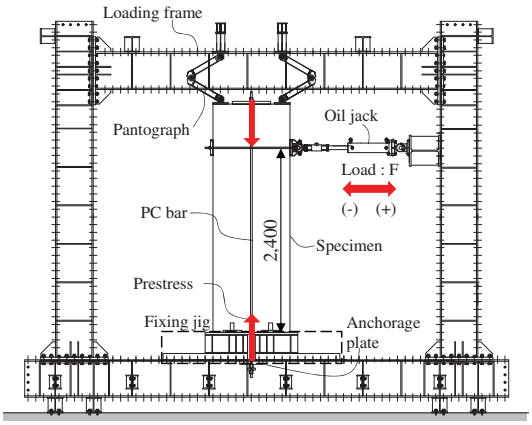

***Figure 3**: Setup*

https://doi.org/10.52202/069179-0044

horizontal displacement of the column base was measured using a contact-type displacement meter (CDP25, Tokyo Sokki). The storey deformation angle θ was obtained by dividing the displacement difference between the column capital and column base by the height of the loaded point. The load was measured using a 200kN load cell attached to the oil jack. Displacement gauges $u_{c\,1}$ and $u_{c\,2}$ were installed on the column base, and the rotation θ_{cb}, uplift u_{cb}, embedded width $x_{n\,cb}$, and bending moment M_{cb} were calculated using Eqs. (1 ~ 4). These equations assume that the embedded triangle and the axial force of the PC bar are balanced. The tensile force acting on the PC bar was measured using a 1000 kN load cell.

2.2 RESULT OF THE EXPERIMENT

Figure 5 shows the relationship between the bending moment of the column base M_{cb} and rotation angle of the column base θ_c. All specimens showed an origin return history and had a high initial stiffness until the bending moment required to release the initial tension was applied. Subsequently, the stiffness decreases as the deformation increases. In (a) RW0, (b) RW30, and (c) RW50, the edge of the column base was damaged, as shown in Figure 6. No CLT damage was observed in (d)RW30φS. (e) RW30φL caused severe damage to the column capital.

(a) RW0 showed no decrease in stress at θ= 1/100 rad (2), indicating that θ= 1/100 rad (1) and θ= 1/100 rad (2) have almost the same history. Therefore, the rocking wall column can be expected to maintain its performance after a severe earthquake. RW0 behaved almost linearly up to 1/50 rad, after which the original return characteristics gradually disappeared.

(b) RW30 showed no decrease in stress at θ= 1/100 rad (2), indicating that θ= 1/100 rad (1) and θ= 1/100 rad (2) had almost the same history. In addition, before θ = 1/30 rad, no significant decrease in yield strength was observed. After experiencing 1/20 rad, the initial stiffness part was lost, and after experiencing maximum deformation, the original return characteristics were also lost. The bending moment required to release the initial tension decreased owing to the decrease in the initial tension of the PC-bar, as shown in Section 2.3.

Considering the initial stiffness in the order of RW-0, RW-30, and RW-50, it can be confirmed that the stiffness increased. In addition, RW50 showed almost the same history at θ= 1/200 rad (2) and θ= 1/200 rad (1), but θ= 1/100 rad (2) is slightly lower than θ= 1/100 rad (1). As

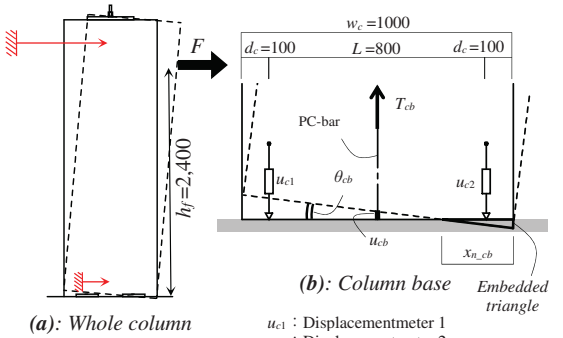

***(a)**: Whole column*

***(b)**: Column base*

$$\theta_{cb} = (u_{c1} - u_{c2})/L \quad (1)$$

$$u_{cb} = (u_{c1} + u_{c2})/2 \quad (2)$$

$$x_{n\_cb} = d_c - u_{c2}/\theta_{cb} \quad (3)$$

$$M_{cb} = F * h_f \quad (4)$$

u_{c1} : Displacementmeter 1
u_{c2} : Displacementmeter 2
θ_{cb} : Rotation angle of column base
L : Distance between displacement meters
x_{n_cb} : Embedded width
d_c : Distance from Displacementmeter to wall-column edge
u_{cb} : Uplift of column base at center
T_{cb} : Tensile force of PC-bar
w_c : Wall width
M_{cb} : Bending moment of column base

***Figure 4**: Measurement items*

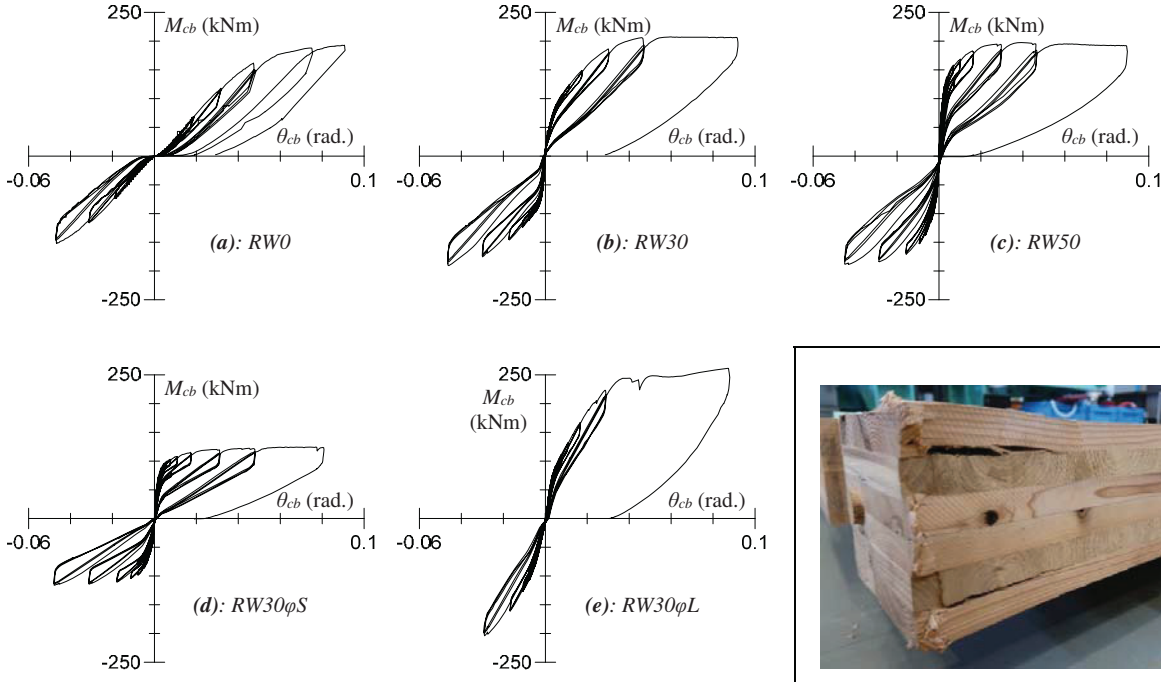

***Figure 5**: Relationship between M_{cb} and θ_{cb}*

***Figure 6**: Destruction property of column base*

https://doi.org/10.52202/069179-0044

the initial tension increased, the initial stiffness increased; however, the CLT was damaged more quickly than RW30. (d) RW30φS of θ=1/100rad(2) is slightly lower than θ=1/100rad(1). After experiencing 1/30 rad, the initial stiffness part was lost, and after experiencing the maximum deformation, the origin return characteristic was also lost.

Observing the order of RW-30φS, RW-30, and RW-30φL, the range in which the initial stiffness is lost decreases. (e) RW-30φL showed no decrease in stress at θ = 1/100 rad(2), indicating that θ = 1/100 rad(1) and θ = 1/100 rad(2) had almost the same history. In addition, before θ = 1/30 rad, no significant decrease in stress was observed, and after experiencing maximum deformation, the original return characteristic was lost.

Figure 7 shows the relationship between the PC-bar tension T_{cb} and uplift of the base column u_{cb}.

RW0 exhibited linear hysteresis, except for the last pull-off, and the maximum yield strength was 389 kN.

RW30 exhibited a maximum yield strength of 419 kN. The hysteresis was linear up to θ=1/50 rad, and the initial stiffness was slightly lower than that of RW0. Subsequently, a decrease in the initial tension was observed when u_{cb} = 0. This decrease in tension is slight at θ = 1/100 rad.(2) and became significant at θ = 1/30 rad.

RW50 had a maximum yield strength of 410 kN. The hysteresis was linear up to θ=1/75 rad, and the initial stiffness was slightly lower than that of RW30. Subsequently, a decrease in the initial tension was observed when u_{cb} = 0.

RW30φS had a maximum yield strength of 230 kN. The hysteresis was linear up to θ=1/150 rad, and the initial stiffness was slightly lower than that of RW30. Subsequently, a decrease in the initial tension was observed when u_{cb} = 0.

RW30φL had a maximum yield strength of 601 kN. The hysteresis was linear up to θ=1/50 rad, and the initial stiffness was slightly higher than that of RW30. Subsequently, a decrease in the initial tension was observed when u_{cb} = 0. Figure 8 shows the anchorage plate of the RW30φL. Just before 1/20 rad, the anchorage plate began to embed into the column capital of CLT while undergoing a large bending deformation, as shown in Figure 8.

Figure 9 shows the changes in the ratio θ_{cb}/θ of the column base rotation angle θ_{cb} and the story deformation angle θ. The vertical axis is θ_{cb}/θ and the horizontal axis is θ. (a) RW0, RW 30, and RW 50 with different prestresses and (b) RW30φS, RW30, and RW30φL with different PC-bar diameters.

RW0 always exhibited a value close to 100%. Because no prestress is introduced in RW0, it is thought that the column base joint behaves closer to a pin joint. The ratio of RW30 was lower at a small deformation than that of RW0 and gradually increased as the deformation increased. Because RW30 has a prestress introduced, it is considered that the ratio of bending deformation and shear deformation of CLT increased, and the behaviour became closer to that of a rigid joint. The ratio of RW50 was lower at a small deformation than that of RW30 and gradually increased as the deformation increased. Because RW50 introduced more prestress than RW30, it is thought that the rate of bending deformation and shear deformation of the CLT increased further. Figure 9(b) shows that there was no significant difference between RW30φS, RW30, and RW30φL.

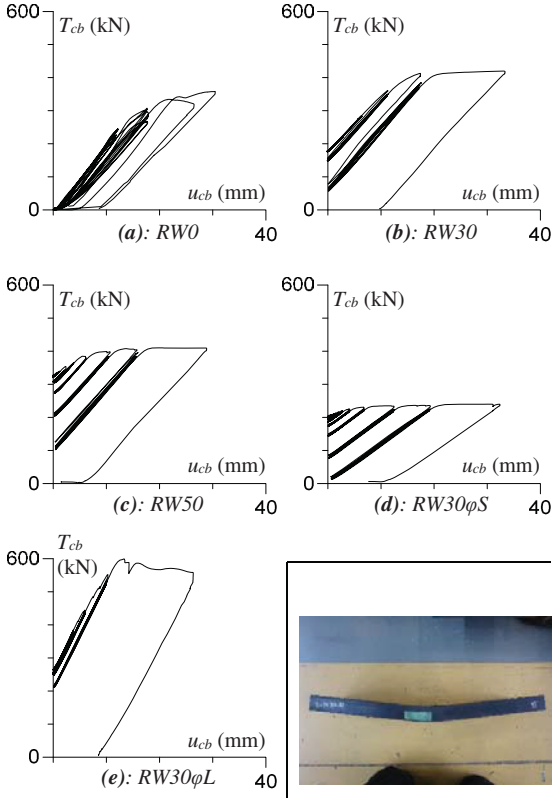

***Figure 7**: Relationship between T_{cb} and u_{cb}*

***Figure 8**: Destruction property of Anchorage plate*

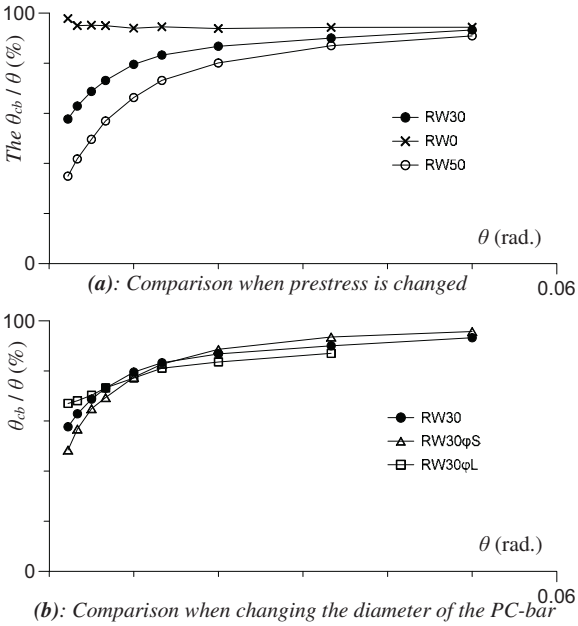

***Figure 9**: Transition in the ratio of θ_{cb} to θ*

https://doi.org/10.52202/069179-0044

3 THEORETICAL EVALUATION METHOD

Figure 10 shows an image of the rotation angle of the column base of the CLT wall column, and Eq. (5) and (6) are the evaluation representing the evaluation methods proposed in [13]. The CLT has a very high in-plane stiffness, and the performance of the column base is directly linked to the performance of the entire CLT wall column. Various parameters, such as M_{cb}, θ_{cb}, and x_{n_cb} must be obtained to evaluate the deformation and stress of the column base. Their parameters are obtained by solving the simultaneous equations of the two equations, the equation of compressive force C_{cb}, Eq. (5), and the equations of compatibility for the embedded triangular, Eq. (6). Their simultaneous equations are solved for θ_{cb} and x_{n_cb} based on the following two points: (i) It is assumed that T_{cb}, tension, and C_{cb}, the compressive force of the embedded triangle, are balanced, (ii) k_g is the slope of the envelope of the CLT-embedded experiment described in Section 3.1. In this case, u_{cb} must be requested in advance.

A mechanical model of u_{cb} is shown in Figure 11. The mechanical model was a spring model with a series combination of K_t: axial stiffness of the PC bar, K_p: embedded stiffness of the anchorage plate, and K_w: compressive stiffness of the CLT middle zone. Here, K_t was created as a skeleton curve with reference to the mill sheet value of the PC-bar. K_p is the envelope of the embedding anchorage plate experiment described in section 3.2. K_w is the envelope of the CLT partial compression experiment described in section 3.3. The skeletal curve of K_t is shown in Table 2 with reference to the mill sheet.

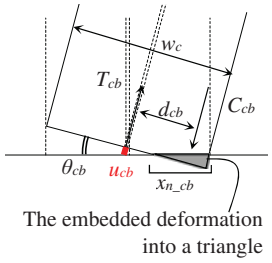

$$T_{cb} = C_{cb} = \frac{1}{2} k_g \theta_{cb} x_{n\_cb}^2 b \quad (5)$$

$$x_{n\_cb} = w_c / 2 - u_{cb} / \theta_{cb} \quad (6)$$

C_{cb} : Compressive force
k_g : Embedding stiffness of column base
b : Wall thickness
d_{cb} : Interval from the point where T_{cb} is applied to the point where C_{cb} is applied

***Figure 10**: Deformation of column base*

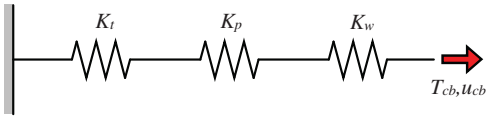

K_t : Axial stiffness of the PC-bar
K_p : Embedded stiffness of the anchorage plate
K_w : Compression stiffness of middle zone in CLT

***Figure 11**: u_{cb} spring model*

***Table 2**: Material characteristic of PC-bar*

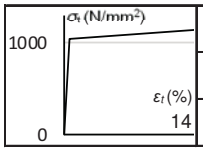

σ_t [N/mm^2]	ε_t [%]
1042	0.51
1136	14

3.1 THE EMBEDDED CLT EXPERIMENT

Figure 12 shows the specimens of the CLT-embedded experiment, which were created by cutting out the less damaged parts of the specimens in the static horizontal loading experiment. The number of specimens is 4. The force position was at the edge of the specimens, and a steel plate (19 × 100 × 260 mm) was used to load vertically downwards. The measurement parameters were the load T_g and absolute vertical displacement δ_g of the steel plate. Figure 13 shows the relationship between the stress σ_g and embedding displacement δ_g. The σ_g–δ_g relations of the four specimens were averaged, and the embedded stiffness was a straight line approximated by the least-squares method between 10% and 40% of the maximum stress. The yield stress was considered as the average value of the highest stress point.

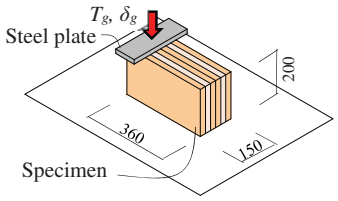

***Figure 12**: The CLT embedded experiment*

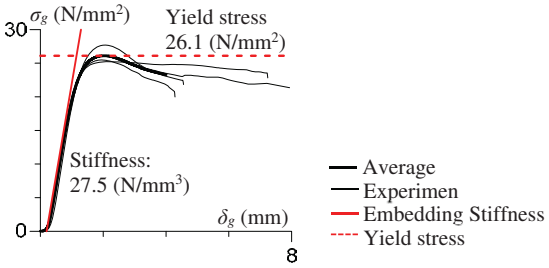

***Figure 13**: The relationships between σ_g and δ_g*

3.2 THE EMBEDDING ANCHORAGE PLATE EXPERIMENT

Figure 14 shows the setup of the embedded anchorage plate. The specimens were created by cutting out the less damaged parts from the wall column specimens. The number of specimens is 3. The anchorage plate was loaded by pulling the PC bar with the centre-hole jack. The measurement items are the tension of the PC-bar, T_p, and the embedding displacement of the anchorage plate, x_p. Figure 15 shows the relationship between T_p and x_p. Note that x_w is the deformation up to 28 mm from the top surface of the CLT.

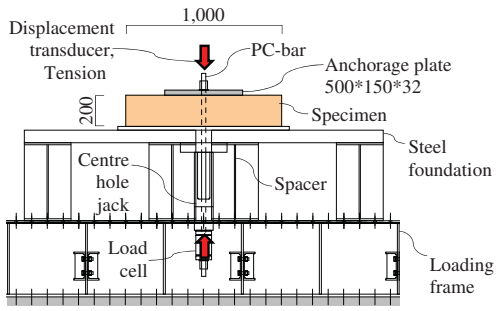

***Figure 14**: The experiment of the embedding anchorage plate*

https://doi.org/10.52202/069179-0044

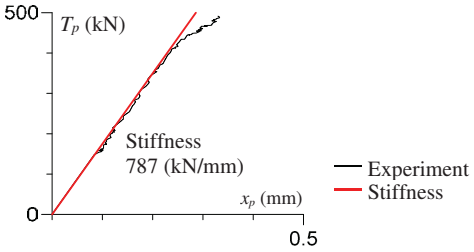

***Figure 15**: The relationships between T_p and x_p*

3.3 THE CLT PARTIAL COMPRESSION EXPERIMENT

Figure 16 shows the setup of the CLT partial compression experiment. The CLT used was different from that used in the static horizontal loading experiment. To understand the difference in the material properties from the CLT of the static horizontal loading experiment, a separate CLT material experiment was conducted. The number of specimens used was one. Assuming a rocked wall column, a load was applied to the centre of the column capital and the edge of the column base. The specimen was loaded with a 500kN oil jack and was placed so that the three points were on the same straight line: (i) the centre of the jack, (ii) the centre of the load-applying surface on the column capital, and (iii) the centre of the load-applying surface on the column base (hereafter referred to as "the load line"). Fifty-ton pins were installed on the column capital and base of the CLT wall column. The 50-ton pin on the column base side was fixed to the loading frame and that on the column capital side was connected to the oil jack. The right end of the oil jack was fixed to the loading frame, and the lower left end of the oil jack was connected to a linear rail that moved only in the direction of the load line. The measurement items were T_w, the load of the jack, and, x_w, the compressive deformation of the CLT on the load line. Note that x_w does not include deformations within 28 mm above and below the CLT. Figure 17 shows the relationship between T_w and x_w.

3.4 METHOD OUTLINE

T_0 evaluate the column base, it is necessary to calculate u_{cb} in advance. The mechanical model of u_{cb} is a spring model with a series combination of K_t, K_p, and K_w. The tension T_{cb} applied to the spring model is the sum of T_0, the initial tension, and dT, the tension change amount after the introduction of the initial tension, as shown in Eq. (7). dT was varied at 0.1 kN increments. The u_{cb} is the sum of dx_t, dx_p, and dx_w; each deformation change amount of the element after the introduction of T_0 as shown in Eq. (8). dx_t, dx_p, and dx_w are the differences between x_t, x_p, x_w, each deformation of the element at T_{cb} and x_{t0}, x_{p0}, x_{w0}, each deformation of the element when T_0 is introduced, as shown in Eqs. (9–11). x_t: The deformation of the PC bar at T_{cb} was calculated using Eq. (12), and x_{t0}, the deformation of the PC-bar when T_0 was introduced and calculated using Eq. (13). x_p, the embedding deformation of the anchorage plate was used as the result of the embedding anchorage plate experiments obtained in Section 3.2. x_w, compression deformation of the CLT middle zone was used as the result of the wall column

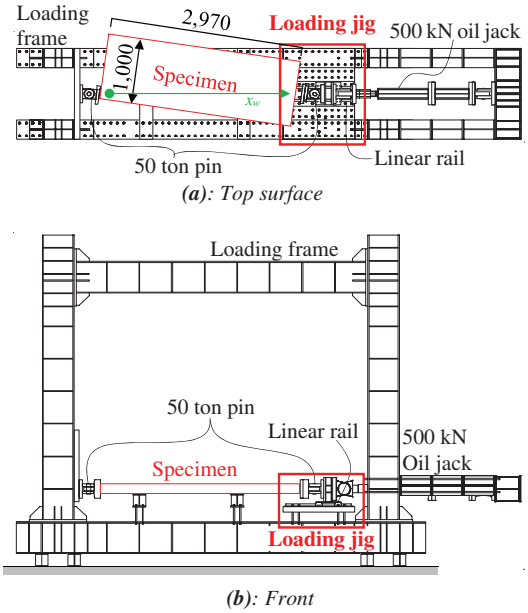

***Figure 16**: The experiment of the CLT partially compressed*

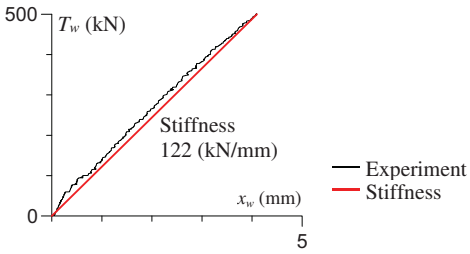

***Figure 17**: The relationships between T_w and x_w*

$$T_{cb} = T_0 + dT \quad (7)$$

$$u_{cb} = dx_t + dx_p + dx_w - x_{g0} \quad (8)$$

$$dx_t = x_t - x_{t0} \quad (9)$$

$$dx_p = x_p - x_{p0} \quad (10)$$

$$dx_w = x_w - x_{w0} \quad (11)$$

$$x_t = T_{cb} / K_t \quad (12)$$

$$x_{t0} = T_0 / K_t \quad (13)$$

$$K_t = A_t E_t / h_t \quad (14)$$

T_0: Initial tension
dT: Tension increase after the introduction of T_0
dx_t: Axial deformation of the PC-bar after the introduction of T_0
dx_p: Embedding deformation of the anchorage plate after the introduction of T_0
dx_w: Compressive deformation of middle zone in CLT after the introduction of T_0
x_{g0}: Embedding deformation of column base after the introduction of T_0
x_t: Axial deformation at PC bar
x_{t0}: x_t after the introduction of T_0
K_t: Axial stiffness of PC bar
A_t: Cross-section area of PC bar
E_t: Elastic modulus of PC bar
h_t: PC bar length
x_p: Embedding deformation at the anchorage plate
x_{p0}: x_p after the introduction of T_0
x_w: Compressive deformation at middle zone in CLT
x_{w0}: x_w after the introduction of T_0

https://doi.org/10.52202/069179-0044

partial compression experiment described in Section 3.3. K_t, the stiffness of the PC bar is the axial stiffness, as shown in Eq. (14).

Figure 18 shows the stress distribution of the column base. For evaluating the column base, two simultaneous equations were solved, and the state of the compressive force was applied according to the degree of deformation. There are five stress distributions of the compressive force: (a) initial point, (b) anchor process, (c) limit anchor point, (d) elastic process, and (e) yield process. (a) The initial point is the state before horizontal deformation when the initial tension T_0 is applied. (b) The anchor process is a state in which the entire cross-section of the column base is in contact with the foundation, although horizontal deformation has occurred. (c) The limit anchor point is the state in which the entire cross-section is in contact, and the edge of the column base has no stress. (d) The elastic process is a state in which the stress distribution is triangular while the column base is uplifted. (e) The yield process is the state in which part of the stress distribution reaches the yield stress when the column base is uplifted.

In (a) Initial point, because horizontal deformation does not occur, there is no need to solve simultaneous equations for θ_{cb} and x_{n_cb}. So that, dT=0 and T_{cb}=T_0 from Eq. (7) and u_{cb}= − x_{g0} from Eq. (8).

Next, (b) anchor process must be evaluated, but this is not performed because it is very difficult to formulate. Therefore, because the deformation is small, (b) the anchor process is assumed to be in the elastic range and a skeletal curve is created by connecting (a) the initial point and (c) the limit anchor point with a straight line.

Next, (c) limit anchor point is presented. As the embedded width x_{n_cb}=w_c, the compressive force equation is given by Eq. (15), and the deformation compatibility equation is expressed by Eq. (16). These two equations were solved.

In (d), elastic process, the solutions of θ_{cb} and x_{n_cb} were obtained from the simultaneous equations of the compressive force C_{cb} (Eq. (17)) and compatibility equation (Eq. (18)).

In (e) yield process, Eq. (19) was used instead of Eq. (17). σ_{gy}, yield stress, and k_g, embedded stiffness, were used as the average yield stress and slope of the envelope obtained in the CLT-embedded experiment in Section 3.1. M_{cb} was calculated using Eq. (20).

The story deformation angle θ of the wall column is the sum of θ_{cb}: the column base rotation angle, θ_b, the storey deformation angle contribution of bending deformation, and θ_s, the storey deformation angle contribution of shear deformation, as shown in Eq. (22). Next, we demonstrate the effect of the stiffness involved in the series u_{cb} spring model on θ_{cb}. Figure 19 shows the deformation of the column base with a focus on θ_{cb}. As shown in Eq. (25), θ_{cb} can be calculated from u_{cb} and x_{ge}. x_{ge} means embedding deformation at the edge of the column base. u_{cb} is the sum of dx_t, dx_p, and dx_w with x_{g0} removed, as in Eq. (8). By rearranging Eq. (8), (22), and (25), Eq. (27) can be obtained. Therefore, θ_{cb} can be expressed as dx_t, dx_p, dx_w, and dx_g. Note that x_{ge} is the product of the rotation angle θ_{cb} and embedded width x_{n_cb} as shown in Eq. (26), and dx_g is the value obtained by subtracting x_{g0} from x_{we}, as shown in Eq. (28).

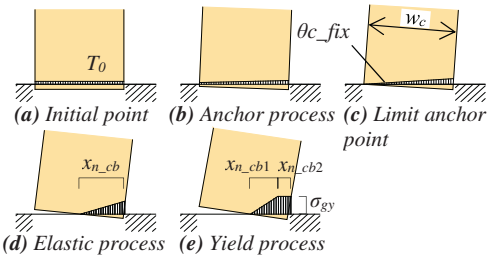

***Figure 18**: Stress distributions of the column base*

$$T_{cb\_fix} = C_{cb\_fix} = \frac{1}{2} k_g \theta_{cb\_fix} w_c^2 b \quad (15)$$

$$\theta_{cb\_fix} = \frac{-u_{cb}}{w_c / 2} \quad (16)$$

$$T_{cb} = C_{cb} = \frac{1}{2} k_g \theta_{cb} x_{n\_cb}^2 b \quad \{\text{same as Eq. (5)}\} \quad (17)$$

$$x_{n\_cb} = w_c / 2 - u_{cb} / \theta_{cb} \quad \{\text{same as Eq. (6)}\} \quad (18)$$

$$T_{cb} = C_{cb} = \frac{1}{2} k_g \theta_{cb} x_{n\_cb1}^2 b + \sigma_{gy} x_{n\_cb2} b \quad \{ x_{n\_cb} = x_{n\_cb1} + x_{n\_cb2} \} \quad (19)$$

$$M_{cb} = T_{cb} d_{cb} = T_{cb} (w_c / 2 - x_{n\_cb} / 3) \quad (20)$$

$$F = M_{cb} / h_f \quad (21)$$

$$\theta = \theta_{cb} + \theta_b + \theta_s \quad (22)$$

$$\theta_b = F h_f^2 / 3 E_w I_w \quad (23)$$

$$\theta_s = F / G_w A_w \quad (24)$$

T_{cb_fix}: Tension at Limit anchor point
C_{cb_fix}: Compressive force at Limit anchor point
θ_{cb_fix}: Rotation angle of column base at Limit anchor point
x_{n_cb1}: Embedded width of stiffness range
x_{n_cb2}: Embedded width of plastic range
σ_{gy}: Embedded yield stress of column base
h_f: Height of the point to apply force
θ_b: Story deformation angle contribution of CLT bending deformation
θ_s: Story deformation angle contribution of CLT shearing deformation
E_w: Elastic modulus of CLT
I_w: Cross-section secondary moment of CLT
G_w: Shear elastic modulus of CLT
A_w: Cross-section of CLT

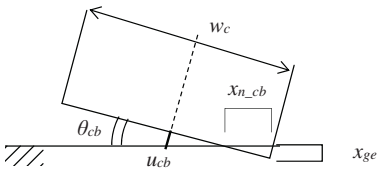

***Figure 19**: Deformation of column base focused on θ_{cb}*

$$\theta_{cb} = \frac{u_{cb} + x_{ge}}{w_c / 2} \quad (25)$$

$$x_{ge} = x_{n\_cb} * \theta_{cb} \quad (26)$$

$$\theta = \frac{2}{w_c} (dx_t + dx_p + dx_w + dx_g) + \theta_b + \theta_s \quad (27)$$

$$dx_g = x_{ge} - x_{g0} \quad (28)$$

x_{ge} : Embedding deformation at the edge of the column base
dx_g : Embedding deformation after the introduction of T_0

https://doi.org/10.52202/069179-0044

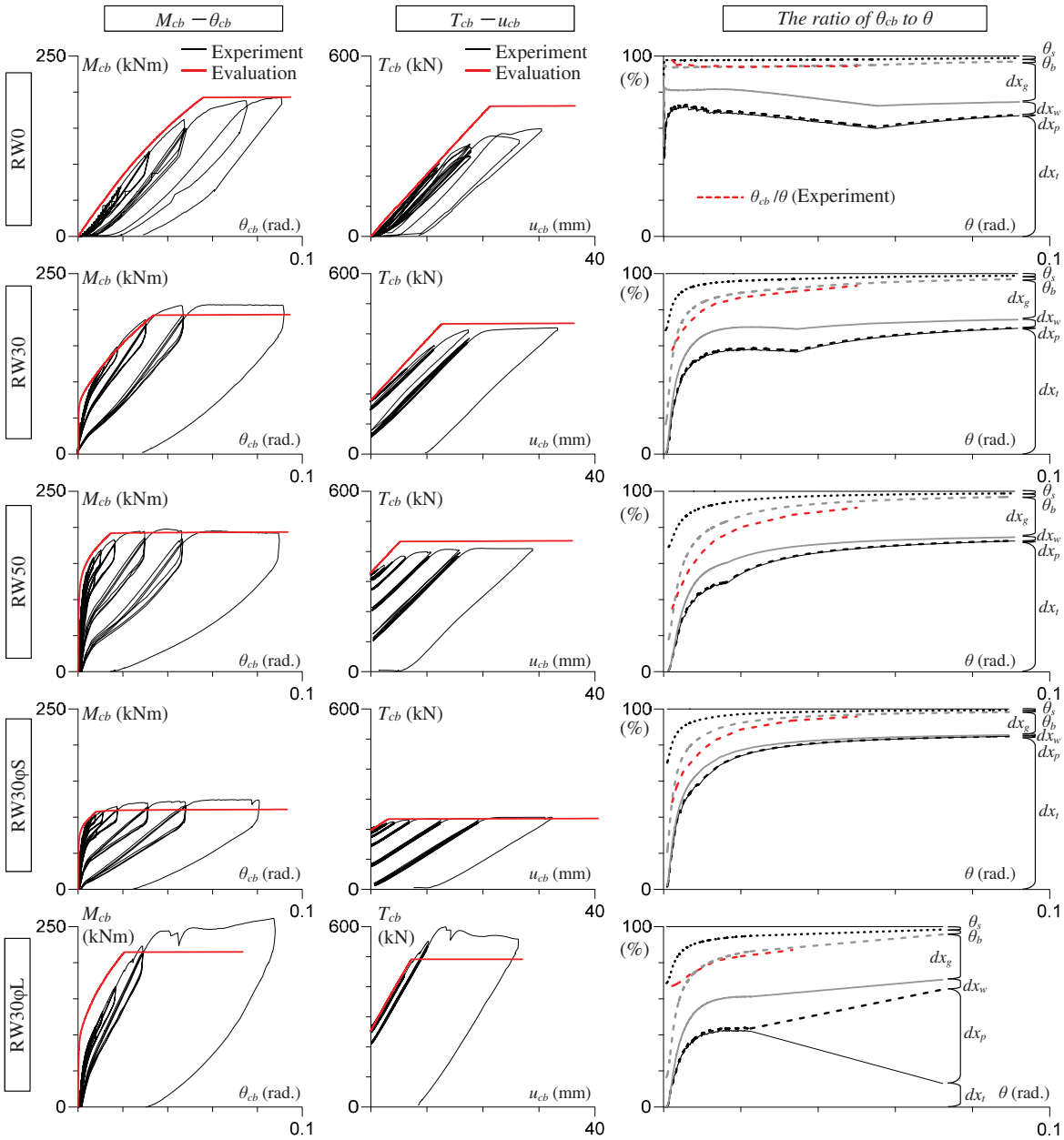

***Figure 20**: Compare the experiment and evaluation*

3.5 COMPARISON BETWEEN THE EXPERIMENT AND EVALUATION

Figure 20 compares the experimental and evaluation values. In the T_{cb}-u_{cb} relationship, the stiffness of RW30 and RW50 is slightly higher than the experimental value, but the evaluated value roughly reproduce the stiffness of the five experimental values. The yield points of RW0, 30, and 50 do not match, but the cause has not been elucidated. For RW30φL, in the experiments conducted to create the spring model in Chapters 3.2 and 3.3, the environment and equipment for applying a load of 500 kN or more could not be prepared. Therefore, deformation after reaching 500kN was not used as a reference.

In the M_{cb}-θ_{cb} relationship, the initial stiffness of RW30 and RW30φL were highly evaluated, but the other specimens reproduced the envelope of the experimental values well. Because T_g-δ_g relationship has a gentle slope when the stress is small, as shown in Figure 13, the experimental values of RW30 and RW30φL show lower initial stiffness than the evaluation values. Because the evaluation value does not reflect the part with low stiffness in the spring model, the evaluation value overestimated the initial stiffness. This aspect needs a more detailed examination in the future.

In θ_{cb}/θ, the horizontal axis is θ and the vertical axis is on the right side of Eq. (27). The distance between the lines corresponds to the proportion of the deformation that occupies θ. The dashed red line represents the experimental value of θ_{cb}/θ, which is compared with the sum of the ratios dx_t, dx_p, dx_w, and dx_g. In other words, the

https://doi.org/10.52202/069179-0044

dashed red line is compared with the dashed gray line. At RW0, dx_t was dominant for θ. Because the experimental (the dashed red line) and evaluation values of θ_{cb}/θ (the dashed gray line) are almost the same, the evaluation value can reproduce the deformation sharing of the rocking wall column without the initial tension. For RW30 and RW50, the effect of dx_t was small at small deformations, and dx_g, θ_b, θ_s were more dominant than RW0. The dashed gray line is the line of close shape to the experimental values of θ_{cb}/θ. RW30φS was influenced more by dx_t than RW30, i.e., the dashed gray line is a curve close to the experimental value of θ_{cb}/θ. In RW30φL, the deformation of the anchorage plate dx_p is dominant. Notably, the deformation of 500 kN or more cannot be used as a reference in relation to T_{cb}-u_{cb}, but the yield load of the PC-bar is approximately 800 kN, and the yield load of the CLT is considered to be even higher. Therefore, yielding at the anchorage plate was considered deterministic. In the experiment (Fig. 8), we confirmed a large deformation of the anchorage plate.

4 CONCLUSIONS

In this study, a static horizontal loading experiment was conducted on CLT wall columns with an origin return characteristic, by introducing prestress, and the mechanical behaviour of the CLT wall columns was investigated. We also proposed a method to evaluate the relationship between the bending moment and rotation angle of the column base. These are summarised as follows:

[Static horizontal loading experiment with CLT rocking-wall columns]

・ We determined the difference in the origin return characteristics and damage of wall columns when the prestress introduced to wall columns and the diameter of the PC steel bar was changed.

[Theoretical evaluation method]

・The proposed evaluation method was characterised by a detailed classification of the stress distribution of the column base and a detailed model of the uplift of the column base.

・Although the evaluation value has issues such as overestimating the initial slope of the M_{cb}–θ_{cb} relationship, the experimental value of some experimental specimens can be roughly reproduced.

ACKNOWLEDGEMENT

This research was supported by the 2016-2019 Grant-in-Aid for Scientific Research, Young Scientists (A): "Development of damping technology and proposal of damping design method for wooden high-scale buildings" (Project number: 16H06107, Research representative: Kazuhiro Matsuda). We would also like to thank Mr. Tomohiro Morimoto of Meiken Kogyo Co., Ltd., for his advice. In the experiment, I received the cooperation of Mr. Chisato Inutsuka, Mr. Keiichiro Goto, Mr. Masaki Sugimori and Mr. Yuta Hisada, former students at Meijo University. Here, we express our gratitude to you.

REFERENCES

[1] Japan Housing and Wood Technology Center: [2016 Building design and construction manual using CLT] CLT wo mochiita kenchikubutu no sekkei sekou manyuaru 2016 (in Japanese).

[2] Shimura S., Tsuda C., Hatakeyama T., Suganumata N., Suzuki K., Okabe M., Nakagawa T., Araki Y. and Tsutimoto T.: Study on Seismic Performance of Building Structure with Cross Laminated Timber Part4 Loading Test on a Frame, Summary of Technical papers of Annual meeting of AIJ, pp.311-312, 2012.9 (In japanese)

[3] Murakami S., Tsuchimoto T., Miura S., Isoda H., Miyake T., Yasumura M.: Study on Seismic Performance of Building Construction with Cross Laminated Timber No. 18 Plane test for large-size-panel of CLT, Summary of Technical papers of Annual meeting of AIJ, pp.569-570,2013.8 (In japanese)

[4] Matsuda, K., Kakuda, Y. and Sakata H.: Experimental Study on Mechanical Behavior of Passively Controlled Timber Structure with Self-Centering-Type CLT Wall Columns, WCTE, Coxe, Seoul, Republic of Korea, 2018.8

[5] Shiling Pei, John W. van de Lindt, Andre R. Barbosa, Jeffrey W. Berman, Eric McDonnell, J. Daniel Dolan, Hans-Erik Blomgren, Reid B. Zimmerman, Da Huang and Sarah Wichman : Experimental Seismic Response of a Resilient 2-Story Mass-Timber Building with Post-Tensioned Rocking Walls, 2019 American Society of Civil Engineers. (2019 ASCE), 2019.9

[6] Francesco Sarti, Allessandro Palermo, Stefano Pampanin: Development and Testin of an Alternative Dissipative Post-tensioned Rocking Timber Wall with Boundary Columns, ASCE Journal of Structural Engineering, E4015011, 2015.8

[7] Asif Iqbal, Stefano Pampanin, Massimo Fragiacomo, Alessandro Palermo, Andrew Buchanan: Seismic Response of Post-Tensioned LVL Walls Coupled with Plywood Sheets, World Conference on Timber Engineering,pp.291-296, 2012.7

[8] Horie Y., Isoda H., Matsuda M. Mori T., Tsuji T., Nakashima S. Araki Y. and Nakagawa T.: Full Scale Shaking Table Test of Structure Using CLT Rocking Shear Walls and Experimental Study of its Seismic Performance. Part 1: Structural System Overview and Pre-Analysis, Summary of Technical papers of Annual meeting of AIJ, pp.497-498,2022.9 (In japanese)

[9] Harada K., Koshihara M.,Araki Y., Tanaka K., Suzuki K, Hayasaki Y, Komoriya M.: Horizontal Loading test of high proof strength earthquake resisting walls using CLT panel(part1: Outline of the test and test models), Summary of Technical papers of Annual meeting of AIJ, pp.188-189, 2016. 8. (In japanese)

[10] Komoriya M., Hayasaki Y., Suzuki K., Harada K., Tanaka K., Araki Y., Koshihara M.: Horizontal Loading Test of High Proof Strength Earthquake Resisting Walls Using CLT Panel（Part2: The In-Plane Shear Test of Earthquake-Resisting Walls Using CLT Panel）, Summary of Technical papers

https://doi.org/10.52202/069179-0044

of Annual meeting of AIJ, pp.189- 190, 2016.8. (In japanese)
[11] Tanaka K., Harada K., Suzuki K., Hayasaki Y., Komoriya M., Araki Y. and Koshihara M.: Horizontal Loading Test of High Proof Strength Earthquake Resisting Walls Using CLT Panel （Part3: Estimation of the Structural Behavior by Elastic-plastic Analysis）, Summary of Technical papers of Annual meeting of AIJ, pp.191-192, 2016.8. (In japanese)
[12] Nagashima T., Tachibana K., Yano M. and Ohashi Y.: DESIGN METHOD FOR POST-TENSIONED TIMBER SHEAR WALL (PART 1): TRIANGULAR EMBEDMENT STIFFNESS AND BEHAVIOR IN ELASTIC RANGE, J. Struct. Constr. Eng., AIJ, Vol.85, No.770, pp. 539-548, 2020.3 (in Japanese)
[13] Inayama M: Study on structural design method of timber semi-rigid column-base joint drawn with tensile bolts, Summary of Technical papers of Annual meeting of AIJ, pp.624-622, Hokkaidou, 2013.8 (In japanese)

https://doi.org/10.52202/069179-0044

World Conference on Timber Engineering Oslo 2023

INVESTIGATION OF CROSS LAMINATED TIMBER'S LONG-TERM PERFORMANCE (CREEP)

Aaron DeSantis[1], Michael Stoner[2], Weichiang Pang[3]

ABSTRACT: Cross laminated timber (CLT) and its use as a structural wood product is relatively new compared to other engineered wood products. While current design standards for CLT subjected to long term deflection or creep provide a value for the time dependent deformation factor (creep factor), direct validation of such a value has not been conducted. The 2018 version of the National Design Specification (NDS) recommends a creep factor of 2.0 be used for CLT. Eurocode recommends a value equivalent to 1.8 for normal moisture and temperature conditions. To provide a point of comparison to the design values suggested in US standards, full scale long-term deflection testing of CLT panels is being conducted under a variety of load levels. The increasing deflections over time give an indication of the creep factor. This paper describes the short-term destructive tests and the first 3 months of progress of the long-term tests. Preliminary results indicate creep factors approaching values glue-laminated timber and solid sawn lumber in the NDS after the first 3 months.

KEYWORDS: Cross laminated timber, CLT, Creep, deflection, wood design

1 INTRODUCTION

With increased use of CLT as a construction material in larger buildings, including midrise and high-rise buildings, the work to fully understand CLT grows in importance. Larger structures, especially commercial use cases require larger spans for gather spaces. This includes meeting rooms, open concept office spaces, recreational spaces and auditoriums. Creep in CLT is of concern for these designs due to wood's low stiffness relative to other building materials such as concrete and steel. As seen in fundamental mechanics lower stiffnesses result in greater deflections for the same spans and strengths. Wood structures, utilizing CLT or not, are therefore more likely to be controlled by deflection limit states rather than strength design.

Current understanding of CLT's performance under creep is lacking. The American Wood Council (AWC) currently group CLT with other panelised products in the 2018 edition of the National Design Specification (NDS) for wood construction [1]. Current provisions from the AWC prescribe equation 1 for calculating long term deflection.

$$\Delta_T = K_{cr}\Delta_{LT} + \Delta_{ST} \quad (1)$$

Where Δ_T is the total deflection of the member, K_{cr} is the time dependent deformation factor also known as the creep factor, Δ_{LT} is the immediate deflection due to the long-term component of the design load, and Δ_{ST} is the deflection due to short term or normal component of design load. [1]. These deflections are calculated using the modified effective bending stiffness shown in equation 2.

$$(EI)'_{eff} = (EI)_{eff} C_M C_t \quad (2)$$

Where $(EI)'_{eff}$ is the adjusted effective bending stiffness, $(EI)_{eff}$ is the effective bending stiffness, C_M is the wet service factor, and C_t is the temperature factor.[1]. The NDS specifies a creep factor of 1.5 to most wood products and lumber in dry service conditions and 2.0 in wet service conditions. CLT is assigned a 2.0 creep factor for both wet and dry service conditions like plywood. Service conditions are based upon expected moisture contents in the structural member. Internal moisture contents above 19% are considered in a wet service condition except for laminar products like CLT and CLT where exceeding 16% is considered wet service. The assignment of the creep factor and the categorization of CLT was made on the recommendation of a study done on European CLT for adoption in Eurocode[4].

Eurocode deals with creep similarly to the NDS though uses a single modification factor, k_{def}, for both the reduction in young's modulus and the magnification of instantaneous deflections where the NDS utilise three different terms, C_M, C_t, and K_{cr}. The modification factor in Eurocode differs by product and service class. The service classes are labelled numerically one to three and are based on escalating moisture content within the material, denotated by averaged ambient temperature and the average relative humidity of the air [4]. Additional discussion on the service classes notes that softwoods in each service class typically stay under certain moisture contents. For service class one softwood moisture content stays below 12%, softwoods in service class two remain below 20% moisture content, and service class three exists for conditions where softwoods are above 20%

[1] Aaron DeSantis, Clemson University, USA, agdesan@g.clemson.edu
[2]Michael Stoner, Clemson University, USA, mwstone@g.clemson.edu
[3]Weichiang Pang, Clemson University, USA, wpang@clemson.edu

https://doi.org/10.52202/069179-0045

moisture content [4]. This system is analogous to the NDS's wet and dry service conditions. Service class one to dry service and service class two and three to wet service. Both deflection magnifications and reductions in member stiffness differ based upon the expected environmental conditions under Eurocode 5. CLT is not explicitly included in the later version as a product though associated standards assign the same values as Type EN 636-2 Plywood for all service classes [5]. For service classes one and two k_{def} is 0.8 and 1.0 respectively. CLT does not have a creep deformation factor for service class three. When these terms are applied, they produce an 80% and 100% magnification in deflections due to long term loads. The NDS only provide one magnification level for long term loads on CLT, a 100% magnification.

The investigation of creep factors for CLT is necessary to provide experimental evidence to support the creep factors suggested in the NDS or propose changes if necessary. To evaluate the long-term performance of CLT panels a series of tests have been conducted. Short term testing to establish the strength and stiffness characteristics of the CLT specimens followed by a long-term creep test. The experimental test setup and current results will be presented and discussed.

2 EXPERIMENTAL TESTING

2.1 SHORT TERM TEST

Two specimens out of the available CLT panels were randomly selected for short term testing. The specimens used throughout the experiment were 5-ply CLT panels with a cross-sectional area of 14.5 cm x 30.5 cm and 5.5 m in length (6.75 in x 12 in x 18 ft). Each panel is a V3 CLT panel per PRG 320 [3] and was tested using four-point loading as shown in Figure 1.

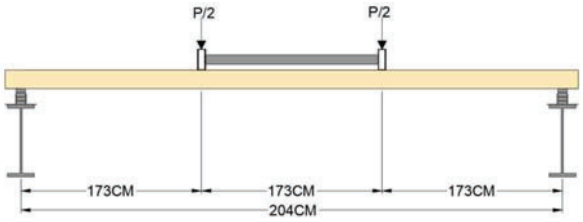

Figure 1: *Loading configuration for short-term testing.*

Four-point loading used for this experiment aligns with previous work for ease of comparison. [4] The load is transferred to the specimen through steel hollow structural sections 7.62 cm (3 in) wide and 20.32 cm (8 in) tall. The specimen rests on top of wood blocks placed on top of steel W-sections as supports spaced at 204 cm (17 ft) center-to-center. Specimens showed no visible signs of crushing at the bearing locations after short term tests.

Specimen subjected to the short-term loading produced moment failure, pictured in figure 2, by fiber rupture in the tension side of the panel. The resulting load displacement graphs are shown in Figure 3.

Figure 2: *Moment failure of specimen in destructive test*

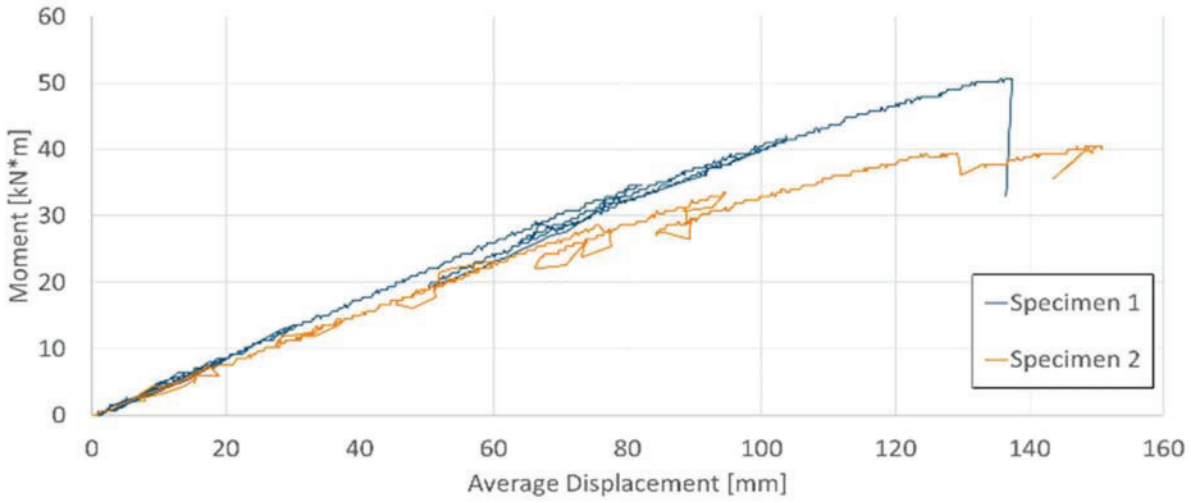

Figure 3: *Short-term test Load-Displacement curves*

https://doi.org/10.52202/069179-0045

The average experimental moment capacity of the CLT specimens was calculated from the following relationship:

$$M = \frac{P}{2}a \quad (3)$$

Where M is the moment capacity, a is the distance from center of bearing to the center of load application (173 cm, 68 in.), and P is the total load applied to the specimen. The load P is split and by a spreader beam and applied evenly according to Figure 1. The moment capacity for each specimen is reported in Table 2 along with the associated peak load and deflection at the peak load. Peak load is reported as total force applied to the specimen. Table 2 also reports the average moment capacity based on the two experimental tests shown in the last row of the table.

Table 2: *Destructive test results and specimen characteristics*

Specimen Number	Peak Load [kN]	Deflection at peak load[mm]	Peak Applied Moment [kN*m]
1	58.7	135.6	50.8
2	46.8	147.1	40.5
Average	52.8	141.5	45.6

2.2 LONG TERM TEST

The primary goal of long-term testing was to measure the creep in a series of CLT specimens. Loading towers were used to maximize the space which was available. Figure 4 shows a representation of the loading towers.

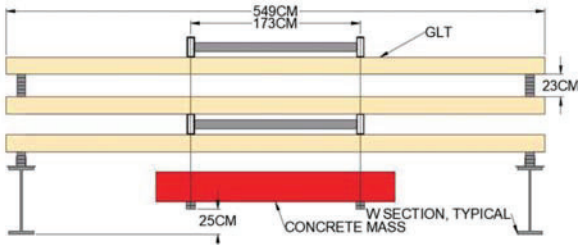

Figure 4: *Schematic view of loading tower for the long-term testing*

Deflection characteristics of the specimen as found during the short-term tests were used to inform the design of the towers such as clearances between specimens within the load towers and the required height of the pedestals to allow sufficient space for the hanging mass. Each tower consists of two CLT panels and a flat-wise glulam beam acting as a transfer member. The load is transferred from the hanging concrete mass below the bottom specimen to the glue laminated timber(GLT) beam using steel threaded rod The GLM beam bends in positive bending and transfers the load to the CLT specimen below at the bearing locations on each end of the beam. The next CLT specimen in the load path will be in negative bending under this load. In total three loading towers have been constructed testing six CLT panels and three GLT beams. Using loading towers introduces variation in the loading due to the accumulation of load due to specimens and equipment self-weights. This additional load was accounted for in all calculations based on an assumed specific gravity for Southern Pine of 0.55, the self-weight of the CLT members were calculated to be 1.57 kN (354 lb). Similarly, the self-weight of the GLT members were calculated to be 1.88 kN (422 lb). LRFD and ASD moment capacities were calculated in accordance with Table 10.3.1 of the 2018 NDS for wood construction. [1] The resulting moment capacities and self-weights of the specimens were used to find the most appropriate load levels to use for the long-term test. The load levels used for the creep test are shown in Table 3. The load levels are reported as a percentage of the average peak moment reported in Table 2 and includes the mass above the specimens and self-weight.

Table 3: *load level information*

Load [kN]	Applied Moment [kN*m]	% Ultimate
P	M	---
8.7	15.1	17
10.6	18.4	20
11.6	20.0	22
13.5	23.3	26
14.7	25.4	28
16.6	28.7	32

The load levels used for this experiment ensure the CLT specimens remained within the linear elastic region ensuring no change in stiffness throughout the creep test. Because the load displacement curves in Figure 1 show no obvious yield point, the 40% rule was used to determine the elastic region of the beam. With this method young's modulus is determined using the load-displacement data associated with 0% to 40% of the failure load. Appendix X2.5-6 of ASTM D198 permits the use of this method when visual inspection of the data is insufficient to identify the yield point.

The creep factors will be back calculated by rearranging equation (1) from the NDS shown as equation (4):

$$K_{cr} = \frac{\Delta_T - \Delta_{ST}}{\Delta_{LT}} \quad (4)$$

Where Δ_T =total deflection, Δ_{LT} =instantaneous deflection due to long-term loadings, Δ_{ST} =instantaneous deflection due to short-term loadings, and k_{cr} = creep factor. For this test there is no short-term loading as all load is applied for the duration of the experiment, therefore equation 4 simplifies to the ratio of total deflection to instantaneous deflection as shown in Equation 5:

$$k_{cr} = \frac{\Delta_T}{\Delta_{LT}} \quad (5)$$

https://doi.org/10.52202/069179-0045

The application of the load for the six CLT specimens and three GLT specimen in three separate stacks was applied on December 20, 2022. The stacks are shown in Figure 5.

Figure 5: *Loading setup of long-term deflection testing.*

3 PRELIMINARY LONG-TERM DEFLECTION RESULTS

The following discussion presents the first 12 weeks of experimental data for the long-term testing. Midspan deflections of each of the six CLT panels and three GLT beams have been collected every minute. Figure 6 reports the daily average deflections for three specimens loaded between two different towers. Daily averages are reported for clarity. Deflection characteristics for the various specimens agree with expected behaviour. Lower load levels produce smaller displacements. Discontinuities in the data are missing data caused by battery and power outages. The instantaneous deflection due to long term loadings were recorded within 3 min of initial loading as per the recommendation of ASTM D6815 [6]. Equation 4 was applied to subsequent readings using this initial deflection to produce the plot in Figure 7.

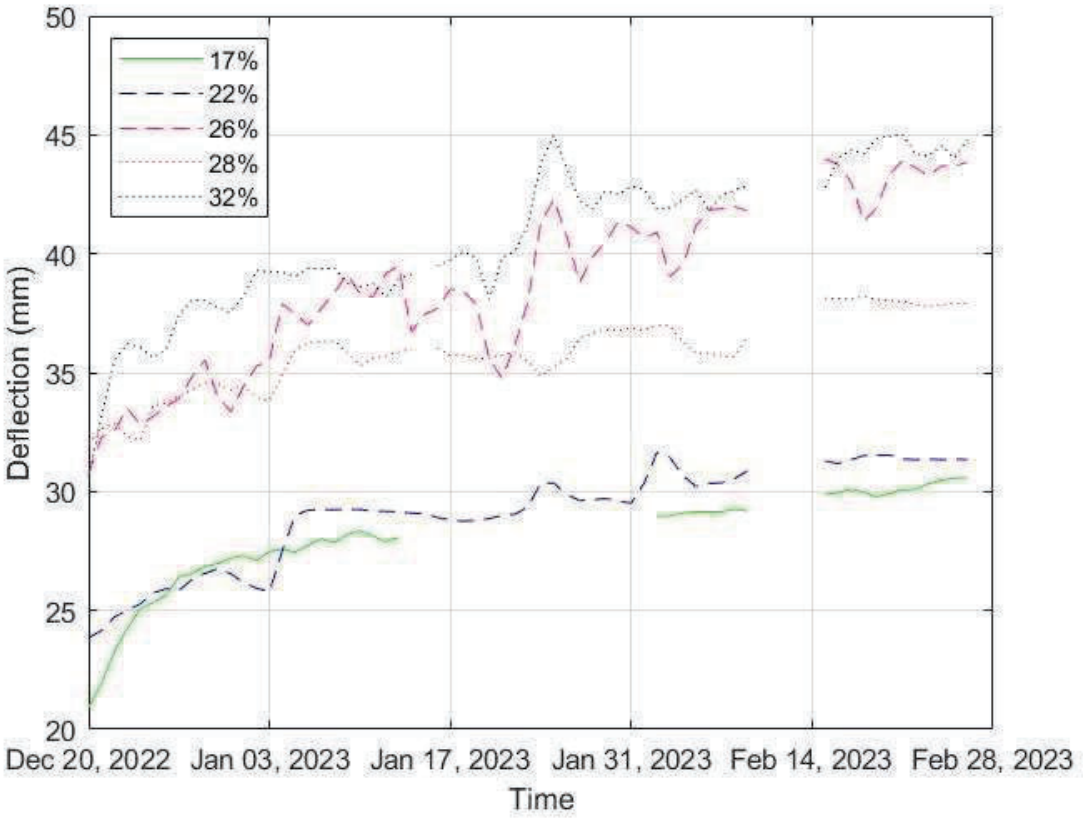

Figure 6: *Daily average deflection time history for all CLT specimen*

https://doi.org/10.52202/069179-0045

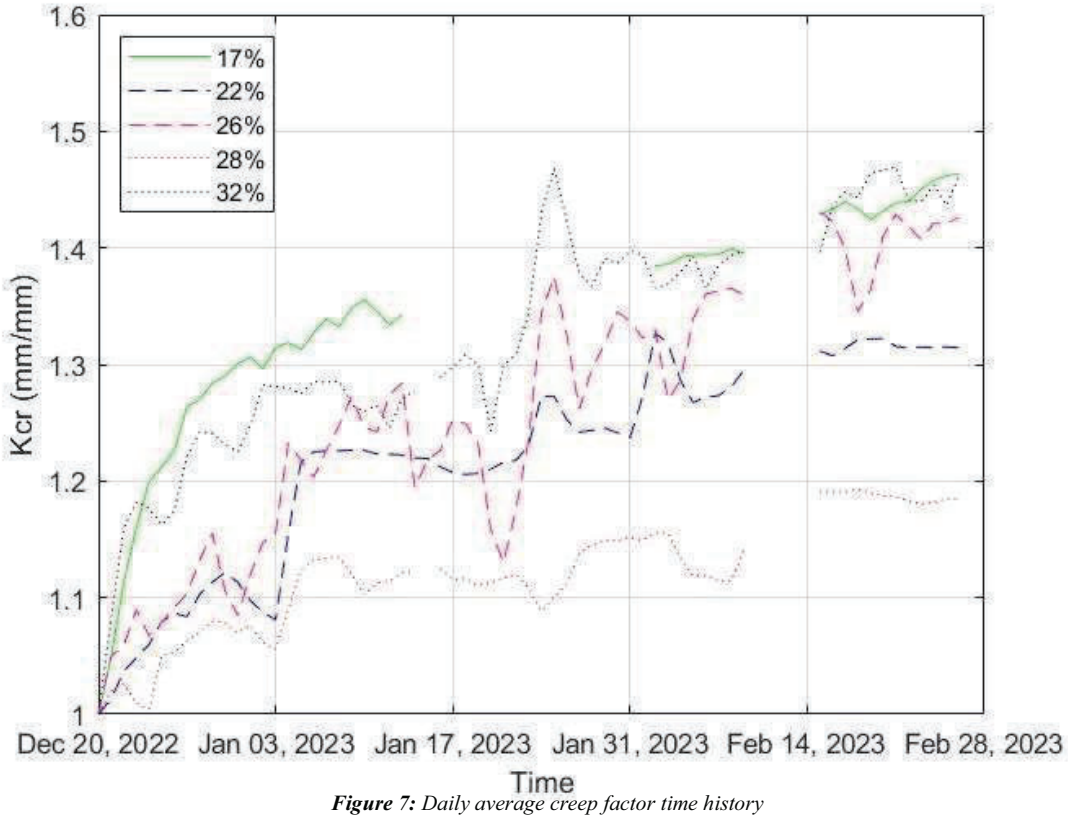

Figure 7: *Daily average creep factor time history*

Figure 6 displays the creep time history for the various specimens at different load levels. Creep factors slowly increase over time as the specimens continue to experience increases in strain. Specimens show a consistent overall creep behaviour, though day-to-day increase in deformation for each specimen differ. The rate of deformation is decreasing over time which is consistent with expected behaviour and previous tests [2]. After three months the CLT specimens experienced 18% to 46% increases in deflection resulting in k_{cr} factors ranging between 1.18 to 1.46. Subjects experienced significant increases in deformation over the first 10 days of the test. The rate of creep then declined significantly and continue to level as the testing period expands. The rate of creep is expected to decline to a level that is considered negligible after 24 months.

4 CONCLUSIONS

An experimental setup was designed to test the long-term deformation (creep) behavior of cross-laminated timber (CLT) to determine the applicability of current design provisions in both the National Design Specification (NDS) and Eurocode. Recommendations for normal temperature and moisture service for NDS recommends amplifying long-term deformations by a factor of 1.5, while Eurocode recommends a factor equivalent to 1.8 for similar conditions. Current time dependent deformation (creep) factors are below the 1.5 recommendation for GLT and solid lumber and below the service class one recommendation under Eurocode, though tests are still ongoing. Past tests indicate that creep continues past the first three months and more time is necessary to obtain an accurate creep factor [2]. Future results will indicate whether the current value prescribed by the NDS is appropriate for CLT or if a lower creep value is appropriate for dry service conditions. Creep factors will continue to be collected and once sufficient data is gathered these values will be evaluated with the currently prescribed values within the NDS.

REFERENCES

[1] American Wood Concil (2018) NDS National Design Standard for Wood Construction with Commentery. AWC – The American Wood Council, Leesburg, VA, USA

[2] American Engineered Wood Products Association, APA (2018). Standard of Performance-Rated Cross-laminated Timber PRG-320. APA – The Engineered Wood Association, Tacoma, WA, USA

[3] Comite Europeen de Normalisation (2004). *Eurocode 5 – Design of Timber Structures. Part1-1: General ules and rules for buildings.* Brussels, Belgum.

[4] Jöbstl, R-A., & Schickhofer, G. (2007). Comparative examination of creep of GLT and CLT slabs in

https://doi.org/10.52202/069179-0045

bending. In *WORKING COMMISSION W18 - TIMBER STRUCTURES* (Vol. 40, pp. 1-15).
[5] Gustafssson, Anders: The CLT Handbook – UK edition. Swedish Proest Industries Federation. Stockholm, Sweden, 2022.
[6] ASTM (2022). Standard Specification for Evaluation of Duration of Load and Creep Effects of Wood and Wood-Based Products. ASTM D6815-22a. West Conshohoken, PA.

World Conference on Timber Engineering Oslo 2023

LOW-TEMPERATURE BONDING OF TIMBER STRUCTURES

Morten Voß*, Tobias Evers* & Till Vallée*

ABSTRACT: Any bonding operation requires a tight control of environmental conditions (most importantly temperature and moisture) to ensure the desired mechanical performance during service life. To overcome these restrictions, the study shows how inductively heated Curie particles can be used to cure wood adhesives (epoxy and polyurethane) under low temperature conditions (+5 and –10 °C). The investigations were carried out using standardised specimens (dogbone / wooden lap shear joints) as well as large Glued-in Rods (GiR). The process is very well suited for the epoxy adhesive, which showed a mechanical performance equal to that of the references. In contrast, the technique is not applicable to polyurethane adhesives bonded on wooden adherends due to moisture diffusion, which interferes with the polymerisation – a problem, which might be solved by using a different particle type with lower Curie temperature, T_c.

KEYWORDS: Low-temperature curing, onsite bonding, induction heating, Curie particles

1 INTRODUCTION

A severe disadvantage of adhesively bonded joints compared to mechanical joining techniques represents the fact that the polymerisation progress is significantly influenced by ambient conditions, most importantly temperature and moisture [1,2]. As a result, practitioners have to costly adapt their production processes to the requirements of the respective adhesive in order to ensure durability and performance of the connections during service life. Furthermore, the bonding-related constraints exclude the use of adhesives for many applications from the start (e.g. onsite bonding in timber engineering).

Up to now, low-temperature curing of polymers is not a well-defined field of research, whereby generally two application approaches may be distinguished: Firstly, the bond may both be produced and cured at low temperatures, secondly, only adhesive application and joining is carried out at low temperatures while the polymerisation is accelerated in the following, e.g. by introducing thermal energy. Both approaches have yet been little studied, with investigations of Moussa et al.[3,4] and Ratsch et al.[5] being available. While Moussa et al. focused on changes in polymer characteristics due to low-temperature curing of a structural adhesive, Ratsch et al. concentrated on providing thermal energy by heating threaded steel bars in a Glued-in Rod (GiR) connection over an external electromagnetic field (EMF).

In order to overcome the temperature-related constraints, the authors investigated if inductively heated Curie particles (CP) can principally be used to cure structural wood adhesives under adverse temperature conditions (+5 and –10 °C). The particles are added to the adhesives and may be heated up to their material-specific Curie temperature, T_c, but not beyond. Thus, a curing process is designed, which automatically reduces the risk of overheating while the heat can be used to enable curing starting from low temperatures.

2 MATERIALS & METHODS

2.1 ADHESIVES

The investigations covered two thermosetting two-component adhesives (epoxy and polyurethane), which are frequently used for different structural applications throughout the German construction sector. In detail, the adhesives Fischer EM390S (abbreviated as Fi390, Fischerwerke GmbH & Co. KG, Germany) and Loctite Purbond CR421 (LP421, Henkel AG & Co. KGaA, Germany) have been selected. Their most important material properties have been listed in Table 1.

Table 1: *Material properties of the adhesives Fi390 and LP421 taken from technical data sheet (TDS) or * that have been measured, ** calculated based upon Arrhenius law* [6]*, tensile strengths measured with v = 1 mm/min and specimens type 1A according to DIN EN ISO 527[7]*

Property	Adhesive	
	Fi390	LP421
Adhesive type	2K-EPX	2K-PUR
Density, ρ [g/cm^3]	1.50	1.35
Pot life at +23 °C [min]	14-30	10
Curing time at +23 °C [h]	18	|240
Curing time at –10 °C [h]	160**	1920**
Young's modulus, E [MPa]	5230*	2760*
Tensile strength, σ_u [MPa]	40.0*	28.6*
Elongation at break, ε_u [%]	1.2*	1.6*
T_g for curing at +23°C [°C]	73.4*	81.3*

2.2 CURIE PARTICLES

Softmagnetic manganese-zinc (MnZn) ferrite particles (Ø0.5–25 µm, cf. Figure 1) with a T_c of 110 °C served as susceptors. The T_c was chosen so to match the heating requirements of the considered adhesives (permissible

**Fraunhofer Institute for Manufacturing Technology and Advanced Materials IFAM, Bremen, Germany*

https://doi.org/10.52202/069179-0046

heating rate / maximum curing temperature), which were determined by preliminary experiments. Moreover, the ceramic particles were selected, since they are corrosion resistant and have a comparatively low coercivity, which ultimately favours heat generation by hysteresis losses. In-depth information about the CP and their characteristics can be found in [8].

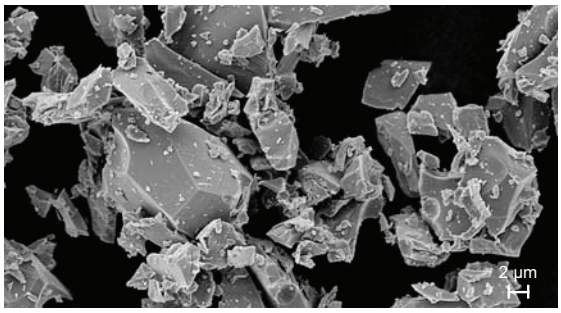

Figure 1: *SEM image of flake-shaped CP (Hengdian Group DMEGC Magnetics Co., Ltd., China)*

2.3 MIXING

All adhesive-CP mixes were prepared under vacuum conditions (100 mbar) using a Speedmixer of type DAC 800.2 VAC-P (Hauschild GmbH & Co. KG, Germany). Mixing was carried out for 60 s at 1.000 rev/min. To maintain comparability, a CP content of 33.3 w/w-% (~8–9 vol-%) was chosen for all produced specimens.

2.4 SPECIMEN TYPES

2.4.1 Dogbone

To analyse the impact of low-temperature curing on tensile properties, dogbone (DB) specimens acc. to DIN EN 527[7] type 1BA were produced, with the adhesive-CP mixes being applied into silicon moulds using a syringe.

2.4.2 Lap shear specimens

In order to characterise the performance of the low-temperature cured adhesives on a small joint scale, single lap shear specimens (SLS, 100 x 25 x 6 mm) acc. to DIN EN 1465[9] were produced using spruce adherends (*picea abies*) with a moisture content of 8.9 ± 0.6 %. The joints overlapped by 12.5 mm. For SLS series bonded with LP421, wood adherends were dried in an oven.

2.4.3 Glued-in Rods

Finally, the experiments were up-scaled to a large joint geometry, so-called Glued-in Rods (GiR). The connection consists of a spruce block (120 x 120 x 300 mm), equipped with bore holes so to embed a reinforcement bar made of glass-fibre reinforced polymer (G-FRP, Ø16 mm). Way more details regarding GiR production and the materials involved can be found in e.g. [10] and will not be repeatedly presented herein.

2.5 LOW-TEMPERATURE EXPERIMENTS

2.5.1 Pre-conditioning at low temperatures

Prior induction heating, all specimens for which low-temperature curing was targeted (cf. Table 2), were pre-conditioned within climate chambers at a temperature of –30 °C (cf. Figure 2). This was done to ensure adhesive temperatures of +5 and –10 °C at the start of inductive heating by letting the specimens re-warm under laboratory RT conditions until the starting temperatures were reached. Depending on the joint geometry, total duration for pre-conditioning differed to ensure that all parts of the joints were cooled to the target temperature.

Figure 2: *Pre-conditioning of wooden SLS joints equipped with thermocouple within climate chamber at –30 °C, adhesive-CP mix applied but not yet cured*

For DB and SLS specimens, the adherends and silicon moulds pre-cooled. Afterwards, adhesive-CP application was done within the climate chambers, which immediately cooled down the mixes and reduced polymerisation progress to a minimum. When the respective DB specimen or SLS series was cooled, they were transported to the induction device (~1 min). Finally, thermocouples were attached to the measurement electronics and the induction device was switched on when thermocouple temperature reached +5 or –10 °C.

2.5.2 Experimental setup & inductive heating

For all low-temperature inductive heating operations, the induction device TrueHeat HF 5010 (Trumpf Hüttinger GmbH & Co. KG, Germany) was used. As an example, Figure 3 shows the inductive heating of a set of five spruce SLS joints (thermocouple attached to middle specimen).

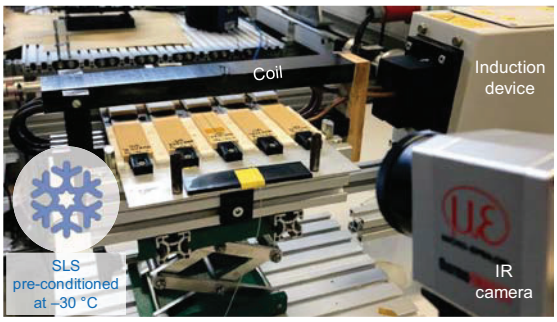

Figure 3: *Experimental setup for inductive heating using five SLS joints (herein bonded with LP421) as an example, P = 2.9 kW, I = 15.8 A, U = 384 V, f = 134 kHz*

All specimen were placed centrally within the induction coils (cf. Figure 3) and cured for 10 min with the EMF in

order to maintain comparability between the specimen types investigated. However, for some low-temperature GiR series, induction time had to be increased to 12.5 min in order to reach high temperatures and thus ensure full cure.

2.6 MECHANICAL TESTING

All specimen types were destructively tested using Zwick||Roell universal testing machines (UTM's). Testing was performed at a speed of 2 mm/min under RT conditions (23 ± 2 °C, 50 ± 10 °C). Testing times were dependent upon the cooling rates of the specimens, with SLS and DB specimens tested ~0.5 h and GiR ~2 h after inductive heating ended. To get an impression of the mechanical tests, Figure 4 shows the setups used for GiR and DB specimens.

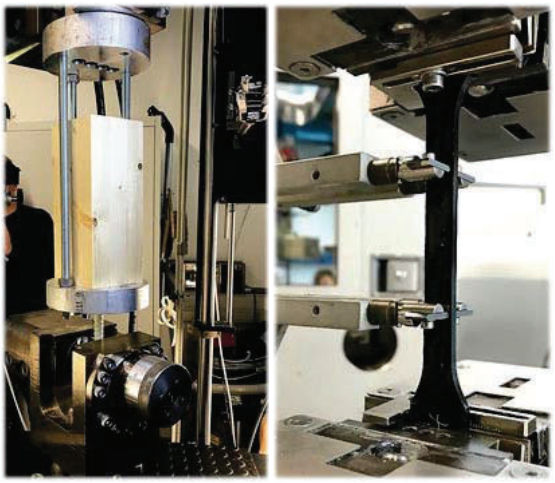

Figure 4: *Setups for mechanical testing of low-temperature cured GiR (left) and DB specimens (right), testing performed at RT*

2.7 EXPERIMENTAL PROGRAM

For a better overview, the complete experimental program has been summarised in Table 2. The experiments included references (unfilled and CP-filled) as well as inductively cured specimens starting from +23, +5 as well as –10 °C for both considered adhesives. The testing times can be found in section 2.6.

Table 2: *Experimental program produced for each Fi390 (2K-EPX) as well as LP421 (2K-PUR), CC = Cold cured at RT, IND = Inductively cured*

Type	Series				
	CC_ Ref	CC_ CP	IND_ +23	IND_ +5	IND_ -10
DB	-	-	5	5	5
SLS	5	5	5	5	5
GiR	5	5	4	4	4

3 RESULTS

3.1 HEATING BEHAVIOUR

In a first step, the heating behaviour for SLS and GiR joints bonded with Fi390 have been visualised in Figure 5. It can be seen that, depending upon specimen geometry, curing temperatures develop fundamentally different. Thus, for the way smaller SLS joints, curing temperatures of roughly 100–110 °C after ~4 min of continuous induction heating can be measured. In contrast, the bigger GiR do not reach the same temperature range although total induction time was 2.5 min longer (12.5 min) as for the SLS specimens (10 min). Consequently, the SLS temperature curve shows a clear flattening around T_c (110 °C), while mean GiR temperatures are still ~90 °C.

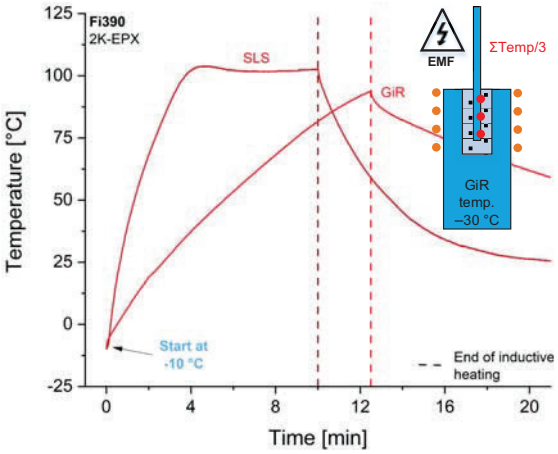

Figure 5: *Curing temperatures during inductive heating of joints bonded with Fi390 recorded with thermocouples embedded within the adhesive-CP mixes*

3.2 MECHANICAL PERFORMANCE

3.2.1 Dogbone

The mechanical results for the inductively cured DB specimens are shown in Figure 6.

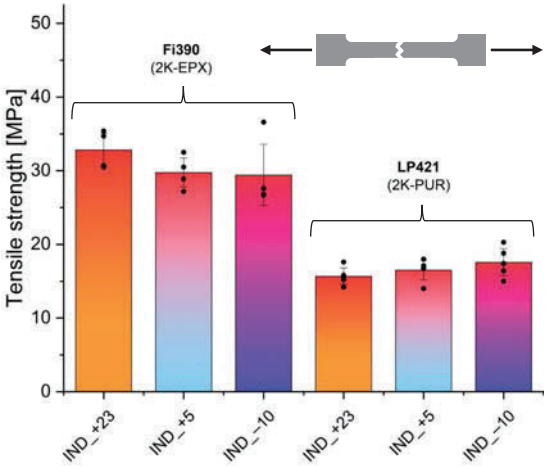

Figure 6: *Mechanical results for tensile strengths measured with DB specimens type 1BA for the two considered adhesives, v = 2 mm/min, tested at RT, Zwick\|Roell UTM 50 kN*

The data reveals that the starting temperature of the induction process has no influence on measurable tensile strengths, which holds true for both considered polymers. At this point, the authors want to point out that a direct comparison with tensile strengths listed in Table 1 is not given since specimens geometry and testing conditions differed.

https://doi.org/10.52202/069179-0046

3.2.2 Lap shear specimens

In the next step, lap shear strengths have been visualised in Figure 7. It can be seen that generally all series result in a tear-off of the wooden fibres, with lap shear strengths of 7–9 MPa being reached. In addition, fracture patterns within the respective series are identical. These observations are valid for both the 2K-EPX as well as the 2K-PUR adhesive.

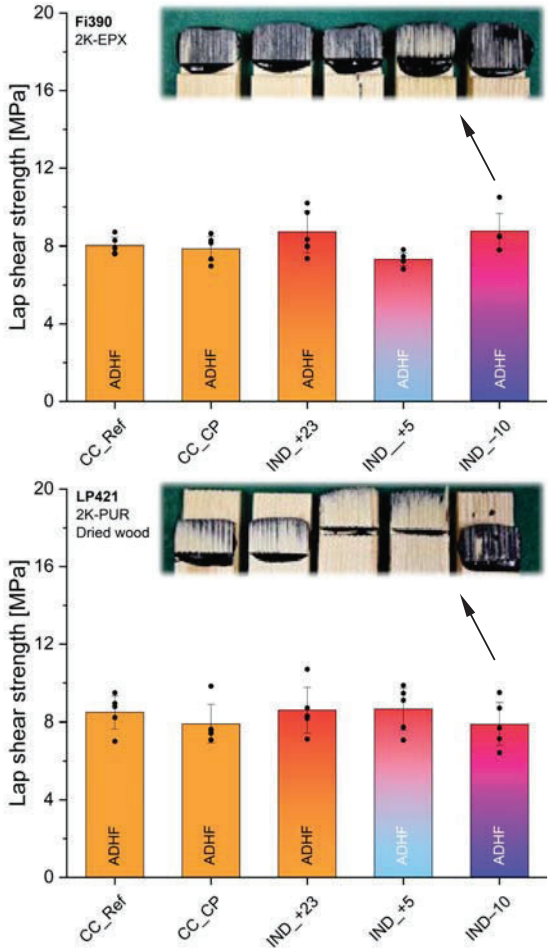

Figure 7: *Mechanical results for spruce SLS joints bonded with the two considered adhesives, v = 2 mm/min, tested at RT, Zwick|Roell UTM 20 kN; ADHF = Adherend failure; adherends for polyurethane dried in oven (moisture content of 0 %, measured immediately prior adhesive-CP application)*

3.2.3 Glued-in Rods

Finally, the mechanical results of the GiR-related mechanical tests have been illustrated in Figure 8. For the first adhesive under investigation, Fi390, all series – independently of the curing conditions considered – resulted in a pull-out of a wooden plug, indicating that the wooden adherends were the weakest part of the connections – a result, which corresponds to the findings on lap shear scale.

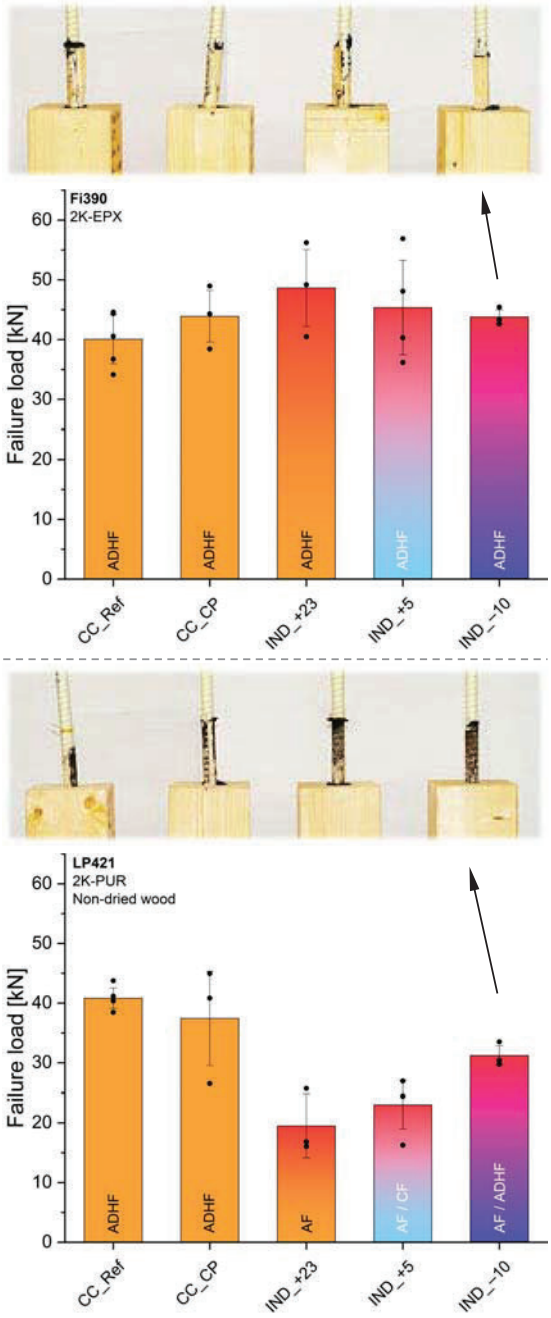

Figure 8: *Mechanical results for GiR joints bonded with the two considered adhesives, v = 1 mm/min, tested at RT, Zwick|Roell UTM 100 kN; ADHF = Adherend failure, all adherends non-dried with moisture content of 8.7 ± 0.9 %*

In contrast, GiR bonded with the 2K-PUR show another behaviour. Thus, for those series that were cured without the use of thermal energy, mechanical tests resulted in a failure of the wooden adherends (wood tear-out). However, when heat is introduced over the particles, failure loads decrease by ~60 % (inductive heating starting from +23 °C), ~50 % (+5 °C) as well as ~25 % (–10 °C), indicating that mechanical performance increases the lower the starting temperature of the joints is chosen. Aforementioned behaviour is accompanied by changes in

fracture patterns from adhesion failure on side of the wood (+23 °C) to mixed adherend / adhesion failure (–10 °C).

4 DISCUSSION

4.1 HEATING BEHAVIOUR

With regard to the curing temperatures (cf. Figure 5), the results revealed a strong influence of joint geometry on the heating behaviour. Compared to the small SLS joints, the way bigger GiR (120 x 120 x 300 mm) needed significantly more time (~10 min) to be heated to the necessary temperature range (> 80 °C) to cure the joints in a decent amount of time. These observations can be traced back to the fact that the comparatively long adhesive layer of the GiR (100 mm) promotes heat dissipation from the adhesive towards the remaining parts of the joints, resulting in lower heating rates in the following. In contrast, the way smaller SLS joints require less heat due to the smaller ratio between adhesive layer thickness and area available for heat transfer. Furthermore, a significantly lower mass of material has to be heated.

A further aspect to be considered is the heat that is released by the exothermic polymerisation, which can be expected to be different depending on the kinetics of the respective polymer. It is already known that this effect may lead to strong inhomogeneity's in heating depending upon joint geometry and adhesive layer thickness[11]. It can thus be concluded that any practical application will require a numerical simulation model, which covers heating-related effects and enables identification of best boundary conditions for optimal and most homogeneous heating. The aforementioned relations have already been presented and discussed in many publications of the authors and will thus not be repeatedly described herein [8,12].

4.2 MECHANICAL PERFORMANCE

4.2.1 Bulk level – Dogbone specimens

The tensile tests on the level of inductively cured DB specimens with different curing conditions resulted in indistinguishable results for both adhesives when the starting temperature of the induction process was varied between +23, +5 as well as –10 °C. These promising results suggest that the general build-up of cohesion is neither hindered nor prevented by the presence of the particles, the inductive heating process as well as the low starting temperatures of the polymerisation. However, from previous investigations it is already known that the mere presence of the much stiffer particles may lead to stress concentrations and earlier failure when unfilled reference and CP-filled DB specimens cured at RT are compared. These negative impacts are, however, counterbalanced when thermal energy is introduced over the susceptors – a process that brings tensile strengths back to the level of the unfilled references [13].

4.2.2 Compound level – Lap shear and Glued-in Rods

The mechanical tests on both the level of SLS as well as GiR joints resulted in promising findings, whereby all EPX-bonded specimens showed a clear adherend failure of the wooden substrates. It can thus be concluded that the general capability of the adhesive to build up significant adhesive strength is not hindered by both the curing process as well as the cold adherend temperatures. The process is thus very well suited for the 2K-EPX adhesive Fi390.

With regard to the LP421-bonded joints (2K-PUR), results behaved differently. In detail, the GiR cured at elevated temperatures showed significantly lower failure loads as well as mixed failure modes (adhesion / cohesion failure). The reason for the deterioration in mechanical performance can be found in the moisture contrained within the wood adherends, which diffuses from the adherends towards the adhesive layer when temperature is applied. In the following, the authors assume that the isocyanate groups of the polyurethane react with the released moisture, leading to both lowered cohesive as well as adhesive strength on side of the wood in the following. These assumptions are supported by the results on lap shear scale (cf. Figure 7-bottom) for which dried adherends were used and thus clear substrate failure could be achieved. In addition, the authors suppose that mechanical performance for low-temperature cured GiR is better due to slower heat development, i.e. slower moisture diffusion (cf. Figure 5, curve for GiR). However, since targeted drying of wooden structures may not represent a realistic solution with regard to practical application, these circumstances might exclude the use of polyurethane adhesives for the technique when temperatures. As a workaround, particles with a lower T_c might offer a way out of the wood-polyurethane-related problems discussed and thus enable their safe CP-curing.

In summary it has been shown that curing of adhesively bonded wooden structures starting in temperature ranges currently not intended by building authorities can be achieved by application of induction heating. Since onsite polymerisation under adverse temperature conditions like those presented would last weeks or not occur at all, the findings might pave the way for additional application fields for bonded timber connections in the future.

5 CONCLUSION

The study focuses on low-temperature curing of structural wood-adhesives (epoxy and polyurethane) using Curie particles (CP), which are added to the polymers and can be heated by an electromagnetic field (EMF) up to T_c but not beyond. For that, experimental investigations were carried out considering three different starting temperatures for the polymerisation (+23, +5 and –10 °C). In a first step, standardised specimen types (dogbone and single lap shear) were produced, after which the investigations were scaled up to the level of large wooden) Glued-in Rods (GiR). The following important findings were made:

- The heating behaviour of low-temperature cured wooden joints using inductively heated particles represents complex due to multifarious conditions such as joint geometry, the materials involved, joint starting temperature,

https://doi.org/10.52202/069179-0046

polymerisation enthalpy as well as the particle type determining the temperature distribution throughout the joint. For better process control, a numerical model would thus be necessary to identify optimal heating conditions and thus avoid cumbersome preliminary experiments.

- The mechanical results showed that tensile strength is identical for different starting temperatures of the induction process (+23, +5, -10 °C). The development of significant cohesive strength takes place, which was observed for both adhesives. In addition, it is known that two counteracting effects have to be considered: Firstly, deterioration of mechanical performance by the mere presence of the particles embedded within the polymers, secondly, counterbalance of negative impact by heat introduction to or above the level of the references[13].
- On the level of small (SLS) and large joints (GiR), a substrate failure could be attained for all EPX-bonded joints, suggesting that the technique is very reliable for EPX adhesives. For the 2K-PUR adhesive, a restriction has to be formulated: When wooden adherends are used and heat is introduced over the particles, moisture diffuses from the wooden adherends and interferes in the cross-linking reaction of the polyurethane. In the following, both adhesive as well as cohesive strength is deteriorated. In order to solve this problem, the authors assume that a lower T_c of the particles will lead to better mechanical results. On the level of SLS joints, polyurethane-bonded dried wood adherends showed a fracture behaviour indistinguishable to those of the references.
- Above all it can be summarised that low-temperature curing of wood structures has been made possible with the presented technique. In detail, the two considered structural adhesives would need weeks to cure at a temperature of –10 °C, which has been reduced to an induction time of ~10 min – a time window, which can be further reduced by e.g. inclusion of the cooling phase for curing or adapting the CP.

ACKNOWLEDGEMENT

The authors sincerely thank Dr. Joachim Schätzel of the Fischerwerke GmbH & Co. KG and Mr. Gordian Stapf from the Henkel AG & co. KGaA for providing the adhesives.

6 References

[1] Rudawska A. The influence of curing conditions on the strength of adhesive joints. The Journal of Adhesion 2020;96(1-4):402–22. https://doi.org/10.1080/00218464.2019.1656615.

[2] Benedetti A, Fernandes P, Granja JL, Sena-Cruz J, Azenha M. Influence of temperature on the curing of an epoxy adhesive and its influence on bond behaviour of NSM-CFRP systems. Composites Part B: Engineering 2016;89:219–29. https://doi.org/10.1016/j.compositesb.2015.11.034.

[3] Moussa, O. Vassilopoulos, A. P., Keller T. Effects of low-temperature curing on physical behavior of cold-curing epoxy adhesives in bridge construction. International Journal of Adhesion and Adhesives 2012;32:15–22. https://doi.org/10.1016/j.ijadhadh.2011.09.001.

[4] Moussa O, Vassilopoulos AP, Castro J de, Keller T. Early-age tensile properties of structural epoxy adhesives subjected to low-temperature curing. International Journal of Adhesion and Adhesives 2012;35:9–16. https://doi.org/10.1016/j.ijadhadh.2012.01.023.

[5] Ratsch N, Burnett-Barking M, Böhm S, Voß M, Adam M, Kaufmann M et al. Accelerated curing of glued-in threaded rods by means of inductive heating — part IV: curing under low temperatures. The Journal of Adhesion 2022;98(2):105–30. https://doi.org/10.1080/00218464.2020.1818562.

[6] Arrhenius S. Über die Dissociationswärme und den Einfluss der Temperatur auf den Dissociationsgrad der Elektrolyte. Zeitschrift für Physikalische Chemie 408(1):96–116.

[7] DIN EN 527-2:2019-07, Büromöbel_- Büro-Arbeitstische_- Teil_2: Anforderungen an die Sicherheit, Festigkeit und Dauerhaltbarkeit; Deutsche Fassung EN_527-2:2016+A1:2019. Berlin: Beuth Verlag GmbH. https://doi.org/10.31030/3030475.

[8] Voß M, Kaufmann M, Vallée T. Curie-supported accelerated curing by means of inductive heating – Part I: Model building. The Journal of Adhesion 2022;98(10):1394–437. https://doi.org/10.1080/00218464.2021.1902810.

[9] DIN EN 1465:2009-07, Klebstoffe_- Bestimmung der Zugscherfestigkeit von Überlappungsklebungen; Deutsche Fassung EN_1465:2009. Berlin: Beuth Verlag GmbH. https://doi.org/10.31030/1507601.

[10] Voß M, Vallée T. Accelerated curing of G-FRP rods glued into timber by means of inductive heating using Curie-particles – large-scale experiments at room temperature. The Journal of Adhesion 2021;97(16):1532–60. https://doi.org/10.1080/00218464.2020.1803067.

[11] Voß M, Vallée T. Accelerated curing of G-FRP rods glued into timber by means of inductive heating – Influences of curing kinetics. The Journal of Adhesion 2022;98(8):1037–75. https://doi.org/10.1080/00218464.2020.1870450.

[12] Voß M, Kaufmann M, Vallée T. Curie–supported accelerated curing by means of inductive heating – Part II Validation and numerical studies. The Journal of Adhesion 2022;98(13):2045–77. https://doi.org/10.1080/00218464.2021.1951712.

[13] Voß M, Vallée T. Effects of Curie particle induced accelerated curing on thermo mechanical performance of 2K structural adhesives – Part I: Bulk properties. The Journal of Adhesion 2022;98(9):1298–339. https://doi.org/10.1080/00218464.2021.1909482.

World Conference on Timber Engineering Oslo 2023

Rapid bonding of timber structures

Morten Voß*, Jona Haupt* & Till Vallée*

**Fraunhofer Institute for Manufacturing Technology and Advanced Materials, IFAM, Bremen, Germany*

ABSTRACT: Adhesively bonded timber-based elements are often manufactured with two-component (2K) adhesives (mostly epoxies and polyurethanes), which usually need many days until full cure, i.e. mechanical performance, has developed. The study shows how wooden components can be bonded in significantly less time by using inductively heated Curie particles (CP), which are added to the polymers and heated by an electromagnetic field (EMF) up to the particle's Curie temperature, T_c, but not beyond. The investigations were carried out using small single lap shear (SLS) as well as medium- and large-sized Glued-in Rods (GiR), all of which produced with spruce adherends. Furthermore, two frequently used 2K adhesives were analysed (epoxy and polyurethane). It could be shown that curing times can be reduced from 1/10 days down to 10 min of inductive heating by application of the technique.

KEYWORDS: Accelerated curing, wood adhesives, induction heating, Curie susceptors

1 INTRODUCTION

Depending on the respective application scenario, polymerisation can be a very slow process. Especially in many structural applications, the usually applied high-strength thermosets – mostly two-component (2K) epoxies (EPX) and polyurethanes (PUR) – require a lot of time (up to many days) until full cure has been achieved and the connections can be stressed or moved for further processing. The reason of these circumstances can be traced back to the comparatively long pot life, which is regarded as a prerequisite to be able to apply the adhesives onto the substrates in time.

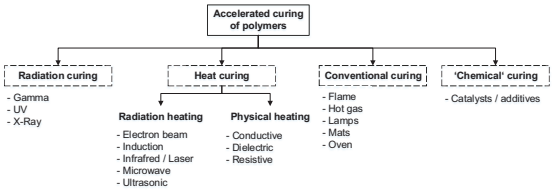

Figure 1: *Methods for accelerated curing of adhesives (no claim to completeness)*

Due to these (and many more) application-related limitations, many techniques for accelerated curing emerged, which can be achieved by different means (cf. Figure 1). The methods range from UV-curing [1], over electron beam[2] or microwave curing [3], to more conventional methods such as ovens. Many of them use heat that is introduced into the adhesive to increase monomer mobility and thus speed up the curing progress.

Probably one of the fastest ways for heat generation represents the use of electromagnetic induction[4] when metallic materials are subjected to an external electromagnetic field (EMF). In context of adhesive bonding technology, induction-based heating can be either used for direct heating of metallic adherends[5] or (when the joint consists of materials that are non-sensitive to EMF) for the heating of susceptors materials (e.g. fibres[6], particles[7], meshes[8] etc.) that are added to the polymers to be cured. In the following, the adhesives are cured 'from the inside'.

In this study, a special type of susceptors, Curie particles (CP), were investigated, which make use of the material-specific Curie temperature, T_c, to control the heating process (no more heat development above T_c) and thus prevent overheating – aspects, which many publications in the field do not consider[9,10]. It was thus targeted to create a self-regulating accelerated curing process, which eliminates the need to store timber-based elements for many days until they can be used.

2 Materials & methods

2.1 Adhesives

The investigations covered two thermosetting 2K adhesives (epoxy and polyurethane), which are frequently used in the German construction sector for wooden applications.

Table 1: *Material properties of the adhesives Fi390 and LP4821 taken from technical data sheet (TDS) or * that have been measured*

Property	Adhesive	
	Fi390	LP821
Adhesive type	2K-EPX	2K-PUR
Density, ρ [g/cm^3]	1.50	1.32
Pot life at +23 °C [min]	14-30	30
Curing time at +23 °C [h]	18	240
Young's modulus, E [MPa]	5230*	1.000
Tensile strength, σ_u [MPa]	40.0*	45.0
Elongation at break, ε_u [%]	1.2*	5.0
T_g for curing at +23°C [°C]	73.4*	71.5*

https://doi.org/10.52202/069179-0047

In detail, Fischer EM390S (abbreviated as Fi390, Fischerwerke GmbH & Co. KG, Germany) and Loctite Purbond CR821 (LP821, Henkel AG & Co. KGaA, Germany) were chosen. Most relevant material properties are listed in Table 1.

2.2 Curie particles

Since no EMF-sensitive materials were involved in all three joint types (cf. section 2.4), particulate Curie susceptors were added to the polymers to be able to heat the adhesives inductively. The particles had a Curie temperature, T_c, of 110 °C, which was selected based upon permissible heating requirements of the polymers. An in-depth characterisation of the CP type has e.g. been presented in [11], which is why it will not be repeatedly described in the present publication.

2.3 Mixing

All adhesive-CP mixes were prepared using a Speedmixer of type DAC 800.2 VAC-P (Hauschild GmbH & Co. KG, Germany). To ensure most homogeneous particle distributions, mixing was carried out under vacuum (100 mbar) using identical parameters for all adhesive-CP mixes prepared (v = 1.000 rev/min, t_{mix} = 60 s). Two different particle contents were used: 33.3 w/-% (~11–13 vol-%) as well as 7.5 w/w-% (2–3 vol-%). Corresponding results have been marked in the result section.

2.4 Specimen types

2.4.1 Lap shear joints

To analyse the performance of the inductively cured adhesives on a small joint scale, single lap shear (SLS) specimens acc. to DIN EN 1465[12] were produced using spruce (*picea abies*) adherends with dimensions 100 x 25 x 6 mm. Their overlap length was 12.5 mm and adhesive layer thickness was selected to be 0.3 mm. The moisture content of the adherends was measured for five adherends at five locations each and amounted to 9.8 ± 0.8 %.

2.4.2 Glued-in Rods

Besides the small SLS joints, experiments were up-scaled in the following to the level of medium- and large-scaled GiR connections, which represent a frequently used timber engineering application[13,14]. The latter consisted of blocks of spruce (*picea abies*, moisture content 8.1 ± 0.3 %) as well as rebars made of glass-fibre reinforced polymer (G-FRP), which were bonded into the wooden blocks. The pultruded rebars are marketed under the name Schöck ComBar® (Schöck Bauteile GmbH, Germany) and have a high resistance against corrosion. The joint geometry of the medium-scaled GiR can be seen in Figure 2.

The complete production approach of the GiR has been described in detail in e.g. [15], which is why detailed information regarding their manufacture will not be repeatedly presented in the present paper. However, the applied steps for induction heating are described in section 2.5.2 of the manuscript.

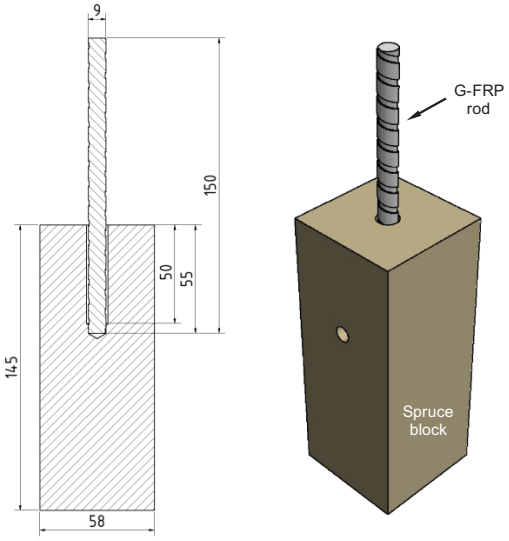

Figure 2: *Geometry of medium-sized wooden Glued-in Rods (GiR) used as an exemplary application for the inductive heating experiments, dimensions for large-scale GiR correspond to a doubling of all dimensions shown, all dimensions in mm*

2.5 Inductive heating

2.5.1 Experimental setup

For all inductive heating operations, the commercially available induction device TrueHeat 5010 (Trumpf Hüttinger GmbH & Co. KG, Germany) was utilised to cure the wooden joints. Depending on coil geometry and mounted capacitors, the system operates in a frequency range of ~50–500 kHz. Essential induction parameters have been summarised in Table 2. For validative purposes, curing temperatures were monitored with thermocouples embedded within the adhesive layers. Figure 3 shows the experimental setup for a medium-sized GiR as an example.

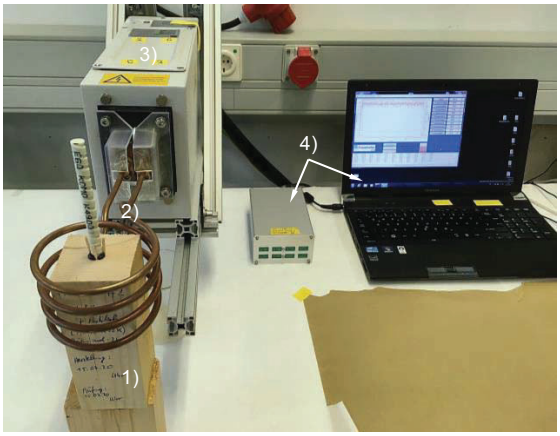

Figure 3: *Experimental setup used for inductive heating with 1) medium-sized GiR (exemplary joint, herein bonded with LP821), 2) induction coil, 3) induction device and 4) measurement electronics / software for thermocouple data evaluation*

https://doi.org/10.52202/069179-0047

Table 2: *Induction parameters for the different joint geometries*

Joint type	P [kW]	I [A]	U [V]	f [kHz]
SLS	4.8	26.3	640	134
GiR_M	4.7	35	650	177
GiR_L	3.8	29.4	795	120

2.5.2 Heating procedure

After mixing was complete, the adhesive-CP mixes were decanted into syringes or 1K disposable cartridges to be able to apply them onto the substrates – a process that has been visualised in Figure 4. All G-FRP rods were degreased with isopropanol 99.9 % and the wood blocks were freed of bore durst using compressed air- If temperature sensors were involved, these were fixed on the substrates using temperature resistant adhesive tape prior adhesive-CP application was performed. To minimise the possibility for air entrapments within the adhesive layer, all GiR joints were filled from bottom to top using a feedhole, which was drilled in the wooden blocks and ended flush with the hole that was used to centre the rods vertically.

Figure 4: *Application of the adhesive-CP mixes to the substrates using syringe for SLS joints (left) as well as 1K disposable cartridge for large-scale GiR (right), application for medium-sized GiR corresponds to right scenario but with syringe*

After adhesive-CP application was complete, the joints were placed within the induction coil (cf. Figure 3), so to ensure that all parts of the adhesive layer were tightly enclosed by the coil. Independently of the different joint geometries, the preparation never exceeded a time window of 7.5 min, which was well within pot life (cf. Table 1).

2.6 Mechanical testing

In order to check the capability of the technique for accelerated curing, the joints were destructively tested at different times after inductive heating ended. However, to exclude any influence of the elevated temperatures on the mechanical results, testing could earliest be performed when the connections had cooled down to RT, which took ~15 min for SLS specimens as well as ~1.5 h, for the GiR. Furthermore, additional time for preparation of the testing devices (~15–30 min) was needed. In detail, testing times of 2, 24, 240 as well as 720 h were investigated, with the GiR setups being illustrated in Figure 5.

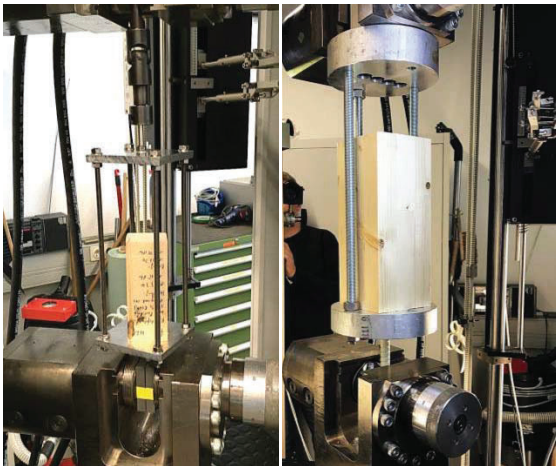

Figure 5: *Configurations for mechanical testing of medium- (left) and large-sized GiR (right), v = 2 mm/min, Zwick\|Roell UTM 100 kN, all tests performed at RT*

2.7 Experimental program

The investigations covered different test series, which have been summarised in Table 3. Besides the inductively cured joints (labelled as IND), reference sets with and without the addition of CP were produced. The latter were 'cold cured' (CC) at RT (23 ± 2 °C, 50 ± 10 % RH) following the protocols that were provided by the adhesive manufacturers. In addition, the expressions GiR_M and GiR_L stand for medium- as well as large-scaled GiR series, respectively.

Table 3: *Experimental program produced for each Fi390 (2K-EPX) as well as LP821 (2K-PUR), CC = Cold cured at RT, IND = Inductively cured, 2h = mechanical testing performed two hours after induction device was switched off*

Type	**Series**					
	CC_ Ref	CC_ CP	IND_ 2h	IND_ 24h	IND_ 240h	IND_ 720h
SLS	5	5	5	5/3	5	5
GiR_M	3	3	3	3	3	-
GiR:L	5	3	3	3	3	-

3 RESULTS

3.1 HEATING BEHAVIOUR

The first step of the evaluation of the results circumvented the analysis of the heating behaviour of the inductively cured joints, as shown in Figure 6. It can be seen that the two adhesives behave fundamentally different during the heating phases of 10 min. Thus, all joints bonded with Fi390 reach the T_c of the particles (110 °C) after different times, whereby ~3 min (SLS), ~5–6 min (GiR_M), as well as 10 min (GiR_L) are needed depending on the respective joint geometry.

In contrast, joints bonded with the 2K-PUR reach slower heating rates, with temperatures recorded for the SLS

https://doi.org/10.52202/069179-0047

joints showing a clear flattening at a curing temperature of approximately 70 °C. Furthermore, both GiR sizes reach temperatures of ~100–110 °C at the end of the inductive heating phase (t = 10 min).

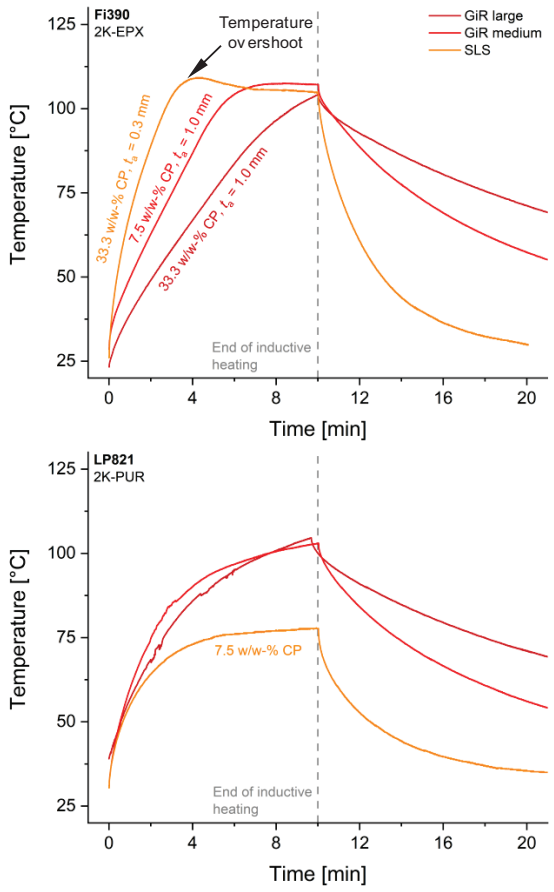

Figure 6: *Heating behaviour recorded with thermocouples embedded within the adhesive-CP mixes for the different joint geometries bonded with the two investigated adhesives, temperatures for medium- and large-sized GiR correspond to arithmetic mean out of three temperature sensors along the rod axis (top, middle, bottom)*

A particularity of the temperature data visualised in Figure 6 can be seen for SLS joints bonded with Fi390 between an induction time of 3–6 min. In this time window, the data reveals a slight temperature overshoot to ~120 °C after which the curve flattens again towards the Curie temperature of 110 °C.

Finally, it can be observed that cooling progresses largely different for the three specimen types, whereby SLS joints – independently of the adhesive – reach RT ~15–20 min after the induction device has been switched off. In contrast, medium- (~30–40 min) and large-sized GiR (~90 min) require significantly more time for cooling.

3.2 MECHANICAL PERFORMANCE

3.2.1 Lap shear specimens

The results for the mechanical SLS tests have been summarised in Figure 7, with the produced series for each adhesive being illustrated as a bar chart. The data shows that both adhesives behave fundamentally different in terms of their lap shear characteristics, i.e. attained lap shear strengths and fracture patterns. In detail, all SLS series produced with Fi390 resulted in a failure of the wooden adherends, indicated by the torn off wood fibres that can be seen in the exemplary failure modes in Figure 7-top. Furthermore, lap shear strengths across all series ranged between ~6–10 MPa independently of the curing conditions considered.

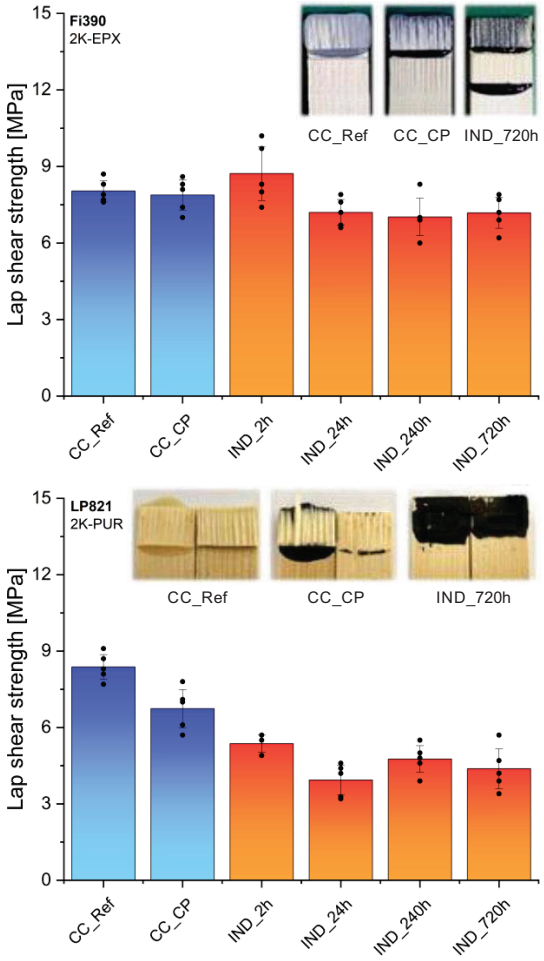

Figure 7: *Mechanical results for wooden SLS joints bonded with the two investigated adhesives, v = 2 mm/min, Zwick|Roell UTM 20 kN, all tests performed at RT*

When the results of the second adhesive (LP821) are compared to those of Fi390, clear differences can be observed. In detail, both series that were cured at RT (with and without added CP) resulted in substrate failure. However, when heat is introduced over the CP, lap shear strengths are lowered to ~3–5 MPa, which is accompanied

by a change in fracture patterns from substrate to cohesive failure (cf. Figure 7-bottom, rightmost pattern). This observation holds true for all inductively cured series of LP821, which were tested at different times (2–720 h) after inductive heating ended.

3.2.2 Glued-in Rods

In the next step, mechanical results for medium- and large-sized GiR were analysed and plotted in the form of bar charts in Figure 8 and Figure 9. Above all, the mechanical tests on GiR level confirmed the findings made on the standardised lap shear scale. Thus, for the 2K-EPX (Fi390) all produced series attained a failure of the wooden adherends, with wood plugs being pulled out of the blocks. Excluding outliners for the medium GiR, shear strengths mainly lie in the range of ~12–19 MPa, whereas large-scale GiR showed failure loads between ~30–55 kN (~4.8–8.8 MPa).

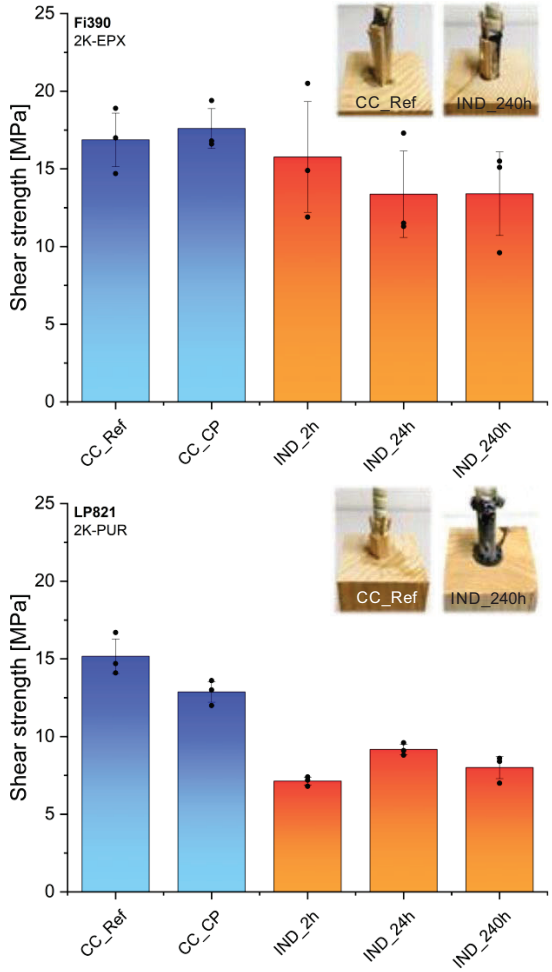

Figure 8: *Mechanical results for medium-sized GiR bonded with the two investigated adhesives; v = 2 mm/min, Zwick|Roell UTM 100 kN, all tests performed at RT*

Focusing on the LP821-related GiR results, the very same trend as on SLS scale became visible, with all CP-cured series cured at elevated temperatures showing a mixed cohesive / adhesive failure (wood side) – a result that is not changed by subsequent conditioning at RT. Furthermore, the mere addition of the susceptors did not impact the fracture behaviour on GiR level, proved by the RT-cured series with added CP.

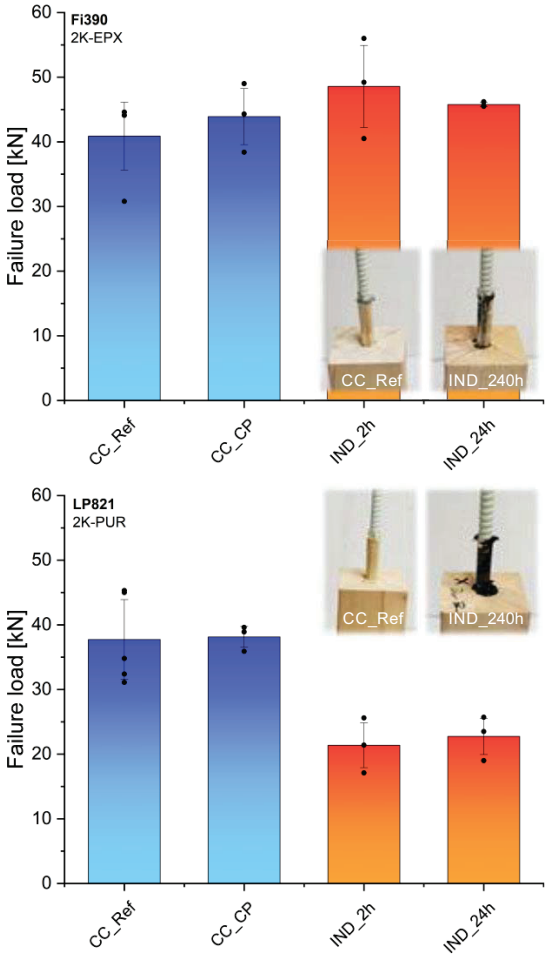

Figure 9: *Mechanical results for large-sized GiR bonded with the two investigated adhesives; v = 2 mm/min, Zwick|Roell UTM 100 kN, all tests performed at RT*

DISCUSSION

3.1 HEATING BEHAVIOUR

In general, the investigations regarding the heating of the different joint geometries revealed slower heating rates for LP821 compared to Fi390 across the specimen types studied. Since all remaining experimental conditions (CP content, coils, induction time, substrates etc.) were kept identical, the authors strongly assume that the curing kinetics, i.e. polymerisation enthalpy and rate of its release, contributed to the temperature distribution throughout the joints. It is already known that the 2K-EPX (Fi390) has faster kinetics and contains more enthalpy [16], which is why the connections can be heated way faster to the relevant temperature ranges. Especially at the beginning of the induction processes, the self-accelerating character of the cross-linking reaction plays a decisive

https://doi.org/10.52202/069179-0047

role, since a lot of enthalpy is released in a relatively narrow time window – a conclusion, which is supported by the enthalpy-related temperature overshoot recorded for Fi390-bonded SLS joints after 3–6 min of inductive heating (cf. Figure 6-top, orange curve).

Besides these adhesive-related differences in heatability, the presented temperature data additionally reveals that the joint type, i.e. the geometry and materials involved, represent a decisive influencing factor for the development of curing temperatures. This becomes particularly clear when the results for Fi390-bonded large-scale GiR and SLS joints (both produced with 33.3w/w-% of CP) are compared (cf. Figure 6-top, dark red and orange curves). Thus for the GiR, a way slower heating can be seen than for the small SLS joints, although adhesive layer thickness, i.e. enthalpy and potential for self-acceleration, is higher. It can thus be surmised that large joints are more difficult to heat but not necessarily excluded for the technique.

From these relations, it becomes clear that an efficient production planning would require a numerical model in which heating-related conditions are mapped to predict the temperature development. Without a simulation model, enthalpy- and geometry-related impacts on the heating can only be determined based upon cumbersome preliminary experiments.

Excluding the slight temperature overshoot for Fi390-bonded SLS joints, it could also be shown that self-regulating heating was successful achieved. However, practitioners have to consider that enthalpy-related overheating can occur if joint and induction conditions favour fast heating – aspects that have to be considered if a numerical model is set up. Parts of such a model have already been presented by the authors [11,17].

3.2 MECHANICAL PERFORMANCE

The extensive experimental campaign revealed a uniform behaviour on the three joint types (SLS, medium and large GiR). For Fi390, all series attained a failure of the wooden substrates – a very promising result. The authors conclude that neither the adhesives capability to build up cohesive as well as adhesive strength is significantly deteriorated by application of the process. However, it is known that both cohesive [18] as well as adhesive strength [19] might be influenced / altered by both the presence of the CP as well as the inductive heating.

In contrast to the EPX adhesive, joints bonded with LP821 systematically showed a mixed failure (adhesive / cohesive) when heat is introduced over the CP. The authors know that this effect does not originate from the nature of the polyurethane adhesive considered, but rather from the moist substrates that were used. In detail, the moisture diffuses out of the wooden adherends when heat is applied and interferes in the polymerisation of the adhesive, i.e. the isocyanate groups react under the formation of CO_2 (indicated by the bubbles that can be seen in the associated fracture patterns). In the following, adhesion / cohesion build-up is significantly deteriorated. It can be expected that the process is also applicable to the 2K-PUR when substrates are changed or the wood is dried before curing.

4 CONCLUSION

The study deals with the accelerated curing of adhesively bonded wooden joints for structural timber applications. For that, so-called Curie particles (CP) were added to two adhesives (2K-EPX and 2K-PUR), which are frequently used throughout the German construction industry. The particles can be heated by an electromagnetic field until their Curie temperature, T_c, is reached, above which the heating is capped by the nature of the particles. Based on these relations a self-regulating curing process is created, which eliminates the need for cumbersome temperature control and enables practitioners to bond under adverse conditions in significantly less time. For the experimental investigations, an up-scaling approach was chosen, with three different specimens types being investigated: standardised single lap shear (SLS) joints as well as medium- and large-scaled Glued-in Rod (GiR) connections – all of which produced with spruce adherends. In addition, the joints were tested at different times after the inductive heating to validate their mechanical performance immediately after and with increasing time after induction curing was complete. After evaluation of all data, the following impotant findings were made:

- The heating behaviour of CP-cured joints is largely determined by component geometry and the adhesive considered, in particular its curing kinetics and polymerisation enthalpy release, which contributes to the curing temperatures. Above all, larger joints are more difficult to heat, especially when long adhesive layers are heated, which offer a larger area for heat dissipation with the remaining parts of the joints.
- With regard to the mechanical performance of the adhesives, the 2K-EPX showed a fracture behaviour indistinguishable to the reference sets, which holds true for all specimen types considered. In contrast, the 2K-PUR showed strengths reductions of ~30–50 % across all joints when heat is applied over the added CP. This was attributed to moisture diffusion from the wooden substrates towards the adhesive layer, which interferes with the cross-linking reaction of the polyurethane. However, this problem might be solved by future investigations by e.g. using a CP type with a lower T_c. In addition, it is already known that the technique works when the adherends are dried prior the induction curing.
- Above all, the findings have to be assessed as very positive, since curing times of both considered adhesives could be reduced from 1 (Fi390) or 10 days (LP821) to an induction time of only 10 min. For future studies, it should be

targeted to include temperatures during the cooling phase or adapt the CP regarding their size and shape to further reduce times needed to cure the joints.

ACKNOWLEDGEMENT

The authors sincerely thank Dr. Joachim Schätzel of the Fischerwerke GmbH & Co. KG and Mr. Gordian Stapf from the Henkel AG & co. KGaA for providing the adhesives.

5 References

[1] Sanai Y, Kubota K. Effect of UV-curing conditions on the polymer structures: a comparison between coating and adhesive. Polym J 2020;52(9):1153–63. https://doi.org/10.1038/s41428-020-0347-4.

[2] Bhowmick AK, Vijayabaskar V. Electron Beam Curing of Elastomers. Rubber Chemistry and Technology 2006;79(3):402–28. https://doi.org/10.5254/1.3547944.

[3] Odom MG, Sweeney CB, Parviz D, Sill LP, Saed MA, Green MJ. Rapid curing and additive manufacturing of thermoset systems using scanning microwave heating of carbon nanotube/epoxy composites. Carbon 2017;120:447–53. https://doi.org/10.1016/j.carbon.2017.05.063.

[4] Rudnev V, Loveless D, Cook R. Handbook of induction heating. Boca Raton, FL: CRC Press, Taylor & Francis Group; 2017.

[5] Ratsch N, Böhm S, Voß M, Adam M, Wirries J, Vallée T. Accelerated curing of glued-in threaded rods by means of inductive heating – Part I: experiments. The Journal of Adhesion 2021;97(3):225–50. https://doi.org/10.1080/00218464.2019.1654864.

[6] Bayerl T, Duhovic M, Mitschang P, Bhattacharyya D. The heating of polymer composites by electromagnetic induction – A review. Composites Part A: Applied Science and Manufacturing 2014;57:27–40. https://doi.org/10.1016/j.compositesa.2013.10.024.

[7] Bayerl T, Schledjewski R, Mitschang P. Induction Heating of Thermoplastic Materials by Particulate Heating Promoters. Polymers and Polymer Composites 2012;20(4):333–42. https://doi.org/10.1177/096739111202000401.

[8] Ferromagnetic nano-particulate and conductive mesh susceptors for induction-based repair of composites; 1998.

[9] Vattathurvalappil SH, Haq M. Thermomechanical characterization of Nano-Fe3O4 reinforced thermoplastic adhesives and single lap-joints. Composites Part B: Engineering 2019;175:107162. https://doi.org/10.1016/j.compositesb.2019.107162.

[10] Bae DH, Shon MY, Oh ST, Kim GN. Study on the Heating Behavior of Fe 3 O 4 -Embedded Thermoplastic Polyurethane Adhesive Film via Induction heating. Bull. Korean Chem. Soc. 2016;37(8):1211–8. https://doi.org/10.1002/bkcs.10841.

[11] Voß M, Kaufmann M, Vallée T. Curie-supported accelerated curing by means of inductive heating – Part I: Model building. The Journal of Adhesion 2022;98(10):1394–437. https://doi.org/10.1080/00218464.2021.1902810.

[12] DIN EN 1465:2009-07, Klebstoffe_- Bestimmung der Zugscherfestigkeit von Überlappungsklebungen; Deutsche Fassung EN_1465:2009. Berlin: Beuth Verlag GmbH. https://doi.org/10.31030/1507601.

[13] Grunwald C, Kaufmann M, Alter B, Vallée T, Tannert T. Numerical investigations and capacity prediction of G-FRP rods glued into timber. Composite Structures 2018;202:47–59. https://doi.org/10.1016/j.compstruct.2017.10.010.

[14] Khelifa M, Oudjene M, Ben Elechi S, Rahim M. FE stress analysis and prediction of the pull-out of FRP rods glued into glulam timber. Wood Material Science & Engineering 2022;17(2):53–62. https://doi.org/10.1080/17480272.2020.1776769.

[15] Voß M, Vallée T. Accelerated curing of G-FRP rods glued into timber by means of inductive heating using Curie-particles – large-scale experiments at room temperature. The Journal of Adhesion 2021;97(16):1532–60. https://doi.org/10.1080/00218464.2020.1803067.

[16] Voß M, Vallée T. Accelerated curing of G-FRP rods glued into timber by means of inductive heating – Influences of curing kinetics. The Journal of Adhesion 2022;98(8):1037–75. https://doi.org/10.1080/00218464.2020.1870450.

[17] Voß M, Kaufmann M, Vallée T. Curie–supported accelerated curing by means of inductive heating – Part II Validation and numerical studies. The Journal of Adhesion 2022;98(13):2045–77. https://doi.org/10.1080/00218464.2021.1951712.

[18] Voß M, Vallée T. Effects of Curie particle induced accelerated curing on thermo mechanical performance of 2K structural adhesives – Part I: Bulk properties. The Journal of Adhesion 2022;98(9):1298–339. https://doi.org/10.1080/00218464.2021.1909482.

[19] Voß M, Vallée T. Effects of Curie particle induced accelerated curing on thermo-mechanical performance of 2K structural adhesives – Part II: Lap shear properties. The Journal of Adhesion 2022;98(9):1167–217. https://doi.org/10.1080/00218464.2021.1884551.

https://doi.org/10.52202/069179-0047

World Conference on Timber Engineering Oslo 2023

EXPERIMENTAL RESEARCH ON POINT-SUPPORTED CLT PANELS: PHASE 1: ROLLING SHEAR STRENGTH

Md Shahnewaz[1], Carla Dickof[2], Houman Ganjali[3], Christian Slotboom[4], Mandy Tam[5], Robert Jackson[6], Marjan Popovski[7], Thomas Tannert[8]

ABSTRACT: Rolling shear strength is one of the key design parameters for point-supported cross-laminated timber (CLT) flat-slab system where the panels are directly supported by columns without any beams. The specified rolling shear strength of CLT in the current Canadian design standard could be conservative estimates considering the variability in wood species, stress grade, thickness of lamellas, layups and grain orientations. To address these gaps in knowledge for the North American market, a Post + Plank research project is being undertaken by Fast+Epp structural engineers in collaborations with the University of Northern British Columbia. In the first phase of the project, presented herein, CLT rolling shear strength under in-plane shear loading was evaluated. A total of 330 specimens (11 series with 30 replicate each, sized 100 mm (width) × 300 mm (length) were tested. The parameters varied were thickness: 3-ply of 89 mm and 105 mm, and 5-ply of 139 mm and 175mm with multiple species and fabricators, and both visual and machine stress graded CLT. The mode of failure was crack development along the growth ring. The results show that the mean rolling shear strength of various Canadian CLT species was between 0.94 MPa to 1.8 MPa. Although thin layers exhibited relatively higher rolling shear strength, these differences were found not to be statistically significant.

KEYWORDS: Point-supported Floors, Cross-laminated Timber, Rolling Shear Strength, Punching Shear Failure.

1 INTRODUCTION

1.1 BACKGROUND

Cross-laminated timber (CLT) has become popular construction material for mid- to high-rise buildings because of its benefits to sustainability, fast installation, design flexibility and overall good acoustic, thermal, fire and seismic performances. Point-supported CLT is a flat-slab building system, where CLT panels are supported directly on columns without drop beams, as designed in the 18 storey Tall Wood House in Vancouver (Figure 1) [1]. This configuration is appealing due to its ease of construction, ease of mechanical and electrical distribution, and reduction of the floor assembly depth. However, the transfer of force at the column faces leads to high shear stress near supports [2].

The strength of CLT in shear is governed by the rolling shear strength in the lamella perpendicular to the direction of loading. In this context, rolling shear refers to stresses causing tension perpendicular to the wood grain in layer perpendicular to the loading, creating a tendency for lamella to roll over each other [3].

Rolling shear strength values adopted in Canadian and American wood design standards [4,5] are much lower than longitudinal shear, and will often govern the capacity of point-supported panels. However, recent studies on [3,6,] suggested that the short-term rolling shear values specified by different standards are overly conservative.

Figure 1: *Point supported CLT floor*

[1] Md Shahnewaz, Fast+Epp, Canada, mshahnewaz@fastepp.com
[2] Carla Dickof, Fast+Epp, Canada, cdickof@fastepp.com
[3] Houman Ganjali, School of Engineering, University of Northern British Columbia, Canada, ganjali@unbc.ca
[4] Christian Slotboom, Fast+Epp, Canada, cslotboom@fastepp.com
[5] Mandy Tam, Fast+Epp, Canada, mtam@fastepp.com
[6] Robert Jackson, Fast+Epp, Canada, rjackson@fastepp.com
[7] Marjan Popovski, FPInnovations, Canada, Marjan.Popovski@fpinnovations.ca
[8] Thomas Tannert, Professor, School of Engineering, U. of Northern British Columbia, Canada, thomas.tannert@unbc.ca

https://doi.org/10.52202/069179-0048

1.2 ROLLING SHEAR STRENGTH IN CLT

Wood is an anisotropic material with three major axes: longitudinal, tangential, and radial relative to the log. Rolling shear occurs in the tangential-radial plane perpendicular to grain direction; failure occurs when the longitudinal fibers roll over each other. Rolling shear strength (f_s) is lower than longitudinal shear strength parallel to grain (f_v), and often "taken as approximately one-third" [3]. The specified CLT rolling shear strengths in Canadian Standard for Engineering Design in Wood [4] range from 0.43 to 0.63 MPa, the allowable stress design values in American Design Standard [5] is between 0.24 to 0.41 MPa depending on the base-material stress grade. For both edge-glued and non-edge-glued CLT made of laminations with a minimum width-to-depth ratio of 4, the recommended rolling shear strength in Europe is 1.4 MPa [7]. If the minimum width-to-depth ratio requirement is not met, then a value of 0.7 MPa is recommended instead.

Rolling shear properties of CLT do not currently have universally standardized test configurations and methods, primarily short span bending tests and in-plane shear tests are conducted. In-plane shear test apply load to a specimen at a 14° angle on the outer lamellas, similar to EN408 [8]. Four-point bending tests for CLT allow to indirectly determine the rolling shear strength. Kumar et al. [9] reported that the in-plane shear test resulted 10-20% higher strength compared to rolling shear estimated from bending tests. EN 16351 [7] adopts both methods and ANSI PRG 320 [10] refers to short span bending tests.

Amongst the several factors that influence the rolling shear properties of CLT: wood species, density of wood, annual ring orientation, the lamella aspect ratio (width to thickness of lamella), knots, and edge gluing or edge gaps, species appears to have the largest impact [9]. Previous studies completed on European species reported the mean rolling shear strength to range from 1.5 MPa to 2.8 MPa for softwoods and up to 5.6 MPa for hardwoods [5]. The mean rolling shear strength observed in North American species ranged from 1.3 MPa to 2.3 MPa [11-13]. The mean rolling shear strength observed for various Australian/New Zealand wood species ranged between 2.0 MPa to 3.6 MPa [3].

Further research found that the shear strength of CLT is increased near column supports [14, 15]. This increase is largely due to two effects: i) the lamella confinement of adjacent layers; and ii) additional confinement against rolling from compression forces. In North America, there have been few tests to confirm these findings, nor has the increase in rolling shear capacity due to confinement s been evaluated for a variety of support conditions. At time of writing, only one research program has completed full-scale panel test [2].

1.3 RESEARCH PROGRAM OVERVIEW

To address these gaps in knowledge for the North American market, a Post + Plank research project is being conducted by Fast+Epp structural engineers in collaborations with the University of Northern British Columbia. This research program will expand industry knowledge on point-supported CLT floors by experimentally testing a wide range of variables critical for point supported CLT construction.

The Post+Plank project will investigate the structural performance of North American CLT panels in point-supported construction through a series of numerical analyses and experimental testing. The experimental testing program will consist of four phases. Phase 1 of testing will use small CLT billets to test short-term rolling shear strength and stiffness of a variety of species, layups, and grades. The results to date from this phase will be reported in-depth in this paper.

In phase 2, the CLT rolling shear strength under 4-point bending loading will be determined for both short-term and long-term duration of load. In phase 3, the punching-shear strength will be evaluated under variation of following parameters: a) support condition (columns at the panel centre, edge, and corner; b) CLT lamella species and grade; c) column support geometry; and d) level of screw reinforcement. Panels sized 1.7×1.8 m, 1.5×1.8 m, and 1.5×1.5 m will be used. Six repetitions per test series for a total of 180 specimens will be tested. Phase 4 will be completed on full-scale floor systems to validate the strength predictions from phases 1 and 3. Six two-span continuous panels will be tested with varying parameters including panel width and presence of penetrations.

2 PHASE 1: SHORT-TERM ROLLING SHEAR STRENGTH

2.1 MATERIALS

In Table 1, and overview of all test series including wood species, stress grade, test layer orientation, and thickness is provided. Tests are completed for E and V rated CLT samples for different species, including Black Spruce and SPF. Each species and grade is tested in both major and minor layer orientations for 3-ply of 89 mm and 105 mm thicknesses and 5-ply of 175mm and 139mm thicknesses CLT panels to evaluate the impact of lamella aspect ratio. The numbers in bold and underlined show the layup, orientation, and thickness of the tested layers.

Table 1: *Test series overview*

Series	Stress Grade	Layup	Species	Tested layer
S1	E1	35/**19**/35	Spruce	Minor
S2	E1	35/**35**/35	Spruce	Minor
S3	E1	35/35/**35**/35/35	Spruce	Major
S4	V2	35/**19**/35	SPF	Minor
S5	V2	35/**35**/35	SPF	Minor
S6	E1	35/35/**35**/35/35	SPF	Major
S9	V2	35/17/**35**/17/35	SPF	Major
S10	V2	35/17/35/**17**/35	SPF	Minor
S11	V2	35/**19**/35	SPF	Minor
S12	V2	35/**35**/35	SPF	Minor
S13	E1	35/35/**35**/35/35	SPF	Major

https://doi.org/10.52202/069179-0048

2.2 METHODS

The specimens were prepared and tested at the University of Northern British Columbia Wood Innovation and Research Laboratory in Prince George. All specimens were conditioned at 20 °C and 65% relative humidity prior to testing. The nominal length and width of each specimen was 300 mm and 100 mm, respectively. The thickness of the lamella of interest varied depending on the layup of the specimen; test specimens of different width are presented in Figure 2. The exact dimensions of the lamellas within the shear plane were measured for each specimen by means of a calliper prior to testing.

Small-scale in-plane shear tests following EN 408 [8] were conducted with the modification where the specimen is inclined against the vertical axis by 14° [16], as shown in Figure 3. The tests were performed using a universal test machine with a calibrated 100kN load cell, at a loading rate of 1 mm/min.

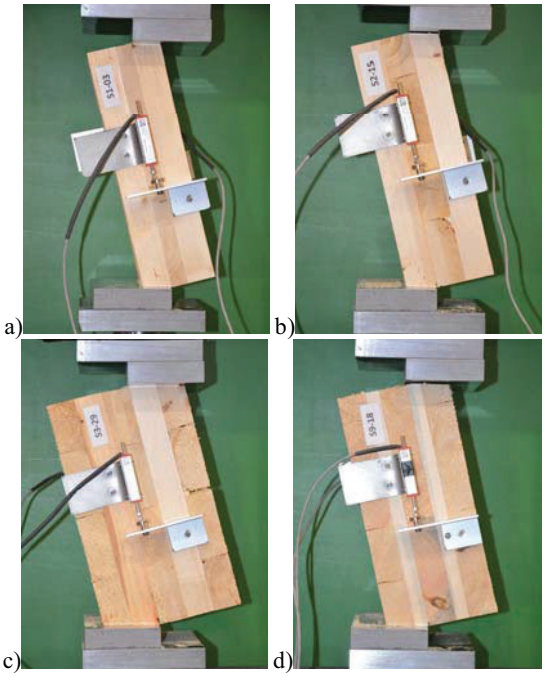

Figure 2: *Test specimen of different width: a) 89mm; b) 105mm; c) 175mm; d) 139mm*

Each specimen was loaded to failure and the rolling shear strength (τ) and shear modulus (G) were calculated by Equation (1) and Equation (2), respectively:

$$\tau = \frac{P_{max}\, cos\alpha}{L\, w} \quad (1)$$

$$G = \frac{t_c}{L\, w}\frac{P}{\Delta}\, cos\alpha \quad (2)$$

Where, P_{max} is the peak load, L and w are the length and the width of the specimen, t_c is the thickness of cross layer, P/Δ is the slope of the linear range of the load deformation curve between 10% and 40%, and ∝ is the angle between the shear plane and the force (14°).

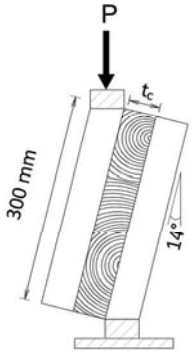

Figure 3: *Modified planar-shear test*

To calculate the average rolling shear modulus of each test series, two linear variable differential transformers (LVDTs) were used to measure the relative displacement between CLT layers adjacent to the loaded layer, on both front and back faces on 15 randomly selected specimens from each series. Load vs. the relative displacement curves of the specimens from S10 are shown in Figure 4. Most specimens exhibited quasi-linear behaviour until failure and sustained some load after peak and failure.

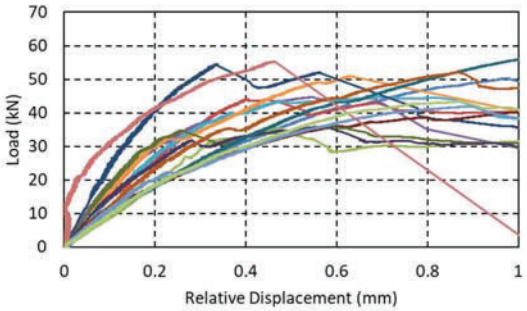

Figure 4: *Load vs. the relative displacement curves of S10.*

Since CSA 086 [4] gives the same value for rolling shear strength of 0.5 MPa for both strength grades, all 13 series were grouped together and the corresponding characteristic rolling shear strength is calculated. Nonparametric percent point estimate (NPE) and parametric tolerance limit (PTL) approaches described in EN 789 [17] were evaluated to calculate the 5th percentile rolling shear strength values. The NPE approach requires fewer assumptions and is deemed more conservative, while the PTL assumptions may lead to inaccurate results, thus NPE is adopted in the rest of this report.

EN 16351 [7] provides rolling shear strength values of CLT panels based on their lamination width-to-depth ratio. Therefore, all specimens with a tested layer thickness of 35 mm were considered as one group called "Thick" and the specimens having tested layer thicknesses of 19 mm and 17 mm were considered as a second group called "Thin". Outliers are excluded from each individual group of specimens. To further groups based on the stress grade of the specimens, E1 and V2, are also created and named accordingly.

https://doi.org/10.52202/069179-0048

2.3 ROLLING SHEAR STRENGTH RESULTS

The results from the in-plane rolling shear tests of all series are summarized in Table 2. The average of the rolling shear strength varied from 0.94 MPa to 1.81 MPa with a coefficient of variation (COV) between 14% to 37%. The average shear moduli range from 84 MPa to 157 MPa with a COV between 11% to 35%. When compared to those obtained in previous research, the measured mean value from this study is in a good agreement with those of the previous studies on the same softwood species.

The characteristic rolling shear strength values of each series are also presented in Table 2. It should be noted that these values need to be adjusted for normal duration of load, i.e., they should be divided by 1.15, if they are to be compared with the specified values in CSA O86 [4].

Table 2: *Summary of test results*

Series	Rolling shear strength			Rolling shear modulus	
	Mean [Mpa]	COV [%]	$\tau_{0.05}$ (NPE), [MPa]	Mean [Mpa]	COV [%]
S1	1.55	18	1.02	157	21
S2	0.94	19	0.60	87	22
S3	1.06	21	0.73	135	32
S4	1.81	23	1.27	104	23
S5	1.72	22	1.23	126	20
S6	1.51	14	1.23	150	11
S9	0.96	24	0.61	140	34
S10	1.54	20	1.10	85	35
S11	1.69	37	0.70	87	21
S12	1.10	20	0.67	102	34
S13	1.48	20	1.08	138	20

Previous findings suggest that the width to thickness ratio of the CLT lamellas influences its rolling shear strength where thinner boards with a higher width to thickness ratio have a greater rolling shear strength were confirmed. For instance, the thinner series, S1 (19 mm) has a greater average rolling shear strength value than the series having thicker test layer from this provider, S2 (35 mm). Similar finding can be observed by comparing values of the series from the panels provided by the same manufacturer.

The cumulative distribution of the rolling shear strength of all E1 and V2 series and the two other combined groups (Thin and Thick) are shown in Figures 5-8. The characteristic rolling shear strength value of E1 and V2 series combined groups are 0.73 MPa and 0.79 MPa, while the characteristic rolling shear strength value of Thin and Thick combined groups are 0.85 MPa and 0.72 MPa respectively.

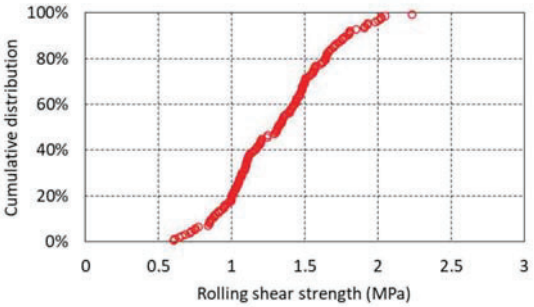

Figure 5: *Cumulative distribution for rolling shear strength of all E1 panel series.*

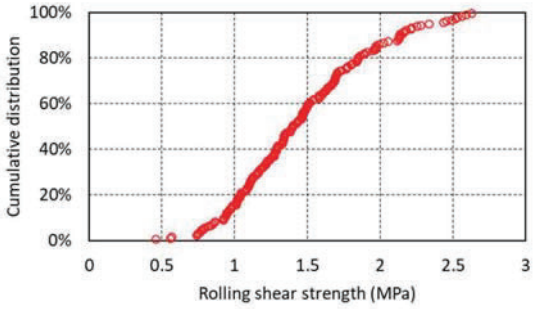

Figure 6: *Cumulative distribution for rolling shear strength of all V2 panel series.*

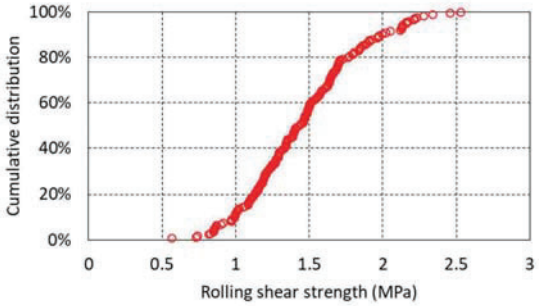

Figure 7: *Cumulative distribution for rolling shear strength of all "Thin" width-to-depth ratio.*

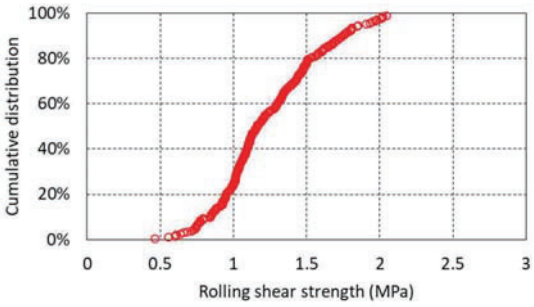

Figure 8: *Cumulative distribution for rolling shear strength of all "Thick" width-to-depth ratio*

https://doi.org/10.52202/069179-0048

For an in-depth investigation of the measured values, one-way ANOVA test [18] was performed with a significance level of 95% and a cut-off *p*-value of 0.05. The obtained *p*-value <0.001 showed that there were statistically significant differences between the test series. Therefore, a Tukey's multiple comparison test was conducted, see Table 4. It can be observed that despite the difference in their average rolling shear strength values, not all *"Thin"* series are different from *"Thick"* series. For instance, it cannot be claimed that S1 is different from S5, S6, and S13. Similarly, it also cannot be claimed that all *"Thick"* are not different from each other; as shown in Table 4, there is a significant difference between S2 and S5.

Table 4: *Tukey's multiple comparison test results.*

Series	Grouping[1]	Grade	Thickness
S1	ca	E1	Thin
S2	b	E1	Thick
S3	b	E1	Thick
S4	c	V2	Thin
S5	ca	V2	Thick
S6	a	E1	Thick
S9	b	V2	Thick
S10	a	V2	Thin
S11	ca	V2	Thin
S12	b	V2	Thick
S13	a	E1	Thick

[1] There is no significant difference at the 0.05 level between groups having at least one letter in common.

2.4 FAILURE MODES

The typical rolling shear failure mechanisms are illustrated in Figure 9. In the most common failure mechanism, cracks formed and propagated along the growth ring and led to a separation. In most tests, the crack(s) stopped at the bonding surface of loading plates and test layer, which resulted in the ultimate fracture. This was occasionally interrupted by steps along the wood ray. The presence of a pith in a specimen also led to the rolling shear failure, where a crack suddenly formed around the pith and then propagated along either the growth ring or a wood ray direction. Same scenario might happen when the wood ray which is a weak zone in a wood section is present. As shown in Figure 9, cracks were caused by tension perpendicular to grain stresses and propagated along the wood ray. During the tests, each or any combination of the above-mentioned mechanisms may have been the reason for initiation of failure, but as the load increased a combination of all three failure mechanisms was likely to be observed.

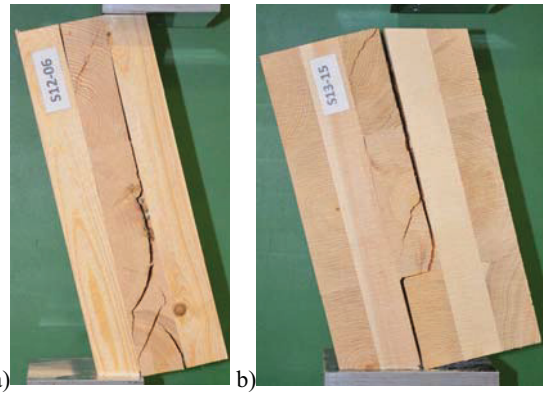

Figure 9: *Typical rolling shear failure of (a) 3-ply, (b) 5-ply*

3 CONCLUSIONS

The Post+Plank program will assess the punching shear capacity of CLT flat slab systems through a large of experimental program. Results for the first phase of testing is overviewed in this paper, showing the base rolling shear strength for North American manufacturers of CLT. The following observations were made:

1. The predominant mode of failure was due to the development and extension of cracks along the growth ring, eventually resulting in separation. Additionally, the presence of a pith in the specimen results in rolling shear failure, wherein a crack abruptly initiates around the pith and extends either along the growth ring or along a wood ray direction.
2. The average of the measured rolling shear strength varied from 0.94 MPa to 1.81 MPa and the average shear moduli ranged from 84 MPa to 157 MPa.
3. The CLT series with a thinner layer exhibited higher average rolling shear strength than the thicker ones, corroborating earlier research that established a positive correlation between width-to-thickness ratio (lamella aspect ratio) and rolling shear strength; however, ANOVA showed these differences not to be consistently statistically significant.
4. The characteristic rolling shear strength values of the combined groups of E1 and V2 series after adjustment for normal duration loading were 0.63 MPa and 0.69 MPa, respectively. These values are 26% and 37% higher than what is specified in the CSA O86 standard [4].

The ongoing structural testing program at Fast + Epp and the University of Northern British Columbia will provide design inputs for point supported CLT.

https://doi.org/10.52202/069179-0048

ACKNOWLEDGEMENTS

The project was supported by the Province of British Columbia Ministry of Energy, Mines and Low Carbon Innovation through a Green Construction Through Wood program and the Natural Sciences and Engineering Research Council of Canada through an Alliance grant. The support by the UNBC technicians James Andal and Ryan Stern is appreciated.

REFERENCES

[1] Fast P, Gafner B, Jackson R, Li J. An 18 Storey Tall Mass Timber Hybrid Student Residence At The University Of British Columbia, Vancouver in 14th World Conference on Timber Engineering, 2016

[2] Popovski M., Chen Z, Gafner B, Structural behaviour of Point-supported CLT floor Systems, World Conference on Timber Engineering, 2016

[3] Ehrhart, T., & Brandner, R. (2018). Rolling shear: Test configurations and properties of some European soft-and hardwood species. Engineering Structures, 172, 554-572

[4] CSA O86 Engineering Design in Wood, Canadian Standards Association Toronto, ON, Canada, 2019.

[5] NDS National Design Specification for Wood Construction. American Wood Council 2015

[6] Aicher S, Christian Z, Hirsch M. (2016). Rolling shear modulus and strength of beech wood laminations. Holzforschung, 70(8), 773-781.

[7] EN 16351, Timber structures -– Cross laminated timber–Requirements. European Committee for Standardization, CEN, Brussels, Belgium, 2015.

[8] EN 408. Timber structures – structural timber and glued laminated timber – Determination of some physical and mechanical properties. European Committee for Standardization, CEN, Brussels, 2010.

[9] Kumar C, Li X, Subhani M, Shanks J, Dakin T, McGavin RL, Ashraf M (2022). A review of factors influencing rolling shear in CLT and test methodology. J. of Testing and Evaluation, 50(2).

[10] ANSI/APA PRG 320 Standard for Performance-Rated Cross-Laminated Timber. APA The Engineered Wood Association, Tacoma, USA, 2019

[11] Wang, Z., Fu, H., Gong, M., Luo, J., Dong, W., Wang, T., & Chui, Y. H. (2017). Planar shear and bending properties of hybrid CLT fabricated with lumber and LVL. Construction and Building Materials, 151, 172-177.

[12] Li M (2017) Evaluating rolling shear strength properties of cross-laminated timber by short-span bending tests and modified planar shear tests. Journal of Wood Science, 63(4), 331-337.

[13] Ruan G, Xiong H, Chen J (2019). Bending and rolling shear properties of cross-laminated timber fabricated with Canadian Hemlock. Structural Durability & Health Monitoring, 13(2), 227.

[14] Mestek P (2011) Punktgestützte Flächentragwerke aus Brettsperrholz (BSP) – Schubbemessung unter Berücksichtigung von Schubverstärkungen, PhD dissertation, Technische Universität München.

[15] Muster M (2020) Column-Slab Connection in Timber Flat Slabs, PhD dissertation, ETH Zurich.

[16] Mestek P, Dietsch P Design concept for CLT-reinforced with self-tapping screws," in Focus Solid Timber Solutions-European Conference on Cross Laminated Timber (CLT), 2013, pp. 103–118.

[17] EN 789, Timber structures. Test methods. Determination of mechanical properties of wood based panels. European Committee for Standardization Brussels, 2004

[18] Barbara I, Susan D. (2013). One-Way ANOVA. In: Introductory Statistics. OpenStax, Houston, Texas.

https://doi.org/10.52202/069179-0048

World Conference on Timber Engineering Oslo 2023

PRELIMINARY TEST RESULTS ON THE IN-PLANE STRENGTHENING OF TIMBER FLOORS WITH THE DOUBLE PLANKING TECHNIQUE

Giovanni Metelli[1], Alessandra Marini[1], Stefania Cominelli[1], Francesca Feroldi[1], Anna Maria Basso Bert[2], Ezio Giuriani[1]

ABSTRACT: The seismic retrofit of existing masonry buildings often needs global interventions to guarantee the box-structural behaviour to inhibit the onset of local mechanisms. However, the so called box structural system requires a correct organization of the diaphragm, as well as its adequate connection to the masonry walls. The use of a new crosswise single layer of wooden planks is here proposed for the in-plane strengthening of existing timber floors. According to this solution, the new layer made with wooden planks has an inclination of 45° with respect to the existing ones that are arranged orthogonally to the wooden beams. The wall-to-floor connection is made of studs fixed to perimeter chord, which is in turn nailed to the wooden planks. The aim of this work is to highlight the role of the type and arrangement of the connections between the wooden planks and the steel plate on the shear behaviour of the diaphragm, as well as on the transmission of the actions from the perimeter chords to the diaphragm inner web-panel by means of an analytical model. The test results on in-plane cyclic shear behaviour of the diaphragm shows a linear trend of shear stresses along the plates, contrary to the usual design practice that assumes a uniform distribution.

KEYWORDS: diaphragm, seismic upgrade, double-planks, nailed connections, in plane shear behaviour

1 INTRODUCTION

The high seismic vulnerability of historical masonry buildings is mainly due to onset of local collapse mechanisms, which involve the detachment of the perimeter walls perpendicular to the inertial actions [1]. In the worst-case scenario, the detachment is followed by the rigid out-of-plane overturning of the masonry blocks or of the whole wall, thus causing also the floors' collapse. Widely used techniques for the retrofitting of masonry buildings rely on the adoption of roof and floor diaphragms. When efficiently connected to the perimeter walls, the diaphragm can collect the inertial forces of the floor and of the wall loaded out-of-plane and transfer them to the shear resistant walls, thus preventing the onset of local mechanism and guaranteeing a box-like behaviour of the whole building [2-5].

Traditional techniques for the construction of a rigid diaphragm entail the use of reinforced concrete slabs. Such a solution was also recommended by past national codes: for example, before the enacting of the Italian building Code (D.M. 2008 [6]), earlier Italian codes recommended replacing the existing timber floor with a new heavy concrete slab, with the exception of historical and monumental buildings for which the conservation of the existing materials was a mandatory requirement for the preservation of the cultural heritage.

Recent Italian earthquakes (2016, 2017) showed the ineffectiveness of the concrete slabs to provide the box-behaviour of stone-masonry buildings, since the walls were not able to withstand significant seismic actions generated mainly by the high mass of this type of diaphragm.

Several techniques were proposed in the past for the construction of in-plane floor diaphragm. Initially, the same techniques proposed for the flexural strengthening of existing wooden floors, fully compliant with the conservation principles of heritage buildings, were further engineered as to also activate a diaphragm action. They rely on the replacement of the non-structural existing screed placed between the wooden planks and the floor, with a structural overlay, stud-connected to the wooden joists, thus generating a composite cross section. The collaborating structural overlay may consist of ordinary [7-8], or natural hydraulic lime mortar [9]. Alternatively, the extrados retrofit may be obtained with a very thin steel plate [10], or of Fiber Reinforced Polymers (FRP) [11]. Recently, efficient dry composite sections were also proposed by using single or double-crossed timber planks [12] or Cross Laminated Timber panels (CLT) [13-16], connected to the existing joists by steel dowels or screws. More recently, specific solutions for wooden floor diaphragms were proposed. The in-plane behaviour under shear loading of strengthened wooden floors was experimentally and numerically investigated by considering: i) composite materials [13, 17-19] ii) single and double diagonal wooden boards, having different thicknesses and orientation of the planks, for varying the connection type and the arrangement between the adjacent boards [13, 17-19]; iii) CLT panels [14, 16]. Other experimental studies investigated retrofitted wooden diaphragms with a different test set-up allowing the development of both the in-plane flexural and shear deformation of diaphragms like in a real building. Several stiffened configurations were considered: i) a single layer of plywood panels or flooring boards connected with

[1] Alessandra Marini, University of Bergamo, Italy, alessandra.marini@unibs.it
[2] Anna Maria Basso Bert, Soprintendenza Archeologia Belle Arti e Paesaggio per le province di Bergamo e Brescia , Italy,

https://doi.org/10.52202/069179-0049

stapled metal sheets [5, 20]; ii) a single overlay of nailed plywood panels [21, 22]; iii) a second diagonal layer of wooden planks, nailed on the existing planks; iv) diagonal bracing consisting of screwed steel plates or epoxy-resin glued FRP strips; v) multi-layers of plywood panels glued on the existing floor; vi) traditional thin reinforced concrete slab connected by means of steel stud to timber joists [23, 24]; vii) a steel truss fixed to the joists' intrados [21].

The experimental results showed that the several proposed configurations can efficiently enhance the in-plane capacity and stiffness of the strengthened timber floor. Furthermore, the experimental results may be considered as an effective benchmark for the validation of numerical and analytical models aiming at shedding light on the capability of flexible diaphragms to affect the global response of the whole buildings, by controlling the out-plane detachment of masonry walls and by contributing to dissipate energy during a seismic event [16; 25].

Among all the cited techniques for the retrofitting of the existing timber floors, it is worth acknowledging that the application of an extrados double crossed planks or timber panels (either plywood or CLT panels) has been widely accepted in the field of architectural restoration as less invasive, with a high degree of reversibility and without the risk of moisture and water percolation. Furthermore, these dry wood-based techniques are very light and the seismic retrofitting of the whole building can benefit from reduced seismic actions with respect to the use of the concrete overlay.

The effectiveness of the retrofit interventions, based on the adoption of either floor or roof diaphragms, is governed by the correct detailing of the connections between the diaphragm and the perimeter walls transferring both the out-of-plane inertial forces of the walls to the floor diaphragm, and the seismic floor actions to the seismic resistant walls. Specific technological, experimental and analytical studies can be found in literature focusing on the local behaviour of steel studs connecting the perimeter diaphragm chords to the masonry walls [26, 27]. This technique has been widely accepted and adopted in the construction practice for the retrofit of many historical monuments since it minimally invasive as opposed, for example, to dovetail joints, and it improves reversibility of intervention.

The literature survey shows that, despite many experimental results on the in-plane strengthening of existing wooden floors, there is a lack of scientific studies focusing on the correct detailing of the connections between the floor diaphragm web panel and the perimeter chords, commonly realized by steel plates. Such a detailing is critical since it governs the distribution of the shear forces/stresses along the diaphragm edges during a seismic event. This paper focuses on the fundamental role of these connections and it aims at presenting design criteria and rules for a correct design of the boundary elements in a wooden diaphragm with double planks.

2 AIMS OF THE RESEARCH

The present research deals with light-dry-wooden diaphragms with double crossed floorboards because this technology complies with the conservation principles of historical buildings, such as compatibility with existing materials, high-reversibility and low-invasiveness. Furthermore, the use of overlaying double planks allows the floor to be breathable while wood panels, like plywood, laminated veneer lumber (LVL) and CLT, can entail vapour barrier due to the presence of adhesive layers which may produce water condensation, thus favouring the degradation of the existing materials.

In the case of the double crossed planks technique, the diaphragm is obtained with the application of new planks overlaying the existing floorboards. the new layer of planks can be placed either perpendicularly (α=90°) or with an inclination of α=±45° to the existing ones. It should be pointed out that the two solutions differ in the capability of transferring the shear actions within the diaphragm. While in the former configuration the resisting shear flow depends both on the width of the overlaid planks and on the number of nails placed at the intersection of the planks, in the latter configuration the resisting shear flow mainly depends on the number of nails placed along the diaphragm boundaries [28]. Furthermore, it can be easily proved that the arrangement with perpendicular planks requires a total amount of nails ten times greater than the configuration with diagonal planks since each intersection between the overlaying timber boards needs at least four nails.

For these reasons, the research work was restricted to the case with diagonal planks only, for which nail connections can be limited, in principle, along the contour to guarantee equilibrium. The connection between the floor diaphragm and the perimeter walls is provided by the diaphragm perimeter chords, usually made with steel profiles (either L-shaped or rectangular section, Fig. 1). The chords are nailed to the double wooden boards and jointed to the seismic-resistant masonry wall by means of shear dowels and to the walls perpendicular to the earthquake direction by means of steel ties which transfer the inertial actions to the diaphragm.

The present work aims at investigating the transfer phenomenon of the shear actions from the boundary steel chords to the diaphragm web panel made of overlaid double planks. Experimental and theoretical studies are presented that focus on the role and the arrangement of the connections on the transmission of actions from the perimetral chords to the inner web of the diaphragm.

As a result, specific design detailing of the boundary connection, with the adoption of additional nails, is proposed to guarantee the effectiveness of the diaphragm. In the first part of the paper, the behaviour of the connections between the overlaying double crossed planks and the perimeter steel chords is analytically studied, whilst in the second part the experimental results of a full-scale test on the proposed wooden diaphragm are presented.

https://doi.org/10.52202/069179-0049

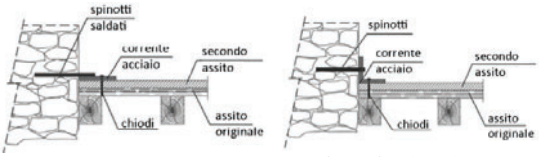

Figure 1: *Diaphragm perimeter chords made of steel plates (a) or L-shaped profiles (b) [29]*

3 DESIGN OF THE CONNECTION

3.1 EFFECT OF SHEAR FLOW DISTRIBUTION ON THE ACTIONS IN THE CONNECTIONS

A rectangular floor diaphragm is considered (Fig. 2). At a given storey, the seismic actions (f_0) produce a uniform distribution of shear flow q= V / L_y, being V the force transferred to the seismic-resistant walls and L_y the diaphragm depth. The shear flow (q) transferred from the perimeter steel chord to the diaphragm web panel depends on the orientation of the timber joists, which can either be perpendicular (case 1 in Fig. 3), or parallel to the diaphragm edge (case 2 in Fig. 3), respectively. In the diagonal configuration, the horizontal and vertical translational equilibriums of a floor length equal to the joist spacing (Δx) allow for the evaluation of the axial action (F_y) in the joist and in the diagonal wooden plank (f_{wd}), as follows:

$$q\,\Delta x = f_{wd}\,\Delta x\,cos^2\alpha \quad F_y = f_{wd}\,\Delta x\,cos\alpha\,sin\alpha \qquad (1)$$

where α is the inclination of the diagonal planks. If α = 45°, the actions in the joists and in the diagonal planks are given by:

$$f_{wd} = 2\,q \qquad F_y = q\,\Delta x \qquad (2)$$

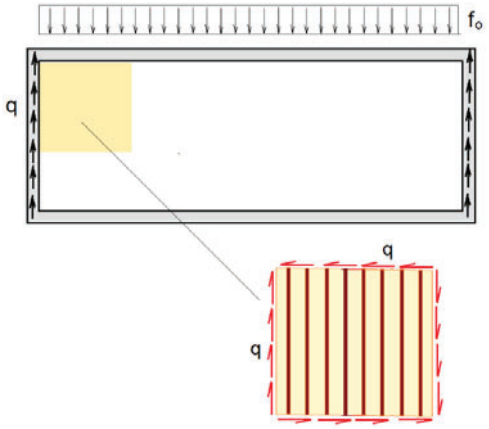

Figure 2: *Shear flow distribution in the diaphragm*

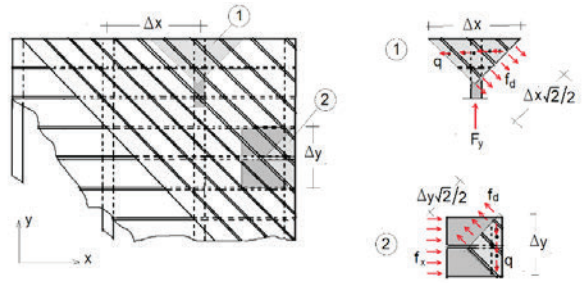

Figure 3*: equilibrium of timber planks along the diaphragm edge*

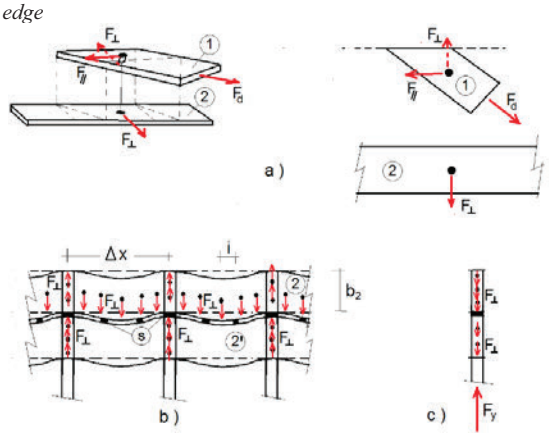

Figure 4: *Portion of the diaphragm with the joist perpendicular to the edge: actions in the nailed connection (a) in the lower existing plank (b) and in the joist (c)*

Furthermore, the shear flow along the diaphragm edge is transferred from the perimeter steel chord to the diaphragm's web panel made of the double-crossed planks through local forces acting in each nailed connection perpendicularly ($F_\perp$) or parallel ($F_{//}$) to the edge (Fig. 4a), as given by the following equation once it is assumed that the steel chord is nailed over the double-crossed planks with a given nail spacing (i) and with plank orientation of α=45°:

$$F_\perp = F_{//} = q\,i \qquad (3)$$

As shown in Figure 4b, the plank parallel and close to the edge is loaded by the bending action induced by the transverse forces $F_\perp$of the nailed connections. Thus, the bending moment (M_2) in the perimeter planks is given by:

$$M_2 = \beta(F_\perp/i)\Delta x^2 \qquad (4)$$

where $\beta = \frac{1}{10} \div \frac{1}{12}$ if the outer plank is modelled as a continuous beam supported by timber joists. As a result, the reaction in the inner supports can be approximately assumed as equal to (Fig. 4c):

$$R = \frac{F_\perp}{i}\Delta x = F_y \qquad (5)$$

It should be noted that each joist has to be connected to the outer plank (labelled as 2 in Fig. 4) by the same number of nails ($n_{nails} = \Delta x/i$) placed along the edge length (Δx). Since in most cases all these nails cannot be placed within a single outer plank (b_2), it is necessary to

https://doi.org/10.52202/069179-0049

include also the inner planks in the connection. In the case of clearance between the existing floor boards, specific wooden or steel wedges have to place between them in order to engage the bending stiffness of the inner plank. Thus, the bending stress of the outer planks having the same width (b_2) (2 and 2' in Figure 4) is:

$$\sigma_2 = \sigma_{2'} = M_2(2t_2 b_2^2/6) \quad (6)$$

The number of nails to connect the steel chord to the double-crossed diaphragm within the joists spacing is:

$$n_{nails} = q\Delta x / V_{Rd,n} \quad (7)$$

where $V_{Rd,n}$ is the shear design strength of each nailed connection. The same number of nails connects the outer planks (2 and 2' in Fig. 4) to each joist.

Along the edge parallel to the joist (case 2 in Fig. 3), the connection does not produce any bending in the perimeter joist since the two layers of planks guarantee the translational equilibrium of the perimeter chord length (Δy). In other words, referring to Fig. 3, the horizontal component of the axial action in the diagonal planks is balanced by the action in the floorboards perpendicular to the joists, while the vertical component by the shear flow along the steel chord length (Δy).

Thus, the translational equilibrium of a diaphragm portion (2 in Fig. 3) along the two directions allows the evaluation of the forces per unit length in the double-planks, as shown by the following equations:

$$q\Delta y = f_{wd}\,\Delta y\, cos\alpha\, sen\alpha \qquad f_x \Delta y = f_{wd}\,\Delta y\, cos^2\alpha \quad (8)$$

By assuming an inclination of the diagonal planks α=45°, the actions in the planks are:

$$f_{wd} = 2q; \qquad f_x = q \quad (9)$$

3.2 STRENGTH AND STIFFNESS OF THE NAILED CONNECTIONS

The bearing capacity of the nailed connections between the steel chord and the double-crossed planks depends on the steel grade of the nail, the nail diameter, and on the local bearing strength of wood (mainly affected by the density of the timber element), and by the angle of the action with respect to the wooden fibers. The nail needs a minimum embedded length of 50÷60 mm in order to connect the three overlaying elements (the existing plank, the new plank and the steel plate). It should be noted that considering the connection between the steel chord and the diagonal plank, the point load acts with an inclination of 45° with respect to the diagonal plank grain direction , while at the interface between the two timber boards the angle to the grain of the point load is equal to 45° in the upper diagonal plank and 90° or 0° in the lower existing plank for the portions 1 and 2, respectively (Fig. 4).

Preliminary tests [28] were carried out according to EN 383 [30] to evaluate the bearing strength and the stiffness of spruce timber for nails with a diameter (ϕ) of 4 mm, commonly used to fix the planks in existing floors. Some test results are presented in Figure 5.

The test results show that the bearing strength (f_{hw}) of spruce wood for ϕ=4 mm nails depends on the load angle with respect to the timber grain, differently from the equations of the main international Codes [31], for which the bearing strength is a function of the wood density and of the nail diameter only. The bearing strength (f_{hw}) is equal to 50, 42 and 37 MPa for an angle to the grain β of 0°, 45° and 90°, respectively, measured for a relative displacement of 4 mm. Furthermore, the local compressive stresses were substantially elastic up to a nail relative displacement of about 1 mm, as it is shown in Figure 5, where the bearing strength is plotted as a function of the nail-to-timber relative displacement. The average initial slope of the curves (Fig. 5) is the elastic stiffness of foundation soil which varied between $k_{w,0}$ = 80 N/mm^3 and $k_{w,90}$= 30 N/mm^3, depending on the action to wooden grain angle.

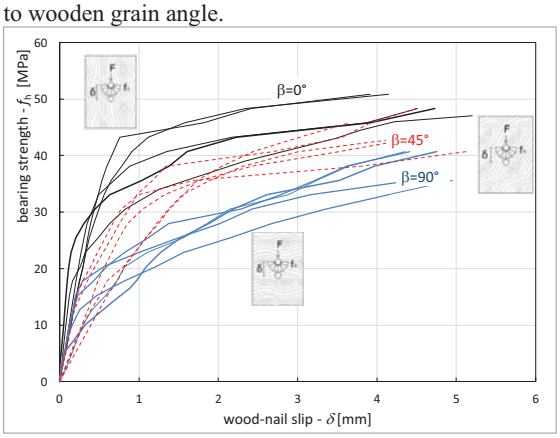

***Figure 5**: Experimental results on the local compressive behaviour of spruce timber (f_{hw}) with 4 mm nails for an action parallel (β=0°), with angle of 45° (b) and perpendicular to the grain (β=90°) (MC=12% during the tests).*

***Table 1**: Bearing strength ($f_{hw,\beta}$) and stiffness $k_{w,\beta}$ of spruce planks for varying direction (β) of the action with respect to wood fibers*

β =0°		β =45°		β =90°	
$f_{hw,0}$ (N/mm^2)	$k_{w,0}$ (N/mm^3)	$f_{hw,45}$ (N/mm^2)	$k_{w,45}$ (N/mm^3)	$f_{hw,90}$ (N/mm^2)	$k_{w,90}$ (N/mm^3)
50	80	40	50	37	30

it is possible to determine the shear stiffness of the nailed connections on the basis of the classical approach of the beam on elastic foundation [9]. Thus, the stiffness of the steel chord - to diagonal plank connection is expressed by the following equation:

$$K_{cp} = 2E_s J \left(\frac{k_{w45}\phi}{4E_s J}\right)^{3/4} \quad (10)$$

while the stiffness of the connection between the existing and the new overlaying diagonal plank in the portion 1 and 2 of the diaphragm are given by the following equations, respectively:

https://doi.org/10.52202/069179-0049

$$K_{pp,1} = 2E_s J \left[\frac{1}{\left(\sqrt[4]{\frac{k_{w45}\phi}{4E_s J}} \right)^3} + \frac{1}{\left(\sqrt[4]{\frac{k_{w90}\phi}{4E_s J}} \right)^3} \right]^{-1} \quad (11)$$

$$K_{pp,2} = 2E_s J \left[\frac{1}{\left(\sqrt[4]{\frac{k_{w45}\phi}{4E_s J}} \right)^3} + \frac{1}{\left(\sqrt[4]{\frac{k_{w0}\phi}{4E_s J}} \right)^3} \right]^{-1} \quad (12)$$

where E_s is the steel modulus of elasticity and J the moment of inertia of the nail cross-section.

For relative displacements greater than 2 mm, the wood local compressive behavior approaches the plastic phase, up to the bearing strength. By assuming a homogeneous isotropic behaviour of the timber and that the bearing strength of the nailed connection does not depend on the ratio between the nail diameter and sapwood thickness, the bearing capacity of the nailed connections can be evaluated by considering the collapse mechanism with two plastic hinges in the nail shank having a fixed end in the steel plate [8]. The strength in the connection depends on the wooden bearing strength in the direction of the applied load, on the yield strength of steel and the nail diameter. The resistance of the steel chord-to-diagonal plank nailed connection is given by the following equation [8]:

$$V_{Rn} = f_h \, \phi \, L_w \quad (14)$$

$$L_w = L'_w - t/2 \quad (15)$$

$$L'_w = L \left\{ -1 + \sqrt{2 + \frac{2}{3}\frac{f_y}{f_{hw,45}} \left(\frac{\phi}{L}\right)^2 + \frac{1}{2}\left(\frac{t}{L}\right)^2} \right\} \quad (16)$$

where t and t_p are the thickness of steel plate and wooden plank, respectively, L_w is the effective length of the nail, f_y the nail yield strength, and $f_{hw,45}$ is the timber bearing strength for an inclination of the shear force of β=45° with respect to grains.

The shear strength of the existing-to-new diagonal timber plank connection depends on the timber bearing strength of the two overlaying planks, which are loaded with a different inclination of the shear action with respect to their grains [31]. The following equations express the shear strength of the existing-to-new plank nailed connection in the portion 1 (with the steel chord perpendicular to the timber joist, Fig. 3) and in the portion 2 of the diaphragm (with the steel chord parallel to the timber joist, Fig. 3), respectively:

$$V_{R,u} = f_{h,90}\Phi^2 \sqrt{\frac{2}{3}\frac{f_y}{f_{hw,90}}\left(1 + \frac{f_{h,90}}{f_{hw,45}}\right)} \frac{1}{1+\frac{f_{hw,90}}{f_{hw,45}}} \quad (17)$$

$$V_{Rn} = f_{h,0}\Phi^2 \sqrt{\frac{2}{3}\frac{f_y}{f_{hw,0}}\left(1 + \frac{f_{h,0}}{f_{hw,45}}\right)} \frac{1}{1+\frac{f_{hw,0}}{f_{h,45}}} \quad (18)$$

In Table 2, the connections stiffness and strength are listed considering a ϕ=4 mm nails, a steel yield strength of 1000 MPa, a thickness of the planks and of the steel chord equal to 22 mm and 3 mm, respectively, along with the bearing strength and the stiffness of the spruce found experimentally (Table 1).

***Table 2**. Stiffness K and strength V_{Rn} of the nailed connections (ϕ=4 mm; t=3 mm; t_p=22 mm)*

Type of connection	K [N/mm]	V_{Rn} [kN]
Steel chord-to timber diagonal plank	1516	1.93
Existing plank – diagonal plank (Portion 1)	614	1.81
Existing plank – diagonal plank (Portion 2)	890	1.95

4 TEST ON DOUBLE-PLANKING DIAPHRAGM

4.1 GEOMETRICAL AND MECHANICAL PROPERTIES OF THE SPECIMEN

A portion of a double planking diaphragm was tested at the University of Brescia with the aim to investigate its in-plane cyclic behaviour under a shear action. A square specimen having a side of 2.0 m was designed on the basis of the seismic actions in a reference two-storeys masonry building with timber floors [28] (Fig. 6). A design shear action V_{Ed}= 30kN was considered in the floor diaphragm during the seismic event. By assuming a design shear resistance $V_{rn,d}$=1.5 kN of the nailed connection, a minimum of 13 nails/m are needed to connect the perimeter steel chord to the wooden diaphragm.

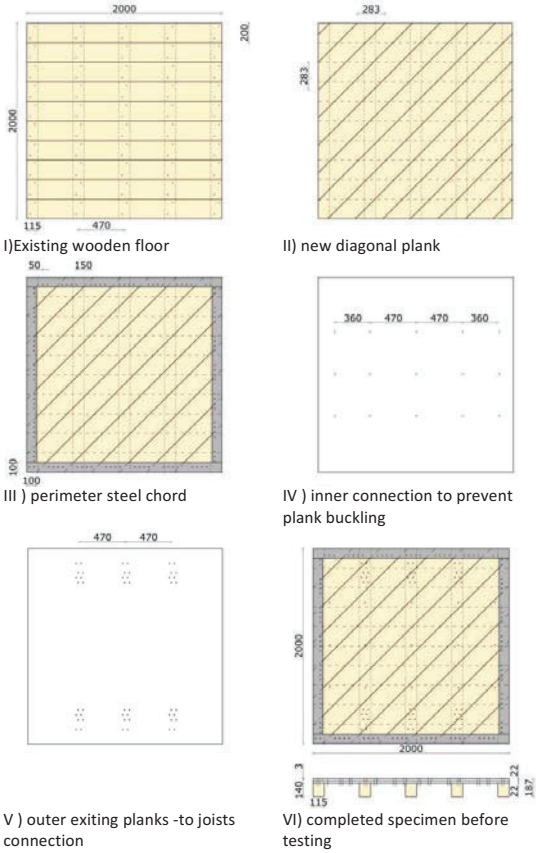

***Figure 6**: Scheme of the assembly stages of the tested specimen*

The specimen consists of spruce joists having a section of 130x110 mm^2 and a spacing of 0.50 m, over which

perpendicular timber planks (190x22 mm^2), resembling the existing floorboards, are connected by means of two 4 mm nails at each joist-to-beam joint. Overlaying diagonal planks are arranged with an inclination of α=45° with respect to the horizontal ones (Fig. 6). Along the perimeter, 3x100 mm steel plates are connected to the double-crossing planks by means of groups of four 4 mm nails (L=70mm) hammered into calibrated holes, corresponding to 13 nails/m. Each group of nails has a spacing of 150 mm; they are inserted into calibrate holes along a single row with a distance of 25 mm to the inner edge of the steel chord (Fig. 6). To avoid the bucking of the diagonal planks, inner screws (d4x70 mm) are set in correspondence of each lower joist. A group of eight nails connects each joist end to the outer horizontal plank to balance the component of the diagonal plank force acting perpendicular to diaphragm edge (Fig. 6). It should be noted that these connections activate the flexural behaviour of the outer existing planks, as already discussed in the previous section.

4.2 TEST SET UP

The testing bench consists of a rigid reaction frame within which the diaphragm specimen is placed. The sample is placed inside the testing bench so that the joists are horizontal (Figure 7). The test was carried out by imposing cyclic displacements of increasing amplitude to the upper chord of the diaphragm using a hydraulic jack fixed to the reaction frame. A steel collector welded to the upper chord of the diaphragm allowed the applied horizontal forces to be distributed as a shear flow along the specimen side. The bottom steel chord of the diaphragm was welded to the supporting beam of the bench.

To measure the specimen deformations and displacements, Linear Variable Differential Transformers (LVDTs) and potentiometers were installed as shown in Figure 7. The horizontal displacement of the diaphragm is measured by a Linear Variable Differential Transformers (LVDTs) while the force acting on the specimen is measured by a load cell placed between the reaction frame and the collector. The deformations of the diagonal planks were measured by potentiometric transducers equipped with extensions, and arranged on the main diagonals of the specimen, one parallel and the other orthogonal to the axis of the plank (diagonal "a" and “b” in Fig. 7). Finally, several potentiometric transducers were placed along two orthogonal sides of the panel, for a continuous acquisition of relative slip between the perimeter steel chord and the diagonal planks. In particular, along two sides of the specimen, three pairs of transducers were arranged to record the relative in plane displacements (slip δ) between the perimeter steel chord and the diagonal planks (detail in Figure 7).

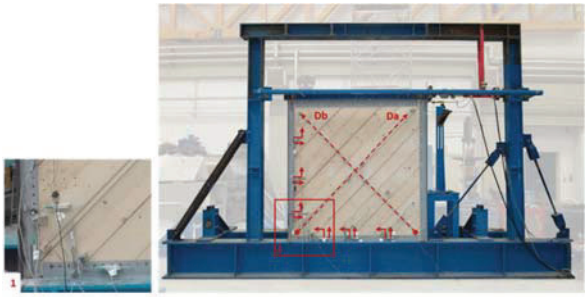

***Figure 7**: Details of the test set up.*

4.3 EXPERIMENTAL RESULTS

Eleven symmetrical cycles of increasing amplitude were applied to the top of the specimen up to a 0.5% drift (corresponding to a lateral displacement η of 10 mm) when a significant damage in the nailed perimeter connections between the steel chord and the diagonal planks was observed. The test started with two cycles with 0.25 mm and 0.5 mm top displacement, respectively, followed by five cycles having an increment of 0.5 mm up to 3.0 mm amplitude. Finally, the last four cycles had an amplitude increment of 2.0 mm.

In Figure 8 the cyclic behaviour of the tested diaphragm is shown in term of shear force (V) versus applied drift (d_r). A symmetrical response of the diaphragm was observed, with an anelastic behaviour beyond a drift of 0.025%, corresponding to a lateral displacement of 0.5 mm and a shear action of 5 kN. The elastic stiffness measured for a drift of 0.025% was K_d=12 kN/mm.

For an applied load equal to the design shear action in the diaphragm of the reference building (V_d=30 kN), a top displacement of 4.55 mm was measured, corresponding to a drift of 0.23%. The secant shear stiffness of the wooden diaphragm is therefore equal to K_d=6.6 kN/mm. The behavior was mainly stable up to the design shear action V_d=30 kN, whilst the failure of the connections at the specimen corners was observed for V=1.5V_d. Then, the test was interrupted to avoid damage in the steel chords.

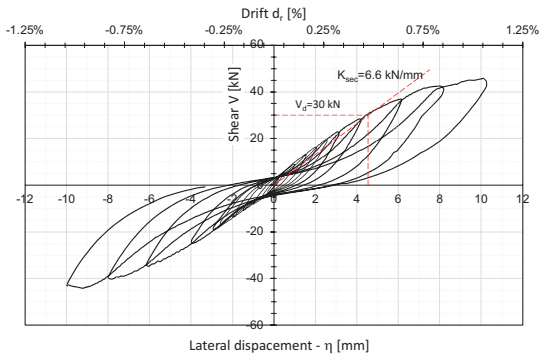

***Figure 8**: Test results: horizontal shear load (V) vs. drift (d_r)*

The measured relative slips between the outer steel chord and the inner web of the diaphragm are shown in Figure 9. It should be noted that the slip parallel to the perimeter

https://doi.org/10.52202/069179-0049

chord (black curves) increases with the applied load, but it gradually reduces along the chord proceeding from the left end (H1), where the longest diagonal plank is located, towards the right corner (H3), where the planks are shorter. A similar trend was measured for the relative slip perpendicular to the perimeter chord (red curves in Figure 9), which shows the maximum value in correspondence to the device (V1) placed on the left longest diagonal plank. Similar values of the relative slips between the outer steel chord and the diaphragm web panel were measured along the vertical left side of the specimen [32]. Based on the experimental results, it can be stated that shear flow between the web and the outer chords of the diaphragm is not uniform, as usually assumed in the current design practice, but it has a linear trend with the maximum value at the corner, where the longest diagonal plank is placed, as shown in Figure 10.

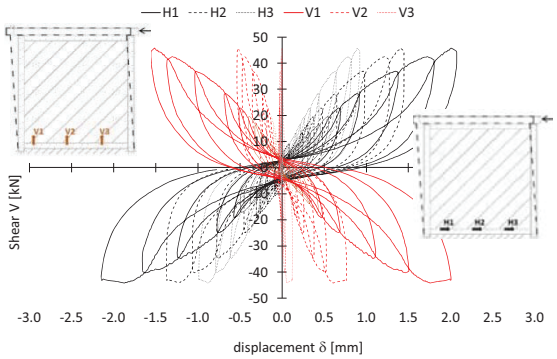

***Figure 9**: Test results: horizontal shear load (V) vs. slip (δ) between the perimeter steel chord and the inner wooden web*

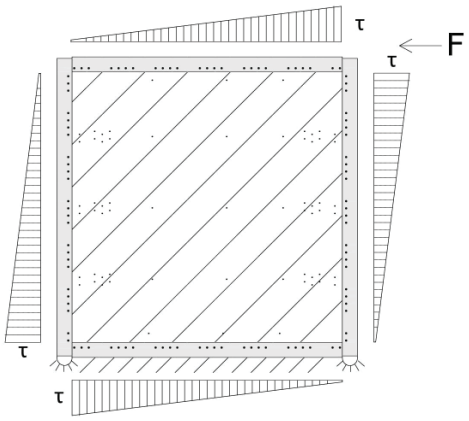

***Figure 10**: Scheme of the distribution of the shear flow along the edges of the diaphragm web.*

5 CONCLUSION

In the seismic retrofit of existing masonry buildings, the global, box-like structural behavior may be guaranteed through the correct organization of the floor diaphragms and their connections to the masonry walls.

Aim of this research is to study the in-plane shear response of wooden diaphragm made with the double planking technique. The proposed technique is characterized by the use of new diagonal planks overlaying the existing planks (which are laid perpendicular to the floor joist). The in-plane shear resisting mechanism of the floor diaphragm is guaranteed by the nailed connections between the perimeter steel chords and the double-crossed overlaying planks. This double planking technique is easy to apply and allows for a significant reduction of the number of nailed connections with the respect to the traditional double crossed timber planks with orthogonal timber boards.

The research focuses on the role and the arrangement of the connections on the transmission of actions from the perimetral chords to the inner web of the diaphragm. An analytical model is proposed to assess the stiffness and the strength of these connections.

The experimental results of a quasi-static cyclic test on a portion of the diaphragm subjected to in-plane shear action show a stable behaviour of the diaphragm up to a load 1.35 times higher than the design shear action. Furthermore, the test results highlight a linear trend of the shear stresses along the perimeter steel chords, contrary to the usual design practice that assumes a uniform distribution.

The shear flow distribution along the edges of the diaphragm is mainly governed by the stiffness of the perimeter nails connections, which is much lower than the axial stiffness of the diaphragm core planks. As a result, the shear flow along the edges of the diaphragm web tends to concentrate where the panel undergoes larger deformation, that is in correspondence of longer planks of the diaphragm core.

ACKNOWLEDGMENTS

The study presented in the paper was partly carried out within the research activities carried out in the frame of the 2022–2023 ReLUIS Project—WP5 funded by the Italian Department of Civil Protection. Note that the opinions and conclusions presented by the authors do not necessarily reflect those of the funding entity. The assistance of Eng. A. Molinari and Eng. M. Rizzi during the experimental campaign is gratefully acknowledged.

REFERENCES

[1] Lourenço, P. B., Mendes, N., Ramos, L. F., and Oliveira, D. V.. Analysis of Masonry Structures Without Box Behavior. International Journal of Architectural Heritage, 5, 369–382, 2011.

[2] Benedetti, D., Benzoni, G., & Parisi, M. A. (1988). Seismic vulnerability and risk evaluation for old urban nuclei. Earthquake Engineering & Structural Dynamics, 16(2):183-201, 1988.

[3] Tomaževič M., 1989. Some aspects of structural strengthening of historic buildings in urban and rural nuclei against earthquakes. *Eur Earthq Eng* 1(1989):19–40

[4] D'Ayala, D., & Speranza, E.. Definition of collapse mechanisms and seismic vulnerability of historic

masonry buildings. *Earthquake Spectra*, 19(3), 479-509. doi:10.1193/1.1599896, 2003.
[5] Giuriani E., Marini A., 2008. Wooden roof box structure for the anti – seismic strengthening of historic buildings, *International Journal of Architectural Heritage* – Conservation, Analysis and Restoration, vol. 2.
[6] D.M. 14 gennaio 2008, Nuove norme tecniche per le costruzioni.
[7] Piazza M., Turrini G. 1983. Una tecnica di recupero statico dei solai in legno, *Recuperare*, 5, 6, 7, Milano.
[8] Gelfi, P., Giuriani, E., Marini, A., Stud shear connection design for composite concrete slab and wood beams. *Journal of Structural Engineering*, 128(12), 1544-1550, 2022.
[9] Marini, A., Cominelli, S., Zanotti, C., & Giuriani, E. 2018. Improved natural hydraulic lime mortar slab for compatible retrofit of wooden floors in historical buildings. *Construction and Building Materials*, *158*, 801-813.
[10] Gelfi, P., and E. Giuriani. 2000. Studio sperimentale del comportamento di travi miste legno-acciaio con connettori a piolo. *V Workshop italiano sulle costruzioni composte*-Palermo. In Italian.
[11] Nowak T.P., Jasiénko J.J., Czepiz D., 2013, Experimental tests and numerical analysis of historic bent timber elements reinforced with CFRP strips, *Constr. Build.* Mater. 40 197–206.
[12] Giuriani E, Marini A, Plizzari G. Experimental behaviour of stud connected wooden floors undergoing seismic action. Restoration of Building and Monuments;11(1):3–24, 2005
[13] Valluzzi M.R., Garbin E., Modena C., Flexural strengthening of timber beams by traditional and innovative techniques, *J. Build.* Appraisal 3 (2) (2007) 125–143, 2007.
[14] Branco, J. M., Kekeliak, M., and Lourenço, P. B., 2014. In- Plane Stiffness of Traditional Timber Floors Strengthened with CLT. *Materials and Joints in Timber Structures*. Ed. by S. Aicher, H. W. Reinhardt, and H. Garrecht, 725–737.
[15] Gubana, A., State-of-the-Art Report on high reversible timber to timber strengthening interventions on wooden floors. *Construction and Building Materials*, 97, 25–33, 2015.
[16] Gubana, A., & Melotto, M. (2018). Experimental tests on wood-based in-plane strengthening solutions for the seismic retrofit of traditional timber floors. *Construction and Building Materials*, 191, 290-299.
[17] Corradi, M., Speranzini, E., Borri, A., and Vignoli, A., 2006. In-plane shear reinforcement of wood beam floors with FRP. Composites Part B: *Engineering* 37, 310–319.
[18] Valluzzi, M. R., Garbin, E., dalla Benetta, M., & Modena, C. (2013). Experimental characterization of timber floors strengthened by in-plane improvement techniques. In *Advanced Materials Research* (Vol. 778, pp. 682-689). Trans Tech Publications.
[19] Gattesco, N. and Macorini, L., 2014. In-plane stiffening techniques with nail plates or CFRP strips for timber floors in historical masonry buildings. *Construction and Building Materials*, 58, 64–76.
[20] Brignola, A., Pampanin, S., and Podestà, S., Experimental Evaluation of the In-Plane Stiffness of Timber Diaphragms. *Earthquake Spectra*, 28(4), 1687– 1709, 2012.
[21] Peralta, D. F., Bracci, J. M., and Hueste, M. B. D., Seismic behavior of wood diaphragms in pre-1950s unreinforced masonry buildings. *Journal of Structural Engineering* 130(12), 2040–2050, 2004.
[22] Wilson, A., Quenneville, P., and Ingham, J. M., 2014. In-plane orthotropic behavior of timber floor diaphragms in unreinforced masonry buildings. *Journal of Structural Engineering*, 140(1).
[23] Piazza M, Baldessari C, Tomasi R., 2008. The role of in-plane floor stiffness in the seismic behaviour of traditional buildings. In: *Proceedings of the 14th world conference on earthquake engineering*, Beijing,
[24] Parisi, M. A., & Piazza, M., Seismic strengthening and seismic improvement of timber structures. *Construction and Building Materials*, 97, 55-66, 2015.
[25] Kallioras, S., Guerrini, G., Tomassetti, U., Marchesi, B., Penna, A., Graziotti, F., & Magenes, G. Experimental seismic performance of a full-scale unreinforced clay-masonry building with flexible timber diaphragms. *Engineering Structures*, 161, 231-249, 2018.
[26] Felicetti R., Gattesco N., Giuriani E., Local phenomena around a steel dowel embedded in a stone masonry wall. *Mater Struct* 30:23, 1997
[27] Marini, A., Giuriani, E., Belleri, A., Cominelli, S., Dowel connections securing roof-diaphragms to perimeter walls in historic masonry buildings and in-field testing for capacity assessment. *Bulletin of Earthquake Engineering*, 16(9), 4001-4025, 2018
[28] Giuriani E., Metelli G., Cominelli S., Marchina E., Diaframmi di piano antisismici di impalcati lignei realizzati con doppio assito. *ReLUIS-2017-PR4_Allegato_05-UR_UNI-BS*, 2017.
[29] Giuriani E., 2012. Consolidamento degli edifici storici. UTET Scienze Tecniche.
[30] EN 383:2007. Timber Structures - Test methods - Determination of embedment strength and foundation values for dowel type fasteners, Brussels, Belgium, CEN, 2007.
[31] EN 1995-1-1:2004. Design of timber structures Part 1-1: general-common rules and rules for building. Brussels, Belgium: CEN, European Committee for Standardization, 2004.
[32] Metelli G., Giuriani E., Cominelli S., Marini A., Feroldi F., Marchina E. e Rizzi M., 2018. Diaframmi di piano antisismici di impalcati lignei realizzati con doppio assito: risultati sperimentali e ruolo delle connessioni tra assito e correnti di bordo sul comportamento a taglio del diaframma. *ReLUIS-2018-PR4_Allegato UR_UNI-BS*.

https://doi.org/10.52202/069179-0049

World Conference on Timber Engineering Oslo 2023

A NEW APPROACH TO DETERMINE AND EVALUATE THE POISSON´S RATIO OF WOOD

Klara Winter[1], Roland Maderebner[2], Philipp Dietsch[3]

ABSTRACT: Modern timber engineering requires increasing application of the finite element method (FEM). In such analyses, the elastic constants including the Poisson´s ratios are required. The latter have mostly been neglected so far, since these vary to a great degree in related literature. Hence, an experimental method based on compression tests was developed and benchmarked on numerous preliminary tests in order to determine the Poisson´s ratios on spruce wood (Picea Abies). For the first time, the extended measurement uncertainty was taken into account. On the basis of these values, a comparison with values from literature was conducted. Several observations indicate that, in addition to the wood properties, the load application as well as the test setup have a significant influence on the Poisson´s ratios. In summary, all obtained values lie in the medium range of the literature values. Consequently, the developed test method for determining the Poisson´s ratios is considered to be suitable. In addition, an expanded Poisson's ratio was determined taking into account the measurement uncertainty in order to obtain a symmetrical compliance matrix.

KEYWORDS: Wood, Spruce (Picea Abies), Poisson´s Ratios, FEM, Elastic behaviour, Measurement uncertainty

1 INTRODUCTION

For numerical calculation of increasingly complex timber structures and three-dimensional timber connections using the finite element method (FEM), the Poisson´s ratios are required. When loading a body in its axial direction this measure indicates the ratio between lateral (ε_l) and axial strain (ε_a). The ratios published so far, vary greatly in their order of magnitude. Therefore, the Poisson´s ratios are often neglected in numerical calculations. Moreover, numerous studies leave uncertainty, which and why a certain test method was applied.

In the context of this work, an own test procedure was developed to clarify, what influences the Poisson´s ratios and what causes the great deviation in the published values. Within this process, the most suitable out of three available measurement techniques was selected. Depending on the measurement technique and the test procedure the extended measurement uncertainty was calculated as well. Thus, a range, in which the true mean value of the determined Poisson´s ratio lies can be stated with a confidence of approx. 95 %. Moreover, computer tomography (CT) measurements were conducted to verify the linear elastic range.

Although there are several different wood species, this study only refers to spruce wood, as this, together with fir, makes up the largest share of construction timber in Central Europe.

Preliminary literature on determining the Poisson's ratios predominantly applied tensile tests (e.g. [1]-7]). For the sake of simplicity and as is stated in [7] and [8] the load type was assumed to have no direct influence on the Poisson's ratio. Only compression tests were performed within this work.

2 MATERIALS AND METHODS

2.1 WOODEN SPECIMENS

All measurements on wood were performed on spruce wood (Picea). The source of the wood was near Iseltal in Austria. The specimens were conditioned in a climate chamber at a temperature of (20 ± 1)°C and a relative humidity of (65 ± 3) % according to [9] and [10]. A total, of three different specimen groups (L, R and T) were prepared in order to perform the preliminary tests and main tests for all six Poisson´s ratios. To achieve the most accurate results, the fibre orientation should be as parallel to the specimen axes as possible. Therefore, the maximum specimen length was examined on the available wood, without having to accept a strong deviation of the fibre orientations. This resulted in specimen dimensions of l x h x b = 100 x 30 x 30 mm³ (Figure 1).

The specimen surfaces were sanded to straighten protruding fibres and saw edges. A total of a 150 specimens per specimen group were manufactured. In this way, it was ensured that enough test specimens were

[1] Klara Winter, Technical University of Munich, Germany, klara.winter@tum.de
[2] Roland Maderebner, Institute for Construction and Material Science, Unit of Timber Engineering, University of Innsbruck, Austria, roland.maderebner@uibk.ac.at
[3] Philipp Dietsch, Timber Structures and Building Construction, Karlsruhe Institute of Technology, Germany, dietsch@kit.edu

https://doi.org/10.52202/069179-0050

available for the preliminary tests and the 20 specimens for each Poisson´s ratio for the main tests.

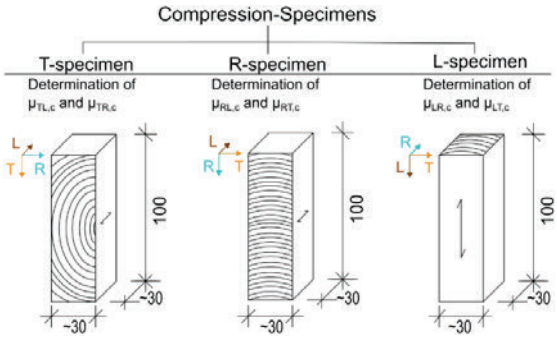

Figure 1: *Different specimen groups including dimensions in [mm]*

The test specimens had further to be pre-drilled on two opposite sides to realize the measurements using DD1 displacement and strain transducers (Figure 2).

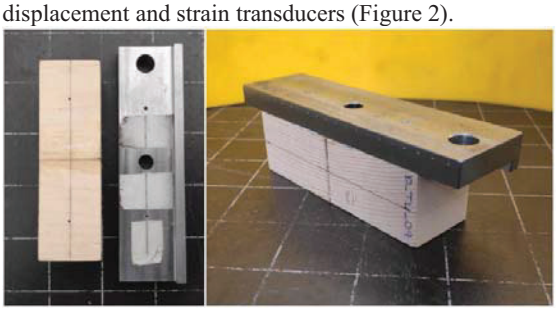

Figure 2: *Metal drilling template on a wooden specimen; left: top view, right: side view*

2.2 ALUMINIUM SPECIMEN

In addition to the wooden test specimens, an aluminium specimen was prepared. This was used as part of the preliminary tests to select the measurement. It was made of the material *EN AW-2007-T4* and its dimensions were l x h x b = 100 x 30 x 30 mm³.
Like the wooden specimens, the aluminium specimen also had to be pre-drilled for the measurements using the strain gauged based DD1 displacement and strain transducers.

2.3 MEASUREMENT TECHNIQUE

The measurement technique was chosen based on comparative measurements preliminary to the main tests. In this regard, the most suitable out of three available measurement techniques including strain gauges, strain gauged based DD1 displacement and strain transducers and videoextensometry was to be selected. The repeatability was investigated by means of the aluminium specimen under compression. Aluminium was chosen as it was expected to not change its properties within the elastic range. The specimen was loaded eight times with each measurement technique. In between the individual loadings the aluminium specimen was removed and inserted into the testing machine again in order to simulate the subsequent test sequence on the wooden specimens as equal as possible. All measurement techniques led to nearly the same average Poisson´s ratio of μ_{alu} = 0,356 but showed significantly different scattering (Figure 3).

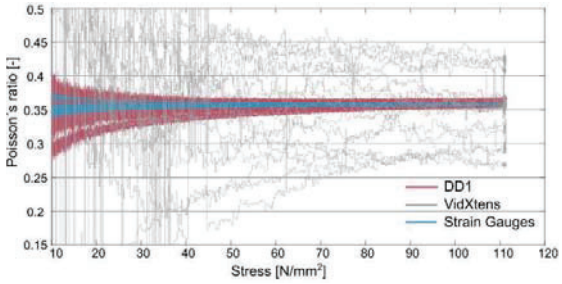

Figure 3: *Comparison of the measurement signals obtained with the three measurement techniques on the aluminium specimen*

The DD1 displacement and strain transducers showed a comparably good repeatability with a standard deviation of 5,33·10^{-3} and a CoV of 1,49 %. As these also required considerably less time for specimen preparation, this technique was chosen for all further measurements. In case of the measurements determining μ_{RL} and μ_{TL} a combination of both DD1 displacement transducers and strain gauges was applied. Reason for this are the significantly smaller lateral strains in grain direction that cause higher signal noise.

2.4 TEST SETUP USING DD1 DISPLACEMENT AND STRAIN TRANSDUCERS

A *Shimadzu Autograph* with an *EDC 580* control unit from *DOLI Elektronik GmbH* was used for all measurements. A spherical cap and a steel cube on top of the wooden specimen ensured uniform load application within all tests (Figure 4).

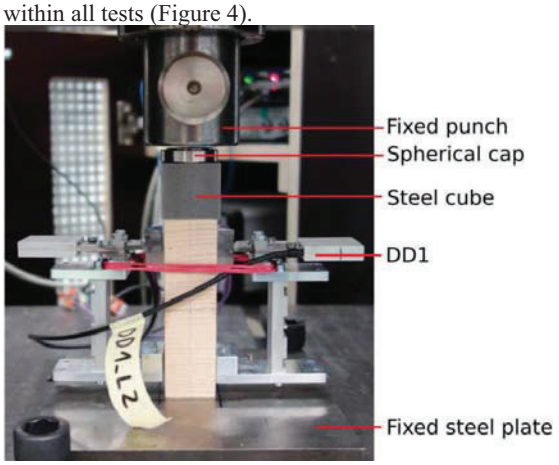

Figure 4: *Load application and strain measurement using DD1 displacement and strain transducers*

The lateral displacement in R- and T-direction could only be recorded using one DD1 displacement and strain transducer. In order to measure the axial displacement two DD1 were attached to opposite sides of the specimen (Figure 5). Thus, possible bending effects could be eliminated. The axial DD1 displacement transducers were attached to the specimen using small nails. Further, two

https://doi.org/10.52202/069179-0050

metal prisms were attached to the upper part of the specimen on opposite sides using small nails as well. The probe tips of the displacement transducers for the axial measurement were in contact with these. The distance between the nails and thus the initial length l was set to 60 mm.

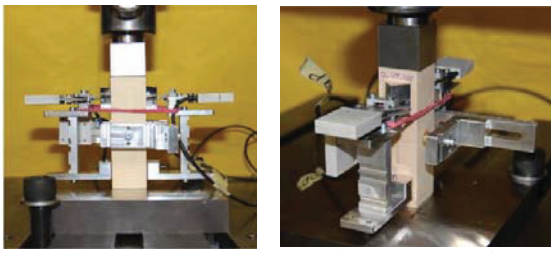

Figure 5: *Test setup with DD1 displacement and strain transducers on wooden specimen; left: Front view; right: Oblique view*

Figure 6 shows the test setup for measuring μ_{RL} and μ_{TL}. For given reasons, two strain gauges were adhered on opposite sides of the specimen in order to measure the lateral displacement in grain direction.

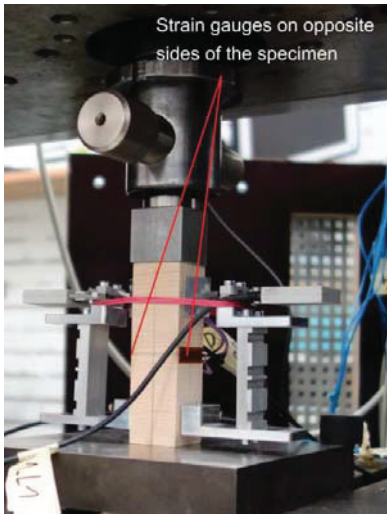

Figure 6: *Measurement configuration used for determining μ_{RL} and μ_{TL}*

2.4.1 Test procedure

All specimens were tested within one hour after removal from the climate chamber, as prescribed in [11]. Preceding the measurement, the specimens were prepared in the measurement room and the duration of the test itself was about 20 minutes. All tests were load-controlled, so that the theoretical compressive strength $F_{c,max}$ would be reached in approx. 90 seconds [9]. Thus, the influence of creep deformations on the Poisson´s ratio are eliminated. The load was applied in such a way that the test specimens were only loaded in their linear-elastic range. Hence, the upper load limit within the preliminary tests was set to 30 % of the compressive strength ($f_{c,90,k}$ resp. $f_{c,0,k}$) given in [12] for spruce wood of class C24. The maximum load applied within the main tests is derived from the CT verification tests described in Section 3.1.3. All measurements were load controlled and started at a load level of 20 N.

Within the determination of the Young´s modulus on concrete, this is loaded in several cycles. Thus, an initial and a stabilized Young´s modulus is defined [13]. Following this procedure, measurements consisting of numerous loading and unloading cycles were performed.

2.4.2 Three-dimensional Hooke´s law for orthotropic materials

The three-dimensional Hooke´s law is based on the assumption that stress σ_{ij} and strain ε_{kl} are linearly related. To describe the three-dimensional elastic behaviour of orthotropic materials 12 compliance coefficients S are necessary [14].

Furthermore, it is valid for orthotropic materials that shear stresses that act in the main direction do not generate normal strains. Normal stresses do not generate shear strains either. Moreover, shear strains are only generated by shear stresses in the same plane. [15] Several compliance parameters of orthotropic materials are therefore zero and the three-dimensional Hooke´s law can be given in the following compliance form:

$$\begin{pmatrix} \varepsilon_1 \\ \varepsilon_2 \\ \varepsilon_3 \\ \gamma_{23} \\ \gamma_{13} \\ \gamma_{12} \end{pmatrix} = \begin{bmatrix} S_{11} & S_{12} & S_{13} & & & \\ S_{12} & S_{22} & S_{23} & & & \\ S_{13} & S_{23} & S_{33} & & & \\ & & & S_{44} & & \\ & & & & S_{55} & \\ & & & & & S_{66} \end{bmatrix} \cdot \begin{pmatrix} \sigma_1 \\ \sigma_2 \\ \sigma_3 \\ \tau_{23} \\ \tau_{13} \\ \tau_{12} \end{pmatrix} \quad (1)$$

where ε = strains [-], γ = shear strains [-], σ = normal stresses [N/mm²], τ = shear stresses [N/mm²], S_{ii} for i = 1,2,3: Strain numbers [mm²/N], S_{ii} for i = 4,5,6: Shear strain numbers [mm²/N], S_{ij} for i,j = 1,2,3: Poisson´s ratios; $i \neq j$ [mm²/N].

Further, the compliance parameters can be replaced by the engineering parameters Young´s modulus E, Shear modulus G and Poisson´s ratio μ. The indices can be replaced with the common labels L, R and T. Hooke´s law then takes the form of Equation (2):

$$\begin{pmatrix} \varepsilon_{LL} \\ \varepsilon_{RR} \\ \varepsilon_{TT} \\ \gamma_{RT} \\ \gamma_{LT} \\ \gamma_{LR} \end{pmatrix} = \begin{bmatrix} \frac{1}{E_L} & -\frac{\mu_{RL}}{E_R} & -\frac{\mu_{TL}}{E_T} & & & \\ -\frac{\mu_{LR}}{E_L} & \frac{1}{E_R} & -\frac{\mu_{TR}}{E_T} & & & \\ -\frac{\mu_{LT}}{E_L} & -\frac{\mu_{RT}}{E_R} & \frac{1}{E_T} & & & \\ & & & \frac{1}{G_{RT}} & & \\ & & & & \frac{1}{G_{LT}} & \\ & & & & & \frac{1}{G_{LR}} \end{bmatrix} \cdot \begin{pmatrix} \sigma_{LL} \\ \sigma_{RR} \\ \sigma_{TT} \\ \tau_{RT} \\ \tau_{LT} \\ \tau_{LR} \end{pmatrix} \quad (2)$$

It is only applicable if the stresses and deformations are referred to the main axes [16]. If the main axes of the wood deviate from the reference system coordinate transformations as described e.g. in [14] and [17] must be applied.

https://doi.org/10.52202/069179-0050

The compliance matrix itself is symmetric. Due to this symmetry condition, only nine of the 12 parameters are independent of each other. It applies:

$$\frac{\mu_{LR}}{E_L} = \frac{\mu_{RL}}{E_R} \tag{3}$$

$$\frac{\mu_{LT}}{E_L} = \frac{\mu_{TL}}{E_T} \tag{4}$$

$$\frac{\mu_{RT}}{E_R} = \frac{\mu_{TR}}{E_T} \tag{5}$$

Further requirements for the compliance matrix are given in [16] and [2].

2.4.3 Calculation of the Poisson´s ratio

The Poisson´s ratio describes the lateral contraction/elongation (ε_l) of a body as it elongates or contracts normal to the force (ε_a) (Equation (6)). Thus, it is also called passive deformation. The Poisson´s ratio is always negative since compression is defined as negative tension.

$$\mu_{al} = -\frac{\varepsilon_l}{\varepsilon_a} \tag{6}$$

2.4.4 Calculation of the Young´s modulus

The Young´s moduli $E_{i,ij}$ were examined on the basis of the tenth loading and unloading cycle between 20 % and 55 % of the estimated upper load limit $F_{c,max,est}$ using Equation (7):

$$E_{i,ij} = \frac{(\sigma_{i,55} - \sigma_{i,20}) \cdot 60mm}{\Delta l_{i,55} - \Delta l_{i,20}} \tag{7}$$

where *i,j* = Anatomical directions resp. load directions, each can attain independently L,R or T [-], $\sigma_{i,20}$, $\sigma_{i,55}$ = stress at 20 % resp. 55 % of $F_{c,max,est}$ when loaded in i-direction [N/mm²] , $\Delta l_{i,20}$, $\Delta l_{i,55}$ = Axial displacement in i-direction at 20 % resp. 55 % of $F_{c,max,est}$.

2.4.5 Data processing

Within the scope of this work, the Poisson's ratios and Young´s moduli were determined on the basis of several loading and unloading paths. However, due to the dissipated energy during specimen deformation, the paths individually would lead to varying results. This effect is called hysteresis [18]. Hence, these were averaged. Figure 7 shows this effect by means of a randomly selected loading and unloading path of a measurement on the aluminium specimen. This specimen was loaded and unloaded once in the stress range between 60 to 105 N/mm². The red path, which is then used for further evaluation represents the average of the loading and the unloading path.

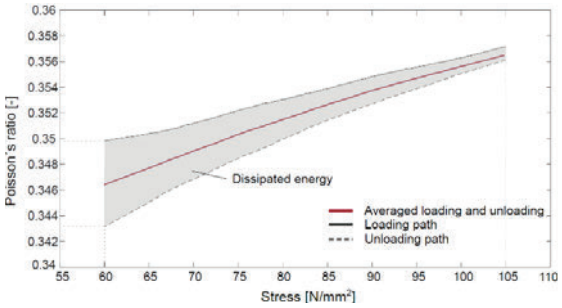

Figure 7: *Hysteresis effect on the basis of a loading and unloading path of the aluminium specimen measured with the DD1 displacement and strain transducers*

Those measurements that still exhibited signal noise after averaging were further denoised, using the *Savitsky-Golay* filter.

2.4.6 Determination of the measurement uncertainty

When specifying a physical variable, it is important to include the measurement uncertainty *u*(x), as all measurement results include errors. The calculation of the measurement uncertainty is described here in detail on the basis of the Poisson's ratio. However, the measurement uncertainty for the Young´s modulus was calculated according to the same systematic.

A physical variable can be given with $\bar{x} \pm s_m$ (absolute specification) or $\bar{x} \pm \frac{s_m}{\bar{x}}$ (relative specification), where s_m is the measurement uncertainty or the standard error.

However, the average Poisson´s ratio does not result from a direct averaged measurement but from a function of several, as is shown in Equation (8). Therefore, the Poisson´s ratio depends on the average lateral displacement Δb, the average axial displacement Δl and both original average lengths l and b ($\mu_{lb} = f(\Delta b; \Delta l; b; l)$).

$$\mu_{lb} = -\frac{\Delta b/b}{\Delta l/l} = -\frac{\Delta b \cdot l}{\Delta l \cdot b} \tag{8}$$

Hence, the uncertainty of the Poisson´s ratio requires the calculation of a combined uncertainty using the *Gaussian error propagation law*. Therefore, all individual variables need to be normally distributed [19]. Using the *Shapiro-Wilk-test* this was checked within this work. However, each individual variable given in Equation (8) is in turn also influenced by several factors. In case of the specimen width *b* for example, the inaccuracy of the calliper and the staff (the lab assistants who measure and prepare the specimens) already influence the variable. Hence, a combined standard error must already be determined for each individual variable included in Equation (8).

The general *Gaussian error propagation law* is given with:

$$u(X) = \sqrt{\left(\frac{\delta X}{\delta y_i} \cdot u(y_i)\right)^2 + \cdots + \left(\frac{\delta X}{\delta y_k} \cdot u(y_k)\right)^2} \tag{9}$$

https://doi.org/10.52202/069179-0050

To determine the combined standard uncertainty of the Poisson´s ratio, this equation takes the following form when formulating the partial derivatives:

$$u(\mu) = \sqrt{\left(-\frac{l \cdot \Delta b}{\Delta l \cdot b^2} \cdot u(b)\right)^2 + \left(\frac{l}{\Delta l \cdot b} \cdot u(\Delta b)\right)^2 + \left(\frac{\Delta b}{\Delta l \cdot b} \cdot u(l)\right)^2 + \left(-\frac{l \cdot \Delta b}{b \cdot \Delta l^2} \cdot u(\Delta l)\right)^2} \quad (10)$$

The extended measurement uncertainty is calculated by multiplying the measurement uncertainty from Equation (10) by the coverage factor 1,96, which is often round up to 2,0.

$$U(\mu) = u(\mu) \cdot 2 \quad (11)$$

By indicating the respective extended measurement uncertainty of each test series a range of values is given. With a certainty of 95 % the true average Poisson´s ratio lies within this range.

3 RESULTS AND DISCUSSION

3.1 PRELIMINARY TESTS

3.1.1 Hygric behaviour of wood as an influence on the Poisson´s ratio

First tests consisted of 15 loading and unloading cycles. However, no convergence of the averaged Poisson´s ratios was noticeable. The hygric behaviour of wood was considered to be the reason for this since the specimens were measured in another climate after being conditioned at 20°C and 65% r.h. . In order to verify this, comparative tests were performed.

Therefore, six μ_{RT}-specimens were stored in two different climates. Three in the climatic chamber and three in the room, where the testing machine was located. The temperature in this measurement room was around 21°C with a relative humidity of approx. 40 %.

In total three comparative tests were performed. Each measurement included two specimens, one that was conditioned in the climatic chamber (CC-specimen) and one that was conditioned in the measurement room (MR-specimen).

All three comparative tests showed very similar results. Figure 8 exemplarily shows one of the resulting graphs.

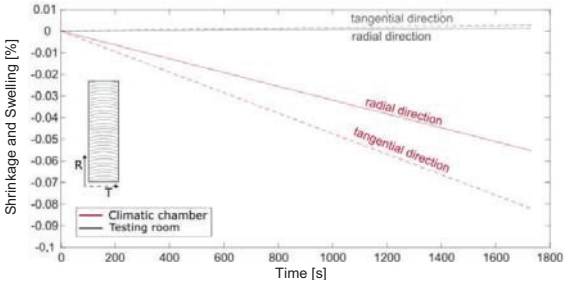

Figure 8: *Shrinkage and swelling deformations in [%] on the basis of comparative measurements*

The specimens conditioned in the climatic chamber show a significantly greater shrinkage in contrast to the specimens conditioned in the measurement room. On the basis of these comparative tests, it is apparent that the change in the ambient climate has a considerable impact measured within one hour after removal from the climatic chamber, as demanded in [11].

Since it was not possible to move the testing machine to the climatic chamber within the scope of this work, all specimens were conditioned in the measurement room.

Figure 9 shows the averaged paths of 15 loading and unloading cycles of two μ_{RT}-specimens conditioned in the measurement room and of one specimen conditioned in the climate chamber. This clearly shows that testing the specimens in the same climate in which these where conditioned leads to a significantly lower dispersion. Hence, the shrinkage and swelling effects on the Poisson´s ratios could be eliminated to a certain degree. Further, it is evident that the Poisson´s ratios of the specimens conditioned and tested in the measurement room are more or less constant over the respective stress range and therefore already show a somewhat linear elastic behaviour. Moreover, a stronger convergence of the cycle paths from the tenth cycle onwards was noticeable for all specimen orientations.

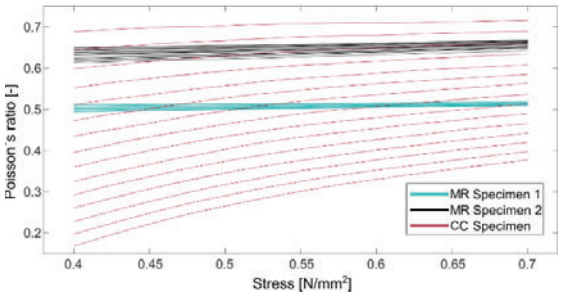

Figure 9: *μ_{RT}-measurements in relation to the stress on the basis of two specimens preconditioned in the measurement room*

3.1.2 Impact of creep deformations on the Poisson's ratio

Subsequently it was to be checked if creep deformations had an influence on the test procedure. For this reason, times of constant load of 20 seconds between loading and unloading were included. These were anticipated to lead to a faster convergence of the paths. Therefore, three specimens already tested without times of constant load were tested again including times of constant load within 15 cycles. In addition, three, yet untested specimens were tested including times of constant load. Figure 10 shows the resulting averaged paths for each specimen over the applied stress range.

The specimens measured for the second time including times of constant load show significantly smaller Poisson´s ratios than before. This is not inevitably due to creeping but could also be the result of compaction of the specimen during the previous measurements. However, this would also indicate that the linear elastic range had already been exceeded.

https://doi.org/10.52202/069179-0050

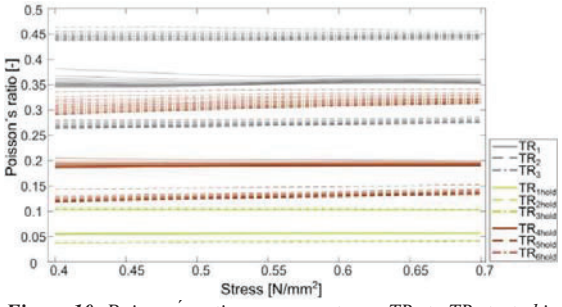

Figure 10: *Poisson´s ratios μ_{TR} over stress; TR_1 to TR_3 tested in 15 load cycles without times of constant load; $TR_{1,hold}$ to $TR_{3,hold}$ tested with times of constant load; $TR_{4,hold}$ to $TR_{6,hold}$ not previously loaded specimens tested with times of constant load*

Considering the specimens that were not previously loaded ($TR_{4,hold}$ to $TR_{6,hold}$) the Poisson´s ratios are approximately 30 % lower ($\mu_{mean,4\text{-}6,hold} = 0{,}213$) compared to the specimens tested without constant loads ($\mu_{mean,1\text{-}3} = 0{,}358$). The latter Poisson's ratios measured without times of constant load fit better with the Poisson's ratios measured on spruce wood in previous literature (e.g. [3],[4]).

In conclusion, including times of constant load appears to have an influence on the Poisson´s ratios. However, only few tests were carried out here including times of constant load. Similar tests in earlier literature are neither found for compression nor tensile loads. Therefore, the observed results would need to be verified in future studies using a significantly higher number of test specimens. Within this work, times of constant load are omitted.

3.1.3 Verification of the linear elastic range

A difficulty often mentioned in previous literature, regarding the Poisson´s ratios, was the occurring asymmetry. Therefore, the assumed linear elastic range was checked prior to the main tests. In order to determine if micro cracks with a width of 10-20 µm occur in the assumed linear elastic range, the specimens were scanned before and after loading in a CT-scanner. Due to dimension restrictions only the middle part (30 x 30 x 30mm³) of the specimens was examined. Figure 11 explains the schematic procedure of the CT-measurements. In order to estimate $F_{c,max}$ two "twin" specimens for each specimen group were taken from the same wooden log at adjacent locations and conditioned in the climate chamber. One of the twins was then loaded till failure. The other twin was used to detect occurring micro cracks following the procedure shown in Figure 11. In total, due to availability reasons of the CT-scanner, only three specimens were tested.

The comparison of individual sections of the generated 3D model, exemplarily shown in Figure 12, showed no noticeable changes at the micro level after loading the specimens up to 60 % of $F_{c,max}$ in all three anatomical directions.

In addition, due to availability reasons, only one specimen per load direction was examined. Concluding, the results obtained suggest that the linear elastic range is not exceeded up to 60 % of $F_{c,max}$. However, this needs to be verified on the basis of further measurements including a larger number of specimens and if possible, scanning a bigger part of the specimens.

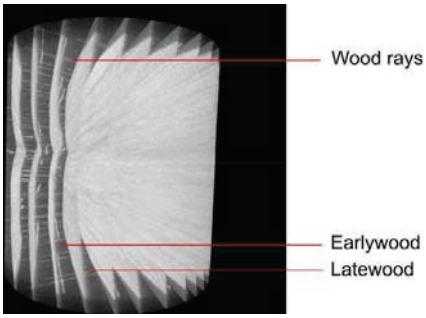

Figure 12: *Exemplary CT-image of the 3D model of the specimen loaded in the tangential direction*

3.1.4 Preliminary tests – Conclusion

The preliminary tests resulted in the following conclusions that were applied within the test procedure of the main tests.

- Conditioning of the specimens in the measurement room as the hygroscopicity of wood makes it impossible to measure the Poisson´s ratios
- The linear elastic range is verified for all three anatomical directions up to 60 % of $F_{c,max,est.}$
- The Poisson´s ratio of each test specimen is evaluated in the range between 20 % and 55 % of the respective applied load

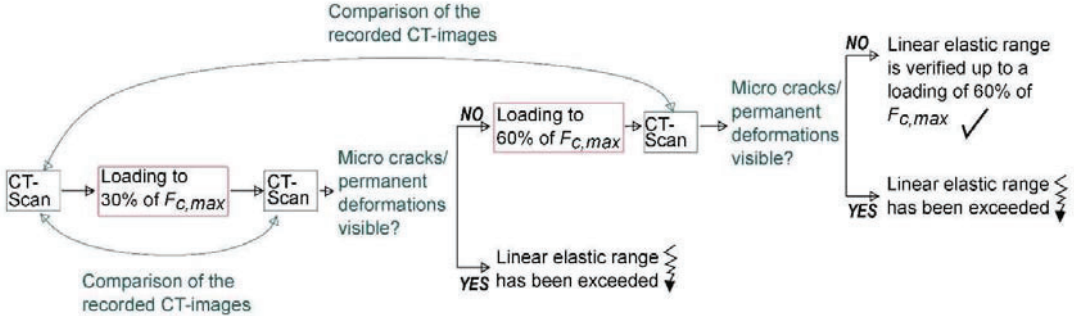

Figure 11: *Schematic procedure of the CT-measurements and the verification of the linear elastic range of spruce wood*

https://doi.org/10.52202/069179-0050

3.2 MAIN TESTS

After the test method and handling of samples was defined in several preliminary tests, the main tests were carried out to determine all Poisson's ratios by means of compression tests on spruce wood. The results are shown on the basis of boxplots in Figure 13 and are directly compared to the Poisson´s ratios found in literature (square markers, Figure 13). The different colours indicate the respective load types (red: tensile test, blue: compression test and green: bending test) that were applied in literature in order to measure the Poisson´s ratios. Table 1 summarizes all Poisson´s ratios and Youngs moduli including the measurement uncertainty and the associated average density and wood moisture contents of the respective test series.

Examining the boxplots in Figure 13 it is evident that almost all Poisson´s ratios determined in Tripolt [7] and Kumpenza et al. [6] are higher than the ratios determined within this work. Both applied tensile tests and used optical measurement techniques (electronic speckle pattern interferometry (ESPI) and a combination of laser- and videoextensometry). For these measurement techniques, Kumpenza et al. [6] specifies the following measurement resolutions: ESPI 0,03 µm, video-extensometry 0,2 µm and laserextensometry 0,11 µm. The Poisson´s ratios in both studies were determined on specimens with a higher wood moisture content (12 %) than present in this work (~7,4 %, Table 1). Further literature values, determined under the same conditions, though, do not show increased values (see NC [4] in Figure 13). As a consequence, neither the wood moisture content nor the load type appear to be responsible for the increased values. In fact, several indications lead to the assumption that the increased values in Kumpenza et al. [6] and Tripolt [7] resulted from strain measurements during the initial loading of the test specimens. Presumably this has to do with the residual stresses still present during the first loading [4].

This was also evident during the preliminary tests realized in the work presented here.

In case of the μ_{LT} values the Poisson´s ratios given in Tripolt [7] lie within the inter-quartile range. Presumably, this is due to creep respectively shrinkage effects during capturing the images when using ESPI. That is why Kumpenza et al. did not give any values for μ_{LT} [6]. Furthermore, Tripolt mentions difficulties using ESPI on flat sawn where early and late wood alternate and thus, cause inhomogeneous stress conditions [7].

Furthermore, the values determined in Kumpenza et al. [6], using a combination of laser- and videoextensometry, are all higher than the ratios determined within this work. As the strains were only recorded on one side of the specimen using this technique possible bending effects

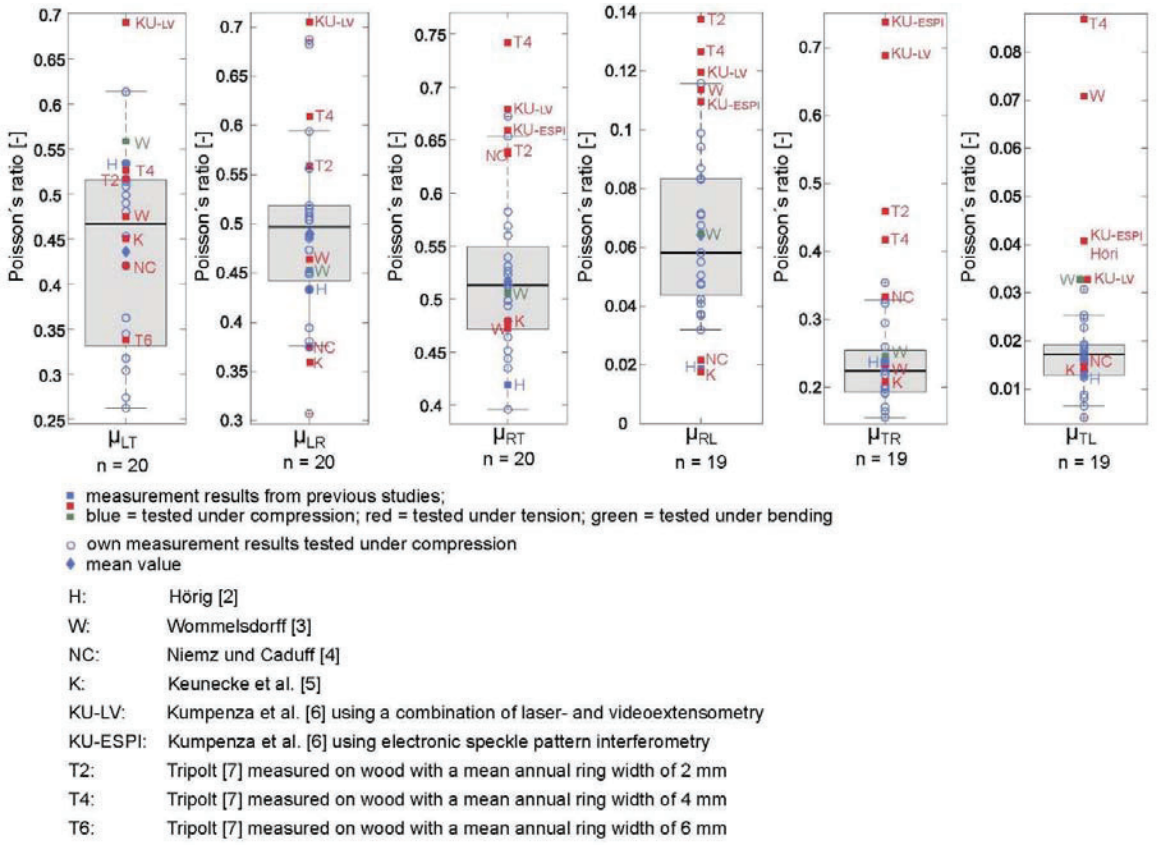

Figure 13: *Boxplot of the Poisson´s ratios of all test series on the basis of n specimens including the Poisson´s ratios determined in previous studies; red: tension tests, blue: compression tests, green: bending tests*

were neglected potentially influencing the resulting Poisson´s ratios.
A quite good agreement of the values determined within in this work is seen regarding the Poisson´s ratios determined in Hörig [2], Wommelsdorff [3], Niemz und Caduff [4] and Keunecke et al. [5]. Here, the test procedure also consisted of several load cycles. Almost all values lie within the inter-quartile range. Only for the RL-series the Poisson´s ratios given in [2], [4] and [5] are below this range. It should be mentioned that the Poisson´s ratio given in Keunecke et al. [5] is a calculated value and not an outcome of a measurement. However, as already mentioned, the measurement of the lateral strain in longitudinal direction is generally problematic due to the higher stiffness in grain direction. Nevertheless, the Poisson´s ratio determined within this work shows a significantly lower deviation (CoV = 38 %) than stated in other studies (e.g.: CoV = 62 % [4], CoV = 59 % [6]). Moreover, the observed wood moisture contents of around 10 to 12 % given in these references are also higher than present in this work. Since the wood moisture content in radial direction has a greater influence, this might be the reason for the higher deviation of the values. Considering the values for μ_{TL} such a deviation cannot be observed which is probably due to the already higher outside temperatures at that time and thus a higher moisture content of around 9,5 % of the specimens. Since the measurement uncertainty has not been a part in previous research further conclusions are difficult to draw.

Table 1: *Determined Poisson´s ratios and Young´s moduli including the measurement uncertainty and associated Density, Moisture content and Annual ring width of all test series*

Poisson´s ratio		[-]
	μ_{RT}	0,517 ± 0,085
	μ_{TR}	0,233 ± 0,044
	μ_{TL}	0,016 ± 0,005
	μ_{LT}	0,436 ± 0,085
	μ_{RL}	0,064 ± 0,017
	μ_{LR}	0,492 ± 0,123
Young´s moduli		[N/mm²]
	E_L	12068 ± 1460
	E_R	966 ± 103
	E_T	302 ± 42
Density		[kg/m³]
	ρ_L	430
	ρ_R	428
	ρ_T	378
Moisture content		[%]
	$u_{L,mean}$	7,4
	$u_{R,mean}$	7,4
	$u_{T,mean}$	9,4
Approx. annual ring width		[mm]
	arw	2

Also noteworthy is the resulting Poisson´s ratio μ_{RT}, that is above 0,5 (Table 1). As a matter of fact, this would indicate that a body under a hydrostatic pressure increases its volume [16]. However, this compressibility condition is only valid for isotropic materials. Wood is an anisotropic material with different Young´s moduli in the three main directions (L,R and T). Therefore, and since Poisson's ratios above 0,5 have also been found in earlier studies, the Poisson's ratio determined for the RT-series is feasible.
The Young´s moduli result in the following ratio $E_T : E_R : E_L$ of 1 : 3,20 : 39,96. For comparison Niemz and Caduff [4] state a ratio of 1 : 2,43 : 25,4, Tripolt [7] a ratio of 1 : 1,57 : 27,6, Kumpenza et al. [6] a ratio of 1: 3,69 : 52,08 and the determined Young´s moduli in Keunecke et al. [5] correspond to a ratio of 1 : 1,57 : 32,24. Overall the determined orders of magnitude are therefore in agreement with the literature. The still persistent differences in the ratio of $E_R : E_T$ can be traced back to the varying annual ring widths [4].
The largest deviation from the literature values is evident regarding the Young´s modulus E_T. This test series also shows a significantly lower density value and the highest moisture content. A possible reason for the lower density might be the small sample geometry combined with the annual ring width [4]. Since the Young´s modulus decreases with lower density [20], this might be the reason for the deviation. The lower moisture content of 9,4% compared to the literature values (~12%) should cause a higher Young´s modulus. Compared to the influence of the density, however, this seems to have less impact on the Young´s modulus.

3.2.1 Symmetry condition

When summarizing all obtained values and inserting these into the compliance matrix, the matrix should fulfil the symmetry condition.

$$\begin{bmatrix} \frac{1}{E_L} & -\frac{\mu_{RL}}{E_R} & -\frac{\mu_{TL}}{E_T} \\ -\frac{\mu_{LR}}{E_L} & \frac{1}{E_R} & -\frac{\mu_{TR}}{E_T} \\ -\frac{\mu_{LT}}{E_L} & -\frac{\mu_{RT}}{E_R} & \frac{1}{E_T} \end{bmatrix} = \begin{bmatrix} \frac{1}{12068} & -\frac{0,064}{966} & -\frac{0,016}{302} \\ -\frac{0,492}{12068} & \frac{1}{966} & -\frac{0,233}{302} \\ -\frac{0,436}{12068} & -\frac{0,517}{966} & \frac{1}{302} \end{bmatrix} = \begin{bmatrix} 8,29 & -6,63 & -5,3 \\ -4,08 & 103,52 & -77,15 \\ -3,61 & -53,52 & 331,13 \end{bmatrix} \cdot 10^{-5} \quad (12)$$

It is seen, that at first glance, based on the presented compliance matrix in Equation (12) the symmetry condition is not identified as fulfilled. This is why the determined measurement uncertainties are additionally considered in the following. Thereby, the symmetry conditions are examined individually.
First symmetry condition:

$$\frac{\mu_{LR}}{E_L} = \frac{\mu_{RL}}{E_R}$$
$$\frac{0,492 \pm 0,123}{12068 \pm 1460} = \frac{0,064 \pm 0,017}{966 \pm 103} \quad (13)$$
$$[2,73;\ 5,88] \cdot 10^{-5} = [4,40;\ 9,39] \cdot 10^{-5}$$

with: [min; max]. This results in an overlapping area of $5,8 \cdot 10^{-5} - 4,4 \cdot 10^{-5} = 1,4 \cdot 10^{-5}$. Therefore, the symmetry condition can theoretically be fulfilled if both values lie within this range. Since the true average

https://doi.org/10.52202/069179-0050

Poisson´s ratio and the true Young´s modulus lie in the respective range with a 95 %-confidence, both values lie in the overlap range with a confidence of approx. 12 %.
Following this example, the second symmetry condition (Equation (14)) is theoretically met on a confidence level of approx. 20 % and the third symmetry condition (Equation (15)) is met on a confidence level of approx. 13 %.

$$\frac{\mu_{LT}}{E_L} = \frac{\mu_{TL}}{E_T} \tag{14}$$

$$\frac{\mu_{RT}}{E_R} = \frac{\mu_{TR}}{E_T} \tag{15}$$

In general, it can therefore be assumed that the compliance matrix determined here corresponds to the symmetry requirement. This supports the developed testing method and the applied measurement technique.
The matrix given in Equation (12) can then take the following symmetrical form and may be applied in the context of FEM.

$$\begin{bmatrix} 8{,}29 \cdot 10^{-5} & -5{,}14 \cdot 10^{-5} & -4{,}11 \cdot 10^{-5} \\ -5{,}14 \cdot 10^{-5} & 1{,}04 \cdot 10^{-3} & -6{,}24 \cdot 10^{-4} \\ -4{,}11 \cdot 10^{-5} & -6{,}24 \cdot 10^{-4} & 3{,}31 \cdot 10^{-3} \end{bmatrix} \tag{16}$$

4 CONCLUSION AND OUTLOOK

This paper takes the extended measurement uncertainty into account. As a result, the six determined average Poisson´s ratios can be stated with a 95 %-confidence. The results obtained seem to be consistent, since the average values lie in the middle range of the results stated in literature. This also includes the Young´s moduli and the density values.
However, it was seen that measurements based on the first loading, lead to significantly higher Poisson´s ratios due to residual stresses. Within future studies it is therefore particularly important to provide more precise information on the test and load procedure. In this context, it is of interest whether measurements using ESPI or a combination of laser- and videoextensometry result in similar Poisson´s ratios as found within this work, when determining the Poisson´s ratio based on the 10th load cycle.
Besides the load procedure, it also appears that the one- or two-sided measurements of the strains on a specimen influence the results. On the one hand this can be concluded from the values determined using laser- and videoextensometry in [6]. There, the strains were determined on only one side of the specimen and are above the determined average in all test series. On the other hand, a measurement on a μ_{TL}-specimen in this work caused an extremely high Poisson´s ratio. This is why this measurement was eliminated within the evaluation here. Reason for this increased Poisson´s ratio was most likely the fact that one of the strain gauges was defective. Thus, the lateral strain was only recorded on one side of the specimen here as well.
Additionally, it should be pointed out, that measuring μ_{TL} and μ_{LT} by means of optical measurement techniques is rather impractical. Difficulties due to different proportions of early- and latewood on the measuring surface were mentioned for example in [7]. Considering that these values, given in Tripolt [7] deviate significantly from the values determined here, this can be confirmed on the basis of this paper.
What could not be confirmed within the present thesis is the stress dependence of individual Poisson´s ratios found in [3]. Prerequisite for an accurately constant Poisson's ratio and thus a stress independent Poisson´s ratio is the accurately linear progression of the axial and lateral strain. On a random basis a linear regression was carried out on these strains over the stress. In each case, the strains run linearly, however, not perfectly. The resulting smallest deviations lead to a deviation of the Poisson's ratio over the stress. As a consequence the partial stress dependence is more an artefact of the measurement fluctuations or measurement uncertainty than an actual stress dependence. This should be verified in detail in future studies, as the above finding is only based on a small sample number. In case it turns out that measurement fluctuations and the measurement uncertainty are not the reason for the partly recognisable stress dependence, the assumption of a rhombic-crystalline behaviour of wood would have to be rejected, as was already mentioned by Wommelsdorff [3].
The present results of the preliminary tests further confirm that in the event of future studies investigating the influence of wood moisture on the Poisson's ratios, special care needs to be taken to perform the measurements in the same climate in which the specimens are conditioned. Otherwise, shrinkage and swelling influences have already a considerable influence on the Poisson´s ratios within a short time periode.
Significant correlations were only evident in a few cases. Moreover, these often differ from the correlations found in [7]. In addition, the Poisson's ratios are not only dependent on the density and the Young's modulus, but also on the microfibril angle and the cell shape angle [21]. These parameters were not recorded within the scope of this paper. Future studies should therefore examine correlations using a larger number of specimens and taking into account more wood properties such as the microfibril angle, the cell shape angle, etc..
Furthermore, creep also seems to have an influence on the measurement results of the Poisson's ratio, as is apparent from the preliminary tests. In this context, it seems reasonable to determine Poisson's ratios including the creep influence in future studies. These could be of particular importance for components subjected to long-term stress.
In summary, the determination of extended Poisson´s ratios of spruce wood has been achieved by integrating the measurement uncertainty. From an engineering perspective subsequent research should validate the Poisson´s ratios determined on clear wood specimens. For this purpose, a combination of finite element method (FEM) calculations in conjunction with associated

measurements on component-sized specimens suggests itself.

ACKNOWLEDGEMENT

This paper is based on my Master's thesis [22] which I was able to write in cooperation between the Technical University of Munich and the University of Innsbruck, supervised by my Co-Authors. Additionally, I would like to thank Dr.-Ing. Patrik Aondio for his support throughout the thesis. Furthermore, I want to acknowledge the entire TVFA team of the University of Innsbruck, without whom I would not have been able to conduct all the measurements. At this point additional thanks go to the Unit of Material Technology at the University of Innsbruck, that enabled the CT-measurements.

REFERENCES

[1] Stamer, J. (1935). Elastizitätsuntersuchungen an Hölzern. *Ingenieur-Archiv*, *6*(1), 1–8. https://doi.org/10.1007/BF02086406

[2] Hörig, H. (1935). Anwendung der Elastizitätstheorie anisotroper Körper auf Messungen an Holz. *Ingenieur-Archiv*, *6*(1), 8–14. https://doi.org/10.1007/BF02086407

[3] Wommelsdorff, O. (1966). *Dehnungs- und Querdehnungszahlen von Hölzern*. Technische Hochschule Hannover, Hannover.

[4] Niemz, P., & Caduff, D. (2008). Untersuchungen zur Bestimmung der Poissonschen Konstanten an Fichtenholz. Holz als Roh- und Werkstoff, 66(1), 1–4. doi: 10.1007/s00107-007-0188-2

[5] Keunecke, D., Hering, S. & Niemz, P. (2008). Three-dimensional elastic behaviour of common yew and Norway spruce. *Wood Science and Technology*, *42*(8), 633–647. https://doi.org/10.1007/s00226-008-0192-7

[6] Kumpenza, C., Matz, P., Halbauer, P., Grabner, M., Steiner, G., Feist, F. et al. (2018). Measuring Poisson's ratio: mechanical characterization of spruce wood by means of non-contact optical gauging techniques. *Wood Science and Technology*, *52*(6), 1451–1471. https://doi.org/10.1007/s00226-018-1045-7

[7] Tripolt, M. (2018). *Prüftechnische Bestimmung des orthotropen Elastizitätsverhaltens von Fichtenholz*. Masterarbeit. Technische Universität Graz, Graz.

[8] Clauß, S., Pescatore, C. & Niemz, P. (2014). Anisotropic elastic properties of common ash (Fraxinus excelsior L.). *Holzforschung*, *68*(8), 941–949. https://doi.org/10.1515/hf-2013-0189

[9] DIN 52185. (1976-09). Bestimmung der Druckfestigkeit parallel zur Faser. Berlin: Deutsches Institut für Normung e.V. Beuth Verlag GmbH.

[10] DIN 52192. (1979-05). Druckversuch quer zur Faserrichtung. Berlin: Deutsches Institut für Normung e.V. Beuth Verlag GmbH.

[11] EN 408. (2012-10). Holzbauwerke - Bauholz für tragende Zwecke und Brettschichtholz: Bestimmung einiger physikalischer und mechanischer Eigenschaften. Berlin: Deutsches Institut für Normung e.V. Beuth Verlag GmbH.

[12] EN 338. (2016-07). Bauholz für tragende Zwecke: Festigkeitsklassen. Berlin: Deutsches Institut für Normung e.V. Beuth Verlag GmbH.

[13] EN 12390-13. (2013-12). Prüfung von Festbeton: Teil 13: Bestimmung des Elastizitätsmduls unter Druckbelastung (Sekantenmodul). Wien: Austrian Standards plus GmbH.

[14] Bodig, J. & Jayne, B. A. (1982). Mechanics of wood and wood composites. New York: Van Nostrand Reinhold

[15] Mang, H. A., Hofstetter, G. & Eberhardsteiner, J. (2013). Festigkeitslehre (Lehrbuch, 4., erw. Aufl.). Berlin, Heidelberg: Springer Vieweg Verlag.

[16] Grimsel, M. (1999). Mechanisches Verhalten von Holz. Struktur- und Parameteridentifikation eines anisotropen Werkstoffes (Dresdner Forschungen Maschinenwesen, Bd. 1). Dresden: w.e.b.-Univ.-Verl.

[17] Albers, K. (1970). Querdehnungs- und Gleitzahlen sowie Schub- und Scherfestigkeiten von Holzwerkstoffen. Dissertation. Universität Hamburg, Hamburg.

[18] Niemz, P., & Sonderegger, W. U. (2017). Holzphysik: Physik des Holzes und der Holzwerkstoffe: mit zahlreichen Bildern und Tabellen. München: Fachbuchverlag Leipzig im Carl Hanser Verlag. Retrieved from http://www.hanser-fachbuch.de/9783446445260

[19] Maul, C., & Dammeyer, T. (2012). Apparatives Praktikum Physikalische Chemie der TU Braunschweig: Messfehler, Fehlerberechnung und Fehlerabschätzung. Technische Universität Braunschweig. Braunschweig.

[20] Neuhaus. (2017). Ingenieurholzbau. Springer Fachmedien Wiesbaden.

[21] Qing, H., & Mishnaevsky, L. (2010). 3D multiscale micromechanical model of wood: From annual rings to microfibrils. International Journal of Solids and Structures (47), 1253–1267. Retrieved from https://www.sciencedirect.com/science/article/pii/S0020768310000259?via%3Dihub

[22] Winter, K. (2021). A new Approach to Determine and Evaluate the Poisson´s Ratio of Spruce Wood. Masterarbeit. Technical University of Munich & University of Innsbruck. Munich

https://doi.org/10.52202/069179-0050

World Conference on Timber Engineering Oslo 2023

THEORETICAL AND EXPERIMENTAL INVESTIGATION ON PREDICTING LONGITUDINAL AND TANGENTIAL ELASTIC CONSTANTS AND RATIOS OF WOOD

Shaghayegh Kurzinski[1], Paul L. Crovella[2]

ABSTRACT: Among all the elastic constants of wood that are required for the engineering design of wood structures, only the modulus of elasticity in the longitudinal (L) direction (E_0 or E_L) is readily available or can be readily measured for the majority of species. Longitudinal and tangential moduli of elasticity and shear moduli are required to predict the structural performance of any composite timber product such as mass timber products. This study selected a low-density local softwood; eastern white pine, and a high-density local hardwood; black locust, to investigate their longitudinal and tangential elastic properties. The eastern white pine and black locust defect-free specimens were prepared and tested under centre-point bending loading (ASTM D198-2015 [1]) alternately on true longitudinal and tangential surfaces. Also, linear regressions with respect to the longitudinal modulus of elasticity were performed on the tangential elastic modulus, and the longitudinal-radial and tangential-radial shear moduli of the softwood and hardwood species with available mechanical properties ratios published in the USDA Wood Handbook [2]. These elastic constants and their ratios from the experiment have been compared to the predicted values and ratios from the regressions using the published values of the species in the USDA Wood Handbook. This provides data on the accuracy of assumed elastic ratios in published references for elastic and shear moduli.

KEYWORDS: Shear modulus, Modulus of elasticity, Centre-point bending test, Elastic ratios of wood, Elastic constants of wood.

1 INTRODUCTION

The arrangement and geometry of wood cells in the tree define three local symmetric axes in the material which are referred to as longitudinal (L, parallel to the grain direction and tangent to the growth rings), tangential (T, perpendicular to the grain) and radial (R, perpendicular to the grain direction and normal to the growth rings) [3]. These three axes determine the mechanical properties of wood by nine elastic constants and related compliances typically used in the engineering design of wood structures. Characterization of these constants in classical mechanics is done in reference to orthogonal axes. However, it should be noted that wood is not a truly orthotropic material because of growth ring curvature. Plain-sawn timber boards are generally used as typical layers of composite engineered timber products when the majority of the surface perpendicular to the major load direction is the tangential surface rather than the radial surface. Therefore, as shown in **Figure 1** the longitudinal and tangential elastic moduli (E_L and E_T) can be referred to as elastic moduli parallel to the grain (E_0) and perpendicular to the grain (E_{90}) respectively. Similarly, the longitudinal-radial and tangential-radial shear moduli can also be referred to as shear moduli parallel to the grain (G_0) and perpendicular to the grain (G_{90}) respectively.

The modulus of elasticity in the longitudinal (L) direction (E_0 or E_L) is readily available or can easily be measured for the majority of wood species. The other elastic constants, such as elastic moduli in the radial (R) and tangential (T) directions, the three Poisson's ratios, and the three shear moduli associated with the three major orthotropic planes, have not been thoroughly examined for most species due to the difficulty of making appropriate experimental measurements.

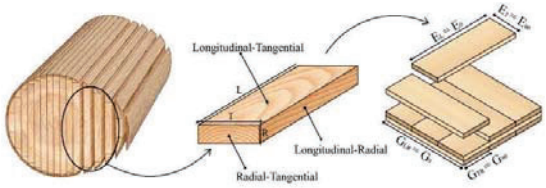

Figure 1: *Plain-sawn Cut Board Details and Usage in a Cross-laminated Timber Panel, multi-layered mass timber product [4]*

To make up for the lack of engineering data on a large number of species, there have been a few methods proposed to predict the elastic constants and their correlations in different species. Adamopoulos [5] studied the difference between the shear modulus in two orientations of longitudinal-radial (G_{LR}) and longitudinal-tangential (G_{LT}), in juvenile and mature black locust wood. They performed centre-point bending tests on 66 small clear specimens and measured the shear modulus in each load direction. Their study showed that the shear moduli in longitudinal-radial and longitudinal-tangential for black locust samples were not significantly different.

[1] Shaghayegh Kurzinski, Ph.D., shaykurzinski@gmail.com
[2] Paul L. Crovella, Ph.D., Assistant Professor, Construction Management, SUNY ESF, Syracuse, NY. USA. plcrovella@esf.edu

https://doi.org/10.52202/069179-0051

The shear moduli values in juvenile wood, however, were slightly lower than the values in mature wood. Divos et al. [6] used three different methods: static bending tests, torsional vibration, and the variation of span method to determine the shear modulus of construction-size timber. They found that between these methods, the static bending test and torsional techniques provided a more precise prediction of the shear constant in different directions.

In research done by Sliker [7], longitudinal-tangential and longitudinal-radial shear moduli of a variety of softwood and hardwood species were determined by two methods: the two-plate shear test and the off-axis tensile test at a 20° angle of load to the grain. In the longitudinal-tangential plane, the shear modulus (G_{LT}), calculated from the off-axis tensile test ranged from 0.87 to 1.25 times the shear modulus (G_{LT}), from the plate test. In the longitudinal-radial plane, the shear modulus (G_{LR}), from the off-axis tensile test ranged from 0.98 to 1.26 times the shear moduli G_{LR}, from the plate test. For the tested species, the linear regressions done for Poisson's ratios in correlation with shear and elastic moduli did not show any significant relationships for either of Poisson's ratios ν_{lr} or ν_{tr} as functions of density, E_L, or E_T.

Yoshihara et al. [8] examined the applicability of Timoshenko's theory and proposed an empirical equation to derive the shear modulus. To validate this empirical approach, three softwoods and three hardwoods were tested. First, the Young's and longitudinal-radial shear moduli were measured by free-free flexural vibration tests. Then three-point static bending tests were undertaken, varying the depth/span ratios. Additionally, the bending tests were simulated by the finite element method (FEM). The longitudinal-radial shear moduli obtained by these methods were then compared. They concluded a new prediction method for determining the longitudinal-radial shear modulus by modifying Timoshenko's theory.

The longitudinal modulus of elasticity to shear modulus ratios of different lumber species is not constant. It varies between 5 and 24 depending on the softwood and hardwood species and the grain direction (L, T, and R). There are published references that assume a typical ratio for longitudinal-radial and tangential-radial shear and tangential elastic moduli regarding the longitudinal elastic modulus (E_L/E_T, E_L/G_{LR}, E_L/G_{TR}). For instance, the North American and European Cross-laminated Timber (CLT) standards; ANSI/APA PRG 320-2019 [9] and EN 16351-2021 [10] assume these ratios to be: E_0/E_{90}=30:1, E_0/G_0=16:1, and E_0/G_{90}=160:1 for softwood species. The timber standards for Australia/New Zealand AS1720-2010 [10] and the Brazilian Timber standard [12] assume the ratio of E_0/G_0 to be around 15:1 for softwoods [13].

This study has selected one local low-density softwood and one local high-density hardwood species to investigate the shear and elastic moduli in two grain directions, longitudinal and tangential. Also, using linear regressions, the study evaluates the elastic ratios of E_0/E_{90}, E_0/G_0, E_0/G_{90} for softwoods and hardwoods with available elastic ratios in the USDA Wood Handbook [2]. The values and ratios of the elastic constants from the experimental testing have been compared to those from the regressions. This study can provide insight into predicting elastic ratios for species with no available published or tested elastic constant values.

2 MATERIALS AND METHODOLOGY

2.1 SPECIMEN PREPARATION AND DIMENSIONS

A total of 20 small black locust specimens and 20 eastern white pine specimens, 19-mm thick and 19-mm wide, with different lengths over a range from 89-mm to 280-mm (as shown in **Table 1**) were cut (respectively) from two defect-free, ungraded, rough-sawn black locust boards obtained from a local sawmill in Newfield, NY and one defect-free NeLMA [14] finish grade board purchased from a local lumber supplier near Syracuse, NY. The specimens' cross-section and lengths have been prepared according to the standard's requirement [1] for the centre-point bending test explained in **Section 2.2**. The boards were surfaced and planed to the desired thickness before the cutting process. The final cut specimens were straight-grained and free from any visible defects. The specimens were conditioned in an environmental chamber set at 20°C and 65% relative humidity until a constant weight was achieved. The final measured moisture content of the boards was approximately in the range of 12±1%. The specimens were prepared to be tested in two different directions relative to the wood grain orientation.

The centre-point bending test has been used to determine the apparent modulus of elasticity by measuring the uniform strain state at the centre of the specimens which is a combination of shear and bending deflection. The relative contribution of bending and shear deflections to the total deflection vary with span-to-depth ratio of the specimen. The measured apparent modulus of elasticity can help determining the shear-free modulus of elasticity by excluding the shear deflection to provide a true bending stiffness.

Table 1 shows the matrix of samples of each species divided into two groups tested under centre-point bending tests in the longitudinal and tangential directions for measuring the apparent modulus of elasticity (E_{app}) in both longitudinal and tangential directions and (respectively) the shear-free longitudinal elastic modulus (E_L) with longitudinal-radial shear moduli (G_{LR}) and shear-free tangential elastic modulus (E_T) with the tangential-radial shear modulus (G_{TR}). **Figure 2** shows the final specimens with different span lengths.

https://doi.org/10.52202/069179-0051

Table 1: *Specimens and Testing Details*

Species	Sample (Test Direction)	Sample Size	Span to Depth (l/d)
Eastern White Pine	Longitudinal-Radial Specimen	10	14:1, 11.3:1, 10.6:1 10:1, 9.3:1, 8.6:1, 8:1, 7.3:1, 6.6:1, 6:1
	Tangential-Radial Specimen	10	10:1, 9.3:1, 8.6:1, 8.3:1, 8:1, 7.6:1, 7.3:1, 7:1, 6.6:1
Black Locust	Longitudinal-Radial Specimen	10	14.8:1, 14.1:1, 13.5:1, 12.8:1, 12.1:1, 9.1:1, 8.4:1, 7.7:1, 7:1, 6:1
	Tangential-Radial Specimen	10	7.6:1, 7.3:1, 7.1:1, 7:1, 6.6:1, 6.5:1, 6.3:1, 6:1, 5.6:1, 5.3:1

Figure 2: *Specimen Samples with Different Span Lengths Prepared for Centre-point Bending Test (Eastern White Pine: Left, Black Locust: Right)*

2.2 CENTRE-POINT BENDING TEST

A non-destructive centre-point bending test as described in ASTM D198-2015 [1] (section 7.3.2.2) was performed on the specimens to provide the shear modulus and modulus of elasticity. The standard requires at least four different span lengths and the same depth such that the span-to-depth ratio (l/d) is between 20:1 and 5:1 ($0.0025 < (d/l)^2 < 0.035$). Using this method, the apparent modulus of elasticity and the shear modulus were predicted. The centre-point bending test was performed using a tabletop Shimadzu Precision Universal Tester 10KN AGX model machine set to a loading rate of 0.889 mm per minute. The test was performed until the proportional limit in the elastic range was reached and before the total failure of the specimen. The data was recorded with Trapezium X Software and a video extensometer. **Figures 3** and **4**, respectively, show illustrative and actual details of the test configuration and the loading direction in each group with respect to the wood grain orientation.

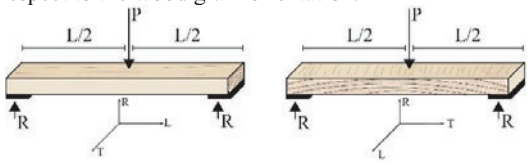

Figure 3: *Center-point Bending Test Details with Respect to Specimens' Grain Orientation*

Figure 4: *Actual Center-point Bending Tests to Determine Shear and Elastic Moduli*

According to ASTM D198-2015 [1] to calculate the shear modulus, first, the value for the apparent modulus of elasticity should be acquired using **Equation 1**:

$$E_{app} = \frac{PL^3}{4bd^3\Delta} \quad (1)$$

where E_{app} is the apparent elastic modulus at a specific span-to-depth ratio and grain orientation, P is the load at the proportional limit, b is the width of the specimen, d is the depth of the specimen and Δ is the deflection that occurs up to the proportional limit.

After determining the values for apparent elastic modulus for different span lengths, their inverses were plotted versus the span-to-depth ratios. The slope of this linear curve is a factor in predicting the shear modulus according to **Equation 2**,

$$G = \frac{6}{5K_1} \quad (2)$$

where G is the shear modulus with respect to the loading direction on the specific grain orientation, and K_1 is the slope of the inverses of apparent elastic moduli versus the span-to-depth ratio (**Error! Reference source not found. 5**).

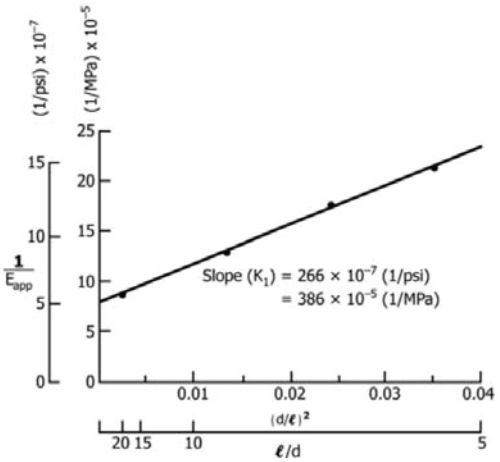

Figure 5: *Shear Modulus Determination based on the Apparent Elastic Modulus and Span-to-Depth Ratio [13]*

After the shear modulus is found for each group of specimens, the shear-free modulus of elasticity can be calculated using **Equation 3**.

$$E_{sf} = \frac{PL^3}{4bd^3\Delta\left(1-\frac{3PL}{10bd\Delta G}\right)} \quad (3)$$

where E_{sf} is the shear-free modulus of elasticity, P is the load at the proportional limit, b is the width of the

specimen, h is the depth of the specimen and Δ is the deflection that occurs up to the proportional limit, and G is the shear modulus with respect to the loading direction on the specific grain orientation.

2.3 THEORETICAL INVESTIGATION OF SHEAR AND ELASTIC MODULI CORRELATION

One of the most easily measured physical properties of wood is the Young's modulus or modulus of elasticity (MoE) in the longitudinal direction (E_0 or E_L). This quantity is available for the majority of the wood species in technical publications, or it can also be obtained on a piece-by-piece basis from non-destructive testing. The USDA Wood Handbook [2] provides ratios for shear moduli in different grain directions (RT, LT, LR) and elastic moduli in tangential and radial directions with respect to the elastic modulus in the longitudinal direction for a few hardwood and softwood species. To predict tangential elastic modulus and longitudinal-radial and tangential-radial shear moduli of eastern white pine and black locust, the Handbook's softwood and hardwood species with available elastic ratios were selected (include the number). The shear moduli in longitudinal-radial and tangential-radial and elastic modulus in tangential directions were calculated for these softwoods and hardwoods using the available elastic ratios. Linear regressions for each elastic constant from the selected species were performed using Microsoft Excel [15] to provide a predicted ratio with respect to the longitudinal elastic modulus. Since the available reference [2] shows a true linear relation of Y=AX, for each elastic constant regarding the longitudinal elastic modulus, an intercept-free linear model was selected for predicting the elastic ratios. These ratios were used to theoretically estimate values for shear moduli in longitudinal-radial and tangential-radial directions (G_{LR} and G_{TR}) and tangential elastic modulus (E_T) for eastern white pine and black locust with respect to their published longitudinal elastic modulus (E_L).

3 RESULTS AND DISCUSSION

3.1 MEASURED ELASTIC CONSTANTS AND RATIOS BY CENTER-POINT BENDING TESTS

The curves showing the correlations between $1/E_{app}$ and span-to-depth ratios (l/d) obtained from the centre-point bending tests for longitudinal-radial and tangential-radial specimens are presented in **Figures 6** and **7**, for eastern white pine, and **Figures 8** and **9** for black locust. The shear moduli values have been calculated from these curves using **Equation 2**. The final values of shear moduli (G_{LR} and G_{TR}) and the measured apparent and shear-free elastic moduli in each loading direction (E_L and E_T) are presented in **Table 2**.

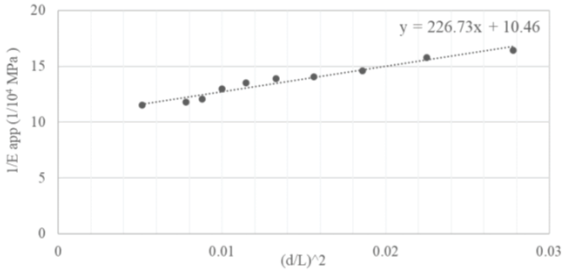

Figure 6: *Apparent Elastic Modulus vs. Span-to-Depth Ratio Curves of Eastern White Pine Specimens in Longitudinal-Radial Direction*

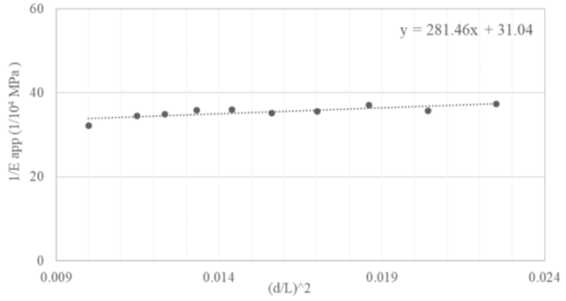

Figure 7: *Apparent Elastic Modulus and Span-to-Depth Ratio Curves of Eastern White Pine Specimens in Tangential-Radial Direction*

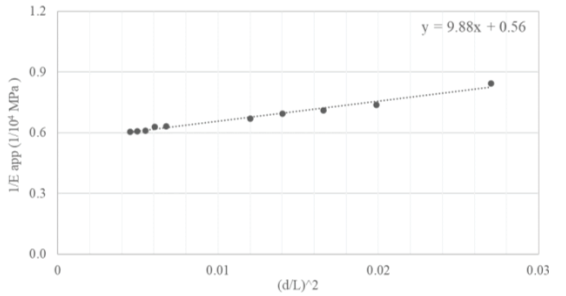

Figure 8: *Apparent Elastic Modulus and Span-to-Depth Ratio Curves of Black Locust Specimens in Longitudinal-Radial Direction*

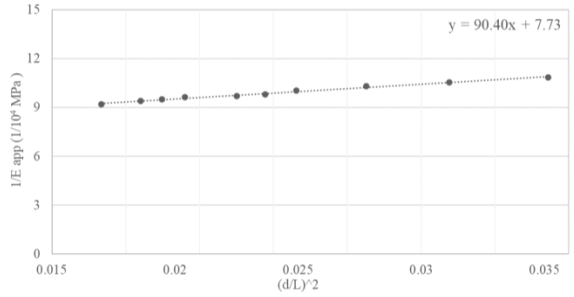

Figure 9: *Apparent Elastic Modulus and Span-to-Depth Ratio Curves of Black Locust Specimens in Tangential-Radial Direction*

https://doi.org/10.52202/069179-0051

Table 2: *Final Measured Values of Apparent Elastic Modulus of Small Specimens Under Centre-point Bending Test*

Species	Properties	Longitudinal	Tangential
Eastern White Pine	Apparent Modulus of Elasticity (MPa)	E_{app} = 7,418	E_{app} = 283
Black Locust	Apparent Modulus of Elasticity (MPa)	E_{app}= 14,993	E_{app}= 1,013

3.2 THEORETICAL PREDICTED ELASTIC CONSTANTS AND RATIOS FROM THE ELASTIC REGRESSIONS

The published longitudinal modulus of elasticity (E_L) values of eastern white pine and black locust have been found from the USDA Wood Handbook [1] to be respectively 8,555 MPa and 14,134 MPa. To theoretically predict the values of longitudinal-radial and tangential-radial shear and tangential elastic moduli of these two species, the estimated elastic ratios from the regressions on the USDA Wood Handbook's [2] softwoods and hardwoods were used. These linear regressions of tangential elastic modulus and shear moduli with respect to longitudinal elastic modulus are presented in **Table 3**. The final theoretical elastic ratios and values of eastern white pine and black locust with respect to the predicted elastic ratios from the regressions are shown and compared to the measured ratios and values, respectively in **Table 4** and **Table 5**.

Table 3: *Linear Regression Components of Tangential Elastic and Shear Moduli of USDA Wood Handbook Softwood and Hardwood Species with Respect to their Longitudinal Modulus Species*

Species	Regression	R^2 Value	Regression Model
Softwood	E_L - E_T	0.9157	Y=0.0547X
	E_L - G_{LR}	0.8631	Y=0.073X
	E_L - G_{TR}	0.7426	Y=0.0057X
Hardwood	E_L - E_T	0.9386	Y=0.061X
	E_L - G_{LR}	0.9403	Y=0.0921X
	E_L - G_{TR}	0.941	Y=0.0194X

Table4: *Predicted and measured Shear and Elastic Moduli Values with Respect to Longitudinal Elastic Modulus (EL) from Regressions on the USDA Wood Handbook Species*

Species	Properties	Longitudinal	Tangential
Eastern White Pine	Predicted Modulus of Elasticity (MPa)	E_L = 8,550	E_T = 468
	Predicted Shear Modulus (MPa)	G_{LR} = 624	G_{TR} = 49
	Measured Modulus of Elasticity (MPa)	E_L = 9,569	E_T = 322
	Measured Shear Modulus (MPa)	G_{LR} = 529	G_{TR} = 43
Black Locust	Predicted Modulus of Elasticity (MPa)	E_L= 14,134	E_T= 862
	Predicted Shear Modulus (MPa)	G_{LR} = 1,302	G_{TR} = 274
	Measured Modulus of Elasticity (MPa)	E_L = 17,925	E_T = 1,294
	Measured Shear Modulus (MPa)	G_{LR} = 1,215	G_{TR} = 133

Table 4: *Measured and Predicted Ratios of Shear and Elastic Moduli (LR: Longitudinal-Radial, TR: Tangential-Radial)*

Species	Ratio	Measured	Predicted
Eastern White Pine	E_L/E_T	29.6	18.3
	E_L/G_{LR}	18.0	13.7
	G_{LR}/G_{TR}	12.4	12.8
Black Locust	E_L/E_T	13.8	16.4
	E_L/G_{LR}	14.8	10.85
	G_{LR}/G_{TR}	9.1	4.7

According to the experimental and theoretical results, the longitudinal shear-free elastic moduli for eastern white pine and black locust from the centre-point bending tests are respectively 11% and 26% higher than the published longitudinal elastic modulus in the USDA Wood Handbook [2]. The predicted shear-free tangential elastic modulus from regressions is approximately 45% higher and 33% lower than the measured tangential elastic modulus for eastern white pine and black locust respectively. The predicted longitudinal-radial shear modulus is 15% and 6% higher than the measured longitudinal-radial shear modulus for eastern white pine and black locust respectively. Also, the predicted tangential-radial shear modulus is 14% and 106% higher than the measured tangential-radial shear modulus for

https://doi.org/10.52202/069179-0051

eastern white pine and black locust respectively. Between the elastic ratios from measured constants, the ratio of eastern white pine longitudinal-radial shear modulus to tangential-radial shear modulus is almost the same (3% difference percentage) as the one predicted from regressions. However, the same ratio (G_{LR} /G_{TR}) for black locust is almost half of what is found based on the measured constants from the centre-point bending tests. Also, the elastic ratio of predicted longitudinal to the tangential modulus of elasticity for eastern white pine is approximately 30% of the measured one while the other predicted elastic ratios from the regressions have a percentage prediction error between 10% and 20% of the measured ratios from the tests.

4 CONCLUSIONS

This research investigated the values and ratios of shear and elastic moduli of black locust and eastern white pine experimentally and empirically. The results showed that longitudinal and tangential shear moduli and tangential elastic modulus can be predicted using longitudinal elastic modulus. The measured elastic ratios of longitudinal to the tangential modulus of elasticity (E_L/E_T) for eastern white pine from the tests were in agreement with the suggested ratios of modulus of elasticity parallel to the grain to the modulus of elasticity perpendicular to the grain (E_0/E_{90}) for softwoods in North American Cross-laminated Timber standard, ANSI/APA PRG 320 [9] to be 30:1. The measured longitudinal elastic modulus to the longitudinal-radial shear modulus ratio (E_L/G_{LR}=18:1) of the eastern white pine was approximately 17% higher than the suggested elastic ratio of shear modulus parallel to the grain to the modulus of elasticity parallel to the grain (E_0/G_0=16:1) for softwoods in ANSI/APA PRG 320 [9]. Therefore, it can be concluded that ANSI/APA PRG 320 [6] provides a conservative prediction of softwoods' elastic ratios compared to the regressions from the USDA Wood Handbook [2] elastic values.

The regression between hardwoods' tangential-radial shear modulus to the longitudinal modulus of elasticity showed a non-conservative agreement with the measured value. The reason for this difference may be the small sample size for the regression. The USDA Wood Handbook [2] provides the tangential-radial shear modulus (G_{TR}) for only six hardwood species. Except for the predicted longitudinal-radial shear modulus of black locust to its published longitudinal modulus of elasticity, the other predicted elastic ratios for this species with respect to the hardwoods' regressions, have predicted a ratio with a percentage prediction error approximately between 10% and 20% of the measured ratios from the tests.

This study provided methods for predicting the shear and elastic moduli in different grain directions of the species without available published elastic constants values. To predict the final stiffness value of any composite or mass timber product (e.g. CLT), the shear and elastic values of the species used in the layers are required. There are several non-standard species that might benefit the timber industry due to density, resource availability, locality, etc. but are not being used for the fabrication since there is no available published value for their elastic constants. Therefore, predicting the elastic constants of different wood species with unknown elastic values can help in using them as individual layers in several mass timber products such as Cross-laminated Timber panels. Further research is recommended to experimentally investigate the elastic values of other softwoods and in particular hardwoods to validate the predicted elastic ratios from the regressions provided in this study.

REFERENCES

[1] Forest Products Laboratory, USDA Wood handbook—Wood as an engineering material. General Technical Report FPL-GTR-190., Madison, WI: U.S, 2021. https://doi.org/10.1161/01.RES.39.4.523.

[2] A.R. de Geus, S.F. da Silva, A.B. Gontijo, F.O. Silva, M.A. Batista, J.R. Souza, An analysis of timber sections and deep learning for wood species classification, Multimedia Tools and Applications. 79 (2020) 34513–34529. https://doi.org/10.1007/s11042-020-09212-x.

[3] Xavier J, Jesus, A, Morais, J, Pinto, J, On the determination of the modulus of elasticity of wood by compression tests parallel to the grain, Revista da Associação Portuguesa de Análise Experimental de Tensões (APAET), 20 (2012), 59-66.

[4] Adamopoulos.S, Flexural Properties of Black Locust (Robinia pseudoacacia) Small Clear Wood Specimens in Relation to the Direction of Load Application, Holz Als Roh-Und Werkstoff, Springer-Verlag. 60 (2002) 325–327.

[5] F. Divos, T. Tanaka, H. Nagao, H. Kato, Determination of shear modulus on construction size timber, Wood Science and Technology. 32 (1998) 393–397.

[6] A. Sliker, A Method for Predicting Non-shear Compliances in the RT Plane of Wood, Wood and Fiber Science. 20 (1988) 44–45.

[7] H. Yoshihara, Y. Kubojima, K. Nagaoka, M. Ohta, Measurement of the shear modulus of wood by static bending tests, Journal of Wood Science, 44 (1998).

[8] American National Standard Institute, ANSI-APA/PRG 320 - Standard for Performance-Rated Cross-Laminated Timber, APA – The Engineered Wood Association, New York, NY, 2019.

[9] CEN National Members., EN 16351-2021, Timber Structures, Cros laminated timber, Requirements., (2021).

[10] Australian Standard Committee TM-001, AS 1720.1-Timber structures - Part 1: Design methods, Council of Standards Australia, Sydney, Australia, 2010.

[11] Brazilian Committee on Civil Construction, ABNT NBR 7190, Brazilian Standard: Design of Timber Structures, ABNT/ CB-02, 2011.

[12] S. Kurzinski, P. Crovella, P. Kremer, Overview of Cross-Laminated Timber (CLT) and Timber

https://doi.org/10.52202/069179-0051

Structure Standards Across the World, Mass Timber Construction Journal. 5 (2022)
[13] American Lumber Standard Committee (ALSC), Northeastern Lumber Manufacturers Association, Standard Grading Rules for Northeastern Lumber, Northeastern Lumber Manufacturers Association, Maine, USA., 2021.
[14] American Society for Testing and Materials Committee, ASTM D198- 15, (2015).
[15] Microsoft Corporation., Microsoft Excel, (2021).

World Conference on Timber Engineering Oslo 2023

PYTHON-BASED PLATE MODEL TO SIMULATE THE EFFECT OF KNOTTY AREAS ON SAWN TIMBER.

Jorge Uribe Cisternas[1], Diego Valdivieso Cascante[2]

ABSTRACT: This paper introduces a computational python-based model of a timber plate of Pinus Radiata D. Don specie grown in Chile. The effect of knotty areas is considered for the simulation of stiffness and resistance in a simply supported plate subjected to out-of-plane bending assessing the failure with the Von Mises normalized and Tsai-Wu criteria. The computational model is implemented based on the Reissner-Mindlin plate theory, considering a rectangular orthotropic model to simulate the behavior of wood. When the knotty area ratio (KAR) reaches its maximal value, 1, stiffness and resistance decrease by 19% and 56%, respectively. Through the Monte-Carlo method, 500 wooden plates are simulated by randomly distributing the lengths of internodes and whorls, which shows a difference of 14% in vertical displacement. It is concluded that the open-source numerical model was able to capture the effect of the knotty areas on the bending behavior of timber elements. The next step involves the calibration of the input parameters of the numerical model from the test results.

KEYWORDS: Plate, KAR, Whorl, Internode, Finite Elements Models, Pinus Radiata

1 INTRODUCTION

Wood has been used repeatedly in Chile for small constructions. Nowadays, the need to carry out sustainable constructions based on renewable materials and with that cause a low impact on the environment makes wood head the list of most required materials in the future.

For the same reason, the Chilean construction industry has evaluated the alternative of building wooden constructions to eventually replace concrete and steel constructions. However, compared to concrete and steel, there is still a lack of knowledge about the behavior of wood products made from Pinus radiata grown in Chile and the effect of their natural defects (i.e., knotty area and its distribution on the tree length) on their mechanical properties [1].

This article aims to contribute to the development of an open-source plate model based on Python that allows quantifying the effects of knotty areas on the bending behavior of wood elements through the finite element method.

2 COMPUTATIONAL MODEL

2.1 GENERAL

A plate is defined as a flat solid whose thickness is much smaller than its other dimensions (length and width). In this paper, a finite element model for plate bending is presented based on the Reissner-Mindlin plate theory for small elastic strains, which includes the transverse shear effect [2,15] (see Figure 1).

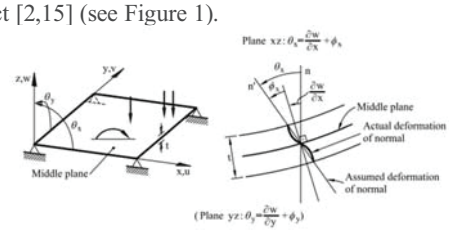

Figure 1: *Reissner-Mindlin plate theory. Sign convention for the displacements and the rotations of the normal. Taken from [9].*

2.2 FORMULATION

2.2.1 Force Formulation

According to [5], the strong formulation of the boundary problem of plate theory is:

$$
\text{(S)}\quad \begin{cases}
\textit{Considering } F, C_\alpha, M_\alpha, Q, W \textit{ and } \Theta_\alpha, \textit{find } w \textit{ and } \theta_\alpha \\
\textit{such that:} \\
\left.\begin{aligned}
m_{\alpha\beta,\beta} - q_\alpha + C_\alpha &= 0 \\
q_{\alpha,\alpha} + F &= 0 \\
m_{\alpha\beta} &= -c_{\alpha\beta\gamma\delta} k_{\gamma\delta} \\
q_\alpha &= c_{\alpha\beta}\gamma_\beta \\
k_{\alpha\beta} &= \theta_{(\alpha,\beta)} \\
\gamma_\alpha &= -\theta_\alpha + w_{,\alpha}
\end{aligned}\right\} \forall x \in A \\
\left.\begin{aligned}
\theta_\alpha &= \Theta_\alpha \\
w &= W \\
m_{\alpha n} = m_{\alpha\beta} n_\beta &= \mathrm{M}_\alpha
\end{aligned}\right\} \begin{aligned}
&\forall x \in \Gamma_{\theta\alpha} \\
&\forall x \in \Gamma_w \\
&\forall x \in \Gamma_M
\end{aligned}
\end{cases}
$$

[1]Jorge Uribe Cisternas, Universidad Nacional Andrés Bello, Chile, j.uribecisternas@uandresbello.edu
[2] Diego Valdivieso, Pontificia Universidad Católica de Chile, Centro Nacional de Excelencia para la Industria de la Madera (CENAMAD) & Centro de Innovación en Madera (CIM UC-CORMA, Chile, dnvaldivieso@uc.cl. University of Colorado at Boulder, USA, diego.valdivieso@colorado.edu

https://doi.org/10.52202/069179-0052

$$q_n = q_\alpha n_\alpha = Q \qquad \} \forall x \in \Gamma_Q$$

Where, F= applied transverse force per unit area, C_α= applied moment couple per unit area, M_α= prescribed moments at the boundary, Q= prescribed shear force at the boundary, W= prescribed displacement at the border. Also $m_{\alpha\beta}$ is the moment tensor, q_α is the shear force vector $k_{\alpha\beta}$ is the curvature tensor and γ_α is the shear strain vector. The $\Gamma'_{(.)S}$ represents the different parts of the boundary.

2.2.2 Finite Element Formulation

We start the weak formulation by defining the spaces:

$$\mathcal{S} = \{w, \theta_1, \theta_2 \in H^1(\Omega, \mathbb{R}) | w = W \ \forall \in \Gamma_w, \theta_\alpha = \Theta_\alpha \ \forall x \in \Gamma_{\theta\alpha}\}$$

$$\mathcal{V}_{\theta\alpha} = \{\delta\theta_\alpha \in H^1(\Omega, \mathbb{R}) | \delta\theta_\alpha = 0, \ \forall x \in \Gamma_{\theta\alpha}\}$$

$$\mathcal{V}_w = \{\delta w \in H^1(\Omega, \mathbb{R}) | \delta w = 0, \ \forall x \in \Gamma_w\}$$

Where $\mathcal{S}$ is the solution space, $\mathcal{V}_{\theta\alpha}$ and $\mathcal{V}_w$ are the test spaces, H^1 is the Sobolev space, W and Ω_α are the prescribed displacements and rotations (essential or Dirichlet conditions), and $\Gamma_{\theta\alpha}$ and Γ_w are the Dirichlet boundaries.

The variational formulation is obtained by multiplying the equations of the strong formulation by the functions test and integrated by parts in the domain $w = A$. Defining $\delta\gamma_\alpha = \delta\theta_\alpha + \delta_{w,\alpha}$ we have:

$$(W)\begin{cases} Considering\ F, C_\alpha, M_\alpha, Q, W\ and\ \Theta_\alpha, find\ w\ and \\ \theta_\alpha \in \mathcal{V}\ such\ that, \forall \delta_w \in \mathcal{V}\ and\ \delta\theta_\alpha \in \mathcal{V}_{\theta\alpha} \\ \int_A \left(-\delta\theta_{(\alpha,\beta)} m_{\alpha,\beta} + q_\alpha \delta\gamma_\alpha\right) = \int_A (\delta_w F - \delta\theta_\alpha C_\alpha) - \\ \int_{\Gamma_M} \delta\theta_\alpha M_\alpha + \int_{\Gamma_Q} \delta_w Q \qquad \forall x \in A \end{cases}$$

Where M_α and Q are the prescribed moments and shear forces (natural or Neumann boundary conditions) Γ_M and Γ_Q are the Neumann frontiers.

From the variational formulation and discretizing the **Ω** domain, the finite element formulation is determined:

$$(L^{FEM})\begin{cases} Considering\ \mathbf{K} \in \mathbb{R}^{NxN}\ and\ \mathbf{F} \in \mathbb{R}^M, \\ find\ \mathbf{d}\ such\ that: \\ \mathbf{K}\,\mathbf{d} = \mathbf{F} \end{cases}$$

Where **d** is the nodal displacement value $\mathbf{d} = \begin{bmatrix} w \\ \theta_1 \\ \theta_2 \end{bmatrix}$

Where:

$$K_{ij} = \iint_A B_i^T \widehat{D} B_j \, dA \ ;$$

$$F = \iint_A N^T p_j - \int_{\Gamma_M} N^T \overline{M} + \int_{\Gamma_Q} N^T \overline{Q}$$

$$p_j = [f_z \quad m_x \quad m_y]^T$$

$\widehat{D}$ is the generalized constitutive matrix.

The stiffness matrix of each element can be divided into bending (k_b) and transverse shear (k_s). The global equilibrium equation is written as

$$(K_b + K_s)d = F \qquad (1)$$

$$K_{ij}^{(e)} = \iint_{A^{(e)}} \begin{bmatrix} B_{bi}^T & B_{si}^T \end{bmatrix}^T \widehat{D} \begin{bmatrix} B_{bj} \\ B_{sj} \end{bmatrix} dA = K_{b_{ij}}^{(e)} + K_{s_{ij}}^{(e)} \qquad (2)$$

Where:

$$B_{bi} = \begin{bmatrix} 0 & N_{i,x} & 0 \\ 0 & 0 & N_{i,y} \\ 0 & N_{i,y} & N_{i,x} \end{bmatrix}; \quad B_{si} = \begin{bmatrix} N_{i,x} & -N_i & 0 \\ N_{i,y} & 0 & -N_i \end{bmatrix}$$

The vector of forces remains:

$$F^{(e)} = \iint_{A^{(e)}} N^{(e)T} p_j - \int_{\Gamma_M^{(e)}} N^{(e)T} \overline{M} + \int_{\Gamma_{Q^{(e)}}} N^{(e)T} \overline{Q}^{(e)} \qquad (3)$$

Where:

$$N_i = \begin{bmatrix} N_i & 0 & 0 \\ 0 & N_i & 0 \\ 0 & 0 & N_i \end{bmatrix}$$

2.3 TYPE OF ELEMENTS CONSIDERED

In order to verify the accuracy of the model, four different elements were implemented: Q4, QS8, QL9, and QH9 based on [9]. The shape functions referring to these elements are presented below:

- Four-node element – Q4

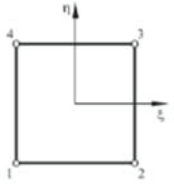

Figure 2: *Bilinear element (Q4).[9]*

$$N_i = \frac{1}{4}(1 + \xi\xi_i)(1 + \eta\eta_i), i = 1,2,3,4 \qquad (4)$$

- Eight-nodes element – QS8

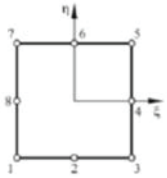

Figure 3: *Serendipity Quadratic element (QS8).[9]*

$$N_i = \frac{1}{4}(1+\xi\xi_i)(1+\eta\eta_i)(\xi\xi_i+\eta\eta_i-1), i = 1,2,3,4$$
$$N_i = \frac{1}{2}(1+\eta\eta_i)(1-\xi^2), i = 5,7 \quad (5)$$
$$N_i = \frac{1}{2}(1+\xi\xi_i)(1-\eta^2), i = 6,8$$

- Nine-nodes element – QL9

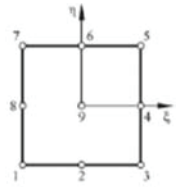

Figure 4: *Lagrangian Biquadratic element (QL9).[9]*

$$N_i = \frac{1}{4}(\xi^2+\xi\xi_i)(\eta^2+\eta\eta_i), i = 1,3,5,7$$
$$N_i = \frac{1}{2}\eta_i^2(\eta^2+\eta\eta_i)(1-\xi^2)+\frac{1}{2}\xi_i^2(\xi^2+\xi\xi_i)(1-\eta^2)$$
$$, i = 2,4,6,8$$
$$N_i = (1-\xi^2)(1-\eta^2), i = 9 \quad (6)$$

- Nine-nodes hierarchical – QH9

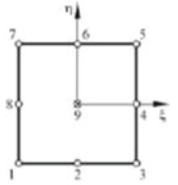

Figure 5: *Hierarchical element (QH9).[9]*

$$\theta_x = \sum_{i=1}^{8} N_i\,\theta_{x_i} \;;\; \theta_y = \sum_{i=1}^{8} N_i\,\theta_{y_i}$$
$$w = \left(\sum_{i=1}^{8} N_i w_i\right) + \overline{N_9} w_9 \quad (7)$$

where N_i are the standard shape functions for the QS8 element and $\overline{N_9} = (1-\xi^2)(1-\eta^2)$. The hierarchical variable w_9 is the difference between the nodal deflections obtained with QS8 and QL9 elements. [9]

2.4 DETERMINATION OF THE BEST ELEMENT TO BE USED

The performance and meshing of the implemented plates with different elements were compared against the analytical solutions from the author S. Timoshenko [12], through the results of the vertical displacement in the center of the plate.

In Figure 6, it shows that the four elements give a result like to Timoshenko formulation due to the low percentage error (i.e., less than 5%) in vertical displacement, however, the QH9 element shows the best accuracy (i.e., 0.002%) due to the addition of a "spring" that eliminates spurious mechanisms [9]. The next steps of this investigation were carried out with the QH9 element.

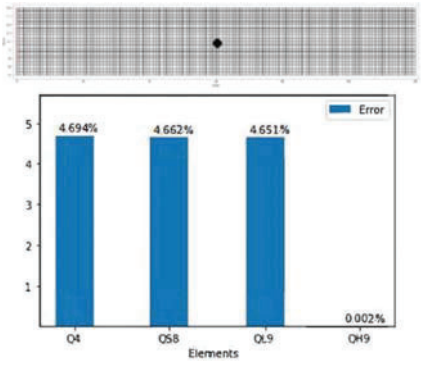

Figure 6: *(up) Evaluation in the center of the discretized plate, (down) Graph of the percentage error of each element.*

3 EVALUATION OF NATURAL DEFECTS ON WOOD PLATES

In each computational model, the displacement and deformation fields were calculated. Subsequently, to evaluate the behavior of the plate, the knotty areas were used, taking as a reference the properties of the Blass study [3], in addition, the properties and distribution of the knotty areas in Radiata Pine specie were replicated. The Knotty Area Ratio (KAR) is varied increasing from 0.1 to 1 to evaluate the impact on the displacement and stress in three control points along the simulated plate (P1, P2, and P3 illustrated in Figure 8). The coordinates of each point are located at (Lx/4, Ly/2), (Lx/2, Ly/2), (3Lx/4, Ly/2) respectively. To evaluate the stress interaction in the plate, the Von Misses Normalized [14] and Tsai-Wu [13] failure criteria were used.

In order to evaluate the effect of knotty area distribution, five hundred wood plates with a fixed KAR but with a different distribution of knotty areas, varying the whorl of internodes and whorls were assessed. The center point of the plate is chosen as the control point and the vertical displacement of the 500 wooden plates is plotted.

3.1 EFFECT OF THE KNOTTY AREA

In order to quantify the accuracy of the model, a virtual test of a representative 120 cm x 20 cm x 6.5cm wood plate made of Radiata Pine grown in Chile was simulated (see Figure 7). A rectangular orthotropic law was considered for the wood constitutive, considering the

https://doi.org/10.52202/069179-0052

mechanical properties from [4]. The model was considered as simply supported and uniformly loaded with 4 [N/cm^2] over the entire surface. The geometry of the element was discretized into 1 cm x 1 cm elements. To include the effect of the knotty area in the model, discrete length stripes were considered whose properties were calculated by means of a linear regression equation determined experimentally in reference [3] based on the knotty area ratio (KAR) (see eq. 8 and 9). The dimensions of the knotty areas (whorl and internode length, see Figure 8) were determined from a study on Radiata Pine grown in Chile (see Table 1) [8].

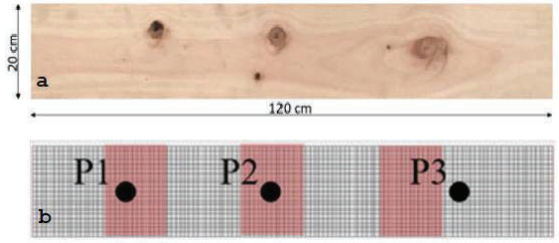

Figure 7: *(a) Representative timber element, (b) Discretization of the wooden plate with the knotty area.*

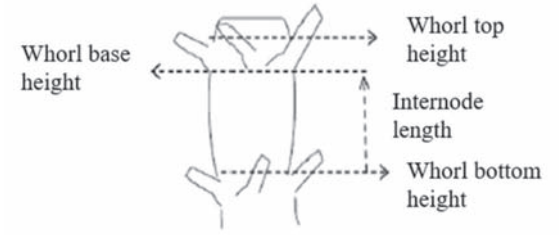

Figure 8: *Base height and top of a whorl. Taken from [8]*

Table 1: *Branch range of the Radiata Pine tree in regions VII and IX of Chile. Take from [8].*

Variable	Range
Internode length [cm]	30 - 110
Whorl length [cm]	20 - 40

$$\ln(\mathrm{E_L}) = 7.90 + 3.81 * 10^{-3} * \rho_0 - 0.369 * KAR$$

With r = 0.773 and S_R = 0.165 (8)

$$\ln(f_\mathrm{L}) = -9.09 + 1.36 * ln(\mathrm{E_L}) - 0.978 * KAR$$

With r = 0.839 and S_R = 0.274 (9)

Where the modulus of elasticity (E_L), resistant tension in flexion (f_L) are in N/mm^2, anhydrous density (ρ_0) in kg/m^3 and the KAR is dimensionless.

3.2 EFFECT OF THE WHORL AND INTERNODE LENGTH

In order to understand the behavior of the timber elements with knotty areas of different lengths of internodes and whorls, a fixed KAR of 66% (KAR = 0.66) was considered to simulate 500 cases with different knotty area dimensions (i.e., whorl and internode length variation) through the Monte-Carlo method.

3.3 FAILURE CRITERIA

3.3.1 VON MISES NORMALIZED

In the reference [14] the authors develop a simplified method for the evaluation of the failure by the resistant tension in flexion (f_L).

$$\frac{\sigma_{vm}}{f_L} = \frac{\sqrt{\sigma_{xx}^2 - \sigma_{xx}\sigma_{yy} + \sigma_{yy}^2 + 3\tau_{xy}^2}}{f_L} \leq 1 \quad (10)$$

Where: σ_{xx}, σ_{yy}, τ_{xy}, are the uniaxial and shearing stress components in the respective directions and sections of an isotropic model and f_L is given by equation 8.

3.3.2 TSAI-WU

For a planar orthotropic model, the failure criteria is given by:

$$F_1\sigma_L + F_2(\sigma_R + \sigma_T) + F_{11}\sigma_L^2 + F_{22}(\sigma_R^2 + \sigma_T^2 + 2\tau_{RT}^2) + F_{66}(\tau_{LR}^2 + \tau_{LT}^2) + 2F_{12}(\sigma_L\sigma_R + \sigma_L\sigma_T) + 2F_{23}(\tau_{RT}^2 - \sigma_R\sigma_T) \leq 1 \quad (11)$$

Where: σ_L, σ_R, σ_T, τ_{LR}, τ_{RT}, τ_{LT} are the uniaxial and shearing stress components in the respective directions and sections of an orthotropic model. F_1, F_2, F_{11}, F_{22}, F_{66} and F_{23} are coefficients obtained from uniaxial stresses (i.e., in tension f_t and compression f_c) and shear stress f_v parallel or perpendicular to the grain (i.e., denoted as 0 or 90 for parallel or perpendicular, respectively), through the reference [7]. F_{12} is a coefficient that represents, the biaxial resistance (parallel and perpendicular).

$$F_1 = \frac{1}{f_{t0}} - \frac{1}{f_{c0}};\ F_2 = \frac{1}{f_{t90}} - \frac{1}{f_{c90}}$$

$$F_{11} = \frac{1}{f_{t0}f_{c0}};\quad F_{22} = \frac{1}{f_{t90}f_{c90}}$$

$$F_{66} = \frac{1}{(0.72f_{v0})^2};\quad F_{23} = \frac{1}{2}\left(\frac{1}{f_{v90}^2} - \frac{1}{f_{t90}f_{c90}}\right)$$

For the factor F_{12} the reference [6] proposes the following:

$$F_{12} = \frac{1}{2}\left(\frac{1}{f_{t0}f_{c90}} + \frac{1}{f_{c0}f_{t90}} - \frac{1}{f_{v0}^2}\right)$$

Experimental data from reference [10] in Radiata Pine is taken into consideration for defining the uniaxial and

shear stress input necessary for calculating the coefficients, F_i. The characteristics will be considered in a dry condition (humidity < 19%).

4 RESULTS

The results of the computational plate model based on QH9 elements are illustrated in Figures 9 to 11, where the displacements and stresses variation as a function of the knotty area ratio (KAR), whorl length, and internode length are evaluated.

4.1 DISPLACEMENT AND DEFORMATION FIELD

The displacements and stresses of the plate are shown in Figure 9 considering a plate without a knotty zone and another with a KAR of 66%. Figure 9.a shows that the vertical displacement at the edge of the plate increases by 12% because of the knotty area effect. Figure 10 shows visually how the KAR influences the stress distribution.

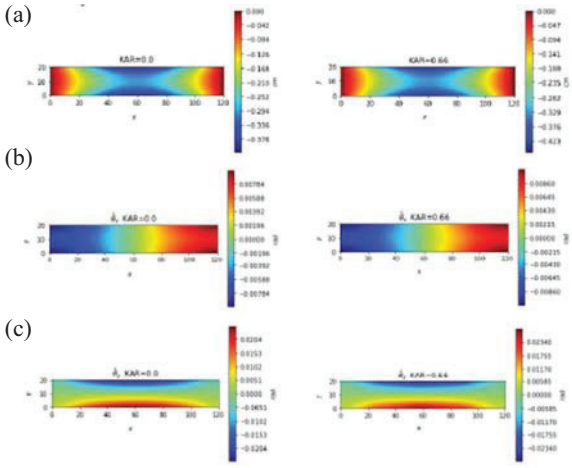

Figure 9: *(left) KAR=0.0, (right) KAR=0.66. (a) Vertical displacement, (b) rotation about X-direction and (c) rotation about Y-direction*

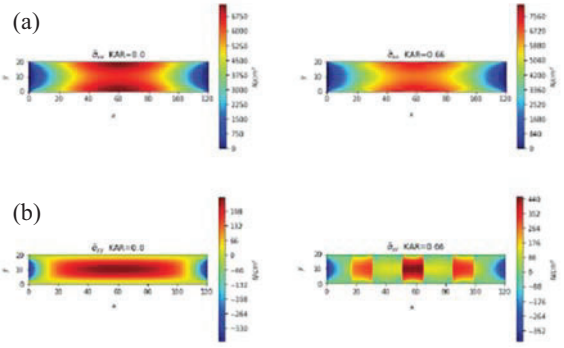

Figure 10: *(left) KAR=0.0, (right) KAR=0.66. Stress field in (a) X and (b) Y direction, respectively*

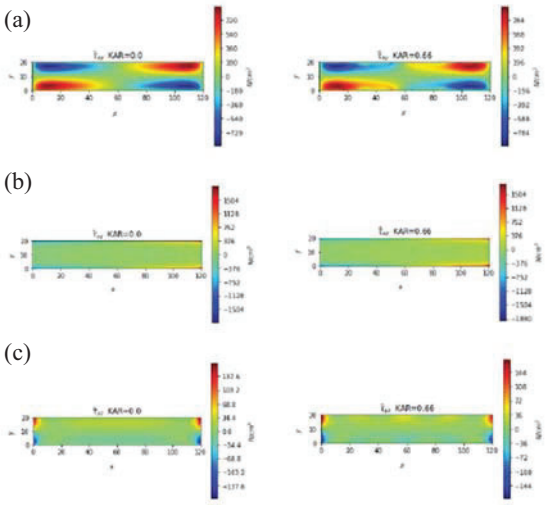

Figure 11: *(left) KAR=0.0, (right) KAR=0.66. Shear stress field (a) XY, (b) XZ and (c) YZ.*

4.2 FAILURE CRITERIA

Two failure criteria were selected to analyze the stress state in the evaluated wood plate. By using the Tsai-Wu criterion, the area where the failure is expected to occur can be identified due to the integration of all the stresses that interact in the plate and the consideration of real Radiata Pine wood coefficients F_i. On the other hand, the Von Mises Normalized criterion does not consider stresses interaction since it is designed for isotropic materials.

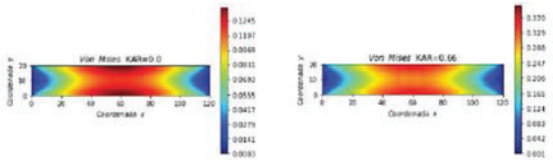

Figure 12: *Failure criterion Von Mises Normalized with (left) KAR=0.0 and (right) KAR=0.66.*

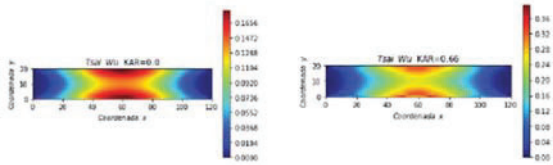

Figure 13: *Failure criterion Tsai Wu with (left) KAR=0.0 and (right) KAR=0.66.*

4.3 EFFECT OF THE KNOTTY AREA

Considering out-of-plane displacement results (see Figure 14), it is observed that as the KAR increases, the vertical displacement increases proportionally, generating an increase of up to 19% in the out-of-plane displacement, being the point P2 with the highest displacement increments, the rotation θ_x increases by 14% at points P1 and P3.

https://doi.org/10.52202/069179-0052

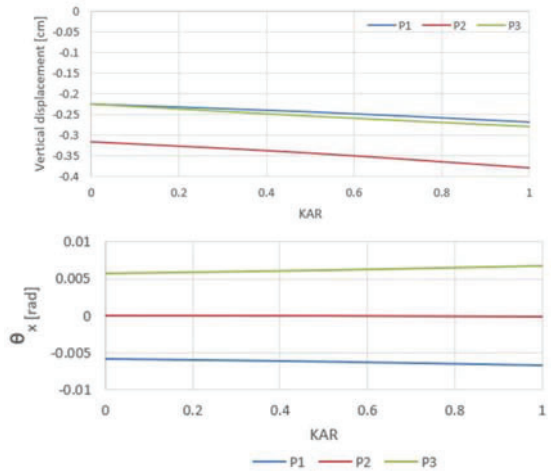

Figure 14: *Effect of the KAR in (top) vertical displacement and (bottom) rotation about X.*

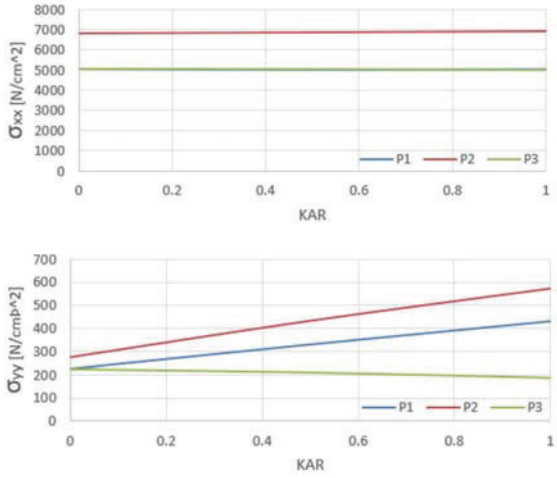

Figure 15: *Effect of the KAR in (top) stress xx and (bottom) stress yy.*

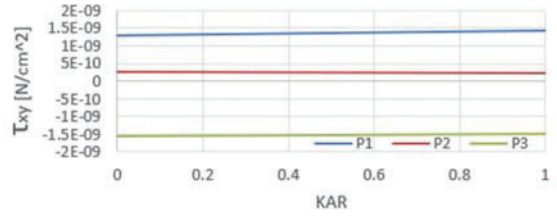

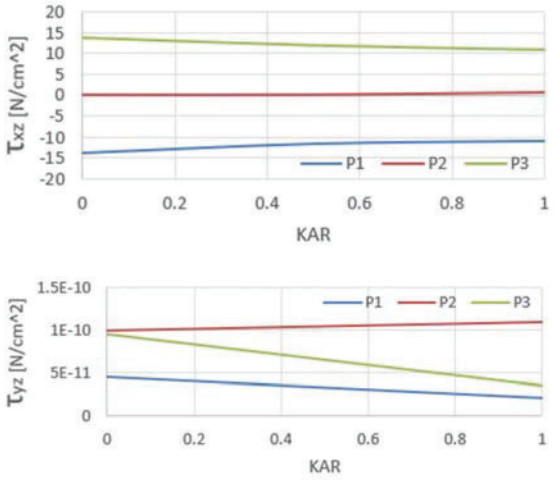

Figure 16: *Effect of the KAR in (top) Taú xy, (middle) Taú xz and (bottom) Taú yz.*

Figure 15 shows that as the KAR increases, the stresses yy (σ_{yy}) increase proportionally, causing a high stress concentration at the points with knotty areas.

Figure 17 shows that for KAR values less than 0.5, the Tsai-Wu criterion is the most conservative in predicting failure whereas for KAR values greater than 0.5 the Von Mises Normalized criterion is the most conservative for failure prediction. The Tsai-Wu criterion utilization factor shows an increment of up to 56% as the KAR increases, while the Von Mises Normalized criterion produces an increment of up to 78%.

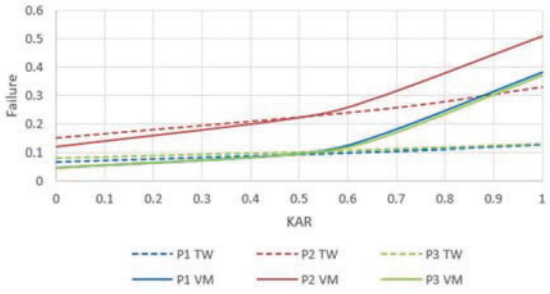

Figure 17: *Effect of the KAR in failure criteria utilization factor.*

4.4 EFFECT OF THE WHORL AND INTERNODE LENGTH

Figure 18 illustrates the evolution of the vertical displacement (*D*) for the 500 simulated cases measured in point P2, considering a KAR=0.66 and varying the lengths of internodes and whorls. Moreover, there is a minimum of one knotty area along the length. From the simulation results, equation 12 is proposed by using the least squares method.

https://doi.org/10.52202/069179-0052

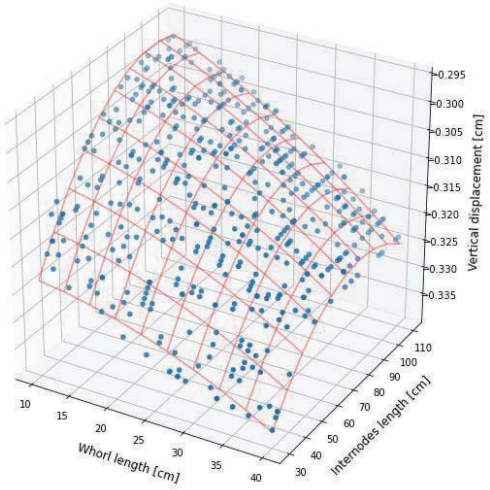

Figure 18: *Vertical displacement at node P2 of the 500 simulated wooden plates with KAR=0.66.*

$$D = 1.879 \cdot 10^{-4} \cdot W + 1.178 \cdot 10^{-3} \cdot I - 1.034 \cdot 10^{-5} \cdot W^2 - 5.256 \cdot 10^{-6} \cdot W \cdot I - 5.803 \cdot 10^{-6} \cdot I^2 \quad (12)$$

Where D= vertical displacement [cm], W= whorl length [cm] and I= internode length [cm].

Figures 19 and 20 show an increment of up to 14% in the vertical displacement depending on internode length or whorl length.

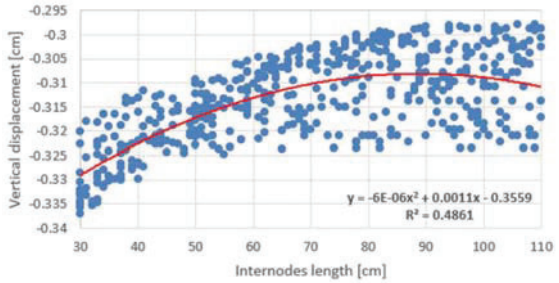

Figure 19: *Vertical displacement v/s internodes length.*

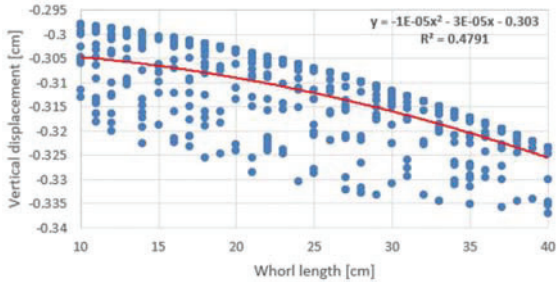

Figure 20: *Vertical displacement v/s whorl length.*

The contour plot shows that the longer the internode length and the shorter the whorl length, the smaller the vertical displacement. On the other hand, between shorter internodes length and greater whorl lengths, the vertical displacement is greater. In the first case, since the length of the internode is so large, it only reaches to one knotty zone along the plate length while the shorter the internode is, there are more knotty zones along the plate. Due to the dimensions of the plates, it only reaches a maximum of three knotty areas.

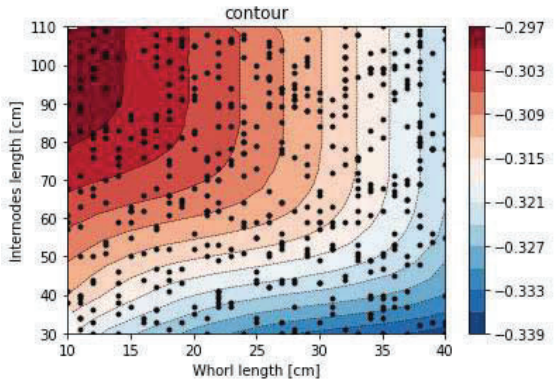

Figure 21: *Internodes length v/s whorl length effect on the vertical displacement at node P2.*

5 CONCLUSIONS

The Python-based model was able to capture the effect of the knotty areas in the response of wood plates subjected to out-of-plane bending. When the KAR reaches its maximum value, the stiffness and strength of the plate decrease by 19% and 56%, respectively. The previous statement can be supported by the failure criteria which takes its maximum values in the wood adjacent to the knotty areas in the center of the plate. Talking about the effect of different lengths of internodes and whorls, the shorter the length of the internode and the longer the whorl, the greater the vertical displacement of the plate, reaching an increment of up to 14%. It is concluded that the open-source numerical model was able to capture the effect of the knotty areas on the bending behavior of timber elements. The next step involves the calibration of the input parameters of the numerical model from the test results.

REFERENCES

[1] Aguilera Fernández, M., Benedetti Ruiz, S., Gallardo Lara, C., & Ulloa, D. *Estudio percepción construcción en madera.* 2020

[2] Cook, R.D., Malkus, D.S., Plesha, M.E., & Witt, R.J.: *Concepts and Applications of Finite Element Analysis.* Fourth edition John Willey and Sons, 2002.

[3] Flaig, M. Blass, H.J.: *Bending strength of cross laminated timber beams loaded in plane.* Proceedings of WCTE 2014, 2014.

[4] Guindos, P.: *Fundamentos del diseño y la construcción con madera. Primera Edición*, 2019.

https://doi.org/10.52202/069179-0052

[5] Hughes, T. J. *The finite element method: linear static and dynamic finite element analysis*. Courier Corporation. 2012
[6] Liu, J. Y. *Evaluation of the tensor polynomial strength theory for wood.* Journal of Composite Materials, 18(3), 216-226. 1984
[7] Mascia, N. T., Nicolas, E. A., Cammpinas, S., & Todeschini, B. R. *Comparison between Tsai-Wu failure criterion and Hankinson´s formula for tension in wood.* Wood Research, 56(4), 499-510. 2011
[8] Millar Ortiz, J.A.: *Análisis del crecimiento diametral de ramas de Pinus Radiata D. Don en distintos sitios entre las Regiones VII y IX*, 2003.
[9] Oñate, E.: *Structural analysis with the finite element method. Linear statics: volume 2: beams, plates and shells.* Springer Science & Business Media, 2013.
[10] Perez, V. *Comprendio de Directrices para enseñanza en ingeniería*. CORMA. 2003
[11] Spiess, A. N., & Neumeyer, N. (2010). An evaluation of R 2 as an inadequate measure for nonlinear models in pharmacological and biochemical research: a Monte Carlo approach. BMC pharmacology, 10(1), 1-11.
[12] Timoshenko, S., & Woinowsky-Krieger, S.: *Teoría de placas y láminas.* Urmo, 1970.
[13] Tsai, S. W., & Wu, E. M. *A general theory of strength for anisotropic materials*. Journal of composite materials, 5(1), 58-80. 1971
[14] Valdivieso D., & Vargas L. *Simulación Númerica del Efecto de los nudos en el Estado Tensional de Placa de Pino Radiata Sometida a Flexión*. 2019.
[15] Zienkiewicz, O.C., Taylor, R.L., J.Z. Zhu.: *The finite element method. Volume 2: Solid Mechanics*. Fifth edition, Butterworth-Heinemann, 2000.

World Conference on Timber Engineering Oslo 2023

SIMULATION OF WOOD FRACTURE MECHANICS USING THE PHASE FIELD METHOD FOR FRACTURE

Sebastian Pech[1], Markus Lukacevic[2], Josef Füssl[3]

ABSTRACT: Fracture mechanics simulations play a crucial role in predicting the failure of materials in various engineering applications. However, modeling fracture in inhomogeneous materials with complex microstructures is challenging. This work applies a non-brittle hybrid multi-phase field model to simulate wood failure. The approach is based on a stress-based split for orthotropic materials and includes multiple phase field variables, incorporating preferable fracture planes. The proposed model is initially applied to two examples, single-edge notched plates with varying fiber inclines and a wooden board with a single knot and spatially varying fiber directions. Both examples show that the model covers the effect of the wood microstructure on macroscopic crack propagation. Subsequently, the model is validated on experimental studies from the literature. We show that by choosing the input parameters, the tensile strength and the fracture energy release rate, in a reasonable range for wood, the model agrees well with the results of the experimental studies. Those findings open the application of the model to more complex situations like wooden boards with multiple knots and show that the used input parameters are not model-specific numerically tuned parameters but rather material-specific quantities.

KEYWORDS: Fracture, phase field method, wood

1 INTRODUCTION

Wood is consequently gaining importance in fields of civil engineering, where mainly steel and concrete constructions have dominated until now. This uprise is primarily due to new developments of high-performance wood-based products, the rediscovery of the excellent performance of wood as a building material and ecological benefits.

Understanding the complex mechanical nature of wood is critical to opening its application in new fields and optimizing its usage.

The microstructure of wood strongly influences its mechanical properties. Crack growth starts on the microscopic scale from defects in the cell wall material. After the localization of a macroscopic crack, a fracture process zone forms [31]. Subsequently, toughening effects like fiber bridging [11,35] set in. Microcracks and toughening effects result in a cohesive material behavior. The microstructure also strongly influences the macroscopic crack orientation. Wood fibers, which were produced at the same time, lie on so-called growth surfaces. Such growth surfaces give structure to the material. With a weak interface between the fibers, cracks tend to follow the direction of least resistance along the fiber [31]. Together with a spatially strongly varying fiber orientation, macroscopic crack topologies become very complex. In summary, for simulating wood fracture, a numerical method is required capable of accounting for an orthotropic constitutive behavior, cohesive fracture, preferable fracture planes, and complex three-dimensional cracks.

At the Institute for Mechanics of Materials and Structures (IMWS), we followed two quite promising methods in recent years: Finite element-based limit analysis [19] and the extended finite element method (XFEM) [21,24]. Both approaches show a good but not yet satisfying performance. Particularly the latter approach suffers geometrical limitations which do not allow for modeling the complex crack paths found in wood fracture.

A method well suited for crack paths of arbitrary complexity is the phase field method for fracture [4,5,12,23]. It is based on Griffith's theory of brittle fracture [13], formulated by a variational approach, minimizing the total energy of the system. An auxiliary field $d \in [0,1]$ models cracks, including a smooth transition between the intact ($d = 0$) and the cracked ($d = 1$) solid.

The original phase field method cannot account for wood fracture phenomena. In particular, the formulation does not include orthotropic materials, cohesive behavior, and favorable fracture planes. In recent years, several publications addressed these issues. In [3], an additional phase field was added to the original formulation. This allows for distinguishing different failure modes like matrix or fiber failure in composite materials. In [8,15,34], the so-called structural tensor was introduced, which accounts for favorable fracture planes by scaling the spatial gradient of the phase field. Failure in composite materials was considered by multiple researchers; actively

[11] Sebastian Pech, Vienna University of Technology (TU Wien), Austria, sebastian.pech@tuwien.ac.at
[2] Markus Lukacevic, Vienna University of Technology (TU Wien), Austria, markus.lukacevic@tuwien.ac.at
[3] Josef Füssl, Vienna University of Technology (TU Wien), Austria, josef.fuessl@tuwien.ac.at

https://doi.org/10.52202/069179-0053

pursued approaches are comprehensively summarized in [6,40]. Research regarding the use of the phase field method for wood was performed in [7] on the microscopic scale, in [33] on the macroscopic scale by incorporation of a representative crack element theory and in [27,28] by a hybrid macroscopic multi-phase field model based on the unified phase field theory. This work focuses on a discussion of the model developed in the latter works.

2 FUNDAMENTALS AND METHODS

Figure 1 shows the approximation of a sharp crack Γ with multiple diffuse representations $\Gamma_i(d_i)$ on a body Ω with the boundary $\partial\Omega$. The model from [27], a hybrid multi-phase field model for orthotropic materials with favorable fracture planes, is based on the unified phase field theory [39]. This adds a cohesive zones model to the formulation to account for effects like micro-cracking and fiber-bridging [31]. As the fracture behavior of wood is highly direction-depended, multiple phase fields [3] are used for cracks perpendicular to the longitudinal, radial and tangential direction.

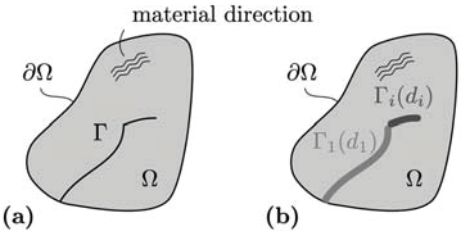

Figure 1: *Sharp and diffuse crack representation*

Excluding body forces and surface tractions, the regularized form of the total energy Π of the system, defined on the domain Ω, reads:

$$\Pi(\mathbf{u},\mathbf{d}) = \int_\Omega \left[\, \psi^+(\boldsymbol{u},\boldsymbol{d}) + \psi^-(\boldsymbol{u})\right] dV + \sum_{i\in\{L,R,T\}} G_{c,i} \int_\Omega \gamma_i(d_i)\, dV, \tag{1}$$

where i denotes the i-th phase field, $\boldsymbol{u}$ the displacement field, $\boldsymbol{d}$ the phase field of dimension 3 and $G_{c,i}$ the critical energy release rate. The strain energy terms $\psi^+(\boldsymbol{u},\boldsymbol{d})$ and $\psi^-(\boldsymbol{u})$ denote the degraded energy and undegraded energy, respectively. The crack geometry is approximated by the volume integral over the crack surface density function $\gamma_i(d_i)$. In the unified phase field theory, $\gamma_i(d_i)$, extended to include the structural tensor, is defined as

$$\gamma_i(d_i) = \frac{1}{c_{0,i}}\left(\frac{1}{l_i}\alpha_i(d_i) + l_i \nabla d_i \boldsymbol{A_i} \nabla d_i\right), \tag{2}$$

with $c_{0,i} = 4\int_0^1 \sqrt{\alpha_i(\beta)}d\beta$, $\alpha_i(d_i) = 2\,d_i - d_i^2$ as the local part of the dissipated fracture energy, and $\boldsymbol{A}_i = \boldsymbol{I} + \beta_i\,(\boldsymbol{I} - \boldsymbol{a}_i \otimes \boldsymbol{a}_i)$ as the structural tensor, where $\boldsymbol{a}_i$ is the material direction and β_i is the scaling factor of the structural tensor for phase field i.

Crack propagation is driven by an energetic force $\psi^+(\boldsymbol{u})$, which also dictates the constitutive behavior through the degraded strain energy $\psi^+(\boldsymbol{u},\boldsymbol{d})$. The phase field model described in [27] uses a stress-based split [32] to decompose the strain energy density into two parts: one that drives cracks and one that is inactive. The crack driving strain energy density is defined based on fracture mechanics failure modes I, II, and III for a crack perpendicular to $\boldsymbol{a}_i$. This includes the assumption that cracks mainly propagate following the principal material directions, which is motivated by the commonly observed "zig-zag" failure pattern of wood shown in Figure 2.

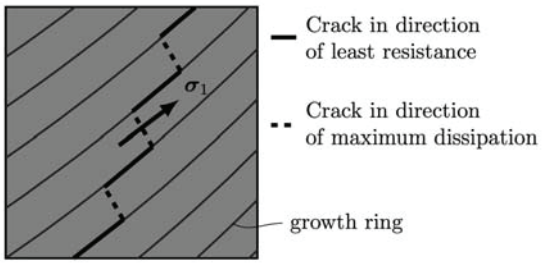

Figure 2: *Typical crack pattern of wood [31]*

The crack driving stress $\boldsymbol{\sigma}^+$ can be determined by projecting the undamaged stress tensor $\boldsymbol{\sigma}$ onto a fictitious crack surface with the crack normal vector $\boldsymbol{a}_i$ [16,27,32]. Subsequently, the mode I, II and III stresses are identified, allowing computation of $\psi_i^+(\boldsymbol{u})$. The crack orientation i that results in the largest energy release, indicated by the largest $\psi_i^+(\boldsymbol{u})$, defines the driving failure mechanism. As a result, Equation (1) is modified by replacing the original strain energy terms by

$$\begin{aligned}\psi_i^+(\boldsymbol{u},\boldsymbol{d}) &= \omega_i(d_i)\,\psi_i^+(\boldsymbol{u}) \text{ and}\\ \psi_i^-(\boldsymbol{u},\boldsymbol{d}) &= \psi_i(\boldsymbol{u}) - \psi_i^+(\boldsymbol{u}).\end{aligned} \tag{3}$$

Cohesive behavior is introduced by tuning the coefficients in the degradation function $\omega_i(d_i)$ and the crack surface density function $\gamma_i(d_i)$ on a one-dimensional bar problem with a single crack and a linear softening law [39].
The resulting energy minimization problem is solved with a staggered algorithm [4,22]. In addition, a hybrid approach [1] is used for degradation. This improves the solver's performance by making the deformation problem linear and, as shown in [27] and further outlined in Section 3.1, is required for adequately modeling the "zig-zag" crack pattern of wood. To prevent the interpenetration of crack faces, the hybrid approach is coupled with a smooth traction-free crack boundary condition [16]. Irreversibility of the phase field is enforced globally by an active-set reduced-space method [41]. An adaptive load increment scheme is adopted for further performance improvement which uses a trial point checker and a step size controller [14], restricting the increment size close to sudden changes in the dissipated energy and maintaining large increments during the linear elastic loading phase. The trial point checker performs an additional, however, very small load step, after a converged solution for the problem was found, and rejects

https://doi.org/10.52202/069179-0053

the converged state if the small additional step resulted in a change in the sign of the strain energy's slope. The step size controller works independently of the trial pointer checker an assures that after a failed load increment, the increment's size is reduced only as much as necessary to meet the convergence criterion.
The entire code is implemented in Julia [2]. For automatically deriving the element stiffness matrices and residual vectors from the energy formulation, the ForwardDiff-Package [30] is used. Pardiso 6.0 [10,18,36] is employed as the sparse linear solver.

3 RESULTS

3.1 VERIFICATION OF THE PHASE FIELD MODEL FOR WOOD

Initially, the described phase field model was verified on single-edge notched plates with varying fiber inclines and a more advanced example of a single knot in a wooden board with spatially varying principal material directions [27].
Figure 3 shows the edge notched plate under tensile loading by prescribing the vertical displacement at the upper edge. The fiber incline rises from 0 to 90 degrees. Initially, the crack path follows the weak interface between the growth rings. In a transition zone, the commonly found "zig-zag" pattern is recovered, and ultimately, the specimen fails with a crack perpendicular to the fiber direction.

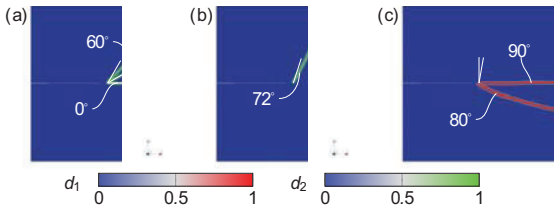

Figure 3: *Transition of failure modes from parallel to perpendicular to the fiber.*

Accurate reproduction of the "zig-zag" pattern in Figure 3 (b) requires applying the hybrid approach. This is related to the stress-based decomposition of the strain energy density described in Section 2. For forming the d_1 crack in Figure 3 (b), an energy state is required with substantial mode I, II and III stresses for the fictitious crack face defined by the normal vector in the longitudinal direction. Figure 4 shows a comparison of the longitudinal stress (i.e., the mode I stress for the d_1 crack) right before the failure of the specimen. Equation (3) is directly used to derive the constitutive relation in the variationally consistent approach. Therefore, the longitudinal stress is not degraded and, thus, peaks at the initial notch, reducing the crack driving energy at the diffuse crack tip for crack d_1. In comparison, in the case of the hybrid approach, everything except compressive mode I stresses is degraded. Therefore, the stress peaks at the diffuse crack tip, thus, allowing propagation of a $d_1$crack.

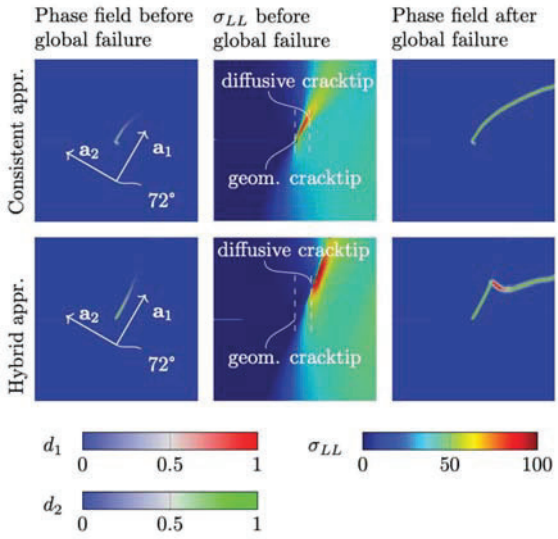

Figure 4: *Comparison of the hybrid and the consistent approach before the specimen's complete failure.*

Subsequently, the phase field model was tested on a more elaborate example. Figure 5 shows a wooden board with a single knot. The board is loaded at the bottom left edge, such that the initial crack is under tensile loading. The spatial fiber course is computed in each integration point using the model from [20]. As expected, the crack follows the fiber direction along the weak interface and shifts downwards in the vicinity of the knot until the whole specimen is cracked.

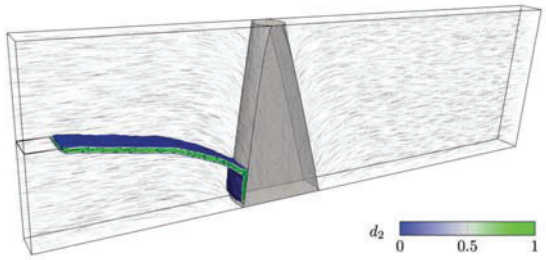

Figure 5: *Phase field crack in a wooden board with a single knot and spatially varying fiber courses.*

The results show that the hybrid multi-phase field model for wood can reproduce commonly found crack patterns of wood. Thus, it can account for the macroscopic structural effects influenced by the wood microstructure. Next, the model was validated on experimental setups in [28].

3.2 VALIDATION OF THE PHASE FIELD MODEL FOR WOOD

Three different types of tests were considered: A single edge-notched beam (SENB) [9,11], a double cantilever beam (DCB) [25] and an end-notched beam (ENB) [29]. Both the SENB and the DCB setups test for mode I

https://doi.org/10.52202/069179-0053

fracture properties; the ENB setup tests for mode II fracture properties.

In Equation (2), the structural tensor $\boldsymbol{A}_i$ is introduced in the formulation of the crack surface density function. The related scale factor β_i is an unknown quantity for wood and defines the intensity of the penalty constraint for invalid crack propagation directions. Due to the configuration of the SENB and the DCB test, β_i does not affect the crack orientation. However, the ENB test is strongly influenced by this quantity. Figure 6 shows the effect of increasing the scale factor for the primary driving failure mode in this test from 0 (isotropic formulation) to 90. This simulation allowed finding a lower bound of the structural tensors scale factor for wood. A value of 70 adequately reproduces the horizontal crack observed in the experiments in [29] and reduces the influence on the maximum load.

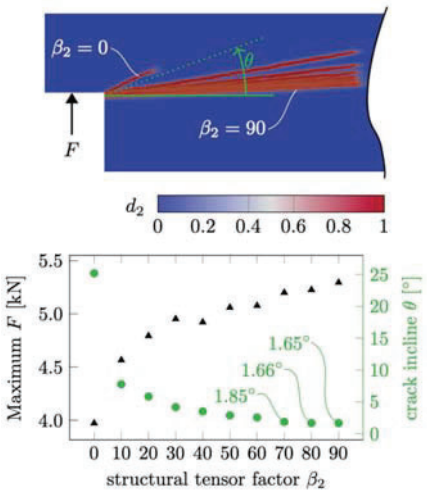

Figure 6: *Influence of the structural tensor's scale factor on the crack orientation and the ultimate load in the ENB test.*

Next, the SENB tests were simulated using the structural tensor scale factor value found for the ENB tests. Figure 7 shows the results for the tests in [9]. Using a multi-phase field model, it was possible to reproduce the experimental data very well with just a single model configuration (tensile strength and fracture energy release rate for L, R and T). Remarkably, the substantial difference in the ultimate load for a crack in the RL-plane and a crack in the TL-plane, also shown in [21], could be captured very well. Figure 8 shows the ultimate crack phase field for the SENB test in the RL-plane.

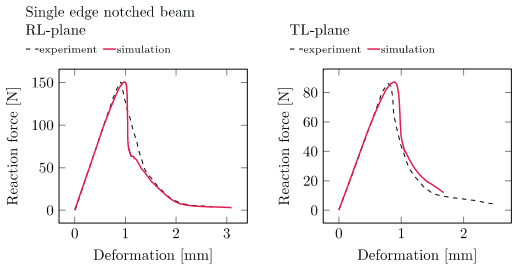

Figure 7: *Simulation and experimental graph of two SENB tests [9] with differently oriented failure planes (crack in RL-plane or TL-plane)*

Figure 8: *Fully cracked SENB specimen for the setup from [9] in the RL-plane*

Subsequently, the model was tested on the DCB tests from [25]. Figure 9 shows a large scatter of the experimental data already in the linear elastic range. This was accounted for in the model by performing simulations for different scale factors of the elastic stiffness from 0.6 to 1.0. Keeping the tensile strength and the fracture energy release constant allowed the reproduction of the experimental data very well. To reduce the computational effort, only the region right after the initial notch was finely discretized. The crack in Figure 10 was sufficient to reproduce a substantial part of the experimental data in Figure 9.

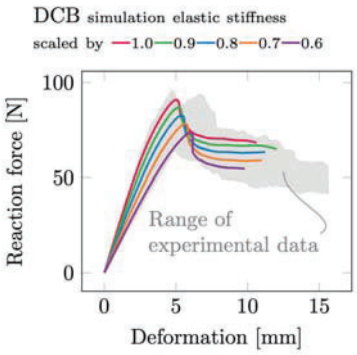

Figure 9: *Simulation and experimental results of a DCB test [25].*

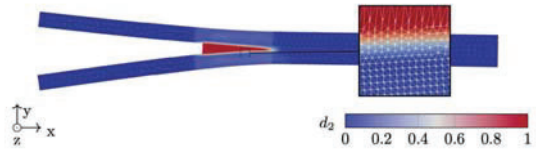

Figure 10: *Cracked DCB specimen*

Finally, the model was validated on the ENB test, which was already used to tune the scale factor of the structural tensor. In addition to a model with a tuned parameter configuration for this specific test, the material parameter found for the SENB tests of [9] were also used in the ENB model. The simulation and experimental results are shown in Figure 11. For both parameter sets, the response was within the experimental results.

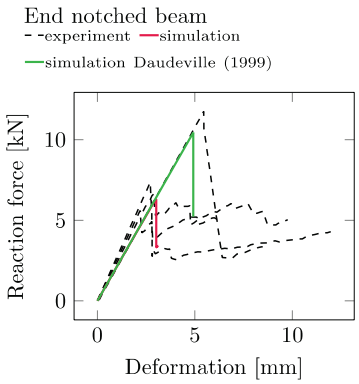

Figure 11: *Simulation and experimental results of the ENB test [29] for tuned model parameters and parameters from the SENB test from [9]*

The validation results in [28] show that the model is very well capable of reproducing experimental results, with the defining material properties, the tensile strength and the fracture energy release rate, well in a range known for wood. Furthermore, a lower bound for the structural tensor's scale factor was found, allowing the reproduction of the horizontal crack in the ENB test.

The phase field model presents a significant advantage over other models commonly used for simulating such experimental studies. Unlike in those models, the crack paths are not predefined. Instead, the model considers the local crack-driving energies and non-local effects induced by the microstructure of wood to form cracks. This approach makes the phase field model more adaptable and suitable for complex situations where the crack path is unknown in advance.

4 CONCLUSION AND SUMMARY

The present work describes implementing, validating, and verifying a phase field model for orthotropic non-brittle fracture of materials with favorable fracture planes and multiple, different failure mechanisms. The model is solved using a generally applicable staggered algorithm with globally enforced irreversibility constraints and an efficient load-stepping scheme. Using this model, it is possible to reproduce commonly found crack patterns of wood and the results of experimental tests. The model's input parameters, the tensile strength, and the fracture energy release rate are for all investigated tests within the range known for wood. Furthermore, values tuned to one experimental setup could be transferred to another setup with a different geometry. This suggests that the input parameters are material-specific rather than model-specific numerical parameters.

Compared to other three-dimensional finite element fracture mechanics simulation frameworks, the main advantage of the phase field method is that cracks of arbitrary complexity can be modeled. This is a fundamental requirement when simulating more complex wooden specimens like knot groups with spatially strongly varying fiber orientations. This work constitutes an important step towards the simulation of such complex models, which allow improved prediction of the load-bearing capacity of wooden boards. Based on an exact simulation using geometrical reconstructions of wooden boards with knots [17], homogenization procedures allow deriving metamodels similar to those in [21]. Such a simplified model allows the application to larger-scale structures or tasks, e.g., for the failure prediction of GTL beams [37], size-effect studies in GLT beams [38] or optimization of GLT beams [26].

ACKNOWLEDGEMENT

This research was funded in whole, or in part, by the Austrian Science Fund (FWF) Y1093-N30. The authors also acknowledge gratefully the support by the ForestValue project InnoCrossLam.

REFERENCES

[1] M. Ambati, T. Gerasimov, L.D. Lorenzis, A review on phase-field models of brittle fracture and a new fast hybrid formulation, Comput. Mech. 55 (2014) 383–405.

[2] J. Bezanson, A. Edelman, S. Karpinski, V.B. Shah, Julia: A fresh approach to numerical computing, SIAM Rev. 59 (2017) 65–98.

[3] J. Bleyer, R. Alessi, Phase-field modeling of anisotropic brittle fracture including several damage mechanisms, Comput. Methods Appl. Mech. Eng. 336 (2018) 213–236.

[4] B. Bourdin, G.A. Francfort, J.-J. Marigo, Numerical experiments in revisited brittle fracture, Journal of the Mechanics and Physics of Solids. 48 (2000) 797–826.

[5] B. Bourdin, G.A. Francfort, J.-J. Marigo, The variational approach to fracture, Springer-Verlag GmbH, 2008.

[6] T.Q. Bui, X. Hu, A review of phase-field models, fundamentals and their applications to composite laminates, Engineering Fracture Mechanics. 248 (2021) 107705.

[7] J. Carlsson, P. Isaksson, Simulating fracture in a wood microstructure using a high-resolution dynamic phase field model, Engineering Fracture Mechanics. 232 (2020) 107030.

[8] J.D. Clayton, J. Knap, Phase field modeling of directional fracture in anisotropic polycrystals, Computational Materials Science. 98 (2015) 158–169.

[9] L. Daudeville, Fracture in spruce: experiment and numerical analysis by linear and non linear fracture mechanics, Holz Als Roh-Und Werkstoff. 57 (1999) 425–432.

https://doi.org/10.52202/069179-0053

[10] A. De Coninck, B. De Baets, D. Kourounis, F. Verbosio, O. Schenk, S. Maenhout, J. Fostier, Needles: Toward Large-Scale Genomic Prediction with Marker-by-Environment Interaction, Genetics. 203 (2016) 543–555.
[11] N. Dourado, S. Morel, M.F.S.F. de Moura, G. Valentin, J. Morais, Comparison of fracture properties of two wood species through cohesive crack simulations, Composites Part A: Applied Science and Manufacturing. 39 (2008) 415–427.
[12] G.A. Francfort, J.-J. Marigo, Revisiting brittle fracture as an energy minimization problem, Journal of the Mechanics and Physics of Solids. 46 (1998) 1319–1342.
[13] A.A. Griffith, G.I. Taylor, VI. The phenomena of rupture and flow in solids, Philosophical Transactions of the Royal Society of London. Series A, Containing Papers of a Mathematical or Physical Character. 221 (1921) 163–198.
[14] A. Gupta, U.M. Krishnan, R. Chowdhury, A. Chakrabarti, An auto-adaptive sub-stepping algorithm for phase-field modeling of brittle fracture, Theoretical and Applied Fracture Mechanics. 108 (2020) 102622.
[15] V. Hakim, A. Karma, Crack Path Prediction in Anisotropic Brittle Materials, Phys. Rev. Lett. 95 (2005) 235501.
[16] T. Hu, J. Guilleminot, J.E. Dolbow, A phase-field model of fracture with frictionless contact and random fracture properties: Application to thin-film fracture and soil desiccation, Computer Methods in Applied Mechanics and Engineering. 368 (2020) 113106.
[17] G. Kandler, M. Lukacevic, J. Füssl, An algorithm for the geometric reconstruction of knots within timber boards based on fibre angle measurements, Constr. and Build. Mater. 124 (2016) 945–960.
[18] D. Kourounis, A. Fuchs, O. Schenk, Toward the Next Generation of Multiperiod Optimal Power Flow Solvers, IEEE Transactions on Power Systems. 33 (2018) 4005–4014.
[19] M. Li, J. Füssl, M. Lukacevic, J. Eberhardsteiner, C. Martin, Strength predictions of clear wood at multiple scales using numerical limit analysis approaches, Computers & Structures. 196 (2018) 200–216.
[20] M. Lukacevic, G. Kandler, M. Hu, A. Olsson, J. Füssl, A 3D model for knots and related fiber deviations in sawn timber for prediction of mechanical properties of boards, Materials & Design. 166 (2019) 107617.
[21] M. Lukacevic, W. Lederer, J. Füssl, A microstructure-based multisurface failure criterion for the description of brittle and ductile failure mechanisms of clear-wood, Engineering Fracture Mechanics. 176 (2017) 83–99.
[22] C. Miehe, M. Hofacker, F. Welschinger, A phase field model for rate-independent crack propagation: Robust algorithmic implementation based on operator splits, Comput. Methods Appl. Mech. Eng. 199 (2010) 2765–2778.
[23] C. Miehe, F. Welschinger, M. Hofacker, Thermodynamically consistent phase-field models of fracture: Variational principles and multi-field FE implementations, Int. J. Numer. Methods Eng. 83 (2010) 1273–1311.
[24] N. Moës, T. Belytschko, Extended finite element method for cohesive crack growth, Engineering Fracture Mechanics. 69 (2002) 813–833.
[25] M.F.S.F. de Moura, J.J.L. Morais, N. Dourado, A new data reduction scheme for mode I wood fracture characterization using the double cantilever beam test, Engineering Fracture Mechanics. 75 (2008) 3852–3865.
[26] S. Pech, G. Kandler, M. Lukacevic, J. Füssl, Metamodel assisted optimization of glued laminated timber beams by using metaheuristic algorithms, Eng. Appl. Artif. Intell. 79 (2019) 129–141.
[27] S. Pech, M. Lukacevic, J. Füssl, A hybrid multi-phase field model to describe cohesive failure in orthotropic materials, assessed by modeling failure mechanisms in wood, Engineering Fracture Mechanics. 271 (2022) 108591.
[28] S. Pech, M. Lukacevic, J. Füssl, Validation of a hybrid multi-phase field model for fracture of wood, Engineering Fracture Mechanics. 275 (2022) 108819.
[29] K. Rautenstrauch, B. Franke, S. Franke, K. Schober, A new design approach for end-notched beams: View in code, in: Paper No. CIB-W18/41-6-2, Proc., Meeting, 2008.
[30] J. Revels, M. Lubin, T. Papamarkou, Forward-Mode Automatic Differentiation in Julia, ArXiv:1607.07892 [Cs]. (2016).
[31] I. Smith, E. Landis, M. Gong, Fracture and fatigue in wood, J. Wiley, Chichester, West Sussex, England ; Hoboken, NJ, 2003.
[32] C. Steinke, M. Kaliske, A phase-field crack model based on directional stress decomposition, Comput. Mech. (2018) 1019--1046.
[33] D. Supriatna, B. Yin, D. Konopka, M. Kaliske, An anisotropic phase-field approach accounting for mixed fracture modes in wood structures within the Representative Crack Element framework, Engineering Fracture Mechanics. 269 (2022) 108514.
[34] S. Teichtmeister, D. Kienle, F. Aldakheel, M.-A. Keip, Phase field modeling of fracture in anisotropic brittle solids, Int. J. Non Linear Mech. 97 (2017) 1–21.
[35] S. Vasic, I. Smith, E. Landis, Fracture zone characterization - Micro-mechanical study, Wood and Fiber Science. 34 (2002) 42–56.
[36] F. Verbosio, A. De Coninck, D. Kourounis, O. Schenk, Enhancing the scalability of selected inversion factorization algorithms in genomic prediction, Journal of Computational Science. 22 (2017) 99–108.
[37] C. Vida, M. Lukacevic, J. Eberhardsteiner, J. Füssl, Modeling approach to estimate the bending strength and failure mechanisms of glued laminated timber beams, Engineering Structures. 255 (2022) 113862.
[38] C. Vida, M. Lukacevic, G. Hochreiner, J. Füssl, Size effect on bending strength of glued laminated timber predicted by a numerical simulation concept including discrete cracking, Materials & Design. 225 (2023) 111550.

[39] J.-Y. Wu, A unified phase-field theory for the mechanics of damage and quasi-brittle failure, J. Mech. Phys. Solids. 103 (2017) 72–99.
[40] J.-Y. Wu, V.P. Nguyen, C.T. Nguyen, D. Sutula, S. Sinaie, S.P.A. Bordas, Phase-field modeling of fracture, in: Advances in Applied Mechanics, Elsevier, 2020: pp. 1–183.
[41] H. Yang, C. Yang, S. Sun, Active-set reduced-space methods with nonlinear elimination for two-phase flow problems in porous media, SIAM J. Sci. Comput. 38 (2016) B593–B618.

https://doi.org/10.52202/069179-0053

World Conference on Timber Engineering Oslo 2023

NUMERICAL SIMULATION OF MOISTURE-INDUCED CRACKING IN INDOOR CLIMATE

Florian Brandstätter[1], Maximilian Autengruber[2], Markus Lukacevic[3], Josef Füssl[4]

ABSTRACT: Wood has the property to absorb and desorb moisture due to its hygroscopicity resulting in dimensional changes. Due to constrained non-uniform direction-depending expansion caused by moisture changes and gradients, respectively, stresses are induced, which may lead to crack initiation and propagation, reducing the load-bearing capacity of timber structures. However, little is known about the correlation between moisture changes or gradients and crack depths, and no quantitative prediction exists of crack depths caused by moisture gradients. Thus, based on numerical simulations, the cracking process for different initial moisture contents (MC) and various relative humidity (RH) reductions is investigated for two solid timber and one glued laminated timber cross-section. As a result, correlations between moisture gradients and maximum crack depths are derived, thus enabling the estimation of crack depths. The investigation revealed that cross-section size significantly influences the relation. In addition, more significant moisture gradients occur in larger cross-sections, resulting in earlier crack initiation compared to smaller ones, and crack development in larger cross-sections tends to last longer.

KEYWORDS: Extended finite element method, Multisurface failure criterion, Crack depth, Indoor climate, Wood

1 INTRODUCTION

Wood is a building material that is significantly affected by moisture. About 50% of the damages in timber constructions subjected to indoor climate conditions are caused by high and low moisture content (MC) as well as MC changes, with about half of the damage being cracks [1]. As wood is a hygroscopic material, the cell walls of wood absorb and desorb moisture from the surrounding climate, resulting in volume changes, which are additionally influenced by temperature. The strains caused by variations in MC and temperature induce stresses, as the non-uniform direction-dependent expansion is constrained. Increasing the stress level can lead to crack initiation and propagation if the strength of wood is exceeded, reducing the load-bearing capacity of timber structures. In addition, MC and temperature also influence material properties, such as strength and stiffness, which vary with the directions characteristic of wood (longitudinal, radial, and tangential). The effect of MC on material properties is limited by the so-called fiber saturation point (FSP) [2], which is the maximum amount of bound water in wooden cells. If further moisture is absorbed, it is present as free water in the lumen in addition to water vapor.

The most intense MC changes for indoor applications occur during the first winter after construction and from the beginning of erection until commissioning [1]. From December to February, the RH indoors can decrease to an average of 30 % [3-6] for two to four weeks resulting in an equilibrium MC of 8.2 % in case of pure desorption. Under uncommon conditions [7], even average RH levels of 25 % (7.2 % MC) over 30 days and 20 % RH (6.2 % MC) over 22.5 days occur. As the initial MC of wooden timber elements after production is usually between 10 % and 12 % [8], and DIN EN 14081-1:2019 allows measurement errors of ±3 % [9], during the first winter, immense moisture differences likely occur, inducing significant stresses, which may result in crack formation. However, it is unknown how deep moisture-induced cracks may propagate, and no quantitative relationship exists between crack depth and MC gradients caused by moisture changes.

Based on numerical simulations, this work aims to find a correlation between crack depth and moisture gradients and quantitatively estimate the crack depth in indoor climate conditions. Therefore, a moisture transport model based on the multi-Fickian theory [10-15] and a model for fracture in wood using the extended finite element method (XFEM) for the simulation of crack development are defined in Section 2. In addition, to find a relation for two solid timber (ST) and one glued laminated timber (GLT) cross-sections, numerous drying scenarios, which are characterized by different initial MCs and different drying loads, are simulated. When the simulation is initialized, the temperature is kept constant, but the initial RH is

[1] Florian Brandstätter, Vienna University of Technology (TU Wien), Austria, florian.brandstaetter@tuwien.ac.at
[2] Maximilian Autengruber, Vienna University of Technology (TU Wien), Austria, maxilian.autengruber@tuwien.ac.at
[3] Markus Lukacevic, Vienna University of Technology (TU Wien), Austria, markus.lukacevic@tuwien.ac.at
[4] Josef Füssl, Vienna University of Technology (TU Wien), Austria, josef.fuessl@tuwien.ac.at

https://doi.org/10.52202/069179-0054

decreased in a single step, which causes the moisture field to change and induce stresses. A multisurface failure criterion [16-19] is used to evaluate whether the induced stresses lead to crack formation. Section 3 illustrates the drying scenarios' results, and the relation between moisture gradient and crack depth is analyzed. In Section 4, the conclusion and outlook are shown.

2 MATERIALS AND METHODS

For the investigation of the relation and the prediction of the crack depth, two simulations per drying scenario are performed. In the first, moisture fields are determined based on the multi-Fickian theory. In the subsequent XFEM simulation, the moisture fields are used as a loading for the stress simulation based on linear-elastic material behavior (viscoelasticity, mechano-sorption, and plastification are not considered). For each increment in each integration point, stresses are calculated, and cracks initiate or propagate if they exceed the wood's strength. The latter is defined by a multisurface failure criterion presented in [16-19].

The commercial finite element software Abaqus (from Dassault Systèmes, Vélizy-Villacoublay, France) was used for the simulations. Quadratic brick elements with linear interpolation functions (C3D8) were used to discretize the cross-sections, and the equations were solved using the modified Newton method. The material is defined as cylindrical-orthotropic in each integration point to enable the consideration of different pith locations of the cross-sections.

2.1 MATHEMATICAL MODEL FOR MOISTURE TRANSPORT IN WOOD

The moisture transport model of [10-15] was used based on the multi-Fickian theory. It describes the transport of water vapor c_v in the lumen, as well as the transport of the bound water c_b in the cells, where the sorption rate $\dot{c}_{bv}$ is used to couple both processes, considering a hysteresis effect. As the MC in the simulations never exceeds the FSP, it is assumed that no free water occurs. To determine the change of the bound water, water vapor and energy, the following three differential equations are used:

Conservation of bound water concentration:

$$\frac{\partial c_b}{\partial t} = \frac{\partial}{\partial x} D_b \frac{\partial c_b}{\partial x} + \dot{c}_{bv} \tag{1}$$

Conservation of water vapor concentration:

$$\frac{\partial c_v}{\partial t} f_{lum} = \frac{\partial}{\partial x} D_v \frac{\partial c_v}{\partial x} f_{lum} - \dot{c}_{bv} \tag{2}$$

Conservation of energy:

$$\begin{aligned} \frac{\partial (ph)}{\partial t} = {} & \frac{\partial}{\partial x} K \frac{\partial T}{\partial x} + \frac{\partial}{\partial x} D_b \frac{\partial c_b}{\partial x} \overline{h}_b + \frac{\partial}{\partial x} D_{bT} \frac{\partial T}{\partial x} \overline{h}_b \\ & + \frac{\partial}{\partial x} D_v \frac{\partial c_v}{\partial x} h_v f_{lum} \\ & + \dot{c}_{bv} (h_v - h_b) \end{aligned} \tag{3}$$

On the left-hand side of Equations (1) to (3) the change rate of the concentrations c_b and c_v as well as of the energy (ph) are defined. The transport tensors of bound water D_b and water vapor D_v describe the diffusion processes, while K accounts for the thermal conduction. While c_b is related to the whole volume of the representative volume element (RVE), c_v is only referred to the volume proportion of the lumen f_{lum}. Whereas $\overline{h}_b$ and h_b define the average and specific enthalpy of bound water, respectively, h_v describes the enthalpy of water vapor.

The constitutive equations for the model are obtained from Autengruber et al. [20]. To implement equations (1) to (3) in Abaqus, the user element subroutine UEL was used.

[13] investigated the interaction between water vapor and bound water, using the sorption rate for description. An isothermal hysteresis was assumed for the simulations, as the temperature was kept constant.

For the initial conditions, it is assumed that the initial bound water concentration $c_{b,ini}$ and the initial water vapor concentration $c_{v,ini}$ are in equilibrium. $c_{b,ini}$ derives from the initial temperature T_{ini} and $c_{v,ini}$, which depends on the initial RH level.

The surrounding climate influences the moisture transport at the wood surfaces, where the effects are considered with Neuman boundary conditions. The given fluxes of water vapor Φ_v and energy Φ_T across the boundary are described by the following equations:

$$\Phi_v = k_{c_v}(c_v - c_{v,0}) f_{lum} \tag{4}$$

$$\Phi_T = k_T(\mathrm{T} - T_0) + k_{c_v}(c_v - c_{v,0}) f_{lum} h_v \tag{5}$$

with

$$k_{c_v} = \frac{Sh}{L} D_{air} \tag{6}$$

k_{c_v} is a film boundary coefficient that considers air flow and convection depending on air speed and surface roughness. Sh is 1 and L is 0.035 m [10] and $D_{air}$is the diffusion coefficient for water vapor in air. k_T defines the heat transfer coefficient and $T_0$is the temperature of distant air, where T is kept constant at 293.15 K.

2.2 MODEL FOR FRACTURE IN WOOD

After the moisture simulation, an XFEM simulation is performed to determine stresses caused by constrained shrinkage deformations, where the moisture fields are used as loading. For the XFEM simulations, moisture-dependent stiffness properties are presented, and the multisurface failure criterion from [16-19], defining the strength of wood, is introduced. The user element subroutine UDMINI was used to implement the criterion in Abaqus. In addition the enrichment regions for all cross-sections are defined and a certain distance is introduced, which is to be referred to as crack depth.

The moisture-dependant material properties of wood are based on the micromechanics material model of [21] with a clear wood dry density of 420 kg m^{-3} for Norway spruce (Picea abies). Based on this, elasticity tensor components for MC levels between 3 % and 30 % were determined and implemented in *Abaqus* (see [22] for details).

For the strength of wood, a multisurface failure criterion from [18], which considers the structure of wood at the

https://doi.org/10.52202/069179-0054

level of annual rings (late- and earlywood), is used. Based on multiple load combinations, the criterion was formulated, leading to eight Tsai-Wu surfaces [23] for the definition of failure:

$$f_i^{cw}(\sigma) = a_{LL,i}\sigma_{LL} + a_{RR,i}\sigma_{RR} + a_{TT,i}\sigma_{TT} + b_{LLLL,i}\sigma_{LL}^2 + b_{RRRR,i}\sigma_{RR}^2 + b_{TTTT,i}\sigma_{TT}^2 + 2b_{RRTT,i}\sigma_{RR}\sigma_{TT} + 4b_{LRLR,i}\tau_{LR}^2 + 4b_{RTRT,i}\tau_{RT}^2 + 4b_{TLTL,i}\tau_{TL}^2 \leq 1 \quad (7)$$

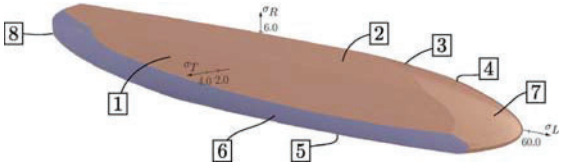

Figure 1: *Surfaces of the failure criterion, illustrated in the* $\boldsymbol{\sigma_{LL} - \sigma_{RR} - \sigma_{TT}}$ *stress space from [18].*

Only the surfaces describing brittle failure (surfaces 1,2,3, and 7) are considered in this work. If the induced stresses exceed the limits of the criterion, the corresponding failure surface defines the orientation of the crack initiation or propagation. The strength limits vary depending on the material orientation (longitudinal 56 MPa, radial 5 MPa, and tangential 2 MPa).

In *Abaqus*, so-called enrichment regions have to be defined to enable cracking. Unless multiple elements violate the failure criterion within the same time increment, only one crack can initiate per region. The enrichment configuration of the cross-sections is based on [22]. While for the GLT cross-section each lamella is divided into two equal-sized regions, one on top of the other, a cross-section configuration of eight rows and three columns is used for the ST cross-sections.

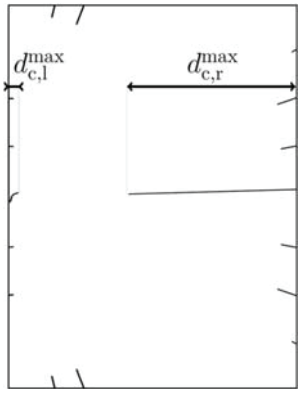

Figure 2: *Exemplary crack pattern of the cross-section ST 6 x 8. The deepest cracks on both the left and right edges are defined as* $\boldsymbol{d_{c,l}^{max}}$ *and* $\boldsymbol{d_{c,r}^{max}}$*, respectively.*

In the XFEM simulations, the crack pattern development is expected to vary depending on cross-section size, initial MC, and drying load. As the deepest cracks affect the safety of structures most, the maximum crack depth is analyzed to describe the evolution of the crack pattern, where the crack depth d_c is defined as the perpendicular distance from the surface to the crack tip. Since cracks on both edges are expected, the maximum crack depths on the left ($d_{c,l}^{max}$) and right ($d_{c,r}^{max}$) edges are determined and subsequently summed, defined as the maximum total crack depth d_c^{max} (see Figure 2).

2.3 DRYING SCENARIOS

Initially, the MC, which results from the surrounding RH, is uniform across the cross-section. When the simulation is initialized, the RH is reduced in a single step to a certain level, which is kept constant for 30 days, leading to moisture field changes. The RH level is reduced so that the expected equilibrium MC is decreased by a Δu_{equ} of 1 % up to 15 % (see Table), considering the desorption isotherm. Due to the non-linear shape of the isotherm, different initial MC levels (10.0 %, 11.9 %, 15.3 %, and 22.0 %) are investigated, which correspond to the RH levels 40.0 %, 50.0 %, 65.0 %, and 85.0 %, respectively. The initial values are based on RH, as this is easier to measure than Δu_{equ} in wood components. The initial RH values derive from the limits of the service classes in EC 5 [24].

Table 1: *Overview of the single-step relative humidity (RH) reductions at the boundary, resulting in differences in equilibrium moisture content* $\boldsymbol{\Delta u_{equ}}$ *of 1 % up to 15 % from four initial RH levels (40 %, 50 %, 65 %, and 85 %) determined with the desorption isotherm.*

Δu_{equ}	initial RH [%] (initial MC [%])			
	40 (10.0)	50 (11.9)	65 (15.3)	85 (22.0)
1	34.6	44.8	61.0	82.6
2	29.0	39.4	56.6	80.0
3	23.8	34.0	51.8	77.4
4	18.8	28.6	46.8	74.4
5	14.4	23.2	41.4	71.0
6	10.6	18.4	36.0	67.6
7	7.4	14.0	30.6	63.6
8	4.4	10.2	25.2	59.6
9	2.0	7.0	20.2	55.0
10	0.0	4.2	15.6	50.2
11	-	1.8	11.6	45.0
12	-	0.0	8.2	39.6
13	-	-	5.2	34.2
14	-	-	2.6	28.8
15	-	-	0.6	23.4

2.4 GEOMETRIES

For the simulations, two solid timber (ST) and one glued laminated timber (GLT) cross-section are studied in this work. The cross-sections are ST 6 x 8, ST 14 x 28, and GLT 20 x 40 (width x height in centimeters), commonly used for timber structures (see Figure 3). The pith location of the ST cross-sections is in the middle of the left edge,

as the deepest cracks are expected for this configuration, as shown by [22]. The lamella height of the GLT cross-section is 4 cm, the pith is located in the middle of the bottom, and the lamellas' orientation is based on common production standards [9]. It is assumed that the glue lines are made of melamine, which only minimally affects moisture transport since the diffusion characteristics of melamine and solid timber are similar [25].

To model plain-strain conditions, only one element with a depth of 1 mm in the longitudinal direction is defined. An overview of the other dimensions of the mesh is presented in Table 2. A hinged support in the center point and a roller support in the middle of the cross-section's right edge are defined for the geometric boundary conditions. Plain-strain conditions are assumed, and therefore, no deformations out-of-plane are allowed. In addition, no initial eigenstresses from, e.g., production processes, are assumed.

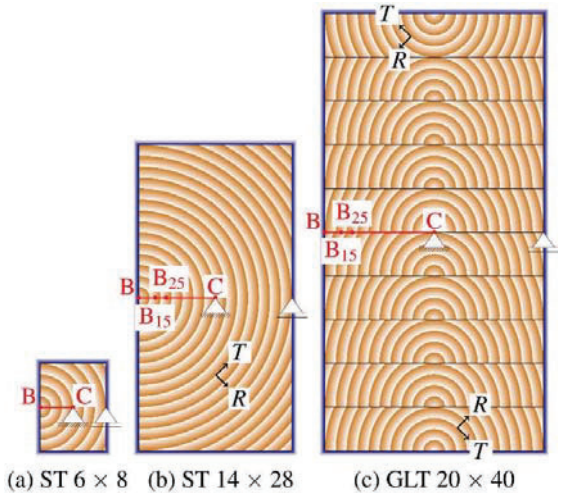

Figure 3: *Illustration of the used cross-sections, including the annual rings, pith locations, the definition of the local coordinate systems, and finite element node reference points: B, B_{15}, B_{25}, and C, where B_{15} and B_{25} are 15 mm and 25 mm, respectively, distant to the boundary. B_{15} and B_{25} are required for the moisture gradient definition in Section 3.2 [26].*

Table 2: *Mesh configurations of the cross-sections*

Elements	ST		GLT
	6 x 8	14 x 28	20 x40
Number	60 x 80	60 x 84	60 x 80
Width [mm]	1	2-4	2-5
Height [mm]	1	2-5	5

3 RESULTS

In the following, the crack initiation and propagation process is presented as well as the development of d_c^{max} for all initial MCs and Δu_{equ} are analyzed. The relationship between moisture gradients and crack depth is investigated based on the development results.

First, the crack initiation and propagation process are described in more detail using Figure 4, where the initial RH was reduced from 65 % to 20.2 % (final state) for the GLT 20 x 40 (see Figure 4 a). This results in a Δu_{equ} of 9 %. When the moisture simulation is initialized, the uniform moisture field adapts to the single-step reduction of the RH, leading to a non-uniform moisture distribution (see Figure 4 b). In the subsequent XFEM simulation, the stresses induced by the moisture field are determined per increment. At the same time, in each integration point, the multisurface failure criterion is evaluated, and if its limits are exceeded, cracks initiate (see Figure 4 c) or propagate (see Figure 4 d and e). Cracking is finished as soon as the criterion is not fulfilled anymore (see Figure 4 f).

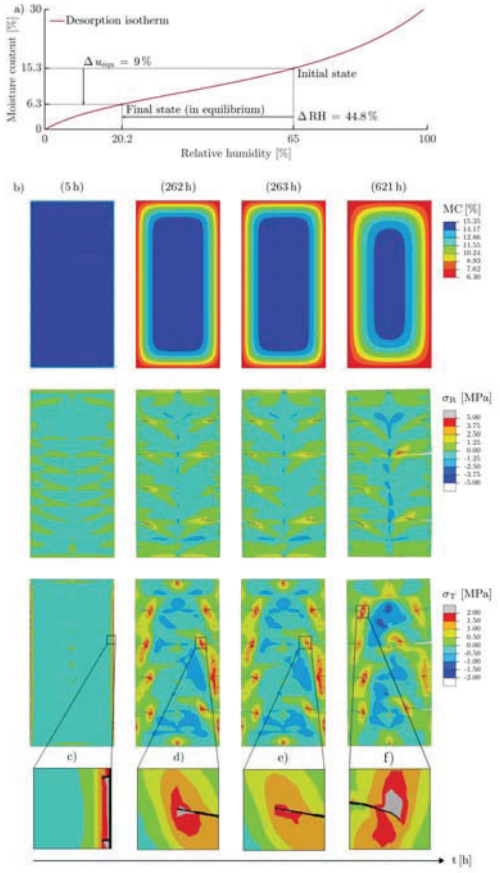

Figure 4: *Cracking process description: (a) Reducing the relative humidity causes moisture field adaptions (b). Stresses, such as $\boldsymbol{\sigma_R}$ and $\boldsymbol{\sigma_T}$, cause (c) initiation and (d-e) propagation of cracks, if the multisurface failure criterion is violated. As soon as the moisture-induced stresses no longer exceed the limits of the criterion, the cracking process is completed [26].*

3.1 CRACK DEPTH DEVELOPMENT

Before the crack depth development investigation, the crack formation at the end of the simulations for all cross-sections is presented, exemplified for an MC reduction from 15.3 % to 2.3 % (Δu_{equ} = 13 %) to show a characteristic crack pattern. For the ST cross-sections, multiple cracks on the top, bottom, and right edge occur,

https://doi.org/10.52202/069179-0054

whereas, on the left edge, only a few cracks can be seen due to the pith's location. However, it is noticeable that for the ST 6 x 8, the deepest crack is located at the middle height, while for the ST 14 x 28, the deepest one is at three quarters of the height. In the case of Δu_{equ} below 12 %, for the ST 14 x 28, the deepest crack also occurs in the middle of the cross-section. Furthermore, additional simulations confirmed that deep vertical cracks can be observed for the ST 14 x 28, which is related to the height-to-width ratio. The GLT 20 x 40 shows a different cracking behavior compared to the ST cross-sections. As the piths are located at the bottom of the lamellas, cracks occur on both the left and right edges. It can be seen that there are lamellas with one deeper and one shorter crack, as well as lamellas with three tiny cracks occur.

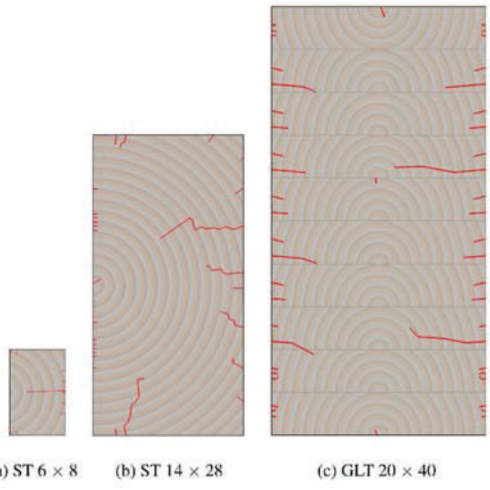

***Figure 5**: Overview of the crack pattern for all cross-sections at the end of the simulation (t = 30 d), exemplified for a reduction of the initial MC from 15.3 % to 2.3 %. In addition, the pith location and the annual rings are illustrated. [26].*

In the following, the development of d_c^{max} is analyzed. Therefore, for all cross-sections, the evolution of d_c^{max} for different MCs and various Δu_{equ} over the complete simulation time is illustrated in Figure 6. For each drying scenario, $d_{c,l}^{max}$ and $d_{c,r}^{max}$ were documented at 0.25 d, 0.5 d, 1 d, 2 d, 3 d, 5 d, 10 d, 15 d, 20 d, 25 d, and 30 d, and subsequently, d_c^{max} was determined. [27] presented that $d_{c,l}^{max}$ and $d_{c,r}^{max}$ of 15 mm to 30 mm are in an acceptable range for timber structures to be considered safe, but the shape of the GLT girder, as well as the type of load, should be matched to the expected crack depth in the design of timber structures. Therefore, for the GLT cross-section in Figure 6, a d_c^{max} of 2 x 15 cm is marked. As the load-bearing capacity of ST cross-sections is also affected by cracking, a depth of 15 mm is highlighted because the pith location results in an asymmetric crack formation.

Figure 6 shows the development of d_c^{max} for all cross-sections under all drying scenarios given in Table 2, where d_c^{max} is given both in mm and in percent (cracked width). For all cross-sections, it can be seen that with increasing cross-section size, cracking stops later under the same conditions. For the ST 6 x 8, cracking ends between 1 d and 3 d, while for the GLT 20 x 40, crack propagation comes to a halt between 5 d and 30 d (in a few cases, the theoretical crack formation can even last longer than 30 d). This is related to the reduction of the MC in the cross-section's center. As soon as the RH is reduced, the MC decreases from both edges toward the center at the same rate. When the center is reached, the MC reduction is accelerated by the contribution of the opposite side. If the boundary condition is applied to only one side, the MC reduction rate would not be increased, as shown in [28]. Therefore, for smaller cross-sections, cracking stops earlier compared to larger cross-sections. In addition, it is noticeable that for the GLT 20 x 40 and the ST 14 x 28, cracking occurs from a Δu_{equ} of 3 %, whereas for the ST 6 x 8, a Δu_{equ} of 4 % is required for cracks to initiate. Only in the case of an initial MC of 22.0 %, a Δu_{equ} of 4 % leads to the first cracks for the ST 14 x 28. Since the moisture distribution is similar during the first hours and the MC in the center is minimally reduced, it can be concluded that cross-section size influences the drying load required to cause crack initiation due to larger moisture-induced stresses. The remaining effects on crack depth development caused by variation in Δu_{equ} are described in detail in [26].

3.2 RELATION OF CRACK DEPTH AND MOISTURE GRADIENT

Since a quantitative prediction of d_c^{max} seems possible for installations where equilibrium MC is given initially, the relation between crack depth and moisture gradient is studied. Dietsch et al. [1] revealed that about 50 % of the damages in timber structures are related to low and high MC and MC changes, resulting in moisture gradients. In [1], they were evaluated between 15 mm and 25 mm from the surface [28]. In this work, a similar approach was chosen: the moisture gradient is defined as the difference in MC between the two points P_1 and P_2, divided by their distance $(\Delta u/\Delta x)_{P_1P_2}$. [22] showed that the deepest moisture-induced cracks occurred when the difference in MC between the surface and the center was at maximum. It follows that the positions where the moisture gradient is evaluated also have to be considered. Therefore, the positions B, B_{15}, B_{25}, and C located on the path between B and C are investigated (see Figure 3), where B_{15} and B_{25} are 15 mm and 25 mm distant to the surface, respectively. For B_{15} and B_{25}, the nodes closest to them define the points for the moisture gradient, as at exactly 15 mm and 25 mm from the surface, there do not have to be finite element nodes (for details see [26]). The following three $(\Delta u/\Delta x)_{P_1P_2}$ configurations are examined: the moisture gradient between B and C $(\Delta u/\Delta x)_{BC}$, between B_{15} and B_{25} $(\Delta u/\Delta x)_{B_{15}B_{25}}$ and between B_{15}^{B} and B_{15}^{c} $(\Delta u/\Delta x)_{B_{15}^{B}B_{25}^{C}}$.

https://doi.org/10.52202/069179-0054

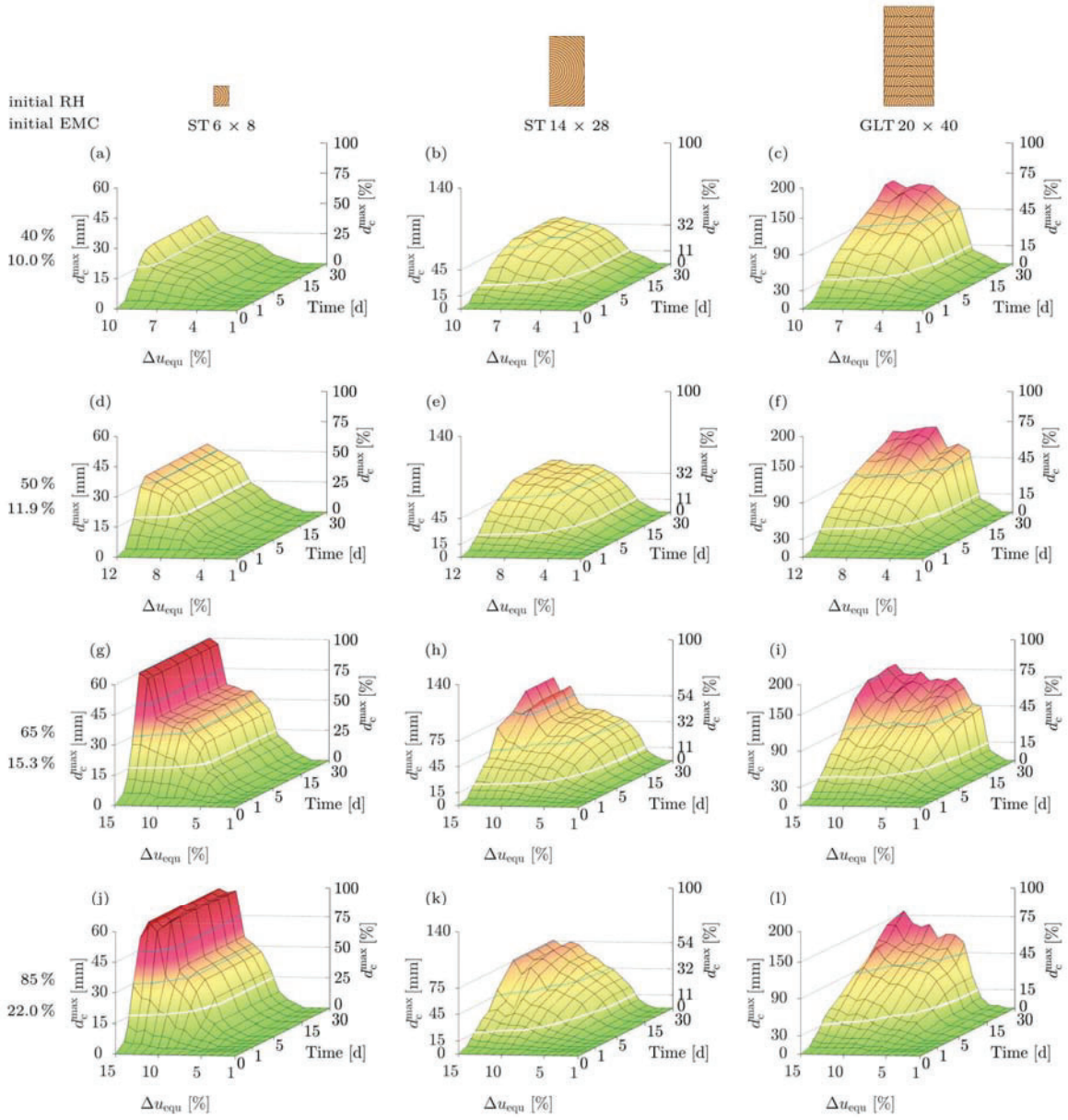

***Figure 6**: Development of the maximum total crack depth $\boldsymbol{d_c^{max}}$ (absolute and in percent of the width) for all cross-sections with initial moisture contents of 10.0 % (a, b and c), 11.9 % (d, e, and f), 15.3 % (g, h and i) and 22.0 % (j, k and l) when the equilibrium moisture content $\boldsymbol{\Delta u_{equ}}$ is reduced from 1 % up to 10 %, 12 % and 15 %, respectively, over 30 days. The white lines mark the limits (ST:15 mm; GLT: 30 mm), above witch the shape of the GLT girder as well as the type of load should be matched to the expected crack depth in the design of timber structures [27]. The blue dotted lines improve the perceptibility of $\boldsymbol{d_c^{max}}$ [26].*

In case of $(\Delta u/\,\Delta x)_{B_{15}^{B}B_{25}^{C}}$, the nodes closest to B15 are used for the definition of the moisture gradient, where one is closer to B (B_{15}^{B}) and the other closer to C (B_{15}^{C}). As the diffusion coefficients in radial and tangential directions are assumed equal, and the mesh is symmetrically along the vertical middle axis, B can be located on the left or on the right edge without affecting $(\Delta u/\Delta x)_{P_1P_2}$.

In the following, the approach to describe the relation between d_c^{max} and, exemplary, $(\Delta u/\Delta x)_{BC}$ is shown, with the result illustrated in Figure 7. For the ST 6 x 8, the developments of d_c^{max} and $(\Delta u/\Delta x)_{BC}$ are displayed with an initial MC of 15.3 % and for a Δu_{equ} of 5 %, 7 %, and 9 % (see Figure 7a). Observing Figure 7a reveals that for each point in time, a d_c^{max} can be connected to a $(\Delta u/\Delta x)_{BC}$, but as the deepest cracks are essential for the design of timber structures, the maximum d_c^{max} is related to the largest $(\Delta u/\Delta x)_{BC}$. More details about the relation and developments of Δu_{equ} and $(\Delta u/\Delta x)_{BC}$ are presented in detail in [26].

https://doi.org/10.52202/069179-0054

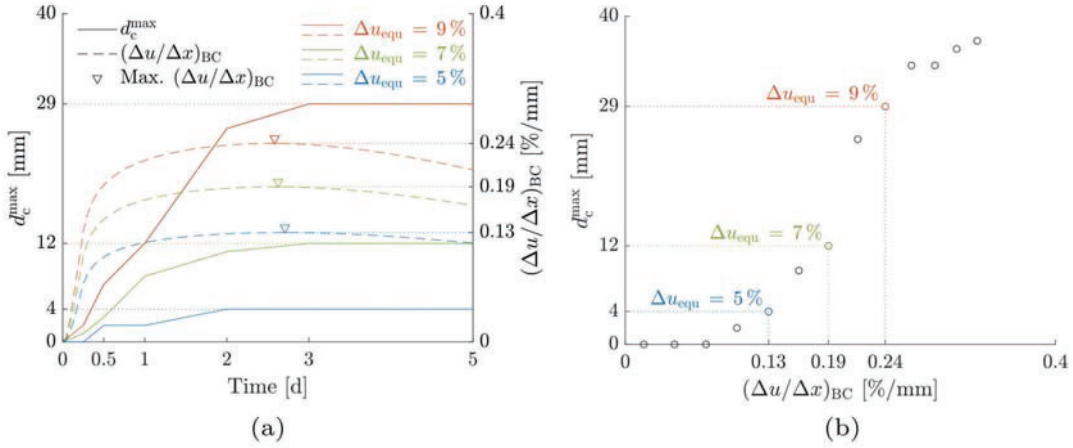

***Figure** 7: Relation between the moisture gradient $(\Delta u/\Delta x)_{BC}$ between the two points B and C (B: boundary; C: centre; see* Figure 3*) and the maximum total crack depth (d_c^{max}) for the ST 6 x 8with an exemplary initial moisture content of 15.3 % In (a), the developments of d_c^{max} and $(\Delta u/\Delta x)_{BC}$. for three different reductions of the equilibrium moisture content Δu_{equ} (*5 %, 7 % and 9 %*) are displayed. In (b), the maxima of d_c^{max} and $(\Delta u/\Delta x)_{BC}$. For Δu_{equ} reductions from 1 % up to 13 % are shown, illustrating the relation between d_c^{max} and $(\Delta u/\Delta x)_{BC}$ [26].*

In Figure 7 b), the maxima of d_c^{max} and $(\Delta u/\Delta x)_{BC}$. For Δu_{equ} reductions from 1 % up to 13 % are shown, excluding 14 % and 15 %, as they are assumed outliers. Observing the data, an exponential increase can be seen, followed by a leveling off of the trend. This behavior can be described with the so-called Gompertz function, which is defined as:

$$d_c^{max}((\Delta u/\Delta x)_{P_1P_2}) = g^{max} e^{-g^l e^{-g^g (\Delta u/\Delta x)_{P_1P_2}}} \quad (8)$$

with d_c^{max} as the maximum total crack depth in mm, the moisture gradient between two points, P1 and P2, $(\Delta u/\Delta x)_{P_1P_2}$ in [%/mm] as well as the function parameters g^{max}, $g^{l,}$ and g^g. g^{max} defines the asymptote and, therefore, the maximum d_c^{max}, g^l sets the displacement along the ordinate axis, and g^g describes the inflection point's growth rate.

Next, the influence of the moisture gradient configuration on the relation is investigated (see Figure *8*). For all cross-sections, the relation between d_c^{max} and $(\Delta u/\Delta x)_{BC}$, $(\Delta u/\Delta x)_{B_{15}B_{25}}$, and $(\Delta u/\Delta x)_{B_{15}^B B_{25}^C}$ with an initial MC of 15.3 % is illustrated, where for each configuration, the best fitting Gompertz function and the corresponding coefficient of determination are shown. As the coefficients of determination are all above 0.97 and the curves fit the data, it follows that such functions can be used to relate the moisture gradients to d_c^{max}, depending on the size of the cross-section. The differences between the configurations are minimal, and therefore, for further investigations, $(\Delta u/\Delta x)_{BC}$ is recommended, due to better possible prediction of the MC at the boundary and the center for larger cross-sections, as presented by [29]. More details about the influence of the moisture gradient configurations on the relation are presented in [26]. In addition, in [26], the effect of varying initial MC on the relation is investigated, and the influence of reducing the RH linearly over time on crack depth development is studied. Furthermore, a simplified crack depth determination for indoor climate conditions is presented.

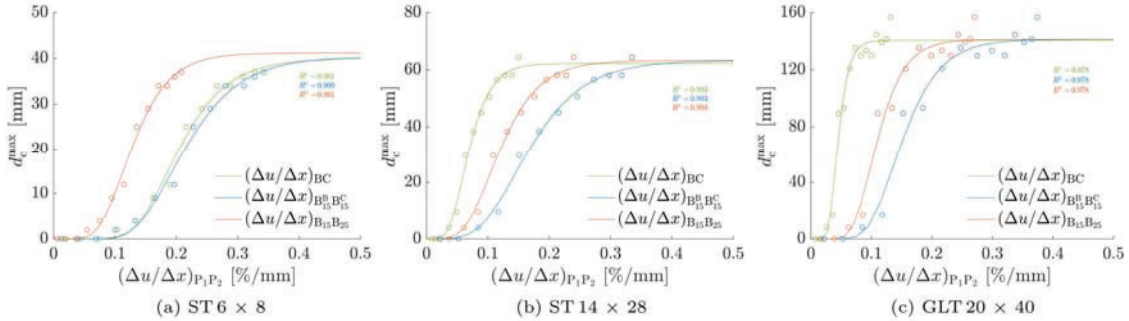

***Figure** 8: Development of the maximum total crack depth d_c^{max} depending on the moisture gradient configuration between two points P_1 and P_2 $(\Delta u/\Delta x)_{P_1P_2}$ to analyse the effect of the positions P_1 and P_2 (B, B_{15}, $B_{25,}$ and C) on the relation with an initial MC of 15.3 % for all cross-sections. The positions are on the path between boundary B and center C (see* Figure 3*). The data illustrated as circles represent the maxima of d_c^{max} related to the maxima of the corresponding $(\Delta u/\Delta x)_{P_1P_2}$ (see Figure 7) [26].*

https://doi.org/10.52202/069179-0054

4 CONCLUSIONS AND OUTLOOK

To quantitatively estimate crack depths in indoor climate conditions and to find a relation between crack depth and moisture gradient, in this work, the crack depth development of two solid timber and one glued laminated timber cross-section for different immediate RH reductions and initial MCs was analyzed numerically. Based on the simulation results, a relation between the maximum total crack depth d_c^{max}, which is the sum of the deepest cracks on the right and left side, and the moisture gradient was established. Thus, the prediction of d_c^{max} in indoor climate conditions for installations, where after production, timber members are protected from environmental influences to have a uniform initial moisture field at the beginning of the operation, seems possible. A multi-Fickian moisture transport model [10-15] was used to simulate the moisture distribution developments within the cross-sections. Those were then used as a loading for the subsequent XFEM simulations, where moisture-induced stresses were determined considering linear-elastic material behavior. For these fracture simulations, a multisurface failure criterion [18] for describing failure behavior and a multiscale material model [21] to determine the moisture-dependant stiffness tensor were used. The main findings are summarised as follows:

- Moisture gradients were correlated to d_c^{max}, where the relation depends on cross-section size.
- In larger cross-sections, larger moisture gradients occurred, which is why cracks initiate earlier compared to smaller cross-sections.
- For larger cross-sections, crack propagation lasted longer than for smaller cross-sections.

For future work, the cracking behavior of different cross-sections or wood products could be analyzed. E.g., [30] used these models to investigate the moisture transport in a timber-concrete composite plate after cast-in-place concrete application, indicating potential moisture-induced cracking behavior due to low surrounding RH.

ACKNOWLEDGEMENT

The funding from the Austrian Science Fund (FWF) through the START project Y1093 "Virtual Wood Labs", the SFB F77 "Advanced Computational Design", and the Forest Value project InnoCrossLam are gratefully acknowledged.

REFERENCES

[1] P. Dietsch, A. Gamper, M. Merk, S. Winter, Monitoring building climate and timber moisture gradient in large-span timber structures, *Journal of Civil Structural Health Monitoring*, 5 (2): 153–165, 2015.

[2] J. Siau: Transport Processes in Wood, Springer-Verlag Berlin Heidelberg, New, York Tokyo, 1984

[3] J. Ferdyn-Grygierek, Indoor environment quality in the museum building and its effect on heating and cooling demand, *Energy and Buildings*, 85: 32-44, 2014.

[4] J. L. Nguyen, J. Schwartz, D. W. Dockery, The relationship between indoor and outdoor temperature, apparent temperature, relative humidity, and absolute humidity, *Indoor Air*, 24 (1): 103–112, 2014.

[5] S. Hameury, T. Lundström, Contribution of indoor exposed massive wood to a good indoor climate: in situ measurement campaign, *Energy and Buildings*, 36 (3): 281–292, 2004.

[6] T. Log, Indoor relative humidity as a fire risk indicator, *Building and Environment*, 111: 238 – 248, 2017.

[7] T. Alsmo, C. Alsmo, Ventilation and relative humidity in swedish buildings, *Journal of Environmental Protection*, 5: 1022 – 1036, 2014.

[8] P. Dietsch, Effect of reinforcement on shrinkage stresses in timber members, *Construction and Building Materials*, 150: 903–915, 2017.

[9] DIN EN 14081-1:2019 10 01: Timber structures – Strength graded structural timber with rectangular cross-section – Part 1: General requirements (Berlin: Deutsches Institut für Normung, 2019).

[10] J. Eitelberger, K. Hofstetter, S. Dvinskikh, A multiscale approach for simulation of transient moisture transport processes in wood below the fiber saturation point. *Compos. Sci. Technol*., 71 (15): 1727–1738, 2011

[11] S. Fortino, A. Genoese, A. Genoese, L. Nunes, P. Palma, Numerical modelling of the hygro-thermal response of timber bridges during their service life: A monitoring case-study. *Constr. Build. Mater*. 47: 1225–1234, 2013

[12] S. Fortino, P. Hradil, G. Metelli, Moisture-induced stresses in large glulam beams. case study: Vihantasalmi bridge. *Wood Material Science & Engineering*, 14 (5): 366–380, 2019

[13] H.L. Frandsen, L. Damkilde, S. Svensson, A revised multi-Fickian moisture transport model to describe non-Fickian effects in wood. *Holzforschung*, 61: 563-572, 2007.

[14] D. Konopka, M. Kaliske, Transient multi-fickian hygro-mechanical analysis of wood. *Computers Struct*., 197: 12–27, 2018

[15] K. Krabbenhoft, L. Damkild: A model for non-fickian moisture transfer in wood, *Materials and Structures*, 37(9): 615–622, 2004.

[16] M. Lukacevic, J. Füssl, R. Lampert: Failure mechanisms of clear wood identified at wood cell level by an approach based on the extended finite element method, *Engineering Fracture Mechanics*, 144:158–175, 2015.

[17] M. Lukacevic, J. Füssl, Application of a multisurface discrete crack model for clear wood taking into account the inherent microstructural characteristics of wood cells. *Holzforschung*, 70 (9): 845–853, 2016

[18] M. Lukacevic, W. Lederer, J. Füssl: A microstructure-based multisurface failure criterion for the description of brittle and ductile failure mechanisms of clear-wood, *Engineering Fracture Mechanics*, 176:83–99, 2017.

https://doi.org/10.52202/069179-0054

[19] M. Li, J. Füssl, M. Lukacevic, J. Eberhardsteiner, C. M. Martin, Strength predictions of clear wood at multiple scales using numerical limit analysis approaches. *Computers & Struct*. 196 200–216, 2018
[20] M. Autengruber, M. Lukacevic, J. Füssl, Finite-element-based moisture transport model for wood including free water above the fiber saturation point. *Int. J. Heat Mass Tran.* 161 (Nov. 2020) 120228.
[21] K. Hofstetter, C. Hellmich, J. Eberhardsteiner, Development and experimental validation of a continuum micromechanics model for the elasticity of wood, European Journal of Mechanics - A/Solids 24 (6) 1030–1053. 2005
[22] M. Autengruber, M. Lukacevic, C. Gröstlinger, J. Füssl. Finite-element-based prediction of moisture-induced crack patterns for cross-sections of solid wood and glued laminated timber exposed to a realistic climate condition. Constr. Build.Mater.;271:121775, 2021
[23] Tsai SW, Wu EM. A general theory of strength for anisotropic materials. *J Compos Mater.* 5(1):58–80, 1971
[24] Austrian Standards International, ÖNORM B 1995-1-1:2019-06-01. Eurocode 5: Design of timber structures – Part 1-1: General – Common rules and rules for buildings – Consolidated version with national specifications national comments and national supplements for the implementation of ÖNORM EN 1995-1-1 (Vienna: Austrian Standards, 2019).
[25] T. Volkmer, J.-A. Schmidt, K. Kranitz, P. Niemz, Untersuchungen zum Einfluss der Klebstoffart auf den Diffusionswidertand von Holzverklebungen, Bauphysik 34 (2) 55–60. 2012
[26] F. Brandstätter, M. Autengruber, M. Lukacevic, J. Füssl. Prediction of moisture-induced cracks in wooden cross-sections using finite element simulations (in revision)
[27] P. Frech, Beurteilungskriterien für rissbildung im konstruktiven holzbau, Fraunhofer IRB Verlag (1998)
[28] S. Svensson, G. Turk, T. Hozjan, Predicting moisture state of timber members in a continuously varying climate, Engineering Structures 33 (11) 3064–3070. 2011
[29] M. Autengruber, M. Lukacevic, C. Gröstlinger, J. Eberhardsteiner, J. Füssl, Numerical assessment of wood moisture content-based assignments to service classes in EC5 and a prediction concept for moisture-induced stresses solely using relative humidity data, Engineering Structures 245 112849. 2021
[30] M. Lukacevic, M. Autengruber, T. Raimer, J. Eberhardsteiner, J. Füssl, Effect of cast-in-place concrete application on moisture distribution in timber-concrete composite floors with notched connections, investigated via finite element simulations, Journal of Building Engineering 42 103005. 2021

World Conference on Timber Engineering Oslo 2023

EXPERIMENTAL DETERMINATION OF R CURVES FOR EUROPEAN SPRUCE USING DCB TESTS

Marija Todorović[1], Marko Pavlović[2], Ivan Glišović[3], Mathieu Koetsier[4]

ABSTRACT: This paper presents an experimental procedure for obtaining the fracture resistance (R curve) of solid wood specimens made of spruce. Double Cantilever Beam (DCB) tests were performed in order to determine energy release rate vs crack length in Mode I wood fracture (crack opening). Ten wood specimens were loaded using the Universal Testing Machine and force-displacement curves were recorded. The most important parameter - crack length was monitored as the crack propagates using Digital Image Correlation (DIC) method. In order to obtain accurate R curve results, procedure which includes calculating cumulative released energy was employed. The cohesive energy G_f was determined based on the R curves. These results can further be analysed in order to obtain cohesive law for Mode I fracture of wood.

KEYWORDS: Mode I fracture, wood, DCB, DIC, R curve

1 INTRODUCTION

Sustainability, renewability and circularity have become great concerns for today's society. Since the construction industry represents one of the biggest sectorial emitters of greenhouse gases causing anthropogenic climate change, application of sustainable and/or natural materials for buildings is advisable as a significant mitigation measure. Aside from its aesthetic appeal, wood represents an eco-friendly material with a significant potential for civil engineering. In order for wood to be implemented correctly for structural purposes, its mechanical behaviour has to be defined for different stress states that can appear in the design process.

Often, timber beam's height needs to be reduced at the supports (notched) so as to satisfy different structural and architectural requirements. Notches represent potentially weak spots in timber structural elements, as stress concentration occurs at the notch corner, decreasing the overall load-carrying capacity. In order to determine possibilities for strengthening and adequate design procedures, comprehensive research has been performed on end-notched timber beams [1]. The research results have proved that a dominant failure mechanism of unreinforced end-notched beams is Mode I fracture - crack opening (Figure 1) caused by excessive tensile stress perpendicular to grain of timber with unstable crack propagation. The unreinforced end-notched have experienced a considerably reduced load-carrying capacity compared to the expected load-carrying capacity of the beams without notches. In order to accurately describe the behaviour of end-notched timber beams, it is necessary to determine Mode I fracture parameters. Therefore, cohesive law for Mode I fracture of wood is necessary for adequate analysis of stress state around the notch area.

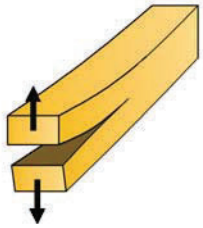

Figure 1: *Mode I fracture – crack opening*

Cohesive law for Mode I fracture can be determined based on the analysis of damage process zone which develops in wood in the case of propagating cracks. Development of the damage process zone causes toughness to change as the crack propagates, which is characteristic of many materials including wood. Process zone development in wood is a direct consequence of fibre-bridging effect (unbroken fibres connect the crack surfaces and slow down the crack growth).

Crack propagation experiments in materials which develop fibre bridging across the crack start with a machined notch that has no process zone [2]. As the load is applied fibre-bridging zone develops with two crack tips. One crack tip is the actual crack tip and one is at the edge of the fibre-bridging zone defined as the notch root, with the distance between them representing the process zone length (Figure 2). At the initial point of fracture, the crack tip moves while the notch root remains stationery

[1] Marija Todorović, University of Belgrade, Faculty of Civil Engineering, Serbia, todorovicm@grf.bg.ac.rs
[2] Marko Pavlović, Delft University of Technology, The Netherlands, M.Pavlovic@tudelft.nl
[3] Ivan Glišović, University of Belgrade, Faculty of Civil Engineering, Serbia, ivang@grf.bg.ac.rs
[4] Mathieu Koetsier, Delft University of Technology, The Netherlands, M.Koetsier@tudelft.nl

https://doi.org/10.52202/069179-0055

and toughness is low. As the process zone develops, since unbroken wood fibres that connect crack surfaces can carry load, toughness tends to raise with crack growth. Once the connecting fibres break, the process zone length stabilizes (steady-state crack propagation). Onward, the process zone propagates together with the developing crack, and the toughness becomes constant. The fracture resistance curve (R curve) is a representation of Mode I fracture toughness of the material in relation to crack propagation. In order to correctly describe the fracture process of any material, including wood, an accurate definition of the R curve is necessary. In accordance with the explained process zone mechanism, the R curve starts at a minimum initial value (corresponding to the low toughness) and then rises with the development of fibre-bridging zone. Once steady-state crack propagation is reached, the R curve becomes constant (corresponding to the constant toughness). The plateau of R-curve represents the cohesive energy - G_f.

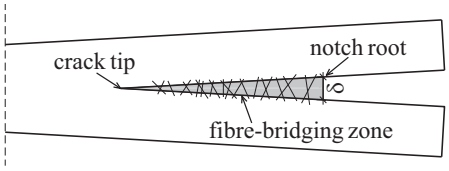

Figure 2: *Crack tip region with fibre-bridging zone*

In order to determine Mode I fracture properties of wood, different methods have been used so far by the researchers. Testing procedures included: three-point bending test [3,4], single-edge-notch specimen [5], wedge-splitting test [6-8], tapered double cantilever beam test [9,10], and double cantilever beam test [11-13]. The single-edge-notch specimen and wedge-splitting test represent standard geometries for determination of fracture energy for wooden products employed in timber engineering. On the other hand, the double cantilever beam test and tapered double cantilever beam test geometries are mostly used in different scientific research activities [14].

In this paper an experimental procedure for determining the fracture resistance curve of wood is explained. Double cantilever beam (DCB) tests were performed in order to determine Mode I fracture (crack opening) properties of spruce wood. As wood represents an orthotropic material, the fracture behaviour of wood is orientation-specific. Hence, six different material fracture planes can be defined - LR, LT, RL, RT, TL, TR (Figure 3), where the first letter indicates the direction perpendicular to the crack plane, and the second letter indicates the direction of crack propagation. The letters L, R and T represent longitudinal, radial and tangential direction of the fibres, respectively. In accordance with the large-scale experiments performed on the end-notched beams crack propagation is considered in the radial-longitudinal direction - RL direction. In order to overcome the main obstacle occurring with the DCB tests, which is crack length measurement, Digital Image Correlation (DIC) method was applied for recording the crack opening and propagation. Jamaaoui et al. [15] demonstrated that DIC method can be successfully used to estimate the crack length and the mechanical state at the crack tip. R curves were obtained from the slope of cumulative energy - crack length curve. The cohesive energy G_f was determined from the R curves. Based on these results, cohesive law for Mode I fracture can be defined.

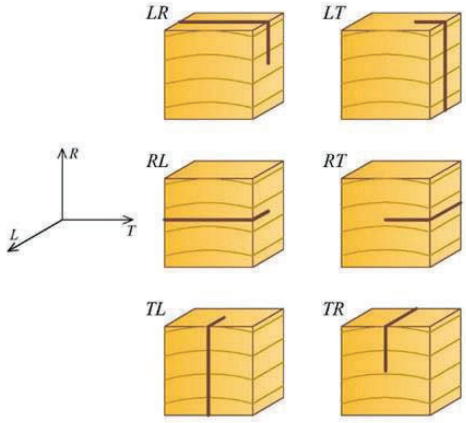

Figure 3: *Fracture planes in wood*

2 MATERIALS AND METHODS

2.1 TEST SET-UP

Altogether ten specimens made from European spruce (Picea Abies) were tested as DCB to the point of failure at the TU Delft, Faculty of Civil Engineering and Geosciences, Department of Engineering Structures. The specimens were made from spruce timber classified in the strength class C22 according to the standard EN 338 [16]. The specimens were made out of the same wood as were the large-scale end-notched beams tested previously, so that the results could be used in further numerical analysis of Mode I fracture.

DCB test set-up and specimen geometry are presented in Figure 4. The specimens' cross section dimensions were 20 x 30 mm and length was 300 mm. They were denoted as S1-S10. The initial 100 mm long crack was formed using a saw with 1 mm thickness. Steel pins with a diameter of 3 mm were used for joining the specimens to the loading fixture.

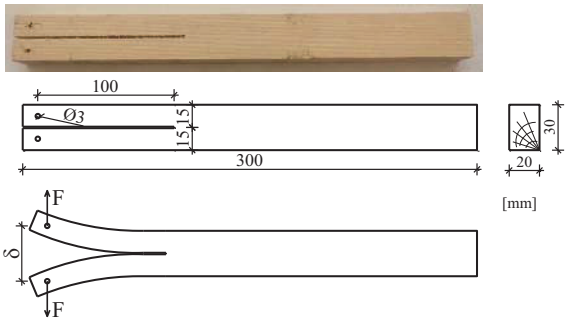

Figure 4: *DCB test set-up and specimen geometry*

https://doi.org/10.52202/069179-0055

Universal testing machine UTM-25 was employed for the experimental testing (Figure 5). Load was applied monotonically with a displacement-controlled rate of 5 mm/min. Load and displacement were recorded using the loading cell with a frequency of 2 Hz. All tests were performed under ambient conditions (at a temperature of about T = 20º C and a relative humidity of about RH = 65%). Using a digital hygrometer moisture content was measured in all the specimens and it had values in a range of 11.0% to 11.9%.

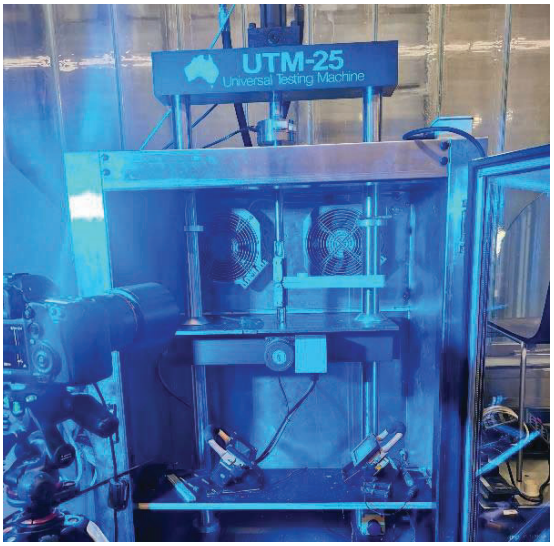

Figure 5: *Experimental set-up*

DIC method was employed for crack length measurement, as well as the measurement of crack opening during the testing. The main problem of this experiment is accurate crack length reading which is necessary for the correct definition of R curves. To overcome this problem, images recorded with a camera were analysed with GOM correlate software. By defining two curves on the upper and lower crack surfaces which are easily visible during the analysis, and measuring the separation between these curves allowed for the accurate crack length reading at each loading step.

2.2 PROCEDURE FOR ENERGY RELEASE RATE

The force-displacement curves recorded during the experimental research were used to obtain R curves (energy release rate vs crack length) based on the procedure explained in the paper by Wilson et al. [17]. This approach can be applied only to fracture mechanics tests with elastic materials (such as European spruce). In elastic materials, the fracture energy is released only due to the development of the damage process zone and the crack growth in the crack plane. For these materials no energy is released due to the non-linear (plastic or damage) behaviour of the materials surrounding the crack plane. Procedure consists of calculating the cumulative energy released up to the certain value of the loading point displacement δ (presented as shaded area in Figure 6). In order to determine cumulative energy, unloading from this point would be required. As Wilson et al. [17] argue in their paper, the fibre-bridging zone would interfere with the unloading and the curve would not return to the origin. Furthermore, authors explain that energy from such crack plane interference during unloading is not a part of the energy released during monotonic crack propagation, and it should not be a part of the cumulative released energy. Therefore, the proposed method assumes that the unloading would return to the origin displacement - δ_0. As suggested, cumulative released energy can be calculated as in accordance with the following expression:

$$U(\delta) = \int_{\delta_0}^{\delta} F(x)dx - \frac{1}{2}F(\delta)(\delta - \delta_0) \quad (1)$$

where U = cumulative energy, δ = displacement, δ_0 = origin displacement and F = force.
Afterwards, cumulative energy is cross-plot in the function of the corresponding crack length (Figure 6). Crack lengths were read from the DIC images for the corresponding force and displacement during the experimental testing. Finally, the R curves represent the slope of cumulative energy - crack length curve, calculated as follows:

$$R = \frac{1}{b}\frac{dU(a)}{da} \quad (2)$$

where R = energy release rate, b = specimen width and a = crack length.

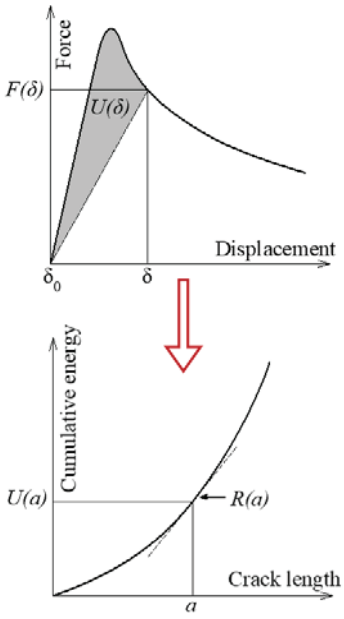

Figure 6: *Procedure for determining R curves based on cumulative released energy [15]*

https://doi.org/10.52202/069179-0055

3 RESULTS AND DISCUSSION

All tested specimens experienced the expected Mode I fracture - crack opening, caused by excessive tensile stress perpendicular to the grain of wood. Typical failure mechanism of tested specimens is presented in Figure 7. Force - displacement curves of all ten tested specimens are presented in Figure 8. As it can be seen from the curves, behaviour of the specimens was entirely linear until ultimate load corresponding to the initial crack opening was reached, with a sudden drop in load at this point. Afterwards, crack propagation and its growth led to a complete separation of the specimens in two parts, with generally clear and straight surfaces between two separated parts. Crack paths followed fibre directions, with minor exceptions in the case of existing defects in wood.

Figure 7: *Typical Mode I failure mechanism of tested specimens*

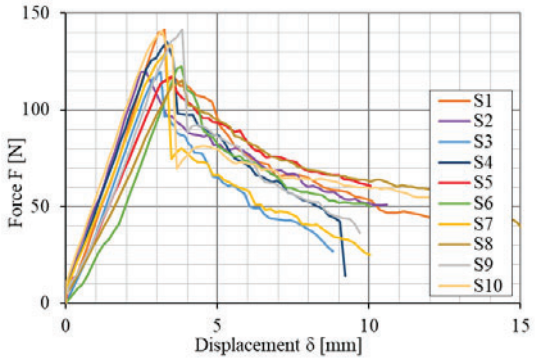

Figure 8: *Force-displacement curves*

After implementing the previously described procedure for energy release rate, cumulative energy vs crack length was calculated from the Equation (1) and presented in Figure 9. Based on these curves, using the Equation (2), R curves of tested specimens were calculated and presented in Figure 10. The recorded data of force - displacement was comprehensive enough to be easily integrated. For each step of loading, corresponding crack length was read from the DIC images analysed with GOM correlate software. Differentiation of the cumulative energy vs crack length curves was performed by fitting them with adequate third-degree polynomial curves. Afterwards, these polynomial curves easily numerically differentiated in order to obtain respective R curves for each specimen.

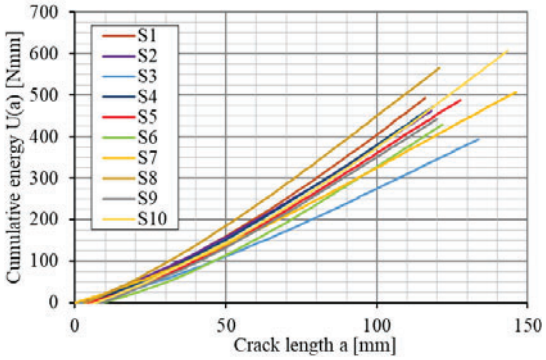

Figure 9: *Cumulative energy-crack length curves and (b) R-curves*

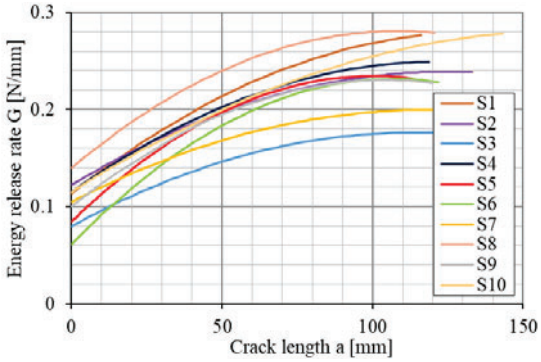

Figure 10: *R-curves*

The cohesive energy or critical value of energy release rate at propagation - G_f corresponds to the plateau value of the R curve [14]. This parameter values are estimated once the toughness stabilized after fibre-bridging process completed and R curves appear to be reaching the steady state. The experimental results for cohesive energy of tested spruce specimens are given in table 1. Cohesive energy values vary between 0.18 - 0.28 N/mm, with the mean value of 0.24 N/mm, and coefficient of variation of 13.7%.

Table 1: *The cohesive energy values*

Specimen	G_f (N/mm)
S1	0.275
S2	0.239
S3	0.181
S4	0.248
S5	0.235
S6	0.231
S7	0.200
S8	0.281
S9	0.230
S10	0.278
Average	0.236
Standard deviation	0.032
Coef. of variation (%)	13.7

https://doi.org/10.52202/069179-0055

The obtained cohesive energy values are comparable to the values obtained in other studies performed in order to determine fracture properties of Norway spruce. Authors Coureau et al. [14] cite cohesive energy values in the range of 0.25 - 0.31 N/mm depending on the test performed (where the value of 0.25 N/mm corresponds to the results of the DCB test). Ostapska and Malo [7] obtained mean cohesive energy value of 0.25 N/mm from the wedge splitting test. Since the results are similar to the ones obtained in this research, it can be said that the proposed procedure for determining R curves in this paper can be considered to be successful in evaluation of the cohesive energy of European spruce.

Crack opening displacement at the initial crack tip was also read from the DIC recorded images uploaded in the GOM correlate software. Crack opening displacement was determined by choosing two points at the initial crack tip, positioned at the future crack surfaces, and measuring their distance in each step as the crack opens and propagates. This parameter was necessary for further analysis in order to obtain the cohesive law for the specimens. Energy release rate plotted against crack opening displacement at the initial crack tip once it is differentiated gives the cohesive law of tested wood specimens [18]:

$$\sigma(\delta^*) = \frac{dG(\delta^*)}{d\delta^*} \tag{3}$$

where σ = nominal stress, δ* = crack opening displacement at the initial crack tip, G = energy release rate. The cohesive law for tested European spruce specimens is given in Figure 11. This was performed using the Equation (3) for an average value of the obtained R curves.

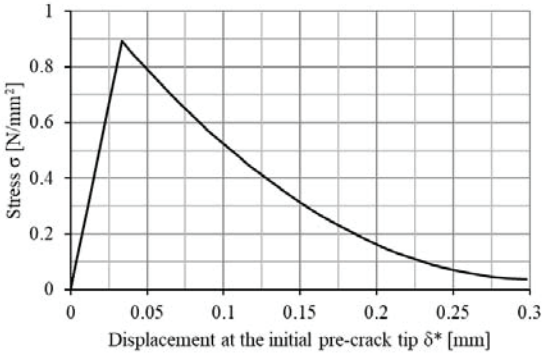

Figure 11: *Cohesive law of tested specimens*

Maximum value of nominal stress equals 0.9 N/mm^2 from the cohesive law curve and it corresponds to the value obtained by Oudjene et al. [19] also from DCB tests. Authors of the mentioned paper also successfully modelled the progressive cracking of the notch details of spruce timber beams using the parameters obtained from the DCB tests.

4 CONCLUSIONS

The condition of steady state crack propagation is required to estimate relevant fracture properties of wood. Adequate test procedure and recording are necessary in order to obtain accurate behaviour of wood in Mode I fracture (crack opening). Comprehending fracture in timber allows to determine the expected behaviour of timber structural elements in terms of load-carrying capacity, ductility and damage tolerance.

An efficient test and analysis procedure to obtain the Mode I fracture energy based on the double cantilever beam (DCB) tests is proposed in this paper. The force-displacement curves recorded during the experimental research were used to obtain fracture resistance curves (R curves). Based on the obtained results, the cohesive energy corresponding to the plateau value of the R curve was determined to be 0.24 N/mm for specimens made of European spruce. Furthermore, R curves were analysed in order to determine cohesive law of wood. The described method has been proven to be successful in determination of Mode I fracture properties of wood.

Cohesive law can be further implemented in the numerical analysis of large-scale timber elements like notched beams and beams with holes. The numerical modelling, as well as the experimental research, can help in better understanding of crack initiation and crack growth phenomenon in timber structures.

ACKNOWLEDGMENTS

This research was supported by the Science Fund of the Republic of Serbia, Serbian Science and Diaspora Collaboration Program: Knowledge Exchange Vouchers: Hybrid structures and connection of timber and FRP. We also acknowledge financial support provided by the Science Fund of the Republic of Serbia on Grant No. 7677448: Towards Sustainable Buildings: Nove Strategies for the Design of Vibration Resistant Cross-Laminated Timber Floors - Substrate4CLT.

The authors express gratitude to personnel of Stevin 2 Laboratory at TU Delft that helped in performing DCB tests with DIC.

REFERENCES

[1] Todorovic M., Stevanovic B., Glisovic I., Stevanovic T.: Experimental Testing of Reinforced End-Notched Glulam Beams. Building Materials and Structures, 61(4):23-36, 2018.

[2] Nairn J.A., Matsumoto N.: Fracture Modeling of Crack Propagation in Wood and Wood Composites Including Crack Tip Processes and Fiber Bridging Mechanics. In: Proceedings of the 12th international conference on fracture, 3411–3418, 2009.

[3] Morel S., Dourado N., Valentin G., Morais J.: Wood: a quasibrittle material R-curve behavior and peak load evaluation. International Journal of Fracture, 131:385-400, 2005.

https://doi.org/10.52202/069179-0055

[4] Dourado N., De Moura M. F. S. F., Morel S., Morais J.: Wood fracture characterization under mode I loading using the three-point-bending test. Experimental investigation of Picea abies L. International Journal of Fracture, 194:1–9, 2015.
[5] Nakao T., Susanti C.M.E., Yoshihara H.: Examination of the failure behavior of wood with a short crack in the radial–longitudinal system by single-edge-notched bending test. Journal of Wood Science, 58:453-458, 2012.
[6] Dubois F., Méité M., Pop O., Absi J.: Characterization of timber fracture using the Digital Image Correlation technique and Finite Element Method. Engineering Fracture Mechanics, 96:107-121, 2012.
[7] Ostapska K., Malo K. A.: Wedge splitting test of wood for fracture parameters estimation of Norway Spruce. Engineering Fracture Mechanics, 232:107024, 2020.
[8] Ostapska K., Malo K. A.: Crack path tracking using DIC and XFEM modelling of mixed-mode fracture in wood. Theoretical and Applied Fracture Mechanics 112:102896, 2021.
[9] Vasic S., Smith I.: Bridging crack model for fracture of spruce. Engineering Fracture Mechanics, 69(6):745-760, 2002.
[10] de Moura M.F.S.F., Dourado N.: Mode I fracture characterization of wood using the TDCB test. Theoretical and Applied Fracture Mechanics, 94:40-45, 2018.
[11] Yoshihara H., Kawamura T.: Mode I fracture toughness estimation of wood by DCB test. Composites Part A: Applied Science and Manufacturing, 37(11):2105-2113, 2006
[12] de Moura M.F.S.F., Morais J.J.L., Dourado N.: A new data reduction scheme for mode I wood fracture characterization using the double cantilever beam test. Engineering Fracture Mechanics, 75(13):3852-3865, 2008.
[13] Zhao, Y., Li, Z., Xu, B.: Mixed-mode (I/II) interlaminar fracture of glued-laminated timber. Materials & Design, 131:210-218, 2017.
[14] Coureau J-L., Morel S., Dourado N.: Cohesive zone model and quasibrittle failure of wood: A new light on the adapted specimen geometries for fracture tests. Engineering Fracture Mechanics, 109:328-340, 2013.
[15] Jamaaoui A., Pop O., Dubois F., Costa G.: Wedge Splitting Test on Douglas genotypes using an integrated mixed-mode approach. Theoretical and Applied Fracture Mechanics, 91:44–51, 2017.
[16] European Committee for Standardization: EN 338: Structural timber - Strength classes. Brussels, 2009.
[17] Wilson E., Mohammadi M. S., Nairn J. A.: Crack Propagation Fracture Toughness of Several Wood Species. Advances in Civil Engineering Materials, 2(1):316–327, 2013.
[18] Gong Y., Hou Y., Zhao L., Li, W., Zhang J., Hu N.: A modified mode I cohesive zone model for the delamination growth in DCB laminates with the effect of fiber bridging. International Journal of Mechanical Sciences, 176:105514, 2020.
[19] Oudjene M., Tran V., Meghlat E., Ait-Aider H.: Numerical Models for Self-Tapping Screws as Reinforcement of Timber Structures and Joints. In: Proceedings of 14th World Conference on Timber Engineering, 2016.

World Conference on Timber Engineering Oslo 2023

THE INFLUENCE OF WOOD COATINGS ON THE MOISTURE BUFFERING CAPACITY OF CLT AND THE INDOOR ENVIRONMENT

Ulrich Hundhausen[1], Robbe Heyvaerts[2], Samee Ullah[3], Dimitrios Kraniotis[4]

ABSTRACT: The objective of the study was to determine the influence of wood coatings for CLT on the moisture buffering capacity and the indoor environment regarding relative humidity and heating demand. Based on the results of a previous screening of a wide range of coatings, three commercial products were chosen: a flooring oil, an alkyd-based interior wall stain and a fire-retardant stain that were considered to provide both, i) high water vapor permeability to maintain wood's hygroscopicity, and ii) adequate protection of CLT under storage, transport, installation and service. A climate chamber test revealed a good moisture buffer capacity of untreated CLT and a limited one of CLT cladded with gypsum. CLT's glue lines in the frontal plane were not found to affect moisture dynamics. The flooring oil and the wall stain reduced the practical moisture buffer value by 39% and 10%, respectively, as compared to the uncoated CLT. CLT coated with the fire-retardant stain had an even higher practical moisture buffer value than uncoated wood, which is explained by the stain's pronounced hygroscopicity. In all elements tested in a heat flux experiment, the theoretical U-values were higher than the experimentally obtained and simulated values. Hygrothermal energy simulations using a room of 50 m^2 as 'reference model' showed that wood's moisture buffer capacity is beneficial for the indoor environment, by means of passive regulation of RH and lower energy demand for humidification and dehumidification.

KEYWORDS: fire retardant, heating demand, indoor environment, moisture buffering, U-value, wood coating

1 INTRODUCTION

Hygroscopic materials change their moisture content (MC) dependent on the ambient climate. As climate conditions permanently vary in real-use conditions and the inertia of sorption, a hygrothermal equilibrium with its surrounding environment is hardly attained [1]. This material property to absorb and desorb moisture and thereby to moderate the indoor variations in relative humidity, RH, is referred to as moisture buffer capacity, MBC [2,3]. The MBC may be utilized to improve indoor climate [e.g. 4] and save energy [e.g. 5,6,7]. Regarding wood, the MBC has been determined in many studies on a wide range of products including solid wood [e.g. 8], plywood [e.g. 9], paneling [e.g. 10], wood-based insulated panels [e.g. 11] and furniture [e.g. 12]. The challenge of fully utilizing wood's MBC is that wood products are usually coated for improving their aesthetics and technical properties; these coatings may significantly reduce the MBC [13,14,15].

The objective of the present study was to determine the influence of coatings for cross laminated timber (CLT) made of Norway spruce (*Picea abies*) on the MBC and the indoor environment regarding RH and the building's energy demand. As producers of CLT claim a need for surface treatments that are industrially applicable, the premise was to find mechanically resistant coatings that protect CLT under storage, transport, installation and service but at the same time maintain wood's hygroscopicity.

2 MATERIALS AND METHODS

The methodological apporach of the study is shown is shown in Figure 1.

In an initial screening, a literature and market study as well as pre-tests on the water vapor permeability, moisture buffer capacity, scratch resistance and blocking were carried out on clearwood specimens to identify potentially suitable coatings for industrial CLT production. Based on those results (not shown in this paper), three commercial coatings were chosen for further

[1] Ulrich Hundhausen, NTI (Norwegian Institute of Wood Technology), Norway, uh@treteknisk.no
[2] Robbe Heyvaerts, HOGENT University of Applied Sciences and Art, Belgium, robbe.heyvaerts@stud.th-rosenheim.de
[3] Samee Ullah, NTI (Norwegian Institute of Wood Technology), Norway, sul@treteknisk.no
[4] Dimitrios Kraniotis, NTI (Norwegian Institute of Wood Technology), OsloMet (Oslo Metropolitan University), Norway, dkr@treteknisk.no

https://doi.org/10.52202/069179-0056

investigations on CLT: a flooring and furniture hardwax oil (RMC Oil Plus C, Rubio Monocoat, Dal, Norway), a waterborne alkyd interior wall stain (Lady Pure Nature, Jotun, Sandefjord, Norway) and a fire-retardant (FR) stain (NT Deco, Nordtreat, Vantaa, Finland). The latter is a certified Euroclass B-s1, d0 treatment for CLT. The coatings were applied according to the producers' specifications on five CLT-elements and one solid wood element with a dimension of 100 x 100 x 60 cm^3 (width x height x thickness). The commercial CLT-elements (KLH Massivholz GmbH, Teufenbach-Katsch, Austria) were composed of five-layers made of Norway spruce (*Picea abies*) glued with an polyurethane adhesive. Uncoated CLT and CLT cladded with gypsum of 12.5 mm thickness served as references. In addition, an uncoated solid wood element was included to study a possible influence of the glue lines in the frontal plane of CLT (Table 1).

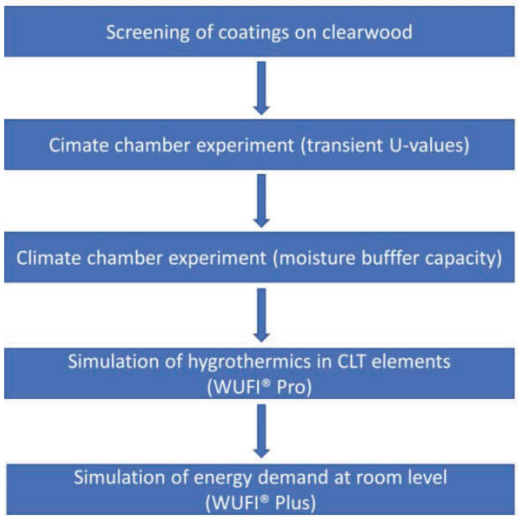

Figure 1. *Methodology of the study*

Table 1. *CLT-elements used in the climate chamber experiment and hygrothermal model. FR = fire retardant*

Element	Coating	Application rate, wet [g/m^2]
1. CLT	/	
2. CLT+gypsum	/	
3. CLT	Hardwax oil	23
4. CLT	Alkyd stain	79
5. CLT	FR-stain	350
6. Solid wood	/	

The elements were installed in a two-room climate chamber that simulated a steady outdoor climate of -2°C/50% and a fluctuating room climate of 23°C/75% and 23°C/33% for 8 h and 16 h, respectively (Figure 2). The interior conditions followed the climate regime described in the NORDTEST protocol to determine the practical moisture buffer value, $MBV_{practical}$ [2]. Before testing, five of the six faces of each element were sealed with vapor barrier tape (FLEX Tape Dampsperre, Isola AS, Porsgrunn, Norway). The unsealed face was exposed to the interior climate. Both air temperature and RH were logged (TH501, Celsicom AB, Varberg, Sweden) in each zone. In addition, the MC in the CLT-elements was logged with electrical resistance moisture meters (MC501, Celsicom AB). In total, five sensors were used, one in each lamella of the elements. The climate chamber experiment provided measurements of the heat flux using plate sensors (TRSYS 02, Hukseflux Thermal Sensors, Delft, The Netherlands), as shown in Figure 3.

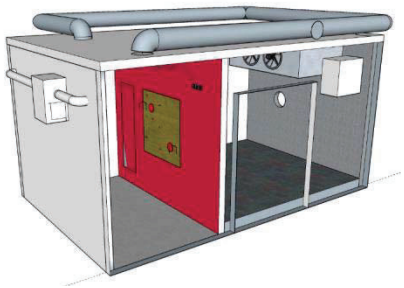

Figure 2*. The two-rooms climate chamber used for measuring the heat flux through the 1 m2 large elements.*

(a)

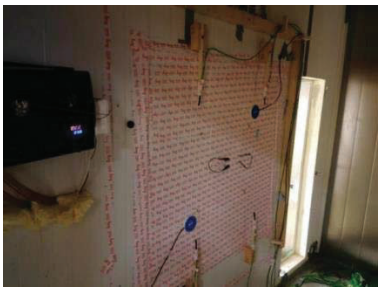

(b)

Figure 3*. The face of the uncoated CLT-element. The red and blue plates are the heat flux sensors, on the interior (a) and exterior (b) surface of the wall.*

https://doi.org/10.52202/069179-0056

The measurements were then used to calculate the thermal trasmittance, i.e. U-values, during the experiments. After the heat flux experiment, specimens were cut from each CLT-element for measuring the wood density and the MC according to the oven-dry method (Figure 4). In addition to the specimens used for density and MC measurements, five specimens were cut from each CLT-element, which were used for determining gravimetrically the $MBV_{practical}$ according to the NORDTEST protocol [2].

The experimental results from the climate chamber test were compared with modelled sorption dynamics and simulated transient U-values in each of the CLT-elements, employing the HAM (heat, air and moisture transport) software WUFI® Pro [16]. The values of T, RH, density and MC measured during the experiment were used as input data. In addition, the S_d-values of the coatings were used for modelling that had been determined in a dry-cup test according to EN ISO 12572:2016 during the screening phase of the study. Eventually, the experimentally obtained U-values (U_{exp}-values) as well as the simulated U-values (U_{sim}-values) in WUFI® Pro were compared with the theoretical (steady state) U-values calculated according to ISO 6946:2017 (U_{th}-values).

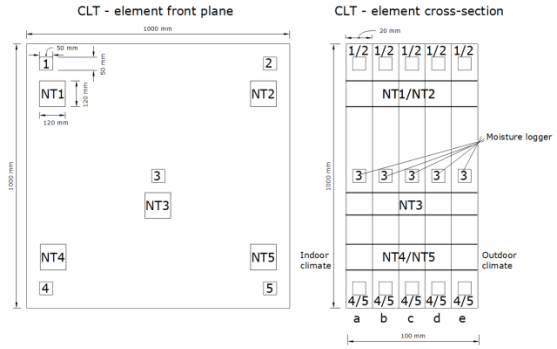

Figure 4. *After the end of the climate chamber test, 25 specimens (five per CLT-lamella) were cut from each CLT-element to measure the density and MC (1 to 5). In addition, five specimens were extracted for determining the $MBV_{practical}$ according to the NORDTEST method (NT1 to NT5).*

To model the moisture dynamics at room level, the hygrothermal energy simulation tool WUFI® Plus [17] was employed. A reference, a room with an area of 5 m x 10 m was used (Figure 5), which is part of a residential building; therefore, the relevant specifications regarding the indoor environment and HVAC systems were followed as described in SN-NSPEK 3031:2020 [18]. The following scenarios were considered:

Two building systems: i) with CLT/solid timber wall systems both as exterior (Figure 6) and interior walls (Figure 7) and ii) a conventional stud wall system as exterior wall (Figure 8 A) and concrete as internal wall (Figure 8 B). All external walls are insulated and the U-value is 0.18 W/m^{2}K. An overview of the scenarios is shown in Table 2.

For the cases with CLT/solid timber wall systems as external and internal walls, the six different cases that had been tested in the climate chamber and validated using the WUFI® Pro 1D were used.

The sixth case consists of a conventional insulated stud wall, with exterior wooden cladding and interior cladding in gypsum board, and a concrete internal wall with only plaster as finishing in both surfaces.

Two different functions in the HVAC system were considered: i) with humidification and dehumidification and ii) without humidification and dehumidification.

Two different functions in the HVAC system were considered: i) with moisture recovery and ii) without moisture recovery. Today, the vast majority of the HVAC systems include only heat recovery but not moisture recovery, which might be important when combined with hygroscopic materials.

Two different levels of mechanical ventilation rate were considered: i) a rate according to the Norwegian Standard SN-NSPEK 3031:2020 for the apartments and ii) a rate reduced by 50% compared to (i).

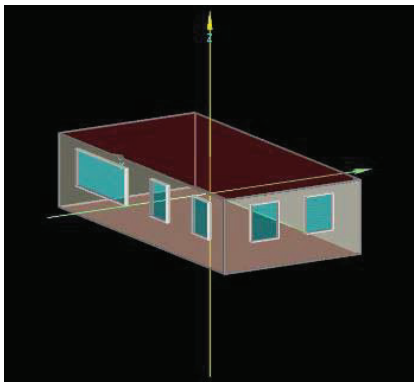

Figure 5. *3D view of the room model used in the hygrothermal energy simulations in WUFI® Plus. The two facades with windows are external walls while the other two are internal walls. The long façade (10 m) and the short façade (5 m) are oriented towards the south and east, respectively.*

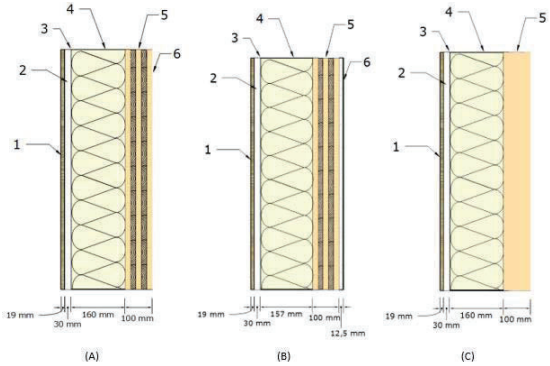

Figure 6. *The three different designs of the external walls in CLT/solid timber: (A) with exposed and uncoated CLT-element, which represents the insulated versions of the elements 1, 3, 4 and 5 in Table 1. (B) CLT-element cladded with gypsum, which represents the insulated version of the element 2 in Table 1. (C) exposed and uncoated solid timber, which represents the insulated version of the element 6 in Table 2.*

https://doi.org/10.52202/069179-0056

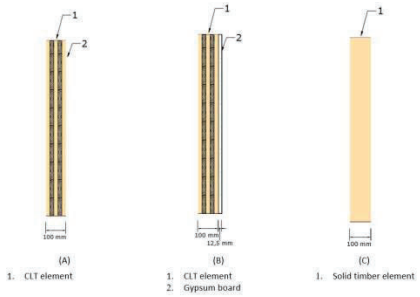

Figure 7. *The three designs of the internal walls in CLT/solid timber: (A) uncoated CLT element,representing the elements 1, 3, 4 and 5 in Table 1. (B) CLT-element cladded with gypsum, representing element 2 in Table 1. (C) exposed and uncoated solid timber, representing element 6 in Table 1.*

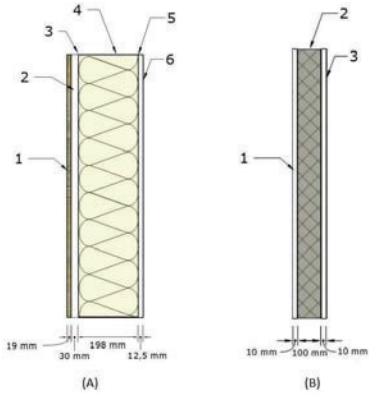

Figure 8*. The exterior (A) and the interior wall (B) for the case #6 in* ***Table 2****, i.e. the case without CLT/solid timber.*

Table 2. *Overview of the wall designs simulated in WUFI® Pro*

Cases	External house wall	Internal house wall
#1	Insulated CLT	Non-insulated CLT, untreated on both surfaces
#2	Insulated CLT with gypsum as interior finishing	Non-insulated CLT wall with gypsum board as interior finishing on both surfaces
#3	Insulated CLT coated with hardwax oil or alkyd stain (S_d = 0.01)	Non-insulated CLT wall coated with hardwax oil or alkyd stain on both surfaces
#4	Insulated CLT coated with FR-stain (S_d = 0.59)	Non-insulated CLT wall coated with FR-stain on both surfaces
#5	Insulated wall in solid timber without glue line in the frontal plane	Non-insulated wall in solid timber without glue line in the frontal plane on both surfaces
#6	Insulated stud wall, with wood panel as exterior cladding and gypsum board as interior cladding	Non-insulated concrete wall, with mortar on both surfaces

3 RESULTS AND DISCUSSION

3.1 MOISTURE BUFFER CAPACITY AND TRANSIENT U-VALUES

Table 3 shows the $MBV_{practical}$, the S_d-values of the three coatings as well as the U_{th}-values, U_{sim}-values and U_{exp}-values. The $MBV_{practical}$ of 1.06 classifies the MBC of uncoated CLT as "good" and of CLT cladded with gypsum as "limited" [2]. $MBV_{practical}$ of untreated Norway spruce found in the literature range from 0.91 [13] to 1.36 [2,8]. The hardwax flooring oil and the alkyd-based interior wall stain decreased the $MBV_{practical}$ by 39% and 10%, respectively, as compared to the uncoated CLT. A reduction by 10% is rather low compared to those reported in other studies on wood coatings [14,15]. Lozhechnikova et al. [13] found for example that a two-layer coating of linseed oil and a spray laquer reduced the $MBV_{practical}$ by approximately 20% and 70%, respectively. CLT coated with the FR-stain had an even higher $MBV_{practical}$ than uncoated wood, which is explained by the stain's pronounced hygroscopicity due to the FR-actives in the formulation. This hypothesis is supported by the observation of small water droplets on the specimen surface (Figure 9 A) and discoloration most likely due to salt crystalization (Figure 9 B), which occured during the moist RH step in both climate chamber tests (Figure 1).

Overall, the $MBV_{practical}$ of the three coated CLT differ more than the SD-values of the coatings suggest (Table 2). A relationship between the MBV and the S_d-values is not found.

Table 3. *The$MBV_{practical}$, the S_d-value of the coatings as well as the theoretical (U_{th}), simulated (U_{sim}) and experimental (U_{exp}) U-values of the six wall elements tested in the climate chamber.*

Element	MBV [g/m² %RH]	S_d [m]	U-value [w/(m²K)]		
			U_{th}	U_{sim}	U_{exp}
1. CLT	1.06		0.93	0.87	0.79
2. CLT+gypsum	0.28		0.89	0.84	0.78
3. CLT+HW linseed oil	0.65	0.01	0.93	0.88	0.80
4. CLT+alkyd-stain	0.95	0.01	0.92	0.87	0.76
5. CLT+FR-stain	1.61	0.59	0.93	0.88	0.75
6. Solid wood	0.98		1.00	0.91	0.92

For all six elements, the U_{th}-values, calculated according to ISO 6946:2017, are higher than the U_{sim}-values and U_{exp}-values (Table 3). Our results confirm the hypothesis that the moisture adsorption and absorption in wood increases the thermal resistance of the element due to the latent heat of sorption, i.e. the heat released due to phase change of water vapor to bounded water in wood. The findings are in agreement with previous studies that have shown the temperature in wood increased with moisture uptake, increasing in this way

https://doi.org/10.52202/069179-0056

the thermal resistance of the element [6,7,19].

(A) (B)

Figure 9. *Water droplets occurred on the CLT-element treated with the FR-stain during the absorption step (A). The discoloration of the surface (B) appeared in the beginning of the absorption step but quickly disappeared again.*

An influence of the three coatings on the U-values does not become apparent (Table 3). This is expected for the U_{th}-values because the thermal resistance of thin materials, with primarly moisture resistive function, like coatings is considered as neglectible and the calculation method does not account for sorption effects. However, we neither observe a significant influence of the coatings on the U_{sim}-values nor the U_{exp}-values although the $MBV_{practical}$ show that the coatings do influence the sorption properties of wood. This suggests that there is no practical difference by means of thermal performance of wood due to moisture uptake between the untreated and treated wood if the latter is coated with highly water vapor permeable coatings.

3.2 MOISTURE DYNAMICS AT ROOM LEVEL

3.2.1 Buffering of RH indoors

Figures 10, 11 and 11 show the minimum and maximum RH indoors in the simulated room when the HVAC system does not include humidification/dehumidification. In Figure 10, the mechanical ventilation is set according to SN-NSPEK 3031:2020, i.e. it is constant at 90 m3/h. In this case, the maximum RH indoors is lowest in case #1 (59.4%) and #5 (59.1%), which is the uncoated CLT-element and the uncoated solid timber element, respectively (Table 2). In comparison, the maximum RH is highest in case #2 (63.2%) and #6 (63.6%), which is the CLT-element cladded with a gypsum board and the stud wall with the gypsum board as interior cladding. The picture is contrary for the minimum RH: the highest values show case #1 (4.9) and #5 (5.0) whereas the lowest values were found for case #2 (3.8%) and #6 (3.4%). The maximum RH is by 4.5% lower and the minimum RH by 1.5% higher in case #5 (most beneficial) than in case #6 (least beneficial). In other words, the wall design with uncoated wood and without gypsum revealed the lowest difference between maximum and minum RH. This behavior is beneficial in terms of passive control of the indoor environment.

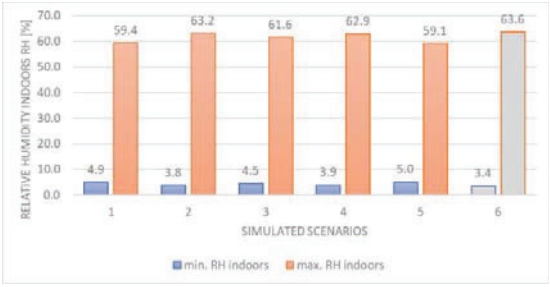

Figure 10. *Simulated minimum and maximum RH indoors in the simulated room without humidification/dehumidification. The mechanical ventilation is set according to SN-NSPEK 3031:2020 and there is no moisture recovery in the HVAC system.*

The moisture buffering effect becomes clearer when moisture recovery is included in the HVAC system (Figure 11). The maximum RH is by 9.4% lower and the minimum RH by 4.6% higher in case #5 (most beneficial) than in case #6 (least beneficial).

A general observation about this set of simulations, i.e. with moisture recovery in the HVAC system (Figure 11), is that the minimum RH is significantly higher than that of the previous set of simulations where moisture recovery was not included in the HVAC system (Figure 10). This means that regardless the type of interior surface, it will be beneficial for the indoor environment if moisture is also recovered, along with heat, in the mechanical ventilation. This seems to be of particular need in spaces/rooms with relatively limited moisture production.

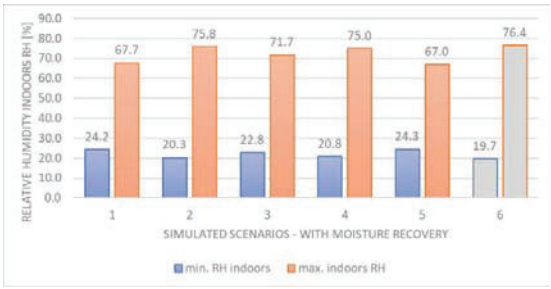

Figure 11. *Simulated minimum and maximum RH_i in the model room without humification/dehumification when moisture recovery is included in the HVAC system.*

Finally, Figure 12 shows the results from the last set of simulations, where the flow rate in the mechanical ventilation was reduced by 50% compared to standard requirements (Figure 10). The reduction resulted in an elevation of both, the maximum and the minimum RH. However, the relationship between the six cases regarding the RH maxima and minima is the same as for the HVAC-systems shown in Figure 10 and Figure 11.

https://doi.org/10.52202/069179-0056

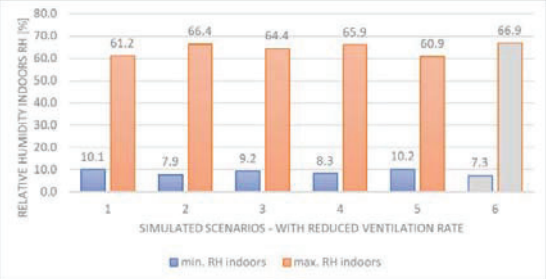

Figure 12. *Simulated minimum and maximum RH indoors in the simulated room without humidification/dehumidification when the mechanical ventilation is reduced by 50% compared to the requirements specified in SN-NSPEK 3031:2020.*

Independent from the type of HVAC-system, the coatings reduce the moisture buffering effect of wood (case #3 and #4, Figure 10, 11 and 12). This applies especially to the FR-stain. Considering the MBV-values (Table 3), the CLT-element coated with the FR-stain (case # 4) should have buffered the RH in the model room best. However, the WUFI® Plus simulations take into account the S_d-values and not the MBV. Against this background, the comparitively high S_d-value of the FR-stain (0.59 m) has a negative impact in the simulations although the MBV of 1.61 W/(m²K) suggests the opposite.

3.2.2 Required energy for humidification and dehumidification

Figure 13, 14 and 15 show the energy used for humidification and dehumidification to maintain the RH indoors within 25% and 60%. Overall, the required energy decreases the better the MBC of the wall system is. However, the impact of the MBC strongly depends on the type of HVAC system.

Figure 13 shows the results of the set of simulations where the mechanical ventilation was set according to SN-NSPEK 3031:2020, i.e. constant to 90 m³/h without moisture recovery in the HVAC system. Case #5 (uncoated solid timber) requires 477.3 kWh for humidification while case #6 (stud wall with gypsum board as interior cladding) requires 502.2 kWh for humidification and 0.3 kWh for dehumidification. Case #1 (uncoated CLT) shows a similar performance like case #5 and case #2 (CLT cladded with gypsum) shows a similar performance like case #6.

The range of 25 to 60% for indoor RH corresponds to the Indoor Environmental Quality class 2, which is the target range for new buildings. Both, Figure 10 and 12 and consequently Figure 13 reveal a large difference between the need for humidification and dehumidification, which shows that the minimum RH is a challenge in modern residential buildings.

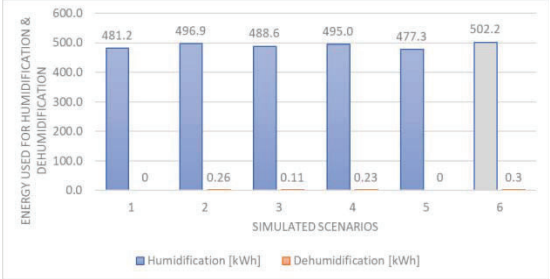

Figure 13. *Energy used for humidification and dehumidification to maintain the RH indoors within 25% and 60% when mechanical ventilation is set according to SN-NSPEK 3031:2020 and there is no moisture recovery in the HVAC system.*

The inclusion of moisture recovery in the HVAC system reduces significantly the need for humidification (Figure 14). In particular, for case #5 (exposed and uncoated solid timber) there is negligible humidification need (0.1 kWh) while for case #6 (stud wall with gypsum board as interior cladding) the humidification need is 4.6 kWh. Case #5 shows also the lowest need for dehumidification (8.2 kWh), which reflects the contribution of this building component to the passive regulation of the RH indoors. In contrast, case #6 shows the highest need for dehumidification (26.9 kWh). As in the other cases, case #1 is similar to case #5, and case #2 is similar to case #6.

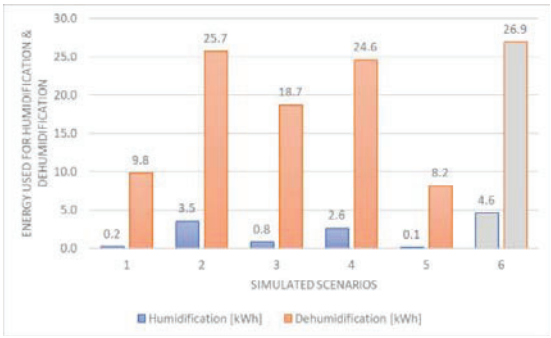

Figure 14. Energy used for humidification and dehumidification when moisture recovery is included in the HVAC system.

Figure 15 shows the results when the flow rate of the mechanical ventilation system is reduced by 50% compared to the standard rate (the indoor air quality (IAQ) was yet exceptional). The results in this set of simulations are similar to the ones of the previous sets.

https://doi.org/10.52202/069179-0056

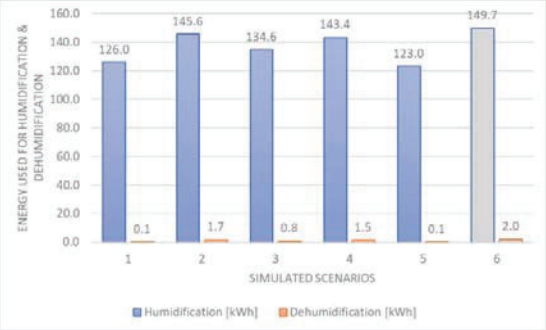

Figure 15. *Energy used for humidification and dehumidification to maintain the RH indoors within 25% and 60% when the mechanical ventilation is reduced by 50% compared to the requirements in SN-NSPEK 3031:2020.*

4 CONCLUSIONS

The study confirms the hypothesis that wood's MBC is beneficial for the indoor environment, by means of RH and energy demand for humidification and dehumidification, as well as for the thermal conductivity of CLT. In other words, there is need to take into consideration the humidity level to calculate a realistic U-value.

Gypsum was found to decrease the MBC of CLT from "good" to "limited" ($MBV_{practical}$ of 0.28). Highly-permeable coatings reduce CLT's $MBV_{practical}$ only slightly. From the practical point of view, a replacement of gypsum is difficult to realize in applications with strict requirements to fire safety. To a certain extent, this might be possible by using an FR-stain, which even increased the $MBV_{practical}$ of untreated CLT from $MBV_{practical}$ 1.06 to 1.61. However, it is to consider that an FR-treatment as its best may improve the reaction-to-fire performance of wood from Euroclass D to B.

Finally, the study on the FR-stain reveals a weakness in the methodology of quantifying the MBC and simulating its impact on the indoor environment and, consequently, on energy requirements related to the HVAC system. The $MBV_{practical}$ of a coating may be high due its hygroscopicity although its water vapor permeability is low.

ACKNOWLEDGEMENT

This study was part of the Build-in-Wood project, funded by the European Union's Horizon 2020 programme under grant agreement No. 862820.

REFERENCES

[1] Engelund E.T., Thygesen L.G., Svensson S., and Hill C.A.: A critical discussion of the physics of wood–water interactions. *Wood science and technology*, 47(1):141-161, 2013.

[2] Rode C., Peuhkuri R.H., Mortensen L.H., Hansen K.K., Time B., Gustavsen A. *et al.* (2005). Nordic Innovation Centre: "Moisture Buffering of Building Materials",proj.no.:04023. Technical University Danmark. BYG Report, NoR-126

[3] Cascione V., Maskell D., Shea A., and Walker P.: A review of moisture buffering capacity: From laboratory testing to full-scale measurement. *Construction and Building Materials*, 200:333-343, 2019.

[4] Hameury S.: Moisture buffering capacity of heavy timber structures directly exposed to an indoor climate: a numerical study. *Building and environment*, 40(10):1400-1412, 2005.

[5] Nore K., Nyrud A.Q., Kraniotis D., Skulberg K.R., Englund F., and Aurlien T.: Moisture buffering, energy potential, and volatile organic compound emissions of wood exposed to indoor environments. *Science and Technology for the Built Environment*, 23(3):512-521, 2017.

[6] Kraniotis D., Nore K., Brückner C., and Nyrud A.Q.: Thermography measurements and latent heat documentation of Norwegian spruce (Picea abies) exposed to dynamic indoor climate. *Journal of Wood Science*, 62(2):203-209, 2016.

[7] Kraniotis D. and Nore K.: Latent heat phenomena in buildings and potential integration into energy balance. *Procedia environmental sciences*, 38:364-371, 2017.

[8] Hameury S.: Influence of coating system on the moisture buffering capacity of panels of Pinus sylvestris L. *Wood Material Science and Engineering*, 2(3-4):97-105, 2007.

[9] Osanyintola O.F. and Simonson C.J.: Moisture buffering capacity of hygroscopic building materials: Experimental facilities and energy impact. *Energy and Buildings*, 38(10),1270-1282, 2006.

[10] Mitamura T., Rode C., and Schultz, J. Full scale testing of indoor humidity and moisture buffering in building materials. In: ASHRAE Conference, IAQ, 1, p.2001, 2001.

[11] Kraniotis D., Langouet N., Orskaug T., Nore K., and Glasø G. Moisture buffering and latent heat sorption phenomena of a wood-based insulating sandwich panel. In: Proceedings of the World Conference on Timber Engineering, pages 22-26, 2016.

[12] Zemitis J. and Borodinecs A. Determination of Moisture Buffering Capabilities of Common Furniture Materials. In: IOP Conference Series: Earth and Environmentl Science. IOP Publishing, 290, p.012090, 2009.

[13] Lozhechnikova A., Vahtikari K., Hughes M., and Österberg M.: Toward energy efficiency through an optimized use of wood: The development of natural hydrophobic coatings that retain moisture-buffering ability. *Energy and Buildings*, 105,37-42, 2015.

[14] Salonvaara M., Ojanen T., Holm A., Künzel H.M., and Karagiozis, A.N. Moisture buffering effects on indoor air quality-experimental and simulation results. In: Proceedings of the Performance of Exterior Envelopes of Whole Buildings, IX International Conference, pages 1-11, 2004.

[15] Mortensen L.H., Rode C., and Peuhkuri R.H. Full scale tests of moisture buffer capacity of wall materials. In: 7th Nordic Symposium on Building Physics, pages 662-669, 2005.

[16] IBP, F. 2020 WUFI® Pro. 6.5 Ed.

[17] IBP, F. 2019 WUFI® Plus. 3.2.0 Ed.

https://doi.org/10.52202/069179-0056

[18] Norway, S. 2020 NSPEK 3031:2020. Energy performance of buildings — Calculation of energy needs and energy supply. Standard Norway, pp. 168.
[19] Charisi S., Kraniotis D., and Nore K. Latent heat sorption phenomena in three building materials: Norwegian spruce (Picea abies), gypsum board and concrete. In: Proceedings of the World Conference on Timber Engineering, pages 1-2, 2016.

World Conference on Timber Engineering Oslo 2023

EVALUATION OF MODELS OF FIBRE ORIENTATION IN SAWN TIMBER USING SYNCHRONISED COMPUTED TOMOGRAPHY AND OPTICAL SCANNING DATA

Johannes A. J. Huber[1], Osama Abdeljaber[2], Johan Oja[3], Anders Olsson[4]

ABSTRACT: Optical scanning and X-ray computed tomography (CT) scanning of sawn timber provide a large number of data points, on which data-driven numerical models can be based for simulations. These models require information about the deviations of the fibre orientations in the vicinity of knots. Optical scanning can be used to measure the in-plane fibre orientation on wood surfaces. In CT scans of sawn timber, the fibre orientation around knots can be estimated using a new fibre reconstruction algorithm based on the density gradient. The goal of this paper is to compare and synchronise optical and CT scanning data of sawn timber and then use the combined data set to evaluate fibre orientations derived from both representations. The material comprised sawn timber of Norway spruce, in which alignment holes were drilled. The timber was scanned in an industrial CT scanner and subsequently in an industrial optical scanner where scanning was repeated after successive planing of the sawn timber surface. The results show that a projective mapping in combination with a spline interpolation are required for synchronisation, and that the in-plane fibre orientations calculated from the density gradients are qualitatively similar to the orientations derived from the optical data.

KEYWORDS: Knots, Tracheid effect, CT scanning, Strength grading, Image analysis, Gradient structure tensor

1 INTRODUCTION

Strength-graded sawn timber constitutes the base of most solid timber-based structures or engineered wood products used in these structures. Knowledge about the mechanical properties of the used timber is therefore imperative for design. For individual pieces of sawn timber, the exact values of these properties are, however, unknown and for strength specifically, they are inherently unknowable without destructive tests.

In machine strength grading, *indicating properties* (IPs) of sawn timber are used in regression models to predict the *grade-determining properties* density, stiffness and strength. For timber graded into C classes, stiffness and strength relate respectively to the bending modulus of elasticity (MoE) and the bending modulus of rupture (MoR), according to the European standard EN 408 [1]. Sawn timber is graded into a few strength classes at sawmills, where the properties of each class are governed by the characteristic values of strength and density, respectively, and by the characteristic mean value of the MoE. IPs can be derived from various measurements using different technologies [2], but usually large variations in the mechanical properties of individual pieces of sawn timber remain, with coefficients of variation often exceeding 20%.

Comparatively high prediction accuracy can be achieved by IPs based on measuring the in-plane fibre orientation on sawn timber surfaces by laser scanning utilising the tracheid effect [3]. This technology accounts for both the presence of knots and the resulting fibre deviations around knots on the board surface. Nevertheless, the plethora of data points needs to be condensed to one or a few scalar parameters for IP-based predictions in regression models.

Recently, some sawmills have also adapted X-ray computed tomography (CT), currently used for sorting logs and to optimise log positioning regarding yield before sawing [4]. The supplied density data in the log volume lends itself for an automated detection of the location of the pith and knots by image analysis [5]. The

[1] Johannes A. J. Huber, Luleå University of Technology, Skellefteå, Sweden, johannes.huber@ltu.se

[2] Osama Abdeljaber, Linnaeus University, Växjö, Sweden, osama.abdeljaber@lnu.se

[3] Johan Oja, Luleå University of Technology, Skellefteå, Sweden, johan.oja@ltu.se

[4] Anders Olsson, Linnaeus University, Växjö, Sweden, anders.olsson@lnu.se

https://doi.org/10.52202/069179-0057

abundant 3D data gathered is however currently not used for prior-to-sawing strength evaluations.

Knots, and the deviations of the fibre orientation caused by them, strongly affect the stiffness and strength of sawn timber. The complex patterns of fibre orientations around knots have been investigated using laser scanning in successively planed sections of sawn timber [6], and in greater detail by using micro-CT scanning [7].

Gathering high-resolution data of sawn timber facilitates the use of numerical models, e.g. 3D finite element (FE) models, for predicting the properties of individual boards. These models require information about wood features like the pith location, the size and shape of knots, and the fibre orientations. Apart from measuring the in-plane fibre orientation, optical surface data can be used to find knots and determine the location of the pith [8]. Surface data has been used previously for FE models, e.g. to predict the bending stiffness profile in [9], where the location of the pith was estimated by fitting concentric circles to growth rings, the knots were idealised as cones and the fibre deviations were calculated on the basis of a mathematical model [10].

In a recent study [11], CT data also has been used to create FE models of the exact shape of sawn timber, whereby image analysis methods were used to locate the pith, detect knots, and furthermore reconstruct the 3D fibre orientations around knots in a new way, which accounts for irregular shapes of knots. To refine the methodology in [11], verifications are required for the fibre orientations and the size of the regions around knots in which the fibres are disturbed. In the future, CT-based modelling could also be used for logs, to predict the mechanical properties of individual virtual boards in logs already before sawing.

Data-driven models which incorporate the rich data of measurements on individual logs or individual pieces of sawn timber can yield accurate predictions and can facilitate the production of timber with bespoke mechanical properties instead of being binned into predefined strength classes with high variability. Tracking individual pieces and their properties also opens the possibility of planning their structural use in a construction already at the sawmill, as part of a purpose-based grading process.

The objective of this study is therefore to compare and synchronise the high-resolution data obtained from optical scanning and CT scanning, respectively, of sawn timber. More specifically, the goal is to use the combined data set to evaluate fibre orientations around knots derived from both data sets.

2 MATERIAL & METHODS

2.1 MATERIAL PREPARATION

Norway spruce (*picea abies*) sawn timber from Sweden with dimensions 45 × 145 × 3600 mm^3 was prepared by drilling positioning holes at equally spaced positions, see Figure 1. Starting at a lengthwise distance of 50 mm from each edge, and subsequently spaced 700 mm from the first position, three holes at each wide face and two holes on each short face were drilled. The outer holes on the wide faces and the holes on the short faces were spaced 15 mm from the edges of the sawn timber. The third hole on the wide face was centred between the edge holes. At 1450 mm from each edge, only a single hole in the middle of the wide faces was drilled.

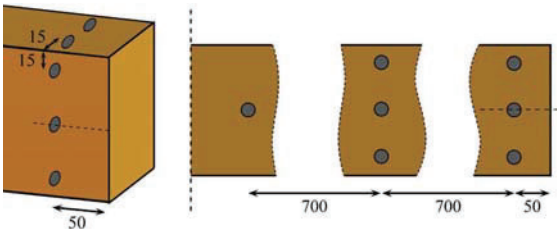

***Figure 1**: Arrangement of the positioning holes*

2.2 DATA ACQUISITION

CT images were acquired of the timber using an industrial CT scanner (Microtec Mito) adapted for research purposes at the facilities of Luleå University of Technology in Skellefteå, Sweden. The sawn timber was wrapped in plastic to contain its moisture content and simply supported at its ends and standing upright, which minimised the bending deflection under its own weight while the scanner moved along the timber, see Figure 2. The reconstructed 3D image stack had a voxel (3D pixel) size of 0.3 × 0.3 × 0.3 mm^3. Each voxel carried a 16-bit grayscale value which represented density in kg/m^3 at the corresponding location.

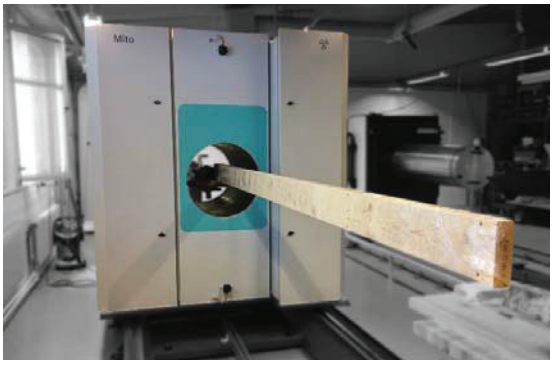

***Figure 2**: CT scanner moving along the sawn timber*

After transport and removal of the plastic wrapping, the sawn timber was scanned using the industrial optical wood scanner Microtec WoodEye (WE) at the facilities of Linnaeus University in Växjö, Sweden. The scanner recorded RGB images of all faces at a pixel size of 0.8 × 0.07 mm^2 (lengthwise × crosswise) and it recorded the in-plane fibre directions using laser tracheid scans at a resolution of 1 × 4.4 mm^2 (lengthwise × crosswise).

To receive a distribution of the in-plane direction in the volume of the boards, the timber was planed successively by a depth of 1 mm at each wide face**,** and after each planing operation, the optical scanning process was repeated, see Figure 3. Nine slices were planed off on each wide face, i.e. 18mm were removed in total.

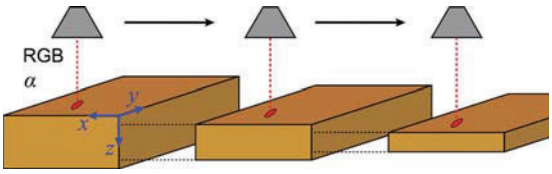

***Figure 3**: Progressively planing and optical scanning*

2.3 CT IMAGE PROCESSING

The CT images represented an equally spaced rectangular grid of density values $\rho(x, y, z)$ in 3D space. The processing of the CT data was primarily performed using code in Julia [12]. For segmenting timber from air, a binary image $B(x, y, z)$ was created by thresholding ρ and filling internal holes.

Since the timber was twisted around its long axis, a misalignment existed between the sawn timber surfaces and the axes of the CT image. To be able to compare flat surfaces in the WE data to corresponding surfaces in the CT images, the latter first needed to be "untwisted". The twist was corrected by rotating and aligning each cross-sectional CT slice to the image axes, see Figure 4. This required estimating the twist angle θ_i of each CT cross-section along a board as well as the translation in both directions (Δx_i and Δz_i) from a fixed reference point. To do so, in each CT cross-section in B the shift in both directions Δx_i and Δz_i from the centroid of the resulting region to the reference point as well as the angle θ_i that the principal axis of the region makes with the horizontal image axis were calculated. These values indicate how much each cross-section should be translated and rotated to straighten the board. The estimates of these values were affected by noise in the CT images, which was partly due to the plastic wrapping around the timber and reconstruction artefacts present in the images. A moving mean filter was therefore applied to denoise the variations of Δx_i, Δz_i, and θ_i before correcting the twist of the board.

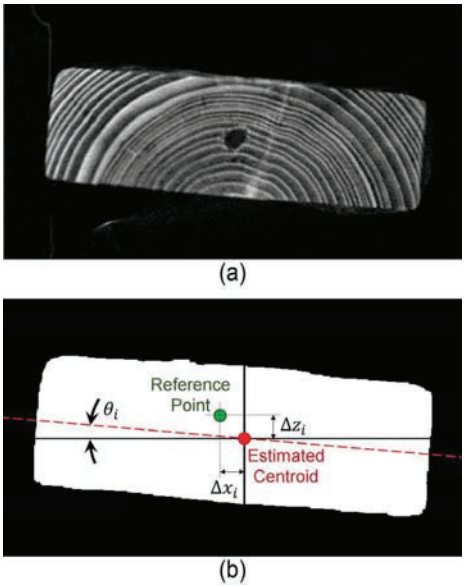

***Figure 4**: Correction of twist in boards; twisted cross-sectional CT image (a), and estimated parameters for untwisting (b)*

To estimate the fibre orientation (*l*-direction) in the untwisted CT image, an adapted version of the method presented in [11] was applied, which is based on finding the smallest gradient in the density field [13]. In a first step, the partial derivatives of the density were calculated by Equation (1).

$$\rho_x = \frac{\partial \rho}{\partial \mathrm{x}} \approx w_{\sigma 1} * (w_{\Delta x} * \rho) \tag{1}$$

where $w_{\Delta x}$ is a convolutional kernel for finite differences [14], $w_{\sigma 1}$ is a Gaussian kernel with a standard deviation of 1 voxel and ρ from here on represents the density of the untwisted CT image. The partial derivatives were equivalently calculated for y and z. In a second step, the *gradient structure tensor* (GST) was constructed, see Equation (2).

$$\mathrm{GST}\big(\rho(x,y,z)\big) = w_{\sigma 2} * \begin{pmatrix} \rho_x^2 & \rho_x\rho_y & \rho_x\rho_z \\ & \rho_y^2 & \rho_y\rho_z \\ \mathrm{sym} & & \rho_z^2 \end{pmatrix} \tag{2}$$

where $w_{\sigma 1}$ is a Gaussian convolutional kernel with standard deviation 3 voxels. In the last step, the eigenvalues and eigenvectors of $\mathrm{GST}(\rho)$ were extracted for each voxel and the eigenvector corresponding to the lowest eigenvalue was taken as the estimated *l*-direction. The result was a vector field $\boldsymbol{l}_{\mathrm{CT}}$ over the entire CT image.

A bounding boxing around the untwisted binary image was calculated to locate the initial surfaces of the sawn timber before planing. The calculation was performed by requiring that the outer slices of the bounding box contained a sufficiently large contiguous area of the untwisted binary image. From the outer slices, consecutive slices corresponding to the planing depths were extracted from the wide faces. For each slice, both the density values and the vector field of the estimated *l*-direction were extracted and exported for the subsequent synchronisation.

2.4 WOODEYE DATA PROCESSING

The WE data consisted of RGB intensity values and the in-plane fibre orientation angle α, which was defined as the shortest angle between the longitudinal scan direction (y) and the measured major axis of the ellipse formed by the laser point due to the tracheid effect. The data processing and the subsequent synchronisation was performed using code in MATLAB [15].

The data corresponded only to the scanned board surfaces and thus made a bounding box search unnecessary. Both the RGB and orientation data were available at points on non-uniform grids. To prepare the synchronisation, all WE data was therefore resampled by bicubic interpolation to the uniform grid of the corresponding slices from the untwisted CT image.

2.5 SYNCHRONISATION

Since some distortions existed in the WE data, e.g. due to the fact that the speed of the conveyor belt placed before the scanner was not perfectly aligned to the operational speed of the scanner, a mapping function needed to be

https://doi.org/10.52202/069179-0057

calculated to synchronise the WE data to the CT images. The synchronisation was based on the resampled WE RGB images of each face and the corresponding grayscale 2D slices obtained from the untwisted CT image.

The predrilled positioning holes served as an easily detectable reference in both representations and their centres were labelled manually in a user dialog in MATLAB by fitting circles, see Figure 4. The circle centres served as an input for calculating the mapping between the WE images to the CT faces. A projective 2D transformation matrix was estimated for performing the first part of the mapping, see Equation (3).

$$\begin{pmatrix} x' \\ y' \\ 1 \end{pmatrix} = \begin{pmatrix} r_1 & r_2 & t_1 \\ r_3 & r_4 & t_2 \\ p_1 & p_2 & 1 \end{pmatrix} \begin{pmatrix} x \\ y \\ 1 \end{pmatrix} \quad (3)$$

where x and y are the original coordinates of the wide face in the WE image, $x'$and y' are the coordinates after the projective transformation, and r_1 to r_4, t_1 and t_2, and p_1 and p_2 are the shear-rotational, translational, and projective coefficients of the transformation, respectively.

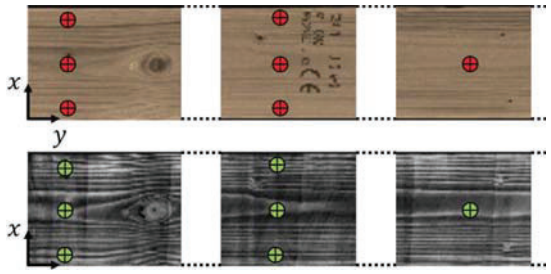

Figure 5: *Circle fitting in WE (top) and CT faces (bottom)*

Since a slight misalignment remained in the y-direction (lengthwise), cubic spline interpolation was used to map the y-coordinates of the transformed WE image (y') to a new set of y-coordinates (y'') that better match the CT image. The coefficients of the spline interpolation were calculated given the y-coordinates of the centres of the holes in the CT image along with the corresponding coordinates in the WE image after the projective transformation. The final transformation was composed of first applying the projective transformation and subsequently the spline interpolation.

The synchronisation needed to be performed separately for each surface of the sawn timber, and for each planing depth. Each calculated final transformation was applied to the corresponding WE data, i.e. both RGB and in-plane fibre orientation.

2.6 COMPARISON

The transformed WE data was compared to the untwisted CT image. The RGB images were converted to grayscale to visually compare it to the grayscale CT images. From the vector field $\boldsymbol{I}_{\mathrm{CT}}$, only the in-plane components were kept and compared to a vector field $\boldsymbol{I}_{\mathrm{WE}}$ which was derived from the WE orientations. Additionally, the absolute value of the in-plane angle $\mathrm{abs}(\alpha)$ of both representations was calculated and qualitatively compared in colour-coded plots.

3 RESULTS AND DISCUSSION

Below, the results of the synchronisation of a single piece of sawn timber are presented, for selected planing depths and primarily for the surface facing to the pith. The results differed little for the surfaces facing away from the pith.

3.1 SYNCHRONISATION MAPPING

Figure 6 shows the relative development of those parameters of the projective transformation matrix which were most different from zero, for increasing planing depth. The parameters associated with the perspective mapping differ before and after planing. The explanation for this is probably that when the holes were drilled with a handheld tool, the drill was not oriented perfectly perpendicular to the board face. Additionally, a human error factor was involved when manually locating the hole centres in the images.

Figure 7 shows the correction in y-direction from the spline interpolation after the projective transformation, for increasing planing depth. The characteristic of the correction is consistent for all planing depths, with decreasing amplitude at increasing planing depth, and with the profile being horizontally mirrored at mid-length of the board. The consistency of this transformation points to a systematic component in the distortion in the data.

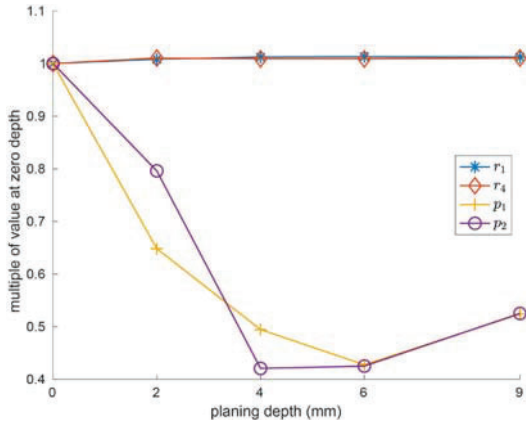

Figure 6*: Parameters of the projective transformation matrix as multiples of their respective values before planing*

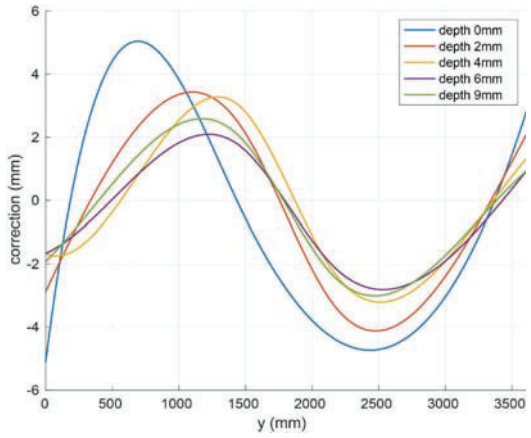

Figure 7*: Spline interpolation correction over the board length*

Figure 8 illustrates the alignment between WE and CT images for the surface of the board before planing, before and after the transformations at the positioning holes of one half of the board. After the projective transformation, a positioning error remained mostly at the holes towards the middle of the board. The error was decreased after the additional spline transformation.

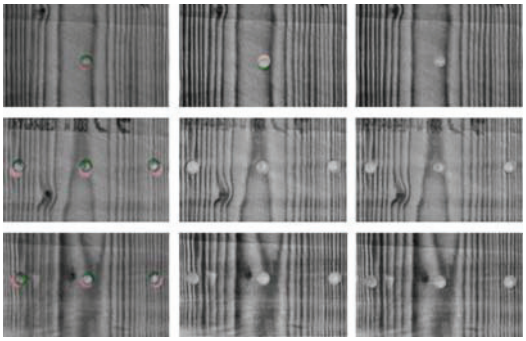

***Figure 8**: Hole alignment before transformation (left column), after projective transformation (middle), and after additional spline transformation (right), differences in red/green*

3.2 IN-PLANE FIBRE ORIENTATION

For a qualitative assessment, three regions along the board containing knots are reported, which comprised lengths of 160 mm in the proximity of the first, second and third row of positioning holes from one end of the board. Those regions will henceforth be referred to as region 1, 2 and 3.

Figures 9, 10 and 11 show the in-plane components of $\boldsymbol{l}_{WE}$ and $\boldsymbol{l}_{CT}$ plotted respectively on the transformed WE RGB image and the untwisted CT slice before planing of the surface facing the pith, and the corresponding angle, for regions 1, 2 and 3, respectively. Figures 12, 13 and 14 show the equivalent plots for a planing depth of 9 mm.

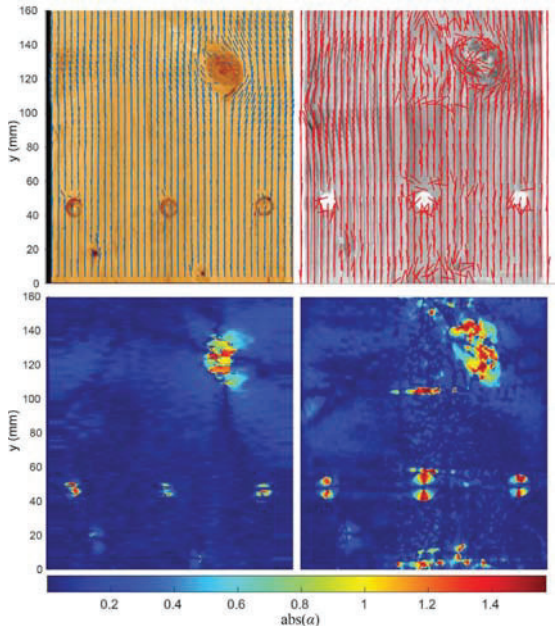

***Figure 9**: WE (left) and CT (right) in-plane vector fields (top) and orientation angle (bottom) for region 1 before planing*

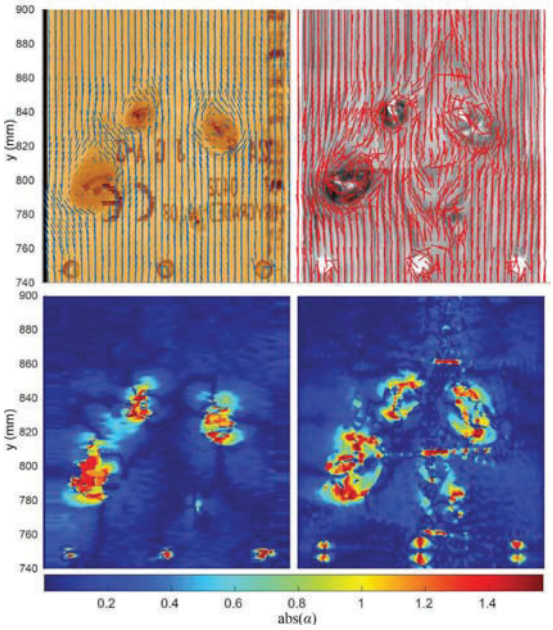

***Figure 10**: WE (left) and CT (right) in-plane vector fields (top) and orientation angle (bottom) for region 2 before planing*

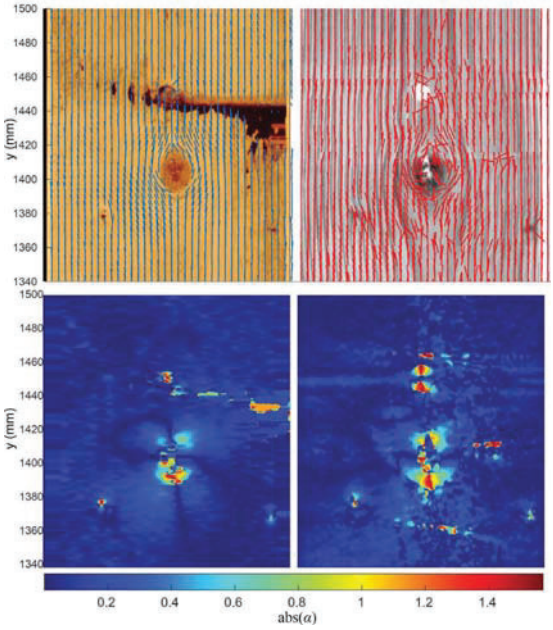

***Figure 11**: WE (left) and CT (right) in-plane vector fields (top) and orientation angle (bottom) for region 3 before planing*

Both, $\boldsymbol{l}_{WE}$ and $\boldsymbol{l}_{CT}$ reproduced a disturbed flow around the knots and a relatively laminar flow in regions without knots. Less variation existed in $\boldsymbol{l}_{WE}$ and the edges of the positioning holes were more clearly visible in $\boldsymbol{l}_{CT}$, due to the large density gradient between wood and air and the smaller pixel size in the CT image. However, $\boldsymbol{l}_{CT}$ was more sensitive to noise than $\boldsymbol{l}_{WE}$, in particular for the surface before planing, where the large density gradient between wood and air in the CT image affected the calculation of the GST. This effect is visible for regions 1 and 2 (Figures 9 and 10), where $\boldsymbol{l}_{CT}$ seems to follow the

https://doi.org/10.52202/069179-0057

apparent grain at the surface before planing, but it is less pronounced for the corresponding planed surfaces (Figures 12 and 13). Additionally, the plastic wrapping disturbed the calculation of $\boldsymbol{l}_{CT}$ in some regions where it was tightly packed. This is most clearly visible in Figure 10, where straight streaks across the surface in the CT image correspond to noise in α along equivalent streaks at the same locations. The field $\boldsymbol{l}_{CT}$ was generally more sensitive than $\boldsymbol{l}_{WE}$ to smaller knots and defects, due to its smaller original pixel size, resulting e.g. in deviations also around pitch pockets, see Figure 12.

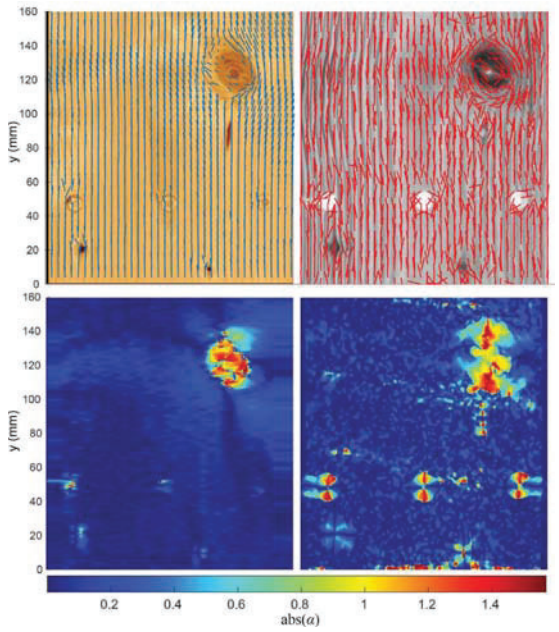

***Figure 12**: WE (left) and CT (right) in-plane vector fields (top) and orientation angle (bottom) for region 1 at a depth of 9 mm*

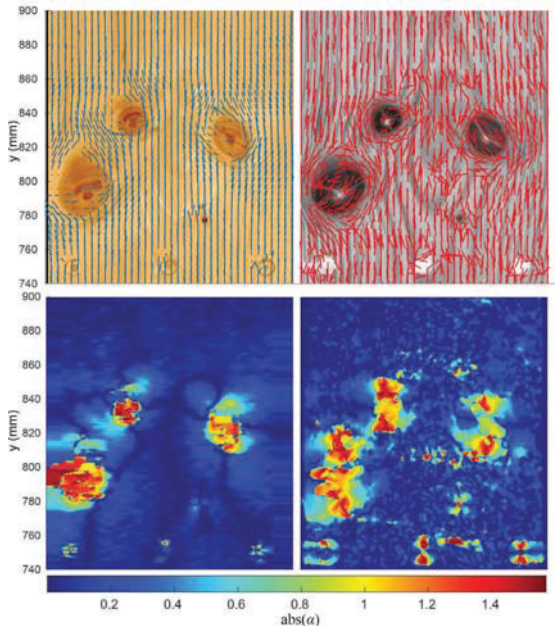

***Figure 13**: WE (left) and CT (right) in-plane vector fields (top) and orientation angle (bottom) for region 2 at a depth of 9 mm*

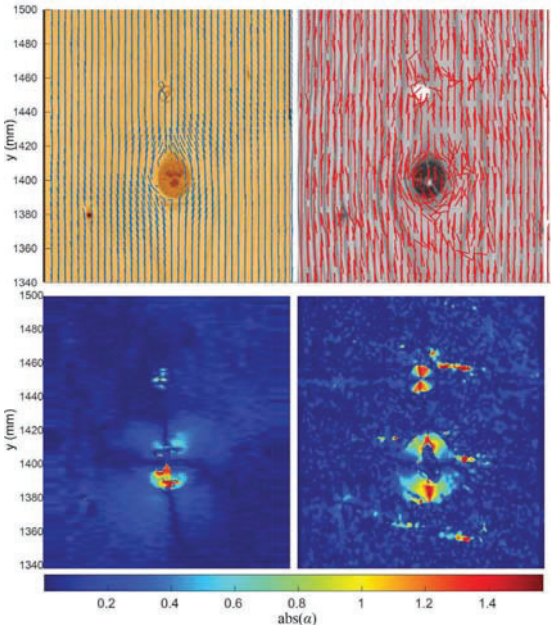

***Figure 14**: WE (left) and CT (right) in-plane vector fields (top) and orientation angle (bottom) for region 3 at a depth of 9 mm*

Figure 15 additionally shows the equivalent plot for region 2 before planing, but for the opposite side, i.e. the surface facing away from the pith. This surface included wane, which consequently affected the derived fibre orientations. For the CT image, vectors in the regions of wane can be removed easily by thresholding on density values. The field $\boldsymbol{l}_{CT}$ is notably affected by the apparent surface grain due to the surface effect described earlier.

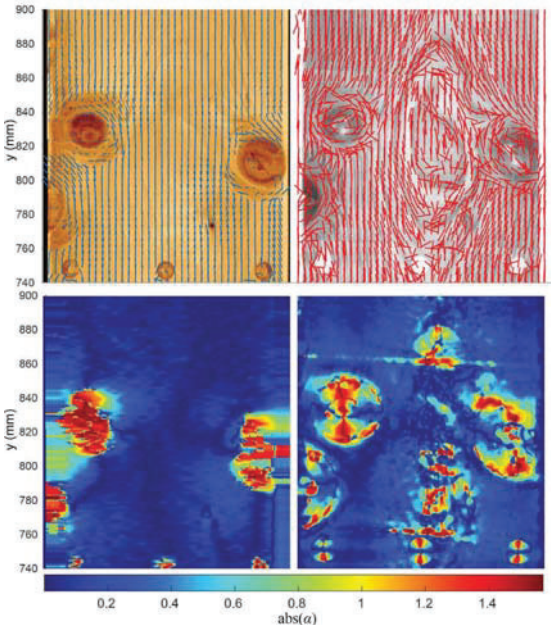

***Figure 15**: WE (left) and CT (right) in-plane vector fields (top) and orientation angle (bottom) for the surface facing away from the pith in region 2 before planing*

The field $\boldsymbol{l}_{CT}$ was strongly affected by the gradient out of plane in the shown image slices, e.g. inside knots where the *l*-direction followed the knot orientation, see Figure 16. For $\boldsymbol{l}_{WE}$, the out-of-plane component also followed the knot direction, but the in-plane component became generally less reliable due to small differences between the major and minor axes of the laser ellipse.

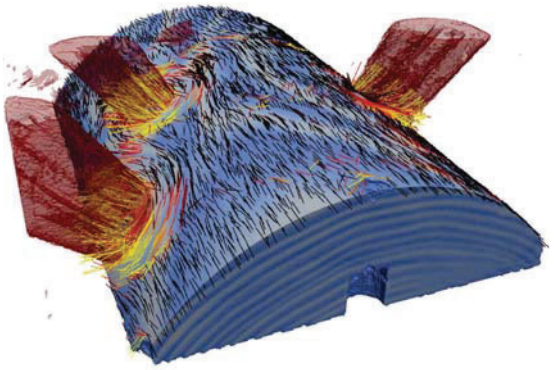

***Figure 16**: The field $\boldsymbol{l}_{CT}$ on a cylindrical cut around the pith in region 2 including segmented knot volumes*

4 CONCLUSION

In this study, optical scanning data of sawn timber was synchronised to corresponding CT images and the combined data set was used to compare and evaluate the fibre orientations derived from laser tracheid scanning and an image analysis-based method based on the density gradient structure. The results show that:

- a projective transformation in combination with a cubic spline interpolation for correction of the lengthwise position can synchronise the optical scanning data to a corresponding surface in the CT image,
- the in-plane fibre orientations calculated from the CT image gradients are qualitatively similar to the orientations derived from the optical data,
- the in-plane orientations from the CT image are more sensitive to noise and small defects, and they are less reliable on the original surface of the sawn timber.

The density gradient-based estimation of the fibre orientation should be further refined to reduce its sensitivity to noise. Further investigations are required on a larger number of samples to quantify the accuracy of this method, both in the vicinity of knots and in clearwood. To improve the accuracy of the synchronisation in future investigations, the location of the centres of the positioning holes should be automated, e.g. by ellipse fitting after an edge detection in the images, to minimise the effects of human error.

ACKNOWLEDGEMENT

The authors thank for the support of the Lennart & Alfhild Gabrielssons foundation, Swedish Wood (Svenskt Trä) and the CT-WOOD research programme in Skellefteå.

REFERENCES

[1] European Committee for Standardization (CEN): EN 408:2010+A1:2012, Timber structures - Structural timber and glued laminated timber - Determination of some physical and mechanical properties. 2012.

[2] Hanhijärvi A., Ranta-Maunus A. and Turk G.: Potential of strength grading of timber with combined measurement techniques. Report of the Combigrade-project - phase 2. VTT Publications 686, 2008.

[3] Olsson A. and Oscarsson J.: Strength grading on the basis of high resolution laser scanning and dynamic excitation: a full scale investigation of performance. *Eur. J. Wood Wood Prod.,* 75(1):17–31, 2017.

[4] Rais A. et al.: The use of the first industrial X-ray CT scanner increases the lumber recovery value: case study on visually strength-graded Douglas-fir timber. *Ann. For. Sci.*, 74(2):28, 2017.

[5] Longuetaud F. et al.: Automatic knot detection and measurements from X-ray CT images of wood: A review and validation of an improved algorithm on softwood samples. *Comput. Electron. Agric.*, 85:77–89, 2012.

[6] Hu M. et al.: Growth layer and fibre orientation around knots in Norway spruce: a laboratory investigation. *Wood Sci. Technol.*, 52: 7–27, 2018

[7] Hu M. et al.: Fibre directions at a branch-stem junction in Norway spruce: a microscale investigation using X-ray computed tomography. *Wood Sci. Technol.*, 56:147–169, 2022.

[8] Habite T., Abdeljaber O. and Olsson A.: Determination of pith location along Norway spruce timber boards using one dimensional convolutional neural networks trained on virtual timber boards. *Constr. Build. Mater.*, 329:127129, 2022.

[9] Lukacevic M. et al.: A 3D model for knots and related fiber deviations in sawn timber for prediction of mechanical properties of boards. *Mater. Des.*, 166:107617, 2019.

[10] Foley C.: Modeling the Effects of Knots in Structural Timber. PhD thesis, Lund University, 2003.

[11] Huber J. A. J. et al.: A method for generating finite element models of wood boards from X-ray computed tomography scans. *Comput. Struct.*, 260:106702, 2022.

[12] Bezanson, J. et al.: Julia: A fresh approach to numerical computing. SIAM review, 59(1): 65-98, 2017.

[13] Huber J. A. J.: Numerical Modelling of Timber Building Components to Prevent Disproportionate Collapse. PhD thesis, Luleå University of Technology, Skellefteå, 2021.

[14] Russ, J. C.: The Image Processing Handbook. 2nd ed. CRC Press, Boca Raton, FL, USA, 1995.

[15] MATLAB. version 9.13.0 (R2022b). Natick, Massachusetts: The MathWorks Inc., 2022.

https://doi.org/10.52202/069179-0057

World Conference on Timber Engineering Oslo 2023

MODELLING THE EFFECT OF THREE-DIMENSIONAL GRAIN ANGLE ON THE TENSION STRENGTH OF BIRCH WOOD

Steven Collins[1], Joonas Jaaranen[2], Gerhard Fink[3]

ABSTRACT: In the present paper, the effect of three-dimensional grain direction on the tension strength of small-scale birch wood specimens is investigated. The grain angles are measured on all four surfaces of the specimens using laser light scattering technique, and afterwards, the specimens are destructively tested in tension. A numerical model is developed to predict the tensile strengths. The model is a combination of a linear elastic finite element model, with local orthotropic material orientations defined based on the measured grain orientations, and stress-based phenomenological failure criteria, with stress averaging. Strength predictions from the numerical model are compared to the experimental results, and, additionally, material strength properties are calibrated by minimizing the difference between the predictions and experimental results. A simple analytic model is further investigated and evaluated against the numerical model. Results indicate that the numerical model can predict the tensile strength of the specimens based on the measured grain angles. Stress averaging improved strength predictions by reducing localized stress peaks. Calibrated strength properties further improved the predictions and are compared with the literature. With only grain angle information, however, the numerical model does not significantly improve predictions, relative to the simple analytical model.

KEYWORDS: Grain angle, Silver birch hardwood, Tension strength, Numerical model, Finite element analysis

1 INTRODUCTION

Wood is a highly orthotropic material with much higher stiffness and strength in the longitudinal direction, compared to the transverse direction. As such, the strength of wood is dependent on fibre orientation (i.e., the grain angle), relative to the loading direction. The inclusion of grain orientation in material models may therefore improve the prediction of strength. For example, in [1], a three-dimensional (3D) material model was developed to consider the effect of knot related grain deviations on the bending strength of Scots pine. The results were validated experimentally, and the effect of knot type and knot combinations were considered in the simulation of various structural timber pieces. In another study [2], the 3D fibre direction was modelled, based on the surface grain direction obtained from laser scanning. The results indicate accurate simulations of local effects for timber boards of Norway spruce.

In previous experimental investigations on birch timber boards [3, 4], tension tests were conducted, and the tension failures often involved clear wood with grain deviations. However, methods for modelling the birch species (a diffuse porous hardwood), which consider grain orientation are lacking. Therefore, the purpose of this study was to develop and evaluate a numerical model for the prediction of tensile strength in birch small-scale clear wood specimens with known grain orientations.

2 EXPERIMENTAL INVESTIGATIONS

Data from small-scale tests specimens of silver birch wood from southern Finland was considered in this study. A total of 119 specimens were investigated. The specimens were sawn from the ends of timber boards with a wide range of grain angles [5]. The specimens are (dog-bone) shaped with a reduced gauge region of 200 mm in length (Figure 1). The radial and tangential directions of the wood are inconsistently oriented in the specimens and as such, a square cross section (w x t = 15 x 15 mm^2) was used in the reduced gauge region. The dimensions of the clamping region were l x w x t = 110 x 45 x 25 mm^3 with a 60 mm transition radius between the clamp and gauge regions. The specimens were conditioned in a climate chamber at 20ºC and 65% RH, according to international standard, ISO 13061-6 [6].

The grain angle was measured on the specimens by means of laser light scattering technique (for softwoods, termed the tracheid effect). Five laser points, spaced at 35 mm intervals, were shone on the surface, in the gauge region of the specimen, and digital images captured the elliptical reflection patterns. Figure 1a shows the laser light reflection patterns and the corresponding measurement locations. All four sides of the specimen were laser imaged. Local fibre direction is determined according to the major axis of an ellipse fit to the reflection patterns, see e.g., [7].

[1] Steven Collin, Aalto University, Department of Civil Engineering, Finland, steven.collins@aalto.fi
[2] Joonas Jaaranen, Aalto University, Department of Civil Engineering, Finland, joonas.jaaranen@aalto.fi
[3] Gerhard Fink, Aalto University, Department of Civil Engineering, Finland, gerhard.fink@aalto.fi

https://doi.org/10.52202/069179-0058

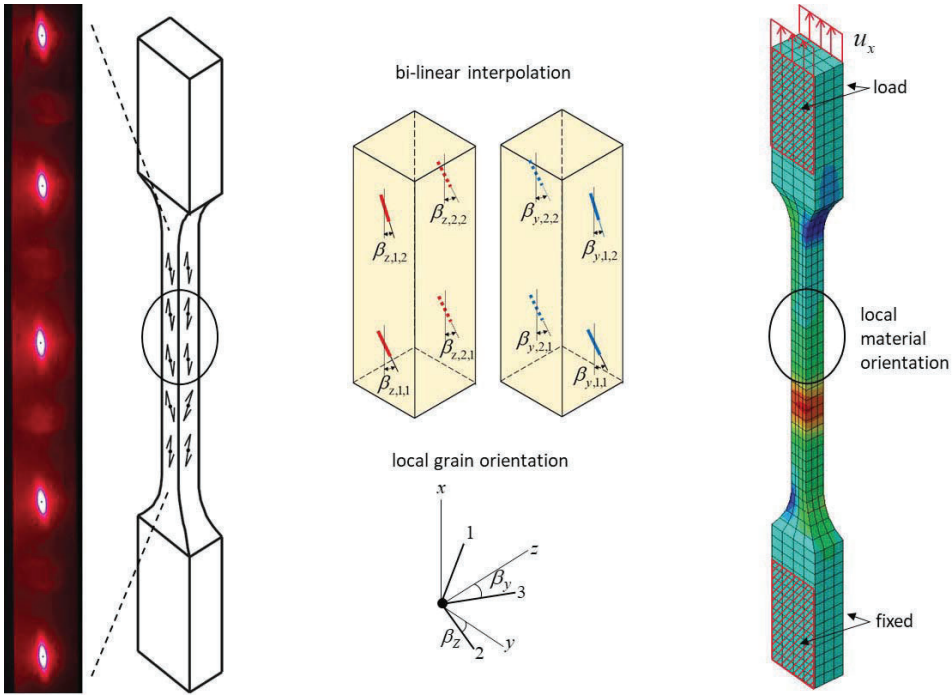

Figure 1. *(a) grain angle measurements by laser light scattering and ellipse fitting; (b) a section of the gauge region with measured grain angles, β_z and β_y used for bi-linear interpolation of the in-plane fibre direction and subsequent determination of the local grain orientation; and (c) finite element model with colour variations indicating local stresses cause by local material orientation. Boundary conditions are shown at the fixed and loaded (μ_x) ends. Element mesh size increased for illustrative purposes.*

Tension tests are subsequently conducted on the specimens using a universal testing device and the tension strength is determined according to the international standard, ISO 13061-6 [6]. The clamped area during testing was 80 x 45 mm^2. After testing, the failure mode of the specimens is analysed and documented [8].

Density was measured from a section of the gauge region after testing and the influence of density on the tension strength of this sample was investigated in a previous study [5]. Wherein, it was found that density had no unambiguous relationship with the tension strength. Therefore, density is not considered in the development of the numerical model.

3 NUMERICAL MODEL

The prediction model combines stress analysis by linear elastic finite element (FE) model with subsequent post-processing. In post processing, strength-based failure criteria with stress averaging were used to estimate the failure loads of the specimens.

3.1 STRESS ANALYSIS

The stress analyses were performed in Abaqus (Dassault Systèmes, Vélizy-Villacoublay, France) with a model of the axially loaded wood specimens, as illustrated in Figure 1c. The geometry follows nominal geometry of the actual specimens, and the model was meshed using eight-node brick elements with eight integration points (C3D8).

The mesh size was selected to have 15 x 10 elements over the specimen cross-section (note: in the figure, larger elements are used for illustration purposes). The material model was orthotropic, linear elastic, with constant properties over the whole specimen. The elastic properties were based on values for birch clear wood in [9] and are summarized in Table 1.

The grain orientations are accounted for by adjusting the local material orientations for each element. The local coordinate system is defined such that the 1-axis aligns with grain orientation and the transverse plane aligns with 23-plane.

The local orientations were determined from two grain angles, β_y and β_z (angles about the global y- and z-axes, respectively). For each element's centre point, local orientations were calculated by bilinear interpolation between the nearest measured in-plane grain angles, on opposite faces of the specimen. This is illustrated in Figure 1b. For example, the grain orientation β_z at arbitrary point (x,y,z) is obtained by interpolating between the four nearest measured grain angles $\beta_{z,i,j}$, with respect to x- and z-coordinates, while the value is constant in the y-direction. The same applies for β_y and the local grain orientation at the point is determined accordingly. Wood regions outside the limits of grain angle measurements, i.e., regions outside the gauge region, were modelled with constant grain direction according to nearest measured values.

https://doi.org/10.52202/069179-0058

Boundary conditions were applied to imitate gripping and loading in the universal testing machine. In the lower end of the specimen, all nodes on the wide faces of the gripping area are fixed in all directions. In the gripping area of the upper end of the specimen, displacement load u_x was applied in x-direction and the other directions were fixed.

For post-processing, the nodal coordinates, nodal stresses, and applied axial load F (sum nodal force in x-direction on loaded faces) were exported from each simulation. The stresses were in local coordinate systems of each node such that they can be directly used in the failure criteria. For the stresses, typical engineering notation convention is used, where σ_i are the axial stresses and τ_{ij} are the shear stresses. The indices refer to local material orientations. When referring to all the stress components at a certain point, a bold symbol $\boldsymbol{\sigma}$ is used to denote a stress vector.

Table 1: *Elastic properties in the FE model*

Property	
MOE par. to the grain E_1 [GPa]	16.3
MOE perp. to the grain $E_2 = E_3$ [GPa]	0.86
Longitudinal shear modulus $G_{12} = G_{13}$ [GPa]	1.05
Rolling shear modulus G_{23} [GPa]	0.19
Poisson's ratio $\nu_{12} = \nu_{13}$	0.46
Poisson's ratio ν_{23}	0.58

3.2 FAILURE CRITERIA

Local stresses, output from the FE model, were input into Matlab (Mathworks, Natick, Massachusetts, USA), where post-processing was performed for the prediction of tensile strength. The tensile strength was defined by most critically stressed point in the gauge region. Since there was data only for the grain orientation (longitudinal axis), but not for rotation angle of the tangential and radial axes of wood, only rotationally invariant transverse isotropic failure criteria were investigated here. Applicable criteria include Hashin criteria [10] and Tsai-Wu criterion [11]. They were originally created for composite materials but have also been widely utilised for wood. Transverse isotropic rotational invariance about 1-axis can be ensured by expressing the stress state in failure criteria in terms of following invariants [10]

$$I_1 = \sigma_1,\ I_2 = \sigma_2 + \sigma_3,\ I_3 = \tau_{23}^2 - \sigma_2\sigma_3,\quad I_4 = \tau_{12}^2 + \tau_{13}^2 \tag{1}$$

The failure criteria were based on the uniaxial strengths, namely, tensile strength parallel to the grain $f_{t,0}$, compressive strength parallel to the grain $f_{c,0}$, tensile strength perpendicular to the grain $f_{t,90}$, compressive strength perpendicular to the grain $f_{c,90}$, longitudinal shear strength f_v and rolling shear strength f_r.

The Hashin failure criterion [10] consist of four separate criteria, two for tensile modes and two for compressive modes. In this study, only the tensile failure modes were considered. The first mode (Equation 2) is "fibre tension" mode, which corresponds to failure parallel to the grain. The second mode (Equation 3) is "matrix tension" mode, which corresponds to failure perpendicular to the grain. In the equations, $\langle\ \rangle$ are Macaulay brackets denoting that $\langle x\rangle = x$ if $x > 0$, and $\langle x\rangle = 0$ otherwise.

$$\left(\frac{\langle\sigma_1\rangle}{f_{t,0}}\right)^2 + \frac{\tau_{12}^2 + \tau_{23}^2}{f_v^2} = 1 \tag{2}$$

$$\left(\frac{\langle\sigma_2 + \sigma_3\rangle}{f_{t,90}}\right)^2 + \frac{\tau_{23}^2 - \sigma_2\sigma_3}{f_r^2} + \frac{\tau_{12}^2 + \tau_{23}^2}{f_v^2} = 1 \tag{3}$$

Tsai-Wu [11] failure criterion consists of a single ellipsoidal failure surface in the stress space. Its transverse isotropic form is

$$\begin{aligned} &F_1\sigma_1 + F_2(\sigma_2 + \sigma_3) \\ &+F_{11}\sigma_1^2 + 2F_{12}\sigma_1(\sigma_2 + \sigma_3) + F_{22}(\sigma_2 + \sigma_3)^2 \\ &+F_{44}(\tau_{23}^2 - \sigma_2\sigma_3) + F_{55}(\tau_{12}^2 + \tau_{23}^2) = 1 \end{aligned} \tag{4}$$

in which F_i and F_{ij} are the strength parameters. They are defined in terms of uniaxial strengths as

$$\begin{aligned} F_1 = \frac{1}{f_{t,0}} - \frac{1}{f_{c,0}}, F_2 = \frac{1}{f_{t,90}} - \frac{1}{f_{c,90}}, \\ F_{11} = \frac{1}{f_{t,0}f_{c,0}}, F_{22} = \frac{1}{f_{t,90}f_{c,90}}, \\ F_{44} = \frac{1}{f_r^2}, F_{55} = \frac{1}{f_v^2} \end{aligned} \tag{5}$$

Parameter F_{12} (in Equation 4) is an off-axis strength parameter that, according to Tsai and Wu [11], should be determined based on off-axis tests. There exist also various approaches to estimate it from the other strength properties in the literature. However, in the present study, the criterion was simplified by setting $F_{12} = 0$.

3.3 STRESS AVERAGING

Purely stress-based strength predictions, without modelling related hardening or softening behaviour, assume a perfectly brittle material behaviour. However, stress-based criteria have been utilised also for quasi-brittle materials by stress averaging method [12, 13], which was also investigated in this study. Here, the averaging length was not derived from fracture mechanics since unambiguous fracture properties were not available, and the existing method for estimating the averaging length has been derived only for plane stress cases.

In the averaging approach adopted, the local stresses $\boldsymbol{\sigma}$ were replaced with average stresses $\overline{\boldsymbol{\sigma}}$ in the failure criteria (Equations 2-4). In this study, the same averaging is applied to all stress components. Averaged stresses at node k are computed by

$$\overline{\boldsymbol{\sigma}}_k = \frac{\sum_{p=1}^{N} w_{kp}\boldsymbol{\sigma}_p}{\sum_{p=1}^{N} w_{kp}} \tag{5}$$

where w_{kp} and $\boldsymbol{\sigma}_p$ are the weight and the stresses at point p. The weights are calculated with a Gaussian smoothing function, based on Euclidian distances d_{kp} between points k and p, as

$$w_{kp} = \exp\left(-\frac{d_{kp}^2}{l_c^2}\right) \quad (6)$$

where l_c is a length scale parameter. The length scale parameter is a distance after which the local stresses have relatively small contribution to the averaged stresses. The relation between the weight function and l_c is shown in Figure 2.

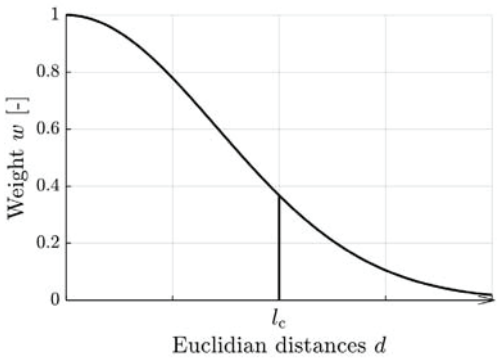

Figure 2: *Stress averaging weight factor w, as a function of Euclidian distance d to the surrounding FE nodes.*

3.4 ULTIMATE LOAD PREDICTION

Prediction of ultimate load was based on utilization ratio in the failure criteria and load F from the FE model. The utilization for point k was defined by the failure function in Equation (7), where $\overline{\boldsymbol{\sigma}}_{\boldsymbol{k}}$ is the averaged stress state at point k. Assuming proportional stresses, the ratio between failure stresses and applied stresses, g_k, was obtained by solving Equation (8). Furthermore, assuming linear elasticity, the ratio between ultimate load and applied load is equal to minimum g_k, and thus, the predicted failure load F_u can be estimated by Equation (9). Coordinates of the point with min(g_k) also give the estimated failure location.

$$f_k = f(\overline{\boldsymbol{\sigma}}_{\boldsymbol{k}}) \quad (7)$$

$$f_k(g_k \overline{\boldsymbol{\sigma}}_{\boldsymbol{k}}) = 1 \quad (8)$$

$$F_u = \min_{k=1\ldots N}(g_k)\, F \quad (9)$$

4 RESULTS

4.1 EXPERIMENTAL DATA

The failure modes were visually inspected and classified according to the five classes shown in Figure 3. A wide range of tension strength values, and grain angles are observed from the experimental investigations. Figure 4 shows the relationship between tension strength and the maximum 3D grain angle measured on the specimens. The grain angle has a clear influence on the strength. In most cases, the failure occurred within the gauge region of the specimens, however, specimens with splintering and longitudinal shear type failures (circle symbols) often had fractures that extend outside the gauge region and into the clamping zone. These specimens have greater scatter and present challenges for strength predictions.

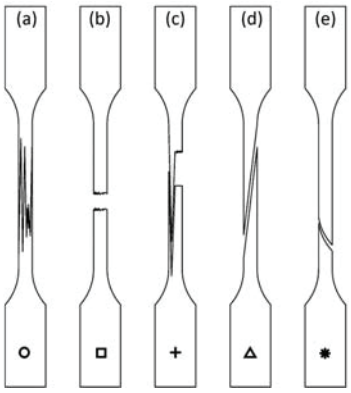

Figure 3. *Typical experimental failure modes used for classification: splintering/longitudinal shear (a), tension (b), combined tension & shear (c), sloping shear (d), and local (curved) grain deviation (e).*

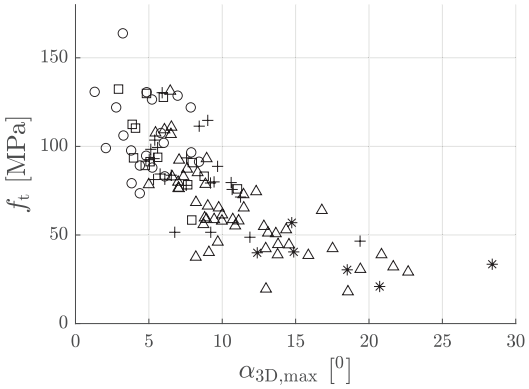

Figure 4: *Comparison between tension strength and measured maximum 3D grain angle.*

4.2 NUMERICAL MODEL

Figure 5 shows comparisons between the tensile strengths from the experimental tests and the predicted strengths according to the numerical models. The results are illustrated for the Hashin and Tsai-Wu failure criteria.

In all cases, stress averaging is applied, whereby the stress values obtained from FE analysis are effectively smoothed, i.e., the peak values are reduced, and the predicted strength values generally increase. Without stress averaging, the predicted strengths, using the initial strength values from literature (Table 2), are significantly underestimated, particularly for specimens of higher strengths. A range of l_c values (from 5 to 15 mm) were investigated and l_c = 5 mm was selected as it improves the initial results, i.e., the fit between predicted and experimental strengths. Nonetheless, l_c values up to 10 mm provide similar improvements. According to literature [14], averaging lengths from 4 mm to 20 mm are typical.

https://doi.org/10.52202/069179-0058

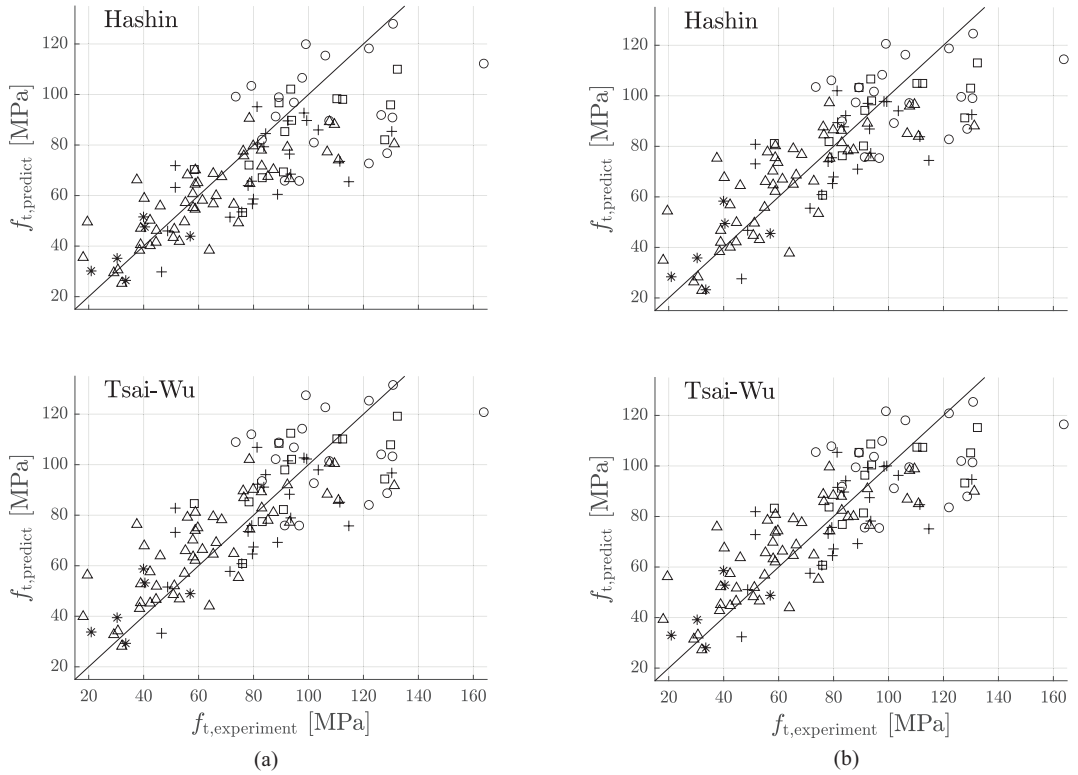

Figure 5. *Comparison between predicted and experimental strength for the Hashin and Tsai-Wu failure criteria when applying (a) strength values from literature, (b) calibrated strength values (calibrated to the whole sample). Stress averaging with l_c = 5 mm is applied in all cases.*

Table 2: *Initial and calibrated strength parameters. References for the initial parameters are shown next the values.*

	Initial	Hashin		Tsai-Wu		Hankinson	
	(uncalibrated)	Whole sample	Gauge	Whole sample	Gauge	Whole sample	Gauge
$f_{t,0}$ [MPa]	137 [15]	130	150	130	140	127	143
$f_{c,0}$ [MPa]	53 [16]	-	-	56	55	-	-
$f_{t,90}$ [MPa]	7.0 [15]	4.4	7.3	6.0	6.6	6.17	8.61
$f_{c,90}$ [MPa]	6.5 [16]	-	-	6.2	6.6	-	-
f_v [MPa]	12 [15]	15	13	13	12	-	-
f_r [MPa]	3.5 [17]	3.3	*	4.2	3.8	-	-
n	-	-	-	-	-	1.79	1.50

*Unstable parameter

Figure 5a illustrates the comparison when the strength properties from literature are considered. It is observed that the Hashin criterion underestimates specimens with higher strengths, yet the Tsai-Wu criterion has a minor bias towards overestimation of strength for the lower strengths and some underestimation for the highest strengths. Since the literature values (of which are generally lacking for silver birch) are from different source materials (excluding the compression strengths, they are determined from the same sample material), the literature values applied may not be ideal for the present sample.

An additional feature captured in the numerical model is the stress concentrations that develop around the curved tapering region of the dog-bone shaped specimen. This leads to predicted failures occurring more frequently in the ends of the gauge region, compared to the inner regions, and this behaviour is also exhibited experimentally.

Investigations into strength properties that are calibrated to the experimental results are conducted. Calibrated strength values are determined by simultaneously optimizing all uniaxial strength properties included in the failure criteria, by minimizing the sum of the squared residuals between

https://doi.org/10.52202/069179-0058

the predicted and experimental strengths. Stress averaging with l_c = 5 mm is maintained. Calibration is performed on both the whole sample and only on specimens that have failed within the gauge region (gauge specimens). Specimens with splintering or longitudinal shear type failure are predominantly those which have failures extending outside the gauge region. Effects from the test setup for specimens with failures extending into clamped region is not captured in the model and may have higher strengths, compared to the model predictions.

The strength properties after calibration are given in Table 2 and Figure 5b illustrates the comparison between experimental and predicted results, according to the calibrated strength properties for the whole sample. The calibrated strengths generally agree with the values from literature, although some considerable differences are obtained. The tension strengths (parallel and perpendicular to grain) calibrated to the whole sample are notably lower than the literature values, especially for Hashin. Calibrations with the gauge specimens and Tsai-Wu criteria largely concur with the literature values. For Hashin, calibrations with the gauge specimens provide similar values to literature except the tension strength parallel to the grain is, in this case, rather high.

Overall, the error when applying calibrated predictions (whether the whole sample or the gauge specimens are considered) is only slightly lower compared to the error when applying literature values, with mean absolute errors around 14 MPa and 15 MPa, respectively. The main difference when calibrating with only the gauge specimens compared to calibrating using the whole sample, is, as expected, larger scatter of the splintering/longitudinal shear type failure but a better estimate of the lower strength specimens, mainly the specimens with sloping shear type failures.

According to the failure criteria, the strength properties with the largest influence on the utilization ratio include tension strength parallel and perpendicular to the grain and the longitudinal shear strength. The model is relatively insensitive to the rolling shear strength values, and as such, the calibrated values may be extreme. The rolling shear was an unstable strength parameter when calibrating to the gauge specimens with Hashin criteria, and for predictions, the literature value was used in this case. It is also mentioned that the compression strength properties in Tsai-Wu may not be representative of the actual compression strengths since they are calibrated in absence of compression experimental data.

4.3 STRENGTH PREDICTION USING THE ANALYTICAL MODEL

To evaluate the numerical model's performance against a well-established analytical model, the generalized Hankinson's formula is considered. It defines off-axis tensile strength $f_{t,\alpha}$ as

$$f_{t,\alpha} = \frac{f_{t,0} f_{t,90}}{f_{t,0} \sin^n \alpha + f_{t,90} \cos^n \alpha} \tag{11}$$

where α is the angle between the load and the grain orientation, and n is a generalization parameter that is optimized by fitting the equation to the sample data, Generalization parameters within the range of 1.5 to 2.0 are typically regarded as suitable for predicting the (off-axis) tensile strength of wood [18].

The maximum 3D grain angle measured on the specimens are used in the formula. The strength properties and generalization parameter are calibrated to the data considering the whole sample and the gauge specimens. The calibrated parameters are given in Table 2. Figure 6 provides a comparison between the experimental and the predicted strengths, according to Hankinson's formula with strength properties calibrated to the whole data set.

The strength predictions of the analytical model are rather similar, in terms of error, when compared to the numerical model developed in this study. Indeed, compared to the analytical model, no significant improvement in the strength predictions was realized with the numerical model. An explanation to the similar results is given by analysis of the predicted failure locations. The location of failure is predicted for each specimen according to the most critical node. The critical node was frequently at the location of maximum 3D grain angle, which (due to the used interpolation method) is near the laser point measurements. In fact, the correlation coefficient between maximum 3D grain angle location and predicted failure location (for both failure criteria) was around 0.9. As such, both the numerical model and analytical model provide strength predictions largely based on the maximum measured 3D grain angle.

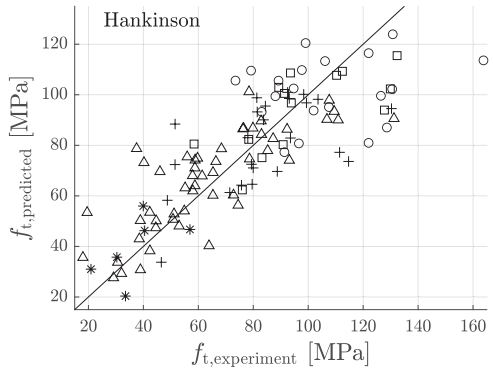

Figure 6: *Comparison between predicted and experimental strength for the Hankinson analytical model with strength properties and exponential parameter n calibrated to the whole sample.*

5 CONCLUSION AND OUTLOOK

In the present paper, a numerical model is developed for the prediction of tension strength of small-scale birch wood specimens with measured grain angles. The strength was predicted according to local stresses obtained from

https://doi.org/10.52202/069179-0058

the finite element model and two failure criteria, Hashin and Tsai-Wu, with a stress averaging approach. The model is compared to the experimental results and a simple analytical model. Results indicate:

- The maximum grain angle is a good indicator of strength. The predicted failure location of the model occurred around the location of the maximum measured 3D grain angles.
- The performance of the numerical model was limited by the information available of the test specimens. With grain angle being the driving indicator for strength, the maximum grain angle within the gauge region was the dominant factor in the strength predictions.

Potential future developments to the presented numerical model include the following:

- Associate the material properties (strength and stiffness) with various growth features identified on each specimen, such as growth ring width, distance to pith, or eigenfrequency. Use correlations between the growth features and the mechanical properties to estimate the material properties applied to the model and corresponding predictions.
- Include information about the location of the pith in the analysis. This way the material can be modelled with cylindrical orthotropy, i.e., tangential, and radial orientations can be defined, and orthotropic failure criteria can be used with related orthotropic strength properties.
- Increase the number of grain angle measurements (laser points) and measure also diving angles to better represent the grain flow of the specimen and the maximum grain angle.
- Consider the actual fracture process in the simulations. This can be implemented via damage or fracture mechanics-based formulations such as smeared crack models (local or non-local damage) or discrete crack models, e.g., cohesive cracks with extended finite element method.

REFERENCES

[1] P. Guindos and M. Guaita, "A three-dimensional wood material model to simulate the behavior of wood with any type of knot at the macro-scale," *Wood science and technology,* vol. 47, no. 3, pp. 585-599, 2013.

[2] M. Lukacevic, G. Kandler, M. Hu, A. Olsson and J. Füssl, "A 3D model for knots and related fiber deviations in sawn timber for prediction of mechanical properties of boards," *Materials & Design,* vol. 166, no. 107617, 2019.

[3] V. Kilde, K. H. Solli, B. Pitzner, P. Lind and J. Bramming, "Bjørk i synlige konstruksjoner (Birch in visible constructions). Rapport nr. 67.," Norsk Treteknisk Institutt, 2006.

[4] S. Collins and G. Fink, "Modeling the tensile mechanical properties of silver birch timber boards," *Construction and Building Materials,* vol. 344, no. 128147, 2022.

[5] S. Collins and G. Fink, "Grain angle determination of silver birch by laser light scattering and tensile fracturing," *Mater Struct,* vol. 55, no. 162, 2022.

[6] ISO 13061-6:2014(E), "Physical and mechanical properties of wood — test methods for small clear wood specimens — part 6: Determination of ultimate tensile stress parallel to grain," International Organization for Standardization, Geneva, 2014.

[7] S.-P. Simonaho, J. Palviainen, Y. Tolonen and R. Silvennoinen, "Determination of wood grain direction from laser light scattering pattern," *Optics and lasers in engineering,* vol. 41, no. 1, pp. 95-103, 2004.

[8] S. Collins, Mechanical behavior of silver birch structural timber under compression and tension loading, Aalto University doctoral thesis 175 Helsinki, 2022.

[9] J. M. Dinwoodie, Timber: its nature and behaviour, CRC Press London, 2000.

[10] Z. Hashin, "Failure criteria for Unidirectional Fiber Composites," *Journal of Applied Mechanics,* vol. 47, pp. 329-334, 1980.

[11] S. Tsai and E. Wu, "A General Theory of Strength for Anisotropic Materials," *Journal of Composite Materials,* vol. 5, pp. 58-80, 1971.

[12] P. Guindos, "Comparison of different failure approaches in knotty wood," *Drewno: prace naukowe, doniesienia, komunikaty,* vol. 57, 2014.

[13] P. J. Gustafsson, "Mean Stress Approach and Initial Crack Approach," in *Fracture mechanics models for strength analysis of timber beams with a hole or a notch - A Report of RILEM TC-133*, Lund, Lund University, Sweden, 2002.

[14] S. Thelandersson and H. J. Larsen, Timber Engineering, first ed, West Sussex: Wiley, 2003.

[15] R. Wagenführ and C. Scheiber, Holzatlas, Leipzig: Fachbuchverlag, 1974.

[16] S. Collins and G. Fink, "Mechanical behaviour of sawn timber of silver," *Wood Material Science & Engineering,* vol. 17, no. 2, pp. 121-128, 2022.

[17] T. Ehrhart and R. Brandner, "Rolling shear: Test configurations and properties of some European soft- and hardwood species," *Engineering Structures,* vol. 172, pp. 554-572, 2018.

[18] F. F. P. Kollmann and W. A. Cote, Principles of Wood Science, New York: Springer-Verlag, 1968.

This page intentionally left blank due to withdrawn paper.

This page intentionally left blank due to withdrawn paper.

This page intentionally left blank due to withdrawn paper.

This page intentionally left blank due to withdrawn paper.

This page intentionally left blank due to withdrawn paper.

This page intentionally left blank due to withdrawn paper.

This page intentionally left blank due to withdrawn paper.

This page intentionally left blank due to withdrawn paper.

World Conference on Timber Engineering Oslo 2023

EFFECTS OF THE CROSS-LINKING OF THE CELLULOSIC FIBRILLAR NETWORK ON THE EFFECTIVE MACROSCOPIC BEHAVIOUR OF WOOD

Nhat-Tung Phan[1], François Auslender[1], Joseph Gril[1,2], Rostand Moutou Pitti1[1,3]

ABSTRACT: This study aims at analysing the influence of the fibrils oscillations and interconnexions on the macroscopic behaviour of wood. For that, a multi-scale model of softwood has been developed, with two options for the cell-wall level: a reference with no oscillations (0S) and oscillations and interconnexions in two directions (2S). The cell-wall and tissue effective behaviours are determined by using numerical homogenization for periodic media, while the succession of earlywood and latewood is dealt with analytically. It is observed that the influence of the fibrils oscillations is significant for some macroscopic moduli, such as the effective shear moduli $\widetilde{G}_{LT}$ and $\widetilde{G}_{LR}$, while it isn't for other moduli at the macroscopic level. Furthermore, although the effect of the interconnexions is quite strong for some components of the elastic behaviour at the cell wall level, it would lose its significance at the macroscopic level, especially for low-density wood. This tendency can be explained by the interaction of layers from two neighbouring cells that compensate for the absence of interaction between fibrils in the 0S model. The effect becomes stronger in the case of a softened matrix.

KEYWORDS: macroscopic behaviour, hierarchical models, numerical homogenization, fibrils oscillations.

1 INTRODUCTION

Wood is one of the longest-standing and most universal materials used by humans. In response to environmental changes, population growth, and increasing standard of living, the global demand for lignocellulose material has accelerated [1]. The advantages of this material are mainly its availability and its excellent mechanical performance relative to the density, explained by its structural organization [2].

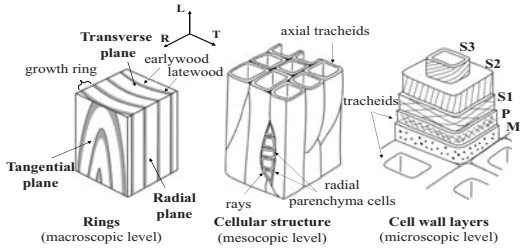

Figure 1: *Hierarchical structure and anisotropy of a softwood*

However, the study of wood has revealed a large variability of mechanical properties and various scales of heterogeneity. Thus, a better understanding of structure-property relationships is required to improve our capacity to design wood-derived products. Since wood is considered as a natural composite material with a complex multiscale organization, its behaviour is a consequence of both the deformation mechanisms of its constituents and their spatial distribution at different scales. In this study, having in mind the case of a softwood, we will then describe wood at three main levels (see Figure 1): the macroscopic level - scale of the grown-rings, the mesoscopic level - scale of the tissues, and the microscopic level - scale of the cell walls.

This paper aims to investigate the influence of a more realistic cell wall morphology on the macroscopic behaviour of wood by considering curved and interconnected fibrils, rather than considering them parallel as classically in the literature [3, 4, 5]. To this end, we develop a multiscale model incorporating three different scales of wood microstructure as described above, ranging from cell walls to annual grown-rings, from which both numerical and analytical homogenization methods will be used to determine their effective behaviour by defining a periodic elementary cell at each scale considered.

2 METHODOLOGY

2.1 MULTI-SCALE MODEL

2.1.1 An anisotropic material at all scales: from the secondary wall to the growth-ring

The illustration of the hierarchical structure of the wood at different scales in Figure 1 highlights the preferred

[1]Nhat-Tung Phan, François Auslender, Joseph Gril, Rostand Moutou Pitti, Université Clermont Auvergne, CNRS, Clermont Auvergne INP, Institut Pascal, F-63000 Clermont Ferrand, FRANCE nhat_tung.phan@uca.fr

[2]Joseph Gril, Université Clermont Auvergne, INRAE, Piaf, F-63000 Clermont Ferrand, FRANCE

[3]Rostand Moutou Pitti, IRT, Libreville Gabon

https://doi.org/10.52202/069179-0060

directions at each level. In this research, we make use of three orthonormal frames with in each case the first direction corresponding to the one with the most resistance and rigidity. They are represented in Figure 2 for the three considered levels. The three reference frames are: (L, R, T) for the growth-rings level, (1', 2', 3') for the tissues level and (1, 2, 3) for the cell walls level.

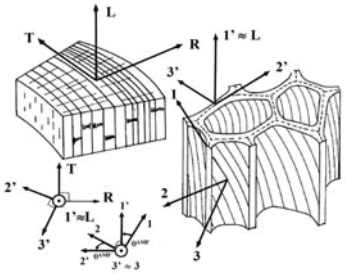

Figure 2: *Macroscopic, mesoscopic and microscopic orientations [6].*

2.1.2 Description of the wood microstructure at the 3 relevant scales

a) Wood cell wall microstructure

In the literature, the macrofibrils have classically been assumed to be straight and parallel to each other (Figure 3a). However, some experimental characterizations [7, 8] suggest that this is not the case and that the macrofibrils are curved and connected to each other [9]. These suggestions are similar to the models of an oscillating cellulose network originally proposed by Boyd [10], and later used by Gril [6].

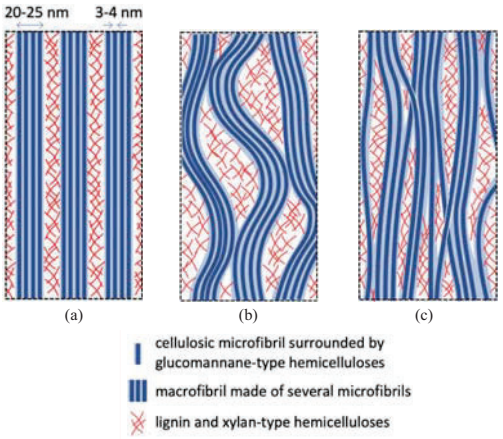

Figure 3: *Interpretation of the interconnexions between macrofibrils:* ***(a)*** *classical representation with straight and parallel microfibrils;* ***(b)*** *Oscillations and lateral contacts between macrofibrils through hydrogen bonding;* ***(c)*** *connexions resulting from the random transfer of oscillating microfibrils between neighbouring macrofibrils [11].*

Furthermore, this oscillating structure may be the reason for the puzzling orientation interpreted from tomography [12]. As to the nature of the links between macrofibrils, it can be speculated that macrofibrils oscillate by slight deviations from their main direction, and occasionally get into contact through hydrogen bonding with neighbouring macrofibrils (Figure 3b). An alternative explanation is that some of the microfibrils composing a macrofibril could occasionally shift to the neighbouring one, resulting in stronger connections (Figure 3c). In any case, it seems reasonable to assume the existence of a network of macrofibrils laterally connected, separated by lignified matrix incrustations with more or less lenticular shapes, and both interpretations would be compatible with the subsequent modelling approach. For the sake of simplification, the macrofibrils will be simply be called fibrils in what follows.

From the schematic description of the secondary walls proposed by Boyd [10], we assume that the fibrils oscillate around a principal direction, that we name direction 1, corresponding to the one defined by the MFA (Figure 4a). Taking the case of perfectly aligned fibrils as a reference (Figure 4b), we will examine the effect of oscillated fibrils (Figure 4c). In this study, we will describe oscillations for which the fibrils can oscillate within both planes (1, 2) and (1, 3).

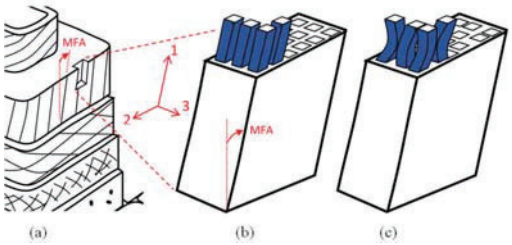

Figure 4: *Representation of the material constituting the secondary cell wall:* ***(a)*** *position and orientation of a portion of the cell wall,* ***(b)*** *classical representation with straight and parallel fibrils and* ***(c)*** *improved description with oscillated and connected fibrils [11].*

In order to analyse the influence of oscillated and connected fibrils on the effective behaviour of the cell wall, two periodic elementary cells that correspond to the 0S and 2S models, respectively, are meshed (Figure 5). The cell wall material is assumed to be the periodic repetition of each of the represented elementary cells.

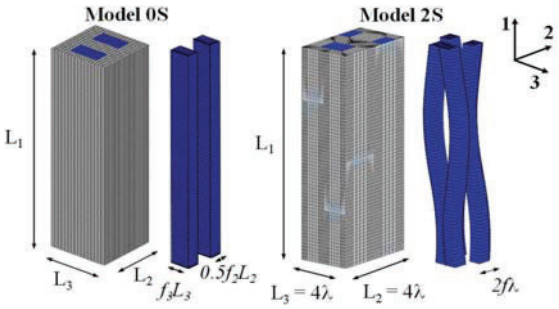

Figure 5: *two different morphological models to describe the periodic elementary cell (Cast3M)*

b) Cellular tissue microstructure

The tissue microstructure of wood is modelled on the basis of anatomical and morphological descriptions of the structure of wood at the tissue level, considering tissues composed only of longitudinal tracheids. We will thus neglect the parenchyma rays which are a minor component of softwood. The studied microstructure being

supposed to be periodic, we will consider a periodic unit cell to represent it and calculate its effective behaviour. Moreover, this elementary cell will be constructed by integrating additional assumptions, frequently used in the literature [13, 14, 15]:

- Invariance of the tissue structure in the longitudinal direction L, i.e. longitudinal irregularities at the points where the tracheids meet end to end are ignored;
- Invariance of the local density in the longitudinal direction.

Based on typical morphological parameters of softwoods at the tissue scale [16], earlywood (EW) and latewood (LW) are described as tissues consisting of a periodic arrangement of tissue microstructures of EW (Figure 6a) and LW (Figure 6b), respectively. Furthermore, each wall of the tissue microstructure consists of 3 layers (S1, S2, and S3), incorporating the primary wall and the middle lamella in the S1 layer.

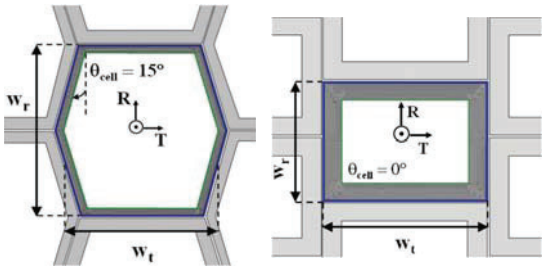

(a) Model EW (a) Model LW

Figure 6: *Geometric description of the two microstructures of EW and LW in the RT plane.*

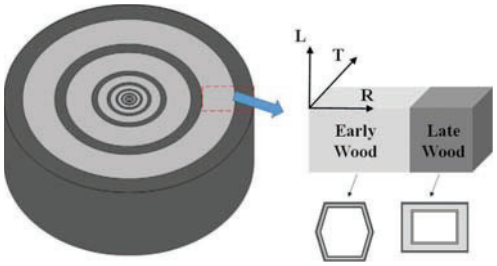

Figure 7: *Schematically idealized model for the annual ring*

c) Growth-ring microstructure

At the macroscopic scale, wood is described as a periodic arrangement of orthotropic homogeneous layers of EW and LW, without taking into account the curvature of the rings (see Figure 7). Although in reality the transition between EW and LW is gradual, the choice of a ring consisting of two layers has been made in order to achieve an equivalent effect in terms of contribution to transverse anisotropy.

2.2 CALCULATION OF THE EFFECTIVE BEHAVIOUR

On the one hand, we determine the effective elastic behaviour at both the cell wall and tissue scales by using a numerical homogenization procedure for its periodic microstructures in the first two steps of the developed multiscale model. On the other hand, the macroscopic elastic properties of the wood corresponding to the succession model of EW and LW are determined analytically and correspond to the last step of the multiscale model. Furthermore, the interaction of the material parameters between the different levels of the multiscale model are also taken into account**.**

2.2.1 Local problem

For determining the effective elastic properties of the different periodic microstructures, we make use of a deformation approach and apply to each periodic unit cell periodic boundary conditions of the type $\underline{u}(\underline{x}) = \underline{\underline{\varepsilon}}\,\underline{x} + \underline{u'}(\underline{x})$ where $\underline{\underline{\varepsilon}}$ is the imposed macroscopic strain and $\underline{u'}(\underline{x})$ a periodic displacement field [17]. The local problem to be solved reads as follows:

$$\left\{\begin{array}{l} \left.\begin{array}{l} \underline{div}\left(\underline{\underline{\sigma}}(\underline{x})\right) = 0 \\ \underline{\underline{\sigma}}(\underline{x}) = \underline{\underline{\underline{\underline{C}}}}(\underline{x}) : \underline{\underline{\varepsilon}}(\underline{x}) \\ \underline{\underline{\varepsilon}}(\underline{x}) = \frac{1}{2}\left(\frac{\partial \underline{u}(\underline{x})}{\partial(\underline{x})} + \frac{\partial \underline{u}(\underline{x})^T}{\partial(\underline{x})}\right) \end{array}\right\} \forall x \in \Omega \\ u(\underline{x}) = \underline{\underline{\varepsilon}}\,\underline{x} + u'(\underline{x}), \text{ with periodic } u', \forall x \in \partial\Omega \end{array}\right. \quad (1)$$

where Ω stands for the RVE, i.e. the periodic unit cell, and $\partial\Omega$ the cell boundary. The fourth-order tensor $\underline{\underline{\underline{\underline{C}}}}(\underline{x})$ is given by:

$$\underline{\underline{\underline{\underline{C}}}}(\underline{x}) = \sum_{r=M,F} \underline{\underline{\underline{\underline{C}}}}^r . \chi^r(\underline{x}) = \underline{\underline{\underline{\underline{C}}}}^M . \chi^M(\underline{x}) + \underline{\underline{\underline{\underline{C}}}}^F . \chi^F(\underline{x})$$

where $\chi^r(\underline{x})$ is the characteristic function of the phase *r,* equal to 1 if $\underline{x}$ belongs to the phase *r* and zero otherwise. The tensors $\underline{\underline{\underline{\underline{C}}}}^r$ are the tensors of the elastic moduli of the phases r.

2.2.2 Numerical homogenization

To calculate the effective behaviour of a periodic elementary cell corresponding to the cell wall (Figure 5) and tissue (Figure 6) microstructures, we make use of a deformation approach and apply periodic boundary conditions (PBC).

By applying 6 different elementary loadings to the periodic unit cell and solving by means of the FE method the local problem, we obtain for each elementary loading the local stress field, thus allowing us to determine the macroscopic stress which is classically defined by:

$$\overline{\underline{\underline{\sigma}}} = \langle \underline{\underline{\sigma}} \rangle = \frac{1}{|\mathrm{VER}|} \int_{\mathrm{VER}} \underline{\underline{\sigma}}(\underline{x}) d\underline{x} \quad (2)$$

The tensor of the effective elastic moduli $\tilde{\mathrm{C}}$ of the cell wall is then obtained by the following relation

$$\overline{\underline{\underline{\sigma}}} = \underline{\underline{\underline{\underline{\tilde{C}}}}} : \overline{\underline{\underline{\varepsilon}}} \quad (3)$$

which, by using Voigt notations, can be rewritten as

$$\begin{pmatrix} \bar{\sigma}_1 \\ \bar{\sigma}_2 \\ \bar{\sigma}_3 \\ \bar{\sigma}_4 \\ \bar{\sigma}_5 \\ \bar{\sigma}_6 \end{pmatrix} = \begin{pmatrix} \tilde{C}_{11} & \tilde{C}_{12} & \tilde{C}_{13} & \tilde{C}_{14} & \tilde{C}_{15} & \tilde{C}_{16} \\ \tilde{C}_{21} & \tilde{C}_{22} & \tilde{C}_{23} & \tilde{C}_{24} & \tilde{C}_{25} & \tilde{C}_{26} \\ \tilde{C}_{31} & \tilde{C}_{32} & \tilde{C}_{33} & \tilde{C}_{34} & \tilde{C}_{35} & \tilde{C}_{36} \\ \tilde{C}_{41} & \tilde{C}_{42} & \tilde{C}_{43} & \tilde{C}_{44} & \tilde{C}_{45} & \tilde{C}_{46} \\ \tilde{C}_{51} & \tilde{C}_{52} & \tilde{C}_{53} & \tilde{C}_{54} & \tilde{C}_{55} & \tilde{C}_{56} \\ \tilde{C}_{61} & \tilde{C}_{62} & \tilde{C}_{63} & \tilde{C}_{64} & \tilde{C}_{65} & \tilde{C}_{66} \end{pmatrix} \begin{pmatrix} \bar{\varepsilon}_1 \\ \bar{\varepsilon}_2 \\ \bar{\varepsilon}_3 \\ \bar{\varepsilon}_4 \\ \bar{\varepsilon}_5 \\ \bar{\varepsilon}_6 \end{pmatrix} \quad (4)$$

https://doi.org/10.52202/069179-0060

where $\overline{\sigma}_i = \overline{\sigma}_{ii}$, $\overline{\varepsilon}_i = \overline{\varepsilon}_{ii}$ for i = 1 to 3 and $\overline{\sigma}_4 = \overline{\sigma}_{23}$; $\overline{\sigma}_5 = \overline{\sigma}_{13}$; $\overline{\sigma}_6 = \overline{\sigma}_{12}$ and $\overline{\varepsilon}_4 = 2\overline{\varepsilon}_{23}$; $\overline{\varepsilon}_5 = 2\overline{\varepsilon}_{13}$; $\overline{\varepsilon}_6 = 2\overline{\varepsilon}_{12}$.

For instance, if we apply an elementary loading of the form $\underline{\underline{\varepsilon}} = \underline{e}_1 \otimes \underline{e}_1$, the first column of the second-order tensor $\underline{\underline{\widetilde{C}}}$ is given by:

$\widetilde{C}_{11} = \overline{\sigma}_1 = \langle\sigma_{11}\rangle$; $\widetilde{C}_{21} = \overline{\sigma}_2 = \langle\sigma_{22}\rangle$; $\widetilde{C}_{31} = \overline{\sigma}_3 = \langle\sigma_{33}\rangle$; $\widetilde{C}_{41} = \overline{\sigma}_4 = \langle\sigma_{23}\rangle$; $\widetilde{C}_{51} = \overline{\sigma}_5 = \langle\sigma_{13}\rangle$; $\widetilde{C}_{61} = \overline{\sigma}_6 = \langle\sigma_{12}\rangle$.

Accordingly, the application of 6 independent elementary loadings provide the whole effective tensor $\underline{\underline{\widetilde{C}}}$ of elastic moduli.

Moreover, by symmetry arguments related to the geometry of the elementary cell and the phase behaviour, it is shown that the effective behaviour of both the cell wall and tissue is necessarily orthotropic.

2.2.3 Analytical homogenization

The macroscopic behaviour of wood in the (L, R, T) directions is calculated by using an analytical solution for a bi-laminate consisting of the periodic repetition of two orthotropic elastic layers of earlywood and latewood (see Figure 7).

3 RESULTS AND DISCUSSION

In this work, we make use of the above-mentioned multiscale approach was used in this research to study the relationships between wood microstructure and its elastic properties. More specifically, this work aims to analyse through parametric studies the influence of oscillated and interconnected fibrils within the cell wall on the elastic effective properties of wood at three different scales.

3.1 THE CELL WALL LEVEL

The parametric studies are performed for both microstructure models (0S) and (2S) of the cell wall by varying different geometrical parameters such as the shape ratio $r_\varphi = L_1/L_2$, the fibril volume fraction c, the ratio of lamellar matrix on lenticular matrix $r_\lambda = V_{\text{lamellar matrix}}/V_{\text{lenticular matrix}}$ and material parameter (phase contrast: ratio E_L^F/E^M where E_L^F is the longitudinal Young's modulus of the fibrils and E^M is the Young's modulus of the matrix). Three effects associated with the fibrils oscillations are highlighted: those induced by the orientation of the fibrils, by the contact between the fibrils, and finally by the heterogeneous spatial distribution of the matrix between the oscillating fibrils (see Figure 8).

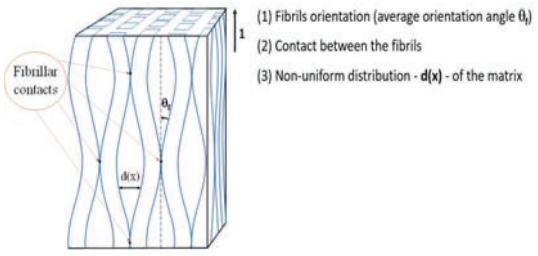

Figure 8: *Illustration of the 3 effects induced by the undulations of the fibrils.*

Furthermore, it is observed that the 2S model have a significant impact on the effective coefficients $\widetilde{C}_{12}$, $\widetilde{C}_{66}$ and $\widetilde{C}_{13}$, $\widetilde{C}_{55}$ which are significantly influenced by the fibril oscillations in the (1, 2) plane and (1, 3) plane, respectively. Besides, the 2S model is able to take into account the influence of oscillated fibrils in the (2, 3) plane by the observations associated with the effective coefficients et $\widetilde{C}_{23}$, $\widetilde{C}_{44}$, respectively.

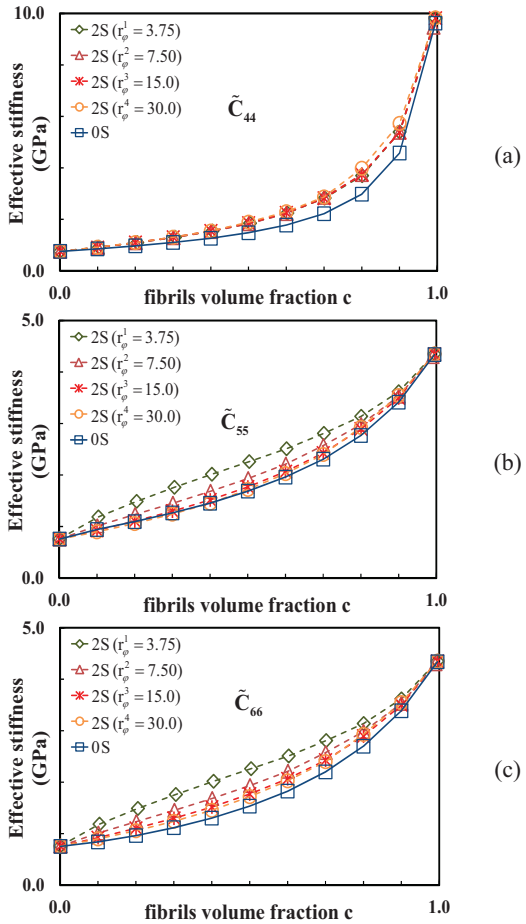

Figure 9*: Variations of the effective moduli $\widetilde{C}_{ij}$ as functions of the volume fraction (r_λ = 1)*

3.2 THE TISSUE LEVEL

Following the observations carried out at the cell wall level, we have shown at the tissue scale that the influence of the oscillated and interconnected fibrils increases with the relative density of the tissue. However, although the effects induced by the fibril oscillations are quite strong for some components of elastic behaviour at the cell wall scale, it loses its importance at the tissue level, especially for low density wood. This trend can be explained by the antisymmetric sloping of microfibrils in adjacent cell walls. Thus, for denser wood where the interaction between adjacent cell walls is less dominant, the effect of fibril oscillations remains significant. To highlight these results, we present in Figure 10 the evolutions of the 3

effective shear moduli $\widetilde{G}_{ij}$ as a function of relative density (wood density divided by cell-wall density) for the latewood case.

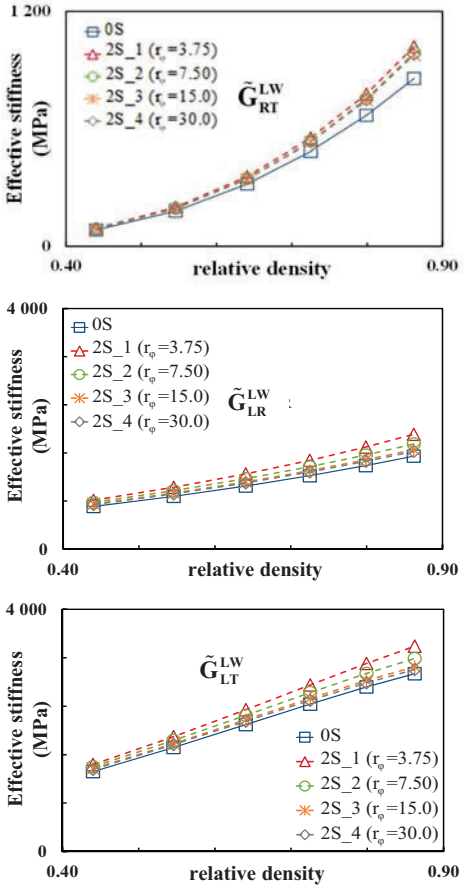

Figure 10: *Evolution of the effective $\widetilde{C}_{ij}$ components as a function of relative density for the LW model with the different data associated with the 0S and 2S models*

3.3 THE GROWN-RING LEVEL

Based on Figure 11, the study of the influence of fibril oscillations on the macroscopic behaviour of wood via the presented multiscale model shows that the results obtained are similar to those observed at the grown-ring level. In addition, we also present for comparison purposes the experimental data of Guitard [18] for softwood.

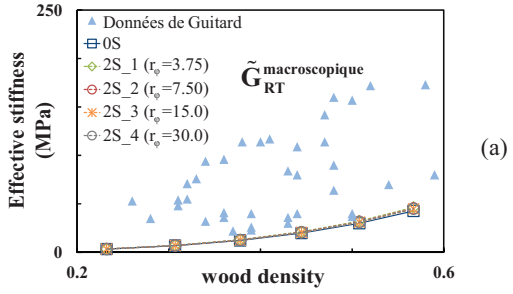

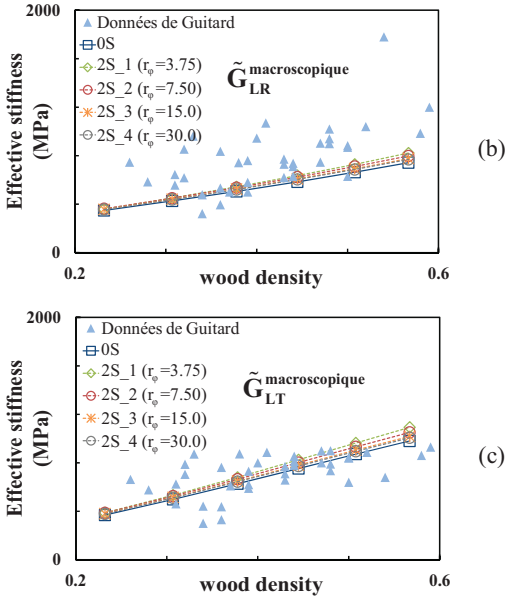

Figure 11: *Evolution of the effective moduli $\widetilde{C}_{ij}$ as a function of wood density for the two microstructures 0S and 2S*

4 CONCLUSION AND PERSPECTIVES

Using the presented multiscale model, we showed that the influence of the oscillated and interconnected fibrils is significant for some macroscopic moduli, such as effective shear moduli, while it is not significant for other moduli at the macroscopic level (grown-ring scale). Furthermore, the proposed multiscale model provides macroscopic elastic properties and their evolutions as a function of wood density which are close to those observed experimentally for softwoods, with the exception of the modulus $\widetilde{G}_{RT}$ which is strongly underestimated. Lastly, although the effect of fibril crosslinks is quite strong for some components of the elastic behaviour at the cell wall level, it loses its importance at the macroscopic level, especially for low-density wood.

In order to study the influence of fibril oscillations not only on the effective elastic properties of wood at the three scales considered, an extension of the presented procedure to the case of linear hygro-elastic behaviour, has been developed within the multiscale model. It is based on FE calculations associated with the linear thermo-elasticity model, has been developed within the multi-scale model. This procedure allows to take into account the deformations induced in the absence of mechanical loading by an increase (respectively a decrease) of the water content which leads to a swelling (respectively a shrinking) of the wood.

https://doi.org/10.52202/069179-0060

REFERENCES

[1] Hansen, E., Juslin, H., 2018. Strategic Marketing in the Global Forest Industries, Oregon State University. Ed.

[2] Salmén, L., 2018. Wood Cell Wall Structure and Organisation in Relation to Mechanics. Springer International Publishing AG.

[3] Harrington, J.J., 2002. Hierarchical modelling of softwood hygro-elastic properties. University of Canterbury, Christchurch, New Zealand.

[4] Persson, K., 2000. Micromechanical modelling of wood and fibre properties (Structural Mechanics). Lund University, Sweden.

[5] Rafsanjani, A.A., 2013. Multiscale poroelastic model - Bridging the gap from cellular to macroscopic scale (Doctor of Sciences). ETH Zurich.

[6] Gril, J., 1988. Une modelisation du comportement hygro-rheologique du bois a partir de sa microstructure. Paris 6.

[7] Bardage, S., Donaldson, L., Tokoh, C., Daniel, G., 2004. Ultrastructure of the cell wall of unbeaten Norwayspruce pulp fibre surfaces. Nordic Pulp & Paper Research Journal 19, 448–452.

[8] Salmén, L., Stevanic, J.S., Holmqvist, C. and Yu, S., 2021. Moisture induced straining of the cellulosic microfibril. Cellulose, 28(6), pp.3347-3357.

[9] Salmén, L. and Burgert, I., 2009. Cell wall features with regard to mechanical performance. A review COST Action E35 2004–2008: Wood machining–micromechanics and fracture.

[10] Boyd, J.D., 1982. An anatomical explanation for visco-elastic and mechano-sorptive creep in wood, and effects of loading rate on strength. New Perspectives in Wood Anatomy 171–222.

[11] Phan NT., Auslender F., Gril J., Moutou Pitti R.. Influence of the cross-linking of the cellulosic fibrillar network on the effective hygro-mechanical behavior of the wood cell wall. Acta Mechanica. 2022.

[12] Reza, M., Ruokolainen, J., Vourinen, T., 2014. Out-of-plane orientation of cellulose elementary fibrils on spruce tracheid wall based on imaging with high-resolution transmission electron microscopy. Planta 240, 565–573.

[13] Astley, R.J., Stol, K.A., Harrington, J.J., 1998. Modelling the elastic properties of softwood. Part II: The cellular microstructure. Holz Als Roh- Werkst. Vol. 56, 43–50.

[14] Koponen, S., Toratti, T., Kanerva, P., 1991. Modelling elastic and shrinkage properties of wood based on cell structure. Wood Sci. Technol. 25, 25–32.

[15] Mishnaevsky Jr, L., Qing, H., 2008. Micromechanical modelling of mechanical behaviour and strength of wood: State-of-the-art review. Comput. Mater. Sci. 44, 363 370.

[16] Fengel, D., 1969. The ultrastructure of cellulose from wood Pat 1: Wood as the basic material for the isolation of cellulose. Wood Science and Technology 3, 203–217.

[17] Bornert, M., Bretheau, T., Gilormini, P., 2001. Homogénéisation en mécanique des matériaux 1 : matériaux aléatoires élastiques et milieux périodiques, Mécanique et Ingénierie des Matériaux.

[18] Guitard, D., 1987. Mécanique du matériau bois et composites, Cépaduès. ed.

World Conference on Timber Engineering Oslo 2023

A MULTI-PHASE HYGRO-THERMAL MODEL FOR WOODEN BRIDGE COMPONENTS EXPOSED TO SOLAR RADIATION

Stefania Fortino[1], Petr Hradil[2], Timo Avikainen[3], Keijo Koski[4], Ludovic Fülöp[5]

ABSTRACT: This study demonstrates the modelling assisted long-term monitoring of wooden bridge components with surfaces exposed to solar radiation. An improved multi-phase finite element model is developed to predict the distribution of moisture content, relative humidity and temperature in wood. Hygro-thermal measurements are collected from the monitoring system of the stress-laminated Tapiola Bridge in Finland. The monitoring uses integrated sensors which provide both the relative humidity and the temperature in given locations of the deck, which are compared to the numerical results. The modelling assisted monitoring can help to reduce the maintenance costs of timber bridges, as well as the cost of instrumentation, and to increase the safety.

KEYWORDS: Wooden bridges, Wood moisture, Solar radiation, Monitoring, Multi-phase models, Finite Element Method

1 INTRODUCTION

Wooden bridges are economical, show an excellent environmental performance and can have a long service life. However, their durability under harsh climates represents one of the main problems for designers and owners. This is due to the material biodegradation caused by moisture content (*MC*) accumulated in wood for long periods, in combination with certain temperatures [1]. Although evidence exists that structural wood can retain its strength through many centuries, the variations of moisture content can strongly influence the structural integrity, the serviceability, and the loading capacity of timber bridges [2].

In this context, the monitoring of moisture content in wood is necessary for both the durability of the material and the performance of the whole structure. In the last decade, several studies have shown that numerical modelling can assist the sensor-based monitoring to get detailed information on the hygro-thermal response of wooden bridge components (see [3] and the related references).

In previous works [2,3], a multi-phase model with separated water phases was found efficient to study the moisture transport in uncoated and coated stress-laminated timber decks below the fibre saturation point (FSP) under outdoor environmental conditions characterized by continuous variations of temperature (T) and relative humidity (RH).

This paper presents a multi-phase hygro-thermal model able to simulate the effects of the external climate, including the solar radiation, on the sun exposed surfaces of timber bridge decks. As a case-study, the hygro-thermal analysis of the stress-laminated timber deck of Tapiola Bridge in Finland [2] is carried out by using the finite element method (FEM).

2 MULTI-PHASE MODEL FOR MOISTURE TRANSPORT IN WOOD

Below the FSP, the phenomena governing the moisture transport in wood are the diffusion of water vapour in the pores, the sorption of bound water and the diffusion of bound water in the cell walls [4]. Above the FSP, there are capillary pressure and gravity for the free water in the pores, sorption between the free water and the bound water phases, evaporation or condensation between the free water and the vapour water phases [5]. In the differential equations describing the above phenomena, the water phases are separated and the coupling between them is defined through conversion rates.

Compared to the previous works by some of the authors, in the present paper the influence of the solar radiation during time is considered by modifying the hygro-thermal boundary conditions for the temperature.

2.1 Governing equations

By using a matrix and vector notation, and considering as variables of the problem the bound water concentration c_b, the water vapour concentration c_v and the temperature T in the wood material, the related governing equations are defined as

[1] Stefania Fortino, VTT Technical Research Centre of Finland Ltd, Finland, stefania.fortino@vtt.fi
[2] Petr Hradil, VTT Technical Research Centre of Finland Ltd, Finland, petr.hradil@vtt.fi
[3] Timo Avikainen, VTT Technical Research Centre of Finland Ltd, Finland, timo.avikainen@vtt.fi
[4] Keijo Koski, VTT Technical Research Centre of Finland Ltd, Finland, keijo.koski@vtt.fi
[5] Ludovic Fülöp, VTT Technical Research Centre of Finland Ltd, Finland, ludovic.fulop@vtt.fi

https://doi.org/10.52202/069179-0061

$$\frac{\partial c_b}{\partial t} = -\nabla \cdot \mathbf{J}_b + \dot{c}_{bv} \quad (1)$$

$$\frac{\partial c_v}{\partial t} = -\nabla \cdot \mathbf{J}_v - \dot{c}_{bv} \quad (2)$$

$$c_w \varrho \frac{\partial T}{\partial t} = -\nabla \cdot \mathbf{J}_T - \nabla \cdot \mathbf{J}_b h_b - \nabla \cdot \mathbf{J}_v h_v + \dot{c}_{bv} h_{bv} \quad (3)$$

In the above equations, $\mathbf{J}_b$ and $\mathbf{J}_v$ represent the fluxes of bound water and water vapour defined as

$$\mathbf{J}_b = -\mathbf{D}_b \nabla c_b;\ \mathbf{J}_v = -\mathbf{D}_v \nabla c_v \quad (4)$$

where ∇ is the nabla operator, $\mathbf{D}_b$ and $\mathbf{D}_v$ are the diffusion matrices for bound water and water vapour phases and the thermal flux $\mathbf{J}_T$ is defined as

$$\mathbf{J}_T = -\mathbf{K} \nabla T \quad (5)$$

where $\mathbf{K}$ is the thermal conductivity matrix. Coupled hygro-thermal terms in fluxes of Equation (4) are not included since their effects were found negligible in the presence of Northern weather conditions [6].
In Equations (1-3) $\dot{c}_{bv}$ represents the conversion rate between the bound water and the water vapour phases. In Equation (3), h_b and h_v are the specific enthalpies and $h_{bv} = h_b - h_v$ the specific transition enthalpy from bound water to water vapour.
The bound water concentration is defined as $c_b = \varrho_0 MC$ where MC is the moisture content and ϱ_0 the dry wood density. The water vapour concentration c_v is a function of the partial vapour pressure p_v through the ideal gas law $c_v = \varphi\, p_v M_{H2O}/RT$ where R is the gas constant and M_{H2O} the molecular mass of water. The vapour pressure is expressed as a function of the relative humidity RH:

$$p_v = RH \cdot p_{vs} \quad (6)$$

where p_{vs} is the saturated vapour pressure given by the semi-empirical Kirchhoff expression [4].
The equation describing the conversion rate between bound water and water vapour is defined as

$$\dot{c}_{bv} = H_c(\varrho_0 MC_{bl} - c_b) \quad (7)$$

where H_c is the moisture dependent reaction rate and MC_{bl} represent the temperature dependent sorption isotherms based on the Anderson-McCarthy model:

$$MC_{bl,\alpha} = -\frac{1}{f_{2\alpha}} \ln\left(\frac{\ln\left(\frac{1}{RH}\right)}{f_{1\alpha}}\right),\ \alpha \in \{a, d\} \quad (8)$$

where a and d refer to adsorption and desorption and $f_{i\alpha} = \sum_{j=0}^{n} b_{ij\alpha} T^j,\ i \in \{1,2\}$.

All material properties of the model equations presented above, as well as the parameters of the Anderson-McCarthy model can be found in [3].

2.2 Hygro-thermal boundary conditions in the presence of solar radiation

The boundary conditions for bound water and water vapour concentrations are defined as:

$$\mathbf{n} \cdot \mathbf{J}_b = \mathbf{0};\quad \mathbf{n} \cdot \mathbf{J}_v = k_v^w c_v' - k_v^a c_v^a \quad (9)$$

where the first equation holds on all the external surfaces considering that the bound water cannot pass them and it is restricted in the cell walls. Therefore the model includes only exchanges of vapour and heat with the ambient air. In the second equation, defined on the surfaces exposed to RH and T, $\mathbf{n}$ represents the outward normal direction to the surface, $c_v' = c_v/\varphi$ is the concentration of water vapour divided by the wood porosity φ, c_v^a is the water vapour concentration of the air, k_v^w and k_v^a represent the surface permeances related to wood temperature and air temperature, respectively.
In the presence of a paint, the permeances of the coated wood referred to wood temperature and air temperature are defined as in [3]:

$$k_v^w = \frac{1}{\frac{1}{k_w} + \frac{1}{k_p}} \frac{RT}{M_{H2O}},\qquad k_v^a = \frac{1}{\frac{1}{k_w} + \frac{1}{k_p}} \frac{RT^a}{M_{H2O}} \quad (10)$$

where k_w is the permeance of uncoated wood and $k_p$the one of the paint.
The boundary condition for the temperature is defined as

$$\mathbf{n} \cdot \mathbf{J}_T = k_T(T - T^a) - q_{r,net} \quad (11)$$

where k_T is the thermal emission coefficient, T^a the temperature of the air, and $q_{r,net}$ represents the so-called net radiance at the wood surface [7]:

$$q_{r,net} = \alpha G + \varepsilon L - \varepsilon \sigma T^4 \quad (12)$$

where α is the solar absorptivity, G the incident solar radiation, ε the longwave emissivity of the surface, L the longwave incident radiation, and σ the Stefan-Boltzmann constant.
The values of dimensionless parameters α and ε depend on the wood material and the type of coating. In [7], the values of α for Korean wood species are around 0.3-0.5 and the values of ε around 0.4-0.7. According to [8], the solar absorptivity increases from a minimum of 0.25 for white paints to a maximum of 0.97 for black paints.
Following [8], the equation that relates the incident angle I on a surface with the solar altitude h, the surface solar azimuth A_{SS} and the orientation of the surface E (i.e. the angle of the surface from the horizontal), is the following:

$$Cos(I) = \cos(h)\cos(A_{SS})\sin(E) + \sin(h)\cos(E) \quad (13)$$

where the solar altitude is a function of the declination angle [9]. Therefore the incident radiation of Equation (12) is multiplied by the $Cos(I)$.

2.2.1 Implementation in Abaqus FEM code

The multi-phase model is implemented in the user subroutine UEL of Abaqus finite element code to describe the three differential equations of the material model and their boundary conditions [3]. At every time increment, the subroutine reads the weather data from the database of measured temperatures, air relative humidities, and solar radiation data. The shape functions for 8-nodes isoparametric brick elements are used to build a finite element with three variables per node (bound water concentration, water vapour concentration and temperature). The time integration is carried out using the fully implicit Euler scheme and the nonlinear system is solved using the Newton method at each time step. The subroutine allows to implement the FEM contributions to the residual vector and to the Jacobian iteration matrix.

3 ANALYSIS OF THE TAPIOLA BRIDGE DECK

The hygro-thermal data in wood are collected from the on-going monitoring of the stress-laminated timber deck of Tapiola Bridge built in the Spring of 2019 in the city of Espoo, Finland (Figure 1).

The Tapiola Bridge is composed of three spans and two of these are stress-laminated timber decks compressed by steel bars in the transverse direction. The bridge deck is composed of 46 timber beams in the width direction. The laminations are 0.215 m wide, and the deck thicknesses are 0.765 m for the 13.45 m span and 1.035 m for the 22.13 m span. The timber decks are 9.89 m wide and are protected with Valtti colour, an oil-based wood stain produced by Tikkurila corporation [10].

Five integrated humidity-temperature sensors, two force sensors and two displacement sensors were installed to monitor the bridge (Figures 3-5). The monitoring unit cabinet is equipped with two thermocouples for tracking its inside and outside temperature. The reader can refer to publication [2] for more details on the bridge structure and the monitoring system.

The parameters used for the boundary conditions of the case-study, are listed in Table 1. For the coated wood, the used parameters consider also the presence of a shading rail on the deck surface.

3.1 Description of the FEM model

The hygro-thermal model proposed in this work is based on the multi-phase moisture transport theory described in Section 2 with the aim to predict the distribution of *MC*, *RH*, and temperature in wood.

Table 1: *Boundary conditions parameters in the presence of solar radiation*

parameter	value	units
k_w	5.0E-9	kg/ m^2 s Pa
k_p	4.0E-9	kg/ m^2 s Pa
k_T	20	W m^{-2} K^{-1}
α (coated wood)	0.35	-
ε (coated wood)	0.5	-
α (asphalt)	0.7	-
ε (asphalt)	1.0	-
Stefan-Boltzmann constant	5.67×10^{-8}	W/m^2 K^4

Figure 1: *View of Tapiola Bridge*

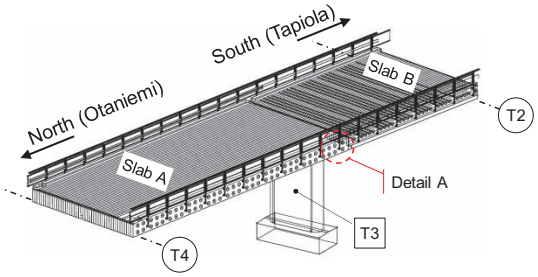

Figure 2: *Scheme of the transverse prestressed glulam wooden slabs of the bridge. The location of the sensors is highlighted as Detail A, in the vicinity of support T3*

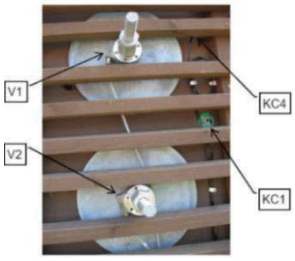

Figure 3: *Photo of the sensor locations. KC1 and KC4: humidity and temperature sensors, V1 and V2: force sensors*

https://doi.org/10.52202/069179-0061

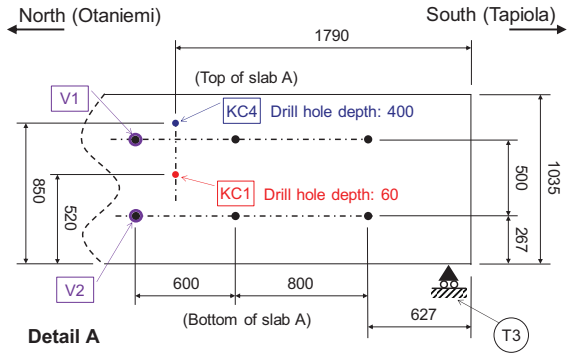

Figure 4: *Sensor locations in the side of the south-west corner of Slab A in the vicinity of support T3*

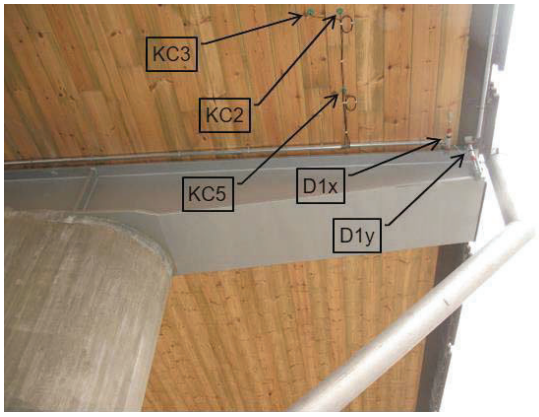

Figure 5: *Photo of the sensor locations on the bottom of the deck. KC2, KC3 and KC5: humidity and temperature sensors, D1x (slab longitudinal displacement) and D1y (slab vertical displacement)*

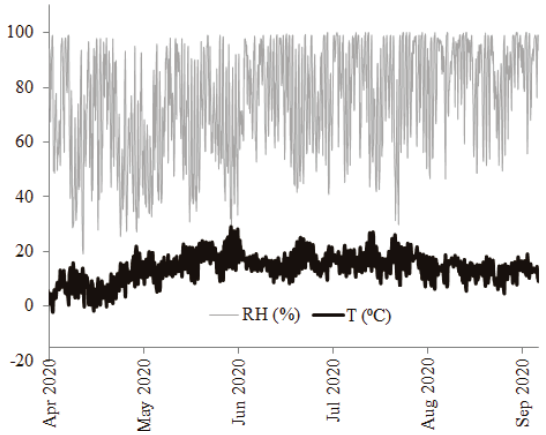

Figure 6: *Hourly relative humidity (RH) and temperature (T) of the air*

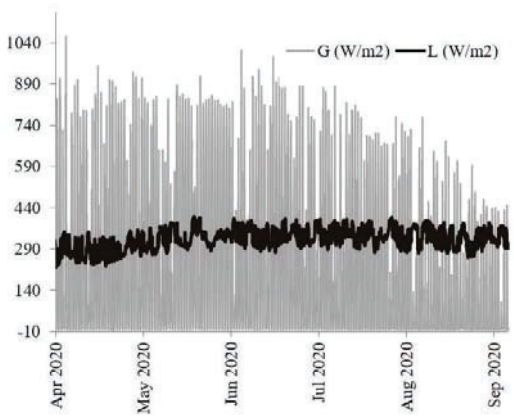

Figure 7: *Hourly incident solar radiation (G) and longwave incident radiation (L) on the exposed surface*

To investigate the hygro-thermal response of the timber deck during the sunny months, characterized by higher temperatures, a six month numerical analysis is carried out from the beginning of April 2020 to the end of September 2020. The hourly air temperature and *RH* are shown in Figure 6, while Figure 7 presents the hourly incident solar radiation and longwave incident radiation.
According to the approach proposed in [2], the modelling of the deck for the case-study investigated in this paper is based on the following scheme and assumptions:

- The deck model is schematized as a representative three-dimensional slice having a width of 215 mm (width of the lamination), height 1035 mm (thickness of the deck) and a thickness of 5 mm.
- Since the top surface is protected from moisture by the asphalt layer, it is considered to be exposed only to a thermal flux.
- The asphalt layer is not modelled as material, but higher values of solar absorptivity and longwave emissivity are applied on the top surface of the modelled slice (see Table 1).
- Compared to the model for internal lamination presented in [2], both fluxes of temperature and relative humidity act on the bottom surface as well as on the lateral surface of the lamination exposed to the air. The solar radiation acts on the lateral surface (Figures 3,4).
- The effect of the glue between laminations is not considered.

The used mesh size of the finite element model for the Abaqus analysis is set between 5 and 10 mm.
The solar radiation on the surfaces exposed to the sun affects the whole hygro-thermal response of the analyzed volume of wood because of the temperature increase on the surface. As observed in [8], the temperature of a vertical surface increases faster than for a horizontal surface because the vertical one receives more solar radiation in the early morning. When the sun rises, the incident angle on the vertical surface decreases while the incident angle on a horizontal surface increases. Therefore

https://doi.org/10.52202/069179-0061

the temperature of a horizontal surface can reach higher values than a vertical surface. The lateral surface of Tapiola Bridge's deck with sensor KC1 is north-west oriented and receives solar radiation during the afternoon.

3.2 RESULTS AND DISCUSSION

Figures 8 and 9 present the temperatures and the vapor pressures in the wood predicted by the model in the middle height of lamination at a distance of 60 mm from the lateral surface exposed to the afternoon solar radiation. The comparison with the measured temperatures and the vapor pressures in KC1 sensor are in good agreement. This also means that the parameters listed in Table 1 are suitable for the model used in the present case-study. The reported vapor pressure is based on the measured relative humidity. The numerical moisture content in the same location and the *MC* on the surface exposed to the sun are drawn in Figure 10. Table 2 summarizes the maximum and minimum numerical values of moisture contents in the sensor location affected by solar radiation (KC1) and on the sensor location at 60 mm from the bottom of the deck (KC2) previously investigated in [2]. It can be observed that the moisture contents are lower in the presence of solar radiation, and the differences are around 5%. On the exposed surface at the middle height of lamination, the predicted moisture contents in the studied period (Figure 10) are very similar to the ones founded at the bottom surface in a previous study [2]. It should be noticed that the lateral surface of the deck is also exposed to the variable relative humidity and this effect is coupled with the increase of temperature due to the solar radiation.

For future work, it is suggested to simulate cases of untreated wood and wood protected by different coatings to better evaluate the performance of the proposed model. Locations closer to the external surfaces should also be monitored by humidity-temperature sensors for accurate validation of the numerical model. In addition, different climates should be tested, especially in Southern Europe environments.

Developments of coupled hygro-thermal models for timber decks allow the accurate evaluation of moisture contents which is important for the prediction of moisture induced stresses (MIS) by using a sequential mechanical analysis [11]. The MIS can cause surface cracking, cupping deformations and losses of the pre-stress force in steel bars [1]. The accurate prediction of temperature increase due to solar radiation is also important for the investigation of wood decay and resistance of wood in connection with dose models [12].

Table 2: *Maximum and minimum predicted MCs in sensor locations from April 2002 to September 2020*

location	max *MC* (%)	min *MC* (%)
KC1	15.9	15
KC2	16.7	15.8

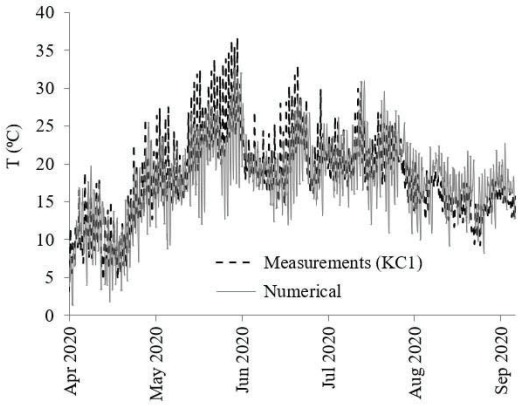

Figure 8: *Measured and predicted temperatures in KC1 sensor location*

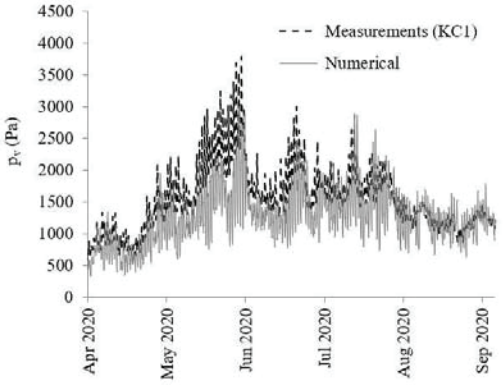

Figure 9: *Measured and predicted vapor pressures in KC1 sensor location*

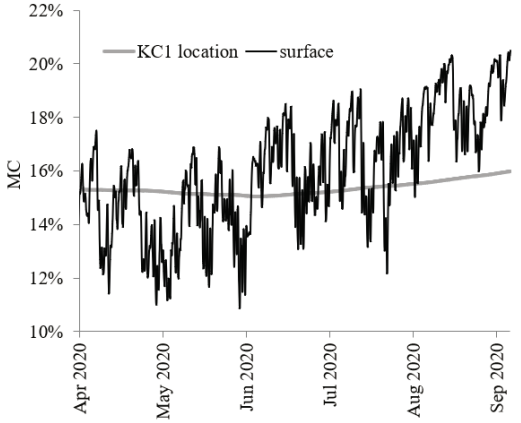

Figure 10: *Predicted moisture contents in KC1 sensor location and on the surface exposed to sun*

https://doi.org/10.52202/069179-0061

In future work, a more general model able to simulate the effects of external climates in wood also in the presence of rain, should consider the free water in lumens above the fibre saturation point [5].
Improved hygro-thermal models, along with sequential mechanical analyses, can reduce the whole costs of timber bridge monitoring and maintenance and increase their safety. The integration of numerical models with sensor-based instrumentation, will indeed reduce the number of needed sensors. In addition, predictions of moisture contents, moisture gradients and the possible crack risk due to the related surface MIS, provide important suggestions for optimal maintenance and eventual repair of the protective system. For instance, it would be practical to check the conditions of paints in certain seasons of the year, as the beginning of summer, characterized by drying in wood.

4 CONCLUSIONS

This paper proposed a multi-phase model for moisture transport able to simulate the hygro-thermal behaviour of a coated wooden bridge deck also considering the effects of solar radiation. The deck is schematized as a three-dimensional slice with the hygro-thermal fluxes on the exposed surfaces and therefore the related FEM analysis is efficient. The results of the model are in good agreement with the monitored data.
To the knowledge of the authors, the effect of solar radiation has not been deeply investigated within multi-phase models with separated water phases previously. Therefore, the proposed model contributes to the scientific advances of this field of research. However, further work is needed to properly validate the model for untreated wood materials and different coatings.
The improved model, used to assist the monitoring, can help to reduce the maintenance costs of timber bridges, as well as the cost of instrumentation, and to increase the safety of these structures.

ACKNOWLEDGEMENT

A part of this research was funded by project “Delivering Fingertip Knowledge to Enable Service Life Performance Specification of Wood - Click Design”, under ERA-NET action ForestValue co-found by the European Union’s Horizon 2020 research and innovation programme, grant agreement No 773324, and the Finnish Ministry of the Environment. The authors wish to thank the Finnish Transport Infrastructure Agency (Väylävirasto) and the City of Espoo for supporting the monitoring of Tapiola Bridge. This research was also funded by project “Image-based Modelling of Water Transport In Wood including material biodegradation – WaterInWood”, Academy of Finland, decision number 349194.

REFERENCES

[1] Pousette A., Malo K., Thelandersson S., Fortino S., Salokangas L., Wacker J. Durable Timber Bridges - Final Report and Guidelines. SP Report 25. Research Institutes of Sweden RISE, Skellefteå, Sweden, 2017.
[2] Fortino S, Hradil P, Koski K, Korkealaakso A, Fülöp L, Burkart H, Tirkkonen T. Health Monitoring of Stress-Laminated Timber Bridges Assisted by a Hygro-Thermal Model for Wood Material. *Applied Sciences* 11(1):98, 2021.
[3] Fortino S., Hradil P., Genoese A., Genoese A., Pousette A. Numerical hygro-thermal analysis of coated wooden bridge members exposed to Northern European climates. *Construction and Building Materials* 208, 492–505, 2019.
[4] Frandsen, H.L. Selected Constitutive models for simulating the hygromechanical response of wood. Ph.D. Thesis, Dept. of Civil Engineering Aalborg University, Aalborg, Denmark, 2007.
[5] Autengruber M., Lukacevic M., Füssl J. Finite-element-based moisture transport model for wood including free water above the fiber saturation point. *International Journal of Heat and Mass Transfer* 161, 120228:1–120228:21, 2020.
[6] Fortino S. Hradil P., Genoese A., Genoese A., Pousette A., Fjellström P.A. A multi-Fickian hygro-thermal model for timber bridge elements under Northern Europe climates. Proceedings of World conference in Timber Engineering (WCTE 2016) conference, August 22-25.2015, Vienna, Austria.
[7] Kang W., Lee Y-H., Kang C-W., Chung W-Y., Xu H-L., Matsamura J. Using the Inverse Method to Estimate the Solar Absorptivity and Emissivity of Wood Exposed to the Outdoor Environment. *Journal of the Faculty of Agriculture*, Kyushu Univ., 56 (1), 139–148, 2011.
[8] Castenmiller C.J.J. Surface temperature of wooden window frames under influence of solar radiation. HERON, Vol. 49, No. 4, 2004.
[9] Karafil A., Ozbay H., Kesler M. and Parmaksiz H. Calculation of optimum fixed tilt angle of PV panels depending on solar angles and comparison of the results with experimental study conducted in summer in Bilecik, Turkey. *2015 9th International Conference on Electrical and Electronics Engineering (ELECO)*, Bursa, Turkey, 2015, pp. 971-976, doi: 10.1109/ELECO.2015.7394517.
[10] Tikkurila Valtti color safety data sheet. Available online: https://tikkurila.com/sites/default/files/valtti-color-sds-en.pdf (accessed on 10 March 2023).
[11] Fortino S, Hradil P. Metelli G. Moisture-induced stresses in large glulam beams. Case study: Vihantasalmi Bridge. *Wood Materials Science and Engineering* 14, 366-380, 2019.
[12] Brischke C., Alfredsen G., Humar M. Conti E., Cookson L., Emmerich L., Flæte P.O., Fortino S., Francis L., Hundhausen U. et al. Modeling the Material Resistance of Wood—Part 2: Validation and Optimization of the Meyer-Veltrup Model. *Forests* 12, 576, 2021.

World Conference on Timber Engineering Oslo 2023

NUMERICAL HOMOGENISATION OF MECHANICAL PROPERTIES OF PINUS PINASTER (AIT.) LAMELLAE CONSTITUTING GLUED LAMINATED TIMBER

Romain Chevalier[1], Bruno Vuillod[2], Mathilde Zani[3], Marco Montemurro[4], Régis Pommier[5], Anita Catapano[6]

ABSTRACT:

Pinus pinaster (Ait.) is a softwood species considerably employed in the current wood industry in the Southwest of France. In a context of new environmental constraints, describing and predicting the behaviour of this local species becomes a matter of high priority. Nonetheless, the vast majority of industrial and research works still use classical softwood properties to determine various engineered Pinus pinaster (Ait.) products characteristics such as glued laminated and cross laminated timber.

This work proposes to employ general numerical homogenisation techniques used in the field of composite materials to obtain mechanical properties of Pinus pinaster (Ait.) as well as wood products such as glued laminated timber (Glulam). The proposed approach consists in decomposing and modelling glued laminated timber in four working scales: scale of glulam products, lamellae of several typologies composing such wood products (macroscopic scale), wood volumes considered analogous to laminar composites (mesoscopic scale) and composed of a few growth rings (microscopic scale) of initial and final wood. The homogenisation technique, adopted to compute properties from the microscopic to the macroscopic scale, is combined with approximation methods reposing on non-uniform rational basis spline entities to compute the mechanical properties of lamellae constituting glulam.

KEYWORDS: Numerical Homogenisation, Approximation methods, Pinus pinaster (Ait.), Glulam, Composite Materials

[1] Romain Chevalier, **Université de Bordeaux**, **Gascogne Bois**, Arts et Métiers Institute of Technology, Bordeaux INP, CNRS, INRA, HESAM Université, I2M UMR 5295, F-33400 Talence, France, romain.chevalier@ensam.eu
[2] Bruno Vuillod, **French Atomic Energy Commission**, Route des Gargails, BP2, Le Barp Cedex, FranceArts et Metiers Institute of Technology, Univ. Bordeaux, CNRS, Bordeaux INP, Hesam Universite, I2M, UMR 5295, F-33400 Talence, France, bruno.vuillod@ensam.eu
[3] Mathilde Zani, **Arts et Métiers Institute of Technology**, Université de Bordeaux, CNRS, INRA, Bordeaux INP, HESAM Université, I2M UMR 5295, F-33400 Talence, France, mathilde.zani@ensam.eu
[4] Marco Montemurro, **Arts et Métiers Institute of Technology**, Université de Bordeaux, CNRS, INRA, Bordeaux INP, HESAM Université, I2M UMR 5295, F-33400 Talence, France, marco.montemurro@ensam.eu
[5] Régis Pommier, **Université de Bordeaux**, Arts et Métiers Institute of Technology, Bordeaux INP, CNRS, INRA, HESAM Université, I2M UMR 5295, F-33400 Talence, France, regis.pommier@u-bordeaux.fr
[6] Anita Catapano, **Bordeaux INP**, Université de Bordeaux, Arts et Métiers Institute of Technology, CNRS, INRA, HESAM Université, I2M UMR 5295, F-33400 Talence, France, anita.catapano@bordeaux-inp.fr

https://doi.org/10.52202/069179-0062

1 INTRODUCTION

Wood is a natural material whose importance has risen exponentially over the last few years. Indeed, this renewable material perfectly fits several "Sustainable Development Goals" set by the United Nations and is highly recommended by the IPCC's "Global Warming of 1.5°C" report [1] as a solution to reduce carbon footprints in building and civil-engineering. In the South West of France, the current wood industry (including the company Gascogne Bois (GB)) is particularly related to Pinus pinaster (Ait.), a softwood species indigenous of the South West of Europe, because of its vast presence across the whole area (between 75% to 84% of total forest area in two French departments [2]).

Glued laminated timber (glulam) is a wood product manufactured by gluing and finger-jointing multiple wood lamellae allowing flexibility in size and shape. Furthermore, wood distortions issued from thermo-hygric variations can be considerably reduced in glulam by assembling a disparity of lamellae properties [3]. This advantage is noticeably reduced when using Pinus pinaster (Ait.) timber. Several studies [4,5] tried to estimate the shape stability of multiple configurations of softwoods glulam. However, the vast majority of studies are focused on others softwood species or use classical softwood properties taken from [6]. Moreover, the variability of wood properties are also neglected.

Hence, the main purpose of this work is to propose a multi-scale mechanical model of lamellae constituting glulam able to take into account the physical properties and related variability of Pinus pinaster (Ait.).

The paper is organiser as follows : modelling of physical and mechanical properties of the two phases of initial and final wood constituting growth rings is presented in Section 2. Section 3 is dedicated to the description of the numerical homogenisation procedure of the mechanical properties of elementary volumes of Pinus pinaster (Ait.). The results of the numerical study is presented in Section 4. Approximation methods are then used to compute the properties of multiple typologies of lamellae in Section 5. Finally, conclusions and perspectives are dispensed in Section 6.

2 PINUS PINASTER (AIT.) STRUCTURE AND PROPERTIES

2.1 MULTI-SCALE DEFINITION

Wood is a highly heterogeneous and anisotropic natural composite whose structure can be defined at three working scales:

- Growth ring composed by the accumulation of wood cells (90% of longitudinal tracheids) at the microscopic scale.
- Elementary volume emerging from the alternation of a few initial wood (IW) and final wood (FW) growth rings at the mesoscopic scale considered as lamellar composite.
- Wood lamellae formed by the combination of elementary volumes of multiple growth ring patterns at the macroscopic scale.

2.2 MODELLING OF PINUS PINASTER (AIT.) LOG

A local orthotropic coordinate system is used to describe wood properties defined by three preferred directions according to Figure 1: longitudinal direction L, radial direction R corresponding to the diametrical growth direction, and tangential direction T to the annual growth rings. Three planes can be identified in this system: the transverse plane RT, the radial longitudinal plane LR and the tangential longitudinal plane LT.

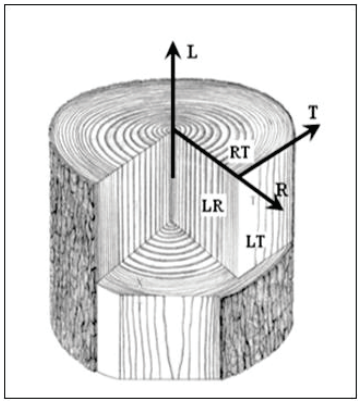

Figure 1: *Local reference system [7]*

The proposed model takes into consideration the difference between initial and final wood and the difference between juvenile and adult wood for growth rings from pith to bark.

Tree trunks are considered straight, with concentric growth rings, centred pith, and a circular shape of the transversal section (plane RT) across the whole L direction. Heartwood formation (no real influence on mechanical properties [8]), presence of knots, and reaction wood are neglected. Grain angle is considered null.

As for the physical properties, ring widths RW, mean relative density d, mean FW relative density FWd, and final wood proportion FWp (proportion of FW in a ring) are regarded at each ring number i. Globally, their variation is considered as function of the distance from the

https://doi.org/10.52202/069179-0062

pith R. Their dependency to the height H is neglected. Variability of such properties is considered at every growth ring. Properties are considered constant in the adult wood, which begins at the 15th ring (juvenile-adult wood limit at 12 years old [9] in the case of Pinus pinaster (Ait.)).

The physical properties relative to ring number i for our Pinus pinaster (Ait.) model are presented in Table 1. They are qualitatively extracted from several references [9,10,11]. The RW properties are adapted to match the data of GB company. Regarding FWp, d, and FWd, their evolution is considered linear with ring number in the juvenile wood and constant in the adult wood.

Table 1: *Physical properties for the Pinus pinaster (Ait) model.*

Ring N° i	RW [mm]	FWp [%]	d	FWd
1	2.5	8	0.43	0.56
2	9.4	10	0.439	0.57
3	10.0	12	0.447	0.58
4	10.2	14	0.456	0.59
5	10.1	16	0.464	0.60
6	9.9	18	0.473	0.61
7	9.0	20	0.481	0.62
8	7.8	22	0.490	0.63
9	6.5	24	0.499	0.64
10	5.3	26	0.507	0.65
11	4.3	28	0.516	0.66
12	3.4	30	0.524	0.67
13	2.8	32	0.533	0.68
14	2.3	34	0.541	0.69
15	2	36	0.55	0.70

In analogy to [12] in the case of a natural material, wood properties defined in this study are governed by uncertainty and their variability is described by a normal distribution at each ring number i (except the first three rings considered constant because of the lack of information in the scientific literature). For a generic property q_i, Equation (1) describes the normal probability density function $\psi(q_i)$ with $\lambda(q_i)$ and $\xi(q_i)$, respectively, the mean value and the standard deviation of the distribution of the property q_i:

$$\psi(q_i) = \frac{1}{\xi(q_i)\sqrt{2\pi}} exp\left(-\frac{\left(q_i - \lambda(q_i)\right)^2}{2\xi(q_i)^2}\right). \quad (1)$$

The mean value $\lambda(q_i)$, standard deviation $\xi(q_i)$, and coefficient of variation $C_v(q_i)$ [%] can be expressed as follows :

$$\lambda(q_i) = \frac{1}{N_v}\sum_{j=1}^{N_v} q_{i,j}\ ,$$
$$\xi(q_i) = \sqrt{\lambda\left(\left(q_i - \lambda(q_i)\right)^2\right)}, \quad (2)$$
$$C_v(q_i) = 100\frac{\xi(q_i)}{\lambda(q_i)}\ ,$$

where $q_{i,j}$ is the jth value of q_i occurring for N_v values :

Regarding the RW and the FWp, the coefficient of variation at each ring number is considered equal to 20% as to be in the same order of magnitude as the references in the scientific literature [11,13]. In the case of d and FWd, a hypothesis is made to consider the wood mass produced by a ring as constant. Hence, a modification of RW and FWp induce a variation of the densities values d and FWd.

The number of ring is defined by the age of the trees considered. In the Landes of Gascogne, 92% of the local forest is private property. Hence, traceability of stands processed by GB company is not ensured and tree ages are unknown.

Nonetheless, GB company possesses dendrological data on the mean and standard deviation of log diameter evaluated on 149727 logs. The measurements were performed for logs of 2.5m extracted between 0m-8m. (Note: GB standard deviation results are overvalued because referenced as 120 stacks of 2500 tree). Few information exists on the trees treated by GB including a minimal age of 40 years old and the possibility to reach 60 years old.

Our model has to take into consideration the heterogeneity of tree ages resulting in a varying number of rings relative to match the GB data. To this end, a hypothesis is introduced : in the following of this paper a half normal distribution with a mean age of 40 and a standard deviation of 7.5 admitting that age cannot be less than 40 years (99% of the ages are included between 40 and 62 years old) is considered. The mean diameter and standard deviation for the GB sample and for the numerical model, performed on a sample of 500 simulations, are presented in Table 2.

Table 2: *Mean diameter and standard deviation for wood logs taken from GB data and the parametric model.*

	GB sample	Parametric Model
Mean diameter [mm]	313.1	314.2
Standard deviation [mm]	19.15	20.34

2.3 ELASTIC PROPERTIES OF INITIAL AND FINAL WOODS AT THE MICROSCPIC SCALE

IW and FW elastic behaviour can be modelled at the microscopic scale through Hooke's law whose compliance matrix for wood is uniquely defined via 9 independent elastic constants: three Young's moduli E_m (m = L,R,T), three shear moduli G_{mn} (m,n = L,R,T and $m \neq n$), and three Poisson's ratios υ_{mn} (m,n = L,R,T and $m \neq n$):

https://doi.org/10.52202/069179-0062

$$\begin{Bmatrix} \varepsilon_L \\ \varepsilon_R \\ \varepsilon_T \\ \gamma_{LR} \\ \gamma_{TL} \\ \gamma_{RT} \end{Bmatrix} = \begin{bmatrix} \frac{1}{E_L} & -\frac{\upsilon_{RL}}{E_R} & -\frac{\upsilon_{TL}}{E_T} & 0 & 0 & 0 \\ -\frac{\upsilon_{LR}}{E_L} & \frac{1}{E_R} & -\frac{\upsilon_{TR}}{E_T} & 0 & 0 & 0 \\ -\frac{\upsilon_{LT}}{E_L} & -\frac{\upsilon_{RT}}{E_R} & \frac{1}{E_T} & 0 & 0 & 0 \\ 0 & 0 & 0 & \frac{1}{G_{LR}} & 0 & 0 \\ 0 & 0 & 0 & 0 & \frac{1}{G_{TL}} & 0 \\ 0 & 0 & 0 & 0 & 0 & \frac{1}{G_{RT}} \end{bmatrix} \begin{Bmatrix} \sigma_L \\ \sigma_R \\ \sigma_T \\ \tau_{LR} \\ \tau_{TL} \\ \tau_{RT} \end{Bmatrix} \quad (3)$$

where ε_m and σ_m are the normal strain and stress, respectively, along m-th axis, whilst γ_{mn} and τ_{mn} are the shear strain and stress, respectively, in the mn plane.

In the scientific literature, wood elastic properties can be expressed as a linear function of the relative density [14]. In [6], the authors proposed a linear model to compute softwoods elastic properties based on experimental results on a large variety of softwood species which is frequently used in most studies. Nonetheless, this model is fairly accurate for lower relative densities; it looses in precision in the case of high density softwood such as Pinus pinaster (Ait.), whereas the model proposed in this paper takes into consideration a FW phase of high relative density.
In this study, we propose to employ data relative to Pinus pinaster (Ait.) mechanical properties taken from the scientific literature [15,16,17,18,19] to establish elastic laws accurately describing the behaviour of IW and FW relative to this softwood species while taking into consideration the dependency to density. To this end, we also admit a linear relationship of the Young's and shear moduli with relative density similarly to the one presented in [6]. Regarding the Poisson's ratios, there is not enough information in the case of Pinus pinaster (Ait.) and their values are considered constant.

2.3.1 Young's moduli

In the case of the trend of the longitudinal Young's modulus with the relative density, eight values were provided in [15], which are reported in Table 3.

Table 3: *Mean longitudinal Young's modulus and density obtained through flexural tests in [15]*

d	0.46	0.60	0.635	0.64	0.65	0.693	0.705	0.715
E_L [GPa]	13.2	15.7	16.11	16.6	16.435	16.794	17.775	17.1

A linear relationship between the mean longitudinal modulus E_L [MPa] and mean relative density d is found and is described in Equation 4 with a coefficient of determination of ${R_d}^2 = 0.9581$.

$$E_L = 5875 + 16209\, d\,. \quad (4)$$

Three references, [16,17,18], estimated Young's moduli but omitting the relative density of the specimens. By considering a similar behaviour in traction and compression from wood samples, the linear relationship Equation (4) allows to estimate the density of the samples from the above studies. The densities estimations and the elastic properties are displayed in Table 4.

Table 4: *Mean Young's moduli and with estimated relative densities from [16,17,18].*

	E_L	E_R	E_T	d
Cariou [16]	11369	/	703	0.3390
Pereira et al. [17]	15100	1910	1010	0.5690
Lahna [18]	16140	2086	/	0.6439

Thus, it is now possible to propose linear relationship with associated density d_k associated to the phase k =IW,FW for the three Young's moduli that are presented in Equation (5):

$$\begin{aligned} E_{L_k} &= 16209\, d_k + 5874.7, \\ E_{R_k} &= 2972.2\, d_k + 238.70, \\ E_{T_k} &= 1334.8\, d_k + 250.51, \end{aligned} \quad (5)$$

with E_{L_k}, E_{R_k}, and E_{T_k} the Young's moduli associated to the phase k = IW,FW.

2.3.2 Shear moduli

[19] characterised the shear moduli of Pinus pinaster (Ait.) by carrying out two shear test methods (Iosipescu and off-axis). Equation (6) presents the models proposed to link shear moduli in [MPa] with infra-density (IF) [20]. They are considered applicable on the densities examined in our study.

$$\begin{aligned} G_{RT_k} &= 495\, IF_k, \\ G_{TL_k} &= 2072\, IF_k, \\ G_{LR_k} &= 2402\, IF_k, \end{aligned} \quad (6)$$

where $IF_k = \frac{d_k}{1.12+0.159\, d_k}$, G_{RT_k}, G_{TL_k}, and G_{LR_k}, respectively, with k = IW,FW.

2.3.3 Poisson's ratios

In [16], the author characterised the elastic properties of Pinus pinaster (Ait.) thanks to experimental tests. Table 5 presents the Poisson's ratio obtained in [16]. As there is too few information in the literature about the variation of Poisson's ratios as a function of the relative density, the ratios υ_{RT_k}, υ_{TL_k}, and υ_{RL_k}, are considered constant for the two phases k = IW,FW.

Table 5: *Pinus pinaster (Ait.) Poisson's ratio, [16] with k=IW,FW.*

υ_{RT_k}	υ_{TL_k}	υ_{RL_k}
0.58	0.03	0.04

2.3.4 Validity of the model

It is necessary to check the conformity of the model with respect to the true wood behaviour. In [6,16], the authors expressed the plausibility for several ratios between elastic properties to be quasi-constant such as E_{L_k}/E_{T_k}, E_{L_k}/E_{R_k}, G_{LR_k}/G_{RT_k}, and G_{TL_k}/G_{LR_k}. In this study, a ratio is considered quasi-constant if the maximum precentage difference between the properties computed over the density range [0.40,0.80] with the mean property computed at the relative density of 0.55 is lower than 10%. All ratios are considered quasi-constant as the condition aforementioned is fulfilled. Furthermore, the positive definiteness of the stiffness tensors is verified for the whole density range.

3 DETERMINATION OF THE ELASTIC PROPERTIES AT THE MESOSCOPIC SCALE

At the microscopic scale, the bibliographic data and the multiple hypotheses done on the properties of Pinus pinaster (Ait.) allow to propose two different material models for both initial and final woods taking into consideration their variability into the stem according to their corresponding relative density.

At the mesoscopic scale, the representative volume element (RVE), which can be seen as a lamellar composite, is modelled by an alternation of growth rings composed by both initial and final wood of varying width. The well-known numerical homogenisation method based on the strain energy of periodic media [21] is then employed to compute the mechanical properties of 3D cubic FE-model of the RVE of wood specimens extracted from several positions in the modelled logs of Pinus pinaster (Ait.).

This technique is based on the use of periodic boundary conditions (PBCs) to calculate the equivalent stiffness matrix of the material at the mesoscopic scale. However, PBCs cannot be applied directly to the lamellae at the mesoscopic scale because of growth ring patterns. Hence, lamellae are separated into several elementary cubes of relatively small dimensions to consider growth rings as rectangular parallelepipeds and to apply the homogenisation technique.

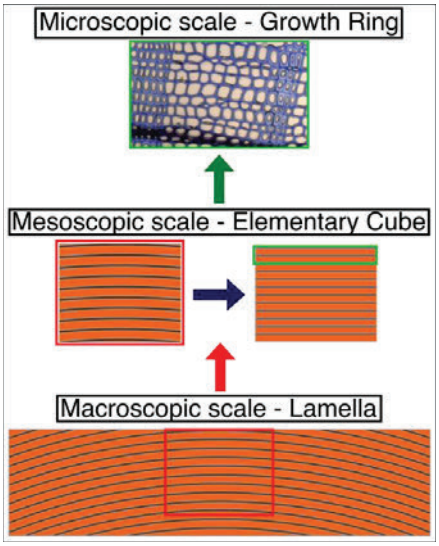

Figure 2 : *Multi-scale modelling of Pinus pinaster (Ait.) Glulam (Microscopic scale image adapted from [22])*

To consider the growth rings as rectangular parallelepipeds, a trigonometric study is realised on the elementary volumes considered as cubes of dimension h. The condition will be fulfilled over the whole range R ∈ [0;150]mm if the dimension h respects the following inequality h≤ 12mm.

The homogenisation procedure will then be coupled with a stochastic approach, the Monte-Carlo method, to efficiently compute the mesoscopic properties impacted by the overall variability.

The following assumptions are made to determine the effective properties at the mesoscopic scale:

• linear orthotropic behaviour defined in a local cylindrical reference system for all phases of initial and final wood;

• perfect bonding condition at the phases interface is considered.

3.1 The numerical homogenisation method

The geometry used for the RVE is the one depicted in Figure 2 with a cube considered as a lamellar composite. The geometric variable parameters used are the dimension of the cube h, the position of the centroid of the RVE R, the properties of the rectangular parallelepiped approximating the growth rings RW and FWp depending on the distance to the pith. The volume of the RVE is defined in Equation (7) in a local Cartesian reference system (O; x_1, x_2, x_3) defined at the centre of the RVE, with a_1, a_2, and a_3 the length of the RVE sides along the x_1, x_2, and x_3 axis, respectively.

$$V_{\mathrm{RVE}} = a_1\, a_2\, a_3 \; = h^3. \qquad (7)$$

The generation of synthetic logs is first coded in Python® environment. The parametric FE-model is then created within the commercial FE code Ansys®. 20-node solid elements SOLID186 with three Degree of Freedom

https://doi.org/10.52202/069179-0062

(DOF) per node have been used. The "Layered" element option has been selected to create and mesh only the RVE volume and model each ring as an equivalent layered section with 3 integration points per layer. In the 3D case, the generalised Hooke's law for the equivalent elastic material corresponding to the RVE can be written as:

$$\begin{Bmatrix} \bar{\sigma}_1 \\ \bar{\sigma}_2 \\ \bar{\sigma}_3 \\ \bar{\sigma}_4 \\ \bar{\sigma}_5 \\ \bar{\sigma}_6 \end{Bmatrix} = \begin{bmatrix} \bar{C}_{11} & \bar{C}_{12} & \bar{C}_{13} & \bar{C}_{14} & \bar{C}_{15} & \bar{C}_{16} \\ \bar{C}_{21} & \bar{C}_{22} & \bar{C}_{23} & \bar{C}_{24} & \bar{C}_{25} & \bar{C}_{26} \\ \bar{C}_{31} & \bar{C}_{32} & \bar{C}_{33} & \bar{C}_{34} & \bar{C}_{35} & \bar{C}_{36} \\ \bar{C}_{41} & \bar{C}_{42} & \bar{C}_{43} & \bar{C}_{44} & \bar{C}_{45} & \bar{C}_{46} \\ \bar{C}_{51} & \bar{C}_{52} & \bar{C}_{53} & \bar{C}_{54} & \bar{C}_{55} & \bar{C}_{56} \\ \bar{C}_{61} & \bar{C}_{62} & \bar{C}_{63} & \bar{C}_{64} & \bar{C}_{65} & \bar{C}_{66} \end{bmatrix} \begin{Bmatrix} \bar{\varepsilon}_1 \\ \bar{\varepsilon}_2 \\ \bar{\varepsilon}_3 \\ \bar{\varepsilon}_4 \\ \bar{\varepsilon}_5 \\ \bar{\varepsilon}_6 \end{Bmatrix}, \quad (8)$$

where $\bar{\sigma}$ and $\bar{\varepsilon}$ are the stress and strain tensors expressed in Voigt's notation, respectively associated with the equivalent homogeneous solid and as such are volume averaged, see [23] for more details.
The goal of this method is to evaluate all the components of the stiffness tensor $\bar{\mathbf{C}}$ by applying successively 6 load cases to the cubic RVE through classical PBCs [21].

After determining the components of the volume-averaged stress tensor (according to the procedure presented in [23]), the components of the elasticity matrix at the mesoscopic scale are calculated, for each set of PBCs, as:

$$\bar{C}_{\alpha\beta} = \frac{\bar{\sigma}_\alpha}{\bar{\varepsilon}_\beta} \text{ with } \beta = 1,2,\dots,6, \quad (9)$$

and $\bar{\varepsilon}_\gamma = 0$, with $\gamma = 1,2,\dots,6$ and $\gamma \neq \beta$.

Furthermore, it is possible to evaluate the effective elastic moduli of the composite material from the compliance tensor $\bar{\mathbf{S}} = \bar{\mathbf{C}}^{-1}$, as shown below [23].

Three Young's moduli:

$$E_1 = \frac{1}{\bar{S}_{11}}, E_2 = \frac{1}{\bar{S}_{22}}, E_3 = \frac{1}{\bar{S}_{33}}.$$

Three shear moduli:

$$G_{23} = \frac{1}{\bar{S}_{44}}, G_{13} = \frac{1}{\bar{S}_{55}}, G_{12} = \frac{1}{\bar{S}_{66}}.$$

Three Poisson's ratios:

$$\upsilon_{23} = -\frac{\bar{S}_{32}}{\bar{S}_{22}}, \ \upsilon_{13} = -\frac{\bar{S}_{31}}{\bar{S}_{11}}, \ \upsilon_{12} = -\frac{\bar{S}_{21}}{\bar{S}_{11}}.$$

Three Chentsov's coefficients:

$$\mu_{23,31} = \frac{\bar{S}_{45}}{\bar{S}_{55}}, \ \mu_{23,12} = \frac{\bar{S}_{46}}{\bar{S}_{66}}, \ \mu_{31,12} = \frac{\bar{S}_{56}}{\bar{S}_{66}}.$$

Nine mutual influence coefficients:

$$\eta_{1,23} = \frac{\bar{S}_{14}}{\bar{S}_{44}}, \eta_{1,31} = \frac{\bar{S}_{15}}{\bar{S}_{55}}, \eta_{1,12} = \frac{\bar{S}_{16}}{\bar{S}_{66}},$$
$$\eta_{2,23} = \frac{\bar{S}_{14}}{\bar{S}_{44}}, \eta_{2,31} = \frac{\bar{S}_{15}}{\bar{S}_{55}}, \eta_{2,12} = \frac{\bar{S}_{16}}{\bar{S}_{66}},$$
$$\eta_{3,23} = \frac{\bar{S}_{14}}{\bar{S}_{44}}, \eta_{3,31} = \frac{\bar{S}_{15}}{\bar{S}_{55}}, \eta_{3,12} = \frac{\bar{S}_{16}}{\bar{S}_{66}}.$$

Moreover, the degree of anisotropy is now available by defining 9 independent symmetry criteria f_a, expressed in [%], reposing on the effective mechanical properties, as presented in the following. A criterion f_a is considered valid if its value, expressed in [%], respects the condition $f_a \leq 1\%$.

Two criteria on the Young's moduli:

$$f_1 = \frac{|E_3 - E_2|}{E_2}, f_2 = \frac{|E_1 - E_2|}{E_2}.$$

Two criteria on the shear's moduli:

$$f_3 = \frac{|G_{31} - G_{23}|}{G_{23}}, f_4 = \frac{|G_{12} - G_{23}|}{G_{23}}.$$

Two criteria on the Poisson's ratios:

$$f_5 = \frac{|\upsilon_{31} - \upsilon_{23}|}{\upsilon_{23}}, f_6 = \frac{|\upsilon_{12} - \upsilon_{23}|}{\upsilon_{23}}.$$

One criterion on the relationship between previous properties:

$$f_7 = \frac{\left| G_{23} - \frac{E_2}{2(1+\upsilon_{23})} \right|}{G_{23}}.$$

Two criteria on the Chentsov's and mutual influence coefficients sets μ and η, respectively:

$$f_8 = max(|\mu|), f_9 = max(|\eta|)$$

4 NUMERICAL RESULTS AT THE MESOSCOPIC SCALE

4.1 Convergence analyses

To validate the accuracy and effectiveness of the FE model of the RVE, convergence analyses on the RVE size and on the mesh size are realised on the equivalent elastic properties results while optimising the computational time. The study is realised in the case of the mean values of physical parameters on the whole range of distance to the pith R.
The details of these sensitivity analyses will be presented during the speech. In the case of the RVE size, for a supposed constant mesh size of $e_{size} = 0.5$mm for 3D element, an optimal RVE size of h = 8mm is selected which respect the condition for rectangular parallelepiped rings. Furthermore, this condition allows to superimpose the local coordinate cylindrical reference system to the local Cartesian reference system. In the case of the mesh size convergence, for a RVE size of h = 8mm, the optimal mesh size is constant and equal to $e_{size} = 1\text{mm} = h/8$. Here, the study is realised on the mean values of physical parameters for only the smaller growth rings at $R >$ 100mm. The computational time needed for 1 simulation is about t = 3.0 seconds.

4.2 Monte-Carlo Method

The Monte-Carlo (MC) method is commonly used to estimate the probabilistic distribution of simulation results and have already been used in the case of natural material [12]. In our specific case, for a RVE volume positioned at a certain distance to the pith R, the variability of physical parameters and mechanical properties at the microscopic scale induce uncertainty on the resulting effective properties at the mesoscopic scale, which can be assessed thanks to the MC method coupled with the numerical homogenisation technique. The probabilistic distribution is supposed to follow a normal distribution for the resulting elastic properties. The MC method applied in our study relies on four main steps.

• Step 1: The parametric FE model takes into consideration the variability of each input parameter, as presented in Section.2.
• Step 2: In the statistical domain, it is mandatory to obtain information on a given population by performing a random sampling. Its main purpose is to select a statistically representative number of samples of our studied population.
• Step 3: The homogenisation process is carried out on each sample to obtain the probabilistic distribution of the equivalent elastic properties at the upper scale at a given distance to the pith R.
• Step 4: Step 1-3 are repeated for some values of R in the range R ∈ [4,150]mm with an increment of 1mm. The number of samples n adequate in the case of our study has been estimated by studying the convergence of equivalent elastic properties mean and standard deviation of RVE volume over the whole range of R for different values of n. For the sake of brevity, this analysis is not presented here and will be discussed during the speech. The number of samples to achieve convergence is n = 250. Hence, the whole MC method takes approximately t_{tot}= 30 hours.

4.3 Numerical results for the effective properties.

In this section, the results of the numerical study are presented. To show the effectiveness of the proposed approach, a comparison between our numerical model and the analytical model of Reuss-Voigt over the range of interest R is accomplished. Furthermore, scientific literature data of interest are juxtaposed to the results as further comparison term. They are taken from various studies such as [15,16,24,25,26,27,28]. Over the whole range of R, only the criteria f_8 and f_9 are verified. Therefore, the homogenised material at the upper scale can be considered as an orthotropic material. For the sake of brevity, only the equivalent properties E_1 and G_{23} are presented in Figure 3.

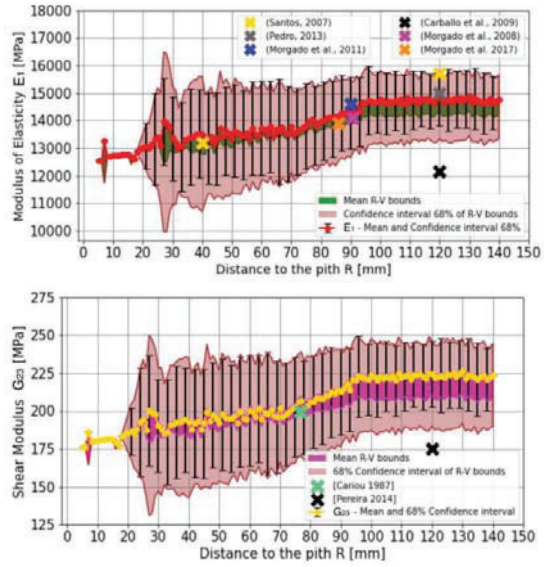

Figure 3: *Numerical results for the equivalent properties* $\boldsymbol{E_1}$ *and* $\boldsymbol{G_{23}}$ *over the whole range [5,140]mm versus experimental results.*

5 LAMELLAE PROPERTIES AT THE MACROSCOPIC SCALE

The purpose of this section is to obtain the equivalent mechanical properties of lamellae at the macroscopic scale. The lamellae are rectangular parallelepipeds of dimensions $A_1 = 500$mm, $A_2 = 95$mm, and $A_3 = 24$mm, along the X_1, X_2, and X_3 axis, respectively, of a global Cartesian reference system (O; X_1, X_2, X_3) defined at the centre of the log.
The lamellae and the RVE positions are defined by the position of their centre, respectively by the distances L, R, and the angle φ in the cylindrical reference system (O; L, R,T) with L the longitudinal axis, as illustrated in Figure 4.

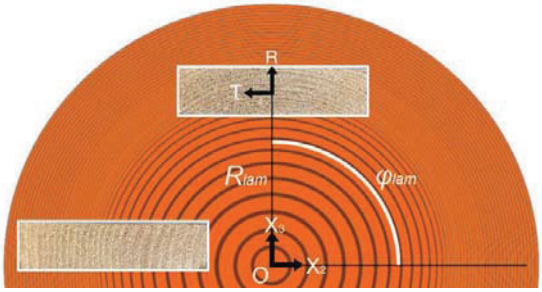

Figure 4: *Reference systems and position of the lamellae in the log.*

In Section 4, the equivalent properties of Pinus pinaster (Ait.) have been computed at the mesoscopic scale thanks to a homogenisation technique coupled with a stochastic approach. These properties are dependent only of the distance to the pith of the volumes R and are independent from the angle φ.
As the X_1 direction has no influence on the lamellae and cubes properties, we will consider only a section of dimensions $A_2 = 95$mm and $A_3 = 24$mm to describe the lamellae in the plane (O; X_2, X_3). To estimate the properties at the mesoscopic scale, we propose to discretise the lamellae as a combination of elementary sections with respect to their corresponding local orientation in the cylindrical reference system.
Finally, approximation methods resting on the utilisation of NURBS surfaces are used to compute the lamellae equivalent properties at the mesoscopic scale from the discretised mechanical properties found in Section 4.

5.1 Non-uniform rational basis-spline (NURBS) hyper-surfaces theory

This section gives a brief reminder of NURBS surfaces theory. These entities generalise the B-Splines surfaces, which generalise the Bézier surfaces [29]. Originally employed in Computer Aided Design (CAD) in the 1990's, these entities are now used in multiples domains, such as topology optimisation [32, 33, 34], shape optimisation [31, 38], anisotropy field optimisation for variable stiffness composites [36, 37], and surrogate model generation [30].

https://doi.org/10.52202/069179-0062

In this work, the NURBS surfaces entities are used as response surfaces (or surrogate models). Their aim is to fit the discrete mechanical properties of a material section or Target Points (TP) to homogenise and render a proper physical interpretation over the entire section. In other words, NURBS surfaces are used as approximation surfaces to fit the TP scalar data identified by their coordinates (X_2, X_3).

NURBS surfaces are used to approximate a model $M : \mathbb{R}^n \mapsto \mathbb{R}^m$, where $n = 2$ and $m = 12$ correspond to the dimensions of (X_2, X_3) coordinates, and to the dimensions of the set of desired mean and standard deviation mechanical properties extracted from the numerical study of Section 4, respectively. In the present case, these properties are the Young's moduli, the shear moduli and the corresponding standard deviations.
The parametric explicit form of each coordinate of a NURBS entity with only two input parameters reads:

$$s_b(u_2, u_3) = \frac{\sum_{i_2=0}^{n_2} \sum_{i_3=0}^{n_3} N_{i_2,p_2}(u_2)\, N_{i_3,p_3}(u_3) \omega_{i_2,i_3} P_{b,i_2,i_3}}{\sum_{i_2=0}^{n_2} \sum_{i_3=0}^{n_3} N_{i_3,p_3}(u_2)\, N_{i_3,p_3}(u_3) \omega_{i_2,i_3}} \tag{10}$$

with $s_b(u_2, u_3)$ the NURBS output b-mechanical property $(b \in [1, m])$ evaluated at the normalised input coordinates $(u_2 \in [0,1], u_3 \in [0,1])$. $n_k + 1 \;\; (k = 2,3)$is the number of control points (CPs) along the u_k parametric direction. ω_{i_2,i_3} corresponds to the weight assigned to the CP of indices i_2, i_3 . In this case, it is taken equal to 1 for every CP. P_{b,i_2,i_3} represents the $(n_2 + 1)(n_3 + 1)$ CPs coordinates. $N_{i_k,p_k}(u_k)$ $(k \in [2,3])$ are the basis functions of degree p_k (equal to 2 in our study) and are evaluated recursively with the Cox de Boor algorithm, based on Bernstein's polynomials [35]. For more information on this matter, the interested reader is referred to [29].
Each timber section is discretised with $N_{TP} = N_2 N_3$ TPs and the number of CPs of the NURBS entity vary as $N_{CP} = \delta\, N_{TP}$. Employing the surface fitting algorithm of [30], the CPs drive the NURBS surface across each output to obtain the distribution of the equivalent elastic properties of the lamellae at the macroscopic scale.

5.2 Sensitivity of the results to the number of target points and control points.

Firstly, a NURBS of degree 3 and $\delta = 1/4$ is applied to the input mechanical properties at the mesoscopic scale computed in Section 4 to smoothen the input curves. For the sake of conciseness, this interpolation process is not presented in this paper and will be presented during the speech.
To validate the interpolation method to compute the lamellae effective properties at the mesoscopic scale, convergence analyses must be made in terms of number of TPs and CPs. As the section geometry is defined in a Cartesian reference system, the TP and CP are also defined in the same reference system and are distributed uniformly across the directions X_2 and X_3.

The results of the sensitivity analysis allow to achieve convergence for a number of TPs equal to $N_{\mathrm{TP}} = 75 \times 30$ for all typologies of lamellae studied.
Regarding the number of CPs, the convergence is achieved with $\delta = 2/3$ to maximise the coefficient of correlation.
The precision of the NURBS surfaces is evaluated by comparing the relative differences between input and output values (a set of TPs different from the one used to determine the approximating NURBS entity). As the relative difference is under 2% for every mechanical properties, the interpolation method is validated.
Finally, defining the TPs and CPs in a Cartesian reference system induce variability of the output properties according to φ (should depend solely on the distance to the pith R) and is evaluated to 5% for a constant value of R.

5.3 Lamellae properties at the macroscopic scale

The NURBS entities are used to compute the equivalent properties of lamellae of two typologies. The first typology is a lamella whose centre is positioned at $R_1 =$ 50mm and $\varphi_1 = 0$ while the second is positioned at $R_1 =$ 80mm and $\varphi_1 = \pi/2$ and are presented in Figure 5. Only the input data (TP) and the output NURBS effective properties for the mean longitudinal modulus are presented for the sake of brevity.

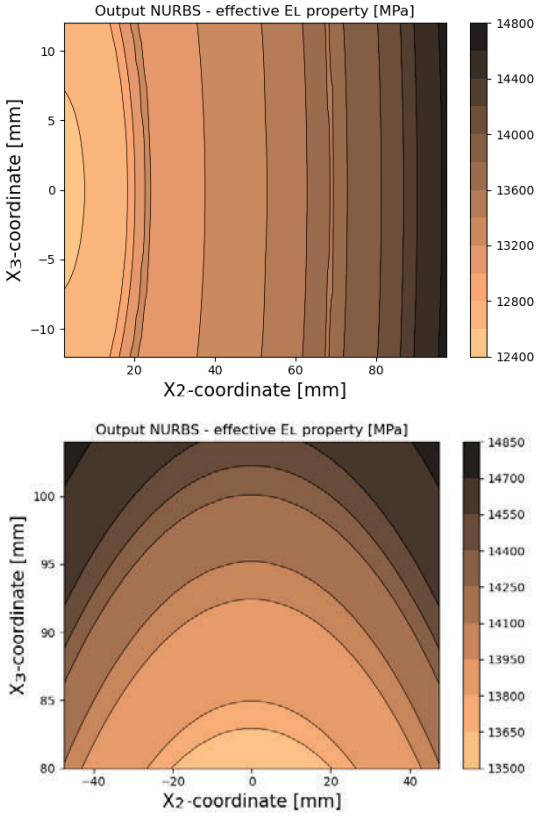

Figure 5: *Output NURBS effective properties (longitudinal modulus) of two typologies of lamellae at the macroscopic scale.*

6 CONCLUSIONS

Effective elastic properties of lamellae of Pinus pinaster (Ait.) at the macroscopic scale have been computed. The model took into account the several sources of variability and their propagation across the scales.

The scientific literature allowed to propose several models of elastic behaviour dependent on the density for the initial and final wood at the microscopic scale.

Numerical composite homogenisation techniques have been used in the case of elementary volumes considered as lamellar composites of initial and final woods.

The "Strain Homogenization Technique" has been used on the RVE to homogenise the effective properties at the mesoscopic scale (including the associated variability).

The lamellae are then discredited into several data reference. An approximation method reposing on the use of NURBS entities has been used to model the elastic behaviour of some configurations of lamellae.

This work focuses on computing homogenised properties to be used for Pinus pinaster (Ait.) instead of the classical softwood properties classically chosen.

These properties adapted to the case of Pinus pinaster (Ait.) can be imported into a model representing multiples configurations of glulam at the macroscopic scale by taking into account the finger-jointing and gluing of the components.

The next step would be to model the impact of grain angle, conical angle, micro-fibril angle, reaction wood, log shape, and centred pith on the results as additional sources of variability to better represent the reality of wood growth.

REFERENCES

[1] IPCC, (2018): Global Warming of 1.5°C.An IPCC Special Report on the impacts of global warming of 1.5°C above pre-industrial levels and related global greenhouse gas emission pathways, in the context of strengthening the global response to the threat of climate change, sustainable development, and efforts to eradicate poverty [Masson-Delmotte, V., P. Zhai, H.-O. Pörtner, D. Roberts, J. Skea, P.R. Shukla, A. Pirani, W. Moufouma-Okia, C. Péan, R. Pidcock, S. Connors, J.B.R. Matthews, Y. Chen, X. Zhou, M.I. Gomis, E. Lonnoy, T. Maycock, M. Tignor, and T. Waterfield (eds.)]. In Press

[2] Vidal, M. (2016). Optimisation des stratégies d'amélioration génétique du pin maritime grâce à l'utilisation de marqueurs moléculaires [Phdthesis, Université de Bordeaux]. https://tel.archives-ouvertes.fr/tel-01359191

[3] Ormarsson, S., Dahlblom, O., Petersson, H. (2000). A numerical study of the shape stability of sawn timber subjected to moisture variation. Wood Science and Technology. 34. 207-219. 10.1007/s002260000042.

[4] Lasserre, B. (2000). Modélisation thermo-hygro-mécanique du comportement différé de poutres de structure en bois [These de doctorat, Bordeaux 1]. http://www.theses.fr/2000BOR10561

[5] Clouet, B. (2014). Comportement hydromécanique d'assemblages bois collés à l'état vert : Approches expérimentale et numérique [These de doctorat, Bordeaux]. https://www.theses.fr/2014BORD0036

[6] Guitard, D. (1987). Mécanique du matériau bois et composites / Préface de Polge H.. Cépaduès-Editions.

[7] Grazide, C. (2014). Une modélisation de la résistance en flexion du pin maritime utilisé en construction [PhD Thesis, Université de Bordeaux]. https://tel.archives-ouvertes.fr/tel-01176734

[8] Berthier, B., A.D., Kokutse, A. Stokes, T. Fourcaud (2001). Irregular Heartwood Formation in Maritime Pine (Pinus pinaster Ait.): Consequences for Biomechanical and Hydraulic Tree Functioning. Annals of Botany, 87(1):19–25.

[9] Moreau, J. (2010). Impact de pratiques sylvicoles intensives sur les proprietés du bois de pin maritime. Phd thesis, Université de Bordeaux 1. URL: https://www.theses.fr/2010BOR14200

[10] Nicholls, J.W.P., H.E., Dadswell, and D.H., Perry (1963). Assessment of wood qualities for tree breeding. II. In Pinus Pinaster Ait. from Western Australia. Silvae Genet, 12(4):105–110.

[11] Gaspar, M.J., J., Louzada, M., Silva, A., Aguiar, and M.H., Almeida (2008). Age trends in genetic parameters of wood density components in 46 half-sibling families of Pinus pinaster. Canadian Journal of Forest Research, 38(6):1470–1477.

[12] Delucia, .M., A., Catapano, M., Montemurro, J., Pailh´es (2020). A stochastic approach for predicting the temperature-dependent elastic properties of cork-based composites. Mechanics of Materials, 145103399.

[13] Louzada, J.L.P.C. (2003). Genetic correlations between wood density components in Pinus pinaster Ait. Annals of Forest Science, 60(3):285–294.

https://doi.org/10.52202/069179-0062

[14] Kasal, B. (2004). Chapter : Wood formation and properties — Mechanical Properties of Wood. In book: Encyclopedia of Forest Sciences Copyright: Academic Press. pp.1815-1828
[15] Santos, J. (2007). Estudo de Modelos e Caracterização do Comportamento Mecânico da Madeira. PhD thesis, UNIVERSIDADE DO MINHO.
[16] Cariou, J.-L. (1987). Caractérisation d'un matériau viscoélastique anisotrope: le bois. PhD thesis, Universit´e Bordeaux I. OCLC: 489807750.
[17] Pereira, J.L. (2005). Comportamento mecânico da madeira em tracção nas direcões de simetria material. Master's thesis, Universidade de Tràs-os-Montes e Alto Douro, Vila Real, Portugal.
[18] Lahna, F. (1983). Mécanique de la rupture des matériaux orthotropes-Application au bois. Phdthesis, Université de Bordeaux 1. URL: http://www.theses.fr/2010BOR14200.
[19] Xavier, J.C., N.M,. Garrido, M., Oliveira, J.L., Morais, P.P., Camanho, F., Pierron (2004). A comparison between the Iosipescu and off-axis shear test methods for the characterization of Pinus Pinaster Ait. Composites Part A: Applied Science and Manufacturing, 35(7-8):827–840.
[20] FPL (2010). Wood Handbook, Wood as an Engineering Material. General Technical Report FPLGTR-190, U.S. Departement of Agriculture, Forest Service, Madison.
[21] Barbero, E. J. (2007). Finite Element Analysis of Composite Materials. CRC Press.
[22] Vieira, J., Campelo, F., Rossi, S., Carvalho, A., Freitas, H., & Nabais, C. (2015). Adjustment Capacity of Maritime Pine Cambial Activity in Drought-Prone Environments. PLOS ONE, 10(5), e0126223. https://doi.org/10.1371/journal.pone.0126223
[23] Catapano,. A., J., Jumel (2015). A numerical approach for determining the effective elastic symmetries of particulate-polymer composites. Composites Part B: Engineering, 78227–243.
[24] Pereira, J., J., Xavier, J., Morais, J., Louzada (2014). Assessing wood quality by spatial variation of elastic properties within the stem: Case study of Pinus pinaster in the transverse plane1. Canadian Journal of Forest Research, 44:107–117. Plomion, C., C., Pionneau, J., Brach, P., Costa.
[25] Pedro, J. (2013). Avaliação destrutiva e não destrutiva de elementos retangulares de madeira de pinho bravo. Master's thesis, Faculdade de Ciencias e Tecnologia da Universidade de Coimbra, Portugal.
[26] Morgado, T.F.M., J.S., Machado, A.M.P.G., Dias, H., Cruz, J.N.A., Rodrigues (2011). Caracteristicas mecânicas et classifição da madeira de secção circular de Pinheiro Bravo CIMAD 11 -1°Congresso Ibero-LatinoAmericano da Madeira na Construção, 7-9/06-2011, Coimbra, Portugal.
[27] Morgado, T.F.M., A.M.P.G., Dias, J.S., Machado, J.H.J.O., Negrao, A., Marques (2017). Grading of Portuguese Maritime Pine Small-Diameter Roundwood. Journal of Materials in Civil Engineering, 29(2):04016209.
[28] Carballo, J., E., Hermoso, J.I., Fernandez-Golfin (2009). Mechanical properties of structural maritime pine sawn timber from Galicia (Pinus pinaster Ait. ssp.atlantica) Investigacion Agraria: Sistemas y Recursos Forestales,18(2):152–158.
[29] Les Piegl and Wayne Tiller. The NURBS books. Springer-Verlag, New York, NY, USA, second edition, 1996.
[30] Yohann Audoux, Marco Montemurro, and Jérôme Pailhès. A metamodel based on non-uniform rational basis spline hyper-surfaces for optimisation of composite structures. Composite Structures, 247 :112439, 2020
[31] Giulia Bertolino, Marco Montemurro, and Giorgio Pasquale. Multi-scale shape optimisation of lattice structures: an evolutionary-based approach. International Journal for Interactive Design and Manufacturing (IJIDeM), 12 2019.
[32] Giulio Costa, Marco Montemurro, and Jérôme Pailhès. Minimum length scale control in a nurbsbased simp method. Computer Methods in Applied Mechanics and Engineering, 354 :963-989, 2019.
[33] Thibaut Rodriguez, Marco Montemurro, Paul Le Texier, and Jérôme Pailhès. Structural displacement requirement in a topology optimization algorithm based on isogeometric entities. Journal of Optimization Theory and Applications, 184 :250-276, 2020.
[34] Giulio Costa, Marco Montemurro, and Jérôme Pailhès. Nurbs hyper-surfaces for 3d topology optimization problems. Mechanics of Advanced Materials and Structures, 28(7) :665-684, 2021.
[35] Carl De Boor. On calculating with B-Spline. Journal of Approximation theory, 6(1) :50-62, 1972.
[36] Marco Montemurro and Anita Catapano. On the effective integration of manufacturability constraints within the multi-scale methodology for designing variable angle-tow laminates. Composite Structures, 161 :145-159, 02 2017.
[37] Marco Montemurro and Anita Catapano. A general b-spline surfaces theoretical framework for optimisation of variable angle-tow laminates. Composite Structures, 209 :561-578, 2019.
[38] Marco Montemurro, Anita Catapano, and Dominique Doroszewski. A multi-scale approach for the simultaneous shape and material optimisation of sandwich panels with cellular core. Composites Part B : Engineering, 91 :458-472, 2016.

World Conference on Timber Engineering Oslo 2023

SIZE EFFECT OF LARGE GLUED LAMINATED TIMBER BEAMS – CONTRIBUTION TO THE ONGOING DISCUSSION

Christoffer Vida[1], Markus Lukacevic[2], Georg Hochreiner[3], Milena Stavric[4], Josef Füssl[5]

ABSTRACT: The effort to experimentally test glued laminated timber (GLT) beams is tremendous, especially for large beams. Such beams are increasingly used to realise wide-span timber structures, but experimental investigations of large beams are missing. In the literature, numerical simulation studies can be found instead to estimate the influence of the beam size. However, these studies come to partly different conclusions regarding the size effect, which confirms the high influence of the modelling strategy. Therefore, we conducted an extensive simulation program covering more than 8000 simulations to research the size effect, including large GLT beams of up to 3300 mm depth.

The developed modelling concept considered the morphology of timber boards deterministically and accounts for discrete cracking to simulate the bending strengths of GLT beams subjected to four-point bending tests. We predicted the size effect on the characteristic bending strength for two commonly used strength classes. We found that the strength decreased with increasing beam size. The results showed that the strength decrease is not only caused by the beam depth but also the length. Furthermore, the influence of different global failure criteria was investigated, with which the results from the existing studies could successfully be reproduced.

KEYWORDS: Glued laminated timber, XFEM, Size effect, Global failure criterion

1 INTRODUCTION

Glued laminated timber (GLT) is a building material suitable to realise a large variety of wide-span structures, e.g., hall constructions as well as office or apartment buildings. In recent decades, the dimensions, especially the beam depth, of GLT beams have increased continuously. The versatile use of GLT requires a comprehensive understanding of the mechanical behaviour and effective properties of the material. However, there is a debate among experts about the influence of the size of GLT beams on their bending strength.

This so-called size effect on the characteristic bending strength $f_{\mathrm{b,k}}$ can be described by applying the commonly used factor k_{h} to a characteristic reference bending strength $f_{\mathrm{b,k,ref}}$:

$$f_{\mathrm{b,k}} = f_{\mathrm{b,k,ref}} \cdot k_{\mathrm{h}} \,. \tag{1}$$

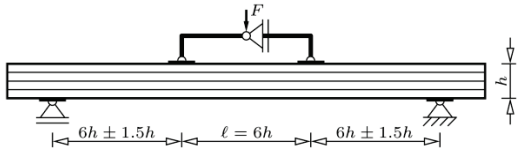

Figure 1: *Four-point bending test setup for a GLT beam according to DIN EN 408 [1] with the depth h and length ℓ.*

According to DIN EN 1995-1-1 [2], $f_{\mathrm{b,k,ref}}$ is provided in DIN EN 14080 [3] ($f_{\mathrm{m,g,k}}$) for beams with the reference beam depth $h_{\mathrm{ref}} = 600\,\mathrm{mm}$ of individual strength classes. The experimental test setup for GLT beams, according to DIN EN 408 [1], is a four-point bending test (Fig. 1), where the beam length is always proportional to the beam depth. Further, the factor k_{h} in [2] is only applicable for smaller beams, reading:

$$k_h = \min\begin{cases}\left(\dfrac{600}{h}\right)^{0.1} \\ 1.1\end{cases}, \tag{2}$$

with a maximum strength increase that is limited to 10 %.

The power law given in Eq. (2) is consistent with the one for wooden members presented by Bohannan [4] based on Weibull's strength theory [5]. Colling [6] also proposed considering the beam volume V and the loading configuration. Here we focus on the size effect k_{h} based on the volumes that reads as:

$$k_{\mathrm{h}} = \left(\frac{V_{\mathrm{ref}}}{V}\right)^{1/m}, \tag{3}$$

where V_{ref} is the reference Volume.

The effort involved in the experimental testing of larger GLT beams is tremendous. Thus, experimental investigations on the size effect in the literature [7–9] focused on smaller GLT beams with depths up to

[1] Christoffer Vida, TU Wien, Austria, christoffer.vida@tuwien.ac.at
[2] Markus Lukacevic, TU Wien, Austria, markus.lukacivic@tuwien.ac.at
[3] Georg Hochreiner, TU Wien, Austria, goerg.hochreiner@tuwien.ac.at
[4] Milena Stavric, TU Graz, Austria, mstavric@tugraz.at
[5] Josef Füssl, TU Wien, Austria, josef.fuessl@tuwien.ac.at

https://doi.org/10.52202/069179-0063

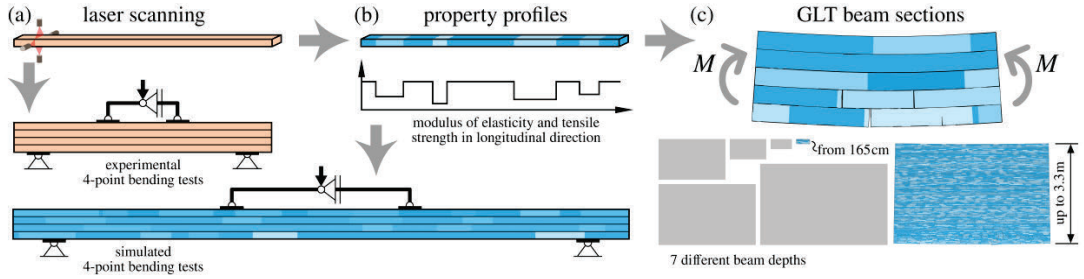

Figure 2: *Modelling concept that was based on (a) GLT beams assembled by real timber boards [8], (b) GLT beams reconstructed by virtual boards using derived material property profiles of real wooden boards [13], and (c) GLT beam sections employed to estimate the size effect [12].*

600 mm. For the larger sizes, numerical studies were conducted, e.g., by Frese and Blaß [10] and Fink et al. [11], covering beam depths up to 3000 mm and 1200 mm, respectively. These studies, however, provided partly contradictory results.

Therefore, we conducted an extensive simulation campaign to study the size effect for beams having depths up to 3300 mm [12]. The applied approach was based on a previous approach that simulates the entire loading process of GLT beams subjected to four-point bending tests [13]. Herein, we present the modelling concept that enabled us to predict the size effect for different beam depths and lengths. Furthermore, global failure criteria similar to the ones used in the literature [10, 11] could be implemented and investigated, which will be presented in detail in [14].

The present paper gives an overview of these studies. The structure is as follows: Section 2 presents the modelling concept to simulate the bending strength of GLT beams subjected to four-point bending tests. The investigation of the size effect and different global failure criteria is presented in Section 3. The paper closes with conclusions and an outlook.

2 MODELLING CONCEPT

The modelling concept builds upon a set of virtual boards to assemble GLT beams (Fig. 2). An experimental study [8] on GLT beams provided the morphological details of real wooden boards based on surface laser scans (Fig. 2a). This enabled the virtual replication of each individual board with deterministic material properties, as outlaid in [15]. The approaches by Frese and Blaß [10] and Fink et al. [11] used, in contrast, stochastic methods to construct the boards and their material properties. Vida et al. [13] presented a modelling approach to simulate the entire loading course of GLT beams subjected to four-point bending tests (Fig. 2b). For the study on the size effect [12], the approach was adjusted to suit the research scope and its efficiency was increased by reducing its model size (Fig. 2c). There, only a beam section anywhere between the two loading points of a four-point bending test was considered, which allowed applying the constant bending moment M directly.

An overview of the procedure deriving the used material properties is presented in Section 2.1. Section 2.2 describes the modelling approach for beam sections before Section 2.3 continues with its validation. The realisation of different beam lengths is discussed in Section 2.4.

2.1 MATERIAL PROPERTIES

The material properties were based on the deterministic estimation procedure presented by Kandler et al. [15]. Therein, the boards were virtually reconstructed and parted in sections. The section length ℓ_s was based on the corresponding knot configuration in the real wooden board, and thus the sections were of individual size (Fig. 3). Each section refers either to defect-free wood, so-called clear wood, or to sections with single large knots or knot clusters, referred to as knot sections.

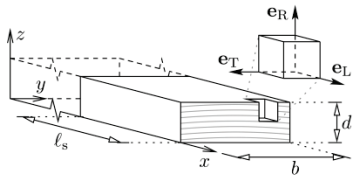

Figure 3: *Board section with homogeneous material properties. [13]*

The material properties of each section were constant, and the material behaviour was orthotropic. The stiffness properties for the clear wood sections were based on a micromechanical multiscale model proposed by Hofstetter et al. [16]. The model used density and moisture content as the primary input parameters. Consequently, each board had its own individual stiffness tensor $\mathbb{C}$. A separate FE approach [15] estimated the longitudinal modulus of elasticity (MOE) $E_{L,i}$ for each knot section i individually. The stiffness tensor $\mathbb{C}$ was then modified along the board by $E_{L,i}$. The tensile strength in longitudinal direction $f_{t,i}$ was assumed to be $55\ \mathrm{N/mm^2}$ for the clear wood sections of all boards. However, the clear wood strength represents an upper strength limit having only a minor influence on the load-bearing capacity [13]. Within knot sections, $f_{t,i}$ was estimated by the knot-area ratio according to the study presented by Lukacevic et al. [17]. Finally, the section-wise constant effective MOE $E_{L,i}$ and tensile strength $f_{t,i}$ in the longitudinal direction were provided for each board by two material property profiles (Fig. 4a,d). Two strength classes, T14 and T22, were considered.

https://doi.org/10.52202/069179-0063

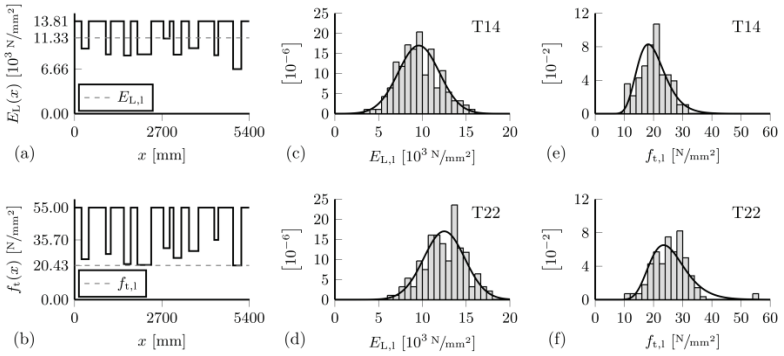

Figure 4: *Example of a board's property profiles providing (a) the effective longitudinal MOE $E_L(x)$ and (b) the effective tensile strength $f_t(x)$ as well as histograms considering all boards and PDFs fitted by maximum likelihood estimations for (c,d) the MOE $E_{L,l}$ and (e,f) the tensile strengths $f_{t,l}$, separate for both strength classes T14 and T22. [13]*

In total, 140 boards of each strength class were available. The board's length was 5400 mm, the width 90 mm, and the thickness 33 mm. The longitudinal MOE of an entire board $E_{L,l}$ considered all sections i of the board as a chain of linear springs:

$$E_{L,l} = \frac{\ell_{tot}}{\sum_i \frac{\ell_{s,i}}{E_{L,i}}} \quad \text{with} \quad \ell_{tot} = \sum_i \ell_{s,i}\,, \tag{4}$$

where $\ell_{s,i}$ is the length corresponding to the section-wise constant $E_{L,i}$ from its stiffness profile (Fig. 4a). Figure 4c,d shows the histograms and the fitted normal probability distribution functions (PDFs) of $E_{L,l}$ according to Eq. (4) for both strength classes T14 and T22, respectively. The board tensile strength $f_{t,l}$ is assumed as the lowest strength $f_{t,i}$ of section i within the strength profile of the considered board (Fig. 4b):

$$f_{t,l} = \min_i \{f_{t,i}\}\,. \tag{5}$$

Figure 2e,f shows the histograms and the fitted log-normal PDFs of $f_{t,l}$ according to Eq. (5) again for both strength classes, respectively. A comparison of the characteristic tensile board strength and the mean longitudinal board MOE to the values according to DIN EN 14080 [3] is given in Tab. 1. Generally, the simulated values are lower than those specified in the standard. The underestimation could be due to different board lengths in the test setup, especially regarding the strengths.

2.2 MODELLING APPROACH

We used a non-linear FE approach to simulate GLT beam sections (Fig. 5) by employing the FE software Abaqus [18]. Details about the approach are published in [12]. The beam layout was assembled by the virtually reconstructed boards from Section 2.1, and the beam structure was designed to be homogeneous. Consequently, only boards corresponding to strength class T14 or T22 were used to simulate beams of strength class GL 24h or GL 30h, respectively. The boards within a beam were arranged by a uniformly distributed pseudo-random process of the following steps:

1. Random picking a full-length board from the entire pool of virtual boards.
2. Random longitudinal displacement of the board within the GLT beam section to define the start and end positions of the lamella.
3. Random choice of the lamella's orientation in the GLT beam layout.

Typically, restrictions on the length of boards are reversed by connecting individual boards with finger joints. Herein, weak points due to finger joints were neglected. We assumed that the structural behaviour and failure is covered by the random allocation of natural weak spots, as it was found by experimental studies [7, 19].

The beam section (Fig. 5) was modelled with the variable length-to-depth ratio ℓ/h, where $h = k \cdot 33$ mm depending on the number of laminations k. The length $e = 100$ mm was added on both ends to avoid disturbing the area of interest by load application effects. The constant bending moment M was applied at the reference points R_1 and R_2 by prescribing a reversed rotation. During the loading, the cross-sections at both beam ends stayed planar. The beam width b was according to the used boards, and the symmetry in the

Table 1: *Comparison of the mean and characteristic values of the histograms in Fig. 2c–f to values according to DIN EN 14080 [3]. [13]*

Strength class	$E_{L,l,mean}$ (N/mm²)	$E_{L,0,l,mean}$ (N/mm²)	$f_{t,0,l,k}$ (N/mm²)	$f_{t,0,l,k}$ (N/mm²)
T14	9 592	11 000	11.6	14.0
T22	12 497	13 000	16.6	22.0

https://doi.org/10.52202/069179-0063

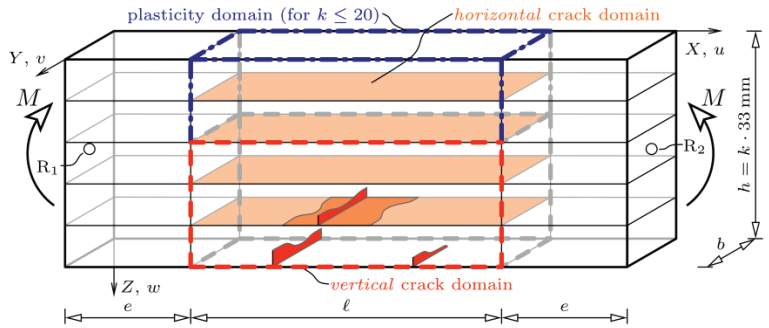

Figure 5: *Representative GLT beam section of length ℓ as used for the numerical simulations with k lamellas resulting in the depth h. The constant bending moment M and the bearing were applied at the reference points R_1 and R_2. [12]*

width direction was exploited to reduce the model size further.

We considered different kinds of local failure mechanisms within the approach, i.e., discrete cracks in the vertical and horizontal direction as well as plastic deformations. All failure mechanisms could only take place within the region of the length ℓ as marked in Fig. 5.

The vertical cracks could occur within the lamellas on the tensile side, and the horizontal cracks between all adjacent laminations building up the beam section (Fig. 5). Both crack directions enabled the formation of a continuous crack over multiple laminations. Two vertical cracks with a horizontal offset and in adjacent laminations could be connected by a horizontal crack. Their implementation is briefly outlined in the following:

- *Vertical* cracks were realised within the framework of XFEM, which was proposed by Tapia Camú and Aicher [20]. The application of XFEM enabled an element to split into two parts with planar and opposing crack surfaces. The split was initiated by an initiation criterion, i.e., the tensile stress in the centroid of an element exceeding the tensile strength $f_{t,i}$. The maximum traction stress t^* between the crack surfaces was, thus, $f_{t,i}$. A linear traction–separation (t–δ) law (Fig. 6a) governed the interaction between the crack surfaces in conjunction of a constant fracture energy $G_{f,v} = 30\ \mathrm{Nmm/mm^2}$.
- *Horizontal* cracks were implemented with cohesive surfaces. The traction–separation (t–δ) relation between the two parts was linear elastic until the initiation of damage and its evolution (Fig. 6b). The maximum traction stress t^* is set to $5.0\ \mathrm{Nmm/mm^2}$ and $6.0\ \mathrm{Nmm/mm^2}$ for transversal tensile stresses and shear stresses, respectively. An uncoupled stiffness tensor defined the traction t between the surfaces and their separation δ. A constant fracture energy $G_{f,h} = 0.6\ \mathrm{Nmm/mm^2}$ was used.

The applied constant properties were assumed because of the lack of available data, e.g., for the fracture energies.

The plastic deformations in compressive zones were considered by implementing ideal plastic behaviour with a multisurface failure criterion [21–23]. The relevance of plastic deformations on the load-bearing capacity was assumed to be limited to smaller beam depths based on an experimental study [8]. Thus, ideal plasticity was only implemented for beams consisting of a maximum of 20 lamellas corresponding to a depth of 660 mm (Fig. 5).

The applied global failure criterion determined the load-bearing capacity M_{max} by the first load decline of at least 3 % from the so far maximum total load M. Finally, the calculated bending strength of the beam reads as:

$$f_b = \frac{6\,M_{max}}{bh^2}, \tag{6}$$

where the dimensions b and h can be found in Fig. 5.

Next is the validation of the approach. The influence of the element size and the plastic deformations on the bending strength are additionally discussed in [12].

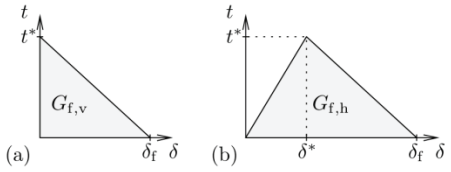

Figure 6: *Traction–separation (t–δ) law with the area representing the fracture energy G_f for (a) vertical cracks and (b) horizontal cracks, where t^* and δ^* are the traction and separation at damage initiation, respectively, and δ_f is the separation at fully evolved damage. [13]*

2.3 VALIDATION

To validate the approach, we compared the results of 40 tested GLT beams with simulation results, i.e., the effective MOE E_{GLT} and bending strength f_b (Fig. 7). The experimental study [8] focused on GLT beams with well-known knot morphology without containing any finger joints. The beams were manufactured using the same boards from the virtual reconstruction process presented in Section 2.1. Thus, it was possible to recreate each tested beam with the unique beam layout and material properties for the simulations.

The validation covered two strength classes, i.e., GL 24h and GL 30h, and two beam sizes with 132 mm and 330 mm depth. The different beam configurations were classified by four types, A, B, D, and E, designated according to their strength class and number of lamellas:

https://doi.org/10.52202/069179-0063

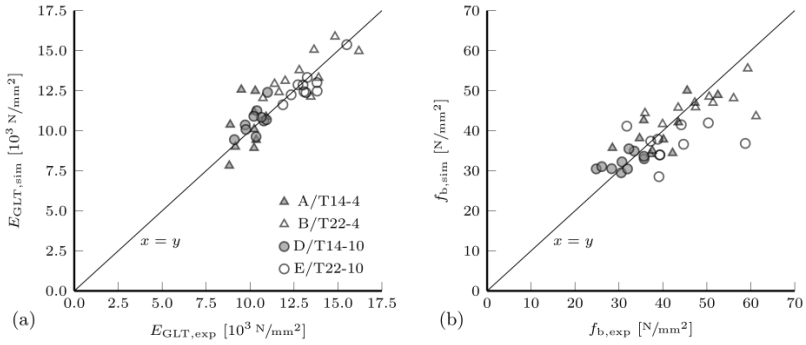

Figure 7: *Comparison of experimental results (subscript exp) to simulation results (subscript sim) for (a) the effective MOE E_{GLT} and (b) bending strength f_b. [12]*

A/T14-4, B/T22-4, D/T14-10, and E/T22-10. The test setup of the experiments was according to DIN EN 408 [1].

The simulations reconstructed the tested beams in the range between the two loading points with a dimensional ratio $\ell/h = 6.0$. The simulation results successfully reproduced the characteristics of the experimental results for the different strength classes and beam sizes, as shown in Fig. 7.

2.4 CONSIDERATION OF DIFFERENT DIMENSIONAL RATIOS

The ratio of beam length to depth ℓ/h, also referred to as dimensional ratio, influences the structural response, as presented in [12]. This was shown by simulating beam sections having ratios ℓ/h of 6.0 and 1.5 for beam depths of h of 165 mm, 330 mm, and 660 mm. However, the larger dimensional ratio requires larger finite element models for which the computation time of the nonlinear calculations became quite long. Therefore, the bending strength prediction of different dimensional ratios based on models having only a ratio of $\ell/h = 1.5$ would be very valuable.

The applied solution to this problem was to estimate the bending strength of larger dimensional ratios $p \times 1.5$ in the following way:

$$f_{b,i} = \min\left\{f_{b,(i-1)\cdot p+1}, f_{b,(i-1)\cdot p+2}, \cdots, f_{b,(i-1)\cdot p+p}\right\}, \quad (7)$$

with $i \in \{1, \ldots, \lfloor n/p \rfloor\}$, where n denotes the number of simulation results from models with $\ell/h = 1.5$ and $\lfloor\cdot\rfloor$ is the floor function that rounds the included number to the nearest smaller integer.

A rough validation was done by comparing the PDFs (Fig. 8) corresponding to the simulation results having the ratio ℓ/h of 6.0 and 4×1.5. The PDFs of f_b were log-normal distributions fitted by maximum likelihood estimations. Considering the simplicity of Eq. (7), the agreement with the simulation results was surprisingly good. The maximum deviation of the mean bending strength was 3.3 % and of the characteristic bending strength 2.2 %. Consequently, the influence of different dimensional ratios can be estimated by this method.

3 COMPUTATIONAL STUDY ON THE SIZE EFFECT

To study the size effect on the bending strength of large GLT beams, we carried out an extensive simulation campaign that is summarised in the following and presented in detail in [12]. The study covered beam sizes ranging from 165 mm up to 3300 mm for two strength classes, i.e., GL 24h and GL 30h. The number of simulations performed depended on the beam size but was the same for both strength classes (Tab. 2). All simulations were carried out with a dimensional ratio of $\ell/h = 1.5$ using the 140 virtually reconstructed wooden boards of each strength class from Section 2.1.

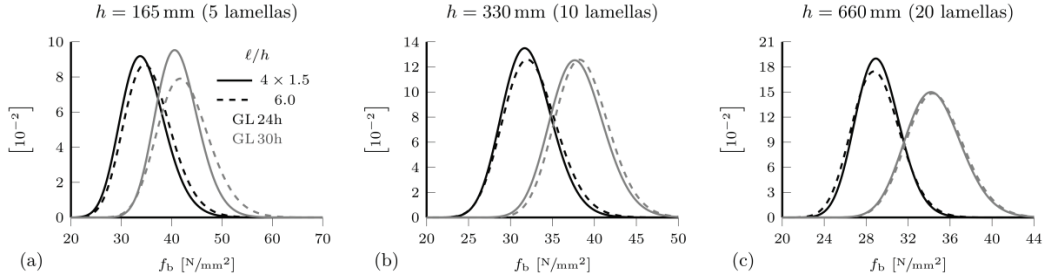

Figure 8: *Comparison of PDFs for the bending strength f_b obtained from simulations with the dimensional ratios of 6.0 or 4×1.5 covering both strength classes for three beam depths: (a) 165 mm, (b) 330 mm, and (c) 660 mm. [12]*

https://doi.org/10.52202/069179-0063

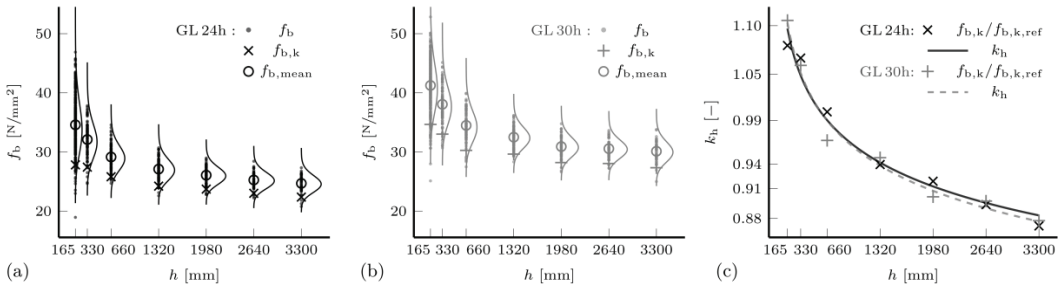

Figure 9: *Bending strength f_b values and PDFs obtained from simulations with the beam depth h and a dimensional ratio of 4×1.5 for strength classes (a) GL 24h and (b) GL 30h, which are used to derive (c) the factor k_h commonly used to describe the size effect. [12]*

The study [12] covered GLT beams having fixed dimensional ratios (Section 3.1) and variable dimensional ratios (Section 3.2). Additionally, the influence of the applied global failure criterion was investigated (Section 3.3), and the results will be published in [14].

Table 2: *Studied beam depths with the corresponding number of lamellas and simulations. [12]*

Depth h (mm)	Lamellas k (–)	Sample size[a] (–)
165	5	1600
330	10	400
660	20	400
1320	40	400
1980	60	300
2640	80	200
3000	100	200

[a] For each strength class with $\ell/h = 1.5$

3.1 BEAM SECTIONS WITH FIXED DIMENSIONAL RATIO

The test setup, according to DIN EN 408 [1], always requires a dimensional ratio $\ell/h = 6.0$ for the maximum loaded range. Consequently, the beam length ℓ increases when increasing the depth h. The effective bending strengths were calculated using the simulation results in conjunction with Eqs. (6) and (7) to obtain representative results for the required dimensional ratio $\ell/h = 6.0$.

The effective bending strengths decreased for both strength classes with increasing beam size (Fig. 9a,b). The decrease was present for the mean and characteristic bending strength, $f_{b,mean}$ and $f_{b,k}$, respectively. The mean and characteristic values were obtained from the two-parameter log-normal PDFs, which were fitted to the entire sample by maximum likelihood estimations. Additionally, the PDFs showed a decreasing variation with increasing beam size. The decreasing variation results in a lower decrease of $f_{b,k}$ compared to $f_{b,mean}$.

On the level of $f_{b,k}$, the size effect k_h according to Eq. (3) was clearly present for the entire range of simulated beam sizes (Fig. 9c). For the analytical solution represented by Eq. (3), the characteristic reference bending strength $f_{b,k,ref}$ and the power law parameter m were fitted to the simulation results by the least squares method. The reference depth h_{ref} was set to 600 mm according to DIN EN 14080 [3].

The characteristic reference bending strengths $f_{b,k,ref}$ found through fitting overestimate the values provided in DIN EN 14080 [3] by about 7 % and 4 % for GL 24h and GL 30h, respectively (Tab. 3). The found parameter m is quite similar for both strength classes having a mean value of 26.2.

Both strength classes showed about the same decrease. The largest simulated beams ($h = 3300$ mm) showed a reduced $f_{b,k}$ of about 12 % compared to $f_{b,k,ref}$ (Fig. 9c). For smaller beam depths than h_{ref}, the predicted k_h agrees well with the modification according to Eq. (2) from DIN EN 1995-1-1 [2]. Additionally, our results agreed very well with two experimental studies from the literature testing beams with depths of about 300 mm and 600 mm. Aasheim and Solli [7] and Schickhofer [9] identified k_h as 1.07 and 1.04, respectively. For the same beam depths, our approach predicted k_h to be 1.05. The result was obtained using the mean value of the parameter m corresponding to both strength classes in Eq. (3).

Table 3: *Characteristic reference bending strength $f_{b,k,ref}$ and power law parameter m fitted to the simulation results. [12]*

	GL 24h		GL 30h	
	$f_{b,k,ref}$ (N/mm²)	m (N/mm²)	$f_{b,k,ref}$ (N/mm²)	m (N/mm²)
Load drop	25.74	27.00	31.23	25.38

3.2 BEAM SECTIONS WITH DIFFERENT DIMENSIONAL RATIO

As already pointed out, the test setup, according to DIN EN 408 [1], defines a fixed ratio of the length ℓ between the two loading points and the beam depth h. However, the dimensional ratio ℓ/h of GLT beams is determined during the design process and might not coincide with the fixed dimensional ratio of the experiments. Therefore, investigating the size effect on $f_{b,k}$ for different dimensional ratios ℓ/h is highly relevant for practical application.

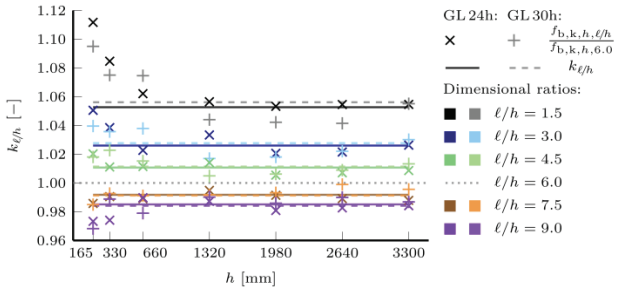

Figure 10: *Comparison of the normalised values $k_{\ell/h}$ of each individual beam depth h: the scatters refer to the simulated results in conjunction with Eq. (7), and the horizontal lines are according to Eq. (3). [12]*

The different ratios ℓ/h were realised using the procedure presented in Section 2.4. The simulation results stemmed from the models having a dimensional ratio of 1.5. For each of the seven simulated beam depths h, five different lengths ℓ were investigated, covering ratios ℓ/h ranging from 1.5 to 9.0. The obtained characteristic bending strengths $f_{b,k,h}$ for each ratio of a specific beam depth h were normalised by $f_{b,k,h,6.0}$ of the same beam depth h with a ratio $\ell/h = 6.0$ (4×1.5). This normalised value is herein denoted as $k_{\ell/h}$.

The simulation results indicated that the ratio ℓ/h heavily influences the bending strength of a GLT beam (Fig. 10). By changing the ratio for a specific beam depth h, the investigated beam length changes. When looking at a particular beam depth, the characteristic bending strength of a beam with a shorter length was smaller than that of a longer length. Especially beams with a depth smaller than 660 mm showed a more pronounced influence of the dimensional ratio ℓ/h. For each individual ratio, the larger beams showed an almost constant factor $k_{\ell/h}$. Consequently, the same size effect is present for only changing the beam length or depth. The horizontal lines in Fig. 10 render the results of Eq. (3) in conjunction with the results provided in Tab. 3. The simulation results agreed well with the analytical concept.

3.3 INFLUENCE OF THE APPLIED GLOBAL FAILURE CRITERION

The applied modelling approach enabled the investigation of different global failure criteria for each simulation. This was possible by simulating the entire loading process and determining the load-bearing capacity afterwards. The size effect on $f_{b,k}$ of large GLT beams had been estimated before by Fink et al. [11] and Frese and Blaß [10]. However, their results diverged from each other. To investigate the influence of applied global failure criteria, we implemented similar criteria within our approach. The modelling strategies of each approach were different, making a completely identical description of the failure criteria impossible, e.g., due to a different mesh size or the implementation of discrete cracking. Nevertheless, we tried to implement the criteria as closely to the proposed one as possible. The implementation of the global failure criteria and the main differences between the modelling strategies will be discussed in detail in [14].

The applied global failure criterion defined the simulated load-bearing capacity M_{max} used to further calculate the corresponding bending strength f_b according to Eq. (6). Additional to our already presented load drop criterion (Section 2.2), we implemented the following global failure criteria:

- The global stiffness reduction criterion is met by the first global stiffness reduction of at least 1 % compared to the initial global stiffness of the first loading increment. The global stiffness is calculated in each increment with the current bending moment and rotation. The load-bearing capacity is then the maximum load during the loading before the criterion is fulfilled. This implementation is similar to the criterion applied by Fink et al. [11].
- The first crack initiation criterion focuses only on the initiation of the first crack in the outermost tensile lamination to identify the load-bearing capacity. The load-bearing capacity is then the maximum bending moment observed during the entire simulation up to this point. During the loading process, an arbitrary number of cracks can occur within the other laminations of the beam. This criterion is comparable with the one used by Frese and Blaß [10] and Frese [24].

The estimated individual trends of the size effect k_h for each global failure criterion (Fig. 11) agreed very well with the results presented in the literature. The stiffness reduction criterion predicted basically no influence of the beam size on $f_{b,k}$, which agrees with the result presented in Fink et al. [11]. The first crack initiation criterion resulted in a decrease only a bit larger than proposed by Frese and Blaß [10]. The characteristic bending strengths of all criteria were taken from fitted log-normal PDFs.

4 CONCLUSION AND OUTLOOK

The development of reliable modelling concepts is of significant importance to effectively investigate wood products such as GLT beams. In the present study, a comprehensive simulation campaign of more than 8000 simulations could predict the size effect for large GLT beams of up to 3300 mm depth. It was further shown that not only the beam depth influences the characteristic bending strength but also the beam length. The size effect,

https://doi.org/10.52202/069179-0063

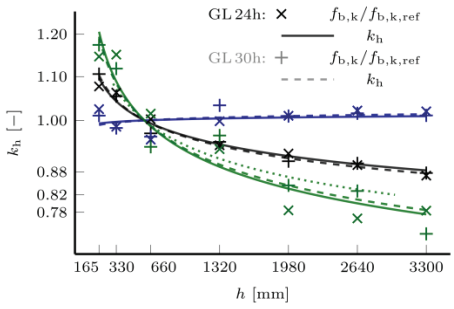

Figure 11: *Size effect k_h according to Eq. (3) based on three different global failure criteria: (i) the load drop criterion in black, (ii) the system stiffness reduction criterion in blue, and (iii) the first crack initiation in the outermost tensile lamination criterion in green compared to (iv) the proposed result by Frese and Blaß [10] with the dotted line in green. [14]*

including changes in beam length and depth, could adequately be described by the concept proposed by Colling [6], at least for beams with depths greater than 660 mm. Additionally, results of numerical studies from the literature could be reproduced by using corresponding global failure criteria.

Numerical simulations offer an efficient way to perform extensive parameter studies of different kinds to make reasonable predictions. Nevertheless, simulation results need to be carefully validated as they might heavily depend on their modelling strategy. Experimental testing of such large GLT beams is unfortunately missing, which would strengthen the value of such studies.

As for future research focus, the aim is to obtain section-wise constant fracture energies for individual knot sections, which then can be used to replace the for now constant one. This could be achieved by employing the so-called phase-field method [25, 26], which is one of our main current research focuses.

ACKNOWLEDGEMENT

The authors gratefully acknowledged the funding from the Austrian Science Fund (FWF) through START grant Y1093 “Virtual Wood Labs” and SFB F77 “Advanced Computational Design”.

REFERENCES

[1] DIN EN 408: Holzbauwerke – Bauholz für tragende Zwecke Und Brettschichtholz – Bestimmung einiger physikalischer und mechanischer Eigenschaften; Deutsche Fassung EN 408:2010+A1:2012. Berlin, Germany: DIN, 2012.

[2] DIN EN 1995-1-1: Eurocode 5: Bemessung und Konstruktion von Holzbauten – Teil 1-1: Allgemeines – Allgemeine Regeln und Regeln für den Hochbau; Deutsche Fassung EN 1995-1-1:2004 + AC:2006 + A1:2008. Berlin, Germany: DIN, 2010.

[3] DIN EN 14080: Holzbauwerke – Brettschichtholz und Balkenschichtholz – Anforderungen; Deutsche Fassung EN 14080:2013. Berlin, Germany: DIN, 2013.

[4] B. Bohannan: Effect of Size on Bending Strength of Wood Members. Research Paper FPL-56. Madison, WI: U.S. Department of Agriculture, Forest Service, Forest Products Laboratory, 1966.

[5] Weibull, W.: A Statistical Theory of the Strength of Materials. Handlingar Nr. 151. Stockholm, Sweden: Ingeniörsvetenskapsakademiens, Generalstabens litografiska anstalts förlag, 1939.

[6] F. Colling: Einfluß des Volumens und der Spannungsverteilung auf die Festigkeit eines Rechteckträgers: Herleitung einer allgemeinen Beziehung mit Hilfe der 2-parametrigen Weibull-Verteilung. *Holz Als Roh- Und Werkstoff*, 44(4):121–125, 1986. doi:10.1007/BF02612013

[7] E. Aasheim, K. H. Solli: Size Factor of Norwegian Glued Laminated Beams. In: *CIB-W18 Meeting 28.* Copenhagen, Denmark, 1995.

[8] G. Kandler, M. Lukacevic, J. Füssl: Experimental Study on Glued Laminated Timber Beams with Well-Known Knot Morphology. *European Journal of Wood and Wood Products*, 76(5):1435–1452, 2018. doi:10.1007/s00107-018-1328-6

[9] G. Schickhofer: Development of Efficient Glued Laminated Timber. In: *CIB-W18 Meeting 29.* Bordeaux, France, 1996.

[10] M. Frese, H. J. Blaß: Numerical Description of Size and Load Configuration Effects in Glulam Structures. In: *Proceedings of the 12th International Conference on Applications of Statistics and Probability in Civil Engineering (ICASP12).* Vancouver, Canada: The University of British Columbia, 2015. doi:10.14288/1.0076135

[11] G. Fink, A. Frangi, J. Kohler: Probabilistic Approach for Modelling the Load-Bearing Capacity of Glued Laminated Timber. *Engineering Structures*, 100:751–762, 2015. doi:10.1016/j.engstruct.2015.06.015

[12] C. Vida, M. Lukacevic, G. Hochreiner, J. Füssl: Size Effect on Bending Strength of Glued Laminated Timber Predicted by a Numerical Simulation Concept Including Discrete Cracking.

Materials & Design, 225:111550, 2023. doi:10.1016/j.matdes.2022.111550

[13] C. Vida, M. Lukacevic, J. Eberhardsteiner, J. Füssl: Modeling Approach to Estimate the Bending Strength and Failure Mechanisms of Glued Laminated Timber Beams. *Engineering Structures*, 255:113862, 2022. doi:10.1016/j.engstruct.2022.113862

[14] C. Vida, M. Lukacevic, G. Hochreiner, J. Füssl: Size Effect of Glued Laminated Timber Predicted by Simulation Concepts – Influence of Global Failure Criterion Definition on Bending Strength and Failure Mechanism. 2023. (manuscript in preparation)

[15] G. Kandler, M. Lukacevic, C. Zechmeister, S. Wolff, J. Füssl: Stochastic Engineering Framework for Timber Structural Elements and Its Application to Glued Laminated Timber Beams. *Construction and Building Materials*, 190(5):573–592, 2018. doi:10.1016/j.conbuildmat.2018.09.129

[16] K. Hofstetter, C. Hellmich, J. Eberhardsteiner: Micromechanical Modeling of Solid-Type and Plate-Type Deformation Patterns within Softwood Materials. A Review and an Improved Approach. *Holzforschung*, 61(4):343–351, 2007. doi:10.1515/HF.2007.058

[17] M. Lukacevic, J. Füssl, J. Eberhardsteiner: Discussion of Common and New Indicating Properties for the Strength Grading of Wooden Boards. *Wood Science and Technology,* 49(3):551–576, 2015. doi:10.1007/s00226-015-0712-1

[18] Abaqus: Abaqus 2021 HF5. Providence, RI, USA, 2021.

[19] Pischl, R.; Schickhofer, G.; Seiner, C.; Steinberger, A.; Gehri, E.; Mauritz, R. (1995). *Entwicklung leistungsfähiger Holzleimbauteile: Zusammenfassender Bericht zum FFF-Forschungsprojekt* (FFF-Forschungsprojekt)Graz/A – Zürich/CH – Wien/A

[20] C. Tapia Camú, S. Aicher: A Stochastic Finite Element Model for Glulam Beams of Hardwoods. *Proceedings of the 2018 World Conference on Timber Engineering (WCTE 2018).* Seoul, Republic of Korea, 2018.

[21] M. Lukacevic, J. Füssl, R. Lampert: Failure Mechanisms of Clear Wood Identified at Wood Cell Level by an Approach Based on the Extended Finite Element Method. *Engineering Fracture Mechanics*, 144:158–175, 2015. doi:10.1016/j.engfracmech.2015.06.066

[22] M. Lukacevic, W. Lederer, J. Füssl: A Microstructure-Based Multisurface Failure Criterion for the Description of Brittle and Ductile Failure Mechanisms of Clear-Wood. *Engineering Fracture Mechanics*, 176:83–99, 2017. doi:10.1016/j.engfracmech.2017.02.020

[23] S. Pech, M. Lukacevic, J. Füssl: A Robust Multisurface Return-Mapping Algorithm and Its Implementation in Abaqus. *Finite Elements in Analysis and Design*, 190:103531, 2021. doi:10.1016/j.finel.2021.103531

[24] M. Frese: *Computergestützte Verfahren zur pragmatischen Beurteilung der Tragwiderstände von Brettschichtholz: Zusammenfassung exemplarischer Simulationsstudien.* Habilitation. Karlsruhe, Germany: KIT Scientific Publishing, 2016.

[25] S. Pech, M. Lukacevic, J. Füssl: A Hybrid Multi-Phase Field Model to Describe Cohesive Failure in Orthotropic Materials, Assessed by Modeling Failure Mechanisms in Wood. *Engineering Fracture Mechanics*, 271:108591, 2022. doi:10.1016/j.engfracmech.2022.108591

[26] S. Pech, M. Lukacevic, J. Füssl: Validation of a hybrid multi-phase field model for fracture of wood. *Engineering Fracture Mechanics*, 275:108819, 2022. doi:10.1016/j.engfracmech.2022.108819

https://doi.org/10.52202/069179-0063

World Conference on Timber Engineering Oslo 2023

MODE I FRACTURE ENERGY OF AUSTRALIAN NATIVE HARDWOOD SPOTTED GUM AT VARIOUS MOISTURE CONTENTS

Peiqing Lu[1], Benoit P. Gilbert[2], Chandan Kumar[3], Robbie L. McGavin[4], Hassan Karampour[5]

ABSTRACT: While there is an industry drive to use Australian hardwood spotted gum (*Corymbia citriodora*) boards in the manufacturing of glulam beams, such beams frequently fail the delamination requirements in the Australian and New-Zealand standard AS/NZS 1328.1 (1998). Delamination likely occurs due to (a) the difficulty in gluing this species and (b) the combination of large shrinkage coefficients and high moduli of elasticity of the material, resulting in large moisture-induced stresses developing in the gluelines during the wetting and drying cycles of the delamination test. The paper forms part of a research aiming at finding mechanical solutions to reduce the moisture-induced stresses in the gluelines, allowing spotted gum glulam beams to pass the delamination requirements and land on the market. Especially, this paper introduces the reader to the overall project and focuses on measuring the Mode I fracture energy of the spotted gum material in the tangential-longitudinal crack system and of the glueline between spotted gum boards at 8%, 12% and 16% moisture contents. The relationship between the Mode I fracture energies and moisture content are then discussed and analysed statistically to determine whether fracture energy is sensitive to the moisture content for the analysed range.

KEYWORDS: Australian hardwood glulam, fracture energy, moisture content

1 INTRODUCTION

With the current drive towards sustainable and green construction, the demand for high-performance engineered wood products is increasing. This brings opportunities and challenges to Australia's hardwood industry, such as for native forest grown spotted gum (SPG - *Corymbia citriodora*), a dense hardwood with superior mechanical properties and durability [1]. Spotted gum occupies about 70% of the annual hardwood logs supplied by Queensland (QLD) native forests [2]. There is a drive to manufacture glulam out of this species to be used as beams, columns or bridge elements. However, for SPG glulam to be commercialised, the bond between boards must satisfy the delamination requirements in the Australian and New Zealand Standard AS/NZS 1328.1 (1998) [3]. The delamination test consists of vacuum water impregnation followed by a drying process. The parameters of these two processes depend on the service class of the final product, i.e., its intended environmental application. However, despite best efforts to improve the gluability of SPG [4], SPG glulam products commonly do not pass the requirements in [3] for external applications, with outcomes from a typical delamination test shown in Figure 1. This phenomenon is thought to be attributed to (1) the difficulty in gluing the species from little adhesive penetration [5] and (2) the high moisture shrinkage coefficients combined with high elastic moduli of the material, resulting in large moisture-induced internal stresses developing in the gluelines during the delamination test.

As delamination develops from over-stressed gluelines [6], reducing the internal stresses could represent an effective mechanical solution to prevent delamination. Several approaches may potentially achieve this. First, as the shrinkage and swelling coefficients of SPG (and timber in general) are different along the radial and tangential directions [7], designing the glulam with boards stacked in a specific grain orientation combination could improve results from the delamination test. Second, cutting stress relief grooves in the boards, with specific shape and arrangement, could also reduce the internal stresses [8]. Finally, adjusting the board geometry (width

[1] Peiqing Lu, Griffith University, Australia, peiqing.lu@griffithuni.edu.au
[2] Benoit Gilbert, Queensland Government Department of Agriculture and Fisheries & Griffith University, Australia, benoit.gilbert@daf.qld.gov.au & b.gilbert@griffith.edu.au
[3] Chandan Kumar, Queensland Government Department of Agriculture and Fisheries, Australia, Chandan.Kumar@daf.qld.gov.au
[4] Robbie McGavin, Queensland Government Department of Agriculture and Fisheries, Australia, Robbie.McGavin@daf.qld.gov.au
[5] Hassan Karampour, Griffith University, Australia, h.karampour@griffith.edu.au

https://doi.org/10.52202/069179-0064

to thickness ratio) could also affect the internal stresses and thereby decrease the stresses imposed to the gluelines during the delamination test.

To study the delamination problem and find mechanical solutions to reduce the moisture-induced stresses in the gluelines, a numerical model that can reproduce (i) the heat-and-mass transfer in the timber during drying, (ii) the associated drying stresses and (iii) crack initiation and propagation in both the timber and gluelines, would represent an economical and efficient method to investigate potential solutions [8, 10]. The physical and mechanical properties of the SPG material and its associated gluelines need to be collected to establish such a model. The SPG physical properties, such as permeability, diffusion coefficient and desorption-isotherm, are already available in [7]. However, there is a lack of information regarding the mechanical properties, especially the fracture properties and their relationship with moisture content. This paper aims to determine the Mode I fracture energy of the SPG material and associated gluelines. As the mechanical properties of timber are moisture sensitive [9] and the SPG glulam moisture content varies during the delamination test in the AS/NZS 1328.1 (1998) [3], the fracture energies along the crack paths experienced during the delamination tests are determined in this paper at different moisture content, namely 8%, 12% and 16%. First, published fracture energy test methods for fracture Mode I are reviewed, and the most appropriate method for timber is selected. Second, the Mode I fracture energies of the timber with a Tangential (T)-Longitudinal (L) crack system, i.e., with the crack occurring in the RL plane and propagating along the longitudinal direction, and of the "glueline" crack system, i.e., with the crack normal to the glueline, at different moisture content are measured experimentally. Note that the timber orientation in the Tangential (T), Radial (R) and Longitudinal (L) directions is shown in Figure 2. The crack systems investigated are shown in Figure 3.

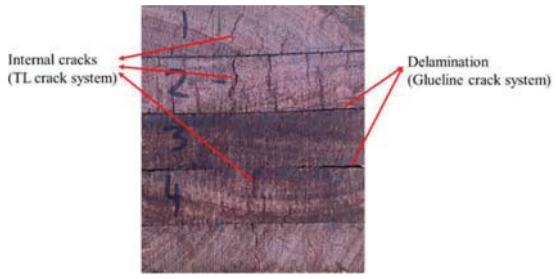

Figure 1: *Spotted gum glulam after delamination test*

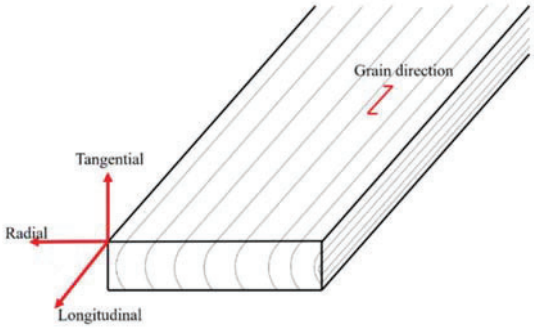

Figure 2: *Timber Tangential (T), Radial (R) and Longitudinal (L) directions*

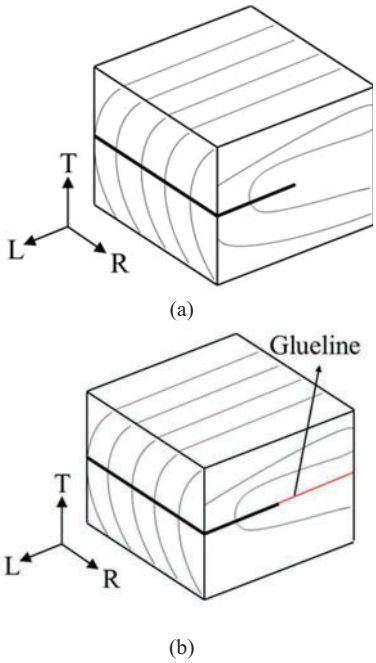

Figure 3*: Timber crack systems (a) TL and (b) glueline*

2 METHODOLOGY

The methodology to obtain the Mode I fracture energies consists of three main steps: (a) determining the test setup used for Mode I fracture energy experiment, (b) preparing the timber and glulam samples and (c) analysing the Mode I fracture energy results statistically by one-way ANOVA.

2.1 MATERIAL, GLUEING AND CONDITIONING

Australian's native forest SPG sawn boards, with the trees harvested in QLD, were used to investigate the Mode I fracture energy and its sensitivity to the moisture content. After the drying process of the delamination test [3], the cracks typically developed within the timber normal to the tangential direction and along the gluelines, as shown in

https://doi.org/10.52202/069179-0064

Figure 1. Therefore, in view of modelling, the fracture Mode I energies in the TL and glueline crack systems were investigated in this study.

When boards needed to be glued to manufacture the samples, as detailed in Section 0, boards were bonded following the results in [4, 10-12] to maximise adhesion, consisting of face milling the boards to a thickness of 22 mm to activate the surface and using commercial resorcinol–formaldehyde adhesive (RF) manufactured by Jowat Adhesive. The gluing process consisted of: (1) mixing the resorcinol with formaldehyde by 4:1 for 5 mins and letting it stand for 10 mins, (2) face milling the surfaces to be glued with a Rotoles 400 D-S manufactured by Ledinek [5], (3) manually applying the adhesive on the milled surfaces, immediately after milling, at a glue spread rate of 450 g/m^2, and (4) pressing the boards together under a pressure of 1.4 MPa for a period of 12 hours.

After the gluing process was finished, the samples were put into different conditioning chambers with targeted equilibrium moisture content of 8%, 12% and 16%, corresponding to the conditioning chambers set at 20℃/40% relatively humidity (RH), 20℃/65% RH and 60℃/90% RH, respectively [13]. The moisture content were selected based on measurements on the glulam samples during delamination tests which reached moisture content up to 16% after vacuum impregnation and down to 8% after kiln drying.

Immediately after testing (Section 2.2), the actual moisture content of each sample was determined following the oven-dry method in the Australian standard AS/NZS 1080.1 [14].

2.2 FRACTURE MODE I TEST SETUP

Different test methods have been adopted in the literature to measure the Mode I fracture energy of timber specimens. Ostapska and Malo [15] applied to timber the wedge splitting test method that was proposed by Brühwiler and Wittmann [16] for concrete. However, this test method is complex and laborious if only fracture energy is required [15]. Franke and Quenneville [17] applied the compact tension shear (CTS) test setup, which was proposed by Richard and Benitz [18], to Radiata Pine Laminated Veneer Lumber (LVL) and sawn timber. The advantage of the CTS is that either Mode I, Mode II or mixed Mode fracture energies can be measured with one test rig by changing the angle of the applied load. However, the CTS specimens must be carefully prepared with high accuracy to avoid that unsymmetrical loading occurs which would significantly affect the applied stress and resulting fracture energy [17]. In addition, De Moura et al. [19], applied the double cantilever beam (DCB) test for fracture Mode I to Pinus pinaster sawn timber and stable crack propagations were achieved.

The most adopted method to measure the Mode I fracture energy of timber samples was proposed by Gustafsson [20] and was used in [17, 21, 22]. It is referred to as single end notched beam specimen (SENB). A notched specimen is glued to two pieces of timber to form a beam. The specimen is loaded in three-point bending, forcing the crack to open and propagate. Due to the gluing involved in preparing the specimens, the manufacturing process is time-consuming if a large number of tests are required. Ardalany et al. [21] improved the setup and replaced the side timber pieces with steel sections to which the notched timber specimens can easily be connected to, significantly simplifying the manufacturing process. A counterbalance weight is placed on each steel section to offset the effect of the self-weight of the test rig into the calculations of the fracture energy. This method was used herein due to its simplicity and its common adoption for timber.

The Mode I tested samples are presented in Figure 4 (a) for the TL crack system and Figure 4 (b) for the glueline crack system. In Figure 4 (a), 100 mm deep × 90 mm wide × 44 mm thick samples were produced. To produce the 44 mm thick samples from the 22 mm thick boards, two SPG pieces, cut from the same board, were face glued together. All boards were selected for grain orientation so that the cracks developed in the chosen system, with the orientation shown in Figure 4 (a). For each sample, (1) a 5 mm thick × 60 mm deep notch was cut by a V-shaped blade in the middle of the sample from which the crack can initiate and (2) two 25 mm deep side notches were cut to connect the sample to the test rig shown in Figure 5 (photo) and Figure 6 (schematic).

In Figure 4 (b) for the glueline crack system samples, four 22 mm thick pieces were glued together to form an 88 mm thick glulam. The two middle pieces came from the same sawn board and were selected to have the grain orientation relative to the glueline making an angle of 1-4 degrees and converging towards the glueline. This configuration encourages the crack to propagate along the glueline as explained in [23, 24]. A thin adhesive tape was positioned over 60 mm on the two middle pieces before gluing to prevent adhesion and create a notch equivalent to the samples shown in Figure 4 (a) and from where the crack can propagate. The produced samples were 100 mm deep × 88 mm wide × 44 mm thick sample with the orientation shown in Figure 4 (b). Two 25 mm deep side notches were cut to connect the sample to the test rig as shown in the figure.

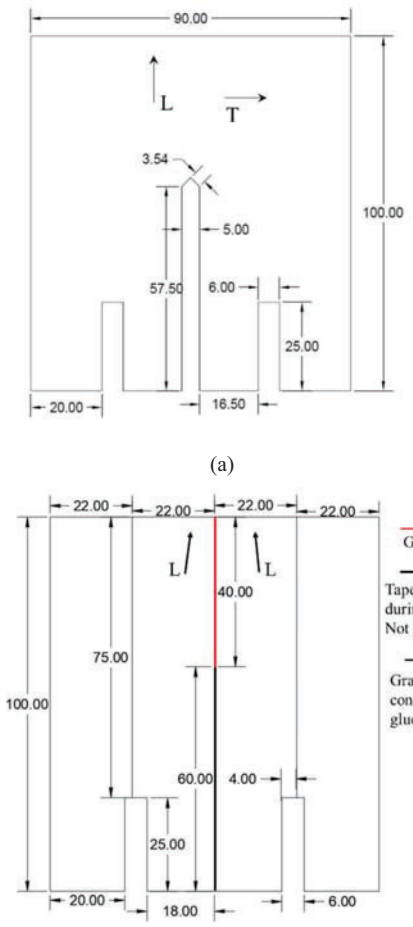

Figure 4: *Sample geometry for (a) TL and (b) glueline crack systems (unit in mm)*

The samples were then connected to two aluminium beams, as shown in Figure 5 (photo) and Figure 6 (schematic) to form a beam. The beam was positioned on two roller supports to be loaded in 3-point bending in a 100 kN capacity INSTRON universal testing machine fitted with a 2.5 kN load cell. A half-round was connected to the load cell to load the specimens at mid-span. Counterbalance weights were also used at the extremity of the aluminium beams to offset both the self-weight of the timber samples and the beams themselves.

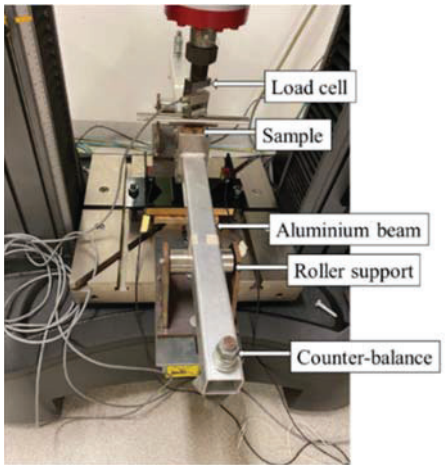

Figure 5: *Experimental setup for fracture Mode I*

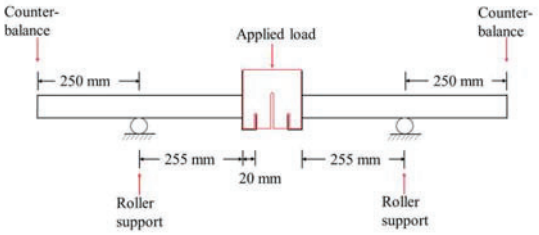

Figure 6: *Fracture Mode I test setup sketch*

A loading rate of 8 mm/min and 1.2 mm/min were selected for TL and glueline crack system samples, respectively, to target failure in 3-5 mins.

The Mode I fracture energy G_{If} was calculated as [22, 25], as.

$$G_{If} = \frac{Q}{h_c b} \quad (1.)$$

where Q is the work performed to fully fracture the sample and calculated from the load-displacement curve, h_c is the measured depth of the specimen above the crack tip and b is the measured specimen thickness. Note that despite the displacement provided by the testing machine may different to the actual displacement of the specimens, as outlined in [26], the testing machine behaves linearly and the work performed by the testing machine is equal to the work needed to fully fracture the samples.

2.3 STATISTICALLY ANALYSIS

After the fracture energy was obtained, a one-way ANOVA statistical analysis was conducted to determine whether there was a statistically significant difference between the mean of various moisture content groups.

https://doi.org/10.52202/069179-0064

3 RESULTS AND DISCUSSION

3.1 FRACTURE MODE I TEST RESULTS

The stress-displacement curves for all the fracture Mode I tests relative to the different crack systems and moisture contents are presented in Figure 7. Nominal and actual moisture content, average measured fracture energies, with associated coefficient of variation (CoV), are summarised in Based on test results presented in Table 1, the Mode I fracture energy in the TL crack system is about four times higher than the fracture energy of the gluelines. This likely reflects the difficulty in gluing this species [5] and indicates that the fracture would propagate faster in the glueline than the timber.

Table 1

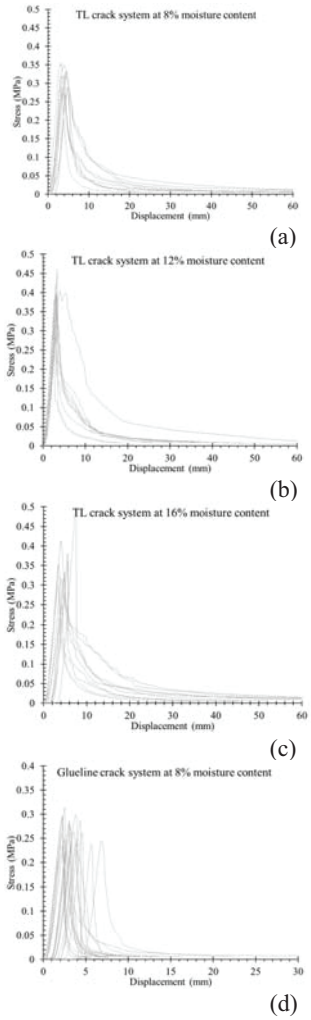

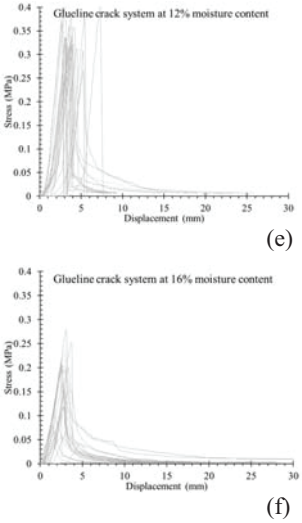

Figure 7: *Load-displacement curves for the Mode I fracture energy tests for TL crack system at (a) 8%, (b) 12% and (c) 16% moisture content, and glueline crack system at (d) 8%, (e) 12% and (f) 16% moisture content*

Based on test results presented in Table 1, the Mode I fracture energy in the TL crack system is about four times higher than the fracture energy of the gluelines. This likely reflects the difficulty in gluing this species [5] and indicates that the fracture would propagate faster in the glueline than the timber.

Table 1: *Fracture Mode I test results*

Crack system	Moisture content *(%)*			Fracture energy G_{If}		
	Nominal	Actual	CoV *(%)*	No. of tests	Mean *(N/mm)*	CoV *(%)*
TL	8	8.3	2.2	10	1.99	44.4
	12	12.5	2.3	10	2.02	55.5
	16	15.8	2.0	10	2.31	42.6
Glueline	8	8.2	3.5	20	0.46	38.1
	12	12.4	1.9	20	0.56	32.0
	16	16.1	1.6	20	0.42	49.6

The results from one-way ANOVA statistical analyses between the different moisture content groups show that for the fracture energies of (1) the TL crack system: $F(2,27) = 0.318$, $p = 0.7301$, and (2) the glueline crack system: $F(2,57) = 1.913$, $p = 0.157$. This implies that there was no statistically significant difference between group means for both TL and glueline crack systems, and therefore that the Mode I fracture energy is independent

of the range of moisture content analysed for both crack systems. This result also indicates that the fracture energy does not seem to follow the same trend as the "common" mechanical properties which vary with the moisture content. According to [27], the difference in mechanical properties between 8% and 16% would be of 27%.

Since it is found statistically that the Mode I fracture energy in both TL and glueline crack systems for SPG is not sensitive to moisture content, the average fracture energy of the three moisture content groups would be taken as future numerical model input.

Figure 8 shows the typical failure modes for the Mode I fracture tests. The cracks initiated either at the tip of notch or non-glued area, and propagated up straight or along the glueline for the TL and glueline system samples, respectively.

(a) (b)

Figure 8: *Fracture Mode I typical failure for (a) TL system and (b) Glueline system*

3.2 COMPARISON TO OTHER STUDIES

Table 2 compares the fracture test results to published studies.

Leka [28] applied the same test setup to the same material presented in this paper and found an average fracture energy 37.9% lower than the one in Table 1. Leka [28] tested both TL and RL crack systems, all together (i.e., with no distinction between the two systems), which could explain the above difference. Franke [17] measured the Mode I fracture energy of softwood Radiata Pine in the TL crack system, which resulted in a fracture energy 74.4% lower than this study. Ammann [24] conducted European beech hardwood glulam glueline fracture tests, with boards bounded with RF as in the present study. The fracture energy presented in Table 1 was only about half compared to Ammann's [24] tests, with 50% of the tests failing in timber rather than glueline in [24].

Table 2: *Mode I fracture energy from other studies*

Species/ type	Test setup	Crack system	Fracture energy (N/mm)	Reference
SPG sawn boards	Three-point-bending	TL	2.11	This study
SPG sawn boards	Three-point-bending	TL/RL	1.53	[28]
Radiata Pine LVL	CTS	TL	1.21	[17]
SPG Glulam	Three-point-bending	Glueline	0.48	This study
European beech Glulam	DCB	Glueline	1.00	[24]

4 CONCLUSIONS

The Mode I fracture energies of SPG sawn timber in the TL crack system and associated gluelines at various moisture contents were measured in this paper. The sensitivity of the fracture energy to the moisture content was analysed statistically. It was found that the average Mode I fracture energies were of 2.11 N/mm and 0.48 N/mm for the TL and glueline crack systems, respectively. The statistical analysis (one-way ANOVA) showed that the Mode I fracture energy of the analysed crack systems was not sensitive to moisture content variation. Therefore, a unique value can be considered for future numerical models which simulate crack initiation and propagation of SPG glulam during the delamination test.

ACKNOWLEDGEMENT

This research was supported by the Australian Centre for International Agricultural Research, project FST/2019/128. The authors would like to thank the technical team at the Salisbury Research Facility of the Queensland Department of Agriculture and Fisheries (DAF) for helping with the specimen preparation and the Griffith University technical team for manufacturing the testing jigs.

https://doi.org/10.52202/069179-0064

REFERENCES

[1]. Bootle, K.R., *Wood in Australia. Types, properties and uses*. 1983: McGraw-Hill book company.

[2]. Queensland Government Department of Agriculture and Fisheries, *Queensland Forest & Timber Industry. An Overview*. 2016.

[3]. AS/NZS 1328.1, *Glued laminated structural timber Part 1: Performance requirements and minimum production requirements*. 2011, Standards Australia: Standards Australia.

[4]. Leggate, W., Outhwaite, A., McGavin, R.L., Gilbert, B.P., and Gunalan, S., *The Effects of the Addition of Surfactants and the Machining Method on the Adhesive Bond Quality of Spotted Gum Glue-laminated Beams.* BioResources, 2022. **17**(2): p. 3413-3434.

[5]. Leggate, W., McGavin, R., Outhwaite, A., Kumar, C., Faircloth, A., and Knackstedt, M., *Influence of mechanical surface preparation methods on the bonding of southern pine and spotted gum: Tensile shear strength of lap joints.* BioResources, 2021. **16**(1): p. 46-61.

[6]. Vella, R., Heitzmann, M.T., Redman, A., and Bailleres, H., *Comparison of test methods for the determination of delamination in glued laminated timber.* BioResources, 2019. **14**(4): p. 7920-7934.

[7]. Redman, A., *Modelling of vacuum drying of Australian hardwood species*. 2017, Queensland University of Technology.

[8]. Raftery, G.M. and Whelan, C., *Low-grade glued laminated timber beams reinforced using improved arrangements of bonded-in GFRP rods.* Construction and building materials, 2014. **52**: p. 209-220.

[9]. Ross, R.J., *Wood handbook: wood as an engineering material.* USDA Forest Service, Forest Products Laboratory, General Technical Report FPL-GTR-190, 2010: 509 p. 1 v., 2010. **190**.

[10]. Leggate, W., McGavin, R.L., Miao, C., Outhwaite, A., Chandra, K., Dorries, J., Kumar, C., and Knackstedt, M., *The influence of mechanical surface preparation methods on southern pine and spotted gum wood properties: Wettability and permeability.* BioResources, 2020. **15**(4): p. 8554.

[11]. Leggate, W., McGavin, R.L., Outhwaite, A., Dorries, J., Robinson, R., Kumar, C., Faircloth, A., and Knackstedt, M., *The Influence of Mechanical Surface Preparation Method, Adhesive Type, and Curing Temperature on the Bonding of Darwin Stringybark.* BioResources, 2021. **16**(1).

[12]. Leggate, W., Shirmohammadi, M., McGavin, R.L., Outhwaite, A., Knackstedt, M., and Brookhouse, M., *Examination of Wood Adhesive Bonds via MicroCT: The Influence of Pre-Gluing Surface Machining Treatments for Southern Pine, Spotted Gum, and Darwin Stringybark Timbers.* BioResources, 2021. **16**(3).

[13]. CSIRO, *Decay of Timber Flooring.* Information Service, 1977: p. Sheet No 10-36.

[14]. AS/NZS1080.1, *Timber-Methods of test Method 1: Moisture Content.* 2012, Standards Australia: Sydney, Australia.

[15]. Ostapska, K. and Malo, K.A., *Wedge splitting test of wood for fracture parameters estimation of Norway Spruce.* Engineering Fracture Mechanics, 2020. **232**: p. 107024.

[16]. Brühwiler, E. and Wittmann, F., *The wedge splitting test, a new method of performing stable fracture mechanics tests.* Engineering fracture mechanics, 1990. **35**(1-3): p. 117-125.

[17]. Franke, B. and Quenneville, P., *Analysis of the fracture behavior of Radiata Pine timber and Laminated Veneer Lumber.* Engineering Fracture Mechanics, 2014. **116**: p. 1-12.

[18]. Richard, H. and Benitz, K., *A loading device for the creation of mixed mode in fracture mechanics.* international Journal of Fracture, 1983. **22**(2): p. R55-R58.

[19]. De Moura, M., Oliveira, J., Morais, J., and Xavier, J., *Mixed-mode I/II wood fracture characterization using the mixed-mode bending test.* Engineering Fracture Mechanics, 2010. **77**(1): p. 144-152.

[20]. Gustafsson, P.J. *A study of strength of notched beams*. in *Proceedings of 21st Meeting of CIB-W18, Parksville, Canada, 1988*. 1988.

[21]. Ardalany, M., Deam, B., and Fragiacomo, M., *Experimental results of fracture energy and fracture toughness of Radiata Pine laminated veneer lumber (LVL) in mode I (opening).* Materials and Structures, 2012. **45**(8): p. 1189-1205.

[22]. Larsen, H. and Gustafsson, P. *The fracture energy of wood in tension perpendicular to the grain. Errata, and annex A12 and A13 to CIB paper W18A/23-19-2. Results from a joint testing project*. in *Proceedings of CIB W18 meeting 24. Princes Risborough, United Kingdom. 1989.: CIB-W18A/24-19-1*. 1991.

[23]. Komatsu, K., Sasaki, H., and Maku, T., *Evaluation of fracture toughness for wood-epoxy adhesive system under external shear force.* Wood research: bulletin of the Wood Research Institute Kyoto University, 1974. **57**: p. 10-22.

[24]. Ammann, S. and Niemz, P., *Specific fracture energy at glue joints in European beech wood.* International Journal of Adhesion and Adhesives, 2015. **60**: p. 47-53.

[25]. Rug, W., Badstube, M., and Schone, W., *Determination of fracture energy of wood for tension perpendicular to grain.* CIB-W18 on Timber Structures, Lisbon, 1990.

[26]. Gilbert, B.P., Fernando, D., and Pham, C.H. *Experimental techniques in structural Testing: Common Mistakes, how to avoid them and other advice*. in *Structures*. 2022. Elsevier.
[27]. Guitard, D., *Mécanique du matériau bois et composites*. 1987: Cépaduès.
[28]. Leka, Y., *Determining key mechanical properties for connection design of softwood and hardwood sawn timber at various strain rates*. 2022, Griffith University.

https://doi.org/10.52202/069179-0064

World Conference on Timber Engineering Oslo 2023

FLEXURAL REINFORCEMENT OF TIMBER ELEMENTS ON-SITE WITH PRF ADHESIVE AND WOOD-BASED PRODUCTS

Andreas Stenstad[1], Karl Christian Mahnert[2], Kristine Vik[3]

ABSTRACT: In this study, the potential application of a two-component phenol-resorcinol-formaldehyde adhesive for on-site reinforcement of glued laminated timber (GLT) and a recovered spruce beam was investigated. Different spread rates (500 – 2000 g/m^2), means of pressurization of the bond lines (clamps, screws and the reinforcements own mass) were applied to establish bond lines between the substrate to be reinforced and the reinforcements, GLT and plywood (PLW). The surface conditions (not planed, partly coated/ sanded, varying surface moisture content) were chosen to resemble situations that might be encountered during on-site reinforcement. The bond lines of two of the 11 different combinations fulfilled the required shear strength according to EN 14080. The investigations show that thicker bond lines and low pressure on the bond lines result in lower bond strength. Coating and partial removal of the coating by sanding are expected to have amplified the effect of the chemically weak boundary layer. Bond lines between materials with similar surfaces yield higher shear strength compared to bond lines between materials with differing surfaces.

KEYWORDS: Flexural reinforcement, phenol-resorcinol-formaldehyde, glulam, plywood, shear strength

1 INTRODUCTION

1.1 BACKGROUND

There are several different motivations to reinforce timber elements. The first one, reinforcement of glulam beams during production serves the purpose of increasing the span of that beam by replacing the outer lamellae with lamellae of hardwood or engineered wood products [1, 2], steel or aluminium [3, 4 5], natural fibres (hemp, flax, basalt, bamboo etc.) [6] or glass fibre reinforced polymers [7]

The second motivation might be to reinforce elements of load-bearing structures after mechanical or biological damage [8] as well as after boring of holes for ventilation and sewage pipes [9]. To avoid the reinforcement of regular glulam beams with holes, [10] propose the use of GLT-LVL composite beams which they proved to make reinforcement of one or multiple large rectangular multiple holes obsolete.

As the term circular economy finds its way into the building industry, the third scenario, reinforcing existing wooden structures to upgrade them for change of use or after changes in regulatory specifications for instance an increase in snow or wind loads as reaction to climate change, comes into play. To increase the lifetime of structural timber elements such as trusses or floor beams by on-site flexural reinforcement, the following approaches are described in the literature:

1) Application of self-tapping screws to avoid splitting of glulam along the grain [11, 12, 13].

2) Inserting of glued-in rods in the wooden element, a technique that has been successfully used for almost 40 years, a comprehensive state of the art report has been presented by [14]. The geometry of the timber, the adhesive area and the rod area, the size of the anchoring zone, the material stiffness and strength, fracture mechanical properties of timber and adhesive, variability of all properties and loading conditions as well as other parameters like wood species and manufacturing practices are defined as key parameters for the load bearing capacity of glued-in rod connections [15]. The rods must be fixed with an adhesive system that provides a continuous bond between the reinforcement and the timber, fills voids and cavities and is able to transfer and sustain loads. Epoxy resins are identified as specifically suitable as structural adhesives in repair [16], acrylic, polyurethane and phenol-resorcinol-formaldehyde adhesive types showed cohesive adhesive failures of adhesion failures [8]. However, the development of adhesive systems is ongoing, and it is obvious that these findings do not represent the state of the art within adhesive technology.

3) Addition of fibre reinforced polymers as described by [17] who tested intentionally damaged timber beams from a 32-year-old storage building reinforced by two types of carbon fibre reinforced polymer (CFRP). The reinforcement yielded an improvement in load-carrying by up to 184% compared to the controls without reinforcement. [18] studied the effect of combining basalt and carbon fibres as reinforcement of timber beams. They compared different grammages of basalt fibres and

[1] Andreas Stenstad, Norwegian Institute of Wood Technology (NTI), Norway, ast@treteknisk.no
[2] Karl-Christian Mahnert, Norwegian Institute of Wood Technology (NTI), Norway, kcm@treteknisk.no
[3] Kristine Vik, kristinestine.vik@gmail.com

https://doi.org/10.52202/069179-0065

unidirectional and bidirectional carbon composites. The results showed better effect of bidirectional fabrics compared to unidirectional fabrics and an increase of the beam stiffness with increasing grammage of basalt fibres. Besides grammage and orientation of the components of a CFRP, prestressing of the sheets was found to increase the bending strength of the reinforced beams significantly compared to those beams that were reinforced with non-prestressed CFRP was found [19].
4) Addition of wood-based panels [20].

1.2 FOCUS OF THIS STUDY

Generally, the reinforcing elements can be attached to the structural element by mechanical fixings, structural adhesives, or a combination of both to hold the reinforcing element in place and apply pressure during the curing phase of the adhesive.
When reinforcing on-site, engineers normally only consider load transfer due to mechanical fasteners. Adhesives are not considered due to uncertainty linked to the application process and whether the quality of the bond line is sufficient to enable the transfer of the load from the substrate to the reinforcement. There is a need for a better understanding on how on-site reinforcement using adhesives can be performed, and to identify the limitations. Currently only EN 17481 [21] covers adhesives explicitly for on-site repair of timber structures. Two-component epoxy and polyurethane adhesives which fulfil the requirements given in the standard are approved for the repair of cracked timber structures. However, two-component phenol-resorcinol-formaldehyde (PRF) adhesive systems which are widely used in the production of block glued glulam according to EN 14080 [22] might be suitable alternatives due to the ease of their application and the gap filling properties.
The aim of this study was to characterize the shear strength of the bond line between solid wood substrates of various qualities and selected wood based reinforcing elements.

2 MATERIALS AND METHODS

2.1 PREPARATION OF THE SHEAR SAMPLES

Pieces of recently produced commercial spruce glulam (GLT) and parts of a recovered spruce beam from an old barn were reinforced with GLT or plywood plates (PLW). A total of 18 sample blocks were prepared.

2.1.1 Materials to be reinforced

Two of the 11 GLT pieces (48 x 250 x 10400 mm) (b x h x l) were conditioned to 9-10 % (L) and 23 % (H) superficial moisture content. The remaining GLT samples were stored at 20 ˚C and 65 % relative humidity (M), one half of the surface of two of those samples was coated with a wall paint (C). The coated surface of one of the pieces was partly sanded (C+S).
Five pieces from a recovered spruce beam (RSB) (92 x180 x 152 mm) (b x h x l) were recovered from an old barn and stored at 20˚C and 65 % relative humidity prior to production of the sample blocks. Three of those pieces were sanded prior to the reinforcement.

2.1.2 Reinforcement

The GLT (36 x 250 x 10400 mm) and the pine plywood (PLW) (9 ply, 12 mm thickness) were stored at 20˚C and 65 % RH.

2.1.3 Assembly of sample blocks

The reinforcing element was bonded to the material to be reinforced with the PRF-adhesive Prefere 4094 and the hardener Prefere 5827, both supplied by Dynea AS. Adhesive and hardener were mixed at a ratio of 100:20, the application rate was varied between 500 g/m^2 to 2000 g/m^2. The adhesive was applied one-sided. Screws (5.0 x 50 mm) (SCR) (Figure 1), clamps tightened by hand (CLA) or the reinforcing elements` own weight (OW) provided pressure during curing of the adhesive.

Figure 1: *Sample blocks of two pieces of split GLT pressurized with screws.*

2.2 SHEAR TESTS OF BOND LINES

The samples were cut from the sample blocks at least 20 mm from the edges (Figure 2). Compressive shear strength (CSS) was tested according EN 14080 [2], Annex D (Figure 3). The shear area for the bond line was approximately 50 x 50 mm.
The Tukey-Kramer test and t-test in JMP 10 (JMP Statistical Discovery LLC) was used for respectively overall or pairwise statistical analysis of the data.

https://doi.org/10.52202/069179-0065

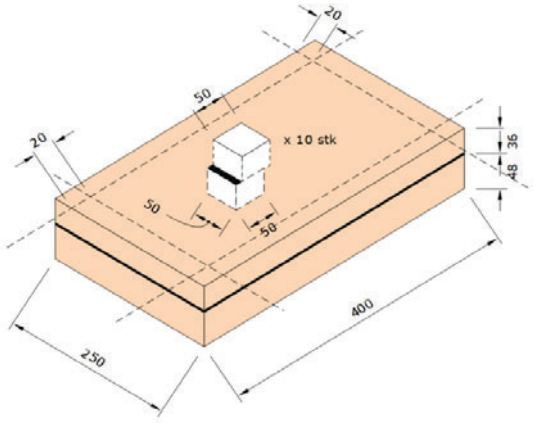

Figure 2: *Production of samples to test compressive shear strength.*

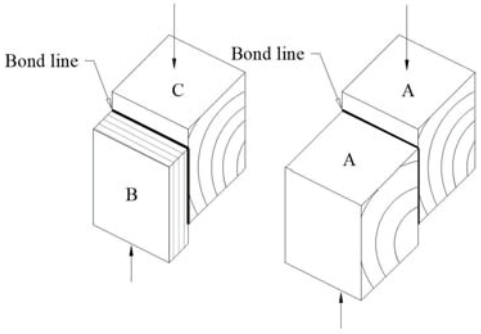

Figure 3: *Samples for compressive shear test of bond lines*

3 RESULTS AND DISCUSSION

3.1 REINFORCEMENT OF GLULAM

The average CSS of the bond lines between the material to be reinforced and the reinforcement was 7.1 N/mm^2 with significant difference between reinforcement GLT (7.6 N/mm^2) and PLY (5.5 N/mm^2), (Table 1). This can be explained by the combination of different surfaces in the samples reinforced with PLW compared to the similar surfaces of the reinforcement with GLT. Treatments 7 and 10 fulfilled the requirements for CSS in timber structures according to EN 14080. Detailed results are presented in Table 2.

Pressurizing the bond line with screws or clamps compared to the reinforcements` own weight increased the CSS of the bond lines significantly (Figure 4). The same applies for the wood failure percentage. This is most likely due to the higher pressure applied on the adhesive joint during curing by screws and clamps compared to the mass of the plywood panel. Thus, the latter results in lower penetration of the adhesive into the wood surface compared to the first, yielding a stronger bond and higher wood failure percentage.

Table 1: *Average compressive shear strength (CCS) of the bond lines between the recovered spruce beam and plywood (PLW) as reinforcement, S: sanded, OW: own weight.*

#	Treatment Name	Samples	CSS [N/mm^2] $\bar{x}$	σ_x
1	GLT(C)_GLT_1000_OW	10	4.3	2.2
2	GLT(C+S)_GLT_1000_OW	10	4.6	2.3
3	GLT(H)_GLT_1000_OW	10	4.3	1.1
4	GLT(H)_GLT_2000_OW	10	6.2	0.7
5	GLT(L)_GLT_1000_OW	9	6.3	1.1
6	GLT(L)_GLT_2000_OW	10	5.7	1.1
7	GLT_GLT_1000_CLA	10	7.4	0.6
8	GLT_GLT_1000_SCR	10	7.5	0.5
9	GLT_GLT_500_CLA	10	7.4	0.9
10	GLT_GLT_500_SCR	10	7.9	1.0
11	GLT_PLW_500_SCR	14	5.5	1.3

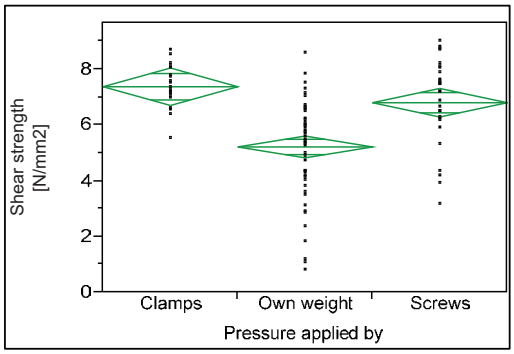

Figure 4: *Compressive shear strength of bond lines between GLT and reinforcement as result of pressurizing method*

A spread rate of 500 g/m^2 resulted in significantly higher CCS than a spread rate of 1000 g/m^2 (6.8 N/mm^2 versus 5.8 N/mm^2) (Figure 5), the same applies for the wood failure percentage. The reason for that is the supposedly thicker bond line resulting from the higher application rate. The lower shear strength of thicker bond lines compared to thinner bond lines is a known fact which is accounted for by the lower requirements for tensile shear strength of thick bond lines compared to close contact bond lines in EN 301 [23].

https://doi.org/10.52202/069179-0065

Table 2: *Average compressive shear strength (CCS) of the bond lines between GLT and reinforcements, C: coated, C+S: coated and sanded, H: high surface moisture content, L: low surface moisture content, PLW: plywood, OW: own weight, CLA: clamps, SCR: screws.*

Treatment		Samples	CSS [N/mm²]		Wood failure [%]		Adhesive failure [%]		Invalid samples
#	Name		$\bar{x}$	σ_x	$\bar{x}$	Min	$\bar{x}$	Min	
1	GLT(C)_GLT_1000_OW	10	4.3	2.2	58	10	42	0	7/10
2	GLT(C+S)_GLT_1000_OW	10	4.6	2.3	61	10	39	0	7/10
3	GLT(H)_GLT_1000_OW	10	4.3	1.1	13	0	87	40	10/10
4	GLT(H)_GLT_2000_OW	10	6.2	0.7	100	100	0	0	0/10
5	GLT(L)_GLT_1000_OW	9	6.3	1.1	88	70	13	0	3/10
6	GLT(L)_GLT_2000_OW	10	5.7	1.1	99	90	2	0	1/10
7	GLT_GLT_1000_CLA	10	7.4	0.6	89	10	2	0	1/10
8	GLT_GLT_1000_SCR	10	7.5	0.5	100	100	0	0	0/10
9	GLT_GLT_500_CLA	10	7.4	0.9	97	90	3	0	1/10
10	GLT_GLT_500_SCR	10	7.9	1.0	100	100	0	0	0/10
11	GLT_PLW_500_SCR	14	5.5	1.3	91	30	0	0	6/14
12	RSB_PLW_1000_OW	4	2.9	1.3	58	40	43	10	4/4
13	RSB_PLW_2000_OW	4	3.4	1.1	78	50	23	10	4/4
14	RSB(S)_PLW_500_OW	4	3.9	1.7	30	100	0	70	3/4
15	RSB(S)_PLW_1000_OW	4	4.1	1.8	90	100	0	10	3/4
16	RSB(S)_PLW_2000_OW	4	5.6	1.9	98	90	3	0	1/4

An influence of the superficial moisture content of the GLT on the CSS was not found. High superficial moisture content, however, resulted in significantly lower wood failure percentage compared to medium and low surface moisture content. This might be due to water saturation of the fibres on the surface of the wetted sample hindering the penetration of the adhesive followed and the subsequent anchoring in the superficial fibres.

Coating of the GLT and sanding of the coated surface resulted in significantly lower CSS of the bond lines compared to the bond lines between untreated GLT and reinforcement (Figure 6). This result can be ascribed to the coating/ coating and sanding of the surface which intensifies the effect of the chemically weak boundary layer on the wooden surfaces that were not machined [24]. [25] did not find significant differences between the tensile shear strength of bond lines between substrates that were prepared by sanding on a professional sander and substrates prepared by planing. Sanding in the current study, however, was conducted manually, lacking the homogeneity of machine sanding.
Our findings underpin the importance of clean surfaces, often accomplished by machining of the material, as prerequisite for good bonding results. This is an issue especially when it comes to the reinforcement of aged wood structures with surfaces that are not accessible for machining.

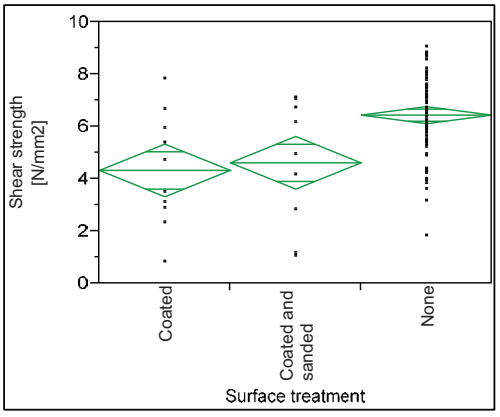

Figure 6: *Influence of surface treatment on the compressive shear strength of the bond lines between GLT and reinforcement*

3.2 REINFORCEMENT OF RECOVERED WOOD

The average CSS of the bond line between the recovered spruce beam and PLW was 3.0 N/mm², see Table 3 for average results per treatment. Neither spread rate nor sanding of the surface influenced the CSS or the wood failure percentage. None of the treatments fulfilled the requirements for CSS given in EN 14080. This is most likely due to the neglected machining of the recovered spruce beam with the resulting chemically weak boundary layer [25]. Ageing of the bulk wood material [26] may contribute, too.

https://doi.org/10.52202/069179-0065

Table 3: *Average compressive shear strength (CCS) of the bond lines between the recovered spruce beam and plywood (PLW) as reinforcement, S: sanded, OW: own weight.*

Treatment		Samples	CSS [N/mm²]	
#	Name		$\bar{x}$	σ_x
12	RSB_PLW_1000_OW	4	2.9	1.3
13	RSB_PLW_2000_OW	4	3.4	1.1
14	RSB(S)_PLW_500_OW	4	3.9	1.7
15	RSB(S)_PLW_1000_OW	4	4.1	1.8
16	RSB(S)_PLW_2000_OW	4	5.6	1.9

3.3 COMPARISON OF REINFORCEMENTS

This comparison covers exclusively samples from blocks consisting of GLT reinforced with GLT or PLW with a spread rate of 500g/m² and bond lines pressurised by screws. Reinforcement with GLT resulted in bond lines with significantly higher CCS compared to reinforcement with PLW (Figure 7). This finding is in line with the significant difference between the CSS of the bond lines of all samples reinforced with GLT compared to PLW.

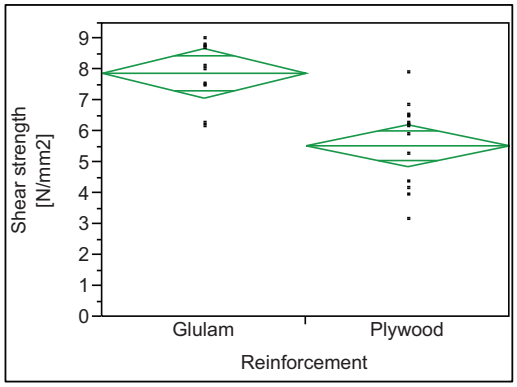

Figure 7: *Compressive shear strength of reinforcement with GLT compared to PLW*

4 CONCLUSIONS

The results suggest the potential of a combination of PRF adhesive and wood-based products as solution for on-site structural reinforcement of glued laminated timber and recovered wood. This application, however, implies neglecting generally accepted principles for wood bonding such as machining of surfaces and controlled application of pressure. These deficits were resembled by the design of the samples and explain the deficient bond strengths of most of the samples compared to the requirements defined in EN 14080. Further investigations should include higher numbers of replicates and reference samples prepared according to current practice of wood bonding.

Another aspect of reinforcing wooden structures on-site, especially in countries with extended periods of low air temperature, is the influence of these low temperatures on the curing of an adhesive and the definition of thresholds for reasonable use of the adhesives. This parameter should also be included in future research.

REFERENCES

[1] Dill-Langer, G.: Hochleistungsverbundträger aus Vollholz- und Furnierschichtholz-Lamellen. 23. Internationales Holzbau-Forum IHF 2017, 2017.

[2] Dziurka, D., Derkowski, A., Wieruszewski, M., Kuliński, M., Mirski, R.: GL Beams reinforced with plywood in the outer layer. Materials, 15(11), 2022.

[3] Sliker A.: Reinforced wood laminated beams. Forest Products Journal, 12(1):91–6, 1962.

[4] Hoyle, RJ.: Steel-reinforced wood beam design. Forest Products Journal 25(4), 17-23, 1975.

[5] Corradi, M.; Osofero, A.I.; Borri, A.: Repair and reinforcement of historic timber structures with stainless steel—a review. *Metals 9(1),* 2019.

[6] Borri, A. Corradi, E. Speranzini, M.: Reinforcement of wood with natural fibers. Composites Part B: Engineering, Volume 53, Pages 1-8, 2013

[7] Corradi, M., Borri, A.: Fir and chestnut timber beams reinforced with GFRP pultruded elements. Composites Part B: Engineering, 38(2), 2007.

[8] Broughton, J. G., Hutchinson, A. R.: Adhesive systems for structural connections in timber. International Journal of Adhesion and Adhesives 21(3), 177-186, 2001.

[9] Danzer, M., Dietsch, P., Winter, S.: Reinforcement of round holes in glulam beams eccentrically of in groups. World Conference on Timber Engineering, 2016.

[10] Aicher, S., Tapia, C.: Novel internally LVL-reinforced glued laminated timber beams with large holes. Construction and Building Materials 169, 662-677, 2018.

[11] Jönsson, J.: Load carrying capacity of curved glulam beams reinforced with self-tapping screws. Holz als Roh- und Werkstoff, 63(5), 342-346, 2005.

[12] Blass, H. J., Bejtka, I.: Querzugversterkungen in gefährdeten Bereichen mit selbstbohrenden Holzschrauben. Kurzberichte aus der Bauforschung, 226-234, 2003.

[13] Angst, V., Malo, K. A.: Effect of self-tapping screws on moisture induced stresses in glulam. Engineering Structures 45, 299-306, 2012.

[14] Steiger, R., Serrano, E., Stepinac, M., Rajčić, V., O'Neill, C., McPolin, D., Widmann, R.: Strengthening of timber structures with glued-in rods. Construction and building materials, 97, 90-105, 2015.

[15] Tlustochowicz, G., Serrano, E., Steiger, R.: State-of-the-art review on timber connections with glued-in steel rods. Materials and structures, 44, 997-1020, 2011.

[16] Van Gemert, D., Vanden Bosch, M.: Structural restoration of wooden beams by means of epoxy resin. Materials and Structures, 20, 165-170, 1987.

[17] Kim, Yail J., Mozahid, H., Kent A. Harries, K. S.: CFRP strengthening of timber beams recovered from a 32 year old Quonset. Element and system level tests, Engineering structures 57213-221, 2013.
[18] de la Rosa García, P., Escamilla, A. C., García, M. N. G.: Bending reinforcement of timber beams with composite carbon fiber and basalt fiber materials. Composites Part B: Engineering, 55, 528-536, 2013.
[19] Triantafillou, T. C., Deskovic, N.: Prestressed FRP sheets as external reinforcement of wood members. Journal of Structural Engineering, 118(5), 1270-1284, 1992.
[20] Szabo, T.: Plywood reinforcement for structural wood members with internal defects. Bulletin of the Association for Preservation Technology, 9(1), 11-15, 1977.
[21] Comité Européen De Normalisation (CEN): EN 17481 Two-component epoxy and polyurethane ahdesives for on-site repair of cracked timber structures – Testing, requirements and repair strength verification, 2021.
[22] Comité Européen De Normalisation (CEN): EN 14080 Timber structures – Glued laminated timber and glued solid timber – Requirements, 2013.
[23] Comité Européen De Normalisation (CEN): EN 301 Adhesives, phenolic and aminoplastic, for load-bearing timber structures — Classification and performance requirements, 2017
[24] Stehr, M., Johansson, I.: Weak boundary layers on wood surfaces. Journal of adhesion science and technology, 14(10), 1211-1224, 2000.
[25] Kläusler, O., Rehm, K., Elstermann, F., Niemz, P.: Influence of wood machining on tensile shear strength and wood failure percentage of one-component polyurethane bonded wooden joints after wetting. International Wood Products Journal, 5(1), 18-26, 2014.
[26] Hänsel, A., Sandak, J., Sandak, A., Mai, J., Niemz, P.: Selected previous findings on the factors influencing the gluing quality of solid wood products in timber construction and possible developments: A review. Wood Material Science & Engineering, 17(3), 230-241, 2022.

https://doi.org/10.52202/069179-0065

World Conference on Timber Engineering Oslo 2023

WEAR RESISTANT PROTECTION OF WOODEN POLES IN ADVERSE ENVIRONMENTS

Thomas Lindblad[1], Knut Magnar Sandland[2], Andreas Treu[2]

ABSTRACT: Wood protection is needed for wood products in outdoor applications due to biodeterioration of this natural material. While bulk treatments of wood have their disadvantages related to impregnation and costs, coatings can protect wood products to large extent. However, harsh environments such as outdoor use classes 3-5 can lead to unfavourable levels of wood moisture content because of the permeable character of most coatings. Water-tight coatings could be an alternative for certain areas of use. This treatment has been identified as a promising approach for prolonging service life in adverse environments. However, installation in larger scale may need connections and fasteners which perforate the coating material. This study shows various solutions of bolt connections including sealants which can be used for installations without significant penetration of water into the wood core. The study also makes reference to a full-scale installation survey covering the same time period, as well as an ageing test of the same coating.

KEYWORDS: coating, outdoor applications, poles, sealant, wood protection

1 INTRODUCTION

Wood protection in adverse climates is obtained by bulk treatments using biocides or wood modification agents. Both approaches require penetrability of the wood substrate and can be challenging with regards to environmental concerns or price. Being independent of the refractory behaviour of some wood species and avoiding any form of impregnation treatment is therefore an asset. However, exposure of unprotected wood products in harsh environments such as outside use, the use in ground contact and sea water contact are particularly demanding. Outside use areas are defined by the incidence of rain and changes in temperature and relative humidity, which can lead to deterioration of unprotected products by fungi and insects. Exposure of wood products in ground contact is dominated by bacteria and fungi due to the constant moist surroundings. Products, which combine both use classes, such as telegraph poles, need therefore not only wood protection for above ground (use class 3), but also in-ground contact (use class 4). In addition, the marine environment (use class 5) represents a different challenge which can only be prevented when the attachment of shipworm larvae on the wood surface and the boring through the wood substrate can be avoided. In addition, gribble can attack the wood surface area, which leads to extensive damage as well [1].

The use of coatings is beneficial for products in outdoor use areas (use class 3-4) and could even prevent marine borer attack (class 5). Coatings help to drastically reduce the uptake of water by the underlying wood substrate, and when airtight it also limits the access of oxygen. This is widely used on wooden facades of many private houses in the Northern European countries. However, coatings for cladding are usually not fully watertight, but allow an exchange with the surrounding relative humidity. Measurements of wood moisture content underneath a wood coating prove the permeable character of some coating types [2,3].

Water-tight coatings could be an alternative for certain areas of use. One example is the full coverage of wooden poles with polyethylene (PE) via an extrusion process [4]. The use of several millimetres of PE on the wood surface leads to high resistance against wear of the coating and to protection against deterioration of the wood core. Given the shore D hardness of 62, it also neutralises the risks of marine borer attacks. WOPAS uses such PE extrusion technology to wood which can be of different shape, square, cylindrical, or tapered. The wood is first dried to a target moisture content of 14%. WOPAS standard PE thickness for marine piles and pole building poles is 6 mm, and for power poles 9 mm. The thicker dimension for power poles stems from the frequent use of climbing shoes causing 2-3 mm recess. However, the installation of these poles often makes it necessary to perforate the protective PE layer if bolts and other mounting parts need to be connected. Sealing of the joints need to make sure that water and oxygen ingress is prevented. However, the type of technical solution for the fastening and the sealing material needs to be investigated.

The aim of the study was to analyse different fastening and sealing solutions in both a short-term submersion test and a long-term outdoor weathering and to select the solution where water ingress could be strongly reduced or prevented. Furthermore, the specific objectives were to include recommended solutions, non-recommended solutions, deliberately damaged coating, references without penetration and references for full scale

[1] Thomas Lindblad, WOPAS, Norway, thomas.lindblad@wopas.net
[2] Knut Magnar Sandland, Andreas Treu, Norwegian Institute of Bioeconomy Research (NIBIO), Norway, knut.magnar.sandland@nibio.no, andreas.treu@nibio.no

https://doi.org/10.52202/069179-0066

installations covering the same time period, as well as an ageing test of the PE.

2 MATERIAL AND METHODS

2.1 BOLTS AND FASTENERS

Starting in May 2019, different connection solutions (see table 1 and example in figure 1) were analysed using water submersion test at the NIBIO laboratory for 1600 hours. The samples were stored between submersion cycles in the freezer and in room climate. Thereafter, the test pieces were exposed to outdoor climate for 700 days (figure 3). Measurements were done twice per year. The weight change during submersion and exposure were measured gravimetrically using a 0.1 g readability scale. (Mettler ToledoPG5002-S DeltaRange), except for test series 21-25 where a 0.5 g readability scale was used (KERN DE 6K0,5N).

Table 1: *Connection material used for the test.*

Connection type	Name
8 pcs stainless steel building board screws, 4,9 mm x 35 mm, incl. gasket	Screws with sealant
20 mm pin bolt with curved washer and mastic. Pre-drilled 20 mm diameter	Bolt with insulation putty
10 mm French bolt, circular washer and mastic. Pre-drilled 7 mm diameter	French bolt
20 mm pin bolt with curved washer. Pre-drilled 20 mm, EPDM gasket	Pin bolt EPDM
Plastic removed from the poles in small flakes	Partly removed plastic
No connections used	Reference

Figure 1: *20 mm pin bolt with curved washer and mastic.*

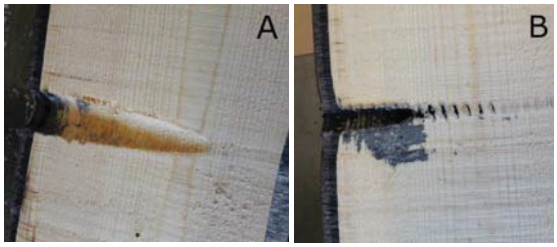

Figure 2: *After the first test period was finalized 15 July 2019, one sample of each series was split. Pictures show: Longitudinal cut from A) 20 mm pin bolt with curved washer and mastic and B) 10 mm French bolt, circular washer and mastic after two months of outdoor weathering.*

Figure 3: *Exposure to outdoor climate.*

2.2 FULL-SCALE INSTALLATION

A 40 kV overhead line with 108 WOPAS poles was installed early 2019 and finalised in May the same year (see figure 4). The fitters used WOPAS recommended fasteners, i.e. pin bolts with curved washer and mastic, French bolts with mastic and building board screws with gasket. The installation was surveyed in June 2022 by a third-party wooden pole expert, representatives from the grid owner and WOPAS. The time frame between installation and survey equals the time frame for the accounted laboratory tests in 2.1.

Of the 108 poles a selection of eight poles was installed in different environments, such as arable land, forest, swamp, rocky ground and gravel. Several methods were used for the survey, such as classical hammer sound surveying, non-destructive electronical moisture meter by Tramex and drilling resistance measurement by use of an IML Resi F400-SX. Drilling was either made just above the ground or close to penetrating fittings, as shown in figure 5. The drilling resistance measurement method enabled recording and print outs, as shown in figure 11. Neither the drilling resistance measurements, nor the survey in general, showed sign of deterioration of the poles.

Figure 4: *Fitters from Linde Energi using French bolts with mastic to prevent sliding and rotation of cross arm fitting.*

https://doi.org/10.52202/069179-0066

Figure 5 *Drilling measurement using a resistograph, close to pin bolt with curved washer and mastic.*

2.3 AGING TEST

Critical to the sealing function is the integrity of the PE over time. Test laboratory CESI of Milan, Italy, on behalf of power grid owner Enel Grids has conducted a test programme of 8 repeating steps during 2022. In addition to mechanical tests like impact protection[5] (IK), bending fatigue and flame test, an ageing test was made to simulate outdoor daily cycle. The testing was made by placing a pole in an insulated steel tube filled with water, figure 7. The water temperature was controlled and varied between 20 and 80 °C (figure 6). The cycle consisted of 8 hours of heating and 16 hours of cooling. The thermal conditions of the cycle were described as consistent with climatic extremes to constitute an acceleration factor of the real stresses to which the pole is subject to in operation. The test was conducted for 1000 hours. The pole, sealed at the ends, is placed in a cylindrical chamber where water is circulated. The water was coloured to enable a subsequent verification of water ingress. At the end of 1000 hours the pole was extracted from the steel tube and inspected for cracks to the PE and welded end caps. The pole was then tested with a bending test to compare any deviation to other non-aged WOPAS poles. The PE layer was thereafter separated from the wood, and the moisture content of the wood was measured, as well as visual inspection tracing any coloured water penetration.

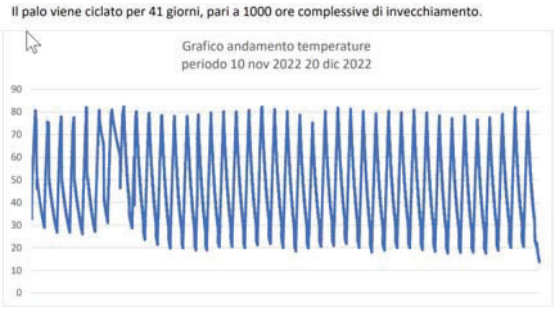

Figure 6: *Temperature variation during 1000 hours of water aging test.*

Figure 7: *Steel tube containing a WOPAS pole for age testing.*

3 RESULTS

3.1 THE INFLUENCE OF BOLTS AND FASTENERS ON WATER UPTAKE

Minor weight changes during submersion and outside exposure were observed (figure 1 and figure 2). The water penetration through the used connections was therefore almost insignificant for all solutions except the use of bolts with insulation butty, which even showed mass loss during the exposure. This could have been caused by the different scale, which was used for these samples or by degradation of the washer. Reference poles with partly removed plastic coating showed higher water uptake during water submersion and outside exposure. The test proved the good performance of the sealants and underlines therefore the importance of the sealing material and the care during installation.

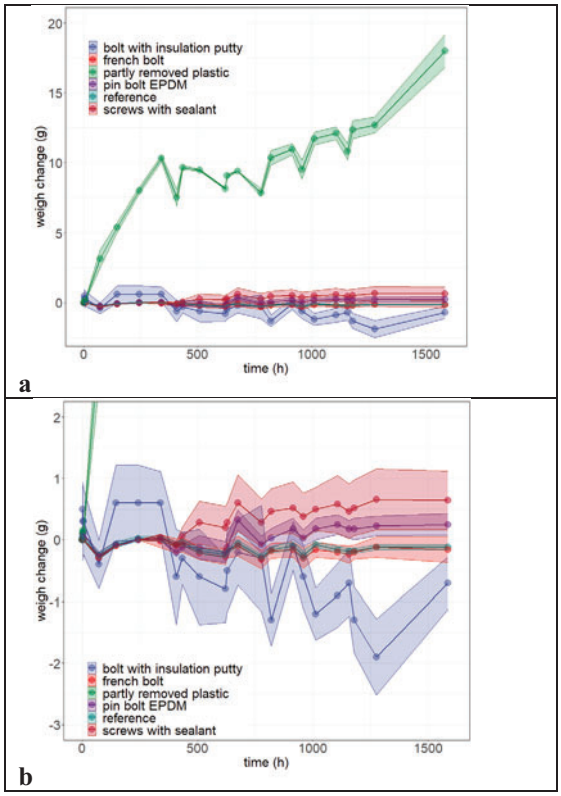

Figure 8: *Weight change due to water uptake during submersion test for more than 2 months. a) note the scale from 0-20, b) note the scale from -2 – 1. The colour-shaded areas show the standard deviation (N=5).*

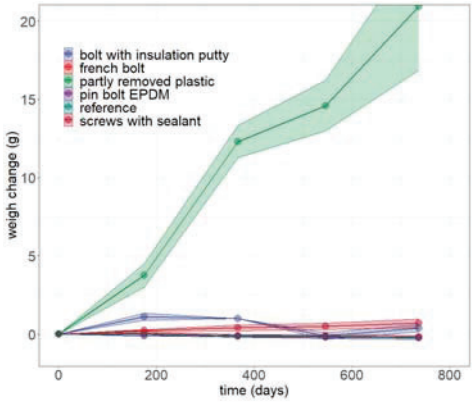

Figure 9 *Weight change due to water uptake during more than two years of outside exposure. The colour-shaded areas show the standard deviation (N=5).*

3.2 SURVEY OF FULL-SCALE INSTALLATION

The visual inspection showed no deviations. The construction was described as very well built by third party Vattenfall Eldistribution. The moisture measurements demonstrated no elevated values of wood moisture content. In addition, the resistograph showed no unusual values, which could indicate deterioration of wood components. See below the photograph of resistograph printouts, figure 11.

The hammer control noted two anomalous sounds, one behind a mark caused by the installation of the poles using excavator grab john (hydraulic pin grab on the back side of the bucket) and another at a random place. Both locations were examined with moisture measurement and resistograph, but without anomalous values. One hypothesis discussed was that the pressure from excavator grab john caused some kind of local sound change, and natural cracks that occur in the wood may have caused abnormal sounds as well.

Figure 10: *Anomalous sound from hammer was followed up using resistograph, in turn showing normal values.*

https://doi.org/10.52202/069179-0066

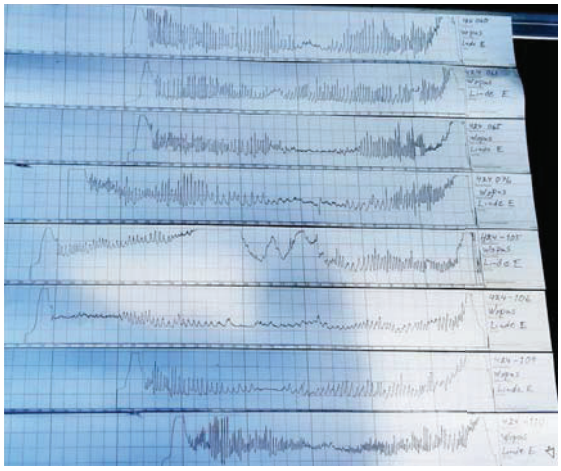

Figure 11: *Paper print-outs of drilling measurement using a resistograph*

3.3 THE RESISTANCE OF THE COATING TO HEAT AND WATER

After the aging test, the pole was tested for bending, impact (IK) and the PE was removed to measure the moisture level and for visual inspection of any coloured fluid. Even after the bending test, no damages were found on the PE, and no water ingress could be noted. The moisture level was observed at two positions, as shown in figure 12, and the moisture level was 10,5-10,7%.

It has been pointed out by CESI and Enel Grids that the specification and aging method have been defined by them for their test, and cannot be extrapolated.

Furthermore, it was described that the PE was well attached to the wood and is able to fill even the natural cracks. In this way the PE is not free to move, which was also verified during the torsion test.

The PE-welded end caps were considered the weakest point before the test. However, it demonstrated to be adequately robust for the intended use as power pole, both in terms of aging and impact. In fact, the impact protection rating corresponded to IK10 according to norm IEC 62262, or 20 Joule (weight of 5 kg from a height of 400 mm).

Figure 12: *Moisture content observation after the aging test*

4 CONCLUSIONS

Several connections through polyethylene coated poles were analysed during water submersion and long-term outdoor exposure. Sealant and careful installation play a crucial role for the long-term performance of installed poles in service. Various solutions of bolt connections including sealants can be used in large-scale installations. In addition, the performance in service as poles for electrical power lines shows promising results so far.

The characteristics and lifetime of polyethylene of PE100 quality is witnessed from water infrastructure, automotive, sea farming and other adverse environments. The combination with wood represents an interesting use, without the need for using biocides or wood modification agents.

ACKNOWLEDGEMENT

We are grateful for the support of the wooden pole experts Kenneth Stefansson and Arnold Solmar with Vattenfall Eldistribution, and the representatives from Linde Energi. Many thanks also to Enel Grids S.r.l. sharing data and Kema labs, CESI, S.p.A, Roberto Piccin performing tests with great dedication.

REFERENCES

[1] Treu A, Zimmer K, Brischke C, et al. Durability and Protection of Timber Structures in Marine Environments in Europe: An Overview. Bioresources. 2019;14(4):10161-10184.

[2] Gezici-Koc O, Erich SJF, Huinink HP, van der Ven LGJ, Adan OCG. Moisture content of the coating determines the water permeability as measured by 1D magnetic resonance imaging. Progress in Organic Coatings. 2019;130:114-123.

[3] van Meel PA, Erich SJF, Huinink HP, Kopinga K, de Jong J, Adan OCG. Moisture transport in coated wood. Progress in Organic Coatings. 2011;72(4):686-694.

[4] Mahnert KC, Hundhausen U. Encapsulation of poles to prevent moisture uptake – a laboratory test. The International Research Group on Wood Protection; 2016.

[5] IEC - International Electrotechnical Commission 2002. Degrees of Protection Provided by Enclosures for Electrical Equipment Against External Mechanical Impacts (IK Code), IEC 62262.

World Conference on Timber Engineering Oslo 2023

WOOD AND STEEL VISCOELASTIC DAMPERS: SHORT AND LONG-TERM PERFORMANCE

David W. Dinehart[1], Edward D. Bolte[2], David E. Lewicki[3]

ABSTRACT: The objective of this study is to characterize the performance and quantify the short-term and long-term differences between viscoelastic dampers constructed with steel and wood. Static and cyclic tests were conducted on steel and wood dampers utilizing 3M ISD-111 viscoelastic polymer. Initially, twelve specimens, six wood and six steel, were loaded statically to failure. Six dampers, three wood and three steel, were subjected to ten fully reversed cycles of sinusoidal displacement at various strains and frequencies. Twenty years later two of the dampers were retested under identical conditions to confirm material integrity and structural performance. For all dampers, the shear area of the VE was held constant, while the thickness varied. The initial static investigation demonstrated that the failure mode for all wood specimens was a shearing of the material at strains over 500%. There was no debonding of the VE material from the wood. After twenty years, the failure mode was delaminating from the wood at a strain of greater than 300%. The results of the cyclic tests showed good agreement between the stiffness and energy dissipations for the wood and steel dampers immediately after construction and twenty years later.

KEYWORDS: viscoelastic dampers, wood, energy dissipation, supplemental damping, polymer bond, time dependent

1 INTRODUCTION

Historically, viscoelastic (VE) dampers have been used exclusively in steel and reinforced concrete structures. Conventional VE dampers are constructed with the polymer bonded to steel plates which connect the dampers to the structure. With the recent increase in mid and high-rise structures constructed from wood, there exists a need to provide supplemental damping to wood structures.

2 BACKGROUND

When first implemented into the design of civil structures, viscoelastic dampers were aimed at decreasing the motion that the structure underwent because of wind. The original World Trade Center Towers in New York City, constructed in 1969, were the first applications of VE dampers in a tall building (Mahmoodi, 1969). The two towers used a combined 20,000 dampers made with VE material located between the lower chord of the floor system and the outside wall column at lateral bracing. VE dampers were utilized in the Columbia Center Building, located in Seattle, Washington, to reduce its acceleration levels (Keel and Mahmoodi, et. al. 1990; Samali and Kwok, 1995). The decision to use viscoelastic dampers in this structure was partially the result of how economic this material was for the overall cost.

The success of viscoelastic dampers in response to wind loading has led to the investigation of this material with respect to seismic activity. Research has shown that steel and reinforced concrete structures have seen improved performance through use of viscoelastic dampers. While wood structures are currently designed such that structural collapse is not a concern, they still experience considerable damage, both structural and nonstructural. A study conducted by Dinehart et. al. (1999a, 1999b) analyzed the performance of conventional shear walls to those constructed with viscoelastic dampers. This research concluded that there was significantly higher stiffness and energy dissipation ability displayed from the tests with viscoelastic dampers than the conventional shear walls.

The research previously conducted into the performance of viscoelastic material in wood structures has been promising, but not enough to fully justify implementation in wood structures. This paper discusses the performance of wood dampers made with viscoelastic material in both the short term and long term, as well as compares its performance to that of a similarly designed steel damper. The utilization of viscoelastic material in the design of wood dampers is an effective way to provide sufficient stiffness and energy dissipation capacity, while maintaining structural integrity. This VE design proves to

[1] David W. Dinehart, Villanova University, Department of Civil and Environmental Engineering, United States, david.dinehart@villanova.edu
[2] Edward D. Bolte, Associate II at Wiss, Janney, Elstner Associates, Inc, formerly undergraduate research assistant at Villanova University, 2020-2021, tbolte@wje.com
[3] David E. Lewicki, McDermott International Inc., Charlotte, NC, formerly research assistant at Villanova University, 1998-2000, david.lewicki@mcdermott.com

https://doi.org/10.52202/069179-0067

be successful in improving the performance of wood dampers not only in the short term, but it maintains its performance when investigated twenty years later. Furthermore, the evaluation of the steel damper confirms the durability of the viscoelastic material over time and its ability to withstand variable dynamic loading. Structures designed with viscoelastic dampers will not only have improved performance, but also decreased economic cost associated with maintaining these structures following seismic events.

3 TEST SPECIMENS

3.1 Polymer

This study utilized two specimens that were constructed and tested in 2000 and then tested again in 2021. The VE material used to construct these dampers was an ISD-111 VE polymer which was manufactured by 3M Corporation. It is important to note that this material is self-adhering. One damper, which will be referred to as "the wood damper", was constructed by adhering the VE material to a wood surface. The second damper, "the steel damper", had the VE material adhered to a steel surface. A double-lap configuration was used to create these dampers so they could resist load in pure shear when loaded axially.

3.2 Wood Damper

The wood damper was constructed by utilizing four-ply American Plywood Associated (APA) rated, 11.9 mm (15/32 in.) thick, plywood and Standard Spruce-Pine Fir (SPF) 50.8 mm by 101.6 mm (2 in. by 4 in.), to model the sheathing to stud connection. ISD-111 VE polymer with a thickness of 15.2 mm (0.6 in.) and a width of 50.8 mm (2 in.) was used to manufacture the wood damper and Grade 8 hex bolts were used opposite the VE material to fasten the damper to an A36 steel plate. Elevation and plan views of the wood damper can be seen in **Figure 1**.

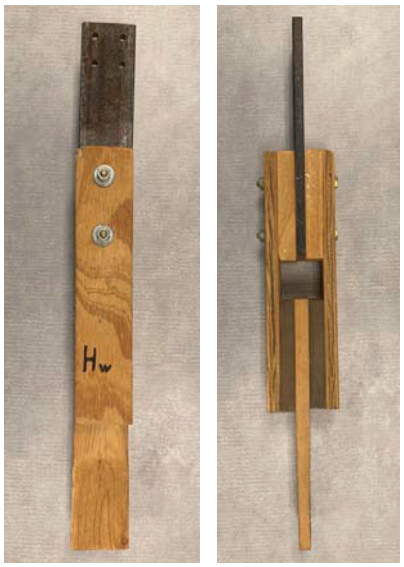

Figure 1: *Wood Damper*

3.3 Steel Damper

The steel damper was created in a manner consistent to that of the wood damper. The specimen utilized 9.5 mm (0.375 in.) thick, A36 steel and ISD-111 VE polymer with a thickness of 5.08 mm (0.2 in.) and a width of 50.8 mm (2 in.). Adjacent to the viscoelastic material, this damper was also fastened using four Grade 8 hex bolts. An example of a steel damper in the testing machine is presented in **Figure 2**. For both specimens, after the VE material was self-adhered, it was compressed to 20% of its initial thickness for 24 hours to ensure complete bonding, as instructed by the manufacturer.

Figure 2: *Steel Damper in test machine.*

3.4 Specimen Modifications

The wood damper was modified, as described in the following section, to allow for attachment to the test apparatus as. Two 6.35 mm (0.25 in.) thick A36 steel plates were added to the SPF Stud and then a third A36 steel plate was placed in between to allow for the damper to be gripped by the test apparatus. The same modifications were made on the opposite side of the damper to the existing 9.5 mm (0.375 in.) A36 Steel Plate. These modifications did not impact the integrity of the specimen, nor alter the results in a way that would make them incomparable to the results collected in 2000.

https://doi.org/10.52202/069179-0067

4 EXPERIMENTAL SETUP AND PROCEDURE

4.1 Testing Apparatus

All the tests conducted on the two dampers were done by an MTS TestStar Materials Testing Workstation. This apparatus has two hydraulic wedge grips that can handle a maximum load of 24.9 tons. The bottom grip functions as the actuator, which is controlled by both the load unit control panel and a multi-tasked TestWare SX program. It is powered by the hydraulic power supply, which provides pressure to the servovalves that then regulate the flow of fluid between the hydraulic power supply and the actuator in a closed loop control mode. An image of the test apparatus that was used in 2000 can be seen in **Figure 3**. A similar test apparatus was utilized again in 2021 for testing consistency.

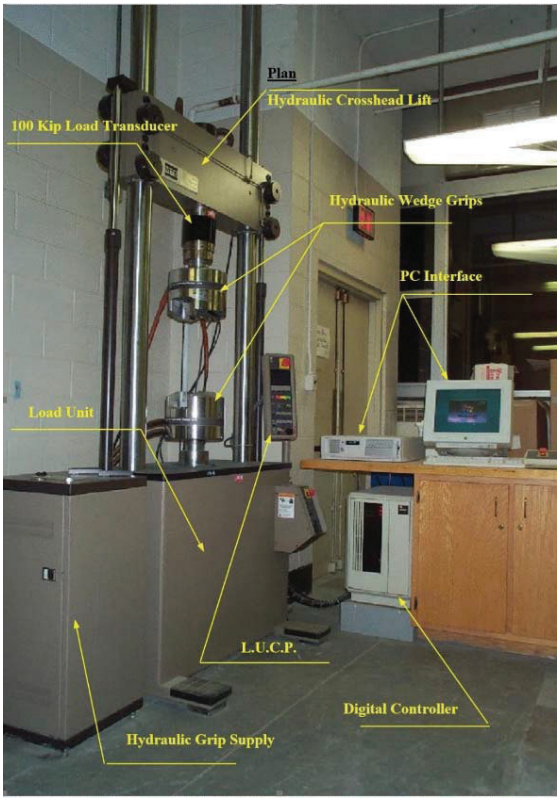

Figure 3: *MTS Workstation*

4.2 Displacement Protocol

The two dampers were subjected to 10 cycles under various frequencies and strains in 2000 and then retested in 2021 under similar frequencies and strains to evaluate their behavior and response. Temperature conditions for 2021 were chosen to ensure that the data would be comparable to the results obtained in 2000.

The wood damper was tested under the following conditions in both 2000 and 2021: 1.0 Hz at 10% strain, 0.5 Hz and 1.0 Hz at 20% strain, and 0.5 Hz at 80% strain. This produced four sets of data to be compared over time. The steel damper was tested at 1.0 Hz at 10% strain and 0.5 Hz at 80% strain in 2000 and then tested at the same strains and frequencies as the wood damper was in 2021. **Figure 4** shows the displacement protocol for the wood damper tested at 1.0Hz and 10% strain.

The tests were originally conducted at a temperature of 26.7°C, a condition that was recreated in 2021 to ensure testing consistency since the VE material is temperature dependent. Both specimens were removed from the testing apparatus between tests and allowed to rest for a predetermined time of thirty minutes to allow the damper to set before undergoing more testing, thus maintaining the integrity of each test's individual results.

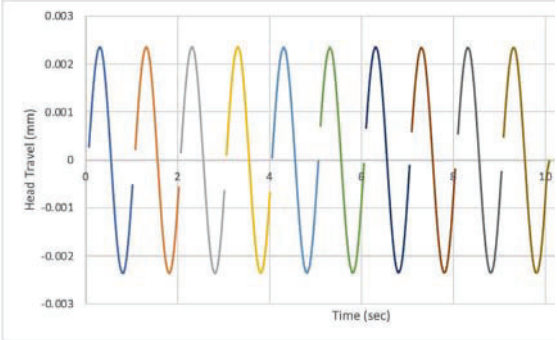

Figure 4: *Displacement versus time test input.*

5 EXPERIMENTAL RESULTS

The data collected from the tests were used to generate hysteresis loops, which display the cyclic response of the damper. **Figure 5** shows a hysteresis loop obtained for a single cycle.

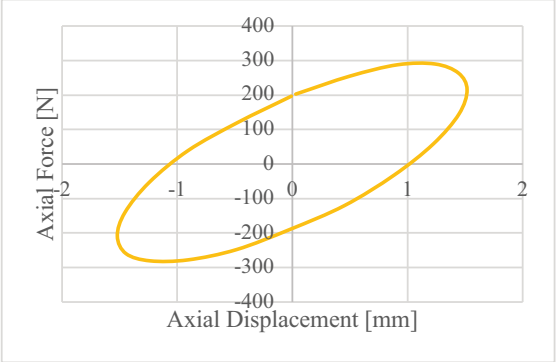

Figure 5: *Example hysteresis loop*

Hysteresis loops were created for each of the tests that were run on the dampers. The hysteresis loops produced from tests conducted at a frequency of 1.0Hz and 10%

https://doi.org/10.52202/069179-0067

strain are shown for the wood and steel dampers in **Figures 6 and 7**, respectively.

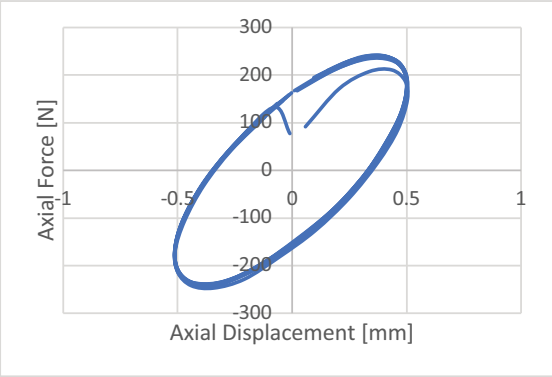

Figure 6: *Wood damper results from tests at a frequency of 1.0Hz and 10% strain*

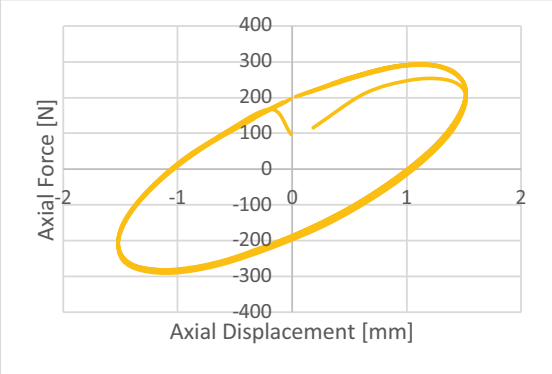

Figure 7: *Steel damper results from tests at a frequency of 1.0Hz and 10% strain*

The slope of the diagonal of the hysteresis loop is equal to the effective stiffness of that cycle. This was calculated using Equation (1):

$$K_{effective} = \frac{P_{x_o} - \bar{} P_{x_o}}{x_o - \bar{} x_o} \quad (1)$$

where P_{xo} = load correlating to the maximum displacement, $\bar{P}_{xo}$ = load correlating to the minimum displacement, x_o = maximum displacement, and $\bar{x}_o$ = minimum displacement.

The area bound by each of the hysteresis loops determines the energy dissipation of that cycle. This was determined utilizing Equation (2):

$$E_D = \pi \gamma_o^2 G'' A h \quad (2)$$

where γ_o = peak shear strain amplitude, G" = the loss modulus, A = shear area, and h = thickness of the VE material.

The hysteresis loops shown for the first cycle of the tests have lower values initially than the rest of the cycles which is the result of this being the initiation cycle for the test. At the completion of the final cycle, the hysteresis loop can be seen decreasing away from the other cycles', which is a result of the test ending and is not necessarily representative of a decrease in material performance. These trends were observed for all the tests conducted on the two dampers.

Average effective stiffness values were obtained for each of the tests conducted in 2000 and 2021 for the two dampers. The average effective stiffness was determined by calculating the mean effective stiffness over all ten cycles of a given test. The values obtained for the wood and steel dampers are shown in **Table 1** and **2**, respectively. A positive percent change value denotes an increase in the effective stiffness between the results obtained in 2000 and 2021.

Table 1: *Average Effective Stiffness (N/mm) for the Wood Damper*

Frequency	Strain	2000	2021	Percent Change
1.0 Hz	10%	115	141	22%
0.5 Hz	20%	93	105	13%
1.0 Hz	20%	119	133	12%
0.5 Hz	80%	81	92	14%

Table 2: *Average Effective Stiffness (N/mm) for the Steel Damper*

Frequency	Strain	2000	2021	Percent Change
1.0 Hz	10%	417	356	-15%
0.5 Hz	80%	283	240	-15%

The wood damper (**Table 1**) shows a relatively consistent increase in average effective stiffness from the tests conducted in 2000 to those conducted in 2021. The steel damper (**Table 2**) saw a 15% decrease in average effective stiffness for the two tests being compared.

The average energy dissipation capacity of the dampers was determined by calculating the area bound by the load-displacement ellipse using Equation (2) for each cycle and taking the mean over the ten cycles of each test. Average energy dissipation values for the wood and steel dampers from each of the tests conducted in 2000 and 2021 can be seen in **Table 3** and **4**, respectively.

https://doi.org/10.52202/069179-0067

Table 3: *Average Energy Dissipation (N-mm) for the Wood Damper*

Frequency	Strain	2000	2021	Percent Change
1.0 Hz	10%	746	786	5%
0.5 Hz	20%	2203	1919	-13%
1.0 Hz	20%	3141	2826	-10%
0.5 Hz	80%	30054	25137	-16%

Table 4: *Average Energy Dissipation (N-mm) for the Steel Damper*

Frequency	Strain	2000	2021	Percent Change
1.0 Hz	10%	316	114	-64%
0.5 Hz	80%	12685	10247	-19%

All the tests, with one exception, experienced a decrease in average energy dissipation from the results obtained in 2000 when retested in 2021. The exception to this trend was the wood damper when tested at a frequency of 1.0Hz and 10% strain, which saw a minor increase of 5%. The steel damper saw a decrease of 64% between 2000 and 2021 when tested at a frequency of 1.0Hz and 10% strain. This appreciable difference in performance is a byproduct of the low energy dissipation capacity of the steel damper under these testing conditions.

6 CONCLUSIONS

From these tests, the following conclusions can be drawn:
1. There was minimal change in the average effective stiffness of the two dampers over twenty years. The wood damper saw an average increase of approximately 15%, while the steel damper saw an average decrease of 15%.
2. The wood damper displayed consistent energy dissipation over time, only experiencing a decrease of about 10%, on average, when tested in 2021. Comparatively, the steel damper had minimal energy dissipation abilities when originally tested, which held true when the tests were conducted again in 2021.
3. The structural integrity of the two dampers held up well between tests and over time, with minimal damage observed between the two dampers.

The results from this research display the promise of using viscoelastic polymers more prominently in structural design of wood structures. These results show that there was no appreciable difference in performance between the steel and wood specimens. Based on this study, engineers can now investigate innovative applications of VE material in mid and high-rise wood frame structures without concern for the long-term effects of connecting VE material directly to wood. The next step in evaluating the performance of this material is to test it on a larger scale within a shear wall and compare the data to traditional shear walls.

ACKNOWLEDGEMENT

The authors greatly appreciate the support of Villanova University in providing and maintaining the equipment used in this study. Technical training of undergraduate researchers by Jeff Cook, Director, Structural Engineering Teaching and Research Laboratory, is also appreciated.

REFERENCES

[1] Bathe K.-J.: Finite-Elemente-Methoden. Springer-Verlag Berlin Heidelberg New York, 2002.

[2] R. Mahnken. A Newton-multigrid algorithm for elasto-plastic/viscoplastic problems. *Comp. Mechs*., 15:408-425, 1995.

[3] Zener C., Hollomon J. H.: Effect of strain rate upon plastic flow of steel. Journal of Applied Physics, 15(1):22-32, 1944.

[4] Johnson G. R., Cook W. H.: A constitutive model and data for metals subjected to large strains, high strain rates and high temperatures. In: 7th International Symposium on Ballistics, 514-546, 1983

[5] H. Vegter, Y. An, H. H. Pijlman, B. D. Carleer, and J. Huétink. Advanced material models in simulation of sheet forming processes and prediction of forming limits. In *First ESAFORM Conference on Material Forming*, pages 499–502, 1998.

[6] J. K. Lee, G. L. Kinzel, and R. H. Wagoner, editors. *Proceedings of the 3rd International Conference: Numisheet '96*, 1996. The Ohio State University.

[7] M. H. A. Bonte, A. H. van den Boogaard, and J. Huétink. A metamodel based optimisation algorithm for metal forming processes. In D. Banabic, editor, A*dvanced Methods in Material Forming*, pages 55–72. Springer Verlag, Heidelberg, Germany, 2007.

https://doi.org/10.52202/069179-0067

World Conference on Timber Engineering Oslo 2023

DURATION OF LOAD UNDER LONG-TERM BENDING LOAD OF LAMINATED VENEER LUMBER AND WOODEN I-BEAM

Ryuya Takanashi[1], Takahiro Tsuchimoto[2], Yoshinori Ohashi[3], Wataru Ishihara[4]

ABSTRACT: A wide range of wooden materials have been developed and used in construction. Although wood-based composites are important structural materials, few studies focusing on their creep rupture properties have been reported. We conducted long-term bending tests and investigated long-term allowable loading levels of laminated veneer lumber (LVL) and wooden I-beams made of LVL flanges and oriented-strand-board (OSB) web. Creep rupture of wooden I-beam specimens occurred in their LVL flanges. At the same time, LVL and I-beam specimens showed similar estimated long-term (50 years) allowable stress levels, which were equal or higher values than that of lumber. Survival analysis of the obtained data indicated no effect of the specimen type (LVL or I-beam) on survival distribution. The duration of load of wood-based composite materials could be estimated based on that of its component members.

KEYWORDS: Creep rupture, Bending, LVL, Constant environment

1 INTRODUCTION

Wood and wooden materials are important building materials. In recent years, timber construction has attracted increasing interest globally for use in many fields [1]. A wide range of wooden materials has been developed and used in construction to make various construction design. Wooden I-beams, which are often called I-joists, are I-shaped engineered wood structural members. They consist of top and bottom flanges, typically of laminated veneer lumber (LVL) or solid sawn lumber, and the web made of plywood or oriented-strand-board (OSB). I-beams possess multiple advantageous properties, such as stiffness, strength, and light weight, and are well-suited for long-span joist and rafter applications [2].

Wood materials demonstrate characteristic behaviors under constant load. When the stress is sufficiently high, failure eventually occurs under constant load. This type of failure is called creep rupture [3]. Creep rupture is an important factor in timber construction, it must be considered to ensure the long-term safety of wooden structures. Several studies have investigated the creep rupture properties of solid lumber [4, 5, 6], wood-based structural panels [7], and cross-laminated timber [8, 9]. However, few studies have been conducted on the duration of load of wood-based composite materials such as wooden I-beams. At the same time, the bending performance [10, 11, 12], shear performance [10], and creep performance [11, 13, 14] of wooden I-beams have been comprehensively investigated. To the best of our knowledge, there have been no reports on the duration of load of wooden I-beams. In addition, wood-based composite materials often have large dimensions, then it is difficult to conduct long-term loading tests because it requires special equipment for long-term loading and takes a long time for the test. If the relationship between the creep rupture properties of a composite and those of its element is elucidated, the creep rupture properties of wood-based composites could be estimated based on tests of their elements with small dimensions. In the present study, we conducted long-term bending tests on LVL and wooden I-beams composed of LVL flanges and OSB web to investigate and compare their long-term bending properties.

2 MATERIALS AND METHODS

2.1 SPECIMENS

2.1.1 LVL

LVL specimens were comprised of eleven-ply veneer of Japanese Larch (*Larix kaempferi*) glued with phenol resin adhesive. Specimens were 53 mm in width (veneer face), 35 mm in thickness (lamination direction), and 700 mm in length. The criterion for stress grading was 120E of Japanese Agricultural Standard for LVL (12.0 kN/mm^2 in mean and 10.5 kN/mm^2 in lower limit for bending modulus of elasticity). LVL specimens were collected from nine LVL motherboards with 1200 mm width. Figure 1 shows the cutting pattern of LVL specimens. Nine specimens were cut from each LVL motherboard: five side-matched specimens for a short-term loading test and four specimens for a long-term loading test. Thus, the total numbers of LVL specimens were 45 and 36 for short-term and long-term loading tests, respectively.

[1] Ryuya Takanashi, Forest Products Research Institute, Hokkaido Research Organization, Japan, takanashi-ryuuya@hro.or.jp
[2] Takahiro Tsuchimoto, Building Research Institute, Japan
[3] Yoshinori Ohashi, Forest Products Research Institute, Hokkaido Research Organization, Japan
[4] Wataru Ishihara, Forest Products Research Institute, Hokkaido Research Organization, Japan

https://doi.org/10.52202/069179-0068

2.1.2 Wooden I-beam

Wooden I-beam specimens were composed of LVL flanges and OSB web glued together by resorcinol resin adhesive. LVL flanges had the same dimensions as LVL specimens and were end-matched with them. Thus, the number of I-beam specimens with side-matched flanges was 81: 45 for short-term and 36 for long-term loading tests. Figure 1 shows the cutting pattern of flanges of I-beam specimens. LVL flanges were 53 mm in width and 35 mm in thickness. The thickness of the OSB web was 9.5 mm. I-beam specimens were 235 mm in height and 4700 mm in length.

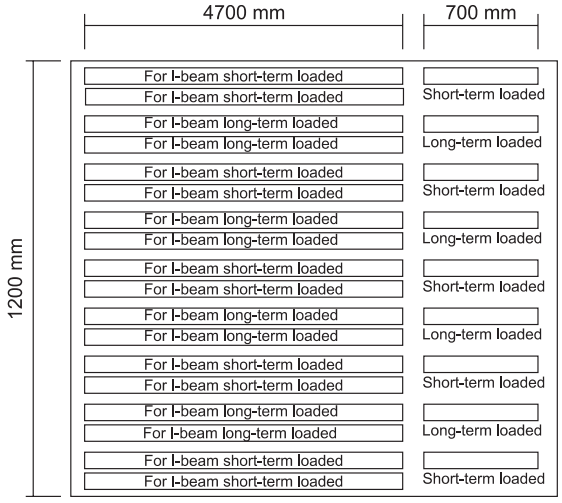

Figure 1: *Cutting pattern of LVL specimens from LVL motherboard*

2.2 SHORT-TERM LOADING TEST

2.2.1 LVL

LVL specimens were conditioned at 20°C and 65% relative humidity (RH) prior to the four-point bending test conducted using a testing machine (ORIENTEC Co. LTD; maximum loading capacity of 100 kN) in an unconditioned room. The specimens were loaded in the vertical direction to lamination at their third-point across a 630 mm supported span at a cross-head moving speed of 2 mm/min. Both the load (P) and displacement at the span center of a specimen from the ground (δ) were measured. Then, the bending modulus of elasticity (E_m) and the bending strength (σ_b) were, respectively, calculated as follows:

$$E_m = \frac{23\Delta P L_1^3}{108\Delta\delta b h^3} \quad (1)$$

$$\sigma_b = \frac{P_{max} L_1}{b h^2} \quad (2)$$

where P_{max} is the maximum load, ΔP is the load increase in an elastic range ($0.4P_{max} - 0.1P_{max}$ for this study), $\Delta\delta$ is an increase in δ with ΔP, L_1 is the length of the support span (630 mm), b is the specimen width, and h is the specimen thickness.

The moisture content of the specimens was measured after the tests based on the oven-dried weight of specimen pieces.

2.2.2 Wooden I-beam

I-beam specimens were conditioned at 20°C and 65%RH prior to the four-point bending test conducted using a testing machine (TOKYO KOKI TESTING MACHINE Co. LTD; maximum bending load capacity of 200 kN) in an unconditioned room. The specimens were loaded at their third-point across a 4410 mm supported span. The tests were conducted with lateral supports on a specimen to prevent horizontal buckling. Cross-head movement speed was 12 mm/min. The load (P) was measured and the maximum bending moment (M_{max}) was calculated as follows:

$$M_{max} = \frac{P_{max} L_2}{6} \quad (3)$$

where P_{max} is the maximum load, and L_2 is the length of the support span (4410 mm).

The moisture content of the specimens was measured after the tests based on the oven-dried weight of specimen pieces.

2.3 LONG-TERM LOADING TEST

Figures 2 and 3 show the experimental setup for the long-term loading tests for LVL and I-beam specimens, respectively. The testing instruments were capable of loading approximately 14 and 17 times the weight suspended at the end of the moment arm to specimens, respectively. The tests were conducted at a constant temperature (20°C) and relative humidity (65%RH). A four-point bending setup was used, which is equivalent to the short-term loading test. In the tests of I-beam specimens, lateral supports on the specimens were used to prevent horizontal buckling of the specimens. The mean maximum load of two both-side-matched short-term loading specimens to a long-term loading specimen was assumed to be the standard (100%) load of a long-term loading. The applied constant load (stress level: SL) was 90, 80, and 75% of the standard load. Thirty-six LVL and I-beam specimens were tested: 12 specimens for each stress level. The displacement was measured at a span center for LVL specimens and the moment arm for I-beam specimens at the measurement interval of 1 min. The measurements were proceeded until specimen failure. The duration of load (time to failure) was calculated as the duration between the completion of loading and specimen failure.

https://doi.org/10.52202/069179-0068

Figure 2: *Experimental setup for the long-term loading tests of LVL*

Figure 3: *Experimental setup for the long-term loading tests of I-beam specimens*

3 RESULTS AND DISCUSSIONS

3.1 SHORT-TERM LOADING TEST

Tables 1 and 2 show the results of the short-term loading tests. All specimens demonstrated bending failure. Most LVL specimens broke at a scarf joint on the tensile surface, and most I-beam specimens broke in the bottom LVL flange (tensile surface). Test duration from the beginning of loading to specimen failure was less than 10 min for most specimens.

Table 1: *Results of the short-term loading test for LVL*

	Density (kg/m^3)	MOE (kN/mm^2)	MOR (N/mm^2)	MC (%)	Test duration (minute)
Mean	621	12.60	57.0	10.2	6.4
SD	23	0.90	8.2	0.7	2.3
Max	667	14.46	75.4	11.6	13.6
Min	580	10.73	38.5	9.1	3.4

MOE: Modulus of elasticity (see Eq. (1)), MOR: Modulus of rupture (see Eq. (2)), MC: Moisture content, SD: Standard Deviation.

Table 2: *Results of the short-term loading tests for I-beams*

	M_{max} (kNm)	MC (%)	Test duration (minute)
Mean	14.9	9.6	4.9
SD	1.7	0.3	0.5
Max	18.1	10.5	6.4
Min	10.9	8.9	3.7

M_{max}: Maximum bending moment (see Eq. (3)), MC: Moisture content, SD: Standard Deviation.

3.2 LONG-TERM LOADING TEST

Tables 3 and 4 show the duration of load in the long-term loading tests. One I-beam specimen loaded at 80% stress level showed horizontal buckling before the completion of loading and this data was not used for analysis. In addition, specimens with blank data in Tables 3 and 4 experienced failure before the completion of loading. Two LVL specimens loaded at 75% stress level that did not fail and two I-beam specimens loaded at 90% stress level that showed horizontal buckling were censored (marked with an asterisk in Tables 3 and 4). Most LVL specimens broke at a scarf joint on the tensile surface and most I-beam specimens broke in the bottom LVL flange, similar to the short-term loading tests. Figures 4 and 5 show the relationship between the duration of load and stress level. Figures 6 and 7 show this relationship with the stress level converted to the ratio of practical stress to the overall mean value for short-term loading specimens. The black solid line in Figures 4–7 represents an empirical hyperbolic curve based on clear and small specimens [4]. This curve is called the Madison Curve, which is expressed as follows:

$$SL = 108.4t^{-0.04635} + 18.3 \quad (4)$$

where SL is stress level and t is time in seconds.

Most specimens show almost equal or longer duration of load than Madison Curve. These specimens exhibit equivalent long-term bending properties to clear solid lumber. The red and blue dashed lines are regression lines fitted by the following models:

$$SL = a_1 \ln(t) + b_1 \quad (5)$$

$$\ln(t) = a_2 SL + b_2 \quad (6)$$

where SL is stress level, t is time in seconds, and a_1, a_2, b_1, and b_2 are coefficients.

Table 5 shows regression coefficients, coefficients of determination, and extrapolation values of SL in 50 years (SL_{50y}) as a long-term performance of the specimens. Duration of load of specimens that showed failure before the completion of loading were assumed to be 1 s in the calculations. Those of censored specimens were assumed to be durations until censoring. First, I-beam specimens show better coefficients of determination of the stress level relative to the overall mean of short-term loading (SL_2). Second, SL_{50y} values for LVL and I-beam

https://doi.org/10.52202/069179-0068

specimens are similar for the same stress level methodology. Finally, specimens in this study show equal or better long-term bending properties than lumber. Long-term strength of lumber is assumed to be 60% of short-term strength [3], and the Japanese building code assumes 55%. The Japanese building code assumes "long-term" as 50 years. Most SL_{50y} for all models in this study exceeds this value. I-beams with the composition and dimensions used in this study are widely employed in practice. Therefore, general I-beams may show equal or higher long-term bending strength than conventional wood members. Furthermore, long-term bending properties of I-beams could be estimated based on those of LVL members in which creep rupture of I-beams occurred. The reasoning behind these claims is discussed further in the next section.

Table 3: *Duration of load of LVL specimens*

SL_1	SL_2	Duration of load (second)	
0.90	0.91	2962	
0.90	0.89	1296867	
0.90	0.87	5426623	
0.90	1.01	-	
0.90	0.90	196321	
0.90	1.11	-	
0.90	0.96	-	
0.90	0.77	179	
0.90	0.98	-	
0.90	0.74	1981	
0.90	0.71	8219	
0.90	0.95	769	
0.80	0.69	15476105	
0.80	0.72	19373016	
0.80	0.95	17222	
0.80	0.96	1953918	
0.80	0.79	5407475	
0.80	0.82	236178	
0.80	0.63	55417421	
0.80	0.57	49179681	
0.80	0.79	1156993	
0.80	0.79	265990	
0.80	0.91	7363	
0.80	0.88	51869517	
0.75	0.67	42338326	
0.75	0.67	29914617	
0.75	0.67	99467792	*1
0.75	0.87	118791	
0.75	0.79	5097780	
0.75	0.79	2206961	
0.75	0.87	4977956	
0.75	0.74	3111670	
0.75	0.76	3558795	
0.75	0.76	90660315	*1
0.75	0.68	26321924	
0.75	0.82	848069	

Note: Blanks represent failure before the completion of loading. SL_1: Stress level relative to that of side-matched specimens, SL_2: Stress level relative to the overall mean of short-term loading, and *1: Censored specimens that did not fail.

Table 4: *Duration of load of I-beam specimens*

SL_1	SL_2	Duration of load (second)	
0.90	0.98	118	
0.90	0.92	1536	
0.90	0.81	1822	
0.90	0.93	3736	
0.90	0.99	793	
0.90	0.74	7952184	
0.90	0.81	120491	
0.90	0.88	1911	*2
0.90	0.98	848	
0.90	0.84	18304	
0.90	0.93	976	
0.90	0.85	1482538	*2
0.80	0.82	65908	
0.80	0.69	5824379	
0.80	0.84	72763	
0.80	0.78	404043	
0.80	0.87	NA	
0.80	0.70	3061833	
0.80	0.80	25404261	
0.80	0.86	-	
0.80	0.78	1335314	
0.80	0.84	14423	
0.80	0.82	31672	
0.80	0.86	4123	
0.75	0.72	570224	
0.75	0.74	9503275	
0.75	0.78	62135	
0.75	0.69	6833192	
0.75	0.78	3073888	
0.75	0.74	35189705	
0.75	0.65	6278815	
0.75	0.77	3140010	
0.75	0.78	502737	
0.75	0.87	159480	
0.75	0.71	31780333	
0.75	0.76	6665934	

Note: Blanks represent failure before the completion of loading. NA: Data not used for analysis due to horizontal buckling before the completion of loading, SL_1: Stress level relative to that of side-matched specimens, SL_2: Stress level relative to the overall mean of short-term loading, and *2: Censored specimens that showed horizontal buckling.

https://doi.org/10.52202/069179-0068

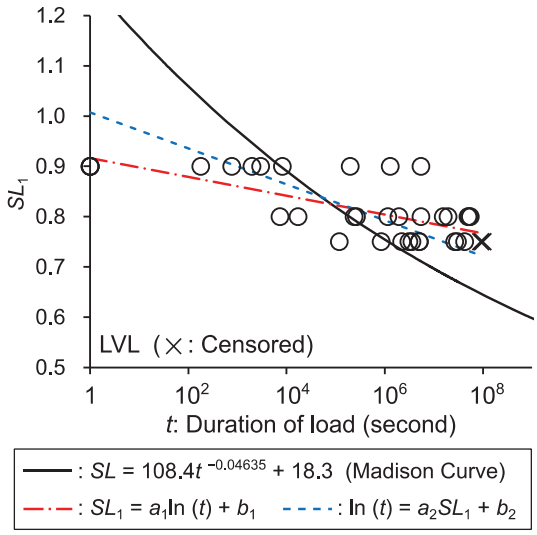

Figure 4: *Relationship between the duration of load and stress level for LVL specimens*
SL_1: Stress level relative to that of side-matched specimens.

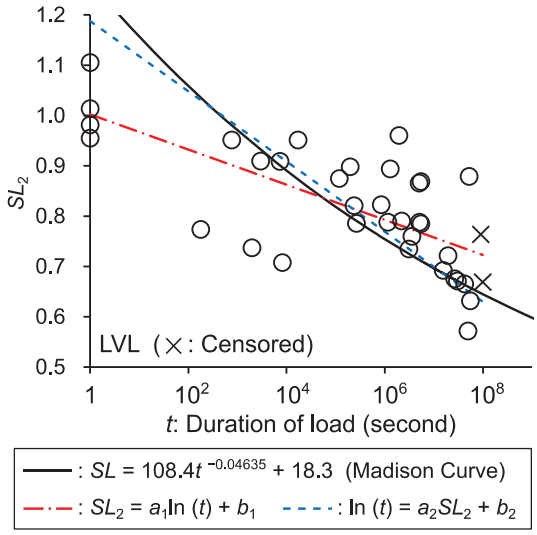

Figure 5: *Relationship between the duration of load and stress level for I-beam specimens*
SL_1: Stress level relative to that of side-matched specimens.

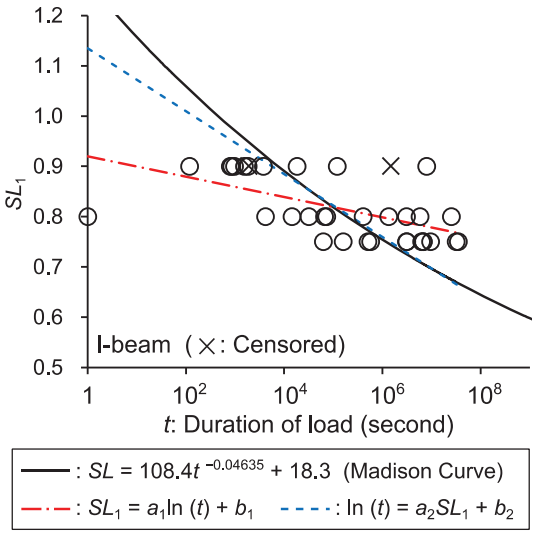

Figure 6: *Relationship between the duration of load and stress level (relative to the overall mean) for LVL specimens*
SL_2: Stress level relative to the overall mean of short-term loading.

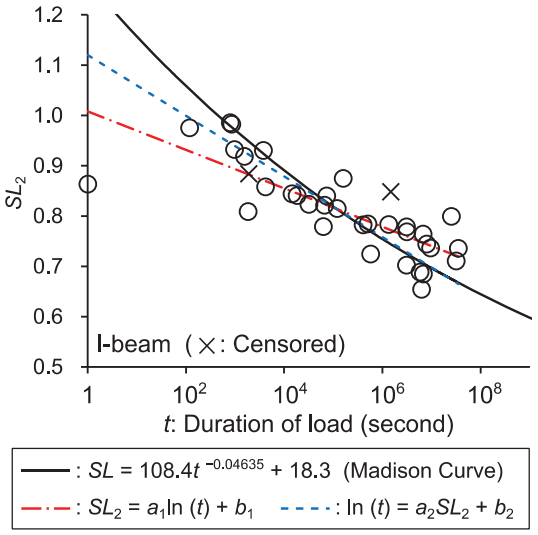

Figure 7: *Relationship between the duration of load and stress level (relative to the overall mean) for I-beam specimens*
SL_2: Stress level relative to the overall mean of short-term loading.

https://doi.org/10.52202/069179-0068

Table 5: *Results of model fitting*

	Stress level	Model	Slope	Intercept	R^2	SL_{50y}
LVL	SL_1	Eq. (5)	−0.008	0.917	0.524	0.744
		Eq. (6)	−64.39	64.86	0.524	0.678
	SL_2	Eq. (5)	−0.015	1.003	0.501	0.681
		Eq. (6)	−32.98	39.18	0.501	0.546
I-beam	SL_1	Eq. (5)	−0.009	0.920	0.323	0.734
		Eq. (6)	−36.83	41.80	0.323	0.560
	SL_2	Eq. (5)	−0.017	1.008	0.634	0.656
		Eq. (6)	−38.19	42.77	0.634	0.565

SL_1: Stress level relative to that of side-matched specimens, SL_2: Stress level relative to the overall mean of short-term loading, R^2: Coefficients of determination, and SL_{50y}: extrapolation values of stress level in 50 years.

3.3 SURVIVAL ANALYSIS

Survival analysis is a collection of statistical procedures for data analysis in which the variable of interest is time until an event occurs [15]. It is a popular data analysis approach in epidemiologic and reliability engineering, which can be used for censored data. In the present study, survival analysis was conducted for the duration of load, which is time until failure. Figures 8–10 show survival curves derived from survival analysis using the Kaplan–Meier method (a non-parametric method). This analysis was performed using the statistical software R version 4.2.2 [16]. One second was used as the duration of load for specimens that failed before the completion of loading. Survival function shows no significant differences ($p > 0.05$) between LVL and I-beam specimens at all stress levels using the log–rank test. In addition, Cox proportional hazard model [17] was applied to data in this study as follows:

$$h(t|x) = h_0(t)\exp(\beta_1 SL_1 + \beta_2 x) \quad (7)$$

where $h(t|x)$ is the hazard function with covariance, $h_0(t)$ is baseline hazard, β_1 and β_2 are coefficients, SL_1 is the stress level relative to that of side-matched specimens, and x is specimen type (LVL: $x = 0$, I-beam: $x = 1$). The hazard function represents the instantaneous failure rate. This model assumes that the hazard ratio depends only on covariance, not on t. Table 6 shows the estimated values of the coefficients. The coefficient of specimen type (β_2) shows no significant differences. In this case, the hazard ratio of the I-beam specimen to the LVL specimen is exp (β_2). This value includes 1.0 in the confidence interval. Therefore, survival functions also show no significant differences between the LVL and I-beam specimens. Considering the discussion in this and former sections, the duration of load of I-beams could be evaluated from that of LVL, which is an element of I-beam in this study.

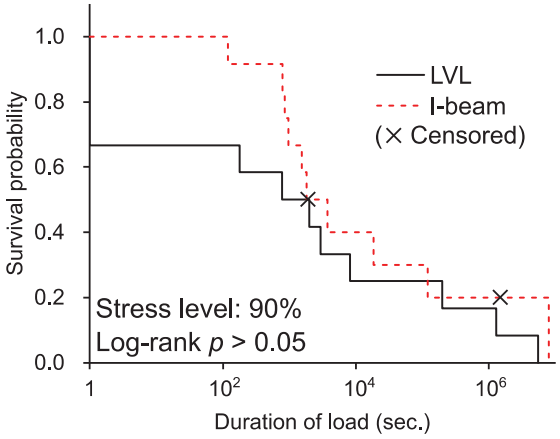

Figure 8: *Kaplan–Meier curves for the stress level of 90%*

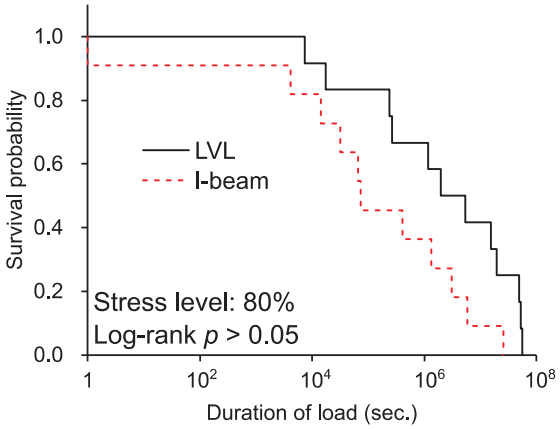

Figure 9: *Kaplan–Meier curves for the stress level of 80%*

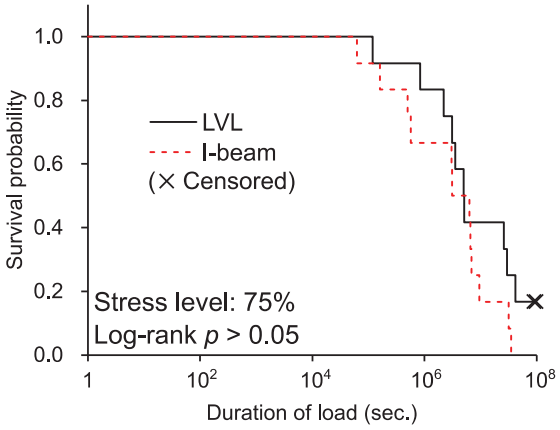

Figure 10: *Kaplan–Meier curves for the stress level of 75%*

https://doi.org/10.52202/069179-0068

Table 6: *Coefficients estimated using the Cox proportional hazard model*

β_1	β_2	exp (β_1)	exp (β_2)
10.69*	0.383^{ns}	43868 (612–3147000)	1.467 (0.883–2.437)

*: p <0.000001, *ns*: not significant (null hypothesis is $H_0 = 0$), with 95% confidence interval.

4 CONCLUSIONS

Long-term bending tests were conducted on LVL and wooden I-beam specimens composed of LVL flanges and OSB web to investigate and compare their long-term bending properties. The results of this study are as follows.

1. Creep rupture of I-beam specimens occurred in the bottom LVL flange, in which the tensile stress occurred.
2. LVL and I-beam specimens showed similar estimated long-term (50 years) allowable stress levels in all fitted models.
3. Specimens in this study show equal or better long-term bending properties than lumber.
4. Survival analysis of the data in this study indicates no significant differences between survival distributions for the LVL and I-beam specimens. Additionally, the duration of load of I-beam specimens could be estimated from that of LVL flange members.
5. Thus, the duration of load of wooden composite materials may be estimated from that of element members that contribute to the failure mode of the composites.

ACKNOWLEDGMENT

This work was supported by JSPS KAKENHI Grant number JP21K14893.

REFERENCES

[1] Brandner R., Flatscher G., Ringhofer A., Schickhofer G., Thiel A.: Cross laminated timber (CLT): overview and development. European Journal of Wood and Wood Products 74:331-351, 2016.

[2] Leichti R., Falk R., Laufenverg T.: Prefabricated wood I-joists: an industry overview. Forest Products Journal 40: 15-20, 1990

[3] USDA Forest Products Laboratory. Mechanical properties of wood. In: Wood handbook: wood as an engineering material, pages 39-40. Madison, US, 2010.

[4] Wood L.: Relation of strength of wood to duration of load. USDA Forest Service Forest Products Laboratory Report No. R1916, 1951.

[5] Schniewind A., Lyon D.: Further experiment on creep-rupture life under cyclic environmental conditions. Wood and Fiber Science 4: 334-341, 1973.

[6] Gerhards C., Link C.: A cumulative damage model to predict load duration characteristics of lumber. Wood and Fiber Science 19:147-164, 1987.

[7] Lufenberg T., Palka L., McNatt J.: Creep and creep-rupture behavior of wood-based structural panels. Research paper FPL; RP-574:20 p, 1999.

[8] Nakajima S., Miyatake A., Shibusawa T., Araki Y., Yamaguchi N., Haramiishi T., Ando N., Yasumura M.: Creep and duration of load characteristics of cross laminated timber. In: World conference on timber engineering, Quebec City, Canada, August 2014

[9] Takanashi R., Ohashi Y., Ishihara W., Matsumoto K.: Long-term bending properties of cross-laminated timber made from Japanese larch under constant environment. Journal of Wood Science 67:65, 2021.

[10] Ohashi Y., Toda M., Fujiwara T., Sato T., Hirai T.: Mechanical properties of wooden I-beams with plantation timber materials in Hokkaido I: bending, shear and partial bearing propeties. Mokuzai Gakkaishi 54: 24-32, 2008 (in Japanese).

[11] Davids W.G., Rancourt D.G., Dagher H.J.: Bending performance of composite wood I-joist/oriented strand board panel assenblies. Forest Products Journal 61: 246-256, 2011.

[12] King D., Sinha A., Morrell J.: Effects of outdoor exposure on properties of I-joists. Wood and Fiber Science 46: 394-400, 2014.

[13] Ohashi Y., Matsumoto K., Sato T., Hirai T.: Mechanical properties of wooden I-beams with plantation timber materials in Hokkaido II: long term bending creep properties. Mokuzai Gakkaishi 54: 174-182, 2008 (in Japanese).

[14] Ohashi Y., Matsumoto K., Sato T., Hirai T.: Mechanical properties of wooden I-beams with plantation timber materials in Hokkaido III: shear creep properties. Mokuzai Gakkaishi 55: 217-225, 2009 (in Japanese).

[15] Kleinbaum D., Klein M.: Introduction to survival analysis. Survival analysis. Springer, New York, pp 1-54, 2012.

[16] R Core Team (2022) R: a language and environment for statistical computing. R Foundation for Statistical Computing, Vienna, Austria, https://www.R- proje ct. org/. Accessed 2 Dec 2022

[17] Cox D.R.: Regression models and life-tables. Journal of the Royal Statistical Society: Series B (Methodological) 34: 187-202, 1972.

World Conference on Timber Engineering Oslo 2023

DERIVATION FROM EN927 METHOD FOR EVALUATING THE OUTDOOR DURABILITY OF COATED FIRE-RETARDANT-TREATED WOOD

Ryo Takase [1], Atsuko Ishikawa[2], Daisuke Kamikawa[3]

ABSTRACT: Conducting an artificial weathering test using UV lamps and water spraying is necessary to predict the outdoor durability of coated fire-retardant–treated wood. This paper describes the results of prototypes derived from the EN927-6 methods, which are artificial weathering methods for coated wood. Modified tests using QUV demonstrated that testing conditions such as the duration of each spray or temperature have different effects on coatings. Thus, low-build coatings tend to be evaluated poorly under the standard cycle. Moreover, maintaining a high moisture content by raising the initial moisture content or lowering the testing temperature speeds up leaching from high-build coatings.

KEYWORDS: Fire retardant, Exterior claddings, Durability, Artificial weathering

1 INTRODUCTION

Fire-retardant chemicals (FRC) effectively reduce the flame spread and heat release in wooden claddings when exposed to fire. The chemical content near the surface is an especially important factor in suppressing the flame spread along fire-retardant–treated (FRT) materials. Under repeated drying–wetting environment, the impregnated chemicals move toward the wood surface [1] because most chemicals are water soluble. If used outdoors, then these accumulated chemicals are easily lost to condensed water or rain. Thus, protection with coatings is important not only from an aesthetic point of view but also to reduce fire risks.

Conducting an artificial weathering test using UV lamps and water spraying is necessary to speed up the development of new coating materials to evaluate how long coated FRT wood maintains the desired amount of FRC. This paper describes the results of modified versions of EN-927 standards [2], which are known as the methods for coated untreated wood.

The degradation of FRT wood is possibly caused by wetting, exposure to the sunlight, and drying. In some existing studies, degradation of coated untreated wood during exterior use is considered [3-5], and in some studies, accelerated tests using a xenon arc lamp method or UV fluorescent lamp method by QUV reproduced aesthetical deteriorations to some extent. Surface cracks and changes in gloss were reproduced using QUV, and changes in colors were correlated using QUV and a Xenon arc lamp [3]. However, attempts to predict FRC retention based on accelerated tests are rarely reported other than in study such as literature [6], while there are some reports related to the outdoor durability such as [7, 8] and fire testing methods for FRT wood after accelerated weathering test [9].

In the evaluation of the durability of FRT wood, moisture absorption should be considered. Figure 1 shows a diagram of the typical deterioration in coated FRT wood. After long-term outdoor exposure, coating cracks and efflorescence followed by leaching of chemicals are common, and many of them originate owing to moisture absorption or desorption.

(a) FRT absorbs more water than untreated wood [10], which means less dimensional stability and more stress on coatings.
(b) Efflorescence occurs at the wood coating boundary [11], which could break the wood coating bonding (only in the case of high-build types of coating).
(c) Water leaches FRC out of wood.

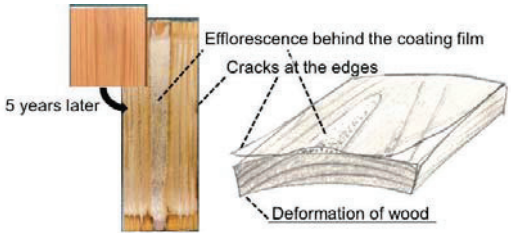

Figure 1: *Typical degradation of FRT wood coated with film-forming type material*

In this study, most of the testing conditions in EN927-6 were applied, and only conditions related to water absorption and desorption were modified to allow the leaching speeds of FRC to catch up with the degradation (i.e., changes in color) speed of coating materials.

There is also a fire testing method called NT Fire 053 [9, 12] that targets the outdoor usages of FRT wood products. The materials eventually undergo the fire spreading test after being repeatedly exposed to spray and drying (UV

[1] Ryo Takase, Ph. D., Forestry and Forest Products Research Institute, Japan, ryotakase@ffpri.affrc.go.jp
[2] Atsuko Ishikawa, Ph. D., Forestry and Forest Products Research Institute, Japan, aishi@ffpri.affrc.go.jp
[3] Daisuke Kamikawa, Ph. D., Forestry and Forest Products Research Institute, Japan, daikami@ffpri.affrc.go.jp

https://doi.org/10.52202/069179-0069

light is also added in Method 2). Except for the absence of the condensation function in NT Fire 053, this method has similar functions as QUV. Thus, some findings from this study provide implications for a better correlation between NT Fire testing and outdoor exposure.

2 EXPERIMENTAL SECTION

Pieces of *Sugi* (*Cryptomeria japonica*) FRT wood with several types of coatings (Figure 2) underwent each test, as shown in Figure 3. In this study, QUV accelerated tests, one year of outdoor exposure test, and steady sorption test were carried out.

In the one year of outdoor exposure test, the moisture content of each coated FRT and untreated wood was measured to grasp the extent of absorption and desorption in actual conditions.

QUV tests that have different testing conditions were conducted, and chemical retention after each accelerated test was compared with the four-year-outdoor exposure reported elsewhere [8].

Alongside these unsteady tests, the diffusion coefficient (ID) of each material was measured to discuss how the moisture absorption speeds are affected by testing conditions, as the temperature in the present QUV equipment is often higher than it is outdoors.

2.1 SPECIMENS

As shown in Table 1, three groups of specimens of different sizes were prepared. For outdoor exposure, specimens with a size of 300 mm (longitudinal, L), 18 mm (radial, R), and 70 or 105 mm (tangential, T) were prepared. For artificial weathering, specimens with a size of 300 mm (L), 18 mm (R), and 70 mm (T) were prepared. They were treated with 25 wt% of FRC aqueous under a pressure of 0.95 MPa and dried. The FRC used herein was a guanidine phosphate based FRC.

After impregnation, each front face and both edge grains were coated with one of the five types of coatings as shown in Figure 2. For the remaining faces, the procedures are the same among the coating types. The back face of the specimens were coated with film-forming alkyd (same one as coating D), and both end-grain faces were sealed with epoxy resin and foil tapes. The above procedures are the same as in previous studies [6, 8].

For ID measurement, wood blocks with a size of 30 mm (L), 18 mm (R), and 30 mm (T) were prepared. Sheets of aluminum foil were directly glued to the remaining five faces with epoxy resin to achieve strict one-dimensional absorption.

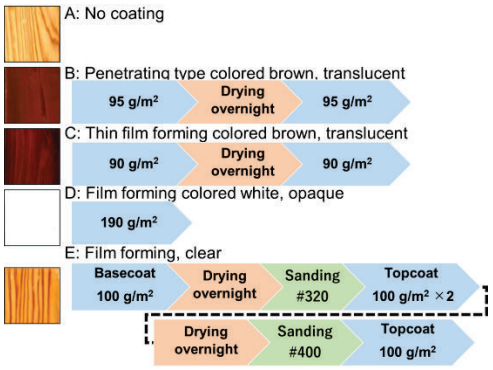

Figure 2: *Coating procedures for weathering tests*

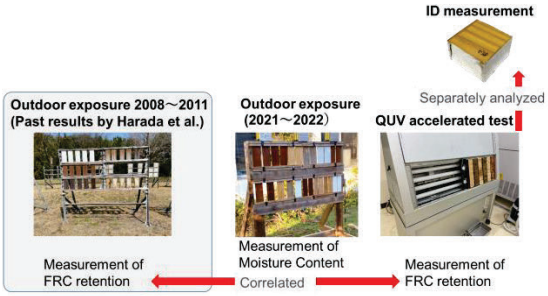

Figure 3: *Experiment schemes*

2.2 MEASUREMENT OF MOISTURE CONTENT DURING OUTDOOR EXPOSURE

On the basis of the outdoor exposure testing method described in Japanese Industrial Standards [13], each specimen in Table 1 underwent outdoor exposure. The site is located in Tsukuba, Japan. Specimens were fixed vertically facing due south. During the exposure, the moisture content was monitored by weighing each specimen almost three times a week. Measurements of moisture content are often performed using electrodes [14-16], but this approach is unsuitable for FRT wood because chemicals are electrically conductive.

Table 1: *List of specimens*

Testing	Number of repetitions (for each coating)	Fire retardant treatment	Specifications of specimens				
			Lengtial [mm]	Radial [mm]	Tangential [mm]	Coating procedures	
Outdoor exposure (2021-2022)	2	None	300	18	105	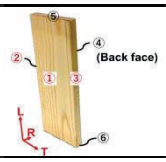	Face ① to ③ : Either coating system A to E Face ④ : Coating system D Face ⑤ and ⑥ : Epoxy resin covered with foil tapes
	2	Phosphate guanidine based	300	18	70		
QUV	1 or 2	Phosphate guanidine based	300	18	70		
ID measurement	1 or 2	None	30	18	30	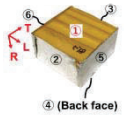	Face ① : Either coating system A to E Face ② to ⑥: Aluminum foil glued with epoxy resin
		Phosphate guanidine based					

The experiment for untreated wood was conducted from May 2021 to Sep. 2022. For FRT wood, the experiment was conducted from July 2021 to Sep. 2022. The rainy season in Japan is typically between June to the end of July. Thus, the exposure of FRT wood started later to minimize the interference of weight changes due to the loss of FRC.

Values of moisture content were calculated as demonstrated in Figure 4 and Equation (1), which defines the weight of each untreated wood piece as 100%.

$$M = \frac{W_g - W_{FRC} - W_w}{W_w} \times 100 \qquad (1),$$

where M is the moisture content [%], W_g is the gross weight [g], W_{FRC} is the weight of FRC approximated with exponential function [g], and W_w is the wood weight [g].

To correct the baseline for the FRC loss during exposure, one specimen for each coating system was separately prepared, exposed to the same environment, and oven dried every 4 or 6 months to be weighed. From the weights measured above, FRC retentions over time were approximated using the exponential function.

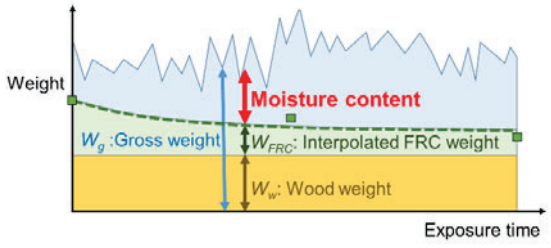

Figure 4: *Estimation scheme of moisture content within FRT wood*

2.3 MODIFICATION OF QUV CONDITIONS

Six conditions that differ in cycles and preconditioning environments were considered as shown in Table 2. The functions named "Condensation", "UV exposure" and "Spray" in Table 2 come standard with Q-LAB QUV/spray equipment. Condensation is typical for QUV equipment and is achieved by condensing hot vapor from a water pan at the specimen surface cooled by ambient air. Among these conditions, cycle S-25% is the closest condition to the EN927-6 standard. The tests were conducted over 504 h of testing time (three repetitions of 168 h cycles) as a unit. All specimens were conditioned beforehand until they reached equivalent moisture content (abbreviated as EMC in Table 2 and later figures), and oven-dried weights were measured subsequently. FRC retentions were calculated using Equation (2). Oven drying took place for three weeks for interim weighing (504, 1008, and 1512 h) and six weeks for the initial and final weights.

$$R_T = \frac{W_t - W_w - W_c}{W_0 - W_w - W_c} \times 100 \qquad (2),$$

where W_0 is the gross initial weight [g], W_t is the gross weight after t hours of QUV test [g], W_w is the wood weight [g], and W_c is the weight of coating materials [g].

Changes in colors are estimated to be approximately 17.4 times faster than that under vertical exposure outdoors under QUV standard condition [5]. The amount of water sprayed in QUV is at least 30 times greater than wall precipitation outdoors; 5.76 L/cm^2 of water is sprayed within 2016 hours in QUV, whereas the wall precipitation at the testing site is estimated to be less than 0.83 L/cm^2 per year, according to Equation (3) [17].

$$R_w = aR_hU\cos\delta \qquad (3),$$

where R_w is the wall precipitation [mm], a is a constant value determined by building size, R_h is the horizontal precipitation [mm], U is the wind speed [m/s], and δ is the horizontal attack angle between a wall and raindrops.

2.3.1 Initial Moisture Content

For some coating materials, conditioning moisture content is practically difficult because of the low permeability of the coating. Conditioning times could be even longer than the testing time. To figure out how much attention should be paid to controlling the initial moisture content, specimens with initial moisture content near 0% and 25% were compared.

Table 2: *Conditions of QUV tests*

Cycle	Testing shedule as a unit: Pre-conditioning → QUV exposure 168h × 3 → Oven dry 60°C, 3 weeks → weighing		QUV details		
	Preconditioning	QUV exposure cycle as a 1/3 unit	Condensation	Spray	UV Exposure
S-0%	60°C incubator; EMC<2%	-24h condensation -(2.5h UV exposure then 0.5h spray) during 144h Condensation 24h; Repetition 48times (UV2.5h then 0.5h spray); Total = 168h	45°C	6~7L/min	· 0.89W/m^2 at 340nm wavelength · 60°C of ambient temperature
S-25%	45°C 65%RH incubator; EMC ≃ 25% for FRT wood				
M1-0%	60°C incubator	**-(16h UV exposure then 8h intermittent spray and condensation) during 144h -24h UV exposure** 2h 1.3h Spray; 2h Cond. 1.3h Spray; Cond. 1.3h Spray; 16h UV; 24h UV; Total = 168h	45°C	6~7L/min	· 0.89W/m^2 at 340nm wavelength · 60°C of ambient temperature
M1-25%	45°C 65%RH incubator				
M2-0%	60°C incubator		45°C	6~7L/min	· 0.89W/m^2 at 340nm wavelength **· 50°C of ambient temperature**
M2-25%	45°C 65%RH incubator				

https://doi.org/10.52202/069179-0069

2.3.2 Duration of Each Cycle

Condensation and spray were alternately repeated for eight hours in cycle M1 to enhance water absorption in one wetting cycle. The total durations of each function (condensation, spray, and UV exposure) are the same between cycles S and M1.

2.3.3 Temperature During UV Cycles

To evaluate the effect of temperature on the leaching speed, cycle M2 that differs from cycle M1 only in the ambient temperature during UV exposure was considered. Cycle M2 is the combination of the lowest temperature available in Q-LAB QUV/spray equipment in each function. High temperatures are available (up to 60°C for condensation and UV exposure) but not considered in this study.

2.4 MEASUREMENT OF DIFFUSION COEFFICIENTS

The diffusion coefficient of each material in Table 1 was calculated from weight change under constant temperature (23°C, 45°C, and 63°C) and humidity (65% RH). These environments were achieved using containers with saturated salt (sherbet-like aqueous of NaCl) placed in incubators. Tests under a high humidity (95% RH) were also attempted, but they provided unstable results due to deliquescence, swelling, and seal failure.

3 RESULTS AND DISCUSSION

3.1 MOISTURE CONTENT DURING OUTDOOR EXPOSURE

Figure 5 shows the yearly transitions of moisture content and the weather record. The weather record from the nearest observatory was retrieved from the database of the Japan Meteorological Agency [18]. The actual peak values of the moisture content are expected to be a little high because the measurement did not necessarily take place right after rainfall. Also, the data earlier than day 40 should be excluded because of its unsteadiness. During the testing period at the site (Tsukuba), the equivalent moisture content estimated by relative humidity and temperature [19] is between 12% to 27%. The results for the coated untreated wood generally agreed with this estimation. The FRT wood had considerably high and unsteady values. The eventual moisture content exceeded 30%, allowing the presence of free water even after a short rainfall.

3.2 EFFECTS OF QUV CONDITIONS

Figure 6 shows the amount of FRC lost after 2016 hours of each test. The following sections show comparisons from some aspects.

3.2.1 Initial Moisture Content

Cycle S-25% is the closest condition to the EN927-6 standard. For specimens C, D, and E (considerably high-build types of coatings), more FRC leached under the cycle S-25% than under S-0%. The influence of initial moisture content becomes unclear for cycles M1 and M2. Initial moisture content seems more important for high-build coatings exposed to short-term spray, due to the low permeability of the coatings.

3.2.2 Duration of Each Cycle

Cycle M1 is the rearranged version of a standard cycle (cycle S). Judging from the fact that most of the specimens leached more under the cycle S than M1, combining condensation and spray as one wetting cycle seems insufficient to enhance the sorption of the coated wood.

3.2.3 Temperature during UV Cycles

Cycle M2 was designed to combine the lowest temperatures available in the present QUV equipment. However, it differs from M1 only in the ambient temperatures during UV exposure. Regardless of the initial moisture content, more FRC tended to leach under cycle M2 than under M1 in the case of specimens A (no coating), D, and E (high-build types of coating).

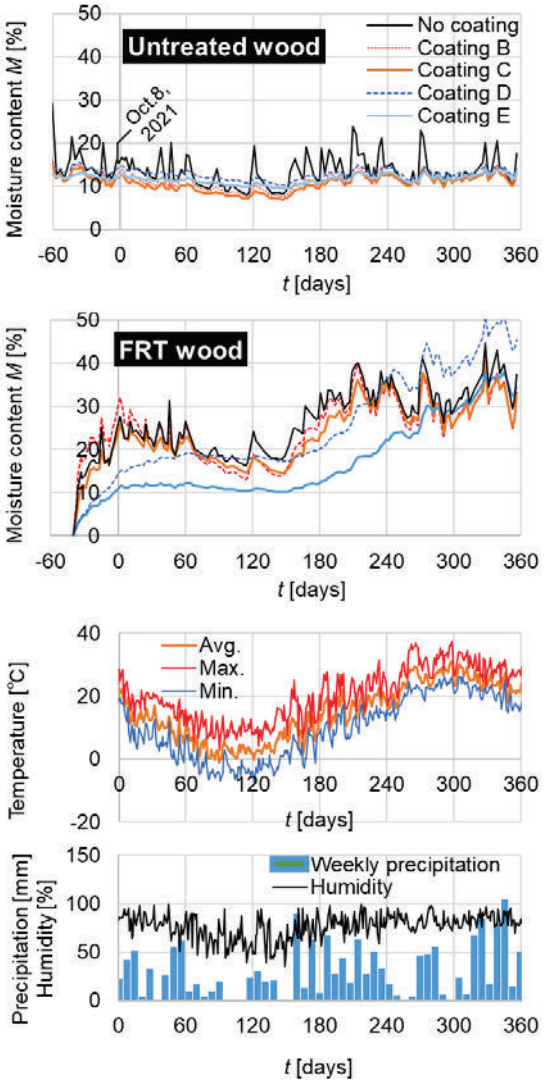

Figure 5: Moisture content and the weather at the site

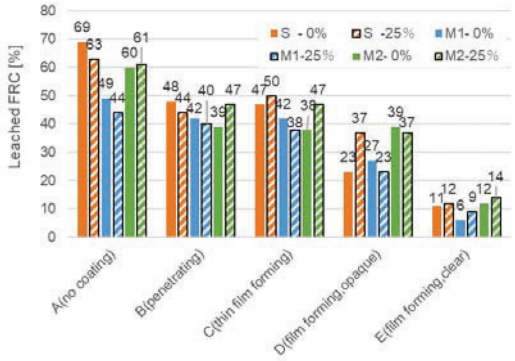

Figure 6: *Leached FRC during 2016h of accelerated tests*

3.3 RELATIONS BETWEEN LEACHING SPEEDS AND DIFFUSION COEFFICIENTS

Table 3 shows the gross (moisture excluding effectiveness of the coating is included) diffusion coefficients according to the method in reports such as [20]. With E defined as shown in Equation (4), its value against the square root of time increases linearly if the sorption follows Fick's law. Figure 7 shows an example of the sorption curves plotted against the square root of time.

$$E = M_t / M_\infty \qquad (4),$$

where E is the dimensionless moisture, $M_t$is the moisture content over time, and $M_\infty$is the equivalent moisture content in the ambient air.

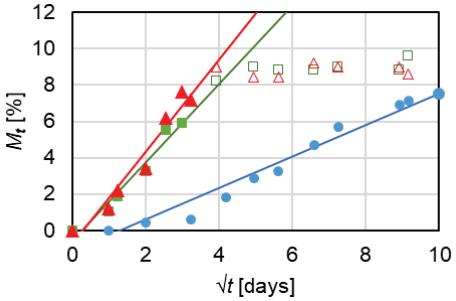

Figure 7: *Examples of sorption under steady environments*

With the use of the slope up to E = 0.8, the diffusion coefficients were calculated using Equation (5)

$$\mathrm{ID} = \frac{l^2}{5.1}\left(\frac{dE}{d\sqrt{t}}\right)^2 \qquad (5),$$

where ID is the diffusion coefficient [m^2/s], l is the length equal to twice of the sample thickness [m], and t is the time [s].

As shown in Table 3, the ratios of ID among the coatings are not maintained as long as the testing temperature is higher than that outdoors. The temperature dependence of IDs differs according to the base material (FR treated or not) and the coating materials, and tends to be highly temperature dependent in the cases of specimens D and E (relatively high-build coatings are applied).

3.4 COMPARISON WITH OUTDOOR RESULTS

In deducting the test method for new coating materials, the degree of acceleration is preferably uniform among the types of coatings. With this degree defined as the acceleration coefficient (Figure 8g), their ratio among specimens A to E is presented in Figure 8. For instance, figure 8d shows that the testing under standard condition (cycle S-25%) for specimens A (no coating), D and E (high-build type of coating) is not as efficient as that for specimens B and C.

In all conditions, the acceleration coefficients for the first 504 h are scattered and larger than the values afterwards. The gradual decrease of acceleration coefficients typical for specimen B and C (considerably low-build types of coatings) agrees with Table 3 in that the ID difference between untreated and FRT wood becomes large at high temperatures.

3.4.1 Effects of Testing Cycles

Regardless of the initial moisture content, the acceleration coefficient is reduced especially in specimens A (untreated), D, and E (high-build type of coating) by modifying the cycle from S to M1. As mentioned in 3.2.2,

Table 3: *Temperature dependence of diffusion coefficients*

	Temperature [°C]		No coating N=2	Coating B N=1	Coating C N=1	Coating D N=1	Coating E N=1
Control	23	ID* [×10^{-11}]	13.75	8.88	9.76	2.78	2.98
	45	ID* [×10^{-11}]	40.68	38.34	46.49	16.15	27.94
		(Ratio to 23°C)	(3)	(4.3)	(4.8)	(5.8)	(9.4)
	60	ID* [×10^{-11}]	57.5	49.0	46.5	35.7	38.5
		(Ratio to 23°C)	(4.2)	(5.52)	(4.8)	(12.8)	(12.9)
FRT wood	23	ID* [×10^{-11}]	22.0	13.1	10.3	0.8	2.6
	45	ID* [×10^{-11}]	91.1	58.8	77.5	21.8	28.6
		(Ratio to 23°C)	(4.1)	(4.5)	(7.5)	(27.1)	(11)
	60	ID* [×10^{-11}]	232.9	121.7	141.3	68.7	71.4
		(Ratio to 23°C)	(10.6)	(9.31)	(13.7)	(85.4)	(27.5)

https://doi.org/10.52202/069179-0069

combining condensation and spray as one wetting cycle seems insufficient to enhance the sorption of coated wood. In addition, no specimen reached an acceleration coefficient of ~30 just because 30 times more water is sprayed in QUV. These findings imply that most of the water sprayed in QUV simply runs down to wash out FRC on the surface of the specimens. Thus, the amount of water in QUV is greater than that absorbed by the wood.

3.4.2 Effects of Testing Temperature

The variation in acceleration coefficient evaluated from RSD is smaller in M2 than M1.

In spite of the ID tendencies shown in Table 3, the acceleration coefficients for specimen D and E shown in figure 8 do not decrease when the testing temperature is lowered from M1 to M2. This finding indicates that, due to the increase of equivalent moisture content by lowering the temperature during UV cycles, the absorbed water was able to remain as free water and enhance the leaching of FRC.

4 CONCLUSIONS

The preferable conditions of artificial weathering tests for FRT wood are narrowed down through the following findings:

1. FRT wood exposed outdoors in Tsukuba could exceed 30% of moisture content, regardless of their coating type.
2. The temperature dependence of the diffusion coefficient differs among the coating materials and base materials, resulting in various acceleration coefficients during QUV tests.
3. Keeping moisture content high by raising the initial moisture content or lowering the testing temperature speeds up the leaching from FRT wood coated with high-build coatings. In other words, the durability of FRT wood combined with these coatings tends to be overestimated under the QUV standard condition if the initial moisture content is low. This finding suggests that tests merely following EN 927-6 could also overestimate durability of these materials because it could take more than a year for these materials to reach equilibrium if the specimens are conditioned at 20°C, designated temperature in the EN 927-6.

A single type of fire-retardant chemical and five types of coatings demonstrated the difficulty of accelerating their degradation to the same degree, especially at high temperature. Acceleration coefficients can be more stabilized not by speeding up unsteady sorption during spray but by keeping testing chamber more humid throughout the testing time. Reducing the thickness of the specimens might be another effective way of speeding up moisture absorption without raising the temperature. Further experiments are being conducted.

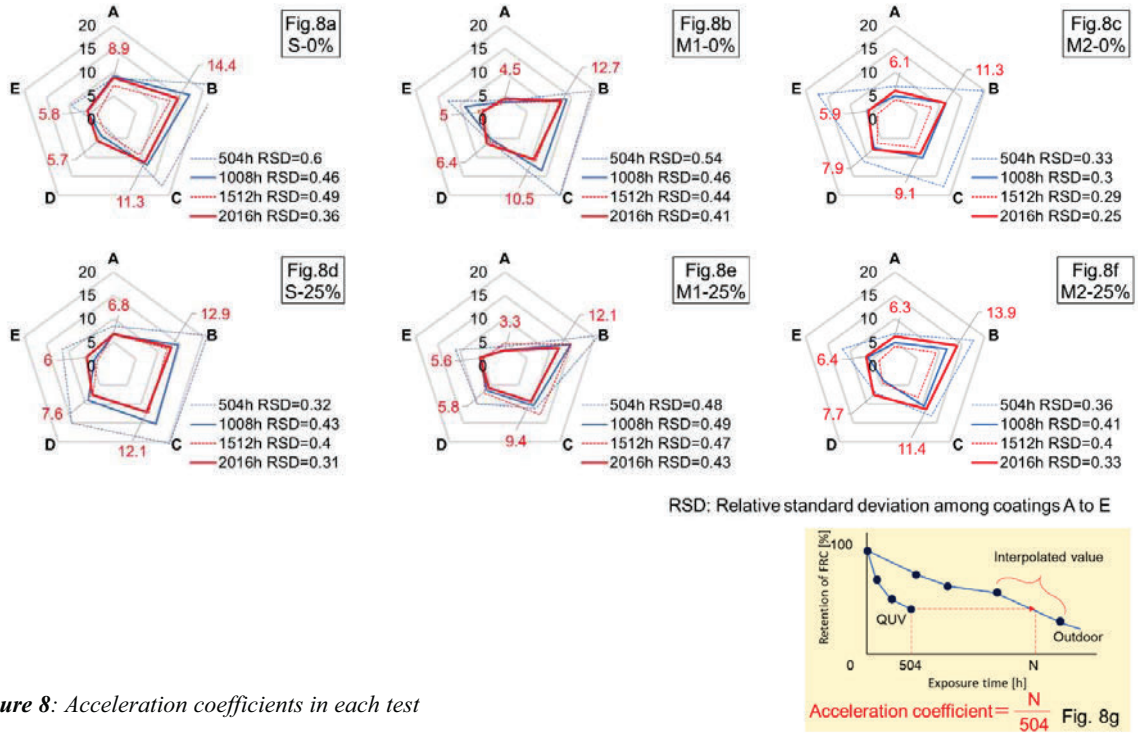

***Figure 8**: Acceleration coefficients in each test*

REFERENCES

[1] B. Östman and L. Tsantaridis: Fire retardant treated wood products – Properties and uses. *Proceedings 47th IRG Annual Meeting*, 2016.

[2] European standard: EN927-6, https://www.sis.se/api/document/preview/80007353/, accessed Feb. 2023.

[3] Podgorski, L., Arnold, M. and Hora, G.: A reliable artificial weathering test for wood coatings. *Coatings World*, 2:39-46, 2003.

[4] G. Grüll, F. Tscherne, I. Spitaler and B. Forsthuber: Comparison of wood coating durability in natural weathering and artificial weathering using fluorescent UV-lamps and water. *European Journal of Wood and Wood Product,* 72:367–376, 2014.

[5] A. Ishikawa, Y. Kataoka, S. Kawamoto, M. Matsunaga, M. Kobayashi and M. Kiguchi: Correlation between natural and accelerated weathering of coated wood. *Wood Protection,* 40(2):55-63, 2014.

[6] R. Takase, A. Ishikawa, D. Kamikawa, H. Matsunaga and T. Harada: Influence of moisture absorption on the degradation of fire-retardant-treated and surface-coated wood: Effect of water spray duration under accelerated weathering. *Wood Protection*, 46(2): 80-88, 2020.

[7] S. L. LeVan, C. A. Holmes: Effectiveness of fire-retardant treatments for shingles after 10 years of outdoor weathering. *Research paper FPL*, 474, 1986.

[8] T. Harada, Y. Kataoka, H. Matsunaga, D. Kamikawa, Y. Kameoka and M. Kiguchi: Weatherability and combustibility of fire-retardant impregnated and surface-coated wood after natural weathering test. *Wood Protection* 39(1):16-23, 2013.

[9] M. Nakamura, M. Kanematsu, Y. Nishio, H. Yoshioka, S. Hagihara, T. Sugita, K. Shimizu and T. Noguchi: Evaluation of durability of reaction-to-fire performance of fire-retardant treated wooden facades by accelerated weathering test. *AIJ Journal of Technology and Design,* 25(60): 709-714, 2019.

[10] M. Kawarasaki and Y. Hirabayashi: Investigation of factors in the efflorescence of fire retardant woods, *Wood Protection*, 40(1):17-24, 2014.

[11] M. Kawarasaki, R. Hiradate, Y. Hirabayashi, S. Kikuchi, Y. Ohmiya, J. Lee, M. Noaki and N. Nakamura: Fire Retardancy of Fire-retardant-impregnated Wood after Natural Weathering I: Effects of chemical types and coatings at up to 60-114, 2018.

[12] NORDTEST: Accelerated weathering of fire-Retardant treated wood for fire testing (NT FIRE 053)

[13] Japanese Industrial Standards: Testing methods for paints−Part 7 Long-period performance of film−Section 6 Natural weathering, JIS K-5600-6, 2002.

[14] Derbyshire, H. and Miller, E.R.: Moisture conditions in coated exterior wood Part 2: the relation between coating permeability and timber moisture content. *Journal of the Institute of Wood Science* 14(4):162-168, 1997.

[15] Derbyshire, H. and Miller, E.R.: Moisture conditions in coated exterior wood. Part 3: Moisture content during natural weathering. *Journal of the Institute of Wood Science,* 14(4):69-174, 1997.

[16] J. Niklewski, M. Fredriksson, T. Isaksson Moisture content prediction of rain-exposed wood: Test and evaluation of a simple numerical model for durability applications. *Building and Environment*, 97:126-136, 2016.

[17] H. Ishikawa and Y. Hashimoto: Estimation of impinging angle of driving rain against wall surfaces : Fundamental study on evaluating exposure severity of external walls to driving rain. *Journal of Structural and Construction Engineering*, 72(611):13-20, 2007.

[18] retrieved from Japan Meteorological Agency https://www.jma.go.jp/jma/indexe.html, accessed Feb. 2023.

[19] William T. Simpson: Equilibrium Moisture Content of Wood in Outdoor Locations in the United States and Worldwide. *Forest Products Laboratory Research Note,* FPL-RN-0268, 1998.

[20] de Meijer, M. and Militz, H.: Moisture transport in coated wood. Part 1: Analysis of sorption rates and moisture content profiles in spruce during liquid water uptake. *Holz als Roh- und Werkstoff*, 58:354–362, 2000.

https://doi.org/10.52202/069179-0069

World Conference on Timber Engineering Oslo 2023

DIMENSIONAL VARIATIONS MONITORING OF RADIATA PINE CLT PANELS: A CASE STUDY IN CONCEPCIÓN, CHILE

Víctor Rosales[1], Fernanda Pascal[2], Franco Benedetti[3], Pedro Rebolledo[4], Alan Jara-Cisterna[5], Mauricio Vargas[6]

ABSTRACT: Variations in wood moisture content lead to changes in virtually all physical and mechanical properties of timber. Besides, the damage to building elements is usually associated with unfavorable changes in material properties, support conditions, geometry, or load variations that can influence the structure's performance or durability. This research is oriented to monitoring the behavior of a CLT module prototype under the action of humidity, simulating the possible changes resulting from its use as a habitable space. With these field measurements, we study the dimensional variation of wall elements and moisture content in the structural panels in order to explore the possible behavior of the PymeLAB experimental building PymeLAB, a 5-story living laboratory that was installed on campus from the University of Bío-Bío during 2022. In this study, a prototype has been manufactured with conditioned 3-layer Radiata pine CLT panels with an initial moisture content of 11.6%. Dimensional changes caused by different humidification cycles were measured. The change in the moisture content of the internal face of the CLT panels exposed to the indoor climate showed increases in deformations of up to 1.74 mm/m.

KEYWORDS: Monitorig CLT, Moisture expansion, hydrothermal performance, CLT Radiata pine.

1 INTRODUCTION

Since the climate of Chile is quite varied, the moisture content of the wood in service varies from one region to another according to the differences in temperature and humidity. Consequently, there are 9 climatic zones, from the desert north to the extreme south [1].

Each building must be subject to a site assessment that considers the impact of seasonal weather conditions associated with the location, the structure, and its behavior in use. Its conditions of use will also have repercussions on the behavior of the building. For example, structures with exposed CLT are not usually used due to construction regulations associated with fire. However, knowing the behavior of uncovered CLT panels allows us to propose its behavior for combination with other interior and exterior cladding materials.

Hygroscopic materials can absorb moisture from the air when its relative humidity rises and release moisture into the air when it falls. These humidity variations result in dimensional variations in the wooden elements, which can cause problems in their connections or sheathings [2], resulting in post-sale costs in the buildings. The damp-absorbing effect of building materials can greatly influence the indoor hygrothermal environment [3]. Moisture absorption/release by hygroscopic materials can be calculated with the basic MBV factor, where the density and porosity of the materials are essential properties in the theoretical calculation of moisture buffering because these factors are likely to influence moisture transport. In addition, air velocity plays a relevant role in the sorption performance of materials. To obtain comparable results, various humidity buffering protocols require that the air velocity be constant and around 0.1 m/s during the tests [4]. Humidity and buffering capacity depend on several factors, from which porosity and temperature are influential; therefore, the moisture buffer values for bio-based materials have been measured at a constant temperature of 23°C [5].

One of the performance demands for buildings is durability, which in the case of wood can be greatly affected by prolonged exposure to moisture [6]. Moisture changes in wood are accompanied by deformations such as shrinkage and swelling. In particular, the prolonged exposure of wooden constructions to the effects of

[1] Victor Rosales, University of Bio Bio, Chile, vrosaleg@ubiobio.cl Centro Nacional de Excelencia para la Industria de la Madera (CENAMAD), Pontificia Universidad Católica de Chile.
[2] Fernanda Pascal, University of Bio Bio, Chile, fernanda.pascal1801@alumnos.ubiobio.cl
[3] Franco Benedetti, University of Bio Bio, Chile, fbenedet@ubiobio.cl
[4] Pedro Rebolledo, University of Bio Bio, Chile, prebolle@ubiobio.cl
[5] Alan Jara-Cisternas, University of Bio Bio, Chile, afjara@ubiobio.cl
[6] Mauricio Vargas, University of Bio Bio, Chile, mvargas@ubiobio.cl

https://doi.org/10.52202/069179-0070

humidity affects the durability and safety of the constructions [7].

Wang et al. (2018) point out that dimensional changes [8], moisture damage and microbial growth must be considered. These can eventually occur with short-term wetting or high relative humidity (RH) (80% to 95%), where the cycles of contraction and swelling of the wood can compromise the mechanical connections due to the degree of humidity exposure. On the other hand, it is pointed out that cracks are attributed to seasonal variations influenced by the internal climate that occurred in the buildings, which is associated with the process of contraction and swelling of the wooden elements. Also, shrinkage and swelling can affect the durability and stiffness of the connections [9].

Sung & Gi (2019) studied the swelling and contraction behavior of Larix kaempferi and Pinus koraiensis, analyzing CLT boards in a controlled environment [10]. From the results, they were able to distinguish that larger deformations were observed in the "y axis" (radial axis, perpendicular to the growth of the fibers) with respect to those perceived in the "x" and "z" axes. They also discriminated that the thickness does not lead to a tendency in the swelling and contraction behavior. However, the combination of the layers is of great relevance since the layers in the longitudinal direction of the panel give it dimensional stability in the x and z axes. According to the research carried out by the authors Schmidt et al. (2017), it is possible to accelerate or stimulate the wetting process to evaluate the performance of CLT panels against deformationsn using a multi-chamber modular environmental conditioning method.

Authors as McClung et al., Wang, Lepage et al., Kordziel and Schmidt et al., cited in the work of Schmidt et al. [6], carried out laboratory-scale experiments emphasizing the monitoring of the wetting and drying behaviors of large CLT samples, thought as the effect of water attacking the faces of the panels (rain). In addition, McClung et al. found that 5-layer CLT samples soaked by immersion for one week with epoxy-sealed edges and subsequently integrated into assemblies of variable permeability were generally within acceptable MC ranges (<26%) after one month, and most of them were dry after 4 to 6 months [6].
According to EN16351 [11], Service Class (SC) 1 is characterized by a moisture content in materials corresponding to a temperature of 20°C, and the relative humidity of the surrounding air only exceeds 65% for a few weeks in a year. In SC 1, the average moisture content in most softwoods will not exceed 12%. Service class 2 is characterized by a moisture content in the materials corresponding to a temperature of 20 °C, and the relative humidity of the surrounding air only exceeds 85% for a few weeks of the year. In SC 2, the average moisture content in most softwoods will not exceed 20%. For its part, SC 3 is characterized by climatic conditions that lead to higher moisture content than in SC 2. Additionally, the standard propose values for the adjustment of the in-plane moisture deformation (0.0002) and perpendicular to the plane (0.0024). These parameters are considered in an expression for the correction of the size for moisture contents within the range from 6% to 25% in the species recognized in the standard. The existing formula in the EN standard predicts CLT contraction and expansion as a function of the CLT coefficient. The limitation of this approach is that the dimensional change of CLT cannot be estimated before measuring the actual CLT coefficient. CLTs of various layer combinations can be manufactured, thus, the dimensional characteristics would differ depending on the layer combinations [10].
A study on moisture in edge-glued wood panels found that a 1 percent change in moisture in White Pine will change the width of a 75mm wide board by 0.05 to 0.15mm. In addition, the study showed that boards gain or lose moisture 10 to 15 times faster from the ends than from the faces and sides of the panel. In contrast, for CLT panels, this is less due to the element's configuration, but a different behavior is expected at the ends of the pieces.

Han et al. [7] used samples with different moisture contents in the layers that make up the CLT elements to study the effect of the moisture difference. The humidification processes were carried out within a period of 3 weeks. After humidification, the changes in width and thickness of the samples were measured during drying under two conditions (80% and 40% relative humidity). The results showed that the dimensional changes of the CLT samples tended to be repeated in shrinkage and swelling, which depended on the humidity variation. Both the shrinkage and the swelling in the width of each sample varied from 0.492 to 2.145 % and from 0.459 to 2.542 %, respectively [7]. For the samples made with a similar moisture content between the inner and outer layers (difference less than 1.6%), the variation in shrinkage and swelling were less than 1.5%.

Schwab et al. [12] investigated the swelling coefficient for a thickness of 20 mm in sheets of European spruce CLT. They found that in the X,Y,Z directions the swelling ceofficient was from 0.00031 to 0.00038, respectively. For their part, Gereke et al. [13] investigated the swelling coefficient for a 30 mm sheet thickness Fagus sylvatica CLT. The swelling coefficient found for the X,Y,Z direction was 0.00011, 0.0023, and 0.00009, respectively. The swelling shrinkage coefficient in the Y direction was approximately 21 and 26 times higher than in the X and Z directions, respectively.
3-layer panels (90 mm thick) of Korean larch (larix kaempferi, 500 kg/m3) and Korean pine (pinus koraiensis, 410 kg/m3) were investigated to predict the dimensional change of CLT from the dimensional change of the sheets. In order to know the swelling, small samples were conditioned at 7.7% moisture

https://doi.org/10.52202/069179-0070

content, which were then brought to 19% and later to a saturated state. For this type of panels of the Korean larch species, in the x direction, a swelling and contraction value of 0.000217 and 0.000507 respectively was achieved; for the z direction 0.000150 and 0.000223 respectively. Using the same CLT panel configuration, but of the Korean pine species, in the x-direction, a swelling and contraction value of 0.000216 and 0.000467 respectively was achieved; for the z direction 0.000117 and 0.000183 respectively. [10]

Given the lack of knowledge about the moisture-deformation behavior of Radiata pine CLT boards subjected to temperature and humidity variations under operation conditions, this work studies the dimensional variation of a full-scale CLT module located in the University of Bio-Bio (Concepción, Chile).

2 MATERIALS AND METHODS

This work focuses on the behavior of a CLT prototype against inner climate variation by monitoring the variation in the in-plane CLT climate response. The workflow considered five humidity cycles of 3 weeks long each.

During the entire test period, the University of Bío-Bío on-site weather station recorded the outdoor weather data, and monitoring equipment recorded the indoor weather. A daily humidity production cycle was chosen, whose maximums are short but intense depending on the relative humidity level necessary to reach the value established by the control equipment.

Sensors were installed in the prototype to continuously record the following parameters: temperature and relative humidity in the center of the module. Here only the measurement parameters temperature and relative humidity are considered.

The interior temperature is maintained at 20°C by a control regulating an electric radiator. The relative humidity is measured in the center of the room at a height of 1.2 m. In addition, the air from the fans is kept at 0.1 m/s.

The ambient temperature remained constant at 20 °C except for a few days, in which this temperature was exceeded for some hours due to intense solar radiation. The damping effect on humidity is more important over 50% in relative air humidity, an environment in which fungal growth is favored. According to the type of panels used in this research, those with no treatment, sealing, or sheathing, are defined as open type, which is not always the case employed in common practice.

2.1 PROTOTYPE DESCRIPTION

The CLT panels were manufactured in the Wood Design and Technology Laboratory facilities of the University of Bío-Bío, Concepción. Kiln-dried radiata pine lumber having a 12% (+/-2%) moisture contente were used. The average density of the lumber boards was 398 kg/m^3, and were mechanically classifiedas C16 according to EN338 [14]. Boards were planed to 18 x 130 and 33 x 130 mm thicknesses, and then edge and face glued with PU-1 K polyurethane adhesive. For the curing of the adhesive, a hydraulic press was employed, applaying a pressure of 0.8MPa. The final dimensions of the CLT panles was 99 x 1200 x 1960 mm (33 x + 33 y + 33 x) for the walls and 84 x 850 x 3600 mm (33 x + 18 y + 33 x) for the floor and ceiling. In one of the panels, electrodes were installed to measure and monitor the moisture content from the beginning of the process.

In order to make the joints, a half-wood milling process is carried out on the edges of the CLT panels, with a dimension of 33 x 60 mm. A C16 Radiata Pine board of 33x119mm was employed to produce the joint between panels, fastened with screws arranged every 70 mm. The elements are assembled using the traditional techniques for this type of construction system, which is based on the use of screws in the corners for the wall-wall connection, angle bracket for the wall-floor connection, and screws for the wall-ceiling connection. Figure 1 presents general views of the module used for the study.

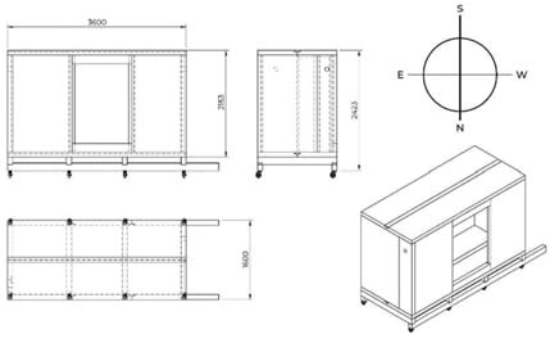

Figure 1: *Floors and elevation plan (left) and 3D view of prototype.*

After the assembly, the sealing tasks were carried out with tapes and membranes that reduce the infiltration and transfer of steam. The edges of the CLT panels were not sealed. Besides, thermal insulation and sheathings were installed on the exterior face. The module has an access door of 42 x 600 x 2300 mm and windows of 500 x 1600 mm located on the north side, which use a thermopanel with a U value of 1.8 W/m^{2}K. The thermal transmittance value of the envelope for the wall is U=0.46 W/m^{2}K, which is obtained from the constructive

conformation of the wall (99 mm CLT of Radiata Pine with 50 mm of mineral wool).

On the outside and at the height of 2500 mm, a temperature and relative humidity recorder was located in the shade, which captures the climate data of the surrounding zone. Inside, two Yowexa-Japan temperature and relative humidity recorders were installed, located at the same interior height (1200 mm) but in 2 different positions. To regulate the indoor climate, a climate unit and a series of humidifiers are installed and connected to an automatic temperature and humidity control system, which was set to control each cycle.

2.2 INSTRUMENTATION

The panels were coded as N, S, E, O (North, South, East, and West), gridded every 300 mm, and in selected zones of the grid, humidity sensors (electrodes) and digital transducers were installed on a Whittemore-type device. The humidity sensors were installed at different depths (P1=21 mm, P2=27 mm, and P3=32 mm), completing a thickness of 1 lamina constituting the CLT, as shown in Figure 2.

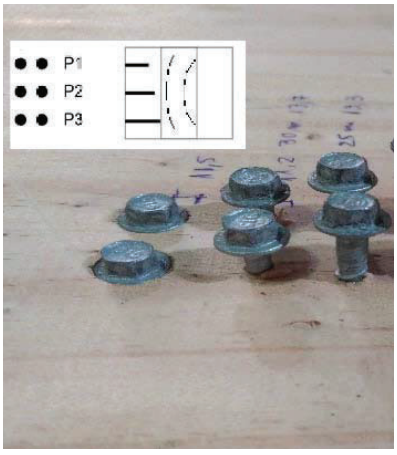

***Figure 2**: Installation of the moisture monitoring electrodes at different depths (P1, P2 y P3)*

Displacement transducers were installed in the area close to the moisture measurement points to evaluate the in-plane deformations of the panel (X, Z plane). Two measurement zones were considered to evaluate the horizontal deformations in the same panel (SX1, SX2), one to measure the complete deformation of the panel plus one joint (SX3), and one for the evaluation of the vertical deformation (SZ3). Depending on the sensor installed, the distance between these two points is around 500 mm to 600 mm. and 1085 mm for SZ3. The layout of the instruments is schematized in Figure 3.

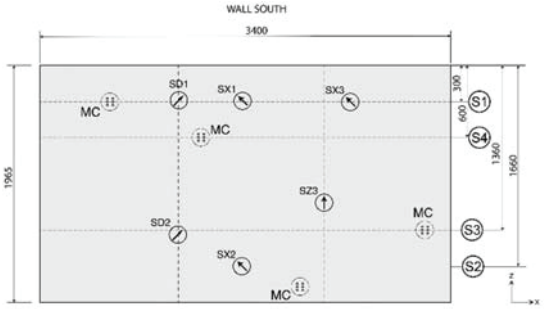

***Figure 3:** Layout for moisture (MC) and displacement metering (S X and SZ) metering.*

2.3 CLIMATE CONDITIONS

The climate used to develop of the experiment considers a temperature of 20 ° (+/- 2°C), and relative humidity (RH) that varies by stages, increasing from 60% to 90% (+/- 3%). Consequently, five stages of indoor climate conditions were defined (Table 1), distinguishing Stage 1: (conditioning) 60% RH; Stage 2: 65% RH; Stage 3: 75% RH; Stage 4: 85% RH and Stage 5: 90% RH. The measurements began on November 2, 2021, and ended on February 3, 2022. The module's external weather conditions corresponded to the Nonguén area's climate (Concepción, Chile) during spring 2021 and summer 2022.

***Table 1:** Climate conditions during the experiment*

Cycle	Days	Inside		Outside	
		Mean RH (%)	Mean temp (°C)	Mean RH (%)	Mean temp (°C)
Stage 1	0-20	59,6	20,5	64,6	16,3
Stage 2	21-43	66,0	21,0	65,3	16,8
Stage 3	44-62	77,1	21,7	68,2	17,7
Stage 4	63-78	84,7	21,7	70,4	18,1
Stage 5	79-94	90,6	21,4	70,1	17,2

2.4 MONITORING SETUP

The deformations in the CLT panels were recorded at constant intervals (two times a day) using Mitutoyo instruments. In addition, the moisture content of the different panels was recorded three times a week, through a RDM[3] Delmhorst resistive xylohygrometer (Figure 4). Additionally, it was necessary to measure the interior climate of the module (Temperature and Relative Humidity) at 30 min intervals, measuring the room temperature at two different points.

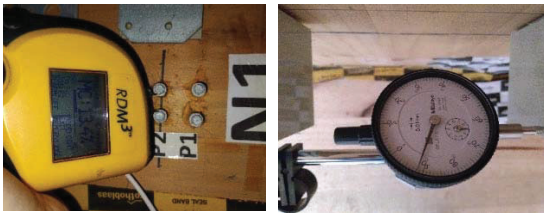

https://doi.org/10.52202/069179-0070

Figure 4: *Moisture content (left) and displacement (right) measurement instrument.*

Critical aspects of installing the moisture content electrodes and the measurements included: (1) avoiding gaps and knots between electrodes, (2) using guides for exact electrode spacing, (3) drilling holes to the exact length of the insulated casing used for the electrode, (4) insert the screws at the same speed and leaving the insulated base leveled with the wood, and (5) ensuring communication with the manual system [15].
The analog displacement gauge has a measuring range of 12mm with a resolution of 0.01mm. However, Huston et al. suggest that electronic instruments are more practical for long-term measurements [16].
The instrumentation arrangement on the wall was intended to monitor the displacements and moisture content of the wood in the nearby area (Figure N°5).

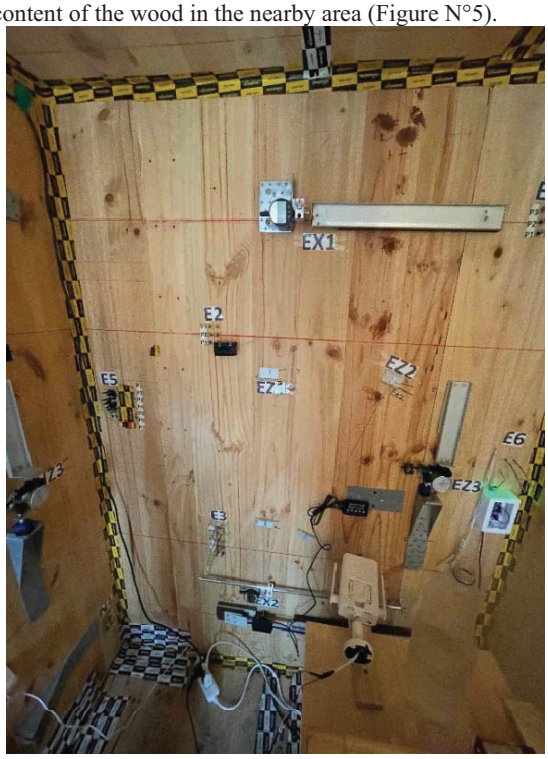

Figure 5: *Instrumentation and monitoring system arrangement for the East Wall.*

2.5 DIMENSIONAL CHANGE IN CLT WALLS

The expression proposed in the EN16351 standard was used to determine the dimensional change, which establishes a coefficient that depends on the direction (in-plane or out of plane).

$$a_{cor} = a_a \, x \, (1 + K_{cor,\propto} x \, (H_{ref} - \, H_a)) \qquad (1)$$

Where a_{cor} = effective dimension (mm); a_a = actual dimension (mm); $K_{cor,\alpha}$ can be either $K_{cor,90}$ = stability coefficient perpendicular to the fiber or $K_{cor,0}$ = stability coefficient in the plane, both expressed for to 1% variation in moisture content between 6% and 28%; H_{ref} = 12%, reference moisture content; and H_a = actual moisture content (%).

3 RESULTS AND DISCUSSION

3.1 POST PROCESAMIENTO DE DATOS Y LA INCERTIDUMBRE DE MEDICIÓN

The literature provides estimates of measurement uncertainty for moisture content based on wood strength, biological variability within a given wood species, and at different moisture contents [15]. In this study, the discontinuous readings were not corrected for the radiate pine CLT given the calibration of the instrument manufacturer for this specie. Moreover, the data collected during the assessments suggest that most of the time, local moisture content fluctuations were clearly correlated with internal weather conditions and the depth of masurement in the CLT panels.

To keep under control the uncertainty, two pieces of 100 x 300 x 450 mm of radiata pine CLT were placed inside the monitored module, and the moisture content was controlled through the instrument and in the laboratory. The moisture content sensors' performance in the CLT module's different positions during the 90 days of the evaluation was consistent with the data obtained from the control samples.

For their part, the instruments that captured the module's temperature and relative humidity were permanently contrasted. Their measurements resulted in being consistent.

The obtained data consist of discontinuous readings for the moisture contents in different positions (North, South, East, and West walls) and depths (P1, P2, and P3), for the deformation of the panel on its corresponding X or Z position. On the other hand, the internal and exterior climate values were recorded continuously.

Both the moisture content data and displacements in the CLT walls are presented in the tables in the following sections. The indoor climate data, as well as the exterior climate data (temperature and relative humidity) are shown as 1-day central moving averages.

https://doi.org/10.52202/069179-0070

3.2 MOISTURE CONTENT MEASUREMENTS

The increase in moisture content inside the prototype module induces an increase in the moisture content of the different panels that set up the walls. Figure 6 shows a comparison of the increases in moisture content at depth P1in the different positions of the module walls (North, South, East, and West).

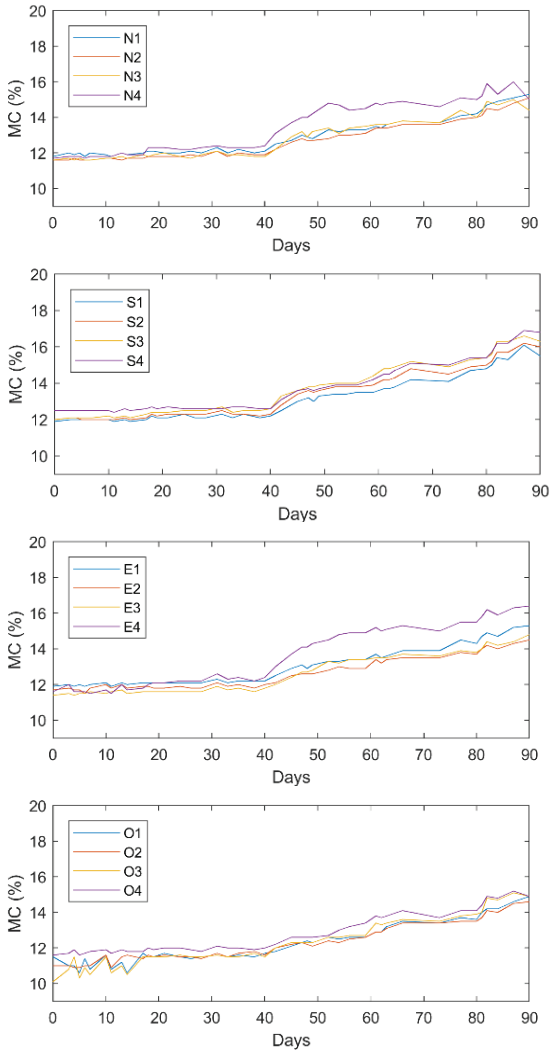

Figure 6: *Moisture content variations at P1 depth in walls North, South, East, and West.*

In cycle 1 with a temperature of 20 °C and 60% relative humidity (days 1 to 20), the values of moisture content in position P1 have an average value of 11.6 %; which is very similar to the averages at depths P2 and P3 (11.7% and 11.5%, respectively). Besides, for cycle 2 with a temperature of 20°C and 65% relative humidity (days 21 to 43), the moisture content in position P1 is 11.8% on average. In contrast, the moisture contents increase in the other two depths (P2 and P3).

In cycle 3 (days 44 to 62, temperature of 20°C and 75% relative humidity), the moisture content average in the three depths tends to be 12%. For cycle 4 (days 63 to 78, temperature of 20°C and 85% relative humidity), once again, the three depths showed similar average values equal to 13.5%. Finally, in cycle 5 (days 79 to 94, temperature of 20°C and 90% relative humidity), the average moisture content in position P1 are slightly higher than P2 and P3, with values of 14%, 13.7%, and 13.3%, respevctively. The different data are shown in Table 2.

Table 2: *Moisture content mena values in the CLT walls for each climate cycle and measurement depth*

Stage	RH (%)	Measurement Depth	Initial MC (%)		Final MC (%)	
			Mean	SD	Mean	SD
1	60	P1	11.6	2.11	11.8	0.78
2	65		11.8	0.78	12.0	0.79
3	75		12.0	0.79	13.5	0.65
4	85		13.5	0.65	14.0	0.82
5	90		14.0	0.82	15.4	1.15
1	60	P2	11.7	2.13	11.9	0.81
2	65		11.9	0.81	12,0	0.81
3	75		12,0	0.81	13,0	0.89
4	85		13,0	0.89	13.7	0.84
5	90		13.7	0.84	14.7	1.16
1	60	P3	11.5	2.15	11.8	0.84
2	65		11.8	0.84	11.9	0.82
3	75		11.9	0.82	12.8	0.89
4	85		12.8	0.89	13.3	0.84
5	90		13.3	0.84	14.2	1.17

The results show an important moisture content gradient for cycle 5 in the three measurement depths. The percentage variations of the moisture contents are 15.4% for P1, 14.7% for P2, and 14.2% for P3. These increasings are related to moisture content increments of 3.8%, 3%, and 2.7% for P1, P2, and P3, respectively.

The moisture content measurements also highlighted the trend of the moisture to concentrate at the interface of the first two CLT layers rather than just on the surface. A recent Morrell et al. [17] study also showed this trend. In the results obtained, the damping effect of the CLT without protection can be noticed since the temperature and relative humidity of the environment should have induced an equilibrium moisture content close to 18 %. However, this value is closer to some measurements of the wall panels on the module's south side, as seen in Figure 7.

https://doi.org/10.52202/069179-0070

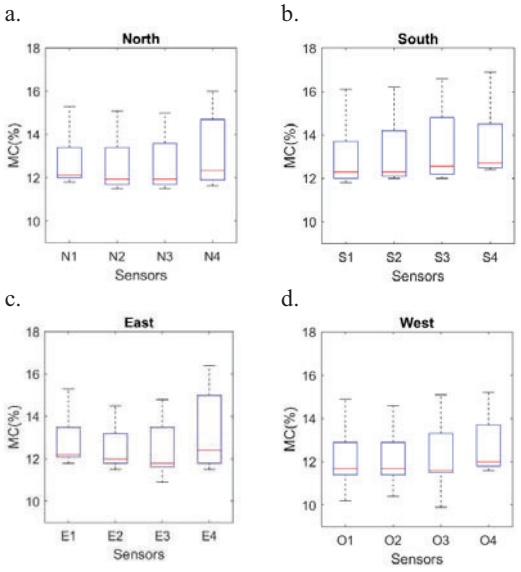

***Figure 7**: P1 depth moisture content box plots for walls a) North; b) South; c) East; and d) West.*

The difference between the moisture content measured the north and east wall, appears to be related to the overheating of the wall due to solar exposure in the summer season.

3.3 DIMENSIONAL STABILITY

The dimensional variation suffered by the CLT module during the experiment is presented in Figure 8, which presents the south side wall results. The expressed values correspond to the differentials that happened in the measurement zone (from 500 to 600 mm) detected by the Whittemore gauge system.

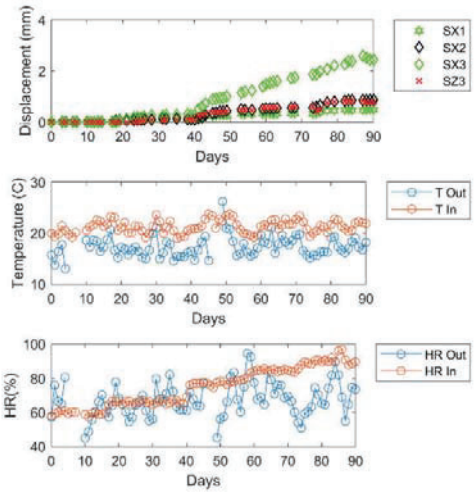

***Figure 8:** In-plane dimensional change of South panel (top), interior and exterior average temperature (middle) and relative humidity (RH, bottom).*

The results of absolute experimental dimensional variations for the different walls are shown in Table 3 for the North, East, and South walls. It is noticed that the total displacement values fluctuate from 0.45 mm to 1.59 mm (SX1 and NX2, respectively), depending on the CLT panel and its orientation. The value measured by the SX3 sensor is not considered for mean value, since it is an evaluation that takes the entire width of one panel and half of the connection with the other panel, having an evaluation length of 1085 mm. Besides, the nominal value is determined considering the experimental dimensional variation evaluated in one meter of length.

***Table 3:** Total dimensional variation in the different analysis directions in each sensor position and orientation.*

Direction	Sensor	Instrumental value (mm)		Total dimensional Variation	
		Initial	Final	Experimental (mm)	Nominal (mm/m)
X	NX1	0.12	1.29	1.17	2.34
	NX2	0.27	1.86	1.59	3.18
	EX1	10.51	11.37	0.86	1.72
	EX2	-0.06	-0.56	0.50	1,00
	SX1	-0.03	-0.48	0.45	0.76
	SX2	-0.01	-0.87	0.86	1.45
	SX3	0,00	2.45	2.45	2.26
Z	NZ3	-0.02	0.52	0.54	1.03
	EZ3	0.00	0.39	0.39	0.73
	SZ3	0.00	0.77	0.77	1.43

For the X direction (wall width) the average results variate 60% more than in the Z direction (wall height), as presented in Table 4. Besides, it is observed that the nominal displacement that would occur in the panels of 1 meter width (1.74 mm/m) should be considered in the gaps or construction tolerances in order to avoid problems in the connections or differences with the interior sheathings, particularly in wet areas.

***Table 4:** Mean total dimensional variation for X and Z directions*

Climate Variation	Direction - Axis	Mean total dimensional variation	
		Experimental (mm)	Nominal (mm/m)
20 °C; RH 60 to 90 (%)	Z	0,57	1,06
	X	0,91	1,74

Due to the constraining action of the cross laminations, CLT has (relative to uniaxial glulam products) more stable in-plane dimensions when it interacts with the environment. The wall samples tested expanded a maximum of 1.59 mm in width (measured transverse to the surface layers) and 0.77 mm in length (measured longitudinally to the surface layers) during all wetting cycles. These deformations are still notably smaller than the nominal calculated values using recommended standard rates that do not take into account the intrinsic characteristics of the Radiata Pine employed.

https://doi.org/10.52202/069179-0070

3.5 STABILITY COEFFICIENT FOR RADIATA PINE CLT PANELS

Using the moisture content data at depth P1 in the area near the displacement measurement zones, it is possible to calculate the experimental stability coefficients through equation (1). These results are presented in Table 5.

Table 5: *Stability coefficient (swelling) calculated per each measuring sensor.*

Direction	Sensor	Total dimensional Variation		Delta MC	K cor,0	Mean Kcor,0
		Experimental (mm)	Nominal (mm/m)			
X	NX1	1.17	2.34	3.5	0.00067	0.00048
	NX2	1.59	3.18	3.3	0.00096	
	EX1	0.86	1.72	3.5	0.00049	
	EX2	0.50	1,00	4.8	0.00021	
	SX1	0.45	0.76	3.7	0.00020	
	SX2	0.86	1.45	4.3	0.00034	
	SX3	2.45	2.26	4.4	0.00051	0.00051
Z	NZ3	0.54	1.03	3.2	0.00032	0.00029
	EZ3	0.39	0.73	3.4	0.00021	
	SZ3	0.77	1.43	4.2	0.00034	

The average value achieved for the plane in the X direction of the CLT walls is 0.00048, 2.4 times higher than the coefficient recommended in the EN16351 standard for the Radiata Pine species. Moreover, the value of the SX3 sensor, which has a longer evaluation length, is close to the mean coefficient calculated, being 0.00051. In the other direction of the plane, Z or longitudinal direction, the average value is 0.00029.

Figure 9 presents a graphical comparison of the experimental stability coefficients with respect to the recommended values of the EN16351 standard.

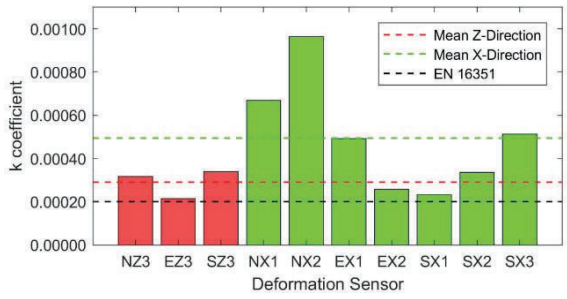

Figure 9: *Comparison of the experimental and recommended stability coefficient values for Radiara Pine CLT panels.*

Finally, in Table 6 is possible to appreciate the values of the swelling coefficient that different authors have achieved.

Table 6: *Comparison of experimental stability coefficient values recommended in different studies.*

Author	Specie	Swelling Value	
		X	Z
Pang S. & Jeang G.	Korean larch	0,000217	0,000150
	Korean pine	0,000216	0,000117
Gereke et al.	Fagus sylvatica	0,000110	0,000090
EN16351	Radiata pine	0,000200	0,000200
Experimental	Radiata pine	0,000479	0,000290

4 CONCLUSIONS

This research monitored the moisture content and dimensional variation based on the relative humidity of the internal climate of a conditioned CLT module, aiming to evaluate if the dimensional changes are within the parameters established in the EN 16351 standard: 2016.

The deformation of the CLT elements under humidity cycles was measured. The in-plane deformations of the CLT increase as the relative humidity of the environment increases in the experimental module. The most important deformations appear when the relative humidity of the environment rises above 75%. After these cycles, the deformations continue to increase.

The Radiata Pine CLT wall panels appear to be dimensionally stable during the development of the experiment. The observed zones expanded on mean 0.91 mm in width and 0.57 mm in height during the conditioning cycles. During the conditioning, the CLT moisture content increased 5.1% at a depth of 21 mm from the surface. The experiment was carried out considering potential conditions of short and long periods of climatic exposure. Even though the construction configuration of the prototype CLT module is atypical (no lining or sheathings were used), this type of test revealed the most critical behavior that the system could have in service. Therefore, it provides relevant information for the variety of climates existing in Chile.

The experience only considered the increase in humidity in the interior climate; thus, only the swelling coefficient was studied to stablish stability. It is suggested to develop experimets to study the behavior of Radiata Pine CLT panels under contraction cycles.

In the tested configuration, the direction of the outer most layer produces a distortion of the CLT laminations on the surface. Those points in which the outer layers of the CLT have pith or central wood suffered larger displacements, especially in the north wall.

Regarding the in-plane dimensional change that the CLT elements of the prototype module experienced, it was observed that these were greater than the values determined using the coefficient recommended in the

https://doi.org/10.52202/069179-0070

EN16351 standard, especially in the direction which is related to the direction of the cut of the wood.

ACKNOWLEDGEMENT

Collaborations of SIMPSON Strong-Tie, CMPC Maderas, Alto Horizonte, Promaest, Forestal Tricahue, JMS Ingenieros, Premad, Cortelima, Constructora IMB, Oxiquim S.A., Láminas Chile, Lemu Products, EBCO, as well as the funding and support provided by MacroFacultad, CIPYCS, and CORFO are deeply acknowledged. Finally, we also thank ANID BASAL FB210015 for their ongoing scientific collaboration with our academic departments.

REFERENCES

[1] Instituto Nacional de Normalización (2008): Nch1079:2008: Arquitectura y construcción - Zonificación climático habitacional para Chile y recomendaciones para el diseño arquitectónico. Santiago, C.
[2] Riggio M., Schmidt E., and Mustapha G.: Moisture Monitoring Data of Mass Timber Elements During Prolonged Construction Exposure: The Case of the Forest Science Complex (Peavy Hall) at Oregon State University. Front. Built Environ. 5:98. 2019 hile:INN
[3] M. Zhang, M. Qin, Z. Chen Moisture buffer effect and its impact on indoor environment IERI Procedia, 2005 (2017), pp. 1123-1129.
[4] Cascione, V.; Cavone, E.; Maskell, D.; Shea, A.; Walker, P. The effect of air velocity on moisture buffering. In MATEC Web of Conferences; EDP Sciences: Les Ulis, France, 2019; Volume 282, p. 02007.
[5] Igue, F.D.; Tran Le, A.D.; Bourdot, A.; Promis, G.; Nguyen, S.T.; Douzane, O.; Lahoche, L.; Langlet, T. Impact of Temperature on the Moisture Buffering Performance of Palm and Sunflower Concretes. *Appl. Sci.* 2021, *11*, 5420.
[6] Schmidt E., Riggio M., Barbosa A., and Mugabo I.: Environmental response of a CLT floor panel: Lessons for moisture management and monitoring of mass timber buildings. Building and Environment Volume 148, January 15 2019, Pages 609-622
[7] Han, Y., Park, Y., Yang, S.-Y., Chung, H., Chang, Y.-S., and Yeo, H. (2019). "Dimensional changes of cross-laminated specimens produced under different conditions due to humidity variation," BioRes. 14(2), 4035-4046
[8] Wang J.Y., Stirling R., Morris P.I., Taylor A., Lloyd J., Kirker G., Lebow S., Mankowski M.E., Barnes H.M., and Morrell, J.J. 2018. Durability of Mass Timber Structures: A review of the biological risks. Wood and Fiber Science. 50: 110-127
[9] Silva C., Ringhofer A., Branco J., Lourenço P., and Schickhofer G.: Influence of moisture content and gaps on the withdrawal resistance of self tapping screws in CLT. In 9º Congresso Nacional de Mecânica Experimental Aveiro, 15-17 de Out., 2014
[10] S.-J. Pang, G.Y. Jeong 2020. Swelling and shrinkage behaviors of cross-laminated timber made of different species with various lamina thickness and combinations Constr. Build. Mater., 240 (2020), Article 117924
[11] EN 16351, Timber structures, cross laminated timber, requirements, European standard, 2016.
[12] E. Schwab, A. Steffen, C. Korte In-plane swelling and shrinkage of wood-based panels Holz Als Roh-Und Werkst, 55 (4) (1997), pp. 227-233
[13] Gereke T, Schnider T, Niemz HA P (2009) Identification of moisture-induced stresses in crosslaminated wood panels from beech wood (Fagus sylvatica L). Wood Sci Technol 43(3):301–315
[14] EN338: Structural timber Strength classes; CEN. 2016
[15] Schmidt, E.; Riggio, M. Monitoring Moisture Performance of Cross-Laminated Timber Building Elements during Construction. *Buildings* 2019, *9*, 144.
[16] Huston, D., Structural sensing, health monitoring, and performance evaluation. 2010: CRC Press.
[17]J. Morrell, I. Morrell, A. Sinha, D. Trebelhorn Moisture intrusion in cross laminated timber and the potential for fungal attack Proc. WCTE 2018 World Conf. Timber Eng. Seoul/S. Korea (2018)

World Conference on Timber Engineering Oslo 2023

EFFECTS OF PANEL DIRECTION, LOAD LEVEL AND AMBIENT HUMIDITY ON THE CREEP OF DOWNSCALED CROSS-LAMINATED TIMBER

Dawei Wang[1], Meizhen Chen[1], Meng Gong[2], Zhuo Cheng[3]

ABSTRACT: The creep behaviour of wood or engineered wood products is an important factor in the consideration of the serviceability of a timber structure. This study evaluated the effect of creep of downscaled cross-laminated timber *(CLT)* specimens by considering panel direction, load level and relative humidity *(RH)*. The test materials were spruce-pine-fir (*SPF*) lumber and polyurethane adhesive. Static bending, one-week creep and four-month creep tests were conducted. It was found that: 1) *CLT* specimens had an average proportional limit *(PL)* of around 3,024 N and 817 N in the "Major-strength" and "Minor-strength" directions, respectively; 2) Panel direction strongly impacted time-dependent deflection, with the "Minor-strength" specimens exhibiting a 2 to 2.5 times as large deflection as the "Major-strength" ones; 3) Load level clearly affected the load-deflection behaviour due to the layup of the specimens; 4) Ambient humidity had a little effect on 7-day creep, but impacted the 4-month mechano-sorptive creep to some degree; and 5) The "Generalized Kelvin" model seemed to be suitable in simulation the creep of the downscaled *CLT* specimens used in this study. The upper limit of the model at 95% confidence level could be a good approach to simulate the creep of the specimens under cyclic *RH*.

KEYWORDS: Cross-laminated timber, Relative humidity, Load level, Panel direction, Creep, Mechano-sorptive behaviour, Modelling

1 INTRODUCTION

The use of cross-laminated timber (*CLT*), an innovative green building material, has gained widespread popularity in recent years, particularly for the construction of mid- and high-rise timber structures. The advanced cross-laminate technology utilized in *CLT* production provides the panels with improved dimensional stability and high in- and out-of-plane stiffness and strength properties, leading to its two-way action capability and enhanced high-strength construction [1]. Additionally, *CLT* offers a cost-effective alternative to traditional building materials such as concrete and steel, as its light weight reduces the size and cost of foundations. The great seismic and fire performance of *CLT* panels further adds to their suitability for use in various building environments [1].

The evaluation of the serviceability of a timber structure requires a thorough understanding of the concept of creep, which can be classified into two types: "pure" creep and mechano-sorptive creep. "Pure" creep is defined as the time-dependent deformation caused by a material under constant load [2], while mechano-sorptive creep is the deformation affected by an interaction between humidity variations and mechanical loading [3]. The creep behaviour of wood is subject to various factors, including temperature, relative humidity (*RH*), grain direction of wood, strength direction of a product, loading condition, member size, and anatomical features of wood. However, the mechano-sorptive creep of *CLT* is specifically influenced by the ambient temperature and humidity when it happens [2]. Despite its importance, research on the mechano-sorptive creep of *CLT* remains limited.

In the early stage of research, the evaluation of creep behaviour in wood materials was primarily conducted through experiments utilizing both small clear wood specimens and full-scale timber products [4-5]. These wood materials were analysed by utilizing rheological and viscoelastic theories, leading to a thorough understanding of their creep behaviour. Under variable temperature and moisture conditions, the time-dependent behaviour of wood is highly complex [6]. Phenomenological studies, similar to those conducted by Schniewind [4], were performed to investigate the impact of environmental factors on creep behaviour, with results obtained for both constant and varying conditions during the course of an experiment. Subsequent studies indicated that creep was often more vulnerable to changes in temperature, moisture content (*MC*), and physical ageing than its elastic properties [2, 7]. Since then, efforts have been made on the studies that included creep by considering multiple influencing factors such as humidity effect, as well as the development of creep models. Over the past several decades, there has been a remarkable advancement in the study of the viscoelastic properties of wood. This has been achieved largely through the innovation and improvement

[1] Dawei Wang, Faculty of Forestry and Environmental Management, University of New Brunswick, Canada, dwang12@unb.ca
[1] Meizhen Chen, Faculty of Forestry and Environmental Management, University of New Brunswick, Canada, meizhen.chen@unb.ca
[2] Meng Gong, Wood Science and Technology Centre, University of New Brunswick, Canada, mgong@unb.ca
[3] Zhuo Cheng, Off-site Construction Research Centre, University of New Brunswick, Canada, zcheng2@unb.ca.

https://doi.org/10.52202/069179-0071

of testing methods, the collection of experimental data, and the formation of rheological models. These progresses have occurred in parallel with the rapid expansion of the wood-based products industry and uses of wood-based products in construction, leading to a corresponding invention and development of various types of engineered wood products (*EWPs*), such as *CLT*. Bengtsson [8] conducted a third-point bending test using Norway spruce (*Picea abies*) specimens and observed that *MC* and density strongly influence the creep behaviour of timber. The study also demonstrated a strong correlation between the relative creep and modulus of elasticity. O'Ceallagh et al. [9] conducted third-point bending tests under constant stress levels using Sitka spruce (*Picea sitchensis*) for 75 weeks to investigate the mechano-sorptive creep behaviour of unreinforced and fiber-reinforced polymer (*FRP*) plate-reinforced glued laminated timber beams with the variable *RH* ranging from 65±5% to 90±5%. The results indicated that variable *RH* values significantly influenced creep behaviour. The first *RH* cycle caused a statistically significant reduction in both total and creep deflection. Takanashi et al. [10] conducted long-term out-of-plane bending tests on full-scale seven-layer Japanese larch (*Larix kaempferi*) *CLT* panels and estimated a mean relative creep of 1.49 after 50 years using a power-law function developed by Holzer [6]. The authors also recommended avoiding *CLT* products made from Japanese larch when subjected to loading levels of 70% or more. Hunt [11] proposed a unified approach to modelling the creep behaviour of Ponderosa pine (*Pinus ponderosa*), who was aimed at developing a mathematical model that could accurately predict the long-term deformation of wood under varying stress levels and environmental conditions. He reported that the full extent of the mechano-sorptive effect would require the timber to reach equilibrium moisture content (*EMC*) under new environmental conditions. Therefore, multiple changes of *RH* in full-scale tests may yield inaccurate results. Due to the lack of a harmonized standard for examining the mechano-sorptive effect in *EWPs*, the duration of creep tests and *RH* cycles vary significantly between test programs. Liu et al. [4] analysed different models for simulating creep in laminated veneer lumber products by using third-point bending test under short- and long-term constant loading and found that the modified Burger model provided good simulation. Cai et al. [12] used the specimens of southern pine (*Pinus spp.*) to give two sets of tests for creep and creep recovery, which presented new models for creep and creep recovery, which could be well fitted to both primary and secondary stages of creep deformation using modified power-law functions.

This study was aimed at investigating and simulating the creep behaviour of *CLT* using the downscaled specimens by considering panel direction, load level and ambient humidity.

2 MATEIRALS AND METHODS

2.1 MATERIALS AND SPECIMENS

Downscaled *CLT* specimens consisting of three-layers were produced using 2×6 No.2 Spruce-Pine-Fir (*SPF*) with moisture-activated polyurethane adhesive (*PUR*) with reference to the standard ANSI/APA PRG 320 and *CLT* Handbook [13-14]. The dimensions of each lamination were 11 mm in thickness, 63 mm in width, and 710 mm in length. The dimensions of each three-layer downscaled *CLT* were 33 mm in thickness, 63 mm in width, and 710 mm in length. Two types of three-layer specimens were fabricated, taking into account the panel direction, i.e., "Major-strength" and "Minor-strength" directions. Table 1 provides the specimen information, in which the notation "S" stands for static bending, "A" for "Major-strength" direction, "O" for "Minor-strength" direction, and "C" and "D" for one-week and four-month creep tests. The manufacturing process is illustrated in Fig. 1. The test specimens were conditioned at 20°C and 65% *RH* until they achieved a constant *MC* of 12%.

Table 1: *Groups and sets labelling of specimens.*

Tests		Panel direction	Load level	RH level	Groups/ sets
Static (S)		Major	/	/	SA
		Minor	/	/	SO
Creep	7-day (C)	Major	30%	65%	CA1
				30%	CA2
			60%	65%	CA3
				30%	CA4
		Minor	30%	65%	CO1
				30%	CO2
			60%	65%	CO3
				30%	CO4
	4-month (D)	Major	30%	30-65% Cyclic	DA1
			60%		DA2
		Minor	30%	30-65% Cyclic	DO1
			60%		DO2

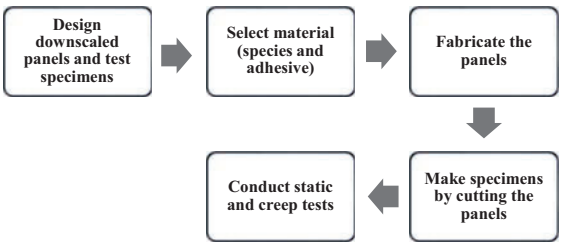

Figure 1: *Design and manufacturing of downscaled CLT.*

2.2 METHODS

2.2.1 Static bending test

The third-point bending tests were conducted at a loading rate of 5 mm/min and a span ratio of 16.4 with reference

to ASTM D198–15 [15] with an aim at determining the limits of proportion (*PL*s) of the *CLT* specimens in the "Major-strength" and "Minor-strength" directions, Fig. 2. A Linear variable differential transformer (*LVDT*) was used to measure the deflection at the mid-span of each specimen, Fig. 2.

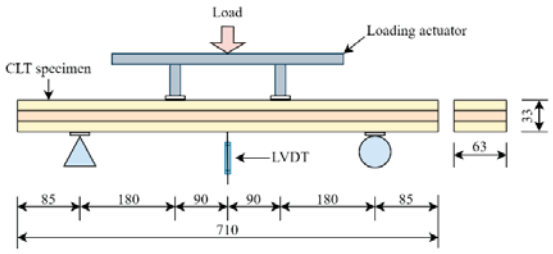

***Figure 2**: Static bending test setup (Unit-mm).*

2.2.2 One-week creep test

A third-point bending setup was employed to conduct a one-week creep test in a conditioning chamber, with a temperature of 20±1°C, Figs. 3 and 4. Two types of specimens were used, "Major-strength" and "Minor-strength". Two levels of *RH* were employed, 30±5% and 65±5%. Two load levels were set at 30% and 60% of the *PL*. The target load was achieved by placing steel plates on each specimen, Fig. 3.

***Figure 3**: Creep test setup with an LVDT at the mid-span of each specimen.*

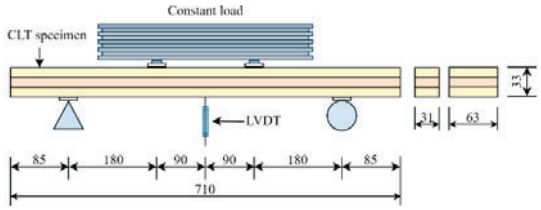

***Figure 4**: Creep test setup (Unit-mm).*

The deflection at the mid-span of each specimen was recorded using an *LVDT* connected to a data logger with a frequency of 1 Hz. In order to safely and efficiently apply the constant load up to 60% *PL* on those specimens, a given *CLT* specimen was ripped into two narrow specimens along the middle line, see the two different cross sections in Fig. 4. The load applied on each narrow specimen (i.e., after ripping) was half of that on the specimen of full width (i.e., before ripping). The loading duration was of 7 days. Six specimens (three specimens per type) were tested at a given load level and *RH*, generating a total of 24 specimens in this phase of testing.

2.2.3 Four-month mechano-sorptive creep test

The four-month mechano-sorptive creep tests were carried out using the same setup as that in the one-week one, Figs. 3 and 4. The load level and panel direction considered were the same as those of 7-day creep tests. The tests were conducted under a constant temperature of 20±1°C in a conditioning chamber with two levels of *RH* (i.e., 30±5% and 65±5%) with an interval of 7 days. The test specimens for the four-month mechano-sorptive creep tests were obtained from the same specimens that had been subjected to a 7-day loading duration and recovered in the chamber for about one year in a conditioning chamber of a temperature of 20°C and 65% *RH*. This allowed the completely release of any residual stress in a specimen. The specimens at 30% *PL* were completed a 4-month mechano-sorptive creep. However, the specimens at 60% *PL* were only terminated to 2 months because of the relatively large deflection that caused a specimen to fracture and/or collapse.

2.2.4 Modelling

Great efforts on modelling the creep behaviour of wood and wood composites have been made [16]. Classical models have been developed that can provide a meaningful approximation of the time-dependent deformation of wood, which offer valuable insights into the mechanical behaviour of wood and wood composites. These models are typically based on a combination of a spring(s) and a Newtonian dashpot(s), representing the elastic and viscoelastic nature of a composite such as wood [12]. The models such as the "Maxwell" model, "Kelvin" model, "Generalized Kelvin (*GK*)" model, and "Burger (*B*)" model are commonly used to describe the mechanical response of viscoelastic materials and involve the arrangement of elastic and viscous elements in either series or parallel configurations [2, 16-17].

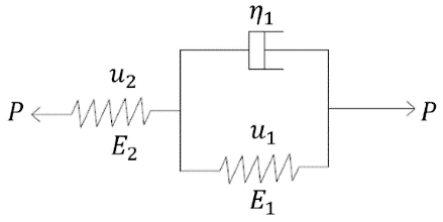

***Figure 5**: "Generalized Kelvin" model [2].*

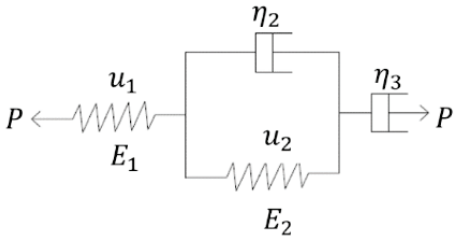

***Figure 6**: "Burger" model [2].*

https://doi.org/10.52202/069179-0071

This study adopted the "*GK*" model and "*B*" model to simulate the creep behaviour of the downscaled *CLT* specimens. The "*GK*" model was chosen due to that it is a derivation from the widely used "Kelvin" model, which can accurately represent the delayed elastic component of a material. The "*B*" model was selected due to its simplicity as well as the model parameters are expressed on a unit basis, relating time-dependent stress-strain behaviour to the modulus of elasticity and rigidity and to the coefficients of the viscosity of a composite [2].
These two models are illustrated in Figs. 5 and 6, in which, E is the modulus of elasticity of a spring; η is the viscosity coefficient of a dashpot; P is the force applied; τ is the relaxation-time constant which is η/E; u is the displacement; t is creep time [4].

***Table 2**: Two creep model equations.*

Creep Model	Creep Equation
"Generalized Kelvin" model	$u = -Ae^{-Bt} + D$
"Burger" model	$u = -Ae^{-Bt} + Ct + D$

Table 2 gives the simplified forms (equations) of two creep models. Where, $A = P_1/E_1$, $B = 1/\tau_1$, and $D = P_1/E_1 + P_2/E_2$, in "*GK*" model; $A = P/E_2$, $B = 1/\tau_2$, $C = P/\eta_3$ and $D = P/E_1 + P/E_2$, in "*B*" model.

3 RESULTS AND DISCUSSION

3.1 STATIC BENDING TEST

Fig. 7 illustrates the load-deflection curves of two groups. Groups SA and SO represent the groups in the "Major-strength" and "Minor-strength" directions. It can be found most specimens failed in a brittle way. It can also be found that one specimen in group SA exhibited an abnormal response, which could be due to the existence of imperfects during manufacturing of specimens such as lack of adhesive causing delamination between laminations. Consequently, this specimen was eliminated from the data analysis. The average peak loads of groups SA and SO were approximately 6,094 N and 1,249 N, respectively. The average *PL* values of groups SA and SO were around 3,024 N and 817 N, respectively. The average stiffness of group SA was approximately 610 N/mm, which was approximately 10 times larger than that of group SO.
Table 3 summarizes the test results of two groups including stiffness, *PL* and P_{max}, plus the deflection at P_{max}. It is not surprising that the group SA (i.e., the "Major-strength" group) exhibit higher strength and stiffness. The deflection at the peak load is around 11 mm, which is about 35% lower than that of the group SO. The maximum bending capacity of the group SA was about 3 times greater than that of the group SO. Subsequent to the static bending test, two load levels were then determined, based on the *PL,* to be 30% *PL* and 60% *PL* for the "Major-strength" and "Minor-strength" groups for the following creep tests.

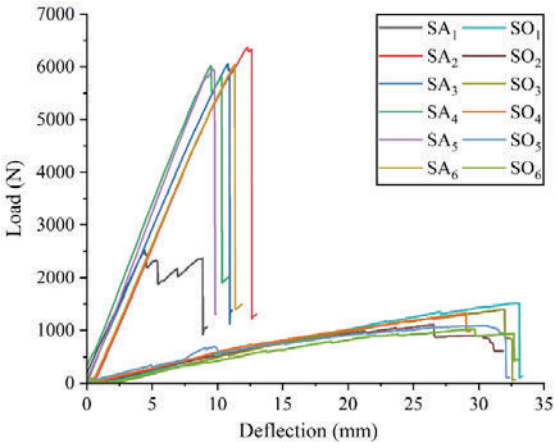

***Figure 7**: Load-deflection curves in the "Major-strength" and "Minor-strength" directions.*

***Table 3**: Mean properties of downscale CLT specimens under the static bending tests (Note: Numbers in parentheses are standard deviations).*

Property	Mean	
	Group SA	**Group SO**
Stiffness (N/mm)	610 (4)	60 (0)
PL (N)	3,024 (431)	817 (238)
P_{max} (N)	6,094 (163)	1,249 (196)
Deflection (mm)	11.36 (1.16)	32.13 (1.46)

3.2 ONE-WEEK CREEP TEST

Fig. 8 was used to illustrate the creep deflections of all specimens under two-panel directions, two load levels, and two *RH* conditions, with each curve representing the average deflection-time response of the corresponding set. It can be obviously seen that the load level had a significant impact on the creep. Each curve consists of two stages, namely the initial creep stage and the steady creep stage. The maximum load applied on a specimen in this study was 60% of *PL*, the accelerated creep stage did not appear in the 7-day creep test, which suggests that the maximum deflection had not exceeded the specimen's deflection limit and caused failure in the 7-day [18]. Thus, only the initial creep stage and steady creep stage were discussed and simulated in 7-day creep test. It can be discovered that the eight sets largely conformed to the general law of creep.
It can be found from Fig. 8 that 1) For the panel direction: the average deflection reached by the "Minor-strength" groups (sets CO1 and CO2) loaded at 30% *PL* are approximately 11.85 mm, which is 2.2 times larger than that made by the "Major-strength" groups (sets CA1 and CA2). For the sets loaded at 60% *PL*, the average deflection of the "Minor-strength" groups (sets CO3 and CO4) was approximately 21.83 mm at 172 hours, which is 2.71 times larger than that of the "Major-strength" groups (sets CA3 and CA4) with a deflection of 8.07 mm.

https://doi.org/10.52202/069179-0071

This is well in agreement with the findings by He et al. [19]; 2) For the load level: "Major-strength" groups bewteen sets CA1-2 and CA3-4 were compared, which revealed a small difference in deflection values at the termination of testing, with average values of 5.39 mm and 8.07 mm, respectively. "Minor-strength" groups bewteen sets CO1-2 and CO3-4 exhibited a much larger difference with the average values of 11.83 mm and 21.83 mm. Especially, set CO3 is about 22.74 mm, the maximum deflection set in 7-day creep test, which is 1.93 times that of set CO1 with a deflection of 11.81 mm at the time of 172 hours; 3) For the *RH*: A comparison made between two *RH*s revealed that the deflection in higher *RH* sets was greater than lower *RH* sets, while keeping other conditions unchanged. This observation can be attributed to the difference in the *MC* of the specimens used, which well aligns with other findings [2, 7-8].

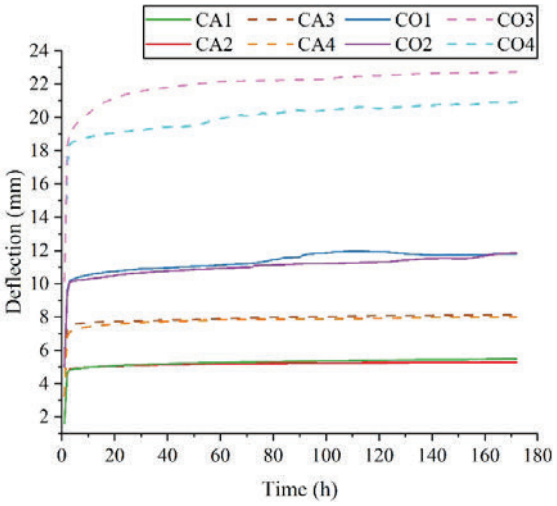

***Figure 8**: Average 7-day creeps of eight sets tested.*

3.3 FOUR-MONTH MECHANO-SORPTIVE CREEP TEST

Fig. 9 depicts the 4-month mechano-sorptive creeps of all sets under two-panel directions, two load levels, and cyclic *RH* ranging from 30% to 60% with a time interval of 7 days. Each curve represents the average deflection-time response of a given set. It can be clearly seen that all setting factors mentioned above had a significant effect on the creep of the specimens tested. It can be discovered that sets DA1 and DO1 largely conformed to the general law of mechano-sorptive creep.

Fig. 9 shows that sets DA2 and DO2, which were loaded at 60% *PL*, had to be halted at the time of about 900 hours due to the collapse of two "Major-strength" *CLT* specimens and the destruction of one "Minor-strength" *CLT* specimen. Based on Fig. 9 and Table 3, the initial deflections of sets DA1-2 and DO1-2 were 1.61 mm and 3.27 mm in the "Major-strength" direction and were 4.99 mm and 10.14 mm in the "Minor-strength" direction, as presented in Table 4. Those initial deflections were using average static bending test data. Additionally, Table 4 presented the total deflection that the specimens experienced on average, derived by considering initial deflection and maximum creep deflection together. Remarkably, the deflections of sets DA2 and DO2 at the end of loading were 9.64 mm and 28.88 mm, respectively, which almost reached the ultimate deflection at a given direction, Table 3, namely, 11.36 mm or 32.13 mm for the "Major-strength" or "Minor-strength" direction. The specimens in sets DA2 and DO2 were speculated to have exceeded the bending yield point and created a high creep deflection causing the specimens to collapse or destroy during the test. Therefore, only the 4-month mechano-sorptive creeps of sets DA2 and DO2, i.e., those subjected to 60% *PL* load level, were excluded from the data analysis and discussion in this study.

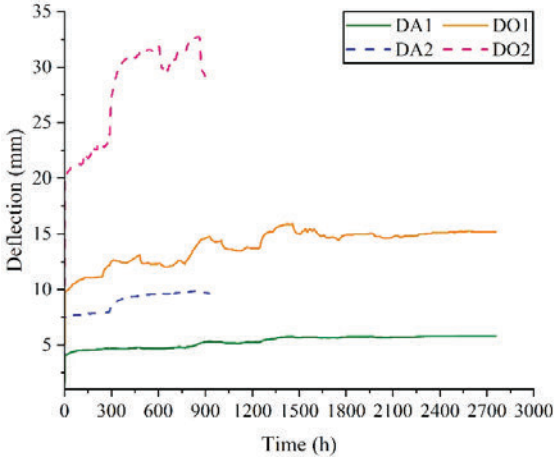

***Figure 9**: Average four-month mechano-sorptive creeps of four sets tested.*

***Table 4**: Average deflections of the specimens tested under the cyclic RH (Unit-mm).*

Test sets	Initial deflection	Deflection at the end of testing	Total deflection
DA1	1.61	4.18	5.79
DA2	3.27	6.37	9.64
DO1	4.99	10.20	15.19
DO2	10.14	18.74	28.88

It can be discovered from Fig. 9 that the panel direction significantly affected the creeps of the specimens under 30% *PL*. Specifically, set DO1 exhibited a deflection of approximately 14.59 mm at 900 hours, which is 277% larger than set DA1 that had a deflection of 5.27 mm. As the testing of sets DA1 and DO1, the deflection curve gradually increased from the initial stage. The sets DA1 and DO1 reached the maximum discrepancy in deflection at 1459 hours, with deflections of 5.76 mm and 15.90 mm, respectively. At the steady stage, which is at 2755 hours, the deflection was 5.79 mm and 15.19 mm for the sets DA1 and DO1, respectively. It is apparent that the

https://doi.org/10.52202/069179-0071

deflection of set DO1 was 262% larger than that of set DA1 to a large degree.

Fig. 10 illustrates the changes in temperature and *RH* values during the 4-month mechano-sorptive creep tests. It can be found thatt temperature was well mainained at 20°C, while *RH* was not well controled at the preset range, i.e., from 30±5% to 65±5%, due to the out-of-control of the chamber during the creep test duration. Fig. 9 indicates that significant increases in deflection were observed at approximately 300, 900, and 1300 hours. The increase in deflection of set DO1 ranged from 12.49 to 15.13 mm, while that of set DA1 was only 4.68 to 5.49 mm when the *RH* increased from 30% to 70% at the times of about 300, 900 and 1300 hours.

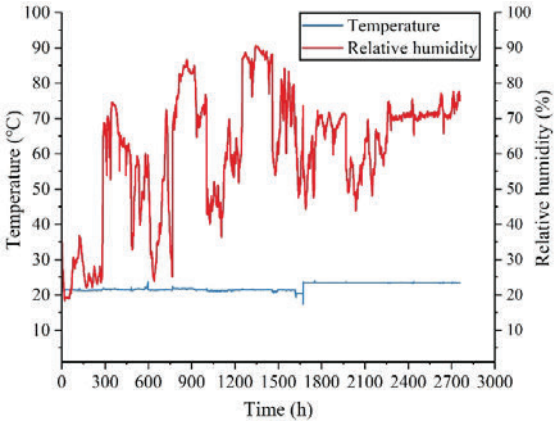

***Figure 10**: Changes in temperature and RH during the creep tests of sets DA1 and DO1.*

There are some shortcomings existed during the mechano-sorptive creep tests in this study, resulting in unsatisfactory results. Firstly, the application of a 60% *PL* load level for the long-term creep test was inappropriate (sets DA2 and DO2) since it could cause a relatively large deflection at 900 hours, which exceeded that at the maximum load under the static tests. Secondly, the *RH* in the conditioning chamber used was not well controlled to some degree as planned. Thirdly, the 4-month duration of the mechano-sorptive creep test could not be sufficient, which was due to the duration (only 1 year) of a project-based master's student's study. Finally, the downsized *CLT* specimens were not good enough to represent the full size *CLT* panels. Hence, there is a need for further research to overcome these shortcomings.

3.4 MODELLING

The "*GK*" model and "*B*" model were selected to simulate the creep of downscaled *CLT* specimens loaded at 30% *PL* in this study. The Curve Fitting Function in Origin software developed by OriginLab Corporation was used to determine the parameters in each model by the non-linear fitting method. The fitting results are provided in Table 5, and Figs. 11 to 12. The R-square values of over 0.85 suggests that both models well fit the experimental data and seems the fitting curve of the "Major-strength" set is slightly better than that of the "Minor-strength" one at a given model. The 95% of prediction bands (filled colour) of each model are plotted in Figs. 11 and 12 as well. Considering the fluctuation of time-dependent deflection due to the cyclic *RH*, the upper limit of 95% confidence level is employed to build "*GK*" model or "*B*" model, which reflects the worst-case scenario for downscaled *CLT* specimens used in this study in a given direction. The creep models developed in this study are given in Table 6.

***Table 5**: Determination of model parameters based on the 4-month creep test results of two sets (DA1 and DO1) in both "Major-strength" and "Minor-strength" directions.*

Sets	Model	Parameters				R-Square
		A	*B*	*C*	*D*	
DA1	GK	1.9317	0.0007	/	6.1452	0.9235
	B	0.2452	-0.0008	0.0012	4.5253	0.9384
DO1	GK	5.4571	0.0013	/	15.4085	0.8786
	B	13.6279	0.0006	-0.0022	23.7686	0.8842

The deflections of specimens DA1 and DO1 at 3 months, 6 months, 1 year, 10 years, and 50 years can be predicted using the models developed above, which are listed in Table 6. It can be found that the "*GK*" model could produce more reasonable results than the "*B*" model based on the data in this study. Also, it could be discovered that the deflections predicted by the "*GK*" model become a constant after 1 year. This suggests that a duration of 1 year, or even 6 months, could be good enough for building a creep mode for *CLT* specimens. However, such a speculation requires further verification. Also, a more complex model should be developed by considering panel direction, load level and relative humidity.

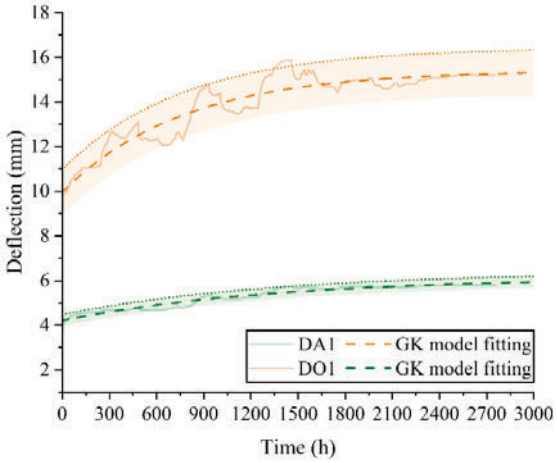

***Figure 11**: "GK" models and prediction bands at 95% confidence level for 4-month mechano-sorptive creep.*

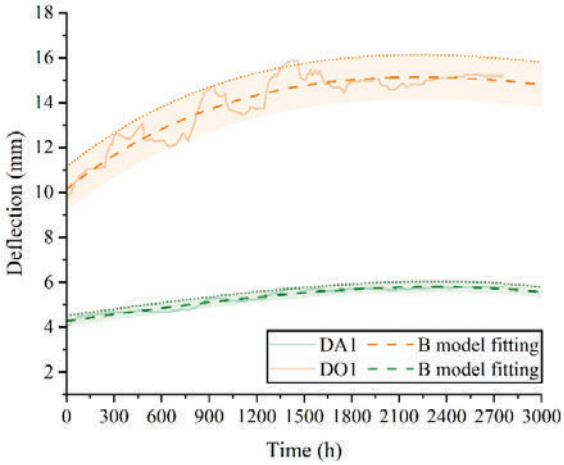

***Figure 12**: "B" models and prediction bands at 95% confidence level for 4-month mechano-sorptive creep.*

***Table 6**: Creep models and predicted deflections at given times.*

Set	Model	Equation	Deflection (mm)				
			Month 3	Month 6	Year 1	Year 10	Year 50
DA1	GK	$u=-1.9319e^{-7.3109t}+6.4080$	6.01	6.33	6.40	6.41	6.41
	B	$u=-0.2518e^{0.0008t}+0.0012t+4.7672$	6.03	2.71	-216.19	-1.09×10^{29}	-3.82×10^{147}
DO1	GK	$u=-5.4555e^{-0.0013t}+16.4243$	16.10	16.40	16.42	16.42	16.42
	B	$u=-13.5727e^{-0.0006t}-0.0022t+24.7067$	16.12	14.20	5.59	-165.55	-926.60

4 CONCLSUIONS

Based on the above analysis and discussion, the following conclusions could be drawn:

(1) The *CLT* specimens had average *PL*s of approximately 3,024 N and 817 N in the "Major-strength" and "Minor-strength" directions, respectively.

(2) The results of the one-week creep tests indicated that the panel direction of *CLT* specimens was the most influencing factor on their creep behaviour, with the "Minor-strength" specimens exhibiting an average creep deflection being 2 to 2.5 times larger than that of the "Major-strength" ones. The initial deflection of those specimens loaded at a level of 60% *PL* was approximate twice as large as that at a level of under 30% *PL*. The effect of *RH* on the creep of the specimens during the one-week loading was found to be less significant than that of the panel direction or load level.

(3) The four-month mechano-sorptive creep results showed that the panel direction, load level and *RH* all played a critical role in contribution to the creep of downscaled *CLT* specimens. A reduction of *RH* to 30% from 65% reduced the creep to some degree.

(4) The "Generalized Kelvin" model seemed to be suitable in simulation the creep of the downscaled *CLT* specimens used in this study. The upper limit of the model at 95% confidence level could be a good approach to simulate the creep of the specimens under cyclic *RH*.

ACKNOWLEDGEMENTS

The authors wish to acknowledge the financial support from the New Brunswick Innovation Research Chair Initiative Program by the New Brunswick Innovation Foundation (Canada), the 3+1+1 Program between the University of New Brunswick (Canada) and Nanjing Forestry University (China), and the technical support from the University of New Brunswick's Wood Science Technology Centre, Canada.

REFERENCES

[1] Gong M. Lumber-based mass timber products in construction. In Timber Buildings and Sustainability. IntechOpen. 10 Lower Thames Street, London, UK. 2019.

[2] Bodig J., & Jayne B.A. Mechanics of wood and wood composites. Van Nostrand Reinhold. New York. 1982.

[3] Martensson A. Creep behavior of structure timber under varying humidity conditions. Journal of Structure Engineering, University of Lund, Lund, Sweden. 1994.

[4] Liu Y., Tang S., Sun X., Gao Z., Gong M. Testing and modeling of creep of poplar laminated veneer lumber beams. World Conference on Timber Engineering. Santiago, Chile. 2020.

https://doi.org/10.52202/069179-0071

[5] Schniewind P. Recent progress in the study of the rheology of wood. Wood Science and Technology, 2(3): 188-20. 1968.
[6] Holzer S., Loferski J., and Dillard D. A review of creep in wood: concepts relevant to develop long-term behavior predictions for wood structures. Wood and Fiber Science, pp: 376-392. 1989.
[7] Armstrong L.D., and Christensen G.N. Influence of moisture changes on deformation of wood under stress. Nature, 191(4791), 869-870. 1961.
[8] Bengtsson C. Mechano-sorptive bending creep of timber-influence of material parameters. Holz als Roh-und Werkstoff, 59(4), 229-236. 2001.
[9] O'Ceallagh C., Sikora K., McPolin D., and Harte A. Mechano-sorptive creep in reinforced glulam. World Conference on Timber Engineering. Seoul, Republic of Korea. 2018.
[10] Takanashi R., Ohashi Y., Ishihara W., and Matsumoto K. Long-term bending properties of cross-laminated timber made from Japanese larch under constant environment. Journal of Wood Science, 67(1), 1-10. 2021.
[11] Hunt D.G., A unifed approach to creep of wood. Proc. R. Soc. London Ser. a-Mathematical Phys. Eng. Sci. 455 4077–4095. 1999.
[12] Cai Z., Fridley K.J., Hunt M.O., and Rosowsky D.V. Creep and creep-recovery models for wood under high stress levels. Wood and Fiber Science, 425-433. 2002.
[13] APA -The Engineered Wood Association. Standard for Performance-Rated Cross Laminated Timber, ANSI/APA PRG 320. Tacoma, WA, USA. 2019.
[14] Karacabeyli E., & Gagnon. Introduction to cross-laminated timber (Chapter 1). Cross-laminated Timber (CLT) Handbook. FPInnovations. Pointe-Claire, Quebec, Canada. 2019.
[15] American Society for Testing and Materials (ASTM) International. Standard test methods of static tests of lumber in structural sizes. Designation: D198-15, ASTM International, West Conshohocken, PA, USA. 2015.
[16] Gittus J. Creep, viscoelasticity, and creep fracture in solids. John Wiley and Sons, Inc., New York, NY. Chapter 7. 1975.
[17] Hanhijärvi A. Computational method for predicting the long-term performance of timber beams in variable climates. Materials and Structures, 33, 127-134. 2000.
[18] Peng H., Jiang J., Zhan T., Lü J. A Review of Pure Viscoelastic Creep and Mechano-Sorptive Creep of Wood. Scientia Silvae Sinicae, 52(4): 116-126. 2016. (in Chinese)
[19] He M., Sun X., and Li Z. Bending and compressive properties of cross-laminated timber (CLT) panels made from Canadian hemlock. Construction and Building Materials. 185, 175-183. 2018.

World Conference on Timber Engineering Oslo 2023

SHEAR CREEP OF POLYSTYRENE CORES IN WOOD-BASED PANELS

André Jorissen[1], Johnny van Rie[2], Jeff Modderman[3], Hèrm Hofmeyer [4]

ABSTRACT: This paper reports on an experimental study of shear creep in load bearing sandwich panels with a polystyrene core and wood-based faces. This is ongoing research at Eindhoven University of Technology (TU/e), in cooperation with industry, to provide scientific and experimental backgrounds to roof panels used for residential housing. For these panels, loaded perpendicular to plane, faces are loaded in tension or compression, whereas the core is mainly loaded in shear. Both the polystyrene core and the wood-based faces show time dependent behaviour (creep) of which only the time dependent behaviour of the core is dealt with in this paper. This by including experiments on panels of which the wood-based faces are replaced by steel, thus isolating the creep of the core. Furthermore, conform other studies on this subject, e.g. Taylor et al. [1], and Kilpeläinen et al. [2], the study presented in this paper indicates that the creep depends on the load ratio, i.e. the quasi-permanent shear relative to the shear stress at failure (strength). Therefore, load ratios were systematically varied. Results indicate that when the shear stress exceeds more than 50% of the shear strength, the tertiary creep phase is reached, and collapse will occur within 4 -5 years. When the shear stress is lower than 40% of the shear strength, the deformation is likely to stabilise in the secondary creep phase.

KEYWORDS: Sandwich panels, Shear creep, Polystyrene (EPS), Wood-based faces

1 BACKGROUND RESEARCH

When using sandwich panels with rigid foam cores for roofs, the panels are predominantly loaded perpendicular to plane. The deflection is usually decisive for the maximum allowed span. Suggested by current European regulations [3], the shear deformation is often the largest part of total deformation, regardless the type of rigid foam applied for the core. For the rigid foam the creep factor k_{def}, defined as $k_{def} = \frac{u_{fin} - u_{inst}}{u_{inst}}$ with u_{fin} = final and u_{inst} = instantaneous deflection, is set to k_{def}=7.0 [3], which causes high predicted deformations. For steel sandwiches, which are usually loaded with low permanent loads at large spans this is not a problem, but for residential building roofs covered with tiles, i.e. large permanent loads at short spans, shear deformation is a considerable part of the total deformation and therefore has a serious impact.

Since there is obviously a difference in behaviour of thermosetting and thermoplastic materials, as shown by Gibson et al. [4], it was seen as an opportunity to allow for higher performance of wood-based sandwich panels by demonstrating that the value for k_{def} for polystyrene loaded in shear is much lower than specified above. Knowing that the core is mainly loaded in shear, as shown in figure 1, and that the shear zones mainly occur in the vicinity of the supports, the research focuses on the shear creep. Furthermore, shear stresses in the core are relative low compared to the shear capacity: In a practical example, e.g. a sandwich panel with a thickness of 200 mm and a span of 4 m, with a dead load (self-weight and roof tiles combined) of 0.65 kN/m², a maximum shear stress of 6.5 kPA results, whereas the characteristic shear strength of a polystyrene core is approximately 80 kPA. Consequently, the deflection is governing the design and therefore, as figure 2 illustrates, an accurate value for k_{def} is necessary.

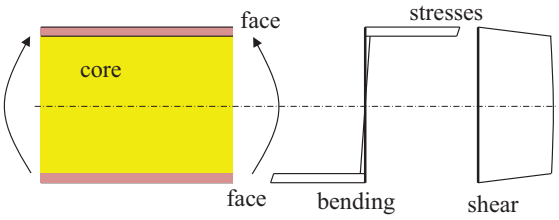

Figure 1: *Stresses in a sandwich panel with thin faces: by approximation, uniform axial stresses in the faces and uniform shear stresses in the core exist* [5]

[1] André Jorissen, Eindhoven University of Technology (TU/e), Den Dolech 2, 5612 AZ Eindhoven and SHR Timber Research, Nieuwe Kanaal 9b, 6709 PA, Wageningen, The Netherlands. Email: a.jorissen@hetnet.nl
[2]Johnny van Rie, Kingspan Unidek, Scheiweg 26, Gemert, The Netherlands. Email:Johnny.vanRie@kingspan.com
[3]Jeff Modderman, Amsterdam.
Email:Jeff.modderman@live.nl,
[4] Hèrm Hofmeyer, Eindhoven University of Technology (TU/e), Den Dolech 2, 5612 AZ Eindhoven.
Email:h.hofmeyer@tue.nl

https://doi.org/10.52202/069179-0072

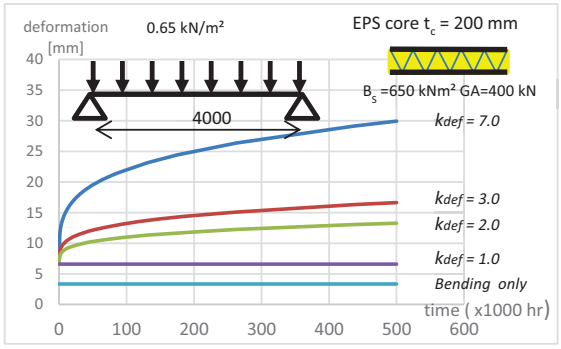

Figure 2: *Effect of different values of k_{def} on time dependent deformation of a given single span sandwich beam.*

2 OBJECTIVE

The objective of this study is to describe the shear creep as a function of the shear load relative to the shear strength of a polystyrene core as applied in wood-based sandwich panels. Therefore, two types of tests are carried out. Pure compact shear tests, according to EN 12090 [6], and tests on beams with Uniform Distributed Loads (UDL), for which the shear stresses and deformations are analysed. The objective of these tests is to show that the different set-ups, for which the bending test is the more realistic one, result in comparable finding for time dependent behaviour. Comparable time dependent behaviour allows small and simple tests on creep in the future, while making sure the creep results do agree with the end use situation. Furthermore, after unloading, being loaded for a long period, the specimen are loaded up to failure and the characteristic residual strength is determined to provide an indication on the strength degradation in time. Results are compared with the results found in previous studies [1,2].

2.1 TIME DEPENDENT DEFORMATION BEHAVIOUR

In engineering practice, time dependent deformations (creep) are calculated according to Equation (1) showing a proportional relationship between the instantaneous deformation u_{inst} and the creep deformation u_{creep} (= u_{fin} – u_{inst}).

$$u_{creep} = k_{def} u_{inst} \qquad (1)$$

Due to creep, part of the stress strain behaviour is non-linear. Furthermore, part of the creep deformation obtained during loading will not recover; part of the deformation remains at time *t*. Figure 3 shows the qualitative deformation behaviour of a polymer affected by creep (or a structure consisting of this material), including unloading after time *t*.

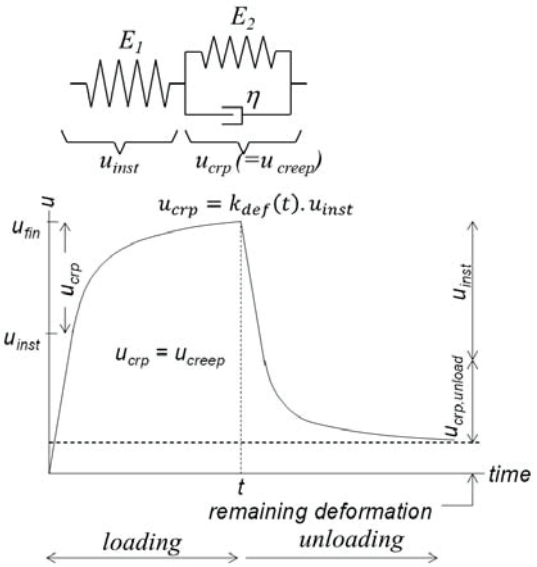

Figure 3*: Top: Shear creep model, Bottom: Deformation behaviour of a polymer affected by creep* [7]

Consequently, both the instantaneous deformation u_{inst} and the creep deformation = k_{def} * u_{inst} are governing the final deformation u_{fin}. The creep factor k_{def} is generally assumed to be only time dependent and is defined as a fixed value for the ratio u_{creep}/u_{inst} after 50 years of permanent loading. Furthermore, at least for wood and wood-based products, the creep factor is influenced by the material moisture content and its fluctuations. In engineering practice, the creep factor is generally assumed not to be affected by the load. For polymers however, the creep factor does not only depend on time but also on the load (stress) level, and significantly so, as shown in Figure 4. The dotted line indicates the stress level which is not to be exceeded. If stress levels are high, progressively higher strains will occur, the so-called tertiary phase is reached, and collapse is due to happen.

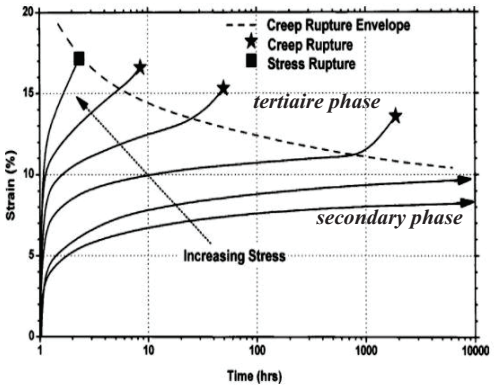

Figure 4: *Strain over time for different stress levels* [8]

https://doi.org/10.52202/069179-0072

At lower stress levels the creep rate decreases and creep stabilises, reaching the secondary phase, as such avoiding failure.

3 MODELLING SHEAR CREEP

3.1 SHEAR CREEP AS NONLINEAR MATERIAL BEHAVIOUR

Previous studies have shown that polystyrene foam reacts differently to various load types. When compressed, the foam behaves as a cellular material, i.e. it has an elastic, by approximation quadratic stress-strain relationship, whereas most solids are about linear [1]; under stresses due to bending it will react purely elastic until failure (brittle) [1]. As discussed in relation to figure 1, in a sandwich panel the core is predominantly loaded in shear and consequently this research focuses solely on shear and the determination of the shear creep. Models describing shear creep both as linear and nonlinear have been developed by Taylor et al. [1], Kilpeläinen et al. [2], and Findley et al. [7], and will be introduced by first presenting the so-called Burgers Model for which the arrangement of the spring and dashpot elements are shown in figure 5.

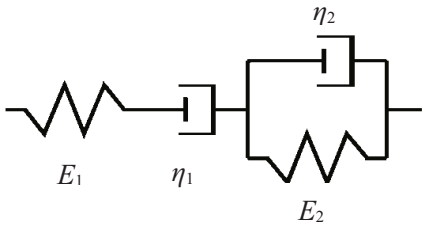

Figure 5*: Creep according Burgers model*

Representing for the spring elements $\sigma = E\varepsilon$ and for the dashpots $\sigma = \eta\frac{d\varepsilon}{dt}$, the Burgers model results in:

$$\varepsilon(t) = \sigma\left[\frac{1}{E_1} + \frac{t^p}{\eta_1} + \frac{1}{E_2}\left(1 - e^{-\frac{E_2}{\eta_2}t}\right)\right] \qquad (2)$$

in which t equals the time, and p is a factor to be determined. If p=1, the behaviour of the first part of the model, represented by the spring (E_1) and dashpot (η_1) is completely linear in time. With p < 1, the tertiary phase can be postponed or avoided. With p > 1, creep will grow progressively, entering the tertiary phase, which must be avoided.

Findley et. al [7] used the above model, and demonstrated it functioned correctly for viscoelastic materials, such as polymers, with their typical time dependent behaviour: They start with instantaneous elasticity, followed by delayed elasticity and visco-elastic flow.

Taylor et al. [1] tried several different creep deflection models, to fit the data measured over 3 months and to predict the creep after 6 months, and concluded that the so-called power model and the 5-element model are suitable to predict relative deflection on beams with EPS or PUR cores. To derive the 5-element model, they

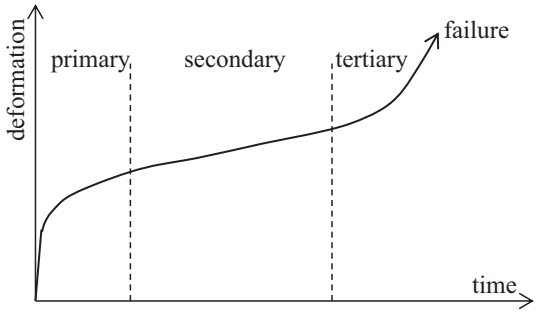

Figure 6: *Creep phases*

rephrased the Burgers model and changed η_1 into $\eta_1(t)$, resulting in Equation (3).

$$\Delta(t) = \Delta_0 + B_1(1 - e^{-B_2 t}) + B_3 t^{B_4} \qquad (3)$$

In which $\Delta(t)$ is the deformation, Δ_0, B_1, B_2, B_3 and B_4 are parameters, and k_{def} can be found by equation (1).

Kilpeläinen et al. [2] applied the power model, and used Equation (4) as a method to fit the data:

$$k_{def}(t) = A_1\, t^{A_2} \qquad (4)$$

Based on this latter model, the k_{def} is low for steel sandwich panels since these panels are used for long spans and relatively low loaded.

3.2 PANEL STRENGTH

Given the presented studies, it is obvious that to find the proper value for k_{def} of a sandwich panel with steel faces, the focus must be on the shear creep in the polystyrene core. Additionally, it should be realised that polystyrene foam transfers shear via and along the walls of each cell, thus the proper fusion, the so-called sealing of the cells, is important. Therefore, in the experiments below not only identical grades of EPS foam are used, but also exactly identical procedures for the production of the core are applied, and fusion strength is tested too. This is not only carried out on "fresh" elements, before applying loads, but also after the experiments, to demonstrate that the residual strength is hardly degraded in time, thus showing that the polystyrene is still in the secondary phase, where the load level is below a certain upper limit.

4 EXPERIMENTS

Two different types of experiments have been carried out: (a) polystyrene specimens loaded in shear (compact shear test according to EN 12090) and (b) panels loaded in bending. Both test setups are shown in Figure 6a and 6b respectively. The bending tests are positioned and monitored in a climate-controlled environment.

https://doi.org/10.52202/069179-0072

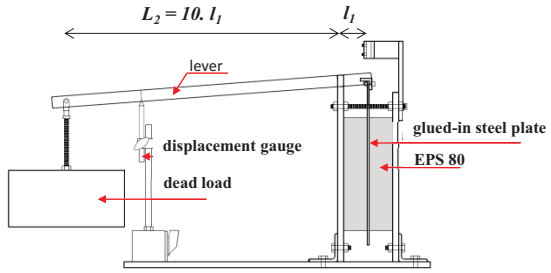

(a)

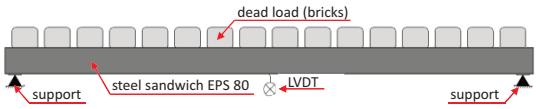

(b)

Figure 6: (a) *Shear test EN 12090 as modified for long term loading.* l_1 *=40 mm;* l_2 *= 400 mm;* (b) *Bending test setup for long term loading. Core thickness = 100 mm. Steel plate thickness = 0.4mm. Panel width =200 mm. Panel length =2100 mm.*

The compact shear tests (See Figure 6a and 7) comprise of 3 series of 6 samples each, loaded relative to the average shear strength by 27%, 41% and 54% respectively (no round percentages due to recalibration and resulting shear strength adjustments). These shear tests ran from June 2011 to April 2020, in a dry and heated, but not climate-controlled environment. After the tests ended, a shear test up to failure was carried out to check the residual strength.

Figure 7: *Overview of compact shear tests*

Measurements were carried out at "regular" time intervals: a small time period (30s) in the beginning (June 2011) going up to once a month at the end (April 2020). This since at the end hardly any changes were visible, using a displacement resolution of 0.05 mm.

The second type of experiments consists of series of simply supported panels carrying bricks as a Uniform Dead Load (UDL), see Figure 6b, 8 and 9. These tests were done in a climate-controlled room at Eindhoven University of Technology.

Figure 8 *side view of all UDL samples, showing data loggers and LVDT's*

Figure 9: *front view of the UDL samples, percentage per column, 6 samples per percentage*

For the specimens in bending, the focus is on the study of the polystyrene core, and the normally wood-based faces are replaced by steel faces.
Four different load levels are applied: 10%, 20%, 30%, and 40% relative to the characteristic shear strength of the

https://doi.org/10.52202/069179-0072

polystyrene core (80 kPA). These percentages differ slightly from those used for the compact shear tests. The reason for that is that the percentages for the compact shear tests are determined after loading comparable specimen to failure.

The measurement of the total deflection is carried out at bottom side of the beam, in the middle, thus excluding measuring compression at the supports. Also these experiments were part of a long running experimental program, which was halted after 5 years due to a failure in the climate room. Afterwards the residual shear capacity was tested. In order to test a part of the polystyrene core that was well loaded by shear, the test specimens were taken near the supports.

5 RESULTS

5.1 PANELS LOADED IN BENDING

The single span tests show, although there are quantitative differences between series, very similar qualitative behaviour. Since the frequency of sampling is rather high, it is possible to discern even climate effects and similar.

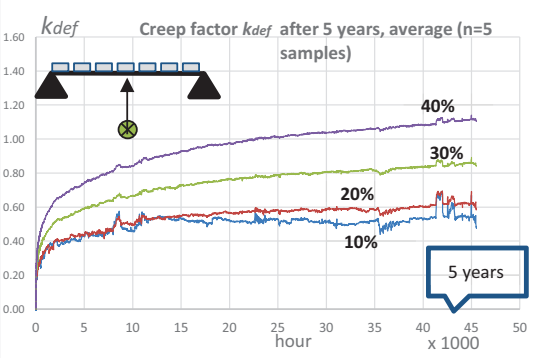

***Figure 10**: averages for series loaded from 10% to 40% of the characteristic strength; single span uniform distributed load experiment.*

Figure 10 shows there is a strong relation between the load and the relative displacement over time. Also, the smaller the load, the more vigorously the beam responds to other events, mostly climate effects. Also, the lower load levels show a lower increase of creep, and thus a lower strain rate. At 42000 hours a serious disturbance occurred, visible for all series. The reason for the disturbance is unknown.

5.2 COMPACT SHEAR TESTS

As mentioned earlier, the compact shear tests consist of three series, namely using load ratios equal to 27%, 41%, and 54%. Also here, a strong dependency on the relative shear stress was visible, as shown in figure 11. The most interesting result was that all samples of the 54% series failed after 4 years, indicated by the cross.

Exact failure times cannot be determined, for data logging was carried out at quite large intervals (700h). It is obvious that since the load was active for a very long period, the degradation of the core was due to progressive creep, and it may be concluded that a shear stress of 54% is well within the tertiary phase. The series of 27% and 41% were monitored for 9 years. After that period, these samples had still not failed.

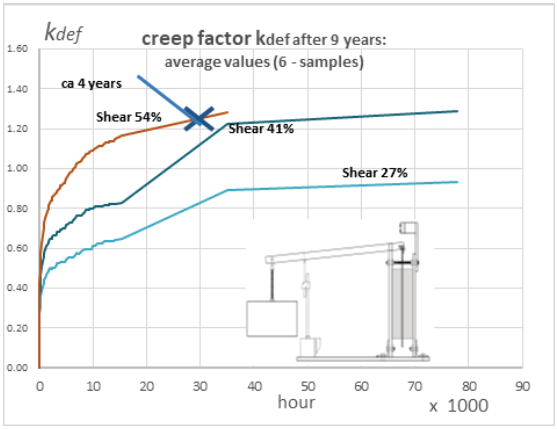

***Figure 11:** average per series of shear tests*

Final measurements were carried out after 12 years, but since the tests were not monitored properly in between 9 and 12 years, the deformations after 9 years were excluded from the study. However, since the samples did not fail, the residual strength could still be determined. At least it is known that 41% still holds after 12 years, so it is likely that when the shear stress is lower than 40% of the shear strength, the deformation stabilises in the secondary creep phase.

5.3 COMPARISON COMPACT SHEAR TEST WITH PANELS LOADED IN BENDING

All experimental results, but as average values of the 6 samples per series, are shown in figure 12.

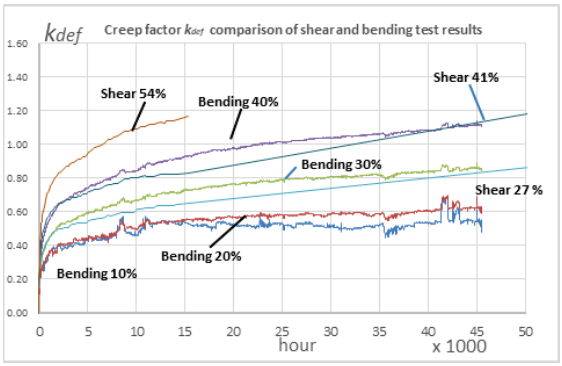

***Figure 12:** Comparison averages of all experiments*

The compact shear experiments show resemblance with the panels loaded in bending, particularly for load ratios up to 30%. It seems that the k_{def}'s found in shear tests are slightly higher than those found in the bending tests.

https://doi.org/10.52202/069179-0072

5.4 COMPARISON PANELS IN BENDING WITH RESULTS OF KILPELÄINEN

Kilpeläinen et al. [2] performed bending tests and modelled the results according to the power model. Using equation (4) for fitting the data, Kilpeläinen found for A_1 = 0.195 and for A_2 = 0.177.

Figure 13 shows the Kilpeläinen et al. predictions for our bending experiments (dotted lines), equation (4) with the above values by the "Design envelope", and our panels in bending.

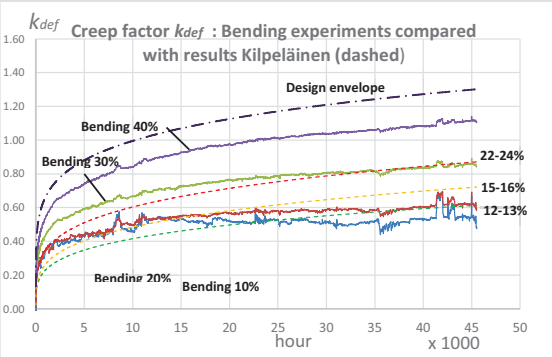

Figure 13: *Comparison averages of beam experiments with* [2]

Overall, predictions agree reasonably well. The power model used by Kilpeläinen et al. seems to underestimate at the start, but agrees after 5 years. Also the proposed upper limit ("Design envelope") is well above the 40% level; This design curve indicates a value for k_{def} = 1.95. For Finnish conditions (following Kilpeläinen et al.), including high quasi-permanent snow loads this is understandable, but for more average conditions, a 40% shear stress level will not be reached.

5.5 DESIGN LIMITS AND EXPERIMENTS

Three design limits are compared with both type of experiments. The design limits are the equation (3) as found by Kilpeläinen et al. [2]; the envelope equation by Kilpeläinen et al. [2], which leads to a k_{def} = 1.49 based on the power model (Equation 5); and the limit using the five points model of Taylor et al., leading to k_{def} = 1.60, Equation 6. This last equation (6) shows only four parameters, however, for determining k_{def} the parameter Δ_0 (Equation 2) vanishes.

$$k_{def}(t) = 0.053\, t^{0.275} \qquad (5)$$

$$k_{def}(t) = 0.171(1 - e^{0.0065\, t}) + 0.143\, t^{0.174} \qquad (6)$$

Kilpeläinen et al. [2] equation (3) is the dashed line almost at top. Clearly the 54% compact shear test was above this line and would have been rejected by all design limits. The second limit, the envelope equation by Kilpeläinen et al. [2] is just above the 30% and well above the 20% bending results. Finally, the Taylor et al. approach (Equation 6) is fitted on the data of this experiment and extrapolated to k_{def} (t=50 years) = 1.60. It is almost coincident with the 30% bending tests.

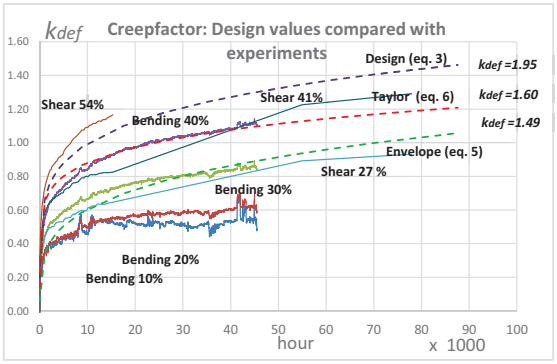

Figure 14: Compact shear and bending experiments compared with 3 proposed design limits

This latter design limit shows a better similarity up to 10.000 hr compared to the power model, which obviously is due to the higher number of parameters fitted. Also, when the permanent relative shear stress is lower than 25%, using k_{def} = 1.60 is an upper limit for the expected relative deformation after 50 years. This is a sound limit, since in the Ultimate Limit State (ULS) state (following EAD 140022 [3]) the EPS for the load duration class "permanent" is limited to 25%. Besides, applying k_{mod} and γ_m also will reduce the actual occurring stress in the Service Limit State (SLS). The limit by the envelope equation of Kilpeläinen et al., green dotted in figure 14, represents the 25% relative shear stress and is derived from results in [2], so it is similar to the design limit but considerably lower. If this later limit (envelope equation) is applied for permanent load duration in SLS states then the conclusion would be that indeed the bending experiments at 10% and 20% are acceptable, and that the compact shear tests at 54% and 41% are rejected. The 27% compact shear test is close to the Envelope (Eq.5), just slightly above, but is rather uncertain in development in time, so no conclusion can be drawn here. At least there is no safety margin. The 30% bending test seems to get under the 25%, but to be sure, this measurement is simply too short.

5.6 RESIDUAL STRENGTH AFTER CREEP TESTS

To determine the residual strength of the bending tests afterwards, several parts of their cores were tested for shear. These parts were taken near the support of the beams, and results are shown in Table 1. The results agree with the shear capacity at the start of the experiment, which was characteristically 80 kPA: the strength of most of the specimen was above 80 kPA, and the characteristic value was about 80 kPA, so it seems that the capacity was not affected. Possibly because stresses were too low, or that there was some 'restoring' effect: For the series up to 20% strains are most likely to be recoverably. For the 27% and 41% series, this is more uncertain.

Table 1*: Residual shear strength of samples bending tests*

https://doi.org/10.52202/069179-0072

No.	S10% [kPa]	S20% [kPa]	S30% [kPa]	S40% [kPa]
1	92.84	86.17	97.44	88.03
2	85.30	86.89	96.03	92.59
3	92.22	83.84	93.29	89.52
4	90.72	82.40	90.82	92.59
5	95.23	83.95	92.76	86.35
6	94.79	81.09	95.37	89.69
7	95.04	81.39	96.34	89.05
Char. 5%	**84.94**	**78.97**	**89.66**	**84.91**

Also, the compact shear test samples were tested for strength, by placing the entire setup in a pressure bench. Results on average were slightly lower than the original 80 kPA, see Table 2.

***Table 2**: Residual shear strength of shear samples*

No.	S27% [kPa]	S41% [kPa]	S54%
1	91.59	77.05	x
2	91.34	79.04	x
3	82.95	86.91	x
4	79.23	91.18	x
5	76.86	86.46	x
6	94.33	x*	x
Char. 5%		**72.88**	
*Sample used for calibration			

This may be the effect of the series 41%, since these are a bit lower, but not dramatically. Sample 6 was lost while measuring; the value was 72 kPa, but Young's Modulus was suspiciously low, and so results were not trusted.

6 CONCLUSIONS

The study in this paper shows for EPS a strong relationship between creep (deformation) and load levels. Also, it is demonstrated that different experimental set-ups (bending and compact shear) agree well with respect to determination of shear creep, with the notion that compact shear tests seem to lead to slightly higher creep values. Furthermore, it shows that, the bandwidth in between tertiary creep (5 years at 54%) and the upper limit of secondary creep (9 years at 40%) is rather small.

Those samples that 'survived' the bending experiments still have the original shear load capacity, which supports the small bandwidth hypotheses. In general, when a shear stress at 25% of the shear strength is applied in serviceability limit state conditions, the creep factor k_{def} will never be larger than 1.6 after 50 years. This is the case for a power model similar to Kilpeläinen et al. [2] as well as for a model according to Taylor et al. [1].
The residual strength of the samples after the test is reassuring. It proves that a long-sustained load on polystyrene can be accepted. Additional details related to this paper can be found in Modderman [9].

ACKNOWLEDGEMENTS

This research was supported by Kingspan Unidek. We thank the staff from the department of quality assurance at Unidek Gemert, and the laboratory staff at the Structures Laboratory Eindhoven, and last but not least Jeff Modderman, by the time student at Eindhoven University of Technology, for his research regarding this subject.

REFERENCES

[1] S.B. Taylor, H.B. Manbeck, J.J. Janowiak, D.R. Hiltunen, Modelling Structural Insulated Panel (SIP) Flexural Creep Deflection, Journal of Structural Engineering 123, 1658-1665, 1997.
[2] T. Kilpeläinen, P. Hassinen, Long-term and fire behaviour of an eps-foam sandwich panel product, Sandwich Construction 3, 911-920, 1996. Chameleon Press LTD London
[3] EAD 140022-00-0304 Prefabricated wood-based loadbearing stressed skin panels, Published by EOTA 2020.
[4] L.J. Gibson, M.F. Ashby, J. Zhang, T.C. Triantafillou, Failure surfaces for cellular materials under multiaxial loads–Modelling, International Journal of Mechanical Sciences 31, 635-663, 1989.
[5] J.M Davies, Lightweight sandwich construction, Blackwell Science Ltd, 2001
[6] NEN-EN 12090:1997, Thermal insulation products for building applications-Determination of shear behaviour, NEN, The Netherlands.
[7] W.N Findley, J.S. Lai, K Onaran, Creep and Relaxation of Nonlinear viscoelastic materials, Dover Publications, 1989.
[8] L.C.E. Struik, Physical Aging in Plastics and Other glassy materials, Polymer Engineering and science 17, 165-173, 1977.
[9] J. Modderman, Non-linear behaviour of stiffened sandwich panels and creep behaviour of EPS, M.Sc.-thesis Eindhoven University of Technology, The Netherlands, 2017.

https://doi.org/10.52202/069179-0072

World Conference on Timber Engineering Oslo 2023

INTEGRATED APPROACH TO PREDICT DETERIORATION OF MECHANICAL PROPERTIES OF DECAYING WOOD

Petr Hradil[1], Stefania Fortino[2]

ABSTRACT: The aim of this paper is to present a methodology to predict bending or compression resistance of structural wooden elements during the onset and growth of the material decay. Two methods are proposed to calculate remaining bending and compression resistance under the attack of brown rot and white rot are presented: (1) reduction of material strength or (2) reduction of the cross-section of the wooden element. The methods are based on the bending and compression tests of material exposed to extreme moisture and are demonstrated as a part of the structural integrity online calculation tool introduced in this paper. They are applicable to planed wood where the decay is expected to progress from the surface inwards. It should be noted that the prediction of structural resistance is in the present state limited to specific loading conditions and decay mechanisms and it is not recommended to replace structural design according to the building codes. However, the estimation of the remaining structural integrity of the material may be very important for the planning of maintenance actions in the structures, such as bridges, where the immediate replacement is not possible or for better safety measures in removing, renovating or demolishing decaying wooden construction.

KEYWORDS: Structural Integrity, Wood decay, Dose-response model, Mass loss, Bending, Compression

1 INTRODUCTION

Exposure of timber products to the external climate, condensate or accumulated water in interiors may lead to biotic degradation of the material. One of the common problems related to the prolonged periods of high moisture is rotting that can lead to material loss and degradation of its mechanical properties [1].

Wood rot, also known as decay, affects the durability and integrity of wood products. It is caused by fungi that grow and feed on the cellulose, hemicellulose, and lignin, breaking down these materials and causing the wood to soften, weaken, and eventually collapse. This paper focuses on the effect of two most common types of rot, brown and white, on the mechanical properties of wood. Brown rot is the most common type of rot and causes the wood to become brittle and crumbly. White rot, on the other hand, affects the lignin in the wood, causing the wood to become stringy and fibrous. The less common forms of decay such as soft rot are not discussed herewith, but the methodology presented in this paper can be easily extended to account for their effect as well.

In order to prevent the decay, it is important to control the moisture levels in the environment surrounding the wood. This can be done by properly sealing and finishing the wood elements to prevent moisture from penetrating, providing adequate ventilation to prevent moisture build-up, and keeping the wood away from sources of moisture like leaky pipes or standing water. If wood rot has already occurred, it is often necessary to remove and replace the affected wood to restore its structural integrity.

The severity of degradation caused by the rot is typically described as decay rating and can be tested on site [2]. The loss of wood mass and mechanical properties due to the decay can be verified experimentally [3].

It was observed that both, the decay rating and mass loss, correlate with the cumulative duration of the high-moisture state above the fibre saturation point at suitable temperature rate (see Figure 1).

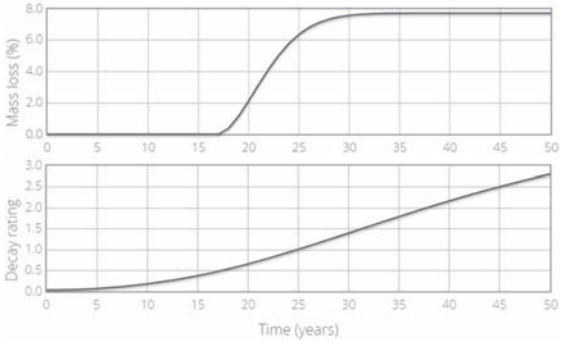

Figure 1: *Example of mass loss (top) and decay rating (bottom) prediction due to brown rot in 80x160 mm softwood member exposed to a constant dose of 10 points per year [4].*

[1] Petr Hradil, VTT Technical Research Centre of Finland Ltd, Finland, petr.hradil@vtt.fi
[2] Stefania Fortino, VTT Technical Research Centre of Finland Ltd, Finland, stefania.fortino@vtt.fi

https://doi.org/10.52202/069179-0073

In order to predict those effects several so-called dose models were introduced earlier [4] by some of the partners of ClickDesign project (Delivering fingertip knowledge to enable service life performance specification of wood) coordinated by the Building Research Establishment in UK. Dose stands for the normalized time of exposure of the material to temperature and moisture levels favourable for the development and growth of wood decay. The aim of the work under the ClickDesign project was to extend the knowledge of the dose-related material loss and to provide practical indicators about the structural integrity of decaying material under the external loads. The tool developed in the ClickDesign project will be then used in Horizon Europe research project 5G-Timber [5] to provide estimation of the quality of the wood waste generated during the service life of modular wooden building.

2 PREDICTIVE MODELS

The most computationally demanding part of the estimation of moisture-induced effects is the numerical prediction of the moisture and temperature dose from the external conditions. This is typically done by hygro-thermal simulation of moisture diffusion, heat conduction and their respective surface emissions implemented in finite element or finite difference models with boundary conditions corresponding to the external climate. For the practical reasons, we assume that the total yearly dose is pre-calculated for untreated wood and the effect of wood treatment, impregnation and surface coating that affects the moisture dose is added explicitly. The following predictive models are based on the existing theories, extended and modified for the practical use in the structural verification of sawn timber

2.1 Mass loss

The loss of material mass ML in % can be modelled by the dose-response function in Equation (1), where the accumulated dose D is obtained either by logistic dose model (LM) or simplified logistic dose model (SLM) [4] and the initial dose before the onset of decay D_0 is assumed to be 150 days. It should be noted that the time before decay cannot be estimated very precisely and in the case of verification of material already contaminated by fungi, we recommend the term $D - D_0$ to be the cumulative dose during the real observed decay period. The final (reduced) mass m_{red} of the wooden element can be then calculated from Equation (2) where its original mass is m.

$$ML = A_{ML}\left(1 - exp(-k_{ML}(D - D_0)^{n_{ML}})\right) \quad (1)$$

$$m_{red} = m(1 - ML) \quad (2)$$

The regression parameters A_{ML}, k_{ML} and n_{ML} in Table 1 and Table 2 were obtained on 15 x 25 x 50 mm specimens of sapwood from *Pinus sylvestris* L.(Scots pine, softwood) and *Fagus sylvatica* (Beech, hardwood) inoculated by *Coniophora puteana* (brown rot) and *Trametes versicolor* (white rot) [6].

Table 1: *Parameters of the mass loss prediction based on logistic dose model LM [6].*

Decay type	A_{ML}	k_{ML}	n_{ML}
Brown rot			
- softwood	52.15172	0.00092	1.72185
- hardwood	41.03166	0.00102	1.69278
White rot			
- softwood	21.557946	0.000732	1.66255
- hardwood	21.188634	0.001542	1.947474

Table 2: *Parameters of the mass loss prediction based on simplified logistic model SLM [6].*

Decay type	A_{ML}	k_{ML}	n_{ML}
Brown rot			
- softwood	42.12828	0.00109	1.86345
- hardwood	32.78056	0.00104	1.88263
White rot			
- softwood	12.776551	0.000591	2.011779
- hardwood	20.833677	0.001235	2.166626

In this paper, the wood decay is assumed to be surface phenomenon (progressing from the surface inwards), and therefore the mass loss ML will be different for wood components with different cross-section from the test samples. In order to generalize mass loss calculation, the value of ML has to be corrected by the shape factor k_{sh} depending on the real width b and height h of the cross-section (see Equation (3)).

$$k_{sh} = 7.9\frac{b + h}{bh} \quad (3)$$

2.2 Decay rating

Decay rating DR is modelled in this paper by the dose-response function in Equation (4). The parameters a_{DR} and b_{DR} are calibrated on the softwood samples of from *Pinus sylvestris* L. (Scots pine), *Pseudotsuga menziesii* Franco (Douglas fir), *Larix decidua* Mill. (European larch) and *Picea abies* Karst. (Norway spruce) and presented in Table 3 [7]. The hardwood rating is not used in the present decay rating model.

$$DR = 4 \cdot exp\left(-exp(a_{DR} - b_{DR}D)\right) \quad (4)$$

Table 3: *Parameters of the softwood decay rating model [7].*

Decay type	a_{DR}	b_{DR}
Brown rot (shade)	2.026	0.0037
Brown rot (no shade)	1.564	0.0054
White and soft rot	1.7716	0.0032

https://doi.org/10.52202/069179-0073

2.3 Structural integrity

Apart from the loss of wood mass, decay causes changes in the material behaviour, especially reduction of its strength. The knowledge of wooden element cross-section and characteristic strength of the material is typically needed to estimate the element's resistance to external loads. For the practical reasons, only one of those parameters can be modified, while the engineers may continue using the nominal value of the second one (nominal cross-section with reduced equivalent strength or vice versa).

Therefore, two methods to calculate bending and compression resistance were developed: reduction of material strength and reduction of element's cross-section. They are based on the bending and compression tests [9] and are demonstrated as a part of the structural integrity online calculation tool [10] introduced in this paper.

2.3.1 Reduction of the material strength

The calculation of reduced material strength is directly based on the approximation model of tested bending or compression resistance at different levels of mass loss [9]. It represents equivalent strength of the homogeneous material with the nominal cross-section (see Figure 2).

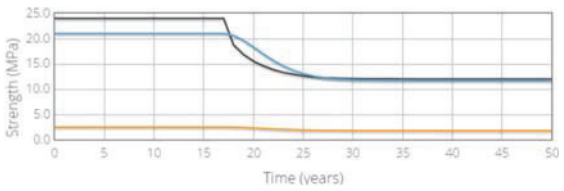

Figure 2: *Example of predicted material characteristic strength degradation in bending (black line), compression parallel to the grain (blue line) and perpendicular to the grain (yellow line) of 80x160 mm member from C24 grade wood.*

The loss of material strength FL can be calculated from the mass loss ML using sigmoid function in Equation (5) with parameters A_{FL}, k_{FL} and n_{FL} fitted to the experimental data for bending [8] and compression [9] in Table 4, Table 5 and Table 6 and the shape factor k_{sh} is obtained from Equation (3). The reduced material strength f_{red} can be then obtained from Equation (6), where f is the characteristic strength of the specified timber grade.

$$FL = A_{FL}\left(1 - exp(-k_{FL}(k_{sh}ML)^{n_{FL}})\right) \quad (5)$$

$$f_{red} = f(1 - FL) \quad (6)$$

In our models, we use experimentally calibrated parameters for bending and compressive strengths, and therefore the applicability of the method is currently limited to structural components subjected to the respective loads.

Table 4: *Parameters of the bending strength reduction model [8]*

Decay type	A_{FL}	k_{FL}	n_{FL}
Brown rot			
- softwood	0.8833	9.6601	0.6155
- hardwood	0.7256	1048.283	2.0538
White rot			
- softwood	2.7368	1.9995	0.7448
- hardwood	54.7094	49.0366	3.2411

Table 5: *Parameters of the compressive strength parallel to gran reduction model in softwood [9].*

Decay type	A_{FL}	k_{FL}	n_{FL}
Brown rot	0.901353	13.069994	1.155478
White rot	1.085979	7.631163	1.248356

Table 6: *Parameters of the compressive strength perpendicular to gran reduction model in softwood [9].*

Decay type	A_{FL}	k_{FL}	n_{FL}
Brown rot	0.989291	5.823211	1.103143
White rot	1.049224	3.977650	0.775042

2.3.2 Reduction of the cross-section

Alternatively, it is possible to describe the effect of degrading resistance as an artificial reduction of structural member's cross-section from the surface towards its centre. The reduced cross-section represents equivalent section of the wooden member and shall be used together with the original material strength (see Figure 3). The reduction depth d is equal from all sides and will be different in different loading situations.

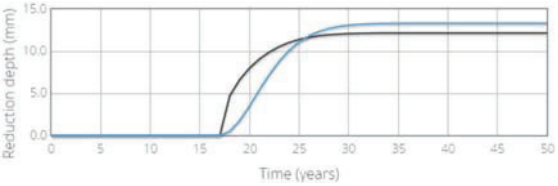

Figure 3: *Example of predicted depth of nominal cross-section reduction in bending (black line) and compression parallel to the grain (blue line) of 80x160 mm member from C24 grade wood.*

It is assumed that the equivalent rectangular cross-sectional area of the compressed member is proportional to the reduction of material strength as in Equation (7).

$$A_{red} = A(1 - FL) \quad (7)$$

We can then express the depth d in compression from Equation (6) as function of cross-section b width and height h and strength loss FL. The solution for root of quadratic Equation (8) is expressed in Equation (9).

$$(b-2d)(h-2d) = bh(1-FL) \tag{8}$$

$$d = \frac{bh - \sqrt{(bh)^2 - 4bh \cdot FL}}{4} \tag{9}$$

Similarly, the bending load requires proportional reduction of the section modulus in Equation (10).

$$W_{red} = W(1-FL) \tag{10}$$

For bending along the horizontal axis of rectangular cross-section, the root of cubic Equation (11) has analytical solution in Equation (12) with coefficients k_1 to k_6 present in Equations (13) to (18).

$$\frac{(b-2d)(h-2d)^2}{6} = \frac{bh^2}{6}(1-FL) \tag{11}$$

$$d = k_1 - \frac{k_2}{3k_1} - \frac{k_3}{3} \tag{12}$$

$$k_1 = -\left(\frac{k_4 + \sqrt{k_4^2 - 4\,k_2/27}}{2}\right)^{1/3} \tag{13}$$

$$k_2 = k_5 - \frac{k_3^2}{3} \tag{14}$$

$$k_3 = \frac{(4b+8h)/bh^2}{k_6} \tag{15}$$

$$k_4 = \frac{FL}{k_6} + \frac{2k_3^3 - 9k_3k_5}{27} \tag{16}$$

$$k_5 = \frac{(-4b-2h)/bh}{k_6} \tag{17}$$

$$k_6 = -\frac{8}{bh^2} \tag{18}$$

2.4 The effect of surface treatment

If the moisture and temperature dose is pre-calculated for untreated wood, it can be later modified (reduced) concerning a specific material protection. This is not as computationally demanding as numerical pre-calculation of dose for every specific surface treatment. Moreover, it enables a wide range of possible treatments, coatings or structural protective measures with temporal variation of their performance. For instance, the effect of paint that starts degrading after 15 years and is renewed after 25 years is demonstrated in Figure 4. Similar scenarios can be studied in real-time using the ClickDesign structural integrity calculator [10].

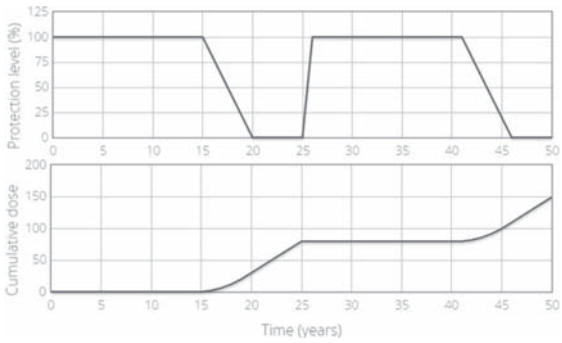

Figure 4: *Example of simulated performance of surface paint (top) and a corresponding delayed dose response (bottom).*

Such behaviour can be modelled using the following three parameters affecting the cumulative dose D entering Equations (1) and (4): treatment maximum protection k_p is the percentage of dose of untreated wood that is avoided by the surface treatment during the first year after its application; treatment durability t_0 expresses the duration (in years) of the maximum level of protection; and finally, the third factor, treatment degradation rate k_d, stands for the percentage loss of the maximum protection k_p per year. Then the total yearly dose of treated wood D_t can be obtained from the pre-calculated yearly dose of untreated wood D_u following Equation (19) where t is the time (in years) from the last renewal of the surface treatment. The value of D_t is limited to interval $\langle 0, D_u \rangle$.

$$D_t = D_u\Big(1 - \big(k_p - k_d(t - t_0)\big)\Big) \tag{19}$$

Figure 4 (top) shows the protection level $k_p - k_d(t-t_0)$ for parameters $k_p = 1$, $k_d = 0.25$ and $t_0 = 15$ years. The cumulative dose D in Figure 4 (bottom) is then a sum of the total yearly doses D_t calculated over a given period (e.g. design life of a building).

3 STRUCTURAL INTEGRITY TOOL

The predictive models described in the previous Section are included in the Python script and integrated in VTT's Modelling Factory simulation environment "modellingfactory.org". This platform enables efficient online publication of various calculation tools developed in different programming languages or spreadsheet editors and it provides powerful user interface builder with links to the calculation inputs and outputs. The source code of the scripts and user interface are typically published with the Modelling Factory tools.

3.1 Architecture of the tool

The Python script calculates a series of values of cumulative dose D by summing up the yearly dose D_t modified by the optionally defined effect of surface treatment (see Section 2.4) from 0 years until the design life of the wooden element a_{max}. Then the calculation follows the flowchart in Figure 5 generating time series data of different model variables.

https://doi.org/10.52202/069179-0073

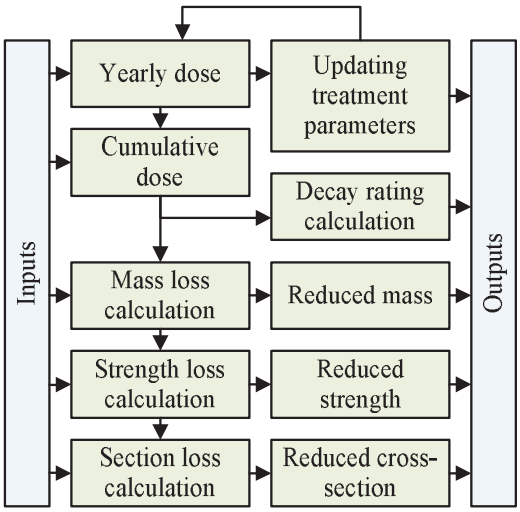

Figure 5: *Architecture of the structural integrity tool with elements of user interface (blue) and Python script (green).*

Mass loss ML and decay rating DR are calculated according to methodology described in Sections 2.1 and 2.2 respectively. Then the value of mass loss is used to estimate the loss of material strength FL in bending or in compression. The prediction of reduced characteristic strength or cross-section is then based on the FL value and follows the methods described in Sections 2.3.1 and 2.3.2.

3.2 User interface

In the case of ClickDesign structural integrity calculator [10], the user interface is divided into two parts: input forms on the left side (Figures 6-8) and output graphs on the right side (Figures 1-4). Since there is no numerical simulation of moisture transport (yearly dose D_u is entered directly in the form), the graphs on the right side are regenerated in real time. The graph data can be also downloaded in a spreadsheet form. For the convenience of the user, brief explanation of the required inputs is provided after clicking on the top-right button next to each input form. The irrelevant parts of the form are automatically hidden.

The dimensions of the wooden element in mm (width b, height h and length l) are entered in the first form (see Figure 6) together with the hardwood or softwood strength class according to EN 338 [11], design life a_{max} (e.g. based on the Eurocodes [12]) and method of structural integrity calculation according to sections 2.3.1 and 2.3.2 of this paper. The length of the member l is used only for the estimation of the full material volume in LCA calculation, which is not discussed in this paper. The design life a_{max} sets the limits of the calculated yearly results. The script then automatically selects the nominal characteristic strength f according to the selected material class. Structural engineers are typically familiar with those design parameters.

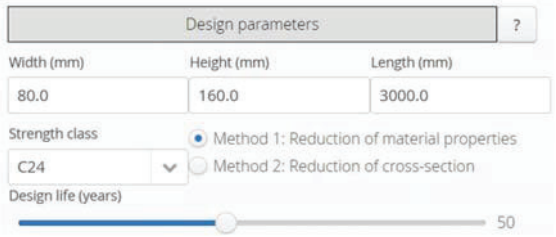

Figure 6: *Basic design values such as dimensions, strength class and design life, and selection of the reduction method.*

The second form (Figure 7) asks the user for additional parameters required for the predictive models. Our goal was to simplify this part and reduce the number of inputs as much as possible. The main requirement is the pre-calculated yearly dose D_u and the method, how it was obtained (logistic model or simplified logistic model [4]). The parameters of decay can be changed by the user, but the default selection (brown rot, no shade) represent the most conservative assumption.

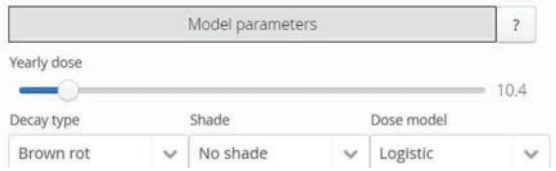

Figure 7: *Additional parameters required for the decay models.*

If the user wishes to simulate the effect of surface treatment, optional form is displayed with the parameters affecting the yearly dose calculation. Those values are not standardized and at the moment there is no experimental procedure how to determine them directly. Therefore, this part is non-compulsory and is hidden from the user by default. The link between commonly used properties of wood treatment (such as surface emissivity) and the model parameters can be the topic for further research and development of the tool.

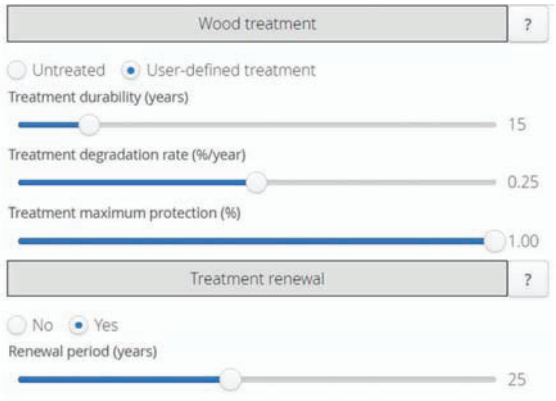

Figure 8: *Optional inputs for the surface treatment simulation.*

https://doi.org/10.52202/069179-0073

It should be noted that it is still possible to utilize the knowledge of the surface emissivity or water vapour resistance by providing pre-calculated yearly dose of the model with appropriate surface properties corresponding to the selected treatment in the "Model parameters" form. However, then the model will lose its real-time regeneration capabilities and possibility to simulate surface renewal in the pre-defined periods.

4 SUMMARY AND CONCLUSIONS

The estimation of the remaining structural integrity of the material is important for planning of maintenance actions in the structures, such as bridges, where the immediate replacement is not possible or for better safety measures in removing, renovating or demolishing decaying wooden construction. It is also useful for estimation of the quality of the end-of-life material in order to optimize wood waste recovery, reuse and recycling.

The presented tool and models integrated in the tool can be a powerful instrument to estimate remaining structural capacity of the wooden elements affected by rot. However, they are at the moment limited to specific loading conditions and rot types and are applicable only to planed wood where the decay is expected to progress from the surface inwards.

The next step in the model development are:

- to integrate material circularity and lifecycle indicators for the assessment of the embodied carbon and generated waste quality of the simulated solution;
- to connect numerical (finite element or finite difference) calculation of the moisture in wood such as already existing Modelling Factory tool called Hygro [13] together with the appropriate dose model;
- to extend the scope of the tool with the knowledge of more wood and fungi species and additional mechanical properties of wood;
- to provide full guidance how the values can be used together with the new Eurocode 5 and the future Eurocode provisions for the assessment of the existing structures [14].

ACKNOWLEDGEMENT

This study and its presentation was supported by Horizon Europe project 5G-TIMBER (Secure 5G-Enabled Twin Transition for Europe's TIMBER Industry Sector), Call: HORIZON-CL4-2021-TWIN-TRANSITION-01, Project number: 101058505. Development of the calculation toolset was supported by ClickDesign project under ERA-NET action ForestValue co-found by the European Union's Horizon 2020 research and innovation programme under grant agreement No 773324 and the Finnish Ministry of the Environment.

REFERENCES

[1] Brischke C., Welzbacher C.R., Huckfeldt T.: Influence of fungal decay by different basidiomycetes on the structural integrity of Norway spruce wood. *Holz als Roh- und Werkstoff*, 66, 433-438, 2008.

[2] CEN/EN 252: Field test method for determining the relative protective effectiveness of a wood preservative in ground contact, European Committee for Standardization, Brussels, 2014.

[3] CEN/EN 350: Durability of wood and wood-based products - Testing and classification of the durability to biological agents of wood and wood-based materials. European Committee for Standardization, Brussels, 2016.

[4] Brischke C., Rapp. A.O.: Dose–Response Relationships between Wood Moisture Content, Wood Temperature and Fungal Decay Determined for 23 European Field Test Sites. *Wood Sci. Technol.* 42:507–518, 2008.

[5] 5G-Timber project webpage, available online at https://www.5g-timber.eu/, 2023.

[6] Oluwademilade J.A.: Impact of micro-environmental temperature on wood decay induced by basidiomycetes, Master thesis. Georg-August Universität Göttingen, Göttingen, 2021.

[7] Brischke C., Meyer-Veltrup L.: Modelling timber decay caused by brown rot fungi, *Materials and Structures* 49:3281–3291, 2016.

[8] Bollmus S., Bester van Niekerk P., Brischke C.: Impact of fungal decay on the bending properties of wood. In *Proceedings IRG Annual Meeting 2020 The International Research Group on Wood Protection*, 2020.

[9] Bester van Niekerk P., Experimental results obtained within the ClickDesign research project, internal communication, 2021.

[10] ClickDesign structural integrity calculation tool available online at Modelling Factory https://modellingfactory.simupedia.com, VTT Technical Research Centre of Finland, 2022.

[11] CEN/EN 338: Structural timber - Strength classes. European Committee for Standardization, Brussels, 2016.

[12] CEN/EN 1990: Eurocode - Basis of structural design. European Committee for Standardization, Brussels, 2005.

[13] Hygro tool available online at Modelling Factory https://modellingfactory.simupedia.com, VTT Technical Research Centre of Finland, 2022.

[14] CEN/TS 17440: Assessment and retrofitting of existing structures. European Committee for Standardization, Brussels, 2020.

https://doi.org/10.52202/069179-0073

World Conference on Timber Engineering Oslo 2023

CREEP TESTS ON PARTIALLY DRIED NOTCHED BEAMS OF SILVER FIR WOOD (ABIES ALBA)

Arthur Bontemps[1], Gaël Godi[2], Rostand Moutou Pitti[3,4], Eric Fournely[5], Joseph Gril[6,7]

ABSTRACT: Silver fir is an important species in the wood French industry but its application is facing drying issues. This paper presents the results of displacement-imposed bending tests and bending creep tests made on green or partially dried silver fir notched beams. The material consists in a batch of thirty beams that were characterised by measurements of basic density and longitudinal modulus of elasticity. The results suggest that the instantaneous strength is independent from the moisture content. During the creep tests, central deflection, crack parameters, shrinkage-swelling and meteorological parameters were measured. The time-dependent compliance is computed and takes into account crack propagation and multi-steps loading. The results show that the initial moisture content has an impact on the maximum time-dependent compliance reached but solar exposure and knots position are also significant parameters. The contribution of cracks to the deflection was also estimated and never exceeded 10% of the total deflection. Finally, observations showed that all crack trajectories were rising whatever the grain angle.

KEYWORDS: Creep, wood, Silver fir, notched beam, bending

1 INTRODUCTION

Silver fir (*Abies alba*) is an important species for European wood industry and accounts for 8% of the French forest. Its wood is mainly used in timber construction but is currently facing drying issues due to wetwood in Auvergne-Rhône-Alpes region [1]. Understanding and forecasting the mechanical behaviour of green or partially dried wood could promote the industrial development of new construction techniques. Traditional frameworks, made with undried wood for many centuries, could inspire the design of agricultural buildings or historical restoration. However, constraints imposed on building construction must be considered. Indeed, Eurocode 5 penalizes green wood by considering a higher final deflection, to account for mechano-sorptive effect resulting from drying under load [2]. However, creep of green timber structural elements depends on several complex factors that are not completely understood. There are several studies on green wood long-term mechanical properties, but mainly realised on small clearwood samples under controlled environments [3], [4]. This paper presents results of an experimental campaign on green or partially dried full-scale notched wooden beams in outdoor semi-sheltered conditions. Scientific challenges involve full-scale outdoor measurements and coupling between fracture mechanics and creep.

2 MATERIAL AND METHODS

2.1 NON-DESTRUCTIVE EXAMINATIONS

The material consists in a batch of 30 notched beams from local silver fir at structural element scale, Figure 1. Most of it is quarter sawn lumber (21/30), and the rest is rift sawn. The batch has been received in green wood state and characterised by non-destructive examination.

[1] Arthur Bontemps, Université Clermont Auvergne, CNRS, Clermont Auvergne INP, Institut Pascal, F-63000 Clermont-Ferrand, France, arthur.bontemps@uca.fr
[2] Gaël Godi, Université Clermont Auvergne, CNRS, Clermont Auvergne INP, Institut Pascal, F-63000 Clermont-Ferrand, France, gael.godi@uca.fr
[3] Rostand Moutou Pitti, Université Clermont Auvergne, CNRS, Clermont Auvergne INP, Institut Pascal, F-63000 Clermont-Ferrand, France, rostand.moutou_pitti@uca.fr
[4] Rostand Moutou Pitti, CENAREST, IRT, BP 14070, Libreville, Gabon
[5] Eric Fournely, Université Clermont Auvergne, CNRS, Clermont Auvergne INP, Institut Pascal, F-63000 Clermont-Ferrand, France
[6] Joseph Gril, Université Clermont Auvergne, CNRS, Institut Pascal, F-63000 Clermont-Ferrand, France, joseph.gril@cnrs.fr
[7] Joseph Gril, Université Clermont Auvergne, INRAE, PIAF, Clermont-Ferrand, France

https://doi.org/10.52202/069179-0074

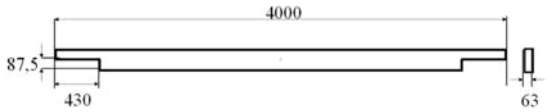

Figure 1: *Beam dimensions (mm).*

2.1.1 Natural vibration tests

The BING© method has been used to measure longitudinal modulus of elasticity (MOE) and shear modulus. It consists in measuring the frequency spectrum of free vibrations of a beam and calculating the stiffness properties using the resonant frequencies. This test was realised before notching the beams. The dynamic MOE measured with this method is known to be 4% higher than the static one [5]. Results are given in Table 1. E^d is the dynamic MOE and G^d is the dynamic shear modulus in the longitudinal-tangential plane. It is observed that the batch is highly heterogeneous, E^d varying from 7.54 to 16.34 GPa.

Table 1: *Free vibration results*

	E^d [GPa]	G^d [GPa]
Minimum	7.54	0.451
Maximum	16.34	0.672
Mean	11.01	0.553
Standard deviation	2.3	0.055

2.1.2 Basic-density measurements

A thin slice of each beam where the green volume V_g and the ovendried mass m_{anh} were measured allowed to calculate the basic density as $\rho_{BD} = (m_{anh}/V_g)$.

The basic density is supposed to be an intensive property, hence the same for the thin slice and for the rest of the beam. As the beams were received in green wood state, their initial volume was V_g and the basic density allows to compute m_{anh} of the whole beams and thus the moisture content (MC) at each weighing. Finally, the basic specific modulus is computed as $E_S^d = (E^d/\rho_{BD})$. The results are given in Table 2.

Table 2: *Basic-density measurements, MC at receipt and* $\boldsymbol{E_S^d}$ *computations.*

	MC [%]	ρ_{BD} [kg.m^{-3}]	E_S^d [Mm^2.s^{-2}]
Minimum	25.1	333	21.49
Maximum	117.5	430	40.84
Mean	60.3	379	28.9
Std	23.9	27.4	4.7

The unit of E_S^d is Mm^2.s^{-2} as it is the square of the sound speed in the material [6]. It is observed that the initial MC is also highly heterogeneous, from 25.1% to 117.5%. However, the hypothesis that the beams are all initially in green state was not verified for every beam and led to approximate results of MC and E_S^d.

2.1.3 Repartition

The experimental campaign was divided into 4-points bending tests with incremental imposed displacement to study the strength as a function of MC, and 4-points bending creep tests to study the long-term mechanical evolution. Both types of tests were realised on wood above fibre saturation point (FSP, MC > 30%), partially dried wood (20% < MC < 30%) and dried wood (MC < 20%). For the creep tests 6 beams were loaded in Spring-Summer 2021, 6 in Autumn-winter 2021-2022 and 6 in Spring-Summer 2022. Figure 2 shows their repartition regarding their mechanical properties (E_S^d and ρ_{BD}). The whole range of mechanical properties has been tested at different MC.

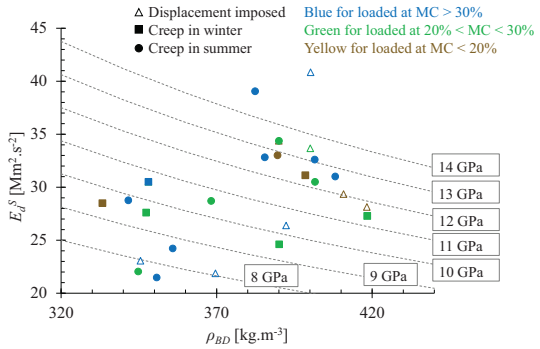

Figure 2: *Beam repartition plotted with specific modulus* ($\boldsymbol{E_S^d}$) *as a function of basic density* ($\boldsymbol{\rho_{BD}}$). *Filled circle: creep test in Summer; filled square: creep test in Winter; empty triangle: displacement-imposed test. Colours indicate initial moisture content (MC). Iso-module curves are added in grey dashed lines.*

2.2 BENDING TESTS

2.2.1 Displacement-imposed

The displacement-imposed 4-points bending tests were performed to correlate the strength with the initial MC and mechanical characteristics. The experimental set-up complies with the norm NF EN 408+A1 [7] and is represented in Figure 3. The central and intermediate deflections (respectively U_c, U_l and U_r) and the crack opening on the "left" and on the "right" (respectively C_{Ol} and C_{Or}) are measured using linear displacement transducers (LDT). The applied load is measured using two load cells.

(a)

https://doi.org/10.52202/069179-0074

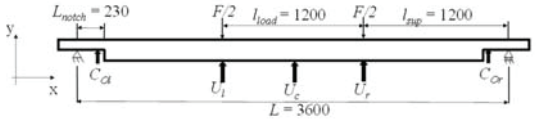

(b)

Figure 3: *Experimental set-up of the displacement-imposed tests: (a) picture of a test; (b) position of the devices. Numerical values are in millimetres.*

2.2.2 Creep tests

The creep tests aimed at studying the long-term mechanical behaviour of partially dried wood. The experimental set-up, shown in Figure 4, was in outdoor semi-sheltered conditions (i.e., sheltered from the rain but some beams were not sheltered from solar radiation). The load was applied using 350 kg waterproofed concrete blocks, incremented by 30 kg every month for 5 months and then every day, so that the duration of the tests never exceeded 7 months. Linear variable differential transformer (LVDT) sensors were used to measure the central deflection. A weather station close to the tests recorded temperature (T), relative humidity (RH) and solar radiation. Furthermore, two thermometers were stuck in the centre of each beam. A marker-tracking technique developed for these tests was used [8]. The relative displacement between markers allowed to measure the variation of beam height due to shrinkage-swelling and the crack opening, length and tip height.

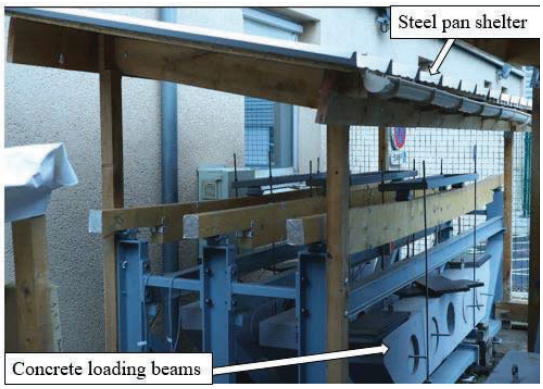

(a)

(b)

Figure 4: *Experimental set-up of creep tests: (a) picture of three loaded beams; (b) positions of measurement (values in mm).*

3 RESULTS AND DISCUSSION

3.1 INSTANTANEOUS RESPONSE

3.1.1 Comparison with non-destructive data

The displacement-imposed bending tests never exceeded 30 min and the mechanical response is hence considered as instantaneous. The axial stress is computed according to beam theory, and the strain, following [9], is given by:

$$\varepsilon \approx \frac{4\Delta U_{spa-r} H}{l_{load}^2} \quad (1)$$

where ε is the maximum normal strain in the centre of the beam, H the height of the beam, l_{load} the distance between the loading points and $\Delta U_{spa-r} = U_c - (U_l + U_r)/2$ the spatial-relative deflection. This allows to plot the stress-strain curves and calculate the static MOE with the slope of the linear part. An "instantaneous" central deflection of the creep tests was estimated by considering the central deflection at 10 minutes U_c^{10min}. An approach adapted from [10] allows computing the static MOE E using U_c^{10min} of the notched beam:

$$E = \frac{A \times f(\beta_0) \times \Delta F}{\Delta U_c^{10min}} \quad (2)$$

with:

$$A = \frac{23 l_{sup} L^2}{36 e H^3} \quad (3)$$

where e is the beam's thickness, L the beam length and l_{sup} the distance between support and loading point. Also:

$$f(\beta_0) = \left(1 + \frac{189\beta_0^3}{23}\right) \times \left[1 + \frac{108}{115}\left(\frac{H}{L}\right)^2 \left(\frac{E}{G}\right)^d \frac{1 + (3/2)\beta_0}{1 + (189/23)\beta_0^3}\right] \quad (4)$$

where $\beta_0 = (2L_{notch})/L$ is the notch factor. The comparison between the instantaneous results with the non-destructive examinations is given in Table 3.

Table 3: *Comparison between dynamic (E^d) and static (E) MOE. ΔE_{rel} corresponds to the relative difference such that $\Delta E_{rel} = (E^d\text{-}E)/E^d$.*

	E^d [GPa]	E [GPa]	ΔE_{rel} [%]
Minimum	7.54	6.02	-23
Maximum	16.34	13.96	32.8
Mean	11.25	9.74	12.4
Std	2.34	2.27	14.5

If the initial MC in a static test is below 30%, E is corrected by 0.15 GPa/% [11] as E^d is supposed to had been measured in green state. The relative difference $\Delta E_{rel} = (E^d\text{-}E)/E^d$ is explained by the natural dynamic and static difference and because E^d was measured on unnotched beams rather than E on notched beams.

3.1.2 Instantaneous strength

In Figure 5 the maximum force reached during the displacement-imposed tests is plotted as a function of ρ_{BD}, with the indication of MC.

https://doi.org/10.52202/069179-0074

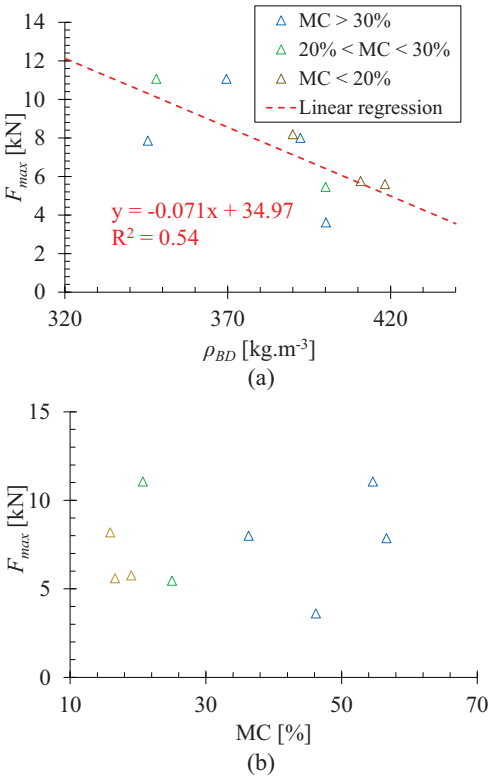

Figure 5: *Maximum force reached during the displacement-imposed tests: (a) as a function of the basic density; (b) as a function of MC.*

Although with a bad coefficient of determination ($R^2 = 0.54$, Figure 5(a)), F_{max} seems to be inversely proportional to ρ_{BD}. This is counterintuitive as the density should increase the MOE and thus F_{max}. As fracture mechanics occur in notched beams, it is supposed that a low MOE implicitly involves several knots that are reinforcements against crack propagation, increasing F_{max}. No correlation is observed between instantaneous F_{max} and initial MC of the tests, Figure 5(b).

3.2 DELAYED RESPONSE

3.2.1 Time-dependent deflection

The delayed response of the creep tests is observed using the time-relative central deflection $U_{time-r}(t)$ defined by:

$$U_{time-r}(t) = q(t) \times \frac{U_c(t) - U_c^{10min}}{U_c^{10min}} \qquad (5)$$

where $q(t)$ is the ratio of initial applied mass m_{ini} over total mass $m_{tot}(t)$ that is increased with load increments and the self-weight of the beam: $q(t) = m_{ini}/m_{tot}(t)$. The height variations due to shrinkage-swelling are measured by the marker tracking, hence correcting their impact on the central deflection: $U_c(t) = U_c(t) - \Delta H(t)/2$. Therefore, $U_{time-r}(t)$ is equivalent to the so-called K_{def} that takes creep into account in Eurocode 5, such that $U_{fin} = U_{inst}(1 + K_{def})$ for permanent load. For a class of service 3 (MC > 20% due to outdoor condition) and starting from green state, K_{def} is fixed at 3.

In Figure 6 the time-dependent deflection for all creep tests is plotted.

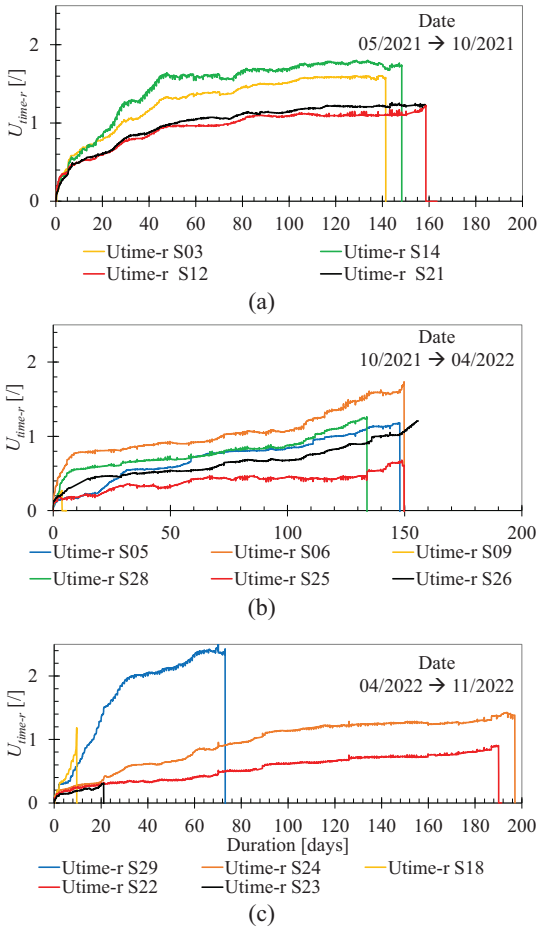

Figure 6: *Time-relative deflection as a function of time: (a) for the first 6 loaded beams in summer 2021; (b) for the 6 beams loaded in winter 2021-2022; (c) for the 6 beams loaded in summer 2022. Sij indicates the number of the considered beam.*

The measured time-dependent deflection never reached 3 as predicted for K_{def}, suggesting that it indeed integrates a safety factor. The beams loaded during Summer show on average a higher $U_{time-r}(t)$. Similar creep tests on initially dried silver fir wood never reached a time-dependent deflection above 2 for 2-years loading [9].

3.2.2 Time-dependent compliance

The time-dependent compliance J_{time-r} was calculated as:

$$J_{time-r} = \frac{E}{E(C_L, t)} - 1 \qquad (6)$$

where E is the initial computed MOE and $E(C_L, t)$ the stiffness evolution based on Equation (2), given by:

https://doi.org/10.52202/069179-0074

$$E(C_L,t) = \frac{A \times f(\beta) \times F(t)}{U_c(t)} \quad (7)$$

where *F(t)* is the updated applied force (adding load increments), $f(\beta)$ uses the crack factor β instead of β_0 by considering the crack length measurement as a notch extension:

$$\beta = \frac{2(L_{notch} + C_L)}{L} \quad (8)$$

This procedure discards the impact of crack propagation and load increments on J_{time-r} and allows comparing beams independently from these effects and from initial MOE. J_{time-r} should depends only on the wood creep itself that is impacted by MC and environmental conditions. In Figure 7 the maximum time-relative compliance reached is plotted as a function of the initial MC at the beginning of the creep test. The external beams exposed to solar radiation (Figure 4(a)) are indicated on the Figure as it has a significant impact on the maximum J_{time-r} reached.

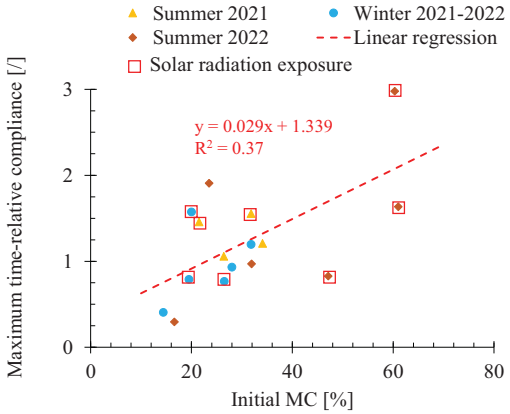

Figure 7: *Maximum time-relative compliance reached as a function of the initial MC at the beginning of the creep tests. Exposure to solar radiation is highlighted by red square.*

There is a slight tendency for the most dried beams to have a lower creep, but there is no strong correlation between initial MC at the beginning of a creep test and maximum time-relative compliance reached after 7 months ($R^2 = 0.37$). Exposure to solar radiations increases creep and brings an unpredicted factor in long-term wood mechanics. Therefore, it should be considered in the same way as moisture content.

3.3 FRACTURE MECHANICS

3.3.1 Deflection involved by fracture

Starting from the function of the notch factor β_0 in Equation (4), the ratio $f(\beta_0)/f(\beta)$, where β is the crack factor that supposes a crack propagation as a notch extension, can be defined. This ratio equals 1 if no crack occurred and decreases with crack propagation. Therefore, a "crack deflection" $U_{crack}(t)$, i.e., a deflection only due to crack propagation, is defined as:

$$U_{crack}(t) = U_c(t)\left(1 - \frac{f(\beta_0)}{f(\beta)}\right) \quad (9)$$

$U_{crack}(t)$ is the total deflection $U_c(t)$ minus the computed deflection as if the beam were free from crack. In Figure 8, $U_{crack}(t)$ is plotted as a function of time for two beams that represent the whole range of observed crack deflection. Thus, $U_{crack}(t)$ varies from 0.8 mm to 4.5 mm, that is at most about 10% of the total deflection. Although assumptions are strong in that computation, it is worth noting that crack seems to have a marginal impact on the observed deflection.

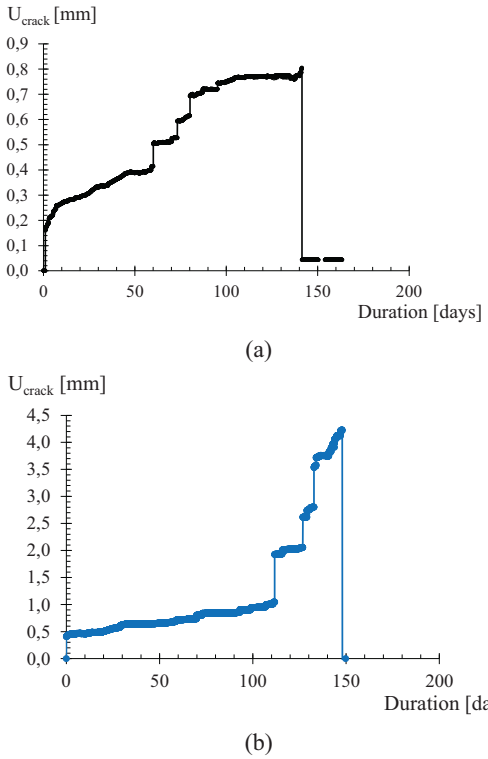

Figure 8: *Crack deflection as a function of time: (a) for beam S03 loaded in summer 2021 with few crack propagation; (b) for beam S05 loaded in winter with lots of crack propagation.*

3.3.2 Fracture facies observation

Observations of fracture facies were made a posteriori. In most cases beams with low strength but high stiffness were free from knots in the crack trajectory. On the contrary, high strength beams with low stiffness had either a knot into the trajectory or slanted facies, Figure 9(b)(c). Indeed, slanted facies requires more energy to propagates because surfaces that must be separated are larger. This result support the assumption that knots and anatomical configurations may increase a beam's strength. Furthermore, it is worth noting that all crack propagations occurred through rising toward the compression zone, whatever the grain angle (Figure 9(a)). It is surprising because the crack usually follows the grain. Reasons that may explain this observation are: (i) a descending crack would not break the beam but only

remove a piece; (ii) in a rising crack trajectory the section is progressively reduced and that is the opposite with a descending trajectory; (iii) in softwoods the overlapping of tracheids [12] allows a crack to rise slightly with no additional energetic cost.

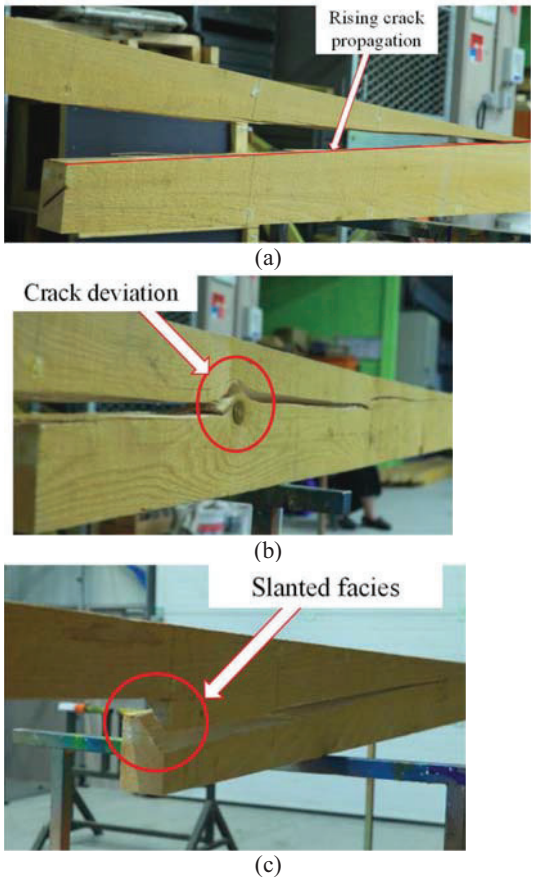

Figure 9: *Fracture facies observations: (a) A low strength beam with a rising crack propagation without knots; (b) crack deviation due to a knot; (c) a high strength beam with low basic density but slanted facies.*

4 CONCLUSION

This paper presents the results of an experimental campaign on full-scale notched beams of silver fir wood. Displacement-imposed bending tests and bending creep tests were realised on wood above FSP, partially dried and dried wood. The studied beam's batch is highly heterogeneous, but the experimental campaign is representative of the mechanical properties range. Both the dynamic and static MOE are consistent, but the estimated MC is not very accurate due to uncertainties on the green volume V_g. All other things being equal, initial MC has no visible impact on instantaneous strength. The basic density seems inversely proportional to that strength, and observations show that low basic density beams with high strength presented either knots on the crack trajectory or slanted facies that increased their strength. On the contrary, the time-dependent central deflection and compliance during creep tests tends to be proportional to the initial MC, but never exceed K_{def} proposed by Eurocode 5. This is explained by the important drying phase that increases the creep due to a mechano-sorptive effect. Nevertheless, exposure to solar radiation and knots position that resists to crack propagation also have a significant impact on the maximum time-relative compliance reached and have to be considered. The deflection only due to crack propagation was estimated to be less than 10% of the total deflection, meaning that crack has a marginal effect on the observed deflection. Finally, all fracture propagations rise whatever the grain angle. This is surprising and only intuitively explained: a rising crack propagation is energetically optimal. A finite element simulation of 4-points loaded notched beams may explain the rising crack trajectory.

ACKNOWLEDGEMENT

The authors would like to thank the Auvergne Rhône-Alpes region for the Ph.D. scholarship as well as the fundings of the Hub-Innovergne program of the Clermont Auvergne University.

REFERENCES

[1] L. Martin, H. Cochard, S. Mayr and E. Badel, "Using electrical resistivity tomography to detect wetwood and estimate moisture content in silver fir (Abies alba Mill.)," *Annals of Forest Science,* vol. 78, no. 65, 2021.

[2] D. Hunt, "A unified approach to creep of wood," *The Royal Society,* vol. 455, no. 1991, 1999.

[3] J. Dlouha, B. Clair, O. Arnould, P. Horacek and J. Gril, "On the time-temperature equivalency in green wood: Characterisation of viscoelastic properties in longitudinal direction," *Holzforschung,* vol. 63, no. 3, pp. 327-333, 2009.

[4] G. Pot, E. Toussaint, C. Coutand and J.-B. Le Cam, "Viscoelastic behaviour of maturing green poplar wood," in *SEM XIII International Congress and Exposition on Experimental and Applied Mechanics*, 2013.

[5] L. Brancheriau, Expertise mécanique des sciages par analyse des vibrations dans le domaine acoustique, Université Aix Marseille II, 2002.

[6] B. Thibaut and J. Gril , "Tree growth forces and wood properties," *Peer Community Journal Section: Forest & Wood Sciences,* 2021.

[7] AFNOR, "Structures en bois : Bois de structure et bois lamellé-collé. Détermination de certaines propriétés physiques et mécaniques," *NF EN 408+A1,* p. 38, 2012.

https://doi.org/10.52202/069179-0074

[8] A. Bontemps, G. Godi, E. Fournely , R. Moutou Pitti and J. Gril, “Implementation of an optical measurement method for monitoring mechanical behaviour. UNDER REVIEW,” *Experimental Techniques,* 2023.

[9] C. F. Pambou Nziengui, «Fissuration du bois en climat variable sous charges de longues durées : applications aux essences européennes et gabonaises,» Clermont-Ferrand, 2019.

[10] C. F. Pambou Nziengui, R. Moutou Pitti, E. Fournely , J. Gril, G. Godi and S. Ikogou, “Notched-beam creep of Douglas fir and white fir in outdoor conditions: Experimental study,” *Construction and Building Materials,* p. 13, 2019.

[11] D.Guitard, Mécanique du matériau bois et composites, 1987.

[12] M.-C. Trouy et P. Triboulot, «Matériau bois - Structure et caractéristiques,» *Techniques de l'ingénieur,* 2019.

World Conference on Timber Engineering Oslo 2023

SIMPLIFIED ENVIRONMENTAL ANALYSIS OF THE LONG-TERM PERFORMANCE OF WOOD CLADDING AND DECKING

Jonas Niklewski[1], Jakub Sandak[2], Philip Bester van Niekerk[3], Christian Brischke[4], Richard Acquah[2], Anna Sandak[2]

ABSTRACT: The performance of timber in exposed environments is affected by several biotic and abiotic factors. For timber cladding and decking, two important aspects include reduced structural performance due to fungal decay and aesthetical changes resulting from superficial effects such as photodegradation and moulds. Predicting the long-term performance of timber is important because it enables rational material (species and treatment) and design (detailing) choices and reduce the risks of unexpected repairs and premature replacement of timber products. In this paper, we use available data on material performance in conjunction with environmental analysis to model, in a simplified way, (1) the time until onset of fungal decay and (2) the long-term aesthetical appearance of timber facades and decking. The results demonstrate how the analysis can be used on a detailed geometry where wooden boards were modelled as separate objects and the choice of material affects the outcome. Several steps needing further development were identified, including a dose model linking microclimate to colour change and a better model for predicting moisture content. The study is part of a long-term effort to make holistic performance-based assessment of wood available for public use through easy-to-use procedures and accessible open-source software.

KEYWORDS: Wood, Aesthetics, Fungal decay, Durability, Long-term performance, Material database

1 INTRODUCTION

There are many different wood species, treatments, and material modifications available on the market. Selecting a material that meets a set of defined user criteria is far from trivial, in part because knowledge of long-term performance is fragmented or incomplete. The long-term performance of timber is affected by both biotic and abiotic mechanisms, and the time until non-performance depends on several aspects. In addition, the definition of non-performance depends on the application. For example, the main concern in the design of structural timber in outdoor applications, such as timber bridges, is generally the impaired structural performance caused by fungal decay. For other applications, such as cladding and decking, both structural integrity and long-term aesthetical performance/visual appearance are important aspects to consider.

Fungal decay leads to wood mass loss and reduced structural integrity, with wood moisture content being one of the main vectors for material deterioration. Free water is a prerequisite for the degradation process, so attack by decay fungi is usually not seen as a risk when the wood moisture content is below cell-wall saturation or when the wood temperature is below freezing [1]. Wood in outdoor exposure is also subject to superficial damage and colour changes not directly associated with structural damage. Colour change is caused by both chemical changes and biological growth. Solar irradiance and wind-driven rain have been cited as the most influential factors driving colour change [2]. Surfaces exposed to UV and visible light will develop a cellulose-rich grayish surface layer, in part due to the decomposition and leaching of lignin [3].

While these two modes of material deterioration lead to different outcomes and consequences, both can be described as functions of material characteristics and environmental exposures. Figure 1 shows, conceptually, a model for deterioration caused by environmental effects. The material database describes how the material (species and modification/ treatment) in question responds to environmental exposure. The environmental exposure can be modelled from the local weather and the geometry of the building envelope. The dose model evaluates these exposures (e.g. rain, temperature) and converts them to a unitless measure of dose. If other input variables are required, such as as moisture content and surface temperature, then those are derived from environmental exposures prior to dose modelling. The exposure dose can then be compared against the resistance to infer the material's response.

[1] Jonas Niklewski, Lund University, Department of Building and Environmental Technology, Sweden, jonas.niklewski@kstr.lth.se
[2] Jakub Sandak, Anna Sandak, Richard Acquah, InnoRenew CoE, Slovenia / University of Primorska, Slovenia, jakub.sandak@innorenew.eu
[3] Philip Bester van Niekerk, University of Goettingen, Wood Biology and Wood Products, Germany, philipbester.niekerk@uni-goettingen.de
[4] Christian Brischke, Thuenen-Institute of Wood Research, Hamburg, Germany, christian.brischke@thuenen.de

https://doi.org/10.52202/069179-0075

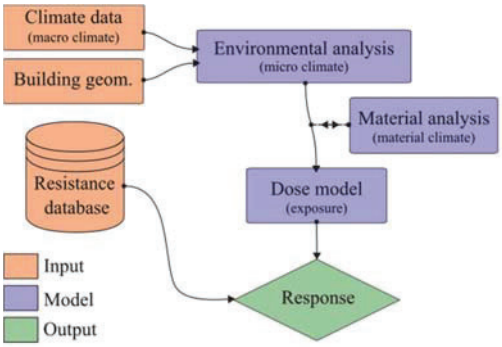

Figure 1: *Conceptual illustration of the models linking the material database to environmental exposures.*

Dose modelling has previously been used as a basis for factorised guidelines targeting service life of wood in above-ground applications [4]. Here, a 'factor' is a unitless measure describing the relative change in service life of a reference case stemming from, for example, a variation in climate conditions or design detailing. Dose models allow factors to be derived from moisture- and temperature conditions, which can be measured or simulated. Factorisation generally relies on simplified interaction between exposures, meaning that synergistic or antagonistic effects are not adequately accounted for. To address this problem, some efforts have been made to limit the use of factorisation by instead expanding the scope of moisture modelling [5]. This study is a continuation of this work, targeting wind-driven rain and shelter through environmental analysis.

Environmental conditions affect the performance of the building envelope. Exposure to wind-driven rain (WDR) and sunlight both vary with orientation and surface tilt, but also depend on design detailing. For example, deep roof eaves have long been used to limit the exposure of WDR on walls. Solar radiation is relatively predictable and can be modelled by ray-tracing. WDR is more chaotic, but can be modelled by computational fluid dynamics (CFD) [6]. As a simpler alternative to the computationally heavy CFD analysis, WDR can also be modelled through ray-tracing [7]. A simple method for environmental analysis of buildings using ray-tracing has previously been proposed by Charisi et al. [8], including both WDR and solar radiation.

The focus of the present paper is to demonstrate how (simplified) environmental analysis combines with other models to link environmental exposures to existing material databases for fungal decay and photodeterioration. WDR and solar radiation were modelled in Blender 3D [9] through particle- and ray-tracing, respectively. The resulting exposures were used as input to calculate moisture content and combined fungal dose. A basic fuzzy inference system (FIS) was used to create semi-realistic colour changes from exposure to WDR and solar radiation. While the FIS model assumptions are subjective, the system can easily be tuned when additional validation data becomes available. The analysis as a whole is simple, relatively fast and relies entirely on OA software to ensure high accessibility.

2 METHODS

This section describes the models involved in predicting aesthetical and decay performance of wooden cladding and decking. The nature of the models involved differs depending on the deteriorating mechanism in question. In both cases, the analysis is based on a specific 3D geometry of the building and the local climate. Climate data were obtained from the Swedish Metereological and Hydrological Institute (SMHI), measured in Gothenburg, Sweden, between 1st of January and 31st of December in 2021.

2.1 MATERIAL DATABASE

Material data for the relative resistance to fungal decay of treated, modified and natural wood species were obtained from Brischke et al. [10]. The data are based on a meta-analysis of measured data on moisture dynamics and inherent resistance. These measurements were used with the Meyer-Veltrup resistance model [11] to estimate the resistance to fungal attack in above-ground applications.

Material data for the colour change of modified and treated wood species were obtained from Sandak et al. [12]. The data set is based on a test-setup where the colour of different wood products was recorded monthly during 24 months of outdoor exposure. The database describes how the late- and earlywood colours vary over time. While a dose model for linking the colour change to weather variables has not yet been developed, the material data alone can be used in conjunction with a simplified exposure criterion to predict the final visual appearance of wood cladding and decking.

2.2 ENVIRONMENTAL ANALYSIS

The environmental analysis is performed in Blender 3D (v.2.83.20.0), an open-source 3D-modelling environment with limited physics-based simulation and analysis capabilities. Since Blender is not a dedicated numerical software, some simplifications are necessary. It should be noted, however, that the functionality to use the software for more sophisticated environment analysis, even CFD, is possible by integration of other open-source software [13].

The 3D geometry of a smaller playhouse (see Figure 2) is used here to demonstrate the concept. The model was obtained from a third party, meaning that the geometry was not tailored to simplify the analysis. The cladding is designed with vertical boards (125x20 mm^2) and battens (45x20 mm^2), i.e. vertical boards in two planes. Each board is modelled as a separate object, with eight vertices and six faces. The geometry was never remodelled or manipulated to facilitate the analysis.

https://doi.org/10.52202/069179-0075

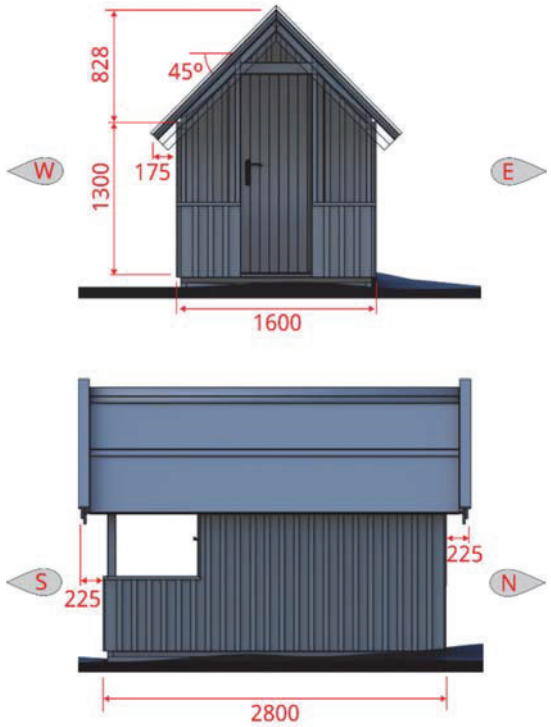

Figure 2: *Object geometry and dimensions. The annotated arrows (E and N) indicate orientation.*

After importing the geometry to Blender 3D, wooden objects to be included in the environmental analysis are inspected to verify that surface normals are consistent with respect to their orientation. The object surfaces are then projected onto a combined flat surface (UV map), using a method to maintain consistent scale between objects. The UV map is a flat representation of object surfaces linking vertex coordinates (xyz) to texture coordinates (uv). This map is used here to store the results from the environmental analysis, such as WDR and solar radiation. With a resolution of 1024x1024, a single pixel represents an area of about 10x10 mm^2, meaning that the width of a board (125 mm) is about 13 px with a thickness (20 mm) of 2 px. A single pixel is hereafter referred to as a node.

The methodology for calculating WDR and direct radiation follows the same principle. Both effects are assumed to follow straight trajectories. The trajectory of direct beam radiation depends on the sun's position, and that of precipitation depends on the wind speed, wind direction and terminal velocity. Following the assumption of straight trajectories, hourly solar radiation and WDR obtained from climate data were projected onto the surface normals of the geometry. In a subsequent step, binary masks were used to filter out exposure in shaded or sheltered regions of the geometry. The binary masks were obtained through different methods depending on the exposure in question, as explained in the following sections.

2.2.1 Exposure to wind-driven rain

The protocol for simplified environmental analysis of WDR presented here builds on a set of software-specific features, including animations, particle physics, 'dynamic paint' and 'texture baking'.

WDR is modelled as a particle system using the Blender physics engine. A particle system has two components: an emitter plane and particles. Particles are emitted from the emitter plane with an initial velocity and follows trajectory based on predefined physics , see Figure 3. The particle behaviour on collision with other objects can be set to, for example, disappearing, sticking or bouncing off the surface with or without damping. Here, particles are set to drop all momentum on collision and then continue in the direction of gravity, thus emulating water runoff.

The feature 'dynamic paint' is used to map particle collisions to the geometry. In general, dynamic paint is used to modify a surface (canvas) based on its proximity to another object (brush). Here, the particle system was defined as brush and the wooden objects (cladding/deck) were defined as canvas. The canvas was set to change colour from white to black (binary) on direct contact with a particle. The radius of brush (particle) on contact was set to 10 mm. The radius of the resulting patch was set to expand to a final radius of about 40 mm. The latter ensured that regions near the point of particle collision were also categorised as exposed.

A square horizontal emitter plane (8x8 m^2) was defined approximately 1 m above the geometry. The plane was set to emit particles in a uniform grid with a resolution of 250x250, which for the given geometry resulted in sufficient detail. The initial vertical velocity (v_z) of the particles was set to 4.5 m/s. This value is commonly used as the terminal velocity of raindrops with a drop diameter of 1.2 mm and can be used for light to moderate intensity rain spells [6]. The horizontal velocity (v_x,v_y) was varied to simulate different wind speeds and directions. Wind directions and speeds were modelled between 0 and 315 degrees in increments of 45 degrees and 0 to 6 m/s in increments of 1 m/s, respectively, resulting in 49 different unique scenarios. Note that v=0 m/s is was not run for varying orientations. The simulations were run programmatically in batch using the Blender API for Python. The outcome of the analysis resulted in 49 binary masks describing the exposed regions for each scenario of precipitation.

The terminal velocity of rain-drops combined with the wind direction and velocity gives the trajectory, $\mathbf{R}$. The projection of $\mathbf{R}$ on the surface (unit) normal of each node $\hat{\mathbf{n}}_{uv}$ is given by the dot-product. The magnitude of this vector divided by the terminal velocity gives the ratio of WDR in the node relative to rain passing through a fictive horizontal plane, which is also known as the wall factor. The wall factor is a convenient metric which can be multiplied by precipitation measured through a horizontal

https://doi.org/10.52202/069179-0075

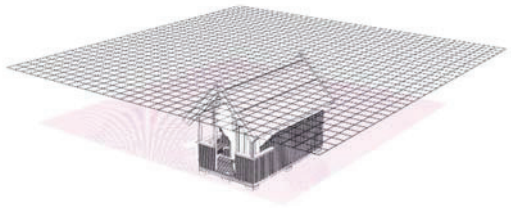

Figure 3: *Particle system simulating rain from a southeast orientation. The corresponding binary exposure map is projected on the cladding/deck, where white colour indicate sheltered areas.*

plane to calculate the amount of rain on a surface with arbitrary orientation and inclination. The binary maps obtained in the previous step were then used to zero out any nodes which were sheltered from rain. For each hour, the binary map corresponding to the nearest velocity (wind speed) and orientation was used.

2.2.2 Exposure to solar irradiance

Solar irradiation is limited to direct (beam) and diffuse irradiation. Here, the effect of reflected irradiance is not considered. Similar to the analysis of WDR, the calculation of solar irradiation on surfaces with different shading, tilt and orientation is performed in two steps. In a first step, the exposed regions of the geometry are identified using ray-tracing. In the second step, the irradiation incident on each node is calculated by projection onto the surface normals.

Regions shaded from direct solar irradiation were identified using the built-in ray- tracing algorithm of the 'cycles' renderer, a 'sun' light source and the built-in sun path algorithm. In Blender, the 'sun' is a directional light source with constant intensity, meaning that the scene lightning depends only on a given angle. This angle is given by the position of the sun in the sky relative to the location of the building, i.e. the azimuth, α, and altitude, β. The position of the sun is a function of geographical coordinates and time. For each hour, the shadow caused by the sun is mapped, resulting in 8760 binary images.

The hourly direct irradiation in each node was calculated from the direct normal irradiance, I_d, measured via satellite by SMHI [14]. The azimuth and elevation angles translate to a unit vector, $\hat{\boldsymbol{n}}_{\mathrm{Id}}$, which multipled by scalar I_d gives the vector, $\mathbf{I}_d$. The procedure is then analogous to the one presented in section 2.2.1, but the vector $\mathbf{R}$ is substituted by $\mathbf{I}_d$. For each hour, the direct beam irradiance normal to each surface was calculated by the projection of $\mathbf{I}_d$ on the surface normal of each node $\hat{\boldsymbol{n}}_{\mathrm{uv}}$. The corresponding shadowmap, as described in the previous paragraph, was then used to zero out any shaded nodes on the geometry.

Figure 4: *Skydome used to estimate the sky view factor.*

Diffuse isotropic irradiation was modelled using the sky view factor (SVF). The SVF is a dimensionless value describing the proportion of visible sky from a node. The SVF depends on surface tilt and obstacles. For example, the SVF of a vertical wall facing a free horizon is 0.5. The diffuse irradiation incident on any node on the geometry can be calculated by multiplying the measured diffuse radiation by the corresponding SVF.

The SVF was calculated by modelling the atmosphere as a dome discretizised into 600 triangular sky patches having equal area, see Figure 4. The surface normal of each sky patch was used to set the direction of a sun light source. The built-in ray-tracing algorithm was then used to map the visible part of the geometry from each sky patch. For this part of the geometry, the incident irradiation in every node was calculated. Finally, the sum total irradiation in every node were divided by that of a horizontal unobstructed surface, to obtain the SVF.

2.3 DECAY PERFORMANCE

The development of fungal decay over time is a function of the material climate (moisture content and temperature) and the material resistance (presence of extractives, treatment, etc.) to decay. The material climate depends on the environmental conditions (exposure) but is also inherently dependent on the moisture dynamics (permeability) of the wood product. For a simplified analysis following the structure in Figure 1, the exposure dose is modelled as material independent, and the moisture performance is instead considered as part of the material resistance.

2.3.1 Moisture performance

The moisture content is estimated from daily averages of relative humidity and temperature and daily sums of precipitation using an existing model developed by Frühwald et al. [15]. The equilibrium moisture content, u, is here calculated as follows:

$$u(\phi) = 0.7\phi^3 - 0.8\phi^2 + 0.42\phi + 0.0077 \qquad (1)$$

where ϕ is the daily average relative humidity. The daily average moisture content of a fictive sheltered board, u_{01}, is calculated from the average equilibrium moisture content over two consecutive days. During rainy periods, the actual moisture content of a board will increase and temporarily exceed that of the sheltered board. In the

https://doi.org/10.52202/069179-0075

model, a rainy day is defined by the daily sum of precipitation exceeding 4 mm, and a rainy period, t_r, is defined by the number of consecutive days when this condition is met. The moisture content during rainy periods, u_1, is then described as:

$$u_1(t_i) = u_{01}(t_i)[1 + k_r] \quad (2)$$

where k_r depends on the wood species and duration of the rain event. Here, a value of k_r=0.8 was used, as proposed by Frühwald et al. [15]. When the rainy period ends, the moisture content, u_1, will decrease towards the moisture content of the sheltered board, u_{01}. The duration of this decrease, t_d, depends on the length of the previous rainy period (number of consecutive days with rain), and is described as t_d=2.5t_r. The moisture content *k* days after a rainy period can then be calculated as:

$$u_1(t) = \max\begin{pmatrix} k(u_{01}k_r)/t_d \\ u_{01} \end{pmatrix} \quad (3)$$

The exposure to precipitation [mm/day] depends on the surface normal (orientation and inclination) and the degree of sheltering. Every node in the geometry is associated with a time-series of precipitation, obtained from the environmental analysis. Relative humidity and temperature were obtained from the weather data and were assumed uniform over the building geometry. In practice, solar irradiance will affect the temperature and relative humidity of the wood surface.

2.3.2 Dose model

In this paper, the 'logistic' dose model from [16] was used to estimate the progression of decay from the moisture- and temperature variation. The model is comprised of two functions: the moisture-induced dose, $D_u(u)$, and the temperature-induced dose, $D_T(T)$, as shown in Figure 5. The dose is a dimensionless value which describes the development of fungal decay between unfavourable (0) and ideal (1) conditions. The functions are mechanistic in the sense that their cardinal points (minimum, maximum, optimum) are based on mycology research [1]. If either D_T or D_u is zero, then it is assumed that no decay development can occur on that day. If both terms are positive, then the daily dose is calculated as a weighted average of the two components, according to:

$$D = \frac{3.2D_T + D_u}{4.2} \quad (4)$$

The dose, D, accumulates over time, with no setback, and relates directly to the decay rating. The relationship between decay rating and dose is based on long-term field trials where the moisture content, temperature and decay rating of Scots pine sapwood (*Pinus sylvestris*) and Douglas-fir heartwood (*Pseudotsuga menziensii*) were monitored [17]. It was found that decay rating 1 corresponds to a dose of approximately D=325, meaning that the species used in the test sustain about 325 days in ideal conditions (for fungal decay) prior to the initiation of fungal decay [18].

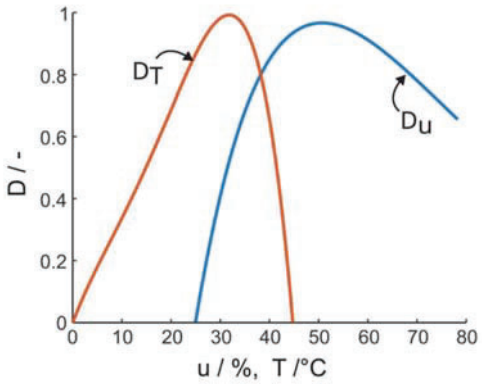

Figure 5: *Dose functions describing the relative temperature- and moisture conditions for fungal decay.*

The limit state is herein defined as the time until the onset of decay. The time until the limit state is reached is calculated as the ratio D_{Rd}/D_{Ed}, where D_{Rd} is the resistance dose obtained from the material database based on [10].

2.3.3 Factorisation

Due to its simplicity, the factorised approach has been commonly used for design guidelines. Here, the annual exposure dose, D_{Ed}, is calculated as follows:

$$D_{Ed} = D_0 k_1 k_2 k_3 \quad (5)$$

where D_0 is a reference value depending on the ambient climate and k_1, k_2 and k_3 are factors to account for moisture trapping, sheltering and distance to ground, respectively. Other factors can also be included.

In this paper, the dose derived from the environmental analysis explicitly considers ambient conditions, D_0, and sheltering, k_2, in the process of modelling moisture content variation. Distance to ground is considered in analogy with the factor-based method by calculating the distance in every node to a ground plane and then using the relationship in [19] to calculate the relative increase in dose:

$$k_3 = \begin{cases} \dfrac{700 - a}{300} & a < 400 \\ 1.0 & a \geq 400 \end{cases} \quad (6)$$

The distance in every node was here obtained through dynamic paint by defining the ground plane as a brush and the wooden elements collectively as canvas. Each node on the canvas was then coloured based on proximity to the brush with a linear falling intensity from direct contact with the ground (1) to a distance exceeding 400 mm (0).

2.4 AESTHETICAL PERFORMANCE

The change in visual appearance is modelled by combining a map of exposure dose and a generic procedural wood texture with the colour database from [12]. A fully functional dose model linking microclimate to colour change does not yet exist. Instead, conditional

https://doi.org/10.52202/069179-0075

statements and fuzzy logic were used to create pseudorealistic weathering patterns.

Colour change caused by photodegradation requires solar radiation to break down the wood cell structure and water to wash off the by-products [20,21]. Whether or not a surface is subject to weathering can thus be infered from a conditional statement. It can futher be assumed that, given a sufficiently long time horizon, surfaces exposed to both solar irradiance and WDR converge to a fully weathered state. This logic is useful for binary classification but is unable to reproduce the characteristic gradual weathering patterns between weathered and non-weathered regions. Here, a multivalued conditional approach based on (fuzzy) logic was used to define a function for interpolating between the two extremes. To demonstrate the concept, a set of subjective assumptions was made.

The function describing the degree of weathering depends on two crisp (numeric) input variables: solar radiation and precipitation. To make use of fuzzy logic, these input variables were fuzzified into two linguistic terms: low, and high exposure. Similarly, the output was described as low and high degree of weathering. The following rules were defined:

1. D == low || R == low → W = low
2. D ~= low & R~=low → W = high

The first rule states that both precipitation and solar radiation may limit the rate of degradation, i.e. if either of the two is zero, then no degradation will occur. The second rule simply describes that if (1) is false, then the degree of weathering is high. Membership functions and the resulting response surface are shown in Figure 6. The membership functions were, for simplicity, assumed triangular with their centre of gravity at 0 and 1, respectively. The resulting response surface shows that no weathering occurs if the node is subject to less than about 5% of the maximum precipitation or solar irradiance, respectively. The shape of the interpolated region between 5% and 10% is determined by the shape of the input membership functions.

The node colour is determined from wood texture and the degree of weathering using colour data from the database. The FIS determines the degree of weathering in each node and the resulting distribution is hereafter referred to as the 'dose map'. In addition to the degree of weathering, the colour depends on whether the node is late- or earlywood, which is determined from the material texture. Here, a procedural wood texture is used where the intensity describes the wood type, i.e. white (1) being earlywood and black (0) being latewood. A value between 0 and 1 describes a mix of latewood and earlywood where the colour is interpolated.

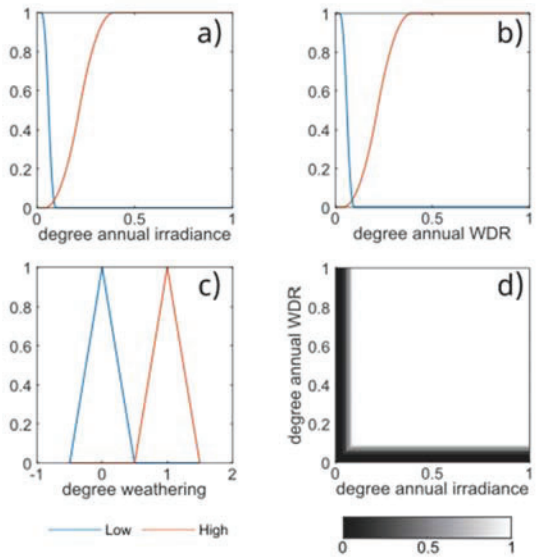

Figure 6: *Input membership functions (a,b), output membership functions (c) and response surface (d).*

3 RESULTS AND DISCUSSION

3.1 ENVIRONMENTAL ANALYSIS

Figure 7 shows the sky view factor (SVF) of the geometry, the total irradiance (direct + diffuse) and the annual exposure to wind-driven rain. The SVF shows that isotropic diffuse radiation is not orientation-dependent, but depends on the degree of sheltering and surface tilt. Therefore, horizontal surfaces on the cladding absorb approximately the same amount of diffuse radiation. The vague light vertical lines on the façade is a result of the design of the cladding, where the outer layer (battens) partially shades the inner layer (boards).

Exposure to solar radiation is higher in the southern orientation, which is typical for buildings in the northern hemisphere. The southern cladding is also subject to more WDR than the other vertical faces, which is typical for Sweden. The maximum WDR (500-600 mm) can be observed on the horizontal boards of the deck. Vertical surfaces close to the ground facing south, west, east and north were subject to approximately 300, 150, 150 and 100 mm of WDR, respectively. These values are consistent with values calculated without considering any sheltering effects.

The environmental analysis was performed for a given time, site, and geometry. However, redoing the entire analysis is necessary only when the geometry is changed. This is an advantage stemming from the fact that weather data was not integrated directly with ray-tracing and particle simulations. Particle simulations were performed based on generic scenarios and are therefore independent of both time-period and location. Ray-tracing on the other hand depends on geometry, location and time-period. The effect of calender year on the sun position is for practical

https://doi.org/10.52202/069179-0075

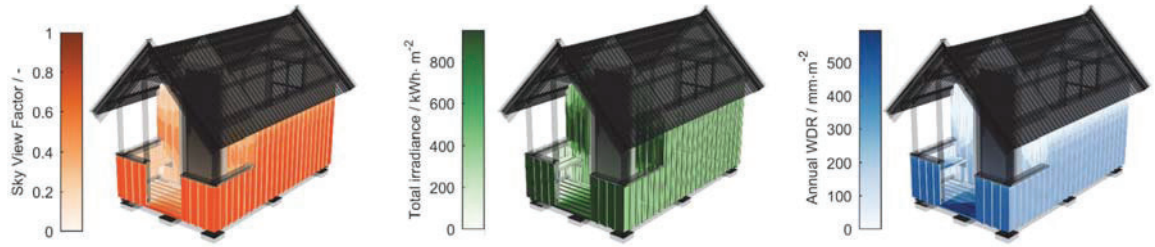

Figure 7: *Sky view factor (a), total solar irradiance (b) and annual wind-driven rain (c), viewed from southeast.*

purposes negligible, so the analysis can be reused for different years. Similarly, location can be varied within reasonable limits without introducing major errors stemming from variatrions in sun position. Alternatively, ray-tracing could be made independent of time-period and location by using generic scenarios of sun position. The analysis of sky view factor is only dependent on the geometry.

3.2 Fungal decay

Figure 8 shows the variation of exposure dose. The dose values range between 1 and 50, depending on orientation, tilt, degree of shelter and distance to the ground. The highest dose values are found close to the ground on the horizontal decking boards, while values close to zero are found on interior surfaces and other locations completely protected from rain, e.g. below the roof eaves. The high dose values seen on the decking boards can be explained by them being exposed to WDR from the most severe (south) orientation in conjunction with unfavorable surface normals (horizontal boards) and small distance to the ground.

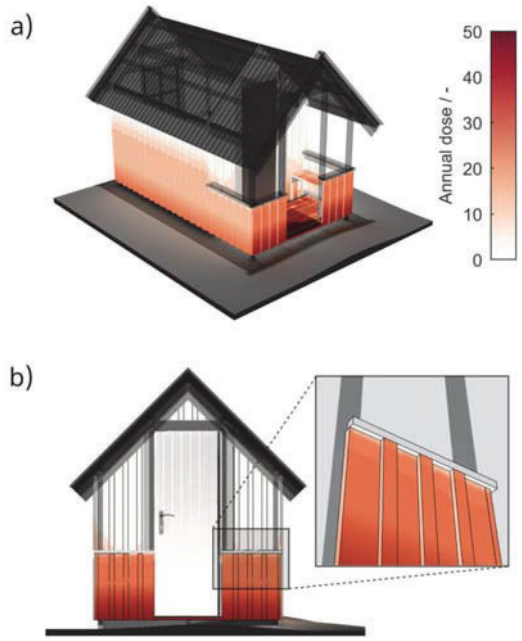

Figure 8: *Distribution of fungal dose viewed from southwest (top) and south (bottom).*

Fully sheltered elements categorised in use class 2 [22] would, under normal circumstances, not be expected to decay. Yet, the results indicate a non-zero dose also for surfaces completely sheltered from WDR. This can be explained by the moisture model employed, specifically equation 2 exceeding the lower threshold for fungal decay (25%) when the relative humidity exceeds 90%. However, the dose values registered on surfaces sheltered from WDR are very small relative the values on exposed surfaces, and therefore have little or no influence on the service life of the building as a whole.

It should be noted that the dose shown Figure 8 does neither account for detailing nor for end-grain absorption. Therefore, the depicted dose should be regarded as a reference value to be multiplied by factor k_3 in regions affected by moisture trapping or exposed end-grain. For example, Figure 8b shows a southern view with a set of vertical exposed boards connected to a horizontal member. The vertical boards are subject to a dose of approximately 20 in the connection to the horizontal board. If the end-grain is directly exposed to precipitation and no ventilated gap (minimum 5-8 mm to facilitate drying) is provided, then the dose will increase by a factor of k_3=1.6 up to 32, following the guideline by Isaksson et al. [19].

The dose shown in Figure 8 is only dependent on the exposure conditions and is thus independent of the wood species, treatment and modification used. The actual service life depends to a great extent on the moisture-performance and inherent resistance of the wood product. These factors are considered by the material resistance dose, which is listed [10] for many different wood products. For example, untreated Norway spruce (*Picea abies*) and European larch (*Larix decidua*) have material resistances in above-ground applications of D_{Rd}=325 and D_{Rd}=1800, respectively.

3.3 AESTHETICAL PERFORMANCE

Figure 9 shows the change in colour from newly built to weathered, with materials including natural and treated pine wood. The wooden materials were rendered without passing the materials through a shader. This means that interaction between material and lightning was not modelled. For demonstrative purposes this was deemed desirable.

https://doi.org/10.52202/069179-0075

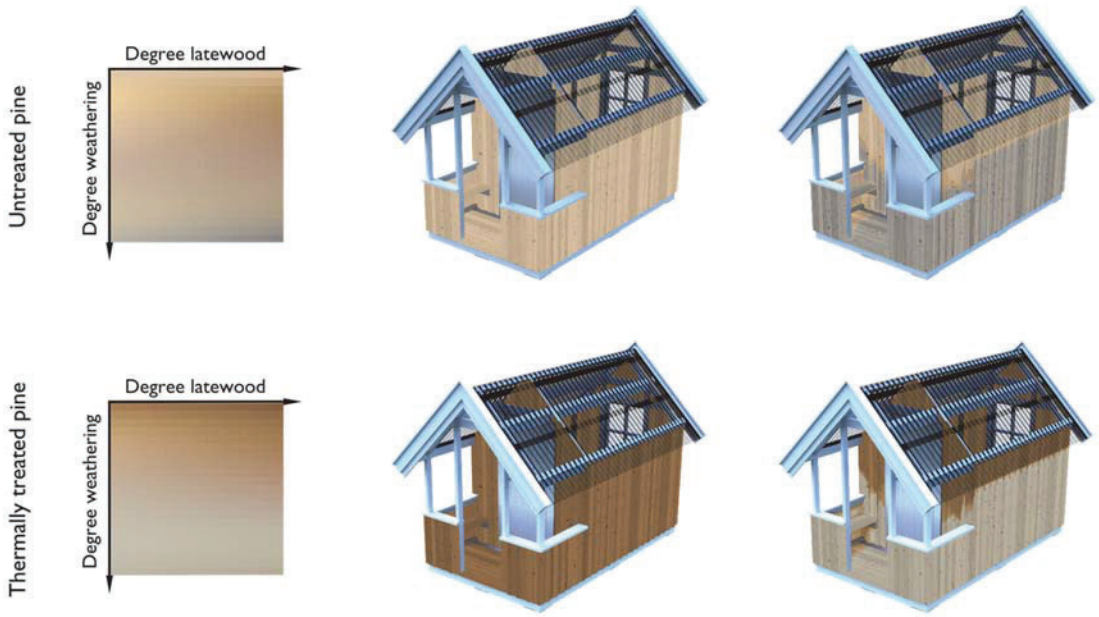

Figure 9: *Colour of newly built (centre column) and fully weathered building (right column) made from natural (top row) and thermally modified (bottom row) pine wood, viewed from southeast. The left column shows the interpolated colour maps, based on the database.*

As can be seen by comparison to Figure 7, the extent of the weathered regions correspond quite well with the coverage of WDR. The reason for this is that the FIS require both exposure to precipitation and solar irradiance for weathering to occur. Regions exposed to WDR are predominantely exposed also to direct and/or diffuse radiation, thus making exposure to precipitation the limiting factor.

It should be reiterated that the FIS model used to determine the dose map is very simplified and is used in lieu of an accurate dose model. The approach presented here can be used for binary classification of regions subjected or not subjected to weathering and for smooth interpolation between those regions. However, the model cannot be used to describe the kinetics of weathering, i.e. the aesthetical appearance at a specific point in time.

4 CONCLUSIONS

Exposures to WDR and solar radiation were modelled on a multi-object geometry. Ray-tracing for solar radiation and particle tracing for WDR were performed in the open-source software Blender 3D. The results were then used to model exposure to fungal decay and to identify areas subject to surface deterioration, respectively. These results, in conjunction with existing material databases, can be used as a basis for service life prediction.

The methods demonstrated here can be used to support decision-makers in the choice of material and design. The results provide a visual overview which can be used to qualitatively identify critical locations where detailing should be designed with caution, as well as regions where detailing is less important. Based on the results, the designer can decide whether the long-term performance, in terms of service life and aesthetics, is acceptable. If not, then the design can easily be adapted with material less prone to weathering and/or with higher resistance to fungal decay.

Future work will focus on improving the model used to estimate moisture content and developing a quantitative dose-response model relating colour change to environmental effects. The scope of the moisture content calculation could also be expanded to include distance to ground and detailing, further reducing the need for factorised design. Finally, the method can be integrated with life cycle costing and maintenance scheduling, as it provides detailed information of exposure for individual components. However, model validation against real examples is needed.

ACKNOWLEDGEMENT

Authors received funding in the frame of the research projects CLICK*design* and WoodLCC, both supported under the umbrella of ERA-NET Cofund ForestValue through the national funders of the participating countries. ForestValue has received funding from the European Union's Horizon2020 research and innovation programme under GA N° 773324. JS, RA and AS gratefully acknowledge the European Commission for funding the InnoRenew CoE project (GA #739574) under the Horizon2020 Widespread-Teaming program and the Republic of Slovenia (investment funding from the Republic of Slovenia and the European Regional Development Fund).

REFERENCES

[1] Schmidt O.: Wood and tree fungi, Springer, 2006.

[2] Rüther P., Jelle B.P.: Color changes of wood and wood-based materials due to natural and artificial weathering. Wood Material Science & Engineering, 8:13–25, 2013.

[3] Kalnins M.A., Feist W.C.: Increase in wettability of wood with weathering. Forest Products Journal, 43(2):55-57, 1993.

[4] Thelandersson S., Isaksson T., Frühwald E., Toratti T., Viitanen H., Grüll G., Jermer J., Suttie E.: Service life of wood in outdoor above ground applications: Engeneering design guideline. Lund University, Lund, 2011.

[5] Niklewski J., Van Niekerk P.B., Brischke C., Frühwald Hansson E.: Evaluation of moisture and decay models for a new design framework for decay prediction of wood. Forests. 12:721, 2021.

[6] Blocken B., Carmeliet J.: Validation of CFD simulations of wind-driven rain on a low-rise building façade. Building and Environment, 42:2530–2548, 2007.

[7] Tsoka S., Thiis T.K.: Calculation of the driving rain wall factor using ray tracing. Journal of Wind Engineering and Industrial Aerodynamics, 179:190–199, 2018.

[8] Charisi S., Thiis T.K., Stefansson P., Burud I.: Prediction model of microclimatic surface conditions on building façades. Building and Environment, 128: 46–54, 2018.

[9] Blender Online Community: Blender - a 3D modelling and rendering package. Blender Foundation, Blender Institute, Amsterdam, http://www.blender.org, 2022.

[10] Brischke C., Alfredsen G., Humar M., Conti E., Cookson L., Emmerich L., Flæte P.O., Fortino S., Francis L., Hundhausen U., et al: Modelling the material resistance of wood—Part 3: Relative resistance in above-and in-ground situations—Results of a global survey. Forests, 12(5): 590, 2021.

[11] Brischke C., Alfredsen G., Humar M., Conti E., Cookson L., Emmerich L., Flæte P.O., Fortino S., Francis L., Hundhausen U., et al.: Modelling the material resistance of wood—Part 2: Validation and Optimization of the Meyer-Veltrup Model. Forests, 12(5):576, 2021.

[12] Sandak A., Sandak J., Brzezicki M., Kutnar A.: Bio-based building skin. Springer Nature, 2019.

[13] Southall R., Biljecki F.: The VI-Suite: a set of environmental analysis tools with geospatial data applications. Open Geospatial Data, Software and Standards, 2: 1–13, 2017.

[14] Swedish Meteorological and Hydrological Institute, (n.d.). www.strang.smhi.se (accessed January 12, 2023).

[15] Frühwald Hansson E., Brischke C., Meyer L., Isaksson T., Thelandersson S., Kavurmaci D.: Durability of timber outdoor structures: modelling performance and climate impacts. In: Proceedings of the World Conference on Timber Engineering 2012 (WCTE 2012), Auckland, New Zealand, 2012.

[16] Isaksson T., Brischke C., Thelandersson S.: Development of decay performance models for outdoor timber structures. Materials and Structures, 46: 1209–1225, 2013.

[17] Brischke C., Rapp A.O.: Dose–response relationships between wood moisture content, wood temperature and fungal decay determined for 23 European field test sites. Wood Science and Technology, 42: 507-518, 2008.

[18] Alfredsen G., Brischke C., Marais B.N., Stein R.F., Zimmer K., Humar M.: Modelling the material resistance of wood—Part 1: Utilizing durability test data based on different reference wood species. Forests, 12(5):558, 2021.

[19] Isaksson T., Thelandersson S., Jermer J., Brischke C.: Beständighet för utomhusträ ovan mark (in English: service life of wood above ground). Structural Engineering, Lund, 2011.

[20] Derbyshire H., Miller E.R.: The photodegradation of wood during solar irradiation. Holz Als Roh-Und Werkstoff, 39: 341–350, 1981.

[21] George B., Suttie E., Merlin A., Deglise X.: Photodegradation and photostabilisation of wood–the state of the art. Polymer Degradation and Stability, 88(2):268–274, 2005.

[22] EN 335: Durability of wood and wood-based products - Use classes: definition, application to solid wood and wood-based products, 2013.

https://doi.org/10.52202/069179-0075

World Conference on Timber Engineering Oslo 2023

ON THE USE OF ARUCO MARKERS IN LONG TERM MONITORING OF TIMBER STRUCTURES

Jiří Kunecký[1]

ABSTRACT: For research and monitoring purposes, there is a need to measure long-term displacements of parts, joints, etc. Of course, existing solutions (LVDT, Tell tales, etc.) can be used, but they are relatively expensive or inaccurate. The article describes a simple procedure based on an optical method using ArUco markers originating from computer vision applications (robotics). This technique uses not only marker tracking, but also along with it image rectification using projective transformation, and thus works well in 2D structures (beams, walls). The illustrated principle allows to take only two images (the original and another one after a certain time) and to quantify the displacement and rotation of the markers identified in the images. Reference points have to be specified. The displacement fields are then interpolated and a final map is produced. This can be of interest to anyone working in practice, conducting research on the long-term behavior of joints, monitoring the creep of wooden structures or for any monitoring purpose - including laboratory tasks. The article describes accuracy and error estimation and shows an example of use.

KEYWORDS: Monitoring of timber structures, ArUco markers, measurement of displacement, long term monitoring.

1 INTRODUCTION

The work presented in the article was created and inspired in everyday practice, both in the laboratory and in-situ. Measuring long-term displacement fields in wood joints or in wood research in general (e.g. shrinkage due to moisture changes) is a complicated matter, as expensive in-situ equipment is not preferred due to possible damage, suffering also from issues like a need of stable power supply, data storage or simply because of the fact that the device is blocked for a period of time for further activities, etc. What is then needed for reliable displacement measurement not only in the wood engineering industry? It is an inexpensive practice that can be used repeatedly, which keeps the data for further analysis and is sufficiently accurate. Such a solution can be attained when taking the advantage of computer vision algorithms. Since many algorithms in this field have been already developed [1], the users need to understand them and use them properly to ensure a reliable result of the analysis.
Optical measurement of movements or strain fields can be performed using marker tracking (e.g. the ones commonly spotted in car crash tests) or based on minimization of warping of a subset in a sequence of images leading directly to digital image correlation (DIC). Because digital image correlation is very sensitive to any moves of the camera, usually it is the choice for laboratory testing, where there is no need of repositioning of the optical device etc. Further text is thus focused on CV [1] and marker-based procedures, which allow (re)moving the camera and return it later after some time.

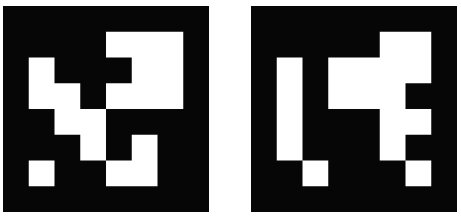

Figure 1: *Samples of two distinct ArUco markers*

The idea is to use an industrial camera (or even an ordinary one) to obtain a picture of the scene and compute the precise position of markers of known dimensions. There are more types of markers [7], but the very simple ones, the ArUco markers [2] have multiple advantages: their area and corners are relatively big to ensure good contrast. The markers have been developed for use in robotics, where cameras are serving as the eyes of the robot and let it orientate in 3D space using found points. Such a marker has simple geometry (see Figure 1) and has also an ID coded in the binary map. That allows to recognize the markers from each other and use further processes to track their relative change. It should be noted that these markers can be printed out very cheap way by a standard laser printer (whose precision 1200 DPI is expected) and glued to the surface use a glue or an adhesive gum. This setup is the starting point for further analysis.
Of course, measurement of precise point displacement can be done using standard geodetic approaches, such as total station or laser-based methods, however, this article goes

[1] Jiří Kunecký, Czech Acad Sci, Inst Theoret & Appl Mech, Czech Republic, kunecky@itam.cas.cz

https://doi.org/10.52202/069179-0076

its own way because a gap in monitoring techniques has been found, especially for rigid body motion assessment: a very cheap technique, that can be done using basic equipment without additional cost and which is relatively powerful. To attract the interest of the professionals and public, the author decided to spread and discuss it in the conference.

2 METHODS

2.1 PRINCIPLE

Theoretical starting point is the image rectification based on projective transformation [3,4]. The method uses the alignment of the image sequence to one image plane (usually to the reference one). The principle requires presence of four rigid reference points in the scene. In next step the algorithm determines the point differences in this (already aligned) reference image plane. Because of this fact the validity of the method is to 2D planar problems because projective transformation is limited to it. The number of problems where this approach can be used is high in civil engineering (beams from the side, walls, crack monitoring). Clearly enough, there is a lot of errors that can be made during the process and which are more in detail discussed later.

2.2 STEP BY STEP ANALYSIS

For clarity the methodology is outlined in following steps and commented more in detail in the paragraphs below:

1. Choose the object for monitoring
2. Print the markers in corresponding size and resolution
3. Select the 'reference part' in the scene and glue 4 markers to represent it
4. Glue the rest of the markers; the more, the better
5. Prepare the camera and perform the camera calibration (needed just once for given lens-camera system)
6. Take one reference image (t_0)
7. Come after some time and place the camera in similar place
8. Take another image (t_n)
9. Repeat step 7 and 8 as many times as needed
10. Analyze the result using the above outlined CV procedures
11. Interpolate and review the displacement field

The object dimension of course affects the precision of the process, since the precision of determination of the marker corners can be in practice considered 0.1 pixel (sub-pixel resolution up to 0.01 px is possible, but not realistic). That is also the key parameter to consider the size of the marker, as minimum 50x50 pixels representation of one marker in the whole scene can be recommended for reliable analysis. Generation of ArUco markers is included in the ArUco OpenCV-contrib package [1], and is coded using a simple Python script. Parameters of such a generation are image size and ID range to generate. The markers should be printed using a laser printer with high resolution; here the method uses the fact, that laser printer is usually the most precise mass-produced device in the office: 1200 DPI means 21 μm dot size! Markers do not have to be printed only on paper, but there exist also vinyl (PVC) sheets for printing. This is very important in the case of humid conditions when paper and timber can have significant shape changes.

The scene has to include the part which is rigid and not moving, since tiny shifts of reference points can jeopardize heavily the analysis results. That is why it is not good to measure members (or joints), which have still strong moisture-related volumetric changes, namely joints made of fresh timber. Such problems can be solved different way: using a matrix of reference points which can be after analysis of their relative displacement (distribution of strain has to be even) reduced to 4 reference points (rarely used). Highest precision is attained if the four reference points are close to four corners of the image, but this is rather an uncommon case, since the part that is monitored has to be inside the reference area. Reference points and actually the whole monitored object should be in the paraxial part of the picture, centered, which ensures lowest distortion.

Markers should be glued using a glue that does not change the shape with change of conditions and which is cheap, standard office glue is often the best one. For rough surfaces can be used an elastic adhesive gum glue.

Camera and lens should be selected carefully. Here an understanding of basic optical principles is needed. Best solution is a HQ camera with at least 5 MP resolution as is used during testing of the setup here: Basler Aca2440-20gm (see Figure 2). Global electronic (preferably not mechanic) shutter with rather bigger chip size should be selected. Field of view (FOV) is the key for proper lens selection, nevertheless, avoid fish-eye effect as much as possible, go for longer lens if the chip size allows it. Always use fixed focal length. In the test a Basler C23-1620-5M-P 16 mm lens with polarizing filter to evite reflections. Camera can be mounted to any camera stand, preferably with all DOFs adjustable.

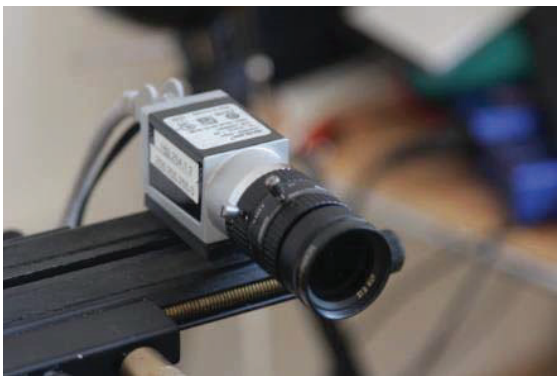

Figure 2: *Camera and lens used in the tests*

For proper measurement, camera has to be properly calibrated [6] and its intrinsic matrix assessed. This technology allows for rectification of the images taken and remove the lens distortion (undistort them). Such a process is made using OpenCV routines described in [7] and a simple chessboard, see Figure 3.

https://doi.org/10.52202/069179-0076

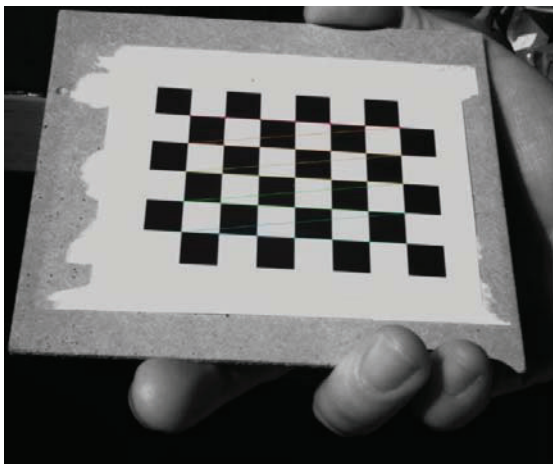

Figure 3: *Camera calibration using a chessboard*

The image acquisition is best, if the takes multiple images and computes an average out of them, since it significantly removes the noise and increases the precision of the measurement. Highest possible illumination along with highest aperture is always preferred.
The whole procedure is programmed using Python and is available for download in [5] under 3-clause BSD license. All people interested in the details can go through the code and look at the solution row by row.
Doubts arise about precision of camera repositioning when the image acquisition is repeated after some time and the camera was removed in between. As an answer it is important to assess the error. Abstractly the error estimation consists of multiple sources of possible error: lens distortion, chip noise, marker position assessment, marker printing, camera calibration error, paraxiality of the marker position (it is always not preferable to undistort the images as it is another idealization), camera repositioning (distance and angular), roundoffs in the CV algorithms. It is not possible to describe such a complexity here, the error estimation would be valid for the particular case and cannot be simply evaluated here in the extent of this article. That is why an example is shown here, which shows the method when focused on *absolutely stable testing plane*: in such case all movements measured would be made by errors of the measurement itself and not made by the displacements. That is how the reader of the article can have an idea about the error present in the measurement.

2.3 TEST AND ERROR ESTIMATION

The test can be shown in Figure 4, when four markers in the left paper (A4, 297x210 mm) are taken as reference points and four in the right are being evaluated. Marker size was 25 mm, their distance was horizontally 120 mm and vertically 169 mm (center-center), working distance 1.382 m, height of the optical axis (chip axis) was 0.819 m.
The goal of the test was to estimate the error if the camera is moved with precision that one can achieve in-situ if there is a marker on the floor for example. Two linear sliding plates were mounted on each other to be able to simulate the precise displacement simulating errors in repositioning, see Figure 5.

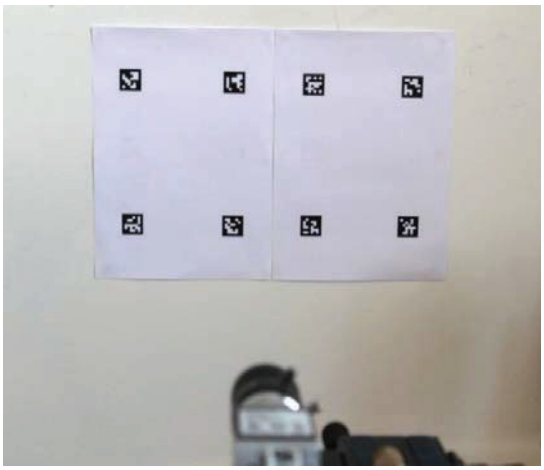

Figure 4: *Testing rig (papers not moved) for the error estimation*

The precise position changed to (points are referred later in results as e.g. 2.3.1 – the first one):
1) -5 cm in X and -5 cm in Z axis (for orientation see Figure 5, going to the left and farther from the object),
2) +5 cm in Z direction (moving closer to the object)
3) yaw - rotate 5 degrees (rotation towards upper left corner in the image)

Output of the analysis is shown in the results section.

Figure 5: M*ount allows for defined camera (re)positioning in two axes (x and z, bottom)*

2.4 EXAMPLE FROM TIMBER JOINTS MONITORING

To show the measurement system described here more in the context of timber structures, another artificial example of use has been made: lap timber joint with slight rotational move – 5 mm timber peg was placed under the joint (see Figure 5). The movement amplitude is not important here, this case is for illustration of use only. The height of the joint is in reality 60 mm, marker size 8 mm. The same camera was used, lens was 55 mm telecentric

(not fully) Computar TEC-M55MPW, same procedure as described above, however, camera was only removed and clicked back to the stand.

Figure 6: *Illustration of use in a timber joint, two images are aligned onto each other and the relative move of the markers is computed*

3 RESULTS

3.1 TEST AND ERROR ESTIMATION

For the analysis of the camera movement see Figure 6-8. The results are very positive, case -5 cm in both axes is depicted in Figure 6. Maximal error is 0.09 mm, however, remember the whole area is 300 mm by 150 mm.

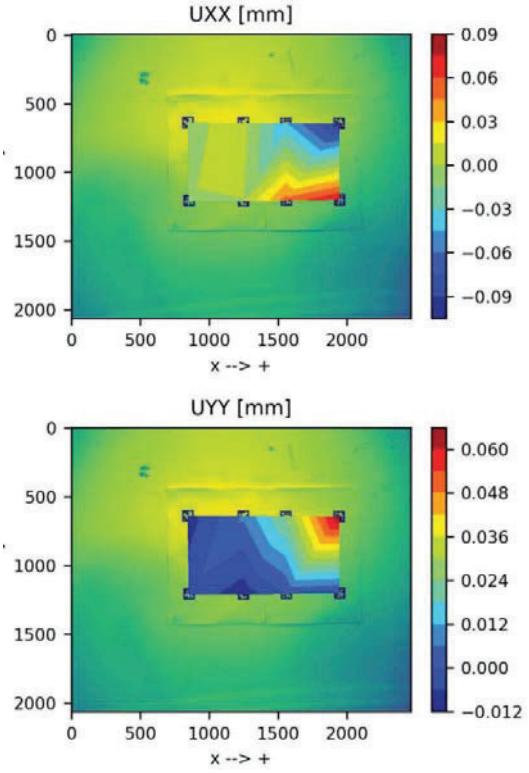

Figure 7: *Interpolated displacement field case 2.3.1)*

Second configuration, 5 cm movement towards the object provides even better results, maximum is 0.016 mm.

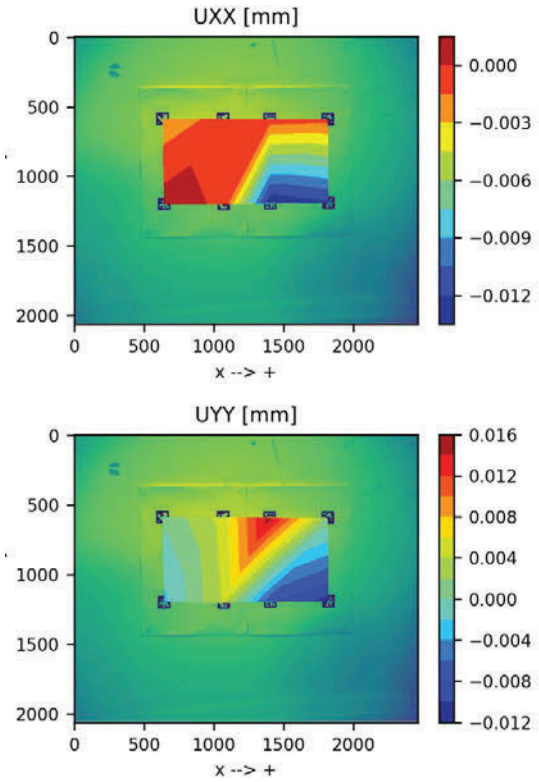

Figure 8: *Interpolated displacement field case 2.3.2)*

As the worst can be seen the angular rotation 5°, as can be seen in Figure 8. However, the results are still not bad, only 0.12 mm. So, the usability of the method is dependent on the precision in structure displacement one wants to measure and can expect.

If case 2) is compared to 1) and 3) it can be concluded, that biggest errors are present in case there is a big move for from the optical axis outside the paraxial area and the curvature of the lens can produce this amount of distortion (although the image was undistorted). Based on the lens focal length and thus its curvature, this error will be higher in case smaller chip size and shorter focal length is selected.

3.2 EXAMPLE FROM TIMBER JOINTS MONITORING

The results of this analysis from 2.4 can be found in Figure 9. Because not precise prescribed move was made using universal testing machine or similar machine, the results cannot be compared directly to the 5 mm peg size. This example is of course intended to show the potential of the methodology for monitoring of structures in time. Note the fact, that the number of colors in the images is directly specified as the number of contours during plotting of the graphs.

https://doi.org/10.52202/069179-0076

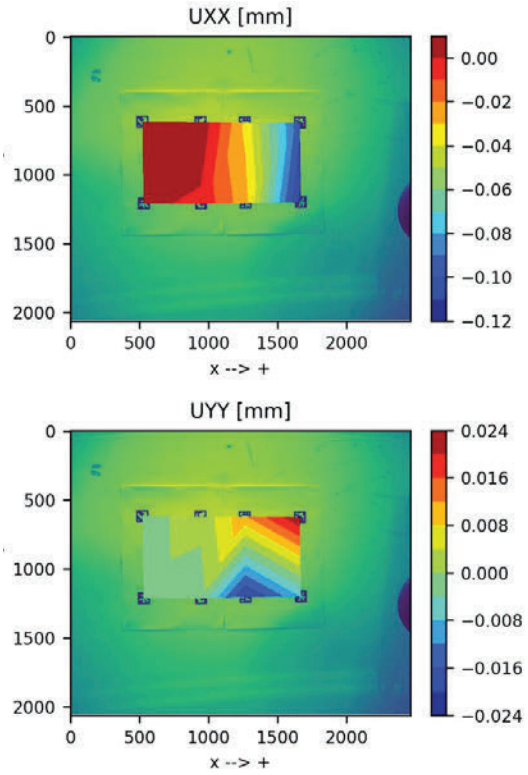

Figure 9: *Interpolated displacement field case 2.3.3)*

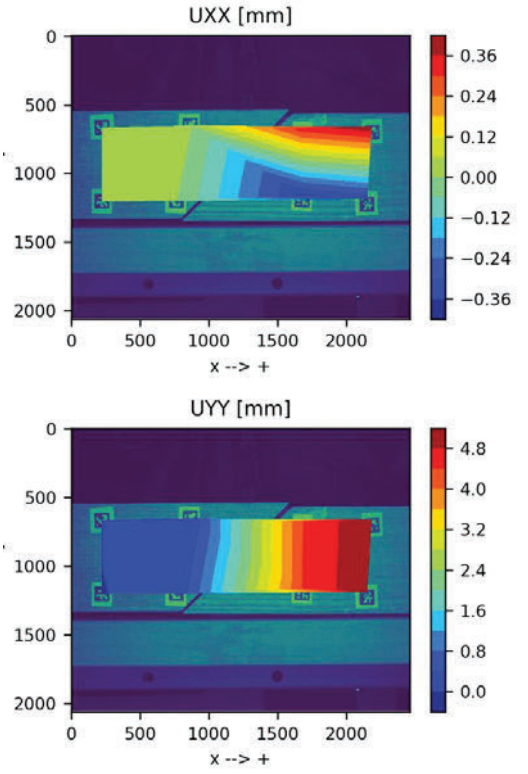

Figure 10: *Interpolated displacement field – half lap joint*

3.3 FINAL REMARKS AND DISCUSSION

The results show according to the author very precise determination of the studied quantities. This enables the method to be used in many applications, where some reference can be found and where only 2D movements take place.

It is good to mention that the displacement field is not continuous enough due to low number of points. That is also the case why one cannot think about strain measurement and stay only in the domain of displacements. Of course, more markers can be glued, the mesh densified and the computed field smoothed using splines; but the quality of strain field will be never the one seen in DIC.

It is a question if one is able to place precisely the camera with say 5 cm error to the place where it was before; from author's experience it definitely is possible, and, actually, it is possible even with higher precision.

The marker-based approach is very convenient because it does not need the same light conditions – markers are recognized even in different light intensity. Such a thing would be never possible when thinking about time-lapse digital image correlation. It should be pointed out that the technique overgoes the problems with shadows in DIC, a problem very often found in rough surfaces and annual rings when the light is repositioned back. The markers can be also removed without any stain remaining on the body. If swelling or shrinking is present, the inspector can put a reference piece of (metal or glass) ruler. Another option is to use markers made of material that do not swell (e.g. silicone-based).

The algorithm takes images which are saved and which can be also analyzed by somebody else later. This can play a significant role when survey of the joint shape is required. It can be used in relatively short periods to quantify the amount of creep, and the results are so precise, that the trend can be assessed (is the crack active or is it already not moving/opening?). Big magnification can be used as well, in this case the precision of repositioning is a very sensitive parameter.

As the biggest disadvantage thus remains the need of reference points inside the picture. This can be, however, solved using another precise positioning system: a rigid and stable object can be mounted before the 2D object and use the advantage of depth of field to focus properly both objects. ArUco detection of not well focused markers is possible and can be valid.

4 CONCLUSIONS

The paper describes a procedure that is able to monitor very precisely marker displacement in time. The marker position and density as well as the whole procedure is based on experience and precision, and thus depends also on the person who prepares it. Error estimation and a sample of use is described. The marker tracking itself – not along with the projective transformation - can be used for other uses as well – e.g. assessment of stiffness of a testing rig using optical measurement (MMB test). However, the original use could be broad and might be very cheap and fruitful for all interested in long term

https://doi.org/10.52202/069179-0076

monitoring of timber structures or in-situ survey. Since it is not based on a commercial code, the method is provided to the scientific community as is. The technique is not a solution for everything and needs proper selection of use. For some types of long-term structure monitoring it is perfectly suitable.

ACKNOWLEDGEMENT

This paper was created with a financial support from grant project of Grant Agency of the Czech Republic GACR No. 21-29389S “Experimental and numerical assessment of the bearing capacity of notches in timber beams at arbitrary locations using LEFM”.

REFERENCES

[1] OpenCV and OpenCV-contrib, www.opencv.org, https://github.com/opencv.

[2] Garrido-Jurado, S., Muñoz-Salinas, R., Madrid-Cuevas, F. J. and Marín-Jiménez, M.J. 2014. "Automatic generation and detection of highly reliable fiducial markers under occlusion". Pattern Recogn. 47, 6 (June 2014), 2280-2292.

[3] Projective transformation, Wikipedia, online. https://en.wikipedia.org/wiki/Homography_(computer_vision)

[4] Image rectification, Wikipedia, online. https://en.wikipedia.org/wiki/Image_rectification

[5] Jiří Kunecký, ArucoLT monitor, open source software documentation, see online http://www.itam.cas.cz/Software/ArucoLT_monitor/index.html

[6] Camera calibration theory, online https://www.mathworks.com/help/vision/ug/camera-calibration.html

[7] OpenCV camera calibration Tutorial, online https://docs.opencv.org/4.x/dc/dbb/tutorial_py_calibration.html

[8] Kalaitzakis, M., Cain, B., Carroll, S. et al. Fiducial Markers for Pose Estimation. J Intell Robot Syst 101, 71 (2021).

https://doi.org/10.52202/069179-0076

World Conference on Timber Engineering Oslo 2023

EXPERIMENTAL STUDY OF THE EFFECTS OF ACCELERATED AGING CYCLES ON THE FIRE REACTION PERFORMANCE OF FIVE WOOD SPECIES

María Pilar Giraldo[1], Alina Avellaneda[2] Laia Haurie [2], Marcel Vilches[1], Ana M. Lacasta[2].

ABSTRACT: The objective of this study is to evaluate the influence of the degradation caused by atmospheric agents' exposure over time (weathering) on the fire behaviour of five species of wood with different natural durability, according to known durability classes (UNE-EN 350:2016). Two laboratory tests were carried out for assessing the wood of Chestnut (Castanea sativa), European larch (Larix decidua), Black pine (Pinus uncinata), Paulownia (Paulownia tomentosa) and Scots pine (Pinus sylvestris), the later with and without durability impregnation-treatment by autoclave. Laboratory tests involved two processes of accelerated aging cycles (without and with spray) for four weeks following the protocols based on the ASTM G154:2016 and UNE-EN 927-6:2019 standards, in order to make reference to the use classes of exposure to humidity 3.1 and 3.2 defined in the UNE-EN 335:2013 standard. Analysis of the variation of the colour and the appearance of deformations and splitting after accelerated aging were performed. Flammability tests were also carried out to analyse the fire reaction performance of the samples in each stage of the aging test. Differences in colour changes were observed depending on the spraying presence in the aging processes. The results indicated that weathering significantly influences the fire reaction on a wooden surface, especially in softwoods with a medium and low degree of natural durability. Surface roughness and splitting hinder the ability to extinguish the flame. On the other hand, larch proved to have both a good resistance to degradation and good fire behaviour.

KEYWORDS: Natural durability of wood, weathering degradation, fire performance of wood, aging cycles.

1 INTRODUCTION

Natural wood durability is generally associated with hardwoods and tropical woods. Their density, hardness, and composition (extractive compounds) make them highly resistant to degradation by abiotic agents (weathering) and attack by organisms such as fungi and insects.

However, some resinous softwood species, such as larch (Larix decidua) (*L in this study)*, offer better-than-average natural degradation resistance, so it is widely used for facade claddings.

Durability varies, not only between different wood species but also within each species. In most wood species, the heartwood, which is the inner part of a log, is naturally more durable than the sapwood, the outer layers of the log [1].

When wood is exposed to outdoor conditions, a complex combination of chemical, mechanical, and light energy factors contribute to natural weathering [2].

The three primary sources of wood degradation are fungi (decay or rot), insects, and weathering. So, we can distinguish between wood decay and wood degradation. The repeated actions of wet (rain) and dry, the changing exposure to high and low temperatures and sunlight results in physical and chemical degradation of the wood over time. Physical deterioration consists of surface roughening, checking, splitting, and wood cell erosion [2,3]. Chemical deterioration involves a complex sequence of free-radical reactions. The degradation of wood by any biotic or abiotic agent modifies some of the organic components of wood [2]. These components are primarily polysaccharides (cellulose, hemicelluloses) and polyphenols (lignin).

One of the most relevant weathering factors responsible for changes in the wood surface is moisture in all its varieties: dew, rain, snow, and humidity. The classes of use described in the UNE-EN 335:2013 standard consider the risks to which a wooden building element may be subjected depending on its exposure to ambient moisture. A facade cladding is subject to use classes 3.1 and 3.2,

[1]María Pilar Giraldo, Forest Science and Technology Centre of Catalonia (CTFC), Spain. pilar.giraldo@incafust.cat.
[2]Alina Avellaneda, Universitat Politècnica de Catalunya UPC, Spain. alina.avellaneda@upc.edu.
[2]Laia Haurie, Universitat Politècnica de Catalunya UPC, Spain. laia.haurie@upc.edu.
[1]Marcel Vilches, Forest Science and Technology Centre of Catalonia (CTFC), Spain. marcel.vilches@fbs.cat.
[2]Ana María Lacasta, Universitat Politècnica de Catalunya UPC, Spain. ana.maria.lacasta@upc.edu.

https://doi.org/10.52202/069179-0077

which consider outdoor exposure without contact with the ground. Class 3.1 refers to limited wetting conditions with wood temporarily above 20% of moisture content (MC), while class 3.2 refers to prolonged wetting conditions with wood frequently above 20% MC (Fig. 1). Accordingly, the design of appropriate construction details facilitates fast and constant water removal and quick wood drying.

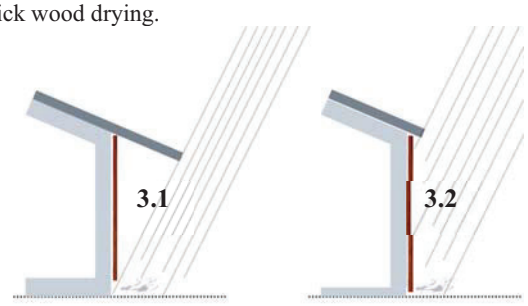

Figure 1. *The use classes of facade cladding are 3.1 or 3.2, depending on ambient moisture exposition. Building details are essential to avoid moisture excess and prevent water sorption by capillarity from taking place causing decay effects.*

Colour is one of the main attributes of wood from an aesthetic point of view, and it is therefore important to analyse its stability against weathering [4]. One of the most important causes of photodegradation in wood is ultraviolet (UV) (visible, and infrared light), light, which induces chemical reactions between its main constituents. Colour differences can be determined according to the CIE-L*a*b* (CIELAB) standard from the International Commission on Illumination CIE. The determination of the colour coordinates according to this standard, before and after aging, allows the quantification of their variations. Research on different wood species reveals an important darkening effect depending on the time and type of aging (natural or accelerated) [5,6].

Wood is a combustible material that exhibits smouldering due to the char layer generated during its burning process. Many research papers focusing on the reaction to fire of wood define the most important factors influencing the fire characteristics of wood are mainly density, orientation concerning the heat source, moisture content, and quality of wood surface treatment [7,8]. In some wood species, particularly rich in extractive substances and exudates, the composition may have more influence on fire behaviour than the density [9]. Weathering factors, especially rain moisture cause leaching which degrades lignin the most thermally stable component of wood as well as the least thermally stable hemicelluloses and extractive substances [10]. As a result, the cellulose in the fibres becomes more apparent and can protrude and produce a fibrous surface and roughness [1]. Defects of wood and cracks influence the persistence of flames on the surface [11].

This study intends to focus on the long-term degradation of wood and how this affects its fire behaviour. This issue is especially important in façade claddings, given the increasing use of this material in both private and public building construction. In some countries, such as Spain, the height limit for timber cladding (D, S2,d0 reaction to fire classification) is 10 m, and the use of flame retardants to improve the fire performance of wood is not an option, because guaranteeing the durability of these products against weathering remains a challenge.

2 MATERIALS

Five wood species were studied. Two hardwoods: chestnut (C) and Paulownia (P) and three softwoods: European Larch (L) Black Pine (PN) and Scots pine, the latest with (PRN) and without treatment (PRT). The natural durability of the heartwood in each of them according to UNE-EN 350:2016 standard is shown in table 1.

Table 1*: Natural durability of studied species*

Code	Density Kg/m^3	wood-decay attack	Insects attack	
C	520	2 (1)	DC2	(D) Durable
L	584	3 - 4	DC2	(D) Durable
*PN	517	-	-	(P) Not very durable
PRN	516	3 - 4	DC2	(D) Durable
P	266	5	DC5	(ND) Not durable

Wood-decay from better to worst 1 → 5. *Data from [12]

Scots pine (*Pinus sylvestris*) has an excellent impregnation capacity (Class 1), a natural (PRN) and treated (PRT) sample was tested. The treatment preventive and curative were impregnated by autoclave with a penetration level of NP5 (UNE-EN 351).

3 METHODS

3.1 TESTINGS

In order to carry out the accelerated aging processes on the wood samples and the subsequent analysis of the colour degradation and the fire behaviour analysis the tests described below were performed.

3.1.1 Accelerating aging tests

Two different exposure conditions (A1 and A2) have been tested for four weeks through an equipment QUV/spray accelerated weathering tester. The A1 process (no sprayed) was conducted according to the protocol of ASTM G154:2016 cycle 1, consisting of 56 alternating cycles of an 8-hour UV-A 340 radiation period and 4 hours of condensation. The A2 process was carried out following the protocol of the standard UNE-EN 927-6:2019. In this process, a one-week exposure cycle begins with 24 hours of condensation, followed by 48 cycles of 3 hours that combine a 2.5-hour UV-A 340 radiation period and a water spray period of 0.5 h. Table 2 shows the total time for each period. The A1 and A2 aging conditions represent the use class 3.1 and 3.2 respectively according to UNE-EN 335:2013 standard.

Wood specimens of 300 x 100 x 15 mm were previously stabilized in a climatic chamber for one week under controlled conditions of 20 ± 2 ° C temperature and 65 ± 5% relative humidity.

https://doi.org/10.52202/069179-0077

An accelerated aging process of 4 weeks resulted in a significant deterioration of the samples. Some studies indicate that 4 weeks under accelerated aging may be equivalent to 2 years of natural aging [13]. Table 2 shows details on the total hours of each cycle.

***Table 2**: Protocols followed for accelerated aging processes A1 and A2.*

Standard	Tests	Exposure periods throughout the trial (h)			
		Condensation	UV-A	Water spray	Total test time
ASTM G154:2016 C.1	A1	224	448	No	672
UNE-EN 927-6:2019	A2	96	480	96	672

3.1.2 Colour measurements

A PCE-TCR 200 colorimeter has been used to measure the CIELAB colour coordinates L^*, a^* and b^*. L^* is the lightness, going from 0 (black) to 100 (white) whereas a^* and b^* are the colour coordinates, from green (negative) to red (positive) and from blue (negative) to yellow (positive) respectively. The total colour differences ΔE_{ab}^* can be calculated as:

$$\Delta E_{ab}^* = \sqrt{(L^* - L_0^*)^2 + (a^* - a_0^*)^2 + (b^* - b_0^*)^2}$$

where L^*, a^* and b^* are the measured values after aging and L_0^*, a_0^* and b_0^* are the corresponding reference values from non-aged samples. Each colour data corresponds to the average of measurements taken from four different points.

***Figure 2.** Points on the sample for colour analysis*

3.1.3 Epiradiator test

Wood samples of 100 x 100 x 15 mm were tested with the device described in the Spanish standard UNE 23727-90. The samples were placed on a metallic grid 3 cm below a heat source of 500 W. The heating source was removed and put back after each ignition and extinction. The parameters determined were the time to ignition, the number of ignitions, and the average time of flame persistence during the first 5 minutes of testing. The results obtained are detailed in section 4.3.

4 RESULTS AND DISCUSSION

4.1 VISUAL OBSERVATIONS

Overall, the degradation of all samples during the four weeks is significant. Remarkable differences are observed between the specimens exposed to the aging cycles without spray (A1) and with spray (A2). Samples tested under A2 testing showed greater surface degradation consisting of cracks and fissures.

The Scots pine (PRN and PRT) and Black pine (PN) samples showed the most significant degradation. These samples developed different sizes of checking and cracking, some of them deep, especially in PRN. Additionally, some of the PRN specimens were curved (Fig. 3).

However, no cracks or texture changes were observed on the surface of the Paulownia (P) samples. Paulownia pieces exhibited exceptional dimensional stability and smooth surface without roughness or cracks, even for the specimens of week 4. Larch (L) also showed a good appearance and dimensional integrity during the 4 weeks, with some small cracks.

***Figure 3.** Photographs of three of the samples studied in three different views: (left) lateral side, (middle) frontal, and (right) fontal after the flammability test. All of them aged with the A2 process (with sprayed). (a) Scots pine (PRN) after 2 weeks of aging. The specimen exhibits several cracks and curved deformation. (b) Paulownia (P) after 4 weeks of aging. The sample remains smooth, with a good appearance, without deformations and no cracks are visible to the naked eye. (c) Larch (L) after 4 weeks of aging. The specimen remains with a good appearance without deformations, with small cracks little perceptible.*

Figure 4 shows a series of photographs, comparing non-aged samples (NA) with those subjected to accelerated aging according to the two procedures summarized in table 2, for 1, 2, 3 and 4 weeks. Samples exposed to the test without spraying (A1) show a progressive darkening and a colour change towards reddish tones. On the other hand, after the A2 test, the samples show less noticeable colour changes. The general trend is towards darkening, except in the case of paulownia (P) which becomes progressively lighter. The tonalities after A2 exposure are bluish.

4.2 COLORIMETRY RESULTS

The colour changes observed visually and discussed in the previous section can be quantified by the CIELAB colour parameters in Figure 5, the lightness L* is shown for both accelerated aging processes A1 (top) and A2 (bottom). In the non-spraying case (A1), for all the wood species, there is a significant decrease in L*, i.e. a darkening of the surface, in the first week of exposure. Over the following

weeks, the samples continue to darken, although at a slower rate. The behaviour is similar for all species, being more remarkable for paulownia (P), where L* is reduced by about 45%. The Scots pine samples darken the least, showing no significant differences between natural (PRN) and treated (PRT) Scots pine. In the case of the A2 aging process, which introduces periods of water spraying but has a shorter condensation time, the samples hardly darken at all. Indeed, in the case of paulownia, some lightning is observed.

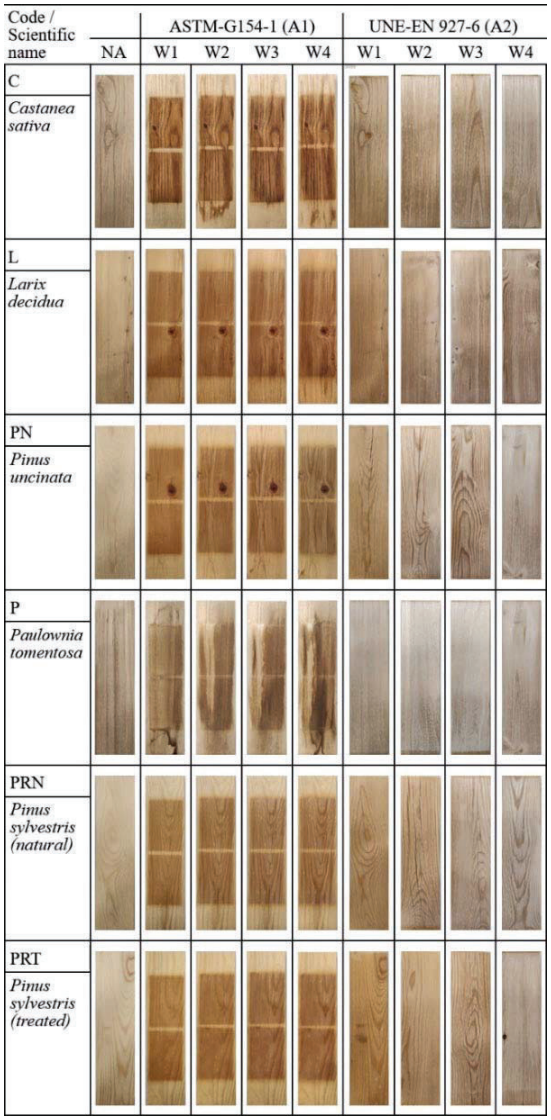

Figure 4. *Four-week aging test. For each specie, photographs of a non-aging (NA) sample and for each week under aging procedures A1 and A2 are present.*

The differences between the two types of aging can be seen more clearly in Figures 6-7, where only the results of week 4 (W4) are compared. Figure 6-top represents the L* values corresponding to no-aging (NA), aging type A1 and aging type A2. Figure 6 (bottom) plots the difference in colour coordinates a* and b* from the initial condition to the situation after 4 weeks of exposure. The arrows show the direction of change for each wood specie, both for A1 (left) and A2 (right) aging. The results obtained in both cases concerning the colour coordinates are quite different. While the unsprayed aging process (A1) increases the values of a* (red) and b* (yellow), the sprayed process (A2) decreases both coordinates. These results are in good agreement with the tonalities towards red in the case of procedure A1 and blue in the case of procedure A2 that were observed in Figure 4.

Finally, as an indicator of the total colour differences, figure 7 shows the ΔE_{ab}^{*}parameter. As expected, the overall changes are more significant for the A1 procedure than for A2 for all species, with Paulownia showing the most significant differences.

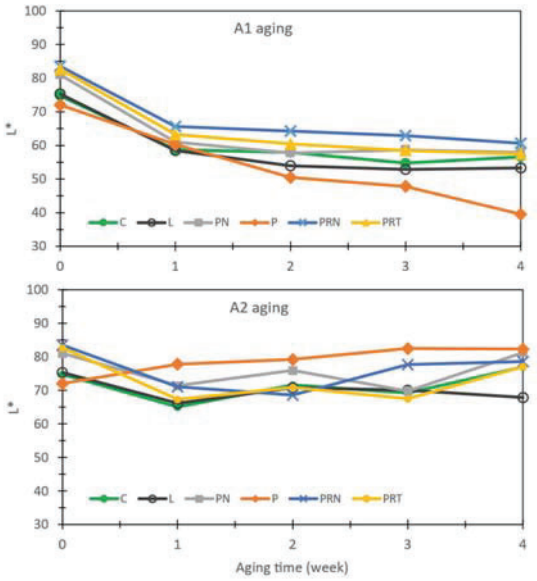

Figure 5. *Lightness L*, as a function of the aging weeks, for the different species analysed. The figures correspond to the accelerated aging processes A1 (top) and A2 (bottom).*

https://doi.org/10.52202/069179-0077

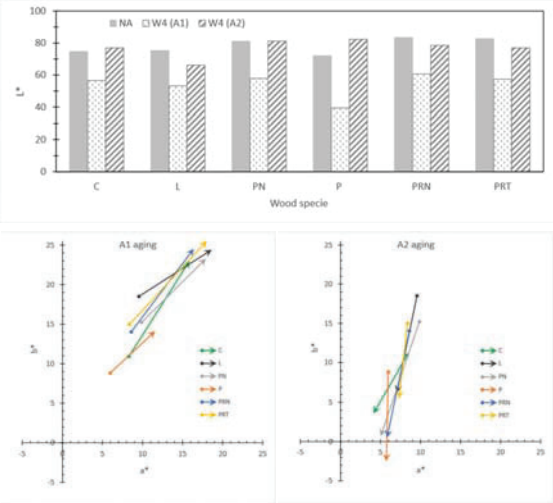

Figure 6. *CIELAB colour parameters for the different species. Top panel: lightness L* corresponding to non-aging (NA) and 4 weeks of exposure according to procedures A1 and A2. Bottom panels: colour coordinates a* and b* showing the difference from the initial measurements (NA) to those determined after 4 weeks of exposure type A1 (left) and A2 (right). The arrows indicate the direction of the change, from the initial to the final situation.*

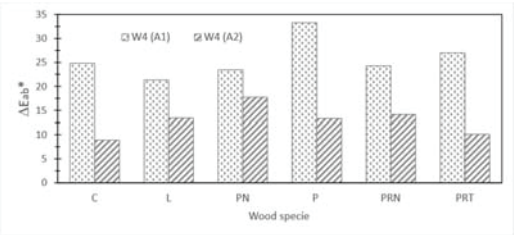

Figure 7. *Total colour differences after 4 weeks of exposure according to aging procedures A1 and A2*

4.3 FIRE BEHAVIOUR

Fire behaviour of the different wood species without aging and after A1 and A2 accelerated aging programs have been evaluated with the epiradiator test. In the case of the non-sprayed aging procedure (A1), samples of each species were tested after 4 weeks of aging, while for the sprayed aging procedure (A2) the fire tests were performed after each week of aging up to 4 weeks.

Figure 8 shows the time at which the first ignition occurs for non-aged, and samples aged under A2 spray conditions. It can be observed that Paulownia has a significantly lower initial ignition time. This hardwood has a low density, 266 kg/m^3, and therefore a highly porous structure that facilitates the release of flammable gases. Larch and Scots pine exhibit higher initial ignition times for non-aged samples with a density of 584 and 516 kg/m^3 respectively.

The time of the first ignition tends to increase with aging which can be explained by the leaching of low thermal stable constituents of wood such as extractives and low molecular weight polysaccharides from hemicellulose [10,14]. The self-extinguish ability of wood samples is related to the average value of flame duration depicted in figure 8 (bottom). Larch exhibits the best behaviour both for non-aged and aged samples. Its good durability and the absence of remarkable cracks are responsible for its good fire behaviour. On the other hand, the porous structure of Paulownia contributes to increasing the duration of the combustions and the propagation rate.

Although there exists some variability, the general trend is a worsening of the fire behaviour with A2 aging, observed through an increase in the persistence of the flames. Several factors can explain this behaviour, one of them is the reduction of the charring ability of wood samples due to the loss and photodegradation of hemicellulose and lignin [10,14]. Hemicellulose and lignin play an important role in wood charring, which is one of the main mechanisms for wood protection in case of fire [15,16]. Another effect is the occurrence of splitting after the dry and wet cycles of aging, as can be observed in figure 3. The presence of cracks favours the release of flammable gases and the persistence of the flames. Black pine and Scots pine are the species that show a higher level of splitting with aging.

Aging under spraying conditions (A2) is more aggressive than non-spraying aging (A1) and the variations in the first ignition values and the average flame durations are more pronounced for A2 samples after 4 weeks of aging.

Figure 10 compares the behaviour of non-treated (PRN) and treated (PRT) Scots pine. The presence of an organic protective treatment shows a positive effect on delaying the ignition of non-aged samples. This could be due to the clogging of the cellular structure that hinders the release of flammable gases. PRT sample also exhibits a smaller number of cracks after aging and this can explain the lower flame duration of week 4 samples aged under A2 procedure. However, in order to assess the effect of the treatment on splitting a higher number of samples would be needed.

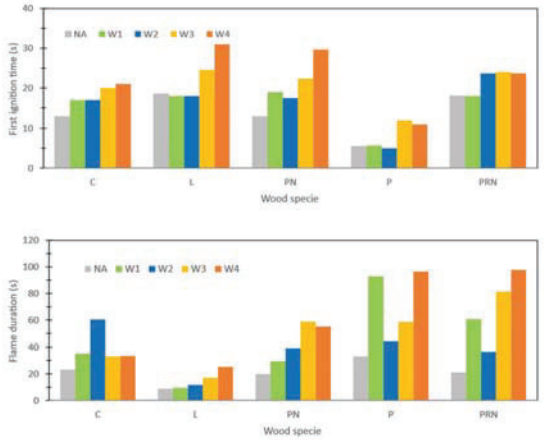

Figure 8. *Comparison of the flammability between species for each week of the A2 accelerated aging procedure. The graphics correspond to the first ignition time (top) and flame duration (bottom).*

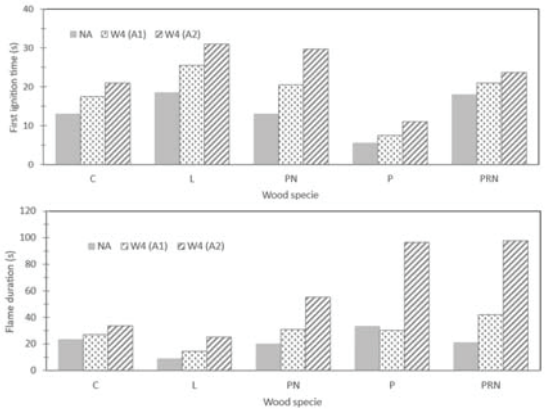

Figure 9. *Comparison between species for no aging (NA) and aged samples in both procedures A1 and A2 at week 4. The graphics show the comparison of first ignition time (top) and flame duration (bottom).*

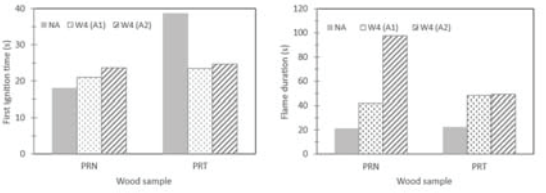

Figure 10. *Comparison between Scots pine non-treated (PRN) and treated (PRT) for no aging (NA) and aged samples in both procedures A1 and A2 at week 4. First ignition (Left) and Flame duration (right).*

5 CONCLUSIONS

Overall, the results show a correlation between weathering degradation and a gradual worsening in the fire behaviour of the samples. Despite the initial ignition time increases for the samples aged with both procedures, the self-extinguish ability worsens leading to a higher flame persistence. Photodegradation and leaching of different components of wood and the appearance of cracks and deformations play a major role in fire behaviour. The good durability of Larch and the absence of remarkable cracks contribute to a good response in fire reaction. On the other hand, although Paulownia does not present cracks and deformations after aging, it exhibits fast propagation of flame and low time of ignition due to its low density and porous structure. Aging causes darkening in most of the samples and changes in colour, being more significant for the non-spraying procedure (A1). The aging process (A2) also produces a progressive darkening of the specimens except for Paulownia, which becomes increasingly lighter. In both cases, Paulownia shows the most relevant differences in its appearance.

6 ACKNOWLEDGMENTS

The authors express their gratitude to the MCIN/AEI/10.13039/ 501100011033 through the research project BioSAFE (PID2020-117530RB-I00) for the financial support received under the scope of the “State R+D+I Program Oriented to the challenges of society” and to the operational program for investment in growth and employment FEDER of Catalunya 2014 and funds from the Lleida's Council in the framework of the PECT project "El bosc, primer recurs de l'economia verda".
Also, they want to thank the Generalitat de Catalunya for the quality accreditation given to the research group GICITED (2021 SGR 01405).

REFERENCES

[1] Zimmer, K., Flindall, O., Gobakken, L., Nygaard, M. (2020). Weathering of unpainted wooden façades: Experience and examples. Wood Be Better, NIBIO, Norwegian Institute of Bioeconomy Research, Vol 6, No 5.
[2] Feist, W. (1990) Outdoor Wood Weathering and Protection. U.S. Department of Agriculture, Forest Service, Forest Products. Laboratory, Madison, WI 53705-2398.
[3] Shupe, T., Stan, L., Ring, D. (2008). Causes and control of wood decay, degradation & stain. LSU. Ag. Center Research & Extension. Pub. 2703.
[4] Kržišnik, D., Lesar, B., Thaler, N., Humar, M. (2018). Influence of natural and artificial weathering on the colour change of different wood and wood-based materials. Forests, 9(8), 488.
[5] Liu, Ru, et al.: Comparison on the aging of woods exposed to natural sunlight and artificial xenon light." Polymers 11.4: 709. 2019.
[6] De Moura, L. F., Brito, J. O., Nolasco, A. M., Uliana, L. R., De Muniz, G. I. B. (2013). Evaluation of coating performance and color stability on thermally rectified Eucalyptus grandis and Pinus caribaea var. Hondurensis woods. Wood Research, 58(2), 231-242.
[7] Friquin, K. (2011). Material properties and external factors influencing the charing rate of solid wood and glue-laminated timber, Fire Mater. 35 303–327.
[8] Bartlett, A.I., Hadden, R.M., Bisby, L.A. (2029). A review of factors affecting the burning behaviour of wood for application to tall timber construction, Fire Technol. 55 (1) 1–49.
[9] Haurie, L., Giraldo, M.P., Lacasta, A.M., Montón, J., Sonnier, R. (20219). Influence of different parameters in the fire behaviour of seven hardwood species, Fire Safety Journal. 107. 193–201.
[10] Panek, M., Kubovský,I., Oberhofnerov, E., Sterbov, I., Niemz , P.,Osvald, A., Kacík, F. (2021). Influence of natural weathering on the ignition and relative burning rate of selected softwoods. Construction and Building Materials. 304. 124615.
[11] Cimer, Z., Czoboly, O., Harmann, B., Lublóy, E. The Effect of the Wood Defects on Fire Resistance. (2020). Periodica Polytechnica Civil Engineering, 64(1), pp. 60–64.
[12] Correal, Eduard, et al.: Physico-mechanical properties, durability, and treatability of Pinus Uncinata from the Pyrenees: WCTE 2016.
[13] Liu, X. Y., Liu, M., Lv, M. Q., Lv, J. F. (2019). Photodegradation of three hardwood species by sunlight and xenon light sources. BioResources, 14(3), 6909-6922.
[14] Nuopponen, M., Wikberg, H., Vuorinen, T., Maunu, S.L., Jämsä, S. and Viitaniemi, P. (2004), Heat-treated softwood exposed to weathering. J. Appl. Polym. Sci., 91: 2128-2134.
[15] Shen, D. K., Gu, S., Bridgwater, A. V. (2010). The thermal performance of the polysaccharides extracted from

https://doi.org/10.52202/069179-0077

hardwood: Cellulose and hemicellulose. Carbohydrate Polymers. 82, 39-45.
[16] Dorez, G., Ferry, L., Sonnier, R., Taguet, A., Lopez-Cuesta, J. M. (2014). Effect of cellulose, hemicellulose and lignin contents on pyrolysis and combustion of natural fibers. Journal of Analytical and Applied Pyrolysis. 107(5), 223-331.
[17] Kránitz, K., Sonderegger, W., Bues, C. T., & Niemz, P. (2016). Effects of aging on wood: a literature review. Wood Science and Technology, 50, 7-22.
[18] de Almeida, T. H., de Almeida, D. H., Gonçalves, D., Lahr, F. A. (2021). Color variations in CIELAB coordinates for softwoods and hardwoods under the influence of artificial and natural weathering. Journal of Building Engineering, 35, 101965.

World Conference on Timber Engineering Oslo 2023

LONG TERM BEHAVIOUR OF A TWO-WAY SPANNING TIMBER CONCRETE COMPOSITE SLAB WITH STEEL TUBE CONNECTOR

Julian Brogli[1], Andrea Frangi[1]

ABSTRACT: Timber-concrete composite (TCC) plays increasingly important roles in today's timber construction. Using timber in the tension zone and concrete in the compression zone uses both materials to their strengths. A novel two-way spanning TCC slab using steel tubes as connectors of the timber and the concrete members was developed at ETH Zurich. As both, concrete and timber have independent long-term behaviours the long-term effects of the slab system are to be determined. This paper discusses the set-up of planned long-term tests and the development of a finite element model to describe the long-term behaviour of the slab system that then can be verified once enough data is acquired.

KEYWORDS: Timber-concrete-composite, TCC, Long-term, Numerical modelling, Steel tube connector, Biaxial

1 INTRODUCTION

Due to the ongoing discussions about the climate in recent years, sustainable construction has become increasingly important. The increasing use of wood in construction leads to a long-term storage of CO_2 and a lower expenditure of gray energy. Since it is estimated that 4 - 7 % of global anthropogenic CO_2 emissions come from cement production, it is not sufficient to modify only manufacturing methods or cement composition [1].

As floor slabs account for one of the largest shares of volume in any building and have been made largely out of reinforced concrete a way of addressing this concern is the development of more climate-friendly alternative systems. Today slabs often are made of high-performance timber products as cross-laminated timber, dowel-laminated timber or timber concrete composite (TCC) [2]. Uniaxial line-bearing timber-concrete composite slabs have already been researched with extensive experimental and numerical investigations, and reliable design bases have been developed [3] [4] [5].

With the current increase in demand for wooden high-rise buildings, the need for slab systems that enable their construction is also growing. In addition to the load-bearing capacity, important requirements for the ceiling system include the need for architectural freedom concerning the floor plan, the thickness and the weight of the slab. Architectural freedom can be achieved by using a two-way spanning system and low weight and thickness of a slab directly translate to a more efficient building as less foundation measures are needed and more usable floor area can be achieved with the same amount of total building height.

With these boundary conditions in mind, a novel biaxial-bearing TCC slab system was developed at ETH Zürich using steel tubes as connectors. The system consists of a 60-100mm thick timber member. Depending on the needed performance, this timber member consists out of beech laminated veneer lumber (LVL), cross-laminated timber (CLT) or a newly developed intermediate product of both using 10mm thin birch lamellas. The concrete member is 90mm thick. The novelty of the slab consists in the non-bearing intermediate layer that separates timber and concrete and is filled with cellulose, stone wool. A heavier recycled material can be used as filling instead if it is needed to comply with sound or vibration criteria. The sheer connection between the timber and concrete layers consists of steel tubes. The general concept of the system is depicted in Figure 1.

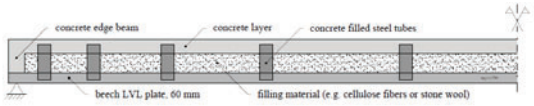

Figure 1: *Concept of the developed TCC slab system with steel tube connector* ***[6]****.*

As a common design problem of timber and TCC slabs are the deflection criteria that need to fulfill a given serviceability limit state (SLS) enforced by structural design guidelines [7] and both concrete and timber have a rheological behaviour, the long-term properties of the slab system have to be investigated.

2 METHODS

2.1 LONG-TERM TESTS

To investigate the long-term behaviour of the slab system long-term tests are investigated in a climate-controlled bunker chamber in Niderweningen, Switzerland. The specimens installed include:

- Uniaxial bending specimens for different two materialisations in both loading directions and 3 loading levels

[1] Institute of Structural Engineering, ETH Zürich Switzerland.
Julian Brogli, brogli@ibk.baug.ethz.ch
Andrea Frangi, frangi@ibk.baug.ethz.ch

https://doi.org/10.52202/069179-0078

- Several connection specimens in a double shear push-out layout to investigate the behaviour on a connection level, with different types of connection layouts,
- bending tests on timber-only beams to investigate the long-term behaviour of different timber materialisations

Space limitations prevent long-term investigations on a biaxial-bearing specimen.

2.1.1 Bending specimens design

The beech LVL configurations timber member consists of a 60mm thick beech LVL (BauBuche Q) plate. For both loading directions (longitudinal and transverse to grain) 5000mm long, 600mm wide and 240mm high bending specimens on three different loading levels in each grain direction are investigated. The steel tubes are arranged according to the expected shear force distribution. The outer steel tube diameter is 101.6mm with a wall thickness of 3.6mm. The steel tubes are embedded into the timber member using a 2mm thick layer of 2C-epoxy resin. The embedment depth of the steel tube into the timber member is 50mm. The embedment depth of the steel tube into the concrete (C40/50) is 60mm. Except for the concrete layer everything was prefabricated by Implenia Holzbau AG. The specimens tested in transverse to grain direction additionally feature two BARTEC connections that connect the timber members, as the maximal production width of BauBuche Q is 1850mm. Therefore, 3 individual pieces have to be connected for the total 5000mm lenght. The layout and dimensions for the specimens in the longitudinal direction are depicted in Figure 23.

2.1.2 Push-out specimens design

As previously conducted short-term tests conducted showed [6], that the global slab behaviour is highly influenced by the local connection behaviour, investigations on the connection level are carried out. For this investigation adapted versions of a double shear push-out test with an appearance as depicted in Figure 2 are used. The outer dimensions of the specimens measure 480 x 400 x 220 mm. With these specimens, the influence on the connection configuration is investigated. These tests include investigations on:

- the type of glue used,
- the thickness of the glue line,
- the local behaviour of different materialisations,
- the embedment depth in eighter layers and
- the influence of the steel tube diameter.

The push-out specimens are carried out in a symmetrical single-material set-up to be able to retrieve the local stiffness behaviour for every embedment type. The combined connection behaviour can be later predicted with a procedure developed by Kreis [6].

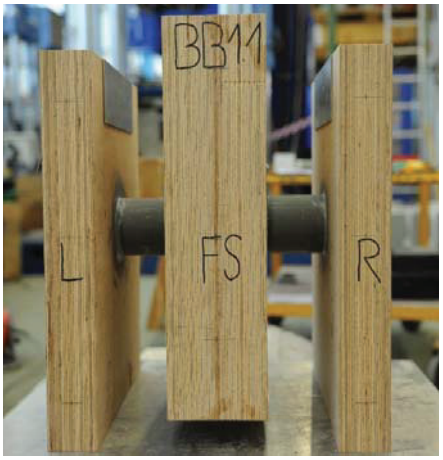

Figure 2:*Example of push-out specimen in beech LVL*

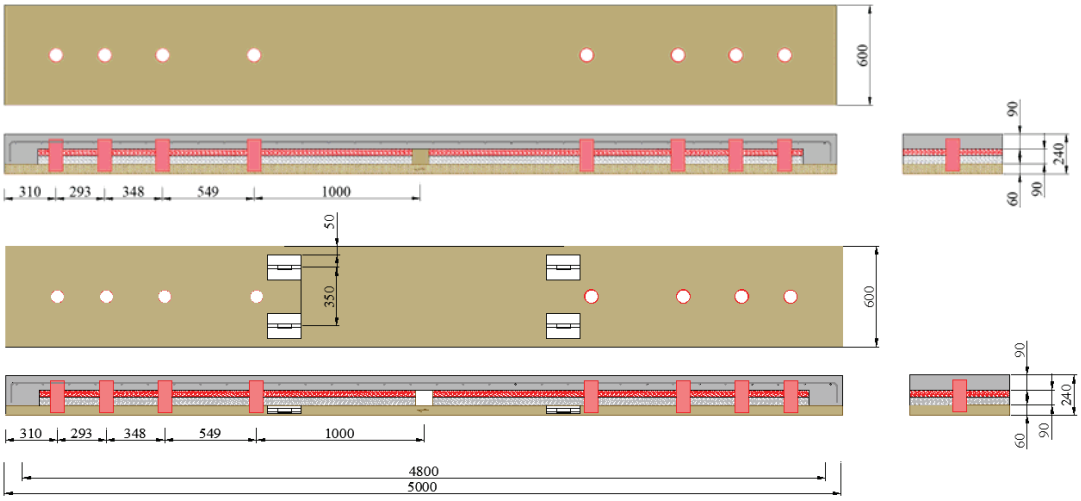

Figure 3: *Uniaxial bending specimen series with dimension longitudinal (top) and transverse (bottom) to grain loading direction.*

2.2 NUMERICAL MODELLING

2.2.1 Software and Subroutines

As the adjustable parameters of the slab systems are extensive and the number of possible experimental tests limited a numerical a parametric simulation model was developed for a 3D analysis. The commercial software Abaqus FEA of the company Dassault Systèmes was used. For the Finite Element analysis, the Abaqus/Standard solver was used. The choice to use Abaqus for the modelling process was strengthened by the fact that the user can adapt functionalities with the use of user subroutines. For the modelling process described in this work the user subroutines UMAT and UEXPAN were applied to define user specific material behaviour and thermal expansion.

2.2.2 System

A separate model for the uniaxial bending and the push-out set-up was developed to be able to simulate the outcomes on both levels of detail. The model of the connection level (push-out) is primarily used to simulate the (non-linear) short-term behaviour that the system shows for short-term push-out tests. With this data the short-term behaviour of the whole slab can be predicted reliably as shown by Kreis [6]. The assembly and boundary conditions are shown in Figure 5. Symmetry conditions help to reduce the total calculation costs.

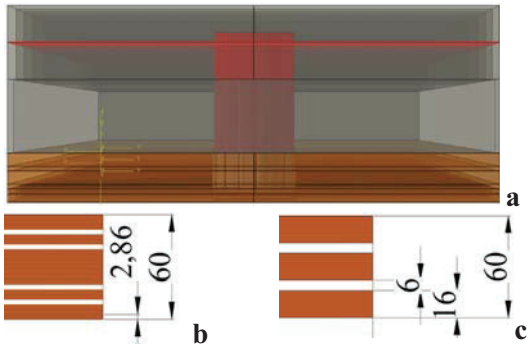

Figure 4:*(a) face view of the model, (b)timber member structure in reality and (c)model simplification, with layers loaded parallel to grain in brown layers loaded transverse to grain in white.*

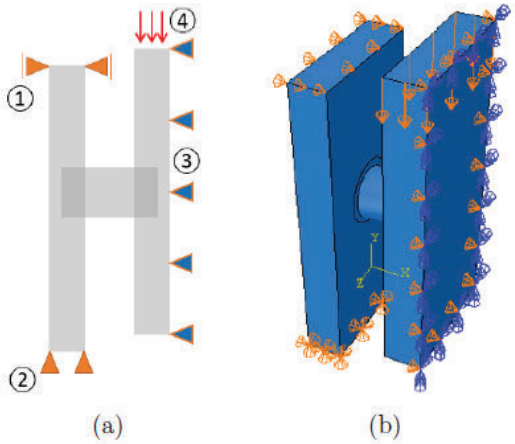

Figure 5 *(a) Boundary conditions: ①support in horizontal direction ② support in vertical, horizontal and out of planel direction ③symmetry conditions ④loading (b) boundary conditions on the 3D model.*

For long-term modelling primarily the bending-test set-up is used. If the whole slab is simulated the time-dependent rheological processing can be captured and processed. Further, they can be translated into a beam midspan deflection, which can be compared to hand calculations or SLS conditions.

The bending set-up model with the configuration using beech-LVL as a timber-member is visualized in Figure 6. This configuration is exemplatory used for the further proceedings of this work. The model consists of an LVL-plate, eight steel-tubes, gluelines connecting steel and timber and the concrete layer that is reinforced with shrinkage reinforcement-bars.

To model the LVL layer some simplifications are made. For numeric reasons the real structure of the beech LVL shown in Figure 4b is simplified with the approach depicted in Figure 4c. The four transverse layers are reduced to two so a simpler 5-layered structure is achieved.

The individually modelled lamellas of the timber member, the steel tubes and the timber, the glue-lines and the concrete layer are connected with tie-constraints with the other parts they are connecing with respectively. For the mechanical modelling, this leads to connections with

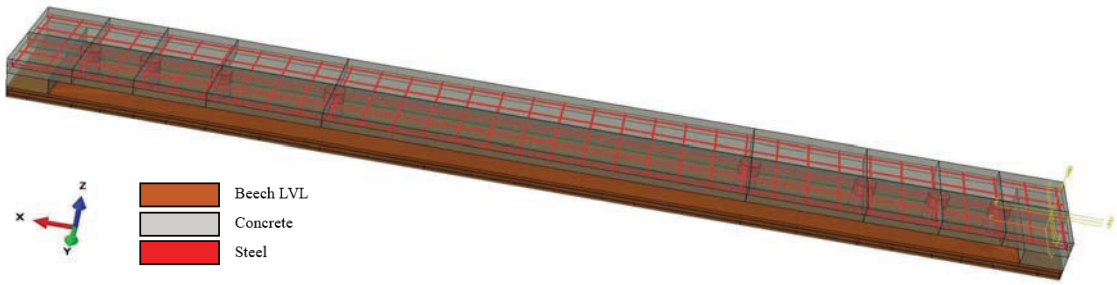

Figure 6: *Visualisation of the model in the uniaxial bending set-up.*

https://doi.org/10.52202/069179-0078

higher stiffnesses as in reality. For the purpose of long-term modelling this is assumed to be acceptable as a lot of computing cost can be saved.

2.2.3 Material models

As both main materials (timber and concrete) used have distinct but different long-term behaviour according material models have to be introduced for the finite element (FE) simulation.

To describe the complex time-, load- and moisture dependent behaviour of european beech (*fagus sylvatica*) the rheological model of Hassani [8] is used. The model was numerically implemented via a UMAT subroutine, as the available Abaqus tools could not provide the needed material behaviour. The basis of the model lays in the implementation of a series of serial-switched Kevin-Voigt-elements, representing the elastic and plastic strains, hygroexpansion (swelling and shrinking) and the strains resulting from visco-elastic and mechano-sorptive creep (see Figure 7).

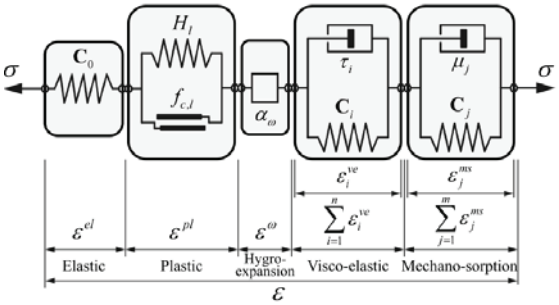

Figure 7:*Rheological material model to describe the time-dependent behaviour of timber* ***[8]****.*

Because of the serial switched strains in the system the total strains can be calculated with Equation (1):

$$\epsilon = \epsilon^{el} + \epsilon^{pl} + \epsilon^{\omega} + \sum_{i=1}^{n} \epsilon_i^{ve} + \sum_{j=1}^{n} \epsilon_j^{ms} \qquad (1)$$

A more detailed description of the numerical implementation of the timber member will not be given in this paper.

The E-modulus of concrete is assumed to be linear-elastic for the model. Modelling a plastic material behaviour in concrete would be possible, but it is assumed that the stresses in the concrete will not reach the plastic range for the this application. A plastic model would unnecessarily increase the already high computational costs. Due to continuous hydration of concrete the E-modulus of concrete is time-dependent. The expected development is described with the CEB-FIB-90 model [9] in Equations (2) – (4)

$$E_{ci}(t) = \beta_E(t) \cdot E_{ct} \qquad (2)$$

$$\beta_E(t) = \sqrt{\beta_{cc}(t)} \qquad (3)$$

$$\beta_{cc}(t) = e^{s\left(1-\sqrt{\frac{28}{t}}\right)} \qquad (4)$$

with s=0.2 and E_{ci} = E-modulus after 28 days.

The modelling of the shrinking and creep- behaviour that is part of the long-term effects of concrete is done by implementing the CEB-FIB-90-Modell that is part of EC 2 [10]. This is numerically done using the UEXPAN subroutine developed by Hampel [11]. With this subroutine the strains coming from shrinking and creep effects calculated after EC2 can be introduced into the model for each time-step. For this the creep and shrinkage effects have to be rewritten as increments $\Delta\epsilon$ that is calculated for each time step $\Delta t = t_n - t_{n-1}$

A more detailed description of the numerical implementation of concrete will not be given in this paper.

2.2.4 Loads

The long-term simulation is made for a time span of 61 months to simulate the first five years after the experimental set-up additional to the first 28day hardening time after concreting. In the first 28 days only 10% of the dead load is simulated as exterior load for convergence purposes. After 28 days the full dead load and an additional areal load is enabled to act on the model. For the exemplatory model presented in this paper the areal load sums up to a total of 3.5 kN/m² representing the 2 kN/m² live load and the additional weight of the slab structure above the load-bearing layer of 1.5 kN/m². The changing moisture content of the air that leads to changing moisture contents in the timber due to its hygroscopic behaviour is simplified. During the simulation process the exposed surfaces of the timber specimen is subjected to a changing surface moisture content that is varying with a sinoical function between 8% and 12%. This is representing a effective moisture content change of 4% in the timber during a year. In Figure 8 the loading conditions for the first 2 years is shown.

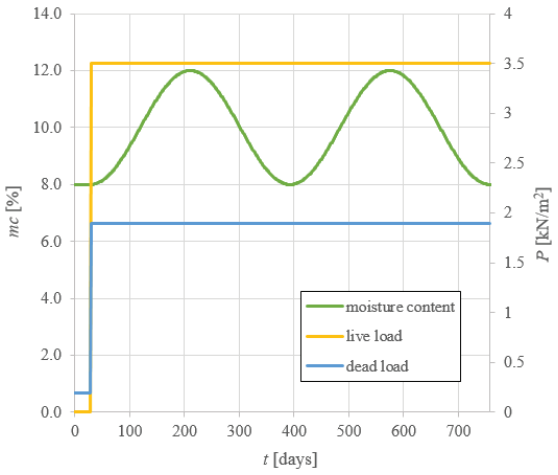

Figure 8: *Loads and subjected moisture content to exposed surfaces for the first 2 years of the model.*

https://doi.org/10.52202/069179-0078

2.2.5 Modelling process and elements

As the moisture content distribution within the timber over time is initially unknown, first an analysis is made with the only external load being the induced moisture content on the exposed timber surfaces. For this process DC3D20 elements are used. In this step the moisture content for each node in the timber member for the total simulation time of 5 years is calculated.

In a second step a mechanical analysis can be carried out using C3D20R Elements. In this second step all loads and boundary conditions are enabled. The moisture content needed to calculate the additional stresses and strains considering the rheologicals effects in the timber are read from the output- file of the first analysis.

3 RESULTS

3.1 MOISTURE DISTRIBUTION

The resulting moisture distribution for the first simulated year is shown in Figure 10. At day 0 the initially defined moisture content of 8% throughout the whole timber member is visible. After 198 days the moister content induced to the models exposed surfaces reaches its maximum of 12%. It can be observed that somewhere around the 300 day mark a maximal moisture content just short of 11% is reached in the middle of the timber member. It can be seen, that when all 4 sides of the timber member are exposed to a seasonal change in relative humidity in the environment, the whole timber cross-section is subjected to significant changes in equivalent moisture contents.

3.2 MIDSPAN DEFLECTIONS

The simulated midspan deflections are displayed in Figure 9. It can be observed, that the changing moisture content has a high influence on the midspan deflections. The initial high displacements due to initial loading appear to slow down after 2 years of simulation. Going forward a slight increase in midspan deflection is observed every year.

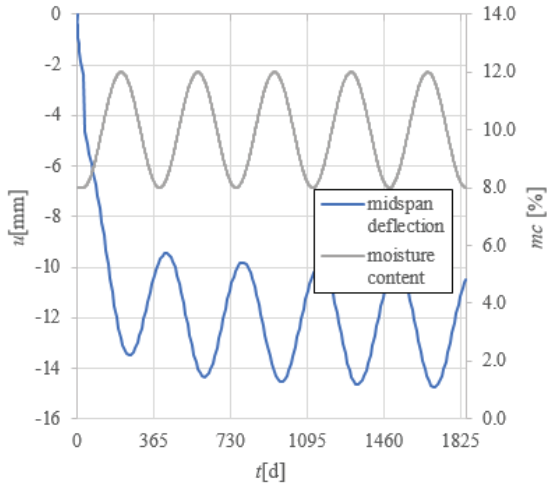

Figure 9: *Midspan deflections of the slab system in relation to the moisture content of the timber member.*

3.3 MIDSPAN STRAINS

For a point on the bottom of the timber member the strain componets are displayed in Figure 11. The total strains consist of shares from elastic, visco-elastic, swelling/shrinkage and mechano-sorptive strains. It can be observed that the swelling and shrinking component is the highest compared to the other strain components. After that the visco-elastic creep component appears to have the second highest influence. The mechano-sorptive creep has the least influence on the total strains even with the high moisture change during a simulated year.
In Figure 12 the midspan strains in a representative point on the concrete member area are shown. The total strains consist of shares from creep shrinkage and elastic strains.

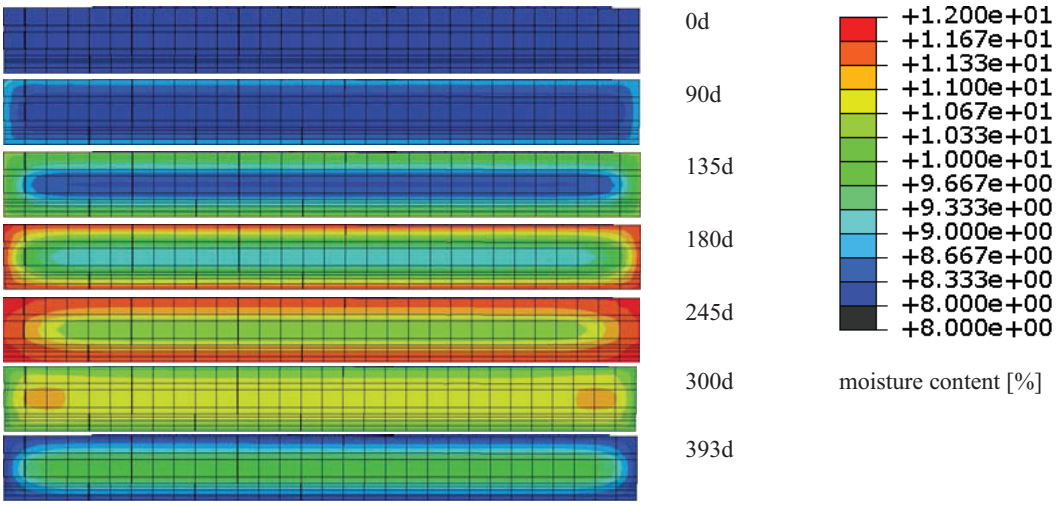

Figure 10: *Moisture distribution at midspan inside in the timber member with four exposed sides during the first year of simulation.*

https://doi.org/10.52202/069179-0078

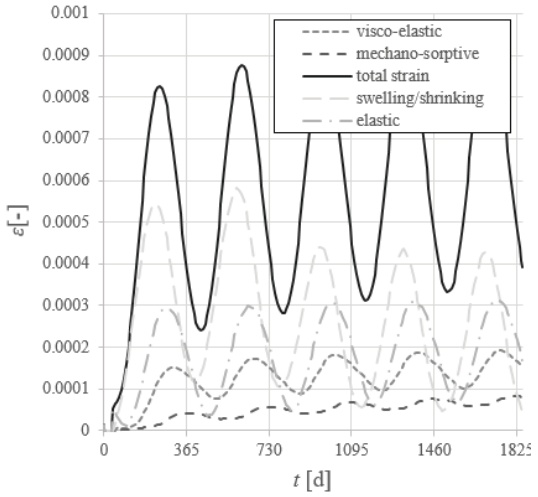

Figure 11: *Visualisation of the strains components at midspan in the timber member*

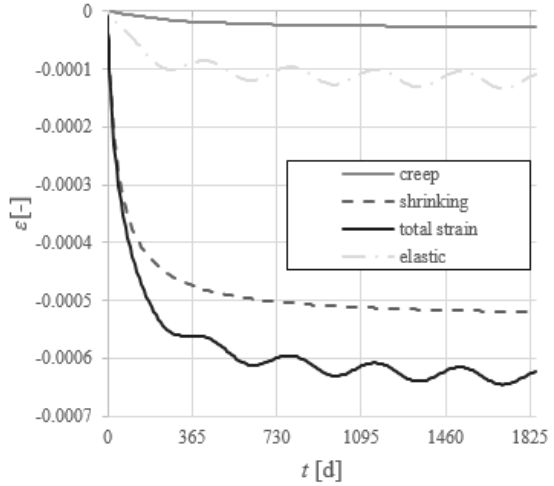

Figure 12: *Visualisation of the strains components at midspan in the topsurface of concrete member.*

4 DISCUSSION

4.1 MOISTURE DISTRIBUTION

The assumption of a 4-sided exposure to moisture of the timber member in the testing set-up can be justified by the fact, that contrary to an area-wide system (real case) the sides of the specimen are exposed. Additionally, the filling material of the interlayer is permeable to moisture. With this chosen 4-sided exposure the moisture content inside the timber member changes almost uniformly. As in the real slab system only exposure from the bottom side is to be expected it has to be accounted for in the proceeding investigations.
It has to be noted, that the way the LVL plate is modelled could have a big bias on the resulting moisture distribution. The simplifications used do not take into account the possible reduction in moisture transport through the glue lines. Especially in a LVL, where the veneers are only 3-4 mm thick, this can have a big influence on the resulting moisture distribution. It is assumed that in reality the moisture is less able to spread through the thickness of the board. This has especially an influence on the result when only one-sided (real case szenario) moisture penetration can take place.
Furthermore, the exact moisture transport conditions in beech LVL is still unknown and has yet to be investigated.

4.2 MIDSPAN DEFLECTIONS

In the first 28 days of the simulation the shrinking of the concrete member presumably is the driving factor for a large amount if the initial midspan deflections. Reducing these shrinking deformations to a minimum within the production process has to be a goal. It is obvious that also the changing moisture content has a big influence on the midspan deflections. The assumed 4% change in yearly moisture change within the timber member is with high probability on the safe side. It is assumed that in reality the resulting moisture exchange is much lower. Nevertheless, it is shown that the moisture content at the time of installation can have a big influence on the total deflections and has to be considered.

4.3 MIDSPAN STRAINS

The high amplitudes of the swelling and shrinking strains in the timber member stand in direct context with the changing moisture content. Because of the 4-side exposed timber specimen moisture exchange happens rapidly and thus high swelling and shrinking is simulated. Only a slight time deviation between the maximally induced moisture and maximal swelling and shrinking components is registered. It is assumed, that with only one side exposed to moisture change, this deviation in time will be bigger.

For the concrete member, the biggest influence on the total strains is coming from shrinkage. After five years the total value for the shrinkage strain corresponds to the analytical solution of EC 2 which is $5{,}13 \cdot 10^{-4}$. This is the result of autogenic and drying shrinkage only being dependent on the time. In the contrary creep is dependent on the elastic strains at the respective time. Through creep the concrete escapes external loads and thus reduces elastic strains.

4.4 GENERAL DISCUSSION

The manual calculation of the presented slab system is based on many assumptions due to the complex geometry and the only partially explored connection. Because the model also still has to make do with many assumptions and not enough experimental data could be collected yet, no verification and validation of the model can be shown within the scope of this work. It is therefore to be noted that up to this point the model shown is only theoretical.

https://doi.org/10.52202/069179-0078

Nevertheless, the model can be used to further understand the system and its general behaviour.
For a reliable simulation of the long-term behaviour of beech LVL, input-material parameters are also missing. Up to now, one has to make do with solid wood parameters for certain parameters that influence the long-term behaviour. However, it can be argued if beech LVL has a lot in common with solid beech wood, if one takes a closer look at its production process.
In addition, further studies with Hassani's material model are necessary. No validation of the model is available for a simulation period longer than one year [8].

5 CONCLUSION

It has to be stated that the presented results exemplify what the model output can be and can not be regarded as concluding. The main task of this paper is to show to opportunities and challenges of long-term modelling with Abaqus.
Modelling such a complex system seems in many parts a balancing act between the level of detail and the introduction of necessary simplifications to keep the computational costs under control.
In the next step acquired experimental data will be used to validate the model for the push-out and uniaxial bending set-up.
Further ahead lies the challenge to adapt the model to an actual biaxial bearing system. Although the system can also be used uniaxial-only it's full potential is only reached with the biaxial application and it's additional influence on the load-bearing behaviour.

ACKNOWLEDGMENTS

The authors acknowledge the financial support by Innosuisse (former CTI – Commission of Technology and Innovation) and the industrial and conceptual support of WaltGalmarini AG and Implenia Schweiz AG

REFERENCES

[1] R. Andrew, "Global CO2 emissions from cemet production," *Earth Systems Science Data,* vol. 10, pp. 195-217, 2018.

[2] D. Yeoh, M. Frangiacomo and M. D. F. a. K. Boon, "State of the Art on Timber-Concrete Composite Structures," *Structural Engineering,* vol. 10, pp. 1085-1095, 2011.

[3] A. Frangi, «Brandverhalten von Holz-Beton-Verbunddecken,» 2001.

[4] A. Dias, "Mechanical behaviour of timber-concrete joints.," 2005.

[5] M. Fraingiacomo, "Long-term behaviour of timber-concrete composite structures.," University of Venice, 2001.

[6] B. Kreis, "Two-Way Spanning Timber-Concrete Composite Slabs made of Beech Laminated Veneer Lumber with Steel Tube Connection," 2021.

[7] CEN European Committee for Standardisation, *Eurocode 5: Design of timber structures - Part 1-1: General- Common rules and rules for buildings,* 2004, pp. 1-123.

[8] M. Hassani, F. Wittel and S. Hering, "Rheological model for wood.," *Computer Methods in Applied Mechanics and Engineering,* 2015.

[9] *CEB-FIP model code 1990 final draft,* 1991.

[10] CEN European Committee for Standardisation , "Eurocode 2. Bemessung und Konstruktion von Stahlbeton- und Spannbeton-Tragwerken". Zürich, SN Bauwesen 2004.

[11] D. Hampel, "Modellieren des Langzeitverhaltens von Holz-Beton-Verbundelementen mit Buchen-Stabschichtholz," Zürich, 2021.

https://doi.org/10.52202/069179-0078

World Conference on Timber Engineering Oslo 2023

INVESTIGATING THE EFFECTS OF MOISTURE INGRESS ON THE PERFORMANCE AND SERVICE LIFE OF AUSTRALIAN MASS TIMBER PANELS-CHARACTERIZATION OUTCOMES.

Maryam Shirmohammadi[1]

ABSTRACT: Composite timber systems made of timber and massive wood products used in construction are susceptible to moisture fluctuations during transport, construction, and post-construction. The wetting dynamics, both ingress and egress, of Australian timber species and mass panels exposed to Australian climate conditions have not been extensively explored. Understanding moisture movement in timber is crucial for predicting the design life of timber products and developing decay modelling protocols. An experimental testing has been conducted in detail to comprehend water movement and moisture gradients in massive wood-based composites. The testing results presented in this paper include the density, porosity, gas, and liquid permeability of three Australian timber species (radiata pine, southern pine and shining gum). The experiments have been designed to explore the hygroscopic properties of timber species in different directions, including face, edge and end and of CLT (2P and 3P) and LVL sections. The porosity values for the three tested species were 56% ± 5, 57% ± 3 and 42% ± 8 for radiata pine, southern pine and shining gum respectively. The experimental results presented in this paper showed that CLT samples made from radiata pine with edge gap (3P) had higher porosity and permeability values than solid radiata sample sections. The CLT 2P sections had lower porosity values than the solid radiata pine samples. The porosity values determined for LVL (made from pine) samples (51% ± 3) were slightly lower than southern pine samples tested. The outcomes of this project will facilitate the prediction of product response to moisture and enable the development of maintenance protocols and remedial solutions for the industry to minimize the potential impacts of moisture penetration in mass timber products in the future.

KEYWORDS: Mass timber panels, moisture ingress, service life, cross laminated timber, laminated veneer lumber.

1 INTRODUCTION

Timber and composite timber systems as building materials provide significant advantages such as low embodied energy, excellent insulation properties, and cost-effective construction processes. However, they are vulnerable to dimensional instability, aesthetic deterioration, and fungal decay if exposed to moisture for a prolonged period. Additionally, poorly designed or maintained timber products and buildings can be impacted by biodegradation. The extent and rate of damage can vary, depending on the environmental conditions to which the products are exposed [1-8]. Moisture intrusion into solid timber or mass panel composites and cyclic variation in moisture during and post-construction could cause changes in appearance and structural properties that can be difficult and costly to repair. Southern pine (*Pinus elliottii x Pinus caribaea)* (SP), radiata pine (*Pinus radiata)* (RP) and shining gum (*Eucalyptus nitens)* (SG) are three commercially available timber species in Australia. Various studies [9-12] have focused on the properties of wood during drying; however, the movement of water in these three species during periodic and long-term wetting when exposed to free water still requires further research. Specifically, the effects of species' anatomical features (cell arrangement and direction) and variations between solid timber products and engineered wood products (EWPs), on the wetting and drying process need to be investigated [9-12]. The differences between species and the effects of their anatomical characteristics (such as pore size/types, permeability, chemistry and cell size) on moisture movement over time are important when longer-term durability and structural stability of products are estimated [13-17]. The hygroscopic properties of building elements affect the different aspects of building design and performance, including durability, performance and thermal comfort [18-21]. The EWPs' structure specifically the direction of boards/the arrangement of veneers, glue lines, edge gaps and cracks, impact the EWPs' long-term performance in-service [19, 22-26]. Moisture ingress into solid wood and EWPs could occur through different wetting events and due to poor site management during erection, poor building design, types of construction or poor maintenance [27]. In addition to the complexity of moisture ingress and egress scenarios for EWPs, there is also a need for further research relevant to long-term performance aspects of these components when used in the wide variety of Australian environments in which timber is employed (e.g. higher decay hazard situations)

[1]Maryam Shirmohammadi, Principal research scientist,
Queensland department of agriculture and fisheries,
Brisbane, Australia,
Maryam.shirmohammadi@daf.qld.gov.au

https://doi.org/10.52202/069179-0079

[28, 29]. This paper discusses porosity, density, and permeability measurements of solid timber (sawn timber) from three Australian species and Australian mass timber panels. The study was conducted as a part of a larger project developing a mathematical model of moisture ingress/egress into EWPs.

2 MATERIALS AND METHODS

2.1 SAMPLES

Kiln-dried boards of radiata pine (*Pinus radiata* D. Don), Caribbean pine/Slash pine hybrid (*Pinus caribaea* Morelet/*P. elliottii* Engelm,), and shining gum (*Eucalyptus nitens* H. Deane & Maiden) were cut into samples oriented to allow moisture movement to be studied in three different directions. Before testing, three-layer radiata pine cross-laminated timber (CLT) and laminated veneer lumber (LVL) were cut into small sections. Figure 1 shows the sample directions, including the end grain orientation (L (longitudinal)/ D3, R (radial)/D1 or T(tangential)/D2) of boards; for CLT samples, directions included face/D1 (radial/tangential), edge/D3 and end/D2. For LVL samples, directions included face/D1 (radial/tangential), edge/D3 (mostly radial) and end/D2 (longitudinal). All samples were conditioned to constant weight (65%RH/25°C) at approximate 12% EMC, and the initial dimensions of each were recorded.

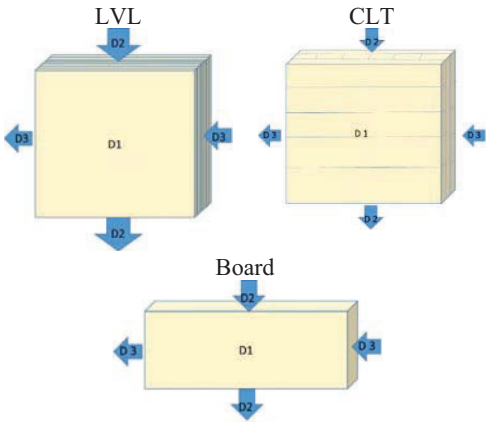

Figure 1: *Directions of water movement that were studied.*

2.2 DENSITY AND POROSITY

The density porosity of samples was determined for blocks of 20x20x20 mm that were conditioned at 12% EMC before being weighed, and their dimensions were measured to determine the density (Table 1). A helium pycnometer [30] was used to measure the density and porosity of the samples. Five replication of material type was used for the density and porosity measurements.

Table 1: *The average sample weights and density used to determine the samples' porosity.*

Material Type	Weight (g)	Density (kg/m3)
Shining gum	4.72 ± 0.2	589.82 ± 32
Radiata pine	4.53± 0.2	583.69 ± 58
Southern pine	4.81± 0.3	607.45 ± 87
LVL	5.98 ± 0.2	688.65 ± 23
CLT-3P	4.04 ± 0.1	506.13 ± 12
CLT 2p	4.1 ± 0.1	519.20 ± 17

Note: ± are standard deviation values

For CLT and LVL sample types are presented in Figure 2. Apparent density (D_a) in kgm^{-3} using the volume of the piece, including void space, was calculated using Eq. 1. For true density (D_t), the density of samples without voids, samples were placed in a gas pycnometer where density was recorded five times and average values were used for data analysis.

$$D_a = \frac{Mass}{Volume} \qquad \textit{Eq. 1}$$

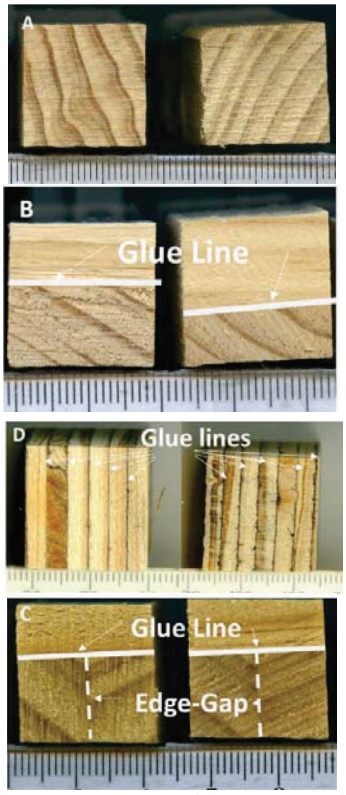

Figure 2: *Sample blocks used for porosity and density measurement ((A)solid, (B)CLT-2P (sample with glue line), (C)CLT-3P (sample with glue line and edge gap) and (D)LVL)*

The porosity of samples was calculated using the true and apparent density values. The porosity (∅) of samples was calculated using Eq. 2.

$$\emptyset = \left(1 - \left(\frac{D_a}{D_t}\right)\right) \times 100 \qquad \textit{Eq. 2}$$

https://doi.org/10.52202/069179-0079

MICROSCOPIC IMAGING AND CELL DIMENSION MEASUREMENT

In this study, the impact of cell pore size and porosity was evaluated on samples obtained from different surfaces (i.e., face, end, and edge) of a given material. To examine and quantify the cell type and size of the samples, a Nikon ECLIPSE LV100ND/LV100NDA microscope was used, and the images were captured at magnifications of 10x, 20x, and 50x (Figure 3). The average size of the cell lumen was determined for 3-5 anatomical images of each species using ImageJ software [34]. In softwood samples, the size of the cells in earlywood and latewood sections was measured, along with the diameter of resin canals and vessels (Figure 3).

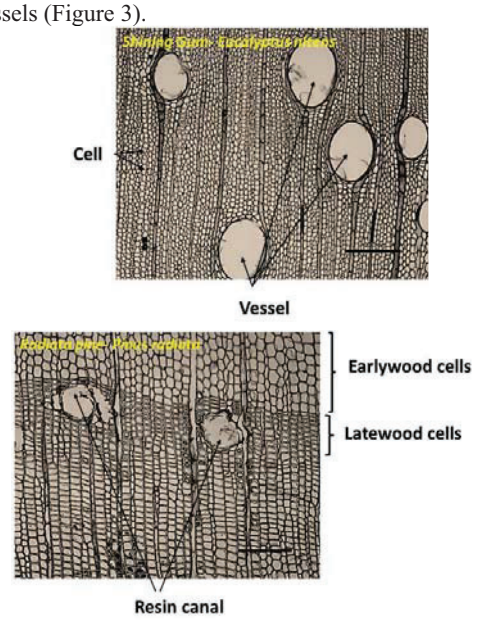

Figure 3: *Example images used for determining the cell dimension at 10x magnification [31] .*

2.3 PERMEABILITY

The gas and liquid permeability of the three solid timber species, CLT and LVL composite panels were determined in the laboratory. Gas permeability was calculated using Darcy's law (Eq. 3) as shown in [15, 32].

$$K = \frac{Q\mu eP}{A\Delta P\overline{P}} \qquad \textit{Eq. 3}$$

In this equation, K is the intrinsic permeability (m^2); Q is the air flux ($m^2\ s^{-1}$); μ is the dynamic viscosity of air (Pa); e is the sample thickness (m); P is the pressure at which flux Q is measured (Pa); A is the sample area (m^2); ΔP is the pressure difference between the air outlet and inlet sides of the sample (Pa); and $\overline{P}$ is the average pressure inside the sample (Pa). Samples (8-10 mm thick) were cut along the radial, tangential and longitudinal direcitons using a 24 mm diameter hole-saw. Ten replicates were tested per sample type and direction. Water movement into the side surfaces of the sample and guarantee air tightness was restricted by the application of two layers of epoxy resin [15].

The effects of glue line and edge gaps were studied for LVL and CLT samples using the sample shown in Figure 4.

Figure 4: *Sample sections (A) CLT (2Piece/2P) (B) CLT (3Piece/3P), (C) LVL (End), (D) LVL (face- one glue line), and (E) LVL (face- two glue lines).*

The study tested the permeability of LVL samples with one (4-5 mm thick) and two (7-8 mm thick) glue lines.

3 RESULTS AND DISCUSSION

3.1 POROSITY

The type and size of wood cells influence the hygroscopic properties of products exposed to in-service conditions. Previous research has explored the relationship between pore size and porosity, permeability, and treatability of products, with a focus on natural weathering and water absorption, porosity and sorption isotherm, and capillary condensation in mass timber buildings [33-36].

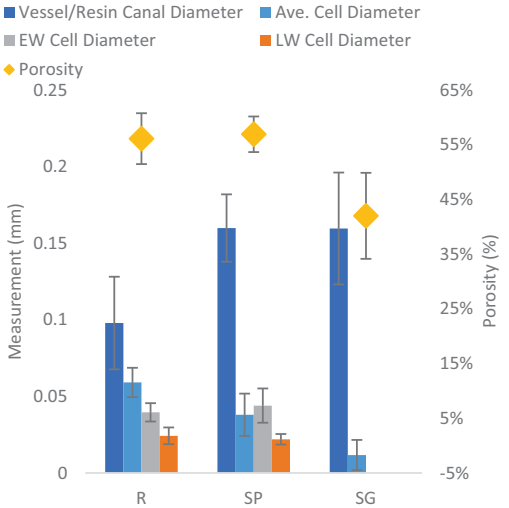

Figure 5: *Anatomical features measurements for radiata pine, southern pine , and shining gum samples and calculated porosity. Errors bars represent one standard deviation.*

The relationship between the porosity values and anatomical features showed higher cell diameter and porosity values following similar trends (Figure 5). Similarly, previous studies showed higher porosity of timber species linked to lower resistance to moisture flow in the product's structure [30]. The porosity of southern pine samples was higher than that of radiata pine samples, and the anatomical features measured were similar except for a higher resin canal diameter for southern pine samples. Shining gum had lower porosity than the pine samples. A higher percentage of pore in timber product's structure can lead to higher water gain when exposed to moisture [37, 38], so it is important to consider product and species porosity values when modelling wetting and drying processes.

As shown in Figure 5, porosity and true density values were higher for radiata pine and southern pine than for shining gum samples. Southern and radiata pine samples had higher true density than shining gum samples. The bulk densities of all three species were in the sample range (as reported in Table 1).

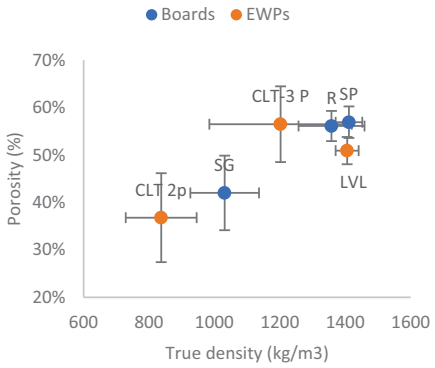

Figure 6: *Average porosity versus true density of solid shining gum (SG), radiata pine (R), Caribbean/slash pine (SP) hybrid timbers, radiata pine LVL, or southern pine CLT with 2 or 3 glue lines.*

The CLT 3P sections (with glue line and edge gap) showed higher porosity values than CLT 2P (with glue line only) samples. The presence of an edge gap can affect the higher values. The average porosity value for solid radiata pine samples was slightly higher than for CLT 2P. This can result from the glue line in the 2P sample structure. Previously, the effects of cracks and edge gaps in the timber product structure are reported to increase the liquid flow and water trapping into the bulk material. This has been considered a factor affecting the structural and aesthetic performance issues of EWPs if not managed appropriately [39, 40]. The average porosity and density value for LVL samples was lower than the average value for southern pine solid samples.

3.2 PERMEABILITY

As expected, solid wood's gas and liquid permeability results were higher in the longitudinal direction than in the tangential and radial directions for the three species [14, 15, 41]. Shining gum samples showed higher variability in gas permeability data in the longitudinal direction. The gas permeability values determined for shining gum were close to zero in the radial and tangential directions (Figure 7). Southern pine samples had the highest gas permeability than southern pine and shining gum samples.

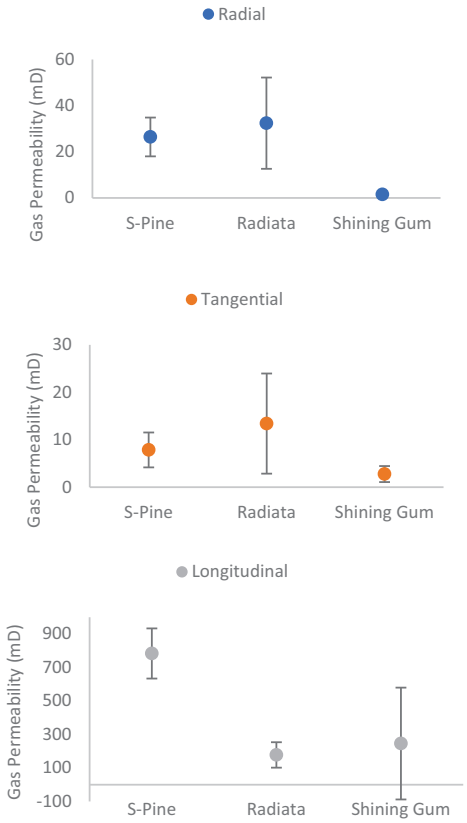

Figure 7: *Gas permeability data for species tested, (SP is southern pine, R is radiata pine, SG is shining gum and L, R and T refer to longitudinal, radial and tangential directions).*

A higher ratio of gas permeability anisotropy was observed for shining gum in K_L/K_R than radiata or southern pine samples (Table 2). The longitudinal to tangential liquid permeability ratio (K_L/K_T) was much higher for shining gum compared to southern pine and radiata pine. The longitudinal to tangential gas permeability ratio (K_L/K_T) was higher for southern pine and shining gum and lower for radiata pine. These ratios suggest that the pressure required for the movement of liquid and gas in the sample affects the hygroscopic properties of timber boards and composites when exposed to free water. The same process happens when the product is exposed to repeated wetting and drying, which leads to a moisture gradient development inside the product's structure [36]. It is reported that the anisotropic ratios could influence the scale of wetting and drying processes and lead to dimensional changes and internal stresses that are critical factors, especially in CLT connection design

https://doi.org/10.52202/069179-0079

and maintenance [13, 14, 17]. The ratios (K_R/K_T) were much lower for both gas and liquid permeability values in the radial to tangential direction than K_L/K_T and K_L/K_R and shining gum had lower values than the pine samples. The very low permeability caused the high KL/KT (ratio of K in longitudinal over tangential directions) value for southern pine in the tangential direction.

Table 2: *Anisotropy ratios of sample permeability values determined for solid timber of three species.*

Species	Permeability	K_L/K_R	K_L/K_T	K_R/K_T
Southern pine (SP)	Gas	29.65	99.80	3.37
	Liquid	202.66	1396.53	0.00071
Radiata pine (R)	Gas	5.48	13.25	2.42
	Liquid	16.46	233.62	0.0043
Shining gum (SG)	Gas	159.35	88.88	0.56
	Liquid	-	7579	0.00013

± values are the standard deviation.

Figure 8 shows that southern pine samples had a higher liquid permeability in the longitudinal direction when compared to radiata and shining gum samples. Shining gum had the lowest radial and tangential liquid permeability, while radiata pine samples had the lowest longitudinal liquid permeability.

Figure 8*: Liquid permeability data for species tested.*

The lower permeability rates in shining gum can be attributed to its small cell size arrangement compared to the softwood samples [45]. The other factors, including the extractive and resin content, must be considered when permeability. Southern pine samples had the highest gas permeability compared to other species tested. Southern pine samples also had the highest longitudinal permeability than the other two species.

Figure 9 shows the permeability values determined for CLT 2P and 3P samples. Higher gas and liquid permeability was observed for CLT 3P sections. This result shows the importance of moisture management programs, especially when CLT panels are exposed to weathering, such as flash flooding and heavy rain during construction. The CLT structure and pathways for higher water ingress into the structure (due to edge gaps and cracks) can result in accelerated moisture intrusion leading to more conducive conditions for the fungal attack in the longer term. The LVL gas permeability values determined were 28.8 ±17 and 20.4±13 mD for samples with one and two glue lines, respectively. The liquid permeabilities were 1.21 ± 1 and 0.63 ± 1 mD for samples with one and two glue lines, respectively.

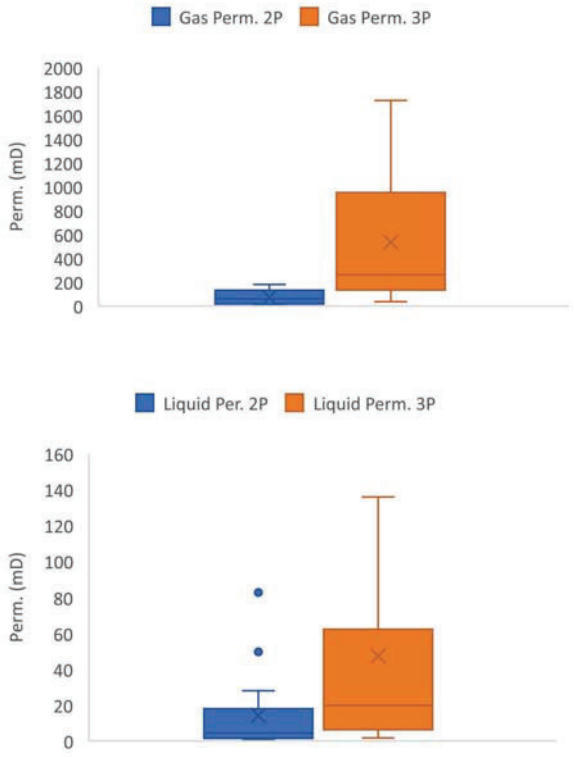

Figure 9: *Average gas and liquid permeability values recorded for CLT 2P and 3P sections.*

4 CONCLUSIONS

This study determined some hygroscopic properties of Australian timber species and EWP (CLT and LVL) samples. The study focused on determining the porosity, density and permeability properties of the products tested. The determined porosity showed that CLT 2P (sections with glue line) made from radiata pine had lower porosity than the radiata pine samples tested. The CLT section with glue line and edge gaps had higher porosity values than the 2P sections. LVL samples had lower porosity than the radiata and southern pine samples tested. Southern pine samples had higher gas permeability in all directions than radiata pine and shining gum samples. The liquid permeability of southern pine samples was higher in the longitudinal direction than the other two species tested. The observed variations in porosity and permeability values between CLT sections with glue line (2P) and glue line and edge gap (3P) should be considered as potential factors that could affect moisture gain and the development of moisture gradients within the CLT layered structure.

ACKNOWLEDGEMENT

The paper's author would like to acknowledge the National Centre for Timber Durability and Design life (NCTDDL) for funding this study and the technical team at the Salisbury research facility for assistance during sample preparation and experimental testing.

REFERENCES

[1] Brischke, C. and G. Alfredsen, *Wood-water relationships and their role for wood susceptibility to fungal decay.* Applied Microbiology and Biotechnology, 2020. **104**(9): p. 3781-3795.

[2] Isaksson, T., C. Brischke, and S. Thelandersson, *Development of decay performance models for outdoor timber structures.* Materials and Structures, 2013. **46**(7): p. 1209-1225.

[3] Libralato, M., et al. *Damage risk assessment of building materials with moisture hysteresis*. in *Journal of Physics: Conference Series*. 2021. IOP Publishing.

[4] Libralato, M., et al. *Multiyear hygrothermal performance simulation of historic building envelopes*. in *IOP Conference Series: Earth and Environmental Science*. 2021. IOP Publishing.

[5] Libralato, M., et al., *Effects of considering moisture hysteresis on wood decay risk simulations of building envelopes.* Journal of Building Engineering, 2021. **42**: p. 102444.

[6] Viitanen, H., et al., *Towards modelling of decay risk of wooden materials.* Eur. J. Wood Prod, 2010. **68**: p. 303-313.

[7] Viitaneu, H., *Factors affecting the development of mould and brown rot decay in wooden material and wooden structures: Effect of humidity, temperature and exposure time.* 1998.

[8] Shirmohammadi, M. and W. Leggate, *Investigating the effects of moisture ingress on the performance and service life of mass timber panels in Australian climates - Experimental tetsing plan* Q.G. Department of Agriculture and Fisheries, Editor. 2020.

[9] Gereke, T., *Moisture-induced stresses in cross-laminated wood panels*. 2009, Dipl.-Ing., University of Leipzig.

[10] Gereke, T., P. Hass, and P. Niemz, *Moisture-induced stresses and distortions in spruce cross-laminates and composite laminates.* Holzforschung, 2010. **64**(1): p. 127-133.

[11] Gereke, T., et al., *Experimental and numerical determination of the hygroscopic warping of cross-laminated solid wood panels.* Holzforschung, 2009. **63**(3): p. 340-347.

[12] Gereke, T., et al., *Identification of moisture-induced stresses in cross-laminated wood panels from beech wood (Fagus sylvatica L.).* Wood science and technology, 2009. **43**(3-4): p. 301.

[13] Taghiyari, H.R. and S. Avramidis, *Specific gas permeability of normal and nanosilver-impregnated solid wood species as influenced by*

https://doi.org/10.52202/069179-0079

heat-treatment. Maderas. Ciencia y tecnología, 2019. **21**(1): p. 89-96.
[14] Redman, A., et al., *Mass transfer properties (permeability and mass diffusivity) of four Australian hardwood species.* BioResources, 2012. **7**(3): p. 3410-3424.
[15] Redman, A., *Modelling of vacuum drying of Australian hardwood species*. 2017, Queensland University of Technology.
[16] Popper, R., P. Niemz, and S. Croptier, *Adsorption and desorption measurements on selected exotic wood species: Analysis with the Hailwood-Horrobin model to describe the sorption hysteresis.* Wood research, 2009. **54**.
[17] Jang, E.-S., J.-H. Yuk, and C.-W. Kang, *An experimental study on change of gas permeability depending on pore structures in three species (hinoki, Douglas fir, and hemlock) of softwood.* Journal of Wood Science, 2020. **66**(1): p. 1-12.
[18] Kukk, V., et al., *Designing highly insulated cross-laminated timber external walls in terms of hygrothermal performance: Field measurements and simulations.* Building and Environment, 2022. **212**: p. 108805.
[19] Chang, S.J., et al., *Assessment of effect of climate change on hygrothermal performance of cross-laminated timber building envelope with modular construction.* Case Studies in Thermal Engineering, 2021. **28**: p. 101703.
[20] Schiavoni, S., F. Bianchi, and F. Asdrubali, *Insulation materials for the building sector: A review and comparative analysis.* Renewable and Sustainable Energy Reviews, 2016. **62**: p. 988-1011.
[21] Balaji, N., M. Mani, and B.V. Reddy, *Discerning heat transfer in building materials.* Energy Procedia, 2014. **54**: p. 654-668.
[22] Leggate, W., et al., *Influence of Wood's Anatomical and Resin Traits on the Radial Permeability of the Hybrid Pine (Pinus elliottii× Pinus caribaea) Wood in Australia.* BioResources, 2020. **15**(3): p. 6851-6873.
[23] Schmidt, E.L., et al., *Environmental response of a CLT floor panel: Lessons for moisture management and monitoring of mass timber buildings.* Building and Environment, 2019. **148**: p. 609-622.
[24] Quesada-Pineda, H., et al., *A Visual Assessment of Cross-laminated Timber Structures in Austria.* BioProducts Business, 2020: p. 51-62.
[25] MacKenzie, C., et al., *Timber Service Life Design Guide*. 2007, Forest & Wood Products Australia Limited.
[26] Bucklin, O., et al., *Mono-material wood wall: Novel building envelope using subtractive manufacturing of timber profiles to improve thermal performance and airtightness of solid wood construction.* Energy and Buildings, 2022. **254**: p. 111597.
[27] Beebe, K. and M. Kam-Biron, *five Ds of moisture management: deflection, drainage, drying, distance and durable materials* in *SEAOC 2016*. 2016. p. 18.
[28] Niklewski, J., et al., *Moisture conditions of rain-exposed glue-laminated timber members: the effect of different detailing.* Wood Material Science & Engineering, 2018. **13**(3): p. 129-140.
[29] Franke, B., et al. *Moisture diffusion in wood–Experimental and numerical investigations*. in *CD-ROM Proceedings of the World Conference on Timber Engineering*. 2016.
[30] RuthMcClung, et al., *Hygrothermal performance of cross-laminated timber wall assemblies with built-in moisture: field measurements and simulations.* Building and Environment, 2014. **71**(January 2014): p. 95-110.
[31] *Wood Reference Collection*. Department of Agriculture and Fosheries Queensland Government.
[32] Manh, H.T., et al., *Mass transfer properties of Acacia mangium plantation wood.* Maderas. Ciencia y tecnología, 2022. **24**.
[33] Cai, C., et al., *Effect of natural weathering on water absorption and pore size distribution in thermally modified wood determined by nuclear magnetic resonance.* Cellulose, 2020. **27**(8): p. 4235-4247.
[34] Peng, L.M., et al., *Analysis of wood pore characteristics with mercury intrusion porosimetry and X-ray micro-computed tomography.* Wood research, 2015. **60**(6): p. 857-864.
[35] Zauer, M., A. Pfriem, and A. Wagenführ, *Toward improved understanding of the cell-wall density and porosity of wood determined by gas pycnometry.* Wood science and technology, 2013. **47**(6): p. 1197-1211.
[36] Friquin, K.L., *Material properties and external factors influencing the charring rate of solid wood and glue-laminated timber.* Fire and materials, 2011. **35**(5): p. 303-327.
[37] De Ligne, L., et al., *Moisture dynamics of wood-based panels and wood fibre insulation materials.* Frontiers in Plant Science, 2022. **13**.
[38] Plötze, M. and P. Niemz, *Porosity and pore size distribution of different wood types as determined by mercury intrusion porosimetry.* European journal of wood and wood products, 2011. **69**(4): p. 649-657.
[39] Sarkar, K. and B. Bhattacharjee, *Modeling of tropical rainfall exposure for the study of moisture penetration in porous building materials.* Journal of Hydrologic Engineering, 2017. **22**(8): p. 04017017.

[40] Bobadilha, G.d.S., et al., *Physical, optical, and visual performance of coated cross-laminated timber during natural and artificial weathering.* Coatings, 2021. **11**(2): p. 252.
[41] Redman, A.L., et al., *Characterisation of wood–water relationships and transverse anatomy and their relationship to drying degrade.* Wood Science and Technology, 2016. **50**: p. 739-757.

https://doi.org/10.52202/069179-0079

World Conference on Timber Engineering Oslo 2023

EXPERIMENTAL INVESTIGATION ON LONG-TERM BEHAVIOR OF TIMBER-TO-TIMBER SHEAR CONNECTIONS MADE BY INCLINED SELF-TAPPING SCREWS

Alessandra Gubana[1], Massimo Melotto[1], Luca De Cillia[1], Alessandro Mazelli[1]

ABSTRACT: Self-tapping screws are an interesting solution for timber-to-timber shear connections due to their performance, their economic advantages and their ease of use. The screws are preferably used inclined with respect to the shear flow direction, to improve the stiffness and the strength of the connection. The shear transfer mechanism is influenced also by the withdrawal capacity of the screw and by friction between timber elements.
These connections are useful for the bending reinforcement of existing timber floors, but the design of these composite-sections requires the knowledge of the connection behaviour. However, very few data are available on the long-term behaviour.
An experimental campaign to follow the connection behaviour during time has been performed. The results of a first group of twenty-four identic specimens were already presented. The last results of another group of sixty-three specimens are here reported. One half of the specimens was stored in a controlled environment, one half was stored in a not-controlled environment. Air temperature and humidity were regularly recorded. Push-out tests (as soon as built and after 6, 12 and 24 months) were performed and the main mechanical parameters of the connections as strength, stiffness and ductility at different ages are here compared.

KEYWORDS: Timber-to-Timber Shear Connections, Self-Tapping Screws, Long Term Behavior

1 INTRODUCTION

Self-tapping screws are nowadays commonly used for the connections and for the reinforcement of timber structural elements due to their performance, their economic advantages and their ease of use. This type of connection is largely applied for local reinforcement [1-5] and in timber-to-timber connections [6]. Besides, self-tapping screws are particularly useful for structural interventions on existing timber structures, reinforced by overlaying and joining timber or timber-based elements. The so created composite section is able to increase the bending strength and stiffness of the floor and to reduce vibrations under service loads. Examples of refurbishments of timber floors by means of timber-to-timber solutions are presented in [7-10]. Several studies in literature face the application of self-tapping screws to join together Cross Laminated panels [11,12], Cross Laminated panel and light frame timber structures [13] and to obtain timber-to-concrete composite sections [14]. The screws are preferably used inclined with respect to the shear flow direction as, in this case, the stiffness and the strength of the connection are strongly improved. The shear transfer mechanism is influenced also by the withdrawal capacity of the fastener and by the friction between the timber elements.

Several short-term tests have been performed [7-9, 15] and formulations have been proposed in literature to calculate the load-bearing capacity and the stiffness under shear/compression or shear/tension load [6, 14-17]. In addition, recent studies provide correlation approaches for Push-Out tests [18,19].
However, very few data are available on the long-term behavior [20], which can be influenced by timber moisture variation, shrinkage and creep.
An experimental campaign to follow the connection behavior during time has been performed. The results of a first group of twenty-four identic specimens were already presented [21]. Another group of sixty-three specimens were prepared in May 2020 to be tested, in clusters of nine. One half of the specimens was stored in a controlled environment, the other half was stored in a not-controlled environment, to simulate the real weathering. Air temperature and humidity were regularly recorded. Push-out tests (as soon as built, after 6 months, after 12 months and after 24 months) were performed and the experimental results are here presented. The main mechanical parameters of the connections as strength, stiffness and ductility at different ages are compared.

[1]DPIA Polytechnic Department of Engineering and Architecture, University of Udine (Italy).
alessandro.mazelli@uniud.it

https://doi.org/10.52202/069179-0080

2 MATERIALS AND METHODOLOGY

The experimental campaign on the long-term behaviour of wood connections was conducted in the laboratory of the University of Udine (Italy), between May 2020 and May 2022.
Seven sets of nine specimens were built in May 2020. A first group was tested immediately. The others were left to age in the laboratory. Half of the specimens was stored in a controlled environment, the other in a non-controlled environment. Air temperature and humidity were recorded regularly for the non-controlled environment.
The mechanical behaviour of the connections at different aging times was characterized in terms of strength, stiffness and ductility with push-out tests.

2.1 TEST SPECIMENS

The specimens consist of one glued-laminated spruce timber element of strength class GL24h (EN 14080:2013 [22]), and two CLT elements symmetrically arranged (Figure 1). The connection is made by four VGZ 7X180 single-thread self-tapping screws. The screws are inclined at 45°, two for each side of the specimen, and they are subjected to shear-tension loading during the test.
The screws are inserted in order to have half of the thread length in the central element and half of the length in the lateral element. The central element has a cross-section of 160x160 mm, whereas the side elements 60x160 mm. The timber longitudinal grain is aligned with the loading direction.

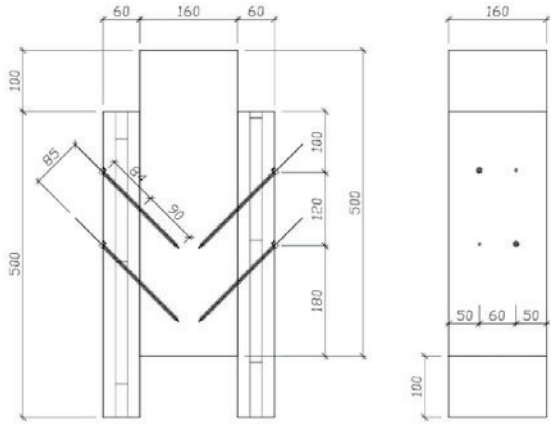

Figure 1: *Specimen geometry.*

The connections were realized by means of VGZ screws (Figure 2), which are characterized by a total thread, by a cylindrical head and by a pronounced cutter on the tip. The geometrical and mechanical properties were provided by the manufacturer and are reported in the relative European Technical Assessment ETA-11/0030 [23] and in Table 1, where $M_{y,k}$ is the characteristic yield moment, $f_{ax,k}$ is the characteristic extraction strength, $F_{tens,k}$ is the characteristic tensile strength and $f_{y,k}$ is the characteristic yield strength.
Seven groups of nine specimens each were built on the same day in May 2020.

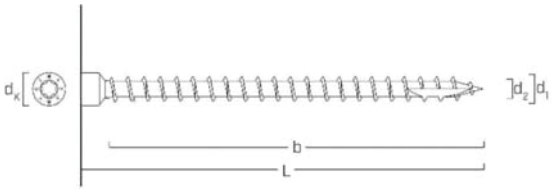

Figure 2: *Geometry of the VGZ 7x180 self-tapping screw.*

Table 1: *Geometrical and mechanical properties of the VGZ 7x180 self-tapping screw.*

Property	Symbol	Value
Length	L	180 mm
Nominal diameter	d_1	7 mm
Head diameter	d_k	9.5 mm
Tip diameter	d_2	4.6 mm
Characteristic yield moment	$M_{y,k}$	14174 Nmm
Characteristic extraction-resistance parameter	$f_{ax,k}$	11.7 MPa
Characteristic tensile strength	$F_{tens,k}$	15.4 kN
Characteristic yield strength	$f_{y,k}$	1000 MPa

All the specimens have the same configuration. A template was used to guarantee homogeneous geometrical characteristic and to correctly incline the screws on all the specimens. The timber elements were cut from different GL beams and CLT panels of the same supplies in order to reduce as much as possible the differences in terms of mechanical properties among the specimens. Every connection sample is identified by an acronym.
The first letter (from A to G) identifies the specimen group. Each group refers to a different age of testing, from 0 months (the test was performed in the same day when the specimens were built) to 24 months. The number (from 1 to 9) identifies the specimen in its group. The test groups are summarized in Table 2, where the time of testing T, the Controlled (C) or Non-Controlled (NC) environment (Env), average mass and average moisture content at time T are also reported.

Table 2: *Specimens description.*

Group	Time of testing T	Env	Avg. Mass at T [g]	Avg. Moisture content at T
A	0 months		9424	10.9
B	6 months	NC	9897	10.5
C	6 months	C	9466	10.8
D	12 months	NC	9560	10.2
E	12 months	C	9488	10.7
F	24 months	NC	9795	10.6
G	24 months	C	9407	9.9

https://doi.org/10.52202/069179-0080

Environmental conditions were constantly monitored and recorded during the ageing of the NC groups specimens. A thermo-hygrometer FHT70 with datalogger was used to register air temperature and humidity every 15 minutes (accuracy ±1°C on temperature and ±2% on air humidity). The moisture content of the specimens was measured before each push-out test by averaging 5 measurements. The electronic moisture meter "Aqua-boy" by KPM (accuracy ±0.1%) was used.

The recorded air temperature and humidity are shown in Figure 3, where the test dates are also highlighted. It can be noted a period without record due to the second phase of the Covid19 pandemic, when the laboratory was not accessible.

On the other hand, the specimens of the controlled environment were stored in a separate room of the laboratory, in order to avoid wide fluctuations in temperature and humidity.

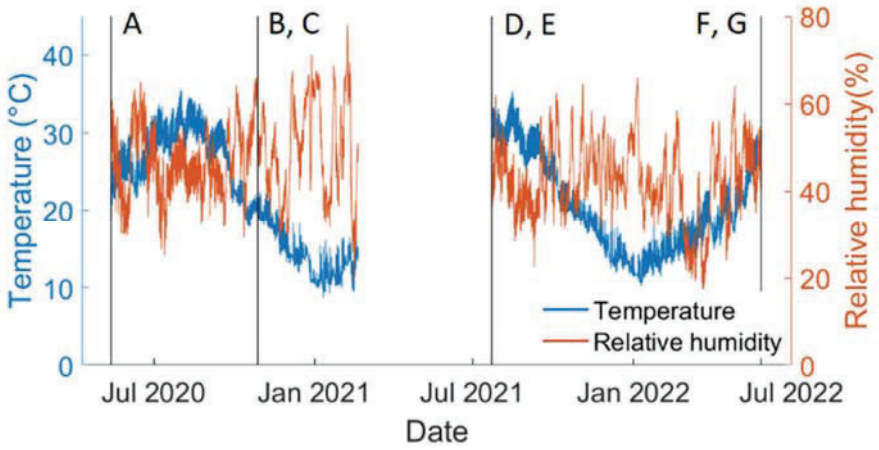

Figure 3: *Temperature (in blue) and relative humidity (in orange) during the test campaign.*

2.2 TEST SETUP AND PROCEDURE

The load-slip behaviour of the connections was obtained by push-out tests according to EN26891:1991 [17]. All the specimens are symmetric with respect to the loading plane and 4 screws are tested at time, 2 for each side of the specimen.

The test setup is shown in Figure 4.

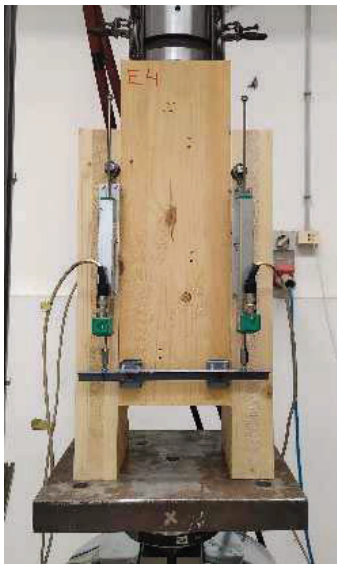

Figure 4: *Test setup.*

Load was applied in compression by a universal testing machine through a hydraulic actuator. During the test, the load was recorded by means of a load cell and the relative displacement was acquired by 4 transducers Gefran PY-150 (150 mm stroke, ±0.05% linearity). Two transducers were located on the front of the specimen and two on the back. The slip is then evaluated as the mean value of the four measures.

The load procedure according to EN 26981:1991 [17] is shown in Figure 5.

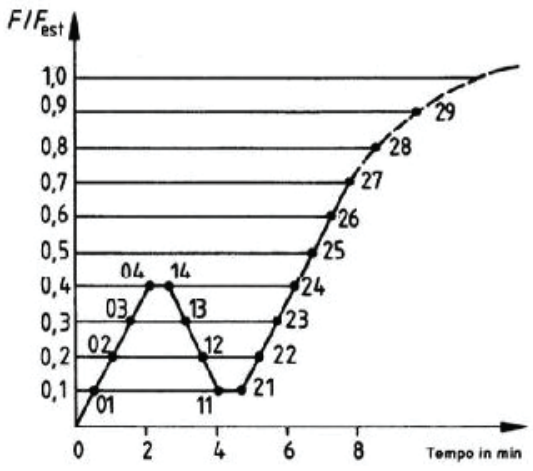

Figure 5: *Loading procedure according to EN 26981:1991 [17].*

https://doi.org/10.52202/069179-0080

The load is applied up to a value of $0.4F_{est}$, where F_{est} is the expected resistance, and maintained for 30s. Then, the load is reduced to $0.1F_{est}$ and again increased up to $0.7F_{est}$. After the reaching of this value, the machine is set into displacement control (speed of 0.05 mm/s). The specimen is pushed up to the actual failure limit state, in order to evaluate the residual capacity also for high values of displacement. As prescribed, the collapse load or a slip of 15 mm is considered as ultimate condition.
The estimated load F_{est} was assumed after the first test, and then it was considered constant for all the specimens.

2.3 ESTIMATION OF THE MECHANICAL PARAMETERS

Stiffness, strength and ductility are evaluated for each connection according to EN12512:2006 [24].
The secant stiffness K is evaluated by means of equation (1):

$$K = \frac{0.4F'_{max} - 0.1F'_{max}}{s_{0.4} - s_{0.1}} \quad (1)$$

where F'_{max} is the actual maximum value when the corresponding slip is less than 15 mm, otherwise the load corresponding to a 15 mm slip is chosen, and $s_{0.4}$ and $s_{0.1}$ are the slip of the connection corresponding to loads equal to $0.4F'_{max}$ and $0.1F'_{max}$ respectively.
The ductility of the connection μ is defined in equation (2):

$$\mu = \frac{s_u}{s_y} \quad (2)$$

where s_u and s_y are the ultimate slip and the slip at the yield point respectively.
The ultimate slip corresponds to $0.80F'_{max}$. According to [24], when the curve does not have two well-defined linear parts, yield value is determined by the intersection of the following two lines: the first is the line drawn between points $0.4\ F'_{max}$ and $0.1\ F'_{max}$ of the curve, the second is the tangent line with an inclination of ⅙K. (Figure 6).

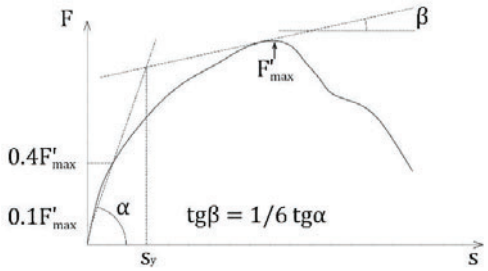

Figure 6: *Evaluation of the yield slip s_y according to EN 12512:2006 [24].*

3 EXPERIMENTAL RESULTS AND DISCUSSION

Figure 7 shows a few specimens at the end of the push-out test. Most of them gave evidence of a ductile rupture mode, consisting in the occurrence of two plastic hinges in the screws. In several samples, at the ultimate condition, screw head penetration was observed, in some cases the tip withdrawal took place.
The specimen experimental results for each group are shown in Figure 8, where the load-displacement relationships are illustrated. The reported load is the one on a single screw (i.e. the total measured load divided by 4). The slip is the average reading of the 4 transducers.
The results are generally dispersed. The dispersion is lower in groups A, D and G. It is worth noticing that specimen B2, D2 and G4 were damaged and the results are not shown.
Maximum load F_{max}, secant stiffness K and ductility μ are evaluated for each specimen with the procedure previously described. Average value (Avg) and coefficient of variation (CoV) are reported in Table 3.

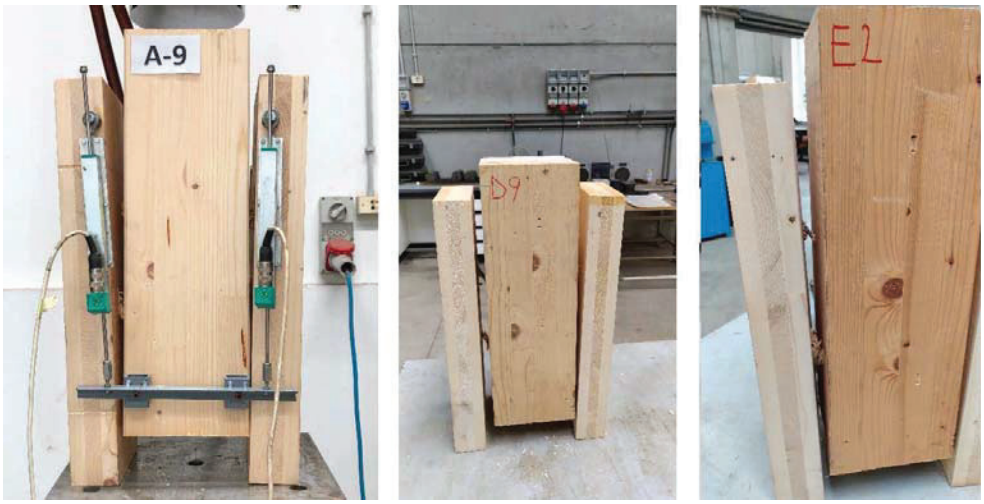

Figure 7: *Specimens of different groups after the tests.*

https://doi.org/10.52202/069179-0080

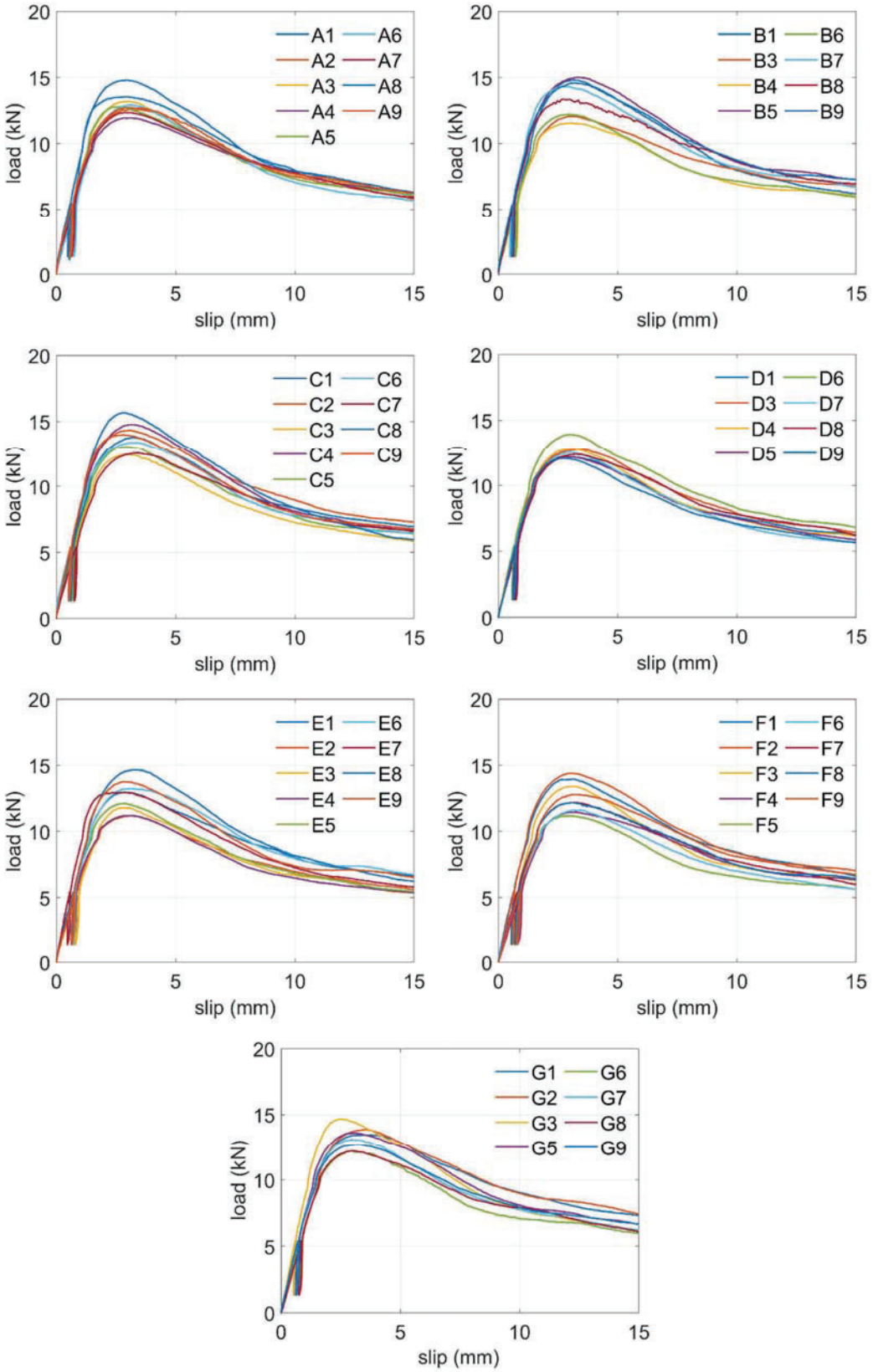

Figure 8: *Load-slip experimental curves for each specimen of the 7 tested groups.*

https://doi.org/10.52202/069179-0080

Table 3: Summary of the test results. (NC: Non-Controlled environment, C: Controlled environment).

Group	Environment	Time of testing	Secant Stiffness K		Maximum Load F_{max}		Ductility μ	
			Avg [kN/mm]	CoV	Avg [kN]	CoV	Avg [-]	CoV
A	-	0 months	7.21	8.9%	12.99	6.0%	4.06	11.9%
B	NC	6 months	7.24	10.4%	13.49	9.6%	4.06	10.3%
C	C	6 months	7.28	7.2%	13.77	7.3%	3.86	9.0%
D	NC	12 months	7.37	7.5%	12.59	4.5%	4.24	9.4%
E	C	12 months	7.06	13.2%	12.66	8.8%	3.91	12.9%
F	NC	24 months	6.87	9.7%	12.58	8.5%	4.04	6.9%
G	C	24 months	7.18	12.2%	13.22	6.1%	3.98	9.7%

For an overall view of the results, all the curves are reported together in Figure 9, where the unload-reload branches were removed to improve the clarity of the chart. The results highlight a difference of 7% between the maximum and the minimum value of the secant stiffness, which reached a minimum after 24 months (6.87 kN/mm). The maximum force reached a peak value after 6 months, both in the controlled and in the non-controlled environment (maximum load increased by 6%). The results highlighted a slight decrease of F_{max} after 12 and 24 months.

Ductility showed variation for specimens of the same age but stored in different environments (difference of 5% between groups B and C, 8% between groups D and E, 1% between groups F and G). The ductility values calculated in the controlled environment are always lower than the starting ductility value of group A (ductility decreased by 5%).

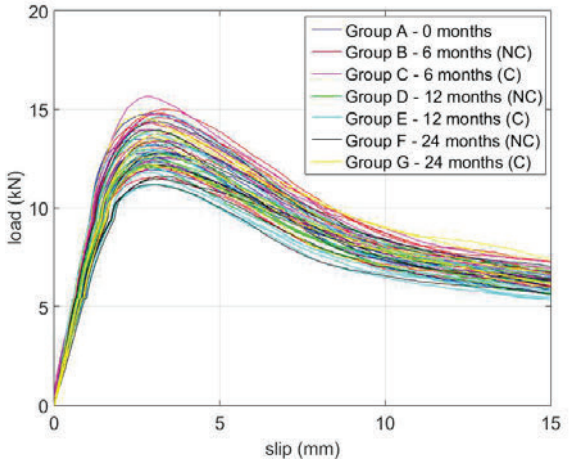

Figure 9: Load-slip curves of the 7 tested groups. (NC: Non-Controlled environment, C: Controlled environment).

4 CONCLUSIONS

An experimental campaign to study the self-tapping screw timber-to-timber connection during time was performed at University of Udine between 2020 and 2022. Samples of different ages were tested by a push-out procedure. The tests were performed for specimens as soon as built and after 6, 12 and 24 months. Half of the specimens was stored in a controlled environment, the other in a non-controlled environment. Air temperature and humidity were recorded regularly for the non-controlled environment.

The mechanical parameters of the connections were calculated after each test. In this paper, the results in term of secant stiffness, maximum force and ductility were compared. The trend now seems to signal only a slight variation of the mechanical characteristics over time. A minimum value of the secant stiffness was reached after 24 months and a peak in term of maximum strength was found after 6 months. Besides, the results showed a decrease in ductility for samples stored in a controlled environment compared to those in the non-controlled environment.

In the following post-processing phase of the data, it will be necessary to highlight the influence of the environmental humidity and the consequent variation of wood moisture content on the mechanical characteristics of the connections.

ACKNOWLEDGEMENT

This research was partly financed by the ReLUIS consortium (Italian University Network of Seismic Engineering Laboratories), within the frame ReLUIS-DPC 2019-2021 project “WP13 Contributi normativi relativi a strutture in legno” and the frame ReLUIS-DPC 2022-2024 “Contributi normativi – Strutture in legno”. The support of ROTHOBLAAS S.r.l.m Cortaccia (BZ), Italy, that offered the self-tapping screws, is gratefully acknowledged.

REFERENCES

[1] Blaß H.J., Bejtka I., Aicher, S., and Reinhardt, H.W.: Screws with continuous threads in timber connections. In: Proceedings of International RILEM Symposium on Joints in Timber Structures, Stuttgart, Germany, pp. 193-201, 2001.

[2] Blaß H.J., Bejtka I.: Reinforcements perpendicular to the grain using self-tapping screws. In: Proceedings of WCTE 2004, Lahiti, Finland, 2004.

[3] Bejtka I., Blaß H.J.: Self-tapping screws as reinforcements in connections with dowel-type fasteners. In: Proceedings of the CIB-W18/38 Meeting, Karlsruhe, Germany, Vol. 38, p. 20, 2005.

https://doi.org/10.52202/069179-0080

[4] Bejtka I., Blaß H.J.: Self-tapping screws as reinforcements in beam supports. CIB-W18/39 Meeting, Florence, Italy, 2006.
[5] Dietsch P., Brandner R.: Self-tapping screws and threaded rods as reinforcement for structural timber elements. A state-of-the-art report. Construction and Building Materials, 97, pp. 78-89, 2015. doi:10.1016/j.conbuildmat.2015.04.028
[6] Tomasi R., Crosatti A. and Piazza M.: Theoretical and experimental analysis of timber-to-timber joints connected with inclined screws. Construction and Building Materials, 24(9), pp.1560-1571, 2010.
[7] Giongo I., Piazza M. and Tomasi R.: Out of plane refurbishment techniques of existing timber floors by means of timber to timber composite structures. In: Proceedings of WCTE 2012, Auckland, New Zealand, 2012.
[8] Riggio M, Tomasi R. and Piazza M.: Refurbishment of a Traditional Timber Floor with a Reversible Technique: Importance of the Investigation Campaign for Design and Control of the Intervention. International Journal of Architectural Heritage, 8:1, 74-93, 2014. doi:10.1080/15583058.2012.670364
[9] Roensmaens B., Van Parys L., Carpentier O. and Descamps T.: Refurbishment of existing timber floors with screwed CLT panels. International Journal of Architectural Heritage, 12 (4), pp. 622-631, 2018. doi: 10.1080/15583058.2018.1442522
[10] Gubana A., Melotto M.: Experimental tests on wood-based in-plane strengthening solutions for the seismic retrofit of traditional timber floors. Construction and Building Materials, 191, pp. 290-299, 2018. doi:10.1016/j.conbuildmat.2018.09.177
[11] Hossain A., Danzig I. and Tannert T.: Cross-laminated timber shear connections with double-angled self-tapping screw assemblies. Journal of Structural Engineering, ASCE, 142(11), 2016. doi: 10.1061/(ASCE)ST.1943-541X.0001572
[12] Brown J.R., Li M.,Tannert T., Moroder D.: Experimental study on orthogonal joints in cross-laminated timber with self-tapping screws installed with mixed angles. Engineering Structures, 228, 111560, 2021. doi: https://doi.org/10.1016/j.engstruct.2020.111560
[13] Eini A., Zhou L., Ni C.: Behavior of Self-Tapping Screws Used in Hybrid Light Wood Frame Structures Connected to a CLT Core. Buildings, 12, 1018, 2022. doi: https://doi.org/10.3390/buildings12071018
[14] Marchi L., Scotta R. and Pozza L.: Experimental and theoretical evaluation of TCC connections with inclined self-tapping screws. Materials and Structures, 50 (3), 2017. doi:10.1617/s11527-017-1047-1
[15] Schiro G., Giongo I., Sebastian W., Riccadonna D. and Piazza M.: Testing of timber-to-timber screw-connections in hybrid configurations. Construction and Building Materials, 171, pp. 170-186, 2018. doi: 10.1016/j.conbuildmat.2018.03.07
[16] Bejtka I. and Blaß H.J.: Joints with inclined screws. In: Proceedings of the CIB-W18/35 Meeting, Kyoto, Japan, 2002.
[17] EN 26891:1991. Timber structures. Joints made with mechanical fasteners. General principles for the determination of strength and deformation characteristics.
[18] Bedon C., Sciomenta M., Fragiacomo M.: Mechanical Characterization of Timber-to-Timber Composite (TTC) Joints with selftapping Screws in a Standard Push-Out Setup. Applied Sciences, 10, 6534, 2020. doi:10.3390/app10186534
[19] Bedon C., Sciomenta M., Fragiacomo M.: Correlation approach for the Push-Out and full-size bending short-term performances of timber-to-timber slabs with Self-Tapping Screws. Engineering Structures, 238, 112232, 2021. doi: https://doi.org/10.1016/j.engstruct.2021.112232
[20] Giongo I., Schiro G., Piazza M. and Tomasi R.: Long-term out-of-plane testing of timber floors strengthened with innovative timber-to-timber solutions. In: Proceedings of WCTE 2016 - World Conference on Timber Engineering, 2016.
[21] Gubana A., Melotto M., and De Cillia L.; Long Term behavior of Timber-to-Timber Shear Connections made by inclined Self-tapping Screws. In: Proceedings of the International Conference on Structural Health Assessment of Timber Structures, SHATiS'2019 25-27 September 2019, Guimarães Portugal, 457-466, 2019.
[22] EN 14080:2013. Timber structures. Glued laminated timber and glued solid timber. Requirements.
[23] ETA European Technical Approval 11/0030: RothoBlaas self-tapping screws.
[24] EN 12512:2006. Timber structures. Test methods. Cyclic testing of joints made with mechanical fasteners.

World Conference on Timber Engineering Oslo 2023

PATINA AND ITS FORMATION ON A WOODEN CHURCH FLOOR – CASE PETÄJÄVESI OLD CHURCH AND VIIKKI CHURCH IN HELSINKI

Jonna Silvo[1]

ABSTRACT: Scratches and other kind of wearing on the floor are caused by everyday actions, such as walking, soiling or for example dropping goods on the floor. During the time they might transform into patina. The aim of this study is to examine wooden patina in selected church floors: an old wooden floor and a modern one. The study also discusses the possibilities of a modern wooden floor to be patinated, when the modern maintaining culture is strong today. The research was done using both literature research and own observations. This study shows that aging and patination of wooden floors, especially new ones, is a wide and sometimes also complex combination of people's opinions, traditions, and maintenance concerns.

KEYWORDS: Patina, Wooden floors, Church, Finland

1 INTRODUCTION

Patina is an obvious and natural thing when looking the old wooden floors in historic churches. The wooden floors have worn for decades and centuries because of use, and most people think they are beautiful. Scratches and other kind of wearing on the floor are caused by everyday actions, such as walking, soiling or for example dropping goods on the floor. Technical features and choices such as wood species, wood structure and wood surface treatment affect how permanently the traces of use remain on the floor. Heating and air conditioning together with the outdoor conditions, determine the current conditions every time when wearing of the wooden floor happens.

The aim of this study is to examine wooden patina in selected church floors. What is patina, how does it appear in old wooden church floors in Finland, for example in Petäjävesi Old Church. What kind of thoughts are faced concerning the wearing of the modern wooden floor in Viikki Church where the floor is expected to patinate over time. This study also discusses the possibilities of a modern wooden floor to be patinated, when the modern maintaining culture is strong today. The research was done using both literature and own observations.

In previous studies wood and wooden floors have been evaluated from the viewpoint of how wood feels and how it influences people. Rametsteiner [1] has found out that people consider wood as a pleasant material and they feel that the presence of wood make them comfortable. It is also known that wood has a healthy and calming effect on people [2]. Rice et al. [3] has noticed that people have a natural understanding of that wood creates a healthy environment. Tuuva-Hongisto [4] adds that in people's minds feeling of aesthetic, warmness and authenticity is connected to wood.

In Finland the attitudes towards using wooden floors are contradictory. On the one hand wood as material is considered natural, warm, ecological and in all ways pleasant to use, on the other hand wood is often considered a material with poorer durability than other common floor materials such as laminate and plastic in Finland have [5].

2 PATINA

The word patina has multiple origins [1]. It is partly a borrowing from Latin but also partly a borrowing from Italian. The word paten was used already in 17th century to mean the layer coming to the surface of the copper. In Latin, paten means a shallow flat vessel or bowl from which the Italian word patena is inspired. As a descriptive concept, patina means a gloss or sheen; specification that on wooden furniture or surface is produced by age and polishing.

All buildings carry their history on their surfaces and that means that also time is written in every building. Mattinen [7] writes that buildings are not static entities; they are constantly evolving and changing, and their appearance

[1] Jonna Silvo, Oulu School of Architecture,
Faculty of Technology, University of Oulu, Finland,
jonna.a.silvo@gmail.com

https://doi.org/10.52202/069179-0081

reflects the changes that have taken place over time. The different signs and marks on buildings, whether they are intentional or unintentional, contribute to the overall character and story of the building [7].

An old environment can be comforting and familiar, offering a sense of safety and continuity. This is because the built environment serves as a tangible reminder of the past, offering a message that can be deeply personal and meaningful. In this way, the patina that accumulates on a building's surfaces can serve as a bridge between the past and present, connecting us to the people and ideas that came before us [7].

The concept of patina refers generally to the desirable surface changes that occur over time due to natural weathering, aging, or use. These changes can add character and depth to a building, giving it a sense of history and uniqueness. In contrast, soil and dirt usually refer to unwanted surface contaminants that accumulate on a building due to neglect or lack of maintenance [7].

2.1 PATINA AND WOOD

In Finland there are naturally just a bit more than 20 wood species [8]. Most utilized species in Finland are pine (Pinus sylvestris), spruce (Picea abies) and birch (Betula pubescens and Betula pendula). Wood patination refers to the natural aging and weathering of wood, which often results in changes in color, texture, and overall appearance (Figure 1.). This process is influenced by several factors, including the wood species, exposure to light and moisture, and the presence of microorganisms.

Figure 1: *An old patinated wooden floor in Finland. Wearing is characteristic for wooden floors.*

Understanding the mechanisms and effects of wood patination is useful for several reasons in modern wood architecture. First, it can provide valuable insights into the durability and long-term performance of wood-based materials in various applications. Second, it can enhance the aesthetic appeal of wood products, particularly in fields such as architecture and interior design.

Sometimes there is only a fine line between what is patina, wearing and what is soiling in people's opinions. When designing modern wide solid wooden floors in public buildings, wearing of the surface must be taken into consideration. Even though wearing is characteristic for wooden floors, people doesn't "know" wood as they did in the past. And that makes it harder for them to accept all the changes on the surface of the wood and changes on the surfaces of wooden floors.

3 PETÄJÄVESI OLD CHURCH

The oldest still existing wooden floors in churches in Finland are from the 18th and 19th centuries. Petäjävesi Old Church (Figure 2.) is one of the UNESCO World Heritage Sites located around the world.

Figure 2: *Petäjävesi Old Church. Photo taken in the beginning of the 21th century.*

The architecture of the church has been described as follows [9]:

> *Petäjävesi Old Church is representative of the architectural tradition of wooden churches in northern Europe. The Old Church is a unique example of traditional log construction techniques applied by the local peasant population in northern coniferous forest areas. European architectural trends, which have influenced the external form and layout of the church, have been masterfully applied to traditional log construction. The adaption of forms and techniques of varied provenance makes this church a multi-layered landmark and an outstanding example of Nordic church architecture. The church is built entirely of pine wood, worked in a constructive and economical manner.*
>
> *The interior's hand-carved log surfaces with their silky patina and the silvery sheen on the seasoned walls lend the hall its unique atmosphere, which is further enhanced by the slightly irregular placement of the floor beams and pews. The distinctive features of the interior are the elaborately carved pulpit, pews,*

https://doi.org/10.52202/069179-0081

chandeliers, and galleries with balustrades, which are entirely the work of local craftsmen and artists.

The interior of the church is presented in Figure 3. and 4.

Figure 3: *The dimensions of wooden planks of Petäjävesi Old Church floor are large, which was the standard at that time when the sawing was not industrial as today. The surface of the floor has worn unevenly.*

Figure 4: *The patinated interior of Petäjävesi Old Church somehow feels timeless.*

3.1 PATINA OF THE FLOOR OF PETÄJÄVESI OLD CHURCH

The wooden floor of Petäjävesi Old Church is a good example of an old patinated wooden plank floor. The patination process of the floor in this church or in others as well has thought not been documented. It is unknown what the Petäjävesi Old Church floor looked like, for instance, 20 or 50 years after its construction.

Today the church floor is beautiful, and the surface of the wooden planks has worn very smooth. The floor is thought uneven. The knots and other harder places have not worn as much as the softer parts of the planks. The surface of the floor is untreated.

4 VIIKKI CHURCH IN HELSINKI

Viikki Church (Figure 5.), built in 2005 and designed by JKMM Architects, represents modern Finnish wood architecture [10]. The main parts of the church are wooden. In the church the bundle-like glulam pillars function as load-bearing vertical designs. The frame has been partly braced with reinforced concrete. The spruce panels and boards of the hall walls and all the floors are of radially sawn spruce, which minimizes the movement of the wood indoors. The flooring material is massive spruce boards and the base floor is stone structured. The furniture has been tailor-made to suit the church activities. The interior of the church hall is presented in Figure 6.

Figure 5: *Viikki Church in winter 2006. The exterior of Viikki church is clad in cleft aspen shingles and they have turn grey during time as originally planned.*

The large wooden floor of the Viikki Church (Figure 3.) is made of feathered spruce floor boards (30 mm x 120 mm) sawn between the tangential and radial directions. The floor is treated with a mixture of lye and oil.

https://doi.org/10.52202/069179-0081

Figure 6: *The large wooden floor of Viikki Church is built with the combination of under-floor heating together with a reinforced concrete foundation. When the floor is serviced annually, the chairs are moved out of the way.*

4.1 PATINA OF THE FLOOR OF VIIKKI CHURCH

When designing a wide solid wooden floor in a public building, wearing of the surface must be taken into consideration. Wearing is characteristic for wooden floors, still sometimes there is only a fine line between what is wearing and what soiling in people's opinions.

The spruce floor in Viikki Church has worn during the past 15 years after completion of the floor (Figure 7). When designing the church, the original idea was that like in many old churches the floor would patinate beautifully over time. In Viikki Church, however, soon after the building was completed it was noticed that the wearing of the floor was very uneven. Some of the boards were also splitting. In discussions with the persons responsible of the maintenance in Viikki church in Finland it has occurred that these persons fear that the users of the church consider a worn floor as a soiled one and not aesthetically pleasant.

For getting more information the users of the Viikki Church were interviewed around this theme [11]. In the comments from Viikki Churh the sticks splitting of the floor came up. Some of the respondents connected the wearing of the floor to the splitting of the boards. If the splitting would not have occurred, the wearing would not have disturbed that much. The splitting of the boards (Figure 8.) were especially irritating parents of children that were visiting the church. Unlike the adults, children did walk with socks on the church floor and got sticks on their foots.

One interviewee commented concerning patina that: *"After all, patina is not dirt and sticks, but how is patina then created!?"*. The changes in the floor led to discussions of what patina is and could the changes of the surface of the floor even be called patina in such a new modern building.

Figure 7: *The wearing of the floor in front of a frequently used cabinet, has been intense compared to the surrounded floor.*

Figure 8: *Splitting of the boards in has been a problem in Viikki Church.*

5 DISCUSSION

In the Viikki Church the user and visitors have been quite satisfied with the wooden floor in the church hall, but some of the people think that wood as material has not been technically the best choice because of splitting of the boards.

There was a small experiment to change the lye-oil treatment to lacquer in the secondary rooms, but this was

not considered as a successful solution. In addition to that lacquer changes the feeling and atmosphere of the whole floor compared to the natural lye-oil treatment.

In retrospect can be said that splitting and sticking of the boards could probably have been prevented by being more precise about the quality of the floorboards, so that all the boards would have been exactly radially sawn. Even if the costs in this way would have been higher in the design and building phase, from a wood technical point of view, the better quality floor probably would have paid for itself during the decades if the floor does not have to be maintained as often.

A random visitor in the church does of course not face the same problems with the floors that a permanent visitor, or people working in the churches every day do. It is true that it does not help that a floor looks beautiful if it complicates you of doing your work for example when you are cleaning (Figure 9.). It can be stated that wearing of the floors has been more a functional problem than an aesthetic one.

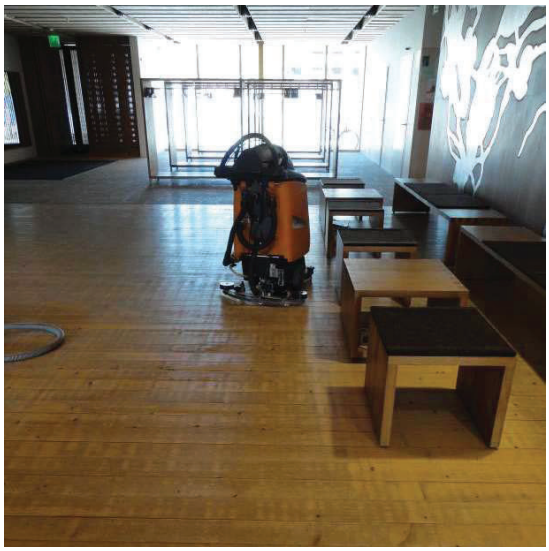

Figure 9: *The wooden floor of Viikki Church is regularly machine washed but only some moisture is absorbed in the floor.*

Besides the wearing of the wooden floors, the floors have of course also been soiled during the years and it is impossible to have them look like new ones with the existing cleaning methods. Still, it can be asked should a wooden floor look like a new one when time goes by. In figures 10. and 11. we can see the difference between a worn floor and a newly sanded floor.

Figure 10: *The floor before it had been sanded. The small round marks are caused by the spikes of the anti-slip pads people use on the shoes when it is slippery during winter time in Finland.*

Figure 11: *The floor after it had been sanded the first time after fifteen years. If the floor will be sanded regularly, it is impossible that the surface would start to patinate as the old wooden floor. On the other hand also the used dimensions are smaller than in the past.*

6 CONCLUSIONS

In this study patina has been examinated and the difference between patina, soil and wearing discussed. The wooden floor of Petäjävesi Old Church is a beautiful example of patination. The wearing of the young wooden floor in Viikki Church has instead caused debate throughout the life cycle of the floor.

It is impossible to know for sure how the floor of the Viikki church will begin to patinate and how the floor will look like during decades, as well as what kind the patinate result will be. It may be that it will look very different

https://doi.org/10.52202/069179-0081

from of what the floor of Petäjävesi Old Church does today. Probably it will not look the same because the dimensions of the floor planks were much larger in the old durable wooden floors. In addition to that the wood material used in past was usually denser in average.

One viewpoint is to think what the wearing and patination of wooden floors bring to architecture and the way we experience it. Could the qualities of wood that are considered problems, such as marks of use and inhomogeneity, also be considered as positive signs of the naturalness of the material. Thinking in this way, the characteristics typical of wood would be precisely those that connect people with nature and thereby affect the experience of the space and material.

However, the main question remains – what is the balance between soil, wearing and patina. How much can both be tolerated, and can they even be completely separated from each other.

It is not known if the wearing of the floor will turn to patina during time. On the other hand, patina is not only aging but also marks of use and wear on the surface. The question remains how much wearing can be tolerated in a new building to obtain patination in the future. This study shows that aging and patination of wooden floors, especially new ones, is a wide and sometimes also complex combination of people's opinions, traditions, and maintenance concerns.

ACKNOWLEDGEMENT

The Finnish Cultural Foundation has funded this work.

REFERENCES

[1] E. Rametsteiner, R. Oberwimmer and I. Gschwandtl. Europeans and Wood: What Do Europeans Think about Wood and Its Uses: a Review of Consumer and Business Surveys in Europe. *Ministerial Conference on the Protection of Forests in Europe,* Liaison Unit Warsaw, 2007

[2] T. Morikawa, Y. Miyazaki, and S. Kobayashi. Time-series variations of blood pressure due to contact with wood. *Journal of wood science,* 44(6):495-497, 1998.

[3] J. Rice, R. A. Kozak, M. J. Meitner and D. H. Cohen. Appearance wood products and psychological well-being. *Wood and fiber science,* 38(4): 644-659, 2006.

[4] S. Tuuva-Hongisto. Puu asumisessa: kuluttajanäkökulma puurakentamiseen. (Wood and living: A consumer view to building with wood). *Report,* University of Eastern Finland. (In Finnish), 2010

[5] K. Vahtikari, J. Silvo and T. Vainio-Kaila. 2010. Are wooden floorings difficult to maintain? In *Conference CD of the WCTE 2010 – World Conference on Timber Engineering 2010.* Riva del Garda, Italy.

[6] Patina. Oxford English Dictionary. Viewed 28 March 2022. https://www-oed-com.libproxy.aalto.fi/view/Entry/138829?redirectedFrom=patina#eid

[7] Mattinen, M. Rakentaminen ja ajan kosketus. Teoksessa: Aika ja kaupunki. (Building and the touch of time. Time and the city). Espoo: Teknillinen korkeakoulu, Yhdyskuntasuunnittelun täydennyskoulutuskeskus, julkaisu C. 1997.

[8] Vepsä M.: Puiden äärillä. In: E. Paloheimo, editor, Metsä ja puu I –Elävä puu, pages 160-180. Helsinki University of Technology, Chair of Wood Construction and Rakennustieto Oy, Helsinki, Finland, 2000.

[9] Petäjävesi Old Church. UNESCO World Heritage Convention. Viewed 22 February 2023. https://whc.unesco.org/en/list/584/

[10] S. Miettinen.Viikin kirkko (Viikki Church, Helsinki). *PuuWoodHolzBois*, 25(4):12-19, 2005.

[11] J. Silvo and L. Rautkari. 2014. User perspective on the wearing of wooden floors – Cases Viikki Church and Kuokkala Church. In *Conference proceedings of the WCTE 2014 – World Conference on Timber Engineering 2014.* Quebec, Kanada.

World Conference on Timber Engineering Oslo 2023

ON THE UTILISATION OF THE WORKSPACE OF AN INDUSTRIAL ROBOT FOR MILLING STRUCTURAL TIMBER COMPONENTS – EXPERIMENTAL TRIALS WITH DIFFERENT ARM POSITIONS AND EVALUATION OF MACHINING QUALITY

Marc Pantscharowitsch[1], Finn Linzer[2], Hans-Berndt Neuner[3] Benjamin Kromoser[4]

ABSTRACT:

Within subtractive manufacturing of timber construction components, industrial robots equipped with a milling spindle hold great potential for efficiency increases and new production methods. A key difference to modern joinery machines is the larger workspace, especially in the horizontal and vertical direction. This pushes the limits for the dimensions of workpiece cross sections and allows for newly thought-out workpiece placement and possibilities for batch processing. However, a basis must be created to assess the quality and to evaluate the effects of different robot positions on the machining quality. The subject of this paper is therefore the machining of pockets in glued laminated timber using the same parameters yet in two test series: A) four different robot positions and tool orientations B) the reach is set to four different values with each two workpiece orientations. The processing quality is then assessed based on four different scales of magnitude: 1) nominal/actual geometry comparison; 2) optical and haptic surface quality assessment; 3) stylus method surface roughness measurements; 4) 3D scans. The results show effects of the position especially in machining directions influenced by longer static levers and mass inertia. Nevertheless, compared to reference workpieces the machining quality is competitive.

KEYWORDS: 3D Scan, Automation in Construction, Glued Laminated Timber, Glulam, Quality Assessment, Robotic Manufacturing

1 INTRODUCTION

Industrial robots (IR) are already state of the art in the automotive and electronics industries [1]. Equipped with a machining spindle they have a high potential to increase the efficiency of subtractive manufacturing of engineered timber construction components. The advantages of IRs over the widely used joinery machines (JM) lie in the lower acquisition costs, the higher technological development and innovation, as well as the availability of robots and spare parts. In terms of their machining properties, they offer opportunities to increase productivity through higher degrees of freedom (DOF), larger workspace and higher flexibility. [2] To determine the applicability of IRs in engineered timber construction, a comprehensive scientific study is required. Therefore, as a first step, the quality of the machining results of IRs was analysed by the authors [3]. The milling of elementary geometries such as lines, rings and pockets using an IR was investigated and showed that the surface quality is satisfactory for the use in timber construction. Furthermore, the geometry and surface quality of milled pockets was compared to pockets manufactured with JMs. The comparison showed that the mean machining quality of the IRs is 11.52 % higher (indicated by the quality deviation value QDV) than that of the JMs. [4] Following these results, the same assessment methods were applied to another type of timber connection: the tenon. This study showed a 24.53 % higher machining quality of the JM compared to the highest quality IR specimen. Nevertheless the surface quality and geometry precision of the IR manufactured specimens was still high enough to meet industry standards. [5]

Having demonstrated the feasibility of subtractive machining using IRs by studying elementary geometries and application examples (pockets and tenons), this investigation looks into the potential of the larger workspace available when using IRs, specifically if the machining quality meets the requirements in terms of dimensional accuracy and surface quality. The idea is to identify potential causes for instability and ultimately lower machining quality.

2 EXPERIMENTAL SETUP

The machines, tools, the specific machining parameters, and the investigated specimens within the two test series are described in this section. In order to investigate the potential of IRs a reference with state of practice

[1] Marc Pantscharowitsch, University of Natural Resources and Life Sciences, Vienna (BOKU), Austria, marc.pantscharowitsch@students.boku.ac.at
[2] Finn Linzer, Technical University Vienna (TUW), Austria, finn.linzer@tuwien.ac.at
[3] Hans-Berndt Neuner, Technical University Vienna (TUW), Austria, hans.neuner@tuwien.ac.at
[4] Benjamin Kromoser, University of Natural Resources and Life Sciences, Vienna (BOKU), Austria, benjamin.kromoser@boku.ac.at

https://doi.org/10.52202/069179-0082

machinery, in this case JMs, needs to be additionally looked into.

2.1 MACHINES AND TOOLS

First the machines and tools of both used within the investigations are described.

2.1.1 IR

The BOKU robot laboratory (Figure 1) is the home of an ABB IRB 7600-325 IR mounted on an ABB IRBT 6004 external linear axis with the following properties: reach 3.10 m; payload 325 kg; position repeat accuracy 0.19 mm, trajectory repeat accuracy 0.4 mm (according to manufacturer) [6]. The IR can be equipped with various end effectors (EE), however within this study a HSD ES951 A 1112 S spindle with 13.2 kW and 10.5 Nm at 12,000 rpm was used. The machining was done with an insert cutter by Leitz (tool ID: 41927) as depicted in Figure 2 with a diameter Ø of 40 mm, an edge height of 160 mm, and two Z2 carbide milling inserts (HeliCut 11 mm x 11 mm x 1,5 mm and one drill cutting edge), with a cutting angle of 20°, a clearance angle of 20° and helix angle of 15° complemented by the HSK F-63 tool holder. The cutting inserts were unused before and showed no tool wear. A solid 2,400 mm by 1,200 mm steel worktable was used as the machining bed, comprising of 24 lamellae parallel to the short side with slots in between to allow for workpiece attachment.

Figure 1: *BOKU robot laboratory with ABB IRB 7600-325 industrial robot mounted on ABB IRBT 6004 external linear axis with the end effector (EE): HSD ES951 A 1112 S and the steel worktable in the back.*

2.1.2 JM

The reference workpieces were machined on a Hundegger k2i joinery machine (JM) using a 5-axis universal milling unit (15 kW up to 5,200 rpm) at the facilities of Rubner Holzbau GmbH. The tool used was an end mill with a diameter Ø of 36 mm, and a length L of 150 mm.

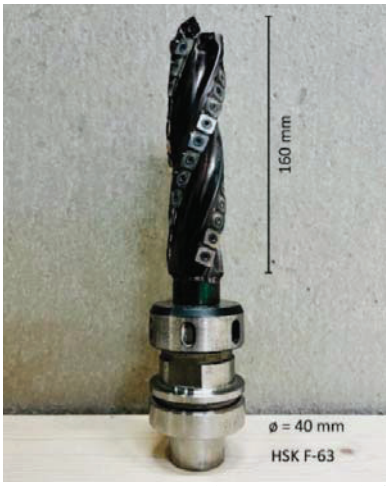

Figure 2: *Leitz insert cutter (tool ID: 41927) with diameter = 40 mm, edge height = 160 mm, 2 x Z2 carbide milling inserts (HeliCut 11 x 11 x 1,5 mm and 1 x drill cutting edge), cutting angle = 20°, clearance angle = 20°, helix angle = 15° and HSK F-63 tool holder.*

2.2 MACHINING PARAMETERS

As not only the used machinery but also the specific machining parameters are of importance within the potential assessment, a statement in regard to the latter is given below.

2.2.1 IR

The machining parameters of the IR were set the same for both test series. The spindle speed was set to 17,900 rpm, with a feed rate of 5,500 mm/min, a radial depth of cut of 35 mm and an axial depth of cut of 20 mm while climb cutting. The machining strategy is visualised blue in Figure 3.

2.2.2 JM

The authors did not have any influence on the machining parameters of the JM as they were set according to the machine operator's experience, relying on best practice and recommendations of the tool manufacturer: spindle speed = 4,000 rpm, feed rate = trajectory speed 5, unknown radial depth of cut, axial depth of cut = 20 mm while climb and conventional cutting. The trajectory speed, as reported by the machine manufacturer Hundegger in an interview [7], is indicated by an integer value from 1 to n. This integer represents the ratio of the set machining speed to the maximum machining speed, which is unique for each toolpath. When looking at a given machining process including cutting, milling and conveying processes and increasing the trajectory speed, the cutting and milling time is reduced but not the conveying time. Therefore, it is not possible to express the speed in SI units as there is no linear relationship. The machining strategy and trajectory of the tool centre point (TCP) are marked red in Figure 3.

2.3 SPECIMENS

The investigated workpieces consisted of four pockets (263 mm x 111 mm x 20 mm) with rounded corners (radius R = 20 mm) as presented in Figure 3. The

https://doi.org/10.52202/069179-0082

machining tests of both series were carried out on glued laminated timber (GLT: Gl24h, spruce, Picea abies L. Kars.).

2.3.1 Reference series

As a reference, two specimens were machined by the previously described JM on a GLT beam workpiece (cross section 200 mm x 200 mm).

2.3.2 Series A

Series A was conducted on a GLT beam with the cross-sectional dimensions of 200 x 200 mm, with the direction of the fibres and lamellae parallel to the long edge of the beam and pockets. The pockets were machined once at the end of the beam on four different opposing surfaces, each with a different orientation. The machining parameters were kept unchanged throughout the investigations, allowing for a comparison of the milling results depending on the robot position as shown in Figure 4. The workpiece was placed upon two vertical supports during all machining trials to achieve the reachability of the workpiece when machining overhead (Figure 4 D).

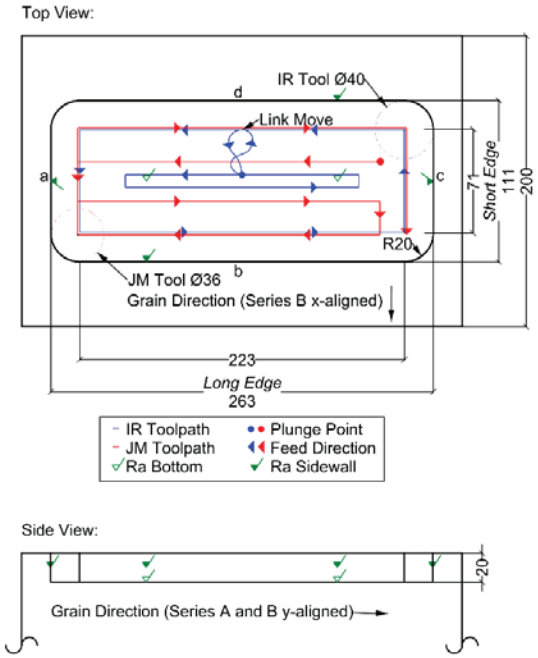

Figure 3: *Specimen [mm]: machined pocket with radial corners. The trajectory of the tool centre point of the toolpath, plunge point and feed direction is represented in blue (IR) and red (JM). Average surface roughness measurement points are marked green. Workpiece of series A and reference series: GLT beam (cross section 200 mm x 200 mm).*

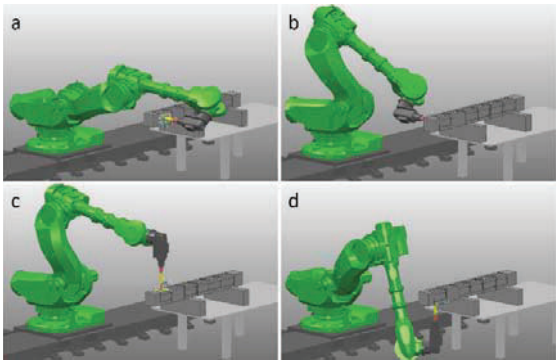

Figure 4: *ABB IRB 7600-325 industrial robot in the four different analysed positions and orientations. A) Long reach, B) Short reach, C) Vertical, D) Overhead.*

2.3.3 Series B

The trials of Series B were conducted on GLT workpieces measuring 2,000 mm x 600 mm x100 mm with the fibre direction parallel to the long edge of the workpiece. This series was subdivided into two subseries. In the first subseries, the pockets were aligned parallel to the long edge of the workpiece (further referred to as y-aligned due to the robots` coordinate system visualised in Figure 5). In the second subseries, the pockets were aligned normal to the long edge of the workpiece (further referred to as x-aligned). Each alignment and reach were machined three times for redundance. The reason for the two different investigated orientations of the specimens relative to the grain is not due to the anatomical structure of the wood but rather the robot motion direction while machining. With the pockets being y-aligned, the longer longitudinal motion requires the robot to increase its reach, while for the x-aligned pockets it is demanding the robot primarily to move laterally and also needs to turn. In Figure 5 top, the workpiece placement in the robot workspace is illustrated with the IR located directly over the central axis of the pockets in y-direction. The four investigated workpiece placement positions are visualised in Figure 5 and were chosen to exploit the entirety of the workspace limits. Position 1 was chosen as close as possible to the robot base while position 4 represented the opposite (farthest away placement still allowing for a undisturbed milling). Positions 2 and 3 were evenly distributed between 1 and 4. As a result, the reach of all four positions varies between the x- and y-aligned test series, as listed in Table 1. Reach is defined by the distance between the robot base (centre of rotation of axis 1 as marked with 0 mm reach in Figure 5 top) and the mid of the pocket. To allow for the investigations of the defined placements with an adequate secure stability, the worktable was extended (marked red) by moving every second lamellae in y- direction.

https://doi.org/10.52202/069179-0082

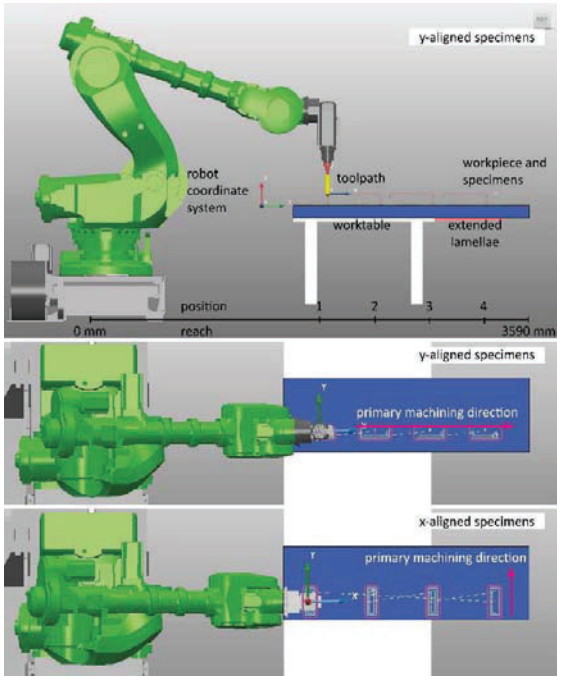

Figure 5: *Top: Workpiece placement, robot positions and reach of y-aligned specimens. Mid: Top view of workpiece placement and primary machining direction of y-aligned specimens. Bottom: Top view of workpiece placement and primary machining direction of x-aligned specimens.*

Table 1: *Specimens positions. * reach is measured from robot base (centre of rotation of axis 1 as marked with 0 mm reach in Figure 5 top) to specimen centre parallel to the y-axis of the robot coordinate system. Δ describes the distance between the positions in y-direction.*

Position	Specimen x-aligned	Reach x-aligned* [mm]	Specimen y-aligned	Reach y-aligned* [mm]
Δ	-	*500*	-	*450*
1	X1	1806	Y1	1882
2	X2	2306	Y2	2332
3	X3	2806	Y3	2782
4	X4	3306	Y4	3232

3 EVALUATION METHODS

In Austria, manufacturing requirements for structural timber can be found in ÖNORM EN 336 [8], with the dimensional accuracy specified in Table NA.L.5 in Eurocode 5 DIN EN 1995 [9] while characteristics for timbre materials like GLT are defined in ÖNORM EN 14080 [10]. Despite these regulations, surface roughness and local geometrical deviations are not considered within the regulations. To evaluate the influence of the different positions and reaches of IRs, the following references and criteria were considered.

3.1 DIMENSIONAL ASSESSMENT

Dimensional measurements were carried out on all specimens of Series A and B using two methods: by hand and by laser profile scans. The results of both methods were combined into mean values before calculating the actual-nominal deviation. Subsequently, the utilisation factor (UF) of each dimension (Length L, Width W, Height H) of every specimen was calculated based on the actual-nominal deviation and regulations specified by ÖNORM EN 14080 [10] (height h ≤ 400 mm: +4 to -2 mm and length l ≤ 2 m: ±2 mm). Note, these regulations do not specify timber in connections. Finally, the cumulated utilisation factor (CUF) of each individual specimen was calculated by determining the mean value of the three individual UFs.

3.1.1 Measurement by Hand

The dimensions (L, W, H) of all specimens were measured by hand using a carpenter´s square. Each measurement was taken three times to avoid discrepancies before the mean values were calculated.

3.1.2 Laser profile Scans

The profile scans were performed using a Keyence LJ-X8900 profile scanner. Mounted to the EE of the robot, the laser profile is aligned parallel to the y-axis of the robot coordinate system (as pictured in Figure 5) producing 2D data. Combined with the robot motion in x-direction, 16,000 profiles are combined into one 3D image. The accuracy in the x-direction is dependent on the robots` speed and the scanners` capture frequency, or in other words the distance travelled in acquiring all the profiles, resulting in this case in 4,000 mm / 16,000 profiles = 0,25 mm. In the y-direction along the profile, the accuracy is given with 25 µm and in the z-direction with 10 µm. The collected data was analysed by the Keyence controller firmware for LJ-X8000 (3D mode) version 1.4. The specimens lengths and widths were measured with the tool gap pitch (edge pairs) from light to dark with 55% edge sensitivity, edge filter width 50 and lower edge intensity 10. The specimen´s pocket depths were assessed with the tool height measurement where the peak-to-peak height was extracted.

3.2 QDV

Currently, there are neither normative regulations nor a consensus within science on an objective assessment system for machined surfaces in timber construction [11]. Therefore, the authors have introduced the quality deviation value (QDV) [3], which is composed of optical and haptic assessment of the geometry as well as the surface roughness R_a measured using the stylus method in addition to optical and haptic inspection.

3.2.1 Geometry Assessment: Optical and Haptic

The geometric quality was assessed both optically and haptically evaluating z-deviations in the bottom area and x- / y- deviations in the sidewall surfaces. The subjective optical and haptic inspection was conducted by two parties to increase objectivity. The characteristics were described by three values: “height criterium” for z-deviations in the bottom area, “lateral criterium short edge” and “lateral criterium long edge” for x- / y- deviations in the sidewall areas with QDV ratings from 1-6 (lower values indicating lower quality). The optic and haptic assessment also includes wood surface defects such as fuzzy grain, which describes wood fibres or fibre collectives that protrude from the surface, or torn

fibre, defined by torn-out wood pieces that do not break directly when cut [12].

3.2.2 Roughness Assessment: Optical and Haptic

Optical and haptic inspection was carried out additionally to analyse the surface roughness caused by the anatomical structure of the wood and machining of the three investigated areas (bottom and short/long sidewalls). Again, the inspection was conducted by two independent parties. As a reference, Figure 6 shows various machined surfaces with associated QDV ratings (min = 1 – good quality, max = 6 – poor quality).[3]

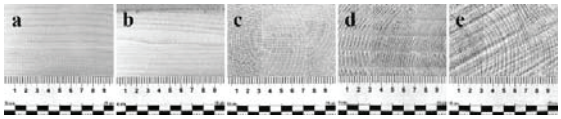

Figure 6: *Assessment of the optical/haptic surface roughness, dependent on the growth direction and machining process. Bottom surface and long edge sidewall surfaces (parallel to the grain): (a) radial/tangential planed, QDV = 1 (b) radial/tangential robot milling with 40 mm insert cutter, QDV = 2. Short edge sidewall surfaces (perpendicular to the grain): (c) axial blade saw cutting, QDV = 3 (d) axial manual chain saw cutting, QDV = 6. [3]*

3.2.3 Surface Roughness Measurement

The stylus method was used to measure the surface roughness of all inspected areas (bottom and short/long sidewalls). The measuring device was a MarSurf PS 10 (PHT 350, 2 µm probe) as shown in Figure 7 with the following settings: evaluation length Lt: 12.50 mm, Gaussian profile filter Ls: 8.00 µm, Lc = 2.5 µm, number of measured subsections N = 5 measuring velocity Vt: 0.5 mm/s, measured points: 30,000. The average surface roughness R_a was chosen as the measured quantity and the data acquisition was performed according to ÖNORM EN ISO 4287 [13] and ÖNORM ISO 16610 [9]. The measured values were scaled by applying a scaling factor (= maximum measured R_a value divided by 6) in order to not distort the QDV.

Figure 7: *MarSurf PS 10 device collecting surface roughness data on bottom area of a specimen of Series B. The stylus is located below the bottom left black tube.*

To increase the validity and reduce the influence of anisotropic and inhomogeneous wood properties, three measurements were conducted on each measuring point. The location of measurement points is depicted in Figure 3 and was marked on the specimens to increase the transparency of the study as recommended by Gurau and Irle [11].

3.3 3D SCANS: POINT CLOUDS

For the micro-scale assessment of the machining irregularities and tracing of tool paths, 3D point cloud scans of Series A were performed. First assessments can be found in [4], [5]. A Leica Absolute Tracker with a Leica T-Scan TS 50-A was used during the examinations to create a point cloud consisting of approximately 1 million points per specimen with the measurement uncertainty to plane surfaces of 80 µm (2 sigma). The data was analysed in the following three steps:

1) Division of the pocket geometry into five sections as presented in Figure 3: bottom surface, left short edge side wall a, lower long edge side wall b, right short edge side wall c and top long edge side wall d.

2) Analysis of the obtained point clouds using the CloudCompare software in the following steps: 2a) Fitting a reference plane to each machined surface a-d and bottom. 2b) Calculation of the difference of each point of the point cloud normal to the reference plane and subdivision into classes. 2c) Assessment of the number of points per class and visualisation in a histogram including a gaussian function graph.

3) Assessment of the data using RStudio. 3a) Preparation and inspection of the QQ-plots of the histograms for normal distribution as this is a precondition for the Wilcoxon rank-sum test. 3b) Assessment of the date using the Wilcoxon rank-sum test to compare the congruency of two identical sections of two different pockets (e.g. bottom surface specimen 1 with bottom surface specimen 2) by their mean values per class. As the null hypothesis states that the true location shift is equal to 0, its rejection ($p < 0.05$) indicates a major difference between the inspected surfaces. The Wilcoxon rank-sum test was performed on pairs of all five congruent areas of Series A specimens Vertical vs. Overhead and Series A specimens Short reach vs. Long reach.

4 RESULTS

In this section, the results of each series and evaluation method are reported.

4.1 SERIES A

Series A concludes the investigation of the four different robot positions Vertical, Overhead, Short reach and Long Reach.

4.1.1 Dimensional Assessment

The results of the dimensional assessment (measurements by hand and laser scanner) are displayed in Figure 8 as nominal-actual deviations. The mean deviations and UF, as described in Section 3.1, were L = 1.85 mm (UF = 92%), W = -1.47 mm (UF = 74%) and H = -0.33 mm (UF = 25%). The CUF per specimen was Vertical = 64%; Overhead = 60%; Short reach = 68% and Long reach = 62%. Calculated differences of CUF for the compared pairs resulted in 4% higher CUF when machined Vertical

https://doi.org/10.52202/069179-0082

against Overhead and 6% higher when machining Short reach against Long reach.

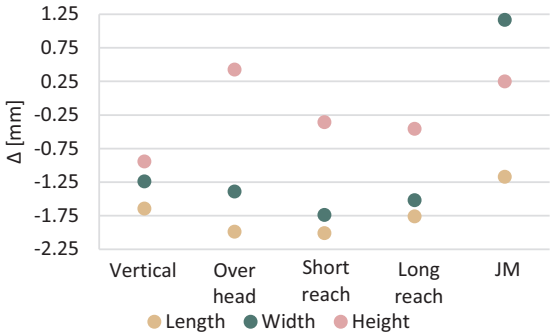

Figure 8: *Nominal-actual deviations for specimens of Series A.*

4.1.2 QDV

The results of the QDV assessment for Series A are displayed in Figure 9 with higher values indicating more deviations and irregularities. The calculated mean QDV of Series A is 19.68 (maximum achievable value 42), while the mean surface roughness R_a equalled 4.7 µm. The mean result of the JM machined reference specimens is also included. The main differences of QDV were observed for the height and lateral criteria and optical and haptic surface roughness assessment.

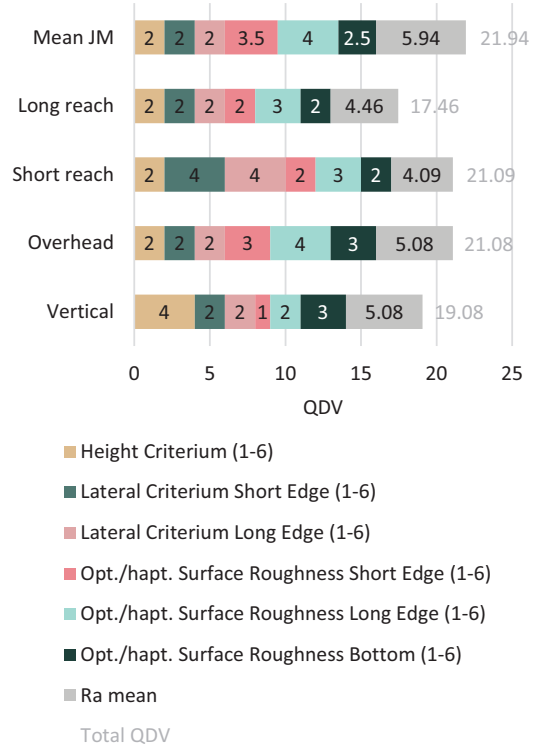

Figure 9: *Quality deviation value (QDV) of individual specimens of Series A. Higher QDVs represent more deviations and irregularities.*

4.1.3 3D Scans

The results of the Shapiro-Wilk normality test (see Table 2) for all inspected surfaces are $p < 0.05$ so the null hypothesis is denied and no normal distribution is present. This is a precondition for the following Wilcoxon rank-sum test for the statistical comparison of two surfaces.

Table 2: *Shapiro-Wilk normality test results. P-values < 0.05 indicate that the null hypothesis is denied and no normal distribution is present.*

Specimen	Inspection area	W	p
Vertical	bottom	0.94628	4.36E-05
Vertical	a	0.85753	6.96E-03
Vertical	b	0.9641	4.00E-07
Vertical	c	0.93584	1.08E-08
Vertical	d	0.95862	1.34E-02
Overhead	bottom	0.77529	2.20E-16
Overhead	a	0.92619	4.06E-03
Overhead	b	0.93049	8.06E-07
Overhead	c	0.90321	1.43E-12
Overhead	d	0.96777	4.07E-04
Short reach	bottom	0.88432	2.20E-16
Short reach	a	0.8998	7.76E-06
Short reach	b	0.88563	2.48E-09
Short reach	c	0.90724	4.40E-06
Short reach	d	0.9673	1.27E-04
Long reach	bottom	0.95337	2.20E-16
Long reach	a	0.92536	4.91E-08
Long reach	b	0.96997	1.80E-04
Long reach	c	0.93647	6.48E-06
Long reach	d	0.93212	9.72E-06

The Wilcoxon rank-sum test was conducted to compare two surfaces of the same type (e.g.: sidewall a). The results in Table 3 represent the significance level for every pair. If $p < 0.05$, the null hypothesis (no significant difference) is denied. In this comparison, the sidewall a of Vertical and Overhead machining and bottom areas of the Short reach and Long reach specimens are significantly different. All other pairs show no significant difference in the point to reference plane distance. As presented in Figure 10 the point cloud to reference plane distances overlaid with an image of the specimen clearly reveal the tool marks and micro-scale irregularities.

Table 3: *Wilcoxon rank-sum test results.*

Specimen and inspection area	W	p	Significant difference
Vertical vs. Overhead			
bottom	90022	0.8573	No
a	2914	0.03946	Yes
b	72058	0.6398	No
c	78927	0.8323	No
d	18428	0.5463	No
Short reach vs. Long reach			
bottom	379543	0.003089	Yes
a	25497	0.0783	No
b	27214	0.07479	No
c	23762	0.1591	No
d	20904	0.1349	No

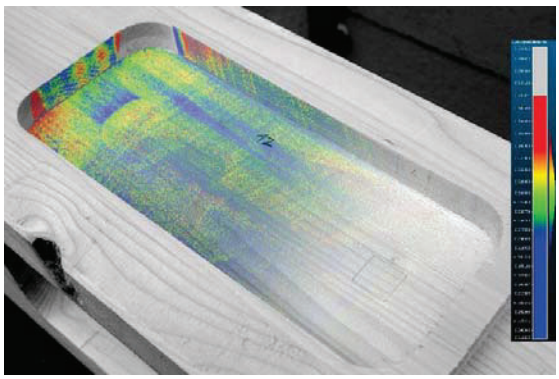

Figure 10: *Specimen 12 with overlaid point cloud with the scalar field indicating calculated point to reference plane distances.*

4.2 SERIES B

Series B includes the analysis of four different reach positions and two different workpiece alignments.

4.2.1 Dimensional Assessment

The results of the dimensional assessment are displayed in Figure 11 as nominal-actual deviations for each measurand and specimen orientation. The mean deviations and UF for the whole test series were L = 1.10 mm (UF = 55%), W = 0.66 mm (UF = 33%) and H = 0.55 mm (UF = 33%). Differentiated for x-aligned specimens the mean deviations and UF were L = 1.33 mm (UF = 66%), W = 0.57 mm (UF = 29%) and H = 0.34 mm (UF = 17%). The CUF per specimen was X1 = 39%; X2 = 32%; X3 = 32% and X4 = 47%. And for y-aligned specimens: L = 0.88 mm (UF = 44%), W = 0.76 mm (UF = 38%) and H = 0.99 mm (UF = 49%). The CUF per specimen was Y1 = 31%; Y2 = 45%; Y3 = 45% and Y4 = 54%. With increased reach, the overall CUF of both alignments and three dimensions increased from 35% to 50%.

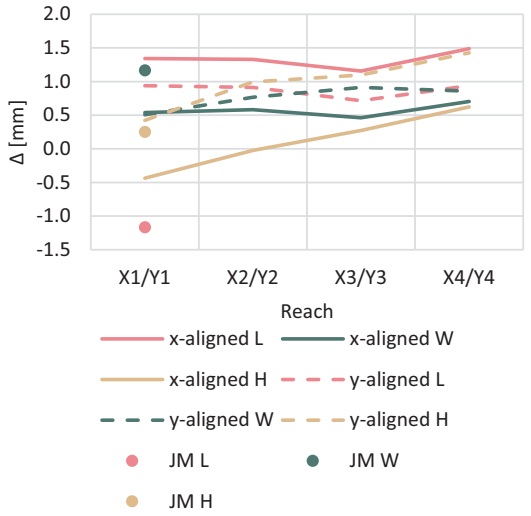

Figure 11: *Nominal-actual deviations and reach for x- and y-aligned specimens of series B as lines and JM reference values as points. Length deviations are marked red, width deviations green and height deviations brown.*

4.2.2 QDV

The QDV assessment was also conducted for Series B with the results displayed in Figure 12 with, as in Series A, the mean results of the two JM specimens also included. The mean QDV of Series B equals 19.52 (maximum value 42), with the x-aligned specimens showing a higher value with 20.55 and therefore more deviations, while the y-aligned show a value of 18.48 (10% difference). The total mean surface roughness is R_a = 4.1 µm, with again the x-aligned specimens showing higher values than the y-aligned specimens with 4.6 µm and 3.7 µm, respectively. The inspection of the short sidewall areas shows a sum over all four specimens and two values (lateral criterium and optical and haptic surface roughness) of QDV = 19 for x-aligned specimens and QDV = 20 for y-aligned indicating slightly higher deviations for y-aligned specimens.

In Figure 13 the QDV of Series B is plotted against the four positions with different reaches for both, the x- and y-aligned specimens. The trend line indicates rising QDV with increased reach implicating more deviations for both alignments. Further, the y-aligned specimens show lower QDV than the x-aligned. As a reference the mean QDV of the JM specimens is marked brown. All specimens of Series A and B except one (x-aligned reach 4) are below those of the JM.

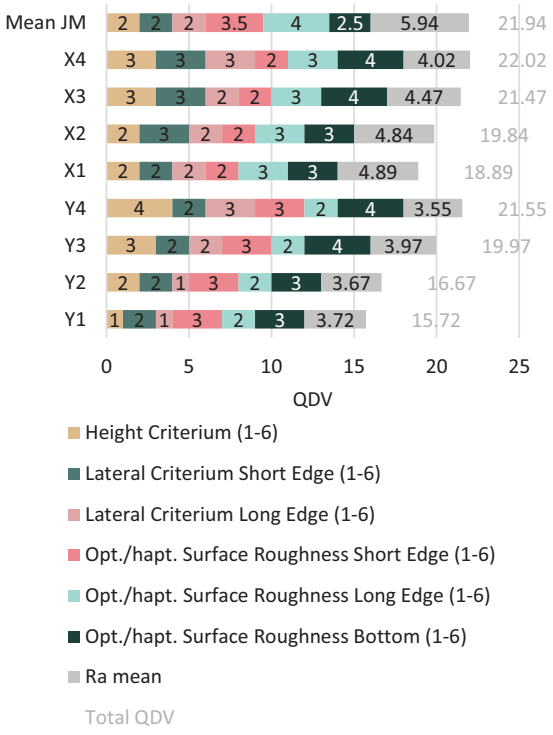

Figure 12: *Quality deviation value (QDV) of individual specimens of Series B. Higher QDVs represent more deviations and irregularities.*

When inspecting the results of the profile line scans, presented in Figure 14, the previously reported change in the pocket depth with varied reach becomes visible. It should however be noted that the height deviations listed

https://doi.org/10.52202/069179-0082

in Figure 11 were measured relative from the bottom to upper edge of the specimens while Figure 14 displays global height differences that could be affected by an uneven workpiece and worktable. The images in Figure 14 are primarily a valuable tool to trace tool marks and irregularities such as fuzzy grain defect that is visible in at least one spot of every specimen where tool trajectories overlap. The bottom pocket machined with a reach of 1806 mm (X1) shows two spots with fuzzy grain defects. Torn fibre defects occur within the specimens with maximum reach in the bottom right corner of the pocket.

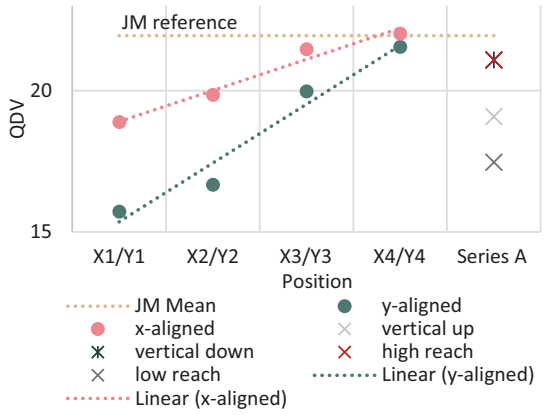

Figure 13: *Quality deviation value (QDV) of x- and y-aligned specimens of Series B. Additionally, Series A values are marked with crosses and the reference specimens machined by JM are marked as lines. Higher QDVs represent more deviations and irregularities.*

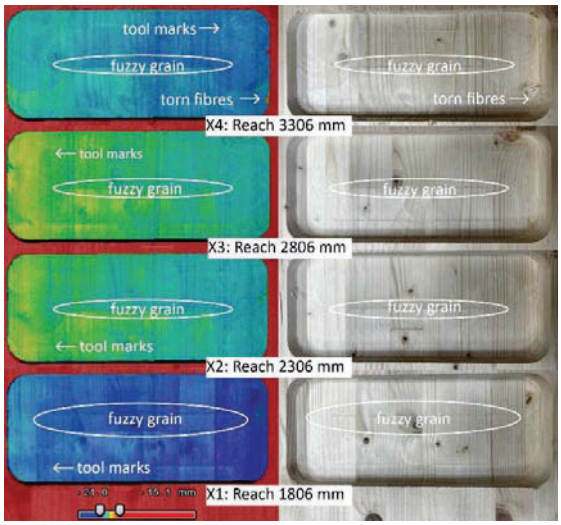

Figure 14: *Topography (left) and photographs (right) of series B x-aligned. The reach was increased from bottom to top. Note: The displayed height is global height difference between sensor and specimen.*

5 DISCUSSION

5.1 General

The dimensional deviations of all specimens of Series A apart from Short reach height and B are within the regulations´ margins defined in ÖNORM EN 14080 [10] with a maximum of -2 mm (UF = 100%).When comparing the dimensional deviations of the IR machined Series A (mean deviations L = 1.85 mm, W = -1.47 mm, H = -0.33) and B (mean deviations L = 1.10 mm, W = 0.67 mm and H = 0.55 mm). with the JM (mean deviations L = 1.17 mm, W = -1.17 mm and H = 0.25 mm) machined references, the results of the JM are more evenly distributed around zero deviation while having a similar span (span IR = 2.44 mm, span JM=2.33 mm). Overall, the achieved machining quality can be considered as sufficiently high with mean deviations of the JM = 0.86 mm as a reference and with slightly higher deviations with Δ = 0.19 mm the mean deviations of the IR = 1.05 mm. The QDV of all except one IR machined specimen is lower than for the JM machined indicating less irregularities. However, the IR tools were previously sharpened as the tool wear of the JM is not known. The main conclusion is therefore that the required machining accuracy and surface quality can be maintained in all positions and reaches when applying the machining parameters validated by previous studies [3], [4]. In addition, the results are equal to those of JMs.

5.2 Series A

When comparing the IR-machined Vertical and Overhead specimens the dimensional deviations in length and width are smaller when machining vertical (ΔL = 0.34 mm, ΔW = 0.15 mm). The nominal-actual difference of height is smaller when machining overhead compared to Vertical (ΔH = 0.49 mm), Short Reach and Long Reach (ΔH = 0.09 mm). Reason for this can be the different robot axis configuration of the compared positions leading to smaller deviations when milling forces are introduced. Another reason can be found in the robot or workpiece support system which is loaded in two opposite directions while machining as lifting and pressing forces can cause different system reactions such as vibrations.

If the QDV is factored in, the previous explanation of smaller horizontal deviations but larger height differences is reinforced by the QDV of the Vertical specimens. At a closer look the larger height deviation when machining vertical is also represented in the QDV height criterium where the vertical value is double that of the overhead manufacturing. When the QDV optical and haptic surface roughness values are inspected, indicating higher values for the sidewalls of the Overhead specimen, the thesis of robot or support system reactions such as vibrations can be underlined. When comparing the QDV of JM with IR specimens, the JM with 21.94 shows 2.31 points (11%) higher results than the IR with 19.63.

The 3D scans show no significant difference between most areas, except for sidewall a. This goes hand in hand with the QDV optical and haptic surface roughness inspection of the short edge and the large length deviation of the overhead specimen which affects the short edge as well. Altogether the mentioned factors indicate lower machining quality for the Overhead compared to the Vertical machined specimen.

During the comparison of short and long reach specimens no significant difference of the dimensional deviations can be identified. On the one hand, the QDV of the short reach specimen is noticeably higher with variance

predominantly in the lateral criteria of the short and long edge.
When inspecting the 3D point clouds, this can statistically not be confirmed. On the other hand, the point cloud indicates a statistically significant difference between the short and long reach bottom areas which cannot be supported by neither the dimensional nor QDV analysis. To sum up the comparison between short and long reach, there is no difference in dimensions but in surface quality favouring the long reach position.
When the 3D point cloud assessment method is applied, the results can be evaluated from two different perspectives. From the timber machining point of view, the deviations are on a scale that is almost irrelevant for practice but conclusions like tool marks and wood defects can be drawn. From the geodetic perspective there is a need of development of a testing strategy similar to the Wilcoxon rank-sum test that fits the quality assessment of both domains.

5.3 Series B

When the reach is increased, the height deviation of both, x- and y-aligned specimens increased (mean increase = 1.03 mm) while length (mean increase = 0.28 mm) and width (mean increase = 0.32 mm) deviations are subject to measuring noise. This effect can be traced back to both, the robot accuracy as well as the inaccurate alignment of the worktable coordinate system that determines workpiece placement. The total QDV is also affected by the reach and increases almost linearly with rising reach (mean increase = 4.48 points). The increased height deviations with rising reach can be supported by the QDV height criterium for both alignments. When looking into detail of the laser profile scans and optical inspection of the specimens, fuzzy grain defect occur more often at short reach, while torn fibre defects are sighted more frequently at high reach. Apart from all that, the tool marks get clearer with increased reach.
The main difference between the milling of x- and y-aligned pockets is, that the turning point of the trajectories requires the robot to primarily change its reach (y-aligned) or to change its lateral position and rotate (x-aligned). In the case of x-aligned specimens, there is not only motion straight in the direction of the reach but also lateral, allowing mass inertia to gain relevance. This is clearly visible in the results, with the larger deviations in length for the x-aligned specimens compared to the y-aligned ones. The investigation of QDV values does support this argument with slightly higher lateral criterium short edge values for the x-aligned specimens. The width measurements on the other hand show similar deviations at minimum and maximum reach. The smaller lateral criterium long edge values indicate less geometrical irregularities of the long edge when they are x- aligned.
The measurement of the average surface roughness R_a indicates a surface with less deviations when machining y-aligned specimens due to the fact that the robot is primarily moving along one direction parallel to the y-axis.

6 CONCLUSION

This study proves that the larger workspace - one of the main benefits of IRs compared to JMs - can be fully utilised without loss in milling accuracy. The required machining quality measured by dimensional deviations is within the margins of both regulations and the JM produced reference specimens. The surface quality of the IR-machined specimens, in the vast majority of cases, remains higher than the JM-produced reference specimens. To sum up, the following observations need to be particularly highlighted:

- The required machining accuracy and surface quality can be maintained in all investigated positions of Series A and B and levels of reach while the results are of higher or equal quality compared to those of a JM.
- The comparison of vertical and overhead machining of Series A reveals slightly higher quality results in terms of horizontal dimensions and surface quality for vertical machining.
- When comparing the opposite short and long reach specimens of Series A, no clear dimensional difference was found, yet the surface quality was higher when machining long reach specimens.
- The dimensional deviations, surface deviations and irregularities (QDV) of specimens machined with identical tool orientation increases when the robots´ reach is increased.
- The dimensional and surface (QDV) quality is decreased when the robot machining trajectories are primarily lateral (x-aligned) compared to primarily longitudinal (y-aligned).

Further research is planned on the machining accuracy of different robot positions in the workspace. For this the location of the tool centre point tracked by ABB´s online signal analysis will be compared with the accuracy of machining results measured by the laser profile scanner.

ACKNOWLEDGEMENT

The authors would like to show their gratitude to Rubner Holzbau GmbH, Leitz GmbH & Co. KG and the Research Unit of Engineering Geodesy at TU Wien for the cooperation. The project is grant by the Austrian Research Promotion Agency (FFG) (project no. 878081).

REFERENCES

[1] International Federation of Robotics, “World Robotics 2021,” Oct. 28, 2021.
[2] M. Pantscharowitsch and B. Kromoser, “Automated Subtractive Timber Manufacturing – Joinery Machines vs. Industrial Robots,” *Journal of Manufacturing Science and Engineering*, 2022.
[3] M. Pantscharowitsch and B. Kromoser, “Influence of Machining Parameters on Subtractive Manufacturing of Elementary Geometries in Glued Laminated Timber Using an Industrial Robot,” *Wood Material Science and Engineering*, p. 37, 2021.
[4] M. Pantscharowitsch and B. Kromoser, “Investigation of Industrial Robots vs. Joinery Machines for Milling Pockets in Glulam –

https://doi.org/10.52202/069179-0082

Comparison Based on Surface Quality and 3D Scans," *Civil Engineering Design - Conference (Green Civil Engineering 2022)*, 2022.
[5] M. Pantscharowitsch and B. Kromoser, "Milling Tenons on GLT Beams Using an Industrial Robot and Joinery Machine – Comparison Based on Surface Quality and 3D Scans," Portland, OR, 14-04 2022.
[6] B. Kromoser, M. Braun, and M. Ortner, "Construction of All-Wood Trusses with Plywood Nodes and Wooden Pegs: A Strategy towards Resource-Efficient Timber Construction," *Applied Sciences*, vol. 11, no. 6, p. 2568, Mar. 2021, doi: 10.3390/app11062568.
[7] W. Piatke, "Interview: Wolfgang Piatke, Vertriebsleiter Hundegger AG," Jan. 14, 2021.
[8] CEN, Austrian Standards, *EN 336:2013 10 - IDT - Structural timber - Sizes, permitted deviations*.
[9] CEN, Austrian Standards, *Önorm EN 1995-1-1:2010-12 Eurocode 5: Design of timber structures - Part 1-1: General - Common rules and rules for buildings*. Brussels: European Committee for Standardization, 2010.
[10] CEN, *ÖNORM EN 14080: 2013 08 01: Timber structures - Glued laminated timber and glued solid timber - Requirements*. Brussels: European Committee for Standardization, 2013.
[11] L. Gurau and M. Irle, "Surface Roughness Evaluation Methods for Wood Products: a Review," *Curr Forestry Rep*, vol. 3, no. 2, pp. 119–131, Jun. 2017, doi: 10.1007/s40725-017-0053-4.
[12] Forest Products Laboratory, "Raised, Loosened, Torn, Chipped and Fuzzy Grain in Lumber." US Forest Service, 1955.
[13] CEN, *ÖNORM EN ISO 4287:2012 02 01 - Geometrical Product Specifiations (GPS) - Surface Texture: Profile Method- Terms, Definitions and Surface Texture Parameters*, vol. 4287:2012 02. 2012.
[14] CEN, *ÖNORM EN ISO 16610-21:2013 07 01 - Geometrical product specifications (GPS) - Filtration Part 21*. 2013.

World Conference on Timber Engineering Oslo 2023

SHEAR THROUGH THE THICKNESS PROPERTY OF SCREW LAMINATED CROSS LAMINATED TIMBER

Shiro Nakajima[1]

ABSTRACT: This paper focus on the shear through the thickness properties of screw laminated cross laminated timber. The shear through the thickness properties of screw laminated cross laminated timber was verified from the results of the shear through the thickness test. Four test specimens with different joint configuration and one test specimen with opening were tested to verify the effect of the number of joints and the length from the screwed joints to the center point of an over wrapping part of the laminations i.e. the length of the moment arm. The test results indicated that the shear through the thickness properties of screw laminated cross laminated timber depends on the number of screwed joints and the length of the moment arm. To estimate the shear through the thickness properties of screw laminated cross laminated timber a structural model and a calculation method were proposed. The load deformation curve of the screw laminated cross laminated timber derived from the proposed structural model and calculation method well estimated the test results at relatively small deformation level. The force caused by the embedment between the laminations brought a difference at the relatively large deformation level.

KEYWORDS: Shear through the thickness, Screw joint, Cross laminated timber, Structural modelling

1 INTRODUCTION

Cross laminated timber (CLT) is composed of sawn boards cross laminated and jointed with glue. The gluing procedure in manufacturing CLT requires high quality control to confirm adequate performance of gluing. And gluing also requires heavy-duty manufacturing facilities. Alternative methodologies for jointing sawn boards such as using mechanical joints will provide the possibility to simplify the manufacturing procedure of CLT and give a chance for relatively small mills to produce CLT.

The bending behaviour of nailed jointed CLT is reported by Sung-Jun Pang et.al [1]. And in Europe the Massiv-Holz-Mauer (MHM) is manufactured and the characteristic values of the panels are evaluated by European Technical Assessment [2]. To provide design methodologies and characteristic values for CLT composed of mechanically jointed laminations it is important to accumulate data and knowledge. This paper focus on the shear through the thickness properties of screw laminated cross laminated timber (SL-CLT). Screw laminated cross laminated timber discussed in this paper is illustrated in Figure 1. The screw laminated cross laminated timber discussed in this paper is composed of lumbers of domestic species and the laminations are jointed with structural screws. The shear through the thickness properties of SL-CLT was verified from the results of the shear test. And the structural model and calculation method to evaluate the shear through the thickness properties of SL-CLT was proposed.

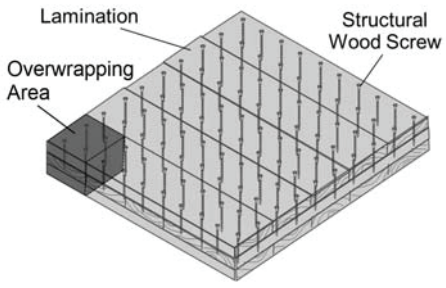

Figure 1: *Screw laminated cross laminated timber (SL-CLT)*

2 SHEAR THROUGH THE THICKNESS TEST

2.1 TEST SPECIMENS

The test specimens are composed of 3 layers of laminations. Each layer is composed of 15 laminations (sawn boards) sized 1800mm in length, 120mm in width and 30mm in thickness (see Figure 2). The species of the lumbers is Japanese Cedar (*Cryptomeria japonica*) of averaged MOE 9.76 (GPa). The detail characteristic

Table 1: *Characteristic values of the lumber*

	Average	Standard deviation
Density (kg/m^3)	386	35.8
MOE (kN/mm^2)	9.75	1.62
Moisture Contents (%)	10.0	1.30

[1] Shiro Nakajima, University of Utsunomiya, Japan, s-nakajima@cc.utsunomiya-u.ac.jp

https://doi.org/10.52202/069179-0083

values of the of the sawn boards composing the test specimens are given in Table.1.

Laminations of adjoining layers are jointed with structural wood screws 5mm in diameter and 80mm in length. The overwrapping parts of the adjoining laminations were jointed with 4 wood screws. The location of the joints is illustrated in Figure 2. There are two different joint configurations, Type A and Type B. Joint Type A has an edge distance of 20mm and for this edge distance the length of the moment arm is approximately 56.6mm. In this paper the moment arm is defined as the distance from the center of the overwrapping part of the adjoining laminations to the wood screw joints. For Type B the edge distance is 30mm and the length of the moment arm is approximately 43.4mm.

For test specimens Type 1 all the part the adjoining laminations overwrap are jointed with four structural wood screws. For test specimens Type 2 half of the overwrapping part are jointed with four structural wood screws. The number of wood screws used to compose the test specimen is 900 for test specimen Type 1 and 452 for test specimen Type 2. Test specimen Type 3 has an opening at the center of the panel and every overwrapping part are jointed with four structural wood screws.

Five types of test specimens with different combination of length of the moment arm, number of screw joints and existence of the openings were prepared and tested. The configuration of the five test specimens is given in Figure 3. All the overwrapping part of the laminations are jointed for test specimen A1 and B1 and the difference between the two test specimens is the length of the moment arm 56.6mm for A1 and 43.4mm for B1. And almost half of the overwrapping part of the laminations are jointed for test specimen A2 and B2 and the length of the moment arm is 56.6mm for A2 and 43.4mm for B2. Test specimen A3 has an opening at the center of the panel and the length of the moment arm is 56.6mm. All the overwrapping part of the laminations are jointed for test specimen A3.

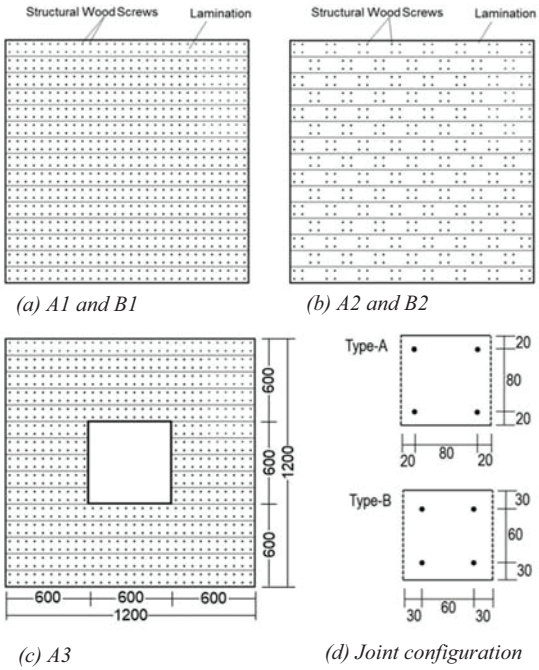

Figure 3: *Type and symbol of the test specimens*

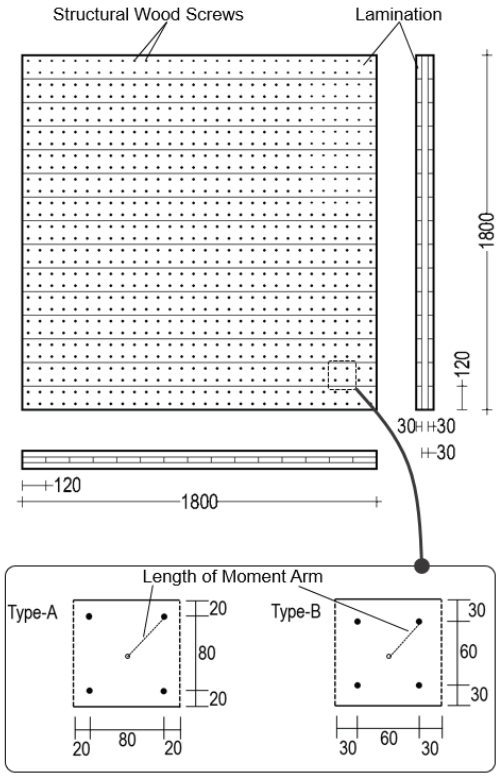

Figure 2: *Configuration of the test specimens*

Note: *The figures in the square line shows the configuration of the joints at the overwrapping part of the laminations.*

2.2 TESTING METHOD

The setup of the shear through the thickness test is given in Figure 4. The out most layer of the laminations located at the top and bottom of the test specimens are extruded to a certain length to setup the test specimens to the testing facilities. And a girder was put on the top of the test specimens to adequately load to the test specimens. The left and right end of the girder were connected to the base frame of the testing equipment by tiedown rods.

Reverse cyclic load was applied to the top of the test specimens. Three repetitive reverse cyclic load was applied at the shear deformation level of approximately $1.67x10^{-3}$ (1/600) rad, $2.22x10^{-3}$ (1/450) rad, $3.33x10^{-3}$ (1/300) rad, $6.67x10^{-3}$ (1/150) rad, $10.0x10^{-3}$ (1/100) rad, $13.3x10^{-3}$ (1/75) rad, $20.0x10^{-3}$ (1/50) rad, $33.3x10^{-3}$ (1/30) rad. And after this cyclic loading the test specimens were loaded to the shear deformation level $83.3x10^{-3}$ (1/15) rad.

The horizontal displacement of the top and bottom of the test specimens were measured and the vertical

https://doi.org/10.52202/069179-0083

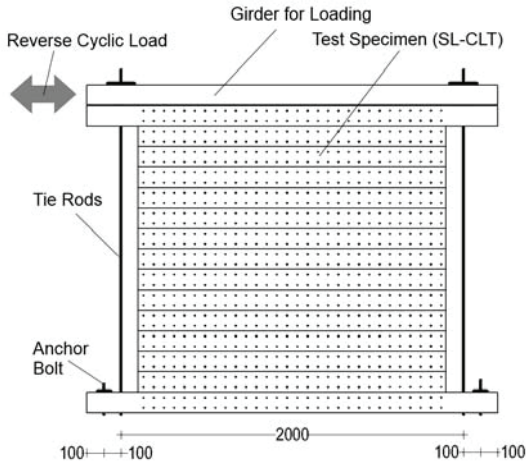

Figure 4: *Setup of the shear through the thickness test*

displacement at both left and right bottom of the test specimens were also measured. The rotation angle of the adjoining laminations was also measured at the vertical cut side of the test specimens.

3 TEST RESULTS

3.1 LOAD DEFORMATION CURVE

The envelope curves of the load deformation curves are given and compared in Figure 5. With an exception for test specimen A1 in general test specimens with longer moment arm length had higher load carrying capacity. And in general, the load carrying capacity was proportional to the number of joints.

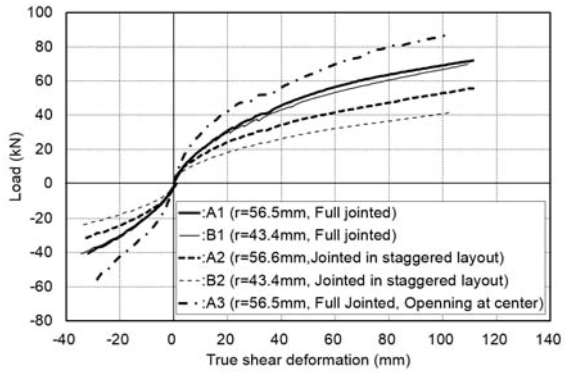

Figure 5: *Envelope curves of the load deformation curves*

Note: *True shear deformation (δ_{true})is calculated by the following formula.*

$$\delta_{true} = \left(\frac{\delta_{h-top} - \delta_{h-bottom}}{H} - \frac{\delta_{v-act} - \delta_{v-free}}{L} \right) \times H$$

Where, $\delta_{h\text{-}top}$ is horizontal displacement at the top of the test specimen,
$\delta_{h\text{-}bottom}$ is horizontal displacement at the bottom of the test specimen,
$\delta_{v\text{-}act}$ is vertical displacement of the bottom edge the loaded side of test specimen,
$\delta_{v\text{-}free}$ is vertical displacement of the bottom edge the unloaded side of test specimen,
H is the hight of the test specimen,
L is the length of the test specimen.

3.2 LOAD DEFORMATION CURVE

The yield load (*Py*), maximum load (P_{max}), ultimate load (*Pu*) and initial stiffness (*K*) are given in Table 2. Each characteristic value is assumed to has a positive correlation with the value obtained by multiplying the length of moment arm multiplied and the number of joints.

Table 2: *Characteristic values of the SL-CLTs*

Test specimens	Characteristic values			
	Py (kN)	P_{max} (kN)	*Pu* (kN)	*K* (kN/mm)
A1	37.5	71.9	63.2	1.30
B1	35.8	69.8	60.0	1.25
A2	28.2	56.1	46.8	1.06
B2	21.1	41.5	35.1	0.81
A3	41.6	86.7	71.6	2.20

Note: *Maximum load (P_{max}) is the load measured when the specimens had the true shear deformation of $6.67x10^{-3}$ rad..*

The relationship between the values above mentioned and the characteristic values is given in Figure 6. With an exception for test specimen A1 the yield load, maximum load and ultimate load had a positive correlation with the value obtained by multiplying the moment arm length and the number of joints. And with an exception for test

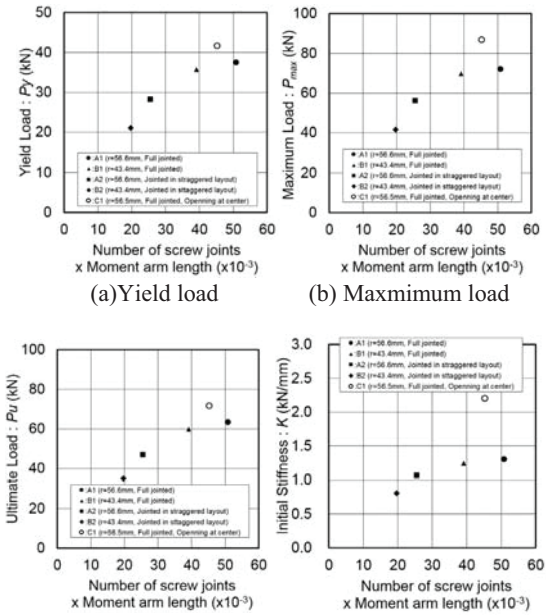

(a)Yield load (b) Maxmimum load

(c) Ultimate load (d) Initial stiffness

Figure 6: *Relationship between each characteristic value and the value obtained by multiplying length of moment arm and number of joints*

https://doi.org/10.52202/069179-0083

specimen A1 and B1 the initial stiffness had a positive correlation with the value obtained by multiplying the moment arm length and the number of joints.

3.3 DEFORMATION OF THE TEST SPECIMEN

Deformation of the test specimen A3 is shown as an example in Photo 1. The photo shows the deformation of the panel when the top of the panel was deformed to 120mm. Slippage can be observed between he vertically adjoining laminations.

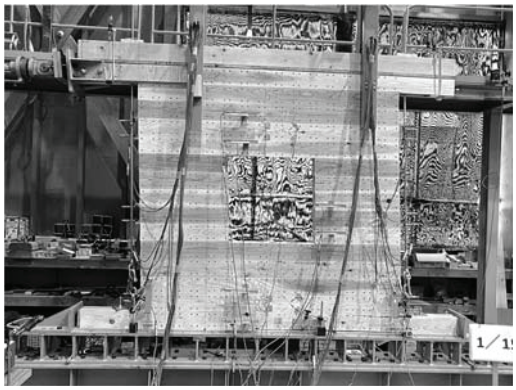

(a) Deformation of the SL-CLT panel

(b) Slippage between the vertically adjoining laminations

Photo 1: *Deformation of the SL-CLT panel A3*

4 ESTIMATION OF LOAD DEFORMATION CURVE

4.1 MODELING AND CALCULATION

The deformation of the overwrapping parts of the screw laminated CLT subjected to in-plane shear force can be model as shown in Figure 7.
When the SL-CLT panel has a shear deformation angle θ (rad) the deformation of the top of the panel x (mm) can be calculated by equation 1.

$$x = \theta \cdot (n \cdot H_{element}) \tag{1}$$

Where n is the number of lamination in vertical direction and $H_{element}$ is width of the lamination.
When the shear deformation angle of the panel is θ (rad) the shear force $F(\theta)$ (kN) generated at the screw joints can be calculated as equation 2.

$$F(\theta) = K_S(\theta) \cdot r \cdot \theta \tag{2}$$

Where $K_s(\theta)$ is shear stiffness of the screw joints at the shear deformation angle θ (rad) and r (mm) is the length of the moment arm.
The internal energy consumption ($E_{INT}(\theta)$) caused by the shear deformation at a single screw joint can be calculated as equation 3.

$$E_{INT}(\theta) = \int_{\theta 1}^{\theta 2} F(\theta) \cdot \theta d\theta = \int_{\theta 1}^{\theta 2} K_S(\theta) \cdot r\theta d\theta \tag{3}$$

The number of screw joints N_s can be calculated by equation 4.

$$N_S = m \cdot n \cdot 4 \tag{4}$$

Where m is the number of lamination in horizontal direction, n is the number of lamination in vertical direction and 4 is the number of screw joints existing at one overlapping part. By inserting equation 4 to equation

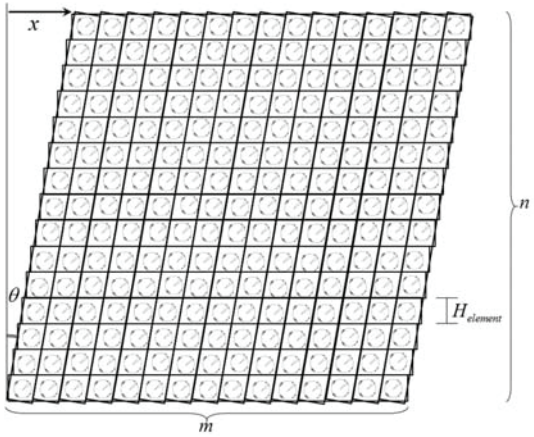

(a) Stuructral model for SL-CLT

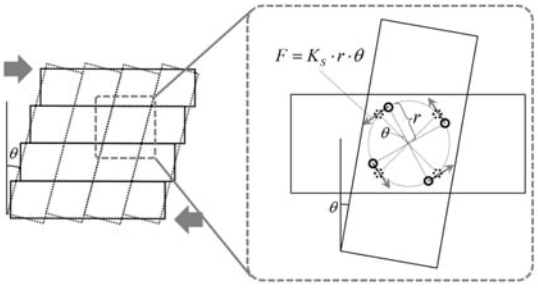

(b) Detail of the model

Figure 7: *Structural modelling of SL-CLT*

https://doi.org/10.52202/069179-0083

3 the internal energy consumption for the entire panel $E_{INT\text{-}total}(\theta)$ that is the energy consumed at all screw joints can be calculated as equation 5.

$$E_{INT-total}(\theta) = m \cdot n \cdot 4 \cdot \int_{\theta 1}^{\theta 2} K_S(\theta) \cdot r\theta d\theta \quad (5)$$

The external energy consumption $E_{EXT}(\theta)$ caused by the shear deformation θ (rad) of SL-CLT panel can be calculated as equation 6.

$$E_{EXT}(\theta) = \int_{x1}^{x2} P(x) \cdot x dx = \int_{\theta 1}^{\theta 2} P\{\theta \cdot (n \cdot H_{element})\}\{\theta \cdot (n \cdot H_{element})\} d\theta \quad (6)$$

Where P is the load applied at the top of the SL-CLT panel. As $E_{INT\text{-}total}(\theta)$ is equal to $E_{EXT}(\theta)$ and the stiffness of the screw joint at a certain deformation level θ is known the load necessary to apply at the top of panel to give a certain deformation at the top of the panel can be calculated.
By conducting an incremental displacement analysis, the load deformation curve of the SL-CLT panels was estimated.

4.2 LOAD DEFORMATION CURVE OF THE SCREW JOINT

The load deformation curve of the screw joint was derived from the test results of the joints. When a torsional deformation occurs at the overwrapping part of the adjoining laminations the screw joints will deform at an angle of 45 degrees against the grain direction of wood. The load deformation curve for screw joint loaded at an angle of 45 degrees was estimated by the test results of screw joints loaded at parallel to grain and perpendicular to gran.
Figure 8 gives the load deformation curve of the screw joints. The load deformation curve for screw joint loaded at an angle of 45 degrees was calculated by the Hankinson's formula.

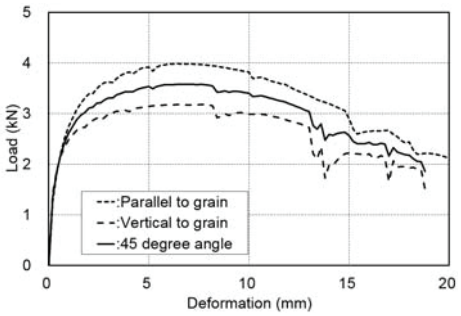

Figure 8: *Load deformation curve the screw joints*

4.3 RESULTS OF CALCULATION

The results of the calculation are given in Figure 9 in comparison with the test results. With an exception for test specimen A1 the calculated load deformation curve well estimated the test results at deformation level

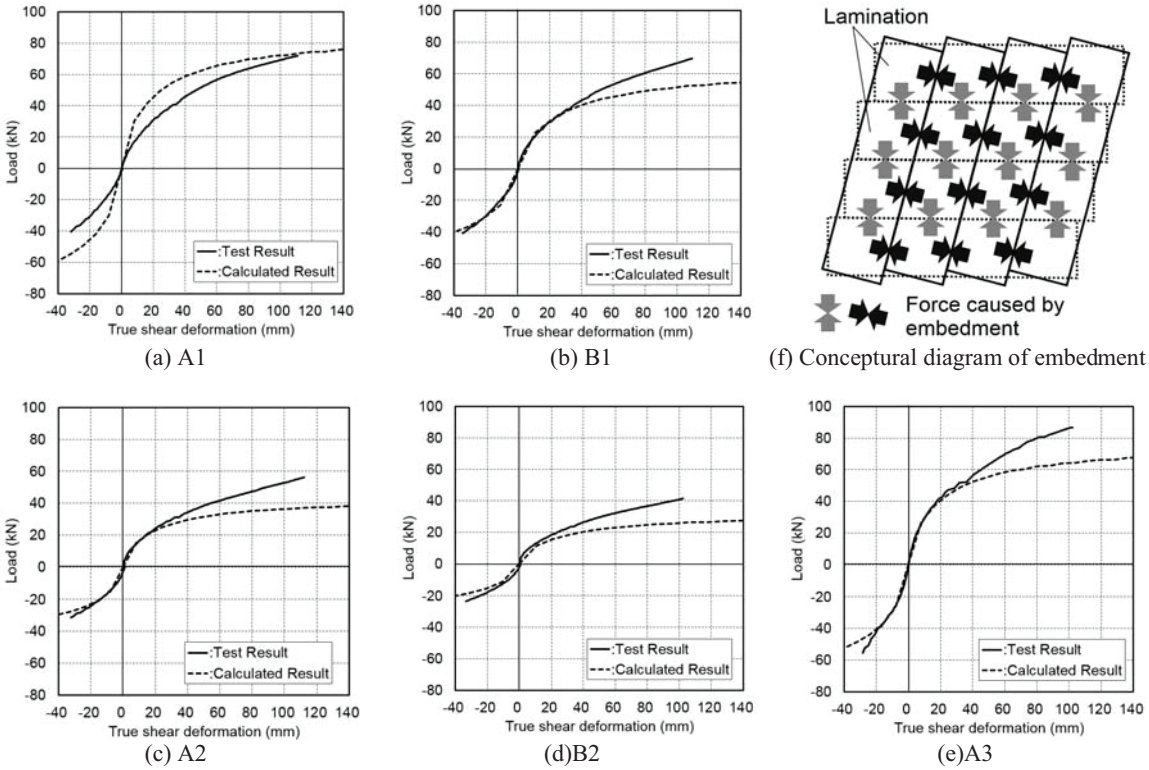

(a) A1 (b) B1 (f) Conceptural diagram of embedment

(c) A2 (d)B2 (e)A3

Figure 9: *Load deformation curve, comparison of experimental results and calculated results*

https://doi.org/10.52202/069179-0083

approximately up to 20mm. Though the load was under estimated when the deformation was approximately 20mm or more. The difference between the calculated load and measured load increased as the deformation increased. The reason for this difference is assumed as follows. When the shear deformation of the SL-CLT increase the gap between the laminations next to each other decrease. And as a result embedment will occur on the side face of the laminations. And the force derived by this embedment will increase as the shear deformation increase. Due to this embedment the load deformation curve calculated only by considering the force derived from the screw joints under estimate the load. The conceptual diagram of the embedment of laminations is given in Figure 9.

The difference between the measured and calculated load deformation curve of test specimen A1 was caused by the high moisture content of the lumbers composing the laminations. The test specimen A1 was manufactured with wet lumbers due to bad storage condition. And the lumbers dried and shrunk after being connected with structural wood screws. Small cracks may propagate and decreased the load carrying capacity of the joints but to conclude the correct reason further test should be conducted.

5 CONCLUSION

The shear through the thickness properties of screw laminated CLT was clarified through testing and the effect of the joint configuration on the shear stiffness was evaluated. A structural model and calculation method was proposed to estimate the load deformation curve. The proposed structural model and calculation method well estimated the load deformation relationship at a relatively small deformation level though at larger deformation level the load was under estimated. The force derived from the embedment between the laminations is supposed increased the load and led this under estimation. A model including the embedment characteristic of the laminations should be considered to accurately estimate the load deformation relationship of SL-CLT.

ACKNOWLEDGEMENT

This research was financially supported by the Maeda Engineering Foundation. The test was supported by Tochigi Prefecture Forest Research Center and Mr. Nobuya Namatame an undergraduate student of Utsunomiya University.

REFERENCES

[1] Sung-Jun Pang, Kwang-Mo Kim, Sun-Hyang Park and Sang-Joon Lee. Bending behavior of nailed-jointed cross-laminated timber loaded perpendicular to plane. Journal of Korean Wood Science. 45(6):728-726, 2017.

[2] European Technical Assessment, ETA-15/0760 of 27.04.2018, Austrian Institute of Construction Engineering.

World Conference on Timber Engineering Oslo 2023

BIRCH FOR ENGINEERED TIMBER PRODUCTS :: PART II

David Obernosterer[1], Georg Jeitler[2], Gerhard Schickhofer[3]

ABSTRACT: Even though birch (*Betula pendula*) is one of the main tree species in the north of Europe, it is currently hardly used for structural products, except plywood. Due to its excellent mechanical properties, the HASSLACHER group decided to see it as a future tree species for their products. In a series of projects, the material was characterised and products like Glued Laminated Timber (GLT) or Cross Laminated Timber (CLT) made from birch were developed and tested. To improve the properties of the material, a new type of lamella was developed and tested, the so-called "Strip Lamella". By using homogenisation effects, the characteristic values of the mechanical properties were strongly improved compared to birch solid wood lamellas. First tests on GLT beams out of Strip Lamella show, that this effect not only occurs in the lamella, but also in structural timber products using this lamella, leading to higher properties compared to birch solid timber GLT.

KEYWORDS: birch, hardwood, Strip Lamella, homogenization

1 INTRODUCTION

Spruce, by far the main wood species in timber construction in Europe, is under high pressure. Droughts, storm and heavy snowfalls weaken the European spruce forests, followed by enormous bark beetle attacks. In Austria, some mountain areas are already cleared prophylactically from any spruce growing there, because it is just a matter of time until they will be infested.

Meanwhile the demand for structural timber products is constantly increasing. To be able to sustainably meet this demand in the future, new strategies are needed. There are different ways to cope with these challenges:

- **Production efficiency** could be **increased**, by better production techniques or less resource-intensive new products.
- **Old timber elements** from demolished buildings could go into **Reuse** instead of being downcycled to particleboards immediately or even being burned.
- Use of **new timber species** for structural timber products, to increase the resources available for sawmilling industry.

All topics are important to further increase the share of timber buildings while maintaining a sustainable use of forests in Europe. This paper will especially focus on the last one, the use of a new timber species which can create new opportunities in the timber construction industry.

Birch (*Betula pendula*) is one of the main wood species in Russia (11,023 Mio. m³), Scandinavia (817 Mio m³) and the Baltic States (325 Mio. m³) [1]. But birch is not only interesting for the north of Europe, also in Central European countries like Austria, Germany or the Czech Republic this wood species will be more important in the future. Currently for example there just around 6.6 Mio m³ Birch growing in Austria [2], but as the climate changes so does the forest. Especially in areas where spruce is facing more difficulties due to drought, birch-pine-forest could be of interest.

Despite these large amounts available in the north of Europe, birch is currently almost not used for structural applications, except as plywood. In a series of projects, the HASSLACHER group together with the Institute of Timber Engineering and Wood Technology and the Centre of Competence holz.bau forschungs gmbh at Graz University of Technology tried to gain more knowledge on the birch timber. Based on these findings, different products like GLT or CLT made from birch were developed [3].

But when working with new timber species, new challenges can occur. In case of using birch for structural timber products, the more difficult drying of the boards, grading and cutting efficiency due to the smaller log diameters were just some of them. Instead of trying to optimize currently existing standard methods for producing GLT and CLT made from spruce, the HASSLACHER group decided to work on new ways to face these challenges going beyond standard practices.

[1] David Obernosterer, HASSLACHER Holding GmbH, Austria, david.obernosterer@hasslacher.com
[2] Georg Jeitler, HASSLACHER Holding GmbH, Austria, georg.jeitler@hasslacher.com
[3] Gerhard Schickhofer, Graz University of Technology, Austria, gerhard.schickhofer@tugraz.at

https://doi.org/10.52202/069179-0084

2 IDEA

The basic idea of the Strip Lamella, already shown e.g. in [4], is to use thinner boards (with a thickness of about 20 mm) than usually used for GLT production. The advantage of using smaller dimensions is the reduced kiln drying time (~ -65 % compared to 40 mm boards) while maintaining a higher yield in the cutting process.
The boards are then glued together to a so called "mini-GLT", which is then cut again into lamellas. The production steps are shown in Figure 1.

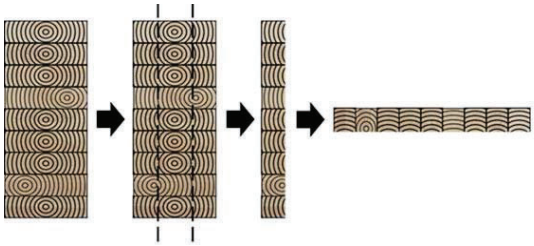

Figure 1: *Process steps of Strip Lamella production*

Despite having higher production effort due to an additional gluing and cutting step, this process is thought to have higher yield. Since production of Strip Lamellas lead to a more homogeneous product, the impact of defects from the original board is reduced. For example, a large knot with a diameter of 50 mm would reduce the strength of the original board dramatically, in the Strip Lamella it is reduced to a maximum width of 20 mm (width of strip), with straight fibres next to it in the adjacent strips.
This leads to fewer rejects when grading and eliminates any cutting of defects in the final Strip Lamella and with that to less loss in the whole production process.

3 STRIP LAMELLA TESTING

3.1 TEST MATERIAL

For production of the test specimen, boards with a dimension of 24 x 150 x 4,000 mm were dried and planed to a thickness of 20 mm. They were then graded following strength class LS7+ [5] and were glued together to a "mini-GLT"-beam with nine boards each using a two component MUF adhesive. The beams were then cut into three lamellas with a dimension of 43 x 169 x 4,000 mm as shown in Figure 1 schematically. A more detailed description of the production process can be found in [4].

As already described in [4], the Strip Lamella was divided into two groups, which were separately tested and analysed:

- **Basic:** middle lamella containing the pith and the pith-near areas, juvenile wood
- **Premium:** outer lamellas without pith, mature wood

Part of the Strip Lamellas produced were cut into shorter sections and finger-jointed together using a two component MUF adhesive.

3.2 TEST METHODS

3.2.1 Tensile Tests

To gain more knowledge on the mechanical properties of the Strip Lamella, tension tests were performed on specimen with and without finger-joints.

Strip Lamellas without finger-joints

For this test 159 Strip Lamellas were cut into specimen with a length of 3,000 mm, while the remaining part was used für the flatwise bending tests described in 3.2.2. The tensile tests were performed using a GEZU 850 tensile testing machine according to [6] with a free span length of 2,300 mm. The test setup and measurements are shown in Figure 2.

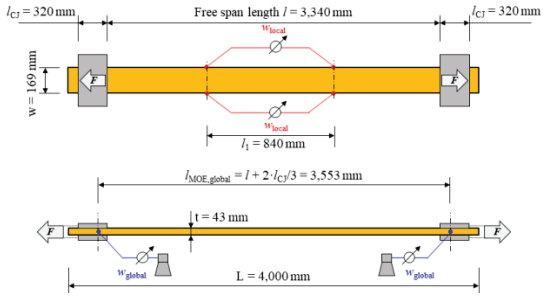

Figure 2: Setup tensile tests | Specimen without finger-joints

Strip Lamellas with finger-joints

The tests on Strip Lamellas with finger-joints were performed at Holzforschung Austria in Vienna. The samples were cut and planed to a size of 40 x 160 x 2,200 mm and were tested according to [7] with a free span length of 200 mm. The test setup can be found in Figure 3.

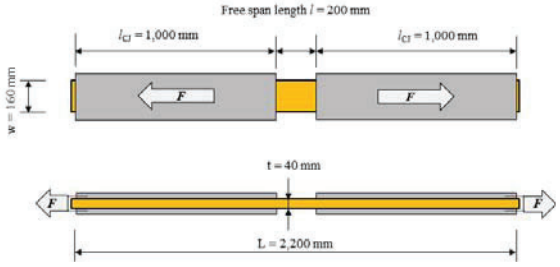

Figure 3: Setup tensile tests | Specimen with finger-joints

https://doi.org/10.52202/069179-0084

3.2.2 Bending Test

The bending tests were performed according to [6] using a Zwick Universal Testing Machine 275. To gain more insight on the bending behaviour in the two different directions, edgewise and flatwise bending tests were performed on Strip Lamellas with and without finger-joints.

Strip Lamellas without finger-joints

The test setup used for the bending tests on Strip Lamellas without finger-joints is shown in Figure 4.

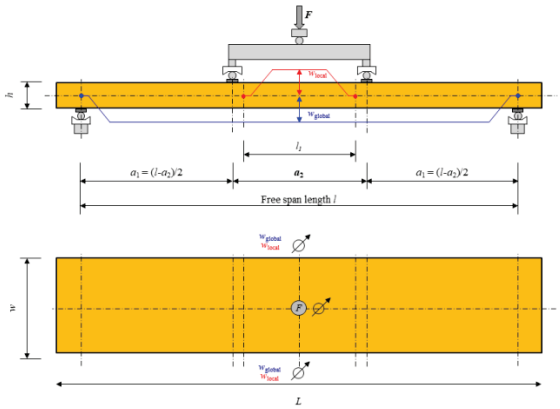

Figure 4: *Bending test setup for lamellas without finger-joint*

Since the test samples were tested flatwise and edgewise, different dimensions had to be used to fulfil the requirements according to [6]. They can be found in Table 1.

Table 1: *Dimensions for test setup of Strip Lamellas without finger-joints in flatwise and edgewise bending in [mm]*

		flatwise	edgewise
Height	h	43	169
Width	w	169	43
Length	L	816	3,211
Free span length	l	774	3,042
Distance force application	a_2	258	1,014
Distance local MOE	l_1	215	845

Strip Lamellas with finger-joints

Since it is not relevant for the characterization of finger-joints, no evaluation of the MOE was performed within these tests. The setup is shown in Figure 5.

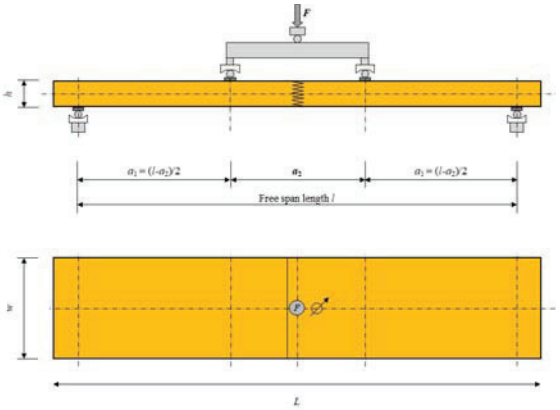

Figure 5: *Bending test setup for lamellas with finger-joint*

The finger-joint was always manufactured horizontally, so the finger-joint profile was visible on the broadside. The dimensions for the tests on Strip Lamellas with finger-joints are shown in Table 2.

Table 2: *Dimensions for test setup of Strip Lamellas with finger-joints in flatwise and edgewise bending in [mm]*

		flatwise	edgewise
Height	h	40	160
Width	w	160	40
Length	L	760	3,040
Free span length	l	720	2,880
Distance force application	a_2	240	960

3.3 Results

3.3.1 Strip Lamella

The mechanical properties of the Strip Lamellas tested are shown in Table 3. Here, the same effect as already discussed in [4] can be observed for all tests: When looking at the "Total" group containing all testes samples, the values are comparable to solid wood boards as shown in Chapter 4. By dividing into the two groups "Basic" and "Premium" according to the position in the log (juvenile vs. mature wood) as shown in Chapter 3.1 and the dynamic MOE as shown in [4], more homogeneous properties can be achieved. This leads to higher characteristic values for bending and tensile strength.

Due to the separation of juvenile and mature wood in the two different groups, also a difference in MOE can be observed, leading to almost 17,000 N/mm² in tensile testing. This shows the high potential birch can have in modern timber construction.

https://doi.org/10.52202/069179-0084

Table 3: *Results of mechanical tests on Strip Lamellas in [N/mm²]*

Results of Strip Lamella testing width: 169 mm | thickness: 43 mm				
		Total	**Basic**	**Premium**
Tensile strength	$f_{t,mean}$	43.7	35.7	47.7
	$f_{t,k}$	29.4	26.1	35.0
Coefficient of variation	COV	20.7 %	16.4 %	15.9 %
MOE	$E_{t,mean}$	15,682	13,238	16,892
Bending strength flatwise	$f_{m,flat,mean}$	81.6	68,3	88.2
	$f_{m,flat,k}$	62.5	57.5	76.4
Coefficient of variation	COV	14.2 %	9.3 %	7.9 %
MOE	$E_{m,flat,mean}$	15,184	13,422	16,084
Bending strength edgewise	$f_{m,edge,mean}$	55.4*	47.7*	59.2*
	$f_{m,edge,k}$	33.6*	33.7*	34.7*
Coefficient of variation	COV	25.3 %	17.7 %	24.8 %
MOE	$E_{m,edge,mean}$	16,523	14,331	17,591

Note: Since the gluing of the Strip Lamellas was not sufficient, the strength values in edgewise bending do not represent the full capabilities of this products but are reduced due to failures in the glue line. These insufficiencies were solved after the here presented test samples were produced and tested, further tests determining this property will follow.

3.3.2 Strip Lamella with finger-joints

The results of testing of finger-joints in Strip Lamellas presented in Table 4 show no significant difference to the values shown for the Strip Lamella itself. This leads to the conclusion, that finger-joints are not reducing the strength of the lamella itself in a critical way, which is essential for developing GLT or CLT using Strip Lamellas.

Table 4: *Results of mechanical tests on Strip Lamellas with finger-joints in [N/mm²]*

Results of Strip Lamella testing width: 160 mm | thickness: 40 mm				
		Total	**Basic**	**Premium**
Tensile strength	$f_{t,j,mean}$	52.8	42.6	58.0
	$f_{t,j,k}$	35.6	30.2	44.9
Coefficient of variation	COV	20.2 %	16.3 %	14.1 %
Bending strength flatwise	$f_{m,j,flat,mean}$	74.1	61.9	80.4
	$f_{m,j,flat,k}$	55.9	49.6	70.7
Coefficient of variation	COV	14.5 %	11.5 %	7.0 %
Bending strength edgewise	$f_{m,j,edge,mean}$	52.5	44.7	56.9
	$f_{m,j,edge,k}$	32.6	28.0	37.3
Coefficient of variation	COV	24.2 %	21.9 %	21.2 %

4 Birch solid wood lamella testing

A randomly selected part of the birch solid wood boards already described in [4] were used for testing using the same methods and dimensions as described in Chapter 3.2. Since they are not in the main focus of this paper, no further discussion will be published here on the preparation of the test samples, but it seems still absolutely relevant to show the results to be able to have a comparison of the newly developed Strip Lamella to more common birch solid wood boards.

Table 5: *Results of mechanical tests on solid wood boards in [N/mm²]*

Results of solid wood board testing width: 165 mm | thickness: 43 mm		
Tensile strength	$f_{t,mean}$	43.9
	$f_{t,k}$	24.2
Coefficient of variation	COV	31.4 %
MOE	$E_{t,mean}$	15,370
Bending strength flatwise	$f_{m,flat,mean}$	89.5
	$f_{m,flat,k}$	64.9
Coefficient of variation	COV	16.8 %
MOE	$E_{m,flat,mean}$	14,851
Bending strength edgewise	$f_{m,edge,mean}$	70.1
	$f_{m,edge,k}$	42.1
Coefficient of variation	COV	24.0 %
MOE	$E_{m,edge,mean}$	16,646

The results of the mechanical tests performed is shown in Table 5 for the solid wood boards and in Table 6 for birch solid wood boards with finger-joints.

Table 6: *Results of mechanical tests on solid wood boards with finger-joints in [N/mm²]*

Results of solid wood board testing with finger-joints width: 160 mm | thickness: 40 mm		
Tensile strength	$f_{t,j,mean}$	53.9
	$f_{t,j,k}$	36.0
Coefficient of variation	COV	21.2 %
Bending strength flatwise	$f_{m,j,flat,mean}$	72.2
	$f_{m,j,flat,k}$	55.8
Coefficient of variation	COV	13.4 %
Bending strength edgewise	$f_{m,j,edge,mean}$	61.4
	$f_{m,j,edge,k}$	36.6
Coefficient of variation	COV	26.2 %

https://doi.org/10.52202/069179-0084

5 GLT FROM STRIP LAMELLA

To further test the mechanical properties, GLT made from Strip Lamellas was produced and tested. The tests were performed at the Institute of Timber Engineering and Wood Technology in Graz.

5.1 TEST MATERIAL AND METHODS

Strip-lamellas with a width of 120 mm (≙ 6 strips) and a thickness of 40 mm were manufactured as described in Chapter 2. Since Basic and Premium lamellas were produced with a ratio of 1:2, a combined beam layup with two Premium lamellas each on top and bottom of the beam and two Basic lamellas in the middle was chosen.

The bending tests were performed according to [6] with a ratio of free span length to height of 1:16. The test setup and measurements are shown in Figure 6.

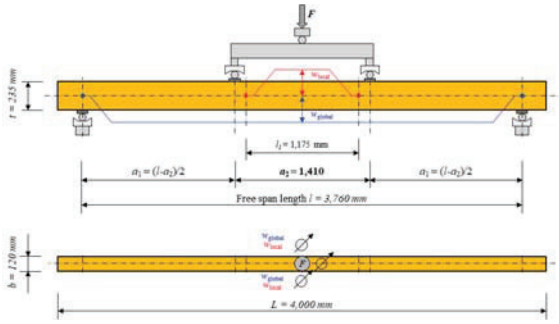

Figure 6: *Test setup for bending tests of GLT made from Strip Lamellas*

5.2 RESULTS

The results of the bending tests in Table 7 show the enormous potential of GLT out of birch Strip Lamellas. With a characteristic bending strength of almost 58 N/mm², this product exceeds the properties of solid birch GLT [8] by 80 % coming close to the values of BauBuche by Pollmeier.

Table 7: *Results of bending tests on GLT made from birch Strip Lamella*

Bending tests on GLT made from Strip Lamella		
width: 120 mm | height: 235 mm		15 specimen
Bending strength	$f_{m,g,mean}$	86.8 N/mm²
	$f_{m,g,k}$	57.8 N/mm²
Coefficient of variation	COV	8.6 %
MOE	$E_{0,g,mean}$	17,813 N/mm²
Coefficient of variation	COV	4.2 %
Density	$\rho_{g,mean}$	616 kg/m³
	$\rho_{g,k}$	557 kg/m³
Coefficient of variation	COV	1.4 %

The MOE on the other hand exceeds not just the solid birch GLT, with 17,800 N/mm² it is the highest value currently available in timber construction products.

6 CONCLUSION AND OUTLOOK

This paper shows the potential modern timber construction products have, when using birch. While current processes are sufficient to achieve very good mechanical properties in the product compared to spruce, new technologies have the chance to further increase them.

To further asses the mechanical properties of the Strip Lamella, more tests will be performed on the lamellas themselves, but also on products like GLT or CLT made from them. There will also be further investigation on connections in these new products to be able to use the in large timber buildings properly.

This will all finally lead to the application for an European Technical Assessment (ETA), to be able to have approved timber construction products.

ACKNOWLEDGEMENT

This project is funded by the Austrian Research Promotion Agency (FFG) via the program "Industrial PhD". The Dissertation is carried out at the Institute of Timber Engineering and Wood Technology at Graz University of Technology and is supervised by Univ.-Prof. Dipl.-Ing. Dr. Gerhard Schickhofer and co-supervised by Univ.-Prof. Dipl.-Ing. Dr. Johannes Konnerth from the Institute of Wood Technology and Renewable Materials at the University of Natural Resources and Life Sciences in Vienna.
Special thanks also to all employees of the HASSLACHER Group, which are involved in this project.

https://doi.org/10.52202/069179-0084

REFERENCES

[1] Hynynen, J.; Niemistö, P.; Viherä-Aarnio, A.; Brunner, A.; Hein, S.; Velling, P.: Silviculture of birch (Betula pendula Roth and Betula pubescens Ehrh.) in northern Europe, Forestry: An International Journal of Forest Research, Volume 83, Issue 1, January 2010, Pages 103–119

[2] Bundesforschungszentrum für Wald: Austrian National Forest Inventory, Vienna: 2022, https://waldinventur.at

[3] Jeitler, G.; Augustin, M.; Schickhofer, G.: Birch | GLT & CLT - Mechanical properties of Glued Laminated Timber and Cross Laminated Timber produced with the wood species birch, Vienna: WCTE, 2016

[4] Obernosterer, D.; Jeitler, G: Birch for engineered timber products, Santiago de Chile: WCTE, 2021

[5] ON DIN 4074-5: Sortierung von Holz nach der Tragfähigkeit – Teil 1: Laubschnittholz, Vienna: Österreichisches Normungsinstitut, 2009

[6] ON EN 408: Timber structures - Structural timber and glued laminated timber - Determination of some physical and mechanical properties, Vienna: Österreichisches Normungsinstitut, 2012

[7] ON EN 14080: Timber structures - Glued laminated timber and glued solid timber - Requirements, Vienna: Österreichisches Normungsinstitut, 2013

[8] European Technical Assessment ETA-19/0031: HASSLACHER GLT Birch, Vienna: Österreichisches Institut für Bautechnik, 2021

World Conference on Timber Engineering Oslo 2023

INVESTIGATIONS ON MULTIFUNCTIONAL TIMBER ELEMENTS IMPREGNATED WITH PARAFFINIC PHASE CHANGE MATERIALS

Jens U. Hartig[1], Peer Haller[2]

ABSTRACT: In this contribution, investigations on multifunctional timber elements impregnated with phase change materials (PCM) are presented. The purpose of the PCM impregnation is a passive air-conditioning by structural timber elements like beams, walls or ceilings. PCM have the ability to take up substantial thermal energy within a narrow, latent temperature range without increasing their temperature. The high specific heat capacity combined with low additional mass can improve the room climate in timber buildings, which have often especially in the summer unpleasant temperature amplitudes without air-conditioning due to low thermal mass.

In order to produce large size PCM-impregnated timber elements several investigations are performed. Besides fundamental impregnation and leakage tests for several wood species, also construction related investigations are carried out. Glue-lamination is important for producing large size structural elements. Thus, different adhesives like, epoxy resin, polyurethane and phenol-based resins are tested for suitability of gluing PCM-impregnated wood. This is also a key aspect for supressing leakage on the surface of the structural element by arranging there a thin layer of not impregnated wood. Other investigations are related to the experimental determination of the mechanical behaviour of PCM-impregnated wood and the combustion behaviour.

KEYWORDS: phase change materials, glue lamination, mechanical properties, combustion behaviour, reaction to fire

1 INTRODUCTION

The use of fossil energy for thermal conditioning of buildings contributes significantly to the global warming by CO_2 emissions. There are several techniques established to reduce the energy consumption of a building for thermal conditioning like thermal insulation, shading, orientation of the building or positioning of the windows etc.

An aspect, which is often not specifically designed is thermal mass or heat capacity, although it is well known that wood buildings have especially in the summer drawbacks compared to heavy buildings made, e.g., of concrete or brick due to low thermal mass. This often results in the necessity of active air-conditioning.

Heat capacity is defined as the product of mass by specific heat capacity of the material. Thus, in order to increase the heat capacity of a building either the amount of material can be increased or a material with higher specific heat capacity can be used. With regard to limited resources, increasing mass just for the purpose of improving thermal conditions seems not to be desirable as it increases the CO_2 footprint and is usually also associated with decreasing usable space or increasing the volume of the building. On the other hand, modifying the specific thermal mass of a material is not easily possible.

However, wood has a cellular structure, which can be used for impregnation to increase the mass and depending on the specific heat capacity of the impregnation materials also the heat capacity of the building element. A special class of materials, so-called phase change materials (PCM), possess a very high specific heat capacity in a narrow temperature range and might be good candidates for impregnation of wood. Especially paraffinic PCM seem to be suitable as they are inert and do not react with the chemicals of the wood. Thus, a long endurance of the PCM is expected. Literature reviews on the impregnation of wood with PCM are given in [1],[2].

By applying PCM, a low amount of additional mass leads to a high increase of heat capacity of a timber element. Previous investigations [1],[3] showed that it is realistic to deposit about 200 kg of PCM per m³ of wood. Thus, depending on the applied wood species the mass is increased by about 30 to 50 %. At the same time, the storable thermal energy is increased in the phase transition range of the PCM by 400 to 600 % (assuming a sensible enthalpy of wood of about 20 J/g and a latent enthalpy of PCM of about 200 J/g in the range of +/- 5°C around the phase transition temperature). By placing PCM in wood elements, temperature amplitudes are passively reduced inside a room over the day by energy uptake of the PCM. By natural ventilation, the room temperature can be decreased over the night below the phase change temperature of the PCM and the stored thermal energy is released.

Most of the previous investigations from literature concentrate on the application of PCM-impregnated wood for interior elements without structural functions like

[1] Jens U. Hartig, Technische Universität Dresden, Germany, jens.hartig@tu-dresden.de
[2] Peer Haller, Technische Universität Dresden, Germany, peer.haller@tu-dresden.de

https://doi.org/10.52202/069179-0085

flooring [10], etc. In the current investigations, elements like beams, walls or ceilings, bearing structural loads are intended. For practical applications, several aspects need to be investigated. A selection will be addressed in this contribution and is briefly summarized in the following.

2 MATERIAL AND METHODS

2.1 IMPREGNATION OF TIMBER

Results on the impregnation of solid wood were already presented in [1]. Pressure impregnation processes in an autoclave with a maximum pressure of 0.8 MPa were carried out. In this contribution, an update is given. The used PCM is the commercially available paraffin-based PCM RT35HC produced by the company Rubitherm, Germany. Four wood species (spruce, beech, poplar and oak) were applied for the investigations. The effectiveness of the impregnation is described by the PCM uptake, which is the mass of PCM within a certain volume of wood.

2.2 LEAKAGE AND ITS SUPPRESSION

Significant leakage was observed for some wood species, which can be substantially suppressed with increasing the viscosity of the PCM [1]. As a new development, the addition of mineral particles (cement Mikrodur R-X by the company Dyckerhoff, Germany) was tested to reduce leakage with promising results. However, for improving serviceability of timber elements, leakage on the surface needs to be securely suppressed. Therefore, a not impregnated timber layer on the surface is applied, which is able to seal the surface.

2.3 HEAT CAPACITY

The specific heat capacity of the impregnated wood is measured with dynamic differential scanning calorimetry (DSC) using a device Netzsch DSC 204 F1 Phoenix. For calibration, the sapphire standard was used. By integration of the specific heat capacity over a temperature range, the enthalpy can be determined, which is a measure for the storable heat of the material in the temperature range. A detailed description of the test procedure is given in [1].

2.4 MECHANICAL BEHAVIOUR

For structural purposes, the mechanical behaviour of the impregnated timber is important. As the PCM might be available in the solid and the liquid state, the mechanical behaviour is determined for both states. As a first indicator of structural performance, three point bending tests (span 420 mm) were carried out according to DIN 52186 [4]. The dimensions of the samples were 450 mm by 20 mm by 25 mm (length by width by height). Both, clear and impregnated samples of beech, spruce and poplar were tested. The impregnated samples of beech and spruce had a PCM uptake of about 200 kg/m³. Poplar had with about 250 kg/m³ a higher PCM uptake. The tests were performed at room temperature with the PCM either in the solid state or after a conditioning of the respective samples at 50°C (60% r. h.) in the liquid state. For each parametric combination 10 samples, thus, in total 120 samples, were tested.

2.5 GLUE-LAMINATION

For producing large size structural elements of timber, glue-lamination is important. Moreover, smaller dimensions of timber pieces support impregnation and reduce the treatment time. As gluing of paraffin impregnated wood is not standardised, investigations are performed to determine effective lamination techniques. Besides the option of producing large timber elements, a high-quality glue-line also supports the sealing of the impregnated timber parts and the suppression of leakage as pointed out previously.

In order to produce engineered timber elements, the gluability of PCM-impregnated wood was investigated. As a first indicator, the shear strength of the glue line was tested corresponding to EN 205 [5], which is a lap joint tension shear test, with different commercial adhesives: an epoxy resin (Vosschemie Epoxy-BK), a phenol resol resin (Bakelite PF 0283 HL) and a one-component polyurethane adhesive (Collano Semparoc I 12 NV). Impregnated and not impregnated reference samples of beech, spruce, poplar and oak were tested. Each four impregnated and two reference samples were tested. The tests were performed at room temperature, when the PCM was in its solid state. The small sized specimens had a glued area of 10 by 20 mm² (length by width).

2.6 COMBUSTION BEHAVIOUR

The combustion behaviour of materials can be tested with a so-called cone calorimeter according to ISO 5660-1 [6]. In this test, a quadratic board shaped sample is heated at the top side. The sample is wrapped with aluminium foil to avoid the loss of leached PCM during the test, while the top side remains open. Afterwards, the sample is placed on the sample holder, which is attached to a weighing cell continuously measuring the mass of the sample during the test. Above the sample an electrical radiant heater is placed, which heats the sample continuously with 50 kW/m².

For the ignition, a spark plug is additionally placed on top of the sample. It is removed as soon as the samples starts burning. The time for ignition t_{ig} is documented for later evaluation. After ignition, the radiant heater is heating the sample for 30 minutes. Besides the continuous measuring of the weight of the sample, the oxygen content of the air, which is collected via the conical head above the sample, is determined. Based on the oxygen content of the air, the heat release by the sample is calculated. Moreover, the smoke production is determined with a photocell.

Each two samples were prepared for the wood species beech, spruce, poplar and oak, which were either impregnated with clear PCM or a PCM-cement mixture. As a reference, also clear wood samples were tested. The samples had dimensions of 100 mm by 100 mm by 30 mm (length by width by thickness). While the longitudinal material orientation was parallel to the length

https://doi.org/10.52202/069179-0085

direction, there was no special alignment of radial and tangential direction.

The PCM uptake of the samples was different depending on the wood species: the beech samples possessed an uptake of about 130-180 kg/m³, the spruce samples of about 140-180 kg/m³, the poplar samples of about 260-280 kg/m³ and the oak samples of 120-150 kg/m³. The samples were conditioned before the testing at 23°C and 50 % relative humidity.

In a second test, the combustion behaviour of a construction element was tested in a setup according to EN ISO 9239-1 [7]. The element was a three-layer wood flooring with a PCM-impregnated middle layer of 8 mm thickness. The PCM uptake was about 200 kg of PCM per m³ of wood. The PCM contained cement particles. The top layer as well as the counteracting lower layer were not impregnated and had a thickness of 3 mm and 2 mm, respectively. The middle layer and the lower layer were made of spruce. The top layer, which was coated with a commercial lacquer, was made of oak. As a reference, elements without PCM were tested. The reference elements are commercially available.

The specimens had a length of 1050 mm and a width of 230 mm. Since the flooring elements are connected mechanically in practice, these joints have to be considered also in the tests. Thus, for the PCM-impregnated and the reference elements one test with a connection in longitudinal direction and one test with joints in transverse direction were performed. During the tests, the samples were placed on a fibre cement board of 8 mm thickness.

The detailed testing procedure is given in EN ISO 9239-1 [7]. Essentially, the sample is heated for the first 10 minutes with a gas burner at one end of the sample over the entire width. After 10 minutes, the burner is turned off. The flame propagation is observed for another 20 minutes. The flame propagation at the sample is recorded over the entire testing time (1800 s).

Moreover, the smoke development is recorded. For achieving a certain fire class according to EN 13501-1 [8], a certain limit of the critical heat flux *CHF* as well as the smoke density integral $\int R$ needs to be complied. The limits for the fire classes according to EN 13501-1 [8] are summarized in Table 1.

Table 1: *Limits for fire classes according to EN 13501-1*

	Fire class			
	B_{fl}	C_{fl}	D_{fl}	E_{fl}
CHF [kW/m²]	≥ 8.0	≥ 4.5	≥ 3.0	Test acc. to EN ISO 11925-2 [9] necessary
	Smoke development			
	s_1	s_2		
$\int R$ [min·%]	≤ 750	> 750		s1, s2 only for B_{fl}, C_{fl}, D_{fl},

3 RESULTS AND DISCUSSION

3.1 IMPREGNATION AND LEAKAGE

Investigations on the impregnation of wood with PCM RT35HC and leakage of PCM out of the wood were already presented in [1],[3]. Thus, these results are only summarised here briefly. It was shown that a high PCM uptake of up to 400 kg of PCM per m³ of wood, which is close to the theoretical maximum corresponding to the available lumen, could be achieved for poplar with pressure processes. For beech, the achieved uptake is with about 250 kg of PCM per m³ of wood less, which is associated with the smaller lumen. The impregnation of beech can be carried out, in principle, by soaking. Pressure processes only decrease the necessary treatment time. Although the impregnability of spruce is worse, a PCM uptake of about 200 kg of PCM per m³ of wood was achieved with pressure processes. However, there is considerable variation in the results of spruce. Oak is very hard to impregnate and even with the applied pressure of 0.8 MPa only an uptake of about 100 kg of PCM per m³ of wood was achieved. It shall be noted that in the respective investigations, the end grain of the samples was sealed in order to simulate the behaviour for big timber elements in the industry. For smaller elements and with open end grain, higher PCM uptake can be achieved.

The addition of thermoplastic additives for increasing the viscosity and, thus, reducing leakage resulted in reduced PCM uptake. For beech and poplar, still high PCM uptake was achieved. As a new development, cement particles with a diameter of less than 5 µm were added to the PCM for reducing leakage by closing the tips of the wood cells. The achieved PCM uptake is comparable with the values when thermoplastic additives are added. Specific values are given related to the description of the other investigations.

Since the wood has a more or less open porous structure, PCM can leach out of the wood volume, which is undesirable for the practical application. The proneness to leakage depends on the wood species. Poplar shows a maximum leakage of about 10 % of the initial amount of PCM. Leakage depends on the PCM uptake, which means that with lower PCM uptake also less leakage occurs, both absolute and relative. For oak, the observed leakage was less than 10 % and, supposedly, limited to PCM in the outermost cell layers. While leakage can be reduced for both wood species by increasing the viscosity of the PCM or by addition of cement particles, a post-treatment at a temperature above the phase transition temperature allowing excessive PCM to leach is advisable and sufficient.

For spruce and beech, leakage of more than 60 % of the initial volume was observed, especially with high amounts of PCM uptake. The addition of thermoplastic or cement particles can reduce leakage significantly to less than 20 % of the initial amount of PCM in the wood. Thus, a post-treatment for leaching excessive PCM is advisable but additionally a careful sealing is necessary to avoid leakage permanently.

https://doi.org/10.52202/069179-0085

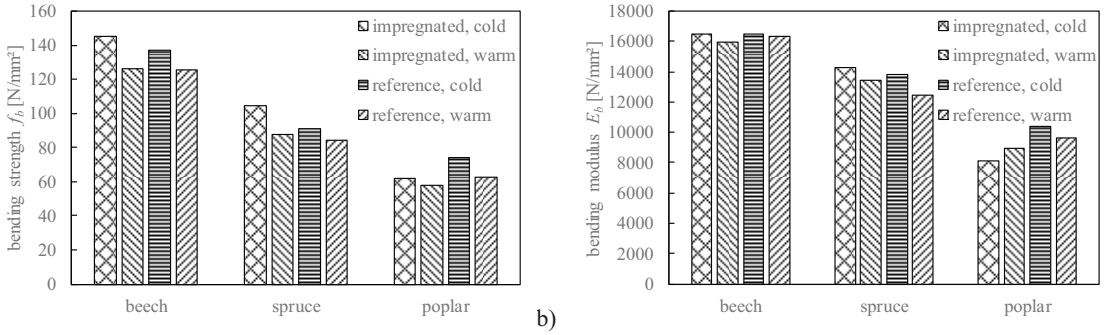

Figure 1: *Results of the bending tests; a) Bending strength, b) Bending modulus*

3.2 HEAT CAPACITY

Results regarding the determination of the heat capacity of the PCM-containing wood were already presented in detail in [1]. Thus, only a summary is given here. The determination of the specific heat capacity of PCM around the phase transition temperature is associated with some challenges due to a dependency on the applied temperature gradient and the amount of the tested material in the DSC. However, the enthalpy, which is the integral of the specific heat capacity over a temperature range, in this case the phase transition range, is independent of the temperature gradient and the amount of material.

Moreover, the enthalpy might be more useful for evaluation of the influence of the PCM on the thermal mass since it gives the total amount of storable heat around the phase transition temperature. In contrast, the specific heat capacity of PCM shows only a peak at the phase transition temperature and has before and after a value in the magnitude of the respective value of wood. Thus, the peak value is not representative for the entire temperature range in service. The results of the investigations presented in [1] show that the phase transition enthalpy of the impregnated wood is proportional to the PCM uptake.

Thus, the enthalpy of fusion or solidification of about 200 J/g of the applied PCM RT35HC and the amount of PCM in the element, i.e. the PCM uptake, can be directly used for estimating the influence on the room temperature e.g. in climatic simulations.

3.3 MECHANICAL BEHAVIOUR

Figure 1 shows the evaluation of the results of the bending tests in terms of bending strength f_b and bending modulus E_b. It can be seen that, as well known, the three wood species have different strength and elasticity values.

Moreover, the known effect of a reduction of f_b and E_b with increasing temperature is observable. In the solid state, the impregnation with PCM results in increasing f_b compared to clear wood for beech and spruce. To lower extent, this is also observable for spruce for E_b. In the liquid state of the PCM, the increase of f_b and E_b vanishes. For poplar, both f_b and E_b were smaller for the impregnated samples than the clear samples. This was also associated with a significantly more brittle failure behaviour.

For the practical application, it can be assumed that at least for the common species for construction purposes spruce and beech, the mechanical properties are not significantly influenced by the impregnation with PCM. This corresponds also to findings in [11]. For poplar, a reduced PCM uptake might result in more favourable mechanical properties and less brittleness.

3.4 COMBUSTION BEHAVIOUR

The combustion behaviour of PCM-containing wood was investigated with two different tests. Figure 2 shows the results of the cone calorimetry for the different wood species and impregnations. It can be seen that the mass of the samples decreases quasi-linearly during the combustion process. Only short before the end of the combustion an increasing mass loss rate is observable. This can be explained by a bending deformation of the samples, which results in a better access of oxygen to the bottom of the sample and an increasing burning surface.

The mass loss rate during the undisturbed combustion before bulging of the sample is approx. the same for the impregnated and the clear reference samples. Except of beech, the mass loss rate is also similar for all the wood species. Nevertheless, it can be seen that the combustion time is longer for the PCM-containing samples due to the higher total mass and has for some samples not ended at the end of the test after 1800 s. The heat release is larger for the PCM-impregnated samples than for the clear reference samples. While the heat release rate *HRR* during undisturbed combustion is except for beech approx. the same for the clear samples of the different wood species, it depends for the impregnated samples on the PCM uptake. Corresponding to the PCM uptake, *HRR* of the PCM-impregnated samples is the lowest for oak and the highest for poplar. There is no significant difference due to the addition of cement observable. The somewhat higher *HRR* for the cement-containing samples of beech can be explained by a higher PCM uptake compared to impregnated samples without cement.

Based on the measured quantities, indicators characterizing the fire ignition hazard and the provided energy for fire propagation can be calculated [12].

https://doi.org/10.52202/069179-0085

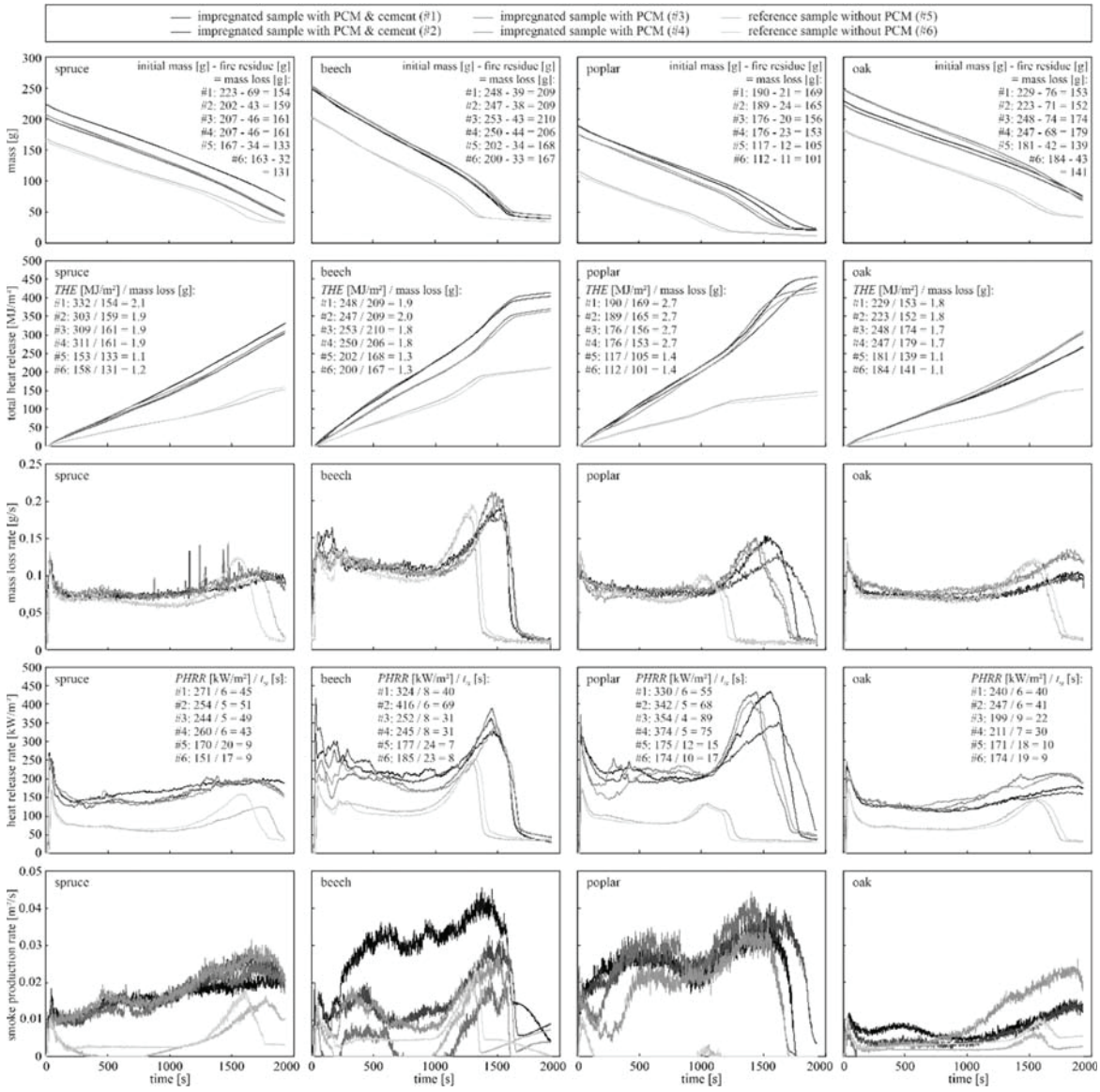

Figure 2: *Results of the cone calorimetry tests*

A first indicator is the ratio of the peak heat release rate *PHRR* and the time to ignition t_{ig}. Both values as well as the ratio are given in Figure 2 in the diagrams of the heat release rate versus time. It can be seen that t_{ig} is substantially smaller for the impregnated samples compared to clear reference samples while the PHRR values are considerably larger. The ratio PHRR / t_{ig} is approx. four to five times larger for the impregnated samples, which means that the PCM acts as fire accelerant.

A second indicator is the ratio of the total heat release at the end of the test *THE* and the mass loss of the sample. This ratio is for the impregnated samples less than twice as large as for the clear reference samples. Thus, for the propagating fire the PCM has a less significant influence than for ignition.

As a conclusion, it can be stated that unprotected PCM-containing wood ignites faster and provides more heat during combustion for fire propagation than clear wood. However, the results of the cone calorimeter tests cannot directly be transferred to real fire events due to a large dependency on length scale [12]. Thus, further tests are necessary.

As described in Section 2.6 also fire tests according to EN ISO 9239-1 [7] on wood flooring containing PCM were performed. Table 2 shows the achieved values of the fire tests with the flooring samples. Besides the *CHF* and $\int R$ values, also the maximum flame spread L_{max} and the

https://doi.org/10.52202/069179-0085

maximum light absorption R_{max} are given. The flame spread propagated in all samples until the end of the test after 1800 s.

Figure 3 shows diagrams of the flame spread vs. time and the characteristic relation for determining *CHF*. From Table 2 and Figure 3, it can be seen that *CHF* of the samples containing PCM has a higher value than the reference samples without PCM. Thus, the flooring containing PCM has with C_{fl} a more favourable fire class than the reference flooring, which achieves only D_{fl}. This probably unexpected result can be explained with the higher heat capacity of the PCM-containing elements, which initially absorb the heat and cool the flamed top layer. This is possible because the PCM is not directly flamed but protected by the not impregnated top layer. Thus, the flash point of the PCM at 177°C is not instantaneously reached like in the tests with the cone calorimeter previously described.

It should be considered that the PCM was in its solid state at the beginning of the test and, thus, a significant additional heat uptake was possible. It remains to be tested, how the behaviour is when the PCM is in its liquid state right from the beginning of the test and, thus, the cooling effect is not existing. It can be assumed that in this case also the PCM-containing elements achieve only fire class D_{fl}.

The second characteristic for the definition of the fire class is the smoke development. As Table 2 shows, the PCM-containing elements behave less favourable with stronger smoke development in terms of $\int R$ and R_{max} compared to the reference samples. Still, the values are considerably below the acceptable values as given in Table 1 for classification s_1, which, thus, both the PCM-containing samples and the reference samples reach.

As a conclusion, it can be stated that a protection of the PCM-containing wood improves the fire behaviour significantly and can compensate the fire accelerating properties of the PCM when directly flamed.

Table 2: *Results of the reaction to fire test according to EN ISO 9239-1 on wood flooring with PCM*

Value	Sample without PCM (long. joint)	Sample without PCM (trans. joints)	Sample with PCM (long. joint)	Sample without PCM (trans. joints)
CHF [kW/m²]	3.98 (D_{fl})	3.71 (D_{fl})	4.58 (C_{fl})	4.67 (C_{fl})
$\int R$ [min·%]	42.1 (s_1)	50.4 (s_1)	175.7 (s_1)	110.7 (s_1)
L_{max} [mm]	480	498	440	434
R_{max} [%]	8.7	11.1	20.7	15.8

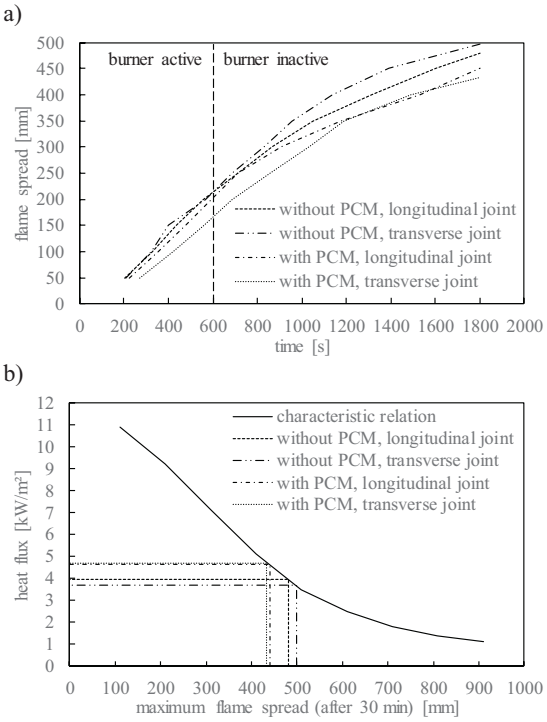

Figure 3: *Results of the fire tests acc. to DIN EN ISO 9239-1 on flooring elements; a) Flame spread vs. time, b) heat flux vs. flame spread (characteristic relation)*

3.5 GLUABILITY

The previously shown results regarding leakage and combustion behaviour indicate that it is advantageous to place the PCM-containing wood not at the surface of the building element. One technique for this purpose is glue lamination.

Figure 4 shows the results of the gluing tests as described in Section 2.5 in terms of the shear strength. It can be seen that the results depend on the wood species and the adhesive. The lowest strength of the glue line was observed for the epoxy resin. Except of beech, the PCM impregnated samples showed higher strength of the glue line compared to the reference samples. This somewhat unexpected behaviour might be explained by the cell lumen filled with PCM preventing a deeper intrusion of the resin, which is associated in the reference case with an insufficient amount of adhesive at the glue line.

The strength of the glue line is larger for the phenol-resol adhesive than for the epoxy resin. However, no clear tendency can be seen whether the performance is impaired by the PCM or not. It depends on the wood species. While for poplar and beech, the strength of the glue line is clearly impaired by the PCM, it is improved for spruce and seems to be not influenced for oak. A similar result can be seen for the PUR adhesive.

Although for poplar and beech the highest values of the reference samples are not achieved for the PCM-impregnated samples, a high-quality glue line can be

https://doi.org/10.52202/069179-0085

produced. The gluability of oak, which has a comparatively low PCM uptake, was not significantly changed by the PCM. For spruce, the PCM resulted in an improved performance of the glue line for the tested adhesives.
Besides these promising results, it shall be noted that tests with the PCM in the liquid state need to be performed. Moreover, long term and cyclic loading tests should be performed for a final evaluation.

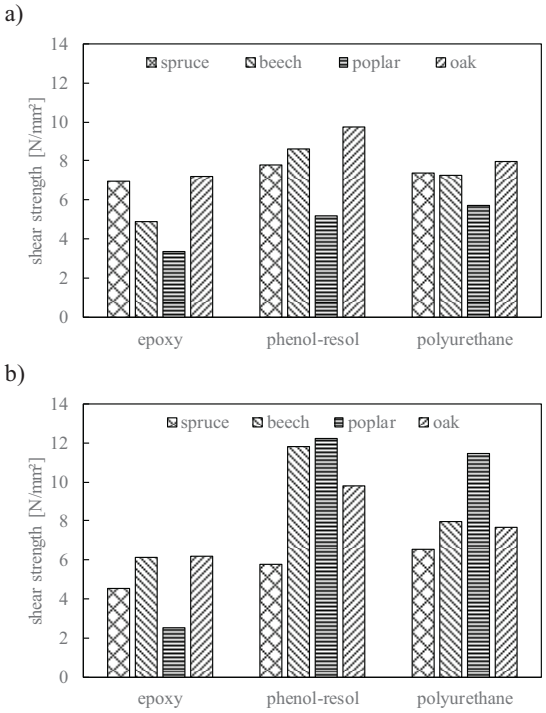

Figure 4: *Results of the gluing tests; a) PCM impregnated samples, b) not impregnated reference samples*

4 SUMMARY AND CONCLUSIONS

In this contribution, different investigations with regard to an application of PCM-containing wood in load-bearing timber elements were presented. A key aspect is the mechanical properties. The results of the bending tests showed that the PCM impregnation does not impair the strength and the modulus for commonly used wood like spruce and beech. In order to produce large sized timber elements from small sized pieces, the gluability is a key aspect. The investigations showed that high-quality glue lines could be achieved for PCM-containing wood. Although further investigations might be necessary, glue lamination is possible for PCM-containing wood. With this regard, using smaller timber pieces also facilitates the impregnation with PCM.
An exemplary glue-laminated timber element is shown in Figure 5. The element takes the aforementioned findings into account. The element consists of a core of clear glue-laminated spruce. The core remains without PCM since the heat penetration over the day is assumed to be limited and the PCM would not be activated at this position. On the side and the bottom faces of the core, PCM-impregnated spruce boards are laminated for locally increased heat capacity. In the case that the side faces are not ventilated in the room, the PCM-containing layer could be also placed only at the bottom face. As top and PCM-free, sealing layer, a thin board, which could be also a veneer, of oak is glue-laminated. Oak is hard to impregnate and serves as a barrier against leakage of the PCM. On the other hand, it has also decorative value. If the latter is not intended or necessary, other wood species, which possess a bad impregnability, like spruce could be used. However, it should be considered that knots and cracks could impair the barrier against leakage.
The PCM-free top layer also improves the fire behaviour. As the respective investigations showed, the direct flaming of the PCM-containing pieces should be prevented. Then, the PCM can even have advantageous properties regarding the fire behaviour by absorbing heat and, thus, cooling the flamed surface of the element, which delay the fire propagation.
The general concept might be applied also to other engineered timber elements like cross-laminated timber.

Figure 5: *Glue-laminated timber element*

ACKNOWLEDGEMENT

The authors gratefully acknowledge the financial support from German Federal Ministry of Food and Agriculture for the FNR research project “PCM-WOOD: Impregnation of wood with phase change materials for latent heat storage in buildings” (grant number 22014318). The authors also thank the project partner ter Hürne GmbH & Co. KG, Südlohn, Germany for collaboration.

https://doi.org/10.52202/069179-0085

REFERENCES

[1] Hartig, J.U., Hilkert, F., Wehsener, J., Haller, P.: Impregnation of wood with a paraffinic phase change material for increasing heat capacity, *Wood Mater. Sci. Eng.*, DOI: 10.1080/17480272.2022.2133630, 2022

[2] Sulaiman, N.S.; Mohamad Amini, M.H.: Review on the Phase Change Materials in Wood for Thermal Regulative Wood-Based Products. *Forests*, 13:1622, 2022.

[3] Hartig J.U., Hilkert F., Wehsener J., Haller P.: Potential of reducing energy consumption in timber buildings by impregnation of wood with phase-change materials. In *World Conference on Timber Engineering 2021*, paper WPC0319, 2021

[4] DIN 52186: Testing of wood; bending test, 1978.

[5] EN 205: Adhesives - Wood adhesives for non-structural applications - Determination of tensile shear strength of lap joints, 2016.

[6] ISO 5660-1: Reaction-to-fire tests - Heat release, smoke production and mass loss rate - Part 1: Heat release rate (cone calorimeter method) and smoke production rate (dynamic measurement), 2015.

[7] EN ISO 9239-1: Reaction to fire tests for floorings - Part 1: Determination of the burning behaviour using a radiant heat source, 2010.

[8] EN 13501-1: Fire classification of construction products and building elements – Part 1: Classification using data from reaction to fire tests, 2018.

[9] EN ISO 11925-2: Reaction to fire tests - Ignitability of products subjected to direct impingement of flame - Part 2: Single-flame source test, 2020.

[10] Mathis D., Blanchet P., Landry V., Lagière P.: Impregnation of Wood with Microencapsulated Bio-Based Phase Change Materials for High Thermal Mass Engineered Wood Flooring. *Appl. Sci.* 8:2696, 2018

[11] Saavedra, H., Garcia-Herrera, C., Vasco, D., Salinas-Lira, C.: Characterization of mechanical performance of Pinus radiata wood impregnated with octadecane as phase change material. *J. Build. Eng.*, 34:101913, 2021.

[12] Schartel, B., Hull, T.R.: Development of fire-retarded materials – Interpretation of cone calorimeter data. *Fire Mater.*, 31: 327-354, 2007.

World Conference on Timber Engineering Oslo 2023

ADDITIVE MANUFACTURING OF WOOD COMPOSITE PARTS BY INDIVIDUAL LAYER FABRICATION-THE PRODUCTION PROCESS AND RESPECTIVE MACHINERY

Birger Buschmann[1], Daniel Talke[2], Klaudius Henke[3], Carsten Asshoff[4], Frauke Bunzel[5], Bettina Saile[6],

ABSTRACT: Additive manufacturing processes that are using wood particles as feedstock material either require large amounts of binder or have relatively poor mechanical properties. This paper details the novel Individual Layer Fabrication (ILF) process and the respective machinery which allow for the additive manufacturing of objects with a low binder content and high strength values. With flexural properties exceeding those of conventional particle boards, an application of objects produced via ILF in the construction industry is possible.

KEYWORDS: additive manufacturing, 3D-printing, binder jetting, sheet lamination, wood composites, wood adhesive processing

1 INTRODUCTION

1.1 CHALLENGES IN THE CONSTRUCTION INDUSTRY

The construction industry is currently facing a multitude of challenges. A deficit in skilled labor inhibits growth and delays or even prevents building projects and the demographic change will most likely worsen this issue in the coming years [1]. Digitalization and automation could offer a solution to this problem, where robots or other machinery fill gaps in the work force, especially for labor intensive and hazardous tasks [2]. A further challenge for the construction industry is to reduce its high environmental impact. According to the 2020 Global Status Report for Buildings and Construction [3] the construction industry as a whole is responsible for around 38 % of the global CO_2-emissions. The report recommends using digital solutions, like automated prefabrication or additive manufacturing (AM - colloquially called "3D-printing") to minimize waste and improve logistics during building construction. Another benefit of digital methods is the possibility to optimize buildings concerning their energy demand during use, which is an even larger contribution to emissions than the construction itself [3]. Employing additive manufacturing processes in the construction industry offers a multitude of opportunities such as improving workplace conditions, reducing construction time and minimizing waste material [4].

Another way of reducing the environmental impact of the construction industry is the usage of wood and other bio-based materials. These can serve as carbon sinks and thus offset CO_2-emissions that were created during construction [3, 5]. However, an increased usage of wood as building material also leads to an increased amount of logging, which can damage and even destroy whole ecosystems [6]. At the same time the waste from the wood industry (during harvest, during processing and at the end of life) is increasing continuously [7]. Hence, using this waste is essential to employ the full sustainability potential of the wood industry. If this is then coupled with additive manufacturing processes, the overall construction industry gains a powerful tool to become more environmentally friendly.

1.2 ADDITIVE MANUFACTURING OF WOOD COMPOSITES

While for example the AM process of concrete extrusion is on its way to commercial success [8], large scale processes that use wood as feedstock material have not yet moved past the experimental or laboratory status [9].

Using wood particles incorporated into a thermoplastic matrix in the fused filament fabrication process for small-scale objects is well established. Here the mixture is

[1] Birger Buschmann, Technical University of Munich TUM, Chair of Timber Structure and Building Construction, Germany, birger.buschmann@tum.de
[2] Daniel Talke, Technical University of Munich TUM, Chair of Timber Structure and Building Construction, Germany, talke@tum.de
[3] Klaudius Henke, Technical University of Munich TUM, Chair of Timber Structure and Building Construction, Germany, henke@tum.de
[4] Carsten Asshoff, Fraunhofer Institute for Wood Research, Wilhelm-Klauditz-Institut WKI, Germany, carsten.asshoff@wki.fraunhofer.de
[5] Frauke Bunzel, Fraunhofer Institute for Wood Research, Wilhelm-Klauditz-Institut WKI, Germany, frauke.bunzel@wki.fraunhofer.de
[6] Bettina Saile, Technical University of Munich TUM, Chair of Timber Structure and Building Construction, Germany

https://doi.org/10.52202/069179-0086

molten and then extruded in strands on top of each other thereby creating objects layer by layer. The respective material is commercially available for example from [10]. Also, a large number of projects have investigated the properties of wood particles mixed into various polymeric materials like PLA [11] or ABS [12]. However, comparatively few projects used this method to build large-scale objects. Gardner et al. [13], for example, used PLA and 20 wt% of wood particles to create a boat roof tooling mould. A Finnish Company, UPM, 3d-printed a small pedestrian bridge using an undisclosed thermoplastic material with 20 wt% wood particles [14]. In the United States, in a collaboration between the University of Maine and the Oak Ridge National Laboratory, researchers printed a fully bio-based house out of an also undisclosed polymer containing wood particles [15]. The disadvantage of mixing wood particles into a polymer matrix for the fused filament fabrication process is that higher contents of wood particles (above 40 wt%) drastically reduce the mechanical properties of the composite [16]. Hence, wood is limited to the role of filler material with this process.

Significantly higher contents of wood can be achieved with the so-called liquid deposition modeling process. As in concrete extrusion, a paste of wood particles, binder and water is extruded in strands. Here, a wood content of up to 89 wt% is possible [17]. Various binders were investigated so far, ranging from synthetic urea formaldehyde binders [18] to fully biodegradable mycelia [19]. As the paste liquefier water evaporates during hardening, significant shrinkage makes the process challenging to control [20] and only comparatively low mechanical strength values are achieved [18, 20].

Kromoser et al. [21] propose a different extrusion process to create degradable “3DP Biowalls”. A mixture of wood particles, starch and lignosulfonate is extruded in a strand, activated by water and then pressed under heightened temperature to create a rigid wall, layer by layer.

Already in 2012 Henke & Treml [22] investigated the possibility to additively create objects through selective binding of wood particles with mineral and biodegradable binders for the use in construction. The binder (cement, gypsum or starch) was dry mixed with wood particles and spread thinly over a vertically movable build plate. Then one layer of the object was created by locally applying water to activate the binder. This spreading and selective activation was repeated until the desired object was finished (see Figure 1: Truncated cone generated by 3D printing with chips of spruce and gypsum as binder (Credit: [22])Figure 1).

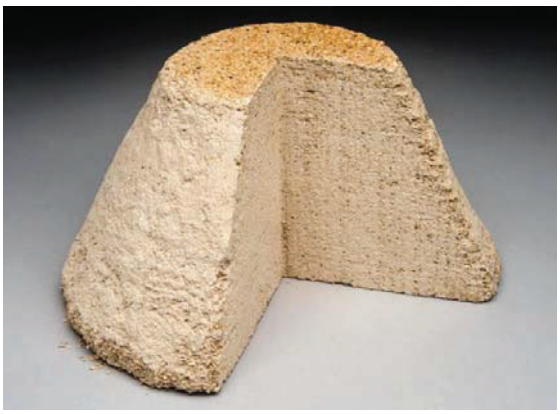

Figure 1: *Truncated cone generated by 3D printing with chips of spruce and gypsum as binder (Credit: [22])*

2 THE ILF PROCESS

2.1 GENERAL PRINCIPLE

The approach of the project presented in the following differs from the previously described ones. The main goal is to develop a process to additively manufacture large-scale, wood composite objects with a high content of wood material and strength values suited for applications in construction. This is accomplished by additively manufacturing thin, individually contoured panels that are stacked and laminated onto one another, thus forming the desired object. [23]

In the course of the project multiple process variants are explored and the necessary machinery is developed in iterative steps. Evaluation of these variants is done by investigating the mechanical properties of the resulting objects as well as the geometric capacity of the processes. Additionally, multiple demonstrators are fabricated for showcase purposes (see Figure 2).

Figure 2: *An Enneper minimal surface demonstrator made via the ILF process.*

The general principle of the ILF process, depicted in Figure 3, can be divided into the following steps. A thin layer of wood particles is scattered (a) and bound by selectively dispensing adhesive according to the target geometry of the object (b). After dispensing the adhesive, the wood particle layer is pressed under heat, curing the adhesive (c). By pressing the amount of required adhesive is drastically reduced while, at the same time, the mechanical properties of the wood composite are increased. Finally, the unbound material is removed and the contoured panel of bound material is laminated onto the stack of previously produced panels (d). [24]

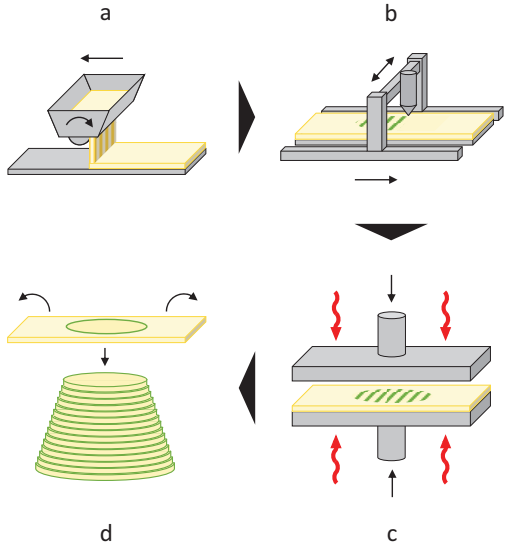

Figure 3: *The basic principle of the ILF process (Credit: [24])*

2.2 MACHINERY

Each step of the ILF process requires specialized machinery. It is either developed or acquired and modified if necessary. In the course of the overall project, multiple process variants and machines are tested and evaluated. The currently used process variant and machinery, with which the object in Figure 2 was created, will be presented in the following chapter.

Initially, a layer of wood particles is scattered on a horizontal moving transportation plate with a size of 500 mm by 500 mm. This is accomplished identically as described in [24], where the particles are picked up out of a material hopper by the needles (length: 10 mm) of a scatter roller. A brush roller (bristle length: 25 mm) rotating faster than the scatter roller brushes out the particles from the needles onto the moving plate below (see Figure 4).

Figure 4: *The particle scattering station*

The plate with the scattered particles then moves to the adhesive dispensing station, displayed in Figure 5, where the pattern of one slice of the final desired object is applied. This is done line by line similar to [24], where one line of adhesive consisted of multiple droplets. However, now the adhesive is not dispensed dropwise but in a continuous stream, thereby drastically increasing the life expectancy of the valve. An increase of temperature, and thus a significantly decrease in adhesive viscosity, allows for this method.

https://doi.org/10.52202/069179-0086

Figure 5: *The adhesive dispensing station*

After dispensing of the pattern, a second layer of wood particles is scattered onto the plate, forming a sandwich structure with the adhesive between two particle layers. This sandwich structure is then pressed under heat (up to 40 bar and 200°C), distributing and solidifying the adhesive and creating a panel with bound and unbound wood particles. The two scattered layers of particles are always of such a thickness that no adhesive can intrude them down- or upwards and preventing the panel from sticking to the press plates. The panel production is done fully automatic by the Panel Printer displayed in Figure 6.

Figure 6: *Panel Printer consisting of the scattering station in the middle, the dispensing station in the front with the transportation plate and the heat press in the back.*

In the following process steps, the unbound particles are removed and the individually contoured panels are laminated onto one another to form the final object. First automated methods and prototypes have been developed for these tasks. However, as these prototypes are not yet reliable, especially for more complex geometries, manual labor is still involved. All demonstrators displayed in this paper were cleaned and laminated by hand. However, all test specimens were processed with the automated machines to ensure reproducible results.

3 MATERIAL TESTS

3.1 MATERIAL PROPERTIES OF INDIVIDUAL PANELS

Already in [24] multiple flexural test specimens were fabricated from the processes intermediate product, the panels, and investigated according to DIN EN 310: 1993-08 [25]. In doing so, a comparison to conventionally fabricated particle boards is possible. As wood particles spruce particles produced by Fraunhofer WKI with a sieve retention mesh size between 0.6 mm and 1.25 mm were used. As adhesive a polymeric methylene diphenyl diisocyanate (pMDI) called I-BOND PB PM 4350 from Huntsman LLC was used. The results are displayed in Figure 7 where the modulus of rupture (MOR) is displayed in megapascal (MPa) and the modulus of elasticity (MOE) is displayed in gigapascal (GPa). Through an alteration of processing parameters, the adhesive content and connected with that the density of the specimens was varied.

The specimens had an average flexural strength of 25.95 to 52.45 MPa and an average stiffness of 3.04 to 5.34 GPa. With these values they all fulfill and largely surpass the flexural requirements of particle boards according to DIN EN 312: 2010-12 [26]. Similarly, also the investigation of tensile properties showed strength and stiffness values exceeding those of conventional particle boards.

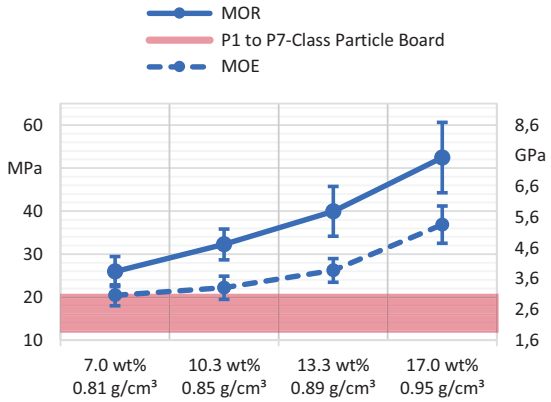

Figure 7: *Flexural properties of individual panels. MOR (left) and MOE (right) as a result of adhesive content (upper) and density (lower). The red area contains bending requirements for P1 to P7 particle boards.*

3.2 PROCESS PARAMETER STUDY

Further investigations regarding the influence of process parameters on flexural strength (MOR in MPa) and density (in g/cm³) of the panels were done. As these flexural test specimens were directly printed and not cut or milled, they deviated from the geometry required according to DIN EN 310: 2010-12. On average they had a thickness of 3 mm, a width of 55 mm and a length of 160 mm. Furthermore, they were stored at room temperature and humidity and not at a precisely defined climate. Because of this the values displayed in Figures 8

https://doi.org/10.52202/069179-0086

to 10 cannot be seen as absolute but rather their change is important. All test specimens were produced in the same way with the parameters displayed in Table 1 kept constant, except for the one that was varied. The results of varying the adhesive content is displayed in Figure 8, the result of varying the pressing force in Figure 9 and the results of varying the pressing duration in Figure 10. Cubic wood particles with the name of Lignocel 9 from J. Rettenmaier & Söhne GmbH were used with a moisture content of 7 wt%. These wood particles have an average diameter of 0.8 mm to 1.1 mm. As adhesive the same type of pMDI as in [24] was used.

Table 1: *Constant production parameters for the parameter variation study*

Parameter	Value
Adhesive Content	12.5 wt%
Pressing Force	31.25 bar
Pressing Duration	180 seconds

Generally, the test specimens behaved as expected from conventional engineered wood. An increase in adhesive content and an increase in pressing force increased the density of the panels, which in turn increased the mechanical properties [27].

When comparing the flexural strength values in Figure 7 with the ones in Figure 8, the significantly lower values of the latter become apparent. Partly this is due to the lower density values of the test specimen in Figure 8. However, the factor of particle morphology also has to be taken into consideration. The test specimens of Figure 7 were fabricated with wood particles specifically produced for particle boards with a relatively high length to width ratio [27]. For the specimens in Figure 8 commercially available wood particles for smoking of foods or horse bedding were used. The two kinds of particles are displayed in Figure 11. A high length to width ratio significantly improves the mechanical properties of the final composite.

A comparison of Figure 8 and 9 indicates that while an increase of density certainly increases mechanical properties, the process parameter of pressing force has only a limited influence. An increase of adhesive content, and a consecutive slight increase in density, leads to a significant increase in mechanical properties in Figure 8. Whereas a very large variation of density through pressing force only marginally varies the mechanical properties in Figure 9. These results seem to contradict the findings of [28] where the main factor of increased flexural strength was panel density and not adhesive content.

The graphs of Figure 10 suggest only a minor influence of pressing duration on flexural strength if a certain time has passed. In this case the minimal necessary pressing time for maximal mechanical properties lies between 30 and 60 seconds or 10 and 20 mm/s (at 3 mm thickness). This is in accordance with literature [29] where a pressing duration of 12 seconds per mm thickness of material is given as necessary for full curing of the adhesive.

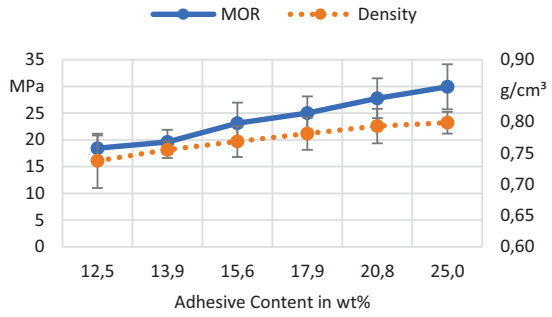

Figure 8: *Flexural modulus of rupture (left) and density (right) as a result of adhesive content variation*

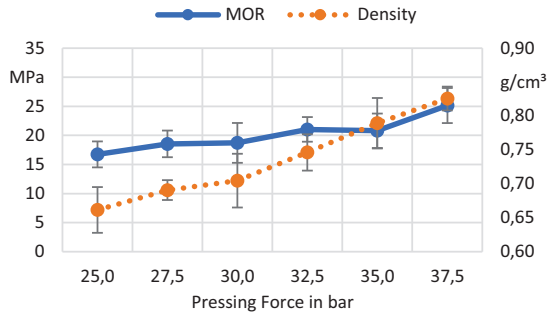

Figure 9: *Flexural modulus of rupture (left) and density (right) as a result of pressing force variation*

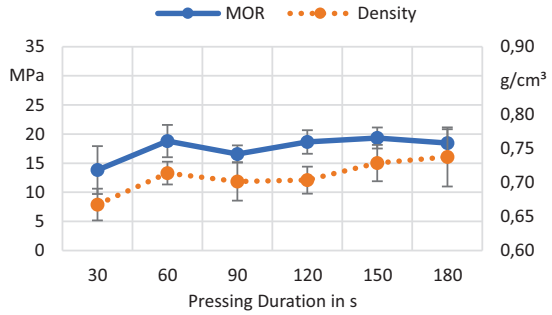

Figure 10: *Flexural modulus of rupture (left) and density (right) as a result of pressing time variation*

Figure 11: *On the left side the wood particles with a high length to width ratio and on the right side the more cubic particles.*

https://doi.org/10.52202/069179-0086

3.3 ANISOTROPIC PROPERTIES OF ILF-OBJECTS

With the same materials as in the parameter study (Lignocel 9 as wood particles and I-BOND PB PM 4350 as adhesive), square panels with the process parameters displayed in Table 2 were fabricated. 50 of these single panels were laminated onto one another with the polyurethane adhesive Jowapur 686.60 from JOWAT Swiss AG. After adhesive application they were pressed. The lamination's adhesive application and pressing parameters are also displayed in Table 2. From the resulting blocks two kinds of flexural test specimen were cut out to the dimensions of 150 mm length, 50 mm width and 10 mm thickness as given in DIN EN 310: 1993-08 [25]. Eight test specimens were cut in a way so that the orientation parallel to the stacked panels could be tested. Another eight were cut in a way so that the orientation perpendicular to the panels could be tested. This made it possible to analyse the anisotropic behaviour of the overall material properties.

Table 2: *Production parameters for anisotropic flexural test specimens*

Parameter	Value
Panel Adhesive Content	8.9 wt%
Panel Pressing Force	31.25 bar
Panel Pressing Duration	180 seconds
Lamination Adhesive Content	9.4 wt%
Lamination Pressing Force	7.50 bar
Lamination Pressing Duration	24 hours

The results of the density and flexural investigation are shown in Table 3 with the average (AVG) values of the eight specimen and the respective standard deviation (SD). Similar to the 25.0 wt% adhesive content specimens from Figure 8, which have a MOR of 29.92 MPa, the parallel oriented specimens, with a total adhesive content of 18.3 wt%, have a MOR of 29.86 MPa. However, as two different materials are compared, such a comparison must be considered with care.

A significant difference in MOR and MOE can be observed between the parallel and perpendicular oriented specimen. The MOR of the parallel oriented specimen is greater than the ones of the perpendicular oriented by a factor of 20. The MOE is greater by a factor of 10. This behaviour is well known from conventional engineered wood materials, where the tensile strength perpendicular to the fibres is only a fraction of the one parallel to the fibres [27]. Also in [28] the transverse tensile strength of the panels was identified to be in the same order of magnitude as the one observed for the perpendicular oriented flexural specimens. In the investigations of single panels some form of arithmetic average of mechanical properties is calculated. Whereas, in a stack of laminated panels only the weakest panel is decisive for the overall mechanical properties.

Table 3: *Results of the anisotropic to panel orientation done flexural and density investigations.*

Parallel oriented	AVG	SD
Density	0.88 g/cm³	0.04 g/cm³
MOR	29.86 MPa	4.73 MPa
MOE	3.31 GPa	0.23 GPa

Perpendicular oriented	AVG	SD
Density	0.88 g/cm³	0.02 g/cm³
MOR	1.44 MPa	0.26 MPa
MOE	0.31 GPa	0.05 GPa

4 APPLICATION

In the course of the overall project multiple demonstrators are fabricated. Next to purely geometric demonstrators, like the Enneper minimal surface in Figure 2 that demonstrate the capabilities of the ILF process, also functional demonstrators are produced. One example is shown in Figure 12. Here a Helmholtz resonator is displayed. A Helmholtz resonator is a bottle like unit made of an airtight material that has a defined cavity. Additionally, the resonator has a neck with an opening that connects the cavity with the surrounding air. This geometry can absorb a certain sound frequency from the surrounding atmosphere. By changing the size of the cavity volume and the length and width of the neck, the sound frequency that is absorbed is changed as well [30]. One possible application for the ILF process is to create wall or ceiling elements that contain a multitude of different sized Helmholtz resonators. With these elements it would be possible to change the sound or filter unwanted acoustic frequencies in e.g. concert halls or lecture rooms.

Another possible application of the ILF-process is to use it as a tool to fabricate optimized parts. This optimization can be in regard to e.g. weight reduction, thermal insulation, fire safety or even combinations thereof. As designs that are created this way are oftentimes geometrically complex their fabrication using conventional methods can become challenging. However, with additive manufacturing methods, like the ILF-process, where the required effort and cost are largely independent of the design's complexity, creating optimized parts is easily feasible. This makes optimization and additive manufacturing an ideal match. Accordingly, optimization tools, like topology or shape optimization, have already been applied to additively manufactured construction elements [31].

Figure 12: *Bottle like Helmholtz resonator (Credit: Korbinian Schwab & Birger Buschmann)*

An example of combining structural optimization with the ILF process is shown in Figure 13. Here, a ceiling element was designed with topology optimization. This was done in such a way that the total volume was reduced by around 75 % in comparison to a massive block. At the same time the original stiffness in regard to an even distributed force from the top was maintained. One corner of this design was selected and printed. The result is shown in Figure 13 (bottom) while the original design can be seen in Figure 13 (top). With conventional fabrication this object would have resulted in a large amount of waste material, whereas with the ILF-process it can be created out of waste material.

5 CONCLUSION

In this paper a new process was presented that enables the additive manufacturing of large-scale wood composite objects. The process was detailed and the respective machinery presented. At more than 80 wt% wood content the objects produced with the process showcased comparatively high mechanical properties at a flexural strength of 29.86 MPa and a stiffness of 3.31 GPa. The overall material properties were identified to be anisotropic in regard to panel orientation with a difference in flexural strength by a factor of 20 and in flexural stiffness by a factor of 10. As relevant production parameters the particle morphology, the adhesive content and the pressing force were identified.
Furthermore, first examples of possible application fields were presented. These include functionalized objects that can e.g. be used for building acoustics or structural elements, designed with the aid of digital optimization tools. Hence, the ILF-process allows for the production of individualized, free-formed structures made primarily of renewable material and with mechanical properties suited for applications in construction.

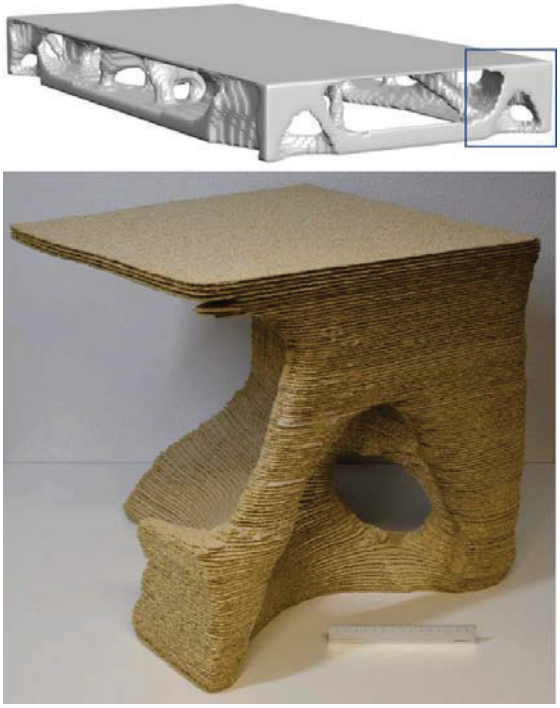

Figure 13: *A topology optimized ceiling element (top) and a corner of the ceiling element produced with the ILF process (bottom). (Credit: Dr. Reza Najian Asl & Birger Buschmann)*

ACKNOWLEDGMENTS

The project is funded by the Deutsche Forschungsgemeinschaft (DFG, German Research Foundation) project number 414265976–TRR 277.
A special thanks to Dr. Reza Najian Asl for supporting us with structurally optimized geometries and Korbinian Schwab for his insightful research.

REFERENCES

[1] M. Müller, *Fachkräfteengpässe im Bauhandwerk beeinträchtigen zunehmend den Wohnungsbau.* [Online]. Available: https://www.kfw.de/PDF/Download-Center/Konzernthemen/Research/PDF-Dokumente-Fokus-Volkswirtschaft/Fokus-2018/Fokus-Nr.-221-August-2018-Fachkraefteengpaesse-im-Bauhandwerk.pdf (accessed: Jan. 7 2022).

[2] Bauen Aktuell, *Automatisierung in der Baubranche: Welches Potenzial Roboter bieten.* [Online]. Available: https://www.bauen-aktuell.eu/automatisierung-in-der-baubranche-welches-potenzial-roboter-bieten/

[3] United Nations Environment Programme, “2020 Global Status Report for Buildings and

https://doi.org/10.52202/069179-0086

Construction: Towards a Zero-emission, Efficient and Resilient Buildings and Construction Sector," Global Alliance for Buildings and Construction, Nairobi, 2020. [Online]. Available: https://globalabc.org/sites/default/files/inline-files/2020%20Buildings%20GSR_FULL%20REPORT.pdf

[4] M. A. Hossain, A. Zhumabekova, S. C. Paul, and J. R. Kim, "A Review of 3D Printing in Construction and its Impact on the Labor Market," *Sustainability*, vol. 12, no. 20, p. 8492, 2020, doi: 10.3390/su12208492.

[5] G. Churkina *et al.,* "Buildings as a global carbon sink," *Nat Sustain*, vol. 3, no. 4, pp. 269–276, 2020, doi: 10.1038/s41893-019-0462-4.

[6] M. Beck-O'Brien, V. Egenolf, S. Winter, J. Zahnen, and N. Griesshammer, *Everything from Wood: The Resource of the Future or the Next Crisis?* How footprints, benchmarks and targets can support a balanced bioeconomy transition. [Online]. Available: https://www.wwf.de/fileadmin/fm-wwf/Publikationen-PDF/Wald/WWF-Study-Everything-from-wood.pdf (accessed: Feb. 2 2023).

[7] Zimmer, A., T., K. Weitz, A. Padhye, S. Sifleet, and Gabriele, H., S., "Wood Waste Inventory: Final Report," United States Environmental Protection Agency, Cincinnati, USA, Jul. 2018. Accessed: Jan. 9 2022. [Online]. Available: https://cfpub.epa.gov/si/si_public_file_download.cfm?p_download_id=537332&Lab=NRMRL

[8] G. Ma, R. Buswell, W. R. Da Leal Silva, L. Wang, J. Xu, and S. Z. Jones, "Technology readiness: A global snapshot of 3D concrete printing and the frontiers for development," *Cement and Concrete Research*, vol. 156, p. 106774, 2022, doi: 10.1016/j.cemconres.2022.106774.

[9] K. Henke, D. Talke, and B. Buschmann, "Use of Wood in Additive Manufacturing in Construction," in *Proceedings of the 17th Rapid.Tech 3D Conference Erfurt, Germany, 22 -23 June 2021*, M. Kynast, Ed., München: Hanser, Carl, 2021, pp. 177–187.

[10] Stora Enso, *DuraSense® for 3D printing.* [Online]. Available: https://www.storaenso.com/en/products/granules/3dprinting (accessed: May 21 2021).

[11] N. Knez, M. Karič, F. Knez, N. Ayrilmis, and M. Kitek Kuzman, "Effects of Selected Printing Parameters on the Fire Properties of 3D-Printed Neat Polylactic Acid (PLA) and Wood/PLA Composites," *Journal of Renewable Materials*, vol. 9, no. 11, pp. 1883–1895, 2021, doi: 10.32604/jrm.2021.016128.

[12] Y. Huang, S. Löschke, and G. Proust, "In the mix: The effect of wood composition on the 3D printability and mechanical performance of wood-plastic composites," *Composites Part C: Open Access*, vol. 5, p. 100140, 2021, doi: 10.1016/j.jcomc.2021.100140.

[13] D. J. Gardner, J. Anderson, H. L. Tekinalp, S. Ozcan, and P. Sauerbier, "Lignocellulosic-filled polymer feedstocks for large scale additive manufacturing of low cost composites," in *Proceedings of the Internaional Forest Products Congress, Trabzon, Turkey, 2018*, pp. 12–22.

[14] S. Peltola, *Steps on a 3D-printed bridge.* [Online]. Available: https://www.upm.com/news-and-stories/articles/2018/10/steps-on-a-3d-printed-bridge/ (accessed: Jan. 30 2022).

[15] T. Ward, *First 100% bio-based 3D-printed home unveiled at the University of Maine.* [Online]. Available: https://umaine.edu/news/blog/2022/11/21/first-100-bio-based-3d-printed-home-unveiled-at-the-university-of-maine/ (accessed: Jan. 20 2023).

[16] M. Karič, M. Sernek, M. Obućina, and M. K. Kuzman, "Effect of wood content in FDM filament on properties of 3D printed parts," *Materials Today Communications*, vol. 14, pp. 135–140, 2018, doi: 10.1016/j.mtcomm.2017.12.016.

[17] M. Rosenthal, C. Henneberger, A. Gutkes, and C.-T. Bues, "Liquid Deposition Modeling: a promising approach for 3D printing of wood," *Eur. J. Wood Prod.*, vol. 76, no. 2, pp. 797–799, 2018, doi: 10.1007/s00107-017-1274-8.

[18] M. Karič, M. Sernek, and M. K. Kuzman, "Use of wood powder and adhesive as a mixture for 3D printing," *Eur. J. Wood Prod.*, vol. 74, no. 1, pp. 123–126, 2016, doi: 10.1007/s00107-015-0987-9.

[19] E. Soh, Z. Y. Chew, N. Saeidi, A. Javadian, D. Hebel, and H. Le Ferrand, "Development of an extrudable paste to build mycelium-bound composites," *Materials & Design*, vol. 195, p. 109058, 2020, doi: 10.1016/j.matdes.2020.109058.

[20] M. Rosenthal, M. Rüggeberg, C. Gerber, L. Beyrich, and J. Faludi, "Physical properties of wood-based materials for liquid deposition modeling," *RPJ*, 2022, doi: 10.1108/RPJ-09-2022-0322.

[21] B. Kromoser, S. Reichenbach, R. Hellmayr, R. Myna, and R. Wimmer, "Circular economy in wood construction – Additive manufacturing of fully recyclable walls made from renewables: Proof of concept and preliminary data," *Construction and Building Materials*, vol. 344, p. 128219, 2022, doi: 10.1016/j.conbuildmat.2022.128219.

[22] K. Henke and S. Treml, "Wood based bulk material in 3D printing processes for applications in construction," *Eur. J. Wood Prod.*, vol. 71, no. 1, pp. 139–141, 2012, doi: 10.1007/s00107-012-0658-z.

[23] K. Henke, D. Talke, F. Bunzel, B. Buschmann, and C. Asshoff, "Individual layer fabrication (ILF): a novel approach to additive manufacturing by the use of wood," *Eur. J. Wood Prod.*, 2021, doi: 10.1007/s00107-020-01646-2.

[24] B. Buschmann, K. Henke, D. Talke, B. Saile, C. Asshoff, and F. Bunzel, "Additive Manufacturing

of Wood Composite Panels for Individual Layer Fabrication (ILF)," *Polymers*, vol. 13, no. 19, 2021, doi: 10.3390/polym13193423.
[25] *DIN EN 310:1993-08, Holzwerkstoffe; Bestimmung des Biege-Elastizitätsmoduls und der Biegefestigkeit; Deutsche Fassung EN_310:1993*, Berlin.
[26] *DIN EN 312:2010-12, Spanplatten_- Anforderungen; Deutsche Fassung EN_312:2010*, Berlin.
[27] P. Niemz and W. U. Sonderegger, *Holzphysik: Physik des Holzes und der Holzwerkstoffe : mit zahlreichen Bildern und Tabellen*. München: Fachbuchverlag Leipzig im Carl Hanser Verlag, 2017. Accessed: Aug. 22 2021.
[28] C. Asshoff, F. Bunzel, B. Buschmann, D. Talke, B. Saile, and K. Henke, "Individual Layer Fabrication (ILF) - Additive Fertigung durch selectives Binden von Holzspänen zu Einzelschichten," *Holztechnologie*, vol. 62, no. 4, pp. 5–13, 2021.
[29] M. Dunky and P. Niemz, *Holzwerkstoffe und Leime*. Berlin, Heidelberg: Springer Berlin Heidelberg, 2002.
[30] A. I. Komkin, M. A. Mironov, and A. I. Bykov, "Sound absorption by a Helmholtz resonator," *Acoust. Phys.*, vol. 63, no. 4, pp. 385–392, 2017, doi: 10.1134/S1063771017030071.
[31] G. Vantyghem, W. de Corte, M. Steeman, and V. Boel, "Density-based topology optimization for 3D-printable building structures," *Struct Multidisc Optim*, vol. 60, no. 6, pp. 2391–2403, 2019, doi: 10.1007/s00158-019-02330-7.

https://doi.org/10.52202/069179-0086

ELASTOMECHANICAL PROPERTIES OF GLUED LAMINATED TIMBER MADE OF STRENGTH GRADED OIL PALM LUMBER

Katja Fruehwald-Koenig[1]

ABSTRACT: The wood from oil palm trunks exhibits significant variations in distribution of structural tissue, density and elastomechanical properties across and along the trunk. Its reliable, safe, and economic usage for load-bearing purposes, such as glued laminated timber (GLT), requires a precise definition of its elastomechanical properties through appropriate strength grading procedures. Oil palm lumber is strength graded according to its density using an X-ray technique in which 50 % of the lamellas are ripped, graded, edge glued and therefore density homogenized, and 50 % are cut only according to their geometry. Lamellas are tested in tension parallel to the vascular bundles; combined GLT is produced from strength-graded lamellas and tested in bending parallel and compression parallel and perpendicular to the vascular bundles. The characteristic strength values for C10 and C14 according to EN 338 are achieved. A correlation between density and elastomechanical properties is established. GLT from density-homogenized lamellas achieve higher bending properties than from lamellas with a "natural" density gradient across the width.

KEYWORDS: Oil palm lumber, glue laminated timber, GLT, strength grading, elastomechanical properties

1 INTRODUCTION

Oil palm trees (*Elaeis guineensis* JACQ.) are mainly cultivated in large plantations for palm oil production to be used for food, chemicals, pharmaceuticals and bioenergy. The palms' oil productivity decreases after 20 years of age. Therefore, plantations are renewed after 25 to 30 years. Each year, there is a large supply of oil palm trunks (approximately 200 Mio. m³ per year, of which over 80 % are in SE-Asia) traditionally considered as waste. Recent research, however, has explored the potential commercial uses of oil palm wood [1]. In many cases, the wood can substitute tropical hardwoods, e.g. as panels (blockboards, flash doors multi-layer solid wood panels) and softwoods in construction timber (glued laminated timber, GLT; cross laminated timber, CLT). In the past 35 years, the macro-mechanical properties of oil palm trunk wood have been widely studied. Because of the property gradients within the cross-section and within the height of the trunk [2,3], all investigations on elastomechanical properties of oil palm wood were performed using small, defect-free test specimens (e.g. [4]) and describe strength and stiffness variations over the cross-section and the trunk height and/or depending on the density, the number or the share of vascular bundles. Only a few investigations focus on oil palm wood in construction size. Jumaat et al. [5] tested trussed rafters from oil palm wood, Srivaro [6] and Srivaro et al. [7] tested sandwich panels with oil palm wood core and rubberwood veneer faces in bending, compression and indentation. Srivaro et al. [8] investigated finger-jointed oil palm wood products in bending and compression parallel to the vascular bundles. Srivaro et al. [9] tested cross laminated timber (CLT) in compression, the hygroscopic properties and the rolling shear. Hoffmann [10] dealt with hybrid CLT from bamboo (surface layer) and oil palm wood (core layer) in bending and compression.

The anatomic wood structure of monocotyledonous palms differs from deciduous and coniferous trees. Palms have no secondary thickness growth, due to the absence of a peripheral cambium. Palm wood consists of high density, rather long vascular bundles embedded in soft (low density) parenchymatous ground tissue. Knots, probably the most important grading criteria for common tree species, are not present in palm lumber. Hence, on the macroscopic level, palm wood is in some aspects homogeneous compared to dicotyledonous wood.

Within the context of a research project [11,12], combined GLT from density graded oil palm wood is tested in bending (f_m, E_m) as well as compression parallel ($f_{c,0}$, $E_{c,0}$) and perpendicular ($f_{c,90}$, $E_{c,90}$) to the vascular bundles and glulam lamellas are tested in tension parallel to the vascular bundles ($f_{t,0}$, $E_{t,0}$). Strength, respectively Young's modulus are related to the density and the performance indices for minimum weight design according to Ashby et al. [13] are calculated. The results are compared with those of

[1] Katja Fruehwald-Koenig, Ostwestfalen-Lippe University of Applied Sciences and Arts, Germany, katja.fruehwald@th-owl.de

https://doi.org/10.52202/069179-0087

small, defect-free specimens of oil palm wood [4] and with building components from palm wood and common wood species found in the literature.

2 MATERIAL

2.1 LAMELLAS FROM OIL PALM WOOD

The material is taken from 30-year-old oil palms (*Elaeis guineensis* JACQ.) grown near Kluang/Johor, Malaysia. The denser material from the periphery is cut to 30 mm (fresh) and has a thickness after kiln drying of 27 mm, the lower dense material from the centre is cut into 55 mm (fresh) resp. 50 mm (kiln-dried) boards. The kiln-dried material is shipped to Germany. For the GLT production, 70 boards of 27 mm thickness from 20 different logs and two different trunk heights (1 – 4 m and 4 – 7 m above ground) are taken. The mean length of the boards is 2.8 m and mean width 0.22 m.

Due to the anatomical structure of monocotyledons (rotationally symmetrical around the stem axis), it is assumed that opposite boards have comparable elastomechanical properties. For the pairwise comparison in this investigation, two outer and two inner 27 mm boards placed opposite to each other are selected by visual inspection. Boards with cracks or cell collapse are not used. The edges of the boards are trimmed along the cortex using a table saw. Due to the natural taper of the oil palm trunks (some 0.8 cm per meter trunk length), the boards have different widths at each end (approx. 2–3 cm difference). The rough-cut lamellas are calibrated using a two-side planer with HeliPlan tools from Leitz, Germany, one board of each pair to a thickness of 20 mm, the other to 17 mm. Details on the material preparation are given in Heister and Fruehwald-Koenig [11]. Some of the 17 mm lamellas are used for the tension test parallel to the vascular bundles (Table 1).

2.2 CALCULATION OF LAMELLA STRENGTH CLASS LIMITS

No strength grading standard exists for oil palm wood. Because of the small dimensions of the GLT specimens produced within this investigation, the strength grading of the oil palm lumber is based on the European strength class system for coniferous lumber (C-classes) according to EN 338 [14] and EN 14081-2 [15]. Fruehwald-Koenig and Heister [4] showed that most elastomechanical properties of oil palm wood depend on the density. Therefore, the statistic calculation model of EN 14081-2 attachment B [15] is used in modified form to calculate the density limits for the strength classes. The calculations are based on the relationships between density (indicating property (IP)) and tensile strength ($f_{t,0}$) resp. compression strength ($f_{c,0}$) parallel to the vascular bundles for MOR determined in preliminary investigations on small test specimens, published in Fruehwald-Koenig and Heister [4] and linearized by the natural logarithm. Details on the calculation of lamella strength class limits are described in Heister and Fruehwald-Koenig [11].

For strength class C14, the characteristic tensile strength value parallel to the vascular bundles ($f_{t,0,k}$ = 7.2 MPa) leads to a density limit value of >427 kg/m^3 and the characteristic compression strength ($f_{c,0,k}$ = 16 MPa) to a density range of 363 – 427 kg/m^3. Because of the high share of oil palm wood material with densities below 350 kg/m^3, property values for an assumed strength class C10 are extrapolated with 290 – 335 kg/m^3 for the compression lamellas and 335 – 363 kg/m^3 for the tension lamellas. The density limit value for the shear lamellas is <290 kg/m^3 for both beam setups.

2.3 STRENGTH GRADING OF THE BOARDS

When grading oil palm boards according to their density, the average density of the board must not be assumed because of the density gradient over the trunk's cross-section (which is higher than the gradient along the trunk height) [3]. Figure 1 shows the density profile across the 140 mm width of a board from the outer area of the trunk.

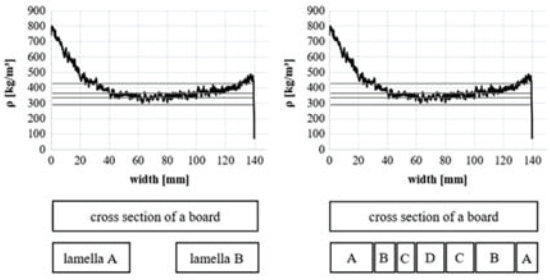

Figure 1: *Density profile of a board from the outer area of an oil palm trunk with a high density gradient over the board width. Cutting of "full size" lamellas according to their geometry with inhomogeneous density (left) and cutting strips with individual width and homogeneous density (right)*

The 17 mm thick board of each pair is used to "conventionally" cut the boards according to their geometry in two 55 mm wide and 2200 mm long lamellas from each side of the board, which results in "full size" cross-section (= non-ripped) lamellas (Figure 1, left) with a density gradient over the cross-section from approximately 800 – 350 kg/m^3. The mean density of each non-ripped lamella is determined from mass and volume.

The 20 mm thick board of each pair is density measured over the board width using X-ray. Therefore, 5 cm long specimens are cut from both ends of the boards. The specimens are planed, rectangular cut and conditioned at a standard climate of 20 °C/65% rh [16]. The X-ray measurements are performed using DENSE-LAB X from Electronic Wood Systems (EWS), Hameln. Measurements are taken at every 0.1 mm of the specimen. Based on the measured density profile from the end with the lower density (according to Koelli [3], it is assumed that this is the upper end), the cutting positions of each board are calculated from the smoothed density profile with a specially developed software. The minimum strip width is 10 mm. The boards are ripped lengthwise from the upper end to strips with individual width (Figure 1, right). The grade assigned to each strip is verified by determining the mean density of each strip from mass and volume. Due to the longitudinal density distribution, the density is higher at

https://doi.org/10.52202/069179-0087

the lower end of the board. This leads to a deviation between the calculated X-ray density class and the measured mean density of the strip. The strips are grouped according to their grade and randomly (within the grading class) edge-glued into boards. Two to six strips are required to achieve a board width of 175 mm. A fibre-reinforced, one-component polyurethane adhesive (Jowapur® 686.60) is used for the edge-gluing. After curing and conditioning, the edge-glued timber boards are calibrated to the final thickness of 17 mm. Three ripped lamellas are cut in width (55 mm) and length (2200 mm) from each edge-glued board. After lamella preparation, the average density is determined from mass and volume. Ultimately, the ripped lamellas show a more uniform density over their width compared to the non-ripped lamellas.

2.4 PRODUCTION OF GLT FOR BENDING AND COMPRESSION TESTS PARALLEL

Six strength-graded lamellas are arranged within the combined GLT beam according to Figure 2. Due to the low number of ripped and non-ripped lamellas of grading class <290 kg/m³, additional non-ripped lamellas are produced from the low density boards from the center of the same trunk sections. The boards are processed in accordance with the manufacturing steps of the non-ripped lamellas described in Sect. 2.3.

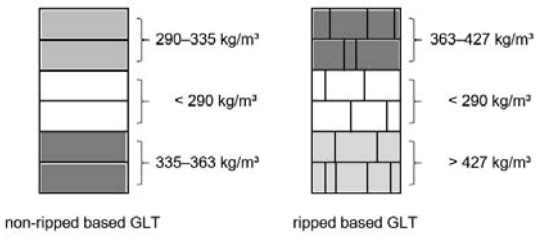

Figure 2: *Examples for lamella arrangement in the 6-lamella GLT test specimens for bending and compression test parallel produced from non-ripped (left) and ripped (right) lamellas, dimensions cf. table 1*

The same resin is used for gluing the GLT as for the edge-gluing (Jowapur® 686.60). The mean adhesive application rate is approx. 350 g/m². Pressing the GLT is done with a specific pressure of 0.75 MPa for a minimum of 240 min on a modified press, TimberPress X 300, commonly used to produce CLT at MINDA Industrieanlagen in Minden, Germany. After storing the beams in a standard climate [16], they are calibrated to the final width of 50 mm and stored again in the standard climate until testing. In summary, 20 beams with different beam setups and from different lamella strength classes are produced, which are used for the bending tests (cf. Sect. 3.2). After the bending test, two specimen sizes are cut from ends of the bending specimens for the compression tests parallel to the vascular bundles. Large specimens are taken over the entire cross-section of the GLT beams with a dimension of 100 x 50 x 300 mm³ (height x width x length) according to EN 408+A1 [17] (= 6 lamellas). Small specimens are taken from the compression and tension zones with a dimension of 34 x 50 x 205 mm³ (= 2 lamellas) (table 1).

2.5 PRODUCTION OF GLT FOR COMPRESSION TESTS PERPENDICULAR

For the compression tests perpendicular to the vascular bundles, test specimens with dimensions of 250 x 204 x 100 mm³ (length x height x width) according to EN 408+A1 [17] are produced out of twelve lamellas each. The arrangement of the lamellas over the cross-section of the specimens is comparable to that of the test specimens for the bending and compression test parallel to the vascular bundles. Figure 3 shows the arrangement of six lamellas as taken for the GLT beams, which are arranged mirror inverted. The two outer lamellas (top and bottom) have the highest densities, the four core lamellas medium density and the two intermediate lamellas are of low density. For the high and medium density lamellas, the 17 mm material described in Sect. 2.1 and 2.3 is used. The low density lamellas are produced from oil palm wood scantlings with dimensions of approximately 1300 x 75 x 45 mm³ (length x width x height), treated with about 2 % of boron by using the vacuum-pressure method. The scantlings are imported to Germany in dry state and visually graded. Due to the width of the scantlings (75 mm), two scantlings are edge-glued together after planning and trimming. For gluing one-component PUR adhesive (Jowapur® 686.60) is used.

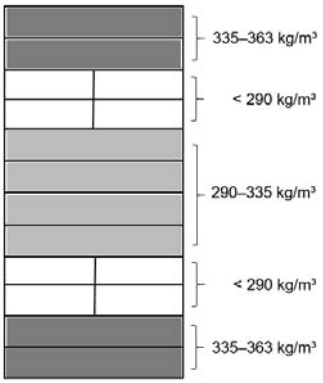

Figure 3: *Compression test specimen perpendicular to the vascular bundles, dimensions cf. table 1*

2.6 OVERVIEW TEST SPECIMENS

Before testing all specimens are stored in a climate chamber at a climate of 20 °C and 65 % relative humidity according to DIN 50014 [16]. An overview on all test specimens is given in Table 1.

Table 1: *Number and dimensions of test specimens, 2l = 2 lamellas, 6 l = 6 lamellas*

test	# specimens	dimension (length x height x width) [mm³]
f_m E_m	20	2,200 x 102 x 50
$f_{c,0,2l}$ $E_{c,0,2l}$	150 48	205 x 50 x 34
$f_{c,0,6l}$ $E_{c,0,6l}$	41	300 x 102 x 50
$f_{c,90}$ $E_{c,90}$	15 22	250 x 204 x 100
$f_{t,0}$ $E_{t,0}$	88	610 x 17 x 50

3 METHODS

3.1 DETERMINATION OF DENSITY

Contrary to EN 408+A1 [17], for all test specimens the density is not determined on a section from the immediate vicinity of the fracture after destructive testing, but as an average from the mass and volume of the entire specimen before testing.

3.2 BENDING TEST

Modulus of rupture (MOR) and local and global modulus of elasticity (MOE) are determined in a four-point bending test according to EN 408+A1 [17]. A 20 kN testing machine is used for the C10 and a 100 kN testing machine for the C14 beams. For measuring the local and global MOE of the C10 beams, three inductive displacement transducers are used (two of type WA50 and one of type WA100; Hottinger Baldwin Messtechnik (HBM), Germany). Plywood and oil palm wood supports of various dimensions are used to protect against support roller imprints when testing the C10 beams, plywood supports are used for the C14 beams (length of all supports three times the specimen width). Specimen geometry and test setup are corrected with k_h and k_l according to EN 384 [18] and the calculation of the characteristic values is done according to EN 14358 [19] (parametric approach for calculation of characteristic density (ρ_k) and strength ($f_{m,k}$) values). Instead of the reduction factor k_s (n), which depends on the number of specimens, the value of the 5 % quantile for a standard normal distribution (p0.05=1.645) is used in all calculations of the characteristic values in addition to the calculation according to the normalized reduction value for k_s (n). Details on the bending test and the calculation of the results are described in Heister and Fruehwald-Koenig [11].

3.3 COMPRESSION TEST

The compression tests parallel and perpendicular to the vascular bundles are carried out according to EN 408+A1 [17] using a 200 kN universal testing machine (FORM+TEST Seidner&Co. GmbH). In deviation to EN 408+A1 [17], the force used to calculate the compression strength perpendicular ($f_{c,90}$) is determined at 1 % plastic strain of the specimen height and the strain measurement for the Young's modulus is carried out by means of digital image correlation (DIC) with a camera system (type GOM Aramis 5M, Carl Zeiss GOM Metrology GmbH). The strain measurements are evaluated with GOM Correlate 2019 (Carl Zeiss GOM Metrology GmbH). Details on the compression test and the DIC strain measurement are described in Fruehwald-Koenig and Heister [12].

3.4 TENSION TEST

The tension test on glulam lamellas parallel to the vascular bundles is carried out according to EN 408+A1 [17] on the FORM + TEST universal testing machine with a clamping length of 80 mm (resulting in a free test length of 9 x width = 450 mm). The elongation is measured with a long-travel extensometer up to approximately 50 % of the tensile strength ($f_{t,0}$) of small, defect-free specimens according to Fruehwald-Koenig and Heister [4]. In deviation to EN 408+A1 [17], the measuring distance of the sensors is 200 mm. To avoid compression failure in the clamping area, the specimens are reinforced with birch plywood on both face sides.

4 RESULTS AND DISCUSSION

4.1 INFLUENCE OF THE DENSITY ON THE PROPERTIES

Figure 4 shows the tensile properties parallel, compressive properties parallel and perpendicular and bending properties of oil palm wood as a function of density for full-size and small, defect-free test specimens. Independent of the specimen size, they show a higher correlation to the density compared to dicotyledons. This is caused by the much larger density range of the oil palm wood and the resulting large range of property values. All strength and stiffness values of the full-size specimens parallel to the vascular bundles increase with the density by power law relationship with similar exponents, except the higher exponent for the bending properties ($f_{m,0}$ and $E_{m,0,global}$), which might be due to the lower number of test specimens in a much lower density range. Properties from compression test perpendicular to the vascular bundles ($f_{c,90}$ and $E_{c,90}$) on full-size test specimen are constant, which might be due to the low number of test specimen and the very low density range. The exponents correspond to the results for oil palm wood on small test specimens according to Fruehwald-Koenig and Heister [4], Srivaro et al. [20] and Srivaro et al. [21] and for other palm species according to Rich [22]. But the determined exponents are very different from those of softwood and hardwood species from modelling [23-25] or from experimental results [26-28], which might be due to the different anatomical structures. The concentration of vascular bundles, as well as the concentration of fibers within the bundles, is greater in the periphery of the trunk than in the central tissue [2,29]. Cell wall thickening is more pronounced in the peripheral tissue than in the central tissue and more in the bottom of the trunk than in the top of the trunk [30], because the bending stresses on the arborescent palm are greatest on the bottom at the periphery of the trunk. Furthermore, the cell wall properties themselves are not constant. Cell wall thickening means that as the palm tissue (vascular bundles and parenchymatous ground tissue)

https://doi.org/10.52202/069179-0087

ages, more cell wall layers are added on the cell wall towards the lumen of the cells resulting in smaller lumina diameters and thicker cell walls with a higher cellulose content [29]. The density in the peripheral zone at the bottom of the trunk rises over time because the trunk volume increase is lower than the mass increase by added volume of additional cell wall layers. But, the density increase due to cell wall thickening is lower than the increase of the elastomechanical properties, which leads to exponents > 1 of the power law relationship.

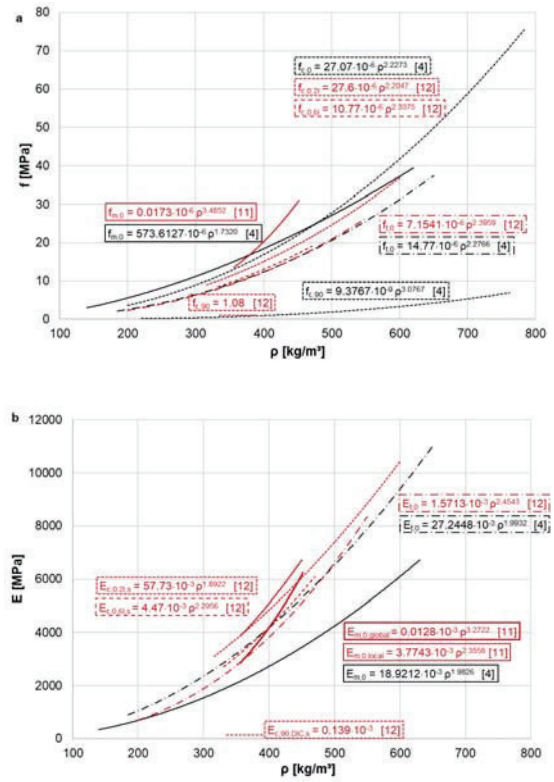

Figure 4: *Elastomechanical properties in relationship to the density (ρ), a strength properties, b stiffness properties (full-size specimens in red, small-size specimens in black)*

4.2 INFLUENCE OF THE TEST SPECIMEN SIZE ON THE PROPERTIES

In contrast to common wood species, the strength of the full-size test specimens is above ($f_{c,90}$), in the same range ($f_{t,0}$, f_m) or only slightly below ($f_{c,0}$) that of small, defect-free test specimens, cf. Figure 4a. Therefore, for oil palm wood specimen size does not influence the strength values.

When testing common wood species a clear distinction must be made between

- "material testing" of small, defect-free specimens that fail on a microscopic level as a result of many small, randomly distributed structural defects in the specimen, and
- "(building) component testing" with macroscopic structural defects due to natural growth characteristics, which mostly fail as a result of these structural defects (especially knots and fiber deviation). For most strength types, the properties of the defect-free wood between the structural defects have no influence on the properties of the building component respectively it´s influence is superimposed by the structural defects.

Both, material and component testing show different failure modes depending on the type and direction of loading and results in significantly different property values.

In contrast to the dicotyledonous common wood species, monocotyledonous palm tissue consists of vascular bundles (having honeycomb-like prismatic cells and dense fibers aligned along the stem) surrounded by parenchymatous ground tissue (made up of thin-walled polyhedral parenchyma like close cell foam-like structure) [31]. From a structural mechanics perspective, if the vascular bundles are considered as reinforcements (fibers) and the ground tissue as the matrix, oil palm wood can be seen as a unidirectional long-fiber-reinforced biocomposite. Therefore, on the microscopic level, palms as monocotyledons have a more heterogeneous structure in comparison to dicotyledons. Since monocotyledons only grow at the top part of the trunk where the apical meristem is located; no radial growth occurs and therefore, palms do not possess radial oriented ray cells or an annual ring structure. The tissue does not contain the typical macroscopic structural defects due to natural growth characteristics (e.g. knots) like dicotyledones. The elastomechanical properties of oil palm wood depend on the anatomical structure at the microscopic level and are therefore not influenced by the specimen size. Main influencing factors on the elastomechanical properties are the density, but also the age of the palm, the location within the trunk (height and cross section) and probably also the oil palm subspecies, differences between individual palms and the plantation sites.

4.3 RELATIONS OF THE PROPERTIES

For the full-size test specimens, the compressive strength parallel to the vascular bundles ($f_{c,0}$) is only approx. 1.2 times the tensile strength parallel (($f_{t,0}$) Figure 4a), whereas it is much higher for low grade softwood (e.g. 2.2 for C14 $f_{c,0,k}/f_{t,0,k}$ according to EN 338 [14]). The ratio of bending and tensile strength parallel to the vascular bundles (Figure 4a) rises with the density from 0.8…1.7…2.6 : 1 within the relevant density range of ρ = 200…400…600 kg/m³ and is in the range of low grade softwood (e.g. 1.9 for C14 $f_{m,k}/f_{t,0,k}$ according to EN 338 [14]). Similarly, the ratio of compression strength parallel and perpendicular to the vascular bundles (Figure 4a) rises with the density from 2.7…13.0…32.6 : 1 for ρ = 200…400…600 kg/m³ and is therefore for most densities above that for low grade softwood (e.g. 8.0 for C14 $f_{c,0,k}/f_{c,90,k}$ according to EN 338 [14]). Figure 4b shows that for oil palm wood $E_{m,0,local} : E_{c,0} : E_{t,0}$ = 1.3 : 1.2 : 1 for ρ = 400 kg/m³. This is in contrast to common wood species according to Egner [32], who stated that $E_m < E_{t,0}$. and according to Kretschmann [27], who stated that E_m includes an effect of shear deflection and therefore can be increased by 10 %.

4.4 PERFORMANCE INDICES FOR MINIMUM WEIGHT DESIGN

Because of the power law relationship between strength respectively stiffness and density, the performance indices for minimum weight design by Ashby et al. [13] calculated for oil palm wood rise with the density and are shown in Table 2. They are comparable to that of small size oil palm, coconut palm and date palm wood test specimens. The strength-density performance index M_4 (strength of a tie under uniaxial load) of oil palm wood is comparable to that of structural size softwood, M_5 (strength of a beam in flexure) and M_6 (strength of a plate in flexure) are only slightly lower than that of structural size softwood. However, the modulus-density performance indices ($M_1 – M_3$) of oil palm wood are much lower than that for structural size softwood. The performance index for elastic design M_8 to allow large, recoverable deformation based on tensile tests is above and that based on compression tests in the range of structural size softwood lamellas.

Table 2: *Performance indices for minimum weight design as proposed by Ashby et al. [13] for ρ = 200…600 kg/m³*

	full-size oil palm wood	softwood lamellas T8…T30 [14]
$M_1 = E/\rho$	3.5…17.2[a]	20.0…30.6[a]
(GPa (Mg m^{-3})$^{-1}$)	4.3…17.8[b]	
$M_2 = E^{1/2}/\rho$	4.2…5.4[a]	7.5…7.9[a]
(GPa$^{1/2}$ (Mg m^{-3})$^{-1}$)	5.7…4.6[b]	
$M_3 = E^{1/3}/\rho$	4.4…3.6[a]	5.5…4.8[a]
(GPa$^{1/3}$ (Mg m^{-3})$^{-1}$)	5.5…3.6[b]	
$M_4 = \sigma_f/\rho$	11.7…54.0[a]	27.6…69.8[ad]
(MPa (Mg m^{-3})$^{-1}$)	12.9…61.3[b]	55.2…70.7[bd]
$M_5 = \sigma_f^{2/3}/\rho$	8.8…16.9[a]	13.8…22.5[ad]
(MPa$^{2/3}$ (Mg m^{-3})$^{-1}$)	9.4…18.4[b]	21.9…23.0[bd]
$M_6 = \sigma_f^{1/2}/\rho$	7.6…9.5[a]	9.8…12.7[ad]
(MPa$^{1/2}$ (Mg m^{-3})$^{-1}$)	8.0…10.1[b]	13.8…13.1[bd]
$M_8 = \sigma_f/E$ [-]	0.0033…0.0031[a]	0.0017…0.0028[acd]
	0.0025…0.0035[b]	0.0034…0.0028 [bcd]

[a] based on tensile tests
[b] based on compression tests
[c] E based on bending tests
[d] calculation based on the 5th quantile

4.5 INFLUENCE OF RIPPED LAMELLAS ON BENDING PROPERTIES

Figure 5 shows the positive trend between density (ρ) and bending strength ($f_{m,0,rf}$) after taking the reduction factors k_h and k_l into account. The bending strength of the ripped beams ($f_{m,0,rf,r}$) is higher than that of the non-ripped beams at the same density and ranges between 22…27 MPa for the ripped C14 and 17…24.5 MPa for the ripped C10 beams. At a density of 400 kg/m³, the ripped C10 and C14 beams show almost the same bending strength of 22.5…24 MPa. The characteristic bending strength ($f_{m,k}^{0.05}$) of the ripped C14 beams is 21 MPa and comparable to that of the ripped C10 beams with 20 MPa (Table 3). The difference between the characteristic bending strength of the non-ripped C10 (11 MPa) and C14 (16 MPa) beams is higher. The characteristic values $f_{m,k}^{k(s)}$ according to EN 14358 [19] are 2…3 MPa lower than the $f_{m,k}^{0.05}$ values. The coefficient of variation ranges between 9…13 % for the C14 and 7…8 % for the C10 beams. The oil palm wood GLT C10 and C14 achieves the target MOR ($f_{m,k}$) according to EN 338 [14]. Applying the reduction factor for coniferous wood according to EN 14358 [19], the target $f_{m,k}$ is not fulfilled by the non-ripped C10 beams. Therefore, the calculated density limits for achieving a target characteristic strength and the calculation method are reasonable.

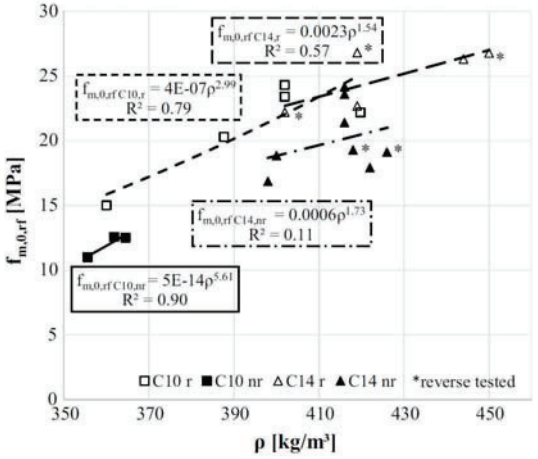

Figure 5: *Relationship between bending strength ($f_{m,0,rf}$) after considering the reduction factors k_h and k_l [18] and the GLT density*

Table 3: *Bending strength properties of GLT beams class C10 and C14*

	C10		C14	
	non-ripped	ripped	non-ripped	ripped
n (-)	3	4	8	5
$f_{m,\bar{x}}$ (MPa)	12	23	20	25
cv (%)	7	8	13	9
$f_{m,k}^{0.05}$ (MPa)	11	20	16	21
$f_{m,k}^{k(s)}$ (MPa)	9	17	14	19
$E_{m,0,l,\bar{x}}$ (GPa)	4.27	5.21	5.64	5.80
cv (%)	14	14	14	19
$E_{m,0,mean,l}^{0.05}$ (GPa)	3.28	4.00	4.32	3.99
$E_{m,0,mean,l}^{k(s)}$ (GPa)	3.99	4.86	5.37	5.44

$f_{m,k}^{0.05}$ = reduction factor k(s) = p(0.05) = 1.645
$f_{m,k}^{k(s)}$ = reduction factor k(s) according to EN 14358 [19]
$E_{m,0,mean,l}^{0.05}$ = reduction factor k(s) = p(0.05) = 1.645
$E_{m,0,mean,l}^{k(s)}$ = reduction factor k(s) according to EN 14358 [19]

Figure 6 shows the local MOE ($E_{m,0,l}$) for the different beam setups and strength classes. The range of the local MOE ($E_{m,0,l}$) of C14, especially the ripped beams, is the highest for all setups and strength classes. The lower values of the C14 are similar to the higher values of C10. The statistical values for the local MOE are shown in Table 3. The ripped beams show a higher mean local MOE ($E_{m,0,l,\bar{x}}$) than the non-ripped beams and the C14 are higher than the C10. $E_{m,0,mean,l}^{0.05}$ of the non-ripped C14 beams is higher (4.32 GPa) than that of the ripped C14 beams (3.99 GPa) (due to one very low MOE value in the C14r group, cf. Figure 5). In contrast, $E_{m,0,mean,l}^{0.05}$ of the ripped C10 beams is higher (4.00 GPa) than that of the non-ripped

https://doi.org/10.52202/069179-0087

C10 beams (3.28 GPa). $E_{m,0,mean,l}^{0.05}$ for ripped beams of both strength classes is almost similar (3.99 GPa for C14 and 4.00 GPa for C10). The target MOE for C14 according to EN 338 [14] ($E_{m,0,mean}$ = 7 GPa) is far from achieved. In contrast, the target density (ρ_k = 290 kg/m³) of C14 according to EN 338 [14] is achieved by all oil palm wood beams.

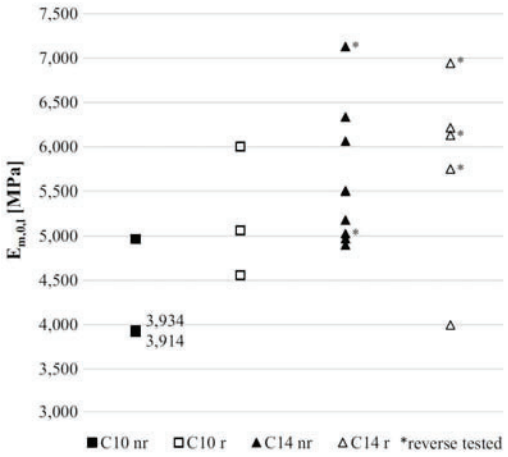

Figure 6: *Local MOE ($E_{m,0,l}$) of the different beam setups and strength classes*

4.6 LOCAL VS. GLOBAL MOE

Figure 7 shows the relationship between the local MOE ($E_{m,0,l}$) and global MOE ($E_{m,0,g}$) for oil palm wood beams with different setups and strength classes and the linear relationship for coniferous wood species according to EN 384 [18]. For all specimens, the local MOE ($E_{m,0,l}$) is above the global MOE ($E_{m,0,g}$). All oil palm wood beams tested showed a positive linear correlation between the global and local MOE, but the linear relationship for softwoods according to EN 384 [18] does not apply to oil palm wood.

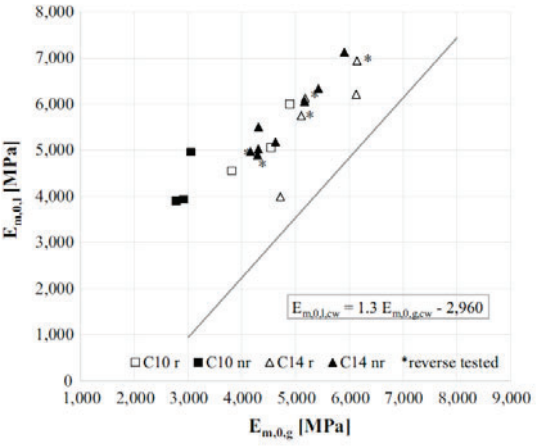

Figure 7: *Relationship between global MOE ($E_{m,0,g}$) and local MOE ($E_{m,0,l}$) for oil palm wood GLT and the linear relationship for coniferous wood species according to EN 384 [18]*

5 CONCLUSIONS

Oil palm wood availability provides good opportunities for supplementing respectively substituting common tropical timber species especially in Asia and timber from pine plantations. Due to its elastomechanical properties, medium and high-density oil palm wood can be used for load bearing products like GLT, but the elastomechanical properties are slightly lower compared to common wood species. The challenge with regard to load-bearing construction products such as GLT and CLT from oil palm wood lies in the comparatively low stiffness of oil palm wood compared to common wood species. The high variation of oil palm wood´s properties compared to common wood species requires grading the oil palm wood, e.g., according to density, because most design values are based on 5th percentiles and high variations result in low product performance. The strength grading according to density and the defined density limits used in this study appear to be reasonable in principle, the targeted strength classes of EN 338 [14] are achieved. Designing beams with lamella positions according to their density has a significant influence on the properties. Ripping boards according to their density into stripes and edge-gluing the stripes to density homogeneous lamellas results in higher MOR and MOE values (no difference is shown for compression properties parallel to the vascular bundles).

As the oil palm wood (similar to other palms) differs in its structure and properties compared to common wood species, special product development (including material respectively product modelling) and process development is necessary to achieve market competitiveness. Hackel [33] modelled the bending properties described in this paper using the finite element method (FEM). For load bearing products, grading and trimming of the lumber, long term durability under load (and wet climate) and design values as well as standardization (matching with building codes) are significant challenges. Standards for common wood species do not automatically fit for oil palm wood. For example, the effect of test specimen size, especially the difference between small-size and construction-size test specimens, is much smaller compared to common wood species; for some properties, the full-size test specimens show higher values than small-size test specimens at the same density (which is likely caused by the complex macroscopic structure of the oil palm wood). The equation between local and global MOE for solid construction timber from softwoods according to EN 384 [18] does not apply for oil palm wood GLT. The relationship between the characteristic values for strength and density of coniferous timber according to EN 338 [14] fits for GLT from oil palm, but not the relationship between the mean MOE and density. The MOE is – in relation to strength and density – much lower for oil palm wood. The correlations between lamella and GLT quality (“GLT model”) and the various properties among themselves, which are well-known for common wood species, do not apply to oil palm wood. Therefore, the building codes need to be adapted for oil palm wood.

https://doi.org/10.52202/069179-0087

ACKNOWLEDGEMENT

The project was funded by the German Federal Ministry of Education and Research through the "Bioökonomie International 2017" project "Oilpalmsugar (031B0767A)". The procurement of the oil palm material was supported by the Malaysian Timber Industry Board (MTIB) and the Fibre and Biocomposite Development Centre (FIDEC) represented by Dr. Loh Yueh Feng as well as Profina Plywood Sdn Bhd. Sawmilling of some of the material was provided by the Forest Research Institute Malaysia (FRIM). Leitz GmbH & Co. KG provided the wood processing tools, Electronic Wood Systems, Hameln the X-ray measurement devices, Jowat SE the adhesives and MINDA Industrieanlagen GmbH the press. Dipl.-Ing. Claus Deis, M.Sc. Lena Heister. M.Sc. Nico Ferlemann and M.Sc. Martin Hackel did the laboratory work.

REFERENCES

[1] Fruehwald A., Fruehwald-Koenig K.: The Use of Oil Palm Trunks for Wood Products. By-Products of Palm Trees and Their Applications, Materials Research Proceedings 11:69-80, 2019.

[2] Fathi L.: Structural and Mechanical Properties of the Wood from Coconut Palms, Oil Palms and Date Palms. PhD Thesis, University of Hamburg, Zentrum Holzwirtschaft, Hamburg, 181 pages, 2014.

[3] Koelli N.: Density and Moisture Distribution in Oil Palm Trunks from Peninsular Malaysia. BSc Thesis, University of Hamburg, Zentrum Holzwirtschaft, Hamburg, 2016.

[4] Fruehwald-Koenig K., Heister, L.: Macromechanical and Micromechanical Behavior of Oil Palm Wood (*Elaeis guineensis* JACQ.): Tensile, Compression and Bending Properties. European Journal of Wood and Wood Products, submitted 2023.

[5] Jumaat M. Z., Rahim, A. H. A., Othman, J., Midon, M. S.: Strength evaluation of oil palm stem trussed rafters. Construction and Building Materials, 20(9):812-818, 2006.

[6] Srivaro S.: Flatwise compressive properties of oil palm core sandwich panel subjected to static compressive load. Journal of the Indian Academy of Wood Science 12(2):110-115, 2015.

[7] Srivaro S., Matan N., Lam F.: Stiffness and strength of oil palm wood core sandwich panel under center point bending. Materials & Design, 84:154-162, 2015.

[8] Srivaro S., Cherdchim B., Pasztory Z.: Bending and Compressive Properties of Finger-jointed Oil Palm Wood Products. BioResources, 14(3):6341-6352, 2019.

[9] Srivaro S., Matan N., Lam F.: Performance of cross laminated timber made of oil palm trunk waste for building construction: a pilot study. European Journal of Wood and Wood Products, 77(3):353-365, 2019.

[10] Hoffmann, J.: Investigation on the application of an engineered bamboo board in cross laminated timber. BSc Thesis, Rosenheim Technical University of Applied Sciences, Rosenheim, 2018.

[11] Heister L., Fruehwald-Koenig K.: Glued Laminated Timber from Oil Palm Timber – Beam Structure, Production and Elastomechanical Properties. In Proceedings of 2nd World Conference on Byproducts of Palms and Their Applications, Springer Nature Singapore, Singapore, 2023.

[12] Fruehwald-Koenig K., Heister L.: Compression and Tensile Properties of Oil Palm Wood (*Elaeis guineensis* JACQ.) in Construction Size. Construction and Building Materials, submitted 2023.

[13] Ashby M. F., Gibson L. J., Wegst, U., Olive R.: The mechanical properties of natural materials. I. Material property charts. Proc. R. Soc. Lond. A. 450(1938): 123-140, 1995.

[14] EN 338: Structural timber – Strength classes. CEN European Committee for Standardization, 11 pages, 2016.

[15] EN 14081-2: Timber Structures – Strength graded structural timber with rectangular cross section – Part 2: Machine grading; additional requirements for type testing. CEN European Committee for Standardization, 39 pages, 2018.

[16] DIN 50014: Normalklimate für Vorbehandlung und/oder Prüfung – Festlegungen. Beuth Verlag, Berlin. 7 pages, 2018.

[17] EN 408+A1: Timber structures – Structural timber and glued laminated timber – Determination of some physical and mechanical properties. CEN European Committee for Standardization, 38 pages, 2012.

[18] EN 384: Structural timber – Determination of characteristic values of mechanical properties and density. CEN European Committee for Standardization, 21 pages, 2019.

[19] EN 14358: Timber structures – Calculation and verification of characteristic values. CEN European Committee for Standardization, 17 pages, 2016..

[20] Srivaro S., Matan N., Lam F.: Property gradients in oil palm trunk (*Elaeis guineensis*). Journal of Wood Science, 64(6):709-719, 2018.

[21] Srivaro S., Rattanarat J., Noothong P.: Comparison of the anatomical characteristics and physical and mechanical properties of oil palm and bamboo trunks. Journal of Wood Science, 64(3):186-192, 2018.

[22] Rich P. M.: Mechanical structure of the stem of arborescent palms. BOT. GAZ., 148(1):42-50, 1987.

[23] Easterling K. E., Harrysson R., Gibson L. J., Ashby, M. F.: On the mechanics of balsa and other woods. Proc. R. Soc. Lond. A, 383(1784):31-41, 1982.

[24] Gibson L. J., Ashby M. F.: Cellular solids: structure and properties. 2 ed., Cambridge University Press, Camebridge, 1999.

[25] Price A.: I. A mathematical discussion on the structure of wood in relation to its elastic properties. Phil. Trans. R. Soc. Lond. A., 228(659-669):1-62, 1929.

[26] Bodig J., Goodman J. R.: Prediction of elastic parameters of wood. Wood Sci., 5(4):249-264, 1973.

[27] Kretschmann, D. E.: Wood Handbook – Wood as an Engineering Material, Chapter 5: Mechanical Properties of Wood. General Technical Report FPL-GTR-190, U. S. Department of Agriculture, Forest Service, Forest Products Laboratory, United States Department of Agriculture, Madison, WI, 509 pages, 2010.

https://doi.org/10.52202/069179-0087

[28] Markwardt L. J., Wilson T. R. C.: Strength and related properties of woods grown in the United States. Forest Products Laboratory, United States Department of Agriculture. Vol. 479, US Government Printing Office, Washington D.C., 1935.
[29] Lim S., Khoo K.: Characteristics of oil palm trunk and its utilization. Malaysian Forester, 49(1-2):3-22, 1986.
[30] Rich P. M.: Developmental anatomy of the stem of Welfia georgii, Iriartea gigantea, and other arborescent palms: implications for mechanical support. Am. J. Bot., 74(6):792-802, 1987.
[31] Gibson L. J.: The hierarchical structure and mechanics of plant materials. J. R. Soc. Interface, 9(76):2749-2766, 2012.
[32] Egner K.: Bestimmung der Elastizität der Hölzer. In Graf O. (ed.), Die Prüfung nichtmetallischer Baustoffe. Springer-Verlag, Berlin, Göttingen, Heidelberg. p. 89-92, 1957.
[33] Hackel M.: Flexural Properties of Oil Palm Wood (*Elaeis guineensis* JACQ.) based Glued Laminated Timber (GLT) using Finite Element Method (FEM). Submitted at the World Conference on Timber Engineering, World Conference on Timber Engineering, Oslo, 19.-22. June, 2023.

World Conference on Timber Engineering Oslo 2023

FLEXURAL PROPERTIES OF OIL PALM WOOD (*ELAEIS GUINEENSIS* JACQ.) BASED GLUED LAMINATED TIMBER (GLT) USING FINITE ELEMENT METHOD (FEM)

Martin Hackel[1]

ABSTRACT: The anatomical structure of oil palm wood is only to a limited extent comparable to common wood species used in construction. Typical for monocotyledons, the material is composed of high density vascular bundles and a parenchymatous tissue of lower density. In three experiment sets, the local and global moduli of elasticity (MOE) and the flexural strength of oil palm wood based GLT are determined using FEM and various influencing parameters are investigated in a sensitivity analysis. Furthermore, the application of densified tension lamellas is studied. The results of the modelling are compared with the results from mechanical tests. Significant differences, mainly attributed to the specific parameters of the selected material, are observed. The results of this preliminary study serve as a starting point for computer-aided optimisation and modelling of other oil palm-based products.

KEYWORDS: Oil palm wood, finite element method (FEM), GLT, modulus of elasticity, flexural strength

1 INTRODUCTION

The rising population in recent decades has led to increased demand for raw materials, especially in the food, chemical and pharmaceutical industries as well as the construction and energy sectors. Oil palms *(Elaeis guineensis* JACQ.) are a versatile raw material producing crop. Oil palm provides raw materials in the form of palm and palm kernel oil, for all industry sectors mentioned. As a result, the global oil palm cultivation area, concentrated in Southeast Asia, increased between 1996 and 2021 by 328 % to 28.9 million hectares [1]. Declining crop yields limit the economic lifespan of oil palms to about 25 to 30 years [2]. The clearing of plantation areas after the end of the economic lifespan results in up to 180 million m³ of usable oil palm wood per year [3]. Its actual use, however, is limited by a lack of knowledge regarding the wood's material properties. Possible substitution potentials of the material are also unrecognised and accordingly not utilised. Influenced by the shortage of building products caused by various factors, such as the conflict in Ukraine, droughts and bark beetle calamities in Europe and North America as well as the effects of the Covid pandemic, building products have been identified as a possible field for substitution approaches.

The development of construction materials from renewable raw materials (e. g. wood or wood like materials) is economically intensive. These raw materials are characterized by inherent variations of their material properties and naturally occurring inhomogeneity. Common building materials such as glued laminated timber (GLT) use layer-based approaches to reduce the property variations respectively the inhomogeneity. The application, production and properties of GLT are specified by e.g. European standards [4, 5]. Before oil palm based GLT can be introduced to the market, it is necessary to create a lamella grading [6] and develop various beam structures in regard to the requirements in the standards. Therefore, expensive material tests need to be performed. A way to reduce costs is through digitalisation. Larger series of experiments can be performed using the finite element method (FEM) without material expense and in a comparatively short investigation period. The quality of FEM-modelling depends on the quality of the material parameters used as input parameters. But suitable material parameters of oil palm wood are only published to a limited extent in the literature. Currently, no modelling of oil palm wood based products has been published.

The aim of the work is to evaluate the suitability of FEM for determining the flexural properties of oil palm GLT by comparing the modelling results with the results of Heister and Fruehwald-Koenig [7] (static tests). Furthermore, possible relationships of the flexural properties with other material properties, primarily density, are evaluated. In the form of a sensitivity analysis, possible influences of different material properties on the flexural strength are examined. Furthermore, the influence of densified tension lamellae on the flexural strength is evaluated.

The objectives of the work are achieved through a multi-stage process. Based on a literature research, suitable relationships between the density and elastomechanical material properties are determined. Missing relationships are established by own investigations or approximation. The beams tested by Heister and Fruehwald-Koenig [7] are implemented in the modelling software RFEM 6.02. Using suitable statistical methods, the results of the different experiments are compared and evaluated.

[1] Martin Hackel, OWL University of Applied Sciences and Arts, Lemgo, Germany, martin.hackel@th-owl.de

https://doi.org/10.52202/069179-0088

Subsequently, correlations of the modelling results with different specimen properties are investigated. Following this, the results of the modelling are compared with the results of the experiments by Heister and Fruehwald-Koenig [7]. Finally, the results are discussed and placed in the context of existing literature.

2 STATE OF THE ART

2.1 ANATOMICAL FEATURES OF OIL PALM WOOD

Oil palms (*Elaeis guineensis* JACQ.) are monocotyledons and show differences in the anatomical structure to dicotyledons (deciduous and coniferous trees). Monocotyledons have no cambium, which results in a lack of annual rings (no secondary thickness growth). Furthermore, oil palms have no wood rays, no differentiation between heartwood and sapwood and no knots. Oil palm wood is composed of vascular bundles of high density and parenchymatous ground tissue of low density. The vascular bundles are mainly parallel to the mantle, but also helical orientations are widespread [8]. Deviations from the stem axis occur due to direct contact with the palm fronds and are therefore also referred to as leaf trace bundle [9].

Lim and Khoo [2] define three zones within the oil palm stem. The “outer” or “peripheral” zone of the stem includes about 20 % of the stem volume, irregular vascular bundles and a low parenchyma content characterise this zone [10]. The “inner” zone (about 40 % of the stem volume) has a high parenchyma content and widely distributed vascular bundles. The “central” zone (approx. 40 % stem volume) forms a transition between the peripheral and inner zone. Lim and Khoo [2] report densities of 170 kg/m³ from the “inner” zone to 700 kg/m³ in the “outer” zone. Kölli [11] confirms this density range (180 kg/m³ - 561 kg/m³). With increasing trunk height, the density of oil palm wood decreases. Kölli [11] shows exponential relationships between the position in the trunk and the density (horizontal and vertical). The “wood” tissue of oil palms is anisotropic, but only small property differences between radial and tangential directions are reported [2, 10]. Nevertheless, orthotropic material behaviour is assumed in the context of this work.

2.2 ELASTOMECHANICAL PROPERTIES OF OIL PALM WOOD

In compression tests (longitudinal), Fathi [12] determines Young's moduli of 1856 to 8238 MPa with a linear relationship ($R^2 = 0.99$) to the density. Srivaro et al. [13] determine values for the Young's modulus (longitudinal) of 114 to 996 MPa and an exponential relationship with the density ($R^2 = 0.64$, exponent 2.67). In the tensile test in fibre direction, Fruehwald-Koenig and Heister [14] determine a Young's modulus of 488 to 13102 MPa and report an exponential relationship to the density ($R^2 = 0.53$, exponent 2.41). A determination of the Young's modulus along all anatomical axes is performed by Fruehwald-Koenig and Faust [15] using ultrasonic measurements. Values of 4368 to 11695 MPa and a linear correlation with the density ($R^2 = 0.75$) are determined for the longitudinal Young's modulus. The values of the radial Young's modulus range from 100 to 501 MPa. The correlation to the density is low ($R^2 = 0.04$). The tangential Young's modulus is determined with values from 91 to 743 MPa and a linear relationship with density is shown ($R^2 = 0.26$).

G_{TL} and G_{RL}, respectively, are determined by Koelli [16] in static shear tests. The reported relationships are determined using linear or exponential regression models and provide coefficients of determination of $R^2 = 0.39$ (linear) or $R^2 = 0.43$ (exponential). Fruehwald-Koenig and Faust [15] determine the G-moduli in all three planes by dynamic ultrasound measurements. The results for G_{LR} range from 189 to 472 MPa, for G_{TL} from 196 to 555 MPa and for G_{RT} from 167 to 345 MPa. For all G-moduli, linear relationships with density are evident ($R^2 = 0.69$ - 0.85).

The Poisson's constants are determined by Fruehwald-Koenig and Faust [15] by dynamic ultrasonic measurements. The mean values of the individual constants are given as follows: $\mu_{LR} = 0.389$, $\mu_{RL} = 0.026$, $\mu_{LT} = 0.911$, $\mu_{TL} = 0.044$, $\mu_{RT} = 0.647$ and $\mu_{TR} = 0.707$. Fruehwald-Koenig et al. [17] determine Poisson's constants on specimens in service dimensions. The measurements do not distinguish between radial and tangential directions. Mean values for $\mu_{L/RT}$ from 0.379 to 0.523 and μ_{RT} of 0.117 are reported. Relationships between density and Poisson`s constants are not pronounced ($R^2 = 0.0024$).

For oil palm wood, no data on hardening moduli are available at the time of writing. Fruehwald-Koenig and Heister [14] determine the tensile strength (longitudinal) with values from 1.9 to 47 MPa and show an exponential relationship to the density ($R^2 = 0.76$, exponent 2.24). Furthermore, tensile strength (radial/tangential) with values of 0.4 to 2.3 MPa and an exponential relationship ($R^2 = 0.5$, exponent 1.4) are reported.

Fathi [12] determines compressive strengths (longitudinal) with values from 4.4 to 27.6 MPa and shows a linear relationship with density ($R^2 = 0.6$). Fruehwald-Koenig and Heister [14] demonstrate an exponential relationship ($R^2 = 0.76$, exponent 2.24) and reported values from 3.1 to 64.6 MPa. For the compressive strength (radial/tangential) an exponential relationship ($R^2 = 0.73$, exponent 3.08) and values from 0.1 to 12.2 MPa are reported.

Investigations by Fathi [12] regarding the shear strength in RL-plane with longitudinal load provide results of approximately 2 to 4 MPa and a linear relationship with density ($R^2 = 0.998$). Fruehwald-Koenig et al. [17] determine an exponential relationship with density ($R^2 = 0.52$, exponent 1.36) for the shear strength in RL plane under longitudinal load and report values from 0.2 to 7.8 MPa. In addition, rolling shear strengths with values from 0.1 to 3.1 MPa and a moderate exponential relationship with density ($R^2 = 0.17$, exponent 1.05) are determined.

2.3 FEM FOR LAYER BASED WOODEN PRODUCTS

FEM is used to model the material behaviour of GLT beams and other layer-based wooden materials. Ehlbeck et al. [18] use FEM to predict the load-bearing capacity of glulam beams made of spruce. The material behaviour is assumed to be linearly elastic. The load is increased

stepwise. Within each stage, all elements are tested against reaching the tensile or compressive strength. When the tensile strength is reached, a case distinction is made. If the applied load is greater than in the previous load level, the material properties of the element are set to zero and the load is increased further. If the load is less than in the previous load level, the load-bearing capacity is reached. When the compressive strength is reached, the properties of the element are changed so that no further load absorption is possible [18]. Blaß et al. [19] and Frese [20] transfer the approach of Ehlbeck et al. [18] to beech wood. Orthotropic linear elastic material behaviour is assigned to the tension zone. The failure of the beam is defined by reaching the tensile strength in one element of the tension lamella. The elements of the compression zone are assigned an ideal elastic-plastic material model [19–20]. If the compressive strength is exceeded, ideal plastic material behaviour is assumed. The deviations between modelling and laboratory tests are between -6.9 % and +2.5 % (flexural strength) and -8.1 % and +1.9 % (global MOE) [20]. Gao et al. [21] transfer the aforementioned approach to Cathay poplar. Deviating from Blaß et al. [19], a three-dimensional model and steel intermediate layers (riders) are used in the load application points. In addition, the adhesive bond is investigated. Isotropic material properties are assigned to the adhesive layers. The bond between adhesive and timber layers is assumed to be rigid. The assignment of the material models in tension and compression zone is realised analogous to Frese [20]. Modelling underestimates the flexural strength by 3.9 % and overestimates the global MOE by 2.8 %.

3 MATERIAL

3.1 MATERIAL ORIGIN

The material used in the laboratory tests [7] originates from two cultivation regions in Malaysia. The material of the specimens with the identifiers ZA and ZN is obtained from approximately 30-year-old oil palms from the Kedah region. The material is transported to Germany in frozen state. Further processing takes place in Germany. Information on processing and drying can be found in Heister and Fruehwald-Koenig [7]. The material of specimen identifiers A and N originates from the Johor region. The cutting of the palms (approximately 30 years old) as well as the drying are carried out within the framework of a research project of the Forest Research Institute of Malaysia (FRIM). Further information on the processing of the material is provided by Heister and Fruehwald-Koenig [7].

3.2 BEAM STRUCTURES

Within the scope of this work, combined GLT beams are investigated. The beams have the dimension 2200 mm x 50 mm x 102 mm and consist of six lamellas each (2200 mm x 50 mm x 17 mm, L x W x H). The chosen beam design aims to achieve strength classes C14 and C 10 (definition by [7]) with density graded lamellas for the compression, shear and tension zones The lamellas of the highest density class are assigned to the tension zone 335…363 kg/m³ for C 10, respectively >427 kg/m³ for C 14. Medium density lamellas are in the compression zone (289…335 kg/m³ for C 10 respectively 363…427 kg/m³ for C 14). Low density lamellas are in the shear zone (<289 kg/m³ for C10 and C14).

For the production of the beams, the two lamella types "natural lamellae" (specimen identification N, cut according to geometry from wider boards and therefore show high density and property gradients) and "assembled lamellas" (specimen identification A, edge-glued of narrow, density graded strips and therefore show more homogeneous density and properties over the width) are used.

3.3 DENSIFIED MATERIAL

To investigate the influence of the densification of lamellas on the GLT properties, material properties of densified oil palm wood are used as input parameters for tension lamellas (only in FEM modelling, no laboratory test). The material is mechanically dewatered and thermo-hydro-mechanically densified using two densification rates (40 % and 60 %). Further information on the process and elastomechanical properties are given in Fruehwald-Koenig et al. [22] and Koelli and Fruehwald-Koenig [23].

3.4 ELASTIC MATERIAL PARAMETERS

Modelling is carried out using two sets of material constants from ultrasonic testing and static testing. The Young´s moduli and shear moduli are taken from Fruehwald-Koenig and Faust [16], who described them related on density from ultrasonic tests. Equations (1) - (3) provide the relationships for the Young´s moduli and (4) – (6) for the shear moduli [15].

$$E_L(\rho) = 22.345\,\rho + 204.89 \quad (1)$$

$$E_R(\rho) = 0.318\,\rho + 223.38 \quad (2)$$

$$E_T(\rho) = 1.37\,\rho - 42.164 \quad (3)$$

$$G_{RT}(\rho) = 0.6917\,\rho - 16.657 \quad (4)$$

$$G_{TL}(\rho) = 1.3857\,\rho - 91.621 \quad (5)$$

$$G_{LR}(\rho) = 1.0738\,\rho - 37.963 \quad (6)$$

where $E_{L,R,T}$ = Young´s moduli along the anatomical axes (ultrasonic test), $G_{RT,TL,LR}$ = Shear moduli in symmetry planes (ultrasonic test), ρ = density

Equation (7) provides the relationship between Young´s modulus in longitudinal direction and density from static test [14].

$$E_{t,0}(\rho) = 0.0021\,\rho^{2.41} \quad (7)$$

where $E_{t,0}$ = Young´s modulus longitudinal (static test), ρ = density.

Equation (8) shows the relationship between shear modulus in the longitudinal direction and density from static test [16].

https://doi.org/10.52202/069179-0088

$$G_{RL,stat}(\rho) = 0.2812\,\rho - 1.7586 \quad (8)$$

where $G_{RL,static}$ = Shear modulus TL-plane (static test), ρ = density.
Due to limited data on static tests, the dynamically determined elastic constants are converted in "reduced" (static) properties using the Equations (9) and (10).

$$E_{R,T\,reduced}(\rho) = \left(\frac{E_L(\rho)}{E_{t,0}(\rho)}\right) E_{R,T}(\rho) \quad (9)$$

$$G_{RT,LR\,reduced}(\rho) = \left(\frac{G_{TL}(\rho)}{G_{RL,stat}(\rho)}\right) G_{RT,LR}(\rho) \quad (10)$$

where $E_{R,T,reduced}$ = reduced Young´s moduli along R and T axis, $E_{L,R,T}$ = Young´s moduli along the anatomical axes (ultrasonic test) (Equations (1) – (3)), $E_{t,0}$ = Young´s modulus longitudinal (static test) (Equation (7)), $G_{RT,LR,reduced}$ = reduced shear moduli in RT, LR plane, $G_{RT,TL,LR}$ = Shear moduli in symmetry planes (ultrasonic test) (Equations (4) – (6)), $G_{RL,static}$ = Shear modulus TL-plane (static test) (Equation (8)), ρ = density.
According to Fruehwald-Koenig et al. [17], Poisson's ratios are not density dependent. Therefore, the mean values μ_{LT} = 0.497, μ_{LR} = 0.497 and μ_{RT} = 0.117 are used. For the densified lamellas, the E- and G-values given in Table 1 are used. They are determined using Equations stated in Koelli and Fruehwald-Koenig [23] estimating a density of 550 kg/m³ and adjustments as described above. As Poisson's ratios, the ratios for undensified material as stated above are used.

Table 1: *Material parameters densified tension lamellas*

	E_L [MPa]	E_R [MPa]	E_T [MPa]	G_{RT} [MPa]	G_{LT} [MPa]	G_{LR} [MPa]
40 %	6301.4	212.3	125.4	43	139.6	148.6
60 %	3741.3	211.6	36.7	43	139.6	157.5

3.5 PLASTIC MATERIAL PARAMETERS

The compressive yield strength is defined as the strength of a material at the transition from elastic to plastic material behaviour. The determination of the compressive yield strength is realised using [4] and [24] and based on the stress-strain diagrams of the compression tests of oil palm wood in service dimensions carried out by Heister and Fruehwald-Koenig [25].
Starting the determination, a straight line is formed through the linear area of the stress-strain diagram. Subsequent this line is shifted parallel by a plastic strain of 0.02 %. The intersection of the shifted line and the test curve defines the elastic limit. The stress in the intersection point corresponds to the compressive yield strength.
The compressive yield strength longitudinal (L) ranges from 5.3 to 34 MPa (mean 15 MPa). An exponential relationship with density is observed (R^2 = 0.76, see Equation (11)).

$$f_{c,L}(\rho) = 1.6115\,e^{0.0052\rho} \quad (11)$$

where $f_{c,L}$ = compressive Yield-strength longitudinal, ρ = density.
The compressive yield strength radial/tangential (R/T) ranges from 0.42 to 0.60 MPa. No relationship with density (R^2 = 0.08) can be proven. The mean value of 0.499 MPa is used as input parameter.
Due to the brittle material behaviour of oil palm wood under tensile load, the tensile yield strength is assumed to be equal to the tensile strength. Equation (12) and (13) show the relationship between density and tensile strength (L) $f_{t,L}$ and tensile strength (R/T) $f_{t,RT}$ [14].

$$f_{t,L}(\rho) = 0.00004\,\rho^{2.12} \quad (12)$$

$$f_{t,RT}(\rho) = 0.0002\,\rho^{1.4} \quad (13)$$

where $f_{t,L}$ = tensile strength (longitudinal), $f_{t,RT}$ = tensile strength (radial / tangential), ρ = density.
Due to limited data on the plastic behaviour of oil palm wood under shear stress, shear yield strengths are assumed to be equal to shear strengths.
Equations (14) and (15) show relationships between density and rolling shear strength and shear strength in the R/T plane (longitudinal loading) [14].

$$f_{v,RT}(\rho) = 0{,}001\,\rho^{1{,}0539} \quad (14)$$

$$f_{v,RL}(\rho) = 0{,}0004\,\rho^{1{,}3573} \quad (15)$$

where $f_{v,RT}$ = rolling shear strength, $f_{v,RL}$ =shear strength (tangential plane, longitudinal load), ρ = density.
For shear strengths in the transverse plane, no correlations are available in the literature. To approximate the shear strengths in the transverse plane, ratios of shear strengths in different plane-load combinations of beech wood according to Kollmann [26] are used to adjust the rolling shear strength and shear strength in the radial/tangential plane (L).
The hardening modulus is defined as the slope between the compressive yield strength and the compressive strength. The hardening modulus (L) reaches values of 526 to 3193 MPa (mean value 1486 MPa). An relationship with density is observed (R^2 = 0.50, see Equation (16)).

$$E_{p,L}(\rho) = 254.14\,e^{0.004\rho} \quad (16)$$

where $E_{p,L}$ = hardening modulus (L), ρ = density.
The hardening modulus (R/T) reaches values from 33.79 to 47.61 MPa. No relationship with density (R^2 = 0.00) can be proven. The mean value of the hardening modulus (R/T) (41.86 MPa) is used as input parameter.

4 METHODS

4.1 DETERMINATION OF FLEXURAL PROPERTIES

The flexural properties of glued laminated timber are determined in accordance with [4] using a four-point bending test. The support points are spaced 18 times the height of the beam (h) corresponding to 1836 mm. Load application points are required to be spaced 6 h (612 mm) apart. In the laboratory tests [7] partially deviating distances of 646 mm, 612 mm and 595 mm are used. Deviating from the requirements of the aforementioned standard solid wood (pine, oil palm) and plywood (beech, birch) riders instead of steel are used [7]. Local and global MOE as well as flexural strength are determined according to [4].

4.2 DETERMINATION OF MODELLING PARAMETERS AND EXPERIMENTS

The effects of varying parameters on the results of the modelling of GLT beams are investigated. The effects are tested in three experiment sets. In the first experiment set (I), the influences of the parameters geometry (2D / 3D), material model (isotropic, orthotropic), material parameter determination (non-destructive, destructive) implementation of riders and element size (8.5 mm, 5.66 mm) on the elastic flexural properties are investigated. Between each experiment one parameter is changed at a time, this enables the observation of the parameter effect. In each individual experiment, 23 beams are investigated and six experiments are carried out.

In the second experiment set (II), the general suitability of FEM for determining the flexural strength of oil palm-based GLT is investigated. Furthermore, the influence of the implementation of riders is again investigated. In addition, densified tension lamellas (cf. section 3.3) are examined separately in two individual experiments. Four different experiments are carried out on 22 GLT beams.

In the third experiment set (III), the influence of variations in the material parameters hardening moduli ($E_{p,L}$, $E_{p,R}$, $E_{p,T}$), compressive yield strengths (R/T) ($f_{c,R}$, $f_{c,T}$), material model (orthotropic plastic: compression zone / total specimen), tensile yield strength (L) ($f_{t,L}$) and shear yield strengths ($f_{v,RT}$, $f_{v,LT}$, $f_{v,LR}$) are investigated on a homogeneous beam model with lamellas of the same density. The total sum of the individual experiments of the third experiment set is 17.

4.3 EXPERIMENT IMPLEMENTATION IN MODELLING SOFTWARE

The modelling is realised using RFEM 6.02 (Dlubal Software GmbH). The beams are represented as two- or three-dimensional geometric models. The lamellas are represented by planes or volume elements. A solid bond is assumed between the lamellas. Modelling of the adhesive joints is omitted in this work, as no failure of the adhesive joints is reported in the laboratory tests.

Isotropic linear and orthotropic linear elastic material models are used to model the local and global MOE. For modelling the flexural strength orthotropic plastic material behaviour is assigned to the compression zone, tension and shear zone are described by orthotropic linear elastic material behaviour. For the description of the material behaviour, nine (orthotropic linear elastic) respectively 21 (orthotropic plastic) material parameters are necessary. The material parameters are determined as described in sections 3.4 and 3.5.

The support is realised as nodal supports or line supports. Displacements along the Y- and Z-axes are omitted. Along the X-axis displacements are possible. The bearings in the X-direction are described by a spring (k = 0.1 kN/m).

The lamellas are modelled with the help of two- and three-dimensional, rectangular plate or cubic volume elements. The element size is set to 5.66 mm or 8.5 mm, which corresponds to two respectively three elements over the height of one lamella. Depending on the settings the models are formed out of 3108 – 366019 elements with 3380 - 110802 nodes.

Loads are applied as nodal or line loads. Half of the total load is applied at each of the two load application points. For the determination of the elastic flexural properties, the loads are applied in two steps representing 10 % and 40 % of the estimated maximum load. The application of the orthotropic plastic material model requires stepwise calculations. Within each load step, equilibrium is determined using the Newton-Raphson method with a maximum of 100 iterations. The load is increased in steps of 50 N as a compromise between accuracy and calculation time.

Four nodal supports are used to determine the deflection necessary to calculate the elastic flexural properties. The supports are arranged according to [4]. To determine the maximum load required to calculate the flexural strength, the longitudinal stresses at raster points on the tensile lamellas are compared to the tensile strength of the corresponding lamella. Failure occurs when the recorded stress exceeds the tensile strength. Tensile strengths and stresses are compared at each load level. Load and stress of the failure load level and the previous load level are used to determine the maximum load by interpolation.

The deformation and stresses are calculated using the solver implemented in RFEM 6.02 and according to first-order theory. The results are presented in the form of graphical representations of the result gradients and tabular output of results in nodes and at grid points (10 mm spacing, total 7120 grid points) on the boundary surfaces of the tension lamellas.

5 RESULTS AND DISCUSSION

5.1 RESULTS FOR LOCAL MOE

Table 2 shows statistical variation parameters of the first experiment set regarding the local MOE. The mean values reach from 4050 MPa to 9625 MPa (laboratory tests 5422 MPa).

Normal distribution can be assumed for all experiments and laboratory tests acc. to an Anderson-Darling test. A one-factor ANOVA and a posterior pairwise t-test with alpha error correction according to Bonferroni shows significant differences of the mean values.

https://doi.org/10.52202/069179-0088

Table 2: *Statistical variation parameters local MOE*

	Parameter	Min [MPa]	Max [MPa]	Mean [MPa]	Sd [MPa]	COV [%]
Exp. I.1	2D, iso, nr, nd, 8.5	7934	10848	9347	838	8.97
Exp. I.2	3D, iso, nr, nd, 8.5	8238	11078	9625	832	8.64
Exp. I.3	3D, ortho, nr, nd, 8.5	7961	10701	9313	815	8.75
Exp. I.4	3D, ortho, nr, d, 8.5	2759	5768	4155	864	20.78
Exp. I.5	3D, ortho, r, d, 8.5	2756	5613	4051	820	20.23
Exp. I.6	3D, ortho, r, d, 5.66	2746	5603	4050	823	20.32
laboratory test [7]		3151	7128	5422	1055	19.46

2D/3D: model dimension, iso/ortho: iso-/orthotropic, r/n.r.: rider, no rider, d./n.d: destructive, non-destructive material parameter, 5.66/8.5: element size

Figure 1 shows the relationships between density and local MOE (experiments and laboratory test). The results of the local MOE show linear correlations with the density in all individual experiments with R^2 between 0.52 and 0.55. The slopes of the linear relationships are lower than that of the laboratory test. Differences between the equations of the regression lines are limited to the ordinate intercept. The regression lines are parallel shifted.

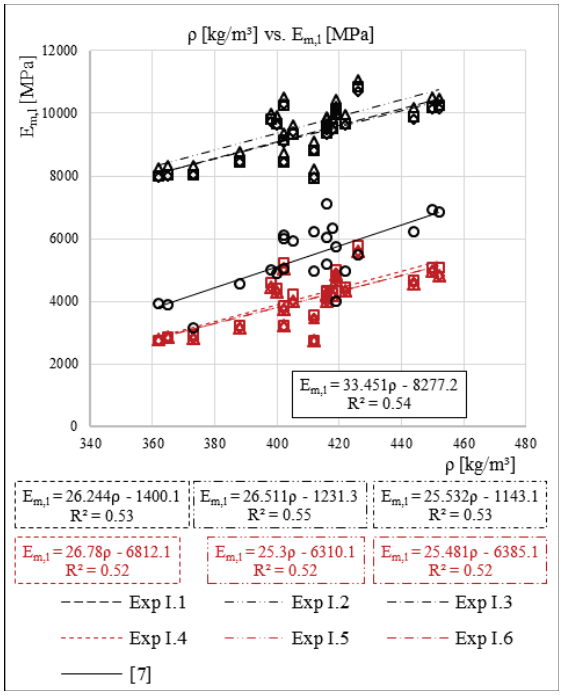

Figure 1: *Relationship between density and local MOE (statistical variation parameters see Table 2)*

5.2 RESULTS FOR GLOBAL MOE

Table 2 shows statistical variation parameters of the first experiment set regarding the global MOE. The mean values reach from 7447 MPa to 18513 MPa (laboratory tests 4562 MPa). Normal distribution can be assumed for all experiments and laboratory tests acc. to an Anderson-Darling test.

A one-factor ANOVA and a posterior pairwise t-test with alpha error correction according to Bonferroni shows significant differences of the mean values.

Table 3: *Statistical variation parameters global MOE*

	Parameter	Min [MPa]	Max [MPa]	Mean [MPa]	Sd [MPa]	COV [%]
Exp. I.1	2D, iso, nr, nd, 8.5	15806	21414	18513	1666	9.00
Exp. I.2	3D, iso, nr, nd, 8.5	15475	20500	18053	1544	8.55
Exp. I.3	3D, ortho, nr, nd, 8.5	14955	19911	17501	1515	8.66
Exp. I.4	3D, ortho, nr, d, 8.5	5092	9953	7447	1442	19.37
Exp. I.5	3D, ortho, r, d, 8.5	5128	10350	7773	1562	20.10
Exp. I.6	3D, ortho, r, d, 5.66	5128	10335	7779	1544	19.85
laboratory test [7]		2541	6142	4562	1022	22.41

2D/3D: model dimension, iso/ortho: iso-/orthotropic, r/n.r.: rider, no rider, d./n.d: destructive, non-destructive material parameter, 5.66/8.5: element size

Figure 2 shows the relationships between density and global MOE (experiments and laboratory test). The results of the global MOE show linear correlations with the density in all individual experiments with R^2 between 0.53 and 0.57. The slopes of the linear relationships are higher than that of the laboratory test differences between the equations of the regression lines are limited to the ordinate intercept. The regression lines are parallel shifted.

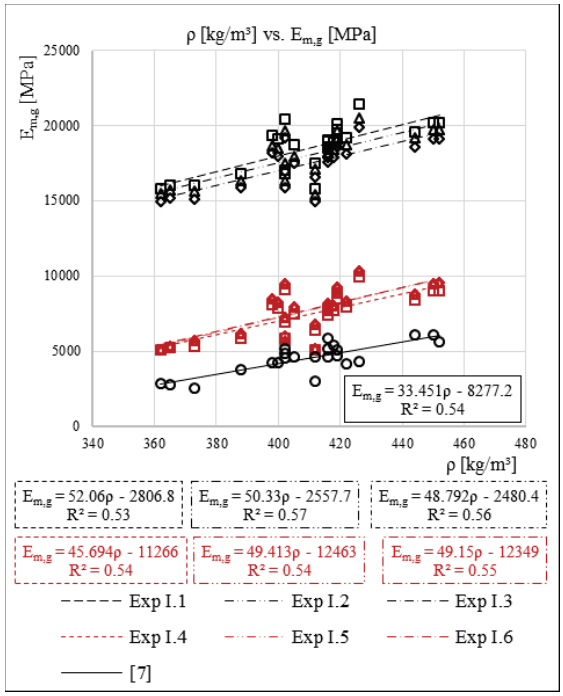

Figure 2: *Relationship between density and global MOE (statistical variation parameters see Table 3)*

5.3 DISCUSSION LOCAL AND GLOBAL MOE

The differences between the experiments can be attributed to varying factors. The difference between experiment I.1 and I.2 is the geometrical dimension (2D, 3D). Only minor effects for components homogeneous across the width occur. The small difference between experiment I.2 and I.3 after changing the material model is attributed to the load case. In four-point bending tests, stresses primarily occur in fibre direction. According to Ehlbeck et al. [18], the Young´s modulus in the fibre direction is the dominating factor for the flexural properties of GLT beams. The Young´s modulus in fibre direction is not varied between experiment I.2 and I.3. The implementation of riders according to [4] in experiments I.5 and I.6 shows no significant effect. The modelling is carried out in the elastic range of the material behaviour of the oil palm wood (no plastic deformations occur). The riders serve to distribute and transmit the load. Minimising the element size (experiment I.6) shows no significant effect in this study. Discretisation by using two or three elements over the lamella thickness is considered sufficient [28]. The significant differences between experiment groups I.1 – I.3 and I.4 – I.6 are attributed to the choice of material parameters. The difference of the Young´s modulus in the fibre direction as one of the main influencing parameters corresponds to 55.4 %. The differences for local MOE (56.7 %) and global MOE (57.5 %) between the experiment groups show similar percentages.

Comparison of the local and global MOE shows that the global MOE exceeds the local MOE in all experiments. Heister and Fruehwald-Koenig [7] report an opposite relationship for the laboratory tests (local MOE > global MOE). The ratio of the mean values of local to global MOE ranges from 0.505 to 0.558. The laboratory tests provide a ratio of 1.189 (0.99 spruce [29]). Thus, the modelled values are below the comparative literature values. Boström [30] reports for spruce, that the local MOE > global MOE if the global MOE is > 10 GPa and local MOE < global MOE if the global is < 10 GPa. Boström [29] attributes the differences between local and global MOE to shear deformations and the influence of timber defects in small cross-sections. The effects described are consistent with the results of experiments I.4 – I.6. Applying one density the whole lamella, leads to a reduction of the natural property gradients (artificial homogenisation). The absence of these natural property variations and defects results in comparably higher values for the global MOE, the influence on the local MOE is less pronounced.

5.4 RESULTS FOR FLEXURAL STRENGTH

Table 4 shows statistical variation parameters of the second experiment set regarding the flexural strength. The mean values are 13.3 MPa and 13.9 MPa (laboratory tests 22.1 MPa). Normal distribution cannot be proven for all experiments. Only the laboratory test shows normal distribution according to an Anderson-Darling test. A Friedman-Test and a posterior pairwise, paired Wilcoxon-Test with alpha error correction according to Bonferroni shows significant differences between the experiments and the laboratory test.

Table 4: *Statistical variation parameters flexural strength*

	Parameter	Min [MPa]	Max [MPa]	Mean [MPa]	Sd [MPa]	COV [%]
Exp. II.1	nr	9.5	15.7	13.3	2.2	16.5
Exp. II.2	r	9.7	16.5	13.9	2.4	17.5
laboratory test [7]		11.7	29.7	22.14	5.57	25.16

r/n.r.: rider, no rider

Figure 3 shows the relationships between density and flexural strength divided for specimen groups A (assembled) and N (natural). R^2 ranges from 0.53 to 0.55. The slope of the laboratory test is steeper than the experimental slopes for specimen group N. The regression lines of the laboratory results from Heister and Fruehwald-Koenig [7] lie above the regression lines of the experiments. Specimen group A (assembled) shows similar slopes for experiments and laboratory tests. The regression lines of specimen group N (natural) agree for the experiments, but differ to that from laboratory testing. This leads to the conclusion, that inhomogeneity and variations in material properties influence the results of the flexural test. Further tests are recommended to enable reliable statements about the stochastic behaviour of the flexural properties of oil palm based GLT.

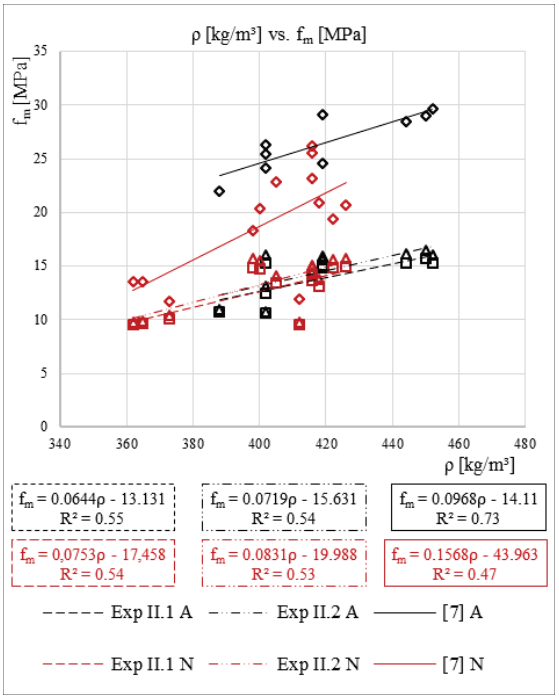

Figure 3: *Relationship between density and flexural strength divided by specimen group A (assembled) and N (natural)*

https://doi.org/10.52202/069179-0088

The comparison with the results of Heister and Fruehwald-Koenig [7] shows mean percentage deviations of -38.6 %. These deviations tend to correspond to the deviations of the local MOE (-25.5 %). Increasing the values of the elastic constants leads to stiffer material behaviour. This in turn results in loads being transferred with a certain delay and thus the critical tensile strengths in the tensile zone are reached later. The flexural strength increases. Further, the choice of the material model influences the flexural strength. Blaß et al. [19] point out that the use of the linear elastic material model in the tensile zone leads to an underestimation of the flexural strength. Plastic material behaviour in the tensile zone results in stress redistributions and thus a delayed attainment of the critical tensile stress. The sensitivity analysis (see section 5.8) shows that the application of the orthotropic plastic material model in the tensile zone results in an increase of the flexural strength of about 3.8 %.

Figure 4 shows the relationships between the density of the tensile lamellas and the flexural strength. Linear relationships are observed (R^2 = 0.83 Exp. II.1, R^2 = 0.84 Exp. II.2). R^2 (0.39) for the laboratory is lower compared to the experiments. Deviation from the behaviour observed for specimen group N (natural) in Figure 3, the regression line of the data from Heister and Fruehwald-Koenig [7] runs roughly parallel above the regression lines of the experiments. It can be observed that the density of the tension lamellas shows better correlations to the flexural strength than the overall density of the GLT beams.

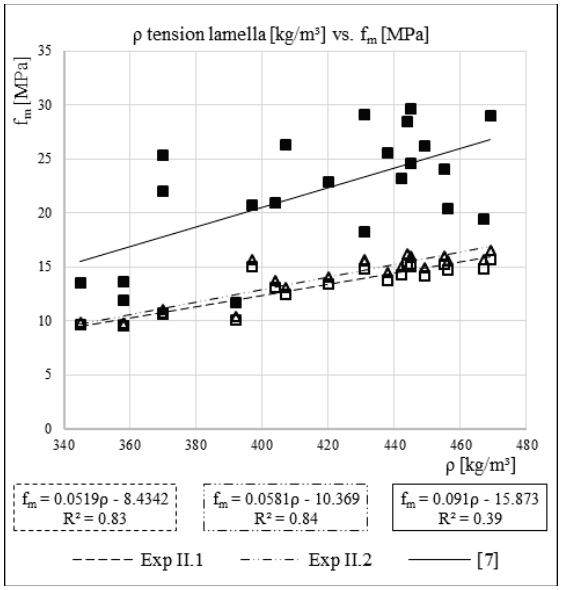

Figure 4: *Relationship between density tension lamella and flexural strength*

The differences between experiment II.1 and experiment II.2 are due to the change in the supports and load application points. Two effects can be observed due to the introduction of riders. The first effect is that plastic deformations are initiated later due to the load distribution over a larger area. Frese [20] confirms this effect by modelling homogeneous comparison beams. The second effect is the change in the stress profile within the tension lamella. As described by Frese [20], a rounding of the stress profile can be observed, which leads to the critical tensile stress being reached later. The mean percentage deviation between the experiments of 4.6 % exceeds the value of 1 % reported by Frese [20] for beech. The effect of load distribution by the riders therefore is higher for oil palm wood. The observed behaviour might be explained by the comparably low compressive strength (R/T) of oil palm wood.

5.5 INFLUENCE OF DENISFIED TENSION LAMELLAS

The use of tension lamellas of uniform density (550 kg/m³) in all test specimens results in a reduction of the observed variations. These variations represent the influence of the remaining test specimen structure. The flexural strength is increased compared to the comparison experiment (Exp. II.2) up to a density of 398 kg/m³ (40 % dens.) and 434 kg/m³ (60 % dens.). Surpassing those aforementioned thresholds, the flexural strength is decreased. This reflects the results of Koelli and Fruehwald-Koenig [23], who report that at the same density, undensified specimens show higher flexural strengths than densified specimens. This explains why despite the higher density of the densified tensile lamellas (550 kg/m³), no improvement in flexural strength can be achieved when the thresholds are exceeded. Densified tension lamellas are therefore particularly suitable for improving the flexural properties of low-density beam structures.

5.6 SENSITIVITY ANALYSIS

Within the sensitivity analysis, influences of the factors listed in section 4.2 on the flexural strength are investigated on the basis of percentage deviations from the comparison experiments III.C1 and III.C2 (Table 5).

Reducing the hardening modulus (R/T) from 41.9 MPa to 4.4 MPa in experiment III.1.1 reduces the flexural strength to 12.0 MPa (-3.6 %). A further reduction of the hardening modulus (R/T) to 0.2 MPa in experiment II.1.2 results in a further reduction of the flexural strength to 10.8 MPa (-13.7 %).

Variation of the compressive yield strength (R/T) shows little influence on the modelling results. Increasing the compressive yield strength (R/T) to 1 MPa (100 % increase) in experiment III.2.1 results in an increase in flexural strength of 0.005 MPa (+0.03 %). Increasing the compressive yield strength (R/T) to 4 MPa (700 % increase) in experiment III.2.2 results in an increase in flexural strength of 0.1 MPa (+0.3 %).

In experiment III.C2, the orthotropic plastic material model is assigned to all lamellas of the comparative specimen. Due to this change, the flexural strength of the reference specimen is increased to 13.0 MPa (+3.8 %). The change of the material model, reduces the compressive stresses in the support area. As described by Blaß et al. [19], stress redistributions in the tensile zone are possible using orthotropic plastic material behaviour, which lead to the critical tensile stress being reached later.

Experiments III.3 and III.4 evaluate the effects of a combination of the change of the material model and increased tensile yield strength (L). When changing the tensile yield strength (L), two separate considerations are to be carried out depending on the chosen comparative tensile strength (L) of the tensile lamellas (cf. section 4.3). Not increasing the critical tensile strength (L) and keeping it at 13.1 MPa (Exp. III.3.2 and III.4.2), results in flexural strengths of 13.0 MPa (-0.1 %, Exp. III.3.2 and Exp. III.4.2). Increasing the critical tensile strength (L) according to the increased tensile yield strength (L), results in flexural strengths of 19.6 MPa (+50.9 %, Exp. III.3.1) and 28.9 MPa (+123.3 %, Exp. III.4.1). The recorded percentage increases of flexural strengths are equal to the percentage increases of the applied tensile yield strengths (L) of 52.32 % and 128.48 %.

The increase of the shear yield strengths (Exp. III.5) shows only little influence on the flexural strength of the comparative specimen, (increase of 0.02 %) because of the choice of test arrangement. In four-point bending tests, only low shear stresses occur.

The sensitivity analysis shows that variations in the hardening moduli have a large influence on the flexural bending strength and needs further investigations. Variations of tensile yield strengths (L) with simultaneous adjustment of the critical tensile strength shows strong effects and needs further investigations. Variations in compressive yield strength and shear yield strength have small influence on the flexural strength. The parameters are applicable in the chosen form.

Table 5: *Sensitivity analysis result and percentage deviations*

	III.C1	III.1.1	III.1.2	III.2.1	III.2.2	
f_m [MPa]	12.5	12.0	10.8	12.5	12.5	
Deviation [%]		3.6	13.7	0.03	0.3	
	III.C2	III.3.1	III.3.2	III.4.1	III.4.2	III.5
f_m [MPa]	13.0	19.6	13.0	28.9	13.0	13.0
Deviation [%]		50.9	0.06	123.3	0.07	0.04

Exp. III.1: reduction hardening moduli (R/T), Exp. III.2: increase compressive yield strength, Exp. III.3: change material model, increase tensile yield strength (L), Exp. III.4: change material model, increase tensile yield strength (L), Exp. III.5: change material model, increase shear yield strength

6 CONCLUSION AND OUTLOOK

The results of the modelling confirm the applicability of the finite element method for modelling oil palm wood-based GLT. The selected geometric models as volume and plane models based on individual layers with varying material properties as well as the chosen support and load application implementation are suitable for a realistic representation of the comparative tests.

Geometric representation, material model, riders as well as element size show no significant influence on the results of the modelling of the local and global MOE, whereas the material parameter determination has a significant influence on the modelled MOE. Deviating from this, the implementation of riders shows a significant influence on the modelling results of the flexural strength. In further investigations, an implementation of riders is strongly recommended.

The comparison of the flexural properties (MOE and flexural strength) with the results of the laboratory tests by Heister and Fruehwald-Koenig [7] shows significant differences due to the material constants used (elastic constants and tensile strength) and the material model used in the tensile zone. The effects of material constants and material model adjustments have to be investigated in experiments on a larger scale.

The relationships between density and local and global MOE proven in this work show comparable forms to Heister and Fruehwald-Koenig [7], whose differences lie primarily in the ordinate intercepts determined. Comparable behaviour is shown by the relationships between density of the specimens and flexural strength (for specimen group A (assembled lamella)) and between tensile lamella density and flexural strength (overall collective). The overall collective as well as specimen group N (natural lamella) show uniform shapes within the modelling for the relationship between density and flexural strength but deviate strongly from the results of Heister and Fruehwald-Koenig [7]. An adjustment of the ordinate intercept is not expedient. The observed behaviour offers a starting point for further investigations regarding the optimisation of the modelling results. The use of densified tension lamellas results in a homogenisation of the flexural strength. Especially the performance of lower density specimens can be improved by using densified tension lamellas. The level of improvement is higher for higher densification rates.

The local and global MOE of the modelling show a different behaviour compared to the literature. The global MOE exceeds the local MOE in all experiments. Further investigations on the global MOE are recommended. An effect of the artificial homogenisation, by applying only one density for one lamella and reducing the natural property gradients, on the results of the global MOE can be demonstrated for specimen group N (natural).

The sensitivity analysis identifies the hardening modulus, the tensile yield strength (L) and the choice of material model in the tensile zone as parameters that strongly influence the results of the flexural strength. The parameters compressive yield strength (R/T) and shear yield strength show much lower influence. The sensitivity analysis is suitable for determining parameter influences.

The results of this work offer starting points for further investigations, in particular the consideration of the influencing factors identified in this work, the modelling of oil palm-based cross laminated timber as well as the application of statistically varying material constants for the representation of larger specimen collectives and the improved representation of natural property variations within the lamellas.

ACKNOWLEDGEMENTS

The laboratory tests referred to in this study were carried out by Prof.'in Dipl.-Holzwirtin Katja Fruehwald-Koenig (creation of a grading system for oil palms, lamella grading and determination of the GLT structure) and Lena Heister M.Sc. (production and testing of the GLT beams).

https://doi.org/10.52202/069179-0088

The evaluation and results of the investigations can be found in the publication by Heister and Fruehwald-Koenig [7]. The investigation was financed by the German Federal Ministry of Education and Research through the “Bioökonomie International 2017” project “Oilpalmsugar (031B0767A)”, as well as the Ministry of Culture and Science of the State of North Rhine-Westphalia through the project “005-2105-0054”.

REFERENCES

[1] Food and Agriculture Organization of the United Nations: Crops and livestock products. https://www.fao.org/faostat/en/#data/QCL, 2023.

[2] Lim S. C., Khoo K. C.: Characteristics of oil palm trunk and its potential utilization. Malaysian Forest, 49:3–22, 1986.

[3] Fruehwald A., Fruehwald-Koenig K.: The Use of Oil Palm Trunks for Wood Products. In: By-Products of Palm Trees and Their Applications, 69–80, 2019

[4] EN 408+A1:2012-07: Timber structures - Structural timber and glued laminated timber - Determination of some physical and mechanical properties. CEN European Committee for Standardization, 2012.

[5] EN 14080:2013-06: Timber structures - Glued laminated timber and glued solid timber - Requirements. CEN European Committee for Standardization, 2013.

[6] Fruehwald-Koenig K.: Properties and Grading of Oil Palm Lumber. In: Proceedings: 21st International Nondestructive Testing and Evaluation of Wood Symposium, 204–212, 2019

[7] Heister L., Fruehwald-Koenig K.: Glued Laminated Timber from Oil Palm Timber – Beam Structure, Production and Elastomechanical Properties. In: Proceedings of 2nd World Conference on Byproducts of Palms and Their Applications, 29–44, 2022.

[8] Tomlinson P. B., Horn J. W. and Fisher J. B.: The anatomy of palms: Arecaceae - Palmae. Oxford University Press, 2011.

[9] E. S. Bakar, M. H. Sahri, and P. S. H’ng. Anatomical characteristics and utilization of oil palm wood. In T. Nobuchi, M. H. Sahri, *The formation of wood in tropical forest trees–a challenge from the perspective of functional wood anatomy*, pages161–178. Penerbit Universiti Putra, Malaysia, 2008.

[10] Killmann W., Lim S. C.: Anatomy and properties of oil palm stem. In: Proceedings National Symposium of Oil Palm By-Products, 1–25, 1985.

[11] Koelli N.: Density and Moisture Distribution in Oil Palm Trunks from Peninsular Malaysia. Bachelor-Thesis, University of Hamburg, Hamburg, 2016.

[12] Fathi L.: Structural and mechanical properties of the wood from coconut palms, oil palms and date palms. PhD-Thesis, University of Hamburg, Hamburg, 2014.

[13] Srivaro S., Matan N., Lam F.: Property gradients in oil palm trunk (*Elaeis guineensis*). Journal of Wood Science, 64(6):709–719, 2018.

[14] Fruehwald-Koenig K., Heister L.: Macro- and Micromechanical Behavior of Oil Palm Wood (*Elaeis guineensis* JACQ.): Tensile, Compression and Bending Properties. Submitted publication, 2023.

[15] Fruehwald-Koenig K., Faust B.: Evaluation of Elastic Constants of Oil Palm Wood using Ultrasonic Measurement. In: Proceedings: 22st International Nondestructive Testing and Evaluation of Wood Symposium, 29–39, 2022.

[16] Koelli N.: Relation shear modulus and densitiy for oil palm wood (*Elaeis guineensis* JACQ.). Personal communication, 2022.

[17] Fruehwald-Koenig K., Faust B., Hackel M.: Macromechanical and Micromechanical Behavior of Oil Palm Wood (*Elaeis guineensis* JACQ.): Elastic Constants and Shear Strength. Publication in preparation, 2023.

[18] Ehlbeck J., Colling F., Görlacher R.: Einfluß keilgezinkter Lamellen auf die Biegefestigkeit von Brettschichtholzträgern. Holz als Roh-und Werkstoff. 43(8):333–337, 1985.

[19] Blaß H. J., Denzler J., Frese M., Glos P. and Linsemann P.: Biegefestigkeit von Brettschichtholz aus Buche. Universitätsverlag Karlsruhe, 2005.

[20] Frese M.: Die Biegefestigkeit von Brettschichtholz aus Buche. Experimentelle und numerische Untersuchungen zum Laminierungseffekt. Universitätsverlag Karlsruhe, 2006.

[21] Gao Y., Wu Y., Zhu X., Zhu L., Yu Z., Wu Y.: Numerical Analysis of the Bending Properties of Cathay Poplar Glulam. Materials 8(10):7059-7073, 2015

[22] Fruehwald-Koenig K., Koelli N., Fruehwald A.: Mechanical Dewatering of Wet Oil Palm Lumber Prior to Press-Drying. In: Proceedings of 2nd World Conference on Byproducts of Palms and Their Applications, 11–27, 2022.

[23] Koelli N., Fruehwald-Koenig K.: Elastomechanical Properties of Thermo-Hygro-Mechanical (THM) Densified Oil Palm Lumber. Submitted publication, 2023.

[5] DIN 50099:2018-12: Tensile testing of metallic cellular materials. DIN Deutsches Institut für Normung e. V., 2018.

[25] Heister L., Fruehwald-Koenig K.: Compression and Tensile Properties Oil Palm Wood (*Elaeis guineensis* JACQ.) Specimen in Dimension of Use. Submitted publication, 2023b.

[26] Kollmann F.: Technologie des Holzes und der Holzwerkstoffe: Anatomie und Pathologie, Chemie, Physik, Elastizität und Festigkeit. 2nd ed. Springer Berlin Heidelberg, 1951.

[27] Vida C., Lukacevic M., Eberhardsteiner J., Füssl J.: Modeling approach to estimate the bending strength and failure mechanisms of glued laminated timber beams. Engineering Structures, 255:113862, 2022.

[28] Boström L.: Determination of the modulus of elasticity in bending of structural timber - comparison of two methods. Holz als Roh-und Werkstoff, 57(2):145–149, 1999.

World Conference on Timber Engineering Oslo 2023

BENDING PROPERTIES OF 100 NARROW CLT-BASED BOARDS – STATIC AND DYNAMIC TESTS AND DIC ANALYSIS

Mikael Perstorper[1], Johan Vessby[2], Emil Lockner[3]

ABSTRACT: Production of CLT-panels typically results in 5-10% cut-offs due to window and door openings. CLT-boards can be made by slicing these cut-offs and finger-jointing them. This paper presents bending properties of 100 narrow CLT-boards (45x95x1800) made from 5-ply CLT panels made of Norway spruce. A limited variation in E-modulus (CV=9%) and bending strength (CV=20%) was found with gross section values not far from typical structural C24-timber. The tests indicate that narrow CLT-boards have sufficient bending properties for being used as structural components, also where the bending capacity is formally utilized. However, the variation was slightly higher than for typical tests on larger CLT-elements (CV=8-16%), probably due to the smaller homogenization effect when fewer sub-parts carry the load. The rolling shear modulus was estimated to be G_r= 65 MPa, which is to be expected due to the distance from the pith of the cross layer boards. The surprisingly high net flatwise bending strength ($f_{m,05}$=49 MPa) can likely be attributed, for the most part, to the reinforcing effect from the cross layers that limit the slope of grain cracking near knots in the longitudinal layers. DIC-tests revealed an indication of a non-plane normal strain distribution over the beam depth in the shear-free zone between the inner loading points. This might lead to an underestimation of the shear-free local E-modulus according to EN 408.

KEYWORDS: CLT, bending strength, E-modulus, rolling shear modulus, strain distribution, DIC-analysis

1 INTRODUCTION

The background of this study is the urge to find smart use of cut-offs from production of Cross Laminated Timber (CLT), see Figure 1. Due to window and door openings, 5-10% of all CLT material is typically chipped up to become biofuel. The idea here is to slice these cut-offs and finger-joint them to CLT-boards with sizes similar to structural timber. It has been verified that this kind of boards can successfully be finger-jointed.

The cross-layers weaken the bending properties compared with solid wood, but give the CLT-boards superior properties when loaded in the perpendicular direction as with horizontal rails in a wall frame. An up to fivefold increase in capacity has been found, see Vessby et al. [1]. However, in this paper the focus is on the bending properties of this kind of narrow CLT-based boards to verify that they have properties that allow for typical handling in the production of timber frame elements. Tests are also warranted in view of applications of the CLT-boards where the bending properties are critical also for formal load-bearing.

It has been shown in many studies that the variation in bending strength is much smaller in CLT, thanks to the fact that many boards carry the load together. One severe defect in an individual is not critical for the strength as neighboring boards carry the load. The coefficient of variation is typically CV=8-16%. Structural timber has a greater variation, especially if the classification is done to only one low grade like C24 and reject: (CV=30-35%). However, most studies on CLT has been done on quite large elements, typically 600 mm wide, which contain several boards. It is not clear how much narrower CLT-boards behave in bending where defects in single boards potentially are more critical for the overall behavior.

In the standardization work in Europe, the size limitations for the applicability of the CLT-standard for small sizes are discussed [2]. This study may contribute to the discussion about such limits. Furthermore, few studies have been done on the in-plane bending strength, especially with small sizes. One of few studies of small size CLT is the one reported by Flaig and Blaß. (2014). [3]. They studied the in-plane bending properties of smaller specimens down to 100x150 mm^2 with a focus on the lamination (system) effect. Their results are encouraging and indicated a substantial positive effect of the cross layers on the in-plane bending strength. However, the narrow CLT-boards focused on here are much smaller and only 45 mm deep for the in-plane bending mode (flatwise in this case).

The objective of this study was to investigate not only the edgewise properties but also the flatwise bending properties as the latter is of importance for practical handling at the construction site and/or at the pre-fabrication factory.

[1] Mikael Perstorper, Karlstad University and Dynalyse AB, Sweden, mikael.perstorper@kau.se
[2] Johan Vessby, Karlstad University, Sweden, johan.vessby@kau.se
[3] Emil Lockner, Karlstad University, Sweden, emil.lockner@kau.se

https://doi.org/10.52202/069179-0089

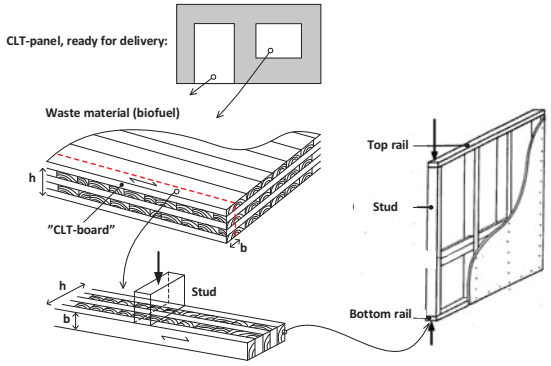

Figure 1: *Illustration of one of many possible uses of the cut-offs from CLT panels — horizontal rails (CLT-board).*

2 MATERIAL AND METHODS

2.1 MATERIAL

The material for the study came from the normal CLT-production at the Stora Enso mill in Gruvön, Sweden. A so called C5s panel with the intended use as a wall element was chosen. This 100 mm thick 5-ply CLT consisted of 20 mm thick layers of Norway spruce boards, strength graded as a single grade to T15. In this case it is comparable to C24, which for Nordic material gives a grading yield of about 99%. The boards were side-glued.
A total of 100 CLT-boards (slices) were produced and planed to the desired standard size (45x95x1800 mm^3) according to Figure 2. The thickness of the layers were: 17.25+20.3+20.3+20.3+17.25 mm resulting in an actual width of 95.4 mm. The boards were in this case cut from one full-size CLT-panel and not from cut-offs. Therefore, there was no need for finger-jointing of board parts from cut-offs. However, it should be noted that the individual boards in the CLT-panel were finger-jointed as usual. The layers were made of 100 mm wide, flat sawn side boards with an average distance from the board center to the pith of approximately 120 mm, see Figure 2. It can also be noted that some longitudinal layers were laminated and contained material from two different side-glued boards. Approximately 80% of the boards had one or more laminated layers.
The average moisture content of the boards was 9.4% and all reported elastic properties were adjusted to the reference moisture content 12%.

Figure 2: *Flatwise view and section of CLT-board where layer 3 and 5 is laminated (consists of two side-glued boards).*

2.2 STATIC TESTS AND DIC MEASUREMENTS

The CLT-boards were tested to determine the edgewise (50 pcs) and flatwise (50 pcs) static bending properties following the EN 408 standard [4]. One deviation was that the flatwise tests were done using the same test set-up as for the edgewise test with a span of 18 times the width (1710 mm), see Figure 3. Unfortunately, the measurement of the local E-modulus between the loading points using a yoke on the tension edge did not give reliable results and is not reported here. The global E-modulus E_{gl} is based on the overall mid-span deflection and the value presented here is not corrected for shear deformations, which are considerable due to the weak cross layers. Properties for the gross and net section were calculated. In the latter case the transverse E-modulus of the cross layers was assumed to be zero, E_{90}=0 MPa. The net E-modulus, without shear deformation influence, was calculated from the global value using the gamma method [5], assuming E_{90}=0 MPa and a rolling shear modulus of G_{90}=65 GPa based on dynamic test analysis.
Strain and displacement data from a Digital Image Correlation (DIC) system was gathered for 5 edgewise boards for the area between the loading points, see Figure 3.

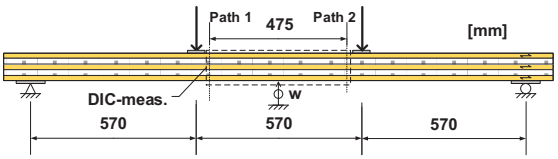

Figure 3: *Bending test set-up according to EN 408 [4] and zone for DIC strain measurement.*

2.3 DYNAMIC TESTS

The 50 boards that were tested in edgewise bending were also subjected to dynamic tests whereby the specimens were suspended in springs to simulate free-free boundary conditions, see Figure 4. Based on geometry, density and resonance frequencies for different vibration modes, E-moduli and shear moduli were determined. The first 3-4 modes of vibrations were analyzed for axial ($E_{d,ax}$), flatwise and edgewise bending ($E_{d,bf}$ + $E_{d,be}$) and torsion ($G_{d,t}$). For the bending vibrations, evaluation was made using beam theory according to both Euler-Bernoulli (Eu) and Timoshenko (Ti). In the latter case the influence of shear deformations and rotatory inertia is taken into account and the approximate solution suggested by Goens [6] was used. See also Hearmon [7] and Perstorper [8] for details on the evaluation of dynamic elastic properties. Since knowledge of the shear modulus G and the ratio E/G is needed for the evaluation, an iterative procedure was used for each board individually until the E-moduli for the first 3 modes of bending vibration coincided as much as possible. This shear-free E-modulus is denoted $E_{d,bf,Ti}$ and $E_{d,be,Ti}$ for flatwise and edgewise bending. As a result of the iteration, a gross shear modulus associated with bending was determined ($G_{d,be}$).

https://doi.org/10.52202/069179-0089

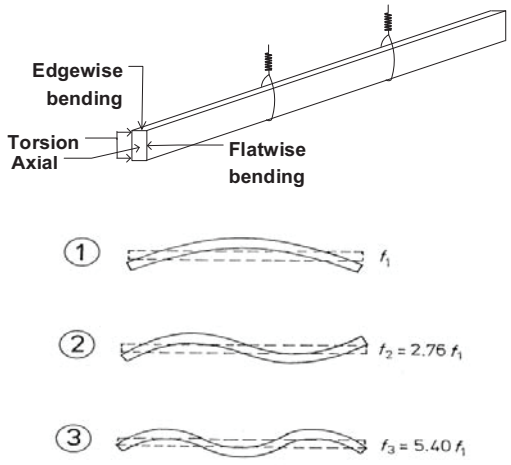

Figure 4: *Dynamic test set-up with indication of excitation directions and accelerometer positions. Visualisation of the mode shape of the first three bending modes.*

A shear mode was observed in the axial tests, for which the outermost layers slide on the weak cross layers, see Figure 5. This vibration mode is governed by the shear stiffness of the cross layers and an attempt was made to establish a model that allowed for an estimation of the rolling shear modulus G_r. In this simplified SDOF-model, the outer layer was modelled as a mass with infinite stiffness and the cross layer below as a shear spring with zero mass.

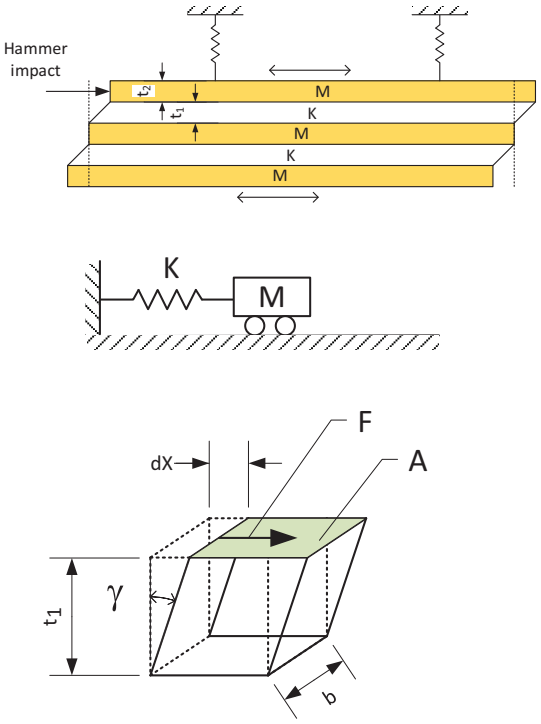

Figure 5: *Shear mode model.*

$$K = \frac{G \cdot A}{t_1} \tag{1}$$

$$f = \frac{1}{2\pi} \times \sqrt{\frac{K}{M}} = \frac{1}{2\pi} \times \sqrt{\frac{G}{\rho \cdot t_1 \cdot t_2}} \tag{2}$$

$$G_{d,r,sh} = (f \cdot 2 \cdot \pi)^2 \cdot \rho \cdot t_1 \cdot t_2 \tag{3}$$

The evaluated mode was the one where layer 3 was a node that did not move. The resulting Equation (3) for the rolling shear modulus $G_{d,r,sh}$ included the thickness (t_2) and density (ρ) of the outer layer, the thickness of the transverse layer (t_1) and the resonance frequency f.

3 RESULTS

3.1 STATIC PROPERTIES

3.1.1 Gross section analysis and overall product performance

The results from the static tests are presented in Table 1 for both the net section and the gross section. The reason for presenting the gross values is that it is easier to compare the overall practical performance of the CLT-boards to solid structural timber. In this sense, the CLT-boards had an edgewise and flatwise bending stiffness that were approximately 30% lower than C24 timber. On the other hand, and as expected, the variation was much smaller for the CLT-boards with a coefficient of variation (CV) of only 9% compared to the usual level for C24 of CV=20-25% for the E-modulus, see Figure 6 and Table 1. At the 5%-percentile level the gross stiffness of the CLT-boards was only 12% lower than the nominal level for C24 ($E_{0,05}$=7.4 GPa).

A similar pattern was found for the gross bending strength, where the bending capacity of the CLT-boards were lower on average but with a smaller variation compared with C24, see Table 1 and Figure 7. The gross average capacity was about 30% (edgewise) and 15% (flatwise) lower for the CLT-boards compared to typical values for single grade C24 ($f_{m,avg}$=45 MPa). The coefficient of variation was 22% and 19% for edgewise and flatwise capacity compared to the typical 30-35% for C24. Thanks to the limited variation, the 5%-percentile value for the gross bending capacity was only 16% lower for the edgewise tests, compared with the nominal value for C24 ($f_{m,05}$=24 MPa). For the gross flatwise bending capacity, the 5%-percentile was actually 19% higher than the C24-value.

In summary, one can conclude that the narrow CLT-boards have gross average bending properties that are not so far from typical structural timber (15-30% lower than C24). Thanks to the limited property variation, the gross 5%-percentile values of the CLT-boards are almost on a par with solid timber. The tests indicate that narrow CLT-boards have sufficient bending properties for being used as structural components, not only as rails but also for situations where the bending capacity is formally utilized.

https://doi.org/10.52202/069179-0089

Table 1: *Results from static bending test and physical properties representing the gross and net section. Average values and standard deviation within brackets. Density and E-modulus adjusted to the reference moisture content 12%. The 5%-percentiles were determined using ranking.*

Property		Edgewise	Flatwise
Basic data			
Number	n	50	50
Thickness	T (mm)	45 (0.2)	44.8 (0.2)
Width	W (mm)	95.4 (0.1)	95.3 (0.2)
Moisture content	u (%)	9.4 (0.4)	9.4 (0.4)
Density	ρ (kg/m^3)	487 (14)	483 (21)
Gross section			
Global E-modulus (shear infl.)	E_{gl} (GPa)	7.54 (0.70)	7.81 (0.73)
Global E-modulus 5%-perc.	$E_{gl,05}$ (GPa)	6.53	6.77
Bending strength	f_m (MPa)	32.2 (7.0)	38.3 (7.2)
Bending strength, 5%-perc.	$f_{m,05}$ (MPa)	20.2	28.6
Net section assuming E_{90}=0 and G_{90}=65 MPa			
Estim. net E-modulus	E_{net} (GPa)	12.2 (1.13)	13.6 (1.27)
Estim. net E-modulus 5%-perc.	$E_{net,05}$ (GPa)	10.6	11.8
Bending strength	$f_{m,net}$ (MPa)	42.9 (9.3)	66.7 (12.5)
Bending strength, 5%-perc.	$f_{m,net,05}$ (MPa)	27.0	49.1

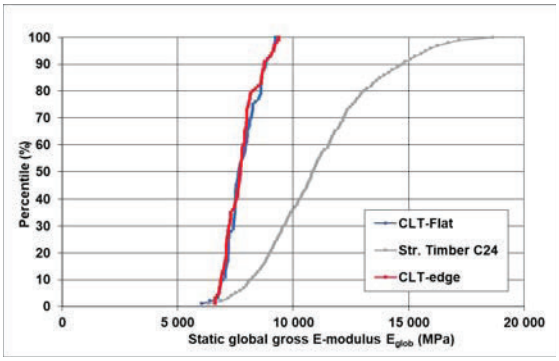

Figure 6: *Variation in edgewise and flatwise gross global E-modulus and comparison with typical Nordic structural timber (C24).*

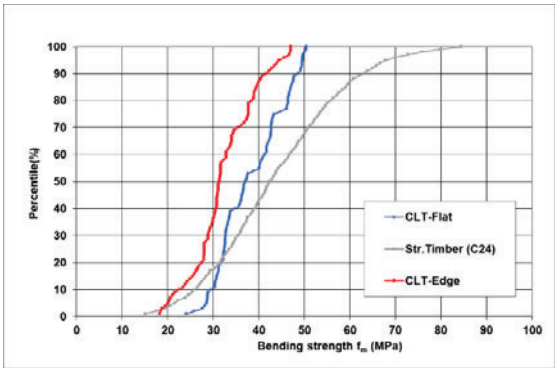

Figure 7: *Variation in edgewise and flatwise gross bending strength and comparison with typical Nordic structural timber (C24).*

3.1.2 Detailed evaluation and net section analysis

The net section properties presented here are based on an assumption that the E-modulus of the cross layers is zero (E_{90}=0). Furthermore, the effective rolling shear modulus of the cross layers is assumed to be G_r= 65 MPa, based on the dynamic tests, see below (section 3.2).

Based on the edgewise global E-modulus, and using the gamma method [5], the net local E-modulus is calculated to be $E_{net,be}$=12.2 GPa, which is higher than the nominal level of C24 of 11 GPa.

The corresponding net E-modulus for the flatwise tests was much higher: $E_{net,bf}$=13.6 GPa, indicating that the material in these boards might have been of a higher structural quality, despite the fact that the boards for the edgewise and flatwise tests were produced at the same time and came from the same batch. The higher net bending strength of the flatwise tests supports this idea, but the almost equal density does not, see Table 1.

However, side boards cut far from the pith as here has been found to have higher E-modulus and strength in many studies, e.g. Oscarsson et al. [9]

One might argue that a too high rolling shear modulus was assumed for the edgewise gamma evaluation, but it would require a value of G_r=44 MPa to get the edgewise net E-modulus $E_{net,be}$ to 13.6 GPa, which is not likely.

A third possible explanation would be a systematically higher E-modulus of the middle lamella (#3) compared to the outer lamellas (#1 and #5). The dynamic tests of the edgewise boards indicate such a tendency, since the edgewise net E-modulus $E_{d,be,Ti,net}$=12.9 was lower than the flatwise $E_{d,bf,Ti,net}$=13.5 MPa and axial E-modulus $E_{d,ax,net}$=13.8 MPa, see Table 3.

A fourth possible explanation would be if there is a lamination effect that is enhancing the E-modulus of the flatwise tests in another way compared with the edgewise direction. It can be noted that the 36 boards with laminated layers had a higher flatwise E-modulus than the 14 boards without laminations: $E_{net,bf}$ = 13.9 GPa vs 12.6 GPa, see Figure 11. For edgewise tests the effect was smaller: $E_{net,be}$ = 12.2 for the 37 boards with lamination vs. $E_{net,be}$ = 11.8 GPa for the 13 boards without laminations. This might indicate that there is a lamination effect for the E-modulus that possibly work differently in flatwise loading (in-plane) compared with edgewise loading (out-of-plane).

https://doi.org/10.52202/069179-0089

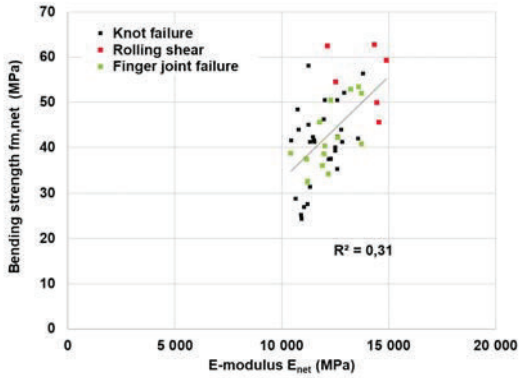

Figure 8: *Correlation between net static edgewise global E-modulus and net bending strength and indication of boards which capacity was limited by rolling shear failure.*

Most boards tested on edge, failed in bending due to knots or finger joints at the tension (predominantly) or compression edge, see Table 2 and Figure 8. However, six boards showed a rolling shear failure outside the loading points. This is quite common for bending tests of CLT with a span of 18 times the beam depth but does not influence the 5%-percentile value. These boards had a higher average failure load and E-modulus compared with the boards that failed in bending, see Figure 8 and Table 2.

The estimated shear stress in the cross layers at failure for the six boards was on average 1.36 MPa, with a range from 1.11 – 1.53 MPa. This is slightly lower than the rolling shear strength reported for Norway spruce by Ehrhart et al [10] but close to the tabled value for C24 for which the characteristic 5%-percentile value is $f_{v,90,k}$=1.1 MPa. It should be noted that there were drying cracks in the cross layers prior to testing, which may have had an influence, see Figure 2. Such cracks are common in CLT when the moisture content in service is lower than it was at the time of production.

It can be noted that the boards with finger joint failure had an average bending strength and E-modulus on a par with boards that failed due to knots. At the lower end of the strength distribution, there were only knot failures. Finger joints seem not to introduce weaknesses that lower the bending strength distribution, see Figure 9.

Table 2: *E-modulus and bending strength for different failure modes for edgewise tests, net section: Rolling shear failure in cross layers and tension/compression failure in outer layers due to knots or finger joints.*

Failure mode	No.	E-modulus	Bending strength
		E_{net} (GPa)	$f_{m,net}$ (MPa)
Rolling shear	6	13.8	55.7
Finger joint (tension or compression)	12	12.2	41.6
Knot (tension or compression)	32	11.9	40.6
All	50	12.2	42.9

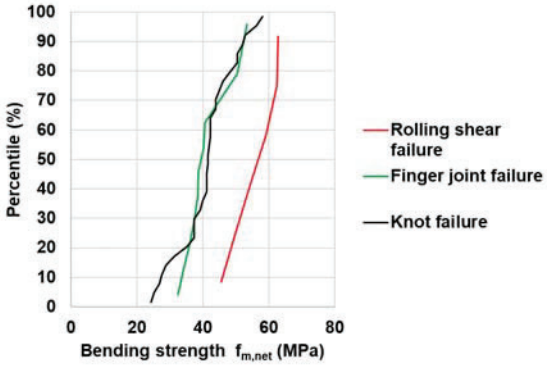

Figure 9: *Percentile plot of net edgewise bending strength for different failure modes.*

Figure 10a: *Examples of failure modes in edgewise bending. Rolling shear (top), knot in tension zone (mid), finger joint in tension zone (bottom).*

https://doi.org/10.52202/069179-0089

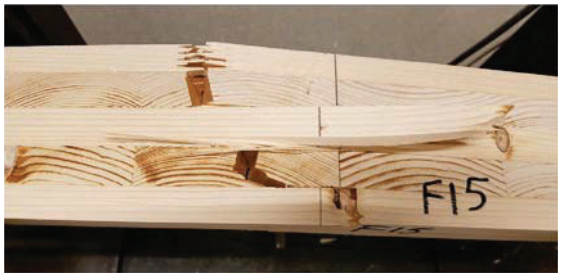

Figure 10b: *Example of bending failure in flatwise bending.*

The net edgewise bending strength was on average $f_{m,net}$=42.9 MPa, which is close to the typical value for Nordic Norway spruce graded to C24 (single grade). The lower variation thanks to the homogenization in CLT led to a 5%-percentile value of $f_{m,05,net}$ = 27 MPa which exceeds the nominal C24-value by 12%, see Table 1. This indicates a lamination effect of 12%, which is stronger than expected for these narrow boards.

However, it shall be noted that 80% of the boards had one or more laminated layers, see Figure 2. The boards without any laminated layers had a 5%-percentile edgewise bending strength of 24 MPa, indicating no difference to the board strength, see Figure 11.

For the flatwise tests, the net bending strength was surprisingly high with an average of $f_{m,net}$=66.7 MPa; almost 50% above the typical value for C24. The 5%-percentile of $f_{m,05,net}$=49.1 MPa was more than double the value for C24.

The net E-modulus was also high (13.6 GPa) for the flatwise tests, supporting the idea of a quality difference. However, it is not likely that a quality difference is the sole reason, since an average E-modulus of 13.6 GPa corresponds to an average bending strength of approximately 50 MPa and a 5%-percentile of 30 MPa, using a database for Nordic Norway spruce from approval tests of grading machines.

Other contributing factors might be that the middle layer (#3) were stronger than the outer layers (#1 and #5), see discussion above for the E-modulus. This would lead to a higher flatwise net strength than edgewise.

An important influencing factor is likely the lamination effect (homogenization). It is plausible that the lamination effect is stronger for flatwise loading, where three layers carry the load in parallel, see Figure CC. In edgewise loading a single defect in the outer lamellas is more critical for these narrow boards.

In the study by Flaig and Blass [3] the lamination effect for in-plane bending was estimated to 8-9% for a lay-up with 3 longitudinal layers in parallel, which would indicate a 5%-percentile bending strength of a single board to 49.1/1.085=45 MPa.

Furthermore, the same study showed a substantial effect of the cross layers on the bending strength. A 5 mm thin cross layer on the side of a board, tested in edgewise bending, increased the average bending strength by 18% (34.0 vs 40.3 MPa). Based on estimations from a graph in the report, the difference at the 5%-percentile level could be more than 60% (13.4 vs 22.2 MPa). Apparently, the cross layers, with a high cross stiffness, strengthened the weak sections by limiting cracking associated with grain deviations around knots.

If one assumes a cross layer enhancement effect of 50% on the 5%-percentile bending strength, and a lamination effect of 8.5%, the 5%-percentile bending strength of the individual layers would be 30 MPa to fit the strength of the CLT-board. This is in fact close to the strength corresponding to the measured flatwise net E-modulus of 13.6 GPa.

If one or more layers were laminated (two side-glued boards), the bending strength was higher compared to CLT-boards where each layer consisted of only one board, see Figure 2 and 11. Out of the 50 CLT-boards tested edgewise, 13 pcs had no laminations and the corresponding number for the flatwise tests was 14 CLT-boards.

The influence of laminations was more pronounced for the boards tested in flatwise bending compared to the edgewise tests at the median level, but the opposite at the 5%-percentile level.

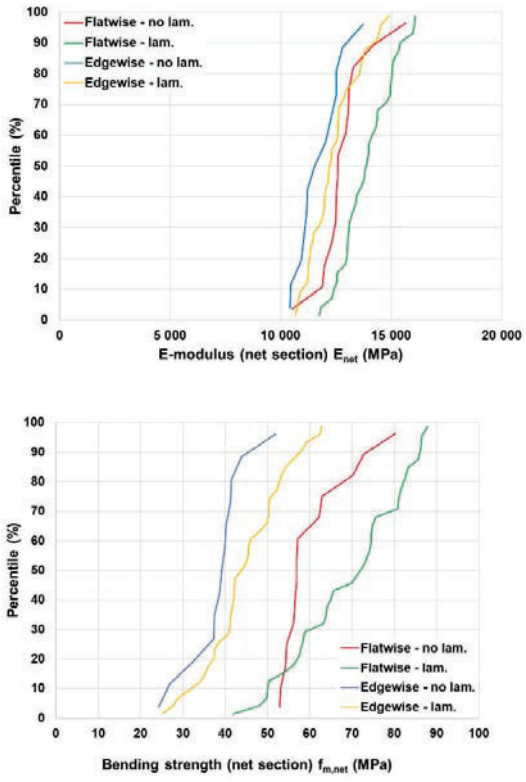

Figure 11: *Percentile plots of net E-modulus and net bending strength for boards that had no laminated layers compared with boards that had one or more layers with lamination (layer with two side-glued boards, see Figure 2).*

https://doi.org/10.52202/069179-0089

3.2 DYNAMIC PROPERTIES AND COMPARISON WITH STATIC RESULTS

A very strong correlation (R^2=0.96) was found between gross dynamic edgewise E-modulus (Euler) $E_{d,be,Eu.gross}$ and gross static global E-modulus $E_{gl,be,gross}$ see Figure 12. Both moduli are influenced by shear deformations more or less in the same way. The dynamic E-modulus was 5,5% higher than the static one, which is found in most studies and is attributed to the large difference in loading speed and the viscoelastic nature of wood.

It can be noted that the shear-free net dynamic E-modulus $E_{d,be,Ti,net}$ = 12.9 GPa coincide very well with the corresponding static E-modulus E_{net} = 12.2 GPa, when taking into account the typical static-dynamic difference.

The average shear-free (Timoshenko beam theory) net E-modulus from edgewise bending vibration was $E_{d,be,Ti,net}$ = 12.9 GPa, see Table 3.

In order to match the gross global E-modulus $E_{d,be,Eu,gross}$ =7.96 GPa the rolling shear modulus of the cross layers must be $G_{d,r,gm}$= 69 MPa using the gamma method [5]. Assuming the usual 5.5% difference, the static rolling shear value would be G_r = 65 MPa, which was used when estimating the shear-free static E-modulus in Table 1.

A rolling shear modulus of G_r = 65 MPa is not far from other studies on Norway spruce for boards cut far from the pith: Erhart et al [10] reported an average value of G_r=56 MPa for boards cut 100 mm from the pith.

Görlacher [11] studied the influence of annual ring geometry on the rolling shear modulus of Norway spruce. For the material in the present study, the angle between the tangential ring direction and rolling shear loading was on average 13 degrees, which points at a rolling shear modulus of 60-65 MPa according to the results of Görlacher.

It can be noted that the nominal value for C24 is 50 MPa, which is considered to be a conservative value for typical CLT-boards. However, it is likely a rather good estimate of the constitutive material parameter G_{RT} for Norway spruce to be used in FE-modelling (valid for boards with zero annual ring curvature and purely tangential or radial ring orientation in relation to board geometry).

The analysis of the shear mode, see Figure 5, resulted in a slightly lower rolling shear modulus of $G_{d,r,sh}$ =55 MPa. One reason for the difference is likely that one needs to account for parts of the mass of the cross layers in the model and this would increase the evaluated shear modulus.

The dynamic shear modulus from analysis of three edgewise bending modes was $G_{d,r,be}$ = 132 MPa. This is a weighted gross average over the cross section including influence of both lengthwise and cross layers. A common way of calculating the effective gross shear modulus for a layered material is given in Eq. 4 where V_{cross} and $V_{lengthwise}$ is the volume fractions of the layers; 43% and 57% in this case.

$$\frac{1}{G_{gross}} = \frac{V_{cross}}{G_{cross}} + \frac{V_{lengtwise}}{G_{lengtwise}} \quad (4)$$

Based on the experimental gross shear modulus of $G_{d,r,be}$=132 MPa and by assuming a shear modulus of G_l = 650 MPa for the lengthwise layers, the rolling shear modulus of the cross layers is $G_{d,r}$= 64 MPa, which is quite close to other estimates in this study.

The gross section shear modulus from torsional vibration was $G_{d,t}$ = 266 MPa, which is less than half of the level for solid timber, but not alarming with respect to practical handling at production. It can be noted that in torsion, the cross layers are not subjected to purely rolling shear stresses as in bending. Furthermore, the shear stresses have a more pronounced maximum in the middle layer (#3) in torsion. Both these factors increase the gross section shear modulus for torsion compared to gross shear modulus related to edgewise bending ($G_{d,r,be}$ =132 MPa).

Table 3: *Results from dynamic tests of the 50 boards that were tested in static edgewise bending. Average values and standard deviation within brackets. The stiffness properties are adjusted to the reference moisture content 12%.*

Property and vibration mode		Gross section	Net section
Dynamic E-modulus (GPa)			
Axial	$E_{d,ax}$	7.91 (0.69)	13.8 (1.2)
Flatwise bending, Timoshenko theory	$E_{d,bf,Ti}$	7.77 (0.66)	13.5 (1.1)
Edgewise bending, Euler theory	$E_{d,be,Eu}$	7.96 (0.74)	-
Edgewise bending, Timoshenko theory	$E_{d,be,Ti}$	9.65 (1.1)	12.9 (1.5)
Dynamic shear modulus (MPa)			
Torsion	$G_{d,t}$	266 (13)	-
Edgewise bending Timoshenko theory	$G_{d,r,be}$	132 (8.7)	64
Rolling shear mode Cross layer value	$G_{d,r,sh}$	-	55 (4.4)
Estimate using gamma method, Cross layer est.	$G_{d,r,gm}$	-	69

The dynamic edgewise E-modulus was correlated to the bending strength. Due to the limited property variation of the multi-ply CLT-board, the coefficient of determination was only R^2= 0.38 but the standard error was quite small: SEE=5.6 MPa, see Figure 13. The results indicate a possibility to use dynamic methods to grade the CLT-boards to a bending strength quality comparable to C24. The average E-modulus of C24 will obviously be harder to achieve.

https://doi.org/10.52202/069179-0089

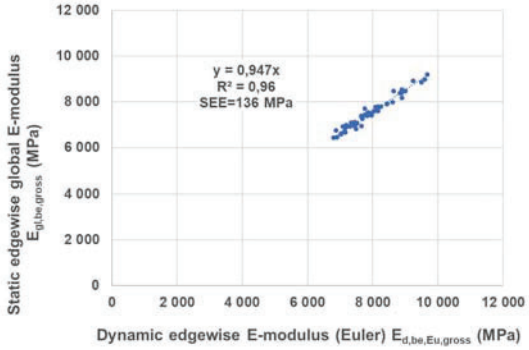

Figure 12: *Correlation between gross dynamic edgewise E-modulus (Euler) $E_{d,be,Eu,gross}$ and gross static global edgewise E-modulus $E_{g,be,gross}$.*

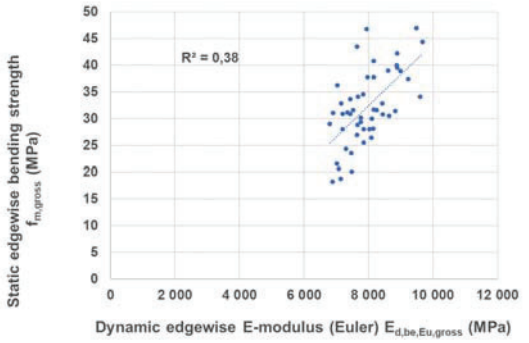

Figure 13: *Correlation between dynamic edgewise E-modulus (Euler) $E_{d,be,Eu,gross}$ and bending strength $f_{m,gross}$ (gross section values).*

3.3 NON-PLANE STRAIN DISTRIBUTION BETWEEN LOADING POINTS - INFLUENCE ON LOCAL E-MODULUS

A DIC-analysis of 5 CLT-boards was done regarding the bending deflections and normal strains in the area between the inner loading points. The bending deflections at the neutral layer were determined over a length of 475 mm (5h), corresponding to the method of determining the local shear-free E-modulus according to EN408 [4]. A deviation was that the measurements were only done on one of the faces, whereas the standard prescribes measurements on both sides to account for twisting.

The average net local E-modulus $E_{loc,DIC}$ for the 5 boards was 10.8 GPa which is lower than expected. Based on the gross static global E-modulus E_{gl} = 7.42 GPa for these boards, a rolling shear modulus of 65 MPa and using the gamma method, the net local E-modulus should be 11.9 MPa. Furthermore, the gross dynamic edgewise E-modulus using Timoshenko beam theory (shear-free) for the 5 boards was 12.4 GPa, which translates to a comparable static value of 11.8 GPa (5.5% reduction). Thus, both static and dynamic data supports that the static local E-modulus seems to be underestimated by approximately 10%.

A possible reason for the underestimation is that the assumption of plane normal strain in the shear-free zone between the loading points is not valid. In order to check this an analysis was made for a load step of 2.5 kN. The strains were calculated based on the normal deformations (x-direction) in path 1 and 2, at each mm of the beam depth, see Figure 3. The idea was to get a strain distribution that represents an average for the measurement zone and thereby minimize local effects that blur the picture. This revealed a non-plane strain distribution over the beam depth with a steeper strain gradient in layer 1, 3 and 5 compared with the overall inclination, see Figure 14. The degree of deviation from a plane strain varied between the boards, possibly depending on local defects close to the paths chosen. The strain gradient was on average 10% steeper in layer 1,3 and 5 compared to a plane strain situation. It is quite possible that this non-plane strain distribution explains the underestimation of the local shear-free E-modulus. Similar strain distributions have been presented in other studies on models for CLT [12].

Although this part of the beam is not subjected to vertical force causing shear stresses, the beam layers are subjected to the non-plane stress distribution from the beam parts outside the loading points, where the shear-weak cross layers influence the normal stress distribution in the manner seen in Figure 14. The general implication of this is that an evaluation of the local shear free E-modulus according to EN 408 [4] might lead to an underestimation if the beam to be tested has a low shear stiffness, like in this case with very shear-weak cross layers. The increased span-to-depth ratio typically used in CLT-tests to avoid rolling shear failure is beneficial in this respect as the shear deformations are diminished.

However, due to the small amount of boards analysed and the variation, one cannot draw any firm conclusions. Further tests and analysis will be done to see if this effect can be verified.

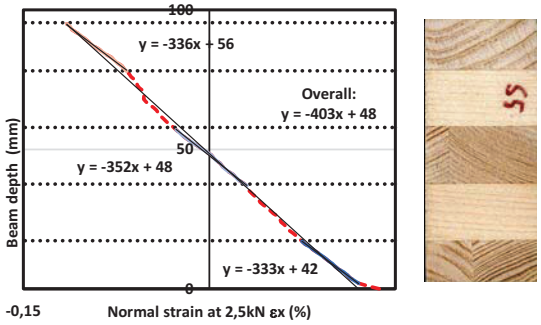

Figure 14: *Non-linear normal strain distribution for board E5, in the shear free portion of the beam between the inner loading points.*

https://doi.org/10.52202/069179-0089

4 CONCLUSIONS

1. The narrow CLT-boards (45x95 mm^2) in this study show gross average bending properties that are not so far from typical structural timber (15-30% lower than C24). Thanks to the limited property variation, the gross 5%-percentile values of the CLT-boards are almost on a par with solid timber. The tests indicate that narrow CLT-boards have sufficient bending properties for being used as structural components, not only with regards to handling but also for situations where the bending capacity is formally utilized.
2. The dominating failure mode in edgewise bending tests was knot failure at the tension edge. The 12 boards that failed at a finger joint had strength on a par with the boards that failed at a knot.
3. Six boards out of 50 exhibited a rolling shear failure. The estimated rolling shear strength was 1.36 MPa, with a range from 1.11 to 1.53 MPa, which is slightly lower than comparable studies on Norway spruce. However, the failure load for these boards were on average 35% higher than the boards that failed in bending.
4. The coefficient of variation for the bending strength was about 20% for both edgewise and flatwise loading, which is in between typical values for CLT (8-16%) and C24 (30-35%, single grade). The small size compared to other CLT-tests seems to reduce the homogenization effect (many sub-parts share the load).
5. The surprisingly high net flatwise bending strength ($f_{m,05}$=49 MPa) can likely, to a high degree, be attributed to the reinforcing effect from the cross layers that limit slope of grain cracking near knots in the longitudinal layers.
6. The rolling shear modulus of the cross layers was estimated to G_r = 65 MPa. This is in line with other studies of flat-sawn Norway spruce side-boards cut far away from the pith.
7. Dynamic E-modulus from edgewise vibration was very well correlated to the global static E-modulus with R^2=0.96. The correlation to bending strength was less strong (R^2=0.38) but with a low standard error (SEE=5.6 MPa).This indicates a possibility for non-destructive testing and grading of CLT-boards to achieve a superior quality for specialty applications.
8. Analysis of the local E-modulus between the loading points of 5 boards based on DIC-measurements indicated a 10% lower level than expected. The analysis also revealed a non-plane normal strain distribution that is likely linked to the low local E-modulus. Further studies are warranted to see if the “shear-free” local E-modulus determined according to EN408 might be underestimated for very shear-weak beams where the non-plane stress distribution outside the loading points have an influence.

ACKNOWLEDGEMENT

The support from several wood construction companies in Sweden, Stora Enso, the innovation program Bioinnovation/Vinnova, and the Knowledge Foundation is gratefully acknowledged.

REFERENCES

[1] J. Vessby, M. Perstorper, M, F. DeMonte, and J. Eriksson.: Structural use of cut-offs from clt-production – three examples that utilize the unique properties. In: World Conference on Timber Engineering, Oslo, 2023

[2] R. Brandner, R. Tomasi, T Moosbrugger, E. Serrano, P. Dietsch (eds.): Properties, Testing and Design of Cross Laminated Timber: A state-of-the-art report by COST Action FP1402/WG2, Shaker Verlag Aachen, 2018.

[3] M. Flaig, and H. Blaß, (2014). Bending strength of cross laminated timber beams loaded in plane. In: World Conference on Timber Engineering, Quebéc, 2014.

[4] EN 408:2010+A1:2012 - Timber structures - Structural timber and glued laminated timber - Determination of some physical and mechanical properties. European Standard.

[5] K. Möhler: Über das Tragverhalten von Biegeträgern und Druckstäben mit zusammengesetzten Querschnitten und nachgiebigen Verbindungsmitteln [About the load bearing capacity of beams in bending and bars in compression with composite cross sections and flexible connections], Habilitation, 1962, TH Karlsruhe (in German).

[6] E. Goens, Determination of Young´s modulus from flexural vibrations (in German). Annalen der Physic 11(6):649-678, 1931.

[7] R. F. S. Hearmon: Theory of the vibration testing of wood. Forest Products Journal, 16(8):29-40, 1966.

[8] M. Perstorper: Dynamic modal tests of timber – evaluation according to the Euler and Timoshenko theories. In: Ninth Int. Symposium on Nondestructive Testing of Wood, 45-54, 1994.

[9] J. Oscarsson, A. Olsson, M. Johansson, B. Enquist and E. Serrano: Strength grading of narrow dimension Norway spruce side boards in the wet state using first axial resonance frequency. International Wood Products Journal, 2(2):108-114.

[10] T. Erhart, R. Brandner, G. Schickhofer, and A. Frangi: Rolling shear properties of some European timber species with focus on cross laminated timber (CLT): test configuration and parameter study. In: Second INTER meeting, Sibenik, Croatia, 2015.

[11] R. Görlacher: A method for determining the rolling shear modulus of timber (Ein Verfahren zur Ermittlung des Rollschubmodulus von Holz), Holz als Roh-und Werkstoff 60:317-322, 2002.

[12] R. Stürzenbecher, K. Hofstetterand J. Eberhardssteiner: Cross laminated timber: a multi-layer, shear compliant plate and its mechanical behaviour. World Conference on Timber Engineering 2010.

https://doi.org/10.52202/069179-0089

World Conference on Timber Engineering Oslo 2023

DENSIFIED WOODEN NAIL FOR ADHESIVE- AND METAL-FREE TIMBER ASSEMBLES

Lei Han[1], Dusan Pauliny[2], Anna Sandak[3], Mariapaola Riggio[4], Andreja Kutnar[5], Dick Sandberg[6] and Jakub Sandak[7]

ABSTRACT: The widespread utilisation of adhesives to assemble engineered wood products may lead to environment and recycle concerns. To improve materials sustainability and recovery at the end-of-life, it is preferable to replace adhesive with mechanical lock-in fasteners such as wood-based connectors. Nowadays, the development of robotic fabrication technologies and wood modification technologies brings the opportunity to rejuvenate traditional wood-joining methods. In this study, thermo-hydro-mechanical densified wooden nail were proposed as an adhesive- and metal-free connector for timber assembles. The densification ratio varied between 40 to 68%. Research has been performed in order to determine the effect of densification on the compression behaviour of wood in the form of nails. The result showed that densification with high compression ratio can successfully increase the density and modulus of rupture of wood, while its influence on modulus of elasticity is not obvious. A set of prototype nails made of densified wood was manufactured. In addition, preliminary insertion tests into wood samples were carried out and served for insertion process understanding. The results obtained reveal a potential for using the densified wooden nail connectors for substitution of adhesive or metal connectors. However, the "success ratio" for proper inserting of wooden nails was not satisfactory. It was observed that the excessive dynamical loading induced buckling failure of the nail during hand-operated insertion.

KEYWORDS: Nail laminated timber; Thermo-hydro-mechanical densification; Compression behaviour

1 INTRODUCTION

Climate change and its dramatic consequences are stimulating a transformation towards sustainable development. The long-term solution of slowing down climate change is to close carbon cycles and reduce greenhouse gas (GHG). In Europe, buildings sectors account for 40% of total energy consumption and 36% of total carbon dioxide emission [1], and it is therefore a key sector for improvements. Compared with other materials used in construction, wood products have much better ecological and environmental performance [2]. In the past decade, the demand to use wood for applications in both residential and non-residential building construction has been increasing. This development has partially result out from the emergence of new engineered wood products (EWPs) and the potential economic benefits of prefabrication and rapid on-site construction [3].

However, EWPs are in majority of cases assembled by adhesives or metal fasteners, which reduce their machinability, sustainability, and limit recyclability. Furthermore, the use of adhesives in EWPs may affect the environment and human health by emitting non-healthy volatile organic compounds (VOC) such as formaldehyde, that increase during use-periods under the high-temperature and varying relative humidity conditions. Therefore, there is a need in the modern timber construction sector for an ecofriendly and recyclable technologies substituting or replacing adhesive and/or metal fasteners [4].

Assembling timber by hardwood connectors like dowels, nails, wedges, and tenon-mortise joints has been invented and applied in furniture making and timber construction from the ancient time [5]. Among these methods, nail connection represent the easiest and fastest method to assemble timber members [6], as metal nails could be successfully inserted into wood and make connection without pre-drilling holes. However, the high thermal conductivity of metal nails affects the overall energetic performance and energy requirements of structures during its service life. The machinability of components joined with metal nails is limited during both, construction and end-of-life transformation. Other problems may occur due to interaction of metal fasteners with tannic acids causing black colored spots on the surface of wooden elements. Therefore, Hasan et al. [7] suggested that wooden nails could be an alternative for renewable fastener used in a robotic fabrication process of nailed laminated timber.

[1] Lei Han, InnoRenew CoE, University of Primorska, Slovenia, lei.han@innorenew.eu
[2] Dusan Pauliny, IPM ENGINEERING s.r.o., Slovakia, pauliny@ipmeng.sk
[3] Anna Sandak, InnoRenew CoE, University of Primorska, Slovenia, anna.sandak@innorenew.eu
[4] Mariapaola Riggio, Oregon State University, USA, Mariapaola.Riggio@oregonstate.edu
[5] Andreja Kutnar, InnoRenew CoE, University of Primorska, Slovenia, andreja.kutnar@innorenew.eu
[6] Dick Sandberg, Luleå University of Technology, Sweden, dick.sandberg@ltu.se
[7] Jakub Sandak, InnoRenew CoE, University of Primorska, Slovenia, jakub.sandak@innorenew.eu

https://doi.org/10.52202/069179-0090

Hand-operated hammer and pneumatic nailing guns are usually used to drive nails into wood. When inserting by pneumatic nailing guns, the friction between the nail and the surrounding surfaces heats the interface to the glass-transition temperature and softens the cell-wall lignin. The following solidification of the softened lignin when the joint's temperature drops results in additional chemical-physical bonding the wood members [8]. Moreover, wooden nails ensure a firm fixing of the elements as they expand when exposed to moisture, that corresponds to same mechanism as observer in the case of wood dowels [9].

The wooden-nail assembling technology was combined recently with other wood modification technologies such as resin impregnation and/or THM wood densification [10–13]. THM densification involves heating the wood above its glass-transition temperature in the presence of moisture. A compression force can be applied in the transverse direction to make the wood cells collapse without fracturing their cell walls. It leads to the reduction in the lumen volume and in the increase of cell density. It is known that there is a strong relationship between wood density and its mechanical properties. Therefore, THM densification is frequently used to improve the mechanical performance of wood, including advanced use of wood in load-bearing timber construction [14,15].

An important research aspect that has received less attention in the context of wooden nails is the compression behaviour in the longitudinal direction of the elongated beams of densified wood forming the nail. Better understanding of densified wood behaviour under compression stress is extremely important for ensuring appropriate quality of the nailing connection. The nail damage occurring during insertion may disqualify the joint as well as may affect the further behaviour of the connection in the service conditions. A proper use of this knowledge may lead to designing nails with high slenderness ratio useable to assemble thicker panels. It would be a greatly appreciated functionality resulting in expansion of wooden nails usage in construction. The goal of this report if to present a set of preliminary results describing the compression behavior of densified wood in the form of nails made from three different species and various compression ratios.

2 MATERIAL AND METHOD

2.1 MATERIAL

Industrial kiln-dried beech (*Fagus sylvatica* L.), poplar (*Populus tremula* L.), and spruce (*Picea abies* L.) were used to produce the densified wood specimens for compression tests. The boards selected for test were detects-free and conditioned at 20°C and 65% RH to achieve an equilibrium moisture content. Standard metal fasteners (nails) were tested for comparison.

2.2 WOOD DENSIFICATION

The densified wood specimens were manufactured by carrying out the THM densification in the radial direction in an open-system hydraulic hot press. The densification cycle was composed of 10 minutes pre-heating (plasticization), 10 minutes densification, 5 minutes post treatment and 5 minutes cooling (Figure 1). The final cooling of the densified samples was performed out of the press, assuring limitation of the sample flatness changes, by applying clamping. The achieved compression ratio (CR) after densification is calculated as in equation 1:

$$\text{Compression ratio (CR)} = \frac{T_0 - T_d}{T_0} * 100\% \quad [1]$$

Where T_0 is the initial thickness and T_d is the thickness after densification

The densified specimens with different CR were conditioned at 20 °C and 65% RH then sawn to final dimensions of 55 mm (longitudinal) × 3 mm (radial) × 3 mm (tangential) before the compression tests.

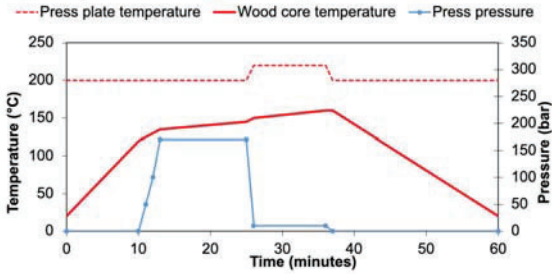

Figure 1: *Schedule of thermo-hydro-mechanical (THM) densification.*

2.3 COMPRESSION TEST

Compression tests were carried out to evaluate the influence of densification on the mechanical behavior of the wooden nails during insertion (Figure 2). Tests were done with the intention to notice the maximum force to be applied during nail insertion, including analysis of the buckling behavior of the nail. For these reasons, the slenderness ratio (which is defined as the ratio of the column length over its diameter) is higher than that recommended for the standard compression tests according to the EN 408 [16]. The ratio of the maximum force to the specimen cross-sectional area was computed here instead of modulus of rapture (MOR) as defined in EN 408. A custom-made mechanical testing machine equipped with a load cell (5 kN) was adopted to conduct the compression load experiments.

https://doi.org/10.52202/069179-0090

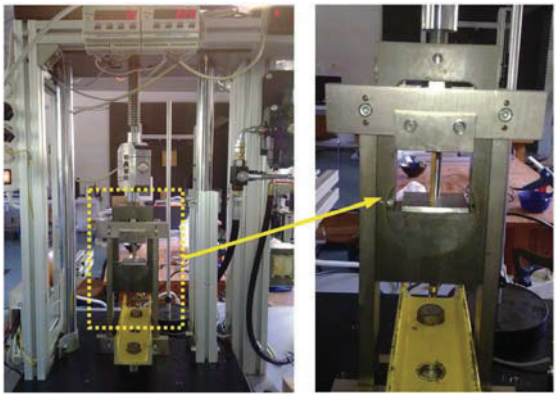

Figure 2: *Compression test setup*

3 RESULTS AND DISCUSSION

3.1 PHYSICAL AND COMPRESSION PROPERTIES

Figure 3 and Figure 4 presnts the density and mechanical properties of the wood densified with different CR. It can be noticed that there is a strong positive correlation between CR and densified wood density as well as modulus of rapture (MOR). However, it is also evident that after certain level of CR the MOR is reduced (for example densified poplar wood with 68% CR). It might result from excessive damage of the cellular structure of wood induced by densification. By contrast, there is no clear correlation between the CR and modulus of elastic (MOE). Majority of the samples have been damaged during test by excessive buckling. Only few of compressed samples were damaged by typical collapse of wood cells. The compression tests have been also performed on the standard metal nails with dimension as densified wooden nails. As expected, the performance of the metal nail was superior compared to wooden nail. Both MOR and MOE under compression of metal nails were more than four times higher than the highest value achieved by wooden nails.

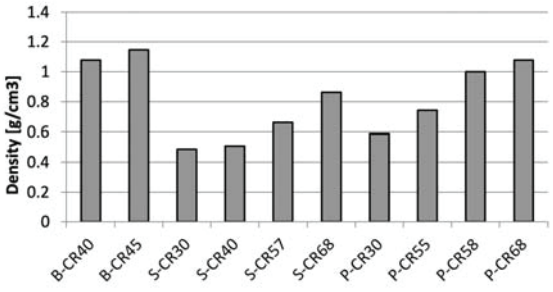

Figure 3: *Density of densified specimens*

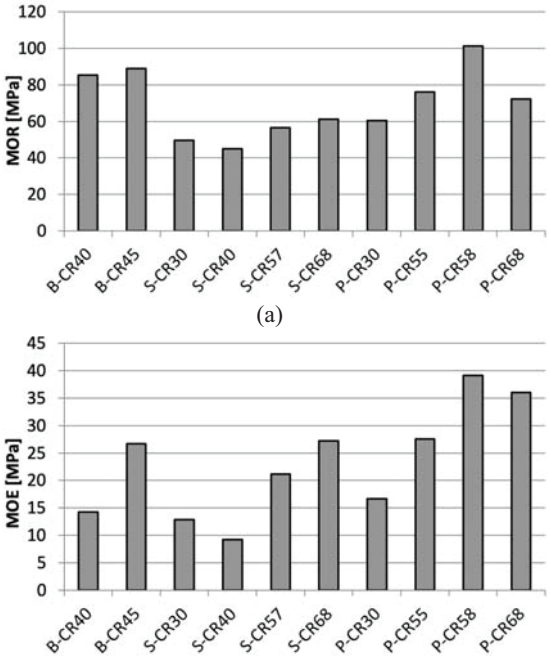

Figure 4: *Mechanical properties of densified specimens measured during compression test (a), modulus of rapture (MOR)(b), modulus of elasticity (MOE)*

3.2 DENSIFIED WOODEN NAIL PROTORTYPE AND PRELIMIARY NAILING TEST

Based on the above observations, it was possible to design a prototype of densified wooden nails. The image of the proposed nail is presented in Figure 5. The slenderness ratio (L/d) depends on the integrity of densified wood. As a rule of thumb, the insertion force is suggested nu exceed the critical buckling load of the nail. The nail's tip geometry depends strongly on the joined material hardness and its anatomical structure. The tip shall never be too sharp. The recommended tip angle (α) is ~30°.

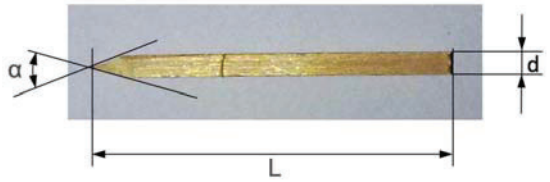

Figure 5: *Image of the developed wooden nail and recommendations for its design.*

The example of the wood pieces joined by densified wooden nails with hand-operated hammer is presented in Figure 6. It should be mentioned here that the ability of the wooden nail to join the other wood pieces is limited by the hardness and anatomical structure of the joined material. Simplifying, the technology developed can be only applied to join wood species of rather low densities. Up to data experiences show acceptable performance if

https://doi.org/10.52202/069179-0090

spruce, fir or poplar to be joined together. Any trials to join higher density species or pieces having certain defects (such as knots) have not been successful.

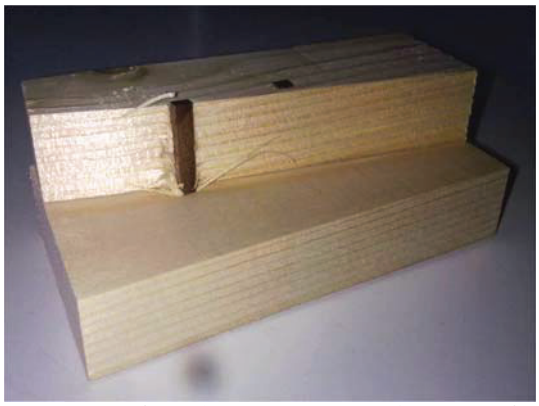

Figure 6. *Wooden nails joining two pieces of spruce wood.*

The "success ratio" of the insertion wooden nails was not exceptionally high. The most typical failures of the nails are presented in Figure 7. Splitting the nail over the surface of joined wood (Figure 7a) occurs if the force direction is not parallel to the nail axis direction. On the other hand, the overload of wood nail (effect in the collapse of wood fibers within the nail structure (Figure 7b). Anyway, the final effect is not satisfactory joint and usually the broken nail protruded over the joined surface.

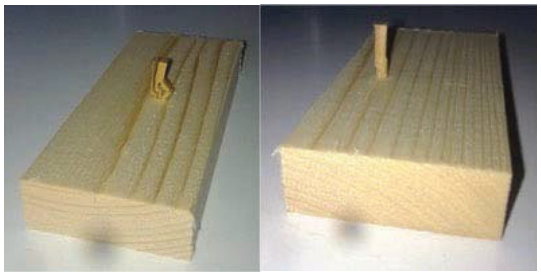

(a) (b)

Figure 7: *Typical damages to the wooden nail occurring during insertion; (a) splitting of the nail, (b) collapse of the wood fibre due to excessive compression stress.*

4 CONCLUSIONS AND FUTURE WORK

The research was dedicated for development of the novel technology of wood assembling by means of densified wooden nails. The results obtained shows a potential of such joins as an alternative to adhesive and traditional metal nails. However, it should be pointed, in general the "success ratio" for proper inserting of wooden nails was much lower that corresponding to metal joints because of excessive dynamical loading, especially when nailing with hand-operated hammer. The necessary loading to insert a wooden nail result in extensive buckling of the nail column, and this may lead to fracture during nail insertion. Another damaging factor was a compressive stress concentration at the tip of the nail limiting the penetration into the wood components to be joined.

The buckling failure of the nail under compression could be influence by many factors. For example, loading type (either dynamical or static loading), nail tip geometry, slenderness ratio, MOE, tribological properties of the wooden nail etc. Therefore, the future work will be focused on studying how those factors affects the buckling behavior of densified wood. An assist tool will also be designed and test to avoid buckling failure during nailing (Figure 8).

Figure 8. *Concept for the assist tool for avoid buckling during nailing.*

ACKNOWLEDGEMENT

The authors acknowledge project WoodLCC, which is supported under the umbrella of ERA-NET Cofund ForestValue, which has received funding from the European Union's Horizon 2020 research and innovation program. The authors acknowledge the European Commission for funding the InnoRenew project (Grant Agreement #739574) under the Horizon 2020 Widespread-Teaming program and the Republic of Slovenia (investment funding of the Republic of Slovenia and the European Regional Development Fund) and the Slovenian Research Agency ARRS for funding project J4-3087. The support of CT WOOD - a centre of excellence at Luleå University of Technology supported by the Swedish wood industry - is also gratefully acknowledged. Authors are grateful to Dr Gabriele Bonamini for his valuable suggestions and support.

https://doi.org/10.52202/069179-0090

REFERENCES

[1]. Official Journal of the European *DIRECTIVE 2010/31/EU OF THE EUROPEAN PARLIAMENT AND OF THE COUNCIL of 19 May 2010 on the Energy Performance of Buildings*; 2010;

[2]. Stark, N.M. *Wood Handbook, Chapter 11: Wood-Based Composite Materials-Panel Products-Glued-Laminated Timber, Structural Composite Lumber, and Wood–Nonwood Composite Materials*; 2010; Vol. 190;.

[3]. Gerard, R.; Barber, D.; Wolski, A. Fire Safety Challenges of Tall Wood Buildings: Final Report. *Natl. Fire Prot. Assoc.* **2013**, 162.

[4]. Han, L.; Kutnar, A.; Sandak, J.; Šušteršič, I.; Sandberg, D. Adhesive-and Metal-Free Assembly Techniques for Prefabricated Multi-Layer Engineered Wood Products: A Review on Wooden Connectors. *Forests* **2023**, *14*, doi:10.3390/f14020311.

[5]. Sotayo, A.; Bradley, D.; Bather, M.; Sareh, P.; Oudjene, M.; El-Houjeyri, I.; Harte, A.M.; Mehra, S.; O'Ceallaigh, C.; Haller, P.; et al. Review of State of the Art of Dowel Laminated Timber Members and Densified Wood Materials as Sustainable Engineered Wood Products for Construction and Building Applications. *Dev. Built Environ.* **2020**, *1*, 100004, doi:10.1016/j.dibe.2019.100004.

[6]. Leban, J.M.; Pizzi, A.; Properzi, M.; Pichelin, F.; Gelhaye, P.; Rose, C. Wood Welding: A Challenging Alternative to Conventional Wood Gluing. *Scand. J. For. Res.* **2005**, *20*, 534–538, doi:10.1080/02827580500432305.

[7]. Hasan, H.; Reddy, A.; TsayJacobs, A. Robotic Fabrication of Nail Laminated Timber. *Proc. 36th Int. Symp. Autom. Robot. Constr. ISARC 2019* **2019**, 1210–1216, doi:10.22260/isarc2019/0162.

[8]. Korte, H.; Koch, G.; Krause, K.C.; Koddenberg, T.; Siemers, S. Wood Nails to Fix Softwoods: Characterization of Structural Deformation and Lignin Modification. *Eur. J. Wood Wood Prod.* **2018**, *76*, 979–988, doi:10.1007/S00107-018-1288-X/FIGURES/10.

[9]. Gerber, C.; Collado, K.; Morrell, J.J. Impact of Moisture Cycling on Lateral Resistance of Resin-Impregnated Compressed Beech Nails in Radiata Pine Timber. *Int. Wood Prod. J.* **2021**, *12*, 147–151, doi:10.1080/20426445.2021.1906389.

[10]. Ruan, G.; Filz, G.H.; Fink, G. Shear Capacity of Timber-to-Timber Connections Using Wooden Nails. *Wood Mater. Sci. Eng.* **2022**, *17*, 20–29, doi:10.1080/17480272.2021.1964595.

[11]. Xudong, Z.; Xue, Y.; Qi, P.; Lan, Q.; Qian, L.; Shen, J.; Gao, Y.; Li, J.; Mei, C.; Li, S. Flexural Properties of Wooden Nail Friction Welding of Laminated Timber. *BioResources* **2023**, *18*, 1166–1176.

[12]. Ganne-Chedeville, C.; Pizzi, A.; Thomas, A.; Leban, J.M.; Bocquet, J.F.; Despres, A.; Mansouri, H. Parameter Interactions in Two-Block Welding and the Wood Nail Concept in Wood Dowel Welding. *J. Adhes. Sci. Technol.* **2005**, *19*, 1157–1174, doi:10.1163/156856105774429037.

[13]. Riggio, M.; Sandak, J.; Sandak, A. Densified Wooden Nails for New Timber Assemblies and Restoration Works: A Pilot Research. *Constr. Build. Mater.* **2016**, *102*, 1084–1092, doi:10.1016/j.conbuildmat.2015.06.045.

[14]. Sandberg, D.; Kutnar, A.; Karlsson, O.; Jones, D. *Wood Modification Technologies*; CRC Press, 2021; ISBN 9781351028226.

[15]. Cabral, J.P.; Kafle, B.; Subhani, M.; Reiner, J.; Ashraf, M. Densification of Timber: A Review on the Process, Material Properties, and Application. *J. Wood Sci.* **2022**, *68*, doi:10.1186/s10086-022-02028-3.

[16]. CEN EN 408 - Timber Structures Structural Timber and Glued Laminated Timber Determination of Some Physical and Mechanical Properties. **2003**.

World Conference on Timber Engineering Oslo 2023

EXPERIMENTAL INVESTIGATION OF FINGER JOINTS UNDER TENSILE AND BENDING LOADS

Farid Vafadar[1], Steven Collins[2], Gerhard Fink[3]

ABSTRACT: Finger joints are commonly used to fabricate endless lamella for engineered wood products such as glued laminated timber beams. The finger joints' properties are important for the mechanical characteristics of glued laminated timber beams, particularly those fabricated from higher-strength-graded lamellas. In the present study, 120 spruce timber boards were used to fabricate finger joints. Each timber board was assessed for quality by measuring the eigenfrequency and the density before the finger joint fabrication. The timber boards were cut in half, and both sets were arranged in the same order and afterward fabricated to endless lamellas, such that the finger joints were fabricated from the same timber boards in both sets. On one set, the tensile strength and on the other one, the flatwise bending strength and stiffness were investigated. This paper presents a statistical summary of the finger joint tensile and bending test results and correlation analyses between the mechanical properties and the relevant quality assessment indicators. A significant relationship between the finger joint tensile and bending strength is observed. Furthermore, the dynamic modulus of elasticity is identified to be a useful indicator of finger joint strength and stiffness.

KEYWORDS: Spruce, finger joint, tensile experiments, bending experiments, correlation analysis

1 INTRODUCTION

A finger joint (FJ) is the longitudinal interlocked connection between two timber boards. It is broadly used in the wood industry to fabricate endless lamella, mainly to produce engineered wood products such as glued laminated timber (GLT) or cross-laminated timber. Particularly for GLT beams fabricated from higher strength graded timber boards, which are typically characterized by fewer and smaller knots, the mechanical properties of the beams are influenced by the properties of the FJs [1].

The mechanical properties of FJs were investigated in several studies. In [2], the relationship between tensile strength and flexural modulus of elasticity in the bending of FJs from spruce timber was investigated. In [3], experiments were reported on the bending and tensile strength of finger-jointed pine lamellas from ten GLT factories. The aim was to compare bending and tensile strengths. As a result, a relatively constant ratio between the mean values of the tensile and bending strengths was found, such that the tensile strength was about 60% of the bending strength. In [4], bending and tensile experiments were performed on 700 FJs to investigate the ratio between the characteristic value (5th percentile-Guassian distribution) of finger joints' tensile and bending strength. Overall, a ratio between the characteristic values of the tensile and bending strength of approx. 0.65 was identified. However, it should be noted that in [4], a reduced testing length was used, and specimens with failures outside the FJ were not considered for analysis.

The importance of FJ is also considered in the respective standard for GLT beam mechanical behavior (EN 14080 [5]), where the mechanical properties of FJs are addressed. According to [5], the strength class of a GLT beam is estimated based on the tensile properties of the used timber boards and the flat-wise-bending properties of the FJ. In this case, the required value of the characteristic strength for FJs tested in tension is $f_{t,0,j,k} = f_{m,j,k}/1.4$.

A few studies have also been carried out to identify the correlation between various strength and stiffness-related indicators and the FJ properties. For instance, in [6], the mechanical performance of structural finger joints was investigated in four-point bending. The results indicated a positive relationship between the density and the bending strength. In [7], the results of 40 FJ tensile experiments were used to develop a model to predict the tensile strength of FJ based on the dynamic modulus of elasticity (E_{dyn}) of the connected timber boards. Nonetheless, the literature in this direction is lacking, particularly for studies investigating the influence of indicators on the FJ mechanical properties.

In the present study, the relationships between the FJ tensile and bending properties on paired specimens and the influences of timber board indicators (stiffness and density) on the FJ mechanical properties are investigated.

[1] Farid Vafadar, Dept. of Civil Engineering, Aalto University, farid.vafadarestiar@aalto.fi
[2] Steven Collins, Dept. of Civil Engineering, Aalto University, steven.collins@aalto.fi
[3] Gerhard Fink, , Dept. of Civil Engineering, Aalto University, gerhard.fink@aalto.fi

https://doi.org/10.52202/069179-0091

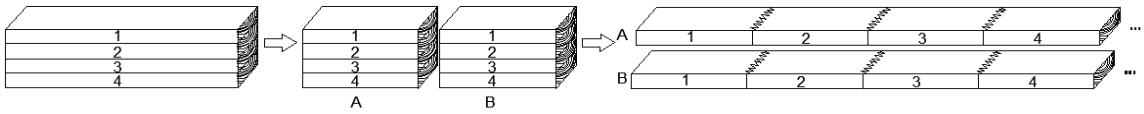

Figure 1: *Schematic of the fabrication process of FJs*

2 MATERIAL AND METHOD

2.1 SPECIMEN

Spruce timber boards (w x t = 125 x 50 mm with a length between 3800 mm and 4700 mm) were used to study the FJ tensile and bending mechanical properties. All timber boards were investigated for quality with a commercial grading device (Precigrader), which grades based on the timber board's E_{dyn} and measures the density. Based on the grader information, the boards were classified into R (rejected), T14, and T22 classes. The descriptive statistics of E_{dyn} for each class are mentioned in Table 1.

The timber boards were cut in half and finger-jointed into two equivalent sets of endless lamellas, according to Figure 1. Thus, the timber boards were arranged in the same order in both sets so that paired (tension and bending) FJs were fabricated. The two endless lamellas were cut into 8 m long segments to transport to the Aalto University testing laboratory. Then the FJs were cut out of each segment. Due to the cutting procedure (for transporting), some FJs could not be used for further testing. In total, 227 finger-jointed specimens (110 FJs for tension and 117 for bending test) were investigated, of which 98 were paired. The order of the timber boards was random, i.e., they were not grouped according to the strength grades[1]. The finger-jointed specimen groups were determined based on the class of the two connected timber boards (see Tables 2 and 3).

For the tensile and bending tests, the specimens were planed to the final dimensions of w x t x l = 115 x 45 x 1300 mm and w x t x l = 115 x 45 x 1000 mm, respectively. In the bending tests, eight specimens had a shorter span (distance between the supports) of 700 mm. All specimens were conditioned in a climate chamber at 20°C, with a relative humidity of 65%.

2.2 TENSILE TEST

The specimens were tested in tension according to EN 408 [8]. The test setup with failure at the FJ is shown in Figure 2. The test length clear of grips was 560 mm (> 9 x 45 mm) with 370 mm clamping length on each side. To secure the specimens in the grips while testing, lateral pressure was applied. However, 14 specimens slipped from the grips. Ten of these were re-clamped and tested for a second time to achieve failure, although it was not possible to test four FJs again because of damage at the clamping region. An actuator with a tensile capacity of 500 kN applied the force. A force control testing protocol with a 30 kN/min loading rate was used.

[1]Initially the study was planned to be performed with graded timber boards, although due to a technical error the boards were not sorted.

Table 1: *Descriptive statistics of E_{dyn} for the used timber boards*

Class	Mean value [MPa]	COV [-]	Range [MPa]
R	8795	0.06	< 9600
T14	10966	0.07	9600-12300
T22	13625	0.08	> 12300

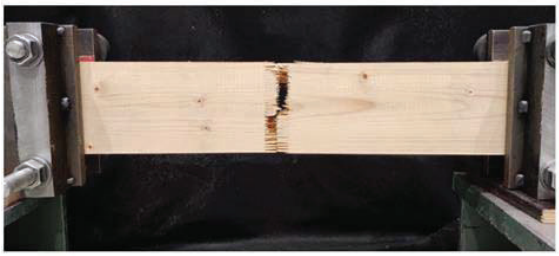

Figure 2: *FJ after failure in a tensile test*

2.3 BENDING TEST

The bending experiments were performed according to EN 408 [8]. The test setup and a specimen during the test are shown in Figure 3. A universal testing machine with a capacity of 200 kN was used. The testing protocol was force control with a 2.5 kN/min loading rate. One linear variable differential transformer (LVDT) in the center of the specimen, at the bottom surface, was installed for global stiffness. For local deflection measurement, two LVDTs were installed on both side faces at the neutral axis and the FJ location. The average value of deflection was considered for local stiffness calculation. The LVDTs were removed from the specimens at an estimated 40% of the maximum force to prevent damage during failure.

2.4 VISUAL INSPECTION

After testing, the specimens were visually inspected. Following the approach presented in [9], the specimens were categorized into four groups according to their fracture pattern: Finger joint failure (FF), wood failure (WF), mixed failure (MF), and the slip of the grip without failure (S) which happened only in tensile tests.

The four specimens that slipped from the grips were considered slipped specimens (S). Conditions for classification are such that if at least two-thirds of the failed cross-section was within the finger joint (failure in adhesion and joint failure at fusion or net section), the specimen was categorized as finger joint failure (FF).

https://doi.org/10.52202/069179-0091

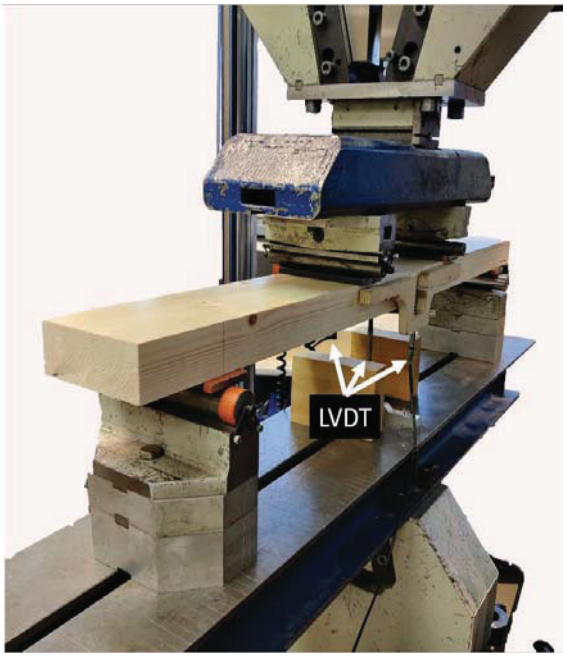

Figure 3: *Flatwise four-point bending test setup and location of the linear variable differential transformer (LVDT)*

Likewise, if two-thirds of the failed cross section was within a wood section, the specimen was considered with a wood failure (WF). All other specimens were defined as mixed failure (MF).

In addition to the failure type, the timber board in which the failure occurred was identified. It was targeted only for specimens where the failure could be allocated to a specific timber board. From the tensile and bending experiments, specimens are considered where at least two-thirds of the failed cross section was within one timber board. For the bending tests, the tension zone of the specimens was investigated. All other specimens, meaning specimens where the failure could not be directly allocated to one specific timber board, are not considered for related investigations.

3 RESULTS

The tensile and bending test results are summarised in Tables 2 and 3, respectively. Descriptive statistics of strength values are given for specimens with the same failure type and all FJs within each FJ group. In the latter case, the specimens with WF, MF, and S failures are considered censored from the perspective of FJ strength since the exact strength of the FJ is unknown, and only a lower bound is known; see [7] for more information. As a result, the tensile and bending strength of the FJs were calculated using equality data (FF) and censored data (WF, MF, S).

In this paper, it is distinguished between (a) the tensile and bending strength of tested specimens denoted with $f_{t,s}$ and $f_{m,s}$ and (b) the tensile and bending strength of FJ denoted with $f_{t,j}$ and $f_{m,j}$.

Table 2: *Expected values and coefficient of variations of tensile strength of FJ (calculated for all specimens considering censored data) and tensile strength of the specimens (categorized according to the failure type).*

FJ group (Based on the quality of the timber boards)	Failure type	n [-]	Tensile strength E(·) [Mpa]	COV [-]
R-T14	FF	4	20.9	0.10
	MF	3	22.8	0.23
	WF	7	18.3	0.29
All finger joints $f_{t,j}$	**-**	**14**	**25.3**	**0.18**
R-T22	FF	4	29.2	0.17
	MF	1	25.0	-
	WF	6	23.2	0.17
All finger joints $f_{t,j}$	**-**	**11**	**30.4**	**0.12**
T14-T14	FF	11	27.9	0.20
	MF	4	25.3	0.07
	WF	9	24.2	0.25
All finger joints $f_{t,j}$	**-**	**24**	**30.4**	**0.18**
T14-T22	FF	24	31.5	0.19
	MF	6	32.4	0.16
	WF	10	26.6	0.31
	S	1	36.3	-
All finger joints $f_{t,j}$	**-**	**41**	**34.2**	**0.20**
T22-T22	FF	14	33.1	0.14
	MF	2	32.4	0.16
	WF	1	38.5	-
	S	3	43.9	0.09
All finger joints $f_{t,j}$	**-**	**20**	**36.6**	**0.20**

About half of the specimens in the tensile experiments failed in the FJ (type FF). Slipped specimens have the highest mean tensile strength value. About 75% of the specimens in bending tests failed in the FJ (type FF).

The mean value of local and global bending stiffness increases with the quality of the timber boards. The global stiffness mean values are lower than the local stiffness. In addition, it is noted that the local deflection data in four specimens and the global deflection of one specimen are missing due to measurement errors of the LVDTs.

General results concerning the tensile and bending tests indicate that the relative frequency of the specimens with FF failure type increases with the quality of the timber boards, particularly for tensile-loaded specimens. This is expected since, in higher-quality timber boards, there are (in general) fewer natural defects that may cause failure outside of the FJs.

4 CORRELATION ANALYSIS

4.1 MECHANICAL PROPERTIES

A scatter plot of the tensile and bending strength for all the paired specimens is shown in Figure 4. In total, 41 pairs failed within FJ in both the bending and the tensile tests. This case is classified as FF-FF. For illustrative reasons, the "Other" specimens are illustrated together, representing specimens in which a failure occurred outside the FJ in tension and/or bending. According to the scatter plot, the relationship is associated with a rather large scatter.

https://doi.org/10.52202/069179-0091

Table 3 *Expected values and coefficient of variations of bending strength and stiffness (local and global). Bending strength of FJ (calculated for all specimens considering censored data) and bending strength of the specimens (categorized according to the failure type).*

FJ group (Based on the quality of the timber boards)	Failure type	Bending strength n [-]	E(·) [Mpa]	COV [-]	Local bending stiffness E_L n [-]	E(E_L) [Mpa]	COV [-]	Global bending stiffness E_G n [-]	E(E_G) [Mpa]	COV [-]
R-T14	FF	11	38.4	0.11						
	MF	3	40.7	0.11						
	WF	2	35.2	0.26						
All finger joints $f_{m,j}$	**-**	**16**	**40.2**	**0.12**	**15**	**9496**	**0.13**	**16**	**8524**	**0.15**
R-T22	FF	8	39.2	0.20						
	MF	2	30.4	0.06						
	WF	3	33.6	0.34						
All finger joints $f_{m,j}$	**-**	**13**	**41.0**	**0.18**	**13**	**9812**	**0.17**	**12**	**9294**	**0.14**
T14-T14	FF	23	42.4	0.18						
	MF	5	43.7	0.15						
	WF	3	44.8	0.17						
All finger joints $f_{m,j}$	**-**	**31**	**44.7**	**0.18**	**31**	**10147**	**0.16**	**31**	**9532**	**0.14**
T14-T22	FF	36	46.5	0.17						
	MF	5	46.9	0.19						
	WF	1	45.5	-						
All finger joints $f_{m,j}$	**-**	**42**	**47.6**	**0.17**	**40**	**11408**	**0.12**	**42**	**10666**	**0.12**
T22-T22	FF	11	53.5	0.11						
	MF	1	44.2	-						
	WF	3	54.1	0.08						
All finger joints $f_{m,j}$	**-**	**15**	**54.8**	**0.10**	**14**	**12348**	**0.19**	**15**	**12009**	**0.16**

Significant relationships are observed between the specimens' tensile and bending strength. The corresponding correlation coefficient for all paired specimens is $r(f_{t,s}, f_{m,s}) = 0.50$, and for the FF-FF case, the correlation is $r(f_{t,j}, f_{m,j}) = 0.48$.

Regarding the relationships between strength and stiffness, notable correlations are found between the bending strengths ($f_{m,s}$ and $f_{m,j}$) and local and global bending stiffness (E_L and E_G), with correlations of $r \approx 0.70$ for all relationships. However, the correlations between tensile strengths and local bending stiffness are lower: for all paired specimens, $r(f_{t,s}, E_L) = 0.44$, and for specimens with FF, $r(f_{t,j}, E_L) = 0.34$. Similar trends for the relationship between tensile strength and global bending stiffness are identified with $r(f_{t,s}, E_G) = 0.51$ (all paired specimens) and $r(f_{t,j}, E_G) = 0.33$ (specimens with FF).

4.2 MECHANICAL PROPERTIES VS. INDICATORS

Correlation analyses are made between the mechanical properties and selected strength and stiffness-related indicators. For the strength properties, the lower quality timber board of the connected timber boards is expected to influence the strength predominantly. Accordingly, the investigated parameters are the minimum characteristics: $E_{dyn,min}$, and ρ_{min}. Based on visual inspection, the timber board in which the failure occurred was identified for each specimen with FF. Of all the specimens tested in tension and bending with FF (57 tensile specimens and 89 bending specimens), 63% and 78% of specimens failed in the timber board with lower E_{dyn}, respectively.

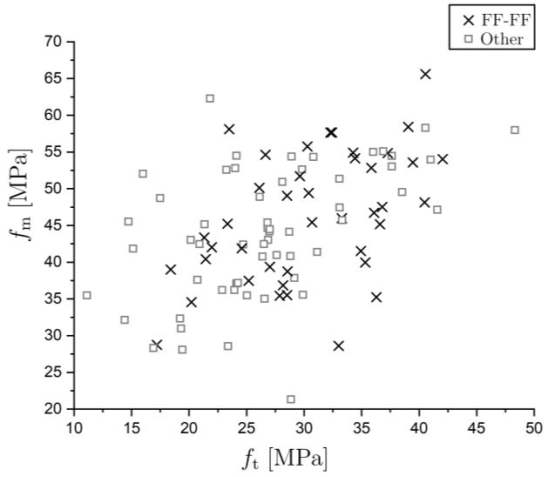

Figure 4: *Scatter plot of all the paired FJs' bending strength versus tensile strength. FF-FF represents FJ failures in both paired bending and tension specimens.*

Further investigation showed that most failures within the stiffer boards were characterized by natural defects, such as knot clusters close to or within the FJs. Since the ρ_{min} and $E_{dyn,min}$ are highly correlated, similar results are expected when considering the minimum density. Therefore, results suggest that FJs fail more frequently within a lower-quality timber board.

A scatter plot of FJ tensile strength and $E_{dyn,min}$, and ρ_{min} are shown in Figure 5. For $E_{dyn,min}$, when all failure types are considered together, the correlation is apparent, and a significant correlation coefficient of $r(f_{t,s}, E_{dyn,min}) = 0.59$ is obtained.

https://doi.org/10.52202/069179-0091

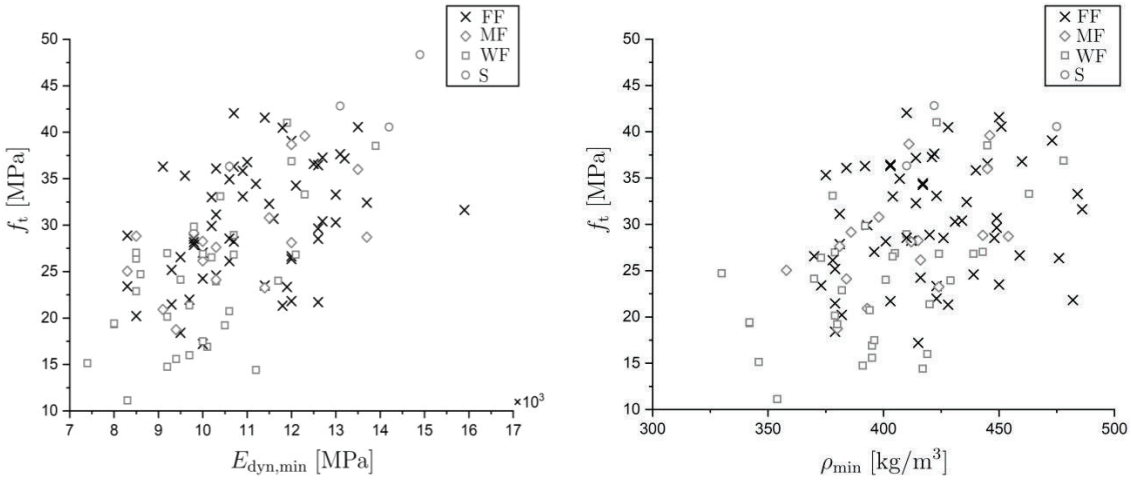

Figure 5: *Scatter plot of FJ tensile strength versus (left) $E_{dyn,min}$ (right) $\boldsymbol{\rho}_{min}$ of the connected boards.*

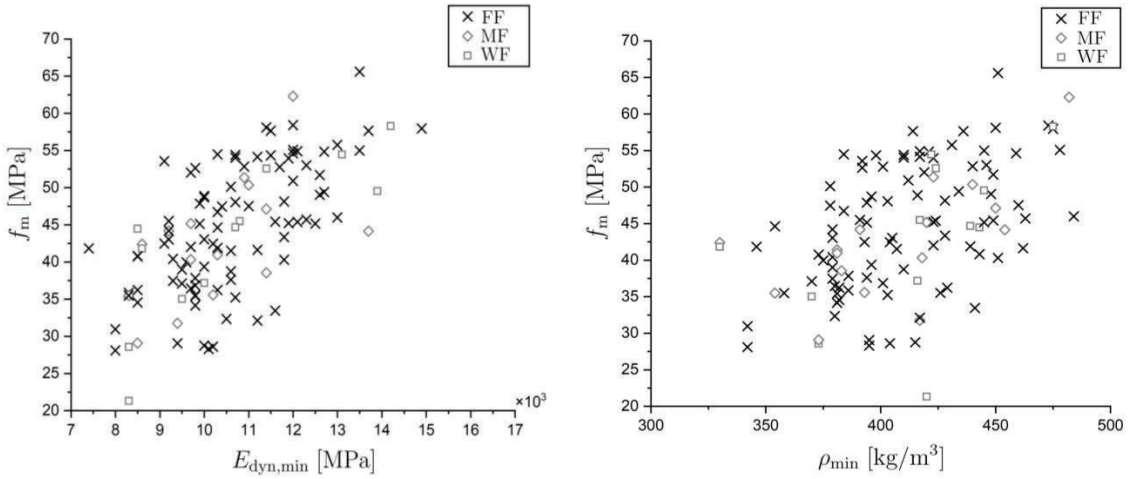

Figure 6: *Scatter plot of FJ bending strength versus (left) $E_{dyn,min}$ (right) $\boldsymbol{\rho}_{min}$ of the connected boards.*

However, for specimens with FF, the relationship between tensile strength and $E_{dyn,min}$ is comparatively lower: $r(f_{t,j}, E_{dyn,min}) = 0.36$. The reason for this difference may be related to the failure types: some of the strongest and stiffest specimens slipped from the testing grips (type S), and some of the weakest specimens failed outside the FJ (e.g., WF); both are not accounted for in the FF group. Therefore, the overall effect is a stronger correlation when all failure types are considered and a lower correlation when FF failure is considered individually. From the scatter plot, the influence of ρ_{min} on the tensile strength for specimens with FF is not unambiguous and associated with a rather large scatter. Overall, the influence of density on the tensile strength is minor. The correlation coefficient is $r(f_{t,s}, \rho_{min}) = 0.47$ and $r(f_{t,j}, \rho_{min}) = 0.20$. It is noted that a few specimens significantly influence this correlation coefficient, with WF having some very low values.

The scatter plot of the FJs bending strength versus the $E_{dyn,min,}$ and ρ_{min} are shown in Figure 6. Overall, the relationship between bending strength and $E_{dyn,min}$ is more significant than the tensile strength. The correlation coefficients are $r(f_{m,s}, E_{dyn,min}) = 0.64$ and for specimens with FF, $r(f_{m,j}, E_{dyn,min}) = 0.62$. In addition, an apparent influence of density on the bending strength is observed, although the scatter is relatively large. The correlation coefficients are $r(f_{m,s}, \rho_{min}) = 0.50$ and $r(f_{m,j}, \rho_{min}) = 0.48$.

The relationships between the local bending stiffness (considered more relevant to FJ, compared to global stiffness) and the indicators are presented in Figure 7. The mean values of the indicators ($E_{dyn,mean,}$ ρ_{mean}) are, in this case, considered to be the relevant characteristics. The corresponding correlation coefficient between E_L and $E_{dyn,mean}$ is $r = 0.59$. However, E_G and $E_{dyn,mean}$ has a higher correlation with $r = 0.67$. The correlation between E_L and ρ_{mean} is $r = 0.42$. A similar correlation is found between E_G and ρ_{mean} ($r = 0.43$). These results suggest that the $E_{dyn,mean,}$ and ρ_{mean} are related to FJ bending stiffness, with $E_{dyn,mean}$ being an important indicator.

https://doi.org/10.52202/069179-0091

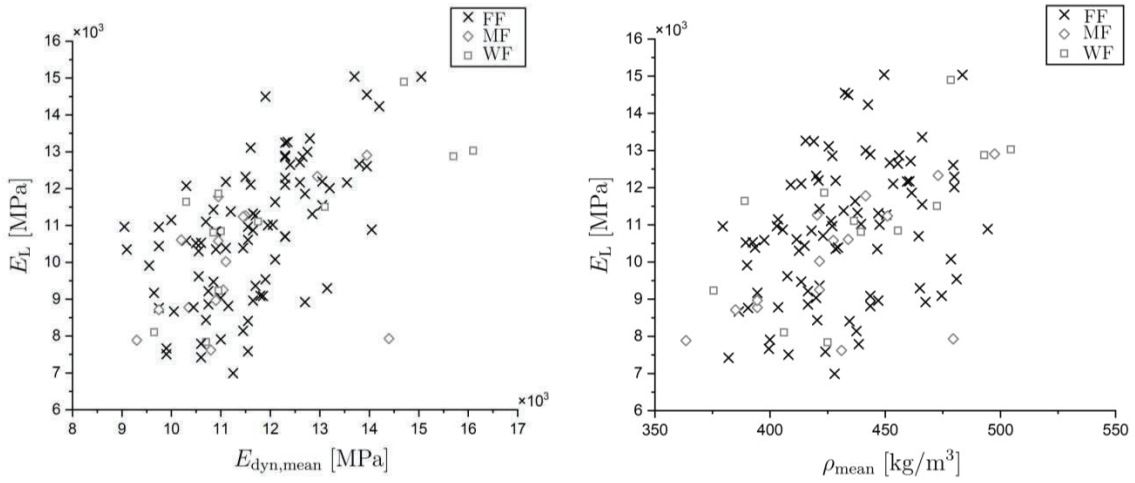

Figure 7: *Scatter plot of FJ local bending stiffness versus (left)* $E_{dyn,mean}$ *(right)* ρ_{mean} *of the connected boards.*

5 CONCLUSION AND OUTLOOK

The tensile and bending mechanical properties of finger joints are investigated. Overall, 227 finger-jointed specimens in five quality groups were tested in tension and bending. The statistical properties of the test results are presented along with a correlation analysis for the relationships between FJ tensile and bending mechanical properties and their relationship to non-destructive indicators. Results indicate:

- On average, the bending strength of finger joints is stronger than tensile strength.
- A significant relationship is identified between the FJ tensile and bending strength with a correlation coefficient of approximately 0.5.
- The mean value of the FJ tensile and bending mechanical properties increases with the quality of the joined timber boards.
- The connected boards' minimum dynamic modulus of elasticity significantly correlates with the FJ tensile and bending strength. The minimum density is also correlated, although to a lesser extent due to a rather large scatter.
- The mean value of the dynamic modulus of elasticity of the jointed boards correlates with the FJ bending stiffness properties.

This research contributes knowledge on the mechanical properties and behavior of finger joints. In addition, it will serve as the base for the development of material models, incorporating the relationship between FJ bending and tensile properties and relevant non-destructive strength and stiffness indicators.

ACKNOWLEDGEMENT

The authors thank Versowood Company for their support and cooperation during specimen fabrication and transportation.

This research has been conducted with funding from the Academy of Finland (decision no. 13334004).

REFERENCES

[1] G. Fink, A. Frangi, and J. Kohler. Bending tests on GLT beams having well-known local material properties. *Mater. Struct. Constr.*, vol. 48, no. 11, pp. 3571–3584, 2015.

[2] B. Heimeshoff and P. GIos. Zugfestigkeit und Biege-E-Modul yon Fichten-Brettlamellen. *Holz als Roh - und Werkst.*, vol. 38, 1980.

[3] H. J. Larsen.: Strength of finger joint. In Prins, C.F.L, editor, *Production, Marketing and Use of Finger-Jointed Sawnwood: An Overview,* In *Proceedings of an international seminar organized by the timber committee of the united nations economic commission for Europe*, 1980.

[4] G. R. Colling F, Ehlbeck J. Glued laminated timber—contribution to the determination of the bending strength of glulam beams. Oxford, United Kingdom, 1991.

[5] SFS-EN 14080: Timber structures - Glued laminated timber and glued solid timber - Requirements, Standard, Finnish Standards Association, Helsinki, 2013.

[6] C. B. Ong, M. P. Ansell, W. S. Chang, and P. Walker. Bending properties of finger-jointed Malaysian dark red meranti. *Int. Wood Prod. J.*, vol. 10, no. 2, pp. 49–54, 2019.

[7] G. Fink, P. Stadelmann, and A. Frangi. Bending test on large-scale GLT beams with well-known beam setup using machine grading indicator. *Int. Wood Prod. J.*, pp. 1–9, 2021.

[8] SFS-EN 408: Timber structures - Structural timber and glued laminated timber - Determination of some physical and mechanical properties, Standard, Finnish Standards Association, Helsinki, 2012.

[9] G. Fink, P. Stadelmann, and A. Frangi. Tensile capacity of finger joint connections - Considering censored data. In *WCTE 2018 - World Conf. Timber Eng.*, pp. 1–8, 2018.

World Conference on Timber Engineering Oslo 2023

POTENTIAL OF REUSING SALVAGED WOODEN MATERIALS IN FABRICATING STRUCTURAL DOWEL LAMINATED TIMBER

Mohammad Derikvand[1], Gerhard Fink[2]

ABSTRACT: Reusing salvaged wooden materials in new structural products offers a promising approach towards a circular economy. In this paper, the potentials and challenges related to reusing salvaged wooden materials in mass laminated timber are explored. Furthermore, the research activities at the group for Wooden Structures (Aalto University) related to the reuse of salvaged timber materials in fabricating dowel laminated timber (DLT) are discussed and the outlook of the subject and the future research needs are summarized. Among others, the research group focuses on the use of DLT in structural applications both as a beam-type element and as a slab-type element. The results show that salvaged plywood plates, which are e.g., used in the construction sector as concrete formwork, can be used effectively to produce tenon connectors for DLT fabrication. In addition, the combination of salvaged timber and new full-scale timber boards in alternate layers have shown to be a promising alternative. In this method, short, salvaged timber elements can be used without any end-to-end joining or gluing. Minimizing the required processing procedures can make salvaged timber more profitable and more attractive to the timber products manufacturing sector.

KEYWORDS: salvaged timber, dowel-laminated timber, wooden connectors, circular economy, climate change, reuse, low processing

1 INTRODUCTION

Over the past years, interest in biobased materials such as timber has increased in different sectors, e.g., due to the challenges related to the climate change. Accordingly, several studies have expected difficulties in meeting the demands for timber in the near future [e.g., 1]. In the case of the construction sector, the cascade use of timber has shown promising potentials for addressing the anticipated demands for timber solutions [1]. In addition, reusing wooden materials could be an effective approach in battling the climate change, and therefore, this subject has been the focus of numerous studies in the recent years [e.g., 2-8].

In this paper, the case of reusing salvaged wooden materials in mass laminated structural elements made with wooden connectors is discussed. A description of the related research and development works at the group for Wooden Structures (Aalto University, Finland) on this topic is also provided. The focus here is on the reuse of salvaged wooden materials in fabricating dowel laminated timber (DLT), both as a beam-type element and as a slab-type element. Finally, the outlook and research needs for breakthrough innovation in the subject area are summarized.

2 POTENTIALS AND CHALLANGES

The concept of reusing salvaged wooden materials is related not only to meeting the future demands for timber solutions, but also to addressing the climate change. Reusing wooden materials offers a potential to reduce the need for new materials, and therefore, preserve the natural resources. Furthermore, salvaged wooden materials are theoretically cheaper than new materials; therefore, if processed economically, they can be used to produce more affordable products. Here, salvaged wooden materials refer to both salvaged timber and salvaged engineered wood products that are often obtained either from a primary application or as waste from a timber production process. Figure 1 shows two examples: cut-offs from a regional housing company and falsework for a concrete bridge. Depending on the material type, several approaches exist in the literature to reuse salvaged wooden materials in new products and applications. Most of the approaches require additional processing on the salvaged wooden materials, e.g., particleboard production or cross laminated timber (CLT) production.

[1] Mohammad Derikvand, Department of Civil Engineering, Aalto University, Finland, mohammad.derikvand@aalto.fi
[2] Gerhard Fink, Department of Civil Engineering, Aalto University, Finland, gerhard.fink@aalto.fi

https://doi.org/10.52202/069179-0092

Figure 1: *Examples of salvaged wooden materials; cut-offs from a housing company (top) and falsework for a concrete bridge (bottom).*

Despite the existence of some methods for the case of reuse, it should be acknowledged that no single method can be effective for all types of salvaged wooden materials, considering the variabilities in e.g., type, shape, dimensions, irregularities, and material characteristics. Some salvaged wooden materials may be only good enough to be used for energy. However, for others a fit-for-purpose approach might be best in order to develop certain types of wooden products.

In terms of new products development, the interest in reusing salvaged timber in fabricating mass laminated timber products for structural applications has increased in recent years. Some research works have also already been conducted on this topic (examples of those studies are summarized in Table 1), most of them focused on non-finger jointed CLT.

Nevertheless, the concept of reusing salvaged timber has several challenges that need to be acknowledged, some of which are described in the following:

- Unknown material source: salvaged timber materials come from different sources and usually their original strength class and or their species are unknown. Assigning the correct species for salvaged timber could be quite difficult [13,14] and this creates further obstacles in the segregation and grading of the salvaged timber materials.

Table 1: *Examples of mass laminated timber products developed from salvaged timber materials in the literature. CLT (cross laminated timber), GLT (glued laminated timber), NLT (nail laminated timber).*

Materials used	Product	Ref.
Salvaged timber and new timber	CLT	[4]
	CLT	[7]
	GLT	[9]
Salvaged timber	CLT	[6]
	CLT	[8]
	CLT	[10]
	NLT*	[11]
	NLT	[12]

*Using wooden nails

- Unknown load history: the previous load history of salvaged timber is typically unknown, especially when the source of the materials is not identified. This makes it more difficult to account for issues such as the duration of load effect on the material properties [15].

- Uncertainties related to the mechanical properties: as the initial grade and the previous load history are usually unknown, the salvaged timber materials that are obtained from different sites might have a wide range of mechanical characteristics. In addition, previous research works [e.g., 5] have demonstrated that it is often quite difficult to identify any clear trend on how much some of the mechanical properties of timber may change over time.

- Grading rules: the classification of the material properties is essential for reusing salvaged timber in structural applications; however, the existing grading rules are in general valid only for new timber. One exception is the Australian interim industry standard for recycled timber [16], however, for most regions a strength grading regulation still does not exist.

- Distortions and damages: distortion and other shape irregularities are usually common in salvaged timber. The presence of damages such as fastener holes, slots, or cracks are also common and can affect the performance of salvaged timber [see, e.g., 17].

- Length limitation: another common challenge for reusing salvaged timber is the length limitation. Usually, the usable part of a salvaged timber board could be relatively small and the additional costs for end-to-end joining can affect the profitability of reusing salvaged timber.

- Presence of metallic fasteners: salvaged timber may contain metallic fasters such as nails or screws from the previous applications. This can make the

processing of salvaged timber more challenging and time-consuming. In this regard, automated systems have been recently developed for processing salvaged timber, including nail and screw removals; see e.g. [18]. Nevertheless, until such technologies become widely available, post processing of salvaged timber can be difficult and costly.

- Contamination: salvaged timber could be also sometimes contaminated due to exposure to chemicals e.g., wood preservatives or other substances such as wet concrete in falseworks.

- Limited availability and supply: although a large volume of salvaged timber is produced every year, currently the number of companies that are involved in sourcing and distributing salvaged timber is quite limited compared to those for new timber. Therefore, access to continued supply of usable salvaged timber can be difficult for manufacturers of timber products and or builders who may want to use salvaged timber in their projects.

The existence of such challenges warrants in-depth research in order to establish effective approaches to achieve the full extent of advantages that can arise from reusing salvaged wooden materials. This could include e.g., establishing an assessment scheme and or grading criteria that could quantify the mechanical properties of salvaged timber as well as implementing design for deconstruction concepts that could ease the end-of-life disassembly processes and streamline the reuse of salvaged timber.

3 EXPERIMENTAL RESEARCH ON DLT

Given the environmental benefits, the full sustainability potential of reusing salvaged wooden materials in new applications can be achieved if, preferably, no synthetic glues or metallic fasteners are utilized. In this regard, wooden connectors have received particular attention as an alternative solution. In this section, two related projects recently carried out by the authors of this paper are summarized.

3.1 DLT FABRICATED WITH CONNECTORS FROM SALVAGED ENGINEERED WOOD PRODUCTS

The use of wooden connectors in fabricating DLT has been studied intensively [e.g., 19-24]. DLT has been used as a slab-type element by the construction industry in several projects worldwide and a design guide is already available for its application as well, see: [25]. Nevertheless, wooden connectors result in flexible connections; therefore, the composite action of DLT is a challenge to be met when it is used as a beam-type element.

In [26], we aimed to reuse salvaged engineered wood products in fabricating connectors for DLT beams. One of the assumptions was that the superior mechanical properties of connectors from engineered wood products can improve the composite action and, at the same time, enhance the sustainability aspects of DLT beams. The project involved push-out shear tests on dowel and tenon connectors made from Oak, salvaged laminated veneer lumber (LVL), and salvaged plywood. Based on the findings, we then performed four-point bending tests on DLT beams made with the selected connectors (i.e., salvaged plywood tenons, Oak tenons, and conventional Oak dowels as a reference).

The project demonstrated that the DLT beams fabricated with salvaged plywood tenons were efficient and led to approximately 40% higher bending stiffness compared to the conventional DLT beams made with Oak dowels. This approach not only improves the bending stiffness of the DLT beams, but also has the potential to contribute to the circular economy by offering a method for reusing salvaged plywood materials.

3.2 DLT FABRICATED WITH SALVAGED TIMBER LAMELLAE AND SALVAGED PLYWOOD TENONS

Length limitation was identified earlier as a challenge for reusing salvaged timber. Reusing short, salvaged timber elements in mass laminated timber products normally requires significant processing, including gluing and end-to-end joining. However, the associated costs of the additional processing and gluing can make salvaged timber less profitable, and therefore, less attractive to the timber products manufacturing sector. On the other hand, without end-to-end joining and gluing the existing methods of mass laminated timber production may not lead to a product that could meet the structural performance requirements.

A recent project conducted at our group aimed to address this issue by developing DLT floor slabs with a mixture of new (full-scale) timber boards and short salvaged timber elements [27]. The idea was to reuse the salvaged timber elements in every other layer of the DLT slab without end-to-end joining or gluing to reduce the cost associated with reusing the short, salvaged timber elements and to reduce the volume of the full-scale boards that would normally be needed in the conventional DLT.

The concept was evaluated on large-scale DLT specimens. The specimens were composed of three layers of new timber boards (l = 3.5 m) and two layers of salvaged timber elements. The specimens were fabricated with six voids located along the two layers of salvaged timber elements (Stage A in Figure 2). The voids were filled by inserting short, salvaged timber elements with about 2 mm larger lengths (Stage B in Figure 2). The specimens were laminated using salvaged plywood tenons.

https://doi.org/10.52202/069179-0092

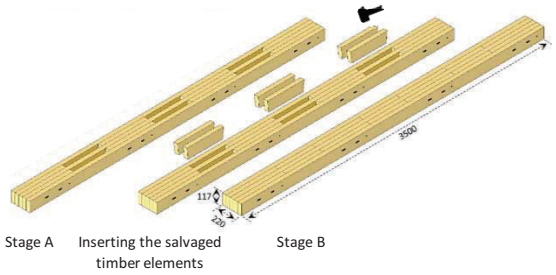

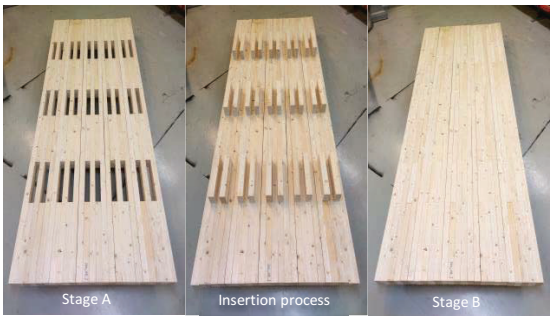

Figure 4: *The fabrication process of the large-scale DLT specimens (top), the actual specimens placed side-by-side to resemble a wider panel (middle), recreated based on [27].*

The vibration characteristics and the bending properties of the specimens were examined in both stages. The results exhibited substantial increase in the bending stiffness and relatively improved vibration characteristics. Overall, the average bending stiffness of the Stage B specimens was about 84% of the expected average bending stiffness of a conventional DLT made with five full-scale timber boards.

Another important finding was that the bending failures occurred almost exclusively in the full-scale timber boards, suggesting that the proposed system may not be so much dependent on the bending strength of the salvaged timber elements. This was due to the fact that the salvaged timber elements were used without end-to-end joining. Therefore, the tension stress caused by the bending loads is resisted predominantly by the full-scale boards.

4 OUTLOOK

Given the current research trends, a promising outlook could be anticipated for the subject of reusing salvaged wooden materials in structural laminated products. In this context, DLT represents a great potential, as it is a cost-effective alternative that does not require gluing. This can directly improve the profitability of salvaged timber materials which may promote their further application in the timber sector. In addition, DLT could be a good option for the construction of affordable housing in less developed areas around the world where access to advanced mass timber production technologies may not be available.

Nevertheless, as highlighted in this paper, there are also important challenges that need to be investigated in order to enable breakthrough innovation in the subject area. Therefore, future research can focus on evaluating ways in which the challenges related to the reuse of salvaged wooden materials can be addressed. Furthermore, when a mixture of new timber and salvaged timber boards are used to fabricate laminated timber products with wooden connectors, different lay ups of the salvaged timber layers could be investigated to identify an efficient lamination system. Investigating the long-term performance under variable service conditions as well as establishing analytical models to predict the mechanical performance are also other vital areas that require further development.

Finally, to better realize the future potentials of salvaged timber, some regulations need to be implemented that can ensure proper ways of sourcing and handling of salvaged timber as well as certifications that can verify its quality. Furthermore, education and awareness about salvaged timber need to be increased in order to improve the consumers perception, create demand, and make products from salvaged timber more available on the market.

ACKNOWLEDGEMENT

The authors would like to thank Serveh Hosseinzadeh (from Tarbiat Modares University) and Lorenzo Giordano (formerly from Aalto University) for their involvement in the experimental research works that were introduced in this paper.

REFERENCES

[1] Szichta P., Risse M., Weber-Blaschke G., and Richter K.: Potentials for wood cascading: A model for the prediction of the recovery of timber in Germany. Resources, Conservation and Recycling, 178, 106101, 2022.

[2] Niu Y., Rasi K., Hughes M., Halme M., and Fink G.: Prolonging life cycles of construction materials and combating climate change by cascading: The case of reusing timber in Finland. Resources, Conservation and Recycling, 170, 105555, 2021.

[3] Huuhka S.: Tectonic use of reclaimed timber: Design principles for turning scrap into architecture. Architectural Research in Finland, 2(1), 130-151, 2018.

[4] Llana D. F., González-Alegre V., Portela M., and Íñiguez-González G.: Cross Laminated Timber (CLT) manufactured with European oak recovered from demolition: Structural properties and non-destructive evaluation. Construction and Building Materials, 339, 127635, 2022.

[5] Cavalli A., Cibecchini D., Togni M., and Sousa H. S.: A review on the mechanical properties of aged wood and salvaged timber. Construction and Building Materials, 114, 681-687, 2016.

[6] Ma Y., Wang X., Begel M., Dai Q., Dickinson Y., Xie X., and Ross R. J.: Flexural and shear performance of CLT panels made from salvaged beetle-killed white spruce. Construction and Building Materials, 302, 124381, 2021.
[7] Arbelaez R., Schimleck L., and Sinha A.: Salvaged lumber for Structural Mass Timber Panels: Manufacturing and Testing. Wood and Fiber Science, 52(2), 178-190, 2020.
[8] Rose C. M., Bergsagel D., Dufresne T., Unubreme E., Lyu T., Duffour P., and Stegemann J. A.: Cross-laminated secondary timber: Experimental testing and modelling the effect of defects and reduced feedstock properties. Sustainability, 10(11), 4118, 2018.
[9] Piao C., Monlezun C. J., Gibson M. D., and Groom L. H.: Recycling of pentachlorophenol-treated southern Pine utility poles. Part II: Mechanical and Delamination properties of laminated beams. Forest products journal, 61(7), 517-525, 2011.
[10] Munandar W. A., Purba R. H., and Christiyanto A.: Exploratory study on the utilization of recycled wood as raw material for cross laminated timber. In: IOP Conference Series: Materials Science and Engineering, 669, (1), p. 012011, IOP Publishing, 2019.
[11] Fink G., Ruan G., and Filz G. H.: Sustainable design concepts for short span, timber-only structures. In *the Annual Symposium of the International Association for Shell and Spatial Structures (IASS)*, 1–8, 2019.
[12] Janowiak J. J., Falk R. H., Gething B. A., and Tsirigotis J. A.: Mechanical Performance of Nail-Laminated Posts Manufactured from Reclaimed Chromated Copper Arsenate–Treated Decking Lumber. Forest Products Journal, 64(1-2), 55-63, 2014.
[13] Crews K.: Development of grading rules for re-cycled timber used in structural applications. International Council for Research and Innovation in Building and Construction, Working Commission W18 – Timber Structures, CIB-W18/40-5-1, Bled, Slovenia, 2007.
[14] Falk R. H., Maul D. G., Cramer S. M., Evans J., and Herian V.: Engineering properties of Douglas-fir lumber reclaimed from deconstructed buildings. Research Paper FPL-RP-650, Madison, WI: U.S. Department of Agriculture, Forest Service, Forest Products Laboratory, 47 p, 2008.
[15] Brandner R., and Ottenhaus L. M.: Properties of salvaged structural timber components: How to account for long-term loading effects given unknown load histories?. In COST ACTION CA 20139 Holistic design of taller timber buildings (HELEN): STATE OF THE ART REPORT (pp. 71-75), 2022.
[16] Crews K., Hayward D., and MacKenzie C.: Interim industry standard recycled timber – visually stress graded recycled timber for structural purposes. Forest & Wood Products Australia, Project No. PN06.1039, ISBN 978-1-920883-35-5, 2008.
[17] Fridley K. J., Williams J. M., and Cofer W. F.: Reliability of reused sawn lumber: effect of fastener holes. Journal of Structural Engineering, 127(4), 412–417, 2001.
[18] Vinoski J.: The urban machine team is using robotics to reclaim waste construction wood. In: Forbes. https://www.forbes.com/sites/jimvinoski/2022/12/08/the-urban-machine-team-is-using-robotics-to-reclaim-waste-construction-wood/?sh=26fdd65a2ff5. Accessed 13 Jan 2023.
[19] Sotayo A., Bradley D., Bather M., Sareh P., Oudjene M., El-Houjeyri I., Harte A. M., Mehra S., O'Ceallaigh C., Haller P., Namari S., Makradi A., Belouettar S., Bouhala L., Deneufbourg F., and Guan Z.: Review of state of the art of dowel laminated timber members and densified wood materials as sustainable engineered wood products for construction and building applications. Developments in the Built Environment, 1, 100004, 2020.
[20] Sotayo A., Bradley D. F., Bather, M., Oudjene M., El-Houjeyri I., and Guan Z.: Development and structural behaviour of adhesive free laminated timber beams and cross laminated panels. Construction and Building Materials, 259, 119821, 2020.
[21] de Moraes Pereira M. C., Sohier L. A. P., Descamps T., and Junior C. C.: Doweled cross laminated timber: Experimental and analytical study. Construction and Building Materials, 273, 121820, 2021.
[22] Bouhala L., Fiorelli D., Makradi A., Belouettar S., Sotayo A., Bradley D. F., and Guan Z.: Advanced numerical investigation on adhesive free timber structures. Composite Structures, 246, 112389, 2020.
[23] Ogunrinde O.: Evaluation of bending performance of nail laminated and dowel laminated timber. Masters dissertation, University of New Brunswick, Canada, 2019.
[24] El-Houjeyri I., Thi V. D., Oudjene M., Khelifa M., Rogaume Y., Sotayo A., and Guan Z.: Experimental investigations on adhesive free laminated oak timber beams and timber-to-timber joints assembled using thermo-mechanically compressed wood dowels. Construction and Building Materials, 222, 288-299, 2019.
[25] StructureCraft.: Dowel laminated timber-the all wood panel-mass timber design guide. 2020. Available online: https://structurecraft.com/blog/dowel-laminated-timber-design-guide-and-profile-handbook. Accessed 11 Jan 2023.
[26] Derikvand M., Hosseinzadeh S., and Fink G.: Mechanical Properties of Dowel Laminated Timber Beams with Connectors Made of Salvaged Wooden Materials. Journal of Architectural Engineering, 27(4), 04021035, 2021. https://doi.org/10.1061/(ASCE)AE.1943-5568.0000513

https://doi.org/10.52202/069179-0092

[27] Giordano L., Derikvand M., and Fink G.: Bending properties and vibration characteristics of dowel-laminated timber panels made with short salvaged timber elements. Buildings, 13, 199, 2023. https://doi.org/10.3390/buildings13010199

World Conference on Timber Engineering Oslo 2023

STRUCTURAL SAWN WOOD PRODUCTION IN THE CHILIEAN SAWMILL INDUSTRY, DATA ANALYSIS FROM SURVEYS CARRIED OUT FOR 4 YEARS

Pamela Poblete[1], Janina Gysling[2], Carlos Kahler[3], Wilson Mejías[4], Daniel Soto[5], Verónica álvarez[6], Evaristo Pardo[7].

ABSTRACT

The sawmill industry produce around of 8 million cubic meters annually, setting Chile as the tenth world producer of sawn wood. Since Chile is a foretry country, the current sectoral policy has among its strategic axis the promotion of quality wood construction. From here it emerges the necesity of reinforce graded structural sawn wood supply, boosting this product demand by the construction industry.

In this context, INFOR began to generates specific statistics on structural sawn wood (MAE), this activity accumulates four years of measurments. In the present research, it is presented the main results of the analysis of data obtained from these measurments, through surveying in the sawmill industry. To carry out the survey on MAE (structural sawn wood), sawmills with production higher than 10,000 cubic meters annually were selected, gathering information from a sample of 100 sawmills per year, from 2018 to 2021; these sawmills represents near of 80% of the sawn wood national production.

Results indicate that the knowledge about MAE concept has just slightly increased during four years of measurments; while the interest of sawmill in participating in MAE production it is determined by the greater access to higher pirces, a more stable demand, and a greater reliability in logs availiability.

KEYWORDS: Structural lumber market; classified structural lumber, structural lumber production

1 INTRODUCTION

In 2021, the sawmill industry in Chile had 1,233 sawmills, from which 922 were in operation. The industry consumed 16.7 million cubic meters of wood in logs, resulting in a production of 8.7 million cubic meters of sawn wood, from which 97.7% corresponds to *Pinus radiata.* From the national total production, 24.8% it is destined to exports, while 75.2% stays in the internal market [1]. According to FAO, these levels of production place Chile in the eleventh position at world level as a sawn wood producer [2].

Regarding the sawmills production range, historically plants with production lower than 5,000 m³/year have been the most numerous, representing 80% of the total number of sawmills in operation in 2021 [3].

In terms of mobility, sawmills are divided in permanent, and mobile. The number of permanent sawmills reaches a share of 48.6% in a historical growing trend, and a decrease of mobile sawmills. This is mainly due to a significant decrease in native sawn wood production, where mobile sawmills dominated [1].

In 2021, La Araucanía region concentrated the greater number of sawmills in operation with 202 units (21.9%), followed by Biobío region, and Los Lagos region with 144 units each, and Maule region with 135 units. These four regions concentrate 67.8% of the total in-operation sawmills in the country [3].

[1] Pamela Poblete, (INFOR) Instituto Forestal, Chile. ppoblete@infor.cl
[2] Janina Gysling, (INFOR) Instituto Forestal, Chile. jgysling@infor.cl
[3] Carlos Kahler, (INFOR) Instituto Forestal, Chile. ckahler@infor.cl
[4] Wilson Mejías, (INFOR) Instituto Forestal, Chile. wmejias@infor.cl
[5] Daniel Soto, (INFOR) Instituto Forestal, Chile. dsoto@infor.cl
[6] Verónica Álvarez, (INFOR) Instituto Forestal, Chile. valvarez@infor.cl
[7] Evaristo Pardo, (INFOR) Instituto Forestal, Chile. epardo@infor.cl

https://doi.org/10.52202/069179-0093

Since Chile is a forestry country, with a highlighted roll as a wood producer, the supply of sawn wood for structural use in construction, graded as such, and in accordance with requirements demanded by the norm in force, is very low. On the other hand, from building statistics it is deduced that 60.7% of predominant materiality in walls was concrete, far surpassing wood as a structural material, which reached 10.6% of the total housing, and non-housing authorized area of new works in 2020 (13.1 million m²) [1]. These figures differ a lot when compared with other wood-producer countries, where the structural use of this material in housing construction exceeds 85% as in case of United States, and Canada, and above 60% in case of Australia, and New Zealand [4].

The promotion of wood construction is a challenge that has been considered as a strategic axis in the current forestry policy. State agencies, companies, and private associations related to the forestry, and construction sectors, as well as the academies, and I+D centers, are developing several initiatives focused on promoting wood as a construction material.

In this regard, INFOR has surveyed during four year a representative statistical sample of sawmills in the country, in order to gather information that allows to know the wood supply for construction. From this information, in the present research, a characterization, and an analysis of the structural sawn wood production is provided.

1.1 DEFINITIONS

1.1.1 Sawn wood for structural use

The sawn wood refers to solid pieces of wood obtained from a sawmill, with different features, and dimensions, which are used in construction with structural ends, mainly in roofing, and walls, but without being subjected to a formal classification process.

1.1.2 Graded structural sawn wood and its requirements

In order for radiata pine sawn wood to meet the structural requirements in construction, there are certain essential specifications that allow to ensure its good performance inside the structure. These are: structural grade, dimensions, moisture content, and preservation. [5].

a) Structural grade

The structural grade corresponds to a category of pieces of sawn wood having the same capacity to resist loads, and stress, that can be measured through the visual grading technique (NCh1207 [5], and NCh1198 [6]), which assign a structural grade to the sawn wood in terms of size, and knots location, pith, missing edges, wrapping, among others; The visual grading results in the following classifications: GS, G1, and G2; or also through a mechanical grading, based on a set of non-destructive tests, which allows to determinate the stiffness, and to be classified in a structural grade, which are: C16, C14, MGP10, and MGP12. (NCh3028 [7] part 1, and part 2, and NCh1198).

In table 1 [5], the different types of structural classifications that the sawn wood can be graded into are presented.

Table 1: *Structural grades for Radiata pine sawn wood, and its mechanical features*

Allowable stress for radiata pine wood							
Grading system	Structural grade	Bending (Mpa)	Parallel compression (Mpa)	Parallel traction (Mpa)	Normal compression (Mpa)	Shearing (Mpa)	Modulus of elasticity in bending (Mpa)
Visual	GS	11	8.5	6	2.5	1.1	10,500
	G1	7.5	7.5	5	2.5	1.1	10,000
	G2	5.4	6.5	4	2.5	1.1	8,900
Mechanical	C24	9.3	8	4.7	2.5	1.1	10,200
	C16	5.2	7.5	3.5	2.5	1.1	7,900
	MGP12	13.5	15.5	6	2.5	1.1	12,700
	MGP10	8.4	10	4	2.5	1.1	10,000

b) Dimensions

In compliance with the 1207 Chilean norm regarding the visual grading, it is stipulated that the allowed dimension tolerance in sawn wood must be in compliance with the 2824 Chilean norm [8]. This stipulates the nominal thickness, and width of the sawn and planed radiata pine wood, establishing a dimensional tolerance for the use of sawn wood of +3 mm thickness, and +5 mm wide. The length of the pieces permits a maximum tolerance of 0.1m.

c) Moisture content

Each piece of radiata pine sawn, or planed wood destined for structural use must be dry, with a moisture content lower or equal to 19%, as stated in the norm NCh 2150 [6].

d) Preservation

In compliance with the *Odenanza General de Urbanismo y Construcciones*, the different species of wood used more frequently are classified in 5 categories according to its durability: very durable, durable, moderately durable, low durability, and non-durable. The radiata pine wood is located in the category of non-durable, consequently, as the *Ordenanza* stipulates, must be preserved in compliance with the NCh 819 [10].

2 MATERIALS AND METHODS

INFOR carry out a sampling of the sawmill industry each year, where information is gathered from around a thousand sawmills from Coquimbo region, to Magallanes region. Since 2019, sawmills are selected to an additional survey on structural sawn wood. The selection requirements are: a production higher than 10,000 cubic meters annually, with a facility with minimum

https://doi.org/10.52202/069179-0093

infrastructure to produce graded sawn wood, as in case of wood drying chambers, or the access to them.
The number of sawmills selected in each year of measurement is: 116 sawmills in 2018, 119 sawmills in 2019, 134 sawmills in 2020, and 136 sawmills in 2021. From the second year, the selection is in accordance with the follow-up of productive units surveyed last year.

The sawmills in the sample were classified in 8 ranges of annual production: lower or equal to 5 thousand m³; 5 thousand to 10 thousand m³; 10 thousand to 20 thousand m³; 20 thousand to 50 thousand m³; 50 thousand to 100 thousand m³; 100 thousand to 200 thousand m³; 200 thousand to 300 thousand m³; and higher than 300 thousand m³.

The quantitative, and qualitative information collected on structural sawn wood consist in: the knowledge on the concept of graded structural sawn wood, and the requirements for its production; annual amount produced; sales orders received, and business done; number of trained operators in wood grading; available equipment to produce structural wood, interest in producing it, and main factors in making the decision to enter the business.

Through the Forestry Statistics Platform from INFOR, the data was stored, and processed to its following analysis.

The information obtained was subjected to a correlation analysis to search for relations between the MAE volume produced, and other variables collected through surveys. The Spearman's rank correlation coefficient was used, since this is a non-parametric measure of statistical dependency between two variables [11]. The statistical significance of correlation between two variables was evaluated with a 95% confidence level.

3 RESULTS

The selected sample to characterize MAE production represents 28.3% average of the period from active permanent sawmills in the country, and around of 13% of the total of sawmills. The 2021 production of sawmills in the sample represents 88.3% of the national sawn wood production.

Table 2: *Number of surveyed sawmills, permanent, and in total in the 2018-2021 period.*

Year	2018	2019	2020	2021
Sawmills Sample MAE	116	119	134	136
Permanent sawmills	448	448	440	448
Active sawmills in the country	984	957	938	922

The surveyed sawmills are concentrated in the southern-central zone of the country, being Maule, Biobío, and La Araucanía regions the ones concentrating approximately 80% of the surveyed sawmills in average during four years of analysis.

In regard of sawmills size in the sample, more than half is concentrated in a production range of 10,000 to 50,000 cubic meters annually.

The sawmills were consulted about their knowledge on the concept MAE (Structural sawn wood), which indicated a positive result, going from 75.0% in 2018, to 86.8% in 2021. This represent a broad knowledge of the concept, which could be helpful in generating classified wood supply.

It is important to mention that, in all production ranges, the knowledge is superior to 66.7%, reaching near to 100% in higher production ranges sawmills, slightly decreasing in lower production ranges.

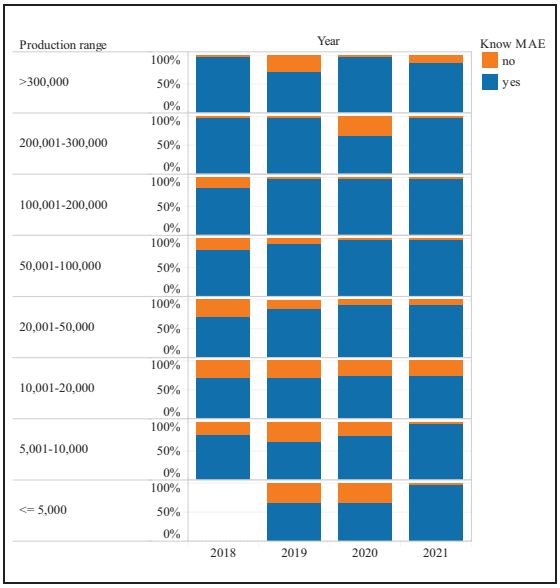

Figure 1: *Knowledge on MAE by production range, and year.*

In case of geographical location, Biobío region is the one with the greater knowledge on the concept, while Los Rios region is the one with lowest levels of knowledge on the concept.

It should be noted that when consulting about MAE concept, it was not mentioned the requirements this product must fulfil. At the period's beginning, 34.5% of the sample declared they produce structural wood, while in 2021, 45.6% of sawmills in the sample declared they produce it, they being located in production ranges of 10,000 to 20,000 m³.

The knowledge of the requirements has also had a slight variation, but negative, from 51.7% of sawmills in 2018 that indeed knew the requirements, to 47.8% in 2021.

https://doi.org/10.52202/069179-0093

In practice, structural sawn wood is identified in a lot of sawmills by its use in construction, however, in few opportunities this wood is subjected to a formal classification process. As a consequence of this, there is no certainty in meeting the structural requirements.

In regard of MAE orders, in the first measurement in 2018, 15 units claimed they had received orders to produce MAE, it was not different in 2021, confirming the orders by 15 sawmills; in average during the period's study, 11.6% of sawmills in the sample received MAE production orders. It should be highlighted that MAE production orders are concentrated in ranges of 10,000 to 20,000 m³, and 20,000 to 50,000 m³.

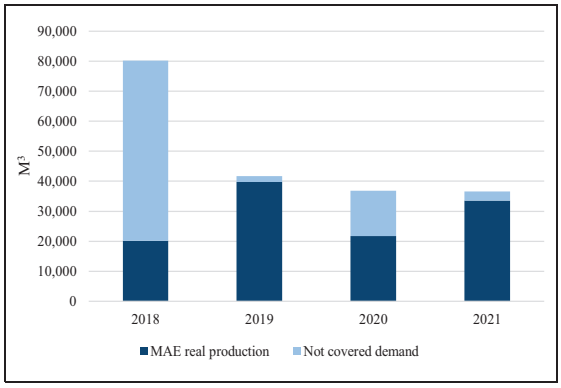

Figure 2: *Structural Sawn Wood demand, and production in 2018-2021 period.*

The volume of MAE requested has had a negative evolution, dropping from 80,120 m³ in 2018, to 36,607 m³ in 2021. On the other hand, the MAE's effective volume produced, and sold presents an increase of 66.1% since 2018 to 2021, amounting a total of 115,109 m³ during the period, meeting 59.9% of the demand in the period.

The demand unmet by sawmills, that is to say, the volume of MAE requested minus the effective produced volume has decreased (See Figure 2), representing in 2021 near of 3 thousand m³, this great variation can be explained by the increase in MAE knowledge y the real capacity of sawmills to produce this product, it is observed that requests in last three years have been adjusting to the real production.

The trained operators to carry out classification tasks have increased from 66 workers in 2018, to 92 in 2021, showing a certain interest by the sawmills in MAE production, promoting external training over internal training.

The main decision factors considered by sawmills during the period to produce, and sell MAE are: obtaining better prices for the product, reach a more stable demand, and reliability in log supply.

Another interesting way of examining the variables was though the correlation analysis, in Figure 3 are presented the main variables, those with a greater correlation with each other, excluding other variables less like-minded with the elements of the survey.

In figure 3, when the variables are closer to 1 (blue), it means a greater correlation. In case of "x", these indicates correlations without statistical significance.

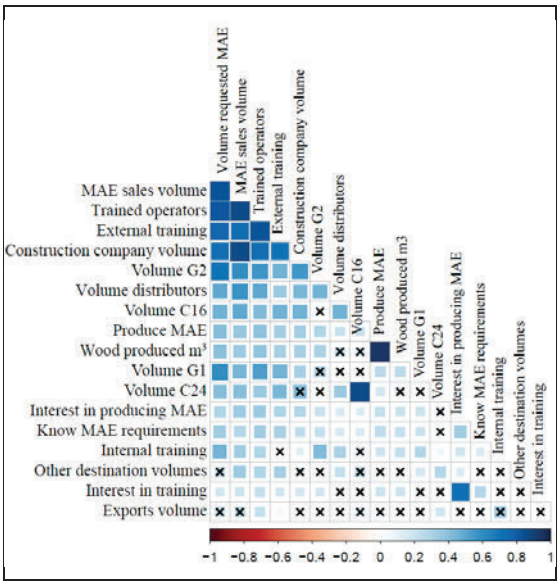

Figure 3: *Outline of main variables correlation of MAE survey*

It is observed that exist a high correlation between MAE requested volume, and actual MAE sales, in addition to trained operators, a key factor in visual grading. It also emerges that MAE requests come from construction companies, which prefer wood graded as G2, followed by G1.

To address the question if sawmills are interested in producing MAE, it is observed that this is linked to the interest in training operators, followed by the knowledge of requirements to produce MAE.

4 CONCLUSIONS

Four years of analyzed samples shows the following:

- Slight increase in knowledge of the graded structural sawn wood concept.
- In average only 5.7% of the wood for structural use marketed in construction corresponds to MAE.
- 59.0% of MAE demand was met by sawmills, of a total of 195,000 cubic meters requested during the research period.
- From the selected sawmills total production, 0.4% corresponds to MAE sales.
- Approximately, per year 10 sawmills participates actively in MAE sales, however, around of 40 are interested in production.

https://doi.org/10.52202/069179-0093

- The main decision factors observed by sawmills in order to produce, and sell MAE during the research period were: higher prices, more stable demand, and reliability in logs availability.

- While there is an interest in producing MAE, the industry recognizes the importance of training their operators externally in order for them to be able to carry out a proper wood grading.

After 4 years of measurements on MAE production, and its features, it is observed that there have been no fundamental changes in supply nor in demand of the product, thus sawmills are still under observations, since MAE production is still not an attractive business in which they can rely on a certain level of demand, and prices.

For this reason, it is necessary to implement policies, and public instruments with biding effect, wood labeling or promoting instruments like subsidies in grading training, to trigger production, supply, and demand to massive level.

The current forestry industry development, new technologies in construction, in addition to sawn wood, and logs prices, it emerges the necessity of making a difference, and to add value to production in sawmills, creating opportunities to exploit graded structural sawn wood production destined to construction.

ACKNOWLEDGEMENT

The present research have been carry out under the framework of the project entitled: *"Fortalecimiento de las Capacidades Tecnológicas del Instituto Forestal (INFOR), para el desarrollo de la Industria Secundaria de la Madera, a través de bienes públicos, orientados al sector de la construcción"*. The project was funded by *Corporación de Fomento a la Producción* (CORFO) and INFOR.

REFERENCES

[1] Álvarez González, V., Poblete Hernández, P., Soto Aguirre, D., *et al.* Anuario Forestal 2022. Santiago, Chile. Instituto Forestal (INFOR). 276p. 2022.

[2] INFOR. El Sector Forestal Chileno 2020. Instituto Forestal. 52p. 2021.

[3] Álvarez González, V., Pardo Velásquez, E., Poblete Hernández, P. La Industria del Aserrío 2022. Instituto Forestal. 136p. 2022.

[4] Gysling Caselli, J., Kahler González, C., Soto Aguirre, D., *et al.* Madera y Construcción, Hacia una Simbiosis Estratégica. Instituto Forestal. 224p. 2021.

[5] Gysling Caselli, J., Kahler González, C., Soto Aguirre, D., *et al.* El Mercado de la Madera Aserrada para Uso Estructural en Chile. Instituto Forestal. 138p. 2020.

[6] Instituto Nacional de Normalización. Pino radiata-Clasificación visual para uso estructural - Especificaciones de los grados de calidad. (NCh N° 1207). Santiago, Chile: INN. 23p. 2005.

[7] Instituto Nacional de Normalización. Madera - Construcciones en madera - Cálculo. (NCh N° 1198). Santiago, Chile: INN. 214p. 2014.

[8] Instituto Nacional de Normalización (INN). Madera estructural - Determinación de propiedades físicas y mecánicas de la madera clasificada por su resistencia - Parte 1: Métodos de ensayo en tamaño estructural. (NCh N°3028). Santiago, Chile: INN. 14p. 2017.

[9] Instituto Nacional de Normalización. Madera Preservada - Madera - Pino radiata - Unidades, dimensiones y tolerancias. (NCh N° 2824). Santiago, Chile: INN. 9p. 2003.

[10] Instituto Nacional de Normalización. Pino radiata-Clasificación visual para uso estructural - Especificaciones de los grados de calidad. (NCh N° 819). Santiago, Chile: INN. 22p. 2012.

[11] Spearman, C. The Proof and Measurement of Association Between Two Things. In J. J. Jenkins & D. G. Paterson (Eds.), *Studies in individual differences: The search for intelligence* (pp. 45–58). Appleton-Century-Crofts, 1961

https://doi.org/10.52202/069179-0093

World Conference on
Timber Engineering
Oslo 2023

ROTATIONAL STIFFNESS OF NEWLY DEVELOPED LVL-BASED COLUMN-HEAD REINFORCEMENT FOR POINT-SUPPORTED SLAB-COLUMN BUILDING SYSTEMS

Cristóbal Tapia[1], Felix Amtsberg[2], Aaron Münzer[3], Simon Aicher[4], Achim Menges[5]

ABSTRACT: The paper presents a recently developed concept for the transmission of vertical loads between columns in point-supported timber slab systems. The concept consists of a specially milled beech LVL element inserted into the end of a GLT column, thus allowing to receive concentrated loads from an also specially milled LVL pin element. Under axial compression the LVL insert proved being able to redistribute the compression stresses effectively before transferring the stresses to the lower GLT column. This paper investigates the rotational stiffness of this concept, both numerically and experimentally with two manufactured specimens. For the studied geometry the obtained rotational stiffness was 3.4×10^2 kNm/rad, being in good agreement with the finite element simulations. Relevant aspects of the robotic manufacturing relating to the tight tolerances needed are discussed.

KEYWORDS: multi-storey timber buildings, GLT, beech LVL, rotational stiffness, robotic manufacturing, point-supports

1 INTRODUCTION

The construction of high-rise buildings based on modern wood engineered products has been a reality for the past decade, with the number of new projects steadily rising worldwide (see e.g. [2, 11]). This development has been fostered by a variety of interacting factors, associated with mechanical, environmental, architectonic and social aspects. Timber, having an excellent weight/strength ratio and enabling a high degree of prefabrication for rapid on-site assembly, fits perfectly the needs of multi-storey building construction. Furthermore, the increasing urge to transit to more CO_2-neutral building technologies has lead to an increasing interest in timber—a natural CO_2 container—as a viable option for high-rise buildings, up until now almost exclusively dominated by reinforced concrete and steel.

This relatively new field of multi-storey timber buildings has not come free of challenges, mostly represented by the need for new performant, bespoken connection solutions for the different components. Examples of problematic joints are found especially in column-slab type of structures, typically consisting of glued laminated timber (GLT) columns and cross-laminated timber (CLT) plates with an additional lateral bracing system. Here, the point-support situation leads to highly demanding requirements for the connection system. In such a situation two main problems arise: firstly, the point-support condition of the plate induces high shear and bending stresses in the immediate region of the CLT surrounding the column. This poses a problem for the CLT plate due to its relative low rolling strength values, normally about three times lower than the shear strength of timber parallel to the fiber. Secondly, the vertical load originating from the upper floors and carried by the upper column needs to be transferred to the bottom column supporting the CLT plate. Owed to the low compressive strength perpendicular to the grain of timber, $f_{c,90}$, the column cannot be supported directly on the CLT plate, and therefore the column force is normally transferred through a hole in the CLT plate (e.g. [10, 11]). This further worsens the stress situation in the CLT in the column region, as tensile stress concentrations will develop in the vicinity of the hole on the bending tension side [13]. Solutions for the reinforcement of CLT plates under these loading conditions are implemented or have been proposed in [10, 13, 18].

The transfer of the vertical loads has been addressed by Fast et al. [11] for columns at the edges of the CLT plate and in [10] for columns placed at the inner field of the CLT plate. In both cases the concept applied to transfer the vertical loads is very similar, consisting on a cylindrical steel profile used to transfer the loads through the reduced cross-section of the column. This steel profile has attached at both ends steel plates, which are fixed to the columns.

[1]Materials Testing Institute (MPA), University of Stuttgart, Pfaffenwaldring 4b, 70569 Stuttgart, Germany, cristobal.tapia-camu@mpa.uni-stuttgart.de
[2]Institute for Computational Design and Construction (ICD), University of Stuttgart, Keplerstraße 11, 70174 Stuttgart, Germany, felix.amtsberg@icd.uni-stuttgart.de
[3]Materials Testing Institute (MPA), University of Stuttgart, Pfaffenwaldring 4b, 70569 Stuttgart, Germany, simon.aicher@mpa.uni-stuttgart.de
[4]Materials Testing Institute (MPA), University of Stuttgart, Pfaffenwaldring 4b, 70569 Stuttgart, Germany, aaron.muenzer@mpa.uni-stuttgart.de
[5]Institute for Computational Design and Construction (ICD), University of Stuttgart, Keplerstraße 11, 70174 Stuttgart, Germany, achim.menges@icd.uni-stuttgart.de

https://doi.org/10.52202/069179-0094

The efficacy of these solutions has been verified by means of full-sized experimental campaigns, for example in [4], where also two additional concepts were tested. Nevertheless, as mentioned in [4], the inclusion of the special steel connectors is costly and alternatives should be explored that require less steel.

Within the context of Research Project 3 of the Cluster of Excellence "Integrative Computational Design and Construction for Architecture" (IntCDC), at the University of Stuttgart, the problem of timber connections for multi-storey timber buildings was addressed. One of the specific objectives was to develop an almost pure timber column-to-column connection. The concept leverages modern digital fabrication methods to combine and glue different timber products with the required tolerances ($\approx$ 1 mm), enabling complex geometries for an efficient use of material and transfer of loads. This paper presents first experimental and finite element results on the newly developed connection concept. Especially, the behavior under vertical and lateral load situations is analyzed, and manufacturing aspects will be discussed.

2 DESCRIPTION OF THE CONNECTION CONCEPT

2.1 GEOMETRY

The newly developed connection consists of an assemblage of three specially milled timber components as illustrated in Fig. 1. The load coming from the top GLT column is first transferred to a stepped, pyramid-shaped beech laminated veneer lumber (LVL) element embedded in an equal negatively shaped pyramid cavity in the column. Then the load is transferred to a hardwood pin element with a similar stepped geometry. From there, the load travels to the bottom column through the same, but inverted, beech LVL component.

The number and dimensions of the steps of each component is variable. The radius, r, of the milled corners (see Fig. 2) is bound to the diameter of the used milling tool, which for the studied case was $r = 8$ mm.

The idea behind the chosen geometry for the beech LVL insert is to enable a gradual transfer of stresses from the smaller cross-section of the pin element to the GLT column. In other words, the stronger LVL insert serves as transition zone for the spreading of the compressive stresses, which are then transferred to the column. The same principle applies to the geometry of the hardwood pin element.

2.2 MATERIALS

In terms of used materials, it is evident that the pin element, owed to its reduced cross-section, is subjected to higher compression stresses as the GLT column. Thus, a strong material is required. For the present study, unidirectional, CE-marked beech LVL according to EN 14374 [7] was used for this component. According to the producer's Declaration of Performance [14] the characteristic compressive strength parallel to grain can be assumed as $57.5 \times 1.2 = 69$ MPa for use in service class 1. However, it should be noted that the performed experiments suggest that an even stronger material—e.g. from tropical hardwoods or densified veneer wood—is required to fully utilize the connection. Similarly, the transition pyramid-shaped insert element is also subjected to rather high stresses, reason for which beech LVL was used as well. The LVL blocks from which the pyramid insert elements were milled consisted of block-glued LVL plates.

Each component is glued into the next one by means of a two-component polyurethane adhesive. For a proper functioning of the connection, the different elements must fit precisely into each other. Otherwise, the loads would concentrate on a subset of the contact surfaces, leading to premature local damage and reducing the capacity of the connection. Small gaps can be effectively bridged by the used gap-filling adhesive, however only to a certain degree. Therefore, it is essential to achieve very small tolerances ($<$ 1 mm) during the manufacturing process. The components can easily be pre-assembled, leaving only one last on-site bonding step per connection during the construction phase.

Due to the geometry of the LVL pyramid insert, stresses perpendicular to the grain are expected in the column. In order to avoid an early failure due to splitting, the GLT column can be reinforced by means of self-tapping screws. The effect of this reinforcement measure was experimentally studied in [17], where a Weibull-based design approach is presented, and will not be further addressed in this paper.

2.3 BEHAVIOR UNDER AXIAL COMPRESSION LOADING

The column was previously investigated numerically and experimentally under axial compression in [17]. In

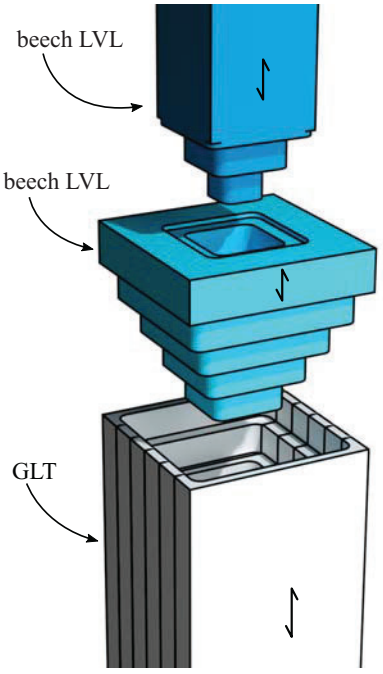

Figure 1: *Concept for the proposed connection for the vertical transfer of loads from upper columns*

https://doi.org/10.52202/069179-0094

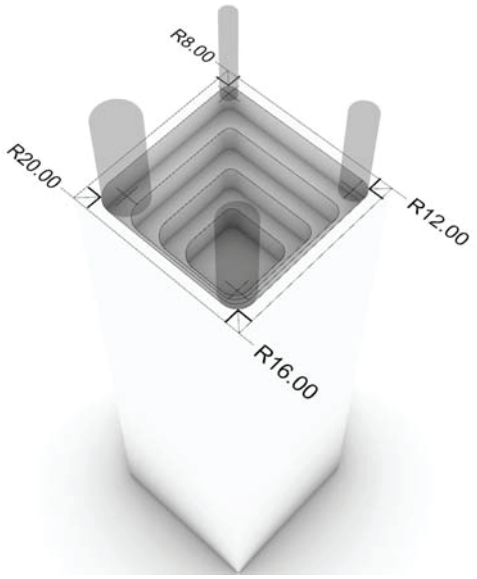

Figure 2: *Example of an automatically generated column detail based on 4 different milling tool diameters*

that study, a series of five specimens was manufactured and tested in order to obtain maximum capacities and to understand the failure mode under axial compression, where the load was introduced exclusively through the LVL pin element. The specimens had identical dimensions as those presented in this paper. The general concept of the connection can be understood by looking at Fig. 3a, where the stresses in the z-direction obtained by a 3D finite element (FE) model are shown.

The rather concentrated load coming from the LVL pin on the top induces a region of high stresses directly below the pin element. However, by placing a strong material in this region—in this case beech LVL aligned vertically—, the stresses can be taken and spread downwards. By using the special stepped geometry, the high stresses can be kept inside the LVL insert, roughly following the stress-isolines as shown in Fig. 3a. The σ_z stresses at the interface between LVL insert and GLT column can be accurately estimated by an analytical model, making this a suitable tool for the design of the connection, without requiring a full 3D FE model [17].

A further analyzed issue was the formation of a region of tensile stresses perpendicular to the fiber, directly below the LVL insert, as illustrated in Fig. 3b. The experiments showed that these stresses were responsible for the failure of the specimens, as splitting triggered the maximum capacity of all tested specimens. The consideration of these stresses was tackled in a first approximation by a Weibull-based design approach, similar as done in [3]. However, local crushing in the GLT, directly underneath the LVL insert was also observed. Therefore, the exact failure model is owed most likely to a more complex combination of compression and splitting stresses.

A further analysis was also made to assess the influence of the application of loads directly on the top surface of the LVL insert, simulating a CLT plate being supported by

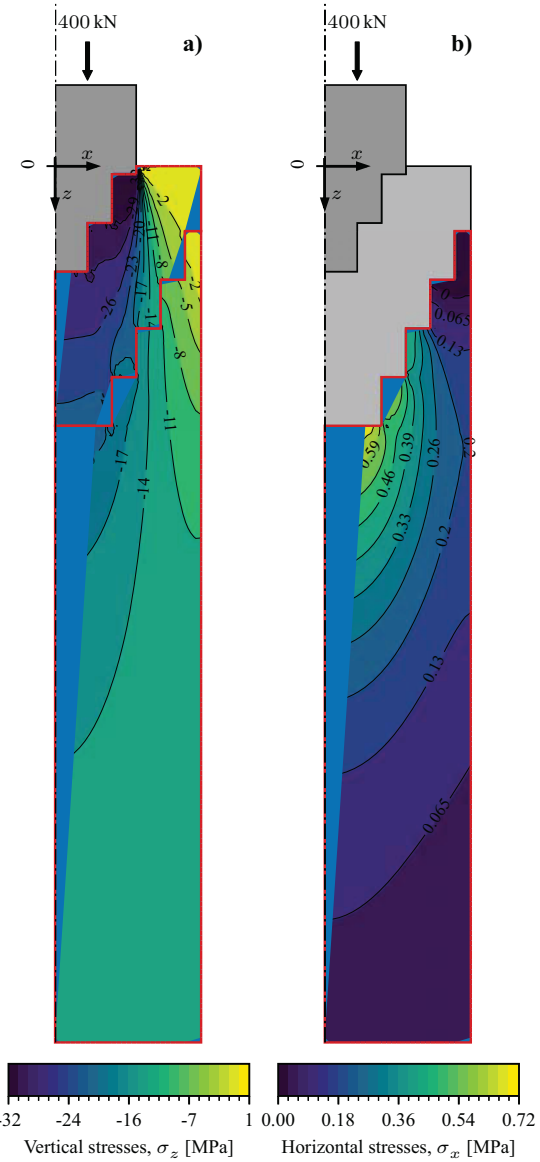

Figure 3: *Contour plots of vertical stresses σ_z (a) and horizontal stresses σ_x (b) for a load of* 400 kN *applied on top of the LVL pin element*

the column. The numerical results showed that the vertical stresses, σ_z, were rather evenly distributed and that the splitting stresses, σ_x, decreased by a factor of two to three.

2.4 MANUFACTURING CONSIDERATIONS

In the digital process chain, parametric models were developed specifically to produce the design details of the outlined column-to-column connections. These allowed an effortless generation of the geometry and resulting milling paths to produce and test various configurations of, for example, the column cross-section steps. Other parameters that were automatically generated include the infeed and path planning according to the selected cutter geometry and blank, feed rate and speed. Rhinoceros 6 [12] and Grasshopper were used as the development environment

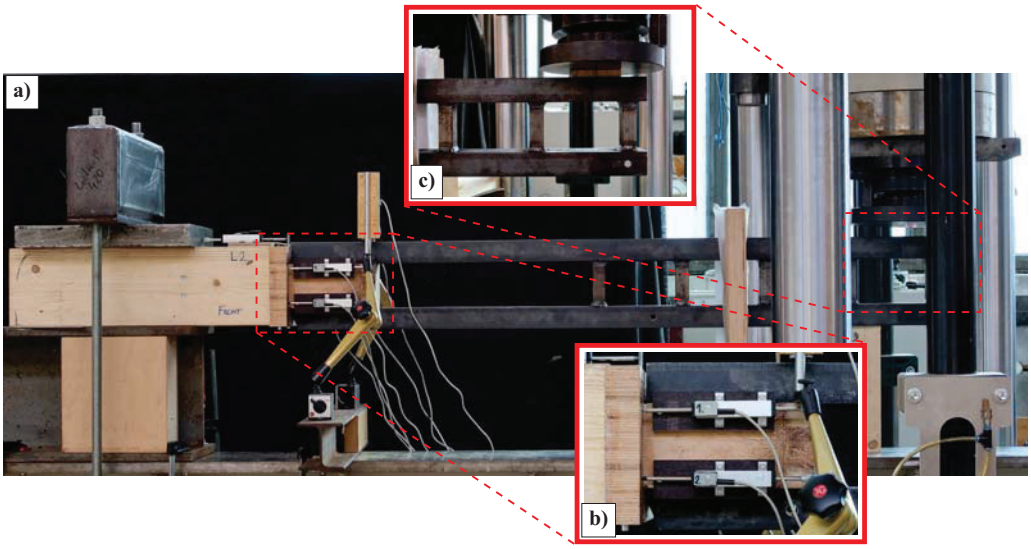

Figure 4: *Example of the realized experimental set-up for the lateral loading testing of the connection concept*

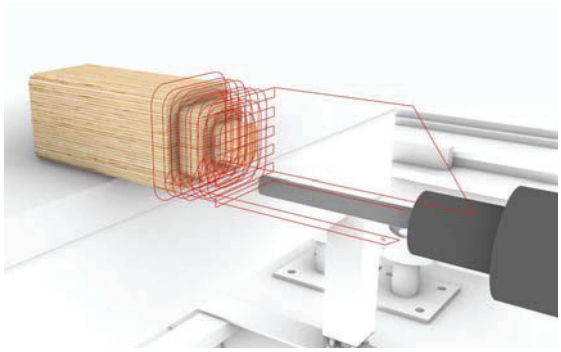

Figure 5: *Rhino Model of the geometry and automatically generated toolpath (red)*

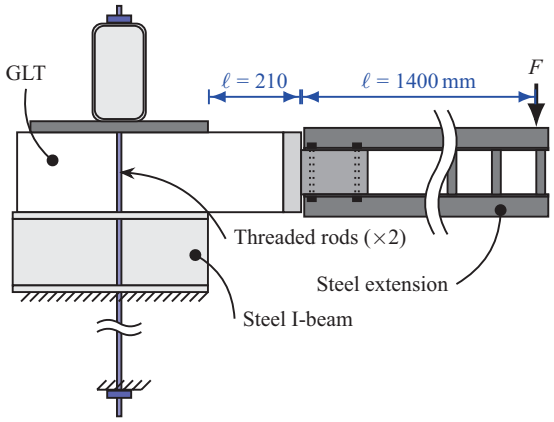

Figure 6: *Experimental setup for the lateral loading configuration*

for tool path, NC code generation and simulation. The data were then transferred to KUKA-CNC and implemented (see Fig. 5).

3 EXPERIMENTAL INVESTIGATIONS

3.1 STUDIED CONFIGURATIONS

The reported connection was studied under lateral loading in order to obtain the moment capacity, as well as the rotational stiffness. The specimens are composed of a softwood GLT column with a cross-section of 180 mm × 180 mm and a length of 600 mm; the dimensions of the LVL insert and the pin elements are described in [17]. The specimens of both configurations were tested at the Division of Timber Constructions of the Materials Testing Institute, University of Stuttgart, with a servo-hydraulic machine with a maximum loading capacity of 1.6 MN. The load was applied in displacement-controlled manner with a stroke rate of 1.5 mm/sec until failure occurred. Since the achieved loads were rather small compared to the maximum capacity of the machine (about 2 kN compared to 1.6 MN), the data recording was accompanied by a significant amount of electronic noise. Future experiments will use an independent load measuring cell, appropriate for the expected load range.

The experimental set-up with its relevant dimensions is illustrated in Fig. 6. Here, an extension made from two steel profiles welded together was attached to the LVL pin element by means of threaded rods. This increases the lever arm, thus increasing the moment to shear force ratio on the connection. The steel extension had a total weight of 14.2 kg. The specimens were clamped to a large steel profile, to achieve a cantilever situation, as presented in Fig. 4.

In both configurations the specimens were reinforced by means of full-threaded self-tapping screws. This was done in order to delay splitting due to stresses perpendicular to the grain. The position of the used screws can be seen in Fig. 7.

https://doi.org/10.52202/069179-0094

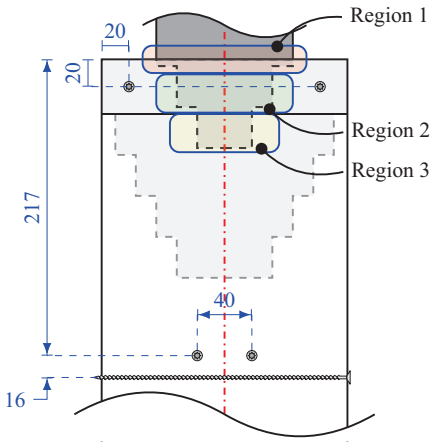

Figure 7: *Position of screws used to reinforce the connection during the lateral loading experiments and definition of regions in the interface between LVL-insert and LVL-pin elements (dimensions in millimeter)*

3.2 MANUFACTURE OF PROTOTYPES

The fabrication setup used to produce the joints from softwood GLT and beech LVL consists of a KUKA 420 R3031 industrial robot mounted on a KUKA KL 4000 linear axis with a travel distance of 11 m. The system is designed and tested for a machining accuracy of $\leq$ 0.4 mm. An air-cooled HSD 929L spindle with a power of 14.40 kW was used for subtractive machining. The column-to-column connection was produced using a coated spiral roughing/finishing cutter with a useful length of 30 mm, a total length of 205 mm and a diameter of 16 mm. After three tests with varying step geometries a total of 12 assemblies were fabricated for experimental testing. The GLT column and LVL pin were machined horizontally (see Fig. 8), while the LVL pocket element was manufactured vertically (see Fig. 9). These were also reclamped to be machined on both sides. Other parameters are feed rate (3000 mm/min GLT, 600 mm/min LVL), speed (12 000 rpm), final infeed (0.25 mm) and offset (0.25 mm). The bond line thickness resulting from this milling set-up was analyzed on a parallel milled sample using an electronic stereo microscope [5]. Predominantly thin (<1 mm) bond line thicknesses were observed. The mean glue joint thickness and the corresponding coefficient of variation were 0.14 mm and 40 % respectively (see Fig. 10). This indicates a high accuracy of the milling process and that, if necessary, the programmed tolerances could be further reduced.

3.3 RESULTS

3.3.1 General observed behavior and failure mode

Figure 11 shows the global moment-displacement curve of specimens L1 and L2 (displacement as machine piston displacement). Both specimens presented a linear behavior until about 1.5 kNm, where first audible failure noise could be heard. This is clearly shown in Fig. 11 for specimen L2, but not for specimen L1. The reason for this is that for the case of specimen L1 this initial failure occurred during the first attempt of testing this specimen, which had to be

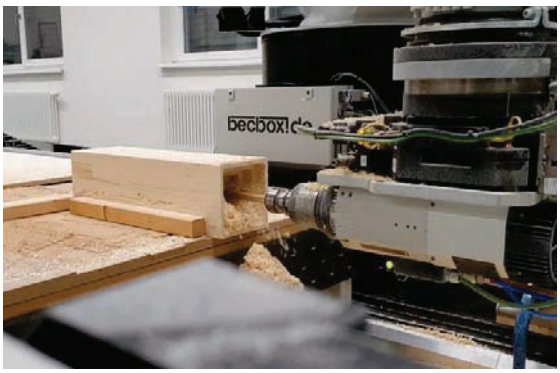

Figure 8: *Horizontal milling of the GLT column*

Figure 9: *Vertical milling of the LVL pocket*

interrupted, as the used steel extension proved to have a far too low shear stiffness—initially both steel profiles were held together exclusively by threaded rods, which were then welded together to increase the shear stiffness.

After the first load drop-down a second failure took place. A further increase in the load triggered the global failure at about M_1 = 2.57 kNm and M_2 = 2.46 kNm for specimens L1 and L2, respectively. Beyond this point the upper part of the pin element began to visibly to be pulled out from the cavity of the LVL insert (see Fig 12). A summary of the achieved maximum loads and corresponding moments is presented in Table 1.

The first can most probably be attributed to the failure of the interface between LVL-pin and LVL-insert elements

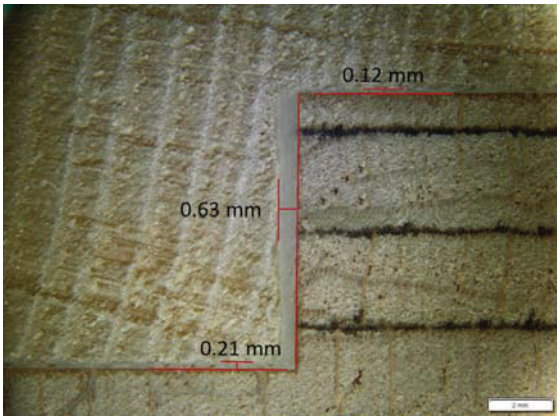

Figure 10: *Adhesive joint thickness of a milled sample*

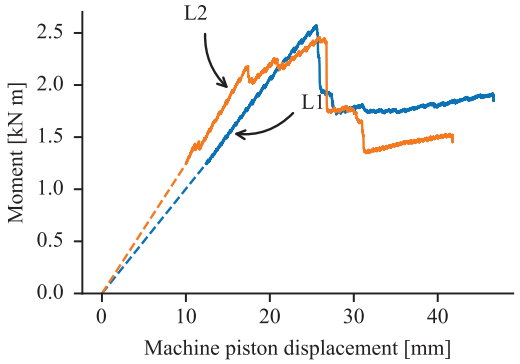

Figure 11: *Load-displacement curves of both tested specimens.*

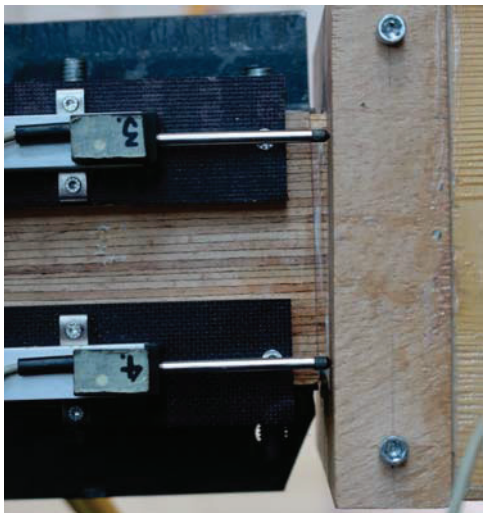

Figure 12: *Pin element of specimen L1 being pulled-out of the LVL insert after reaching maximum load.*

in the vertical surfaces of region 1 shown in Fig. 7. As the damage progressed, the horizontal faces in region 1 failed, causing the second load drop. Finally, the vertical and horizontal bond faces of region 2 failed, causing the global failure of the connection. The bond faces of region 3 probably failed together with those of region 2, as they show a smaller total area to transfer the loads and the lever arm is smaller compared to region 2, thus increasing the bending stresses. Figure 13 shows the failed vertical surface of region 2 for Specimen L1, where a rather low percentage of fiber breakage can be observed.

Table 1: *Maximum loads and moments achieved by specimens L1 and L2, and estimated rotational stiffness*

Specimen	Maximum Load [kN]	Maximum Moment [kN m]	Rotational Stiffness [kNm/rad]
L1	1.84	2.57	3.4×10^2
L2	1.76	2.46	–

Figure 13: *Shear failure on the vertical surface of region 2, corresponding to the vertical surface of the second step of the LVL-pin element*

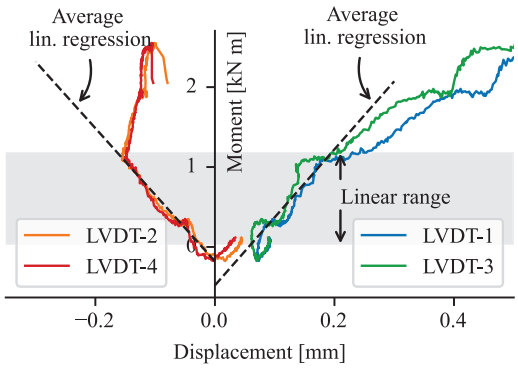

Figure 14: *Measured relative displacement between pin element and LVL insert of specimen L1. LVDT's 1 and 3: tension side; LVDT's 2 and 4: compression side. Grey region marks the load limits used to compute the average linear regression on both sides.*

3.3.2 LVDT measurements

Figure 14 presents the moment-displacement curves for the LVDT's which measure the displacements in the tension (1 and 3) and compression (2 and 4) regions of specimen L1. Although the data is rather noisy, the expected behavior of positive and negative displacements in the tension and compression regions, respectively, can be clearly observed. The dashed lines in Fig. 14 represent the linear regression of the averaged curves from LVDT's in tension and compression within the linear range denoted by the shaded region.

The corresponding measurements from Specimen L2 are not presented here, as problems with the fixation of the steel extension lever arm caused a relative shift between steel and pin-element, resulting in erroneous data. Future experiments will consider a more robust concept for the clamping of the steel extension to the LVL-pin element.

3.3.3 Rotational stiffness

The rotational stiffness of the connection can be obtained from the LVDT measurements at positions 1 and 3 (bending tension side), and 2 and 4 (bending compression side), as shown in Fig 14. To estimate the rotational stiffness, k_θ, the rotation angle between the LVL-insert and the LVL-pin

https://doi.org/10.52202/069179-0094

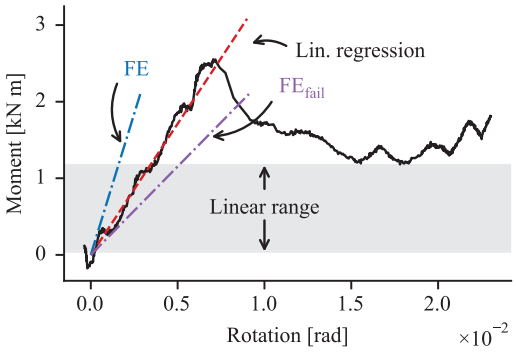

Figure 15: *Moment-rotation-rotation curve computed for specimen L1. The rotation was computed from the averaged results of the front and rear LVDT's*

elements was computed as

$$\theta = \arctan\left(\frac{\bar{u}_t - \bar{u}_c}{d}\right), \tag{1}$$

where $\bar{u}_t$ and $\bar{u}_c$ are the averages of the displacements measured in tension and compression, respectively, and d is the vertical distance between the LVDT's, in this case $d = 80$ mm.

Figure 15 shows the moment-rotation curve obtained for Specimen L1, from which the rotational stiffness can be estimated by means of a linear regression. The linear regression was computed for the data within the linear range defined in Fig. 14. Finally, a rotational stiffness $k_\theta = 3.43 \times 10^2$ kNm/rad was obtained for Specimen L1.

4 NUMERICAL ANALYSIS

4.1 DESCRIPTION OF FE MODEL

A parametric 3D finite element model was programmed in Abaqus V2022 [1] with the available Python API. The model consists of three parts (GLT column, LVL insert and LVL pin) bonded by means of cohesive interactions on the respective vertical faces and contact behavior for the horizontal surfaces (i.e. end grain can take up compressive loading but not tension). This can be seen in Fig. 16, where the different cohesive and contact regions, as well as the used mesh is shown. Symmetry along the YZ-plane was used to reduce the total number of elements. The boundary conditions corresponding to the clamping where applied on the side surfaces according to Fig. 6, by restraining all degrees of freedom. The load was applied as a shear force-moment pair on a reference point placed at the center of the top face of the LVL pin part. This reference point controls a rigid surface, which is "tied" to the top face of the pin.

The geometry was meshed with linear 3D brick elements with incompatible modes of type C3D8I, with an approximate size of 3 mm. The elastic material properties used are shown in Table 2, while the cohesive interaction was defined with stiffness parameters $k_{nn} = k_{tt} = 1000$ N/mm^3, with finite sliding. A failure of the bond line of the vertical surfaces of region 1 (see Fig. 7), in the bending tension side of the connection, was simulated by deactivating the cohesive behavior in this region. The full model is available in [16]. For the post-processing and visualization the results were saved in the ASCII format *.fil and were then analyzed with the Python library Pybaqus [15].

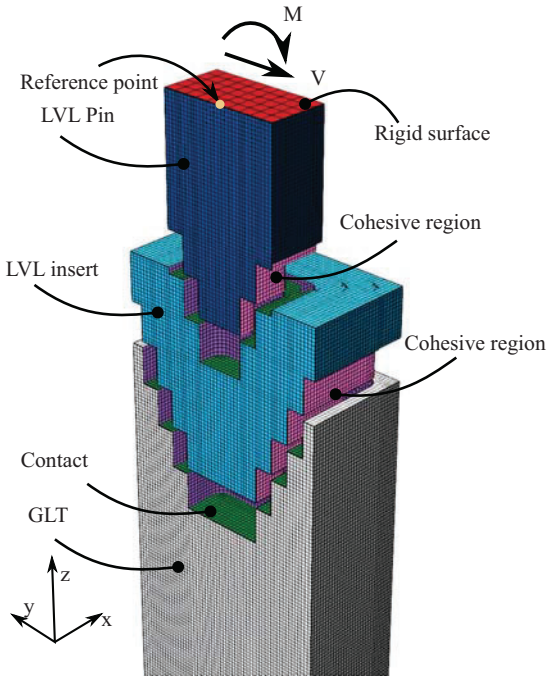

Figure 16: *Illustration of the FE mesh, together with the definition of cohesive regions and load application*

Table 2: *Elastic material stiffness properties used for the FEM simulations*

Material	E_0* [MPa]	E_{90} [MPa]	ν_{12} [–]	ν_{23} [–]	G [MPa]	G_r [MPa]
CLT[1)]	11 000	370	0.2	0.02	690	50
LVL[2)]	12 800	2000	0.2	0.02	430	43

[1)] acc. to values in [8] for softwood boards strength class C24 as indicated in [9]

[2)] acc. to values in [6, 19] (except ν_{ij})

* E_0: MOE parallel to fiber; E_{90}: MOE perpendicular to fiber; G: shear modulus; G_r: rolling shear modulus; $\nu_{12} = \nu_{13}$: Poisson coefficient between the fiber direction and the other two orthogonal directions; ν_{23} Poisson coefficient between both directions perpendicular to the fiber direction.

4.2 ROTATIONAL STIFFNESS

The numerical results for the moment-rotation behavior are shown in Fig. 15, where both models—with and without simulated failure in region 1—are shown along with the experimental curve. It can be seen that the experimental results yield values in-between the two models, which most probably means that in reality the horizontal faces are not fully unused. The rotational stiffness for the model with and without simulated failure is 7.4×10^2 kNm/rad and 2.3 kNm/rad, respectively. The experimentally measured stiffness is 3.4×10^2 kNm/rad.

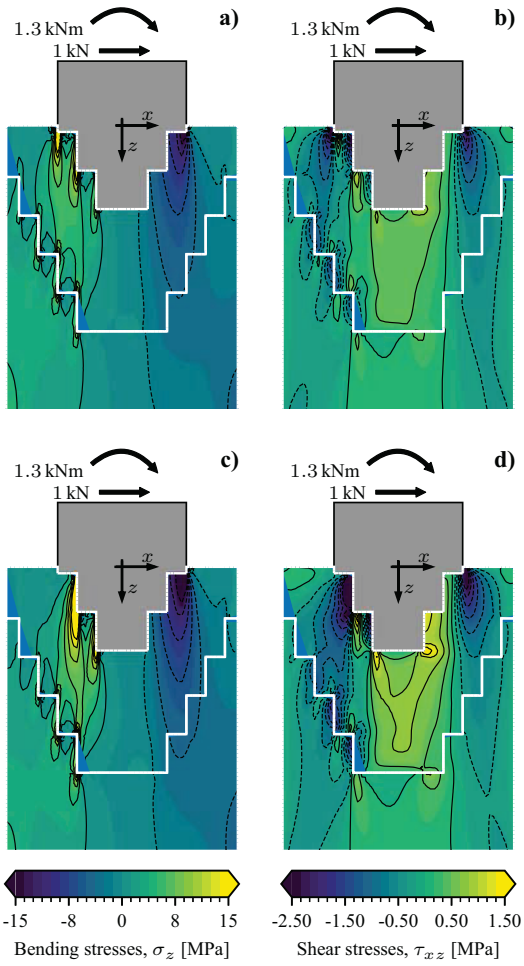

Figure 17: *Stresses in the region of the column-head for the intact connection and with the simulated failure of bonded faces of region 1; (a) Stresses parallel to column axis, σ_z ans (b) shear stresses τ_{xz} for intact connection; (c) Stresses parallel to column axis σ_z and (d) shear stresses τ_{xz} for simulated damaged connection.*

The current analysis did not consider any form of fracture mechanics based softening in the bonded surface, assuming a very simple mixture of cohesive and contact behavior. It can be expected that a much better agreement with the experiments can be obtained, if a more realistic mechanical behavior for the bonded region is used. This could be done by considering softening or by simply adjusting the stiffness properties of the cohesive region.

4.3 STRESSES IN THE COLUMN-HEAD REGION

Figure 17a presents the stresses parallel to the fiber and column axis for the intact model (no failure), where regions of high tensile and compressive stresses are seen at the interface between LVL pin and LVL insert element. The observed asymmetry in the stress distribution is due to the assumption that tensile stresses are not transferred through the horizontally bonded surfaces (endgrain bonding). Figure 17b shows the shear stresses, τ_{xz}, in the same region, where high stressed regions are evidenced on the vertical bond faces on the left side (bending tension side).

Figures 17c,d present the analog results for the model with the simulated failure in region 1. It is evident that the stresses increase significantly due to the reduced cross-section. These high stresses remain mostly in the LVL insert element. From Fig. 17d it can be seen that the shear stresses on the bonded surface are above 2.5 MPa with a moment of 1.4 kN m directly on the top face of the insert element. The characteristic shear strength of the used beech material is 4.5 MPa, which explains the observed failure during the experiments (at about 2.5 kN m).

5 DISCUSSION

5.1 GEOMETRY OF THE CONNECTION

The initial development of the presented connection considered only the effects of vertical loads, as the horizontal loads were assumed to be taken by a stiffening element, such as a reinforced concrete core. However, unless a pin joint is used, some amount of moment will still be transferred to the columnhead, in which case it is important to understand the behavior under moment action, thus justifying this analysis. The most evident problem with the current geometry is the small depth of the vertical step of region 1, which leads to a rather early failure due to the small available shear surface to transfer the stresses. A simple solution for an improvement is to make the first step deeper, hence, increasing the shear surface and resulting in a more robust concept.

5.2 UTILIZED ADHESIVE

Although the bonding of the different components worked very good—as can be judged from the observed axial compression experiments from [17]—, the aspect of the shear failure from Fig. 13 hints a possible limitation of the chosen two-component PUR adhesive. This is due to the rather low percentage of fiber breakage observed. However, it must be stated that the used beech LVL cannot be judged by the same parameters as e.g. softwoods, due to the marked differences in strengths of both materials. Further studies with different gap-filling adhesives should be performed in order to better assess the here presented results.

6 CONCLUSIONS AND OUTLOOK

The current state of a new column-to-column connection was presented. Following one of the project's objective of only using wooden materials if possible, a concept based on softwood GLT and beech LVL was conceived, where the GLT column head is reinforced by embedding a stepped beech LVL insert. Relevant aspects of the mechanical behavior as well as of the manufacture process were presented and discussed, from which the following conclusions can be distilled:

1. The robotic-based manufacturing process proved to be suitable for the precise milling of components with tight tolerances of about 1 mm, enabling the experimental testing of the concept.

https://doi.org/10.52202/069179-0094

2. The rotational stiffness was shown to lay within the range predicted by finite element simulations if damage in region 1 (top most level) is assumed. An improved agreement with the experiments could be achieved by using more realistic material behavior such as softening.

3. The data acquisition during the experiment was problematic due to the rather low fracture load level (about 2 kN) as compared to the maximum load of the machine (1.6 MN). Further experiments will consider a separate load measuring cell, appropriate for the expected load range.

4. The observed failure mode on the shear surface indicates possible limitations with the chosen two-component PUR, which needs to be further assessed experimentally.

5. Finally, although the current geometry is rather weak under bending induced by lateral loading, simple modifications to the geometry can be introduced to improve this if needed.

ACKNOWLEDGEMENTS

The presented ongoing research is partially supported by the Deutsche Forschungsgemeinschaft (DFG, German Research Foundation) under Germany's Excellence Strategy – EXC 2120/1 – 390831618. The authors owe many thanks to the company Pollmeier (Creuzburg, Germany) for generously sponsoring the beech LVL plates (Baubuche) for the presented tests. Further gratitude is owed to the Company Henkel AG & Co. KGaA, Düsseldorf, Germany for supporting the project with tailor-made adhesives.

DATA AVAILABILITY

Some or all data, models, or code generated or used during the study are available in a repository or online in accordance with funder data retention policies. (doi: 10.18419/darus-3388, Ref. [16])

REFERENCES

[1] Abaqus v2022. *ABAQUS/Standard User's Manual, Version 2020*. Providence, RI, USA: Dassault Systèmes, 2022.

[2] R. Abrahamsen. "Mjøstårnet – 18 storey timber building completed." In: *Proc. 24. Internationales Holzbau-Forum (IHF)*. Garmisch-Partenkirchen, Germany, 2018.

[3] S. Aicher and L. Höfflin. "Weibull based design approach of round holes in glulam." In: *International Council for Research and Innovation in Building and Construction – Working Commission W18 – Timber Structures*. Colorado, USA, 2003.

[4] N. S. Bergen. "Case study of UBC Brock Commons - construction details and methods." In: *Proceedings of the World Conference on Timber Engineering (WCTE 2016)*. Austria: Vienna University of Technology, Austria, 2016. ISBN: 978-3-903039-00-1.

[5] M. Claus, C. Tapia, and S. Aicher. "Bond line characteristics of new edge connections of cross-laminated timber in the weak direction based on milled profiled connection plates from laminated veneer lumber made of beech." In: *Otto-Graf-Journal* 20 (2021), pp. 39–60. ISSN: 0938-409X.

[6] DOP PM–017–2022. *Pollmeier Furnierwerkstoffe GmbH: Laminated veneer lumber made from beech for non-load bearing, load bearing and stiffening elements – Board BauBuche S and BauBuche Q*. Declaration of Performance. 2022.

[7] EN 14374. *Timber structures – Structural laminated veneer lumber – Requirements*. Brussels, Belgium: European Committee for Standardization, 2004.

[8] EN 338. *Structural timber – Strength classes*. Brussels, Belgium: European Committee for Standardization, 2016.

[9] ETA-06/0009. *Binderholz Brettsperrholz – Massives plattenförmiges Holzbauelement zur Verwendung als tragendes Bauteil in Bauwerken*. European Technical Assessment. Berlin, Germany, 2017.

[10] ETA-19/0700. *SPIDER Connector and PILLAR Connector*. European Technical Assessment. Vienna, Austria: Austrian Insitute of Construction Engineering (OiB), 2020.

[11] P. Fast, B. Gafner, R. Jackson, and J. Li. "Case study: an 18 storey tall mass timber hybrid student residence at the University of British Columbia, Vancouver." In: *Proceedings of the World Conference on Timber Engineering (WCTE 2016)*. Austria: Vienna University of Technology, 2016. ISBN: 978-3-903039-00-1.

[12] R. McNeel et al. "Rhinoceros 3D, Version 6.0." In: *Robert McNeel & Associates, Seattle, WA* (2010).

[13] M. Muster and A. Frangi. "Experimental analysis and structural modelling of the punching behaviour of continuous two-way CLT flat slabs." In: *Engineering Structures* 205 (2020), p. 110046. DOI: 10.1016/j.engstruct.2019.110046.

[14] Pollmeier Furnierwerkstoffe GmbH. *Declaration of Performance No.: PM–005–2018 – Laminated veneer lumber made from beech – Laminated veneer lumber according to EN 14374:2005-02 for non-load bearing, load bearing and stiffening elements*. Austrian Institute of Construction Engineering. Viena, Austria, 2018.

[15] C. Tapia. *Pybaqus: A Python library for the visualization and post-processing of Abaqus ASCII result files*. Version 0.2.9. 2023. URL: https://github.com/cristobaltapia/pybaqus.

[16] C. Tapia. *Replication Data for: Rotational stiffness of newly developed LVL-based column-head reinforcement for point-supported slab-column building systems*. Version V1. 2023. DOI: 10.18419/darus-3388.

[17] C. Tapia and S. Aicher. “Numerical and experimental investigations on a new concept for column-to-column connections for multi-storey timber buildings.” In: *Materials and Building Construction* (2023). In review.

[18] C. Tapia, L. Stimpfle, and S. Aicher. “A scalable column-CLT-slab connection for open-plan high-rise timber buildings.” In: *Proceedings of the World Conference on Timber Engineering (WCTE 2021)*. Santiago, Chile, 2021.

[19] Z-9.1-775. *Technical Approval, Brettschichtholz mit dem Keilstoß-System “Hess Limiteless” für tragende Holzkonstruktionen – Approval holder: Hasslacher Holding GmbH*. Berlin, Germany: issued by Deutsches Institut für Bautechnik, 2020.

https://doi.org/10.52202/069179-0094

World Conference on Timber Engineering Oslo 2023

MECHANICAL PROPERTIES TESTS OF DELIGNIFIED AND DENSIFIED WOOD

Jörg Wehsener[1], Martina Bremer[2], Peer Haller[1]

ABSTRACT: Wood modification has a long tradition. The target is in many case to improve the mechanical properties, durability or other properties. In this study was investigated a combination of delignification and densification to enhance bending strength and ASE. Both wood treatments change properties in different ways depending on the conditions and the wood species. The primary objective of this treatment combination was the improvement of mechanical properties by partly extraction of lignin components. The treated structure retains cellulose and hemicellulose chains aligned. The densification perpendicular to the grain will reduce the cell lumina and compress the wood structure more than 70% together, afterwards. As a result, the cell walls become entangled and hydrogen bonds between adjacent cellulose nanofibers according [1].
The combined processes were applied to the green and dried poplar (*Populus nigra* L.). Firstly: delignification procedure was done with small samples in NaOH and Na_2SO_3 solution by more than 100°C, 130°C and 150°C for 7h. After washing and analyse wood components second step followed: densification. The wood was compressed perpendicular to the grain in different temperature levels (100°C, 130°C, 160°C) and holding times up to 80% of the original thickness. After the treatment, ASE, MoR and MoE were determined. The bending strength was meanly depending on the solution temperature and compression time and temperature. Bending strength has the optimum by around 90% lignin removal and 130°C pressing time over 24h. The bending strength will increase up to 450MPa compare to the densified reference of 250MPa and the untreated polar app. 65MPa. ASE was reduced by strong delignification and increase temperature.
.

KEYWORDS: tension, bending strength, recovery set, delignification, densification

1 INTRODUCTION

Investigations on modification processes have been done since the last decades. All types of processes (chemical, physical or biological) improve the material behavior in different ways. Thus, better material properties must be achieved. Samples of wood modification – like thermo hydro mechanical densification - was produced as LIGNOSTONE, STAYPAK or LIGNIFOL [8, 20]. Inoue et al. [6] and other authors tried to solve the recovery problem by superheated steam, [12] and [9] by heated oil, [10] in combination by both. Other treatment with chemical components and different types of resin impregnation (DMDHEU, melamine, phenol, furfuryl) were investigated by e.g. [19, 13, 21, 14, 11, 17] and many more. Beside of the published study from [4] using alkaline, densification and partial extraction of wood polymers will attract attention. The dependency of densification time and temperature to improve the dimensional stability of are well known: first, decrease in the very hydrophilic hemicelluloses means a decrease in the water affinity. Second, the resulting furfurals bind to the lignin and provide additional crosslinking through this adhesion. In this way, the stresses that arose during compaction can be relieved by re-crosslinking the microfibrils of the cellulose. According to [10], these stresses are the main cause of recovery. Also the moisture influence reduced the glass transition temperature of lignin. It appears less tensions during densification process caused by wood plasticizing. Moisture also contributes to further hydrolysis of the polysaccharides, which supports hydrophobicity, but also leads to a shortening of cellulose chain length and an associated loss of strength. Results of those treatments show significant increase of mechanical properties and dimensional stability. In this point of view, success appear, but modification processes are dealing with small and thin wood samples.

[1] Jörg Wehsener, Technische Universität Dresden, Germany, joerg.wehsener@tu-dresden.de
[1] Peer Haller, Technische Universität Dresden, Germany, peer.haller@tu-dresden.de
[2] Martina Bremer, Technische Universität Dresden, Germany, martina bremer@tu-dresden.de

https://doi.org/10.52202/069179-0095

Poplar, as fast growing wood species has the potential to become high strength properties by chemical and mechanical modification. It is well-known that densification transverse to grain will improve the mechanical properties [18, 22, 15]. Delignification influence wood structure, dimensional stability and bond strength of cellulose [23, 25]. By using both, there is stronger increase of mechanical properties caused by breaking and reformation new hydrogen bonds [1, 16, 26]. A new approach is a partial delignification combined with a compression of the wood was described by [2, 3]. As a structure-forming polymer, lignin plays an important role in plants. It penetrates the cellulose fibers and stick them together whereby it contributes significantly to the strength properties. With partial removal of the lignin, a higher compression of the cellulose fibers is possible [24]. In addition, fewer cracks form in the cell wall during densification and the density and associated strength increase. According to [5] and [4] new intermolecular interactions between the cellulose chains are formed during compression, which further increases the strength. In addition, the dimensional stability is improved due to reduced water accessibility and other solvents. Another positive benefit of this material is the improved surface hardness [7]. These modified properties result in new applications potentials such as parts of music instruments, timber joints like wood nails or connection plats, machine parts or others.

2 MATERIAL AND PROCESS

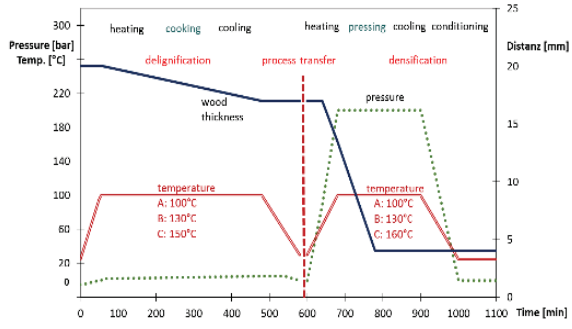

***Figure 1**: Process parameters during thermal delignification and thermo-mechanical densification (schematically)*

2.1 MATERIAL

Green sawn and dried poplar wood (*Populus nigra* L.) was used for the investigations. The wood samples, with the dimensions of 200 mm (longitudinal) x 100 mm (tangential) and 20 mm (radial), were cut from green log with initial oven dry density of 0.44 g/cm³). The same log-material were used for all treatments, respectively, were used as untreated reference specimens. The initial moisture content (mc) of green specimens was 90%, 124% and 162% at the beginning of delignification process (temperature of 100°C, 130 °C and 150°C). The dried one were treated at 9% moisture. Green and dried specimens were delignified in digester, washed and conditioned (20°C/65%RH) for two weeks. Afterwards, densification was applied in heating press. In each case, twin specimens were produced in order to be able to determine the changes in chemical composition caused by the delignification and to be able to proof hornification effects on delignification. In total, 12 specimens were modified by each process. Figure 1 shows both modification processes schematically:

2.2 DELIGNIFICATION

Delignification takes place in a 20 Litre autoclave with circulation pump (Figure 2). The delignification liquor contained sodium hydroxide (2.5 molar) and sodium bisulfite (0.4 molar). Wood specimens were placed in the digester with the help of a grid to ensure even circulation of the cooking liquor around all specimens. The temperature during delignification was varied whereby the delignification time was counted from reaching 100°C. Digestion time was seven hours for each.

For removing the chemicals and dissolved wood components, several washing steps were carried out after the cooking process. At first, the specimens were washed inside the autoclave with hot water (80°C) two times. In the next step, the samples were placed in green water for at least 18h hours. This was followed by two short rinsing cycles with cold water. Finally, the samples were stored again in water for 2 days.

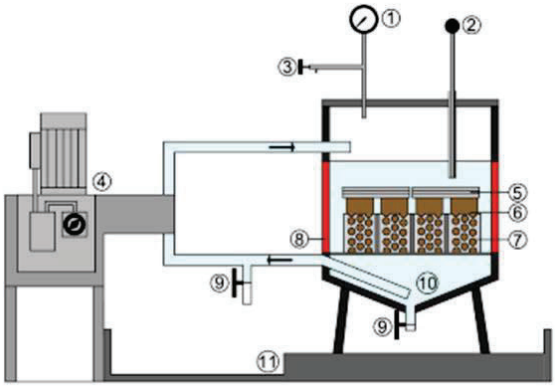

***Figure 2:** Digester equipment for delignification (1 pressure gauge with pressure relief valve, 2 temperature sensors, 3 valve, 4 circulation pump, 5 stainless steel perforated plates, 6 specimens, 7 stainless steel perforated grilles, 8 wall heating, 9 drain valve, 10 solution, 11 drip tray)*

2.3 CHEMICAL CARACTERIZATION

The delignified as well as the twin specimens were characterized for their chemical composition. For that, the specimens were dried at 103°C and milled by a cross beater mill using a 4 mm sieve. All contents relate to the dry matter of the specimens. Content of extracts were estimated by Soxhlet extraction with a mixture of ethanol and toluene (1:1 v/v) for 6 h. Since there is a mass loss

https://doi.org/10.52202/069179-0095

during delignification, the reference mass for the chemical analysis of the contents of the individual wood components changes. Therefore, the wet-chemically determined contents were corrected on the basis of the mass loss.

2.3.1 Cellulose

For determination of cellulose content about 1 g of the specimens were cooked three times under reflux in 25 % nitric acid in ethanol for a half hour each. After that the cellulose was separated by filtration using glass filter crucible of pore size 40 – 100 µm. The separated cellulose was cooked again in water for 1 h and washed acid free with water. Masses of cellulose were determined after drying at 103°C.

2.3.2 Holocellulose

About 0.3 g of specimens were used for estimation of holocellulose by delignification with sodium chlorite. For this, the specimens were shacked in a solution of 60 µL glacial acetic acid and 0.3 g sodium chlorite in 45 mL deionized water five times for 1 h at 70°C. After each hour glacial acetic acid as well as sodium chlorite was added again in the same amounts. Then the holocellulose was separated by filtration using glass filter crucible of pore size 16 – 40 µm and washed acid free with water. Masses of holocellulose were determined after drying at 103°C.

2.3.3 Hemicelluloses

Content of hemicelluloses results from the difference between holocellulose and cellulose.

2.3.4 Klason lignin

Content of Klason lignin was determined by dissolving of the Polysaccharides. About 0.5 g of specimens were mixed with 15 mL of 72 % sulphuric acid. This mixture was hold at room temperature for 2 h with occasional stirring. After that, the mixture was diluted with 560 mL of deionized water and cooked for 4 h under reflux. The resulting Klason lignin was separated by filtration using glass filter crucible of pore size < 16 µm and washed acid free with hot water. Masses of lignin were determined after drying at 103°C.

2.4 DENSIFICATION

The specimens were conditioned in a climate chamber at 20°C and 90 % *RH*. At a wood moisture content (*MC*) of approx. 20 %, 12 boards of each species were thermo-mechanically densified transverse to the grain to a thickness of 4 mm. It was carried out as a thermo-mechanical pressure deformation in an open system (Figure 3). The process was applied in three steps: 1) heating for 60 min by using temperature of 100,130 and 160°C, 2) densifying during next 120 min by maximum pressure of 40 N/mm² followed by a second phase of thermosetting for 4 h, 20 h or 24 h, and 3) cooling to 40°C within 60 min.

During the densification process, *MC* was reduced. Metal spacers were used to limit the degree of densification but there was no limitation in width. Volumetric density measurements were performed subsequently on densified specimens. After conditioning, specimens were cut parallel to fibre in original thickness for mechanical tests. Compression set *C* was evaluated as.

$$C = \frac{R_0 - R_c}{R_0} \quad (1)$$

were R_0 is the initial thickness and R_C is the thickness of compressed specimens. The compression set was 80 % caused by inhomogeneous cross section of delignified specimens.

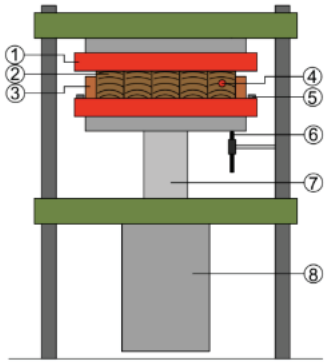

***Figure 3**: Hot press (1 hot plate, 2 specimens, 3 fixer, 4 temperature sensors, 5 metal spacer, 6 transducers, 7 plunger, 8 hydraulic cylinder)*

2.4.1 Three-point bending test

The modulus of rupture (*MoR*) was determined in a three-point bending test according to DIN 52186 (1978) with a span of 120 mm parallel to the grain and 3 replicate (n) specimens of 140 mm (longitudinal) x 10 mm x 4 mm (radial) for each test modification parameter. The direction of densification was equal to the direction of loading. Test speed was 6 mm per minute.

2.4.2 Determination of dimensional stability (ASE)

Based on the DIN 52184 modified material was stored in normal conditions for 10 days. Specimens of 10 mm (longitudinal) x 20 mm x 4 mm (n = 3) were tested with five cycles of oven drying at 103 ± 2°C for 18 h. This was followed by a soaking phase by means of water vacuum-pressure impregnation (50 kPa and 15 min followed by 800 kPa and 20 min) with subsequent water storage for 24 h to determine the change of volume due to the treatment. *ASE* was calculated as

$$ASE = \frac{a_{untreated} - a_{treated}}{a_{untrated}} \quad (2)$$

where $a_{\text{untreated}}$ is the maximal swelling before and a_{treated} is the maximal swelling after treatment.

Additional were determined compression-set-recovery C_R according Equation (3), which

express permanent thickness after swelling. It was calculated as

$$C_R = \frac{R_{C,wet} - R_c}{R_0 - R_c} \quad (3)$$

where $R_{C,\,wet}$ is the thickness of dried compressed specimens after swelling.

3 RESULTS AND DISCUSSION

3.1 PROCESSES

Washing was done two times 15 min and repeated after 18 h water storage. Depending on treatment temperature, surface colour changed from white to dark brown. This may be explained by contact of black liquid, caused by lignin. Green and dried specimens were soft after processing and distorted after drying. Particularly with regard to the dried poplar specimens showed drying cracks and loose fibers (reduced bonds due to removed lignin). After conditioning, densification, the determination of chemical components took place. Mean density of green and dried specimens after treatment are shown in Table 1. As expected, the poplar density was multiplied by densification and once again more by delignification.

In generally, on dried specimens were measured higher density than on the green one, significantly. The density of green sawn specimens was slightly affected at delignification temperature of 100°C and 130°C, but degreased of 150°C significantly. Higher process temperatures result in more defibration and degradation of the cell composite.

Table 1: *Oven-dry density of poplar (reference=0.44g/cm³), only densified poplar (1.22g/cm³) specimens after delignification and densification (treatment temperature/ treatment time)*

Delignification temperature (°C)		Densified, delignified 100°C/4h (g/cm³)	Densified, delignified 130°C/4h (g/cm³)	Densified, delignified 160°C/4h (g/cm³)
100	green	1.46	1.39	1.41
	dried	1.50	1.51	1.49
130	green	1.44	1.36	1.44
	dried	1.55	1.51	1.53
150	green	1.09	0.93	0.98
	dried	1.38	1.41	1.34

3.2 CHEMICAL COMPOSITION

It can already be seen from the measured loss of mass due to delignification that there is a significant difference between the green and pre-dried wood. While the mass loss of the green specimens is independent of the temperature, in the dry specimens the mass loss increases with rising delignification temperature. A comparison of mass loss with the summarized changes in the contents of the wood components, which were determined by wet-chemical methods, shows the same trends. In the case of green specimens the absolute value of measured loss is significantly smaller than the summarized changes in contents of wood components. This suggests that depolymerizations occur. The resulting low molecular weight (oligomeric) products cannot be determined with the wet chemical methods. For the technical-dried specimens, the values of the measured mass losses and the sum of changes of wood components are closer together. Beside this, the mass loss at delignification temperature of 150°C is much higher for the dried specimens.

If one considers the change in the individual wood components (Table 2), the different behaviour of the green compared to the technical dried specimens can also be seen here. With the exception of cellulose, in the dried specimens the proportion of all components decreases with increasing temperature. The lignin is then completely removed. Extracts and hemicelluloses are only about 80% present after delignification at 150°C. The change in the cellulose content shows a minimum at 130°C, which is caused by the binding of reactive degradation products of lignin or hemicelluloses to cellulose. At 150°C, the degradation of hemicelluloses and lignin leads to less reactive substances with condensed structures and low content of functional groups.

Table 2: *Changes in contents of wood components*

Sample	$T_{Delignification}$ (°C)	Change in contents (% (w/w)) EXTRACTIVES	LIGNIN	CELLULOSE	HEMICELLULOSE	ASH
green	100	15	-19	6	-68	169
	130	1	-44	13	-62	87
	150	-14	-91	47	-68	202
dry	100	-21	-5	-15	-42	1265
	130	-42	-54	-7	-52	372
	150	-81	-99	-20	-77	287

For green specimens the change of lignin content correlates also with the temperature. In contrast, the degradation of hemicelluloses seems to be almost independent of temperature. The increase of cellulose content can be explained with the binding of reactive degradation products. Change in extractive content varies with temperature. Indeed, the content of extractives in green specimens is in general less. Digestion chemicals that have not been removed completely cause the sharp increase in the ash content for all specimens. These results show that the accessibility of the digestion chemicals is better in technical dried wood than in green wood.

3.3 DENSIFIED WOOD

Delignified specimens were app. 4 mm thick after densification. The average density after the treatment varied from 0.9 g/cm³ to 1.5 g/cm³, depending of different delignification. Deformation of cross section does not influence compression quality result in very tightly

https://doi.org/10.52202/069179-0095

packed, stiff and hard material. Only highly delignified specimens show loose fibres on the surface.

3.4 BENDING STRENGTH

Bending strength was determined by 3-point bending test. MoR of undensified poplar was according *Wehsener et al. (2018)* approx. 62 MPa by mean density of 0.36 g/cm³ and on 50 % densified specimens MoR of 107 MPa (0.69 g/cm³) was achieved. The MoR of tested only densified reference (approx 75%) increased to 234 MPa by density of 1.219 kg/m³.

Results of MoR from green cut and dried poplar (4 h and 20/24 h densification process) were summarized in Figure 4. Densification of delignified poplar lead to increased MoR depending on treatment temperature and time.

Delignified specimens by 100°C (lignin content 19%) show high MoR (440 MPa) after long densification process (24 h, 130°C), as well as after short process of 4 hours and 160°C (426 MPa). There was not remarkable influence of using green sawn or dried poplar on bending strentgh after delignification at temperatures of 100°C or 130°C.

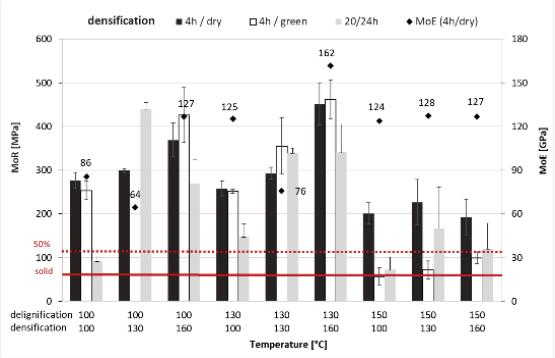

***Figure 4**: Bending strength of poplar (red), 50% densified (red dotted) and 80% densified and delignified by 100°C, 130°C and 150°C; lignin content by delignification temperature was 19% (100°C), 13% (130°C) and 2% (150°C)*

Delignification temperature of 130°C and 4 h on 160°C densified shows also high MoR of 462 MPa (dry) and 452 MPa (green). Specimens treated by 150°C, MoR degrease all about, but twice on green sawn specimens at the same time.

MoE of 150°C delignified specimens sustained at the high level close to 120 GPa, but shows also indifferent behaviour on lower temperature. In generall, it can be seen, the MoR values are higher on lower temperature and longer pressing time (130°C, 24h) even on short time and high temperature (160°C, 4h). For obtaning optimum results, the delignification temperature should be on mild temperatures (100°C or 130°C) for partial delignification (reduced lignin between 20 and 60%) and high temperatures for densification (130°C; 160°C). The treatment process achive maximal bending strength on less than 50% reduced hemicellulose and elevated densification temperature.

The delignification reduces density and hence characteristics like mechanical properties are affected. The measured bending strength are indifferent in regards to the expected results. Figure 5 shows the MoR results of the untreated, densified, and delignified and densified specimens (densification: 4 h) in relationship to the density. High delignified green sawn wood (2% lignin) show similar results close to 100 MPa, but very high density differences (0.44 to 1.4 g/cm³). Dried and high modified wood achieved MoR twice time compared to green sawn specimens. Specimens low delignified (13% and 19% lignin) tend to high density up to 1.5 g/cm³ and MoR (up to 250 MPa). All specimens show maximum MoR independent of the initial moisture content. Only 80% densified specimens double MoR nearly and density compared to 50% densification. Values of around 200 MPa were measured.

Material of 2% lignin remaining are less compact and dense than mild delignified wood. Specimens failed interlaminar and show defibration. High delignification reduced bonding of cellulose fibers, caused by lignin removing. Bending tests show MoE around 120 GPa, but low MoR on 100 MPa by green sawn specimens. In opposite to the high treated material (2% lignin) the mild delignified material (13% and 19% lignin) shows high elasticity and no brittle failure. Material has compact and dense structure across the section. Bending strength increased up to 440MPa and the specimens failed very ductile. Green sawn specimens failed by shear and on several specimens fiber splitting appeared.

Considering the densification time it can be stated that long densification time of 24 hours combined by mild delignification leads to high mechanical properties. In the tests, the MoR showed similar tendency and increased when densification time chosen for 4 hours and densification temperature was high.

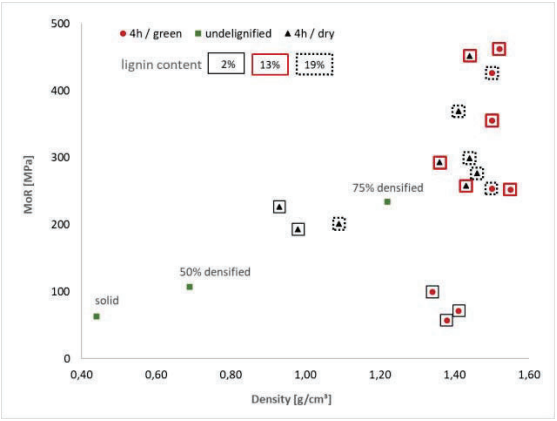

***Figure 5**: MoR in comparison to density modified on green and dried poplar with reduced lignin content and densification ratio*

3.5 ANTI-SWELLING EFFICIENCY (ASE)

During five cycles of swelling and shrinking the recovery-set of the modified material was reduced. As previously reported by [15], recovery-set of densified wood is decreasing with increasing intensity of a thermal

modification. In this study, solid, densified and densified combined with delignified modification processes were tested. Highly delignified specimens showed different layers by loose fibres. In general, swelling is reduced by increased temperature and compression time compared to only densified specimens. Influence of different lignin content was not detectable. Swelling of green sawn specimens was smaller than dried one. The results showed similar behaviour of maximum swelling and recovery, basically. Specimens (lignin 13%) densified by 100°C and 20 hours and also densified by 130°C and 4 hours, recovery decrease to 62.4% and 59.4%. The treatment (19% lignin content) reduces recovery less than 50% (Table 3). The material obtained from the combined process of thermo-mechanical densification and delignification was, thus, more dimensionally stable.

Table 3: *ASE and C_R of modified specimens (*-failed)*

Lignin (%)		Densification time (h)	Densification temperature (°C)	ASE	C_R
19	green	24	100	0.49	0.15
	dried	4	100	0.27	0.48
	dried	24	130	0.31	0.49
	dried	4	160	0.32	0.40
	dried	24	160	0.45	0.24
13	green	20	100	0.62	0.9
	dried	4	100	0.38	0.31
	dried	4	130	0.22	0.50
	dried	4	160	0.59	0.23
	dried	20	100	0.29	0.37
	dried	24	130	0.38	0.41
	dried	24	160	0.47	0.27
2	green	4	100	0.23	0.35
	dried	4	130	0.33	0.36
	dried	4	160	0.23	0.31
	dried	20	100	0.26	0.36
	dried	20	130	0.5	-*
	dried	20	160	0.34	0.24

4 CONCLUSIONS

The results obtained in this study confirmed the potential of the combined treatment to improve material properties e.g. bending strength and ASE. It showed also the absolute requirement to determine the optimum between process temperature and time of delignification and densification. The rate of delignification depends strongly on temperature. At 100°C, lignin degradation only takes place to a small extent. At 150°C, on the other hand, lignin is almost completely degraded. The degradation of the hemicellulose does not show this strong temperature influence. Strong delignified material shows less compact structure than mild delignified. Mechanical properties increase by extended densification and high temperatures. Improved bending strength was gained by partly removed lignin and temperature of 130°C on both processes. The bending strength increase up to 450 MPa compared to the densified reference of 250 MPa and the untreated poplar of 65 MPa. The densification time had the strongest influence parameter on the dimensional stability. High delignification rate as well as decrease of polar polysaccharides reduces ASE. However, there was no clear correlation to bending strength and the density.

ACKNOWLEDGEMENT

The authors gratefully acknowledge the financial support from German Federal Ministry of Food and Agriculture for the FNR research projects “Development of high-performance material for electronic card systems - WoodCard” (grant numbers 2220HV094B.

REFERENCES

[1] Cheng, S., Huang, A., Wang, S., Zhang, Q. (2016) Effect of Different Heat Treatment Temperatures on the Chemical Composition and Structure of Chinese Fir Wood. *BioResources* 11(2), 4006-4016, doi: 10.15376/biores.11.2.4006-4016

[2] Frey, M., Widner, D., Segmehl, J., Casdorff, K., Keplinger, T., Burgert, I., (2018) Delignified and densified cellulose bulk materials with excellent tensile properties for sustainable engineering. *ACS Applied Material Interfaces* 10(5): 5030-5037, doi: 10.1021/acsami.7b18646.

[3] Frey, M., Schneider, L., Masania, K., Keplinger, T., Burgert, I. (2019) Delignified Wood-Polymer Interpenetrating Composites Exceeding the Rule of Mixtures. *ACS Applied Material Interfaces* 11, 35305-35311, doi 10.1021/acsami.9b11105.

[4] Song, J., Chen, C., Zhu, S. *et al.* (2018) Processing bulk natural wood into a high-performance structural material. *Nature* 554, 224–228, doi: 10.1038/nature25476.

[5] Ugolov, B., (2014) Wood as natural smart material. *Wood Science and Technology* 48(3), 553–568, doi: 10.1007/s00226-013-0611-2.

[6] Inoue, M., Norimoto, M., Tanahashi, M., Rowell, R.M. (1993) Steam or heat fixation of compressed wood. *Wood Fiber Science* 25(3), 224–235.

[7] Neyses, B., Rautkari, L., Yamamoto, A., Sandberg, D. (2017) Pre-treatment with sodium silicate, sodium hydroxide, ionic liquids or methacrylate resin to reduce the set-recovery and increase the hardness of surface-densified Scots pine. *iForest - Biogeosciences and Forestry*, 10(5), 857-864, doi: 10.3832/ifor2385-010.

[8] Kollmann, F.P. (1936) Technologie des Holzes. Springer, Berlin

[9] Welzbacher, C.R., Wehsener, J., Rapp, A.O., Haller, P. (2008) Thermomechanical densification combined with thermal modification of Norway spruce (Picea abies Karst) in industrial scale—dimensional stability and durability aspects. *Holz als Roh- Werkstoff* 66(1), 39–49, doi: 10.1007/s00107-007-0198-0.

[10] Navi, P., Heger, F. (2004) Combined densification and thermo-hydro-mechanical processing of wood. *Material Research Society Bulletin* 29(5), 332–336

https://doi.org/10.52202/069179-0095

[11] Pfriem, A., Dietrich, T., Buchelt, B. (2012) Furfuryl alcohol impregnation for improved plasticization and fixation during the densification of wood. *Holzforschung*, 66(2), 215–218, doi: 10.1515/HF.2011.134.
[12] Rapp, A. O., Sailer, M. (2001) Oil-heat treatment of wood in Germany - State of the art. In: Rapp AO (Ed.) Proceedings of special seminar on heat treatments, Antibes, France. Office for official publications of the European communities. Luxembourg.
[13] Militz, H. (1993) Treatment of timber with water-soluble dimethylol resin to improve their dimensional stability and durability. *Wood Science & Technology* 27, 347–355, doi.org/10.1007/BF00192221.
[14] Gindl, W., Zargar-Yaghubi, F., Wimmer, R. (2003) Impregnation of softwood cell walls with melamine-formaldehyde resin. *Bioresource Technology* 87(3), 325-330, doi: 10.1016/s0960-8524(02)00233-x.
[15] Wehsener, J., Brischke, C., Meyer-Veltrup, L., Hartig, J., Haller, P. (2018) Physical, mechanical and biological properties of thermo-mechanically densified and thermally modified timber using the Vacu³-process. *European Journal of Wood and Wood Products* 76(3), 809-821, doi: 10.1007/s00107-017-1278-4
[16] Jakob, M., Gaugeler, J., Gindl-Altmutter, W. (2020) Effects of Fiber Angle on the Tensile Properties of Partially Delignified and Densified Wood. *Materials* 13, doi 10.3390/ma13235405.
[17] Liu, Y., Li, B., Mao, W., Hu, W., Chen, G., Liu, Y., Fang, Z. (2019) Strong Cellulose-Based Materials by Coupling Sodium Hydroxide-Anthraquinone (NaOH-AQ) Pulping with Hot Pressing from Wood. *ACS Omega* 4, 7861-7865, doi 10.1021/acsomega.9b00411.
[18] Perkitny, T., Jablonsky, W. (1984) On the assessment of mechanical properties of densified wood. Holz als Roh und Werkstoff 42, 81-84, doi 10.1007/BF02628857.
[19] Stamm, A.J., Seborg, R.M. (1941) Resin-treated, laminated, compressed wood. *Material Science* (37), 0385-0398.
[20] Seborg, R.M., Millett, M.A., Stamm, A.J. (1945) Heat-stabilized compressed wood (Staypak). Mechanical Engineering 67(1), 25–31
[21] Yano, H., Hirose, A., Collins, P.J., Yazaki, Y. (2001) Effects of the removal of matrix substances as a pretreatment in the production of high strength resin impregnated wood based materials. *Journal Material Science Letters* 20(12), 1125-1126. https://doi.org/10.1023/A:1010992307614.
[22] Haller, P., Wehsener, J. (2004) Festigkeitsuntersuchungen an Fichtenpressholz (FPH). *Holz als Roh- und Werkstoff*, 62, 452-454, doi 10.1007/s00107-004-0516-8.
[23] Wang, Q., Xiao, S., Shi, S.Q., Cai, L. (2018) Effect of light-delignification on mechanical, hydrophobic, and thermal properties of high-strength molded fiber materials. *Scientific Reports* 8(1), 955, doi 10.1038/s41598-018-19623-4.
[24] Wang, J., Fishwild, S.J., Begel, M., Zhu, J.Y. (2020) Properties of densified poplar wood through partial delignification with alkali and acid pretreatment. *Journal Material Science & Engineering* 55(29), 14664–14676, doi.org/10.1007/s10853-020-05034-2.
[25] Wang, J.; Liu, J.; Li, J.; Zhu, J.Y. (2021) Characterization of microstructure, chemical, and physical properties of delignified and densified poplar wood. *Materials* 14(19), 5709, doi 10.3390/ma14195709.
[26] He, Z., Qi, Y., Zhang, G., Zhao, Y., Dai, Y., Liu, B., Lian, C., Dong, X., Li, Y. (2022) Mechanical properties and dimensional stability of poplar wood modified by pre-compression and post-vacuum-thermo treatments. *Polymers* 14(8), 1571, doi 10.3390/polym14081571.

World Conference on Timber Engineering Oslo 2023

DEVELOPMENT OF CONSTRUCTION METHODS WITH NATURALLY GROWN TIMBER AND BENDING-RESISTANT JOINTS

Kevin Moreno Gata[1], Alex Seiter[2], Denis Grizmann[3], Martin Trautz[4].

ABSTRACT: Timber is a highly versatile material that can be used for a wide range of applications and products, including standardized construction elements such as bars, boards, and beams. However, these traditional timber constructions typically rely on straight logs, with naturally grown irregular elements like tree branches, forks, or curved logs often being discarded.

Advancements in digitization tools, such as 3D scanning and image-based processing in parametric environments, allow architects and engineers to upcycle these discarded materials innovatively. This study proposes a method integrating discarded tree parts collected from timber harvesting forests. We have developed a structural joint-free knot system using timber forks that can be employed in bar-type structures. Therefore, we analyzed the morphological possibilities of the timber forks and used an optimization system based on their length and angle variations. The proposed knot system can seamlessly integrate into architectural designs with minimal processing and rapid assembly, providing a solution to managing this intelligently grown material. This approach can expand the application of grown timber in construction by utilizing naturally irregular elements that would otherwise be discarded. We suggest that this approach can extend the application of grown timber and provide a solution to managing this intelligently grown material.

KEYWORDS: naturally grown timber, image-based modeling, bar structures, construction methodology

1 TREE PARTS AS LOAD-BEARING ELEMENTS IN CONSTRUCTION

Grown timber parts are usually irregular and discarded due to their unique geometry. However, their use is frequent in temporary constructions in agricultural areas, small industrial roofs, or structures for decorative purposes using cultivated structural round timber (SRT), see [1].

Novel digital applications, such as Photogrammetry or Laser Scanning, allow the combination of natural and digital geometries and mapping tree parts as load-bearing elements in construction. Incorporating and cataloging tree forks (bifurcations) [2] with digital standardization techniques enhances the design and manufacturing process for such a construction method [3]. Robotized manufacturing strategies allow for exploring new possibilities for augmenting the design of structures [4]. Other design explorations incorporate tree forks in a digital workflow to assist in creating reticular shells [5].

Furthermore, the study of tree growth allows us to understand its geometry to make alterations or guidance during its early age, being able to design constructive elements that grow [6]. A computational approach and geometric simplification of tree growth enable mechanical growth simulations to understand the internal geometry of the tree and study its cross-sections [7].

In this paper, we explore how to generate bar-type structure typologies based on the characteristic geometric dimensions of the timber elements, Figure 1.

Figure 1: *a) Bar-type structure with naturally grown timber elements: flat, curved bars and fork b) construction detail development. c) Tree-fork as an off-knot element.*

2 RECONSTRUCTION OF GROWN TIMBER BASED ON IMAGES

Theoretically, trees and plants grow according to L-Systems [8] growth rules. However, they adapt to the conditions of the environment generating three-dimensional structures that are difficult to simplify into axes or main growth lines. These shapes are classified into lines, curves, and forks (bifurcations). They can be simplified into three-dimensional axes, which, sectioned into parts, can be contained and approximated in two-dimensional planes. In this work, we have studied methods of simplification and automation to find the most

[1] Moreno Gata, Kevin, Chair of Structures and Structural Design, RWTH Aachen University, Germany, morenogata@trako.arch.rwth-aachen.de
[2] Seiter, Alex, Chair of Structures and Structural Design, RWTH Aachen University, Germany, seiter@trako.arch.rwth-aachen.de
[3] Grizmann, Denis, Chair of Structures and Structural Design, RWTH Aachen University, Germany, grizmann@trako.arch.rwth-aachen.de
[4] Trautz, Martin, Chair of Structures and Structural Design, RWTH Aachen University, Germany, trautz@trako.arch.rwth-aachen.de

https://doi.org/10.52202/069179-0096

suitable geometries and sections to manage the grown elements for documentation.

2.1 3D SCAN AUTOMATIZATION INTO 2D AND CLASSIFICATION

The process starts with a 3D scan of the elements. We developed an automatization to contain these shapes in bounding boxes. These boxes can be positioned in 3D. Additionally, we vary the scan's position to reduce the box's volume. This box acts as a basic geometry where we contain the scan, and therefore we determine the most optimal 2D positioning for further processing, see Figure 4.

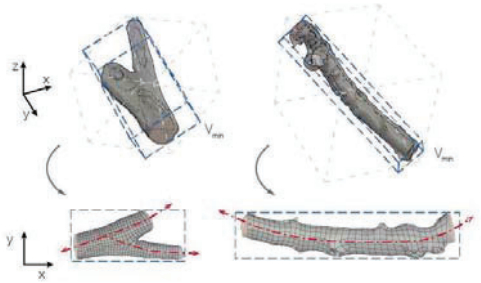

Figure 2: *Minimal volume bounding box automatization and 2D reorientation.*

2.2 GEOMETRIC PROCESSING AND CLASSIFICATION

After the previous procedure, we generate a series of additional automation in which we convert the mesh into NURBS volumes. We can automate and define the main growth line (in red) through this volume, see Figure 3. We finally geometrically process the elements and generate a library of objects with their angle and dimension classification.

Figure 3: *Image-based 3D modeling method, from 3d mesh to NURBS and growth trajectories.*

This process involved 60 elements, which were analyzed and digitized. An example can be seen in Figure 4. The studied specimens of oak, beech, and birch provide geometric variations of angles that were considered for developing constructive structures later in the methodology used in 3.2.

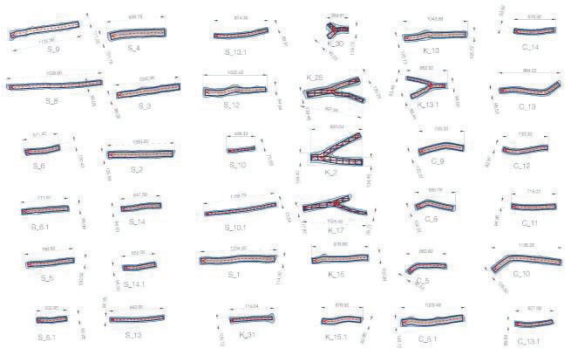

Figure 4: *Analysis of selected elements based on the image-based methodology.*

3 CONSTRUCTION METHODS

The analyzed and documented elements allow for estimating the load capacities of the analyzed elements according to their geometry. These elements can be applied in structures individually, making it necessary to explore structural typologies. Based on the examples in the literature [1-5], we carried out a constructive design approach in bar structures. These elements may be straight, curved, or forks (or bifurcations), and their structural connections (P) must be located at the ends of the growth trajectories.

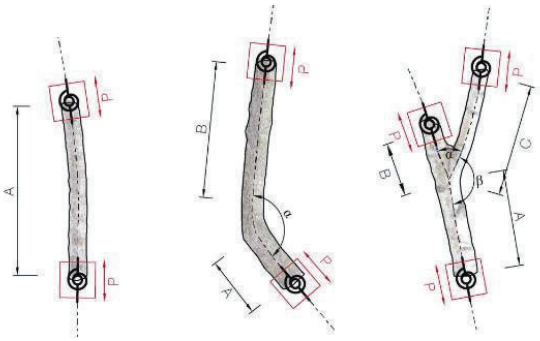

Figure 5 *Elements definition (straight, curved, and bifurcations) and main parameters end (P) as rotational springs, member axis (A, B, C), and angles (α, β)*

3.1 BAR-STRUCTURES DESIGN

Timber bar structures, generally designed as trusses, require complex connection nodes mainly executed with slotted steel plates. These connections are therefore located at the structural nodes. The present design method studies the construction of these trusses and frameworks with rigid nodes. Taking advantage of the capacity of naturally grown timber, we develop free, "off-knot" structural nodes. The moment curves in the frameworks are characteristic of Vierendeel and frame systems.

https://doi.org/10.52202/069179-0096

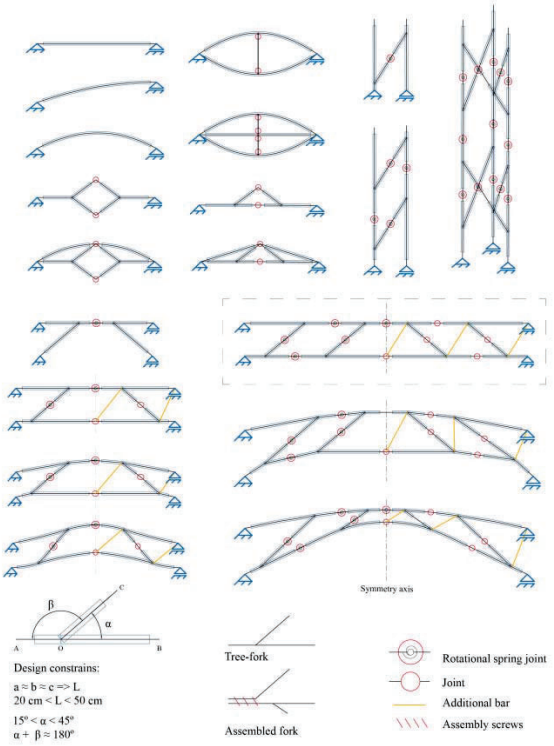

Figure 6: *Above: frameworks and bar-structures design. Below: the design constraints for a joint definition based on grown timber.*

In addition to the cross-sectional dimensions of the tree forks, the position of the joints of the "straight bars" are decisive for the structural design of the grown timber structures. While the bifurcations are optimally suited for moment loads thanks to their bending strength due to the unbent cross-section, the joints of the straight bars should be subjected to normal forces.

3.2 JOINT METHODOLOGY

In this section, we define a method for positioning the joints, and applying it to one of the simplified typologies. The proposed methodology for determining the most appropriate location of the joints utilizes multi-objective optimization. The location of the joints along the member axis ($0 < x_{joint} < L$) serve as input parameters. Joints are implemented as rotational springs. Geometric restrictions derived from databases of raw timber elements, such as maximum and minimum fork angles and lengths, can be considered (e.g., by the following condition $0.1\ L < x_{joint} < 0.9\ L$). Optimization objectives are reduction of total system deflection, maximum deflection, summed bending moments, and maximum fork moment. All load cases are considered.

The automated selection of fitting elements can thus only be done after the static analysis. Such a process see can be based on [2]. In addition to lengths and angles, minimum section dimensions derived from the determined internal forces can be specified as search criteria in the data beacons. This method is similar to the common cross-section optimizations, where only a structural element's minimum and maximum cross-sections are considered. The process integrated the modeling part in Rhino & Grasshopper [9], used MOO engine Octopus [10], [11], and used Karamba [12] for the static analysis.

3.3 OPTIMIZATION RESULTS

Figure 7 shows a Vierendeel-girder under a vertical and 45° inclined traveling load. Each of the 16-point loads (P01-P16) represents a separate load case (LC01-LC16). The joint positions were determined under the optimization objectives of a minimum sum of moments, a minimum sum of deflections, and a minimum maximal deflection of the girder.

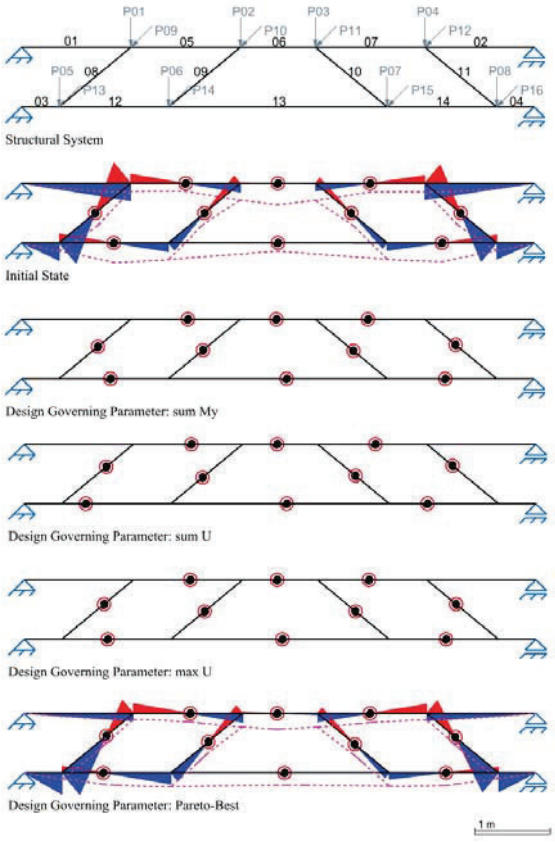

Figure 7: *Vierendeel-girder system*

Table 1 shows that optimization of the joint position results in up to 23% less total deflection (sum U) and 21% less maximum deflection (max U). The total moment summed up over the girder (sum My, magnitude sum) increases by 7% to 78%. For asymmetrical governing load cases or systems, more favorable moment distributions and lower deflection can be achieved by optimization.

https://doi.org/10.52202/069179-0096

The method is especially beneficial since the grown timber elements from the databases do not always allow joint positions in the center of the member.

		Design Governing Parameter				
		initial state	sum My	sum U	max U	**Pareto-best***
		Relative hinge location from bar starting point				
bar no.	01	-	-	-	-	-
	02	-	-	-	-	-
	03	-	-	-	-	-
	04	-	-	-	-	-
	05	0.50	0.52	0.53	0.52	**0.52**
	06	0.50	0.52	0.54	0.54	**0.54**
	07	0.50	0.52	0.47	0.53	**0.52**
	08	0.50	0.54	0.62	0.59	**0.62**
	09	0.50	0.52	0.56	0.53	**0.48**
	10	0.50	0.53	0.53	0.52	**0.52**
	11	0.50	0.57	0.64	0.59	**0.60**
	12	0.50	0.53	0.78	0.58	**0.62**
	13	0.50	0.54	0.53	0.51	**0.52**
	14	0.50	0.53	0.35	0.52	**0.52**
Results	sum My	*100%*	*107%*	*178%*	*119%*	***126%***
	sum U	*100%*	*84%*	*77%*	*80%*	***79%***
	max U	*100%*	*84%*	*87%*	*79%*	***82%***

Table 1: *Optimization results*

4 CONSTRUCTION DETAILS

The criteria for defining the construction details were to meet the static analysis results. The result of the image processing allows us to know the stock material with its dimensions and the direction of the wood grain. In addition, the optimized bar structure shows the load-bearing trajectories. This combination defines the construction development and its joints.

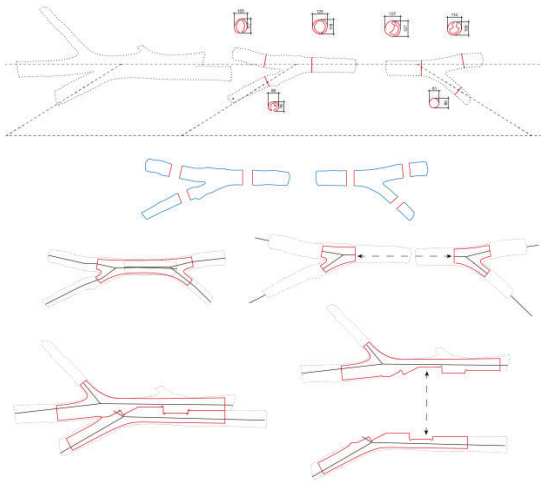

Figure 8: *Framework division in individual off-knot elements, according to their growth trajectories and cross-section.*

4.1 CONSTRUCTION DEVELOPMENT

Using natural timber allows the development of multiple construction details (Figure 1b) based on traditional Timber construction in many cases. The incorporation of robotic fabrication methods also allows to the incorporation of three-dimensional curved elements in a practical way, which also using dowel joints [13] can withstand normal forces and certain bending moments. In this project, we develop 2-dimensional elements based on the examples analyzed in 3.1.

The documented elements (Figure 4) were examined with the optimized structure to determine joining methods. In addition to incorporating interlocked joints with dowels for the connections (Figure 9), the possibility of using fully threaded screws is also experimented with. Examples from the literature [14] [15] show how using these screws enables homogenization in solid wood. This allows us to combine curved/straight elements or forks to generate solid joints as "hybrid" forks (Figure 10).

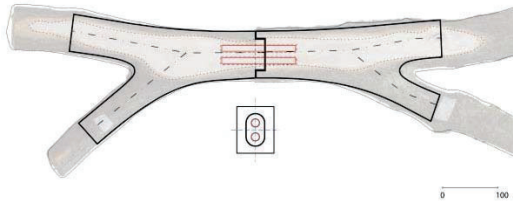

Figure 9: *Detail of a butt joint with two oak elements with inserted dowel. Scale in cm.*

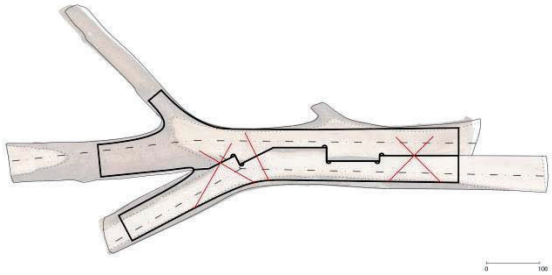

Figure 10: *Detail development of a bending-resistant connection from two elements of maple and beech in a hybrid fork using fully threaded screws. Scale in cm.*

4.2 FABRICATION METHODS

In this manufacturing method, the elements (stock material) are minimally processed with a planning machine following the positioning of the bounding box (Figure 2). As it is a 2D process based on optimization, the pre-processing is quick. After the stock is pre-processed, the construction details are adapted for 2D-CNC fabrication (Figure 8). From the automated information about the positioning of the Bounding box we reposition the cutting lines (in red). Then the stock material position is transmitted through informative sensors and the CNC programming is performed. The manufacturing of butt-joints takes place by milling in 2D the sides of the fabricated parts.

https://doi.org/10.52202/069179-0096

Figure 11: *Projection of the fabrication outlines for the CNC cutting operation.*

5 FABRICATION RESULTS

As a sample, we fabricated several elements. The first specimen was made as the central element of the structural system, manufactured with two oak elements, Figure 12. The ends were made with beech dowels, see Figure 13. Secondly, we made a joint of two parts to form a hybrid element (Figure 14 and 15). This shows that it is possible to use two different materials (beech and maple) to vary the mechanical properties of the construction element. As a last example, we experimented with three-dimensional joints (Figure 16 and 17), which were executed in an interlocking geometry in two birch specimens.

Figure 12: *Photo of a fabricated, grown timber element in oak.*

Figure 13: *Photo detail of the butt joint with dowels.*

Figure 14: *Photo of a fabricated hybrid fork made with two specimens of beech and maple, joined together with fully threaded screws.*

Figure 15: *Photo detail of the butt joint, and the position of the fully threaded screws.*

Figure 16: *Photo of a three-dimensional experimental component produced from two 2D tree forks of birch*

Figure 17: *Photos detail of the interlocked joint.*

6 CONCLUSIONS

The work detailed in this study demonstrates a novel approach for automating the integration of naturally grown elements into structural design, focusing on bending-resistant joints. We propose construction methodologies to incorporate the inherent geometries of these elements into minimally processed structural components. The proposed procedures can be applied to both planar and three-dimensional structures whose constituent parts are described in two dimensions. Furthermore, we leverage image processing techniques to

https://doi.org/10.52202/069179-0096

automate the design and production processes, as evidenced by construction demonstrations.

7 FUTURE WORK

The subsequent phases of the project will prioritize evaluating the load-bearing capacity of the elements, utilizing their respective cross-sectional dimensions as a basis. The remaining tasks include numerical simulation of the scanned elements and conducting load tests. We are also investigating the feasibility of integrating the joint simulation process with tree felling operations to streamline the selection of suitable specimens within the same forest. Augmented reality tools may also be employed to enhance the integration of tree specimens with the overall structure.

ACKNOWLEDGEMENTS

The methods presented here are part of preliminary work carried out during the summer semester of 2022 in the academic project "Tree-based constructions" at the Faculty of Architecture of the RWTH-Aachen; special thanks to Mr. Viktor Wages for his bachelor thesis with the same title. This paper is part of the preliminary work of the recently started interdisciplinary research project. Special gratitude for the financial support to the Deutsche Forschungsgemeinschaft (DFG, German Research Foundation). Project-ID: 512769030

REFERENCES

[1] "WholeTrees Structures," *WholeTrees Structures*. https://wholetrees.com/ (accessed Feb. 07, 2023).

[2] F. Amtsberg, Y. Huang, D. Marshall, K. Moreno Gata, and C. Mueller, “Structural Up-cycling : Matching Digital and Natural Geometry,” 2021. Accessed: Dec. 10, 2021. [Online]. Available: https://publications.rwth-aachen.de/record/822362

[3] M. Self, E. Vercruysse, A. Menges, B. Sheil, R. Glynn, and M. Skavara, "Infinite Variations, Radical Strategies," in *Fabricate 2017*, UCL Press, 2017, pp. 30–35. doi: 10.2307/j.ctt1n7qkg7.8.

[4] P. Von Buelow, O. Oliyan Torghabehi, S. Mankouche, and K. Vliet, "Combining parametric form generation and design exploration to produce a wooden reticulated shell using natural tree crotches," *Proceedings of IASS Annual Symposia*, vol. 2018, no. 20, pp. 1–8, Jul. 2018.

[5] Niels Martin Larsen & Anders Kruse Aagaard, "Robotic processing of crooked sawlogs for use in architectural construction | SpringerLink." https://link.springer.com/article/10.1007/s41693-020-00028-7 (accessed Dec. 11, 2022).

[6] K. Moreno Gata, M. Trautz, and D. Grizmann, “Guiding the Tree Growth for Timber Structures Design,” 2021. Accessed: Dec. 10, 2021. [Online]. Available: https://publications.rwth-aachen.de/record/825087

[7] K. Moreno Gata, J. Musto, and M. Trautz, "Growing Construction Components - Design and simulation strategy for self-formation following tree growth," in *Werner, L and Koering, D (eds.), Anthropologic: Architecture and Fabrication in the cognitive age - Proceedings of the 38th eCAADe Conference - Volume 2, TU Berlin, Berlin, Germany, 16-18 September 2020, pp. 51-59*, 2020. Accessed: Sep. 30, 2020. [Online]. Available: http://papers.cumincad.org/cgi-bin/works/paper/ecaade2020_312

[8] P. Prusinkiewicz and A. Lindenmayer, *The Algorithmic Beauty of Plants (The Virtual Laboratory)*. New York, Berlin, Heidelberg: Springer-Verlag, 1996.

[9] R. McNeel and others, "Rhinoceros 3D, Version 6.0," *Robert McNeel & Associates, Seattle, WA*, 2010.

[10] "Octopus," *Food4Rhino*, Dec. 06, 2012. https://www.food4rhino.com/en/app/octopus (accessed Feb. 07, 2023).

[11] R. Vierlinger, "Multi Objective Design Interface," Master Thesis, TU Wien, Faculty of Civil and Environmental Engineering, 2013. doi: 10.13140/RG.2.1.3401.0324.

[12] C. Preisinger, "Linking Structure and Parametric Geometry," *Architectural Design*, vol. 83, no. 2, pp. 110–113, 2013, doi: 10.1002/ad.1564.

[13] N. M. Larsen, A. K. Aagaard, M. Hudert, and L. W. Rahbek, "Timber structures made of naturally curved oak wood: prototypes and processes," *Archit. Struct. Constr.*, vol. 2, no. 4, pp. 493–507, Dec. 2022, doi: 10.1007/s44150-022-00046-9.

[14] M. Ayoubi and M. Trautz, “Verbundverhalten von Vollgewindeschrauben in Brettschichtholzbauteilen. - Teil 1: Experimentelle Untersuchungen zum Einsatz der Schrauben mit großen Einbindelängen als Bewehrung,” *790-799*, 2015, doi: 10.1002/bate.201400098.

[15] M. Trautz *et al.*, "Laser predrilling for high-precision positioning and installation of fully threaded screws in glued-laminated timber (glulam)," *Wood Material Science & Engineering*, vol. 0, no. 0, pp. 1–16, Apr. 2022, doi: 10.1080/17480272.2022.2051735.

World Conference on Timber Engineering Oslo 2023

GREEN OAK BUILDING WITH HIGH-TECH METHODS, PART 1: CHARACTERISATION OF THE RAW MATERIAL

Nicolas Hofmann[1], Franka Brüchert[2], Udo H. Sauter[3], Kay-Uwe Schober[4], Beate Hörnel-Metzger[5], Maximilian L. Müller[6]

ABSTRACT: In Germany, only half of the annual increment of oak stands is used. Especially small-diameter oaks are currently either not used or only used as firewood. This research project aims on making small-diameter oak logs available as structural timber members. For this purpose, the mechanical properties of the logs and factors influencing them must be determined.

In the experimental program, (oven-dry) wood density, moisture content, internal and external wood defects and round wood geometry properties were measured by non-destructive and destructive methods. Additionally, dynamic and static modulus of elasticity and modulus of rupture were determined for log characterisation. The test material (210 oak logs, *Quercus petraea* (Matt.) Liebl.) originated from one stand at age of 90 years in Rhineland-Palatinate which developed from stump sprouts.

The results show that the strength and stiffness of small-diameter oak logs are well sufficient for the use in load-bearing structures. Initial analysis on strength prediction of individual logs based on non-destructive methodologies reveal large heterogeneity at the small sample size and thus only restricted prediction strength. Among the investigated predictors, oven-dry wood density and log dynamic modulus of elasticity showed the best correlation with strength.

Improvement of the strength prediction, which could then allow strength grading, would be desirable for even more efficient utilization of small-diameter oak wood. This could possibly be achieved by finalizing the assessment of the internal knot features in this study and by increasing the sample size (number of oak logs) in a subsequent study.

KEYWORDS: structural timber, NDT, wood properties, wood density, external quality grading, *Quercus petraea*

1 INTRODUCTION

In Germany, only half of the annual increment is used in oak stands [1]. Especially small-diameter oaks are currently either not used or only used as firewood. The use of wood as a construction material has several advantages. On the one hand, the carbon is sequestered much longer compared to firewood, and on the other hand, energy-intensive materials such as steel or concrete are substituted. In addition, there is a higher added value for the forest owner.

In order to exploit these opportunities, our research project aims on making small-diameter oak logs available as structural timber members, e. g. for columns, frameworks and agricultural buildings, like barns. For this purpose, the mechanical properties of such logs and the factors influencing them must be determined, as these have only been insufficiently investigated so far. Most of the previous studies on strength properties have been conducted on softwoods, since softwoods have been used much more frequently for load-bearing structures than hardwoods in recent decades due to their straightness and better predictable mechanical properties. As a consequence, one goal of the project was to apply conventional NDT technology already in use for (board strength) grading, with which we can infer the strength of green oak logs.

The second part of this project deals with the implementation of log bending tests (strength and stiffness) to obtain reference values, the third part with the construction of a demonstration hall from a subset of the investigated oak logs. Part two was also presented at this conference and included in the proceedings [2].

2 MATERIAL AND METHODS

As test material, 210 oak logs (*Quercus petraea* (Matt.) Liebl.) with a length of 5 m and an average mid diameter of about 25 cm were cut from one stand at age of 90 years in Rhineland-Palatinate. The trees have developed from

[1] Nicolas Hofmann, FVA Forest Research Institute of Baden-Württemberg, Germany, nicolas.hofmann@forst.bwl.de
[2] Franka Brüchert, FVA Forest Research Institute of Baden-Württemberg, Germany, franka.bruechert@forst.bwl.de
[3] Udo H. Sauter, FVA Forest Research Institute of Baden-Württemberg, Germany, udo.sauter@forst.bwl.de
[4] Kay-Uwe Schober, Mainz University of Applied Sciences, Germany, kay-uwe.schober@hs-mainz.de
[5] Beate Hörnel-Metzger, Mainz University of Applied Sciences, Germany, beate.hoernel-metzger@hs-mainz.de
[6] Maximilian L. Müller, Mainz University of Applied Sciences, Germany, maximilian.mueller@hs-mainz.de

https://doi.org/10.52202/069179-0097

stump sprouts. The logs were divided into three subsamples (n = 70, each) to facilitate the measuring process. Subsample 3 was used for the construction of the demonstration hall [2] and underwent a shorter test program without destructive measurements. In this article, we only present the results from the subsamples 1 and 2 which underwent the complete measurement programme in non-destructive and destructive testing for characterisation. From these subsamples, 80 logs were debarked, 30 logs were edged on two sides and 30 logs were edged on four sides. Debarking was executed for faster drying, edging for a simplified construction geometry (Figure 1).

Figure 1: *Oak logs from subsample 1 (n = 70). Edged on two or four sides (left) and debarked (right).*

In the experimental program, green density distribution and internal knot features of the logs were determined by computed tomography scans (MiCROTEC® CT.LOG, Figure 2).

Figure 2: *Measurement of natural frequency (Viscan), left, and of raw density and geometry (CT.LOG and DiShape), right.*

The dry wood density distribution was measured on 2 × 1 cm small clear samples, which were taken in four spatial directions from a ~2 cm thick log slice from the top end of the log (Figure 3). The samples were dried to constant weight at 103 °C, followed by immersion weighing to determine sample volume. Moisture content of the logs (MC, moisture mass fraction on dry basis) was determined by sampling of seven slices per log at the end of the trial (Figure 3). In conjunction with the mass measurement of the log at all phases of the test programme, we were able to determine the moisture content of the logs at earlier points in time as well.

External wood defects, i.e. knots, were investigated by log quality grading following the German Framework Agreement for Timber Trade (RVR) [3]. Geometry properties were measured using a 3D laser scanner (MiCROTEC® DiShape, Figure 2).

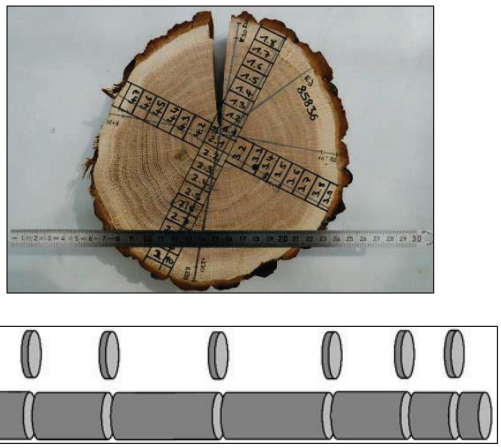

Figure 3: *Samples for determination of oven-dry density distribution (MC = 0 %) on a log slice from the top end of the log (top). Slice samples for determination of the final moisture content and dry mass of the log (bottom).*

The curvature was calculated from the DiShape data as the maximum bow height divided by the log length, excluding the 50 cm butt end of the log, according to [4] to avoid buttresses.

The dynamic modulus of elasticity (MOE_{dyn}) of the logs has been calculated from measurements of the natural frequency (MiCROTEC® Viscan, Figure 2), the green density and length of the logs. The static modulus of elasticity (MOE_{stat}) and the bending strength (MOR) have been investigated by our project partners according to DIN EN 14251 [5] (see part 2 of this project) [2].

3 RESULTS AND DISCUSSION

Round wood grading according to RVR show that most logs were graded in quality class C, which represents intermediate quality logs characterised by a large number

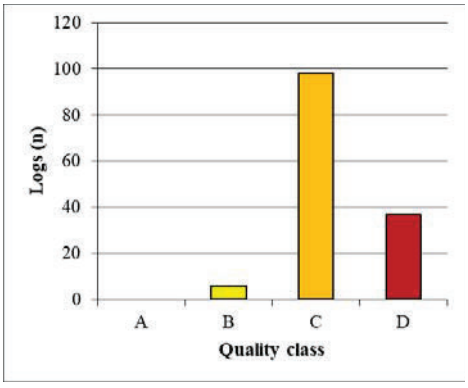

Figure 4: *Frequency distribution of the oak logs from subsample 1 and 2 (n = 140) in different quality classes (A = best quality, D = worst quality) according to the German Framework Agreement for Timber Trade [3].*

https://doi.org/10.52202/069179-0097

of small to medium sized knots, the presence of curvature and other features (Figure 4). Mean number of externally visible knots and burls per log was 24.9 (± 17.9) and mean curvature was 1.7 % (± 0.8 %), with multiple curvatures occurring frequently.

Wood density in oven-dry condition (Figure 5) was within the range found for oak in the literature [6]. Heartwood showed a slightly higher dry density than sapwood, probably due to narrower annual rings in sapwood affected by increasing competition between the trees. Incorporation of chemical substances in heartwood seems to have a minor effect on dry wood density [6].

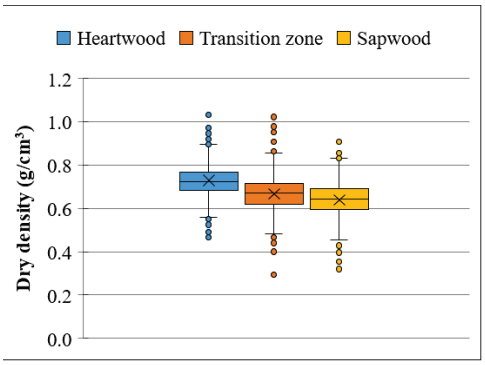

Figure 5: *Dry wood density distribution (MC = 0 %) of different wood compartments for the 140 oak logs from subsample 1 and 2, determined on 4720 wood samples.*

Moisture content in fresh condition was, compared to other studies [7], relatively low at 66.8 % (mean value for subsample 2, not measured for subsample 1), which is probably due to the very dry weather conditions over the last years. The logs dried to an average moisture content of 35.4 % within ~20 months (Figure 6) until the testing programme terminated with destructive testing. When the bending tests were performed, all but two logs from subsamples 1 & 2 were still above the fibre saturation point (FSP), which is at approx. 25 % MC for oak wood [8].

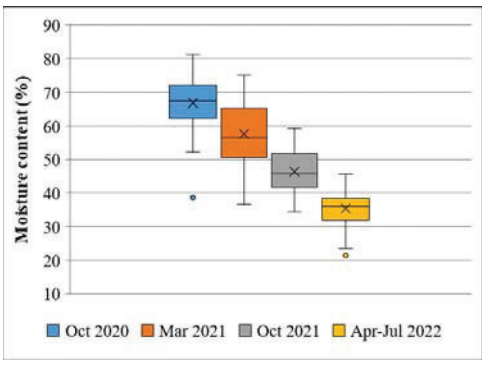

Figure 6: *Moisture content distribution of subsample 2 (n = 70 oak logs) over time, determined by regular weighing and measurement of the dry mass of the logs at the end of the trial. Felling was conducted in September 2020, bending tests from April to July 2022.*

Dynamic modulus of elasticity ranged from 5,481 MPa to 18,754 MPa (median 12,070 MPa) for all logs. Mean dynamic MOE was about 3.5 % higher than mean static MOE (see part 2 of this project [2]). Static MOE showed several extremely high values with a maximum of 32,956 MPa. Consequently, the median of MOE_{stat} was only 10,647 MPa, and therefore 13.4 % lower than the median of MOE_{dyn}, which is in accordance with other studies comparing non-destructive and destructive methodologies for mechanical characterisation of timber [9]. Modulus of rupture (MOR) ranged from 27.4 MPa to 135.0 MPa (median 66.1 MPa) for all logs [2]. Conventional classification of stiffness and strength results to standard seemed not appropriate, as dimension/geometry and moisture content of our test specimens (logs) were not in line with common test standards. Literature values were mostly determined on small clear oak specimens at a moisture content of 12 %. For such specimens, a range of 9,200-13,500 MPa for MOE_{stat} and of 78-117 MPa for MOR is given by [10] and a mean of 12,300 MPa for MOE_{stat} and of 105 MPa for MOR were reported by [11]. In green condition, a mean MOE_{stat} of 8,600 MPa and a mean MOR of 57 MPa was specified [11]. Consequently, the strength and stiffness values measured in this study appear to be within the natural range for oak, or even slightly higher if the high moisture content of the logs is taken into account.

ANOVA and bivariate linear regression analysis to clarify the influence of the external and internal log structures and characteristics on the bending strength revealed the necessity to deal with the different geometric variants separately. Hereafter, only the results for the round logs are presented. In future, round logs will probably play a more important role in the processing of small-size oak construction timber than edged logs, since less material is wasted and no sawing is required. Bending tests were performed on 71 of the 80 round logs. Three round logs were used for compression tests, the six remaining logs had either too strong curvature or too large drying cracks to perform the bending tests safely.

Oven-dry wood density and dynamic modulus of elasticity of the logs contributed most to the variation in log MOR (Figure 7). Both variables were statistically significant positively correlated with the bending strength, oven-dry density even quite closely (Pearson test, $\alpha = 0.05$ with $r = 0.61$ and $p = 0.000$ for dry density and $r = 0.51$ and $p = 0.000$ for MOE_{dyn}).

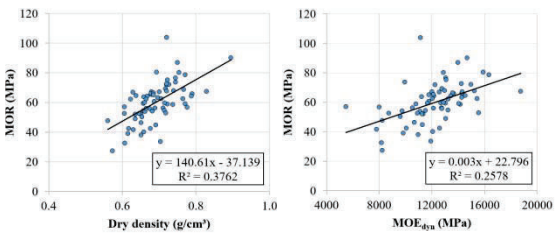

Figure 7: *Relation and linear regression between modulus of rupture and mean oven-dry wood density at MC = 0 % (left) and dynamic modulus of elasticity (right) for the debarked round wood (n = 71).*

https://doi.org/10.52202/069179-0097

In a study on a strength prediction model for pine wood, density and MOE_{dyn} were also the variables with the best explanatory power [12]. Compared to the present study, the coefficients of determination were slightly lower and the MOE_{dyn} had a slightly higher explanatory power than the wood density. In addition, study [12] did not investigate oven-dry density, but density at 12 % moisture content. However, this low and uniform MC is unlikely to have had a large effect on the strength of the correlation.

Considering a log grading procedure based on these characteristics, measurement of MOE_{dyn} can be described as non-destructive and relatively fast. The measurement of oven-dry density, on the other hand, is only possible based on destructive wood sampling. Since these samples originated from the very top end of the log, the log's subsequent use is hardly restricted. However, for an on-line work-flow, a disadvantage is the long time required for this measurement.

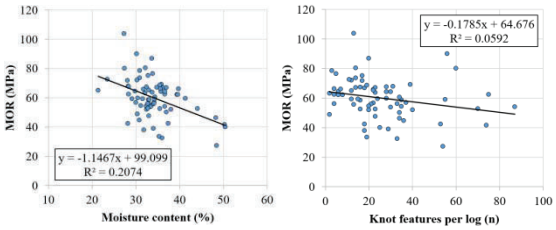

Figure 8: *Relation and linear regression between modulus of rupture and mean moisture content of the logs (left) and number of knot features per log according to [3] (right) for the debarked round wood (n = 71).*

In contrast to the literature, a statistically significant correlation (Pearson test, $\alpha = 0.05$ with $r = -0.46$ and $p = 0.000$) was also found between bending strength and moisture content of the logs (Figure 8, left). The literature states that the mechanical properties only change below the fibre saturation point (FSP) [13]. In this context, a mean log moisture measure over the whole cross section could be misleading as significantly drier areas below the FSP located in mechanical important peripheral stress zones might have a greater influence on the strength in a bending test than the core areas. An evaluation of additional moisture measurements by means of impact electrodes (resistance-based, Hydromette CH 17, GANN Mess- u. Regeltechnik GmbH) at peripheral log depths of 2 cm and 4 cm frequently showed values below the FSP, but explained the variation in strength distinctly worse instead of better. This indicates that we have a spurious negative correlation based on other, unknown causes in case of Figure 8 (left).

The number of externally visible knots and burls per log also showed a statistically significant, but very weak negative correlation (Pearson test, $\alpha = 0.05$ with $r = -0.24$ and $p = 0.045$) with bending strength (Figure 8, right). In a study on the effect of knots on the bending strength of boards from two different poplar clones, the correlation coefficients r range from -0.12 to -0.60, depending on the position and diameter ratio of the knots [14].

For a better interpretation of our results, a deeper analysis of the knot data is necessary. Above all, the internal knot structures of the logs must also be taken into account. For this purpose, all knot features in CT scans of five logs were manually annotated (over 10,000 polygons in total) and categorized (Figure 9). A machine learning algorithm was trained with these scans to develop an automated knot detection procedure for knot segmentation for further use on such CT scans (Figure 10). This process has not yet been completed, but due to the accuracy achieved so far stronger correlations between knot architecture of oak logs and their strength is expected.

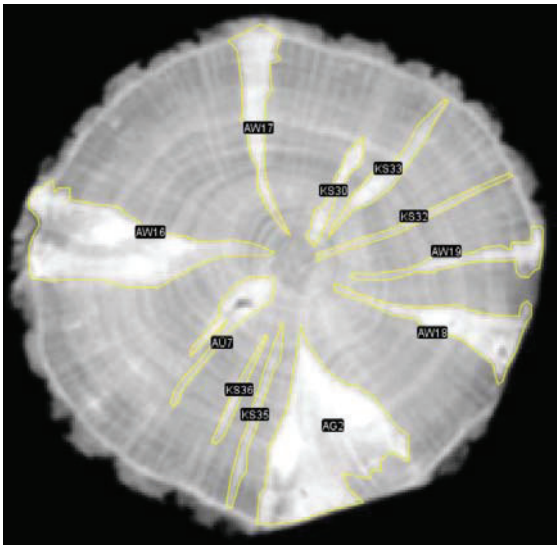

Figure 9: *Manually annotated and categorized knot features in a CT slice of an oak log. KS = bud trace, AW = burl, AG = sound knot, AÜ = overgrown knot; followed by the consecutive number of the feature within the log.*

Figure 10: *Comparison of manual (left) and machine learning based automated (right) segmentations of knot features in the same CT slice of an oak log.*

Mean curvature of the round logs was 1.9 % (± 0.8 %). Curvature showed no statistically significant correlation with bending strength. Strong stem deviation leads to stem eccentricity and severe tension wood formation in hardwoods which usually shows a lower strength. Obviously, the curvature recorded in the test material did not lead to the formation of tension wood with different mechanical properties. This assumption was visually confirmed during the sampling of numerous log slices after the bending test.

Measurement of knot features as defined in visual log grading regulations and CT scanning works non-

destructively. In contrast, measuring a precise moisture content is only possible by the collection of representative wood samples and their subsequent kiln-drying [15]. The disadvantage of this method is that it is time-consuming and destructive. Non-destructive rapid MC determination devices usually show high deviations in their measurement precision from the reference method [16].

Although small-diameter oak logs are well suited for construction purposes, grading procedures of individual logs similar to softwood board strength grading still requires further evaluation of our data. Furthermore, an increase in the sample number in additional studies could significantly improve this strength prediction.

4 CONCLUSIONS

The results of our collaborative research project indicate that small-diameter oak logs appear well suitable for load-bearing structures. This application seems to be the best option, since such logs cannot be used for the production of lumber or even veneer due to their knottiness, small diameter and strong curvature.

For even more efficient use, it would be beneficial to predict the strength of individual logs by non-destructive measurements. In this study, the best explanation for the variation in bending strength was obtained by the measurement of the oven-dry density at the top end of the logs, followed by the measurement of the global dynamic modulus of elasticity. Moisture content of the logs also showed a significant correlation with bending strength, but this relation appears to be coincidental since almost all logs were still above the fibre saturation point at the time of testing. Log curvature in the range found in the test material had no effect on bending strength, probably because it was not related to tension wood occurrence. Number of knots and burls quantified in course of external quality grading was weakly correlated with strength. However, the influence of knots is still under evaluation. In particular, innovative machine learning procedures applied to CT scans with respect to internal knot features could lead to a better strength prediction.

After completion of data evaluation, all measured parameters and log characteristics will be integrated into a strength prediction model for oak logs.

ACKNOWLEDGEMENT

This project (support code 2218WK18C3) was funded by the Federal Ministry of Food and Agriculture (BMEL) and the Federal Ministry for the Environment, Nature Conservation, Nuclear Safety and Consumer Protection (BMUV) through the Agency for Renewable Resources (FNR) from the Forest Climate Fund (WKF).

The authors would like to thank Oswald Keller, Heike Laux, Christoph Beilharz, Adrian Kölz, Elias Maurer, Jakob Fei and Nikolaj Markgrander for their great help with sampling and practical measurements, Werner Rützler for the CT/DiShape scanning and Martin Huber, Elisa Kammer, Omoyemi Edun, Hannah Staiger and Tushar Maske for the detailed processing of the CT scans.

REFERENCES

[1] BMEL: Federal Ministry of Food and Agriculture, Results of the National Forest Inventory 2012 https://www.bundeswaldinventur.de, Germany, 2022.

[2] Schober, K.U.; Hörnel-Metzger, B.; Müller, M.L.; Hofmann, N.; Brüchert, F.; Sauter, U.H.: Green oak building with high-tech methods, Part 2: Log bending tests for determination of strength and stiffness. Proceedings of the 17th World Conference on Timber Engineering (WCTE 2023), Oslo, Norway, 2023.

[3] Deutscher Forstwirtschaftsrat; Deutscher Holzwirtschaftsrat: German Framework Agreement for Timber Trade (RVR), 3rd Edition, Agency for Renewable Resources (FNR): Gülzow-Prüzen, Germany, 2020.

[4] Gorges, J.; Huber, M.; Sauter, U.H.; Dormann, C.F.: Curvature of Logs – Development of and Comparison between Different Calculation Approaches. *Forests* 2021, 12, 857.

[5] DIN EN 14251:2022-10. Structural round timber - Test methods; German version EN 14251:2003, DIN, Berlin, Germany.

[6] Merela, M.; Cufar, K.: Mechanical properties of sapwood versus heartwood, in three different oak species. *Drvna Industrija* 64 (4): 323-334, 2013.

[7] Bues, C.T.; Schulz, H.: Festigkeit und Feuchtegehalt von Eichenholz aus Waldschadensgebieten. *Holz als Roh- und Werkstoff* 48: 85-89, 1990.

[8] Krpan, J.: Untersuchungen über den Fasersättigungspunkt des Buchen-, Eichen-, Tannen- und Fichtenholzes. *Holz als Roh- und Werkstoff* 12 (3): 84-91, 1954.

[9] Zhou, Z.; Zhao, M.C.; Wang, Z.; Wang, B.J.; Guan, X.: Acoustic testing and sorting of Chinese poplar logs for structural LVL products. *Bioresources* 8 (3): 4101-4116, 2013.

[10] Wagenführ, R.: Holzatlas. 6th ed., Carl Hanser Verlag München, Leipzig, 816 pages, 2007.

[11] Lavers, G.M.: The strength properties of timber. Dept. of the Environment, Building Research Establishment report, H.M.S.O., 3rd ed., Garston, Watford, London, 60 pages, 1983.

https://doi.org/10.52202/069179-0097

[12] Franca, F.J.N.; Franca, T.S.F.A.; Seale, R.D.: Use of longitudinal vibration and visual characteristics to predict mechanical properties of No. 2 Southern Pine 2 × 4 and 2 × 10 lumber. *Wood and Fiber Science* 52 (3): 280-291, 2020.
[13] Glass, S.V; Zelinka, S.L.: Chapter 4: Moisture relations and physical properties of wood. In: Wood handbook – wood as an engineering material. General Technical Report FPL-GTR-282. Madison, WI: U.S. Department of Agriculture, Forest Service, Forest Products Laboratory. 22 pp, 2021.
[14] Koman, S.; Feher, S.; Abraham, J.; Taschner, R.: Effect of knots on the bending strength and the modulus of elasticity of wood. *Wood Research* 58 (4): 617-626, 2013.
[15] Dietz, P.: Dry Matter Content Determination of Pulp Wood. *Holz als Roh- und Werkstoff* 25 (7): 255-265, 1967.
[16] Reisinger, K.; Hartmann, H.; Turowski, P.; Nürnberger, K.: Schnellbestimmung des Wassergehaltes im Holzscheit – Vergleich marktgängiger Messgeräte. Berichte aus dem TFZ Nr. 16, Straubing, 115 pages, 2009.

World Conference on Timber Engineering Oslo 2023

VARIATION IN MECHANICAL PROPERTIES WITHIN AND BETWEEN PLANTATION-GROWN *GMELINA ARBOREA* TREES

Stanley Emeka Iwuoha[1], **Werner Seim**[2]

ABSTRACT: Recent studies have shown that the material properties of Gmelina - a fast-growing hardwood species, are comparable with those of European-grown softwood species and are suitable for construction purposes. Information on the variation in the material properties which could aid the end use, such as sorting the logs with respect to end user requirement, is lacking. This work is an investigation into the variation of the mechanical properties along the height and between different Gmelina trees, to aid an efficient and effective end use of the material. 10 material properties were experimentally and statistically investigated. The results showed that the material properties of Gmelina do not vary along its height as much as is observed for other timber species. Between the trees, a variation range of 11 – 14 % was determined.

KEYWORDS: ANOVA, *Gmelina arborea*, Mechanical properties, Statistical analysis, Tropical timber species, Variation

1 INTRODUCTION

Gmelina arborea is a fast-growing tropical hardwood species which is capable of reaching a mean diameter at breast height of between 60 - 80 cm in 20 years [1]. It has a low cost of establishment, is suitable for paper and pulp and for making solid wood products, and has been described as a very promising tree species [2]. It has also become one of the most important plantation species in tropical areas due to its low cost of establishment and the fact that it can be developed extensively where it has never existed before [3]. Gmelina is not a threatened species and grows across different continents of the world. Recent studies on its mechanical properties and embedment strength, show that it has great potential for use as a construction material [4]. For an optimal use of the material in the construction industry however, a proper understanding of the variation of its strength properties along its height, and between different trees is required to provide valuable information to aid decisions on how to sort the logs in accordance with end-user requirements. For Gmelina however, this information is not yet available. This study aims at determining the variation in the mechanical properties between and within (along the height of) three Gmelina trees (see Figure 2) by means of experimental and statistical investigations.

2 MATERIALS AND METHODS

2.1 MATERIALS

The material used for this study was collected from three plantation grown *Gmelina arborea* trees obtain in Akure in southwestern Nigeria (see Figure 1).

Figure 1: *Map of Nigeria, showing Akure, the location where the materials were obtained (Map was obtained from Google).*

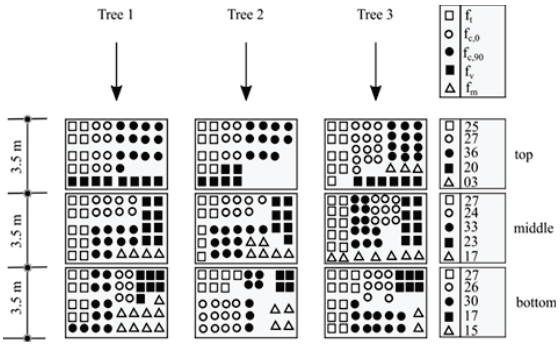

Figure 2: *Location and number of specimens tested.*

[1] Stanley Emeka Iwuoha, Timber Structures and Building Rehabilitation, University of Kassel, 34125 Kassel, Germany (iwuoha@uni-kassel.de)

[1] Werner Seim, Timber Structures and Building Rehabilitation, University of Kassel, 34125 Kassel, Germany (wseim@uni-kassel.de)

https://doi.org/10.52202/069179-0098

2.2 METHODS

The collected specimens were prepared and tested in accordance with EN 408 [5], except for the tensile strength test, which was conducted in accordance with the German standard DIN 52188 [6]. The specimens for investigating the variation in the material properties between the trees were separated according to trees as trees 1, 2, and 3 while those for investigating the variation in the material properties along the height were separated according to location as top, middle, and bottom (see Figure 2). The number of specimens, the type of tests conducted, and the location from which the tested specimens were obtained, are all shown in Figure 2.

Details of the procedures leading to the experimental data shown in Table 1, are published in [4]. After obtaining the experimental data, statistical analyses such as the analysis of variance (ANOVA) and the Tukey HSD test were conducted on them using the R-programming language. The ANOVA was conducted to determine the variation in the various material properties along the height and between the trees, while the Tukey HSD test was conducted to determine further insights on the nature of the variations both within and between the trees.

The ANOVA, being a process of testing for the similarity or difference between two or more groups of data by testing the means of the different groups, is done under the null hypothesis H_0 that the sample means are equal, or do not have significant differences. The result of this test is generally given in terms of the F-statistic (f-value), which is then compared with critical f-values obtained from statistical tables. The null hypothesis is true if the calculated or observed f-value ($F_{observed}$) from a set of data is less than the corresponding critical f-value ($F_{critical}$) from statistical tables. Since this is a relatively complex calculation, its result from the R programming language is given both as the f-value as well as the p-value (an evidence in support of the null hypothesis). Considering a significance level (α-value) of 0.05, p-values > 0.05 would mean that there is no significant difference in the sample means of the set of data tested. P-value < 0.05 means that the means of the tested group of data are different. In such cases, the Tukey HSD test (conducted under the null hypothesis that the means of the various groups are equal) is carried out by determining the q-statistic. This is then compared with critical q-statistic values of the studentized range distribution, to uncover the source of the difference in the tested data. Using the R-programming language, the results are also given as p-values, which can be interpreted as already explained.

Ten material properties including the tensile strength ($f_{t,0}$), compressive strength parallel to the grain ($f_{c,0}$), compressive strength perpendicular to the grain ($f_{c,90}$) shear strength (f_v), bending strength (f_m), density (ρ) the elastic moduli in tension ($E_{t,0}$), bending (E_m) compression parallel ($E_{c,0}$) and the MoE in compression perpendicular to the grain ($E_{c,90}$) were all investigated in the study and the results obtained are presented and discussed in Section 3.

3 RESULTS

3.1 EXPERIMENTAL RESULTS

Results of the complete experimental investigations are shown in Table 1.

Table 1: *Experimental results*

Material property	Minimum (MPa)	Maximum (MPa)	Mean (MPa)
$f_{t,0}$	36.89	98.72	67.91
$f_{c,0}$	23.88	41.38	34.02
$f_{c,90}$	3.97	9.53	4.51
f_v	3.91	7.83	6.30
f_m	29.79	72.73	55.64
E_t	7,855	18,888	11,840
$E_{c,0}$	6,321	21,051	11,027
$E_{c,90}$	161.00	701.00	419.42
E_m	9,446	15,540	12,340
ρ (kg/m^3)	387.00	528.00	452.00

3.2 STATISTICAL ANALYSIS RESULTS: WITHIN-TREE VARIATION

The ANOVA results for the within-tree variation are shown in Table 2 and those for the between-tree variation, are shown in Table 4.

Table 2: *ANOVA results for within-tree variation*

Material Property	Within tree variation		
	$F_{observed}$	$F_{critical}$	p-value
$f_{t,0}$	2.902	3.129	0.061
$f_{c,0}$	10.02	3.131	< 0.01
$f_{c,90}$	2.428	3.102	0.093
f_v	3.316	3.102	0.044
f_m	1.595	3.302	0.219
$E_{t,0}$	0.298	3.149	0.744
$E_{c,0}$	0.146	3.130	0.865
$E_{c,90}$	1.418	3.149	0.248
E_m	0.358	3.133	0.702
ρ	3.985	3.000	0.020

The result in Table 2 shows that apart from the $f_{c,0}$, f_v, and ρ, whose p-values < 0.05, the material properties of the Gmelina trees considered in this study do not vary along the height. This findings agree with those of [7] who reported no variation in the MoE in bending, bending strength and in the compressive strength parallel to the grain of Blackwood grown in Portugal.

The variation along the height of Gmelina determined in Table 2 for $f_{c,o}$, f_v, and density also agrees with [8] who reported a variation in density and compressive strength parallel to the grain along the height of beech wood. The nature of the variation determined for these material properties along the height of Gmelina, was further investigated by comparing the mean value of one of the groups (e.g., the top) with the mean value from each of the other groups (middle and bottom respectively), using

the Tukey HSD test. The result of this is shown in Table 3. In Table 3, the results of the Tukey test are shown in the first three columns, while the mean material property values obtained from the different parts of the trees are presented and compared in the other columns.

Within-tree variation in the compressive strength parallel to the grain – $f_{c,0}$

Table 2, shows the results of comparing the strengths of one part of the trees (e.g., the top), with the other parts (middle or bottom respectively) to determine the part or parts of the tree that are different from the others. Based on the data in Table 2, one sees that there is no statistical significance in the compressive strength parallel to the grain obtained from the top and bottom parts of the trees.

A comparison between the middle and bottom parts as well as the top and the middle parts, as shown in Table 3, are seen to be statistically significant (p-values < 0.05). Furthermore, the differences of the mean strength values between the middle and bottom as well as the top and middle parts are respectively 8 % and 14 %, while that between the top and bottom part is 5 %. A look at the mean values, shows that the compressive strength parallel to the grain obtained at the middle parts of the trees, is smaller than those obtained from the top and bottom parts. This shows that the difference in the strength values detected by the ANOVA, is due to the strength obtained from the middle part of the trees. The variation in compressive strength along the height (as shown in Table 3) is thus a slight reduction in the strength from the bottom to the middle and then a slight increase from the middle to the top.

Table 3: *Within-tree Tukey HSD test results*

Material Property	Parts tested	p-values.	Mean values (MPa)			Bottom	Top	Top
			Top	Middle	Bottom	Middle	Bottom	Middle
$f_{c,0}$	Middle-Bottom	0.0008	35.88	31.60	34.23	1.08	1.05	1.14
	Top -Bottom	0.1945						
	Top-Middle	0.0219						
f_v	Middle-Bottom	0.1663	5.92	6.70	6.13	0.91	0.97	0.88
	Top-Bottom	0.7995						
	Top-Middle	0.0497						
ρ	Middle-Bottom	0.0835	448	450	458	1.02	0.98	1.00
	Top-Bottom	0.0216						
	Top-Middle	0.8476						

Within-tree variation in shear strength parallel to the grain - f_v

On the variation of the shear strength, Table 3 shows that there is no variation in the shear strength obtained from the middle and bottom parts of the trees as well as those obtained from the top and bottom parts (all having p-values > 0.05). However, comparison of results obtained between the top and middle parts is seen to be statistically significant, with a p-value of approximately 0.05. This shows that the difference detected in the ANOVA test for the shear strength tests, is due to the results obtained from the middle part of the trees, whose mean values as seen in Table 3 are relatively higher. Based on data in Table 3 however, the difference in the mean values obtained from the top and the middle parts is 12 %. The variation in shear strength is seen to increase slightly from the bottom to the middle, and then reduces slightly from the middle towards the top.

Within-tree variation in the density values

No statistical difference was determined in the density values between the top and the middle parts of the trees as well as between the middle and bottom parts of the trees. A comparison between the top and bottom parts however, showed to be statistically significant (having a p-value of 0.0216, which is < 0.05). Looking at the mean density values in Table 3, one sees that the mean density obtained from the bottom part of the trees is comparatively higher than those obtained from the middle and top parts, respectively. This shows that the difference in the density values identified by the ANOVA, is owed to the value from the bottom part of the trees. It can also be seen that the mean density value at the middle is higher than that at the top. This implies that the density values as considered in this study, fall slightly with increase in height. Although studies by different researchers as compiled in [9] show exceptions with differing along the height of different wood species, it can be understood from the formation and growth of wood in trees, as well as the influence and presence of juvenile wood up the trunk that the heaviest wood should be at the base of the tree, with a gradual decrease in density up the trunk [10]. Other density variation patterns discussed in [9] are inconsistent

https://doi.org/10.52202/069179-0098

with this rule and are not within the scope of discussion of the current study. The results (slight reduction of density with height) obtained in this study for the variation of density along the height of Gmelina, was also reported by Lamb [11] for Gmelina, as well as by other researchers [7], [8], [12] for other tree species.

3.3 STATISTICAL ANALYSIS RESULTS: BETWEEN-TREE VARIATION

Results of the between tree variation in the Gmelina trees examined in this study are shown in Table 4 and Table 5. The data in Table 4, shows that there is no variation in the shear strength, the bending strength, and the MoE in compression parallel to the grain between the Gmelina trees considered in this study, whereas the other material properties showed to vary between the trees. The nature of the variation in the mechanical properties between the trees as determined from the Tukey HSD test are detailed in Table 5 and discussed in the sections that follow.

Table 4: *ANOVA results for the between-tree variation*

Material Property	Between tree variation		
	$F_{observed}$	$F_{critical}$	p-value
$f_{t,0}$	3.261	3.129	0.044
$f_{c,0}$	6.119	3.131	0.003
$f_{c,90}$	11.93	3.102	< 0.01
f_v	2.905	3.102	0.064
f_m	0.461	3.302	0.635
E_t	15.83	3.149	< 0.01
$E_{c,0}$	2.626	3.130	0.079
$E_{c,90}$	3.641	3.149	0.030
E_m	19.13	3.133	< 0.01
ρ	3.225	3.000	0.041

Table 5: *Between tree Tukey HSD test results*

Material property	Trees compared	p-values	Mean values (MPa)			Tree 1 / Tree 2	Tree 1 / Tree 3	Tree 2 / Tree 3
			Tree 1	Tree 2	Tree 3			
$f_{t,0}$	T2 - T1	0.0507						
	T3 - T1	0.1171	73.13	64.29	66.33	1.14	1.10	0.97
	T3 - T2	0.8304						
$f_{c,0}$	T2 - T1	0.0624						
	T3 - T1	0.0024	36.13	33.72	32.64	1.07	1.11	1.03
	T3 - T2	0.5072						
$f_{c,90}$	T2 - T1	< 0.01						
	T3 - T1	0.2809	3.96	5.33	4.38	0.74	0.90	1.22
	T3 - T2	0.0037						
$E_{t,0}$	T2 - T1	< 0.01						
	T3 - T1	0.995	12,775	9828	12,831	1.30	1.00	0.77
	T3 - T2	< 0.01						
$E_{c,90}$	T2 - T1	0.0509						
	T3 - T1	0.9993	387	499.93	385.5	0.77	1.00	1.30
	T3 - T2	0.0509						
E_m	T2 - T1	0.9959						
	T3 - T1	< 0.01	11,475	11,435	13,849	1.00	0.83	0.83
	T3 - T2	< 0.01						
ρ	T2 - T1	0.9699						
	T3 - T1	0.0967	455	456	447	1.00	1.02	1.02
	T3 - T2	0.0638						

Between-tree variation in the strength properties

The between tree variation in tensile strength as obtained by the Tukey HSD test and as presented in Table 5, shows no variation between the trees (p-values > 0.05 for all cases). Though different from the ANOVA results, this can be attributed to the level of sensitivity of the tests used. Considering that for all cases, the ANOVA has been proven to be very robust [13], the maximum difference detected by the ANOVA in the between-trees tensile strength (based on the mean tree values), as shown in column 7 of Table 5, is 14 %. This shows that the maximum difference was obtained by comparing the values from trees 1 and 2. Following the same procedure applied for determining the sources of differences in the material properties along the height of the trees, one sees

that the maximum difference in the compressive strength parallel to the grain between the trees is 11 %, stemming from tree 1. Considering the compressive strengths perpendicular to the grain, the maximum variation (26 %) between the trees was obtained from comparing trees 1 and tree 2. From the mean values presented in Table 5, this can easily be understood as stemming from tree 2. In general, the variation in the strength properties (both within and between the Gmelina trees species considered in this study) falls between 11 % to 14 %. The exception to this, is the compressive strength perpendicular to the grain which, although did not vary within the trees, showed a maximum variation between the trees of 26 %. It can thus, be firmly stated that for the materials considered in this study, the compressive strength perpendicular to the grain, between the trees, was the most varied.

Between-tree variation in the elastic moduli values

A comparison between trees 1 and 3 as well as trees 2 and 3 as shown in Table 5, shows that there is a significant variation in the MoE in bending between the trees. This difference however, is 17 % and agrees with the 16.9 % reported in [14] for Blackwood. The value (30 %) obtained for the MoE in compression perpendicular to the grain and for the MoE in tension, is seen to be the highest of all variations observed in this study for Gmelina.

Between-tree variation in the Density values

Considering the density variation between the trees, data in Table 5 strongly declares no between-tree density variation. This is validated by the fact that for all the cases compared, the p-values were consistently above the limits of 0.05. The maximum difference in density computed between the trees as seen in columns 8 and 9 of Table 5 is 2 % and confirms that the mean density values obtained for the different trees as presented in Table 5 are within the same range. It can thenceforth be conclusively stated that the density of Gmelina as considered in this study does not vary between the trees. Any difference between the Tukey HSD and ANOVA tests would be due to the difference in the level of sensitivity of the different tests.

4 FINDINGS

Using 10 material properties which were experimentally determined from different parts of three Gmelina trees obtained from Southwestern Nigeria, this study has shown that at 95 % confidence level:

i. There is no consideration variation in the tensile strength, compressive strength perpendicular to the grain, bending strength, MoE in tension, MoE in compression parallel to the grain, MoE in compression perpendicular to the grain, and the MoE in bending along the height of the Gmelina sample considered in this study.

ii. The compressive strength of Gmelina parallel to the grain ($f_{c,0}$) varies along the height; with mean values from the middle parts being 8 % and 14 % lower than those from the bottom and top parts, respectively.

iii. Even though the shear strength varies with height, no difference was determined for the middle and the bottom parts as well as for the top and the bottom parts, respectively. A comparison between the top and the middle parts however, showed to be statistically significant. This difference (in terms of the mean shear strength values) was observed to be 12 %.

iv. Variation in the shear and compressive strength parallel to the grain along the height of Gmelina as obtained in this study, ranged between 11 % and 14 %, and was the same as was obtained between the trees for the tensile and compressive strength parallel to the grain. The only exception was the compressive strength perpendicular to the grain whose variation between the trees was obtained to be 26 %.

v. The shear strength, bending strength, MoE in compression parallel to the grain and density did not vary between the trees considered in this study, whereas the other material properties did vary.

vi. The density variation within and between Gmelina trees is constant at 2 %. The variation along the height is a slight reduction with increase in height of the trees. No statistical significance was determined for the top and middle parts of the trees. However, a comparison between the other parts showed to be statistically significant. Considering the mean density values, the variation between the bottom and the middle parts and that between the top and the bottom parts are respectively 2 % and 3 %. This variation in the density as seen, does not influence the variation in the mechanical properties. This is because the variation pattern exhibited by the density data (slight reduction from the bottom to the top) is quite different from that exhibited by the mechanical properties (compressive strength parallel to the grain and the shear strength) which varied along the height. The variation pattern observed for the density in this study, agrees with that reported for Gmelina in [11].

vii. The variation in the MoE in bending between the trees is 17 % and agrees with 16.9 % reported in the literature for Blackwood [7].

viii. The mechanical properties of Gmelina as considered in this study (except for the shear and compressive strengths parallel to the grain which vary along its height), are not location dependent as is the case with some wood species. The

https://doi.org/10.52202/069179-0098

overall variation (combined variation both within and between the trees) of Gmelina is less than is obtainable for spruce (*Picea abies*) and pine (*Pinus sylvestri*) grown in Europe. The nature of the variation along the height of Gmelina would be useful in aiding end users on how to optimally and profitable apply Gmelina trunks for practical use.

5 CONCLUSION

This study has discussed the variation in the material properties between and within three plantation - grown *Gmelina arborea* trees obtained from Akure, in southwestern Nigeria, thus contributing to existing research efforts on the characterization and use of Gmelina as a construction material. Having elaborated on how the various material properties vary within and between the trees that were investigated, the study has presented information that would be useful in facilitating an efficient and optimal use of the material for effective applications. Further areas of research on Gmelina as a structural material are its long-term behaviour under load and temperature, determination of applicable modification and deformation factors for the timber, and similar investigations using materials from different sites to complement the results reported both in the current as well as previous studies.

AKNOWLEDGEMENT

The authors would like to thank the Petroleum Technology Development Fund (PTDF) and the German Academic Exchange Service (DAAD) for sponsoring this research.

REFERENCES

[1] J. C. Onyekwelu, “Silviculture, productivity and propects of afforestation with Gmelina arborea in Nigeria.,” *Niger. J. For.*, vol. 35, no. 1, pp. 66–80, 2005.

[2] J. A. Espinoza, “Within-tree density gradients in Gmelina arborea in Venezuela,” *New For.*, vol. 28, no. 2–3, pp. 309–317, 2004.

[3] C. O. Ataguba, C. Enwelu, W. Aderibigbe, and E. . Okiwe, “A comparative study of some mechanical properties of Gmelina arborea, Parkia biglobosa and prosopis africana timbers for structural use,” *International Journal of Technical Research and Applications*, vol. 3, no. 3, pp. 320–324, 2015.

[4] S. E. Iwuoha, W. Seim, and J. C. Onyekwelu, “Mechanical properties of Gmelina arborea for engineering design,” *Constr. Build. Mater.*, vol. 288, p. 123123, 2021.

[5] EN 408:2010+A1:2012, “Timber structures-Structural timber and glued laminated timber-Determination of some physical and mechanical properties,” 2012.

[6] DIN 52188, “Bestimmung der Zugfestigkeit parallel zur Faser,” 1979.

[7] J. S. Machado *et al.*, “Variation of wood density and mechanical properties of blackwood (Acacia melanoxylon R. Br.),” *Mater. Des.*, vol. 56, no. April, pp. 975–980, 2014.

[8] E. Topaloglu and E. Erisir, “Longitudinal variation in selected wood properties of oriental beech and caucasian fir,” *Maderas Cienc. y Tecnol.*, vol. 20, no. 3, pp. 403–416, 2018.

[9] B. J. Zobel and J. P. van Buijtenen, *Wood Variation, Its causes and control*, vol. 1. Berlin: Springer Verlag, 1989.

[10] H. . Desch and J. . Dinwoodie, *Timber Structures, Properties, Conversion and Use*, 7th ed., no. c. Macmillan Press Ltd, 1996.

[11] A. F. . Lamb, “Fast growing timber trees of the lowland tropics,” *Commonw. For. Inst.*, vol. 1, 1968.

[12] M. Kiaei and M. Farsi, “Vertical variation of density, flexural strength and stiffness of Persian silk wood,” *Madera y Bosques*, vol. 22, no. 1, pp. 169–175, 2016.

[13] M. J. Blanca, R. Alarcón, J. Arnau, R. Bono, and R. Bendayan, “Non-normal data: Is ANOVA still a valid option?,” *Psicothema*, vol. 29, no. 4, pp. 552–557, 2017.

[14] J. S. Machado and H. P. Cruz, “Within stem variation of Maritime Pine timber mechanichal properties,” *Holz als Roh - und Werkst.*, vol. 63, no. 2, pp. 154–159, 2005.

World Conference on Timber Engineering Oslo 2023

IN-GRADE CLT FROM UNGRADED PINUS RADIATA BOARDS.

Paolo Lavisci [1], Marco Molinari [2] and Michele Brunetti [3]

ABSTRACT: Within the feasibility analysis for a Cross Laminated Timber (CLT) plant, the possibility to produce in-grade panels from boards that were not strength-graded according to the applicable standard was demonstrated by tests on panels produced in industrial conditions. The "cross-lamination effect" that explains this result was observed, and an innovative CLT lay-up with inner boards at 45deg angles was tested for the first time on Pinus Radiata. A set of scans and sorting feedback information, executed by Microtec on a sub-sample of the boards, provided a very useful insight and allowed significant resource optimization, particularly in the case of knotty boards. The comparison with a benchmark of C24 Spruce CLT, produced and tested in identical conditions, showed that higher in-plane shear resistance and modulus were achievable with ungraded Radiata Pine; this is a desirable performance for mid-rise construction (buildings of at least 4-storey high), which is a growing market trend, able to generate more value for the fraction of this fast-grown plantation timber which is currently not meeting the stud framing market specifications.

KEYWORDS: Ungraded boards, CLT, Radiata Pine, supply chain resilience

1 INTRODUCTION

Cross Laminated Timber (CLT) is changing the way architects and engineers look at wood construction systems as a viable alternative to concrete and steel in mid-rise construction, and beyond. Different countries have different definitions and regulations, and in Australia "mid-rise" means buildings with 25m maximum effective height (i.e. 4-9 storeys), but some projects have already successfully been built that exceed this height limit, through a specific "Performance Solution" addressing all the design specifications. Therefore, CLT is increasingly being selected by specifiers for several reasons including safer and quicker installation, lighter weight resulting in lower requirement for foundations (and/or consolidation of existing structures in vertical extensions of buildings), excellent sustainability credentials, wellness and comfort and, last but not least, cost-efficiency when the projects are well optimized for timber construction. Consistently with its mandate, Forest and Wood Products Australia (FWPA) has coordinated a number of initiatives in this field, including some R&D projects with industry stakeholders, one of which is described here.

Radiata Pine plantations are the major source of Australian structural products and therefore, when a local Company started considering the possibility to invest in a CLT plant, it was decided to run a feasibility analysis which included a research on the mechanical properties that might be obtained from their wood resources. Information is disclosed in this paper with some restrictions, consistently with the confidentiality agreements that the authors signed with the Company.

Machine-Graded Pine (MGP) was introduced in 1996 by Pine Australia (now Plantation Timber Association Australia), following an extensive, nationwide in-grade testing program of Australian Pine (radiata pine, pinaster pine, slash pine and Caribbean pine), undertaken by CSIRO and State Forests of NSW. The MGP grades are the result of a substantial research and development program by the pine industry to ensure that accurate and reliable design properties are available for structural pine timber in Australia, through standardized test methods [1]. The benefits of increased reliability for MGP products are not only based on MGP having more accurate information on the grade proper-ties, but also on the fact that all mills producing MGP are subject to stringent third-party auditing. This assesses appropriate machine grading and monitors property and other quality control procedures to ensure the validity and consistency of the MGP design properties. Therefore, MGP10 and MGP12 grades are currently the market standard for structural timber, and ungraded boards are not used by the frame & truss manufacturing industry that supplies the largest part of the low-rise construction market (detached houses, townhouses and multi-residential apartment blocks up to 3-storey). As a consequence, at the state of the art it was difficult to imagine that a structural product like CLT, which targets the mid-rise market, would not use MGP graded boards.

But to explore this possibility, which was considered potentially very significant for the optimization of the

[1] Paolo Lavisci, FWPA, Australia, paolo.lavisci@woodsolutions.com.au
[2] Marco Molinari, Universita' degli Studi di Trento; marco.molinari@unitn.it
[3] Michele Brunetti, CNR-IBE, Istituto per la BioEconomia; michele.brunetti@cnr.it

https://doi.org/10.52202/069179-0099

project's feasibility, we suggested to perform research with the aim to understand and quantify the potential benefits of innovative grading and/or layup strategies, possibly by using ungraded boards and deriving the characteristic values for structural engineering only from tests performed on the CLT panels. There are a few basic reasons why this scope of works was relevant for the Company:

- Even using only a fraction of their MGP10 and MGP12 boards for a new product, which is also potentially competing with frame & truss elements, would distract them from the established client base, therefore creating a major commercial risk;
- The MGP grading system is finalized to selecting boards for use as slender elements where buckling plays a significant role. Therefore, a single and isolated defect such as a knots or wane can already downgrade a whole board which, only a few centimetres away from that defect, may have very good mechanical qualities. The state-of-the-art solution to this problem (finger-jointing) is costly and may create a bottleneck in a CLT production;
- The effect of lamination, and even more of cross lamination, is known to "dilute" the influence of defects and therefore provide better performances than those measured on the single boards [2]. Bringing it within the grading and testing procedures may allow to optimize the yield from a fiber resource where knots and wane are relatively large (especially with respect to the board widths) like the fast-growing Radiata Pine plantation logs, which are currently considered having lower quality with respect to competing slow-growth logs.

In solid timber grading, the "reverse engineering" concept is sometimes used for in-grade testing to check production or to obtain the values representing the strength/stiffness distribution of available products as the basis for design, e.g. when a batch of ungraded timber needs to be used for a structural purpose. But so far, to our knowledge, this approach has not been applied to obtaining proprietary design values directly from product testing of CLT, instead of calculating them from the grades of the boards that are used to manufacture it. This is particularly strange because CLT is very similar to plywood in its mechanical behaviour: a few decades ago, before veneer grading machines were developed, plywood factories were testing samples from the pro-duction to derive the product's design strengths and stiffness values, as this was the only possibility. But when CLT was developed, producers and researchers were considering it more like solid timber or glulam, than a product with its own logic. Also, testing large amounts of panel samples being quite expensive, the use of available sawn timber grades to calculate the performances of CLT panels was preferred, and embedded into the Euro-pean Technical Approval Guidelines to become a market standard for many years. But this approach has proven to be particularly non-efficient for CLT, where the boards are used mostly in just two dominant stress modes (tensile bending or rolling shear), and cross lamination has a well demonstrated effect on the reduction of both fracture initiation and growth [3, 4].

The recent EN standard for CLT [5], whose drafting and approval took a very long time, has finally introduced the additional possibility to "recalculate" the mechanical properties of the timber layers from full-scale tests on panel samples. This acknowledgement of the applicability of the reverse engineering approach validates the scope and the methodology of this research.

2 MATERIALS AND METHODS

A container of Radiata Pine boards (Table 1), randomly sampled from the production at a sawmill in Australia, was shipped to XlamDolomiti's CLT factory in Italy. A narrow board width, also with respect to board thickness, was purposely chosen to maximize the influence of knots and wane, in a "worst case scenario" approach. The board cross section dimensions shown are net values, as used in the CLT after dressing before bonding.

Table 1: *Grades, sizes and quantities of the Radiata Pine boards used. The letter "U" means "Ungraded", while the letters "A" and "B" refer to two alternative sawing patterns.*

Grade	Width (mm)	Thickness (mm)	Length (mm)	Quantity (pcs)
MGP12	90	30	3300	128
MGP12	90	30	2400	128
MGP10	90	30	3300	256
MGP10	90	30	2400	256
U-A	90	30	3300	384
U-A	90	30	2400	384
U-B	90	30	3300	768
U-B	90	30	2400	768

As a first step, a random subsample of the rough sawn boards (4 packs = 512 boards) was sent to Microtec for a full non-destructive scanning, coding and grading with their GoldenEye 706 and Viscan equipment (which has a well-established correlation with MGP grades for plantation-grown Radiata Pine from the same area), in order to collect data enabling a subsequent, targeted panel layup optimization and the interpretation of failure modes (if needed). Then the boards were sent back to XlamDolomiti, for processing in their standard mill conditions, following the cycle described in the European Technical Approval (1-component PU adhesive, no edge bonding, top and side pressure).

A preliminary batch of 4x 90mm/3-layers panels was produced to test all the settings and perform the routine controls of bonding quality, then 14x 150mm/5-layers panels were produced for the mechanical testing, all in a 3300x2400mm size (LxW). A higher amount of rather small panels was preferred to a lower number of bigger panels to keep the boards' positions and alignment more easily under control. Table 2 describes the panel types and the tests which were planned on the resulting CLT samples.

The CLT panel layup is kept confidential, being part of the Company's intellectual property, but the "Purpose"

https://doi.org/10.52202/069179-0099

column in Table 2 clearly describes the logic that was followed in selecting the ungraded boards, based on the data provided by Microtec. The 45deg crossbands layup was inspired by the positive experiences reported for slow-growth Nordic Pine [6], therefore it was decided to replicate them with a fast-growth pine species. MGP12 boards were not used in the CLT manufacturing.
The samples in Table 2 were cut at XlamDolomiti and sent for testing at Universita' degli Studi di Trento, after the routine controls on bonding quality.

Table 2: *Grades, sizes and quantities of the Radiata Pine boards used. The letter "U" means "Ungraded", while the letters "A" and "B" refer to two alternative sawing patterns.*

Type	Purpose of the type's lay-up	BL	BG	DC	GT
Spruce	European benchmark	4	2	-	4
MGP10	Structural grade reference	4	2	4	4
U-A	Use the best ungraded boards	4	2	4	4
U-B_a	Understand the lower limit	4	2	4	4
U-B_b	Improve with respect to U-B_a	4	2	-	4
U-B_{45}	Try the 45deg crossbands	2	2	-	4

Table 3: *Explanation of the test codes used in Table 2.*

Code	Test type
BL	Four-point **Bending** tests perpendicular to the plan to failure on 450x3150x150mm CLT panels, according to EN 16351 Annex C2.1 for bending MOR and MOE (**Local**)
BG	Four-point **Bending** tests perpendicular to the plan to failure on 450x1950x150mm CLT panels, according to EN 16351 Annex C2.3 for rolling shear strength, rolling shear modulus and **Global** bending modulus
DC	In-plane shear tests with **Diagonal Compression** for in-plane shear strength and in-plane shear modulus, according to [7]
GT	Rolling shear tests, according to EN 16351 Annex C2.2 (**Guillotine Test**)

The test series is very similar to what is required for product development and/or approval of CLT panels, with just a reduced number of samples because the aim of the research was not obtaining statistically significant characteristic values for design, but just a proof of concept. Moreover, the test panels and then the samples were accurately assembled, based on the data provided by Microtec, to reflect the purposes described in Table 2 and to allow for the interpretation of any possible unclear fracture patterns.
In all the tests, the load was applied by means of an MTS 244.51 actuator with 1000kN capacity and 500mm stoke.

For the bending tests an MTS FT60 controller was used, endowed with 16 +/- 10V acquisition channels: two couples of AEP strain gage displacement transducers were installed and ac-quired directly by the controller. Two 10 mm instruments acquired the relative displacement of the central joke, whilst two 100 mm jokes acquired the global displacements in the central position. Instruments were applied at both sides of the panel, in the central point, thus allowing to correct effects of any unwanted torsion deriving by alignment errors and/or specimen asymmetry.
In-plane shear tests were carried out according to [7]. This method induces shear failure by axially loading a square CLT panel at two opposite corners, like shear tests carried out on masonry, and it is a good alternative to a four-point bending test with in-plane oriented panels, where unwanted bending failure often arises. This test can single out the actual type of shear failure, either torsional on the glued surfaces or perpendicular to the grain. The set-up was adapted to the reduced size of the specimens, therefore the size of the plates on which the loads were applied were reduced proportionally to the expected, reduced failure load, to 150mm length. The same MTS 244.51 hydraulic actuator was controlled by an MTS Test Star 2 system. The actuator was clamped at the top and hinged at the bottom edge, and the panel was resting on the 150mm long steel plates, leaving a "free" core failure area a*a equal to 240*240mm wide. To acquire the panel deformation, two couples of jokes, each supporting a displacement transducer, were hinged at the corners of the core. As for previous tests, AEP 10 mm stroke, strain gage linear displacement transducers were used. For panels with 45deg crossbands this in-plane shear test was not performed because it is meaningless: with 5-layer panels, there's always at least one layer with internal boards parallel to the load direction, therefore a very high load is reached, with local crushing in correspondence to the load and rest plates. Moreover, the boards loaded parallel to the grain are present only on one side, so there is a geometrical asymmetry leading to a lateral bending during test, which is evident and dangerous (during testing) since the specimen instability can be reached.
Rolling shear tests were carried out according to EN 16351 by removing two external layers from the original 5 layers, leaving a 90 mm thick, 3 layers panel. The 361 mm length of the panel was chosen in order to obtain the necessary inclination of the acting force resultant: arctan(90/361) = 14deg. The outer layers are aligned to the direction of the load, which was applied by two stiff steel plates 30 mm wide, i.e. as wide as the outer layers. The upper plate was centred above the lower hinge of the actuator. The controller, acquisition cards and transducers were the same used in the bending tests. The transducers were aligned in the load direction and acquired the relative displacement of the mid-planes of the outer layers.
Figures 1-3 show some of the panels and test setups:

- The panels with diagonal crossbands
- The 4-point bending setup, and
- The planar shear tests setup.

https://doi.org/10.52202/069179-0099

3 RESULTS

The results from the board scanning are summarized in Table 4, and those from the tests on CLT panels are summarized in Table 5.
From the data in Table 4, it is quite clear that also the ungraded boards have rather good strength and stiffness properties, and in particular:

- "A" has a predicted MOR/MOE profile which falls in between MGP10 and MGP12,
- "B" is lower in density and predicted MOR/MOE, while it is higher in knottiness.

Table 4: *Values of density, knottiness, MOR and MOE of the board types. Each value is the average of 128 boards, the number between brackets is its Coefficient of Variation. The knottiness is an index developed by Microtec for their grading algorithms, the MOR is the predicted lowest 5th percentile bending strength of the board, and the 3 different MOEs are, respectively: measured by a dynamic tool (Viscan), predicted from knottiness and density, and the average of the previous two. The table is split in 2 parts, with the same left column.*

Board Type	**Density** kg/m3	**Knottiness** -	**MOR** MPa
MGP12	547 (8%)	1,930 (50%)	39.9 (16%)
MGP10	499 (10%)	2,965 (46%)	29.6 (33%)
A	504 (8%)	2,402 (50%)	34.7 (24%)
B	483 (7%)	3,484 (34%)	24.6 (33%)

Board Type	**MOE_{dyn}** MPa	**MOE_{pred}** MPa	**MOE_{avg}** MPa
MGP12	14,251 (14%)	11,036 (13%)	13,538 (14%)
MGP10	10,852 (26%)	8,552 (25%)	10,309 (26%)
A	12,788 (17%)	9,967 (16%)	12,149 (17%)
B	9,488 (18%)	7,555 (17%)	9,014 (18%)

The main result of the tests on CLT is that with ungraded Radiata Pine boards randomly selected from the current sawmill production output (which is additional to the MGP grades output) it was possible to obtain panels whose mechanical performances matched, and in some case even exceeded, those of both the reference Radiata Pine panels made with MGP10 boards, and of the Spruce panel (which provided a significant bench-mark because it was made of boards with a very good quality).
Moreover, the effect of the two different sawing patterns ("A" and "B") was clearly visible from the tests, as was the result of using crossbands layered at 45deg, consistently with previous findings [6]. The improvement sought from the U-Bb sample by optimizing the cost-effective layup adopted in U-Ba was indeed obtained, validating the underlying hypothesis and the use of the scanning results to inform the selection of the boards with criteria that differ from the MGP grading rules. The U-B boards being very knotty, they would have a low yield if graded according to MGP10 rules, therefore discouraging the use of this sawing pattern for the frame & truss market, but they can become a valuable resource when used correctly for CLT, where an optimized layup results in good panel performances.

Table 5: *Average values (MPa) of the mechanical parameters measured on the CLT panels. The table is split in 2 parts, with the same left column. Note 1 - Timber boards on the single panel used as benchmark were of very good quality, with no significant defects, much better than an average C24 grade. Note 2 - Grs is computed based on the reduced area Ars. Note 3 - Average published data, from [7].*

Test	**Spruce**	**MGP10**	**U-A**
Bending strength (MOR)	38.40 (1)	29.29	33.51
Bending modulus (MOE)	11,070	8,359	10,565
Global bending modulus (E_{global})	9,055	7,392	9,133
Rolling shear strength (bending)	1.48	2.40	2.48
Rolling shear modulus (bending) (2)	-	65.4	65.5
In-plane shear strength	4.67 (3)	8.22	8.13
In-plane shear modulus	543 (3)	944	730
Rolling shear strength (guillotine)	1.36	2.18	2.26
Rolling shear modulus (guillotine)	72.7	170	208

Test	**$U\text{-}B_a$**	**$U\text{-}B_b$**	**$U\text{-}B_{45}$**
Bending strength (MOR)	24.65	31.28	33.31
Bending modulus (MOE)	7,169	8,813	9,379
Global bending modulus (E_{global})	6,594	8,419	8,128
Rolling shear strength (bending)	2.15	1.95	2.33
Rolling shear modulus (bending) (2)	7.4	-	65.9
In-plane shear strength	7.99	-	-
In-plane shear modulus	688	-	-
Rolling shear strength (guillotine)	2.34	2.40	3.16
Rolling shear modulus (guillotine)	198	164	277

The confidentiality agreements in place do not allow for further disclosure on the results.

https://doi.org/10.52202/069179-0099

4 DISCUSSION

When CLT panels are used as floor slabs, the bending stiffness is typically more important than the shear stiffness in reducing the structural deformability that often governs design; indeed, higher shear resistance is important for short span slabs with heavy loads, but this is rarely the case in residential design.

It is interesting to compare the estimate of the rolling shear parameters using bending or guillotine tests: the resistance is similar in both tests, but the guillotine test offers a simpler way to measure shear stiffness, and it can be easily carried out also to evaluate the bonding quality during production, therefore leading to higher number of measurements and providing a statistically more reliable information. Modelling of Radiata Pine CLT [4] have shown a 40% reduction of the critical load (associated with rolling shear failure) when edge-gluing is not considered in the manufacturing process, like in the present case. Therefore (and from some of the author's unpublished experiences), we can certainly expect that this would apply also to the use of the U-A and U-B panel types described here. Similar results were found by [8] for Pinus Taeda from Brazil and [9] for Southern Pine from the USA.

Other factors which were not addressed by this research, but will provide further optimization opportunities, are the variation of the lamella thickness and, if edge bonding is not considered, the aspect ratio of the boards (thickness divided by width). Specimens with 35mm and 20mm thick laminations were studied in [10] to evaluate the influence of this parameter on the rolling shear strength. The test results indicated that the recommended characteristic rolling shear strength values of CLT products in Europe and Canada might be over-conservative and it might be more efficient to specify different rolling shear strength values for CLT with different lamination thickness.

Lower grade lumber with a higher percentage of knots was recommended in [11] for the crossbands, which are mainly responsible for resisting shear stresses. The authors found that using the shear analogy method to interpret their results led to underestimations of rolling shear strength, especially in the case of CLT specimens containing knots. Clearly, also within this research, knottiness has proven to be a positive factor for the stiffness of crossbands, which mostly govern panel shear performances in bending, but close attention should be paid in the panel manufacturing to avoid excessive knots (and especially excessive wane) at the upper and lower layers of the panel, since the efficiency of some types of mechanical connections could be negatively affected; this certainly re-quires further research.

It is also worthwhile to mention the increased bending resistance of U-B45 panels with respect to their counterparts: simply changing the internal board inclination the rolling shear resistance increases by 50 % and – more importantly – the bending resistance and stiffness increase by 30%, thus deserving further research for a proper evaluation of the industrial feasibility.

The assessment of the mechanical properties of CLT panels based on four-point bending tests and guillotine tests, instead of the calculation based on the board grades, is a very promising opportunity for both the producers and the specifiers because it may result in getting "more from less" in terms of performances, and a higher product reliability, therefore making the whole production, design, and construction process a more sustainable one. This assessment approach, finally embedded into the European standard, can be rather easily applied in mill conditions due to the typical availability of offcuts from the CNC machining of large panels to produce the different elements in a building. Different analytical theories have been implemented and were used in [9] to estimate stiffness and strength properties under loads perpendicular or parallel to the principal plane of CLT panels from laboratory tests, predicting the associated deformation and failure mechanisms and assessing the reliability of the estimated properties with respect to the expected design values (and in terms of consistency among specimens with different layer configurations); the bending response is on average well represented in the theories currently used, for the two cases of loading, while for loads perpendicular to the plane the characteristic rolling shear strength appears to have a significant variability among the different layups, and for loads in plane a combined rolling and torsional shear failure criterion would provide more consistent results with respect to a less rigorous approach. Again, further experiences will provide better calibrations for the foreseen industrial quality control and in-grade testing routines.

5 CONCLUSIONS

The possibility to produce in-grade CLT panels from boards that were not strength-graded according to the applicable standard was demonstrated. The "cross-lamination effect" that explains this result was observed also for fast-grown Radiata Pine plantation logs, and particularly for sawing patterns that are not optimized for obtaining MGP grades and are therefore more cost efficient of MGP-specific patterns.

A set of scans and sorting feedback, executed by Microtec on a sub-sample of the boards, provided a very useful insight and suggested that significant resource optimization is possible, particularly for very knotty boards, leading to CLT panels which com-pared well also with a benchmark of C24 Spruce CLT which was produced and tested in identical conditions, showing that higher in-plane shear resistance and modulus were also achievable with ungraded Radiata Pine, a desirable performance for mid-rise which is a growing market trend.

These results will contribute to generating more value from a significant fraction of the Radiata Pine fibre resource which is currently not meeting the stud framing specifications and the MGP grading rules, therefore enhancing the resilience of the Australia supply chain.

https://doi.org/10.52202/069179-0099

Figure 1 *– The U-B45 panels (diagonal crossbands).*

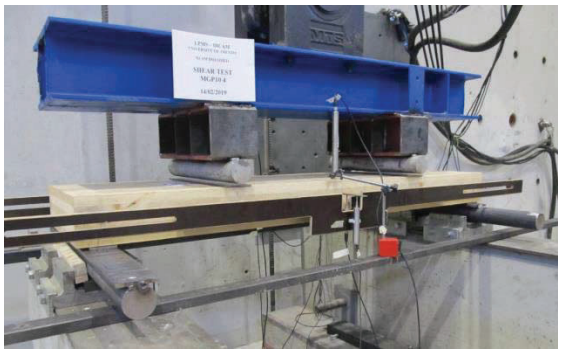

Figure 2 *– The 4-point bending tests setup.*

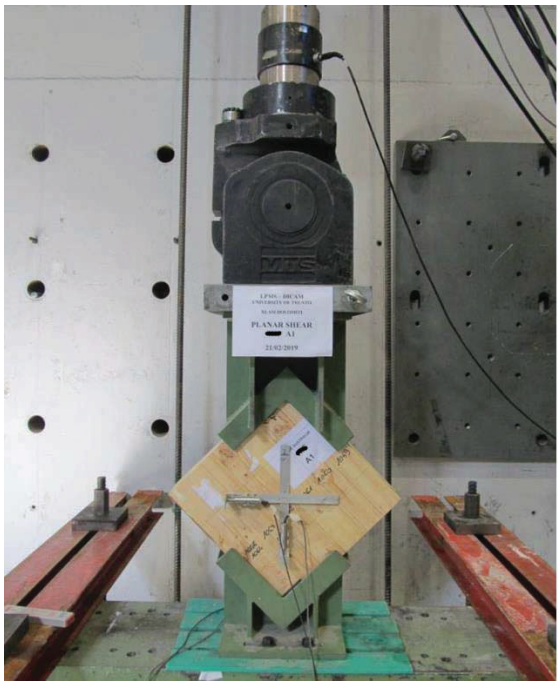

Figure 3 *– The planar shear tests setup.*

ACKNOWLEDGEMENT

Significant technical support to this research was offered from, and performed by, https://www.xlamdolomiti.it/ and https://microtec.eu/

REFERENCES

[1] AS 3519 Timber Machine Proof Grading.
[2] Blass, H.J.; Fellmoser, P. Design of solid wood panels with cross layers. Proceedings of the World Conference of Timber Engineering (WCTE) 2004, Lahti, Finland
[3] Naim, J.A. Predicting layer cracks in cross-laminated timber with evaluations of strategies for suppressing them. European Journal of Wood and Wood Products 2019, 77(10):1-15
[4] Saavedra Flores, E.I.; Saavedra K.; Hinojosa, J.; Chandra, Y.; Dasd, R. Multi-scale modelling of rolling shear failure in cross-laminated timber structures by homogenisation and cohesive zone models. International Journal of Solids and Structures 2016, Volume 81, Pages 219-232
[5] EN 16351. Timber structures. Cross laminated timber. Requirements.
[6] Buch, D.; Hagman, O. Mechanics of diagonally-layered cross laminated timber. Proceedings of the World Conference of Timber Engineering (WCTE) 2018, Seoul, South Korea
[7] Andreolli, M.; Rigamonti, M.; Tomasi, R. Diagonal Compression Test on Cross Laminated Timber Panels"; Proceedings of the World Conference of Timber Engineering (WCTE) 2014, Quebec City, Canada
[8] Bello Mussi Alencar, J.; Daniel de Melo Moura, J. Mechanical Behavior of Cross-Laminated Timber Panels Made of Low-Added-Value Timber. Forest Products Journal 2019, 69 (3): 177–184
[9] Hindman, D. Mechanical Properties of Southern Pine Cross-Laminated Timber. Journal of Materials in Civil Engineering, 2014 27(9):04014251
[10] Li, M. Evaluating rolling shear strength properties of cross-laminated timber by short-span bending tests and modified planar shear tests. Journal of Wood Science 2017 Vol.63 No.4 pp.331-337
[11] Cao, Y.; Street, J.; Lim, H. Analytical and Experimental Evaluation of the Effect of Knots on Rolling Shear Properties of Cross Laminated Timber (CLT). Proceedings of the World Conference of Timber Engineering (WCTE) 2018, Seoul, South Korea
[12] Christovasilis, I.P.; Brunetti, M.; Follesa, M.; Nocetti, M.; Vassallo, D. Evaluation of the mechanical properties of cross laminated timber with elementary beam theories. Construction and Building Materials 2016, Volume 122, Pages 202-213

World Conference on Timber Engineering Oslo 2023

COLLAGE QUALITY OF BRAZILIAN WOODS FOR USE IN GLUED LAMINATED TIMBER BEAMS

Julio Cesar Molina[1], Natália Andrade Bianchi[2], Felipe Dutra Lisboa [3] Nádia Barros Gomes[4]

ABSTRACT: The glued laminated timber industries in Brazil have been looking for alternatives that improve the quality of their products, by choosing the correct wood used in the composition of the structural elements, type of adhesive, as well as by monitoring the quality of the material's manufacturing process. This study evaluated the percentage of delamination and shear strength of glue lines in glulam beams constructed with Brazilian reforestation woods (pine and eucalyptus) and structural adhesives (Cascophen RS 216M and Polyurethane Jowat 686.60). For that, the Brazilian test method [1] based on the [2] was used. To qualify the percentage of failure in the gluing areas, the ImageJ software was used. Complementary microscopy analyzes were used to evaluate the gluing areas. As a result, it was observed that the best bonding quality results were obtained for pine and eucalyptus woods bonded with Cascophen RS 216M adhesive. There were no statistically significant differences between the shear strengths of the glue lines of the cross sections of the tested beams. The wood density and the adhesive viscosity had an influence on the bonding quality of glulam beams. The microscopic analyzes indicated that pine woods have an anatomical structure that allows better bonding quality.

KEYWORDS: Glulam, Delamination, Glue line strength, Image analysis, Microscopy

1 INTRODUCTION

The correct choice of the “specie/adhesive combination” in the manufacture of the glulam elements is fundamental to guarantee the structural quality of the element in service. In the manufacture of glulam elements, different polyurethane structural adhesives and resorcinol-based adhesives are used, as well as different types of Brazilian woods. The most common species of Brazilian reforestation woods are pine and eucalyptus, [9]. In addition, in Brazil there is a great availability of reforestation woods, [10]. There are several factors that can influence the wood glue quality response with structural adhesives. According [3] an important factor is the density of the wood. Denser woods tend to be more difficult for the adhesive to penetrate. The viscosity of the adhesive is another factor to be considered. Higher viscosities result in greater resistance to movement and, consequently, less ability of the adhesive to penetrate the wood. High viscosity values are undesirable due to the difficulty of uniformly distributing the adhesive over the wood. On the other hand, using low viscosity adhesives can result in a hungry glue line or excessive absorption by the wood [3].

The Brazilian test method [1] for evaluating the quality of bonding is based on the delamination and shear strength tests of the glue lines, proposed by the European standard [2] for the external environment.

This study proposed the evaluation of the bonding quality of glulam beams based on the recommendations of the Brazilian test method [1]. In the manufacture of the glulam beams were used two species of reforestation wood (Eucalyptus and Pine) glued with two different types of structural adhesives: one polyurethane and another based on resorcinol. Complementary microscopy and image analysis tests were realized in the evaluation of the bonding regions of the glulam specimens.

2 MATERIALS AND METHOD

The woods used in gluing the glulam beams (dimensions: 50 mm x 100 mm x 1200 mm) were Eucalyptus salligna (C30) and average density equal to 592 kg/m^3 and Pine elliottii (C25), average density equal 447 kg/m^3, without preservative treatment. For gluing the glulam beams, Cascophen RS 216M (bicomponent) and polyurethane Jowapur 686.60 (single component) adhesives were used. The viscosities considered for the adhesives were those indicated by their manufacturers. The viscosity value of Cascophen RS 216M adhesive varied between 500-1000 Pa.s and of Jowat 686.60 polyurethane adhesive between 10200 ± 2500 mPa.s. All tests were carried out at the Materials Properties Laboratory of UNESP in Itapeva,

[1] Julio Cesar Molina, EESC/USP – São Carlos School of Engineering of the University of Sao Paulo, Brazil, julio.molina@usp.br
[2] Natália Andrade Bianchi, FEG - University of Sao Paulo State, Brazil, nataliabianchi95@gmail.com
[3] Felipe Dutra Lisboa, UNESP - University of Sao Paulo State, Brazil, felipe.lisboa@unesp.br
[4] Nádia Barros Gomes, FEG - University of Sao Paulo State, Brazil, nadia.b.gomes@unesp.br

https://doi.org/10.52202/069179-0100

State of São Paulo, Brazil, [4]. Wood characterization tests and tests to evaluate the bonding quality of the four different specie/adhesive combinations were carried out, in this research, as shown schematically in Figure 1.

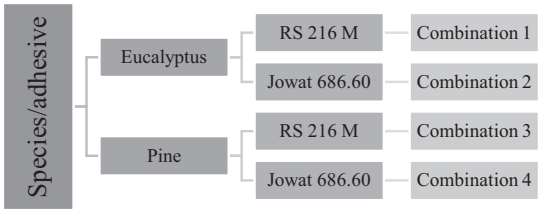

Figure 1: *Specie/adhesive combinations tested in this research*

2.1 GLUING PRESSURE FOR THE BEAMS

The bonding pressures used for the pine and eucalyptus glulam beams with different adhesives were 0.7 MPa (wood density ≤ 0,5 g/cm^3) and 1.2 MPa (wood density > 0,5 g/cm^3), respectively [5]. Pressure values were measured using a torquemeter and the gluing of the beams was made in a floor press (Figure 2). The moisture content of the wooden lamellae at the time of gluing was 12% ± 1% [5]. The glulam beams, after the pressing process, remained at rest for 72 hours for the complete curing of the adhesives and, later, they were machined to remove the specimens for the tests (delamination and shear strength of the glue lines), according to [1].

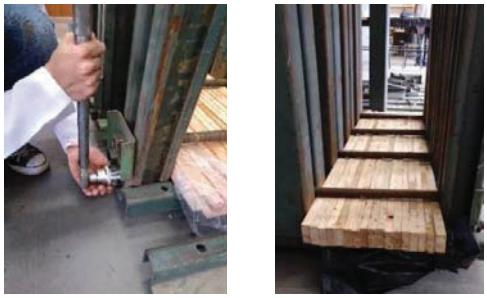

Figure 2: *Pressure control in glulam beams*

2.2 TEST SPECIMENS

All lamellae used in the glulam beams were visually and mechanically graded [5,6]. The lamellae classified in visual Class 1 were positioned at the edge of the cross section (lamellae 1, 2, 4 and 5, Figure 3) while the lamellae classified in visual Class 2 were positioned in the central part of the cross section (lamella 3). Thus, a total of four lines of glue and five lamellae were considered per beam (see Figure 3). The thickness of each lamella was 20 mm [5]. For bonding the glulam beams with the Cascophen RS 216-M adhesive (two-component), the weight considered was 240 g/m^2, applied on a single side of the lamella. A ratio of 10:2 (adhesive:catalyst) was used, i.e., 12 g of adhesive to 2.4 g of catalyst. For the Jowapur 686.60 polyurethane adhesive (one-component), a weight of 200 g/m^2 was used, with the adhesive applied to a single side of the lamella [7].

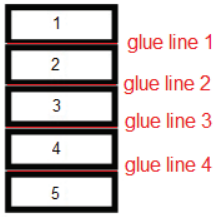

Figure 3: *Cross section of the glulam beams*

The specimens (50 mm x 100 mm x 75 mm) for the delamination and shear strength of the glue lines tests were obtained from the glulam beams, Figure 4. Six glulam beams (B1 – B6) were made for each specie/adhesive combination (total of 24 beams). From each glulam beam, 16 specimens were obtained, 7 for the delamination tests and another 7 for the glue lines shear tests. The two specimens of the edge of the beams were excluded.

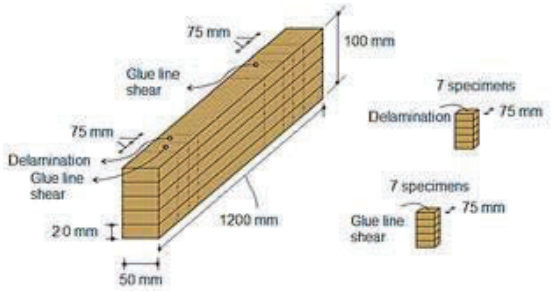

Figure 4: *Specimens for bonding quality tests*

2.3 GLUE LINE SHEAR AS A FUNCION OF POSITION IN THE CROSS SECTION

It was also analyzed whether the glue lines of the glulam beams showed differences of shear strength in relation to the height of the neutral line (LN), as lamellae arrangement shown in Figure 5. Thus, it was verified whether the two lines of glue (2 and 3) from the center of the cross section showed differences with relationship to the two other glue lines (1 and 4) at the edge of the cross section. This analysis was performed with the use of box plots for the values of the pairs of internal glue lines and external, compared to the total number of glue lines in the cross section of each analyzed combination in Figure 1.

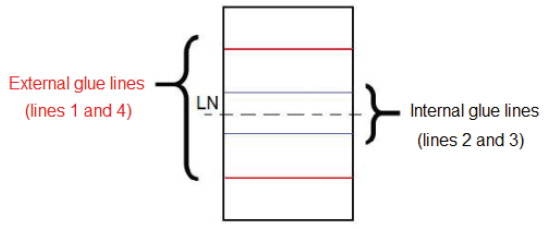

Figure 5: *Internal and external glue lines in the cross section*

https://doi.org/10.52202/069179-0100

2.4 COLLAGE QUALITY TESTS

To evaluate the bonding quality of the specie/adhesive combinations, delamination and shear of the glue lines tests were carried out on the specimens (Figure 4).

2.4.1 Delamination tests

The delamination and shear strength tests of the glue lines were carried out based on the recommendations of the Brazilian test method [1], for external environment, which is based on the European standard [2] and is recommended by the [5]. The delamination specimens initially had their masses determined. At the beginning of the test, the specimens were submerged in water, inside an autoclave, at a temperature of 20 ºC (Figure 6). Then, a vacuum of 80 kPa was applied for 30 minutes. Subsequently, the specimens were subjected to a pressure of 550 kPa for 2 hours. A metallic grid was positioned on the specimens inside the autoclave to ensure that the specimens were submerged in water during the delamination tests. After a single vacuum-pressure cycle, the specimens were placed in a drying kiln at 70 °C. Inside the drying kiln, the air flow had a velocity of 2 m/s and a relative humidity of approximately 8%. During drying, the specimens were spaced 50 mm apart, with the cut cross sections positioned parallel to the air flow. The drying of the specimens continued until the mass of the specimens reached a value between 0% and 10% above the original mass obtained before the autoclave process. The drying process of the specimens in the drying kiln lasted between 19 and 22 hours.

Figure 6: *Details of delamination tests*

The percentage of total delamination of each specimen was obtained by Equation (1) based on Figure 7.

$$D_T = \frac{L_a}{L_a} x100 \qquad (1)$$

Where:
Dt: total delamination, in %;
La: sum of the length of the opening of all glue lines on the faces of the cross section, in mm;
Lt: total length of all glue lines on the faces of the cross section, in mm.

For all delamination tests, the evaluation of the opening of the glue lines was carried out by measuring the glue lines on the front and back faces of the specimens taken from the glulam element, without considering the delamination of the lateral glue lines. The delamination limit considered for coniferous woods, according to the [1] test method was 4% and 6% for dicotyledonous woods. According to [8] the delamination lengths must be measured on the biggest face of the specimen, which generally correspond to the front and back faces of the cross section of the glulam specimen (Figure 7). In addition, according to method A of the [8] standard, the delamination limit after the third pressure and vacuum cycle is 10%.

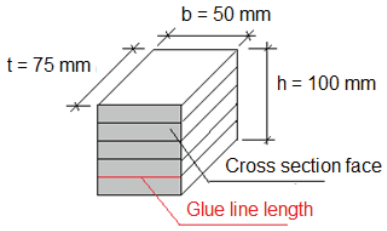

Figure 7: *Cross section of the specimen considered in the evaluation of the percentage of delamination*

2.4.2 Shear tests of glued lines

The shear strength of the glue lines and the percentage of wood failure in the sheared area were also recorded. The shear strength for the glue lines was obtained through Equation (2). The four lines of glue (Figure 3) were broken by shear for each of the specimens tested. For the shear tests, a metallic device coupled to the EMIC testing machine was used (Figure 8). The percentages of rupture, in the gluing regions, after the shear tests of the glue lines, were quantified using the ImageJ software.

$$f_v = \frac{F_{v,max}}{(b.t)} \qquad (2)$$

Where:
f_v: shear strength of the glue line, in MPa;
$F_{v,max}$: maximum shear load applied to the rupture lamella, in N;
b: width of the specimen, in mm (Figure 7);
t: height of the specimen, in mm (Figure 7).

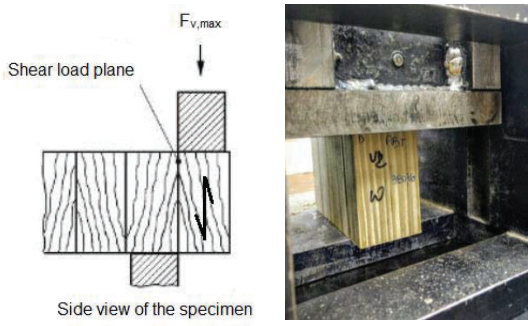

Figure 8: *Glue line shear test details*

https://doi.org/10.52202/069179-0100

2.4.3 Microscopy analysis

The surfaces of the lamellae before bonding were analyzed using optical microscopy. A LEICA M80 optical microscope with lighting was used.

From lamellas with initial dimensions of 5 x 2 x 120 cm, before gluing the glulam beams, samples with dimensions 50 x 20 x 75 mm were taken to analyze the quality of these surfaces. The variations in the thickness of the glue lines of the glulam specimens were also analyzed by microscopy.

2.5 STATISTICAL ANALYSIS OF THE RESULTS

The delamination and shear strength results of the glue lines were analyzed using the Minitab statistical analysis software. Initially, the normality of the data was verified using the Anderson-Darling test.

Subsequently, an analysis of variance was performed based on Student T test with determination of the p-value. It was verified whether there were significant differences between the means obtained for a significant level of 5%.

3 RESULTS AND DISCUSSION

3.1 DELAMINATION TESTS

Tables 1 and 2 show the delamination results of the glulam beams (eucalyptus and pine) glued with RS 216M and Jowapur 686.6 adhesives, calculated by equation (1).

Table 1: *Average delamination percentages of eucalyptus beams glued with Cascophen RS 216M and Jowapur 686.60 adhesives.*

Beams	Combination 1 (%)	Combination 2 (%)
B1	0.00	6.78
B2	0.42	7.44
B3	1.37	6.95
B4	1.23	6.70
B5	0.00	8.50
B6	0.78	6.91
Average	0.63	7.21

Note: an average of 7 specimens was considered for each glulam beam

Table 2: *Average delamination percentages of pine beams glued with Cascophen RS 216M and Jowapur 686.60 adhesives.*

Beams	Combination 3 (%)	Combination 4 (%)
B1	2.49	0.30
B2	2.40	3.84
B3	2.13	7.99
B4	2.17	1.79
B5	1.70	2.78
B6	2.12	8.97
Average	2.17	4.28

Note: an average of 7 specimens was considered for each glulam beam

The Cascophen RS 216M adhesive showed good delamination results, both for eucalyptus wood (average percentage lower than the 6% limit) and for pine woods (average percentage lower than the of 4%). The Jowapur 686.60 adhesive showed higher viscosity during application on the lamellae. Higher viscosity for the adhesive associated with higher density wood (eucalyptus) resulted in poor bonding quality.

3.2 GLUED LINE SHEAR TESTS

Tables 3 and 4 present the results of shear strength of the glue lines (Equation 2) and respective percentages of failure in the wood obtained for the glued areas (ImageJ).

Table 3: *Results of shear tests of glue lines of glulam beams with eucalyptus woods.*

Beams	Combination 1		Combination 2	
	$f_{v,m}$ (MPa)	FW (%)	$f_{v,m}$ (MPa)	FW (%)
B1	8.94	96.00	8.33	91.00
B2	8.15	95.00	7.13	92.00
B3	9.13	97.00	6.41	92.00
B4	8.51	95.00	7.51	91.00
B5	8.45	95.00	8.98	92.00
B6	8.21	94.00	5.81	89.00
Average	8.41	95.33	7.02	91.20
$f_{v,k}$	5.99	66.73	5.15	63.84
DP	0.36	0,94	1.08	1.07
CV (%)	4.28	0,99	15.38	1.17

Notes: an average of 7 specimens was considered for each glulam beam. $f_{v,m}$= average value of shear strength of the glue lines of the beams; FW= wood failure (ImageJ); CV= coefficient of variation (DP/mean*100); DP = standard deviation; $f_{v,k}$ = characteristic value of shear strength according to [3].

Table 4: *Results of shear tests of glue lines of glulam beams with pine woods.*

Beams	Combination 3		Combination 4	
	$f_{v,m}$ (MPa)	FW (%)	$f_{v,m}$ (MPa)	FW (%)
B1	7.15	86.00	4.26	79.00
B2	434	83.00	4.06	78.00
B3	6.39	85.00	4.71	80.00
B4	8.64	87.00	5.39	81.00
B5	9.10	88.00	5.73	81.00
B6	6.16	84.00	6.13	82.00
Average	7.18	85.50	4.93	80.20
$f_{v,k}$	4.87	59.85	3.54	56.14
DP	1.60	1.71	0.76	1.34
CV (%)	22.28	2.00	15.41	1.67

Notes: an average of 7 specimens was considered for each glulam beam. $f_{v,m}$= average value of shear strength of the glue lines of the beams; FW= wood failure (ImageJ); CV= coefficient of variation (DP/mean*100); DP = standard deviation; $f_{v,k}$ = characteristic value of shear strength according to [3].

For all specie/adhesive combinations (Figure 1), the failure in the collage area occurred in the wood, indicating good gluing results. The average values of the shear

strengths of the glue lines were higher for the eucalyptus beams glued with the Cascophen RS 216M adhesive (combination 1) when compared to the values obtained for the beams glued with Jowapur 686.60 adhesive (combination 2). However, from a statistical point of view these differences were not significant (p-value equal to $0.08 > \alpha = 0.05$). For the combinations of the glulam beams with pine woods (combinations 3 and 4), the average shear strengths of the glue lines were statistically significant (p-value equal to $0.03 < \alpha = 0.05$).

3.3 GLUE LINE SHEAR AS A FUNCION OF POSITION IN THE CROSS SECTION

The box-plot graphs for the values of the pairs of internal and external glue lines, compared to the number of total glue lines in the cross section of each analyzed combination are show in Figures 9 to 12.

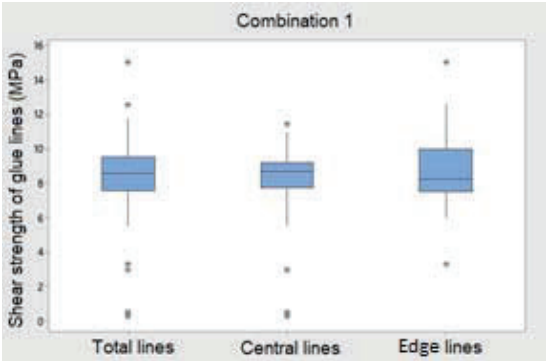

Figure 9: *Box plot of the shear strengths of the glue lines as a function of their location in the cross section (Combination 1).*

For combination 1, the central portion of the graphs showed a median (8.67 MPa) very similar to the glue lines of the extreme regions (8.26 MPa) and the total (8.30 MPa). In addition, the central value showed lower data dispersion (1.46 MPa).

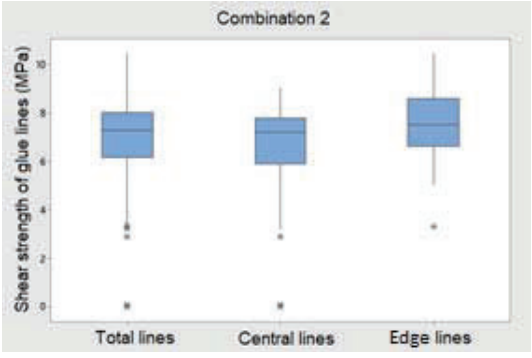

Figure 10: *Box plot of the shear strengths of the glue lines as a function of their location in the cross section. (Combination 2)*

For combination 2, the lines in the central part presented median (7.21 MPa) like the edge lines (7.52 MPa) and total (7.28 MPa). The lines in the central part showed lower data dispersion (1.88 MPa).

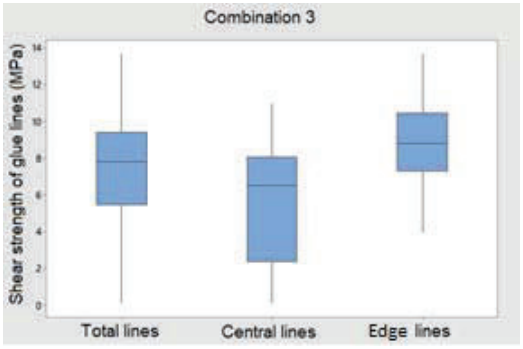

Figure 11: *Box plot of the shear strengths of the glue lines as a function of their location in the cross section. (Combination 3)*

In combination 3 (Figure 12), the median value of the center lines (6.52 MPa) was below the median of the edge lines (8.81 MPa) and total (7.81 MPa). The central lines showed the greatest dispersion (5.67 MPa).

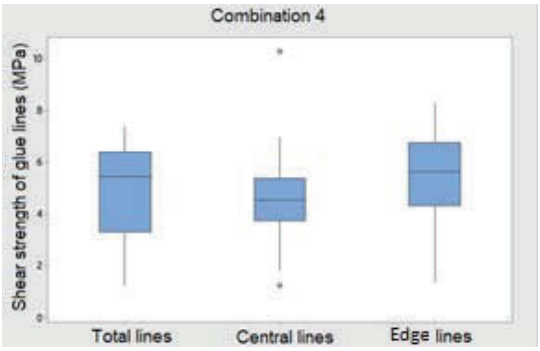

Figure 12: *Box plot of the shear strengths of the glue lines as a function of their location in the cross section. (Combination 4)*

For combination 4, the total glue lines dataset showed a median (5.45 MPa) very close to the edge glue lines (5.62 MPa). However, the central glue lines showed lower data dispersion (1.62 MPa) and median (4.52 MPa) a little lower than the others.

3.4 MICROSCOPIC ANALYSIS

Figure 13 shows the microscopy details of the surfaces of the machined lamellae before bonding.

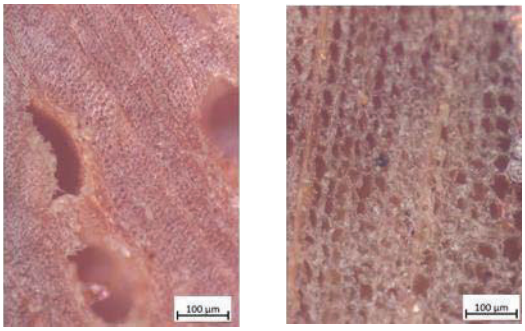

Figure 13: *Microscopy of lamellae surfaces before bonding.*

https://doi.org/10.52202/069179-0100

In the enlarged images of the lamellae surfaces, it was observed that the eucalyptus lamella presented open vessels with irregular shapes. The pine lamella exhibited a more homogeneous surface due to the presence of early and late wood tracheid's distributed throughout the lamella bonding area. The average variation of the thicknesses of the glue lines on the glulam beams are presented in Table 5.

Table 5: *Variation of glue line thickness for different specie/adhesive combinations*

Adhesives	Thickness of glue lines (μm)	
	Eucalyptus	Pinus
RS 216-M	112.8 – 119.9	69.2 – 155.0
Jowapur 686.60	225.1 – 319.0	89.6 – 211.8

When gluing pressure is applied to the glulam element, the adhesive layer acquires a narrow and continuous thickness which should obtain thicknesses between 76 and 152 μm [3]. From the analysis of Table 5, it was observed that, except for glulam elements made with eucalyptus wood and glued with Jowapur 686.60 adhesive (combination 2), all other specie/adhesive combinations (1, 3 and 4) showed variations in the thickness of the glue lines in agreement with the results of the literature [3].

4 CONCLUSIONS

The results obtained from the delamination and shear strength tests of the glue lines indicated that the wood density and the adhesive viscosity are important factors in the gluing of glulam beams.

In general, bonding the wooden lamellas with Cascophen RS 216M adhesive resulted in better bonding quality for the glulam beams. Except for combination 2 (eucalyptus glued with Jowapur 686.60 adhesive), all other combinations presented acceptable delamination limits (< 4% for gluing coniferous wood and < 6% for gluing dicotyledons) according to the Brazilian test method [1].

For all specie/adhesive combinations evaluated, the predominant failure in the specimens' bonding areas, in the shear tests of the glue lines, occurred due to failure in the wood.

In general, the shear strengths (in the glue lines of the glulam specimens made with eucalyptus wood were higher than those obtained for the specimens with pine wood.

There were no statistically significant differences between the shear strengths of the glue lines evaluated in the same cross-section of the specimens. Thus, the number of analyzes in the shear tests of the glue lines can be reduced since the test in the central region of the cross section of the specimen is prioritized, due to the higher concentration of shear stresses.

The microscopic analysis of the surfaces of the wooden lamellae indicated that the pine woods, due to their anatomy, present a greater regularity of the surface with greater porosity provided by the presence of the tracheids of the early and late wood, which facilitates the penetration of the adhesive with respect to eucalyptus woods.

The microscopy analyzes also indicated that, in general, the thickness of the glue lines for the specie/adhesive combinations analyzed agreed with the values in the literature (76 and 152 μm) except for gluing eucalyptus wood with Jowapur 686.60 adhesive.

ACKNOWLEDGEMENT

The authors thank FAPESP (São Paulo State Research Support Foundation, Brazil) for its financial backing of this work. Process number 2017/19974-6.

REFERENCES

[1] ASSOCIAÇÃO BRASILEIRA DE NORMAS TÉCNICAS. NBR 7190-6: projeto de estruturas de madeira – métodos de ensaio para caracterização de madeira lamelada colada estrutural, 2022.

[2] BRITSH STANDARD INSTITUTION. EN 14080: Timber structures – glued Laminated timber and glued solid timber – requirements, 2013.

[3] Juliana J. B., Angelica C. O. C., João P. S. L., Ana P. M. T., Flavia A. P., Bráulio S. O.: Shear strength in the glue line of Eucalyptus sp. and Pinus sp. wood Revista Árvore, 40(6):1109-1117, 2016.

[4] ASSOCIAÇÃO BRASILEIRA DE NORMAS TÉCNICAS. NBR 7190-3: projeto de estruturas de madeira – métodos de ensaio para corpos de prova isentos de defeitos para madeiras de florestas nativas, 2022.

[5] ASSOCIAÇÃO BRASILEIRA DE NORMAS TÉCNICAS. NBR 7190-1: projeto de estruturas de madeira, 2022.

[6] ASSOCIAÇÃO BRASILEIRA DE NORMAS TÉCNICAS. NBR 7190-2: projeto de estruturas de madeira – métodos de ensaio para classificação visual e mecânica de peças estruturais de madeira, 2022.

[7] BIANCHI, N. A. Avaliação da delaminação e da resistência da linha de cola de elementos de MLC com base no projeto de revisão da norma ABNT NBR 7190:2013 considerando madeiras de reflorestamento tratadas com CCA e sem tratamento preservativo. Dissertação (Mestrado em Engenharia Mecânica). Faculdade de Engenharia de Guaratinguetá, Universidade Estadual Paulista. 77f. Guaratinguetá. 2020.

[8] EUROPEAN STANDARD. EN 391: Glued laminated timber – delamination tests of glue lines, 1995.

[9] Soares, L. S. Z. R.; Fraga, I. F.; Paula, L. S.; Arroyo, F. N.; Ruthes, H. C.; Aquino, V. B. M.; Molina, J. C.; Panzera, T. H.; Branco, L. A. M. N.; Chahud, E.; Christoforo, A. L.; Lahr, F. A. R.: Influence of moisture contente on physical and mechanical properties of cedrelinga catenaeformis wood Bioresources, 16(4):6758-6765, 2021.

[10] Karina, A. O., Carolina A. B., Julio C. M.: Physical, chemical and mechanical characterization of Acrocarpus Fraxinifolius cultivated in Sao Paulo. Maderas-Ciencia y Tecnologia, v. 24, 1-8, 2022.

World Conference on Timber Engineering Oslo 2023

NON-PARAMETRIC LOWER CONFIDENCE BOUNDS FOR THE FIFTH PERCENTILE – EN 14358 IN COMPARISON TO A FULLY NON-PARAMETRIC APPROACH

Andreas Weidenhiller[1], Dan Ridley-Ellis[2], Andreas Neumüller[3]

ABSTRACT: In Europe, fifth percentile values are required for the calculation of characteristic values of strength and density. The European standard EN 14358:2016 defined three ways to calculate a 75% lower confidence bound (LCB) for such fifth percentile values, based either on a lognormal parametric approach, on a normal parametric approach or on a non-parametric approach. Using simulated data with different sample sizes and with different underlying distributions, this paper studied the effects of using each of the three approaches of EN 14358. As the third approach in EN 14358 did not seem to be fully non-parametric, the simulation study included, as a fourth approach, a fully non-parametric calculation of the LCB for the fifth percentile. The simulation study confirmed that both non-parametric approaches led to acceptable results for some important distributions, although the non-parametric approach defined in EN 14358 seemed to be more conservative especially for data with a non-normal distribution. The study also confirmed that the use of an incorrect parametric assumption can lead to systematically misleading LCB values for the fifth percentile. The authors recommend replacing the non-parametric approach currently defined in EN 14358 by a fully non-parametric approach. This approach can easily be implemented in a standard.

KEYWORDS: timber strength; fifth percentile; lower confidence bound; simulation study; distribution assumptions

1 INTRODUCTION

Fifth percentile values are frequently required when assessing strength. Such values are also used for assessing the strength of timber, timber products and timber structures. In recent years, the European standard EN 14358 [1] has evolved towards encompassing a number of cases for calculating fifth percentile values.

In its original form from 2006, the standard EN 14358 [2] contained instructions for calculating 75% lower confidence bounds (LCB) for the fifth percentile assuming a lognormal distribution; the purpose was to assess test results for connections and wood-based products. Construction timber was explicitly excluded and was dealt with in a separate standard (EN 384 [3]). The calculation in EN 384 differed from the one in EN 14358 in two important aspects: it was a nonparametric fifth percentile (in contrast to the parametric lognormal distribution assumption in EN 14358), and the fifth percentile itself was reported as the result (in contrast, EN 14358 required to report the 75% LCB). With the revision of both standards in the year 2016 [1, 4], the calculation of the fifth percentiles was completely moved from EN 384 to EN 14358. In the course of this revision, EN 14358 was extended to encompass, in addition to lognormal fifth percentiles, also fifth percentiles for normally distributed quantiles, nonparametric fifth percentile calculation, and mean values of normally distributed quantities, all with a 75% LCB [1].

For the parametric quantities, the standard gives three options for calculation: using an exact formula, using a rational approximation, and using tabled coefficients. For the 75% LCB m_k of the nonparametric fifth percentile $y_{0,5}$, only an approximation formula is given [1]:

$$m_k = y_{0,5}\left(1 - \frac{k_{0,5,0,75}V}{\sqrt{n}}\right) \quad (1)$$

where n is the sample size, V is the coefficient of variation (CoV), and $k_{0,5,0,75}$ is a factor of which the standard claims that it leads to the 75% LCB [1]:

$$k_{0,5,0,75} = \frac{0.49n + 17}{0.28n + 7.1} \quad (2)$$

The authors could not trace the origins of these formulas and the underlying assumptions remained unclear. But the use of the coefficient of variation V in formula (1) makes it clear that some parametric assumptions have to be involved.

On the other hand, there is a well-known method to calculate a fully nonparametric LCB (see, for example [5]). This method is discussed in more detail in section 2.1 below.

[1] Andreas Weidenhiller, Holzforschung Austria, Austria, a.weidenhiller@holzforschung.at
[2] Dan Ridley-Ellis, Edinburgh Napier University, UK, dan.ridley-ellis@napier.ac.uk
[3] Andreas Neumüller, Holzforschung Austria, Austria, a.neumueller@holzforschung.at

https://doi.org/10.52202/069179-0101

How does this method perform in comparison to the approaches defined in EN 14358 [1]?
In the long run (after, say, 1000 repetitions), we would expect that, in 75% of the cases, the true fifth percentile value is above the 75% LCB. This fact was used in the present paper to compare the 75% LCB calculation approaches from EN 14358 [1] and from the fully nonparametric approach with the true fifth percentile values for simulated data with a known distribution.

2 MATERIAL AND METHODS

2.1 FULLY NONPARAMETRIC 75% LOWER CONFIDENCE BOUND FOR THE FIFTH PERCENTILE

To get a non-parametric LCB for the fifth percentile of a sample with n measurement values, we order the measurement values by increasing value, so that x_1 is the smallest value, x_2 the second smallest value, and x_n the largest value. We say that these values have rank 1, 2 and n, respectively.
The probability with which the measurement value x_i with rank i underestimates the fifth percentile can be calculated using the binomial distribution [6].
This probability is independent of the actual values x_i – it only depends on the ranks i. Therefore, one can calculate a table which tells, for each sample size n, the maximum rank i_{max} which fulfils the following condition: The probability that $x_{i_{max}}$ underestimates the fifth percentile is 75% or more. Underestimating the fifth percentile means that we get a conservative estimate of the fifth percentile.
Table 1 lists such values i_{max} (ranks) for selected values of n. Such a table could easily be incorporated in a standard. For intermediate values of n, one would have to pick the smaller rank value (e.g., for $n = 50$, still the value x_1 with rank 1 would have to be picked as the 75% LCB).

Table 1: *Lowest sample size n for which the element with a given rank (counted from the smallest to the largest value) is a nonparametric 75% lower confidence bound (LCB) for the fifth percentile.*

rank	n	rank	n	rank	n
1	28	8	193	15	347
2	53	9	215	16	368
3	78	10	237	17	390
4	102	11	259	18	412
5	125	12	281	19	433
6	148	13	303	20	455
7	170	14	325	21	476

Due to the discrete nature of the binomial distribution, for intermediate values of n, the probability that $x_{i_{max}}$ underestimates the fifth percentile can be quite a bit higher than the 75% which we aimed for – for example, the probability for $n = 40$ is 87%. However, it is also possible to determine interpolated ranks directly at the desired probability of 75%, for example, by using the R package cbinom which provides a continuous analog of the binomial distribution [7].
In the present study, we used the sample sizes $n = 40$, 80, 500, 1000 and 100000 (see 2.3) – for these, the interpolated ranks are 1.488, 3.107, 22.13, 45.77 and 4954, respectively. These ranks were used for the calculation of the fully non-parametric LCB values in the study.

2.2 INCLUDED PROBABILITY DISTRIBUTIONS

We included normal and lognormal distributions, because they are included in EN 14358. For normal distributions, the location parameter does not influence the results, so we chose 420 (required mean density in kg/m³ for C24 in EN 338 [8]) and used CoV values of 5%, 10% and 20%. For the lognormal distribution, the location parameter also changes the shape of the distribution, so we calculated mean strength values corresponding to the requirements for C16, C24 and C35 in EN 338 [8] together with CoV values of 5%, 10% and 20%. A further important class of distributions are truncated normal distributions, because these represent an extreme case of what efficient strength grading can do. Here we took the normal distributions defined above but cut off everything below 310, 350, respectively 390 (required fifth percentile of density in kg/m³ for C16, C24 respectively C35). The calculations on the truncated normal distributions were handled using the R package truncnorm [9].
Regarding normal distributions, it is important to note that those always include negative values (if maybe only with a small probability). Negative values are not realistic in the application and cause the calculation of parametric lognormal LCB values to fail. Therefore, the normal distributions are actually modelled as truncated normal distributions truncated below 1.
The parameterization of the different distributions is listed in Table 2.

2.3 SIMULATION STUDY

We simulated 1000 samples of each of the distributions given in Table 2, for each of the following sample sizes: 40, 80, 500, 1000 and 100000. 40 was chosen as the smallest sample size, because below that, the nonparametric calculation according to EN 14358 may not be used [1]. 100000 was chosen as an "almost infinite" sample size, where we expected the LCB to be almost equal to the sample fifth percentile, and we expected the sample fifth percentile to almost perfectly match the true fifth percentile according to the distribution.

2.4 STATISTICAL ANALYSIS

For each simulated sample, we calculated parametric 75% LCB values for the fifth percentile according to EN 14358 [1] assuming a normal or lognormal distribution. Further, nonparametric LCB values according to EN 14358 [1] and according to the procedure outlined in section 2.1 were calculated.

https://doi.org/10.52202/069179-0101

Table 2: *Parameters for the simulated distributions. mu and sigma describe location and spread. "lower bound" is a parameter for the truncated normal distribution that ensures that no values below the lower bound are included in the distribution. For simulation, this is implemented using accept-reject sampling (see help on rtruncnorm in [6]). Additionally, the fifth percentile of the distribution is given.*

distribution	mu	sigma	lower bound	fifth percentile
normal	420	21	1	385
	420	42	1	351
	420	84	1	282
lognormal	2,85	0,05		15,9
	2,94	0,0998		16,1
	3,1	0,198		16,0
	3,26	0,05		24,0
	3,34	0,0998		23,9
	3,5	0,198		23,9
	3,64	0,05		35,1
	3,72	0,0998		35,0
	3,88	0,198		35,0
truncated normal	420	21	310	385
	420	42	310	353
	420	84	310	329
	420	21	350	386
	420	42	350	365
	420	84	350	361
	420	21	390	396
	420	42	390	395
	420	84	390	397

For each simulated sample and each calculated LCB value, we determined the "true percentile" this LCB value corresponded to according to the distribution by which the sample was generated.
For example, the "true percentile" of 350 in a normal distribution with mean 420 and a CoV of 10% is 4.78. The "true percentile" value 4.78 in this example is lower than five. This means that 350 is a conservative estimate of the fifth percentile of the underlying distribution – in fact, the actual fifth percentile of the underlying distribution is 351.
All calculations were performed using R 4.2.1 [10].

3 RESULTS AND DISCUSSION

In Figure 1, the results of the simulation study were summarised using boxplots. On the vertical axis, for each 75% LCB value, the "true percentile" value in the respective underlying distribution was plotted. The upper end of each box corresponded to the threshold below which we found 75% of the observed values. For the 75% LCB, we would expect 75% of the observed values to be below the target value five, which is indicated by the black horizontal line.
For an optimal 75% LCB, the upper end of the box would be at the target value five, which means that 75% of the calculated values would be conservative estimates of the fifth percentile of the underlying distribution.
If the upper end of the box is above five, the calculated LCB values are too optimistic. If the upper end of the box is far below five, the calculated LCB values are very conservative. If the height of the box is large, the LCB values have a large spread. The ideal situation would be a box with low height with its upper end at or closely below five.
In Figure 1a, the true percentiles for the parametric normal calculation of 75% LCB values according to EN 14358 are shown. When the underlying distribution was normal (leftmost five boxes in Figure 1a), the height of the boxes as well as the distance of the true percentiles to the target value five decreased with increasing sample size n. For $n = 100000$, there were almost no deviations of the true percentile from the target value five. However, for the other underlying distributions in Figure 1a, the heights of the boxes and the distances from the target value five did not decrease. In particular, even for $n = 100000$, the true percentile values could be far away from the target value five. Even if the discrepancies are on the conservative side, it is clear that the parametric normal LCB calculation was misleading when the underlying distribution was not normal.
A similar pattern could be observed for the parametric lognormal calculation of 75% LCB values (Figure 1b). When the underlying distribution was lognormal (central five boxes in Figure 1b), the parametric lognormal calculation was close to optimal. For other underlying distributions, the parametric lognormal LCB calculation was misleading. When the underlying distribution was normal, the upper ends of the boxes were above the target value five, meaning that more than 25% of the LCB values were too optimistic, and this share increased with increasing n. For $n = 1000$, 75% of the LCB values were

https://doi.org/10.52202/069179-0101

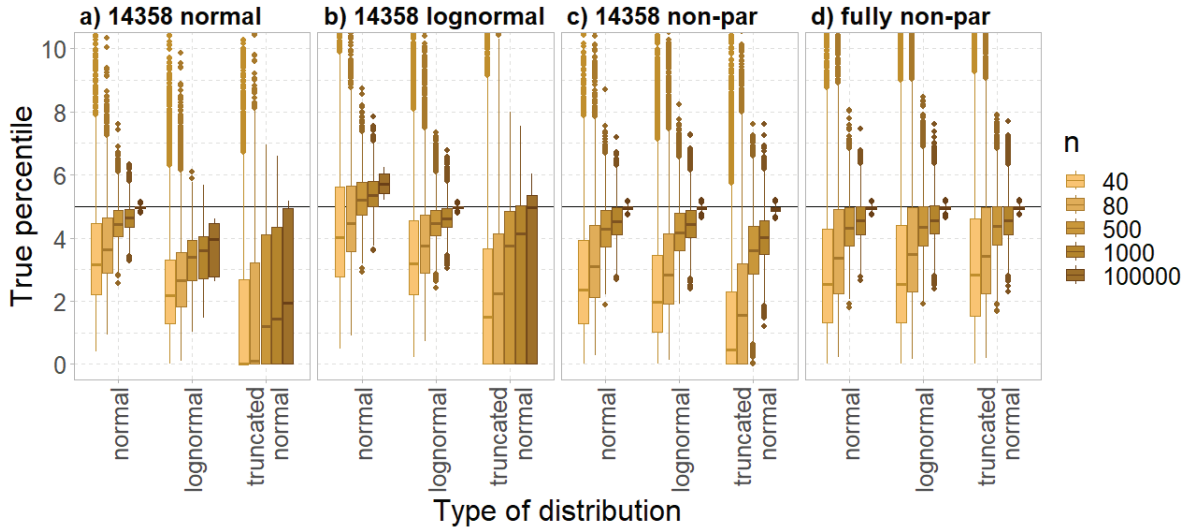

Figure 1: *Boxplots of "true percentiles" (the percentile which a calculated 75% LCB corresponds to in the true underlying distribution) separated by underlying distribution (horizontal axis), sample size n (colour scale) and mode of calculation for the 75% LCB of the sample fifth percentile. a) parametric normal LCB acc. to EN 14358, b) parametric lognormal LCB acc. to EN 14358, c) non-parametric LCB acc. to EN 14358, d) fully non-parametric LCB as outlined in section 2.1. The range of the vertical axis is optimised for the boxes – not all extreme values are included. Each box summarises 1000 runs times the number of different parameterisations for each type of distribution – see also Table 2.*

too optimistic, and for $n = 100000$, all parametric lognormal LCB values were above the target value 5.

Both nonparametric approaches to calculating 75% LCB values (Figure 1c and d) worked for all underlying distributions examined in this study. In all the cases, the height of the boxes as well as the distance of the true percentiles to the target value five decreased with increasing sample size n. For $n = 100000$, there were almost no deviations of the true percentile from the target value five.

In Figure 2, the boxes from Figure 1c and d were rearranged to facilitate comparisons between the two nonparametric approaches to calculating 75% LCB values. When the underlying distribution was normal, the two approaches behaved similarly, with the fully non-parametric LCB values being slightly closer to the target. For an underlying lognormal distribution, and even more for an underlying truncated normal distribution, the fully non-parametric LCB values were distinctly closer to the target fifth percentile.

In Figure 1, the dangers of using a parametric calculation of the 75% LCB can be observed. If the distribution assumptions are not met, there is a risk of obtaining misleading results.

The non-parametric approaches to calculating the 75% LCB seemed to work well for very different types of distributions, at the cost of a higher spread of the values (indicated by greater heights of the boxes in the plots).

To facilitate the inclusion of the fully non-parametric approach in a standard, it would be helpful to have an approximation function for the interpolated ranks which are needed to calculate the fully non-parametric LCB values (section 2.1). Using linear regression, such an approximation was calculated for all sample sizes from 40 to 10000.

The rank r can thus be calculated as

$$r = 0.422 + 0.05\,n - 0.147\,\sqrt{n} \qquad (3)$$

where n is the sample size. The relative errors of this approximation in the range from $n = 40$ to $n = 10000$ are in the range between -0.01% and +0.26%.

4 CONCLUSIONS

In this paper, different approaches to calculating 75% lower confidence bound (LCB) values for the fifth percentile of a sample were compared by means of a simulation study.

Both parametric and non-parametric approaches were included, focusing on approaches defined in the European standard EN 14358 [1]. As the non-parametric calculation of 75% LCB values defined in the standard EN 14358 [1] is not fully non-parametric, a fully non-parametric approach was also included in the study.

Samples of sizes 40, 80, 500, 1000 and 100000 were simulated for the following underlying distributions: normal, lognormal, and truncated normal. For all distributions, different coefficients of variation were included, and for the lognormal and truncated normal distributions, the mean respectively the lower bound parameter were also varied.

The study highlighted the risk of misleading results if a parametric approach to calculating 75% LCB values is used when the assumptions about the type of underlying distribution are not met.

https://doi.org/10.52202/069179-0101

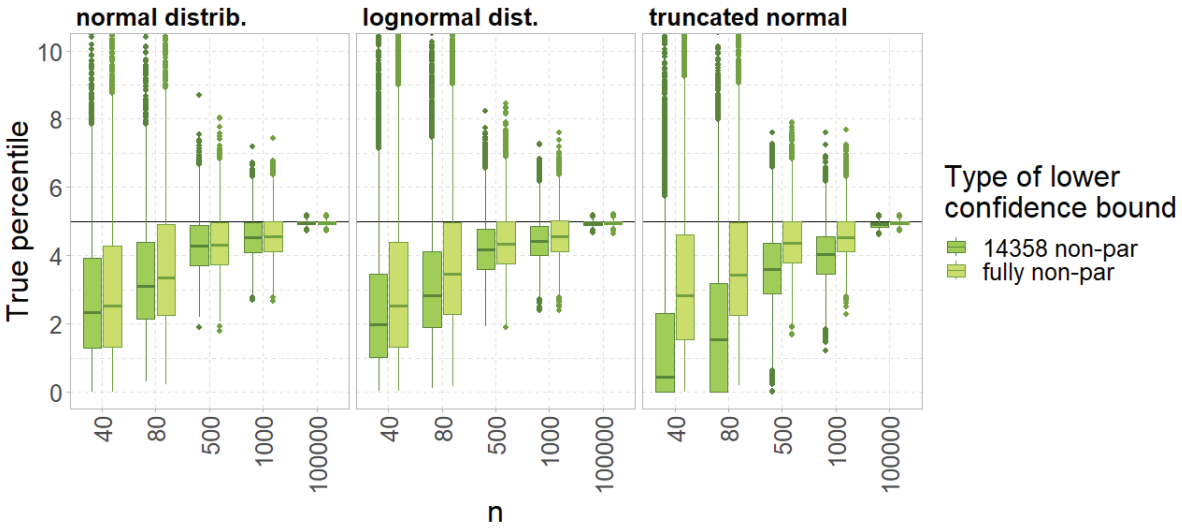

Figure 2: *Rearranged boxplots of "true percentiles" from Figure 1 for the two non-parametric approaches to calculating the 75% LCB ("14358 non-par" and "fully non-par"). For each combination of sample size n and type of distribution, the boxes for the two approaches "14358 non-par" and "fully non-par" are plotted side by side to facilitate pairwise comparison.*

Both non-parametric approaches to calculating 75% LCB values led to acceptable results. However, the non-parametric approach defined in EN 14358 [1] led to 75% LCB values which were more conservative than necessary, especially if the underlying distribution was not normal.

Therefore, the authors recommend revising the standard EN 14358 [1], replacing the current non-parametric approach to calculating 75% LCB values by a fully non-parametric approach.

The fully non-parametric approach is suitable for implementation in the standard. Implementation could be done using tabled values, an approximation formula and/or an exact formula, in a similar manner to the way in which the parametric approaches to calculating 75% LCB values are currently implemented in EN 14358 [1].

ACKNOWLEDGEMENT

Part of the research for this paper has been conducted within the InnoGrading project funded by the Austrian Research Promotion Agency FFG (grant nr. 869170).

REFERENCES

[1] CEN European Committee for Standardization. EN 14358:2016. Timber structures – calculation and verification of characteristic values. Brussels; 2016.

[2] CEN European Committee for Standardization. EN 14358:2006. Timber structures - Calculation of characteristic 5-percentile values and acceptance criteria for a sample. Brussels; 2006.

[3] CEN European Committee for Standardization. EN 384:2004. Structural timber – Determination of characteristic values of mechanical properties and density. Brussels; 2004.

[4] CEN European Committee for Standardization. EN 384:2016. Structural timber – Determination of characteristic values of mechanical properties and density. Brussels; 2016.

[5] David HA, Nagaraja HN. Order Statistics. 3rd ed. New York, NY: John Wiley & Sons 2004.

[6] Nagaraja CH, Nagaraja HN. Distribution-free Approximate Methods for Constructing Confidence Intervals for Quantiles. International Statistical Review 2020; 88(1): 75–100.

[7] Dalthorp D. cbinom: Continuous Analog of a Binomial Distribution; 2021. Available from: URL: https://CRAN.R-project.org/package=cbinom.

[8] CEN European Committee for Standardization. EN 338:2016. Structural timber – Strength classes. Brussels; 2016.

[9] Mersmann O, Trautmann H, Steuer D, Bornkamp B. truncnorm: Truncated Normal Distribution; 2018. Available from: URL: https://CRAN.R-project.org/package=truncnorm.

[10] R Core Team. R: A Language and Environment for Statistical Computing. Vienna, Austria; 2022. Available from: URL: https://www.R-project.org/.

https://doi.org/10.52202/069179-0101

World Conference on Timber Engineering Oslo 2023

NEW CRITERIA FOR VISUAL STRENGTH GRADING OF SAWN TIMBER FROM BIRCH GROWN IN SWEDEN

Ulf Lemke[1], Marie Johansson[2], Rune Ziethén[3], Andreas Briggert[4]

ABSTRACT: Today there is no standard for strength grading and CE-marking sawn timber of Birch grown in Sweden, which makes it impossible to use this material as structural timber. Internationally, there are standards for visual grading of hardwood in several European countries. However, these standards may not be used to classify Birch timber grown in Sweden without having been tested and verified to meet the standard's requirements. In a project (BizWOOD) run by RISE, 600 pieces of sawn birch wood from Sweden is visually graded and strength tested.

The project aims to result in grading rules for birch, either by using international standards or where international standards will be used as references for the identification of defects that will be included in the grading model. This paper summarizes parts of the BizWOOD project and includes 1) description of sampling and timber origin, 2) visual grading according to international standards, 3) strength testing of the material, 4) evaluation of mechanical characteristics, 5) evaluation of grading techniques.

KEYWORDS: Birch (*Betula spp.),* density, bending strength, modulus of elasticity, MOR, MOE, strength grading.

1 INTRODUCTION

The Swedish forests consists of about 18% hardwood and this proportion is increasing as a result of environmental goals [1] and certification criteria [2]. The largest proportion of the deciduous forests are located in Southern Sweden [3], where pure stands of deciduous trees are found. However, the market for sawn timber from deciduous trees is very limited today and for several tree species the market is largely non-existent. A large proportion of the Swedish hardwood that is felled is used as pulpwood or firewood, only a very limited proportion is used as sawn timber in Sweden and a small proportion is exported as logs. The problem is often explained by a Catch-22 within the value chain - no demand leads to no production and no production leads to no demand. The large players in the market find it difficult to rationally handle the relatively small quantities of hardwoods that come out of the market. This means that the hardwood market is dominated by a few larger companies specializing mainly in floor manufacturing. In addition, the market consists of many small sawmills, all of which are included in the small and medium sized enterprises category.

The Swedish deciduous forest is dominated by Birch, a combination of *Betula pendula* and *Betula pubescens*. The total timber stock of Birch in the Swedish forest is about 386 million m^3sk (forest cubic meters), where the growth is about 14 million m^3sk per year [3]. The felling in Sweden is about 8 million m^3sk, i.e. the growth is significantly higher than the felling but of which only 77 000 m^3sk is used in the four larger sawmills in Sweden [4] for furniture and joinery without strength grading, e.g. about 1% of the total volume. The remaining material is used in pulp mills or as firewood. One of the reasons for this is that, today, there is no strength grading standard that can be used for strength grading sawn birch timber grown in Sweden. This makes it very difficult to use birch wood as structural timber in Sweden.

The objective of this paper is to present the BizWOOD findings where timber characteristics were measured for birch timber grown in Sweden. Data for strength grading, both for visually- and machine-grading will be presented for about 600 pieces. All specimens were strength tested in four-point bending, in accordance with EN 408 [5], the results for bending strength, modulus of elasticity (MOE) and density will be presented. The possible yields in different grades based on the sampled material will be presented.

The long-term aim is to establish methods that can be used to strength grade sawn timber from birch grown in Sweden and thus make it possible to use birch as a structural material in Sweden. This will broaden the raw material base in the Swedish forestry sector. The work is done as part of a larger project BizWOOD, with the aim

[1] Ulf Lemke, RISE Research institutes of Sweden, Sweden, ulf.lemke@ri.se
[2] Marie Johansson, RISE Research institutes of Sweden, Sweden, marie.johansson@ri.se
[3] Rune Ziethén, RISE Research institutes of Sweden, Sweden, rune.ziethen@ri.se
[4] Andreas Briggert, RISE Research institutes of Sweden, Sweden & Jönköping University, Sweden, andreas.briggert@ri.se

https://doi.org/10.52202/069179-0102

of finding more use of hardwood timber grown in Sweden.

2 MATERIAL AND METHODS

The sampling and measurements were done according to the principles used when setting initial values for machine strength grading in accordance with EN 14081 [6]. This meant sampling and testing more than 450 pieces of timber from the growth area. A growth area is defined, according to EN 14081-2 [7], as the source from which timber is intended to be strength graded.

2.1 Sampling of material

The sampling was carried out at 5 different sawmills in Sweden, see Figure 1, and a total number of 600 specimens of sawn timber were collected. The specimens were divided into four so-called verification samples (sub-sample): North Sweden, Mid Sweden, Southeast Sweden and Southwest Sweden. The material from the two sawmills in Mid Sweden was grouped as one sub-sample as their source areas are overlapping.

The thickness of the specimens varied between 22 mm to 66 mm, and the width from 60 mm to 200 mm. The length of the specimens was between 2,9 and 3,2 meters, which is the standard length of birch timber in Sweden. The number of specimens in each sub-sample, together with corresponding dimensions and origin, is summarized in Table 1.

Figure 1. *Locations of the five sawmills represented in the study. The material from the two sawmills in Mid Sweden was grouped into one sub-sample as the catchment area for the two sawmills were overlapping.*

The total sample of specimens were later broadened to include an additional sub-sample consisting of 120 specimens from Norway. However, these specimens are not included in the evaluation presented in this paper.

The birch grown in Swedish forest consists of a mix of *Betula pendula* and *Betula pubescens* which are not distinguishable visually when sawn to boards. Due to this reason the birch species *Betula pendula* and *Betula pubescens* are processed as one species, the number of specimens of each species in the sample is unknown. The sawmills processing birch timber are relatively small and not all of them uses kiln drying. The specimens included in sub-samples Mid Sweden and Southeast Sweden were kiln dried to approximately 12% moisture content. The specimens in the other subsamples were air-dried. All specimens were planed before testing.

Table 1. *Number of specimens from different sub-samples (geographical sources) and their dimensions and tested length (span length) in four-point bending. The dimensions marked with * could not be tested with a span length of 18h.*

Sub-sample	Nominal dimension [mm x mm]	Span length [m]	Number
North	22 x 75	1.35	40
North	48 x 75	1.35	42
North	48 x 100	1.80	41
Mid	48 x 200	3.00*	42
Mid	36 x 70	1.26	52
Mid	39 x 150	2.70	51
Mid	47 x 60	1.08	79
Mid	50 x 125	2.25	50
Southeast	45 x 95	1.71	43
Southeast	45 x 70	1.26	39
Southeast	45 x 150	2.70	24
Southwest	45 x150	2.70	27
Southwest	45 x 170	2.72*	33
Southwest	66 x 125	2.25	37
Total			600

2.2 Measurements – visual, physical, and mechanical characteristics

In the laboratory the visual characteristics were recorded, and the mechanical properties were tested for each specimen.

2.2.1 Visual characteristics

Visual characteristics of each specimen were recorded in the form of; knot sizes in the critical cross section, rot, cracks, slope of grain, and wane according to INSTA 142 [8]. If other defects were found these were noted in the protocol. The measurements were done by hand. The parameters distortion and annual ring width were not recorded.

Knots were recorded for a length of 150 mm at the critical cross section within the middle 6h of the length, i.e. the

https://doi.org/10.52202/069179-0102

part of the specimen used as the middle span in the bending tests.

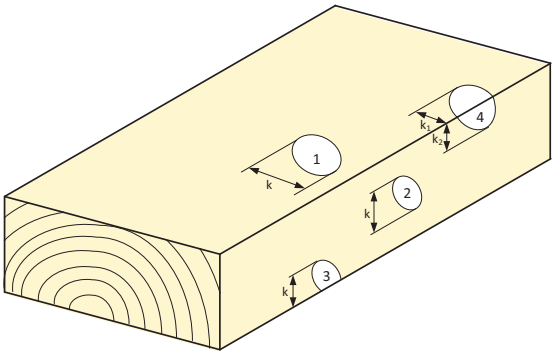

Figure 2. *Principal definition of knot measurement for five different types of knots.*

The main principle for the knot measurement was that a factor (k) was determined as length of the knot in the right angle to the length of the piece, see for example illustration of knot 1 in Figure 2. This is the principle described in INSTA 142 [8].

The knot measurement of knots fully on the edge side are measured perpendicular to the longitudinal axis (knot 2). Knots on the corner between heartwood face of the sample and the edge are measured on the edge side and counted as edge knots (knot 3). Knots on the corner between the sapwood face and the edge side (knot 4) are measured as:

$$k = k_1 + 0.5k_2 \qquad \text{(Eq. 2)}$$

and classified as an edge knot. Knots going through the specimen from one flat face to the other are measured on the sapwood face of the specimen. If the through going knot is closer to the edge than the measure (k), the knot is classified as an edge knot. If the knot is visible on the whole edge side, it is classified as an edge knot with the knot measure equal to the thickness of the specimen. Overlapping knots are not taken into account, each knot was measured as a single knot.

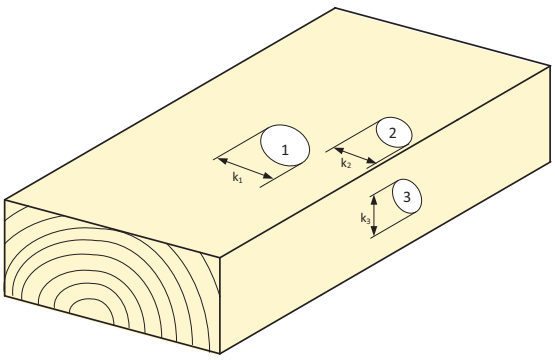

Figure 3. *Principal definition of knot group measurement.*

Knots are counted as knot group if they occur within the same 150 mm specimen length, see Figure 3. The knot measure for a knot group is defined as: the sum of the face knots (on the sapwood face) and the edge knots on both edges.

$$k_g = k_1 + k_2 + k_3 \qquad \text{(Eq. 3)}$$

Slope of grain was measured using a scribe on the sapwood face of the samples and expressed as a ratio between the "fiber deviation/ measurement length".

2.2.2 Density and moisture content

Clear wood density (ρ) was measured on a section of each sample after the bending test according to EN 408 [5]. This means measurement of the dimensions and the weight of the specimen. The test specimen was taken as close as possible to the fracture in clear wood. Clear wood density is defined as:

$$\rho = \frac{m}{V} \qquad \text{(Eq. 4)}$$

where (m) is the mass of the test sample and (V) the volume of the test sample. The volume was measured by Archimedes principle i.e., the mass of water displaced by the specimen.

Moisture content was determined using the oven drying method according to EN 13183 [9], and on the same samples as used for determining density. The moisture content (u) in percent was calculated as:

$$u = \frac{m_1 - m_0}{m_0} \cdot 100 \qquad \text{(Eq. 4)}$$

where (m_1) is the mass of the sample before drying and (m_0) the mass of the sample after oven drying.

2.2.3 Dynamic modulus of elasticity

The dynamic modulus of elasticity was evaluated for each specimen using the first resonance frequency in the axial direction. The measurement of the resonance frequency can be summarized as follows: the specimen was firstly placed on a rubber foam to simulate free-free conditions. An accelerometer was then placed at one of the ends of the specimen and a hammer was used to produce an axial shock wave through the specimen. The time signal from the accelerometer was registered and a Fast Fourier Transform (FFT) was performed. The first resonance frequency, (f_{A-1}) was picked as the first peak in the frequency spectra. The first axial resonance frequency together with the measured length and density of the specimen was then used to calculate the dynamical modulus of elasticity (E_{dyn}) according to [10] using Eq. 2.

$$E_{dyn} = 4 \cdot \rho \cdot L^2 \cdot f_{A-1}^2 \qquad \text{(Eq. 2)}$$

Where (ρ) is the density of the specimen at the measurement time based on volume and weight of the whole board, (L) is the length of the specimen and (f_{A-1}) is the first resonance frequency in the axial direction.

https://doi.org/10.52202/069179-0102

Measurement for E_{dyn} are missing for one series, why this series is omitted in figures presenting (E_{dyn}) below.

2.3 Strength testing according to EN 408

The static bending tests were performed at RISE test laboratory in Borås, accredited as testing laboratory according to EN 408 [5]. According to EN 408 [5] and EN 384 [11] each specimen was tested in edgewise four-point bending. A span length of 18 times the depth (h) of the specimen between the outer supports was used. The inner span length, i.e., the length between the loading points, was $6h$. Local and global modulus of elasticity were measured. The local modulus of elasticity was measured as curvature over a span of $5h$, see Figure 4. The global deflection was also measured giving an alternative value for modulus of elasticity.

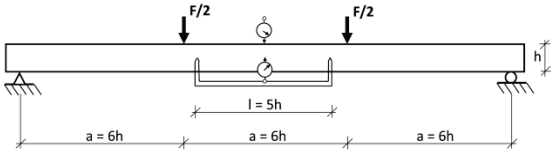

Figure 4. *Four-point bending test including span length and measurement of local and global deflection.*

The critical cross section was, if possible, centred between the loading points. The measured defects were placed randomly in either tension or compression.

The standard log length when harvesting birch in Swedish forest is about three meters. This meant that for the series with specimen depth of 170 and 200 mm it was not possible to use the length of 18 h between the supports. The span length between the outer supports were adjusted to $15h$ for the specimens with depth of 200 mm, and to $16h$ for the specimens with a depth of 170 mm.

2.4 Strength reducing characteristics and machine grading visual override

The regulations for machine strength grading includes a visual override where specimens including some strength reducing characteristics results in the specimens being assigned to a grade with a lower strength class. These characteristics include values for cracks, distortion, wane and rot. In the protocol 25 pieces were recorded as having rot to some extent. Wane was recorded in 46 pieces; where some extended over the limit of 1/3 of the face or edge. Slope of grain above 1/10 was recorded in 20% of the pieces. Other defects were noted in 10% of the protocol entries. No specimens were rejected due to the visual override. The distortion: bow, spring, twist and cup were not measured, and no specimens were rejected for testing because of distortion.

2.5 Evaluation of data

Based on the test results from the bending tests the characteristics local MOE ($E_{m,l}$), global MOE ($E_{m,g}$) and bending strength (f_m) was evaluated as:

$$E_{m,l} = \frac{a l_1^2 (F_2 - F_1)}{16 \frac{bh^3}{12} (w_2 - w_1)} \quad \text{(Eq. 6)}$$

$$E_{m,g} = \frac{3al^2 - 4a^3}{2bh^3 \left(2 \frac{w_2 - w_1}{F_2 - F_1}\right)} \quad \text{(Eq. 7)}$$

$$f_m = \frac{3Fa}{bh^2} \quad \text{(Eq. 8)}$$

where the measures (a) and (l) are defined in Figure 4, ($F_2 - F_1$) is the increment in load between 0.1 max load (F) and 0.4 of the max load (F), and ($w_2 - w_1$) the corresponding deformations either measured locally or globally. The dimensions of the specimen are depth (h) and width (b).

The evaluated data was adjusted for moisture content, depth, and length. Test values for density were adjusted to a moisture content u_{12} = 12%, according to the formula in clause 5.4.2.2 in EN 384 [11], Eq. 9. Test values for modulus of elasticity were adjusted to a moisture content u =12%, according to the formula in clause 5.4.2.3 in EN 384 [11], see Eq. 10.

$$\rho = \rho_u (1 - 0.005(u - u_{12\%})) \quad \text{(Eq. 9)}$$

$$E_0 = E_{0,u} (1 - 0.005(u - u_{12\%})) \quad \text{(Eq. 10)}$$

The measured bending strength for samples with a depth less than 150 mm was adjusted with a (k_h) factor given in EN 384 [11]. The measured bending strength for the two tested dimensions with a span shorter than the stated 18h, for these series the bending strength has been adjusted with factor (k_l) given in EN 384 [11].

$$k_h = min \left\{ \left(\frac{150}{h} \right)^{0.2} \right. \quad \text{(Eq. 9)}$$
$$\left. 1.3 \right\}$$

$$k_l = \left(\frac{48h}{l_{ef}} \right)^{0.2} \quad \text{(Eq. 10)}$$
$$l_{ef} = l + 5a$$

Where (l) is the distance between the two outer support points and (a) is the distance between the two inner loading points.

3 RESULTS

3.1 Knot size distribution

Knot size is the most important parameter for visual grading. Figure 5 shows the knot size distribution on the face side of the specimens. The majority of the knots cover less than 20% of the face side of the specimens.

https://doi.org/10.52202/069179-0102

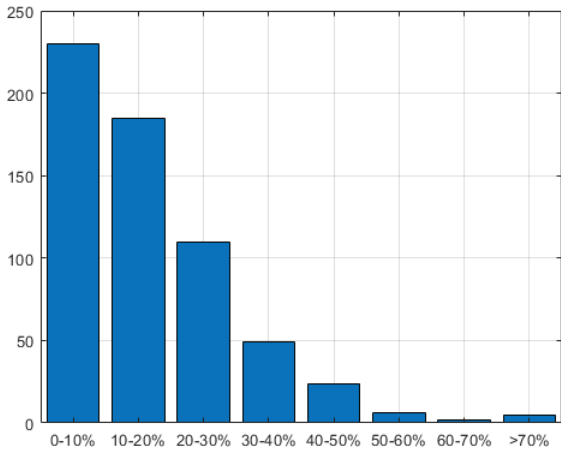

Figure 5. *Histogram of knot size (as percent of the total face) on flat face of the specimens.*

Figure 6 shows the knot size distribution on the edge sides of the specimens. The majority of the knots cover less than 10% of the edge sides of the specimens.

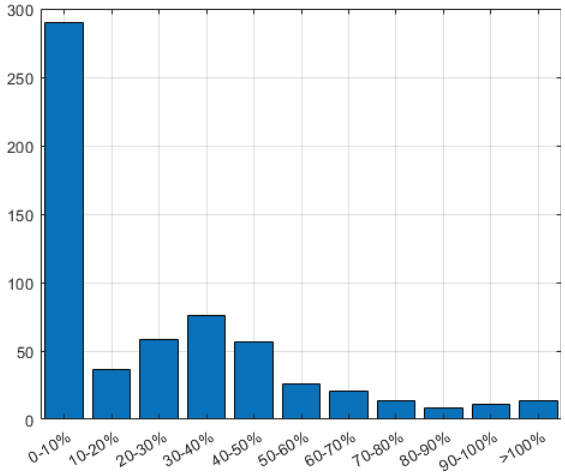

Figure 6. *Histogram of knot size on edge sides (as percent of the total sides) of the specimens.*

3.2 Variation in density, modulus of elasticity and bending strength

The parameters density, stiffness and bending strength are all defined as grade determining properties in strength grading. Figure 7 shows the distribution of density in the 600 specimens.

Figure 8 and Figure 9 show the distribution of local MOE ($E_{m,l}$) and bending strength (f_m), respectively, for all 600 specimens.

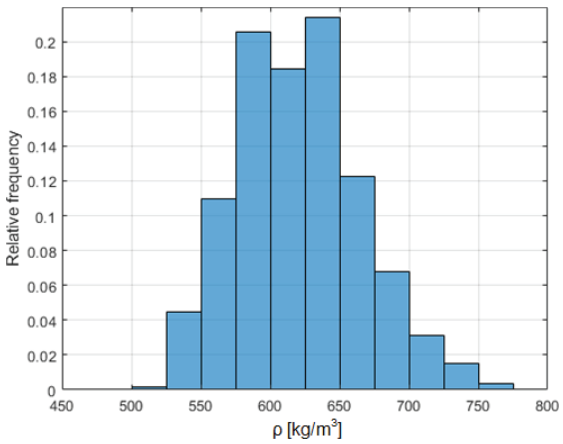

Figure 7. *Histogram for the distribution of density (**ρ**).*

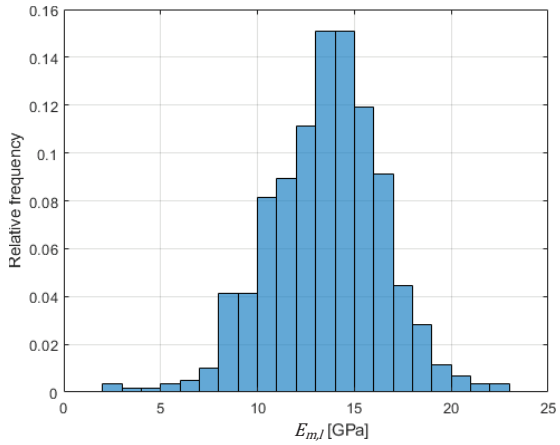

Figure 8. *Histogram for the distribution of local modulus of elasticity MOE (**$E_{m,l}$**).*

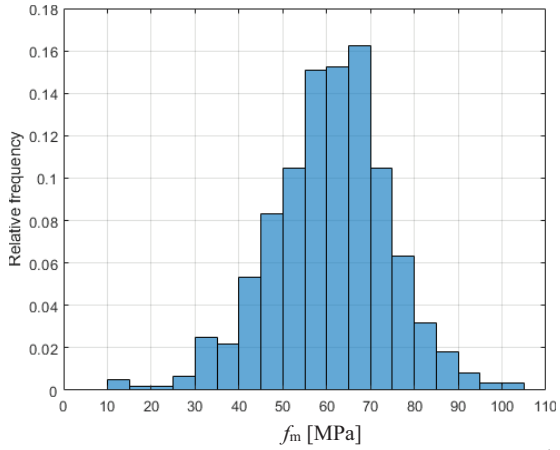

Figure 9. *Histogram for the distribution bending strength (**f_m**).*

The data was evaluated to investigate the mean values for density, modulus of elasticity and bending strength as well as the coefficient of variation (CoV) and the 5% percentile value (characteristic value) according to EN 14358 [12].

https://doi.org/10.52202/069179-0102

The mean value for bending strength shows a value of 60.9 MPa with a value for the characteristic bending strength of 38.6 MPa (5% percentile), see Table 3. The results in Table 3 also shows that the different geographical sources have similar values for both strength and Coefficient of Variation (CoV). The latter indicates that the sampling worked well and that no discrepancy can be found between the subsamples. Splitting the bending strength values between different sizes of samples shows also similar results and the same depth adjustment factor used for softwood in EN 384 [11] works also for birch.

The mean modulus of elasticity for all the samples is 13.6 GPa, when splitting between different geographical sources there is a difference in mean value varying from 12.3 to 14.6 GPa. The mean density is just over 600 kg/m^3 for all samples and varying between 603-638 kg/m^3 when split between the different geographical sources.

3.3 Visual grading

All specimens were assigned to a single grade class (T0–T4) according to INSTA 142 [8], using the requirements for knots on the edge side (k), the flat face (k), knot groups (k_g) and slope of grain as described in Table 4. The number of specimens assigned to each grade class can be found in Table 2.

Table 2. *Number of samples in each assign grade according to requirements in Table 4.*

Grade	N
Reject	21
T0	45
T1	132
T2	188
T3	214
Sum	600

Table 3. *Compiled mean value, coefficient of variation and 5% percentile (characteristic value) for bending strength (f_m), local modulus of elasticity ($E_{m,l}$) and density (ρ) for all specimens and divided for geographical source and for specimen size.*

	Geographical source					Specimen depth		
	All	North	Mid	Southeast	Southwest	<90	90-150	>150
f_m [MPa]	60,9	59,8	62,2	65,0	54,1	61,8	62,3	58,5
CoV [%]	22%	19%	24%	23%	22%	26%	24%	19%
5% percentile	38,6	42,1	34,5	42,0	33,1	32,1	34,5	41,2
$E_{m,l}$ [GPa]	13.6	14.6	13.4	13.3	12.3	12.7	13.4	14.3
CoV [%]	21%	20%	24%	19%	20%	25%	24%	18%
ρ [kg/m^3]	620	603	619	638	613	620	620	604
CoV [%]	7%	13%	7%	11%	7%	7%	7%	6%
5% percentile	551	544	556	580	544	554	556	547

Table 4. *Used requirements from INSTA 142* [8] *for strength reducing characteristics used for assigning grades.*

	Grade class			
Characteristics	**T3**	**T2**	**T1**	**T0**
Single knot – edge side	k < 1/3 b	k < 1/2 b	k < 4/5 b	k = b
Single knot – flat face	k < 1/6 h	k < 1/4 h	k < 2/5 h	k < 1/2 h
Knot group	k_g < 1/3 b + 1/6 h	k_g < 1/2 b + 1/4 h	k_g < 4/5 b + 2/5 h	k_g < b + 1/2 h
Spiral grain angle	< 1:10	< 1:8	< 1:6	< 1:4

Table 5. *Comparison of mechanical properties, mean bending strength (f_m), mean modulus of elasticity ($E_{m,l}$) and mean density (ρ) from this study compared to other studies of birch timber and for two large studies for Norway spruce.*

Mean value	f_m [MPa]	$E_{m,l}$ [GPa]	ρ [kg/m^3]
Birch			
BizWOOD	61.0	13.6	620
Kilde 2006 [13]	43.5 (tension strength)	13.3	625
Obernoster & Jeitler 2021 [14]		15.1	603
Dunham et al. 1999 [15]	47.3-63.8	8.1-12.7	655-723
Norway spruce			
Olsson & Oscarsson 2017 [16]	42.1	11.6	441
Ranta-Maunas et al. 2011 [17]	40.2	11.2	428

https://doi.org/10.52202/069179-0102

3.4 Correlation between strength and stiffness

The correlation between stiffness and strength is an important parameter for machine strength grading. Using all the data the correlation between local modulus of elasticity and bending strength is $r^2 = 0.41$, see Figure 10.

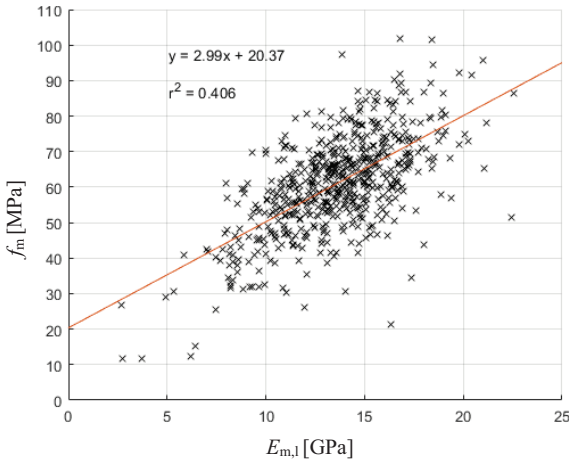

Figure 10. *Correlation between local MOE ($E_{m,l}$) and bending strength (f_m).*

4 ANALYSIS AND DISCUSSION

4.1 Mechanical properties

The mechanical properties for birch from this study can be compared to data from other studies, see Table 6. The results show that the values are similar to values obtained in Norway [13] but higher than for studies performed in Austria [14] or the UK [15] for full size timber members with defects. Note that the Norwegian and Austrian values are obtained from tensile tests.

The values are also much higher than for the normally used Norway spruce, see Table 5. The bending strength for Norway spruce from the Nordic countries are normally just over 40 MPa, with a mean MOE of about 11.5 GPa and a mean density much lower than measured for the birch in this study.

4.1 Strength and stiffness of Birch timber from the Nordic countries compared to strength classes

Sawn timber is, in Europe, normally graded into different strength classes according to EN 338 [18]. The grading is done based on the characteristic value for bending strength, mean value for modulus of elasticity and characteristic value for density, see Table 6. Values for the characteristic bending strength (f_m), mean modulus of elasticity ($E_{m,l}$) and characteristic density (ρ) for some C-classes according to EN 338 [18].

Table 1Hardwood species can be graded into D-classes and softwood species into C-classes. The D-classes are designed for denser species like oak, ash and beech. The D-classes are rarely used in the Swedish building industry; therefore, we aim for grading birch into C-classes in this paper.

The results presented in Table 3. Compiled mean value, coefficient of variation and 5% percentile (characteristic value) for bending strength (f_m), local modulus of elasticity ($E_{m,l}$) and density (ρ) for all specimens and divided for geographical source and for specimen size. show that the ungraded birch with the sampled distribution reaches the characteristic values for strength class C35. The grade determining factor that limits the strength grade is the mean modulus of elasticity of the material. The mean value of the modulus of elasticity is 13.6 GPa, which makes it possible to grade the material into C35 but not in a higher grade. The characteristic bending strength is 38.6 MPa which is also clearly in the C35 class. The mean density of 620 kg/m^3 and the characteristic density value of 551 kg/m^3 implies that the birch sample used in this study has a density much higher than required for grade C35.

Table 6. *Values for the characteristic bending strength (f_m), mean modulus of elasticity ($E_{m,l}$) and characteristic density (ρ) for some C-classes according to EN 338* [18].

Grade	f_m [MPa]	$E_{m,l}$ [GPa]	ρ[kg/m^3]
C14	14	7.0	290
C24	24	11.0	350
C30	30	12.0	380
C35	35	13.0	390
C40	40	14.0	400
C45	45	15.0	410

4.2 Strength grading of birch

Two methods for strength grading of sawn timber from birch grown in Sweden were performed in this study:

- Visual grading,
- Machine strength grading.

4.2.1 Visual grading

For visual grading the regulations in INSTA 142 [8] were used. The grading of the material was based on comparing the characteristic bending strength, mean modulus of elasticity and the characteristic density for each T group with the values for the C classes, c.f. Table 6. This gave a result as in **Fel! Hittar inte referenskälla.**, for the different T-classes. No verification has been done for the subsamples, neither has the k_n factor been used.

Table 7. *Yield percentage and C-class for each visually graded T-class.*

Grade	Class	Percent yield
Reject	R	4%
T0	C24	8%
T1	C30	12%
T2	C35	31%
T3	C40	35%

As the material has these natural properties the possibility to use simpler combinations were investigated. The first version was to combine T0 and T1 to one class and T2 and

T3 to one class. This yielded in 66% of the total sample could be assigned into strength class C40, see Table 8.

Table 8. *Yield percentage and C-class for each combination of visually graded T-class.*

Grade	Class	Percent yield
Reject	R	4%
T0 + T1	C30	30%
T2 + T3	C40	66%

The simplest combination is to grade all sawn timber in only T0 and better and reject. That yielded that all material that was not rejected could be assigned to C35, see Table 9. The limiting factor is in most cases the mean modulus of elasticity.

Table 9. *Yield percentage and C-class using only the combination T0 and better.*

Grade	Class	Percent yield
Reject	R	4%
T0 and better	C35	96%

When these thresholds are used for softwood the visually graded material in class T0 are assigned to grade C14 and material in class T2 are assigned to class C24 according to EN 1912 [19].

4.2.1 Machine strength grading

The most common method of machine grading softwood in Sweden is by using the dynamic modulus of elasticity as an indicating property. In the following figures the scatterplots for E_{dyn} versus f_m and E_{dyn} versus $E_{m,l}$ are shown.

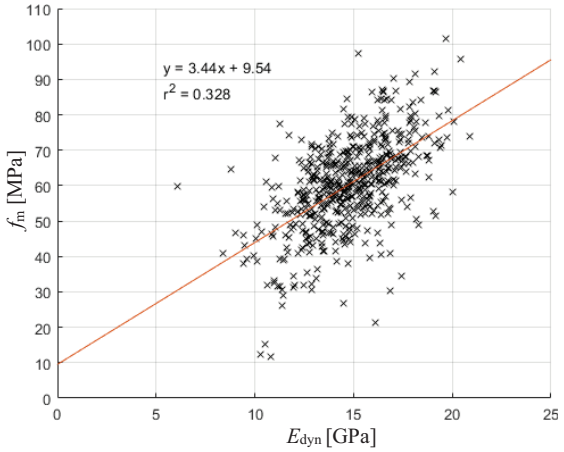

Figure 11. *Bending strength ($\boldsymbol{f_m}$) versus dynamic modulus of elasticity ($\boldsymbol{E_{dyn}}$).*

The relationship r^2 between the mechanical parameters are not as good for birch, as for softwood, see Table 10, [17], [18].

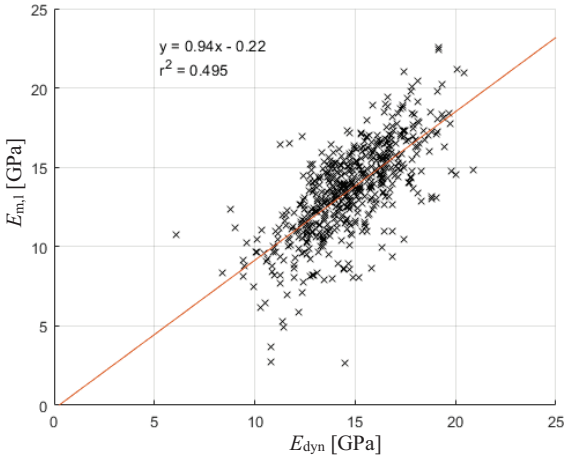

Figure 12. *Local modulus of elasticity ($\boldsymbol{E_{m,l}}$) from the static tests versus dynamic modulus of elasticity ($\boldsymbol{E_{dyn}}$).*

Table 10. *Coefficient of determination, r^2, between $\boldsymbol{E_{dyn}}$ and $\boldsymbol{f_m}$ and between $\boldsymbol{E_{dyn}}$ and $\boldsymbol{E_{m,g}}$ in this study and two studies for spruce, and $\boldsymbol{E_{dyn}}$ and $\boldsymbol{E_{m,l}}$ for birch.*

Species	E_{dyn} v. f_m	E_{dyn}v. $E_{m,g}$	E_{dyn}v. $E_{m,l}$
Birch	0.33	0.73	0.50
Spruce [17]	0.54	0.83	-
Spruce [16]	0.53	0.84	-

For simulating machine strength grading the measured dynamic modulus of elasticity was used as indicative property (IP). Using threshold values for the dynamic modulus of elasticity it was possible to assign 55% of the samples to class C45 and 35% of the samples to assign 35% to class C30. The values for characteristic bending strength and characteristic density were checked so that they fulfilled the requirements for the assigned strength class, c.f. Table 6. The threshold values presented in Table 11 were determined so that the pieces assigned to the grade fulfil the requirement of characteristic strength, characteristic density and mean MOE. No subsample control has been done, neither has the k_n factor been used.

Table 11. *Threshold values for IP ($\boldsymbol{E_{dyn}}$), strength class and percent yield for each class.*

Threshold IP	Class	Percent yield
Reject	R	10%
> 12.0 GPa	C30	35%
> 14.5 GPa	C45	55%

https://doi.org/10.52202/069179-0102

5 CONCLUSIONS

This study shows that the unsorted birch material has a higher mean bending strength, MOE and density than the softwood species used in the Swedish industry today. Studies show that mixed stands of Spruce and Birch give a higher volume growth than spruce monocultures, that is the most common silvicultural choice today.

The findings of this study show that it would be possible to strength grade birch from Sweden by using the existing set of rules from INSTA 142. This study also shows that by the means of using frequency and density measurements for indicating properties, machine strength grading would be possible. Both methods would possibly give good yields in high strength classes, for material of the same distribution as the sampled material. A combination of using both machine grading and visual grading could in some strength class combinations be favourable.

The possibility to strength grade sawn timber of birch is important for the possibility of utilizing also other hard woods grown in Sweden. This is a potential in the Swedish forest that at the moment is not possible to utilise as structural timber. This will increase both the utilisation of existing material in the Swedish forests in products with a long lifetime. This will also improve the possibility for increased biodiversity in the forest by increasing the value of the hardwoods and therefore give the forest owners incentive for also growing hardwood species.

The 600 pieces from this test will together with 120 pieces from Norway be a good foundation for publishing a new grading regulation for birch wood grown in Sweden and Norway.

6 ACKNOWLEDGEMENT

The BizWOOD is financially supported by the Swedish Agency for Economic and Regional Growth through the European Regional Development Fund (Nr: 2035272) and the Swedish Regions; Jönköping, Kalmar and Kronoberg. The authors acknowledge that support with great gratitude.

7 REFERENCES

[1] United Nations, “Goal 15 | Department of Economic and Social Affairs,” 2015. https://sdgs.un.org/goals/goal15 (accessed Mar. 01, 2023).

[2] FSC Sweden, “The FSC National Forest Stewardship Standard of Sweden,” Bonn, 2020.

[3] P. Nilsson, C. Roberge, J. Fridman, and S. Wulff, “Skogsdata 2019 - Aktuella uppgifter om de svenska skogarna från SLU Riksskogstaxeringen,” Umeå, 2019. Accessed: Feb. 09, 2023. [Online]. Available: https://www.slu.se/globalassets/ew/org/centrb/rt/dokument/skogsdata/skogsdata_2019_webb.pdf

[4] N. Fahlvik *et al.*, “The future possibilities for Birch in a climate adapted use of forests. (In Swedish: Björkens möjligheter i ett framtida klimatanpassat brukande av skog),” Uppsala, 2021. Accessed: Feb. 09, 2023. [Online]. Available: https://www.skogforsk.se/cd_20210819163404/contentassets/d137d50a15684623990378edae0ab4c6/bjorkens-mojligheter_low.pdf

[5] SS-EN 408:2010+A1:2012, “Timber structures - Structural timber and glued laminated timber - Determination of some physical and mechanical properties,” Stockholm, 2012.

[6] SS-EN 14081-1:2016+A1:2019, “Timber structures-Strength graded structural timber with rectangular cross section-Part 1: General requirements,” Stockholm, 2019. [Online]. Available: www.sis.se

[7] SS-EN 14081-2:2018+A1:2022, “Timber structures-Strength graded structural timber with rectangular cross section-Part 2: Machine grading; additional requirements for type testing,” Stockholm, 2022. [Online]. Available: www.sis.se

[8] SS 230120:2010, “Nordic visual strength grading rules for timber (INSTA 142),” Stockholm, 2010. [Online]. Available: www.sis.se

[9] SS-EN 13183-1, “Moisture content of a piece of sawn timber –Part 1: Determination by oven dry method,” Stockholm, 2003.

[10] P. Hoffmeyer, “Strength grading gives added value , Part 2 - available technology (In Danish: Styrkesortering ger mervärde, Del 2 - Tilgaenglig teknik),” Copenhagen, 1995.

[11] SS-EN 384:2016+A2:2022, “Structural timber-Determination of characteristic values of mechanical properties and density,” Stockholm, 2022. [Online]. Available: www.sis.se

[12] SS-EN 14358:2016, “Timber structures – Calculation and verification of characteristic values,” Stockholm, 2016. [Online]. Available: www.sis.se

[13] V. Kilde, K. H. Solli, B. Pitzner, P. Lind, and J. Bramming, “Birch in visible structures (In norwegian: Bjørk i synlige konstruksjoner),” Oslo, 2006. Accessed: Feb. 28, 2023. [Online]. Available: https://www.treteknisk.no/resources/filer/publikasjoner/rapporter/Rapport-67.pdf

[14] D. Obernosterer and G. Jeitler, “Birch for engineered timber products,” in *World Conference on Timber Engineering 2021 (WCTE2021)*, 2021. Accessed: Feb. 28, 2023. [Online]. Available: https://www-scopus-com.proxy.lnu.se/record/display.uri?eid=2-s2.0-85120751723&origin=resultslist&sort=plf-f&src=s&st1=mechanical+properties+birch+timber&sid=a07ff0eb868a132292e9c6f9734d9689&sot=b&sdt=b&sl=49&s=TITLE-ABS-KEY%28mechanical+properties+birch+timber%29&relpos=10&citeCnt=0&searchTerm=

[15] R. A. Dunham, A. D. Cameron, and J. A. Petty, “The Effect of Growth Rate on the Strength Properties of Sawn Beams of Silver Birch (Betula

pendula Roth)," *Scand J For Res*, vol. 14, no. 1, pp. 18–26, 1999, doi: 10.1080/02827589908540805.

[16] A. Olsson and J. Oscarsson, "Strength grading on the basis of high resolution laser scanning and dynamic excitation: a full scale investigation of performance," *European Journal of Wood and Wood Products*, vol. 75, no. 1, pp. 17–31, Jan. 2017, doi: 10.1007/S00107-016-1102-6/TABLES/7.

[17] A. Ranta-Maunus, J. K. Denzler, and P. Stapel, "Strength of European Timber. Part 2. Properties of spruce and pine tested in Gradewood project," Helsinki, 2011. [Online]. Available: http://www.vtt.fi/publications/index.jsp

[18] SS-EN 338:2016, "Structural timber – Strength classes," Stockholm, 2016. [Online]. Available: www.sis.se

[19] SS-EN 1912:2012/AC:2013, "Structural Timber - Strength classes - Assignment of visual grades and species," Stockholm, 2013.

https://doi.org/10.52202/069179-0102

World Conference on Timber Engineering Oslo 2023

FIBRE-OPTIC MEASUREMENTS FOR MONITORING ADHESIVELY BONDED TIMBER-CONCRETE COMPOSITE BEAMS

Jens Frohnmüller[1], Werner Seim[2], Ann-Charlotte Spangenberg[3]

ABSTRACT: The technology of fibre-optic sensors (FOS) enables the continuous measurement of strains along the fibre axis. This offers the possibility of studying and monitoring the behaviour of the component to which the fibre is connected at any given point. In this paper, the FOS measurement technique is applied aiming to develop a monitoring tool for checking the integrity of the adhesively bonded joint between timber and concrete. Accordingly, tests with adhesively bonded timber-concrete composite beams, which have been loaded up to ultimate failure, are conducted. The measurement results are presented and checked for plausibility with the aid of an finite element model. Subsequently, a calculation model is presented with which the shear stresses in the adhesive joint can be derived directly from the strain measurements. As a result, it can be stated that it has been possible to monitor the integrity of the bonded joint and derive shear stresses directly from the measurement, however, more research is necessary to get an even better understanding of how to analyse and post-process the measurement data.

KEYWORDS: Fibre-optical measurement, Monitoring, Adhesives, Timber-Concrete Composites, Quality control

1 INTRODUCTION

1.1 FIBRE-OPTIC SENSORS – TYPICAL AREAS OF APPLICATION

The technology of fibre-optic sensors (FOS) allows the measurement of strains continuously along the length of the sensor. This offers new and promising possibilities for the testing of structural elements in the laboratory, and especially for the on-site monitoring of load-bearing elements if possible damage can be identified.

The FOS were used, for example, by Schmidt-Thrö et al. [1] and Lemcherreq et al. [2] to investigate the basic behaviour of the fibres in the case of the bond between reinforcement steel and concrete. The optic fibre was glued onto the steel-rod in this case.

A quite extensive report on FOS for use in structural bondlines was reported by Könke et al. [3], who also investigated the use of the technology as a monitoring tool for adhesively bonded timber-concrete composite (ATCC) beams. Könke et al. hereby observed, for example, that cracks in the concrete plate could be detected. Similar observations were documented by Spangenberg [4], who identified knot-holes and air bubbles of the adhesive, which had been used to apply the fibre onto an ATCC specimen, as peak values in the measurement.

In the field of timber structures, a comparable measurement method, so-called Fibre Bragg Grating (FBG), was used by Claus et al. [5] to investigate the force distribution in self-tapping screws in timber. New effects regarding the load distribution in the interface between screw and timber could be seen and the effective embedding length of the screws was considered in more detail, comparing it to Volkersen's theory.

1.2 AIM AND APPROACH

The aim is to investigate how FOS can be used for the monitoring of structural elements, focusing on the adhesive bondline. Firstly, the materials and methods are presented. The results of the measurements for two different test series are then presented. In both cases, the strains in the adhesive joint are measured, and in one case, additionally the strains at the bottom edge of the timber (see exemplarily one of the specimens from test series ATCC-A in Figure 1).

In a next step, the experimental measurement data are validated and checked for plausibility by means of a finite element (FE) model. A calculation model is then presented, with which the shear stresses in the bondline can be determined directly from the measurement.

2 MATERIALS & METHODS

2.1 EXPERIMENTAL PROGRAMME AND TEST SET-UP

The experimental programme covers two types of specimens. The cross-section and the location of the FOS are depicted in Figure 1 (ATCC-A) and Figure 2 (ATCC-B).

[1] Jens Frohnmüller, University of Kassel, Timber Structures and Building Rehabilitation, Germany, jens.frohnmueller@uni-kassel.de
[2] Werner Seim, University of Kassel, Timber Structures and Building Rehabilitation, Germany.
[3] Ann-Charlotte Spangenberg, DB Netz AG, Kassel, Germany.

https://doi.org/10.52202/069179-0103

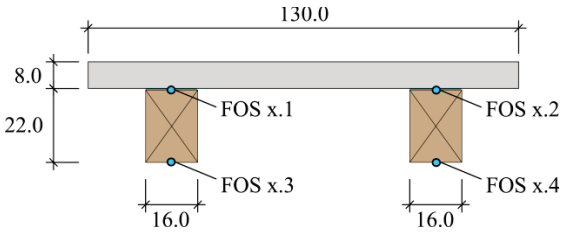

Figure 1: *Geometry and location of FOS for specimens of series ATCC-A*

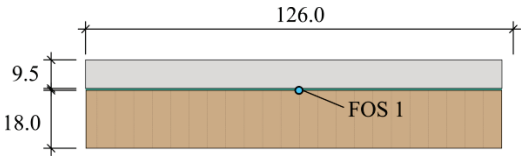

Figure 2: *Geometry and location of the FOS for specimens of series ATCC-B*

Regarding the specimens of the series ATCC-A, the FOS have been placed in the bondline (FOS x.1 and FOS x.2) and on the bottom edge of the timber beam (FOS x.3 and FOS x.4) continuously along its length. Concerning the specimen ATCC-B, one FOS has been installed directly in the bondline. The relevant parameters and decisive differences between the two types are summarised in Table 1.

Table 1: *Experimental programme*

Parameter	Type	
	ATCC-A	ATCC-B
Number of specimens	3	1
Span	6.00 m	7.68 m
Bond arrangement	Continuous (full length)	Discontinuous (strips)
Adhesive	Low viscous epoxy (2EP)	Polymer mortar (2EP)
Timber geometry	Beam	Plate
Timber quality	GL24h	GL28c
Concrete quality	C45/55	C40/50
Number of FOS per specimen	4	1

The bottom surface of the prefabricated concrete parts of ATCC-A has not been further processed after removing the formwork. The bottom surface of the concrete parts of ATCC-B has been sandblasted.

The ATCC specimens were tested in a 4-point bending configuration similar to that by Frohnmüller et al. [6]. The force was measured with a load cell, and the mid-span deflections and the relative displacement between timber and concrete with displacement transducers. The measurement was performed at a sampling rate of 2 Hz. The distance between each measurement point on the sensor length was chosen to be 1.3 mm. This led to approximately 12,000 data points (ATCC-A) and 14,500 data points (ATCC-B) along the span per second.

The strains ε_x could be converted, considering Young's Modulus E_x, into stresses σ_x using Equation 1.

$$\sigma_x = \varepsilon_x \cdot E_x \quad (1)$$

2.2 SPECIMEN MANUFACTURING

The FOS were installed by cutting a small groove at a depth of 5 mm into the timber part, laying the sensors into the groove and filling it up with a low viscosity epoxy adhesive. During hardening, the adhesive was sucked into the timber part at several points due to knot-holes or small cracks. Small air bubbles appeared in these areas, and were then pierced before more adhesive was applied.

The manufacturing process of gluing timber and concrete was different for the two test series.

2.2.1 ATCC-A

The concrete plate was turned on its back and spacers with a thickness of 2 mm were placed on the slab. The timber beams were then placed on top. They had been drilled previously at regular intervals with holes through the height of the beam. After a circumferential sealing of the joint, the adhesive was injected through the holes which were then successively closed utilising beech wood dowels. The bond width was reduced to 75 % of the original width for specimen -02 and to 50 % for specimen -03 for each beam.

2.2.2 ATCC-B

The polymer mortar for the second type was applied on the timber part with a mortar sledge, into which a toothed spatula had been installed. The prefabricated concrete plate was then placed on top of the timber plate. No turning of the concrete plate was necessary.

3 TEST RESULTS

3.1 ATCC-A

The global failure occurred in all three cases as a bending failure in the timber beam at a load level of $F_{u,exp}$ = 109 kN (ATCC-A-01), $F_{u,exp}$ = 153 kN (ATCC-A-02) and $F_{u,exp}$ = 165 kN (ATCC-A-03), whereby $F_{u,exp}$ is the load applied by the actuator. Additionally, the self-weight F_G = 11 kN of the steel structure to transfer the load must be added. The specimen ATCC-A-01 showed the peculiarity that a local bending failure occurred in the outer lamella of one beam of the timber at a load level of $F_{u,exp}$ = 93 kN. Further loading was possible up to global bending failure. The adhesive joint remained intact, with a negligible relative displacement between the timber and the concrete for all specimens.

The results of the FOS measurements along the bond length of all three specimens are shown in Figure 3. The measurement results are all presented for the same load step F_{exp} = 75 kN for reasons of comparability.

https://doi.org/10.52202/069179-0103

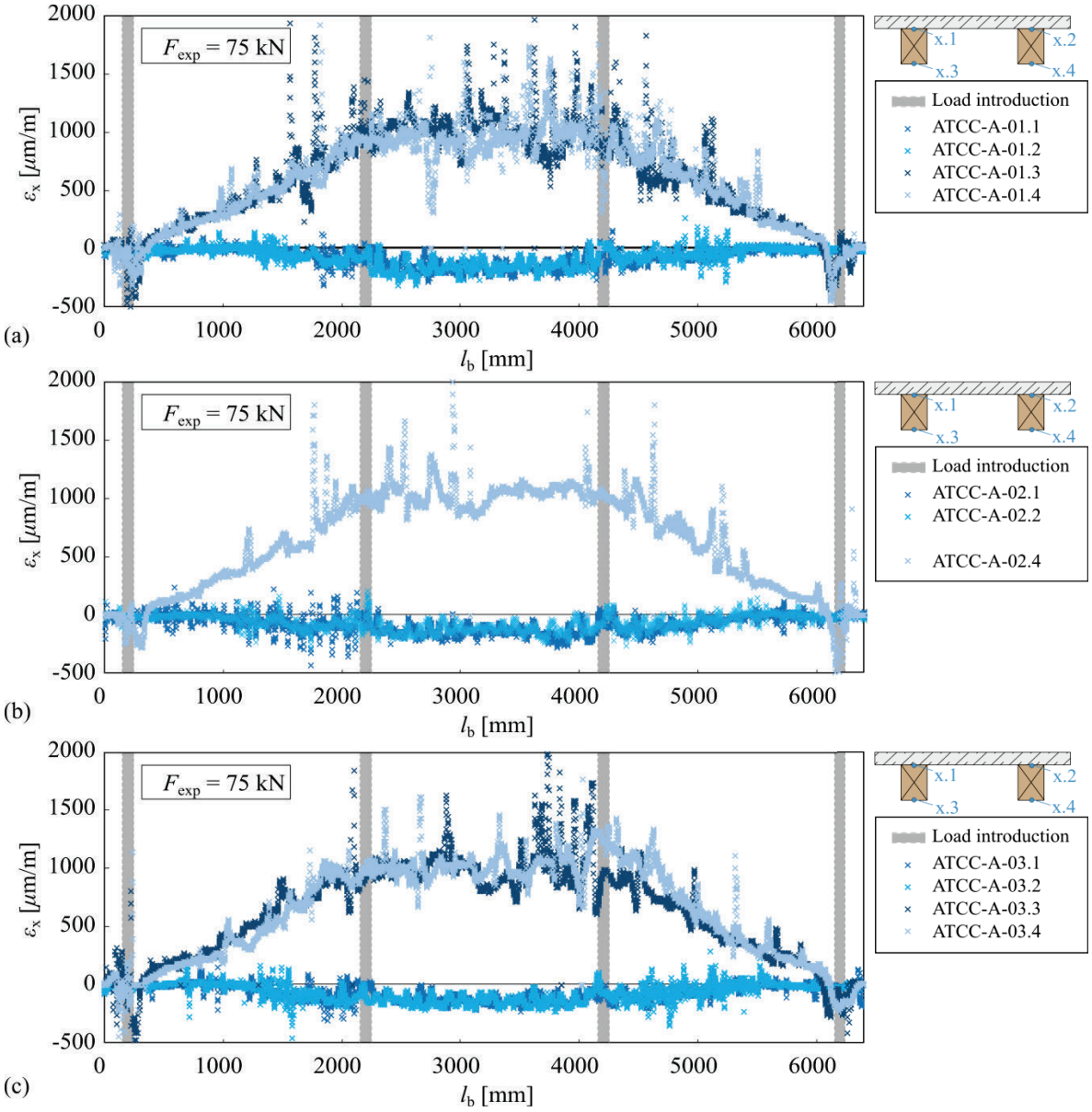

Figure 3: *Results of the fibre-optic measurements – ATCC-A-01 to ATCC-A-03. Strains ε_x along the bond length for the load step F_{exp} = 75 kN (a) ATCC-A-01, (b)B ATCC-A-02 and (c) ATCC-A-03*

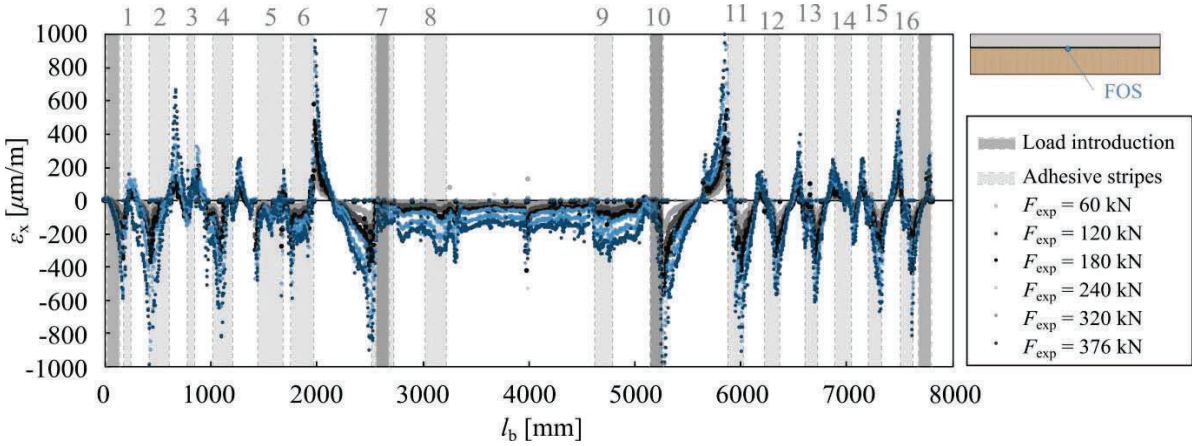

Figure 4: *Results of the fibre-optic measurements – ATCC-B. Strains ε_x along the bond length for the six load steps (The scale in the range of -1000 μm/m to +1000 μm/m is depicted; individual strain values are larger)*

https://doi.org/10.52202/069179-0103

The force from the actuator is F_{exp}, since the measurement was zeroed before the start of the FOS measurement. The steel structure for the load transfer was installed before the start and the zeroing of the measurement. No measurement data is available for the fibre 2.3 in Figure 3b due to a breakage during the installation of the fibre into the testing field.

The large peaks in the measurement (Figure 3) indicate local irregularities in the timber part, such as knot-holes or air bubbles in the adhesive used to glue the fibre into the groove. Smaller deviations are associated with cracks in the concrete, as observed by Könke et al. [3], or knot-holes in the timber, which were in close proximity to the fibre (approximately 10 to 50 mm).

A quasi linear-elastic load-displacement behaviour was observed during all three tests of the series ATCC-A. The same applies to the majority of the FOS measurement data which can be seen in Figure 5, where the normalized strains $\varepsilon_x/\varepsilon_{x,max} < 1.0$ of two different load steps are depicted. The load step $F_{u,exp} = 93$ kN complies with the load step immediately before the failure. However, an irregular behaviour of the strains becomes visible in certain areas.

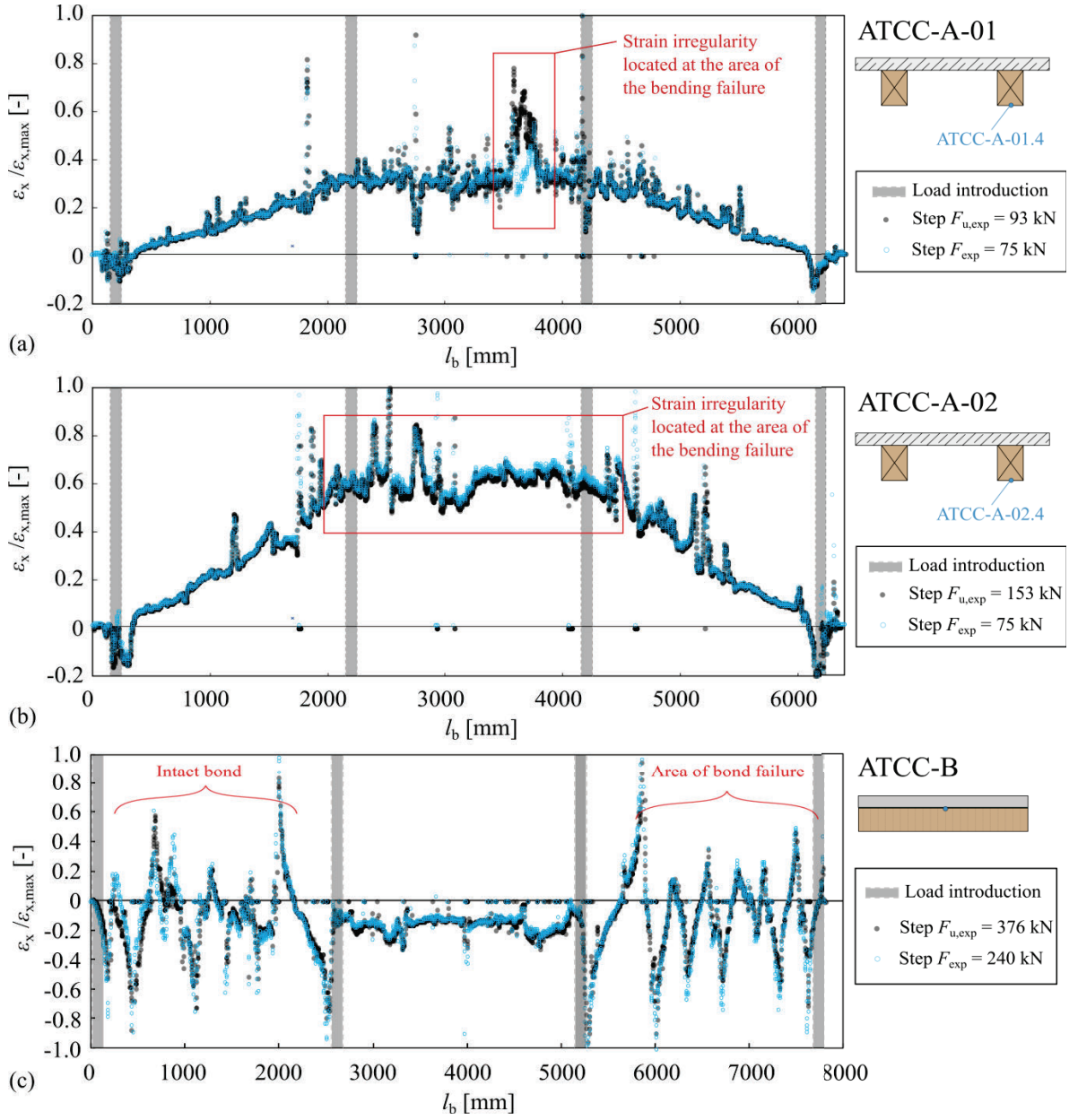

Figure 5: *Comparison of normalised strains $\varepsilon_x/\varepsilon_{x,max}$ for two load steps and (a) ATCC-A-01 (b) ATCC-A-02 and (c) ATCC-B*

https://doi.org/10.52202/069179-0103

The change of the strains of ATCC-A-01.4 happened comparatively suddenly and was concentrated locally on a certain section (Figure 5a). The sensor ATCC-A-03.3 showed a comparable behaviour.

The other sensors, ATCC-A-01.3, ATCC-A-02.4 and ATCC-A-03.4, showed a different behaviour, because the change was not concentrated but distributed mostly in the inner third of the span, where the largest bending stress occurred (Figure 5b). The irregularity in the inner third of the span happened in contrast to the irregularity which was concentrated locally, continuously over time.

3.2 ATCC-B

The failure of the composite beam occurred as expected as a combined bond failure in the timber and the concrete at a load level of $F_{u,exp}$ = 376 kN. The bond failure took place simultaneously at the strips no. 11-16 in the area of l_b = 5.0 …8.0 m and has been characterised purely by a mixed substrate failure in the timber and the concrete and no adhesion or cohesion failure could be documented. Further details of the full-scale test can be found in Frohnmüller et al. [6]. The strains measured are depicted for several load steps in Figure 4. The largest strain gradient in terms of magnitude occurred in the adhesive strip no. 11. The strains generally increased to the same extent as the load steps. Regarding the load-displacement behaviour, a linear elastic behaviour was present. This could also be confirmed for the strains based on Figure 5c, where no explicit irregularities were detected.

4 VALIDATION OF THE MEASUREMENT

4.1 FINITE ELEMENT MODEL

A validation of the strain measurement is possible by means of an FE model. The latter is implemented using the software package ABAQUS and is based on two-dimensional shell elements with a mesh size of a_E = 5.0 mm, which corresponds to about 60 FEs over the height of the component for the test series ATCC-A and 56 for the test series ATCC-B. The model consists of CPS4R elements with four nodes and one integration point in the centre of the element (reduced integration). The path where the strains are evaluated was chosen similar to the location of the FOS. The FE model is depicted exemplarily for one specimen of the type ATCC-A in Figure 6.

Both bending and bond failure occurred in a brittle manner and a linear-elastic load-displacement behaviour could be seen in the tests, therefore, linear-elastic material properties were assigned. Local axes were defined to account for the anisotropy of the timber. This orthotropic material behaviour of the timber is modelled in ABAQUS using parameters as documented in Table 2.

Table 2: *Stiffness properties of timber*

Quality	E_x [N/mm²]	E_z [N/mm²]	ν_{xz} [-]	G_{xz} [N/mm²]
GL24	11.500	510	0.45	650
GL28	12.500	510	0.45	710

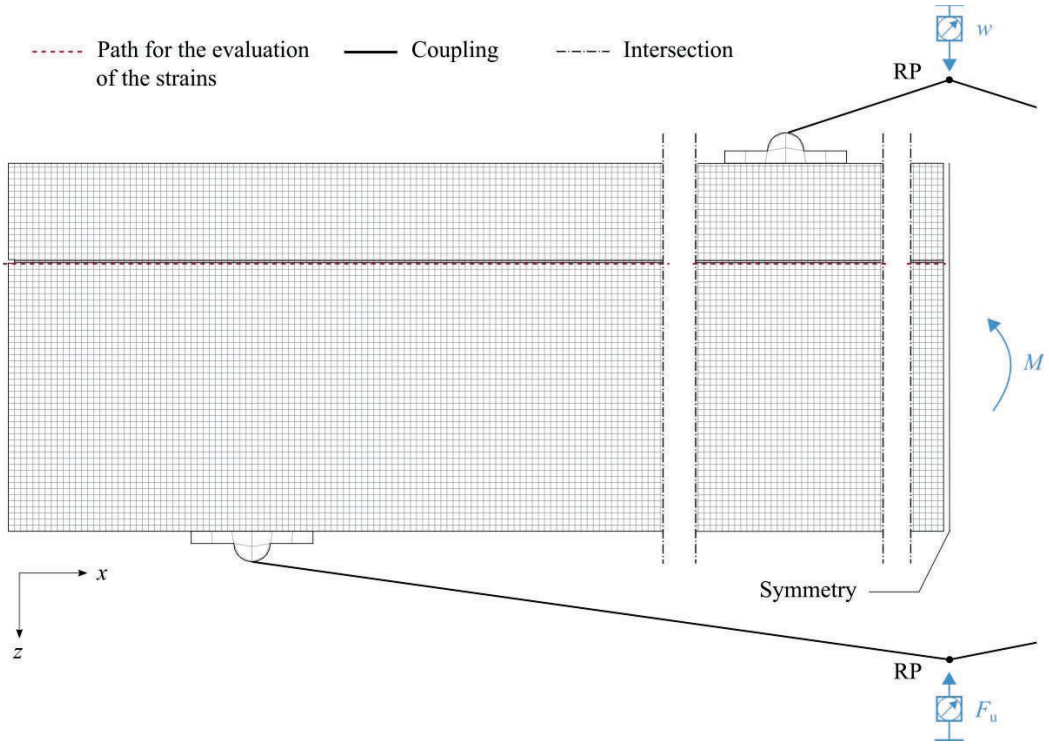

Figure 6: *Finite Element (FE) Model*

https://doi.org/10.52202/069179-0103

The isotropic material properties of concrete and adhesive are summarised in Table 3.

Table 3: *Stiffness properties of concrete and adhesive*

Material	E_x [N/mm²]	ν_{xz} [-]	G_{xz} [N/mm²]
Concrete C40/50	33.000	0.20	13.750
Concrete C45/55	34.500	0.20	14.375
2EP, low viscosity	2.500	0.40	893
Polymer mortar	25.000	0.30	10.500

4.2 COMPARISON OF MEASUREMENT AND FE MODEL

A comparison of the strains between the measurement and the FE model for type ATCC-A is depicted in Figure 7a and Figure 7b exemplarily for both beams of the specimen ATCC-A-03. The results of the FOS are depicted for the ultimate load step $F_{u,exp}$ = 165 kN.

Regarding ATCC-A, the general shape of the measurement data stands in good accordance with the results from the FE calculation. The maximum strains, however, are, in some parts, significantly higher than assumed by the calculation. Some of these peak values may be attributed to air bubbles in the adhesive with

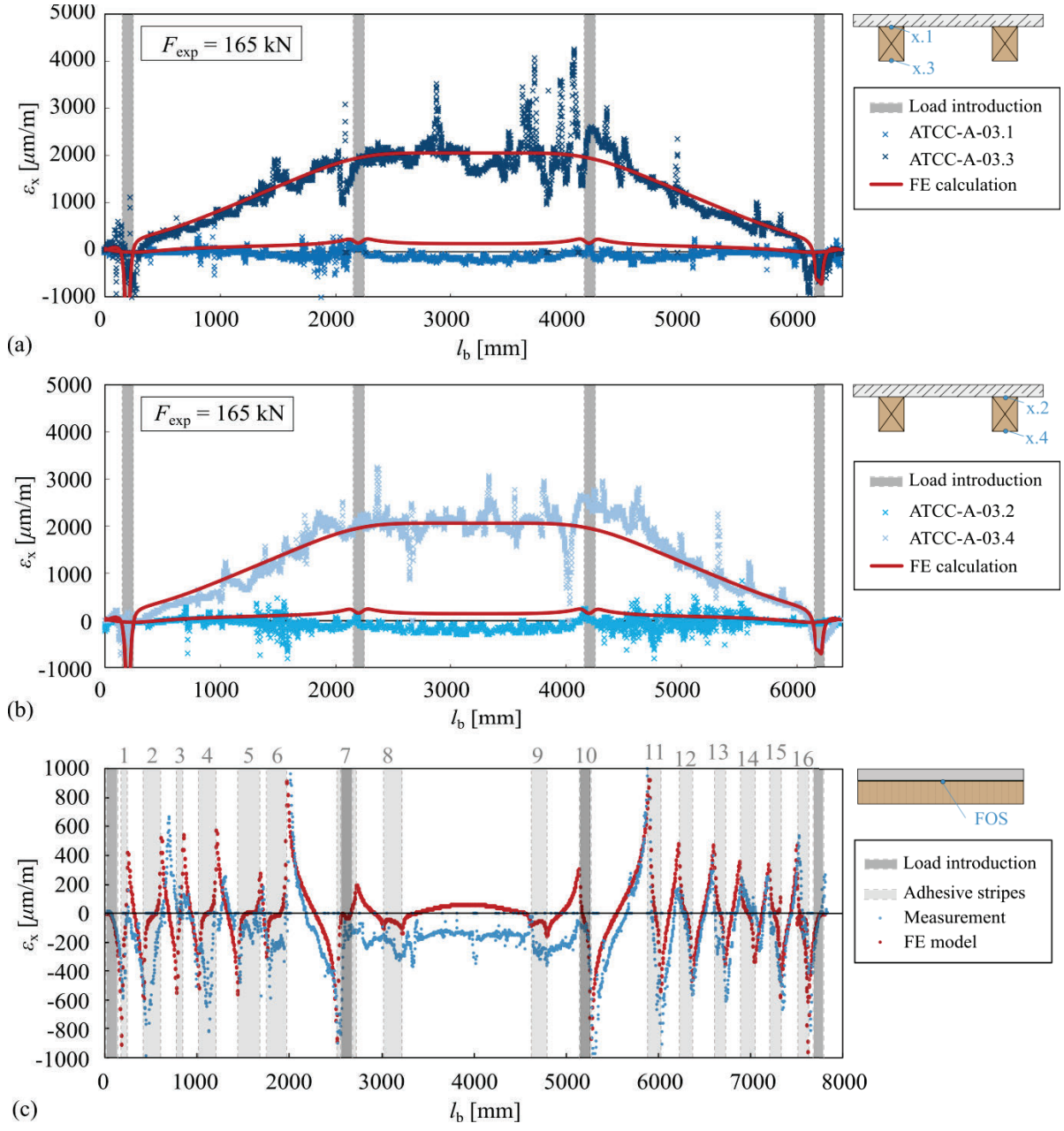

Figure 7: *Strains ε_x – comparison of measurement and FE model for ATCC-A-03*

https://doi.org/10.52202/069179-0103

which the fibre has been glued into the groove or knot-holes in the timber, as noted by Spangenberg [4]. Nevertheless, some strains clearly exceed the calculation.

A comparison of the strains between the measurement and the FE model for the composite of specimen ATCC-B is depicted in Figure 7c. A good accordance in the area of l_b = 5.5 … 8.0 m, where the bond failure occurred, can be seen both in the area of the adhesive strips and between them. It becomes evident that the bond at every strip is active, because otherwise there would no strain gradient.

Certain deviations concerning the beginning and the end of the individual adhesive strip can be seen in the area of l_b = 0 … 2.5 m and, therefore, also in the maximum and minimum values.

It should be noted that the general shape of the data curves in the area between the strips at l_b = 2.5 … 5.5 m are comparable, however, the measurement shows a timber component which is fully under compression, while the FE model indicates that the fibre is more or less located around the neutral axis of the composite beam.

5 SHEAR STRESSES

5.1 DERIVATION FROM MEASUREMENT DATA – PROCEDURE

Regarding the strains measured with FOS, the shear stresses τ_b in the bondline can be calculated directly from the measurement data if the strains have been measured both in the bondline and on the outer edge of the timber beam, resulting in two measurement points per timber beam section, as is the case for test series ATCC-A. The geometric relationships and the step-by-step procedure are shown in Figure 8.

In a first step, the strains measured are converted into stresses using Equation 1. The strains ε_o and ε_u have been averaged for 7 data points, which complies to a length of about 1 cm. The resulting forces in the timber cross-section are then determined by assuming a linear stress distribution over the height of the timber.

$$F_t = \frac{(\sigma_o + \sigma_u)}{2} \cdot A_t \tag{2}$$

The section area A_t is determined considering the height h_t and the width b_t of the timber beam.

$$A_t = h_t \cdot b_t \tag{3}$$

The determination of the force at the right edge of the cut ($F_t + \Delta F_t$) is done in the same way with the stresses at the next measuring point ($\sigma_o + \Delta\sigma_o$) and ($\sigma_u + \Delta\sigma_u$).

$$(F_t + \Delta F_t) = \frac{((\sigma_o + \Delta\sigma_o) + (\sigma_u + \Delta\sigma_u))}{2} \cdot A_t \tag{4}$$

Using the condition of equilibrium of horizontal forces $\sum H = 0$, the shear force in the joint T_b can be determined as:

$$T_b = (F_t + \Delta F_t) - F_t = \Delta F_t \tag{5}$$

The shear stress $\bar{\tau}_b$ derived from the strain can then be calculated by relating T_b to the effective bond area of the surface $A_{\Delta l}$ considered.

When the whole beam width is bonded, the width of the glued joint b_b is equal to the width of the timber beam b_t.

$$\bar{\tau}_b = \frac{T_b}{A_b} \tag{6}$$

with:

$$A_b = b_b \cdot \Delta l \tag{7}$$

The parameter Δl corresponds to the distance between two individual measuring points along the fibre.

The width, the height and the Young's modulus of each timber beam are inserted for the geometrical parameters in Equation 8: b_t = 160 mm, h_t = 220 mm and E_t = 11.500 N/mm². The bond width b_b varies depending on the specimen. For ATCC-A-01, the full width b_b = 160 mm, for ATCC-A-02 the reduced width b_b = 120 mm and for ATCC-A-03 only half of the width b_b = 80 mm is inserted. The length Δl is chosen as Δl = 0.10 m.

5.2 SPECIMENS ATCC-A

The results $\bar{\tau}_b$ of the calculation from section 5.1 are shown exemplarily for the beam 02 of specimen ATCC-A-03 in Figure 9a. The shear stresses $\bar{\tau}_b$ are compared to the shear stresses from the FE calculation. It can be seen that the values of $\bar{\tau}_b$ oscillate around the value of the FE calculation and the maximum and the minimum values differ significantly. A similar behaviour can be

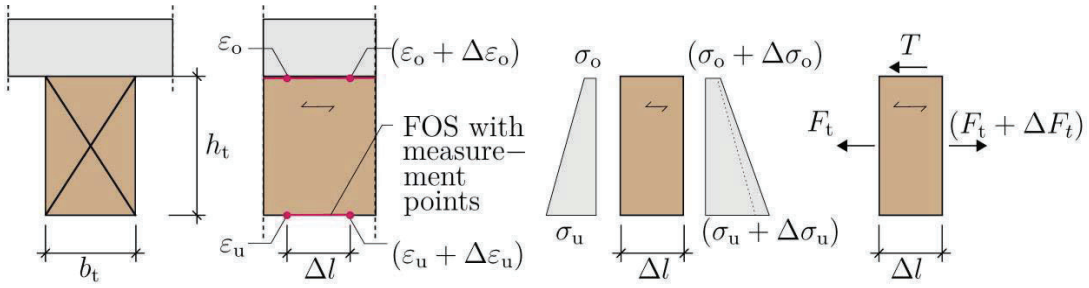

Figure 8: *Model for the derivation of shear stresses*

https://doi.org/10.52202/069179-0103

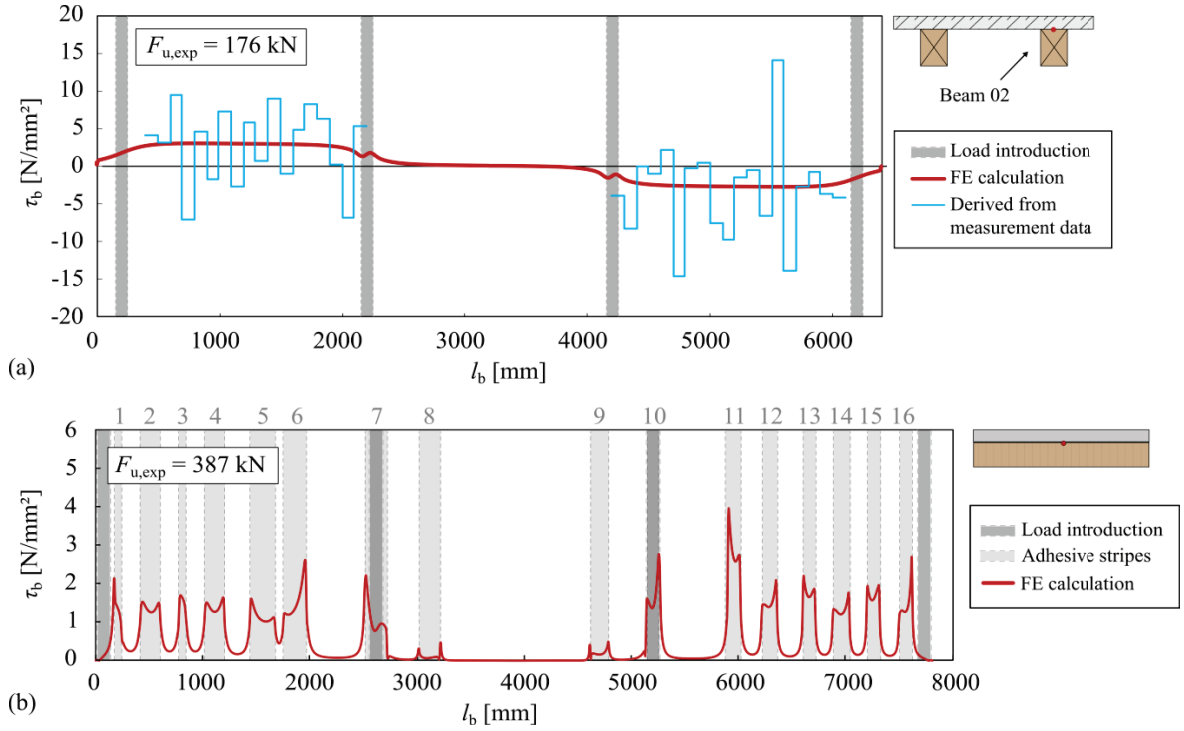

Figure 9: *(a) ATCC-A-03, beam 02: Shear stresses from FE calculation compared to shear stresses derived from measurement data for Δl = 0.10 m, beam 02*
(b) ATCC-B: Shear stresses from the FE calculation

observed for the specimens ATCC-A-01 and ATCC-A-02. At this point, it is important to point out again that these shear stresses are not ultimate shear stresses, since a bending failure in the timber has occurred in the tests and not a bond failure.

5.3 SPECIMEN ATCC-B

Only the shear stresses from the FE calculation for the specimen ATCC-B are shown in Figure 9b, with the maximum shear stress of $\tau_{b,max}$ = 4.0 N/mm² in strip 11. The procedure from section 5.1 cannot be applied there because the derivation of $\bar{\tau}_b$ requires two sensors for each timber beam.

6 CONCLUSIONS & OUTLOOK

The topic of monitoring ATCC components can be subdivided into the question of the control of the bond and the prediction of failure.

In this study, a successful adhesion could be observed by comparing the experimentally determined strains from the measurement with the values from an FE calculation. This applies both for the strains in the actual bondline, since a missing bond would be recognisable from the strain gradient, and the strains in the tension zone, which would have to be significantly greater in the case of a missing bond due to the missing composite action.
The shear transfer could further be visualised for a discontinuous bond arrangement, as is the case with the specimen ATCC-B, by means of a large strain gradient.

Regarding the three specimens from the type ATCC-A, a successful adhesion could be shown based on a calculation model, with which shear stresses have been derived directly from the measurement data. This data, however, is influenced strongly by local irregularities, such as cracks and knot-holes, which lead to a rather unsteady strain curve influenced by peaks and high strain gradients in small increments. Although the shear stresses are basically in a reasonable range, it becomes clear that this procedure is not yet fully matured and that further research is necessary. The aim should be to find either a method to determine a more constant and less unsteady strain measurement or a more robust calculation method for direct shear stress derivation. Approaches to the former can be found, for example, in Galkovski et al. [8] who place a significant emphasis on post-processing of the measurement data.

Regarding the possible prediction of a failure, the strains at the failure load were compared with those from load levels that were more distant from failure. On the basis of three specimens, it could be observed that strains behaved irregularly in some sections. Sudden changes could then indicate an imminent failure. Regarding the other two specimens, no irregular development of the strains could be observed. Whether this different behaviour is due to the fact that the corresponding sensor had not been located at the point of failure or if the irregular strain behaviour just coincided with the failure areas requires further research.
Finally, it can be stated that the FOS technology is a significant improvement compared to strain gauges, because the strips are measured continuously and not only locally, hence, a better understanding of the load transfer in the elements can be achieved.

https://doi.org/10.52202/069179-0103

ACKNOWLEDGEMENTS

The experimental campaigns were part of two research projects. The type ATCC-A has been conducted within the project “Adhesively bonded timber-concrete composites – pilot tests on the suitability of a commercially available epoxy resin adhesive” between the University of Kassel and fischerwerke GmbH & Co. KG, Germany. The type ATCC-B has been conducted within the project “Development of a rapid construction method for ATCC floors by means of bonding prefabricated concrete components” between the University of Kassel and BEWO-Betonfertigteile GmbH, Germany. The latter project is supported by the German Federal Ministry of Economics and Technology under the reference code ZF4147005EB9.

The authors would like to thank the research associations which funded and supervised the projects. Moreover, thanks goes to the associated companies Lübbert Warenhandel GmbH und Co. KG, Gebr. Schütt KG and RAMPF Machine Systems GmbH & Co. KG for their support and provision of materials.

REFERENCES

[1] Schmidt-Thrö G., Scheufer W., Fischer O.: Kontinuierliche faseroptische Dehnungsmessung im Stahlbetonbau, *Beton Stahlbetonbau* 111:496–504, 2016. https://doi.org/10. 1002/best.201600026

[2] Lemcherreq Y., Kaufmann W., Vogel T.: Fatigue of bond: Experimental investigation using pull-out tests with distributed fibre optical sensors. fib Symposium: Concrete Structures for Resilient Society (virtual) 2020.

[3] Könke C., Kuhne M., Beinersdorf H., Hildebrand J., Ganß M.: Monitoring von Klebverbindungen mittels faseroptischen Messsystem, Bauhaus-Universität Weimar and MPA Weimar, Report IGF: 17777 BR, 2015.

[4] Spangenberg A.-C.: Testing the use of fibre-optic measurement technology for monitoring bonded timber-concrete composite structures (Erprobung des Einsatzes faseroptischer Messtechnik für das Monitoring geklebter Holz-Beton-Verbundtragwerke), master thesis, 2022.

[5] Claus T., Seim W., Küllmer J.: Force distribution in self-tapping screws: experimental investigations with fibre Bragg grating measurement screws. *European Journal of Wood and Wood Products* 80:183–197, 2022. https://doi.org/10.1007/s00107-021-01740-z

[6] Frohnmüller J., Fischer J., Seim W.: Full-scale testing of adhesively bonded timber-concrete composite beams. *Materials and Structures* 54(5):1–21, 2021. Doi: https://doi.org/10.1617/s11527-021-01766-y

[7] Frohnmüller J., Seim W., Hummel J., Umbach C.: Adhesively bonded Timber-Concrete-Composite construction method (ATCC) – pilot application in a school building in Germany. WCTE 2023. Oslo, Norway, 2023.

[8] Galkovski T., Lemcherreq Y., Mata-Falcón J., Kaufmann W.: Fundamental Studies on the Use of Distributed Fibre Optical Sensing on Concrete and Reinforcing Bars. *Sensors* 21: 7643, 2021. https://doi.org/10.3390/s21227643

World Conference on Timber Engineering Oslo 2023

ESTIMATION OF MOISTURE DISTRIBUTION IN SAWN TIMBER USING COMPUTED TOMOGRAPHY

Boris Poupet[1], José Couceiro[1], Sara Florisson[2], Lars Hansson[3], Dick Sandberg[1]

ABSTRACT: Most of the physical, mechanical, and esthetic properties of wood products are affected by the drying of sawn timber. A better understanding of moisture transport in wood during kiln drying is necessary to obtain better quality products, shorter drying schedules, lower energy consumption, and a more sustainable process. Four-dimensional X-ray computed tomography (4DCT) (three-dimensional in space and one in time) with image processing techniques can be used to study the moisture content (MC) of sawn timber during kiln drying. The development of the technique is however made difficult by computational complexity and a lack of accurate experimental validation. In this study, a method relying on 4DCT has been developed using state-of-the-art image processing techniques. The method was validated by a regression analysis of the predicted MC against gravimetric measurements for different timber cross sections and different initial MC distributions on a significantly smaller scale than has previously been investigated. It is concluded that the MC can be estimated with an average uncertainty of ±4.8 percentage points on a 10 mm scale. Sawmills could ultimately benefit from a better understanding of wood-water interactions and dry sawn timber more efficiently.

KEYWORDS: four-dimensional, drying, moisture content, elastic-image registration, Norway spruce

1 INTRODUCTION

Wood is a hygroscopic material that attracts and holds water through adsorption from the surrounding environment, but wood-water interactions are still not fully understood [1], Swedish sawmills thus use software based on numerical models dating back to the mid-eighties to determine drying schedules for timber [2]. It has been empirically shown that shorter schedules are possible, reducing energy consumption and time.

X-ray computed tomography is being used in Swedish sawmills to study logs and timber in a non-destructive manner. The investigation of the internal structure of wood by means of tomography started in the mid-eighties with a medical CT scanner with first studies focused on determining the moisture content (MC) through image processing [3]. Since then, several methods have been developed to study the MC distribution with increasing complexity: unidimensional along radial lines [4], two-dimensional by manually deforming tomograms [5] digital image correlation [6], and two-dimensional in time with image registration [7].

However, almost four decades after the first investigations to determine the MC from tomograms, no attempts have been made to expand the idea to four dimensions, i.e., processing volumetric tomographic data repetitively acquired during a certain period. Such a method would be useful to investigate e.g., moisture transport along the fibres, and moisture-induced deformations in the sawn timber. Two-dimensional methods were previously usually validated against a gravimetric reference by averaging the MC determined through CT (predicted MC) of the entire cross-section [8], although this did not allow to assess the reliability of the method on a small scale.

This study contributes to the development of an image processing method to efficiently compute the MC distribution from 4DCT data. The method is validated to quantify its accuracy and precision against a gravimetric reference on a centimetre scale.

2 MATERIALS AND METHODS

2.1 Specimen preparation

Two undried centre-yield planks of Norway spruce (*Picea abies*) were collected in a local sawmill in northern Sweden. One plank, labelled S40, had a green cross-

[1] Division of Wood Science and Engineering, Department of Engineering Sciences and Mathematics, Luleå University of Technology, Sweden, boris.poupet@ltu.se
[2] Department of Materials Science and Engineering, Division of Applied Mechanics, Uppsala University, Sweden, sara.florisson@angstrom.uu.se
[3] Department of Ocean Operations and Civil Engineering, Faculty of Engineering, Norwegian University of Science and Technology, 6025 Ålesund, Norway, laha@ntnu.no

https://doi.org/10.52202/069179-0104

sectional area of 40×160 mm², and the other, labelled S70, 70×160 mm²; both with a length of approx. 5 m. From each plank, three specimens with a length of 200 mm containing only clear wood were cut, sealed on their exposed cross-sections with a layer of silicone Casco SuperFix+ [Sika, Baar, Switzerland], wrapped in plastic film and stored in a frozen condition to limit uncontrolled drying before the start of the experiments.

2.2 Validation

The MC computation from CT data was studied with different MC distributions achieved in three different ways: (1) with no drying (i.e., in the green condition), (2) by drying at 70°C for 1 h, and (3) by drying at 70°C for 3 h. The silicone on the end grain impeded longitudinal moisture transport to obtain MC distributions like those obtained with industrial kilns. After the treatment, two adjacent clear wood samples with a thickness of 20 mm were cut from each specimen, one labelled "CT" and the other "reference". On the exposed cross section of the reference samples, horizontal and vertical lines were drawn at centimetre intervals to form a regular grid (Figure 1).

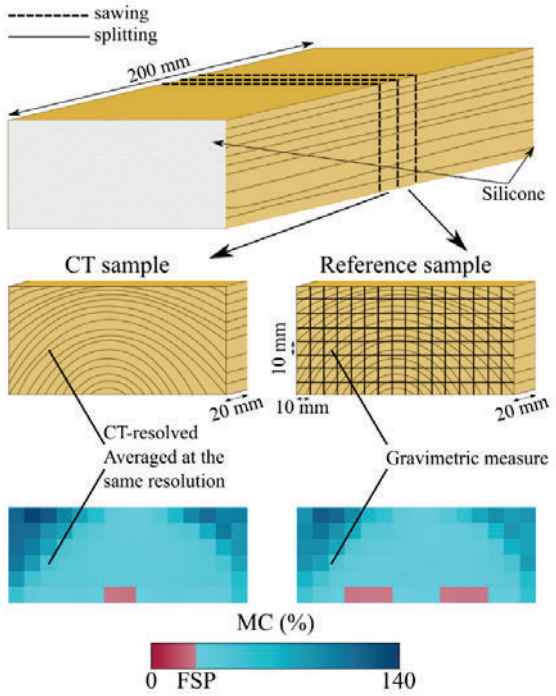

Figure 1: *CT and reference samples prepared after the specimen treatment. The MC distribution of the reference sample was determined gravimetrically by splitting it into test volumes 10 mm×10 mm×20 mm in size. The MC distribution in the CT sample was predicted with the CT method and averaged at the same spatial resolution.*

The CT sample was used to obtain the 2D density distribution ρ_{CT} after drying using a Siemens Somatom Emotion Duo [Siemens, Munich, Germany] CT-scanner at a spatial resolution of 0.98 mm×0.98 mm in the cross-sectional plane and 10 mm lengthwise. The masses after treatment of both CT and reference samples were acquired with a precision balance Ohaus AX523 [Ohaus, Parsippany, USA]. The reference samples were split with a knife along the grid lines into test volumes 10 mm×10 mm×20 mm in size and their initial masses were determined with the precision balance. The samples were oven-dried at 103±2°C (CEN 2002) and reweighed. The CT sample was rescanned with the same settings to evaluate its oven-dry density distribution $\rho_{0,CT}$.

In the reference samples, the gravimetric MC of the jth test volume (w_g^j) was computed using Equation (1):

$$w_g^j = \frac{m_i^j - m_0^j}{m_0^j} \quad (1)$$

where m_i^j is the initial mass of the jth test volume and m_0^j its oven-dry mass. Together, the measures w_g^j form the MC distribution w_g of the reference sample. The MC of the CT sample w_{CT} was predicted on the voxel scale using the method described in 1.3. For comparison with the reference MC distribution, the predicted MC was averaged in test volumes of 10 mm×10 mm×10 mm as w_{CT}^j.

Although these experiments use the 4DCT method to provide the first validation of the method, it was performed in 2D to simplify the process. It was observed in preliminary tests that the cross-sectional directions of the wood are the most troublesome to register. The gravimetric method to which the predicted MC is validated is very time-consuming, it would not be practical to repeatedly implement it for many CT/reference sample pairs contained in the same specimen.

2.3 Image processing

The image processing method was intended for use with 4DCT data, but it is applicable in fewer dimensions. Regardless of the dimensions, data reconstructed by the CT scanner are stacked as a density field in NRRD format. Processing this density data for MC computation involves three steps: image registration, density correction, and MC calculation.

2.3.1 Image registration

To compute the change in MC during drying, the density fields $\rho(\mathbf{X},t)$ at different times (t) must be compared to the oven-dry density field $\rho_0(\mathbf{x})$, where $\mathbf{X} = (X,Y,Z)$ are the material coordinates and $\mathbf{x} = (x,y,z)$ are the spatial coordinates as shown in Figure 2. This operation is made difficult by the anisotropic deformations that sawn timber undergoes while drying, which introduce misalignments between the tomograms. To solve this problem, state-of-the-art elastic image registration based on B-splines was used [9]. This technique computes a coordinate transformation from the material to the spatial coordinates $\mathbf{x} = \mathbf{T}(\mathbf{X},t)$ so that the registered densities $\rho(\mathbf{x},t)$ are spatially aligned with $\rho_0(\mathbf{x})$, as illustrated in Figure 2. The registration is performed in the image-analysis software *3Dslicer* using the *Sequence Registration* module

specially dedicated to 4D registration based on the *Elastix* toolbox [9]. With the different input data tested, the algorithm always converged to a solution as long as the deformations were continuous, i.e., provided that no cracks or material losses occurred.

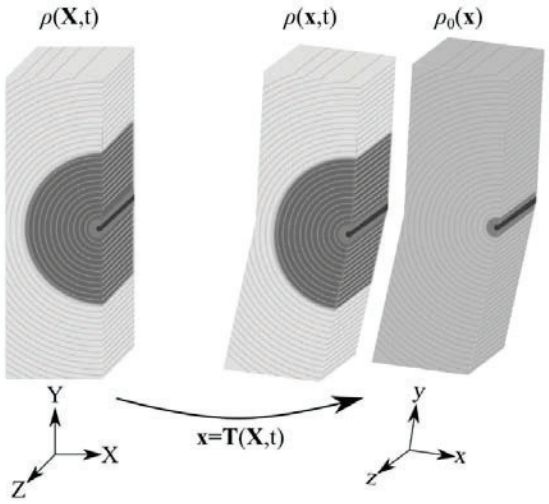

Figure 2: *Lagrangian description of the displacement experienced by a wood volume from an undeformed configuration* $\boldsymbol{\rho(X,t)}$ *to a deformed configuration (oven-dry)* $\boldsymbol{\rho_0(x)}$*. By applying the transformation* $\mathbf{T}(\mathbf{X},t)$*, the volumes become spatially aligned (shifted in the illustration by a rigid-body displacement for visualisation purposes).*

2.3.2 Density correction

The registered densities $\rho(\mathbf{x},t)$ must be interpolated and recalculated. The transformation performed by the image registration allocates the registered densities to non-voxel positions, and interpolation is necessary to assign a single density value to each voxel position. Since the image registration deforms the wood volume, the densities must be recalculated to compensate for the local volumetric strains defined by Equation (2).

$$\varepsilon_V(\mathbf{x},t) = \frac{V_0(\mathbf{x}) - V(\mathbf{X},t)}{V_0(\mathbf{x})} \tag{2}$$

Where $V(\mathbf{X},t)$ is the voxel volume in the undeformed configuration and $V_0(\mathbf{x})$ is its equivalent in the deformed configuration.

Density interpolation and rescaling were performed simultaneously with an algorithm developed by Hansson and Fjellner [10] and based on polygon clipping. The volumetric strain was decomposed as the sum of the elementary strains $\varepsilon_V = \Sigma\varepsilon_j$ computed in the regions enclosed by the undeformed grid. The rescaled densities $\rho'(\mathbf{x},t)$ were computed as shown in Figure 3 using Matlab® [MathWorks, Natick, USA].

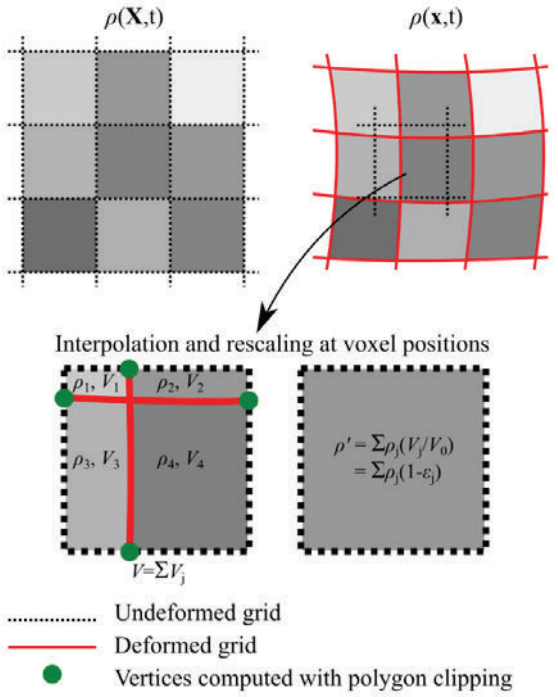

Figure 3: *Density correction. The volumes* V_j *are computed by obtaining the vertex coordinates via polygon clipping. The rescaled density is the sum of the densities weighted by their respective volumetric changes. The illustration is limited to 2D for visualization purposes.*

2.3.3 Moisture content calculation

The MC was computed using Matlab® at the voxel level from the spatial coordinates in Equation (3):

$$w(\mathbf{x},t) = \frac{\rho'(\mathbf{x},t) - \rho_0(\mathbf{x})}{\rho_0(\mathbf{x})} \tag{3}$$

2.4 Uncertainties of measurement and errors

Differences between the gravimetric (w_g) and predicted (w_{CT}) MC distributions were studied with respect to measurement limitations and errors to estimate the uncertainty of the method.

The uncertainty of the gravimetric method u_g^j was estimated in Equation (4) for each test volume as the combined uncertainty of measurement due to the scale precision u_s^j and uncertainty due to the ongoing drying of the reference samples while being splitted (u_d).

$$u_g^j = \sqrt{\left(u_s^j\right)^2 + {u_d}^2} \tag{4}$$

The precision of the balance is given by the manufacturer as $\Delta m = \pm 10^{-6}$ kg. The uncertainty u_s^j is computed in Equation (5) as the total differential of w_g^j defined in Equation (1).

https://doi.org/10.52202/069179-0104

$$u_{\mathrm{s}}^{\mathrm{j}} = \frac{\Delta m}{m_0^{\mathrm{j}}}\left(2 + w_{\mathrm{g}}^{\mathrm{j}}\right) \tag{5}$$

The uncertainty u_{d} is estimated for each reference sample in Equation (6):

$$u_{\mathrm{d}} = w_{\mu}\left(m_{\mathrm{i}}, \Sigma m_0^{\mathrm{j}}\right) - w_{\mu}\left(\Sigma m_{\mathrm{i}}^{\mathrm{j}}, \Sigma m_0^{\mathrm{j}}\right) \tag{6}$$

where $w_{\mu}\left(m_{\mathrm{i}}, \Sigma m_0^{\mathrm{j}}\right)$ is the average MC of the reference sample with initial mass m_{i}, and $w_{\mu}\left(\Sigma m_{\mathrm{i}}^{\mathrm{j}}, \Sigma m_0^{\mathrm{j}}\right)$ its average MC based on the initial mass $\Sigma m_{\mathrm{i}}^{\mathrm{j}}$, i.e., the sum of the initial masses of the test volumes. In both situations, the oven-dry mass was assumed to be Σm_0^{j}, i.e., the sum of the oven-dry masses of each test volume, as the oven-dry masses of the reference samples could not be measured before the splitting.

The uncertainty of the predicted MC ($u_{\mathrm{CT}}^{\mathrm{j}}$) is estimated for each test volume from Equation (7) as the combined uncertainty due to the density measurement of the CT-scanner u_{ρ}^{j} and the errors associated with the image processing steps $u_{\mathrm{im}}^{\mathrm{j}}$:

$$u_{\mathrm{CT}}^{\mathrm{j}} = \sqrt{\left(u_{\rho}^{\mathrm{j}}\right)^2 + \left(u_{\mathrm{im}}^{\mathrm{j}}\right)^2} \tag{7}$$

The precision of density measurement by the CT scanner was taken to be $\Delta\rho_{\mathrm{CT}} = \pm 4$ kg/m³. This value corresponds to the scatter of the density distribution measured for a 1 cm³ volume of a water phantom at thermal equilibrium with a 95% confidence interval.

This uncertainty was propagated by computing the total differential of w_{CT} and estimated for each voxel in Equation (8):

$$u_{\rho} = \frac{\Delta\rho_{\mathrm{CT}}}{\rho_{0,\mathrm{CT}}}\left(2 + w_{\mathrm{CT}}\right) \tag{8}$$

This uncertainty was sufficiently uniform in the capillary and bound water dominated regions to justify averaging the values according to Equation (9):

$$u_{\rho}^{\mathrm{j}} = \begin{cases} u_{\rho,\mathrm{c}}\,, w_{\mathrm{CT}}^{\mathrm{j}} > 0.6 \\ u_{\rho,\mathrm{b}}\,, w_{\mathrm{CT}}^{\mathrm{j}} \leq 0.6 \end{cases} \tag{9}$$

where $u_{\rho,\mathrm{c}}$ and $u_{\rho,\mathrm{b}}$ are the average uncertainties of the capillary and bound water dominated regions respectively.

The uncertainty $\Delta_{\mathrm{z}} w$ accounts for the differences in MC between the CT and reference samples, i.e., the lengthwise gradients of MC, as:

$$\Delta_{\mathrm{z}} w = w_{\mu,\mathrm{CT}} - w_{\mu,\mathrm{r}} \tag{10}$$

where $w_{\mu,\mathrm{CT}}$ and $w_{\mu,\mathrm{r}}$ are the average gravimetric MCs of the CT and reference samples respectively.

The absolute difference between the predicted MC and the gravimetric MC is interpreted as being the combined uncertainty due to the gravimetric method, the CT method, and experimental limitations:

$$\left|w_{\mathrm{g}} - w_{\mathrm{CT}}\right| = \sqrt{{u_{\mathrm{g}}}^2 + {u_{\mathrm{CT}}}^2 + \left(\Delta_{\mathrm{z}}^{\mathrm{j}} w\right)^2} \tag{11}$$

The uncertainty $u_{\mathrm{im}}^{\mathrm{j}}$ corresponding to the errors due to the image processing was not directly estimated in this study but was instead indirectly evaluated in Equation (12) by comparing the observed difference between the CT and reference MC distributions and the previously evaluated uncertainties.

$$u_{\mathrm{im}}^{\mathrm{j}} = \sqrt{\left(w_{\mathrm{g}}^{\mathrm{j}} - w_{\mathrm{CT}}^{\mathrm{j}}\right)^2 - \left(u_{\rho}^{\mathrm{j}}\right)^2 - \left(u_{\mathrm{g}}^{\mathrm{j}}\right)^2 - \left(\Delta_{\mathrm{z}} w\right)^2} \tag{12}$$

Lindgren et al. [3] determined experimentally a maximal deviation of 2 pixels when performing a non-linear transformation for a wood sample between an equilibrium MC state and a state after soaking the sample in water. These authors related this spatial mismatch to an additional density uncertainty $\Delta\rho_{\mathrm{im}} = \pm 6$ kg/m³, which is higher by a factor of 1.5 than the uncertainty due to the CT-scanner. Under this assumption, a threshold was set to evaluate whether the image registration introduced a spatial mismatch (s^{j}) greater or less than 2 pixels:

$$s^{\mathrm{j}} = \begin{cases} \leq 2 \text{ pixels} & \text{if } u_{\mathrm{im}}^{\mathrm{j}} \leq 1.5 u_{\rho}^{\mathrm{j}} \\ > 2 \text{ pixels} & \text{else} \end{cases} \tag{13}$$

3 Results

Linear regressions between the predicted and gravimetric MCs were calculated and the results are shown in Figure 4. The predicted MC tends to be overestimated, since the regression lines are located above the line of equality $w_{\mathrm{CT}} = w_{\mathrm{g}}$.

The cross-sectional area and the MC distribution of the samples were identified as the parameters which had the greatest impact on the reliability of the image processing method. An increase in the cross-sectional area was indeed expected to increase the computation complexity as more voxels must be processed. The MC distribution was expected to influence the performance of the method, since it is correlated to the degree of deformation of the wood. The MC computation should be more complex in an undeformed configuration (green sawn timber) than in an intermediately deformed configuration (between a green and an oven-dry state).

https://doi.org/10.52202/069179-0104

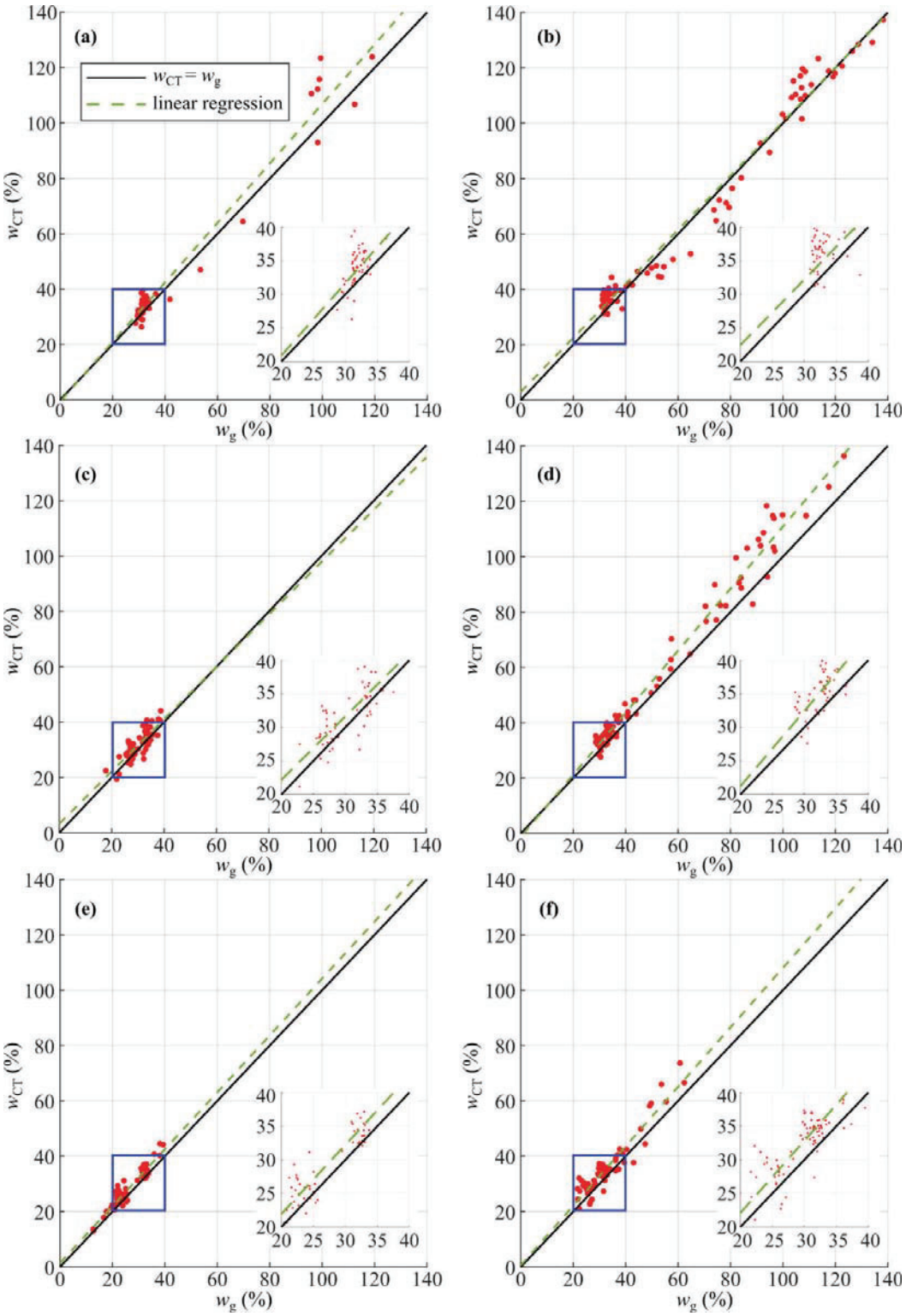

Figure 4: *The predicted MC (w_{CT}) plotted against the gravimetric MC (w_g). (a), (c), and (e) represent the S40 samples with cross-sectional area of 40×160 mm², and (b), (d), and (f) represent the S70 samples with a cross-sectional area of 70×160 mm². (a) and (b) specimens that underwent no drying; (c) and (d) specimens that underwent drying for 1h at 70°C; (e) and (f) specimens that underwent drying for 3h at 70°C. The diagonal plain line represents a perfect match between the two datasets ($w_{CT=}w_g$). The dashed line corresponds to a linear regression. The smaller graph with values from 20 % to 40 % is a region around FSP for better visualization.*

https://doi.org/10.52202/069179-0104

The validation was assessed by the root-mean square error (RMSE) which indicates the precision of the method and the coefficient of determination of the linear regression (R^2) which indicates its accuracy. The results are presented in Figure 5.

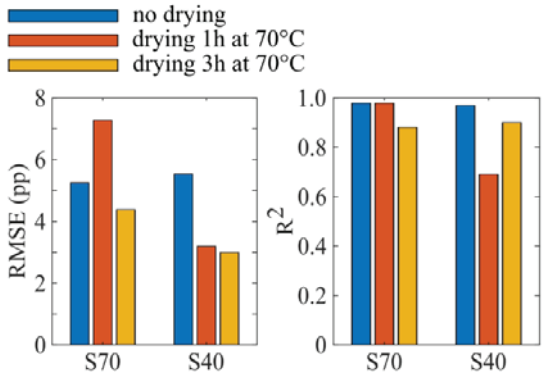

Figure 5: *Precision and accuracy of the CT-method. Root-mean-square-error (left) and R^2 (right) of the linear regressions. "pp" stands for percentage points.*

The average RMSE was higher for the larger S70 specimens than for the smaller S40 specimens, which suggests that a larger cross-sectional area is more complex to process for both image registration and density correction algorithms. The RMSE of the S40 specimens decreased from 5.5 to 3 percentage points (pp) when the drying was extended from 0 h to 3 h. The RMSE of the S70 specimens was 5.25, 7.28, and 4.38 pp for 0 h, 1 h, and 3 h drying respectively. Except for the RMSE peak at 1 h drying for the S70 specimen, these observations suggest that the image processing performs better when the sawn timber is dried, as it is easier to compute smaller deformations. A decrease in the R^2 coefficient was observed for both specimen groups with increasing drying time.

The performance of the image processing method was assessed by quantifying its uncertainty and spatially mapping it within the cross section. The uncertainty was estimated with Equations (12-13) and the results are shown in Figure 6. High uncertainties (>10 pp) considered as outliers were always found for test volumes located at the sample edge, mostly in the sapwood region. Uncertainties corresponding to spatial mismatches greater than 2 pixels (>*) were relatively more frequently found in the S70 than in the S40 samples. Drying lowered the average uncertainty value for both sample sizes.

The occurrence of test volumes with spatial mismatches greater than 2 pixels in CT samples could be related to their respective strain distributions. It was inferred that the image registration was worse for regions experiencing a high strain and shear.

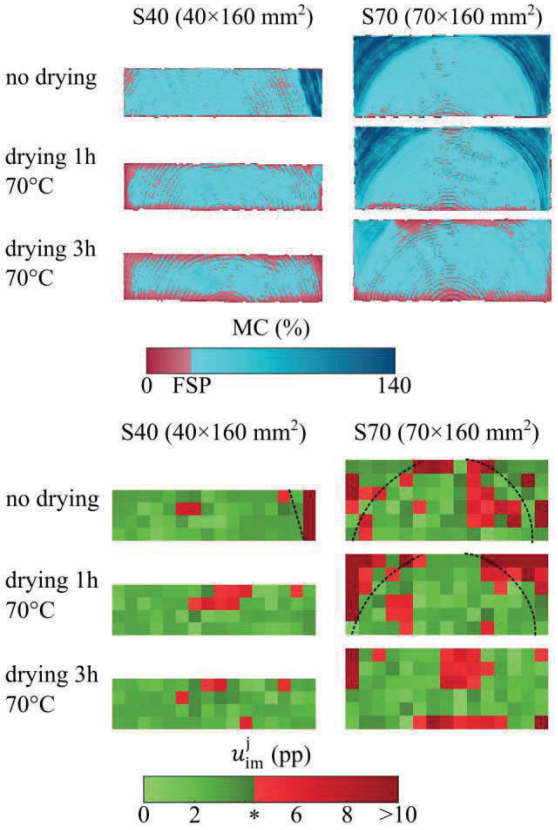

Figure 6: *Predicted MC (top) and uncertainty of the image processing method (below). The threshold marked * is set as described in Equation (13): values below or above it corresponds to spatial mismatches greater or less than 2 pixels. The value of the threshold is slightly different for each situation and ranges from 3.8 to 4.5 pp. The dashed curves indicate the sapwood/heartwood borders when they were visible in the CT data. "pp" stands for percentage points.*

4 CONCLUSIONS

It has been shown that the image processing is a suitable method for the calculation of MC with an average uncertainty ranging from 2.8 to 4.9 pp estimated on a 10 mm scale. A fine adjustment of the image processing parameters might reduce this error. Measurement limitations of the CT scanner increase this range to ±[4.4-7.8] pp, which may be improved by using another image reconstruction algorithm.

The method performed better when the cross section of the specimen was smaller, as the complexity of the image registration decreases with a decreasing amount of data to process. The method was also more precise when the transformation was computed from an intermediate deformed configuration than from an undeformed configuration (green condition). Consequently, the reliability increased with a lower MC, dry enough to initiate the deformation. The cross-sectional area of the specimen was identified as having a greater effect than the MC distribution on the precision of the method.

https://doi.org/10.52202/069179-0104

Extending this method to compute the MC in 4D can be better than existing methods for investigating wood-water relations during the drying of sawn timber, and for other processes such as wood modification or mechanical testing. The method will be expanded to characterize moisture-induced strain fields based on the displacement data obtained by image registration.

ACKNOWLEDGEMENT

The authors acknowledge the considerable support of the CT WOOD research program at Luleå University of Technology in Skellefteå for the development of X-ray computed tomography applications for use in the forest products industry.

REFERENCES

[1] E. E. Thybring, M. Fredriksson, S. L. Zelinka, S. V. Glass. Water in Wood: A Review of Current Understanding and Knowledge Gaps. *Forests,* 13(12):2051, 2022

[2] J. Salin. Simulation models; from a scientific challenge to a kiln operator tool. In *6 th International IUFRO Wood Drying Conference*, pages 25-28, 1999.

[3] O. Lindgren, S. Grundberg, J. R. Davis. Applying digital image processing on CAT-scan images of wood for non-destructive moisture content measurements. Paper VI in *O. Lindgren, 1992. Medical CT-Scanners for Non-Destructive Wood Density and Moisture Content Measurements. Doctoral thesis. Luleå University of Technology, Division of Wood Technology, Skeria 3, SE-931 87 Skellefteå, Sweden. Thesis No. 1992:111D. ISSN 0348-8373,* 1992.

[4] J. R. H. Fromm, I. Sautter, D. Matthies, J. Kremer, P. Schumacher, C. Ganter. Xylem Water Content and Wood Density in Spruce and Oak Trees Detected by High-Resolution Computed Tomography. *Plant Physiology*, 127(2): 416-425, 2001.

[5] C. Lazarescu, K. Watanabe, S. Avramidis. Density and moisture profile evolution during timber drying by CT scanning measurements. *Drying technology,* 28(4): 460-467, 2010.

[6] K. Watanabe, C. Lazarescu, S. Shida, and S. Avramidis. A Novel Method of Measuring Moisture Content Distribution in Timber During Drying Using CT Scanning and Image Processing Techniques. *Drying Technology,* 30(3): 256-262, 2012.

[7] L. Hansson, E. Cherepanova. Determination of wood moisture properties using a CT-scanner in a controlled low-temperature environment. *Wood Material Science and Engineering,* 7(2): 87-92, 2012.

[8] J. Couceiro, D. Elustondo. Implementation of computer aided tool for non-destructive X-ray measurement of moisture content distribution in wood. *Pro Ligno,* 11(4): 330-336, 2015.

[9] S. Klein, M. Staring, K. Murphy, M. A. Viergever, J. Pluim. Elastix: A Toolbox for Intensity-Based Medical Image Registration. *IEEE Transactions on Medical Imaging,* 29(1): 196-205, 2010.

[10] L. Hansson, B-A. Fjellner. Wood shrinkage coefficient and dry weight moisture content estimation from CT-images. *Pro Ligno,* 9(4): 557-561, 2013.

https://doi.org/10.52202/069179-0104

World Conference on Timber Engineering Oslo 2023

PREDICTION OF DOUGLAS-FIR SAWN TIMBER YIELD BASED ON LOG COMPUTED TOMOGRAPHY

Andreas Weidenhiller[1], Boris Sandor[2], Thomas Simlinger[3], Franka Brüchert[4], Johannes A. J. Huber[5]

ABSTRACT: Climate change affects the growth conditions for Norway spruce (*Picea abies*) which is the most important species for the European construction timber industry. As a countermeasure, the species mix in European forests is being changed to include more hardwood, but also more drought-resistant softwood species, for example Douglas-fir (*Pseudotsuga menziesii*). Previous research has shown that Douglas-fir can on the one hand be suitable to produce high-strength material. On the other hand, however, Douglas-fir wood can also have a considerably lower strength than what is expected from spruce. Therefore, there is need for improved strength prediction and strength grading methods for Douglas-fir, to enable the correct allocation of Douglas-fir roundwood to the most suitable target product. In the present study, computed tomography (CT) image reconstructions of 53 Douglas-fir logs were used to predict the strength of the sawn timber and thus to identify logs which are suitable to produce glulam lamellas. To achieve this, statistical modelling was combined with Finite Element (FE) modelling of destructive tensile tests, based on simulated fibre orientations for the boards.

KEYWORDS: Douglas-fir (*Pseudotsuga menziesii*), strength prediction, glulam lamellas, statistical modelling, simulated fibre orientations, Finite Element Analysis

1 INTRODUCTION

Europe aims to proceed towards a sustainable bio-based economy, which should be less dependent on fossil resources [1]. Forest based products, including construction timber products, are an important element in this strategy. At the same time, the growth conditions are declining for spruce (*Picea abies*) which is Europe's most important wood species for construction timber products – due to climate change, temperatures are rising, and the risk of drought is increasing. Douglas-fir (*Pseudotsuga menziesii*) is seen as one of the tree species which could complement spruce in the future, due to its drought resistance, fast growth and interesting material properties [2]. Sauter [3], e.g., observed an average tensile strength of more than 40 N/mm², but with unusually high coefficients of variation (CoV) of 50%-60%. Rais et al. [4] reported, for material from a plant density trial, average tensile strengths between 17 N/mm² and 25 N/mm² with CoV in the range of 30%-40%. Such high variations in sawn timber properties can be a challenge for the construction timber industry. Therefore, our study presents methods to predict the sawn timber strength already at the roundwood stage and thus to allow identification of suitable raw material for glulam production.

2 MATERIAL AND METHODS

2.1 MATERIAL

For this study, 53 Douglas-fir logs from two stands (age of 60 years) close to Vienna (Austria) were selected, focusing on qualities which are typically used for construction timber production. The share of quality class A according to Austrian wood trade practices was 9%, that of quality class B 76%. 15% of the wood corresponded to the quality class C. The roundwood diameters were between 25 cm and 46 cm.

2.2 ROUNDWOOD SCANNING AND SAWING

The logs were scanned with the roundwood CT scanner at the Forest Research Institute Baden-Württemberg in Freiburg, Germany. Based on the CT image reconstruction, several wood properties were extracted, among them heartwood, knots and pith. For the knots, parametric descriptions similar to Johansson et al [5] were computed.

[1] Andreas Weidenhiller, Holzforschung Austria, Franz-Grill-Straße 7, Vienna, Austria, a.weidenhiller@holzforschung.at
[2] Boris Sandor, Holzforschung Austria, Austria, b.sandor@holzforschung.at
[3] Thomas Simlinger, Holzforschung Austria, Austria, th.simlinger@gmail.com
[4] Franka Brüchert, Forest Research Institute Baden-Württemberg, Germany, franka.bruechert@forst.bwl.de
[5] Johannes A. J. Huber, Luleå University of Technology, Sweden, johannes.huber@ltu.se

https://doi.org/10.52202/069179-0105

Further, the longitudinal eigenfrequency f of each log was measured using a Microtec ViScan device, and the dynamic modulus of elasticity $E_{dyn,log}$ was calculated for each log using Equation (1):

$$E_{dyn,log} = 4 \cdot \rho_{log} (l \cdot f)^2 \quad (1)$$

Where ρ_{log} was the average log density from CT scanning and l was the log length.

The logs were sawn according to the cutting patterns given in Figure 1. 14 logs were sawn according to pattern a, 23 logs according to pattern b, and 16 logs according to pattern c. One log in pattern c was accidentally sawn so that it had four more side boards. In total, sawing yielded 267 main boards and 156 side boards. The boards were dried to a target moisture content (MC) of 12%. The main boards were planed to a thickness of 45 mm; the side boards were all planed to a thickness of 25 mm.

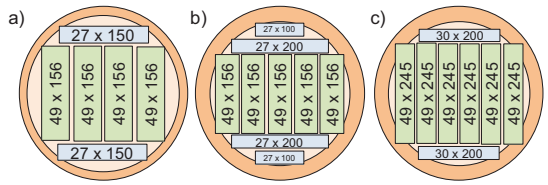

Figure 1: *Cutting patterns used for sawing the Douglas fir logs (board dimensions in mm). One of the logs in pattern c had 4 additional side boards of the dimensions 30 x 100 mm².*

2.3 SAWN TIMBER SCANNING AND TESTING

After planing, the boards were strength graded with a Microtec GoldenEye 706 machine including X-ray and eigenfrequency measurement. At the laboratory of Holzforschung Austria, the boards underwent destructive tensile testing according to EN 408 [6], including measurement of dry wood density and MC on a small clear sample of each tested board, and corrections of the values according to EN 384 [7]. However, it was decided to exclude the 28 side boards of dimension 27x150 mm² from destructive testing, as their number was so small.

Further, 14 main boards and 14 side boards had to be excluded due to various reasons, like breakage during machine strength grading or excessive wane.

The final yield was: 253 main boards with the cross sections 45x145 mm² and 45x230 mm², and 104 side boards with 25x90 mm² and 25x185 mm².

2.4 TRACKING OF TIMBER POSITIONS

The position of each board in the respective log was tracked using log end templates [8]. Those templates were sheets of paper containing the log ID as well as angular information and distance to the pith (see Figure 2a). The sheets were glued to one log end and remained there during sawing, drying, planing, industrial strength grading and destructive testing (Figure 2b). At the end of the process, the templates on the boards were scanned and manually arranged to reconstruct the original positions of the then dry boards in the green log CT reconstruction. To easily arrange the images, a dedicated tool was programmed by the authors (Figure 2c) using R [9] and the shiny package [10].

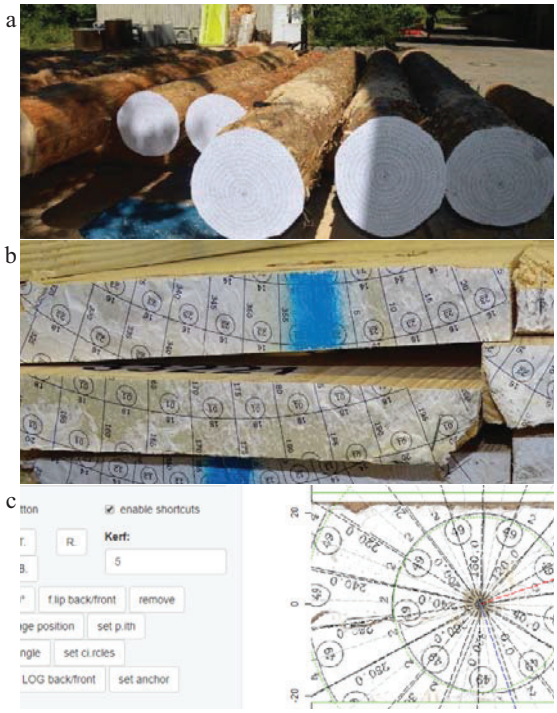

Figure 2: *Log end templates. a) glued to the log end, b) remaining on the board throughout the board processing, c) detail screenshot of the tool to arrange the scans.*

2.5 VIRTUAL SAWING

Using the reconstructed board positions, virtual boards were created from the CT images of the log. For each virtual board, descriptive variables were calculated, including heartwood density, distance from pith and percentage of knot volume. Further, a board X-ray scan was simulated by calculating average densities along the direction of the board thickness, which resulted in density data arrays of the dimensions "board width" by "board length". These green densities were assumed to have been measured at an MC of $u = 29\%$ (fibre saturation point) and were corrected to an MC of $u_{\text{ref}} = 12\%$ using Equation (2) (EN 384 [7]).

$$\rho = \rho(u)\big(1 - 0.005(u - u_{\text{ref}})\big) \quad (2)$$

2.6 SIMULATION OF FIBRE ORIENTATIONS

Based on the parametric knot descriptions calculated on the CT images and using the reconstructed board position, fibre orientations were simulated along the length and width of the central plane for each board at a resolution of one grid point per mm, using the approach described by Huber et al. [11]. A detail of such reconstructed fibre

https://doi.org/10.52202/069179-0105

orientations is shown in Figure 3. For the figure, the resolution was reduced to one grid point per 5mm.

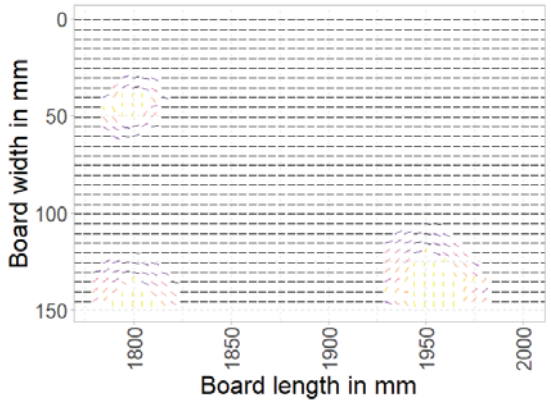

Figure 3: *Detail of simulated fibre orientations: flow of fibres around three knots in board 23047. Each line segment corresponds to one grid point, colours indicate the magnitude of the grain deviation.*

2.7 FINITE ELEMENT MODEL

Using COMSOL Multiphysics® [12], tensile tests were simulated on a two-dimensional plane stress model of each board. The calculated fibre orientations (section 2.6) were used to generate a locally varying coordinate system. This system transforms the three-dimensional cylindrical (LRT) material properties defined by the reference stiffness tensor C [13] to the two-dimensional model of the board – see Equation (3).

$$C(\rho) = \frac{\rho(x,y)}{\rho_{ref}} \begin{bmatrix} 11162 & 504 & 435 & 0 & 0 & 0 \\ & 866 & 281 & 0 & 0 & 0 \\ & & 528 & 0 & 0 & 0 \\ & & & 620 & 0 & 0 \\ & sym & & & 500 & 0 \\ & & & & & 23 \end{bmatrix} \quad (3)$$

Due to the density dependence of this stiffness tensor the local values were linearly scaled from the reference density of $\rho_{ref} = 390$ kg/m³ according to the local density $\rho(x,y)$ obtained from the virtual board (section 2.5). The discretization was performed with a uniform quadrilateral mesh with a resolution of 1 mm. In order to determine the Young's Modulus one side of the board was constrained in both spatial directions while the other side was prescribed a displacement of 5 mm along the x-axis. From the reaction forces, the Young's Modulus was calculated for each board.

2.8 MODELLING THE SAWN TIMBER STRENGTH GRADING

We wanted to predict the grade yield achieved by the GoldenEye 706 sawn timber strength grading machine. For this purpose, we modelled the GoldenEye Indicating Property (IP) for strength with linear regression, based on descriptive variables extracted from the virtual boards, the Young's Modulus from the FE model, as well as the $E_{dyn,log}$ in various combinations. The regression coefficients were calculated on the training data set, which encompassed 60% of the logs in the study (33 logs, 208 boards). The following predictors for the GoldenEye 706 strength IP were calculated:

- VB ("virtual board") using the virtual board's knottiness, heartwood density and distance to pith information (section 2.2);
- VB+FE, using in addition the Young's Modulus from the FE model (section 2.7);
- VB+Edyn,log, which combined the virtual board's knottiness and heartwood density with the $E_{dyn,log}$ (section 2.2).

2.9 YIELD PREDICTION

For the GoldenEye strength IP, a setting S for strength grading into strength class T14 was calculated on the training set, using a simplified approach based on EN 14081-2 [14]. The T14 strength class is defined in EN 338 [15] with the following properties: 5th percentile of tensile strength ($f_{t,k}$) at least 14 N/mm²; average tensile modulus of elasticity ($E_{t,0,mean}$) at least 11 kN/mm², and fifth percentile of the density (ρ_k) at least 350 kg/m³. T14 is one of the most important strength classes for producing glue laminated timber (glulam) of strength class GL24h [16].

Boards with an IP below the setting value S were rejected, and all other boards were assigned to T14. The same setting S was applied to the three IP predictors calculated on the log scanning data (section 2.8). This was used to predict the yield of T14 boards from the sawn timber strength grading.

2.10 LOG PRESORTING

Log pre-sorting was done by assigning only such logs to the production of T14 boards where the predicted yield was above a certain threshold T, which we varied from 0% to 100%.

The efficiency of the pre-sorting was defined as obtaining as many T14 boards as possible from the given logs while producing as few rejected boards during the sawn timber strength grading as possible.

This trade-off was visualised using the following two quantities in Equations (4) and (5).

$$total\ yield\ T14 = \frac{n_{T14,grading}}{n_{boards,sawn}} \quad (4)$$

$$relative\ yield\ T14 = \frac{n_{T14,grading}}{n_{boards,grading}} \quad (5)$$

where $n_{T14,grading}$ means the number of boards assigned to T14 during strength grading, $n_{boards,sawn}$ means the number of all boards sawn from all logs, and $n_{boards,grading}$ means the number of boards sent to the strength grading process. Thus, the $total\ yield\ T14$ is the percentage of T14 boards relative to the number of all

boards sawn from all logs, and the $relative\ yield\ T14$ is the percentage of T14 boards relative to the number of boards sent to strength grading.

To get a more complete picture, the whole range of pre-sorting thresholds was calculated, which resulted in a curve of values in the diagram $total\ yield\ T14$ vs. $relative\ yield\ T14$. These curves were compared between the three predictors VB, VB+FE and VB+Edyn,log.
Finally, the curves for each predictor were compared to those obtained on the test dataset, which encompassed 40% of the logs in the study (20 logs, 149 boards). Similar curves between training and test are an indication that the pre-sorting approach could also work on future unknown data.

2.11 CALCULATIONS AND VISUALISATION

All calculations were done with R 4.2.1 [9]. The diagrams were created in R using the ggplot2 package version 3.4.0 [17].

3 RESULTS AND DISCUSSION

3.1 FINITE ELEMENT SIMULATIONS

In Figure 4, the Young's modulus calculated by the FE models was compared to the modulus of elasticity determined during the destructive tensile tests. We observed a moderate correlation with a coefficient of determination of $r^2 = 0.46$.

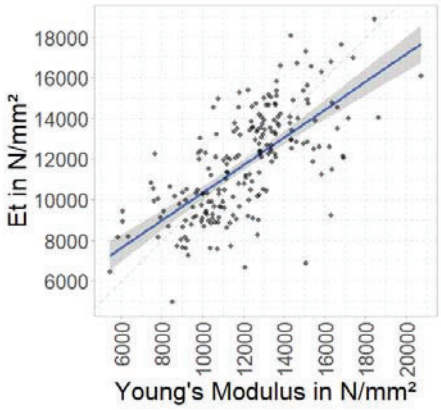

Figure 4: *The Young's modulus obtained from the FE models against the modulus of elasticity* $\boldsymbol{E_t}$ *from the destructive tensile tests for the 208 boards from the training dataset; coefficient of determination* $\boldsymbol{r^2 = 0.46}$.

For comparison: Olsson et al [18] achieved up to $r^2 = 0.70$ of their models with local modulus of elasticity in bending, $r^2 = 0.80$ if they included density, and $r^2 = 0.84$ if they included the longitudinal dynamic modulus of elasticity of the board ($E_{dyn,board}$).
When we used a two-dimensional density array measured on the dry boards during industrial strength grading (section 2.3), the coefficient of determination increased from 0.46 to 0.52, but this information is never available at the log stage. In other words, the knowledge of the boards' dry density improved the FE model – therefore, it would be desirable to develop an improved prediction of the dry density based on the green density.
Also, $E_{dyn,board}$ is never available at the log stage. However, a linear regression model for E_t, based on the Young's modulus from the FE model and on $E_{dyn,log}$ led to an $r^2 = 0.67$. Therefore, we also looked at yield prediction models including $E_{dyn,log}$, even though this quantity is not used in practice in Europe – for logs in intermediate states between frozen and thawed, $E_{dyn,log}$ cannot be determined reliably [19].
A further possibility for improving the prediction of the Young's modulus would be to base the FE model on a three-dimensional grid of fibre orientations instead of on a two-dimensional grid. This is planned as a next step in our research.

3.2 YIELD PREDICTION

Each of the three predictors predicted the correct grade for about 85% of the boards in the training data, with a clear tendency to overestimate the number of T14 boards – between 60% and 70% of the wrongly predicted boards were rejected boards which were assigned to T14 by the predictors.

3.3 LOG PRESORTING

In Figure 5, the *relative yield* was plotted against the *total yield* of T14 boards from the training data. This resulted in three curves for the three yield predictors VB, VB+FE and VB+Edyn,log. In the background of Figure 5, also the curve resulting from perfect yield prediction is displayed as a thin grey line.

An increase in the relative yield could only be achieved at the cost of a decrease in the total yield.

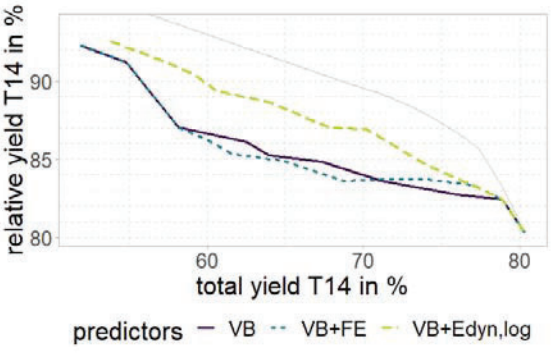

Figure 5: *Relative yield vs. total yield for the three yield predictors VB, VB+FE and VB+Edyn,log, based on the 208 boards from the training data. The thin grey curve to the right is the best possible pre-sorting, resulting from perfect foreknowledge of the final grading result.*

https://doi.org/10.52202/069179-0105

In Figure 5, this is apparent because the curves all decrease from left to right, even the thin grey line based on perfect yield prediction.

This trend is directly related to the pre-sorting strategy (section 2.10). We excluded logs with a predicted yield of T14 which was below a certain threshold *T*. A low predicted yield of T14 means a high predicted number of reject boards. Excluding these logs meant that the logs chosen to produce T14 boards had a lower share of reject and a higher share of T14, i.e. a higher relative yield. However, even from logs with a low yield of T14, we would be able to produce some T14 boards. When those logs were excluded based on the yield threshold *T*, those T14 boards could not be produced, and the total number of produced T14 boards decreased. This implied a lower total yield of T14.

When comparing the curves for the three yield predictors, curves further to the right (i.e., with a higher total yield for any given relative yield) indicate a higher pre-sorting efficiency, because this means that a given relative yield can be achieved while maintaining a higher total yield. Therefore, the thin grey line based on a perfect yield prediction is always furthest to the right. In Figure 5, the curve of the predictor VB+Edyn,log was closest to the perfect prediction curve and thus had the highest pre-sorting efficiency. We had expected that the predictor VB+FE would have a higher pre-sorting efficiency than VB, but, in fact, those two predictors were at the same level. It seems that a more accurate FE simulation of the Young's Modulus is needed to improve the pre-sorting efficiency, for example by basing the FE model on a three-dimensional grid.

In Figure 6, the yield curves were compared between the training data and the test data separately for each predictor. For all three predictors, the training data and the test data led to similar curves, given the rather small number of logs involved. Therefore, the pre-sorting strategies defined in this study should also work on new unknown data, although a repetition of the present study on a larger data set is recommended.

In Table 1, some selected value combinations of total yield and relative yield were extracted from Figure 6. Further, the values for the perfect prediction (as if one knew the result from board strength grading already when pre-sorting the logs) were added. To get a total yield value for a certain given relative yield value for all predictors, the total yield values were linearly interpolated between data points.

A relative yield of 80% was the baseline, where no logs were excluded. Therefore, all predictors had a total yield of 80% for this row. In the test data, this corresponded to 119 T14 boards and 30 reject boards.

A relative yield of 85% (test data), was achieved by the predictors VB and VB+FE at a total yield level of 66%. This corresponded to 99 T14 boards and 22 boards rejected during grading, but by excluding some logs, the opportunity to produce 20 more T14 boards was traded against having 13 less reject boards.

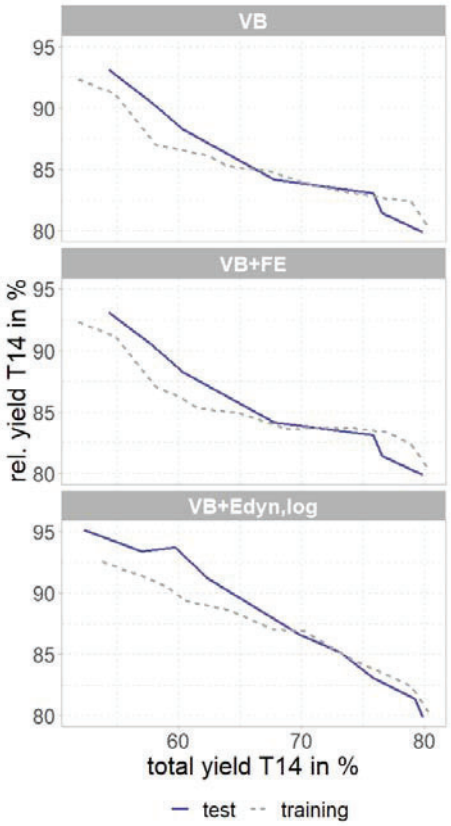

Figure 6: *The yield curves from Figure 5 (training data, 208 boards), compared to the curves resulting from the test data (149 boards).*

Table 1: *Interpolated values for the total yield at a certain level of relative yield for the different predictors and for the perfect prediction, for the training data and the test data.*

	relative yield in %	total yield in %			
		VB	VB+ FE	VB+ Edyn,log	perfect prediction
training (n = 208)	80	80	80	80	80
	85	66	64	73	78
	90	56	56	60	69
	92	52	52	55	62
test (n = 149)	80	80	80	80	80
	85	66	66	73	75
	90	58	58	64	68
	92	55	55	60	64

Again for a relative yield of 85%, the predictor VB+Edyn,log was able to produce 109 T14 boards; here, the trade-off was 10 fewer T14 boards and 11 fewer reject boards, which is considerably more efficient.
At the same level of relative yield, the perfect prediction traded 7 fewer T14 boards against 10 fewer reject boards.
At the highest relative yield level in Table 1 (92%), VB and VB+FE only led to a production of 83 T14 boards, VB+Edyn,log to a production of 89 T14 boards, and the perfect prediction to a production of 96 T14 boards.

4 CONCLUSIONS

In this study, data from log scanning were successfully used to predict the yield of the final strength grading of dried sawn timber. The input data were based on images from log computed tomography (CT) and dynamic modulus of elasticity of the log. As an additional input to the yield prediction models, a Finite Element analysis based on the CT images and using simulated fibre orientations was performed.
Based on these yield predictions, a pre-sorting strategy was tested where only logs with high predicted yield in the strength grade T14 were directed towards producing machine strength graded timber.
Using this approach, the T14 grade yield at the sawn timber strength grading process step could be increased from 80% to up to 92%, at the cost of losing up to 30% of the T14 boards which could have been produced if all of the logs in the study had been sent to the strength grading process.
Although the results on Young's modulus from Finite Element analysis had a coefficient of determination of 0.46 with the tensile modulus of elasticity, using this result for predicting the strength grading yield did not improve the pre-sorting efficiency.
Further research should be directed towards increasing the accuracy of the Finite Element analysis, e.g. by basing it on a three-dimensional board grid instead of a two-dimensional board grid. It is also expected that a better prediction of the density of the dry board from the CT images could improve the accuracy of the Finite Element analysis.

ACKNOWLEDGEMENT

The research for this study was part of the project READiStrength, which was funded by the ERA-NET Cofund Call "ForestValue – Innovating the forest-based bioeconomy" as well as by the national funding agencies Vinnova, Fachagentur Nachwachsende Rohstoffe e.V. and the Austrian Federal Ministry for Agriculture, Regions and Tourism.

REFERENCES

[1] European Commission. Innovating for sustainable growth: A bioeconomy for Europe. Luxembourg: Publications Office of the European Union 2012.
[2] Hintsteiner WJ, van Loo M, Neophytou C, Schueler S, Hasenauer H. The geographic origin of old Douglas-fir stands growing in Central Europe. Eur J Forest Res 2018; 137(4): 447–61.
[3] Sauter UH. Technologische Holzeigenschaften der Douglasie als Ausprägung unterschiedlicher Wachstumsbedingungen: [Technical Douglas fir wood properties as an effect of different growing conditions] Dissertation thesis. University of Freiburg 1992.
[4] Rais A, Poschenrieder W, Pretzsch H, van de Kuilen J-WG. Influence of initial plant density on sawn timber properties for Douglas-fir (Pseudotsuga menziesii (Mirb.) Franco). Ann For Sci 2014; 71(5): 617–26.
[5] Johansson E, Johansson D, Skog J, Fredriksson M. Automated knot detection for high speed computed tomography on Pinus sylvestris L. and Picea abies (L.) Karst. using ellipse fitting in concentric surfaces. Comput Electron Agr 2013; 96: 238–45.
[6] CEN European Committee for Standardization. EN 408:2012. Timber structures – Structural timber and glued laminated timber – Determination of some physical and mechanical properties. EN 408:2010+A1:2012-07. Brussels; 2012.
[7] CEN European Committee for Standardization. EN 384:2018. Structural timber – Determination of characteristic values of mechanical properties and density. EN 384:2015+A1:2018. Brussels; 2018.
[8] Smith RGB, Palmer G, Davies M, Muneri A. A method enabling the reconstruction of internal features of logs from sawn lumber: The log end template. Forest prod j 2003; 53(11-12): 95–8.
[9] R Core Team. R: A Language and Environment for Statistical Computing. Vienna, Austria; 2020. Available from: https://www.R-project.org/.
[10] Chang W, Cheng J, Allaire JJ, Xie Y, McPherson J. shiny: Web Application Framework for R; 2020. Available from: https://CRAN.R-project.org/package=shiny.
[11] Huber JAJ, Broman O, Ekevad M, Oja J, Hansson L. A method for generating finite element models of wood boards from X-ray computed tomography scans. Comput Struct 2022; 260(2): 106702.
[12] COMSOL Multiphysics® v. 6.0. Stockholm, Sweden: COMSOL AB. Available from: www.comsol.com/.
[13] Dinwoodie JM. Timber: Its Nature and Behavior. 2nd ed., revised. New York, Florence: Spon Press [Imprint]; Routledge; Taylor & Francis Group [distributor] June 2000.
[14] CEN European Committee for Standardization. EN 14081-2:2018. Timber structures – Strength graded structural timber with rectangular cross section – Part 2: Machine grading; additional requirements for type testing. Brussels; 2018.
[15] CEN European Committee for Standardization. EN 338:2016. Structural timber – Strength classes. Brussels; 2016.
[16] CEN European Committee for Standardization. EN 14080:2013. Timber structures - Glued laminated

https://doi.org/10.52202/069179-0105

timber and glued solid timber - Requirements. Brussels; 2013.
[17] Wickham H. ggplot2: Elegant graphics for data analysis. Second edition. Cham: Springer International Publishing 2016.
[18] Olsson A, Pot G, Viguier J, Hu M, Oscarsson J. Performance of timber board models for prediction of local bending stiffness and strength - with application on douglas fir sawn timber. Wood Fiber Sci 2022; 54(4): 226–45.
[19] Denzler JK, Weidenhiller A. Pre-grading of spruce logs containing frozen and unfrozen water by means of frequency-based nondestructive testing (NDT). Holzforschung 2016; 70(1): 79–85.

World Conference on Timber Engineering Oslo 2023

CONSIDERATIONS FOR GRADING SPECIES COMBINATIONS. THE EXAMPLE OF DOUGLAS FIR WITH LARCH IN IRELAND AND UK

David Gil-Moreno [1], Dan Ridley-Ellis [2], Annette M. Harte [3]

ABSTRACT: This paper examines the grading of Douglas fir (*Pseudotsuga menziesii*) and larch (*Larix* spp.) as a strength grading species combination for the growth area formed by Ireland and the UK. The two genera produce higher timber quality than Sitka spruce (*Picea sitchensis*), the main commercial timber species in the two countries. Developing this species combination may increase the volume of timber available for the market, making these species more commercially attractive to sawmills, particularly if there are common settings that can be used for either species whether mixed in production or not. Simultaneously, the paper examines the challenges of mixed species grading within the framework of the European standard EN14081 for machine control grading, as the requirements for combining species are not clearly defined. More than 1600 pieces are used for this study. The results found that the ranges of modulus of elasticity, strength and density of both species are similar, but special considerations are required to ensure the safe grading of the timber.

KEYWORDS: Wood properties, Strength grading, Douglas fir, Larch, Species combination, Standards

1 INTRODUCTION

The main timber species grown in Ireland and UK is Sitka spruce (*Picea sitchensis* (Bong.) Carrière). Commercially, it is common to refer to it as "British spruce", WPCS [1], a long-standing commercial combination where Sitka spruce is often mixed in the forest and the sawmills with Norway spruce (*Picea abies* (L.) H.Karst). The amount of each species in the mixture depends on the relative volumes available in the forests, which varies geographically. The overall percentage of Norway spruce is low but nevertheless a batch with 100% Norway spruce could be processed and sold as British spruce. The mixture is possible because the grade determining properties (GDPs) are similar. This paper will focus on GDPs as those primary properties determined for grading on the usual bending strength basis, namely modulus of elasticity (MOE), strength and density. The wood of the two species also has practically identical visual appearance and is not separated in production. Such industry practise species combinations are not uncommon, but this is also potentially a way to combine lesser used conifers with an established species, or grade lesser conifers together, as a convenient route to market.

There are many other species combinations in use. For example, Douglas fir (*Pseudotsuga menziesii* (Mirb.) Franco) and western larch (*Larix occidentalis* Nutt.) are graded together as a species combination, WPSM [1], as well as a part of other species combinations in North America. The properties of both species are somehow similar, and can be mixed for selling [2, 3] following grading rules of different agencies, like WCLIB, WWPA or NLGA. The combination is commonly used for glulam in the US [2].

Although western larch is not grown commercially in Europe, in Ireland, larches and Douglas fir are currently the second and third largest timber species in terms of forest area after spruces [4]. In Great Britain, larch is the third largest timber species, and Douglas fir is the fifth [5]. In 2018 and 2020, as part of the WoodProps programme at the University of Galway, machine grading settings were developed for Douglas fir [6], PSMN, and larch (WLAD: European larch (*Larix decidua*), hybrid larch (*Larix x eurolepis*) and Japanese larch (*Larix kaempferi*)), separately [7], for the grading area formed by Ireland and the United Kingdom (UK). Douglas fir and larch produce higher timber quality than British spruce and it would be desirable to have more material available on the market. However, the relatively small and dispersed volume of these species in Ireland may not always make grading these species on their own attractive to sawmills.

New construction projects in Ireland are now using locally grown Douglas fir (Figure 1). An option to concentrate the timber volume and increase the use of the local timber resources currently available is a combined approach for production and marketing. For this, it is desirable to have common machine grading settings that could be used for either WLAD or PSMN whether mixed in production or not.

[1] David Gil-Moreno, University of Galway, Ireland, david.gil-moreno@universityofgalway.ie
[2] Dan Ridley-Ellis, Edinburgh Napier University, UK, d.ridleyellis@napier.ac.uk
[3] Annette M. Harte, University of Galway, Ireland, annette.harte@ universityofgalway.ie

https://doi.org/10.52202/069179-0106

Figure 1: *Viewing tower at the Avondale Forest Park in Ireland built with locally grown Douglas fir. Source: WIEHAG GmbH.*

There is very little literature on how to develop machine control grading settings for a mixture of two or more species. Regarding the sampling for testing, the standard EN14081-2 [8] says that when species are graded together without being differentiated, the sampling should be representative of the species proportion. The standard thus leaves open the question as to whether the approach should be different if the species are more commonly differentiated, but desired to be graded by a common process. The standard also states that the species within a species combination need to be "sufficiently similar", but it does not explain how to satisfy this requirement.

In order for timber to be graded under the European machine control system, the thresholds (settings) for the machine indicating properties (IPs) are calculated based on their predictive relationship to the GDP values, as determined by a large testing programme. The characteristic values for strength and density are the lower 5th percentiles and for MOE the mean. It would be expected that when populations of different species have similar GDP mean and variances, characteristic values, and correlations with the grading parameters, the species can be graded together as species combination. However, the fact that the relationships between the GDPs can be similar in two species (falling within the confidence intervals), does not guarantee that the relationship between a grading machine's IP and all the GDPs is also similar. Likewise, it is worth knowing what would happen if, in the effort to study "sufficiently similar" samples, timber of higher or lower characteristics is overlooked.

This paper examines the grading of the species combination PSMN with WLAD for the first time in Europe, in particular for the grading area formed by Ireland and the UK, while suggesting an appropriately cautious approach to develop machine settings of species combinations within the scope of EN14081.

2 MATERIALS AND METHODS

2.1 MATERIALS

The study uses timber from normal production runs in sawmills sampled from across the Republic of Ireland and the United Kingdom. As usual for grading work, specification was given to each sawmill that the timber provided should be unsorted for quality, except for the removal of any pieces that fail visual override criteria as described by EN 14081-1 [1, 9]. The sampling also included timber from research studies in the two countries, considered representative of the timber in production. A total of 704 pieces of PSMN and 899 of WLAD were available and split into four verification samples per genus (Table 1) for the analysis, where A to D correspond to PSMN and E to H correspond to WLAD.

Table 1: *Pieces sampled by cross-section size and source.*

Size (mm^2)	Sample	WLAD	PSMN
35x75	H	96	-
37x75	B	-	70
45x100	A, D	-	277, 109
47x100	E, F,	166, 126,	
"	G, H	126, 60	
50x100	C, D	113, 75	-
47x150	E	17	-
75x150	F, G, H	80, 80, 94	
76x225	B	-	60
100x275	F, G	27, 27	

2.2 METHODS

The pieces were tested at the University of Galway using a Zwick/Roell 500 kN Servo Hydraulic testing machine, and at Edinburgh Napier University using a Zwick Z050 universal testing machine. The tests followed the requirements of the European standards EN408 [10] and EN384 [11]. For WLAD, local MOE was used to calculate the settings, whereas for PSMN, global MOE and the correction to shear free MOE (Clause 5.3.2 of EN 384:2016+A2:2022, E_0=1.3 x $E_{global,u=12\%}$ - 2690 N/mm^2) was applied. The choice of one or the other moduli of elasticity influences the grading yields, particularly when MOE limits the allocation to a strength class [12, 13]. MOE and density were adjusted to 12% moisture content and strength to 150 mm depth in accordance with EN384 [11]. The moisture content of every specimen was determined using the oven drying method, or estimated by moisture meter [14]. The symbols and units used in this paper are listed in Table 2.

Table 2: *Symbols and units.*

Symbol		Units
Bending strength, adjusted to 150 mm width		
f_{mean}	Mean	N/mm^2
f_k	5th percentile	N/mm^2
Bending modulus of elasticity, parallel to grain, MOE		
$E_{0,mean}$	Mean, at 12% mc	kN/mm^2
Density		
ρ_{mean}	Mean, at 12% mc	
ρ_k	5th percentile, at 12% mc	

In order for timber to be graded, the dynamic modulus of elasticity (MOE_{dyn}) was chosen as the IP. This IP was developed through modelling using non-destructive acoustic properties as predictor variables of the GDPs. The methodology for the calculation of IP thresholds, or "settings", followed the requirements in EN14081-2:2018+A1:2022, from the calculation of the

optimum grading to the determination of the cost matrix using Annex C. However, this paper focuses on the specific issue of verification for new settings of the whole sample and verification samples, with the aims of investigating how settings can distinguish the upper-grade timber from the lower-grade timber taking species into account, and providing a good practice example for future work on grading of species combinations.

As per the existing approach, in the first step, the calculation sought to determine the lowest IP value that defined a population whose characteristic values met those of the target grade. Secondly, a check was carried out to ensure that that each of the eight verification samples studied (EN14081-2:2018+A1:2022 states that the whole sample must be divided into at least four) achieved at least 90% of the characteristic values of strength and density of the target grade and 95% of the required mean modulus of elasticity. Strictly speaking, these two steps would suffice to verify the grading settings according to the current procedure in EN14081-2. However, developing grading settings must ensure that the assignments are safe beyond the calculations required by the standards. There are questions unanswered when developing grading for a species combination: What happens if one sample is noticeably better or worse than the others? How many samples there must be for each species? What happens if the grading of the species is limited by a different GDP? Can the two species be safely graded separately but using the same settings? In order to address those questions, in particular to ensure that the grading is safe, an additional (not specified by EN14081-2) requirement was added. This was implemented so that the settings fully satisfied (100%) the required strength class values of the GDPs for Douglas fir and larch separately to explicitly confirm correct grading of each species alone. In fact, EN14081-2 does suggest the verification procedure to be applied on non-geographical subsets of the whole, when there is reason to be cautious. This approach is also similar to the expansion check carried out for expansion of existing settings to a larger setting area.

3 RESULTS

3.1 GPDs of UNGRADED TIMBER

The properties of the timber (ungraded) are summarised in Table 3. The moisture content at the time of grading varied between 9.8% and 25.9%, with a mean of 15.3%. The moisture content at the time of testing varied between 8.8% and 22.8%, with a mean of 13.5%. Overall, WLAD had slightly higher strength and density values than PSMN, but lower modulus of elasticity. However, sample A had the highest GDP values of all, and certainly much higher than the rest of PSMN values. This large variation is likely the result of microsite factors and differences in forest management, and it must be understood that this variation can occur in a sawmill and is therefore important to include it in the sampling. In fact, the results are comparable to data reported for PSMN from the UK [15], and data collected within the GradeWood project by BRE (unpublished). The two genera produce higher timber quality than Sitka spruce [7, 16] and the GDPs are comparable enough between themselves producing yields above 80% for the strength class C18 investigated in this paper as shown in Table 3.

Table 3: *Summary of properties by sample.*

	Sample	f_{mean}	f_k	$E_{0,mean}$	ρ_{mean}	ρ_k
PSMN	A	50.4	29.2	13400	561	481
	B	27.8	14.1	8980	454	394
	C	34.3	17.1	8960	453	360
	D	28.7	11.5	8410	452	376
	PSMN	38.0	15.4	10550	495	397
WLAD	E	41.9	21.7	9400	483	405
	F	37.7	22.0	9560	497	404
	G	38.9	20.3	10100	499	415
	H	43.6	25.7	10500	532	426
	WLAD	40.5	22.5	9920	504	410
	All	39.4	19.0	10200	500	405

Figure 2 shows the relationships between the three GDPs and the distribution of values as density plots. The results show that both species have comparable values of GDPs, with a slightly wider distribution of values of the GDPs in PSMN as previously mentioned. The figure also shows that the correlations between density and strength and density and stiffness are stronger in PSMN (orange) than in WLAD (green).

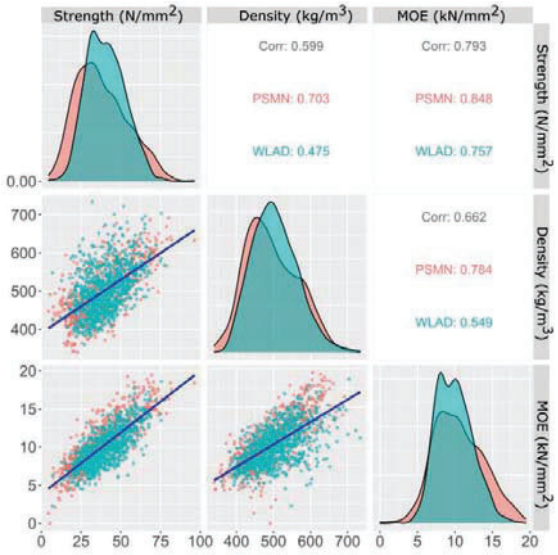

Figure 2: *Distribution of the GDPs and Pearson correlations.*

The optimum grading for the entire population was C20, that is, the one that results from using the values of the destructive tests instead of those based on the IP. For this purpose, the 0.95 factor was applied to the required characteristic value $E_{0,mean}$, and 1.12 to f_k (for non-portable grading machines). However, it can be observed that PSMN on its own would only achieve C18, largely penalised by the low characteristic strength value of sample D. WLAD on the other hand, would achieve C22. Previous studies analysing these datasets in part or in full, reported that the grading of PSMN was in general limited by strength [6], whereas WLAD was typically limited by

https://doi.org/10.52202/069179-0106

MOE [17]. This can be observed in Figure 3 and Figure 4, which illustrate the grading for strength and MOE respectively using MOE_{dyn} as IP. The y-axis represents the characteristic values (f_k and $E_{0,mean}$, respectively), where the lowest value corresponds to the characteristic value of the whole population. Each successive point corresponds to the characteristic value as the ranked board values increase. Thus, f_k and $E_{0,mean}$ typically increase while the yields decrease until the board/s with the highest strength and stiffness, respectively, are reached. Figure 3 shows that the characteristic value of strength for PSMN is lower than that of WLAD for most of the sample. Roughly 60% and 75% of PSMN and WLAD, respectively, are below the 10.5 kN/mm^2 threshold. However, the characteristic value of MOE for PSMN is higher for almost the entirely range of MOE_{dyn} values (Figure 4).

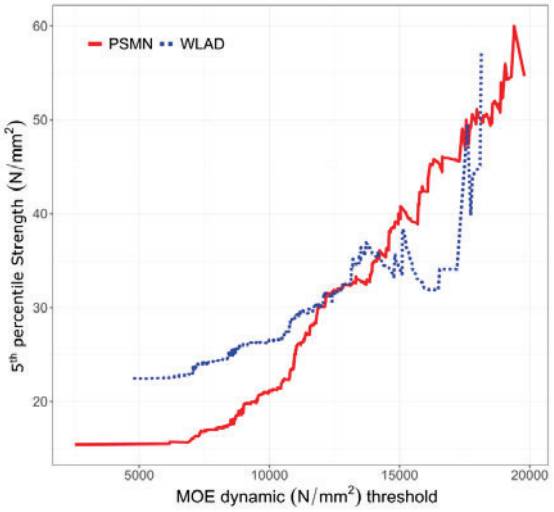

Figure 3. *Timber grading for strength using MOE_{dyn}*

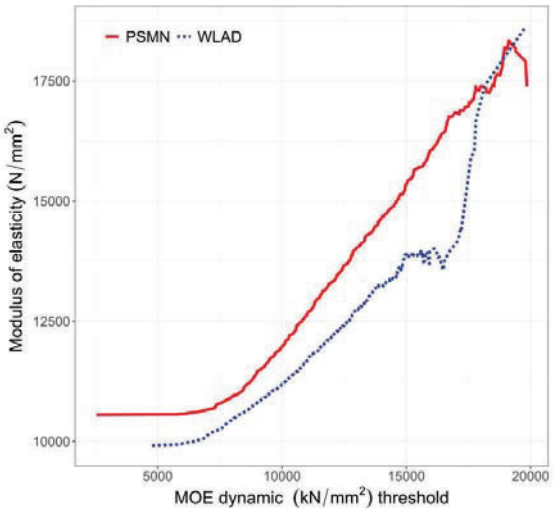

Figure 4. *Timber grading for MOE using MOE_{dyn}*

For the development of grading settings it is typically the limiting GDP that is modelled as priority. In the current dataset, the limiting GDP is different for each species. There is therefore the risk of grading an entire population of PSMN, as part of the species combination with WLAD, based on an IP that predicts MOE (for which the correlation with MOE_{dyn} is typically higher than for strength or density) and that may result in graded timber that does not meet the requirements for strength. For comparison with the derivation of machine settings for a single species, this scenario would be an analogous situation where the required characteristic values of the three GDPs must be met for the whole sample.

Although superficially similar, there are meaningful differences in the species combination that presents, a priori, a great challenge when it comes to develop the grading settings. For this reason, an additional requirement, not required by the letter of the standard but required by the spirit, was added, where it was required to also verify that the settings satisfied 100% the required strength class values of the GDPs for each species separately to confirm correct grading of each species alone.

3.2 CALCULATION OF SETTINGS

The timber of both species was non-destructively assessed with the Viscan Plus (Microtec s.r.l. – GmbH). This device measures the natural frequency of vibration in the longitudinal direction of a board, and together with density enables calculation of dynamic modulus of elasticity MOE_{dyn} using Equation (2):

$$MOE_{dyn} = \rho\,(2Lf)^2 \text{ N/m}^2 \qquad (2)$$

where ρ is the wood density (kg/m^3), L the length of the specimen (meters) and f the first mode resonance frequency (Hz) at which the stress wave propagates.

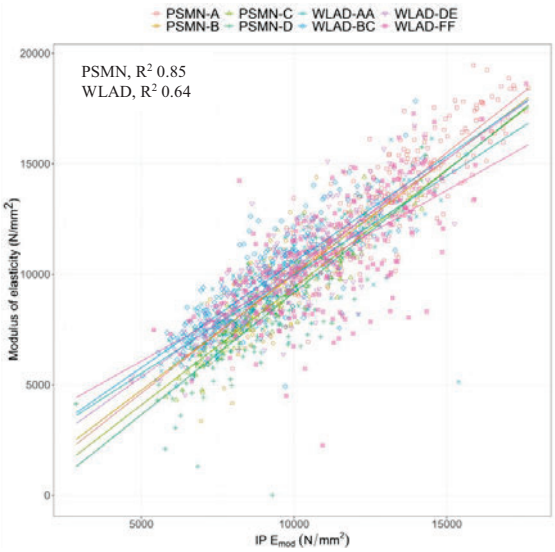

Figure 5: *Relationship between modulus of elasticity and IP by sample (R^2 0.42 to 0.88, overall 0.75)*

The strongest correlation of the IP was with modulus of elasticity (Figure 5), followed by density (Figure 6) and strength (Figure 7). The IP generated by MOE_{dyn} is closely related to the static MOE, therefore the stronger

https://doi.org/10.52202/069179-0106

correlation is expected. By species, MOE_{dyn} explained 85% of the variation in MOE of PSMN and 64% of WLAD. In all the cases, MOE_{dyn} was more strongly related to the GDPs of PSMN than of WLAD.

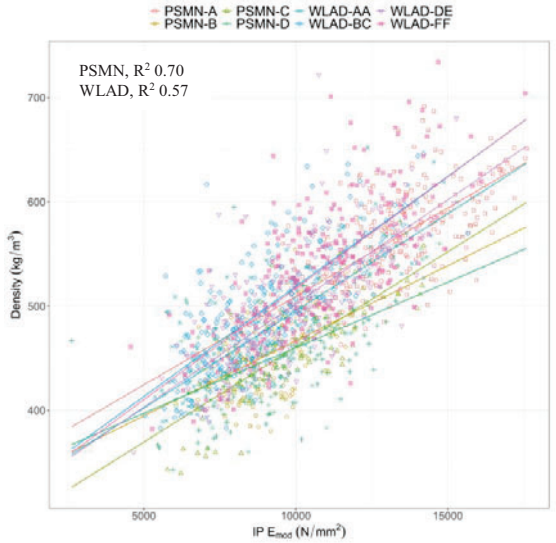

Figure 6: *Relationship between density and IP by sample (R^2 0.19 to 0.65, overall 0.58).*

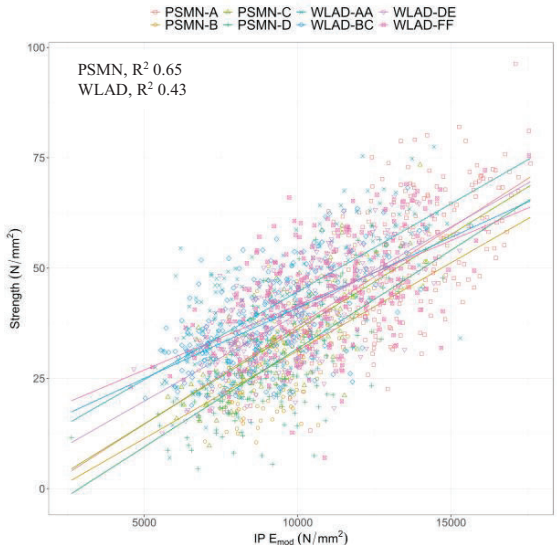

Figure 7: *Relationship between bending strength and IP by sample (R^2 0.22 to 0.56, overall 0.49).*

For grading, the analysis addressed initially the strength class combination C18/C14/reject. The setting must ensure that the whole population assigned to a grade must achieve 100% of the required strength class values of the GDPs. As well as that, at least 90% of the required target value for strength and density and 95% of stiffness must be met for each subsample.

In the first step, the settings for the upper grade was calculated. The first challenge was to find the threshold that would satisfy the requirements of the upper grade for subsamples B and D of PSMN. These samples had the lowest values for strength, and due to the large differences in GDP values between subsamples, it was possible that satisfying the requirements as a whole population was far from satisfying those of each subsample. This issue however, is not specific to the grading of a species combination.

Table 4 shows that the ratios between the derived characteristic values of the whole population and the required strength class values were 100% satisfied. The ratios for the eight subsamples (results not shown) also satisfied the requirements (90% of the target value for strength and density and 95% of stiffness). Under the current specifications of EN14081-2, the derived settings would be within the requirements of the standard. However, the strength of the PSMN population graded as C14 did not achieve 100% of the required value, 12.5 N/mm^2, of the strength class. Since the number of boards graded as C14 in samples A, B and C was less than 40, the parametric method was used to calculate f_k, which as Figure 3 shows is subjected to large fluctuations for a small number of pieces. To satisfy the species requirement it was not possible to simply increase the C14 setting, and that of the higher grade C18 had to be increased in beforehand so that more pieces were assigned to C14. As a result, the number of rejected pieces increased by 0.8 % points. Table 4 also shows settings for the combination C18/batten14. Batten14 is a user-defined strength class with characteristic values of: f_k = 14 N/mm^2; $E_{0,mean}$ = 7.5 kN/mm^2 and ρ_k = 330 kg/m^3 [7]. The peculiarity of this grade is that f_k is the same as in C14, but $E_{0,mean}$ and ρ_k are higher. This combination aimed to investigate how the higher requirement for $E_{0,mean}$ may influence the grading of WLAD. However, without the additional requirement, it was PSMN that did not achieve 100% of $E_{0,mean}$. On the contrary, WLAD, even though limited by MOE, achieved 100% of the GDPs without the additional requirement.

Table 4: *Ratios between the derived characteristic values, of the whole population and of species, and the required strength class values (re for MOE, rf for strength, rd for density).*

Strength Class	*Sample*	re	rf	rd
C18	ALL	1.28	1.33	1.32
C14	ALL	1.12	1.23	1.33
R	ALL			
C18	PSMN	1.32	1.14	1.29
C14	PSMN	1.02	0.91	1.25
R	PSMN			
C18	WLAD	1.25	1.60	1.38
C14	WLAD	1.18	1.67	1.38
R	WLAD			
Strength Class	*Sample*	re	rf	rd
C18	ALL	1.29	1.34	1.32
Batten14	ALL	1.06	1.19	1.18
R	ALL			
C18	PSMN	1.33	1.16	1.29
Batten14	PSMN	0.99	1.01	1.10
R	PSMN			
C18	WLAD	1.26	1.61	1.38
Batten14	WLAD	1.11	1.69	1.21
R	WLAD			

https://doi.org/10.52202/069179-0106

In order to investigate further the effect of the additional species requirement, the analysis for this paper also calculated the settings for C18/reject for the total sample less:

1) the best and worst quality samples;
2) the best quality sample, PSMN-A;
3) the worst quality sample, PSMN-D

Table 5 summarises the resulting yields under the three cases, and the following grading of the remaining pieces. Using the eight samples (case 0), the lowest C18 setting that satisfied the requirements of the whole and verification samples also met the requirement for each species alone. Excluding the best and worst samples (case 1), it was necessary to increase the C18 setting so that PSMN as a whole achieved 100% of the required strength class values. Consequently, the overall yield dropped considerably. Excluding the best subsample (case 2), again PSMN did not achieve 100% unless the additional requirement was applied. As expected, if the setting was calculated excluding the worst subsample (case 3), the setting value was considerably lower, and the overall yield increased. However, this practice would not make grading safe as the strength ratio reached for the otherwise not included PSMN-D was only 81%. EN14081-2 contains a verification procedure for checking that existing settings are grading correctly in a particular location. This requires that the graded timber being checked achieves at least 90% of f_k and ρ_k of the target grade and 95% of the required $E_{0,mean}$. That check would fail for PSMN-D.

As well as that, EN14081-2 requires knowledge and experience to be applied when designing the sampling strategy, and states that *if weak areas* (i.e., low quality) *are known, they should be taken into account accordingly*. While it may be tempting to remove or avoid sampling low performing data from the calculation on the grounds that it is different, it would certainly be incorrect to do so. In the previous version of EN14081-2:2012 [18], the verification checks were applied differently, so that the required characteristic values for each grade were achieved for the total sample less one geographical sample in turn. In that procedure the mean setting could not be more than 15% different from the most conservative setting or otherwise the setting had to be adjusted by 15% towards the mean value. It was realised that this procedure becomes ineffective as more samples are included in the settings calculation even though, as illustrated above, there can be significant issues with individual samples. In revising the standard, the verification checks were made more robust and explicit in their function. The standard also states that the same procedure can be used to check non-geographical samples that are suspected to be different. The standard mentions cross-section size as the example, but it is valid also for species. It is therefore recommended to apply the species check to ensure that the grading is safe.

One might also wonder whether to group the dataset by species and country, resulting in four samples, which is the minimum verification samples required in the standard. This approach gave the lowest rejects for C18/reject, 45 boards over the whole population. However, in view of the results shown in Table 5, it may be advisable from a safety point of view to consider at least four samples per species. Since EN14081-2 requires at least one hundred specimens per sample, four samples per species leads to at least 800 specimens for a combination of two species. This will provide a larger dataset to analyse, and more variability of the timber source than the 450 specimens given in the standard as the minimum number required for deriving settings. In developing grading settings, the first objective must always be safety of grading and it is sometimes necessary to do more than the minimum required by the standard, and accept some loss in yield, in order to achieve that.

Table 5: *Pieces allocated to C18/reject under different cases and the subsequent grading of the remaining pieces without (No Sp. Req.) and with the additional species requirement.*

Case		Samples	PSMN	WLAD	Reject
0	No Sp. Req. Sp. Req.	ALL	605	688	310
1	No Sp. Req.	a)	231	810	101
		PSMN-A & D	442	-	19
	Sp. Req.	a)	193	679	270
		PSMN-A & D	406	-	55
2	No Sp. Req.	b)	329	688	309
		PSMN-A	276	-	1
	Sp. Req.	b)	316	673	337
		PSMN-A	273	-	4
3	No Sp. Req. & Sp. Req.	c)	507	810	102
		PSMN-D	166	-	18

The study here presented used a machine that uses MOE_{dyn} for grading, a relatively simple case due to the direct link between the IP and GDPs. The additional check by species may become more important when grading timber using characteristics such as knottiness. Knots are related to GDPs in a much more complicated way with differences in species and growth conditions. The IPs determined by grading machines using knottiness are typically obtained through linear regression between the knots (and density) and the GDPs on all available test data. If one of the species has small knots compared to the other(s), and is widely represented in the sampling used to develop the settings (which EN14081-2:2018 specifies should broadly similar to that in practice), the influence of the knot characteristics on the model will be less, which may benefit other species with larger knots in the combination.

4 CONCLUSIONS

This paper has shown that it is possible to grade PSMN -Douglas fir- with WLAD -larch- together as a species combination for the grading area formed by Ireland and the UK. In doing so, this paper also outlines an approach to develop machine grading settings for species combinations. In particular, it includes an additional check (in line with EN14081-2, but not

required by it) so that the required characteristic values of the target grade are fully satisfied for the two (or more) species within the combination. The additional requirement aims to ensure that the grading is safe, particularly if the species are graded separately. It is shown that while larch and Douglas-fir look superficially very similar in their properties and grading, there are some meaningful differences. Further, it is shown that as long as differences are accounted for, the strength grading of the species combination can still be safely achieved. The disadvantage is that it requires an even larger testing programme than normal, and the ability to separate the species in testing.

Having common settings that can be used for Douglas fir and larch, whether mixed in production or not, is an advantage both economically and from a logistical point of view to sawmills and may increase the volume of timber available for the market, making these species more commercially attractive for processing.

ACKNOWLEDGEMENTS

This work was developed within the WoodProps programme funded by the Forest Sector Development Division of the Department of Agriculture, Food and the Marine, Ireland. The authors gratefully acknowledge the support of Coillte, Murray Timber Group, and MiCROTEC s.r.l. – GmbH. The contribution of University of Galway staff who one way or another helped to complete this programme is appreciated. The work also draws on data from other projects at University of Galway and the SIRT project at Edinburgh Napier University, and the authors are also grateful to its funders and research partners.

REFERENCES

[1] CEN, Timber structures - Strength graded structural timber with rectangular cross section. Part 1: General Requirements. EN 14081-1:2016. 2016, *European Committee for Standardisation*: Brussels. p. 44.

[2] Forest Products Laboratory, Wood handbook wood as an engineering material. General Technical Report FPL-GTR-282. 2021: Madison, WI: U.S. Department of Agriculture, Forest Service, Forest Products Laboratory. p. 543.

[3] WWPA, Douglas Fir & Western Larch - *Pseudotsuga menziesii* & *Larix occidentalis*, in FS-3/0813e/Rev.5-02. 2002, *Western Wood Products Association*.

[4] DAFM, Forest Statistics Ireland 2022, Department of Agriculture, Food & the Marine, Ireland, Wexford, Editor. 2022.

[5] Forestry Commission, Forestry Statistics 2020. Chapter 1-Woodland Area and Planting. 2020: Edinburgh, UK.

[6] Gil-Moreno, D., Ridley-Ellis, D., and Harte, A.M., Timber grading potential of Douglas fir in the Republic of Ireland and the UK. *International Wood Products Journal*, 2019. **10**(2): p. 64-69.

[7] Ridley-Ellis, D., Gil-Moreno, D., and Harte, A.M., Strength grading of timber in the UK and Ireland in 2021. *International Wood Products Journal*, 2022. **13**(2): p. 127-136.

[8] CEN, Timber structures - Strength graded structural timber with rectangular cross section. Part 2: Machine grading; additional requirements for initial type testing. EN 14081-2:2018+A1:2022. 2022, *European Committee for Standardisation*: Brussels. p. 42.

[9] CEN, Timber structures - Strength graded structural timber with rectangular cross section. Part 1: General Requirements. EN 14081-1:2005+A1:2011. 2011, *European Committee for Standardisation*: Brussels. p. 36.

[10] CEN, Timber structures—structural timber and glued laminated timber—Determination of some physical and mechanical properties. EN408:2010+A1:2012. 2012, *European Committee for Standardization*: Brussels. p. 38.

[11] CEN, Structural timber-Determination of characteristic values of mechanical properties and density. EN 384:2016 + A2:2022. 2022, *European Committee for Standardization*: Brussels. p. 16.

[12] Gil-Moreno, D., Ridley-Ellis, D., and McLean, P., Using the right modulus of elasticity to get the best grades out of softwood timber species in Great Britain, in Proceedings of the World Conference on Timber Engineering (WCTE), August 22-25, 2016. Vienna, Austria.

[13] Gil-Moreno, D., Ridley-Ellis, D., and Harte, A.M., Test machine effect in the determination of modulus of elasticity for strength-graded timber, in Proceedings of the World Conference on Timber Engineering (WCTE), August 9-12, 2021. Santiago de Chile, Chile.

[14] CEN, Moisture content of a piece of sawn timber—Part 1:Determination by oven dry method. EN 13183-1:2002. 2002, *European Committee for Standardisation, Brussels, p.5*.

[15] Bawcombe, J., A study of Douglas-fir anatomical and mechanical properties and their interactions [PhD dissertation]. 2012, *University of Bath*.

[16] Moore, J.R., et al., Within-and between-stand variation in selected properties of Sitka spruce sawn timber in the UK: implications for segregation and grade recovery. *Annals of forest science*, 2013. **70**(4): p. 403-415.

[17] Ridley-Ellis, D., Adams, S., and Lehneke, S., Thinking beyond the usual strength grades–with examples of British spruce and larch, in Proceedings of the World Conference on Timber Engineering (WCTE), August 22-25, 2016. Vienna, Austria.

[18] CEN, Timber structures - Strength graded structural timber with rectangular cross section. Part 2: Machine grading; additional requirements for initial type testing. EN 14081-2:2010+A1:2012. 2012, *European Committee for Standardisation*: Brussels. p. 26.

https://doi.org/10.52202/069179-0106

CONSIDERATIONS FOR GRADING SPECIES COMBINATIONS. GENERAL REMARKS ON SCENARIOS AND REQUIREMENTS.

Dan Ridley-Ellis[1], David Gil-Moreno[2], Annette M. Harte[3]

ABSTRACT: This paper discusses the situations in which timber species might be combined in commercial combinations, and the considerations relating to strength grading work. It is expected that more species combinations will be developed in the years to come, as the timber value chain diversifies. However, it is not clear how the grading standards and associated procedures should best adapt to cover situations where there is no long-standing industry experience. This paper presents some considerations and examples, with the aim of assisting people doing grading work in taking informed, safe steps based on their knowledge of the resource. This paper gives examples from the European standards, and mostly temperate species, but the principles are general.

KEYWORDS: Wood properties, strength grading, species combinations, standards, taxonomy, growth conditions

1 INTRODUCTION

The species of tree from which timber comes is an important consideration for strength grading, since it is part of what influences the wood properties, and the grading process required. For practical convenience (or necessity), species are commonly grouped into species combinations. There are many such species combinations in common and long-standing use. However, the matter of what "species" means exactly, as far as the grading standards are concerned, is not entirely clear. This means that the requirements and considerations for forming new species combinations are also unclear.

There is an increasing need for new species combinations, as hitherto lesser-used timber species come to market. Lesser-used species might be included as a new minor component of an already established species combination, or form a new combination with other relatively lesser-used species. Common species might also be combined in new ways, and familiar species combinations might be created from new growth areas, or be graded by methods that work on new principles.

Continued advances in tree breeding, hybridisation and clones add further complexity since they represent differences below the species level. Taxonomy is also not completely stable for some species, which may be regarded as varieties, subspecies or separate species by different authorities, and consequently be recognised differently in different countries. This raises the question of what a species combination even means.

In future, it is expected that some of what is currently monoculture plantation forestry will move to more diverse and intimate species mixtures for changing forest management objectives, such as climate resilience. It is also expected that species that were previously coming from logging of natural forests will instead come from plantations. Such things change the resource, even though the species is the same.

There is also growing need to be able to assess the strength of timber *in-situ* and grade timber from building deconstruction, where identification might only be possible to a list of likely species.

These give cause to reflect on the purpose of species combinations, the way they should be handled by the standards, and the way that industry can adapt to a changing resource.

It is first important to recognise that, for timber strength grading, the concept of "species" serves a different purpose than it does for botany.

2 NEED FOR SPECIES DISTINCTION

The species is one of the key determinants of timber properties. For structural timber, the important aspects are the species influence on strength, stiffness and density, averages, standard deviations, and correlations. Importantly, this includes the correlations of grade determining properties like strength, with the criteria used for grading (whether that is by visual grading or machine). Density and stiffness could be directly assessed for each piece non-destructively, but strength will always depend on predictive models.

The growth conditions are also key determinants of timber properties, and this interacts with the species and the within-species variation. The phenotype (the resulting timber) is a combination of the genotype and the environment:

- Phenotype, *e.g.*
  - Tree size and log shape
  - Knots (size, distribution, etc.) and ring width

[1] Dan Ridley-Ellis, Edinburgh Napier University, UK, d.ridleyellis@napier.ac.uk
[2] David Gil-Moreno, University of Galway, Ireland, david.gil-moreno@universityofgalway.ie
[3] Annette M. Harte, University of Galway, Ireland, annette.harte@universityofgalway.ie

https://doi.org/10.52202/069179-0107

  - Wood properties
- Genotype, *e.g.*
  - Species
  - Seed provenance
  - Tree selection or genetic improvement
- Environment, *e.g.*
  - Site: soil, climate, wind, temperature, seasons, *etc.*
  - Management: forest type, spacing, pruning, thinning, age at felling, *etc.*
  - Pests, diseases, storms, fires, *etc.*

These complex interactions are the reason why timber strength grading is necessarily linked to species and growth area, and may also change over time.

For example, knots indicate timber strength because of their influence on grain deviation within the sawn timber, but the knots are also determined by growth conditions, which additionally influence wood strength in other ways. The tree's branching results from a combination of genetics and environment, which are things that also change other aspects of the wood microstructure on account of the different biomechanical needs of the tree.

For timber strength grading, it is therefore not possible to completely separate the concept of species from the concept of growth area. It can also connect with timber sizes, since certain cross-sections and lengths come from differently sized trees, which have different growth conditions.

The genotype–environment interaction is part of the reason why it is common in the trade to distinguish between, for example, French oak and English oak as if they were different species, but not necessary to make a distinction between the oak species within these resources: *Quercus robur* and *Q. petrea*. This is also part of the reason why, even after significant research effort toward the aim, there has been little harmonisation of visual strength grading standards in Europe [1,2]. Strength grading across very broad sets of species has been shown to be possible within certain limits, but not completely independently of species due, especially, to the effect of knots when present [3].

3 THE CONCEPT OF SPECIES

For structural timber, unless appearance, durability or some other species aspect is an additional criterion, the species *per se* is less important than the declared structural properties. Indeed, a key concept of general strength class systems such as in the European Standard EN338 [4] is that timber can be specified with almost no regard to its species.

In that sense, the limitation of species in strength grading performs a similar role to the limitation of growth area. These two things are part of what determines how the timber should be graded, and what design properties can be obtained. Indeed, a fine distinction of species may well be a way of indirectly being more specific about growth area within countries that have varied growth conditions.

The taxonomy of trees is done by botanists, rather than timber engineers. Family, genus and species are assigned based on the morphology of the tree's features and, more lately, from genetic sequencing. For wood properties, a fine distinction between species may be of no consequence, but it can also be the case that differences below species level do affect the grading enough that they need to be accounted for. This could be because the subspecies or variety is different because of the growth conditions it has naturally adapted to, or because cultivars, seed provenance or clones have been chosen because of their desirable timber characteristics.

Even the matter of strict botanical species is not necessarily clear cut, and since there is no single central authority on taxonomy, even being specific about species can be tricky; especially when historical trade names and documents do not correspond exactly to the latest botanical state-of-the-art.

Therefore the concept of species in timber grading is not the same as the botanical one. In timber grading we might refer to *Handroanthus* (a genus in taxonomy) and *Pinus nigra* subsp. *nigra* (a subspecies level distinction) both as a "species", and *Larix decidua*, *Larix kaempferi* and *Larix×marschlinsii* as a "species group" (even through the hybridisation of larch is something of a spectrum).

We might even include some other aspect into our concept of species that is to do with the growth conditions. In Europe, machine control grading gives us one example in having a distinction between *Pinus pinaster* and *Pinus pinaster* trees at least 40 years old (Xyloclass F machine settings Table 21-2 [5]).

Less obviously, growth conditions maybe the reason we need to make some subspecies level distinctions, such as for the various types of *Pinus nigra* that appear in European grading rules and standards (see below). This also gives us another example: The description of *Pinus nigra* and *Pinus nigra* subsp. *laricio* each as a "species", and a mixture of *Pinus nigra* subsp. *laricio* and *Pinus nigra* subsp. *nigra* as a "species group".

It is not always clear how best to control species in structural timber grading, and in many respects it might be helpful; to regard all timber as a kind of mixture, even if nominally the same species.

4 THE DESCRIPTION OF A SPECIES COMBINATION

A species combination can be specified at different levels:

1) Listing at genus level.
2) A specific list at species level, but regarded as if a single species
3) A specific list at species level, regarded as a combination of species
4) A list with items below species level, such as subspecies, variety or clone.

A specification at genus level might be more restricted than it first appears, since the way the trade operates might limit in other ways. It is also the case that a list of species might be a long one and it is common to combine species that are only distantly related genetically. As an example, Figure 1 shows a phylogenetic diagram ending in species

https://doi.org/10.52202/069179-0107

and species combinations that appear in European strength grading documents, and Table 1 lists the species combinations. These are not exhaustive since there are additional items in national standards.

In practice, these four ways of describing a species combination are not completely distinct since taxonomy can differ. It is also the case that a specification of a single species, might be regarded as mixture of below species level distinctions. For example, in the European grading system *Pinus sylvestris* is not sub-divided (except by growth area) but it could be considered as a mixture of *P. sylvestris* var. *sylvestris, P. sylvestris* var. *lapponica, P. sylvestris* var. *hamata, and P. sylvestris* var. *elicinii.* Europe also has (non-native) *Pseudotsuga menziesii* var. *glauca* and *P. menziesii* var. *menziesii*, but the two are covered under a single listing of *Pseudotsuga menziesii*, and for timber strength grading the benefit of distinguishing varieties taken out of their native growth conditions is, anyway, questionable.

For timber grading, the matter of whether a resource should be treated as a species combination or not should be about the considerations that can affect grading, and not strict botanical taxonomy, which has no concern to wood properties. This can mean treating a single species as if it was a combination of elements, or ignoring botanical distinctions that are of no consequence to the timber.

5 SOME EXAMPLES

In the most recent draft of the European Standard EN1912 [6], the standard which lists assignments to strength classes (design values) from visual grading, pine from France is specified as a group with the exception of *Pinus pinaster*. This is because the available test data showed that this species (from France) graded less well (had lower design properties) than the other pines (when done to the French visual grading standard). Since it would be possible for a batch of timber to be of a single pine species it was necessary to either exclude *P. pinaster*, or lower strength class assignment (design values) to the level of *P. pinaster*. The first option was chosen as the better compromise for the industry.

The standard EN1912 [6] also lists a very specific entry for poplar from France, *Populus×canadensis* cv 'Robusta', 'Dorskamp', 'I 214', 'I 4551' due to the high level of variability across the poplar cultivars in the country. However, thanks to extensive additional testing, settings for machine control grading with several machines [5] were approved in 2019/20 for the very general species description: *Populus spp.*

Larches readily hybridise where they meet naturally, and where they are planted. This makes strict distinction by species unachievable in some situations. There are machine grading settings for *Larix sibirica* under the European system [5] but also confusion with *Larix gmelinii* (in [7]) with which it hybridises in Siberia and with no distinct line between the two. Some botanists also recognise a species *Larix sukaczewii* separately from *L. sibirica* on the basis of morphological differences that others regard as environmental rather than phylogenetic. In cases like this, the species distinction and growth area distinction are hard to separate.

The latest draft of EN1912 [6] also includes an entry for fir from Türkiye, which combines *Abies cilicica* with *Abies nordmanniana*. However, since some botanists regard the sub-divisions *A. nordmanniana* subsp. *equi-trojani* and *A. nordmanniana* var. *bornmuelleriana* as species in their own right (*Abies bornmuelleriana and Abies equi-trojani*) it is not clear cut whether the combination of Caucasian and taurus fir from Türkiye is two species or four.

6 KINDS OF MIXTURE

It is also necessary to take into account the possible different kinds of species combination, which include:

1) Intimate mixtures in the forest, which are not practical to separate in the wood value chain. The wood is processed, graded and sold as a mix. Batches of processed timber might be expected to contain reasonably consistent ratios of the different species components (although it may not be possible to know this).
2) The species are separate in the forest, but harvested at the same time. They could be separated, but there are commercial reasons not to. The species are processed, graded, and sold as a mixture. Batches might contain quite varied ratios of components, because logs of different species are not so well mixed as in case (1).
3) The species are separate in forest, and are not harvested at same time. Species are processed as individual species but graded on common basis and sold as species combinations for market convenience. Batches contain very varied ratios of components because the species are only combined later in the process.
4) The species are separate in the forest, and not harvested at same time. They are processed and graded as individual species but sold under a species combination for market convenience. Batches of timber are generally always not a mixture when graded, but they could be mixed by merchants and end users.
5) Species are processed and sold separately, but under a common grading process which covers a number of different species.

7 CONSIDERATIONS FOR MIXTURES

7.1 Before strength grading

In the case when sawmills have some choice as to whether or not to process logs of different species together, there are several practical factors to consider including whether the species are similar for debarking, sawing and drying. The way the sawmills process the timber will have an effect on the species mix in the packs of graded timber, but even if the species are well mixed in production, the packs are likely to be less mixed, due to the number of boards that come from individual logs ending up together.

https://doi.org/10.52202/069179-0107

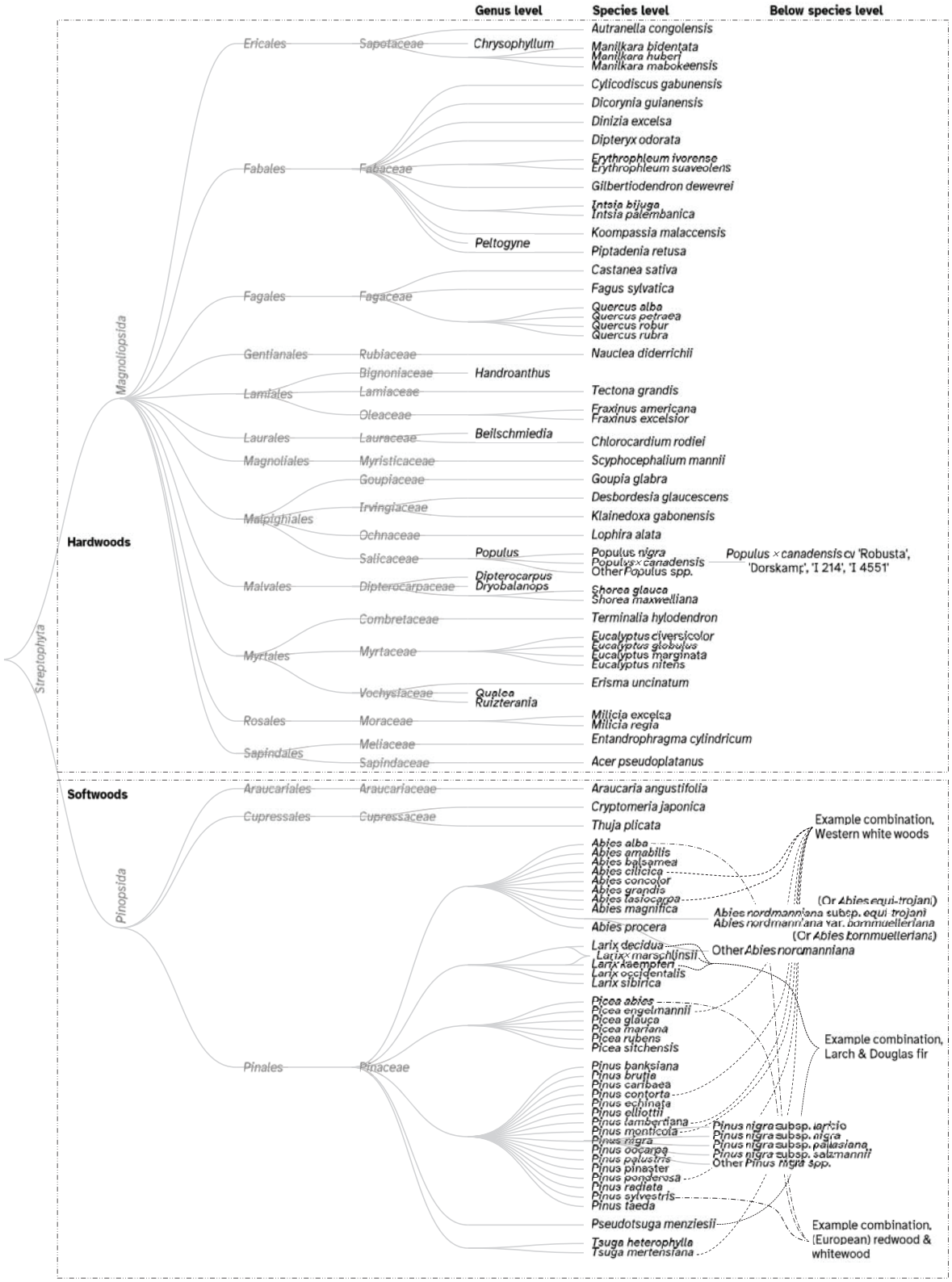

Figure 1: *Phylogeny of species mentioned in European standards [7,8] and machine control grading settings tables [5]*

https://doi.org/10.52202/069179-0107

Table 1: *Example: list of species combinations referenced in European standards [7,8] and machine control grading settings tables [5]*

Genus level as if a single species	
Temperate	
Poplar spp.	Poplars
Tropical	
Qualea spp., Ruizterania spp. *	Mandio (gronfolo)
Chrysophyllum spp. (syn. *Gambeya spp*)	Longhi
Dipterocarpus spp.	Keruing
Dryobalanops spp.	Kapur
Beilschmiedia spp.	Kanda
Handroanthus spp.	Ipé (Ebene verte)
Peltogyne spp.	Amarante (Purpleheart)

A species list as if a single species	
Temperate	
Quercus petraea, Quercus robur	European oak
	Tropical
Erythrophleum ivorense, Erythrophleum suaveolens	Missanda (Tali)
Intsia bijuga, Intsia palembanica	Merbau
Milicia excelsa, Milicia regia	Iroko
Shorea glauca, Shorea maxwelliana	Balau (bangkirai)

A species list as a species combination	
Temperate	
Abies alba, Picea abies	Spruce & fir whitewood
Abies alba, Picea abies, Pinus sylvestris	Redwood & whitewood
Abies amabilis, Abies concolor, Abies grandis, Abies magnifica, Abies procera, Tsuga heterophylla	Hem-fir
Abies balsamea, Abies lasiocarpa, Picea engelmannii, Picea glauca, Picea mariana, Picea rubens, Pinus banksiana, Pinus contorta, Pinus ponderosa	S-P-F (spruce-pine-fir)
Abies balsamea, Abies lasiocarpa, Picea engelmannii, Pinus contorta, Pinus lambertiana, Pinus monticola, Pinus ponderosa, Tsuga mertensiana	Western white woods
Abies nordmanniana, Abies cilicica, Abies bornmuelleriana, Abies equi-trojani	Caucasian and taurus fir
Larix decidua, Larix × marschlinsii, Larix kaempferi	Larch (European, Japanese and hybrid)
Larix decidua, Larix × marschlinsii, Larix kaempferi, Pseudotsuga menziesii	Larch and Douglas fir
Larix occidentalis, Pseudotsuga menziesii	Douglas fir-larch
Manilkara bidentata, Manilkara huberi	Balata Franc (Massaranduba)
Picea abies, Picea sitchensis	British spruce
Picea abies, Pinus sylvestris	Norway spruce and Scots pine
Pinus caribaea, Pinus oocarpa	Caribbean pitch pine
Pinus echinata, Pinus elliottii, Pinus palustris, Pinus taeda	Southern pine
Pinus elliottii, Pinus taeda	Loblolly pine and slash pine
Pinus nigra, Pinus pinaster, Pinus sylvestris	Pines
Pinus nigra subsp. *laricio, Pinus nigra* subsp. *nigra*	Austrian & Corsican pine
Pinus nigra subsp. *laricio, Pinus nigra* subsp. *nigra, Pinus sylvestris*	French pine (not including maritime)
Pinus nigra subsp. *laricio, Pinus sylvestris*	British pine

* EN13556 [8] does not include *Ruizterania*

7.2 During strength grading

The considerations during strength grading depend on the kind of grading, in particular:

- For machine grading, the nature of the things the machine assesses, and how those are combined in the particular indicating property model used for those settings.
- For visual grading, the features possible to assess, how they are quantified (especially knots and ring width) and the grade limits.
- The grade determining properties of the different species (particularly the means, standard deviations and correlations).
- The strength class (design value) requirements, the combination of strength classes being graded, and the particular grade determining property (if any) that is limiting the grading.

Some species influences might not be immediately obvious. For example, the standard EN14081-1 [8] requires visual grading standards to have a rule about ring width or density, with ring width intending to function as a predictor of density when it is not directly measured. However, the kind of species affects this (the transition of earlywood to latewood in softwoods and the ring porous / diffuse porous spectrum for hardwoods), as well as influencing how easy it is to assess ring width. It also interacts with growth condition effects as ring width is also connected to geographical origin and to radial position in the log. Depending on how important ring width is in a particular visual grading scenario, it may or may not limit the possible species combinations.

In the case of grading to a single strength class with near 100% yield the considerations to do with species and grading method may not be so important, especially if the grade limiting property is not the strength. But generally speaking, for effective grading, the species would ideally have similar grade limiting properties, which correlate in a similar way with the grading criteria. Properties that are not grade limiting need not correlate in a similar way with the grading criteria. The degree to which this affects the grading of species combinations depends on both the grading method and the target strength classes (design values).

It is commonly expected that the difference between the species in a combination are ideally of similar variation seen within a single species (within the growth area), but this is not an easy requirement to quantify.

In the case of machine grading, it is also important that the species can be graded with the same indicating property adjustments for moisture content, temperature, cross-section size and machine operating speed.

When grading is controlled via testing in production (known as output control in Europe) the effect of species is only accounted for if the feedback to machine settings is fast enough to adapt to any large deviation in species mix ratio. Measures to separately check individual species in the production testing can mitigate this.

The European strength grading system does not prohibit a species combination that combines both hardwoods and softwoods, although such a thing would need to be based on the "softwood" strength classes due to the secondary properties. It is already the case that lower density hardwoods like *Populus*, *Castanea sativa* and *Eucalyptus nitens* can be given "softwood" strength class assignments.

7.3 After strength grading

Strength grading ensures the key mechanical and physical properties for structural use, but there are still practical considerations such as similar treatability with preservatives and similar workability from the user perspective (finishing, gluing, moisture movement, dead knots, resin pockets, need for pre-drilling etc), especially for use in laminated timber products. Product and usage standards might also have specific restrictions based on species.

To a certain extent there needs to be similar appearance for market acceptability, and similar average density (for predictable self-weight, handling, drilling etc). However, in the European system, the grading is only concerned with a minimum characteristic (5th percentile) density and the mean density is not explicitly controlled.

If the different species are distinguishable as sawn timber, the grading should still be safe even if the end user or merchant separates them for some reason.

8 VERIFICATION OF GRADING

Whether or not species should be included as a specific aspect of the grading verification calculation (and sampling for the testing) depends on the situation. If the species cannot be distinguished before, during and after grading in real production, it is usually appropriate not to treat species separately in the verification. However, it is still necessary to consider how similar those species are to allow for the expected variation in the mixture from sawmill to sawmill and timber pack to timber pack. For that reason, if species can be distinguished in sampling it is advisable to do so.

If species can be distinguished, it is prudent to check each species individually. In the framework of machine control grading in Europe [9] this could be done by creating additional verification samples in a similar manner to the geographical ones. An example of this is provided in an accompanying paper [10].

A full separate check on species is expensive in test data, and if species differences are thought comparable to growth area differences, it may be appropriate to treat the addition of a species to an existing grading route in a similar way to the route for an already included species to an extended growth area.

When it is not economic to do a large enough testing programme to fully resolve the uncertainty, the grading assignment should be correspondingly conservative. It is not enough that a resource as whole grades correctly since it is packs of timber that are used in structures, and grading must work correctly at that level whatever

https://doi.org/10.52202/069179-0107

realistic separation of the species has occurred before, during or after grading.

There are two additional ways in which fully separate grading verification calculations could be combined, although since they require a large amount of testing they are less useful for bringing minor species to market:

1) Separate calculations but with the same indicating property model and thresholds (or visual grading rule and assignment) so that the grading process can be common.
2) Separate calculation and also different grading settings (or visual grading rules), but the graded timber marked and sold as a combination for market convenience.

9 RECOMMENDATIONS

It is recommended that national grading experts work to develop a framework for establishing grading assignments for new species combinations, rather than develop requirements for sampling and verification on an *ad hoc* basis as new grading reports are prepared. This would make it clearer for those developing the grading assignments, and also help to ensure that relevant considerations are accounted for from the planning stage. Nevertheless, it will still be necessary to be able to adapt this framework as more information is revealed through experience. Whatever the approach, it would be important that it is not subservient to strict botanical taxonomy, but rather use taxonomy as part of the way that the resource is defined.

Developing the grading assignments by treating each species (or other relevant resource division) separately is the most robust approach, but requires a very large dataset and it is not always practically possible to distinguish the individual species during the grading development work, while still maintaining the overarching requirement for the sampling to be representative of the resource. The best course of action depends on the context both before and after grading.

For new grade combinations, and lesser-used species, it may be advantageous to also include a mean or upper percentile density to allow for fact that actual density may be considerably higher than the declared value, in order to avoid over-weight problems for handling and transport.

ACKNOWLEDGEMENT

This work is informed by the standardisation support work packages of the SIRT (Strategic Integrated Research in Timber) in the UK funded by Public Sector Forestry and industry, and the WoodProps programme, funded by the Department of Agriculture, Food and the Marine in Ireland.

REFERENCES

[1] P. Stapel, J-W. van de Kuilen. Efficiency of visual strength grading of timber with respect to origin, species, cross section, and grading rules: A critical evaluation of the common standards, *Holzforschung* 68, DOI: 10.1515/hf-2013-0042, 2013.

[2] D.J. Ridley-Ellis, D., P. Stapel, & V. Baño. Strength grading of sawn timber in Europe: an explanation for engineers and researchers. *Eur. J. Wood Prod.* 74, DOI: 10.1007/s00107-016-1034-1, 2016.

[3] G. Ravenshorst. *Species independent strength grading of structural timber*, PhD Thesis, Delft University of Technology, DOI:10.4233/uuid: b2243d5d-3275-4d93-9378-b39f97a39f02, 2015

[4] CEN, *Structural timber. Strength classes.* EN338:2016, European Committee for Standardisation, Brussels, 2016

[5] CEN TC124 WG2 TG1. AGR tables for machine control grading (viewed 10/03/2023)

[6] CEN, *Structural Timber. Strength classes. Assignment of visual grades and species*, EN1912:2012, European Committee for Standardisation, Brussels, 2012 (and most recent draft update to 10/03/2023)

[7] CEN, Round and sawn timber. Nomenclature of timbers used in Europe. EN13556:2003, European Committee for Standardisation, Brussels, 2003.

[8] CEN, *Timber structures. Strength graded structural timber with rectangular cross section. General requirements.* EN14081-1:2005+A1:2011 & EN14081-1:2016+A1:2019, European Committee for Standardisation, Brussels, 2011 & 2019.

[9] CEN, *Timber structures - Strength graded structural timber with rectangular cross section. Part 2: Machine grading; additional requirements for type testing.* EN14081-2:2018+A1:2022, European Committee for Standardisation, Brussels, 2022.

[10] D. Gil-Moreno, D., D. Ridley-Ellis, and A.M. Harte, Considerations for grading species combinations. The example of Douglas fir with larch in Ireland and UK, in *World Conference on Timber Engineering*, Oslo, 2023.

World Conference on Timber Engineering Oslo 2023

PREDICTION OF TIMBER TWISTING BASED ON MEASURED SPIRAL GRAIN OF SPRUCE TRUNKS AND LOGS

Kloiber Michal[1], Kunecký Jiří[2], Kotmel Miroslav[3]

ABSTRACT: This work focuses on the prediction of timber (beam) twisting based on the measurement of spiral grain under the bark of spruce trees (using Fakopp) and the subsequent measurement of spiral grain of logs during manipulation using a slope of grain detector. When selecting wood, it is necessary to take account of the effect of spiral grain on sawing; based on international practice, a spiral grain up to 5% deviation per 1 m of log length is not considered a defect. However, it is important whether the spiral is left-handed or right-handed, as measured on the log perimeter. Left-handed spiral increases after log processing while right-handed spiral decreases. The perimeter of an element from a left-handed log that was within the acceptable 5% angle deviation per 1 m of length manifests a considerably higher deviation when machined, which markedly affects the timber twist during drying. By contrast, beams from right-handed logs with up to 5% deviation per 1 m of length have perimeter without spiral grain, and they are not defected by twist during drying. This phenomenon has been confirmed by the study conducted. Further, a good prediction of spiral grain in trees has been achieved using non-invasive equipment, Fakopp ArborSonic Microsecond Timer.

KEYWORDS: Timber, spiral grain, twist, structural repair.

1 INTRODUCTION

All trees (and also Norway spruce) can contain spiral grain under the bark. Spiral grain trees have better resistance to strong wind and it helps them prevent breaking. When straight grain trunks are loaded, the side closer to the loading force is under tensile stress while the other side is compressed, which causes tension. In spiral grain trunks, the compression and tensile forces are transferred along the spiral to the other side of the trunk, which balances the tension. Many trees begin to grow twisted under the strong pressure of wind and snow. Under such conditions, the grain can deviate up to 30° from the vertical direction of growth. This twisted growth provides the tree with a better protection against mechanical damage; it can be considered a type of protective response [1].

If a tree grew perfectly straight, only the needles above the roots would receive water from them, and the roots directly below the needles would receive nutrients. Damaged roots on one side would then lead to dying of branches on that side. Twisted trees supply water from one root to all the needles, and conversely, nutrients from one branch flow to all the roots [2].

Twisted growth means spiral grain along the pith. In the saw machining practice, the spiral grain within 5% of angle deviation per 1 m of length is not considered a defect, which is very tolerant and often unacceptable for the final user of the timber as the product is damaged by twist. The reasons for spiral grain vary, slanting of cambial cells is most often mentioned. Cambial cells - spindle-shaped initials - are elongated and capable of coordinated reorientation in response to internal and external stimuli. Their intensity decreases rapidly as the tree ages [3]. The bark is very different in this respect because it is produced outside the vascular cambium, without the oriented spindle cells [4]. Therefore, it is not possible to predict the twist on logs without debarking.

The direction of the spiral grain can be left-handed, right-handed, or there is straight grain. The spiral can change along the trunk and there is no regularity. Across the trunk, it can change from a left-handed to a right-handed spiral from the pith towards the perimeter [5][6]. In Norway spruce, the left-handed spiral is usually the greatest in the 4th to 10th tree ring, counted from the pith. Subsequently, the spiral usually decreases and the spruce becomes straight-grained somewhere between the 40th and the 70th tree ring [7]. With the increasing number of tree rings within the rotation period, the spiral gradually turns to the right. This pattern applies to all species within the *Picea*, *Abies* and *Larix* families, plus almost every member of the *Pinus* family [8].

Spiral grain is usually found in trees growing in sparse stands and in avenues of solitary standing trees, which testifies relation to the tree growth speed [9]. This suggests that the decrease in spiral is not only related to

[1] Kloiber Michal, Czech Academy of Sciences, Institute of Theoretical and Applied Mechanics, Czech Republic, kloiber@itam.cas.cz
[2] Kunecký Jiří, Czech Academy of Sciences, Institute of Theoretical and Applied Mechanics, Czech Republic, kunecky@itam.cas.cz
[3] Kotmel Miroslav, Czech University of Life Science Prague, Department of Wood Processing and Biomaterials, Czech Republic

https://doi.org/10.52202/069179-0108

the effect of tree age or diameter, but may be influenced by the availability of nutrients and water to stimulate growth. The effect of wet snow and high winds on the spiral degree has been presented in the past [10], [11].
The spiral grain direction is the same whether you look from the crown to the roots or vice versa. Therefore, the spiral grain direction can be established also for short logs where the bottom and the top cannot be determined.
For Norway spruce, the undesirable left-handed spiral mainly appears in young trees, that is why timber from thin trunks twists more often than that from trunks from a mature stand [12]. Therefore, the central (juvenile) part of spruce logs is not suitable for use as structural timber. The general impact of spiral grain on timber utilization depends on the rate and duration of the development from the pith towards the cambium [8].
The spiral grain may have a considerable impact on the timber behaviour during drying, particularly twisting [13]. In consequence, the angle of spiral grain is an important parameter for each model that aims to describe the sawn timber deformation after drying and the subsequent moisture content changes during storage and use. The higher the spiral grain angle, the greater the timber twist when drying [15], [16], [17].
Various techniques have recently been proposed to determine the degree of the spiral, e.g. [18] developed an automated method for measuring twist on logs; the method uses the light-conducting properties of softwood tracheids to measure the grain orientation on the external side of debarked logs. This method has enabled high resolution measurements over large areas and segregation of material with visible spiral. The applicability of visible light and laser is limited by the presence of bark on the log [19].
Other non-destructive methods for measuring spiral of logs, e.g. using X-rays are presented by authors [20], [21]; use of microwaves is presented in [22], [23]. These techniques require expensive equipment and powerful mathematical modelling; yet, they are increasingly commercially applied. The variation there is up to 10 degrees. The most accurate method to determine the spiral is splitting [24].
A very precise yet simple method is pressing a sharp tip into the wood surface and marking the longitudinal direction of the grain with a slope of grain detector [25]. The slope of grain detector consists of a steel rod, which is loosely placed in a rotating wooden handle at one end, with a needle (tip), which is pressed into the wood, protruding at the other end. This simple tool allows for satisfactory results and can be used with great accuracy if its limitations are understood and measures are taken to eliminate them.
The tendency for spiral grain of tree trunks can be detected directly under the bark or can be seen in the roots [26] and also branches [27]. The spiral grain estimation from branches was used in the past by shingle manufacturers, who thus eliminated unsuitable left-handed logs. However, research has shown that the spiral of branches and trunks is not identical. For example, [27] took detailed measurements of 11 *Larix kaempferi*, *L. gmellinii* trees and found that the mean values for spiral and their standard deviations were twice as large in the trunk as in the branches.
The processes used to detect the spiral grain direction of wood need not be applied to sawn timber or debarked logs only. Some methods can be used for standing trees without permanent damage, e.g. bark stripping. [28] used ultrasonic testing equipment Pol-Tek to determine the direction - sound pulses propagate at maximum speed in the direction along the grain. Our measurements, made by indenting probes through the bark of standing trees, showed the method applicability to determine the spiral grain direction on the tree trunk perimeter under the bark with an accuracy approaching 90 %.
The study reported here was designed to provide information on the spatial variation in Norway spruce trunk spiral grain, using:
• the prediction of spiral grain based on trunk measurement by stress-wave;
• the prediction of timber twisting during drying based on trunk measurement by stress-wave;
• the prediction of timber twisting during drying based on sawlog measurement by a slope of grain detector;
• the prediction of timber twisting during drying based on the actual timber measurement by a slope of grain detector.
Thirty spruce logs from 22 trees were examined to improve our understanding of the spatial variation of spiral grain within a trunk and the ability to predict it given the potential distortion of beams during drying.

2 SPIRAL GRAIN MEASUREMENT

For the purpose of the experiment, the spiral grain was measured in 22 selected trees of Norway spruce (*Picea abies* (L.) H. Karst.) from the forest stand near Oblajovice municipality, which is a part of Natural Park Polánka, in the western part of the Českomoravská vrchovina Highlands (central area of the Czech Republic). The trees grew at an altitude of 650 m a.s.l., i.e. at the bottom line of Norway spruce natural occurrence. The selection of the trees was carried out with exclusion of damaged trees and other defects arising during tree growth (swollen rootstock, crooked trunk, cracks, branched lower part of the trunk, etc.). The breast height diameter of the trees ranged between 40 cm and 60 cm. After harvest, 6m logs were cut out.
The spiral grain was measured at the breast height by means of Fakopp ArborSonic Microsecond Timer. This device is supplied to the market by the Hungarian manufacturer Fakopp Enterprise. The principle consists in measuring the passage time of a stress wave through the trunk [29]. The equipment uses push-in sensors that provide the signal transfer and the contact with the wood. The wave passes through material in a constant speed, the frequency depends on the hammer force on the sensor head. The push-in sensors are fitted using a specialised template (Fig. 1) 50 cm apart from each other in the trunk longitudinal axis and 5 cm far from the trunk axis at the same time, so that the top sensor (excitation) is displaced to the left and the other sensor (receiver) to the right. This sensor placement allowed measuring the speed in the left-handed direction. When the sensors were changed to

measure the right-handed direction, the top sensor was placed 5 cm to the right from the longitudinal axis and the lower sensor 5 cm to the left (Fig. 2).

Figure 1: *Measuring the tree spiral grain in the bark by means of Fakopp ArborSonic Microsecond Timer and a template*

After the time of stress wave passage through the left- and right-handed placement of sensors was measured, the propagation speed ($m.s^{-1}$) was calculated. The difference between right- and left-handed speed measurements were correlated with the real slope of grain on logs after harvest using the slope of grain detector (Fig. 3), consisting of a wooden handle in which a metal rod is inserted so that it can turn freely. The rod is bent in the right angle and its tip is fitted with a metal spike.

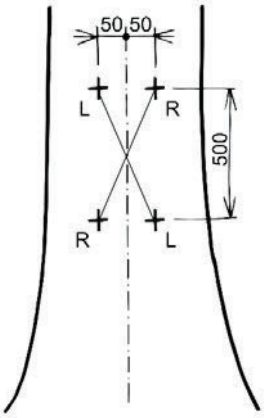

Figure 2: *Positions and placement (mm) of sensors for measuring the stress wave propagation speed in the longitudinal direction of the tree (L-left-handed and R-right-handed measurements)*

Before the slope of grain detector was used, the bark had been removed with a drawshave and the log axis had been marked with a carpenter pencil and a ruler. Then the spike was pushed in the axis marked on the trunk and the real grain deviation was carved. The grain deviation from the log longitudinal axis (mm/m) was measured along a distance of 20 cm and then calculated per 1 m of length, as standards apply, e.g. EN 1310:1997 [31]. The spiral grain established by means of the slope of grain detector was measured on both ends of 6m logs and then averaged for each log. In the case of trees with a large diameter, two 6m logs were used for the measurement: 0-6 m of the tree height (22 pcs) and 6-12 m of the tree height (17 pcs), 39 logs of spruce in total. The diameter of the upper logs had to be large enough to yield a beam of 20×25 cm profile. I.e., the log diameters corresponded to the common processing procedure, in which sometimes two 6m logs are taken out from one tree and sometimes only one is possible. The condition was applied that the final sawmill product (20×25 cm structural beam) needs to have sharp edges without rounding.

Figure 3: *Measuring the spiral grain under the bark by means of slope of grain detector*

When the measurement of logs was finished, they were sawn into 20x25cm beams, 6 m long, which were stored in a pile and dried in a natural way to 16% moisture content. Out of a total of 39 spruce logs, 30 were used for sawing. The naturally dried beams were subjected to twist measuring: one end of the beam was stabilised in the vertical position using a spirit level and the twist deflection was measured on the vertical surface of the other beam end (Fig. 4). The measured deflection was used to calculate the twist angle of the naturally dried beams.

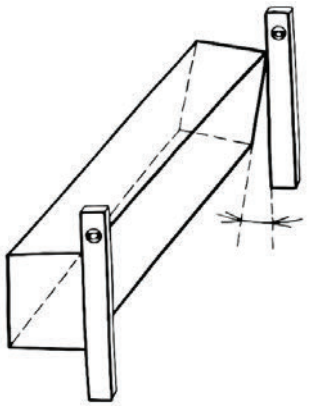

Figure 4: *Measuring the twist angle of beams after natural drying using a spirit level*

https://doi.org/10.52202/069179-0108

3 RESULTS AND DISCUSSION

Recently, emphasis has been placed on the quality of timber, which is dependent on our understanding of spiral grain and its effect on sawmill products [32]. The selection of suitable logs based on the determination of the spiral grain and a prediction of timber behaviour during processing are essential for processing. In this study, a non-invasive approach of detecting spiral grain directly on the tree using the Fakopp 2D instrument has been proven to be effective; the probes of the instrument are arranged in an X-shaped pattern at the breast height of the trunk, i.e. both left- and right-handed directions of stress wave propagation are covered (Fig. 2). The differences in the propagation speed of the stress wave in both directions can predict the direction and especially the degree of the spiral grain with an accuracy of R^2=0.93, which is confirmed by the results presented in Fig. 5. The high accuracy is related to the bottom log, i.e. 0-6 m from the tree base. In the case of the spiral grain prediction for two 6m logs (0-12 m tree height), the coefficient of determination decreases slightly R^2=0.87 (Fig. 6.) In the case of predicting spiral grain only for the upper log (6-12 m tree height), the coefficient of determination is R^2=0.78 (Fig. 7).

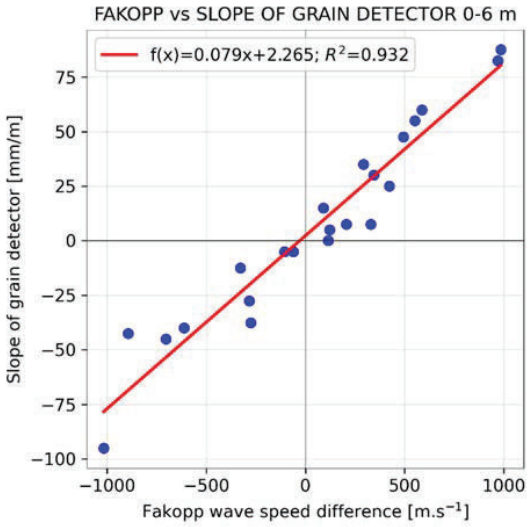

***Figure 5**: Dependence of the difference in longitudinal stress waves speed from Fakopp measured at tree breast height compared to spiral grain as measured by the slope of grain detector, measured on logs 0-6 m from the tree base*

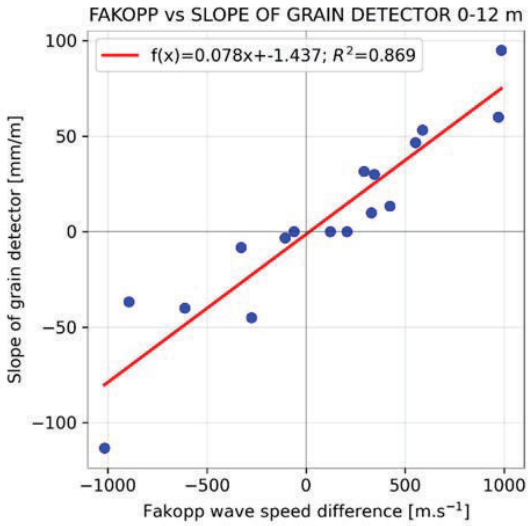

***Figure 6**: Dependence of the difference in longitudinal stress waves speed from Fakopp measured at tree breast height compared to spiral grain as measured by the slope of grain detector, measured on logs 0-12 m from the tree base*

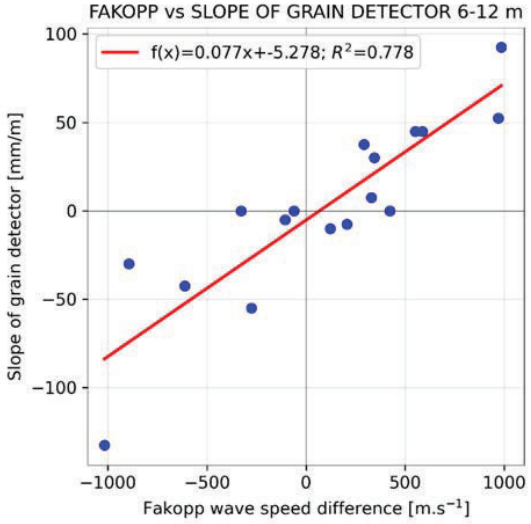

***Figure 7**: Dependence of the difference in longitudinal stress waves speed from Fakopp measured at tree breast height compared to spiral grain as measured by the slope of grain detector, measured on logs 6-12 m from the tree base*

When trying to predict the timber twisting (0-6 m from the tree base) after natural drying from the differences in the stress wave propagation velocity for the two directions of spiral grain measured using the Fakopp 2D instrument, the coefficient of determination is R^2=0.81 (Fig. 8). The upper logs (6-12 m from the tree base) yield an even better coefficient of determination: R^2=0.92 (Fig. 9), and the combined logs (0-12 m from the tree base) reach a coefficient of R^2=0.95 (Fig. 10).

The graphs show that for left-handed spiral, we can accept speeds of up to 250 $m.s^{-1}$ when predicting the spiral grain from differences in the stress wave speed, in order to avoid the undesirable twist (greater than 5° in a 6 m long

log) when drying the timber. Speed differences for left-handed spiral greater than 250 m.s^{-1} mean that such timber should be avoided as it will represent significant loss caused by material acquisition and cutting costs. On the contrary, the differences in the stress wave speed in the case of right-handed spiral indicate that the twist of the sawmill product will be minimal even if the differences in measured speeds reach 1000 m.s^{-1}(Fig. 8-10).

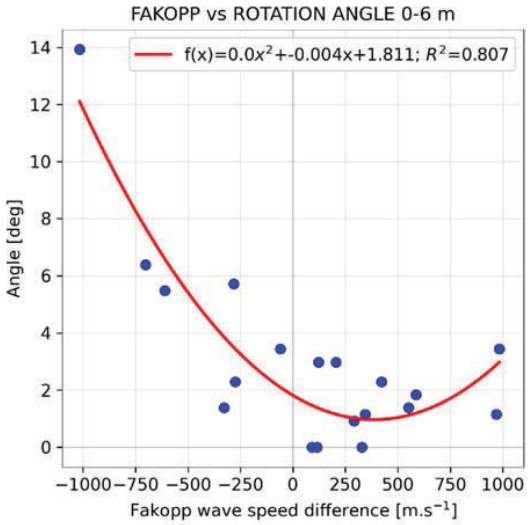

***Figure 8**: Dependence of the difference in longitudinal stress wave speeds from Fakopp measured at the breast height compared to the twist of a 20×25×600 cm beam from a log cut at 0-6 m from the tree base*

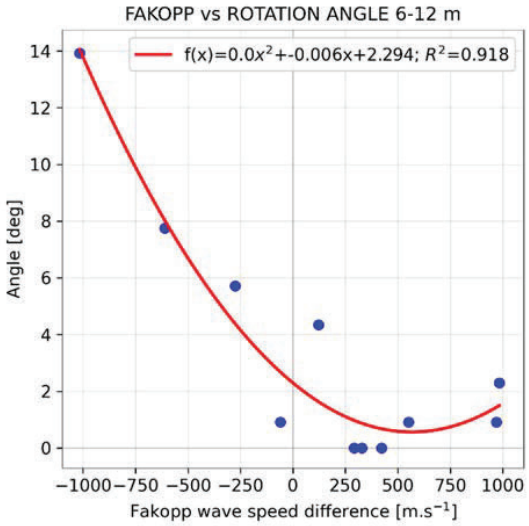

***Figure 9**: Dependence of the difference in longitudinal stress wave speeds from Fakopp measured at the breast height compared to the twist of a 20×25×600 cm beam from a log cut at 6-12 m from the tree base*

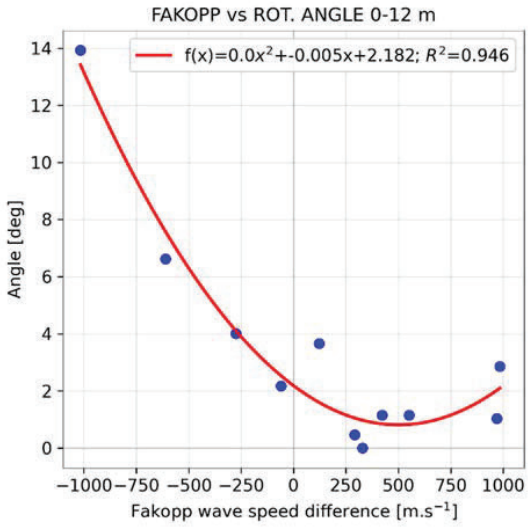

***Figure 10**: Dependence of the difference in longitudinal stress wave speeds from Fakopp measured at the breast height compared to the twist of a 20×25×600 cm beam from a log cut at 0-12 m from the tree base*

The above dependences between the differences in the stress wave speeds measured on a tree with the Fakopp 2D instrument and the beam twisting show that this is a very accurate prediction, which can be obtained directly in the forest using totally non-invasive measurements on the tree. The prediction accuracy is also confirmed by the following graph in which timber twisting is in direct dependence on the spiral grain as measured by the slope of grain detector on logs - the coefficient of determination reaching R^2=0.82 (Fig. 11). It is therefore a prediction that can be carried out in the storage facility or directly in the forest during harvest.

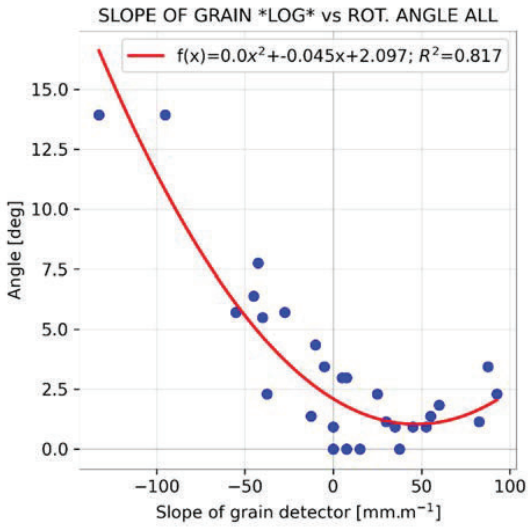

***Figure 11**: Dependence between the spiral grain measured by the slope of grain detector in a 6m log and the timber twisting*

https://doi.org/10.52202/069179-0108

The coefficients of determination reach a similar level to the prediction of speed differences using stress waves measured directly on the tree. In order to gain a twist of maximum 5° per length in a 6m beam, the grain deviation of the left-handed spiral can be 25 mm/m at maximum (Fig. 11). On the other hand, in the case of right-handed spiral, grain deviation detected by the slope of grain detector can be as high as 75 mm/m, and the beam twist will meet the maximum tolerance of 5°.

Therefore, it can be argued that spiral grain and the resulting problems with timber processing for construction purposes can be eliminated directly in the forest when selecting trees, or later in a storage place. Naturally, this concerns small volumes, for example, when selecting timber suitable for repairing structural elements of roof trusses, ceilings or other parts of historic buildings. The results of this study show that the spiral grain is an important variable affecting the twist of timber. Data analysis shows that the direction of spiral and its deviation have a significant effect on the twisting. The data on spirals show that the spiral pattern across the trunk starts from an initial left-handed direction, gradually decreases towards the log perimeter, and in about half of the cases it turns into a right-handed pattern, as already suggested by [13], [14], [17]. The above statement can be supported by the dependence between the grain deviation determined by the slope of grain detector directly on the beam and its twisting during natural drying (Fig. 12). The spiral grain variance at the same angle of beam twist is the same for the left-handed and right-handed sides (ideally 0 mm/m). This is different from the spiral grain found on the perimeter of logs, where the ideal degree was around 40 mm/m to the right.

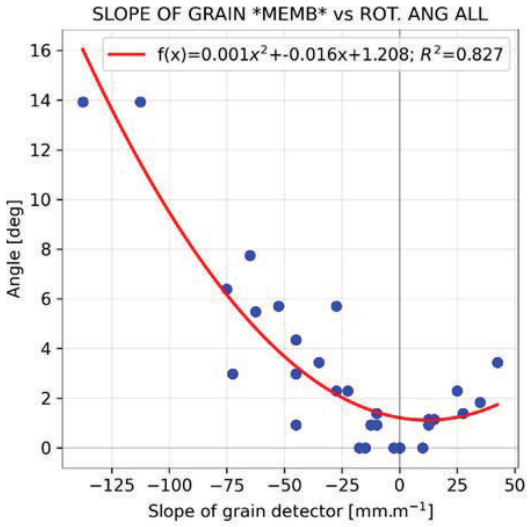

***Figure 12**: Dependence between the spiral grain measured by the slope of grain detector in a 6m beam and the beam twisting*

Previous observations suggested a shortage of straight-grained spruce timber [7]. This finding was confirmed in this study by measurements of 6m logs. Right-handed logs have greater torsion stability than left-handed logs. A likely reason for the greater stability in timber made from logs with a right-handed twist on the perimeter is the balancing of the shrinkage stress during drying [8]. The shrinkage stresses should work against each other, right-handed wood on the log perimeter against the left-handed wood in the central part of the log.

On the other hand, the logs that showed a left-handed spiral grain on the perimeter twist to the left with nothing to prevent them, after the required 20×25cm beams are made. The degree of spiral grain has also been proven to have a significant effect on the timber twist. In addition, previous research shows that left-handed wood has lower strength [21], [33].

4 CONCLUSIONS

The aim was to test the hypothesis that timber selection based on spiral grain measurement on the trunk surface can considerable help reduce the number of sawn timber prone to twist. The quality of timber is markedly affected by the wood spiral grain, which can be non-destructively investigated as early as during the selection of trees in a stand. Fakopp ArborSonic Micosecond Timer proved to be a suitable tool for the spiral grain determination through stress wave propagation speed measurement. The differences in stress wave propagation speed for the left- and right-handed directions, as measured at the breast height, allowed determining the spiral degree with up to 93% accuracy for 6m logs. The impact of left-handed spiral grain on the twist of timber during drying has been confirmed. The optimum log spiral grain proved to be in the range of 0 to 75 mm/m towards the right, then the twist during drying of the structural beams reached a maximum of 5° per 6 m of length. In the case of 0 to 50 mm/m slope of grain to the left, the logs are prone to twist, reaching 7,5° per 6 m of length. A grain deviation greater than 50 mm/m to the left represents a serious damage to timber and this cannot be used for structural purposes.

The problems of timber twisting during the drying process was pointed out by [7], [8], [13], [14]. A possible option to counter the damage is to reduce the tolerance in timber grading. Our recommendation for the production of structural members is to limit the use of logs with a left-handed spiral grain from the 50 mm/m stipulated in standards to 25 mm/m. In the case of right-handed logs, the spiral grain of 50 mm/m is usable as the twist of the final structural member reduces to required deviations close to 0°.

ACKNOWLEDGEMENT

This paper was created with a financial support from grant project GAČR No. 21-29389S ”Experimental and numerical assessment of the bearing capacity of notches in timber beams at arbitrary locations using LEFM”, authors gratefully thank the provider.

REFERENCES

[1] Tributsch, H.: How life learned to live. The MIT Press, Cambridge, 1984. 218 p.

[2] Kubler, H.: Function of spiral grain in trees. Trees, 5(3), 1991. pp. 125-135.

[3] Larson, P.R.: The vascular cambium. Development and structure. Springer series in wood, Springer, Berlin, Heidelberg, New York, 1994. 725 pp.

[4] Kramer, P.J., Kozlowski, T.T.: Physiology of wood plants. In: Academic Press, Orlando, 1979. 811 pp.

[5] Danborg, F.: Spiral grain in plantation trees of Picea abies. In: Canadian Journal of Forest Research, 24, 1994. pp. 1662-1671.

[6] Hannrup, B., Säll, H., Jansson, G.: Genetic parameters for spiral grain in Scots pine and Norway spruce. In: Silvae Genetica, 52(5-6), 2003. pp. 212-215.

[7] Säll, H.: Spiral grain in Norway spruce. Doctoral Thesis. Acta Wexionensia 22. Växjö, Sweden, Växjö University Press. 2002. 171 pp.

[8] Harris, J.M.: Spiral grain and wave phenomena in wood formation. Springer-Verlag, Berlin, 1989. 214 pp.

[9] Eklund, L, Säll, H, Linder, S.: Enhanced growth and ethylene increases spiral grain formation in conifers. In: Trees, 17, 2002. pp. 81-86

[10] Rouvinen, S., Kuuluvinen, T.: Structure and asymmetry of tree crowns in relation to local competition in a natural mature Scots pine forest. Canadian Journal of Forest Research, 27, 1997. pp. 890-902.

[11] Skatter, S., Kucera, B.: Spiral grain – an adaptation of trees to withstand stem breakage caused by wind-induced torsion. In: Holz als Roh und Werkstoff, 55, 1997. pp. 207-213.

[12] Ormarsson, S., Cown, D.J.: Moisture-related distortion of boards and wooden products of radiata pine: comparison with Norway spruce. In: Wood and Fiber Science, 37(3), 2005. pp. 424-436.

[13] Kliger, I.R.: Spiral grain on logs under bark reveals twist-prone raw material. In: Forest Products Journal 51(6), 2001.

[14] Perstorper, M., Pellican, I., Kliger, R., Johansson, G.: Quality of timber products from Norway spruce. In: Wood Science and Technology, 29, 1995. pp. 157-170.

[15] Mishiro, A., Booker, R. E.: Warping in New Crop Radiata Pine 100 x 50 mm (2 by 4) Boards. Bulletin of the Tokyo University Forests, 80, 1988. pp. 37-68.

[16] Cown, D. J., Haslett, A. N., Kimberley, M. O., McConchie, D. L.: The influence of wood quality on lumber drying distortion. In: Annales Des Sciences Forestieres, 53(6), 1996. pp: 1177-1188.

[17] Forsberg, D.: Warp, in particular twist, of sawn wood of Norway spruce (Picea abies). Doctoral thesis, Swedish University of Agricultural Sciences, Uppsala, Sweden. 1999.

[18] Nyström, J.: Automatic measurement of compression wood and spiral grain for the prediction of distortion in sawn wood products. Doctoral Thesis, Division of Wood Technology, Luleå University, Sweden. 2002. 18 pp.

[19] Bernard, P., Chalebois, A., Pearson, N., Samson, M.: Application of infrared ellipsometry to detection of local grain organization and spiral grain in wood. In: 10th Symposium NDT of Wood, 1996. pp. 165-174).

[20] Buksnowitz, C., Muller, U., Evans, R., Teishinger, A., Grabner, M.: The potential of SilviScan's x-ray diffractometry method for the rapid assessment of spiral grain in softwood, evaluated by goniometric measurements. In: Wood Science and Technology, 42(2), 2008. pp. 95-102.

[21] Sepúlveda, P., Kline, D.E., Oja, J.: Prediction of fiber orientation in Norway spruce logs using an X-ray scanner: A preliminary study. In: Wood and Fiber Science, 35(3), 2003. pp. 421-428.

[22] Sjödén, T., Nilsson, B., Nordebo, S.: Microwave modelling and measurements for early detection of spiral grain in wood. In: 14th International Symposium on Nondestructive Testing of Wood, Eberswalde, Germany, 2005.

[23] Nilsson, B., Sjőděn, T., Nordebo, S., Säll, H.: Method for under-bark detection of the wood grain angle radial dependence. In: Wood Material and Engineering, 3-4, 2007. pp. 118-129.

[24] Miyaki, M., Hatakeyama, S., Goshu, K.: Relationship between grain inclination and axis of pith when using the splitting method. In: Journal Japan Forestry Society 65(5), 1983. pp. 183-186.

[25] Koehler, A.: Guide to determining slope of grain in lumber and veneer. In: US For Serv Rep FPL-1585, 1955. 58 pp.

[26] Krempl, H.: Untersuchungen Uber den Drehwuchs bei Fichten. Mitt Forst Bundes-Versuchsanst, Wien, 1970. 118 pp.

[27] Ohkano, T.: Estimate of spirai grain in the stem of standing tree by the branches. In: Proceedings Pacific Regional Wood Anatomy Conference Tsukuba Japan, 1984. pp. 43-45.

[28] Foulger, A.N.: Through-bark measurements of grain direction: pre1iminary results. In: Forestry science 15, 1969. pp. 92-94.

[29] Bucur, V.: Non-destructive characterization and imaging of wood. Springer-Verlag, Berlin, 2003. 354 pp.

[30] Ross, J.R., Brashaw, K.B., Wang, X., White, H.R., Pellerin, F.R.: Wood and Timber Condition Assessment Manual. Forest Products Society Madison, WI., 2004. 73 p.

[31] EN 1310:1997 Round and sawn timber – Method of measurement of features. 1997.

[32] Johansson, G., Kliger, R., Perstorper, M.: Quality of structural timber-product specification system required by end-users. In: Holz als Roh und Werkstoff, 52, 2007. pp. 42-48.

[33] Lowery, D.P., Erickson, E.C.: The effect of spiral grain on pole twist and bending strength. Intermountain Forest & Range Experiment Station, 35, Forest Service, US Department of Agriculture, 1967. 16 pp.

https://doi.org/10.52202/069179-0108

World Conference on Timber Engineering Oslo 2023

ULTRASONIC-BASED DEFECT IDENTIFICATION IN TIMBER USING UNIFORM MANIFOLD APPROXIMATION AND PROJECTION (UMAP)

Prashanth Gunasekaran[1], Mehrisadat Makki Alamdari[2], Hamid Valipour Goudarzi[3]

ABSTRACT: Naturally occurring strength-impacting defects in timber, such as grain deviation and knots, are common in commercial timber. Additionally, defects caused by the environment such as fungal decay and termite damage are also attributed to strength reduction which can lead to the failure of structural timber. This work provides a demonstration, of applying Uniform Manifold Approximation and Projection (UMAP), a novel feature extraction tool, for the purpose of identifying such defects in structural timber, with the use of an ultrasonic-based examination of the test specimens. Two case studies are presented, the first demonstrating UMAP's capability in identifying grain deviation and knots in timber, and the second, showing its ability to distinguish healthy sections from that with known internal damage. In both case studies, 54kHz pressure waves were transmitted transversely through pre-defined sections of known damage state and were analysed with UMAP – producing highly favourable clustering and data separation between defect states, compared to wavelet packet decomposition, a state-of-the-art signal analysis framework. The key contributions of the study are – UMAP is successfully applied for the first time for damage identification in commercial bare timber, and it is demonstrated to be able to identify signals sent through sections of different defect types. This demonstration in this area opens the door to future works, which may then scrutinise in-depth material-specific factors for the aim of defect characterisation in timber and timber composites using UMAP.

KEYWORDS: Ultrasonic testing, Pressure wave, Wavelet decomposition, Feature extraction, Damage identification

1 INTRODUCTION

Strength-reducing defects are highly common in commercial timber and are either naturally occurring at growth, or induced due to the service environment or loading. Some examples of these defects include grain deviations and knots, associated with the former, and that related to termite damage, fungal decay and splitting damage associated with the latter. Additionally, local splitting failure caused by the rupturing of in-service structural timber due to higher loads also leads to the creation of weak zones. These weak zones incited by these defects have been shown to often be the initiation point of further damage [1], and hence their detection while in-service can be used to inform rehabilitation decisions.

Non-destructive testing (NDT) methods used for the purposes of assessing defects in timber have evolved over the last few decades. Current ultrasonic-based NDT techniques adopted on timber [2] to investigate these defects, face challenges in the signal processing stage. Wavelet packet decomposition (WPD) is one of the leading current signal processing approaches adopted for these purposes in the literature [3]. In [4], the structural integrity of timber utility poles was assessed using WPD, and their embedment depth has also been investigated using similar techniques [5]. In these studies, it was found that its chief challenge was parameter calibration. In WPD, different hyperparameters (levels of decomposition, choice of mother wavelet and filter functions) need to be trialled in order to attain separation of data between healthy sections and defective sections – a time-consuming and multi-variate process.

In this paper, a novel dimensionality reduction and feature extraction tool, Uniform Manifold Approximation and Projection (UMAP) [6], is applied for the first time, for the purposes of timber defect identification. The study is presented in two case studies. In the first case study, a timber specimen exhibiting multiple states including healthy sections, a section with visible grain deviation, and one with a visible knot are tested ultrasonically. The choice to adopt a test specimen with visible defects is justified in the study via the following consideration – the received signal is a function of the medium it was propagated through, regardless of the external visibility of the defect. Hence, the same outputs can be drawn from a test specimen with identical defects that were not externally visible. Accordingly, through visual inspection, the ground truth of the defect state of the specimen can be ascertained and thereafter compared with the output of the adopted signal analysis techniques, serving as an evidence-based mechanism in this study to demonstrate the efficacy of the algorithm.

[1] Prashanth Gunasekaran, University of New South Wales p.gunasekaran@unsw.edu.au
[2] Mehrisadat Makki Alamdari, University of New South Wales m.makkialamdari@unsw.edu.au
[3] Hamid Valipour Goudarzi, University of New South Wales h.valipour@unsw.edu.au

https://doi.org/10.52202/069179-0109

54 kHz ultrasonic pressure waves (P-waves) are transmitted between the sections transversely, and the signals are analysed first using WPD. Thereafter, the signals are comparatively analysed using UMAP, with the differences between the two methods examined and the superiority of the latter being demonstrated. In the second case study, a test specimen exhibiting healthy sections is adopted, with a void fabricated internally in the middle, creating loss of material – serving as a proxy for a piece of timber that has experienced interior termite damage, fungal decay or internal splitting damage. 54 kHz P-waves were transmitted transversely through pre-defined discretised locations in the timber. Similar to the first case study, the signals were analysed with WPD first, and thereafter compared with a UMAP analysis, their results further discussed.

2 THEORETICAL BACKGROUND

The theoretical background behind the two signal analysis approaches compared in this study is briefly recalled in the succeeding sections.

2.1 WPD METHODOLOGY

WPD is a technique used to fundamentally capture the frequency characteristics of the assessed signal while time-domain information is still retained [3]. A two-stage process is used in the decomposition: (1) The signal is processed with a wavelet transform, wherein features of the signal similar to the adopted mother wavelet are extracted at a particular scale and time. The mother wavelet is scaled and translated over the input signal with the aid of discrete scaling and translation parameters in the transform function. This wavelet transform is recalled in Equation 1. Thereafter; (2) A pair of low-pass filters (LPF) and high-pass filters (HPF) are used to conduct sub-band coding on the signal to delineate time-frequency features, in which the approximate and detail wavelet coefficients are obtained, respectively. The LPF and HPF formulas are recalled in Equation 2 and 3.

$$G_{k,j} = \int_{-\infty}^{\infty} f(t)\psi_{k,j}(t)\,dt \tag{1}$$

where G = wavelet coefficients, ψ = mother wavelet function, k = scaling parameter and j = translation parameter.

$$y_{low}[v] = \sum_{t} f(t) \cdot c(2v - t) \tag{2}$$

$$y_{high}[v] = \sum_{t} f(t) \cdot u(2v - t) \tag{3}$$

where f = input signal, c = low-pass filter impulse response factor, u = high-pass filter impulse response factor, t = translation parameter and v = subsampling parameter.

The level of decomposition is an inherent hyperparameter to be chosen when conducting the analysis. Representations of both the two-level and three-level sub-band coding schema are presented in Figure 1.

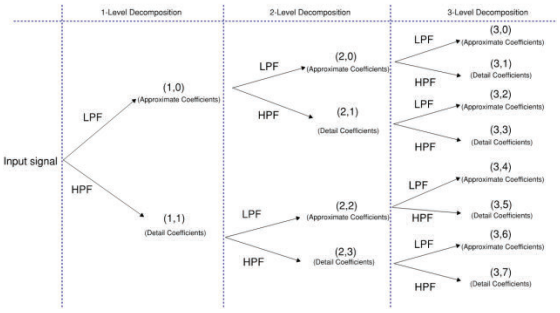

Figure 1: *Illustration of the sub-band coding schema for a 2 and 3-level wavelet packet decomposition.*

Apart from the level of decomposition, another key hyperparameter to select would be the mother wavelet, with a large variety of popular wavelet types adopted in the literature [7-10]. In this study both the Daubechies' 'db2' and 'db4' wavelets were investigated, and both 2 and 3-level decompositions were conducted, their results assessed in the succeeding sections.

2.2 UMAP METHODOLOGY

UMAP as an algorithm exists in the dimensionality reduction space, wherein the signal is represented as a point in a multi-dimensional space whose coordinates correspond to its amplitudes. UMAP then reduces the dimensions of the space to an easily comprehensible output graph.

The aim of the algorithm is to cluster signals with similar characteristics together and accurately and distinctively separate those with differing characteristics. It does so in two main stages. The first stage involves constructing the data's high dimensional topology as simplicial complexes. The Nerve theorem is applied, such that each signal is established as a 0-simplex and connections are made between each closely related signal – thereby approximating the topology of the high dimensional distribution of signals. These connections are made through the following process: (1) Spheres of varying radii are created around each signal based on density, through a fuzzy cover, wherein connections are formed with signals of intersecting radii. Mathematically, this is accomplished by first constructing the high dimensional signals on a Riemannian Manifold and establishing the spheres around each signal with a unit size. The required variable radii property is achieved through the homeomorphisms of these unit sized spheres on the manifold and their counterparts in Euclidian space, the latter allowing for such a property via varying notions of

https://doi.org/10.52202/069179-0109

distance. To maintain the same number of neighbouring signals allowed around each signal, fed into the algorithm as a hyperparameter, smaller notions of distance are used in Euclidian space for regions in the topology with higher density, and vice versa. (2) For efficient processing of the connections for each signal, concepts of Random Projection Trees [11] and Nearest Neighbour Descent [6] are utilised. (3) Connections between signals are mathematically represented through connection probabilities, considered via a 'neighbouring' matrix which holds each individual connection probability between signals in the original high dimension. In some regions of the topology, signals could have multiple connection probabilities associated with neighbouring signals in different metric spaces, due to the overlap of multiple spheres, and hence, distances of notion. Probability theory is utilised to condense these multiple connections to a single ideal connection between pairs of signals, by considering the combined probability of all connections between the signal pair.

In the second stage of the algorithm, the higher dimensional simplicial complex is projected to an easily comprehendible lower dimensional space. This done through a cross-entropy process, applied on the complexes, to cluster signals of similar characteristics together, and separate those with dissimilar features, projecting the topology into a two-dimensional graph [6]. The former, considered an attractive component between signals in the operation, is a commonly found trait of modern dimensionality reduction tools. UMAP's strength lies in the latter component of the cross-entropy process, considered a 'repulsive' operation, wherein the requisite distances between dissimilar signals are established. This results in the final output graph attained at the end of the algorithm.

The key hyperparameters to be calibrated for the algorithm are: (1) 'k' nearest neighbours – the number of nearby signals allowed for a given signal in the local metric space; (2) Minimum distance – referring to that between nearby signals in the final output. This hyperparameter is known to assist with the visualisation and cluster depiction; (3) Distance model – chosen for the mathematical calculation of distance between each signal.

3 ULTRASONIC TESTS ON TIMBER SPECIMENS

3.1 CASE STUDY 1

To investigate the versatility of the algorithm in structural defect detection and localisation in plain timber, the following test was conducted. The test specimen features an externally visible knot and grain deviation.

3.1.1 Specimen description

A 300mm long piece of machine-graded Australian *radiata pine* (MGP10), 90mm in width and 45mm in thickness was utilised, shown in Figure 2. Figure 2 also shows a schematic of the visible features in the test specimen. The knot in the specimen can be considered 'dead' due to a visible loss of fibre continuity between itself and the surrounding pieces of wood. The specimen was discretised into 4 sections. The centre of the knot is aligned with Section 4, and the grain direction change due to the presence of the knot is also within Section 3. Sections 1 and 2 did not show any visible signs of defects in the timber and featured longitudinally aligned grains - hence being classified as healthy sections.

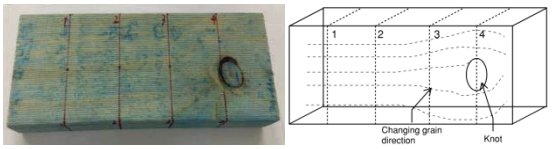

Figure 2: *Machine Graded Pine (MGP10) specimen (left) and schematic expressing defects (right).*

3.1.2 Time signals

P-waves of 54 kHz were transmitted transversely through the specimen, parallel to its 45mm thickness, in the perpendicular to grain direction. At each section of the specimen, 10 signals were transmitted with the transmitter on one end and the receiver on the other, thereafter having their positions swapped and measuring another 10 signals - amounting to a total of 20 signals at each measured section, summarised in Table 1.

Table 1: *Case Study 1 - Section information summary*

Section	Defect Status	Number of signals
1	Healthy	20
2	Healthy	20
3	Grain Deviation	20
4	Knot	20
Total number of signals		80

Figure 3 illustrates a sample of the ultrasonic signals sent through the timber specimen. The vertical axis represents signal energy, and for clearer visualisation, they are translated vertically with respect to each other. From visual inspection of the signals, the presence of the knot in Section 4 causes the most disruption to the received signal relative to the grain deviation in Section 3, when benchmarked against the signals from the healthy sections (1 and 2). The signal from Section 4 exhibits significantly lower wave energy than that of healthy sections, while the signal from Section 3 has similar wave amplitudes.

Prior studies have been conducted using stress waves in timber, wherein recorded phase velocities of signals transmitted transversely (perpendicular to grain) are smaller to that transmitted longitudinally (parallel to grain) - showcasing the significant effect that grain direction has on phase velocities [12,13].

https://doi.org/10.52202/069179-0109

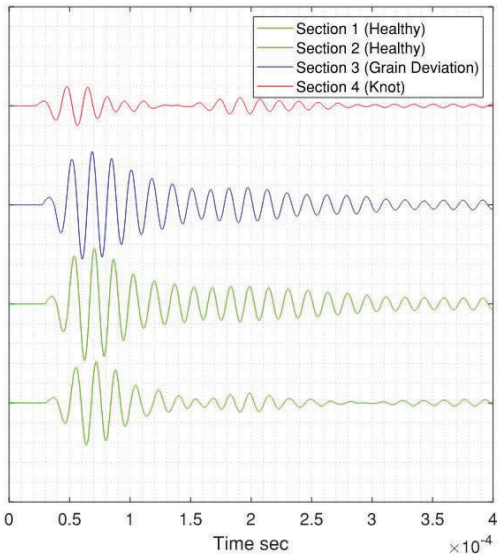

Figure 3: *Sample of time signals measured for each section in Case Study 1. The vertical axis represents signal energy, although each signal has been translated vertically for clarity. The signals are presented in order, with Section 1 featured as the lowermost and Section 4 as the uppermost signal.*

Where phase velocities are concerned in this test, Sections 1 and 2 exhibited similar P-wave speeds, with an average of 1660 m/s. However, in Section 3 with the presence of grain deviation, the average recorded phase velocity was 1838 m/s. In Section 4, wherein the largest disruption of grain direction was visible with the presence of the knot, the recorded average phase velocity of 2340 m/s was the fastest of all sections. This feature is in-line with findings from the aforementioned literature [12,13] demonstrating that in Sections 3 and 4, the grains were deviating in such a way that they were becoming more aligned with the transmitted signals, amounting to a parallel to grain transmission compared to the perpendicular to grain transmission conducted in Sections 1 and 2. This is also complementary with visual inspection of the test specimen shown in Figure 2.

The signal window used for the analysis with UMAP needs to be calibrated prior to use. P-waves exhibit higher phase velocities than surface waves, the latter being a component of ultrasonic signals that are often found to succeed the former [14]. As evidenced in Figure 3, it can be seen that the P-wave component of the signal cannot be easily identified due to significant overlap with the surface wave components. As such, beginning from the largest recorded arrival time from the 80 signals, the upper bound of the signal window used for the analysis needs to be calibrated in order to fine tune the results obtained, while the lower bound of the signal window is set at the start of the signal – although it should be noted that the sensitivity of the output of UMAP to this calibration is low.

3.1.3 Wavelet analysis results and discussion

Firstly, all 80 signals measured in Case Study 1 were analysed using WPD. The two key hyperparameters of WPD to be trialled are levels of decomposition, and mother wavelet type. For this study, both 2 and 3 levels of decomposition are conducted, and both the Daubechies' 'db2' and 'db4' mother wavelets have been trialled in this study.

2-level decomposition

Once both the detail and approximate wavelet coefficients are extracted, following Equation 1 to 3, their wave energies are then calculated. To encapsulate the outputs of the analysis in a single graph, a matrix scatter plot can be used – allowing the relationships of the wave energies of the decomposed signals between frequency band pairs to be expressed. This is represented in the off-diagonal plots presented in Figure 4, making any dependencies between the frequency band pairs easily discernible. The distribution of the wave energies of the decomposed signals within the associated frequency band is plotted on the diagonal plots in Figure 4, allowing single variable dependence to be ascertained.

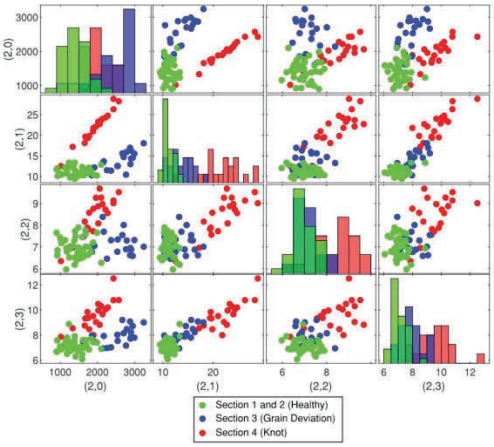

Figure 4: *Case Study 1 - Scatter plot of the signal energies in 4 frequency bands - decomposition level 2 and 'db2' mother wavelet.*

Some of the scatter plots shown in Figure 4 demonstrate some separation between data from Section 4 (knot) and the other sections. In particular, plots comparing frequency bands (2,1 – 2,0) show a promising separation of the majority of the wave energies of Section 4 from the rest, although notably there is still some overlap of the wave energies of some decomposed signals of Section 4 and healthy sections (1 and 2). The same can be said about the overlap of data from Section 3 and that of healthy sections (1 and 2). Investigating the other off-diagonal scatter plots, it can be seen that no distinct separation between data from the sections of each defect type and that of healthy sections can be discerned. The distribution for the wave energies of the individual studied frequency bands computed in each diagonal plot also illustrates

https://doi.org/10.52202/069179-0109

some separation between the section categories, with frequency band (2,1) showcasing the most promise - albeit significant overlap between the studied section categories is still present, with no high-confidence separation between the data.

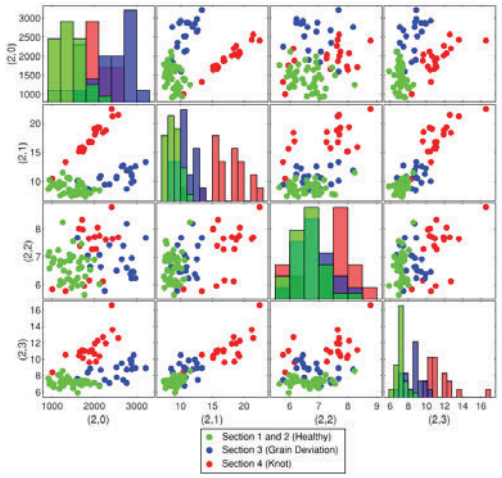

Figure 5: *Case Study 1 - Scatter plot of the signal energies in 4 frequency bands - decomposition level 2 and 'db4' mother wavelet.*

A similar scatter plot to the 'db2' decomposition can be plotted using the 'db4' mother wavelet, as in Figure 5 – the outcome of this analysis also being similar - showing a low sensitivity of the final output to changes in the Daubechies' mother wavelet type. Although some separation in signal energies corresponding to frequency band pairs (2,1 – 2,0) can be seen, none of the off-diagonal scatter plots depict a high-confidence separation of wave energies related to the desired section categories. The distributions of each frequency band plotted on the diagonal also feature large portions of overlap between signal energies of different section categories, also amounting to an undesirable outcome. Ultimately, the analysis using wavelet packet decomposition at 2 levels of decomposition with both the 'db2' and 'db4' mother wavelet does not achieve the desired data separation and clustering required to be able to tell the studied sections apart based on defect status.

3-level decomposition

Similar to the 2-level decomposition, a 3-level decomposition can be conducted on the transmitted signals. As expressed in Figure 1, at the third level of the sub-band coding schema, 8 frequency bands can be analysed, identified from (3,0) to (3,7).

When comparing the wave energies of the 'db2' wavelet decompositions of all 80 measured signals amongst the 8 frequency band pairs in the scatter plot matrix shown in Figure 6, it is clear that the majority of the frequency band pair plots do not show adequate separation between the section categories - a similar result being obtained when a decomposition with the 'db4' wavelet is done, shown in Figure 7. Notably, in Figure 6, some separation of the wave energies of Section 4 is seen, away from that of Sections 1, 2 and 3 in frequency band pairs (3,1 - 3,0) and (3,2 - 3,0).

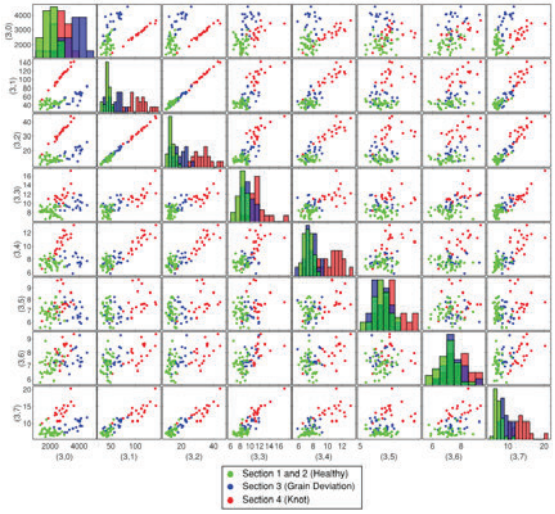

Figure 6: *Case Study 1 - A sample set of decomposed signals over 8 frequency bands with mother wavelet 'db2'.*

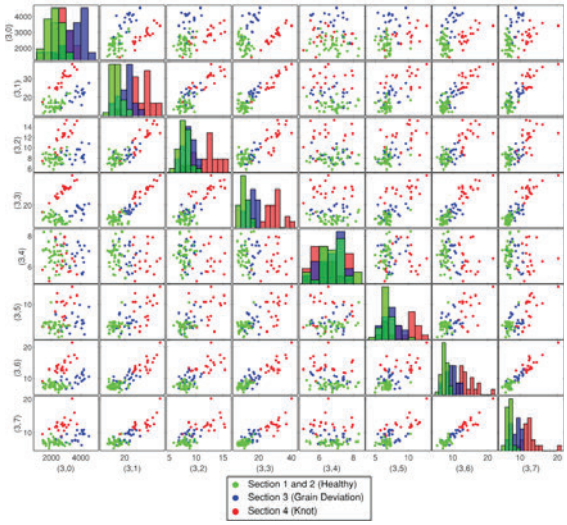

Figure 7: *Case Study 1 - A sample set of decomposed signals over 8 frequency bands with mother wavelet 'db4'.*

However, the distinction of wave energies in Section 3 from Sections 1 and 2 is not sufficient in these frequency band pairs. This feature is missing when studying the scatter plot output of the 'db4' decomposition (Figure 7), revealing the increased sensitivity of the output to the Daubechies' mother wavelet choice at this level of decomposition.

In summary, the preceding investigation could not yield a high-confidence separation between the signals transmitted through healthy sections and defective

sections. Moreover, no separation between signals sent through sections of varying defect types was discernible.

3.1.4 UMAP analysis results and discussion

The UMAP algorithm was also used to analyse the signals. It should be noted that for the UMAP analysis, the same signal window as that used in WPD was adopted. The key hyperparameters needed to be set were: (1) target embedment dimension, (2) k-nearest neighbours, (3) minimum distance, and (4) distance model. (1) refers to the dimension of the final output graph – a value of 2 dimensions being selected for simplicity of comprehension of the final results, additionally allowing for an easy comparison of the UMAP output with that of WPD demonstrated in the preceding sections. (2) and (3) work to control the level of clustering of the signals, changing how condensed or sparsely spaced the data points are, wherein the former sets the number of neighbouring signals which can be associated with a given signal, and the latter controls the minimum separation between neighbouring signals in the output graph. For this investigation, (2) was set at a value of 0.07 and (3) was set to 15 as they provided the most distinct clustering – although it should be noted that the sensitivity of the final output on these parameters is very low. (4) refers to the model used to express the distance between each signal, with many options available in the literature [15-18]. In this study, the Chebyshev distance model [18] was adopted, due to the highly favourable results obtained with this choice.

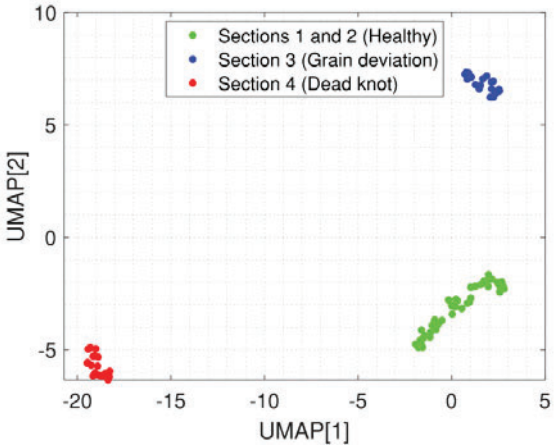

Figure 8: *Case Study 1 - UMAP two-dimensional (2D) reduction output.*

The UMAP results are shown in Figures 8 and 9. There is strong clustering of points with respect to each section. Clusters from both Sections 3 and 4 are separated from that of 1 and 2. Notably, wave behaviour in Section 3 is not clustered together with Section 4, showing the separation between a defect location characterised by grain deviation within a part of the specimen which is still intact with fibre continuity, and a defect location characterised by the centre of a dead knot.

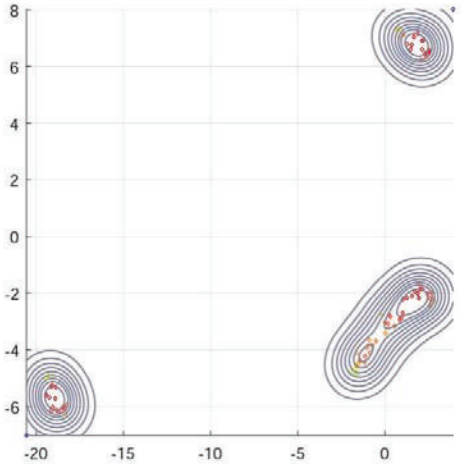

Figure 9: *Case Study 1 - UMAP two-dimensional (2D) cluster topology.*

A schematic of the relevant visual features of the specimen is shown in Figure 2. The outcome is highly desirable, especially since the results are not as sensitive to hyperparameter calibration, compared to the wavelet approach. The results are congruent with visible findings of the timber specimen, clearly distinguishing regions with material defects from those without any. The results demonstrate UMAP's capability of ultimately distinguishing between sections of sound wood and those with strength-reducing characteristics. Additionally, its ability to separate sections experiencing different types of strength-reducing characteristics is highly useful in structural health monitoring applications.

3.2 CASE STUDY 2

To examine the behaviour of both WPD and UMAP for defects caused by fungal decay, termite damage or splitting damage – ultimately eventuating in fibre discontinuity or voids in the centre of the cross-section, Case Study 2 was developed.

3.2.1 Specimen description

A piece of machine-graded Australian *radiata pine* (MGP10), similar to that used in Case Study 1 was employed. The specimen features a 190mm width and 45mm thickness. The specimen was carefully selected, such that no grain deviation or knots were present, with only longitudinally aligned grains visible – signifying a standard healthy section of timber.

3 sections were devised for the case study, a picture of the test specimen and its schematic shown in Figures 10a and 10b, respectively. Sections 1 and 2 are located within the healthy zone of the timber. To simulate the loss of material and fibre discontinuity due to the aforementioned defects, a hole was drilled at the centre of the cross-section, with a 6mm drill bit, as shown in Figures 10a and 10b. This method of simulating either splitting damage or that due to decay or termite attack is justified with two considerations: (1) Termite attack and fungal decay have

https://doi.org/10.52202/069179-0109

been shown to manifest as a material loss with the creation of voids within structural timber [19]; (2) Splitting damage manifests as longitudinally aligned cracks along the length of the timber element, with similar creation of voids used to artificially recreate such damage, as utilised in previous studies [20].

Figure 10a: *Case Study 2 – Test specimen*

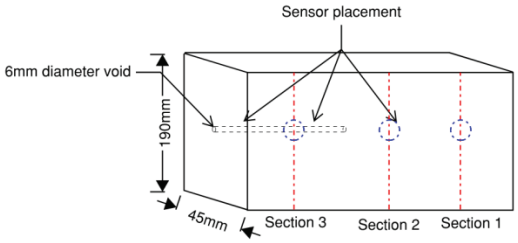

Figure 10b: *Case Study 2 – Specimen schematic*

A point directly aligned over the position of the created void was marked as Section 3, representing the fabricated defective section.

3.2.2 Time signals

54 kHz P-waves were transmitted over each of the sections, similar to the process adopted in Case Study 1. 10 ultrasonic signals were transmitted with a given transmitter and receiver position, and another 10 were recorded with their positions swapped, amounting to 20 signals measured at each location, and 60 signals measured in total for the analysis. A summary of the recorded signals is reflected in Table 2.

Table 2: *Case Study 2 - Section information summary*

Section	Defect Status	Number of signals
1	Healthy	20
2	Healthy	20
3	Drilled	20
Total number of signals		60

The measured time signals reflected a similar phase velocity across all sections, with the recorded averages being 2152 m/s, 2157 m/s and 2159 m/s for Sections 1, 2 and 3 respectively. It can be seen that they have negligible differences between each other, as evidenced by a largely similar wave pattern comparing Section 3 with that of Section 1 and 2, observed in Figure 11, which illustrates a sample of the signals, recorded at each section. This could possibly be due to the small size of the void.

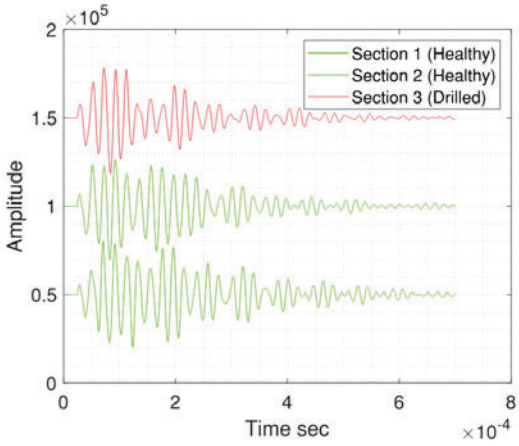

Figure 11: *Sample of time signals measured for each section in Case Study 2. The vertical axis represents signal energy, although each signal has been translated vertically for clarity. The signals are presented in order, with Section 1 featured as the lowermost and Section 3 as the uppermost signal.*

Similar to the observation made in Case Study 1, the distinction between the P-wave component of the signals and the surface waves is not evident from visual inspection and hence, calibration of the signal window for the output of UMAP is required, just as was done in Case Study 1.

3.2.3 Wavelet analysis results and discussion

All 60 recorded signals were analysed using WPD, with both 2 and 3 levels of decomposition trialled, and the 'db2' and 'db4' mother wavelet applied – the identical analysis approach adopted in Case Study 1.

2-level decomposition

Figure 12 provides a depiction of a concise plot comparing the wave energies of all 60 decomposed signals of all 3 sections within pairs of frequency bands to visualise their dependencies, similar to that depicted in Case Study 1. The outcome of the analysis shows significant overlap between the signal energies of the defective section, shown in red, and the healthy sections shown in green, in the off-diagonal scatter plots. The plots comparing wave energies in frequency band pair (2,2 – 2,1) show the strongest positive correlation, with no discernible separation between signals of healthy sections and that of the defective section. The plots comparing frequency band pairs (2,1 – 2,0), and (2,2 – 2,0) show some promising separation, but notably, it can be observed that there is still some overlap between the signals – an unfavourable outcome. This outcome is akin to that demonstrated in Case Study 1.

The same analysis was conducted with the 'db4' mother wavelet, the final scatter plot is shown in Figure 13. Of note, the strong positive correlation of frequency band pairs (2,2 – 2,1) which was evident with the 'db2' mother

wavelet analysis is missing with the 'db4' mother wavelet.

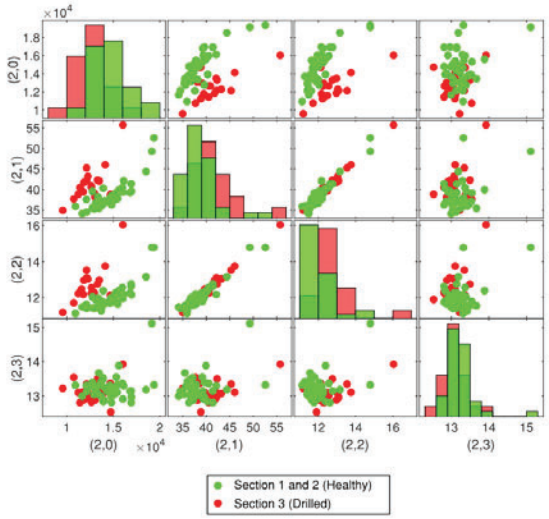

Figure 12: *Case Study 2 - Scatter plot of the signal energies in 4 frequency bands - decomposition level 2 and 'db2' mother wavelet.*

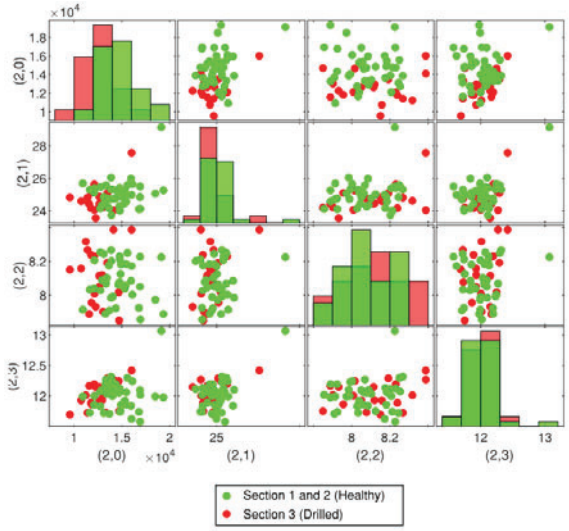

Figure 13: *Case Study 2 - Scatter plot of the signal energies in 4 frequency bands - decomposition level 2 and 'db4' mother wavelet.*

The wave energies are more scattered in the plots compared to that shown in Figure 12, signifying a reduced correlation between the frequency band pairs when 'db4' is adopted, relative to 'db2'. The outcome of the analysis, however, is still not favourable, with no high-confidence separation in the data seen in the bivariate relationship comparisons in the off-diagonal plots, or the univariate analyses depicted on the diagonal plots.

3-level decomposition

Just as was conducted in Case Study 1, 3-level decompositions can also be carried out with the 60 measured signals. As depicted in Figure 1, the 3-level decomposition yields 8 frequency bands ranging from (3,0) to (3,7) – amounting to 56 possible frequency band pair comparisons – shown on the off-diagonal plots, and 8 plots visualising the distribution of wave energies within a given frequency band – shown on the diagonal plots. Figure 14 depicts this analysis with the use of the 'db2' mother wavelet and Figure 15 features that conducted with the 'db4' mother wavelet. In the former, several of the frequency band pairs – (3,2 – 3,1), (3,4 – 3,1), (3,4 – 3,2) – show a strong positive correlation, with high levels of overlap between signals of healthy sections and that of the defective section. This feature is missing from the 'db4' analysis, an artefact also found in the 2-level decomposition described in the preceding section.

Similar to that shown in Case Study 1, both the 'db2' and 'db4' analyses yield an ultimately unfavourable result, with no high-confidence separation of the wave energies between healthy and defective sections, as intended.

In summary, all of the trialled hyperparameter variations in the study – levels of decomposition and mother wavelet type – were unable to yield a desirable outcome. Although some separation of signals was observed in certain cases, as established in the preceding discussion, the lack of complete, high-confidence separation of signal clusters points to an inability of the adopted WPD methodology and trialled hyperparameters to accurately serve the purpose of the detection of a defect of this nature in timber.

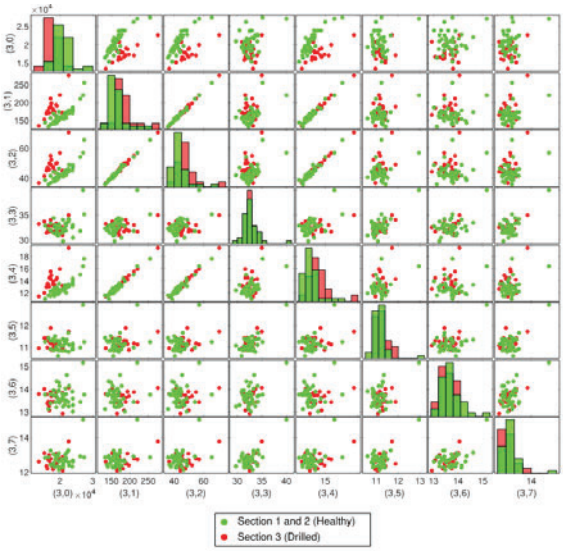

Figure 14: *Case Study 2 - Scatter plot of the signal energies in 4 frequency bands - decomposition level 3 and 'db2' mother wavelet.*

https://doi.org/10.52202/069179-0109

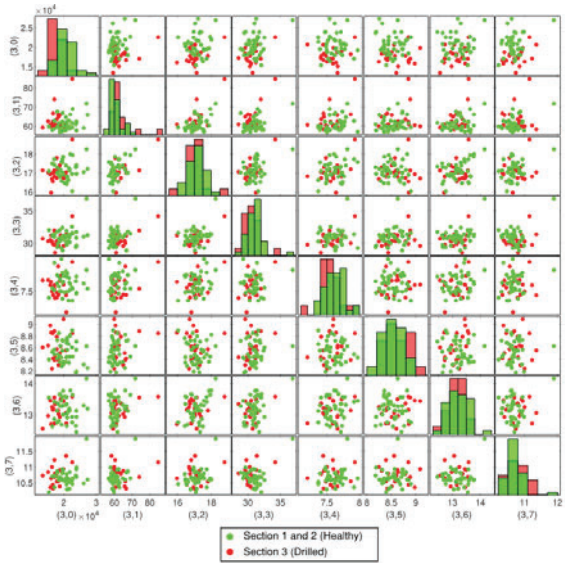

Figure 15: *Case Study 2 - Scatter plot of the signal energies in 4 frequency bands - decomposition level 3 and 'db4' mother wavelet.*

3.2.4 UMAP analysis and results

All 60 signals were thereafter analysed with UMAP, similar to Case Study 1. The hyperparameters used in the analysis were similar to that used in Case Study 1, with minimum distance being set to a value of 0.07 and k-nearest neighbours being set to 15. It should be noted that just as in Case Study 1, the values of both minimum distance and k-nearest neighbours had minimal impact on the output graph, primarily altering the density of the clustering of the signals and influencing the cluster separation. The Chebyshev distance model was adopted for the analysis. The 2-dimensional output graph is shown in Figure 16, with the associated data topology shown in Figure 17.

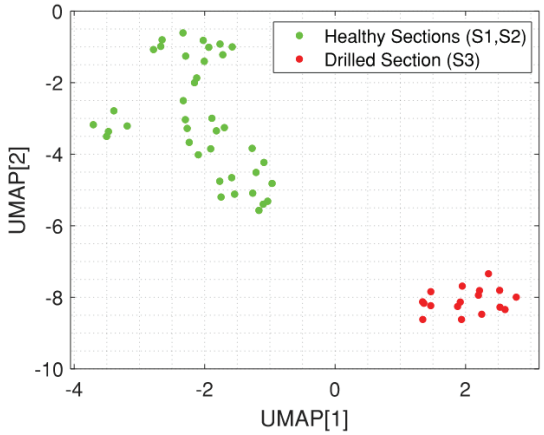

Figure 16: *Case Study 2 - UMAP two-dimensional (2D) reduction output.*

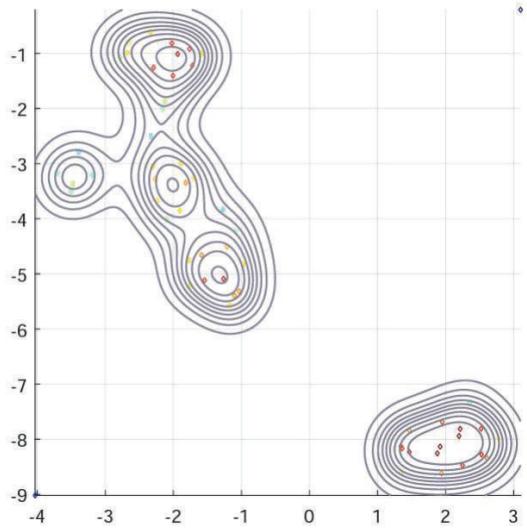

Figure 17: *Case Study 2 - UMAP two-dimensional (2D) cluster topology.*

As depicted, the output of the UMAP analysis is highly favourable, with complete and distinct separation between signals sent through the defective Section 3, and that sent through healthy Sections 1 and 2. Signals from Sections 1 and 2 are treated as being part of the same cluster, as shown in the cluster topology in Figure 17. This positive outcome is congruent to that found in Case Study 1.

4 CONCLUSIONS

This study attempts for the first time to investigate the effectiveness of a novel feature extraction algorithm for the purpose of identifying defects within the timber. UMAP proved to be very effective in separating signals from damaged and healthy sections in timber, requiring little calibration, and providing an easily visualisable output graph. UMAP was versatile in performing successfully under differing defect types in timber. In the first case study, UMAP was able to successfully distinguish between healthy sections and those with naturally occurring defects such as grain deviation and knots. A key positive attribute of the algorithm is its ability to separate the signals of sections featuring differing defect types as opposed to merely clustering them together – providing further insight into the different material characteristics inherent in sections of starkly different grain orientation and fibre make-up. In the second case study, the algorithm proved to be able to successfully distinguish signals transmitted through healthy sections and a defective section fabricated with a void in the centre of the cross-section, meant to simulate material loss and fibre discontinuity caused by defects such as fungal decay, termite damage or splitting damage. The study also juxtaposes the highly favourable outputs of UMAP against competing wavelet-based frameworks, proving the former's robustness and applicability for the intended purpose proposed in the study, compared to the latter. The low sensitivity of the final output of UMAP

due to changes in its hyperparameters, and the versatility of the algorithm in being able to identify various defect types in timber demonstrates the capability of the algorithm for the application of defect identification in timber.

This study acts as an initial proof-of-concept for the viability of UMAP as a signal analysis tool for defect identification in timber. The positive demonstration of the algorithm can hence open the door to future works investigating in-depth the efficacy of the algorithm in more complex, built-up sections of engineered timber, wherein the occurrences of defects are not visible from the exterior of the element. These investigations are currently in progress by the authors.

ACKNOWLEDGEMENT

This work was supported by an Australian Government Research Training Program Scholarship. The assistance provided by Mr Chan Chun-Yen, Mr Jonathan Lui and Ms Benjaporn Samleerangkul is greatly appreciated.

REFERENCES

[1] L. Kia, "Development of Expressive Timber-Steel Hybrid Exoskeletal Systems for Tall Timber Structures," thesis, 2022.

[2] R. H. White and R. J. Ross, Wood and Timber Condition Assessment Manuel. US Forest Service.

[3] W. Ting, Y. Guo-zheng, Y. Bang-hua, and S. Hong, "EEG feature extraction based on wavelet packet decomposition for brain computer interface," Measurement, vol. 41, no. 6, pp. 618–625, 2008.

[4] J. Li, M. Subhani, and B. Samali, "Determination of embedment depth of timber poles and piles using wavelet transform," Advances in Structural Engineering, vol. 15, no. 5, pp. 759–770, 2012.

[5] M. Subhani, J. Li, B. Samali, and N. Yan, "Determination of the embedded lengths of electricity timber poles utilising flexural wave generated from impacts," Australian Journal of Structural Engineering, vol. 14, no. 1, 2013.

[6] L. McInnes, J. Healy, N. Saul, and L. Großberger, "UMAP: Uniform manifold approximation and projection," Journal of Open Source Software, vol. 3, no. 29, p. 861, 2018.

[7] R. S. Stanković and B. J. Falkowski, "The Haar wavelet transform: Its status and achievements," Computers & Electrical Engineering, vol. 29, no. 1, pp. 25–44, 2003.

[8] C. É. Vonesch, T. Blu, and M. Unser, "Generalized daubechies wavelet families," IEEE Transactions on Signal Processing, vol. 55, no. 9, pp. 4415–4429, 2007.

[9] W. Dahmen and C. A. Micchelli, "Biorthogonal wavelet expansions," Constructive Approximation, vol. 13, no. 3, pp. 293–328, 1997.

[10] A. K. Yadav, R. Roy, A. P. Kumar, C. S. Kumar, and S. K. Dhakad, "De-noising of ultrasound image using discrete wavelet transform by symlet wavelet and filters," 2015 International Conference on Advances in Computing, Communications and Informatics (ICACCI), 2015.

[11] S. Dasgupta and Y. Freund, "Random projection trees and low dimensional manifolds," Proceedings of the fortieth annual ACM symposium on Theory of computing, 2008.

[12] U. Dackermann, K. Crews, B. Kasal, J. Li, M. Riggio, F. Rinn, and T. Tannert, "In situ assessment of structural timber using stress-wave measurements," Materials and Structures, vol. 47, no. 5, pp. 787–803, 2013.

[13] X. Wang, F. Divos, C. Pilon, B. K. Brashaw, R. J. Ross, and R. F. Pellerin, "Assessment of decay in standing timber using Stress Wave Timing Nondestructive Evaluation Tools : A guide for use and interpretation," 2004.

[14] H. Zhao, A. Gachagan, G. Dobie, and T. Lardner, "Wavelet analysis of poorly-focused ultrasonic signal of pressure tube inspection in nuclear industry," AIP Conference Proceedings, 2018.

[15] Z. Li, Q. Ding, and W. Zhang, "A comparative study of different distances for similarity estimation," Communications in Computer and Information Science, pp. 483–488, 2011.

[16] S. K. Prabhakar and H. Rajaguru, "Code converters with city block distance measures for classifying epilepsy from EEG signals," Procedia Computer Science, vol. 87, pp. 5–11, 2016.

[17] G. J. McLachlan, "Mahalanobis distance," Resonance, vol. 4, no. 6, pp. 20–26, 1999.

[18] R. Coghetto, "Chebyshev distance," Formalized Mathematics, vol. 24, no. 2, pp. 121–141, 2016.

[19] M. Riggio, R. W. Anthony, F. Augelli, B. Kasal, T. Lechner, W. Muller, and T. Tannert, "In situ assessment of structural timber using non-destructive techniques," Materials and Structures, vol. 47, no. 5, pp. 749–766, 2013.

[20] Y. J. Cai, W. Zhang, and W. P. Zhang, "Experimental study on eccentric compression behavior of timber columns with longitudinal cracks strengthened by CFRP sheets," Advanced Materials Research, vol. 446-449, pp. 3132–3136, 2012.

[21] H. Mitsui, K. Mizutani, and N. Wakatsuki, "Defect detection in square billet using time-of-flight of longitudinal waves," Japanese Journal of Applied Physics, vol. 49, no. 7S, 2010.

https://doi.org/10.52202/069179-0109

World Conference on Timber Engineering Oslo 2023

GLUED-IN HARDWOOD RODS USING BIO-SOURCED ADHESIVES — PART I: INVESTIGATIONS UNDER LABORATORY CONDITIONS

Jana Kolbe[1]*, Stephanie Koesling[2], Till Vallée[3], Nils Monard[4], Jona Haupt[5]

ABSTRACT: Glued-in Rods (GiR) have proven to be a particularly good method for connecting timber structures, in which steel or FRP steel rods are yet commonly bonded with two-component epoxy resin or polyurethane adhesive systems. However, from a sustainability point of view, this poses a problem. This paper summarises preliminary results of a research project investigating to which extent the currently used glued-in steel rods in softwood can be substituted by rods made of hardwood for load-bearing functions. The project also reports on the performance of bio-sources adhesives to substitute the chemical adhesives currently used. The results presented herein focus on the performance of corresponding small scale GiR under laboratory conditions; the companion paper, also presented at the WCTE2023, will extend these findings towards more critical environmental conditions.

KEYWORDS: glued-in-rods, structural, joints, adhesion, bio-sourced

1 INTRODUCTION

1.1 SETTING THE FRAMEWORK

Glued-in-rods (abbreviated as GiR in the following) form a subset of bonded connections, in which load is transferred from one timber block to another via one (or several) bonded rods [1–3]. Design parameters involved for GiR are the choice of materials (timber, adhesive, and rods) and their sizing (cross-section of the timber members, adhesive layer thickness, and embedment length). Because of the complexity of this joint type, failure can take multiple forms. Figure 1 summarises them graphically, for more details refer to [1–3]. Each of these is associated with specific material and geometry parameters of the GiR, which cannot be discussed at length in this paper [4–6].

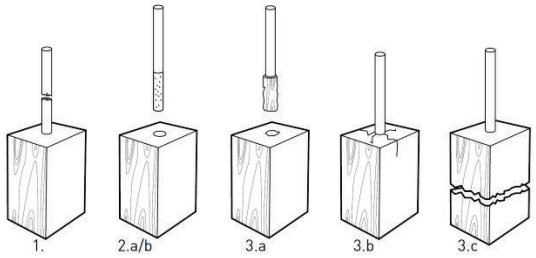

Figure 1: *Failure modes of glued-in-rod connections*

For most current applications, the rods are either threaded rods [7] or rebars [8], seldom fibre reinforced polymers [9]. Regarding the adhesive, almost all experimental investigations consider two-component epoxies (2K-EPX) or 2K-polyurethanes (2K-PUR) [2], both being of petrochemical origin. While timber engineering is widely acclaimed for its sustainability [10], the use of metallic and polymeric material for the joints may be questioned.

The research summarised in this paper addresses the question to which extent the concept of glued-in rods can be pushed towards sustainability by substituting the metallic rods by hardwood ones, and the "chemical" adhesives by bio-sources alternatives.

[1] Jana Kolbe, Fraunhofer Institute for Manufacturing Technology and Advanced Materials, Germany, Jana.Kolbe@ifam.fraunhofer.de
[2] Stephanie Koesling, Fraunhofer Institute for Manufacturing Technology and Advanced Materials, Germany, Stephanie.Koesling@ifam.fraunhofer.de
[3] Till Vallée, Fraunhofer Institute for Manufacturing Technology and Advanced Materials, Germany, Till.Vallee@ifam.fraunhofer.de
[4] Nils Monard, Fraunhofer Institute for Manufacturing Technology and Advanced Materials, Germany, Nils.Monard@ifam.fraunhofer.de
[5] Jona Haupt, Fraunhofer Institute for Manufacturing Technology and Advanced Materials, Germany, jona.haupt@ifam.fraunhofer.de

https://doi.org/10.52202/069179-0110

Surprisingly little research has been documented on gluing-in hardwood rods to connect structures in timber engineering. Among those, Koizumi and Jensen [11–13] presented experimental results on dowels (in fact rods) made of Maple (*Acer saccharum*) glued into Cedar (*Cupressus japonica*). The results showed that average shear strengths of beyond 8 MPa were achieved with a 2K-PUR, and beyond 10 MPa using a 2K-EPX.
Adhesives based on renewable resources have been used since the dawn of humanity in conjunction with timber. Both their availability, and performance, proved sufficient to fulfil all demands up to World War II, where they were still used to manufacture aeroplanes [14]. Nowadays, adhesives based on natural raw materials are classified into glutine (in the following referred to as animal glue), casein, lignin, tannin, and dextrin [15,16]. They achieve, on spruce shear strengths up to 9.6 MPa, and for beech strength up to 11 MPa
.

1.2 OBJECTIVES

The research summarised in this publication aimed to three different objectives: (1) Investigate the potential hardwood dowels (or bars) offer as an ecologically sustainable alternative to steel, and FRP, rods; and (2) extend the sustainability of GiR through the substitution of "chemical adhesives" by "natural" ones.

2 MATERIALS AND METHODS

2.1 Adhesives

The adhesives used in this study were all derivatives of "Technical Gelatine 400/115" from the Company Fritz Häcker GmbH in Germany. The basic adhesive, is a gelatine currently commercially available. A feature relevant for this study is the relatively high water-content during processing of the adhesives.

The technical gelatine is delivered in a dried state in form of granulate. As a first step it is swollen in water. Therefore 25 parts of technical gelatine is mixed with 75 parts of water. The gelatine must be soaked in water for at least two hours before it can be further processed. To improve laboratory workflow, the mixtures are usually soaked overnight. In the next step the adhesive was molten in a water bath at 50 °C. In this state, the adhesive is now ready for processing.

Modifications of the basic formulation involve aspects such as reduction of the water-content, the addition of solid particles (as chalk, saw dust), and further reactants (as tannin etc.) A summary of the modifications, all labelled M*XX*, is shown in Table 1and Table 2

Table 1: Summary of adhesive modifications to improve the formation of larger adhesive layer thickness (% are related to the mass)

REF	Technical Gelatine 400/115: water-content 25:75
M29	REF with water-content reduced to 25:60
M30	REF with water-content reduced to 25:45
M31	REF + 30% chalk
M32	REF + 50% chalk
M33	REF + 30% sawdust

The modifications of the adhesive were performed following two objectives:
Firstly, the one discussed in this part, aimed at enabling the adhesive to form the relatively large layers (0.2 to 0.5mm) required for the glued-in rods, as opposed to the almost nil thickness needed in lap shear samples. The issue herein is related to the large water content of the gelatine-based adhesives.
Secondly, gluing with technical gelatine means that the processed adhesive contains 75 % of water. For the usual applications for this adhesive, like gluing books, folding boxes or cardboard this is not an issue. Animal glues are adhesives which have been used for centuries to bond wood. However, because of their high water-content, they have problems to fill large adhesive layer gaps above 200 µm. To overcome this limitation the idea was to increase the solid content. One way was to work with less water. The other way was to incorporate fillers. Therefor we chose two different fillers: Chalk and sawdust. Chalk is used very often in adhesives. We worked with the product Omyacarb HSB from Omya.GMBH / Germany. And another interesting filler for us was sawdust, due to the application of gluing wood. Working with a filler, is changing a lot of the adhesive characteristics like viscosity, stiffness or the thermal expansion coefficient. By choosing sawdust, we saw a high chance to improve several characteristics of the adhesive and additionally get a bio-based filler so to fulfil the requirement of sustainability. We used the product HAHO 120/F from JELU-WERK J. Ehrler GmbH & Co. KG / Germany for the sawdust. Secondly, improving—if necessary—the mechanical performance of the adhesives under elevated moisture contents, an aspect further developed in the second part of this publication.

Table 2: Summary of adhesive modifications to improve the performance under elevated moisture environment

M7	1 % tannic acid
M10	3 % kalinite
M14	0,3 % gallic acid
M26	1 % tannic acid + 9 % linseed oil
M10C	M10 + 30% chalk
M14C	M14 + 30% chalk

2.2 Investigations on lap shear samples

The preliminary investigations focused on a comparison of the mechanical performance of the adhesive used in lap shear samples (acc. to DIN EN 1465).
The substrates consisted in beech wood (*Fagus sylvatica*) in the dimensions 19.5 × 5.2 × 80.5 mm³, which were conditioned to 23 °C and 50% relative humidity (rH) for at least 7 days prior to bonding.
During the bonding, a pressure of 0.7±0.1 MPa was exerted on the overlap, the resulting adhesive layer thickness was almost nil.

https://doi.org/10.52202/069179-0110

For the results presented in this part, bonded lap shear samples were conditioned for 7d @ 23 °C and 50% rH prior to testing.
Testing occurred in an UTM under displacement control, with 5mm/min, until failure occurred. Ten samples were tested in each series.

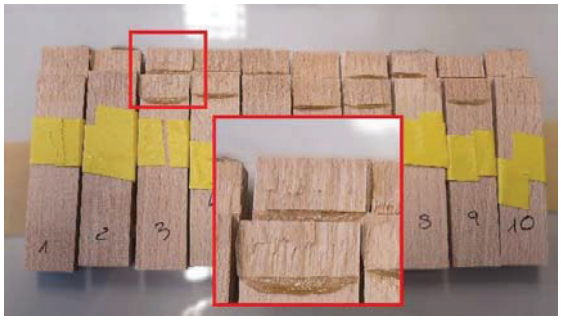

Figure 2: A set of ten lap shear samples after testing (the enlargement shows a typical substrate failure)

The results subsequently presented herein are given as average lap shear strength, which corresponds to the failure load divided by the bonded area surface, which was measure using a calibrated calliper for each individual sample.
Additionally, the fracture surface has been characterised so to distinguish between substrate failure (SF) and adhesive failure (AF).

2.3 Investigations on glued-in rods

The mechanical performance of bio-sourced adhesives was compared to that of widely used "chemical" ones. Tests were performed on the following wood species. Spruce, which constitutes the base material of all GiR, and beech for the rods. Two increasing levels of complexity were considered. Firstly, lap shear samples acc. to DIN EN 302; secondly, small scale GiR consisting of 45x45x120 mm³ spruce blocks in which ø6mm hardwood rods were bonded
The spruce blocks are drilled to precisely 6.4 mm with an automatic drilling machine, to achieve an accurate adhesive layer thickness between the two substrates. This results in a radial distance of 0.2 mm.
To ensure axiality, the glued in rods are centred during the gluing process with thin spacers around the hole top. The wooden rods are deburred and thoroughly cleaned with isopropyl alcohol.

Preparing the lap shear samples with the ecological adhesive is identical to the process of the lap shear samples, however the application process is different. After mixing of the adhesive, the viscous fluid is transferred to a syringe and subsequently used to fill the lateral hole in the spruce block with adhesive. The outside of the hardwood dowel is coated in a film of the same adhesive. The rod is then pressed into the hole with a spring-loaded guide mechanism until it bottoms out, for further details regarding the bonding process cf. [17].
These bonded samples are then cured and conditioned under the same environmental conditions as the lap shear samples (7d @ 23 °C and 50% rH).

Figure 3: Process of injecting the adhesive into the hole, coating the rod and combining them

2.3.1 Test setup

Testing the adhesive performance is conducted by rigidly clamping each side of the sample in the UTM, under displacement control and 2mm/min, until failure.
Clamping the hardwood rod directly did not produce adequate findings, due to deformation of the wood fibres and therefore induced stress fractures and reduced tensile strength of the dowel. This resulted in the premature failure and breakage of the rod during testing.
To limit the compression of the wood across the grain, multiple options were followed.
Bonding an aluminium sleeve with a chemical adhesive to protect the wood from crushing, did not achieve satisfactory results due to poor adhesion between the metal and wooden substrate.
Gluing a block of beech wood to the exposed part of the dowel still resulted in both brittle fractures as well as the wood splitting along the grain.

Figure 4: (Top) Aluminium sleeve bonding failure, (bottom) rod failure with beech block

https://doi.org/10.52202/069179-0110

The hardwood rods therefore not only break due to excessive compression and reduced surface area, but also due to pulling forces not being parallel to its grain structure.
To finally solve the issue, a secondary spruce block with identical dimensions was affixed to the opposite end of the rod using double the adhesive layer length. Either block is also drilled through on the side. A specific testing setup was devised to ensure perfect coaxiality.

During testing the samples are fixed in the UTM by inserting metal rods into these holes. This allows in conjunction with a bearing fixture for up to five degrees of freedom during the test. This setup achieved adhesive or substrate failure every time, and no hardwood rod failed.

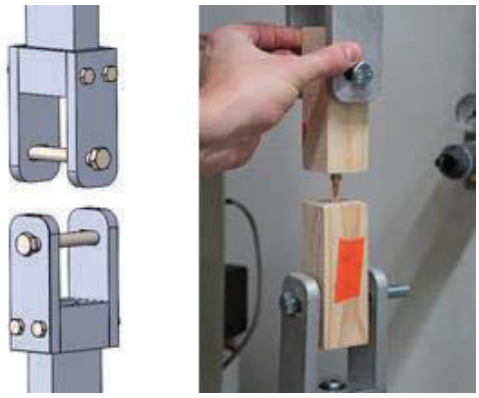

Figure 5: Test setup for the GiR

3 RESULTS AND DISCUSSION

3.1 Investigations on lap shear samples

The results of the lap shear tests with the different adhesive modifications described in

Table 1 are summarised below in Figure 6.
The original formulation of the adhesive, labelled herein REF, resulted in a lap shear strength of 12.7 MPa, with a variance (defined as standard deviation divided by the average) of 10%. Reducing the water-content, i.e., considering the modification M30, resulted in a reduction of the average lap shear strength by roughly one third, while increasing the variance to a relatively value of 25%. Regarding chalk, it is to be noted that the addition of 30% (M31) did neither affect strength nor variance; for 50% (M32), however, the average lap shear strength increased marginally by 8%, with an almost unchanged variance of 12%. Lastly, adding 30% sawdust to the basic adhesive formulation (M33) reduced the average lap shear strength by 20%, without affecting the variance.

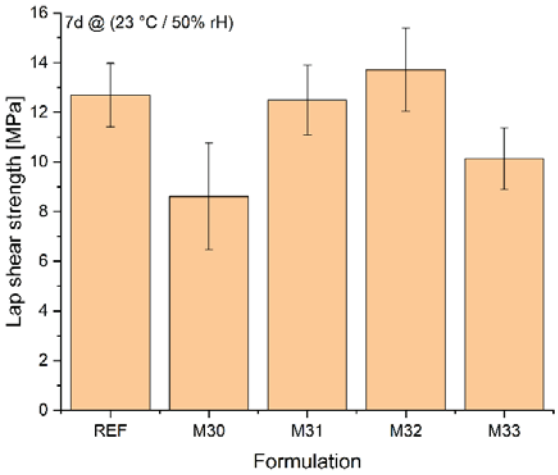

Figure 6: Experimentally determined lap shear strengths with the formulations allowing for larger adhesive layer thickness

Animal glue is made from collagen. While the polymer molecules in collagen are present as a triple helix, in animal glues they are converted into random coils. During swelling, melting (processing of the adhesive) and drying (within the adhesive layer), the polymer molecules partially convert back to triple helix. These triple-helix structures act like nodes in a physical network. Reducing the water content during processing of the gelatine-based adhesive affects this conversion from random coils to triple helix. The decreased adhesive bonding strength of the samples with reduced water content may be an indication of a weaker physical network due to the lower content of these triple-helix structures.

The aforesaid short summary of the results may lead to the conclusion that the different adhesive formulations may be easily ranked in terms of mechanical performance. However, because of the statistical nature of all experimental work, a closer statistical look through an analysis of variance (ANOVA) is required. Accordingly, the data was viewed through Tukey's test at a significance level of 0.05, and allowed for conclusions with regard to the statistical significance of differences. The ANOVA showed that reducing the water content resulted in a significant decrease of strength compared to the reference, both chalk series, but not if compared to the addition of sawdust. On the other hand, adding the chalk (in both proportions, 30 and 50%) did neither significantly increase nor decrease strength. Lastly, the addition of sawdust, although resulting in lower average strength, did not significantly impact the mechanical performance.

https://doi.org/10.52202/069179-0110

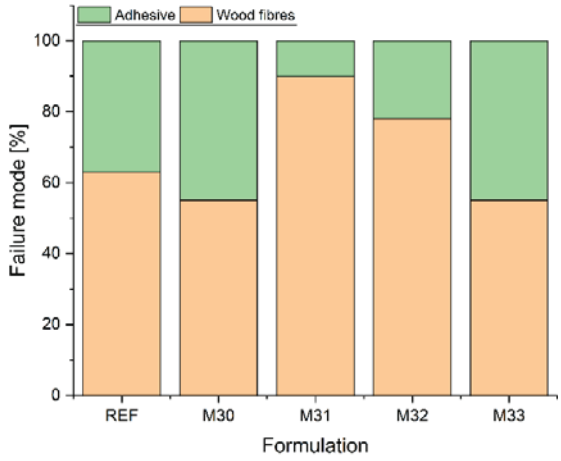

Figure 7: Failure modes observed in the lap shear tests

Focusing on the failure patterns, summarised in Figure 7, it appears that there are significant differences between the different adhesive formulations. While for the reference adhesive, slightly over 60% of all failure surface was withing the wood, this proportion slightly decreases when the water content is reduced. Chalk on the other hand seems to result in much more wood being torn off, although this results also depends on the chalk content, as higher values tend to increase the proportion of adhesive failure. Lastly, the addition of sawdust leads to the lowest observed proportion of wood being ripped-off—barely more than 50%.

Regarding the second aspect, which was to prepare adhesive formulations prone to better perform under moist conditions, and which resulted in the modifications described in Table 2 only preliminary results obtained under "normal" conditions, i.e. +23 °C and 50% rH, are presented herein in Figure 8.

The reference gelatine adhesive mixtures were modified using different techniques. For M7, Technical gelatine was first swollen overnight in demineralized water, and then tannic acid was added. The mixture was heated to 50°C, and a 10% solution of tannic acid (by weight) was introduced, resulting in gelation of the adhesive. For M10, Technical gelatine was first swollen overnight in a solution of gallic acid, and the mixture was then melted and stirred at 50°C. During this process, compressed air was introduced for 1.5 hours to modify the adhesive. In the case of M14, Technical gelatine was first swollen overnight in a solution of kalinite. The mixture was then heated to 50°C and stirred, resulting in adhesive modification. Finally, for M26, Technical gelatine was first swollen overnight in demineralized water and mixed with linseed oil before the addition of tannic acid. The mixture was heated to 50°C and stirred, resulting in the modification of the adhesive. This method is similar to M7, with the addition of linseed oil as a modifying agent.

To improve moisture resistance, we tried two different ideas: using Potassium alum, and crosslinking. Previous studies [18] suggest that Potassium improves the moisture resistance of glutine adhesives. Kalinite is also used as tannin agent and surely as in impact on collagene.

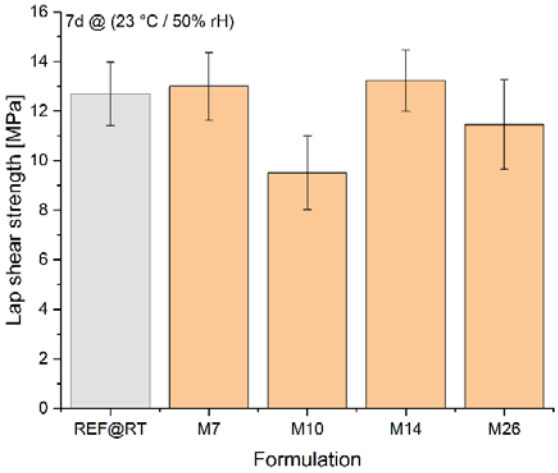

Figure 8: Experimentally determined lap shear strengths with the formulations allowing for higher moisture contents (tested under RT conditions)

It appears that, if related to the original formulation (REF), all but one (M10) modification result in very similar lap shear strengths under normal conditions that cannot be distinguished statistically (using an ANOVA, Tukey's test, p=0.05) from the original one. Similar is the situation regarding the scatter, expressed as variance. The mechanical behaviour under moist conditions will be the subject of the second part of this study.

3.2 Investigations on glued-in rods

An initial round of testing to determine an optimal adhesive layer thickness between the rod and the drilled hole resulted in the results presented in Figure 9. The minimum hole diameter is limited in part due to the natural deviations in roundness of the rod and the pressure required for inserting it into pre-filled holes. With an initial layer thickness of 0.2 mm and a gradual increase in thickness up to 0.5 mm an obvious trend of reduced adhesion strength between the substrates is identifiable.

Figure 10 presents a summary of the results from the GiR tests conducted using the various adhesive modifications. The different formulations include but are not limited to those shown in

Table 1. An epoxy adhesive series was also added as a comparison.

Some increases in average shear strength were observed when comparing the original REF formulation to the subsequent M29 and M30 modifications, which have the same components but differ only in water content. The M29 showed little to no effect on strength, though the variance increased from 14% to 18%. Further reduction of the water content to 60% of the REF formulation with the M30 however, increased shear strength from 4.9 MPa to 5.4 MPa, while also slightly increasing the variance. The addition of chalk to the original formulations as a filler,

https://doi.org/10.52202/069179-0110

resulted in increased adhesive strength in both cases. With M31 outperforming the reference by 27% on average shear strength and decreasing the relative variance by a third.

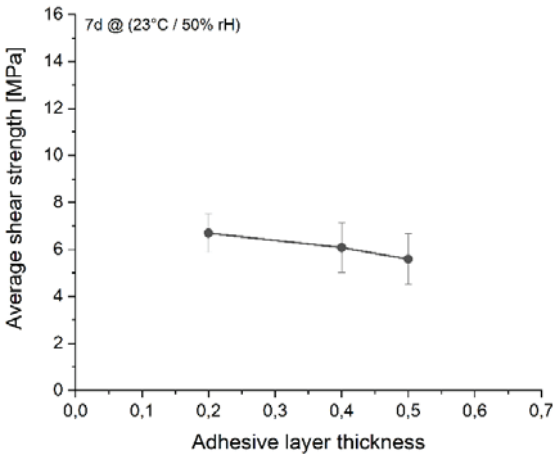

Figure 9: Test results of the GiR with selected ecological adhesives *(t_a indicates the adhesive layer thickness)*

Although still surpassing the previously observed strength values at 5.8 MPa, the M32 modification exhibits a slightly lower mean value compared to M31, with a corresponding increase in variance to 16%. Finally, adding fine sawdust to the adhesive resulted in an improved strength performance compared to the original formulation with 5.2 MPa, though with a comparatively high variance of 32%.

The 2K-epoxy which was chosen as a comparison for an adhesive able to bridge very high layer gaps, was very comparable to the M31, with an average shear strength of 6.7 MPa, which is only around 7% higher than the best ecological adhesive from this series.

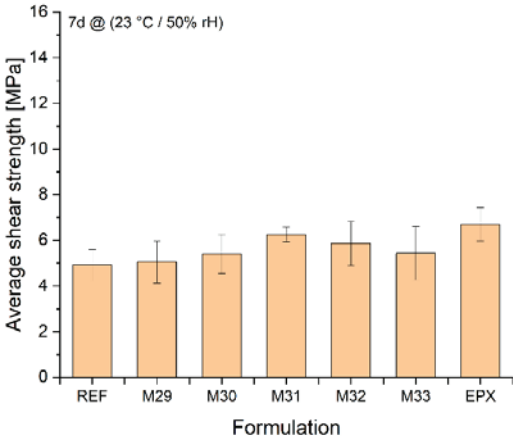

Figure 10: Test results of the GiR with selected adhesive formulations *(0.2 mm adhesive layer thickness, all embedment lengths are 30 mm)*

The testing revealed that the most common failure modes encountered were related to wood tear-out of the spruce block, which is a typical behaviour of this relatively soft material. This kind of failure occurs when the strength of the adhesive exceeds that of the wood, which can cause the wood fibres to tear apart.

Figure 11: *Typical failure of GiR with hardwood rods and eco-sourced adhesives*

Figure 11 depicts a common scenario of wood failure over adhesive failure. However, accurately quantifying the amount of wood tear-out versus adhesive failure is challenging due to the similarities in colour between the adhesive and the substrate. As the embedment length increases, the failure mode shifts from wood tear-out to splitting or fracturing of the hardwood rod either along or across the grain.

Shear strength tests on small, and large, scale glued-in rods (GiR) composed of hardwood rods glued into softwood (spruce) blocks confirmed the results obtained on the lap shear tests; mechanical performance of the "natural" adhesives ranged just slightly below that of the "chemical" ones.

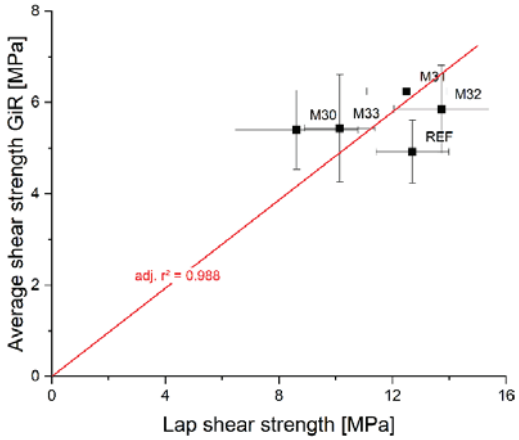

Figure 12: Comparison between lap shear strength (obtained in 1/lap shear samples) and average shear strength (obtained on GiR) for selected adhesives

When comparing the lap shear strengths to the average shear strength of the GiR, it may be difficult to compare the adhesive formulations individually from each testing method. Figure 12 aims to compare each mixture directly between lap shear and average shear strength.

While the absolute strength values differ, a direct correlation between the result can more easily identified. It is shown that some formulations form a close correlation between the two testing methods, like the M31, M32 and M33, showing that the adhesive mixtures are cross-comparable between the glued-in rods and the lap shear samples. However, outliers such as the M30

https://doi.org/10.52202/069179-0110

which performed better in GiR samples, or the reference mixture which performed very well in lap shear samples, show trials of both testing variants has to be done, especially for elevated moisture conditions like those done in the second part of this study [19], to ensure accurate findings.

In order to ensure comparability between the lap shear test samples and the GiR samples for the adhesive formulations designed to perform under moist conditions, their average shear strength was also tested under RT conditions.
To also adapt these formulations to increased adhesive layer thicknesses, a preselection was made for the M10 and M14 and the mixtures were expanded to include a further series with chalk as a filler. For both formulations 30% filler was added, additionally to their original formulation. The results of this series of tests can be seen in Figure 12. For simplified comparability of the results, both the reference formulation and M31, which have the same chalk content as the M10C and the M14C, were included. The M10 adhesive was 25% weaker than the reference mixture at only 3.93 MPa and a variance of around 11%. However, the basic M14 formulation outperformed not only the reference mixture by over 10% at RT, but also some of the formulations directly aimed at improving layer adhesive gaps. The M10C, modified with 30% chalk improved on its adhesive strength, though still underperforming compared to the reference adhesive. The M14C even outperformed the M31 mixture and had very similar strengths to that of the 2K epoxy adhesive at 6.60 MPa and a variance of 8%.

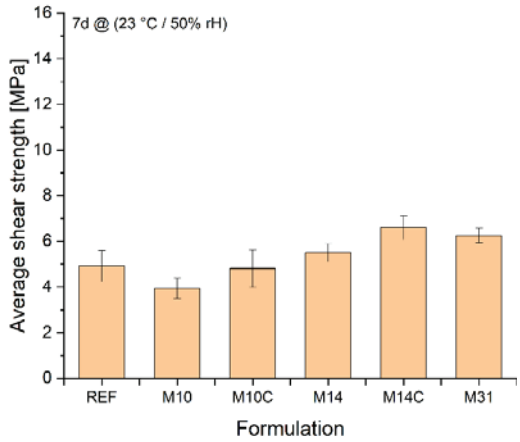

Figure 13: Test results of the GiR with moisture resistant adhesive formulations *(0.2 mm adhesive layer thickness, all embedment lengths are 30 mm)*

4 CONCLUSION

As a first conclusion, it appears that the considered ecological, or naturally sourced, adhesive, has the potential to achieve relatively high levels of lap shear strength. The measures taken to mitigate the effect of the high water-content, most prominently the addition of chalk and sawdust, improved the mechanical performance, especially for increased adhesive layer thicknesses.
Similarly, a series of modifications to ensure that strength is not degraded under moist conditions have been developed. Most of them resulted in lap shear strength in essence statistically not distinguishable from that of the reference formulation. The glued-in rods had very similar results and showed promising improvements for increased strength when additional filler was added to the mixture.
However, due to the different mechanical properties of the hardwood rods, if compared to steel, it proved necessary to adapt geometrical parameters (as embedment length, slenderness ratio l/d). Numerical modelling proved adequate to predict the load bearing capacity of all experimental series with sufficient accuracy.
The follow-up study, also submitted to the WCTE [19], will investigate if these promising results are also obtained under adverse environmental conditions (in particular high moisture content).

REFERENCES

[1] Tlustochowicz G, Serrano E, Steiger R. State-of-the-art review on timber connections with glued-in steel rods. Mater Struct. 2011;44:997–1020.
[2] Grunwald C, Vallée T, Fecht S, et al. Rods glued in engineered hardwood products part I: Experimental results under quasi-static loading. International Journal of Adhesion and Adhesives. 2018. DOI: 10.1016/j.ijadhadh.2018.05.003.
[3] Ayansola GS, Tannert T, Vallee T. Glued-in multiple steel rod connections in cross-laminated timber. The Journal of Adhesion. 2021:1–17.
[4] Blass H, Laskewitz B. Effect of spacing and edge distance on the axial strength of glued-in rods. In: Proceedings CIB-W18 Meeting: Pap. 32-7-12; Graz, Austria; 1999.
[5] Martín E, Estévez J, Otero D. Influence of geometric and mechanical parameters on stress states caused by threaded rods glued in wood. Eur. J. Wood Prod. 2013;71:259–266.
[6] Gonzales E, Tannert T, Vallee T. The impact of defects on the capacity of timber joints with glued-in rods. International Journal of Adhesion and Adhesives. 2016;65:33–40.
[7] Estévez Cimadevila J, Vázquez Rodríguez JA, Otero Chans MD. Experimental behaviour of threaded steel rods glued into high-density hardwood. International Journal of Adhesion and Adhesives. 2007;27:136–144.
[8] He ZW, Xiao Y. Experimental Study on Axial Pull-Out Behavior of Steel Rebars Glued-In Glubam. Journal of Materials in Civil Engineering. 2020;32:4020021.
[9] Grunwald C, Kaufmann M, Alter B, et al. Numerical investigations and capacity prediction of G-FRP rods glued into timber. Composite Structures. 2018;202:47–59.
[10] Ramage MH, Burridge H, Busse-Wicher M, et al. The wood from the trees: The use of timber in construction. Renewable and Sustainable Energy Reviews. 2017;68:333–359.

[11] Koizumi A. Withdrawal properties of hardwood dowels in end joints. I. Evaluation of shear performance of adhesives. Mokuzai Gakkaishi. 1998;44:41–48.
[12] Koizumi A. Withdrawal properties of hardwood dowels in end joints. II. Effrcts of dowel diameters, Young's moduli of adherents, dowel spacings and numbers of dowels. Mokuzai Gakkaishi. 1998;44:109–115.
[13] Jensen JL, Koizumi A, Sasaki T, et al. Axially loaded glued-in hardwood dowels. Wood Sci Technol. 2001;35:73–83.
[14] Allen S, Truax T. Glues used in airplane parts: Report No. 66. (vol. 189). Washington/USA: [publisher unknown]; 1920.
[15] Pizzi A. Recent developments in eco-efficient bio-based adhesives for wood bonding: opportunities and issues. Journal of Adhesion Science and Technology. 2006;20:829–846.
[16] Pizzi A. Wood products and green chemistry. Ann. For. Sci. 2016;73:185–203.
[17] Kohl D, Ratsch N, Böhm S, et al. Influence of manufacturing methods and imperfections on the load capacity of glued-in rods. The Journal of Adhesion. 2018;44:1–22.
[18] Lottermoser A, Matthaes W. Ueber die Einwirkung von Kalialaun auf Gelatine. Kolloid-Zeitschrift [Internet]. 1929;49:103–118.
[19] Jona Haupt, Nils Monard, Cordula Grunwald, Stephanie Koesling, Jana Kolbe. Glued-in hardwood rods using bio-sourced adhesives — Part II: influence of environmental conditions. Proc. of the World Conference on Timber Engineering, Oslo 2023.

https://doi.org/10.52202/069179-0110

World Conference on Timber Engineering Oslo 2023

GLUED-IN HARDWOOD RODS USING BIO-SOURCED ADHESIVES — PART II: IFNFLUENCE OF ENVIRONMENTAL CONDITIONS

Jona Haupt[1], Nils Monard[2], Till Vallée[3], Stephanie Koesling[4], Jana Kolbe[5]*

ABSTRACT: The first of this two-part series presented an ecological alternative to the commonly considered metallic rods glued into wood using conventional, petrochemical based, adhesives. A series of tests spanning from lap shear samples, small-scale glued-in rods (GiR), to large scale GiR featuring hardwood rods in spruce blocks and eco-sourced adhesives, proved the feasibility of a substitution concept under laboratory conditions. This second part investigates the influence of environmental conditions on the load-capacity of aforedescribed GiR.

KEYWORDS: glued-in-rods, structural, joints, adhesion, bio-sourced

1 INTRODUCTION

1.1 SETTING THE FRAMEWORK

Glued-in-rods (abbreviated as GiR in the following) form a subset of bonded connections, in which load is transferred from one timber block to another via one (or several) bonded rods [1–3]. While most investigations focus on so-called laboratory conditions (e.g. 23 °C and 50-65% rel. humidity), it is well known that conditions deviating therefrom are more critical. On one hand, temperature directly affects the performance of the adhesive [4], on the other hand moisture strongly influences the behaviour of wood [5]; additional effects results from the temperature and moisture induced deformations [6]. All these effects potentially lead to a reduction of the load-bearing capacity of bonded joints involving wood. Aforesaid is also true for glued-in rods (GiR) [7–9].

Gelatine adhesive is a type of adhesive that has been used for a long time, but its durability and resistance to environmental conditions have been questioned. Recent studies have shown that gelatine adhesive has good potential for use in various applications, such as wood and paper conservation. However, its performance may depend on factors such as the preparation method and the environmental conditions it is exposed to. Gelatine adhesive may be vulnerable to degradation by factors such as humidity, temperature, and microorganisms, which can affect its long-term stability. Some researchers have suggested that gelatine adhesive can be improved by modifying its properties or using it in combination with other materials. Overall, more research is needed to fully understand the durability of gelatine adhesive and how it can be optimized for different applications. To improve the durability of gelatine-based adhesive to environmental conditions, several additives can be used. One effective approach is to modify the gelatine itself to enhance its properties. For instance, adding crosslinking agents or modifying the gelatine with other polymers or resins can improve its mechanical and water resistance properties. Other additives that may improve the durability of gelatine-based adhesive include plasticizers, which can improve flexibility and reduce brittleness, and preservatives, which can protect against microbial degradation. Additionally, fillers and reinforcement materials, such as cellulose or silica, can be added to improve mechanical properties and reduce shrinkage. The specific choice and amount of additives will depend on the specific application and the desired properties of the adhesive.

1.2 OBJECTIVES

The research summarised in this publication continue those presented in the companion paper [10], in which the potential substitution of metal by hardwood for rods and petrochemical adhesives by eco-sourced ones has been demonstrated under laboratory conditions. The focus of this second part is set on environmental conditions considered critical for most eco-sourced adhesives, and timber engineering in general.

[1] Jona Haupt, Fraunhofer Institute for Manufacturing Technology and Advanced Materials, Germany, jona.haupt@ifam.fraunhofer.de
[2] Nils Monard, Fraunhofer Institute for Manufacturing Technology and Advanced Materials, Germany, Nils.Monard@ifam.fraunhofer.de
[3] Till Vallée, Fraunhofer Institute for Manufacturing Technology and Advanced Materials, Germany, Till.Vallee@ifam.fraunhofer.de
[4] Stephanie Koesling, Fraunhofer Institute for Manufacturing Technology and Advanced Materials, Germany Stephanie.Koesling@ifam.fraunhofer.de
[5] Jana Kolbe, Fraunhofer Institute for Manufacturing Technology and Advanced Materials, Germany, Jana.Kolbe@ifam.fraunhofer.de

https://doi.org/10.52202/069179-0111

2 MATERIALS AND METHODS

2.1 Adhesives

The fundamental information related to the adhesive used, Technische Gelantine 400/115, a gelatine marketed by the German company Fritz Häcker GmbH, was reformulated in several modifications so to result in two types of improvements. Firstly, enabling the adhesive to form the relatively large layers (0.2 to 0.5mm) required for the glued-in rods, as opposed to the almost nil thickness needed in lap shear samples. The issue herein is related to the large water content of the gelatine-based adhesives. Secondly, improving—if necessary—the mechanical performance of the adhesives under elevated moisture contents. Both aims were achieved to a series of modifications summarised in Table 1.

Table 1: Summary of the adhesive formulations

REF	Technical Gelatine 400 / 115
M30	REF with water-content reduced to 25:45
M31	REF + 30% chalk
M32	REF + 50% chalk
M33	REF + 30% sawdust
M7	1 % tannic acid
M10	3 % kalinite
M14	0,3 % gallic acid
M26	1 % tannic acid + 9 % linseed oil
M10C	M10 + 30% chalk
M14C	M14 + 30% chalk

Modification with tannic acid: One part of Technical Gelatine was mixed with three parts of demineralised waters and left to swell overnight. This prepared adhesive was melted in combination with stirring in a water bath at 50 °C. A solution of tannic acid (10 mass %) was adjusted to pH 8 with the aid of NaOH and added to the adhesive. The reaction started immediately and gelation of the adhesive begun.
Modification with gallic acid: A solution of gallic acid (0.1 mass %) was adjusted to pH 8 with the aid of NaOH. One part of Technical gelatine was mixed with three parts of gallic acid solution and left to swell overnight. The adhesive was melted with stirring in a water bath at 50 °C and clean compressed air was introduced into the reaction mixture for 1.5 hours.
Modification with kalinite: One part of Technical gelatine was mixed with three parts of kalinite solution (1 masse %) and left to swell overnight. The adhesive was melted with stirring in a water bath at 50 °C
Modification with tannic acid and linseed oil: same procedure like modification with tannic acid alone. Linseed oil is added to the molten adhesive (before tannic acid is added).

This second part of the study focuses on the mechanical performance of the original adhesive's modification described above. For more details refer to the first part of this study [10]. For that, several series of ten lap shear samples (DIN EN 1465) were manufactured from beech (*Fagus sylvatica*) substrates (19.5 × 5.2 × 80.5 mm³) conditioned at 23 °C and 50% relative humidity (rH), bonded, and subjected to different environmental conditions. The first thereof was a co-called climatic Box briefly described as follows: samples were placed in a lockable plastic box over a saturated salt solution. A sensor recorded temperature and moisture. We worked with saturated solution of sodium chloride. The box was placed in a circulating air-drying cabinet at 40 °C for 7 days. Inside the box 75 % relative humidity was measured; that was exactly what was to be expected. Lap shear samples were removed immediately bevor testing without drying time at room temperature.

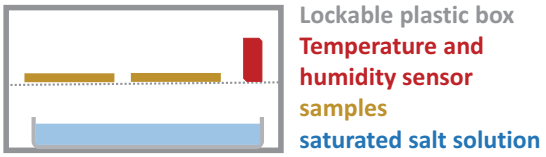

Figure 1: Principle of the climatic box

The second being a classical climate chamber set up for 45 °C and 85% rH. Samples were removed from the chamber and stored at room temperature until tested.

All tests were performed in a UTM under displacement control, with 5mm/min, until failure occurred. The results subsequently presented herein are given as average lap shear strength, which corresponds to the failure load divided by the bonded area surface, which was measure using a calibrated calliper for each individual sample.

2.2 Glued-in rods (GiR)

As part of the second round of testing with changed environmental conditions, the GiR are also subjected to different moisture and temperature levels.

Hence, the adhesives listed in Table 1 were evaluated against commonly used "chemical" adhesives by subjecting them to elevated levels of humidity and thermal conditions to determine their mechanical performance. The tests were conducted on various wood species including spruce, which served as the base material for all GiR, as well as beech, ash, and oak, which were used for the rods. The GiR samples comprised spruce blocks measuring 45 x 45 x 120 mm³, to which ø6 mm hardwood rods were affixed using the adhesives under evaluation.

Overcoming the challenges of manufacturing and testing of the GiR samples was thoroughly discussed in the first part of this study [10]. Therefore, the manufacturing process is herein summarized. The adhesive layer thickness was carefully controlled to achieve a radial adhesive layer thickness of 0.2 mm, and spacers were used during the gluing process to ensure concentricity of the wooden rods. The rods were also cleaned with isopropyl alcohol to remove any debris and left to fully evaporate.

https://doi.org/10.52202/069179-0111

In the initial study described in reference [10], the adhesive application process involved using a syringe to inject the adhesive into the lateral hole in the spruce block, while simultaneously coating the hardwood rod with the adhesive. The rods were then cantered and pressed into the hole using spacers to ensure precise concentricity.
However, during the process of liquefying the M10 adhesives at 50° C, the resulting mixture remained very viscous and would gelatinize immediately. This meant that the adhesive had to be applied immediately, within seconds, after melting so to avoid it solidifying in the syringe.
To speed up the process of pressing the gelatinous adhesive mixture into the gap, a different bonding method was used. Specifically, in large-scale GiR test trials involving chemical adhesives, the adhesive is injected laterally into a hole that is perpendicular to the hole for the hardwood rod. The rods are inserted into the hole beforehand, and the adhesive is then pressed in until it visibly emerges from the sides of the rod at the top opening of the hole. Adopting this process however was not as straight forward.
Because the adhesive layer thickness for the ecological glues is smaller by a factor of 5 than that of chemical adhesives, increased hydraulic pressure was generated when the adhesive was pressed in, which caused the wooden rods to be forced out like a piston. To prevent this from happening, a specially designed bonding device, which is shown in Figure 2, was used to pretension and centre the hardwood rods using tension springs and guide rods.

Figure 2: Bonding device designed for the rapid application of adhesives

After applying the adhesive, all samples were cured and conditioned for 7 days at 23°C and 50% rH. In the same fashion as the second variant of environmental conditions of the lap shear samples, all GiR were placed in a climate chamber at 45°C and 85% rH for 14 days after curing.

Testing the adhesive performance involved rigidly clamping each side of the sample in the UTM under displacement control and 2 mm/min until failure. However, clamping the hardwood rod directly resulted in inadequate findings due to deformation of the wood fibres, inducing stress fractures and reducing tensile strength of the dowel. To limit compression of the wood across the grain, to stop the rod from failing before the adhesive, several options were tried.
Increasing the hardwood rod diameter for instance still did not achieve satisfactory results, due to the dowel still breaking during testing. Other different attempts are thoroughly discussed in part one of the study [10].
The hardwood rods broke due to excessive compression, as well as pulling forces not being parallel to its grain structure. To reduce the pulling forces and combat the other issues a combination of different elements solved this problem.

One of these elements involved reducing the bonding depth of the glued-in rod to decrease the tensile load on the rod during testing. However, the most significant improvement was achieved by affixing a secondary spruce block with identical dimensions to the opposite end of the rod using double the adhesive layer length. Either block was also drilled through on the side, and a specific testing setup was devised to ensure perfect coaxiality. During testing, the samples were held in the UTM by inserting metal rods into the side holes, allowing for up to five degrees of freedom during the test. This setup achieved adhesive or substrate failure every time, and no hardwood rod failed.

3 RESULTS AND DISCUSSION

3.1 Lap shear samples

In a first round of experiments, samples were first conditioned for 7days at 23 °C and 50% rH, and then placed in the aforedescribed climatic box (40 °C and 75% rH) for another 7 days.

The resulting lap shear strengths, shown in Figure 3, ranged from extremely low 0.95 MPa (for the basic formulation, labelled REF) to 12.87 MPa (for M26, with 1 % tannic acid + 9 % linseed oil). The scatter, if expressed as standard deviation divided by the average, ranged from 9 to 15%, which remains acceptable for wood-based samples. The poor performance of the REF-samples was attributed to the favourable conditions for fungi growth in the climatic box, which contrasted with the results observed in the classical climatic chamber. After conducting an analysis of variance using Tukey's test with a significance level of 0.05, it was concluded that there was no statistically significant difference in measured strength among all series except for the REF adhesive, which was excluded from the analysis.

Comparing the performance of the aforesaid adhesive modifications after conditioning in the climatic box with that under RT (i.e., 23 °C and 50% rH) resulted in the

following: save for the REF-series, which exhibited the already presented fungi issue, lap shear strength was on average the same, with M7 presenting a 9% lower and M10 a 20% higher value. The differences series-wise being not statistically significant—again taking out the REF-series.

Turning the focus to the failure modes (again discarding the REF-series for the reasons already stated), almost all series exhibited a clear substrate failure that manifested in ripping of a thin layer of wood, as shown in Figure 4.

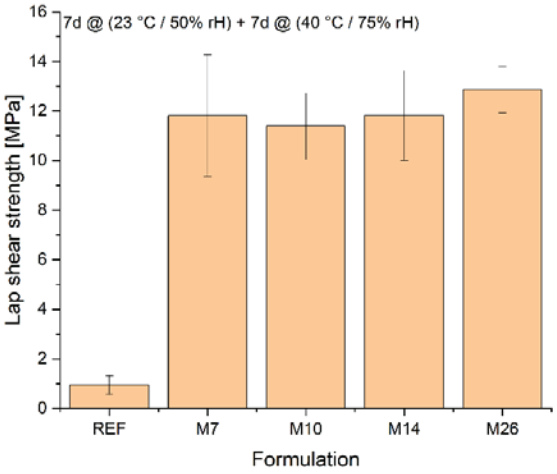

Figure 3: Experimental results obtained in the climatic box (without reconditioning to RT)

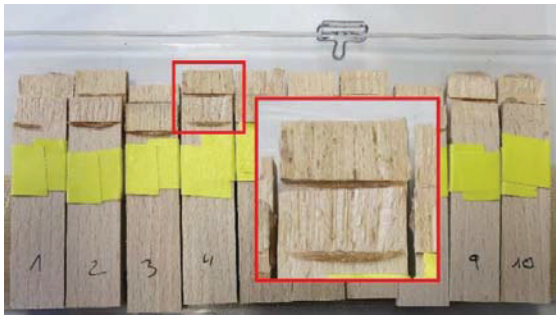

Figure 4: Typical failure mode observed

In the second round of tests, which involved a classical climatic chamber, samples were first conditioned for 7 days at 23 °C and 50% rH, then 14 days at 45 °C and 85% rH before being tested. The experimental results are presented in

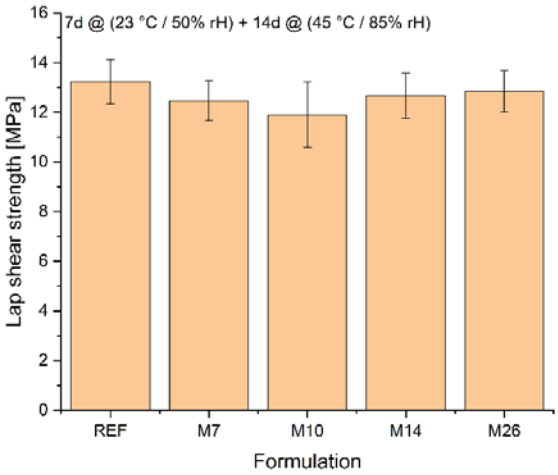

Figure 5: Experimental results obtained in the climatic chamber (with reconditioning to RT)

According to the results, the average lap shear strength for each series ranged from 11.9 MPa (for modification M10) to 13.2 MPa (which was surprisingly observed for the unmodified REF-series that no longer had fungi-related problems). On average, the variation, indicated by the standard deviation relative to the average, was 8% (with M7 having 6% and M10 having 11%).

In comparison to the lap shear strength tests carried out under room temperature (RT) conditions, the lap shear strength was observed to be higher by an average of 7%. However, statistical analysis through ANOVA using Tukey's test with a significance level of 0.05 revealed that these differences are not statistically significant. Similarly, when compared to the lap shear strength tests conducted in the climatic box, the average lap shear strength was higher by 4%, but not statistically significant, except for the REF-series, which exhibited fungal issues.

The issue with the moisture resistance of technical gelatine is due to the fact that technical gelatine can absorb a lot of water and swells. This reduces the mechanical properties, including the cohesive strength.
The first step was storing samples in a climate chamber. After removing the specimens after 7 in the climate chamber, these samples lay for an indefinite time at RT and had the opportunity to dry back. This means that at the time of testing, the technical gelatine was no longer in a swollen state. The test result shows two things:

- The technical gelatine is able to re-dry very well.
- Secondly, no ageing in the form of a loss of strength due to hydrolytic degradation could be detected.

In order to measure the strength of the bonds in the swollen state of the technical gelatine, we carried out the humidification in the box over a saturated NaCl solution. The box was taken to the testing machine after being exposed to the increased temperatures and moisture in the closed state. The samples were removed from the box just

https://doi.org/10.52202/069179-0111

before they were clamped in the testing machine and then tested immediately. The adhesive had no time to dry back. These tests show:
The unmodified technical gelatine has a low bond strength of less than 1 MPa in the swollen state (as was to be expected). The modifications, however, significantly improved the moisture resistance with an average lap shear strength of 12 MPa.

3.2 Glued-in Rods

The measurement of moisture content in the wood is a critical aspect of evaluating and comparing the adhesive strength to those not exposed to higher levels of humidity. To analyse the moisture content of the test samples after conditioning in the climate chamber (14d @ 45°C/85% rH), the glued in rods were measured in regular intervals during their period in the climate-controlled environment.
For this study, we employed two methods to measure the moisture content of wooden blocks. The first method was a pin-type moisture meter, which is a widely used tool for determining the moisture content of wood. This type of moisture meter can only measure the moisture content up to a depth of a few millimetres. This limited depth measurement can be a challenge when trying to assess the overall moisture level of a wooden block, as the surface of the wood can become saturated with ambient humidity very quickly, while the interior may remain dry.

To address this issue, we also measured the weight of each wooden block at regular intervals. This method provides a more accurate and comprehensive assessment of the moisture content of the wood, as it captures the changes in weight over time, reflecting the moisture uptake or loss. Figure 6 shows the results of both the moisture meter and weight measurements.

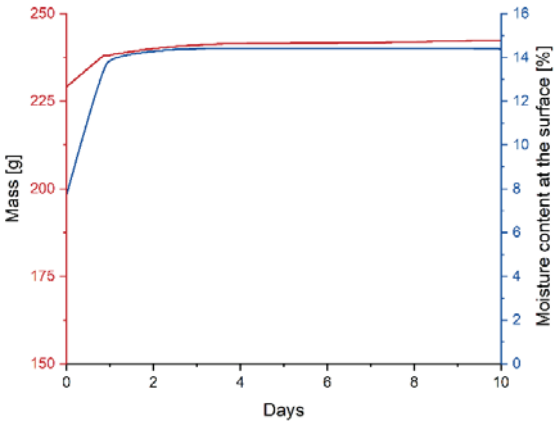

Figure 6: Measured wood moisture in comparison to weight increase over time

Our findings revealed that although the humidity values measured with the moisture meter reached a stable plateau within the first 48 hours, the moisture level in the wooden blocks continued to increase significantly until day four of their exposure in the climate chamber. After that, the moisture content plateaued and did not increase any further.

The first part of this study [10] conducted a series of GiR tests comparing the different variations and mixtures of the adhesive formulations, also listed in Table 1 (Ref, M29-M33). Following the findings of that study, a preselection of those mixtures, based on the adhesive strength for higher layer thickness was made, as seen in Table 2. The highest performing as well as formulations without additional fillers were chosen.

Table 2: GiR adhesive selection

		Shear strength dry [MPa]
M10	3 % kalinite	3.93 ± 11%
M10C	M10 + 30% chalk	4.81 ± 17%
M14	75% gallic acid + 25% gelatine	5.49 ± 7%
M14C	M10 + 30% chalk	6.59 ± 8%
M30	REF with water-content reduced to 60%	5.40 ± 16%
M31	REF + 30% chalk	6.25 ± 5%
M33	REF + 30% sawdust	5.44 ± 22%
EPX	Chemical Epoxy	6.70 ± 11%

The effect of warm temperatures and high moisture levels (45 °C and 85% rH) for 14 days on the adhesive properties was investigated with the aforementioned adhesives. The results as presented in Figure 7 showed that all ecological, gelatine-based adhesives performed poorly.

The ecological formulations exhibited a reduction in tensile strength on average by approximately 80% after exposure in the climate chamber. Differentiating between the different mixtures, the M33 showed the highest average tensile strength of 2.50 MPa with a variance of 5%. On the other hand, the M30 exhibited an average tensile strength of 2.00 MPa similar to the M31, with a variance of 6%.

To compare the GiR samples against an adhesive that is moisture resistant, the same 2 component chemical epoxy from the first study [10] was used. It performed only 20% worse compared to its dry tensile strength counterpart at 5.92 MPa. It is noteworthy that the failure mode exhibited mostly wood tear-out and not adhesive failure. The decreased tensile strength performance can be explained by the fact that when wood is exposed to warm temperatures and high moisture levels, the lignin, which is the natural glue holding the wood fibres together, can degrade and lose its adhesive properties. This can lead to a weakening of the intermolecular bonds between wood fibres and result in decreased strength of the wood. In addition, moisture can cause wood to swell and deform, further reducing its strength and durability.

https://doi.org/10.52202/069179-0111

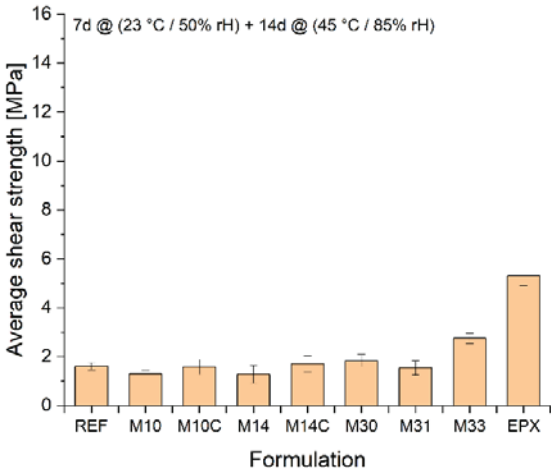

Figure 7: Average shear strength of the GiR (without reconditioning to RT)

In conclusion, the results of the tests of the mixtures tested at RT part one of this study [10] indicate that the ecological adhesive formulations can perform well under room temperature and humidity conditions. However, they are not be suitable for applications where the wood will be exposed to elevated temperatures and high moisture levels for extended periods.

To improve the performance of the ecological, gelatine-based adhesives, the specially formulated mixtures for humid environments (M10, M14 and M10C, M14C) were also tested as GiR samples. A comparison of the M10 and M14 and their chalk modified counterpart, against the other eco-adhesive variations from Table 2: GiR adhesive selectionTable 2 and the chemical epoxy, is depicted in the same Figure 7.

The reference adhesive, consisting of 3-parts water and 1-part technical gelatine, was used as the basis for the new formulations. The M10 mixture, which substituted the water for a kalinite solution, exhibited an average strength of only 1.30 MPa during the climate chamber experiment. Further regression was observed with the M14 formulation, which substituted the water with gallic acid, resulting in a further 2% decrease in adhesive performance. Both eco-adhesives displayed a high variance with the M14 mixture reaching 30%.

When compared to the gelatine-based adhesives not specially formulated to withstand higher levels of moisture, it was evident that the M10 and M14 eco-adhesives were not able to effectively adhere to wood. The series of tests with additional 30% chalk content, while marginally better at 1.57 MPa and 1.69 MPa for the M10C and M14C respectively, could not realistically improve on the adhesive performance.

Figure 8: Wood tear out (left) and adhesion failure (right)

Quantifying the failure modes of the adhesives, all ecological adhesives showed considerable adhesion failure, with little to no wood failure. Figure 8 depicts a comparison of the typical wood tear out experienced during the tests performed at RT versus the same formulation under the increased moisture and temperature levels. The hardwood rod is clear of any adhesive and shows virtually no sign of any adhesion.

4 CONCLUSION

In this second part of a study devoted to ecological, or sustainable adhesives, and their use in a structural context, the investigations presented in [10], which were carried out at RT, were extended towards more severe environmental conditions (+45 °C and 85% rH).

Firstly, an existing gelatine-based adhesive was modified so to improve its performance under the previously mentioned severe environmental conditions. This resulted in four additional mixtures.

Secondly, the lap shear strength of the aforesaid formulations, additionally to that of the reference gelatine, were determined under two different environmental scenarios: in a climatic box, with tests performed without reconditioning at RT, then in a climatic chamber with reconditioning to RT. The results indicated that it is possible to achieve similar lap shear strength under these climatic conditions, if compared to RT. It is to be noted that in the lap shear samples, the adhesive layer thickness was almost zero.

Lastly, tests on glued-in rods (GiR) were performed. A first round of tests was performed with the original formulation, to which different fillers were added (for more details refer to [10])—which were not optimised for humid environments and tested without reconditioning. These were, in a second run, compared to some of the formulations that were optimised, also without reconditioning to RT. Unlike the lap shear samples, the adhesive layer thickness in the GiR tests was set to 0.2 mm due to technological reasons. If compared to the similar tests described in [10], which were performed

https://doi.org/10.52202/069179-0111

under RT, joint capacities significantly decreased by around 80% (averaged over all series). If comparing the performance of a 2K-epoxid taken as reference, exposure to elevated temperature and moisture only resulted in a decrease of roughly 20% in strength.

Regarding the resistance to temperature and moisture of ecological gelatine-based adhesives, the study showed that the influence of the adhesive layer is paramount. It is therefore not sufficient to assess the performance of such adhesives only at the level of lap shear samples (with very thin layer thicknesses).

REFERENCES

[1] Tlustochowicz G, Serrano E, Steiger R. State-of-the-art review on timber connections with glued-in steel rods. Mater Struct. 2011;44:997–1020.

[2] Grunwald C, Vallée T, Fecht S, et al. Rods glued in engineered hardwood products part I: Experimental results under quasi-static loading. International Journal of Adhesion and Adhesives. 2018. DOI: 10.1016/j.ijadhadh.2018.05.003.

[3] Ayansola GS, Tannert T, Vallee T. Glued-in multiple steel rod connections in cross-laminated timber. The Journal of Adhesion. 2021:1–17.

[4] Adams RD, Coppendale J, Mallick V, et al. The effect of temperature on the strength of adhesive joints. International Journal of Adhesion and Adhesives. 1992;12:185–190.

[5] Bazant ZP. Constitutive equation of wood at variable humidity and temperature. Wood Science and Technology. 1985:159–177.

[6] Kläusler O, Clauß S, Lübke L, et al. Influence of moisture on stress–strain behaviour of adhesives used for structural bonding of wood. International Journal of Adhesion and Adhesives. 2013;44:57–65.

[7] Aicher S, Dill-Langer G. Influence of moisture, temperature and load duration on performance of glued-in rods. In: Proceedings RILEM PRO 22: Rilem Symposium 2001 - Joints in Timber Structures; Stuttgart; 2001.

[8] Di Maria V, D'Andria L, Muciaccia G, et al. Influence of elevated temperature on glued-in steel rods for timber elements. Construction and Building Materials. 2017;147:457–465.

[9] Lartigau J, Coureau J-L, Morel S, et al. Effect of temperature on the mechanical performance of glued-in rods in timber structures. International Journal of Adhesion and Adhesives. 2015;57:79–84.

[10] Jana Kolbe, Stephanie Koesling, Cordula Grunwald, Nils Monard, Jona Haupt. Glued-in hardwood rods using bio-sourced adhesives — Part I: investigations under laboratory conditions. Proc. of the World Conference on Timber Engineering, Oslo 2023.

World Conference on Timber Engineering Oslo 2023

MATERIAL FLOW ANALYSIS AND CARBON FOOTPRINT OF FOREST RESOURCES IN JAPAN: A CASE STUDY ON BUILDING MATERIALS

Hongjun Wang[1], Atsushi Takano[2]

ABSTRACT: The importance of wood products' environmental properties, such as renewability and carbon storage capacity, is well recognized in sustainable development. For the sustainable use of wood, the deeply linked supply and demand relationships are important. However, few studies have been conducted to develop a comprehensive understanding of the forest resource flow. The objectives of this study are to conduct holistic analyses on the material flow and carbon footprint of forest resources in Japan, focusing on building materials; draw holistic flowcharts on the basis of the inventory; and based on that, discuss problems and possibilities from resource and environmental points of view. In the material flow, a large amount of forest wood waste is unmanaged, and the replanting ratio is continuously low. Since major GHG emissions originate in manufacturing and waste management, attentions should be paid to the utilization of biomass energy and the choice of waste management.

KEYWORDS: Material Flow Analysis (MFA), Forest resources, Wood products, Carbon storage

1 INTRODUCTION

Due to a decrease in domestic wood supply and an increase in imports, the wood self-sufficiency rate in Japan dropped from 86.7% in 1960 to 18.8% in 2002. To improve this situation, the government has implemented measures to promote the use of domestic wood. As a result of such effort, the wood self-sufficiency rate recovered to 36.2% in 2017 and a goal of 50% or more has been set for 2025 [1]. Meanwhile, the importance of wood and forest product with environmental properties, such as renewability and carbon storage capacity, is widely recognized in the context of sustainable development nowadays. Carbon storage in forests and wood products is especially regarded as a key to tackling climate change. Since forest products such as timber and pulp are produced from the same resource, the linkage between the related industries: forestry, manufacturing, construction, and waste management is important.

Against such background, researchers in various countries have performed Material Flow Analysis (MFA) of forest resources. For instance, Lenglet et al. [2] have made an MFA of the French forest-wood supply chain to compensate for the absence of consistent accounts for wood product production and consumption. They have attempted to fill this gap and evaluate the potential consequences of raw wood export reduction policies in France. Gonçalves et al. [3] have developed an MFA of forest biomass in Portugal to clarify circularity and resource efficiency. They have created material circularity indicators and cascade factors for different product sectors and pointed out heterogeneity in the circulation of wood products in Portugal. For studies on a larger scale, Mantau [4] has assessed wood flow throughout Europe to produce a tool for setting policy targets. He has quantified resource potentials, cascades and carbon effects. In addition to MFA, the carbon footprint of forest resources has been assessed worldwide. For instance, Zhang et al. [5] have created the life-cycle carbon budget for Harvested Wood Products (HWP) in China to clarify the role HWP play in climate change mitigation. They have assessed carbon stock and emissions from HWP in China, considering production, end-use, post-service disposal stages, and pointed out that in-use HWP account for 73.7% of the life-cycle carbon stock. Head et al. [6] have developed a database of greenhouse gas (GHG) life cycle inventory, focusing on the wood used in Canadian buildings, to facilitate comparisons of climate change impact with non-wood materials. They suggested that most wood building products provide net negative climate change impact scores, but there is still a lack of data for the development of this modular database.

In Japan, there are not yet many studies related to MFA or the carbon footprint of forest resources. Kobayashi et al. [7,8] have developed material flow of forest resources and calculated the environmental loads during manufacturing. They have calculated the carbon footprint of timber,

[1] Hongjun Wang, Kagoshima University, Japan, Hongjun_Wang@protonmail.ch

[2] Atsushi Takano, Kagoshima University, Japan, takano@aae.kagoshima-u.ac.jp

https://doi.org/10.52202/069179-0112

plywood and wood waste, and the CO_2 emissions from building materials. They have pointed out the importance of reforestation and suggested that the utilization of wood waste may compensate for the emissions. To compensate for the insufficiency of emission factors, Nambu et al. [9] have developed an LCA database of wood materials, mainly focusing on imports. They have pointed out the lack of evaluation of imported wood materials and the insufficiency of unit values. In many cases, the assessment of forest resources ended with the accomplishment of the material flow or the database of emission factors, and few have gone on to discuss the issue from environmental perspectives. Emissions from the manufacturing sector have been assessed, while emissions from other processes such as forest management, construction, waste management, and so forth were not considered. Additionally, emissions from imported forest products have not been evaluated so far, though emission factors have already been calculated.

Against this background, this study aims to a create comprehensive overall image of the current state of forest resources in Japan through an examination of forestry, manufacturing, construction, and waste management. To fulfill this objective, this study:
1) presents a holistic flowchart of forest resources in Japan, mainly focusing on building materials.
2) performs MFA on the basis of the inventory.
3) analyses carbon footprint: processing GHG emissions and carbon content flow, on the basis of the inventory.
4) discusses the situation and points of improvement in terms of forest resources in Japan from material flow and environmental perspectives.

2 MATERIALS AND METHODS

2.1 SYSTEM BOUNDARIES

The system boundaries of this study are summarized in Figure 1. The life cycle stages studied are named according to the modularity principle of a building life cycle (EN 15978: 2011) [10], which consists of four main stages (module A1-3: product stage, A4-5: construction stage, B: use stage, and C: end-of-life stage) and an additional information module (module D: benefits and loads beyond the system boundary) has been added.

2.2 MFA

The inventory was carried out on the basis of statistical data published by relevant authorities, such as the Ministry of Agriculture, Forestry and Fisheries [11] and the Food and Agricultural Organization (FAO) [12]. The reference year is 2017. The definition of four sectors in the flowcharts are shown in Table 1, and the rules of flowcharts are explained in section 3.1. Most of the data are known in cubic meters, while data that are known in other units are converted by the following rules: data in "ton" are divided by the weight conversion factor from the Japanese Industrial Waste Information center [13], data in "square meter" are multiplied by the wood utilization conversion factors from the Japanese Ministry of Land, Infrastructure, Transport and Tourism [14]. Estimates were made using conversion factors and formulas referenced in the relevant publication by the Japanese Forestry Agency, the FAO and the Japanese Ministry of Environment [1, 12, 15].

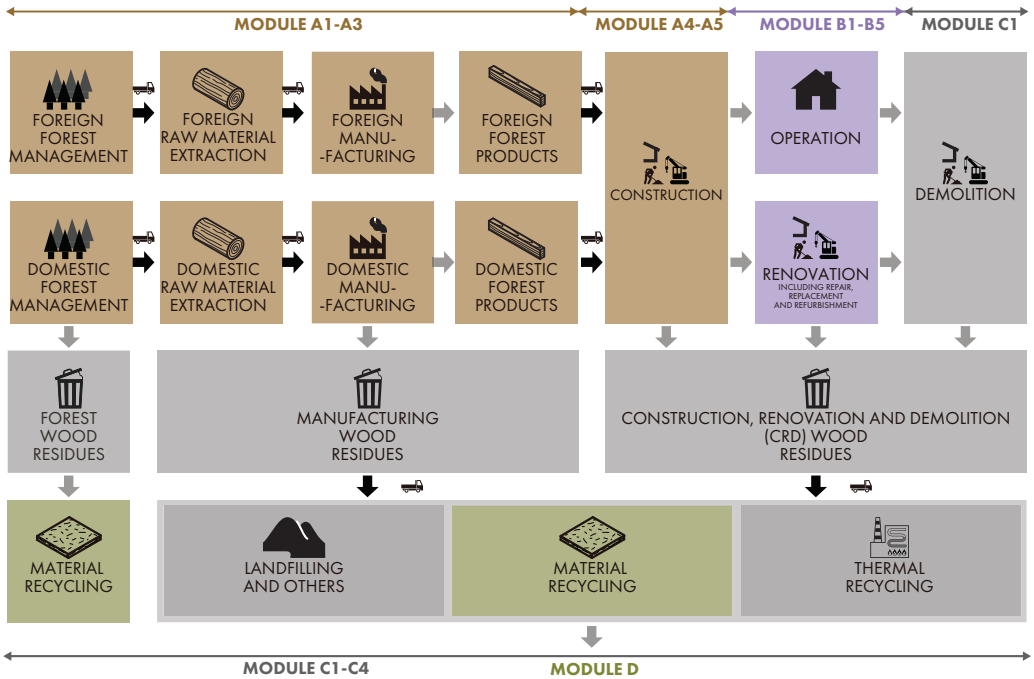

Figure 1: *System boundaries of this study.*

Table 1: Definition of sectors in this study.

Sectors	Contents of each sector
Forestry	Forest management, growing stock (by forest type and age class) and the annual increment of it, forest wood waste
Manufacturing	Production, imports, exports and consumption of forest products, manufacturing wood waste
Building	Wood stock in existing buildings (by construction method) and the annual increment/decrement of it
Disposal	Construction, renovation and demolition (CRD) wood waste, wood waste management

2.3 CARBON FOOTPRINT

2.3.1 Processing GHG emissions

On the basis of the inventory, GHG emissions generated during forest management, forest product processing, construction, demolition, selection, and waste management are assessed. Carbon release from incineration of post-use wood was not counted as processing GHG emissions. Emissions associated with domestic forest product processing, construction, demolition and wood waste management were calculated in accordance with the unit values from the Inventory Database for Environmental Analysis [16]. GHG emissions of imported forest products were calculated using the LCA database created by Nambu et al. [9]. The calculations were carried out by multiplying the unit values by the amount of each product.

2.3.2 Carbon content flow

The carbon content flow of the entire process was also assessed based on the inventory. Carbon content in forest resources was quantified based on the National Greenhouse Gas Inventory Report [15] and Intergovernmental Panel on Climate Change's guidelines for national GHG inventories [17]. In the carbon content flow, "stock" refers to the trees in forests and wood used in buildings; "carbon storage" refers to the carbon in the stock; "carbon uptake" refers to the annual increment of carbon in forests, forest products and wood used in buildings; "carbon release" refers to carbon released after disposal and carbon in exported products. The carbon content related to forests and forest products was calculated using relevant equations and carbon factors [16]. The carbon storage in the existing building stock and carbon uptake in new construction were calculated using relevant carbon fractions [17]. The carbon release was assessed for exported forest products and wood waste by multiplying either the volume or mass according to their carbon fractions [16, 17].

3 RESULTS AND DISCUSSION

3.1 MFA

The result of MFA in Japan is summarized in Figure 2 as a flowchart. Volume of four sectors: forestry, manufacturing, building, and disposal are shown from left to right. In the forestry sector, each tree icon represents $1x10^8$ m^3 of wood volume in growing stock and the dotted circle shows the annual increase of the wood volume. Gradational colors of tree icons represent trees of different age classes, in which trees from young to old are classified by colors from light to dark respectively. In the manufacturing sector, the area of ring is in proportion to the volume of each type of forest product. Each ring with two different colors shows the direct material input (DMI, equals production plus imports): production is shown in the darker color and imports are shown in a lighter color. The lighter ring above the two-color ring shows the exports of forest products. In the building sector, each house icon represents $1x10^8$ m^3 of wood stock in buildings and the dotted circle shows the annual increase of the wood stock. In the disposal sector, the area of the ring is in proportion to the volumetric data. Gradational gray colors from light to dark represent wood waste disposed of by material recycling, thermal-recycling, incineration without electricity production, landfill or other disposal methods.

3.1.1 Forestry

Japan has $25.05x10^6$ ha of forest, of which 51.02% is covered by coniferous trees and the remaining 48.98% is covered by non-coniferous trees. In $5,242x10^6$ of growing stock, 71.08% is coniferous and 28.92% is non-coniferous. Of all the coniferous forest, 52.96% of trees is aged 41~60 years, followed by 21.76% aged 61~80 years and 12.81% aged more than 80 years. There is an average annual increase of $68.26x10^6$ m^3 or 1.40% in growing stock, including 78.26% in planted forests and 21.74% in natural forests. 84,226 ha of forest are harvested, but only 22,069 ha or 26.20% of the harvested area is replanted. The composition of Japanese forest by area is different from the composition by volume, since the density of conifer trees in planted forests is much higher than that of trees in natural forests. As for the age class, of all the coniferous forests, more than 30% is aged 61+ years and ready for harvesting. The non-coniferous forests are generally older than coniferous forests since non-coniferous forests depend on natural regeneration and very few areas are replanted.

3.1.2 Manufacturing

Japan produces $28.68x10^6$ m^3 of roundwood, $9x10^6$ m^3 of timber, $2x10^6$ m^3 of Glulam (Glued Laminated Timber) and CLT (Cross-Laminated Timber), $3.57x10^6$ m^3 of veneer sheets, $3.06x10^6$ m^3 of plywood, $0.18x10^6$ m^3 of LVL (Laminated Veneer Lumber), $5.19x10^6$ m^3 of wood chips, and $1.89x10^6$ m^3 of wood-based panels. Among all roundwood production, 42% is Japanese cedar, 10% is Hinoki cypress, 23% is Japanese larch, Yezo spruce and

https://doi.org/10.52202/069179-0112

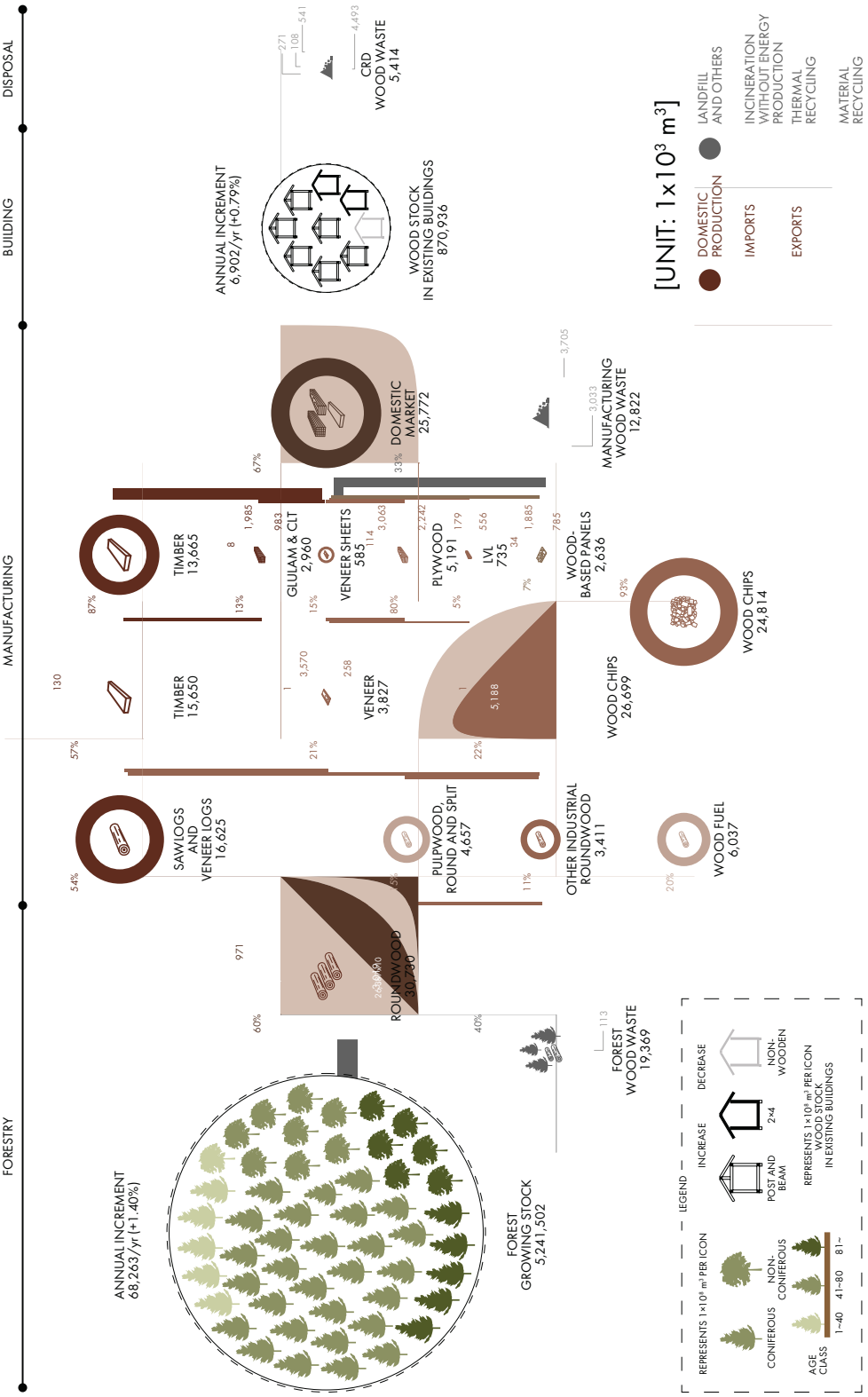

Figure 2: *Material flow of forest resources in Japan (Reference year 2017)*

https://doi.org/10.52202/069179-0112

others, the remaining 25% is unclassified. To meet domestic consumption, approximately 10% of roundwood DMI, 40% of timber DMI, 33% of Glulam & CLT DMI, 7% of veneer sheet DMI, 42% of plywood DMI, 76% of LVL DMI, 81% of wood chip DMI, and 29% of wood-based panel DMI is imported. As for the main source of imports, 85.66% of roundwood imports is from North America, 78.88% of timber imports is from Europe and North America, 81.18% of Glulam imports is from Europe, 83.53% of veneer sheet imports is from Russia, and 92.95% of plywood imports is from Southeast Asia. Of all roundwood consumption, 54% is consumed as sawlogs and veneer logs, 15% is consumed as pulpwood, round and split, 11% is consumed as other industrial roundwood, and 20% is consumed as wood fuel. Of all timber consumption, 13% flowed to glulam and CLT manufacturing, and 87% is used directly in construction and other industries. 25.77×10^6 m^3 of forest products flowed to the domestic market and an average of 1.19% of domestic production is exported. For the composition of the domestic market, 53.02% is timber, 11.48% is glulam and CLT, 2.27% is veneer sheets as the final product, 20.14% is plywood, 2.85% is LVL and 10.23% is wood-based panels. For the sustainability of harvesting, although the increase of most forest types is greater than removals, since the harvesting-replanting ratios are different by forest type, the sustainability of roundwood from different forest types should be evaluated separately and the harvesting should be controlled. For the inflow of forest products, Japan has tried to lower the volume of material imports but still has a great dependency on foreign products. For most types of forest product, the majority of imports are from particular regions, which throws more doubt on the reliability of forest product DMI. For the consumption of forest products, the majority of timber production is still being used directly in construction and other industries. Since the demand for Glulam is increasing because of the recovery of new housing construction and the utilization of CLT is being promoted by the Japanese government, the demand for EWP (Engineered Wood Products) will probably increase in the near future.

3.1.3 Building

Of 81.71×10^6 m^2 of new housing construction, 63.59% is wooden construction (W), 19.66% is reinforced concrete construction (RC), and 16.14% is steel construction (S). Among 52.97×10^6 m^2 of new non-housing construction, 71.85% is S, 15.60% is RC, and 8.64% is W. The volume of the wood stock in total new construction is 12.32×10^6 m^3. Wood stock in new construction is composed of 87.68% in W, 6.72% in RC, and 5.41% in S. Japan has $8{,}381 \times 10^6$ m^2 of existing building stock, which 48.93% is W, 30.52% is S, and 18.51% is RC. The volume of wood stock in existing buildings is 870.94×10^6 m^3, containing 89.94% in W, 6.06% in RC, 3.82% in S, and tiny in SRC and CB. Most of the wood is stocked in wooden housing, while 12% is stocked in non-dwelling buildings using other construction methods because of their large area. Thus, wood stock used in non-wooden constructions should also be accounted for. The composition of the wood stock in new construction are similar to that in existing buildings, but the share of wood stock in wooden constructions in new construction in 2017 is 2.26% smaller than that in existing buildings. Despite the promotion of wooden construction and wood for furnishing these years, the share of it is still lower than in the past.

3.1.4 Disposal

Japan generates 19×10^6 m^3 of forest wood waste, which is 40.31% of the volume of harvested roundwood. Of 5×10^6 m^3 of CRD wood waste, 40% is generated during construction and 60% is generated during demolition. Wood waste generated during renovation is minor. 99% of forest wood waste is unmanaged and less than 1% is material-recycled as wood chips. 47% of manufacturing wood waste is landfilled or disposed of by other waste management, 29% is material-recycled and 24% is thermal-recycled. 83% of CRD wood waste is thermal-recycled, 10% is material-recycled, 5% is incinerated without electricity production, and 2% is landfilled or disposed of by other management method. Although GHG emissions and energy payback ratio in utilization of forest wood waste may be higher than that of fossil fuel [18], the majority of forest wood waste is still unmanaged due to reasons such as the difficulty of collection and the greater cost. Moreover, due to the high water-content ratio very little waste is estimated to be recycled and less than 1% is actually accounted for. Together with the promotion of forest wood waste recycling, methods raising the mechanization rate of collection and lowering the expense should be considered. Since most of the manufacturing wood waste is small particle and ideal as a source of composting material for agricultural purposes, half of the amount is disposed or used by agriculture without recycling. CRD wood waste is usually combined with metals and other matters, which makes the selection time-consuming, so most of it is incinerated for energy use.

3.2 PROCESSING GHG EMISSIONS

The assessments result of processing GHG emissions are summarized in Figure 3 in the same manner as Figure 2. The darker grey line represents processing emissions from domestic production and the lighter grey line represents emissions associated with imported products. The width of each line is relative to the amount of GHG emissions.

3.2.1 Emissions from forest management and roundwood manufacturing

Of 486,306 t-CO_2eq of GHG emissions during roundwood processing, domestic production accounts for 36.80% and importation accounts for 63.20%. Half of the GHG emissions during domestic roundwood manufacturing come from Japanese cedar, followed by 25.51% from unclassified trees and 12.29% from Hinoki cypress.

https://doi.org/10.52202/069179-0112

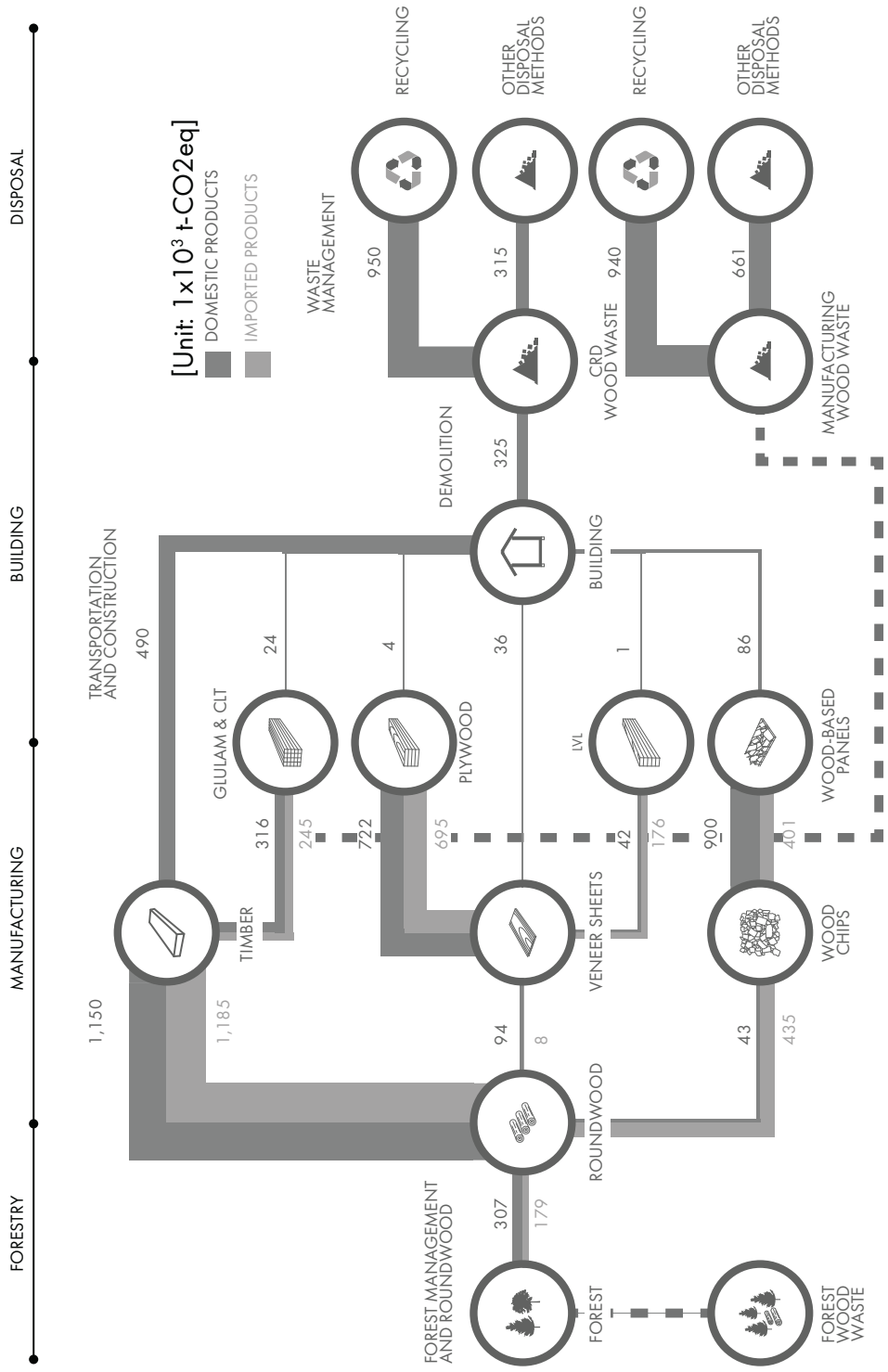

Figure 3: *Processing GHG emission flow of forest resources in Japan (Reference year 2017)*

https://doi.org/10.52202/069179-0112

3.2.2 Emissions from forest product processing

Of $6.41x10^6$ t-CO_2eq of GHG emissions during forest product processing, 51% is from domestic production, 21.40% from Southeast Asia, followed by 10.05% from Europe, 5.90% from North America, 5.79% from Russia and 5.90% from other regions. Of $3.27x10^6$ t-CO_2eq of GHG emissions from production, 35.21% come from timber processing, followed by 27.56% from wood-based panel processing, 22.09% from plywood processing, 9.66% from glulam & CLT processing, and the remaining 5.47% from other processes. Of $3.15x10^6$ t-CO_2eq of GHG emissions from imports, 37.67% come from timber processing, followed by 22.08% from plywood processing, 13.83% from wood chip processing, 12.75% from wood-based panel processing, and the rest 13.77% from other processes.

3.2.3 Emissions from construction and demolition

$0.97x10^6$ t-CO_2eq of GHG emissions come from building material transportation, construction and demolition, of which 66.29% is from building material transportation and construction, 30.20% is from demolition and 3.51% is from the selection of CRD waste. 76.63% of GHG emissions resulting from these processes is from timber, followed by 13.43% from wood-based panels and 9.93% from other forest products. 76.72% of the GHG emissions related to the utilization of forest products come from wooden construction, followed by 12.79% from steel construction, 9.59% from reinforced concrete construction, and less than 1% from others.

3.2.4 Emissions from wood waste management

$1.60x10^6$ t-CO_2eq of GHG emissions come from manufacturing wood waste management, of which 58.71% is from recycling and 41.29% is from other disposal methods. 71.29% is from collection and transportation, followed by 21.14% from thermal-recycling, 7.37% from landfilling and others. $1.26x10^6$ t-CO_2eq of GHG emissions come from CRD wood waste management, of which 75.13% is from recycling and 24.87% is from other disposal methods. 39.62% is from thermal recycling, followed by 38.18% from collection and transportation, 2.39% from pure incineration, and 19.81% from landfilling and others.

3.2.5 Total GHG emissions

The amount of GHG emissions associated with all forest products is $10.67x10^6$ t-CO_2eq, of which 68.84% is from domestic processing and 31.16% is from foreign processing. Of the total GHG emissions resulting from forest resource processing, 59.71% is from forest product processing, followed by 26.85% from wood waste management, 9.05% from CRD activities, and 4.39% from forestry. The most (21.80%) is generated during timber processing, specifically 11.60% from timber imports and 10.70% from domestic timber construction. This amount is tremendous mainly because of the great volume, and the use of fossil fuel during the wood-drying process. To reduce the GHG emissions during timber processing, methods such as biomass substitution during the subprocess of drying should be brought into the discussion. The second largest (15.00%) is generated during manufacturing wood waste management, and as much as 11.86% is from CRD wood waste management. Wood waste in Japan is difficult to collect or select, which transforms into high unit values. The transportation distance and the choice of wood waste management methods may have a great influence on total GHG emissions.

3.3 CARBON CONTENT FLOW

The assessment results of carbon storage, uptake and release (defined in section 2.3.2) are summarized in Figure 4 in the same manner as Figure 2. Most of the rules are the same as for the material flow, while values of carbon storage in forests and buildings are represented by rings with two layers, which are proportionally 25 times larger than single-layer rings.

3.3.1 Carbon storage and uptake

Of $7{,}268x10^6$ t-CO_2eq of carbon storage, 90.11% is stored in the growing stock and 9.89% is stored through wood utilization in existing building stock. More specifically, 55.17% is stocked in coniferous forests, 34.94% in non-coniferous forests, 8.89% in wooden construction buildings, and 1% in other construction. Of $104x10^6$ t-CO_2eq of carbon uptake, 78.56% is from growing stock and 21.44% is from forest products. 45.44% of carbon uptake in forest products is stored in buildings, while the remaining 54.56% is discarded during construction or flows to other industries. Similar to the volumetric composition, $22.36x10^6$ t-CO_2eq of carbon uptake in forest products flowed to the domestic market, with 51.33% being from timber, followed by 22.75% from plywood, 12.71% from wood-based panels, and a combined 26.44% from others. 39.48% is stored in imports and 60.52% is stored in production.

3.3.2 Carbon release

$1.08x10^6$ t-CO_2eq is exported in forest products and $17.69x10^6$ t-CO_2eq is released through wood waste management. Carbon loss consists of 60.36% in forest wood waste, 25.84% in manufacturing wood waste and 13.81% in CRD wood waste. Since the majority of forest wood waste is unmanaged and industrial wood waste is mostly treated through thermal recycling, almost all the carbon in wood waste is released.

4 SCENARIO ANALYSIS

4.1 GOAL OF WOOD SELF-SUFFICIENCY RATE

Although the demand for wood was predicted to decline from $82x10^6$ m^3 in 2017 to $79x10^6$ m^3 in 2025, the goal of wood self-sufficiency has been increased from 36.2% in 2017 to 50% in 2025 [1]. Thus, the amount of self-sufficient wood is assumed to increase from $29x10^6$ m^3 in 2017 to $40x10^6$ m^3 in 2025. This variation may trigger impacts on the sustainability of forest resources.

https://doi.org/10.52202/069179-0112

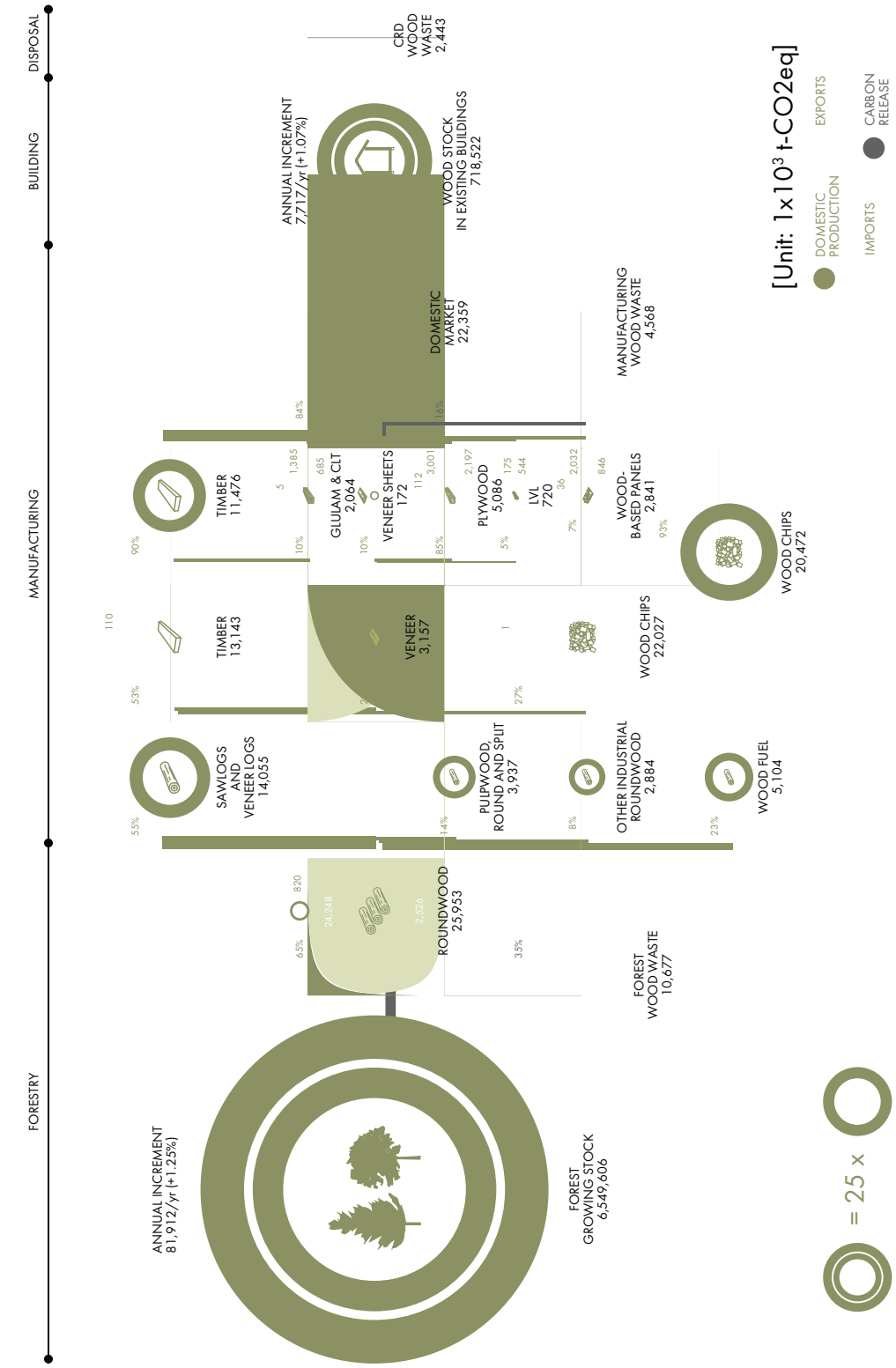

Figure 4: *Carbon content flow of forest resources in Japan (Reference year 2017)*

https://doi.org/10.52202/069179-0112

In 2025, the roundwood removals and imports are predicted to change by +36.29% and -25.27%, respectively. A reduction of forest area by 92,721 ha is predicted to be caused due to the low planting ratio and the difficulties of natural regeneration [18]. In terms of processing GHG emissions, 5.83% more of total GHG emissions is predicted to be generated, which is 14.27% more from forestry, 6.15% more from manufacturing, 6.77% more from disposal, but 3.12% less from building due to the decline in demand. In the carbon content flow, the carbon uptake in forests and forest products is predicted to decline by 25.54% and 3.12%, respectively. This is predicted to lead to a 20.73% decline in total carbon uptake. As a result, there is predicted to be a lower dependency on imports, worse sustainability of forests, a greater amount of GHG emissions, and a lower amount of annual carbon uptake. To solve these potential threats, both the improvement of forest resources sustainability and the reduction of GHG emissions resulting from domestic manufacturing should be taken into consideration. With a higher replanting ratio of harvested forest lands, there are predicted to be more sufficient domestic forest resource and more carbon uptake in forests. This may compensate for the material volume loss by domestic harvesting and the GHG emissions released by domestic manufacturing. The promotion of biomass energy utilization should be also encouraged since the substitution of biomass for fossil fuel is predicted to be efficient in terms of emission reduction (discussed in section 4.3).

4.2 BIOMASS SUBSTITUTION DURING TIMBE R MANUFACTURING

As mentioned before, a large amount of GHG emissions is generated from timber processing. For the details of this process, Komata et al. [19] suggested that most of GHG emissions due to domestic timber processing are from the drying process. They pointed out that the substitution ratio of biomass for fossil fuel in Japan is relatively low (41%), compared to countries in Europe (90%), Oceania (85%) and North America (80%). Thus, this scenario analysis was conducted to discuss the reduction of GHG emissions using different levels of biomass substitution. On the basis of the case study on biomass substitution in different countries [9], and the emission factors for the kiln-drying process [20], three scenarios with different levels of biomass substitution were estimated. S1 was assumed as timber processing without biomass energy use (fossil fuel: 100%, biomass energy: 0%). S2 was assumed as the lowest level of biomass substitution (fossil fuel: 60%, biomass energy: 40%). And S3 was assumed as the highest level of biomass substitution (fossil fuel: 10%, biomass energy: 90%). In S2, the GHG emissions from domestic timber processing is predicted to decrease by 19.26% and the total GHG emissions from forest resource processing is predicted to decrease by 1.89%. In S3, GHG emissions from domestic timber processing is predicted to decrease by 42.28% and the total GHG emissions from forest resource processing is predicted to decrease by 4.15%. Theoretically, the substitution of biomass energy during the wood-drying process of domestic timber manufacturing alone will reduce the GHG emissions by a relatively large amount. Considering the GHG emissions from long-distance overseas transportation of imported timber, the promotion of biomass energy utilization during manufacturing may allow domestic timber to be more competitive in the future.

4.3 OUFLOWS OF WOOD WASTE

When discarded forest products are material-recycled, carbon is not released and it can be stored for a longer period of time [21], material-recycling should be encouraged. However, very little wood waste is material-recycled and flows back to the carbon pool at the moment. Thus, this scenario analysis was conducted to discuss the reduction of GHG emissions and carbon release by two scenarios to the achievable improvement of wood waste management. S1 was assumed as the improvement reducing 10% more volume of total wood waste. S2 was assumed as the improvement with 10% more shares of material-recycling in all disposal methods of wood waste. In S1, there is predicted to be a decline in total GHG emissions by 2.69%. There is predicted to be a decline in carbon outflows by 9.42%. In S2, the GHG emissions are predicted to decrease by 13.36%, specifically manufacturing wood waste management by 5.25% and CRD wood waste management by 23.62%. This leads to a decline in total GHG emissions of 3.59%. The carbon release is predicted to decrease by 11.24%, specifically forest wood waste by 10.06%, manufacturing wood waste by 14.06% and CRD wood waste management by 11.11%. By reducing the volume of wood waste, there would be lower GHG emissions and less carbon release. By disposing more wood waste through material-recycling, the GHG emissions and carbon release would decrease even more. A better choice of recycling methods guarantees less GHG emissions and less carbon release, than the pure reduction of wood waste. To improve wood waste management, efforts should be put into both the reduction of volume and the choice of recycling methods.

5 CONCLUSIONS

The sustainable use of forest resources is one of the main challenges in the society, while the state of forest resources in Japan can be enhanced in terms of material flow and environmental perspectives. To understand the overall image of forest resources in Japan, this research has attempted to perform analyses of material flow and carbon footprint. The results show that the large amount of unmanaged forest wood waste, the low replanting ratio, and the lack of monitoring on supply-demand relationships are some of the main problems of forest resources in Japan at present. By 2025, we have predicted a decrease in the sustainability of forests due to greater domestic production. To solve these problems, policies encouraging waste management and replanting, as well as standards of evaluation on the sustainability level of harvesting are needed. For the carbon footprint of forest resources, major GHG emissions originate in imported

https://doi.org/10.52202/069179-0112

products, waste management, and timber processing. To improve the disposal of wood waste, efforts should be put into both the reduction of volume and the choice of recycling methods simultaneously. Since there is a relatively low biomass substitution ratio in Japan, the promotion of biomass energy may contribute to the decline of emissions from timber processing. This research resulted in inventory and holistic flowcharts of forest resource flow focusing on the quantities, processing GHG emissions, and carbon content flow. The inventory and flowcharts could be used to perform other analysis of forest resources, or as a platform for discussion on the current problems and points of improvement. The results may be useful for environmental policy development.

ACKNOWLEDGEMENT

The authors acknowledge the assistance of all concerned.

REFERENCES

[1] Japanese Ministry of Agriculture, Forestry and Fisheries. Annual Report on Forest and Forestry in Japan, 2018.

[2] J. Lenglet, J. Y. Courtonne, and S. Caurla. Material flow analysis of the forest-wood supply chain: A consequential approach for log export policies in France. Journal of Cleaner Production, Volume 165, 2017, Pages 1296-1305.

[3] M. Gonçalves, F. Freire, and R. Garcia. Material flow analysis of forest biomass in Portugal to support a circular bioeconomy. Resources, Conservation and Recycling, Volume 169, 2021.

[4] U. Mantau. Wood flow analysis: Quantification of resource potentials, cascades and carbon effects. Biomass and Bioenergy, Volume 79, 2015, Pages 28-38.

[5] X. Zhang, H. Yang, and J. Chen. Life-cycle carbon budget of China's harvested wood products in 1900–2015. Forest Policy and Economics, Volume 92, 2018, Pages 181-192.

[6] M. Head, A. Levasseur, R. Beauregard, and M. Margni. Dynamic greenhouse gas life cycle inventory and impact profiles of wood used in Canadian buildings. Building and Environment, Volume 173, 2020.

[7] K. Kobayashi, S. Nakajima, Y. Tsunetsugu, and T. Ikaga. Analytic study on woody material flows in view of carbon reduction: discussing utilization of building-related woody waste and forest wood residues as biomass. Journal of Environmental Engineering, 2011, Volume 76, Issue 659, Pages 91-96.

[8] K. Kobayashi, K. Wakabayashi, K. Fujitsu, and S. Taniguchi. Woody resource utilization for environmental impact reduction with focus on building industry, Journal of Environmental Engineering, 2019, Volume 84, Issue 765, Pages 1019-1027.

[9] Y. Nambu, T. Ikaga, H. Hondo, K. Kobayshi, and Y. Tsunetsugu. Developing a LCA database of wood materials, AIJ Journal of Technology and Design, 2012, Volume 18, Issue 38, Pages 269-274.

[10] British Standards Institution, BS EN 15978 Sustainability of Construction Works–Assessment of Environmental Performance of Buildings–Calculation Method, British Standards Institution, London, 2011.

[11] Japanese Ministry of Agriculture, Forestry and Fisheries, https://www.maff.go.jp/e/ (accessed 11 September 2021).

[12] Food and Agriculture Organization of the United Nations, http://www.fao.org/home/en/ (accessed 11 September 2021).

[13] Japan industrial Waste Information Center. Aggregate units and weight conversion factors for each type of industrial waste Ver.1.4. https://www.jwnet.or.jp/assets/pdf/jwnet/gyouseihoukoku_jyuuryoukanzankeisuu.pdf (Accessed 20 April 2021).

[14] Japanese Ministry of Land, Infrastructure, Transport and Tourism. Survey on Unit Requirements of Labor Force and Materials in Construction Industry, 2017, https://www.e-stat.go.jp/stat-search/files?page=1&toukei=00600040 (Accessed 9 December 2021).

[15] Japanese Ministry of the Environment. National Greenhouse Gas Inventory Report of JAPAN, 2021, Greenhouse Gas Inventory Office of Japan (GIO), http://www.nies.go.jp/gio/archive/nir/jqjm1000000x4g42-att/NIR-JPN-2021-v3.0_GIOweb.pdf (accessed 11 September 2021).

[16] Inventory Database for Environmental Analysis (IDEA). http://idea-lca.com/?lang=en (accessed 11 September 2021).

[17] 2006 IPCC Guidelines for National Greenhouse Gas Inventories; Volume 4 Agriculture, Forestry and Other Land Use. https://www.ipcc-nggip.iges.or.jp/public/2006gl/vol4.html (accessed 11 September 2021).

[18] H. Komata, S. Sakai, Y. Ishikawa, and N. Hattori. GHG emissions and energy payback ratio in utilization of forest residue as fuel for the boiler. Abstracts for ILCAJ meeting, 2010, Volume 2010, The 6th meeting of the institute of Life Cycle Assessment, Japan, Session ID A1-03, Pages 5.

[19] Japanese Ministry of Agriculture, Forestry and Fisheries. Annual Report on Forest and Forestry in Japan, 2017.

[20] H. Komata, Y. Kato, M. Takayama, and Y. I shikawa. Evaluation of Greenhouse Gas Emissions and Problems of the Methods for the Production of Lumber, Glued Laminated Timber and Plywood. Journal of the Hokkaido Forest Products Research Institute, 2010, Volume 539, Pages 1-5.

[21] R. Sikkema, M. Junginger, P. McFarlane, and A. Faaij. The GHG contribution of the cascaded use of harvested wood products in comparison with the use of wood for energy—A case study on available forest resources in Canada. Environmental Science & Policy, Volume 31, 2013, Pages 96-108.

World Conference on Timber Engineering Oslo 2023

GROUND IMPROVEMENT EFFECT OF TIMBER PILES BURIED IN SOFT CLAY GROUND

Tadashi Hara[1], Yoshitaka Kubojima[2], Hidao Kato[3], Satomi Sonoda[4]

ABSTRACT: Promoting use of timber piles for ground reinforcement requires determining the effectiveness and sustainability of ground consolidation and compaction after burial, according to soil type. In this study, from simple soundings we determine penetration resistance near timber piles buried in a soft clay layer and its change over time to analyze the degree of solidification and extent of improvement. The results of a series of field tests showed that penetration resistance in a cohesive soil layer significantly increases in the vicinity of timber piles immediately after their installation, with the consolidation area concentrically expanding over time; that buried timber piles act as drainage columns and caused consolidation phenomena deep in the ground; and that the longer the piles have been buried, the greater the effects. Because the results of this study demonstrate the effectiveness and continuity of timber piles as ground reinforcement materials, we can expect their active use in the future to promote ground disaster prevention and contribute to global warming countermeasures by storing carbon in the ground.

KEYWORDS: Ground improvement, Timber pile, Soft clay layer, Penetration resistance

1 INTRODUCTION

Wood as a civil engineering material is easy to process and environmentally friendly. In a land environment where the population is concentrated on plains, ground-related damage such as loose or sunken road surfaces and sinking or tilting of structures is likely to occur, and damage will be frequent. There is great social interest in the use of wood as a ground improvement material and its application to disaster prevention, for example as a countermeasure against ground deformation and shaking in earthquakes. In Japan, abundant forest resources were actively utilized as civil engineering and construction materials until the period of rapid economic development in the 1950s, and large amounts of timber pile were buried in applications such as pile foundations to support structures and compact reclaimed ground. Even today, many structures have exceeded a service life of 50 years, withstanding earthquakes and other natural disasters as well as providing safety and security [1]. In Venice, which is known for its timber pile foundations, many structures supported by timber piles driven into soft ground (muddy soil) are still in service some four hundred years after their construction [2].

In cooperation with a private company, the authors developed the Log Piling Method for Liquefaction Mitigation and Carbon Stock (LP-LiC) as a measure to mitigate ground liquefaction damage in the event of a Nankai Trough earthquake, which has a high probability of occurrence [3]. Artificial materials for civil engineering are easy to handle and process and are in wide use, so actively utilizing historically popular wood in civil engineering works for disaster prevention will require grasping the presence or absence of cross-sectional loss due to biodeterioration of timber piles in the ground as well as the degree and sustainability of solidification of the ground after construction, according to the soil material in question.

In a study of sandy soil with high liquefaction potential, Yoshida et al. [4] performed model tests to verify the effectiveness of log casting for soil prone to liquefaction, finding that the circumferential friction force of logs greatly affects the bearing capacity of the soil. Hara et al. [5] conducted multiple sounding tests on reclaimed sandy soil improved by the LP-LiC method to investigate the effects of soil improvement depth and casting intervals. In a study focusing on the bearing capacity of timber piles, Yamauchi et al. [6] evaluated the effect of compacting sandy soil from laboratory soil tests by collecting soil samples around pine piles that had been used as bridge foundations for about 70 years. In field loading tests, Mizutani et al. [7] investigated the bearing capacity of cedar timber piles jacked into cohesive soil layers, finding that

[1] Tadashi Hara, Kochi University, Japan, haratd@kochi-u.ac.jp
[2] Yoshitaka Kubojima, Forestry and Forest Products Research Institute, Japan National Research and Development Agency, Japan, kubojima@ffpri.affrc.go.jp
[3] Hideo Kato, Forestry and Forest Products Research Institute, Japan National Research and Development Agency, Japan, kato_hideo@ffpri.affrc.go.jp
[4] Satomi Sonoda, Polytechnic University of Japan, Japan, timber.satomi@gmail.com

https://doi.org/10.52202/069179-0113

the values for the same shape were larger for steel, concrete, and timber piles, in that order. There have thus been several studies on the effects of compaction by timber piles, mainly in sandy soils at some point in time after burial. In contrast, there have been few field studies and experiments involving clayey soil layers, and there are few examples of studies through field investigations that systematically analyze the degree of soil solidification, the extent of improvement, and sustainability of the effects of buried timber piles.

In this study, we performed simple sounding tests to determine softness or hardness near timber piles buried in a soft clay layer and then analyzed changes in properties after piles were buried. Specifically, we evaluated the superiority of timber piles as a ground improvement material by summarizing changes in ground solidification due to timber pile burial, the extent of any improvement, changes in ground solidification immediately after installation, and the durability of effects from the viewpoint of penetration resistance and the elapsed time after installation.

2 GENERAL INSTRUCTIONS OUTLINE OF THE INVESTIGATION SITE AND BURIED TIMBER PILES

The study site was located on the premises of the Forestry Research and Management Organization in Tsukuba City, Ibaraki Prefecture (Figure 1). Figure 2 shows a geologic columnar section from the study site. The target site is a developed alluvial plain, in which soft layers with N values of less than 10 as obtained by standard penetration tests are distributed. Strata where the timber pile was buried consisted of andosol as the buried soil from ground level (GL) −0.50 to −4.5 m and former topsoil surface up to GL−–2.00 m, tuffaceous clay with similar properties from GL −2.00 to −4.70 m, and fine clay mixed with a small amount of medium to coarse sand from GL −4.70 to −5.80 m. Among the tuffaceous cohesive soils, there was extremely soft, clayey blue-gray cohesive soil with $N = 2$ around GL −3.00 to −4.70 m. There was no clear groundwater table throughout the entire formation, but the old topsoil and clay layers were saturated, and borehole logs showed perched groundwater at around GL −2.65 m.

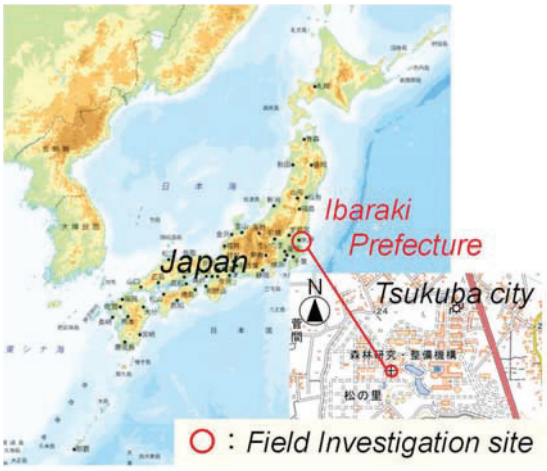

Figure.1: *Field investigation site (Tukuba city, Ibaraki Prefecture, Japan)*

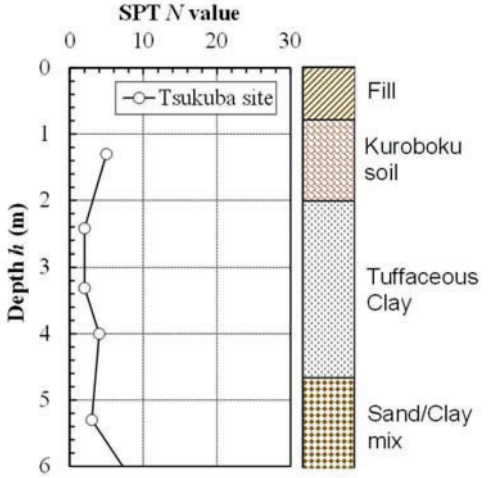

Figure.2: *Layer composition of the ground at the investigation site*

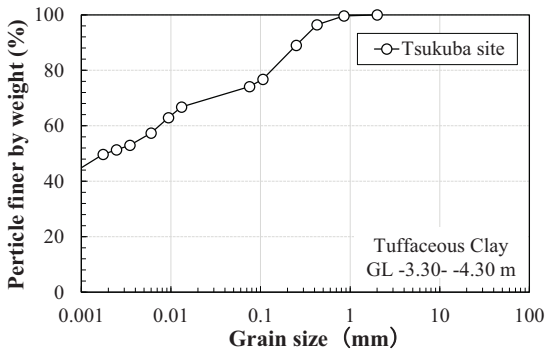

Figure.3: *Particle size distribution curve for tuffaceous clay*

Figure 3 shows a particle size distribution curve for tuffaceous clay collected from the site. The fine-grained content F_c is a large 74.1%, indicating that the soil is predominantly fine-grained. The plasticity index I_p obtained from liquid limit and plasticity limit tests was 60, indicating that the clay content was high.

Figure 4 shows a timber pile buried at the study site. Cedar logs (140 mm in diameter, 4.00 m long) from Fukushima Prefecture were used as timber piles. Young's modulus E_{ft} values for the timber piles as obtained by the longitudinal vibration method were 6.74, 6.76, 6.78, 8.21, and 9.50 GPa [8], showing some variation. The moisture content of timber piles pulled about one year after burial ranged from 74% to 149%, above the fiber saturation point at all sites and increasingly higher with greater depth than the average estimate (94%) prior to burial [9].

We buried the timber piles on 3 Dec 2020. After removing relatively hard pebbles from the ground surface at a depth of −1.00 m, we used a small pile borer (Komatsu BA-100) to continuously and statically jack-in the pile as shown in Figure 5, without prior excavation using an auger, until the pile mouth reached a depth of −0.30 m from the ground surface. The depth of the timber piles, including

https://doi.org/10.52202/069179-0113

Figure.4: *Timber piles buried in the ground*

Figure.5: *State of press-in timber piles*

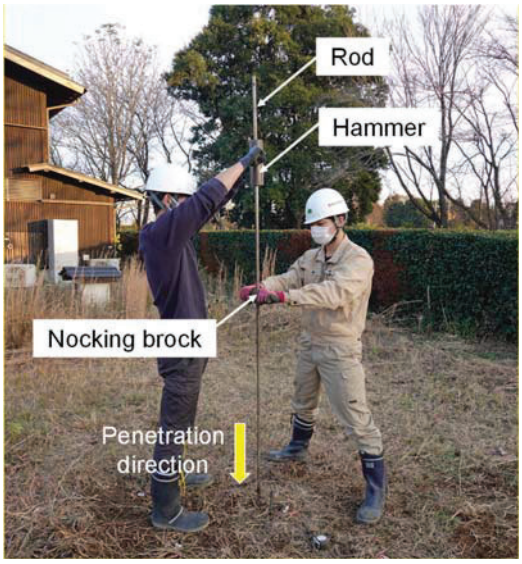

Figure.6: *Status of the Portable Dynamic Cone Penetration (PDCP) test*

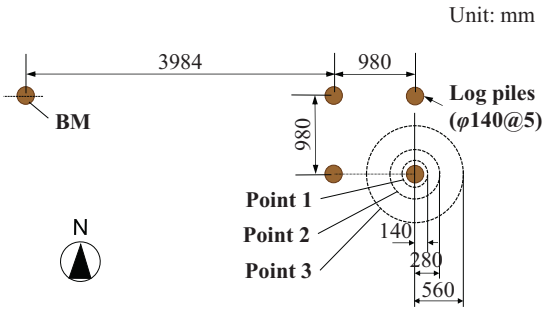

Figure.7: *Location of the build of the timber piles and place to perform PDCP test*

the pile length, was −0.43 m. Spacing between buried timber piles was about seven times the distance between centers of adjacent piles.

3 CHANGES IN PENETRATION RESISTANCE AND SOLIDIFICATION RANGE DUE TO BURIAL OF TIMBER PILES

We performed soundings using the portable dynamic cone penetration (PDCP) test [10] to determine changes in timber pile strength before and after burial. As Figure 6 shows, the PDCP test determines the degree of soil softness or hardness by determining the number of times N_d required to drive a cone attached to the tip of a rod 100 mm into the ground by dropping a 5-kg drive hammer from a height of 500 mm, allowing determination of a relative value for soil softness or hardness. Using continuous sounding blows, we obtained soundings every 100 mm from GL −1.00 to −5.50 m, which was a depth of −1.20 m below the tip of the timber pile (GL −4.30 m). As Figure 7 shows, we selected four basis measurements (BM) not subject to changes in ground properties due to the construction, located close to the sides of the timber piles, about 140 mm from the pile core (Point 1), about 280 mm away (Point 2), about 560 mm away (Point 3), and about 4 m west of where the timber pile was driven.

Figure 8 summarizes the relation between depth from ground surface h and penetration resistance N_d from the results of PDCP tests performed at Points 1, 2, and 3 one day after burial (4 Dec 2020). The same figure also shows BM results from 15 Dec 2020. The BM N_d values show that the ground at the investigation site is continuously below $N_d = 10$ up to about GL −3.50 m, indicating the characteristic properties of extremely soft clay soil, as shown in the results obtained from the standard penetration test in Fig. 2. Comparing the surveyed points, the data of Point 1 near the timber pile shows an increase at almost all layers immediately after the installation, while the data of Points 2 and 3 far from the timber pile shows an increase in a limited area, below GL −3.00 m, and a large change near GL −4.00 m, which is close to the tip of the pile. From this, we can infer that in areas where the timber pile and the ground are in close contact, clay around the

https://doi.org/10.52202/069179-0113

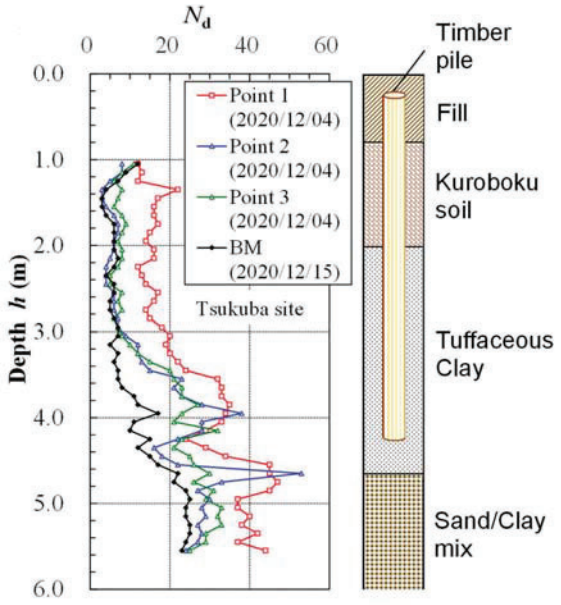

Figure 8: *Relationship between N_d value and Ground depth (1 day after build of a timber piles)*

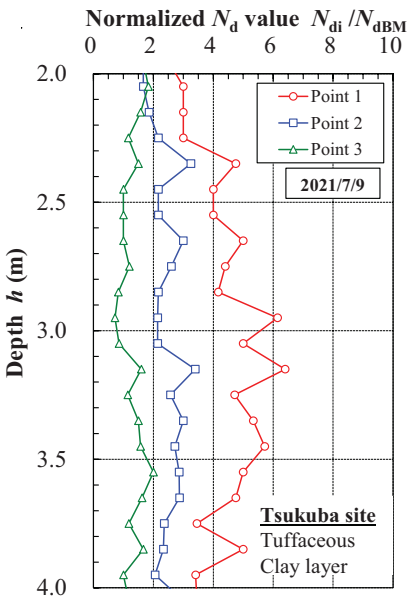

Figure 9: *Relationship between Normalized N_d value and ground depth (218 days after build of timber piles)*

circumference of the timber pile is temporarily disturbed and its strength is reduced during the timber pile burial, but near the pile and at the pile tip, interstitial water moves horizontally to the pile surface and, as seen in sandy soil, is absorbed by the timber pile shortly after installation [10], and consolidation of the clay layer occurs immediately. Values for N_d at GL −3.50 m and below show an increasing trend at all depths, whereas values from GL −5.00 to −5.50 m below the pile tip increase with depth, unlike in the standard penetration test results shown in Fig. 2. This is due to the compressive effect of the ground around the timber pile during jack-in and the increase in apparent penetration resistance due to friction between the penetration rod and the ground [11].

Figure 9 summarizes the results of penetration tests at Points 1 and 3 in tuffaceous clay (GL −2.00 to −4.00 m) about six months after burial (on 9 July 2021) with regards to the depth from the ground surface h and the normalized penetration resistance N_{di}/N_{dBM}. The normalized penetration resistance is the normalized value obtained by dividing the penetration resistance N_{di} obtained at each survey point (i = 1, 2, 3) by the BM penetration resistance N_{dBM}, and is a multiplier of the penetration resistance obtained at the reference point. The largest increase in penetration resistance of about four times is at Point 1, near the timber pile, but even at Points 2 and 3, which are far from the timber pile, the increase over time is about two times, indicating that the area solidified by pile burial extends in concentric circles.

4 CHANGES IN ELAPSED DAYS AND PENETRATION RESISTANCE

Figure 10 shows the results of PDCP tests at each study site one day (4 Dec 2020), one week (14–15 Dec 2020), three months (16 Mar 2021), six months (9 Jul 2021), about one year (30 Nov 2021), and about two year (6 - 7 Dec 2022) after the timber pile was buried, compared with results obtained on 23 Jun 2022, more than 10 years passed the burial on 15 Dec 2011. Although the results show different trends due to local ground variations, the penetration resistance after timber pile burial is globally greater than that of the BM, regardless of the burial period. The penetration resistance N_d at Point 1 shown in Fig. 10(a) increases significantly from relatively shallow depths immediately after construction, whereas those at Points 2 and 3 shown in Figs. 10(b) and 10(c) significantly increase near the timber pile tip at GL −3.00 to −4.50 m. Focusing on the passage of time after installation, at Point 1 in Fig. 10(a), N_d significantly increases immediately after burial in the clay layer near the ground surface below GL −1.50 m, and gradually increases with time after installation near the pile tip at around GL −4.00 m. The results at Point 2 in Fig. 10(b), which show a local increase of only N_d at depths below GL −3.00 m one day after burial, show a significant increase across all layers where the timber pile was buried about three months after burial, with that effect continuing for a long time as with Point 1. At Point 3 in Fig. 10(c), the increase in N_d is slower immediately after the construction than at Points 1 and 2, but gradually increases over time, and soil solidification extends across spread from the center to the tip.

Figure 11 shows PDCP test results obtained at the pile tip at GL −1.05 to −1.35 m, in the middle of the timber pile at GL −2.05 to −2.55 m, and at the pile tip GL −3.85 to −4.35 m as a function of days elapsed from installation and normalized penetration resistance, N_{di}/N_{dBM}. The plots in that figure show normalized penetration resistance values obtained every 100 mm and averaged for the depth of each section of interest. Compared with the

https://doi.org/10.52202/069179-0113

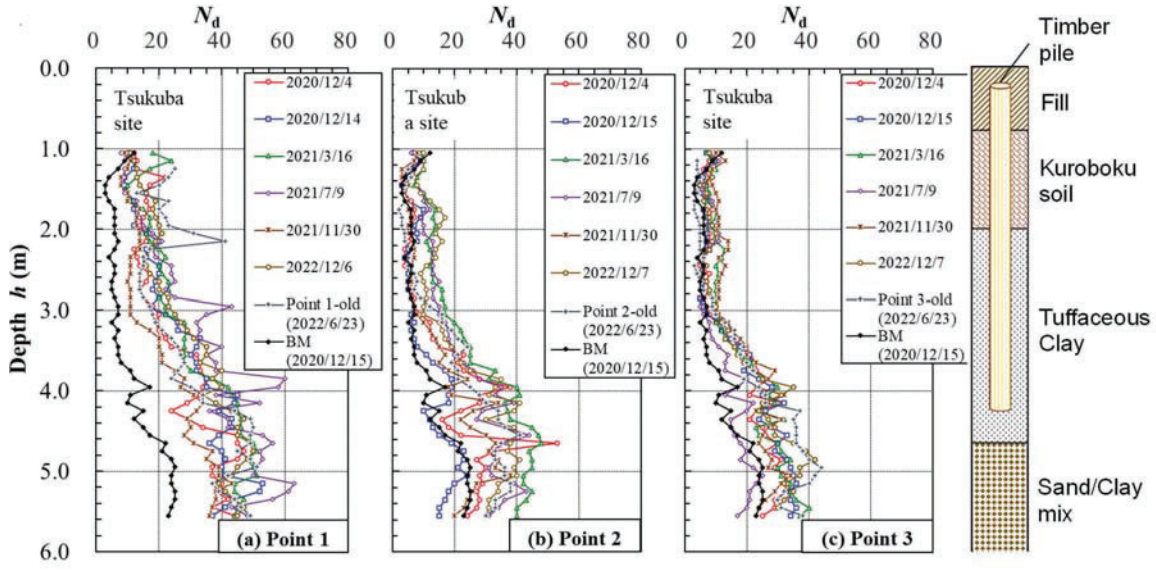

Figure 10: *Relationship between N_d value and ground depth (All investigations)*

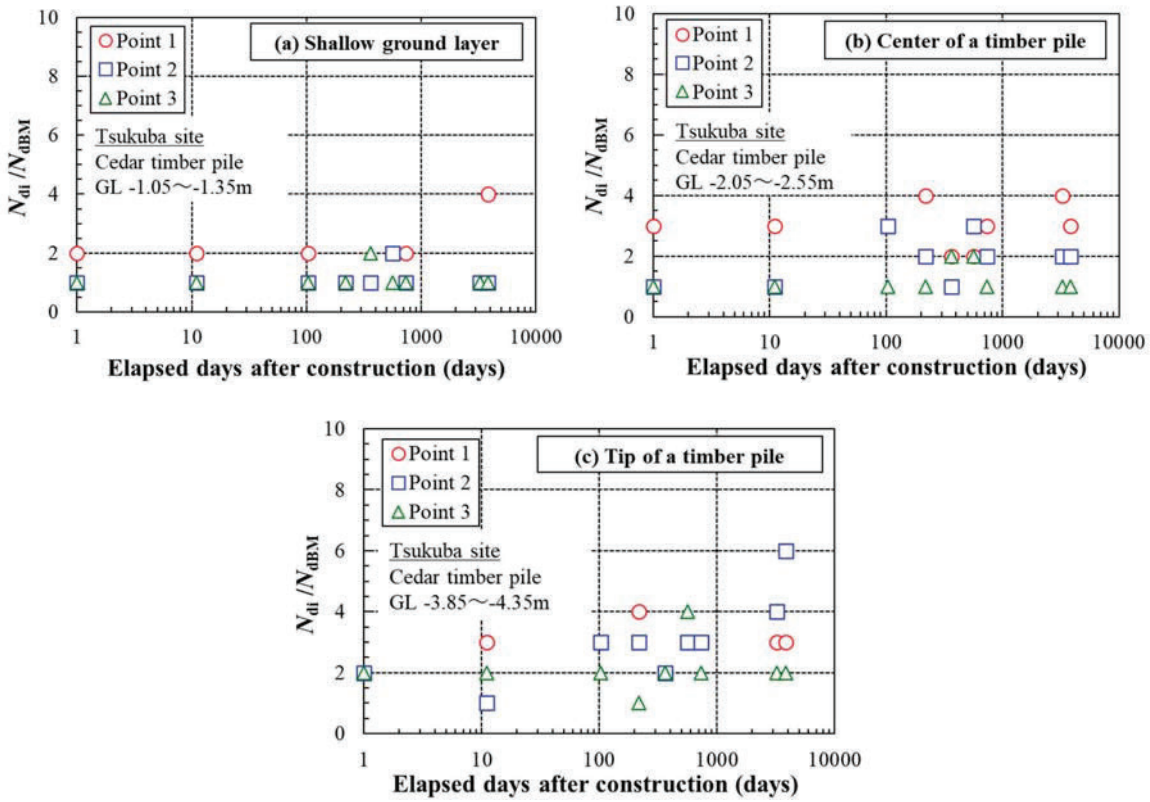

Figure 11: *Relationship between Elapsed days after construction and Normalized N_d value*

BM results, the penetration resistance increased at each depth after timber pile burial, and the effect continued throughout the burial period, but the increase in resistance was more pronounced near the pile at Point 1. Figure 11(c) shows that the increase in N_d at the pile tip was slower than in Figs. 11(a) and 11(b), but that penetration resistance rapidly increases after 200 days at Point 2, and after about ten years the resistance even at Point 3, which is farthest from the timber pile, is two times higher than the BM.

Figure 12 shows results obtained from a series of soundings as the relation between mean depth h and normalized

https://doi.org/10.52202/069179-0113

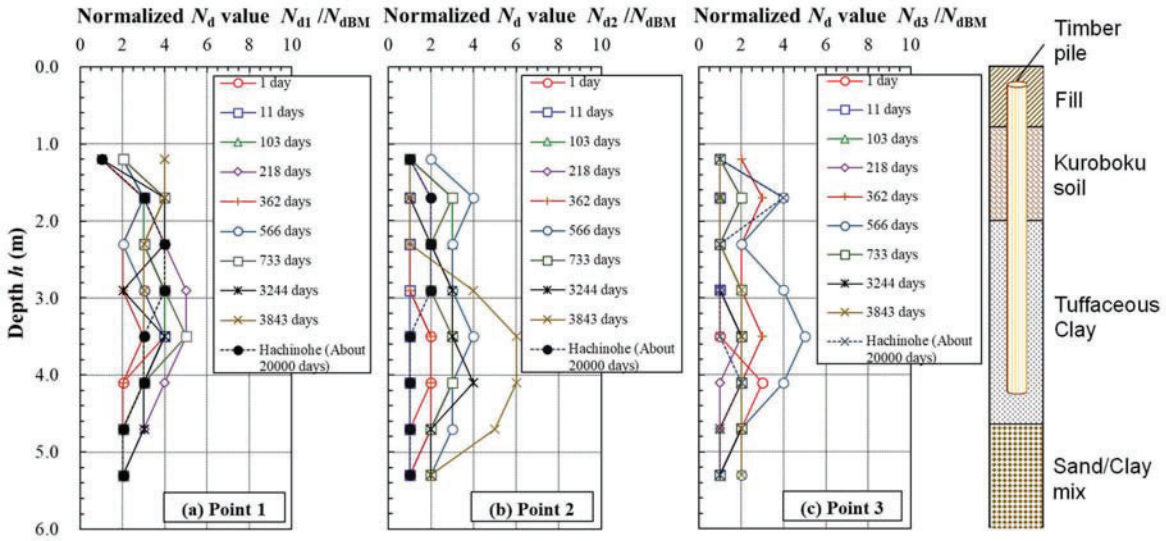

Figure 12: *Relationship between penetration resistance N_{di}/N_{dBM} and average depth (All investigations)*

penetration resistance N_{di}/N_{dBM}. The results in that figure show the normalized penetration resistance from GL −1.05 to −5.55 m as the relation between average depth and average value for normalized penetration resistance at 0.50 m intervals from GL −1.05 m near the ground surface. Although the degree of increase in the values varied depending on the surveyed location, consolidation of the soil based on the normalized penetration resistance values by timber piles embedded in clay were greatest in the center of the timber pile installation at GL −2.00 to −3.00 m for a period of about one year after construction. The trend for normalized penetration resistance about nine years after installation is different from the results from about one year after the installation. From GL −3.00 m at points 2 and 3, slightly deeper than at the center of the timber pile, the normalized penetration resistance of the piles increases in a bulbous manner, becoming greatest from the center of the pile to the tip at GL −3.00 to −4.00 m, and decreasing below about GL −4.00 m. This is presumably because in addition to horizontal interstitial water movement [11], the buried timber pile acts as a drain column that promotes drainage into the ground, where interstitial water in the deep clay layer, which has a higher confining pressure compared with the shallow layer, is absorbed by the wood, and over time consolidation develops from the pile tip. Compared with shallow layers in contact with planks, soil moisture is more easily absorbed by the timber pile in the deeper soil surrounding the wood surface at the pile tip. This accelerates consolidation, which is expected to progress over a wider area, spreading its effect to deeper soil where the timber pile is not buried. Figure 12 also shows results for a timber pile that was buried for approximately 55 years, installed using an impact method in reclaimed sandy soil with pile spacing similar to that in this study [13]. Although the characteristics of this soil are very different from that of the cohesive soil in this study, burial of the timber pile similarly tightens the soil, and the effect concentrically spreads out against the timber pile.

Increased resistance to ground penetration is considered to be influenced by the permeability of the soil type in question and the nature of soil particles. In sandy soils with high hydraulic conductivity, where liquefaction occurs more frequently than in clay soils, excess interstitial water pressure dissipates in a relatively short period at laying and consolidation effects by compaction are present immediately after burial, but this study showed that consolidation and compaction by timber pile burial continues on a yearly basis with higher effects near the timber pile.

5 CONCLUSIONS

From simple soundings, we continuously determined penetration resistance and its change in the vicinity of timber piles buried in a soft clay layer from immediately after burial, and we analyzed the degree and extent of solidification. The results of a series of field tests showed that penetration resistance in cohesive soil layers significantly increases near the timber piles immediately after their burial, that soil consolidation concentrically spreads over time, that buried timber piles act as drainage drain columns and promote the consolidation of cohesive soil, and that these effects are greater in soil in which piles have been buried for longer times. The results of model tests have shown higher water content and heightened consolidation phenomena with vicinity to timber piles, and that the vertical bearing capacity of piles increases with time since installation [14], both of which are consistent with the results of this study. This effect is not seen when using artificial materials such as steel or concrete. Consolidation of clayey soils presumably increases over time due to the combined effects of changes in soil microstructure caused by age effects and leaching of cementation materials from wood, in addition to the above-described accelerated consolidation associated with interstitial water movement into the timber pile immediately after burial. Through field surveys and laboratory tests, we will continue to quantitatively analyze factors promoting soil solidification to elucidate other advantages over artificial materials.

https://doi.org/10.52202/069179-0113

ACKNOWLEDGEMENT

This research was supported by JSPS KAKENHI Grant Number JP19k06170, 20H0305201 and 22H02408. We would like to thank the following people for their cooperation and assistance in this project: Mr. Daiki Nishimura, Mr. Toshiki Matsufuji, and Mr. Riku Ohara at Kochi University.

REFERENCES

[1] Hara, T.: Ground reinforcement technology and evaluation method using logs, *Wood industry*, 76(9), 361-365, 2021. (in Japanese)

[2] Shiono, N.: The Story of the City of the Sea ~ A Thousand Years of the Republic of Venice ~, *Shincho Bunko*, 53-55, 2009. (in Japanese)

[3] Hara, T.: Resilience Efforts in the Kochi Prefecture in Preparation for the Nankai Trough Earthquake, *Journal of Disaster Research*, 12(4), 755-765, 2017.

[4] Yoshida, M., Ishizaki, R., Kino, K., Shirota, T., Miyajima, M., Hamadda, M. and Numatra, A.: Shaking Table Tests on Improvement of Bearing Capacity of liquefiable ground by Piling Japanese Cedar Logs, P*roceedings of the 45th Japan National Conference on Geotechnical Engineering*, 1459-1460, 2010. (in Japanese)

[5] Hara, T., Sakabe, A., Numata, A., Mizutani, Y. and Ikeda, H.: Field Investigation on Liquefied Ground Reinforced by Log Piles, *Paper Reports on Use of Wood for Civil Engineering*, 11, 87-94, 2012. (in Japanese)

[6] Tamauchi, K., Miyata, T., Yamada, H., Matayoshi, K. and Matsumoto, K.: Characteristics of 70-Year-Old Timber Pile Foundation - Vertical Loading Ttest, Horizontal Reciprocal Loading Test -, *Bridge and Foundation Engineering*, 40(11), 29-46, 2006. (in Japanese)

[7] Mizutani, Y., Nakamura, H., Imano, Y. and Numata, A.: Supportability and durability of log piles in clay ground, *Paper Reports on Use of Wood for Civil Engineering*, 10, 62-68, 2011. (in Japanese)

[8] Kubojima, Y, Kato, H., Hara, T. and Sonoda, S.: Vibration phenomenon of logs buried in the ground (Part 4) Underground terminal conditions one year after construction, *The 72nd Annual Meeting of the Japanese Wood Society*, C15-P-13, 2022. (in Japanese)

[9] Kato, H., Kubojima, Y., Sonoda, S. and Hara, T.: Vibration and its application of wooden pile in the ground. Part 6. Underground moisture content for wooden piles one year after construction, *The 72nd Annual Meeting of the Japanese Wood Society,* C15-P-06, 2022. (in Japanese)

[10] Tezuka, D., Igarashi, C. and Hara, T.: Evaluation of the effect of soil and groundwater on ground improvement log piles contained preservative treated piles, *World conference on timber engineering,* WCTE 2021, WPC311,1-6, 2021.

[11] Tezka, D., Igarashi, C. and Hara, T.: Effect of change in properties of ground improvement log piles buried in the early stage, *Journal of JSCE*, 77(5), I_70-I_76, 2021. (in Japanese)

[12] Japanese geotechnical society: Ground survey method and explanation, Chapter 3 Portable cone penetration test, 274-279, 2013. (in Japanese)

[13] Hara, T., Igarashi, C., Tezuka, D., Horisawa, S. and Kato, H.: Evaluation of ground improvement effect and soundness of log piles buried in for an extended period, *World conference on timber engineering*, WCTE 2021, WPC603, pp.1-7, 2021.

[14] Suetsugu, D., Nasu, R., Koyama, A. and Fukubayashi, Y.: Effects of the shape on vertical bearing capacity of the timber pile installed in soft clay ground, *Journal of JSCE*, 77(5), I_77-I_83, 2021. (in Japanese)

https://doi.org/10.52202/069179-0113

World Conference on Timber Engineering Oslo 2023

STUDY ON ENVIRONMENT DECOMPOSITION AND STRENGTH OF CLT WHEN TEMPORARILY USED ON CIVIL ENGINEERING

Naoya Iizawa[1], Kei-ichi Imamoto[2], Chizuru Kiyohara[3], Hideyuki Nasu[4], Satoshi Onishi[5],

ABSTRACT: This study examines the civil engineering use of CLTs; if the civil engineering use of CLTs is promoted, the supply of domestically produced CLTs will increase and stabilize, and the price of CLTs will decrease. The purpose of this study is to verify the conditions of use and decomposition in a civil engineering environment. As initial tests, visual observation, 3-point bending tests, and compression tests were conducted to verify the rate of strength degradation and degradation conditions for each elapsed month. As a result, since there was a large strength fluctuation at the same moisture content in terms of the embedded yield strength, an additional verification using small specimens was conducted. The results suggest that the strength reduction in the buried specimens was due to the absorption of water during the burial period, as well as minor but significant biodeterioration.

KEYWORDS: Timber material, CLT, Civil engineering use, Degradation, Strength reduction rate, Moisture content

1 INTRODUCTION

In recent years, against the backdrop of global environmental issues, Cross Laminated Timber (hereafter, CLT) is expected to become a wood-based building material that can curb CO2 emissions and effectively utilize forest resources. In Japan, however, the post-war period saw a sharp increase in demand for lumber, but a significant shortage in the supply of domestic lumber caused the price of domestic lumber to skyrocket, leading to a massive supply of imported lumber. As a result, the demand for imported lumber increased dramatically, and the demand for high-priced domestic lumber decreased dramatically. In addition, many trees were planted before the supply of imported timber, but the dramatic increase in demand for imported timber has resulted in many the planted trees being left unattended. Furthermore, Japan has many steep mountains that prevent large heavy machinery from entering the mountains, making it difficult to secure a stable distribution volume of lumber, and the complicated transportation system has led to high intermediate costs, which have caused lumber prices to skyrocket. Therefore, CLT is currently used only for low to mid-rise buildings and subsidized projects.

Therefore, we aim to expand the use of CLTs by making them more versatile. One idea is to apply CLTs to civil engineering materials, where the amount of used is small compared to the economic scale and there is room to expand its use. To increase the demand for timber and to utilize forest resources, civil engineering use of timber is already in progress, such as the use of wooden dams and ground improvement using wooden piles. When CLTs are used for this purpose, they can be substituted for the steel plates used to prevent the ground from being dented by the weight of large heavy machinery at construction sites. Usually, steel plates are collected after temporary construction and used again, but this is very disadvantageous in terms of transportation because they are extremely heavy and dangerous to work with. In addition, some people bury it without collecting them after construction is completed, but this is a major burden on the environment. Replacing these materials with CLTs will greatly reduce the weight, thus improving safety during transportation. In addition, since timber can be returned to the soil, even if it is not recovered and buried, it will lead to a reduction in the environmental burden. If the civil engineering use of CLTs is promoted, the supply of domestic lumber will increase and stabilize, which will contribute to a reduction in the price of domestic lumber. However, it is necessary to clarify the conditions under which CLTs can be used and the conditions and length of time required for their return to the natural world, and whether they can be buried and decompose naturally.

Therefore, this study verifies the conditions of use, conditions of return to nature, and the number of years of use of CLTs, and proposes a deterioration prediction equation that serves as an index for the number of years of use. As an initial verification, the strength degradation rate and degradation condition of CLT were verified for each elapsed number of months.

[1] Naoya Iizawa, Graduate Student, Tokyo University of Science, Japan, naoya.iizawa@gmail.com
[2] Kei-ichi Imamoto, PhD. in Eng., Tokyo University of Science, Japan, imamoto@rs.tus.ac.jp
[3] Chizuru Kiyohara, PhD. in Eng., Tokyo University of Science, Japan, ckiyo@rs.tus.ac.jp
[4] Hideyuki Nasu, PhD. in Eng., Nippon Institute of Technology, Japan, hideyuki.nasu@nit.ac.jp
[5] Satoshi Onishi, M. in Eng., Nippon Institute of Technology, Japan, onishi.satoshi@nit.ac.jp

https://doi.org/10.52202/069179-0114

2 SUMMARY OF EXPERIMENT

2.1 STRENGTH TEST

A summary of the specimens is shown in Table 1. The effects on strength and degradation were tested with and without adhesive bonding at the width-bonding area. The effects of different gaps in the width joints on degradation were also examined (Figure 1). In addition, the effects of different fiber orientations on strength and degradation were also verified. For some of the specimens, the difference in deterioration was compared between when the specimens were buried in the soil and when they were left outdoors.

2.2 VISUAL OBSERVATION

The deterioration of the specimens was visually observed, and image analysis was conducted to determine the area ratio of the deteriorated portions on the specimen surface.

Table 1: *List of experimental specimens*

Specimen name	Overview
Japan Standard	Bonding the width-bonded sections
European Standard	No bonding the width-bonded sections
Gap 2.5 mm	2.5 mm gap and bonding at each width joint (Figure 1)
Gap 5.0 mm	5.0 mm gap and bonding at each width joint
Laminated timber	The lamina fibers are aligned, laminated and glued together.

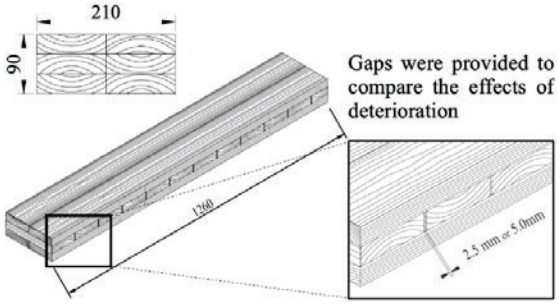

Figure 2: *Gap Specification Diagram*

2.3 EXPERIMENTAL PROCEDURE

2.3.1 BENDING TEST

Three-point bending tests were performed on a 2000 kN universal testing machine (Figure 2). The specimen was a 3-ply, 3-layer, 3-ply CLT of 1260×210×90 mm. After measuring the yield load and initial stiffness, the rate of strength loss was calculated for each elapsed month, and the strength loss and its factors were compared and discussed.

2.3.2 EMBEDDED COMPRESSION TEST

Tests were conducted using a 2000 kN universal testing machine (Figure 3). The specimen was cut out from the part with the least damage after the three-point bending test. The specimen was 210 x 210 x 90 mm in size, and a 100 x 100 mm loading plate was placed in the center of the end face. The test was conducted by loading the specimens until the flexural displacement exceeded 20 mm, measuring the load and flexural stiffness, and then calculating the strength degradation rate for each elapsed month to compare and discuss the strength degradation and its factors.

2.4 MOISTURE CONTENT MEASUREMENT

Moisture content was measured to verify the relationship between strength and moisture content. A high-frequency capacitance moisture content meter (HM-520) was used to measure the moisture content of the specimens.

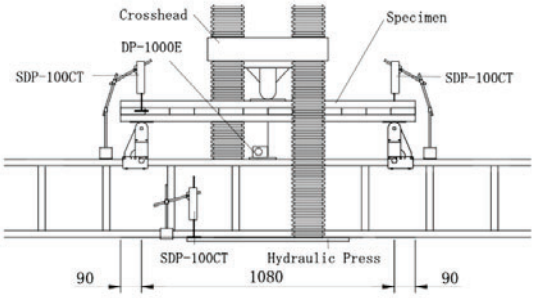

Figure2: *2000kN Universal Testing Machine and Specimen Installation Diagram.*

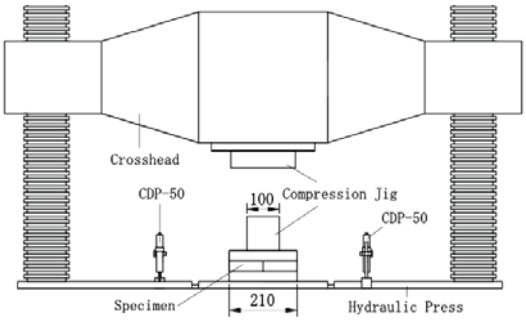

Figure3: *2000kN Universal Testing Machine and Specimen Installation Diagram.*

Table 2: *Image Analysis Result*

Lapsed month	Analysis image	Deterioration rate (%)
2month	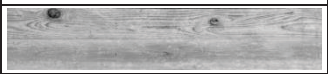	0
4month	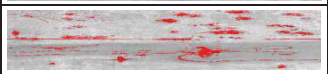	2.1
6month		4.8
8month	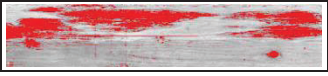	18.0

https://doi.org/10.52202/069179-0114

3 TEST RESULTS AND DISCUSSION

3.1 VISUAL OBSEVATION

The results of image analysis are shown in Table 2, which shows that the surface of the first layer of the specimen showed slight discoloration and insect bite marks starting from the fourth month. 2.1% of the specimen was discolored at the fourth month and 4.8% at the sixth month, which is a very small percentage of degradation, but it was confirmed that the longer the specimen was buried, the more the discolored areas increased. Regarding the deterioration factors, the sapwood, which is lighter in color, showed more damage, while the core timber, which is darker in color, showed less damage. The sapwood has low decay resistance, whereas the core timber has high decay resistance, and the fact that the damage looks like insect bites suggests that the cause of deterioration may be biodeterioration.

3.2 BENDING TEST RESULTS

Test results are shown in Table 3. Compared to CLT, the yield bending strength and bending stiffness of the glued laminated timber were greater. The laminated lumber is laminated in the parallel fiber direction, so all three layers exhibit performance when bending occurs, whereas the CLT is laminated in the transverse fiber direction, so the first and third layers in the fiber direction exhibit performance in bending, but the second layer in the transverse fiber direction has less resistance to bending. In fact, the section modulus for each fiber direction was calculated, and the section modulus of the second layer, which is transverse to the fiber direction, was about one-ninth that of the first and third layers, which are in the fiber direction. This characteristic is also manifested in the fracture properties: the CLT has low resistance to bending in the second layer, since the timber in the second layer often cracks (Figure 4). But no significant difference in bending stiffness of CLT was observed between the different specimen types.

Figure 5 shows the rate of decrease in yield bending strength. All the specimens showed a large decrease in the second month, but the rate of decrease fluctuated afterwards repeatedly since then. Although there was some variation, the rate of decrease in strength of the glued laminated timber was smaller than that of the CLT. Within the scope of this test, there was no clear difference in the effect of securing gaps as a route of entry for rotting fungi and termites, or of the presence or absence of gluing of the width-bonding. It was also confirmed that the strength loss of the specimens exposed outdoors was smaller than that of the specimens buried in the soil.

The specimens were removed from the soil and dried indoors for 5 days before bending strength tests were conducted. Therefore, the moisture content of the specimens at the time of the flexural strength test was different. Figure 6 shows the relationship between the moisture content at the time of measurement and yield bending strength. It was confirmed that the moisture content increased to 30% after 2 months of burial. The strength decreased significantly with moisture content up

Table 3: *Bending Test Results*

Lapsed month	Yield stress (kN)	Strength reducation rate (-)	Yield stress (kN)	Strength reducation rate (-)
	Japan Standard (Buried)		Japan Standard (Exosed)	
0	33.05		33.05	
2	13.54	0.60	23.76	0.28
4	22.18	-0.64	29.25	-0.23
6	17.01	0.23	16.52	0.44
8	19.84	-0.17	26.38	-0.60
	European Standard		Gap 2.5 mm	
0	28.55		24.79	
2	13.89	0.55	15.35	0.32
4	15.37	-0.11	16.32	0.15
6	13.02	0.16	15.62	0.04
8	20.77	0.60	12.06	0.23
	Gap 5.0 mm		Laminated timber	
0	26.20		57.16	
2	17.73	0.32	39.97	0.30
4	15.06	0.15	42.56	-0.06
6	16.74	-0.11	40.53	0.04
8	18.99	-0.13	38.77	0.04

Figure 4: *Fracture Properties*

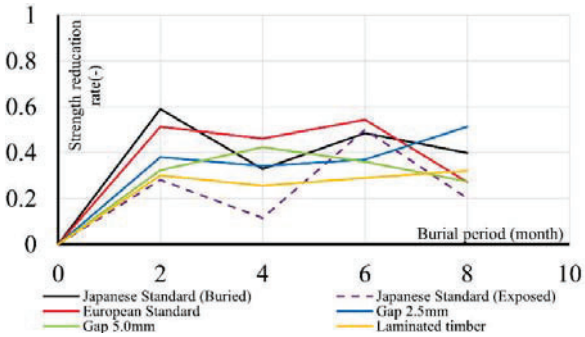

Figure 5: *Yield Bending Strength Reduction Rate*

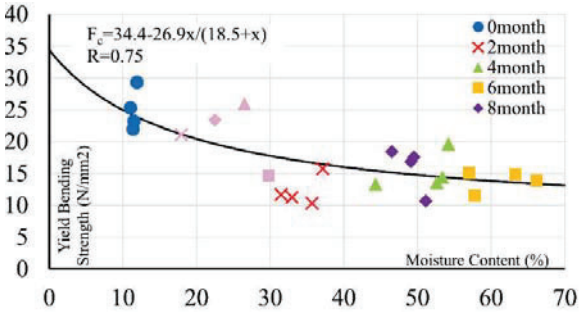

Figure 6: *Yield Bending Strength - Moisture Content*

https://doi.org/10.52202/069179-0114

to the fiber saturation point of 30%, but the decrease in strength with increasing moisture content tended to be small for moisture contents above 40%. The coefficient of variation of yield strength is 17% according to Sasaki et al. [4], and the image analysis results in Table 2 suggest that the factor of yield strength reduction shown in Figure 6 is due to the absorption of moisture during the burial period, and the influence of biological deterioration such as decay fungi and insect damage could not be confirmed within the scope of this test.

3.3 RESULTS OF THE COMPRESSIVE TEST

The test results are shown in Tables 4. Unlike the bending strength properties, there was no significant difference between the glued laminated timber and CLT specimens in terms of the embedded stiffness. The percentage of decrease in yield strength under shear (Figure 7) shows that the percentage of decrease in yield strength under shear was larger than that of yield bending strength for all the specimens. Therefore, in outdoor use of CLTs, it is necessary to consider the decrease in the embedded strength during the service period.

In terms of the embedded yield strength, the rate of strength reduction tends to be greater for glued laminated timber than for CLT. The parallel fiber lamination of the glued-laminated timber may have weakened its resistance to compression. A comparison of fracture properties (Figure 8) shows that timber cracking was concentrated in the first layer of CLT, whereas cracking also occurred in the second and third layers of glued-laminated timber. In addition, in the glued-laminated timber, the timber in the upper layer was embedded into the timber in the lower layer, which is thought to be one of the reasons for the reduction in bearing capacity that is assumed to occur when the timbers are stacked in the parallel direction to the fibers.

Next, Figure 9 shows the relationship between moisture content at the time of the strength test and the yield strength of the specimens with a 2.5 mm gap. As with the yield bending strength, the embedded yield strength decreased significantly with decreasing moisture content up to 30%, the fiber saturation point, and the rate of change in strength with increasing moisture content was small when the moisture content was 45% or higher.

The coefficient of variation of the embedded yield strength is 12% according to Ido et al. [5], and the variation of

the embedded yield strength in this test is large for the same moisture content. Therefore, in the next section, the effect of moisture content on the embedded yield strength of undamaged solid timber and CLT specimens will be examined.

4 RELATIONSHIP BETWEEN EMBEDDED YIELD STRENGTH AND MOISTURE CONTENT

4.1 VERIFICATION USING SMALL SPECIMENS

The change in compressive strength under penetration

Table 4: *Compression Test Results*

Lapsed month	Yield stress (kN)	Strength reducation rate (-)	Yield stress (kN)	Strength reducation rate (-)
	Japan Standard (Buried)		Japan Standard (Exposed)	
0	45.36		45.36	
2	21.16	0.54	19.32	0.58
4	10.62	0.50	7.74	0.60
6	9.90	0.07	31.42	-3.06
8	13.76	0.39	17.84	0.43
	European Sandard		Gap 2.5 mm	
0	31.58		35.66	
2	32.82	-0.07	15.66	0.54
4	7.72	0.76	9.46	0.40
6	22.27	-1.88	13.65	-0.44
8	16.76	0.25	8.74	0.36
	Gap 5.0 mm		Laminated timber	
0	29.94		40.04	
2	14.32	0.52	6.88	0.83
4	7.72	0.46	6.76	0.02
6	17.43	-1.26	14.04	-1.07
8	16.90	0.03	8.67	0.38

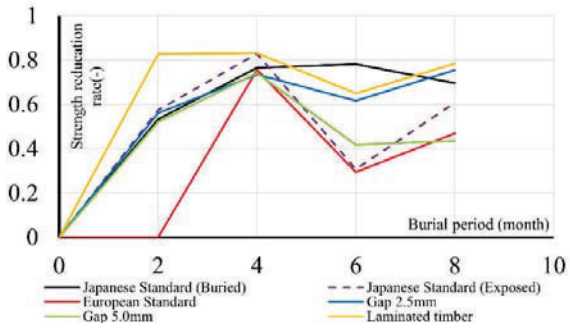

Figure 7: *Embedded Yield Strength Reduction rate*

Figure 8: *Fracture Properties*

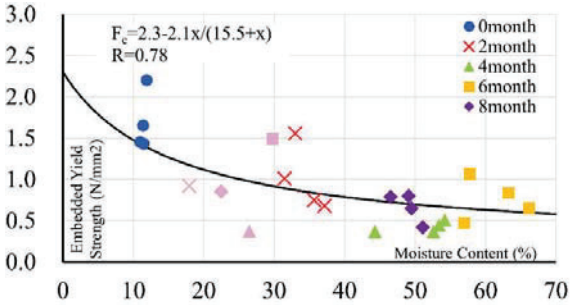

Figure 9: *Embedded Yield Strength - Moisture Content*

https://doi.org/10.52202/069179-0114

was verified using solid Japanese cedar specimens with different moisture contents. All specimens were dried in a constant-temperature room at 40°C and allowed to absorb water naturally to keep the moisture content in the range of 0% to 70%. Since it takes time for the specimens with high moisture content to absorb water, the specimens were vacuumed for 1 hour, allowed to stand for 1 hour after water injection, and then recompressed for 1 day, as shown in Figure 10. The test was conducted using a 50 kN table-top precision universal testing machine with a 10×10mm loading plate. The test was displacement-controlled, and force was applied at a rate of 2 mm/min. The test was terminated when the force reached 5% of the edge length. The embedded yield strength was calculated, and the coefficient of variation was calculated from the mean value and standard deviation to evaluate the variation. The results are shown in Table 5 and Figure 11. While the embedded yield strength decreases significantly as the mass water content changes up to the fiber saturation point of 30%, the strength decrease tends to be smaller when the mass water content is 40% or higher. According to Sawada [6], the coefficient of variation of the embedded yield strength of solid SUGI lumber is estimated to be around 20% to 30%, and in this test, the coefficient of variation of the embedded yield strength was 5 to 20%, which is within the range of variation. Although there was some variation in vacuum water absorption, many of the specimens were within the variation range, suggesting that they could be evaluated in the same manner as the other specimens.

Using these test results as a baseline, similar tests were conducted on smaller CLT specimens in the next section to verify the variation of the yield strength due to the change in moisture content.

4.2 VERIFICATION USING CLT SMALL SPECIMENS

The effect of moisture content on the yield strength of CLT is verified by using a small CLT specimen. The test specimens were 100 mm square pieces of 3-ply CLT after the flexural strength test used in Section 3.2. The test specimens were prepared in the same way as the small specimens, with moisture content ranging from 0 to 70%, and vacuum water absorption was performed for moisture contents of 50% to 70% based on the results of the small specimens. The test method was the same as for the small specimens, and the size of the loading plate was 40 × 40 mm. As with the small specimens, the yielding strength was calculated, and the coefficient of variation was calculated from the mean and standard deviation of the yielding strength to evaluate the variation.

Table 6 and Figure 12 shows the test results. Like the results of the small specimen described above, the yield strength of the specimen decreased significantly as the moisture content increased up to 30%, the fiber saturation point, but the decrease in strength tended to be small when the moisture content increased above 40%. Only one specimen had high embedded yield strength in the moisture content range of 15-30% and 30-50%, but this is due to the presence of knots on the compression surface.

Table 5: *Small Specimens Results*

Parameter		Embedded Yield Strength (N/mm^2)	Moisture Content (%)
0%	Average	1.68	0.50
	Standard Deviations	0.32	0.71
	Variation Coefficient (-)	0.19	1.44
15~30%	Average	0.91	22.71
	Standard Deviations	0.16	3.77
	Variation Coefficient (-)	0.18	0.17
30~50%	Average	0.75	37.92
	Standard Deviations	0.16	4.43
	Variation Coefficient (-)	0.21	0.12
50~70% (Vacuum Suction)	Average	0.76	68.36
	Standard Deviations	0.30	0.95
	Variation Coefficient (-)	0.40	0.01
50~70% (Natural Suction)	Average	0..74	66.39
	Standard Deviations	0.06	0.81
	Variation Coefficient (-)	0.09	0.01

Figure 10: *Vacuum Suction*

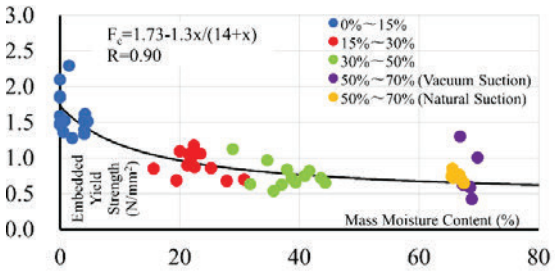

Figure 11: *Embedded Yield Strength - Moisture Content*

The specimens with vacuum-absorbed water also showed some variation. One of the reasons for this may be that CLTs are subjected to a greater load than solid timber because the expansion of CLTs is inhibited by the adhesive, which is a factor in the expansion of timber as a result of water absorption. The adhesive used was a water-based polymer isocyanate adhesive, but the effect of the adhesive needs to be further investigated.

https://doi.org/10.52202/069179-0114

Next, a comparison was made with the small specimens and the strength tests in Section 3, considering the dimensions of the specimens and the pressurized plate, and the yield strength of the specimens was calculated using the following equation (1).

$$Fc = Fy / (b \cdot l) \quad (1)$$

where Fc=Caving-in yield strength (N/mm^2), Fy=Yield load (N), b=Specimen width (mm), l=Length of pressurized plate (mm).

Compared to the small specimen, the yielding strength of this test was slightly higher than that of the small specimen. This is due to the orthogonally stacked CLT fibers. The relationship between the embedded strength and the moisture content in the soil test (Figure 13) is compared. Since the slopes of the approximate formulas are similar before the fiber saturation point, the strength reduction of the buried specimens is due to the absorption of water during the burial period. On the other hand, after the fiber saturation point, the strength difference is larger, suggesting that biodeterioration, although small, has affected the strength of the buried specimens. However, due to the small number of specimens, the approximate formula needs to be further studied.

5 CONCLUSIONS

The findings of this study are as follows.

1) Although differences in strength and stiffness were observed between laminated timber and CLT, no differences in specifications between CLTs were identified at this time.

2) Visual observation suggested the possibility of biodeterioration, but no effect of biodeterioration on the strength of the specimens was observed within the scope of the strength tests in Section 3.

3) The results of the compressive test on small specimens of solid timber and CLT indicated that the strength loss of the buried specimens was due to the absorption of moisture during the burial period as well as to a small amount of biodeterioration

Table 6: *CLT Small Specimens Results*

Parameter		Embedded Yield Strength (N/mm^2)	Moisture Content (%)
0%	Average	2.48	0
	Standard Deviations	0.28	0
	Variation Coefficient (-)	0.11	0
15~30%	Average	1.40	29.20
	Standard Deviations	0.59	8.99
	Variation Coefficient (-)	0.42	0.31
30~50%	Average	1.48	33.28
	Standard Deviations	0.66	5.83
	Variation Coefficient (-)	0.45	0.18
50~70% (Vacuum Suction)	Average	1.12	67.11
	Standard Deviations	0.33	1.13
	Variation Coefficient (-)	0.30	0.02

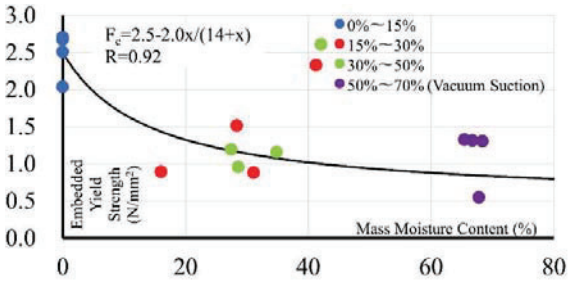

Figure 12: *Embedded Yield Strength - Moisture Content*

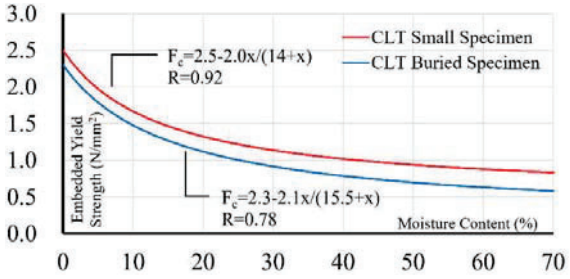

Figure 13: *Approximate Formula Comparisons*

REFERENCES

[1] N.Iizawa et al.; STUDY ON ENVIRONMENT DECOMPOSITION AND STRENGTH OF CLT WHEN TEMPORARILY USED ON CIVIL ENGINEERING, VERIFICATION OF STRENGTH REDUCTION RATE DEGRADATION FACTORS OF CLT. Collection of the Proceedings of the Annual Meeting of the AIJ 2022

[2] S.Onishi, H.Nasu ; STUDY FOR PRACTICAL USE OF NAIL-LAMINATED-TIMBER, EFFECTS OF GAPS AMONG THE LAMINAS DURING MANUFACTURING. Collection of the Proceedings of the Annual Meeting of the AIJ 2021.9

[3] M.Yamada, et al.; FUNDAMENTAL STUDY ON STRNGTHENING OF TERMITE INDUCED DETERIORATED TIMBER MEMBER WITH RESIN. NO.1 COMPRESSION TEST AND BENDING TEST. Collection of the Proceedings of the Annual Meeting of the AIJ 2021.

[4] T.Sasaki et al.; INFLUNCE OF LAYER COMPOSITION AND LAMINA GRADE ON IN-PLANE BENDING PERFORMANCE OF CLT. Collection of the Proceedings of the Annual Meeting of the AIJ 2015.

[5] H.Ido et al.; CAVING STRENGTH PERFORMANCE OF CROS LAMINATED TIMBER (CLT) MANUFACTURED USING JAPANESE CEDAR. Journal of the Japan Society of Wood Science and Technology Vol60, N0.1, p.16-22(2014)

[6] M.Sawada ; DEFORMATION BEHAVIOR OF WOOD. Materials Science Society of Japan, Vol.32, No.358, p.838-847(1983)

https://doi.org/10.52202/069179-0114

World Conference on Timber Engineering Oslo 2023

DEVELOPMENT OF FUTURE-ORIENTED CONCEPTS FOR AGRICULTURAL CONSTRUCTION WITH WOOD

Carina Hartmann[1], Özlem Özdemir[1], Annette Hafner[1]

ABSTRACT: This paper presents the interdisciplinary project "Development of future-oriented concepts for agricultural construction with wood - from planning to deconstruction" (ZukunftLaWiBau). The aim of this project is to increase the share of agricultural buildings in wood construction by means of future-oriented concepts, taking into account technical and socio-economic issues. The result of the project will be a planning guide "Agricultural Building with Wood in the 21st Century". The guide includes current issues of climate protection, animal welfare, regional value creation, durability of wood as a building material, resource efficiency and economic viability as cross-sectional fields. An interdisciplinary research team is working on the issues in a holistic manner. In the following, this interdisciplinary cooperation and the goal will be explained in more detail.

KEYWORDS: Agricultural buildings, timber buildings, wood, circularity, sustainability

1 INTRODUCTION

The goal of becoming nearly emission-free in the building sector by 2045 is important and ambitious, not only because the sector, which includes the construction, maintenance and operation of buildings, is responsible for around 40 % of all greenhouse gas emissions in Germany. Particularly in agricultural construction, large potential is seen in the use of wood, a regionally available and already historically used raw and as construction material. In Germany, the diverse, sustainably managed forests and domestic wood are currently not reflected enough in agricultural construction. The timber construction quota in agricultural construction in Germany was only 35% in 2021 [1]. The use of wood in agricultural construction has been obvious for a long time, as farms often also own forests and could thus utilize their own wood.
To ensure sustainable land management, regional cycles should be included and made usable. An economic evaluation in this respect has been lacking up to now.

2 PROJECT

The use of wood in agricultural construction has a very long tradition. However, in recent decades, the importance of wood decreased compared to other building materials [1]. Regionally, there are differences in the size and typology of the category grouped as agricultural buildings. From the data of the Federal Statistical Office on new non-residential buildings, it is to recognize that there is a tendency for agricultural buildings to be larger in the north and smaller in the south, but that the number of buildings in the south is significantly higher. Farmers traditionally often own (small) private forests, which could provide wood supplies at least for their own needs. Various studies show that the use of domestic wood raw materials can consolidate regional value chains in rural areas [2]. In the current structures, however, there are too few incentives and implementation possibilities to use this potential for own buildings.

The difficulty for the application of wood in agricultural construction, especially regarding the use of spruce in agricultural buildings without preventive chemical wood preservation measures (according to DIN 68800), could already be reduced within the research project of the TUM and the LfL "Agricultural buildings in timber construction without preventive chemical wood preservation (use class 0" [3]. Within the scope of the project, it could be shown that, with a few exceptions (potato storage halls), a classification of all forms of use in livestock and storage through constructive measures, in conjunction with the recommendation to use kiln-dried wood, seems possible in service class 0 (according to DIN 68800). However, the proof of these positive, but still selective results for the breadth of the typologies of wood structures used in agricultural construction in Germany is still pending. Technically, wood can be used in most agricultural buildings, but there are additional requirements for individual components.

However, a central open question with regard to the sustainable use of wood or wood products in livestock farming is the predominantly negative assessment of the hygiene status on the part of the official veterinarians As representatives of public interests in the context of the building permit procedure, but also in their control function for current facilities, they repeatedly complain about barn facilities made of wood or point out that they must be removed and burned in the event of an epidemic. In some cases, requirements are placed on the surface finish that do not comply with the relevant hygiene regulations.

[1] Carina Hartmann, Özlem Özdemir, Annette Hafner, Department of Civil and Environmental Engineering, Resource efficient building, Ruhr-University Bochum, Germany, carina.hartmann@ruhr-uni-bochum.de

https://doi.org/10.52202/069179-0115

There is also uncertainty about the storage of harvested products due to requirements from the relevant regulations. As a result, farmers who build new buildings or remodel existing ones often opt for plastic or steel. Scientific studies on the hygiene status of tools and wooden surfaces (e.g. cutting boards in large slaughterhouses), on the other hand, confirm that certain types of wood have the best germ-inhibiting or killing effect. However, in view of the relevant guidelines, this is obviously not sufficient for the transfer of these results into practice. The situation is aggravated by the fact that no research projects have been carried out on this issue in the last 20 years.

A continuing obstacle is the lack of a broad database for the environmental assessment of agricultural buildings and their use of resources. This is necessary in order to make the data usable for calculating the product store of carbon in wood products and thus to be able to meet the requirements of agricultural construction in the 21st century with regard to climate protection. The project "Development of forward-looking concepts for agricultural construction with wood - from planning to deconstruction (ZukunftLaWiBau)" therefore aims to increase the proportion of agricultural buildings in timber construction again, taking into account technical issues. To this end, planning principles for agricultural buildings are being brought into the 21st century on the basis of model buildings. For this purpose, planning principles for agricultural buildings are used on the basis of a small and a large hall. Regional value chains in rural areas will be taken into account, current issues of hygiene and wood products will be considered and possibilities to use the potential of existing wood will be proposed. In addition, the database on climate and resource protection of agricultural buildings made of wood will be updated and deepened and made usable for the Charter for Wood 2.0 process in Germany.

The result of the project is a planning guide "Agricultural construction with wood in the 21st century". The guide incorporates current issues - climate protection, animal welfare, regional value creation, durability, resource efficiency and economic viability - as cross-cutting fields. Since the subject area is so broad and the expertise of very different stakeholders is needed, a structure with interlocking work packages was developed to be able to answer all questions holistically (see figure 1).

3 PROJECT PARTNERS AND WORK PACKAGES

An interdisciplinary team of project partners is working together to develop a holistic guideline for future agricultural construction. This team consists of the Chair of Resource Efficient Construction at the Ruhr University Bochum (RUB), the Technical University of Munich with the chair wood Science (TUM-WS) and the chair Timber Structures and Building Construction (TUM-TS). Furthermore the Bavarian State Research Center for Agriculture with the Institute for Agricultural Engineering and Animal Husbandry, the working group Agricultural Construction, the Department of Veterinary Medicine, Institute for Animal Hygiene and Environmental Health at the Free University of Berlin and the Friedrich-Loeffler-Institute with the Federal Research Institute for Animal Health are involved.

In order to deal with the interdisciplinary topics in a holistic manner, work packages (WP) were developed (see figure 1). The results from these work packages are linked in the planning guide. The starting point (WP1) is an integrated inventory analysis and data collection of the main building types currently used in agricultural construction in Germany (what is currently being built, including a map of regional differences in construction methods). These data form the basis for a comprehensive analysis in the following areas: Status-quo Analysis (WP 1), Life cycle assessment (LCA) buildings (WP 2), resource potential (WP 3), wooden products (WP 4), hygiene (WP 5), durable constructions (WP 6), design for reuse (WP 7) and economic structures (WP 8). The results of these analyses, as well as the suggestions for improvement derived from them, will be discussed and synthesized. The results from analysis, optimization, discussion and consolidation will be incorporated into the guide .

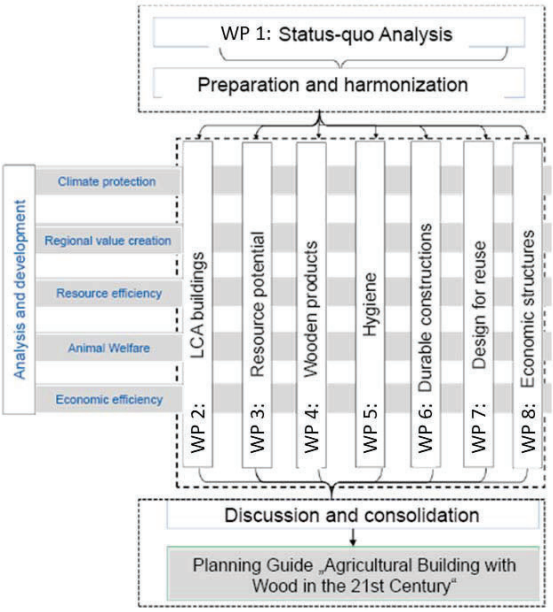

Figure 1: *Work steps within the framework of the development of the design catalog and associated work packages3.1 Status-quo Analysis (WP 1, LfL)*

https://doi.org/10.52202/069179-0115

3.1 Status-quo Analysis (WP 1, LfL)

In WP 1, typical procedures in agricultural animal husbandry and storage in Germany are recorded and systematized for status quo recording and compared with the associated building typologies and building geometries. In the process, not only utility buildings in timber construction are recorded, but also buildings and barn facilities in all otherwise common materials (e.g. concrete, brick, steel, plastic). The resulting catalog serves as the basis for all further work packages of the project partners. Starting with the compilation and allocation/categorization of inventory data (including planning and construction documents, publications, consulting documents) on agricultural buildings for livestock and storage (from the 1970s onwards), the second step is an initial assessment of the substitution potential for non-wood materials with wood products or a comparison of the same processes/building typologies in non-wood construction or wood construction. In the following, the entire data material will be processed (in electronic form) for further use in the following work packages and the selection of sample buildings and processing for further use, especially in WP 2.

3.2 LCA buildings (WP 2, RUB)

In WP 2, the functional unit "building" with its system boundaries is defined in accordance with DIN EN 15978 and the systematics for agricultural building types is adapted and defined by all project partners. For this purpose, the necessary building material data will be updated if necessary and transferred to the LEGEP software and the results on building level will be generated in a calculation program and validated by a critical review according to DIN EN ISO 14040 and ISO TS 14071. The life cycle assessments necessary for calculating the environmental impact of timber buildings and their alternatives in the defined market segment as well as estimating possible efficiency improvements will be calculated. Scientific publications will be developed over the duration of the project, continuously updated data from ÖKOBAUDAT will be entered into the calculation software. The system boundaries and the functional unit for LaWiBau will be defined and standardized according to DIN EN 15978. Data for data acquisition and mass determination of functionally identical LaWiBau are procured and the calculation software LEGEP is adapted accordingly. In the next step, data is collected to form the data basis and enlarge the building data pool. The creation of the data basis takes place by the data acquisition and by the mass determination of functionally identical agricultural buildings. For this purpose, building data from different sources must be obtained, compiled and standardized. Different reference sources, such as the building pool of the LfL, KTBL data sets or also construction plans of already implemented agricultural farm buildings, which contain a proportion of wood in the construction, form the building data pool. The differences in use (e.g. dairy barns, horse barns, machine sheds, etc.) are taken into account in the categorization of the LaWiBau building pools. The LCA of the procured data are calculated over the entire building life cycle using the LEGEP calculation software and subsequently validated via a critical review. The environmental parameters such as GHG emissions, primary energy consumption, raw material use, etc. are worked out and presented for the individual types of use. The existing LaWiBau buildings are mostly formed by hybrid constructions in the existing HolzImBauDat building pool. In a detailed investigation, the environmental influence of the mineral material concept of individual building components on the building will be determined. For example, the influence of individual steel columns (or reinforced concrete columns) in wooden barns on the load-bearing environmental balance is clarified in comparison with an overall structure in wood. The aim is to create economical load-bearing structures while taking environmental aspects into account.

As a result of this work package, the substitution potential in the building sector is presented, which is the savings in greenhouse gas emissions that result when a functionally equivalent wooden building is constructed instead of a conventional building. This is based on standard-compliant calculations of life cycle assessments at product and building level. It also shows the carbon storage, which shows the storage of biogenic carbon in the wood products, represented as global warming potential (GWP) biogenic.

3.3 Resource potential (WP 3, TUM-WS)

In work package 3, resource potentials, in particular of the farmers' own rural forest, are identified for agricultural construction with wood. Existing and potential value chains (Fig. 2) will be analyzed with regard to structure and success factors and evaluated by means of environmental (life cycle assessment) and economic (including value creation) indicators as to whether and how construction with wood can be strengthened, in particular through the involvement of regional actors. Example regions for the analysis of value chains are available through an master thesis of the TUM-HFM (Oberallgäu/Bavaria, Hochsauerlandkreis/North Rhine-Westphalia, Vulkaneifel/Rhineland-Palatinate, here with focus on buildings for dairy farming) as well as further contacts through the LfL (Saxony etc.).

https://doi.org/10.52202/069179-0115

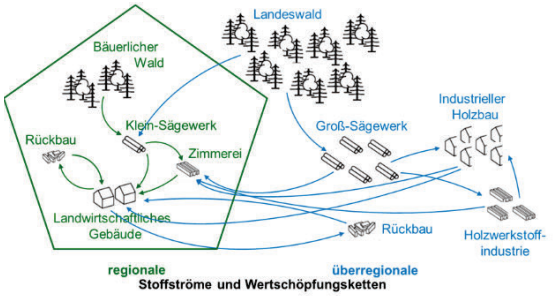

Figure 2: *Illustration of possible value chains for agricultural construction with wood (using Wegener et al. 2010).*

The basic characterization of agricultural farms will be carried out together with WP 1 nationwide with regard to their needs and possibilities of building with wood, using the annual nationwide survey of the test farm network of the BMEL (by means of an additional short questionnaire with regard to characteristic values of forest area, wood types, agricultural building types, priorities in the choice of building material) as well as the annual telephone survey of the small private forest of state authorities in several federal states. From this information, farms in sample regions will be selected and subjected to in-depth quantitative and qualitative analysis. The resource potentials are determined in the example regions, in particular for the farmer with rural forest ownership, by comparing the wood supply (wood species, quantities, assortments), and the previous raw material use with the current raw material/wood use and the wood demand for future construction with wood of the example farms. Data sources are the Federal Forest Inventory (BWI), state statistics, data collections for the small private forest in adherence to the methodology of Wilnhammer et al. [4], as well as queries for realized and planned agricultural buildings (categorization), raw material use of selected building categories (wood species, building materials, components, quantities, costs), and implementation of timber construction (raw material, building material origin, implementing wood processing and timber construction companies). With regard to the analysis of the value chains for agricultural construction, the actors of the value chain used so far as well as the material flows are first determined and interviews are conducted with regard to success factors and obstacles. In doing so, the possibilities of integrating regional actors as well as actors not yet considered are analyzed. For the environmental assessment of the value chains, the regional conditions of the production of the wood products including transport routes are taken into account [5] In this way, possible advantages of the regional value chain can also be considered in the life cycle assessment of the buildings. For the economic evaluation, the cost accounting of local/regional actors (mainly farmers with their own forest, carpentry shops) will be included in cooperation with WP 8 and compared with those of supra-regional actors (mainly state forest, industrial timber construction companies). Based on this, the (supra-)regional value added is calculated [6]. Finally, the potentials of building with own or regional wood will be presented as well as recommendations for an optimization of the value chains especially in the regional context and the feasibility for farmers.

As a conclusion and recommendations for action of this work package, the statement can be made that, in principle, regional, often also farm-owned wood is available for agricultural construction in Germany. The use of other tree species than spruce for the constructive and also non-constructive area offers regionally specific potentials, but due to the regional differences for the promotion of agricultural timber construction a regionally specific approach is necessary.
Furthermore, it can be said that the use of own wood in agricultural construction often shows a cost-efficient and sustainable solution with high potential and especially smaller construction projects can be more easily realized with own / regional wood. In order to ensure the profitability of using own wood, the provision of wood from own forest has to be recognized as eligible. Important success factors in agricultural timber construction are competent and regionally available actors in the value chain as well as support and technical expertise from private and public construction consulting and planning. Building with own / regional wood increases the regional added value by involving a large number of actors, secures jobs and income in rural regions and promotes climate protection by reducing transport distances.

3.4 Wooden products (WP 4, TUM-WS)

Work package 4 compiles the properties for wood products necessary for the special conditions of agricultural construction in a catalog. Existing knowledge as well as experiments and field tests for missing knowledge, especially for hardwood building materials, as well as new materials are used. For the analysis of the suitability of different wood species or wood products and their material properties with respect to specific requirements against gaseous, liquid and, if applicable, mechanical loads in the respective agricultural structures, literature as well as previous experiences of farmers are used for traditional wood products. With regard to the assessment of the use of innovative wood products and materials, not only from spruce, but also from pine (possibly larch and Douglas fir) or hardwood (especially oak and beech), for which no knowledge is yet available with regard to chemical-aggressive stress, laboratory experiments or test methods are used [7]. In worst case scenarios, samples are stored in model atmospheres and the surfaces are examined (e.g. pH, ATR-FTIR or microscopically) or emission measurements are carried out, e.g. by means of chemical sorbers and subsequent pyrolysis GC/MS. Since laboratory tests cannot always represent real-life conditions, field tests (on-site monitoring) are conducted to investigate the durability of wood structures made of selected wood products in agricultural environmental conditions (e.g. glulam, cross-

https://doi.org/10.52202/069179-0115

laminated timber, laminated funicular timber, cement-bonded particleboard or thermowood) under different uses (bay/partition walls as well as exterior walls and ceilings). Based on the results of the laboratory and field tests/monitoring, farmers' previous experience with building with wood, and information from the literature, the advantages and disadvantages of each type of wood or wood-based material and their area of application are compiled in a wood type and product catalog based on selected criteria like the durability class for agricultural construction.

3.5 Hygiene (WP 5, FLI, FUB)

In work package 5, the properties of wood building materials are tested with regard to hygiene requirements. Wood building materials with different surface structures (smoothly planed, rough sawn, etc.) are contaminated with indicator germs (bacteria, fungi and viruses) and with viral animal disease pathogens and the disinfection effect of physical and chemical processes is tested in laboratories of the required biological protection level. Wood products with different surface structure (smoothly planed, rough sawn, etc.) are contaminated with viral animal pathogens (African swine fever virus, foot-and-mouth disease virus, bovine herpesvirus type 1, highly pathogenic avian influenza virus) and the disinfection effect of physical and chemical procedures is tested in laboratories of the required biological protection level. The resistance of the wood products used to the successful disinfection procedures is investigated.

As a result of this work package, the general legal basis as well as the specific legal basis for wood will be presented. In addition, a disinfectant suitable for wooden buildings and their different agricultural use will be proposed, as well as the procedure of barn cleaning and disinfection.

3.6 Durable constructions (WP 6, TUM-TB)

All analyses of damage to buildings in timber construction confirm that the execution of connections has a decisive influence on the durability of timber structures. The main task of this work package is to investigate the connection details used in agricultural timber construction today, which were recorded during the as-built analysis/data collection. The expected damage mechanisms affecting the supporting structure of agricultural buildings can be divided into three categories: mechanical, chemical, and biological-physical attack. Accordingly, topic maps are developed for each category to provide a brief overview of the problems and possible actions. The goal is the same for all topic cards: permanent protection from damage through structural/design measures. The basic hazards and the corresponding structural measures are considered. These topic maps are intended as a first, quick orientation aid, and show that simple and effective measures exist. In the planning process, all corresponding introduced technical building regulations, in particular DIN 68800-2:2022-02, must also be observed.

Other results from this work package include the realization that, regardless of the type of connection, sacrificial boards provide simple and effective protection against all attacks. In conclusion, it can be said that correctly planned and executed agricultural halls made of wood are a durable and sustainable alternative to steel and reinforced concrete halls.

3.7 Design for Reuse (WP 7, TUM-TB, RUB)

Design for recycling and enabling the reusability (= design for reuse) of building materials and permanent connection details are the requirements for the reuse of building components. They enable a cascade use of wood in the first place (Fig. 3). The data necessary for the deconstructability of the connecting materials and their manufacture and static design in relation to the overall structure as necessary basics will be developed in coordination with WP 6. The investigations on the recycling of the agricultural buildings are to prove the nature of this potential. In comparative analyses, open material flow loops of agriculture construction are investigated and modified in feedback with the (building) construction in order to raise the efficiency potential even further, if possible, and thus extend value-added processing to the end of life of product systems. For this purpose, a renewal and extension of the conceptual methods as applied in the investigation of building life cycles (processes) is aimed at.

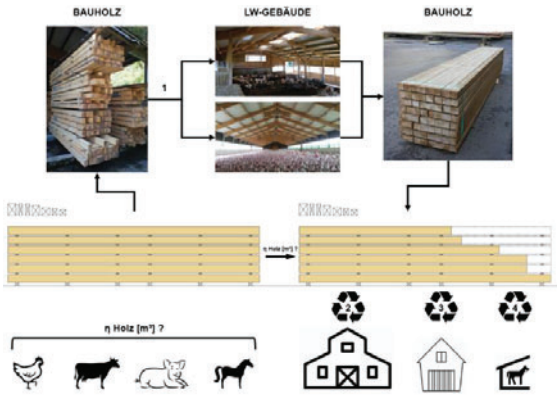

Figure 3: *Concept reuse*

First of all, an investigation of the connection methods of the building pendants takes place on the basis of the previously elaborated data with recording of the components with regard to their assembly and disassembly properties for different building types / materials. Then, the load-bearing structures in timber construction with their components as well as their connection alternatives with their respective manufacturing and assembly methods for the possible improvement of their deconstructability and the assembly

and disassembly and the connections of the components are calculated according to constructional and life cycle assessment methods. The characteristic values about the material stock and to the utilization ways of the wood and wood materials in proportions and geometries are compiled and are available as information for the possible use in a second life cycle or for the cascade use. Finally, an investigation of the economic efficiency and resource efficiency of the hall types through secondary material use and deconstructability over the life cycle takes place. The type of agricultural use results in different heavily used areas in the building. Depending on the type of use, lower loads are present from a certain height in the building, which is addressed here in particular.

3.8 Economical supporting structures (WP 8, LfL)

From the point of view of farmers as building owners, agricultural construction is primarily the manufacture of production facilities, which are subject to high cost pressure due to competition in food production. At the same time, requirements from animal welfare or quality assurance of the stored goods, building physics, optimized work management, expandability, design and the landscape have to be taken into account during planning and construction. In WP 8, first a systematization of typical animal husbandry and storage procedures to characteristic functional, grid and axial dimensions as well as building geometries takes place, and then the development of structural variants, which are previously elaborated building typologies or standardized timber components adapted to an economic utilization, takes place.

Exemplary working drawings are developed for the supporting structures in wood determined from the static pre-dimensioning as a basis for the further investigation steps and supplemented with comprehensive material/parts lists. In the process, the material/parts lists for determining the material consumption (including cross-sections of the load-bearing components, timber requirements, timber fastenings) will be developed and the costs for the design variants will be determined using bills of quantities. The goal is also to develop criteria for estimating the cost consequences of specific design decisions. In addition, the implementation and evaluation of new software add-ons at the interface between CAD work and CNC truss planning for company-specific timber construction projects will be carried out in order to reduce the additional planning effort due to the lack of industry-specific software.

4 RESULTS

The result of the project is a planning guide, which is intended to provide planners and builders with the necessary information from a neutral source. The scientific findings are intended to contribute to implementation in building practice and to show farmers ways in which they can again make greater use of wood as a raw material for their own projects. In addition to a presentation of typical floor plans and load-bearing systems for the majority of agricultural uses, the guide contains reliable information on life cycle assessment, necessary quantities of building materials, individual fraction types and quantities for the reusability of building materials and durable connection details, as well as information on the hygienic properties of wood products as a basis for practice. The preparation of the planning guide is carried out under the condition to enable smaller, regionally working timber companies to participate again in agricultural construction with wood. In addition, politicians as well as industry can use the results, which concern the increase in the use of wood in agricultural construction, resource efficiency and the environmental impact of an overall increase in the use of wood, for an improved basis for decision-making, both in the planning of buildings themselves and in the evaluation of measures in the field of construction.

5 CONCLUSION

The research project "Development of future-oriented concepts for agricultural construction with wood - from planning to deconstruction" will run until the end of 2023. The planning guide mentioned here is currently being compiled and supplemented by a detailed final research report.

ACKNOWLEDGEMENT

This study was carried out on basis of the research project "Development of future-oriented concepts for agricultural construction with wood - from planning to deconstruction" funded by the Federal Ministry of Food and Agriculture (BMEL) under the grant number 2219NR154.

This is a joint project of Ruhr University Bochum, Technical University of Munich, Bavarian State Research Center for Agriculture, Free University of Berlin and Friedrich-Loeffler-Institute.

REFERENCES

[1] Destatis, *Baufertigstellungen von Wohn- und Nichtwohngebäuden (Neubau) nach überwiegend verwendetem Baustoff. Lange Reihen ab 2000.,* 2021.

[2] LfL- Landesanstalt für Landwirtschaft, *INTERREG IV Bayern-Österreich-Projekt „Bauen in regionalen Kreisläufen“, Teil 1: Landwirtschaftliche Nutzgebäude in Holzbauweise, Teil 2: Primärenergiebedarf und Treibhauspotenzial bei landwirtschaftlichen Nutzgebäuden, Teil 3:*

https://doi.org/10.52202/069179-0115

Regionale Wertschöpfung. LfL/ALB (Hrsg.), Freising, 2013.

[3] Jiang, Y., Dietsch, P., Oberhardt, F., Simon, J., *: Landwirtschaftliche Nutzgebäude in Holzbauweise ohne vorbeugenden chemischen Holzschutz (Gebrauchsklasse 0 (GK 0)) - Besondere bauliche Maßnahmen in Anlehnung an DIN 68800. Schlussbericht für das Forschungsvorhaben gefördert durch LWF, Freising. Internet: https://www.hb.bgu.tum.de/fileadmin/w00bpc/www/Forschung/Laufende/Landwirtschaftliche_Nutzgebaeude_in_GK0_Kurzfassung.pdf,* 2018.

[4] Wilnhammer M., Rothe A., Weis W., Wittkopf S., *Estimating forest biomass supply from private forest owners: A case study from Southern Germany. Biomass and Bioenergy 47, 177-187. http://dx.doi.org/10.1016/j.biombioe.2012.09.044,* 2012.

[5] HFM – Holzforschung München, Technische Universität München, *INTERREG IV Bayern-Österreich-Projekt „Bauen in regionalen Kreisläufen“, Teil 2: Primärenergiebedarf und Treibhauspotenzial bei landwirtschaftlichen Nutzgebäuden, LfL/ALB (Hrsg.),* Freising, 2013.

[6] G. Weber-Blaschke, C. Lubenau, M. Wilnhammer, F. Härtl, S. Friedrich, R. Hammerl, S. Helm, D. Helm, H. Borchert, S. Wittkopf, T. Knoke und K. Richter, *Konkurrenz um Holz: Ökologische, soziale und ökonomische Effekte der stofflichen und energetischen Verwertung von Holz. Abschlussbericht der Technischen Universität München, Hochschule Weihenstephan-Triesdorf und Bayerischen Landesanstalt für Wald und Forstwirtschaft, Freising. Kurzbericht, 36 S., Langfassung 266 S.,* 2015.

[7] Weegner, G. Fengel, D., *Untersuchungen zur Beständigkeit von Holzbauteilen in aggressiven Atmosphären. Holz als Roh- und Werkstoff,* 1986.

World Conference on Timber Engineering Oslo 2023

BUILDING TOWARD ZERO EMBODIED CARBON

Richard Hough[1], Carsten Moeller[2]

ABSTRACT: This paper reviews the factors that determine the contribution of timber buildings to CO_2 emissions abatement, and how they are likely to impact our transition to net zero. Factors include projected volume demands of future building construction; building embodied carbon vs operational carbon; the carbon emissions of different construction materials; the growth and benefits of prefabrication; forests as carbon sinks under sustainable harvesting regimes and the impact of COP26; building end-of-life choices, and political drivers for the increased use of timber for carbon sequestration.

KEYWORDS: embedded, carbon, sequestration, end-of-life

1 INTRODUCTION

With global building floor area expected to double by 2050 [1], demand for raw materials is likely to grow proportionally. Embodied carbon emission from so much new construction will grow similarly unless we act to mitigate its effect.

The contribution of buildings to our global carbon emissions is typically estimated in the range 30-40% [2,3,4]. As a portion of those building emissions, embodied carbon emissions from building construction are typically estimated in the range 10-30% [5]. As efforts to reduce building operational carbon emissions begin to take effect, embodied emissions will continue to increase as a percentage of total building emissions. So the balance of mitigation effort will need to shift - attenuating building embodied carbon will play an increasingly important part in helping achieve net zero carbon by 2050, the goal that is consistent with efforts to limit the long-term increase in average global temperature to 1.5 degC [6].

The cement and steel industries are well aware of the challenge and are ramping up efforts to respond. Meanwhile, timber construction appears to offer an attractive alternative to concrete and steel in climate terms. Depending on availability of sustainably managed forest resource and end-of-building-life strategies, it can provide sequestration of biogenic carbon, or displacement of fossil fuel from current energy generation. For timber to fulfil its potential, government policy regarding the abatement of carbon emissions will be key, at international, national, and local levels. These and other factors affecting timber's likely contribution to climate change mitigation are discussed below.

2 OPERATIONAL VS EMBODIED EFFECTS

Building embodied energy (EE) is the energy consumed during production of a building, ie energy expended in extraction, conversion and transportation of raw materials, and in their processing and manufacture as building components. In terms of EN 15978 boundaries [7], it can be extended across modules A1-A3 ('cradle to gate'), or A1-A5 ('cradle to site') if the building's construction phase is to be included. Embodied carbon (EC) refers to the carbon emissions associated with the embodied energy, plus other emissions associated with the creation of materials, such as calcination in the case of cement, reduction in the case of iron, and photosynthesis in the case of timber.

Operational energy (OE) is the energy consumed in using the building over its lifespan, including heating, cooling, ventilating, lighting, appliances and equipment. Operational carbon (OC) refers to carbon emissions associated with the operational energy, typically deriving from electricity generation or on-site fossil fuel combustion.

Studies vary widely in their assessment of the relative portions of EE (or EC) and OE (or OC) in buildings. At the high end, for an energy efficient apartment block in Sweden with a projected lifespan of 50 years, EE accounted for 45% of total energy [8], with recycling potential estimated at 35-45% of EE. A more modest estimate puts EE at 'usually not more than 30%' [9]. One of the most extensive studies [10] covering 73 sample buildings across 13 countries estimated average EE at 10-20% of total life cycle energy, though changes to the EE/OE balance since publication (2010) would likely have seen that range increase.

[1] *Richard Hough, Senior Consultant, Arup Sydney; Adjunct Professor, University of Sydney, richard.hough@arup.com*
[2] *Carsten Moeller, Structural Engineer, Arup Brisbane, carsten.moeller@arup.com*

https://doi.org/10.52202/069179-0116

Regarding changes to these ratios over time, two effects are at play. Firstly, thanks to the historically greater emphasis on reducing operational energy through more energy-efficient heating and cooling systems, improved building insulation, take-up of 'passive' design strategies, changing user behaviours, regulation, and voluntary ratings schemes, OE continues to reduce, so increasing the EE/OE ratio.

Secondly, the transition to renewable energy has acted to reduce the carbon intensity of OE, whereas much of the carbon emission associated with material production, particularly of cement and steel, is not reducible in a similar way, being inherent in the chemical processes underlying the material's production. So the EC/OC ratio is rising faster than the EE/OE ratio, placing more urgency on attenuation of EC if the construction industry is to play its part in reducing global emissions.

3. CONSTRUCTION MATERIALS

The raw materials we extract from the earth and turn into products for building construction contribute significantly to our annual global greenhouse emissions. Concrete and steel currently dominate the choice of construction materials. Both are the subject of substantial R&D investment to reduce their carbon footprints, but reductions are constrained by the fact that conventional production of both materials involves chemical processes that necessarily off-gas CO2 as a by-product.

Cement is typically cited as contributing around 8% of global carbon emissions [11]. Combustion of fuel for kiln heating accounts for around 40% of that, and calcination of limestone around 60% [12]. Calcination is intrinsic to the production of normal Portland cement, and not amenable to reduction.

Cement substitutes hold much promise, with blast furnace slag, fly ash, and silica fume among the most commonly used. Their use in meaningful proportions raises issues for designers and contractors however in terms of lower early strength. This can translate into longer production cycle times for precast components, longer floor-to-floor cycle times for in-situ construction with delayed de-propping of formwork, and delays in application of prestressing for post-tensioned floors and beams.

Recycling of concrete still offers much scope for implementation [13]. It includes recycling into aggregate for road construction or backfilling, recycling into aggregate for new concrete production, and re-use of precast elements, all of which see more take-up in countries with policies constraining landfill dumping.

The steel industry has made big strides in improving energy efficiency but still accounts for around 8% of global emissions [14]. As with cement, emissions from conventional steel production include an irreducible component inherent in the chemical pathway – reduction of iron oxides generating CO2. Some progress has been made experimenting with alternative reduction environments, including the use of hydrogen [15]. Most promising in the short term however may be increasing the extent of recycling, where studies show plenty of room for improvement globally [16,17].

With the challenges faced by cement and steel in transitioning to low carbon production, construction in timber, or timber composites with concrete or steel, presents itself as an attractive third option.

4. EMBODIED CARBON AND PREFABRICATION

Leaving aside the potential benefits from biogenic carbon storage in wood, embodied carbon to produce a building in timber is typically less than a similar building in concrete or steel [47,48]. Production in timber is typically less energy intensive, typically uses renewable fuel, doesn't involve chemical processes that off-gas CO2, and is well-suited to prefabrication.

Fig. 1. The timber in this prefabricated office building for Sky UK represents -1442 t biogenic CO2, ie sequestered from atmosphere. Emissions from manufacture and transport from Austria represented +200 t, leaving embodied CO2 of -1242 t (Module A1-A5 including biogenic). The alternative structure with steel frame and concrete slabs would have cost +553 t embodied CO2 (A1-A5), ie emitted to atmosphere [44]. Given the building's energy saving features like rooftop PV, LED lighting and CCHP, the -1242 t CO2 represents about 13 years of operational emissions. Even if the sequestered carbon is returned to atmosphere at end-of-life, the 353 t benefit (553 t – 200 t) cf the steel/concrete composite alternative, remains. Photo copyright Simon Kennedy.

Prefabrication can reduce the embodied carbon footprint of a manufactured item by concentrating material resources and equipment at a single location, so reducing the transport costs of diverse materials to distributed construction sites, by encouraging optimisation of material usage and minimisation of waste, and by creating more opportunity for recycling. Precast concrete components for example benefit from indefinite reuse of

https://doi.org/10.52202/069179-0116

steel forms compared to more limited reuse of timber formwork typical of in-situ concrete construction.

Because of its easy machinability, timber is particularly well-suited to prefabrication, and this typically leads to local generation of a valuable biomass energy resource during milling and machining. It is common now for manufacturers of glulam, CLT and LVL to operate plants at or near energy self-sufficiency, with a very small carbon footprint. This is achieved by harnessing all residuals for heat/energy generation – harvesting and sawmilling residuals including bark, and offcuts and sawdust from manufacturing.

At its Varkaus LVL mill for example, Stora Enso operates combined heat and power plants using bio- and recycled fuels and is energy self-sufficient (self-reported [18]). Wiehag's glulam plant at Altheim near Stuttgart generates 38 GWh pa of renewable energy by biomass conversion from 10,000t pa of offcuts and sawdust. This is enough to supply all of the plant's electricity and heating needs, including space heating and kiln drying. Excess offcuts are sold as product and excess power is sold to the grid (self-reported [19]). At Nelson Pine's LVL plant in New Zealand, over 70% of energy requirements are for kiln heating, and are almost entirely accounted for by burning of wood residues from sustainably managed forests (self-reported [20]). According to a Canadian study, two-thirds of the country's total energy consumed in converting logs to dry-dressed lumber is attributable to drying operations, and on average 50% of energy use is derived from renewable biomass fuel [21].

Fig. 2. Wiehag's glulam plant at Altheim near Stuttgart. Photo: Wiehag

5. FORESTS AS CARBON SINKS

For current timber markets to expand, the supply of wood from sustainably managed forests also needs to expand. According to the IPCC, increasing the global resource of sustainably managed forests represents a benefit for global draw-down of CO2 : 'In the long term, a sustainable forest management strategy aimed at maintaining or increasing forest carbon stocks, while producing an annual sustained yield of timber, fibre or energy from the forest, will generate the largest sustained mitigation benefit" [22]. Regarding establishment of new plantation forests, they will be subject to competing land use claims, some of which can also point to carbon benefits, such as planting for biofuel crops. Supply of construction round wood from existing plantations is already subject to competition from biomass energy feedstock markets, which also claim carbon benefits, through fossil fuel substitution. More rigorous life-cycle assessment (LCA) will be an important tool in adjudicating between these competing claims in terms of climate change mitigation potential.

Despite competition for land, Europe's forests have increased in area by 9% over the past 30 years [23], to over a third of the continent's land surface. The associated biomass and stored carbon have grown by 50%, with only three quarters of the net annual wood increment harvested [24], so creating a net carbon draw-down benefit.

Fig. 3. Sweden's plan is to achieve net zero carbon by 2045, with forest carbon storage an important part of the plan. Forest stock has doubled in the past 100 years [45], with harvest rarely exceeding growth in any year. In 2018, CO2 drawdown to forests accounted for 80% of Sweden's 52mt CO2-e emissions [46].

Round wood harvesting in Europe benefits from a long tradition of sustainable forest management. Well-regulated extraction practices have earned European forestry its social licence. The same is not true in other temperate regions however, such as Australia, where harvesting in native forests remains controversial and politically sensitive. Foresters refer to the 'abattoir syndrome', where we enjoy timber products but prefer not to see a tree cut down. That is despite studies favouring managed forests over conservation forests for CO2 draw-down potential [43]. Increasing take-up of forest management certification should help alleviate these concerns. Globally, cumulative forest area managed under the major certification schemes has increased over 30-fold since 2000 [25], to around 30% of worldwide round wood production [26].

https://doi.org/10.52202/069179-0116

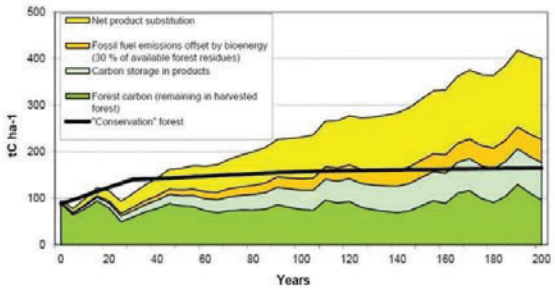

Fig. 4. Native forests in the state of New South Wales, Australia, include 'conservation' forests, with no harvesting, and 'multiple use' forests, with sustainable harvesting. The potential carbon drawdown of each forest type was modelled over a 200 year period. The conservation forest quickly reaches carbon equilibrium (heavy line), as does the multiple use forest. Allowing for potential product substitution benefit and fossil fuel offset benefit from biomass energy conversion of forest residues, the multiple use forest continues to extract carbon from atmosphere (top line) [43].

Deforestation in tropical regions casts a shadow over the timber industry's claims to be contributing to climate change mitigation however. Government responses in temperate regions have included regulation to control importation of illicit product, often with criminal convictions applying. Funding programmes such as UN REDD, the Norwegian Climate and Forest Initiative, the Amazon Fund, and the Billion Tree Campaign have had some effect, and there are now instances of deforestation reversal. Deforestation reached its peak in Costa Rica in the 1980's and has since reversed thanks to legal controls on land use change and stable funding through a PES (payment for ecosystem services) scheme [27]. ITMO's (internationally transferred mitigation outcomes) agreed at COP26 may open the way for funding flows into regions most affected (see 'Political Drivers' below). In the private sector, consumer goods retailers and manufacturers with a combined market value of USD2tr and financial institutions managing USD9tr recently pledged to eliminate deforestation from their supply chains and portfolios [28].

6. END-OF-LIFE CHOICES

LCA allows us to quantify embodied carbon in products and so to encourage behaviours that will move us closer to the circular economy. The challenge with buildings as products is predicting their full life cycle, particularly end-of-life (EOL) scenarios that may occur fifty years or more from construction. That is ambitious if not fanciful, but necessary for the equitable allocation of life-cycle carbon emissions, through fuller application of the LCA toolbox.

Regarding the life cycle of timber buildings, potential EOL scenarios are :

1. *Reuse.* Complete timber components are salvaged for reuse in a future building. Carbon already stored in the timber continues to be stored. Reuse will become more attractive with the increasing use of large section glulam or LVL beams and columns and large CLT floor and wall panels. Elements like these have had enough value added during manufacture to warrant reuse even in the present-day market. A way of quantifying the carbon benefits or disbenefits of reuse is to measure potential outcomes according to Module D of EN 15978 [29], which considers carbon emissions beyond Stage C, End-of-Life. The benefit of reuse is considered to be the emissions difference between reuse of timber components in a hypothetical future building versus the emissions associated with producing a functionally equivalent building using standard practices and market averages.

EOL scenarios are usually uncertain, as are Module D impacts. The benefit of reporting them, even if only qualitatively, is that they offer a measure of 'circularity' of a building project, or its ability to contribute to the low carbon circular economy, which will be key to hastening the decarbonisation of the construction industry. An example is design for deconstruction, which attracts credit in Module D when advantage is taken of reuse.

2. *Recycling*. In this scenario timber is chipped or shredded and repurposed for a variety of potential uses, including OSB or particleboard manufacture, and agricultural uses such as organic mulch for soil nutrition, ground cover for moisture retention and weed suppression, or animal bedding. Depending on the jurisdiction, preservative treated, glued, painted or coated wood may be banned or restricted for some recycling uses.

In LCA terms, recycling of demolition timber into chips for some new use is reported as a C3 transfer of stored carbon to the new product in the same way as for reuse. There are likely however to be additional fossil carbon emissions due to the EOL processing, which is necessary before the new recycled product can be created.

3. *Energy Recovery*. Timber is burned in an energy recovery facility, so the stored CO2 returns to atmosphere, along with small quantities of other greenhouse gases. Applying the EN 15897 Module D approach to the LCA of a timber building where energy recovery is assumed at EOL produces a carbon benefit equal to the difference between the carbon cost of BAU (business as usual) energy production and the carbon neutral cost of the energy retrieved from the timber, assuming of course the equivalent timber is regrown.

Whether the regrowth timber is assumed to have sequestered its carbon before the incineration event or after, raises the question of timelines for biogenic carbon.

https://doi.org/10.52202/069179-0116

'Dynamic LCA' models have been developed to try to account for the relative timings of capture and release of biogenic carbon [30], though they are limited in use by the quality of data available regarding carbon flux in managed forests.

The other uncertainty regarding the calculation of energy recovery from the burning of wood is estimating the Module D benefit in terms of substitution of this carbon-neutral energy for BAU energy. Logically, BAU should refer to conditions likely to prevail at actual EOL, when the substitution occurs. In countries where electricity generation is currently carbon heavy, the future substitution benefit from biomass renewables is likely to be less than currently, assuming progress is made in decarbonising the electricity mix. On the other hand, in countries where hydropower is currently dominant, the substitution benefit would be small both currently and in the future. Less conservative interpretations of Module D calculate BAU energy based on current not future conditions, on the grounds EN 15804:2012 (Sustainability of Construction Works – EPDs) 6.4.3.3 permits this assumption.

Of course when the local grid has converted entirely to renewables, there will be no substitution benefit at all. If CCS (carbon capture and storage) has progressed to commercial feasibility by then, it will open up an alternative means of permanently sequestering the biogenic carbon, by capture and burial of carbon from the flue gases.

Biomass energy conversion raises questions of air pollution, both particulate and gaseous. While incineration of virgin wood is commonly permitted, burning of preservative treated, glued, painted or coated wood is commonly banned or restricted. Scrubbers can neutralise acids in the emission stream; fabric filters and electrostatic precipitators can remove particulates, and higher furnace temperatures can break down combustion chemicals into simpler less harmful compounds, but optimal application of these technologies comes at a price and is far from universal [31].

4. *Storage in Landfill.* While dispatch of EOL timber to landfill is prohibited in some countries and restricted in many others, and while it runs counter to the intention of the circular economy by removing products from circulation, it may nevertheless represent the most effective way of sequestering biogenic carbon from the atmosphere long term in certain circumstances. The landfill scenario in the EN 15804-compliant EPD by FWPA for Australian glulam for example [32] predicts a long-term release from landfill of 62 kgCO2-e/m3, which is just 6% of the biogenic carbon originally sequestered in the wood. The calculation is based on the following assumptions, with technical references provided in the EPD :

Fig. 5. Filbornaverket in Helsingborg, Sweden, is a modern waste-to-energy incineration plant that uses combustible household and commercial / industrial / demolition waste to produce 78MW of electricity and steam for district heating. It was designed to exceed EU standards for cleanliness of exhaust gases [41]. Around half of Sweden's municipal solid waste is burned for energy recovery at end-of-life, the other half is recycled [42]. Photo : Öresundskraft

• Of the gases formed from any degradation of wood in landfill, 50% is methane and 50% is carbon dioxide.
• 36% of the methane is captured, of which a quarter is flared and three quarters is used for energy recovery.
• Of the methane that is not captured, 10% is oxidised and 90% is released to the atmosphere.
• The 'typical' DOCf (degradable organic carbon fraction) is taken as 0.1%, based on bioreactor laboratory research involving testing of various wood waste types in reactors operated to generate maximum methane yields [33], and informed also by excavation of landfill sites to recover old wood samples [34].

Fig. 6. Sections of timber products retrieved from a Sydney landfill site after 46 years of burial [34].

https://doi.org/10.52202/069179-0116

This suggests a remarkable potential for indefinite carbon storage, though assumptions regarding landfill management practices will vary with country and industry practice, particularly regarding methane capture, flaring, and energy recovery. The CO2-e calculation is sensitive to the DOCf assumption, and it relies on the anaerobic conditions commonly found in Australian landfill sites, which will also not be universal.

System Boundaries

In an LCA under EN 15978, a full building system boundary contains Modules A to C, with the 'supplementary' Module D covering the benefits and loads considered to be beyond the system boundary, by giving credit for avoided future use of primary materials and fuels [7]. Module D needs to be reported separately and not aggregated with Modules A to C [49].

Sourced from sustainably managed forests, timber in buildings is generally considered to have biogenic carbon neutrality, meaning biogenic carbon is accounted for when entering (Module A1) and leaving a building (Module C3/C4), producing a net zero effect [29]. In the case of re-use or recycling, carbon benefits are accounted for in the downstream processes of any subsequent product through reduced Module A1-A3 emissions. For European timber products, where Module D energy recovery through incineration is common practice, the benefit is also beyond the system boundary and becomes a broader circular economy benefit. On the other hand, long-term carbon storage in landfill sits in Module C4 and thus within the system boundary of the current project. Adopting the EPD in [32] for example, the landfill option therefore means a considerable biogenic benefit for the current project, compared to the re-use scenario where EN 16485 implies zero benefit, as the captured carbon is passed on. For the current project, landfill therefore wins over re-use, which is at odds with the intent of the circular economy.

The purpose of this discussion about EOL is to highlight the impact that choice of LCA system boundaries can have on allocation of biogenic carbon benefits and therefore the importance of providing a verbal account of project EOL carbon transfer options in addition to the strictly numerical account.

7. POLITICAL DRIVERS

At the international level, a key outcome from the 2021 COP26 in Glasgow was the ratification of Article 6 of the 2015 Paris Agreement, thereby opening the way for international trading of carbon credits via ITMO's (internationally transferred mitigation outcomes), to assist countries in meeting their NDC's (nationally determined contributions) under the Agreement. Applied to forest management for example, this could have big implications for inward investment into countries under pressure to reduce deforestation, such as African countries in the Congo basin, where the world's largest carbon sink is under threat [35,36].

At the national level, governments that have adopted carbon tax or cap-and-trade systems are best placed to monitor and control their progress toward their NDC. Applied to the construction sector, cap-and-trade or other carbon pricing mechanisms will over time favour the transition to greener materials and construction practices [37], providing a market advantage for construction in timber.

Climate Change Conferences (COP's) also host gatherings of regional and city leaders, who continue to advance their own abatement plans alongside national plans. In some local and regional jurisdictions 'timber first' policies have been introduced, including Canada, New Zealand, Germany, Finland, USA, Australia. In most instances there was an active local forest industry advocating, with notable exceptions like the London Borough of Hackney, where the council adopted its policy in 2012 and now has 24 of the UK's largest timber buildings [38].

Some policies have mandated the use of wood in buildings funded with public resources (Canada, France, Sweden); other policies at local government level in Sweden and Finland have required the use of timber on certain sites, and others have funded R&D through public competitions (Austria, Germany, Canada, USA, Norway). Japan introduced its Wood First Law in 2010, which obliges national and local government to use wood for public buildings of three storeys or less [40].

While governments grapple with emissions policy, voluntary green building ratings schemes continue to have a positive effect. These schemes have been evolving too: LEED and BREEAM have moved to recognise LCA as a key assessment tool, thereby allowing more accurate quantification of timber's carbon sequestration potential.

8. CONCLUSION

Construction in timber will not be a primary driver of emissions abatement, but it will make a useful contribution and can also serve as a catalyst for better forest management. The wider adoption of LCA as a criterion for assessing the carbon performance of construction in different materials will be important in maximising the sequestration potential of timber buildings. As part of that, understanding end-of-life choices and their effect on life-cycle outcomes will also be important. LCA conventions that allow credit for biogenic carbon storage to be allocated equitably across building projects will allow clearer present-day choices to be made between the benefits of different construction materials.

Increasingly, an important catalyst for timber building uptake will be government leadership in setting CO2

abatement policy, through stricter implementation of carbon pricing schemes as key platforms for achieving nationally determined contributions under the Paris Agreement.

REFERENCES

[1] UNEP, United Nations Environment Programme : Towards zero-emission efficient and resilient buildings. Global Status Report 2016, prepared by the GABC on the occasion of the 22nd Conference of Parties (COP22) to the United Nations Framework Convention on Climate Change (UNFCCC), UNEP 2016.
https://goo.gl/oWUi3Y

[2] IPCC Working Group III : Climate Change 2022, Mitigation of Climate Change. Assessment Report 6, Chapter 9, 2022
https://www.ipcc.ch/report/ar6/wg3/downloads/report/IPCC_AR6_WGIII_Chapter_09.pdf

[3] World Green Building Council : Bringing Embodied Carbon Upfront. WGBC, Sep 2019
WorldGBC_Bringing_Embodied_Carbon_Upfront.pdf

[4] International Energy Agency : Buildings, Sectorial Overview, Tracking Report. IEA, Sep 2022.
Buildings – Analysis - IEA

[5] See references in 'Operational vs Embedded Effects'

[6] International Energy Agency : Net Zero by 2050, A Roadmap for the Global Energy Sector. IEA, May 2021
https://iea.blob.core.windows.net/assets/7ebafc81-74ed-412b-9c60-5cc32c8396e4/NetZeroby2050-ARoadmapfortheGlobalEnergySector-SummaryforPolicyMakers_CORR.pdf

[7] EN 15978 : 'Sustainability of construction works - Assessment of environmental performance of buildings - Calculation method', Comité Européen de Normalisation (CEN), 2011

[8] Thormark, C : A low energy building in a life cycle—its embodied energy, energy need for operation and recycling potential. Building and Environment, V37, Issue 4, April 2002, Pages 429-435.

[9] Food and Agriculture Association of the United Nations : Forest Products Annual Market Review 2015-2016. UNFAA, p16.
fpamr2016.pdf (unece.org) p16.

[10] T. Ramesh, Ravi Prakash, K.K. Shukla : Life cycle energy analysis of buildings: An overview. In Energy and Buildings, V42, Issue 10, Oct 2010, pp 1592-1600
Life cycle energy analysis of buildings: An overview - ScienceDirect

[11] Chatham House : Making Concrete Change: Innovation in Low-carbon Cement and Concrete. Chatham House Report, 13 June 2018
Making Concrete Change: Innovation in Low-carbon Cement and Concrete | Chatham House – International Affairs Think Tank

[12] Goguen, C : Concrete and CO2. National Precast Concrete Association, 22 May 2013.
Concrete and CO2 - National Precast Concrete Association

[13] European Commission (DG ENV) : Service Contract on Management of Construction and Demolition Waste – SR1 Final Report Task 2. Feb 2011.
https://ec.europa.eu/environment/pdf/waste/2011_CDW_Report.pdf

[14] World Steel Association : Climate change and the production of iron and steel. WSA, 2021.
Climate-change-and-the-production-of-iron-and-steel.pdf (worldsteel.org)

[15] World Steel Association : Hydrogen (H2)-based ironmaking. WSA, June 2022.
https://worldsteel.org/wp-content/uploads/Fact-sheet-Hydrogen-H2-based-ironmaking.pdf

[16] United Nations Environment Program, International Resource Panel : Recycling Rates of Metals, A Status Report. UNEP, 2011.
https://wedocs.unep.org/bitstream/handle/20.500.11822/8702/Recycling_Metals.pdf?sequence=1&isAllowed=y

[17] Boyer J, : Understanding Steel Recovery and Recycling Rates and Limitations to Recycling. Dovetail Partners, 2015.
http://www.dovetailinc.org/report_pdfs/2015/dovetailsteelrecycling0315.pdf

[18] Stora Enso : Varkaus Mill, Satakunnankatu, Finland.
Varkaus Mill - About us | Stora Enso

[19] email from Wiehag to author, 2017

[20] NPIL : Carbon Footprint. Nelson Pine Industries Ltd, 2023.
https://www.nelsonpine.co.nz/environment/carbon-footprint/

[21] Garrahan, P : How Energy Efficient is you Drying Operation ?. In Canadian Forest Industries eNews, December 2, 2011
https://www.woodbusiness.ca/how-energy-efficient-is-your-drying-operation-352/

[22] Nabuurs, G.J. et al : Forestry. In Climate Change – Mitigation, Contribution of Working Group III to the Fourth Assessment Report of the IPCC, Cambridge University Press 2007.

https://doi.org/10.52202/069179-0116

https://www.ipcc.ch/site/assets/uploads/2018/02/ar4-wg3-chapter9-1.pdf p543

[23] Forest Europe, UNECE, UNFAO : State of Europe's Forests, 2020. Forest Europe, 2020. https://foresteurope.org/wp-content/uploads/2016/08/SoEF_2020.pdf

[24] Op. cit. p16.

[25] UN FAO : Global Forest Resources Assessment 2015 - How are the world's forests changing ?. UN Food and Agriculture Organisation, 2015, p4. Global Forest Resources Assessment 2015. How are the World's Forests Changing? (Second edition) (fao.org)

[26] Food and Agriculture Association of the United Nations : Forest Products Annual Market Review 2015-2016, UN FAO, UNECE, p16. fpamr2016.pdf (unece.org)

[27] The World Bank : Costa Rica's Forest Conservation Pays Off. Feature article, World Bank website, 16 Nov 2022. https://www.worldbank.org/en/news/feature/2022/11/16/costa-rica-s-forest-conservation-pays-off

[28] K DeValue, et al : Halting deforestation from agricultural value chains: the role of governments. UN FAO 2022, p viii. https://www.fao.org/3/cc2262en/cc2262en.pdf

[29] EN 16485 : 'Round and sawn timber - Environmental Product Declarations - Product category rules for wood and wood-based products for use in construction'. Comité Européen de Normalisation (CEN), 2014

[30] Hart J, Pomponi F, More Timber in Construction: Unanswered Questions
and Future Challenges, in Sustainability 2020, 12, p10.

[31] R Atkins : Generating power with waste wood. Power Engineering, V99 Issue 2 https://www.power-eng.com/emissions/generating-power-with-waste-wood/#gref

[32] Forest and Wood Products Australia Ltd : Environmental Product Declaration – Glued Laminated Timber, FWPA 2017.

[33] Wang, W., Padgett, J., De La Cruz, F. and Barlaz, M. (2011) : Wood biodegradation in laboratory-scale landfills. Environmental Science & Technology, V45 N16, pp 6864-6871.

[34] Ximenes, F.A. et al. : The decomposition of wood products in landfills in Sydney, Australia. Waste Management, V28 N11, November 2008, Pages 2344-2354.

[35] T. Mohanna : Article 6 of the Paris Agreement: Opportunities for Africa. White and Case, Winter Newsletter 2022. https://www.whitecase.com/insight-our-thinking/africa-focus-winter-2022-article-6-paris-agreement-opportunities-africa

[36] World Bank : Journey into the Congo Basin – The Lungs of Africa and Beating Heart of the World. The World Bank, Newsletter, 24 Oct 2022. https://www.worldbank.org/en/news/feature/2022/10/24/journey-into-the-congo-basin-the-lungs-of-africa-and-beating-heart-of-the-world#:~:text=Known%20as%20the%20%E2%80%9Clungs%20of,critical%20habitat%20for%20endangered%20species

[37] A Feldman et al : Putting a price on pollution: What it means for Australia's property and construction industry. Green Building Council of Australia, post 2011. https://www.gbca.org.au/uploads/203/3787/Carbon%20Paper_LR.pdf

[38] J Gregory : Timber talked up as Town Hall planners discuss importance of building materials in reducing carbon emissions. Hackney Citizen Newsletter, 28 Oct 2021. https://www.hackneycitizen.co.uk/2021/10/28/timber-planners-building-materials-carbon-emissions/#:~:text=In%202012%2C%20the%20council%20adopted,hold%20carbon%20for%2060%20years.

[39] W Hawkins : Timber and carbon sequestration. The Structural Engineer, V99 N1, January 2021, p18.

[40] UN FAO : Law on Promotion of Use of Wood in Public Buildings (Act No 36). UN FAO data entry LEX-FAOC192789, 1 Jan 2010. https://www.fao.org/faolex/results/details/en/c/LEX-FAOC192789/

[41] Öresundskraft : Filbornaverket data sheet. Öresundskraft website. Filbornaverket (öresundskraft.se)

[42] C Kim, R Mauborgne : Turning Waste to Energy: Sweden's Recycling Revolution. Blue Ocean, 2023. https://www.blueoceanstrategy.com/blog/turning-waste-energy-sweden-recycling-revolution/#:~:text=Only%201%25%20of%20Sweden's%20trash,homes%20and%20electricity%20to%20250%2C000

[43] Ximenes, F; George, B; Cowie, A; Williams, J; Kelly, G:'Greenhouse Gas Balance of Native Forests in New South Wales, Australia', Forests, V3, 2012, pp653-683

[44] 'Believe in Better Building, The Wood Awards 2015'; award submission document by Arup Associates, p5.

[45] World Economic Forum : Sweden's forests have doubled in size over the last 100 years. WEF, 13 Dec 2018. https://www.government.se/4a9f07/contentassets/730d6345a5d745b1bc5f084e2f00fff7/revised-national-forestry-accounting-plan-for-sweden p6.

[46] Government Offices of Sweden : Sweden's long-term strategy for reducing greenhouse gas emissions. GOS, Ministry for the Environment, Dec 2020, p17. https://unfccc.int/sites/default/files/resource/LTS1_Sweden.pdf p17.

[47] A Himes, G Busby : Wood buildings as a climate solution. Developments in the Built Environment, V4, Nov 2020. Wood buildings as a climate solution - ScienceDirect

[48] J Hart, B d'Amico, F Pomponi : Whole-life embodied carbon in multistorey buildings. Journal of Industrial Ecology, V25, 2021, pp 403–418. https://www.napier.ac.uk/~/media/worktribe/output-2753394/whole-life-embodied-carbon-in-multi-storey-buildings-steel-concrete-and-timber.pdf

[49] RICS : Whole life carbon assessment for the built environment. Royal Institute of Chartered Surveyors, 1st edition, Nov 2017. https://www.rics.org/uk/upholding-professional-standards/sector-standards/building-surveying/whole-life-carbon-assessment-for-the-built-environment/

https://doi.org/10.52202/069179-0116

World Conference on Timber Engineering Oslo 2023

TRADE-OFFS IN EMBODIED CARBON AND ACOUSTIC INSULATION FOR MASS TIMBER FLOOR ASSEMBLIES

Samantha J. Leonard[1], Mohamad B. Eddin[2], Morgan K. Prichard[3], Jonathan M. Broyles[4], Nathan C. Brown[5], Sylvain Ménard[6]

ABSTRACT: Mass timber structural systems are increasingly used in the design of low and mid-rise buildings. One of the primary motivators for using mass timber structures is their low embodied carbon emissions (EC), which reduces a building's carbon footprint. Despite this advantage, a criticism of mass timber structures in multi-story buildings is often poor air-borne and impact sound insulation. In response, this paper studies common mass timber floor assemblies for their EC and sound insulation performance. EC data is used along with previous experimental acoustic data to evaluate how acoustic insulation affects the sustainability of mass timber floors. This study found that there is no clear relationship between EC and acoustic insulation; while high-EC assemblies exist, there are many low-EC assemblies at all levels of acoustic insulation. Trade-offs instead occur in the types of assemblies that can achieve performance goals and their depth or visible finish. While other factors such as cost or structural requirements may control assembly selection, designers seeking to reduce EC should consider room design needs and select acoustic insulation strategies with favorable EC-to-acoustic insulation ratios.

KEYWORDS: Mass Timber Floors, Sound Transmission Class, Impact Insulation Class, Embodied Carbon Emissions

1 INTRODUCTION

Mass timber structures are increasingly gaining interest among building owners and developers due to their potential to positively affect the triple bottom line: sustainability, society, and economy [1]. Mass timber structural elements have been shown to require less energy during manufacturing compared to traditional structural materials such as steel and concrete [2], can improve occupant wellness [3], and have the potential to revitalize local economies in forested regions [4].

However, the relatively lightweight mass timber floor structures often pose challenges for serviceability requirements such as sound insulation [5, 6]. The 2021 IBC requires that projects meet specific acoustic performance standards for floor and wall assemblies separating dwelling units [7]. The two main acoustic insulation performance quantifiers in North America are Sound Transmission Class (STC), a measure of a floor or wall assembly's ability to prevent airborne-based sound transmission between spaces, and Impact Insulation Class (IIC), a measure of a floor assembly's ability to insulate a space from impact noise (i.e., footfall) from above [8].

Lab-based measurements for mass timber floor systems constructed using Cross Laminated Timber (CLT), a panelized mass timber product, have demonstrated that bare CLT alone cannot meet typical code requirements for acoustic insulation [9]. While several recommendations exist to improve the acoustic performance of a CLT floor system, not every recommendation improves the same acoustical phenomena. Common examples of acoustical treatments include using dense-porosity surfaces that reflect sound, adding mass to reduce vibration amplitudes, including sound-dissipating layers in the assembly to absorb sound, and providing acoustic separation between finishes and the structure to improve sound insulation [5, 10]. These strategies complicate how acoustical performance can be improved for mass timber structures. As sound insulation performance requirements can have significant effects on the floor assembly construction, designers require guidance during project decision-making. Many organizations offer resources with data on mass timber floor assembly acoustic performance, such as the FPInnovations CLT Handbook chapter on acoustics and the WoodWorks Inventory of Acoustically-Tested Mass Timber Assemblies (WW Inventory herein) [5, 11].

[1] Samantha Leonard, The Pennsylvania State University (PSU), Department of Architectural Engineering, USA, sjd5225@psu.edu, Corresponding Author
[2] Mohamad Bader Eddin, University of Quebec at Chicoutimi, Department of Applied Sciences, Canada, mohamad.bader-eddin1@uqac.ca
[3] Morgan Prichard, PSU, Department of Architectural Engineering, USA, mkp5607@psu.edu
[4] Jonathan Broyles, PSU, Department of Architectural Engineering, USA, j.broyles@psu.edu
[5] Nathan Brown, PSU, Department of Architectural Engineering, USA, ncb5048@psu.edu
[6] Sylvain Ménard, University of Quebec at Chicoutimi, Department of Applied Sciences, Canada, Sylvain_Menard@uqac.ca

https://doi.org/10.52202/069179-0117

However, there is limited guidance on how decisions related to sound insulation performance affect a mass timber floor system's carbon produced during material extraction, transportation, and manufacturing, also known as embodied carbon (EC).

Salles E Portugal et al. studied concrete versus cork flooring materials for their environmental impact [12]. Broyles et al. conducted design optimization of concrete floor slabs for embodied carbon and acoustic performance [13, 14]. Tomas M. Echenagucia et al. researched the acoustic optimization of a concrete structure for a concert hall space [15]. Mirdad et al. analyzed 28 mass timber-concrete composite floors for EC and STC and found that increasing timber thickness is generally more beneficial for sound insulation and EC than increasing concrete thickness; however, IIC was omitted, and the types of assemblies are limited [16]. Ilgin et al. reviewed 13 tall mass timber building case studies for various architectural design features, including finding an average floor-to-floor height of 3 m, which is affected by floor assembly construction [17]. Beyond these papers, current literature review did not find a comparison of acoustic performance and embodied carbon for a wide range of mass timber floor assembly types. This study builds on the existing WW Inventory by adding EC data for each assembly. By pairing acoustic insulation ratings and EC data sets, these performance objectives can be compared for a range of assembly types and configurations. Resulting findings are intended to aid early design decision making.

2 METHODS

The studied assemblies for this research come from the WW Inventory, which is the most comprehensive database of mass timber assembly acoustic performance test results found during the literature review process. This study calculated EC for the assemblies based on the inventory's description of their construction, and EC is compared to the inventory's acoustic performance test ratings during the data analysis process.

2.1 ASSEMBLY CONSTRUCTION

The WW Inventory included descriptions and test data for 349 mass timber floor assemblies. The inventory organized floor assemblies into six categories, which was further divided into twelve total categories in this study. The categories included in this study are summarized in Table 1. Assemblies include features such as: structural or non-structural toppings, exposed mass timber panel ceilings, suspended acoustic ceilings, and raised access floors. A variety of materials and products appear in the assemblies, including those of the following types: mass timber panel, concrete or gypsum topping, acoustic mats or systems, acoustic accessories, board-type products such as gypsum board and plywood, insulation, flooring, and acoustical underlayment. Assembly descriptions and typical material properties are used to estimate total assembly depth. In the final EC database, 92 out of 349 assemblies meet the 2021 IBC requirements, have both STC and IIC data, and have sufficient information to estimate EC.

Table 1: *Categories used in this research, based on the WW Inventory. Symbols are referred to later in the results plots. The final main EC database is discussed further in section 2.3.*

Symbol	Assembly Category & Symbol	Typical Assembly Construction	Number of Assemblies	Code-compliant w/ STC/IIC data	In Final Main EC Database
●	Mass timber with ceiling side concealed, with or without finish floor	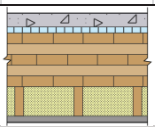	59	39	25
●	Mass timber with ceiling side concealed, with or without finish floor, no topping	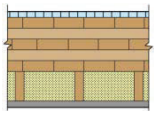	31	22	17
▼	CLT-concrete composite	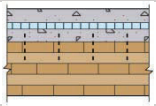	10	10	6
◆	Mass timber with concrete or gypsum topping	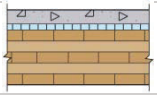	59	16	7
◆	Mass timber with concrete or gypsum topping w/ finish floor	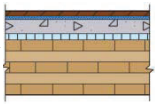	81	17	13
⬟	GLT decking	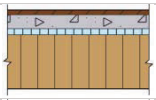	5	1	1
★	NLT decking	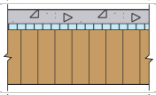	25	8	5
■	CLT without concrete or gypsum topping	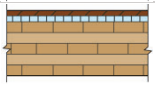	30	5	3
⬢	Mass timber with raised access floor	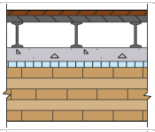	15	7	7
✖	Mass timber with raised wood sleepers	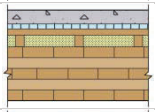	15	5	5
✚	Mass timber with raised wood sleepers, no topping	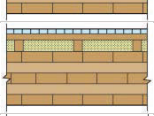	4	2	2
▲	T&G decking	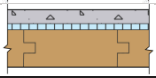	15	5	1
		Total	349	137	92

https://doi.org/10.52202/069179-0117

Most assemblies in the full WW Inventory (266 out of 349, or 76 percent) use five-ply CLT panels, which can typically span about 4 to 5.5 meters [18]. Table 2 shows typical maximum allowable spans for the mass timber panels which appear in the inventory. Spans are based on IBC 2021 residential occupancy loads but can vary depending on factors such as wood species, structural loading requirements, and project-specific fire resistance rating requirements. Mass timber panel structural spans are often controlled by criteria to limit walking-induced floor vibrations. More in-depth calculations of span limits for individual assemblies are out of this paper's scope.

Table 2: *Typical allowable spans for mass timber panels appearing in the WW Index, based on publicly-available manufacturer technical guides* [18–20] *STC and IIC data is from the WW Inventory* [11].

Mass Timber Panel	Panel Depth (mm)	Span (m)	Assumed Panel Construction	STC	IIC
3-ply CLT	104.8	4.0	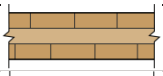	38	22
5-ply CLT	131.8	4.8	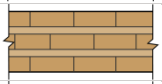	39	22
5-ply CLT	137.2	4.8	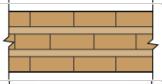	41	27
5-ply CLT	174.6	5.5	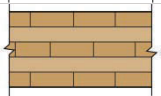	41	25
7-ply CLT	228.6	7.0	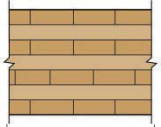	44	30
GLT	88.9	3.7		35	20
2x4 NLT w/ Plywood	88.9	3.7		29	-
2x6 NLT w/ Plywood	139.7	5.2		34	33

2.2 ACOUSTIC PERFORMANCE DATA

Acoustic performance test data for most assemblies consists of one STC rating and one IIC rating (270 assemblies). Some assemblies include only STC or IIC (57 assemblies), while 33 assemblies include one or more of the following ratings: Apparent Sound Transmission Class (ASTC), Apparent Impact Insulation Class (AIIC), Field Impact Insulation Class (FIIC), Field Sound Transmission Class (FSTC), and Normalized Noise Isolation Class (NNIC). Where ASTC, AIIC, FSTC, FIIC, or NNIC ratings are provided in lieu of STC and IIC, an estimated STC and IIC rating were calculated to provide a comparable rating to other assemblies. It is assumed that these metrics generally result in a lower rating by about five points due to field conditions [21], and therefore five points were added to these values to estimate equivalent STC and IIC ratings. The WW Inventory assembly ratings are obtained from various manufacturer and third-party test reports for testing performed in accordance with the ASTM E 90 and ASTM E 492 test standards [22, 23]. A limitation of this data is that there are often rating discrepancies between labs, bringing into question the expected sound insulation performance of an assembly [24]. Additionally, construction quality can vary the acoustic insulation performance [25], as air leaks can reduce performance [26]. Table 3 summarizes the standards and methods used in the WW Inventory assembly data.

Table 3: *Test standards and methods used to quantify sound insulation of assemblies in the WW Inventory.*

Standard (Short Name)	Standard (Long Name)	Number of Assemblies
ASTM E 492 [23]	Standard test method for laboratory measurement of impact sound transmission through floor-ceiling assemblies using the tapping machine	176
ASTM E 90 [22]	Laboratory measurement of airborne sound transmission loss of building partitions and elements	170
Modified ASTM E 90/E 492 [22, 23]	Floor zone testing procedures	68
ISO 12354 (ISO 15712-1) [27]	Building acoustics — Estimation of acoustic performance of buildings from the performance of elements — Part 1: Airborne sound insulation between rooms	36
ASTM E 1007 [28]	Standard test method for field measurement of tapping machine impact sound transmission through floor-ceiling assemblies and associated support structures	26
Multiple Methods	Combination of ASTM E 492 and ASTM E 1007 [23, 28]	20
ASTM E 336 [29]	Standard test method for measurement of airborne sound attenuation between rooms in buildings	19
Legacy from CLT handbook [30]	Various European standards	11

For the purposes of evaluating and comparing designs, levels of acoustic performance are defined per Table 4, based on the performance divisions used by Long [21].

Table 4: *Acoustic performance tier requirements*

Performance Tier	STC/ IIC	Description
Non-code-compliant	<50	Clearly hear normal activities of neighbor
Code Minimum	50	Normal activities of neighbors somewhat muted
Good	55-59	
Better	60-64	Cannot hear normal activities of neighbors
Best	65+	

2.3 EMBODIED CARBON ESTIMATION

The assemblies studied include between 1 and 9 floor materials and components. Embodied carbon material values are obtained for each material from either the Inventory of Carbon and Energy (ICE) V3.0 database [31], product environmental declaration (EPD) sheets, or industry wide EPDs. The ICE database is a collection of EC factors that relate a construction material quantity to its corresponding carbon emissions, using a cradle-to-gate life cycle assessment (LCA). EPDs are often created by manufacturers or third-party groups and are independently validated per ISO 14025:2006. Additionally, technical product data sheets and NRC test reports were referenced to clarify typical information about some material types, and to help inform property assumptions. Note that the analysis includes only the cradle-to-gate LCA boundaries (A1-A3).

From the perspective of calculating embodied carbon, all the materials included in the studied assemblies can be classified based on their coverage, resulting in three coverage categories: area, linear, and discrete. Each material in the WW Inventory had typical properties such that EC per area could be calculated for each material. Most materials in the inventory are area-based, meaning they are installed to cover the full area of the floor. EC per area for these materials is calculated per Equation 1:

$$EC_i = EC_f * t_{i,typical} * \rho \quad (1)$$

Where:

EC_i = EC per area for a given assembly layer of typical thickness [kg CO_2 eq./m^2]

EC_f = EC factor per mass for a given assembly component [kg CO_2 eq./kg]

$t_{i,typical}$ = the baseline layer thickness assumed for the EC_i value [m]

ρ = component density [kg/m^3]

Acoustic accessories include both linear- and discrete-based materials, where linear includes items like wood furring or resilient channels, and discrete includes those such as acoustic clips or rubber isolators. EC for linear and discrete materials can be calculated per Equations 2 and 3, respectively, to determine an equivalent EC per area. Based on Equations 1 through 3, representative assembly material values are summarized in Table 5.

$$EC_i = \frac{EC_f * A_{i,typical} * \rho}{S} \quad (2)$$

Where:

$A_{i,typical}$ = the baseline component cross sectional area assumed for the EC_i value [m^2]

S = component spacing [m]

$$EC_i = \frac{EC_f * m_{i,typical}}{S_\perp * S_\parallel} \quad (3)$$

Where:

$m_{i,typical}$ = the baseline component mass assumed for the EC_i value [kg]

$S_\perp$ = spacing perpendicular to a reference span direction [m]

$S_\parallel$ = spacing parallel to a reference span direction [m]

Table 5: *Embodied carbon of representative mass timber assembly materials (kg CO_2 eq. per m^2 per typical thickness/unit/spacing)*

Coverage Category	Material Type	Material	EC_i	Ref
Area	Mass Timber Panel	CLT (5-ply)	23.9	[32]
		GLT (88.9 mm)	14.3	[33]
	Concrete or Gypsum Topping	NW Concrete (38.1 mm)	12.4	[31]
		LW Concrete (76.2 mm)	12.0	[34]
	Acoustic Mats or Systems	Dimpled Rubber Mat (25.4 mm)	13.7	[35]
		Raised Access Floor	52.5	[36]
	Board-type Products	Gypsum (15.9 mm)	1.79	[37]
		Plywood (19 mm)	7.3	[31]
	Insulation	Fiberglass (92 mm)	0.90	[38]
		Mineral Wool (30 mm)	1.1	[39]
	Finish Flooring	Carpet	12.9	[40]
		Hardwood Flooring	3.5	[31]
	Acoustical Underlayment	Flat Rubber Mat (17 mm)	21.8	[35]
		Foam Mat	3.5	[41]
Linear	Acoustic Accessories	Resilient Channels	1.66	[42]
		Wood Furring	0.35	[31]
Discrete		Sound Isolation Clips	5.35	[31]

https://doi.org/10.52202/069179-0117

In some cases, EC information was not available for materials or products, or there was not enough information in an assembly description to reasonably estimate EC. As a result, only 217 out of 349 assemblies were included in the EC database. 92 of those 217 assemblies meet the 2021 IBC and have both STC and IIC data. Each studied assembly is evaluated for EC by a summation of each material's EC material value. The unit of comparison is kg CO_2 eq. per m^2. Because the layer EC values were first calculated based on typical properties per Equations 1-3, atypical conditions must be accounted for in each assembly estimate. While some modifications were made as needed depending on whether a layer was area, linear, or discrete-based, the general equation to estimate the full assembly EC is summarized and simplified in Equation (4):

$$EC = \sum_{i=1}^{n} EC_i * \frac{d_{i,actual}}{d_{i,typical}} \quad (4)$$

Where:

EC = total assembly EC per area [kg CO_2 eq./m^2]

$d_{i,actual}$ = the actual property (thickness, density, area, spacing, or mass) of the given component if different than typical [mm, kg/m^3, mm^2, m, kg]

$d_{i,typical}$ = the baseline property assumed for the EC_i value [mm, kg/m^3, mm^2, m, kg]

3 RESULTS AND DISCUSSION

3.1 RESULTS

After obtaining the total EC for the corresponding timber floors in the WW Inventory, the EC is plotted against the air-borne (STC) and structure-borne (IIC) acoustic performance. Figure 1 shows STC versus EC, assigning to each data point a hue based on assembly depth and a marker style based on whether the mass timber panel is exposed aesthetically to the underside. Similarly, Figure 2 compares the same data set, but for IIC versus EC. Horizontal lines in both Figures 1 and 2 depict the lowest rating of each acoustic performance tier per Table 4.

Figure 1 shows that there is no clear relationship between STC and EC; all STC performance tiers can be achieved with similar levels of EC (between about 30 to 50 kg CO_2 eq./m^2) if the right assembly is selected. While low-EC options exist, there are numerous assemblies with significantly higher EC (by 2 to 4 times, upwards of 100 to 125 kg CO_2 eq./m^2) which should be avoided if possible. Interestingly, these high-EC assemblies occur more frequently in the lower performance tiers for this data set. Figure 1 also finds that while low-depth options exist at all performance tiers (200 to 300 mm), the highest STC-rated assemblies made use of deep assemblies (of 400 to 450 mm) and concealed ceilings (i.e. underside acoustic treatment is required such that the ceiling cannot be exposed aesthetically.) Some assemblies with exposed ceilings achieve great STC performance but are limited to a maximum of STC-66 within this data set.

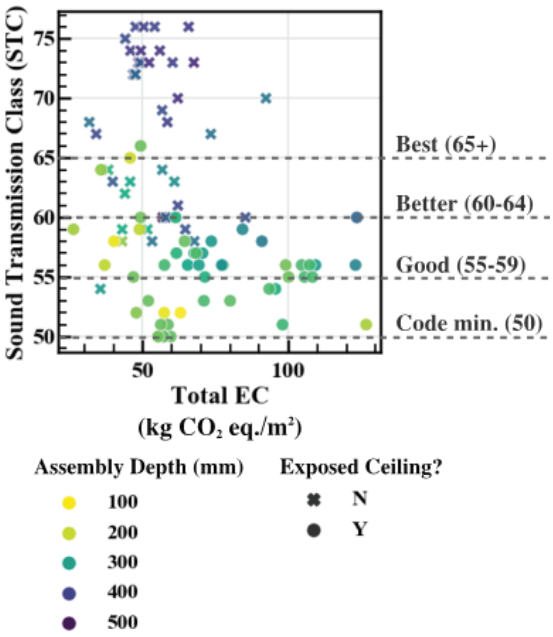

Figure 1: *STC versus EC for all studied code-compliant assemblies. Horizontal lines depict acoustic performance tiers.*

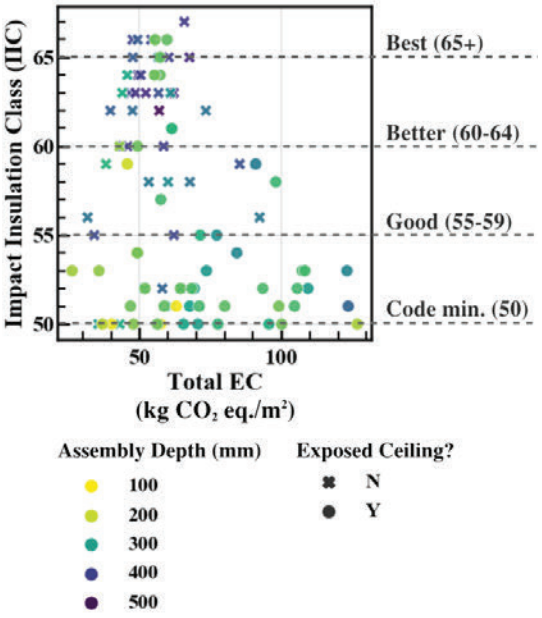

Figure 2: *IIC versus EC for all studied code-compliant assemblies. Horizontal lines depict acoustic performance tiers.*

Figure 2 shows some trends for IIC versus EC similar to those for STC versus EC. There is again no clear relationship between IIC and EC, and while high-EC options exist especially at lower performance tiers, there are low-EC options at all performance tiers. Further, there

are similarly relatively low-depth options (200 to 300 mm) at all performance tiers; however, the highest IIC-ratings are not limited to the deepest assemblies. Note that maximum IIC ratings are lower than the maximum STC ratings for assemblies in this data set, which is consistent with the difficulty of achieving higher IIC ratings in general. Figures 1 and 2 show several assemblies at a given performance rating with different EC values. While designers should attempt to select the lowest-EC option that meets their project's IIC and STC requirements, other factors out of the scope of this study, such as structural requirements, cost, aesthetics, and scheduling, may restrict assembly selection.

Figures 3 and 4 use the full database of assemblies with both STC and IIC test data and sufficient EC data, including non-code-compliant assemblies. These were included here to better understand the relationship between STC and IIC amongst the assemblies included in the WW Inventory, as well as to visualize how estimated EC (Figure 3) and approximate allowable span (Figure 4) are represented within the data set.

Figure 3 shows that STC and IIC have a hyperbolic relationship. Many more of the assemblies in this data set met code for STC than for IIC, as it is often more difficult to achieve higher IIC ratings. The lowest-EC assemblies with 15 to 20 kg CO_2 eq./m^2 often do not meet code. Relatively low-EC assemblies of 40 kg CO_2 eq./m^2 occur at all combined STC and IIC performance tiers (i.e. both STC and IIC are rated at the same performance tier for an assembly.) Assemblies with concealed ceilings generally achieve the best combined STC and IIC performance.

Figure 4 shows the same data as Figure 3, but with data points assigned a hue based on approximate allowable span per Table 2 and a marker based on the presence of a topping. All acoustic performance tiers for STC and IIC have options that can span upwards of 6 meters. Longer spans are likely possible at higher acoustic performance using similar assemblies to the 6-meter-spanning assemblies; however, the number and types of longer-spanning assemblies was limited in the WW inventory.

Figures 5 and 6 take the data from Figure 3 and removes the non-code-compliant assemblies for closer analysis of STC versus IIC (Figure 5) and Depth versus EC (figure 6). In each plot, both marker hue and style are assigned based on the assembly category per Table 1. Per Figures 5 and 6, although many concealed-ceiling assemblies are the deepest assemblies, averaging around 400 mm, these represent most of the best-performing assemblies for STC and IIC while maintaining relatively low EC, with several options in the range of 45 to 50 kg CO_2 eq./m^2.

Figure 5 and 6 also show that for categories that include versions both with and without a concrete or gypsum topping (Ceiling Side Concealed and Raised Wooden Sleepers), those with a topping tended to achieve higher STC and IIC ratings with limited impact to EC. This is likely because the concrete and gypsum toppings are most often paired with an acoustical mat, which together can be a relatively efficient use of material to improve acoustic insulation. While STC and IIC are generally related in Figure 5, some assemblies with flooring can have a high IIC rating even if STC is low.

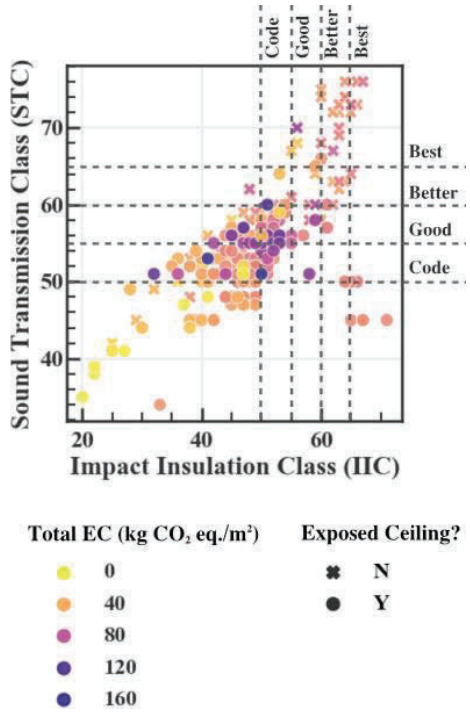

Figure 3: *STC versus IIC for all studied assemblies, including non-code-compliant assemblies.*

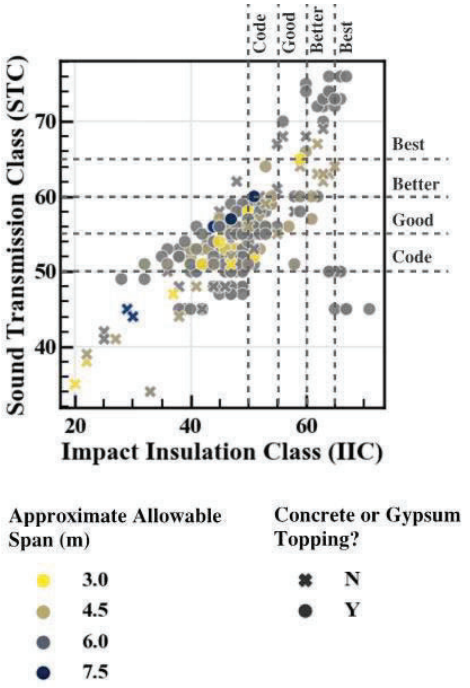

Figure 4: *STC versus IIC for all studied assemblies, including non-code-compliant assemblies.*

https://doi.org/10.52202/069179-0117

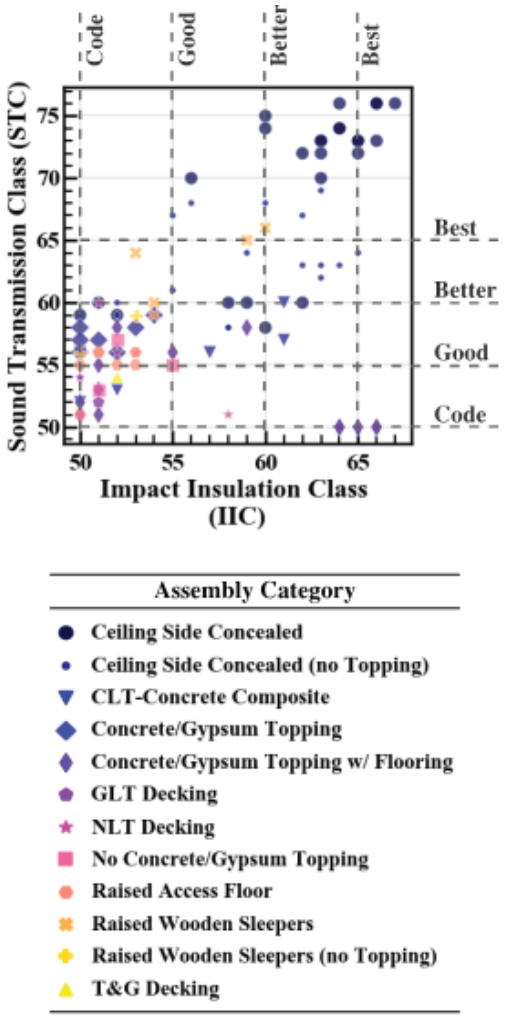

Figure 5: *STC versus IIC for all studied code-compliant assemblies*

Further, there is no relationship between EC and assembly depth, according to Figure 6. Low-EC options of 30 to 40 kg CO_2 eq./m^2 occur at a variety of assembly depths. This is likely because many assemblies use separation and air gaps between assembly components to improve acoustic performance, which makes efficient use of the materials in such assemblies.

Although Figures 1 through 6 indicate no clear relationship between sound insulation and EC, or between assembly depth and EC, options exist with higher EC. While it may be possible for designers to simply select the lowest-EC option that meets their project's STC and IIC requirements, there are most likely other factors that have the potential to control assembly selection, such as structural performance requirements, cost, scheduling, and material availability. Except for the approximate allowable spans shown in Figure 4, these factors are out of the scope of this research. However, by understanding the material efficiency of the components and systems used to improve sound insulation versus their EC, general recommendations and guidance can be provided to help reduce EC during early design decisions. Approximate component and system contributions to EC, STC, and IIC are shown in the bar chart in Figure 7.

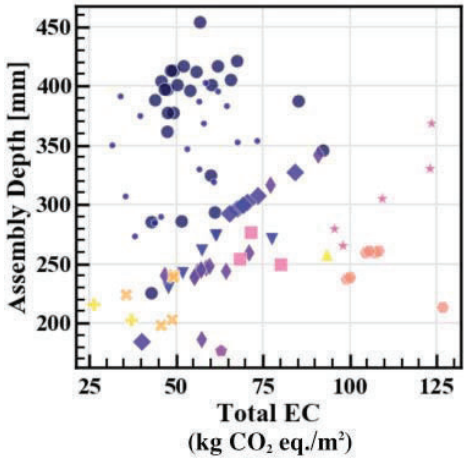

Figure 6: *Assembly depth versus EC per unit of floor area for all studied code-compliant assemblies*

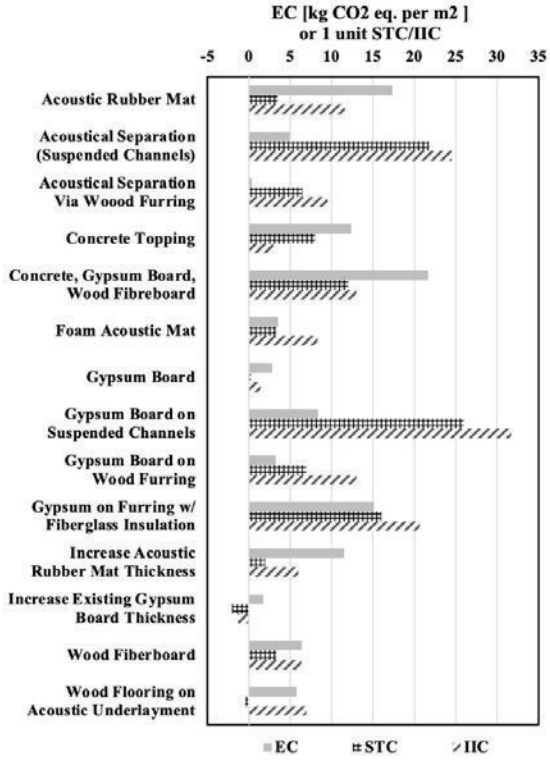

Figure 7: *EC per floor area of various materials or systems of materials and the difference in STC and IIC as compared to existing baseline assemblies without the given material or system. (Based on a selective set of assemblies with 5-ply CLT panel and 38-mm concrete topping)*

https://doi.org/10.52202/069179-0117

Figure 7 shows that increasing gypsum in an assembly that already has some gypsum does not add much EC but does not help STC or IIC either. Additionally, adding a separation between layers via wood furring provides the best STC and IIC improvement per amount of added EC. However, the most significant takeaway is that suspended channels and other means of providing acoustical separation between assembly layers provide high improvements to STC and IIC with relatively low EC impact to the assembly. This further validates that the typical recommendation of providing acoustic separation between layers is a materially-efficient and effective approach to improving sound insulation in an assembly.

3.2 DISCUSSION

Previous studies have shown that many mass timber floor systems without acoustic treatments have unsatisfactory air-borne and structure-borne sound insulation performance. However, adding materials and components to improve sound insulation can affect the EC of mass timber floor assemblies. By combining existing acoustic test results with EC data for a variety of assemblies, comparisons can be made to understand different assembly types and trade-offs with improved sound insulation. Because of data limitations due to lab-to-lab differences in STC and IIC results, as well as the limited availability of EC data, the findings of this research are most helpful during early design when more general and broad design decisions occur. Further analysis is needed to refine a design in the later stages of a project. This research finds that:

- Although adding acoustic treatments or systems to assemblies results in many with high EC, there is no clear relationship between STC and EC or between IIC and EC; relatively low-EC options exist at all acoustic performance tiers.
- In this data set, deeper assemblies are needed to achieve the best STC values, but low-depth options exist for all IIC tiers.
- One trade-off to achieve the best acoustic performance is that a designer may need to sacrifice exposed timber ceilings for underside acoustic treatment, which affects the architecture and results in greater assembly depth. However, because separations and air gaps are often used to achieve improved IIC and STC, these assemblies can still have relatively low EC.
- The best EC per STC or EC per IIC from separating components aligns with typical recommendations to improve sound insulation per the CLT handbook [5].
- An in-depth structural analysis was excluded; however, there are a wide variety of assemblies in this data set that can span up to 6 meters at all acoustic performance tiers.
- Experimental measurements were not taken from the same lab, which could have significant variability in results from lab to lab.
- More holistic studies including other building disciplines (for example, fire proofing, thermal insulation, cost, scheduling, etc.) may continue to reveal what the best assemblies are and for what design scenarios are best.
- There are many buildings for which code will not allow exposed timber ceilings depending on the Construction Type per the 2021 IBC, and in most cases, a non-combustible topping is required for mass timber floors [7].

4 CONCLUSIONS

This study extended the WW inventory that compiled the sound insulation performance of mass timber assemblies by extracting material information and adding EC data. The results showed that there was no direct correlation between EC and acoustic insulation. As a result, designers may select a floor assembly which meets project-specific goals for EC, STC, and IIC. Where several assemblies have similar acoustic performance, but different EC, other factors not in this study's scope may control the design selection. These additional factors include, but are not limited to, structural design requirements, cost, scheduling, and fire resistance requirements. Although this study helps extend existing research on the performance of mass timber assemblies within the built environment, a comprehensive database including additional considerations could improve initial assembly selection.

DATA AVAILABILITY

The WoodWorks Inventory of Acoustically-Tested Mass Timber Assemblies is publicly available at no cost from https://www.woodworks.org/resources/inventory-of-acoustically-tested-mass-timber-assemblies/. EC data generated for this paper, building on the WW Inventory data, is available by request from the corresponding author. Components and data sources in Table 5 are only representative. Data available from the corresponding author includes EPDs, technical data sheets, and reports for the components listed below. Most EPDs are manufacturer-specific, and as such, a multitude of manufacturers are listed below as data sources for this research; however, it is not the authors' intent to promote specific manufacturers or products.

- CLT – average of Product EPDs from various North American manufacturers: Smartlam, [smartlam.com], Structurlam [structurlam.com], Nordic Structures [nordic.ca/en/products], Vaagen [vaagentimbers.com], Kalesnikoff [kalesnikoff.com]
- Glue Laminated Timber (GLT) – Industry-wide EPD, [awc.org/wp-content/uploads/2021/11/AWC_EPD_NorthAmericanGluedLaminatedTimber_20200605.pdf]
- Mass Plywood Panel (MPP) – Product EPDs from Freres, [frereswood.com]

https://doi.org/10.52202/069179-0117

- Lightweight Concrete – Paper by Kanavaris et al. [34]
- Gypsum-based Toppings – USG Product EPD, [www.usg.com]
- Acoustic ceilings, sound reduction board, and other generic gypsum-, cement-, or fiber-based boards – Product EPDs by USG, [usg.com]
- Flooring Underlayment and Acoustic Membranes: Product EPDs by Autex Acoustics, [autexacoustics.com], Fermacell [fermacell.com/en], Isolon [isolon.lv/en], QT Sound Control, [qtsoundcontrol.com/], and Sto [stocorp.com]; Technical product data by AcoustiTech [acousti-tech.com/en], Kinetics [kineticsnoise.com/], Maxxon [maxxon.com], Pliteq [pliteq.com], Regupol [regupol.us], Soprema [soprema.us], and Sto [stocorp.com].
- Proprietary Subflooring – Product EPD by HuberWood, [huberwood.com/advantech]
- Raised Access Floor – Product EPD by Teccrete, [globalifs.com/raf-teccrete]
- Metal Channels, Studs, and Ceiling Framing – Product EPDs by Cemco [cemcosteel.com], and Clark Dietrich [clarkdietrich.com]; Design guide by USG [43].
- Insulation – Product EPDs and Technical data sheets by Johns Manville [jm.com/en/], Owens Corning [owenscorning.com/en-us/insulation], and Rockwool [rockwool.com/north-america/].
- Bamboo Plywood – Product EPD by Plyboo, [plyboo.com]
- Roof Board – Product EPD by Georgia Pacific, [buildgp.com/densdeck]
- Sand – Report by the National Stone Sand & Gravel Association [44].
- Flooring – Product EPDs by Mannington Commercial [manningtoncommercial.com] and Tarkett [home.tarkett.com/en_EU]; Industry-wide EPDs by TCNA [tcnatile.com] and RFCi [armstrongflooringpartner.force.com/ArmstrongConnect/s/article/Environmental-Product-Declaration-EPD-Luxury-Vinyl-Tile].

The ICE v3.0 database values were used for Nail Laminated Timber (NLT), tongue and groove (T&G) decking, wood subfloor, cement mortar, normal weight concrete, sound isolation clips, wood furring, wood board products such as plywood, hardwood flooring, and laminate flooring [31]. Finally, NRC reports on sound insulation research and assembly test results were used to clarify assembly construction where relevant [45],[46].

ACKNOWLEDGEMENTS

The authors would like to thank Ryan Solnosky, Kevin Parfitt, Dr. Ali Memari, and Corey Gracie-Griffin for their advisement on this work. This research is supported in part by the Graduate Assistance in Areas of National Need (GAANN) Fellowship and the J. Roger Glunt Graduate Fellowship in Housing, hosted by the Pennsylvania Housing Research Center (PHRC). Neither fellowship had any role or input in the planning and implementation of this research, and the included results do not reflect the views of these organizations.

REFERENCES

[1] P. F. Oldfield, *Tall buildings and sustainability. PhD thesis, University of Nottingham.* 2012.

[2] M. D. Webster, 'Achieving Net Zero Embodied Carbon in Structural Materials by 2050', 2020.

[3] G. Lowe, 'Wood , well-being and performance: The human and organizational benefits of wood buildings', British Columbia, 2020.

[4] H. K. D'Errico, 'Tall, cross-laminated and massive timber buildings: A United States perspective', Mississippi State University, 2016.

[5] L. Hu and S. Gagnon, 'Acoustic performance of cross-laminated timber assemblies', in *Cross Laminated Timber Handbook: 2019 Canadian Edition*, E. Karacabeyli and S. Gagnon, Eds. Pointe-Claire, Quebec, Canada: FPInnovations, 2019.

[6] M. Caniato, F. Bettarello, P. Fausti, A. Ferluga, L. Marsich, and C. Schmid, 'Impact sound of timber floors in sustainable buildings', *Build Environ*, vol. 120, pp. 110–122, 2017, doi: 10.1016/j.buildenv.2017.05.015.

[7] International Code Council Inc., *2021 International Building Code*. Country Club Hills, IL: International Code Council Inc., 2020. [Online]. Available: https://codes.iccsafe.org/content/IBC2021P1

[8] T. E. Vigran, *Building Acoustics*. New York City, NY: Taylor & Francis, 2008.

[9] D. P. Hindman and M. V. Golden, 'Acoustical Properties of Southern Pine Cross-Laminated Timber Panels', *Journal of Architectural Engineering*, vol. 26, no. 2, pp. 1–8, 2020, doi: 10.1061/(ASCE)AE.1943-5568.0000407.

[10] F. Asdrubali, S. Schiavoni, and K. v Horoshenkov, 'A Review of Sustainable Materials for Acoustic Applications', *Building Acoustics*, vol. 19, no. 4, pp. 283–311, 2012, doi: 10.1260/1351-010X.19.4.283.

[11] WoodWorks, 'Acoustically-tested mass timber assemblies'. 2022.

[12] R. Salles E Portugal, B. Lawrence, P. F. Laleicke, and A. Sinha, 'Technical note: A preliminary study to quantify the environmental impacts of concrete and cork flooring', *Wood and Fiber Science*, vol. 50, no. 1, pp. 104–112, 2018, doi: 10.22382/wfs-2018-011.

[13] J. M. Broyles, M. R. Shepherd, and N. C. Brown, 'Design Optimization of Structural–Acoustic Spanning Concrete Elements in Buildings', *Journal of Architectural Engineering*, vol. 28, no. 1, pp. 1–11, 2022, doi: 10.1061/(asce)ae.1943-5568.0000520.

[14] J. M. Broyles *et al.*, 'Shape optimization of a concrete floor systems for sustainability, acoustical, and thermal objectives', in *Structures and Architecture A Viable Urban Perspective?*, CRC Press, 2022, pp. 1121–1128.
[15] T. M. Echenagucia, A. Astolfi, M. Jansen, and M. Sassone, 'Architectural Acoustic and Structural Form', *Journal of the International Association for Shell and Spatial Structures*, vol. 49, no. 3, Dec. 2008.
[16] M. A. H. Mirdad, H. Daneshvar, T. Joyce, and Y. H. Chui, 'Sustainability Design Considerations for Timber-Concrete Composite Floor Systems', *Advances in Civil Engineering*, vol. 2021, 2021, doi: 10.1155/2021/6688076.
[17] H. E. Ilgın, M. Karjalainen, and S. Pelsmakers, 'Contemporary tall residential timber buildings: what are the main architectural and structural design considerations?', *International Journal of Building Pathology and Adaptation*, 2022, doi: 10.1108/IJBPA-10-2021-0142.
[18] Structurlam, 'Mass Timber Technical Guide for CrossLam CLT and GlulamPLUS'. Sructurlam, 2021.
[19] Structurlam, 'StructurDek GLT'. Penticon, BC.
[20] Binational Softwood Lumber Council, 'Nail-Laminated Timber Design & Construction Guide v1.0'. 2017.
[21] M. Long, *Architectural Acoustics*. Elsevier, 2005.
[22] ASTM International, 'ASTM E90: Standard Test Method for Laboratory Measurement of Airborne Sound Transmission Loss of Building Partitions and Elements'. 2016.
[23] ASTM International, 'ASTM E492: Standard Test Method for Laboratory Measurement of Impact Sound Transmission Through Floor-Ceiling Assemblies Using the Tapping Machine'. 2012.
[24] A. Meier, A. Schmitz, and G. Raabe, 'Inter-Laboratory Test of Sound Insulation Measurements on Heavy Walls : Part II – Results of Main Test', pp. 171–186, 1999.
[25] R. Öqvist, F. Ljunggren, and A. Ågren, 'On the uncertainty of building acoustic measurements – Case study of a cross-laminated timber construction', *Applied Acoustics*, vol. 73, pp. 904–912, 2012, doi: 10.1016/j.apacoust.2012.03.012.
[26] O. A. B. Hassan, 'An alternative method for evaluating the air tightness of building components', *Build Environ*, vol. 67, pp. 82–86, 2013, doi: 10.1016/j.buildenv.2013.05.007.
[27] Technical Committee : ISO/TC 43/SC 2 Building acoustics, 'ISO 12354-1:2017 Building acoustics — Estimation of acoustic performance of buildings from the performance of elements — Part 1: Airborne sound insulation between rooms', 2017.
[28] ASTM International, 'ASTM E1007-21: Standard Test Method for Field Measurement of Tapping Machine Impact Sound Transmission Through Floor-Ceiling Assemblies and Associated Support Structures', West Conshohocken, PA, 2021.
[29] ASTM International, 'ASTM E336-20: Standard Test Method for Measurement of Airborne Sound Attenuation between Rooms in Buildings', West Conshohocken, PA, 2020.
[30] E. Karacabeyli and S. Gagnon, *Canadian Cross Laminated Timber Handbook: 2019 Edition*. Pointe-Claire, Quebec, Canada: FPInnovations, 2019.
[31] G. Hammond, C. Jones, F. Lowrie, and P. Tse, 'Inventory of carbon & energy: ICE database version V3.0'. 2019.
[32] Athena Sustainable Materials Institute, 'EPD: Structurlam Crosslam CLT', Okanagan Falls, BC, 2020.
[33] UL Environment, 'EPD: North American Glued Laminated Timber - American Wood Council, Canadian Wood Council', American Wood Council, Canadian Wood Council, 2020.
[34] A. A. Abbas *et al.*, 'Reducing the carbon footprint of lightweight aggregate concrete', pp. 1–7, 2020.
[35] SCS Global Services, 'EPD: ECORE Products', ECORE, 2015.
[36] Intertek Health Sciences Inc., 'EPD: Global IFS TecCrete Raised Access Floor', 2020.
[37] T. Brooke, 'EPD: USG 5/8 in. (15.9mm) Sheetrock Brand Firecode X Panels', 2021.
[38] UL Environment, 'EPD: Owens Corning EcoTouch Pink Fiberglas Batt & Roll Insulation - Unfaced and Faced', 2018.
[39] Institut Bauen und Umwelt e.V., 'EPD: ROCKWOOL Stone Wool Insulation', 2019.
[40] E. Griffing and M. Overcash, 'EPD: AtlasMasland - Modular Carpet Family', 2020.
[41] L. G. F. Tellnes, 'EPD: ISOLON TX Cross-linked PE foam SkumTech AS', 2021.
[42] UL Environment, 'EPD: CEMCO Cold-Formed Steel Framing Systems', 2016.
[43] USG, 'Chapter 2 - Framing', in *The Gypsum Construction Handbook*, 7th Editio., 2014, pp. 88–100.
[44] National Stone Sand & Gravel Association, 'The Aggregates Industry - Greenhouse Gases: Low Emissions, High Resiliency', 2021.
[45] I. Sabourin, 'Measurement of airborne sound insulation of 8 wall assemblies measurement of airborne and impact sound insulation of 29 floor assemblies', 2015.
[46] S. Schoenwald, B. Zeitler, F. King, and I. Sabourin, 'Acoustics summary: sound insulation in mid-rise wood building: report to Research Consortium for Wood and Wood-Hybrid Mid-Rise Buildings', 2014.

https://doi.org/10.52202/069179-0117

World Conference on Timber Engineering Oslo 2023

ECOLOGICAL PERFORMANCE AND RECYCLABILITY OF TIMBER-BASED CONSTRUCTIONS

Alireza Fadai[1], Daniel Stephan[2]

ABSTRACT: The growing importance of large-volume timber construction in European metropolitan areas leads to the investigation of a possible optimization potential in the use of timber in combination with other materials. This results in further investigations to gain synergies from a combination of the individual composite systems. For this reason, different types of combined timber composite constructions are developed and evaluated with regard to structural implementation and environmental optimization. Through a suitable combination, a construction-optimized design with increased resource efficiency can be achieved both at the component level and at the level of the overall structure.

For a holistic ecological assessment of building structures, the whole life cycle of the construction system needs to be investigated. Sustainable recycling means employing the materials used for the construction and operation of a building after the initial use for a new purpose. In a progressive design process, recyclability of the materials has to be considered in the planning stage of construction projects. If possible, recyclable components or already recycled components should be used. The factors separability and absence homogeneity are particularly decisive for the assessment of the possible recyclability of materials. For this reason, various life cycle phases and exploitation scenarios beyond the production phase of the building materials ("from cradle to gate") are evaluated. Especially the timber-wood lightweight concrete-glass-façade, developed and further investigated at the research department "Structural Design and Timber Construction" at the Vienna University of Technology, is set in context to standardized exterior façades to demonstrate a sensible design process regarding recyclability, resource efficiency and ecological advantages.

In addition, the thermal behavior is assessed in multiple studies. In the process, different construction methods, including timber, reinforced concrete and brick construction, are investigated and impact factors such as the orientation and size of the windows, the total solar energy transmittance of the glazing and solar shading devices are evaluated.

KEYWORDS: Wood-based construction, Sustainable building, Environmental impacts, Recyclability, Energy efficiency

1 INTRODUCTION

The growing importance of large-volume timber construction in European metropolitan areas leads to the investigation of a possible optimization potential in the use of timber in combination with other building materials. This results in further investigations to gain synergies from a combination of the individual composite systems.
For this reason, different types of combined timber composite constructions are developed and evaluated with regard to structural implementation and environmental optimization. Through a suitable combination, a construction-optimized design with increased resource efficiency can be achieved both at the component level and at the level of the overall structure.
Within the scope of subprojects, material-specific potentials could be identified for the respective materials used, which combine timber in the form of integrated timber ribbed panels (HCLTP elements [1]), wood lightweight concrete (WLC) and glass to increase the overall resource efficiency. This construction is in the focus of the current research project (cf. Figure 1 and [2, 3]).
When timber-WLC-glass-façades are used, the combined panel and ribbed component geometry offers an ideal basis for the execution of a multi-layer polyvalent composite construction.

The ribbed structure makes it possible to mount stiffening glass elements on the outside of the ribs and to create a buffer plane in the space between the ribs. By using an additional adaptive planking made of WLC, this gap can contribute to the structural optimization of the supporting structure [4].

[1] Alireza Fadai, TU Wien, Research Unit of Structural Design and Timber Engineering, Austria, alireza.fadai@tuwien.ac.at
[2] Daniel Stephan, TU Wien, Austria, daniel.stephan@tuwien.ac.at

https://doi.org/10.52202/069179-0118

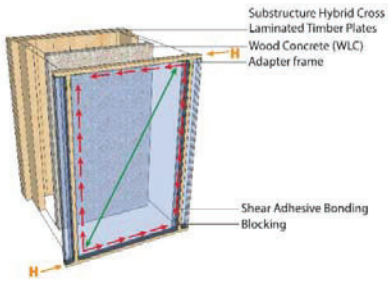

Figure 1: *Timber-wood lightweight concrete-glass façade*

The amount of glass used in this façade not only increases the resource efficiency of the construction, it also gives the opportunity to design optimal ratios of opaque and transparent elements. Nowadays the people feel the consequences of climate change very clearly. Especially in dense city areas the importance of climate resistant planning is invaluable. One of the key elements of climate resilient planning is designing glass façades to increase solar gains in the winter to reduce the heating demand but to look out for overheating in the summer.
To figure out clear factors for the design process, various simulations of different construction methods are carried out and put in context to the timber-WLC-glass-façade design decision. In the process, impact factors like orientation, window size, total solar energy transmittance (g-value) and solar shading devices are valuated.

2 LIFE CYCLE ASSESSMENT

Sustainable recycling means employing the materials used for the construction and operation of a building after the initial use for a new purpose. Waste products turn into secondary raw material. Easier dismantlability of an object into its components means that this object shows a better deconstruction. [5].
In a progressive design process, recyclability of the materials has to be considered in the planning stage of construction projects. If possible, recyclable components or already recycled components should be used. The factors separability and absence homogeneity are particularly decisive for the assessment of the possible recyclability of materials.
In consideration of their recyclability the lifecycle of different construction alternatives with a focus on timber and glass as building material is being analyzed and evaluated. For a holistic ecological assessment of building structures, the whole life cycle of the construction system needs to be investigated. For this reason, various life cycle stages and exploitation scenarios beyond the production phase of the building materials ("from cradle to gate") are evaluated according to the European standards EN 15804 [6] and EN 15978 [7], including the use and end of life cycle stages, such as energy consumption, maintenance and repair, respectively deconstruction, disposal and recycling ("from cradle to grave").

Thereby considered assessment criteria are the renewable **P**rimary **E**nery **I**nput (PEI_e), the non-renewable **P**rimary **E**nergy **I**nput (PEI_{ne}) and the **G**lobal **W**arming **P**otential over 100-year time horizon (GWP_{100}).
With these environmental computations, the ecological properties and impacts of wood-based construction systems can be shown. Furthermore, decisively design criteria for sustainable structural systems can be derived thereof [8].
The ecological assessments are calculated with integration of the databases "IBU-EPD" [9] and "ÖKOBAUDAT" [10], both managed by the German Federal Ministry of Housing, Urban Development and Building (BMWSB). In the last years the database updated from EN 15804 (now called EN 15804 + A1) [6] to the new system EN 15804 + A2 [11] because the new standard DIN EN 15804 + A2 [11] is introduced. With this change the ecological parameters differ a lot from the old ones and must not be mixed in the calculation process. The new system will be the basis of future calculations, especially within the Assessment System for Sustainable Building (BNB) [12]. The ecological assessment in this paper focuses in the comparison of different materials and the timber-WLC-glass-façade from before the change, so the used data is based on the system according to EN 15804 + A1 [6].
To put the decision to use wood- and glass-based materials as primary investigation in the timber-WLC-glass-façades in a clear context, different building materials and components are compared [13].

Figure 2 compares the primary energy demand, categorized in renewable and non-renewable (grey energy), of different building materials per m³ for the life cycle stages A-D (production, construction process, use and end of life stage as well as supplementary beyond the building life cycle).

The comparison of the materials concrete (different compressive strength classes), brick (insulating and non-insulating), timber (coated, structural and medium density fiberboard) and glass panels shows that timber and glass have high primary energy values. Nevertheless, most of the primary energy of timber is the renewable part (mostly solar power in the production phase) and glass is calculated as 1 x 1 x 1m block (of glass) to ensure comparability. Concrete with low compressive strength (C25/30) has lower primary energy demand than concrete with higher compressive strength (C50/60). Bricks without insulation and lower density of 740kg/m³ lead to lower environmental impact than its perlite filled version with 800kg/m³. In need of insulation material later on in most cases, the low-density version is more likely to be used within a solid brick construction.

https://doi.org/10.52202/069179-0118

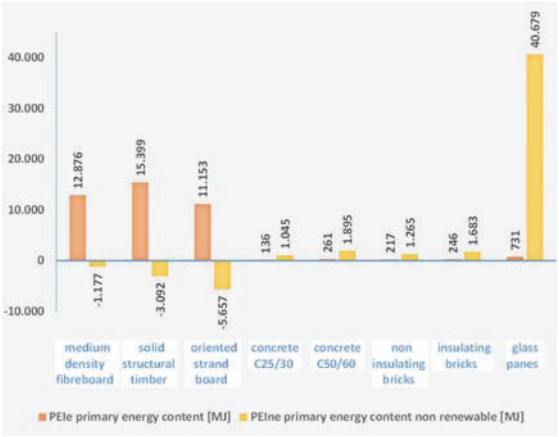

Figure 2: *Primary energy demand of building materials per m³ for the life cycle phases A-D*

Figure 3 illustrates one of the great advantages of timber-based materials. With a negative input for the global warming potential, wood has a considerable environmental balance. In contrast, concrete and brick materials cause more environmental impacts depending on density and compressive strength, similar to the calculations of the primary energy demand. Glass materials again cause the most GWP value due to the framework conditions, but have a high potential when used as individual panes.

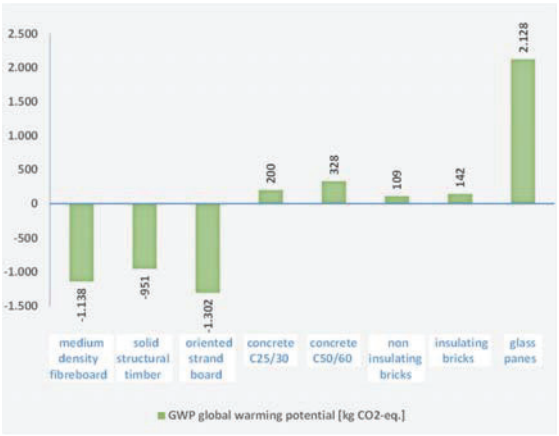

Figure 3: *Global warming potential of building materials per m³ for the life cycle phases A-D*

In a comparison of different exterior walls with concrete and brick materials (cf. Figure 4), vertically perforated brick and monolithic concrete require the most primary energy. Monolithic brick, perlite-filled brick and concrete with **e**xternal **t**hermal **i**nsulation **c**omposite **s**ystem (ETICS) roughly tie here.

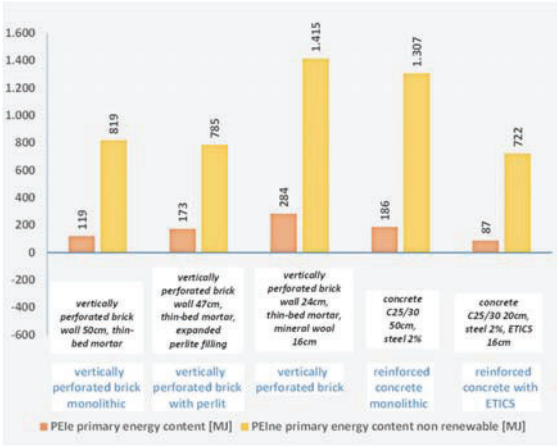

Figure 4: *Primary energy demand of brick and concrete exterior walls per m² for the life cycle phases A-D*

As can be seen in Figure 5, the perlite-filled brick in particular stands out in comparison, because of its high GWP value due to its filling. The GWP data of the other exterior walls are similar, with the ETICS concrete and the monolithic brick having the lowest GWP values.

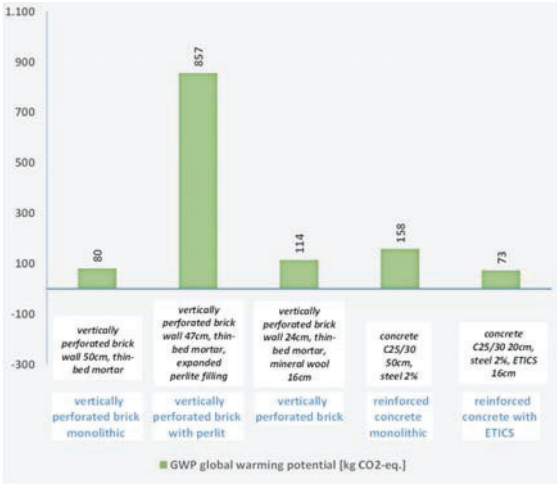

Figure 5: *Global warming potential of brick and concrete walls per m² for the life cycle phases A-D*

The analyzed timber exterior walls perform significantly better in terms of primary energy demand, especially the non-renewable part (cf. Figure 6).

https://doi.org/10.52202/069179-0118

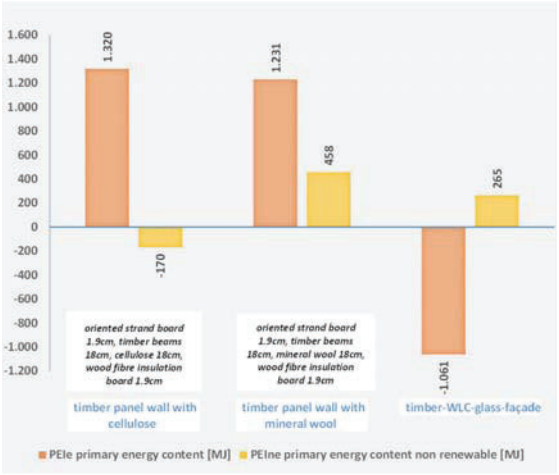

Figure 6: *Primary energy demand of timber exterior walls per m² for the life cycle phases A-D*

The results of the timber-WLC-glass-façade are particularly interesting and noteworthy. In the calculations per m² of façade, the strength of a mixed construction method from an ecological point of view is clearly shown by the very low primary energy values.

The same tendency is just as evident when considering the global warming potential. The timber exterior walls have a lower GWP value than the concrete or brick walls, especially the timber panel with cellulose and the timber-WLC-glass-façade (cf. Figure 7).

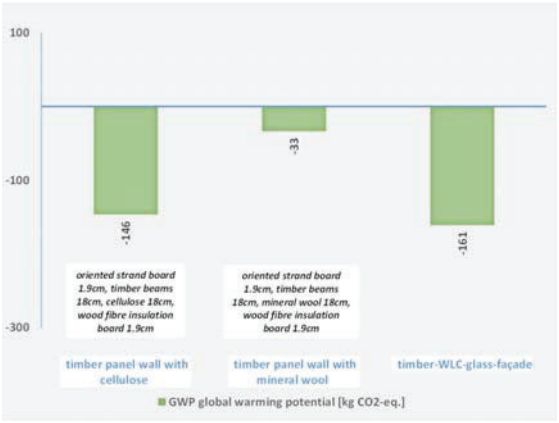

Figure 7: *Global warming potential of timber exterior walls per m² for the life cycle phases A-D*

A sensitive mixture of building materials (including glass) in a façade can therefore lead to ecological advantages if connected correctly. These studies show the potential of hybrid timber façades especially in case of the overall resource efficiency and recyclability potential.

3 ENERGY EFFICIENCY

At the present time, the required energy standard of buildings according to building regulation is at the level of a low-energy house. By introducing the "Energy Performance of Buildings Directive", the European council established the basis for uniform valuation. These guidelines indicate that a building has to be sustainable, the used construction materials and components have to be recyclable and the use of environmentally friendly resources and secondary materials is welcome [14].
Coherences of sustainability and energy efficiency on component and on overall system level can most suitable be shown by the assessment of a building model with a maximum geometrical simplicity. Consequently, a quadratic one-storied simulation model in different variations (wood-based and conventional building structures) is defined (cf. Figure 8) and subsequently investigated and compared with regard to its thermal behavior (heating energy demand and operative room temperature).

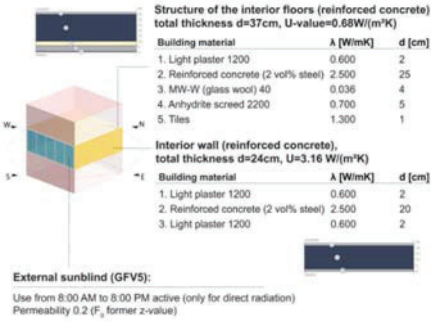

Figure 8: *Isometric view of the simulation model*

The simulations are carried out with the 3D online tool Thesim 3D [15]. Thesim 3D simulates the thermal behavior of a room in a steady-state, periodic condition (period length: 1 day). It is therefore particularly suitable for standardized summer overheating tests according to EN ISO 13791 [16] or ÖNORM B 8110-3 [17].
To evaluate these assessments, different types of conventional constructions are compared with the timber-WLC-glass-façade. The comparison is made with respect to materialization at the component level as well as at the overall structure level, which allows a scale-independent evaluation of the investigated types of construction to be achieved. This evaluation is made possible by a broad spectrum of calculations, ranging from static and dynamic thermal simulations for annual heating-up and overheating periods to the resulting various ecological impact calculations.

As a starting point for the simulations, a critical room with the dimensions 4 x 4 x 6m is defined (cf. Figure 9), which is initially calculated with the timber-WLC-façade in Vienna, Austria (average temperature is 24.9°C ± 7K). In the first calculation neither shading nor night ventilation is applied, the windows are triple glazing (U-value = 0,5; g-value = 0,48).

https://doi.org/10.52202/069179-0118

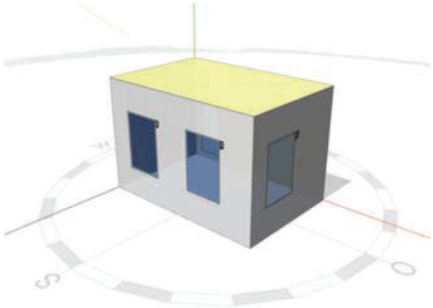

Figure 9: *Isometric view of the critical room model*

As shown clearly in Figure 10, the operative room temperature far exceeds the 27°C limit according to ÖNORM B 8110-3 [17]. Due to the closed windows facing south and lack of ventilation, the heat in the critical visibly accumulates and cannot escape.

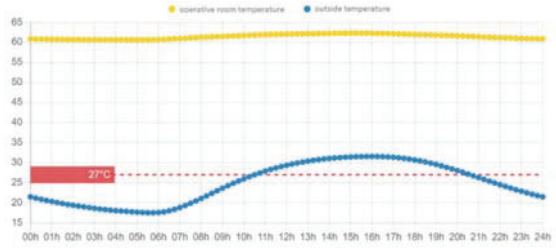

Figure 10: *Thermal simulation of the critical room*

Therefore, some optimization measures has to be taken (cf. Figure 11). This time shading (F_c = 0.2) in direct sunlight and night ventilation from 08:00 PM to 08:00 AM (tilted window) is applied.

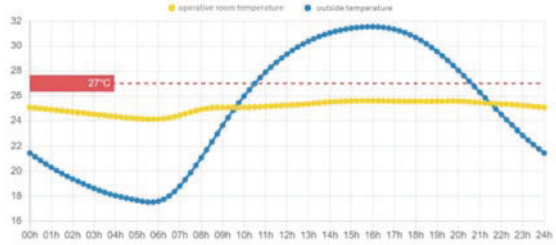

Figure 11: *Thermal simulation of the critical room with optimization measures*

As a result, the critical room does not exceed an operative room temperature of 25.8°C even during the hottest summer days.

Furthermore, to evaluate other influencing factors several thermal simulations of existing buildings in the cities Vienna and Wels (Austria), Bochum (Germany) as well as London (England) are carried out. The critical room dimensions are congruent, but other framework conditions are unquestionably different in these European cities. The wide range of climatic conditions and various construction made out of timber, reinforced concrete and brick should lead to nuanced solutions. To save energy on the one hand and to avoid summer overheating on the other hand the factors "orientation and size of windows", "g-values of window panes" and "awnings" are identified.

As the studies show, the building design contributes significantly to the desired indoor climate in summer. Independent of the location the highest solar radiation occurred in the south and west zones of the buildings and has no shading available. Consequently, the placement and size of windows as well as the use of balconies and shading devices are crucial for the overheating aspect.
In terms of g-value of window panes the case study in London with a solid wood building (daily average exterior temperature: 16.3°C) shows that a lot of emphasis must be placed on orientation and the g-value during the planning phase.
Especially in this context, the question between double and triple glazing arises. In winter, triple glazing (U-value = 0.7; g-value = 0.48) is more advantageous than double glazing (U-value = 1.4; g-value = 0.27) because of its low U-value. In summer, however, low U-values and higher g-values are counterproductive, as less heat is lost through the windows and overheating occurs (cf. Figure 12).

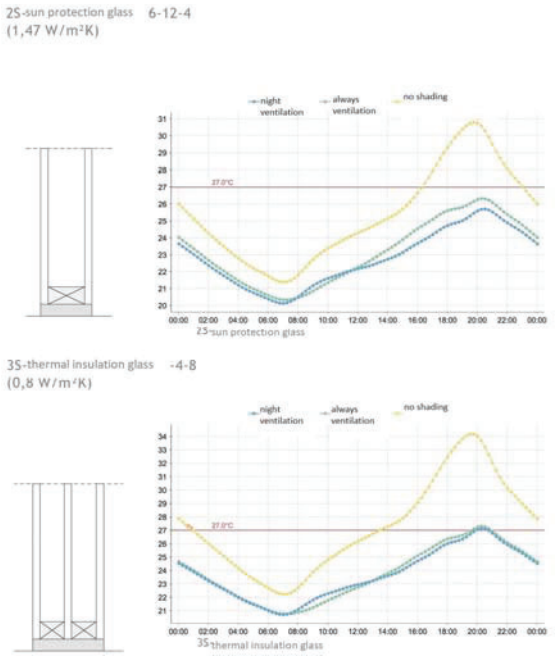

Figure 12: *Thermal dynamic building simulations with double and triple glazing, building in London (© ITI/TU Wien)*

https://doi.org/10.52202/069179-0118

4 CONCLUSIONS

This paper illustrates how timber-based structures can be used both optimally and sustainably in terms of their ecological value, recyclability and energy efficiency. On the basis of these investigations, the competitiveness of timber construction compared to conventional construction methods is demonstrated. Especially the timber-WLC-glass-façade, developed and further investigated at the research department "Structural Design and Timber Construction" at the TU Wien is set in context to standardized exterior façades to demonstrate a sensible design process regarding recyclability, resource efficiency and ecological advantages.

When looking at the ecological values of individual building materials, it is apparent that in terms of non-renewable primary energy input (primary energy necessary to construct a building; so-called "*grey energy*") and global warming potential, timber-based materials have a good environmental balance. Nevertheless, building materials such as concrete or even glass can also offer an ecological advantage in certain building components. The timber-WLC-glass-façade is an example of the environmental benefits that mixed construction can have, as long as it meets the structural requirements.

Furthermore, multiple studies are carried out to assess the thermal behavior of the timber-WLC-glass-façade and other materials. In the process, different construction methods, including timber, reinforced concrete and brick construction, are investigated and impact factors such as the orientation and size of the windows, the g-value of the glazing and solar shading devices are evaluated. In conclusion a thermal sensitive design should always consider structural sun protection, the situational number of glass layers in windows, appropriate ventilation behavior and orientation of the most critical room in the given location.

Ultimately, a well-thought-out planning process requires many factors. In order to move towards a sustainable circular economy, the issues of environmental sustainability, recyclability and resource efficiency must be considered in particular.

REFERENCES

[1] Sustersic, Iztok, et al., "Hybrid cross-laminated timber plates (HCLTP)–numerical optimisation modelling and experimental tests," in *World Conference on Timber Engineering (WCTE 2016), Wien*, Vienna, 2016.

[2] Fadai, Alireza; Winter, W., "Ressource-efficient wood lightweight concrete composites in building constructions," in *Structural Engineering International 27(2), pp. 197-204*, 2017.

[3] Fadai, Alireza; Rinnhofer, M.; Winter, W., "Development of Timber-Wood Lightweight Concrete-Glass Composite for Multi-Story Facades," in *Applied Mechanics and Materials, Vol. 887, pp. 30-39*, 2019.

[4] Fadai, Alireza, "Develop Innovative Load-Bearing Structures For Use Of Wood-Based Raw Materials," in *Proceedings of the International Conference on Structural Health Assessment of Timber Structures, SHATiS´2019*, Guimarães, Portugal, 2019.

[5] Schneider, Patricia; Pfoh, S.; Grimm, F., "Projektplattform Energie - Leitfaden 01 Ökologische Kenndaten Baustoffe und Bauteile," TU Wien, 2016.

[6] *ÖNORM EN 15804:2012+A1:2013 Sustainability of construction works - Environmental product declarations - Core rules for the product category of construction products,* Austrian Standards, 2014.

[7] *ÖNORM EN 15978 - Sustainability of construction works - Assessment of environmental performance of buildings - Calculation method,* Austrian Standards, 2012-10-01.

[8] Fadai, Alireza; Stephan, D., "Zur Bewertung der Ressourceneffizienz entwickelter hybriden Holz-Glas-Hülle im mehrgeschossigen Hochbau," in *Glasbau 2021*, 2021.

[9] "Institut Bauen und Umwelt e.V., "IBU-EPD" Institute of Building and Environment e.V., 2019.," [Online]. Available: https://ibu-epd.com. [Accessed 15 02 2019].

[10] "ÖKOBAUDAT platform," Federal Ministry of Housing, Urban Development and Building, [Online]. Available: https://www.oekobaudat.de/en.html. [Accessed 11 March 2023].

[11] *ÖNORM EN 15804 - Sustainability of construction works - Environmental product declarations - Core rules for the product category of construction products,* Austrian Standards, 2022-02-15.

[12] "Assessment System for Sustainable Building (BNB)," German Federal Ministry of the Interior, Building and Community, [Online]. Available: https://www.bnb-nachhaltigesbauen.de/en/assessment-system/. [Accessed 11 March 2023].

[13] A. Fadai and D. Stephan, "Ecological performance of reversible constructions," in *Sustainable Built Environment D-A-CH Conferenz*, Berlin, 2022.

[14] P. J. Sölkner, A. Oberhuber, S. Spaun, R. Preininger, F. Dolezal, H. Mötzl, A. Passer and G. Fischer, "Innovative Gebäudekonzepte im ökologischen und ökonomischen Vergleich über den Lebenszyklus," Austrian Ministry for Transport, Innovation and Technology, Vienna, 2014.

https://doi.org/10.52202/069179-0118

[15] J. Nackler, "Thesim," 2022. [Online]. Available: www.thesim.at. [Accessed 15 Juli 2022].

[16] EN ISO 13791, *Wärmetechnisches Verhalten von Gebäuden - Sommerliche Raumtemperaturen bei Gebäuden ohne Anlagentechnik - Allgemeine Kriterien und Validierungsverfahren,* 2010.

[17] *ÖNORM B 8110-3, Wärmeschutz im Hochbau - Teil 3: Ermittlung der operativen Temperatur im Sommerfall (Parameter zur Vermeidung sommerlicher Überwärmung),* 2020-06-01.

World Conference on Timber Engineering Oslo 2023

EMBEDMENT STRENGTH OF RECOVERED SPRUCE AND OAK

Caitríona Uí Chúláin[1], David Gil-Moreno[2], Daniel F. Llana[3], Mitja Plos[4], Goran Turk[5], Paul Hogan[6], Annette M. Harte[7]

ABSTRACT: The circular use of construction materials is an essential step in the drive to reduce the environmental impact of the construction sector. One of the factors that currently limits the ability to reuse timber recovered from demolition in structural applications is the lack of data relating to its structural performance, which would allow for the certification of its characteristics and the development of design guidelines.

This paper presents a study on the embedment performance of recovered timber by determining the embedment strength of spruce and oak specimens recovered from demolition sites in Ireland and Slovenia. Tests were carried out in the parallel and in the perpendicular to the grain directions using three different dowel diameters. The results were comparable with mean values reported in the literature and with the empirical Eurocode 5 predictions. Based on these findings, it can be concluded that the embedment performance of the recovered spruce and oak is equivalent to that of new timber. Further studies on recovered timber of different origin, species, ages and history of use are needed to confirm these findings.

KEYWORDS: Embedment strength, connections, circular construction, recovered timber, spruce, oak

1 INTRODUCTION

More than a third of all waste within the EU comes from construction and demolition [1]. This waste contains valuable natural resources with significant potential for reuse and recycling. In Europe, timber recovered from buildings at the end of life, often referred to as recovered or secondary timber, is, for the most part, converted into chips for use in energy production and, to a lesser extent, for the manufacture of particle boards or pallet blocks [2-4].

Recovered timber is considered to have great reuse potential [5] with maximum environmental benefits achieved through reuse in products with long lifespan, such as those for structural applications in buildings. However, the realisation of this potential is currently inhibited by the lack of grading standards and design guidelines for use of this resource. Recent European projects have begun to address this issue including the Buildings as Material Banks project (BAMB2020) [6], the CaReWood project [7] and the InFutUReWood project [8]. These projects have identified problem areas and proposed technical and methodological solutions to maximise reuse of timber from current buildings especially as a structural material. The most important issue to be addressed is of lack of knowledge of the material properties after the end of its first life.

Some recent studies have applied visual grading and non-destructive testing to characterise the flexural properties of recovered softwoods and hardwoods. Nakajima and Nakagawa [9] developed a visual grading approach for recovered timber boards which acocunts for holes and fissures. Non-destructive evaluation of recovered softwood [10-13] and hardwood [14] timber boards using acoustic methods was used to sort timber for the manufacture of CLT panels, which were subsequently tested in bending.

The issue of connections between recovered wood members has not been addressed to date and the development of design guidelines for such connections will be key to the successful implementation of the circular use of wood in construction.

Dowel-type connections are commonly used to connect structural timber members. For laterally-loaded fasteners, Eurocode 5 (EN1995) [15] provides guidelines derived from the Johansen yield model [16] for the connection capacity. The embedment strength of the timber elements being connected is a required property. For this, the embedment strength may be determined by test or calculation. The embedment strength may be established from experimental tests in accordance with standards, which for Europe is EN 383 [17]. Many studies have reported on embedment strength tests on new timber. Ehlbeck and Werner [18] tested seven different wood

[1] Caitríona Uí Chúláin, University of Galway, Ireland, caitriona.uichulain@universityofgalway.ie
[2] David Gil-Moreno, University of Galway, Ireland, david.gil-moreno@universityofgalway.ie
[3] Daniel F Llana, Universidad Politécnica de Madrid, Spain, d.f.llana@upm.es
[4] Mitja Plos, University of Ljubljana,Slovenia, mitja.plos@fgg.uni-lj.si
[5] Goran Turk, University of Ljubljana, Slovenia, goran.turk@fgg.uni-lj.si
[6] Paul Hogan, Hegarty Demolition, Ireland, paul@hegartydemolition.ie
[7] Annette M Harte, University of Galway, Ireland annette.harte@universityofgalway.ie

https://doi.org/10.52202/069179-0119

species (including softwood and hardwoods) using dowel diameters ranging from 8 mm to 30 mm under different load to grain angles. The tests were made in accordance with the then proposed standardised European embedment test method prEN 383 in compression and in tension. The test findings indicated that the embedment strength increases linearly with increasing wood density and that results depend significantly on the fastener diameter. A formula was proposed where the strength is proportional to the timber density with a correction depending on the diameter of the dowel. Sawata and Yasumura [19] tested four grades of Japanese softwood under loading parallel and perpendicular to grain using dowel diameters ranging from 8 mm to 20 mm. The study found that there is significant correlation between embedding strength and density but found that the dowel diameter did not significantly influence results. Sandhaas *et al*. [20][21] compiled a data set of softwood and hardwood embedment tests. Six different wood species with densities ranging from 465 kg/m^3 to over 1200 kg/m^3 were tested, using 12 mm and 24 mm diameter dowels of two different steel grades. All embedment tests were carried out in compression. The influence of the dowel diameter on the embedment strength was found to be of low significance. They presented a simplified formula, discounting any influence of the dowel-to-wood surface area, that gave a more straight-forward design equation to that proposed by Ehlbeck and Werner [18]. Santos et al. [22] found that results of embedment testing to European EN 383 [17] and American ASTM D5764 [23] standards were comparable.

As an alternative to testing, embedment strength may be determined by calculation. Eurocode-5 [15] provides expressions for the embedment strength of new timber, which are a function of the characteristic timber density (the 5th percentile), the dowel diameter, the angle between the load direction and the timber grain, and the timber type. These empirical equations were adapted from those proposed by Ehlbeck and Werner [18] and were derived based on tests on new timber. Their applicability to recovered timber has yet to be established.

This paper presents a study carried out as part of the InFutUReWood project [8] to determine the embedment strength of recovered softwood and hardwood timber. The test programme includes the determination of embedment strength of timber from demolition projects in Ireland and Slovenia. Recovered spruce and oak specimens were tested in compression using dowels of three different diameters in the parallel and perpendicular to the grain directions in accordance with EN 383 [17]**.** Values obtained are compared with published data for new timber and with values from the Eurocode 5 empirical equations [15].

2 MATERIALS AND METHODS

2.1 RECOVERED TIMBER SAMPLES

The three types of recovered timber samples were investigated in the study were: Irish-sourced spruce, Slovenian-sourced spruce, and Slovenian-sourced oak. The Irish-sourced spruce sample was recovered from the roof trusses of a 1970s office block in Dublin, which had been vacant for over two years before its demolition. Grade stamps were visible on some of the boards indicating that the timber was grade TR26 imported spruce. This timber grade is commonly used in Ireland and the UK for roof trusses. TR26 grade timber has characterisitic and mean densities of and 370 kg/m^3 and 444 kg/m^3, respectively [24]. The moisture content of the timber boards at the time of recovery was estimated using a hand-held moisture meter to be between 18% and 23%. This high moisture content was attributed to water ingress onto the structural timber through damaged slates and sarking felt in the roof envelope for a period of time prior to demolition.

The Slovenian spruce was recovered during the refurbishment of the roof of a faculty building at Ljubljana University. The building is estimated to have been built in the years from 1947 to 1949 so the specimens were about 70 years old. The strength grade of the timber is unknown as at that time the JUS (Yugoslavian) norms were not yet in use. During their use in the building the specimens were protected against rain and not insulated. Therefore, they were not exposed to water, but were subjected to varying temperature estimated between -20° C and 50° C. The moisture content estimated with a resistance moisture meter was between 6.5 % and 12.4 %, with an average of 8.9 %. The density of the specimens at moisture equilibrium was between 362 kg/m^3 and 526 kg/m^3, with an average of 426 kg/m^3.

The Slovenian oak sample was recovered during the reconstruction of an external vehicle bridge over the river Sava, which was constructed between 1930 and 1935. During their use on the bridge, the specimens first served as the driving surface, and later they were covered with a new driving surface also made from wood. At first the water and salt from the vehicles would drip onto the specimens directly, and later only partially. The whole time they were exposed to moisture from the surrounding moist air over the river, but they were protected from direct rain by the roof of the bridge. The moisture content of the beams was between 9.1 % and 11.2 % at the time of recovery. The density of the specimens at moisture equilibrium was between 609 kg/m^3 and 860 kg/m^3, with an average of 739 kg/m^3.

Before preparation of the embedment specimens, the timber was conditioned in a chamber with a relative humidity of 65 ± 5% and temperature 20° ± 2° C. The specimens were then cut to the dimensions outlined in EN 383 [17] where the size of the specimen varies with the dowel size used, and with the load direction relative to the wood grain. The cut specimens were returned to the conditioning chamber until testing. The moisture content of all the timber specimens at the time of embedment testing was determined in accordance with EN 13183-1:2002 [25].

2.2 EMBEDMENT TESTING

Specimens for embedment testing were prepared in accordance with EN383 [17] (Figure 1). Smooth high strength steel dowels with diameters of 10 mm, 12 mm and 14 mm were used. A minimum of 10 specimens were tested for each combination of timber source, dowel diameter and loading direction where possible giving a

total of 191 specimens tested (Table 1). The exception was the 14 mm dowel tests perpendicular to the grain on the Irish-source spruce where only 8 specimens could be manufactured from the available resource. In all, 59 and 65 specimens of Irish-sourced and Slovenian-sourced recovered spruce were tested along with 67 specimens of Slovenian recovered oak.

Each dowel was loaded perpendicular to its axis in accordance with the loading procedure outline in EN 383 [17] and EN 26891 [26]. The dowel deformation was measured using two LDVTs. Tests were terminated when the deformation reached 5 mm or when the specimen failed due to splitting.

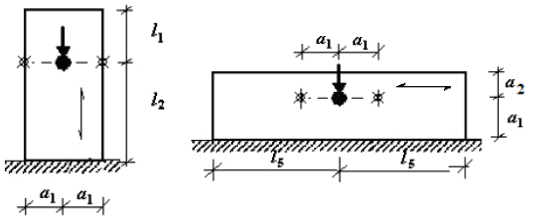

Figure 1: *Test set up for embedment tests parallel to the grain (left) and perpendicular to the grain (right) [2]*

Table 1: *Embedment test series by dowel diameter (dia)*

Series	Dowel dia (mm)	No. Tests Parallel	No. Tests Perpendicular
Spruce Ireland	10	11	10
	12	10	10
	14	10	8
Spruce Slovenia	10	12	11
	12	11	10
	14	10	11
Oak Slovenia	10	12	13
	12	10	10
	14	11	11

3 RESULTS

3.1 LOAD-DISPLACEMENT RESPONSE AND FAILURE MODES

The mean load-displacement responses for tests carried out using 10 mm dowels in the parallel to grain and 14 mm dowels in the perpendicular to grain directions are shown in Figures 2 and 3, respectively. Similar trends were found with other dowels diameters in the respective loaded directions. For all tests, no significant difference was found between the Irish-sourced and Slovenian-sourced spruce. The higher density oak sample was clearly stiffer than the two spruce samples. For the parallel to the grain tests, the peak load was reached before the 5 mm displacement limit specified in EN 383 [17]. This occurred at a displacement of 2 mm for the spruce and 3.5 mm for the oak specimens. As previously reported [21], specimens tested in the parallel to the grain direction are prone to splitting. For the present study, the proportion of specimens failing by splitting reduced with increasing dowel diameter as seen in Table 2. The occurrence of splitting failures occurred for the most part after the peak load had been reached in the tests and therefore does not impact on the embedment strength. This agrees with the findings of Sandhaas *et al*. [21] who found that there was no difference in embedment strength for unreinforced specimens and those reinforced to prevent splitting.

For the perpendicular to the grain tests, the load continued to increase up to the 5 mm displacement limit without reaching a steady state. All of the 94 specimens except one of the 10 mm Slovenian spruce specimens failed in embedment without splitting.

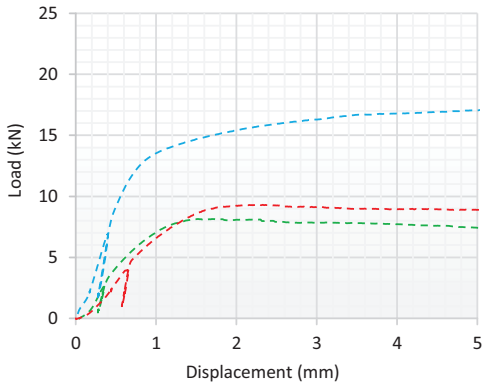

Figure 2: *Embedment test results for 10 mm dowel loaded parallel to the grain (Irish Spruce- green; Slovenian spruce-red; Slovenian oak-blue)*

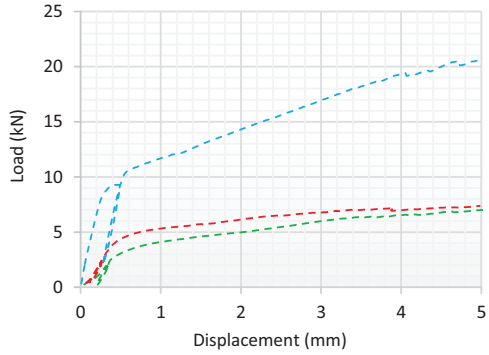

Figure 3: *Embedment test results for 14 mm dowel loaded perpendicular to the grain (Irish Spruce- green; Slovenian spruce-red; Slovenian oak-blue)*

Table 2: *Splitting failures by dowel diameter (dia)*

Series	Dowel dia (mm)	Splitting (%) Parallel	Splitting (%) Perpendicular
Spruce Ireland	10	27	0
	12	10	0
	14	10	0
Spruce Slovenia	10	33	9
	12	18	0
	14	10	0
Oak Slovenia	10	33	0
	12	20	0
	14	18	0

https://doi.org/10.52202/069179-0119

3.2 EMBEDMENT STRENGTH

The embedment strength for each specimen was determined from the maximum load divided by the area of contact between the dowel and the timber element using Eq. (1).

$$f_h = \frac{F_{max}}{dt} \quad (1)$$

where f_h, in N/mm^2, is the embedment strength, F_{max}, in N, is the maximum load at 5 mm dowel embedment (or failure load due to splitting), d, in mm, denotes the dowel diameter and, t, in mm, represents the thickness of the timber specimen. The mean values of embedment strength and density of the test specimens in each series together with their respective coefficients of variation (COV) are given in Tables 3 and 4 for the parallel to and perpendicular to the grain tests, respectively.

Table 3: *Mean density and embedment strength parallel*

Series	Dowel diameter (mm)	Density kg/m^3 (COV %)	Embedment strength N/mm^2 (COV %)
Spruce Ireland	10	426 (18)	30.2 (30)
	12	408 (6)	26.8 (14)
	14	424 (9)	29.2 (18)
Spruce Slovenia	10	368 (5)	28.7 (10)
	12	374 (12)	27.8 (15)
	14	371 (7)	28.6 (12)
Oak Slovenia	10	628 (9)	55.5 (16)
	12	581 (12)	47.3 (18)
	14	609 (9)	51.5 (14)

Table 4: *Mean density and embedment strength perpendicular*

Series	Dowel diameter (mm)	Density kg/m^3 (COV %)	Embedment strength N/mm^2 (COV %)
Spruce Ireland	10	416 (6)	20.5 (9)
	12	378 (6)	17.4 (23)
	14	399 (8)	16.5 (12)
Spruce Slovenia	10	407 (6)	25.6 (45)
	12	367 (3)	16.4 (13)
	14	393 (8)	17.6 (21)
Oak Slovenia	10	631 (10)	46.2 (29)
	12	653 (10)	50.3 (22)
	14	669 (7)	48.6 (19)

For the parallel to grain direction, the mean embedment strength varied between 26.8 and 30.2 N/mm^2 for the recovered spruce specimens and between 47.3 and 55.5 N/mm^2 for the recovered oak. The COV was 18% or less except for the 10 mm Irish spruce series which was 30%. For the perpendicular to the grain tests, the embedment strength for the recovered spruce specimens varied between 16.4 and 25.6 N/mm^2 while the values for the recovered oak varied from 46.2 to 50.3 N/mm^2. Overall, there was greater variability in the perpendicular to grain results with COV of over 20% in five of the nine series with the largest COV in the 10 mm Slovenian spruce series at 45%.

Boxplots of the embedment strength for the parallel to grain tests by diameter and species are given in Figure 4.

There was no significant difference between the embedment properties of the spruce recovered in Ireland and that in Slovenia, regardless the diameter. The higher embedment strength of the oak specimens is likely to be due to their higher density. Similar conclusions can be drawn for the perpendicular to the grain direction.

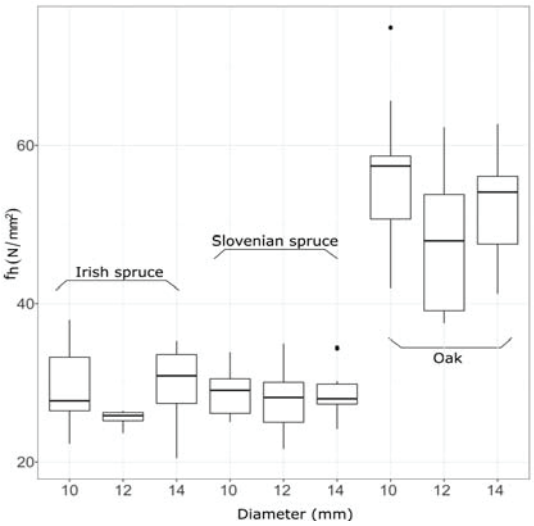

Figure 4: *Box plots of embedment strength parallel to the grain results*

Embedment strength results in the parallel and perpendicular to grain directions were strongly influenced by density as can be seen in Figure 5.

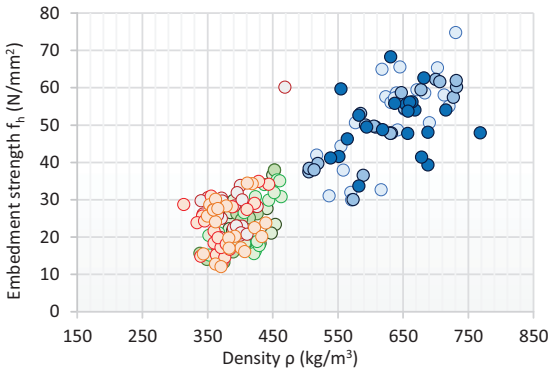

Figure 5: *Embedment strength v density – all specimens (Irish spruce-green; Slovenian spruce –red; Oak – blue)*

For the full dataset of parallel to grain data, the linear relationship between density and embedment strength was very strong (R^2 = 0.90). Including diameter as an additional explanatory variable in the linear regression had a negligible effect on the overall fit of the regression (R^2 = 0.91). The effect of the diameter on the slope and intercept of a linear regression was investigated with ANOVA. The results showed that the diameter affects the intercept ($F_{2\ 94}$ *=3.99, P= 0.02*) but not the slope ($F_{2\ 92}$ *=0.78, P= 0.46*). A multiple comparison at the 95% confidence level showed that 12 mm diameter had an intercept term 3 kN/mm^2 lower than the other two

diameters, with no significant differences between the intercept for the 10 mm and 14 mm diameters. It is important to note that these findings are based on the limited dataset in the study and more testing of recovered timber will be needed before any definitive conclusions can be reached.

The overall relationship between density and embedment strength in the perpendicular to grain direction was also very strong ($R^2 = 0.90$). An ANOVA of the softwood data showed that the diameter affects the intercept ($F_{2\,55} = 9.01$, $P < 0.001$) but not the slope ($F_{2\,53} = 1.32$, $P = 0.28$). In the softwoods, the 10 mm diameter was about 3 kN/mm^2 higher than those of the 12 mm and 14 mm. The differences between the latter were not statistically significant. For the hardwood, the effect of diameter in the relationship was not significant ($F_{2\,30} = 1.57$, $P < 0.23$), but the number of tests was roughly half that of the softwoods. Figure 6 shows the relationship of perpendicular to the grain strength by timber type. Even though the effect of the diameter was significant for the embedment strength calculation parallel to the grain and in softwoods tested perpendicular to the grain, trends could not be established. As mentioned earlier, the size of the dataset in the current study does not allow for definitive relationships for the embedment strength of recovered timber to be established. Nevertheless, some trends can be identified.

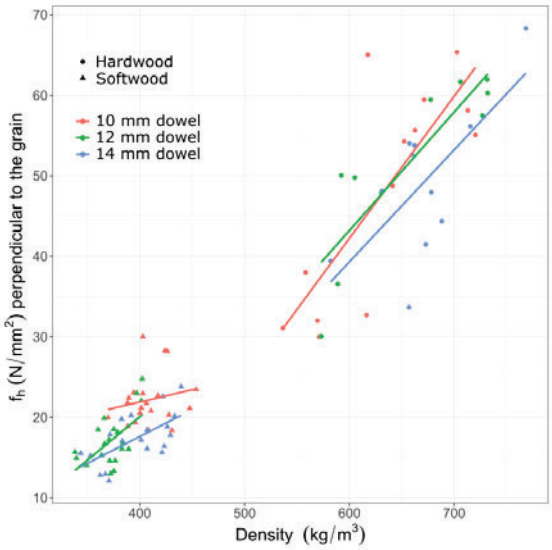

Figure 6: *Relationship between density and embedment strength perpendicular to the grain by dowel diameter*

3.3 COMPARISON WITH PUBLISHED DATA FOR NEW TIMBER AND EC5

The embedment strength values for recovered timber reported here agree reasonably well with values published in the literature from tests on new timber of similar species. Figure 7 shows a comparison of the results for 12 mm dowel parallel to grain tests from the current study compared to data presented by Glišovíc *et al.* [27] and Sandhaas *et al.* [21] for spruce, pine, oak and beech. No impact of aging can be seen in the recovered timber results.

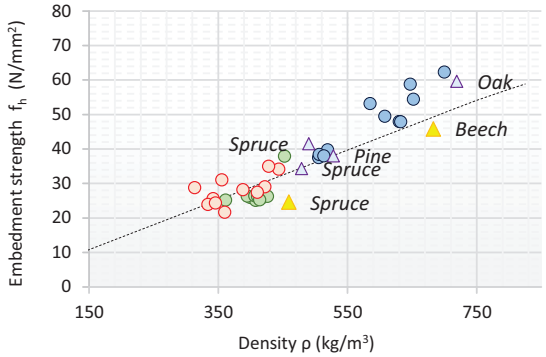

Figure 7: *Embedment strength v density – 12 mm specimens parallel-to-grain (Irish spruce-green; Slovenian spruce – red; oak – blue; Glišovíc et al. [27] – purple; Sandhaas et al. [21] - yellow)*

EC5 [15] provides an empirical equation for embedment strength as a function of density, dowel diameter and angle to grain (Equation (2)).

$$f_{h,\alpha,k} = \frac{0.082\,(1 - 0.01\,d)\rho_k}{k_{90}\,sin^2\alpha\, +\, cos^2\alpha} \qquad (2)$$

where $f_{h,\alpha,k}$, in N/mm^2, represents the characteristic embedment strength, ρ_k, in kg/m^3, denotes the characteristic timber density, d, in mm, represents the dowel diameter, and α, represents the angle of the load to the grain. k_{90}, may be taken as $1.35 + 0.015\,d$ for softwoods, and as $0.90 + 0.015\,d$ for hardwoods. The line representing this equation with the characteristic value replaced by the actual density is shown in Figure 7. For the spruce specimens, the data points are closely aligned with this equation. The equations underpredict the embedment strength of the recovered oak. In general it can be said that the EC5 equation can be used to predict the embedment strength of the recovered timber specimens in the current study. Further work is required to determine its applicability to recovered timber in general.

4 CONCLUSIONS

To support the understanding of the behaviour of recovered timber and support its reuse in new construction, a study was carried out as part of the InFutUReWood project [8] to determine the embedment strength in the parallel and perpendicular to grain directions of recovered spruce and oak. Spruce was recovered during the demolition of roof structures in Ireland and Slovenia and the oak was recovered from the renovation of a vehicle bridge in Slovenia.

Specimens were tested in accordance with EN383 [17] using smooth high strength steel dowels of three different diameters. A total of 191 tests were performed of which 97 were in the parallel to grain direction and 94 perpendicualr to the grain.

For the two spruce series, no significant difference in the embedment strength was found despite the fact that the environmental conditions during the life of the two roof

https://doi.org/10.52202/069179-0119

structures from which the material was recovered was quite different. For the tests in the parallel to grain direction, the peak load was reached at an embedment of approximately 2mm. A high percentage of specimens failed in splitting before reaching the 5 mm embedment value specified in the standard. For the perpendicular to grain tests, only one specimen failed in splitting.

The embedment strength of the recovered oak specimens was significantly higher that that of the spruce, which is likely due to the higher density. Again, splitting occurred in a high proportion of the parallel to grain tests with no evidence of splitting perpendicular to the grain.

A strong linear relationship was found between embedment strength and density for all tests. The influence of dowel diameter on strength was less clear and will require further testing to establish it.

The results were compared with mean values for new softwood and hardwood timber specimens reported in the literature and were found to be generally in line with these values. The empirical Eurocode 5 predictions for the embedment strength of softwoods and hardwoods were good predictors of the embedment strength of the recovered timber specimens investigated in this study.

Based on these preliminary findings, it can be concluded that the embedment performance of recovered spruce and oak seems to be equivalent to that of new timber. However, further studies on recovered timber of different origin, species, ages and history of use are needed to confirm these findings for recovered timber in general.

ACKNOWLEDGEMENTS

This work was carried out in Ireland and Slovenia as part of the InFutUReWood project supported under the umbrella of ERA-NET Cofund ForestValue by the Department of Agriculture, Food and the Marine for Ireland and the Ministry of Education, Science and Sport for Slovenia. This is supported under the umbrella of ERA-NET Cofund ForestValue, and ForestValue has received funding from the European Union's Horizon 2020 research and innovation programme under grant agreement No. 773324.

The authors would like to acknowledge the contribution of Colm Walsh and Peter Fahy, senior technical officers in the School of Engineering, University of Galway, for their assistance with the laboratory test programme.

REFERENCES

[1] European Commission, Construction and demolition waste. Available at: < https://ec.europa.eu/environment/topics/waste-and-recycling/construction-and-demolition-waste_en> Accessed: February 14 2023.

[2] Irle, M., Privat, F., Deroubaix, G., Belloncle, C. Intelligent recycling of solid wood. Pro Ligno 11(4):14-20. 2015.

[3] Llana, D.F., Íñiguez-González, G., de Arana-Fernández, M., Uí Chúláin, C., Harte, A.M., Recovered wood as a raw material for structural timber products. Characteristics, situation and study cases: Ireland and Spain. In *Proceeding of 63rd International Convention of Society of Wood Science and Technology (SWST)*. 117-123, 2020. Online.

[4] Harte, A.M., Uí Chúláin, C., Nasiri, B., Hughes, M., Llana, D.F., Íñiguez-González, G., de Arana-Fernández, M., Shotton, E., Walsh, S-J., Ridley-Ellis, D., Cramer, M., Risse, M., Ivanica, R., Cristescu, C., Sandberg, K., Sandin, Y., Turk, G., Plos, M., Šuligoj, T., Hogan, P., Recovered timber in Europe: sources, classification, existing and potential reuse and recycling. *National University of Ireland Galway* 2020. DOI: 10.13025/r2dt-jp43

[5] Whittaker MJ, Grigoriadis K, Soutsos M, Sha W, Klinge A, Paganoni S, et al. Novel construction and demolition waste (CDW) treatment and uses to maximize reuse and recycling. Adv Build Energy Res.. 15:253–69. 2021. https://doi.org/10.1080/17512549.2019.1702586.

[6] Buildings as Material Banks (BAMB2020). Project website: https://www.bamb2020.eu Accessed: February 14 2023.

[7] CaReWood: Cascading Recovered Wood. Project website https;//carewood.lam.upr.si/ Accessed: February 14 2023.

[8] InFutUReWood: Innovative Design for the Future – Use and Reuse of Wood (Building) Components. Project website https://www.infuturewood.info Accessed April 20 2022.

[9] Nakajima, S., Nakagawa, T, Technologies and environmental benefits to reuse two-by-four salvaged lumbers. In Proceedings of *World Conference on Timber Engineering (WCTE 2010),* Paper No. 675, Riva del Garda, Italy, 2010.

[10] Rose, C.M.., Bergsagel, D., Dufresne, T., Unubreme, E., Lyu, T., Duffour, P., Stegemann, J.A., Cross-laminated secondary timber: experimental testing and modelling the effects of defects and reduced feedstock properties, *Sustainability* 10(11):4118, 2018. doi: 10.3390/su10114118

[11] Stenstad, A., Lønbro Bertelsen, S., Modaresi, R., Comparison of strength tests for evaluating the secondary timber utilisation in Cross Laminated Timber (CLT). In Proceedings of *16th World Conference on Timber Engineering (WCTE 2021),* 2201-2206, Santiago, Chile. Online, 2021.

[12] Arbelaez, R., Schimleck, L., Sinha, A. Salvaged lumber for structural mass timber panels; manufacturing and testing, *Wood Fiber Sci.,* 52(2): 178-190, 2020. doi: 10.22382/wfs-2020-016.

[13] Uí Chúláin, C., Llana, D.F., Hogan, P., McGetrick, P., Harte, A.M., Bending characterisitics of CLT from recovered spruce. In *Proceeding of World Conference on Timber Engineering (WCTE 23)*. Oslo, Jun 2023.

[14] Llana, D.F., González-Alegre, V., Portela, M., Íñiguez-González, G., Cross laminated timber (CLT) manufactured with European oak recovered from demolition: structural properties and non-destructive

evaluation, *Constr. Build. Mat*. 339: 127635, 2022. doi: 10.1016/j.conbuildmat.2022.127635
[15] EN 1995 EN 1995-1-1: 2004 & AC:2006 & A1:2008 & A2:2014. Eurocode 5: Design of timber structures - Part 1-1: General - Common rules and rules for buildings. European Committee of Standardization (CEN), Brussels, Belgium. 2014.
[16] Johansen, K.W., Theory of timber connections, *Int. Assoc. Bridge & Struct Eng*, 9:249-262. 1949.
[17] CEN,EN 383: Timber Structures - Test methods - Determination of embedment strength and foundation values for dowel type fasteners. European Committee of Standardization (CEN), Brussels, Belgium. 2007.
[18] Ehlbeck J, Werner H. Softwood and hardwood embedding strength for dowel-type fasteners. In Proceedings of *CIB-W18 Timber Struct.,* Âhus: p. 25-7–2. 1992.
[19] Sawata K, Yasumura M. Determination of embedding strength of wood for dowel-type fasteners. *J Wood Sci* 48:138–46. 2002. https://doi.org/10.1007/BF00767291.
[20] Sandhaas C. Mechanical behaviour of timber joints with slotted-in steel plates. PhD Thesis: Technical University of Delft, 2012.
[21] Sandhaas C, Ravenshorst GJP, Blass HJ, Van De Kuilen JWG. Embedment tests parallel-to-grain and ductility aspects using various wood species. *Eur J Wood Wood Prod*. 71:599–608. 2013. https://doi.org/10.1007/s00107-013-0718-z.
[22] Santos CL, de Jesus AMP, Morais JJL, Lousada JLPC. A comparison between the EN 383 and ASTM D5764 test methods for dowel-bearing strength assessment of wood: Experimental and numerical investigations. *Strain* 46:159–74. 2010. https://doi.org/10.1111/j.1475-1305.2008.00570.x.
[23] ASTM D5764-97a: Standard test method for evaluating dowel-bearing strength of wood and wood-based products, ASTM International, 2002.
[24] Ridley-Ellis, D., Gil-Moreno, D., and Harte, A.M., Strength grading of timber in the UK and Ireland in 2021. *International Wood Products Journal*, 2022. **13**(2): p. 127-136.
[25] CEN, EN 13183-1: Moisture content of a piece of sawn timber Part 1: Determination of oven dry method. European Committee of Standardization (CEN), Brussels, Belgium. 2002.
[26] CEN, EN 26891: Timber structures - Joints made with mechanical fasteners - General principles for the determination of strength and deformation characteristics. European Committee of Standardization (CEN), Brussels, Belgium. 1991.
[27] Glišovíc I, Stevanovíc B, Kočetov-Mišulić T. Embedment test of wood for dowel-type fasteners. Wood Res 57:639–50. 2012.

https://doi.org/10.52202/069179-0119

World Conference on Timber Engineering Oslo 2023

PROPOSAL OF A METHOD FOR ESTIMATING THE RESIDUAL STRENGTH FROM THE DEPTH OF PILODYN PENETRATING FOR A CYLINDRICAL MEMBER

Makoto Imai[1], Hironobu Kobayashi[2], Tadashi Hara[3]

ABSTRACT: A method for estimating the residual strength from the depth of Pilodyn penetrating for a cylindrical member (thereafter, Pe) was investigated. Conventionally, a relational expression for estimating the residual strength from the results of Pe and the strength test has been sought. However, it is not always possible to carry out a fracture test, and the residual strength should be theoretically derived from Pe and the like. The defect model by Pe was generally a circular cross-section model based on the average value, but since the decay was not uniform, it was thought that the elliptical model could estimate the residual strength more realistically. We acquired Pe and conducted strength tests on members used outdoors, and verified the fit between the residual strength estimation results based on the elliptical model and the actual strength test results. With this method, it is possible to estimate the residual strength simply by acquiring Pe, and it is expected that it will be easier to determine the renewal time of the structure.

KEYWORDS: Pilodyn penetration, Section modulus, Elliptical approximation, Estimating the residual strength

1 INTRODUCTION

Japan is a hot and humid environment that is unfavorable for wood, which is very different from the dry summer conditions in Northern Europe and Canada [1]. Wood and wood products used outdoors are constantly exposed to wind and rain and wood-rotting fungi in such an environment, and deterioration over time such as decay is inevitable. Aging causes not only a deterioration in appearance, but also a reduction in the strength of materials and joints. As a preventive measure against deterioration, treatment with antiseptic agents, protection using other materials, etc. are performed, but deterioration cannot be completely prevented. Therefore, it is necessary to periodically diagnose deterioration.

Deterioration is generally diagnosed by visual observation or palpation, and if any abnormality is confirmed, secondary diagnosis using dedicated equipment is performed to acquire quantitative data [2]. Dedicated equipment used for secondary diagnosis is mainly non-destructive diagnostic equipment such as FFT Analyzer (Hammering sound frequency analyzer) and FAKOPP (Stress wave measuring device), and micro-destructive diagnostic equipment such as RESISTOGRAPH (Penetration resistance measuring instrument) and Pilodyn (Figure 1).

Pilodyn is a device that ejects a steel pin with a diameter of 3 mm and a length of 40 mm by the force of a spring and measures the depth of the pin driven into wood. This equipment diagnoses deterioration by estimating the density from the obtained penetration depth. Since the density has a high correlation with the bending strength, the method of estimating the residual strength by deriving the relational expression between the Pilodyn penetration depth *Pe* and the bending strength σ by strength test is generally performed [3].

Figure 1: A scene of driving a Pilodyn pin into a pillar

Simply put, when Pe exceeds 30 mm, it is considered to be the service life limit [4], but since Pe is affected by the moisture content [5][6], the evaluation may differ depending on the condition of the material to be driven.

[1] Makoto Imai, Hokkaido Research Organization, Japan, imai-makoto@hro.or.jp
[2] Hironobu Kobayashi, Hokkaido Research Organization, Japan, kobayashi-hironobu@hro.or.jp
[3] Tadashi Hara, Kochi University, Japan, haratd@kochi-u.ac.jp

https://doi.org/10.52202/069179-0120

Since Pe fluctuates depending on the moisture content, it is difficult to judge the initial deterioration from Pe within the range of 30 mm from sound material (approximately 15 mm). The authors are also working on an initial deterioration detection method that applies the preventive design technology of quality engineering (MT system) [7]. Mori et al. [4] regarded the rotten part of the processed material as a defect, and defined the ratio of the sound part other than the defect in the cross-sectional area as the cross-sectional survival rate. As a result of the strength test, it was shown that the relationship between the section survival rate and the bending strength fits well when it is hypothesized that decay progresses uniformly from the outer periphery. Based on this result, the average thickness of the cross-sectional loss due to decay (hereinafter referred to as the defect depths) was estimated from the average *Pe* values at multiple points on the outer circumference, and we devised a method to evaluate the residual strength by calculating the section modulus of the remaining circular cross section from the defect depths (hereinafter referred to as the circular approximation method) (Figure 2).

However, in actual wood, it is thought that decay progresses locally from the part where the efficacy barrier of antiseptic agents is weak, and the hypothesis that "decay progresses uniformly from the outer periphery" does not necessarily hold. Therefore, it is necessary to examine the appropriateness of simply averaging the defect depths. In addition, for structures such as fences, it is important to evaluate the soundness against external forces from outside the plane to prevent overturning. If the defects are concentrated in the direction of the external force, the circular approximation method may give a poor evaluation of the out-of-plane external force, resulting in a dangerous judgment result.

Therefore, we devised a method to calculate the residual strength from *Pe* by assuming that the residual cross section is elliptical rather than circular, and using the section modulus that reflects the anisotropy of the defect (Figure 3). This method is hereinafter referred to as the elliptical approximation method.

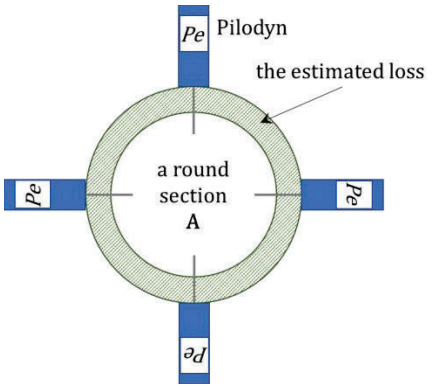

Figure 2: *The method of Mori et al. (Circular approximation)*

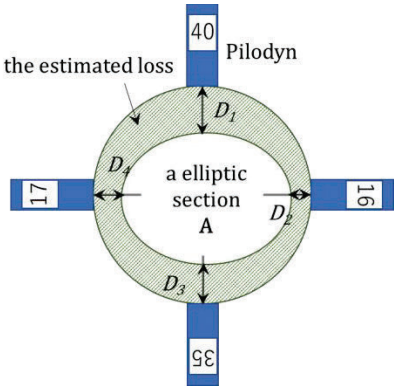

Figure 3: *The new idea of ellipse approximation (Pilodyn values are examples)*

2 SPECIMEN AND TEST METHOD

2.1 OVERVIEW OF THE SPECIMEN

The object of the investigation is a column material (φ150 mm) made of Japanese larch, which has been preserved with antiseptic chemicals for more than 10 years since it was installed as access prevention fences on a high-standard road (Figure 4).

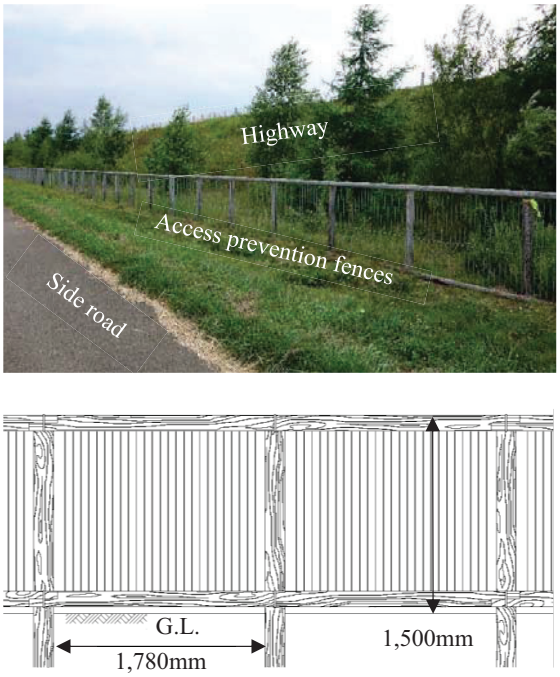

Figure 4: *Access prevention fences on a high-standard road*
Upper: Fences seen from side road, Lower: Fences front view

Two types of bending strength tests were conducted: a full-scale test and a sample test. A full-scale test specimen (n=10) was used for the test with the original cross-sectional dimensions (φ150 mm × 2,900 mm) of the cylindrical material. Sample specimens (n = 307) were prepared by cutting a cylindrical material into rectangular

https://doi.org/10.52202/069179-0120

cross sections of 25 mm × 25 mm × 550 mm. In addition, the samples were taken from the outer part without the heartwood so as to include the rotten part as much as possible (Figure 5).

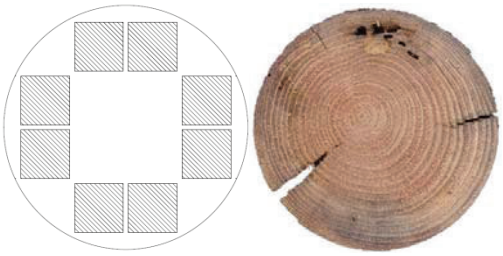

Figure 5: *Image of cutting out sample specimens from a cylindrical material (The shaded area is the sample specimen)*

2.2 BENDING STRENGTH TEST METHOD

The bending strength test was carried out by the trisecting four-point loading method with the bending span set to 18 times the height of the specimen for both the full-scale test and the sample test. In both tests, the decayed surface was taken as the upper surface (Figure 6).

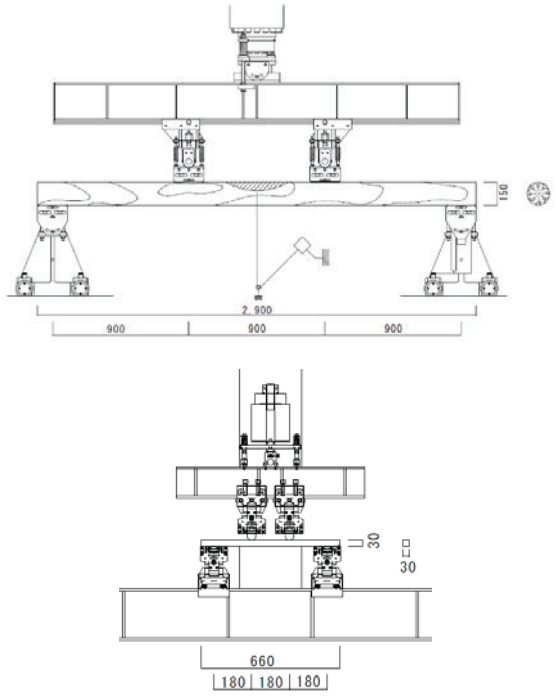

Figure 6: *The trisecting four-point loading method (The shaded area is the decayed area), Upper: full-scale test, Lower: sample test*

For the full-scale test specimen, the presence or absence of decay was visually observed before the test was conducted, and the average *Pe* was calculated from the *Pe* obtained by injecting Pilodyn into four points on the outer periphery of the center of the span.

For the sample specimen, both butt ends were observed before the test, the defect depths *D* due to decay was actually measured (Figure 7), and the section modulus Z_1 was calculated from the remaining cross section. The section modulus reduction rate R_d was calculated from the ratio to the original section modulus Z_0 without defect (Equation(1)).

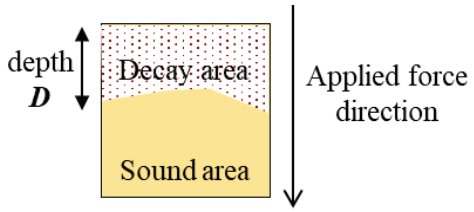

Figure 7: *The cross-sectional defect depth D of the sample specimen*

$$R_d = 1 - \frac{Z_1}{Z_0} \tag{1}$$

The bending strength σ was calculated from the maximum load values P_{max} obtained from the bending test and Z_0. (Equation(2)).

$$\sigma = \frac{aP_{max}}{2Z_0} \tag{2}$$

Here, a = Distance between fulcrum to load points.
Considering the average bending strength of specimens without cross-sectional defects as the bending strength of sound material σ_0, the ratio of the bending strengths σ_1 and σ_0 of each specimen with cross-sectional defects was used to calculate the residual rate of bending strength R_σ (Equation(3)).

$$R_\sigma = \frac{\sigma_1}{\sigma_0} \tag{3}$$

Imai et al. [8] obtained *Pe* by penetrating Pilodyn into larch columns. After that, the material was cut at the place where the pin was driven, the defect depths *D* was measured from the cross section (Figure 8), and the relationship between *Pe* and *D* was derived as Equation(4). This indicates that Pilodyn has enough energy to allow the pin to penetrate the sound larch wood by an average thickness of 14.5 mm. It also indicates that the driving depth of the pin increases as the sound portion and density decrease due to decay or the like. In other words, by using this equation, it is possible to estimate the defect depths (degree of decay) at that location from the measured Pilodyn penetration depth.

$$D = 0.94Pe - 14.5 \quad (\text{n} = 664, \text{R} = 0.946) \tag{4}$$

https://doi.org/10.52202/069179-0120

Using these Equations (1) to (4), a method for estimating residual strength from measured *Pe* is examined.

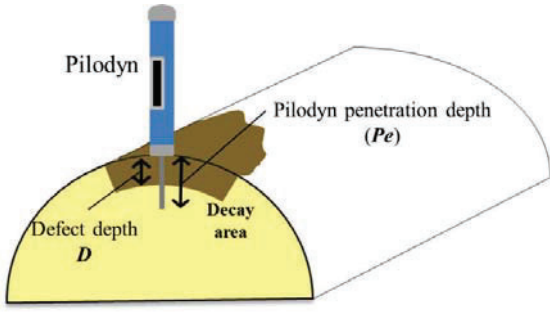

Figure 8: *The defect depth D observed by cutting at the Pilodyn penetration position*

3 VALIDATION OF THE ESTIMATION METHOD

3.1 RELATIONSHIP BETWEEN BENDING STRENGTH AND DRIVING DEPTH OF FULL-SCALE SPECIMEN

As a result of visual observation of full-scale test specimens, decay was confirmed in 5 out of 10 specimens. Table 1 shows the bending test results. The average bending strength σ_d of the 5 specimens with decayed parts is 12.2 N/mm^2 (standard deviation 6.3 N/mm^2), and the average bending strength σ_h of the remaining 5 specimens is 16.1 N/mm^2 (standard deviation 2.4 N/mm^2).

Table 1: *A result of the full-scale specimens bending test*

Specimens	P_{max} (kN)	Bending Strength σ (N/mm^2)
Decay_1	7.6	10.3
Decay_2	14.5	19.7
Decay_3	10.3	14.0
Decay_4	1.9	2.6
Decay_5	10.5	14.2
Ave. (S.D.)	**9.0**	**12.2 (6.3)**
C.V.	**52.0**	**51.6**
Sound_1	12.5	16.9
Sound_2	11.3	15.3
Sound_3	10.1	13.7
Sound_4	10.7	14.5
Sound_5	14.6	19.9
Ave. (S.D.)	**11.8**	**16.1 (2.4)**
C.V.	**15.2**	**14.9**

Table 2 shows the Pilodyn measurement results. Figure 9 shows the relationship between the bending strength σ calculated from the results of the full-scale test and the average value of *Pe*, and the regression equation is shown in Equation(5). A strong correlation was found between σ and the average *Pe* (R = 0.887).

$$\sigma = 125.37e^{-0.146Pe} \quad (R^2 = 0.760,\ P < 0.01) \qquad (5)$$

Table 2: *A result of Pilodyn measurement results*

Specimens	Pe_1 (mm)	Pe_2 (mm)	Pe_3 (mm)	Pe_4 (mm)	***Ave.* (mm)**
Decay_1	12.0	40.0	14.0	17.0	**20.8**
Decay_2	11.0	11.0	13.0	13.0	**12.0**
Decay_3	14.0	13.0	16.0	13.0	**14.0**
Decay_4	40.0	23.0	14.0	11.0	**22.0**
Decay_5	13.0	23.0	16.0	14.0	**16.5**
Sound_1	13.0	15.0	17.0	13.0	**14.5**
Sound_2	13.0	14.0	18.0	13.0	**14.5**
Sound_3	12.0	14.0	14.0	13.0	**13.3**
Sound_4	17.0	15.0	18.0	17.0	**16.8**
Sound_5	12.0	13.0	15.0	11.0	**12.8**

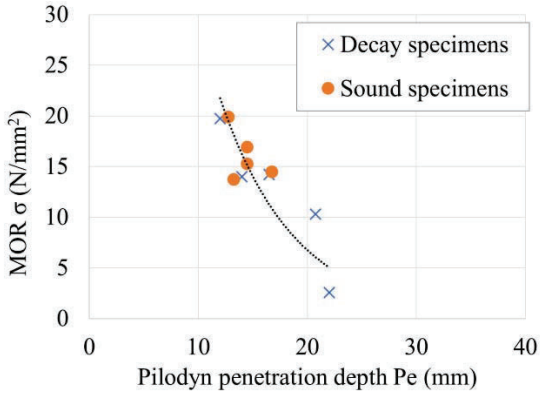

Figure 9: *A relationship between bending strength and Pilodyn penetration depth*

3.2 RELATIONSHIP BETWEEN SECTION MODULUS REDUCTION RATE AND BENDING STRENGTH RETENTION RATE

As a result of observing the butt end of the sample specimen, 224 specimens out of 307 specimens were sound specimens without defects. Table 3 shows the bending test results. The average bending strength σ_0 of the sound body was 56.4 N/mm^2 (standard deviation 12.5 N/mm^2).

The section modulus reduction rate R_d was calculated from the specimen in which defects were observed, and the relationship between the bending strength residual rate R_σ calculated from the bending strength obtained in the test and R_d is shown in Figure 10, and the regression equation is expressed by the Equation(6). A strong negative correlation was observed between R_σ and R_d (R = 0.755).

$$R_\sigma = 1.1015e^{-2.75R_d} \quad (R^2 = 0.565,\ P < 0.01) \qquad (6)$$

https://doi.org/10.52202/069179-0120

Table 3: *A result of the sample specimens bending test*

Specimens	Quantity	Ave. D (mm)	**Ave. σ** (S.D.) (N/mm^2)
Decay	83	3.7	**40.0** (23.3)
Sound	224	0.0	**56.4** (12.5)

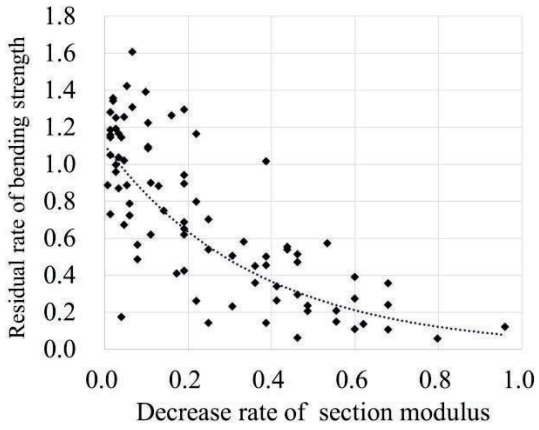

Figure 10: *A relationship between Residual rate of bending strength and decrease rate of section modulus*

3.3 EXAMINATION OF APPROXIMATION METHOD OF RESIDUAL CROSS-SECTIONAL SHAPE

First, Pe_1 to Pe_4 obtained from four points on the circumference of the full-scale specimen were substituted into Equation(4) to estimate the cross-sectional defect depths D_1 to D_4. The section modulus was obtained using the Equation(7) for the circular approximation method and the Equation(8) for the elliptical approximation method, and the section modulus reduction rate was calculated from the Equation(1). R_σ was estimated from the calculated R_d using Equation(6).

$$Z_{CA} = \frac{\pi(r - D_{ave})^3}{4} \quad (7)$$

$$Z_{EA} = \frac{\pi(2r - D_1 - D_3)(2r - D_2 - D_4)^2}{32} \quad (8)$$

Here, r = original cross-sectional radius of the cylindrical material, D_{ave} = average value of D_1 to D_4, D_1 and D_3 are cross-sectional defect depths in the width direction, and D_2 and D_4 are cross-sectional defect depths in the external force direction.

Using the average bending strength σ_h of sound materials, the initial strength σ_0 is assumed to be 16.1 N/mm^2, and the estimated R_σ is substituted into Equation(3) to estimate the bending strength (remaining strength). Figure 11 shows the relationship between the estimated residual strength and the residual strength obtained from the full-scale strength test.

If the circular approximation plot is higher than the elliptical approximation plot, it means that the circular approximation method underestimates the effects of decay. 6 out of 10 specimens corresponded to this, but the remaining 2 out of 4 specimens were clearly underestimated by the elliptical approximation method rather than by the circular approximation method. In the elliptical approximation method, the major axis of the ellipse is in the direction of less decay, and the minor axis is in the direction of more decay, but there are cases in which there is less decay in the direction of applied force. In other words, it is thought that decay was concentrated in the areas perpendicular to the direction of the applied force in these two bodies, and it was found that the elliptical approximation method does not always result in a safer evaluation than the circular approximation method. In addition, almost all approximation methods lead the residual strength from *Pe*, but the estimated value exceeded the measured value. This is because, in the case of cylindrical timbers with heartwood, unlike rectangular sample specimens with small cross-sections, there are areas with high strength on the outside (mature timbers, etc.) [9]. In this case, it is considered that the reduction in strength is greater than the defect thickness estimated from Equation(4).

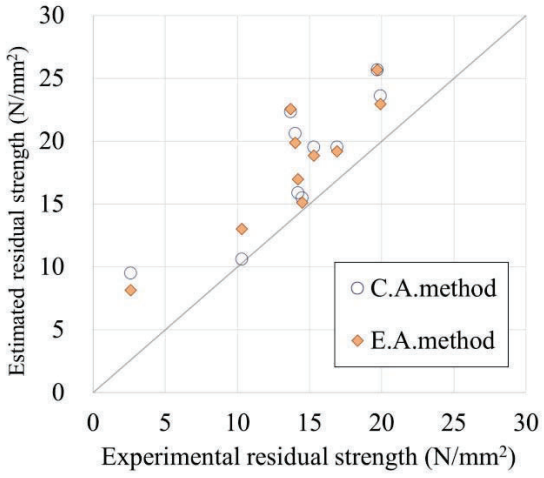

Figure 11: *A relationship between estimated residual strength and experimental residual strength*

4 CONCLUSION

The proposed method for estimating the residual strength by elliptical approximation of the residual cross section is

to calculate the section modulus appropriately from the defect depths estimated by driving Pilodyn, considering the direction of the external force applied to the structure, and to calculate the residual strength against the external force. It is a method to estimate the intensity, and it was found that it is possible to make a sufficient estimation. In this test, the number of subjects was limited to 10, so it was not possible to fully confirm the merits of the elliptical approximation method. However, it is clear that it is a residual strength estimation technique that takes into consideration.

In the future, we would like to recommend the elliptical approximation method by proving the usefulness of the method through the enrichment of empirical data.

We are also considering applying this method to a diagnostic method at the field level. The elliptical approximation method requires calculation of the section modulus once, and is not suitable for diagnosing the state of deterioration immediately on site. Therefore, it is considered preferable to utilize *Pe* directly as a diagnostic parameter while maintaining the concept of the elliptical approximation method, that is, the concept of section modulus. In other words, this is a method of giving weight to *Pe* in the direction of force application for evaluation. For example, *Pe* in the applied direction is squared, and Pe in the orthogonal direction is treated as it is.

If it is possible to derive the relationship between the value calculated by this method and the state of deterioration (for example, residual bending strength, etc.), it will be possible to diagnose the state of deterioration without complicated calculations even at the site level.

ACKNOWLEDGEMENT

This research was carried out by the 2016-2018 Hokkaido Research Organization Priority Research and 2022-2023 Ordinary Research. We received cooperation from the Performance Department of the Forest Products Research Institute and research support staff in preparing sample specimens and assisting in bending tests. I would like to take this opportunity to express my deep gratitude.

In addition, Mr. Kasama, Researcher of the Regional Landscape Unit of the Civil Engineering Research Institute for Cold Region, provided valuable advice on the provision of the site, the provision of the full-scale test specimen, and the construction method. Thank you from the bottom of my heart.

REFERENCES

[1] Proposal Promoting the use of wood in construction as a countermeasure against global warming, *Science Council of Japan Committee on Agriculture, Forestry Subcommittee*, pp.15, 2020, https://www.scj.go.jp/en/info/kohyo/pdf/kohyo-24-t289-3.pdf (Reference 21 Feb 2023).

[2] Mitsunori Mori: Special feature on ``Deterioration diagnosis of wood"-Deterioration diagnosis for extending the life of houses-, *Rinsanshi dayori(Online), January 2010 issue*, https://www.hro.or.jp/list/forest/research/fpri/dayori/1001/2.htm (Reference 6 Feb 2023).

[3] Yoshlharu Ishikawa, Youji Naitou, Hirotaka Ochiai, Isamu kamihara: Durability of wooden facilities based on various tests, Evaluation method of rot and bending strength, *Journal of sabo Society Vol.56 No.4* (249) November 2003.

[4] Mitsunori Mori, Shu Moriizumi, Teruhisa Miyauchi, Tomoaki Sugiyama, Noriaki Maeda, Takuya Fujiwara, Makoto Imai: Development of specification standards for civil engineering structures using thinned wood, *2003 Priority Area Special Research Report Of Hokkaido Forest Products Research Institute*, pp.73-78, 2004.

[5] Makoto Imai, Hironori Kobayashi: Effect of incising on moisture content and depth of pyrodine implantation, *Abstracts of the 68th Annual Meeting of the Japan Wood Research Society*, 2018.

[6] Yamada, M., Hara, T., Mizutani, Y., Mimura, K., Numata, A., Yoshida, M., Mori, M., Suetsugu, D., Noda, R., Umezu, H.: Moisture content of wood depends on pyrodin test value and penetration depth of driver. Influences, *Wood Utilization Research Papers 16*, pp.63-70, 2017.

[7] Makoto Imai, Hironobu Kobayashi, Tadashi Hara: Degradation determination method using pyrodine using MT system, *Abstracts of the 73rd Annual Meeting of the Japan Wood Research Society*, 2023.

[8] Makoto Imai, Hironobu Kobayashi, Satoshi Kasama: Estimation of the useful life of larch wood-made access prevention fences installed on high-standard highways in Hokkaido, *Reports On Papers On Wood use 18, Japan Society of Civil Engineers*, pp. 25-33, 2019, http://committees.jsce.or.jp/mokuzai07/system/files/r1808.pdf (6 Feb. 2023).

[9] Kazushige Matsumoto: Development of high-strength laminated lumber from Hokkaido larch, *Rinsanshi Dayori (Online), September 2020 issue*, pp.2-3, https://www.hro.or.jp/list/forest/research/fpri/dayori/2009/2009-2.pdf (Reference 6 Feb. 2023).

https://doi.org/10.52202/069179-0120

World Conference on Timber Engineering Oslo 2023

BENDING CHARACTERISTICS OF CLT FROM RECOVERED SPRUCE

Caitríona Uí Chúláin[1], Daniel F. Llana[2], Paul Hogan[3], Patrick McGetrick[4], Annette M. Harte[5]

ABSTRACT: The circular use of construction materials is an essential step in the drive to reduce the environmental impact of the construction sector. Structural materials, such as timber, recovered from demolition of buildings is a valuable resource. Reuse or recycling these materials in new buildings products reduces waste and the overall carbon footprint of the build environment. This paper investigates the use of spruce recovered from demolition of a roof structure in the manufacture of CLT panels. Bending tests are performed on 3-layer panels made from this recovered material and also on panels made from new timber and hybrid panels with mixed new and recovered timber. Results show that the performance of CLT panels using recovered timber is equivalent to that of panels from new timber in terms of bending strength and stiffness.

KEYWORDS: recovered timber, circular construction, mass timber, spruce, Douglas fir, secondary timber, salvaged, reclaimed

1 INTRODUCTION

The construction sector is the largest consumer of raw materials and accounts for about 50% of all extracted materials [1,2] and the built environment is responsible for 25-40% of global carbon emissions [1]. At the same time, the OECD has predicted that the world's consumption of raw materials will more than double over the period 2017-2060 [3] and the construction sector will account for much of this increase.

To address this, policy initiatives aimed at enhancing the sustainability of the construction sector have been introduced as a key priority for Europe. As part of the European Green Deal, the European Commission in 2020 adopted a new Circular Economy Plan [2], which promotes circularity principles throughout the lifecycle of buildings. It is addressing the sustainability performance of construction products through revision of the Construction Product Regulation, including the possible introduction of recycled content requirements for certain construction products and revising material recovery targets set in EU legislation for construction and demolition waste.

As construction and demolition is currently responsible for more than a third of all waste within the EU [4], reuse and recycling of building materials has the potential to significantly reduce this waste and also reduce the carbon footprint of the built environment through extending the life span of building components.

Timber recovered from buildings at the end of life, often referred to as recovered or secondary timber, is a valuable natural resource with significant potential for reuse and recycling. To optimise the environmental benefits of reuse and recycling and support the circular economy, recovered timber should be used in long-life products, such as structural products for buildings. However, in most European countries timber construction and demolition waste is, for the most part, converted into chips for use in energy production with smaller amounts used for particle board or pallet block manufacture and for composting [5-7]. Key factors inhibiting reuse of recovered timber in the manufacture of structural products are the fact that it is currently prohibited by regulations and that grading standards are not available. To support the development of standards on the reuse of timber, further research is necessary concerning the properties of recovered timber and identification and characterisation

[1] Caitríona Uí Chúláin, Timber Engineering Research Group (TERG), University of Galway, Ireland, caitriona.uichulain@universityofgalway.ie
[2] Daniel F. Llana, Timber Construction Research Group, Universidad Politécnica de Madrid, Spain, d.f.llana@upm.es
[3] Paul Hogan, Hegarty Demolition, Ireland, paul@hegartydemolition.ie
[4] Patrick McGetrick, TERG, University of Galway, Ireland, patrick.mcgetrick@universityofgalway.ie
[5] Annette M. Harte, TERG, University of Galway, Ireland, annette.harte@universityofgalway.ie

https://doi.org/10.52202/069179-0121

of new engineered timber structural products suitable for use of this material.

This work has already begun with a number of European projects focussing on circular use of building materials. The Buildings as Material Banks project (BAMB2020) [8] investigated ways to increase the value of building materials through flexible, circular building design. The CaReWood project [9] introduced an upgrading concept for recovered solid timber as a source of clean and reliable secondary wooden products. In the InFutUReWood project, [10] key problem areas were identified and technical and methodological solutions were proposed to maximise reuse of timber from current buildings especially as a structural material.

The recent growth in interest in timber construction across the globe can be credited not only to the necessity to reuse the embodied carbon of construction materials but also to the development of cross-laminated timber (CLT), which is a high-performance panel product that can displace reinforced concrete and steel in demanding structural applications [11]. CLT was first commercialised in Austria in the 1990s [12] and production in Europe has grown exponentially in the intervening years. While most European CLT is manufactured from Norway spruce, many studies have been carried out to investigate the potential use of locally-grown timber, including lower grade species, for CLT production [13-15]. In the future, it will be challenging to meet the growing demand for timber to produce CLT and other products from the finite supply of new timber from our forests. Supplementing the new timber with suitable material recovered from buildings at the end of life offers a potential solution.

Some recent studies have started to investigate the potential use of recovered timber for CLT production. Llana *et al.* [16] investigated the flexural performance of three-layer CLT panels manufactured using 200-year-old recovered oak. Four different designs were investigated: all new oak, all recovered oak, outer lamina recovered oak with new oak core and outer lamina new oak with recovered oak core. Based on results from tests on three replicates of each design, they found no significant different in the flexural stiffness of the four designs. However, the bending strength of the panels with new oak on the outer layers was about double that of the panels with recovered oak on the outer layers. Rose *et al.* [17] compared the properties of three-layer CLT panels manufactured from recovered mixed-species softwoods with those made from new Scandinavian pine timber. Comparing results from bending tests of three specimens of each type, the modulus of elasticity of the panels made from recovered timber were found to be double that of the panels from new timber. However, the bending strength of the recovered timber panels was only 60% of those from new timber. The fact that 70% of specimens failed at finger joints may have contributed to the difference in strength values.

In a Norwegian study, Stenstad *et al*. [18] used recovered timber with a variety of defects, such as holes, in the cross-layer of three-layer CLT panels. All the boards had their original grade stamps indicate that they were C24. New timber of grade T22 was used in the outer layers. The bending stiffnesses of these panels were found to be the same as those manufactured using new timber in all layers. Arbelaez *et al.* [19] also found similar bending stiffness in 3-layer panels manufactured from new and recovered Douglas fir.

Within the InFutUReWood project [20], the recycling potential of recovered timber in new mass timber products has been investigated. This paper presents results of a study carried out as part of this project to investigate the processing of recovered spruce onto cross-laminated timber panels and to compare their structural performance with equivalent products from new timber.

2 MATERIALS AND METHODS

Norway spruce (*Picea abies* (L.) Karst.) timber boards were recovered from the roof trusses of an office building in Dublin, Ireland. The building was constructed in the 1970s and had been unoccupied for over two years before its demolition. The building was demolished mechanically and materials were sorted at ground level (Figure 1). A sample of 78 boards was recovered, most of which had cross-sectional dimensions of 142 mm x 35 mm. Grade stamps visible on some of the boards indicated that the timber was imported grade TR26 spruce. This timber grade is commonly used in Ireland and the UK for roof trusses. TR26 grade timber has a mean modulus of elasticity in bending of 11000 MPa and a characterisitic bending strength of 28.3 MPa [21].

Using a hand-held moisture meter, the moisture content of the timber boards at the site was estimated to be between 18% and 23%. This high moisture content is attributed to rain penetration of the roof through damaged slates and felt over an extended period of time prior to demolition. Punched metal plates and other metal content were removed on site where possible.

Figure 1: *Recovered timber on site awaiting collection.*

The material was moved to the Timber Engineering Laboratory at the University of Galway where all remaining detectable metal content was removed and it was stored in a conditioning room at 65% relative humidity and 20°C until it reached the equilibrium moisture content.

2.1 NON-DESTRUCTIVE TESTING

Non-destructive testing based on acoustic measurements is widely used for the evaluation of timber mechanical

https://doi.org/10.52202/069179-0121

properties [22]. In this study, non-destructive evaluation of the recovered timber boards was carried out using a handheld acoustic grader (MTG, Brookhuis, Netherlands) to record the longitudinal vibration frequency *f*. The dynamic modulus of elasticity E_{dyn} was then determined using Equation (1), where the density ρ for each board was determined based on measurements of mass and dimensions and *L* is the board length. Values were then adjusted to a reference moisture content of 12% in accordance with EN 14081-2 [23].

$$E_{dyn} = 4\,\rho\, f^2 L^2 \quad (1)$$

For the boards, the adjusted values, $E_{dyn,12,adj}$, ranged between 8000 N/mm^2 and 15000 N/mm^2. To reduce variability between specimens, from the full sample boards with $E_{dyn,12,adj}$ values between 11000 N/mm^2 and 13900 N/mm^2 were selected for the manufacture of CLT panels.

A matching sample of new timber was sourced for manufacturing reference CLT panels and hybrid panels. As Irish-grown spruce is normally graded to C16, its properties are not equivalent to TR26 material and so it deemed unsuitable as reference new timber. The most suitable available material was Irish grown Douglas fir (*Pseudotsuga menziesii* (Mirb.) Franco). Based on acoustic measurements of 101 new boards, a batch of timber boards with $E_{dyn,12,adj}$ values between 10600 N/mm^2 and 14600 N/mm^2 was chosen for processing into CLT panels. The nominal cross-section of these boards was 110 mm x 45 mm.

2.2 CLT MANUFACTURE AND TESTING

Three-layer 60 mm thick CLT panels were manufactured using recovered and new timber, as shown in Figure 2. Three different material combinations were used: recovered timber in all layers, new timber in all layers, and hybrid with new timber in top and bottom layers and recovered timber in the core. Three panels of each material combination were manufactured for testing. All boards were planed to a final cross-section of 90 mm x 20 mm. Additional nails that had not previously been detected in the recovered timber were removed at this stage. Panels were bonded using a one-component polyurethane adhesive using a pressure of 0.6 MPa for a minimum of 2 hours. The adhesive selection and processing parameters were based on previous studies carried out in the University of Galway using new spruce timber [24, 25]. The final panel dimensions were 1620 mm x 360 mm.

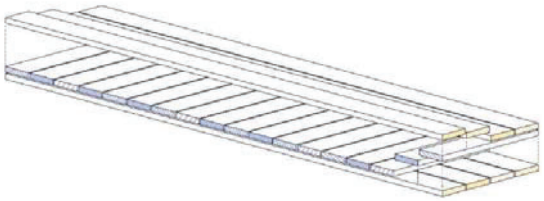

Figure 2: *60 mm x 360 mm x 1620 mm three-layer CLT panel*

All panels were conditioned at 65% relative humidity and 20°C prior to testing in out-of-plane bending in accordance with EN408 [26] and EN 16351 [27]. The four-point bending tests were carried out over a span of 1560 mm (equivalent to 26 times the depth *h*) with the load heads spaced at 6*h*. Global deflection of the panels was measured at each edge at midspan using two 100 mm linear variable differential transformers (LVDTs).

The global modulus of elasticity was calculated from Equation (2) [adapted from EN 408 [26] 10.3 Equation (2)].

$$E_{m,g}\, I = \frac{3al^2 - 4a^3}{24\left(2\frac{w_2 - w_1}{F_2 - F_1} - \frac{6a}{5Gbh}\right)} \quad (2)$$

where l, b, h , in mm, represent the span, panel width, and depth, respectively. The mean shear modulus *G* is taken as 650 N/mm^2 in accordance with EN 408 [26] and EN 16351 [27].

The bending strength was calculated using Equation (3)

$$f_m = \frac{F_{max}\, a h}{4\, I_{tr}} \quad (3)$$

where F_{max} is the failure load, I_{tr} is the transformed second moment of area and other terms are as defined above and in EN 408 [26].

3 RESULTS AND DISCUSSION

3.1 LOAD-DISPLACEMENT RESPONSE

The load-displacement response of the recovered, new and hybrid CLT panels are presented in Figures 3, 4, and 5, respectively. The displacement in each case is the average of the displacement measurements from the two LVDTs mounted at the panel edges.

Similar linear responses until close to failure are seen in each panel type.

https://doi.org/10.52202/069179-0121

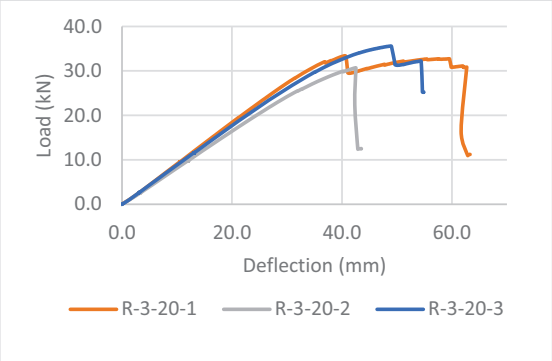

Figure 3: *Load-deflection response – recovered timber panels*

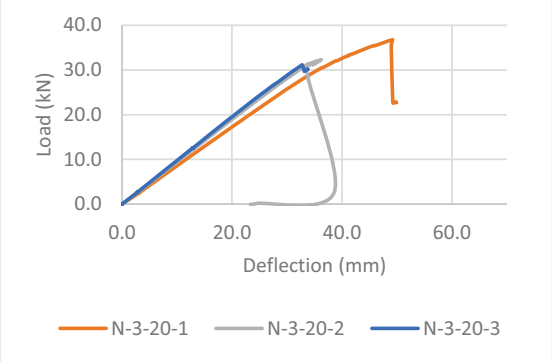

Figure 4: *Load-deflection response – new timber panels*

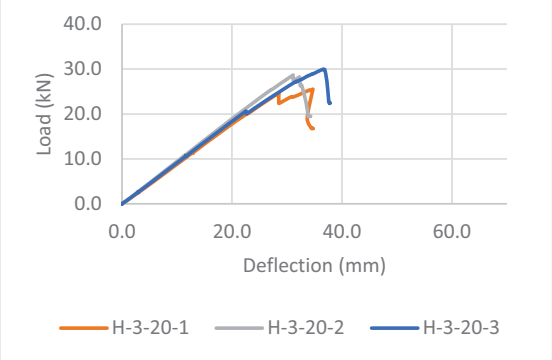

Figure 5: *Load-deflection response – hybrid timber panels*

All panels failed in bending, which initiated at the location of a knot or large slope of grain on the underside of the panel and then propagated through the thickness of the panel as seen in Figure 6.

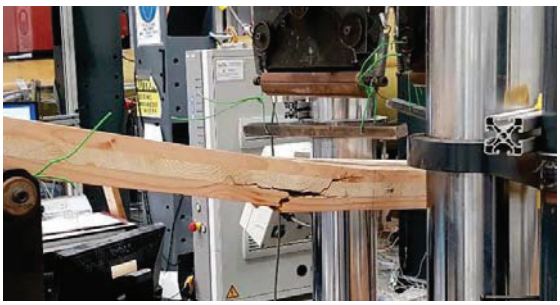

Figure 6: *Bending failure of hybrid CLT panel*

3.2 MODULUS OF ELASTICITY

The mean global modulus of elasticity and bending strength for each test series together with the coefficients of variation are given in Table 1. The mean modulus of elasticity was 10300 N/mm^2, 10900 N/mm^2 and 10800 N/mm^2 for the recovered, new and hybrid panels, respectively. There is no significant difference between the means of each group as can be observed visually in Figure 7. This is to be expected as the panels were manufactured with timber boards with similar dynamic modulus of elasticity values. This finding is consistent with other studies [16, 18, 19].

As the modulus of elasticity values of the CLT panels are consistent with the modulus of elasticity of the boards used in their manufacture, it indicates that the bonding of the layers was successful for both recovered and new timber.

Table 1: *Bending test results*

Panel type	Panel #	$E_{m,g}$ N/mm^2	f_m N/mm^2
Recovered	R-3-20-1	10900	50
	R-3-20-2	9700	46
	R-3-20-3	10420	53
	Mean	*10300*	*49*
	COV %	*5.9*	*7.5*
New	N-3-20-1	10100	55
	N-3-20-2	11100	48
	N-3-20-3	11400	46
	Mean	*10900*	*50*
	COV %	*6.1*	*8.7*
Hybrid	H-3-20-1	10500	38
	H-3-20-2	11100	43
	H-3-20-3	10800	45
	Mean	*10800*	*42*
	COV %	*2.8*	*8.2*

https://doi.org/10.52202/069179-0121

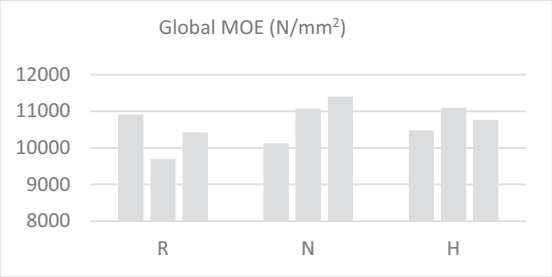

Figure 7: *Global Modulus of elasticity – all panels*

3.3 BENDING STRENGTH

The mean bending strength was 49 N/mm^2, 50 N/mm^2 and 42 N/mm^2 for the recovered, new and hybrid panels, respectively (Table 1), with low coefficients of variation in the range 7.5%-8.7%. The strength values for the hybrid panels were consistently lower than those of the recovered and new panels (Figure 8). There was no obvious reason for this detected during testing. However, as only three panels were tested in each series and significant variability is expected in timber strength due to the influence of features such as knots, these differences in strength values may not be significant.

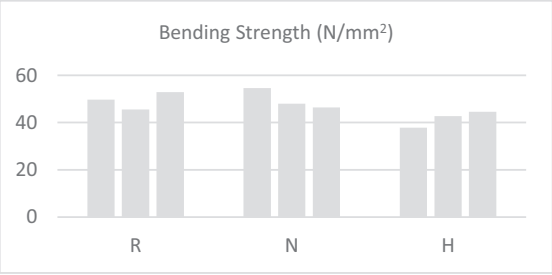

Figure 8: *Bending strength – all panels*

This finding is different to that reported by Rose *et al.* [17] who reported a 60% lower bending strength for recovered softwood panels compared to new panels. These panels had a different failure mode to the current study which may be a factor in the different outcomes. For hardwoods, Llana *et al.* [16] recorded a 50% reduction in bending strength for panels using recovered oak compared to those made from new oak. Kránitz *et al.* [28] in their extensive literature review on the effects of aging on wood, reported a decrease in bending strength for hardwoods. However, this review indicated that for softwoods there was no difference in the bending strength between new and wood up to 400 years old. For the present study, the age of the recovered timber was about 50 years so no deterioration would be expected based on the conclusions of five different studies.

While bending strength and stiffness do not appear to be adversely affected by being under load for 50 years, other properties need to be investigated. Kránitz *et al.* [28] reported an increase in brittleness, which may affect the properties perpendicular to the grain.

4. YIELD OF CLT

Regarding the yield from the recovered timber, the recovered timber cross-section (142 x 35 mm^2) was significantly larger than the board dimensions required for panel manufacture (90 x 20 mm^2) and this resulted in a yield of about 28% when length reductions are included. The yield would be greatly increased if recovered timber dimensions closer to the final board dimension were available. For example, using 130 mm x 30 mm boards to produce a 90 mm thick panel would have increased the yield to 70%. The commercial availability of recovered timber in a range of sizes close to those required for panel manufacture will be necessary to ensure efficient reuse of the material.

5. CONCLUSIONS

Spruce members were recovered from the demolition of a timber roof truss that had been under load for about 50 years and which was exposed high relative humidity during its later years. A sample of new timber with a similar range of dynamic modulus of elasticity values was source. CLT panels of three different designs were successfully manufactured and tested in bending from this material. These included panels made entirely from recovered timber, panels from new timber and hybrid panels with new timber in the outer layer and recovered timber in the cross-layer. Overall, this study has found no difference in the mechanical properties in bending of CLT manufactured from recovered and new softwood timber.

While these results are very positive, it should be borne in mind that the number of specimens tested was small and used recovered timber from a single source. Further testing of panels manufactured from a wide range of sources is recommended to confirm these findings.

In terms of yield, mass timber products are a good option for recycling of recovered timber subject to availability of boards with cross-sections close to the final size required.

ACKNOWLEDGEMENTS

This work was carried out in Ireland as part of the InFutUReWood project supported under the umbrella of ERA-NET Cofund ForestValue by the Department of Agriculture, Food and the Marine. ForestValue has received funding from the European Union's Horizon 2020 research and innovation programme under grant agreement No. 773324.

The authors would like to acknowledge the contribution of Colm Walsh and Peter Fahy, senior technical officers in the School of Engineering, University of Galway, for their assistance with the laboratory test programme.

REFERENCES

[1] World Economic Forum 2016. *Shaping the Future of Construction. A Breakthrough in Mindset and Technology.*

https://www3.weforum.org/docs/WEF_Shaping_the_Future_of_Construction_full_report__.pdf. Accessed January 19 2023.
[2] European Commission, 2020, *A new Circular Action Economy Plan. For a cleaner and more competitive Europe.* https://environment.ec.europa.eu/strategy/circular-economy-action-plan_en. Accessed January 19 2023.
[3] OECD (2017) *Global Material Resources Outlook to 2060 – Economic Drivers and Environmental Conseq* https://www.oecd.org/environment/raw-materials-use-to-double-by-2060-with-severe-environmental-consequences.htm. Accessed January 19 2023.
[4] Construction and Demolition Waste. European Commission website. https://ec.europa.eu/environment/topics/waste-and-recycling/construction-and-demolition-waste_en Accessed 20th April 2022.
[5] Irle, M., Privat, F., Deroubaix, G., Belloncle, C. (2015) Intelligent recycling of solid wood. Pro Ligno 11(4):14-20
[6] Llana, D.F., Íñiguez-González, G., de Arana-Fernández, M., Uí Chúláin, C., Harte, A.M., Recovered wood as a raw material for structural timber products. Characteristics, situation and study cases: Ireland and Spain. In *Proceeding of 63rd International Convention of Society of Wood Science and Technology (SWST)*. 117-123, 2020. Online.
[7] Harte, A.M., Uí Chúláin, C., Nasiri, B., Hughes, M., Llana, D.F., Íñiguez-González, G., de Arana-Fernández, M., Shotton, E., Walsh, S-J., Ridley-Ellis, D., Cramer, M., Risse, M., Ivanica, R., Cristescu, C., Sandberg, K., Sandin, Y., Turk, G., Plos, M., Šuligoj, T., Hogan, P., Recovered timber in Europe: sources, classification, existing and potential reuse and recycling. *National University of Ireland Galway 2020.* Doi: 10.13025/r2dt-jp43
[8] Buildings as Material Banks (BAMB2020) project website: https://www.bamb2020.eu Accessed: February 14 2023.
[9] CaReWood: Cascading Recovered Wood project website https;//carewood.lam.upr.si/ Accessed: February 14 2023.
[10] InFutUReWood: Innovative Design for the Future – Use and Reuse of Wood (Building) Components Project website https://www.infuturewood.info Accessed April 20 2022.
[11] Harte, A.M., Mass timber – the emergence of a modern construction material*, J Struct. Integ. Mtce*., 2 (3), 121-132. 2017. doi: 10.1080/24705314.2017.1354156
[12] Brandner, R., Flatsher, G., Ringhofer, A., Schickhofer, G., Thiel, S, Cross laminated timber (CLT): overview and development. *Eur. J Wood Prod.*, 74(3):331-351, 2016. doi: 10.1007/s00107-015-0999-5
[13] Azambuja, R.R., De Vallance, D.B., McNeel, J., Hassler, C., Dahle, G., CLT panels from below-grade yellow-poplar sorted by non-destructive proof loading. In *Proceeding of 63rd International Convention of Society of Wood Science and Technology (SWST)*. 106-107, 2020. Online.
[14] Sikora, K.S., McPolin, D.O., Harte, A.M., Effects of the thickness of cross-laminated timber (CLT) panels made from Irish Sitka spruce on mechanical performance in bending and shear, *Constr. Build. Mater*., 116: 141-150. 2016. doi: 10.1016/j.conbuildmat.2016.04.145
[15] Hindman, D.P., Bouldin, J.C., Mechanical properties of Southern yellow pine cross-laminated timber, J. *Mater. Civil. Eng.,* 27: 1-7. 2015. doi: 10.1061/(ASCE)MT.1943-5533.0001203
[16] Llana, D.F., González-Alegre, V., Portela, M., Íñiguez-González, G., Cross laminated timber (CLT) manufactured with European oak recovered from demolition: structural properties and non-destructive evaluation, *Constr. Build. Mat*. 339: 127635, 2022. doi: 10.1016/j.conbuildmat.2022.127635
[17] Rose, C.M.., Bergsagel, D., Dufresne, T., Unubreme, E., Lyu, T., Duffour, P., Stegemann, J.A., Cross-laminated secondary timber: experimental testing and modelling the effects of defects and reduced feedstock properties, *Sustainability* 10(11):4118, 2018. doi: 10.3390/su10114118
[18] Stenstad, A., Lønbro Bertelsen, S., Modaresi, R., Comparison of strength tests for evaluating the secondary timber utilisation in Cross Laminated Timber (CLT). In Proceedings of *16th World Conference on Timber Engineering (WCTE 2021),* 2201-2206, Santiago, Chile. Online, , 2021.
[19] Arbelaez, R., Schimleck, L., Sinha, A. Salvaged lumber for structural mass timber panels; manufacturing and testing, *Wood Fiber Sci.,* 52(2): 178-190, 2020. doi: 10.22382/wfs-2020-016.
[20] Sandberg, K., Sandin, Y., Harte, A.M., Shotton, E., Hughes, M., Ridley-Ellis, D., Turk, G., Íñiguez-González, G., Cristescu, C., *Summary reportInFutUReWood – Innovative Design for the Future – Use and Reuse of Wood (Building) Components. RISE, Sweden 2022. doi: 10.23699/p41e-ae46*
[21] EN 14081-4:2009 Timber structures – Strength graded structural timber with rectangular cross section – Part 4: Machine grading – Grading machine settings for machine controlled systems. European Committee of Standardization (CEN), Brussels, Belgium. 2009.
[22] Gil-Moreno, D., O'Ceallaigh, C., Ridley-Ellis, D., Harte. A.M. Use of nondestructive techniques for determination of tension parallel-to-grain properties of spruce. In *Proceedings of the 21st International Nondestructive Testing and Evaluation of Wood Symposium.* 233-240. Freiburg, Germany. 2019
[23] EN 14081-2:2018 Timber structures – Strength graded structural timber with rectangular cross section – Part 2: Machine grading; additional requirements for type testing. European Committee of Standardization (CEN), Brussels, Belgium. 2018.
[24] Raftery G., Harte A.M., Rodd P. Qualification of

https://doi.org/10.52202/069179-0121

wood adhesives for structural softwood glulam with large juvenile wood content, *J. Inst of Wood Science*, 18(1):24-34, 2008. doi:10.1179/wsc.2008.18.1.24

[25] Sikora K.S., McPolin D.O., Harte A.M. Shear strength and durability testing of adhesive bonds in cross-laminated timber*, J. Adhesion* (2(7-9):758-777, 2016. doi: 10.1080/00218464.2015.1094391

[26] EN 408:2010+A1 Timber structures - Structural timber and glued laminated timber - Determination of some physical and mechanical properties. European Committee of Standardization (CEN), Brussels, Belgium. 2012.

[27] EN 16351 Timber structures - Cross laminated timber - Requirements. European Committee of Standardization (CEN), Brussels, Belgium. 2015.

[28] Kránitz, K., Sonderegger, W., Bues, C.-T., Niemz, P., Effects of aging on wood: a literature review, Wood Sc. Technol., 50:7-22, 2016. doi: 10.1007/ s00226-015-0766-0.

World Conference on Timber Engineering Oslo 2023

COMPARISON OF ENERGY EFFICIENCY BETWEEN WOODEN-BASED HYBRID STRUCTURE SYSTEM AND RC STRUCTURE SYSTEM IN SUBTROPICAL AND TROPICAL AREA

Cheng-Chieh Hsu [1], Meng-Ting Tsai [2], Shao-Chi Wu [3]

ABSTRACT: In response to the environmental problems of global warming, the need to save energy and carbon emissions, the energy usage in building sector accounts for 40% of global energy consumption, and its greenhouse gas emissions account for more than three-thirds of its global emissions. It is the largest source of emissions in most countries. However, previous research has mostly focused on comparing the energy-saving efficiency between wooden and RC structures in high-latitude regions, energy-saving efficiency between wooden and RC structures in low-latitude regions, especially in sub-tropical or tropical area in Asia, has not been focused. In this study, in order to examine the energy consumption differences in sub-tropic and tropic area, the energy consumptions in Taipei, Kaohsiung, Hochimin City and Singapore were compared. Moreover, considering the common-used construction materials in buildings in the selected Asian cities, hybrid structure system comprises RC beams/columns and various floors and walls system such as brick, wood and so on was used for the comparison. Simulation method was used to compare the energy efficiency of the four-story and ten-story wooden structures, RC structures, and other types of hybrid system focusing on the usage phase of the building in this study. The research method is to establish a simulation model based on the literature review to set the basic building parameters for analysis. The software called Green Building Studio in Revit was used to simulate the energy consumption in different types of buildings. The carbon emission was calculated to compare the difference in energy efficiency between different structures. Moreover, the combination of different wooden based structural system which was influenced by the energy consumption was evaluated as well, in order to understand the advantage of applying wooden components. The results of the study show that, the use of CLT in four-story and ten-story buildings has a common energy-saving trend in the energy consumption. For the hybrid structural system, the average energy saving are up to 7.49% to 8.12%, depending on the different types of wooden based hybrid system, when the numbers of the original RC buildings were replaced by wooden buildings.

KEYWORDS: Wood structure, RC structure, building energy use, building energy simulation

1 INTRODUCTION

Due to the environmental problems caused by global warming, energy consumption and carbon emissions must be reduced. The building density in an area rapidly increases with increasing population. A report of the United Nations Environment Program indicates that the energy consumption of the construction sector accounts for 40% of the global energy consumption. In addition, the greenhouse gas emissions of the construction sector account for over 33% of the total global emissions, and the construction sector is considered the largest emission source. Consequently, to reduce their environmental impact, construction-related industries should aim to reduce their energy consumption and carbon dioxide emissions in the usage stage of the building life cycle.

Wood construction is becoming increasingly popular internationally, and various new types of wooden building materials and wood construction methods are constantly emerging. From the environmental perspective, wooden structures are favorable insulators that are suitable for carbon fixation. The thermal conductivity of concrete is 1.4 w/m·k, which is 10 times the conductivity of wood. In this study, in order to examine the energy consumption differences in sub-tropic and tropic area, the energy consumptions in Taipei, Kaohsiung, Hochimin City and Singapore were compared. Moreover, considering the common-used construction materials in buildings in the selected Asian cities, hybrid structure system comprises RC beams/columns and various floors and walls system such as brick, wood and so on was used for the comparison. The amounts of the carbon emission was calculated to compare the difference in energy efficiency between different structure systems. Moreover, the power reserve capacity (rate) in the power station which was influenced by the energy consumption was evaluated as well, in order to understand the advantage of applying wooden components in to the wooden-based hybrid structure system in tropical and subtropical area.

[1] Cheng-Chieh, Hsu, National Taiwan University of Science and Technology, Taiwan, b10000085@gmail.com
[2] Meng-Ting, Tsai, National Taiwan University of Science and Technology, Taiwan, tsai@mail.ntust.edu.tw
[3] Shao-Chi, Wu, National Taiwan University of Science and Technology, Taiwan, tim29341405@hotmail.com

https://doi.org/10.52202/069179-0122

2 METHODOLOGY

2.1 ASSESSMENT OF ENERGY CONSUMPTION

Autodesk Green Building-rating System (GBS) was used for simulating the structure energy consumption in this study. GBS can be used as an independent cloud-service-based program or a plug-in component of the Revit program for energy analysis. GBS comprises the DOE-2.2 analysis core and can provide extremely detailed analysis. As a cloud-based tool, GBS can facilitate rapid computation on the Autodesk server. In general, the DOE-2.2 analysis core requires extremely detailed information on the building envelope and electromechanical system for computation. However, GBS presets numerous building envelope and electromechanical system parameters according to the ASHRAE standard. Thus, architects can focus more on the design factors that have decisive influences on the overall energy consumption of buildings and can ignore technical details. In addition to the building energy consumption, electricity consumption, and annual carbon emissions, GBS can calculate the Energy Star score of buildings. It can also evaluate the glass property and water usage efficiency scores according to the LEED evaluation system published by the U.S. Green Building Council. GBS can even determine the solar energy usage potential.

2.2 ASSESSMENT OF CO2 EMISSION

The Guidelines for National Greenhouse Gas Inventories published by the Intergovernmental Panel on Climate Change were used for the assessment of carbon dioxide emissions. In this study, the calculation method for the emissions of carbon dioxide, methane, and nitrous oxide was adopted to calculate the carbon emissions of different countries. GBS calculates the energy consumption of buildings according to two major parameters: electricity consumption and fuel consumption. The calculated carbon emission of electricity consumption differs according to the electricity carbon emission coefficients of different countries. The carbon emissions can be calculated using equation (1). The emission coefficients of different countries are listed in Table 1. For calculating the carbon emission of fuel consumption, the fuel volume (m3) is first converted into energy units. An energy of 38 MJ or 10.6 kWh can be generated by burning 1 m3 of natural gas. The carbon emission of fuel consumption can then be calculated using equation 2. The carbon emissions coefficient of fuel is listed in Table 2, and all the compared countries have the same carbon emissions coefficient of fuel. The carbon emissions of the total energy consumption of a building can be obtained by summing the carbon emissions of electricity and fuel.

(A) Electricity consumption is converted into carbon emissions by using the following formula:
Electricity usage (kWh) × electricity emissions coefficient (kg CO_2e/kWh) = carbon dioxide emissions(kg) (1)

(B) Fuel consumption is converted into carbon emissions by using the following equation:
Fuel usage (m^3) × natural gas emissions coefficient (kg CO_2e/m^3) = carbon dioxide emissions (kg) (2)

(C) The carbon emission of total energy consumption is calculated as follows:
Carbon emission of total energy consumption (kg)
= equation (1) + (2) (3)

3 SIMULATION MODELING

To determine the energy usage efficiencies under different conditions, the energy consumption and carbon emission were compared for different numbers of stories (4 and 10), different construction materials (RC and CLT), and cities with different latitudes (from north to south, Taipei, Kaohsiung, Hochimin City and Singapore). The related structure usage situations and air admission timing of the air-conditioning system were set. In addition, the energy simulation was only conducted for the daily usage stage in the structure life cycle. When GBS was used for structure energy simulation, the basic settings, simulation parameters, weather data, electromechanical system, indoor load, and operation schedules had to be input in the simulation process. The basic parameters and settings of this study are as follows:

1. According to the descriptions on the official website of Autodesk, the data on weather stations were obtained from the World Meteorological Organization.
2. For concrete materials, the pre-existing data in the program were used. The parameters of CLT walls were obtained from relevant research.
3. For the electromechanical system and indoor load, detailed data were required from the DOE-2.2 analysis core to the electromechanical system for the operation. However, the building envelope and electromechanical system parameters were preset in GBS according to the ASHRAE standards. Different air-conditioning systems are used in different countries. The preset parameters were used for the mechanical system and indoor load in this study. The preset parameters of heating, ventilation, and air-conditioning (HVAC) systems were a central variable air volume system, hot-water heating, a performance coefficient of 5.96 for the freezer, and a boiler efficiency of 84.5.

Because this study was a preliminary study, a 24/7 operation schedule was set. Thus, simulations were conducted 7 days a week and 24 hours a day. Then, GBS was used to analyze the simulated building energy consumption. In the comparison of the energy consumptions of different building materials (RC and CLT) in cities at different latitudes, only the energy consumption in the operation stage was considered. In

https://doi.org/10.52202/069179-0122

addition, the following assumptions were made in the simulation process for the energy consumption:
(1) The window positions remained the same when switching from an RC structure to a CLT structure; thus, the illumination demands remained the same.
(2) Except for the balcony, the indoor temperatures of all the rooms were controlled between 18 and 26 °C.
(3) No heating or cooling was conducted in the stair areas.
(4) Electricity was used for the air-conditioning system and illumination, and fuel was used for heating.

3.1 TARGET BUILDING

To determine the energy usage efficiencies for different numbers of stories and different weather conditions, the standard floor of social housing in Taipei City was used as the standard floor in this study. The layouts and basic information of a four-story building and a 10-story building are listed in Table 3.

3.2 BUILDING MATERIALS

The influence of the floor height on the energy-saving efficiency was examined. In addition, the energy consumption efficiencies of the RC and wooden-based hybrid structures were compared. In this study, only the energy consumption in the daily life stage of the building was examined. The simulated building was an RC structure with fixed floor plans on different floors, the building height, building direction, total area, and opening such as windows and doors were fixed for the building simulation. The layout and the structure of the other types of buildings follow the RC structure, which was the target building, however, the material of structures floors and walls, was replaced with wooden components. The building types are illustrated and as shown in Fig 2.

Table 1. Electricity carbon emission coefficients of different countries.

Country	Electricity carbon emission coefficient (kg CO2e/kWh)
Taiwan (Taipei/Kaohisung)	0.53
Vietnam (Hochumin City)	0.57
Singapore	0.41

The physical properties of RC and CLT, including their heat transfer coefficient, specific heat, and density, were also determine for complete analysis. As presented in Table 4, RC has a higher heat transfer coefficient, specific heat, and density than CLT does. Thermal resistance and heat loss are inversely correlated. Thus, an increase in the thermal resistance of the wall material between the interior and exterior of a building can reduce the heat loss of the building (equation 4). As presented in Table 4, CLT walls have a higher thermal resistance than RC walls do. The thermal resistance of a 300-mm-thick external CLT wall is up to 3.3 m2·K/W. The thermal resistance of a 300-mm-thick RC external wall is only 0.25 m2·K/W, which is approximately 1/13th the thermal resistance of a 300-mm-thick CLT external wall. Table 5 lists the physical properties of RC and CLT walls of different thicknesses. Fig. 2 displays the models of numerical analysis. Four- and Ten-story CLT and RC buildings were constructed for comparing the energy consumptions in their daily life stages.

$$\text{Heat loss} = (A/R) \times (T_{indoor} - T_{outdoor}) \quad (4)$$

A : external surface area of the building
R : thermal resistance (R value)
T_{indoor}: indoor air temperature
$T_{outdoor}$: outdoor air temperature

Table 2. Fuel carbon emission coefficient.

Item	Carbon emission coefficient (CO2e/m3)
Natural gas	1.88

Table 3. Basic information on the target buildings.

Building type	4F	10F
Single-story floor area	192.8 m²	702.6 m²
Total floor area	771.2 m²	7026.0 m²
Total surface area	1161.2 m²	3906.6 m²
Exterior window ratio	16.4%	19.9%
User number per unit area	3 people/100 m²	3 people/100 m²
Total user number	23 people	211 people
Average illumination power	6.6 W/m²	6.6 W/m²

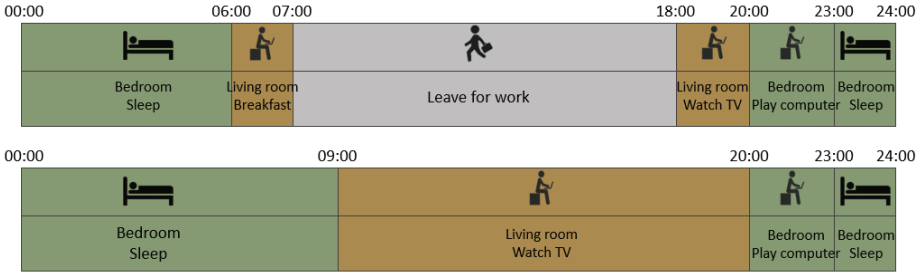

Fig. 1. Life trajectory for simulation

https://doi.org/10.52202/069179-0122

3.3 CITIES IN SUB- AND TROPICAL AREA

Cities at different latitudes have different climates, which influence the energy consumption of buildings. The climate includes the highest and lowest outdoor temperatures and humidity.

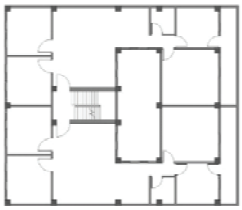

(a) 4-story building

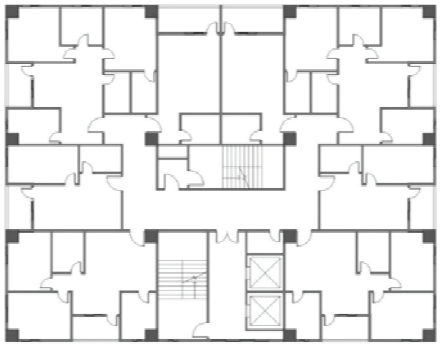

(a) 10-story building

Fig. 2. Standard floor plans of the target buildings

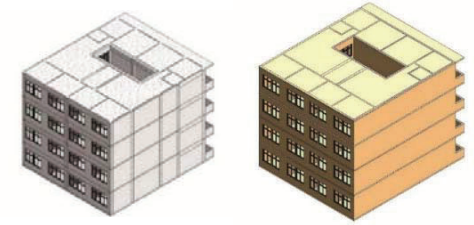

(a) Analysis models of the 4-story RC and CLT structures.

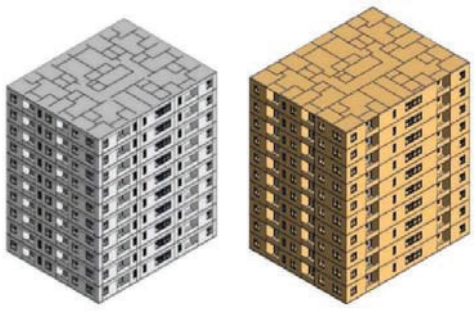

(b) Analysis models of the 10-story RC and CLT structures.

Fig. 3. Simulation modelling.

In this study, the energy consumptions of buildings in cities at different latitudes were also simulated to determine how the overall energy usage efficiency varied with the latitude. The latitude of Taipei was selected as the standard. The other cities selected for comparison were Tokyo and Harbin, which are located to the north of Taipei, as well as Singapore, which is located close to the equator and to the south of Taipei. These cities were selected for comparing the energy-saving efficiencies of RC and CLT buildings of different heights in different environmental conditions. The monthly average temperatures of the aforementioned cities in 2021 are presented in Fig. 4. The lowest monthly average temperature in Taipei, which is located at a high latitude of subtropical zone, was 17.7 °C in January, and the highest monthly average temperature in Taipei was 30.6 °C in July. Thus, the largest monthly average temperature difference was approximately13 °C in Taipei. The lowest monthly average temperatures in Singapore, which is located at a low latitude, near Equator, were 27 °C in December, and the highest monthly average temperatures in Singapore were 29 °C in August and September, respectively. The highest monthly average temperature difference in Singapore was only 2 °C. The highest monthly average temperatures of Kaohisung and Hochimin City, which are located inbetween the tropical zone, were 28.6 °C in August and 30.6 °C in April, respectively. These temperatures were comparable to the high temperatures in Singapore, which is located in the tropics as shown in Fig. 4 and Fig. 5.

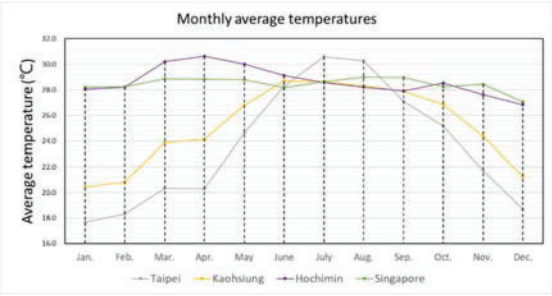

Fig. 4. Monthly average temperatures of the cities.

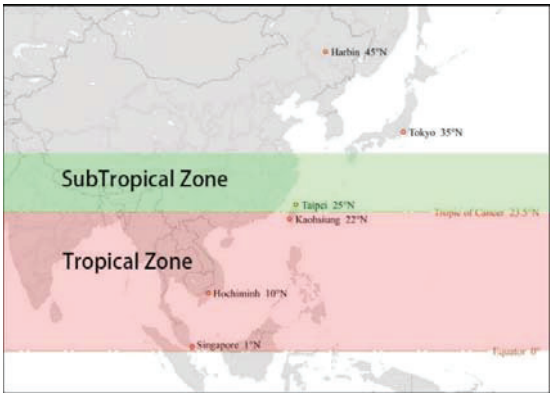

Fig. 5. Cities in Sub- and Tropical Zone

https://doi.org/10.52202/069179-0122

Table 5. Interior materials of different wall types.

Wall material	Wall purpose	Total thickness (mm)	Wall schematic	Interior material	Thickness (mm)
RC	Exterior wall	150		Ceramic tile	10
				Cement mortar	10
				Concrete	120
				Cement mortar	10
	Interior wall	120		Cement mortar	10
				Concrete	100
				Cement mortar	10
CLT	Exterior wall (10F)	300		Plasterboard	15
				Rigid insulation wall	50
				CLT	220
				Plasterboard	15
	Exterior wall (4F)	215		Plasterboard	15
				Rigid insulation wall	50
				CLT	135
				Plasterboard	15
	Interior wall	150		Plywood	10
				Rigid insulation wall	20
				CLT	110
				Plywood	10

4 RESULT AND DISCUSSION

4.1 ENERGY CONSUMPTION

In the simulation, electricity was used by the HVAC system, illumination equipment, and other equipment. Fuel was used by the HVAC and domestic water heating systems. Table 6 presents the simulation results for the 4- and 10-story building made of different building materials and located in cities at different latitudes.

Taking10-story building in Taipei for example, which is located at the highest latitude among the considered cities, the annual electricity consumptions of the RC and CLT structures were 157 and 151 kWh/m^2, respectively. For Singapore, which is at the lowest latitude, the annual electricity consumptions of the RC and CLT buildings were 202 and 190 kWh/m^2, respectively. For both 4- and 10-story building, the simulation results indicated that the electricity consumption of RC buildings was considerably higher than that of CLT structures at higher and lower latitudes. However, at low latitudes, the difference in the electricity consumptions of RC and CLT buildings was relatively higher. The different trend was observed for the fuel energy usage though. Overall, the energy-saving efficiencies of CLT buildings were higher than those of RC structures. The differences in the energy-saving efficiencies considering both electricity and fuel of CLT and RC buildings were higher at higher latitudes.

A comparison of the total energy consumptions of RC and CLT buildings is presented in Table 6 as well. For four-story buildings, the total energy consumptions of the CLT buildings were approximately 98.7%, 99.6%, and 98.7% those of the RC buildings in Kaohsiung, Hochimin City, and Singapore, respectively. No significant difference was observed in the total energy consumptions of the four-story CLT and RC buildings in these cities. Greater difference of the total energy consumptions of RC and CLT buildings is observed in Taipei, which is approximately 89.6% difference. For 10-story buildings, the total energy consumptions of the CLT buildings were approximately 95.9%, 97.3%, and 96.1% those of the RC buildings in Kaohsiung, Hochimin City, and Singapore, respectively. For Taipei, the difference between the total energy consumptions of the 10-story CLT Buildings and RC buildings was marginally higher than that of the four-story CLT and RC structures, which is 88.8% of the difference.

4.2 CO2 EMISSION

Table 7 presents the carbon dioxide emissions per unit area for 4- and 10-story RC and CLT structures in cities at different latitudes. The carbon emissions of electricity energy consumption mainly originate from air-conditioning systems, illumination systems, and basic facilities of the structure. The carbon emissions of fuel energy consumption mainly originate from the use of heating systems. Electricity carbon emissions were calculated according to the electricity emission coefficients of the countries in which the considered cities are located (Tables 1 and 2). Thus, the carbon emissions from the same electricity energy consumption were different in different countries.

The electricity carbon emissions of four-story RC and CLT buildings were 95 and 93 kg/m^2·yr, respectively, in Taipei; thus, the difference in the electricity carbon emissions of the two types of four-story structures was only 2 kg/m^2·yr in Taipei. In Singapore, the electricity carbon emissions of four-story RC and CLT buildings were 157 and 153 kg/m^2·yr, respectively, which represents an electricity carbon emission difference of 4 kg/m^2·yr. The difference in carbon emissions was small because the monthly average temperature in every month

https://doi.org/10.52202/069179-0122

in Singapore was higher than 26 °C, which was the temperature set in this study for the air-conditioning system to be turned on. The air-conditioning system demands were high. Thus, the demands for carbon emissions from electricity energy consumption were high for both RC and CLT buildings. For Taipei, in addition to the air-conditioning system demands, the heating system demands were slightly high. The carbon emissions of fuel energy consumption for four-story RC and CLT buildings in Taipei were 38 and 30 kg/m^2·yr, respectively, which represents a fuel carbon emission difference of 8 kg/m^2·yr. In Singapore, the fuel carbon emissions of four-story RC and CLT buildings were both 19 kg/m^2·yr. In cities at higher latitudes, the heating system needs were higher. Thus, the fuel carbon emissions and fuel carbon emission differences increased considerably with the latitude. Table 7 indicate that the 10-story buildings had better carbon emission reduction effects to those of the four-story buildings for electricity and fuel energy consumption. For regions at higher latitudes (Taipei), the differences in electricity carbon emissions of 10- and 4-story structures were not significant. However, the carbon emissions reduction efficiencies of buildings with more stories could be shown in the differences of fuel carbon emissions. Thus, greater differences were observed in the carbon emissions of total energy consumption for RC and CLT buildings in Taipei and Singapore for 10 story building.

4.3 HYBRID BUILDING SYSTEM

The results of this study indicate that CLT buildings have higher energy-saving and carbon reduction efficiencies than RC buildings do at different latitudes. These efficiencies increase with the number of floors. Moreover, the differences in the energy consumption efficiencies of CLT and RC buildings increase with the latitude. All the East Asian cities selected in this study have high degrees of urbanization and concentrated high-rise buildings. The existing high-rise buildings in these cites face the problem of aging. For example, in Taipei, most buildings are RC structures that are approximately 30–50 years old. These structures are still usable; however, their overall energy consumption is high because of the RC building material. Consequently, in this study, few strategies are proposed for the renewal of these buildings in the future. The proposed strategy involves preserving existing RC beam structures and renewing the floors and walls with CLT for renovation type 1. Replacing the top 4 floors of the building with wooden system is the renovation type 2 in this study. For renovation type 3, the original service core with RC as major construction material is preserved, while the rest of the living space is replaced by wooden construction. On the basis of this concept, three wooden based hybrid building systems are defined, and the analysis model was established in this study. Fig. 6 illustrates the models of preserving the RC beam structures and replacing the floors and walls with CLT, replacing the top 4 floors of the building with wooden system, and the original service core with RC as major construction material is preserved. The energy consumptions of CLT and RC structures of the same size were also compared. The analysis and simulation conditions were the same as stated previously as shown in Section 3. The simulation results are concluded and as shown in the next section.

Table 6. Energy consumption comparison of structures with different heights in different cities.

		Taipei		Kaohsiung		Hochimin City		Singapore	
		RC	CLT	RC	CLT	RC	CLT	RC	CLT
(A)Electricity	4 storys	175	179	210	211	222	221	232	227
(kWh/m^2/yr)	10 storys	157	151	188	178	193	184	202	190
(B)Electricity	4 storys	631	644	756	761	799	795	833	818
(MJ/m^2/yr)	10 storys	566	543	675	641	695	662	726	682
(C)Fuel	4 storys	761	603	481	460	415	414	390	389
(MJ/m^2/yr)	10 storys	701	583	461	449	407	410	382	382
Sum (B)+(C)	4 storys	1392	1247	1237	1221	1214	1209	1223	1207
(MJ/m^2/yr)	10 storys	1267	1126	1136	1090	1102	1072	1108	1064

Table 7. Carbon emissions comparison of structures with different heights in different cities.

		Taipei		Kaohsiung		Hochimin City		Singapore	
		RC	CLT	RC	CLT	RC	CLT	RC	CLT
(A)Electricity	4 storys	95	93	113	112	127	126	157	153
(kg/m^2/yr)	10 storys	84	81	100	95	110	105	136	128
(C)Fuel	4 storys	38	30	24	23	21	21	19	19
(Kg/m^2/yr)	10 storys	35	29	23	22	20	20	19	19
Sum (A)+(B)	4 storys	133	123	137	135	148	147	176	172
(Kg/m^2/yr)	10 storys	119	110	123	117	130	125	155	147

4.4 SIMULATION RESULTS FOR HYBRID BUILDING SYSTEMS

The analysis results presented in Table 8 indicate that 3 types of different hybrid buildings have better electricity energy consumption performance to the RC structure. The electricity energy consumption performance of the hybrid buildings is only marginally worse (3%–7% lower) than that of the CLT buildings. Thus, the proposed hybrid buildings are close to the CLT buildings in terms of electricity energy consumption. For fuel energy consumption, no significant difference was observed between the different building in Singapore and Hochimin City and Kaohsiung, which is located at a lower latitude. In Taipei, which are located at relatively higher latitudes, the fuel energy consumption of the hybrid buildings is higher than that of the RC buildings and not significantly different from that of the CLT buildings. The CLT and wooden based hybrid buildings exhibited no significant difference in their total energy consumptions. The aforementioned buildings exhibited lower total energy consumptions than the RC buildings did. The energy-saving efficiency of the proposed wooden hybrid structure system, which comprises RC beam structures and CLT floors and walls for hybrid type 1, replacing the top 4 floors of the building with wooden system for hybrid type 2, and original service core with RC as major construction material preserved for hybrid type 3, are close to that of CLT buildings. The advantage of the hybrid building system is obvious if the weight of the material is compared. The total building weight is potentially reduced if part of the building material is replaced from reinforced concrete to wood, due to the light weight property for wood comparing to concrete. In the region with high frequent earthquake, especially in Taipei or Kaohsiung, the reduction of building weight means the seismic force can be potentially reduced, improving the resilience of the building.

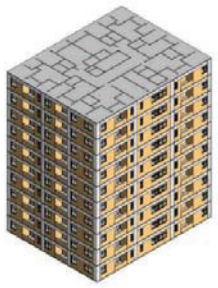

(a) Hybrid Type 1: models of preserving the RC beam structures and replacing the floors and walls with CLT

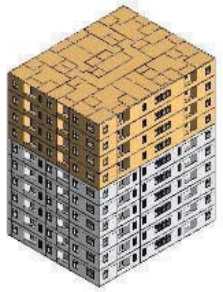

(b) Hybrid Type 2: models of replacing the top 4 floors of the building with wooden system

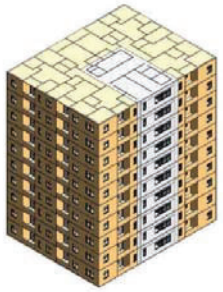

(b) Hybrid Type 3: models of original service core with RC as major construction material preserved

Fig. 6. Models of different hybrid building systems

Table 8. Energy consumption of hybrid buildings with RC and CLT structures.

Taipei					
	RC	CLT	Hybrid Type 1	Hybrid Type 2	Hybrid Type 3
(A) Electricity	566	543	549	549	540
(B) Fuel	701	583	570	638	576
Sum (A)+(B) (MJ/m²/yr)	1267	1126	1119	1187	1116
Kaohsiung					
	RC	CLT	Hybrid 1	Hybrid 2	Hybrid 3
(A) Electricity	675	641	649	654	642
(B) Fuel	461	449	440	442	440
Sum (A)+(B) (MJ/m²/yr)	1136	1090	1089	1096	1082
Hochimin City					
	RC	CLT	Hybrid 1	Hybrid 2	Hybrid 3
(A) Electricity	695	662	673	675	666
(B) Fuel	407	410	407	392	407
Sum (A)+(B) (MJ/m²/yr)	1102	1072	1080	1067	1073
Singapore					
	RC	CLT	Hybrid 1	Hybrid 2	Hybrid 3
(A) Electricity	726	682	692	700	685
(B) Fuel	382	382	382	368	382
Sum (A)+(B) (MJ/m²/yr)	1108	1064	1074	1068	1067

https://doi.org/10.52202/069179-0122

5 CONCLUSIONS

In this study, the differences of energy consumption and carbon emission at sub-tropical and tropical area such as Taipei, Kaohsiung, Hochimin City and Singapore, were compared. The preliminary study clarified that the energy-saving efficiency is higher in the cities in the higher latitude when the construction materials are substituted from RC structure to CLT structure. Generally, the performance of wooden buildings is better than RC buildings and the following results are conclude.

(1) For 10-story buildings, the total energy consumptions of the CLT buildings were approximately 95.9%, 97.3%, and 96.1% those of the RC buildings in Kaohsiung, Hochimin City, and Singapore, respectively. For Taipei, the difference between the total energy consumptions of the 10-story CLT Buildings and RC buildings was marginally higher than that of the four-story CLT and RC structures, which is 88.8% of the difference. For cities located in Subtropical area such as Taipei, archiving a better energy consumption efficiency than the cities located in tropical cities, such as Kaohsiung, Hochimin City, or Singapore.

(2) The greater differences were observed in the carbon emissions of total energy consumption for RC and CLT buildings in Taipei and Singapore for 10 story building, indicating that the 10-story buildings had better carbon emission reduction effects to those of the 4-story buildings for electricity and fuel energy consumption.

(3) The electricity energy consumption performance of the hybrid buildings is only marginally worse (3%–7% lower) than that of the CLT buildings, indicating the energy-saving efficiency of the proposed wooden hybrid structure system, which comprises RC beam structures and CLT floors and walls for hybrid type 1, replacing the top 4 floors of the building with wooden system for hybrid type 2, and original service core with RC as major construction material preserved for hybrid type 3, are close to that of CLT buildings. Thus, it is understood that the proposed hybrid buildings are close to the CLT buildings in terms of total energy consumption.

In conclusion, the proposed hybrid building system, which comprises RC beams, columns and CLT floors and walls, replacing the top 4 floors of the building with wooden system, and original service core with RC as major construction material preserved have less building weight compared to the original RC building, and less energy required for the manufacturing of building materials in the renovation of the aged building, has an energy-saving efficiency close to that of a CLT building. For the cities selected in this study, the proposed hybrid building systems can be effectively used for old building renewal.

ACKNOWLEDGEMENT

This research was financially supported by the Ministry of Science and Technology of Taiwan, R.O.C. under Grant No. MOST 111-2221-E-011-030 -

REFERENCES

[1] Pierrehumbert, R.. There Is No Plan B for Dealing with the Climate Crisis. Bull. At. Sci. 75, 1–7, 2019.
[2] Guidelines on Green Houses of Worship, UN Environment Programme, July. 2020. Available online: https://www.unenvironment.org/resources/publication/guidelines-green-houses-worship (accessed on 5 Oct. 2020).
[3] Tsai M.T., Lin W.T. Efficiency of Energy Consumption between Reinforced Concrete Structure and Cross-Laminated Timber Based Hybrid Structure in East Asian Cities. Energies, 15, 165, 2022.
[4] Nässén, J.; Hedenus, F.; Karlsson, S.; Holmberg, J. Concrete vs. Wood in Buildings—An Energy System Approach. Build. Environ., 51, 361–369, 2012.
[5] Connolly, T.; Moudgil, M.; Loss, C.; Iqbal, A. Feasibility of Cross-Laminated Timber Cores for the UBC Tall Wood Building. In Proceedings of the 15th World Conference on Timber Engineering (15WCTE), Seoul, Korea, 20–23, August 2018.
[6] Taipower Company Sustainabilty Report, 2008. Available online: https://www.taipower.com.tw/upload/85/2018010916401984784.pdf (accessed on 16 January 2021).
[7] Binder M., Wang C.C., Lu Y.P., Houssein M.M., Lin J.T., Chu C., Tsai M.T. Impact of Using Wood as Material for Building Renovation – Taking Research Building in NTUST as Example, 3rd International Conference on Civil Engineering Fundamentals and Applications, Paper No. 135, Seoul, Korea, 24–26, October, 2022.
[8] Tsai M.T. and Koshihara M. The Study and Proposed Application of the Multi-Storey Hybrid Timber Structural System onthe Design Flexibility and Hazard Prevention. World Conference on Timber Engineering (WCTE), Quebec City, Canada, 10–143, August 2014.

World Conference on Timber Engineering Oslo 2023

ENVIRONMENTAL PERFORMANCE OF NEXT-GENERATION TIMBER SCHOOLS FOR CLIMATE ACTION: A SIMULATION APPROACH

Ramit Debnath[1], Antiopi Koronaki[1*], Dario Marino[1], Yiping Meng[1], Darshil U. Shah[1], Peter Hazzard[2], Simon Smith[3], Kirsten Haggart[4], Michael H. Ramage[1]

ABSTRACT: As the global response to climate change intensifies, timber buildings will play an essential role in reducing carbon emissions from the built environment. This study provides a simulation-driven approach to estimating the environmental performance of timber buildings. In doing so, we present a case study of the UK's next generation of timber school buildings, the New Model School (NMS-timber). We perform a sensitivity analysis of the timber school building to concrete construction (NMS-concrete). The methodology involves an environmental performance estimation of the two building cases' operational energy and thermal comfort characteristics. The results show that NMS-timber has an annual energy usage intensity (EUI) of ~132kW/m^2 and ~146kW/m^2 for NMS-concrete, demonstrating a ~9.6% more energy efficiency per square metre for the timber building. We also find that the timber school building will save ~34.30% heating energy compared to the concrete construction while almost eliminating the cooling energy needs. We conclude that the NMS-timber can offer significantly better environmental performance to concrete buildings. When applied in early stages of the design development, the digital workflow presented promotes informed decisions during the project development stages and enhances the construction of energy-efficient structures.

KEYWORDS: Computational modelling, digital twin, simulation, CFD; energy performance; prefabrication

1 INTRODUCTION

With the building and construction sector contributing around 38% of global carbon dioxide emissions [1], natural materials like timber and advancements in their structural applications have been at the forefront of decarbonising the embodied emissions of the built environment [2]–[4]. However, there are several policy and operational challenges to integrating engineered timber structures in the current built environment which hinder the seamless collaboration and material flow across the supply chain [5].

This study contributes to current discussions on the suitability of engineered timber in decarbonisation of the built environment with a focus on school buildings. The significant shortage of school places in the UK and the government's commitment to deliver a platform for low-carbon schools highlight the importance of reducing their embodied and operational emissions [6, 7]. This study explores the potential of engineered timber to address this challenge by evaluating a timber school case-study using environmental performance analysis metrics. In doing so, the novel aspect of this study is the data-driven and computational simulation-based approach that compares the energy-use demand, environmental characteristics, and occupancy-based optimisation of spaces in a proposed timber building in the UK.

This paper generates a comparative basis for engineered timber buildings like schools with their concrete counterparts. The main objectives of this research are, first, to establish a simulation-driven comparative basis for evaluating the environmental performance of engineered timber buildings and enable its reproducibility for architects, designers, policymakers, and researchers, thus contributing a critical step towards developing a digital twin model of timber buildings. Second, to evaluate characteristic environmental factors that differentiate timber schools from existing concrete schools. When carried out in early stages of the design development, such studies promote informed design decisions and the construction of energy-efficient structures.

2 CONTEXT

The case-study analysed in this paper is the New Model School (NMS), a modular engineered timber school building designed as an extension to the Fawcett Primary state school in Cambridge, UK. The existing school is a concrete structure including teaching spaces, a dining hall, sport facilities, offices, and services. The New Model

[1] Centre for Natural Material Innovation, Department of Architecture, University of Cambridge, 1-5 Scroope Terrace, Cambridge CB2 1PX, UK
*Antiopi Koronaki, 1-5 Scroope Terrace, Cambridge CB2 1PX, UK, ak2260@cam.ac.uk
[2] Cundall Engineering Consultants, 15 Colmore Row, Birmingham, B3 2BH
[3] Smith and Wallwork Engineers, 50 St Andrews Street, Cambridge CB23AH
[4] Waugh Thistleton Architects, 77 Leonard Street, London EC2A4QS

https://doi.org/10.52202/069179-0123

School (NMS) extension was developed in collaboration between academia and industry, aiming to demonstrate the potential of a modular kit-of-parts of engineered

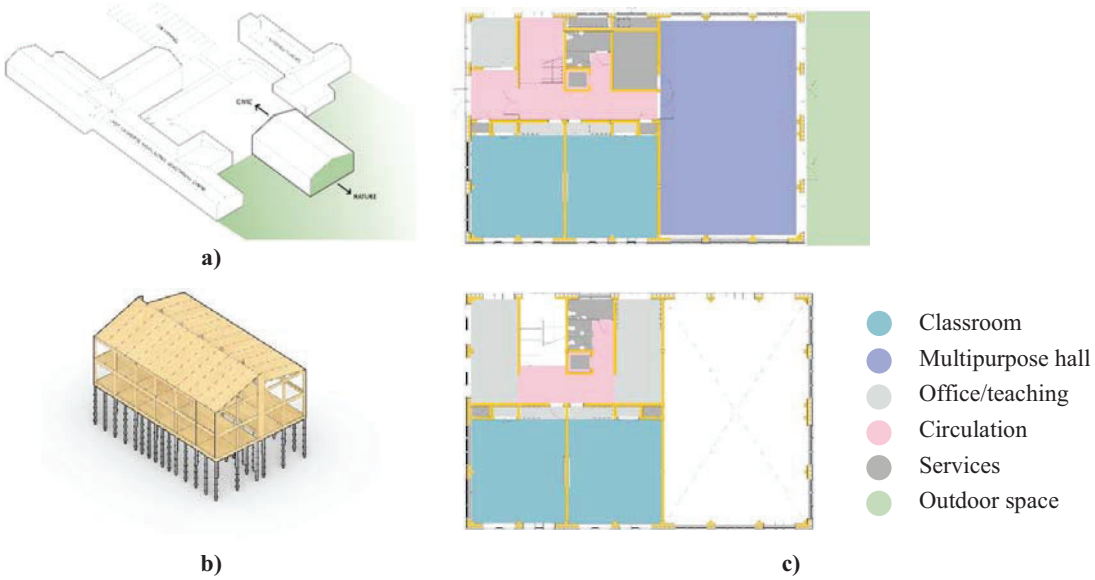

Figure 1: *a) The proposed two-storey engineered timber school extension and its relationship with the existing school building on site. b) The structure of the New Model School, made from engineered timber components. c) Programme distribution on the two storeys.*

timber [8]. The goal of the project was to develop a set of building components that can be combined to create healthy indoor environments and that can then be fully demounted and reconfigured to address a diverse set of programmes and scales. The NMS building is an extension to the existing primary school and has received approval from planning.

The NMS forms a stand-alone two-storey structure of 660m^2 and its design is based on a repeatable grid of size *ca* 56m^2 that meets the spatial and programmatic requirements for primary schools according to the Department for Education, as shown in Fig. 1 [9]. It is a lightweight glulam frame-based structure with composite CLT and ribbed glulam beam components for the roof and first floor slabs. The substructure uses a suspended softwood timber cassette sat atop glulam ground beams supported on recycled steel screw piles. The façade is made of modular insulated timber panels, while a vertical service wall traverses the building and incorporates natural ventilation shafts and service risers.

3 METHODOLOGY

The aim of this study is to assess the impact of the building envelope on the environmental performance of school buildings. The New Model School is used as a case-study and by maintaining the building orientation, programme, and openings identical, we generate two digital models of the school: one using the proposed engineered timber structure and envelope of the New Model School (*NMS-timber*) and one using the conventional construction of the existing school building with a concrete structural frame and brick infill walls (*NMS-concrete*). Since the focus of this study is placed on the impact of the building envelope, the two structural systems are applied interchangeably, without accounting for potential changes in the sizing and configuration of structural elements.

We adopt a simulation-driven methodology to evaluate and compare the environmental performance of the two school models. The simulation has three main components. First, setting up the site parameters and calibrating with climatic parameters; second, setting up the building parameters; third, setting up the energy simulation parameters to evaluate annual thermal comfort variations in the NMS using two variables: operating temperature and mean radiant temperature. These act as guides to assess the thermal comfort of users within the space. Finally, we estimate and compare the annual energy use intensity (EUI, kW/m^2) for heating and cooling demands in the NMS-timber and NMS-concrete, which provide an insight to the operational energy required.

3.1 SITE AND CLIMATE

The historical climate data is accessed from University of Cambridge's Digital Technology Group [10] and diurnal weather data from Cambridge Airport's weather monitoring station [11]. The actual NMS-site is within a 5km radius from these data locations.

https://doi.org/10.52202/069179-0123

3.2 BUILDING DESIGN PARAMETER SETUP

The NMS-timber envelope is an insulated timber frame with air-tight and well-insulated façade panels. Designed for high energy efficiency, it has low U-values (walls: 0.05 W/m2K; windows: 1.36 W/m2K; roof: 0.26 W/m2K; ground: 0.08 W/m2K). The concrete building envelope, on the other hand, is made of brick infill walls with layers of insulation and air gap, concrete floor slabs and an insulated lightweight concrete roof. When applied to the digital model, the respective U-values increase (walls: 0.42 W/m2K; windows: 1.36 W/m2K; roof: 0.39 W/m2K; ground: 0.52 W/m2K). Each classroom is 7.2x7.8m and has four south-facing windows (30% of total surface area), which are partially operable for free cooling in the summer and cross-ventilation through natural ventilation shafts on the service wall. The occupancy ratio of the building is defined according to government guidelines for schools [12]. It is assumed that the local community will use the building for extra-curricular activities; hence the analysis period spans the whole calendar year.

3.3 SIMULATION SETUP

The computational models of NMS were set up as a multizonal energy simulation (MES) using EnergyPlus v22.2.0 [13] and OpenStudio v3.5.1 [14] to estimate energy usage intensity (kW/m^2), season sensitive energy demand, heat balance and thermal comfort estimations (operational and radiant temperatures, and relative humidity (%)), heating and cooling energy demand.

Occupancy scheduling was done on a whole-year basis instead of following a typical UK school term, as the timber school is also designed for community events and activities, apart from the regular classroom services.

3.4 BENCHMARKING

The simulation results of NMS-timber and NMS-concrete are benchmarked against recent studies that used the Non-domestic National Energy Efficiency Data (ND-NEED) [15], the Display Energy Certificates (DEC) database [16] and CIBSE TM46 standards [17]. The ND-NEED provides standards for energy use in non-domestic buildings in Great Britain, based on actual readings. Similarly, the CIBSE TM46 and DEC databases include national-scale statistical data and benchmarks of energy consumption for educational buildings.

4 RESULTS

The analysis was run for a one-year period and the results presented focus on the environmental performance of the four classrooms (c1; c2; c3; c4) to evaluate the impact of building fabric, mainly concrete (NMS-concrete) and engineered timber (NMS-timber). Results show that NMS-timber has higher operating temperature values across all months, especially peaking in July (see Fig 2a). The NMS-timber demonstrates ~2°C higher operating temperature in peak summer months (July) compared to the NMS-concrete model. Similarly, for peak winter (Dec-Feb), NMS-timber shows ~1.8 - 2.2°C higher operating temperatures than NMS-concrete (see Fig 2a). In addition, the relative humidity levels were ~0.9% higher (on average) in the NMS-timber than in NMS-concrete, as shown in Fig 2c. While the peak temperatures in the summer months are on the limits of thermal comfort levels, a more detailed digital model of the school's environmental performance is needed to better understand

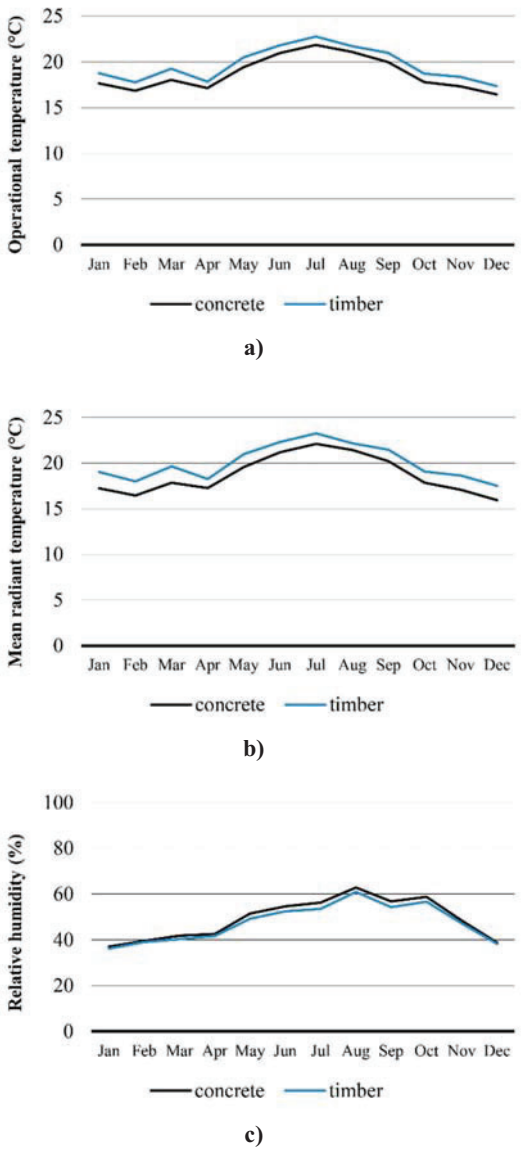

Figure 2: *Simulated annual environmental parameters for NMS-timber and NMS-concrete a) Operational temperature (°C); b) Mean radiant temperature (°C), and c) Relative humidity (%).*

https://doi.org/10.52202/069179-0123

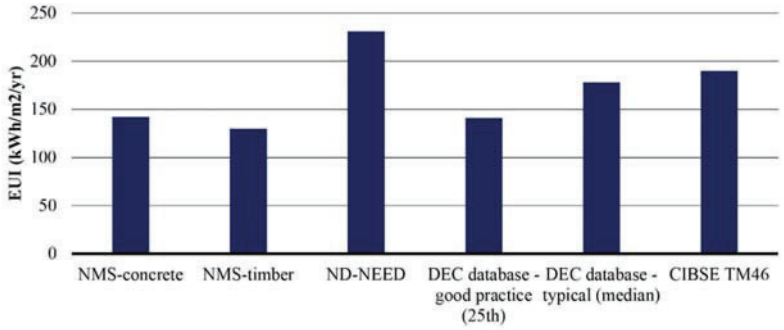

Figure 3: *Energy consumption in kWh/m²/year of the timber and concrete models of the school in comparison to benchmarks from literature.*

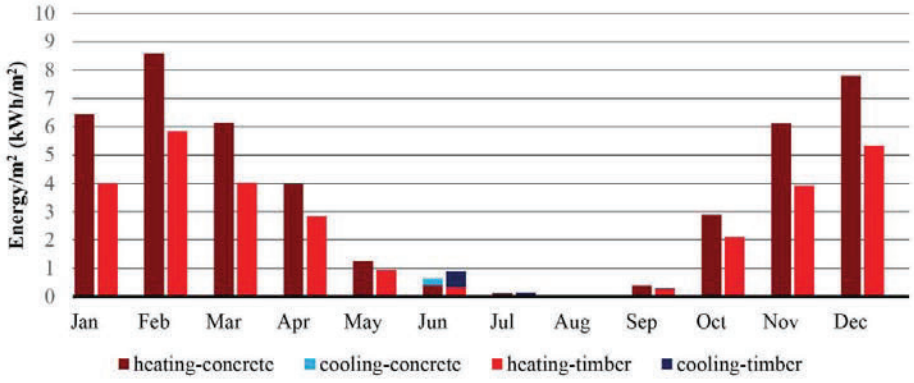

Figure 4: *Monthly energy demand per square metres for cooling and heating of all 4 classrooms for the engineered timber (NMS-timber) and concrete school (NMS-concrete).*

the internal environment, considering airflow characteristics and their impact on temperature and thermal comfort.

However, in terms of mean radiant temperature, the simulated temperature differences were significantly higher in peak winter months ~4°C (see Fig2b) for the timber building compared to the concrete structure. Therefore, NMS-timber can offer greater thermal comfort in winter than NMS-concrete. Similarly, simulated results show that the temperature difference for peak summer months (June - August) is in the range of ~1.9 - 2.1°C, offering NMS-concrete to be cooler. Our ongoing study will use on-site environmental performance measurement to confirm this trend and verify with occupant-led subjective comfort ratings.

The results from the energy performance analysis show that NMS-timber has an annual energy usage intensity (EUI) of ~132kW/m2 and ~146kW/m2 for NMS-concrete (see Fig 3). Therefore, this demonstrates that the timber building is ~9.6% more energy efficient per square metre than the concrete construction of similar configurations. Furthermore, in the benchmarking tests, we find the NMS-timber to be 40%, 9%, 20% and 30.5% less energy intensive per m2 compared to ND-NEED, DEC-good practice, DEC-typical and CIBSE TM46 standards, respectively (see Fig 3).

Fig 4 shows the simulated heating and cooling energy demand for the NMS-timber and NMS-concrete buildings. The timber building in general has less heating and cooling energy demand per square metre by 29.22%. More specifically, the heating energy demand for November - February is 34.30% less in NMS-timber than in NMS-concrete. Similarly, the cooling energy demand for NMS-timber is negligible (~0.08kWh/m^2) between June - August, as compared to NMS-concrete (~0.8kWh/m^2). Thus, emphasising that timber school building has better winter and summer energy performance characteristics.

5 CONCLUSION

This paper presents an environmental performance basis for engineered timber buildings like schools (NMS-timber) with an existing concrete school structure (NMS-concrete). We used an environmental performance simulation approach to estimate the two building cases' operational energy and thermal comfort characteristics. The results from the energy performance analysis show that NMS-timber has an annual energy usage intensity (EUI) of ~132kW/m^2 and ~146kW/m^2 for NMS-concrete, demonstrating a ~9.6% more energy efficiency per square metre for the timber building. Moreover, when benchmarked against recent studies, our results showed the NMS-timber to be 40%, 9%, 20% and 30.5% less

https://doi.org/10.52202/069179-0123

energy intensive per m2 compared to ND-NEED, DEC-good practice, DEC-typical and CIBSE TM46 standards, respectively.

We also find that the timber school building will save ~34.30% heating energy annually compared to the concrete construction while almost eliminating the cooling energy needs. Thus, the NMS-timber building developed can offer significantly better environmental performance to concrete buildings.

Our future work will expand the verification and validation of this study's simulation approach using in-site environmental sensors and establish an experimental protocol for streamlining such measurements for upcoming timber building stocks. It also includes a detailed analysis of the school's Building Integrated Photovoltaics (BiPV) systems that need to be integrated into the timber school, per UK government norms. Moreover, further optimization of the building parameters, BiPV and school ancillary services will be performed to improve the accuracy of the energy simulation. This will include estimating airflow characteristics using a computational fluid dynamics (CFD) workflow, which, when overlaid with the MES analysis, gives a comprehensive insight to the school's environmental performance, In this manner, this study intends to set a workflow for a digital twin model of the school where different materials and emission reduction scenarios can be used to measure its sustainability over the long run.

As the global response to climate change intensifies, timber buildings will play an essential role in reducing embodied carbon emissions of the built environment. Our study proposes a digital workflow that enables the comparative assessment of alternative construction materials based on their environmental performance in a robust and resource-efficient manner. When carried out in the early stages of a project, this approach can promote informed design decisions during the project development stages, improve the environmental performance of new buildings and act as a guide to policymaking.

ACKNOWLEDGEMENTS

This research is in part supported by the Laudes Foundation, the EPSRC Impact Acceleration Account Adventurous Impact Grant and the Centre for Digital Built Britain's work within the Construction Innovation Hub. The funding was provided through the Government's modern industrial strategy by Innovate UK, part of UK Research and Innovation.

REFERENCES

[1] UNEP, '2021 Global Status Report for Buildings and Construction: Towards a Zero-emission, Efficient and Resilient Buildings and Construction Sector'. United Nations Environment Programme, 2021. Accessed: Mar. 18, 2022. [Online]. Available: https://globalabc.org/resources/publications/2021-global-status-report-buildings-and-construction

[2] N. Reyes et al., 'Achieving zero carbon emissions in the construction sector: The role of timber in decarbonising building structures', Engineering, preprint, Nov. 2021. doi: 10.33774/coe-2021-hgd6q-v2.

[3] CCC, 'Biomass in the low-carbon economy'. Climate Change Commitee, 2018. Accessed: Mar. 20, 2022. [Online]. Available: https://www.theccc.org.uk/publication/biomass-in-a-low-carbon-economy/

[4] UNFCCC, 'Climate Action Pathway: Human Settlement'. 2020. Accessed: Dec. 12, 2021. [Online]. Available: https://unfccc.int/sites/default/files/resource/ExecSumm_HS_0.pdf

[5] A. Koronaki, A. Bukauskas, A. Jalia, D. U. Shah, and M. H. Ramage, 'Prefabricated Engineered Timber Schools in the United Kingdom: Challenges and Opportunities', Sustainability, vol. 13, no. 22, p. 12864, Nov. 2021, doi: 10.3390/su132212864.

[6] "The Platform." GenZero. Department for Education. Accessed: Feb 24, 2023. [Online]. Available: https://www.genzero.co.uk/the-platform.

[7] Koronaki, A.; Bukauskas, A.; Jalia, A.; Shah, D.U.; Ramage, M.H. Prefabricated Engineered Timber Schools in the United Kingdom: Challenges and Opportunities. Sustainability 2021, 13, 12864. https://doi.org/10.3390/su132212864

[8] Precision Engineered Timber – Digital design and delivery of healthier schools. 2023. Accessed: Mar 1, 2023. [Online].Available: https://www.cdbb.cam.ac.uk/research/digital-built-environment/precision-engineered-timber-digital-design-and-delivery-healthier

[9] Area guidelines for mainstream schools, Building Bulletin 103, Department for Education. 2014. Accessed: Mar 1, 2023. [Online]. Available: https://assets.publishing.service.gov.uk/government/uploads/system/uploads/attachment_data/file/905692/BB103_Area_Guidelines_for_Mainstream_Schools.pdf

[10] University of Cambridge. Digital Technology Group. 2010, Digital Technology Group - Cambridge Weather - 6.8 C.

[11] http://climate.onebuilding.org/WMO_Region_6_Europe/GBR_United_Kingdom/ENG_England/GBR_ENG_Cambridge.AP.035715_TMYx.zip

[12] School Output Specification technical Annex, Department for Education. Accessed: Feb. 19, 2023. [Online]. Available: https://assets.publishing.service.gov.uk/government/uplo

https://doi.org/10.52202/069179-0123

ads/system/uploads/attachment_data/file/1119959/FE-OS_Annex_2H-Energy-A-C03.pdf

[13] Energy Plus. Accessed: Feb 24, 2023. [Online]. Available: https://energyplus.net/downloads

[14] OpenStudio. Accessed: Feb 24, 2023. [Online]. Available: . https://openstudio.net/

[15] The Non-Domestic National Energy Efficiency Data-Framework (ND-NEED). 2014, The non-domestic National Energy Efficiency Data-Framework (ND-NEED). Accessed: Dec. 15, 2023. [Online]. Available: https://assets.publishing.service.gov.uk/government/uploads/system/uploads/attachment_data/file/314725/non_domestic_need_framework.pdf

[16] Godoy-Shimizu D, Armitage P, Steemers K, et al. Using display energy certificates to quantify schools' energy consumption. Build Res Inform 2011; 39: 535–552.

[17] CIBSE TM46. Accessed : Feb 15, 2023 [Online]. Available: https://www.cibse.org/knowledge-research/knowledge-portal/tm46-energy-benchmarks.

World Conference on Timber Engineering Oslo 2023

DEVELOPMENT OF MATERIAL FOR CIVIL CONSTRUCTION WITH BABASSU PALM FIBERS

Antonio da Silva[1], Francisco Lahr[2], Antonio Costa[3], Joaquim Costa[4]

ABSTRACT: Present in the transition space of the Caatinga, Cerrado and Amazon biomes, distributed between the north and northeast regions of Brazil, it hosts a species that carries with it an economic potential already known by local populations: the babassu (Attalea speciosa).This palm is a source of income for families that depend on babassu extraction in the Brazilian states of Maranhão, Piauí and Tocantins. According to studies by Embrapa, the exploitation of babassu coconut (the most used part of the babassu) is just one of the possibilities involving this native raw material. It is for this reason and for its favorable environmental repercussion, in view of the sustainability of its material, that we aim with this research to enable a new application for babassu, using fibers from its leaf, whose characteristics allow its use in civil construction for internal use and environments exteriors in buildings. Thus, this work intends to evaluate the technical viability of manufacturing, on a laboratory scale, a compact sawn wood board, similar to the Oriented Strand Board (OSB), making a considerable reduction in the final value of the work, as it is an abundant material in the region, easy to produce, sustainable and ecological.

KEY WORDS: Plate, Babassu, Civil Construction, Sustainable

1 INTRODUCTION

The generalities about the Palm of Babassu, its impact on the economy with the products already known, research for its use in civil construction and objectives of this research will be addressed.

1.1 GENERAL CHARACTERISTICS OF THE BABASSU PALM TREE

The Babassu Palm is a species that dominates the ecotonal landscapes, which are areas resulting from the contact between two or more border biomes, in the mid-north region of Brazil (Transition between the Amazon, Cerrado and Caatinga), traditionally exploited in an extractive way by thousands of families, mainly in the states of Maranhão, Piauí and Tocantins. The adult babassu palm can reach between 10 and 30 meters in height and its leaves can reach up to 8 meters in length.

Babassu is still used as a source of raw material for the production of charcoal, fibers for basketry, fences, housing roofs, and even for the preparation of porridge and cakes (Silva et al., 2001). Its importance for the family farmer, the socioeconomic issues and land conflicts arising from its exploitation are widely described in the works of May (1990) and Anderson et al. (1991).

1.2 THE IMPORTANCE IN THE ECONOMY

Several economic activities can be developed from babassu, since the tree is fully utilized, and the fruit has the greatest economic potential for technological and industrial use, being able to produce about 64 products, such as coal, ethanol, methanol, cellulose, flour, fatty acids, glycerin, among others.

The babassu almond, due to the quality of its oil, is the part of the plant that currently has the greatest economic importance, although it represents a small proportion in relation to the total mass of the fruit, having produced a quantity of 48,706 tons in 2019 throughout Brazil, with the state of Maranhão responsible for the production of 45,166 tons, corresponding to 92.73% of the total, and moving about 89,363 thousand reais, according to data provided by the Brazilian Institute of Geography and Statistics (IBGE)..

The above demonstrates that babassu stands out as an important species not only for the subsistence of poor families in a wide geographic region of the country, but also as a non-timber extractive product of enormous value for the industry. In addition, because it spontaneously occupies landscapes with little economic expression in the

[1]Antonio Jorge Parga da Silva, Ph.D, Federal Institute of Maranhão (IFMA, Monte Castelo Campus, Civil Construction Department, São Luís – Maranhão, Brasil, Parga@ifma.edu.br
[2]Francisco Antonio Rocco Lahr, Ph.D. USP-SC, São Carlos – São Paulo, Brasil, Frocco@sc.usp.br
[3]Antonio Willy Alves da Costa, Graduating, Federal Institute of Maranhão (IFMA), Monte Castelo Campus, Civil Construction Department, São Luís – Maranhão, Brasil, W.costa@acad.ifma.edu.br
[4]Joaquim Bezerra Costa, Ph.D. Brazilian Agricultural Research Corporation(Embrapa), São Luís – Maranhão, Brasil, Jbczootecnia@gmail.com

https://doi.org/10.52202/069179-0124

national agricultural scenario, babassu is of strategic-territorial importance for the country.

1.3 USE OF THE PALM TREE IN THE CONSTRUCTION SECTOR AND RESEARCH INCENTIVES

Despite its importance as a non-timber extractive product and its potential for generating energy and co-products, in the field of civil construction, which has been reinventing itself and increasingly seeking sustainable materials, there is little published literature, as well as a scarcity of research in order to use this promising material. In the literature, there are only reports of the use of babassu palm leaves being used to form the roofs of low-income families' houses. In recent years, some actions have been initiated aimed at using babassu parts in civil construction, however, there has been discontinuity of work, lack of integration between different areas of knowledge and lack of long-term research and development policies.

In 1980, the State Institute of Babassu (INEB) was created, an agency of the Government of the State of Maranhão. During its four years of existence, INEB coordinated a research program on babassu, in collaboration with what was then CENARGEN (now Embrapa Genetic Resources and Biotechnology) and the New York Botanical Garden (NYBG) (Pinheiro et al., 2005).

Research on babassu was intensified by the creation of the National Research Program (PNP) on Babaçu, coordinated by EMBRAPA, in 1982. The PNP-Babaçu was organized with the aim of contributing to rationalizing and accelerating the use of babassu. The program's long-term goal would be “the gradual transformation of current babassu extractivism into an economically exploitable crop” (EMBRAPA, 1984), but clearly this goal has not yet been reached.

1.4 OBJECTIVE OF THE ARTICLE

Emphasize research on the technical feasibility of manufacturing, on a laboratory scale, particulate panels similar to OSB (Oriented Strand Board), derived from fibers using babassu leaf or coconut bunch cover as input, a residue originating from the removal of The palm leaf or the top of the bunch falls off the palm tree on its own, together with the fruits when they mature, with the aim of manufacturing a low-cost product with a quality equivalent to products that are at the top of the market today, in addition to providing a new product from the babassu palm tree intended for the civil construction area, using engineering to develop ecologically sustainable materials with low environmental impact, and finally, making available and encouraging studies on an endemic palm tree in Brazil with great economic potential.

2 MATERIALS AND MODEL USED

The main material used in the manufacture of the particulate plate was the babassu leaf, representing about 98% of the product composition and the other 2% correspond to the centrifuged latex that was used as a binder to make the product similar to OSB. A hydraulic press, model SL 10/5, was also used to press the layers of sheets and give better compactability to the plate.

2.1 BABASSU

Babassu is a highlight among the palm trees present on Brazilian soil, it is a large species, reaching up to 30m in height, has leaves up to 8m long, slightly arched and pointed in the vertical direction, which fall when reaching their apex. giving way to new ones (Figure 1), it also has cream-yellowish flowers, clustered in long bunches protected by peduncular bracts, which are foliaceous structures associated with the inflorescence of the palm tree that are highly resistant to humidity and fire, and later give rise to origin to oval and brown fruits, with an almond inside.

Figure 1: *Babassu palm trees located in the parking lot of the Federal Institute of Maranhão (IFMA). (Source: Author)*

The occupation of the landscape by babassu occurs vigorously (Figure 2), and seems to be favored by slash-and-burn family farming systems, as well as the formation of pastures (Anderson et al., 1991). Strongly associated with the local culture, babassu is part of the life history of hundreds of communities that collect and break coconuts in a rudimentary way, to sell the almond, an important complement to their income.

Figure 2: *Great density of palm trees in nature. (Source: Flickr)*

2.2 CENTRIFUGED LIQUID LATEX

Latex is a material extracted directly from the rubber tree, a tree of the genus Hevea, of the Euphorbiaceae family, native to the Amazon rainforest, which stands out for its ability to produce this material (Figure 3). The extraction process begins when the tree trunk reaches a perimeter of 45cm, being measured at a distance of 1 meter over the graft, only then is an incision made in the stem with a special knife, without going beyond the part where the lactiferous vessels, so as not to impair the radial growth of the trunk. When harvested from the tree, latex has an average of 30% rubber, 68% components such as water and substances such as proteins, mineral salts, etc.

Figure 3: *Latex extraction process. (Source: wandee007/shutterstoch.com)*

In this research, Centrifuged Latex 60%, from RICLA colas e resins, a Brazilian company that has been manufacturing adhesive gums since 1989, was used. a) Practicality in use: based on its elasticity and flexibility, practicality is guaranteed in carrying out different types of work, including the manufacture of OSB boards; b) Impermeability: as it is a water-resistant adhesive, latex glue can be used to glue parts that will be exposed to moisture; c) Excellent cost-benefit ratio: it is a material that yields a lot; and d) Ease of adhesion: it showed good adhesion with laminated profiles of babassu leaves.

Figure 4: *Binding material used. (Source: Company catalog).*

2.3 ORIENTES STRAND BOARD (OSB)

The industrial scale production of structural particle boards began in the 1970s, in the United States, under the trade name “waferboard”.

The sheets were produced with particles of larger dimensions, in relation to the particles used in “conventional” agglomerates, but with the same random distribution in the mattress formation process.

The width and length of “OSB” sheets are determined by the production technology and not according to the length of the logs, as in the case of plywood. The current context of the Brazilian forest sector demonstrates the consequences of the predatory exploitation of natural forests, mainly caused by the expansion of the agricultural frontier, by mining activities, by the production of charcoal and others. The lack of an exploitation monitoring policy, via sustained management, also contributes to worsening the situation. Within this context, it seems, more and more, that the logical tendency is to use reconstituted wood from the furniture industry and alternative materials of lignocellulosic fibers.

The OSB panel offers resistance for multiple uses and has a wide application in the field of housing construction, in all existing types, and other applications, among which stand out: floors, walls, I-beams, stairs, ceilings, roofs, fencing, sheds, protective trays. Other applications: furniture, loudspeakers, dividers, packaging (Bins and Paillets), finishing in general and design, according to quotes from Revista de madeira, year 16, nº 97, June/2006.

As it is a product recently produced in Brazil, it can be considered that there is little information available on the market about the variables of its processing, mainly in relation to alternative materials not yet explored in the production process.

https://doi.org/10.52202/069179-0124

3 METHODOLOGY

Analyzing the babassu palm, intriguing characteristics were noted, due to its natural state it presents great resistance to fire and water, making it a very promising material for use in civil construction and in the manufacture of materials used in contact with humidity and temperatures high.

In a field work, the senescent leaves of the palm tree were collected, being removed from the thickest stalk that supports the leaves with the aid of a machete and accommodated in bales that were transported to the Federal Institute of Maranhão (IFMA), Campus Monte Castelo, São Luís (Figure 5).

Figure 5: *Conditioning the raw material in bales for transport to the laboratory. (Source: Author).*

In the civil construction laboratory belonging to the institution, the samples were placed in an oven for drying at a temperature of around 60ºC, during a period of 48 hours. After drying, the material was cut into 14 cm sheets with a natural leaf width of approximately 4 cm, and then we used a brush to spread the 60% centrifuged latex over the leaves, beginning the assembly of the layers that form the panels. After organizing the sheet blades, similar to OSB, the first layer of the panel was taken to the Hydraulic Press SL 10/5, where it was pressed at a pressure of 1.5 ton/cm², for a time of 24 hours. This process was repeated 10 times, forming 10 layers with a thickness of approximately 1 mm (natural thickness of the sheet), which were successively glued and pressed overlapping one by one in crossed directions, respecting the same pressure and time mentioned above, resulting in a plate final with a thickness of 1 cm and dimensions of 50 x 50 cm, weight of 499.28g, total volume of 1250 cm³ and density of 0.399 g/cm³.

Figure 6: *Material cut into 14 cm sheets and natural leaf width of approximately 4 cm. (Source: Author)*

4 RESULTS AND DISCUSSIONS

Babassu is indisputably a raw material of immeasurable value that is still little researched and used. The plate made with the leaf of this palm tree is light, has an excellent design, has low degradation over time, in addition to having a low modulus of elasticity, facilitating its molding. In the initial stage of the first layer, with fibers oriented only in one direction, good flexural strength was observed, being able to significantly support its own weight without excessive deformation. After pressing the ten layers, positioning the fibers crosswise, we obtained a panel with greater resistance than imagined and with very attractive aspects, combining quality and good value for money in a single piece, which will provide satisfaction and pleasure to the consumer public. Due to its characteristics (Table 1), it can be used in civil construction to cover walls in internal and external environments (reconciled with additives), in linings, in decorative details of rooms, in baseboards, among others, making a considerable reduction in the final value of the work because it is a material that is easy to produce, sustainable, renewable and ecological, in addition to collaborating with the preservation of the environment by reducing construction waste, and having the raw material with vast density in the Brazilian territory.

Table 1: *Characteristics of the plate made in the laboratory.*

Material /Character	OSB of Babaçu
Weight	499,28g
Dimension	50x50cm
Average Thickness	1cm
Área	2500cm²
Volume	2500cm³
Density	0,199g/cm³

.

5 CONCLUSIONS

For the realization of the plate similar to OSB, we can emphasize that this new material based on leaves of the Babassu Palm tree as the main raw material has a great benefit in the environmental field and a good use for the most diverse purposes, since it is a material low cost to operate and sustainable, in addition to being a renewable raw material, causing the satisfaction of all who come to use these panels (Figure 7). Observing the need to protect the environment, which is suffering a lot with the development of humanity, both with the production of garbage and pollution, and with the exploitation of finite resources in an unbridled way, the importance of studies and discoveries of ecologically sustainable products and low impact on nature is vital for reducing environmental degradation and increasing people's quality of life in the future. Based on this, the exploitation of babassu palm leaf fibers for the preparation of pressed wood panels similar to OSB, with the intention of being used in the field of civil construction, can have a positive impact because it is an ecological product, without generating toxic waste in its manufacture and revolutionizing the means of producing materials for this branch of engineering that is essential for human development and which is currently one of the main degraders of the environment.

The social aspect of this new product can also be emphasized, as there is the possibility of building houses using these panels, thus lowering their final value and contributing to a more sustainable world.

Therefore, Brazil, as the sole owner of this raw material, will be able to take advantage of this product, which at the moment is unexploited, making it a great benefit both for society and for the economy, which will gain a new production line, generating jobs and influencing the GDP (Gross Domestic Product) of this country.

Figure 7: *Samples of completed babassu leaf fiber boards.*

REFERENCES

[1] Silva, E. M. S., Napolitano, J, E., Bastos, S.: Small Ecosocial Projects of babassu coconut breakers: reflections and lessons leraned. Brasília: ISPN, 2016.

[2] IPHAN - TO: Cultural universe of Palm Babassu. Tocantins, 2017.

[3] EMBRAPA-SNLCS, SUDENE-DRN: Edaphoclimatic zoning of babasse in the states of Maranhão and Piaui. Rio de Janeiro, 1984.

[4] IBGE. PEVS – Production of Plant Extraction and Silciculture, 2019.

[5] Da Silva, A. J. P.: Application of long and oriented sugarcane bagasse particles in the production of particle board similar to OSB. São Carlos, University of Sao Paulo, 15-72, 2006.

[6] European Committee For Standardization. European Standard – EM 300: Particle board and oriented to long timber (OSB) – Definition, classification e specification. Portugal, 2002.

[7] Pinheiro, A, A. Siani, A, C. Guilhermino, J, F. Henriques, M, G, M, O. Quental, C, M. Pizarro, A, P, B. Methodology to manage research and development projects focused on products: a proposal. Rio de Janeiro, 2006.

https://doi.org/10.52202/069179-0124

World Conference on Timber Engineering Oslo 2023

EXPLORING THE STRUCTURAL DESIGN, COST AND DURABILITY OF MASS TIMBER NOISE BARRIER FOR HIGHWAY APPLICATIONS

Weichiang Pang[1], Michael Stoner[2], Harsh Bothra[3], Laura Redmond[4], Patricia Layton[5]

ABSTRACT: The sound generated from vehicular traffics on highways cause noise pollution. To deal with the traffic noise coming from these highways, noise barriers have been erected across major highways. Currently, the primary material used for highway noise barrier is concrete. This paper explores the use of mass timber as highway noise barrier from a structural design, cost, and durability perspective. The structural design of mass timber noise barrier to resist wind and earthquake loadings will be discussed. Cost comparisons between noise barriers constructed using pre-cast concrete panels and cross-laminated timber panels indicate that mass timber noise barrier is cost competitive. As part of this study, a prototype noise barrier was constructed for evaluating the constructability of the proposed design and for monitoring the moisture performance in an exposed weather environment.

KEYWORDS: Cross-Laminated Timber, Noise Barrier, Highway

1 INTRODUCTION

Highways are some of the biggest causes of noise pollution in the United States of America. To deal with the traffic noise coming from these highways, noise barriers have been erected across major highways. Several materials are used for sound barriers, including steel, wood, concrete, composites as well as insulating wool. These materials help to abate noise via reflecting, diffusing or absorbing sound waves. Concrete and steel are the most common materials for highway noise barriers. However, wood products are known to be more environmentally friendly than concrete or steel. Additionally, the use of wood products is also considered to be more aesthetically appealing to most motorists. Wood products also have the benefit of being lighter and thus easier to transport and erect compared to concrete and steel.

The design of a highway noise barrier is typically based on the structural design, sound efficiency, long-term durability, and material and construction cost associated with implementation [1]. A comparative study on the performance of wood highway sound barriers revealed that wood barriers (solid sawn or glue-laminated timber) which were properly installed, designed, and detailed could be designed to achieve similar acoustic performance to precast concrete panels [2]. Given that most mass timber elements are thicker than those measured in this study, it was assumed that a sufficient acoustic performance could be achieved by utilizing mass timber elements.

In this study, wood products, specifically Cross-Laminated Timber (CLT) and Mass plywood Panel (MPP) are considered as potential materials for noise barriers. A representative noise barrier design is presented and compared to typical concrete construction with respect to cost and carbon footprint. Additionally, a prototype sound barrier was constructed and instrumented for long-term moisture monitoring.

2 DESIGN OF MASS TIMBER NOISE BARRIER

Cross-laminated timber (CLT) is made from lumber boards that have been glued to each other forming layers. Structurally, mass timber exhibits high bending strength and has lower weight than a concrete or steel system. A CLT noise barrier was designed considering the wind load and seismic loads across the US following the design procedure of AASHTO (American Association of State Highway and Transportation Officials) [2] and FHWA (Federal Highway Administration) [3]. The panel span width was limited to 6m (20 ft) based on an attempt to maximize the efficiencies of current CLT fabrication facilities and to produce the easiest construction sequence. The analysis results showed that 3-ply CLT panels could withstand winds of up to 80.5 m/s (180 mph), however larger steel posts were required. Seismic analysis was

[1]Weichiang Pang, Professor, Clemson University, USA, wpang@clemson.edu
[2]Michael Stoner, Research Assistant Professor, Clemson University, USA, mwstone@clemson.edu
[3]Harsh Bothra, Project Engineer, Reackon Concrete Pvt Ltd, USA, hbothra@reackon.com
[4]Laura Redmond, Assistant Professor, Clemson University, USA, lmredmo@clemson.edu
[5]Pat Layton, Direction, Clemson University Wood Utilization + Design Institute, USA, platyon@clemson.edu

https://doi.org/10.52202/069179-0125

carried out and a smaller W10x33 steel post was shown to be sufficient for the very high seismic region with an S_s value of 2.25g. Table 1 shows the design criteria for the CLT noise barrier.

***Table 1**: Design Criteria of CLT highway noise barrier*

Design Criteria	*Value*
Design Wind Speed	80.5 m/s (180 mph)
Wind Pressures	2.9 kPa (60 psf)
Spectral Response Acceleration @ 0.2s (S_s)	2.25 g
Peak Ground Acceleration	0.9 g
Steel Post Design	W10 x 33
CLT Panel Design	3-ply V3: 105 mm (4.13 in)

Figure 1 shows the top and isometric views of the noise barrier with two 3-ply CLT panels of 6.1m x 2.4m (20-ft. x 8-ft.) stacked vertically along the long edge and W10x33 structural steel posts. The installation of the noise barrier begins with typically installed foundations concrete foundations. Structural steel posts are installed with four cast-in-place anchor bolts. Figure 2 shows the details of connections used to fasten the CLT panels to the steel posts. After the steel posts are bolted the foundation, shim angles and seating angles are fastened to the post using bolt connections, the CLT panel is then slid into the post from the top (Figure 3). In this example, a second panel is added on top of the first and jointed using a lap joint connection with wood screws.

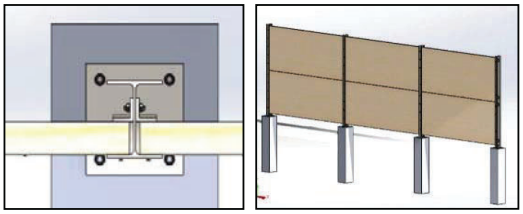

***Figure 1**: Top View of 3-D Model (left), Isometric View of 3-D Model (right)*

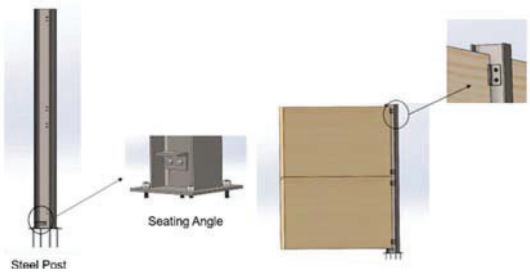

***Figure 2**: Seating Angle (left), Shim Angle (right)*

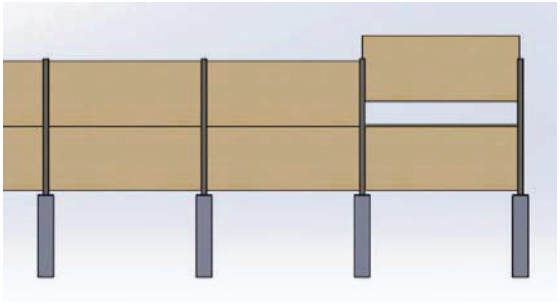

***Figure 3**: Installation of CLT Noise Barrier.*

Additional improvements in the structural design to further increase the structural efficiency, reduce the amount of non-wood components, reduce the number of concrete foundations, and reduce the time for construction of the highway noise barrier system using CLT.

3 COST COMPARISON AND ENVIRONEMNTAL IMPACTS

Factors such as the environmental impacts, costs, waste management, and aesthetics play a role in the selection of what construction materials will be used in a construction project. The use of wood and its different forms and products has substantially reduced environmental pollution and greenhouse gas emissions within the building sector [3]. A carbon emission study on a 6m x 4.9m x 10.4cm (20’ x 16’ x 4.125”) timber panel used as the primary structural component in a highway noise barrier and an equivalent size concrete panel was carried out during this research. It was found that 740 kg (1630 lbs) of CO2e is emitted during the construction process of the concrete panel whereas 2040 kg (4500 lbs) of CO2e will be stored if a CLT panel is used. Therefore, adoption of mass timber noise panels will result in a reduction of up to 2780 kg (6130 lbs) of CO2e for every 6m (20 ft) of noise barrier. These environmental calculations did not include the environmental impacts of the foundations, steel posts, or transportation of such elements.

***Table 2**: Cost Analysis Summary of 800m Case Study*

	CLT	Precast Concrete
Panel Dimensions	6 m x 2.4 m	3 m × 2.4 m
Distance From Project Site	400 km	160 km
Material Cost	\$185.67/m^2 including posts and treatment	\$123.79/m^2 including posts
Total Material Cost	\$ 644,554	\$ 485,760
Transportation & Installation cost	\$ 91.49/m^2	\$145.31/m^2
Total Project Cost	\$1,003,594	\$1,056,000

https://doi.org/10.52202/069179-0125

A cost study for a project in 2020 in Florida was conducted for a representative CLT noise barrier compared to a concrete noise barrier using construction cost data collected for typical concrete noise barriers. The cost study was performed on for an 800m (1/2 mile) length of noise barrier. The factors considered in the cost study include the material cost, transportation cost, and installation cost described in detail in Table 3.

***Table 3**: Detailed Cost Breakdown of Case Study*

	CLT		Precast	
	per m^2	total	per m^2	total
Material	$1.60	$728,640	$1.07	$485,760
Transport	$0.03	$13,563	$0.06	$25,575
Install	$0.76	$345,477	$1.20	$544,665
Total	$2.39	$1.00 mil	$2.32	$1.06 mil

Reductions in the transportation cost for the CLT noise barrier were due to the reduction in weight per panel resulting in 14 truckloads versus 66 truckloads for the precast panels. Additionally, reduction in the installation cost was due to the reduction in foundations and lifting equipment required for the CLT noise barrier. Additional cost was included for the treatment of the CLT panels, though the maintenance cost was not included as the extent of such costs was unknown at the time of the study.

It was determined for the 800m (½ mile) case study length, a cost reduction of around 5.2% was achieved. The saving mainly comes from transportation and installation costs as wood is about 1/5 of the weight of concrete.

4 MOCK-UP CONSTRUCTION AND MOISTURE MONITORING

A 2.4m x 2.4m (8 ft x 8 ft) prototype CLT noise barrier was built and installed at the Clemson University Built Environment Laboratory located in Pendleton, South Carolina. Two different Sansin coatings applied on the CLT panel to protect the panels from UV and moisture (Figure 4). Each coating was applied in two coats per the manufacturer recommendation with sanding of the surface between each coat. The total thickness of the coating after both layers were applied was 0.3 mm (11-12 mils).

***Figure 4:** Application of UV and moisture protection*

The prototype noise barrier was constructed in accordance with the design procedures mentioned (Figure 5). The panel was instrumented with temperature and moisture sensors to measure the moisture fluctuation in the panels. SMT Research sensors were used to instrument the prototype noise barrier and obtain moisture, temperature, and rainfall data. In total, 18 moisture sensors, 2 rain gauges and 2 temperature sensors were installed in the panel and data is being collected remotely. The sensors were installed at depths of 2.5 cm (1 in.), 5.1 cm (2 in.), and 7.6 cm (3 in.) at three locations on each of the two coatings. Figure 6 and Figure 7 represent the location and depths of the moisture sensors installed in the prototype panel.

***Figure 5:** Front view of prototype noise barrier (left), Rear view of prototype noise barrier (right).*

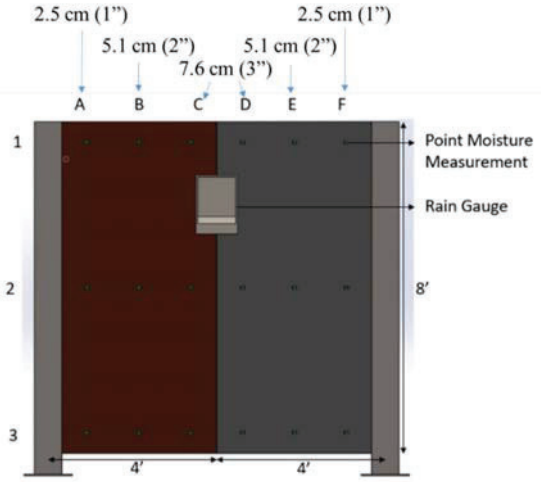

***Figure 6:** Schematic view of sensors installed in the prototype noise barrier.*

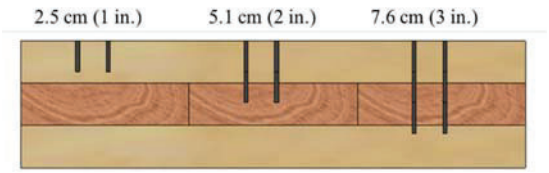

***Figure 7**: Depth of moisture sensors in prototype noise barrier*

https://doi.org/10.52202/069179-0125

The intent of the sensors was to determine the moisture content fluctuations in the CLT panel due to rainfall events. Information such as the peak moisture content after a rainfall event, the variation in moisture in each layer, and the rate at which the moisture content returned to pre-rainfall event levels were all of interest. The amount of rainfall in each rainfall event was captured by rain gauges located on either side of the prototype panel. These rainfall events are summarized in Figure 8. Gaps in the data between October 2022 and January 2023 exist due to battery outages in the sensors. In total 105 measurable rainfall events were recorded by the system over the time of the measurement.

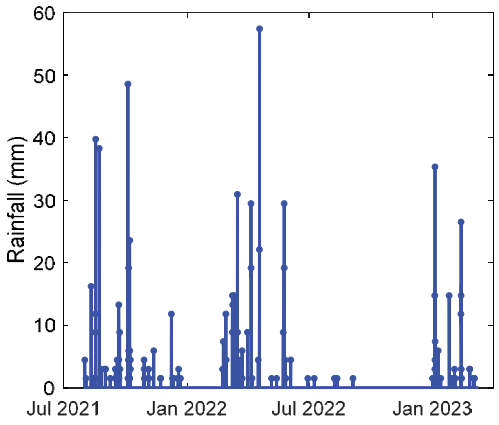

***Figure 8**: Rainfall events July 2021-Mar 2023*

The moisture content in the CLT panels were quantified in terms of the peak moisture content after the rainfall event. In data presented in Figure 9 shows the distribution of the peak moisture content after each event as an average of the three sensors placed at identical depths in each of the two coatings. After rainfall events, the moisture content increases to between 15% to approaching the fiber saturation point of wood. Though differences in the moisture content by layer were evident, no trend was found consistent between the two coatings. The average peak moisture content measured between 20% and 23.5%, which is just above the point at which the effects of increased can begin to occur, usually around 20% [5].

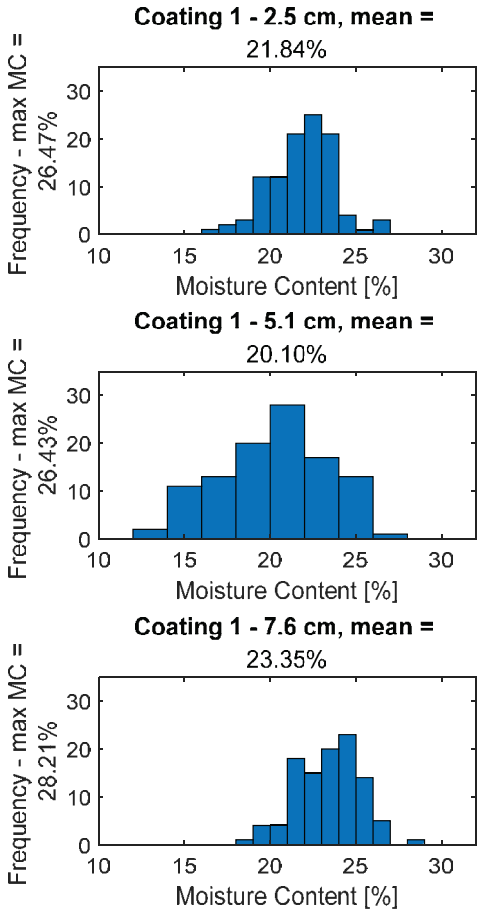

***Figure 9:** Distribution of peak moisture content readings after rainfall event for Coating 1*

https://doi.org/10.52202/069179-0125

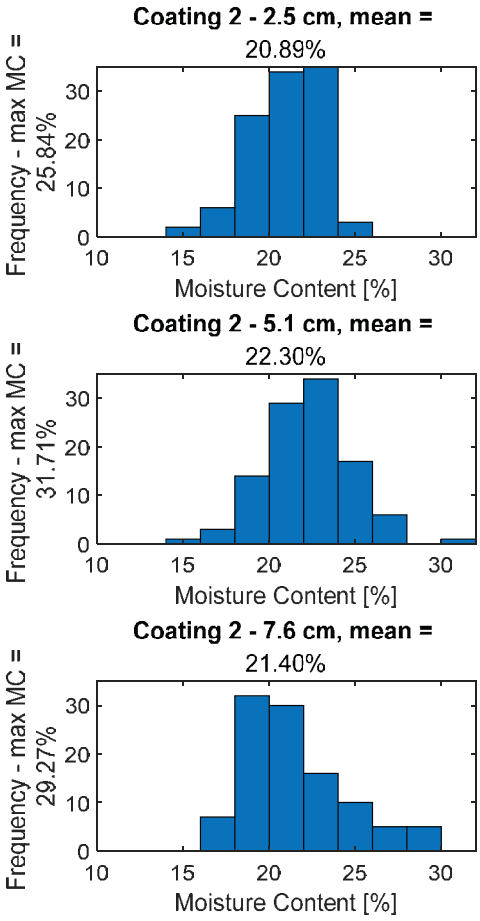

Figure 10: *Distribution of peak moisture content readings after rainfall event for Coating 2*

In addition to the peak average moisture content, the return of moisture content to pre-event levels was tracked by the sensors. As the moisture content exceeded the point at which decay to the wood fibers, it became important to track the amount of time to return to a moisture content below 20% and below 16%, the recommended moisture content for dry service conditions specified in the National Design Specification [6]. Figure 10 represents the average moisture content after a peak rainfall event and the subsequent 24 hours following the event. It shows that within the first two hours after the peak moisture content was measured, the moisture content in the wood drops below the 20% threshold. After approximately 5-7 hours, the moisture content returns to at or below 16% indicating that the wood fibers do not experience elevated moisture content for very long.

The qualitative degradation of the noise barrier over time was measured through periodic inspections of the panel. Discoloration of the noise barrier over the 20+ months of exposure was minimal, indicating the coatings were performing as intended. Delamination of a single piece of the outer layer of the CLT barrier at the top of the wall was observed, likely due to the repetitive moisture cycling (Figure 12). For future installations of the panel, it is recommended that a steel cap be placed on top of the noise barrier to prevent such delamination from occurring and to prevent moisture intake on the panel end-grain. An additional CLT noise barrier with no coating will be installed and monitored in the same way to compare the moisture and degradation performance.

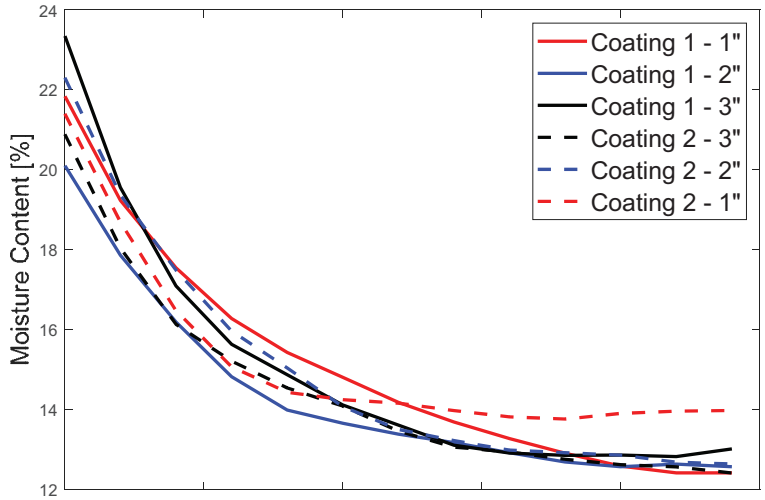

Figure 11*: Moisture content after rainfall event*

https://doi.org/10.52202/069179-0125

Figure 12: *Delamination of top of CLT noise barrier*

5 SUMMARY AND CONCLUSIONS

Cross-laminated timber has the potential to serve as the primary structural material for highway noise barriers in an effort to reduce environmental impact and sequester carbon from the atmosphere. Based on the structural design and cost estimates presented, such a noise barrier is comparable to a similarly designed barrier made of precast concrete with substantial carbon advantages. A prototype noise barrier was installed and instrumented ot determine the long-term moisture performance and degradation of the panels. The data from the prototype noise barrier has been monitored since mid-August 2021 and will be continually monitored as part of a long-term study. For the initial monitoring period from August 2021 to November 2021, the moisture content in the CLT goes up to 28% during heavy rain and drops down to 10% within 24 hours under dry conditions. Using durable and high-quality breathable coating appears to be a viable solution that addresses the effect of moisture retention in CLT panels.

ACKNOWLEDGEMENT

The materials presented in this paper is supported in part by the by USDA Forest Service under agreement #19-DG11083150-014.

REFERENCES

[1] Klingner, R. E., McNerney, M. T., & Busch-Vishniac, I. J. (2003). *Design guide for highway noise barriers* (No. 1471-1474). Austin, TX, USA: Center for Transportation Research, Bureau of Engineering Research, University of Texas at Austin.

[2] AASHTO, LRFD bridge design specifications. (2020). Washington, D.C. :American Association of State Highway and Transportation Officials

[3] FHWA, FHWA highway construction noise handbook, (2006). DOT-VNTSC-FHWA-06-02;FHWA-HEP-06-015 https://rosap.ntl.bts.gov/view/dot/8837

[4] Albee, R. R. (2019). Global overview of the Cross-Laminated Timber Industry. MS Thesis. Oregon State University.

[5] Baker, M. C. (1969). Decay of Wood. Canadian Building Digest. CBD-111

[6] American Wood Concil (2018) NDS National Design Standard for Wood Construction with Commentery. AWC – The American Wood Council, Leesburg, VA, USA

https://doi.org/10.52202/069179-0125

World Conference on Timber Engineering Oslo 2023

CORROSION INHIBITOR POTENCIAL WITH BOLDO BRASILEIRO COMPARED TO COMMERCIAL INHIBITOR OI WOOD CONNECTIONS

Letícia Costa[1], Ana Farias[2], Antonio da Silva[3], Francisco Lahr[4]

ABSTRACT: The corrosion caused in metallic elements in connection with wood is a relevant fact for scientific research, since this problem directly affects the strength and service life of structures. When metal alloys are subjected to wood, exposure to corrosion is noticeable, due to the presence of water and oxygen in the cellular structure of wood, as well as chemical reactions between its constituents. Although metals have definite and advantageous mechanical properties, they are still not sufficient to contain the oxidation content. It is observed that these connecting pieces embedded in wood present easy degradation, bringing high economic, environmental and technological costs in their maintenance or replacement. Through analysis, a comparison was made between the corrosion rates and protection efficiency of different corrosion inhibitors that are often marketed, replacing them with green inhibitors, also known as natural inhibitors, used to prevent the corrosion process in metals. In the tests, several specimens were tested, with and without the presence of the natural additive, thus being able to evaluate satisfactory results in which the extract plectranthus barbatus Andrews, also known as Brazilian boldo, formed a protective layer on the metals. In summary, it is notorious that these natural inhibitors do not harm the environment, as well as economic advantages when compared to the commercial inhibitor, which is harmful and toxic to the environment.

KEYWORDS: **Corrosion, natural inhibitors, plectranthus barbatus Andrews.**

1. INTRODUCTION

Wood is a precursor material, widely used in civil construction. It has several applicability because it is a massive and versatile element, used in structures, especially in roofs or finishes (MATIELLO and NESPOLO, 2015). According to Nagaoka (2014), wood has been a material that is not very resistant, but with a high market value, generally used in craft techniques. In countries in the northern hemisphere, it is also used as a structural material, due to its technological devices. Its geometry, areas and proportions allow the creation of different parts, and allows the realization of amendments and/or connections with metallic elements that make up the structure. On the other hand, it is observed in several conventional constructions the use of nails, pegs and screws, which are interconnection components for elements that have the same material or different materials. For large industries, a good example of this, which has the possibility of quick assembly and standardization in the connections, are the Gang Nail connectors, an element made of hot-dip galvanized steel. In general, steels are widely sold in several industrial sectors due to their other properties and resistance to the effects of corrosion and oxidation. In theory, they are alloys composed of iron and carbon, which respond positively to the way they are exposed to weather and stress, as a result of their composition, microstructure, morphology, electrical resistivity, heat treatments, among other factors. The metallic elements are fundamental pieces that strongly contribute to the wood-metal junction, making it a technological and comprehensive innovation. In the constructive system, the combination of these materials can cause a series of damages in the structures, due to a phenomenon called corrosion (NAPPI, Manuela Marques Lalane et al, 2012)ɜIt is known that despite the high resistance of metals, corrosion is a redox process that occurs in the

[1]Letícia do Nascimento Costa, Graduate Student, Federal Institute of Maranhão (IFMA), São Luís – Maranhão, Brazil, c.leticia@acad.ifma.edu.br

[2]Ana Patrícia Pinto Farias, Master in Analytical Chemistry (PPGQUIM) at the Federal University of Maranhão (UFMA), São Luís- Maranhão, Brazil, ana004397@ceuma.com.br

[3]Antonio Jorge Parga da Silva, Ph.D. Federal Institute of Maranhão (IFMA), São Luís – Maranhão, Brazil, parga@ifma.edu.br

[4]Francisco Antonio Rocco Lahr, Ph.D. USP-SC, São Carlos – São Paulo. frocco@sc.usp.br

https://doi.org/10.52202/069179-0126

midst of natural agents, and thus compromises the performance and functionality of the material. Therefore, the present work aimed to study corrosion in marine environments, since seawater has a high concentration of sodium chloride (NaCl), magnesium chloride (MgCl2), magnesium sulfate (MgSo4), calcium sulfate (CaSo4), potassium chloride (KCL) and other dissolved and particulate gases. It is noteworthy that the atmospheric environment also influences the high percentage of relative humidity, solar radiation and tidal effects. According to De Melo, Grazielma Ferreira; et al (2021, p.68) are "factors that act as propellants and catalysts in the corrosion process". Therefore, the following research has investigative data sources for the plectranthus barbatus Andrews extract, also known as Brazilian Boldo, against corrosive media to inhibit the corrosion process in metals, acting as a protective layer. Among the metals, galvanized steel was studied, which served as studies for testing specimens together with the natural extract, serving as a main additive in the concentration that will be mentioned in topic 3 of the methodology. But before, it will be presented in topic 2, the materials that were made to obtain the specimens.

2. MATERIALS

2.1 PLECTRANTHUS BARBATUS ANDREWS

The Plectranthus barbatus Andrews also known as Brazilian Boldo, from the lamiaceae family, originating in Africa is widely used in Brazilian territory. Because it is a bushy, aromatic, perennial plant with erect branches, it can reach a height of up to 1.5 meters, has oval, hairy and thick leaves, its flowers have a bluish color and grow like spikes in rainy seasons. Plectranthus barbatus Andrews is an herb recognized in Brazil as a medicine for the treatment of liver diseases, infections, liver problems and food digestion. Due to the presence of flavonoids, tannins and alkaloids in their composition, these substances have antioxidant actions, making the natural extract an excellent inhibitor in combating corrosion, which justifies and makes it important to study this plant, since it has a good inhibition efficiency shown in previous researches.

2.2 GALVANIZED STEEL

Galvanized steel is a material that undergoes several processes, one of which is the galvanizing process where it is coated with a very thin layer of zinc, which provides resistance against corrosion. Steel itself is a material that is widely marketed and used in building structures. It is worth remembering that its initial material, which is iron or zinc, is not yet as resistant and ends up being corroded by rust, over time, bringing expenses and maintenance to companies.

2.3 HDF- HIGH DENSITY FIBERBOARD

HDF is its abbreviation for High Density Fiberboard or Industrialized Wood Panel. HDF is a material derived from wood, produced with fibers from selected Pine or Eucalyptus woods from reforestation, introduced by thermosetting resins by pressure and high temperature. In the quality certificate and in its technical reports, it offers great resistance, homogeneity and dimensional stability. of furniture, side and bottom of drawers. It offers excellent cutting and machining capacity, not to mention that it has a great cost benefit. However, when this wooden panel is subjected with pins, screws, or any type of metal exposed to room temperature, it is subject to oxidation, corrosion and other types of degradation, leading to the useful life of wooden structures.

3. METHODS

3.1 PRODUCTION OF EXTRACTS

In the production of extracts, it was first necessary to analyze the leaves of the Brazilian Boldo. They were removed from the herbarium at Ceuma University, and selected for the drying process. The research continued in the laboratory of the Federal Institute of Maranhão (IFMA), where a new plantation of Brazilian boldo was made with the same species of leaves that were cultivated at the Ceuma university. Then, the leaves were placed in an oven at a temperature of 100° degrees celsius for 24 hours to carry out a new drying, after this procedure, the leaves were sent to the materials laboratory, then they were removed from the oven and part of them were introduced on a precision balance to obtain its original mass. Therefore, the leaves were transferred to a mortar to carry out the maceration process, previously grinding the leaves for the preparation of tea in order to reduce the size of the particles and facilitate dissolution in an aqueous medium. Then, in a closed glass container, 500 grams of macerated leaves, as weighed by the volumetric balance, and 500 ml of H2O were added, subject to room temperature for a few hours. The following figures show the procedures for making the extracts.

https://doi.org/10.52202/069179-0126

Figure 1. *Brazilian Boldo Plantation (Source: Author, 2023)*

Figure 2. *Leaves inserted in the oven- Drying Process (Source: Author, 2023)*

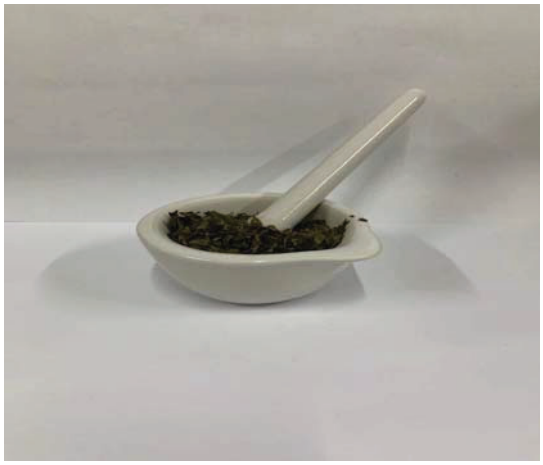

Figure 3. *Maceration process (Source: Author, 2023)*

Figure 4. *Brazilian Boldo Extract (Source: Author, 2023)*

3.2 MANUFACTURE OF TEST SPECIMENS

In this research, galvanized steel screws and pins were used fixed in 4 sheets of laminated flooring composed of HDF, wood fibers in its structure, specifically mentioned in the materials in topic 2. Before being submitted to their sheets, the materials were weighed to obtain their referred initial masses, then they were bathed each in their respective beakers. Each container having a mixture and concentration of different extracts. The first CP (Proof body) having only H2O, the second CP only with natural extract (additive) and H2O, the third CP with H2O and NaCl (sodium chloride) popularly known as table salt, and the fourth and last CP, was obtained from all mixtures previously formed (H2O + Nacl + natural extract). In the research, 4 divergent CPS were used, precisely to compare the efficiency of inhibition in each test requested. The figures below show the respective samples that were prepared to bathe the 4 HDF sheets which were tested in the gravimetric tests.

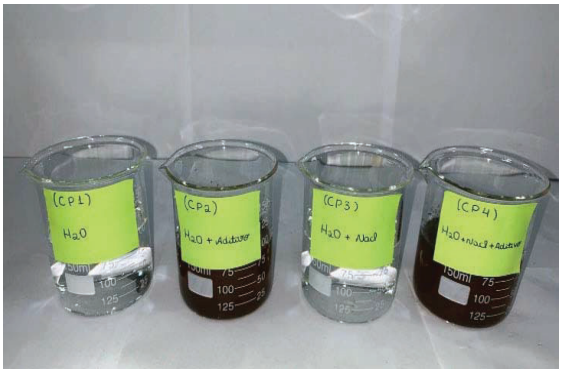

Figure 5. *Samples (Source: Author, 2023)*

.

Figure 6. *Representation of inserted pins and screws on the HDFsheet (Source**:** Author, 2023)*

3.3 MANUFACTURE OF SPECIMENS WITH COMMERCIAL INHIBITOR

As the research was intended to compare the natural inhibitor with the commercial inhibitor, it was necessary to carry out new tests by bathing other HDF sheets made using TF7 (industrial inhibitor), an excellent rust converter sold in Brazil to eliminate rust in surfaces, forming films that eliminate and prevent corrosion. Therefore, 3 beakers were prepared to carry out new tests and serve as a comparison for the other specimens. Figure 7 shows the CPs with TF7 and HCL (hydrochloric acid). In this test, 90 ml of TF7 and 10 ml of HCL were used in concentration.

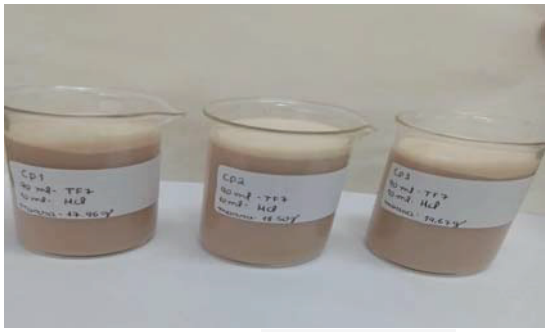

Figure 7. *CP1, CP2 e CP3 (Source: Author, 2023)*

3.4 CORROSION RATE AND INHIBITION EFFICIENCY CALCULATIONS

The fraction from the extraction of plectranthus barbatus Andrews, with the presence of H2O and Nacl acid, was evaluated as a potential corrosion inhibitor for galvanized steel, using gravimetric tests for mass loss. The intensity of corrosive processing was determined by calculating the corrosion rate (TC), which, according to ASTM G1-03 (2011), is represented by the following formula:

TC = (K.W) / A t p (equation 1)
Where:
K=Specific Constant (8.76 x 10^4)
W= mass loss (in grams)
A= area (in cm^2)
t= time (in hours)
p= specific mass (in $g.cm^{-3}$)

As a final result, the average corrosion rates were applied to the first 4 specimens of each test. The inhibition efficiency (EI) of the extract as a corrosion inhibitor was calculated from the corrosion rates (TC) by the following formula: (OLIVEIRA, T.M.de; CARDOSO, S.P., 2014).

EI = (T0 – T1) / T0 (equation 2)
Where:
T0= corrosion rate without the presence of the inhibitor;
T1= corrosion rate with the presence of the inhibitor.

4. DISCUSSION AND RESULTS

Mass loss tests were carried out according to the proposed methodology, in figure 8 shows the CP1, specimen that was submitted in a container containing only H2O. Note some corrosion spots on screws and pins. Figure 9 shows CP2, a specimen that was inserted into a container containing H2O along with the natural extract. A yellowish coloration is observed, due to some antioxidant substances contained in its composition, which implies and makes the research even more investigative. It is likely that this coloration presented in metals is a protective layer in the fight against corrosion.

Figure 8. *CP1 (H2O) (Source: Author, 2023)*

https://doi.org/10.52202/069179-0126

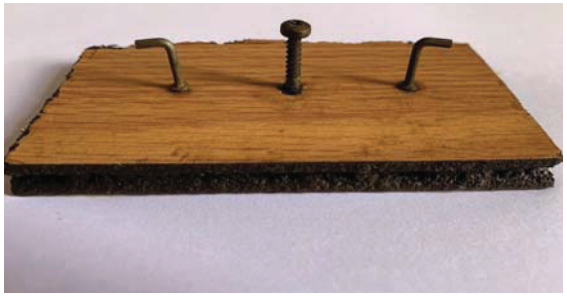

Figure 9. *CP2 (H2O+ Natural Extract (Source: Author, 2023)*

In view of this analysis, two more CPS were tested to obtain results. CP3, a specimen containing H2O + Nacl without the presence of the natural natural extract, was tested precisely to compare its corrosion rates. With this, it was possible to observe how much metals corrode, especially when they are close to saline areas. Finally, CP4 was performed, a specimen containing H2O + Nacl + natural extract (Brazilian boldo additive). In this CP, it presented a behavior equivalent to CP3, and also similar to CP2. It is observed that the compounds of this mixture act against and in favor of corrosion, a factor that provokes and induces researchers to look for results. Image 10 and 11 show the behavior of the CP tested at 14 days, which were soaked with their respective extracts.

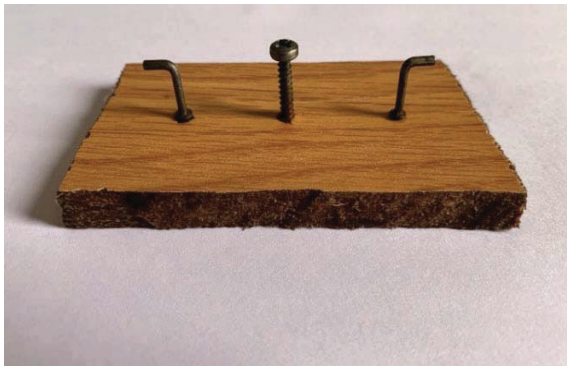

Figure 10. *CP3 (H2O + Nacl)(Source: Author, 2023)*

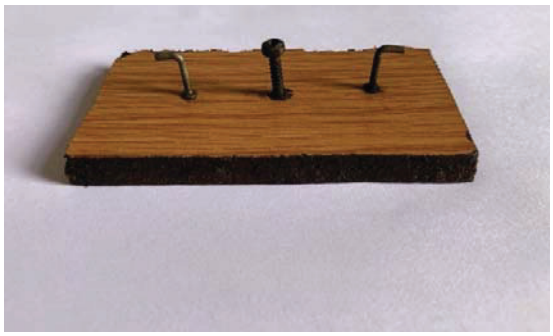

Figure 11. *CP4 (H2O + Natural Extract + Nacl) (Source: Author, 2023)*

Table 1 first shows the initial mass of the specimens referring to all the pins and screws that were embedded in the HDF sheets, before being inserted in their respective extracts.

Table 1. *Initial mass of pins and screws*

MATERIAL	STEEL TYPE	INITIAL MASS
PIN 1	GALVANIZED	0.68 g
PIN 2	GALVANIZED	0.68 g
SCREW	GALVANIZED	1.35g

Source: *Own authorship*

Tables 2 and 3 show the initial mass as well as the final mass of the test specimens of pins and screws. Finally, they present the total mass loss (W), when placed in a mixture after the CPS were wetted and dried at room temperature after 14 days of testing.

Table 2. *Initial mass, final mass and mass loss of pins (W)*

PROOF BODIES	INITIAL MASS	FINAL MASS	WEIGHT LOSS(W)
CP1	0.68 g	0.68 g	0g
CP2	0.68 g	0.67g	0.10g
CP3	0.68 g	0.66 g	0.20g
CP4	0.68 g	0.70 g	0.20g

Source: *Own authorship*

Table 3. *Initial mass, final mass and mass loss of screws (W)*

PROOF BODIES	INITIAL MASS	FINAL MASS	WEIGHT LOSS (W)
CP1	1.35 g	1.35 g	0g
CP2	1.35 g	1.34 g	0.10g
CP3	1.35 g	1.33 g	0.20g
CP4	1.35 g	1.37 g	0.20g

Source: *Own authorship*

Tables 4 and 5 show the aggressiveness in the corrosive medium of all the concentrations that were submitted, which can be proven by gravimetric tests and by equations 1 and 2 mentioned in the methodology, in topic 3.4. With the data provided by Tables 2 and 3, we acquired the initial and final mass of the materials, making it possible to calculate the corrosion rate and inhibition efficiency. (FERNANDES, L.D.; RUAS, L.V.; et al 2019)

Table 4. *Corrosion rate and inhibition efficiency- Pin*

CP	CORROSION RATE	INHIBITION EFFICIENCY (EI)%
CP1	0.66	95%
CP2	0.66	95%
CP3	0.43	74%
CP4	0.61	90%

Source: *Own authorship*

Table 5. *Corrosion rate and inhibition efficiency- Screw*

CP	CORROSION RATE	INHIBITION EFFICIENCY (EI)%
CP1	0.66	95%
CP2	0.66	95%
CP3	0.34	73%
CP4	0.61	90%

Source: Own authorship

With the information obtained in the tables above, it was observed the growth of the inhibition efficiency, obtained by the corrosion rate. The graphs below show partial results of the specimens.

Graph 1. *Corrosion rate analysis and inhibition efficiency- Pin*

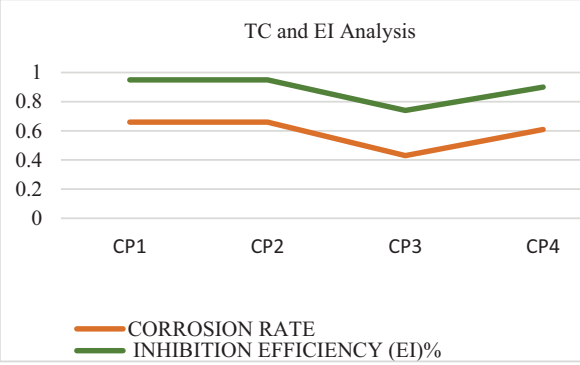

Source: Own authorship

Graph 2. *Corrosion rate analysis and inhibition efficiency- Screw*

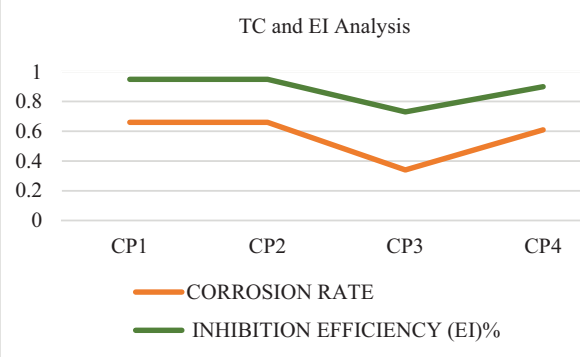

Source: Own authorship

According to the results provided by the research, there is a satisfactory reduction in the speed of the corrosive process of the CPS, this behavior is satisfactory, since there is use of the natural inhibitor in the concentrations. The data in the table and graph were calculated and compared with CP1, a neutral specimen with H2O only, which was tested without the presence of extract and Nacl in the composition. It is noteworthy that due to the delay in weight loss (w) of metals and the search for a commercial inhibitor for galvanized steel, it has not yet been possible to calculate the weight loss of pins and screws subjected to industrial anticorrosive. However, the specimens are still being tested and after 14 working days it will be possible to compare the efficiency rate with the Brazilian boldo, a natural inhibitor under study.

5. CONCLUSIONS

In the tests carried out, the loss of mass of the galvanized steel in the absence and presence of the inhibitor is verified. Even without the results of mass loss from the commercial inhibitor, it is clear that the Brazilian boldo extract presents a satisfactory inhibitory behavior for research. It can be seen in the specimens presented, a reduction in the speed in the corrosive process, leading to an efficiency of 90% and 95% of inhibition. Studies indicate that this efficiency can provide protection for both steel and wooden structures, which are subject to damage from corrosion. Given this analysis, we can conclude that Plectranthus barbatus Andrews extract becomes an excellent natural extract, as it meets the inhibition requirements. Because it uses a clean, renewable and sustainable technology, minimizing the deterioration of metals and benefiting in economic and environmental aspects when compared to other commercial inhibitors.

ACKNOWLEDGEMENT

First of all, I would like to thank God for allowing me to have health and determination not to lose heart during this work, to my parents and my sisters for all the support and help in my most difficult moments, to my teachers for all the advice and guidance and for all the patience with which they guided my learning. To the IFMA teaching institution, essential in my professional training process, for the dedication and for everything I have been learning over these years in the Civil Engineering course.

https://doi.org/10.52202/069179-0126

REFERENCES

[1] ASTM G1-03. Standard practical for preparing, cleaning, and evaluating corrosion test specimens, 2011.

[2] FERNANDES, L.D.; RUAS, L. V.; SILVA, A. A. da; CASTRO, D.L. in; CARDOSO, S. P. Extracts of leaves and flowers as corrosion inhibitors of plant origin. Research, Society and Development, 2019.

[3] MATIELLO, Nigian; NESPOLO, Samara. Study of the behavior of the connections of wooden pieces with stamped teeth plates, for use in light shears with reforestation wood. 2015. 105 f. Completion of course work (Graduation) - Federal Technological University of Paraná, Pato Branco, 2015.

[4] MELO, G. F.; LAURENTINO, J. V. A.; SANTOS, L. O. Comparative study of the efficiencies of commercial corrosion inhibitors in marine reinforced concrete structures. Engineering Sciences, v.9, n.2, p.66-80, 2021.

[5] NAGAOKA, Rai. K. Mechanical behavior of wooden truss with connections by stamped tooth plates. 2014. 46 f. Completion of course work (Graduation) - Civil Engineering. Federal Technological University of Paraná. Campo Mourao, 2014.

[6] NAPPI, Manuela Marques Lalane et al. Corrosion of metallic elements embedded in different wood species. 2012.

[7] OLIVEIRA, T.M.de; CARDOSO, SP. Camellia sinensis (L.) Kuntze extract (THEACEAE) as a corrosion inhibitor of vegetable origin. Perspectives of science and technology, v .6, n.1/2, 2014.

World Conference on Timber Engineering Oslo 2023

REVIEW AND COMPARISON OF DIFFERENT TIMBER BUILDING PRODUCTS' EMBODIED EMISSIONS USING FREE DATABASES.

Felipe Victorero[1,2,3] , Daniela Mendez[1,2], Felipe Bascuñan[1,2], Waldo Bustamante[3,4].

ABSTRACT: This paper aims to present a brief review of sources of information for studying the variability of embodied carbon emissions in structural wood products commonly used in construction. The review considered 13 primary sources, focused on EPDs and generic databases, and allowed the collection of data for the study of 140 products divided into Sawn lumber, Glulam, OSB, and Plywood. The information collected made it possible to identify factors such as the variability of density properties, wood species, the origin of the products, among others. In addition to analyzing the variations in the biogenic carbon of the different products studied. The results allow us to conclude that although the variability of wood products can be significant, like any product of natural origin, when they are studied within the framework of the analysis of the materials of a building, they can present a smaller fluctuation than other materials such as concrete. Moreover, this effect can be accentuated in wood products with greater density or have undergone processes that increase the mass of biogenic carbon per cubic meter in the final product.

KEYWORDS: CO2 Emissions, Embodied Carbon, Global Warming Potential, Biogenic carbon.

1 INTRODUCTION

The building sector is one of the main contributors to the global warming crisis, associated with anthropogenic GHG, with nearly 39% of the global CO2eq emissions. Moreover, when we disaggregate this percentage, we realize that almost 23% of the worldwide CO2eq emissions correspond to building materials production and transport, such as steel and cement, which represent nearly 11% of the global total [1]; while 9% of the emissions to the building's operation, and especially the energy required for space heating [2]. Even more, recent studies have raised evidence that in 2020 the anthropogenic mass became equivalent to the whole planet's biomass. More importantly, approximately 70% of this anthropogenic mass corresponds to concrete and aggregates, the most abundant manmade materials in the world and with the highest environmental impact on the planet's emissions [3].

As a result, the materials we use in our built environment are of utmost importance, since their production and effects on a building's life cycle have been responsible for a good part of the anthropogenic GHG emissions. This could also be extended to other environmental indicators such as energy use, waste production, and water pollution. Therefore, previous research has suggested that replacing steel and concrete with bio-based construction materials could help answer the current construction sector environmental problem. Likewise, studies such as the one led by the researcher Churquina [3] also present a scenario in which massive timber buildings and cities could not only reduce CO2eq emissions but also help to capture it from the environment. Turning cities into long-term carbon storages and promoting a more sustainable forest sector that could foment reforestation and afforestation processes worldwide, also helping to keep capturing carbon from the atmosphere and eventually even returning it underneath the Earth.

On the other hand, although there have been attempts to reduce the building sector's GHG emissions during the past decades, these have been insufficient and carried out primarily in developed countries. Moreover, developed countries' new and increasing attempts to reduce building sector emissions during the following decades might still be unsuccessful. This is because it is expected that the world population will increase by nearly 20% by 2050, although this will not be concentrated in developed countries but developing countries. In this matter, the need for new housing and infrastructure, in regions such as Asia, Africa, and Latin America, will be decisive if we want to decrease anthropogenic GHG emissions and limit global temperature rise under 2°C before the 2050 tipping point.

Developing countries, such as Chile, have made great efforts to commit to achieving carbon neutrality before 2050. Mostly relying upon increasing their renewable energies share, from the current 40% to an ambitious 70%

[1] Centro Nacional de Excelencia para la Industria de la Madera (CENAMAD), Pontificia Universidad Católica de Chile, Santiago, Chile.
[2] UC Timber Innovation Center, Pontifical Catholic University of Chile, Chile.
[3] School of Architecture, Pontifical Catholic University of Chile, Chile.
[4] Center for Sustainable Urban Development (CEDEUS), Pontificia Universidad Católica de Chile, El Comendador 1916, Santiago, RM, 7520245, Chile.

https://doi.org/10.52202/069179-0127

by 2050; but also by increasing their CO2 sequestration through new forest plantations, capturing almost 50% of the total country's emission. Moreover, this presents a scenario where buildings would benefit from a cleaner energy source, drastically reducing their operational emissions. Still, it also means that buildings' embodied emissions would become more relevant to achieve carbon neutrality emissions in the Chilean building sector. Also, creating an opportunity to get the advantage of the new forest plantation and the promotion of low embodied carbon timber buildings, which may kickstart a more sustainable development model.

2 GLOBAL WARMING POTENTIAL AND TIMBER PRODUCTS

CO2 is the most common anthropogenic GHG emission and a by-product of burning fossil fuels or biomass, being determined as the reference by which other GHG are compared in their effects on the Earth's radiative balance and global warming over a known period. Therefore, the global warming potential or GWP defines the amount of energy that the emissions of 1 ton of a determined GHG will absorb compared to 1 ton of CO2 over 100 years. In this matter, gases such as methane tend to have a GWP twenty times higher than CO2, while hydrochlorofluorocarbon gases can reach tens of thousands more GWP.

To compare the effects of different GHGs emissions with independent GWP, it is usual to multiply the GWP for a 100 years period by the total gas emission, this way obtaining a CO2 equivalent or CO2eq value. This equivalent emission allows comparing the radiative and global warming effect of different GHG, or even mixed emissions from the same or different production process. Moreover, diverse GHG emissions associated with a specific building product manufacturing can be grouped under a total global CO2eq value.

This CO2eq emission data, associated with GHG GWP factors, is usually used by designers and investors to select building products to reduce a project's overall CO2eq emissions in the early design stages. This is done mainly by comparing the buildings products' embodied equivalent CO2 emissions; when considering raw materials extraction, transport, and manufacturing prosses. Generally corresponding to a cradle-to-gate stage analysis of the life cycle or "Product stage" A1-A3 according to the EN 15978's "System Boundary."

For the designers to obtain the embodied emission information of building materials, they usually must ask manufacturers for the Environmental Product Declaration or EPD for their specific products. EPDs that consider technical standards, such as EN 15804, give detailed information on the product's environmental impact and declare the stages considered on the system boundary for evaluation. Another way to obtain the emission data is to check building products' emissions inventories databases or use specialized tools to estimate emissions through a specific material manufacturing process analysis. Although depending on the data source, emissions could drastically vary their results between products and manufacturers, depending on the process or methodology applied.

It is also important to state, especially for this review, that materials such as wood can also have biogenic carbon sequestration, considered in EPDs and databases that use more up-to-date standards, such as EN15804. This biogenic carbon corresponds to carbon captured from the CO2 in the atmosphere when the tree grows and becomes part of the final timber product structure. Therefore, depending on the process involved in timber product manufacturing and the methodology used to account for emissions, the balance between emissions and CO2 capture can be negative.

Nevertheless, obtaining the embodied emission data can be challenging, especially for timber building products. Data gathering for producing EPDs, or product inventories, is extremely time-consuming and too expensive for many companies. Moreover, free access databases are rare, limited, outdated, and usually constrained to some regions in developed countries. Thus, this is especially complicated in developing countries, where data is almost non-existent, and designers have few tools to select building materials according to their embodied CO2eq performance.

3 METHODOLOGY

This document seeks to review the most used and free access, building product's embodied emission catalogs, focusing on databases that gather EPDs and generic product inventories. Thus, comparing the GWP CO2eq emission variability of more common timber structural products with fewer production prosses, such as saw wood, and those more sophisticated such as plywood or CLT. Meanwhile, other private or paid access databases are not considered since; although they might be more comprehensive, updated, and have a friendlier user interface; they are less used by designers and project managers. A situation that is most frequent in developing countries where the requirements for this analysis are less usual, and paying for this information is not part of a project's budget.

For this purpose, the reviewed sources prioritize first more detailed data from EPDs Program Operators under the ISO 14025 standard; and second, generic environmental impact data from public catalogs and databases worldwide. Moreover, it is important to notice that the catalogs presented later are the ones that declared timber construction products at the moment of the review. In contrast, other discarded catalogs did not have timber products or any construction data, or it was impossible to access them or the information within their platforms. Also, the information needed to be accessed remotely and

in English to be useful for designers' decision-making worldwide. Yet, some specific countries' databases were language exclusive for global use purposes and, therefore, not considered.
Although data from the EPDS's Program Operators and catalogs might have differences that could make their study difficult, such as their Product Category Rules (PCR) conventions, an effort is made to homogenize de data for comparison. This is done by applying data selection criteria, simplifying their analysis, and converting functional units for comparison. Moreover, a minimum of ten different data sources is required to have representative data to analyze a specific structural timber product, such as glulam. This way, a product with little information that might distort the comparative analysis is not considered.

The criteria for selecting the data and subsequently compare results, from the mentioned sources, consider; i) selecting information from timber structural products commonly available in the market, non-structural timber products such as floors or sheathing are not considered; ii) that the EPD data considered the inclusion of EN 15804:2012+A1:2013, EN 15804:2012+A2:2019 or ISO 21930:2017 standards, which are specific for building products and give more comparable information; iii) that the LCA data consider at least product stage information, modules A1-A3 regarding extraction, material transport and manufacturing; that the global warming potential data available for the product stage, includes separate wood biogenic information; iv) that the wood spices, water content and/or density is declared, in order to identify if the product consists of softwood or hardwood; v) that the functional unit is in cubic meters or there is enough information to make a suitable conversion; vi) that the data is not older than five years, in accordance with international standard. If any previous criteria are not fulfilled, the product is not included in the study. Moreover, timber building products EPDs that could be part of multiple Program Operators or Catalogues are assigned to only one data source to avoid duplicated information.

In addition, to uniform data, functional units expressed in kilograms or square meters, when available, are transformed to cubic meters using equivalent density data and product thickness. Moreover, for timber products that declare their biogenic carbon in kilograms, in accordance with EN 16449:2014 and the atomic weight of carbon and CO2, a factor of 3.67 is used to transform it to CO2eq. Even more, for specific timber product cases, where the total Global Warming Potential excluding the biogenic carbon is not given, this is estimated by resting the informed biogenic CO2eq from the total GWP.

At last, to identify the impact of using different GWP data in a specific case, a Chilean timber frame representative 6-story dwelling building is also studied. Therefore, allowing the understanding of using different timber products' embodied emissions data versus a traditional concrete structure. Moreover, considering the overall effect of the structural material quantities analysis in a complete building evaluation.

4 RESULTS & DISCUSSION

4.1 Timber structural database.

A total of 34 EPDs Program Operators, catalogs, and databases are reviewed, remaining only 13. Most of the sources reviewed considered a specific section for construction material data and filters that allows identifying particular materials such as wood products or capabilities as structural performance. Also, most sources consider digital EPDs documents in PDF format, and only a few have additional data in other forms, such as spreadsheets or HTML data.

Table 1: *Data source*

Data source	Type of data	Source origin	N° products
Environdec	EPDs	Europe	40
EPD Hub	EPDs	Europe	3
ASTM	EPDs	America	10
SPOT UL	EPDs	America	5
EPD Irland	EPDs	Europe	8
EDP Denmark	EPDs	Europe	8
EPD Norway	EPDs	Europe	1
INIES	EPDs	Europe	26
INIES	Generic	Europe	3
IBU EPD	EPDs	Europe	4
ECO Platform [a]	EPDs	Europe	2
ICE 2019	Generic	Europe	7
Quartz	Generic	America	5
ÖKOBAUDAT	Generic	Europe	18

[a] *Although ECO Platform is one of the most significant sources of EPDs information, the data comes from other Program Operators and therefore are assigned to the original source. The remaining data correspond to EPDs that were not accessible through their Program Operators.*

The final list of EPDs Program Operators and catalogue data bases, that can be seen with more detail in table 1, consist of the EPD Environdec System [4], owned by EPD International AB, and part of the Global EPD program for publication of ISO 14025 and EN 15804 compliant EPDs; the EPD Hub [5], based in Europe and in compliant with ISO 14025; the ASTM EPD program [6], managed by the ASTM International, North American organization devoted to standards development; SPOT UL [7], program operated by UL Solutions; EPD Ireland [8], consisting of a program managed by the Irish Green Building Council; EPD Denmark [9], focused in the construction sector and with del EN 15804 European standard; EPD Norway [10], established by the Norwegian Confederation of Business and Industry; INIES EPDs data [11], French national organization which gathers materials and construction system environmental data; IBU.dat [12], which is a data base created by the Institut Bauen und Umwelt oriented to the

https://doi.org/10.52202/069179-0127

European region (IBU EPD); and ECO Platform [13], International association of private and public EPD's Program Operators. Meanwhile, regarding generic data for timber construction products, the sources compromise of the University of Bath ICE 2019 database [14], which collects data from reports and EPDs; Quartz project [15], which gathers information from EPDs, the Pharos project, and GaBi database; the ÖKOBAUDAT platform [16], from the German Federal Ministry for Housing, Urban Development and Building; and the INIES's generic data [11], built from French EPDs representative data.

Regarding the revised structural timber products, more than 30 products were discarded from the study, primarily due to lack of information, having old data, being innovative products with low market share, and/or not meeting other methodological requirements for this study. Also, some product types, such as Laminated Veneer Lumber (LVL), Nailed Laminated Timber (NLT), Dowel Laminated Timber, Laminated Stand lumber (LSL), and I-joist beams, did not meet the minimum number of product data to be included.

Consequently, the remaining list consists of 140 entries, with information not older than 2018, representing five different structural timber products. Thus, they separate into 40 sawn wood products, finger-joints are not included in this group because of the lack of representative data; 35 glued laminated timber (Glulam), this combining different elements such as columns and beans; 26 Cross Laminated Timber (CLT) products, considering panels of various sizes; 26 Plywood boards, with different representative thickness and manufacturing process; and, 18 Oriented Strained Board (OSB), with different origins and layers.

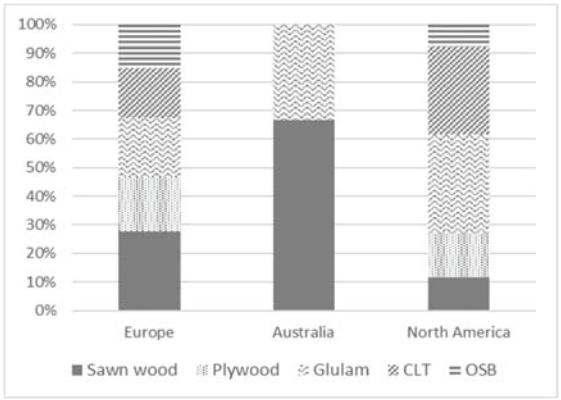

Figure 1: *Timber product share by region of origin. South America is not considered since it only has two EPDs***.**

4.2 Timber products properties.

It is well known that wood, as a natural product, presents different properties depending on various factors such as the species, growing considerations, carbon capture, water content, among many others. This has meant that many researchers have concluded that determining the global warming potential of wood products is particularly difficult. However, the properties of structural wood products are more similar to each other when compared to other non-structural products such as flooring, cladding, furniture, tools, decoration, etc. This is mostly due to the types of wood used for building structural purposes, which commonly consist of softwoods with similar properties. Moreover, engineering wood products used in building structures often have production standards that set similar physical properties to control their humidity and strength.

Therefore, from the data collected from EPD information and generic data, it is possible to identify that most of the timber structural products evaluated in this study consist of dried softwoods with an average density between 471kg/m^3 and 623kg/m^3, depending on the product type. Although some wood, such as Cypress, can have a density of more than 800kg/m^3.

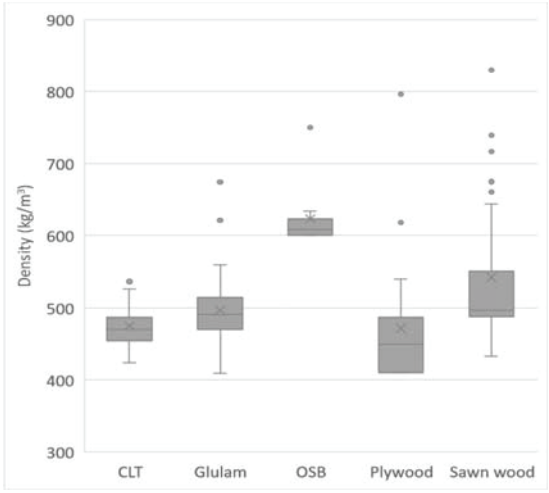

Figure 2: *Timber products and their density range.*

Moreover, the most common species within this study are different softwoods such as Spruce, Pine, and Douglas-Fir. Other hardwoods such as Poplar, Beech, or Oak are also present in products like plywood or sawn wood; nevertheless, they only represent less than 13% of the whole sample.

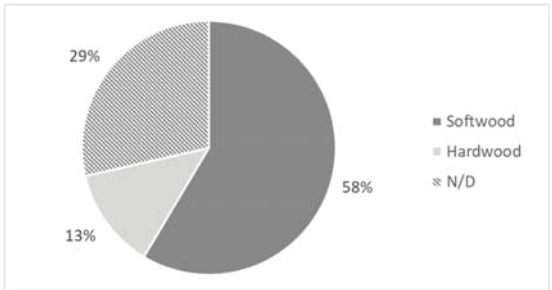

Figure 3: *Wood classification by softwood or hardwood, according to EPDs' data.*

4.3 Global Warming Potential and biogenic carbon

The wood products' Global Warming Potential results show that when biogenic carbon sequestration is considered in the product stage, the total GWP is negative in all the cases. Despite the variability in results within each timber product and the important difference that arise between product types. By comparison, products that require more manufacturing processes, have a higher adhesive or additives to wood mass relation, and present a more significant range of wood species, such as Plywood and OSB, tend to have considerable variability in their GWP results. While on the other hand, timber products with a lower manufacturing process, reduced adhesive to wood mass rates, and more consistent wood species use, such as the sawn wood, CLT, and glulam, present more consequent GWP results. Nevertheless, products with a more complex manufacturing process, such as OSB, still present lower GWP values than sawn wood.

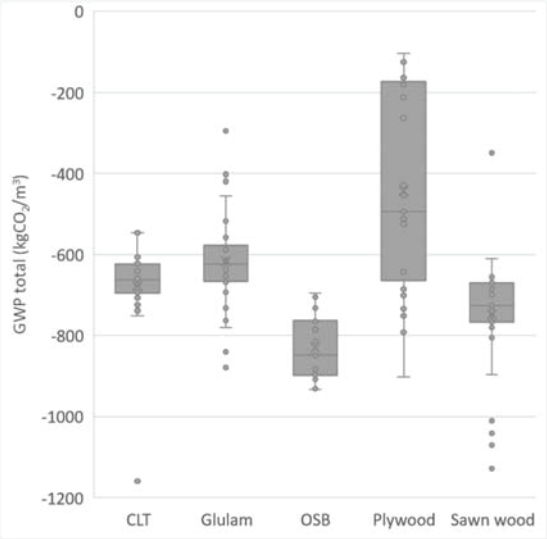

Figure 4: *GWP total by timber product, for product stage (cradle to gate), considering carbon biogenic captured in the wood mass.*

Regarding the manufacturing process, it is essential to notice that less complex manufacturing products will present lower GWP results when biogenic carbon is not considered. Explaining why, in this scenario, the sawn wood has a lower impact than the OSB and Plywood. Therefore, the final dry wood density of the product, regardless of the original wood product density before the manufacturing process, is a crucial factor to consider when studying the GWP of wood base products.

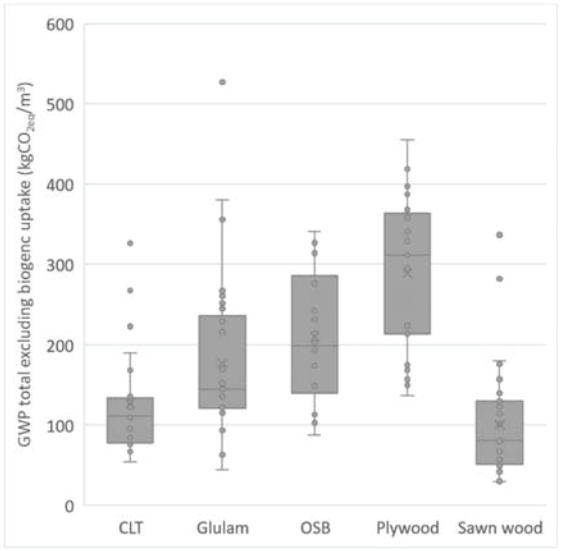

Figure 5: *GWP total by timber product, for product stage (cradle to gate), excluding biogenic carbon uptake by the wood mass.*

However, density and moisture content are crucial to determine the carbon captured in wood products, as presented in EN 16449 standard. Therefore, since structural timber products must be dry, the wood mass density would be the main factor in determining a product's biogenic carbon content. In this sense, the denser the wood used in a product, the more biogenic carbon and CO2eq are sequestered. For example, a cubic meter of dried saw Pine wood with a density of 450kg/m3 and 12% moisture content would have approximately 200.8kg of carbon or a biogenic GWP of -737.3 kgCO2eq. In comparison, a cubic meter of dried sawn Beech wood with a density of 740kg/m3 and a 12% moisture content would have 330.3kg of carbon and a biogenic GWP of -1,212.4 kgCO2eq.

Depending on the product manufacturing process, the amount of dry wood may vary. Therefore, timber products that compress wood might have a higher density than the original piece of wood used for its manufacturing and, therefore, more biogenic carbon by the cubic meter of product. On the other hand, the mass of an engineering timber product could be conformed of wood and other products such as adhesives or preservatives, reducing the amount of biogenic carbon by volume of product. For example, the density of an OSB board could be higher than the pine wood used for its production, but it is also important to take into account the adhesive density in the product to determine the total biogenic carbon. Nevertheless, and weighing their production process, an OSB board made from Pine could have a lower GWP than a Sawn wood piece of the same Pine when biogenic carbon is considered by volume in the product stage.

https://doi.org/10.52202/069179-0127

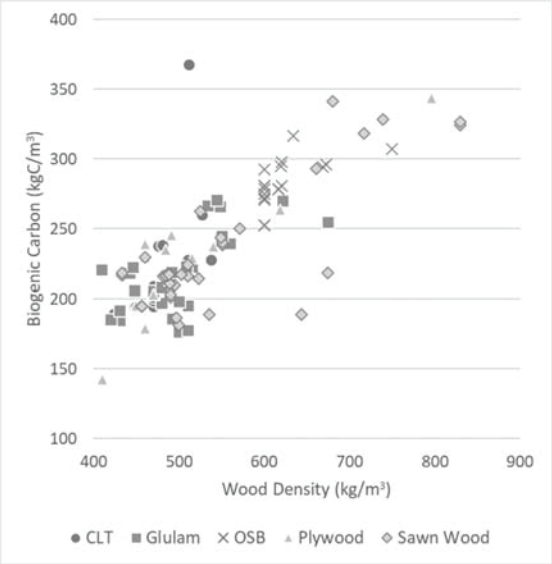

Figure 6: *Timber products' density and biogenic carbon content.*

4.3.1 Chilean case

As it is stated at the beginning of this document, the Chilean renewable energy growth scenario for the next decades is a particularly interesting case to evaluate buildings' embodied carbon versus operational emissions. Consequently, Chilean buildings that rely completely on electricity for their operation might become, in the future, almost net-zero without any important upgrades. And therefore, new building GWP emissions would mainly depend on the embodied emissions of materials.

On the other hand, Chilean structural timber is produced almost entirely in sustainable certified forests, making it possible to presume that carbon sequestration is taking place in the life cycle of a wood product. Moreover, Chilean structural timber consists exclusively of Radiata Pine, a softwood similar to the one found in the northern hemisphere market, allowing the promotion of knowledge transfer with other countries.

Nonetheless, Chile lacks information regarding the environmental impact of building materials, and the use of international EPDs or generic data is the only option in many cases. Most of the time, presenting uncertainty about the adequacy of the data and doubts about the obtained results, especially for wood-based products that also need to consider carbon sequestration as a critical factor. Moreover, the only two structural wood base products EPDs registered in South America by this study are Plywood boards from Chile, made from softwood Pine and with GWP results raging from -525kgCO2eq and -454 kgCO2eq.

Figure 7 presents the GWP totals of three 6-story buildings' structure materials, one with a timber frame construction system, a second with a mass timber structure in CLT, and a third with a traditional reinforced concrete configuration. It is essential to notice that this data does not consider a whole life cycle assessment, and it is only intended to compare the GWP of three structural building products to verify if wood-based products have higher variability in a project. For this purpose, non-wood product-stage carbon emissions are obtained from the international Institution of Structural Engineers [17] and used in the analysis along with the building's structure mass quantification.

Table 2: *Material GWP product stage (cradle to gate) in kgCO2eq/m³*

Material [a]	Avg. GWP	Min. GWP	Max. GWP	Var. GWP
Concrete C32/40 [b]	420	333.6	504	170.4
Steel plate [c]	12,403	4,451	19.233	14,782
Steel bar [d]	15,386	3,100	31,164	28,064
CLT	-678.6	-750.8	-546.7	204.1
Glulam	-617.2	-780.0	-456.8	323.2
OSB	-829.7	-933.3	-694.9	238.4
Plywood	-443.5	-901.7	-103.7	798.0
Sawn wood	-748.9	-897.2	-611.0	286.2

[a] Concrete and steel data obtained from the Institution of Structural Engineers.
[b] density of concrete 2400kg/m³
[c] Steel plate min and max GWP correspond to UK data, while average value to global data. Density 7850kg/m³
[d] Density of Steel bar 7850kg/m³

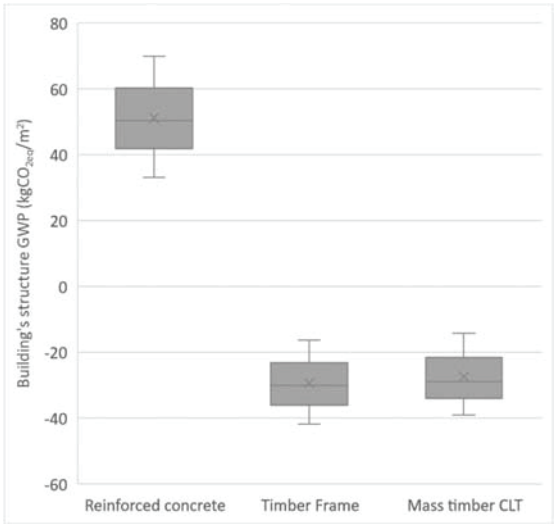

Figure 6: *Timber products' density and biogenic carbon content.*

The buildings' structural material analysis shows first, as expected, that the overall CO2eq emissions of the timber structures are lower than the reinforced concrete

alternative. It also presents that timber building structural materials' total emissions are negative, despite considering steel connectors and concrete foundations in their carbon balance. But what might be more interesting is that the variability of the CO2eq emissions is lower in the timber cases than in the concrete. This condition is explained by the higher mass of concrete in the buildings, compared to timber, and its greater importance contrasted to the structural products' GWP variability.

In the same way, although the volume of wood is higher in the mass timber case, the greater density of wood in OSB boards compensates for the embodied biogenic carbon. This makes the two structural timber systems have almost the same emissions performance for this 6-story building case. This raises the question of which timber structure is most suitable for reducing materials' carbon emissions when building mid-height structures. Tambien entre maderas mayor densidad.

5 CONCLUSIONS

First, it is relevant to remember that this is a brief study of the most popular free-access carbon emissions database for timber structural materials. Therefore it was never intended to address all the information available. Also important, it only focuses on the product stage emissions, not taking into account other important stages in a whole life cycle analysis, such as maintenance or renovations during the life span of the building product or disposal of the material at the end of life. Nevertheless, the previously mentioned stages will depend drastically on design and operation considerations and the scenarios defined for waste management. For example, burning wood products at the end of life would release biogenic carbon, although if it is reused, recycled, or buried in landfills, it might prolong the capture or even become permanent.

The study shows that most data comes from European sources, presumably because of more developed regulations and standards, along with a more informed population and industry. A condition is also reflected in the products data covering, having a similar number of EPDs available for common products such as sawn wood and more innovative products like CLT. Moreover, regions such as North America and Australia have fewer data and, in some cases, concentrate on a couple of timber structural products. Nonetheless, other developing areas have little or no data available at all, like South America, where only two timber structural products' EPDs were identified.

On the other hand, the known variability in wood's Global Warming Potential properties might be less in timber structural products than in non-structural elements. This might be explained by a more standardized manufacturing process and the preference for a small number of softwood species. Therefore spices such as Pine and Spruce are the most mentioned in the EPDs reviewed. Also, the higher density of the wood or timber products, the more significant the reduction in the total GWP associated with the biogenic carbon uptake.

Consequently, considering biogenic carbon and its mass in structural wood products used in a building shows that, although wood may have a higher GWP variability, this is offset by the lower mass required by other materials such as concrete. Thus, a concrete building may have a higher variability in its overall performance, despite concrete having more limited GWP data variability. Therefore, timber structural average GWP data, like the one presented by this study, might have less variability than other traditional material data, such as concrete, when a whole structure building is considered.

Finally, when comparing timber-frame and CLT structures, it is interesting that although their mass volume may vary, the greater density of products such as OSB boards make them have almost the same CO2eq emission for a 6-story building. Because even though the CLT and the OSB can be made of the same tree, the density of the second would have more biogenic carbon per cubic meter due to the manufacturing process and the increase in density. Nonetheless, there are several other factors to consider when studying timber products' environmental impact, apart from GWP, which could have significant implications in a whole life cycle assessment of a product and building. Therefore it is expected that more complete and detailed studies in this matter will follow the present work.

ACKNOWLEDGEMENT

The authors acknowledge the funding provided by the Chilean Ministry of Housing and Urban Planning (MINVU), the support of the ANID BASAL FB210015 CENAMAD, and the UC Timber Innovation Center of the Pontifical Catholic University of Chile.

REFERENCES

[1] UN Environment programme (2021), 2021 *Global Status Report for Buildings and Construction: Towards a Zero-emission, Efficient and Resilient Buildings and Construction Sector*. Nairobi.

[2] Elhacham, E., Ben-Uri, L., Grozovski, J. et al. (2020). Global human-made mass exceeds all living biomass. *Nature* 588, 442–444 (2020). https://doi.org/10.1038/s41586-020-3010-5

[3] Churkina, G., Organschi, A., Reyer, C. P. O., Ruff, A., Vinke, K., Liu, Z., Reck, B. K., Graedel, T. E., & Schellnhuber, H. J. (2020). Buildings as a global carbon sink. *Nature Sustainability*, 3(4), 269-276. https://doi.org/10.1038/s41893-019-0462-4

[4] EPD International AB. (n.d.). *The International EPD System. EPD Library*. Retrieved 15 February 2023, from https://www.environdec.com/library

[5] EPD HUB LIMITED. (n.d.). *EPD-Hub. EPD Library*. Retrieved 15 February 2023, from https://manage.epdhub.com/

[6] ASTM International. (1996, 2023). *Certifications. Environmental Product Declarations*.

https://doi.org/10.52202/069179-0127

https://www.astm.org/products-services/certification/environmental-product-declarations/epd-pcr.html
[7] SPOT. (n.d.). *Sustainable Product Database. Products Catalog, Certifications*. Retrieved 15 February 2023, from https://spot.ul.com/
[8] Irish Green Building Council. (n.d.). *EPD Ireland. EPD Search*. Retrieved 15 February 2023, from https://www.igbc.ie/epd-home/
[9] EPD Danmark. (n.d.). *EPD Database. Epddanmark*. Retrieved 15 February 2023, from https://www.epddanmark.dk/uk/epd-database/
[10] Global Program Operator. (n.d.). *EPD Norge. Forsiden.* Retrieved 15 February 2023, from https://www.epd-norge.no/
[11] INIES. (n.d.). *La base INIES. Espace de Consultation, Les Données Environnementales et Sanitaires de Référence Pour Le Bâtiment*. Retrieved 15 February 2023, from https://www.inies.fr/
[12] Institut Bauen und Umwelt e.V. (n.d.). *IBU.data. EPD-Datensätze*. Retrieved 15 February 2023, from https://ibu-epd.com/ibu-data-start/
[13] Eco Platform. (n.d.). *ECO PORTAL*. Retrieved 15 February 2023, from https://www.eco-platform.org/epd-data.html
[14] Circular Ecology. (n.d.). *Embodied Carbon Assessment. The ICE Database*. Retrieved 15 February 2023, from https://circularecology.com/embodied-carbon-footprint-database.html
[15] Healthy Building Network. (n.d.). *Pharos. Common Products.* Retrieved 15 February 2023, from https://pharosproject.net/common-products#cp%20
[16] Bundesministerium für Wohnen, S. und B. (n.d.). *ÖKOBAUDAT. Sustainable Construction Information Portal*. Retrieved 15 February 2023, from https://www.oekobaudat.de/
[17] 17 The Institution of Structural Engineers. (2022). *How to calculate embodied carbon* (2nd ed.)

World Conference on Timber Engineering Oslo 2023

LIFE CYCLE ASSESSMENT ON DIFFERNET TIMBER BRIDGE TYPES: DECK BRIDGE, BLOCK GIRDER BRIDGE, TROUGH BRIDGE, PYLON BRIDGE

Özlem Özdemir[1], Annette Hafner[2]

ABSTRACT: Germany's national climate targets set the ambitious goal of achieving net zero emissions by 2045, which is in line with the Paris Agreement. The construction sector is a key player in reducing greenhouse gas emissions. In Germany, the focus has always been on the building sector, while little attention has been paid to civil infrastructures. At the international level, civil infrastructures are increasingly assessed and analysed for their environmental impact using life cycle assessment (LCA), although here, too, the use category of foot and bicycle bridges has hardly been studied. In the context of local mobility, foot and bicycle bridges (FBB) play an important role in the regional and local transportation network. Since in Germany timber bridges are used for FBB this paper presents, a standardized approach for life cycle assessment of bicycle bridges. A total of four different types of timber bridges are distinguished: deck, block girder, trough and pylon. The LCAs were performed following the applicable standards. The results show that the impact is influenced by different bridge components, although provides a basis that allows a first impression of the LCA results.

KEYWORDS: life cycle assessment, timber bridges, environmental footprint, carbon storage

1 INTRODUCTION

In line with the Paris agreement of 2015 [1] and in view of sustainable development goals, Europe has defined ambitious climate protection targets to be achieved by 2050. With 95 percent probability, human action has the greatest impact on climate change. [2] The use of resources is directly related to environmental impacts such as global warming and greenhouse gas emissions. Neverless, demand for natural resources will increase due the growth of the world population and increasing urbanization, as well as the needs of built city infrastructure. [3,4]

In the context of local mobility, foot and bicycle bridges (FBB) play an important role in the regional and local transportation network. The municipal budget situation is often a decisive criterion for awarding contracts. The construction of infrastructure demands nearly 40 % of all raw material consumption.

Bridge structures under municipal responsibility are assumed to be in similar condition to bridge structures under federal or state responsibility, increased replacement can be expected. It is therefore important to create basic data and to develop a uniform application system and to demonstrate the applicability and advantages to decision-makers.

The European Commission promotes the use of organic building materials such as wood from sustainable forestry to minimise the footprint of constructions through resource efficiency and circularity combined with transform parts of the construction sector into a carbon sink [5].

The primary energy non-renewable (PENRT) input in the life cycle represents the use of primary raw materials, the global warming potential (GWP) shows the impact on the global environment.

2 LITERATURE

The literature shows the beginnings and the developments of LCA in the field of bridges.

The beginning of LCA conducting on bridges were made by Horvath and Hendrickson [6], Widman [7] and Lünser [8] in 1998 wherein they compared different bridges on the environmental impact through the choice of material. Further LCA studies were conducted to analyse the impact of the of new materials compared to conventional materials [9]. Comparing of similar bridge components and materials with different maintenance scenarios were carried out by Penadés-Plà et al. [10]. Itoh et al. investigated for example whether the overall environmental impact of a bridge with increased maintenance is lower [11]. There have also been studies that examined the environmental impact of different bridge forms in different material categories by considering the construction and maintenance phases in terms of energy consumption and CO2 emissions [12].

[1] Özlem Özdemir, Ruhr University Bochum, Faculty of Civil and Environmental Engineering, Germany
oezlem.oezdemir@rub.de
[2] Annette Hafner, Ruhr University Bochum, Faculty of Civil and Environmental Engineering, Germany

https://doi.org/10.52202/069179-0128

In a further study, an approach is being developed in which the risk of natural events, such as earthquakes, is to be taken into account in the life cycle assessment of a bridge [13].
Although LCA has been applied in the research context of bridges since 1998 and a wide range of impacts have been studied taking into account varying aspects, it has not yet found its way into practice and is still rarely used in decision making. This is mainly due to the application method, which has not yet been harmonized.
To identify the significant differences in the methodological approach a literature survey were conducted. The main differences were identified, for example, in the:
- functional unit
- system boundaries
- functional equivalence
- period of consideration
- considered product systems

The functional unit (FU) is the basis for comparing LCA results. The survey has shown that the FUs are consistent within the studies but differ between studies, as follows:
- m² superstructure.
- m² roadway
- absolute or percentage comparison
- m superstructure.
The differences in the FUs complicates the comparison of different studies, regardless of functional equivalence and system boundaries.

system boundaries
The determination of the spatial and temporal system boundaries makes it possible to limit the system to be considered, in this case the bridge structure, so that concrete results can be obtained.
The spatial system boundaries include different observation areas in the studies carried out. For example, in some studies, the system boundaries are set such that the entire structure falls within the observation space. In other studies, however, the system boundaries are based only on the superstructure, or/and the effects of potential traffic disruptions due to rehabilitation measures are included.
The temporal system boundary allows the system to be divided into specific phases over the life cycle phases in order to identify specific hotspots. Thus, the historical development of the databases shows that more and more detailed life cycle phases could be included in the investigations.

functional equivalence
The definition of functional equivalence according DIN EN 15643-5 is, in which the function is described by the functional equivalence. The functional equivalence describes the quantified functional requirement and/ or technical requirements of an engineering structure or of a assembled component, and serves as a basis for comparisons. [14]

Most studies compared two alternative variants designed for the same conditions and for the same location.

period of consideration
The period under consideration can vary depending on the category of use, the main material or the objective of the study. Within the survey the period of consideration varies between 50 and 200 years. For the use categories, the time periods considered were defined as follows:
- Foot- and Bicycle bridge 50 years
- Railroad bridge: 100 to 120 years
- Highway bridges: 50 to 200 years

considered product systems
Bridge structures are examined in varying detail in the studies within the areas of consideration. Component groups are defined as the umbrella term for the grouping of components that serve similar purposes. The levels of detail differ from study to study. For example, bridge structures are only considered subdivided into the component groups substructure and superstructure (cf. [15]) or more detailed levels of detail are formed (cf. [8,16–18]).

The literature survey has also shown that most LCA studies were conducted for road bridges. And most of the conductions were not always in line with the standards.
Different studies has approved that the materials use in the construction has a variable of environmental impacts (e. g.: [6–10,19]).

3 METHODOLOGY

3.1 LIFE CYCLE ASSESSMENT

Life cycle assessment (LCA) is a methodical approach to assessing the environmental impacts associated with all phases of a construction's life, i.e., from raw material extraction through material processing and use to the end of use stage. The generally applicable standards are specified by the principles and framework in ISO 14040 [20] and the requirements and guidance in ISO 14044 [21]. Applied LCA for the construction sector is specified by EN 15804 [22], in which the framework is related to the building product level, and by EN 15978 [23], in which the framework conditions for assessing the environmental performance of buildings is defined.
The modular structure of the entire life cycle is in accordance to EN 15643: 2021 [24], which includes the production and construction phase (module A), the use phase (module B) and the end-of-life phase (module C).

3.2 LCA FOR FOOT AND BICYCLE BRIDGES

The framework for the conduction of LCA is explained step by step for the calculated bridges. The step of categorisation by main materials use will be skipped within this study.

3.2.1 Use category

In the first step the considered use category is defined. Within this study the considered use category is FBB and

FB and is defined analogously to the recommendations of the *Forschungsgesellschaft für Straßen und Verkehrswesen e. V.*, in which the geometric framework is defined. Accordingly, it is determined that a FB should have a minimum walkway width of 1.80m and a FBB a minimum path width of 2.5m. Figure 1 illustrates the distinction.

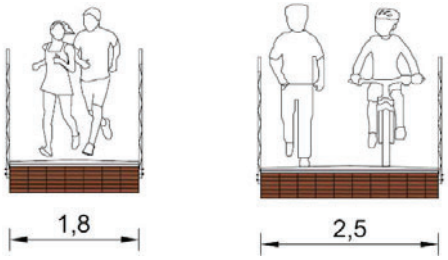

Figure 1: *Minimum path widths accordingly EFA und ERA, a) FB, b) FBB*

3.2.2 Bridge types

The different types of timber bridges which were considered as for foot and bicycle bridges (FBB) are as follows.

Deck bridge (DH): The main girder of the timber deck bridge consists of at least two solid girders and spans the entire bridge cross-section. The deck is attached to the longitudinal girders. The deck can be either waterproof or water-bearing. Depending on the decking, the structural timber protection is designed. [25]

Figure 1: *Example of a deck bridge*

Block girder bridge (BH): A further development of the traditional deck bridge is the timber block girder bridge. The timber block girder is composed of a solid block glued with timber and spans the entire cross-section of the bridge. The entire block cross-section can be used as a roadway, with the roadway itself serving as additional weather protection. Structural timber protection is established by the shape of the cross-section, the overhangs, and adequate air circulation. [25]

Figure 2: *Example of a Block girder bridge*

Through bridge (TH): The main structure of a wooden trough bridge is formed by two main girders and is located between the roadway and the railing at the railing level and is secured against tipping by a stiffening steel to prevent overturning. Structural wood protection is provided by the top cover and lateral cladding of the main girders. main girders. [25]

Figure 3: *Example of a Through bridge*

Pylon bridge (PH): The main component of the load-bearing system of cable-stayed or suspension bridges are pylons. The pylons are used to transfer loads from the superstructure to the substructure via stay cables or via hangers. The superstructure is formed by a bracing girder so that the loads from the deck are distributed to the cables or suspension cables. The stiffening of the superstructure eliminates the need for supporting structures. The types of construction described above are suitable as superstructure. [26]

Figure 4: *Example of a Through bridge*

https://doi.org/10.52202/069179-0128

3.2.3 Period of consideration
Within this study the considered period is 50 years.

3.2.4 Bridge size
The study includes a total of 10 bridges of different size and bridge type. The sizes of the considered bridges are listed in Table 1 and vary between 63 to 288 m².

Table 1: *Bridges and road areas*

Bridge	Road Area [m²]
DH4	69
BH1	288
BH2	68
PH1	114
PH3	146
PH4	125
PH5	141
TH1	85
TH3	63
TH4	169

3.2.5 Considered product systems
Despite the different types of construction, bridges are basically of comparable design and can be divided into main components and subcomponents. In bridge construction, a distinction is made between superstructure, substructure and equipment as main assemblies. Whereby a component group includes components that serve similar purposes.
In the context of this study, the superstructure is considered, which integrates the component group of equipment.

3.2.6 Functional equivalence
As the aim of this study is not to compare but to generate results to create a database the functional equivalence as it is defined is not given. Al considered bridges belong to the use category of foot and bicycle bridge.

3.2.7 Database and calculation program
Since 2013, the dataset Oekobau.dat comply with the standard DIN EN 15804 and includes information on the environmental impact of construction, transportation, energy disposal processes and building materials, enabling life cycle assessment over the entire life cycle.
The results base on Oekobau.dat Version 2020-I.
The calculations were conducted with the R_ENI-LCA Tool. The Tool is explained details in Özdemir [27].

4 RESULTS
The LCA-Results for the indicators GWP and PENRT are shown in Figure 5 and Figure 6.

The Database for the indicator GWP and timber bridges are between 3 and 7 [kg CO2 eq./m²*a]. Whereby the minimum GWP value was calculated for the bridge TH1 and the maximum Value for the bridge PH1.

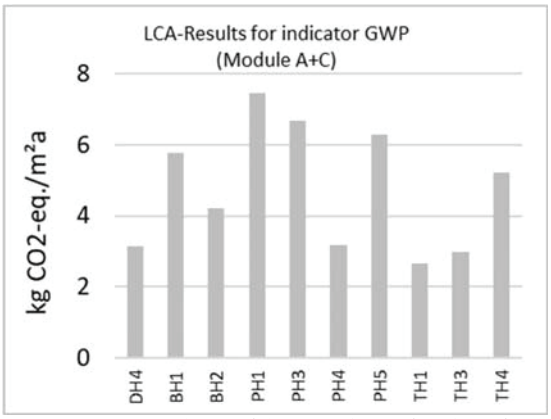

Figure 5: *LCA Results (Module A+C) for Bridges for indicator GWP [27]*

The Database for the indicator PENRT and timber bridges are between 32 and 92 [MJ/m²*a]. Whereby the minimum PENRT value was calculated for the bridge TH1 and the maximum Value for the bridge TH4.

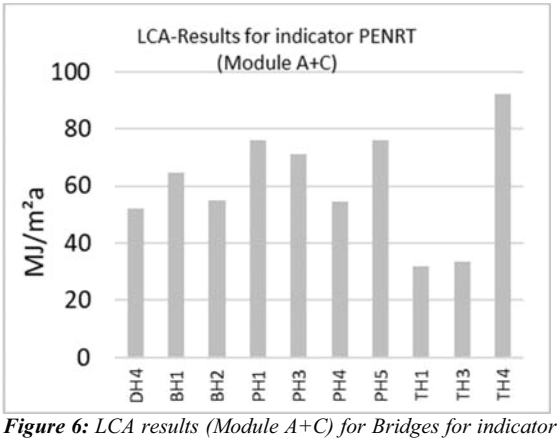

Figure 6: *LCA results (Module A+C) for Bridges for indicator PENRT [27]*

5 CONCLUSIONS
This study considers in detail the environmental impacts of municipal bridge structures, timber FBB, over the entire life cycle. The area of the use category GRB does not play a role in previous research on LCA. The present work forms the basis for further research projects.
An LCA bridge database can assist decision makers in decision making and facilitate the classification of LCA results. In the context of local mobility, foot and bicycle bridges (FBB) play an important role in the regional and local transportation network and focusing on timber bridges here could be an interesting focus for additional climate protection.

Acknowledgement
This paper is an outcome of the PhD thesis [27].

6 References

[1] United Nations. Paris Agreement to the United Nations Framework Convention on Climate Change, Dec. 12, 2015. Paris: United Nations; 2015.

[2] Intergovernmental Panel on Climate Change. Climate Change 2014 - Synthesis Report - Summary for Policymakers: Fifth Assessment Report (AR5); 2014.

[3] Elmqvist T, Fragkias M, Goodness J, Güneralp B, Marcotullio PJ, McDonald RI et al. Urbanization, Biodiversity and Ecosystem Services: Challenges and Opportunities. Dordrecht: Springer Netherlands; 2013.

[4] Seitzinger SP, Svedin U, Crumley CL, Steffen W, Abdullah SA, Alfsen C et al. Planetary stewardship in an urbanizing world: beyond city limits. Ambio 2012;41(8):787–94. https://doi.org/10.1007/s13280-012-0353-7.

[5] European Commission. A Renovation Wave for Europe - greening our buildings, creating jobs, improving lives. COM(2020) 662 final. Communication from the commission to the european parliament, the council, the european economic and social committee and the committee of the regions; Available from: https://eur-lex.europa.eu/legal-content/EN/TXT/HTML/?uri=CELEX:52020DC0662&rid=5.

[6] Horvath A, Hendrickson C. Steel versus Steel-Reinforced Concrete Bridges: Environmental Assessment. Journal of Infrastructure Systems 1998;4(3):111–7. https://doi.org/10.1061/(ASCE)1076-0342(1998)4:3(111).

[7] Widman J. Environmental impact assessment of steel bridges. Journal of Constructional Steel Research 1998;46(1-3):291–3.

[8] Lünser H. Ökobilanzen im Brückenbau: Eine umweltbezogene, ganzheitliche Bewertung. Basel: Birkhäuser Basel; 1998.

[9] Keoleian GA, Kendall A, Dettling JE, Smith VM, Chandler RF, Lepech MD et al. Life Cycle Modeling of Concrete Bridge Design: Comparison of Engineered Cementitious Composite Link Slabs and Conventional Steel Expansion Joints. J. Infrastruct. Syst. 2005;11(1):51–60. https://doi.org/10.1061/(ASCE)1076-0342(2005)11:1(51).

[10] Penadés-Plà V, Martí JV, García-Segura T, Yepes V. Life-Cycle Assessment: A Comparison between Two Optimal Post-Tensioned Concrete Box-Girder Road Bridges. Sustainability 2017;9(10):1864. https://doi.org/10.3390/su9101864.

[11] Itoh Y, Nagata H, Liu C, Nishikawa K. Comparative Study of Optimized and Conventional Bridges: Life Cycle Cost and Environmental Impact. In: Frangopol DM, Furuta H, editors. Life-Cycle Cost Analysis and Design of Civil Infrastructure Systems. Reston, VA: American Society of Civil Engineers; 2000, p. 130–148.

[12] Collings D. An environmental comparison of bridge forms. Proceedings of the Institution of Civil Engineers - Bridge Engineering 2006;159(4):163–8. https://doi.org/10.1680/bren.2006.159.4.163.

[13] Itoh Y, Wada M, Liu C. Lifecycle environmental impact and cost analyses of steel bridge piers with seismic risk. In: Augusti G, editor. Safety and reliability of engineering systems and structures: Proceedings of the Ninth International Conference on Structural Safety and Reliability, ICOSSAR '05, Rome, Italy, 19 - 23 June 2005. Rotterdam: Millpress; 2005, p. 1581–1588.

[14] Deutsches Institut für Normung e. V. Nachhaltigkeit von Bauwerken - Bewertung der Nachhaltigkeit von Gebäuden und Ingenieurbauwerken - Teil 5: Leitfaden zu den Grundsätzen für und den Anforderungen an Ingenieurbauwerke; Deutsche Fassung EN 15643-5:2017;91.040.01(15643-5). Berlin: Beuth Verlag GmbH; 2018.

[15] Mara V, Haghani R, Sagemo A, Strock L, Nilsson D. Comparative study of different bridge concepts based on life-cycle cost analyses and life-cycle assessment. Asia-Pacific Conference on FRP in Structures (APFIS 2013) 2013.

[16] Zinke T, Ummenhofer T, Schneider S, Beck T, Lenz K, Neudeck M et al. Ganzheitliche Analyse von Stahl- und Verbundeisenbahnbrücken. Stahlbau 2017;86(2):112–22. https://doi.org/10.1002/stab.201710458.

[17] Du G, Karoumi R. Environmental life cycle assessment comparison between two bridge types: reinforced concrete bridge and steel composite bridge: 18. - 21.08.2013. Third International

https://doi.org/10.52202/069179-0128

Conference on Sustainable Construction Materials and Technologies 2013.

[18] Hammervold J, Reenaas M, Brattebø H. ETSI Stage 2 - Sub-Project 2: Environmental Effects - Life Cycle Assessment of Bridges. ETSI - Bridge Life Cycle Optimisation - ETSI Stage 2; 2009.

[19] Hafner A, Rüter S, Ebert S, Schäfer S, König H, Cristofaro L et al. Treibhausgasbilanzierung von Holzgebäuden – Umsetzung neuer Anforderungen an Ökobilanzen und Ermittlung empirischer Substitutionsfaktoren (THG-Holzbau): Forschungsprojekt: 28W-B-3-054-01 Waldklimafonds BMEL/BMUB; 2017.

[20] DIN Deutsches Institut für Normung e. V. ISO 14040:2006 + Amd 1:2020, Environmental management - Life cycle assessment - Principles and framework; German version EN ISO 14040:2006 + A1:2020;13.020.10, 13.020.60(14040). Berlin: Beuth Verlag GmbH. https://doi.org/10.31030/3179655.

[21] ISO 14044. ISO 14044:2006 + Amd 1:2017 + Amd 2:2020, Environmental management - Life cycle assessment - Requirements and guidelines; German version EN ISO 14044:2006 + A1:2018 + A2:2020: International Organization for Standardization.

[22] DIN Deutsches Institut für Normung e. V. DIN EN 15804:2020-03, Sustainability of construction works - Environmental product declarations - Core rules for the product category of construction products;91.010.99, 91.040.01(15804). Berlin: Beuth Verlag GmbH. https://doi.org/10.31030/3054172.

[23] DIN Deutsches Institut für Normung e. V. DIN EN 15978:2012-10 Sustainability of construction works - Assessment of environmental performance of buildings - Calculation method; German version EN 15978:2011;91.040.99(15978). Berlin: Beuth Verlag GmbH. https://doi.org/10.31030/1917049.

[24] EN 15643:2021. DIN EN 15643:2021-12 Sustainability of construction works - Framework for assessment of buildings and civil engineering works; German version EN 15643:2021: European Committee for Standardization.

[25] Qualitätsgemeinschaft Holzbrückenbau e.V. (ed.). Entwurf von Holzbrücken. Friolzheim; 2019.

[26] Freundt U. Unterbauten. In: Mehlhorn G, Curbach M, editors. Handbuch Brücken: Entwerfen, Konstruieren, Berechnen, Bauen und Erhalten, 3rd ed. Wiesbaden: Springer Vieweg; 2014, p. 661–685.

[27] Özdemir Ö. Erstellung einer Datenbasis zur Einschätzung der Umweltauswirkungen von Geh- und Radwegbrücken und Entwicklung eines LCA-Tools für Infrastrukturbauwerke. Bochum: Dissertation; 2022.

World Conference on Timber Engineering Oslo 2023

STRUCTURAL AND LIFE CYCLE ANALYSES FOR A TIMBER-CONCRETE HYBRID BUILDING

Xiaoyue Zhang [1], Wanru Huang [2], Mehdi Khajehpour [3], Mehrdad Asgari [4], Thomas Tannert [5],

ABSTRACT: The concerns related to the impact of construction materials are increasing globally. Timber-based hybrid buildings combine the structural benefits of multiple materials, reduce the carbon footprint, shorten construction times, and potentially improve seismic and building physics performances. In this paper, a ten-story timber-concrete hybrid building, designed for a location in the Guizhou Province, China, is compared to a pure concrete building. The structural analysis showed that the self-weight of the hybrid structure was reduced by 30% compared with the concrete structure, and the base shear forces in X- and Y-directions decreased by 43% and 29%, respectively. The life-cycle analysis showed that hybrid building had lower impacts than the concrete building in six categories: global warming potential, acidification potential, human health particulate, eutrophication potential, ozone depletion potential, and photochemical ozone formation potential. Specifically, in terms of global warming potential, the hybrid building had nearly 65% lower emissions, and the wood components have the additional advantage to store carbon over their lifetime. These results promote the development and application of high-rise timber-based hybrid buildings in China.

KEYWORDS: Tall Timber, Hybrid Building, Structural Design, Life Cycle Analysis

1 INTRODUCTION

1.1 BACKGROUND

Timber-concrete hybrid buildings combine the benefits of both materials, specifically the environmental benefits of timber and the fact that concrete is non-combustible. The most common type of tall wood hybrid structures is combining a cast-in-place concrete core that resists the lateral loads, with the timber structure carrying the gravity load [1]. Many feasibility studies have confirmed the significant potential of timber-concrete and timber-steel hybrid systems in terms of structural performance, sustainability, and construction speed [2-5].

Several timber-hybrid buildings have been successfully constructed. The 8-storey LifeCycle Tower ONE has concrete foundations and a concrete core, with glulam columns and hybrid slabs that span up to 9 meters [6]. The world's tallest hybrid wood-based building, the 18-story "Brock Commons" in Vancouver, Canada, features a cast-in-place concrete ground floor and two elevator cores with CLT floors and Glulam columns [7]. The 17 stories of mass-timber superstructure carry all gravity loads, while two concrete cores act as LLRS.

These successful examples illustrate the potential of timber-concrete hybrid buildings in offering a combination of structural and environmental benefits.

1.2 LIFE CYCLE ASSESSMENT

To evaluate the environmental impact of buildings, Life Cycle Assessment (LCA) has been developed to provide an in-depth assessment of the life cycle performances of entire buildings, construction materials, and components, from the "cradle" to the "grave" [8]. Designers use LCA to assess the impact of a building's energy and materials on the environment, systematically integrating the complete life cycle of products to develop sustainable building solutions [9]. LCA allows estimating the environmental impact over the entire lifespan of residential, commercial, and industrial buildings, from resource extraction to land filling and beyond [10].

Numerous previous studies have compared wood to other building materials such as reinforced concrete. For instance, Robertson et al. [11] demonstrated that the environmental impact from the cradle-to-construction site of traditional cast-in-place concrete is higher than that of wood products (hybrid CLT and glulam).

[1] Xiaoyue Zhang, Chongqing University, Chongqing China, xiaoyuezhang@cqu.edu.cn

[2] Wanru Huang, Chongqing University, Chongqing China, 13364030956@163.com

[3] Mehdi Khajehpour, University of Northern British Columbia, Prince George BC Canada

[4] Mehrdad Asgari <masgari@unbc.ca

[5] Thomas Tannert, University of Northern British Columbia, BC Canada, Thomas.Tannert@unbc.ca

https://doi.org/10.52202/069179-0129

Basaglia et al. [12] compared the LCA of three materials (GLT, CLT, and concrete) and showed that the embodied energy of CLT is almost 2.5 times higher than that of concrete. Lu et al. [13] sowed that emissions of engineered wood in the environmental categories of greenhouse gas, acidification, human toxicity, and fission depletion are all low compared to concrete and steel for multi-storey residential buildings. Jayalath et al. [14] assessed the environmental impact of high-rise residential buildings in CLT and showed that the carbon dioxide emissions were reduced by up to 34% compared with reinforced concrete residential buildings. However, there is limited research on LCA for timber-concrete hybrid systems.

1.3 OBJECTIVE

The objective of this research was to promote the development of timber-based hybrid high-rise construction systems in China. To meet this objective, the structural and environmental performance a 10-storey case-study glulam timber frame with concrete core structure is compared to that of a pure concrete building.

1.4 BUILDING DESCRIPTION

A hybrid system composed of wood frames and concrete shear walls for a 10-storey hotel, located in Jianhe County, Guizhou province of China, was designed. The storey height was 3.9 m, for a total building height of 46.4 m to the top of the roof, with a typical story floor area of 924 m^2 (23.1 × 40 m) for a total 10,000 m^2 building area.

The hybrid building, shown in Figure 1a, consisted of a concrete core, concrete base, and a glulam frame system. The first concrete floor is the parking lot, and the upper nine stories consist of mass-timber superstructure, carrying all gravity loads. The concrete core acts as the wind and seismic lateral load-resisting system [15]. The structure was designed in accordance with the structural design codes and technical standards of China. For some connection and component design, i.e., the timber-concrete composite (TCC) beams, Eurocode 5 [16] was used as a reference.

The pure concrete building, illustrated in Figure 1b, also consisted of a concrete core and a concrete base used as the parking lot, but instead of using wood frames for the gravity system, it had a reinforced concrete gravity framing. The design was based on Chinese building code GB50010-2010[17].

2 METHODS

2.1 STRUCTURAL DESIGN

The gravity loads included dead load, live load, and snow load. The total dead load for typical floor (including 100 mm concrete topping, partition load and miscellaneous) was 380 kg/m^2. For the roof, the total dead load was 280 kg/m^2. The live load was 250 kg/m^2, and the roof snow load was 500 kg/m^2, based on the location. All values are typical for Chinese hotels and were obtained from GB 50009-2012 [18]. According to GB50011-2010 [19], the lateral systems were designed for seismic intensity 7 with a basic ground acceleration of 0.1 g for a site class II.

The hybrid model adopted Glulam frames to transfer the gravity loads to the foundation. Grade TC_T21 was used for both girders and columns [15,18]. Based on the vertical loads, the typical column size was 580 × 580 mm. The Glulam girders as the main framing beams span between 9 and 11 m in north-south direction with secondary glulam beams placed on top in east-west direction, see Figure 2. The depth of girders was 580 mm to satisfy the structural clearance requirements. The 290 × 290 mm cross section was selected for the glulam beam girders and 240 × 400 mm cross section was selected for secondary glulam beams, all based on the Chinese timber building design codes GB 50009-2012 [18], GB5005-2017 [20], GB 50206-2012 [21], and GB T 50329 2002 [22].

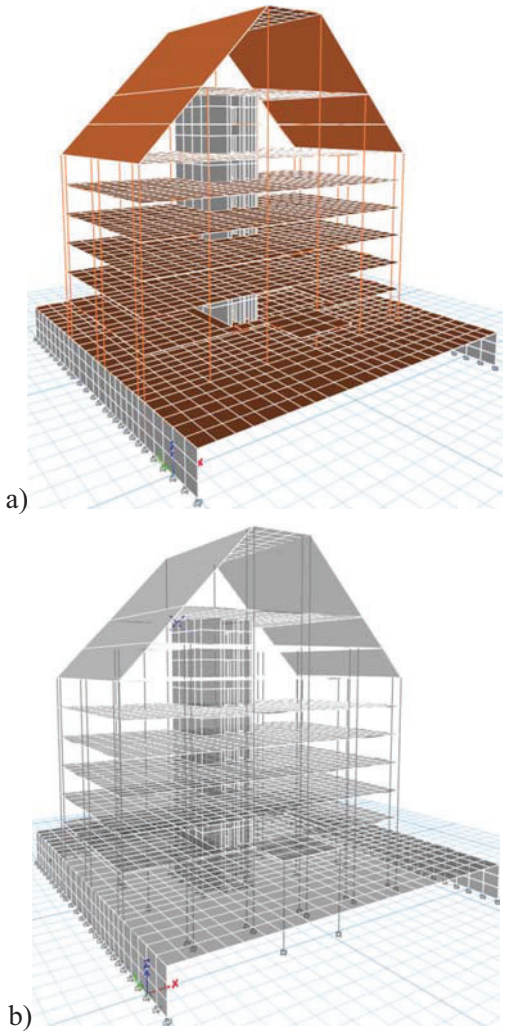

Figure 1: *3D ETABS models: a) hybrid building; b) concrete building*

Figure 2: *Typical floor plan for both buildings*

2.2 STRUCTURAL ANALYSIS

Both buildings were modelled in ETABS [23]. In the hybrid model, the wood frames were used to transfer the gravity loads. The columns were pinned to avoid imposing any lateral stiffness on the lateral load-resisting system. P-Delta effects, which are created from the lateral deflections, were also considered.

The concrete building design was based on GB 50010-2010 [17]. There, concrete slabs and columns transfer the gravity loads, and the slab/beams and columns were connected through a fixed connection. Normal density concrete with a strength grade of C30 was used.

For both models, the main structure (top 9 stories) stands on the underground floor with perimeter retaining walls. The loads coming from the soil pressure were also taken into account and imposed on the retaining walls. The column bases were modelled as pinned to the ground to neglect the stiffness of the base column connections, which is negligible compared to the stiffness of the shear walls. The foundations were composed of strip footing under the columns and perimeter retaining walls, with a slab (pad) footing under the core shear wall.

Regarding the lateral load resisting system, ductile-reinforced concrete shear walls were assigned to both models. In the hybrid model, the walls were put in the middle of the plan as a “core” system to accommodate architectural elements. Concrete slabs on the metal deck, which seats on the wood frames, were modelled to carry the gravity loads, and to act as the diaphragm to transfer the seismic shear to the core shear walls. For the concrete model, the shear walls were optimized along with the reinforced concrete moment frames to transfer the seismic loads.

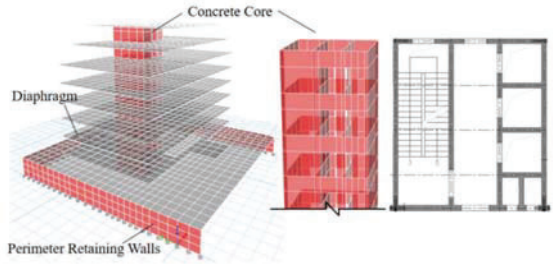

Figure 3: *Lateral Load Resisting System for both models*

2.3 LIFE CYCLE ASSESSMENT

The Athena Impact Estimator for Building (IE4B) [24], an open-source software, was used to assess the environmental impact of both buildings. It can be applied to any type of new construction, renovations, and additions projects in North America.

Athena IE4B contains life cycle inventory (LCI) called the Athena database, or TRACI [25]. LCI is the data collection portion of the LCA [26]. These methods focus on the following impact categories: ozone depletion climate change, acidification, eutrophication, smog formation, and non-renewable energy consumption [27]. The material inputs for LCA came from the building's design blueprints and were included in the Data collection report. 60 years was selected as the service life for a commercial structure. The cradle-to-grave LCA data found within the various LCI databases conform to ISO 14040 standards [28].

To conduct LCA and compare the environmental impact of the hybrid and pure concrete buildings, six impact categories of the TRACI protocol were used. The calculation process is divided into three main parts: (i) estimate of quantities of materials and processes in the building; (ii) estimate of environmental impacts for each material and process; (iii) estimate of the total environmental impact of the building. The scope of this LCA was a cradle-to-grave assessment of the material effect of structure, envelope, and operating energy and water use during 60 years modelled by IE4B [24].

3 RESULTS

3.1 BASE SHEAR COMPARISON

The base shear forces were obtained from the ETABS models based on the seismic provisions of the Chinese code. As shown in Figure 4, the seismic base shear forces for hybrid model (timber-concrete hybrid structure) and concrete model (pure concrete structure) in the X direction are 3,449 kN and 4,716 kN respectively, which is 43% different. The values in the Y direction are 3,084 kN and 3,983 kN, almost 29% different. The lower base shear of the hybrid model shows the efficiency of replacing the concrete framing.

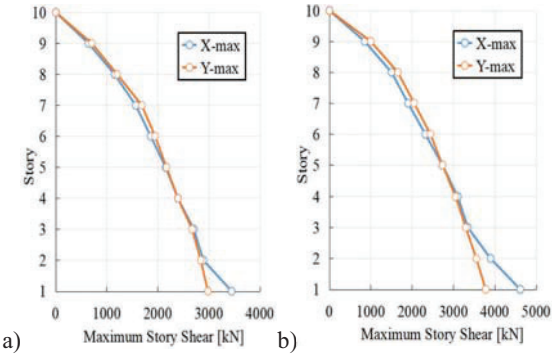

Figure 4: *Storey shear: a) hybrid building; b) concrete building*

https://doi.org/10.52202/069179-0129

3.2 INTER-STORY DRIFT

The current Chinese Code for Seismic Design of Building (GB50011-2010) [19] limits the elastic and elastic-plastic inter-story drift to 1/800 and 1/100, respectively, to limit the damages to the lateral load resisting systems and the non-structural components and sensitive elements of a structure. Figure 5 shows the "elastic" story drifts of hybrid and pure concrete structures, respectively, under the response spectrum in the X direction.

For the real "inelastic" story drifts, these values must be multiplied by the corresponding ductility coefficient of the structure. Since the intention of this article is simply to compare these two systems, we will only consider the elastic story drift ratios. The drift of storey 2 in the hybrid structure is nearly half of that in the pure concrete structure (0.030% versus 0.056%), which were below the drift limit of 1/800. The reason for this large difference is that the weight of the super-structure is much higher in the pure concrete structure.

On the other side, the stiffness of the storey 2 lateral load-resisting system in both buildings is almost the same, since both buildings' shear wall thicknesses are the same. The reason is that, in Chinese concrete code, the shear wall thickness is usually governed by the "minimum" wall thickness based on the level of "ductility" and the height and width of the walls, in other words the geometry. Therefore, both buildings required the same wall thickness. The second main observation is that, for the higher stories, the drift ratios for the pure concrete structure are higher than the hybrid structure, however, this difference is lower, around 25% to 50%.

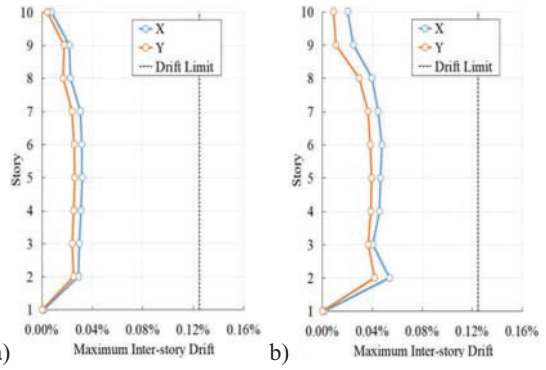

Figure 5: *Maximum story drift in X direction: a) hybrid building; b) concrete building*

3.3 BUILDING MATERIAL INVENTORY

The 10-storey concrete building set the baseline for the Bill of Material (BOM). The BOM of the buildings exported from ETABS includes foundations, columns, beams, floors, and walls. The pure concrete structure consists of a shear wall, concrete slabs, concrete columns and beams, and all the rebars related. On the other hand, the hybrid structure includes a foundation, concrete shear walls, concrete topping of the slab, and glulam beams and columns.

After inputting the BOM of the two buildings, the total mass value of materials used in each building component was computed. As shown in Table 1, replacing concrete frames with wood frames has reduced material consumption. The amount of concrete used in timber-concrete hybrid structure is 5632000 kg, versus 9189000 kg used in the pure concrete structure, which is 40% less. Additionally, the foundation in the hybrid building is only 700 mm thick under the core wall, versus 900 mm thick core wall slab footing under the concrete footing. This will require less excavation and a faster construction procedure. Lower concrete consumption along with the lower base shear has also resulted in less steel reinforcement needed for the composite structure. The hybrid structure only used 39% steel reinforcement of the amount used in the pure concrete structure. This reduction in concrete and steel consumption will have a great impact not only financially, but also in terms of CO_2 emission and environmental effects.

Table 1: *Bill of Material for hybrid and pure concrete building*

Hybrid model			
Materials	Concrete (m^3)	Glulam (m^3)	Steel (kg)
Columns, beams	0	304	0
Floors	1041	1251	26000
Foundation	599	0	16000
Roof	0	0	0
Wall	791	0	35000
Total Volume (m^3)	2431	1555	-
Total Mass (kg)	5632000	727000	77000
Pure concrete model			
Materials	Concrete (m^3)	Glulam (m^3)	Steel (kg)
Columns, beams	210	0	42000
Floors	1933	0	100000
Foundation	889	0	19000
Roof	0	0	0
Wall	791	0	39000
Total Volume (m^3)	3823	0	-
Total Mass (kg)	9189000	0	200000

3.4 LIFE CYCLE ANALYSES

Table 2 shows the comparison of the overall impacts of the two buildings. The hybrid building performs better in all analyzed impact categories. The critical part of these results is the difference in Global Warming Potential (GWP) where the hybrid building has 65% lower value. The tropospheric ozone formation potential (Smog or POCP) value of forest operations is affected by the emissions of a chainsaw, but the wooden material still performs better than concrete with 18.4 kg O_3 eq /m^2 less. Stratospheric Ozone Depletion (ODP) and Acidification Potential of the hybrid building are 9% and 15%, respectively.

Table 2: *Cradle to Grave LCA comparison for two functionally equivalent buildings*

Summary measure	Hybrid building	Concrete building
Global warming potential (kg CO_2 eq)	1.79E+06	6.26E+05
Stratospheric ozone depletion (kg CFC-11 eq)	1.58E-02	1.44E-02
Acidification potential (kg SO_2 eq)	8.76E+03	7.42E+03
Eutrophication (kg N eq)	8.02E+02	7.01E+02
Tropospheri ozone formation (kg O_3 eq)	1.84E+05	1.48E+05
Depletion of non-renewable energy resources (MJ)	1.66E+07	1.25E+07

Figure 6 displays the percentage contributions of the building components to six environmental impact categories using LCA results. For the concrete building, the foundation which was the second most concrete and the floor and roof which was primarily concrete by volume contributed approximately 50% of the building material. Similarly, the timber-concrete hybrid building was separated into the same components, except that the mass-timber superstructure, responsible for carrying all gravity loads, rested on a concrete core that acted as both the wind and seismic lateral load-resisting systems.

The environmental impact indicators for both buildings were primarily attributed to the floors and roof, with roughly 50% impact in all categories, except for Global Warming Potential (GWP), which had a lower emission rate of 15% in the hybrid building due to the use of mass timber. As a result, the GWP was reduced by 35% in the timber-concrete building. In the pure concrete structure, the foundation was responsible for the second-highest emission portion, with 23% in Ozone Depletion Potential (ODP), 22% in Acidification Potential (AP), Human Health (HH) potential, Eutrophication Potential, and 21% in Smog Potential. However, the foundation's contribution decreased to approximately 17% in the timber-concrete hybrid building, while it remained the second-highest emitter in GWP with 42%. Shear walls had similar emissions in both buildings, with approximately 21% in the concrete structure and around 22%, except for GWP with 57%, in the hybrid building. The columns and beams had the lowest contribution to environmental impact, with approximately 7% in the pure concrete building and around 6% in the hybrid building. However, this decreased to -14% in GWP due to the glulam material used.

Overall, the use of timber in the hybrid building results in a lower environmental impact across all indicators, especially in terms of GWP. The environmental emissions of the hybrid building are improved by incorporating TCC floors, replacing the traditional cast-in-place concrete floors. As a result, the GWP of a 10-story timber-concrete hybrid building is estimated to be reduced by approximately 35%.

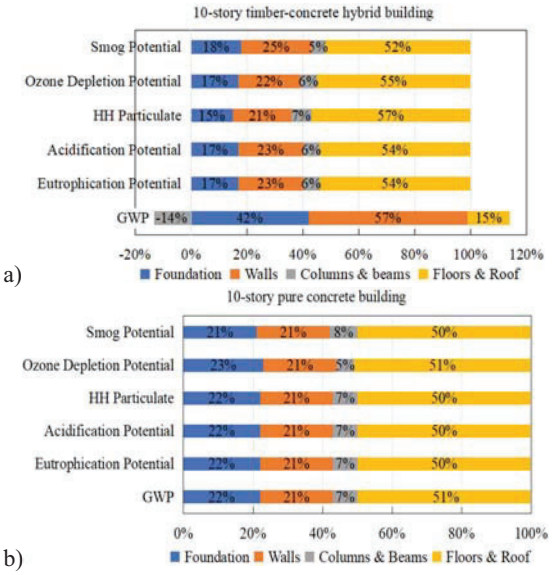

Figure 6: *Percentage of contribution to environmental impact category: a) hybrid building; b) concrete building*

Figure 7 presents the emissions of concrete and mass timber buildings separated by life-cycle stage for the categories of GWP, acidification potential, human health particulate, eutrophication potential, ozone depletion potential, smog potential, and total primary energy. The A1-A3 stage contributed 88% and 87% of the total GWP emissions for concrete and mass timber buildings, respectively. The construction (A4 and A5) and end-of-life (C) stages contributed more to the total emissions of the hybrid buildings than the concrete building. In addition to GWP, ozone depletion potential, and human health particulate, eutrophication potential has a significant environmental impact on both buildings, with total eutrophication potential emissions of 829 and 712 kgN eq for pure concrete and timber-concrete hybrid buildings, respectively, of which 80% and 84% are attributed to the production stage (A1-A3).

The beyond-life considerations are difficult to predict decades into the future. For mass timber buildings, the GWP impact category can be highly influenced by the beyond-building life stage (D) and how carbon emissions are accounted for. Figure 8 studies the beyond-building life emissions (stage D), including the biogenic carbon of the mass timber buildings. The results show that the amount of sequestered carbon for the hybrid building, stage A-D, is significantly lower than the total amount of embodied carbon for stages A-C. It should be noted that this study does not include the contributions of non-structural interior building components, such as partition walls, carpeting, windows, etc. Therefore, the timber-concrete hybrid building has a significantly lower environmental impact than the concrete structure, mainly due to the much smaller amount of sequestered carbon related to the timber-concrete hybrid building.

https://doi.org/10.52202/069179-0129

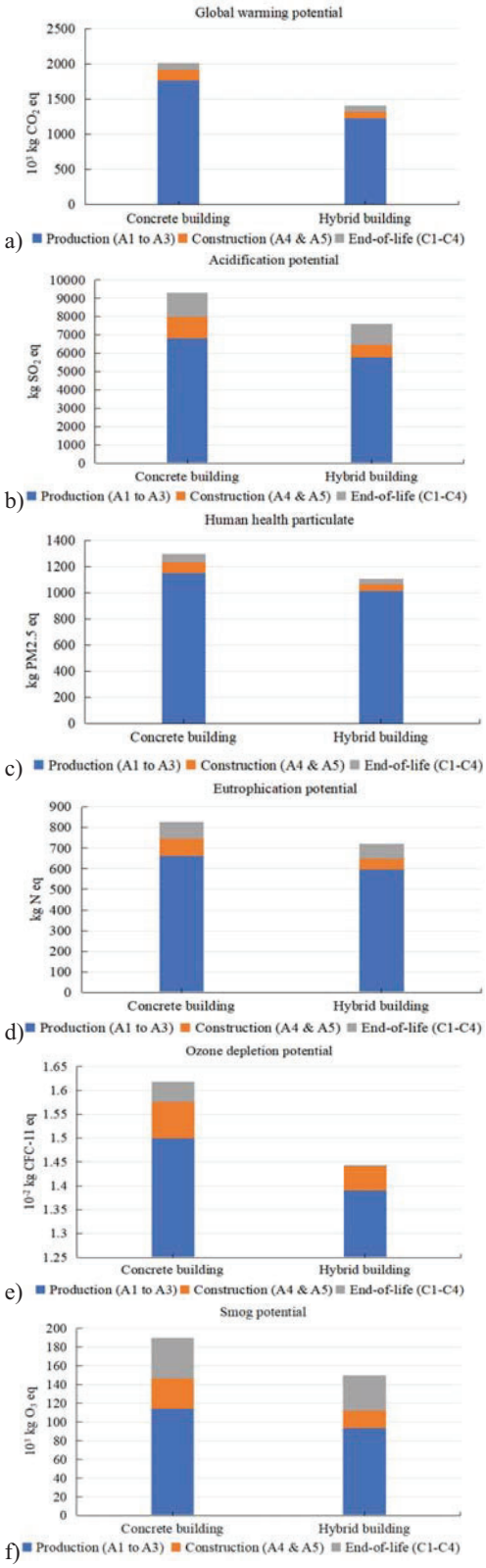

Figure 7: *LCA environmental impact data: a) GWP; b) AP; c) HH; d) EP; e) ODP; f) Smog*

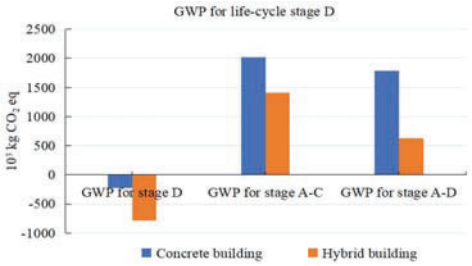

Figure 8: *LCA global warming potential for life-cycle stage D*

4 CONCLUSIONS

The structural and environmental performance of two ten-storey buildings with different frames was compared: one with a wood frame and the other with a concrete frame. The following main conclusions were drawn:

1) Using wood in the hybrid building led to a significant reduction in weight of about 30%. Additionally, the hybrid building had superior seismic performance, which reduced foundation requirements, resulting in time and cost savings. The maximum inter-storey drift in the hybrid structure was almost half that of the all-concrete structure, which was below the drift limit of 1/800.

The LCA results indicated that the hybrid building had favourable values for all categories considered, such as global warming potential, stratospheric ozone depletion, acidification potential, eutrophication, smog potential, human health particulate, non-renewable energy consumption, fossil fuel consumption, and total primary energy consumption. The hybrid building emitted nearly 65% less CO_2, and the wooden components acted as carbon storage for its entire lifetime.

Based on the structural and environmental performance of the hybrid building, this study can serve as a useful guide for the design of timber-based hybrid high-rises in China. The results demonstrate the benefits of using wood in construction, including reduced weight and improved seismic performance, which can save on foundation requirements, time, and cost. Moreover, the significant reduction in CO2 emissions and the carbon storage potential of wooden components in hybrid structures can contribute to mitigating the effects of climate change.

ACKNOWLEDGEMENT

The authors also would like to thank the National Natural Science Foundation of China (Grant Nos. 52108192); China Postdoctoral Science Foundation (Grant Nos. 2022M710528); The Chongqing Technology Innovation and Application Development Project (CSTB2022TIAD-KPX0138); the OEICDI fund (Grant Nos. B13041); the Entrepreneurship and Innovation Support Program for Overseas-educated student in Chongqing China (Grant Nos. CX2021085).

REFERENCES

[1] Poirier, E., Moudgil, M., Fallahi, A., Staub-French, S., & Tannert, T. (2016). Design and construction of a 53-meter-tall timber building at the University of British Columbia. Proceedings of WCTE.

[2] Minjuan, H., Duo, T., and Zheng, L. (2016). Research progress of multi-story and high-rise timber and timber hybrid structures. Journal of Building Structures, 37(10), 1-9.

[3] Zhang, X., Azim, M. R., Bhat, P., Popovski, M., and Tannert, T. (2017). Seismic performance of embedded steel beam connection in cross-laminated timber panels for tall-wood hybrid system. Canadian Journal of Civil Engineering, 44(8), 611-618.

[4] Dias, A. M. P. G., Skinner, J., Crews, K., and Tannert, T. (2016). Timber-concrete-composites increasing the use of timber in construction. European Journal of Wood and Wood Products, 74, 443-451.

[5] Pan, Y., Tannert, T., Kaushik, K., Xiong, H., & Ventura, C. E. (2021). Seismic performance of a proposed wood-concrete hybrid system for high-rise buildings. Engineering Structures, 238, 112194.

[6] M. Zangerl and N. Tahan, "LCT ONE," Wood design & building, Vols. Winter 2012-13, 2012.

[7] Connolly, T., Loss, C., Iqbal, A., and Tannert, T. (2018). Feasibility study of mass-timber cores for the UBC tall wood building. Buildings, 8(8), 98.

[8] Curran, M. A. (Ed.). (2012). Life cycle assessment handbook: a guide for environmentally sustainable products. John Wiley & Sons.

[9] Sharma, A., Saxena, A., Sethi, M., and Shree, V. (2011). Life cycle assessment of buildings: a review. Renewable and Sustainable Energy Reviews, 15(1), 871-875.

[10] Hernandez, P., Oregi, X., Longo, S., and Cellura, M. (2019). Life-cycle assessment of buildings. In Handbook of Energy Efficiency in Buildings (pp. 207-261). Butterworth-Heinemann.

[11] Robertson, A. B., Lam, F. C., and Cole, R. J. (2012). A comparative cradle-to-gate life cycle assessment of mid-rise office building construction alternatives: Laminated timber or reinforced concrete. Buildings, 2(3), 245-270.

[12] Basaglia, B., Lewis, K., Shrestha, R., and Crews, K. (2015). A comparative life cycle assessment approach of two innovative long span timber floors with its reinforced concrete equivalent in an Australian context.

[13] Lu, H. R., El Hanandeh, A., and Gilbert, B. P. (2017). A comparative life cycle study of alternative materials for Australian multi-storey apartment building frame constructions: Environmental and economic perspective. Journal of cleaner production, 166, 458-473.

[14] Jayalath, A., Navaratnam, S., Ngo, T., Mendis, P., Hewson, N., and Aye, L. (2020). Life cycle performance of Cross Laminated Timber mid-rise residential buildings in Australia. Energy and Buildings, 223, 110091.

[15] Zhang, X., Xuan, L., Huang, W., Yuan, L., and Li, P. (2022). Structural Design and Analysis for a Timber-Concrete Hybrid Building. Advanced Concretes and Their Structural Applications. doi: 10.3389/fmats.2022.844398.

[16] Steer, P. J. (2001, November). EN1995 Eurocode 5: Design of timber structures. In Proceedings of the Institution of Civil Engineers-Civil Engineering (Vol. 144, No. 6, pp. 39-43). Thomas Telford Ltd. doi:10.1680/cien.2001.144.6.39.

[17] GB 50010-2010 Code for Design of Concrete Structures (2015). National Standards of the People's Republic of China, Ministry of Construction, PRC. Beijing: China Building Industry Press.

[18] GB 50009-2012 Load code for the design of building structures (2012). National Standards of the People's Republic of China, Ministry of Construction, PRC. Beijing: China Building Industry Press.

[19] GB50011-2010 Code for Seismic Design of Buildings (2016). National Standards of the People's Republic of China, Ministry of Construction, PRC. Beijing: China Building Industry Press.

[20] GB5005-2017: Standard for design of timber structures (2017). National Standards of the People's Republic of China, Ministry of Construction, PRC. Beijing: China Building Industry Press.

[21] GB 50206-2012 Code for construction quality acceptance of timber structures (2012). National Standards of the People's Republic of China, Ministry of Construction, PRC. Beijing: China Building Industry Press.

[22] GB T 50329 2002 (2002). Technical Standard for Methods Testing of Timber Structures . Beijing: China Building Industry Press.

[23] Guleria, A. (2014). Structural analysis of a multi-storeyed building using ETABS for different plan configurations. Int. J. Eng. Res. Technol, 3(5), 1481-1485.

[24] Athena Sustainable Materials Institute, 2018a. LCA, LCI, LCIA, LCC: what's the difference? http://www.athenasmi.org.

[25] Wu, T., Gong, M., and Xiao, J. (2020). Preliminary sensitivity study on an life cycle assessment (LCA) tool via assessing a hybrid timber building. Journal of Bioresources and Bioproducts, 5(2), 108-113. doi: 10.1016/j.jobab.2020.04.004.

[26] Athena Sustainable Materials Institute, 2018b. LCI database. http://www.athenasmi.org/

[27] Bare, J. C. (2002). TRACI: The tool for the reduction and assessment of chemical and other environmental impacts. Journal of industrial ecology, 6(3-4), 49-78. doi: 10.1162/108819802766269539.

[28] Geneva, S. (2006). Environmental Management–Life Cycle Assessment–Principles and Framework. ISO, 14040, 2006.

https://doi.org/10.52202/069179-0129

World Conference on Timber Engineering Oslo 2023

EVALUATION OF THE RECYCLABILITY OF WOODEN BEAM STRUCTURES

Zsofia Varga.[1], Antonia Birkholz[2], Anna Wagner[3] Stefan Winter,[4]

ABSTRACT: The aim of this paper is to present a methodology for increasing the material recyclability of wooden beam structures. The methodology was developed as part of a research project in which the deconstructability of wooden beam structures of agricultural halls was investigated. The load bearing structure of six agricultural halls was documented and the connection points of their main structure were evaluated with regard to their recyclability. In the following, it will be investigated to what extent the choice of fasteners is relevant with regard to the recyclability of the timber. For further development the methodology could be applied to other beam structures such as roof trusses or a combination of plates and beam structures such as wood panel construction.

KEYWORDS: recycling, reuse, wood, material recycling, material utilization, deconstruction

1 INTRODUCTION

The increasing scarcity of resources and augmenting material costs are leading to a rethinking in the construction industry.
The aim of the German Resource Efficiency Program (ProgGressIII), which serves to implement the German sustainability strategy, is to identify ways of using resources sparingly and thus reducing the burden on the environment. One measure is to promote the use of renewable raw materials such as timber from sustainable forestry as a construction product. [1]
Timber as a construction material serves as a carbon store and should be kept in the material cycle for as long as possible, which is why reusing timber is in line with the German resource efficiency program. To keep the timber in the material cycle for as long as possible is necessary to not only extend one material life cycle for as long as possible, but also to use the wooden resource in cascades which means to reuse, recycle or utilize material substitution. Due to photosynthesis, timber stores CO_2 during the growth of the tree, which is why it is called a carbon reservoir. After the timber has been used to generate energy, the CO_2 is released back into the atmosphere. Therefore, the goal should be to keep timber in the material cycle for as long as possible in the form of cascade utilization. This means that the timber should be downcycled in another form. For example, a beam can be processed into a wooden slat and then into a chipboard.[2]

The research project is about developing a concept for design for reuse and recycling of the hall supporting structures made of timber. This should enable reuse, re-utilisation and thus a cascade use of timber. The aim is the renewal and extension of conceptual methods for the investigation of life cycle processes of bar supporting structures made of timber.
Reuse means that the timber beam can be used again in the same way as a beam in a new supporting structure. [3]
Recovery means that the beam can be used materially for the same application (equivalent material recovery) [4] or be downcycled, e.g. in the form of a chipboard, final material recovered or final energetical recovered as firewood [5].
According to [6] the reuse of timber components depends mainly on their installation situation and on the type of fastener used to join the components. In the case of detachable connections, disassembly is mostly possible in a non-destructive manner [6]. The choice of fasteners should be considered at the very beginning of the design of timber structures. The fasteners should be easy to find, accessible, and detachable with standard tools. Also, as few nail and adhesive connections as necessary should be used to promote non-destructive disassembly. [6]
In principle, as few and similar fasteners as possible should be used. In this way, faster dismantling is possible. In addition, there is less damage to the assembled components. By using similar, uniform fasteners, there is no need to change tools, which would otherwise slow down the dismantling process. The dismantling effort is

[1]Zsofia Varga, Research Associate, Technical University Munich, Chair for Timber Structures and Building Construction, Arcisstraße 21, D-80333 München. Email: zsofia.varga@tum.de
[2] Antonia Birkholz, former Research Assistant, Technical University Munich, Chair for Timber Structures and Building Construction, Arcisstraße 21, D-80333 München. Email: antonia.birkholz@web.de
[3] Anna Wagner, Research Associate, Technical University Munich, Chair for Timber Structures and Building Construction, Arcisstraße 21, D-80333 München. Email: anna.wagner@tum.de
[4] Stefan Winter, Professor, Technical University Munich, Chair for Timber Structures and Building Construction, Arcisstraße 21, D-80333 München. Email: winter@tum.de

https://doi.org/10.52202/069179-0130

reduced and disassembly is faster, which reduces costs. To ensure rapid deconstruction, the fasteners should be easily identifiable and accessible even after the planned service life. [3] It is important to detach the fasteners after service life, because sometimes the building is be used longer then its planned service life.

The ongoing research project „*Entwicklung zukunftsweisender Konzepte zum landwirtschaftlichen Bauen mit Holz - von der Planung bis zum Rückbau (ZukunftLaWiBau)*“ is intended to give farmers the opportunity to take timber from their own forest and use it as building material for their agricultural halls. At the end of their life cycle, it should be possible to dismantle the halls as efficiently as possible, while leaving as much running meter of undisturbed timber as possible. Thus, farmers should be given the opportunity to use their timber for other purposes.

In the following, a methodology developed to evaluate and to increase the material recyclability of wooden hall structures is presented.

2 BACKGROUND AND METHOD

To apply the method, six agricultural halls made of timber with span widths equal to the modular construction hall shown in Figure 1 Figure 6[7], were inspected. The beam structures of the halls consist of solid timber wood, glued laminated timber and steel fasteners. The foundations are made of reinforced concrete. An as-built survey helped to identify and to record the dimensions as well as the type of detail points of the main supporting structures.

Further, the inspection and documentation of the detail points helped to find out in which way and by using which fasteners the detail points have been assembled. Based on the results of the as-built survey, the **equivalent material recovery** of the timber structures could be determined. The detail points were assessed in terms of their **deconstructability**. To do so, a ranking of the fasteners of each detail point was carried out, and the results were included in a detail catalogue. Based on this, a methodology could be developed to increase the recyclability of timber structures.

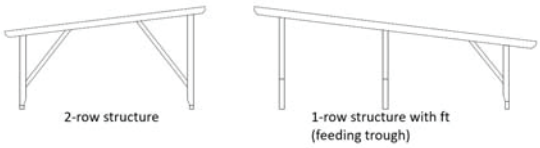

Figure 1: *Profile modular construction hall, Modulbausystem Grub-Weihenstephan according to [7]*

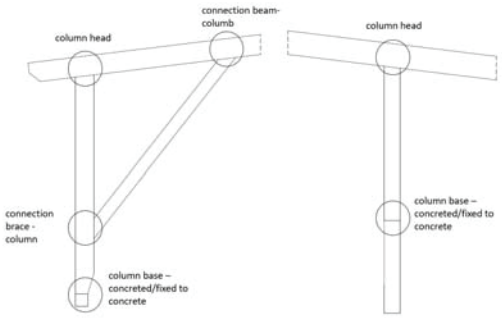

Figure 2: *Considered detail points of main structure*

2.1 EQUIVALENT MATERIAL RECOVERY OF THE TIMBER

By equivalent material recovery amount of recyclable material within one wooden beam is meant after the areas affected by fasteners would have to be cut out by a saw in the worst case. It is being assumed that the saw cut is made with the maximum necessary edge distance to the fastener. The edge distances were determined according to DIN EN 1995-1-1/NA:2013-08, p.45 ff.; DIN EN 1995-1, p.78ff [8]

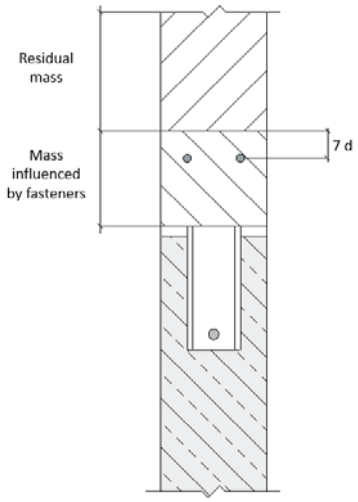

Figure 3: *detail column base, connection wood-concrete*

2.2 DECONSTRUCTABILITY

In addition to the equivalent material recovery, the evaluation of the fastener regarding fast deconstruction was carried out in terms of removability, accessibility and recognizability, because these aspects ensure fast deconstruction according to [5].

https://doi.org/10.52202/069179-0130

Table 1: *definition and evaluation of removability according to DIN 8593-0 [9]*

	removability sign	evaluation
without damage	+	(3)
with (sufficiently) low damage	0	(2)
with damage	-	(1)

For the evaluation of the removability, the recycling tool of the research project *Ressourcennutzung Gebäude* [10] was used and modified. (Table 1)
A subdivision was made according to the accessibility of the detail points and the fasteners.

Table 2: *definition and evaluation of the accessibility of the detail points according to VDI 2243[5]*

		accessibility sign
directly accessible	no optimization necessary	+
indirectly accessible	improve possible disassembly depth	0
not accessible	check modification for axial accessibility	-

The evaluation of the accessibility of the detail points was neglected, because in a hall structure all detail points are accessible with a ladder. (Table 2)
The accessibility of the fasteners was evaluated according to VDI 2243. [5] The shortcut F stands for fastener

Table 3: *definition and evaluation of the accessibility of the fasteners according to VDI 2243[5]*

		sign	fastener	accessibility of the fastener element
directly accessible	no optimization necessary	F +		
Indirectly accessible	improve possible disassembly depth check modification for axial accessibility	F 0	slotted-in steel plate	when fish plate removable
not accessible		F -	hidden slotted-in steel plate, split ring	completely hidden by the element

The third evaluation was made according to the recognizability of the connecting means. The definition of recognizability of the connecting means of the bar supporting structures is based on VDI 2243 [5].

Table 4: *definition and evaluation of the recognizability of the fasteners according to VDI 2243[5]*

		sign	Recognizability of the fastener
definitely visible	No optimization necessary	R +	fastener carpenter joints
Not visible, but with indication	Provide labeling	R 0	slotted-in steel plate
Not visible, no indication	Provide notice and labeling	R -	split ring

The recognizability of the fasteners was evaluated according to VDI 2243 [5]. The shortcut (R) stands for recognizability. The *slotted-in steel plate* was defined as not visible, but with indication (R0), since it was hidden by the timber structure on the outside as an internal fastener, but the bar dowels give an indication of it from the outside. *Split ring* was considered to be a non-findable fastener (R-). The fastener is *not directly visible*, only after removing the timber structure. There is also no indication

of the fastener. All other fasteners, as well as *carpenter joints* were defined as definitely visible (R+), because the type of the fastener is definitely visible.

3 EVALUATION METHOD

3.1 EVALUATION OF EQUIVALENT MATERIAL RECOVERY

To evaluate the part of a wooden beam structures, which could be equivalent material recovered, it was necessary to determine how much additional timber, potentially damaged, had to be removed by a saw in the area influenced by the fasteners.
For example, if the fasteners cannot be removed due to aging, such as rust, or there are other reasons, the fasteners can be cut out with a saw. In this way, a wooden beam is obtained which can be equivalent material recovered. The remaining material around the fastener can be further processed and be recycled. Sawing out the fasteners is possible in this case of the bar structure, since it is not a flat component consisting of several layers.

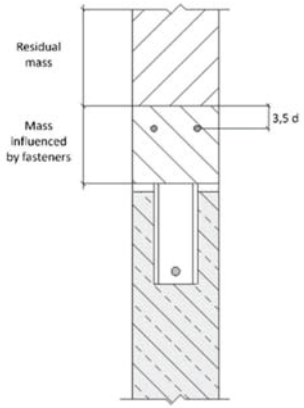

Figure 4: *detail column base, connection wood-concrete*

3.2 DECONSTRUCTABILITY, EVALUATION OF THE FASTENERS

The evaluation method should be shown as an example on Figure 5.

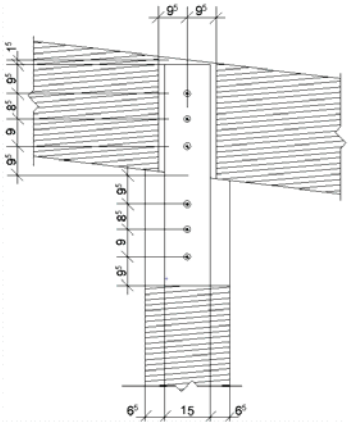

Figure 5: *Detail column head-beam: bracket + fully threaded screw*

First, the individual joints of the components and fasteners were evaluated among themselves. For this purpose, the individual components and fasteners that come into contact with each other were compared in a table. Based on the documented detail point, the removability of the layers was evaluated with numbers (Figure 5) (+ (3); 0 (2); - (1)) and divided by the maximum possible scoring combination ((3) for each joint). Thus, the percentage evaluation of the removability of the detail point was obtained. (Figure 6)

Table 5: *definition and evaluation of the removability of fastener according to [11]*

	removability of the fastener
	sign
without damage removable	+
removable with sufficiently low damage	0
with damage removable	-

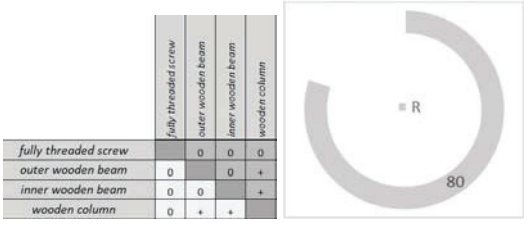

Figure 6: *removability of the layers, Graphical evaluation of removability*

https://doi.org/10.52202/069179-0130

4 EVALUATION OF THE AGRICULTURAL HALLS

As both detail points, the column head and the connection beam column, are constructed in the same way with the same fasteners (Figure 2), the removability of the column head is the same.
Therefore, the faster deconstruction of the detail points

1. column base
2. connection beam-columb
3. column head

is discussed below. Since all detail points of the 2-row structure are represented in the 1-row structure, only the 1-row structure is considered in the following. (Figure 1)

4.1 EQUIVALENT MATERIAL RECOVERY OF THE TIMBER

In order to determine the equivalent material recovery of the timber, the amount and the type of fasteners were calculated and dimensioned for the load case of the worst load case. A sensitivity analysis was carried out to find out to what extent the choice of fasteners plays a role for the equivalent material recovery of the timber or if deconstruction of the fasteners plays a neglectable role.

For this purpose, the main structure was divided into different areas. Their beginning and end were delimited by the detail points (DP). The sections were named according to their location; *apex column* (*AC*), *center column (CC)*, *eaves column (EC)*, *eaves brace (EB)*, *apex brace (AB)*). The beam (B) was divided into five sections (B1-B5). (Figure 7)

The aim was to find out to what extent the choice of fasteners has an influence on the length of the timber components after the removal of the areas affected by the fasteners. For this purpose, the distances between the fasteners were determined for the respective structural members according to the standard. [8]
The minimum edge distances for the worst case to remove the fasteners were calculated.

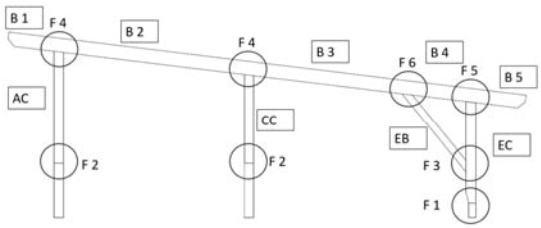

Figure 7: *1-row feeding trough (ft) structure: overview elements and detail points*

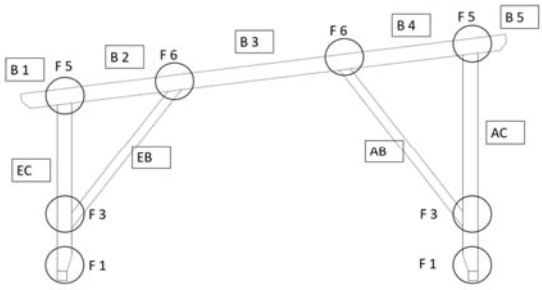

Figure 8: 2-row structure: elements and detail points

The shortcuts for the fasteners are listed in Table 6 and Table 7:

Table 6:*acronyms for different fasteners*

fastener	acronym
slotted-in steel plate	SP
split ring	SR
staggered joint	SJ
pin	P
fully threaded screw	FS
ear	E
U-steel profil	U
Steel profil	S
steel dowel pin	DP
staggered joint	SJ

Table 7: *Overview of possible combinations within one detail point (F)*

F1	F2	F3	F4	F5	F6
SP	SR + P +S	SJ+P	SP +DP	SR + P +E	E+FS
U+ SR	SP	SP +DP	SR + P	SR + P	SR +P+E
S+SP+DP	U+SR		SR +P+E		
	E+FS	SR + P			

In (Figure 9-Figure 11) the remaining lengths after cutting out the areas of the connection points for the different variants are compared to the initial length. It was found out, that there was no fastener which was responsible for cutting the less wood out. When comparing the different variants, only one recommendation can be made for the choice of the connection means of column base (F1 and F2) (Figure 9 and Figure 10) and the connection eaves column bottom (F3) (Figure 11). For this detail points following fasteners should be taken, so that the smallest area is cut off from the supports around the fasteners: F1:S+SP+SD/ SP, F2:SP and F3:SJ +P. By choosing these fasteners, the maximal length of the beams could be achieved.
The highlighted dark beams indicate the maximum and minimum, respectively, after cutting out the fasteners.

https://doi.org/10.52202/069179-0130

The empty frame indicates the original length of the beam. The shortcut F stands for the fasteners in the respective detail points. Figure 7

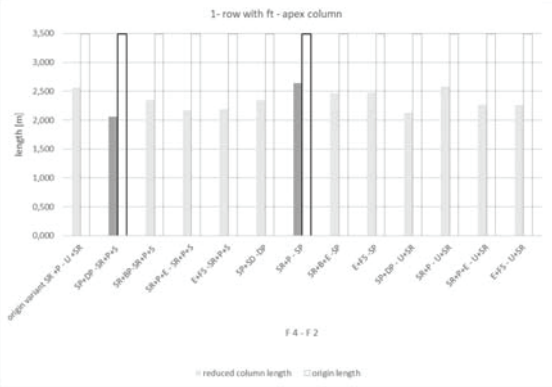

Figure 9:*1-row ft structure - apex column*

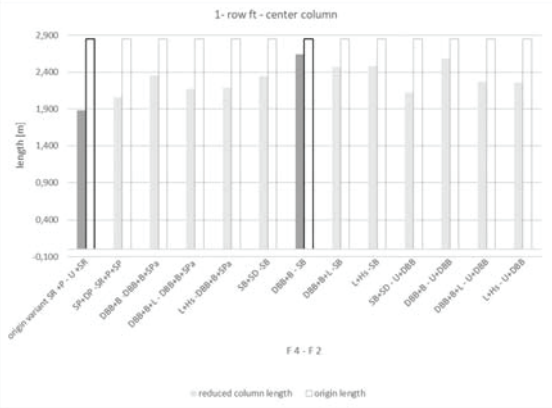

Figure 10:*1-row ft structure - center column*

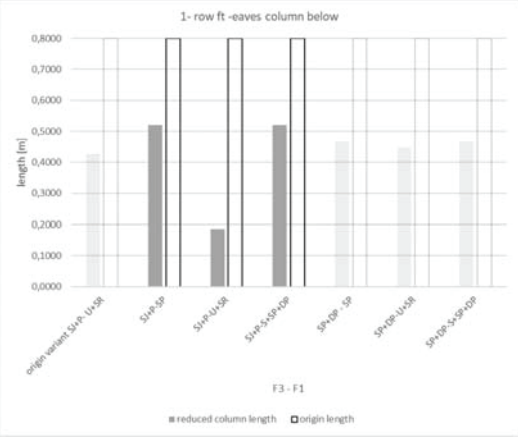

Figure 11: *1-row ft structure – eaves column bottom*

In all three cases, the variant with staggered joint and dowel pins has led to more residual length of the column, regardless of whether or not the staggered joint was concreted into the column base or the one attached to the concrete column. (Figure 11 and Figure 12)

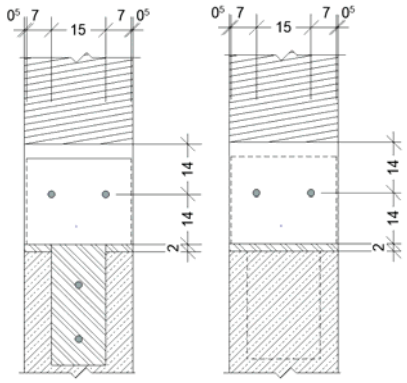

Figure 12: *slotted-in steel plate und dowel pins fixed on concrete column(le.) slotted-in steel plate und dowel pins, Steel profile set in concrete in support (ri.), F2*

For the fastener F, pin *eaves diagonal-eaves column*, the staggered joint and pin performed best in terms of the amount to be cut off and is preferable to the fixation slotted-in steel plate and dowel pins .(Figure 13)

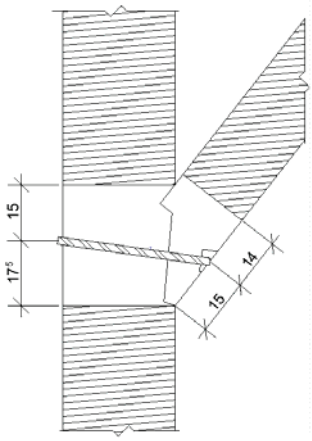

Figure 13: *staggered joint and pin, F3*

The evaluations of the detail point are shown in Figure 14-Figure 16

https://doi.org/10.52202/069179-0130

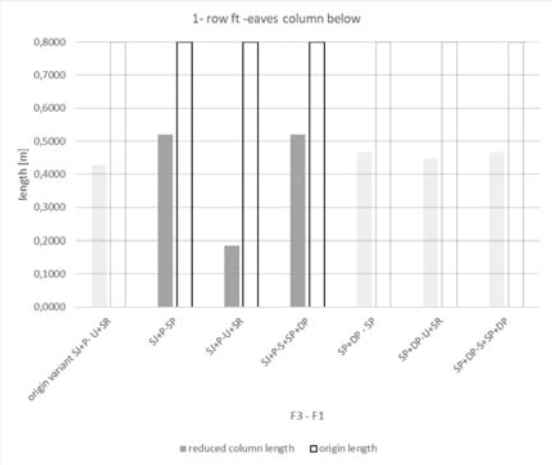

Figure 14: *1-row FT structure – eaves column, bottom*

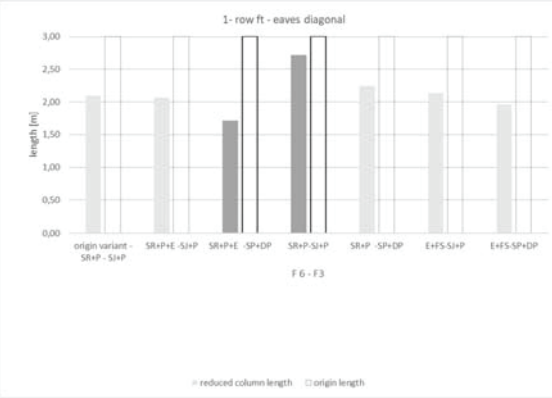

Figure 15: *1-row FT structure – eaves diagonal*

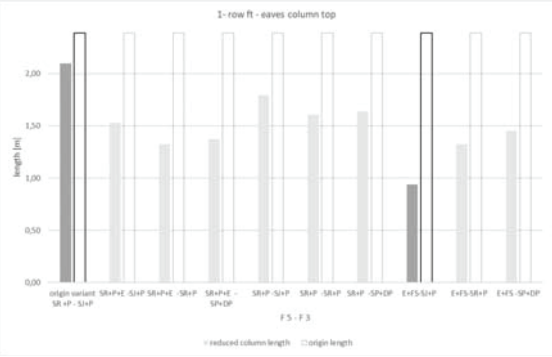

Figure 16: *1-row ft structure – eaves column top*

For the fasteners connecting the columns/diagonals to the beams, always different fasteners performed best or worst, depending on the combination.
The choice of fastener does not seem to have a significant influence on reusability.

4.2 FAST DECONSTRUCTABILITY

Since all fasteners are accessible with a ladder and, in the case of agricultural sheds, the structural components are generally not cladded, an evaluation with regard to recognizability and accessibility is neglected. The classification of fasteners according to their accessibility and recognizability was already conducted in chapter 3.1 and could easily be applied to all considered connections. Only the removability of the fasteners will be considered in more detail.
Of the variants identified, the fasteners for the best possible removability of the detail points are presented:

4.2.1 Column base

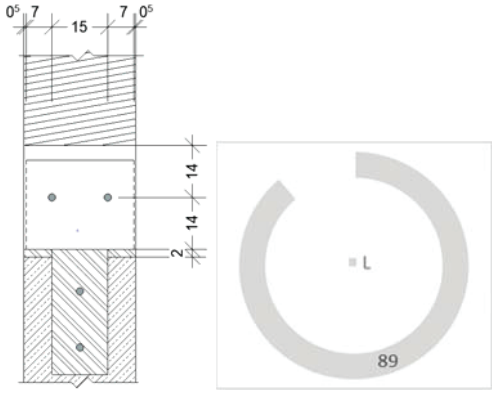

Figure 17: *slotted-in steel plate laterally fixed to concrete (left), removability [%] (right)*

The highest removability of 89% was achieved for the detail column base by the fastener alternatives *slotted-in steel plate laterally fixed to concrete.* (Figure 17)

4.2.2 connection brace – column

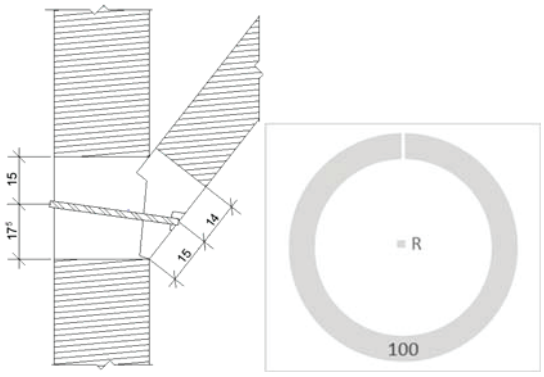

Figure 18: *staggered joint and pin (left), removability [%] (right)*

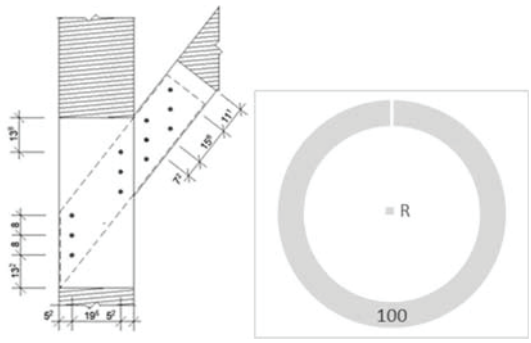

Figure 19: *slotted-in steel plate und dowel pins (left), removability [%] (right)*

The highest removability with 100% was achieved for the connection brace-column fastener alternatives *staggered joint and pin* and *slotted-in steel plate and bar dowels.(*Figure 18-Figure 19)

4.2.3 Connection column head

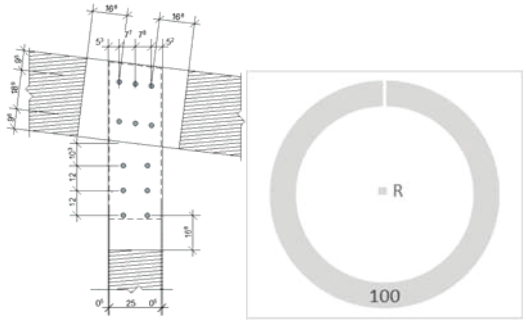

Figure 20: *slotted-in steel plate and dowel pins (left), removability [%] (right)*

The highest removability of 100% for the detail column head fastener alternatives had *slotted-in steel plate and dowel pins.* (Figure 20)

5 CONCLUSIONS

In the worst case, the areas of the construction affected by the fasteners can be removed by means of a saw, which is why the focus was on the rapid recoverability of the hall and thus, in a narrower sense, the detail points. [11]
A recommendation regarding the equivalent material recovery of the wood can only be given for the detail points *brace -column connection*. For the remaining detail points, no fastener can be identified that could significantly account for an increased number of running meter (lfm) of equivalent material recovered timber.
With regard to the fast deconstructability of the fasteners, the variant *slotted-in steel plate und dowel pins fixed on concrete column* can be recommended for the column base, for the connection brace-column: staggered joint and pin and slotted-in steel plate und dowel pins and for the detail point connection column head the fasteners *slotted-in steel plate* and *dowel pins* can be recommended. The only match between the two criteria of equivalent material recovery of the timber and fast deconstructability is in the detail item *staggered joint and pin.*
The general equivalent material recovery of the timber could not be clearly attributed to a fastener.
In order to determine the equivalent material recovery of wooden beam structures, it should not first be determined as fast deconstructability and equivalent material recovery of the timber as assumed at the beginning. Rather, the focus should be on the removability of the fasteners, since the fastener selection does not significantly affect the beam length remaining after deconstruction.
Accordingly, the methodology for determining the recyclability of timber agricultural beam structures can be further developed and transferred to other beam structures or a combination of beam and sheet structures made of timber. For example, the deconstruction potential of roof structures or elements of wood panel construction could be determined. The focus should also be on further development with regard to the evaluation of the removability of the fasteners.

ACKNOWLEDGEMENT

Thanks go to the LfL [7] for providing the plans and to the farmers who allowed us to examine their agricultural halls. The project is funded by Fachagentur Nachwachsende Rohstoffe e.V, FNR FKZ 2220HV 036B.

REFERENCES

[1] Bundesministerium für Umwelt; Naturschutz und nukleare Sicherheit (Hg.) (2020): Deutsches Ressourceneffizienzprogramm 3 – 2020 bis 2023. Bundesministerium für Umwelt, Naturschutz und nukleare Sicherheit (BMU). Available online via https://www.bmuv.de/publikation/deutsches-ressourceneffizienzprogramm-iii-2020-bis-2023, last checked on 27.06.2022

[2] Rüter, Sebastian (2016): Der Beitrag der stofflichen Nutzung von Holz zum Klimaschutz - Das Modell WoodCarbonMonitor. Dissertation. Technische Universität München, München.

[3] Office P (2008) Richtlinie 2008/98/EG des europäischen Parlaments und Rates vom 19. November 2008 über Abfälle und zur Aufhebung bestimmter Richtlinie

[4] (2012) Gesetz zur Förderung der Kreislaufwirtschaft und Sicherung der umweltverträglichen Bewirtschaftung von Abfällen (Kreislaufwirtschaftsgesetz - KrWG).

[5] (2012) Gesetz zur Förderung der Kreislaufwirtschaft und Sicherung der umweltverträglichen Bewirtschaftung von Abfällen (Kreislaufwirtschaftsgesetz - KrWG).

https://doi.org/10.52202/069179-0130

[6] Dechantsreiter, Ute; Horst, Peter; Mettke,, Dr. Angelika; Asmus, Stefan; Schmidt, Stephanie; Knappe, Florian et al.: Instrumente zur Wiederverwendung von Bauteilen und hochwertigen Verwertung von Baustoffen. Hg. v. Umweltbundesamt. Oktober 2015. Dessau-Roßlau

[7] Bayerische Landesanstalt für Landwirtschaft (LfL), Institut für Landtechnik und Tierhaltung, (Arbeitsgruppe Landwirtschaftliches Bauwesen (ILT 4c), Dipl.-Ing. Architekt Jochen Simon).

[8] Norm DIN EN 1995-1-1/NA:2013-08, August 2013: Nationaler Anhang – National festgelegte Parameter – Eurocode 5: Bemessung und Konstruktion von Holzbauten.

[9] Norm 8593-0, September 2003: Fertigungsverfahren Fügen.

[10] Hafner, Anette; Krause, Karina; Ebert, Samuel; Ott, Stephan; Krechel, Marco: Ressourcennutzung Gebäude: Entwicklung eines Nachweisverfahrens Ressourcennutzung Gebäude: Entwicklung eines Nachweisverfahrens zur Bewertung der nachhaltigen Nutzung natürlicher Ressourcen in Bauwerken. Hg. v. Ruhr-Universität Bochum, Fakultät Bau- und Umweltingenieurwissenschaften, Ressourceneffizientes Bauen, Prof. Dr.-Ing. Annette Hafner (S1).

[11] Schwede, Dirk; Störl, Elke (2017): Methode zur Analyse der Rezyklierbarkeit von Baukonstruktionen (1). Available online via https://onlinelibrary.wiley.com/doi/epdf/10.1002/bate.201600025.

World Conference on Timber Engineering Oslo 2023

SUSTAINABLE ASSESSMENT: A CONTRIBUTION TO IMPROVE THE RELIABILITY OF NDT ON OLD CHESTNUT PURLINS

Vittoria Borghese[1], Silvia Santini[2], Lorena Sguerri[3]

ABSTRACT: The aim of this study is to give an additional contribution to the improvement of a sustainable diagnostic practice to be used for the assessment of ancient wooden structures, in order to limit the damage of the existing ones through destructive tests, and to have a reliable prediction of old element properties, with their historical value, reducing demolition and substitution with consumption of new materials. To achieve this purpose, correlation laws and methodologies that can be used to facilitate the performance of non-destructive testing (NDT) in situ, will be highlighted. Seventeen chestnut purlins, dated between the 19th century and the 20th century and coming from the roof of the Cloister of Michelangelo at the Baths of Diocletian in Rome, are tested. As the first part of a wider experimentation, the aim is to identify the best practice for three relevant unknowns that characterize a wooden structural element: the geometry, through the survey and the BIM modelling; the density by means of the penetrometric tests (Resistograph and Woodpecker); the elastic module through direct and indirect ultra-sonic tests.

KEYWORDS: Assessment, chestnut, NDT

1 INTRODUCTION

The proposed research aims to combine the best diagnostic practices with the most recent dictates of sustainability, giving itself as a meeting point between the assessment commonly understood and the application of the best methodologies to preserve the environment.
Usually, a critical point is represented by the scheduled maintenance operations in order to protect the historical heritage and ensure greater sustainability of the restoration. The aim is to highlight sustainability in historic buildings through methodologies and correlations useful to facilitate the performance of non-destructive testing (NDT) *in situ* on existing timber structures without altering the characteristics of the analysed element and to limit the consumption of new materials or the damage of existing ones through destructive tests.
Moreover, several Countries have a wooden historical-artistic heritage plagued by aging and bad reworkings, all factors that aggravate its conservation. For this reason, it is important to provide a sustainable and reliable methodology for the assessment of this heritage developing procedures for the historical timber structures.
As the first phase of wider experimentation that includes destructive tests too, this study aims to develop the best practices for the estimation of three important unknowns that characterize a wooden structural element: the geometry, through the visual survey and the photogrammetry; the density by means of the penetrometric tests, such as the Resistograph and the Woodpecker [1]; the elastic module through direct and indirect ultra-sonic tests [2], thanks to the relationship that connects the static modulus with the dynamic one calculated by density and the stress wave speed parallel to the grain. However, at the moment, only the correlation between the direct and indirect measures was investigated To achieve this purpose, chestnut (*Castanea Sativa Mill.*) roof purlins were used, all dated between the 19th century and 20th century and coming from the Cloister of Michelangelo at the Baths of Diocletian in Rome (Figure 1).

Figure 1: *Reference sections and position of the penetrometric tests*

In conclusion, the aim of this study is to give an additional contribution, with new data and analysis, in order to improve a sustainable methodology, that can be used on-

[1] Vittoria Borghese, University of Roma Tre – Department of Architecture, Italy, vittoria.borghese@uniroma3.it
[2] Silvia Santini, University of Roma Tre – Department of Architecture, Italy, silvia.santini@uniroma3.it
[3] Lorena Sguerri, University of Roma Tre – Department of Architecture, Italy, lorena.sguerri@uniroma3.it

https://doi.org/10.52202/069179-0131

site, able to estimate these three fundamental characteristics of an ancient wooden structural element.

2 CASE STUDY

To carry out the proposed research, seventeen purlins coming from Michelangelo's Cloister of the Baths of Diocletian in Rome were examined.

2.1 CLOISTER OF MICHELANGELO

The Cloister of Michelangelo is part of the complex of the Diocletian's Baths in Rome, located near the Termini station [3].
The famous Baths of Diocletian were immediately considered witnesses of Roman greatness, built in 302 A. C. and they were the largest in Roman times by extension [4].
Each side of the internal Cloister consists of the ground floor of 25 spans of vaults and Tuscan columns in travertine. The structure ends with a roof inclined to a wooden pitch.
Since the 80s of the last century, the building of the Cloister has undergone many interventions of structural consolidation, due to the critical conditions of the supporting structure. The few diagnostic operations carried out in the last 40 years have led to low knowledge of the load-bearing capacity and countless consolidation interventions throughout the structure.

2.2 PREVIOUS WORKS

This research is the prosecution of two previous works carried out on the first part of the sample that originally counted 40 purlins. The first work addresses the issue of sustainability for interventions on ancient wooden structures, proposing a methodology of analysis of NDT, aimed at limiting the decommissioning and replacement of roofing, suggesting non-invasive methods of analysis to understand the bearing capacity of the primary elements [5].
The second work focuses on the assessment of the sustainability of the interventions carried out over the decades on the Cloister of Michelangelo. The aim is to demonstrate how the development of NDT can be more sustainable than the complete replacement but also compared with local structural reinforcement interventions carried out without careful analysis. Classic rehabilitation interventions are also compared and a multi-criteria Decision Analysis (MCDA) based method is provided to assess sustainability and establish a ranking of intervention alternatives [6].

3 GEOMETRY

3.1 SAMPLE PROPERTIES

The elements analyzed are in chestnut wood and date back a period included between 1865 and 1911 and had the function of purlins in the roof of the Cloister.
The purlins examined are seventeen. Eight of them are confined with an old metallic continuous spiral (from F6 to F15) while the others are free (from SF6 to SF21). All the specimens were submitted to the NDT. Section dimensions and length vary from one to the other and the average values are given in Table 1.

3.2 VISUAL INSPECTION

Wood is a living material defined, which has continuous exchanges with the external environment, heterogeneous and anisotropic (also defined as orthotropic). It is a complex material to analyze and it presents defects that are part of its nature and that are partially eliminated in innovative engineered timber elements, but that are present in historic ones. Wood defects produce a material discontinuity that causes a change in physical and mechanical characteristics, resulting in the formation of critical zones that affect the overall strength.
In Italy, there is a specific standard, the UNI 11119:2004, that provides criteria for the visual strength grading of the ancient timber elements when they are still in place [7].
The Standard requires a visual survey of the geometry (maximum dimensions and presence of wanes) and the defects (knots, knot clusters, mechanical cracks, splits, ring shakes and slope of the grain). It is returned, by tree species, a classification in three different categories of strength with the relative modulus of elasticity in bending (MoE) and allowable tension and compression stress values. Regarding the purlins, 7 samples were classified in class II with a corresponding MoE value of 9000 N/mm^2 and the remaining 10 in class I with a MoE of 10000 N/mm^2.
The visual grading was made excluding the section wanes, since the geometrical limitations provided by the standard are considered too penalizing for historical timber elements.

Table 1: *Purlin dimensions and strength-classes given by the visual grading*

Purlin	Strength Class	Width (cm)	Hight (cm)	Lenght (cm)
F06	II	16,0	18,0	262
F07	II	14,0	13,0	265
F08	II	18,0	16,0	264
F09	I	14,0	15,0	263
F11	II	12,0	10,5	301
F12	I	13,0	12,0	255
F13	I	13,0	14,5	299
F15	I	11,5	15,5	297
SF06	I	15,0	13,0	263
SF07	I	15,5	19,0	263
SF09	II	16,0	15,0	260
SF10	I	15,5	15,5	306
SF12	II	12,5	12,5	271
SF13	II	17,5	17,0	263
SF14	I	16,0	16,0	240
SF15	I	13,0	18,0	263
SF21	I	18,5	13,0	306

3.3 VOLUME ESTIMATION

In order to estimate the correlation laws between the NDT and the chestnut density, it is required to determine the density of the 17 purlins. For this purpose, it is necessary

to derive the actual volume and weight, the latter measured by a dynamometer, of the specimens. For the volume the task is more complex, being the beams very irregular in every direction. Two measurement methods were applied. The first one detects a detailed geometry in several sections approximating the variations in shape along the purlin. The sections were recreated in the HBIM environment, linking them and obtaining the volume (Figure 2a). The second one employs the photogrammetric technique creating a PointCloud dataset of points, giving a very accurate geometry elaborated with a Matlab code and also with the identification of cracks [8] (Figure 2b).

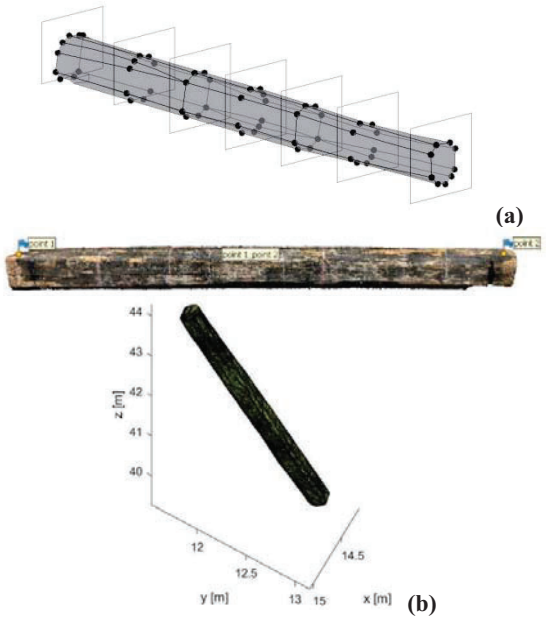

***Figure 2: (a)** BIM element created by sections; **(b)** Photogrammetry Point Cloud and MatLab elaboration*

In Table 2 the volumes and the resulting densities obtained by the two methods (V_{BIM}, V_{PHG}, ρ_{BIM}, ρ_{PHG}) are reported and compared. However, the photogrammetric method was applied to the purlins without confinement only, since the presence of the metal band causes an important alteration of the computed volume. The change in density associated with the change in the volume estimation is expressed as a percentage variation and may have significant values included between 3% and 21%.
In the following, the density obtained by sections and then computed for the whole sample will be considered as the actual density ρ on which to estimate the correlation laws.

4 DENSITY

4.1 PENETROMETRIC METHODS

The penetrometric methods include all those tests performed with devices that involve penetrating the wood with a needle. The needle can be short or long. In the first case the superficial layer is involved only, while in the second case the entire section can be crossed. In any case, these types of tests cause little damage to the material and then they can be counted among the non-destructive methods (NDT). For the actual experimentation the Woodpecker and the Resistograph were employed both alone and by combining the results.

***Table 2:** Volume, density and percentage variation results for the third and fourth methods.*

Purlins	V_{BIM} (m^3)	ρ_{BIM} (Kg/mc)	V_{PHG} (m^3)	ρ_{PHG} (Kg/mc)	$\frac{\rho_{BIM}}{\rho_{PHG}}$ (%)
F06	0,068	524	-	-	-
F07	0,055	545	-	-	-
F08	0,069	560	-	-	-
F09	0,059	588	-	-	-
F11	0,053	618	-	-	-
F12	0,042	602	-	-	-
F13	0,055	547	-	-	-
F15	0,061	595	-	-	-
SF6	0,057	676	0.055	658	3%
SF7	0,073	569	0.081	512	11%
SF9	0,061	597	0.067	546	9%
SF10	0,050	595	0.052	578	3%
SF12	0,054	518	0.061	461	12%
SF13	0,068	639	0.072	608	5%
SF14	0,059	631	0.067	563	12%
SF15	0,065	610	0.078	505	21%
SF21	0,082	630	0.088	583	8%

Considering the medium purlin length and the intention to perform bending tests in the future, three reference sections have been chosen in order to execute the penetrometric tests: the central one and the two sections delimiting the middle third as illustrated in Figure 3.

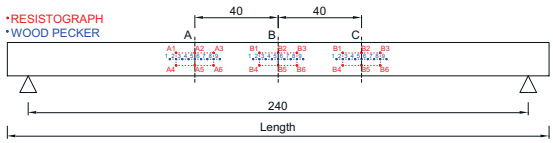

***Figure 3:** Reference sections and position of the penetrometric tests*

4.1.1 Woodpecker

The Woodpecker (WP), produced by the Italian company DRC, is a modified Schmidt hammer. On the percussion, the rod was added a removable needle in hardened steel with a conical tip, a diameter of 2,5 mm and a total length of 50 mm. The test is to insert the needle into the wood with a given number of shots. Then, the penetration depth (*PD*) is obtained by measuring the exposed part of the needle.
The penetration depth is related to the superficial density of the wooden element and the manufacturer gives some correlation laws *PD*-ρ concerning different wood species,

https://doi.org/10.52202/069179-0131

including chestnut. These relationships were estimated on the basis of experimental research conducted on a limited number of new timber specimens with dimensions 80x80x1300 mm [9]
In order to use these results, the manufacturer recommends to drive the needle with 5 consecutive shots and to execute at least 9 insertions in the same area following a grid with 25÷30 mm interaxis. Obviously, the test must be performed by choosing a possible defect-free area along the wooden surface.
Few studies have been performed on the reliability of the WP up to now. Lliana et al. 2018 [10] utilized twelve Norway spruce joist specimens, extracted from a dismantled 19th century building, in order to compare four different test methodologies suitable for *in-situ* density estimation: the needle penetration resistance (NPR) including both the Woodpecker and the Pylodin, the screw withdrawal resistance (SWR), the core drilling (CD) and the drilling chips extraction (DCE). Concerning the WP, the authors evaluated the test results driving the needle with one, three and five shots. The last option, which is the one recommended by the manufacturer, gave the best correlation with density with a coefficient of determination of 0,33. This value is higher than the one obtained with the Pylodin, but lower than those related to the other three test methodologies.
Similarly, Osuna-Sequera et al. 2019 [11] compared the NPR, SWR and DCE methods in order to optimize the number of measurements to be performed along extended wooden elements where the density variation, due to the growth of the original tree, becomes important from one end to the other. Then, they demonstrate that the penetration depth measured with the WP is considerably influenced by the position of the test area reaching differences up to 5 mm between the bottom of the original tree and a section 10 meters high. Anyway, performing ten measurements along the element they obtain R^2=0,55. In this case, the coefficient of determination is higher than the one obtained with the Pylodin and with the SWR method too.
Regarding chestnut, Faggiano et al. [12] used the WP upon 24 wooden elements extracted from a dismantled roof of an ancient building in Naples. In this case, the authors made the tests following the producer's recommendations. In detail, they performed 10 tests, including 9 measurements each, along with all the specimens.
According to the description they gave, the surface conditions of the 24 elements seem to be very similar to the actual ones with an extended decay due to the attacks of xylophagous insects in addition to the presence of defects as knots, cracks and holes. The correlation that they found between the penetration depth and the density was quite low with R^2 = 0,30 and the regression line was:

$$\rho = -11{,}40 \times PD + 777{,}69 \quad (1)$$

where *PD* is included in the range 13÷19 mm, while the manufacturer's correlation law, calibrated on new chestnut samples, covers a depth range between 9 and 14 mm.
Besides, it seems to be obvious that the superficial decay makes the cortical layer of an old wooden element softer, permitting the needle of the WP to penetrate deeper. This is a very crucial factor since it is not easy to quantify the amount of this decay and the way it is distributed along the surface, being inhomogeneous.
In order to investigate, with more data, the relationship between the penetration depth and the density of old chestnut structural elements, 6 tests, with 9 measurements each, were performed along the 17 purlins. The test grids were located next to the three central reference sections and on two opposite sides of the specimen (Figure 3). The spacing of the grid was about 30 mm and the area with the best superficial condition, without knots and at least 25 mm far from any crack or hole was chosen.

4.1.2 Resistograph

The Resistograph was developed from the second half of 80s by a german researcher: Frank Rinn. The device is characterized by a thin needle that can be 400 mm long and penetrates, like the tip of a drill, inside the wood. Then, the drilling resistance is measured, registered and displayed by a graph that highlights density variations due to the annual growth circles of the trunk and to the presence of eventual defects as cracks or decay with a sharp drop in resistance, or knots with peaks of resistance. Moreover, the relationship between the drill resistance and the density of the wood was demonstrated in 1996 by comparison with some X-ray tests [13].
Given the results of the test, the Resistograph is very suitable to detect possible states of decay hidden inside a wooden element and then not identifiable by a visual survey. However, given also the relationship with the material density, several attempts to correlate the outcome of the test directly with the density and even with the mechanical properties of the wood, as the elastic and the rupture modulus, were done. In fact, if *DR* (%) is the drilling resistance, expressed as a percentage of the amplitude, and *h* (mm) is the progressive drilling depth up to *H*, a medium rate (DR_m) may be calculated by the integral of the graph (Figure 4):

$$DR_m = \frac{\int_0^H DR \cdot dh}{H} \quad (2)$$

The outcomes of these correlation attempts are very discordant [13]. On the other hand, the result of the test depends on several factors including, first of all, the tree species and then the moisture content, the drilling direction in relation to the growth circles, the model of the Resistograph, the drilling speed and many more.
Some experimental works aimed to find the correlation laws between the drilling resistance and the physical and mechanical properties of wood were made about chestnut too. With regard to density, processing the data obtained by Faggiano et al. [12] who tested 24 ancient chestnut beams by means of a Resistograph IML RESI F400, a correlation with R^2 = 0,43 was obtained, while the authors themselves, with the same device, found a correlation with R^2 = 0,32, performing the test along 9 purlins of the late nineteenth century [5].

For the actual experimentation, a Resistograph IML RESI PD400 was employed. This tool can provide not only the drill rate (*DR*) but also the feed rate (*FR*). The outcomes are two different graphs where *DR* and *FR* are both expressed in percentage of the amplitude. In either case, it is possible to detect an eventual decay within the wooden element and to calculate a medium rate, however, the drill rate is generally affected by the friction that develops between the needle and the wood during the test. This friction is affected by several factors as the tree species, the density, the moisture content and the penetration depth. In any case, a very simple linear model, with friction depending only on the drilling depth, can be assumed. In this way, the drill graph can be easily corrected just by subtracting the increasing friction along the path [14] (Figure 4).

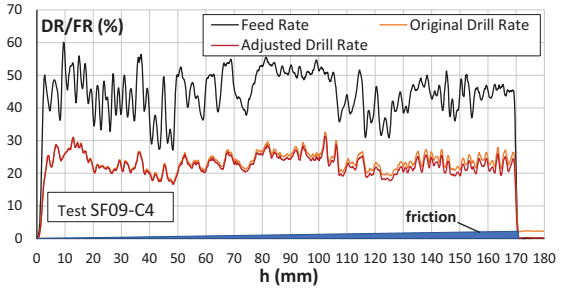

Figure 4: *Resistograph - Comparison between the original drill rate graph, the adjusted one and the federate graph*

The comparison between the correlations found for the feed rate and the drill rate with the mechanical and physical properties of four tree species developed by Sharapov et al. [15] suggests that *DR* is more reliable than FR. In detail, about the relationship *DR*-ρ, coefficient of determinations generally higher than 0,76 were found.
In a similar way, the tests performed along the 17 purlins were processed considering both the drill rate and the feed rate (Figure 4). For each element, 6 tests around the three reference sections, were executed, for a total of 18 tests (Figure 3). The rotational speed was set at 3000 rpm, while the feed speed at 100 cm/min.
When processing, both FR_m and DR_m were calculated, the latter having subtracted the friction component. In both cases the medium resistance was computed excluding all the inhomogeneous parts of the graphs as peaks or drops due to the presence of knots, cracks or decay.

4.1.3 Combined method

The superficial decay that generally affects the ancient timber structural elements and its randomness compromise the reliability of the Woodpecker, since this kind of test involves just a thin layer of material close to the surface. On the other hand, the Resistograph involves all section thickness, but any correlation laws with density are strictly connected with the model of the instrument and with the drilling speed. In order to overcome these limits, it is proposed to combine the two methods as already suggested by the authors [5], although in place of the Woodpecker, the Pylodin was used.

If the WP producer law is considered reliable enough for any value of the penetration depth, the resulting density (ρ_{WP}) can be related with the medium resistance computed along the initial or the final section of the Resistograph graph for a length equal to PD_m ($R_{m,PD}$). Then, the following ratio can be calculated;

$$C = \frac{\rho_{WP}}{R_{m,PD}} \tag{3}$$

Assuming that this ratio remains constant along the entire section thickness, the wood density can be estimated multiplying the coefficient C by the medium resistance computed on the remaining part of the graph:

$$\rho_{comb} = C \cdot R_{m,(H-PD)} \tag{4}$$

Obviously, both tests must be executed close to each other so that their combination makes sense. In fact, regarding the 17 purlins, the two tests were performed at the three reference sections (Figure 3). Then, the WP was executed both on the inlet and outlet side of the Resistograph so that both the initial and final parts of the feed rate and drill rate graphs were considered.

4.2 RESULTS

Regarding the WP, the mean penetration depth of one purlin is calculated as the average value of the six tests outcomes, while the single test result is evaluated as the mean value of 9 measures. In Table 3, the mean penetration depths (PD_m) and the related coefficients of variation (*CV*) are reported for each purlin, together with the maximum and minimum values (PD_{min} and PD_{max}) registered by the six tests.

Table 3: *Wood Pecker tests results*

Purlin	PD_m (mm)	*CV* (%)	PD_{min} (mm)	PD_{max} (mm)
F06	18,83	10,9	17,02	22,89
F07	18,02	1,8	17,50	18,38
F08	17,63	4,9	16,30	18,52
F09	16,52	2,0	15,94	16,84
F11	17,89	9,4	16,39	20,71
F12	16,88	3,4	16,46	17,97
F13	19,07	3,7	17,94	19,66
F15	17,96	7,4	16,66	20,49
SF06	18,04	7,8	15,60	19,40
SF07	16,94	6,5	15,61	18,44
SF09	16,29	5,6	15,46	17,64
SF10	16,54	3,6	17,58	16,83
SF12	20,18	6,2	17,92	21,64
SF13	16,95	10,2	15,67	19,31
SF14	17,10	5,9	16,37	18,88
SF15	17,04	7,3	15,74	19,21
SF21	16,19	5,9	15,52	18,06

It can be observed, that the mean penetration depths are included between 16,2 mm and 20,2 mm, while the results of the single tests have a wider range from 15,5 mm to 23

https://doi.org/10.52202/069179-0131

mm. The coefficients of variation, as well as the minimum and maximum depths, highlight that the experimental data are quite scattered along the same purlin, probably due to the inhomogeneity of the surface decay. In addition, the conditions of the cortical layer make completely inadequate the producer's law as illustrated in Figure 5.
On the other hand, Figure 6 shows the regression line built on the actual data (ρ and PD_m) with the related 95% confidence and prediction intervals. The purlin SF06 was excluded from the analysis, since the related data seems to be an outlier (Figure 5). The coefficient of determination is $R^2 = 0,55$.
The actual regression line is compared with the one obtained by Faggiano et al. [12] (Eq. (1)). The two lines have a quite different slopes, however they are strictly connected considering that the second one falls almost completely within the confidence limits of the first one. Anyway, the general randomness of the superficial decay and the lack of knowledge about the sample that Faggiano et al. used, does not encourage data to be merged to achieve a single law.

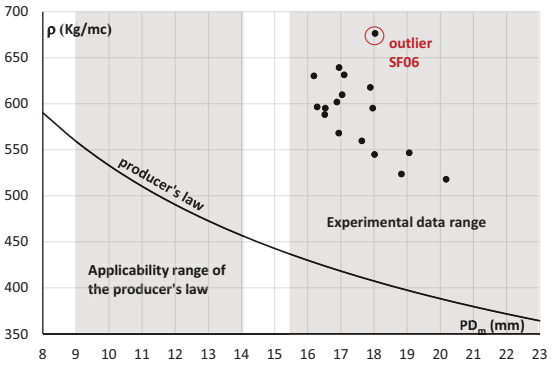

Figure 5: *WP - Comparison between the experimental data and the producer's law*

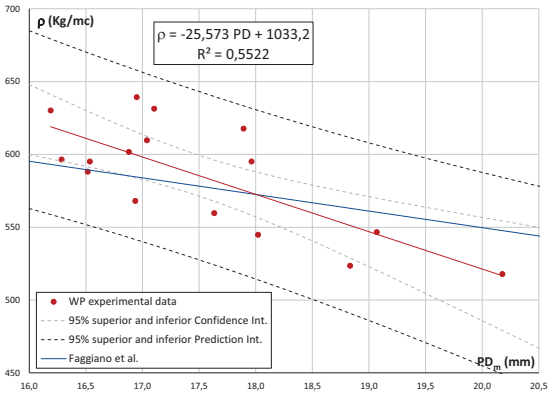

Figure 6: *WP - Correlation between the penetration depth and the actual density*

Better results are obtained by means of the Resistograph, probably because this method involves the entire section, rather than just the cortical layer, and therefore the superficial decay is irrelevant.

In Table 4 the medium feed rate (FR_m) and the medium drill rate (DR_m) are reported together with the respective coefficient of variation (CV_{FR} and CV_{DR}).

Table 4: *Resistograph tests results*

Purlin	FR_m (%)	CV_{FR} (%)	DR_m (%)	CV_{DR} (%)
F06	32,1	5,3	18,8	10,9
F07	38,8	14,2	18,0	13,4
F08	39,3	4,3	18,7	5,6
F09	44,9	8,3	20,4	8,7
F11	47,2	5,3	22,0	10,9
F12	44,7	10,0	20,9	10,8
F13	39,2	11,8	17,3	8,9
F15	41,5	7,3	19,3	7,1
SF06	53,4	6,1	25,9	8,4
SF07	38,9	7,7	18,0	5,5
SF09	42,6	6,5	20,8	10,9
SF10	38,8	6,8	17,9	5,9
SF12	30,7	11,2	14,6	8,7
SF13	46,2	4,3	21,9	6,6
SF14	47,5	9,5	22,8	11,2
SF15	46,3	4,0	22,2	5,7
SF21	46,8	8,1	22,0	9,6

In both cases, the correlations between FR_m and DR_m and the actual density of the purlins are strong. However, the regression line FR_m - ρ is slightly more reliable than the other one with a coefficient of determination $R^2 = 0,89$ versus $R^2 = 0,82$. In Figures 7 a/b the regression lines with the related 95% confidence and prediction intervals are reported. Then, the chestnut density may be estimated through the following relationships:

$$\rho = 7{,}011 \cdot FR_m + 294{,}26 \mp 37 \left(\frac{Kg}{mc}\right) \quad (5)$$

$$\rho = 14{,}71 \cdot DR_m + 295{,}15 \mp 47 \left(\frac{Kg}{mc}\right) \quad (6)$$

Finally, it is necessary to point out that these correlation laws may be considered a reference just if the tests are performed with the Resistograph IML RESI PD400 with the same rotational and feed velocities set.
Regarding the combined method, for each section, the average values of all densities estimated by combining the penetration depth with the inlet and outlet sections of both the feed rate ($\rho_{comb,FR}$) and drill rate ($\rho_{comb,DR}$) graphs were computed. During processing, those combined densities that were lower than the ones estimated with the Wood Pecker only were excluded, as well as those ones higher than 700 Kg/mc. In Table 5 the combined densities estimated with both the graphs and the relative coefficients of variation are reported. These last highlight an important dispersion of the data.

https://doi.org/10.52202/069179-0131

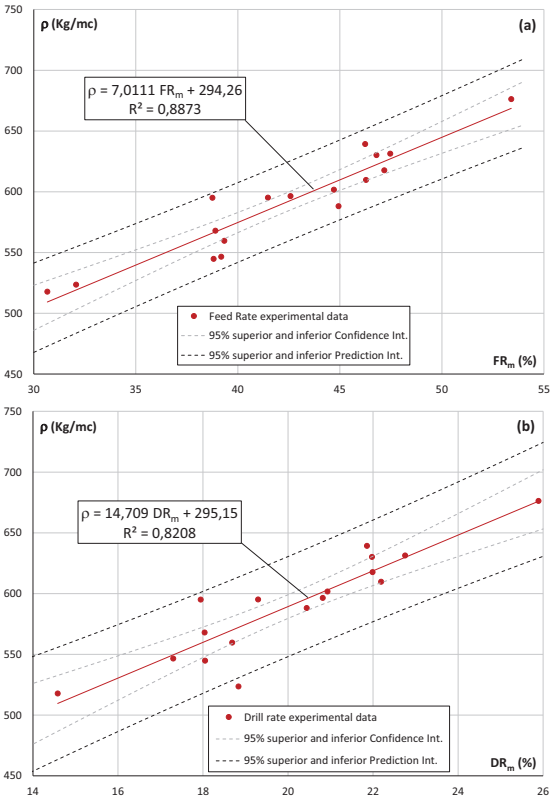

Figure 7: *Resistograph - Correlation between the Feed Rate (a) and the Drill Rate (b) and the actual density*

Table 5: *Combined method results*

Purlin	$\rho_{comb,FR}$ (Kg/mc)	CV_{FR} (%)	$\rho_{comb,DR}$ (Kg/mc)	CV_{DR} (%)
F06	491	9,5	468	8,1
F07	476	11,7	491	14,5
F08	469	11,6	493	10,7
F09	503	11,1	507	11,3
F11	491	12,5	505	13,4
F12	499	12,4	509	11,9
F13	490	13,0	485	14,2
F15	480	9,5	509	15,8
SF06	520	16,5	520	14,1
SF07	500	10,0	493	12,3
SF09	475	12,8	513	16,0
SF10	486	11,2	502	9,8
SF12	430	7,6	430	6,7
SF13	575	13,8	558	14,4
SF14	491	10,9	498	13,6
SF15	509	12,3	538	15,8
SF21	502	14,7	476	10,4

As can be seen from Table 5, the estimated densities are very conservative, anyway, the correlation between the actual densities and the ones evaluated through the drill rate graph has some interesting aspects. Considering the whole sample, the regression line is quite parallel to the equality one ($\rho_{comb,DR} = \rho$) with $R^2 = 0,48$ (Figure 8). Anyway, the data concerning the specimens SF06 and SF21 can be considered outlier and then they can be excluded from the correlation. In this case, the coefficient of determination increases up to 0,69, while the regression line slightly lowers keeping the slope almost the same. Considering the 95% prediction intervals, it can be assumed that:

$$\rho = 1{,}0838 \cdot \rho_{comb,DR} + 40{,}4 \mp 57 \left(\frac{Kg}{mc}\right) \tag{7}$$

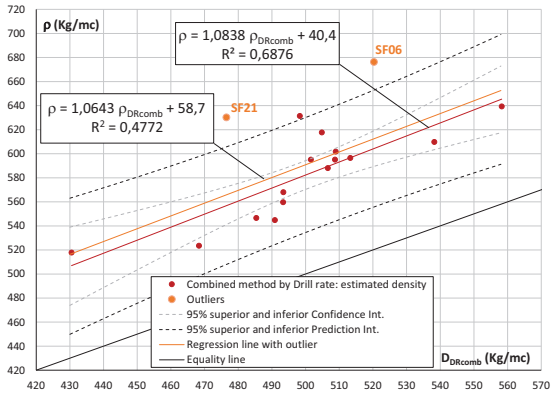

Figure 8: *Combined method - Correlation between the estimated densities evaluated through the Drill Rate graph and the actual densities*

5 MODULUS OF ELASTICITY

5.1 ULTRASONIC PULSE VELOCITY

The elastic properties of wood may be estimated through the so-called dynamic methods including the ultrasonic pulse velocity measurement (V). This velocity is strictly connected with the density of wood (ρ), with its dynamic modulus of elasticity (E_{dyn}) and with the Poisson modulus (ν). Since the latter is often ignored, the relationship between the remaining quantities becomes very simple:

$$V = \sqrt{\frac{E_{dyn}}{\rho}} \tag{8}$$

However, the correct application of the method and the subsequent interpretation of the data is not as simple.
First of all, wood is an orthotropic and inhomogeneous material with very different structural characteristics depending on the species. Then, the stress wave speed is influenced by the direction, the internal "architecture" of the material, the presence of any defect as knots, cracks or decay, as well as by the moisture content and even by the equipment employed for the test. Therefore, also among the same species, the ultrasonic pulse velocity measurement can vary greatly depending on the test conditions, compromising the reliability of the dynamic modulus estimation.
Second, the existing relationship between the dynamic modulus of elasticity and the static one is still discussed.

https://doi.org/10.52202/069179-0131

With regard to chestnut, some studies have been conducted on old structural elements with different results. Faggiano et al. [12] found a strong correlation between E_{dyn} and the bending modulus (E_b) with $R^2 = 0,76$ as well as Santini et al. [5] although in this case, the correlation involved the compression modulus ($E_{C,0}$). On the other hand, Koca et al. [16] found a weak correlation between E_{dyn} and E_b with $R^2 = 0,32$.

In any case, the stress wave speed is generally measured parallel to the grain (V_L). In fact, along this direction, it reaches the highest value and it is less influenced by local defects and by the arrangement of the growth circles of the wood since there is an important difference between the velocity along the radial or the tangential direction ($V_R \approx 1/2V_L$ and $V_T \approx 1/3V_L$) [17]. Then, a practical problem is added. During *in-situ* surveys, the ends of the investigated wooden elements are often not accessible making it impossible to measure the longitudinal pulse velocity by direct way.

In this case, a solution may be given by the indirect measure (V_{ind}), placing the two transducers along the same face of the element with an appropriate distance between them. Some studies highlighted that in this way it is possible to obtain a good approximation of the longitudinal velocity. Oh [18] finds out, by some tests performed on spruce lumber specimens, that the ratio V_{ind}/V_L increases with the distance (d) asymptotically tending to 0,87 for $d = 20$ cm. However, Machado et al. [19] demonstrate that when some superficial defects occur it is important to further increase the distance in order to involve deeper wood layers in the propagation path. In this case, they obtained a ratio V_{ind}/V_L greater than 0,90 with $d = 40$ cm.

These studies are all performed on small clear wood specimens without defects or with planned defects. On the contrary, the ultrasonic tests executed on the 17 purlins are aimed to estimate the ratio V_{ind}/V_L when the indirect method is applied directly on site and to evaluate the best methodology to perform it. The equipment employed is an ultrasonic system CMS HLF-P SG02_0128 series with 55 kHz piezoelectric transducers equipped with tips.

The direct longitudinal velocity was calculated for each purlin as the average value of five tests performed between the ends: one in the middle of the section and the others close to the four edges (Figure 9).

The indirect measures were executed along the four sides of each element and the transducers were placed at both a distance of 40 cm ($V_{ind,40}$) and 60 cm ($V_{ind,60}$) as illustrated in Figure 9. The chosen paths were apparently free from macroscopic defects as knots and holes or important decay and they were not cut by significant fractures.

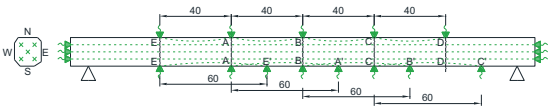

Figure 9: *Direct and indirect measures of the ultrasonic pulse velocity*

5.2 RESULTS

Following the tests, with regard to the choice of the distance between the transducers, it was observed that:

- the ratio V_{ind}/V_L remains approximately the same despite the variation of the distance ($V_{ind,40}/V_L$=0,85 - $V_{ind,60}/V_L$=0,86);
- it is more difficult to find a path with a length of 60 cm free of defects than one of 40 cm;
- the attenuation of the signal over 60 cm makes sometimes too difficult to read the time of flight of the stress wave.

For all these reasons the authors chose to deepen and analyse only the method that provide the shortest distance. The results of the direct (V_L) and indirect tests ($V_{ind,40}$) are given in Table 6. The indirect velocity is the medium value computed on 12÷15 different paths (N) for each purlin. In fact, despite a careful choice of the wave trajectory, the indirect velocities along the same element may be quite scattered with a coefficient of variation (CV) that can rise up to 10,63% (specimen F09). On the other hand, a relatively high number of measurements allows to maintain stable enough the ratio $V_{ind,40}/V_L$ with a CV less than 2%.

Table 6: *Direct and indirect ultrasonic tests results*

Purlin	V_L (m/s)	N	$V_{ind,40}$ (m/s)	CV (%)	$V_{ind,40}/V_L$
F06	5181	13	4521	5,55	0,873
F07	5264	12	4460	7,75	0,847
F08	5548	12	4653	5,69	0,839
F09	5392	12	4603	10,63	0,854
F11	5345	12	4597	4,67	0,860
F12	4948	12	4199	9,01	0,849
F13	5113	12	4530	7,80	0,886
F15	5358	12	4427	9,91	0,826
SF06	4944	12	4290	4,67	0,868
SF07	5316	12	4398	6,18	0,827
SF09	5248	12	4400	8,27	0,838
SF10	5397	12	4620	8,88	0,856
SF12	4944	12	4291	8,50	0,868
SF13	5638	15	4737	4,46	0,840
SF14	5645	13	4744	4,82	0,840
SF15	5379	14	4547	9,04	0,845
SF21	5260	12	4597	6,06	0,874
	Medium value of the ratio $V_{ind,40}/V_L$				0,852
	CV of the ratio $V_{ind,40}/V_L$ (%)				1,94

Figure 10 shows the correlation between the direct and the indirect readings. The coefficient of determination (R^2) is good and particularly it may be observed that there is quite no difference between the best fit regression line and the one forced to pass through the origin. Then, the latter may be considered reliable enough and, according to the related 95% prediction intervals, the longitudinal velocity can be estimated through the following relationship:

$$V_L = 1,174 \cdot V_{ind,40} \mp 229 \left(\frac{m}{s}\right) \quad (9)$$

where the slope is given by the ratio $V_L/V_{ind,40}$, which is 1/0,852.

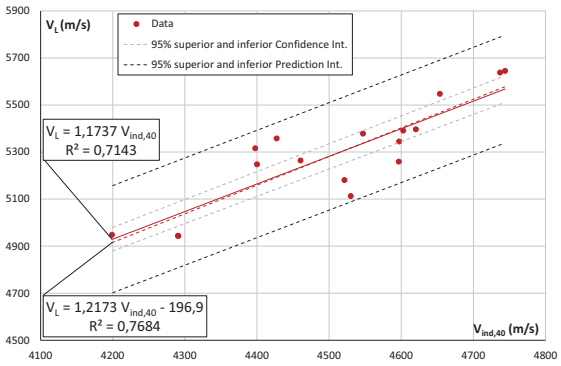

Figure 10: *Correlation between direct and indirect velocities*

6 SUSTAINABILITY CONSIDERATIONS

When addressing the issue of sustainability it is necessary to do so with full knowledge of the facts. In this research, authors talked about sustainability as material saving, but in reality, the considerations to be made are several.

In the first instance to conduct the experimental diagnostic operations on the samples were made of operations that have caused consumption and emissions that the proposed methodology offers to avoid. So the transport from the Diocletian Baths to the laboratory and the replacement of the elements are exactly the phases that, opting for non-destructive diagnostic operations, the research aims to avoid in the future.

On the basis of these considerations, it is necessary to think about actual consumption from a multi-parametric point of view, as carried out in previous research, as mentioned before. In this sense, NDT were analysed from an environmental, social, economic and structural point of view. There is no doubt, however, about savings in terms of assessment, transport, economics in the face of replacement works, and the social and cultural value of preserving not only the historical heritage but also the technology and materials.

This analysis compared various interventional alternatives, modelled using Heritage-Building Information Modelling (HBIM) technology, assessed using the multi-criteria decision analysis Analytic Hierarchy Process (AHP), and quantified sustainability using the multi-criteria Modelo Integrado de Valor para Evaluacin Sostenible (MIVES) methodology. To do this, the study offers a methodology to assess various interventions, including NDT diagnosis: i. replacement with the insertion of braces; ii. non-destructive testing and steel jacketing with shaped retaining profiles welded in situ; iii. non-destructive test and support beams bolted with braces; iv. NDT and simple braces addition.

Wood is a material that can be understood as a witness for such research and insights since it is often underestimated its strength in structural terms and the consequent economic and environmental savings resulting from its assessment.

Moreover, in the absence of many ancient wooden roof structures, it is also relevant for a cultural and architectural tradition that must be preserved and that must also be available to posterity.

7 CONCLUSIONS

The research aims to suggest a methodology that can provide a wide assessment examination for historic timber structures also taking into account sustainability, emphasizing the correlation that diagnostic tests can have with the environmental impact.

Non-destructive tests, given the low invasiveness, can be a set of scheduled maintenance operations that allow having a complete and constant overview of structural behavior over the years. Considering also the few analyses that are carried out on historic wooden buildings and the randomness of the results present due to the heterogeneity of the material, a procedural method is proposed in the research through combinations of different test results in order to obtain a complete assessment of the structure, without it being damaged or replaced.

The aim is to derive the estimates of the three unknowns concerning the wooden elements: geometry, density and elastic modulus.

The first, especially with regard to volume, is difficult to estimate on the construction site. The proposed analysis of several relevant techniques compared, allows having a general overview and a correlation between the data obtained. From the simple measurement of only the main dimensions to the photogrammetric survey, the authors have seen the influence that the estimated volume change can have on the density of the material.

The visual investigation deepens these analyses by providing a mechanical classification based on the defects observable from the outside.

The non-destructive tests provide estimation values of the physical and mechanical properties of the material, so the other two unknowns (density and elastic modulus) must be obtained through correlations that can make the results obtained reliably.

The correlations obtained from the proposed combined procedure, which are useful to derive the density estimate by comparing surface and depth results, have the limit of being able to be used only with the instrumentation used and with the same settings as those used in this research. In addition, the conservative state of the surface layer was also a key factor. Poor maintenance and deterioration of the wood surface layer is an important variable to consider especially with regard to surface testing.

For the modulus of elasticity through ultrasonic tests, instead, a comparison between estimated speeds based on the distance of the probes has been proposed, to understand which is more suitable for the use in situ.

The set of data and results obtained is useful in order to propose a useful methodology on site to carry out non-invasive diagnostic tests that can limit the consumption of material and maintain the historical value of ancient structures and technologies.

It is therefore intended to provide a method that can prevent the cultural, historical and architectural heritage

https://doi.org/10.52202/069179-0131

too many invasive changes and alterations that prevent their preservation, through timely diagnostic operations.

REFERENCES

[1] Liana D.F., Iniguez-Gonzales G., Diez M.R., Arriaga F.: Nondestructive testing used on timber in Spain: A literature review. Maderas. Ciencia y tecnologìa, 22(2), 2020.

[2] Machado J., Palma P., Simoes S.: Ultrasonic indirect method for evaluating clear wood strength and stiffness. In: NDTCE'09, Nantes, 2009.

[3] Serlorenzi M., Laurenti S.: Terme di Diocleziano & S. Maria degli Angeli. EdUP Strenne, 192, 2013. ISBN: 8884210461.

[4] Aurigemma S.: Terme di Diocleziano e il Museo Nazionale Romano. La Libreria dello Stato Roma, 176, 1954.

[5] Santini S., Baggio C. and Sguerri L.: Sustainable interventions: conservation of old timber roof of Michelangelo's Cloister in Diocletian's Bath. International Journal of Architectural Heritage, DOI: 10.1080/15583058.2021.1938747

[6] Santini S., Borghese V., Baggio C.: HBIM-Based Decision-Making Approach for Sustainable Diagnosis and Conservation of Historical Timber Structures. Sustainability, 15, 3003, 2023.

[7] UNI 11119:2004 "Cultural heritage. Wooden artefacts. Load-bearing structures – On site inspections for the diagnosis of timber members". Ente Nazionale Italiano di Unificazione (Italian Organization for Standardization)

[8] Barazzetti, L., Banfi, F., Brumana, R., Gusmeroli, G., Previtali, M., Schiantarelli, G.: Cloud-to-BIM-to-FEM: Structural Simulation with Accurate Historic BIM from Laser Scans. Simul. Modeling Pract. Theory, 57, 71–87, 2015.

[9] Menditto, G., Bufarini, S., D'Aria V. and Massaccesi M.: Risultati sperimentali di una ampia campagna di prove per il tracciamento di curve di correlazione per lo sclerometro per legno. *Proceedings of the 11° Congresso Nazionale sulle Prove non Distruttive Monitoraggio Diagnostica*, Milano, 2005.

[10] Llana D.F., Íñiguez-González G., Montón J. and Arriaga F.: *In-situ* density estimation by four non-destructive techniques on Norway spruce from built-in wood structures. Holzforshung, 72(10):871-879, 2018

[11] Osuna-Sequera C., Llana D.F., Esteban M. and Arriaga F.: Improving density estimation in large cross-section timber from existing structures optimizing the number of non-destructive measurements. Construction and Building materials 211: 199-206, 2019.

[12] Faggiano B., Grippa M.R., Marzo A., Arriaga F. and Mazzolani F.M.: Combined non -destructive tests for the mechanical characterization of old structural timbers elements. In 3AESE: *Proceedings of the 3rd International Conference on Advances in Experimental Structural Engineering*, pages 657-666, San Francisco, 2009.

[13] Nowak T.P, Jasienko J., Hamrol-Bielecka K.: In situ assessment of structural timber using the resistance drilling method – Evaluation of usefulness. Construction and Building Materials 102: 403-415, 2016.

[14] Sharapov E., Wang X., Smirnova E.: Drill bit friction and its effect on resistance drilling measurements in logs. In: *Proceedings of the 20th International Nondestructive Testing and Evaluation of Wood Symposium,* Madison, 2017.

[15] Sharapov E., Brischke C., Militz H., Smirnova E.: Prediction of modulus of elasticity in static bending and density of wood at different moisture contents and feed rates by drilling resistance measurements. European Journal of Wood and Wood Products 77: 833-842, 2019.

[16] Koca G., Dündar T. and Nusret A.S.: Using the ultrasonic stress wave technique to evaluate structural timber members of an old masonry building. Kastamonu University, Journal of Forestry Faculty, 18(3):341-349, 2018.

[17] Hasegawa M., takata M., Matsumura J. and Oda K.: Effect of wood properties on within-tree variation in ultrasonic wave velocity in softwood. Ultrasonics, 51(3): 296-302, 2011.

[18] Oh S.C.: Comparison of Ultrasonic Velocities between direct and indirect methods on 30 mm x 300 mm spruce lumber. Korean Wood Sci Technol., 48(4): 562-568, 2020.

[19] Machado J., Palma P., Simoes S.: Ultrasonic indirect method for evaluating clear wood strength and stiffness. In: NDTCE'09, Nantes, 2009.

World Conference on Timber Engineering Oslo 2023

COMPARATIVE LIFE CYCLE ASSESSMENT OF TIMBER-CONCRETE-COMPOSITE WALLS WITH CONCRETE AND CLT-WALL ELEMENTS

Anna Wagner[1], Klara Winter[2], Anna Nestmann[3], Stephan Ott[4], Stefan Winter[5], Oliver Fischer[6]

ABSTRACT: In this study, Life Cycle Assessment of a new hybrid timber-concrete wall element was conducted. Furthermore, the results for the hybrid wall element were compared with the LCA results of a functional equivalent reinforced concrete wall element and a cross-laminated timber wall element. The thickness of the cross-section of the wall element (1 m² wall area) varied dependent on the applied load which was equal for every construction method. Modules A1-3, B4 as well as C1-4 and module D were considered. The results were analysed in terms of Global Warming Potential. The evaluation of the results indicated that, from an environmental impact point of view, the concrete-wall element is the least-reasonable option. The CLT wall element is the most suitable for small loads. However, with increasing load, a tipping point was reached. From this point on, the hybrid wall element showed lower environmental burden than the CLT wall element. This is because the thickness of the CLT used for the hybrid wall element and hence, its volume significantly increased compared with the volume of the hybrid wall element. Dependent on the applied load level, the difference in thickness among the cross-sections of the three construction methods can vary significantly.

KEYWORDS: comparative Life Cycle Assessment, hybrid construction element, timber-concrete wall

1 INTRODUCTION

In a completed research project, new hybrid timber-concrete wall elements were investigated by *Oberndorfer et al.* [1]. The wall elements consist of core lamellas in Ultra High Performance Concrete (UHPC) and exterior cross-laminated wooden lamellas. This composition should lead to a reduced use of concrete and at the same time, to a minimized component thickness compared to a Cross Laminated Timber (CLT) wall element. The reason for this is, that the combination of these two materials and their different properties enables an optimised utilisation for load-bearing purposes compared to CLT wall elements. [1]

The investigations of *Oberndorfer et al.* [1] focused on the force-fit adhesion of wooden lamellas to UHPC lamellas, showing promising results for a one-part polyurethane adhesive applied on a sanded UHPC lamella. In a follow-up research project, these hybrid CLT wall elements are now further investigated to evaluate their feasibility in practice. Thus, amongst other aspects such as hygrothermal behaviour and fire resistance, the environmental impacts of the wall elements are investigated.

To study the environmental performance of such wall elements, this article analyses the environmental impacts over their life cycle, in comparison with CLT and reinforced concrete (RC) wall elements dependent on the applied load.

By conducting a comparative assessment approach, the following research-questions should be answered:

- What are the environmental impacts of such hybrid CLT walls?
- What influence does the End-of-Life stage have on the results?
- Do these hybrid CLT walls have advantages over the environmental impact of common construction methods, such as reinforced concrete or CLT?

To enable prefabrication and the transport to the construction site, the focus is on wall elements. In this study, the term “wall” refers to wall elements.

2 BACKGROUND

2.1 Hybrid CLT walls

2.1.1 Composition of hybrid CLT walls

The investigated hybrid CLT wall resembles a common CLT wall. However, the core wooden lamella of the wall is replaced by an UHPC lamella (see Figure 1). This UHPC lamella can either be included continuously or, in the event of local load peaks, in an alternating way (see Figure 1).

[1] Anna Wagner, Technical University of Munich, Chair of Timber Structures and Building Construction, Germany, anna.wagner@tum.de
[2] Klara Winter, Technical University of Munich, Chair of Concrete and Masonry Structures, Germany, klara.winter@tum.de
[3] Anna Nestmann, Technical University of Munich, Germany, anna.nestmann@tum.de
[4] Stephan Ott, Technical University of Munich, Chair of Timber Structures and Building Construction, Germany, ott@tum.de
[5] Stefan Winter, Technical University of Munich, Chair of Timber Structures and Building Construction, Germany, winter@tum.de
[6] Oliver Fischer, Technical University of Munich, Chair of Concrete and Masonry Structures, Germany, oliver.fischer@tum.de

https://doi.org/10.52202/069179-0132

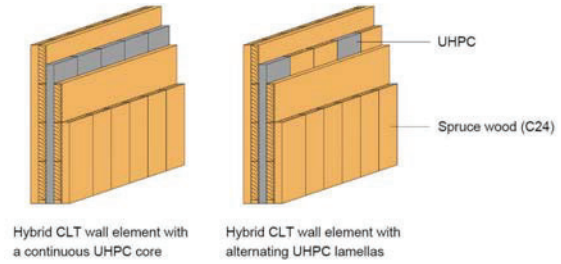

Figure 1: *Exemplary composition of Hybrid CLT walls*

The advantage of UHPC is that it shows much higher compressive strength than commonly used concrete, leading to thinner elements in comparison to concrete elements [2]. A one-component polyurethane adhesive is used to bond the lamellas (not bonded on the narrow sides). For an optimised application of timber and concrete, the UHPC lamella mainly bears the compressive force, whereas the outer wooden lamellas bear both compressive and tensile forces resulting from bending.

2.1.2 Production of hybrid CLT walls

In this study, the production process described in *Oberndorfer et al.* [1] is considered (see Figure 2). The production of hybrid CLT walls within the scope of the research project was partly manually conducted. For future practical applications, it is intended to produce the hybrid CLT walls on an assembly line that is comparable to the assembly line of CLT. The UHPC lamellas can be manufactured precisely because they are dimensionally stable in the setting process and are then precisely ground to size. Therefore, the processing steps can be automated. The extent to which the energy input for automated production influences environmental impact will have to be further investigated in the future.

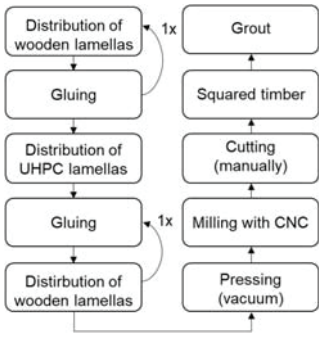

Figure 2: *Production process of hybrid CLT wall according to [1]*

The production process is similar to that of CLT walls. To produce the hybrid CLT walls, the wooden lamellas are slightly longer than the UHPC lamellas. Hence, after pressing, the wooden lamellas are milled with a CNC mill and manually cut without damaging the blades. After this process, a squared timber is inserted on the narrow sides. A small gap between the wooden and the UHPC lamellas results, which is filled with grout. [1]

2.2 LCA of hybrid construction components and of UHPC

2.2.1 LCA of hybrid construction components

To investigate the environmental performance of complex construction components and to compare different construction methods, Life Cycle Assessment (LCA) can be applied [3].

In different studies [4,5], LCA of hybrid timber-concrete components was conducted. In these studies, only the production stage was investigated based on already existing product-datasets. However, for a holistic consideration, all life cycle stages should be considered [3], because, especially for hybrid structures, the End-of-Life stage influences the environmental impact results of the full life cycle [6].

According to the European waste directive [7] and in terms of resource conservation and avoiding emissions, reuse or high-level material recycling should be favoured, instead of final material recovery, energy recovery or disposal. In 2020, around 57 % of construction waste in Germany was used as recycling material for street and earth work, 16 % was used to produce asphalt and concrete, while the resting percentage was disposed or landfilled [8]. Moreover, approximately 80 % of waste wood in Germany is incinerated [9]. This shows that, for both concrete and construction wood, high-level recycling or even reuse as required by the European waste directive [7] is not yet broadly established in practice.

To enable the reuse or high-level recycling of construction products, separability into homogenous and identifiable materials must be given [10,11]. Hence, for hybrid timber-concrete construction components, it is necessary to ensure the separability of timber and concrete at End-of-Life to enable the recycling of the different materials [6]. Solutions such as deconstructable connectors for Timber-Concrete-Composite floors may ease separation [12]. Further, the adjustment of legislations is necessary to allow the use of secondary materials in new products [11].

2.2.2 LCA of UHPC

Several studies have been conducted to assess the environmental impacts and resource consumption of UHPC production [e.g. 12–14]. Additionally, standard UHPC mixtures with eventually more sustainable UHPC mixtures have been compared, for example, by partly replacing cement with blast furnace sly or fly ash [13]. The environmental performance of UHPC compared to common concrete is comparatively assessed by, for example, *Sameer at al.* [12] and *Ji et al.* [14]. The results show, that the environmental impacts of UHPC are much higher than of commonly used concrete related to a functional unit of 1 m³ [14]. This is mainly because less than 50 % of the amount of cement used in UHPC is necessary for the concrete [14]. For common German concrete C20/25, the cement production is responsible for 82 % of the global warming potential (178 kgCO2-eq./m³) and approximately 56 % of non-renewable primary energy consumption (912 MJ) of the concrete production [15]. This is significantly influenced by the

https://doi.org/10.52202/069179-0132

deacidification process of limestone as well as the energy required for that process during the production of cement clinker [15,16]. Nevertheless, UHPC shows higher strength properties and hence, dependent on the boundary conditions such as geometry and load, smaller cross-sectional dimensions can be required for an UHPC element than for a common concrete element [13,17].

2.3 Functional equivalency in comparative LCA

For a comparative assessment of different construction components, a functional equivalent must be determined by defining the main functional requirements combined with the intended purpose of use [18,3]. In the study of *Kromoser and Holzhaider* [4] for example, for the comparison of different timber-concrete composite ceilings, the functional equivalent of load-bearing capacity was chosen. In other studies, the U-value of walls is taken into consideration, because outer walls and the secondary structure are considered [e.g. 10]. Nevertheless, it has to be mentioned, that according to the European Construction Product Regulation (EU CPR), construction products have to fulfil several basic requirements at once to ensure "[…] health and safety of persons involved throughout the life cycle […]" [19]. These requirements do not only include static and hygrothermal aspects, but also e.g. fire resistance, sound insulation, energy consumption, health aspects and sustainable resource consumption [19].

3 METHOD – GOAL AND SCOPE DEFINITION

3.1 GOAL

The aim is to conduct a life cycle analysis of the hybrid CLT walls in comparison with CLT and reinforced concrete walls. The comparison is intended to provide a comparative statement on the environmental performance of the walls in terms of the load-bearing capacity. In such way it should be investigated if the hybrid CLT wall brings advantages concerning the environmental impacts.

3.2 SCOPE

3.2.1 Product system

For the comparative life cycle assessment, walls in three different construction methods are evaluated: A hybrid CLT wall, a CLT wall and a reinforced concrete wall (see Figure 3)

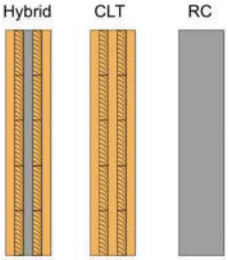

Figure 3: *Vertical sections of the three studies product systems for the comparative LCA*

The hybrid CLT wall consists of lamellas equal to CLT-lamellas, but the core is replaced by ultra-high performing concrete (UHPC) lamellas. The number of layers can, equal to CLT, vary between three, five, and seven layers. In this study, the focus is only on 5 layered CLT and hybrid CLT walls, as this is a very commonly used composition in practice. This study considers a continuous UHPC lamella instead of accounting a squared timber and a specific amount of grout.

3.2.2 System boundaries and data

The LCA is conducted for the functional unit of 1 m² surface area of a wall. The thickness of the wall varies dependent on the applied load and is therefore part of the functional equivalent for the comparison.

For the assessment only *GaBi* Datasets with Germany as regional system boundary are considered.

The LCA covers the manufacturing stage A1-3 (A4-5 is neglected because of lacking data), as well as the deconstruction stage C1-4. The loads and advantages of recycling and recovery are separately shown outside the system boundary in module D [18]. An exchange of the primary load-bearing structure during the life cycle is not necessary (Module B4) because the secondary structure (e.g. insulation, cladding) is responsible for its durable protection during the life cycle. In this study, the consideration of the "full life cycle" refers to modules A1-3 (production stage), module B4 and modules C1-4 (End-of-Life stage).

This study does not consider material losses during production and waste treatment. Further, side streams during the production stage are assumed to be insignificant or are covered by the applied *GaBi* datasets. Moreover, concerning concrete and UHPC, it should be noted that the environmental benefits of carbonation during the life cycle are not considered in this research.

Concerning the consideration at End-of-Life, the instructions of DIN 15804 are followed [18]. The End-of-Life scenarios shown in Figure 4 are evaluated for the walls in different construction methods.

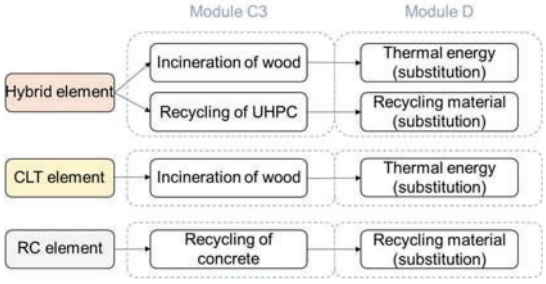

Figure 4: *End-of-Life scenarios for the studied walls in different construction methods*

For the reinforced concrete wall, neither loads nor benefits are accounted for the steel in module C3, similar to the dataset for *ready-mixed concrete C20/25* of the *Ökobaudat* database [20]. Additionally, in the dataset, it is supposed that 25 % of the material is landfilled and 75 % of the inert material is further used as filling material e.g. for streets (substitution) [20]. In this research a

https://doi.org/10.52202/069179-0132

simplified approach is used, assuming that 100 % of the inert material substitutes primary filling material.
For the CLT wall, a thermal recovery scenario is assumed. Hence, the environmental impacts due to the incineration of the wall are accounted in module C3 and only the benefits of the substitution of the recovered energy are accounted in module D.
For the hybrid CLT wall, a separation into wooden lamellas and UHPC-lamellas seems possible, because the two materials could be separated either by e.g. using an excavator to scrape off the wood or by using a mill or a saw to separate the wall. The milling or sawing is possible due to the very precise production of the hybrid CLT wall. In such way the thermal recovery of the wood as well as the treatment and use of the UHPC as filling material is seen as a realistic future scenario. Consequently, the assumptions and simplifications made for CLT and reinforced concrete are also made for the hybrid CLT wall.

3.3 Functional equivalent

Since the load-bearing capacity is the main functional requirement of the considered internal walls, this is the necessary functional equivalent for the comparison.
For this purpose, an equal load is applied to the walls of the different construction methods. This load is then linearly increased until the maximum load-bearing capacity of the walls is reached. The environmental impacts related to the resulting cross-sections of the walls should then give answers to the above-mentioned research questions. For the sake of simplicity, further basic functions required by the EU CPR [19], like fire safety or sound protection are neglected in this article. Moreover, the thermal conductivity is not part of the consideration, because this would be relevant for the assessment of external walls.

3.4 Impact indicators

To calculate information about the environmental impacts, the impact indicator climate change Global Warming Potential (GWP) is considered. As required in DIN EN 15804+A2 [18], the GWP_{total} is separated into GWP_{fossil}, $GWP_{biogenic}$ and GWP_{luluc} (land use and land use change). GWP_{luluc} does not have to be declared when it contributes to less than 5% of the GWP_{total} caused in the declared modules (module D excluded).

4 LIFE CYCLE INVENTORY

4.1 Variations of cross-sectional dimensions

To compare the environmental impacts of functionally equivalent walls in terms of their load-bearing capacity, an equal design load F_d [kN] has been applied, as shown in Figure 2. By stepwise increasing the load, the cross-sectional dimensions of the walls of different construction methods change. Only five layered CLT and hybrid CLT walls were assessed. However, cross-sections of wooden lamellas with a longitudinal layer thickness of more than 40 mm consist of two adhered lamellas (see Figure 5). These seven layered walls were still considered, because the lamella orientation and consequently the load-bearing principle does not change.

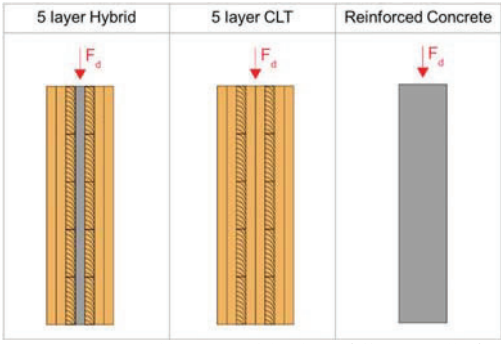

Figure 5: *Vertical sections of the three different walls dependent on the construction method*

F_d was stepwise increased by 100 kN/m considering a 1 m long wall. For dimensioning, a 3 m high hinged column was investigated. This leads to an imperfection of approximately 8 mm regarding 2nd order theory [21]. Fire safety was not included within the calculations.
The CLT and hybrid CLT walls were calculated according to shear-force analogy. All reinforced concrete walls were calculated according to DIN EN 1992-1-1:2011-01 [22]. Table 1 summarizes all strength values and further boundary conditions considered in the calculation.

Table 1: *Boundary conditions for the calculation of the walls under a load increase in steps of 100 kN*

CLT	
•	CLT layers - strength class: C24
Hybrid CLT	
•	Separate wooden layers - strength class: C24
•	UHPC lamella - strength values:
	Youngs modulus: 45000 [MN/m²]
	Shear modulus: 19489 [MN/m²]
	Compressive strength: 132,5 [MN/m²]
Reinforced concrete	
•	Exposure class: XC1
•	Steel grade: S 355
•	Strength class: C 25/30

To obtain functional equivalent results in terms of the load-bearing capacity, the aim was to consider the loads and respective cross-sectional dimensions with, at best, equal performance ratios. Since standard lamella thicknesses were used for the calculations, a performance ratio between 0.75 to 1.0 has been assumed as “equal”. For the reinforced concrete walls, a minimum thickness of 100 mm is required [22,23]. Nevertheless, in this study, a minimum thickness of 150 mm was considered to ensure the practical feasibility of mounting such walls and to compact the concrete despite the required minimum amount of reinforcement. Hence, due to the wall thickness

of the reinforced concrete of 150 mm, the performance ratio is below 0.75 up to a load of 2100 kN.
Figure 6 exemplarily shows the results for different construction methods under increasing loads. Here, the thickness per 1 m² surface area, and hence, the volume of the different walls, is shown.

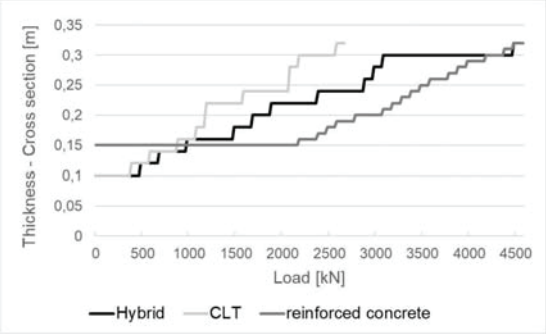

Figure 6: *Wall thickness [m] dependent on the applied load for a hybrid CLT, a CLT and a reinforced concrete wall*

For a standard CLT wall with five layers, the maximum load is reached at 2600 kN (cross-section: 80-40-80-40-80). The hybrid CLT wall with five layers reaches a maximum possible load of 4500 kN. A further increase in the load would lead to larger CLT or hybrid CLT wall cross-sections, which are normally not available on the market. Therefore, no additional cross-sections are calculated for increased loads in the case of these two construction methods.
No such limitation regarding wall thickness exists when considering reinforced concrete. Therefore, the cross-sections for the reinforced concrete wall are shown for loads of up to 4600 kN. At load levels higher than 1000 kN, the cross-section of the reinforced concrete wall is constantly smaller than that of the CLT and the hybrid CLT wall. At 4400 kN, this changes and the cross-section of the reinforced concrete wall becomes ticker than that of the hybrid CLT wall. In this study, the strength class of the concrete is constantly set to C25/30. Under the same load, the use of a higher strength class could lead to thinner cross-sections. However, an equivalent volume of concrete with a higher strength class also has greater environmental impacts [15]. For simplification, the effect of this correlation on the environmental impact results for reinforced concrete, is not part of this study but should be further investigated in detail.

4.2 Production stage - LCI

4.2.1 UHPC lamellas - LCI and LCIA

To calculate the environmental impacts of a hybrid CLT wall, the environmental impacts of UHPC (raw density of 2.500 kg/m³) must be determined. For the LCA modelling of the UHPC, the walls and further background data, the *GaBi Software and Database for Life Cycle Engineering* (*GaBi*) from *Sphera Solutions* was used. The *GaBi* database does not provide any dataset for UHPC. Hence UHPC production had to be modelled.

The calculation of the environmental impacts of 1 m³ UHPC was based on a composition without reinforcing steel fibers, which has been used for the completed research project [1]. Additionally, the research results of *Sameer et al.* [12] for 1 m³ precast UHPC have been considered. The transportation distances as well as the consumption of fuel and electricity are calculated to produce 1 m³ of precast UHPC [12]. Similar to *Sameer et al.* [12], material losses during production are neglected in this consideration. Further, the formwork is not considered because, like for common concrete, it is assumed to have no significant impact due to the number of uses [24]. Moreover, the electricity and fuel consumption for the treatment of the UHPC lamella after stripping the formwork are neglected according to the cut-off criteria of DIN EN 15804 [18], because it is assumed, that they account for less than 5 % of the energy and resource inputs for UHPC production.
Figure 7 shows the GWP_{fossil} results for 1 m³ UHPC in comparison with 1 m³ concrete C25/30. These results are used in the following sections to calculate the environmental impacts of the hybrid walls. Compared to the results for a concrete C25/30, the $GWP_{fossil.}$ of UHPC is nearly 60% higher.

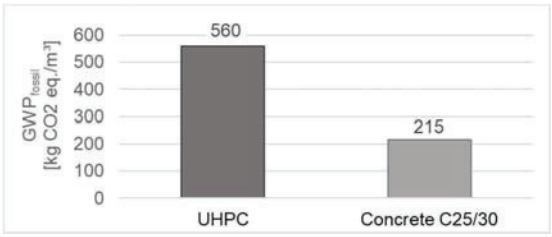

Figure 7: *GWP_{fossil} results for 1 m³ UHPC in comparison to 1 m³ concrete C25/30*

4.2.2 Hybrid CLT wall - LCI

To produce a hybrid CLT wall, the production steps described in the research of *Oberndorfer et al.* [1] are necessary. Table 2 lists the flows and processes required for the production stage of the hybrid CLT wall. Dependent on the cross-sectional dimensions of the wall and the corresponding thicknesses of the lamellas, the quantity of the input flows concerning the UHPC and the wooden lamellas varies.

Table 2: *Input flows to produce 1 m² hybrid CLT wall*

Input flow	quantity	Source
UHPC	*Varies [kg]	[*]
Wooden lamellas (adhesive included)	*Varies [kg]	[*]
Adhesive between UHPC and wooden lamellas	0,34 [kg]	[1]
Truck transport	*Varies [tkm]	[**]

*Dependent on applied load
**Dependent on amount of adhesive and UHPC-lamella thickness

https://doi.org/10.52202/069179-0132

It is assumed that the production of the hybrid CLT wall takes place in a CLT-factory. As the hybrid CLT wall basically is a CLT wall with a different core lamella, the production process is supposed to be equal to the one of a CLT wall, except for the adhesion of the core UHPC-lamellas to the wooden lamellas. For 1 m² surface area, 170 g of adhesive was applied. Hence, both sides of the UHPC lamella require 340 g/m² [1]. As until now, the adhesion process is manually conducted, no further electricity or fuel is consumed.
Due to similar production steps and because the focus is on the comparison of the different construction methods, the data set being used for the CLT wall is used for the bonded lamellas of the hybrid CLT wall. Until now, the *GaBi* database does not contain any dataset for CLT. In the German database *Ökobaudat*, datasets for Glue Laminated Timber (GLT) and CLT can be found. These datasets are based on the findings of *Rüter and Diederichs* [25], who used *Gabi* for simulation. The dataset for modules A1-3 of 1 m³ GLT shows a slightly higher share of GWP_{fossil} and a lower share of $GWP_{biogenic}$ than the dataset for 1 m³ CLT. This might result in slightly higher results for GWP_{fossil} and lower results for $GWP_{biogenic}$. Hence, because the focus of this study is on the comparison of different walls, the dataset for GLT has been used.

4.3 Deconstruction stage - LCI

For the End-of-Life consideration, the deconstruction processes for the walls (module C1) as well as the transportation distances (module C2) are considered as equal for the three different construction methods.
For the demolition scenario, the findings of *Sameer et al.* [12], who focused on the demolition of precast UHPC, are taken into account. Due to lacking robust data for buildings, an average transport distance of 20 km from the demolition site to the waste treatment factory is considered.
For waste separation (module C3) of the hybrid CLT wall an electricity consumption for the milling process of 3,4 kWh/m² is assumed due to lacking robust data.
The benefits from the substitution of gravel as filling material with recycled concrete and the benefits of the energy substituted by the thermal recovery of wood are separately accounted in module D (see Figure 4).

5 ENVIRONMENTAL IMPACT ASSESSMENT AND COMPARISON

5.1 Production stage - LCIA

5.1.1 Hybrid CLT wall - LCIA

With increasing load steps, the UHPC lamella changes its thickness from 20 mm (0-1000 kN) to 40 mm (1000-3100 kN) to 80 mm (3100-4500 kN). Figure 8 presents GWP_{fossil} and $GWP_{biogenic}$ of selected cross-sections. The cross-sections are selected at the minimum and maximum loads resulting in the three UHPC lamella thicknesses.

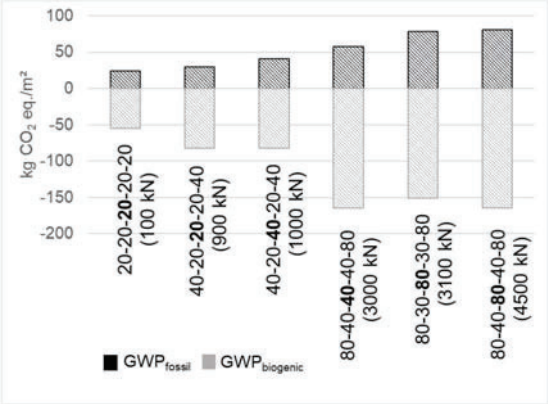

Figure 8: *GWP_{fossil} and $GWP_{biogenic}$ (modules A1-3) of 1 m² hybrid CLT wall for selected cross-sections at the corresponding minimum and maximum loads (UHPC lamella in **bold**)*

With increasing thickness of the cross-section, the GWP_{fossil} increases. This is not only due to the increase in UHPC, but also due to the increasing amount of wood, because an increasing amount of these two materials requires higher process inputs. Moreover, $GWP_{biogenic}$ mainly depends on the overall thickness of the wooden lamellas. Looking at the cross-sections 80-40-40-40-80 (3000 kN) and 80-30-80-30-80 (3100 kN), the UHPC lamella becomes thicker and at the same time the total thickness of the wooden lamellas diminishes. As less carbon can be stored in the wooden lamellas, the $GWP_{biogenic}$ increases.

5.1.2 Comparison of different construction methods

Figure 9 exemplarily shows the results for GWP_{fossil} for life cycle modules A1-3 for the different construction methods under increasing load steps. It must be mentioned that the reinforcement content of the reinforced concrete was constantly set to 4 %.

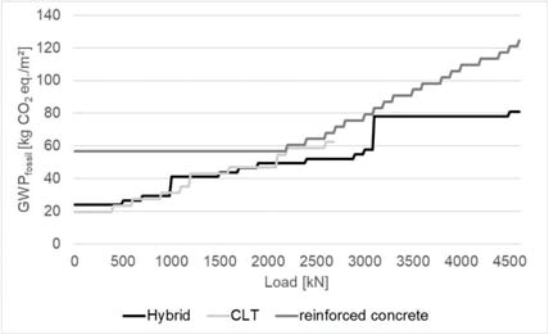

Figure 9: *GWP_{fossil} for 1 m² wall area (modules A1-3) for the different construction methods under increasing load*

The results indicate that, in general, the CLT and the hybrid wall have a lower environmental impact than the reinforced concrete wall. This is under small loads boosted due to the minimum thickness of the concrete wall of 150 mm. At 2100 kN, the GWP_{fossil} of the CLT and reinforced concrete wall is nearly equal due to the difference in thicknesses of the walls. The thicknesses are

directly related to the volume of the wall and hence, the amount of associated environmental impacts resulting from the corresponding production processes.
Until 2100 kN the CLT wall mostly performs slightly better than the hybrid wall. This is because of the comparatively low greenhouse gas emissions during the production processes of the CLT wall. As the environmental impacts of the CLT wall increase relative to the thickness (volume), the increase in the environmental impacts is higher than that of the hybrid CLT walls. Thus, at 2100kN, a tipping point is reached. From that point on, the hybrid CLT wall constantly shows lower environmental burdens than the CLT wall until the maximum carrying capacity of the CLT wall is reached.
As already shown in Figure 8, when the thickness of the UHPC-lamella changes from 20 to 40 mm (1000 kN) and from 40 to 80 mm (3100kN), a strong increase in the GWP_{fossil} of the hybrid CLT wall results. When the UHPC lamella thickness turns to 80 mm, the GWP_{fossil} of the hybrid CLT wall (300 m) nearly becomes as high as that of the reinforced concrete wall (220 mm). A further increase in the load does not change the cross-section of the hybrid CLT wall (300 mm) and hence, its environmental impacts. Simultaneously, the thickness of the reinforced concrete wall and consequently, GWP_{fossil} increases.
To not only assess the $GWP_{fossil,}$, Figure 10 additionally shows the $GWP_{biogenic}$ of the walls for three selected load steps. GWP_{luluc} is not shown, because it is responsible for less than 5 % of the GWP_{total} caused in the considered modules.

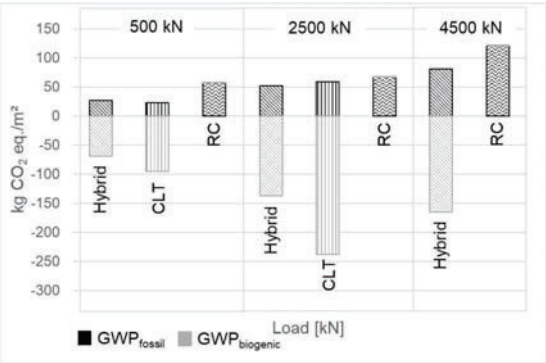

Figure 10: *GWP_{fossil} and $GWP_{biogenic}$ per 1 m² wall area (modules A1-3) of the different construction methods for three selected load steps*

$GWP_{biogenic}$ shows a negative value for both the CLT and the hybrid CLT wall. The reason for this is mainly the carbon stored inside the wooden lamellas during the life cycle. This biogenic carbon leaves the product system at End-of-Life in module C3. During the life cycle of a building the long-term storage of carbon might have a positive effect on counteracting climate change by contributing to cities as global carbon sinks [26].

5.2 End-of-Life - LCIA

To determine the influence of the End-of-Life stage, Figure 11 shows the GWP_{fossil} and $GWP_{biogenic}$ results for the full life cycle as well as for module D (outside system boundaries) for a load level of 500 kN.

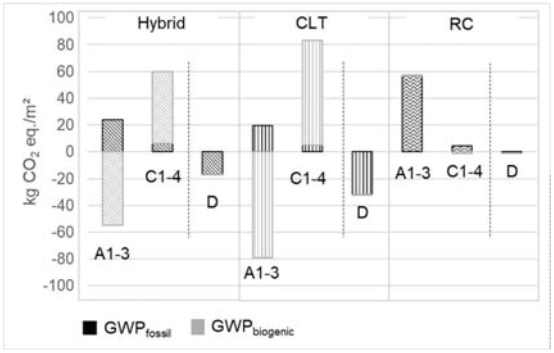

Figure 11: *GWP_{fossil} and $GWP_{biogenic}$ per 1 m² wall area for the full life cycle (modules A1-3, C1-4, D) of the three construction methods*

When considering modules A1-3 and C1-4, the $GWP_{biogenc}$ equals nearly zero, because the carbon stored in the wood is released at the end of the life cycle. This shows that fossil greenhouse gas emissions are dominant for all three walls. The highest share of GWP_{fossil} for every construction method is caused in the production stage and the impact of the deconstruction stage in the case of the walls is comparatively low. For the hybrid CLT wall, the GWP_{fossil} of modules C1-4 accounts for approximately 25 % of the GWP_{fossil} of modules A1-3.
Looking at the benefits and losses outside the system boundaries makes clear that the benefits for the CLT due to the thermal recovery of the wood are the highest, followed by the hybrid CLT wall due to the thermal recovery of the lamellas. The replacement of primary material with recycled concrete at the End of Live brings only a very small amount of benefits. This shows that even if module D is considered separately, it may influence decisions when taking Circular Economy principles into account.
The dominant GWP_{fossil} as well as the considerations of module D point out the importance of enabling separability and hence ensuring a high-level recyclability of the products.

6 CONCLUSION

The LCA results for the full life cycle indicate that, dependent on the load level and the resulting thicknesses, the use of hybrid CLT walls can show less greenhouse gas emissions and can be a structurally reasonable alternative to concrete and CLT.
Regarding GWP_{fossil} for the production stage, the reinforced concrete wall constantly shows the highest greenhouse-gas emissions. Under small loads, the CLT wall emits the lowest greenhouse gases. At 2600 kN, the CLT wall reaches its carrying capacity. At 2100 kN a tipping point is reached and the hybrid CLT wall shows

https://doi.org/10.52202/069179-0132

the lowest global warming potential. At even higher load levels, the hybrid CLT wall shows less environmental impacts than the concrete wall. The change in the thickness of the UHPC lamella in the hybrid CLT wall, has a significant influence on the global warming potential. When the thickness of the UHPC lamella changes from 40 mm to 80 mm, the GWP_{fossil} of the hybrid CLT wall differs only slightly from that of the reinforced concrete wall. However, with further increasing loads, this difference increases again until the hybrid CLT wall reaches its carrying capacity. Applying only the UHPC lamella where high loads are expected (alternating), may lead to a decrease of the environmental impacts of the wall.

A consideration of GWP_{total} or $GWP_{biogenic}$ only for the production stage could be misleading. because of the negative accounting of the biogenic carbon in the wood when entering the product system. The production stage of the hybrid CLT as well as the CLT wall seems to be carbon neutral or even positive, but when accounting for the benefits and loads resulting from the processes and especially from the biogenic carbon leaving the system boundary at End-of-Life, all three construction methods lead to greenhouse gas emissions. Nevertheless, further investigations on long-term carbon storage in buildings and their components should be conducted to explore this possible potential.

These carbon emissions during the life cycle and the End-of-Life considerations for all three construction methods show the necessity to bring solutions into practice that enable high-level recycling, or even reuse of the walls for further cycles instead of final disposal or incineration.

To improve the LCA results, background data, other impact indicators, different End-of-Life options, and practical deconstruction and separation trials of the hybrid CLT wall must be further researched. Dependent on the load level, the thicknesses of the walls can differ from 10 mm to more than 100 mm. The wall thickness is directly related to the volume. This aspect must be further evaluated.

For the comparison of construction components, this study highlights the importance of defining a robust functional equivalent for LCA comparisons dependent on the main functions of the component and the goal of the study. Here, only the load-bearing capacity was considered. To improve the validity of the results, it is further necessary, to consider not only the load-bearing capacity. For the functional equivalence of inner walls especially fire safety and sound protection play an important role. These requirements will be further considered in the ongoing research project as the focus is on the building level. In addition, for the comparison of external walls, thermal behaviour should be considered.

ACKNOWLEDGEMENT

This paper is an outcome of a research project with funds from the *Zukunft Bau* research programme of the *Federal Institute for Research on Building, Urban Affairs and Spatial Development* in the *Federal Office for Building and Regional Planning* (reference number: 10-08.18.7-20.29).

REFERENCES

[1] Oberndorfer, T., Hunger, F., and Fischer, O.: Ultra High Performing Timber Walls - Einsatz von schlanken Lamellen aus ultrahochfestem Beton in Brettsperrholzelementen zur Steigerung der Tragfähigkeit, Fraunhofer IRB Verlag, 2021.

[2] Schmidt, M., and Fehling, E. (eds.): Ultra-Hochfester Beton Planung und Bau der ersten Brücken mit UHPC in Europa, kassel university press GmbH, 2003.

[3] Deutsches Institut für Normung e.V.: DIN EN 15978:2012-10. Nachhaltigkeit von Bauwerken – Bewertung der umweltbezogenen Qualität von Gebäuden – Berechnungsmethode, Beuth Verlag GmbH, Berlin.

[4] Kromoser, B., and Holzhaider, P.: An innovative resource-efficient timber-concrete-composite ceiling system: Feasibility and environmental performance, Civil Engineering Design (3), 2021, pages 179–191.

[5] Fortuna, S., Mora, T. D., Peron, F., and Romagnoni, P.: Environmental Performances of a Timber-concrete Prefabricated Composite Wall System, Energy Procedia, 2017, pages 90–97.

[6] Agustí-Juan, I., Sharon, Z., and Guillaume, H.: End-of-life consideration for hybrid material systems, in: 14th International Conference on Durability of Building Materials and Components, pages 377–378.

[7] European Parliament and the council of the European Union: Directive 2008/98/EC of the European Parliament and of the Council of 19 November 2008 on waste and repealing certain Directives, 2008.

[8] Bundesverband Baustoffe – Steine und Erden e. V.: Mineralische Bauabfälle Monitoring 2020, Druckwerkstatt Lunow, Berlin (Germany).

[9] Mantau, U., Weimar, H., and Kloock, T.: Standorte der Holzwirtschaft, Holzrohstoffmonitoring, Abschlussbericht, 2012.

[10] Ebert, S., Ott, S., Krause, K., Hafner, A., and Krechel, M.: Modell der Recyclingfähigkeit auf Bauteilebene, Bautechnik (S1), 2020, pages 14–25.

[11] Kanters, J.: Design for Deconstruction in the Design Process: State of the Art, Buildings (8), 2018.

[12] Sameer, H., Weber, V., Mostert, C., Bringezu, S., Fehling, E., et al.: Environmental Assessment of Ultra-High-Performance Concrete Using Carbon, Material, and Water Footprint, Materials (12), 2019.

[13] Randl, N., Steiner, T., Ofner, S., Baumgartner, E., and Mészöly, T.: Development of UHPC mixtures from an ecological point of view, Construction and Building Materials, 2014, pages 373–378.

[14] Ji, C., Wu, Y., Zhao, Z., Chen, C., and Yao, L.: Life Cycle Assessment of Off-Site Construction Using Ultra-High-Performance Concrete, Sustainability (14), 2022.
[15] Becke, A., Reiners, J., and Tuan Phan, A.: Beton Umweltproduktdeklarationen, Verlag Bau+Technik GmbH, 2020.
[16] Bergmeister, K., Fingerloos, F., and Wörner, J.-D.: Nachhaltigkeit, Digitalisierung, Instandhaltung, 111. Jahrgang (2022), 111st ed., Ernst & Sohn a Wiley brand, Berlin, 2022.
[17] Schmidt, M., and Fehling, E. (eds.): Ultra-Hochfester Beton, 2nd ed.
[18] Deutsches Institut für Normung e.V.: DIN EN 15804:2022-03. Nachhaltigkeit von Bauwerken – Umweltproduktdeklarationen – Grundregeln für die Produktkategorie Bauprodukte, Beuth Verlag GmbH, Berlin.
[19] European Parliament and the council of the European Union: Regulation (EU) No 305/2011 of the European Parliament and of the Council of 9 March 2011 laying down harmonised conditions for the marketing of construction products and repealing Council Directive 89/106/EEC, 2011.
[20] Ökobaudat database, Sphera Solutions GmbH (owner): Transportbeton C20/25, 2021.
[21] Deutsches Institut für Normung e.V.: DIN EN 1995-1-1:2010-12. Eurocode 5: Bemessung und Konstruktion von Holzbauten – Teil 1-1: Allgemeines – Allgemeine Regeln und Regeln für den Hochbau, Beuth Verlag GmbH, Berlin (Germany).
[22] Deutsches Institut für Normung e.V.: DIN EN 1992-1-1:2011-01. Eurocode 2: Bemessung und Konstruktion von Stahlbeton- und Spannbetontragwerken - Teil 1-1: Allgemeine Bemessungsregeln und Regeln für den Hochbau, Beuth Verlag GmbH, Berlin.
[23] Deutsches Institut für Normung e.V.: DIN EN 1992-1-1/NA:2013-04. Nationaler Anhang – National festgelegte Parameter – Eurocode 2: Bemessung und Konstruktion von Stahlbeton- und Spannbetontragwerken – Teil 1-1: Allgemeine Bemessungsregeln und Regeln für den Hochbau, Beuth Verlag GmbH, Berlin (Germany).
[24] Institut Bauen und Umwelt e.V. (IBU): Umweltproduktdeklaration - Beton der Druckfestigkeitsklasse C30/37, 2018.
[25] Rüter, S., and Diederichs, S.: Ökobilanz-Basisdaten für Bauprodukte aus Holz, 1 Jan. 2012.
[26] Churkina, G., Organschi, A., Reyer, C. P. O., Ruff, A., Vinke, K., et al.: Buildings as a global carbon sink, Nature Sustainability (3), 2020, pages 269–276.

https://doi.org/10.52202/069179-0132

World Conference on Timber Engineering Oslo 2023

GHGs EMISSIONS FROM SAWNWOOD PRODUCTS IN NORWAY– THE IMPORTANCE OF HARMONISED LCA METHODOLOGY IN ENVIRONMENTAL PRODUCT DECLARATIONS (EPDs)

Johann Kristian Næss[1], Ana Maria Santos Bouzada[1], Roja Modaresi [1]*

ABSTRACT: Wood is often considered a low-emission and sustainable material. However, there is always potential for the industry to further reduce environmental impacts if hotspots in the production phases are identified. When a contribution analysis is performed in LCA for building materials, the different processes, raw materials or life cycle stages contribution to a functional unit's overall impact can be compared. However, methodological choices in the LCA can be decisive for how a contribution analysis should be interpreted. This study has two main purposes; 1) to perform a contribution analysis for planed timber products in terms of Global Warming Potential, representative for sawmill industry in Norway, 2) to highlight the importance of harmonised LCA methodology in Environmental Product Declarations (EPDs) by performing a sensitivity analysis for the choice of allocation assumptions, as Product Category Rules (PCRs) can be interpreted differently by EPD practitioners. Calculations are based on data from five timber manufacturers in Norway, whereas three of these also had facilities for surface treatment on site. The uptake of carbon dioxide in the timber products was not considered in the GWP calculations. Results show that forestry and sawlog transport contribute the most to the GWP of planed timber. Furthermore, results for A1 and A2 modules (A1: raw material, A2: transport of raw material) are sensitive to allocation assumptions defined in A3 of the LCA model (A3: manufacturing). Using physical properties instead of economic values for allocation of these upstream emissions in forestry and transport, reduces the GWP emissions by approximately 30%, from 59.1 to 41.6 kg CO_2-eq/m^3. This demonstrates how allocation choices across life cycle stages matters. Inconsistency in allocation practices impairs the comparability of EPDs developed for wood building materials and deteriorates rationale environmental decisioning for the building sector.

KEYWORDS: Sawmills, Emissions, Forestry, EPD, EN15804, Allocation, LCA

INTRODUCTION

Wood increases its legitimacy in comparison to other materials, often associated with relatively low greenhouse gas emissions (GHGs) in processing, in addition to the carbon sequestration possibilities in the use phase [1-4]. Norway has an annual production of about 13 Mm^3 of roundwood [5, 6]. 2.7 Mm^3 of sawn timber are produced in Norway annually by relatively small sawmills, where 75% of the total production is coming from 18 sawmills with a capacity of above 50 000 m^3 [7]. Several LCA studies on forestry have been conducted since the early 1990s, however, there are differences in assumptions, background data, and their subsequent results [8]. GHGs from Norwegian forestry and transport to industry has previously been well documented for roundwood [9]. However, there has been a lack of similar studies that includes downstream production activities from the forest, such as sawmilling and planing of timber. This makes it difficult to compare the GHGs from different stages in the Norwegian value chain for timber building materials. Such an assessment exists for individual sawmills in other countries. For example, Lauri et. al compared different allocation methods for timber products and included results for different life cycle stages, using manufacturers data from three sawmills in Europe [10]. Beside all the existing studies, interpretation of LCA results for the production phases of sawn timber must be made with caution in EPDs and LCA studies. This difference in practice, becomes important when joint co-production processes are present in one or more of these life cycle stages. Such processes can be defined as undividable processes that has more than one output product with positive economic value. In these cases, environmental impacts associated with the joint-co production process including upstream impacts from materials and energy needed, must be partitioned to the products in a rational way. Partitioning of the flows to different products are often referred to as allocation in LCA. Allocation is usually based on physical properties such as mass or energy content. However, flows shall be allocated by economic value for the distinct co-products when the differences in the respective revenues are high, >25% according to a 'Note' in EN 15 804 [11]. A typical joint-co production process in the value chain of wood building materials is the sawing process, with outputs of sawn timber, chips and sawdust. For these co-products, the differences in revenues are relatively high. Different interpretations for the interlink between life cycle stages are made in LCA of wood materials in Nordic countries, where mainly two different methodical frameworks have been established for the development of EPDs. Two

[1] NTI Norwegian Institute of Wood Technology, Norway
* Corresponding author: Roja Modaresi Norwegian Institute of Wood Technology, rmo@treteknisk.no +47 402 95 791

https://doi.org/10.52202/069179-0133

different program operators are publishing EPDs, in Norway (EPD-Norge) and Sweden (International EPD system (IES)). Program operators provides guidelines for the development of EPDs by providing PCRs for specific product groups, but the rules must follow PCRs' higher in the hierarchy, such as EN 15804 [11] and EN 16485 [12], the latter is currently being revised. Rules for accounting of greenhouse gas emissions are also increasingly being governed by law, which can affect the new revisions of EPD standards. LCA is still a field under development, and despite the great number of PCRs that exist to harmonise methods for calculations, rules in standards and Product Category Rules (PCRs) are still open for interpretation [10]. There is a lack of knowledge among the EPD users [13]; and problems especially occurs when EPDs from different program operators are compared, with the aim of selecting a product with a better environmental profile. It is clearly shown in a study of 436 EPDs which were published under two different programme operator and therefore two different PCRs; that almost 90% of EPDs were incomparable [14].

The aim of this study is to perform; 1) GWP assessment for surface treated claddings, and planed timber products produced in Norway, using a contribution analysis format and LCA principles from development of EPDs 2) sensitivity analysis of using two different methodical frameworks that is present in EPD development in Nordic countries.

METHODOLOGY

A cradle-to-gate GHG assessment was made for planed timber and surface treated cladding in a contribution analysis format, meaning that the contribution of different products or processes impacts to the final result can be examined. Furthermore, a sensitivity analysis was performed for different methodical frameworks practiced for EPDs in Norway and Sweden; "NO method", following NPCR 015 and the older version of EN 16485. Also referred to as the traditional value chain calculation, "SE method", which differentiates from the value chain calculation by allocating upstream activities (roundwood) in forestry (A1) and transport of roundwood to sawmills (A2) after mass in joint co-production processes at sawmills.

Contribution analysis

Included activities inventoried in this assessment are highlighted in Figure 1. The system boundary is defined by the outer grid in the figure, which includes processes from rejuvenation activities in forestry until the finished product (planed timber or surface treated cladding) is packaged and stored within the factory gate. The functional units are 1 m³ of planed timber and 1 m² of surface treated timber cladding. Planed timber includes a varieties of untreated timber products that has undergone sawing, drying and planing and are used as building materials for both structural and non-structural purposes, indoor or outdoor. Cladding is used for exterior façade of houses and buildings, and one layer of primer and paint is applied in the manufacturing (industrially coated) for this functional unit. In the contribution analysis for planed timber, the same production activities within the dotted border in Figure 1 represents the grouping of sawmill activities, and in addition, Forestry and roundwood transport are also a separate group. For surface treated cladding, only the timber cladding and the surface treatment constitutes the two contribution groups in this analysis. Other important activities that are not depicted by Figure 1 is the production of paint and diesel, emissions from the manufacturing of these raw materials are included in the analysis groups for surface treatment and internal transport, respectively.

Five sawmills, located in the South-eastern parts of Norway, constitutes the providers of specific manufacturers data in this study. The results are represented by the mid-point category for greenhouse gas emissions, GWP-IOBC (Global Warming Potential assuming instantaneous oxidation of biogenic carbon). This means that the uptake of carbon dioxide into biogenic carbon in the wood material is not included in the GWP result. This indicator is described in more detail in PCR part A from EPD-Norway [15]. The correct characterisation for methane in the PCR is not clear enough. Therefore, this study follows IPCC 2019 guidelines [16], in addition to EN 15 804.

Life Cycle Inventory (LCI)

The background LCI is built on a selection of Ecoinvent v3.7.1 data [17], combined with datasets tailormade for the Norwegian wood industry, e.g. roundwood production [18]. The specific data was gathered in EPD projects, involving five manufacturers of sawn timber, whereas three of these manufacturers had facilities for industrial surface treatment. A flow chart highlighting the included wood value chain activities in this study are presented in Figure 1.

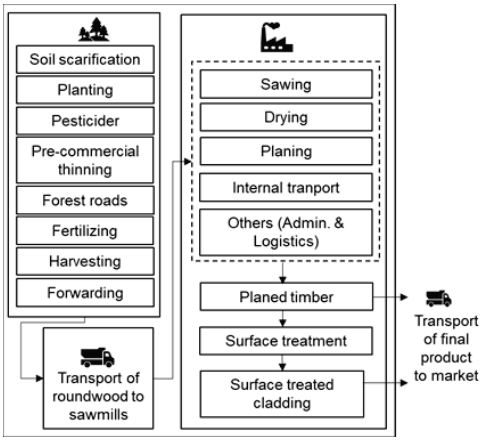

Figure 1: *Flow chart that summarizes included processes for processing of wood throughout the wood value chain.*

The reference year for annual activity data varies for the different subprocesses in forestry, but all are within the years 2016-2020, and based on national statistics data [19-21]. Otherwise, the LCI for forestry processes is taken from previous studies [9, 22]. LCI for fuel used is taken

https://doi.org/10.52202/069179-0133

from Vennesland et al. [23]. Regarding the silvicultural activity of fertilizing, it is assumed that 150 kg of nitrogen are used per ha of forest and that the secondary release of dinitrogen monoxide into the atmosphere due to the added fertilizer are 2,75 kg per ha [24]. The total area fertilized are based on national statistics data from the reference year of 2020 [25]. The allocation between sawlog and pulpwood has been adjusted to be in line with the requirements in EN 15804 [11] and NPCR 015 [26]. This means an economic allocation of silviculture operations and harvesting, except for the activity of forwarding (terrain transport of roundwood from the felling to the forest gravel road). It is assumed that the forwarding is not affected by the demand for roundwood, or pulpwood and these assortments can be transported separately from each other.

The dataset used for the road transport of roundwood is originally Ecoinvent data that has been modified at NTI to be more suitable for roundwood transport in Norway. The adjusted parameter values on fuel consumption, lorry weight, fuel blend, average load weight, and vehicle load capacity are based on information from actors within forestry operating in Eastern Norway (Norsk Virkesmåling, Viken Skog and Trekk Tømmer). A mix of 7% biofuel in the diesel is assumed, following NS-EN 590 [27]. For logs transported by sea, the background data are based on generic Ecoinvent data [17].

The process for industrial heat production, which is generated by the combustion of wood biomass by-products at the sawmill plants, is based on Ecoinvent data [17] for a 5000 megawatt wood furnace. But the process input inventory has been adjusted, by changing the inputs of wood by-products to specific data modelled in the EPD projects. In this way LCI flows are allocated back to the timber production, e.g. in the drying process of timber where heat energy is important. Bark is the most important fuel in the furnaces, in addition to sawdust. The data is validated by using a bioenergy calculator developed at NTI [28].

The upstream data for infrastructure and electricity are taken from Ecoinvent [17]. Data for alkyd coating applied in the surface treatment process are also based on generic Ecoinvent data for both the primer and paint. Similarly, the acryl coatings added for this alternative are based on generic Ecoinvent data for losses of chemicals, energy use and waste treatment, but the components in the acryl coatings is based on literature study [29]. The amount of paint applied on the claddings is based on the dried weight amount of coating on the claddings as stated in the original EPD projects. Furthermore, this amount is assumed for both acryl and alkyd coating application in this assessment, although correct application amounts for such paints can vary between coating manufacturer and type of binder used.

Weighting averages

Weighted average of the five sawmills are calculated based on the production capacity of the factories (total output of finished timber products). The process of industrial surface treatment is averaged by the production capacity of the different factories in terms of finished timber products with coating. The wood timber input in surface treatment (untreated cladding) are however weighted in the same way as for planed timber and in fact are the same cradle to gate (A1-A3) average result for planed timber for the five different factories, only adjusted for conversion to m² assuming a 19 mm thick cladding with a simple profile, giving 0,019 m³/m² of cladding.

Sensitivity analysis for different allocation practices in Nordic countries

Considerable differences in the EPDs' results of similar products from Norway and Sweden were recognized. Therefore, NTI initiated the communication with two national associations, Treindustrien in Norway and SvenskTrä in Sweden, which took over the administrative lead to figure out the differences present between EPD actors and harmonise the methodical differences present. Two different approaches were recognised in the communication, which are applied in this sensitivity analysis carried out for planed timber. All other assumptions in the LCA are kept constant to show how the methodical frameworks may affect the results.

Allocation of upstream emissions from forestry activities and the transport of roundwood (A1 and A2) was different for the two modelling approaches. Minor differences were also present for allocation of emissions occurring in the manufacturing (A3), but this consequence was considered less important for affecting final results and was modelled in the same way for both approaches in the sensitivity analysis.

The model framework applied for the 'NO model' are similar to Ecoinvent models [17], similar approaches are also present in other published LCAs for wood products [30-33]. The main difference of the SE and NO models is that special treatment is made for allocation of upstream emissions in the SE model, i.e., emissions not a part of energy use or direct emissions at the manufacturing. These can be emissions occurring in forestry or transport of roundwood, which are allocated by mass in joint co-allocation processes at sawmill, in contrast to economic value which are used in the NO model.

In the SE model, the roundwood input including transport to the sawmill is held constant at 1.15 m³, where 1 m³ represents the forestry emissions and transport of logs allocated to the climate impact for planed timber, and 0,15 m³ likewise are allocated to bioheat purposes at the sawmill factories, which are then allocated back to the planed timber. This means that also 1,15 m³ of roundwood is assumed transported from the forest to the sawmill, as shown in Table 1. Sometimes additional allocation procedures are made for the forestry part in the SE model, leading to a higher input of roundwood than shown in the table. A perfect mass balance approach was however assumed for SE in this analysis, to recognise the biggest possible differences present for sawn timber products in EPDs today. In the NO model, the wood raw material needed in the timber manufacturing will accumulate throughout the value chain, for every joint-co production process dividing the flow of emissions to main and by-products. This leads to accumulated use of roundwood along the value chain, and as shown in Table 1, 1,65 m³

illustrate the use of roundwood for the 1 m^3 of sawn timber production. While 2,14 m^3 are the use of roundwood produced in forestry, accumulated during the allocation to pulpwood and roundwood from forestry sub processes. NO amounts in Table 1 are approximate amounts used for the harmonisation meetings and planed timber is assessed for this sensitivity analysis and not rough sawn timber (the wood input in the planing process), as in the table. The planing process also leads to accumulation of roundwood needed, following the NO model.

Table 1: *Assumptions for roundwood consumption in the production of rough sawn timber in Nordic countries. The outcome from the EPD harmonisation work by Treindustrien and Svensk Trä.*

Scenario no.	Roundwood (Forestry) (A1) [m^3]	Transport of roundwood (A2) [m^3*km]
NO Method	2.14	1.65
SE method	1.15	1.15

Note: The NO method is not developed in Norway nor limited to EPD development in Norway and the same applies for the SE method, but the abbreviations were used in the harmonisation work, which has been started between the two countries.

RESULTS

The average result of GWP-IOBC for 1 m^2 of planed wood and surface treatment activity for a façade product with a 19 mm thickness is shown in Figure 2. Production of 1 m^2 planed wood correspond to 1.1 kg CO_2-eq. While almost 1 kg CO_2-eq is emitted for the industrial surface treatment process including the production of paint, which are the average result for the three sawmills with surface treatment combination plants.

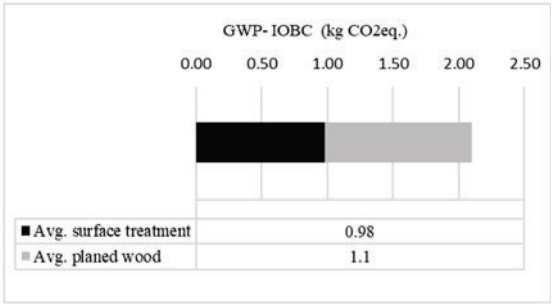

Figure 2: *GWP-IOBC for 1 m^2 of surface treated cladding products for an average of Norwegian sawmills.*

Figure 3 presents the results as a contribution analysis for planed timber production per activity, average for the five sawmills using the two defined methodical frameworks: 'NO method' and 'SE method'. All upstream forestry processes mentioned in Figure 1 are grouped together to represent a single forestry activity. While other sawmill processes are presented separately. Forestry shows the highest contribution, followed by roundwood transport. There is a distinct difference in the result for forestry and roundwood transport for the different methods.

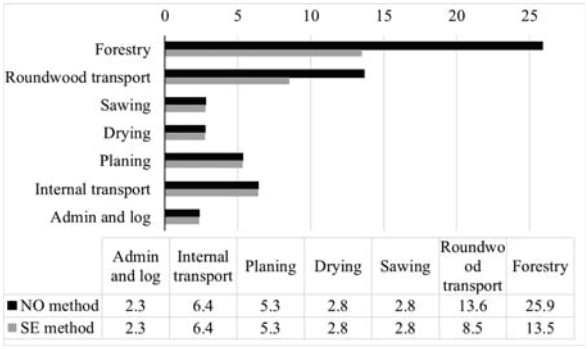

	Admin and log	Internal transport	Planing	Drying	Sawing	Roundwood transport	Forestry
NO method	2.3	6.4	5.3	2.8	2.8	13.6	25.9
SE method	2.3	6.4	5.3	2.8	2.8	8.5	13.5

Figure 3: *Weighted average for GWP- IOBC contribution [kg CO_2 eq] per activity to produce 1 m^3 of planed timber in the five selected Norwegian sawmills.*

The two methods can be compared in Figure 1, by the ratio for contribution for GWP in A1-A3. In the SE method, sawmill activities show the highest share, due to the different approach for calculating upstream emissions. While in NO method, the forestry has the highest share in the overall contribution.

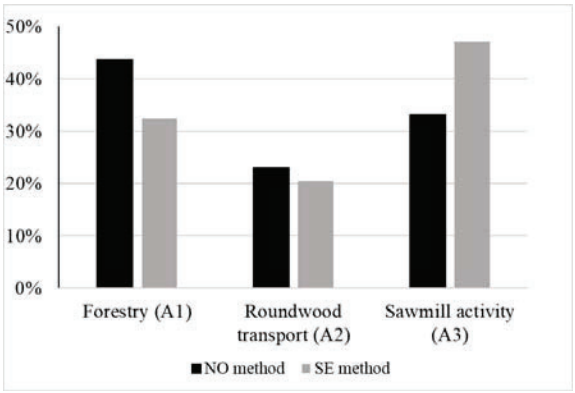

Figure 4: *Contribution by different production stages to GWP-IOBC for planed timber.*

DISCUSSION

The planed wood and surface treatment are having almost equal contribution for production of surface treated cladding. In addition, one layer of surface treatment is advised after the installation, and during each maintenance interval of the façade in the use phase of buildings. Considering the application of paint during the lifetime of a building, a previous study showed that the contribution of paint is dominating throughout the lifecycle [34].

Forestry is the highest contributor for planed timber, because of several energy intensive silvicultural activities. Roundwood transport from forest to sawmills has a considerable effect. However, this can vary depending on the sawmill location and the forest resources.

Results in EPDs are sensitive to the choice of allocation assumptions across the production phases. The author's interpretation is that the EPD standard (EN 15804) is not

https://doi.org/10.52202/069179-0133

explicit enough for the allocation treatment of upstream raw material acquisition and processing, including the transport thereof, and requires a better common understanding between EPD practitioners.

The different production stages (modules) are treated more separately in the SE model compared to the NO model, resulting in a lower amount for the assumption of roundwood consumption in the production of sawn timber. In the harmonisation discussions, argumentation for using the SE method is that forestry products and residues can be input for a wide range of products, and that this is not known at the time of harvest. The owner structure from forest management to the production of wood building materials are often merged in Sweden, which can make it difficult to estimate the economic value of intermediate wood products and therefore apply the allocation principles demanded in EN 15 804. The NO model is the rationale choice for partitioning of emissions throughout the value chain of wood in many trade regions around the world, but this is put on the test by ownership structures in some regions and the market situation for raw wood and intermediate products. However, differences in results that are not due to actual conditions in production are unwanted by anyone producing or using LCA data. Nor is this wanted by regulatory law either, which set new rules for environmental documentation and performance at an increasing rate. Finally, inconsistency in methodology will deteriorate manufacturers possibility of comparing themselves with other manufacturers.

The result demonstrates how methodology choices across life cycle stages matters. Inconsistency in allocation practices impairs the comparability of EPDs developed for wood building materials and deteriorates rationale environmental decisioning for the building sector when performing building LCA. With increasing use of EPDs, it is important to have comparable methods for timber material between different countries. In addition to that, it is important to be able to compare timber material with similar functionality with other types of building materials, such as steel and concrete. EN 16485 is currently under revision, and it may bring the solution for harmonising methodical choices in LCA for EPDs on wood building materials.

ACKNOWLEDGEMENT

This work has been funded by Norwegian Institute of Wood Technology. Special thanks to Vegard Ruttenborg for technical support and initiation of the work. Silje Unander for commenting the abstract.

REFERENCES

[1] Sjølie, H.K., Analyses of the use of the Norwegian forest sector in climate change mitigation. 2011.

[2] Skog, K.E. and G.A. Nicholson, Carbon cycling through wood products: the role of wood and paper products in carbon sequestration. Forest Products Journal, 1998. 48(7): p. 75-83.

[3] Iordan, C.-M., et al., Contribution of forest wood products to negative emissions: historical comparative analysis from 1960 to 2015 in Norway, Sweden and Finland. Carbon balance and management, 2018. 13(1): p. 12.

[4] Bache-Andreassen, L., Harvested wood products in the context of climate change: A comparison of different models and approaches for the Norwegian greenhouse gas inventory. 2009.

[5] Svensson, A., Bærekraftig skogbruk i Norge - Tilvekst og skogavvirkning, L.S. Dalen, Editor. 2021, Norsk institutt for bioøkonomi.

[6] SSB. Fakta om skogbruk - Statistisk sentralbyrå. Statistisk sentralbyrå 2022; Available from: https://www.ssb.no/jord-skog-jakt-og-fiskeri/faktaside/skogbruk.

[7] Vendt, M.R., Energy management in the Norwegian sawmill industry, in Industrial Efficiency 2020. 2020: Gothenburg, Sweden.

[8] Klein, D., et al., 20 years of life cycle assessment (LCA) in the forestry sector: state of the art and a methodical proposal for the LCA of forest production. The International Journal of Life Cycle Assessment, 2015. 20(4): p. 556-575.

[9] Timmermann, V. and J. Dibdiakova, Greenhouse gas emissions from forestry in East Norway. The International Journal of Life Cycle Assessment, 2014. 19(9): p. 1593-1606.

[10] Lauri, L., et al., Environmental product declaration of timber products: The impact of allocation method to the impact categories. Journal of Cleaner Production, 2020. 256: p. 120386.

[11] NS-EN 15804:2012+A2:2019 - Sustainability of construction works -- Environmental product declarations -- Core rules for the product category of construction products. 2019, Standard Norge.

[12] CEN, NS-EN 16485:2014 - Round and sawn timber -- Environmental Product Declarations -- Product category rules for wood and wood-based products for use in construction. 2014, Standard Norge. p. 32.

[13] Ibáñez-Forés, V., et al., Environmental Product Declarations: exploring their evolution and the factors affecting their demand in Europe. Journal of cleaner production, 2016. 116: p. 157-169.

[14] Moré, F.B., B.M. Galindro, and S.R. Soares, Assessing the completeness and comparability of environmental product declarations. Journal of Cleaner Production, 2022. 375: p. 133999.

[15] NPCR, PART A: Construction products and services. 2021, The Norwegian EPD foundation.

[16] Myhre, G.S., D; Bréon, FM; Collins, W; Fuglestvedt, J; Huang, J; Koch, D; Lamarque, JF; Lee, D; Mendoza, B; Nakajima, T; Robock, A; Stephens, G; Takemura, T; Zhang, H Anthropogenic and natural radiative forcing in Climate change 2013: The physical science basis. Contribution of working group I to the fifth assessment report of the Intergovernmental Panel on Climate Change. Stocker, TF; Qin, D; Plattner, GK; Tignor, MMB; Allen, SK; Boschung, J; Nauels, A; Xia, Y; Bex, V; Midgley, PM. 2013, Cambridge University Press Cambridge, UK. p. 659-740.

[17] Ecoinvent system model 3.7.1: Allocation, cut-off by classification. 2021, Ecoinvent.

[18] Norsk treteknisk insitutt, N.T.I., Forestry, sawlog, spruce, at forest road {NO – Norenviro, in NorEnviro. 2022.
[19] Ldir, Kommunevis avvirkning pr kjøper - 2017. Fylke, kommune, kjøper, volum *). Årlig. 2018.
[20] Skogfrøverket. Publication - Årsmelding 2017 (Annual report 2017). Statistics - (sales of forest plants) 2017 med tall for godkjent import. 2019; Available from: www.skogfroverket.no
[21] SSB, Statistisk sentralbyrå (Statistics Norway). Agriculture, forestry, hunting and fishing: Forestry (data from 2017). 2017.
[22] Timmermann, V. and J. Dibdiakova, Klimagassutslipp i skogbruket - fra frø til industriport. Vugge-til-port livsløpsanalyse (LCA). in Rapport fra Skog og landskap;20/2013. 2013, Norsk institutt for skog og landskap.
[23] Vennesland, B., et al., Prosjektrapport KlimaTre. Energiforbruk og kostnader - Skog og bioenergi. 2013, Norsk institutt for skog og landskap.
[24] Hege Haugland, E.B.B., Else Marie Løbersli, Odd-Kristian Selboe, Helga Gunnarsdottir, Aksel Granhus, Gunnhild Søgaard, Kjersti Holt Hanssen, Torleif Terum, Jørn Lileng og Hans Asbjørn Sørlie, Målrettet gjødsling av skog som klimatiltak - Egnede arealer og miljøkriterier. 2014, Miljødirektoratet, Statens landbruksforvaltning og Norsk institutt for skog og landskap.
[25] SSB, Statistikkområde: Skogkultur, Skogsveier. 2020.
[26] PCR - Part B for wood and wood-based products for use in construction, in NPCR 015 version 4.0. 2021, The Norwegian EPD Foundation.
[27] CEN, T.E.C.f.S., NS-EN 590:2013+A1:2017 - Automotive fuels — Diesel — Requirements and test methods. 2017, Standard Norge.
[28] NTI, N.I.o.W.T., Bioenergi fra treindustrien, in Teknisk småskrift. 2002. p. 32.
[29] Strömberg, L., Integrated life-cycle design of coatings on exterior wood. Part 2: Life-cycle assessment. Surface Coatings International Part B: Coatings Transactions, 2004. 87: p. 211-220.
[30] Puettmann, M., E. Oneil, and R. Bergman, Cradle to gate life cycle assessment of softwood lumber production from the Northeast-North Central. Consortium for Research on Renewable Industrial Materials. University of Washington. Seattle, WA. April 2013. 33 p., 2013: p. 1-33.
[31] Jungmeier, G., et al., Allocation in lca of wood-based products experiences of cost action E9 - part i. methodology. The International Journal of Life Cycle Assessment, 2002. 7(5): p. 290-294.
[32] Taylor, A.M., et al., Impacts of the Allocation Assumption in Life-Cycle Assessments of Wood-Based Panels*. Forest Products Journal, 2017. 67(5-6): p. 390-396.
[33] Werner, F., et al., Life Cycle Inventories of Wood as Fuel and Construction Material, in ecoinvent report 2007, Swiss Centre for Life Cycle Inventories: Dübendorf, September 2007.
[34] Roja Modaresi, Johann K.Næss., The environmental impacts of the planed timber production in Norwegian sawmills vs. coated timber cladding, in 18th Annual Meeting of the Northern European Network for Wood Science and Engineering. 2022: Germany.

https://doi.org/10.52202/069179-0133

World Conference on Timber Engineering Oslo 2023

INFLUENCE OF DIFFERENT END-OF-LIFE CYCLE SCENARIOS ON THE ENVIRONMENTAL IMPACTS OF TIMBER-CONCRETE COMPOSITE FLOOR SYSTEMS

Hooman Eslami[1], Alireza Yaghma[2], Laddu Bhagya Jayasinghe[3], Daniele Waldmann[4]

ABSTRACT: Timber-concrete composite (TCC) floor systems attracted attention in the construction industry because of their low environmental impacts while demonstrating decent load-bearing capacity. However, the environmental impacts of possible end-of-life scenarios of TCC floors have not been extensively studied. To address this gap, a comprehensive life cycle assessment (LCA) study was conducted on three different slabs: a Reinforced concrete slab, a Steel concrete composite slab, and a CLT-concrete composite slab. The study revealed that the CLT-concrete composite slab has the lowest Global Warming Potential (GWP) among the three slabs. Subsequently, a more detailed LCA is performed on the CLT-concrete composite slab considering three different end-of-life scenarios of the CLT: 1. Energy recovery via incineration, 2. The prevailing scenario in Europe (a combination of energy recovery, recycling, and disposal), and 3. Reuse. The results show all three scenarios are beneficial in terms of GWP whereas the 3rd scenario is the most beneficial one.

KEYWORDS: Timber-concrete composite floor system, Life cycle assessment, Environmental impact, Reusable slab

1 INTRODUCTION

The construction industry is a major consumer of global resources and contributes greatly to waste generation and greenhouse gas emissions [1, 2]. In the last few decades, with the aim to reduce the environmental impacts of the construction industry, the use of renewable and more environmentally friendly materials such as timber and engineered wood products have gained more attention due to their green properties such as low carbon footprint and low embodied energy. Previous studies have shown that Timber-Concrete Composite (TCC) floor systems are promising sustainable solutions since they have decent structural behavior while having low environmental impacts [3].

TCC slabs have several advantages over conventional Reinforced Concrete (RC) slabs. By replacing concrete with timber, the environmental impacts of the floor system can be reduced about 30 to 50 percent [4]. Moreover, TCC can be used for resource-saving and lightweight constructions. These advantages can be expanded if the TCC slabs are designed to ensure the concrete is only subjected to compression and that all or most of the timber is stressed in tension. Consequently, TCC slabs should be designed so that shear between the timber and concrete components is transferred effectively through a proper shear connector system. The degree of composite action of the slab depends on the efficiency of the shear transfer system between the two materials. Furthermore, the connection system influences the sustainability of the TCC slab since it manipulates the fabrication, installation, maintenance, and End-of-Life (EoL) scenario. Hence, important aspects of sustainability such as prefabrication, deconstruction, recycling, and reuse must be considered during the design of the shear connection. A shear connection system that bonds the two materials permanently makes the deconstruction, reuse, or recycling difficult while a demountable shear connection facilitates these processes. This encouraged researchers to develop new shear connections suitable for prefabrication [5–7] and deconstruction [8, 9]. Having these new solutions which facilitate the recycling and reuse of TCC slabs, it is important to evaluate and compare the environmental impact of different EoL cycle possibilities for TCC floor systems.

This paper aims to study the environmental impacts of different floor systems for identical loading and span length. Then, a comparison between different EoL scenarios for the timber used in TCC floors is studied to identify the best solution considering the environmental impacts.

[1] Hooman Eslami, FSTM University of Luxembourg, Luxembourg, Hooman.eslami@uni.lu
[2] Alireza Yaghma Carbonel, FSTM University of Luxembourg, Luxembourg
[3] Laddu Bhagya Jayasinghe, FSTM University of Luxembourg, Luxembourg
[4] Daniele Waldmann, Massivbau TU Darmstadt, Germany, waldmann@massivbau.tu-darmstadt.de

https://doi.org/10.52202/069179-0134

2 ASSESSMENT OF THE ENVIRONMENTAL IMPACT

Life-Cycle Assessment (LCA) is a common method that is used for the analysis of the environmental impact of products [10]. It is an analysis technique that evaluates the environmental impacts of different stages of a designed product during its life cycle. In an LCA study, an inventory of the energy and materials which are used for the product is determined and the corresponding potential environmental impacts are calculated to improve the environmental profile of a product or compare it to another one.

Many studies evaluate the environmental impacts, considering the Global Warming Potential (GWP) and Primary Energy (PE), for some or all of the life cycle stages of a designed product [11]. GWP is a metric to quantify the total global warming effect of a substance over a specified time horizon. The GWP of a substance is defined as the ratio of the cumulative radiative forcing over a specified life cycle stage due to the emission of a unit mass of a substance, relative to the equivalent emissions of CO_2. PE states to the energy that is first extracted from natural sources and then used to generate electricity, heat, or power for other purposes. The sources of primary energy include renewable energy sources such as wind, solar, hydro, and geothermal, as well as non-renewable energy like coal, oil, and natural gas [12]. For construction materials and components, the stages which are mostly considered are Production and Construction (A), Use(B), End of Life (C), and Benefits and Loads (D) [13]. The considered stages in this study are demonstrated in Figure 1 which are the most relevant ones to the floor systems.

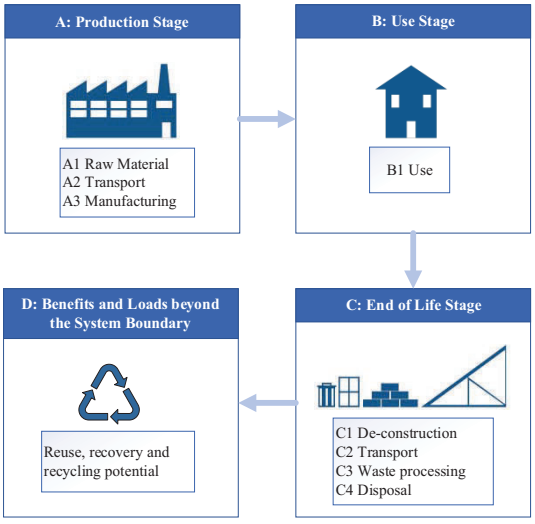

Figure 1: *Lifecycle stages of construction materials and components. Based on [13]*

Stage A includes the extraction and processing of the raw materials, as well as their transportation to the manufactory where the floor component is produced. The construction process stage is not considered here because it does not have a noticeable influence compared to the other stages on a component level of analysis. Stage B only considers the use phase, assuming that the floor systems will not require any maintenance, repair, replacement, refurbishment, energy, or water during their service life. Stage C includes the deconstruction of the component, transportation, waste processing, and disposal. Stage D depends on the method that is used to derive benefits from the materials or components through reuse, recovery, or recycling. Although all the stages influence the environmental impacts of construction materials, stages A, C, and D are the decisive ones since stage B has no or a very small contribution to the environmental impacts.

Depending on the scope of an LCA analysis, different stages are considered in a study. A cradle-to-grave (CTG) scope considers stages A, B, and C, whereas a cradle-to-cradle (CTC) scope includes stages A, B, C, and D. The CTG approach examines the environmental impacts of a product from the extraction of raw materials to its disposal. On the other hand, the CTC approach takes into account the possibility of reusing, recovering or recycling the materials and components of the product at the end of its life. This approach considers the grave of a structure as the new cradle for its materials and components, enabling them to be used again in the manufacturing process of new products, reducing waste and the need for additional raw materials.

3 ASSESSMENT OF DIFFERENT FLOOR SYSTEMS

The Eco-Construction for Sustainable Development (ECON4SD) project at the University of Luxembourg has the objective of advancing toward a sustainable and circular society. This initiative aims to accomplish this goal by developing innovative architectural and structural design models that are resource and energy-efficient. The underlying purpose of this project is to create constructions that utilize sustainable practices, thereby minimizing their environmental impact. This paper study the environmental impacts of different possible floor systems to find a suitable floor system for the prototype 3 building in the ECON4SD project [14], which is a demountable building made of standard prefabricated modules. Each module has a length of 10.8 meters, a width of 10.8 meters, and a height of 3 meters. The building is made by adding these modules and expanding the building horizontally and vertically as it is shown in Figure 2. The architectural concept is designed for adaptive usage over the life cycle such as residential, office, and public buildings. After each lifecycle, the building can be modified for a new purpose or can be demounted and reused in another building site.

To find a suitable floor system for this prototype building, 3 different floor systems are designed statically. Then, the environmental impacts of the floor systems are compared through a cradle-to-grave LCA analysis. The proposed floor systems are Reinforced Concrete (RC), Steel-

https://doi.org/10.52202/069179-0134

Concrete Composite (SCC), and Timber-Concrete Composite (TCC). The floor systems which are depicted in Figure 3, are designed for an office building loading condition and a 10.8 meters single-span system. The design considers both load-bearing capacity and serviceability of the floor for a lifespan of 50 years. Since the building is meant for prefabrication and demounting, floor modules are designed as prefabricated slabs with 1.8 meters in width.

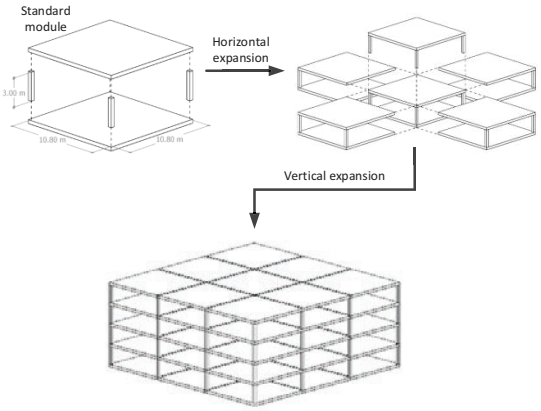

Figure 2: *Architectural concept and standard module expansion for ECON4SD building prototype 3. From: [14]*

The TCC slab includes a 60 mm deep concrete slab on top of a Cross-Laminated Timber (CLT) panel with a thickness of 300 mm. CLT is a type of engineered wood product that is made from layers of solid-sawn lumber and is used in construction as floors, walls, roofs, etc. The layers are stacked in alternating orthogonal directions and then glued together under pressure to form a solid, stable panel. The CLT and concrete are connected by shear connections. The SCC slab is made of an IPE 360 steel profile with a 65 mm deep concrete slab. The RC floor has the highest thickness of 440 mm and The TCC has the lowest thickness of 360 mm.

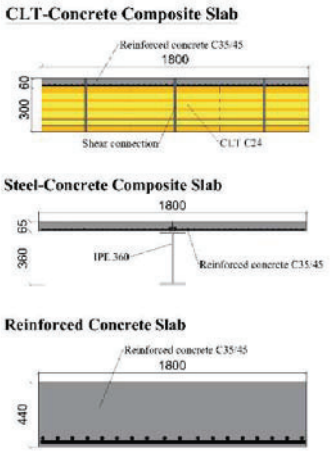

Figure 3: *The investigated floor systems (dimensions in mm).*

Based on the designed floor systems, all material quantities required for each slab module are calculated. Then, the ÖKOBAUDAT German database [15] which provides data on the environmental impacts of the construction products, is used to calculate the GWP and PE of all the materials in each stage except for CLT whose environmental impact is extracted from Stora Enso environmental product declaration [16]. Figure 4 and Figure 5 show the results of the LCA analysis in GWP and PE, respectively. For each floor system, the results are calculated for all stages and the total CTG is presented. The GWP results for the TCC and SCC floors are similar with a small advantage for the TCC slab while the result for the RC slab is about 3 times higher than the other two floors. This is due to the high CO_2 footprint of cement in the production stage. For TCC, the production stage of timber contributes to removing CO_2 from the environment while the EoL stage releases CO_2 back into the environment due to incineration. Since the steel in the SCC slab will be recycled in stage C, the CO_2 contribution comes mostly from the production stage. Stage B contribution for all the slabs is negligible since it counts only the insignificant recovered CO_2 by concrete carbonation during the utilization stage.

The results for PE are different since the SCC slab requires about 30% less energy compared to the TCC slab. Yet, the RC slab requires the highest PE with about 2 times more than the TCC slab. The majority of the demanded PE is used in the production stage for all of the slabs. Only for the TCC slab, there is recovered PE which belongs to the heat recovery of the timber by incineration in stage C. Figure 5 also demonstrates the proportion of the renewable and non-renewable energy. Although the TCC slab requires more primary energy, it is mostly acquired from renewable energy. This is contrary to the SCC slab. Therefore, one can claim that the TCC slab is more sustainable compared to the other two slabs in a cradle-to-grave LCA analysis.

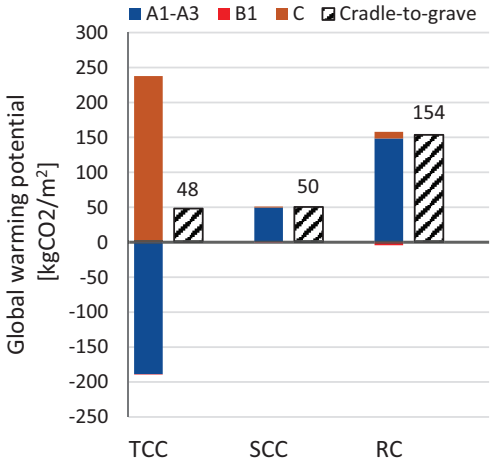

Figure 4: *CTG global warming potentials of TCC, SCC, and RC slabs*

https://doi.org/10.52202/069179-0134

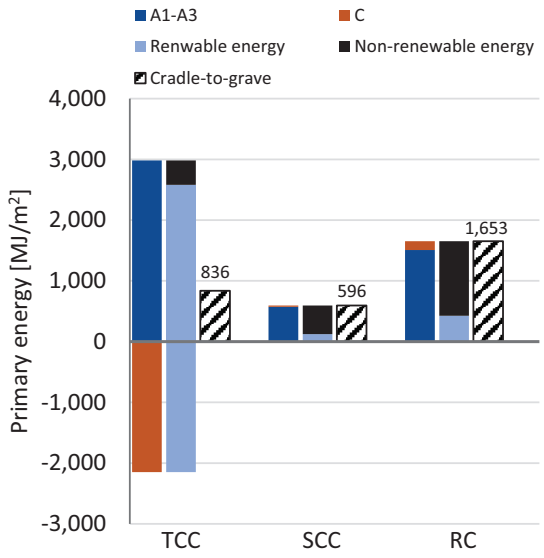

Figure 5: *CTG primary energy of TCC, CLT, and RC slabs*

To have a cradle-to-cradle LCA, the potential GWP and PE relevant to stage D of each slab are calculated to determine the loads and benefits of each substance from its reuse, recycling, or recovery. For both GWP and PE measures, as it is shown in Figure 6 and Figure 7, respectively, the TCC slab stands significantly more beneficial than the other two slabs. For GWP this goes from 6 times compared to the RC slab up to 12 times better compared to the SCC slab. For PE the same trend exists when comparing TCC with RC and SCC slabs with 18 times and 53 times more recovered energy, respectively.

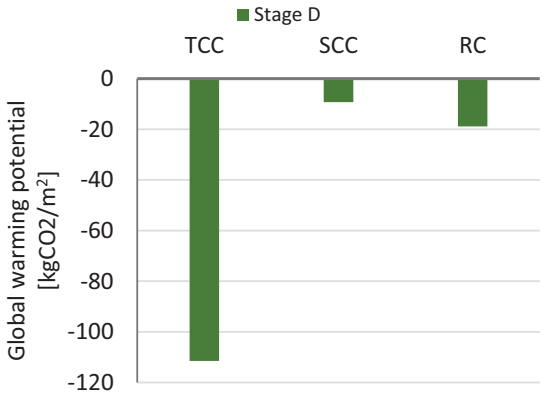

Figure 6: *Comparison of the GWP from benefits and loads beyond the system boundary for TCC, SCC, and RC floor system*

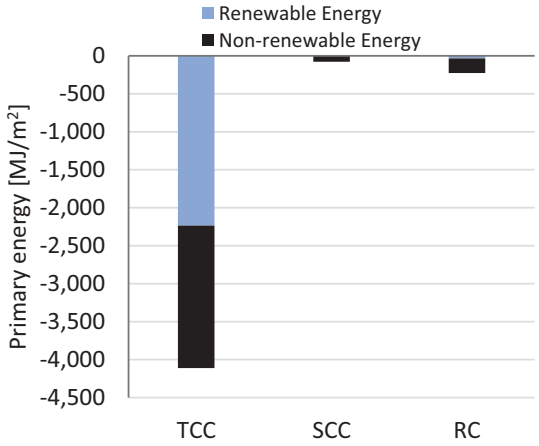

Figure 7: *Comparison of the PE from benefits and loads beyond the system boundary for TCC, SCC, and RC floor system*

4 COMPARISON OF POSSIBLE END-OF-LIFE SCENARIOS FOR TCC

Knowing the TCC floor system has sustainable advantages compared to SCC and RC floors, different possible EoL cycle scenarios can be studied to compare their benefits toward finding a more sustainable solution. The assumed EoL cycle stages are shown in Figure 8. Since the production and use stages are identical, only stages C and D vary between the scenarios. For all the scenarios, the materials in the TCC slab are considered for de-construction (C1), transportation (C2), and waste processing (C3). The steel parts such as reinforcements and the bolts are recycled and the concrete is downcycled. Then, three different scenarios are studied for the CLT panel. The first scenario is identical to the one in the previous part which considers the benefits of timber for full energy recovery by incineration of wood to generate steam heat energy or electricity. On the other hand, a study [17] shows that in Europe on average 37% of wood products go to disposal while 33 % is recycled and the rest is used to produce energy. For disposal, the wood is interred in a landfill where the methane produced from its decomposition can also be harnessed to produce electricity. As for recycling, wood waste can be processed into engineered wood products and paper [18]. Therefore, the second scenario is considered the prevailing scenario in Europe with the combination of the mentioned proportions for disposal, recycling, and energy production. Then again, the environmental impact of a component can be reduced significantly when it is designed for deconstruction and reuse which is the aim of the ECON4SD building prototype 3. Therefore, the third scenario considers that the CLT panel of the composite slab is fully reused with the assumption that the shear connection allows for such operation.

https://doi.org/10.52202/069179-0134

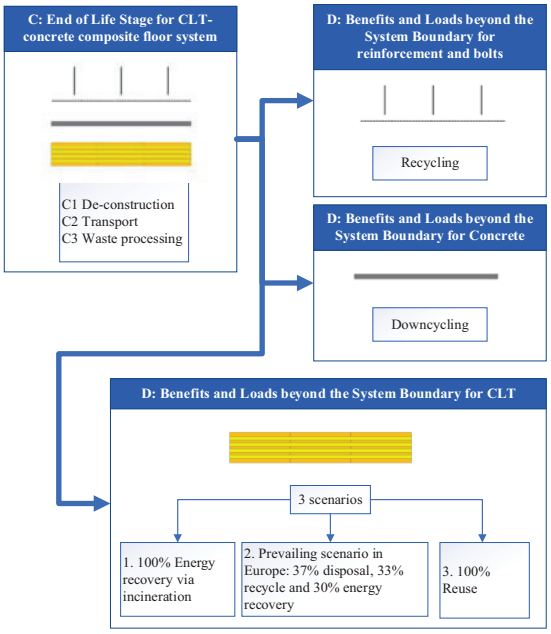

Figure 8: *End-of-life scenarios of CLT-concrete composite floor system*

Although the different EoL scenarios do not affect the environmental impact in C1 and C2 stages, they influence the C3 stage. This impact can be seen in Figure 9 and Figure 10 with the CTG calculation of the GWP and PE. The second scenario has about two times more GWP than the other two scenarios. The third scenario has about 25% less GWP than the first scenario. Considering PE, the renewable required energy is almost the same for all scenarios. However, regarding the non-renewable PE, the third scenario is again the most sustainable solution demanding about 15% and 7% less PE compared to the first and second scenarios, respectively.

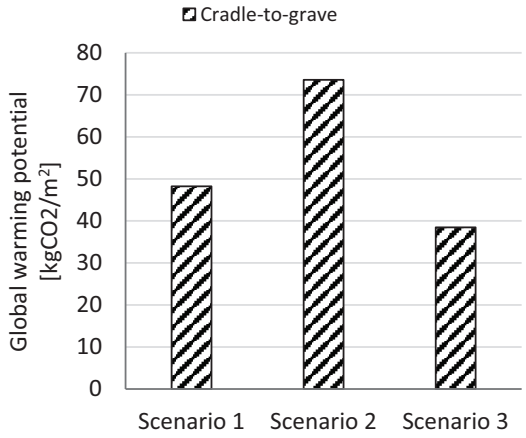

Figure 9: *Cradle-to-grave GWP of the three different EoL scenarios for the TCC floor system*

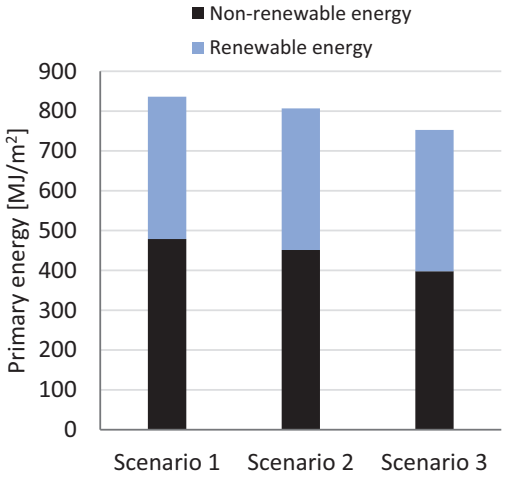

Figure 10: *Cradle-to-grave PE of the three different EoL scenarios for the TCC floor system*

The benefits and loads of the three scenarios in stage D are compared in Figure 11 and Figure 12 as recovered GWP and PE, respectively. The first and second scenarios have almost the same GWP potential benefits while the GWP for the third scenario is more than 2 times higher compared to the other two scenarios. The maximum possible recovered primary energy is from the first scenario followed by the third and second scenarios. This is due to the recovered energy from the incineration of the timber in the first scenario. However, the third scenario has the most renewable energy. Therefore, among the three scenarios, the third scenario has the least environmental impact and the most benefits beyond the system boundary.

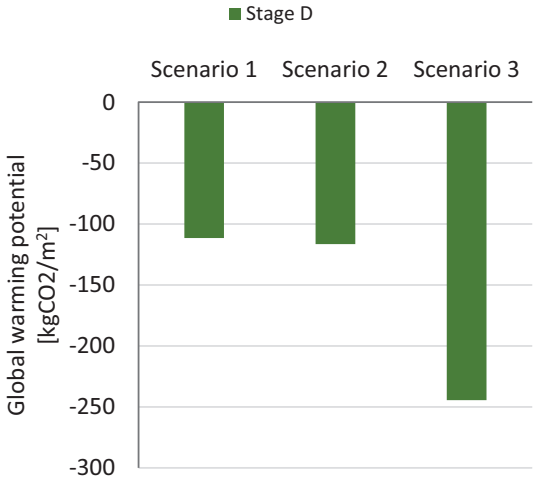

Figure 11: *Stage D potential benefits for GWP of the three different EoL scenarios for the TCC floor system*

https://doi.org/10.52202/069179-0134

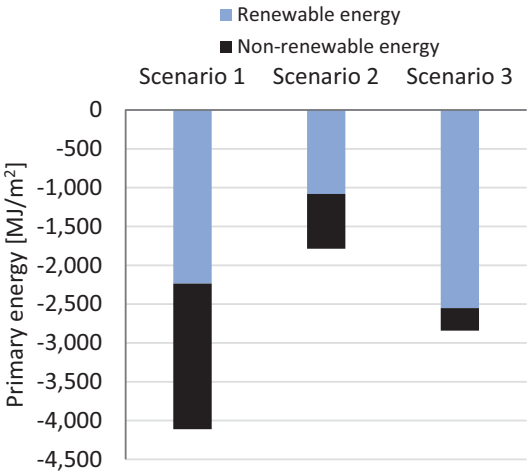

Figure 12: *Stage D potential PE recovery of the three different EoL scenarios for the TCC floor system*

5 CONCLUSION

Three different floor systems are designed for the prototype building of the ECON4SD project considering the same loading condition and life span. The results show that:

- The global warming potential of the TCC floor system is one-third of the RC floor.
- The demanded primary energy of the TCC floor system is half of the RC floor.
- The TCC floor has significantly higher environmental benefits in stage D of the LCA compared to the other two floor systems.

Additionally, three different EoL cycle scenarios are compared for the CLT panel including full energy recovery, the prevailing scenario in Europe with a combination of energy recovery, disposal and recycling, and full reuse of the CLT. The comparison shows that reusing the CLT is the most sustainable solution since it has the lowest GWP and required PE. Also, the environmental benefits of the reuse scenario are more sustainable considering both GWP and PE measures. Therefore, for the studied building, a demountable and reusable TCC floor system is the most sustainable solution.

REFERENCES

[1] Jayasinghe L. B., Waldmann D.: Development of a BIM-based web tool as a material and component bank for a sustainable construction industry. *Sustainability*, 12(5), 2020, 1766, doi: 10.3390/su12051766.

[2] Abd Rashid A. F., Yusoff S.: A review of life cycle assessment method for building industry. *Renewable and Sustainable Energy Reviews*, 45:244-248, 2015. doi: 10.1016/j.rser.2015.01.043.

[3] Holschemacher K., Hoffmann L., Heiden B.,: Environmental impact of timber-concrete composite slabs in comparison to other floor systems. *In: World Conference on Timber Engineering*, 2021

[4] Basaglia B., Lewis K., Shrestha R., Crews K.: A comparative life cycle assessment approach of two innovative long span timber floors with its reinforced concrete equivalent in an Australian context. In *International Conference on Performance-based and Life-cycle Structural Engineering*, pages 1433–1442, 2015. doi: https://doi.org/10.14264/uql.2016.714.

[5] E. Lukaszewska, M. Fragiacomo, and H. Johnsson, "Laboratory Tests and Numerical Analyses of Prefabricated Timber-Concrete Composite Floors," *J. Struct. Eng.*, vol. 136, no. 1, pp. 46–55, Jan. 2010, doi: 10.1061/(ASCE)ST.1943-541X.0000080.

[6] B. Shi, W. Zhu, H. Yang, W. Liu, H. Tao, and Z. Ling, "Experimental and theoretical investigation of prefabricated timber-concrete composite beams with and without prestress," *Engineering Structures*, vol. 204, 2020, doi: 10.1016/j.engstruct.2019.109901.

[7] S. Yilmaz, S. Demir, and N. Vural, "Experimental investigation of a prefabricated timber-concrete composite floor structure: Notched-slab approach," *Advances in concrete construction*, vol. 12, no. 1, pp. 13–23, Jul. 2021, doi: 10.12989/ACC.2021.12.1.013.

[8] N. Khorsandnia, H. Valipour, J. Schänzlin, and K. Crews, "Experimental Investigations of Deconstructable Timber–Concrete Composite Beams," *J. Struct. Eng.*, vol. 142, no. 12, Dec. 2016, doi: 10.1061/(ASCE)ST.1943-541X.0001607.

[9] M. Derikvand and G. Fink, "Bending properties of deconstructable cross-laminated timber-concrete composite floor elements," *Wood Material Science & Engineering*, pp. 1–8, May 2022, doi: 10.1080/17480272.2022.2077658.

[10] A. Luximon and L. Jiang, "The Role of Footwear Fitting and Comfort in the Environmental Impact of Footwear," in Advances in Physical Ergonomics and Human Factors, Cham, 2016, pp. 183–190.

[11] Algren M., Fisher W., Landis A.E.: Chapter 8 - Machine learning in life cycle assessment. In J. Dunn and P. Balaprakash, editors, *Data Science Applied to Sustainability Analysis*, pages 167–190. Elsevier, 2021, doi: 10.1016/B978-0-12-817976-5.00009-7.

[12] Shahzad, U. (2012). The need for renewable energy sources. energy, 2, 16-18.

[13] Enzo S.: Environmental product declaration in accordance with ISO 14025 and EN 15804 for: CLT, 2021.

[14] Silva M. F., Jayasinghe L. B., Waldmann D., Hertweck F.: Recyclable architecture: prefabricated and recyclable typologies," *Sustainability.*, 12(4), 2020, doi: 10.3390/su12041342.

[15] B. a. C. Federal MInistry of the Interior, "oekobaudat.de," [Online]. Available: https://www.oekobaudat.de/en.html.

https://doi.org/10.52202/069179-0134

[16] The International EPD system, “S-P-02033 EPD CLT (Cross Laminated Timber).” Stora Enso Oyj, May 11, 2020. Accessed: Feb. 13, 2023. [Online]. Available: https://www.storaenso.com/-/media/documents/download-center/certificates/wood-products-approvals-and-certificates/epd/stora-enso-epd-clt-2021.pdf

[17] Besserer A., Troilo S., Girods P., Rogaume Y., Brosse N.: Cascading recycling of wood waste: a review. *Polymers* 13, 1751, 2021.

[18] J. Morris, “Recycle, Bury, or Burn Wood Waste Biomass?: LCA Answer Depends on Carbon Accounting, Emissions Controls, Displaced Fuels, and Impact Costs: Recycle, Bury, or Burn Wood Waste Biomass?,” Journal of Industrial Ecology, vol. 21, no. 4, pp. 844–856, Aug. 2017, doi: 10.1111/jiec.12469.

World Conference on Timber Engineering Oslo 2023

A STRUCTURAL-MEMBER LEVEL ASSESSMENT OF THE ENVIRONMENTAL IMPACT OF TIMBER, REINFORCED CONCRETE AND STEEL IN BUILDING CONSTRUCTION

Jae-Won Oh[1], Sung-Jun Pang[2], Kyung-Sun Ahn[3], Jung-Kwon Oh[4]*

ABSTRACT: This study evaluates and compares the environmental impact of timber, concrete, and steel as building materials. This study designed a target member (beam) with equivalent structural performance under the same design conditions, such as span and live load, and compared the environmental impact. The carbon footprint analysis was conducted using Life Cycle Assessment (LCA) methodology, with a functional unit of 1-meter length of the designed beam and a cradle-to-gate system boundary. The study found that timber has a lower carbon footprint than steel and concrete, with the lowest carbon emissions during the product stage. Notably, the study also found a significant difference between the two environmental impact comparison methods, unit volume-based and structural performance-based. The findings demonstrate the sustainability of timber in high-rise construction and its potential to contribute to carbon neutrality while offering exceptional engineering capabilities. Further research is needed to improve the structural assumptions and LCA to evaluate the environmental impact of building materials more accurately.

KEYWORDS: Environmental Impact, Timber, Concrete, Steel, LCA, Equivalent structural performance

1 INTRODUCTION

The construction industry has recently been focusing on environmental concerns, such as climate change and global warming, leading to a growing emphasis on assessing the environmental impact of building materials. The building sector dramatically impacts the environment, accounting for over 40% of global energy consumption and roughly 30% of greenhouse gas emissions [1]. As a result, the building sector must take responsibility and play a role in addressing the challenge of climate change. Timber presents a range of substantial environmental advantages over other building materials, emitting fewer greenhouse gases during production and serving as a carbon sink. As a result, timber has gained recognition as an environmentally friendly material that has the potential to contribute to carbon neutrality while offering exceptional engineering capabilities. Despite its potential benefits, the utilization of timber in modern high-rise construction is still in its early stages, and there remains a need for a deeper understanding of its comparative environmental impact when compared to other building materials, such as steel and concrete.

Evaluating timber as a building material from an environmental perspective poses several challenges. One of the significant difficulties is that direct comparison of the environmental impact of buildings is limited. This is because the total environmental impact of a building is influenced by a multitude of factors, such as size, energy consumption during use, and the materials used. It is often difficult to determine the relative impact of each factor. In addition, the number of timber buildings is smaller than that of other buildings, limiting statistical analysis. Some researchers have attempted to address this challenge by utilizing a methodology that compares the environmental impact of existing buildings virtually by redesigning them as equivalent buildings of the same usage and layout [2-3]. However, this methodology may have limitations as there is no guarantee that the structural system of a building designed with a different material will be as efficient as the original building.

Consequently, this study aims to compare the environmental impact of timber as a building material with steel and concrete. Structural members were designed to achieve this with equivalent performance under controlled design conditions while considering the mentioned issues. Furthermore, this study aims to comprehensively understand the sustainability of timber in modern high-rise construction and identify each material's strengths and weaknesses.

2 STRUCTURAL DESIGN

2.1 TARGET MEMBER AND EQUIVALENT STRUCTURAL PERFORMANCE

This study designed members with equivalent structural performances and compared their environmental effects.

[1] Jae-Won Oh, Seoul National University, Republic of Korea, redhurse@snu.ac.kr
[2] Sung-Jun Pang, Seoul National University, Republic of Korea, pangsungjun@snu.ac.kr
[3] Kyung-Sun Ahn, Seoul National University, Republic of Korea, rudtjs6339@snu.ac.kr
[4] Jung-Kwon Oh, Seoul National University, Republic of Korea, jungoh@snu.ac.kr
*: Corresponding author

https://doi.org/10.52202/069179-0135

To objectively compare the environmental impact of different materials, selecting a target for comparison and defining equivalent structural performance as a criterion is necessary.

As a specific building was not designated in this study, making necessary assumptions may become complicated and increase research limitations. Hence, due to its relatively simple design conditions, the target member was selected as a beam supporting mainly gravity loads.

Even though beams with different materials may have different moment and shear strengths, they can provide the same space and function as long as their design conditions, such as span and load, are the same. Thus, in this study, equivalent structural performance was defined through design conditions, not calculated indicators such as moment and shear strength. Additionally, all members were designed to have similar depth as steel beams using Products produced according to standard specifications, even if the structural performance is the same. This was done to ensure that the overhead clearance is not greatly affected, as a difference in beam depth would result in a difference in usable space, as shown in Figure 1.

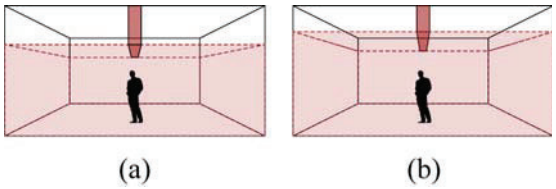

Figure 1: *Example of usable space and overhead clearance according to beam depth: (a) large beam depth, (b) small beam depth.*

2.2 MATERIALS

Three types of materials were used in the beam design: timber, steel, and reinforced concrete (RC). The timber beam was assumed to a glued-laminated timber (GLT) using larch (*Larix kaempferi*), a mechanically graded dimensional lumber. The materials used in the design are listed in the following Table 1, and the design was based on the KS standard [4–7]. All materials were chosen from those commonly used in the industry. The dead load was calculated using the density data from the Ministry of Land, Infrastructure, and Transport [8].

Table 1: *Material properties*

Type	Material	Density [kg/m^3]	Strength [MPa]	MOE [MPa]
Timber	10S-30B	580	10 (f_b)	9,000
Steel	SM355A	7,850	355 (f_y)	210,000
RC	C30	2,300	30 (f_{ck})	27,500
	SD400	7,850	400 (f_y)	200,000

Where MOE=modulus of elasticity, f_b=bending strength, f_y=yield strength, f_{ck}=compressive strength.

2.3 STRUCTURAL MEMBER DESIGN

The beams were designed based on the following structure (Figure 2). In order to simplify, it was assumed that the plane has a square shape and that the beam is located at the center. The design was carried out considering a span ranging from 3 to 8 meters and a live load ranging from 2 to 6kN/m^2. The design followed the Korean design standard (KDS), and the timber structure was designed using the allowable strength design (ASD) method. In contrast, the steel and concrete were designed using the ultimate strength design method (USM) and the load and resistance factor design method (LRFD), respectively. In order to design optimally, All beams were designed with the minimum member weight in each condition.

The following assumptions were additionally made in the design:

1) The shape of the timber and concrete beams was rectangular, and the shape of the steel beams was an I-beam (Figure 3).
2) The beams were assumed to be a simple beam condition in which all boundary conditions are pin connections and were designed only for dead and live loads.
3) The slab's weight was calculated by designing a CLT slab for timber and a concrete slab for RC and steel. The weight of the finishing and equipment was not included.
4) Fire-resistance design was not considered.

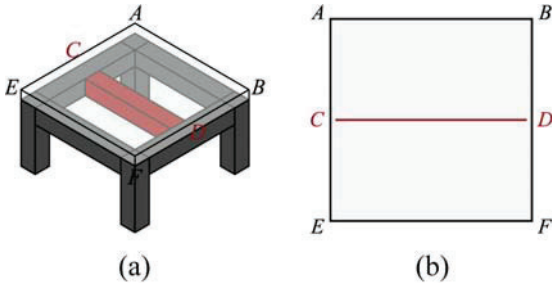

Figure 2: *Assumed structural diagram for the beam design: (a)elevation and (b)floor plan.*

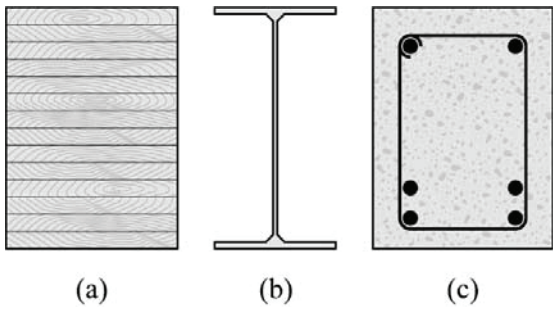

Figure 3: *Cross-sectional schematic diagram of beams designed for (a)GLT, (b)Steel, and (c)RC.*

https://doi.org/10.52202/069179-0135

3 CARBON FOOTPRINT ANALYSIS

3.1 FUNCTIONAL UNIT AND SYSTEM BOUNDARY

This study evaluated the environmental impacts by carbon emissions through Life Cycle Assessment (LCA) methodology. To perform LCA, defining a functional unit and a system boundary is necessary. The functional unit was set as the 1-meter length of the designed beam, and the final quantity was calculated by dividing the total quantity of the beam by the span. The system boundary was defined as cradle-to-gate (product stage), and only the environmental impacts during raw material extraction and processing, transportation, and manufacturing were considered (Figure 4). The reference service life of the building was assumed to be 50 years.

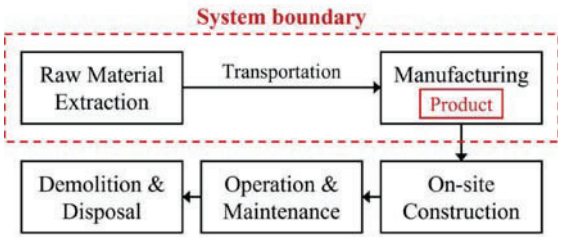

Figure 4: *Building life cycle and system boundary.*

3.2 CARBON EMISSION EVALUATION

The data used to evaluate the carbon emission was taken from a publicly accessible environmental product declaration (EPD) database. The carbon emission data of steel and concrete materials were obtained from the database of the Ministry of Environment. In contrast, data for GLT was taken from the database of the Forest Science Institute, as there was no EPD database available in Korea. The used data is presented in the following Table 2. The total CO_2 emissions were calculated by multiplying the material quantities by the CO_2 emissions factor per unit.

Table 2: *The equivalent carbon emission factor of materials*

Material	CO_2 emission	Unit	Reference
GLT	87.64	$kgCO_2$-eq/m^3	[9]
Steel	11,241		[10]
Concrete	3,532		[10]
Rebar	259		[10]

3.3 LIMITATIONS

This study has similar assumptions as previous studies [11], and similarly, it has the following limitations:

1) This study used the equivalent carbon emission factor from the EPD database developed in Korea. This study did not account for environmentally improved products such as low-carbon concrete. Therefore, it is essential to note that the results may be limited to the conditions of Korea at the time of this study. Production processes, transportation methods, and efficiencies vary by region and time, which may result in different findings from this study.
2) The system boundary of this study was limited to the product stage, from raw material extraction to manufacturing, thereby excluding the impact in the use and disposal stages.
3) The findings of this study should be separate from other building components (e.g., columns) or structural systems (e.g., continuous structural systems). For instance, vertical members, such as columns and walls, are highly influenced by upper-level loads. Thus, an increase in load caused by the building size, material density, and member volume increases, leading to an increase in the cross-sectional size of the vertical member. Additionally, the moment distribution in the member may change for a continuous structural system, which could result in different findings. This study also did not apply any load factor to timber beam design.
4) It is also important to note that this study did not consider the fire-resistance design. Therefore, the findings may not be suitable for fire-resistance design purposes.

4 RESULTS AND DISCUSSIONS

4.1 COMPARISON CARBON EMISSIONS ACROSS SPANS

Figure 5 presents the carbon emissions results along the span for each live load. As the span increased, a greater structural performance was necessary, which led to an increase in the cross-sectional size and quantity of materials, and consequently resulted in a rise in carbon emissions. The analysis indicates that GLT emitted the lowest carbon across all scenarios with equivalent structural performance, while RC and Steel followed in that order.

To clearly compare the ratio between each material, the data was normalized by the steel, which has the highest carbon emission, as shown in Figure 6. The results indicate that, on average, timber and RC exhibited a reduction of 85.52% and 37.29% in carbon emissions compared to steel.

Although no distinct patterns in carbon emissions were discernible across the span, the data indicated the presence of fluctuations. The observed fluctuations in the results can be attributed to discontinuities in the cross-sectional design of the beams. Since steel beams were used as ready-made products, the section properties were not continuous across spans. Furthermore, considering the workability, the cross sections of timber and RC were designed with 10mm increments. Consequently, the strength-to-load ratio of each beam differed across spans, leading to the observed fluctuations.

4.2 COMPARISON CARBON EMISSIONS ACROSS LIVE LOADS

In Figure 7, the equivalent carbon emissions along the live load are shown for a span length of 6m. It was observed that the change in carbon emissions along the live load is

https://doi.org/10.52202/069179-0135

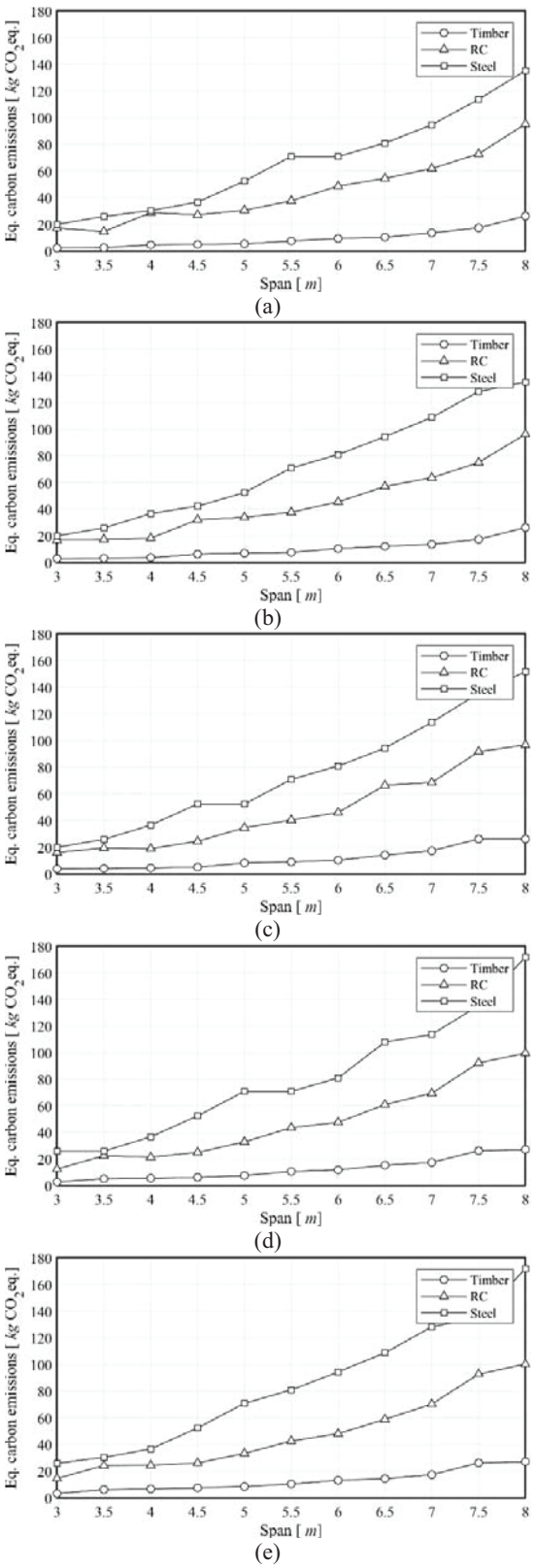

Figure 5: Equivalent carbon emissions along the span when the live load was (a)2kN/m², (b)3kN/m², (c)4kN/m², (d)5kN/m², and (e)6kN/m².

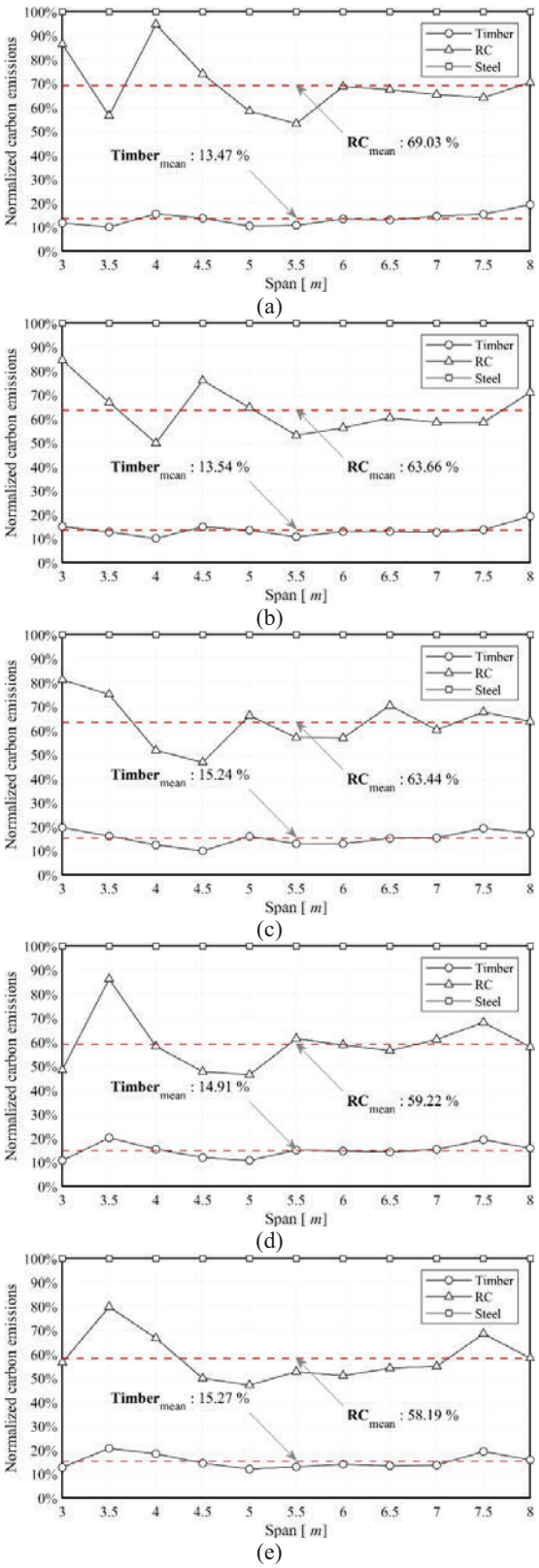

Figure 6: Normalized equivalent carbon emissions along the span when the live load was (a)2kN/m², (b)3kN/m², (c)4kN/m², (d)5kN/m², and (e)6kN/m².

https://doi.org/10.52202/069179-0135

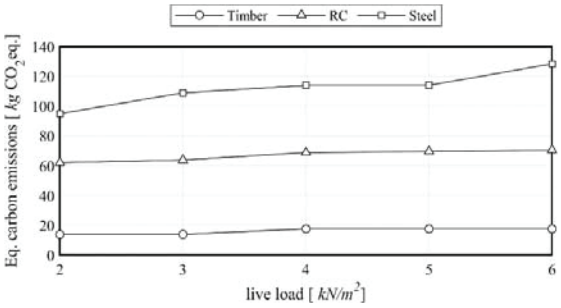

Figure 7: *Equivalent carbon emissions along the live load when the span was 6m.*

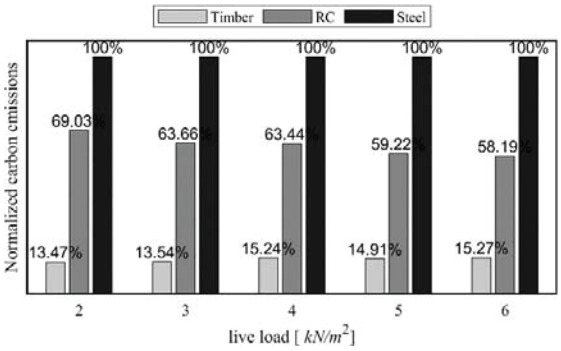

Figure 8: *Comparison of normalized equivalent carbon emissions along the live load.*

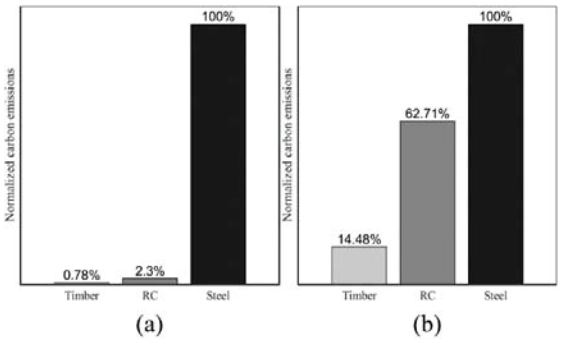

Figure 9: *Comparison of normalized equivalent carbon emissions by (a)volume-based and (b)performance-based comparisons.*

not greater than the change along the span. This arises from the influence of live load and span on required strength and deformation. The required strength and deformation increase proportionally to the load's first power. In contrast, the required strength increases proportionally to the span's square, and the deformation increases proportionally to the span's fourth power. Consequently, the required structural performance was predominantly influenced by the span, resulting in a more pronounced alteration in the environmental impact as the span varied, compared to the effects caused by changes in the live load.

Figure 8 also presents the average normalized equivalent carbon emissions along the live load. In this case, the changes in carbon emissions caused by the live load were not substantial, and no distinct patterns could be identified as well.

4.3 CARBON EMISSION RATIOS FOR SUSTAINABLE BUILDING MATERIALS

Figure 9 reveals that the carbon emission ratio by material varies significantly between a unit volume-based comparison and a structural performance-based comparison. This difference can be attributed to the specific structural performance of each material, indicating that direct comparisons of carbon emissions per unit volume may lead to substantial errors.

Notably, when comparing the results of volume-based and performance-based comparisons, there has been a decrease in the steel/timber ratio and an increase in the RC/timber ratio. This observation may suggest that, from an environmental standpoint, the structural efficacy of timber is relatively inferior to that of steel but superior to that of RC. Such a finding may have significant implications for sustainable construction practices, as it highlights the potential of timber as a viable alternative to traditional building materials, particularly in the context of reducing the carbon footprint of construction projects.

5 CONCLUSIONS

In conclusion, this study analyzed and compared the environmental impact of timber, concrete, and steel in building construction at the structural member level. The results revealed that timber and concrete had significantly lower equivalent carbon emissions than steel, with timber having the lowest emissions. Although the carbon emissions of all materials increased with the increasing span, there was no specific trend according to span and live load.

A significant difference was observed when comparing the environmental impact ratio of volume-based and performance-based comparisons. This indicates that the structural efficiency of timber was found to be relatively inferior to steel but superior to concrete. This finding suggest that timber could be a feasible alternative to conventional building materials and could have important implications for sustainable construction practices.

However, this study has limitations, and further research is required to improve the structural assumption and life-cycle assessment. Future studies should consider diverse structural systems, design conditions, and target members. Furthermore, comprehensive life cycle assessments covering various impact categories should be conducted to obtain a more comprehensive understanding of the environmental impact of these building materials.

REFERENCES

[1] Birgisdottir, H., Moncaster, A., Wiberg, A. H., Chae, C., Yokoyama, K., Balouktsi, M., Seo, S., Oka, T., Lützkendorf, T., and Malmqvist, T.: IEA EBC annex 57 ‘evaluation of embodied energy and CO2eq for building construction’. *Energy and Buildings.* 154:72-80, 2017.

[2] Robertson, A., Lam, F., and Cole, R.: A comparative cradle-to-gate life cycle assessment of mid-rise office

https://doi.org/10.52202/069179-0135

building construction alternatives: Laminated timber or reinforced concrete. *Buildings*, 2(3):245-270, 2012.
[3] Liang, S., Gu, H., Bergman, R., and Kelley, S.: Comparative life-cycle assessment of a mass timber building and concrete alternative. *Wood and Fiber Science*, 52(2):217-229, 2020.
[4] Korean Standards Association. KS F 3021 Structural glued laminated timber. 2022.
[5] Korean Standards Association. KS D 3515 Rolled steels for welded structures. 2018.
[6] Korean Standards Association. KS F 4009 Ready-mixed Concrete. 2011.
[7] Korean Standards Association. KS D 3504: Steel Bars for Concrete Reinforcement. 2011.
[8] Korea Institute of Civil Engineering and Building Technology. Standard of Construction Estimate. Jinhan M&B, 2021.
[9] Chang, Y.S., Chun, S., and Shin, Y.J. Establishment of Environmental Load DB According to Improvement of Domestic Lumber Production Process. National Institute of Forest Science, 2021.
[10] Korea Environmental Industry & Technology Institude. Environmental Product Declaration. The Ministry of Environment. https://www.greenproduct.go.kr/epd/ (accessed Sep. 18, 2022).
[11] Oh, J.W., Park, K.S., Kim, H.S., Kim, I., Pang, S.J., Ahn, K.S., Oh, J.K. Comparative CO2 emissions of concrete and timber slabs with equivalent structural performance. *Energy and Buildings*, 281:112768, 2023.

World Conference on Timber Engineering Oslo 2023

MEETING THE 2050 PARIS AGREEMENT TARGETS USING MASSIVE TIMBER IN SCHOOL BUILDINGS

Efthymia R. Stæhr[1], Thomas K. Thiis[2],Arnkell J. Petersen [3] Leif D. Houck[4]

ABSTRACT: Due to the importance of global warming and the signature of the Paris agreement, Norway has committed to reducing greenhouse gas emissions by 95% by 2050. Using school buildings that have already been designed with high environmental standards as case studies, one can identify the building elements that contribute the most to embodied energy and develop methods to reduce them even more. This article presents a review of 4 schools that include massive timber elements, the correlation between their CO_2 emissions and the gross floor area per year and compares this ratio to the Paris agreement targets set for 2050. The study revealed that the case studies comply with the current median environmental performance standards but lack to reach the 2050 targets. Added to this, the importance of using more massive timber in school buildings was highlighted and the need for an upgraded timber material was underlined.

KEYWORDS: LCA, timber schools , school buildings, sustainable schools

1 INTRODUCTION

It is widely recognized that the construction industry is greatly contributing to greenhouse gas (GHG) emissions in Europe [1]. The European Union (EU), in recognition of the climatic change and the impact of global warming, decided that impending action is needed to lower GHG emissions in Europe [1]. The Paris Agreement which was signed by a great number of nations represents the decarbonization efforts of the EU and sets a reduction target of GHG emissions by 91-94% of 1990 levels by 2050 [1]. In 2021, Norway updated its intended nationally determined contribution (INDC) to reduce the emissions by 95% in 2050 compared to 1990 levels [2].

The challenge to comply with the Paris Agreement includes reducing the GHG emissions connected with both the operational energy of the building, as well as the embodied emissions associated with the building materials. According to EN 15978:2011 the life cycle of the building materials is divided into different phases: the manufacturing phase (A1-A3), the maintenance phase (B3), the disposal and refurbishment phase (B4-B5) and the end-of-life phase (D) [3].With measures implemented to reduce buildings' operational energy over the last couple of years and with the effort required to reach the Paris Agreement target, the embodied-operational ratio has shifted. Currently, the embodied energy of a building represents a considerable percentage of the total building emissions. [4,5].

In the last 20 years, considerable effort has been made in developing timber structural products which also contributed to the reduction of GHG emissions [6,7]. This has resulted in a variety of engineered wood products (EWP) that have been used broadly in the construction industry. Cross-laminated timber (CLT), also known as massive timber or X-lam [8], is a versatile wood product with properties that make it suitable for the structural support frame of a building [9].

CLT products have been gaining popularity in the Norwegian construction industry. When public buildings and especially schools are concerned, the massive timber usage seems to be increasing. Data indicates that the investment in timber for school buildings from 1,7 billion NOK in 2012 increased to 3,4 billion NOK in 2021 [10].

As sustainability awareness has increased and massive timber construction has risen, a gap has been created in knowledge about whether those newly built school buildings can fulfil the Paris agreement targets.

Scholars have shown that massive timber buildings can have up to 30% lower GHG emissions when compared with conventional materials such as concrete and steel [11, 12]. But even though today much effort has been put

[1] Efthymia Ratsou Stæhr, Norwegian University of Life Sciences (NMBU), Norway, efthymia.ratsou.staehr@nmbu.no
[2] Thomas Kringlebotn Thiis, Norwegian University of Life Sciences (NMBU), NTNU Norwegian University of Science and Technology (NTNU) Norway, thomas.thiis@nmbu.no
[3] Arnkell Jonas Petersen, Norwegian University of Life Sciences (NMBU), Norway, arnkell.jonas.petersen@nmbu.no
[4] Leif Daniel Houck , Norwegian University of Life Sciences (NMBU), Norway, leif.daniel.houck@nmbu.no

https://doi.org/10.52202/069179-0136

into designing buildings that hold high environmental standards, it is unclear if these buildings can fulfil the 2050 Paris agreement targets [13].

As the world population rises, a great investment is done in school buildings. Norwegian Municipalities have set up high building standards following sustainability commitments. Data from the industry show that more than 339 billion NOK has been invested in school buildings, and from this amount, 218 billion NOK is invested in new buildings [10].

The objective of this work is to present and study a selection of school buildings that include CLT in their construction. A case study of four schools is used to answer the following research questions:

- How do CLT school buildings with high environmental standards perform regarding their GHG emissions?
- How do those results compare with the Paris Agreement sustainability targets for 2050?

2 METHODS

In Norway, GHG emission targets from embodied energy in buildings until recently have been expressed as percentage reductions relative to so-called reference buildings [14]. This approach turned out to be inconclusive since all case studies were evaluated relatively to a customized reference for each building. The Research Centre for Zero Emission Neighborhoods (ZEN) created the only Norwegian GHG emission database by collecting different building typology case studies for both the material production phase (A1-A3) as well as the replacement phase (B4) of the building process. This was done through the usage of different Life Cycle Analysis (LCA) software such as Powerhouse, OneClickLCA, SimaPro and an MS Excel-based ZEN algorithm. Through this method, ZEN managed to depict the GHG 2050 targets for all building typologies. A benchmark of the environmental impact value of 5,4 $kgCO_2/m^2$/year was determined as a 2020 starting point, with an endpoint of 0,4 $kgCO_2/m^2$/year for 95% reduction or 1,4 $kgCO_2/m^2$/year for 80% reduction [15].

The main objective of this study is to establish the environmental impact ratio ($kgCO_2/m^2$/year) of the chosen school buildings and compare it with the 2050 benchmark that has been established by ZEN.

Additionally, the correlation between the materials used and the GHG emissions of each case study will be explored. This will be done, by a case study of newly constructed elementary schools that also include cross-laminated timber in their building modules. In the analysis, the volume of materials per square meter of heated floor area (HFA) will be highlighted ($\frac{m^3}{m^2}$ HFA), so as to give a justification concerning the association between material usage and GHG emissions in the building envelope.

The criteria for choosing the case studies rely on their similar building timeframe (2019-2021), and construction materials (usage of CLT, steel, and concrete). Added to this, all case studies are considered multi-functional buildings which contain teaching areas, sports halls, and cultural spaces.

2.1 DATA COLLECTION

The first step of this study includes the analysis of the building modules using Building Information Modeling (BIM). Through correspondence with the architects, we could acquire the International Foundation Class (IFC) files of the buildings. From there, we created inventories (schedules) in BIM software such as Archicad v. 25 and Solibri v. 9.12.10 that could differentiate the material quantities used in every part of the building. After that, through correspondence with the architects and contractors of the case studies, we acquired some of the Environmental Product Declaration (EPD) of the materials used in the construction. For the building modules that we were not able to acquire the EPD, a standard benchmark was used from the Ecoinvent database v 3.8 [16, 17]. An EPD, also referred to as type III environmental declaration, is *a standardized (ISO 14025) and LCA-based tool to communicate the environmental performance of a product* (Schmincke, 2007). Through the EPD, information was gathered concerning the GHG emissions of each building component. That information included CO_2 quantities from the raw material production to the transport of the processing facilities and finally to the transport of the building site (A1-A3 phase). Additionally, information regarding the replacement and refurbishment phase (B4-B5) was given.

2.2 LIFE CYCLE ANALYSIS (LCA)

To accomplish the scope of the research, a Life Cycle Analysis was next used to determine the overall building GHG emissions of the case studies and which elements of the building envelope contributed the most. Through standardization, LCA has gained global support as the most important tool for furthering more environmentally friendly choices in the sector. The functional unit for this analysis, in reference to the school buildings, was defined

as one square meter of floor area for a period of the lifecycle (1 m2); The life cycle of the school buildings was set to 60 years as this enables comparisons with similar studies. The system boundary for a building's life cycle consists of material manufacturing, transportation, construction, operation(A1-A3), and maintenance phases (B4-B5). The LCA methodology software that was used for all 4 case studies is the OneClickLCA. The specific software was chosen as it follows the requirements of NS 3720 Norwegian standard which is based on EN 15978:2011 and ISO international standard [19].

After the overall GHG emissions of the buildings were calculated, the required environmental impact ratio was established by dividing the CO_2 emissions by the area and the life cycle of the building. The final ratio of $kgCO_2/m^2$/year is compared with the ZEN 2020 median ratio and the ZEN 2050 prognosis.

2.3 THE CASE STUDIES

The criteria of choosing the case studies include the same material choice (a combination of CLT, steel and concrete) as well as the addition of multifunctional spaces (sports and cultural halls). Furthermore, all 4 buildings follow the Norwegian TEK 17 building legislation [20], hence the same regulations on technical requirements. In addition, all school buildings have been designed with high sustainability standards in mind and received sustainability certifications after their completion.

Case A - Flesberg school (2017-2019)

Flesberg is a school building built according to Passive house sustainability standards. It consists of 4 individual building volumes that link together through a connecting area. The concept of this project indicated that each volume has a different purpose; the more acoustically challenging volumes, such as the swimming hall, and the sports hall are isolated from the last two volumes which are used for teaching spaces. The connecting area between the building volumes serves as a common area for students between the library, the amphitheatre and the administrative space. The building is placed partly under the terrain because of the topography of the chosen site. The parts of the building that are under the terrain, are constructed in concrete. Above ground level, massive timber is used in various parts of the building frame, including the walls of the sports hall and the swimming hall.

Case B - Bamble school (2018-2021)

Bamble is a BREEAM -very good accredited school that consists of 3 building volumes; the first two that inhabit the teaching spaces are connected through a common area, while the third one that accommodates the sports, swimming hall and the gym, is independent. The concept has separated the building volumes to protect the main teaching spaces (classrooms) from the more acoustically challenging volumes (sports hall, swimming hall, gym). The building volumes that host teaching facilities are constructed in massive timber, while for the swimming hall, concrete was used. Although the site was flat, a volume was placed under the terrain to host sports facilities.

Case C - Huseby school (2017-2021)

The school received a BREEAM-Very good certification and consists of 2 different building volumes that connect through a concert hall and a sports hall. The school's concept was to separate the different age groups (each age group has a different entrance) but at the same time unite them under the cultural and activity spaces. The main teaching spaces (classrooms) are constructed in massive timber, while the common spaces (sports hall, concert hall) are constructed out of steel and placed under the terrain.

Case D - Nordre Ål school (2017-2019)

Nordre Ål school is built according to Passive house standards and consists of 4 different building volumes. All volumes are connected through an amphitheatre which represents the heart of the school. The foundations, elevator shafts and ground floor slabs are made of concrete, while the remaining structural elements are predominantly made of massive timber.

https://doi.org/10.52202/069179-0136

Table 1. *The table shows an overview of the characteristic parameters for the different cases.*

	Case A	Case B	Case C	Case D
Facilities	Teaching spaces Sports hall Swimming hall Library Cultural space	Teaching spaces Sports hall Swimming hall Gym Cultural space	Teaching spaces Sports hall Cultural space	Teaching spaces Sports hall Cultural space
Building data received	IFC model	IFC model	IFC model	Solibri model
Material data received	EPD massive timber EPD steel	EPD massive timber EPD steel	EPD massive timber EPD steel	EPD massive timber EPD steel EPD plasterboard
Gross Area (m^2)	8884	14565	12933	8109
Sustainability Certificate	Passive house	BREEAM very good	BREEAM very good	Passivhaus
Sub. volumes	yes	yes	yes	no

3 FINDINGS

In this section, the outcomes of the life cycle GHG emissions were analyzed and compared with the given ZEN benchmarks. Additionally, the volume of material per square meter of heated floor area is highlighted.

3.1 BUILDING ENVELOPE FINDINGS

In all four buildings due to the requirement of sustainability certifications, an effort was made for good environmental performance. When embodied energy is concerned, that effort was reflected in the addiction of massive timber in the building envelope.

In the two case studies (Case A and Case C) that we have inclined site topography, the building volumes that are below the earth are made in concrete while the timber is used mainly above terrain levels. That has resulted in a higher concrete volume than massive timber per square meter of HFA. (Table 2). In Case B, even though there wasn't any inclined site topography, a requirement of a basement was made, making the concrete volume almost equal to the massive timber used (Table 2).In Case D, as being the only school without the need for a basement, a great differentiation is shown between the massive timber and concrete volume used per square meter, with massive timber volume being more than double. (Table 2)

Table 2. *The table shows the summary of the environmental data of 4 massive timber school buildings.*

	Case A	Case B	Case C	Case D
$kgCO_2$ (A1-A3)	1,9 million	2,1 million	2,9 million	1,3 million
$kgCO_2$ (B4-B5)	128 407	945 510	195 277	41 448
$kgCO_2/m^2/year$	3,8	3,5	4,1	2,9
Timber ($\frac{m^3}{m^2}$ HFA)	0,18	0,18	0,29	0,43
Concrete ($\frac{m^3}{m^2}$ HFA)	0,32	0,19	0,9	0,17

3.2 LCA FINDINGS

The LCA data showed that all case studies have achieved lower emissions than the median 2020 benchmark of 4.5 $kgCO_2/m^2/year$.

Nordre Ål school (Case D), with the highest percentage of massive timber compared to concrete, and without underground volumes seems to perform the best with a 2,9 $kgCO_2/m^2/year$ while Huseby (Case C) seems to perform the worst with 4,1 $kgCO_2/m^2/year$. When placed in the 2030 and 2050 GHG emission scenario, Huseby's (Case C)ratio depicts the 2025 target, while Flesberg's (Case A) 3,8 $kgCO_2/m^2/year$ ratio is the 2027 target. Bamble school (Case B) , with a ratio of 3,5 $kgCO_2/m^2/year$ represents the 2029 target, while Nordre Ål (Case D) 2,9 $kgCO_2/m^2/year$ ratio for the 2032 GHG reduction, exceeding the 2030 commitment. (Fig 1)

https://doi.org/10.52202/069179-0136

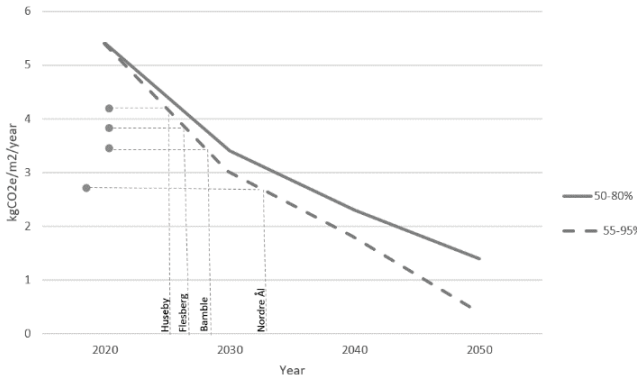

Figure 1. *The Figure shows the comparison of kgCO₂/m²/year ratio of the case studies to the 2030 and 2050 GHG reduction scenarios. The scenario benchmark values were calculated by ZEN (M. Kjendseth Wiik, 2020)*

4 DISCUSSION

As Norway is in the process of lowering its GHG emissions, all four case studies represent newly built sustainable schools. It is greatly understood that massive timber when used as a building material bears environmental benefits [21, 22] hence seems to be promoted for usage in all case studies. The initial results of the research confirm that indeed the percentage of low carbon materials such as CLT that are used in building modules, play the biggest role in the reduction of total emissions, making all case studies perform better than the median set by ZEN.

It is also understood that the overarching goal of these case studies is to achieve the best environmental performance according to the 2020 benchmark standards with great success. But still, fail to reach the 2050 goal. Massive timber, a material with a low carbon footprint, was used mostly in less acoustically challenging areas with smaller span such as classrooms and meeting rooms. Subsequently, if the use of massive timber was greater, the case studies might have shown better lower-emission performance.

Added to this, the preliminary results show that buildings that require subterrain volumes due to the formation of the terrain or due to other circumstances, perform worse emission wise. Concrete, as a building material, is currently regarded as the only option when building volumes under the earth level. Even though great research has been put into reducing its carbon footprint [23], still concrete is concerned a high emission material when compared to massive timber. Although it is difficult to draw definite conclusions, to be able to tackle the 2050 targets, the usage of concrete needs to be further reduced in the building envelope. This may be done by either reducing the number of subterrain volumes or changing the way those volumes are constructed.

5 CONCLUSIONS AND FURTHER RESEARCH

To play a role in restricting the global temperature increase to a safe level of 1.5°C and hence follow the Paris agreement targets, a greater effort in the use of low carbon materials such as massive timber is required. This research revealed that to design a school with high environmental standards, a great percentage of massive timber should be used. But even though those buildings broadcast lower GHG emissions than the average benchmark, they need more improvement to reach the 2050 targets.

For the next step, it would be interesting to address more case studies to examine deeply the connection between the emissions related to material use and the overall GHG emissions in school buildings.

ACKNOWLEDGEMENT

This study has been made possible with the help of Kristian Funderud, who has contributed to the gathering of LCA data.

https://doi.org/10.52202/069179-0136

REFERENCES

[1] COMMISSION, E. 2018. *Clean Planet for all. A European long-term strategic vision for a prosperous, modern, competitive, and climate neutral economy.*

[2] GOVERNMENT, N. 2021. *Lov om endringer i klimaloven (klimamål for 2030 og 2050). In: ENVIRONEMNT, M. O. C. A. (ed.).* https://lovdata.no/dokument/LTI/lov/2021-06-18-129.

[3] STANDARDS, EU. 2012. *BS EN 15978:2011. Sustainability of construction works. Assessment of environmental performance of buildings. Calculation method.*

[4] RÖCK, M., SAADE, M. R. M., BALOUKTSI, M., RASMUSSEN, F. N., BIRGISDOTTIR, H., FRISCHKNECHT, R., HABERT, G., LÜTZKENDORF, T. & PASSER, A. 2020. *Embodied GHG emissions of buildings – The hidden challenge for effective climate change mitigation. Applied Energy, 258, 114107.*

[5] GIORDANO, R., SERRA, V., DEMARIA, E. & DUZEL, A. 2017. *Embodied Energy Versus Operational Energy in a Nearly Zero Energy Building Case Study. Energy Procedia, 111, 367-376.*

[6] HEEREN, N., MUTEL, C. L., STEUBING, B., OSTERMEYER, Y., WALLBAUM, H. & HELLWEG, S. 2015. *Environmental Impact of Buildings—What Matters? Environmental Science & Technology, 49, 9832-9841.*

[7] HILDEBRANDT, J., HAGEMANN, N. & THRÄN, D. 2017. *The contribution of wood-based construction materials for leveraging a low carbon building sector in Europe. Sustainable cities and society, 34, 405-418.*

[8] SANTI, S., PIEROBON, F., CORRADINI, G., CAVALLI, R. & ZANETTI, M. 2016. *Massive wood material for sustainable building design: the Massiv–Holz–Mauer wall system. Journal of wood science, 62, 416-428.*

[9] BRANDNER, R., FLATSCHER, G., RINGHOFER, A., SCHICKHOFER, G. & THIEL, A. 2016. Cross-laminated timber (CLT): overview and development. *European Journal of Wood and Wood Products,* 74**,** 331-351

[10] BYGGFAKTA. 2021. *RE: School building construction materials in Norway. Email communication*

[11] LIANG S, GU H, BERGMAN R, 2021 *Environmental Life-Cycle Assessment and Life-Cycle Cost Analysis of a High-Rise Mass Timber Building: A Case Study in Pacific Northwestern United States Sustainability 2021 Vol. 13 Issue 14 Pages 7831*

[12] JAYALATH A, NAVARATNAM T,NGO P,MENDIS N, HEWSON N, & AYE L, 2020 *Life cycle performance of Cross Laminated Timber mid-rise residential buildings in Australia, Energy and Buildings 2020 Vol. 223 Pages 1100910*

[13] MAIERHOFER,R RÖCK M. RUSCHI M, MENDES M, SAADE E, HOXHA & PASSER A, 2022 *Critical life cycle assessment of the innovative passive nZEB building concept 'be 2226' in view of net-zero carbon targets, Building and Environment 2022 Vol. 223 Pages 109476*

[14] ZEN CENTER, R. 2022. *Zero emission neighborhoods in smart cities. Definition , assessment criteria and key performance indicators.: Zero emission neighborhoods research center*

[15] M. KJENDSETH WIIK, E. S., M. FUGLSETH, E. RESCH, C. LAUSSELET, I. ANDRESEN, H. BRATTEBØ, U. HAHN 2020. *Klimagasskrav til materialbruk i bygninger.* https://fmezen.no*: ZEN Research centre*

[16]] WERNET, G., BAUER, C., STEUBING, B., REINHARD, J., MORENO-RUIZ, E. & WEIDEMA, B. 2016. *The ecoinvent database version 3 (part I): overview and methodology. The International Journal of Life Cycle Assessment, 21, 1218-1230.*

[17] ASSOCIATION, E. 2022. *Ecoinvent material database [Online]. Available:* https://ecoinvent.org/the-ecoinvent-database/ *[Accessed]*

[18] Schmincke, E& GRAHL B, 2007. *The part of LCA in ISO type III environmental declarations International Journal of Life Cycle Assessment 2007 Vol. 12 Pages 38-45*

[19] BIONOVA. 2015. Available: https://www.oneclicklca.com/wp-content/uploads/2016/11/360optimi-verification-ITB-Certificate-scanned-1.pdf [Accessed].

[20] DIBK 2017. *TEK 17. In: ADMINISTRATION, N. O. O. B. T. A. (ed.) TEK 17 Regulations for technical building limitations Online*

[21] BUCHANAN, A. H. & LEVINE, S. B. 1999. Wood-based building materials and atmospheric carbon emissions. *Environmental Science & Policy,* 2**,** 427-437.

[22] YOUNIS, A. & DODOO, A. 2022. *Cross-laminated timber for building construction: A life-cycle-assessment overview. Journal of Building Engineering, 52, 104482*EN 15978:2011*, Sustainability of construction works - Assessment of environmental performance of buildings - Calculation method, in: European Committee for Standardization, Brussels, Belgium, 2012*

[23] KIM, T., TAE, S. & ROH, S. 2013. *Assessment of the CO2 emission and cost reduction performance of a low-carbon-emission concrete mix design using an optimal mix design system. Renewable and Sustainable Energy Reviews, 25, 729-741.*

World Conference on Timber Engineering Oslo 2023

HOLISTIC DESIGN OF TALLER TIMBER BUILDINGS – COST ACTION HELEN (CA20139)

Gerhard Fink[1], Robert Jockwer[2], Iztok Šušteršič[3], Mislav Stepinac[4], Pedro Palma[5], Chiara Bedon[6], Daniele Casagrande[7], Steffen Franke[8], Giuseppe D'Arenzo[9], Daniel Brandon[10], Christian Viau[11]

ABSTRACT: With the worldwide construction sector being responsible for one third of carbon dioxide emissions, as well as forty percent of the world's energy use and waste production, a shift to sustainable and renewable construction techniques is crucial. Engineered timber, a champion of sustainable construction materials, has evolved to a stage that enables the construction of not only family housing but also taller buildings so far commonly built from concrete or steel. Designing taller timber buildings made is more demanding than their concrete and steel counterparts. Whereas different design aspects (architectural, structural, fire safety, acoustics, etc.) of concrete buildings can work almost independently, the design of taller timber buildings should be performed with intensive collaboration among the design teams. It is therefore crucial to address taller multi-storey timber buildings from a collaborative and interdisciplinary perspective, considering static, dynamic, fire, acoustic, human health, and other aspects in parallel and not in isolation. Only through interdisciplinary analysis and interaction can a set of holistic design guidelines be developed that will enable the safe construction of taller timber buildings, as well as respect human wellbeing demands. In this paper, the COST Action CA20139 will be presented and the main aims will be discussed.

KEYWORDS: COST, holistic design, tall timber buildings, sustainability, multi-storey timber, robustness, design for adaptability and reuse, deformation and vibrations, durability, seismic design, fire

1 INTRODUCTION

The number and height of multi-storey timber buildings substantially increased over the past decade [1, 2]. The envelope is being pushed every year, and the current record (as of 2020) for a purely timber multi-storey apartment building stands at 18 storeys (85 m), while for a timber-concrete hybrid it stands at 24 storeys (84 m). Hence, timber buildings up to 10 storeys are in the meanwhile already considered as midrise.

Due to targets regarding a more sustainable and healthier environment, contemporary multi-storey timber buildings are being recognised as a long-term sustainable solution, especially in urban areas where they present an environmentally friendly alternative to concrete and steel buildings [3].

The design of taller timber buildings so far has always been made by highly specialised engineering teams that were well aware of the unique demands and challenges that multi-storey timber buildings are associated with. Despite that several midrise and a few taller timber buildings have been already built, the knowledge level as well as the number of recognised experts on taller timber buildings is still far from its concrete and steel counterparts.

Additionally, there are also new and most likely more challenges to be tackled with taller timber buildings [4]. Despite efforts, practically all the worldwide research performed in the field of multi-storey timber buildings was performed partially with intense focus on individual fields (connections, vibrations, acoustics, fire, durability [5-6]) and not considered from a wider perspective, namely in a holistic manner. However, a well-integrated design is absolutely crucial for designing taller timber buildings.

[1] Gerhard Fink, Department of Civil Engineering, Aalto University, Finland, gerhard.fink@aalto.fi
[2] Robert Jockwer, Department of Architecture and Civil Engineering, Chalmers University of Technology, Sweden, robert.jockwer@chalmers.se
[3] Iztok Šušteršič, Innorenew CoE, Slovenia, iztok.sustersic@innorenew.eu
[4] Mislav Stepinac, Faculty of Civil Engineering, University of Zagreb, Croatia, mstepinac@grad.hr
[5] Pedro Palma, Empa – Swiss Federal Laboratories for Materials Science and Technology, Structural Engineering Research Lab, Switzerland, pedro.palma@empa.ch
[6] Chiara Bedon, University of Trieste, Italy, chiara.bedon@dia.units.it
[7] Daniele Casagrande, National Research Council of Italy, Italy, daniele.casagrande@ibe.cnr.it
[8] Steffen Franke, Bern University of Applied Sciences, Switzerland, steffen.franke@bfh.ch
[9] Giuseppe D'Arenzo, University of Kassel, Germany, giuseppe.darenzo@uni-kassel.de
[10] Daniel Brandon, RISE Research Institutes of Sweden, Sweden, daniel.brando@ri.se;
[11] Christian Viau, Carleton University, Canada, ChristianViau@cunet.carleton.ca;

https://doi.org/10.52202/069179-0137

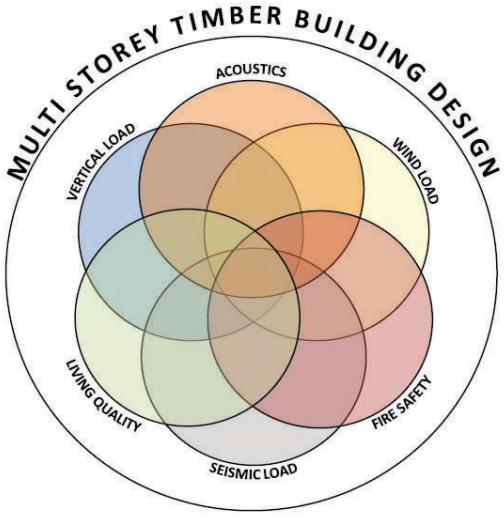

INTERACTIONS + positive - negative N neutral	VERTICAL LOAD	WIND LOAD	SEISMIC LOAD	FIRE SAFETY	ACOUSTICS	LIVING QUALITY
VERTICAL LOAD		+	-	-	+	N
WIND LOAD	+		+	N	-	N
SEISMIC LOAD	-	+		N	-	N
FIRE SAFETY	-	N	N		+	-
ACOUSTICS	+	-	-	+		-
LIVING QUALITY	N	N	N	-	-	

***Figure 1**: Interaction of a few different building design fields and their inherent collisions, either positive or negative, that need to be resolved for multi-storey taller timber buildings.*

2 CHALLENGES AND AIMS OF THE COST ACTION

COST Action CA20139 – Holistic design of taller timber buildings (HELEN) was started on 12/10/2021 and runs until 11/10/2025. It will try to change the paradigm of building construction research, shifting R&D from isolated topics to an integrated interdisciplinary approach, which is critically necessary to safely design and build as well as correctly maintain and recycle taller timber buildings. There are several reasons why: less general experience with them; codes for timber buildings are not as developed as they are for concrete or steel [7,8]; and less suitable literature is available for practicing designers. However, a key difference is the design complexity of timber buildings due to basic material properties. Whereas different designers (architects and structural, fire and acoustic engineers) of concrete buildings can work almost independently, the design of taller timber buildings should be performed with intensive collaboration among the design team members [9]. Otherwise, serious conflicts can arise (Figure 1) that effect both the load resisting and serviceability criteria of a building.

Counting purely on design codes is not sufficient as the code information and offered solutions only partly address the full range of concerns for timber buildings. Therefore, it is crucial to address taller multi-storey timber buildings from a collaborative and interdisciplinary perspective, considering static, dynamic, fire, acoustic, human health and other aspects in parallel and not in isolation. Only through interdisciplinary analysis and interaction can a set of holistic design guidelines be developed that will enable safe construction of taller timber buildings that respect human well-being demands.

The main objective of HELEN is to foster international interest and effort in developing a shared understanding and deriving common guidelines for the holistic design of taller timber buildings. This will be carried out through the sharing of technical and scientific skills from the different and diverse research profiles within the network as well as their research facilities. Cooperation within this network will allow for coordinated research efforts and achievement of the following objectives:

- Coordinate, compare and bring together results of related research with the aim of defining optimized holistic approaches to improve the performance of taller timber buildings.
- Collect case studies that show flagship examples describing taller timber building design.
- Foster the transfer of knowledge among different actors in order to find suitable applications in various multidisciplinary fields (e.g. vibrations of buildings, material response and influence).
- Serve as a hub to combine existing knowledge and identify common issues and problems in order to develop new holistic taller timber building design guidelines.
- Suggest new design approaches, processes and technologies that can build and improve upon existing best practices and finally presented in the design guidelines suggesting the optimal holistic design of taller timber buildings.
- Identify and address regulatory, governance, financial and legal drivers and barriers for a wider implementation and use of taller timber buildings.

https://doi.org/10.52202/069179-0137

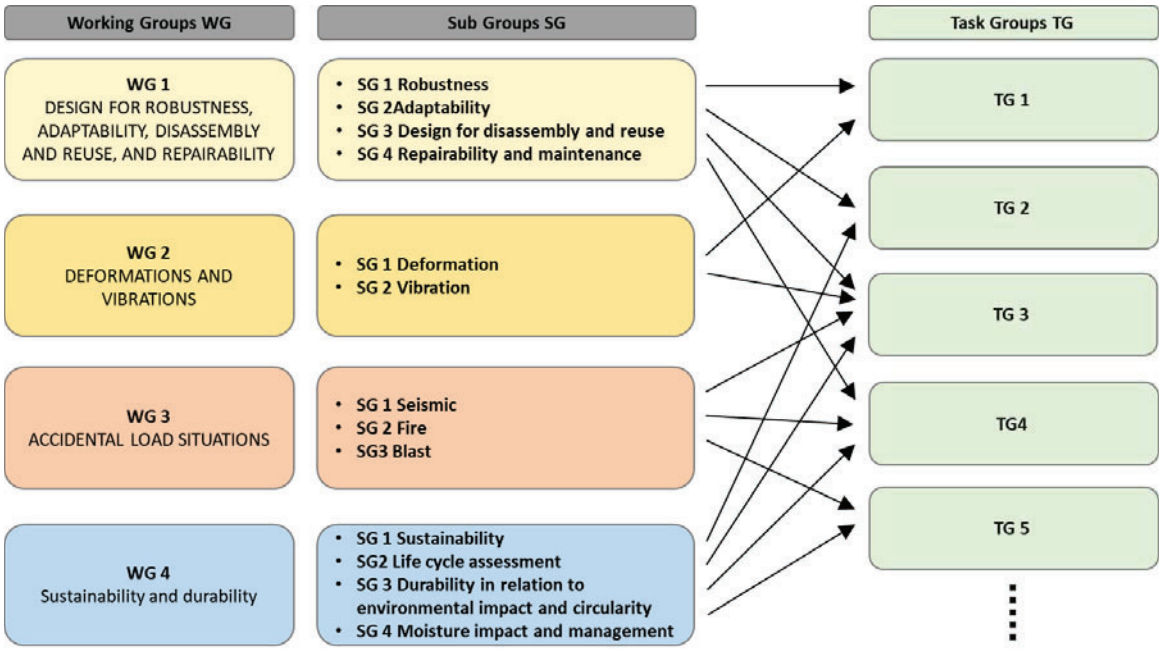

***Figure 2**: Structure of COST Action CA* 20139

3 STATE-OF-THE-ART REPORT

HELEN is organised in four Working Groups (WGs), each containing several subgroups (SGs). An overview is presented in Figure 2. As a result of the multidisciplinary aspects considered in HELEN, the COST Action is rapidly growing with currently 282 members from 44 countries (status March 2023).

One of the first targets on HELEN was the development of a state-of-the-art report in taller multi-storey timber building design fields: 1) Design for robustness, adaptability, and reuse and repair; 2) Deformations and vibrations; 3) Accidental load situations and 4) Sustainability and durability. In this chapter, the WGs and the content of the State-of-the-Art report is shortly introduced.

One of the main activities of the action is the identification of multidisciplinary tasks and research questions, for which the expertise of several WGs can be combined in task groups (TG) in a multidisciplinary effort (Figure 2). The State-of-the-Art Report was a first step in the identification of such multidisciplinary issues.

3.1 WG 1 – DESIGN FOR ROBUSTNESS, ADAPTABILITY, DISASSEMBLY AND REUSE, AND REPAIRABILITY

WG1 deals with aspects related to *robustness, adaptability, design for disassembly and reuse, and repairability*. Given the broad range and interdisciplinary nature of the topics assigned to WG 1, it has members with different backgrounds in both engineering and architecture and in research and practice. WG 1 is organised in four Sub-Groups (Figure 2) i) SG *Robustness*; ii) SG *Adaptability*; iii) SG *Design for disassembly and reuse (DfDR)*; and iv) SG *Repairability and maintenance*. The contribution of WG 1 to the State-of-the-Art Report [10] includes a total of 20 documents from all SGs.

Robustness:

SG *Robustness* deals with the topics of resistance to disproportionate damages, including structural and non-structural robustness and resistance to progressive collapse. The SG has worked on developing a framework for the design of timber buildings against disproportionate collapse, which includes identifying all stakeholders and their interests and responsibilities. Case studies of structural design for increased robustness have been analysed and most important strategies summarised. The key issues identified by the SG are the: experimental validation of sudden element-removal scenarios; simplified structural analysis models for alternative load-paths (ALPs), e.g. with dynamic amplification factors; the behaviour of connections in ALPs; connections as fuse elements in segmentation strategies, which has similarities with *capacity design* for earthquake resistance; "power storeys" for vertical segmentation in taller timber buildings. The members of SG *Robustness* contributed with five documents to the State-of-the-Art Report.

https://doi.org/10.52202/069179-0137

Adaptability:
SG *Adaptability* deals with topics related to changes in the functional use of buildings, how the design of tall timber buildings can account for adaptability-related requirements (e.g. versatility, convertibility, expandability), and with the interactions between these and other requirements (e.g. robustness, durability). The SG created a definition of adaptability of a taller timber building an identified key challenges and advantages of timber buildings. The SG is currently focusing on: identifying spatial structures and constructions that allow for the highest degree of interaction, flexibility and adaptability; identifying key parameters for adaptability; identifying conflicts between adaptability and other requirements (e.g. acoustics, fire safety); socioeconomic factors for higher adaptability; digitalisation, information management and computational methods for adaptability, repairability and reusability of timber buildings; development of reversible connection systems.

Design for disassembly and reuse:
SG *Design for disassembly and reuse (DfDR)* addresses the topics of design for disassembly and reusability in the context of tall timber buildings. This includes the design of new timber buildings taking into account future needs of disassembly and maximising reuse possibilities, but also the reuse of reclaimed materials in new buildings. The SG has been working on: identification of circular materials flows in tall timber buildings; assessment of the mechanical properties of reclaimed timber members; and identification of barriers to the design for disassembly and reuse.

Repairability and maintenance:
SG *Repairability and maintenance* deals with issues of maintenance of buildings during their planned service life and of restoring the original conditions in case of damages. The work of this SG has focused on: maintenance strategies for tall timber buildings; design strategies to take into account eventual need for repairs; repair strategies for tall timber buildings; and how to extend the service life of taller timber buildings.

3.2 WG 2 – DEFORMATIONS AND VIBRATIONS

WG2 deals with aspects and design issues related to *deformations and vibrations* in the framework of taller timber structures. Basically, scientist and professional engineers contributing to the activities of WG2 are representative of research institutions, universities and industrial partners. Actually, major activities of WG2 are divided into two major Sub-Groups: SG1 – Deformations and SG2 – Vibrations, see [11] and Figure 2. Besides, many tasks and sub-topics represent a critical input and vital part of discussion and elaboration in SG1 and SG2.

Deformations:
Talking about *deformations* in tall timber structures, the attention goes to a multitude of aspects and issues that have major effects in research and industrial applications and are often fairly addressed by existing standards and regulations. As a matter of fact, deformations in timber structures are primarily associated to joints and connections. There are however no doubts about the complexity and variability of possible technological solutions in the field of *joints* and *connections* for timber structures. Also, the type of load, the boundary conditions and the assessment of their mechanical performance suggests the need of a robust background in support of optimal and safe mechanical design of these systems.

Vibrations:
The issue of *vibrations*, which is also addressed by WG2 members, is implicitly related to deformations and corresponding gaps in engineering knowledge / design tasks. Starting from the assumption that *vibrations* itself is a rather general definition and can cover a multitude of practical / technical aspects in the framework of timber structures, WG2 members actively contributed to the elaboration of a State-of-the-Art document in which most of engineering terms and problems could be first defined in their context. So far, do we implicitly talk about vibrations in floors or partition walls for timber structures? And which kind of design action should be primarily addressed in terms of vibration serviceability, for the specific solutions in use in tall timber structures? But indeed, how can we monitor and control, or possibly minimize and mitigate the effect of vibrations in typical load-bearing components for tall timber structures?
The first elaboration from WG2 members, in this sense, resulted in the detection of rather wide and complex tasks in which – under the assumption of a joint primary goal of design – basic engineering knowledge for vibration assessment and mitigation is still represented by the need of standardized operational procedures and guidelines which could be efficiently applied to any type of building component (floors for instance, but not only). This need implicitly recalls the complexity of possible design actions (WG3 topic) and their effect and assessment in terms of vibrations. Human-induced loads on timber floors, for example, are totally different in dynamic and mechanical features (and effects) from wind pressure or seismic actions (and corresponding vibrations).
There are no doubts, finally, about the inter-correlation of *vibrations* and *deformations*, which again suggest an intrinsic mutual interaction of load-bearing components for tall timber structures and the final user / the design actions.

3.3 WG 3 – ACCIDENTAL LOAD SITUATIONS

The activities conducted in the first year on accidental load situations have been summarized in the form of a State-of-the-Art report [12]. The State-of-the-Art, developed with the contribution of 45 people from 17 different countries, aims to reflect the current knowledge on the development, design, and construction of taller timber buildings subjected to accidental load situations due to earthquakes, fires, and blasts. Particular attention was paid to the efforts and the proposals made to overcome the limitations for the progress in the

https://doi.org/10.52202/069179-0137

construction market of mid-rise and taller timber building. The report is the result of a deep review of scientific literature, international collaborations, national regulations, design guidelines, as well as case studies. Potential interactions with other fields of design and to the efforts made in the recent years to overcome the limitations for the progress in the construction market of timber buildings were investigated. The indications collected represent the starting point of discussion to identify solutions, research targets, methods, and resources for the future of taller timber buildings under seismic, fire, and blast loads following a holistic design approach. Three different sub-groups (SGs) have been defined for WG3 State-of-the-Art activities, namely SG1 - Seismic Loads, SG2 - Fire and SG3 - Blast. For each SG, different subtopics have been analysed and discussed.

Seismic:

With potentially devastating effects on occupant safety and economic stability, earthquakes represent one the main hazard to consider when designing buildings in seismic prone areas. Despite possessing properties that make them well-suited for seismic design (i.e. lightness), timber structures are not immune to the effects of earthquakes. In light of the current timber construction sector growth, investigating the effects of earthquakes on taller timber structures is crucial to ensure life safety and minimal economic losses.

The primary focus of SG1 was to analyse how seismic activities impact tall timber buildings. In particular, eight topics were identified (Figure 3) and deeply examined, including: Lateral Load Resisting Systems (LLRSs), high performance connections, seismic protection technologies, seismic design strategies and analyses, standards and codes, analysis of case studies, and interaction and conflict in holistic design.

The State-of-the-Art report reveals that different LLRSs including shear walls, heavy frames and hybrid structural systems are typically adopted for taller timber buildings. Regardless of the structural system considered, connections are crucial for the seismic performance of timber buildings, as they determine their stiffness, capacity, and ductility. Two categories of connections were identified, namely traditional and innovative, and the need of connections with significant resistance and ductility was pointed out. Seismic protection technologies such as supplementary damping systems [13] and passive control systems can be used as viable solutions to reduce structural and non-structural damages and related economic losses, especially in areas with high seismic hazard.

The analysis of the design strategies and the seismic analyses indicates that capacity-design principles should be employed to ensure energy dissipation and optimal structural performance. Also, modern performance-based design, both force-based [14] and displacement-based [15], can be adopted to reach specific target performance. However, to date only a limited number of international codes has specific design guidelines for timber buildings

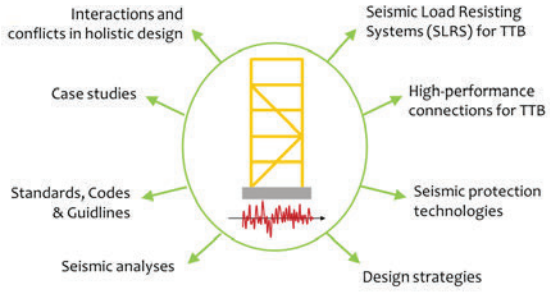

Figure 3: *topics analysed by SG1 for seismic load on taller timber buildings.*

subjected to seismic load. Further research is required in the near future to address seismic design-related issues, such as the in-plane behaviour of floor diaphragms, prediction of connection mechanical properties, and the interaction of structural elements. Finally, the analysis of case studies and discussions with designers emphasized the need for integrated design methodologies that optimize functions, minimize costs and errors, and avoid conflicts between different design strategies.

Fire:

Structural timber is often cited for its carbon storage and subsequently for offering a possible response to the current climate crisis. For fire safety implementation in buildings, it is, however, important to note that the presence of more potential fuel is a consequence of this carbon storage. The State-of-the-Art report indicates that the contribution of structural timber as a fuel to the fire can, among other things, increase the fire growth [16], the structural damage, and the external exposure of fires [17]. However, only a handful of countries to date have adopted provisions aimed at limiting the fuel contribution for the whole duration of the expected fire scenarios, such as by limiting the exposed surfaces of mass timber [18] and preventing glue line integrity failure [19], or accounting for its impact (e.g. by having construction type specific fire resistance requirements [20]). Although most previous research focussed on the performance of timber in standard fire resistance tests, knowledge gaps regarding connections, multi-span structures, point loaded panels, and connections [21] relevant for taller timber buildings were identified. These gaps are especially pertinent when considered for the combined action of earthquakes or blasts and fires. The State-of-the-Art report also indicated that only a small amount of data was found relevant for robustness, post-fire repair, fire suppression strategies, which are topics mainly related to the protection of property.

Blast:

The increase in market share of the timber construction industry brings with it an increase in potential exposure to accidental and intentional blast explosions, such as that emanating from gas leaks and vehicle bombs, respectively. Understanding how wood behaves under high strain-rates and having well-established mitigation

https://doi.org/10.52202/069179-0137

strategies to minimize the risk of progressive collapse is required to ensure occupant safety during these rare events. As an organic material, high strain rate effects and failure modes were found to be affected by the direction and rate of the load in both members [21-23] and connections [24-25]. With that being said, present-day blast design codes were developed based on preliminary data which are no longer applicable to the novel engineered wood products. As in the case of connections for seismic detailing, connections of timber assemblies under blast load must be designed to concentrate the majority of the deformations within ductile connectors, to protect the load-bearing timber element against unwanted damage [e.g. 26- 27].
Particular attention should be given to the brittle behaviour of timber in order to minimize the risk associated with progressive collapse in timber structures. Another consideration was ensuring that connections and main elements had sufficient ductility and strength in addition to ties consideration in the main principal directions [28]. While simplified modelling methodologies were praised for their proven efficacy and low computational costs [29], they lack the ability to consider and capture multiple failure modes. This may be circumvented using finite element modelling (FEM); however, proper attention is required to develop a representative material model that can treat wood and its many failure modes, including both brittle and ductile failure modes.

3.4 WG 4 – Sustainability and durability

A holistic design approach can make taller timber buildings even more sustainable compared to conventional buildings made mainly of steel, concrete, or masonry. Durability is meant in terms of moisture safety for longevity of timber products, assemblies and structures, and the possibility to increase utility by e.g., reuse or quality cascading in upcoming product life. Robustness should express the general resistance of timber against moisture within certain limits. To not exceed these limits, a proper moisture management is necessary and must be considered already in the holistic design for taller timber structures, considering the different stages from factory until operation. Robustness also has to do with the resilience of structures and assemblies and their repairability to maintain most of the moisture affected situations. This robustness concept exercised for entire buildings also enables to additionally lower environmental footprint because it allows to keep buildings in service as long as technically possible. Therefore, many crosslinks with Working group 1 - Robustness, Reuse and Repair of CA20139 exists.

To benefit from these advantages, tall timber buildings must have a similar or almost equal durability compared to conventional buildings. Otherwise, the sustainability advantages would be compromised. Therefore, tall timber buildings must be designed, considering the special properties of timber as construction material. The goal is to maximize resistance of this type of timber structures and envelope systems against various moisture exposure scenarios causing deterioration and damage. Not only design but also execution of timber structures is of relevance namely construction site activities and prevention from severe moisture impact. Further operation and maintenance of large and tall timber buildings need a focus on risk reduction measures.

Despite these special requests for the designers, tall timber structures are already built in Europe, but also North America and Australia are competing since a few years. Thus, a lot of research work and development have been done especially in Europe on this field.

The aim of Working Group 4 is to report the state of the art in terms of research and practice of durability and sustainability of tall timber building systems, in order to summarize the existing knowledge in the single countries and to develop a common understanding of the design for moisture safe and robust execution and operation of tall timber buildings. The State-of-the-art report reflects parts of the work and the discussions within WG 4 [30] and covers the SG topics given Figure 2. It intends to give information and studies available around the world, but especially in Europe through the active contribution and participation of experts from various countries involved in this Action.

Exchanges of experts are planned in order to achieve a harmonisation of concepts, approaches and methods, e.g. in the field of life cycle assessment for taller timber buildings. Gaps in knowledge over all four parts of WG 4 (Figure 2) will be defined and built up the framework for further research projects and collaborations. Existing expertise's are to be presented and passed on to a wider range, of timber engineers and practitioners within training schools, online seminars or specific short term scientific missions educating especially the younger generation, the engineers of our future.

4 SHORT-TERM SCIENTIFIC MISSIONS

Short Term Scientific Missions (STSM) are aimed at supporting individual mobility and at strengthening the existing networks and fostering collaborations by allowing scientists to visit an institution or laboratory in another Participating COST Country or an approved institution. A STSM should specifically contribute to the scientific objectives of the COST Action, while at the same time allowing applicants to learn new techniques or gain access to specific instruments and/or methods not available in their institutions. In doing so, the COST Action addresses with the STSMs in particular the needs of young scientists to build and strengthen their network and supports diversity in the field. In the first Grant period of HELEN (the year 2022), six STSMs were conducted, covering the following topics:

- Experimental and numerical assessment of soundproofing interlayers influence on the

strength and stiffness of timber to steel screw connections
- Fire induced delamination
- Influence of elevated temperature on the adhesive used in hollow glue-laminated timber elements
- State-of-the-art report on realistic fire exposure in fire design of taller timber buildings
- Towards Zero Carbon Buildings: Timber structure for sustainable buildings
- Environmental impact assessment of multi-storey residential timber buildings – integrated approach

The COST Action is committed to promoting the development of novel applications and will consistently allocate additional resources towards new research initiatives.

5 COMMUNICATION

The HELEN COST Action has generated interest from a broad range of stakeholders, who are involved in the WGs, such as representatives of the timber construction industry, architects, structural engineers, consultants, builders, product developers in the sector of timber structures, authorities and policy makers at regional and European levels, research community, relevant standardization bodies and code writers, teachers, lecturers and students of structural design, engineering, and architectural schools.

The COST Action aims at connecting these stakeholders and communicate its activities to the stakeholders, research community, and society, amongst others by:
- Sharing research results
- Stimulating new research projects
- Raising awareness of the Action topics in general public and among scientific societies
- Engaging the stakeholders
- Influencing policy making
- Exchanging ideas on sustainable development of the built environment

The discussion of the research efforts and the development of the research results are realized through workshops, seminars, and STSMs. The consolidated results of the action are disseminated and communicated through conferences, training schools, and the joint elaboration of state-of-the-art papers, best practice examples and final design guidelines for a holistic design and construction of taller timber buildings.

The workshops, conferences, and training schools to be carried out within this Action promote the interdisciplinary research in the fields of wood science and technology, timber engineering and structural reliability. The first training school in 2023 covers the holistic design of connections in timber structures and all WGs are involved in its preparation. Further training schools on interdisciplinary topics are planned for the following years.

6 CONCLUSIONS

The very essence and key to a successful COST Action will be intense interdisciplinary work with in-depth discussions and debate over a series of hypothetical and real case studies, followed by focused research work. Contrary to common building research work done in the past, where individual topics were assessed in depth by specialised teams working on isolated topics (i.e. just timber connections or just vibration of floor plates), research within HELEN will be intensely collaborative and integrated.

ACKNOWLEDGEMENT

This research was funded by the COST ACTION HELEN (Holistic design of taller timber buildings – CA20139): https://cahelen.eu/.

The authors thank all members of the COST Action CA20139, for the discussions, presentations, and contributions. A special acknowledgment is owed to the authors of the documents prepared for the State of the Art Report and the Sub-Group coordinators (listed alphabetically by surname and by Sub-Group): Reinhard Brandner, José Manuel Cabrero, Maria Felicita, Kristina Kröll, Lisa Ottenhaus, Felipe Riola-Parada (WG 1); Thomas Reynolds and Angelo Aloisio (WG 2); David Barber (WG 3); Shady Attia, Bettina Franke, Jens Frohnmüller, and Stephan Ott (WG 4).

REFERENCES

[1] Carvalho, L. F., Carvalho Jorge, L. F., & Jerónimo, R. (2020). Plug-and-Play Multistory Mass Timber Buildings: Achievements and Potentials. Journal of Architectural Engineering, 26(2), 1–22
[2] Kuzmanovska, I., Gasparri, E., Monne, D. T., & Aitchison, M. (2018). Tall Timber Buildings : Emerging Trends and Typologies. World Conference on Timber Engineering 2018.
[3] FPInnovations. (2013). Technical Guide for the Design and Construction of Tall Wood Buildings in Canada (E. Karacabeyli & C. Lum, eds.). Conference on Timber Engineering.
[4] Buchanan, A. H. (2016). The challenges for designers of tall timber buildings. WCTE 2016
[5] Sustersic, I., Fragiacomo, M., & Dujic, B. (2012). Influence of the connection behaviour on the seismic resistance of multi-storey crosslam buildings. WCTE 2012 - World Conference on Timber Engineering, 402–410.
[6] Pei, S., Berman, J., Dolan, D., Lindt, J. Van De, Ricles, J., Sause, R., … Rammer, D. (2014). Progress on the Development of Seismic Resilient Tall CLT Buildings in the Pacific Northwest. World Conference on Timber Engineering 2014.
[7] Smith, T., Moroder, D., Sarti, F., & Pampanin, Stefano, Buchanan, A. H. (2015). The reality of

https://doi.org/10.52202/069179-0137

seismic engineering in a modern timber world. Proceedings INTER, 2015.
[8] Kleinhenz, M., Winter, S., & Dietsch, P. (2016). Eurocode 5 - A halftime summary of the revision process. WCTE 2016 - World Conference on Timber Engineering.
[9] Aberger, E., Koppelhuber, J., & Heck, D. (2018). Building information modeling in timber onstruction – A solution for planning process, design phases and the unification of scope of works. WCTE 2018 – World Conference on Timber Engineering.
[10] Palma P., Fink G., Design for robustness, adaptability, disassembly and reuse, and repairability of taller timber buildings: a state of the art report, COST Action CA 20139 Holistic design of taller timber buildings (HELEN), 2022.
[11] Bedon C., Reynolds T., Aloisio A., Design of taller timber buildings against deformations and vibrations: a state-of-the-art review, COST Action CA 20139 Holistic design of taller timber buildings (HELEN), 2022.
[12] Casagrande, D., Brandon, D., D'Arenzo, G., & Viau, C. Design of taller timber buildings subjected to accidental loads: a state-of-the-art review. COST Action CA 20139 Holistic design of taller timber buildings (HELEN), 2022.
[13] Ugalde D, Almazán JL, Santa María H, Guindos P. (2019) Seismic protection technologies for timber structures: a review. Eur. J. Wood Wood Prod., 77(2), 173–194. Springer Berlin Heidelberg.
[14] Seim W, Hummel J, Vogt T. (2014) Earthquake design of timber structures - Remarks on force-based design procedures for different wall systems. Eng. Struct., 76, 124–137. Elsevier Ltd.
[15] Loss C, Tannert T, Tesfamariam S. (2018) State-of-the-art review of displacement-based seismic design of timber buildings. Constr. Build. Mater., 191, 481–497. The Author(s).
[16] Nothard, S., Lange, D., Hidalgo, J.P., Gupta, V., McLaggan, M.S., Wiesner, F., Torero, J.L., (2022). Factors influencing the fire dynamics in open-plan compartments with an exposed timber ceiling. Fire Safety Journal 129, 103564.
[17] Su, J., Lafrance, P.-S., Hoehler, M., Bundy, M., (2018a). Fire Safety Challenges of Tall Wood Buildings - Phase 2: Task 3 - Cross Laminated Timber Compartment Fire Tests.
[18] IBC (2021) International Building Code (USA). International Code Council.
[19] ANSI/APA PRG 320 (2018) Standard for Performance-Rated Cross-Laminated Timber, ANSI standards.
[20] Brandon, D. et al (2019). High-fire-resistance glulam connections for Tall Timber Buildings. RISE Rapport; 2019:26, Sweden.
[21] Lacroix, D.N. and G. Doudak, *Determining the Dynamic Increase Factor for Glued-Laminated Timber Beams.* Journal of Structural Engineering, 2018. 144(9): p. 04018160.
[22] Poulin, M., C. Viau, D.N. Lacroix, and G. Doudak, *Experimental and Analytical Investigation of Cross-Laminated Timber Panels Subjected to Out-of-Plane Blast Loads.* Journal of Structural Engineering, 2018. 144(2): p. 04017197.
[23] Lacroix, D.N. and G. Doudak, *Investigation of Dynamic Increase Factors in Light-Frame Wood Stud Walls Subjected to Out-of-Plane Blast Loading.* Journal of Structural Engineering, 2015. 141(6): p. 04014159.
[24] McGrath, A., C. Viau, and G. Doudak, *Investigating the Response of Bolted Wood Connections to the Effects of Blast Loading*, in *CSCE 2019 Annual Conference*. 2019, Canadian Society for Civil Engineering: Laval, QC.
[25] Viau, C. and G. Doudak, *Behaviour and modelling of cross-laminated timber panels with boundary connections subjected to blast loads.* Engineering Structures, 2019. 197: p. 109404.
[26] Viau, C. and G. Doudak, *Behavior and Modeling of Glulam Beams with Bolted Connections Subjected to Shock Tube-Simulated Blast Loads.* Journal of Structural Engineering, 2021. 147(1): p. 04020305.
[27] Viau, C. and G. Doudak, *Energy-Absorbing Connection for Heavy-Timber Assemblies Subjected to Blast Loads–Concept Development and Application.* Journal of Structural Engineering, 2021. 147(4): p. 04021027.
[28] Sørensen, J.D., *Framework for robustness assessment of timber structures.* Engineering Structures, 2011. 33(11): p. 3087-3092.
[29] Viau, C. and G. Doudak, *Dynamic analysis methods for modelling timber assemblies subjected to blast loading.* Engineering Structures, 2021. 233: p. 111945.
[30] Franke, S. (Ed.) 2022. Sustainability and Durability of Taller Timber Buildings: A state-of-the-art report. COST Action CA20139 Holistic design of taller timber buildings (HELEN)

World Conference on Timber Engineering Oslo 2023

DESIGN AND CRADLE-TO-GRAVE LIFE-CYCLE ASSESSMENT: FULL-SCALE SIX-STORY SHAKE-TABLE TEST BUILDING LATERAL SYSTEMS

Steven Kontra[1], Andre R. Barbosa[2], Arijit Sinha[3], Gustavo A. Araujo R.[4], Patricio Uarac P.[5], Nathan C. Brown[6], Jace Furley[7], Tu X. Ho[8], Gustavo F. Orozco O.[5], Barbara G. Simpson[9], John W. van de Lindt[10], Seyed Hossein Zargar[11]

ABSTRACT: This paper describes the lateral force resisting system (LFRS) design in a full-scale six-story shake-table test building and presents a comparative cradle-to-grave life-cycle assessment of alternative LFRSs. The test building features the reuse of material from a ten-story shake-table structure comprised of engineered mass timber (MT) products. These include MT floors (cross-, glue-, nail-, and dowel-laminated timber [CLT], [GLT], [NLT], [DLT]); MT post-tensioned rocking walls (CLT and mass ply panels [MPP]); and a gravity system consisting of laminated-veneer lumber (LVL) beams and columns. Shake-table testing will benchmark innovative, low-damage design solutions for the LFRSs. To supplement this test, the environmental impact of a MT LFRS is determined relative to design alternatives that use conventional materials. The Athena Impact Estimator for Buildings was used to perform a comparative, cradle-to-grave life-cycle assessment (LCA) of the prototype MT LFRS with respect to an alternative, functionally equivalent reinforced concrete (RC) shear wall design. The LCA results showed reduced environmental impacts across some impact metrics, with a significant reduction in Global Warming Potential for the MT LFRS when accounting for biogenic carbon.

KEYWORDS: Engineered wood products; Life-cycle assessment; Rocking wall; Seismic Design; Shake-table test

1 INTRODUCTION

The rapid development of MT engineered wood products has resulted in a suite of new design opportunities for architects and engineers. As many building types using these MT products have not yet been codified, liberty in their use has fuelled the development of new engineering design solutions that strive to meet both resilience and sustainability criteria. These innovative designs would benefit from experimental benchmarking to accelerate acceptance from various regulatory jurisdictions and agencies for design code adoption.

A full-scale six-story MT building testing program will be implemented at the National Hazards Engineering Research Infrastructure outdoor shake-table testing facility at University of California San Diego (NHERI@UCSD) by the Converging Design Project team [1]. The testing program is intended to benchmark low-damage MT LFRS design solutions, provide data for numerical models employing MT, and inform design methodologies and life-cycle analyses.

This paper summarizes the designs of the shake-table specimen LFRS and provides insight into the relative environmental sustainability of these design choices. A cradle-to-grave LCA was used to investigate the

[1] Graduate Research Assistant, Civil Engineering and Wood Science & Engineering, Oregon State University, Corvallis, U.S.A., kontras@oregonstate.edu
[2] Professor, School of Civil and Construction Engineering, Oregon State University, Corvallis, U.S.A., andre.barbosa@oregonstate.edu
[3] Professor, JELD-WEN Endowed Chair, Wood Science & Engineering, Oregon State University, Corvallis, U.S.A.
[4] Graduate Research Assistant, Civil Engineering, Stanford University, Stanford, U.S.A.
[5] Graduate Research Assistant, Civil Engineering and Wood Science & Engineering, Oregon State University, Corvallis, U.S.A.
[6] Assistant Professor, Dept. of Architectural Engineering, Penn State University, University Park, U.S.A.
[7] Graduate Research Assistant, Dept. of Civil and Environmental Engineering, Colorado State University, Fort Collins, U.S.A.
[8] Postdoctoral Scholar, Wood Science & Engineering, Oregon State University, Corvallis, U.S.A.
[9] Assistant Professor, Dept. of Civil and Environmental Engineering, Stanford University, Stanford, U.S.A.
[10] Harold H. Short Endowed Chaired Professor, Dept. of Civil and Environmental Engineering, Colorado State University, Fort Collins, U.S.A.
[11] Graduate Research Assistant, Dept. of Architectural Engineering, Penn State University, University Park, U.S.A.

https://doi.org/10.52202/069179-0138

environmental impact of the MT LFRS, as compared to a functionally equivalent RC design solution.

2 SPECIMEN REUSE AND SHAKE-TABLE TESTING

This study highlights a six-story MT test building, which will feature the reuse of a ten-story MT test building from the NHERI TallWood test program [2]. The top four stories and non-structural elements of the original ten-story building will be deconstructed to form the new six-story specimen that will consist of various engineered MT products, as shown in Figure 1.

The ten-story building was designed to feature post-tensioned (PT) MT rocking walls with U-shaped flexural plates (UFPs) as energy dissipators. The four rocking walls are connected to the timber diaphragm through a shear key connection designed for the transfer of horizontal shear forces while allowing for wall rotation and vertical displacement relative to the diaphragm. Self-centering capabilities are included through a series of four PT high-strength steel rods located near the center of the wall section and spanning across the entire wall height. Figure 2 shows the UFP-wall configuration, illustrating key components such as PT rods and shear keys for lateral force transfer.

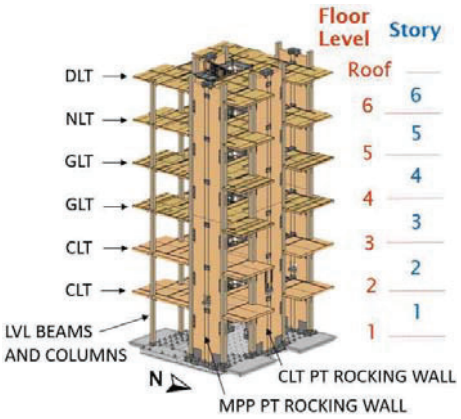

Figure 1: *Six-story MT test building*

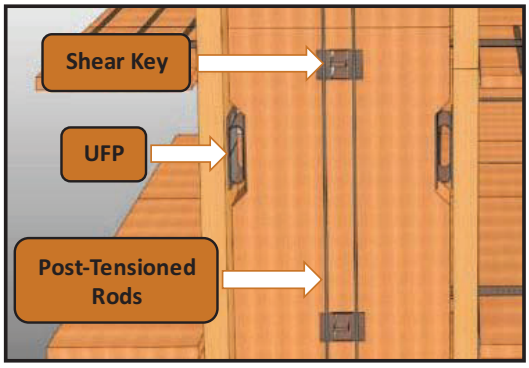

Figure 2: *PT rocking wall with UFPs*

Following deconstruction and inspection for any damage that may have resulted from the ten-story testing program, the new six-story building specimen will consist of three phases, in which three different LFRSs will be tested.

In the first phase of the six-story testing, the inherited shear wall panels in both directions will be cut to size and reused. A new UFP-wall configuration will then be installed, along with a new PT rod setup, based on the Direct Displacement-Based Seismic Design (DDBD) method. This methodology has been proposed as an alternative design procedure that allows the designer to achieve strain-limit- or drift-limit-based performance objectives [3,4]. The UFPs were designed as the main component that will behave in the inelastic range, in which its displacement was defined as the performance objective. The panels and post-tensioned rods are designed and expected to remain essentially elastic. Wall system design limit states and performance objectives are described in more detail in section 3.2.3.

The plan for the second phase of testing involves the replacement of the two MPP walls resisting lateral forces in the N-S direction. In their place, a new LFRS will be installed featuring MPP panels with buckling-restrained braces (BRBs) whose design is informed by LFRS prototype testing at Oregon State University (OSU) [5,6]. The BRBs are installed at the wall boundaries in the first story, acting as high-ductility hold-downs, while the MPP walls are designed to remain essentially elastic above the base [7]. The proposed lateral system takes inspiration from previous research on steel elastic frames, and concrete and mass timber walls employing buckling-restrained columns as energy dissipators [8–10]. The BRBs are bolted at both ends to gusset plates. The top gusset plate is ultimately connected to the MPP wall through steel side plates and 45-deg inclined, fully threaded screws. The design detail takes advantage of the high strength and stiffness of inclined screws in tension [11,12], while compressive forces are transferred through bearing of the MPP on top of the timber to BRB connection.

The planned final phase of testing involves the removal of the LFRS installed in the second phase of testing and installation of a new LFRS design that is still under development.

3 LIFE-CYCLE ASSESSMENT

3.1 BACKGROUND

One of the many aspects driving the innovation and development of new MT design solutions is the potential for enhanced building system sustainability through environmental impact reduction. This relative environmental utility can be quantified and analyzed using a cradle-to-grave LCA – a systematic method for compilation of lifetime product system inputs and outputs, and their potential environmental impacts [13].

https://doi.org/10.52202/069179-0138

Several studies [14–17], using an established LCA framework [13] have investigated the environmental performance of MT building systems with respect to functionally equivalent reinforced concrete and steel design alternatives. Findings from the various studies indicate significant environmental impact savings associated with the use of MT structural systems.

3.2 METHODS

3.2.1 Goal and scope

The objective of this study is to contribute to the existing body of research contrasting the environmental impacts of MT and conventional design alternatives using the LCA framework developed in ISO 14040 [13]. The study scope involves a comparative LCA focusing specifically on the MT LFRS presented for the phase I design (UFP-wall configuration) in contrast with a functionally equivalent RC shear wall design. For this study, functional equivalence is defined as a wall design with a lateral force-resisting ability in compliance with seismic provisions specified in relevant building codes and standards [18,19]. The defined functional unit is a LFRS for a six-story building with approximately 500 square meters of usable space, designed to resist a Risk-Targeted Maximum Considered Earthquake (MCE_R) in Seattle, Washington, USA. This study follows the LCA framework developed in ISO 21930 [20], which defines four life-cycle stages: Production, Construction, Use, and End-of-Life. In addition, the framework includes an option to add Beyond Building Life (BBL) net benefits sourced from reuse, recycling, energy recovery, and carbon sequestration occurring outside the system boundary.

The system boundary defined for this analysis is cradle-to-grave; thus, environmental impacts are tracked from the point of raw material extraction to their end-of-life, with consideration given to BBL net credits from the timber and steel material after departing the defined system boundary. The Use stage is omitted from this analysis, as it relates to building operation. This aspect is not relevant to this study, which focuses solely on the LFRS. Figure 3 summarizes the four life-cycle stages, the modules within each stage, and the study system boundary with the Use stage omitted.

3.2.2 Seismic design parameters

The alternative RC walls were designed to achieve functional equivalence with the MT rocking walls and, therefore, used the same seismic parameters in design, as summarized in Figure 3.

3.2.3 MT phase 1 wall design

As previously described, the MT LFRS used in phase 1 is comprised of four MT rocking walls. A pair of stacked, 9-ply (314 mm) CLT panels [21] resist forces in the E-W direction, while a pair of thinner (233 mm), stacked 9-ply MPP panels [22] resist lateral forces in the N-S direction. For each wall, two UFPs are provided at each level along the height to provide energy dissipation and increase system ductility. The MPP walls include a double UFP configuration at the first story. Four post-tensioned rods are also included for each MT wall to provide recentering capability. These wall systems were designed using the DDBD, considering limit states that enable enhanced resilience performance objectives. Table 2 provides a summary of the considered limit states and performance objectives.

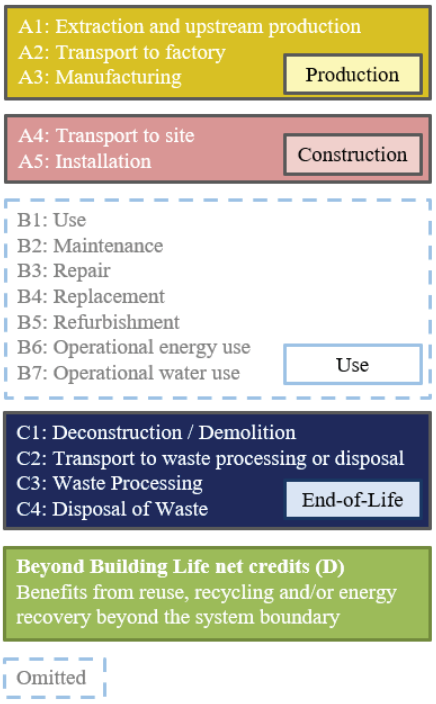

Figure 3: *ISO 21930 life-cycle stages and study system boundary*

Table 1: *Seismic design parameters*

Location	Seattle, Washington (USA)	
Risk Category	II	
Site Class	C	
Importance Factor	1.0	
Seismic Design Ctgy.	D	
MCE_R Hazard Level	$S_S = 1.378$	$S_{1} = 0.48$
	$F_a = 1.2$	$F_v = 1.2$
	$S_{MS} = 1.378$	$S_{M1} = 0.48$

3.2.4 RC shear wall design

To perform the comparative assessment, a functionally equivalent RC shear wall was designed consistent with the previously described functional unit. A design software tool, ETABS [23], was used to determine the required steel reinforcement. Relevant US building codes and standards were followed, including ACI 318-19 [18] and ASCE 7-16 [19]. The wall was designed with 34.4 MPa (5000 psi) concrete and includes special reinforced

https://doi.org/10.52202/069179-0138

boundary elements in the first two stories in accordance with code provisions [18]. Table 3 provides a summary of seismic design coefficients and factors used for a special reinforced concrete shear wall per [19].

Table 2. MT wall seismic design criteria

Limit states	
UFPs	Yielding at SLE, UFP ultimate displacement at MCE_R
PT Rods	Yielding at MCE_R
Walls	Yielding at DE; crushing at MCE_R
Global level performance objectives	
SLE	0.5% roof drift ratio
DE	2% roof drift ratio
MCE_R	4% roof drift ratio*

* Beyond 3% drift limit specified in ASCE 7-16

Table 3: *RC wall design coefficients and factors*

Response Mod. Coeff.	R = 6
Overstrength Factor	$\Omega_0 = 2.5$
Deflection Amp. Factor	$C_d = 5$

Figure 4 shows the rebar detailing along the height of the N-S RC shear walls. Wall detailing is similar for N-S and E-W walls, with the exception that the N-S walls are 2980 mm (9'-9") and E-W walls 2675 mm (8'-9") in width. All dimensioning and rebar sizing was calculated according to US standards, which are converted to SI units for approximate dimensions, and "soft metric" rebar sizes.

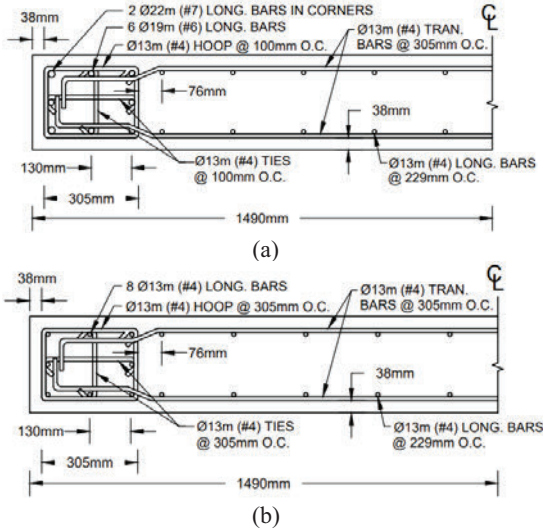

Figure 4: *RC N-S wall steel reinforcement detail (a) Level 1 – 3; (b) Level 3-7*

3.2.5 Bill of materials

Upon design completion, a bill of materials (BOM) was assembled from the RC wall and phase I MT rocking wall designs. Note, although the MT LFRS to be tested in Phase I will contain a steel foundation beam for enhanced compatibility with the shake-table surface, the MT LFRS will be redesigned with a RC foundation, as this is the planned foundation system for future implementation of these LFRSs. Table 4 provides a high-level summary of the timber, steel, and concrete materials and material quantities present in the MT and RC design alternatives.

Table 4: *MT and RC wall BOM summary*

MT rocking wall			
Element	**Mat.**	**Unit**	**Qty**
N-S Rocking Wall	CLT	m^3	37.6
E-W Rocking Wall	MPP	m^3	24.9
Bounding Columns	LVL	m^3	23.3
Out-of-Plane Bracing	Steel	kg	1494
Splice Connections	Steel	kg	2673
Shear Trans. (Found./Wall)	Steel	kg	2793
Shear Trans. (Wall/Dia.)	Steel	kg	4715
Recentering Mechanism	Steel	kg	5657
Damping System	Steel	kg	5583
Wall Foundation	Concrete	m^3	3.1
Wall Foundation	Steel	kg	211
Column Base Connection	Steel	kg	836
Fasteners	Steel	kg	1811
RC shear wall			
Shear Walls	Concrete	m^3	72.6
Shear Wall Reinforcement	Steel	kg	5454
Shear Trans. (Wall/Dia.)	Steel	kg	2560
Wall Foundation	Concrete	m^3	5.2
Wall Foundation	Steel	kg	228
Fasteners	Steel	kg	86.2

3.2.6 LCA tools

The comparative cradle-to-grave LCA framework was applied using the Athena Impact Estimator for Buildings (IE4B). This IE4B tool draws upon a highly developed, proprietary life-cycle inventory (LCI) database that complies with the framework used in [13]. The environmental impacts associated with LCI outputs are aggregated following procedures developed in the Tool for the Reduction and Assessment of Chemical and Other Environmental Impacts (TRACI) [24] methodology in accordance with ISO 21930 [20].

IE4B also provides data for energy use, transportation, construction, maintenance, demolition, and other processes in addition to the data developed for building materials [25]. To account for material waste in construction, transport to disposal, and other processes, IE4B also attributes material specific waste factors. At the End-of-Life stage, IE4B assumes that the current practices of material disposal will be the same as in the future. For steel, a "closed material loop recycling methodology" is

https://doi.org/10.52202/069179-0138

followed, where percentages of material recycled are tabulated per [26], and the avoided burdens of steel manufacturing are added to the BBL stage in accordance with [13]. For timber materials, the End-of-Life pathway assumption is 80% landfill, 10% combustion, and 10% recycling, where 77% of the biogenic carbon in the MT sent to landfill remains permanently sequestered, and 23% decomposes and is released back into the atmosphere. This accounting system results in 61.6% of the total initial biogenic carbon being permanently sequestered. IE4B assigns net credits from biogenic carbon sequestration in the BBL stage in agreement with international standards, including [27–29]. In this way, IE4B attempts to capture the holistic environmental impact.

3.2.7 Study limitations

While the IE4B tool can help users get a general sense of the environmental impacts associated with different design alternatives, the results may lack precision due to the assumptions and simplifications inherent within the tool and present in any LCA calculation. Some of these uncertainties arise from the method IE4B uses for determining LCI results, which involves averaging regional data for emissions associated with the modules listed in Figure 3, as well as other simplifications assumed for construction and deconstruction energy. To account for this, the IE4B tool suggests that LCA results be viewed with a 15% margin of error, where alternative designs within this margin can be considered close to equal in terms of environmental impact [25].

Other study limitations involve the simplified design of the RC shear wall in contrast with the MT rocking wall design. This RC design does not include many of the design features that help the MT design achieve enhanced resilience performance objectives. These features include recentering and energy dissipation mechanisms that assist in reducing residual displacements and limiting damage. Lacking these elements, the RC wall does not achieve 100% functional equivalence in design objectives and may provide a conservative environmental impact estimate.

3.3 RESULTS AND DISCUSSION

The environmental impacts of the MT and RC design alternatives were tabulated by way of importing the assembled BOM into the IE4B software program. Data for several evaluation metrics were produced, including global warming potential (GWP), acidification potential (AP), human health particulate (HHP), eutrophication potential (EP), ozone depletion potential (ODP), smog potential (SP), and total primary energy (TPE). While all metrics are important, this study will highlight the associated carbon footprint of each design alternative, best represented by the GWP metric (CO_2 equivalent mass over a 100-year time horizon). Figure 5 presents the comparative life-cycle environmental impacts of the two design alternatives without beyond building life (BBL) net credits added for carbon sequestration and metal recycling. The data was normalized by the greater of the two impacts for ease in comparison.

A mixed result can be observed from the seven environmental metrics analyzed. Note again, a significant amount of steel was added to the MT rocking wall system to meet performance objectives (energy dissipation, recentering, etc.), while the RC wall was designed to be similar to traditional shear wall systems that do not include these elements. Ultimately, without considering BBL net credits, the GWP associated with each wall design is similar. However, when including the BBL net credits in the LCA, the GWP disparity between the two designs grows substantially.

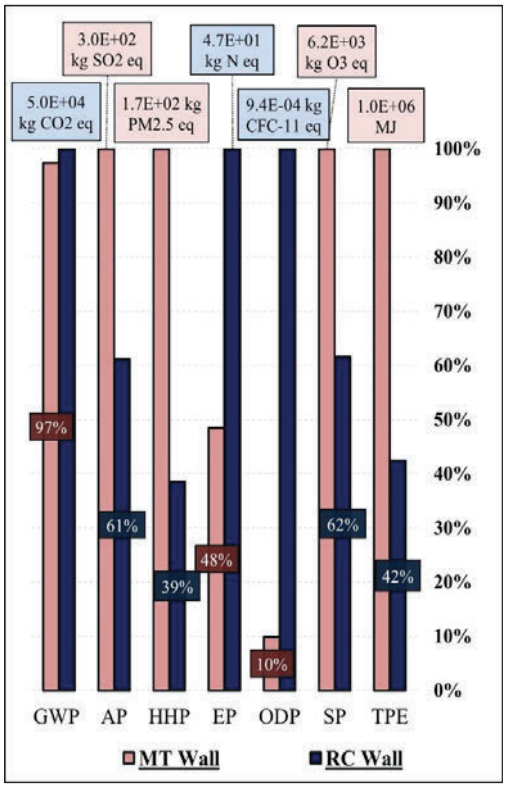

Figure 5: *Normalized impact metrics for MT and RC walls without BBL net credits*

Figure 6 shows the comparative environmental impacts with BBL net credits included. It can be observed that the MT shear wall design has only 42% of the GWP that is associated with the RC design when BBL net credits are included. This decrease in total GWP for the MT design is expected per the IE4B methodology, as described in section 3.2.6., considering permanent carbon sequestration and steel recycling. While knowing the total impact of the seven environmental metrics is important, any steps toward impact mitigation will require a more refined analysis of how each life-cycle stage contributes to the LCA.

https://doi.org/10.52202/069179-0138

Figure 7 shows a comparative breakdown of the GWP impacts from each life-cycle stage. It can be observed that the GWP associated with the Production, Construction, and End-of-Life phases were relatively similar for both designs. However, BBL net credits reduced the total impact of the MT design and increased the total impact of the RC design.

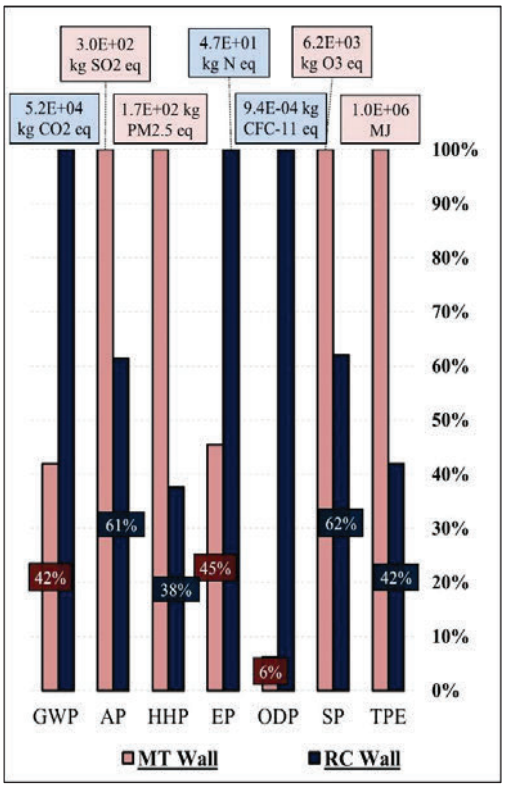

Figure 6: *Normalized impact metrics for MT and RC walls with BBL net credits*

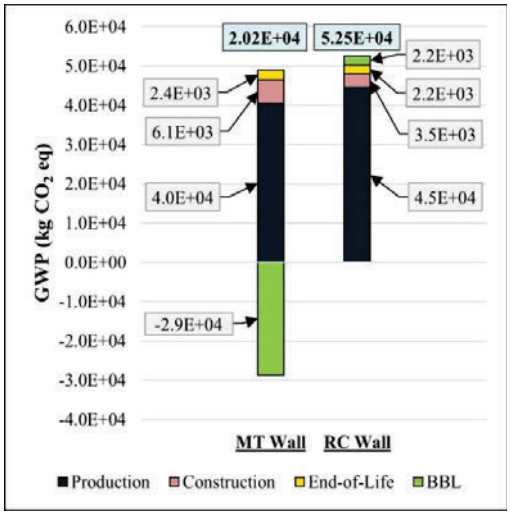

Figure 7: *GWP by life-cycle stage for MT and RC walls*

Figure 8 shows a breakdown of the cradle-to-grave GWP contribution including BBL net credits of each element grouping as described in Table 4. When considering environmental impacts (particularly GWP) associated with the MT wall design, examining how each element grouping contributes to the total GWP can be insightful. The data presented in Figure 8 shows that while the timber elements are associated with a net negative GWP, the large amount of steel in the system significantly increases the total GWP.

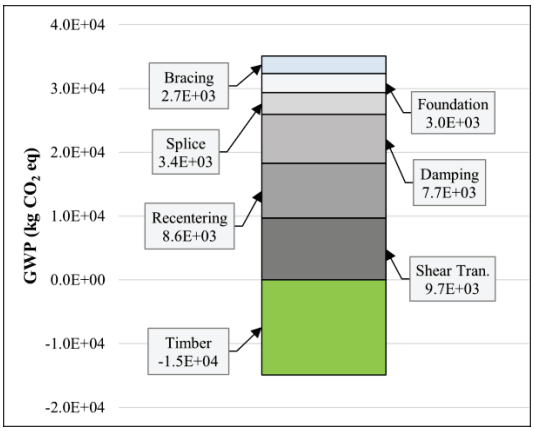

Figure 8: *MT wall: GWP by element grouping*

Beyond the environmental impact metrics discussed in Figure 5 to Figure 8, it is important to interpret LCA results within the proper context. While consideration of environmental sustainability is a growing factor for architects and engineers during the preliminary design stage, it is certainly not the only evaluation criteria, and, most times, not the most important in accordance with current practice. When performing a holistic review of design alternatives, it is not uncommon for sustainability goals to be overshadowed by economic, perception, and logistical design criteria. Thus, while MT designs can be associated with reduced environmental impacts, particularly GWP, it is critical to understand that there are other important design criteria that must also be carefully considered, balanced, and factored into the final design choices.

3.4 FUTURE WORK

The presented cradle-to-grave analysis compares environmental impacts of RC and MT lateral systems using Athena IE4B to give high-level insight into the sustainability of the two design alternatives. The environmental impact metrics were mixed across designs, while the GWP associated with the timber design decreased from 97% to 42% of the RC design when accounting for permanently sequestered carbon and recycled steel.

However, opportunity exists to broaden the study scope and calculate environmental impact metrics with increased precision. Subsequent work will expand the

https://doi.org/10.52202/069179-0138

shake-table specimen case study to include a Whole Building Life-Cycle Assessment (WBLCA) for the six and original ten-story shake-table test building. This study will develop a higher resolution analysis, where opportunities for population of all WBLCA modules will be explored using a mixture of primary and secondary data.

Additionally, the short lifespan of the shake-table test building will be leveraged for insight into the End-of-Life stage for MT construction. Prior to testing, a variety of End-of-Life scenarios for the building material will be examined to determine the most practical and sustainable End-of-Life pathways. Following completion of testing, empirical data will be collected throughout deconstruction, e.g., deconstruction time, labor requirements, specialized equipment needs, transportation, waste generated, and potential material reuse opportunities. Based on the data collected, the LCA will be revisited, and the impact of the information collected evaluated. These efforts will highlight logistical challenges and opportunities associated with various MT End-of-Life pathways, with particular emphasis on the feasibility of MT reuse in the context of circular economy [30, 31].

Ultimately, understanding the relative cradle-to-grave environmental impacts on design choices within building systems has become progressively more relevant for practicing architects and engineers and may become increasingly so as monetary implications of low embodied carbon designs gain traction. In the past several years, many governmental regulatory programs, such as cap and trade [32], have surged in popularity. A primary objective, among many, of these programs has been to assign dollar values to environmental impacts to help provide a business incentive for impact reduction. When applied to the building sector, the usage of renewable, low-impact materials, such as the engineered MT products herein, stand to benefit. Future studies will further explore the convergence of economic and environmental criteria into a singular design methodology.

4 CONCLUSIONS

Shake-table testing of a full-scale six-story MT structure will be conducted to benchmark the design of three LFRSs. All design phases feature PT CLT rocking walls resisting forces in the E-W direction, while three independent LFRSs will be tested for lateral force resistance in the N-S direction for each phase. For these LFRSs, the phase I design will feature MPP walls with UFPs, phase II will consist of new MPP walls with BRBs, and phase III design is still under development.

The LFRS designed in phase I was compared with a functionally equivalent RC design to contrast cradle-to-grave environmental impacts of the two design alternatives. The Athena IE4B tool was employed to tabulate impact metrics and showed a mixed comparative performance between the MT and RC designs, with significant GWP advantage given to the MT solution when accounting for BBL net credits. Examining the GWP at each life-cycle stage, it was observed that the Production, Construction, and End-of-Life stages were similar between design alternatives, with a major disparity in accounted BBL net credits. Considering each element group in the MT wall system, it was shown that the timber elements have a net negative GWP contribution, while the other steel elements contribute significantly to the total GWP.

Overall, this research examines the comparative environmental sustainability of MT design solutions, while also investigating their structural performance in seismic regions.

ACKNOWLEDGEMENT

This material is based upon work supported by the National Science Foundation (NSF) under awards #2120683, #2120692, and #2120684. We would also like to acknowledge the USDA Agricultural Research Service, the TallWood Design Institute, and our industry partners for supporting this experimental program. Any opinions, findings, and conclusions are those of the authors and do not necessarily reflect views of the supporting agencies.

REFERENCES

[1] S. Kontra. Converging Design. *TallWood Design Institute*, 2022. https://tallwoodinstitute.org/converging-design-home/

[2] S. Pei. Shake Table Testing of a Full-Scale Resilient 10-Story Mass-Timber Building. *NHERI TALLWOOD*, 2016. http://nheritallwood.mines.edu/

[3] A. di Cesare, F. Ponzo, S. Pampanin, T. Smith, D. Nigro, and N. Lamarucciola. Displacement based design of post-tensioned timber framed buildings with dissipative rocking mechanism. *Soil Dynamics and Earthquake Engineering,* 116:317–330, 2019.

[4] W. Pang, D. Rosowsky, J. Lindt, and S. Pei. Simplified direct displacement design of six-story NEESwood Capstone Building and pre-test seismic performance assessment. In *World Conference on Timber Engineering*, 2010.

[5] G. Orozco, G. Araujo, A. Barbosa, A. Sinha, and B. Simpson. Innovative mass timber seismic lateral force-resisting systems: Testing of a full-scale three-story building with mass ply panels (MPP) rocking walls. In 12 NCEE EERI, 2022.

[6] G. A. Araújo R. Design, Experimental Testing, and Numerical Analysis of a Three-Story Mass Timber Building with a Pivoting Spine and Buckling-Restrained Energy Dissipators. *MS Thesis*, Oregon State University, Corvallis, OR, 2022.

https://doi.org/10.52202/069179-0138

[7] R. B. Zimmerman, H.-E. Blomgren, J. McCutcheon, and A. Sinha. Catalyst - A Mass Timber Core Wall Building with High Ductility Hold-Downs in a Seismic Region. In *2020 World Conference on Timber Engineering*, 2020.

[8] Q. Jiang, Y. Zhou, Y. Feng, X. Chong, H. Wang, X. Wang, and Q. Yang. Experimental study and numerical simulation of a reinforced concrete hinged wall with BRBs at the base. *Journal of Building Engineering,* 49: 104030, 2022.

[9] T. Takeuchi, X. Chen, and R. Matsui. Seismic performance of controlled spine frames with energy-dissipating members. *J Constr Steel Res*., 114:51–65, 2015.

[10] M. Massari, M. Savoia, and A. R. Barbosa. Experimental and Numerical Study of Two-Story Post-Tensioned Seismic Resisting CLT Wall with External Hysteretic Energy Dissipaters. In *XVII Convegno ANIDIS L'ingegneria Sismica in Italia*, pages 72–82, 2017.

[11] Z. Chen, M. Popovski, and A. Iqbal. Structural Performance of Post-Tensioned CLT Shear Walls with Energy Dissipators. *Journal of Structural Engineering*, 146:04020035, 2020.

[12] W. Dong, M. Li, C. L. Lee, G. MacRae, and A. Abu. Experimental testing of full-scale glulam frames with buckling restrained braces. *Eng Struct.,* 222:111081, 2020

[13] International Standards Organization. ISO 14040:2006 Environmental management — Life cycle assessment — Principles and framework. 2006.

[14] K. Allan and A. R. Phillips. Comparative cradle-to-grave life cycle assessment of low and mid-rise mass timber buildings with equivalent structural steel alternatives. *Sustainability (Switzerland)*, 13.6:3401, 2021

[15] Z. Chen, H. Gu, R. D. Bergman, and S. Liang. Comparative life-cycle assessment of a high-rise mass timber building with an equivalent reinforced concrete alternative using the athena impact estimator for buildings. *Sustainability (Switzerland)*, 12.11:4708, 2020.

[16] K. Milaj, A. Sinha, T. H. Miller, and J. A. Tokarczyk. Environmental Utility of Wood Substitution in Commercial Buildings using Life-Cycle Analysis. *Wood Fiber Sci*., 49.3:338-358, 2017

[17] A. B. Robertson, F. C. F. Lam, and R. J. Cole. A comparative cradle-to-gate life cycle assessment of mid-rise office building construction alternatives: Laminated timber or reinforced concrete. *Buildings*, 2.3:245–270, 2012

[18] ACI 318-19: Building Code Requirements for Structural Concrete. American Concrete Institute, Farmington Hills, Michigan, 2019.

[20] ASCE/SEI 7-16: Minimum Design Loads and Associated Criteria for Buildings and Other Structures. American Society of Civil Engineers, Reston, Virginia, 2016.

[21] Smartlam North America. Cross-Laminated Timber. https://www.smartlam.com/product-line/

[22] Freres Lumber. Mass Ply Panel. *Freres Engineered Wood*. https://frereswood.com/products-and-services/mass-ply-products/mass-ply-panel/

[23] Computers and Structures, Inc. ETABS v.20. [computer software] Walnut Creek, California, 2021.

[24] M. Ryberg, M. Viera, M. Zgola, J. Bare, and R. Rosenbaum. Updated US and Canadian normalization factors for TRACI 2.1. *Clean Technol Environ Policy*, 16:329–339, 2014.

[25] Athena Sustainable Buildings Institute (ASMI). Impact Estimator for Buildings v.5: User Manual and Transparency Document, 2019.

[26] World Steel Association. Life cycle assessment methodology report. Brussels, Belgium, 2011.

[27] British Standards Institute. Publicly Available Specification (PAS) for the assessment of the life cycle greenhouse gas emissions of goods and services. *Bsi Br. Stand, 978:580,* 2011.

[28] International Standards Organization. ISO/TC 14067 Greenhouse gases — Carbon footprint of products — Requirements and guidelines for quantification and communication. 2013.

[29] P. Bhatia, C. Cummins, L. Draucker, D. Rich, H. Lahd, and A. Brown. Greenhouse Gas Protocol Product Life Cycle Accounting and Reporting Standard. 2011.

[30] N. Ahn, A. Dodoo, M. Riggio, L. Muszynski, L. Schimleck, and M. Puettmann. Circular economy in mass timber construction: State-of-the-art, gaps and pressing research needs. *Journal of Building Engineering*, 53:104562, 2022.

[31] R. N. Passarelli. The Environmental Impact of Reused CLT Panels: Study of a Single-Storey Commercial Building in Japan. In *World Conference on Timber Engineering*, 2018.

[32] L. Goulder and A. Schein. Carbon taxes versus cap and trade: a critical review. *Clim Chang Econ (Singap)*, 4.03: 1350010, 2013.

World Conference on Timber Engineering Oslo 2023

HYBRID STRUCTURES IN HIGH-RISE BUILDINGS: THE USE OF APPROPRIATE MATERIALS

Guido Nieri [1], Carsten Hein [2], Stuart Smith [3]

ABSTRACT: Architectural and engineering evolution has seldomly been characterised by a smooth transition, but rather by rapid changes. Currently, we are living in the time of a "sustainability revolution" and "timber renaissance". Based on the recently emerging awareness for sustainability, a new architectural and construction language has developed. This requires a complete review of the old materials used in the last two centuries in favour of more "sustainable" and "natural" ones. This new approach has sparked a dynamic debate about construction materials. Since wood is the only regrowing building material, there is a natural inclination to believe that building with wood is good for the environment. But under which conditions is this really the case? What should we build with wood? What is the best way to achieve an optimal solution? This article examines the current state of the building industry with a holistic approach, exploring the use of structural timber and its combination with other materials for the design of medium and high-rise buildings.

KEYWORDS: Sustainability, embodied carbon, circularity, timber, hybrid structures, high-rise building.

1 INTRODUCTION

Timber is without a doubt the oldest building material ever used. However, following the advent of steel and reinforced concrete, the use of this material was almost exclusively limited to small constructions, such as family homes. The recently emerging awareness and profound interest in sustainable development, as well as the introduction of new engineered timber materials, such as Glulam or Cross Laminated Timber (CLT), have given this material a comeback, and as a result the construction of tall buildings made entirely or partly of timber is experiencing a boom on a scale never seen before.

Even though timber is the only renewable building material and there is a natural inclination to believe that building with timber is good for the environment, the environmental benefits of using it are not unequivocal. Critique has been expressed at the fact that only a portion of the harvested wood can be utilised as a building material. Additionally, the high energy demand required for the drying process of the wood as well as the problem of deforestation have sparked interest amongst critics.

Although this article does not aim to find answers to all these complex questions, we examine the benefits and drawbacks of using timber as a building material. This article does not claim to be exhaustive but is merely intended to give the audience an overview and some key points characterising design with timber and timber-hybrid constructions. With a holistic approach, we try to evaluate the feasibility of timber as a construction material in comparison to and in combination with other technical solutions and materials, also analysing environmental and financial aspects to achieve greater benefits for people and the planet.

2 THE CHALLENGE

Rising temperatures, melting glaciers, floods, desertification: All these well-known topics – summarised under the term "climate change" – are no longer just potential problems for the future, but already a reality. As we know, the above-mentioned aspects are closely related to us humans, to our activities and ultimately to the emissions we produce. Accounting for almost 38% of total global CO_2 emissions, the construction industry is one of the main contributors to climate change. From this, 28% is related to the operational energy, while the other 10% are attributed to so-called embodied carbon. This includes energy associated with the construction, demolition, and renovation of buildings as well as the extraction, production, transportation, and installation of all necessary elements [2]. Conventional building materials are responsible for around 2 billion tonnes of CO_2 emissions annually [5]. If we assume that on average, 50 trees would have to grow for one year to absorb 1 tonne of CO2, that would mean that we would require 100 billion trees to offset these emissions.

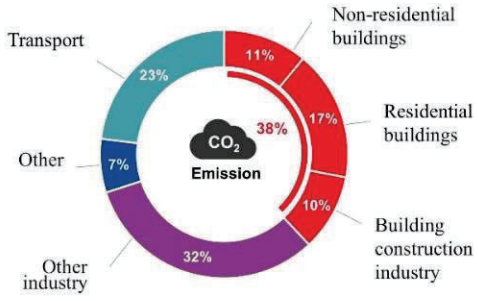

Figure 1: *Emissions in the Building Sector (© Arup)*

[1] Guido Nieri, Arup, Germany, Guido.Nieri@arup.com
[2] Carsten Hein, Arup, Germany, Carsten.Hein@arup.com
[3] Stuart Smith, Arup, Germany, Stuart.Smith@arup.com

https://doi.org/10.52202/069179-0139

These figures alone make it clear that reducing CO_2 emissions is a very ambitious goal. In addition, two other aspects must be considered: exponential growth of the world's population and the limitation of available non-renewable raw materials.

According to the United Nations: Today, the world's population is more than three times larger than it was in the mid-twentieth century. The global human population reached 8.0 billion in 2022 from an estimated 2.5 billion people in 1950. It is estimated to rise to over 10 billion by 2060 [8]. This means that the world's population will have quadrupled in almost 100 years and the demand for buildings and infrastructure – considering the rising standard of living – is going to increase exponentially.

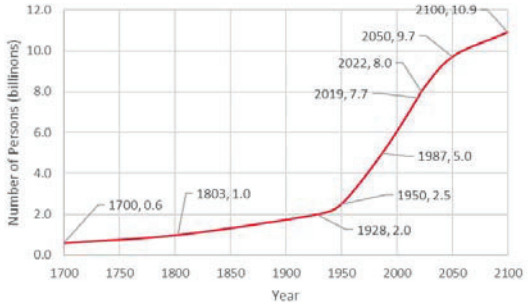

Figure 2: *World's population (©Arup, source: United Nations)*

Conventional building materials like reinforced concrete are composed of slow-renewable or completely non-renewable raw materials such as sand and aggregate. Concrete is one of most used substances in the world, second only to water, and it is the most used building material, twice as much as steel, wood, plastic and aluminium combined. According to the World Economic Forum, demand for sand mining has tripled in the past two decades, reaching 50 billion tonnes per annum in 2019 [7]. Sand mining or aggregate extraction – where sand and gravel are removed from riverbeds, lakes, oceans, and beaches for use in construction – is happening at a rate faster than the materials can be renewed, which is having a huge impact on the environment.

Figure 3: *Sand mining (© Dmitry Rukhlenko)*

For all these reasons, the most important matter of our time is a multiparametric challenge named sustainability: the necessity to build for an exponentially growing number of people using fewer non-renewable raw materials and producing lower emissions.

Dealing with this challenge requires a change in design and construction philosophy, not merely a change in materials. In other worlds, it requires the definition of a new architectural and structural language.

The first step of this revolution should be to consider limiting the construction of new buildings (aiming to the paradox build nothing) and instead transforming, reusing and retrofitting existing structures. In parallel, the focus should be on optimising the structure using materials wisely, using low-emission materials such as timber or recycled materials where appropriate, and conventional materials such as reinforced concrete where necessary.

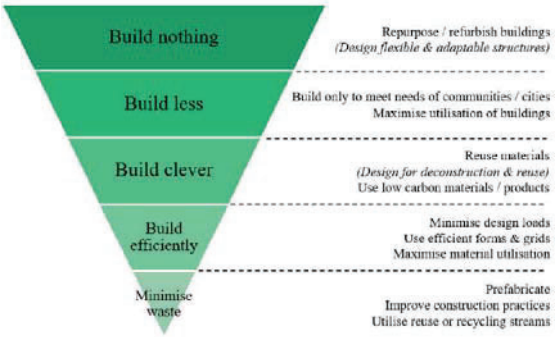

Figure 4: *Sustainable Design scheme (© Arup)*

3 SUSTAINIBILITY

3.1 What really is sustainability?

After decades in which the construction industry – except for few players – only aimed at minimising costs, a reorientation is taking place making sustainability one of the main targets. Defining the goal (e.g., designing a sustainable office building) is easier than defining the objectives or the way to get there. In fact, for each individual project there are a variety of approaches that can lead to a more sustainable outcome, and only the experience of the designers and the wisdom of the client can help to define the right solution for the specific project.

For example, in the project Coal Drops Yard in King's Cross, a derelict industrial site from the 19th century was transformed into a new shopping district for London. The design was refined and engineered to retain as much of the existing structure as possible, while upgrading building performance. In this project, it was possible to achieve an exceptionally sustainable result even with almost no use of timber.

https://doi.org/10.52202/069179-0139

Figure 5: *Coal Drops Yard, London (© Hufton Crow)*

3.2 Industrial-based and / or bio-based material?

The transition between industrial-based materials like concrete or steel, to bio-based materials like timber is a turning point for the entire building industry, affecting investors, architects, and engineers. Engineered timber offers the possibility of creating a new visual language and at the same time poses new challenges in terms of structural design as well as building physics, acoustics, and fire protection. Exposed timber also modifies the internal climate of buildings and has a positive effect on the wellbeing of inhabitants and users (biophilia).

Mass timber has relatively decent strength, but it also has its own specific characteristics and limitations, which call for a change in the construction techniques and design concepts. Currently, we can see a general tendency to replace conventional materials with this "new one" by forcing the "new material" into traditional structural schemes. This leads to a tendency to use timber everywhere without considering whether other materials such as reinforced concrete or steel would be more suitable for a particular purpose, which in turn can lead to significantly higher material quantities, thus having an adverse effect on the costs associated with the construction of the building.

3.3 Materials follow purpose

To achieve a truly sustainable design on a large scale, ideally in every new project, we believe that a new "manifesto" for the use of materials must be established: materials follow purpose. Since the amount of building materials – and this also applies to timber – is limited, we must use them wisely and use timber, concrete, or steel to achieve an overall material reduction. With this principle in mind, we can experiment with new configurations and define a new architectural and structural language that reflects the demands of our time, such as sustainability, while considering the material properties.

3.4 Circularity, prefabrication, and modularity

The use of timber in hybrid structures opens new possibilities for the construction industry, namely prefabrication and modularity. Thanks to these two methodologies, construction time can be drastically reduced, construction costs optimised, and, above all, waste reduced to a minimum. The life-cycle of prefabricated systems can be extended beyond the once-off life of the building. The fact that the elements are not monolithically connected (as opposed to reinforced concrete structures), but can be assembled, dis-assembled, and re-assembled increases the possibility of using the individual components even after their first "life". This transforms the building industry from a linear process from construction to disposal to a circular process in which the individual components can be used multiple times and ideally never become waste. Circular economy principals are driving reuse and recycling of entire areas of the built environment. Refurbishment plays a vital part in this economy, and the whole industry needs to prepare for the future life of buildings. The principles of the circular economy enable far more than just decarbonisation. They help us to keep finite resources and healthy materials in endless loops. They help us to eliminate waste and to regenerate natural systems. Furthermore, they also help us to keep assets flexible and adaptable for any future use.

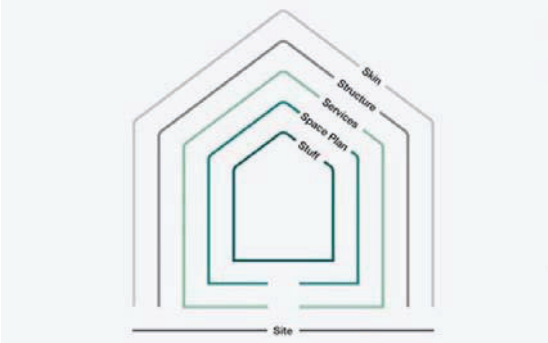

Figure 6: *Circular principles (© Arup)*

Using circular principles, the various components are designed for assembly Design for manufacturing and assembly (DfMA), but also for disassembly (DfD). In addition, the construction-relevant information is retained throughout the life of a building, making its reinvention more likely and less complicated. Under these principles, the different components are designed considering a different lifespan based on the technical possibilities and not only on the first use of the building. In this process, some components such as the structure have a longer lifespan – a correctly designed and maintained structure can last much longer than the typical 50 years specified in the regulations – while others such as the façade or the building services tend to require replacement at shorter intervals (usually 20-25 years). Modular building systems can be added to, expanded, downsized and repurposed, as needed. The modules can even be easily relocated from one place to another as needed. This is, for example, the main concept of the project "Adaptive Buildings", developed by Arup in collaboration with Futur2K, using a modular timber structure as the main part of the project.

https://doi.org/10.52202/069179-0139

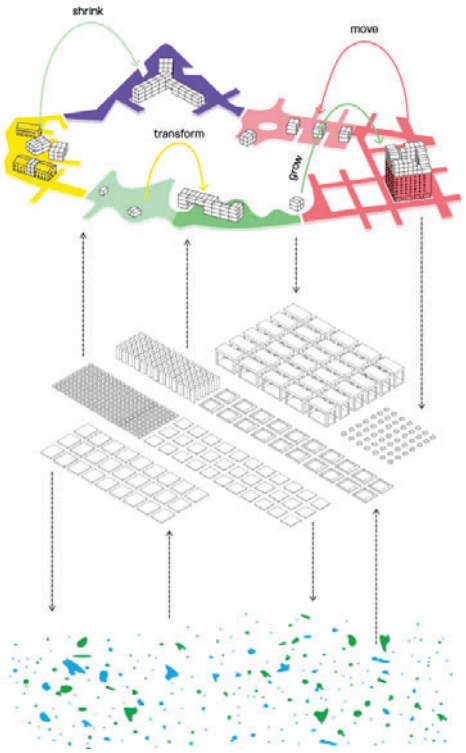

Figure 7: *Adaptive buildings (© Arup)*

3.5 Legislations, certifications, and financial aspects

Emerging sustainability regulations in individual countries are increasingly imposing mandatory sustainability requirements and financial incentives for sustainable design. It has also been proven that sustainable buildings are more attractive on the market and generate higher revenues. These facts have a direct impact on the use of timber, and from various experiences we have found that the additional costs associated with using this material are offset by the financial benefits and higher revenues.

Certifications (BREEAM, LEED, or DGNB) play an important role in defining the materials used. Timber structures can help projects acquire the desired sustainability rating score. For most clients, the direct higher revenues from a Gold or Platinum certified building or the reduction of risk in their investment strategy by decarbonising their portfolio is one of the main reasons for using timber. Other clients really embrace that as a framework for innovation and to unlock new growth opportunities for instance by rethinking their asset operation strategy or by applying new circular business models for the built environment.

Construction-grade timber and engineered forest products are some of the highest valued products from trees. This suggests that the structural use is important for economies that rely on forestry, and to further the development of the forest itself by planting new trees.[9]

4 PURE TIMBER STRUCTURES

4.1 Timber: a lightweight and strong material

Timber has a strength (parallel to grain) similar to reinforced concrete: hardwood is slightly stronger, and softwood slightly weaker, although timber cannot match modern high-strength concrete in compression. Timber is less stiff than concrete, and both materials are far less stiff and strong than steel. However, timber has a low density compared with these other conventional structural materials [9]. For this reason, considering strength-to-weight and modulus-to-weight ratios softwood performs similarly to steel by those measures.

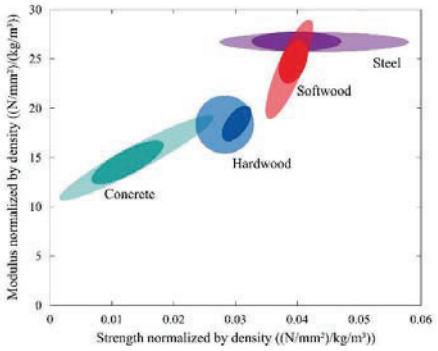

Figure 8: *Compression strength and modulus of elasticity materials normalised by density. (Source: [9])*

This suggests that timber is a particularly structurally efficient material in structures, or parts of structures, in which a high proportion of the load to be resisted is the self-weight of the structure. Examples are roofs, some bridges, and the gravity load resisting system of tall buildings [9]. However, in structures for which the load to be resisted is largely independent of the weight of the structure – such as the wind load on a tall building – the higher absolute strength of steel or reinforced concrete may make them more efficient, in terms of the amount of material required [9].

In an earthquake, the force imposed on the structure depends strongly on its mass, with heavier structures experiencing larger seismic forces. Light timber residential buildings have therefore been observed to perform well in seismic events [9]. The seismic behaviour of taller timber buildings is an active field of research. WG3 of COST Action CA20139 “Holistic design of taller timber buildings”, of which one of the authors (Guido Nieri) is a member, is researching this topic (see [4]).

As wood is 6 times lighter than reinforced concrete and almost 20 times lighter than structural steel, the use of timber as a construction material has numerous advantages. The reduced weight (especially when compared to reinforced concrete) can lead to the reduction in foundation sizes or avoiding the necessity for deep foundations, thus resulting in a more economical design. Furthermore, it increases the possibility for vertical

https://doi.org/10.52202/069179-0139

extensions of existing buildings. Indeed, by using a more lightweight material than concrete or steel, it allows for quicker construction and minimises strengthening of the existing structure. By doing so, structures that might have otherwise been demolished or lain empty can be modernised using eco-friendly building standards. They can retrofit existing structures and create additional income with new leasable area. For example, in the project 80M Located in Washington D.C. lightweight engineered timber was used as a carbon-friendly construction technique to retrofit the existing structure with three additional storeys.

Figure 9: *Project 80M, Washington D.C. (© Ron Blunt)*

Complex geometries can be produced economically and efficiently by utilising timber. This is perhaps wood's most important advantage. Being both lightweight and machined to high tolerances means that wooden buildings can be assembled rapidly when compared to concrete, which requires several activities to construct (falsework, formwork, reinforcement, pouring) and then curing time after construction before follow-on trades can gain access to the structure [1]. BIM to CNC fabrication allow designers and fabricators to create a smooth transition between design and production [1].

Figure 10: *Metropol Parasol, Seville, (© Hufton + Crow)*

4.2 Possibilities and limitations of pure timber structures in medium and high-rise buildings

The use of pure timber structures for medium and high-rise building is still a challenge today, but – up to a certain height – certainly feasible. Projects like the Mjøstårnet tower in Norway, with its 18 storeys, is the best example of today's possibilities but also of the critical aspects. In this case, for example, additional mass (screed/concrete slabs without composite action) have been added to control sway and vibration, and the diagonals of the stabilisation system are visible and sometimes limit functionality.

A structure's complexity increases with the overall height of the building. For low-rise buildings (3 to 5 storeys), where the forces to be resisted are relatively low, shear wall systems mainly made of CLT panels can be used.
The structural and mechanical behaviour of cross laminated timber and its use to support lateral loads has been extensively researched in recent years. Arup department of Specialist Technology & Research in London (Lawrence, Abeysekera, and Smith) has produced detailed research and design guidelines and have published their findings [12] on which this chapter, among others, is based.

To resist lateral loads, the individual walls act primarily as vertical cantilevers subjected to bending. The stiffness of the connections plays an important role in the stiffness of an individual wall and that of the entire system. The fact that each wall is divided into several interconnected panels and that different loads may act on the individual connections, which are characterised by different stiffnesses, leads to quite complex mechanical behaviour even when observing an individual wall. This can be theoretically described by the superposition of 4 different behaviours, which are shown in the following figure.

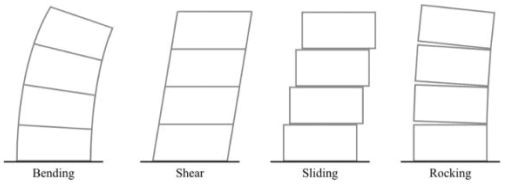

Figure 11: *Mechanical Behaviour CLT walls (© Arup, I. Abeysekera)*

Furthermore, stability systems generally consist of different walls connected to form a statically indeterminate system. However, since timber, like glass, is a brittle material, there is no redistribution of forces based on plasticity, therefore determining the actual load path is not straightforward. For these reasons, the correct dimensioning of the structural components and the connection is very demanding. In addition, questions about the robustness of the system, especially for use in seismic zones, have not yet been clarified and the guidance given in codes is very limited.

https://doi.org/10.52202/069179-0139

As timber structures increase in height, all-timber stability systems can become increasingly expensive (due to the cost of connections). In addition, due to fire safety requirements, CLT walls must usually be completely covered (typically with plasterboard), so that the wooden structure is completely invisible. For these reasons, CLT stability systems are not very common.

Alternatively, timber frame systems arranged around the perimeter can be provided by bracing. The bending moment (e.g., from wind loads) is converted into tension and compression forces in the bracing, but diagonals are required limiting functionality. Moment-bearing structures (rigid frames) rely on the interaction between beams and columns that transfer the moment caused by horizontal forces directly at the connection. The rotational stiffness of the connection influences the horizontal deflection of the building, and the strength of the connection determines the load-bearing capacity of the structure. Due to the typically low strength and stiffness of timber moment connections, this type of system is not very common.

4.3 Key design criteria: acoustics and vibration

Although being lightweight has certain advantages in terms of transportation and erection, it does inevitably make the building more susceptible to dynamic excitation issues and sound transmission. The required acoustics and vibration performance of timber structures can be achieved by careful layout and design and should be addressed at an early stage of the design process so that proper cost allowances can be made.

4.3.1 Vibration

Vibrations are usually the governing factor in the design of mass timber buildings. For slab design, the comfort criteria for human-induced vibrations is reached when the bending stresses in the elements are still far below their load-bearing capacity. Longer spanning floors especially, need careful attention to vibration from an early design stage. Simplified approaches like static deflection methods can, in some cases, lead to lively floors which attract adverse comment. For this reason, conducting a full dynamic computational analysis at an early stage is recommended [1]. Test results on real buildings also demonstrate that damping by structural and non-structural elements also play an integral role in defining the dynamic property of the system.

4.3.2 Acoustics

Best practice in acoustic design of building projects using standard reinforced concrete structures is well established and the regulations cover the typical configurations comprehensively. However, this is not the case when it comes to timber. Due to the low mass, to meet acoustic requirements additional mass may need to be added to the floor build-up. This can be in the form of an additional layer of either concrete, or a similar rigidly bonded mass layer (e.g., bound gravel). A wet screed on sound insulation or a raised floor system with acoustic absorbers are needed to create a mass-spring-mass system which takes away some of the benefit of the low-mass timber slab. Decoupling of floor panels or screed from the CLT slab by using an acoustic batten build up or acoustic insulation on top of the CLT helps to improve acoustic insulation and is an important part of maximising impact sound insulation. Furthermore, it is also important to consider sound flanking transmission.

4.4 Fire protection

In addition to the structural, acoustic and vibration requirements, the building must have sufficient fire safety and fire protection systems for occupant life safety, prevention of fire spread and protection of fire fighters. Considering the brevity of this article and the complexity of the topic fire design in timber construction, only a few comments are addressed here. A detailed analysis of this topic is demanded in separate articles (e.g., Barber et al. [13],[14]). There are a range of fire safety systems that can be implemented to achieve safety goals, such as sprinkler protection, or reducing the area of exposed timber through the installation of non-combustible panels (e.g., gypsum boards). Different local regulations, approaches, and interpretations of some critical aspects of timber design lead to project-specific challenges that affect the design process and the building itself. The requirements for structural fire resistance rating increase with the height of the building and can sometimes even be met without additional protective layers, but only by considering sacrificial depths in the design of the elements.

4.5 Costs

As cost is the driving parameter in the industry, these aspects cannot be neglected. Although for a long time the difference between timber structures and standard structures was relevant, currently it looks like carefully designed timber systems (using timber only where it is possible and really the best choice) can economically challenge traditional concrete structures.

4.6 Holistic approach

As is evident from the topics presented in this chapter, the complexity of timber high-rise buildings is neither linked to individual subjects nor limited to individual disciplines. In each project it is necessary to find bespoke solutions that represents the best compromise between different requirements. Unlike other construction materials, where a single aspect can govern the design, in the case of timber, it is a combination of requirements which drive the design, which in turn is what makes timber unique. As shown by the experience in daily practice at Arup, but also shown by different institutions and research (e.g., COST Action CA20139), a holistic approach is required to improve the performance of taller timber buildings and increase their competitiveness when compared with other materials. For this reason, only with a multidisciplinary design strategy is it possible to maximise the real advantages of timber.

https://doi.org/10.52202/069179-0139

5 HYBRID STRUCTURES

The term “hybrid structures” describes systems that consist of two or more structural materials, in this case: timber and reinforced concrete or steel. The combination of materials can be limited to a single structural component, such as timber-concrete composite panels, or to the entire building, such as the use of reinforced concrete cores as a stability system for horizontal forces. In both cases, the term “hybrid” is used as an antithesis to the purist approach described in the previous chapter. The reason for combining the two materials is the need to improve the properties of timber related to such aspects as acoustics, vibrations or fire performance.

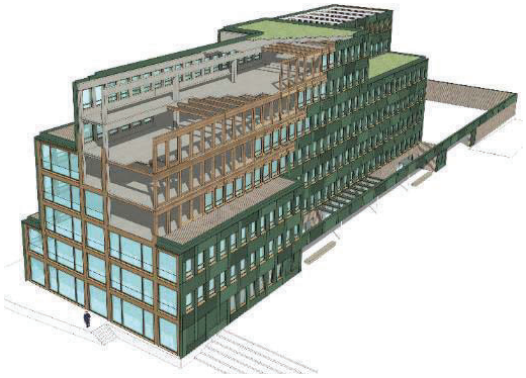

Figure 12: *Projekt H7 in Münster, Germany. (© Andreas Heupel Architekten BDA)*

In projects like H7 in Münster (Germany) or the project HAUT in Amsterdam the design was driven exactly by this priniple: timber where possible, concrete and steel when necessary. As a result, the foundations, basements, and cores were built using concrete. The concrete cores provide stability to the structure and contribute to the fire safety of the building. Based on this it was possible to achieve a highly optimised design with a total embodied carbon reduction of 50% when compared to a conventional building. Furthermore, looking for ways to use as much timber as technically possible, Arup embarked on a quest for an innovative and affordable technical solution comprising almost entirely of precast timber-concrete composite floor systems.

Figure 13: *Project HAUT, Amsterdam (© Jannes Linder)*

5.1 Stability Systems

As introduced in the previous chapter, lateral support for seismic and wind loads is one of the major challenges associated with the design of high-rise buildings in general and for timber buildings in particular. Wood-based lateral timber-bearing systems, such as CLT walls/cores, braced wood frames (but also more advanced post-tensioned/self-centring systems), are feasible design options today. However, the fire safety requirements, the uncertainty about the stiffness of the elements and the connections and thus about the load path, the required tests, and the time and costs involved in obtaining official approvals would have had an adverse impact on the cost and complexity of the building. For this reason, in daily practice for medium and tall timber buildings, the primary lateral support for earthquake and wind forces is usually provided by concrete cores.

As discussed in [11], a typical 50-60 m tall timber high-rise building usually consists of a concrete core (to meet fire protection, acoustic and structural requirements) in combination with timber or timber-concrete composite floors and possibly timber columns along the façade (at relatively short intervals). For taller buildings, additional bracing for sway vibration and comfort requirements or additional stability systems are usually also required.

5.2 Slabs: Timber Concrete Composite (TCC)

Timber Concrete Composite (TCC) consists of a timber beam or panel (glulam or CLT) and a concrete slab mechanically connected by a fastener, e.g., with self-tapping screws and/or notches in the timber beam/panel. From a structural point of view TCC can double the imposed load carrying capacity and have up to three times the flexural rigidity of traditional timber floor systems, when compared to the same depth system acting non-compositely, leading to reduced deflections and decreased susceptibility to vibrations. The combination of timber and concrete is not only an efficient mechanical use of materials, but also offers better fire performance and acoustic properties compared to pure timber systems.

Even though the system itself could be more expensive than a standard slab system, the overall cost of TCC floors can compete with other floor systems when cost savings such as fast construction and reduced foundation costs are considered. There are many variations on the construction market at present, and there are projects where a timber or hybrid floor system are very competitive with conventional reinforced concrete. In addition, the savings in embodied carbon make TCC an attractive construction method compared to concrete/steel counterparts. The concrete topping also provides a good level of thermal mass that can help reduce building operating costs and energy consumption when combined with an effective ventilation system.

Recent research suggests that an optimal slab build-up could consist of two layers: a structural layer of reinforced

https://doi.org/10.52202/069179-0139

concrete, reduced to a minimum to achieve structural performance, and a top layer of wet screed to improve acoustics. The validity of this solution has been corroborated in various projects such as the recently completed 21-storey HAUT in Amsterdam [1]. The deployment of this new technology comes with its own challenges, as these new systems are not fully regulated and different systems with different short- and long-term structural behaviours and costs are available on the market. In addition, as is common with composite structures, the possible future separation of the two materials and their reuse has not yet been fully explored.

Currently, Arup is conducting internal research to incorporate latest design codes and optimise the TCC systems to provide best performance for structures, dynamics, acoustics, and fire.

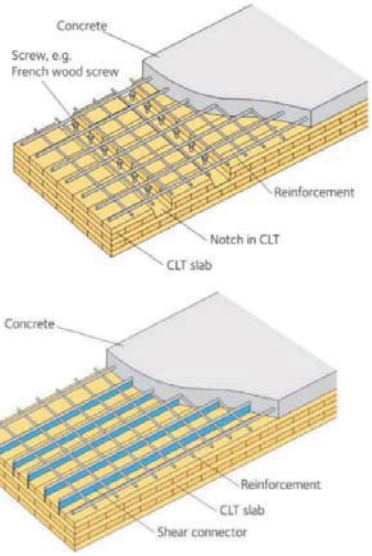

Figure 14: *Timber Concrete Composite Floor System (© Arup, S. Tang)*

5.2.1 The mechanics of the system

The typical shear connections used for TCC are not infinitely stiff. Due to the sliding and creep of the connection, there is only partial composite action. This must be considered when determining the proportion of bending and axial stresses in each element and in the design. Due to the partial shear interaction, the assumption that plane sections remain plane is invalid for the whole composite section. The analysis must check the overall stresses resulting from the bending moments in both the concrete and timber in combination with the axial compression and tension forces respectively owing to the shear transferred across the connection.

The section of the Timber Eurocode (EC5) covering TCCs has been revised and published as a Pre-Standard (CEN/TS 19103:2022-02). This standard has been updated and includes new design methods. This underlines the importance of TCC and will promote its wider application in practice.

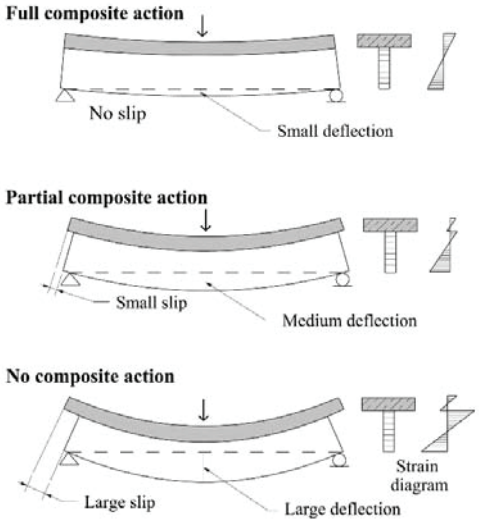

Figure 15: *Mechanical behaviour of TCC (© Arup)*

5.2.2 Possible shear connections

The most important aspects of the Timber Concrete Composites are, of course, the shear connections. These are the elements that connect the timber and concrete layers and allows the materials to act together as one structural material. A stiff connection between the two materials enables a slimmer design of the slab system, whereas a softer connection results in larger cross-sections. Shear connections are not only relevant from a mechanical point of view, but also play a key role for the cost and constructability of the system. The most common shear connectors in TCC are:

- Screws with partial embedment into the timber and partial embedment into the concrete,
- Perforated plates (HBV mesh) glued into the timber and protruding upwards into the concrete,
- Notches (indentations) in the timber beam or panels into which the concrete is poured.

In addition, many combinations of dowels, epoxied bars, nail plates, etc. have been explored in the past. Unique and new types of connections are usually more complex and expensive or lack data from tests. They are also usually not very stiff and sometimes do not have sufficient ductility, which limits the performance of the composite. Two promising new types of connections still being researched are:

- Glued connections: these have almost not slip.
- Micro-notches defined and tested by Prof. Frangi et. Al from ETH Zurich.

https://doi.org/10.52202/069179-0139

5.2.3 Multi-span continuous timber–concrete composite floors

TCC floors which have been researched and built are almost exclusively simply supported single spans. Multi-span continuity can be used to enhance the stiffness, strength, robustness, and ductility of TCC floors [10]. These configurations are currently only being investigated in research or test laboratories, with very few innovative projects exploring their possible applications in practice.

5.3 Vertical structural systems

The vertical system of a building is composed of walls and columns. While the walls can also serve as a stability system (as described in the previous chapter), the columns are usually only loaded in compression. In the case of columns, the material is used as it is in a living tree. Up to 10-15 storeys (30-60 m), the use of timber columns is practically state of the art, although not without challenges. The requirements for fire protection increase with the height of the building and can usually be met without additional protective layers, but only by considering sacrificial depths in the design of the elements. In Germany, for example, the required fire resistance time is 90 minutes up to a height of 60 m, and 120 minutes above 60 m.

The load-bearing capacity of the vertical structural systems is usually not the main challenge. Taller buildings simply require larger cross-sections. The only limits here are the architectural requirements and the costs. Major challenges are the shortening of the timber columns and the definition of an adequate robustness concept that prevents e.g., progressive failure in case of column loss.

5.4 Timber skyscraper

In terms of vertical load capacity, it would be possible to build a skyscraper several hundred metres high entirely with timber columns. However, there are strong reasons associated with fire performance, resistance to disproportionate collapse and carbon impact resulting from inefficient use of the wood for not doing so.
For these reasons it seems much more appropriate to think about hybrid solutions aimed at limiting (but not avoid completely) the use of reinforced concrete on a large scale and defining a smooth transition to the new era. With this vision in mind, it would also be possible to consider implementing the construction principle of medieval towers, with stronger materials (such as reinforced concrete) in the lower part and lighter materials (timber) in the upper parts of the structure. Alternatively, a combination of reinforced concrete superstructure with a modular timber system could also be a viable alternative.

Figure 16: *Case study on combination of reinforced concrete superstructure with modular timber system (© Arup)*

6 Conclusion

Sustainability is no longer a choice, but an obligation for each of us towards future generations. Sustainability cannot be reduced to the simple approach of using a sustainable material but rather is a multi-parametric challenge. Sustainability is a necessity to enable us to build for an exponentially growing number of people using fewer non-renewable raw materials and producing lower emissions. To properly address this challenge, we need to go beyond considering a single aspect such as energy efficiency or embodied carbon and instead approach the multiple faceted issue in a holistic manner to avoid an over-simplistic approach that can only lead to greenwashing.

As with other technical breakthroughs, architects, designers, engineers, and all consultants should explore the limits of technical feasibility for new applications in a safe and responsible manner. This requires a good understanding of the materials and the behaviour of the components, backed up by rigorous analysis and extensive testing. Timber should be used where it adds value to the project, considering all technical, economic and environmental parameters along with the properties and limitations of the material.

Hybrid constructions are one of the best choices for medium and tall buildings, as they use the best properties of timber, concrete, and steel without the need to oversize some components to compensate for the limitations of pure timber (e.g., acoustics, vibrations) or have the high embodied carbon and material consumption characteristic of reinforced concrete construction.

https://doi.org/10.52202/069179-0139

Acknowledgements

The authors would like to thank the company Arup for the support provided for this work globally and furthermore for its commitment to sustainability, efficient structures, and multidisciplinary design.

We would like to extend special appreciation to the entire Arup team for their continuous research and development, which forms the basis for most of the topics covered in this article. The knowledge, dedication and passion of various colleagues and experts from different disciplines, who are not directly mentioned here, have been invaluable to the successful realisation of the projects we are involved in and this article.

Very special thanks go to Andrew Lawrence and David Barber, as main reviewer of this article and also to Ishan Abeysekera, Iris Halm, Ulrike Elbers, Albert Dwan, Stefan Löffel, Tom Finger and Cinthia Buchheister who supported the authors in writing the manuscript and provided valuable comments and feedback.

REFERENCES

[1] A. Lawrence, J. Lauppe, T. Snelson: Three Step to make Timber a Standard Material for Multi-Storey building. WCTE 2016

[2] U. Elbers: "Ressourcenschonendes Bauen – Wege und Strategien der Tragwerksplanung". Bautechnik 99. 2022

[3] C. Hein, L. Kaluzni, B. Twohig: Timber-Concrete-Composite slabs – research for optimisation. WCTE 2016

[4] CA20139 WG3: Design of taller timber buildings subjected to accidental loads: a state-of-the-art review. Cost Action CA20139 Holistic design of taller timber buildings – HELEN. October 2022

[5] M. Löcker: Potenziale für den Holzbau aus Sicht eines Immobilienentwicklers. 26. Internationales Holzbau-Forum IHF 2022

[6] T. W. Crowther et al.: Mapping tree density at a global scale. Nature September 2015

[7] World Economic Forum: Sand mining: the environmental challenge you've probably never heard of. 30th June 2022. https://www.weforum.org/agenda/2022/06/global-sand-mining-demand-impacting-environment/

[8] United Nations: World Population prospects 2022. September 2022

[9] M. H. Ramage et al.: The wood from the trees: The use of timber in construction. Renewable and Sustainable Energy Reviews 68 (2017) 333–359

[10] W. Sebastian, A. Lawrence, A. Smith: Commentary: The potential for multi-span continuous timber–concrete composite floors. Proceedings of the Institution of Civil Engineers – Structures and Buildings 171(9): 661–662

[11] C. Hein Mehrgeschossiger Holzhochbau – gibt es Grenzen nach oben? Interaktion von Statik, Brandschutz, Bauphysik und Wirtschaftlichkeit at IHF, Garmisch-Partenkirchen, 2018

[12] I.K Abeysekera, A.J.R Smith & A.C. Lawrence: Safe design of an indeterminate system in a brittle material. European cooperation in science and technology (COST), State-of-the-art report by COST Action FP1402 / WG2, 2018

[13] D. Barber et al.: Exposed Mass Timber in High-Rise Structures: a practical Discussion of a Complex Fire Problem. CTBUH Journal, 2022 Issue I

[14] D. Barber et al.: Implications on mass timber structures from the findings of the very large compartment fire experiments. SiF 2022– The 12th International Conference on Structures in Fire. Hong Kong Polytechnic University, Nov 30 - Dec 2, 2022

World Conference on Timber Engineering Oslo 2023

BENCHMARK LIFE-CYCLE AND CONSTRUCTABILITY ASSESSMENT OF COMPOSITE STEEL-TIMBER SYSTEMS

Emma E. Rohde[1], David B. Roueche[2], Kadir C. Sener[3], Brian K. Via[4]

ABSTRACT: This study presents comparative structural designs and life cycle assessment of the impact of composite steel-timber flooring systems in mid- to high-rise construction. Four architecturally consistent benchmark buildings are analysed, two each with steel-concrete and steel-timber structural systems. Additional comparisons are made between a steel-timber composite and a steel-timber hybrid structural system. The life-cycle assessment focuses primarily on the structural system and its direct impacts, assuming building use and architectural elements remain the same across the structural systems. The Life-Cycle Assessment evaluates global warming impact, total embodied energy, material quantities, combined life-cycle energy, and energy consumption, primarily relying on the commercial LCA software Tally. Contextualization is provided of the steel-timber composite system within recent studies on constructability of mass timber and other modular construction techniques. The study finds significant benefits to the steel-timber composite systems from a life-cycle assessment perspective, with room for further benefits if the systems can be better optimized for vibration.

KEYWORDS: LCA, Composite, Constructability, Mass Timber, Steel.

1 INTRODUCTION

Despite significant advancements in the acceptance and recognition of the benefits of mass timber construction, the building industry in the United States is still dominated by steel and concrete structural systems for non-residential and multi-story residential construction (Figure 1).

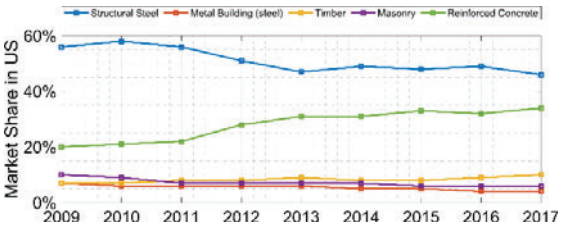

Figure 1. Market share by construction material in the US based on building footprint area. Data from Dodge Analytics [1].

One promising avenue to increasing the use of mass timber in commercial construction is through replacing concrete floors in steel buildings with mass timber floors. This approach has been successfully applied in hybrid steel-mass timber systems, but the structural benefits of the composite behaviour of the mass timber with the steel framing has typically been ignored, despite some recent studies demonstrating feasibility (e.g., [2], [3]). Given the structural benefits, there is a need to quantify the potential global impacts of using composite steel-mass timber systems relative to other common structural systems. In parallel with a separate experimental study being conducted by the authors [4], the objective of this study is to provide benchmark life-cycle assessments (LCA) of composite steel-mass timber systems relative to other traditional structural systems.

2 BENCHMARK BUILDINGS

The focus of this study was on mid- to high-rise commercial and mixed-use buildings. Steel-timber composite (STC) and steel-concrete composite (SCC) structural systems are compared. The steel-timber structural system consisted of steel columns and floor beams with cross-laminated timber (CLT) spanning between floor beams to form the floor system. The benchmark buildings are architecturally consistent, with one seven story building and one eighteen story building for each structural system. All buildings have a story height of 3.66 m and column spacing of 9.14 m (Figure 2) and are assumed to have the same usage (business) and architectural elements. The geometric constraints for the design of the structure were in accordance with IBC 2021, and specifically met the requirements for Occupancy B, Type IV. Total building heights were 25.6 m and 66 m in

[1] Emma E. Rhode, KPFF, Structural Engineer, emma.rohde@kpff.com
[2] David B. Roueche, Department of Civil and Environmental Engineering, Auburn University, dbroueche@auburn.edu
[3] Kadir C. Sener, Department of Civil and Environmental Engineering, Auburn University, sener@auburn.edu
[4] Brian K. Via, School of Forestry and Wildlife Sciences, Auburn University, brianvia@auburn.edu

https://doi.org/10.52202/069179-0140

the 7-story (conforming to Type IV-C) and 18-story (conforming to Type IV-A) structures. Similarly, 9.1 m by 9.1 m bay sizes were chosen to maintain dimensional consistency in framing plans. Spans of 3.0 m and 4.6 m were chosen for the concrete and timber slabs respectively.

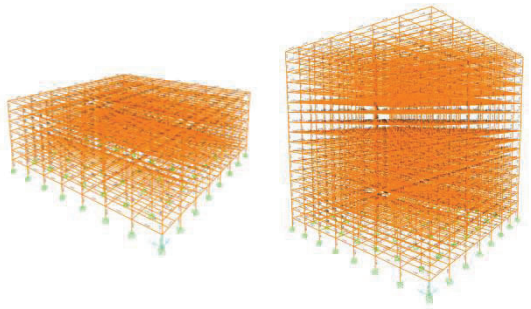

Figure 2. Structural layout of the (left) seven story, and (right) eighteen story benchmark buildings.

2.1 STRUCTURAL DESIGN METHODS

Buildings were structurally designed for gravity loads only, assuming an office occupancy to determine appropriate live loads (3.11 kPa) and superimposed dead load (0.5 kPa). Deflection criteria was considered, including superimposed load deflections and live load deflections. Vibration due to walking excitation was also considered based on a limit of $a_p/g \leq 0.005$, using AISC Design Guide 11 [5] for the steel-concrete floor systems and the US Mass Timber Floor Vibration Design Guide [6] for the steel-timber floor systems. CLT floor slabs were additionally sized to meet fire resistance requirements. Both steel-timber and steel-concrete floor systems utilized a normal weight concrete topping slab, as this is common practice to mitigate vibration, meet acoustical requirements, and support flooring products.

Structural designs were performed using a combination of manual calculations and structural design software, specifically CSI ETABS. Roof and floor beams were first sized for gravity loads, including dead and live loads, and deflection and vibration criteria, using the relevant material-specific design standards. The manually sized floor and roof beams were then defined in the structural analysis software along with the gravity loads, and the software was allowed to optimize the column designs accordingly. Foundations and lateral force resisting systems were not considered.

For steel-timber composite designs, for which no design guides yet exist, a method consistent with steel-concrete composite design was utilized [7]. A partial composite action corresponding to 25% was assumed to be achieved by self-tapping screws transferring interfacial shear that connect steel floor beams/girders and CLT panels. The flexural capacity of a STC member was resultant of the internal resisting force couple and the force couple moment arm. The compressive capacity of the CLT was a summation of the compressive strength of each lamination, which is dependent on orientation to the beam span and therefore varied with panel orientation. Because the STC members were designed to 25% composite action, the depth of the compression block corresponded to 25% of the compressive strength of the full CLT section. Tension in the CLT was ignored in this study; therefore, tension capacity was resultant of the tensile capacity of the steel wide-flange sections alone.

2.2 STRUCTURAL DESIGN RESULTS

Typical beam and girder cross-sections for the STC and SCC systems are shown in Figure 3. All STC floor systems were composed of 5-ply Southern Pine CLT with 38 mm normal weight concrete topping. Typical floor framing consisted of W18x40 beams, framing into W24x55 girders. Typical roof framing consisted of W14x22 beams, framing into W18x35 girders. Columns in the 7-story STC varied in size between W12x26 and W14x61, while in the 18-story buildings, columns varied in size between W12x30 and W14x145. All SCC floor systems were composed of a 127 mm slab on a 51 mm deep 20-gauge steel deck. Typical floor framing consisted of W12x26 beams, framing into W21x50 girders. The roof decking systems were 89 mm slabs on a 38.1 mm deep 20-gauge deck. Typical roof framing consisted of W12x19 beams, framing into W18x40 girders. Floor beams and girders for the SCC system were also designed to approximately 25% composite action. Columns varied in size between W12x30 and W12x65, and between W12x30 and W14x159 for the 7-story and 18-story buildings respectively.

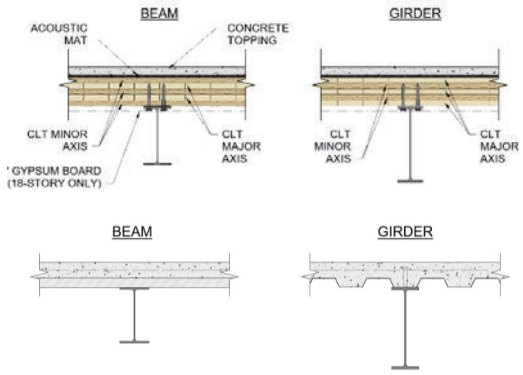

Figure 3. Typical cross-sections for (top) steel-timber composite and (bottom) steel-concrete composite structural floor systems.

The inclusion of the vibration design criteria tended to dominate the beam member for the STC designs relative to the strength and deflection criteria, despite the use of service level live loads (0.6 kPa) and assumption of 100% composite action for vibration design. With the chosen beam span of 9.1 m, the STC beams with 38 mm NWC had a utilization rate (ratio of usage to capacity) of 0.98 for vibration, but only 0.57 and 0.62 for strength and deflection criteria respectively. A parametric study was conducted to evaluate the role of vibration in controlling

https://doi.org/10.52202/069179-0140

member design for a range of beam spans (Figure 4). The parametric study showed that longer beam spans, and increased topping thickness, both helped balance the utilization ratio across all three criteria. More rigorous studies are needed, but the preliminary results highlight the importance of the architectural layout of the building in optimizing the utilization of steel-timber composite systems.

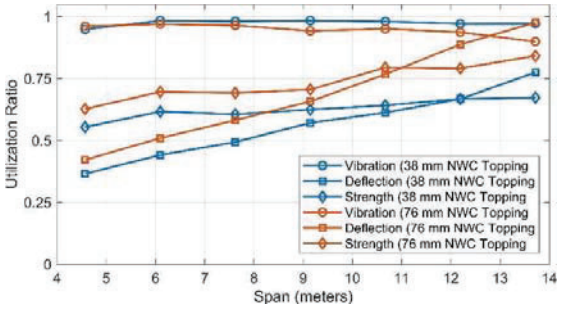

Figure 4. Utilization ratios considering vibration, deflection, and strength criteria for STC beams with 38 mm and 76 mm topping slabs and variable CLT floor spans.

2.3 STEEL-TIMBER COMPOSITE VS HYBRID

While steel-timber composite floor systems are a relatively new structural system, steel-timber hybrid (STH) floor systems have become relatively popular in mass timber construction. In the STH system, CLT floor slabs are still mechanically fastened to the steel beams and girders, but the composite behaviour is ignored in the design. The current study provided an opportunity to evaluate the benefits of composite design by taking the beam sections required to meet the vibration criteria and comparing their utilization rate for strength and deflection criteria both with and without consideration of composite action (i.e., 25% composition action compared to 0% composite action) for two different concrete topping slab thicknesses. The results showed that if the composite action were ignored in the design, the deflection and strength utilization ratios began to govern the design over the vibration criteria. For spans greater than 6.1 m, utilization ratios for deflection criteria were greater than 1.0 (Figure 5), indicating the steel beams would need increased cross-sections if designs assumed hybrid performance. In summary, explicitly accounting for composite action in the steel-timber floor systems likely provides marginal benefits if vibration criteria is part of the design, but stands to provide much greater benefits if vibration criteria is not necessary in the design.

3 LIFE-CYCLE ASSESSMENT

3.1 METHODS

The environmental impacts of the STC and SCC systems were quantified using LCA. The LCA was constrained to include cradle-to-gate (which measures the environmental footprint up to the point where it leaves the manufacturing facility), construction transportation, and end-of-life impacts [8]. The LCA did not include operational use of the buildings, nor the environmental impacts of on-site construction, as these are assumed to be nominally independent of the structural system relative to the impacts in the other stages. The building life expectancy was taken to be 60 years for all structures. Biogenic carbon was accounted for in the cradle-to-gate phase. The study includes raw materials supply, transport, manufacturing, construction process, and end of life stage.

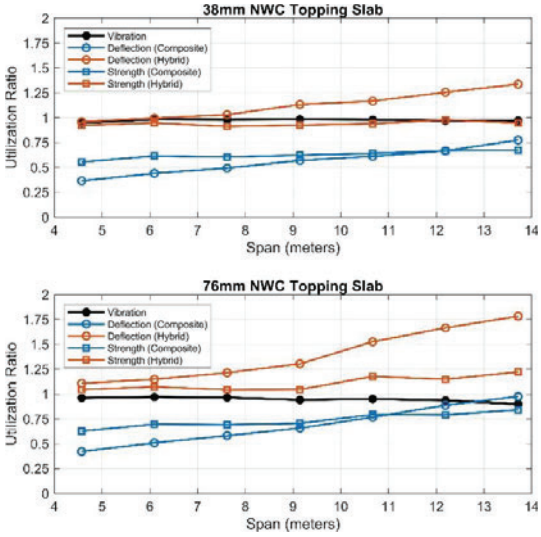

Figure 5. Utilization ratios for composite and hybrid STC designs considering vibration, strength, and deflection with 38 mm and 76 mm topping slabs for variable CLT spans.

To conduct the LCA study, the structural analysis models for the benchmark buildings that were generated using the structural design software ETABS were then imported into Revit, where the Tally Revit application was used to perform the LC assessments, which is widely used for comparative building LCA ([9], [10]). The outputs considered are mass, embodied carbon, and embodied energy, both as raw values and normalized by the net floor area (28,679 m^2 and 73,746 m^2 for the 7- and 18-story buildings respectively) or material mass.

The life cycle inventory (LCI) was compiled using Revit's built-in capabilities to calculate total material quantities based on the defined structural sections and geometries. Tally leverages the commercial GaBi 8.5 database along with the EC3 Environmental Product Declaration (EPD) database to perform LCA. Review of the environmental impacts assigned to the various materials used from the GaBi database found that a few manual adjustments were needed. Specifically, the generic CLT in the GaBi database reported environmental impacts were not representative of the EPDs from US CLT manufacturers (primarily with respect to the embodied energy), and further, the database lacked a suitable rubber material analogous to an acoustic mat. The CLT environmental impacts reported by Tally were therefore scaled to match the unit environmental impacts reported in the EPD from a CLT manufacturer in the Southeast US. A similar

https://doi.org/10.52202/069179-0140

procedure was used for the acoustic mat, adjusting the environmental impacts of a rubber high-traffic commercial flooring product to match the EPD from a US-based acoustic underlayment mat.

Several assumptions were required to complete the LCA analysis, most of which followed the assumptions standard to the Tally software. It was assumed that all individual elements have life spans greater than or equal to the building service life; essentially ignoring repair and replacement activities. Hot-rolled steel and steel decks were assumed to have been fabricated with 100% and 28% recycled material, respectively. Average transportation distances for each product for the US as estimated by Tally were used rather than tying transportation distance to a specific site. This resulted in transportation distances of 332 km for CLT, 431 km for the steel, and 24 km for concrete materials. End-of-life scope varied by material. For CLT, 14.5% was assumed recovered, 22% incinerated with energy recovery, and 63.5% landfilled. Steel was assumed to be 98% recovered. Concrete was assumed to be 55% recycled and 45% landfilled.

3.2 LCA RESULTS

LCA results are presented for the 7-story steel-timber composite (STC), steel-timber hybrid (STH), and steel-concrete composite (SCC), and 18-story steel-timber composite (STC) and steel-concrete composite (SCC).

The total mass varied only slightly across the various structural systems as presented in Figure 6. The STC system had the lowest mass for both stories considered, but the total mass in the 7-story STH and SCC were only 2% and 11% higher than the 7-story STC. Only a 4% increase in total mass was observed in the 18-story SCC relative to the 18-story STC. Floor systems, including the CLT, acoustic mat, metal deck, concrete slab and topping, and gypsum, accounted for between 84% and 87% of the total mass of the structure for all systems considered. Ignoring the composite action in the STC resulted in a 12.7% increase in steel framing mass, but this difference would be significantly higher if vibration criteria were ignored and utilizations were optimized for strength and deflection criteria only.

Differences in environmental impacts, specifically embodied carbon (Figure 7) and embodied energy (Figure 8) were more pronounced between the structural systems for the scope considered (cradle-to-gate, construction transportation, and end-of-life). Total embodied carbon was lowest in the STC, with the SCC system containing almost 200% of the total embodied carbon for the 7-story building, and 171% for the 18-story. Conversely, embodied carbon and embodied energy were 40% and 22% lower in the 18-story STC compared to the 18-story SCC respectively. Most of these differences are driven by the choice to include biogenic carbon in the CLT embodied energy, which results in a net negative effect from the CLT. The differences between the 7-story STC and STH are less pronounced, with only 10% higher embodied carbon in the STH compared to the STC. The high embodied carbon density of steel is clearly evident, with the steel framing accounting for between 41% and 82% of the total embodied energy in each structural systems despite only accounting for less than 15% of the total mass.

Environmental impacts for the studied structural systems were also quantified for each considered LCA stage in terms of embodied carbon (Table 1) and embodied energy (Table 2). According to Table 1, carbon sequestration of lumber products causes the largest portions of the STC structures' carbon footprints to appear at the end-of-life stages. This is because extraction of lumber avoids net carbon emissions due to the large amount of carbon sequestered in lumber. Conversely, the SCC structures' carbon footprints are heavily front-loaded. This is due to the production stages accounting for the bulk of SCC structures' embodied carbon. Conversely, the end-of-life and post-life stages of concrete are associated with the material's environmental credits, due to recycling and re-use. Similarly, the energy required to produce CLT is relatively low compared to the energy required to produce concrete and metal decking. However, the STC structures have no avoided energy burdens throughout their life cycles; whereas, the SCC structures have a net negative embodied energy value in the reuse and recycling phase.

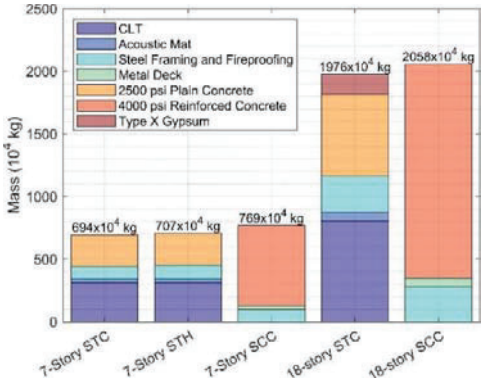

Figure 6. Total mass by structural system and material type.

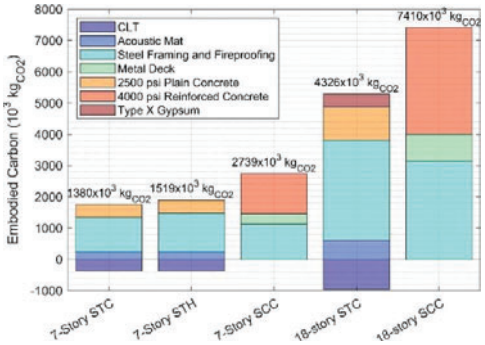

Figure 7. Total embodied carbon by structural system and material type.

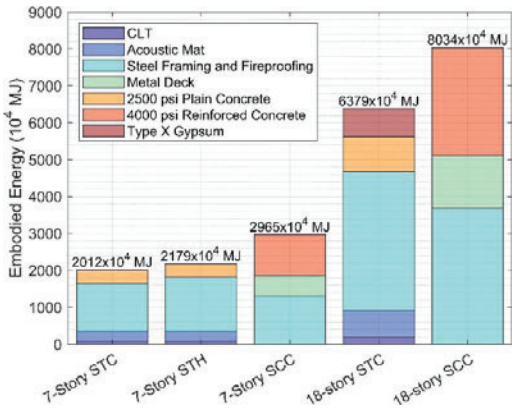

Figure 8. Total embodied energy by structural system and material type.

The net effect is that embodied energy is also heavily concentrated in the Production stage for all systems (Table 2), with the lower energy requirements for CLT production reflected in the slightly lower concentration of embodied energy for the STC and STH systems in the Production stage relative to the SCC systems.

Table 1. Distribution of embodied carbon in each structural system by LCA stage.

Structural System	LCA Stage			
	Production	Transportation	End-of-Life	Post-Life
7S STC	-120%	5%	195%	20%
7S STH	-101%	5%	177%	19%
7S SCC	96%	1%	10%	-8%
18S STC	-83%	4%	161%	17%
18S SCC	96%	1%	10%	-7%

Table 2. Distribution of embodied energy in each structural system by LCA stage.

Structural System	LCA Stage			
	Production	Transportation	End-of-Life	Post-Life
7S STC	90%	2%	6%	2%
7S STH	90%	2%	5%	2%
7S SCC	96%	2%	8%	-6%
18S STC	89%	2%	7%	2%
18S SCC	96%	2%	8%	-5%

4 CONSTRUCTABILITY

Beyond biophilic aesthetics and a decreased environmental impact, the use of mass timber panels in composite timber-steel floor systems has become increasingly attractive to owners, installers, and designers because of its benefits for on-site safety and scheduling efficiencies [10]. These benefits are largely attributed to the modular installation process, which decreases the number of required employees and can reduce construction schedules by 30 to 50 percent [11]. Given the potential constructability benefits, there is a need to quantify the potential labour hours and schedule duration of composite steel-mass timber structural systems relative to other common structural systems.

Unfortunately, such studies are difficult due to lack of building-specific construction data and lack of established modelling methods, although a few limited studies do exist. Bhandari et al. [12] evaluated construction duration per 1000 m^2 of actual buildings that used CLT and reported 10 hybrid CLT with concrete mid-rise buildings were constructed in under 4 weeks. However, no steel-CLT hybrid buildings were included in the dataset. Brisland et al. [13] found daily productivity rates between 67 m^2 and 111 m^2 for multi-story mass-timber buildings. Mirando and Onsarigo [14] tracked construction progress in a multi-story mass timber building and measured a productivity rate of 33 m^2 per person-day, a rate nearly three times that estimated by the authors for cast-in-place concrete based on literature reviews. Real-time data was collected through daily reports generated by the onsite foreman, digital photographs taken by two time-lapse cameras placed on the jobsite, and a 360-degree construction photo documentation system. Tavares et al. [15] evaluated life-cycle effects of prefabrication across a range of building materials and reported that pre-fabrication reduces construction time by between 33-50%. The study did not explicitly consider steel-timber hybrid or composite structures though, and primarily focused on low-rise buildings. Reduced waste, material use, and environmental impacts were also noted in prefabricated structural systems. Mofolasayo [16] noted the benefits of modular construction were closely tied to transportation distances, with long transportation distances limiting the benefits of modularity. In this regard, the constructability of steel-timber composite may be negatively affected relative to steel-concrete composite, given the longer transportation distances typically associated with mass timber relative to concrete (see Section 3.1).

In summary, a literature review of constructability reveals clear benefits to modular construction, which steel-timber systems would benefit from, in terms of costs, erection time, and environmental impacts. These benefits are limited if transportation distances are long. Constructability data is still relatively scarce however, particularly for steel-timber hybrid or composite systems.

https://doi.org/10.52202/069179-0140

Future efforts are needed to collect research-suitable data during actual construction projects.

5 CONCLUSIONS

Structural designs for gravity loads were completed for functionally-equivalent 7-story and 18-story buildings with steel-timber and steel-concrete structural systems. Lateral force resisting systems and foundation designs were ignored at this time. Life-cycle assessment was then performed on the structures using the material inventories from the structural designs and environmental product declarations primarily obtained through the GaBi database integrated into the Tally LCA software. The following conclusions can be formed from the analysis:

1. Vibration dominated the sizing of steel beam elements in the floor for the considered spans and spacings, with steel members underutilized for strength and deflection criteria as a result. Better understanding of vibration behavior of steel-timber composite systems is needed to develop more optimized design guidelines and enable more efficient overall designs.
2. CLT panel depth was controlled by fire-resistance requirements, resulting in 5-ply panels for all systems. The fire requirements led to an optimal floor panel span of 4.5 meters, demonstrating how secondary design considerations such as vibration, fire, and even acoustics can oftentimes control the overall framing layout in steel-timber composite systems.
3. Significant advantages were found to be associated with STC design relative to non-composite (hybrid) design, with larger beam sizes being needed for the hybrid design relative to the composite design.
4. Embodied carbon and embodied energy were both lower in the steel-timber composite systems relative to the steel-concrete composite systems, with differences in the 18-story buildings as much as 40% for embodied carbon and 22% for embodied energy.
5. The environmental impacts of all structural systems were disproportionately driven by the steel framing, despite its low mass relative to the other building materials.
6. Steel-timber composite structural systems are expected to be advantageous from a constructability standpoint due to the potential for modular construction, but relative to other modular construction techniques, may still be limited by the longer transportation distances associated with steel framing and mass timber procurement.

While this study provides an initial life-cycle assessment of steel-timber structural systems, many knowledge gaps remain. Better guidelines for vibration design of steel-timber composite systems are needed. The relative impacts for lateral force-resisting systems and foundations are also needed. And finally, attempts to evaluate constructability would greatly benefit from focused studies tracking scheduling and manpower for real construction projects.

ACKNOWLEDGEMENT

This research is financially supported by the United States Department of Agriculture under the Wood Innovations Grant, 21-DG-11083150-150. Additional financial support was provided by the Southern Lumber Board and material donations by the American Institute for Steel Construction.

REFERENCES

[1] Dodge Data & Analytics, “Market share by construction material,” Bedford, MA, USA, 2018.

[2] A. Hassanieh, H. R. Valipour, and M. A. Bradford, “Experimental and analytical behaviour of steel-timber composite connections,” *Constr. Build. Mater.*, vol. 118, pp. 63–75, Aug. 2016, doi: 10.1016/j.conbuildmat.2016.05.052.

[3] R. Yang, H. Li, R. Lorenzo, M. Ashraf, Y. Sun, and Q. Yuan, “Mechanical behaviour of steel timber composite shear connections,” *Constr. Build. Mater.*, vol. 258, p. 119605, Oct. 2020, doi: 10.1016/j.conbuildmat.2020.119605.

[4] H. Merryday, M. Potuzak, K. Sener, and D. Roueche, “On The Usage of CLT Panels to Form Timber-Steel Composite Floor Systems,” presented at the World Conference on Timber Engineering (WCTE) 2023, Oslo, Norway, 2023.

[5] T. Murray, D. Allen, and E. Ungar, “Design Guide 11: Vibrations of Steel-Framed Structural Systems Due to Human Activity,” American Institute of Steel Construction, 2016. Accessed: Mar. 09, 2023. [Online]. Available: https://www.aisc.org/Design-Guide-11-Vibrations-of-Steel-Framed-Structural-Systems-Due-to-Human-Activity-Second-Edition

[6] S. Breneman *et al.*, “U.S. Mass Timber Floor Vibration Design Guide,” WoodWorks, 2021.

[7] W. T. Segui, *Steel design*, 6th edition. Mason, OH: Cengage Learning, 2017.

[8] Z. Duan, Q. Huang, and Q. Zhang, “Life cycle assessment of mass timber construction: A review,” *Build. Environ.*, vol. 221, p. 109320, Aug. 2022, doi: 10.1016/j.buildenv.2022.109320.

[9] D. Davies, L. Johnson, B. Doepker, and M. Hedlund, “Quantifying Environmental Impacts of Structural Material Choices Using Life Cycle Assessment: A Case Study,” in *Embodied Carbon in Buildings: Measurement, Management, and Mitigation*, F. Pomponi, C. De Wolf, and A. Moncaster, Eds. Cham: Springer International Publishing, 2018, pp. 123–142. doi: 10.1007/978-3-319-72796-7_6.

[10] J. Zuo *et al.*, “Green building evaluation from a life-cycle perspective in Australia: A critical review,” *Renew. Sustain. Energy Rev.*, vol. 70, pp. 358–368, Apr. 2017, doi: 10.1016/j.rser.2016.11.251.

[11] D. Atkins, R. Anderson, E. Dawson, and L. Muszynski, “2022 International Mass Timber Report,” Forest Business Network, 2022. Accessed: Mar. 09, 2023. [Online]. Available: https://workdrive.zohoexternal.com/external/19514eca4c17dc14004806d4679e86603204c6e861b2e02ab893de74532c8964

[12] S. Bhandari, M. Riggio, S. Jahedi, E. C. Fischer, L. Muszynski, and Z. Luo, “A review of modular cross laminated timber construction: Implications for temporary housing in seismic areas,” *J. Build. Eng.*, vol. 63, p. 105485, Jan. 2023, doi: 10.1016/j.jobe.2022.105485.

[13] R. E. Brisland, P. Forsythe, and A. A. F. Fini, “Mass Timber Productivity- the Significance of Reduction in Non-Value Add Activities during On-Site Installation Sequence.,” *Modul. Offsite Constr. MOC Summit Proc.*, pp. 227–234, May 2019, doi: 10.29173/mocs98.

[14] A. Mirando and L. Onsarigo, “Construction Productivity Comparison Between Cast-in-Place Concrete and Mass-Timber Framing: A Case Study of the Nation’s Largest Mass-Timber Building,” in *EPiC Series in Built Environment*, May 2022, vol. 3, pp. 443–451. doi: 10.29007/qttp.

[15] V. Tavares, N. Soares, N. Raposo, P. Marques, and F. Freire, “Prefabricated versus conventional construction: Comparing life-cycle impacts of alternative structural materials,” *J. Build. Eng.*, vol. 41, p. 102705, Sep. 2021, doi: 10.1016/j.jobe.2021.102705.

[16] A. Mofolasayo, “A framework for the evaluation of the decision between onsite and offsite construction using life cycle analysis (LCA) concepts and system dynamics modeling,” *World J. Civ. Eng. Archit.*, vol. 2, no. 1, Art. no. 1, Jan. 2023.

https://doi.org/10.52202/069179-0140

World Conference on Timber Engineering Oslo 2023

DEVELOPING AN APPLICATION FOR MASS PLYWOOD PANELS IN SEISMIC AND ENERGY WALL RETROFITS

Mark Fretz[1], Jason Stenson [2], Gustavo Fernando O. Orozco[3], Payton Narancic[4], Flynn Casey[5], Dale Northcutt[6], Kevin Van Den Wymelenberg[7], Judith Sheine[8], Andre R. Barbosa[9]

University of Oregon and Oregon State University are collaborating through the TallWood Design Institute (TDI) to upgrade aging multi-family housing, which is energy inefficient and does not meet current code lateral force resistance, by developing a mass ply panel (MPP) façade retrofit panel assembly that employs digital workflows and small diameter logs (down to 127mm) to create an economically viable energy/seismic retrofit model for the West Coast of the United States (U.S.) and beyond. The design and testing of the retrofit panelised system for upgraded energy and seismic resilience of existing light-wood-frame multi-family housing stock were completed at TDI's Emmerson Laboratory for a full-scale one-story mock-up. The research program includes structural and energy performance design, and benchmarking of digital to physical workflows and construction methods. The next iteration is a three-story prototype fabricated by a commercial contractor to validate the design, scanning techniques, fabrication, construction, and cost models resulting from the initial prototype construction, with the intent of commercializing designs for immediate adoption.

KEYWORDS: Seismic Resilience, Energy Upgrades, Retrofits, Mass Plywood Panels

1 INTRODUCTION

In the past decade, humans have witnessed the convergence of global, regional, and local natural and human-made crises. On the U.S. West Coast, extreme weather events, forest fires, and power outages have exposed millions of Americans to the loss of life, property, and livelihood. Skyrocketing housing prices have depleted the market of available housing that is affordable, exacerbating social inequities and homelessness [1]. Moreover, reductions in timber harvest have depressed rural manufacturing and economic development. Therefore, the building design and construction industry, manufacturing, and government agencies are working to respond to multiple crises simultaneously by developing creative solutions to multifaceted problems.

The U.S. Forest Service has responded to extreme forest fires with healthy forest initiatives [2] that include selective harvesting of small-diameter trees to reduce fuels and wildfire risk; however, this form of harvesting is labour intensive, costly, and the resulting harvest of small-diameter logs has low market value [3], resulting in this wood fibre being commonly sold for products that have only short-term biogenic carbon storage (e.g., paper, biomass fuel), thus, reducing the climate benefit of wood to sequester carbon dioxide. Thus, there is great interest in finding higher value utilization of small-diameter logs that provide long-term carbon sequestration in building materials.

At the same time, local, state, and federal investments in energy efficiency and decarbonization have been increasing. At the local level, the City of Portland, Oregon created and approved in 2018 a unique funding stream to support climate action by providing clean energy home upgrades and associated jobs to vulnerable communities [4]. The fund, called the Portland Clean Energy Fund (PCEF), initially anticipated local investments of USD 44-61 million annually [5]; however, in 2022, the fund made its largest award of USD107 million to 65 projects fighting climate change [6]. The State of California is also aggressively pursuing an energy code to achieve zero net energy to mitigate climate change. The California Energy Commission is advancing novel energy efficient technologies through Electric Program Investment Charge (EPIC) funding to develop and commercialize

[1] Mark Fretz, University of Oregon, United States, mfretz@uoregon.edu
[2] Jason Stenson, University of Oregon, United States, jstenson@uoregon.edu
[3] Gustavo Fernando O. Orozco, Oregon State University, United States, gustavo.orozco@oregonstate.edu
[4] Payton Narancic, University of Oregon, United States, pcn@uoregon.edu
[5] Flynn Casey, University of Oregon, United States, fcasey@uoregon.edu
[6] Dale Northcutt, University of Oregon, United States, tdnorth@uoregon.edu
[7] Kevin Van Den Wymelenberg, University of Oregon, United States, kevinvdw@uoregon.edu
[8] Judith Sheine, University of Oregon, United States, jesheine@uoregon.edu
[9] Andre Barbosa, Oregon State University, United States, andre.barbosa@oregonstate.edu

https://doi.org/10.52202/069179-0141

deep energy retrofit solutions for existing buildings [7]. In August 2022, the U.S. Congress passed the Inflation Reduction Act, which includes USD369 billion for energy and climate resilience, targeted at building decarbonization, energy efficiency, and affordability [8].

In the U.S., buildings account for approximately one-third of carbon dioxide equivalent emissions each year [9]. Moreover, existing low-rise multifamily building stock is ubiquitous and much of it is affordable but also aging and not climate resilient. According to the Northwest Energy Efficiency Alliance (NEEA) Residential Building Stock Assessment, 88% of this housing stock in the Pacific Northwest is one- to three-story light-wood-frame and was constructed between 1960-1994 with very low wall insulation levels (64% had R8-R12 wall insulation) [10].

While urgent, the focus on building energy and decarbonization does not address the other critical West Coast need for seismic retrofits for pre-1990's era buildings [11]. In Oregon, the building seismic code has evolved since the 1970s to include a better understanding of seismic risks and associated base shear forces, beginning at 5% in the 1973 Uniform Building Code (UBC) [12], slowly ramping to 16.41% in the 1997 UBC following an initial understanding of the Cascadia Subduction Zone risk, and back down to 11.30% in the 2003 International Residential Code (IRC) [13]. Unfortunately, the preponderance of existing multifamily housing units in the Pacific Northwest was constructed well before the increased base shear code requirements ramped up in the 1990s [10]. Moreover, many low-rise multifamily buildings typically found in this housing group include a soft story, such as open bays without horizontal bracing or shear walls to accommodate parking at the ground level, further escalating the urgency of seismic retrofit.

Although there is increased recognition of the need to address multifamily housing climate and seismic resilience in the Pacific Northwest, the states of Oregon and Washington currently do not require these upgrades and there has been resistance to making these retrofits mandatory due, in part, to their construction costs and potential for tenant displacement. Prevailing seismic upgrade techniques often require extended building vacancy or at least significant occupant disturbance, which cannot be tolerated in an environment of housing scarcity. In fact, due to years of housing underproduction on the U.S. West Coast, Oregon alone predicts that it will need 584,000 new homes over the next 20 years [14]. To meet that goal, existing housing must be maintained, in addition to creating new housing units. Therefore, there is an urgent need for cost-effective, low-impact energy and seismic upgrades to extend the useful life of this critical housing stock.

Housing projects in Europe have begun to address deep energy upgrades with minimal tenant disturbance using prefabricated façade retrofits. For example, the *Energiesprong* [15] method developed in the Netherlands employs a technique of digital scanning of existing facades and using these scans to fabricate new façade systems off-site, complete with insulation, high-performance windows, doors, and cladding. Since the panelised systems are manufactured in a factory, fabrication can employ digital workflows, such as computer numerical control (CNC) machining, with high environmental and quality control over the manufacturing process. The resulting products are then applied over the existing facade with minimal time and occupant disruption on site.

While the *Energiesprong* method provides many lessons for the U.S., deep energy façade retrofits on the West Coast must also contend with seismic activity; adding an increase of 10% to an existing building's weight in an insulative wall system triggers seismic upgrade requirements in many jurisdictions. The mass ply panel (MPP) system that is described in this paper is a building assembly that could provide for both energy and seismic resilience while minimizing occupant disturbance with few necessary interior disruptions through off-site prefabrication. MPP, developed in rural Oregon by Freres Engineered Wood, is a veneer-based mass timber panel that utilizes small diameter logs (down to 127 mm), which can be sourced from healthy forest initiatives, thereby making forest restoration products more economically viable while providing a building product that supports the housing industry. Since panels are available in nominal sizes as large as 3.7 m x 14.6 m with thicknesses starting at 52 mm and increasing by additional lamella thicknesses of 26 mm, there is a wide range of flexibility for their use as secondary facade systems.

The estimated total available U.S. multifamily market for the MPP panel system is close to 18 million housing units [16]. Even narrowing this to the serviceable available market (California/Oregon/Washington region, pre-1990 construction in a high seismic zone, not previously upgraded seismically), there are slightly more than 3 million housing units. By employing MPP that are 52 mm to 78 mm thick using an efficient process of prefabrication with digital workflows, retrofit wall panels spanning one- to three-stories can be efficiently constructed and provide both energy upgrades and seismic resilience to aging multifamily housing.

The project is a collaboration between the University of Oregon (UO)'s Energy Studies in Buildings Laboratory and Oregon State University (OSU) through the TallWood Design Institute (TDI), a collaboration between UO's College of Design and OSU's College of Forestry and College of Engineering that advances engineered timber products and their application through research and testing. This project demonstrates a system of prefabricated panels built with MPP that can be rapidly applied onsite over existing building cladding to upgrade older light-wood-frame one- to three-story buildings to meet or exceed current energy and seismic codes.

https://doi.org/10.52202/069179-0141

2 METHODS

To develop the panelised wall system, we divided the project into discrete phases: *predesign, structural design, envelope design*, then created an existing condition mock-up to test digital workflows during *panel fabrication and construction.* Structural connection and envelope details were developed over a series of iterations and a full-scale mock-up resulting in construction and assembly details.

2.1 PRE-DESIGN

At the outset of the project, we surveyed the morphologies of pre-1990 multifamily housing in Portland, Oregon USA to characterize common aspects of building, site, and existing utility infrastructure that would impact or even preclude a façade retrofit. We found predominantly two-story light-wood-frame structures with repeated stacked housing units and regular façade elements, such as window size and placement. Concrete stem wall foundations with a shallow crawlspace were most common, though slab-on-grade was found as well.

Often units were sited with priority given to on-site vehicle surface parking, leaving limited lot building setbacks and minimal landscaping. Access to upper-floor units is typical via exterior stairs with circulation zones occurring either between sets of units or by incorporating an outdoor walkway in front of units.

Electrical service in the area is from overhead power lines but is brought to larger multifamily structures below grade from the street. On-site distribution usually incorporates an exterior façade-mounted electric meter for each unit. Natural gas service is not typical for this housing typology in this location in Portland, Oregon. Additional façade penetrations may include exhaust fan venting, which predominantly occurs through the roof, but can be found located at the façade for ground floor units.

Figure 1: *Visualization of case study multifamily building used for façade retrofit study, pre-retrofit*

The case study building selected, pictured in Figure 1 and detailed in Figure 2, offers an example of typical existing multifamily construction found in the study region while also representing a reasonable candidate for façade retrofit. Exterior circulation occurs between units, leaving the façade unobstructed by walkways or other large overhangs. Window openings are large, but sufficient two-story wall area remains between openings to locate full-height shear panels. Furthermore, the building is set back sufficiently far from the property line, so additional wall thickness will not encroach into the setback zone.

The central on-site parking area offers a straightforward staging and crane location, eliminating the need for crane access from multiple street frontage locations or over other structures not involved in the retrofit. The location of electric meters, distribution conduit, and exhaust vents, though spread across the structure, are all found on the façade opposite the parking area, which minimizes the continuous lineal footage of the façade where services will need to be factored into more complex retrofit panel design and installation.

2.2 STRUCTURAL DESIGN

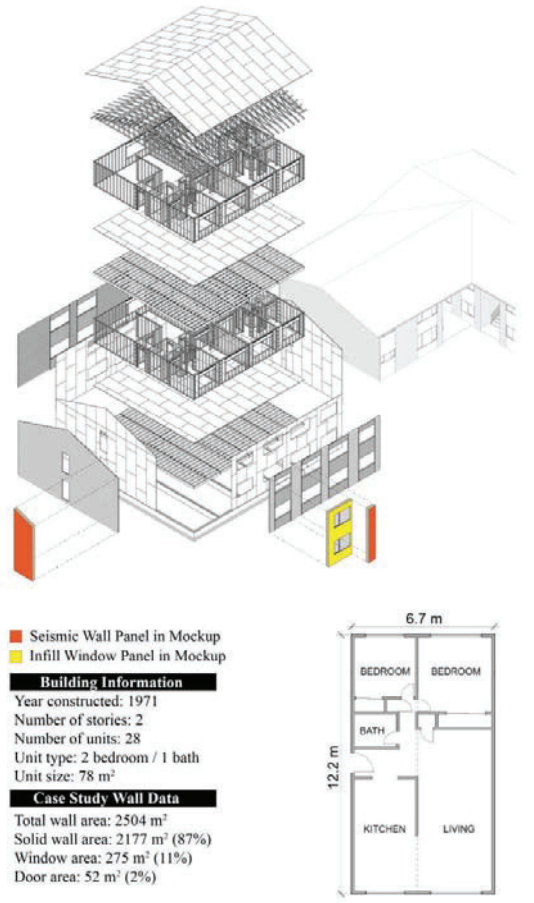

Figure 2: *Case study multifamily building: building information, typical unit design, exploded view of existing light-wood frame structural system, wall area data and panels tested during mock-up.*

With the focus of structural design on the development of a façade retrofit lateral force resisting system (LFRS) which incorporates the use of MPP, a foundation upgrade

https://doi.org/10.52202/069179-0141

was identified early on as a requirement to both account for the added gravity load of the MPP and new façade elements, but also to help resolve concentrated seismic loads delivered through the stiffer and stronger MPP as compared to the conventional plywood shear walls found in existing light-wood-frame structures.

The MPP could be attached to this additional concrete footing which would be tied back into the existing foundation, but a solution would also be required to transfer lateral loads between the existing wood structure and the MPP. At the elevation of each floor diaphragm, as well as at the roof diaphragm, a transition joist was planned to wrap the entire existing building and be securely fastened to the building's existing load-carrying elements. The MPP would then be attached to these transition joists to accomplish the load transfer between the existing structure and the retrofit LFRS.

The entire façade would not need this type of LFRS; infill panels could be used in between these panels and would not require the same level and type of connection. Infill panels could still be designed with MPP to simplify the material palette and assembly complexity.

The lateral resistance provided by an MPP LFRS is expected to significantly reduce inter-story drifts and overall building deformation in the event of a seismic event. This should limit overall damage to the building, including interior finishes, and could shorten the timeline for re-occupancy of light-wood-frame multifamily housing, therefore providing for a more resilient design.

2.3 ENVELOPE DESIGN

The wall insulation of existing pre-1990 multifamily housing in the study region can be assumed to be below the current code requirements of RSI-3.7 for new construction, and the degree to which the walls are insulated is a primary design criterion for a façade energy upgrade. Leaving the existing wall in place minimizes renovation disturbance, and adds the existing insulation value to the overall effective insulation value of the retrofit solution.

With the MPP façade retrofit panel, insulation can be included on either or both sides of the MPP. A natural insulation cavity is created behind the MPP where the depth of the transition joist at each diaphragm location holds the MPP off the existing façade everywhere else. A compressible insulation allows for managing some of the inevitable construction irregularities of the existing façade, such as areas with trim elements protruding or an area being out of true. It also offers a location for new services to be run, should they be required. The depth of insulation added outboard of the MPP can be easily modified in the design phase to meet the energy code needs of a different climate zone or to increase the thermal performance target of the envelope. Table 1 lists a range of performance criteria by level of retrofit target.

Table 1: *Range of Energy Retrofit: Comprehensive, Moderate, Low-Cost and Current Energy Code Standard. [1]Indicates typical existing conditions per NEEA Residential Building Stock Assessment.*

RETROFIT ENERGY PERFORMANCE LEVEL				
	1 (Comprehensive)	**2** (Moderate)	**3** (Low-cost)	**0** (No retrofit)
STANDARD	PHIUS	DOE - ZERO ENERGY READY HOME (ZERH)	OREGON CODE (2021 ORSC)	TYPICAL EXISTING CONDITIONS[1]
WALLS	RSI-8.3	CZ 4-5: RSI-3.5 OR RSI-2.3 + RSI-0.9 CZ 6: RSI-3.5 +0.9 OR RSI-2.3 + 1.8	RSI-2.6 (EXISTING) RSI-3.7 (NEW)	RSI-1.4 – RSI-2.1
CEILING	RSI-15.7	CZ 4-6: RSI-8.6	(EXISTING) RSI-3.7 – RSI-8.6 (NEW) RSI-5.3 – RSI-8.6	RSI-5.3+
FLOOR	RSI-9.0	CZ 4-6: RSI-5.3 SLAB CZ 4,5:RSI-1.8, 61cm CZ 6:RSI-1.8, 122cm	(EXISTING) RSI-4.4 – RSI-5.3 (NEW) RSI-5.3 (SLAB EDGE) RSI-2.6	UNINSULATED SLAB
WINDOWS	U-0.91 OR LESS	CZ 4-6: U-1.53 CZ 4C & 5: U-1.70	U-1.48 OR LESS	SINGLE PANE ALUMINUM TYPICAL
DOORS	RSI-1.8	NO REQUIREMENT	U-1.14 WITH <= 0.23 m^2 GLAZING U-2.27 WITH >= 0.23 m^2 GLAZING	NO REQUIREMENT
INFILTRATION	0.30 L/s50/m2 ENVELOPE AREA	LESS THAN 3 ACH 50	LESS THAN 3 ACH 50	NO REQUIREMENT

New windows offer the most tangible feature of energy upgrades for occupants through perceptibly improved thermal comfort. Installing them in the MPP retrofit panel in the factory as part of a prefabricated façade assembly allows for greater quality control and speed of on-site installation. Existing windows would be removed just prior to retrofit panel installation, and interior finish carpentry would immediately follow the panel installation, minimizing occupant disturbance. The precision CNC fabrication of the MPP also achieves a very predictable tolerance for window rough openings in the panels so that gaps between the window and MPP can be far smaller than site-built rough openings.

Air tightness or infiltration is another key envelope criterion for reducing operational energy use in buildings for heating and cooling. The large format, multi-story MPP limits the number of joints where air leakage can occur. Panel-to-panel joints closed in the field become critical details that need to be executed precisely to achieve anticipated performance.

One concern in covering the existing envelope with new additional enclosure layers is that moisture could become trapped in the combined wall assembly. For this reason, we used WUFI 2D (version 3.4) moisture transmission simulation [17] and analysis for the proposed retrofit solution over an existing wall assembly. All materials were assumed to have an elevated starting water content

https://doi.org/10.52202/069179-0141

equivalent to 80% relative humidity and the simulation was run for one year with modelled climate and weather. For each material in the assembly and every hour over one year, the duration at a given water content is converted to mould index ranging from 0 - no growth to 6 - 100% coverage with visible growth [18]. Results for all materials demonstrate that moisture is not being trapped in the overall wall assembly at any time, which translates to <1% coverage of microscopic growth. At the conclusion of the one-year simulation, all materials have dried, having a mould index of 0, or no growth.

2.4 EXISTING CONDITION MOCK-UP, PANEL FABRICATION AND CONSTRUCTION

We constructed a full-size mock-up using a corner and window condition from the case study building (Figures 2, 3) to test design, detail, fabrication, and installation assumptions. Research questions addressed with the mock-up included: 1) how much data generated from the scan of an irregular building topography can and should we ignore with the high tolerance capabilities of CNC; 2) what digital actions can minimize our time on site through the use of a digital model compared to simple physical interactions with the existing physical object; 3) what are the out of plane tolerances of an existing building; 4) how do we make structural connections while prefabricating and closing as much of the panel as possible; and 5) how do we rig and lift the panel in a vertical orientation to not damage foundation connections and navigate the eave. We used video and still photography to capture key elements and events during the testing process.

First, we created a mock existing condition. Although the shear panel foundation connectors were sized for the two-story case study building, we determined that a one-story section of the existing structure was sufficient to allow us to test the foundation, roof eave, rake details, and a panel-to-panel field and corner condition. The existing structure included plywood T1-11 siding, a typical vinyl frame sliding window, gutter, downspout, dryer vent, and trim.

Next, we scanned the existing condition as in Figure 3a. We evaluated different scanning techniques, including Matterport Pro2, Leica BLK360, and Artec Ray. The Matterport Pro2 camera is a professional, high-resolution 3D camera. Both the Leika BLK360 and the Artec Ray are Light Detection and Ranging (LiDAR) equipment. The Leica BLK 360 provides 3D captures with indoor and outdoor capabilities and excellent measurement accuracy for an extended range of 20 m. However, the Artec Ray is designed for large objects with up to 110 m distance and proved to work well with the large scale of a building façade, yielding clean, complete scans. The point-cloud software, Artec Studio, was used to merge Artec Ray scans into a singular model (Figure 3b) and to fit planes through the existing T1-11 wall surface (Figure 3c). Once planes were established, we could develop a topographical map of wall surface tolerance (Figure 3d) and use Autodesk ReCap Pro (Figure 3e) to link the model

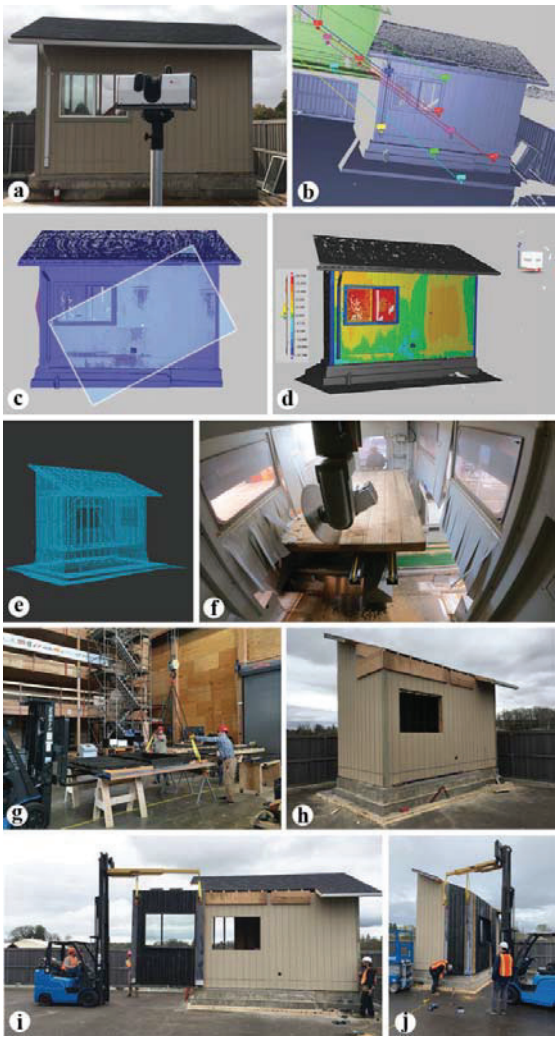

Figure 3: *Process for facade energy + seismic panelized retrofit: a) LiDAR scan existing building; b) process multiple scans into singular digital model; c) fit plane to wall surface; d) surface irregularity establishes tolerances; e) digital scan to Autodesk ReCap Pro; f) digital CNC fabrication of MPP structural core for facade panel assemblies; g) factory pre-assembly of facade panels with weather barriers, insulation, windows and cladding; h) site preparation including removing eave, trim, existing window and installation of MPP transfer joists at roof diaphragm; i) individual panels lifted into position on existing façade; j) panel connections completed at foundation beam and transfer joists. Panel-to-panel joints completed with elastomeric sealant, WRB, connector plates, insulation, and cladding.*

into Autodesk Revit 2022, in which we modelled the new facade. The façade models were exported from Revit and imported into DDX EasyWOOD for the generation of CNC toolpaths. CNC processing (Biesse Uniteam UT-9) of MPP occurred at TDI's Emmerson Laboratory at OSU (Figure 3f) along with the subsequent addition of weather barrier, window, flashing, insulation, and cladding (Figure 3g).

https://doi.org/10.52202/069179-0141

Finally, we tested prefabricated panels for ease of installation. On-site work included the installation of a 52 mm MPP transfer joist at the roof diaphragm, removing the existing eave for ease of installation, then gutter, downspout, trim, dryer vent, and existing window (Figure 3h). Once the existing condition was prepared, we flew panels into position, beginning with the infill window panel to align the window with a framed rough opening (Figure 3i) and continued with the seismic shear panels at the corner and panel-to-panel location with approximately 6 mm tolerance between panels. After completing all structural connections, we closed the joints with sealant, weather barrier, in-plane panel-to-panel plates, insulation, and cladding (Figure 3j). Lastly, we installed the roof blocking, sheathing, shingles, and the foundation rigid insulation with cementitious board over the newly installed seismic connections.

3 RESULTS

The main structural components of the system include an upgraded foundation system using a new 102 mm concrete beam and footing bonded to the existing stem wall and footing using epoxy rods. Wall panels consist of a rocking shear wall panel that resists panel flexural and shear forces, two hold-downs connected to an upgraded concrete foundation, resisting design forces induced by rocking of the wall either in tension (T) or compression (C), and a shear plate that transfers the horizontal base shear (V_b) between the wall and the concrete foundation. Forces between the shear wall panels are transferred to steel plates through fasteners (screws). Forces between the steel plates and the concrete foundation are transferred by the concrete shear anchor bolts (Figure 4b). At floor levels, shear wall panels are connected to the MPP transfer joist via eight fasteners at each edge of the panel, transferring diaphragm forces between the building and the shear wall (Figure 4a). Infill wall panels are connected to the MPP transfer joist via slotted steel plate connections (not shown in the figure).

The MPP walls selected for the two-story case study building are 1.22 m in width, 6.10 m in height, and 78 mm thick. The design of the shear wall panel followed existing standards, including ASCE 41-17 [19] and ASCE 7-16 [20], and consisted of determining (1) the tributary seismic weight to be resisted by the shear wall panel, (2) the seismic base shear, (3) forces and verification of the design of the main elements of the wall lateral force resisting system, (4) a drift analysis, and (5) capacity-based design of elements that are designed to remain essentially elastic. For a total base shear of 7.88 kN, tension and compression forces equalling 36.61 kN are generated at the base of the wall. Further description of the structural analysis of the system, and details on connections are described in the structural retrofit paper of the project [21].

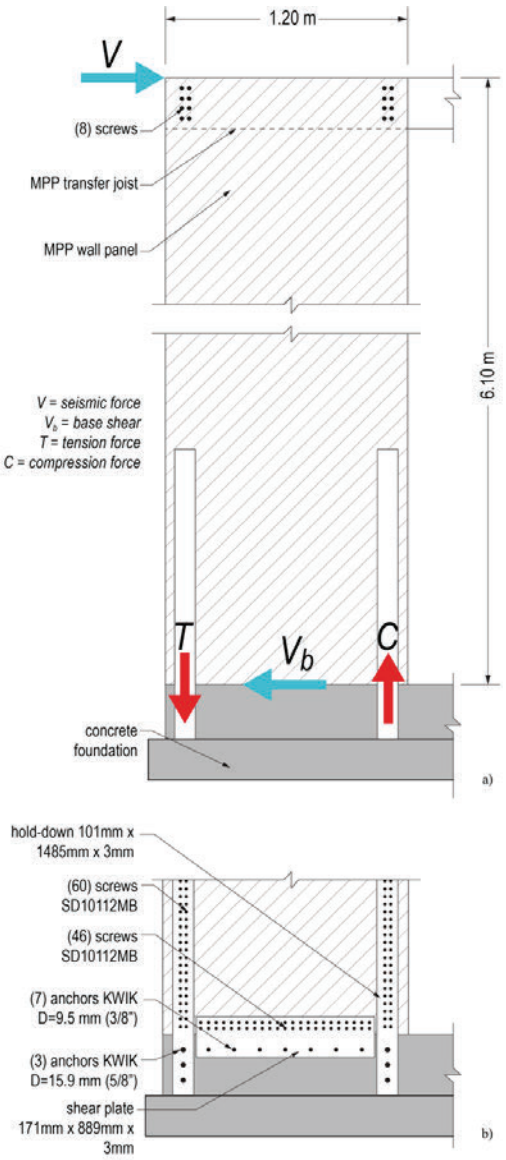

Figure 4: *a) Panel dimensions and reaction forces for connection design, b) foundation connection design*

Due to the MPP structural core, the panel system is designed to accept a wide range of outboard insulation levels, thus, a wide range of energy performance possibilities for a given climate. The existing case study wall assembly included (from inside to outside) 13 mm gypsum board, 89 mm stud frame with fiberglass batt insulation, and 13 mm T1-11 plywood siding for an insulation value of RSI-2.5. The retrofit system developed for the case study included (from inside to outside) 60 mm Steico flex wood batt insulation, 78 mm MPP, 60 mm Steico special dry board insulation, Soprema VP Sopraseal weather barrier, 19 mm ventilated cavity and 16

https://doi.org/10.52202/069179-0141

mm T1-11 plywood siding for an insulation value of RSI-3.1 (Figures 5-7). The combined system (existing condition and retrofit assembly) insulation value exceeded code in Portland, Oregon for a wall insulation value of RSI-5.6.

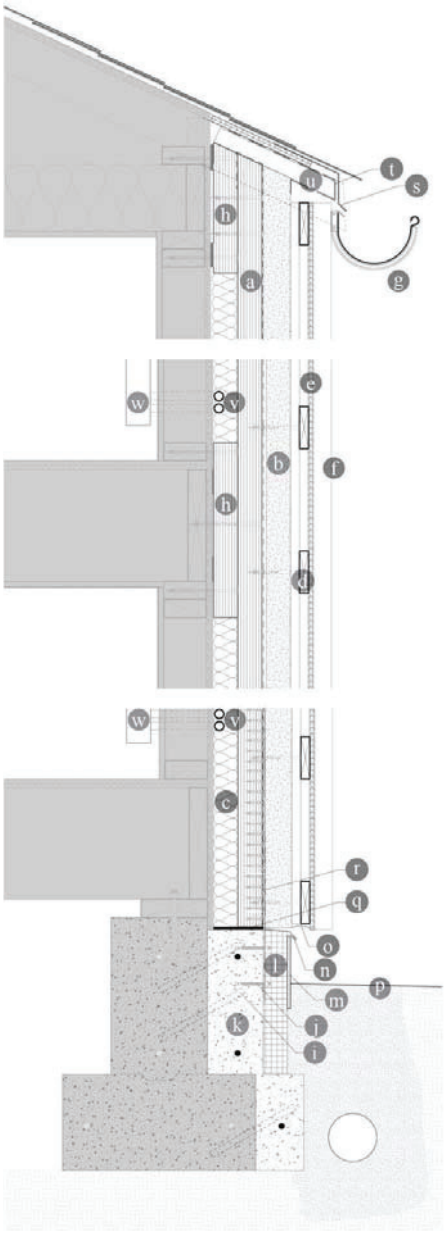

Figure 5: *Detail section view of façade retrofit assembly: a) 51mm MPP panel b) shop-applied mineral wool board; c) shop-applied 51mm mineral wool batt; d) horizontal batten; e) rough-sawn T1-11 plywood f) reclaimed wood batten; g) half-round gutter; h) 51mm MPP transfer joist; i) epoxy rod; j) steel expansion anchor; k) new 102mm concrete beam and footing; l) 51mm XPS insulation; m) cementitious board; n) flashing; o) insect screen; p) existing grade; q) neoprene pad; r) foundation seismic connector; s) flashing; t) insect screen; u) vented attic intake; v) hydronic retrofit piping; w) hydronic fan coil unit*

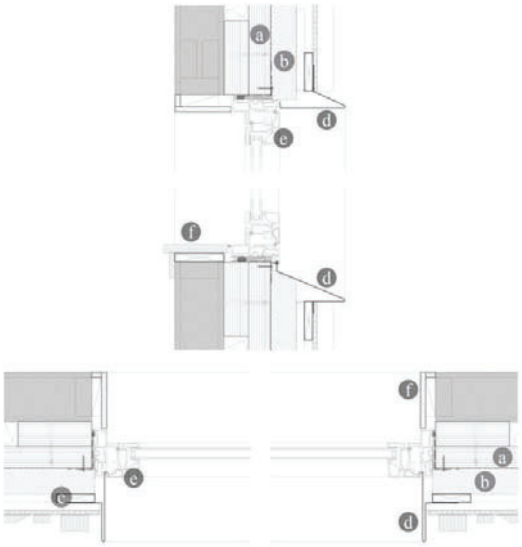

Figure 6: *Detail section and plan views of façade retrofit at window: a) 51mm MPP panel; b) shop-applied mineral wool board; c) vertical batten; d) brake-form steel window enclosure; e) fiberglass window; f) new interior finish.*

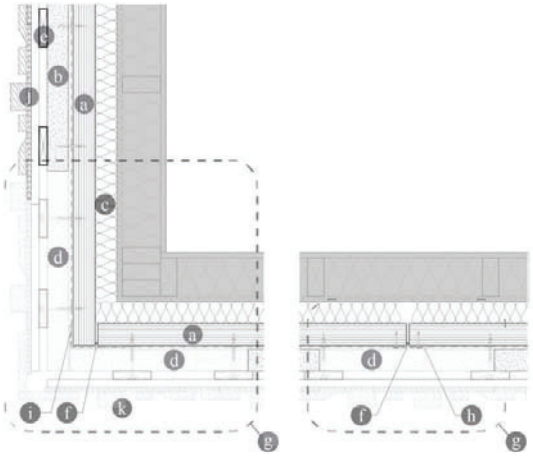

Figure 7: *Detail plan view of façade retrofit at panel-to-panel corner and field joint condition: a) 51mm MPP panel; b) shop-applied mineral wool board; c) shop-applied 51mm mineral wool batt; d) field-applied mineral wool board; e) vertical batten; f) elastomeric sealant; g) panel-to-panel field joint; h) panel-to-panel field connector plate; i) panel-to-panel corner connector plate; j) rough-sawn T1-11 plywood; k) reclaimed wood batten*

4 DISCUSSION

4.1 CONSIDERATIONS FROM MOCK-UP

Several light detection and ranging (LiDAR) scanning technologies are commercially available with a wide range in both capability and cost. Of the three systems we tested for this project, we found the Artec Ray (Artec 3D, Senningerberg, Luxembourg) to provide a suitable solution for our intended use case. This three-dimensional scanner is intended for large objects and in our experience

captured high quality dimensionally accurate information of building facades. In addition, the ease and sophistication of post-processing into one clean usable model and compatibility with other software required for panel design and fabrication was an important consideration in developing the digital workflow used in the project. The scan resolution allowed irregularities in the finish of the retrofit concrete foundation to even be translated to a cut file and milled into the bottom edge of the MPP for an exact fit when installed.

Figure 8: *Mock-up pre-retrofit (top image) and Mock-up post-retrofit (bottom image).*

Where deep overhangs from existing eaves impede retrofit façade panel installation, two methods are possible. Some *Energiesprong* projects in Europe have employed specialty lifting attachments for crane-assisted positioning of panels that keep the attachment clear of the eave while allowing the suspended panel to be placed flush against the existing wall. We chose the other method: removing the existing eave so retrofit panels can be placed by conventional lifting attachments (Figure 8).

Though the scope of the current project is limited to façade retrofit only, it is reasonable to assume that if a building were to undergo such a retrofit the roof may also be considered for an upgrade. In this case, a parallel chord roof truss may be selected to span the existing roof while adding space for additional roof insulation and transferring the added load to the perimeter walls where façade retrofit panels can be designed to accommodate this. In this whole building retrofit scenario, the removal of existing eaves would be advantageous for more than just ease of placing retrofit wall panels.

Figure 9: *Reflected view of installed seismic retrofit panel.*

In rigging the panels for lifting and installation two Dragon lifting belts (Rothoblaas, Cortaccia, Italy) were used suspended from a boom (Figure 3i). This method required 35mm through-holes to be drilled through the MPP panel. The method was successful from an installation perspective, with the lifting belts easily retrievable and reusable once the panels were secured. However, the two holes are large envelope penetrations that must be properly sealed in the field as part of completing the panel-to-panel joints. An alternative approach to rigging attachments that eliminates these through holes would be desirable as a future installation refinement to avoid any possibility of these penetrations being missed or improperly finished.

https://doi.org/10.52202/069179-0141

Some elements of façade panel assemblies are best accomplished with panels oriented flat. For example, bonding wood fibre insulation to the MPP prior to CNC milling of the composite panel was piloted and proved a successful means of reducing the overall fabrication labour. The panels not only need to be rotated in the factory for fabrication, but also for transportation, and again while being lifted into place. The panel stiffness, factoring in window openings and added weight from the built-up façade assembly, must be sufficient to allow for panel rotation in any configuration. Panel flex is also undesirable for machining operations. If the panel must be stiffened or attached to a spoil board to be accurately cut, this will add time and in turn cost.

One important consideration concerning the positioning of steel seismic connectors on each panel is that some of each connector must be left exposed for attachment to the building and to adjacent panels during installation. The plates must then be covered as part of the process of sealing and finishing panel-to-panel joints once attached to the building. Limiting the size and location of these areas to be finished in the field reduces installation time and complexity. It also should be part of a cohesive design strategy focused on how panels and seams are conceived to work visually with the overall completed façade aesthetic. Seismic connectors were intended to be limited to exposed vertical edges of each panel (Figure 9), with field-installed vertical siding elements used to conceal panel-to-panel joints on the completed façade. However, the seismic connection to the foundation is best accomplished with the inclusion of a horizontal steel plate at the base of the MPP panel (Figure 4b). This area, if left exposed for installation, needs future consideration for how it will be detailed to be incorporated into the overall façade design.

4.2 FUTURE RESEARCH DIRECTION

We are now planning to construct and test a three-story prototype fabricated and installed by a commercial contractor to test the validity of design, scanning techniques, fabrication and construction methods, and cost models resulting from the initial prototype construction. Construction-ready documents will be made publicly available and given the potential market for these retrofits, a significant market increase for mass timber products is anticipated.

Along with this project, the team is exploring mass timber façade retrofits for energy and seismic resilience in low-rise commercial buildings. Other future related research may include designs for a prefabricated MPP roof retrofit with insulation and integrated photovoltaics.

5 CONCLUSIONS

This project produced a physical demonstration mock-up of a seismic/energy panelised retrofit, utilizing MPP as the structural core, with performance upgrades to meet U.S. Department of Energy Zero Energy Ready Home (ZERH) Standard [22] and current seismic code, that is capable of initially being rolled out across U.S. West Coast markets and beyond. The desired result is to use the innovative design solution produced by UO/OSU as a demonstration and cost model for industry adoption, including manufacturers, developers, and contractors.

Figure 10: *Visualization of case study multifamily building using the façade retrofit system developed.*

We recognize that each retrofit project will need this prototype design adapted for each existing building. In particular, the seismic design will vary depending on the existing conditions in the building, including its size and shape. Some buildings may need additional structural interventions across floors to connect to exterior walls and these will have to be designed to cause minimal interior disruption. However, using scans of existing buildings, translated into digital files for fabrication and panel assembly in a factory setting, we believe that the custom solutions can be more efficiently accomplished than with each project constructed on-site. With the substantial need for upgrading this existing stock of housing for energy and seismic resilience, this solution can have a significant impact on lowering carbon emissions and extending the useful life of much-needed existing housing.

ACKNOWLEDGEMENT

We would like to acknowledge Phillip Mann, technical director of the Emmerson Lab, for his assistance in CNC file preparation, milling, panel construction, and installation, and Mark Gerig, lab technician at Emmerson Lab, for his assistance with panel construction and installation. We would also like to acknowledge Carly Loving, MS graduate student at Oregon State University, for her assistance with the Leica BLK360 scans. This work was generously supported by a U.S. Forest Service Wood Innovation Grant #2020-DG-11062765-737 and by the TallWood Design Institute. This work was further supported by generous donations from HawkRidge Systems, who donated equipment, software, time, and support using the Artec Ray scanner; New Energy Works, who donated Steico wood fibre board insulation; Bensonwood, who donated wood fibre batt insulation, Simpson Strong-Tie, who donated mechanical fasteners and Soprema, who donated Sopraseal Stick VP weather barrier.

REFERENCES

[1] Thomas, B.H., Henwood, B.F., Orlando, A.W.: A rising tide drowns unstable boats: How inequality creates homelessness. *The ANNALS of the American Academy of Political and Social Science* 693, no. 1: 28-45, 2021.

[2] Congress, U. S. Healthy Forests Restoration Act of 2003: HR 1904. in *108th Congress of the United States of America* vol. 7 (2003).

[3] Cumbo, D. W., Smith, R. L. & Becker, C. W., III. Value analysis of lumber produced from small-diameter timber. *For. Prod. J.* 54, (2004).

[4] Portland Clean Energy Community Benefits Initiative 2018 (2018, February 18). Retrieved from https://www.portlandoregon.gov/auditor/article/674246

[5] Portland Clean Energy Fund. (n.d.). About the Portland Clean Energy Fund, Retrieved from https://portlandcleanenergyfund.org/about

[6] City of Portland, Planning and Sustainability (BPS). (2022, July 20). Portland City Council unanimously approves largest single investment in climate justice in City history [Blog post]. Retrieved from https://www.portland.gov/bps/cleanenergy/news/2022/7/20/portland-city-council-unanimously-approves-largest-single-investment

[7] Doughman, P. *Electric Program Investment Charge 2020 Annual Report*. https://www.energy.ca.gov/publications/2021/electric-program-investment-charge-2020-annual-report (2021).

[8] Bipartisan Policy Center. (2023, February 11). What does the Inflation Reduction Act Mean for Housing? Retrieved from https://bipartisanpolicy.org/blog/inflation-reduction-act-mean-for-housing/

[9] United States Energy Information Administration, *Monthly Energy Review*, Tables 11.1-11.6, April 2022.

[10] Northwest Energy Efficiency Alliance. Residential Building Stock Assessment II: Multifamily Buildings Report 2016-2017, Revised 2019.

[11] Flynn, J., Slovic, P., Mertz, C. K. & Carlisle, C. Public support for earthquake risk mitigation in Portland, Oregon. *Risk Anal*. 19, 205–216 (1999).

[12] International Council of Building Officials (ICBO), 1973, Uniform Building Code (UBC). Whittier, CA. (1973).

[13] International Codes Council (ICC) International residential code for one- and two-family dwellings (IRC), Falls Church, Va. (2003)

[14] Oregon Housing and Community Services: Building on New Ground: Meeting Oregon's Housing Need, February 2021.

[15] Energiesprong. (2023, February 11). [Website]. Retrieved from https://energiesprong.org.

[16] United States Census Bureau [Website] Retrieved from https://www.census.gov/topics/housing.html.

[17] Sedlbauer, K., Krus, M., Zillig, W. and Kunzel, H.M., Mold growth prediction by computational simulation. *Fraunhofer Institute for Building Physics,* 2001

[18] Viitanen, H., Krus, M., Ojanen, T., Eitner, V., Zirkelbach, D. Mold Risk Classification Based on Comparative Evaluation of Two Established Growth Models. In: Energy Procedia, 1425-1430, 2015

[19] ASCE/SEI 41-17: seismic evaluation and retrofit of existing buildings, American Society of Civil Engineers, Reston, VA. (2017).

[20] ASCE/SEI 7-16: Minimum Design Loads and Associated Criteria for Buildings and Other Structures, American Society of Civil Engineers, Reston, VA. (2016).

[21] Orozco, G., Barbosa, A. R., Fretz M., Sheine, J., Stenson, J., Van Den Wymelenberg, K., Narancic, P., Casey, F. Seismic and Energy Retrofit of Light-Frame Timber Multifamily Residential Buildings Using Mass Ply Panel (MPP) Shear Wall Façade System. In: 2023 World Conference in Timber Engineering (WCTE 2023). (2023).

[22] Gilbride, T. L. *DOE Zero Energy Ready Homes*. https://www.osti.gov/biblio/1525975 (2017).

https://doi.org/10.52202/069179-0141

World Conference on Timber Engineering Oslo 2023

EMISSION OF VOLATILE ORGANIC COMPOUNDS FROM WOOD MATERIALS AND IMPACT ON INDOOR AIR QUALITY

Ingrid Bakke[1], Anders Nyrud[2], Roland Kallenborn[3], Lina Aarsbog[4]

ABSTRACT: The main purpose of this study was to investigate the emission of volatile organic compounds (VOCs) during construction of a cross-laminated timber (CLT) building. Bjølstad student housing complex was built in 2020, with a main frame of Norway Spruce (*Picea abies)* CLT. Emission concentrations of six selected VOCs (hexanal, α-pinene, camphene, β-myrcene, β-pinene and 3-carene) were measured during the nine last weeks of construction, in dormitories with different loading rates of visible CLT. All VOCs were detected above limits of quantification, although 3-carene and β-pinene were detected above the linear ranges in some samples. The variation and trends in VOC emission indicated considerable sources in addition to CLT. None of the measured VOC concentrations exceeded the recommended LCI values.

KEYWORDS: VOC, Engineered Wood, Indoor Air Quality, Human Health, Environmental Impact

1 INTRODUCTION

Outdoor air pollution has long been a topic of concern while indoor air pollution has been paid too little attention, especially considering the higher concentration of air pollutants indoors and the fact that most people spend 90% of their time in indoor spaces [1]. With energy efficient building designs comes airtight buildings and accumulation of pollutants in the indoor environment. To guarantee sustainable building designs both regarding low carbon footprint and good occupant health it is important to consider sources and sinks of air pollutants to the indoor environment. Volatile organic compounds (VOC) make up a main group of indoor air pollutants and are of high concern as some VOCs are considered leading causes of SBS (Sick-Building-Syndrome) and other negative health effects from air pollution. VOCs can originate from multiple sources, such as outdoor air, cleaning agents, personal hygiene products, paint, wood furniture and building materials. The relative impacts of these sources on indoor air quality differ greatly, but in most cases outdoor air dilutes the polluted indoor air.

Cross-laminated timber (CLT) has good thermal and mechanical properties and is easily cut to preferred dimensions. In addition to wood being more sustainable material than other building materials such as concrete or plaster, the quick assembly, prefabrication, and lighter weight of CLT often makes it more beneficial alternative for construction. The solid wood surface of CLT introduces a buffer capacity with the surrounding environment, establishing an equilibrium of physiochemical properties between the wood surface and ambient air. This buffering property can impact the long-term emission of VOCs and it is hypothesized that low-emitting wood surfaces adsorb VOCs from highly polluted air [2].

Previous studies have shown that different wood building materials have different emission concentrations of VOCs and indicate that untreated wood surfaces lead to high emissions compared to coated wood [3]. In addition, the profile of VOC emission from solid wood surfaces differs from that of other building materials and of glued or surface treated wood materials. Coniferous wood surfaces emit mostly terpenes such as mono-, di- and sesquiterpenes followed by aldehydes such as hexanal and pentanal. These biogenic VOCs occur naturally in green vegetation, while anthropogenic sources of VOCs include petrochemical refinement, burning of fuels and manufacturing and use of consumer products [1]. Engineered wood building materials may emit VOCs originating from anthropogenic activity and may pose a different environmental impact on the indoor air. Liu et al. (2020) found that the largest contributor to VOC emissions from particle board was 1,2-dichloropropane, which is most likely not a compound found naturally in wood as it is halogenated [4]. It is classified as hazardous to human health and there are indications that it might be a carcinogen. Liu et al. (2020) found in total 11 hazardous air pollutants emitted from wood-based panels and found that approximately 50% of the total VOC was aldehydes,

[1] Ingrid Bakke, Norwegian University of Life Sciences (NMBU), Faculty of Environmental Sciences and Natural Resource Management, ingrid.m.bakke@nmbu.no
[2] Anders Qvale Nyrud, Norwegian University of Life Sciences (NMBU), Faculty of Environmental Sciences and Natural Resource Management, anders.qvale.nyrud@nmbu.no
[3] Roland Kallenborn, Norwegian University of Life Sciences (NMBU), Faculty of Chemistry, Biotechnology and Food Science, roland.kallenborn@nmbu.no
[4] Lina Aarsbog, Norwegian Institute of Bioeconomy Research (Nibio), lina.aarsbog@nibio.no

https://doi.org/10.52202/069179-0142

while less than 40% was terpenes. This difference in VOC emission profile between solid wood and highly processed wood products is largely due to the physiochemical conditions wood chips are subjected to during production [1, 5].

Previous studies have found that emission of VOCs from wood construction products decrease over time after installation. The European Standard 16516 limits the measuring period to 28 days, indicating that the VOC emissions will have stabilized 28 days after production or processing of the wood surface [6]. As VOC emissions are highest right after installation it is relevant to measure the VOC emissions during construction of a wood building, to maximize the indoor air concentrations and regard the associated risk. Usage and surface planing of wood construction materials influence the subsequent VOC emissions strongly as creating a new surface gives rise to a new source of VOC emission. As wood surfaces are in equilibrium with ambient air temperature, relative humidity along with other physiochemical parameters also impact VOC emissions [7, 8].

High exposure of VOCs in a short period of time is associated with negative health effects such as SBS [9]. SBS is allocated to buildings where symptoms like headache, irritation of nose, eyes and throat, nausea and asthma have been reported by building users without other probable cause [9, 5]. One study showed an increase in eye dryness and xylene metabolite in urine for test subjects exposed to new buildings containing high levels of VOCs [10]. A Swedish study showed an increase in prevalence of asthma and inflammatory symptoms in airways related to exposure to newly painted surfaces [11]. In the Swedish study, the VOC levels increased by 100 $\mu g/m^3$ in the newly painted dwellings compared to prior to painting. High exposure to VOCs over a long period of time is associated with more adverse health effects like damage to liver, kidney, and carcinogenic effects [1, 9].

On the other hand, recent studies have reported health benefits from exposure to solid wood surfaces and to VOCs emitted from wood [12]. Grote et al. found that test subjects sleeping in beds of *Pinus cembra* solid wood had improved cardio-respiratory interactions, decreased heart rate, and increased vagal activity compared to sleeping in chipboard beds [12]. Another study showed that wood odor such as α-pinene had a positive psychophysiological effect on test subjects [13]. The VOCs emitted from wood products are what give rise to the characteristic pleasant smell of wood, and Dematté et al. (2018) found that a higher level of comfort was induced in wooden rooms compared to plaster rooms [14]. There are indications that monoterpenes such as α-pinene and limonene may decrease heart rate and have anti-inflammatory effects [15]. Skulberg et al. (2019) investigated the respiratory health effects and neuropsychological performance of participants exposed to fresh Scots pine (*Pinus sylvestris*) and aged Norway spruce (*Picea abies)* as a control. The study was double-blinded and randomized, and they found no significant difference in physical health or test performance between the spruce control room and the pine room with much higher VOC concentrations [16]. The perception of wood surfaces is closely interrelated to the psychophysiological effects of wood. Alapieti et al. (2022) reported a positive perception of indoor air quality in wooden rooms. VOC concentrations and perceived air quality (percentage of people dissatisfied) was measured in pine and gypsum board rooms [17]. At low ventilation rates the gypsum board room had lower satisfaction rates than pine room, though the pine room had higher VOC concentrations. Although indoor air quality perception and psychophysiological effects are connected, factors such as culture and background influence consumer's perception of wood building materials [18]. Interestingly, Matsubara et al. (2018) reported that women were affected by the presence of wood in indoor environments to a higher degree than men [19]. In a study where an environment with VOCs from Japanese cedar (mainly sesquiterpenes such as δ-cadinene) was compared to a control environment, women experienced a suppression of α-amylase in saliva in the cedar room and an increase of cortisol in the control room. It was also noted that men experienced a similar suppression of the nervous system at higher VOC concentrations rom cedar, indicating that the relaxation effects from wood VOCs such as δ-cadinene occur at lower concentrations for women than for men [20].

Several European certificates for building materials have now included criteria for VOC emissions in their evaluation. There are over ten different voluntary classification schemes from various European countries, which all include a limit value for TVOC and a weighted evaluation of the health risk of each VOC present, called the R-value. This R-value is based on substance-specific Lowest Concentrations of Interest (LCI), derived by the European Commission [21]. LCI values are based on toxicological data of VOCs from 12 different compound groups.

2 METHODS

Measurement of VOC concentration in indoor air was performed following the Norwegian standard NS-EN 16516:2017+A1 [6]. The student housing at Bjølstad had a supporting structure in Norway Spruce (*Picea abies*) CLT, and all indoor ceiling in addition to some walls was left visible. After inspection of the site, two dorm rooms were chosen as sampling locations. One room had visible CLT in the ceiling (H0310d of 10.8m^2) and the other in one wall and ceiling (H0311d of 9.4m^2).

2.1 SAMPLE COLLECTION BJØLSTAD

Air samples were collected from the construction site between 24.06.2020 to 11.08.2020. At this point the floor was cast, and plaster walls were painted. Samples were collected on conditioned sorbent tubes with 300mg Tenax

https://doi.org/10.52202/069179-0142

TA using handheld SKC pumps. Each sample was collected by pumping approximately 16L of air at a flowrate of 250mL/min. A total of 36 samples were collected on site: two samples from each dorm room for each of the nine weeks of sampling. Blank samples were collected by opening sorbent tubes at the sampling location without starting the pumps. Sorbent tubes were kept in the freezer before subsequent analysis on TD-GC-MS. Temperature and relative humidity sensors were placed in the common area outside dorm rooms, registering the temperature and relative humidity four times a day from 05.05.2020 to 10.07.2020.

2.2 MEASUREMENT OF VOC CONCENTRATIONS

Chemical analysis was performed at NMBU, using an Agilent 7890B GC coupled to a 7000C QQQMS and a Perkin Elmer ATD-400 injector [22]. The sorbent tubes were desorbed for 30min at 250°C and transferred to the GC by a heated deactivated silica transfer line. The GC was equipped with an HP-VOC column (60m, 0.2mm, 1.1µm) and the flow rate was set to 1mL/min. The temperature program was started at 50°C, heated to 150°C at a rate of 5°C/min before heating to 290°C at 50°C/min and holding for 10min. The MS was operated in EI mode (70eV), the source temperature and the quadrupole temperature were set to 200°C. Agilent MassHunter Quantitative Analysis B.07.00 was utilized for method evaluation and quantification of analytes. Concentration, *C*, of an analyse, *i*, in the sampled air, was calculated by equation (1).

$$C_i = \frac{m_i}{V_i} - \frac{m_b}{V_b} \quad (1)$$

Where m = mass, V = air volume and b = blank. The R-value for evaluation of risk of negative health effect is shown in equation (2).

$$R = \sum \frac{C_i}{LCI_i} \quad (2)$$

Where *C* = concentration of compound *i*, *LCI* = Lowest Concentration of Interest of compound *i*.

3 RESULTS AND DISCUSSION

VOC concentration measurements in indoor environment in the student dormitories resulted in the detection of five terpenes and one aldehyde. The six individual VOCs were detected above the limit of quantification in all samples, although 3-carene was only semi-quantified as the concentrations exceeded the linear range in all but one sample. β-pinene concentrations exceeded the linear range in two samples. LOQ and linear range data is shown in Table 1. Average concentrations of the six VOCs during the sampling period 24.06.2020 to 11.08.2020 are shown in Figure 1. All six VOC concentration profiles followed similar trends in the dormitories, indicating common sources of the substances in both rooms, either placed inside the rooms or originating from a common outside source. The changes in VOC concentrations in the two rooms over time were similar. The VOC concentrations reached a maximum during week 6 and 7.

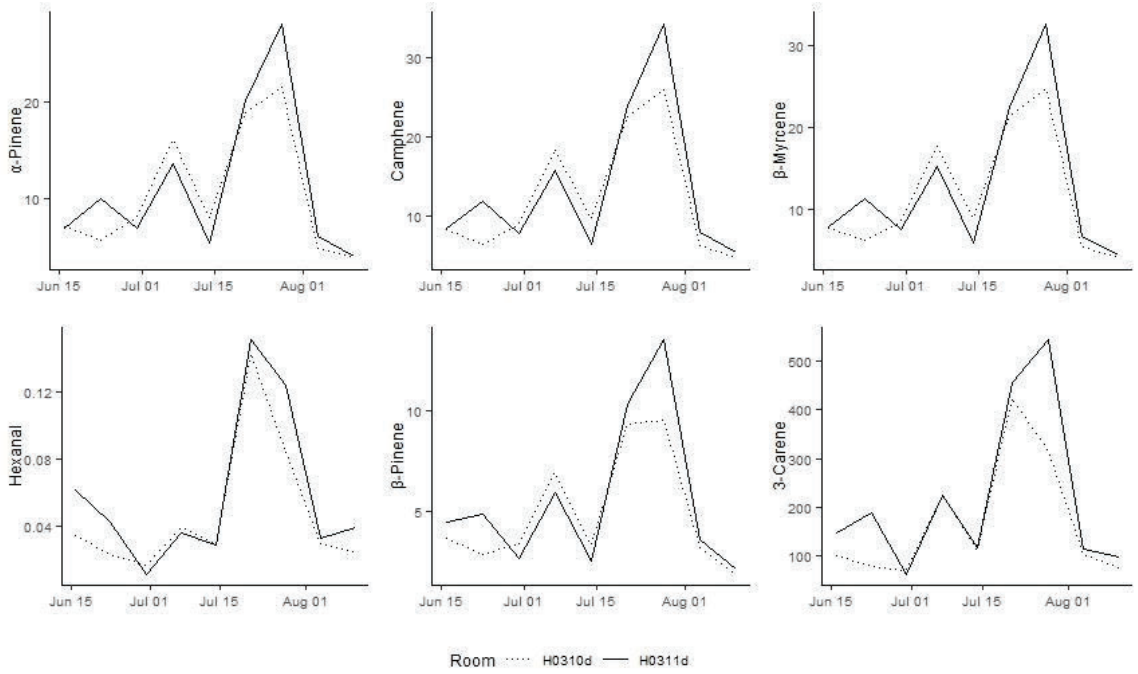

Figure 1. *VOC emission [µg/m3] measured during nine weeks of construction in room designed with visible cross-laminated timber in ceiling (H0310d) and in ceiling and wall (H0311d).*

https://doi.org/10.52202/069179-0142

Table 1. *Limits of quantification and linear range for the six target VOCs.*

	LOQ [µg/m^3]	Linear range [µg/m^3] (min – max)
Hexanal	$2.2 \cdot 10^{-4}$	0.00063 – 0.19
α-Pinene	$1.4 \cdot 10^{-1}$	0.031 – 63
Camphene	$2.2 \cdot 10^{-2}$	0.063 – 63
β-myrcene	$4.3 \cdot 10^{-2}$	0.31 – 63
β-Pinene	$6.4 \cdot 10^{-3}$	0.013 – 63
3-Carene	$1.5 \cdot 10^{-2}$	0.031 – 63

As VOC emission from wood surfaces has shown to decrease over time in a handful of published work emissions from CLT would be expected to decrease after time of installation at the Bjølstad site as well. VOC concentrations measured at the construction site were therefore presumed to come from additional sources.

The concentrations of individual VOCs differed greatly; hexane emitting at the lowest concentration and 3-carene at the highest for all samples. High concentrations of terpenes and low of the aldehyde hexanal coincides with the previously reported emission profile of spruce wood [23]. However, the concentration of 3-carene was almost tenfold that reported from spruce heartwood by Czajka et al. (2020) [24].

The VOC concentration in the room with a larger surface area of CLT (CW) were slightly higher than in the room with less wood surface (C) in week 2 and after week 5. However, during weeks 3-5 VOC concentrations were slightly higher in the room with less visible CLT, indicating a source of VOCs other than the spruce wood and adhesive in CLT. As the room with visible CLT in wall and ceiling was smaller it had a considerably higher loading rate of solid spruce surface, approximately 0.95m^2/m^3 in room H0310d, compared to 0.45m^2/m^3 CLT in room H0311d.

As the VOC concentrations varied greatly during the sampling period the construction site activities were registered in Table 2.

Table 2. *Overview of visits to construction site, including purpose (I=inspection, TRH=placing (1) and removing (2) of sensors for temperature and RH measurement, S=sampling) and description of construction site activity.*

Date	Purpose	Construction site progress
29.04	I	Visible CLT in floor, ceiling, and selected walls
06.05	TRH1	Preparation for casting of floors
16.06	S (W1)	Floor casting done. Wardrobe and kitchen cabinets
23.06	S (W2)	Shelf and bathroom doors
30.06	S (W3)	Closet doors and more kitchen furniture
07.07	S (W4)	-
10.07	TRH2	-
14.07	S (W5)	Plate tops in kitchen
21.07	S (W6)	Curtains and sofas
28.07	S (W7)	Desk and office chair
04.08	S (W8)	Table, chairs and wood wool ceiling in common area, beds in rooms
11.08	S (W9)	-

During the weeks of maximum VOC concentrations, week 6 (21.07) and 7 (28.07), the rooms were furnished with curtains, desks and office chairs, and sofas were placed in the common area. To assess the additional VOC emission from these changes at the construction site, the textiles and pieces of furniture must be tested for their individual VOC emissions separately.

Besides the introduction of furniture and appliances at the construction site, factors such as human activities, use of cleaning agents and rate of ventilation shortly before collection of air samples most likely has an impact on the subsequent VOC concentration in the rooms.

3.1 HEALTH IMPACT OF MEASURED VOCS

When evaluating the health impact of VOCs in indoor environments it is imperative to regard effects from individual volatile compounds. According to Salthammer et al. (2022) total VOC (TVOC) concentration cannot be used as an indicator of health in an indoor air study [25]. TVOC concentrations are not always comparable as there is inconsistency in the four methods for measuring TVOC specified in the indoor air standard ISO 16000-6. Additionally, the additive dose approach used when evaluating mixed effects of VOCs with their respective LCI values does not account for cocktail effects and different modes of action of the volatile compounds. Lastly, the LCI values established by the European Commission are mostly based on safety data sheets and animal studies which are not always transferrable to human toxicology. In this study, individual LCI values were compared to the maximum concentrations of individual VOCs, as shown in Table 3.

Table 3. *Maximum VOC concentrations and LCI values.*

	Maximum conc. [µg/m^3]	LCI [µg/m^3] [a]
Hexanal	0.17	900
α-pinene	32	2500
Camphene	39	1400
β-myrcene	37	1400
β-pinene	15	1400
3-carene	622	1500

[a] LCI values from the European Commission [21].

All individual VOC concentrations were below recommended LCI values, indicating no risk related to occupying the building during the last weeks of construction. The R-value for the VOC concentration at the student housing was 0.49. In most voluntary classification schemes the criteria for VOC concentration is an R-value less than or equal to 1. However, as 3-Carene was only semi-quantified and detected in high

https://doi.org/10.52202/069179-0142

concentrations, further measurements are recommended to confirm concentrations were below LCI for this compound.

4 CONCLUSIONS

The results from VOC measurements at Bjølstad showed indications of VOC sources in addition to the spruce CLT surfaces. Concentration profiles with regard to chemical species, loading rates and increase in concentration over time was not characteristic for spaces where spruce is the main source of VOCs. To assess this issue a chamber test of the spruce CLT is necessary. A more comprehensive approach to better map the VOC profile at Bjølstad student housing may also be beneficial. However, all individual VOC concentrations were detected below LCI values, and no health risk was associated with the investigated VOC levels in the student housing. Source appointment of VOC emission in a wooden indoor environment is a difficult task as both natural and anthropogenic sources are present at all times and testing uncertainties for available methods are high. More knowledge of the toxicity of characteristic VOC emission from spruce is needed to ensure safe use of building materials such as CLT in the future.

ACKNOWLEDGEMENT

This study was supported by grants from the Norwegian University of Life Sciences, Skogtiltaksfondet and Innovation Norway. Sample collection and analysis of air samples from the construction site in Bjølstad, Fredrikstad was conducted by Lina Aarsbog.

REFERENCES

[1] T. Adamová, J. Hradecký and M. Pánek. Volatile organic compounds (VOCs) from wood and wood-based panels: Methods for evaluation, potential health risks, and mitigation. *Polymers,* vol. 12, pp. 1-21, 2020.

[2] S. Niedermayer, C. Fürhapper, S. Nagl, S. Polleres and K. P. Schober. VOC sorption and diffusion behavior of building materials. *European Journal of Wood and Wood Products,* vol. 71, no. 5, pp. 563-571, 2013.

[3] L. Salo, E. Castagnoli, T. Alapieti, C. Vornanen-Winqvist, R. Mikkola and H. Salonen. The effects of coatings on the indoor air emissions from pinewood building materials. *Sisäilmastoseminaari*, Helsinki, 2018.

[4] Y. Liu, X. Zhu, X. Qin, W. Wang, Y. Hu and D. Yuan. Identification and characterization of odorous volatile organic compounds emitted from wood-based panels. *Environmental Monitoring and Assessment,* vol. 192, no. 6, p. 348, 2020.

[5] J. Pohleven, M. D. Burnard and A. and Kutnar. Volatile organic compounds emitted from untreated and thermally modified wood - a review. *Wood and Fiber Science,* vol. 51, no. 3, pp. 231-254, 2019.

[6] European Committee for Standardization. NS-EN 16516:2017+A1:2020. Construction products - assessment of release of dangerous sunstances: Determination of emissions into indoor air. Standard Norge, 2020.

[7] T. Alapieti, E. Castagnoli, L. Salo, R. Mikkola, P. Pasanen and H. Salonen. The effects of paints and moisture content on the indoor air emissions from pinewood (Pinus sylvestris) boards. *Indoor Air,* vol. 31, no. 5, pp. 1563-1576, 2021.

[8] K. Harčárová, S. Vilčeková and M. Bálintová. Building materials as potential emission sources of VOC in the indoor environment of buildings. *Key Engineering Materials,* vol. 838, pp. 74-80, 2020.

[9] R. Kishi, D. Norbäck and A. Araki. Indoor Environmental Quality and Health Risk Toward Healthier Environment for All. *Springer Nature Singapore Pte Ltd.,* 2020.

[10] J. Kwon, H. Park, H. Kim, W. Kim, M. Kim and S. Lee. Exposure to volatile organic compounds and airway inflammation. *Environmental Health,* vol. 17, no. 1, p. 65, 2018.

[11] G. Wieslander, D. Norbäck, E. Björnsson, C. Janson and G. Boman. Asthma and the indoor environment: the significance of emission of formaldehyde and volatile organic compounds from newly painted indoor surfaces. *Sweden Int Arch Occup Environ Health,* vol. 69, pp. 115-124, 1997.

[12] V. Grote, M. Frühwirth, H. K. Lackner, N. Goswami, M. Köstenberger, R. Likar and M. Moser. Cardiorespiratory interaction and autonomic sleep quality improve during sleep in beds made from pinus cembra (Stone pine) solid wood. *Environmental Research,* vol. 18, p. 9749, 2021.

[13] L. Schreiner, B. Karacan and S. Blakenagel. Out of the woods: psychophysiological investigations on wood odors to estimate their suitability as ambient scents. *Wood Science and Technology,* vol. 54, no. 5, pp. 1385-1400, 2020.

[14] M. L. Demattè, G. M. Zucco, S. Roncato, E. Paulon, R. Cavalli and M. Zanetti. New insights into the psychological dimension of wood–human interaction. *European Journal of Wood and Wood Products,* vol. 76, no. 4, pp. 1093-1100, 2018.

[15] P. Wolkoff. Indoor air chemistry: Terpene reaction products and airway effects. *International Journal of Hygiene and Environmental Health,* vol. 225, p. 113439, 2020.

[16] K. Skulberg, A. Nyrud, L. Goeffeng and A. Wisthaler. Health and Exposure to VOCs From Pinewood in Indoor Environments. *Frontiers in Built Environment,* vol. 5, p. 107, 2019.

[17] T. Alapieti, C. Vornanen-Winqvist, R. Mikkola and H. Salonen. Measured and perceived indoor air quality in three low-energy wooden test buildings. *Wood Material Science and Engineering,* 2022.

[18] L. Häyrinen, A. Topppinen and R. Toivonen. Finnish young adults' perceptions of the health, well-being and sustainability of wooden interior materials. *Scandinavian Journal of Forest Research,* vol. 35, no. 7, pp. 394-402, 2020.

[19] E. Matsubara and S. Kawai. Gender differences in the psychophysiological effects induced by VOCs emitted from Japanese cedar (Cryptomeria japonica). *Environmental Health and Preventative Medicine,* vol. 23, no. 10, 2018.

[20] E. Matsubara and S. Kawai. VOCs emitted from Japanese cedar (Cryptomeria japonica) interior walls induce physiological relaxation. *Building and Environment,* vol. 72, pp. 125-130, 2014.

[21] European Commission. Agreed EU-LCI values (December 2021). 16 03 2022. [Online]. Available: https://ec.europa.eu/docsroom/documents/49239.

[22] L. B. Aarsbog, "Solvent-free quantification for selected volatile organics in Arctic air : application of thermal desorption-gas chromatography-mass spectrometry Lina Aarsbog," NMBU, KBM, Ås, 2019.

[23] F. Englund and R. M. Nussbaum. Emission of volatile organic compounds from heartwood and sapwood of selected coniferous species. *Holzforschung,* vol. 54, pp. 449-456, 2000.

[24] M. Czajka, B. Fabisiak and E. Fabisiak. Emission of volatile organic compounds from heartwood and sapwood of selected coniferous species. *Forests,* vol. 92, p. 11, 2020.

[25] T. Salthammer. TVOC - Revisited. *Environment International,* vol. 167, p. 107440, 2022.

https://doi.org/10.52202/069179-0142

World Conference on Timber Engineering Oslo 2023

COMBINED EFFECTS OF VISUAL AND OLFACTORY STIMULATION BY INTRODUCING WOOD WHILE WORKING OR RESTING

Takashi Shima[1], Katsuhiko Sakata[2], Motoki Yairi[3], Daisuke Fujii[4], Haruki Momose[5], Yuko Tsunetsugu[6]

ABSTRACT: This study aimed to investigate the impact of visual and olfactory stimulation related to wood on subjective evaluation indices by incorporating wooden interiors and wood scents in simulations of real-life work and rest scenarios. We conducted subjective evaluations while participants performed tasks on a computer or rested to assess the combined effects of visual and olfactory stimulation. The working and resting rooms were either covered with wooden material or concrete-looking wallpaper, and the scent of Hinoki cypress (*Chamaecyparis obtusa*) was introduced into some of the rooms. The results of the experiment suggest that the introduction of both the Hinoki scent and wooden panels may enhance the olfactory impression during work and weaken it during rest, but the visual impression remains unchanged. Additionally, the results of the mood states suggest that the combined introduction of visual and olfactory stimulation from wood may improve mood state during work and rest. The results of the subjective fatigue also suggest that individual stimuli can affect subjective feelings of fatigue, and the Hinoki cypress scent may have potential in reducing various forms of fatigue. Overall, the results indicate that the combined visual and olfactory stimulation from wood may affect individuals differently depending on their activities.

KEYWORDS: Hinoki cypress, wooden interior, combined effect, subjective evaluation

1 INTRODUCTION

An increasing number of companies have been prioritizing environmentally friendly practices, including the development of eco-friendly materials and space design. The demand for low-carbon, CO2-emitting wooden structures has increased as companies aim to become more carbon neutral, which has enhanced the value of wooden spaces. Furthermore, wooden spaces may potentially have a stress-relieving effect on people.

Lowering stress is of great significance in contemporary society. In Japan, a significant portion of employees are reported to endure high stress levels in their jobs and daily life. A space that fosters a strong connection to nature can serve as an effective setting for individuals to recuperate from stress [1].

The suitability of wood as a material for stress relief is being explored in various studies [2]. These studies focus on examining the comfort provided by spaces that utilize wood and the stress-reducing effects of the material.

While many studies have explored the visual and olfactory effects of wood [3-4], most have centered around a single stimulus, and few have investigated the combined effect of both the visual and olfactory elements. To effectively utilize wooden stimuli in the workplace, the psychophysiological effects of incorporating wood and utilizing wooden spaces (e.g., for work and rest) need to be understood more comprehensively.

In this study, we aim to examine the impact of both visual and olfactory stimulation related to wood by incorporating wooden interiors and wood scents into simulations of real-life work and rest scenarios. The findings of this study are focused on the effects of the combined stimulation on subjective evaluation indices.

2 MATERIALS AND METHODS

2.1 PARTICIPANTS

Twelve adults (three men and three women in their 30s, and three men and three women in their 40s) were recruited for this study. All participants were confirmed to not have a habit of smoking. In addition, they did not have any symptoms of nasal inflammation or consume alcohol the day prior. This study was performed in accordance with the regulations of the Ethics Committee of Kajima Technical Research Institute.

2.2 STUDY PROTOCOL

In this experiment, the ambient conditions in the rooms were maintained at 23–26 °C and 40–60% relative humidity. The illuminance near the participant's head was

[1] Takashi Shima, Kajima Technical Research Institute, Kajima Corporation, Japan, shimata@kajima.com
[2] Katsuhiko Sakata, Kajima Technical Research Institute, Kajima Corporation, Japan, sakatak@kajima.com
[3] Motoki Yairi, Kajima Technical Research Institute, Kajima Corporation, Japan, yairi@kajima.com
[4] Daisuke Fujii, Kajima Technical Research Institute, Kajima Corporation, Japan, fujiid@kajima.com
[5] Haruki Momose, Kajima Technical Research Institute, Kajima Corporation, Japan, momoseh@kajima.com
[6] Yuko Tsunetsugu, Graduate School of Agricultural and Life Sciences, The University of Tokyo, Japan, a-yukot@g.ecc.u-tokyo.ac.jp

https://doi.org/10.52202/069179-0143

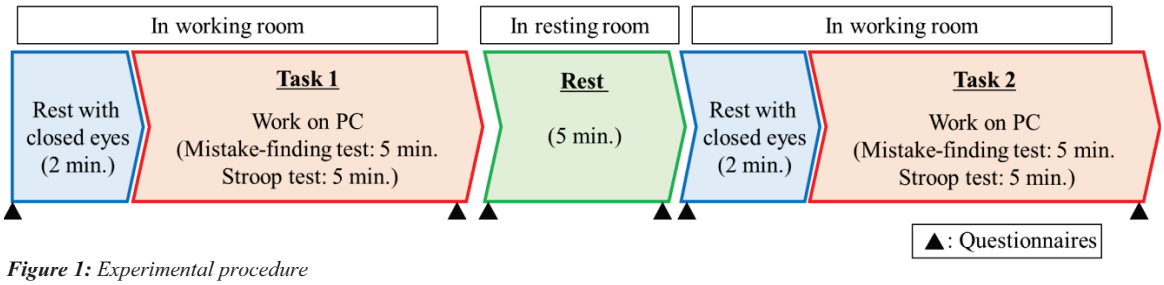

Figure 1: *Experimental procedure*

maintained at about 500 lx. The overall experimental procedure is illustrated in *Figure 1*. The experiments were conducted every other day for seven days. On the day of the experiment, each participant entered the room to work on a PC. The participants were instructed to close their eyes for 2 min and then start working on the PC (Task 1). After working for 10 min, each participant left the room and entered the resting room, where they rested for 5 min (Rest) before returning to the working room. The participants were again instructed to close their eyes for 2 min and work on the PC for 10 min (Task 2).

The experimental conditions are listed in *Table 1*. Except for Condition I, either or both the visual stimulation by the wooden room and/or the scent of Hinoki cypress were introduced in the experiment.

Table 1: *Experimental conditions*
(words in red indicate introduction of wooden stimulation)

Conditions	Working room stimulation		Rest room stimulation	
	visual	olfactory	visual	olfactory
Ⅰ: N-N	Concrete	None	Concrete	None
Ⅱ:W-N_Work	Wooden	None	Concrete	None
Ⅲ: N-H_Work	Concrete	Hinoki	Concrete	None
Ⅳ: W-H_Work	Wooden	Hinoki	Concrete	None
Ⅴ:W-N_Rest	Concrete	None	Wooden	None
Ⅵ:N-H_Rest	Concrete	None	Concrete	Hinoki
Ⅶ: W-H_Rest	Concrete	None	Wooden	Hinoki

2.3 VISUAL STIMULATION

Two rooms of 10 square meters each were set up and furnished with wooden (walnut) paneling and concrete-style wallpapers on the ceilings and walls, as illustrated in *Figure 2*. To enhance the illusion of open space behind the walls, photos of the company's training center were affixed to the front and right sides of the rooms. The training center was designed with a wood-like texture, and in the room with concrete wallpaper, a grayscale version of the same photo was used.

2.4 OLFACTORY STIMULATION

The scent of Hinoki cypress (*Chamaecyparis obtusa*) was introduced into either one or none of the rooms using an aroma diffuser (Tree of Life Co., LTD; *Figure 2*). For the wood condition, 1 ml of Hinoki essential oil was mixed with 10 ml of water, and water (without essential oil) was used in the control conditions. The concentration of the mixture was determined through a preliminary experiment conducted on 12 individuals in their 20s, separate from the main experiment. The participants performed 10 deep breaths in the room where the scent of Hinoki cypress was generated, then responded to a subsequent survey on the odor intensity. The concentration that fell between the average range of "weak odor" to "easily noticeable odor" was used. The composition of the odor was analyzed by collecting air at nose level and conducting gas chromatography. When introducing the scent of Hinoki cypress, we confirmed that the concentration of the main aromatic component, α-pinene, did not exceed the concentration described in previous papers as "slightly unpleasant".

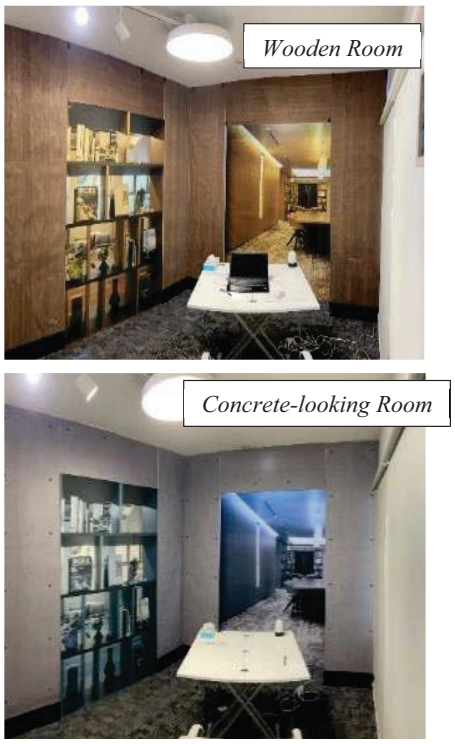

Figure 2: *Experiment rooms covered with sliced walnut veneer (wooden room) (top) and concrete-patterned wallpaper (concrete-looking room) (bottom)*

https://doi.org/10.52202/069179-0143

2.5 PC TASKS

The study required the participants to perform two PC tasks. In the first 5 minutes, the participants were asked to compare two slips on a PC and identify a character that was different, which they entered using a keyboard. For the latter 5 minutes, a Stroop test was administered. Participants are presented with color names written in a color and it evaluates the phenomenon where naming the color takes longer when the color and the written word do not match compared to when they do match. The Stroop test is originally designed to assess selective attention [5], but in this study, it is introduced as a stress task. In this experiment, characters written in red, blue, yellow, and green were displayed every second. There were 16 possible combinations of colors and characters. Participants were required to read the characters as they were displayed and respond by pressing the corresponding key on a keyboard to match the character's color.

2.6 MEASUREMENT

Three questionnaires for subjective evaluation were administered before and after the participants entered the rooms. Subjective ratings were given on a 7-point scale to describe the effects of visual or olfactory impressions. The visual impression was evaluated using six items, which were "like-dislike," "familiar-unfamiliar," "settling-unsettling," "luxurious-simple," "spacious-small," and "natural-artificial." The olfactory impression was evaluated using six items, which are "good-bad," "like-dislike," "familiar-unfamiliar," "settling-unsettling," "luxurious-simple," and "mild-pungent."

The Japanese version of the Profile of Mood States 2nd Edition Short Form (POMS2; Kaneko Shobo Co., Tokyo, Japan [6]) was administered to assess negative mood states. The POMS2 evaluates the state of mood and emotion using seven scales: “anger-hostility,” “confusion-bewilderment,” “depression-dejection,” “fatigue-inertia,” “tension-anxiety,” “vigor-activity,” and “friendliness”. There are five questions for each scale, and each question is evaluated on a scale of 0 to 4, representing the individual's mood. The Total Mood Disturbance (TMD) score, indicating a comprehensive negative mood, is calculated by the scores of all scales except "friendliness."

The Jikaku-sho Shirabe (Industrial Fatigue Research Committee of Japan [7]) was utilized to measure subjective fatigue. This tool provides a subjective evaluation of fatigue on five scales, i.e., drowsiness, unsteadiness, discomfort, sluggishness, and haziness. Each dimension comprises five questions, to which the participant answered on a five-point scale from 1 to 5. By observing changes in scores over time, the extent of the participants’ fatigue complaints can be assessed.

2.7 STATISTICAL ANALYSIS

We conducted statistical tests between the conditions to determine the differences in impression scores after Task 1, after rest, and after Task 2. To verify the effects of visual stimulation alone and the combination of visual and olfactory stimulation, statistical tests were performed between conditions I, II, and IV after the tasks and between conditions I, V, and VII after rest for the visual impression items. To determine the individual effects of olfactory stimulation and the combined effects of visual and olfactory stimulation, statistical tests were conducted between conditions I, III, and IV after Task 1 and between conditions I, VI, and VII after rest for the olfactory impression items.

Statistical tests were performed between each condition regarding the changes in scores of the Jikaku-sho Shirabe and POMS2 before and after Task 1, before and after rest, and before and after Task 2. To compare the effects of individual and combined stimulation, the changes in scores before and after tasks were compared between conditions I, II, III, and IV, and those before and after rest were compared between conditions I, V, VI, and VII.

The differences between the conditions were tested using the Wilcoxon signed-rank sum test (Bonferroni correction) (SPSS 28.0.1.1, IBM). The significance in difference was set at 5%.

3 RESULTS AND DISCUSSION

3.1 IMPRESSION EVALUATION

The visual impression scores after the tasks and rest are shown in *Figure 3*. After Task 1, the impression scores of settling-unsettling were significantly higher in both conditions II (introduced only wooden panels) and IV (introduced both wooden panels and the scent of Hinoki cypress) than in condition I (nothing introduced). The scores of luxurious-simple were significantly higher in condition II (p<0.05) than in condition I. After rest, the scores of like-dislike significantly increased in condition VII (introduced both wooden panels and the scent of Hinoki cypress) compared to condition I (p<0.05). After Task 2, the scores for the impression of luxurious-modest significantly increased compared to condition I in both conditions II and IV (p<0.05).

The olfactory impression scores after tasks and rest are shown in *Figure 4*. After Task 1, the scores of like-dislike and luxurious-simple were significantly higher compared to condition I in both conditions III (introduced only the scent of Hinoki cypress) and IV, and the scores of good-bad were significantly higher compared to condition I in condition IV (p<0.05). After rest, the impression score of luxurious-simple was significantly higher compared to condition I in both conditions III and IV, and the scores of good-bad, like-dislike and familiar-unfamiliar were significantly higher compared to condition I in condition III (p<0.05). After Task 2, the scores of good-bad, like-dislike, settling-unsettling, and luxurious-simple were significantly higher in both conditions VI (introduced only the scent of Hinoki cypress) and VII than in condition I (p<0.05).

The results of this experiment showed that the visual impression after the tasks and after rest did not differ. On the other hand, the assessment of olfactory impression

showed that during tasks, most items tended to be higher when both stimulations were introduced compared to when only olfactory stimulation was introduced, whereas during rest, the condition in which only olfactory stimulation was introduced showed a significant improvement over the control condition.
The results of this study suggest that the introduction of both the scent of Hinoki cypress and wooden interior did not alter the visual impression but led to an improvement in the olfactory impression during work, while the olfactory impression may have weakened during rest. This implies that the combined stimulation of the wooden material and scent may have an impact on the perception of the space.

3.2 MOOD STATES

The changes in the mood state scores before and after the tasks and rest are shown in *Figure 5*. The changes in scores on the anger-hostility, confusion-bewilderment, fatigue-inertia, and TMD scales depicted in *Figures 3-5* showed significant differences between the conditions. The change in scores of anger-hostility was larger in condition I (nothing introduced) than in condition IV and VII (introduced both wooden panels and the scent of Hinoki cypress) during both Task 1 and rest, with a significant increase during Task 1 and a significant decrease during rest (p<0.05). The change in confusion-bewilderment scores was significantly smaller for condition II (introduced only wooden panels) compared to condition I during Task 1 (p<0.05), while during rest, condition VII showed a larger decrease than condition V (introduced only wooden panels) (p<0.05). During Task 2, condition IV as found to have a smaller increase compared to condition I (p<0.05). The change in scores of fatigue-inertia was significantly smaller for condition II compared to condition I during Task 2 (p<0.05). The change in TMD scores was significantly smaller for condition IV compared to condition I during Task 2 (p<0.05). No significant differences were observed in the changes in the depression-dejection, tension-anxiety, and vigor-activity scores between conditions.
In many evaluation scales of POMS2, introducing visual or olfactory stimulation, or both, has been observed to improve mood states during both work and rest. Additionally, the improvement in mood states was significantly higher only in the confusion-bewilderment scale when both visual and olfactory stimulation were introduced compared to when only visual stimulation was introduced. No significant differences were observed between the conditions of introducing only olfactory stimulation and introducing both stimulation in all scales. However, significant differences were observed between the conditions where both visual and olfactory stimulation

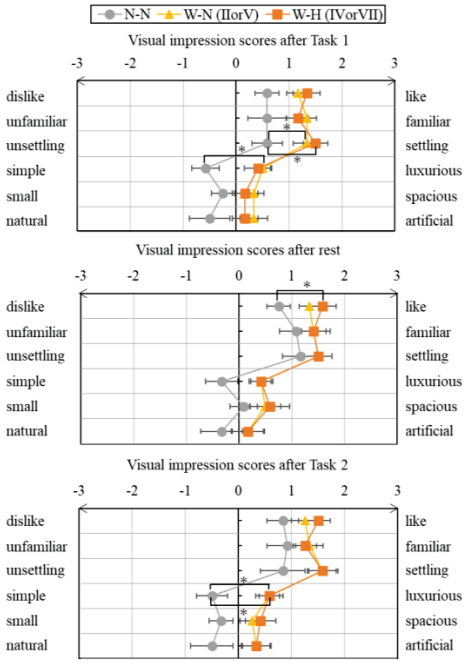

Figure 3: *Visual impression scores after tasks and rest with different visual conditions as mean ± S.E. (n=12).*
** p<0.05, Wilcoxon signed-rank sum test (Bonferroni correction)*

Figure 4: *Olfactory impression scores after tasks and rest with different olfactory conditions as mean ± S.E. (n=12).*
** p<0.05, Wilcoxon signed-rank sum test (Bonferroni correction)*

https://doi.org/10.52202/069179-0143

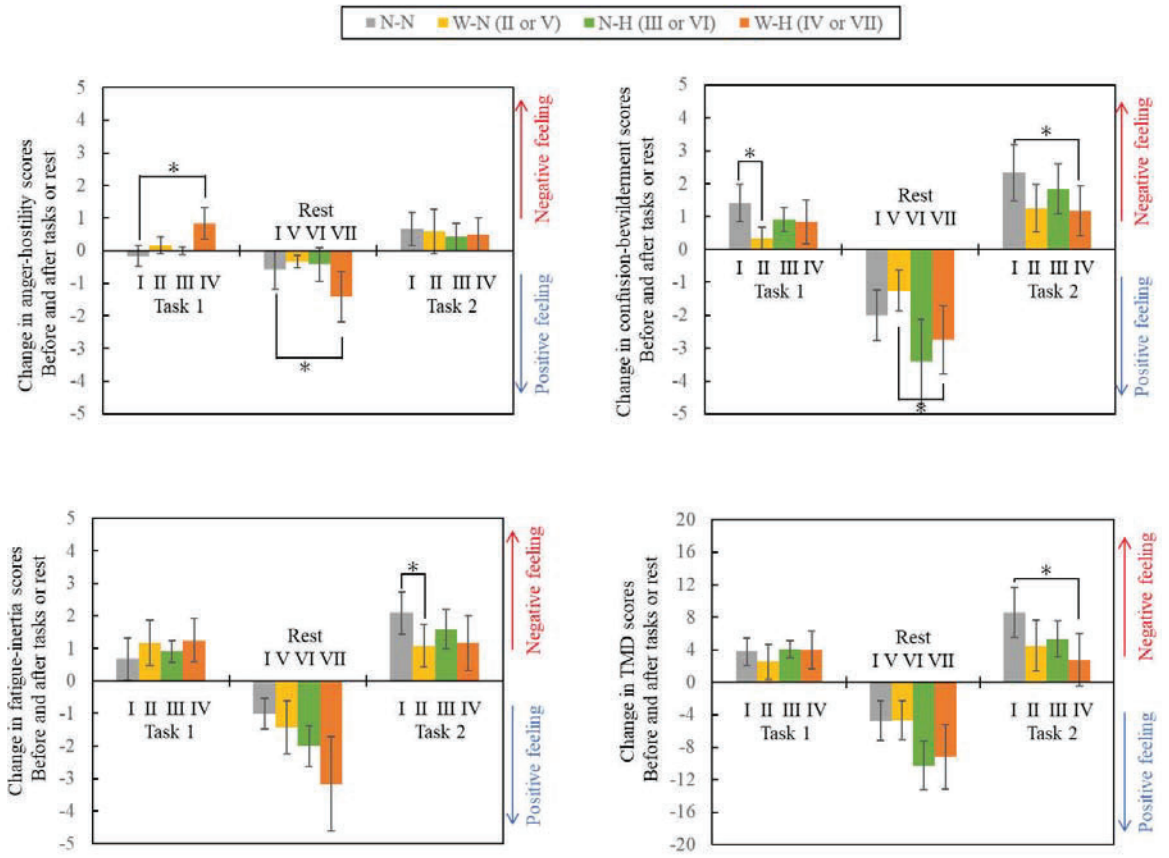

Figure 5: *Changes in mood state scores ("anger-hostility," "confusion-bewilderment," "fatigue-inertia," and TMD) before and after tasks and rest with different olfactory conditions as mean ± S.E. (n=12).*
** $p<0.05$, Wilcoxon signed-rank sum test (Bonferroni correction)*

were introduced and the control conditions on many scales, indicating the potential to enhance stress relief during work and rest by incorporating both visual and olfactory stimulation of wood in the office space.

3.3 SUBJECTIVE FATIGUE

The changes in the subjective fatigue scores (from the Jikaku-sho Shirabe) before and after tasks and rest are shown in *Figure 6.* The changes in drowsiness, discomfort, and haziness scores depicted in *Figures 3-5* showed significant differences between conditions. The change in drowsiness scores was found to be significantly larger for condition III (introduced only the scent of Hinoki cypress) compared to condition II (introduced only wooden panels) during Task 1 ($p<0.05$). The discomfort scores significantly decreased more in condition III than in condition I (introduced nothing) during rest ($p<0.05$). Condition VI (introduced both wooden panels and the scent of Hinoki cypress) showed a larger decrease than condition V (introduced only wooden panels) ($p<0.05$). The haziness scores showed significantly less change compared to condition I during Task 2 in conditions II and III. No significant differences were observed in the score changes of unsteadiness and sluggishness between the conditions.

In the Jikaku-sho Shirabe, the scale of discomfort showed a reduction in fatigue during rest in the condition where the scent of Hinoki cypress was introduced compared to when nothing was introduced. The scale of haziness indicated that fatigue from the task was relieved in the condition where visual or olfactory stimulation was introduced. On the other hand, during Task 1, the increase in drowsiness after Task 1 was greater in the condition where the scent of Hinoki cypress was introduced than when the wooden panels was introduced. While the results might seem conflicting when considering subjective fatigue as a whole, drowsiness can occur as a feeling state even during relaxation. Therefore, this result aligns with previous research [4] and demonstrates the relaxing effects of the scent of Hinoki cypress.

The combined effects of both olfactory and visual stimulation were not observed in this measurement. The subjective fatigue was affected by the individual stimulus,

and the potential for reducing various types of fatigue was particularly evident when the scent of Hinoki cypress was introduced.

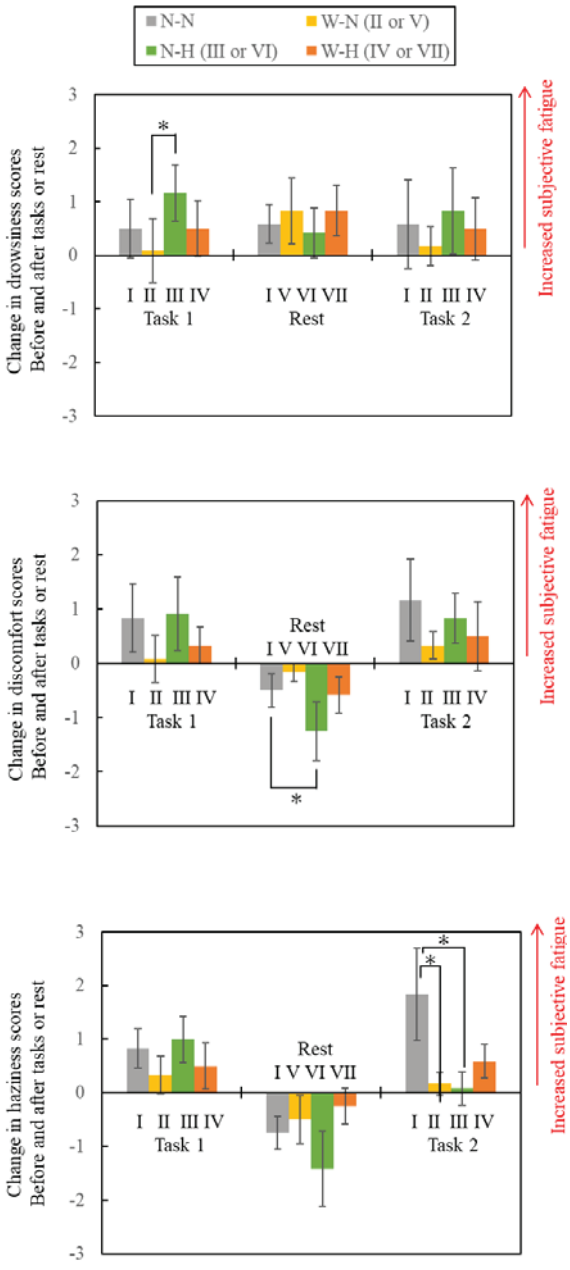

Figure 6: *Changes in subjective fatigue score (drowsiness, discomfort, and haziness) before and after tasks and rest with different olfactory conditions as mean ± S.E. (n=12).*
** p<0.05, Wilcoxon signed-rank sum test (Bonferroni correction)*

4 CONCLUSION

The aim of this study was to examine the combined effects of olfactory and visual stimulation derived from wood materials. We conducted a subjective experiment where participants performed tasks and rested in a space containing wood panels and the scent of Hinoki cypress. The results of the experiment suggest that when both the Hinoki scent and wooden panels were introduced, the visual impression did not change, but the olfactory impression may improve during work and weaken during rest. The results of the POMS2 also suggested that the combined introduction of visual and olfactory stimulation from wood into the space may further improve mood state during work and rest. The results of the Jikaku-sho Shirabe suggest that individual stimuli can impact subjective feelings of fatigue, and the introduction of Hinoki cypress scent shows potential in reducing various forms of fatigue. The results suggest that the combined visual and olfactory stimulation from wood may affect individuals in different ways, depending on the activities in which they are engaged.

REFERENCES

[1] Ministry of Health, Labour and Welfare. Overview of the Results of the Labor Safety and Health Survey (Actual Conditions Survey). Available: r03-46-50_kekka-gaiyo02.pdf (mhlw.go.jp)

[2] Burnard M. D. Kutnar A. Wood and human stress in the built indoor environment: a review. Wood Science and Technology. 49; 969–986. 2015

[3] Tsunetsugu Y. Miyazaki Y. Sato H. Physiological effects in humans induced by the visual stimulation of room interiors with different wood quantities. Journal of Wood Science, 53:11-16, 2007.

[4] Ikei H. Song C. Miyazaki Y. Physiological effect of olfactory stimulation by Hinoki cypress (*Chamaecyparis obtusa*) leaf oil. Journal of Physiological Anthropology, 34:44, 2015.

[5] Stroop J. R. Studies of interference in serial verbal reactions. Journal of Experimental Psychology 18: 643-661, 1935

[6] Heuchert J. McNair D. Yokoyama K. Profile of Mood States 2nd Edition (in Japanese). Kaneko Shobo, 2015.

[7] Sakai K. Revision Work of the "Self-Check Survey" by the Industrial Fatigue Research Society of the Japanese Society of Industrial Health. Science of Labor, 57; 295-298. 2002

https://doi.org/10.52202/069179-0143

World Conference on Timber Engineering Oslo 2023

WOOD INTERIORS IN ARCHITECTURE: AN EYE-TRACKING STUDY

Pasi Aalto[1], Martin Steinert[2]

ABSTRACT: In this architecture study, we examine the gaze patterns of participants (n=20) when presented with a selection of images featuring building materials (concrete, stone, brick, wood and painted wood) and interiors (church, lobby and work area with high, medium and low levels of wood use). We utilize eye-tracking to quantify the fixations, saccades, blinks, and pupil dilations within the participants gaze pattern. This gaze pattern is then compared to the participants perception of naturalness and pleasantness. We show that naturalness and pleasantness strongly positively correlate with each other, and that material choice plays a role in the participants perception of these values. Gaze patterns do not clearly correlate with naturalness nor pleasantness, although we report indications that pupil diameter, blink count and saccade amplitude should be investigated further in separate experiments.

KEYWORDS: Eye-tracking, Architecture, Wood, Materials, Cognition

1 INTRODUCTION

First discovered in the 1970's [1] by examining the views from hospital patients windows, a significant body of research has been developed to better quantify and understand the positive effects of nature on building users [2], [3]. More recently, the use of wood has become more prevalent in the Nordic building industry due to its cultural acceptance, low emissions, and increased availability. This has also spurred research interest into the health effects of wood use on the habitants of buildings [4]–[7] that seem to suggest that multiple positive effects are achievable through thoughtful use of building materials. At the same time, more research is needed to better understand and quantify the effects.

1.1 RESEARCH QUESTIONS

In this study, we examine the relationship between gaze patterns and participant perception of naturalness and pleasantness. We hypothesise that and strive to answer the following research questions:

RQ1: Is there a correlation between naturalness and pleasantness?
RQ2: Is there a correlation between wood use and perceived naturalness and pleasantness?
RQ3: Do different building materials have a different gaze response?
RQ4: Is there a correlation between a gaze response and the perception of naturalness and pleasantness?

2 THEORY

Quantifying the perception and impact of architecture has gained more research interest in the recent years [2]. Two central aspects of this development have been the validity and usability of different quantifying methods as well as connecting the research to an existing body of research in environmental well-being.

2.1 EYE-TRACKING

The use of eye-tracking (ET) is an effective method to determine the gaze pattern of a person, which mainly consists of rapid movements with intermittent stops. Fixations are instances where the gaze dwells on a specific area, such as a flower or an oncoming car. Fixations vary in length but are generally in the 80-300ms range and indicate where the participants cognitive system engages with the visual stimuli. The opposite, a saccade, is a rapid eye-movement between fixations where the participant is not consciously registering what the eyes are looking at [8]. In Video Oculography (VOG) – based eye-tracking [9], a video recording of the eyes, when calibrated, analysed and correlated with a synchronized video of the world view in front of the participant allows for a relatively easy analysis of gaze patterns at both individual level and in a group, even with idiosyncratic differences between the participants.

Several measurements are available from current ET devices. Reduced saccade amplitude can indicate during increased mental effort, inspection, or high-frequency visual information. Alternatively, saccadic velocity decreases with low vigilance. Pupil dilation increases with arousal and mental workload. Long fixation durations indicate low arousal and shorter fixations can indicate stress responses. For a more thorough discussion on measures, see Holmqvist et al., part III [8]. Additionally, more complex relations are being investigated, such as the correlation between participants preferences and their gaze patterns [10].

[1] Pasi Aalto, NTNU Norwegian University of Science and Technology, Norway, pasi.aalto@ntnu.no
[2] Martin Steinert, NTNU Norwegian University of Science and Technology, Norway, martin.steinert@ntnu.no

https://doi.org/10.52202/069179-0144

2.2 NATURE, WOOD USE AND HEALTH

Previous ET research into architectural material use is inconclusive, and it is difficult to examine the validity and generality of using ET to examine materials in architecture. The general correlation between pupil dilation and emotional reactions has been observed when looking at architectural interiors [11] and also linked to preference to stay [12]. When comparing natural environments to urban settings, [13] and in interiors [14], fewer but longer fixations were observed. Contrastingly, fixation time was found to be independent of vegetation when looking at indoor workplace design and the amount of vegetation in front of the participant [14]. Also material choice might be a factor as average fixation duration has been shown to differ between stone and mixed material facades, as well as experts and non-experts [15].

Wood materials exhibit positive effects similar to nature [4], are preferred by participants [7] and generally considered natural materials [16]. Eye-tracking studies of wood interiors has so far received little interest in research, although there are indicators that wood exhibits a similar gaze pattern as nature [17] and affect staying durations [12].

3 METHOD

This experiment is a within-subjects laboratory experiment using gaze pattern and survey answers as data.

3.1 STIMULI

The experiment used 2 sets of stimuli. For the 5 most common architectural materials in the Nordics (concrete, stone, brick, untreated and painted wood), 5 images of each were selected to cover the innate variation in the use of the material in a building context. This also provided an extra control to examine variations within material groups and to compare this to results between groups. Additionally, two images were baseline photographs, one of plants (i.e., purely nature stimuli) and another of a graphical plate with multiple overlays of texts (i.e., high visual density stimuli). The total amount of images in the first set of stimuli was 27. An example of material stimuli is seen in Figure 1.

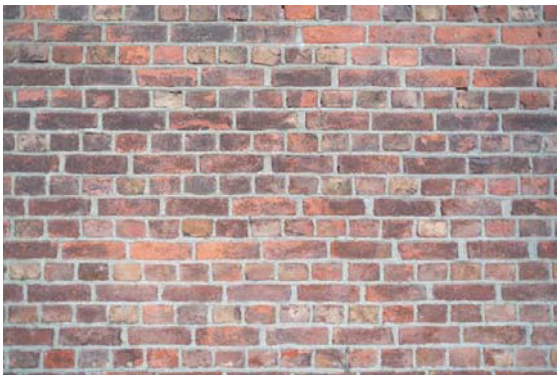

Figure 1: *Example image of a material stimuli, brick-3.*

Material images were taken with a Nikon D750 digital SLR with a 20mm f2,8 Nikon AF Nikkor lens. Both camera and lens were optically clean. The images were taken from a distance of 1.2 - 1.4 meters with suitable exposure settings to avoid clipped highlights or movement artefacts.

The second set of stimuli consists of 17 interior images showing 5 images each of 3 distinct spaces: church/sacral, lobby and an informal learning space in academia. Each group has 1 stimulus with high level of wood use, 2 with medium levels and 2 with low levels or no wood use at all. In addition, 2 baseline images were included, a nature image displaying a beautiful waterfall as well as a high visual density stimuli image of a city scape in Trondheim, Norway.

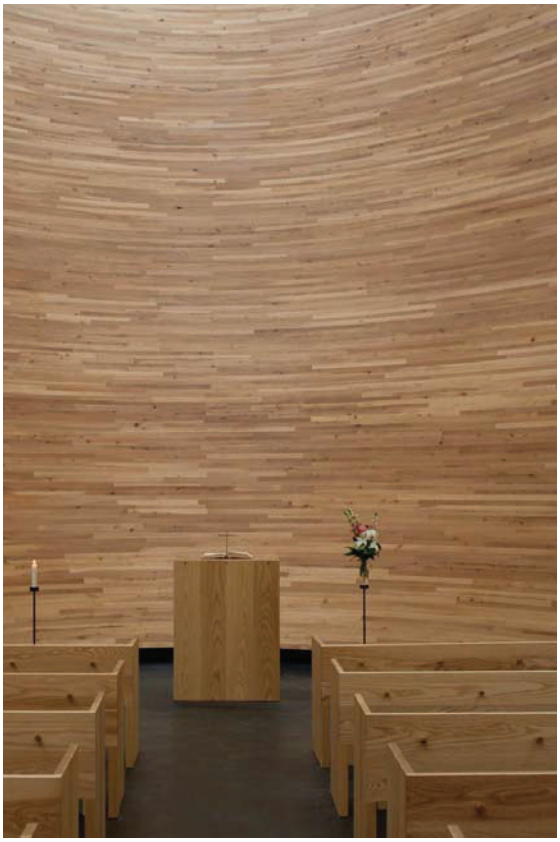

Figure 2: *Example image of a interior stimuli, church-2, exhibiting high level of wood use.*

The interior images were taken with either a Nikon D750 or D700 digital SLR with a 20mm f2,8 Nikon AF Nikkor or 17-35 f2,8 Nikon AF-S Nikkor lens. Both camera and lens were optically kept clean and suitable exposure settings were used to avoid clipped highlights or movement artefacts.

Each image was edited in Adobe Lightroom with a profile-based correction to chromatic aberration as well as

https://doi.org/10.52202/069179-0144

distortion and vignetting. The images were manually corrected for residual distortion, vertical and horizontal parallel lines as well as image rotation. The exposure, contrast, texture, and clarity were adjusted to ensure an even lightness and tonality across images, as well as a natural look. Finally, the images were cropped to the same format, 3:2 landscape for the material images and 3:2 portrait for the interior images.

3.2 PARTICIPANTS

This study included 20 healthy participants of which 8 were female. The participants had either perfect eyesight or their eyesight was corrected with contact lenses. The average age of the participants was 23,5 years (SD=4,49). 3 participants had an educational background focused on buildings. Four of the participants were left-handed.

3.3 PRESENTATION

The participants were welcomed to the experiment space where they receive a short formal introduction to the study and give consent. Eligibility to the study is confirmed. The participants are fitted with a Pupil Labs Core [18] mobile binocular eye-tracking glasses recording 120 Hz video with 192x192 pixels of each eye. In addition, a 1280 x 720 world cam at 30 Hz is recorded. The participants view stimuli shown on a 27" Dell ultrasharp U2719DC screen with 1920 x 1200 pixels at 60 Hz. Each participant underwent a calibration and verification procedure to ensure accuracy of the recorded data (0.5 - 1.5 degrees from eye-tracker, corresponding to approx. 7-25mm accuracy on screen with 80 cm viewing distance). All images and survey are displayed using PsychoPy stimuli presentation software [19] linked with Pupil Capture through dynamic link. For each ET capture, Apriltag36_11 QR codes were present in the corners of the screen to allow surface tracking of the screen as seen in Figure 1.

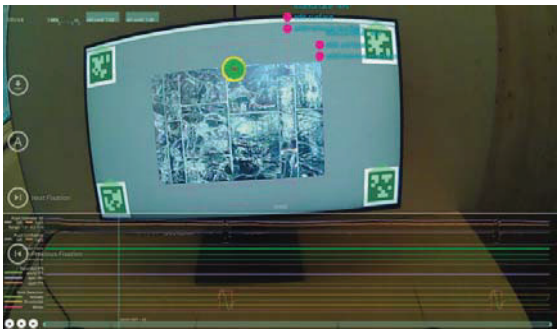

Figure 3: *Experiment setup from Pupil Player as seen by the participant world camera, showing Apriltag36_11 QR codes around stone-1 image. On screen is also pupil dilation, confidence, and blink data, while fixations are shown with a yellow circle around the gaze point when active.*

After setup, each participant is first presented with the 27 material images in randomized order. Each image is displayed for 10 seconds with a 2 second pause between images showing a re-focusing cross in the middle of the screen. The images were 1076 x 690 pixels, giving an on-screen size of 21 x 14 cm in landscape format. This approach leaves ample grey background area on screen to minimize luminosity changes from the stimuli, as this might affect pupil dilation. The stimuli size corresponds to approximately 10 x 15 degrees eye movement when viewed from 80 cm away.

In the second part, the participant reviews the re-randomized images one at a time and ranks them with 2 sliders, unnatural (0) – natural (10) and unpleasant (0) – pleasant (10), verified by an OK button.

In the third part, the participant similarly first views the interior images, followed by the fourth and final part where they assess the interiors with the same sliders. Before each part, the participant is given clear instructions on screen as to the next part of the experiment.

3.4 RESPONSE DATA ANALYSIS

Participants evaluation of the naturalness and pleasantness of each stimulus is recorded in PsychoPy as a value of 0-10. The sliders are by default valued as 5 (middle) and if the participant does not move the slider but clicks OK, this number is used in the analysis.

3.5 ET DATA EXTRACTION AND STRUCTURING

For each participant, 33 trials were captured, consisting of one video for each eye and one world view video per trial. Pupil Player was used to analyse each trial. The first analysis included fixation detection using 1,5-degree movement threshold and 100-500ms as duration, both on stimuli surface as well as during the entire trial. Secondly, gaze positions and pupil dilation were extracted. Finally, a blink detection analysis was performed to count the number and duration of blinks in each trial.

Exported data from Pupil Player and PsychoPy was structured into folders per participant and a custom Python script was developed to extract, structure, and output a joint CSV that included all trials for all participants. The data was structured by case, where each row represented a single stimulus, viewed by a single participant. For each case, the dataset included averages over the entire viewing duration of a given stimuli by the given participant. The structured data included average saccade amplitude and velocity, blink count and duration, average and total fixation duration, and count for both surfaces and in total, average pupil dilation for both eyes as well as participant responses and the order the stimulus was presented.

3.6 ET DATA ANALYSIS

SPSS (Version 29) was used for the statistical analysis. To explore the relationship between variables, partial correlation was used while controlling for the presentation order of the stimuli. To assess outliers and anomalies,

SPSS' Identify unusual cases-function was used and the identified data checked to ensure correct representation.

4 RESULTS

The data quality of the experiment was assessed to be good. All participants responded to the survey. During material and interior trials, 93% and 90% of fixations were within the presented stimuli boundaries, respectively. This indicates that the participants were actively engaging in the task.

4.1 CORRELATION BETWEEN NATURALNESS AND PLEASANTNESS

To explore the relationship between naturalness and pleasantness responses from the participants, two-tailed partial correlation was used while controlling for the presentation order of the stimuli. Statistical assumptions of normality and linearity were assessed.

When looking at material images (n=27), there is a strong, significant partial correlation between perceived naturalness and pleasantness when controlling for stimuli order, $r = .513$, $n = 540$, $p < .001$, where high levels of naturalness are associated with high levels for perceived pleasantness.

This partial correlation also held true when looking at interior images with an equally strong correlation, $r = .547$, $n = 340$, $p < .001$, indicating that naturalness and pleasantness are strongly positively related.

4.2 WOOD USE, NATURALNESS AND PLEASANTESS

A one-way ANOVA was conducted to examine the effect of material use on naturalness and pleasantness. During the first trial presenting only groups of materials, a statistically significant result was found for both naturalness, $F (6, 533) = 32.758$, $p < .001$, and pleasantness, $F (6, 533) = 15.574$, $p < .001$. A post-hoc Tukey test indicated distinct, homogenous subsets in the groupwise comparison for both naturalness and pleasantness as presented in Tables 1 and 2. However, when investigating the responses for each stimuli using a Tukey test, the results show that images within each group can be assessed very differently, although similarities exist within groups as well. To exemplify, concrete scored poorly in groupwise naturalness and pleasantness while the individual images of concrete also were among the bottom 6 in naturalness and bottom 7 in pleasantness, together with the graphic stimuli. Contrastingly, the wood-5 stimuli, showing OSB is ranked 10th in unnaturalness and 4th in unpleasantness, while wood-4, showing a worn, slightly damp, pressure treated wood cladding, was ranked second only to nature in pleasantness and 4th most natural stimuli.

Table 1: *Homogenous groups based on groupwise Tukey analysis on means of naturalness scores from 0 (unnatural) to 10 (natural).*

Material Group	N	1	2	3	4	5
Graphic	20	1.9				
Concrete	100		3.9			
Brick	100		5.0	5.0		
Wood Paint	100			5.5	5.5	
Wood	100			5.8	5.8	
Stone	100				6.4	
Nature	20					9.6

Table 2: *Homogenous groups based on groupwise Tukey analysis on means of pleasantness scores from 0 (unpleasant) to 10 (pleasant).*

Material Group	N	1	2	3	5
Graphic	20	3.2			
Concrete	100	4.1	4.1		
Wood	100		5.2	5.2	
Brick	100			5.4	
Wood Paint	100			5.6	
Stone	100			5.7	
Nature	20				9.6

An ANOVA looking at the wood-use in interiors revealed similar results. First, groupwise analysis between high, medium, and low wood use, as well as a nature image and an image of Trondheim city was conducted. Naturalness, $F (4, 335) = 15.691$, $p < .001$, and pleasantness, $F (4, 335) = 9.148$, $p < .001$, both showed significant differences between the groups. A post-hoc Tukey test showed that in both cases, the nature image was distinctly both more natural and more pleasant than the other images. In pleasantness, all other images showed the same grouping regardless of wood use, while in naturalness, both low and medium wood use scored lower than high wood use. An alternative grouping of the space functions (lobby, church, and work area) was conducted to compare results. This yielded similar results for both naturalness, $F (4, 335) = 22.323$, $p < .001$, and pleasantness, $F (4, 335) = 18.956$, $p < .001$, with work areas and lobbies scoring less than churches and the city, while nature again was the most natural and pleasant choice. Finally, the images were analysed individually using a Tukey test to see whether the defined groups were coherent as evaluated by the participants. In both naturalness and pleasantness, spatial functions and wood-use groupings showed variation within the groups.

4.3 GAZE RESPONSES

The participants gaze responses were examined using a one-way ANOVA, followed by a post-hoc Tukey test if the significance was nearing $p < .05$.

https://doi.org/10.52202/069179-0144

4.3.1 Material trials

The ANOVA test showed no significant differences ($p < .05$) between gaze responses between the material groups, nor the individual stimulus, apart from the pupil dilation of eye 1 ($F\ 6, 553) = 2.232$, $p < .039$ for groupwise analysis, $F\ (26, 513) = 1.493$, $p < .057$ for individual stimulus analysis. When examining the Tukey post hoc test, the most significant difference was found to be between nature and concrete groups. Contrastingly, the dilation of eye 0 differed widely, $F\ (6, 553) = .659$, $p < .683$ for groupwise analysis, $F\ (26, 513) = .644$, $p < 0.914$ for individual stimulus analysis but this eye was considered more uncertain due to a single participant having a miscalculated 3d gaze parameter resulting in a very small pupil diameter.

4.3.2 Interior trials

Three ANOVA tests were conducted to examine gaze variables in interior images. The factors considered were the level of wood use (no significances $p < .05$), the spaces function (no significances $p < .05$) and individual images (no significances $p < .05$). However, a 2-tailed partial correlation test showed a weak negative correlation between blink count and naturalness, $r = -.153$, $n = 340$, $p = .005$, as well as a weak negative correlation between saccade amplitude and naturalness, $r = -.098$, $n = 340$, $p = .071$.

5 DISCUSSION

The aim of this study was to examine possible relationships between perceived naturalness, pleasantness, and gaze patterns in an explorative manner.

5.1 NATURALNESS, PLEASANTNESS AND WOOD

The participants show a strong positive correlation between perceived naturalness and pleasantness. The most consistently perceived stimulus, regardless of the stimulus set, are the 2 images of nature. When viewing material surfaces, a picture of chaotic graphic is clearly perceived as both unnatural and unpleasant, while an image of the city is more ambiguous as a baseline when compared to interiors.

A significant finding is the variation within material groups. While concrete surfaces were perceived as uniformly unnatural and unpleasant, wood surfaces varied to a larger degree. This internal variation should be expressly addressed in future experiments by selecting multiple stimuli within each material group. This affects both the validity and generality of the experiment as variation within groups can be better understood and the results be discussed in relation to practical everyday utilisation of building materials.

5.2 GAZE PATTERN, NATURALNESS AND PLEASANTNESS

The relationship between gaze patterns, naturalness and pleasantness is inconclusive. The study cannot confirm the relationship between saccade amplitude, blinks, pupil dilation and the survey responses, nor can we outright reject them. More advanced analysis might be needed to discover relationships between the variables. We have however identified some patterns that could help design better experiments in the future. Firstly, the viewing behaviour between purely material stimuli and interiors varies. Pupil dilation was found to be significant in viewing materials but not to the degree that it could differentiate multiple material groups. For interiors, blinks seem significant, as well as saccade amplitude. Secondly, variations within material groups needs to be accounted for. Thirdly, comparisons across studies will be essential to build systematic knowledge over time. Reporting threshold values, dispersion factors and specific analyses performed will speed development.

5.3 LIMITATIONS

Our approach has several limitations. Firstly, it was designed to explore potential gaze patterns rather than targeting a single measurement. The experimental setup for some of these measurements are contrary. To exhibit large saccade movements when searching, a bigger stimulus should be used. At the same time, pupil dilation will be affected as the size of the stimuli on screen increases to the grey background.

While a balance between trial length and the number of stimuli was necessary in this study, increasing the amount of images in fewer material categories would increase generality and validity of the results.

Finally, increasing the number of participants will provide a sounder base for statistical analysis that might uncover more nuanced results.

6 CONCLUSIONS

In this study, we performed a controlled within-subjects ($n=20$) laboratory experiment using gaze pattern and survey answers as data. We used 2 sets of stimuli, consisting of materials ($n = 27$) and interiors ($n = 17$). Our results show a strong positive correlation between naturalness and pleasantness when viewing images of both materials and interiors. We also demonstrated a that material groups score differently on naturalness and pleasantness, although variation within material groups exists.

We cannot confirm differences in gaze patterns between different building materials, nor a correlation between gaze response and naturalness or pleasantness. However, indications of pupil dilation, blink counts and saccade amplitudes being affected by materials were found.

7 ADDENDUM

7.1 AVAILABILITY OF MATERIALS

We support the replication and verification of experiments. The used images, data, PsychoPy files and Python scripts, as well detailed analysis files are available upon request.

7.2 CONFLICT OF INTEREST AND FUNDING

The authors declare no conflict of interest. This study was in its entirety funded by the Norwegian University of Science and Technology, NTNU.

REFERENCES

[1] R. S. Ulrich, "Visual landscapes and psychological well-being," *Landsc. Res.*, vol. 4, no. 1, pp. 17–23, Mar. 1979, doi: 10.1080/01426397908705892.

[2] W. Zhong, T. Schröder, and J. Bekkering, "Biophilic design in architecture and its contributions to health, well-being, and sustainability: A critical review," *Front. Archit. Res.*, vol. 11, no. 1, pp. 114–141, Feb. 2022, doi: 10.1016/j.foar.2021.07.006.

[3] G. N. Bratman, J. P. Hamilton, and G. C. Daily, "The impacts of nature experience on human cognitive function and mental health: Nature experience, cognitive function, and mental health," *Ann. N. Y. Acad. Sci.*, vol. 1249, no. 1, pp. 118–136, Feb. 2012, doi: 10.1111/j.1749-6632.2011.06400.x.

[4] T. Alapieti, R. Mikkola, P. Pasanen, and H. Salonen, "The influence of wooden interior materials on indoor environment: a review," *Eur. J. Wood Wood Prod.*, vol. 78, no. 4, pp. 617–634, Jul. 2020, doi: 10.1007/s00107-020-01532-x.

[5] M. D. Burnard and A. Kutnar, "Wood and human stress in the built indoor environment: a review," *Wood Sci. Technol.*, vol. 49, no. 5, pp. 969–986, Sep. 2015, doi: 10.1007/s00226-015-0747-3.

[6] M. D. Burnard and A. Kutnar, "Human stress responses in office-like environments with wood furniture," *Build. Res. Inf.*, vol. 48, no. 3, pp. 316–330, Apr. 2020, doi: 10.1080/09613218.2019.1660609.

[7] A. Q. Nyrud, T. Bringslimark, and K. Bysheim, "Benefits from wood interior in a hospital room: a preference study," *Archit. Sci. Rev.*, vol. 57, no. 2, pp. 125–131, Apr. 2014, doi: 10.1080/00038628.2013.816933.

[8] K. Holmqvist, M. Nyström, R. Andersson, R. Dewhurst, H. Jarodzka, and J. Van de Weijer, *Eye tracking: a comprehensive guide to methods and measures*. Oxford ; New York: Oxford University Press, 2011.

[9] H. Singh and J. Singh, "Human eye tracking and related issues: A review," *Int. J. Sci. Res. Publ.*, vol. 2, no. 9, pp. 1–9, 2012.

[10] S. Shimojo, C. Simion, E. Shimojo, and C. Scheier, "Gaze bias both reflects and influences preference," *Nat. Neurosci.*, vol. 6, no. 12, pp. 1317–1322, Dec. 2003, doi: 10.1038/nn1150.

[11] W. Tuszyńska-Bogucka *et al.*, "The effects of interior design on wellness - Eye tracking analysis in determining emotional experience of architectural space. A survey on a group of volunteers from the Lublin Region, Eastern Poland," *Wwwaaempl Ann. Agric. Environ. Med.*, vol. 27, no. 1, Art. no. 1, 2020, doi: 10.26444/aaem/106233.

[12] J. Cho and J. Suh, "Spatial Color Efficacy in Perceived Luxury and Preference to Stay: An Eye-Tracking Study of Retail Interior Environment," *Front. Psychol.*, Art. no. Query date: 2021-01-07 06:34:32, 2020, [Online]. Available: https://www.ncbi.nlm.nih.gov/pmc/articles/PMC7136482/

[13] M. Franěk, J. Petružálek, and D. Šefara, "Eye movements in viewing urban images and natural images in diverse vegetation periods," *Urban For. Urban Green.*, vol. 46, p. 126477, 2019, doi: 10.1016/j.ufug.2019.126477.

[14] Q. Lei, C. Yuan, and S. S. Y. Lau, "A quantitative study for indoor workplace biophilic design to improve health and productivity performance," *J. Clean. Prod.*, vol. 324, p. 129168, Nov. 2021, doi: 10.1016/j.jclepro.2021.129168.

[15] F. Jam, H. R. Azemati, A. Ghanbaran, J. Esmaily, and R. Ebrahimpour, "The role of expertise in visual exploration and aesthetic judgment of residential building façades: An eye-tracking study.," *Psychol. Aesthet. Creat. Arts*, vol. Advance online publication, no. Query date: 2022-01-03 10:37:28, Feb. 2021, doi: http://dx.doi.org/10.1037/aca0000377.

[16] K. Strobel, A. Q. Nyrud, and K. Bysheim, "Interior wood use: linking user perceptions to physical properties," *Scand. J. For. Res.*, vol. 32, no. 8, pp. 798–806, Nov. 2017, doi: 10.1080/02827581.2017.1287299.

[17] S. Song, Q. Wan, and G. Wang, "Eye movement evaluation of different wood interior decoration space," *Wood Res.*, vol. 61, no. 5, Art. no. Query date: 2021-01-07 06:34:32, 2016, [Online]. Available: http://www.woodresearch.sk/wr/201605/15.pdf

[18] M. Kassner, W. Patera, and A. Bulling, "Pupil: an open source platform for pervasive eye tracking and mobile gaze-based interaction," in *Proceedings of the 2014 ACM International Joint Conference on Pervasive and Ubiquitous Computing: Adjunct Publication*, Seattle Washington, Sep. 2014, pp. 1151–1160. doi: 10.1145/2638728.2641695.

[19] J. Peirce *et al.*, "PsychoPy2: Experiments in behavior made easy," *Behav. Res. Methods*, vol. 51, no. 1, pp. 195–203, Feb. 2019, doi: 10.3758/s13428-018-01193-y.

https://doi.org/10.52202/069179-0144

World Conference on Timber Engineering Oslo 2023

CROSS-LAMINATED WOOD PANELS IN A PATIENT ROOM AND STUDIES OF INTERIOR ENVIRONMENT

Bror Sundkvist [1], Olena Myronycheva [1], Sarka Langer[2], Ingrid Liljelind[3], , Bo Glas[3], Tomas Nord[4], Björn Nordin[5]

ABSTRACT: Studies on the effect from biobased materials and products on humans have indicated positive effects. This has earlier been shown in studies for e.g. hospitals, where indications of lower stress and pain in patients with wood as part of interior solutions.

This paper describes the first step of a larger study that investigates the interior environment and the response of patients. The study presented here measured RH, temperature, emissions of volatile organic compounds (VOC) and microbial activities in two rooms at a hospital in Skellefteå, Orthopaedic ward. One room had a cross-laminated wood panel covering 42% of walls, window reveal and doors, and the other a control room with standard coverings.

Results indicated only a small difference between the rooms in terms of temperature and RH. VOC emissions varied in both rooms but all concentrations were lower or much lower than threshold values for interior air quality standard limits. Biological contamination of the surfaces and from air sampling was also performed.

Conclusions of this experimental study shows that from a regulatory perspective it is possible and safe to use wood as interior product.

KEYWORDS: wood, hospital environment, volatile organic compounds, ozone, microbial populations

1 INTRODUCTION

Studies on the effect of biobased materials and products on humans have indicated positive effects. What properties of wood as a material give these positive results? Do they come from what [1] showed as being natural (less strong medication to patients with a forest view compared with a "built" view), or what [2] measured as indications of lower stress and pain in patients with wood as part of interior solutions? Or is it from the anisotropic and hygroscopic properties affecting the interior air quality [3]. Hospital care is currently often performed in very sterile indoor environments with smooth painted walls and no components with natural materials. Applying a biophilic approach in places of recovery and recuperation has been considered as a means of improving recovery and reducing durations of stay. This was illustrated recently in a paper [4] that considered the contrasting effects of Sick Building Syndrome (SBS) and Building Related Illnesses (BRI) and a high Indoor Environmental Quality (IEQ). The use of wooden materials has been related to positive effects in terms of aesthetics, smell, air humidity and well-being [5].
The aim of this study is to investigate indoor air quality in two patient rooms in Skellefteå Hospital. One room (Room 4) is an ordinary patient room with painted concrete walls, while wooden wall panels have been installed in the other room (Room 5).

2 MATERIALS AND METHODS

2.1 SUB-CHAPTER TITLE

The measurements of indoor climate parameters temperature, relative humidity (RH) and concentration of carbon dioxide (CO_2) as well as concentrations of air pollutants nitrogen dioxide (NO_2), ozone (O_3), volatile organic compounds (VOCs) and aldehydes have been performed in the two rooms during one year. NO_2 and ozone were also measured in the outdoor air, and outdoor temperature and relative humidity were retrieved from SMHI:s measurement station at Skellefteå airport. Temperature, relative humidity and concentration of CO_2

[1] Bror Sundqvist, Olena Myronycheva, LTU Lulea University of Technology, Sweden, bror.sundqvist@ltu.se, olena.myronycheva@ltu.se
[2] Sarka Langer, IVL Swedish Environmental Research Institute, Sweden, sarka.langer@ivl.se
[3] Ingrid Liljelind, Bo Glas, Umeå University, Sweden, ingrid.liljelind@umu.se bo.glas@umu.se
[4] Tomas Nord, Research Institutes of Sweden (RISE), Sweden, tomas.nord@ri.se
[5] Björn Nordin, Swedish Wood, Sweden, bjorn.nordin@svenskttra.se

https://doi.org/10.52202/069179-0145

were measured with Wöhler CDL 210 CO_2-logger with a time resolution of 2 minutes. The chemical compounds were measured by passive/ diffusive samplers.

For measurements of NO_2 and ozone concentrations, IVL passive/ diffusive samplers were used [6]. These compounds were analysed by wet chemical techniques using a spectrophotometric method (NO_2) and ion chromatography (O_3). The analytical procedures are accredited by the Swedish accreditation agency SWEDAC.

Volatile organic compounds were passively sampled on Tenax TA (Perkin-Elmer) adsorbent tubes and analysed in compliance with the standard ISO 16017-2 [7]. The Tenax tubes were thermally desorbed (Markes International, Unity 1 and Ultra) and analysed by gas chromatography/ mass spectrometry (GC/MS) in electron impact ionization mode. The sum of individual VOCs in a sample (TVOC, Total Volatile Organic Compounds) was quantified in toluene equivalent, *i.e.* using the uptake rate and the response factor of toluene.

Formaldehyde was measured using passive samplers – DSD-DNPH Aldehyde Diffusive sampling Device (Supelco, Bellefonte,PA). The sampling period and the analytical technique (solvent extraction and high-performance liquid chromatography) followed the ISO 16000-4 standard [8].

The estimation of the water amount in dry air was done by using Mollier-Diagram [9].

Enumeration of the moulds in indoor and outdoor air was done by SS-ISO 16000-17:2008 [10]. The data represents the number of colony-forming units (CFU) of fungi or bacteria per sample. The malt-extract agar, potato-dextrose agar, dichloran 18% glycerol agar (DG18 agar) and nutrient broth agar were used as culture media. The plates were checked regularly for up to 7 days. The temperatures 25°C and 37° were used for the incubation. Calculations of the results were based on the colony count of the agar where the best growth occurs. The results are presented in colony-forming units per cubic meter.
The sampling from the walls and other surfaces was done according to ISO 16000-21:2013(E) [11] by sterile cotton swabs cultured on malt extract agar nutrient media. Incubation was done at 25°C.
The Adenosine Tri-Phosphate ATP bioluminescence was used to rapidly evaluate material surface cleanness [12]. The method is based on the correlation of biological residuals with the light generated during the reaction with luciferin/luciferase enzyme and measured by a luminometer 3M Clean-Trace™ Luminometer, St. Paul Minnesota, USA. The general acceptance for the cleanness is below 20 RLUs or Relative Light Units.
The sampling locations for swabbing and ATP measurement were:
- left and right dry walls of the left window
- left and right dry walls of the right window
- left and right walls of the room ca. 1.5 m from the floor
- left and right sides of the ceiling about 1 m from the ventilation channel
- nearby the ventilation channel
- doors of the patient lockers

The sampling periods are summarized in Table 1.

Table 1: *Sampling periods*

Week	Month, year	Start	Stop
1	October 2021	2021-10-04	2021-10-12
10	December 2021	2021-12-06	2021-12-13
19	February 2022	2022-02-07	2022-02-14
27	April 2022	2022-04-04	2022-04-11
35	May 2022	2022-05-31	2022-06-07
44	August 2022	2022-08-01	2022-08-08
53	October 2022	2022-10-02	2022-10-10

3 RESULTS AND DISCUSSION

3.1 INDOOR CLIMATE PARAMETERS

The values of temperature (Figure 1) were within the range of 20–24 ◦C defined by the EN 16798 standard [13] and by the Swedish regulations [14,15] during the whole period of measurements for one year. The values of relative humidity (Figure 2) were within the range defined by the EN 16798–1:2019 standard (25–60% RH) only during the non-heating season. During the heating season, the RH was <20%.

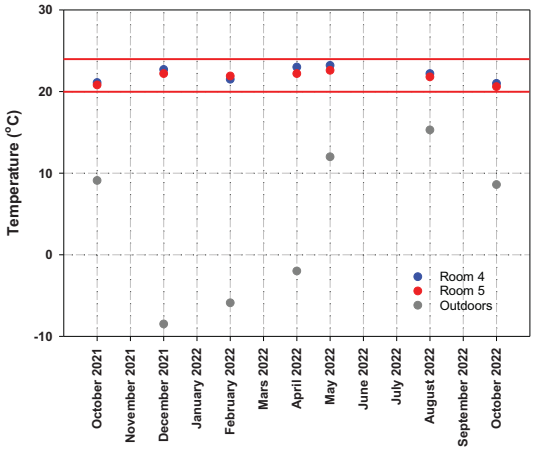

Figure 1*. The temperature in the studied rooms and in outdoor air. The full red lines indicate the range of comfortable indoor air temperature stated in standards.*

https://doi.org/10.52202/069179-0145

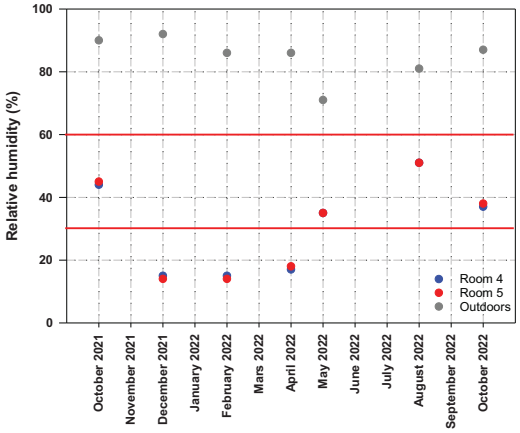

Figure 2. *Relative humidity in the studied rooms and in outdoor air. The red line indicates the range of comfortable indoor air relative humidity stated in standard.*

3.2 INDOOR AIR POLLUTANTS

The TVOC concentrations (Figure 3) were below the recommended long-term guideline value of 300 µg/m^3 in both rooms [16]. The TVOC concentrations did not differed significantly between the two rooms.

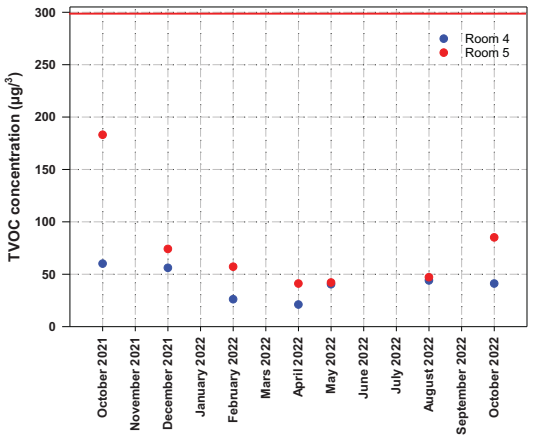

Figure 3. *Concentration of TVOC in the studied rooms. The red line indicates the recommended guideline value for TVOC of 300 µg/m^3.*

3.3 OUTDOOR/INDOOR WATER CONTENT IN DRY AIR

According to Swedish Public Health Agency's general advice on moisture and microorganisms "that the average value of the humidity should not exceeds 7 g water/kg dry air for a longer period during the heating season, which corresponds to approx. 45% relative humidity at 21° C" in a public building [17]. Such conditions might be favorable for microbial growth [19].

The evaluation of the climate was done to find the risk dates. The graph is presented in Figure 4.

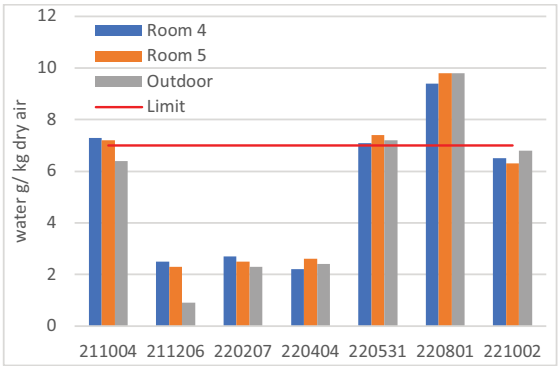

Figure 4. *The amount of water in g per 1 kg of dry air. The red line is a limit and parameters above are favourable for the microbial growth.*

3.4 INDOOR AIR MICROORGANISMS

The threshold limit values for biological contaminants such as microorganisms are difficult to define, and particularly for mould fungi the World Health Organisation (WHO) did not provide such values in their Indoor air quality guideline [18]. The threshold amount > 1000 CFU/m^3 in the whole mould is proposed as considered for dwellings at risk for allergic patients [19]. The total amount of microorganisms in the air of the sampling areas grown at 25°C and 37°C is presented in Figure 5 below.

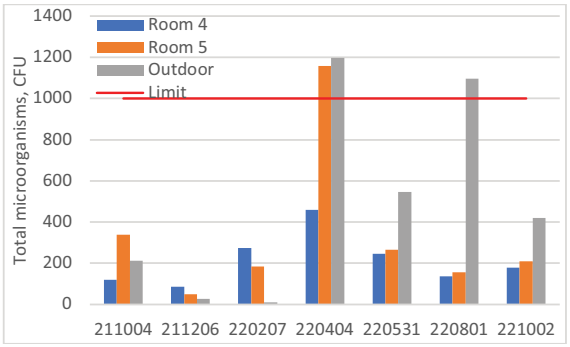

Figure 5. *Total amount of microorganisms CFU/m^3 grown at the temperature 25°C and 37°C. The red line shows the threshold value.*

The dominating effect of indoor/outdoor fungi is proposed for the determination of dominating effect of the microbial concentrations for the data interpretation [20]. The indoor: outdoor (I/O) concentration ratios related to the presence of indoor sources of microorganisms. I/O ratios are typically less than 1.0. However, if there is a strong microbial source indoors exists the ratio can exceed 1.0. Table 2 represents the ration of total microorganisms in the rooms for the sampling time.

https://doi.org/10.52202/069179-0145

Table 2. *The I/O concentration ratio for sampled time and locations in air samples of the microorganisms*

Day	I/O	
	Room 4	Room 5
211004	0.6	1.6
211206	3.3	1.9
220207	27.3	18.3
220404	0.4	0.9
220531	0.5	0.5
220801	0.1	0.1
221002	0.4	0.5

3.5 MICROBIOLOGICAL ASSESSMENT OF MATERIAL SURFACE

The ATP bioluminescence is applied essentially for hygiene status of the surfaces. It is an effective system to verify cleaning of surfaces from biological residues and microorganisms. The value below 20 RLU is considered moderate clean, when below 5 it is efficiently clean. Since the hospital environment is quite full of biological contaminations the value showed that surfaces are unclean. The distribution of the contaminated areas in the room showed in Figure 6.

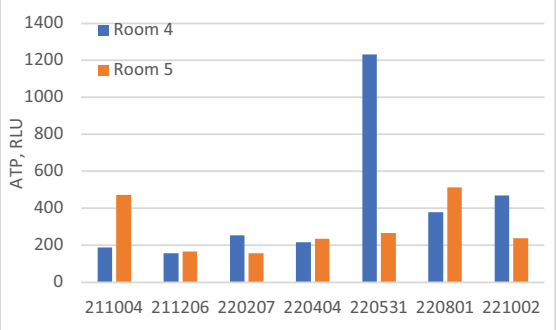

Figure 6. *The average value of ATP per room in RLU.*

The total amounts of the colony-forming units for fungal and bacterial microbial species are presented in Figure 7 and the number of fungi was much less than the amount of bacterial species on material surfaces.

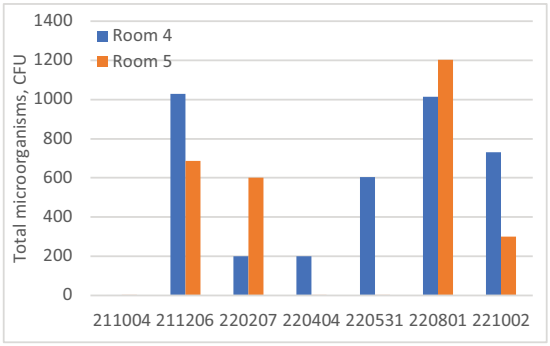

Figure 7. *Total amount of microorganisms CFU isolated from the material surface.*

4 CONCLUSIONS

The temperature was within the recommended comfort limits. The relative humidity was also within the recommended comfort limits with exception for the heating season (low RH) when the outdoor temperature was low.

The concentrations of all the TVOCs were low and below recommended guideline values and quite similar in both rooms.

The microbial contamination was low regarding generally suggested limits but influenced by indoor microbial source during heating season. The material surface was subjected to microbial contamination but mainly by bacterial isolates in both rooms.

From both the indoor climate and microbiological measurements, the values are within or well below limits for what standard regulations require for an acceptable indoor climate. Moreover, there was no or little difference between the rooms, this shows that it's possible to include biophilic design also in hospital environments.

These findings are a part of an ongoing study, and more results will be published, that involves clinical trials on patients and a survey for the staff of their perception of the rooms investigated. For the whole study at the hospital, we hope to gain new results and findings that clarifies the relation between indoor environments and human well-being.

ACKNOWLEDGEMENT

The research for this article was funded by Swedish Wood and EU regional funds. We would like to thank the persons involved from Skellefteå Hospital for their effort, support, and patience during difficult pandemic situations.

REFERENCES

[1] Ulrich R (1984) View through a window may influence recovery from surgery. Science 224(4647):420–421

https://doi.org/10.52202/069179-0145

[2] Nyrud, A.Q., Bysheim, K., Bringslimark, T. Forthcoming. Do elements of nature have a healing effect? The impact of wooden materials and landscape pictures in patient rooms. Arkitektur N.

[3] Vahtikari K, Noponen T, Hughes M (2016). The effect of wood anatomy and coatings on the moisture buffering performance of wooden surfaces. In: Eberhardsteiner J, Winter W, Fadai A, Pöll M 2016, World Conference on Timber Engineering (WCTE 2016) August 22-25, 2016, Vienna, Austria

[4] Sadek, A.H., Nofal, E.M. Indoor Environmental Quality Effects of Indoor Environmental Quality on Occupant Satisfaction in Healing Environments. Building Simulation Cairo 2013 - Towards Sustainable & Green Life, Cairo.

[5] Vos, T., et al., (2020). Global burden of 369 diseases and injuries in 204 countries and territories, 1990–2019: a systematic analysis for the Global Burden of Disease Study 2019. The Lancet (British edition), 396(10258), 1204-1222.

[6] Ferm M, Rodhe H. 1997. Measurements of air concentrations of SO_2, NO_2 and NH_3 at rural and remote sites in Asia. Journal of Atmospheric Chemistry 27, 17-29.

[7] ISO 16017-2. Indoor, ambient and workplace air - sampling and analysis of volatile organic compounds by sorbent tube/thermal desorption/capillary gas chromatography - Part 2: diffusive sampling. Geneva: International Organization of Standardization; 2003.

[8] ISO 16000-4. Indoor air - part 4: determination of formaldehyde - diffusive sampling method. International Organization of Standardization, Geneva, 2004.

[9] Bernard. 2023. 'Mollier Diagram Calculator and Sketcher'. Mollier-Diagram.Com. 2023. https://www.mollier-diagram.com.

[10] SS-ISO 16000-17:2008. 2008. 'Indoor Air - Part 17: Detection and Enumeration of Moulds - Culture-Based Method. Geneva: International Organization of Standardization; 2008.

[11] SS-ISO 16000-21:2015. 2015. 'Indoor Air - Part 21: Detection and Enumeration of Moulds - Sampling from Materials. Geneva: International Organization of Standardization; 2015.

[12] Patel, P. D., ed. 1995. Rapid Analysis Techniques in Food Microbiology. Boston, MA: Springer US. https://doi.org/10.1007/978-1-4615-2662-9.

[13] SS-EN 16798-1. Energy Performance of Buildings – Ventilation for Buildings – Part 1: Indoor Environmental Input Parameters for Design and Assessment of Energy Performance of Buildings Addressing Indoor Air Quality, Thermal Environment, Lighting and Acoustics – Module M1-6, SIS, Swedish Standards Institute, Stockholm, Sweden, 2019.

[14] AFS 2020:1. Arbetsmiljöverket (the Swedish Work Environment Authority) 2020. Workplace design (in Swedish: Arbetsplatsens utformning), Stockholm, Sweden.

[15] FoHMFS 2014:17. Public Health Agency's general advice on indoor temperature (in Swedish: Allmänna råd om temperatur inomhus). Folkhälsomyndigheten, Public Health Agency of Sweden), Stockholm, Sweden, 2014.

[16] Fromme H, Debiak M, Sagunski H, Röhl C, Kraft M., Kolossa-Gehring M. (2019). The German approach to regulate indoor air contaminants, International Journal of Hygiene and Environmental Health 222, 347–354.

[17] FoHMFS 2014:14. 2020. 'Allmänna råd om fukt och mikroorganismer'. Folkhälsomyndigheten. http://www.folkhalsomyndigheten.se/publicerat-material/publikationsarkiv/f/fohmfs-201414/.

[18] Heseltine, E., Rosen, J. and World Health Organization, eds. 2009. WHO Guidelines for Indoor Air Quality: Dampness and Mould. Copenhagen: WHO.Institute of Medicine (U.S.), ed. 2004. Damp Indoor Spaces and Health. Washington, DC: National Academies Press.

[19] Reboux, Gabriel, Steffi Rocchi, Audrey Laboissière, Habiba Ammari, Martine Bochaton, Guillaume Gardin, Jean-Marc Rame, and Laurence Millon. 2019. 'Survey of 1012 Moldy Dwellings by Culture Fungal Analysis: Threshold Proposal for Asthmatic Patient Management'. Indoor Air 29 (1): 5–16.

[20] Shelton, Brian G., Kimberly H. Kirkland, W. Dana Flanders, and George K. Morris. 2002. 'Profiles of Airborne Fungi in Buildings and Outdoor Environments in the United States'. Applied and Environmental Microbiology 68 (4): 1743–53.

World Conference on Timber Engineering Oslo 2023

CIRCULAR WOOD CONSTRUCTION – EXPECTATIONS, EXPERIENCES AND ACCEPTANCE AMONG USERS, ARCHITECTS AND INDUSTRY REPRESENTATIVES

Kaja Heltorp[1], Ute Groba[2], Anders Q. Nyrud[3]

ABSTRACT: Circularity approaches aim at keeping resources "in loop" as long as possible, both resulting in a more efficient use of resources and in avoiding waste production. A prolonged and repeated use of wood-based construction materials enhances their function as carbon sinks and as replacements of more harmful materials. Aiming to systematize circularity measures within the building sector, this paper proposes four different fields of ambition as consecutive focus areas during the life cycle of wooden building materials. The first one of these ambitions, prolonging a building's life span, depends not only on the construction's robustness and maintenance or the layout's adaptability, but also on the building's overall "lovability" and acceptance. This renders the user perspective an important part of understanding building performance and architectural quality. Based on interviews and focus groups from 2016 and 2017, insights have been gained about the experiences, expectations, preferences and values tied to wooden materials both among users and architects and how these impact the acceptance and choice of materials. Substantiated by new data collected in 2022 with architects and wood industry representatives, this paper discusses the expectations, experiences and acceptance of re-used and recycled wooden materials among different stakeholders, and how these may affect all four circularity ambitions. Results suggest that language, together with professional background, experience and responsibility inform the acceptance of re-used and recycled wood both in a short-term and in a long-term perspective; they need to be taken into account when aiming for advancing circular wood construction. The user adds an important perspective on circular wood construction that is not covered by industry representatives.

KEYWORDS: Circularity, reclaimed wood, engineered wood, wood construction, user perspective, qualitative research

1 INTRODUCTION

A circular economy (CE) signifies the continuous use of objects and materials. CE has been gaining increasing attention within the building sector. Circularity approaches aim at keeping resources "in loop" as long as possible (ideally forever, as formulated in "cradle-to-cradle"), both resulting in a more efficient use of resources and in avoiding waste production [1]. A maximised life span is not only highly important for the use of finite resources, but also enhances the ecological benefits of renewable resources. In the case of wood-based construction materials, a prolonged and repeated use increases their function as carbon sinks and the replacement of more harmful materials. It is, however, unlikely that a construction from virgin or pre-used wood will last forever. In order to avoid the dead end of cascading use scenarios in a landfill, wood's circular life involves its combustion or composting at some stage. A number of treatments for aesthetic reasons or to make wood more durable result in turning wood into hazardous waste. In order to establish a circular value chain, it is important to keep all use stage scenarios in mind from the outset when designing wooden architecture, and to avoid harmful treatments.

Aiming to systematize circularity measures within the building sector, this paper proposes four different fields of ambition as consecutive focus areas during the life cycle of wooden building materials.

The first aim ("Plan A") is to prolong a building's life span, which depends on its construction's robustness and its maintenance, the layout's adaptability, and its overall "lovability" and acceptance [2]. When a building nevertheless needs to be taken down at some point, the second focus is on re-using the building's components in the least processed way possible ("Plan B"). The third goal is to recycle the materials contained in building components that are not possible to re-use any longer ("Plan C"). In the fourth and last stage, building materials are composted for soil amendment or combusted to obtain energy, both of which are needed in the production of resources that feed into a new cycle ("Plan D").

In general, in this context, the main focus has been on physical and mechanical properties of materials, and the same is true for wooden materials, both virgin and re-used. However, also the materials' non-physical characteristics determine their life span, as they are part of how users experience and value materials, and partake in informing the users' acceptance of both virgin and re-used materials. The user's acceptance also influences the treatment and detailing of wooden materials, which then inform the material's further potential for circular use.

[1] Kaja Heltorp, Norwegian University of Life Sciences (NMBU), Norway
[2] Ute Groba, The Oslo School of Architecture and Design (AHO), Norway, ute.christina.groba@aho.no
[3] Anders Qvale Nyrud, Norwegian University of Life Sciences (NMBU), Norway, anders.qvale.nyrud@nmbu.no

https://doi.org/10.52202/069179-0146

Circular wood construction can therefore not only rely on the physical and mechanical performance of materials, but must include experience and value based concepts. While the user perspective tends to be underrepresented in conventional design processes, it is however gaining recognition as important part of understanding building performance and architectural quality [3].

The questions this paper addresses include how different stakeholders and decision makers understand, perceive and value wooden materials, and especially their reuse and recycling.

2 METHODS

Qualitative approaches, such as semi-structured interviews and focus groups, have been used both in the precursory studies on wooden building materials that this paper builds on, and in a follow-up study that addresses re-used wooden materials.

2.1 Semi-structured qualitative interviews with architects and inhabitants of urban timber buildings conducted in 2017

27 inhabitants of urban residential timber projects by recognized contemporary timber architects have been interviewed as part of a doctoral research project conducted at The Oslo School of Architecture and Design [4].

The interviewees were chosen on the background of their homes that complied with a number of common denominators, such as timber as the main construction material; housing on an urban scale as a functional typology; and Austria, Germany and Norway as comparable climatic and cultural contexts. Other aspects were deliberately chosen to differ, such as the construction system (massive timber, column-and-beam systems or hybrid structures); the urban typology (referring to building geometry and access system); the type of occupancy (rental or owner-occupied); and the exposure of wooden construction members (covered by gypsum, painted, glazed or with wood's natural surface). The cases' maximum variation strengthens the findings' significance in qualitative research where, as opposed to quantitative research, a limited number of strategically chosen cases is investigated with many variables [5].

Set up as semi-structured qualitative interviews, the conversations were organised around a predefined set of themes and consciously left time to explore topics of special interest to the interviewees in greater detail. Without the presumption of any theoretical framework, the open-ended questions addressed more general architectural values and qualities first, before turning to how these relate to wooden materials. The interview data was analysed by structuring the transcribed conversations according to the topics addressed, and by pinpointing corresponding and contrasting statements.

2.2 Focus groups with users conducted in 2016

Focus groups are carefully planned group discussions, typically with 5–10 participants, that are designed to gather participants' views and opinions on specific topics. The group discussion is led by a moderator. Results from focus groups cannot and should not be generalized to the population as a whole but should rather be seen as the opinions of a small subset that merit further investigation to determine their validity for the population as a whole.

Focus groups were conducted in 2016 in Norway with inhabitants and wood related professionals. The interview guide was directed at gauging the participants' perceptions of topics related to the use of natural materials, and particularly wood, in the interior built environment [6].

2.3 Semi-structured qualitative interviews with architects and stakeholders in the Norwegian sawnwood industry in 2022

As part of a pilot study on drivers of the future demand for sawnwood, another series of semi-structured interviews with industry experts (3), industry representatives (3) and architects (4) was conducted via Teams video calls in 2022. The reuse and recycling of wooden construction parts were part of the topics included in the interview guide developed for the study, aiming to map i. weather and why (or why not) participants believed wood should or could be re-used or recycled, ii. barriers they perceived as preventing the reuse and recycling of wood, and iii. how they envisioned wood to be re-used or recycled. In addition, all participants were asked to appraise the current market value, i.e. the willingness to pay for used wood. Rather than defining a theoretical framework or hypothesis prior to the study, it had an explorative set-up. The industry experts and representatives were purposely sampled based on their assumed knowledge of the industry and the market. Likewise, the architects were sampled because of their experience with wood-based constructions.

The interviews were not recorded; instead, the interviewer took extensive notes. The interview data was assessed by structuring the notes by themes and analysing the content with a focus on i. identifying common perceptions and attitudes and assessing the degree of consensus, and ii. describing the spread or extremes in perceptions and opinions.

3 RESULTS

3.1 Addressing wood through three dimensions of materiality (2016 and 2017)

Two preceding studies have established the importance of involving users (e.g. inhabitants), professionals and other stakeholders in the wood-based construction industry when aiming to understand their perspective on wooden construction materials and to advance the implementation of these. Insights have been gained about the experiences, expectations, preferences and values tied to wooden materials and how these impact the acceptance and choice

https://doi.org/10.52202/069179-0146

of materials. The studies also revealed diverging ways of talking about material related issues.

The focus groups conducted in 2016 in Norway focused on users´, professionals´ and stakeholders´ perception of wood in the interior environment [6]. The study concluded that both professionals and non-professionals can identify and explain relevant physical and immaterial properties of wood, but that the way these properties are expressed differ between professional stakeholders and non-professionals.

Likewise, the interviews conducted in 2017 found that inhabitants and architects talk about the same thematic dimensions when discussing wooden construction materials, but with different views on them, weighting them differently, and with a different vocabulary **[4]**. Three overarching and overlapping thematic dimensions were identified in the interview material, relating to wood's *properties*, *experiences* and *values*.

- Mechanical *properties* were identified as important in the semi-structured interviews, such as the ones that allowed inhabitants to use or modify the wooden structure. Their interpretation as either robust, safe and reliable in the long run, or as unsettling, unstable and vulnerable influenced the users' acceptance. For the interviewed architects, constructive efficiency and systematization was important. Apart from atmospheric qualities, some favoured exposing wooden construction elements as a risk-minimizing measurement, as potential water damages would be detected earlier.
- The *experiences* of wooden materials as something living, healthy, warm and comforting or in contrast as pressing, overwhelming or dated were often tied to associations and memories that would co-determine the acceptance of wooden surfaces. Some inhabitants appreciated the stories weathered or worn surfaces exhibit and how this individualizes buildings, for example through traces of use or from weather exposure. Others wished they could maintain wooden surfaces in such a way that the materials would appear to be new and untouched. They also described bodily reactions to wooden materials. The architects' answers were less detailed and exhaustive in this realm, and not all architects expected the users to be concerned with or sensitive to experiential qualities.
- The *values* associated with wooden building materials included sustainability, a connection to nature and life, and local identity. A personal connection to the materials' origin, to the neighbourhood community the architectural design fostered, and an understanding of leading design principles and ideals were found to impact the users' acceptance and appreciation of the project's materiality in its various dimensions. For architects, important wood related values also included the status of wood related professions and workmanship quality.

3.2 Attitudes among professionals in the wood-based construction sector (2022/2023)

In the follow-up interviews from 2022/23, the four interviewed architects agreed without any reservation that wood always should be re-used if possible. To their mind, burning wooden materials from demolished or deconstructed buildings in heating plants (combustion power plants) for district heating should be the very last option and only considered when all other alternative usage was unrealistic. As of today, burning used wood in heating plants is the most common utilization of this resource in Norway [7,8]. For all architects, minimalizing resource use and waste production as well as limiting carbon emissions were the main motivation for their view. In addition, one architect mentioned the need for limiting the harvesting of fresh wood to preserve natural habitats and to protect vulnerable species.

Among the industry experts and representatives, one participant was uncertain whether the reuse of wood was environmentally and economically sound and thus not convinced that systems for wood reuse or recycling should be implemented. This participant reasoned that as fresh wood from sustainable forestry already had a very low carbon footprint, it was likely that the process of deconstructing, transporting, sorting, rinsing, testing and then possibly processing, producing or reworking the materials into new products would cause more carbon emissions than using fresh wood. The industry representatives also believed that said process would be rather costly and time consuming, so that products from used wood would have a hard time to be economically sustainable and competitive compared to products from fresh wood. Another participant shared some of these doubts, claiming that to be environmentally and economically sound, transportation, processing and handling would need to be kept at a minimum. In addition, they claimed that for some segments of used wood, reuse and recycling would be technically challenging or risky due to a lack of knowledge on for example pre-existing treatments. They argued that using such materials for energy recovery (i.e. district heating) was a sound and established option. Apart from these two, the industry experts and representatives conceded that wood, if possible, should be re-used or alternatively recycled – either because of the need for all industries to minimize carbon emissions, or because external pressure, for example from the EU, would force the sector to do so. However, compared to the architects, the participants from an industry background were more focused on barriers and quick to elaborate on practical issues, obstacles and prerequisites that would need to be addressed before the reuse or recycling on a larger scale would be practically feasible.

Barriers and obstacles towards reuse and recycling surfaced repeatedly throughout most of the interviews, without the interviewer asking. In addition, these themes were a predefined topic in the interview guide, so that all participants assessed barriers and obstacles at least once during the interviews. Barriers and obstacles that surfaced in nearly all the interviews included:

https://doi.org/10.52202/069179-0146

- The lack of infrastructure/ a system for collecting, transporting, testing and sorting, rinsing, processing etc. used materials or alternatively the (perceived) high cost of (establishing infrastructure/ a system for) collecting, transporting etc. wood materials.
- The lack of knowledge regarding the amount of, state of, and quality of used wood materials from demolition and deconstruction, making it challenging to estimate the potential for different types of reuses and recycling.
- The (poor) quality and heterogeneity of (proportions of the) used materials, due to e.g., maintenance level throughout the lifespan of the buildings, impacts like leakages, rot, fungus etc. and the current practice of demolishing rather than deconstructing buildings, resulting in materials being destroyed, poorly sorted or contaminated.
- The (perceived) high cost of changing demolition practices.
- Lack of knowledge about previous treatments and/or lack of ability to/methods for/cost of determining pervious treatments, limiting the potential for reuse and recycling (e.g., due to potential health hazards).
- The notion that used materials lack strength and tolerance which would limit potential uses, and the cost associated with testing these characteristics.

Other, less frequently mentioned barriers included high energy prices and thus the potential competition for the materials from other usages including export for bioenergy purposes. In addition, the relatively cheap price of wood might limit how much effort or resources would be sound to invest in systems for the re-use and recycling of used wood.

Apart from this, several participants mentioned the established conventional building practices and a lack of focus on deconstructability and reusability when the buildings had been planned and built. Interestingly, opinions on whether the more recent building practices (i.e., after 1950) or the older ones constituted the biggest challenges for reuse differed. Some participants argued that prior to around 1950, buildings were generally constructed in a way that allowed deconstruction and reuse. In addition, their opinion was that building materials used in older buildings often were of great quality. Others argued that the knowledge about construction and thus materials used in buildings from before 1950 was neglectable, making it necessary to sort and test all materials and to plan each deconstruction process in detail. Deconstructing newer, more standardized houses and reusing the well-documented materials from them would therefore be more straightforward and less demanding.

Finally, representatives from the sawnwood industry mentioned the high costs of processes such as joining smaller pieces and lengths of wood into more usable dimensions and materials, e.g., using techniques like finger jointing, glue laminating (glulam) and cross laminating timber (CLT). In addition, they thought that such elements and materials engineered from used wood might possibly have poorer properties in terms of strength, tolerance etc. than when using fresh wood. In addition, testing such products would be essential to ensure so that customers could trust their capacity, which again would add costs to the process.

Quite often in the conversations, views on how used wood materials could be re-used or utilized in other ways surfaced without encouragement. In addition, the participants were directly asked to give their view on this. Two of the participants displayed a high level of technical insight on the subject and based their answers on this knowledge. These two gave relatively detailed answers, e.g., they differentiated between materials, gave examples and were quite specific. The other participants talked more generally of wood materials, differentiated less, and although some displayed technical knowledge and based their assessments on this knowledge, there was still a clear difference between these and the first two in how specific and detailed their views and underlying reasonings were.

A common reply to questions regarding how the participants visioned materials being re-used or recycled was “in any way possible”. Elaborating, participants explained that if technically possible, materials should be re-used in the same way they were originally used, i.e., “direct re-use”, keeping handling and processing to a necessary minimum. Materials no longer meeting requirements for the original use, e.g., requirements for load tolerance, should be processed as little as possible and then utilized for the second-best alternative e.g., cladding, cross laminated timber (CLT) or glulam elements. One of the architects stated that if utilized as a layer in CLT-elements, used wood would add extra aesthetical interest.

Shorter bits of wood of high quality could e.g., be joined together using techniques like finger jointing in what several participants called “reversed sawmills”, making new, strong, materials. However, according to sawnwood-industry experts and representatives, the most likely and realistic first step towards more circularity would be the recycling of untreated, used materials in wood-based panels. This alternative was considered the most likely because of the (perceived) low costs and effort required for processing used wood into raw materials for wood-based panels, and the (relatively) low requirements in terms of material heterogeneity (e.g., length, strength, moisture, condition) for this usage. One of the experts was of the opinion that wood-based panels would be the prevalent utilization of used wood materials in the near and intermediate future, together with continuing to burn them in heatplants for energy purposes. In the more distant future, i.e., around 70 years, this would shift, and more direct uses would dominate.

They thought 70 years to be a likely timeframe for such a shift, believing that by then, the majority of buildings to be deconstructed would have been built with techniques and materials intended for deconstruction and reuse. One of the architects believed that planning for reuse soon would become an integrated part of building standards and already had some experience with planning such buildings due to the clients’ requirements.

Table 1: *Table summarizing if and how participants signalled that sawnwood, engineered wood and wood-based panels could be reused, recovered, recycled, composted, or put to other usages.*

	Reusable	Recoverable	Recyclable	Compostable	Other usages
Sawnwood	Yes, a proportion of used sawnwood is almost directly reusable (endings may need to be adjusted etc.), provided that materials are controlled and meet quality standards. In a short-time perspective, increasing the reusable proportion requires a shift from demolition to deconstruction. To upscale the reusable proportion, reuse must already be considered when planning and constructing buildings.	Yes, a proportion of used sawnwood is recoverable, provided that materials are controlled and meet quality standards. Examples of recovery include processing loadbearing wood into cladding, interior products or engineered wood products. In a short-time perspective, recovering more sawnwood requires a shift from demolition to deconstruction. Upscaling requires already considering recoverability when planning and constructing buildings.	Yes, a proportion of used sawnwood may be recycled into wood-based panels or materials for pallets, provided that materials are free from metals and contaminations. Recycling into wood-based panels is considered the most likely and easiest way of keeping the resource in circulation longer at present.	Not discussed	Energy-recovery i.e., burning in heatplants for district heating, is the most likely usage of a considerable part of used sawnwood in a short-time and medium-term perspective.
Engineered wood	Yes, a proportion of used engineered wood is reusable, provided that materials are controlled and meet quality standards. Requirements for increased reuse were not discussed.	Recoverability of engineered wood products were not discussed.	Yes, may be recycled, provided that materials are clean (e.g. glue must be biobased and not constitute a health hazard). Examples of uses were not explicitly mentioned apart from general statements, implying that the participants assumed that if meeting health- and technical requirements, all wood-based materials could be recycled into wood-based panels.		Not explicitly discussed, but general statements implied that the participants assumed that most used wood could be converted into energy.
Wood-based panels	Not explicitly discussed. However, implicitly included as one of the materials when discussing the need for a shift from demolition to deconstruction, i.e., if new, gentile practices are introduced, a larger proportion of used wood-based panels might be reusable.	Recoverability of wood-based panels were not discussed.	Examples of recycling were not explicitly mentioned, apart from general statements implying that the participants assumed that if meeting health- and technical requirements, all wood-based materials could be recycled into wood-based panels.		Not explicitly discussed, but general statements implied that the participants assumed that most used wood could be converted into energy.

https://doi.org/10.52202/069179-0146

Table 1 summarizes the possible forms of re-use discussed by the participants, sorted into the categories "re-usable", "recoverable", "recyclable", "compostable" as proposed by the International Organization of Standardization [9], and "other usages". Most participants focused implicitly or explicitly on sawnwood, while none included explicit details on how wood-based panels could be re-used. From the general statements however, it could be derived that participants assumed that wood-based panels meeting health requirements, e.g., not treated with products or coating containing dangerous chemicals, could be recycled. None of the participants mentioned composting wood-based materials, suggesting that the participants did not associate composting of wood materials with circular economy.

As to whether there was an added value in used wood materials visually appearing to be used, the participants, with a few deviations, suggested that this would depend on the segment, purpose and use of said materials, and the timeframe. For visible materials, at present, many thought that there could be some market advantages if used wood looked used. For non-visible wood, and in a longer perspective, the participants doubted that there would be any such advantage. The few interviewees with a different view focused solely on visible wood and the present market and agreed that used wood with vintage patina would be beneficial. One participant explained how a product literally had been driven over and tossed around by the manufacturer to achieve the desired used look and thought that since this was a product that was popular with some segments, genuinely used materials would probably also be popular with some costumers. Regarding the willingness to pay for used wood, all participants assumed that it would be lower than the willingness to pay for fresh wood.

4 Discussion

Wooden materials can be re-used in many valid ways and play an important role in replacing more harmful materials and in prolonging the storage of CO_2 as "climate sinks" – both when the constructive elements are exposed and when not visible in the building.
The materials can be:

- Hidden between gypsum boards.
- Treated / repaired / refined / renewed, visible and recognizable.
- Recycled, hidden or visible but unrecognizable (e.g. in particle boards).
- More or less in their original state, and visible and recognizable.

Both the precursory interviews and focus groups and the recent interviews showed a tendency among architects and industry representatives to mostly talk about tangible, technical aspects, both when discussing wooden construction materials in general, and the reuse and recycling of such materials. The values they focused most on also coloured their view on the feasibility and the time aspect of reusing and recycling wooden construction materials – some focused more on the short time economic risks and gains for their company and were more sceptical about re-use and recycling becoming common practice before circular construction had become the common and possibly prescribed way to build. These participants were mainly industry representatives. Others highlighted more idealistic values, and ideals that would benefit society at large. They were more prone to seeing opportunities rather than obstacles, to start at a small and experimental scale at once in order to actively contribute to making a change, and to invest in future and more common gains. A subsequent more in-depth analysis of the interview data could include information on the participants being employees or company owners. This might influence how positively one looks at risks – an employee does not have the same responsibilities as a company owner.

In the study from 2022, the interviewer noticed that the architects described qualitative aspects of the material in ways that surprised her and that she hadn't considered herself or not formulated in that way, while interviewees with a technical focus (naturally) focused more on the technical than on the experiential or idealistic aspects, but also used a different and more straightforward language.

However, the experiences of re-used and recycled materials were barely addressed in the recent interviews. In the preceding research cited here [4], it was discovered that the users' (inhabitants') statements about their experiences with wooden construction materials were much more articulate, specific and rich than the architects' (and also than some architects expected). It stands to reason to assume that users also could fill a gap in understanding the experience-related acceptance of re-used and recycled wooden construction materials.

In the previous research, it was argued that these qualitative aspects were an essential part of architecture's "lovability", influencing the life cycle of a building. As cited before [2], loved buildings are expected to motivate the user to a greater degree to adapt to the building even when it is not a perfect match for the user's need any more, to take better care of the building, and to find new functions for the building when users change.

"Lovability" includes tangible, experiential and value related aspects of materiality. Based on interviews with inhabitants. these include:

- Sensory perceptions that cause bodily response (e.g. effects on heart-beat rate, sleep quality, recovery) and mental responses (e.g. stress level, behaviour, interaction with others).
- Associations, either with earlier experiences and memories, or with acquired ideas; these will influence the acceptance and appreciation of materials, of their state and treatments, and of their changing appearance when ageing.
- Individualisation of materials and products – even industrial, standardized products will become unique when weathered and used, and display their situatedness

in a geographical and in a cultural context (e.g., their orientation towards the sun/wind/rain, and habits of use entailing repeated touch).
- Atmospheric qualities
- Narrative (e.g. about the materials' earlier location or user)
- Affordance: the possibilities of use that a material signals. For example, a massive wooden wall suggests which loads it can carry and which tools to use, while a gypsum wall could either cover a void that makes it difficult to hang heavier things (curtains, pictures, furniture), or a concrete wall that requires heavier tools.

In the earlier study, "lovability" has been used in an argument for prolonging the life cycle of buildings, and for including the users' experiences [2,4]. It can also be a useful term when aiming at a greater degree of reuse and recycling.

In the interviews from 2022, architects tended to focus more on the possibilities and were optimistic about the realization of new ideas, while industry representatives tended to focus more on possible obstacles, risks, costs and how long it would take to implement new ways of doing things. A reason may be that architects and industry representatives have different roles in a project - architects are more used to selling new ideas, and industry partners must make ensure the financial feasibility; furthermore, they are already selling wooden products and do not depend on new markets for the re-use and recycling of wood.

A note on value: one interviewee said that materials were handled harshly to create a more used look. Then, "Plan A", the option to give the material a long life in a primary function and in its pristine state, is passed by. Hereby, the values tied to the re-use and recycling of materials are foiled. Then, the entire universe of interrelated material aspects (tangible, experiential and value related) are reduced to visual characteristics.

5 Conclusion

Precursory studies have established that physical properties, sensory and intellectual experiences, together with associated values and narratives are important dimensions to consider when understanding expectations towards and the acceptance of wooden materials. It is important to include the user in the group of stakeholders when discussing these dimensions. It is expected that this is also valid for re-used and recycled wooden materials. Furthermore, in order to include the entire value chain in circular models for wooden construction materials, the combustion for energy gain and the composting of wooden materials have to be part of all considerations.

The recent set of interviews presented in this paper focused on how professional decision makers (stakeholders from the wood industry and architects) relate to the wood-related properties, experiences and values established by users when discussing re-used and recycled materials.

Important findings were that the professionals were detailed and explicit when focusing on mechanical and physical properties, and that their assessment of whether and how to pursue circular construction goals (and how soon) were guided by values, ideals and convictions, and in addition colored by their professional roles and responsibilities. Experiential aspects were largely absent from their statements. However, when developing new products and areas of application for re-used and recycled wooden construction materials, all three wood-related dimensions should be considered; besides properties and values, experiential aspects should be included, and the user perspective should complement the knowledge and insights already at hand in the wood industry.

Among others, this plays an important role when deciding if and how to process and treat wooden materials for aesthetic reasons, as this is greatly based on the users' assumed acceptance and appreciation of wooden materials but might impact the combustibility and compostability of wooden materials negatively. If the full cycle in a circularity perspective is part of how products both from new and from recycled wooden construction materials are promoted, this may also influence public taste and trends. When considering the full cycle of wooden material flows that includes their burning or composting, and when asking oneself if one would like to eat or to breathe in one's building (materials), then preferences of varnish, paint and other decorative treatments may be judged anew and change.

REFERENCES

[1] McDonough, William, and Michael Braungart. *Cradle to Cradle: Remaking the Way We Make Things*. 1st ed. New York: North Point Press, 2002.

[2] "Only things people like get a long life" states architect Dietmar Eberle. Sattrup, Peter Andreas. 'Arkitekter, arkitektur og ressourcer: Interview med Dietmar Eberle'. *Arkitekten* 11 (2008): 42–43. Translation by the author.

[3] Preiser, Wolfgang F. E., and Jack L. Nasar. 'Assessing Building Performance: Its Evolution From Post-Occupancy Evaluation'. *International Journal of Architectural Research:* ArchNet-IJAR 2, no. 1 (2008).

[4] Groba, Ute. 'Timber Tales: A Qualitative Study of Timber Materiality in Housing Projects'. Doctoral dissertation. The Oslo School of Architecture and Design, 2021.

[5] Flyvbjerg, Bent. 'Five Misunderstandings About Case-Study Research'. *Qualitative Inquiry* 12, no. 2 (April 2006): 219–45.

[6] K. Strobel, A. Q. Nyrud and K. Bysheim. 2017. 'Interior wood use: linking user perceptions to physical properties'. *Scandinavian Journal of Forest Research* 32(8): 798-806

[7] Statistisk sentralbyrå, Behandling av avfall fra nybygging, rehabilitering og riving (tonn), etter år, statistikkvariabel, behandlingsmåte og materialtype (Tabell 09781). 2022.

[8] Statistisk sentralbyrå, Avfall frå hushalda, etter nedstrømsløsning, år, statistikkvariabel, region, behandling og materiale. 2022.

[9] International Organization of Standardization, Definitions related to circularity - proposed by ISO/TC 287/WG 3 for use within ISO/TC 287, in ISO/TC 287/WG 3 N192. 2022. p. 6.

https://doi.org/10.52202/069179-0146

World Conference on
Timber Engineering
Oslo 2023

https://doi.org/10.52202/069179-0146

World Conference on Timber Engineering Oslo 2023

FUNDAMENTAL STUDY ON REPAIR BY EPOXY RESIN MIXED WITH CELLULOSE FIBER TO RECOVER BENDING PERFORMANCE OF WOODEN PARTS

Akiko Ohtsuka[1], Nozomi Satou [2], Naoyuki Itagaki[3], Run Minoura[4], Shinichi Terasaki [5]

ABSTRACT: This study conducts basic research on the reinforcement effect achieved by mixing epoxy resin and cellulose fiber to gauge the bending performance. Flowability tests indicated that increasing the amount of cellulose fiber relative to epoxy resin decreases flowability, and resins containing approximately 5% cellulose fiber are easier to apply. The compression test results indicated that the compressive strength of the material decreased upon mixing epoxy resin with cellulose fiber. However, the test piece containing cellulose fiber showed higher compressive strength than Cedar and Douglas fir. Compression test results confirmed that when the wood was filled with epoxy, the reinforcing effect achieved was greater than that of sound wood; it was sufficiently effective as a compression repair material. Furthermore, bending test results showed repair work utilising epoxy resin helped recover the bending performance of the test pieces with a 35% defect. Thus, the composite resin of cellulose fiber and epoxy resin is effective as a repair material for the bending material.

KEYWORDS: Cellulose fiber, Epoxy resin, Termite, Repair method

1 INTRODUCTION

1.1 BACKGROUND

Several historical and cultural properties constructed out of wood still exist in Japan. However, the strength of the wood of these buildings has decreased over time due to decay, insect damage, and deterioration. Therefore, appropriate repairs and restoration should be carried out to preserve the original timber used. Wood deteriorates in several ways; termite damage deteriorates the wood from the inside while fungal decay begins on the surface.

Current methods of repairing degraded areas include traditional techniques, such as root joints, and scientific techniques using synthetic resins and carbon fiber [1]. While each repair method has its advantages, cosmetic surface, workability, construction period, and cost can be concerns. Yamada et al. [2] examined the compressive strength of simulated deteriorated pieces to confirm the reinforcing effect of synthetic resins and the compressive and bending strength of wood exposed outdoors like pine wood, which deteriorates in a short period by Formosan subterranean termites. Their examination confirmed that the repair method using epoxy resin had a stronger reinforcing effect on the compressed material than on sound material; however, no reinforcing effect was confirmed on the bent material.

1.2 PURPOSE OF STUDY

This study aims to focus on the recovery of bending performance of wooden structures and propose a more appropriate and effective repair method. We conducted a basic study on the reinforcing effect achieved by mixing cellulose fiber with epoxy resin. The bending performance of the repair structures was confirmed after evaluating the material performance of the resin mixed with the cellulose fiber by conducting compression tests.

1.3 RESEARCH CONTENT

In this report, the material performance of the resin is evaluated by compression and fluidity tests, and the bending performance of the repaired member is confirmed by ultrasonic propagation velocity measurement and bending test, especially to examine the repair method using synthetic resin.

2 CONSIDERING REPAIR METHODS

Based on the literature survey [1]-[10], the characteristics of repair methods used in the past for cultural property buildings are shown in ***Table 1***. Carbon fiber repair methods are mainly classified as bonding, filling, or strengthening methods. Epoxy resins are often used for bonding and filling, and synthetic resins, such as isocyanate-based prepolymers, are often used for strengthening. The latter penetrate the interior of wood by application or impregnation and react with moisture and cellulose to strengthen the interior of the resin, thereby restoring the strength of the degraded wood [6, 7]. Sekino et al. [6, 7], stated concerns that the excessively high hardness of the resin and the fact that when impregnated,

[1] Akiko Ohtsuka, Akita Prefectural University, Japan, akiko@akita-pu.ac.jp
[2] Nozomi Satou, Akita Prefectural University, Japan
[3] Naoyuki Itagaki, Akita Prefectural University, Japan
[4] Run Minoura, Asante Inc., Japan
[5] Shinichi Terasaki, Maeda Kosen Co, Ltd., Japan

https://doi.org/10.52202/069179-0147

if the surface is not finished again, the texture of the resin may not match with the weathered surface.

Table 1: *Results of bending strength tests*

Method	Strength Recovery	Construction	Design
Carbon Fiber	○	◎	×
Sheet Roll	○	◎	×
Plate Embedding	○	×	◎
Auxiliary	—	○	×
Oblique Scarf Joint	◎	△	×
+Reinforced plastic	△	○	×
Synthetic Resin	○	○	○
Epoxy	△	○	△
Isocyanate prepolymer	—	○	—
Acrylic	○	◎	×

Recent research has examined carbon fiber repairs for cultural properties constructed out of wood [8, 9]. There are two types of repair methods using carbon fiber: the external adhesive type of carbon fiber board and the embedded type into the member, and the rolled type and auxiliary type of carbon fiber sheet [8]. Externally bonded molds and sheet-wound molds of carbon fiber board can be used to attach to damaged members. The external adhesive type of carbon fiber board is made by impregnating carbon fiber with epoxy resin, hardening it, and then affixing it with an adhesive. This makes it easy to install. However, since it is plate-shaped, the use of external adhesive type carbon fiber board is limited to smooth areas. v but they are thin, flexible, and can handle complex shapes. Auxiliary types include the use of carbon fiber rods as anchors or braces. Moreover, except in the case of embedding, the carbon fibers are exposed to the surface, which may prove to be an unsuitable design from design perspective.

Filling termite damage with synthetic resin can be done to prevent wood degradation caused by decay, and insect damage. Yamada et al. [2, 10] investigated the compressive and flexural strengths of pine wood exposed outdoors to Formosan subterranean termites, and that of small pieces subjected to simulated deterioration to confirm the reinforcing effects of synthetic resins. Results revealed that the repair method using epoxy resin was more effective for compressive materials than for sound materials, but not for flexural materials.

3 CELLULOSE FIBER

Cellulose fiber is biomass material derived from plants. Attention to plant biomass materials such as cellulose fiber was sparked by the depletion of oil resources. Consequently, biomass became much discussed whenever crude oil prices soared, leading to calls for the development of technologies to replace petroleum-derived plastics with renewable biomass resources as fuel and raw materials for chemical products [11].

This study also investigated the reinforcing effect of adding cellulose fiber to epoxy resin. Additionally, the cellulose fiber used in this study was extracted from rice straw produced at the University of Tokyo. The materials used in the production process have extremely low environmental impact.

The process of cellulose extraction is as follows:

(1) After adding distilled water into the rice straw and letting it stand, the process of pulverizing the rice straw with a mass collider is repeated to remove lignin and hemicellulose from the cellulose surface in the cell wall. This exposes the cellulose to the surface. The material input is shown in ***Photo 1***.

Photo 1: *Separation work*

(2) Using a vacuum and a flask, only the crushed rice straw is removed from the liquid in the rice straw and distilled water. ***Photo 2*** shows the separation process.

Photo 2: *How the ingredients were added*

(3) Dry in a drying oven (60 °C).

The cellulose condenses and hardens when the cellulose fiber is dried. They are broken up after drying to finish the process. ***Photo 3*** shows how it looks after drying.

Photo 3: *Cellulose fiber after drying*

https://doi.org/10.52202/069179-0147

4 MATERIAL PERFORMANCE OF RESIN

4.1 EPOXY RESIN

4.1.1 Outline of compression tests

To confirm the reinforcing effect of blending epoxy resin with cellulose fiber, test pieces containing a blend of epoxy resin with cellulose fiber by 2%, 5%, and 10% were prepared and subjected to compression tests. The size of each test piece was 20 × 20 × 40 mm compared with the previous studies [2, 10]. ***Photo 4*** shows the state of fabrication. We used formwork plywood wrapped with silicone resin-treated glassine paper to prepare the pieces. The curing period was 23°Cfor four days plus 60°Cfor three days. Additionally, the cellulose fiber B was mixed with the main agent and hardener. We made three pieces for each repair method.

We used a two-liquid mixture (main curing agent) resin. The component of the main agent was an epoxy resin, and that of the curing agent was a polyamine. To confirm the original performance of the epoxy resin used this time, a test piece N without compounding cellulose fiber was prepared, and the compression test was performed.

Photo 4: *The state of fabrication of test pieces*

4.1.2 Compression test results

Figure 1 shows the compression test results**.** Adding cellulose fiber to epoxy resin increased the strength of resin containing 2% cellulose fiber. Contrarily, the resin containing 5% or 10% cellulose fiber decreased compressive strength. However, it acts as an effective repair material for compression in this study because it has a higher value than the design basis quasi-compressive strength of Douglas fir (27.0 N/mm^2). Its compressive strength was about 40 to 50 N/mm^2, which was confirmed to be similar to the experimental results of past studies in which wood was filled in with epoxy resin. [2].

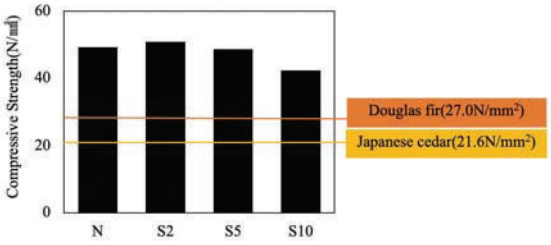

Figure 1: *Results of compressive strength tests*

4.2 WORKABILITY

Viscosity measurements were performed using a B-type viscometer. The B-type viscometer is shown in ***Photo 5***. To measure the viscosity, a sample liquid was placed in a container such as a beaker and the spindle was immersed in the liquid. When the motor was rotated, the spring and spindle also rotated; however, the spring is twisted by the flow resistance of the measured sample. This twist is detected by a torque sensor and obtained as a torque value. The viscosity is calculated from the constant determined by the combination of this torque value and the spindle speed.

Photo 5: *B-type viscometer [13]*

The viscosity values of each resin obtained from the flowability test results are shown in ***Figure 2***. The change in resin fluidity was confirmed by mixing different percentages of cellulose fiber with epoxy resin. The results showed that the more cellulose fiber was added, the higher the viscosity and the lower the fluidity.

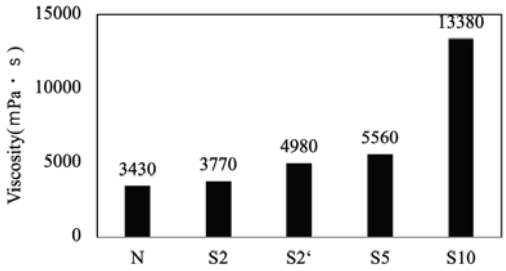

Figure 2: *Viscosity values of epoxy resin and cellulose blends*

As shown in ***Figure3***, it can be confirmed that the fluidity of the pieces with 10% cellulose fiber added to epoxy resin was greatly reduced compared to the pieces with 2% or 5% cellulose fiber added.

It is considered that a highly flowable repair material, which is easy to fill to the back against deterioration of termite paths, is more effective as a repair material at the time of resin filling in deteriorated materials. Contrarily, a less flowable repair material is more effective at the time of curing until the filled resin hardens.

https://doi.org/10.52202/069179-0147

The general liquid viscosity [14] is comparable to a resin containing 10% of the thickest cellulose fiber. It is considered difficult to fill wood materials with this viscosity value. Contrarily, epoxy resin with 2% or 5% cellulose fiber shows the same viscosity value as strawberry jam, and with this viscosity, the resin can be filled deep into the termite path against deteriorated components. Thus, this viscosity is suitable for filling.

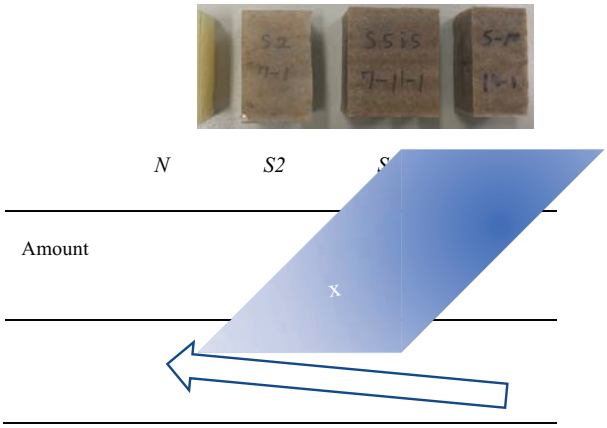

Figure 3: *Relationship between the amount of cellulose fiber and liquidity*

5 VERIFICATION OF BENDING PERFORMANCE FOR SIMULATED DETERIORATED PIECES

5.1 OUTLINE OF BENDING TESTS

A simulated deterioration test piece similar to termite damage deterioration was produced, and a bending test was performed. The bending test was carried out according to JIS Z 2101. ***Figure 4*** shows the parameters of the flexural pieces. To reproduce the wood degradation from termite damage, the simulated degradation test piece was produced. The shape of the test piece was a column of square cross-section with side length a = 20 mm, a total length L = 320 mm, and load span l = 280 mm.

Table 2: *Pieces for bending strength tests*

Piece	Defect (%)	Number
B-0	0	3
None		
	20	3
BS2-20	20	3
	20	3

A longitudinal slit was inserted symmetrically as shown in ***Figure 4***. The defect ratios to the volume of each piece and the wood opening area were about 20%, 30%, and 35%. Pieces were prepared by mixing 2% and 5% cellulose fibers with epoxy resin as shown in ***Photo 5***.

Additionally, to confirm the bending performance recovery before and after each repair method, bending tests were also conducted on sound materials without repair and at each defect rate. The first and second parts of the test piece names in ***Table 2*** indicate the repair method and defect rate, respectively. B is unfilled, BN is filled only with epoxy resin, and BS2 and BS5 are filled with epoxy resin containing 2% or 5% of cellulose fiber, respectively. In this study, Douglas fir was used as the tree

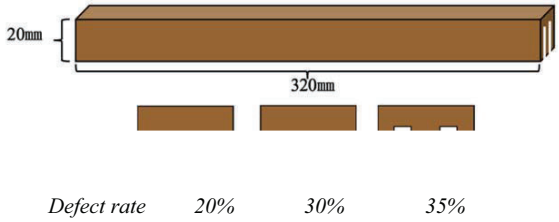

Figure 4: *Shape of the piece*

Photo 5: *Pieces for bending strength tests*

Photo 6: *Conducting bending strength tests*

5.2 BENDING TEST RESULTS

Figure 5 shows the bending test results at each defect rate for each repair method. The results were compared with B-0 (the sound). The bending strength decreased with increasing defect rate. Considering the unrepaired test pieces (B), the bending strength of B-20 (the 20% defect) is decreased by 11% compared to B-0, B-30 (the 30% defect) is decreased by 18%, and B-35 (the 35% defect) is decreased by 20%. The average repair effect at 20% defect across resin-filled pieces(BN, BS2 and BS5) changed compared to the unrepaired piece little.

As for the resin-filled test pieces (BN, BS2, and BS5) with 20% defect, no repair effect was confirmed compared to the unrepaired material (B) regardless of the repair method. On the other hand, in the resin-filled test pieces

https://doi.org/10.52202/069179-0147

with 35% defect, strength recovery was observed in all test pieces compared to the unrepaired test piece (B-35) with the same failure rate. Additionally, with a 35% defect, the test pieces that mixed the cellulose fiber (BS2 and BS5) showed a higher reinforcing effect than the one containing only epoxy resin (BN). It was indicated that the reinforcing effect was higher as the mixing quantity of the cellulose fiber became larger from 2% in BS2 to 5% in BS5. From these results, it is considered that resin mixed with cellulose fiber is an effective repair material for recovering the bending performance in material with a 30% and 35% defect rate. However, there is a dispersion in the obtained strength, and further examination is necessary.

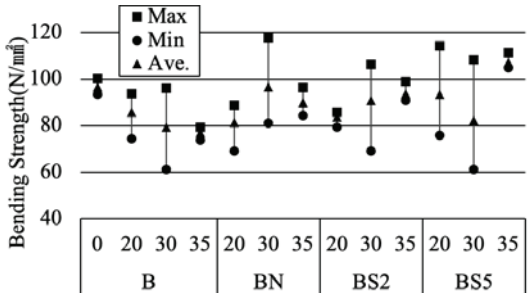

Figure 5: *Results of bending strength tests for repair methods*

To confirm whether the filling was sufficient, ultrasonic propagation velocity measurement, which is a non-destructive diagnosis, was performed before and after filling, and sufficient filling was confirmed from the change in velocity. The height of the terminal was placed at the center of the piece (20 mm each in the short-side direction), and an ultrasonic propagation velocity measuring instrument was used.

The ratio of the ultrasonic propagation velocity measurement results performed after epoxy resin filling of the simulated deteriorated piece to the ultrasonic propagation velocity of the sound piece is shown in ***Figure 6***. The experimental results showed that the rate of change in velocity is comparable or higher for sound pieces. This suggests that the simulated deteriorated pieces were sufficiently filled with epoxy resin.

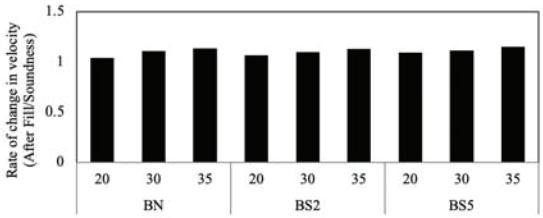

Figure 6: The ratio of ultrasonic propagation velocity after epoxy resin filling to that of the sound piece

The rate of change in ultrasonic propagation velocity before and after resin filling is shown in ***Figure 7.*** In the pieces with a defect rate of 30% and 35%, an increase in the ultrasonic propagation velocity due to resin filling was confirmed. This suggests that ultrasonic propagation measurement may be an effective method for confirming whether defects are sufficiently filled. Contrarily, no significant change was observed in the rate of change in velocity before and after resin filling in the 20% defect piece. It is inferred that the depth and width of the defect at the measurement position affected this as shown in ***Figure 8***.

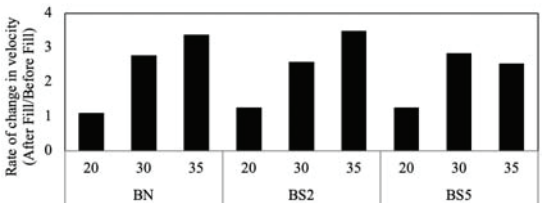

Figure 7: The rate of change in ultrasonic propagation velocity before and after resin filling

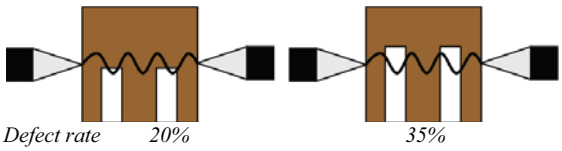

Figure 8: *Results of bending strength tests by defect rate*

6 CONCLUSION

This study mainly focused on the bending performance and carried out basic research on the reinforcing effect of mixing plant-derived cellulose fiber into epoxy resin for the proposal of more appropriate and effective repair.

A literature search revealed that although the winding form of carbon fiber sheets is effective in improving bending performance, design problems remain in cosmetic materials, and no reinforcement effect has been confirmed for bending materials in repair methods using epoxy resins.

From the results of compression tests on resins, it was found that compounding cellulose fibers with epoxy resin tends to reduce the compressive strength. However, the test pieces with cellulose fibers were found to have high compressive strength compared with the standard compressive strength of Cedar and Douglas Fir. Furthermore, the results of ten compression tests conducted when wood members were filled with epoxy resin with a compressive strength of ~40-50 N/mm^2 have confirmed that these materials are more effective than sound materials in reinforcing wood.

Flowability tests showed that with the increase in the amount of cellulose fiber relative to epoxy resin, the flowability decreased. When deteriorated materials are filled with resin, it is considered that highly flowable repair materials, which are easy to fill deep against deterioration of termite, are more effective as repair materials. Less flowable repair materials are more effective when considering the curing time until the filled

https://doi.org/10.52202/069179-0147

resin hardens. Therefore, resins containing about 5% cellulose fiber are the easiest to apply.

Ultrasonic propagation velocity measurements showed a large rate of change before and after filling, suggesting the effectiveness of resin filling in pieces with a defect rate of 30% and 35%.

The results of the bending tests showed that the repair with epoxy resin had a higher reinforcing effect on the members with larger defect rates. Additionally, the recovery of bending performance was confirmed by combining epoxy resin with cellulose fiber for 35% deficient pieces. The composite resin of cellulose fiber to epoxy resin is an effective repair material for bending materials.

ACKNOWLEDGEMENT

This work was supported by JSPS KAKENHI Grant Number 20K14872. We would like to thank Kohshin. H. C Co., Ltd., and other related parties for their great cooperation in the studies presented in this report. We are grateful for the cooperation rendered to us by Associate Professor Eiichi Sakai, Department of Mechanical Engineering, School of Systems Science and Technology, Akita Prefectural University, and the members of the laboratory for the cellulose fiber presented in this paper. The content of this report is based on the research results of Akita Prefectural University graduate Shuto Ochiai. We would like to express our deepest gratitude to everyone involved.

REFERENCES

[1] Wataru Kawanobe: Survey of Synthetic Resins Applied for the Conservation of Japanese Building, Science for conservation, No. 37, p 99-123,1998.3

[2] Mikako Yamada, Masamitsu Sawada, Kei-ichi Imamoto, Chizuru Kiyohara, Akiko Ohtsuka, Shinya Sasaki, Shinichi Terasaki: Study on reinforcement method by filling synthetic resin in timber damaged by termites, Proceeding of the architectural research meetings, 2018, Kanto Chapter, Architectural Institute of Japan, Vol. 89, p 69-72, 2019.3

[3] Wataru Kawanobe: Synthetic resin used in restoration of cultural property, National Museum of Ethnology survey report, Senri Ethnological Reports, Vol. 36, p 103-114, 2003.02

[4] Yutaka Takenouchi, Wataru kawanobe: Study on the Deterioration of Synthetic Resins Used in the Restoration of Wooden Buildings, Science for conservation, Vol. 37, p 124-136, 1998.03

[5] Kentaro Oka, Masaki Tamura, Osamu Goto, Yasunori Tsumura: Architectural Institute of Japan, AIJ J. Technol. Des. Vol. 23, No. 55, p 789-794, 2017.10

[6] Masaru Sekino: Development of Artificial Resin Application Methods in the Conservation and Restoration Work of Wooden Materials of the Rakando of the Former Fukiji, an Important Cultural Property, and the Joan, a National Treasure, Science for conservation, Vol. 10, p 1-8, 1973.03

[7] Yasuda Corporation: Jogan "Phantom Tower" Important Cultural Property Horyuji Rakan-do Hall (former Fuki-ji Temple) Restoration Work Report, Repair Work Report No. 3,1973.

[8] Hyunjjung CHO: THE USE OF CARBON FIBER IN HISTORIC WOODEN ARCHITECTURE -Focusing on the repair of architectural members-, Architectural Institute of Japan, AIJ J. Technol. Des. Vol. 16, No. 34, p 1175-1180, 2010.10

[9] Atsuo Takino, Sara Yagami, Masahide Murakami: Bengig Experiments of timber joints reinforced with carbon fiber, Architectural Institute of Japan, AIJ J. Technol. Des. Vol. 24, No. 56, p 141-146, 2018.2

[10] Mikako Yamada, Masamitsu Sawada, Kei-ichi Imamoto, Chizuru Kiyohara, Akiko Ohtsuka, Shinya Sasaki, Shinichi Terasaki : Fundamental study on strengthening of termite induced deteriorated timber member with resin, No. 1 Compression test and bending test, Summary of Academic Lectures at the Architectural Institute of Japan (Hokuriku), p 821-822,2019.7

[11] Guidelines for the Utilization and Application of Cellulose Nanofiber Towards the Decarbonization and Achievement of a Circular Economy, Ministry of the Environment, 2021.3

[12] 2000.5.31 Ministry of Construction Notice No. 1452: Determination of Standard Strength of Wood Fc, Ft, Fb and Fs. Ministry of Construction (2000). (Amendment: 2015.6. 30 the Ministry of Land, Infrastructure, Transport and Tourism Notification No. 816, Final amendment: 2015.8.4 the Ministry of Land, Infrastructure, Transport and Tourism Notification No. 910)

[13] EKO Hidehiro Seiki Co., Ltd., Brookfield viscometer - Measurement method to capture the characteristics of the sample, (https://eko.co.jp/products/physical-property/maker/maker1/p5001.html), Last viewed date：2022. 3. 7

[14] THINKY (www.thinkymixer.com), Last viewed date: 2023. 1. 10

World Conference on Timber Engineering Oslo 2023

QUALITY ASSURANCE OF TIMBER STRUCTURES BY NEW MONITORING METHODS FOR THE MOISTURE CONTENT OF WOOD

Bettina Franke[1], Steffen Franke[2], Marcus Schiere[3], Andreas Müller[4]

ABSTRACT: Wood is a hygroscopic material and can absorb or release moisture from the surrounding climate. The wood moisture content (MC) influences the material strengths and stiffnesses as well as the long-term load-bearing behaviour. For this reason, the continuous monitoring of wood moisture content is a suitable early warning system to increase the quality of wood structures in a pioneering way and to detect changes in time. The paper presents several suitable measuring methods for the MC and explains their advantages, accuracies, and applications. The explanations are supported by case studies.

KEYWORDS: wood, quality assurance, moisture content, measuring methods, monitoring

1 INTRODUCTION

The continuous monitoring of wood moisture content is a suitable early warning system. The importance of wood moisture in relation to possible damage in timber construction is shown by Frese & Blaß [1], where 50 % of all investigated objects show damages or failures due to wood moisture changes or low and high wood moisture contents. Dietsch & Winter [2] shows that 30% of these objects are damaged due to seasonal or climate-induced wood moisture changes.

Since the distribution of wood moisture is often not constant across the cross-section, internal stresses perpendicular to the grain (moisture-induced stresses, MIS) arise due to the anisotropic moisture-strain behaviour. These stresses can easily exceed the characteristic tensile strength perpendicular to the grain and lead to crack development, [3]. In curved glulam beams, these stresses can also lead directly to the total loss of load-bearing capacity, as shown in [4], [5].

First, the focus must be on the design regarding the load bearing capacity and serviceability. Therefore, the service classes according to the EN 1995-1-1 needs to be considered. For a more detailed assessment of the expected climate, the results from Franke et al. [6] can also be used. Here, continuous monitoring data for one year was evaluated for different uses, such as sports halls, ice rinks and riding arenas, but also storage buildings, bridges, or mountain stations. The curves obtained show the range of variation and the expected wood moisture content per object.

Second, the condition of the structure must be ensured during the whole life cycle - 50 years for buildings and up to 100 years for infrastructural objects. This is usually done by regular visual checks and inspections combined with control measurements. If the control measurements are carried out continuously by means of a monitoring system, trends in the behaviour, damaging events or even damages can be derived from the data and inspections can be planned more time and cost efficiently.

The control of timber structures over ice rinks, riding surfaces, in warehouses and production halls, for facades made of wood, or flat roofs are engineering applications to ensure the quality of timber construction. The variety of monitoring possibilities is e.g., demonstrated at the "House of Natural Resources" at ETH Zurich, [7]. A dense sensor network was installed to measure, among other things, the prestressing force, the deformation, or relative displacements in addition to the wood moisture content to record the behaviour of the building over several years and to quantify the long-term behaviour of this wooden structure.

Monitoring systems can also be used for system controlling. In an apartment building in Büren in Switzerland, four apartments were equipped with sensors to measure air quality, [8]. Air quality has direct effects on the people who spend time indoors. Measurements of air temperature, air quality, CO_2, and volatile organic compounds (VOC) can be used to assess air quality. The air exchange rate can be reduced to the necessary/optimal amount and the control of the air exchange units can be optimized. The result is a constantly very good air quality with simultaneous energy savings due to the reduction of the air exchange rate when no people are in the apartment.

[1] Bettina Franke, Bern University of Applied Sciences, Switzerland, bettina.franke@bfh.ch
[2] Steffen Franke, Bern University of Applied Sciences, Switzerland, steffen.franke@bfh.ch
[3] Marcus J. Schiere, Wijma Kampen B.V., Kampen, Netherland, mjs@hupkeswijma.com
[4] Andreas Müller, Holzbauexperten GmbH, Switzerland, andreas.mueller@holzbauexperten.ch

https://doi.org/10.52202/069179-0148

2 MEASURING METHODS FOR THE WOOD MOISTURE CONTENT

2.1 GENERAL TO THE MEASURING METHODS

For the measurement of wood moisture content, single point and laminar measuring systems can be used, as shown in overview in Figure 1. For the monitoring of small critical areas, the resistance measuring method, the sorption isotherm method and the passive RFID tag method are available. The principal description of the measurement techniques for wood moisture content is given e.g. in [9], [10]. Specifics for monitoring purposes is discussed below.

2.2 ELECTRICAL RESISTANCE METHOD

The electrical resistance method is the most common non-destructive method to monitor moisture content developments. The method allows measurement of moisture content in different depths from the surface and measured resistances can logged over extended periods of time. The principle is to measure the electrical resistance between two installed electrodes, [9]. The electrical resistance depends on the moisture content, temperature, and wood species. The accuracy of the method is about 1 to 2 M% [9]. Factors affecting the accuracy concern the grain orientation, type of electrodes, wood density, and temperature as well as surrounding electrical installations, permanent fitting/bond of electrodes to wood. Resistance between two electrodes roughly ranges between 100 kΩ to 100 GΩ from the fiber saturation point to about 5 M%, respectively. Once resistances are large, electrical currents are extremely small and electrical fields around the monitored structure are considered a possible source of error.

The choice and installation of electrodes should be done carefully, especially for objects subjected to outdoor climate, strong climatic variations, or direct weathering. Due to the shrinkage and swelling of the wood, normal wood screws or nails may have no or poor contact with the wood or the cable. Both lead to distortion of the resistance measurement and mostly indicate lower wood moisture contents than in reality. The use of hanger bolts and a protective box has proved to be successful, see Figure 2. The hanger bolts must be insulated with suitable material except for the tip. The cables are fixed directly to the hanger bolt with nut and locknut. The shrinkage and swelling of wood have almost no influence on the required good electrical contact between wood and electrode. All metallic parts of the electrodes should be made of stainless steel, if possible, [11].

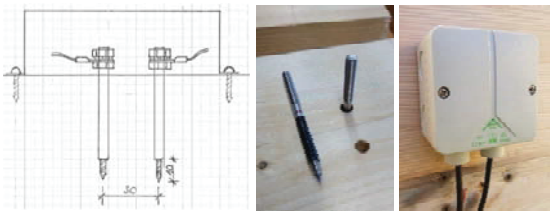

Figure 2: *Principal sketch and photos of the installation of the hanger bolt electrodes and protective box, [11]*

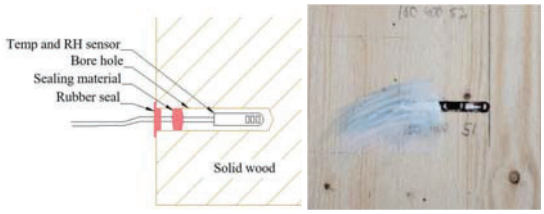

Figure 3: *Installation of air temperature and relative humidity sensors in solid wood*

2.3 SORPTION ISOTHERMS

2.3.1 General

The equilibrium moisture content in the wood can be derived from the temperature and relative humidity, [12]. The implementation of sensors in small, closed cavities in the wood is called the sorption isotherm method. The sorption isotherm method is most suitable in the presence of glue joints, the influence of salts, the use of protective and impregnating agents, or even in the presence of prolonged temperatures below 5 °C. All these factors do not influence the measurement by means of sorption isotherms. The application and implementation of the measuring probe requires a cavity size of 8 to 10 mm in diameter, whereby the depth of the measuring probe can be controlled as desired, see Figure 3.

2.3.2 Moisture sensor developed at BFH-AHB

To simplify the application of the sorption isotherm method, a special very small sensor was developed at Bern University of Applied Sciences, the Institute for Timber Construction, Structures and Architecture and the Institute for Electrical Engineering and Information Technology. An extra small battery-operated sensor for wood moisture measurement with radio data transmission was developed, see Figure 4. The sensor is located at the tip of the pin shaped extension below the electronic facing

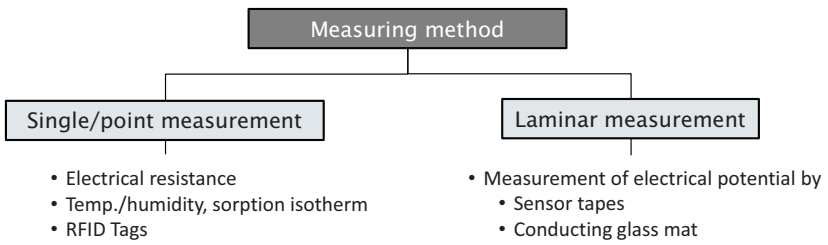

Figure 1: *Overview of selected measurement methods for wood moisture content in the monitoring application*

https://doi.org/10.52202/069179-0148

outwards. The extension which will be screwed into a drill hole. Different extension lengths could be realized to measure in different depths. The device is inexpensive, easy to apply, and measures, the air humidity, and the temperature in a cavity in any material, and transmits it by radio (LoRa) directly to the cloud or to a gateway (Figure 5). The measurement results can then be processed and visualized.

While every node could work and transmit its data individually, the results of several nodes can be synchronized and collected by using a Gateway. It receives the data by LoRaWAN, saves it and transmits them at once via 4G data net. The gateway also provides a remote access for checking the system conditions. Measurements up to two years can be made with one battery.

2.4 RFID SENSORS

Radio Frequency Identification (RFID) sensors are small devices that use low-power radio waves to receive, store, and transmit data to nearby readers (Figure 6). The basic types of RFID sensors are passive, active, and semi-passive or battery-assisted passive (BAP), [12].

- Passive RFID sensors do not have an internal power source but are powered by electromagnetic energy transmitted from an RFID reader.
- Active RFID sensors have their own transmitter and power source on board the tag.

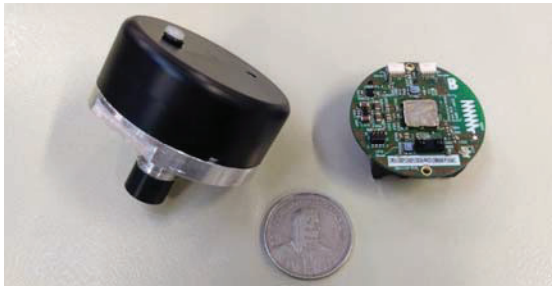

Figure 4: *Moisture-Sensor, system with waterproof housing (left), electronic (right).*

Figure 5: *Gateway to use and control several sensor nodes*

- Semi-passive or battery-assisted passive (BAP) sensors consist of a power source integrated into a passive tag configuration.

In addition, RFID sensors operate in three frequency ranges:

- Ultra-High Frequency (UHF),
- High Frequency (HF) and
- Low Frequency (LF).

RFID sensors can be attached to a variety of surfaces and are available in different sizes, designs, and shapes (e.g. dogbone or patch, Figure 6). Dimensions vary from a few millimeters to several centimeters. The Smartrac company or RFMicron are already provide passive RFID sensors for capacitive measurement of moisture or humidity. These tags have been successfully applied in the fields of construction, energy, but also healthcare.

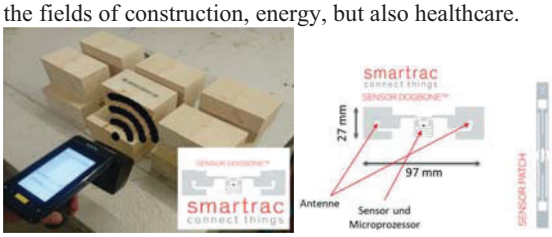

Figure 6: *Simultaneous measurement of several RFID sensors installed in the wood specimen (left) and RFID sensor shapes (right)*

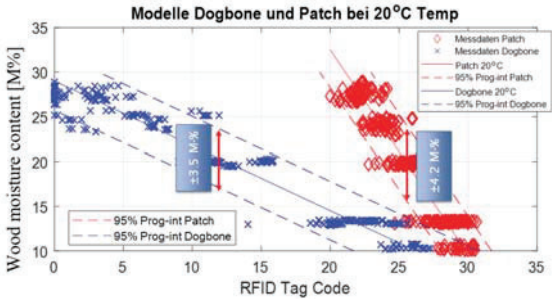

Figure 7: *Correlation between RFID sensors code vs. wood moisture at 20 °C for the dogbone and patch sensor*

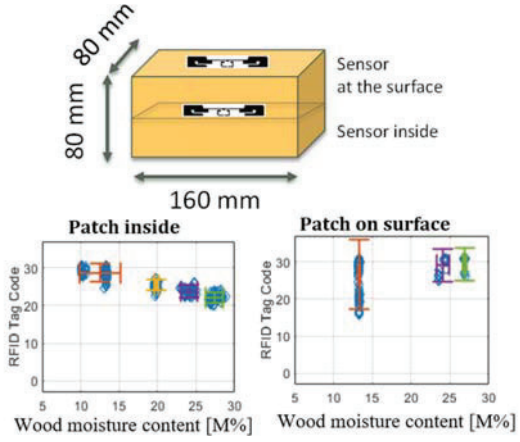

Figure 8: *RFID sensor tests at surface and inside, setup (top), correlations (bottom)*

https://doi.org/10.52202/069179-0148

Figure 9: *Bridge Rupperswill, application of sensor band on the wooden panel of a timber bridge (left) and detail of senor band (right)*

The applications of RFID-sensors have shown that the punctual measurement of the wood moisture content is suitable, but with a greater measurement uncertainty than the electrical resistance or sorption isotherm method. The correlation between the read-out sensor code and the wood moisture must currently still be determined on the basis of reference checks. Figure 7 shows an example correlation between sensor code and wood moisture together with the prediction interval. The width of the prediction interval results from the scatter of the measurement data used to derive the correlation. Depending on the application, temperature compensation of the measurement must also be considered. The application range of the model is between 10 M% and 28 M% for the wood moisture. The measurement error of the dogbone shaped sensor and patch sensor is ± 3.5 M% and ± 4.2 M% respectively, derived from the width of the prediction interval. To improve the measuring accuracy, the RFID sensors should be embedded inside the component. The results of a comparative study show lower variations in the measured values, Figure 8.

Due to the very low price of RFID sensors and their small size, several sensors can be installed at each measuring point and an average of the sensor codes could then be calculated. In this way, a higher measurement accuracy can be achieved, and the system is less susceptible to the failure of individual RFID sensors. RFID- sensors make it possible to monitor hard-to-reach and invisible components even without a power supply. The RFID sensors are said to have a service life of 50 years.

2.5 LAMINAR LEACKAGE MONITORING

2.5.1 Sensor tapes

With sensor tapes, it is possible to detect high moisture or wetness in a linear manner, e.g., under a waterproofing layer of flat roofs or road pavements [14]. This measuring method is mainly used in places where water or moisture can spread under the waterproofing. Depending on the spacing and arrangement of the individual tapes, quasi-laminar monitoring can be achieved with the sensor tapes. During monitoring, a potential measurement is made between two wires in the sensor band. The presence of water causes the electrical resistance to drop and can be detected.

For the application in timber bridge structures, a roadway structure with an unbonded waterproofing layer must be used for a two-dimensional leakage detection with linear sensor tapes. Because, depending on the planned transverse and longitudinal slope of the bridge, any water that has penetrated the separating layer between the waterproofing and the deck slab would flow in the direction of the slope and could be detected here, e.g., at a bridge edge or deck transition.

The foot and cycle path bridge between Rupperswil and Auenstein was equipped with sensor tapes, see Figure 9. The monitoring system monitors the possible leakage of the waterproofing and additionally records climate data, material temperature and wood moisture. The on-site measuring unit evaluates the measurement data and sends it to a cloud. The measurements values can be retrieved worldwide at any time using a browser. Warnings and alarms are triggered when critical values are reached.

2.5.2 Conductive fleece

For laminar leakage detection like in flat roofs or landfills, a conductive glass fleece is installed under the waterproofing and above the insulation, [14], [15]. In an intact waterproofing, there is no water flow and therefore no electrical current flow. In case of a leakage in the waterproofing, water penetrates the waterproofing layer and allows the conduction of electric current in the conductive fleece underneath the waterproofing. The presence of water in the case of a leakage changes the electrical properties, respectively the measured value, thus leakages can be detected. After drying out, the original values are restored. Early detection and the detection of hidden water damage are possible.

3 DATA TRANSFER AND SAVING

For the planning, implementation and evaluation of a monitoring system, an exchange with appropriate experts should take place, [16]. At the beginning, the choice of the measured quantity is a first important step next to the definition of the control points and their number. The density of measurement data must be defined individually from object to object or from control point to control point. Specialists in this field can assist and advice in deciding on a suitable system.

The installation of measurement sensors enables the acquisition of measurement data at defined intervals. Data can be transmitted from individual measuring points, e.g., by WLAN, LoRaWan or LPWan to a central module (gateway) and further to a WebPortal, as shown in Figure 10. If the measurement data are stored on a WebPortal, they can be viewed in quasi real time from the workplace and are available worldwide. The server can evaluate the measurement data and trigger warnings or an alarm. Storage and evaluation of the measurement data can also

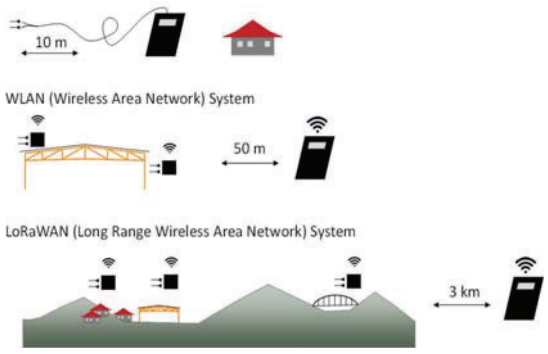

Figure 10: *Application of sensor band on the wooden panel of a timber bridge*

take place directly on the gateway or other measurement/ storage units and release warnings or alarms (e.g., via SMS). After commissioning, these systems operate autonomously.

The various components (measuring points, measuring device, gateway and user interface) form the monitoring system. Battery-powered systems can operate maintenance-free for up to several years, depending on the system and the number of measuring points.

4 CASE STUDIES

4.1 SOLID WOOD WALL MONITORED BY SORPTION ISOTHERM METHODE

The monitoring results for a solid wood wall show the very good functioning of the sorption isotherm method over different component depths, compare Figure 11. The diagram shows the measured wood moisture content and the calculated equilibrium moisture content (green line) from the room climate over a period of two years. It can be seen very clearly that the sensor near the surface in the wall at a depth of 5 - 10 mm (orange line) reacts very quickly to the room climate with a similar rate of change and amplitude as the calculated compensation moisture. Only in the summer months, when the indoor climate becomes more humid very quickly, there are differences between the orange and green lines. However, these differences quickly equalize. In this construction, for example, plaster-board and abrasion are very diffusion-open materials.

Furthermore, the diagram contains the measured wood moisture contents at depths of 20 - 30 mm, 70 - 80 mm and 95 - 105 mm. Already from a depth of 20 mm (purple line), a "damped" behaviour of the wood moisture with respect to calculated equilibrium moisture can be observed. Here, the wood moisture values are lower in summer and higher in winter than the calculated equilibrium moisture. In this case, the sorption isotherm method allows very precise evaluations of the wood moisture content and the interaction between the room climate and the water content in the solid wood wall.

4.2 TIMBER BRIDGE OBERMATT MONITORED BY ELECTRICAL RESISTANCE METHODE

The bridge Obermatt is monitored over several years within the framework of research projects, by the Institute for Timber Construction, Structures and Architecture at the Bern University of Applied Sciences. Some irregularities could be detected in time, as shown in Figure 13. The measuring points are located at different critical points and in different depths. Figure 12 contains the measurement locations shown on the bridge cross-section.

The wood moisture content was measured near the surface, approx. 20 mm deep, and in the cross-section with a depth of 200 mm. The diagram in Figure 13 shows the change of the air temperatures and relative humidity measured on site together with the calculated equilibrium moisture content on the surface of the wood for the timber bridge Obermatt. The wood moisture content measured in the cross-sections are shown in Figure 14. In addition, the

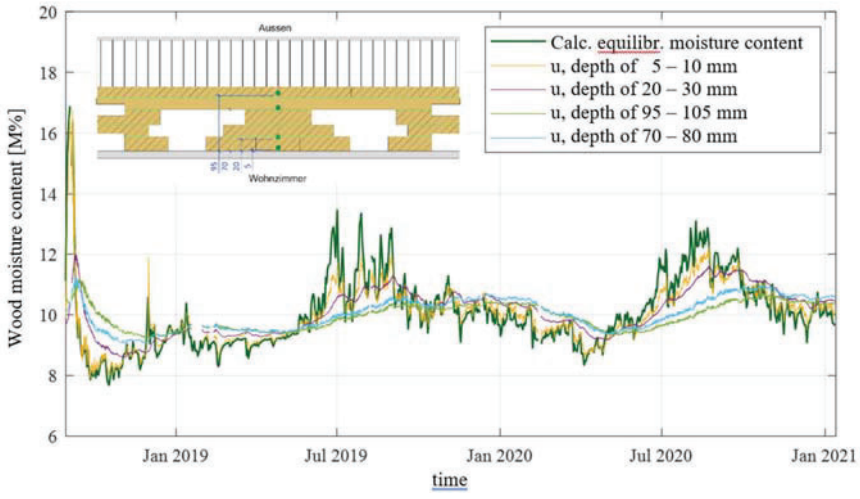

Figure 11: *Evaluation of the wood moisture content measured with the sorption isotherm method at different depths in a solid wood wall, [8]*

https://doi.org/10.52202/069179-0148

calculated equilibrium moisture content was determined for each measuring point; a time delay due to the moisture transport in the wood and the duration of exposure to the climate was not considered. The graph of the measured wood moisture content shows a delayed and damped behaviour compared to the calculated equilibrium moisture content.

On the south side, an increase in wood moisture content for one measurement sensor can be observed from August 2013. This is associated with a partial structural leakage, which has since been corrected and the wood is allowed to dry out again. In this case, the installed monitoring system has acted as an early warning system and later serious structural damage could be avoided at an early stage. Further monitoring results and case studies are explained and shown in [17].

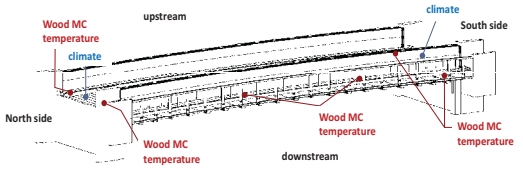

Figure 12: *Positioning of the measuring sensors at the Obermatt bridge*

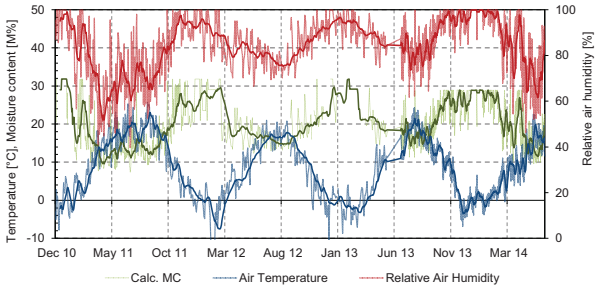

Figure 13: *Climate, wood moisture content and calculated equilibrium moisture content for the Obermatt Bridge*

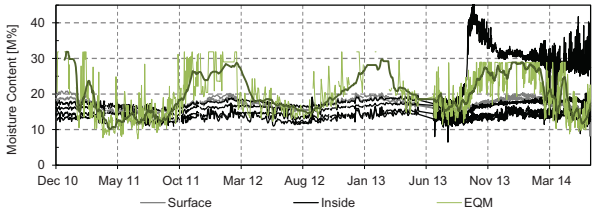

Figure 14: *Wood moisture content and calculated equilibrium moisture Content for the Obermatt Bridge, after August 2013 a leakage is visible in the measuring data*

5 CONCLUSIONS

Wood is a living and recognized construction material. However, wood is also a hygroscopic material and can absorb or release moisture from the surrounding climate. The so-called wood moisture content (MC) influences the material strengths and stiffnesses as well as the long-term load-bearing behaviour. As studies showed, half of the cause of damage to wood structures is due to a change in wood moisture content or seasonal and climate-related changes in wood moisture content. For this reason, continuous monitoring of wood moisture content is a suitable early warning system to increase the quality of wood structures in the future in a pioneering way and to detect changes in time.

The control points in the monitoring should be placed in possible danger zones/hot spots. These can include roadway crossings, support areas, transition areas and penetrations. The various point and area methods presented are suitable for measuring wood moisture content. For the planning, implementation and evaluation of a monitoring system, the number of measuring points, the accuracy and the data storage/transmission should always be defined with a view to the objective. At this stage, an exchange with appropriate subject matter experts can provide positive support.

The electrical resistance measurement method is technically very simple to implement, easy to install and can be replaced from the outside. The sorption isotherm method provides high accuracy by measuring relative humidity and temperature in an insulated cavity. An RFID sensor measures the humidity in the immediate vicinity of the sensor averaged over a certain component depth using the principle of capacitive sensing. The use of RFID sensors is inexpensive and wireless but with less accuracy. Passive RFID sensors even do not require an external power supply or battery and can be used in many applications.

ACKNOWLEDGEMENT

The presented research results have been generated in the projects "Quality Assurance of Wooden Structures" of the Forest and Wood Research Promotion Switzerland (WHFF-CH) of the Swiss Federal Office for the Environment and the "Sealing Systems and Bituminous Layers on Bridges with Pavement Slabs", VSS2016/326 of FEDRO. The funding bodies and accompanying business partners are thanked here for their support.

REFERENCES

[1] M. Frese, H. J. Blass. Statistics of damages to timber structures in Germany, *Engineering Structures 33*, pp. 2969–2977, 2011.

[2] P. Dietsch, S. Winter. Structural failure in large-span timber structures: A comprehensive analysis of 230 cases, *Journal of Structural Safety 71*, pp. 41-46, 2018.

[3] K. Möhler, G. Steck. Untersuchungen über die Rissbildung in Brettschichtholz infolge Klimabeanspruchungen, *Holzbauforschung*, pp. 194-200, 1980.

[4] S. Aicher, G. Dill-Langer, A. Ranta-Maunus. Duration of load effect in tension perpendicular to the grain of glulam in different climates, *Holz als Roh- und Werkstoff 56*, pp. 295-305, 1998.

[5] P. J. Gustafsson, P. Hoffmeyer, G. Valentin. DOL behaviour in end-notched beams, *Holz als Roh- und Werkstoff 56*, pp. 307-317, 1998.

[6] B. Franke, S. Franke, M. Schiere, A. Müller. Quality assurance of timber structures, *Research report*, Bern University of Applied Science, https://www.bfh.ch/dam/jcr:98c05049-9082-4cb3-a6e8-775fed93ac0d/R%20008098%2077FE%20FoBericht%20Qualit%C3%A4tsicherung%20von%20Holztragwerke.pdf Biel/Bienne, Switzerland, 2019.

[7] C. Leyder. Monitoring-Based Performance Assessment of an Innovative Timber-Hybrid Building. *Doctoral Thesis*. ETH Zurich, Switzerland, 2018.

[8] S. Bonifacio. Untersuchung der Grundlagen zur Messung des Raumklimas in einen Holzgebäude, *Msc-Thesis*, Bern University of Applied Sciences, Biel/Bienne, Switzerland, 2020.

[9] P. Dietsch, S. Franke, B. Franke, A. Gamper, S. Winter. Methods to determine wood moisture content and their applicability in monitoring concepts. *Journal of Structural health monitoring 5(2),* pp 115-127, 2014.

[10] P. Grönquist, N. Flexeder, B. Franke, S. Franke. "Monitoring of Wood Moisture Content in Timber Structures by Electrical Resistance and the Sorption Methods: Current Challenges." *Sustainability and Durability of Taller Timber Buildings: A state-of-the-art report.* COST Action CA20139 Holistic design of taller timber buildings (HELEN), 2022.

[11] A. Müller, C. Angst. Sealing systems and bituminous layers on bridges with timber roadway slabs. *Research Report VSS 2016/326*, http://www.mobilityplatform.ch, online 10. Feburary.2023.

[12] W. Simpson. Prediction equilibrium moisture content of wood by mathematical models. *Wood and Fiber* 5(1), 41-49, 1973.

[13] S. Smiley. A Tag, A Label, An Inlay. Atlas RFID store, www.atlasrfidstore.com/rfid-insider/a-tag-a-label-an-inlay, online 1. May 2019.

[14] A. Roedel (2022) "Full-area covering leakage and wetness monitoring on big timber structures using real time monitoring systems." *Sustainability and Durability of Taller Timber Buildings: A state-of-the-art report.* COST Action CA20139 Holistic design of taller timber buildings (HELEN).

[15] K. Burger, P. Elter, K. Holm, U. Kämmer. Das dichte Flachdach, *Bauphysik-Kalender - Feuchteschutz und Bauwerksabdichtung*, 335-360, 2018.

[16] M. Riggio. "Moisture management and monitoring during erection and service life of tall wood buildings." *Sustainability and Durability of Taller Timber Buildings: A state-of-the-art report.* COST Action CA20139 Holistic design of taller timber buildings (HELEN), 2022.

[17] B. Franke, S. Franke, A. Müller. Case studies: long-term monitoring of timber bridges, *Journal of Civil Structural Health Monitoring 5*, p. 195-202, 2015.

https://doi.org/10.52202/069179-0148

World Conference on Timber Engineering Oslo 2023

CURRENT STATUS OF MAINTENANCE OF THATCHED ROOFS IN SHIKOKU

Naoki Kakehashi[1], Miyako Kamatoko[2]

ABSTRACT:

The use of the traditional Japanese construction method, "thatched roofing," is steadily declining despite its considerable environmental performance. Here, thatched roofs in Shikoku were re-roofed without subsidies to clarify preservation of these roofs. We conducted a hearing survey with officers of the city engaged in activities related to the traditional Japanese construction method and obtained opinions on the maintenance method of thatched roofs and the implemented policies in the city. Thatched roof maintenance is possible without subsidies by maintaining and managing roofs that have existed for generations, and thatching replacement, such as procuring thatched roofs independently. Policy implementation, such as increasing the number of thatched-roof events and increasing the subsidy rate for thatched-roofing work, positively impact residents. Three teahouses were re-roofed as demonstration during a workshop. We confirmed the records of traditional construction methods and established the measures of roofing that can be adapted. For durability, the traditional construction method to firmly fix thatched roofs to the base and minimize the influence of rainwater were followed, screws and reinforcing bars were used, and the roof slope was changed. Furthermore, new technology increases the durability of the roof and prolong the number of years before re-roofing is required.

KEYWORDS: Thatched roof, sustainable resource, Chado

1 INTRODUCTION

Grass is sometimes used as a material for thatching walls and roofs. One such grass is *Imperata cylindrica*, or Cogon grass. Thatching has existed as a construction method in various parts of Japan since BC.

Using LC(Life Cycle) system analysis, according to Naoki, the amount of carbon fixation per hectare in grasslands is approximately 8,514 tCO_2/year [1]. In addition to their role in fixating carbon, grasslands also serve as habitat for unique organisms, who in turn play a role in maintaining biodiversity. Moreover, a 2014 study by a Danish research institute performed a life cycle assessment (LCA) of the environmental impact of thatched roofs from pampas grass and reeds growth, thatch field management, thatch transport, and construction. Results showed that, even if domestic and overseas transportation energy is included, these values are negative [2].

After the thatched structure is taken down, the old thatch can be used as fertilizer in the fields. Ando stated, “When re-roofing, the large amount of old thatch produced is decayed to a moderate degree, with a large amount of soot from the hearth adhering to it, making it a great fertilizer.” He also noted that “old thatch from roofs are better as a fertilizer than freshly cut thatch applied directly to mulberry fields” [3].

However, the use of thatched roofs are on the decline. According to a questionnaire survey conducted by Takamido, Takahashi, and Shigematsu, 71.4% of structures in Miyamachō had thatched roofs in 1945, but this number dwindled to only 23.7% by 1986. In addition, a questionnaire survey was conducted on the reasons households had changed from thatched to tin roofs, with 38% of respondents indicating that thatch was hard to acquire, and that it was difficult to find help to install thatched roofing. However, it has become clear that good quality thatch and neighbors that are willing and able to lend a hand, which were easy to obtain in the past, have declined due to labor shortages and changing times (Table.1) [4].

In addition, tiled roofs became the trend around 1930. Furthermore, rapid economic growth, chemical fertilizers, and mechanization due to the modernization of agriculture reduced grassland values.

However, in European countries, the environmental performance of thatched roofs is being reassessed, with thatched roofing still being used in modern buildings. This is especially true in the Netherlands, where some 2,000 to 2,500 structures are outfitted with new thatched roofs annually. These structures include public buildings and housing complexes, in addition to alone standing houses. Below is an example (Figure 1).

In Japan, there is also an environmental-based movement underway to preserve thatched roofs, with

[1] Naoki Kakehashi, Graduate student, Kagawa University, Japan, s22g256@kagawa-u.ac.jp

[2] Miyako Kamatoko, Assistant Professor, Kagawa University, Japan, kamatoko@eng.kagawa-u.ac.jp

https://doi.org/10.52202/069179-0149

methods suitable to contemporary lifestyles, the environment, and resources.

In this study, we focused on Shikoku, where the numbers of craftsmen and thatched buildings are declining rapidly. We clarified what kind of measures are currently being taken where frequent re-roofing is not possible, and examined possibilities and issues involving the use of thatch in modern society moving forward.

Table 1: *Reasons for changing thatched roofs [4]*

The reason for using galvanized steel (Multiple answers up to 3 out of 12)	Respondent households (129) (%)
Can't get thatch	23
If you change it, you won't have to worry about fires	20
No help when reroofing	15
It is more durable to replace	9
Community of thached dependency is falling apart	7
The change fits the modern lifestyle	4
The sense of life has become urban	3
No time to reroof	2
Started doing jobs other than agriculture and forestry	2
Cheaper to change	2
Financially comfortable	1
Others	12

Figure 1: *Dutch thatched roof*

2 METHODS

A hearing survey with related parties and a construction method survey at the construction site of active craftsmen were conducted. The surveys were conducted between 2019 and 2022. The hearing survey was conducted on all the subjects who are currently involved in the maintenance of thatched roofs, i.e., the owner, craftsman, and government. Specifically, the survey was conducted on two houses and four residents namely: Ino Town, Kochi Prefecture, Kumakogen Town, and Ehime Prefecture. The houses were re-roofed with active Kabuki craftsmen and without subsidies. One of the masters (Yusuhara Town, Kochi Prefecture) and two local governments (Miyoshi City, Tokushima Prefecture and Seiyo City, Ehime Prefecture) were working on the preservation of thatched roof in the cultural property department in Shikoku. In the construction method survey, there was only one active thatched-roof craftsman in Shikoku. Therefore, the construction process performed on the thatched roof of the three buildings (Yasuo Chado, Katahira Chado, Koyamati Chado) by the Yusuhara craftsman was recorded in video, and drawings were constructed by an actual measurement. The changes from the traditional construction method were confirmed. The survey area is shown in the Figure 2 below.

Figure 2: *The survey sites*

3 HEARING SURVEY

3.1 OWNERS WHO CONTINUE TO RE-ROOF THATCHED HOUSES

In a previous study [4], reasons that justify the decrease in thatched roofs were "I cannot get thatched roofs" and "I do not have any help when changing the thatched roofs." The two houses that had their homes re-roofed had personally prepared a thatched roof (Figure 3), and spent several years collecting thatched material, saving the material, and re-thatching. In addition, the owners were foresters by profession, and had experience in re-thatching with aid from the village. They also aided craftsmen by assisting their families when re-roofing at a home rice field.

Figure 3: *Kayaba*

3.2 THATCHERS IN YUSUHARA

The only active thatched-roof craftsmen who inherited traditional techniques in Shikoku are the craftsmen in

https://doi.org/10.52202/069179-0149

Yusuhara Town. We interviewed one of the masters regarding the people who often go to the site among the members, and Table 2 outlines our findings. Here, *tego* refers to craftsmen who gather the thatch and *jibashiri* refers to those who clean it. Professional proficiency increases as one moves to the left-hand side of the table. All of them, including their masters, make a living from agriculture, and the average number of thatched-roof jobs is three or four per year. The types and sizes of buildings they re-roof vary from small buildings such as *Chado* to main buildings of about 200 m², Kaya uses Yoshi from Watarase Retarding Ground in Tochigi Prefecture (Figure 4). Unlike Japanese pampas grass, this grass grows in water from May to September, and is harvested after being dried during the dry conditions of October. Although the cost is higher if transportation costs are included, the overall stretch is longer than the local pampas grass and can cover a large area. It is also excellent in durability, hence it is economical in the long run.

Figure 4: *Reeds at Watarase Reservoir in Tochigi Prefecture*

Table 2: *Careers of craftsmen in Yusuhara Town*

	craftsman K	apprentice A	apprentice B	apprentice C	apprentice D	apprentice E
position	master	corner roofing	flat roofing	needle picking	tego	jibashiri
age	70's	late 50's～early 60's	late 50's～early 60's	40's	40's	40's
gender	man	man	man	man	man	man
birthplace	Yusuhara	Yusuhara	Yusuhara	Yusuhara	Yusuhara	Yusuhara
profession	agriculture	agriculture	agriculture	agriculture	agriculture	agriculture

Table 3: *Miyoshi City Cultural Assets*

Thatched facility as a cultural asset						
	district	name	kinds	scale(m²)	remarks	reroofing
1	Otiai	Nagaoka's	Main house	232.0	Recurrent construction: Cultural properties open facility	2010
2		Fusho	Main house	63.9	Recurrent construction: Tourist old private house stay	2011
3		Seiko	Main house	203.0	Recurrent construction: Tourist old private house stay	2012
4		Udoku	Retirement room	126.0	Recurrent construction: Tourist old private house stay	2013
5		Yukyo	Main house	200.0	Recurrent construction: Tourist old private house stay	2014
6		Yukyo	Retirement room	110.0	Recurrent construction: Tourist old private house stay	2014
7		Ungai	Main house	146.0	Recurrent construction: Tourist old private house stay	2014
8		Soten	Retirement room	79.9	Recurrent construction: Tourist old private house stay	2014
9		Tanzai	Main house	248.0	Recurrent construction: Tourist old private house stay	2015
10		Ten-ippo	Main house	240.0	Recurrent construction: Tourist old private house stay	2015
		subtotal		1648.8		
11	Sugeoi	Kone's	Main house	169.0	National important cultural property	2009
12	Turui	Kimura's	Main house	291.0	National important cultural property	2007
13	Turui	Kimura's	Retirement room	169.0	National important cultural property	Iron plate

https://doi.org/10.52202/069179-0149

3.3 CULTURAL PROPERTY-RELATED DEPARTMENT

There are many thatched-roof buildings in Miyoshi City and Seiyo City that are making advanced efforts regarding thatched roofs. In Miyoshi City, under the historical scenic maintenance and improvement plan, thatched roofs were secured to cover the amount required for re-thatching 17 thatched-roof buildings (Table 3). Residents were hired to collect thatched roofs. In case of a surplus of the thatched roof, the building material was sold outside the city. As a future policy, the city is planning to continue its current thatch cutting activities, providing events where local elementary and junior high school students and others who do not know about thatch can learn more about this resource. Premised on a desire to preserve thatched roofs, the city shared its opinion that it would like to continue the maintenance of thatched roofs, using this as a catalyst for the prosperity of the local community and to attract migrants from other regions. In Seiyo City, there are more than 10 thatched-roof teahouses, which are common property in the village. Teahouses are a place of customs for "intangible folk cultural properties for which measures, such as creating records, should be taken." At that time, a mechanism was created to assist the cost for Kaya and others. In addition, in August 2014 a regional development group held an exchange between residents of urban areas and local residents at Yasuo Chado, the aim of which was to utilize thatched roofs as a symbol of farming villages. Using vacant houses and abandoned farmland, the group is busy with revitalization efforts that center on holding migrant exchange meetings, mainly for people living in urban centers.

4 CURRENT THATCH CONSTRUCTION METHODS

The construction method used in the re-roofing work of three buildings (Yasuo Chado, constructed in 2019; Katahira Chado, constructed in 2020; and Koyamachi Chado, constructed in 2021) in Shirokawa-cho, Seiyo City, was implemented by the aforementioned master of Yusuhara Town. The method was plotted based on interviews with craftsmen and actual measurements (Figure 5, 6, 7, 8). Due to the traditional technique of the right person in the right place, the construction method slightly differed depending on conditions such as the amount of kaya gathered and the skill of the builder even in the construction of the three teahouses of the same scale that we witnessed. There have been some changes from traditional methods. First, reinforcing bars were used for the top oshiboko (pressed bamboo) on which the ridge is placed (or Iribanachi [Yokotake at the top of the eaves] depending on the construction) (Figure 9). In addition, the inside of the house and the first Iribanachi were connected by a number line (Figure 10). All of them are particularly strengthening the members that received the load. When fastening the thatched roof to the rafters, instead of rice straw, a thinner and stronger sisal rope was used to improve workability and durability (Figure 11). In addition, we tried to follow the traditional Ehimeroofing method of fixing the rope to the kaya bundle in the corner without penetrating the rope into the hut so that water is not used when fastening the corner (Figure 12). The construction method was selected with consideration of performance improvement and regional characteristics. Next, we summarize the differences in the items noted below for the three *Chado*.

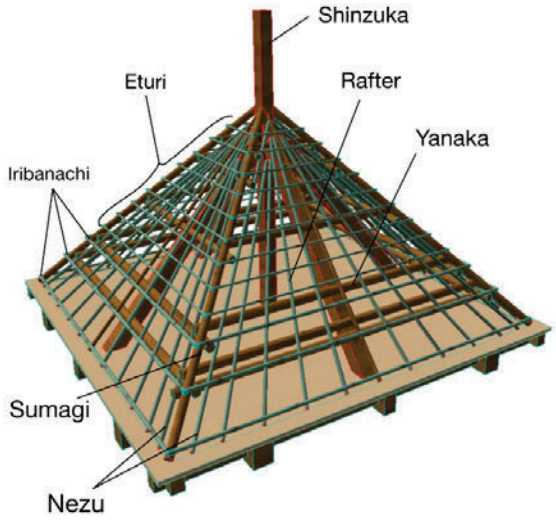

Figure 5: *Names of roof trusses*

Figure 9: *Reinforcing bars are used for the top shavings that support the water bottle*

Figure 10: *Connecting the Yanaka and the first Iribanachi with a number line*

https://doi.org/10.52202/069179-0149

***Figure 11**: Using a sisal rope as a substitute*

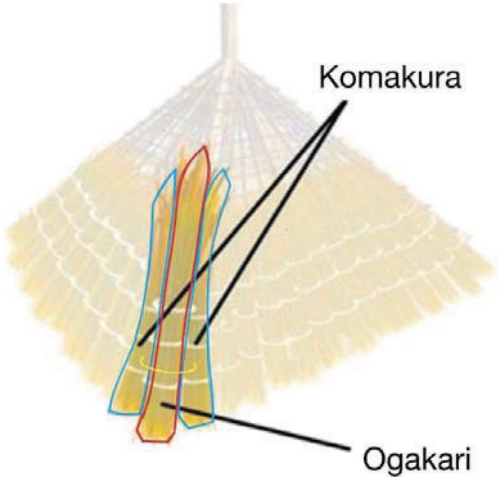

***Figure 12:** Fixing mackerel tuna bundle*

4.1 THATCH THICKNESS

A thatch thickness of 560 mm was recorded for Katahira Chado, which was re-roofed in 2020. This was the only record of thatch thickness exceeding 500 mm. This was thicker than the roofs of other Chado when it was first re-roofed, likely because the site where it was built has better sun exposure than the sites of the other two Chado. Both Yasuo Chado and Koyamachi Chado are flanked by mountains and trees. Just as with the thatch-roofed main house, which had a hearth, thatch is not moisture-resistant and will rot faster if it is not kept dry. For this reason, the thatch of the Katahira Chado, which receives good sun exposure, remained thick. Yasuo Chado and Koyamachi Chado have similar site conditions, but the thatch on Yasuo Chado grew thinner.

4.2 THATCH MATERIALS

All thatch is made from pampas grass or reeds. There is no difference between the two but, as the area is characterized by plentiful rain, Craftsman K said, “Rather than removing the undergrowth, we will leave it and bring the thatch with the undergrowth on to the outside. This will prevent the rain from penetrating.” Thatch roofing naturally has a water-conducting effect, but as the years pass, the thatch becomes thinner, and rainwater begins to penetrate. This undergrowth will fill the gap and prevent leaks.

4.3 EAVES/CEILING

There are two types of ceilings: joist ceilings where the ceiling is closed off with boards, and decorative attics where the beams are left exposed. These differences do not in any way affect the durability of the roof; the joist ceiling prevents birds and animals from entering the roof, while the decorative attic emphasizes ventilation and promotes the drying of the thatch. Hence, each type presents some advantages and disadvantages.

4.4 BASE MATERIAL

The base material consists of a lattice-like structure made of bamboo and rafters and is made at lengths of approximately 200–400 mm or less. Since wood is more durable than bamboo, when bamboo is used, six pieces are used per interval, while for wood, only five are used. For Yasuo Chado (girder line length: 2,133 mm) nine cedar posts are used, while for Katahira Chado (2,193 mm) one cedar post is positioned in the center, surrounded by eleven bamboo posts. For Koyamachi Chado, nice bamboo posts were used, but those had a thicker diameter than the ones used for Katahira Chado, and the interview survey revealed that this was because the craftsmen believed that the robustness would be sufficient.

4.5 MUNESHIMAI

Since the tin originally used for the muneshimai of Yasuo Chado was peeling off, this was repainted the original color. Bamboo and cedar bark were used on the muneshimai of Katahira Chado and Koyamachi Chado. However, as these could not be reused, muneshimai were created using water jars provided by local residents. Because these jars have such wide mouths, they are filled with thatch bundles. The culture of using recycled materials on the muneshimai runs deep.

4.6 ROOF SLOPE

Thatch does not leak because the thin, straw-like strands have a water-conducting effect and thus serve as an effective roofing material. However, if the slope of the roof is too gentle, rainwater will collect in the gaps of the thatch, allowing rot to establish. Based on the slopes of the three buildings, it is thought that a thatched roof slope of 45° or more is preferred.

https://doi.org/10.52202/069179-0149

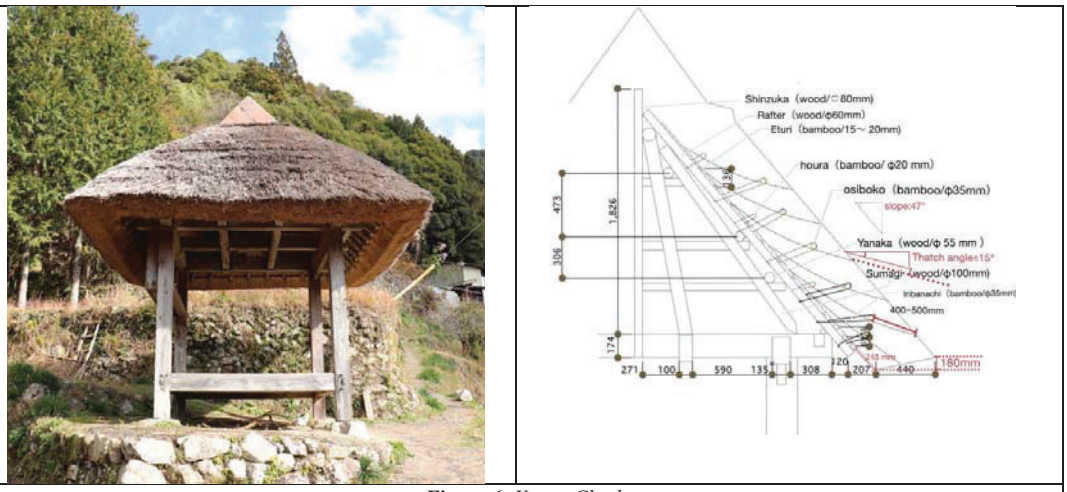

Figure 6: *Yasuo Chado*

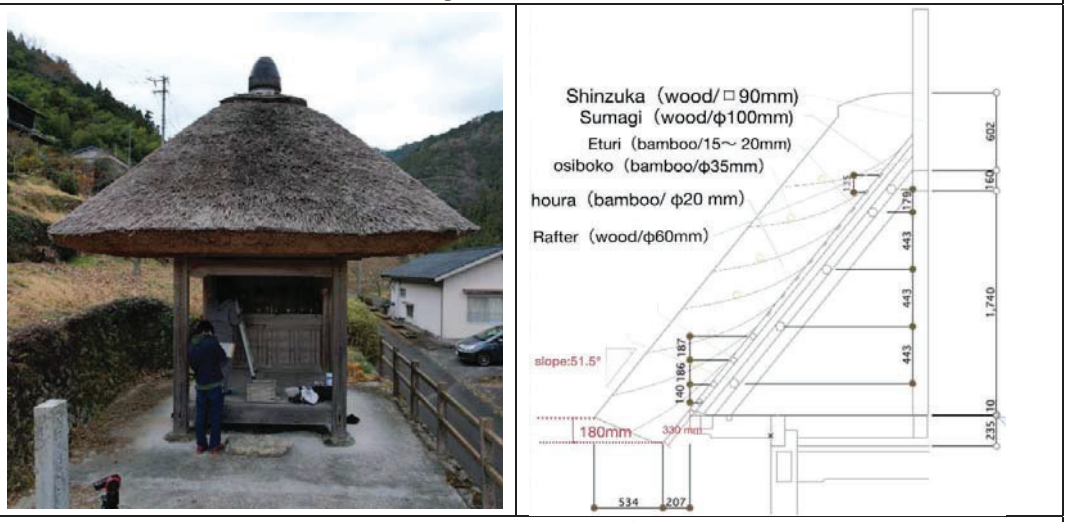

Figure 7: *Katahira Chado*

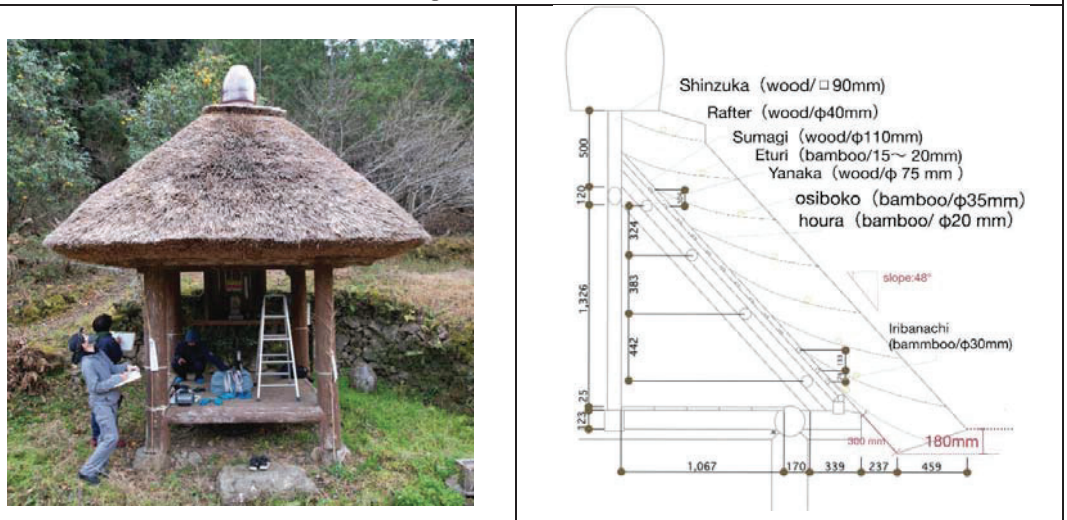

Figure 8: *Koyamachi Chado*

https://doi.org/10.52202/069179-0149

5 CONCLUSIONS

With clarity on the information on thatched roofs, owners, craftsmen, and governments are exploring and practicing methods of maintaining and organizing thatched-roof buildings with consideration that modern thatched roofs, materials, and craftsmen are limited. Considering the situation of the owner who faces challenges in re-roofing frequently, the craftsmen have devised their construction method to improve durability, reduce the frequency of repairs, and tried to replace the material as much as possible. Moreover, present Shikoku craftsman methods can be applied to thatched roofs anywhere in the country, and if these methods can be properly disseminated, we believe that they can greatly contribute to the maintenance of thatch.

In the future, the conditions necessary for growing thatch suitable for roofing require clarification. This is because if thatch, which serves as the chief material of thatched roofs, cannot be harvested, properly maintaining such roofs becomes impossible.

ACKNOWLEDGEMENT

This research was supported by JSPS Grant-in-Aid for Scientific Research JP19K12460 and Nippon Life Foundation. We would like to thank the families of the owners of the thatched-roof houses used in the study, the residents of Shirokawa area who maintain the thatched houses, the thatched-roof craftsmen of Yusuhara town, and the Board of Education of Miyoshi City and Seiyo City rice fields. We would like to thank Editage (www.editage.com) for English language editing.

REFERENCES

[1] Sae Naoki: LC System Analysis of Roof Materials for Thatch Buildings in Japan -Carbon Fixation Properties of Thatch Material Production Based on Establishing System Boundaries - Summary of Master's Thesis, Department of Architecture, Graduate School of Engineering, Kogakuin University, 2020.

[2] Jydsk Tækkemandslaug, Teknologisk Institut：Miljøvurdering af tag med tagrør og tækkemiscanthus, 2014.

[3] K. Ando: Folklore of Thatched Roofs, New Edition,-A private house as a living technique, Haru Shobo, 2017.

[4] M. Takamido, R. Takahashi, T. Shigematsu: Studies on the conservation of thatched roofs as a traditional component of the Village landscape, Journal of rural planning association, 10(1):25-35, 1991.

World Conference on Timber Engineering Oslo 2023

POSSIBILITIES TO PROMOTE CIRCULAR ECONOMY IN MID-RISE TIMBER CONSTRUCTION IN THE PROJECT PLANNING AND EARLY DESIGN PHASES

Ninni Westerholm[1], Juha Franssila[2]

ABSTRACT: This paper examines the client's decisions and actions taking place in the early project planning phase that could promote a circular economy in mid-rise timber construction projects. During the early planning phase, the client has an integral role in setting targets for circularity that the assembled construction actor-network carries out and tries to accomplish. However, the current research lacks concrete conceptualization and categorization of how circular economy principles can be carried out by the client in mid-rise timber projects. Therefore, the paper analyses one mid-rise timber construction project that has promoted circularity in all the life cycle stages. The study is conducted using a qualitative single case study method to identify which actors, resources, and activities can be utilized in the construction actor-network to achieve circularity targets set in project brief. The main finding is that a single actor in the construction actor-network has limited resources to promote circular economy in a mid-rise timber construction project and collective activities among project members are required to achieve circular economy targets. To conclude, the paper adds to the existing research by clarifying the client's role in utilizing the full circular economy potential of the construction actor-network.

KEYWORDS: circular construction, timber buildings, actor-network analysis

1 INTRODUCTION

Globally, the buildings and construction sector uses 36% of the energy, produces 39% of emissions [1], up to 40% of waste [2] and uses 50% of all the extracted materials [1]. Raw material extraction and processing cause 90% of biodiversity loss [3] and it is estimated that only 9% of the extracted resources are circular, meaning that is the amount re-used annually [4]. These numbers highlight the connection between the buildings and construction sector and three current predicaments: climate emergency, resource scarcity and the biodiversity crisis.

Using engineered timber for construction has great potential in climate change mitigation. If 90% of the new urban population would be housed in mid-rise timber buildings, 106 Gt of carbon dioxide emissions could be saved by 2100 [5]. Besides increasing the use of timber in construction, a transition from the now dominant linear economic model towards a circular economy could significantly lower the negative environmental impacts of construction.

A circular economy is based on the principles of designing out waste and pollution, keeping products and materials in use, and regenerating natural systems [6]. In a circular economy, materials and products are not taken out of the loop, but they are kept in the economy for as long, as efficiently and at the highest utility as possible. The emissions and use of virgin and non-renewable resources are minimized and the recycling of materials and products is maximized.

This paper presents design strategies that have been identified in the literature [7–11] to promote circularity in the built environment. Thereafter, circularity targets are presented that can be set to assure or promote the realisation of the strategies.

The paper focuses on the project planning and early design phases and the client's possibilities to promote circularity in the construction actor-network. Three key aspects support the chosen focus. First, research shows that most of the decisions that affect the circularity in construction projects are done in the early design phase [12]. Second, it is advocated in the project management and infrastructure project literature that the project planning phase is where the involved stakeholders have the best possibility to affect the final project and its outcomes [13]. Third, the clients are in a key position,

[1] Ninni Westerholm, Tampere University, Finland, ninni.westerholm@tuni.fi
[2] Juha Franssila, Tampere University, Finland, juha.franssila@tuni.fi

https://doi.org/10.52202/069179-0150

since they can include circularity as a goal in a construction project at an early stage [14].
The role of the client and the requirements and objectives they set for a project are obscure in the transition from linear to circular construction. Therefore, by identifying applicable circularity targets in realized construction projects and key activities in achieving them, a client can make early-phase decisions promoting circular economy during the building's entire life cycle.
This article identifies and describes how the client can utilize assembled construction actor-network to promote a circular economy in mid-rise timber projects. The following research questions were formed for the article: which circularity targets are present in the selected case study's project brief and how have they been met in the final construction (1), which are the key actors in the early design phase to promoting circularity in mid-rise timber projects (2), and what resources are required from the gathered actor-network to carry out the needed activities to reach the set circularity targets (3).
The article is divided into five chapters: introduction, literature survey, research methodology, results and discussion and conclusion. The literature review presents a summary of the identified circular economy strategies and related targets and gives an overview of the actor-network literature. The research method describes the selected case study and how it was analysed. The result chapter consists of three sub-chapters that will present the findings for the set research questions. The aim of the single case study analysis is to understand how the construction actor-network was able to realize the circularity targets in the early design phase of the project. Finally, the article presents a discussion of the findings.

2 LITERATURE SURVEY

2.1 CIRCULARITY STRATEGIES

This chapter discusses and describes design strategies that have been identified to promote circularity in the built environment. These strategies are then combined into a conceptual framework for this research.
The definitions of circular economy vary but optimising resource consumption, waste generation and/or embodied environmental impacts and regenerating natural systems target the main principles of a circular economy [15]. In the buildings and construction sector, circular strategies are of such nature that they promote one or more of the key aspects of a circular economy. 16 circularity strategies were identified through the literature survey (Table 1). Strategies focus on design aspects that can be implemented in the early design phase of the project.

Table 1: *Circularity strategies and their short descriptions. Sources:* [7–11]

Strategy	Description
Design for assembly/ disassembly	Reversible connections that allow easy reuse of components.
Design with circular materials	Choosing or substituting conventional materials with materials that are local, renewable and/or have low negative environmental impacts.
Design for adaptability/ flexibility	Designing buildings that can adapt to future changes regarding use, function, and available materials.
Design with modularity	Lean production and standard solutions that allow easier replacement, flexibility, and recycling.
Design for prefabrication	Off-site construction that allows material and time optimisation.
Design with secondary materials	Using recycled or reused materials instead of virgin materials.
Design for durability	Designing long-lasting buildings with long-lasting components.
Design with standardised solutions	Using standardised solutions (dimensions of components or connections) to ease efficient replacements and recycling.
Design for component and material optimisation	Reducing the amount and variations of materials and components used.
Design optimised shapes/ dimensions	Design with precision and specification to optimise the use of material and space.
Design for accessibility	Providing easy access to connections of components to ease maintenance, repairs, and recycling.
Design for layer independence	Making components and materials independent from each other's lifespan.
Design for short use	Designing buildings for their specific performance span.
Design symbiosis	Using resource outputs from one building as feedstock to other buildings.
Design energy-efficiency	Designing buildings that operate energy-efficiently.
Design for sharing	Buildings where spaces or equipment are in common use and thus reducing the need for private ownership.

2.2 ANALYSING ACTOR-NETWORKS

One way to approach network-based research analysis is to identify and examine the combination of activities, resources and actors that have been organized to work toward a specific goal. This is a focal approach applied in IMP research[16] and is identified as the ARA model focusing on industrial networks where actors undertake

activities using various resources [17]. Actors are individuals, companies or firms [18], resources can be defined as a different mix of competencies and set of assets that are used in conjunction [19] and activities as actions carried out by the actors to reach a specific target [20].

Networks are a general and abstract concept that can be used all the way from describing and modelling a complex business market to understanding a specific relationship between companies [21]. This paper focuses on understanding how a specific group of actors have been promoting circularity in a mid-rise construction project. The article incorporates the ARA-model approach to network analysis to examine the transition from identifying circularity targets in the competition brief to designing how they can be achieved.

3 METHODOLOGY

There is a lack of understanding of how circularity targets can be implemented into mid-rise timber construction projects. Therefore, this paper incorporates a qualitative single-case study [22] to examine one mid-rise timber construction project that has implemented multiple circularity strategies. Therefore, this study examines qualitatively one mid-rise timber project that promotes circularity in many ways [22]. The case study approach was chosen since it provides rich descriptions of the phenomena in the real-world context and is suitable for exploring new research areas where little is known about the subject [23,24]. Additionally, the case study research strategy can be used to investigate and retain information on organisational processes [22,25] by incorporating questions of “how” and “why” to reach a complete understanding of the studied real-world phenomena [32].

The selected case project consists of a densely built cluster of social housing buildings. The 3–4 story buildings have a hybrid structure consisting mainly of timber, concrete, and steel. The buildings have post-and-beam frames of glulam timber, glulam timber slabs, steel connectors, and a concrete core. Additionally, cross-laminated timber (CLT) walls are used in the buildings for stiffening the structure and steel beams are used in places where extra strength is needed. Moreover, the project represents mid-rise timber construction that has been designed and constructed by accounting for the following circularity characteristics:

- low carbon footprint
- energy-efficiency
- the use of renewable low-carbon construction materials
- material-efficiency.

Furthermore, the selected case study has received praise for its architectural design in the media and in the scientific community. Architectural design can be identified as one of the key activities in the project's early design phase but requires other activities' support to reach different circularity targets.

The competition brief was identified as the main data source for understanding the circularity targets set by the client. To complement the case study analysis, photographs of the project during construction were studied and one semi-structured interview was carried out to collect data from one of the key actors in the early design phase. Interviews have an essential role in case studies to fully understand the studied phenomenon [22,26]. The project manager of the design phase was selected as the interviewee because people in this role generally have a good overview of the early design phase of the project. The design phase project manager also acted as the leading architect in the case project.

Interview questions focused on finding out which circularity targets were eventually reached and what activities, resources and capabilities were required from the early design phase actor-network. The interview was audiotaped, transcribed and analysed.

Case studies incorporate different analysis methods such as a thematic analysis where collected case data is categorized into themes through coding [25]. The selected and formed themes were based on the literature survey and two main categories were selected: circular economy and actor-network. The circular economy theme was divided into sub-categories: circular spatial solutions, circular construction materials and circular connections. Firstly, circular spatial solutions prolong the building's lifespan or lower the users' negative environmental impacts, for example, flexible and adaptable spaces, spatially efficient spaces, or spaces in common use. Secondly, the characteristics of circular construction materials can be defined as renewable, low-energy, low-emissions, carbon-storing, healthy, durable, local, resource-efficient, recycled and recyclable (a material does not have to be all the above to be considered circular). Finally, circular connections include joints and other means of assembly that are durable and allow flexibility, disassembly, replacements, and maintenance with little or no loss of the building's or its components' value.

Similarly, the actor-network theme was divided into sub-categories: actors promoting circular economy, activities promoting circular economy and resources required to promote circular economy. The aim is to link the identified actions promoting circular economy to a specific construction actor and understand what resources were required to realize the set circularity targets.

The results chapter is divided into three sub-chapters. The first sub-chapter presents circularity targets found in the competition brief and circular design strategies they promote. The second sub-chapter presents how these targets have been met in the project. The third sub-chapter identifies the key actors in the actor-network and their activities and resources that enabled achieving a circular project.

4 RESULTS

4.1 IDENTIFIED CIRCULARITY TARGETS IN THE COMPETITION BRIEF

This section presents how circular economy has been included in the competition brief. Table 2 summarizes identified targets and connects them to strategies presented in Table 1.

Holistic sustainability, which includes ecological, economic and socio-cultural sustainability is a key goal in

https://doi.org/10.52202/069179-0150

the competition brief. The different aspects of sustainability are repeated throughout the brief, though it is not defined in greater detail how holistic sustainability should be achieved in the project. Even though the brief asked for holistic sustainability, this paper focuses on identifying how environmental sustainability was promoted.

The competition program states that the proposals are evaluated based on environmental quality, economic quality, sociocultural and functional quality, technical quality, process quality, and the quality of the area, including social and locational aspects. How these aspects have been considered must be shown in the requested drawing material and corresponding descriptions. The competition brief also states that interdisciplinary design efforts are highly appreciated.

The program asks for proposals that have a minimal burden on the global and local environments. They have specified that this includes resource-saving principles both during the construction and operation of the buildings and their external areas. Additionally, materials must be selected based on an LCA approach where the focus is on using building materials that can be produced locally or regionally with low energy consumption, and where materials from a renewable raw material resource are preferred. When choosing materials, consideration must also be given to robustness against expected wear and tear, which steers towards durability.

It is also stated that the project must consider efficiency in energy consumption, water consumption, waste management, materials, and land use. The buildings must reach at least a low-energy class in 2015. In addition, an environmental vision for the entire building is desired and its resilience to and handling of climate change is also included.

The competition brief also recommends pursuing a DK-DGNB silver or gold certificate. The competition organizers emphasized that the desire for a certain certification must not be perceived as something limiting further sustainability measures in the answer to the competition task. The DK-DGNB system is a Danish-adapted evaluation system that is based on the DGNB system developed in Germany. The DK-DGNB system is based on the three central pillars of sustainability: ecological, economic and socio-cultural sustainability, and these three are weighted equally in the evaluation process. Therefore, ranking in DK-DGNB can be seen as a tool to measure how well the competition proposal delivers holistic sustainability.

The competition program also included flexibility. The brief describes that apartments should provide space to live that is flexible and has the possibility of adaptation in case living situations change over time. The brief does not directly say that flexibility should be considered in the structural design, but the DNGB classification considers this aspect of flexibility and thus designing with it in mind helps achieve good scores in the ranking, which was required in the brief.

The competition brief also included targets supporting design for layer independence and accessibility. First, by specifying that all materials that have a shorter expected life span than the building must be able to be replaced easily, economically and with little inconvenience for the residents. Second, by stating that easy replacement of parts is highly appreciated.

Design for material and component optimisation is also vaguely promoted in the brief since it is stated that simple construction systems are preferred. Besides simplicity, the brief considers proven constructions preferable, which connects to standardised solutions and modularity.

One of the focuses of the brief is on social sustainability and some aspects of social sustainability promote circularity. Without directly demanding a sharing economy, the brief discusses its benefits and gives examples of it, such as sharing cars, shared guest rooms, and shared spaces to organize events. Moreover, the brief includes the option of constructing a separate community house, which can be used to facilitate sharing.

Table 2: *Targets from the competition brief and connected circular strategies*

Target	Strategy
Flexible apartments that can adapt to changing life situations	Design for adaptability/ flexibility, design for assembly/disassembly
Renewable materials	Design with circular materials
Local or regional materials	Design with circular materials
Materials with low embodied energy	Design with circular materials
Robustness against wear and tear	Design for durability
Low-energy class	Design energy-efficiency
DK-DNGB gold or silver certificate	Design with circular materials, design for assembly/ disassembly, design for durability, design energy-efficiency
Materials with short service-life must be easily replaced	Design for accessibility, design for layer independence
Simple solutions	Design for component and material optimisation
Common spaces	Design for sharing

The competition brief included sustainability targets in various ways. The project that won the competition and got built used a circular economy approach to respond to many of the things asked in the brief. It is to be noted that the brief never actually mentions circular economy. Nonetheless, the key aspects of the economic model were included and described with varying detail.

4.2 IDENTIFIED CIRCULAR ECONOMY RESPONSES IN THE CASE PROJECT

Table 3 explains how the project has responded to the targets set in the competition brief and how these responses have promoted circularity. The table also shows whether the targets were met, exceeded or undershot. In

Table 3: *Identified circular solutions in the case project and how they respond to targets set in the brief and how they promote different circular strategies*

Target	Response	Strategy
Flexible apartments that can adapt to changing life situations	Walls and openings can easily be altered, and apartments can be combined vertically and horizontally	Design for adaptability/ flexibility, design for assembly/disassembly, design for accessibility, design for layer independence
Renewable materials	Timber-based frame, CLT walls that are exposed on the interior, unplaned lye-treated timber boards in the interior, and exterior facades of untreated wood. Because of the vast use of natural materials the carbon footprint is estimated to be 50-70% of the conventional solution.	Design with circular materials
Local or regional materials	Using local or regional materials. The timber was mainly from Sweden and Germany.	Design with circular materials
Materials with low embodied energy	The structure is timber-based and has slow embodied energy	Design with circular materials
Robustness against wear and tear	CLT is used in walls and left exposed. Other interior surfaces of lye-treated timber. Maintenance is limited mainly to sanding and redoing the lye-treatment.	Design for durability
Low-energy class	Energy-efficient buildings with lots of daylight	Design energy-efficiency
DK-DNGB gold or silver certificate	DK-DNGB gold	Design with circular materials, design for assembly/ disassembly, design for durability, design energy-efficiency
Materials with short service-life must be easily replaced	Timber facades and interior panelling are designed to be easily replaced	Design for accessibility, design for layer independence
Simple solutions	Repetitive post-and-beam grid. Exposed CLT walls, untreated facades, lye-treated interior surfaces. Less material-layers than in conventional construction.	Design for component and material optimisation, design with circular materials, design for adaptability/ flexibility, design for assembly/ disassembly, design for accessibility, design for layer independence
Community house	Community house with common activities and community space with kitchen and toilets. Additionally, there is a maintenance-room for sharing of used objects, furniture, books etc	Design for sharing

some cases, when comparing the response to a target, the project delivered solutions that were better at promoting environmental sustainability than what was asked for. For example, the brief asked for flexible apartments that can adapt to changing life situations but the project consists on flexible buildings, in which changes can be made within apartment but also through combining apartments in various ways. However, it is to be noted that it was stated in the competition brief that proven structures are preferred and that the project is contradicting this as the proposed structural system is piloted in this project. However, the new system was deliberately chosen because the benefits to be achieved with it, such as flexibility, were well in line with the other targets in the brief.

4.3 ACTOR-NETWORK AS A CIRCULAR ECONOMY PROMOTER

The single case study revealed that three key actors can be identified from the early design phase that are responsible for promoting circular economy (Picture 1). All the actors were in tight collaboration throughout the design phase with varying roles and complementing resources.

Firstly, the client can be seen as an enabler for the project by first setting targets in the project brief and later collaborating with other network members to achieve and approve a quality product for the tenants. Even though the client's role is more passive than those of the architects and engineers, the choices made by the client have a great impact on the overall sustainability of the process. Specifically in this project, the client was open-minded and allowed the architect and the engineer to create innovative solutions as part of promoting circularity. The client was, understandably, sceptical about some of the suggested solutions, especially of those concerning the

https://doi.org/10.52202/069179-0150

maintenance phase of the building. Nonetheless, with an active discussion between the actors, enough reassurance was produced to clear out doubts concerning for example different material choices and surface treatments. Overall, the client approved all the suggested decisions by the actor network after going through all the possible operational scenarios during the maintenance phase.

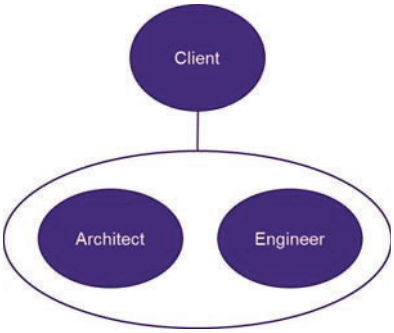

Picture 1: *Key actors in the design phase promoting circular economy targets*

Secondly, the architect and the engineer combined their resources during the planning phase of the project and the interviewee described the collaboration as a 50/50 relationship. However, the architect was the official project manager during the planning phase and took more responsibility for the finalized solutions. The engineer had a role to supplement the actor-network with technical capabilities that enabled the detailed level of planning and provided an additional understanding of the regulatory framework. In particular, the engineer had more understanding of acoustic and fire requirements that are key aspects in timber construction but the architect made sure that the surface materials matched the client's requirements. The interviewee summarized that experience in timber construction and collaboration with the engineer in previous projects enabled the providing of circular solutions for the sustainability targets set by the client.

Thirdly, innovative construction projects are typically perceived as high-risks and high-cost in comparison to conventional solutions. This was also a concern highlighted by the interviewee during the project. However, the project team was able to reach cost-effective results and reach the financial requirements for social housing. To meet the set financial requirements, the interviewee described that they focused resources in the early design phase on understanding how the project contractors should be tendered to reach an optimal outcome. The architect and the engineer came up with a

Table 4 *Activities, resources and actors promoting circular economy in the mid-rise timber construction design phase*

Activities	Resources	Actors
Sustainable material selection	Experience and specialization in timber construction and a circular economy in housing projects to optimize material selection and use with fire and acoustic requirements in mind	Architect, engineer
LCA	Understanding of the building component life spans, environmental impact, cost of their replacement and the possibility to replace them if needed. Collaboration with the client to communicate and ensure good quality building component life cycle performance	Architect, client
Maintenance planning for tenant turnovers	Understanding how wood material will behave under tenant use and agreeing on the surface material tolerance with the client	Architect, client
Design for disassembly and flexibility	Utilizing the spatial expertise of the architect and combining it with the technical understanding of engineers on how timber structures can be designed with mechanical joints	Architect, engineer
Design solutions that enable easy construction phase assembly	Designing the solutions with the tendering process in mind, market must have the operators to realize the design solutions	Engineer, architect
A structural system that enables good-quality moisture control in the building phase	The possibility to erect the building without moisture damage in the structures by using skeleton structure and taking care of façade elements' moisture control	Architect, engineer
Innovation during the design phase to develop solutions for circularity	Collaboration with client to ensure the functionality of new approaches and solutions. Enough financial understanding and resourcing in working with development projects	Client, architect, engineer

solution where the tendering was divided into three tenders, while conventional projects only use one main contractor. This enabled the actor-network to acquire more specialized contractors for the building phase that were able to produce cost-effective solutions. However, the required additional design work affected the architect's commission negatively. Overall, the case project was financially successful.

Finally, a more specific collection was produced from all the identified circularity promoting activities, resources, and the actor responsible for them (Table 4). The interviewee was able to describe how each identified circularity activity was combined with a specific resource to reach the set circularity targets described in Table 3. As a result, a description of how each actor can contribute to promoting a circular economy in the early design phase.

In the interview, it was also mentioned that it would be good to get the product manufacturers involved in the early design stage. It was also noted that this is usually difficult because the product manufacturers are typically selected based on tenders at a later design stage. However, this prompts us to discuss if the tendering and selection of manufacturers should be done earlier or if it would be possible to get product manufacturers involved in early planning by other means.

5 DISCUSSION

The case study analysis showed that it was possible to design a project that is contradicting the competition brief by introducing a new system though the brief clearly states that proven systems are preferred. However, the design team has successfully argued that their system is more in line with sustainability than conventional solutions. The used hybrid construction system is based on mechanical metal connectors that allow easy assembly and disassembly and it is the result of tight cooperation between architects and engineers. Though the system has not been used and proven to function well in advance, the joint effort of the architects and engineers is in line with the competition brief where it was claimed that interdisciplinary cooperations are highly appreciated.

The case study project represents design for disassembly (DfD) even though this was not directly required in the competition program. However, the client and the competition organisers could include DfD in the brief to promote material efficiency. DfD improves the possibilities of reusing the materials, as well as the flexibility of the project.

The strategies to promote a circular economy are many and some are easily measurable, which makes it easier to set targets in the project brief that assure circular measures. For example, if the goal is to use secondary materials, an amount of reused or recycled content can be defined in the project brief [8,27]. Setting a low carbon footprint or carbon balance in the brief would, besides promoting secondary materials, also promote the use of renewable and local materials because of their generally lower carbon footprints [8,28–30]. Setting carbon demands that include Module D (Benefits and loads beyond the system boundary) favour the use of bio-based materials such as timber (carbon storage) and DfD that allows easy reuse and value retention of components.

Whereas recycling targets and carbon goals increase the use of materials with low negative environmental impacts, material passports have been identified to promote circularity after deconstruction. Requiring materials passports means encompassing the life cycle of construction materials during the design phase, making it easier to design for reuse and disassembly and to plan the future of the materials in case of deconstruction [11,31]. Reversible design can also be promoted in the early project planning phase by requiring detailed demolition plans in the design phase and mechanical joints in construction.

Defining technical solutions precisely is challenging in the project planning phase, as it complicates the tendering that takes place later in the project. However, in the project planning phase, the pre-fabrication, modularity and repeatability, which have been identified to promote resource efficiency, can be determined to some extent.

Material efficiency can be promoted through technical design but also through high-quality architectural design. Well-designed buildings are more likely to be well taken care of, which prolongs the buildings' lifespan. Architectural quality can be increased by organizing architecture competitions and selecting the most promising plan and design teams. Additionally, designers can promote sustainability by preparing for possible future scenarios by designing buildings that can adapt. Adaptability or flexibility can be considered in the early project planning phase. In apartment buildings, this could be done by requiring plans for how to combine apartments vertically or horizontally, which was done by the architects in the studied case even though it was not required.

This study was based on only one case project. Therefore, the conclusions from this study cannot be generalized and assumed to be valid in all projects. To form a more generalized understanding of how different construction actor-networks can reach ambitious circularity targets a broader data collection and analysis is required. However, there are a limited amount of realized mid-rise timber projects that follow the key principles of a circular economy. In conclusion, the results of this paper should rather be read as indicative than absolute.

6 CONCLUSIONS

The studied case project showed various ways of promoting circular economy in mid-rise timber buildings. Many key aspects of a circular economy were already present in the early project planning phase. This paper set out to investigate how clients can include circularity in project briefs and how these can be met in the final project, who are the key actors to promote circularity in mid-rise timber projects and what resources are needed for the actors to deliver a circular construction project. The main findings are:

- The client can include targets steering towards circular solutions in the project planning phase by writing them into the project brief. Such targets include: flexibility, local and renewable

https://doi.org/10.52202/069179-0150

materials, materials with low embodied energy, robustness against wear and tear, energy-efficiency, sustainability certificates, easy replaceability of components, simple structural solutions and common spaces.

- The identified key actors from the early design phase that are responsible for promoting circular economy are the client, the architects and the engineers.
- The client's role is more passive in the design phase in comparison to those of the architects and engineers but acts like the enabler of circular solutions
- Even though the client can include circularity in the project brief, a competent design team can exceed the targets and deliver more circular solutions
- When realising circular mid-rise timber buildings, previous collaboration between the architects and engineers, experiences with timber buildings and complex buildings, knowledge of LCA, and a deep understanding of circularity in construction are beneficial for the design team.

ACKNOWLEDGEMENT

We would like to acknowledge Antti Tuure, Aku Aspila, Jesse Lietzen and Harri Sivu from the Graduate School of Industrial Timber Construction, as well as professor Sofie Pelsmakers and post-doctoral researcher Jukka Puhto for the questions they raised and the thoughts they shared that helped shape this research.

REFERENCES

[1] Global ABC., IEA., UNEP. Towards a zero-emissions, efficient and resilient buildings and construction sector. 2019 Global Status report, 2019.

[2] UNEP. Sustainable Buildings and Climate initiative, 2009.

[3] IRP. Global Resources Outlook 2019: Natural Resources for the Future We Want, 2019.

[4] Circle Economy. The Circularity Gap Report: Closing the Circularity Gap in a 9% World. Circle Economy, 2019.

[5] Mishra A., Humpenöder F., Churkina G., Reyer CPO., Beier F., Bodirsky BL., et al. Land use change and carbon emissions of a transformation to timber cities. Nature Communications 13:4889, 2022.

[6] Ellen MacArthur Foundation. What is circular economy, n.d.

[7] Munaro MR., Tavares SF., Bragança L. The ecodesign methodologies to achieve buildings' deconstruction: A review and framework. Sustainable Production and Consumption 30:566–83, 2022.

[8] Kozminska U. Circular design: Reused materials and the future reuse of building elements in architecture. Process, challenges and case studies. IOP Conf Ser Earth Environ Sci, vol. 225, Institute of Physics Publishing, 2019, 2019.

[9] Eberhardt LCM., Birkved M., Birgisdottir H. Building design and construction strategies for a circular economy. Architectural Engineering and Design Management 18:93–113, 2022.

[10] Ellen MacArthur Foundation. Potential for Denmark as a Circular Economy. A Case Study from: Delivering the Circular Economy - A Toolkit for Policy Makers, 2015.

[11] Westerholm N. State of Play for in Europe Circular Built Environment, UN OPN SBC Programme, 2020.

[12] Basbagill J., Flager F., Lepech M., Fischer M. Application of life-cycle assessment to early stage building design for reduced embodied environmental impacts. Building and Environment 60:81–92, 2013.

[13] Heravi A., Coffey V., Trigunarsyah B. Evaluating the level of stakeholder involvement during the project planning processes of building projects. International Journal of Project Management 33:985–97, 2015.

[14] Huovila P., Westerholm N. Circularity and Sustainability in the Construction Value Chain. IOP Conference Series: Earth and Environmental Science 1078:012004, 2022.

[15] Reike D., Vermeulen WJV., Witjes S. The circular economy: New or Refurbished as CE 3.0? — Exploring Controversies in the Conceptualization of the Circular Economy through a Focus on History and Resource Value Retention Options. Resources, Conservation and Recycling 135:246–64, 2018.

[16] Hakansson H., Johanson J. A model of industrial networks. Industrial networks - a new view of reality, , 1992, p. 28–36, 1992.

[17] Håkansson H., Gadde L-E. Four decades of IMP research – the development of a research network. IMP Journal 12:6–36, 2018.

[18] Biem A., Caswell N. A value network model for strategic analysis, 2008.

[19] Barney J. Firm Resources and Sustained Competitive Advantage. Journal of Management 17:99–120, 1991.

[20] Möller K., Rajala A. Rise of strategic nets - New modes of value creation. Industrial Marketing Management 36:895–908, 2007.

[21] Håkansson H., Ford D. How should companies interact in business networks?, 2002.

[22] Yin RK. Applications of case study research, 2003.

[23] Gustafsson J., Gustafsson J. Single case studies vs. multiple case studies: A comparative study, 2017.

[24] Eisenhardt KM., Graebner ME. Theory Building from Cases: Opportunities and Challenges. vol. 50, 2007.

[25] Miles MB. Qualitative data analysis : a methods sourcebook. 4th edition. SAGELos Angeles, 2020.

[26] Knight A., Roddock L. Advanced research methods in the built environment. Wiley-BlackwellOxford, 2008.
[27] United Kingdom Green Building Council. Circular economy guidance for construction clients : How to practically apply circular economy, 2019.
[28] Asdrubali F., D'Alessandro F., Schiavoni S. A review of unconventional sustainable building insulation materials. Sustainable Materials and Technologies 4:1–17, 2015.
[29] Skullestad JL., Bohne RA., Lohne J. High-rise Timber Buildings as a Climate Change Mitigation Measure - A Comparative LCA of Structural System Alternatives. Energy Procedia 96:112–23, 2016.
[30] Takano A., Hughes M., Winter S. A multidisciplinary approach to sustainable building material selection: A case study in a Finnish context. Building and Environment 82:526–35, 2014.
[31] Høibye L., Sand H. Circular economy in the Nordic construction sector Identification and assessment of potential policy instruments that can accelerate a transition toward a circular economy, 2018.

https://doi.org/10.52202/069179-0150

World Conference on Timber Engineering Oslo 2023

EFFECT OF RESIN IMPREGNAITON INTO WOOD CELL ON LATERAL RESISTANCE OF SCREWED JOINT CONNECTING SOLID WOOD AND STEEL PLATE

Keita Ogawa[1], Kenji Kobayashi[2], Satoshi Fukuta[3]

ABSTRACT: During lateral loading to dowel-type timber joints, embedment deformation occurs around the contacting parts of dowels and wood. Hence, the embedment properties of wood are vital to the development of joints with high lateral resistance. In this study, the potential of resin impregnation for strengthening the embedment properties is analyzed. A lateral loading test is conducted using a screwed joint connecting solid wood and a steel plate. Resins are impregnated into the cell walls around the screws. Test results indicate that the initial stiffness is twice that of the control specimen. The yield load and maximum load are not significantly affected by the resin impregnation. Additionally, the resin-impregnated specimens indicate brittle fracture and low deformability, particularly in the case involving sapwood screwing.

KEYWORDS: Screwed joint, Lateral resistance, Resin Impregnation, Initial stiffness

1 INTRODUCTION

Owing to increasing interest in large-scale timber buildings, the development of timber joints with higher resistance performance has received significant attention. Dowel-type joints are one of the most general connecting methods used not only in housing, but also in large-scale buildings.

The lateral resistance of the joints significantly affect the seismic performance of buildings constructed using them. When a lateral load is exerted on a dowel-type joint, the dowel locally embeds the wood member around the contact part between the dowel and wood. Therefore, the strengthening of wood against embedment loads is effective for developing joints with higher lateral resistance.

Based on a micro-level observation of wood embedment, embedment can be regarded as the crushing of wood cells (Figure 1), and a method for preventing this crush is desired. In this regard, the authors investigated the potential of resin impregnation [1], which allows the local impregnation of resin into wood cells. If the wood cells around the dowel are filled with resin before the lateral load is applied, then an improvement in the embedment property can be expected.

Previously, the authors attempted to apply resin impregnation techniques to bolted joints [2]. Consequently, the initial stiffness and yield load improved significantly, i.e., by 104% and 73%, respectively. Additionally, the embedment properties of Japanese cedar (*Cryptomeria japonica* D.DON) were revealed using an embedment test [3], i.e., its stiffness improved by 278% and 94% under parallel and perpendicular loading, respectively. Resin impregnation is expected to improve other dowel-type joints.

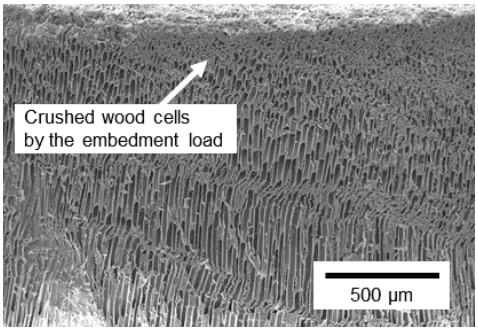

Figure 1: *Crushed wood cells under the embedment load by dowel-type fasteners*

Screwed joints are typically used in modern timber construction. Although the diameter of a screw is smaller than that of a bolt, their main mechanism is similar. In this study, the authors attempted to apply a resin impregnation to a screwed joint. A lateral load test was conducted to evaluate the effects of the impregnation.

2 MATERIALS AND METHOD

2.1 SPECIMEN PREPARATION

A lateral load test with screw joints was conducted based on ASTM D1761-20 [4], as shown in Figure 2. Air-dried

[1] Keita Ogawa, College of Agriculture, Academic Institute, Shizuoka University, Japan, ogawa.keita@shizuoka.ac.jp
[2] Kenji Kobayashi, College of Agriculture, Academic Institute, Shizuoka University, Japan, kobayashi.kenji.b@shizuoka.ac.jp
[3] Satoshi Fukuta, Aichi Center for Industry and Science Technology, Japan, fukuta@aichi-inst.jp

https://doi.org/10.52202/069179-0151

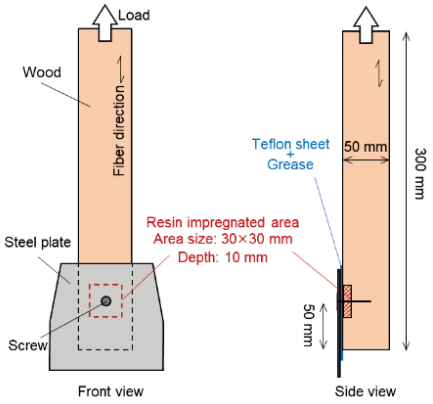

Figure 2: *Screwed joint specimen and loading method*

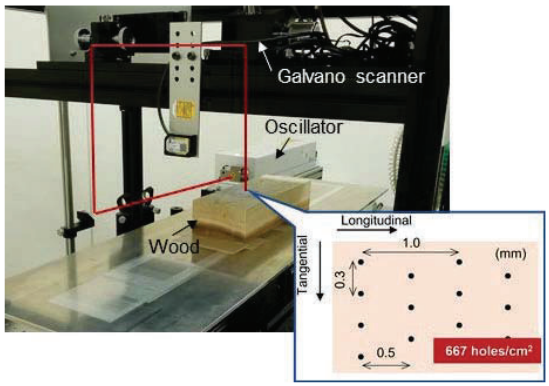

Figure 3: *UV laser incision. Red line shows trajectory of UV laser from oscillator to wood surface*

Japanese cedar (*Cryptomeria japonica* D.DON), a steel plate measuring 2.3 mm thick, a TB-45 screw (Tanaka Co. Ltd.; diameter: 5.1 mm; length: 43 mm) were used. To assemble the joint specimen, Teflon sheets and grease were inserted between the wood member and steel plate to prevent friction [5].

The wood members were treated via resin impregnation on their surfaces. First, microscopic incisions were created using an ultraviolet (UV) laser around the area where the screw was tapped. As shown by the red square in Figure 2, the area measured 30 mm × 30 mm. A diode-pumped solid-state Q-switched laser (Talon355-15SH, Spectra-Physics) was used for laser oscillation, and a Galvano scanner was used to create the incision pattern, as shown in Figure 3. The diameter, depth, and density of the incision were approximately 80 µm, 10 mm, and 667 holes/cm^2, respectively.

Next, the resin was impregnated from the incised area by brush painting operation. Two types of resins were used in this study: acrylic monomers (DIAKITE PE-2730, Toeikasei Co. Ltd.) and urethane prepolymers (PS-NY6, Kotobukikakoku Co. Ltd.); hereinafter, they are referred to as acryl and urethane, respectively. In the case of acryl, 2.2'-azobisisobutyronitrile (0.6 parts by weight) was incorporated as a polymerization initiator; it was heated at 140 ℃ and cured for 30 min. In urethane, the wood members were cured for one week in a testing room. The evaporation residue of urethane was approximately 40%.

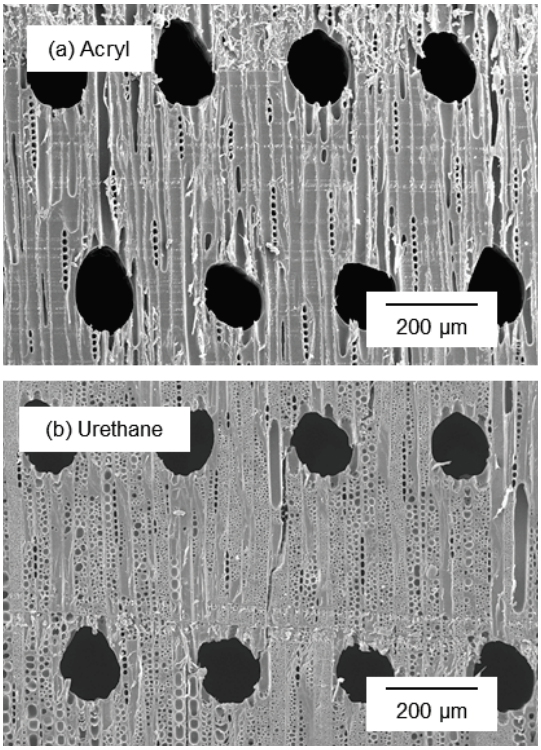

Figure 4: *Holes created using UV laser and resins filled into wood cells*

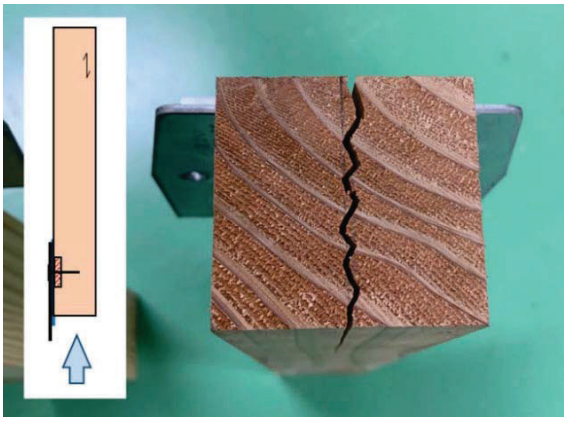

Figure 5: *Crack observed (from blue arrow) at screwing location in test groups with resin impregnation.*

Examples of scanning electron microscopy images are shown in Figure 4. Both images show that the resins filled the wood cells.

The amount of impregnated resin differed for each specimen. As described in our previous study [2], resins impregnate more in sapwood than in heartwood. The specimens used in this study exhibited the same tendency. In one incision area (represented as the red square in Figure 1), 16.32 ± 3.43 g of acryl was impregnated into the sapwood. Subsequently, the amount R per incision volume was calculated as follows:

$$R = \frac{W}{V} = \frac{W}{A \times d}, \quad (1)$$

https://doi.org/10.52202/069179-0151

Table 1: *Number of spesimen for each specimen group*

Group	Resin	Number of speciems			
		Prepared		Tested	
		Heartwood	Sapwood	Heartwood	Sapwood
Control	None	10	8	9	8
Acryl	Acryl	10	8	10	4
Urethane	Urethane	10	8	9	0

where W is the mass of the impregnated resin; V is the incision volume; and A and d are the incision (30 mm × 30 mm) and depth (10 mm), respectively. Using the equation above, the R of acryl impregnated into sapwood was calculated to be 1813 ± 381 kg/m^3, whereas that impregnated into heartwood was 430 ± 413 kg/m^3. Meanwhile, 1971 ± 576 kg/m^3 and 318 ± 2.93 kg/m^3 of urethane were impregnated into the sapwood and heartwood, respectively.

Three testing groups were prepared for this study: two types of resin (acryl and urethane) and a control group. Eighteen specimens were prepared for each group. However, a prominent crack beginning from the screwed point to the bottom face of the wood member occurred in some specimens, as shown in Figure 5. Subsequently, lateral loading tests were halted on the specimens. The replicates for each group are presented in Table 1. Cracks occurred in many specimens of sapwood. This implies that a higher amount of resin impregnation may cause brittleness in wood.

2.2 TESTING METHOD

The lateral loading test was conducted using a universal testing machine (AG-I 250kN, Shimadzu Co., Ltd.), as shown in Figure 6. A steel plate was fixed to the testing machine and an upward load was applied to the wood member. During the test, the load and relative slip between the wood member and steel plate were recorded. A load cell equipped with a testing machine (SFL-50kNAG, Shimadzu Co. Ltd.) was used to measure the load. To measure the relative slip, a displacement transducer (SDP-100CT, Tokyo Measuring Instruments Lab.) was attached to the wood member and the target was attached to the steel plate. The alignment support was adjusted to correct the load axis during the testing.

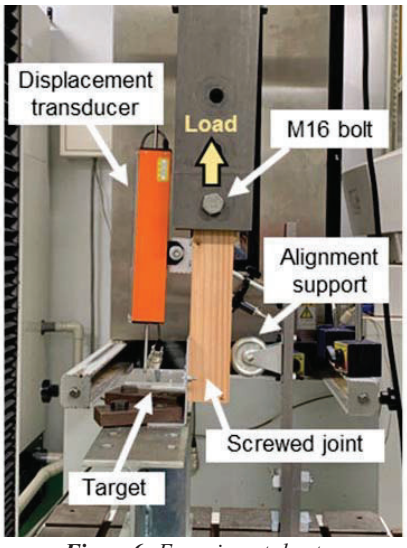

Figure6: *Experimental setup*

3 RESULTS AND DISCUSSIONS

3.1 RELATIONSHIP BETWEEN LOAD AND SLIP

The relationship between the load and slip for each specimen group obtained via the lateral test is shown in Figure 7. For the control group (Figure 7(a)), the load increased linearly with slip at the beginning of testing. When the load reached approximately 1.5 kN, the slope began to decrease. When the slope decreased, the load did not decrease, and most specimens maintained their load until the slip reached approximately 30 mm.

Compared with the control group, acryl and urethane indicated higher slopes at the beginning of the test. However, the load decreased significantly in some specimens after linearity was observed. Cracks occurred from the screwed point to the bottom surface of the wood member. The loads of four of the specimens decreased significantly before the slip reached 5 mm. These specimens were screwed onto sapwood. This result shows that even though cracks did not occur during the joint assembly, the joint was in the limit state of brittle failure. The load of most joint specimens screwed onto the heartwood did not decrease drastically until the slip reached approximately 20 mm.

3.2 CHARACTERISTICS

To evaluate the characteristics of the joint specimens, the relationship between the load and slip was further analyzed using a perfect elasto-plastic model [6, 7]. The method to obtain the characteristic values is explained below and shown in Figure 8. The black line indicates the relationship between the load and slip obtained from the lateral loading test. Here, P_{max} and δ_{max} are the mean maximum load and the slip at the maximum load, respectively. First, a direct line is drawn between $0.1P_{max}$ and $0.4P_{max}$, and between $0.4P_{max}$ and $0.9P_{max}$; the lines drawn for the former and latter are referred to as lines I and II, respectively. Line II shifts until it satisfies the load-slip relationship, and the shifted line is named Line III. Subsequently, a new line parallel to the horizontal axis that passes through the intersection of Lines I and III is

https://doi.org/10.52202/069179-0151

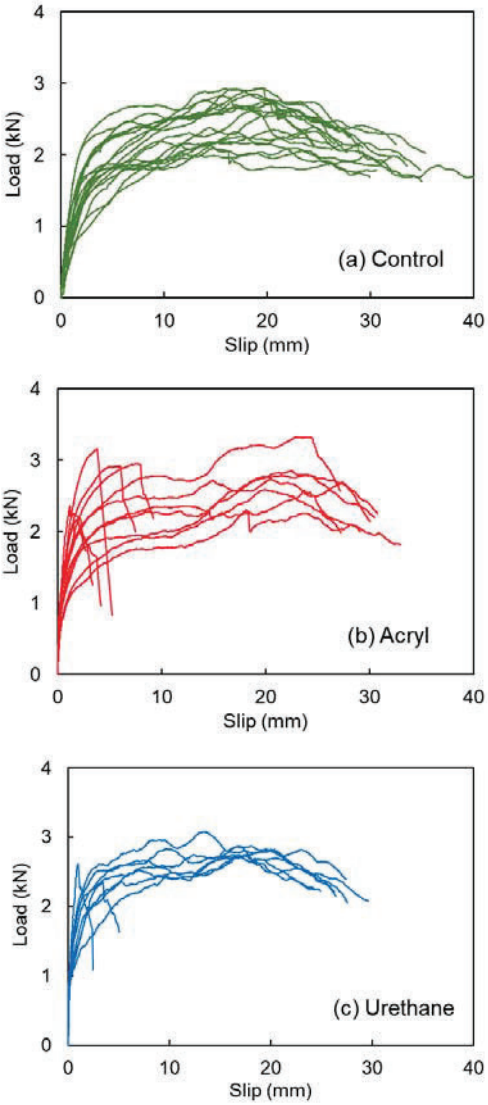

Figure 7: *Relationship between load and slip*

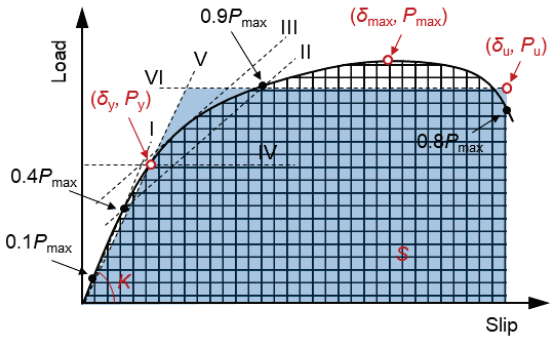

Figure 8: *Perfect elasto-plastic model [7]*

drawn and named Line IV. The intersection of Line IV with the load-slip relationship is regarded as the yield point, and the abscissa and ordinate of the point are the slip at yielding δ_y and the yield load P_y, respectively. The line connecting the origin and yield point is named Line V, and the slope of Line V is regarded as the stiffness K. Next, the slip at the ultimate load δ_u is determined as the abscissa of a point when the load is decreased to $0.8P_{max}$ after surpassing the maximum load. If the load does not decrease until the slip reaches 30 mm, then $\delta_u = 30$ mm is used instead of the point at $0.8P_{max}$. Subsequently, the energy based on the load-slip relationship from the origin to δ_u (hatched region in Figure 8) is determined and denoted as S. Next, a line parallel to the horizontal axis, named Line VI, is drawn such that the area of the trapezoid, which comprises Line V, Line VI, the horizontal axis, and the line $X = \delta_u$ (blue region in Figure 8), is equivalent to the energy S. The ordinate of Line VI is regarded as the ultimate load P_u. The characteristics obtained using the model are listed in Table 2.

The most improved characteristic owing to resin impregnation was the initial stiffness. Whereas the initial stiffness of the control was 0.75 kN/mm, those of acryl and urethane were 1.57 and 2.01 kN/mm, respectively. This implies that the initial stiffness was more than doubled by the resin impregnation. Table 2 shows similar average values for the parameters related to the load, i.e.,

Table 2: *Characteristics obtained using perfect elasto-plastic model*

Group		P_y (kN)	δ_y (mm)	K (kN/mm)	P_{max} (kN)	δ_{max} (mm)	P_u (kN)	δ_u (mm)
Control	Average	1.60	2.47	0.75	2.50	17.78	2.27	30.06
	SD	0.20	1.10	0.28	0.32	3.06	0.27	4.46
Acryl	Average	1.64	1.11	2.01	2.77	12.79	2.47	20.90
	SD	0.31	0.68	1.05	0.19	6.31	0.23	9.65
Urethane	Average	1.56	1.54	1.57	2.68	13.37	2.39	17.93
	SD	0.27	0.97	0.94	0.35	9.23	0.34	12.50

P_y: Yield load; δ_y: Slip at yielding; K: Initial stiffness; P_{max}: Maximum load

δ_{max}: Slip at maximum load; P_u: Ultimate load; δ_u: Slip at ultimate load

https://doi.org/10.52202/069179-0151

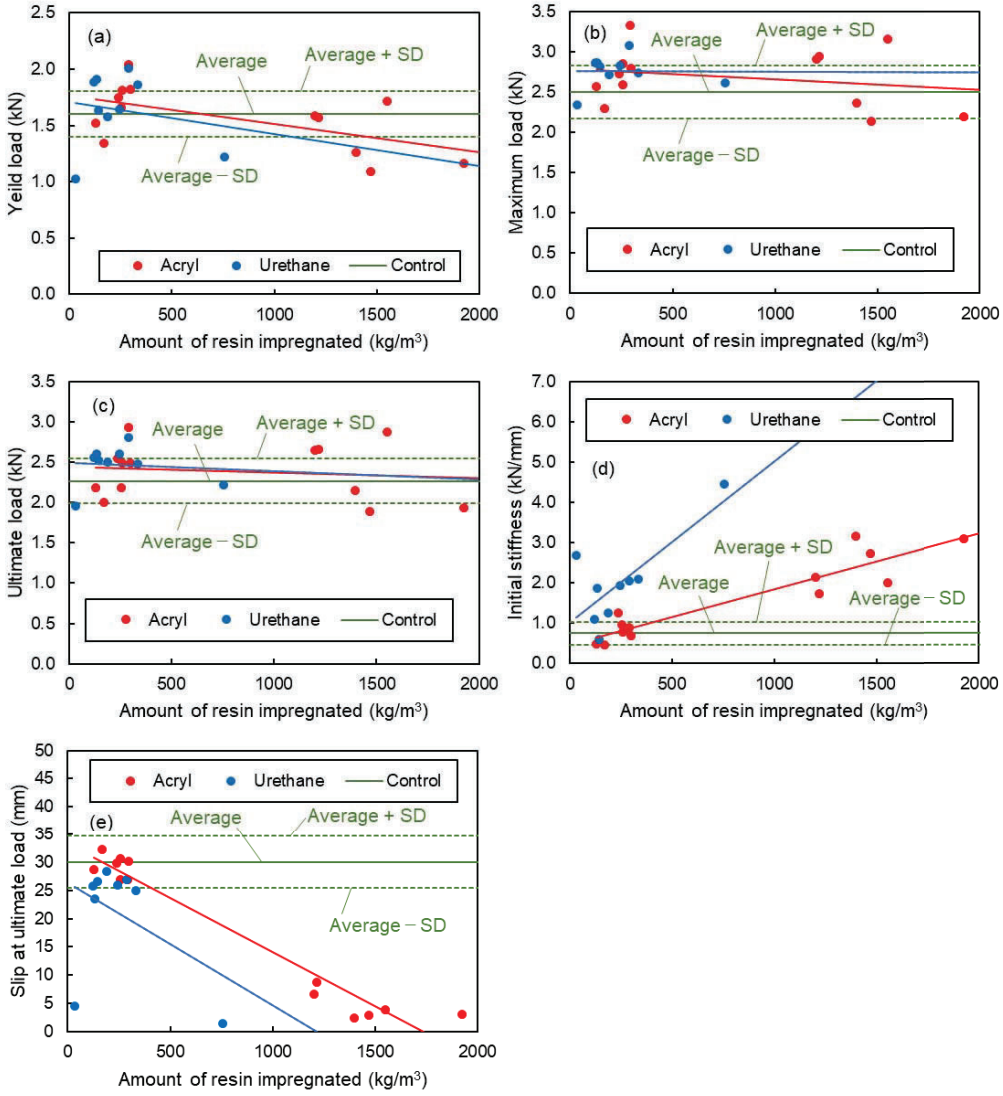

Figure 9: *Relationship between characteristics and amount of resin impregnated*

the yield load, maximum load, and ultimate load. In summary, resin impregnation can improve the lateral resistance of the joint; however, the effect was limited to the range of small slips. Meanwhile, the values of parameters related to deformation, such as slip at yielding, slip at the maximum load, and slip at the ultimate load, decreased due to resin impregnation. This shows that resin impregnation results in decreased deformability. The result indicating the increasing brittleness of the joints is a critical issue that must be addressed closely.

3.3 INFLUENCE OF AMOUNT OF IMPREGNATED RESIN ON CHARACTERISTICS

As described in Section 2.1, the amount of impregnated resin differed between sapwood and heartwood. In this section, the effect of the amount of impregnated resin on the characteristics of sapwood and heartwood is discussed.

Figure 9 shows the relationship between the characteristics and amount R of impregnated resin calculated using Equation (1). The characteristics related to the load, yield load, maximum load, and ultimate load are shown in this figure. Figure 9(a) shows that the yield load decreased as the impregnated resin increased. Specimens with a higher amount of impregnated resin exhibited higher brittleness, and micro-level cracks were assumed to have occurred in the small slip. Meanwhile, the maximum and ultimate loads decreased slightly (as shown in Figures 9 (b) and (c), respectively), as the amount of impregnated resin increased.

As described in the previous section, resin impregnation significantly affected the initial stiffness. Based on Figure 9(d), the initial stiffness increased with the amount of impregnated resin. When a low amount of acryl (less than 500 kg/m^3) was impregnated, the initial stiffness did not differ significantly from that of the control. In specimens with a high amount acryl (more than 1000 kg/m^3), the

initial stiffness increased significantly. Meanwhile, the impregnation of a low amount of urethane resulted in a higher initial stiffness.

To investigate the deformability, the authors examined the relationship between the slip at the ultimate load and the amount of impregnated resin (see Figure 9(e)). In both resins, the slip at the ultimate load decreased as the impregnated amount increased. The specimens with small amount, slip at ultimate load was almost similar with control specimens. In specimens with a high amount of resin (more than 500 kg/m^3), a decrease in slip was clearly observed.

4 CONCLUSION

In this study, the effect of resin impregnation on the lateral resistance of screwed joints connecting wood and steel plates were investigated. Screwed joint specimens impregnated with acryl- and urethane-type resins were tested via lateral loading tests, and the results obtained were compared to those of the control specimen.

A significant improvement in the initial stiffness was indicated. Based on the average value, the initial stiffness more than doubled owing to resin impregnation. For the case of acryl impregnation, the initial stiffness of the specimen was higher than that of the control specimen when the impregnated amount was high. For the case of urethane, the specimen indicated a higher initial stiffness was observed even if the impregnated amount was low.

Additionally, resin impregnation resulted in decreased deformability. When the amount of impregnated resin exceeded 500 kg/m^3, the slip at the ultimate load became much lower than that of the control. The result indicating the increasing brittleness of the joints is a critical issue that must be addressed.

Acknowledgements

This study was financially supported by Emachu Wood Promotion Foundation. The authors thank Mr. Morimoto and Ms. Sakurai, bachelor course students at Shizuoka University, for their great help in specimen preparation and test conduction.

REFERENCES

[1] Fukuta S., Nomura M., Ikeda T., Yoshizawa M., Yamasaki M., Sasaki Y.: UV-laser incision to apply wood-plastic compositions to wood surface. Mokuzai Gakkaishi, 64(1):28-35, 2018. (In Japanese)

[2] Ogawa K., Fukuta S., Kobayashi K.: Experimental study of lateral resistance of bolted joints using Japanese cedar (*Cryptomeria japonica*) treated with resin impregnation. Journal of Wood Science, 66:71, 2020.

[3] Ogawa K., Fukuta S., Kobayashi K.: Embedment properties of Japanese cedar (*Cryptomeria japonica*) trearted with resin impregnation. Journal of Wood Science, 68:9. 2022.

[4] ASTM D1761-20: Standard test method for mechanical fasteners in wood and wood-based materials. West Conshohocken, 2021.

[5] Ogawa K., Mori R., Kobyashi K.: Verification of general methods for inhibiting friction used in mechanical tests of timber joints. Mokuzai Kogyo, 76(10):376-381, 2021 (In Japanese).

[6] Yasumura M., Kawai N.: Evaluation of wood framed shear walls subjected to lateral load. CIB-W18/30-15-4. 1997.

[7] Working group for revising the manuscript of the allowable stress design for wooden framework method (2017) Committee for revising the allowable stress design for wooden framework method (ed). Allowable stress design for wooden framework method. Japan housing and wood technology center, Tokyo (In Japanese).

https://doi.org/10.52202/069179-0151

World Conference on Timber Engineering Oslo 2023

STRUCTURAL PERFORMANCE OF GLULAM TIMBER-STEEL BRACE CONNECTIONS REINFORCED WITH SELF-TAPPING SCREWS

Thomas Breijinck[1], Joshua Woods[2], Colin MacDougall[3]

ABSTRACT: Modern mass timber braced frames rely on connection yielding to provide ductility and energy dissipation capacity under earthquake loads. However, the ductility and energy dissipation capacity of steel dowel connections can be limited by the onset of a brittle failure mechanism in the timber (e.g., row-shear, group tear-out, or tension failure) prior to significant dowel yielding. To address this challenge, this paper presents experimental results on the structural performance of timber-steel dowelled connections reinforced with self-tapping screws. Four full-scale connections were tested under monotonic loading with and without reinforcing screws. The tested connections had two internal steel plates that were fastened to the timber using steel dowels. The unreinforced connection was intentionally designed to exhibit a brittle row shear failure prior to yielding of the steel dowels. Results of the study demonstrated the brittle nature of row shear in timber connections and the potential for using self-tapping screws to promote a more ductile failure. While the unreinforced connections exhibited no ductility, the reinforced connections had an average ductility of 4.8. Overall, results of this study demonstrate the potential for using self-tapping screws to retrofit and reinforce a timber-steel brace connection for situations in which a connection may be predisposed to brittle row shear failure.

KEYWORDS: Mass timber, connections, internal steel plates, self-tapping screws, row shear, ductility

1 INTRODUCTION

In the last twenty years, the use of mass timber in mid-rise and high-rise buildings has increased dramatically and is expected to continue to grow in the coming decades [1]. In Canada, the maximum permissible height for mass timber buildings was recently increased to 12 storeys, which is expected to continue to fuel this demand [2]. However, as the height of tall mass timber buildings increases, so does the demand on the structural elements, requiring larger section sizes and higher-capacity connections to safely transfer loads to the structure's foundation. These connections are also key elements of a structure's seismic force resisting system (SFRS), which must be designed to have sufficient ductility in the event of a design-level earthquake. A European study analysing failures in 127 timber structures found that about one quarter of collapses occurred as a result of connection failure, more than half of which occurred in dowel-type connections [3].

One commonly used SFRS for tall timber structures are braced frames. In the seismic design of mass timber braced frames, the brace connections are typically designed to act as fuses, yielding during a large earthquake, dissipating seismic energy, and protecting surrounding structural elements. A common connection detail used in mass timber braced frames involves the use of steel dowel-type fasteners (e.g., bolts, dowels, or drift pins) in combination with steel plates that are inserted into slots in the timber. This type of connection is appealing because high strength and stiffness can be achieved by incorporating multiple slotted-in steel plates, and these plates are inherently protected from fire by the surrounding timber.

Under axial load, these connections can experience a variety of failure modes, including ductile failure through yielding of the steel fasteners and brittle failure of the timber member. Brittle failure modes include fracture over the net section, row shear failure, or group tear-out. In the design of these connections for tall timber frames, which require high-strength brace connections, one convenient approach to increase capacity is to introduced multiple slotted-in steel plates into the connection. However, this reduces the dowel bending length and results in the potential for brittle shear failure (e.g., row shear or group tear-out) with little-to-no ductility if careful attention is not paid to the design and detailing of the connection.

In the literature, there are few reported experiments on timber connections with multiple slotted-in steel plates and dowel-type fasteners tested at scales required for tall timber structures. Furthermore, there is an increasing need to better understand the behaviour of brittle failure modes in these connections and to develop novel strengthening approaches to improve their seismic performance, including ductility and energy dissipation capacity. One such approach that has been proposed in the literature but not studied in large-scale timber brace connections with

[1] Thomas Breijinck, WSP Engineers, Canada, thomas.breijinck@queensu.ca

[2] Joshua Woods, Queen's University, Canada, joshua.woods@queensu.ca

[3] Colin MacDougall, Queen's University, Canada, macdougc@queensu.ca

https://doi.org/10.52202/069179-0152

slotted-in steel plates is the use of self-tapping screws as reinforcement. This study aims to address these knowledge gaps through experimental testing of four full-scale glulam timber connections with multiple slotted-in steel plates both with and without reinforcement under monotonic loading. The specific objectives of this study are to: (i) study brittle failure mechanisms in a full-scale timber connection with slotted in steel plates, (ii) determine if the use of self-tapping screws can prevent brittle failure in the tested connection and improve ductility and energy dissipation capacity, (iii) study the influence of end distance on the connection behaviour and the performance of the screw reinforcement.

2 BACKGROUND

There have been few studies reported on glulam timber connections for a multi-storey mass timber braced frame with multiple slotted-in steel plates and tested experimentally at full-scale. Several researchers have investigated the performance of small-scale timber-steel connections with a single slotted-in steel plate [4-8]. These studies have shown that the connection ductility depends largely on the connection geometry, fastener spacing, and material properties of the timber. A study by Yurrita et al. [9] examined the potential for brittle failure in large-scale pine glulam and laminated veneer lumber connections with two slotted-in steel plates and nine steel dowels. Fastener spacing and timber thickness were varied, and the results showed that block shear, row shear, net tension, and a combination of block and net shear failure were the observed failure mechanisms.

To determine the potential contribution of self-tapping screws to connection strength and ductility, Piazza et al. [10] tested timber-to-timber self-tapping screw connections with several orientations relative to the shear plane. The results found that that increasing the installation angle of the screw from 0° to 45° improved the load capacity and stiffness of the tested connections. Some researchers have also used reinforcing screws in timber connections with slotted-in steel plates and dowel-type fasteners to prevent brittle failure. In some connections tested by Dorn et al. [11], a clamp was used to simulate the reinforcement provided by self-tapping screws and the results showed the potential for improvements in strength and ductility. Lathuillière et al. [12] tested bolted moment-resisting connections reinforced with self-tapping screws under shear and moment. Although the connections did not simulate a brace connection under direct axial tension, the results did show that reinforcement through self-tapping screws was effective at controlling crack propagation and improving connection ductility.

Studies on small-scale timber connections reinforced with self-tapping screws have also been carried out. Zhang et al. [13] tested small-scale single dowel connections with a single slotted-in steel plate under direct axial tension. The results once again showed potential for reinforcing screws to improve connection ductility.

3 EXPERIMENTAL PROGRAM

The experimental program described in this paper consisted of 4 tests performed on full-scale glulam timber connections with multiple slotted-in steel plates and steel dowel-type fasteners. The specimens included two control connections (without reinforcing screws) and two reinforced connections. Other investigated parameters included the loaded end distance.

3.1 TEST SPECIMENS

Figure 1 shows the geometry of the slotted-in steel plate connections tested in this study. The glulam timber member measured 266 × 265 × 1300 mm. The holes and slots in the glulam member were fabricated using a computer-numerical control (CNC) machine. At one end, each glulam member had two 12 mm wide slots and 6 – 16 mm (5/8”) holes perpendicular-to-grain, for the installation of the steel dowels. At the opposite end of the connection, 16 – 22 mm (7/8”) diameter holes 310 mm (12”) long were drilled in the parallel-to-grain direction for a glued-in-rod connection used to fix the specimen to the test frame, which was fixed to the laboratory floor.

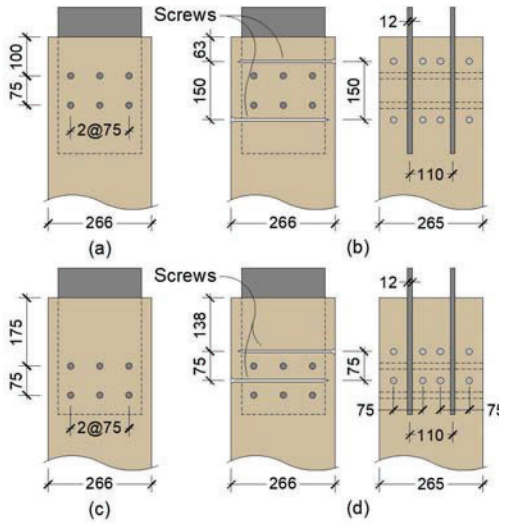

Figure 1: *Tested connections with slotted-in steel plates: (a) C100, (b) C100-R, (c) C175, (d) C175-R*

The tested connection included two 12 × 214 mm internal slotted-in steel plates. The slotted-in steel plates were connected to the timber using 16 mm diameter (*d*) steel dowels that were 266 mm long. The connection, based on the geometry in Figure 1, has a slenderness ratio (λ) of 6.9 (110/16 = 6.9), calculated as the ratio of the thickness of the timber (*t*) between the slotted-in steel plates (110 mm in Figure 1) divided by the dowel diameter (*d*).

Connection tests included those with and without self-tapping screws. The two control connections (without reinforcing screws) were denoted C100 and C175, in which the ‘100’ or ‘175’ is the loaded end distance in each

https://doi.org/10.52202/069179-0152

connection. The two other connections had identical geometry to the control connection but were reinforced with self-tapping screws. These connections are referred to as C100-R and C175-R in this paper.

All connections with screw reinforcement had 8 - 250 mm long fully threaded 11 mm diameter Rothoblaas VGS 9380 self-tapping screws with a countersunk head. The screws were installed in pre-drilled holes measuring 6.35 mm (1/4") in diameter, according to the manufacturer's recommendations [14]. Figure 1 shows the configuration of the screws in the reinforced connections. The goal of this screw orientation was to strengthen the shear failure plane and arrest crack development in the direction of the load. Connection C100-R was reinforced with 4 screws across the shear plane and an additional 4 screws outside the loaded end to prevent timber splitting along the length of the member, which was observed in previous tests. In connection C175-R, 8 screws were placed across the shear plane, to examine the influence of additional screws on connection stiffness, strength, and ductility.

3.2 MATERIAL PROPERTIES

The glulam connections were fabricated of 24f-ES Spruce-Pine-Fir (SPF) glulam supplied by Nordic Structures and produced as per CSA O177-06 [15], as specified by CSA O86-19 *Engineering Design for Wood* [16]. This glulam grade has a density of 560 kg/m^3, a mean relative density (G) of 0.47, and a moisture content of 12%. Typical design characteristics are a modulus of elasticity of 13.1 GPa, a parallel-to-grain tension strength of 20.4 MPa, and a shear strength of 2.5 MPa [17].

The material properties of the steel dowels were determined by conducting direct tension tests on three coupons according to the guidelines in ASTM E8 [18]. Figure 2 shows the stress-displacement response of the dowels used in this study. The 16 mm dowel had an average yield strength, determined using the 0.2% offset method, of 825 MPa and an ultimate strength of 946 MPa. The Rothoblaas VGS 9380 reinforcing screws have a manufacturer's reported characteristic yield moment of 45.9 N-m and a yield strength of 1000 MPa [14].

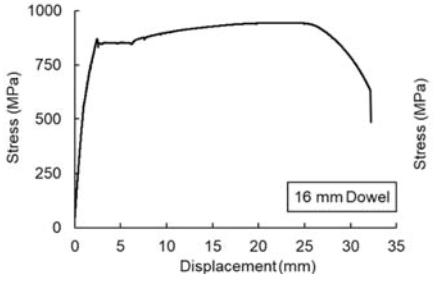

Figure 2: *Stress-displacement behaviour of steel dowel*

3.3 CONNECTION STRENGTH

Prior to the experimental testing, calculation of connection capacity was carried out according to the Canadian Wood Design Standard (CSA O86-19). Table 1 summarizes the calculated resistances of each connection for each failure mode. Additional information on these design calculations is available in [16]. Based on the design provisions in CSA O86-19, the unreinforced connections were expected to fail in brittle row shear Furthermore, the ratio of brittle to ductile failure (φ), taken as the row shear strength divided by the yield resistance, was approximately 0.6 for all of the tested connections. The reinforced connections had additional capacity against row shear and group tear-out because of the self-tapping screws. The results in Table 1 suggest that connection C100-R is still susceptible to row shear failure (φ = 0.9) while connection C175-R had yielding of the steel dowels as a predicted failure mode (φ = 1.2), and thus, was expected to exhibit the highest ductility amongst the tested connections.

Table 1: *Connection design strength*

Specimen	*Net Tension* (kN)	*Row Shear* (kN)	*Group Tear-out* (kN)	*Yielding* (kN)
C100	1071	304	684	501
C100-R	1071	446	826	501
C150	1071	304	684	501
C150-R	1071	589	969	501

3.4 EXPERIMENTAL TEST SETUP

Figure 3 shows the experimental setup for the connection tests. The connections were tested under direct axial tension. At one end of the timber member, a 1350 kN hydraulic actuator was used to apply the load, to which a steel double lap splice connection was used to connect the actuator to the slotted-in steel plates in the timber connection. The slotted-in steel plates were bolted to the actuator connection using two 25.4 mm (1") diameter high-strength (Grade 12) steel bolts.

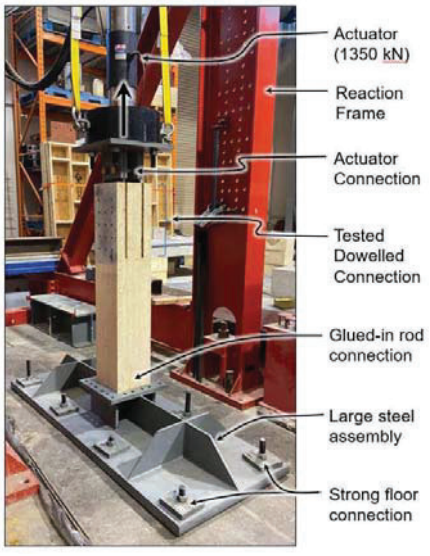

Figure 3: *Experimental test setup*

The connection was fixed to the lab strong floor using a large steel assembly that included a 50.8 mm (2") thick base plate and was connected to the laboratory strong floor using 8 – 28.1 mm (1.5") diameter B7 threaded rods. The timber connection was attached to the steel assembly using a glued-in-rod connection, which was intentionally overdesigned to ensure it remained elastic during the test. The glued-in-rod connection consisted of 16 – 19.1 mm (3/4") threaded rods embedded 305 mm (12") into 22 mm (7/8") holes in the glulam timber. The rods were glued in the timber using Sikadur-35 Hi-Mod LV, which is a two-part high modulus and strength, low-viscosity epoxy resin intended for grouting bolts or dowels in wood [19]. According to the manufacturer, the epoxy has a modulus of elasticity of 2.41 GPa, a tensile strength of 58 MPa, and an elongation at break of 4.2% [19].

3.5 TEST PLAN AND INSTRUMENTATION

The connections were tested under monotonic loading at a constant rate of 1 mm/min up to failure. Figure 4 shows the instrumentation used to measure the response of the connections during the test. The connection deflections were measured using nine linear potentiometers (LPs). Four LPs were installed at the top and bottom of the connection on opposite faces. These LPs were used to measure the displacement of the glued-in rod and actuator connections. Two string potentiometers (SPs) were also used to measure the displacement of the connection. The SPs were affixed beneath the dowelled connection and connected to the underside of the steel plate connected to the actuator. A 2000 kN load cell connected to the hydraulic actuator was used to measure the load applied to the connection during each test. The data was collected at 1 Hz for each test.

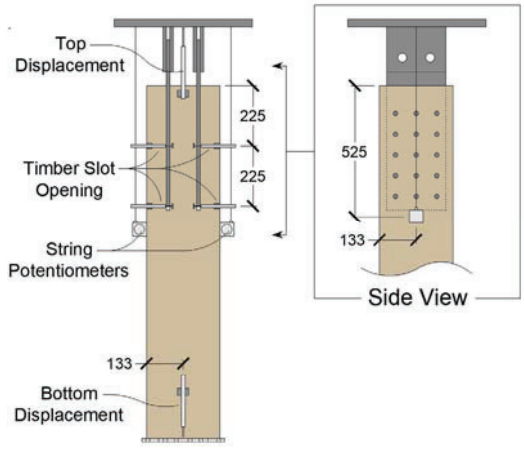

Figure 4: *Typical connection instrumentation*

4 RESULTS AND DISCUSSION

Figure 5 shows the connection force-displacement behaviour, measured using the SPs (see Figure 4) and Table 2 shows the structural response parameters for each connection, including the yield displacement, ultimate load, and ultimate displacement. It is noted that the ultimate displacement was determined as the displacement after the load dropped 20% from the ultimate load. In addition, to assess the potential for the use of self-tapping screws to improve the seismic performance of timber-steel connections, Table 2 also shows the displacement ductility of the connections, which was determined as the ratio of the yield displacement to the ultimate displacement ($\mu_\Delta=\Delta_u/\Delta_y$).

Table 2 *Structural Response Parameters*

Specimen	Δ_y (mm)	P_u (kN)	Δ_u (mm)	μ_Δ (mm/mm)
C100	-	730	2.4	-
C100-R	4.0	671	14.5	3.6
C150	-	692	5.2	-
C150-R	5.3	715	31.8	6.0

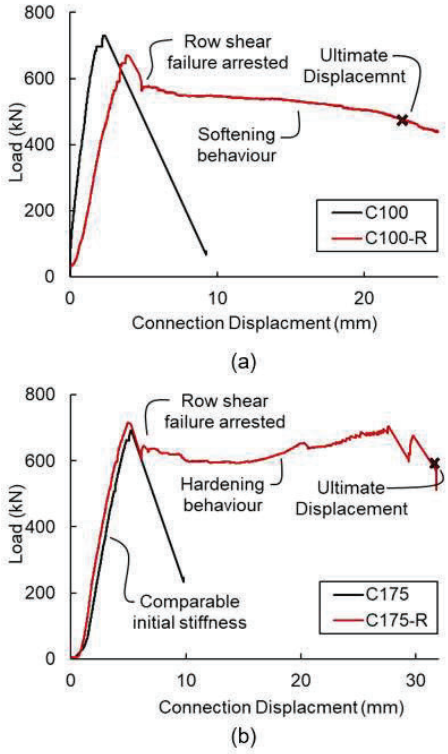

Figure 5: *Connection force-displacement behaviour (a) C100 and C100-R, (b) C175 and C175-R*

4.1 UNREINFORCED CONNECTIONS

The force-deformation responses in Figure 5 show that both unreinforced connections fail in sudden and brittle row shear failure, and as a result, had no ductility. Comparing peak load, the unreinforced connections had an average strength of 711 kN, and the strength of C100 was approximately 5% larger compared with connection C175. The ultimate displacements of the connections were 2.4 and 5.2 mm, respectively, demonstrating the

https://doi.org/10.52202/069179-0152

high stiffness exhibited by these connections as well as the potential for very brittle failure if careful attention is not paid to their detailing during design.

Figure 6 shows the row shear failure for connection C100, which was similar to that of C175. The result shows the formation of a distinct shear failure plane for each row of fasteners. In some cases, timber 'plugs' protrude from the specimen along the shear failure plane. Distinct timber plugs were generally observed in the central portion of the connection (between the steel plates), in which the dowel is supported by the slotted-in steel plate on either side. In the timber side members, the row shear failure plane formed as either a timber plug or as a single splitting crack through the centre of the holes, depending on the row of fasteners in the connection.

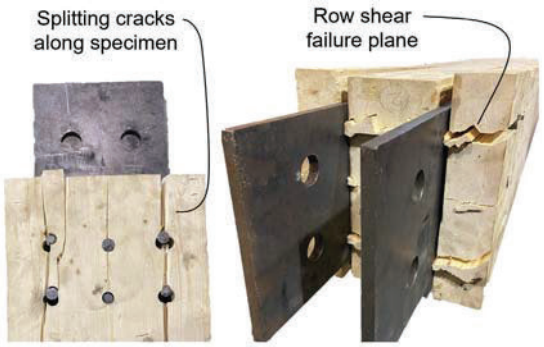

Figure 6: *Row shear failure of connection C100*

Comparing the strength of the unreinforced connections with the design values according to the Canadian Wood Design Standard (CSA O86-19), the results show that the code did correctly predict the mode of failure. However, the observed row shear strength of connections C100 and C175 were 2.4 and 2.3 times greater than the predicted design strengths, respectively. The main difference between connections C100 and C175 was the loaded end distance, which were 100 mm and 175 mm respectively. Despite the increase in loaded end distance, connection C100 had a row shear strength that was within 5% of C175. This suggests that the code requirement that the minimum of the loaded end distance and fastener spacing is an adequate approach to calculating the row shear capacity of the connection. Despite the fact that these design values are based on the characteristic strength of the timber, the results do suggest that current provisions in CSA O86-19 for large timber-steel connections with multiple slotted-in steel plates may be conservative.

4.2 REINFORCED CONNECTIONS

Figure 5 compares the response of the connections reinforced with self-tapping screws with their respective controls. Overall, the results show that the self-tapping screws were effective at altering the behaviour of the connections and preventing sudden and brittle row shear failure. The reinforced connections had ultimate strengths that were within 10% of their respective controls, suggesting that the presence of the self-tapping screws did not have a significant effect on the connection strength. Furthermore, the results also show that the addition of the self-tapping screws also did not have a significant effect on the stiffness of the connections. This could be attributed to the fact that the self-tapping screws were not installed directly adjacent to the fasteners, something that is commonly done in practice. Despite not having a large influence on strength or stiffness, the addition of the self-tapping screws did result in large increases in ductility, as connections C100-R and C175-R had a displacement ductility of 3.6 and 6.0, compared with the unreinforced connections which did not exhibit any ductility. The connections also exhibit large increases in dissipated energy of 22.2 kN-m and 18.3 kN-m, for connections C100-R and C175-R, respectively, which is 5.67 and 7.30 times higher than their respective control connections.

With respect to observed behaviour, Figure 7 shows the failure mode for connection C100-R. At a displacement of approximately 4 mm, connection C100-R experienced a small drop in load carrying capacity (~15% from the maximum load), highlighted on Figure 5, which corresponded to the initiation of a row shear failure in the timber. However, the presence of the reinforcing screws effectively prevented propagation of the shear failure plane to the edge of the timber, which is highlighted in Figure 7(a), which prevented further drop in load carrying capacity.

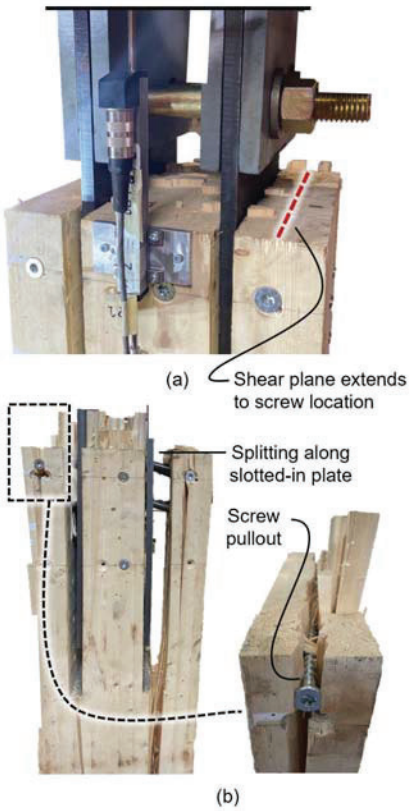

Figure 7: *Glulam timber test specimen*

After the initial drop in load carrying capacity, the force-displacement response of the connection shows a post-peak plateau up to approximately 20 mm, during which the load dropped by 20%. Beyond 25 mm of displacement, the connection exhibited gradual softening to a displacement of 75 mm, at which point the connection was able to carry 15% of its peak load carrying capacity and did not experience any sudden drops in load carrying capacity, and the test was stopped. Gradual softening of the connection was attributed to embedment failure of the self-tapping screws, shown in Figure 7(b), which occurred parallel to the load in a crack along the row of fasteners. Under increasing displacement, the screws (as well as the dowels) were forced out of the splitting cracks in the timber, resulting in a gradual loss in load.

Connection C175-R, which had 8 screws providing additional row shear reinforcement had comparable behaviour to connection C100-R up to the peak load, but the post-peak response was markedly different. Figure 8 shows the failure mode for connection C4-6R. At the peak load, the force deformation behaviour showed a ~15% drop in load carrying capacity which, similar to connection C100-R, corresponded to the formation of a shear failure plane parallel to the load, identified in Figure 8(a). Comparing the deformation patterns in Figure 7(a) and 8(a), the results show indicate that the damage to connection C175-R was much smaller when compared with connection C100-R, which is likely the result of the additional reinforcing screws.

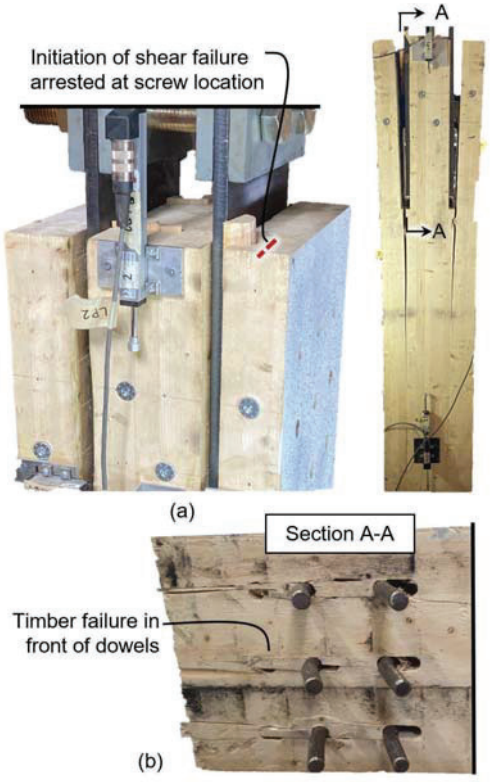

Figure 8: *Glulam timber test specimen*

Examining the force deformation response of connection C175-R in Figure 5, the results once again show that the reinforcing screws were effective at preventing brittle row shear failure of the connection and the force-deformation response shows a relatively constant post-peak plateau following the initial drop in strength up to a connection displacement of approximately 15 mm.

At displacements beyond 15 mm, C175-R shows a hardening response, characterized by an increase in stiffness and strength up to a local maxima of 703 kN, representing 96% of the maximum load, at a connection displacement of 27.5 mm. This behaviour is attributed to interaction between the self-tapping screws and the steel dowels, which come into contact with one another once significant dowel bending has occurred. Eventually, splitting along the length of the slotted-in steel plates resulted in the timber side members separating completely from the main timber member between slotted-in steel plates, shown in Figure 8(b), causing a drop in load carrying capacity of 20% from the peak load. It is worth noting that even after failure of the timber side members, the main member was still capable of carrying over 500 kN of load (roughly 70% of the ultimate capacity).

5 CONCLUSIONS

The goal of this research project was to study the behaviour of large-scale timber-steel connections with multiple slotted-in steel plates and dowel type fasteners prone to brittle row shear failure and investigate the potential use of self-tapping screws to improve their ductility and energy dissipation capacity. The study included tests on 4 large-scale connections under axial monotonic loading. The following specific conclusions are drawn:

1. Connections tested without reinforcing screws failed in sudden and brittle row shear failure with no ductility and little-to-no energy dissipation capacity. The larger loaded end distance in connection C100 was not found to have an influence on the load carrying capacity of the connection.
2. The CSA O86-19 design standard was found to be able to determine the mode of failure in the connections tested without reinforcing screws, however, the standard over-predicted the row shear strength of the connections by 2.3 times on average.
3. The use of self-tapping screws was found to be an effective approach for preventing premature row shear failure and shift the failure mode, permitting a more ductile response. The studied connections with 4 and 8 reinforcing screws had displacement ductilities of 3.6 and 6.0, respectively, a significant improvement in performance when compared to the connections tested without reinforcing screws.
4. The use of self-tapping screws was also found to increase the energy dissipation capacity of the connections by 5.67 and 7.30 times for connections

https://doi.org/10.52202/069179-0152

C2-6R and C4-6R, respectively, compared with the control connections without reinforcing screws.

Overall, the results suggest that timber-steel connections with multiple slotted-in steel plates have the potential to meet the large force demands required for tall mass timber braced frames. However, careful attention must be paid to ensure the connections are detailed to prevent brittle row shear failure. Furthermore, in connections that may be prone to brittle shear failure, results of this study show that the use of self-tapping screws is a feasible approach to shifting the failure mode to a more ductile failure with additional energy dissipation capacity. However, more testing on large-scale connections with varying geometry, dowel slenderness ratio, and self-tapping screw configurations is required.

ACKNOWLEDGEMENT

The Authors would like to gratefully acknowledge support provided by the Natural Sciences and Engineering Research Council of Canada and Nordic Structures. Technical advice provided by Carla Dickof of Fast+Epp and technical assistance in the laboratory provided by Hal Stephens, Justin Bennett, and Zena Lauzon is also acknowledged.

REFERENCES

[1] Natural Resources Canada (2021). State of mass timber in Canada (SMTC) report.

[2] National Research Council (2020). National Building Code of Canada (NBCC). National Research Council of Canada.

[3] Hansson, E. F. (2011). Analysis of structural failures in timber structures: Typical causes for failure and failure modes. Engineering Structures, 33(11), 2978-2982.

[4] Jorissen, A. J. M. (1998) Double shear timber connections with dowel type fasteners (thesis). Delft University Press, Delft.

[5] Pedersen, M. U. (2001) Dowel Type Timber Connections: Strength modelling. Danmarks Tekniske Universitet.

[6] Dorn, M., de Borst, K., and Eberhardsteiner, J. (2013) Experiments on dowel-type timber connections. Journal of Engineering Structures, 47(1):67–80.

[7] Oudjene, M., Tran, V. D., and Khelifa, M. (2017). Cyclic and monotonic responses of double shear single dowelled timber connections made of hardwood species: Experimental investigations. Construction and Building Materials, 132, 188-195.

[8] Jalilifar, E., Koliou, M., and Pang, W. (2021). Experimental and Numerical Characterization of Monotonic and Cyclic Performance of Cross-Laminated Timber Dowel-Type Connections. Journal of Structural Engineering, 147(7), 04021102.

[9] Yurrita, M., Cabrero, J. M., and Quenneville, P. (2019). Brittle failure in the parallel-to-grain direction of multiple shear softwood timber connections with slotted-in steel plates and dowel-type fasteners. Construction and Building Materials, 216, 296-313. https://doi.org/10.1016/j.conbuildmat.2019.04.100

[10] Piazza, M., Polastri, A., and Tomasi, R. (2011). Ductility of timber joints under static and cyclic loads. Proceedings of the Institution of Civil Engineers-Structures and Buildings, 164(2), 79-90.

[11] Dorn, M., de Borst, K., & Eberhardsteiner, J. (2013). Experiments on dowel-type timber connections. *Engineering structures*, *47*, 67-80.

[12] Lathuillière D., Bléron L., Descamps T., Bocquet J. F. (2018) Reinforcement of dowel type connections. Journal of Construction and Building Materials, 97(1):48-54.

[13] Zhang C., Harris R., Chang W. S. (2019). Strain Distribution of Dowel-Type Connections Reinforced with Self-Tapping Screws. Journal of Materials in Civil Engineering, 32(1)

[14] Rothoblaas (2020) VGS Fully Threaded screw with countersunk or hexagonal head data sheet, https://www.rothoblaas.com/products/fastening/screws/screws-structures/vgs accessed: July 10, 2022.

[15] CSA (2006). "Qualification code for manufacturers of structural glued-laminated timber." CSA O177-06, Rexdale, ON, Canada.

[16] CSA (2019) Canadian Wood Design Standard, Canadian Standards Association. Rexdale, Canada.

[17] Nordic Structures. (2022). Mass Timber Construction: Nordic LAM+ Technical Guide, Nordic Structures, Montreal.

[18] ASTM (American Standards and Testing Methods). 2010. Standard Test Methods for Tension Testing of Metallic Materials. West Conshohocken, PA: ASTM.

[19] Sika Canada, (2022). Sikadur-35 Hi-Mod LV Product Data Sheet, Sikadur35HiModLV_pds.pdf accessed: July 10, 2020.

World Conference on Timber Engineering Oslo 2023

PREDICTION OF WITHDRAWAL STIFFNESS OF SELF-TAPPING SCREWS

Md Abdul Hamid Mirdad[1], Jan Niederwestberg[2], Arman Jucutan[3], Ying Hei Chui[4]

ABSTRACT: Self-tapping screw is a new generation of fasteners which is often inserted into the face of timber members at an angle to develop stiff and strong connections. The withdrawal stiffness of self-tapping screws is an important property that influences the performance of the connection. The designs of composite timber hybrids incorporating inclined self-tapping screws, such as timber-concrete and timber-steel, can be governed by the stiffness of their connections, which is in turn influenced by the fastener withdrawal stiffness. This study proposes empirical equations for directly predicting the withdrawal stiffness of the self-tapping screws, based on wood density, fastener diameter, insertion angle and penetration length. These empirical equations were developed based on an analysis of withdrawal test data from several test programs, covering two wood species and two screw diameters. They could be used in conjunction with appropriate models to predict the stiffness of connection containing self-tapping screws inserted at an angle to the wood member surface.

KEYWORDS: Withdrawal stiffness, Non-linear regression, Self-tapping screw, Insertion angle

1 INTRODUCTION

Self-Tapping Screw (STS) is an improved threaded fastener specifically developed for mass timber and is the key factor contributing to the emergence of modern tall mass timber structures. STS mostly features a continuous thread over the whole or partial length leading to a uniform load transfer between the screw and the wood material specifically under withdrawal action while the special self-drilling tip helps to avoid pre-drilling in timber members [1, 2, 3]. Many experimental and theoretical studies of STS connections conducted in timber-to-timber, steel-to-timber and concrete-to-timber have concluded that there is a substantial increase in the strength and stiffness of the STS connection if the screws are installed at an angle (e.g., 45° or 30°) to the surface of the timber member, instead of normal (90°) to the surface [4, 5, 6, 7, 8]. Stiffness of connections is a critical design property that governs the structural performance of timber structures, such as drift of lateral load resisting system, deflection of composite systems under gravity load and dynamic response of structural systems. Despite this, it is a property that is not given much attention in timber design standards compared to strength properties [9, 10, 11]. Withdrawal stiffness is an important input parameter for the evaluation of connection stiffness containing the self-tapping screws, which are measured by conducting tests following standards, such as ASTM D1761-12 [12] and EN 1382 [13]. There is currently limited information in timber design standards on withdrawal stiffness properties to allow designers to utilize any analytical solutions to calculate connection stiffness containing self-tapping screws. Therefore, in this study, withdrawal test data were accumulated from various studies and non-linear regression analyses were performed to derive equations for predicting the withdrawal stiffness of STS, based on wood density, fastener diameter, and angle.

2 WITHDRAWAL TEST

Withdrawal tests of the screws from timber at various angles to the grain were performed according to EN 1382 [4] procedure to evaluate the withdrawal stiffness. With this test setup, the measured withdrawal deformation includes both slips between the wood and screw and the axial elongation of the screw. Fully threaded self-tapping screws with a countersunk head and self-drilling tip were selected. Two screw diameters of 9 and 11 mm from a single manufacturer were tested at five different insertion angles, 0°, 30°, 45°, 60° and 90°. Wood specimens were cut from spruce-pine-fir (SPF) and Douglas fir (DF) Glued Laminated Timber (GLT). Two penetration lengths were studied for each combination of screw diameter and insertion angle. Five replicates were used for each combination of parameters, giving a total of 100 withdrawal tests. The mean density of the SPF and DF woods were 429 kg/m^3 and 533 kg/m^3 respectively. The mean moisture content of SPF and DF woods was 8.3% and 9.2% respectively based on measurements using an electrical resistance moisture meter. Each wood specimen was pre-drilled with a diameter equal to the shank diameter of the screws to avoid any splitting. In each wood specimen, three screws were placed on one side and two on the opposite side at 10d spacing to reduce the amount of wood specimen preparation. The spacing of the fasteners meets the requirement of EN 1382 [13], to avoid any splitting and optimize the wood-effective areas. It should be noted that the wood members were cut to allow the load to be applied which simulates the withdrawal of a screw in a connection when it is inserted at an angle to the wood member surface. A typical withdrawal test setup at a 45° insertion angle is shown in *Figure 1*.

The test specimen was first attached to a 75 mm thick steel plate with a 20 mm hole that was created to accommodate different screw diameters. The steel plate was anchored to

[1] Md Abdul Hamid Mirdad, University of Illinois at Urbana-Champaign, USA, mirdad@illinois.edu
[2] Jan Niederwestberg, TNO, Netherlands, jan.niederwestberg@tno.nl
[3] Arman Jucutan, University of Alberta, Canada, jucutan@ualberta.ca
[4] Ying Hei Chui, University of Alberta, Canada, yhc@ualberta.ca

https://doi.org/10.52202/069179-0153

the laboratory floor. The screw head was then locked to a 50 mm thick steel plate which was attached to the actuator of the test machine. Two Linear Variable Differential Transformers (LVDTs) were attached to the same steel plate which was connected to the test jack to measure the relative displacement between the two steel plates. The tests were conducted at a constant displacement rate of 1.5 mm/min. The load and displacement were recorded during the test and the test was stopped after the withdrawal failure of the screw from the wood. The slope of the load-displacement response at between 10% and 40% of the maximum load was used to calculate the stiffness. The withdrawal stiffness, K_{ax} in N/mm^3, was calculated using equation (1).

$$K_{ax} = \frac{S}{\pi d l_e} \quad (1)$$

where S is the slope of load-displacement response between 10% and 40% of the maximum load (N/mm), d is the nominal thread diameter of the screw (mm) and l_e is the effective penetration length (mm) excluding the length of the tip.

Figure 1: *Withdrawal test of screws at 45 °angle to timber grain*

Table 1: *Withdrawal stiffness of self-tapping screws in timber*

Diameter (mm)	Angle	Penetration Length (mm)	Mean Density (kg/m^3)	Mean Stiffness (N/mm^3)	CoV (%)
11	0°	70	429	4.8	21.2
	30°			4.6	5.5
	45°			4.0	15.8
	60°			4.1	17.5
	90°			3.5	15.1
11	0°	90	429	4.8	11.5
	30°			4.7	11.8
	45°			3.8	11.0
	60°			3.9	11.1
	90°			3.6	14.4
9	0°	80	533	5.7	9.9
	30°			5.4	22.8
	45°			5.0	17.8
	60°			5.0	15.0
	90°			5.2	16.3
9	0°	100	533	6.9	14.7
	30°			6.0	20.0
	45°			6.5	8.2
	60°			5.5	13.5
	90°			5.6	12.6

Withdrawal test results are summarized in *Table 1* for different configurations and the mean wood density for each species. The results are graphically represented in *Figure 2*. Mean withdrawal stiffness per unit area (K_{ax}) are shown with their CoVs in the table, which was calculated using equation (1). It should be noted that the small sample size influences the CoV which is within a range of 5%-22% for stiffness. From the withdrawal test results, it can be seen clearly that the withdrawal stiffness decreased with the increase of insertion angle for both SPF and DF specimens. For each screw diameter, the highest stiffness was found at 0° angle and the lowest was noted at 90° angle. DF specimens showed higher stiffness compared to SPF specimens.

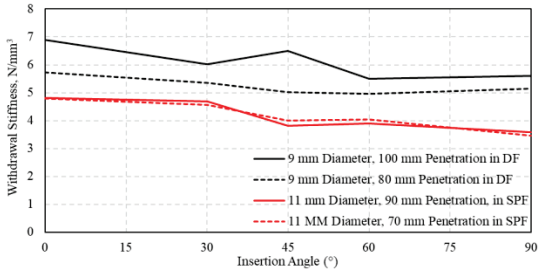

Figure 2: *Withdrawal stiffness of self-tapping screws for different parameters*

The main reason for testing each species/diameter combination with effective different penetration lengths was to explore if the withdrawal stiffness is directly proportional to penetration length, as is commonly assumed in design standards [14] for other dowel-type fasteners such as lag screw, wood screw and nail. To explore this issue, the measured stiffness property at the longer effective penetration length was divided by that at the shorter effective penetration length for each screw diameter/species/angle combination as shown in *Figure 3*. As can be seen in the figure, for the SPF wood with an 11mm screw, the penetration length had practically no impact on withdrawal stiffness, even for a 30% increase in length. For the DF wood with a 9mm screw, the withdrawal stiffness increased with a larger penetration length. However, the property increase does not appear to be directly proportional to the length increase. This issue will require further investigation given that the finding is not in line with the common assumption for other threaded fasteners such as lag screws and wood screws [14].

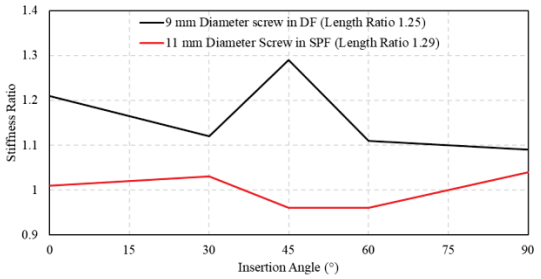

Figure 3: *Influence of the screw penetration length on the withdrawal properties of self-tapping screws*

https://doi.org/10.52202/069179-0153

3. PARAMETRIC ANALYSIS

Parametric analyses were performed by curve-fitting the measured withdrawal stiffness data to develop predictive equations for stiffness. MATLAB programming was used to perform non-linear regression analyses to determine the influence of density, diameter, penetration length and insertion angle on the withdrawal stiffness of the self-tapping screw. Initially, two different regression analyses were performed for SPF and DF data sets to evaluate any potential differences between the two groups. Then, regression analyses were conducted on the combined SPF and DF data to come up with the general stiffness equation.

Non-linear regression analysis was carried out using the SPF and DF data and the following equation was used to determine the relevant coefficients and quantify the results of the test series. The withdrawal stiffness mostly depends on the diameter, penetration length and insertion angle of the screw and density of timber. Therefore, the equation format for the withdrawal stiffness, $K_{ax,\alpha}$ is shown in equation (2).

$$\boldsymbol{K_{ax,\alpha}} = \frac{w_1\ {l_e}^{w_2}\ \rho^{w_3}\ d^{w_4}}{w_5\ cos^2(\alpha) + w_6\ sin^2(\alpha)} \tag{2}$$

where α is the insertion angle to timber grain, d is the nominal diameter of the fastener, l_e is the fastener penetration into wood excluding the tip and ρ is the timber density.

After performing the non-linear regression analysis with the SPF test data, the screw withdrawal stiffness in the SPF timber can be expressed as shown in equation (3).

$$\boldsymbol{K_{ax,\alpha,SPF}} = \frac{0.30{l_e}^{-0.01}\ \rho^{0.18}\ d^{1.09}}{2.37cos^2(\alpha) + 3.22sin^2(\alpha)} \tag{3}$$

The coefficient values and their related errors and p-values are presented in *Table 2*. Analysis of the coefficient of determination (R^2) has revealed a strong correlation, with a value of 0.9. The root mean square error (RMSE) was found to be 0.152. The p-values associated with the length of Equation (3) for SPF data were found to be high indicating that the influence of length was less significant compared with other parameters based on the SPF test results.

Then, a non-linear regression analysis was carried out with the DF test data and the screw withdrawal stiffness in the DF timber can be expressed as shown in equation (4).

$$\boldsymbol{K_{ax,\alpha,DF}} = \frac{0.44{l_e}^{0.69}\ \rho^{2.93}\ d^{-7.82}}{5.32cos^2(\alpha) + 6.32sin^2(\alpha)} \tag{4}$$

The coefficient values and their related errors and p-values are presented in *Table 2* where, the analysis of the coefficient of determination (R^2) has revealed a reasonable correlation, with a value of 0.83. The root mean square error (RMSE) was found to be 0.249. The lower p-value associated with the length of equation (4) indicates that the influence of penetration length in withdrawal stiffness is high based on the test results.

Finally, after performing the non-linear regression analysis with all the SPF and DF test values in this study, the screw withdrawal stiffness for both SPF and DF timber can be expressed as shown in equation (5).

$$\boldsymbol{K_{ax,\alpha,G}} = \frac{0.17{l_e}^{0.41}\ \rho^{0.72}\ d^{-0.51}}{5.09cos^2(\alpha) + 6.35sin^2(\alpha)} \tag{5}$$

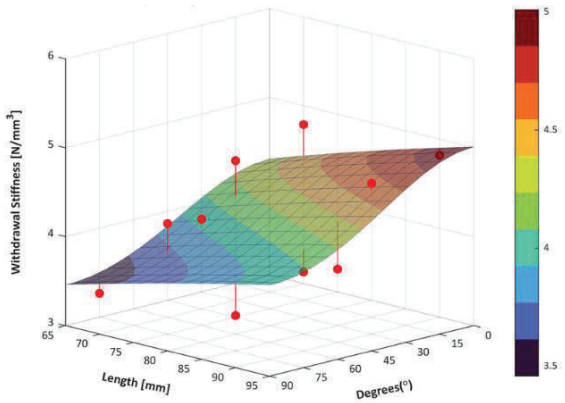

Figure 4: *Surface of withdrawal stiffness vs insertion angle and penetration length for 11 mm diameter SPF data using combined coefficient (ρ=429 kg/m³)*

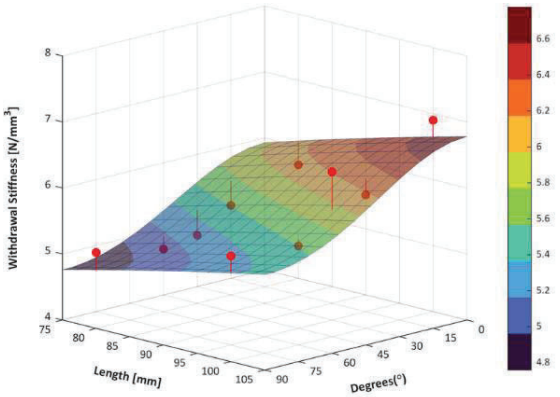

Figure 5*: Surface of withdrawal stiffness vs insertion angle and penetration length for 9 mm diameter DF data using combined coefficient (ρ=533 kg/m³)*

The coefficient values and their related errors and p-values are presented in *Table 2*. Analysis of the coefficient of determination (R^2) and the root mean square error (*RMSE*) has revealed a strong correlation, with a value of 0.885 and 0.315 respectively, which is promising. The standard errors are found within an acceptable range which subsequently yielded a smaller range for a 95% confidence interval for all the coefficients. The surface of the withdrawal stiffness values represented by equation (5) for SPF and DF data associated with their respective diameter are shown in *Figure 4* and *Figure 5* respectively. The surface depicts expected values based on equation (5)

https://doi.org/10.52202/069179-0153

while individual data points depict the experimental withdrawal stiffness. The mean density of 429 kg/m^3 and 533 kg/m^3 was considered for the SPF and DF wood samples in *Figure 4* and *Figure 5* respectively following the test data.

Table 2: *Coefficient estimation for each data set of withdrawal stiffness after parametric studies*

Equation	Species	Coefficients	Values	p-Value	Standard Error	Lower 95%	R^2	RMSE
3	SPF	w_1	**0.30**	0.495	0.419	-0.661	0.900	0.152
		w_2	**-0.01**	0.930	0.118	-0.283		
		w_3	**0.18**	0.621	0.340	-0.607		
		w_4	**1.09**	0.012	0.306	0.382		
		w_5	**2.37**	3.47E-08	0.067	2.214		
		w_6	**3.22**	1.30E-09	0.053	3.096		
4	DF	w_1	**-0.44**	2.09E-06	0.031	-0.515	0.830	0.249
		w_2	**0.69**	0.002	0.150	0.337		
		w_3	**2.93**	4.79E-09	0.086	2.724		
		w_4	**-7.82**	3.24E-15	0.030	-7.888		
		w_5	**-5.32**	2.57E-09	0.142	-5.652		
		w_6	**-6.32**	2.32E-10	0.120	-6.599		
5	DF + SPF	w_1	**0.17**	0.855	0.929	-7.532	0.851	0.315
		w_2	**0.41**	0.011	0.142	0.101		
		w_3	**0.72**	0.271	0.626	-1.551		
		w_4	**-0.51**	0.473	0.696	-3.054		
		w_5	**5.09**	9.511E-16	0.147	-0.566		
		w_6	**6.35**	1.466E-18	0.118	-0.706		

Based on equations (3)-(5), a comparative study was undertaken for all diameters, insertion angles, penetration length and wood species to compare the effectiveness of the general combined equation which is shown in *Figure 6*. The statistical analysis for SPF and DF data concluded that the combined general equation (5) can be used for both the SPF and DF wood species instead of using individual equations (3) and (4) for SPF and DF separately. Therefore, to predict the withdrawal stiffness of the screws with known insertion angle and penetration lengths within the diameter of 9-11 mm, and wood density of 429-533 kg/m^3, the general equation (5) may be utilized based on the parametric studies conducted in this study. However, further studies are required with a wider range of test data to cover more diameter, penetration length and density. In the case of CLT, as long as the input parameters are within the mentioned range, the average value of withdrawal stiffness of all penetrated screw layers can be considered as the final withdrawal stiffness.

Also, the withdrawal stiffness of all possible screw diameters ranging from 8-12 mm at 0°, 30°, 45°, 60° and 90° insertion angles, penetration length from 50-200 mm in SPF and DF wood with a density of 425 and 525 kg/m^3 is calculated and presented in *Figure 7*. From the figure, it can be seen that the withdrawal stiffness decreases with increasing insertion angle to timber grain and the screw diameter but increases with the increase of wood density and screw penetration length. Therefore, withdrawal stiffness is sensitive to the screw penetration length and wood density.

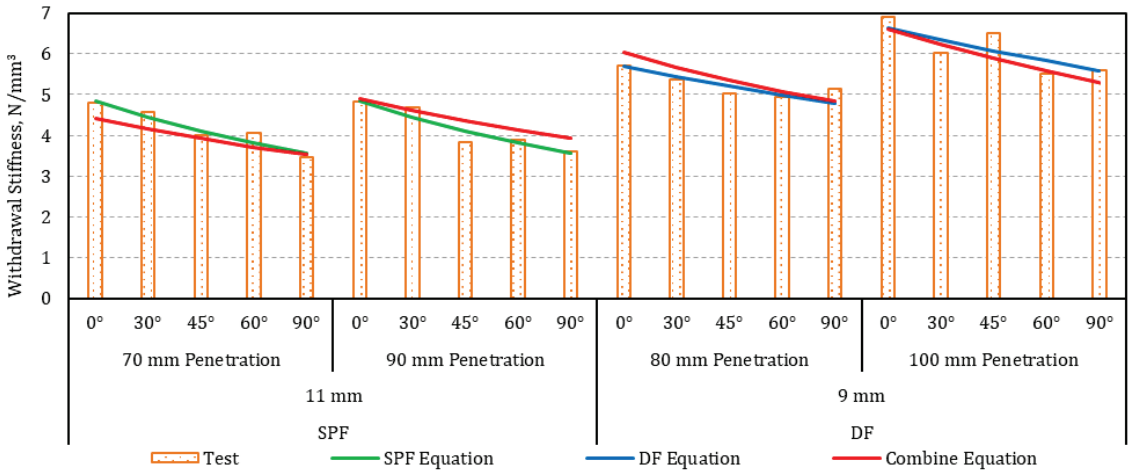

Figure 6: *Withdrawal stiffness comparison*

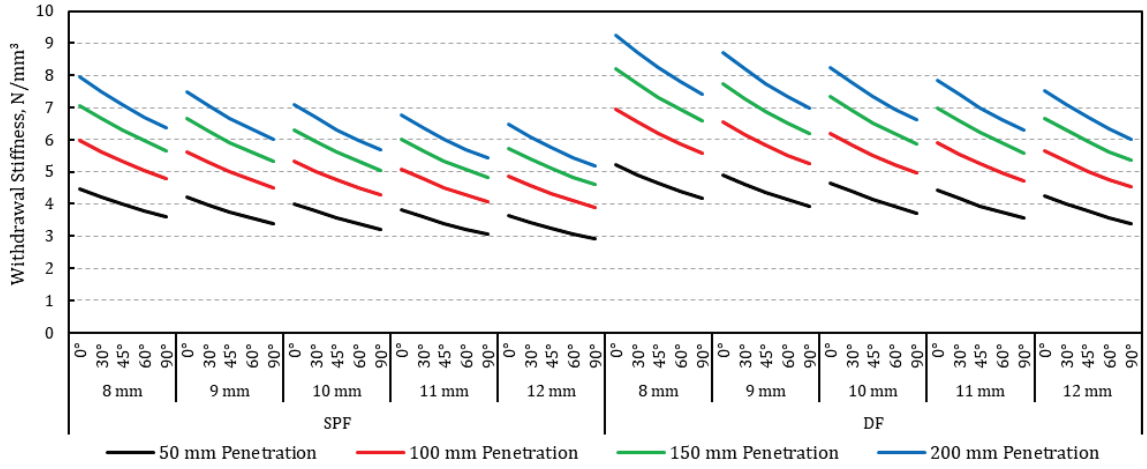

Figure 7: *Predicted withdrawal stiffness of different diameter screws in SPF and DF using general withdrawal stiffness equation for different penetration lengths (ρ_{SPF} = 425 kg/m^3 and ρ_{DF} = kg/m^3)*

4. CONCLUSIONS

Self-tapping screws are often inserted into the face of timber members at an angle to take advantage of their high withdrawal strength and stiffness to resist lateral loads. Because of the inclined arrangement, the calculation of the stiffness of such self-tapping screw connections requires knowledge of withdrawal stiffness at various insertion angles relative to the grain of wood on the timber member surface. From a design calculation perspective, it would be beneficial to express these stiffness properties in terms of wood density and fastener diameter, similar to parallel expressions for withdrawal strength, as well as the insertion angle. The main goal of this study was to provide a preliminary indication if it is feasible to develop empirical equations to express withdrawal stiffnesses in terms of the geometry of the fastener, wood density and insertion angle. Although the databases used in this study were limited in terms of the range of parameters studied, results from non-linear regression analyses performed on the collected data have shown that the withdrawal stiffness of self-tapping screws could be estimated from wood density, screw diameter, insertion angle, and effective penetration length. While the influences of wood density and screw diameter are as expected, it was noted that insertion angle influences withdrawal stiffness directly. Based on this study, withdrawal stiffness decreases with increasing insertion angle.

5. REFERENCES

[1] A. Ringhofer, G. (. Schickhofer and R. (. Brandner, "Axially-loaded self-tapping screws in solid timber and laminated timber products," Monographic Series TU Graz: Timber Engineering & Technology; Vol. TET 5, Verlag der Technischen Universität Graz, Graz, Austria, 2017.

https://doi.org/10.52202/069179-0153

[2] G. Pirnbacher, R. Brandner and G. Schickhofer, “Base Parameters of Self-Tapping Screws,” in *CIB-W18/42-7-1, Proceedings of the international council for research and innovation in building and construction, Working commission W18 –timber structures, Meeting 42*, Duebendorf, Switzerland, 2009.

[3] I. Bejtka and H. Blaß, “Self-tapping screws as reinforcements in connections with dowel-type fasteners,” Meeting 38, International Council for Research and Innovation in Building and Construction, CIB-W18/38-7-4, Universität Karlsruhe, Karlsruhe, Germany, 2005.

[4] R. Brandner, “Properties of axially loaded self-tapping screws with focus on application in hardwood,” *WOOD MATERIAL SCIENCE & ENGINEERING,* vol. 14(5), no. https://doi.org/10.1080/17480272.2019.1635204, p. 254–268, 2019.

[5] R. Brandner, A. Ringhofer and T. Reichinger, “Performance of axially-loaded self-tapping screws in hardwood: Properties and design,” *Engineering Structures,* vol. 188, no. https://doi.org/10.1016/j.engstruct.2019.03.018, p. 677–699, 2019.

[6] T. Uibel and H. Blaß, “Load carrying capacity of joints with dowel type fasteners in solid wood panels,” Karlsruhe, Germany, 2006.

[7] M. A. H. Mirdad and Y. H. Chui, “Load-slip performance of mass timber panel-concrete (MTPC) composite connection with self-tapping screws and insulation layer,” *Construction and Building Materials,* vol. 213 , no. https://doi.org/10.1016/j.conbuildmat.2019.04.117, p. 696–708, 2019.

[8] M. A. H. Mirdad and Y. H. Chui, “Stiffness prediction of Mass Timber Panel-Concrete (MTPC) composite connection with inclined screws and a gap,” *Engineering Structures,* vol. 207: 110215, no. https://doi.org/10.1016/j.engstruct.2020.110215, 2020(b).

[9] A. Ringhofer, R. Brandner and G. Schickhofer, “A Universal Approach for Withdrawal Properties of Self-Tapping Screws in Solid Timber and Laminated Timber Products,” in *International Network on Timber Engineering Research (INTER)*, Sibenik, Croatia, 2015.

[10] R. Khan, J. Niederwestberg and Y. H. Chui, “Influence of insertion angle, diameter and thread on embedment properties of self-tapping screws,” *European Journal of Wood and Wood Products,* vol. 79, no. https://doi.org/10.1007/s00107-020-01651-5, p. 707–718, 2021.

[11] R. Jockwer, R. Steiger and A. Frang, “Fully threaded self-tapping screws subjected to combined axial and lateral loading with different load to grain angles,” *Materials and Joints in Timber Structures, RILEM,* vol. 9, no. https://doi.org/10.1007/978-94-007-7811-5_25, pp. 265-272, 2014.

[12] ASTM, “Standard Test Method for Mechanical Fasteners in Wood,” Designation: D1761 − 12, ASTM International, West Conshohocken, PA, 2012.

[13] EN 1382, “Timber structures - Test methods - Withdrawal capacity of timber fasteners,” European Committee for Standardization, CEN, Brussels, Belgium, 1999.

[14] CSA, “Engineering design in wood,” Designation: CSA O86:19, Canadian Standards Association, Toronto, ON, 2019.

World Conference on Timber Engineering Oslo 2023

RNN-BASED MONOTONIC LOADING BEHAVIOR PREDICTION OF CLT JOINTS

Yewei Ding[1],Haibei Xiong[2],Cheng Yuan[3],Lin Chen[4],Yurong Lu[5]

ABSTRACT: Cross-laminated timber (CLT) joints play an essential role in ensuring co-working performance between CLT structural parts and dissipating seismic energy when structures suffer earthquake. The variation of mechanical properties of CLT joints would further affect the whole structural safety. Thus, evaluating and predicting the loading behaviors of CLT joints is critical. In this research, the authors proposed a recurrent neural network (RNN)-based method to predict monotonic loading behaviors of CLT joints. Two RNNs models were adopted, including long short-term memory (LSTM) and gated recurrent unit (GRU). Further, the prediction performance of two RNNs models was compared using statistical and mechanical property index. Prediction results demonstrate that both LSTM and GRU models can predict the failure stage of the CLT joint with R^2 more than 0.90, λ_S and λ_T larger than 0.98. In the statistical index, the GRU model outperformed the LSTM model, although both models achieved the same accuracy in the mechanical property index. Overall, the RNN-based prediction method proposed in this study can provide an outstanding prediction performance for the monotonic mechanical behavior of CLT joints.

KEYWORDS: CLT joint, Mechanical properties, Monotonic loading, Recurrent neural networks (RNNs)

1 INTRODUCTION

Cross-laminated timber (CLT), as an engineering timber product, has recently become more popular in high-rise building construction due to its low carbon footprint and excellent mechanical properties[1]. For high-rise CLT constructions, joints play important roles in structural safety. Thus, it is significant to understand and predict mechanical properties of CLT joints.

To obtain loading behaviors of the CLT joint, many mechanical researches have been conducted. He et al. tested 3-layer and 5-layer CLT panels for bending, shear, and compressive strength. The research revealed the various failure modes of CLT bending and shear specimens, suggesting that the numerical model of the CLT bending specimens can predict initial elastic stiffness K_e and ultimate load-resisting capacity F_{max} [2]. Dong et al. taken research on the CLT shear wall anchored with tensile connections. The strength, stiffness, and ductility of sixty-eight groups of hold-down connections were investigated. The result demonstrated that the connections employed in their test could produce reasonably high ductility while avoiding the metal bracket fracture failures [3].

Mechanical tests can undoubtedly determine the loading behaviors of the CLT joint, but they are destructive and time-consuming. With the emerging improvement of artificial intelligence, machine learning algorithms have been utilized in predicting loading behaviors non-destructively and validated their feasibility. For example, Chen et al. evaluated and predicted damage degree of the bolt joint in glulam timber constructions via machine learning and received a high predicting accuracy of 96% [4]. When utilized for data-driven prediction, recurrent neural networks (RNNs) have the advantage of boosting efficiency and extracting damaged information from data as one of the machine learning algorithms [5]. In civil engineering, RNN models used to predict loading behaviors have made substantial progress. High accuracy prediction in hysteretic or constitutive behavior and nonlinear seismic response is made using RNN, such as long short-term memory (LSTM) and gated recurrent unit (GRU) [6]. However, no research towards predicting CLT joint loading behaviors has been published.

The purpose of this article is to predict the monotonic loading failure procedure of the CLT joint. Section 2 describes the mechanical tests of the CLT joint and explains the theory of the RNN models utilized in this paper. Section 3 displays the RNN model parameters and prediction result evaluation indexes. Section 4 and 5

[1] Yewei Ding, Tongji University, China, 2111383@tongji.edu.cn
[2] Haibei Xiong, Tongji University, China, xiong204@outlook.com
[3] Cheng Yuan, Tongji University, China, 20310146@tongji.edu.cn
[4] Lin Chen, Tongji University, China, 1710742@tongji.edu.cn
[5] Yurong Lu, Tongji University, China, 15250983931@163.com

https://doi.org/10.52202/069179-0154

contain the discussion and conclusion of the prediction results.

2 METHODOLOGY

Experiments were carried out in the methodology to determine the mechanical properties of the CLT joint and the materials. The tested values were then trained by two RNN models to predict the failure stage in the loading procedure. Finally, multiple indexes were used to evaluate the predicted load value. Figure 1 depicts the methodology's flowchart.

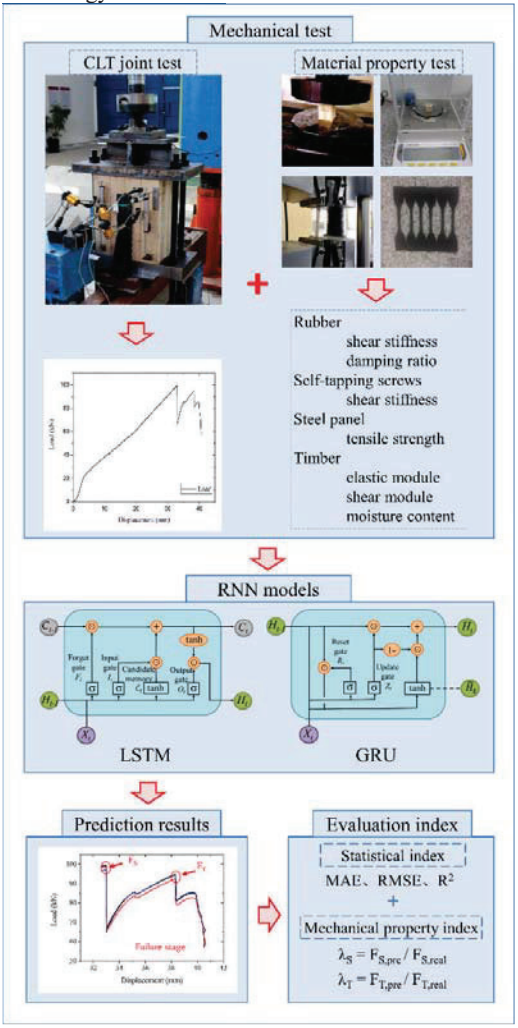

Figure 1: *Flowchart of the methodology*

2.1 MATERIALS AND PROPERTIES

The CLT panel was made with Canadian hemlock lumber and had a width of 300 mm and a height of 400 mm. Each panel was fabricated with 35/35/35 mm layups and a total thickness of 105 mm. According to the formal research, the connection used in this study employed energy-consuming rubber to reduce the interlayer displacement and improve the anti-seismic property, as shown in figure 2 [7]. The loading procedure in Hassanieh and Zhou's study included CLT joint failure with steel panel yielding, self-tapping screw cutting, and CLT panel broking [8,9]. So the mechanical properties of the steel panel, self-tapping screws, and CLT panels would influence the performance of the CLT joint. The mechanical properties of timber, self-tapping screws, and steel are tested according to the relevant standards and listed in table 1.

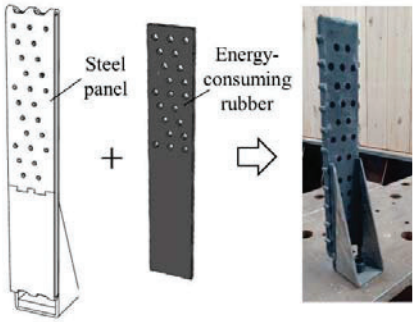

Figure 2: *Connection with energy-consuming rubber*

Table 1: *Value of material properties*

Material properties	Value
Shear stiffness of rubber	0.6 GPa
Damping ratio of rubber	0.2
Number of self-tapping screws	25
Shear stiffness of self-tapping screws	0.31 GPa
Tensile strength of steel	0.32 GPa
Elastic module of timber	15.31 GPa
Shear module of timber	1.17 GPa
Moisture content of timber	10.39%

2.2 TEST SETUP AND PROCEDURE

The monotonic loading approach used a two-stage displacement-control method (preloading procedure and formal loading procedure) according to ASTM D5652 [10]. The load was raised to 10% of the estimated peak load value during the preloading procedure, then unloaded after 2 minutes. In the formal loading procedure, the load was stopped when the joint reached the peak load or the displacement of 60 mm. Throughout the procedure, the loading speed is 1.5 mm/min. The CLT joint specimen and loading equipment are shown in figure 3.

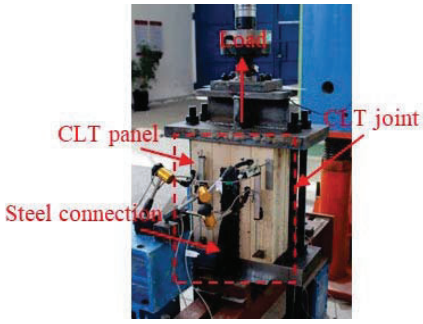

Figure 3: *CLT joint specimen and loading equipment*

2.3 TEST RESULTS

Figure 5 depicts the load-displacement curve of the monotonic loading procedure. The entire procedure, as

shown by the curve, is divided into three stages: elastic, plastic, and failure.

The wood fibers began to cut and crackle when the displacement reached 3 mm, and the joint entered the plastic stage. Following that, a part of the steel panel of the connection broke, causing the load suddenly decrease at the displacement of 33 mm, indicating that the procedure had entered the failure stage. The load was then supported by the energy-consuming rubber, the remaining steel panel, and the self-tapping screws. Finally, at the displacement of 38 mm, shear failure of the self-tapping screws resulted in the joint breaking and the load dropping precipitously.

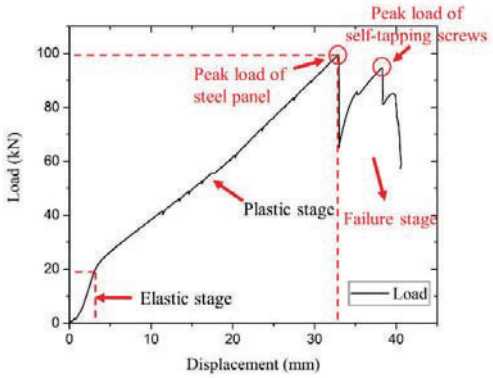

Figure 4: *Load-displacement curve*

2.4 RECURRENT NEURAL NETWORKS

Recurrent neural networks (RNNs) have been widely adopted as a kind of machine learning algorithm to predict sequential data [11]. One of the most widely used RNNs models is long short-term memory (LSTM). Long-term dependencies in the LSTM model are improved over traditional RNN models due to the gate functions introduced in the cell structure. Compared with the LSTM model, the gated recurrent unit (GRU) model has one fewer gate function, which may reduce the computational burden [12]. The LSTM model has been utilized to predict fracture growth rates of L-shape concrete specimens as well as the dynamic response of the nonlinear structure [13,14]. The GRU model has also been used in structural health monitoring (SHM) of civil structure buildings [15]. As a result, both the LSTM and the GRU models are effective methods for predicting loading behavior in civil engineering.

2.4.1 LSTM model

The LSTM model was initially introduced in 1997 and has received much attention in sequence prediction [16]. As shown in figure 3, variable weight matrixes are implemented by adding the input gate (I_t), forget gate (F_t), and output gate (O_t) in LSTM. Each gate includes a σ neural network layer and a pointwise multiply operation:

$$I_t = \sigma(X_t W_{xi} + H_{t-1} W_{hi} + b_i) \quad (1)$$

$$F_t = \sigma(X_t W_{xf} + H_{t-1} W_{hf} + b_f) \quad (2)$$

$$O_t = \sigma(X_t W_{xo} + H_{t-1} W_{ho} + b_o) \quad (3)$$

where X_t means input. H_{t-1} means the hidden state. σ is the activation function. W means the weight matrix, the first subscript of W refers to the input, and the second subscript refers to the gate. b means bias, and the subscript of b refers to the gate.

Candidate memory $\tilde{C}_t$ is expressed as:

$$\tilde{C}_t = tanh(X_t W_{xc} + H_{t-1} W_{hc} + b_c) \quad (4)$$

Memory cell C_t is expressed as:

$$C_t = F_t \odot C_{t-1} + I_t \odot \tilde{C}_t \quad (5)$$

Hidden state H_t is expressed as:

$$H_t = O_t \odot \tanh(C_t) \quad (6)$$

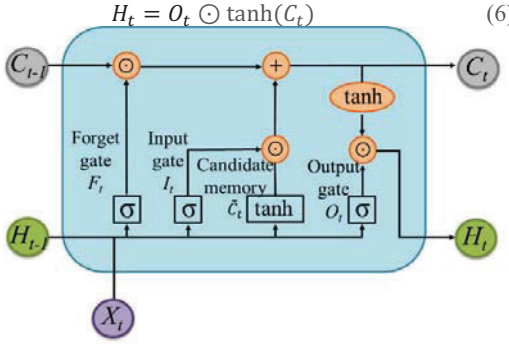

Figure 5: *Frame diagram of LSTM models*

2.4.2 GRU model

To decrease the computation burden, the LSTM model was improved into the GRU model with some cell states improved [17]. As shown in figure 6, the three gates in the LSTM model are integrated into the reset gate (R_t) and the update gate (Z_t) in the GRU model:

$$R_t = \sigma(X_t W_{xr} + H_{t-1} W_{hr} + b_r) \quad (7)$$

$$Z_t = \sigma(X_t W_{xz} + H_{t-1} W_{hz} + b_z) \quad (8)$$

where σ refers to the activation function, X_t means input, H_{t-1} means the hidden state, W represents the weight refers to different inputs and gates, b refers to bias.

The candidate hidden state $\widetilde{H}_t$ is expressed as:

$$\widetilde{H}_t = \tanh(X_t W_{xh} + (R_t \odot H_{t-1}) W_{hh} + b_h) \quad (9)$$

The hidden state H_t is expressed as:

$$H_t = Z_t \odot H_{t-1} + (1 - Z_t) \odot \widetilde{H}_t \quad (10)$$

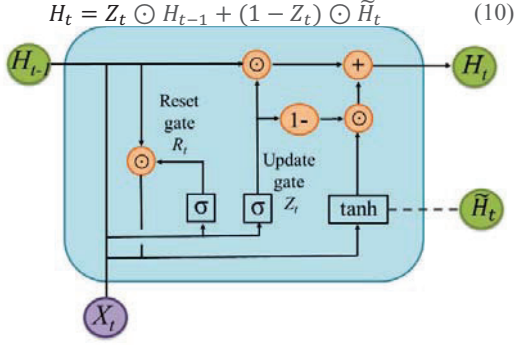

Figure 6: *Frame diagram of GRU models*

3 PREDICTION SETTINGS AND EVALUATION INDEX

3.1 PARAMETER SETTINGS

The load-displacement data obtained from the monotonic loading test are time-sequential. The mechanical testing

https://doi.org/10.52202/069179-0154

machine collected 300 data points per minute, fro a total of 8207 data points in the dataset. At that point, each data point contains the corresponding load, displacement, and material parameter. Although some parameters, such as the mechanical properties of CLT and steel, would change when entering the plastic stage, this study assumes that these material parameters would not change for simplification. In both LSTM and GRU models, the number of neurons is 8. The proportions of training and validation sets are 0.8 and 0.2, respectively.

In this research, rectified linear unit (ReLU) was adopted as the activation function to avoid the problem of disappearing gradients and to speed up training. Explained by equation (11) and figure 7:

$$f_x = \max(0, x) \tag{11}$$

where x is the output value from the previous layer.

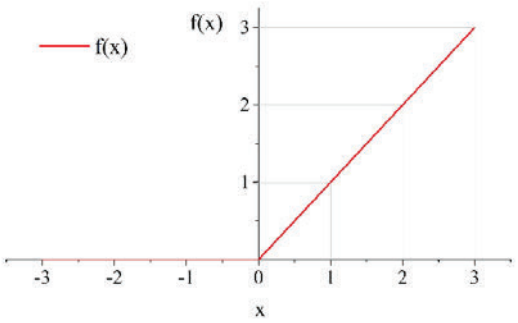

Figure 7: *Function image of ReLU*

Mean square error (MSE) is taken as the loss function in order to facilitate convergence:

$$MSE = \frac{\sum_{i=1}^{n}(y_i - x_i)^2}{n} \tag{12}$$

where x_i means real value, y_i means predicted value, n is the number of data.

Adaptive momentum is adopted to optimize. Furthermore, early stopping is employed for defending overfitting. Other parameter settings are listed in Table 2.

Table 2: *Parameter settings in RNN models*

Parameter	Value
Time step	40
Dropout	0.1
Epoch	100
Validation split	0.1
Batch size	32

3.2 EVALUATION INDEX

This paper presents two kinds of performance evaluation indexes (statistical and mechanical property indexes). Statistical indexes assess the fitness between predicted and real monotonic behavior obtained during the test. Mechanical property indexes are proposed as a mean of estimating predicted mechanical properties.

3.2.1 Statistical index

The statistical index contains mean absolute error (MAE), root mean square error (RMSE), and coefficient of determination (R^2). MAE and RMSE both indicate the error to the real value. Lower values of MAE and RMSE mean better prediction performance. The degree of fitness between predicted and real values is donated by R^2. When R^2 is close to 1.00, the prediction is more accurate. Three indexes are listed in equation (13-15):

$$MAE = \frac{\sum_{i=1}^{n}|y_i - x_i|}{n} \tag{13}$$

$$RMSE = \sqrt{\frac{\sum_{i=1}^{n}(y_i - x_i)^2}{n}} \tag{14}$$

$$R^2 = 1 - \frac{\sum_{i=1}^{n}(x_i - y_i)^2}{\sum_{i=1}^{n}(x_i - \bar{x})^2} \tag{15}$$

where x_i means real load value, $\bar{x}$ means mean real load value, y_i means predicted load value, n is the number of data in the load-displacement curve.

3.2.2 Mechanical property index

It is significant to evaluate the mechanical properties of the predicted results, which represent the loading behavior of the actual experiment. The broken steel panel and self-tapping screws of the CLT joint caused a sudden drop in load. As a result, the load value at these two points is adopted to evaluate the mechanical properties during the failure stage.

Based on the formal research [7], this study takes the coefficient of peak steel panel load λ_S as the normalized value of the predicted peak steel panel load based on the real value:

$$\lambda_S = F_{S,pre}/F_{S,real} \tag{16}$$

where $F_{S,pre}$ means the predicted peak steel panel load, the $F_{S,real}$ means the real peak steel panel load.

The coefficient of peak self-tapping screws load λ_T is similar to λ_S:

$$\lambda_T = F_{T,pre}/F_{T,real} \tag{17}$$

where $F_{T,pre}$ means the predicted peak self-tapping screws load, the $F_{T,real}$ means the real peak self-tapping screws load.

The closer λ_S and λ_T get to 1.00 representing a higher prediction accuracy.

4 RESULTS AND DISCUSSION

Figure 8 depicts the loading behaviors predicted by the LSTM and GRU models. Only the failure procedure is predicted. Load curves predicted by the LSTM and GRU models are both fit closely to the real load curve. Table 3 lists three statistical evaluation indexes. Both MAE and RMSE of the GRU model are lower than LSTM model's, while R^2 is higher, indicting that the GRU model's predicted results are statistically more precise than the LSTM model's.

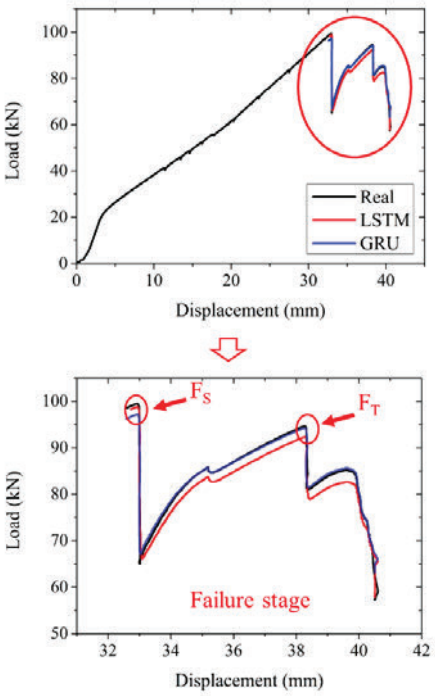

Figure 8: *Real and predicted load-displacement curve*

Table 3: *Statistical index*

Statistical index \ Model	LSTM	GRU
MAE (kN)	2.14	0.67
RMSE (kN)	2.58	1.62
R^2	0.91	0.97

Table 4 lists the peak loads predicted by the LSTM and GRU models for the steel panel and self-tapping screws, respectively. λ_S and λ_T are calculated according to the real and predicted load values. The λ_S and λ_T of the LSTM and GRU model are both higher than 0.98, which are close to 1.00. The LSTM model achieves λ_S of 0.99, which is higher than the 0.98 predicted by the GRU model. While the values of λ_T are the opposite. The high value of mechanical property indexes demonstrates the precise prediction ability of LSTM and GRU models.

Table 4: *Mechanical property index*

Mechanical property index \ Model	Real	LSTM	GRU
F_S (kN)	99.50	98.80	97.20
F_T (kN)	94.61	92.30	94.20
λ_S	--	0.99	0.98
λ_T	--	0.98	1.00

As stated in section 2.4, the GRU model has a lower computational burden than the LSTM model. The LSTM model consumed 14 seconds and 92 milliseconds in this study, while the GRU model took 14 seconds and 54 milliseconds. Given that the number of predicted data points in this monotonic loading test is 1641, the GRU model consums only 38 milliseconds less than the LSTM model. In case of tests containing a large amount of data points, such as hysteretic loading tests or other complex and time-consuming tests, the computation reduction and time-saving effect of the GRU model will be more obvious.

5 CONCLUSIONS AND PROSPECT

The authors proposed an RNNs-based prediction method for the failure procedure of CLT joint under monotonic loading in this paper. Statistical indexes (MAE, RMSE, and R^2) and mechanical property indexes (λ_S and λ_F) are used to evaluate the predicted load-displacement curves.. The MAE of the LSTM and GRU model are both no higher than 2.14 kN, while the RMSE of the two RNN models is no higher than 2.58 kN, and R^2 is greater than 0.91. The values of the three statistical indexes indicated that the error between the predicted value and real value is small. Furthermore, both λ_S and λ_T of the LSTM and GRU model are greater than 0.98, indicating that the two models predict the peak load of the steel panel and self-tapping screws of the joint with a high accuracy . The high value of the prediction indexes demonstrates that both the LSTM and GRU models accurately predicted the failure procedure of CLT joint under monotonic loading precisely, with the GRU model outperforming the LSTM model in terms of statistical indexes.

Prediction accuracy demonstrated the feasibility and effectiveness of using the RNN-based method to predict the failure procedure of CLT joints, providing a reference for CLT construction mechanical properties research.

The mechanical properties of the materials in the RNN model, on the other hand, remained constant throughout the loading procedure, whereas the stress varies with strain during the actual loading procedure. Therefore, in the future work, the constitutive model of the materials would be considered for more accurate physics expression and prediction results.

ACKNOWLEDGEMENT

The authors are thankful for the support of the National Natural Science Foundation of China (51978502).

REFERENCE

[1] Brandner R., Flatscher G. and Ringhofer A. et al. Cross laminated timber (CLT): overview and development. *Eur J Wood Wood Prod*, 74(3): 331-351, 2016.

[2] He M., Sun X. and Li Z. et al. Bending, shear, and compressive properties of three- and five-layer cross-laminated timber fabricated with black spruce. *J Wood Sci*, 66(1), 2020.

[3] Dong W., Li M. and Ottenhaus L. et al. Ductility and overstrength of nailed CLT hold-down connections. *Eng Struct*, 215: 110667, 2020.

https://doi.org/10.52202/069179-0154

[4] Chen L., Xiong H. and Yang Z. et al. Preload measurement of steel-to-timber bolted joint using piezoceramic-based electromechanical impedance method. *Measurement*, 190: 110725, 2022.
[5] Shajihan S. A. V., Wang S. and Zhai G. et al. CNN based data anomaly detection using multi-channel imagery for structural health monitoring. *Smart Struct Syst*, 29(1): 181-193, 2022.
[6] Sajjad M., Khan Z. A. and Ullah A. et al. A Novel CNN-GRU-Based Hybrid Approach for Short-Term Residential Load Forecasting. *Ieee Access*, 8: 143759-143768, 2020.
[7] Chen J., Xiong H. and Furuta T. et al. Experimental and analytical studies on mechanical performance of innovative energy-dissipating hold-down for CLT structures. *Constr Build Mater*, 317: 125966, 2022.
[8] Zhou Q., Gong M. and Chui Y. H. et al. Measurement of rolling shear modulus and strength of cross laminated timber fabricated with black spruce. *Constr Build Mater*, 64: 379-386, 2014.
[9] Hassanieh A., Valipour H. R. and Bradford M. A. Composite connections between CLT slab and steel beam: Experiments and empirical models. *J Constr Steel Res*, 138: 823-836, 2017.
[10] ASTM D5652-21. Standard Test Methods for Single-Bolt Connections in Wood and Wood-Based Products. *ASTM International*, United States, 2021.
[11] Yu Y., Si X. and Hu C. et al. A Review of Recurrent Neural Networks: LSTM Cells and Network Architectures. *Neural Comput*, 7(31): 1235-1270, 2019.
[12] Cho K., van Merrienboer B. and Bahdanau D. et al. On the Properties of Neural Machine Translation: Encoder‐Decoder Approaches. *Statistics-Abingdon*, 2, 2014.
[13] Xue J. and Ou G. Predicting wind-induced structural response with LSTM in transmission tower-line system. *Smart Struct Syst*, 3(28): 391-405, 2021.
[14] Le Hien Nguyen D., Thi Thanh Do D. and Lee J. et al. Forecasting Damage Mechanics by Deep Learning. *Computers, Materials & Continua*, 61(3): 951-977, 2019.
[15] Liu Y. WSN-Based SHM Optimisation Algorithm for Civil Engineering Structures. *Processes*, 10(10): 2113, 2022.
[16] Hochreiter S. and Schmidhuber J. Long Short-Term Memory. *Neural Comput*, 1997.
[17] Dey R. and Salem F. M. Gate-Variants of Gated Recurrent Unit (GRU) Neural Networks. *Statistics-Abingdon*, 2017.

World Conference on Timber Engineering Oslo 2023

CYCLIC BEHAVIOR OF MORTISE-TENON JOINTS REINFORCED BY SELF-TAPPING SCREW

Tianxiao Yin[1], Chenyue Guo[2], Zhiqiang Wang[3,*], Wei Zheng[4], Jianhui Zhou[5], Meng Gong[6]

ABSTRACT: In this study, fully-thread countersunk head self-tapping screw (STS) with outer diameter of 6 mm and 8 mm were used to reinforce the mortise-tenon (MT) joints with horizontal and inclined insertion methods. A total of fifteen cyclic loading tests were carried out for one group of unreinforced joints and five groups of reinforced joints, and the load-carrying capacity, strength, stiffness, ductility and energy dissipation of these joints were evaluated. The results showed that larger diameter STS and more STS could improve the load-carrying capacity and initial stiffness of the joints, although it might accelerate the damage to the joints and change the failure modes of MT joints. In addition, different reinforcement methods had different improvement effect, as the joints reinforced by STS horizontal insertion had a more significant improvement in the load-carrying capacity, while the inclined insertion of STS had a more significant improvement in the initial stiffness. This study provides data for reinforcement of MT joints with STS, and different reinforcement methods can be selected according to different engineering requirements.

KEYWORDS: Timber, Mortise-tenon (MT) joint, Self-tapping screw (STS), Reinforcement, Cyclic loading

1 INTRODUCTION

As a kind of essential connection in Chinese traditional architecture, mortise-tenon (MT) joints are the main energy dissipation components in wood construction, which are easy to install and have good rotation ability [1]. Previous research found that MT joints belongs to semi-rigid joints [2,3]. With the development of modern timber construction, the bearing capacity and stiffness of traditional MT joints can hardly meet the engineering requirements. In order to improve the mechanical properties of MT joints, kinds of different reinforcement methods have been carried out for MT joints.

Currently, the reinforcement methods designed for MT joints can be categorized as three types according to the materials applied: wood component [4,5], metal connector [6-8] and new composite material component [9-11]. However, these methods have some shortcomings to some extent. For instance, the durability of wood components is not ideal, and the appearances of the MT joints reinforced by metal connectors (e.g. steel plate) and composite material (e.g. fiber reinforced polymer) are not clean and tidy. Thus, some new reinforcement methods need to be carried out.

Inspired by the connections in modern timber construction, some new dowel-type connectors can be considered for application in the reinforcement for MT joints. Among them, self-tapping screw (STS) is widely recognized as the state-of-the-art connector for timber construction, for its economic cost and convenient installation as well as its excellent mechanical properties [12-15]. According to former scholars' researches, carpentry joints reinforced by STS can achieve good performance, especially the stiffness and load-carrying capacity, which can compensate for the shortcomings of traditional MT joints [12-16]. Furthermore, previous researches found that the insertion angle of STS had a significant influence on the mechanical properties of those reinforced joints [14, 17-20]. At present, it is generally believed that the STS inserted perpendicular to the surface of the components can obtain better ductility, while STS inclined insertion can achieve better stiffness, both of which can improve the load-carrying capacity of the joints.

This paper presents glulam MT dovetail reinforced by STS with horizontal (perpendicular to the timber surface)

[1] Tianxiao Yin, College of Materials Science and Engineering, Nanjing Forestry University, China, yintianxiao@njfu.edu.cn
[2] Chenyue Guo, School of Engineering, University of Northern British Columbia, Canada, cguo@unbc.ca
[3] Zhiqiang Wang, College of Materials Science and Engineering, Nanjing Forestry University, China, wangzhiqiang@njfu.edu.cn
[4] Wei Zheng, College of Materials Science and Engineering, Nanjing Forestry University, China, zw@njfu.edu.cn
[5] Jianhui Zhou, School of Engineering, University of Northern British Columbia, Canada, jianhui.zhou@unbc.ca
[6] Meng Gong, Wood Science and Technology Centre, University of New Brunswick, Canada, meng.gong@unb.ca
* Corresponding author

https://doi.org/10.52202/069179-0155

and inclined insertion methods. Cyclic loading testes were carried in this study for both unreinforced (CG) and reinforced joints to evaluate their load-carrying capacity, strength, stiffness, ductility and energy dissipation capacity.

2 MATERIALS AND METHODS

2.1 MATERIALS

Four-layer Glulam made of NO.2 SPF (*Spruce-pine-fir*) dimension lumber were used for process of MT joints. The moisture content and density of glulam were 13.3% (COV=6.7%) and 449 kg/m^3 (COV=4.8%), respectively. Fully-thread countersunk head STS (grade 1022 [21]) with a diameter of 6 mm and 8 mm were used in this study. The yield moment ($M_{y,R}$) and the pull-through capacity (F_{head}) of STS were tested and evaluated respectively [22, 23], and the characteristic values were calculated [24], as shown in Table 1.

The dimension of the components was designed according to the Qing Dynasty " *Gong Cheng Zuo Fa Ze Li*" [25] and is shown in Fig. 1. The different reinforcement methods for MT joints are shown in Fig. 2. In order to ensure the uniformity of materials for specimens, the beam, column and crosser (a tamping placed in the groove of mortise upon tenon) used the same material and were assembled without adhesive.

Table 2 shows the grouping of specimens. It should be noted that in the preliminary tests, the tenon would split when the STS with 8mm diameter was applied for inclined insertion, so this diameter was not considered for use as inclined-insertion reinforcement for MT joints in the formal tests.

Table 1 *Properties of STS*

	Outer diameter d (mm)	Length l (mm)	$M_{y,R}$ (N·mm)	F_{head} (N)
STS-6	6	140	11090	3261
STS-8	8	140	34406	3927

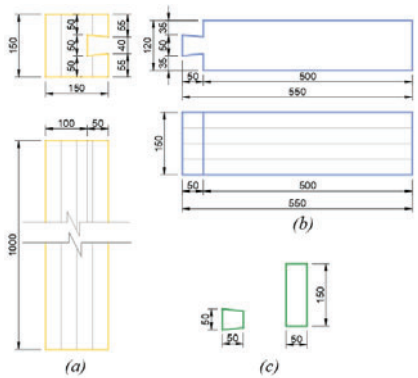

Figure 1: *Dimension of components in joints: (a) Column; (b) Beam and (c) Crosser (Unit: mm).*

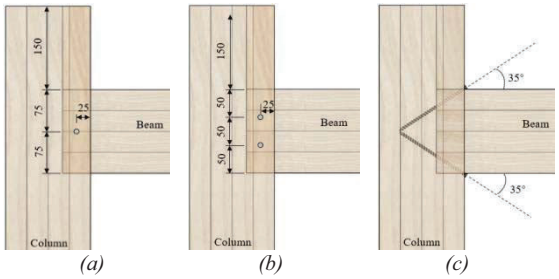

Figure 2: *different reinforcement methods: (a) one STS with horizontal insertion, (b) two STS with horizontal insertion and (c) two STS with inclined insertion.*

Table 2 *Specimen grouping*

Group	Number of STS	Diameter of STS (mm)	Insertion angle (°)	Replicates
CG	/	/	/	3
RSV6	1	6	90°	3
RSV8	1	8	90°	3
RV6	2	6	90°	3
RV8	2	8	90°	3
RI6	1	6	35°	3

2.2 TEST SETUP

During tests, the columns were placed horizontally and horizontal force was acted on the beam end by hydraulic actuator. The rightward push was recorded as positive direction and the leftward pull was recorded as negative direction. Approximately 10 kN horizontal load was applied at the end of the column through a hydraulic jack to simulate the load of the column under actual situation. The whole test setup is shown in Fig.3. The loading protocol referred to ISO-16670 [26]. The cyclic loading tests were repeated three times for each group.

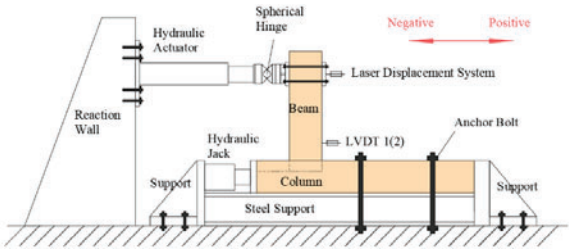

Figure 3: *Test setup.*

2.3 DATA ANALYSIS

The bending moment (M) and the corresponding rotation (θ) in this study were calculated by geometric relations as:

$$M = P \cdot H \quad (1)$$

$$\theta = \frac{\Delta}{H} \quad (2)$$

where P is the load applied, H is the distance between the joint and loading point (400 mm in this study), Δ is the displacement of the loading point in horizontal direction. The yield moment (M_y) of these joints was determined according to EEEP method [27] as:

$$M_y = (\theta_u - \sqrt{\theta_u^2 - \frac{2A}{K_e}})K_e \quad (3)$$

where M_y is the yield moment, θ_u is the ultimate rotation angle, A is the integral area under envelop curve in the interval of [0, θ_u], K_e is the initial stiffness which equals to 0.4 M_m/θ_e, where M_m is the maximum bending moment and θ_e is the rotation angle at 0.4 M_m.

Strength degradation factor (λ) was used to characterize the behavior that the strength of the joints decreases as the number of cycles increases [10], which was calculated as:

$$\lambda_i = \frac{M_{i,3}}{M_{i,1}} \quad (4)$$

where λ_i is the strength degradation factor in the i th displacement amplitude, $M_{i,1}/M_{i,3}$ is the peak bending moment of the first cycle in the i th displacement amplitude.

Stiffness degradation of joints was referred to evaluate the stiffness decreases in this study [28]. The secant stiffness K_i was calculated as:

$$K_i = \frac{|+M_i|+|-M_i|}{|+\theta_i|+|-\theta_i|} \quad (5)$$

where M_i is the peak bending moment of joints at the 1st cycle in the i-stage displacement amplitude while θ_i is the relevant rotation angle of M_i.

The ductility coefficient (D) of the joints in this study was evaluated as the ratio between the ultimate rotation (θ_u) and yield rotation (θ_m):

$$D = \frac{\theta_u}{\theta_y} \quad (6)$$

The ductility of joints into four scopes from brittle ($D \leq 2$) to high ductility ($D > 6$) according to their ductility coefficient [29].

The equivalent viscous damping coefficient (v_{ep}), which is a dimensionless coefficient, can be employed to assess the energy dissipation capacity of these joints [30]. The calculation of the equivalent viscous damping coefficient is as follows:

$$v_{ep} = \frac{E_d}{2\pi E_p} \quad (7)$$

where E_d is the energy dissipated per half cycle, E_p is the available potential energy.

3 RESULTS AND DISCUSSIONS

3.1 FAILURE MODES

The typical failure modes of the CG group were push out of crosser and pull-out of the tenon, together with splitting and crack on the column, as shown in Fig. 4.

As regards to the reinforced groups with STS horizontal insertion, split of the column and yielding of STS were the typical failure modes. Apart from this, the crack and crush of wood on the column below the joints area were also observed in these groups. For RSV6 and RSV8 groups reinforced with one STS, they had similar failure modes during the tests, which were the pull-out of the tenon and splitting on the side of the column, together with the yielding of STS, as shown in Fig. 5 and Fig. 6. Due to the larger diameter of STS, the amount of the pull-out of tenon in RSV6 group was larger than that in RSV8 group. The phenomenon of RV6 and RV8 groups during the initial loading phase was similar to RSV6 and RSV8 groups. Benefitted from the more rigid connection provided by two STS, the amount of tenon pull-out was decreased, compared with that in RSV6 and RSV8 groups. However, on account of the more STS inserted, the joints might suffer more damage at the late loading stage, for example, the column would split or even fracture. The two STS inserted in RV groups were yielded at the late loading stage. Typical failure modes of RV6 and RV8 are shown in Fig. 7 and Fig.8.

Similar to other groups, the pull-out of tenon and crack on the column appeared in RI6 group with STS inclined insertion. However, the difference between RI6 group and other groups was that there was no split on the side of the column in RI6 group and the STS used in it was not found yielding. After cutting the specimens, the withdrawal of STS was found in the RI6 group. The failure mode of RI6 group was shown in Fig. 9.

(a) (b) (c)

Figure 4: *Failure modes of CG group: (a) push-out of crosser; (b) pull-out of tenon and splitting on the side of column and (c) crack on the lower end of mortise of column.*

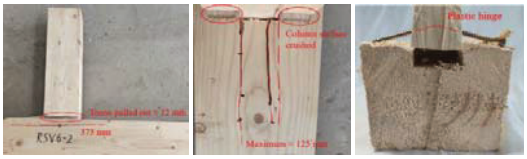

(a) (b) (c)

Figure 5: *Failure modes of RSV6 group: (a) pull-out of tenon and splitting on the side of column; (b) crack on the lower end of mortise of column and crush of wood and (c) STS yielding.*

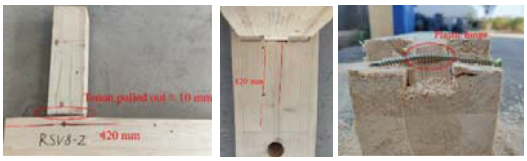

(a) (b) (c)

Figure 6: *Failure modes of RSV8 group: (a) pull-out of tenon and splitting on the side of column; (b) crack on the lower end of mortise of column and crush of wood and (c) STS yielding.*

(a) (b) (c)

Figure 7: *Failure modes of RV6 group: (a) crush and fracture of wood; (b) splitting of wood and (c) STS yielding.*

https://doi.org/10.52202/069179-0155

(a) (b) (c)

Figure 8: *Failure modes of RV8 group: (a) crack, crush and fracture of wood; (b) splitting of wood and (c) STS yielding.*

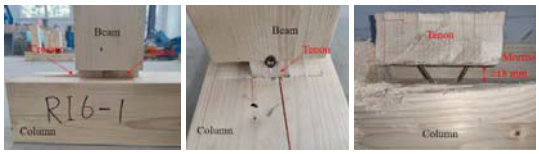

(a) (b) (c)

Figure 9: *Failure modes of RI6 group: (a) pull-out of tenon and crosser; (b) crack on the column and (c) withdrawal of STS.*

3.2 HYSTERETIC AND ENVELOP CURVES

The average hysteretic curves of each group showed different degree of pinching effect and exhibited asymmetry in positive and negative directions, as shown in Fig. 10.

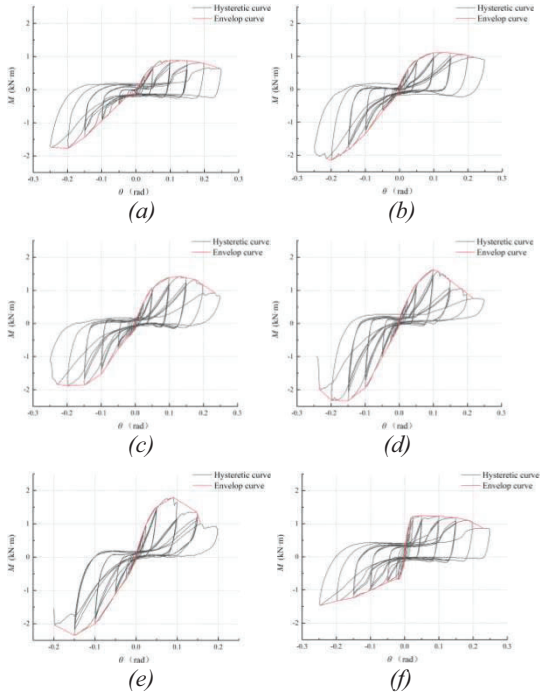

(a) (b) (c) (d) (e) (f)

Figure 10: *Hysteretic curves of: (a) CG group; (b) RSV6 group; (c)RSV8 group; (d) RV6 group; (e) RV8 group and (f) RI6 group.*

These hysteretic curves showed a similar trend. To be specific, the slope of hysteretic curve was small at the initial loading stage because of the processing gap between mortise and tenon. As the increment of displacement amplitude, the friction area between mortise and tenon increased thus caused the rapid increase of the bending moment. It can be obviously seen that the hysteretic curves of each joint have asymmetry, and the absolute value of the peak point of the negative loading curve was higher than that of the positive loading curve, which indicated that the negative loading process had a higher load-carrying capacity. The reason for this was the tenon was constrained differently under these loading directions. Specifically, under positive loading, the pushing out and loosening of the crosser would lead to a decrease in the load-carrying capacity, on the contrary, the rigid constraint had a positive effect on the improvement of the load-carrying capacity under negative loading tests. Different from the curves of the joints with horizontally inserted STS, the hysteretic curve of RI6 group exhibited excellent initial slope and alleviate pinching effect.

For easy comparison, the envelop curves of each group have been extracted and drawn in Fig. 11. It is clear from this figure that the RV groups had the largest load-carrying capacity, followed by the RSV groups and the RI6 group. In a homogeneous group, it can be found that a bigger diameter could provide higher load-carrying capacity. For example, as regard the RV groups, the RV8 group had a higher maximum bending moment than that of RV6 group. In general, the joints reinforced with STS horizontal insertion had significant improvement in terms to load-carrying capacity, while those with STS inclined insertion had obvious improvement in initial stiffness.

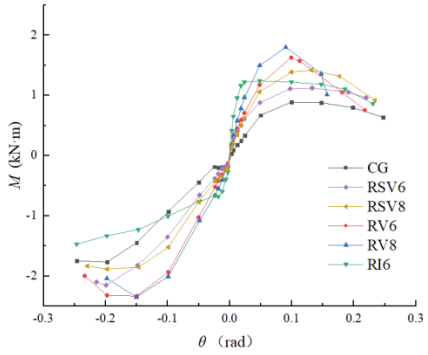

Figure 11: *Envelop curves of each group.*

3.3 MECHANICAL PROPERTIES

The average maximum moment (M_m), ultimate moment (M_u), yield moment (My) and their corresponding rotation together with the initial stiffness (K_e) and ductility coefficient (D) during two loading directions of each group are summarized in Table 3.

The load-carrying capacity and stiffness of MT joints have been improved significantly after being reinforced by STS. Two STS with horizontal insertion (RV group) had obvious improvement in load-carrying capacity, and STS with larger diameter had more improvement. Compared with the CG group, the load-carrying capacity of the RV group joints was 102% and 33% higher in positive and negative loading directions, respectively. As mentioned above, a larger diameter of STS can improve the load-carrying capacity due to its larger bending strength. Moreover, compared with RV groups and RSV groups, it can be concluded that the number of STS had a significant

https://doi.org/10.52202/069179-0155

effect on the load-carrying capacity of MT joints, although it did not meet a liner rule. From the results, it can be seen that the improvements of load-carrying capacity brought by RSV groups were not as good as that brought by RV groups. For instance, the maximum bending moment of the RSV8 and RSV6 groups increased by 59 % and 26%, respectively, which was smaller than the improvement of MT joints in RV groups. Furthermore, the reinforcement effect of RI6 group was small, under positive loading, the load-carrying capacity of MT joints was increased by 39%, while under negative loading, the load-carrying capacity of which was close to that of CG group. This means for this kind of MT joints, using horizontally inserted STS can achieve a higher improvement on load-carrying capacity compared with inclined insertion STS.

Table 3 *Mechanical properties of MT joints*

Group	Loading direction	M_m (kN·m)	θ_m (rad)	M_u (kN·m)	θ_u (rad)	M_y (kN·m)	θ_y (rad)	K_e (kN·m·rad^{-1})	D
CG	Positive	0.89	0.10	0.71	0.22	0.83	0.06	13.21	3.56
RSV6		1.12	0.13	0.96	0.22	1.03	0.03	29.97	6.43
RSV8		1.42	0.13	1.14	0.20	1.29	0.05	27.05	4.26
RV6		1.63	0.10	1.30	0.15	1.42	0.05	31.01	3.22
RV8		1.80	0.09	1.44	0.14	1.57	0.03	45.00	3.92
RI6		1.24	0.05	1.00	0.21	1.18	0.01	124.40	21.76
CG	Negative	1.77	0.20	1.74	0.25	1.83	0.20	9.18	1.23
RSV6		2.15	0.20	2.10	0.21	1.99	0.15	13.45	1.45
RSV8		1.88	0.20	1.83	0.23	1.86	0.12	15.38	1.90
RV6		2.33	0.15	2.00	0.23	2.19	0.11	20.73	2.21
RV8		2.35	0.15	2.04	0.20	2.13	0.09	23.48	2.19
RI6		1.47	0.25	1.47	0.25	1.11	0.02	48.93	10.91

The strength degradation of each group between -0.15 rad to 0.15 rad is shown in Fig. 12. It can be easily seen that the strength degradation factor of each group decreased with the increase of loading amplitude. The strength degradation of CG group was more minor before rotation reached 0.15 rad, which may prove that the wood damage inside the unreinforced joints was slighter. Afterward, the strength of CG group degraded greatly due to the significant increase of tenon pulling out. It is worth noting that the strength degradation of RV groups was more prominent in this test, verifying that those joints suffered more damage in loading. On the contrary, the strength degradation of RSV and RI groups tended to be stable at the late loading stage.

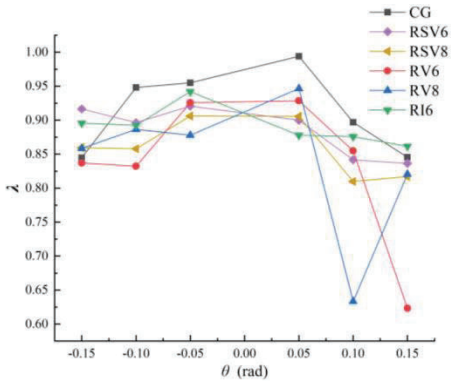

Figure 12: *Strength degradation of each group.*

The stiffness degradation of each group is shown in Fig. 13. In general, the stiffness of each group showed similarity before the rotation came to 0.05 rad, which decreased and then remained stable. When the rotation came to 0.25 rad, each group exhibited similar stiffness in the end, indicating that significant failure had occurred in each group. During the whole loading process, the unreinforced CG group showed a markedly lower stiffness than those of the reinforced group. In the reinforced groups, RI6 group exhibited very large stiffness in the initial loading stage, which could significantly improve the initial stiffness of MT joints, up to 842% and 433% higher than those of CG group, respectively in two loading directions. Comparing the RV groups with RSV groups, it can be found that MT joints reinforced with two STS can obtain higher initial stiffness than that of those reinforced with one STS. Besides, a bigger diameter of STS can also effectively improve the initial stiffness.

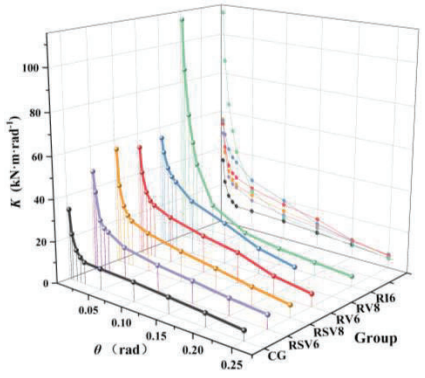

Figure 13: *Stiffness degradation of each group.*

As shown in Table 3, the ductility coefficient (D) of each group under positive loading was higher than that under negative loading. The reason for this was that the joints entered yield stage earlier when they were loaded in positive direction, due to the different constraints under

https://doi.org/10.52202/069179-0155

the two loading directions. It is worth noting that under positive loading, RSV groups had higher ductility coefficient than RV group, while under negative loading the situation was the opposite. The reason for this could be that, as mentioned, the constraints under negative loading were more rigid, thus leading to plastic deformation of wood in RV groups. As a result, RV groups entered the yield stage earlier, which makes the calculation result of ductility coefficient larger. Among these groups, the ductility of RI6 was significantly higher than that of other groups, while the ductility of CG group without reinforcement was relatively lower. According to the classification of ductility proposed by Smith et al. [29], except the RI6 group belongs to high ductility, other groups were classified as low ductility.

The equivalent viscous damping ratios curves of each group during tests are shown in Fig. 14. These joints exhibited similar energy dissipation trend during the whole loading test. To be specific, the energy dissipation capacity was low when the rotation was about 0 rad, before or after that, the energy dissipation capacity reached a high level. Combined with the damage of wood, it is easy to understand that when the rotation angle was about 0 rad, the joints were loose due to the repeated extrusion, leading to a low friction effect. As the displacement amplitude increased, the joints got close contact with surrounding components, the friction effect was enhanced, so the energy dissipation capacity increased. As regards reinforced groups, since joints experienced different extent of damage during loading process, the energy dissipation capacity has not got obvious improvement at late loading stage. On the contrary, CG group showed a stable energy dissipation during tests, and at late loading stage, its energy dissipation capacity was better than that of reinforced groups, even though its cumulative energy dissipation was not as good as others'. Among reinforced groups, RI6 group had the best energy dissipation capacity, especially when the rotation was not large. It can be considered that the friction between the thread of STS and wood hole contributed a lot to the energy dissipation. Generally speaking, the factors that influence the energy dissipation capacity of MT joints were friction and fracture of wood. In this study, the initial energy dissipation of joints depended mostly on the friction between mortise, tenon and STS, as loading continued, the damage of wood could absorb part of the energy, meanwhile, the joints began to loosen.

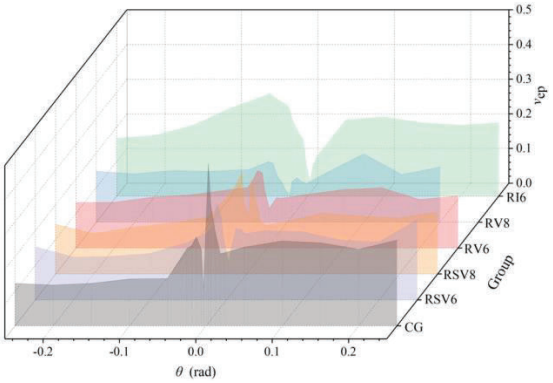

Figure 14: *Equivalent viscous damping ratios of each group.*

4 CONCLUSIONS

The MT joints reinforced by STS with different insertion methods could obtain an improvement on connection performance. Below are some conclusions summarized from this study:

(1) The typical failure modes of the unreinforced joints were the pull-put of tenon and the split on the column. Regarding the reinforced joints, the application of STS could significantly lower the pull-out amount of the tenon, especially when STS were inserted horizontally. On the other hand, the insertion of STS could also accelerate the damage of wood.

(2) Using more STS or increasing the diameter of STS could effectively improve the load-carrying capacity of MT joints, although this might hasten their failure.

(3) Inclined insertion of STS could help the MT joints obtain higher initial stiffness, stable strength degradation and better ductility and energy dissipation capacity.

(4) Further study about the configuration of MT joints and effect of the type of STS are worth conducting.

ACKNOWLEDGEMENT

This work was financially supported by the National Natural Science Foundation of China (Grant No. 32071700), the National Key Research and Development Program of China (Grant No. 2021YFD2200605) and Qing Lan Project.

REFERENCES

[1] P. Yu, Q. Yang, S. Law, Lateral behavior of heritage timber frames with loose nonlinear mortise-tenon connections, Structures. 33(2021) 581-592. DOI: 10.1016/j.istruc.2021.04.061.

[2] D.P. Fang, M.H. Yu, Y. Miyamoto, S. Iwasaki, H. Hikosaka.: Numerical analysis on structural characteristics of ancient timber architecture. Eng. Mech., 18 (1): 137-144, 2001.

[3] D.P. Fang, M.H. Yu, Y. Miyamoto, S. Iwasaki, H. Hikosaka, Experimental studies on structural

characteristics of ancient timber architectures, Eng. Mech. 17 (2) (2000) 75-83.
[4] L. B. Sandberg, W. M. Bulleit, E. H. Reid, Strength and stiffness of oak pegs in traditional timber-frame joints, J. Struct. Eng. 126 (6) (2000) 717-723. DOI: 10.1061/(ASCE)0733-9445(2000)126:6(717).
[5] T. Shiratori, K. Komatsu, A. Leijten, Modified traditional Japanese timber joint system with retrofitting abilities, Struct. Control Health Monit. 15 (7) (2008) 1036-1056. DOI: 10.1002/stc.240.
[6] Q. Zhou, W. Yan, Z. Li, B. Zhang, Experiments on the aseismic behavior of Chinese ancient architecture mortise-and-tenon joints strengthened with iron-hooks, Sci. Conserv. Archaeol. 23 (4) (2011) 17-25. DOI: 10.16334/j.cnki.cn31-1652/k.2011.04.002. [In Chinese].
[7] W. Lu, W. Sun, J. Gu, D. Deng, W. Liu, Experimental study on seismic performance of timber frames strengthened with curved steel dampers, J. Build. Struct. 35 (11) (2014) 151-157. DOI: 10.14006/j.jzjgxb.2014.11.019. [In Chinese].
[8] J. Xue, L. Zhai, F. Zhang, Y. Li, Performance analysis and design recommendations for damaged mortise-tenon joints of ancient timber structure strengthened with flat steel, J. Xi'an Univ. of Arch.& Tech. (Natural Science Edition). 47 (5) (2015) 621-625. DOI: 10.15986/j.1006-7930.2015.05.002. [In Chinese].
[9] K. U. Schober, A. M. Harte, R. Kliger, R. Jockwer, Q. Xu, J.F. Chen, FRP reinforcement of timber structures, Constr. Build. Mater. 97 (2015) 106-118. DOI: 10.1016/j.conbuildmat.2015.06.020.
[10] J. Xue, C. Wu, X. Zhang, Y. Zhang, Experimental study on seismic behavior of mortise-tenon joints reinforced with shape memory alloy, Eng. Struct. 218 (2020) 110839. DOI: 10.1016/j.engstruct.2020.110839.
[11] J. Xue, C. Wu, X. Zhang, Y. Zhang, Effect of pre-tension in superelastic shape memory alloy on cyclic behavior of reinforced mortise-tenon joints, Constr. Build. Mater. 241 (2020) 118136. DOI: 10.1016/j.conbuildmat.2020.118136.
[12] P. Dietsch, R. Brandner, Self-tapping screws and threaded rods as reinforcement for structural timber elements-A state-of-the-art report, Constr. Build. Mater. 97 (2015) 78-89. DOI: 10.1016/j.conbuildmat.2015.04.028.
[13] C. Zhang, H.B. Guo, K. Jung, R. Harris, W.S. Chang, Using self-tapping screw to reinforce dowel-type connection in a timber portal frame, Eng. Struct. 178 (2019) 656-664. DOI: 10.1016/j.engstruct.2018.10.066.
[14] T. Tannert, F. Lam, Self-tapping screws as reinforcement for rounded dovetail connections, Struct. Control Health Monit. 16 (3) (2009) 374-384. DOI: 10.1002/stc.283.
[15] X. Song, K. Li, E. Crayssac, Y. Wu, Lateral performance of traditional heavy timber frames with mortise-tenon joints retrofitted using self-tapping screws, J. Struct. Eng. 144 (10) (2018) 04018187. DOI: 10.1061/(ASCE)ST.1943-541X.0002191.
[16] H. Li, F. Lam, H. Qiu, Comparison of glulam beam-to-beam connections with round dovetail and half-lap joints reinforced with self-tapping screws, Constr. Build. Mater. 227 (2019) 116437. DOI: 10.1016/j.conbuildmat.2019.07.163.
[17] C. Loss, A. Hossain, T. Tannert, Simple cross-laminated timber shear connections with spatially arranged screws, Eng. Struct. 173 (2018) 340-356. DOI: 10.1016/j.engstruct.2018.07.004.
[18] J. R. Brown, M. Li, T. Tannert, D. Moroder, Experimental study on orthogonal joints in cross-laminated timber with self-tapping screws installed with mixed angles, Eng. Struct. 228 (2021) 111560. DOI: 10.1016/j.engstruct.2020.111560.
[19] D. Hanna, T. Tannert, Glulam connections assembled with screws in different installation angles, Maderas-Cienc. Tecnol. 23 (54) (2021) 1-14. DOI: 10.4067/s0718-221x2021000100454.
[20] A. Hossain, M. Popovski, T. Tannert, Cross-laminated timber connections assembled with a combination of screws in withdrawal and screws in shear, Eng. Struct. 168 (2018) 1-11. DOI: 10.1016/j.engstruct.2018.04.052.
[21] ASTM A29/A29M, Standard specification for general requirements for steel bars, carbon and alloy, hot-wrought, ASTM Standards, West Conshohocken, PA, USA, 2015.
[22] ASTM F1575, Standard test method for determining bending yield moment of nails, ASTM Standards, West Conshohocken, PA, USA, 2017.
[23] EN 1383:2016, Timber structures-Test methods-Pull through resistance of timber fasteners, European Committee for Standardization (CEN), Bruxelles, Belgium, 2016.
[24] EN 14358:2016, Timber structures-Calculation and verification of characteristic values, European Committee for Standardization, Bruxelles, Belgium, 2016.
[25] S. Liang, Illustration of Gong Cheng Zuo Fa Ze Li, Tsinghua University Press, Beijing, China, 2006. [In Chinese].
[26] ISO 16670: 2003, Timber structures-Joints made with mechanical fasteners-Quasi-static reversed-cyclic test method, Technical Committee ISO/TC 165, Timber structure, Ottawa, Canada, 2003.
[27] ASTM E2126, Standard test method for cyclic (reversed) load test for shear resistance of walls for buildings, ASTM Standards, West Conshohocken, PA, USA, 2005.
[28] JGJ/T 101-2015, Specification of test methods for earthquake resistant building, Ministry of Housing and Urban-Rural Development of the People's Republic of China, China Architecture & Building Press, Beijing, China, 2015. [In Chinese].
[29] I. Smith, A. Asiz, M. Snow, I. Chui, Possible Canadian/ISO approach to deriving design values from test data, The 39th CIB Working Commission W18-Timber Structures, Florence, Italy, August 2006.
[30] EN12512:2001, Timber structures-Test methods-Cyclic testing of joints made with mechanical fasteners, European Committee for Standardization, Bruxelles, Belgium, 2001.

https://doi.org/10.52202/069179-0155

World Conference on Timber Engineering Oslo 2023

SERVICEABILITY STIFFNESS OF TIMBER CONNECTIONS WITH DOWELS AND SLOTTED-IN STEEL PLATES

Kjell Arne Malo[1], Haris Stamatopoulos[2], Francesco Mirko Massaro[3], Saule Tulebekova[4]

ABSTRACT: The paper presents experimental stiffness measurements from large scale tests on dowel connections with both single and double slotted-in steel plates. The intended use of the results is quantification of the effect connections have on the stiffness of trusswork in glulam buildings. An engineering model of the connection stiffness is proposed and evaluated in view of the test results. The paper also shows comparisons of measured results to guidelines in European standards for timber engineering.

KEYWORDS: Stiffness, connection, dowel, serviceability, experiment, model

1 INTRODUCTION

The height of timber buildings has increased significantly within the last decennium. Several buildings with 10 to 20 stories using load carrying systems purely in wood have been built at various locations throughout the world. However, very little experience has been reported with respect to their in-service properties - like wind-induced vibrations. Dynamical properties are dependent on mass, stiffness and damping properties of the buildings. Several high-rise buildings, like "Treet" (14 stories, 2014) [1], and "Mjøstårnet" (18 stories, 2019, see Figure 1) [2], have used large trusswork in glulam with connections of slotted-in steel plates and dowels. The most exposed connections in the Mjøstårnet trusswork (see Figure 2) have in the order of 800 shear planes in a single connection. Although the stiffness of a single shear plane for a single dowel is given in [3], it is known from experiments that connections having large numbers of dowels cannot be sufficiently evaluated as only a summation of single dowels, see for example [4]. This is an important issue for high-rise buildings as the stiffness of joints is crucial for their dynamic response.

The objective of the experimental investigation has been to perform series of tests to get experimental results for quantification of elastic stiffness of connections with multiple dowels, suitable for modelling of connection stiffness for serviceability evaluations. The test series consists of experiments ranging from a single dowel and one slotted in steel-plate, up to connections with 2 slotted-in steel plates and 35 dowels. The investigation is limited to dowels having 12 mm diameter, which is most used in the Nordic countries.

Figure 1:*Mjøstårnet in Norway, 18 story glulam building.*

2 MATERIALS AND METHODS

2.1 MATERIALS

The wooden materials used was glulam GL30C according to [5]. This type of glulam usually consists of combined lay-up of two or more different strength classes of lamellas. In this case the outer lamellas are of strength

[1] Kjell Arne Malo, NTNU Norwegian University of Science and Technology, Norway. kjell.malo@ntnu.no
[2] Haris Stamatopoulos, NTNU Norwegian University of Science and Technology, Norway.
[3] Francesco Mirko Massaro, NTNU Norwegian University of Science and Technology, Norway
[4] Saule Tulebekova, NTNU Norwegian University of Science and Technology, Norway

https://doi.org/10.52202/069179-0156

class T22, and the inner lamellas T15. However, as the majority of the dowels usually are located in the inner lamellas, the tests have been performed on T15 lamellas and material properties for T15 lamellas are used throughout this paper, see [5]. The mean stiffness moduli are $E_{0,mean} = 11500$ MPa, $G_{mean} = 720$ MPa, while the density is $\rho_{mean} = 430$ kg/m^3.

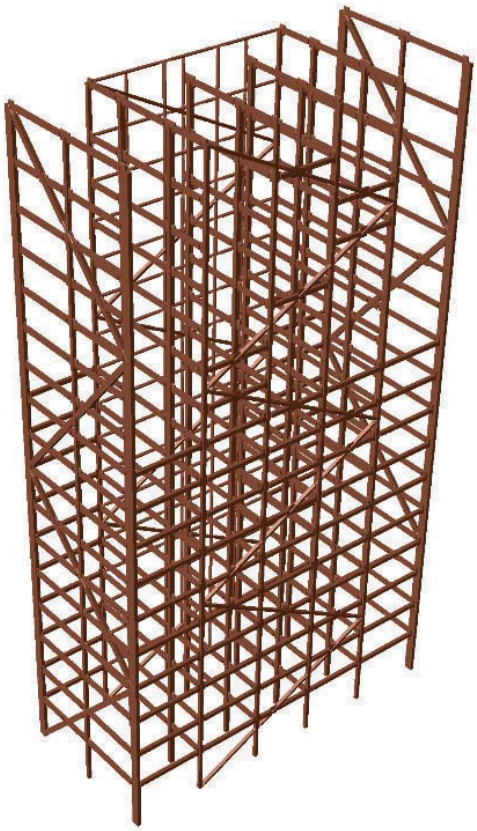

Figure 2 *Numerical model of the glulam trusswork used in Mjøstårnet.*

The steel plates in the slots are of quality S355 and have thickness 10 mm. All dowels have diameter of 12 mm and are of high strength stainless steel (class EN 1.4418) with yield strength 755 MPa. For all specimens the dowel spacing is 60 mm in the grain direction (a_1) and 55 mm in the perpendicular direction (a_2), which is a very common spacing for this type of dowel connections.

2.2 SMALL SCALE AXIAL TESTS

Two series of small-scale tests with one steel plate have been performed: the first is uniaxial tests loaded in the grain direction, confer Figure 3, while the second, shown on Figure 4, is in principle a three-points bending test. Both test series contain results from 1 dowel and up to 3 x 3 dowels, arranged in various layouts and loaded along grain direction, see Figure 3, or perpendicular to grain direction, see Figure 4. The notation used is as follows; a capital indicates a line in the grain direction, while a number indicates a row perpendicular to grain. A dowel in the middle will hence have identification B2, a row of 3 dowels in the middle in grain direction B123, a row perpendicular in the middle A1B1C1, while all dowels in the group becomes A123B123C123.

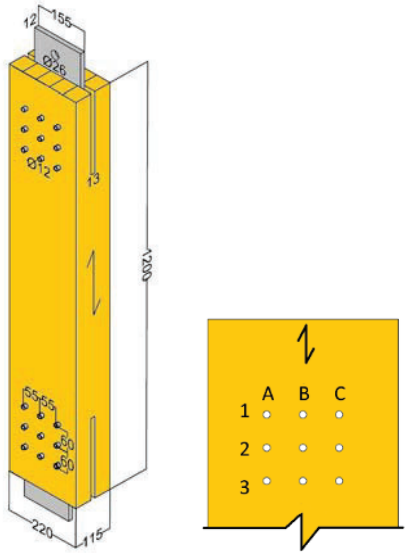

Figure 3:*Specimene for loading parallel to grain and to the right, naming of dowel configurations.*

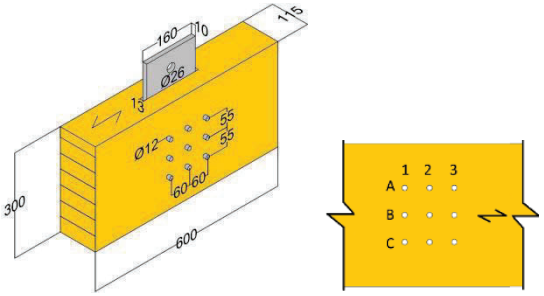

Figure 4:*Specimene for loading perpendicular to grain and to the right, naming of dowel configurations.*

2.3 LARGE SCALE COMPONENT TESTS

The second test series contains three types of connections with two slotted-in steel plates, see Figure 5, and up to 5x7 dowels arranged in various patterns, confer Figure 6. The experimental setup for these tests is depicted in Figure 8. Note that the "Bottom" connection shown in Figure 5 is not evaluated herein.

2.4 INSTRUMENTATION AND MEASUREMENTS

All test setups are statically determined and hence the force distribution is well known. The stiffness is characterized by the applied load and the relative displacement between the steel plate (or plates), and the surrounding wood close to the steel plates. Each steel plate has two LVDTs, one at each edge, in order to cancel

https://doi.org/10.52202/069179-0156

out any rigid body motion by averaging the measurements from the two sides, confer Figure 7 and Figure 8.

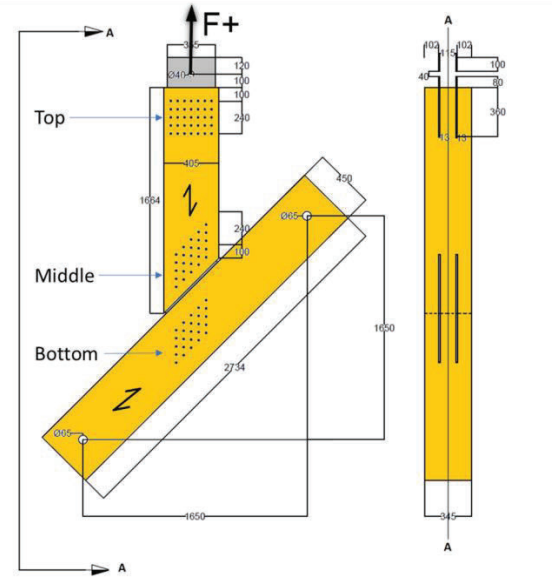

Figure 5:*Setup for large scale glulam diagonal components. Three different connections in one setup; TOP connection, MIDDLE connection and BOTTOM connection.*

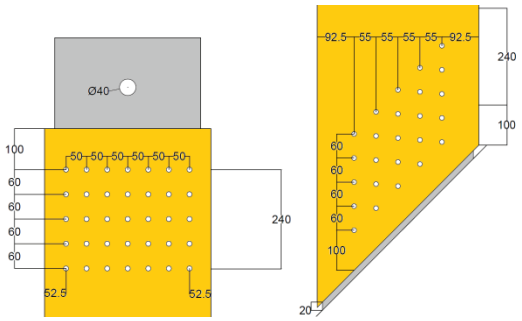

Figure 6:*Lay-out for the diagonal connections loaded along grain. Left: TOP connection and right: MIDDLE connection.*

A connection is here defined as the transfer of forces between a steel plate(s) and a glulam component by use of shear loaded dowels. The steel plates have two connections, either to another glulam component or to the loading or reaction devices.

Figure 7: *Small scale test setup and instrumentation.*

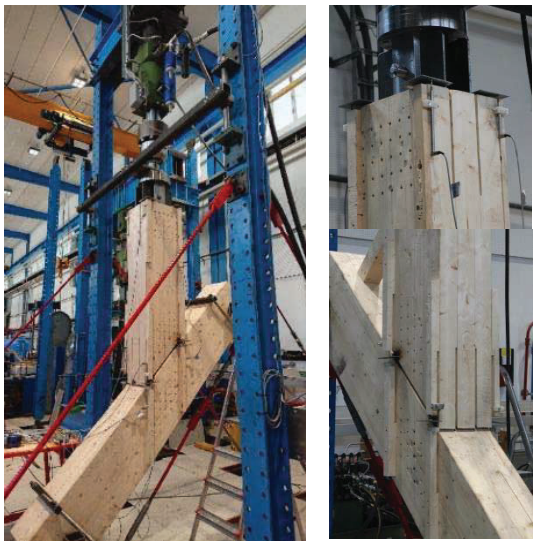

Figure 8: *Diagonal test setup with three dowel connections*

2.5 TEST PROGRAM

For the small-scale tests with loading in grain direction, three glulam specimens with a connection in each end were used (total six different connections). Eight different dowel configurations were used, confer Figure 9.

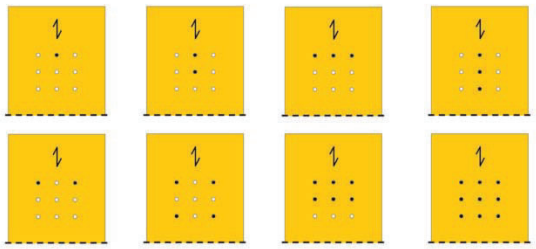

Figure 9: *Dowel configurations for small scale tests, loading in grain direction.*

https://doi.org/10.52202/069179-0156

For loading perpendicular to grain, six configurations shown in Figure 10 were tested, using in total three specimens.

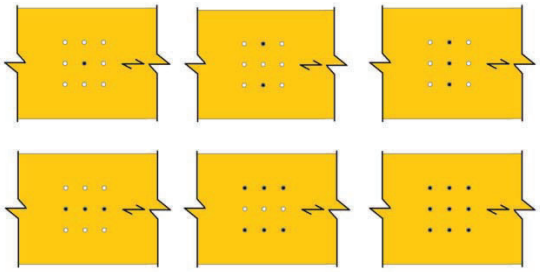

Figure 10: *Dowel configurations for small scale tests, loading perpendicular to grain.*

Only one specimen for the large-scale diagonal test setup was available, and here 5 different configurations were tested. The tests were performed by sequentially installing an additional row of dowels along the grain, starting from the ends of the connections. For the TOP connection the number of dowels perpendicular to grain $n_{90} = 7$ was kept constant, while the MIDDLE connection had $n_{90} = 5$ constantly.

2.6 LOADING PROTOCOL AND EVALUATION

The initial stiffness is not necessarily representative of a building in a wind exposed situation. Wind loading has usually a quasi-static part in addition to the turbulence causing vibrations. Therefore, the zero mean force situation is not likely to occur, as the quasi-static part of the wind loading is commonly large. Consequently, the effect of initial slips is of minor importance in this context.

The methods for evaluation of stiffness in ISO 6891 [6] do not fully cover the needs for quantification of stiffness for dynamic response evaluation. Therefore, a more suitable loading and evaluation protocol has been worked out for the test series and presented in Figure 11. The loading protocol is based on cycling the load between 10 and 40 % of the estimated maximum load, both on the tensile and compressive side. Finally, the load is cycled between +40 % and -40 %, passing through the domain of zero force. As it may be observed from Figure 12, or better from Figure 13, it takes a few cycles before the cycles stabilize and they appear on top of each other on the plots.

The plots in Figure 12 show tensile cycling corresponding to the first sequence in Figure 11, while the second block with cycling on the compressive side is shown on Figure 13. The plots show quite considerable hysteretic loops and picking specific points for stiffness calculation might lead to unnecessary large scatter in results, dependent on the choice of points (shown as pink dots on the plots). In the authors opinion it is much better to utilize all the information in the cycles and use the method of least squares to fit a straight line to the stable cycles (the cycles after stabilization).

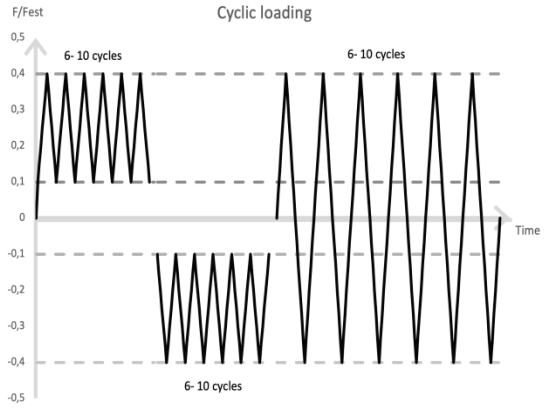

Figure 11: *Loading protocol for stiffness evaluation*

This is shown as dashed lines in the plots, and this stiffness measure is also more consistent with the numerical modelling of structures. Consequently, the latter method is used herein, and typically four values for the stiffness are determined. In the results section, stiffness evaluated from cycling in tension in denoted *tension* (tens), cycling in the compressive domain is denoted *compression* (comp). The large cycles passing through zero force, are called *Fully Reversed* and these cycles are evaluated separately both on the tensile side (FRt) and on the compressive side (FRc), as visualized on Figure 14.
The horizontal distance between the two dashed stiffness lines for fully reversed cycles shown on Figure 14 is a measure of the initial slip in the connection. The initial slip is not further reported herein, but a treatment of this issue can be found in [7].

3 RESULTS

The experimental results are given in tables and plots, where n_0 denotes the number of dowels in grain direction, while n_{90} is the number of dowels perpendicular to grain. As explained in Section 2.6 the stiffness has been evaluated in four different domains, one-sided cycling in tension (tens), in compression (comp), and fully reversed cycling evaluated separately both on the tension side (FRt) and on the compressive side (FRc). The columns denoted “Aver” or “Average” are the average of the four evaluated stiffnesses. All stiffnesses are given as stiffness per fastener and shear plane in kN/mm. For comparison, the Eurocode 5 [3] expression for this is

$$k_{ser} = 2 \cdot \frac{\rho_{mean}^{1.5} \cdot d}{23} = 2 \cdot \frac{430^{1.5} \cdot 12}{23} = 9.304 \text{ kN/mm} \quad (1)$$

where ρ_{mean} is the mean density of wood (kg/m^3) and d is the dowel diameter (mm). The total stiffness of the connection Eurocode 5 [3] is calculated by multiplying the stiffness k_{ser} with number of shear plane per fastener, herein either 2 (small-scale) or 4 (large-scale), and multiplied with the total number of fasteners $n_0 \cdot n_{90}$.

https://doi.org/10.52202/069179-0156

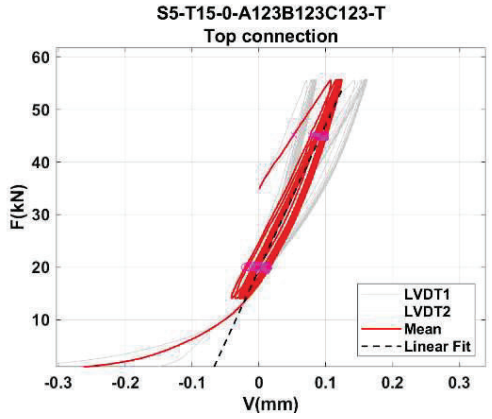

Figure 12: *Example on cycling on the tensile side for small scale specimen.*

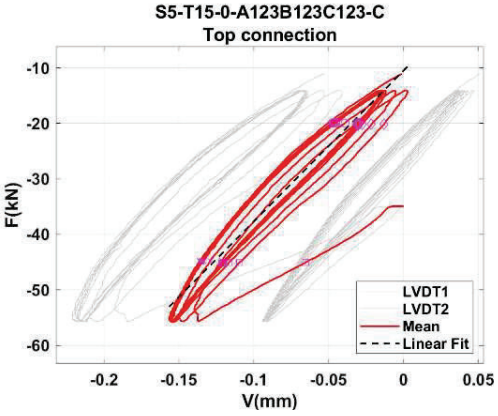

Figure 13: *Example on cycling on the compressive side for small scale specimen.*

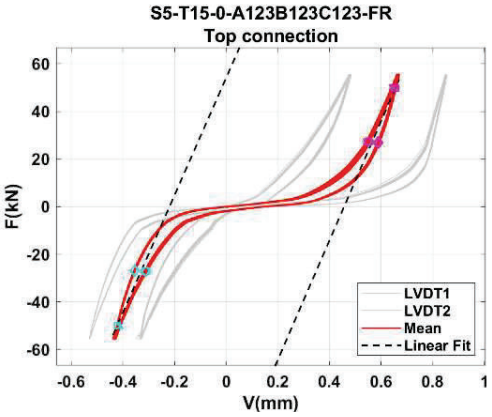

Figure 14: *Example on fully reversed cycles passing through zero force.*

3.1 RESULTS FROM SMALL-SCALE TESTS

Table 1 gives the measured stiffnesses per fastener and shear plane with loading in grain direction. The number of dowels in the grain direction is varied, keeping the number of fasteners perpendicular fixed, either one or three. The average results are plotted in Figure 15, and it may be observed that the stiffness decrease with the number of fasteners in the grain direction n_0. Comparing the blue line having $n_{90} = 1$, to the red line having $n_{90} = 3$, also an interaction between n_0 and n_{90} is probable.

Table 1: *Small scale specimen, loading in grain direction, stiffness per fastener and shear plane.*

Configuration	n	n0	n90	tens	comp	FRt	FRc	Aver
B1	1	1	1	24.64	25.98	19.26	21.69	22.89
B12	2	2	1	14.71	16.50	13.28	14.33	14.71
B123	3	3	1	12.77	15.92	12.05	14.31	13.76
A1B1C1	3	1	3	19.04	19.96	16.33	17.29	18.16
A12B12C12	6	2	3	14.19	15.18	12.88	14.11	14.09
A123B123C123	9	3	3	12.12	14.09	10.98	12.75	12.49

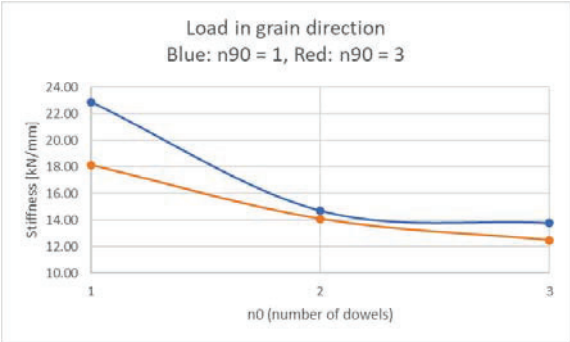

Figure 15: *Average stiffness from small scale specimens, loading in grain direction.*

Configurations with loading perpendicular to grain are given in Table 2 and the average stiffness is plotted in Figure 16, keeping the number of fasteners in grain direction n_0 constant. An increase of fasteners n_{90} in the load direction (here perpendicular) decreases the stiffness. From the plot it is suggested that an increase of n_0 will further decrease the stiffness.

Table 2: *Small scale specimen, loading perpendicular to grain*

Configuration	n	n0	n90	tens	comp	FRt	FRc	Aver
B2	1	1	1	10.51	11.59	10.17	11.27	10.89
A2C2	2	1	2	9.84	11.18	9.52	11.14	10.42
A2B2C2	3	1	3	9.28	10.38	9.16	10.11	9.73
A123C123	6	3	2	7.72	9.08	7.81	9.03	8.41
A123B123C123	9	3	3	6.02	6.87	5.94	6.93	6.44

https://doi.org/10.52202/069179-0156

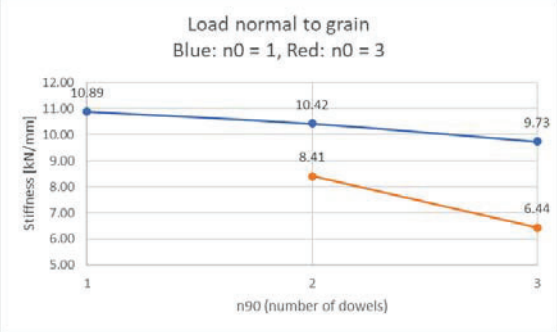

Figure 16: *Small scale, loading perpendicular to grain*

The configurations highlighted with yellow colour in Table 1 and Table 2 are comparable. Letting the stiffnesses obtained for perpendicular loading be scaled with the comparable stiffness obtained for loading in grain direction, we obtain the ratio of stiffness between loading perpendicular and along the grain and these ratios are presented in Table 3. The stiffness ratios based on the average data are between 0.48 and 0.54, i.e. the stiffness for loading perpendicular to grain is roughly only half of the stiffness for loading along the grain.

Table 3*: Stiffness ratios for loading perpendicular to grain vs loading in grain direction. Small scale specimen with comparable configuration*

n0	n90	tens	compr	FRt	FRc	Average
1	1	0.4265	0.4461	0.5280	0.5196	0.4755
1	3	0.4874	0.5200	0.5609	0.5847	0.5360
3	3	0.4967	0.4876	0.5410	0.5435	0.5158

3.2 RESULTS FROM LARGE-SCALE TESTS

The different configurations for the large-scale tests differ only by the number of installed dowels in the grain direction, n_0, while keeping the number of dowels perpendicularly constant at the maximum, which is 7 and 5 for the TOP and MIDDLE connections, respectively. Note that the loading for the TOP and MIDDLE connections is along the grain, while the BOTTOM connection has loading at 45 degrees relative grain and is therefore not included herein. The experimental results are given in Table 4.

The stiffnesses obtained from the four evaluation schemes (cyclic tension, cyclic compression, fully reversed compression and fully reversed tension) are plotted as separate curves in Figure 17 for the TOP connection. Note that the top connection has $n_{90} = 7$ and a rectangular lay-out of dowels. The lay-out for the MIDDLE connection is close to a parallelogram with 45 degrees between crossing lines. The loading for the MIDDLE connection is also along grain and the results for increasing number of dowels along grain n_0 are plotted on Figure 18. All these evaluations and measurements are in good agreement, and there is a clear trend of decreasing stiffness with increasing number of dowels in the grain direction.

Table 4: *Large scale specimen, vertical loading, stiffnesses in kN/mm per fastener and shear plane.*

Connection	n0	n90	tension	compr	FRt	FRc	Average
Top	1	7	7.93	12.49	9.07	11.08	10.14
Middle	1	5	15.15	21.23	10.23	12.30	14.73
Top	2	7	4.23	8.02	4.61	6.45	5.83
Middle	2	5	10.51	12.90	9.07	8.00	10.12
Top	3	7	2.60	5.83	3.72	5.43	4.39
Middle	3	5	7.47	8.53	5.64	6.49	7.03
Top	4	7	2.64	3.66	3.45	3.12	3.22
Middle	4	5	6.06	7.93	5.55	6.58	6.53
Top	5	7	1.99	3.78	2.53	2.95	2.82
Middle	5	5	4.92	6.91	3.82	5.76	5.35

The comparable stiffness from Eurocode 5 is 9.3 kN/mm, Equation (1), and it is obvious that this stiffness can only be achieved for connection having few dowels, roughly 10 dowels at most, independent of configuration. For more dowels the stiffness per fastener and shear plane will be considerably smaller. All configurations for the large-scale tests (and small-scale tests as well) show the same decreasing stiffness with increasing number of dowels in the grain direction.

From the small-scale tests presented on Figure 15 and Figure 16, for loading in grain direction and perpendicular respectively, it seems necessary to take into account the number of dowels in both directions (n_0 and n_{90}) as there is a clear interaction between them.

The obtained stiffness measurements were averaged and are presented on Figure 19, one curve for each large-scale connection. The average stiffness per fastener and shear plane is larger for the MIDDLE connection than for the TOP connection, but they are almost parallel and clearly show the same tendency of decreasing stiffness with increasing n_0. Furthermore, there is a clear trend to approaching an asymptotic value for $n_0 \geq 5$.

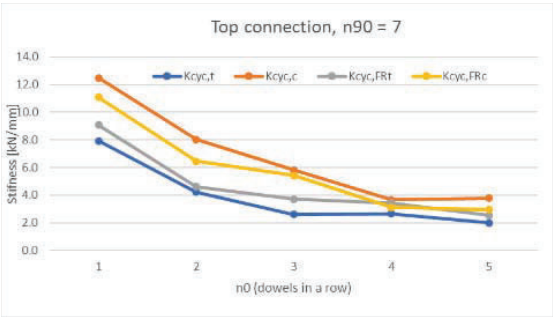

Figure 17: *Large scale diagonal test, TOP connection, loading in grain direction.*

https://doi.org/10.52202/069179-0156

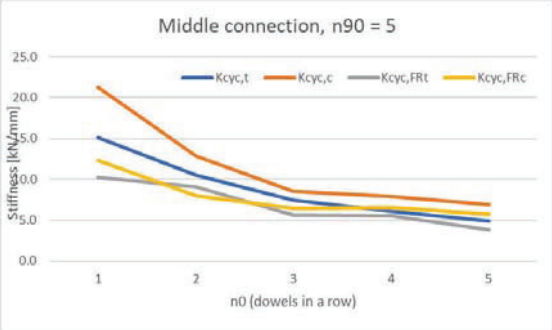

Figure 18: *Large scale MIDDLE connection, loading in grain direction.*

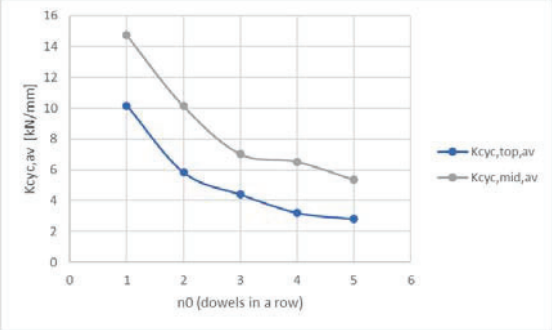

Figure 19: *Stiffness per fastener and shear plane for the two different dowel connections in the diagonal test setup.*

By scaling all stiffnesses with the stiffness value for one dowel in the grain direction, we can express the results by a relative ratio of effective numbers of dowels, depending on the number in grain direction, see plot on Figure 20. Note that the information used here involves the effect from both along and perpendicular to the grain and thus shows the sum of the effects from the number of dowels in both directions simultaneously. The MIDDLE connection has in all cases number of dowels perpendicular grain $n_{90} = 5$, and shows a decreasing trend with n_0. The TOP connection, which has $n_{90} = 7$, shows in comparison smaller effective numbers.

By combining the results from small-scale and large-scale tests, we have configurations which clearly show that there is similar trend from the number of dowels perpendicular to grain, see graphs on Figure 21, where the number of dowels along the grain is kept constant for each curve.

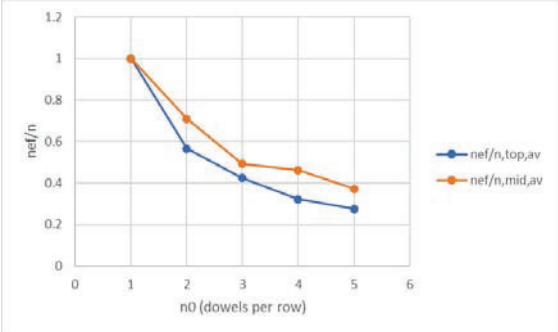

Figure 20: *Effective number of dowels in the grain direction in the diagonal test setup with three different dowel connections.*

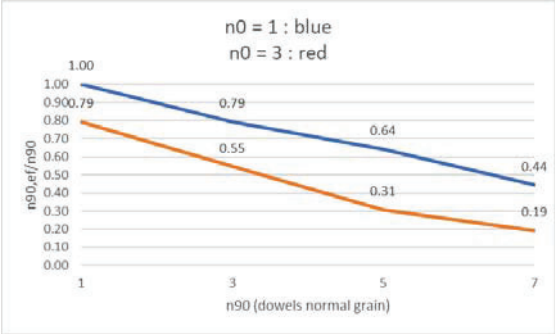

Figure 21: *Effective number of dowels perpendicular to grain, combination of small and large scale tests.*

4 MODEL FOR CONNECTION STIFFNESS OF DOWEL JOINTS

4.1 Model considerations

The stiffness of the dowel connections is dependent on the layout and cannot, with sufficient accuracy, be calculated just by a linear addition of the shear planes. Eurocode 5 [3] underestimates the stiffness for a single dowel, while the stiffness is severely overestimated for connections with large number of dowels. Herein, the number of wooden specimens is low. Therefore, effects of varying embedding stiffnesses of wood, thicknesses of layers and varying spacing cannot be determined from the present test series. The focus has only been on the effect of the number of dowels, keeping all other parameters constant.

4.2 Model

The idea behind the model is to use the information already available in codes like Eurocode 5 [3] together with simple modifications. Hence, the stiffness for a single steel-to-wood dowel connection k_{ser} is modelled by Equation (1).

Assuming that all shear planes contribute with the same stiffness, the method for stiffness evaluation from Eurocode 5 [3] is

$$K_{ser,EC5} = k_{ser} \cdot n_{spd} \cdot n_0 \cdot n_{90} \quad (2)$$

where n_{spd} is the number of shear planes per dowel. A regular dowel pattern is assumed herein such that the total number of dowels equals the product $n_0 \cdot n_{90}$.

Considering all plots on Figure 15 to Figure 21, a decaying behaviour of the average shear plane stiffness is observed. It will be unphysical that the decaying behaviour with increasing number of dowels ends up with zero average stiffness, so an asymptotic behaviour is expected, confer Figure 19.

The introduction on an effective number of fasteners also for stiffness evaluation has been proposed by several authors, see for example [8]. This can simply be introduced in Equation (2) by a non-dimensional modification factor M on the number of fasteners. A simple asymptotic expression for dowels on a single row along the grain can be:

$$M_0 = m_0 \cdot \left(q_{0,1} + q_{0,2} e^{\frac{1-n_0}{r_0}}\right) \quad (3)$$

where m_0 is the calibrated value for one dowel in grain direction. The parameter r_0 together with the parameters $q_{0,1}$ and $q_{0,2}$ govern the non-dimensional asymptotic decrease. A similar approach in the transvers direction reads:

$$M_{90} = m_{90} \cdot \left(q_{90,1} + q_{90,2} e^{\frac{1-n_{90}}{r_0}}\right) \quad (4)$$

By replacing n_0 with the product $n_0 M_0$ and n_{90} with $n_{90} M_{90}$ in Equation (2), the model stiffness becomes:

$$K_{ser,mod} = k_{ser} \cdot n_{spd} \cdot n_0 m_0 \cdot \left(q_{0,1} + q_{0,2} e^{\frac{1-n_0}{r_0}}\right) \cdot n_{90} m_{90} \cdot \left(q_{90,1} + q_{90,2} e^{\frac{1-n_{90}}{r_{90}}}\right) \quad (5)$$

For a single dowel, the exponential term equals unity, and therefore for easy calibration, we let always

$$q_{\alpha,1} + q_{\alpha,2} = 1 \quad (6)$$

Here α denotes 0 or 90 directions and $q_{\alpha,1}$ is the asymptotic value. Furthermore, for only one dowel Equation (5) reduces to

$$K_{ser,mod} = k_{ser} \cdot n_{spd} \cdot m_0 \cdot m_{90} = k_{ser} \cdot n_{spd} \cdot m \quad (7)$$

Equation (7) can be used for calibration in the two orthogonal directions, but as it herein is only dealt with either loading in the grain or perpendicular to grain direction, only one parameter is needed, and hence the simplification $m_0 \cdot m_{90} = m$ has been made.

From Table 1 and configuration B1 (one single dowel), the stiffness per shear plane is about 23 kN/mm and taking $k_{ser} = 9.3$ kN/mm from Equation (1), the parameter m becomes $m = 2.5$. Similarly, utilizing the results in Table 3 and Figure 16, the parameter m for a single dowel loaded perpendicular to grain is $m = 1.3$.

The model for serviceability stiffness of a dowel connection with multiple slotted in steel plates and multiple dowels, loaded either along grain or perpendicular to grain, then becomes:

$$K_{ser,mod} = k_{ser} \cdot m \cdot n_{spd} \cdot n_0 \left(q_{0,1} + q_{0,2} e^{\frac{1-n_0}{r_0}}\right) \cdot n_{90} \cdot \left(q_{90,1} + q_{90,2} e^{\frac{1-n_{90}}{r_{90}}}\right) \quad (8)$$

where k_{ser} is calculated according to Eurocode 5, see Equation (1), and n_{spd} is the number of shear planes per dowel. The effect from an increasing number of dowels in the grain direction has been evaluated from the measured results plotted in Figure 19, while for the effect from the number of dowels perpendicular to grain, the information presented in Figure 21 was used. The resulting model parameters for 12 mm dowels embedded in Norway spruce GL30c are specified in Table 5.

Table 5 *Model parameters for 12 mm dowels*

	Along grain			**Perpendicular grain**		
Number of dowels	n_0			n_{90}		
Model symbols	$q_{0,1}$	$q_{0,2}$	r_0	$q_{90,1}$	$q_{90,2}$	r_{90}
Model values	0.3	0.7	2	0.3	0.7	4
Loading direction	$m = 2.5$			$m = 1.3$		

The resulting model stiffness per shear plane and dowel for loading along grain and for varying number of dowels in grain direction is shown with dashed lines in Figure 22 for the two different diagonal connections, note the difference in n_{90}. For comparison, the continuous lines show the measured stiffness.

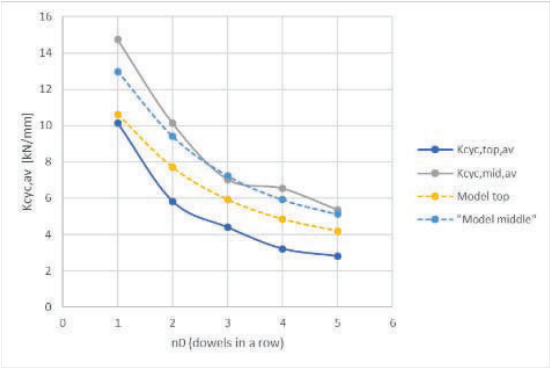

Figure 22 *Modelled and measured stiffness per shear plane and dowels (* $\boldsymbol{n_{90,top} = 7}$ *and* $\boldsymbol{n_{90,middle} = 5}$*.)*

Keeping the number of dowels constant in grain direction and varying the number of dowels in perpendicular direction, the relative reduction in modelled stiffness is shown on Figure 23 using dashed lines, while the measured results are shown with continuous lines.

https://doi.org/10.52202/069179-0156

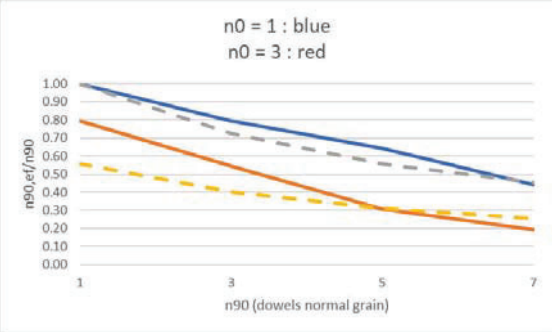

Figure 23 *Relative reduction of stiffness per shear plane and dowel for varying number of dowels perpendicular to grain.*

In the present test series, it has been emphasized to only vary the number of dowels and keep all other parameters constant. However, the test series contain two different lay outs of tests; the small-scale tests having a single slotted in steel plate, and large scale having two plates. The wooden materials are from the same production, but, of course, considerable variation is to be expected due to many local effects like knots etc. Most of the results have been obtained by just installing more dowels in the same specimen. However, for the small-scale specimen several specimens had to be used in order to get the desired configurations without removing any dowels. Therefore, higher variability must be expected in the regime with few dowels. For the determination of the model parameters, most emphasis has been put on the domain where the total number of dowels exceeds 10.

4.3 Verification

Stiffnesses from the connection measurements are compared to the model results in Table 6. Here, Equation (8) has been used with the parameters specified in Table 5 and, and with k_{ser} from Equation (1), (Eurocode 5, [3]). The measured and the modelled stiffness for loading along and perpendicular to grain show the same ratio of stiffness, the grain direction is about 1.9 times stiffer than perpendicular.
Eurocode 5 shows about the same stiffness for loading along grain as the model when the total number of dowels is around 10. For higher number of dowels Eurocode 5 largely overestimates the stiffness, while the developed model is in good agreement with the measurements.

Table 6 *Comparison of connection stiffness from measurements, analytical model and Eurocode 5.*

	Connection			Stiffness kN/mm		
Load directio	n_{spd}	n_0	n_{90}	Measured	Model	EC5
0	2	3	3	225	169	168
90	2	3	3	116	88	168
0	4	5	7	540	586	1303
n	4	5	5	522	512	930

To get a better understanding of the dependency of the number of dowels in the two directions in the model, a plot of the reduction in stiffness is shown on Figure 24 for up to 100 dowels using the parameters from Table 5. The asymptotic value of the reduction of stiffness in the model given by Equation (8) is in this case

$$\frac{K_{ser,mod,asymptote}}{k_{ser} \cdot m \cdot n_{spd} \cdot n_0 \cdot n_{90}} = q_{o,1} \cdot q_{9o,1} = 0.09 \qquad (9)$$

Compared to the Eurocode 5 stiffness computation by Equation (2), the asymptotic value in the model becomes 0.225, as the parameter $m = 2.5$ is required for the fitting of the present model to a single dowel.

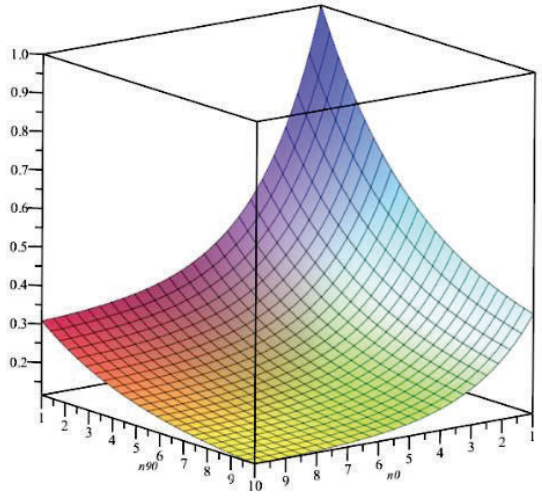

Figure 24 *Average relative stiffness dependent on dowels in the two directions.*

4.4 Limitations and extensions

Available number of tests having many dowels in both directions and multiple slotted in steel plates are few. Furthermore, stiffness measurements are not very well defined and are sensitive to the load level as well as to experimental conditions. Furthermore, the variability in wood material properties is large, and makes comparisons between various tests hard.
The proposed model herein is made in a multiplicative way, such that the various effects might be treated separately. The parameters in Table 5 are given for $a_1 = 60 = 5d$ and $a_2 = 55 = 4.6\,d$. Probably, the q and r parameters in Equation (8) will be dependent on the spacing between the dowels, and this effect can be considered by modifying the parameters and make them dependent on the spacing. This is not a part of the present paper and consequently the bottom connection shown in Figure 5 is not included herein.
Moreover, it is well known that inner and outer parts of a dowel connection with multiple steel plates seldom have the same stiffness per shear plane. This effect can be considered by using an effective number of shear planes n_{spd}. Dowel diameter dependency and dowel surface properties (friction) can put into the k_{ser} parameter.

https://doi.org/10.52202/069179-0156

5 CONCLUSIONS

The paper presents and discusses an approach for stiffness estimation of large dowel connections. Input parameters are the number of dowels on rows parallel and perpendicular to grain, and the number of shear planes per dowel. Both loading along and perpendicular to grain can be evaluated. The shear plane stiffness, and thereby the dependency on dowel diameter and density, is calculated by use of Eurocode 5 [3]. The model is compared to experimental results as well as the simple approach in design standards like Eurocode 5 [3].

The model is developed for dowel connections with 12 mm dowels and commonly used spacing in the Nordic countries.

ACKNOWLEDGEMENT

This research has been conducted as part of the Dynamic Response of Tall Timber Buildings under Service Load project (Dyna-TTB). In Norway, funding was provided by the Norwegian Research Council, grant no. 297513. The master students Elisabeth Frette, Amund Heggheim and Thomas Munkeby are highly acknowledged for their contributions to perform the tests and preparing drawings and photos.

REFERENCES

[1] K.A. Malo, R.B. Abrahamsen and M.A. Bjertnes Some structural design issues of the 14-storey timber framed building “Treet” in Norway. European Journal of Wood and Wood Products, (2016), Vol. 74(3) 74:407–424, DOI 10.1007/s00107-016-1022-5

[2] R. Abrahamsen: Mjøstårnet-Construction of an 81 m tall timber building". In: Inter-nationales Holzbau-Forum IHF (2017), pp. 1-12. url: https://www.moelven.com/globalassets/moelven-limtre/mjostarnet/mjostarnet---construction-of-an-81-m-tall-timber-building.pdf

[3] European Committee for Standardization. NS-EN 1995-1-1:2004 Eurocode 5: Design of timber structures - Part 1-1: General - Common rules and rules for buildings. 2004.

[4] Jockwer, R.and Jorissen, A: Stiffness and deformation of connections with dowel-type fasteners. In: COST Action FP1402 / WG3 (2018): Design of Connections in Timber Structures. Shaker Verlag GmbH, ISBN 978-3-8440-6144-4, ISSN 0945-067X.

[5] European Committee for Standardization. NS-EN 14080:2013+NA2016 Glued laminated timber and glued solid timber - Requirements. 2016.

[6] NS-ISO 6891(1983): Timber Structures. Joints made with mechanical fasteners. General principles for the determination of strength and deformation characteristics. Standard Norge (1991).

[7] Reynolds T.P.S., Miranda W., Trabucco D., Toumpanaki E., Foster R.M., Stiffness and slip in multi-dowel timber connections with slotted-in steel plates. (2022) Engineering Structures, 268, DOI: 10.1016/j.engstruct.2022.114723 Reynolds

[8] Sandhaas, C: Mechanical behaviour of timber joints with slotted-in steel plates. “Proefschrift” for PhD, TU Delft, The Netherlands, 2012. ISBN 978-90-8570-837-7

https://doi.org/10.52202/069179-0156

World Conference on Timber Engineering Oslo 2023

MOISTURE AND ASSEMBLY HISTORY EFFECTS ON EMBEDMENT PROPERTIES OF STEEL DOWELS IN SPRUCE AND BIRCH LOADED IN GRAIN DIRECTION

Michael Schweigler[1], Romain Lemaître[1,2], Zijad Shehadeh[1], Thomas K. Bader[1]

ABSTRACT: Embedment strength and stiffness of steel dowels in spruce and birch solid wood were investigated in an experimental study, taking into account the moisture and connection assembly history. Thus, in addition to the effect of different mechanical properties of wood at different moisture contents, the effect of changes in the moisture content between the steps of: drilling the dowel hole, assembly of the dowel, and testing of the specimen on the embedment strength and stiffness was studied. Full-hole embedment tests with 12 mm steel dowels showed a decrease in embedment strength with increasing wood moisture content, while the elastic embedment stiffness was not influenced. Drying the wood specimens after the dowel was inserted yielded up to 50% higher elastic embedment stiffness compared with connections drilled and assembled when the equilibrium moisture content was reached. Application of an artificial crack showed only a moderate effect on embedment strength and stiffness, while the ductile embedment behavior was maintained.

KEYWORDS: Embedment strength and stiffness, experiments, spruce, birch, moisture content, assembly history

1 INTRODUCTION

Structural timber elements undergo from their production, over drilling boreholes for the fasteners, transportation, to the joint assembly, as well as during the service life, multiple changes in the ambient climate (temperature and relative humidity). This results in changes of the moisture content (MC) in the joint area, which influences the mechanical properties of the wood and thus the mechanical behavior of the joint. In addition, variations in MC lead to geometrical changes of the timber around the steel dowels by means of shrinkage and swelling, while the geometrical shape of the steel dowel itself is unaffected. This can lead to moisture induced pre-stressing of the wood matrix around the dowel, or to shrinkage cracks when the tensile strength of the wood perpendicular to the grain is exceeded.

The embedment strength is the parameter, which represents the mechanical response of wood loaded by a dowel-type fastener in the European Yield Model. The latter is used for the calculation of the capacity of a single-fastener connection according to Eurocode 5 [6]. A possibly reduced capacity due to an increased MC (and the load duration) is considered by multiplication of the characteristic connection capacity with the modification factor, k_{mod}, when calculating a design capacity of a connection. For service class 3, the embedment strength is thus indirectly decreased due to the higher MC, while no reduction due to MC is considered for service classes 1 and 2 [6]. This is however in contradiction to findings from [1]-[4], who found a decreased embedment strength, f_h, for increasing MCs within service classes 1 and 2. Hardly investigated is the influence of the MC on the embedment stiffness, k_{el} (e.g. [4]). In the studies [1]-[4], test specimens were produced after the targeted equilibrium MC was reached, and thus the history of moisture changes was not considered. In contrast, Sjödin et al. [5] conducted an experimental study to investigate the influence of a decreasing MC after assembly of a multi-dowel steel-to-timber connection on the connection capacity, while the connection stiffness was not studied. A decrease in connection capacity with decreasing MC was found, which was explained by moisture gradient induced stresses, initiating small cracks in the connection area. However, to the best of our knowledge such a study was not yet carried-out on the embedment level.

In this contribution, the aim is to investigate the influence of the moisture and assembly history on the embedment strength and stiffness in grain direction by means of an experimental study. Thus, not only the influence of the MC on the embedment properties, but also the influence of different MCs in combination with the manufacturing and assembly history: drilling of the dowel hole, assembly of the dowel, and embedment testing, including even the influence of a crack underneath the dowel-wood interface, is investigated.

[1] Michael Schweigler, Department of Building Technology, Linnaeus University, Universitetsplatsen 1, 351 95 Växjö, Sweden, michael.schweigler@lnu.se, romain.lemaitre@lnu.se, zs222bs@student.lnu.se, thomas.bader@lnu.se
[2] Romain Lemaître, Fire Testing Centre, CERIB, Épernon, France, r.lemaitre@cerib.com

https://doi.org/10.52202/069179-0157

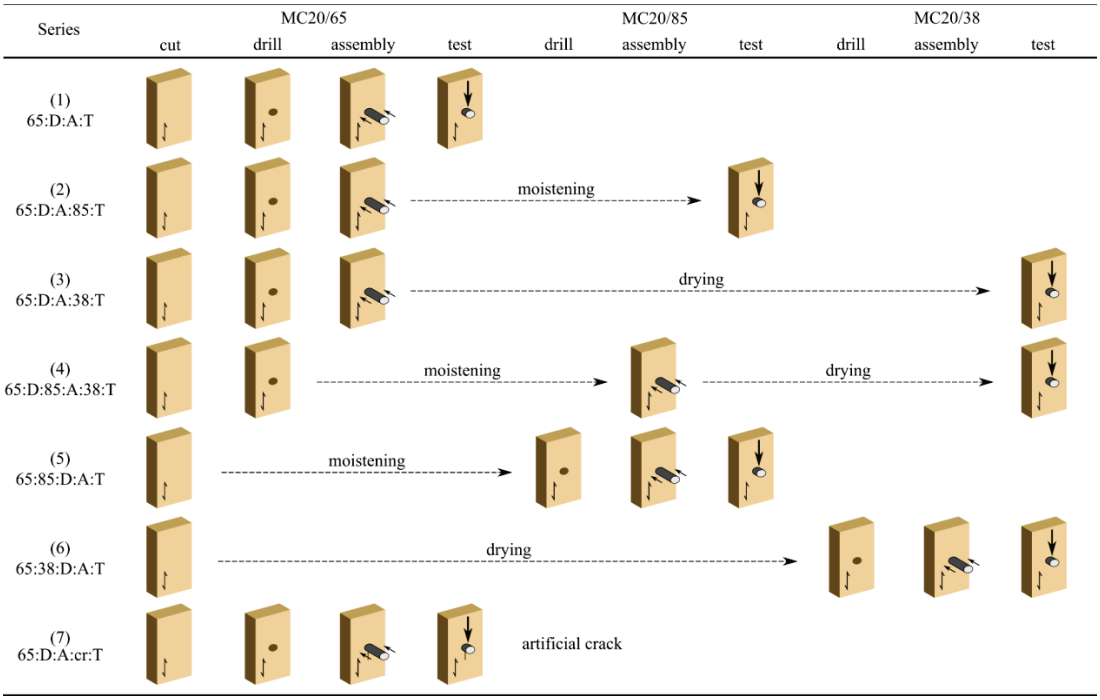

Figure 1: *Embedment test series for spruce and birch, indicating the ambient climate at: specimen cutting (cut), dowel hole drilling (drill), dowel assembly (assembly) and testing (test). Note: D…drill, A…assembly, cr…artificial crack, T…test, 38, 65, 85…corresponding relative humidity in (%).*

2 MATERIAL AND METHODS

2.1 Experimental program and materials

To study the influence of the moisture and assembly history on the embedment strength and stiffness in grain direction, seven groups of ten spruce and birch specimens each, with similar density distribution, were created (Figure 1). These groups differed by the moisture content (MC) of the specimen at the time: the dowel hole was drilled, the dowel was inserted, and the specimen was tested. In total, three different MCs, corresponding to ambient climates of 20°C and 65% RH (MC20/65 as a standard climate condition for testing), 20°C and 85% RH (MC20/85 as a condition with a higher MC), and 20°C and 38% RH (MC20/38 as a condition with lower MC) were used in the experimental program. These three ambient climates could be seen as representative for service class 1-3 in the current European design standard for timber structures, Eurocode 5 [6].

Series (1) served as a reference series, at which drilling, assembly and testing were done at the same MC, i.e. MC20/65 (standard climate condition for testing). The same procedure was followed for Series (5) and (6), but at a condition with high MC (MC20/85), and low MC (MC20/38), respectively. For Series (2) and (3), drilling and assembly were done at the reference condition (MC20/65), while testing was carried out in high MC (MC20/85) and low MC (MC20/38) conditions. Series (4) represents the situation of drilling right after production (MC20/65), assembly on-site after exposure to rain (MC20/85), and subsequent indoor application (testing at (MC20/38)). In addition, Series (7) investigates a damaged state, by application of an artificial crack parallel to the grain underneath the dowel-wood interface and aligned with the dowel hole center (see Figure 1), at MC20/65.

In total, 140 tests were conducted, uniformly distributed over seven different test series, with ten tests each, and two wood species, namely spruce and birch. Embedment test specimens were produced out of solid timber boards according to the corresponding European test standard, EN 383 [7]. Systematic selection of the specimens allowed for similar mean density and similar density distribution in the seven test series (Table 1). This was achieved by sourcing specimens from ten different boards, where each board provided one specimen per test series. The careful specimen selection was of importance in order to avoid large variations in wood characteristics that could influence the embedment properties. More details about the specimen sourcing are given in [8].

The mean density at an ambient climate of 20°C and 65% RH, amounted to 468.4 kg/m^3 (CV= 10.0%) for spruce, and 623.2 kg/m^3 (CV= 5.6%) for birch. The mean moisture content (MC) of the specimens at the time of testing is given per test series and species in Table 1. For determination of the MC, the oven-dry method according to EN 13183-1 [9] was used by placing the specimens in an oven at 103 ± 2°C directly after the embedment test. An ambient climate of 20°C and 65% RH resulted in a mean MC of 13.7% (CV= 2.7%) for spruce, and 11.0% (CV= 3.2%) for birch, while an ambient climate of 20°C and 85% RH resulted in a mean MC of 16.6% (CV= 1.2%) for spruce, and 14.9% (CV= 1.8%) for birch. An ambient climate of 20°C and 38% RH resulted in a mean MC of 8.6% (CV= 2.1%) for spruce, and 7.8% (CV= 2.6%) for birch.

https://doi.org/10.52202/069179-0157

Table 1: *Mean density at 20°C and 65% RH, ρ, (kg/m³), and mean moisture content at testing, MC, (%), and their coefficient of variation, CV, (%) of spruce and birch specimens.*

Series	ρ (kg/m³) Mean | CV (%)	MC (%) Mean | CV (%)
Spruce		
(1) 65:D:A:T	467.7 | 9.9%	14.0 | 2.0%
(2) 65:D:A:85:T	464.7 | 9.6%	16.7 | 1.2%
(3) 65:D:A:38:T	464.7 | 10.2%	8.8 | 0.7%
(4) 65:D:85:A:38:T	473.6 | 9.6%	8.5 | 1.4%
(5) 65:85:D:A:T	468.5 | 10.5%	16.6 | 1.2%
(6) 65:38:D:A:T	472.1 | 9.2%	8.4 | 1.1%
(7) 65:D:A:cr:T	467.5 | 10.6%	13.5 | 2.1%
All specimens	468.4 | 10.0%	
Birch		
(1) 65:D:A:T	624.4 | 5.1%	10.8 | 3.1%
(2) 65:D:A:85:T	625.0 | 6.6%	14.9 | 2.0%
(3) 65:D:A:38:T	618.8 | 5.1%	8.0 | 1.4%
(4) 65:D:85:A:38:T	627.2 | 5.8%	7.7 | 1.5%
(5) 65:85:D:A:T	625.4 | 6.4%	14.9 | 1.6%
(6) 65:38:D:A:T	623.3 | 5.0%	7.6 | 1.8%
(7) 65:D:A:cr:T	618.4 | 5.1%	11.1 | 2.6%
All specimens	623.2 | 5.6%	

Note: D…drill, A…assembly, cr…artificial crack, T…test, 38, 65, 85…corresponding relative humidity in (%)

Specimen dimensions followed the rules of EN 383. Thus, for a dowel with a diameter of d=12 mm, loaded in grain direction, the specimen height, h, (in grain direction) was 168 mm (twice 7d), the width, w, was 72 mm (twice 3d), and the thickness, t, was chosen to 36 mm (3d). All boards were stored in a climate chamber at an ambient environment of 20°C and 65% RH until the equilibrium moisture content was reached. Thereafter, the specimens for all test series were cut, and further processed according to the test program given in Figure 1. Equilibrium moisture content was assumed to be reached when two successive weightings, at an interval of 24 h, did not differ by more than 0.1% of the specimen mass, which is stricter than the rule given in EN 383 [7].

Immediately before testing, all specimens were reinforced with two partly-threaded screws (d=6 mm), to avoid early brittle failure of the specimen, i.e. before the targeted maximum embedment displacement of 15 mm was reached, as it was seen e.g. in [1] and [3]. Two screws, one above and one below the dowel were inserted at a distance of 36.5 mm from the dowel axis (Figure 2). The distance was decided based on results from Lederer et al. [10], to allow for a minimum distance between dowel and screw of one time the dowel diameter, i.e. 12 mm, at the end of the test. Thus, ductile behavior is ensured while a strength increase by the reinforcement screw is avoided. Moreover, this distance is far enough to not affect the elastic behavior of the wood-to-dowel contact.

Depending on the test series, the electrogalvanized dowel of steel quality S235, with d=12 mm was inserted either before the moisture content in the wood was adjusted or directly before testing. The borehole for the dowel was drilled to 12 mm in diameter without any clearance.

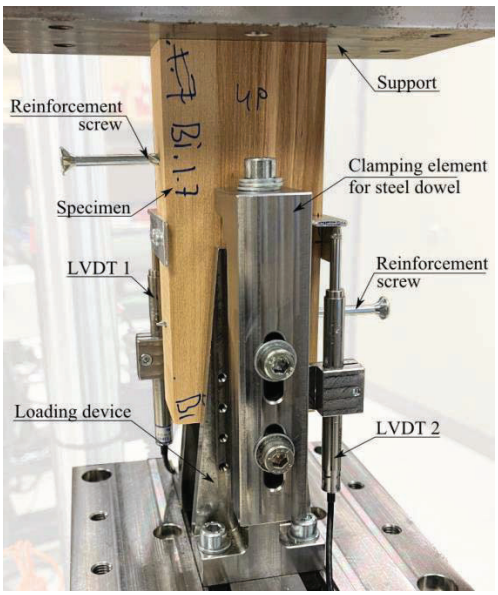

Figure 2: *Embedment setup for loading in grain direction according to EN 383 [7], including reinforcement screws to avoid premature splitting and 2 LVDTs for local displacement measurement.*

An artificial crack below the dowel with a length of 15 mm and a width of 0.5 mm, over the full specimen depth was added for Series (7). For this purpose, a small precision band saw was used. For more details, the reader is referred to [8].

2.2 Test setup and loading protocol

Full-hole embedment tests according to EN 383 [7], of 12 mm steel dowels embedded in spruce and birch specimens, loaded in grain direction were carried-out. The specimens were placed in a uniaxial testing machine (MTS 810, MTS Systems Corporation), by clamping both dowel ends in the loading device (Figure 2). Clamping of the dowel was used to minimize the effect of elastic bending of the dowel to ensure a uniform load transfer to the timber specimen along the dowel. A gap of 1 mm at each side between specimen and loading device was ensured to avoid friction between these elements.

On each side of the test setup, one displacement transducer (LVDT) was attached to measure the relative local displacement, u, between specimen and the loading device, and thus between the dowel and the timber specimen. For this purpose, steel angle brackets were diagonally mounted on the timber specimen's sides, in line with the dowel, to act as counterparts for the LVDTs mounted to the loading device. The force, F, as a result of embedment loading was directly measured by the load cell of the machine. In addition, the displacement of the actuator giving the machine displacement, u_{MTS}, was recorded.

The loading procedure followed the regulations of EN 383 [7], with small modifications. Loading was applied in grain direction until a machine displacement, u_{MTS}, of 17 mm, to ensure a local embedment displacement, u, of at least 15 mm.

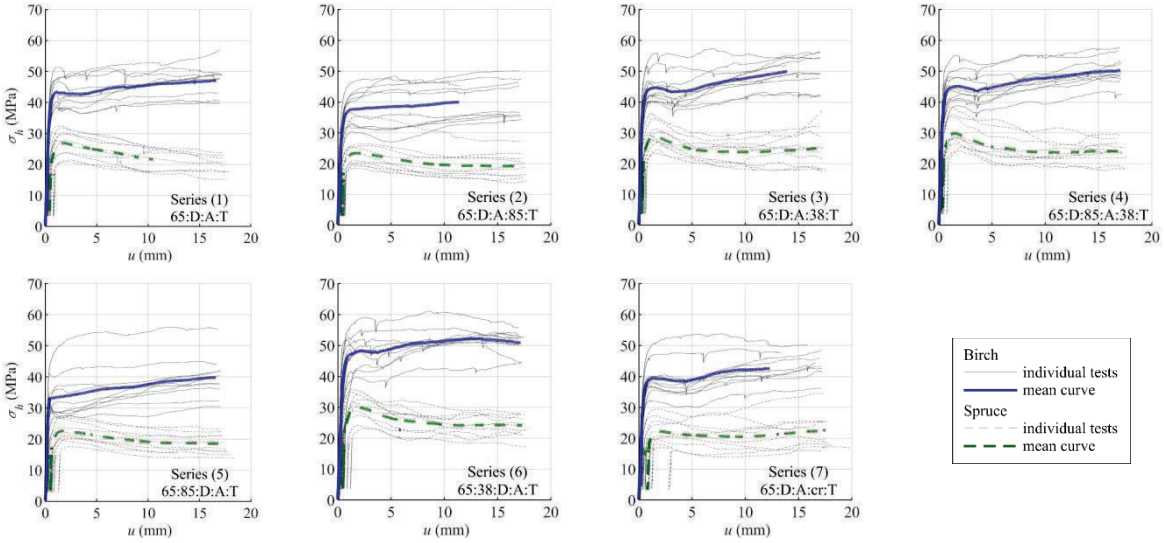

Figure 3: *Embedment stress-displacement curves for Series (1)-(7) of spruce (dashed lines) and birch specimens (continues lines).*

The displacement limit was increased compared to the 5 mm limit in EN 383 [7], to give access to the embedment behavior after yielding to serve as input for numerical models. The specimen was loaded force-controlled until a load level of 50% of the estimated maximum force, F_{est}, within 150 sec. This was followed by a 30 sec holding phase before the specimen was unloaded force-controlled with the same force rate to a force level of 10% of F_{est}. After a 30 sec holding phase, the specimen was re-loaded displacement-controlled with a displacement rate of 1.2 mm/min until u_{MTS} reached 17 mm.

2.3 Test evaluation

The local displacement, u, was determined as the average displacement measured by the two LVDTs. The embedment stress, σ_h, was calculated as the measured force, F, divided by the nominal contact surface of the dowel, i.e. the dowel diameter, d, times the specimen thickness, t. This gives access to the embedment stress-displacement curve for each test, from which the mean curve was determined by taking the average over the ten experiments per series.

The embedment strength, f_h, was defined according to EN 383 [7] as the maximum embedment stress up to a local displacement, u, of 5 mm. The elastic embedment stiffness, k_{el}, was defined as the inclination of the line, resulting from linear regression of the embedment stress-displacement curve between 10% and 40% of f_h as suggested in [8].

3 RESULTS AND DISCUSSION

3.1 Embedment stress-displacement curves

Embedment tests showed a pronounced global ductile behavior until the final displacement of more than 15 mm, thanks to the applied reinforcement screws. Most of the experiments showed local cracks in the wood below the dowel-wood contact surface, which however did not lead to global splitting of the specimen, as cracks were stopped at the reinforcement. These local cracks can be seen by load drops in the embedment stress-displacement curves illustrated in Figure 3. However, it also can be seen, that the force recovered after the crack-initiated load drop, reaching the load level before cracking.

Embedment stress-displacement curves for all seven test series, for both wood species (spruce and birch) are illustrated in Figure 3. Thin gray lines represent the individual tests, while thick green and blue lines give the mean curves of the individual test series per wood species. As typical for the embedment behavior of wood in grain direction, an almost linear behavior, representing the elastic range was observed for the first loading part. As soon as the elastic limit is reached, the stiffness decreases. For most of the tests, a local maximum is seen at this transition between elastic and plastic curve part, which is confirmed by previous tests [4,10,11]. Interestingly, spruce showed for most of the tests a continuous decrease in the embedment stress with increasing displacement, while the opposite was seen for birch, i.e., an embedment stress increase after the local maximum (see Figure 3). As expected, substantially higher embedment resistance was seen for birch compared to spruce, which confirms the correlation of the embedment resistance with the wood density [12,13].

3.2 Embedment strength and elastic stiffness

The embedment strength, f_h, as defined by EN 383 [7] (see Section 2.3), is given for Series (1)-(7) for both wood species, by its mean value and corresponding coefficient of variation (CV in %), in Table 2. For spruce specimens, a mean embedment strength, f_h, of 22.77 MPa to 30.34 MPa was found. The CV amounted to values below 20.5%. Birch specimens showed an f_h of 36.24 MPa to 49.24 MPa, with a CV of less than 19.9%. The difference in the mean embedment strength reflects the difference in MC between the test series. The about 60% higher embedment strength for birch compared to spruce is based

https://doi.org/10.52202/069179-0157

Table 2: *Mean embedment strength, f_h, (MPa), and mean elastic embedment stiffness, k_{el}, (MPa/mm), and their coefficient of variation, CV, (%) of spruce and birch specimens.*

Series	f_h (MPa) Mean | CV (%)	k_{el} (MPa/mm) Mean | CV (%)
Spruce		
(1) 65:D:A:T	27.00 | 14.9%	49.44 | 26.5%
(2) 65:D:A:85:T	23.63 | 20.5%	51.09 | 29.7%
(3) 65:D:A:38:T	29.33 | 13.2%	72.80 | 27.1%
(4) 65:D:85:A:38:T	30.00 | 15.4%	73.29 | 32.6%
(5) 65:85:D:A:T	22.77 | 14.7%	48.88 | 44.4%
(6) 65:38:D:A:T	30.34 | 13.8%	48.85 | 37.7%
(7) 65:D:A:cr:T	22.79 | 17.6%	40.18 | 30.8%
Birch		
(1) 65:D:A:T	44.48 | 10.7%	104.81 | 16.5%
(2) 65:D:A:85:T	39.45 | 16.7%	103.76 | 15.2%
(3) 65:D:A:38:T	45.24 | 11.3%	133.53 | 20.0%
(4) 65:D:85:A:38:T	45.81 | 10.7%	121.45 | 19.0%
(5) 65:85:D:A:T	36.24 | 19.9%	113.83 | 19.3%
(6) 65:38:D:A:T	49.24 | 10.7%	112.07 | 31.5%
(7) 65:D:A:cr:T	39.97 | 14.7%	89.40 | 15.2%

Note: D…drill, A…assembly, cr…artificial crack, T…test, 38, 65, 85…corresponding relative humidity in (%)

on its higher density, even if the magnitude in f_h-difference cannot fully be explained by the density difference, which was only about 30%. One explanation could be the untypical low f_h-results measured for spruce for its corresponding density. Furthermore, different correlations between f_h and density might be applicable for softwoods (e.g. spruce) and hardwoods (e.g. birch) as it was proposed by Ehlbeck and Werner [12].

The elastic embedment stiffness, k_{el}, as defined in Section 2.3, is given for all test series in Table 2. For spruce, a mean elastic stiffness, k_{el}, of 40.18 to 73.29 MPa/mm was found. The CV amounted to values up to 44.4%. Birch specimens showed a k_{el} of 89.40 to 133.52 MPa/mm, with a CV of up to 31.5%. Interestingly, birch specimens showed consistently lower variation in k_{el}-results compared to spruce specimens, while in general the variation for the embedment stiffness was higher than for the embedment strength. This confirms the sensitivity in measuring embedment stiffness, as it was already seen in previous studies [4,11], resulting among others from inaccuracies of the specimen preparation, dowel hole drilling, test setup, and displacement measurement. Birch specimens showed an elastic stiffness, k_{el}, of about twice the stiffness of spruce. This indicates a considerably stronger increase of the elastic stiffness with increasing density as it was found in [13].

3.3 Influence of moisture content

Results form Series (1), (5) and (6), are compared to study the influence of the moisture content (MC) on the embedment behavior, embedment strength, f_h, and elastic embedment stiffness, k_{el}. In these test series, the steps of (i) drilling the dowel hole, (ii) assembly of the dowel, and (iii) testing, were carried out after the equilibrium moisture content was reached. Thus, the only difference between these test series is their MC, while the assembly history and average specimen density was the same for all series. Series (1) corresponds to the standard climate of 20°C and 65% RH (MC20/65), Series (5) to a condition of a higher MC at 20°C and 85% RH (MC20/85), and Series (6) to a condition with a lower MC at 20°C and 38% RH (MC20/38). Corresponding MCs are given in Table 1.

The embedment stress-displacement curves in Figure 4(a) show a clear difference in the embedment resistance when reaching the yield limit. Higher embedment stresses can be reached, the lower the MC of the wood specimen is. Similar curve shapes can be seen for the different MCs, while distinct differences are found in the curve shape between spruce and birch, as discussed in Section 3.1.

The embedment strengths, f_h, presented in Figure 4(b) reflect the increase of resistance with decreasing MC. Series (5) (MC20/85), showed a decrease in the average f_h of about 15% (spruce) and 19% (birch) compared to the reference MC (MC20/65) in Series (1). This corresponds to a decrease in f_h by 5.8% (spruce) and 4.6% (birch) per 1% decrease in MC. Series (6) (MC20/38), showed an increase in the average f_h of 11% (spruce and birch) compared to the reference MC in Series (1). This corresponds to an increase in f_h by 2.0% (spruce) and 3.4% (birch) per 1% decrease in MC. Thus, results from this study suggest a nonlinear correlation of the embedment strength, f_h, with the corresponding wood MC, as well as differences between the two investigated wood species. Nevertheless, values are overall in line with findings from Hübner et al. [3], Sandhaas et al. [2] and van Blokland et al. [4], who found a strength increase of 3-4%, 2%, and 4-7% per 1% MC increase, respectively.

The elastic embedment stiffness, k_{el}, is illustrated in Figure 4(c). Interestingly, neither spruce, nor birch showed a distinct correlation of k_{el} with the corresponding MC. The difference in the average stiffness between Series (1), (5) and (6) were lower than 2% (spruce) and 8% (birch). Results need to be interpreted with care, since the stiffness parameter, k_{el}, showed for most of the test series a considerable variation in the results. These results are to some extend in contradiction to findings from van Blokland et al. [4], who found a significant influence of the MC on the elastic embedment stiffness for the first loading sequence, while almost no influence was seen for the following unloading/reloading sequence.

3.4 Influence of assembly history

Results from Series (2) and (5) are compared in Figure 5 to study the influence of the assembly history at a higher moisture content MC, i.e., at a MC corresponding to an ambient climate of 20°C and 85% RH (MC20/85). The influence of the assembly history at lower MC (MC20/38) is studied by comparing Series (3), (4) and (6) in Figure 6. In series (5) and (6), respectively, the steps of drilling, assembly and testing were done after the equilibrium moisture content was reached, and thus could be seen as reference cases. In contrast, in Series (2) and (3), respectively, the steps of drilling and assembly were done before the MC was adjusted. Furthermore, in Series (4) drilling was done at MC20/65, assembly at MC20/85, and testing at MC20/38. Thus, the only difference between

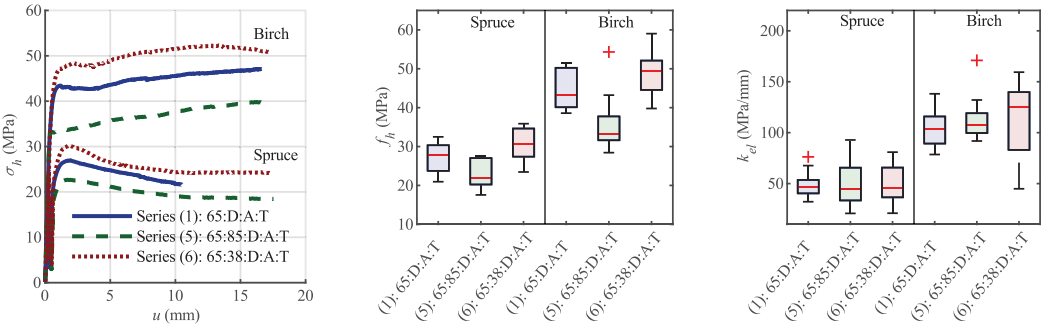

(a) (b) (c)

Figure 4: *Influence of the moisture content, MC, on (a) embedment stress-displacement curve, (b) embedment strength, f_h, and (c) elastic embedment stiffness, k_{el}. For spruce and birch tested in Series (1), (5) and (6), mean curves are given in (a), while boxplots in (b) and (c) express the median values and variation (25th and 75th percentile) for f_h and k_{el}, respectively.*

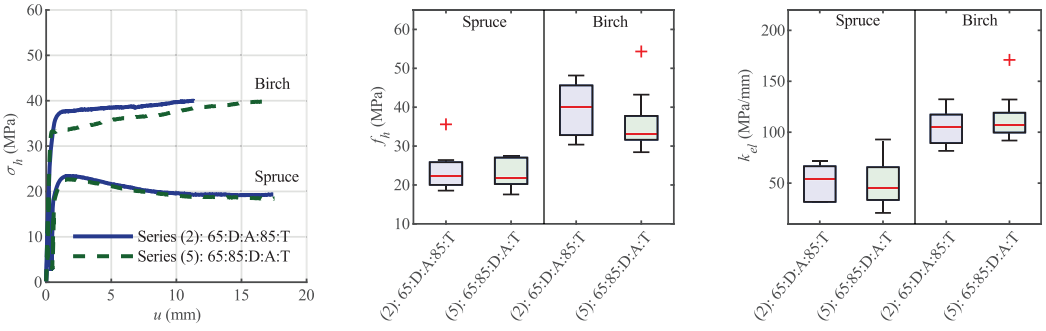

(a) (b) (c)

Figure 5: *Influence of the assembly history, for the high MC condition (tested at MC20/85), on (a) embedment stress-displacement curve, (b) embedment strength, f_h, and (c) elastic embedment stiffness, k_{el}. For spruce and birch tested in Series (2) and (5), mean curves are given in (a), while boxplots in (b) and (c) express the median values and variation (25th and 75th percentile) for f_h and k_{el}, respectively.*

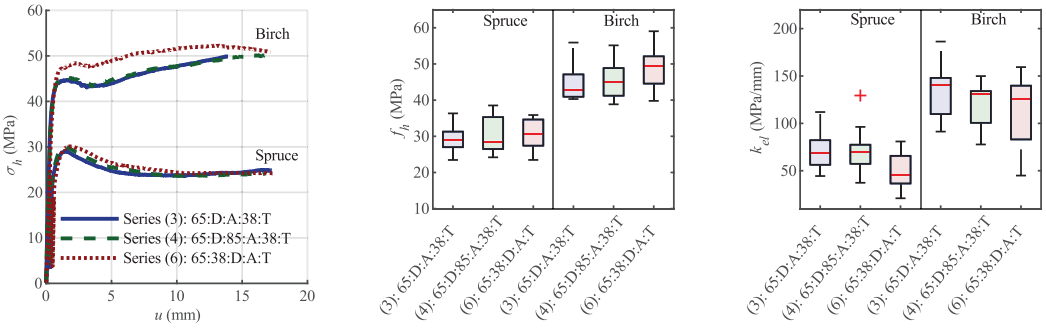

(a) (b) (c)

Figure 6: *Influence of the assembly history, for the low MC condition (tested at MC20/38), on (a) embedment stress-displacement curve, (b) embedment strength, f_h, and (c) elastic embedment stiffness, k_{el}. For spruce and birch tested in Series (3), (4) and (6), mean curves are given in (a), while boxplots in (b) and (c) express the median values and variation (25th and 75th percentile) for f_h and k_{el}, respectively.*

https://doi.org/10.52202/069179-0157

the series compared in this section, is the assembly history, while the MC at testing (either high or low MC) and the mean specimen density are always the same.

The embedment stress-displacement curves in Figure 5(a) and Figure 6(a), show for both wood species similar shapes and stress levels independent from the assembly history. Curves for spruce exhibit an almost perfect overlay. Curves for birch however show small differences, where for high MC condition the reference curve showed lower resistance, while for the low MC condition the reference curve exhibited higher resistance compared to the corresponding reference series.

The embedment strengths, f_h, illustrated by boxplots in Figure 5(b) and Figure 6(b), reflect the observations from the embedment stress-displacement curves. For spruce, the difference in the average f_h between the series was smaller than 5%, in low and high MC conditions. The corresponding difference for birch was slightly larger amounting up to about 10% in the low and high MC cases. Thus, a significant influence of the assembly history on f_h was not observed.

The elastic embedment stiffness, k_{el}, shown in Figure 5(c) and Figure 6(c), exhibited a different behavior for the high and low MC situation. While hardly any influence of the assembly history was seen when the specimens were moistened (less than 10% difference), a more distinct influence was seen when the specimens were dried, especially for spruce. For the cases at which the dowel was assembled before the specimen was dried, namely Series (3) and (4), an about 50% higher average k_{el} was found for spruce (for birch up to 20% difference) compared to the reference case (Series (6)). This might be explained by pre-stressing of the wood matrix around the steel dowel, due to shrinkage caused by decreasing MC. Thus, small gaps might be closed during drying of the specimen, resulting in a tighter fit at testing, and additional friction at the sides of the dowel due to shrinkage in transverse fiber direction, might result in a higher k_{el}. However, results should be treated with care, since the stiffness parameter k_{el} exhibited a considerable variation in the results.

3.5 Influence of artificial cracks

Results from Series (1) and (7) are compared in Figure 7 to study the influence of an artificial crack on the embedment behavior. For both series, all the steps of drilling, assembly and testing were done at a moisture content corresponding to an ambient climate of 20°C and 65% RH. Compared to Series (1), specimens of Series (7) had an artificial crack in the wood below the dowel, representing a crack, which could develop at connectors during the service live of a building, e.g. due to moisture changes.

The embedment stress-displacement curves in Figure 7(a) show a clear difference in the embedment resistance when reaching the yield limit. A consistently higher embedment resistance was seen for the case without artificial crack (Series (1)). Both cases exhibit a similar curve shape, and a similar ductile behavior. Thus, also Series (7) did not show any global brittle failure, which can be explained by the applied reinforcement screws.

The embedment strengths, f_h, illustrated by a boxplot in Figure 7(b), reflect the observations from the embedment stress-displacement curves. Application of an artificial crack reduced the average embedment strength by about 10-15% for both investigated wood species. This might be explained by the reduced contact area below the dowel, and the reduced clamping effect of the dowel, since no tensile forces perpendicular to the grain can be transferred below the dowel, due to the artificial crack.

The elastic embedment stiffness, k_{el}, shown in Figure 7(c), was found to be slightly stronger influenced by the artificial crack as it was found for the embedment strength. The artificial crack reduced the average k_{el} by 15-20% compared to the uncracked case for both wood species. This might be explained by the aforementioned reduced clamping effect, which might affect the embedment stiffness more than the strength.

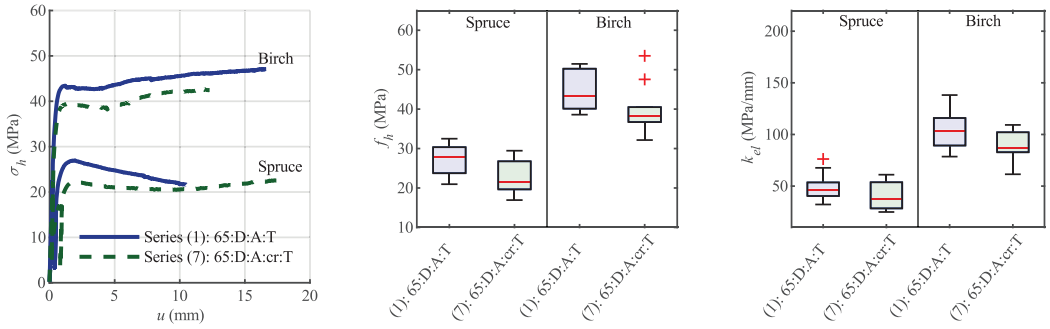

(a) (b) (c)

Figure 7: *Influence of artificial cracks on (a) embedment stress-displacement curve, (b) embedment strength, f_h, and (c) elastic embedment stiffness, k_{el}. For spruce and birch tested in Series (1) and (7), mean curves are given in (a), while boxplots in (b) and (c) express the median values and variation (25th and 75th percentile) for f_h and k_{el}, respectively.*

https://doi.org/10.52202/069179-0157

4 CONCLUSIONS

The comprehensive experimental testing program gave valuable insights into the embedment strength and stiffness, as regards the influence of the moisture conditions relevant for practical applications during production, assembly, and testing. Similar observations for spruce and birch indicate validity of the findings for different wood species with different density. Thorough sampling and accurate production of the test specimens were key to isolate the influence parameters of (i) moisture content, (ii) assembly history, and (iii) artificial cracks, from other major influence parameters like wood density.

The wood moisture content had a distinct influence on the embedment strength. For increased moisture contents compared to the reference MC at 20°C and 65% RH, an increase in strength of 2-4% per % MC was found, while for decreased moisture contents a decrease in strength by 4-6% per % MC as compared to the reference MC. In contrast, no distinct influence of the moisture content on the embedment stiffness was seen.

The assembly history did not show a distinct influence on the embedment strength. However, an increase in the average elastic embedment stiffness of up to 50% was found when drying the specimen after assembly of the steel dowel at the reference condition. In contrast, no influence was seen when the specimen was moistened after dowel assembly.

The artificial cracks applied below the steel dowel over the entire specimen depth resulted in a reduction of the average embedment strength by 10-15%. An even stronger effect was seen for the elastic embedment stiffness, which was reduced by 15-20% by the artificial crack. Due to reinforcement of the specimens, no global brittle failure was seen, despite application of an artificial crack.

These findings are expected to give valuable information for numerical modelling of dowel-type connections, as well as for engineering design. Furthermore, the results of this study might help to interpret findings from structural health monitoring and field measurements, as it shows the development of local connection stiffness with moisture changes in respect to the assembly history. In addition, the study highlighted the challenge of accurate stiffness measurement, which was reflected in a comparable high variation in stiffness results. It is proposed that more attention should be paid to embedment stiffness determination for future experimental studies and to the development of future testing standards, since the need for suitable connection stiffness prediction increases with the development of complex modern timber structures, like taller timber buildings.

ACKNOWLEDGEMENT

This work has been carried out within the project hardwood_joint, which is supported under the umbrella of ERA-NET Cofund ForestValue by BMLFUW (AT), ADEME (FR), FNR (DE), Vinnova, Swedish Energy Agency and Formas (SE). ForestValue has received funding from the European Union's Horizon 2020 research and innovation programme under grant agreement N°773324. Furthermore, the authors like to thank Anders Alrutz for his support with the experiments.

REFERENCES

[1] Rammer, D.R, Winistorfer, S.G.: Effect of moisture content on dowel-bearing strength. *Wood Fiber Sci.*, 33, 126-139, 2001.

[2] Sandhaas, C., Ravenshorst, G., Blass, H.J., van de Kuilen, J.: Embedment tests parallel-to-grain and ductility aspects using various wood species. *Eur J Wood Wood Prod*, 71, 599-608, 2013.

[3] Hübner, U., Bogensberger, T., Schickhofer, G.: Embedding strength of European hardwoods. *In Proceedings of CIB-W18/41-7-5*, 2008.

[4] van Blokland, J., Florisson, S., Schweigler, M., Ekevid, T., Bader, T.K., Adamopoulos, S.: Embedment properties of thermally modified spruce timber with dowel-type fasteners. *Constr Build Mater*, 2021, 313, 125517, 2021.

[5] Sjödin, J., Serrano, E.: An experimental study of the effects of moisture variations and gradients in the joint area in steel-timber dowel joints, *Holzforschung*, 62, 243-247, 2008.

[6] EN 1995-1-1: Eurocode 5: Design of timber structures – Part 1-1: General – Common rules and rules for buildings. *European Committee for Standardization (CEN)*, Brussels, Belgium, 2004.

[7] EN 383: Timber structures - Test method - Determination of embedment strength and foundation values for dowel type fasteners. *CEN*, Brussels, Belgium, 2007 (2007).

[8] Shehadeh, Z.: Embedment Behavior of Steel Dowel in Timber: Influence of Moisture Content, Assembly History, and Artificial Cracks: An experimental and numerical study of embedment strength and stiffness of steel dowel in timber with different wood moisture content and assembly history, *Master Thesis, Linnaeus University,* Växjö, Sweden, 2022.

[9] EN 13183-1: Moisture content of a piece of sawn timber – Part 1: Determination by oven dry method. *European Committee for Standardization (CEN),* Brussels, Belgium, 2002.

[10] Lederer, W., Bader, T. K., Unger, G., Eberhardsteiner, J.: Influence of different types of reinforcements on the embedment behavior of steel dowels in wood. *Eur. J. Wood Wood Prod.*, 74, 793-807, 2016.

[11] Schweigler, M., Bader, T. K., Hochreiner, G., Unger, G., Eberhardsteiner, J.: Load-to-grain angle dependence of the embedment behavior of dowel-type fasteners in laminated veneer lumber. *Constr Build Mater*, 126, 1020-1033, 2016.

[12] Ehlbeck, J., Werner, H.: Softwood and hardwood embedding strength for dowel-type fasteners. *In: CIB-W18 Meeting 25*, Paper 25-7-2, Ahus, Sweden, 1992.

[13] Schweigler, M., Bader, T. K., Bocquet, J. F., Lemaitre, R., Sandhaas, C.: Embedment test analysis and data in the context of phenomenological modeling for dowelled timber joint design. *In: 6th meeting of INTER,* Paper 52-7-8, Tacoma, USA, August 26-29, 2019.

https://doi.org/10.52202/069179-0157

World Conference on Timber Engineering Oslo 2023

EXPERIMENTAL AND NUMERICAL ANALYSES OF A CONNECTION FOR CLT STRUCTURES

Lars Blomqvist[1] , Roberto Crocetti[2], August Claesson[3], Zakaria Ben Osmane[4], Rune Ziethén[5], Marie Johansson[6]

ABSTRACT: Although building systems made of cross-laminated timber (CLT) have become common in Sweden in the past 20 years and they have developed rapidly during the same period, steps remain to be taken to simplify the assembly of such systems, especially at construction sites. Current construction methods, however, remain labour-intensive and thus show room for improvement.

This paper describes a novel connection for the assembly of building elements made of CLT. Simple and inexpensive, the connection is fairly insensitive to manufacturing tolerances and enables rapid, more efficient construction than the connections for CLT structures currently used. Test results show the excellent strength and stiffness of the connection, which also allows the replacement of numerous fasteners, including nails and screws, with only a single steel rod.

KEYWORDS: assembly, connections, cross-laminated timber

1 INTRODUCTION

The deficit of affordable housing in Northern Europe requires the rate of housing production to increase in parallel to a decrease in production costs. Beyond that, construction needs to be more resource-efficient and, as such, more environmentally friendly.

The construction of residential timber buildings with different structural systems has recently increased significantly in Europe. In Sweden, the development of structural systems for timber buildings has taken two paths: one driven by the single-family house industry with industrially built volume elements (i.e. also used for multi-storey buildings) and one driven by manufacturers of engineered wood products such as glulam and cross-laminated timber (CLT).

In CLT's case, the building method is well-suited for traditional construction industries, primarily due to its similarity to the building method used in prefabricated concrete. In Sweden, buildings made of CLT began being built approximately 20 years ago. In that context, the manufacture of CLT has recently shown significant intensification, with several production plants being launched in the past few years. Although CLT construction systems have developed rapidly during those years, steps remain to be taken to simplify the assembly of the CLT elements, especially at construction sites.

This paper reports the development of a connection for the assembly of building elements made of CLT. The proposed connection provides greater precision and enables a faster, more efficient process than typical connections used today. We have already reported a feasibility study [1] which, among other things, revealed how the inspiration of the presented connection comes from the furniture industry.

2 MATERIALS AND METHODS

The tested specimens were cut from five CLT panels of Norway spruce (*Picea abies* L.) into a nominal thickness of 120 mm. The panels were produced with five laminations with a C24 strength class. Regarding thickness, the two outer layers were 30 mm, while the three inner layers were 20 mm. The layers were bonded with a polyurethane reactive adhesive free of urea-formaldehyde, for a bonding that complied with EN 14080, type 1, according to EN 15425. Meanwhile, the density of the panels was in the range of 457–510 kg/cm^3. The two outer layers and the central layer had their grains oriented in the direction perpendicular to the load,

[1] Lars Blomqvist, RISE Research Institutes of Sweden, Sweden, lars.blomqvist@ri.se
[2] Roberto Crocetti, KTH Royal Institute of Technology, Sweden, crocetti@kth.se
[3] August Claesson, KTH Royal Institute of Technology, Sweden, august.claesson@hotmail.com
[4] Zakaria Ben Osmane, KTH Royal Institute of Technology, Sweden, zakariyabenosmane@yahoo.com
[5] Rune Ziethén, RISE Research Institutes of Sweden, Sweden, rune.ziethen@ri.se
[6] Marie Johansson, RISE Research Institutes of Sweden, Sweden, marie.johansson@ri.se

https://doi.org/10.52202/069179-0158

whereas the other two layers were oriented in the direction of the applied load. Last, the laminations were finger-jointed lengthwise but not edge-bonded.

Our study was performed on connections with varying geometries (see Figure 1a and Table 1), chiefly to assess the strength and stiffness of the proposed connection by varying two parameters: distance to end grain (DY) and lateral width (DX).

Altogether, seven specimen types were investigated experimentally, analytically and numerically. Two to three laboratory test repetitions on nominally identical specimens were performed in order to achieve satisfactory statistical relevance, which resulted in a total of 18 tested specimens.

Before commencing the laboratory tests, simplified hand calculations were performed in order to gain an approximate estimation of possible failure modes and corresponding failure load.

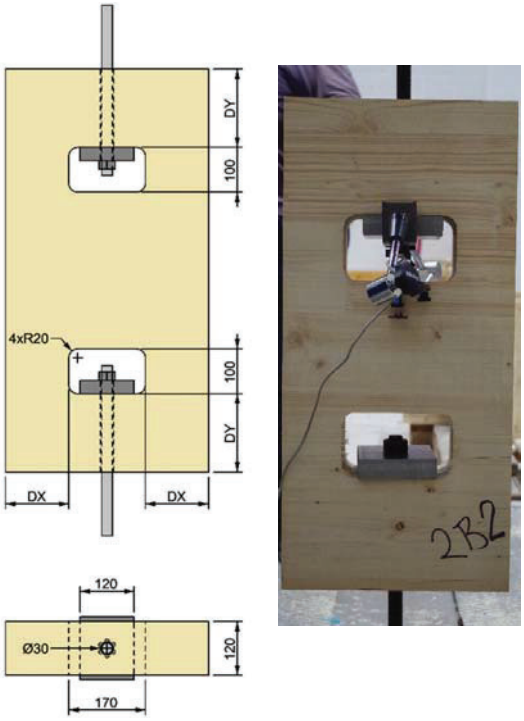

a b

Figure 1: *a) Dimensions of test samples*
b) Test set-up

Table 1: *Dimensions that varied in the samples by group*

Specimen group	DX (mm)	DY (mm)	Quantity (pcs)
1	90	100	3
2	165	100	3
3	90	175	3
4	238	175	3
5	90	250	2
6	155	250	2
7	238	250	2

Specimens were tested in a universal testing machine, and loads and corresponding displacement were recorded during the laboratory tests. The tensile axial load was applied to the specimens through a pair of steel rods 24 mm in diameter that were inserted in holes with a 30 mm diameter vertically drilled into the upper and lower parts of the specimens. The rods were fixed to the specimens by means of rectangular anchoring steel plates with a bearing area of 120 × 120 mm^2 and nuts at the end of the rods. The anchoring plates were allocated in openings made in the specimens that were rectangular in shape and had rounded off corners (Figure 1). Local displacements were measured using linear variable differential transducers (LVDT) placed directly above or directly below the rod's anchoring plate at each opening (Figure 1b). To avoid possible damage, the LVDTs were removed from the specimens when the load was approaching the predicted failure load of the connection.

2.1 The numerical model

Every specimen type was subjected to FE modelling with the commercial software Abaqus. The gap between the laminations within each layer was created by extruding a cut 0.01 mm wide. For each model, only half of the sample was modelled explicitly, and symmetry boundary conditions were used to represent the other half. All models used linear 8-noded brick elements with reduced integration and hourglass control. For groups 1, 3 and 5 of specimens, the FE mesh size was set to 6 mm.

The elastic material properties were the same for all models and are shown in Table 2. The properties are based on ones previously published [2]. For each layer, Direction 1 was oriented parallel to grain, Direction 2 was oriented in the direction perpendicular to the grain, and Direction 3 was set to point out of the plane of the panel.

Table 2: *Material properties, with E_i, υ_{ij} and G_{ij} indicating Young's modulus, Poisson's ratio and the shear modulus, respectively, in Directions 1, 2 and 3*

Name of the mechanical property	Numerical value
E_1	12,000 MPa
E_2	500 MPa
E_3	500 MPa
υ_{12}	0.3
υ_{13}	0.3
υ_{23}	0.3
G_{12}	600 MPa
G_{13}	600 MPa
G_{23}	60 MPa

The load was applied to the rod by using a reference point with a rigid body constraint, which allowed the load to be more evenly distributed over the end face of the rod. The load was modelled as a concentrated force acting on the reference point, its magnitude was set to the max load for each sample, and it was applied incrementally.

The boundary conditions used were different symmetry conditions applied to the symmetry surface of each sample.

https://doi.org/10.52202/069179-0158

The glued interaction between the layers of the CLT was handled by using a cohesive contact condition implemented in the FE software. Following past investigations [2], the bonded connection was given a stiffness of 1000 N/mm^3 in every direction; that condition was applied to all flat face surfaces of CLT, and no interaction between the lamination edges was used. The contact area between the steel anchor plate and the CLT was also simulated by using a special contact condition with hard contact typically for the surfaces and with a frictional behaviour tangential to the surfaces. The coefficient of friction between the steel and the timber was set to 0.4, and the penalty friction formulation was used.
A static general step was used in numerical simulations with Abaqus and with non-linear geometric effects toggled on. The increment was controlled to give curves without significant leaps and to apply the load in reasonably small steps.
The load displacement curves were defined based on displacement at the top edges of the plate and the hole to thereby measure displacement in the same location as the transducers used in the experiments.
For areas with significant tensile stress concentration, a linear elastic stress check based on beam theory was performed, namely by isolating the area of interest (e.g. a single lamination) and using a free body cut to find the forces and moment acting on the cut section with the highest stresses. Those values were subsequently used to determine stresses using Navier's equation.

3 RESULTS AND DISCUSSION

The load capacity of the studied connection in panels 120 mm thick is shown in Figure 6. The results reveal variation in load capacity depending on the geometry of the connection. Nearly all of the tested specimens failed in shear. Both rolling shear failures (i.e. at the bonded area between two adjacent laminations) and planar shear failure (i.e. with a crack parallel to the grain in laminations oriented perpendicularly to the direction of the applied load) were observed (Figure 2). However, it remains unclear which of the two shear failures occurred first.

Figure 2: *Failure mode of a type 1 specimen. The pictures show typical failure modes observed in most of the tested specimens. Both rolling shear in the outer horizontal laminations (upper picture) and longitudinal shear in the two internal vertical laminations (lower picture) can be seen*

https://doi.org/10.52202/069179-0158

The way in which the load is transferred from the openings where the anchoring plates are placed to the surrounding structure can be explained by the simplified model shown in Figure 3.

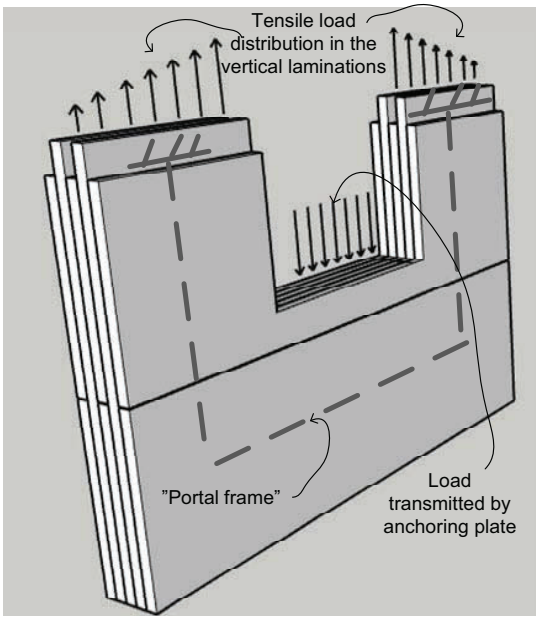

Figure 3: *Simplified model showing how the load is transmitted from the point of its application to the surrounding structure*

The part of the connection shown in Figure 3 suggests that the connection's structural behaviour is rather similar to that of an (upside-down) portal frame loaded with a distributed load at mid-span and rotationally restrained at the bases of the two frame columns. At the column bases, the bending moment and axial force generate a distribution of the reaction forces (virtually taken only by the vertical laminations) similar to that shown in the figure.

During loading, the portal frame is subjected to axial forces, shear forces and the bending moment. Those actions are most prevalently borne by the laminations of the portal frame with the grain parallel to the major stresses. For example, regarding the bending moment action in the frame, it will essentially be resisted by lamination 4 in the rafter part of the frame and by lamination 1 in the columns (Figure 4).

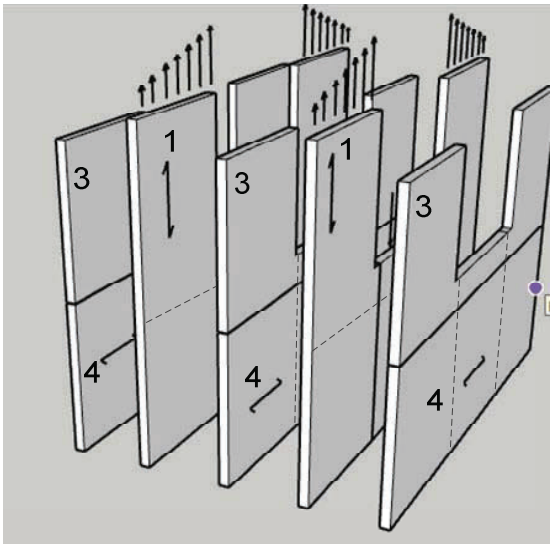

Figure 4: *Exploded sketch of the model shown in Figure 3. Laminations 3 and 4 have the grain in the direction perpendicular to the applied load, whereas Lamination 1's is in the direction parallel to the applied load*

However, because the vertical and horizontal laminations are bonded together, the bending moments and the consequent bending deformations in the load-bearing laminations are restrained by the cross-laminations. That dynamic generates torsional (shear) stresses at the bonded area between two adjacent laminations that might lead to failure due to rolling shear.

Similar considerations apply to the shear force in the frame. When the shear is transferred from the rafter (i.e. lamination 4) to the column (i.e. lamination 1), aside from rolling shear at the bonded areas, planar shear also occurs in lamination 1 (i.e. vertical shear) and in lamination 4 (i.e. horizontal shear) due to the moment gradient.

Finite element simulations revealed especially high shear stresses in all analysed specimens for loads close to the failure load. For example, for specimen type 1, the rolling shear and planar shear stresses at failure load are shown in Figure 5.

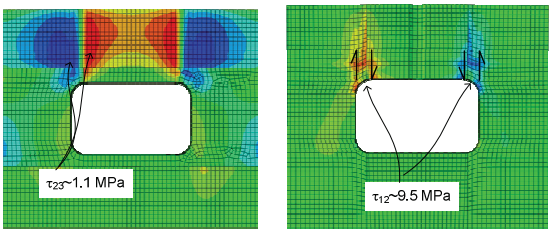

Figure 5: *Left: Rolling shear in outer horizontal lamination at failure load. Right: In-plane longitudinal shear in longitudinal lamination at failure load*

https://doi.org/10.52202/069179-0158

As shown in the analyses, shear stresses close to shear strengths are achieved for both rolling and planar shear, respectively.
In some of the sample with higher shear strength (i.e. specimens with larger DY), local bearing failure under the steel anchoring plate could be observed as well.
Our analysis of the results of laboratory tests suggests that the lateral distance, DX, within the tested range of 90 mm to 238 mm, had very little influence on the load-bearing capacity of the connection (Figure 6).

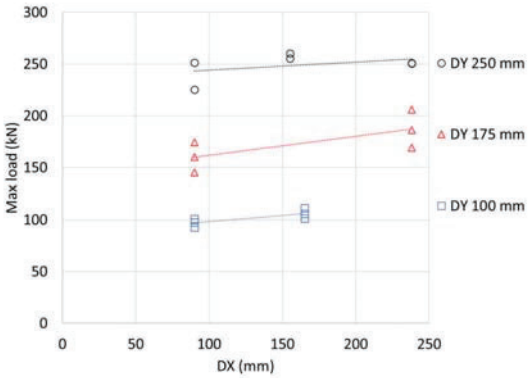

Figure 6: *Load capacity of the different tested specimens as a function of DX*

By contrast, there was also a clear increase in load-carrying capacity as the distance increased between the outer part of the anchoring plate and the upper (or lower) part of the specimen, DY (Figure 7).

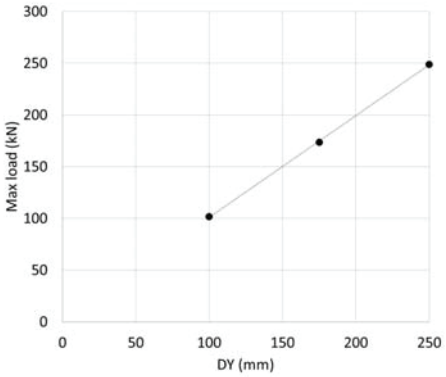

Figure 7: *Mean load capacity of the different tested specimens as a function of DY*

The stiffness of the connection was calculated as the ratio between the applied load and the local deformation measured underneath the anchoring plate. The maximum recorded local deformation for all of the tested specimens was generally small (i.e. approx. 1 mm), which led to very high axial stiffness of the connection. The stiffness was primarily influenced by the distance, DY, and to a lesser extent by DX. Moreover, the greater the distance, the lesser the influence of DX on the stiffness of the connection (Figure 8).

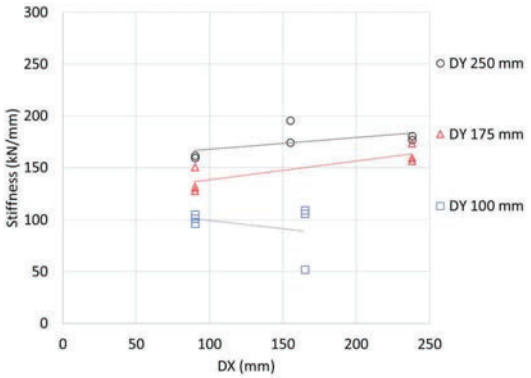

Figure 8: *Stiffness measured from local deformation.*

In terms of load displacement behaviour, FE analyses afforded highly accurate predictions. For example, a comparison of FE analysis and the laboratory results for one of the specimen groups is shown in Figure 9.

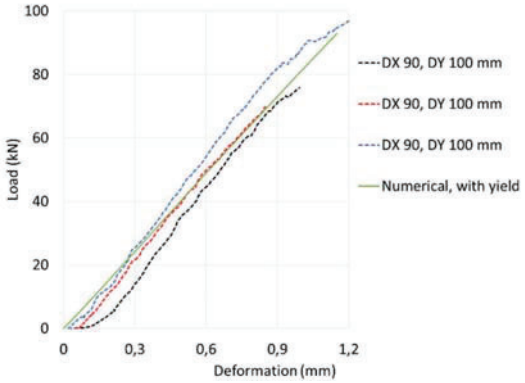

Figure 9: *Load versus local deformation for specimen type 1: comparison of experimental and FE results*

For the tested geometries, a pronounced linear relationship can be observed between the load-carrying capacity of the connection and the distance, DY. That condition, together with the fact that essentially all of the specimens failed in shear, lead to the formulation of a very simple verification model that was valid at least for a preliminary design of the connection within certain geometry boundaries. According to the model, the connection's capacity can be checked similarly to a check of the shear capacity of the rafter of a portal frame (Figure 10).

https://doi.org/10.52202/069179-0158

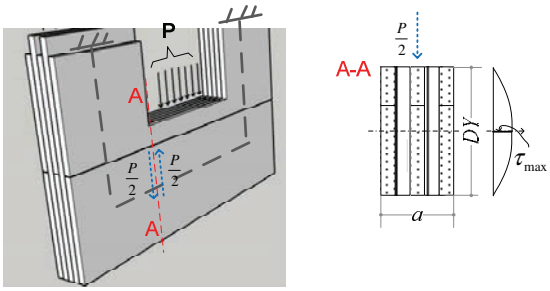

Figure 10: *Simplified verification model for the preliminary design of the proposed connection*

According to the model, the load carrying capacity, P, of the connection can be estimated as:

$$P = \frac{4}{3} \cdot a \cdot DY \cdot f_v \qquad \text{Eq 1}$$

in which a and DY are as explained in Figure 10, and f_v is the shear strength of the gross cross-section. For the tested specimens, the mean value of f_v was approximately 6.2 MPa. That relatively high value of shear strength, however, is suitable only for predictions of the realistic capacity of the connection. For a design situation, a lower shear strength value, presumably in the range of 3 to 4 MPa, is advisable.

4 CONCLUSIONS

The chief findings of our study were that:

- DX's influence on the load bearing capacity of the investigated connection is rather slight
- DY has significant influence on the load bearing capacity of the connection and
- Failure modes and corresponding failure loads are predictable for the geometries tested.

The novel structural connection demonstrates properties of strength and stiffness that are adequate for applications in connections between wall elements and between floor and ground foundations in multi-storey building. A single connection of this type can thus replace hundreds of conventional fasteners such as screws and nails.

ACKNOWLEDGEMENTS

Our research received financial support from the Kamprad Family Foundation (Ref. No. 20200013). We also wish to thank the Södra Skogsägarna forestry cooperative, especially Daniel Anderson and Kristoffer Segerholm, for the CLT used in the specimens.

REFERENCES

[1] Blomqvist, L., Honfi, D., Johansson, M., Ziethén, R., Crocetti, R., Norén, J.: Development of novel structural connections – Inspiration from furniture industry. In: Proceedings of the 2021 World Conference on Timber Engineering (WCTE), 2021.

[2] Basic, A., Amrllahu, K.: Korslimmat trä – styvhet vid belastning i planet. Student thesis (Degree project). Lund, LTH, 2018.

https://doi.org/10.52202/069179-0158

World Conference on Timber Engineering Oslo 2023

ROBUSTNESS OF ADHESIVELY BONDED PANEL-TO-PANEL CONNECTIONS IN CLT FLOORS

Lei Zhang[1], Muster Marcel[2], Thomas Tannert[3], Hercend Mpidi Bita[4]

ABSTRACT: Cross-laminated timber (CLT) panels are increasingly used in floor construction with the individual panels often connected with self-tapping screws (STS) through surface spline, half-lap, and butt joints. An alternative solution is provided by using the Timber Structure 3.0 (TS3) technology that connects butt joints through high-performance adhesives and creates a near-rigid connection; therefore, two-way resistance of CLT panels can be utilized. However, TS3 joints fail in a brittle manner, and floor diaphragms lose integrity after crack develops. In this study, measures to improve the robustness and prevent floor collapse after TS3 joint failure were investigated. Seven panel-to-panel connections with TS3 and a secondary connection system were fabricated and tested under bending to evaluate the joint behaviour and observe crack propagation. After TS3 failed, bending or shear tests were conducted to test the residual strength of the secondary connections. The tests showed that it is possible to increase the robustness of TS3 joints by using additional mechanical connectors; i.e., the secondary connections exhibited residual strength after the TS3 joints failed. More tests are planned to further investigate measures to improve the robustness of TS3 joints.

KEYWORDS: Cross-laminated timber, TS3, Self-tapping screw, X-fix, Robustness

1. INTRODUCTION

1.1 BACKGROUND

Cross-laminated timber (CLT), a plate-like material made from layers of dimension lumber glued crosswise to one another, is commonly used in walls, floors, and roofs [1]. Due to prefabrication limitations, CLT panels are manufactured with width up to approximately 3.4 metres and assembled with panel-to-panel connections on-site. When used as floor diaphragm, the panels resist out-of-plane gravity loads and in-plane lateral (wind and seismic) loads. To successfully build CLT floors, connections between individual panels need to be designed for appropriate strength, stiffness, and ductility.

Traditional panel-to-panel connections employ dowel-type fasteners such as self-tapping screws (STS) to transfer in-plane shear forces. Tests have shown that screw connections display desirable structural performance under in-plane loads [2,3]. An alternative to STS in connecting CLT panels is the X-fix connector [4], which is a double dovetail-shaped wood wedge made of birch or beech veneer plywood.

The desire for open space and clear storey height favours the use of flat-plate system where CLT panels are point supported by columns and span two ways. In such systems, the out-of-plane performance of connections is critical to engage two-way behaviour. However, screw connections have limited moment capacity under out-of-plane loads [5]. As a result, CLT panels are often designed as one-way systems without considering the load-sharing action in the transverse direction.

1.2 TIMBER STRUCTURE 3.0 TECHNOLOGY

The Timber Structure 3.0 (TS3) technology provides a viable alternative to connect butt joints on-site using two-component Polyurethane adhesive [6]. TS3 butt-joints provide near-rigid connection performance under bending moments and shear forces and can realize the biaxial load-carrying timber flat slabs with a column grid up to 8 m × 8 m and a live load of 5 kN/m^2. This construction technology contributes to CLT replacing concrete in constructing large-scale flexible floor slabs.

However, under seismic loads, the ductility of CLT diaphragms relies on the connections, and engineers are reluctant to use adhesive connections due to their brittle failure. The combination of TS3 and mechanical fasteners such as STS or X-fix provides a possible solution for achieving both high stiffness and high ductility in the joints. In this hybrid system, TS3 provides stiffness for the connections under the service loads while STS or X-fix acts as a backup system and can be designed only for the failure loads. The combination of TS3 and STS joints has been successfully utilized in the floor construction of ON5 building in Vancouver, Canada [7].

[1] Lei Zhang, University of Northern British Columbia, Canada, lzhang2@unbc.ca
[2] Muster Marcel, Timber Structures 3.0 AG, Switzerland, marcel.muster@ts3.biz
[3] Thomas Tannert, University of Northern British Columbia, Canada, Thomas.Tannert@unbc.ca
[4] Hercend Mpidi Bita, Timber Engineering Inc., Canada, hercend.mpidibita@timberengineering.ca

https://doi.org/10.52202/069179-0159

1.3 ON5 MASS TIMBER BUILDING

ON5 is an 840 m^2 innovative four-storey mixed-use commercial and office building located on a 7.6 m wide infill lot, as shown in Figure 1. The building was designed to Passive House principles by Hemsworth Architecture, engineered by Timber Engineering Inc., and constructed by Naikoon Contracting Ltd.

(a)

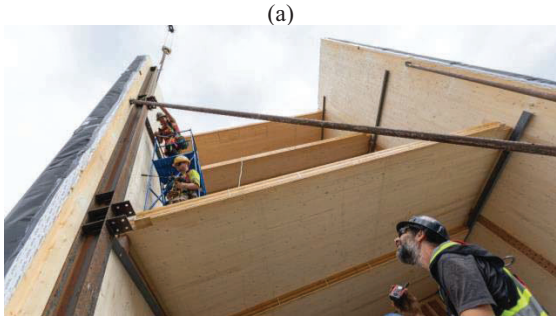

(b)

***Figure 1**: ON5 (a) Completed building (b) During construction (credit KK Law courtesy naturally:wood)*

The building was constructed with three-storey mass timber on top of a concrete and masonry podium. The gravity load-resisting systems of the mass timber portion are the CLT floors, roof, and walls, while the lateral load-resisting system relies on a CLT core, shear walls, and diaphragms. The CLT core uses innovative resilient slip friction hold-downs by Tectonus [8] at four corners to dissipate energy and reduce lateral drift. The CLT floor, roof, and wall panels are 5-ply (175 mm) E1 grade [9] while CLT core has both 7-ply (245 mm) and 5-ply (175 mm) running in East-West (short) and North-South (long) directions, respectively.

CLT floor panels spanning 7 m along East-West direction were sitting on balloon-type CLT walls along North-South direction. Under gravity loads, the design of CLT floor panels is governed by deflection and vibration requirements, while the strength requirements can be met when designed as one-way panel in the major strength direction. To achieve the required span with 5-ply E1 grade, the stiffness of CLT in the secondary direction was engaged by employing TS3 connection between panels. This way, the flat slab system was achieved without additional beams. As shown in Figure 2, the adhesive was injected into the gap between panels, creating a seamless connection. In addition, 220 mm FT/CSK screws [10] with a diameter of 10 mm were installed in 45° at a maximum spacing of 500 mm as the backup to TS3 joints in the event of a failed TS3 connection.

Along East-West direction (short direction), the CLT diaphragm cantilevered about 15 m on both sides of the core. Under seismic loads, CLT diaphragm can deflect due to slips between panels. The TS3 joints between panels eliminate slip of diaphragm between panels and control lateral deflection of floors and roof. With the rigid connection solution, a rigid diaphragm is achieved, and forces are transferred to stiffer CLT walls and core.

***Figure 2**: Application of TS3*

1.4 FLOOR ROBUSTNESS

In addition to the lack of ductility, another challenge towards the widespread adoption of TS3 is the loss of floor integrity after initial failure. At the ultimate strength level, cracks of TS3 appear at locations of imperfect bonding and wood defects. Initial cracks from extreme or abnormal loadings not considered in the design stage have a risk of propagation, which can lead to floor collapse. This is especially important for mass timber floors as existing studies on disproportionate collapse prevention on mass timber buildings are scarce [11-13].

Implementing structural robustness as a floor property is considered the best-suited method for disproportionate collapse prevention. With structural robustness, the floor can withstand initial damage and stop propagation by developing alternative load paths. A floor is considered robust if it can develop collapse-resistance mechanisms to absorb the initial local damage without collapse [14].

For a continuous TS3 joint, it is beneficial to install crack stoppers that block the crack propagation. The goal of crack stoppers is to physically divide the TS3 joints into different sections and allow stress redistribution after some sections fail. The floor should be able to resist dead and live loads without collapse. The simplest crack stoppers could be gaps or dowels that isolate TS3 into different sections. These simple measures can be combined with mechanical connectors that are often used as secondary connections to TS3, such as STS or X-fix, to provide additional strength.

https://doi.org/10.52202/069179-0159

2. EFFECTIVENESS OF CRACK STOPPERS

2.1 OBJECTIVES

For the acceptance of TS3 in CLT panel connections, it is necessary to demonstrate the robustness and ductility of the joints and provide adequate technical information for designers and engineers to use. This study focuses on the effectiveness of crack stoppers in preventing the progressive collapse of TS3. Tests were conducted on seven panel-to-panel connections with combined TS3 and a secondary connection system. The bending stiffness, strength, and shear strength of the joints were determined and compared with each other.

2.2 MATERIALS

The panel-to-panel connections with combined TS3 and a secondary connection system were fabricated and tested at ETH Zurich. The CLT panels were 5-ply with a thickness of 150 mm and a lamella grade of C24 [15]. The panels were 1.3 m long and 1.5 m wide, and connected by butt joints in the major strength direction. The TS3 joints had a thickness of 4 mm. The cross-section of the tested joints is shown in Figure 3. Crack stoppers were spaced 750 mm and divided the joint into three sections. To initiate the crack, two external sections were weakened by drilling holes with a diameter of 5 mm at the bottom after TS3 was cured.

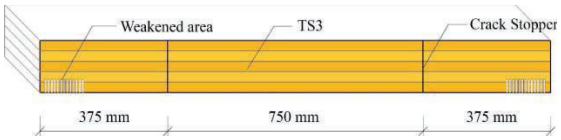

***Figure 3**: Cross-section of tested TS3 joints*

The specimens used the following crack stoppers:

1) Specimen 1 (SP1) was connected with two pairs of STS.
2) Specimen 2 (SP2) was connected with two X-fix connectors, glued to the bottom of the specimen with PU adhesive, as shown in Figure 4(a).
3) Specimen 3 (SP3) was connected with two pairs of STS. In addition, a 20 mm hole was drilled next to each pair of screws, as shown in Figure 4(c).
4) Specimen 4 (SP4) was connected with two mechanically inserted X-fix at the bottom, as shown in Figure 4(b).
5) Specimen 5 (SP5) and specimen 6 (SP6) comprised two pairs of STS. In addition, vertical beech dowels were installed next to screws to separate TS3, as shown in Figure 4(d).
6) Specimen 7 (SP7) was connected with two mechanically inserted X-fix at the top. At the bottom of each connector, a 20 mm hole was drilled.

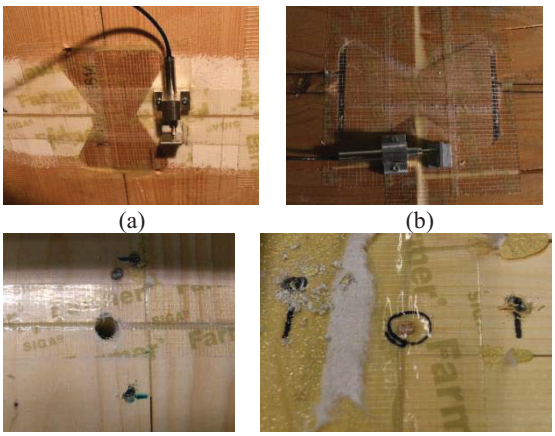

***Figure 4**: Crack stoppers used in the specimens (a) Glued X-fix in SP2; (b) X-fix in SP4 (c) Self-tapping screws and 20mm hole in SP3 (d) Self-tapping screws and beech dowel in SP5.*

Pairs of double-thread SFS WT-T screws [16] with a diameter of 8.2 mm and a length of 160 mm were installed at 45°. The X-fix connectors were 90 mm high, 130 mm long, and 96 mm wide. In SP4 and SP7 where the X-fix was not glued to CLT, the connector transferred tensile forces through interlocking and shear forces through friction. The 20 mm holes in SP3 and SP7 were drilled after TS3 adhesive was cured. The beech dowels in SP5 and SP6 were installed before the application of TS3. The holes and vertical wood dowels only serve as crack stoppers while STS and X-fix can provide additional tensile and shear strengths to the joints. The effectiveness of the crack stoppers is evaluated based on the following criteria: 1) A crack stopper should stop the continuous crack propagation from one section to another; 2) Load increase should be observed between individual cracks.

2.3 METHODS

The specimens were tested under four-point bending and Iosipescu shear as shown in Figure 5 and Figure 6, respectively. Instead of applying loads over the whole width of the panels, loads were only applied at edges of the panels with steel plates under the steel beams to provoke the failure of the glue line in the weakened region. The loading protocol was following the procedure in EN 26891 [17]. The load was applied to 40% of the estimated peak load and maintained at this level for 30 s. The load was then reduced to 10% of the estimated peak load and maintained for another 30 s. Thereafter, the load was increased monotonically until failure. To observe the crack propagation, servo-hydraulic with a displacement control was adopted. The loading rate varied in the range of 1-2 mm/min and was adapted to each specimen so that the specimens failed within 10 min.

https://doi.org/10.52202/069179-0159

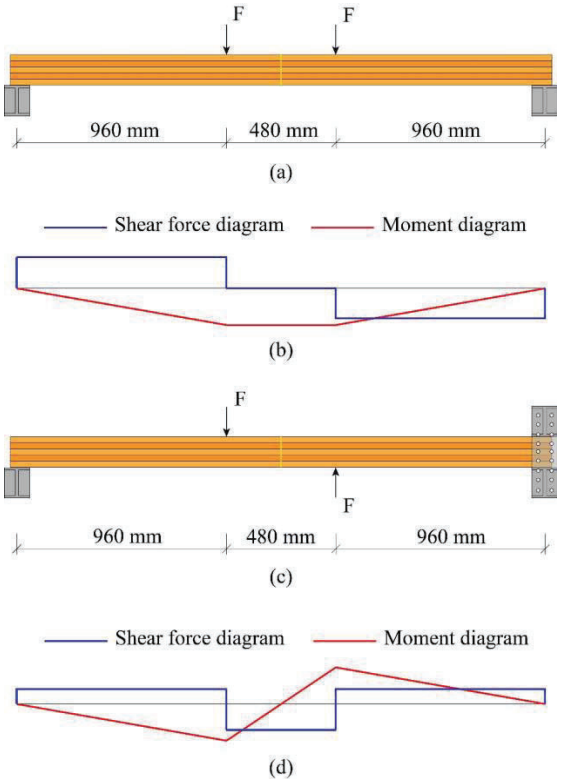

***Figure 5**: Bending and shear tests on panel-to-panel connections (a) Out-of-plane bending tests; (b) Moment and shear diagrams in bending tests; (c) Out-of-plane shear tests; (d) Moment and shear diagrams in the shear tests*

Four Linear Variable Differential Transformers (LVDTs) were mounted at the bottom of the specimens along the glue line to monitor the crack opening. LVDTs were mounted at two edges and locations of crack stoppers, as shown in Figure 7. The vertical deflection of the joint was measured by two LVDTs mounted on the top two edges.

After TS3 joints failed under bending, specimens SP1, SP2, SP5, SP6, and SP7 were re-tested under shear to determine the residual capacities of the secondary connections. The right hydraulic cylinder was kept in position by mounting the steel plates to the panel while the left hydraulic cylinder applied a downward force. The rightmost support was designed in such a manner that it can resist uplift forces. Under the new loading protocol, the joint in the middle was subjected to pure shear forces without any moment, as shown in Figure 5(d). For specimens SP3 and SP4, second bending tests on the failed TS3 joints were conducted to test the residual bending capacities of the secondary connections.

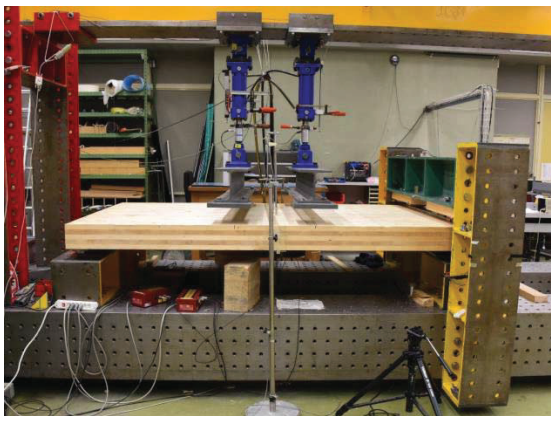

***Figure 6**: Laboratory bending test setup on panel-to-panel connections*

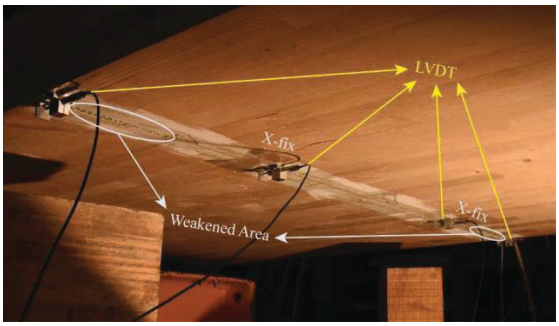

***Figure 7**: LVDTs mounted at bottom of specimens to measure crack opening*

2.4 RESULTS OF FIRST BENDING TESTS

Under bending, the failure of the TS3 joints started from one end at the location of the weakened area. The crack then appeared at the other end and finally in the middle of the joints. An example of crack opening at the bottom of the joint is shown in Figure 8 for SP2. It can be seen that there were three major cracks happening one after another in SP2 before the failure of the entire TS3.

The initial crack of TS3 did not cause the failure of the joint, but resulted in a drop of the applied load, as shown in the load-deflection relation of SP2 in Figure 9 where the vertical deflection was taken as the average of two deflections measured at two edges of the specimen. Following the first crack, the load rose again to the peak load. For most specimens, the second crack happened at the peak load. With more cracks appearing, the TS3 joints failed completely. The failure of a typical TS3 joint under bending is shown in Figure 10. No complete collapse of the specimens was observed due to the secondary connections.

https://doi.org/10.52202/069179-0159

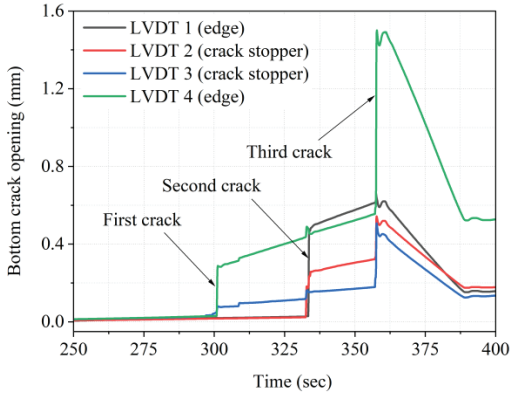

***Figure 8**: Bottom crack opening in SP2*

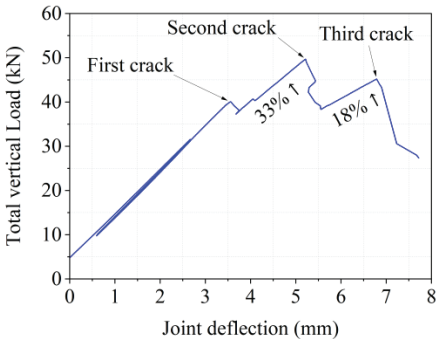

***Figure 9**: Load-deflection relation of SP2*

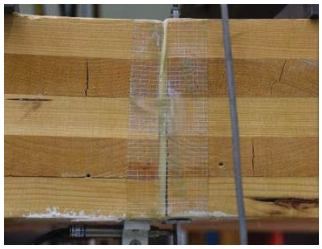

***Figure 10**: Failure of SP5 under bending*

Based on the crack opening and load-deflection relations of specimens, the number of cracks, the load level of each crack, and the load increase after each crack are listed in Table 1. The load level is the ratio between the load when the crack happened and the peak load. The load recovery represents the maximum increase of load following the load drop due to crack. Most specimens had 3-4 major cracks before TS3 failure. SP6 exhibited only two cracks while SP4 had five. It can also be observed that the peak load usually happened at the second crack except for SP5. The load recovery after each load drop indicates stress redistribution in the joints. On the contrary, a continuously decreasing load after the final crack suggests the complete failure of TS3. The most effective crack stopper was found in SP4 with two X-fix at the bottom, while the least effective crack stopper was found in SP6 which contained STS and vertical beech dowels.

***Table 1**: Effectiveness of crack stoppers*

	Crack openings	Load level	Load recovery after crack
SP1	1st	100%	1%
	2nd	100%	16%
	3rd	71%	/
SP2	1st	81%	33%
	2nd	100%	18%
	3rd	91%	/
SP3	1st	99%	1%
	2nd	100%	5%
	3rd	95%	6%
	4th	78%	/
SP4	1st	68%	52%
	2nd	100%	7%
	3rd	97%	17%
	4th	87%	19%
	5th	42%	/
SP5	1st	78%	16%
	2nd	82%	11%
	3rd	77%	34%
	4th	100%	/
SP6	1st	66%	63%
	2nd	100%	/
SP7	1st	85%	23%
	2nd	100%	10%
	3rd	73%	8%
	4th	69%	/

The mechanical properties of the panel-to-panel joints are listed in Table 2. P_{max} is the maximum total vertical load the specimens sustained during bending tests. Based on the maximum load, the moment capacity of TS3 joints can be determined as

$$M_{max} = \frac{P_{max} L_1}{2} \times \frac{2}{3} \quad (1)$$

where L_1 is the distance between loading point and the nearest support, which was 960 mm. The moment resistance has been normalized to 1 m width in Eq. (1). As shown in Table 2, the moment resistance of the joints was in the range of 11.3-20.6 kNm. As a reference, the design strength of C24 CLT is 72 kNm [15]. The lowest bending strength was found in SP5, which was attributed to the defects of TS3 joint. The failed section of TS3 in SP5 showed there was trapped air in the joint during TS3 application process.

The stiffness K of the joints was determined by calculating the slope of load-deflection relations of the specimens in the initial pre-loading phase. From Table 2, it can be observed that the stiffness of the joints showed less variation (COV=13.3%) than the moment resistance of the joints (COV=20.9%). Based on the joint stiffness (K in kN/mm), the apparent bending stiffness EI of the tested cross-section can be determined as:

$$EI = \frac{K}{48}(3L^2 - 4L_1^2)L_1 \quad (2)$$

https://doi.org/10.52202/069179-0159

where L is span which was 2.4 m. The apparent bending stiffness $(EI)_{ap}$ of C24 CLT under four-point bending load can be determined from shear analogy method as

$$(EI)_{ap} = \frac{(EI)_{eff}}{1 + \frac{24(EI)_{eff}}{(3L^2 - 4L_1^2)GA}} \quad (3)$$

where $(EI)_{eff}$ is the pure bending stiffness and GA is the term accounting for shear deformation. The determined bending stiffness of the TS3 joints according to Eq. (2) is in the range of 1122-1818 kNm^2 with an average value of 1560 kNm^2. The determined bending stiffness of C24 CLT according to Eq. (3) is 1916 kNm^2. It can be concluded that TS3 joints can reach more than 80% of the continuous CLT bending stiffness.

***Table 2**: Summary of test results*

	P_{max} kN	M_{max} kNm	K kN/mm	EI kNm^2	M_{re} kNm	V_{re} kN
SP1	52.4	16.8	9.6	1744	/	15.6
SP2	49.7	15.9	10.0	1818	/	58.5
SP3	42.2	13.5	8.1	1469	2.2	/
SP4	38.6	12.4	6.2	1122	3.7	/
SP5	35.4	11.3	8.6	1566	/	45.5
SP6	64.4	20.6	8.6	1558	/	46.8
SP7	37.7	12.1	9.1	1644	/	53.8

Note: P_{max} is the maximum total vertical load the specimens sustained during bending; M_{max} is the moment capacity of TS3 joints normalized to 1 m width; K is the stiffness of TS3 joints based on total vertical load and deflection; EI is the bending stiffness of TS3 joints normalized to 1 m width; M_{re} is the residual moment resistance of the secondary joints normalized to 1 m width; and V_{re} is the residual shear capacity of the secondary joints.

2.5 RESULTS OF SECONDARY TESTS

For specimens SP3 and SP4, bending tests were conducted again on the failed TS3 joints to test the residual moment capacities of STS and X-fix. The failure of X-fix under bending is shown in Figure 11(a) which shows the shear failure of plywood in the wedge and local shear failure of CLT. For the rest of the specimens, shear tests were conducted on the secondary connections and the shear failure of STS and X-fix under out-of-plane shear are demonstrated in Figure 11(b) and (c), respectively, from which the bending of screws, embedment of screws into wood, and sliding of X-fix can be observed.

The load-deflection relations of SP3 and SP4 under secondary bending are plotted in Figure 12. The moment resistances of two secondary connections are listed in Table 2 as M_{re}. While the moment resistances of STS and X-fix were both significantly lower than TS3, X-fix had a higher moment resistance than STS. More importantly, the failure of X-fix joint under bending was in a more ductile manner, as can be seen from the large deflection of the joint in Figure 12(b). The ductility came from bearing of wood fibres between CLT and X-fix.

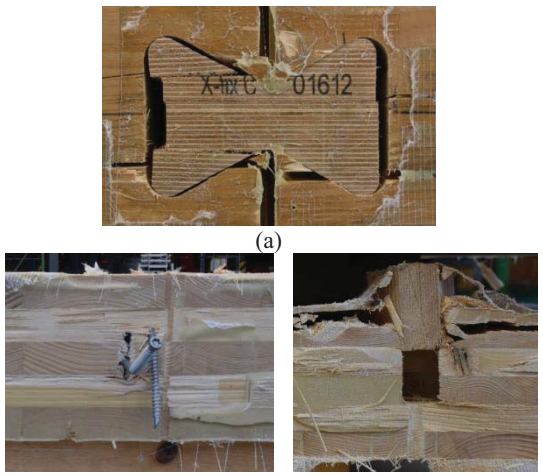

(a) (b) (c)

***Figure 11**: Failure of secondary connections (a) X-fix at the bottom of SP4 under bending (b) STS in SP5 under shear (c) X-fix in SP7 under shear*

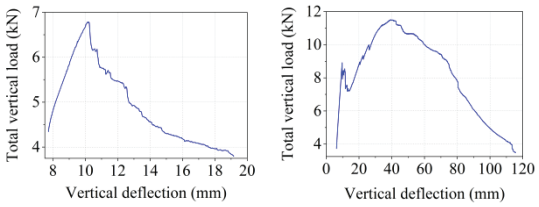

(a) (b)

***Figure 12**: Load-deflection relations in secondary bending tests on (a) STS in SP3 (b) X-fix in SP4*

The residual shear strengths of STS in SP1, SP5, and SP6, and X-fix in SP2 and SP7 are listed in Table 2 as V_{re}. The shear capacities of X-fix in SP2 and SP7 were similar, while the shear capacities of STS in SP5 and SP6 were close to each other. According to [16], the characteristic shear capacity of two pairs of WT-T screws is 19.3 kN which is less than half of the tested values of SP5 and SP6. It should be noted that X-fix connectors have no technical approval for out-of-plane shear loading. Nonetheless, the tests showed that the X-fix connectors had higher shear strength than STS. It is not obvious why the STS in SP1 had a much lower shear strength than the rest of the specimens. As the shear tests were conducted on the failed TS3 joints, it is possible that STS were already loaded in the first bending test.

3. ONGOING EXPERIMENTAL WORK

The experimental study discussed in Section 2 focused on the potential of using crack stoppers to prevent the complete collapse of floors with TS3 joints. The tests were limited to joints in the major strength direction under out-of-plane loading, while TS3 performances in minor strength direction of CLT and under in-plane loads were not investigated. Another critical property of the panel-to-panel connections is the ductility under in-plane and out-

https://doi.org/10.52202/069179-0159

of-plane loads, especially under seismic loads. However, the failure mode of the tested joints was brittle in general.

To address the brittle failure pattern of TS3, metal fasteners such as STS can be installed in a closer spacing than the tested specimens in this study, thus STS is not only used as crack stoppers after TS3 fails, but also as additional fasteners to provide ductility. A research program is underway at University of Northern British Columbia (UNBC) to study the performance of combined TS3-STS joints in connecting CLT panels. The testing program includes combined TS3-STS in both major and minor strength directions under in-plane and out-of-plane loads, as well as two test series under long-term bending load. Figure 13 depicts the proposed testing plan on CLT panel-to-panel connections. The complete testing matrix is shown in Table 3.

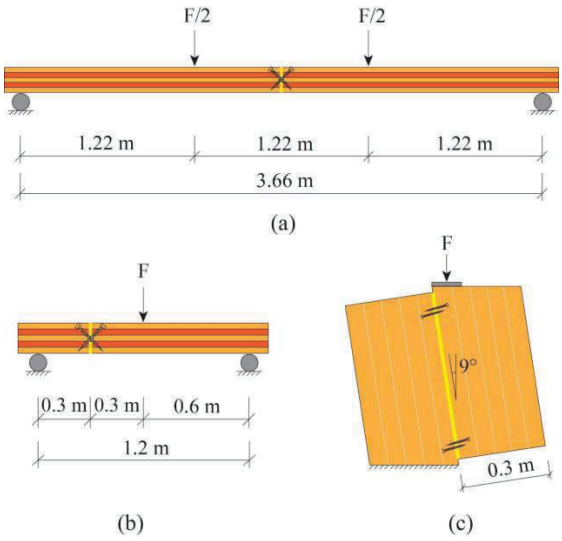

***Figure 13**: Proposed testing on CLT panel-to-panel connections (a) Out-of-plane bending test (b) Out-of-plane shear test (c) In-plane shear test*

Out-of-plane bending tests will be conducted on the panel-to-panel joints, see Figure 13(a). Four-point bending tests will create a pure bending zone for the joints. The variations of the specimens are the CLT layup (5-ply and 7-ply), joint type (TS3, STS, combined TS3 and STS), and panel orientation (major direction and minor direction). Most specimens will be tested under short-term loading while two series will be tested under long-term loading with load levels of 25% and 50% of the short-term peak load, respectively.

The shear tests on the joints will be conducted on a reduced variation of joints. The main variations in the shear tests are the CLT layup and orientation, while only the joints with combined TS3 and STS will be tested. The out-of-plane shear tests on the connections are shown in Figure 13(b). The load applies in the mid-span and the joint is located at a quarter span from the nearest support. This way, the joint is subjected to the highest shear force and reduced bending moment. The combined shear and bending moment mimic the loading case for the joints in real structures. The in-plane shear test is illustrated in Figure 13(c) where the specimen contains a single shear plane, and the vertical load aligns with the centre of the shear plane.

***Table 3** Test matrix of ongoing work*

Series	CLT ply	CLT direction	Load duration	Joint
B5PSA	5	//	ST	TS3
B5PSS1	5	//	ST	STS
B5PSAS1	5	//	ST	TS3+STS
B5PLAS1-1	5	//	LT	TS3+STS
B5PLAS1-2	5	//	LT	TS3+STS
B5TSA	5	⊥	ST	TS3
B5TSS1	5	⊥	ST	STS
B5TSAS1	5	⊥	ST	TS3+STS
B7PSA	7	//	ST	TS3
B7PSS2	7	//	ST	STS
B7PSAS2	7	//	ST	TS3+STS
B7TSA	7	⊥	ST	TS3
B7TSS2	7	⊥	ST	STS
B7TSAS2	7	⊥	ST	TS3+STS
S5PSAS1	5	//	ST	TS3+STS
S5TSAS1	5	⊥	ST	TS3+STS
S7PSAS2	7	//	ST	TS3+STS
S7TSAS2	7	⊥	ST	TS3+STS
I5PSAS1	5	//	ST	TS3+STS
I5TSAS1	5	⊥	ST	TS3+STS
I7PSAS2	7	//	ST	TS3+STS
I7TSAS2	7	⊥	ST	TS3+STS

Note: // and ⊥ represent the major and minor strength directions of CLT, respectively; ST stands for short-term loading; and LT stands for long-term loading.

In all the specimens, the width of CLT is 600 mm. STS are installed in pairs and inclined 45°. For each test series, six replicates will be tested. The connection stiffness, strength, and failure pattern will be evaluated, and then the characteristic values of connections will be provided for the engineering design of connections. The goal of the proposed research is to provide adequate technical guide for designers and engineers to use, thus promoting a growing application of mass timber panels in two-way flat slab floor systems.

4. CONCLUSIONS

The effectiveness of crack stoppers in preventing the collapse of TS3 joints was examined by testing seven panel-to-panel CLT connections under bending and shear. Test results showed promising performance of STS and X-fix as secondary connections in transmitting shear forces and bending moments after TS3 failure. Therefore, in floor construction, X-fix or STS can be used as a

temporary measure to connect CLT panels and hold the panels in position for TS3 applications. In the event of TS3 failure, these connections serve a second purpose as the backup system to maintain the integrity of the joint. Overall, X-fix showed better mechanical performance than pairs of STS as secondary connections. However, due to the limited number of specimens tested, no recommendation concerning the design of secondary connections can be provided. Ongoing experimental work will provide data for the robust design of TS3 joints.

ACKNOWLEDGEMENT

The research project on the crack stoppers was funded by Innosuisse and supported by Timber Structures 3.0 AG, Schilliger Holz AG, and Henkel & Cie AG. The research project was a collaboration between ETH Zurich and the Bern University of Applied Sciences. Funding for the research project on the hybrid joints has been sought from the Natural Sciences and Engineering Research Council of Canada for an Alliance project in collaboration between Timber Engineering Inc. and the University of Northern British Columbia and supported by Timber Structures 3.0 AG.

REFERENCES

[1] FPInnovations. Canadian CLT Handbook. Pointe-Claire, QC, Canada, 2019.

[2] A. Hossain, M. Popovski, T. Tannert. Cross-laminated timber connections assembled with a combination of screws in withdrawal and screws in shear. *Engineering Structures*, 168: 1–11, 2018.

[3] B. Taylor, A. R. Barbosa, A. Sinha. Cyclic performance of in-plane shear cross-laminated timber panel-to-panel surface spline connections. *Engineering Structures*, 218: 110726, 2020.

[4] ETA-18/0254 of 01.09.2020. European Technical Assessment for X-fix C. Austrian Institute of Construction Engineering, 2020.

[5] S. Zhang, Y. H. Chui. Characterizing flexural behaviour of panel-to-panel connections in cross-laminated timber floor systems. *Structures*, 28: 2047-2055, 2020.

[6] S. Franke, S. Zöllig. TS3 – A New Technology for Efficient Timber Structures. *Current Trends in Civil & Structural Engineering*, 4(4): 1-4, 2020.

[7] A. Hashemi, P. Quenneville, H. M. Bita, R. Malczyk, S. Varier, P. Zarnani. Application of resilient rocking cores in low damage mass timber structures: A case study. NZSEE Annual Conference, 2022.

[8] A. Hashemi, T. Fast, C. Dickof, R. Jackson, P. Fast, A. Dunbar, P. Zarnani, P. Quenneville. Seismic Resilient Mass Timber Structures with Damage-Avoidance Connections: Design Methods and Case Studies. SESOC conference, Hamilton, New Zealand, 2021.

[9] ANSI/APA PRG 320: Standard for Performance-Rated Cross-Laminated Timber. APA-The Engineered Wood Association, 2019.

[10] ETA-12/0373 of 03.11.2017. European Technical Assessment for Schmid screws. Austrian Institute of Construction Engineering, 2017.

[11] H. M. Bita, T. Tannert. Experimental Study of Disproportionate Collapse Prevention Mechanisms for Mass-Timber Floor Systems. Journal of Structural Engineering 146(2): 04019199, 2020.

[12] K. Voulpiotis, J. Köhler, R. Jockwer, A. Frangi. A Holistic Framework for Designing for Structural Robustness in Tall Timber Buildings. *Engineering Structures*, 227: 111432, 2021.

[13] K. Voulpiotis, S. Schär, A. Frangi. Quantifying Robustness in Tall Timber Buildings: A Case Study. *Engineering Structures*, 265: 114427, 2022.

[14] H. M. Bita. Disproportionate Collapse Prevention Analysis for Mid-rise Cross-Laminated Timber Platform-type Buildings. Thesis, University of British Columbia, 2019.

[15] EN 338: Structural timber - strength classes. European Committee for Standardization, 2016.

[16] ETA-12/0063 of 15 April 2019. European Technical Assessment for SFS Self-tapping Screws WT. DIBT, 2019.

[17] EN 26891. Timber structures - Joints made with mechanical fasteners - General principles for the determination of strength and deformation characteristics. European Committee for Standardization, 1991.

https://doi.org/10.52202/069179-0159

World Conference on Timber Engineering Oslo 2023

EXPERIMENTAL INVESTIGATIONS ON THE STIFFNESS OF STEEL-TIMBER DOWEL-TYPE CONNECTIONS IN BEECH LVL

Lea Buchholz[1], Ulrike Kuhlmann[2]

ABSTRACT: With the increasing complexity of timber structures, accurate computational prediction of the load-deformation behaviour of joints is becoming more important for design. In particular, the initial stiffness is a relevant parameter. Therefore, a detailed knowledge of the parameters influencing the connection stiffness is required, but is currently not available for hardwoods. A comprehensive database on the load-deformation behaviour of steel-timber dowel-type connections in beech LVL is being developed on the basis of experimental tests currently being carried out at the University of Stuttgart. The aim is to enable the efficient use of hardwoods in high-performance yet easy-to-manufacture connections by realistically predicting connection stiffness. This paper will give an overview on the first results.

KEYWORDS: Steel-timber dowel-type connections, connection stiffness, beech LVL, experimental testing

1 INTRODUCTION

In times of climate change, timber structures are coming under increasing political and social focus as a sustainable and resource-efficient construction method. At the same time, the forest structure in Germany is changing due to extended drought, with the high proportion of spruce being replaced mainly by beech. As a result, beech will have to be increasingly used in construction practice. The prerequisite for this is a reliable and economical design, also for hardwoods. In particular, the prediction of the load-deformation behaviour of high-performance joints is crucial for the design of complex timber structures. However, the current database on the connection stiffness in hardwoods is far too small to derive reliable predictions.

Therefore, the research project "Innovative timber joints by modelling the stiffness for high-performance timber structures made of hard- and softwood" [1] was started at the Institute of Structural Design at the University of Stuttgart in 2021. The aim is to increase the database of stiffness values of steel-timber dowel-type connections in beech laminated veneer lumber (beech LVL) through experimental investigations. This will enable more accurate predictions in order to provide design recommendations for the new version of Eurocode 5 [2].

This paper deals with the first results of these experimental investigations. After an overview of the current normative regulations for stiffness calculation and the state of the art, the test programme and setup as well as the geometry and the material of the above-mentioned tests are described. Afterwards, the first experimental results are presented and discussed.

2 STATE OF THE ART

For the determination of the slip modulus K_{ser} for steel-timber dowel-type connections in the serviceability limit state (SLS), Equation (1) is given in Eurocode 5 [2]. Thus, the slip modulus depends only on the timber density ρ and the fastener diameter d. Other influencing factors such as the load-to-grain angle, the number of fasteners and the slenderness of the connection (failure mode) are not considered.

$$K_{ser,EC5} = \frac{2}{23} \cdot \rho_m^{1.5} \cdot d \tag{1}$$

In comparison, the Swiss standard SIA 265 [3] defines the above-mentioned slip modulus K_{ser} according to Equations (2) and (3). Unlike Eurocode 5, a distinction is made between fasteners loaded parallel and perpendicular to the grain.

$$K_{ser,0,SIA} = 6 \cdot \rho_k^{0.5} \cdot d^{1.7} \tag{2}$$

$$K_{ser,90,SIA} = 3 \cdot \rho_k^{0.5} \cdot d^{1.7} \tag{3}$$

Several studies (see [4]-[9]) have shown that the stiffness calculated according to Eurocode 5 [2] is quite inadequate, even for softwood connections. First experimental investigations on steel-timber dowel-type connections in beech glulam and LVL mainly examined the load-bearing capacity (see [10]-[12]). This is underestimated by approximately 33 % for connections in beech glulam [10]. Kobel et al. [12] have shown that veneer cross-layers have a positive effect on the load-bearing capacity of connections in beech LVL by preventing the timber from

[1] Lea Buchholz, M.Sc., University of Stuttgart, Institute of Structural Design, Stuttgart, Germany, lea.buchholz@ke.uni-stuttgart.de
[2] Prof. Dr.-Ing. Ulrike Kuhlmann, University of Stuttgart, Institute of Structural Design, Stuttgart, Germany, sekretariat@ke.uni-stuttgart.de

https://doi.org/10.52202/069179-0160

Table 1: *Load-bearing capacity F_{max}, initial stiffness K_{ser} and reloading stiffness K_e from tensile tests on steel-timber dowel-type connections (d = 16 mm) [4]*

Series	Mean values			COV [%]		
	F_{max} [kN] (F_{test} / F_{EC5})	K_{ser} [kN/mm] (K_{test} / K_{EC5})	K_e [kN/mm] (K_{test} / K_{EC5})	F_{max}	K_{ser}	K_e
G-SD16 11 0 1_**GL 24h**	47.9 (114 %)	33.0 (138 %)	57.7 (175 %)	4.54	33.1	20.4
G-SD16 11 0 1_**GL 75**	89.4 (154 %)	55.5 (88 %)	88.7 (160 %)	1.49	25.5	18.4

splitting. As a result, higher loads can be achieved with significantly improved ductile behaviour. The aim of the research project presented in this paper [1],[13] is therefore to verify the positive influence of cross-layers on the stiffness. Initial investigations on the stiffness of steel-timber dowel-type connections in beech LVL have already been carried out by Misconel et al [14]. According to this, the formula for stiffness calculation in Eurocode 5 [2] is insufficient for connections in beech LVL. Comparable results were obtained in tests carried out at the University of Stuttgart as part of IGF project no. 20625 N [4]. In addition to a large number of tests on steel-timber dowel-type connections in spruce glulam (GL 24h and GL 28h), tests were also carried out on 12 connections in beech LVL. Table 1 shows the results of two series of tests on spruce glulam and beech LVL and compares them with the corresponding values determined according to Eurocode 5 [2]. The average load-bearing capacity F_{max} of the connection in beech LVL is underestimated by 54 %. This tendency is also in line with the results of Franke & Franke [10]. It is also shown that the initial stiffness K_{ser} is better represented normatively than the reloading stiffness K_e, which is underestimated by 60 % in beech LVL. However, the large scatter of the test results with coefficients of variation (COV) of around 25 % and the small number of tests do not yet allow any precise recommendations to be made with regard to the computational prediction of the connection stiffness in beech LVL. Fundamental investigations of the stiffness of steel-timber dowel-type connections in beech LVL are therefore necessary and are being carried out in an ongoing research project at the University of Stuttgart [1]. The first results of these investigations are presented in this paper.

3 EXPERIMENTAL RESEARCH

3.1 TEST PROGRAMME AND SETUP

Based on a completed research project at the Institute of Structural Design [4],[5], which mainly investigated the stiffness of dowel-type connections in glulam made of spruce, a further 172 tensile tests are carried out on steel-timber dowel-type connections in beech LVL. The aim is to obtain a comprehensive database on the load-deformation behaviour of dowel-type connections. Figure 1 shows the test setup for the single fastener specimens with a load-to-grain angle α of 0° (top) and 90° (bottom). All tensile tests with grain parallel loading are double symmetric, allowing two connections to be tested simultaneously. Therefore, a total of four displacement transducers per specimen (two per connection) were applied. Only two displacement transducers are used for the tensile tests with a load perpendicular to the grain, as the modified test setup tests a single connection. The displacement transducers measure the relative deformation between the slotted-in steel plate and the timber at the level of the centre line of the dowel.

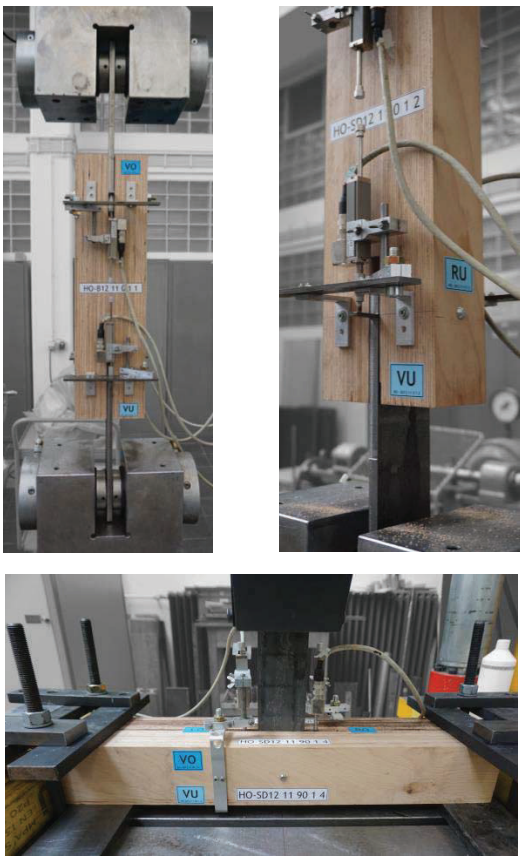

Figure 1: *Test setup for the specimens with a single fastener and load parallel to the grain (top) and with a load-to-grain angle α = 90° (bottom)*

The experimental programme is given in Table 3. In addition to the number of fasteners, the type and diameter $Ø$ of the fasteners, the load-to-grain angle α, the type of reinforcement of the timber element and the side member thickness $t_{1\text{-}3}$ are varied. The reinforcement of the timber is partly achieved by fully threaded screws and partly by internal reinforcement using veneer cross-layers (GL 60Q). The designation of the test specimens is designed as:

https://doi.org/10.52202/069179-0160

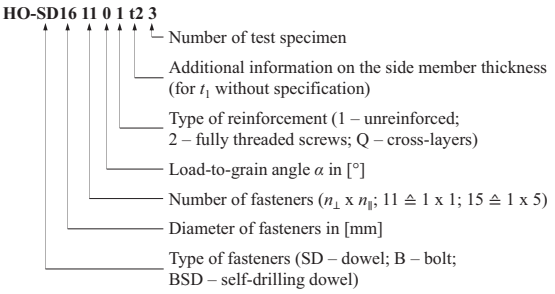

The different side member thicknesses $t_{1\text{-}3}$ are intended to induce all three possible European Yield Model (EYM) failure modes according to Eurocode 5 [2] in the tests. For this purpose, preliminary numerical investigations were carried out using a Beam-on-Foundation (BoF) model already implemented in RFEM (Dlubal) (see [4]-[6]). Figure 2 shows as an example the numerically calculated deformation of the dowel with a diameter of 16 mm plotted over the width of the test specimen for different side member thicknesses with a maximum deformation of the connection of 4 mm.

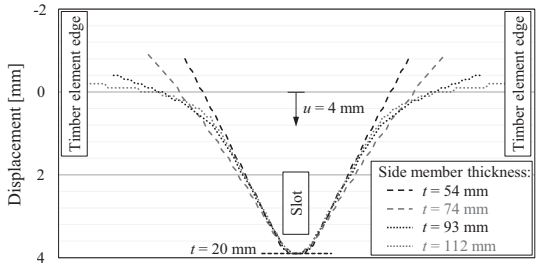

Figure 2: *Deformation of the dowel (Ø = 16 mm) calculated with RFEM plotted over the width of the test specimen for various side member thicknesses (connection deformation 4 mm)*

Using the BoF model, a side member thickness of 20 mm leads to embedment failure in timber (t_1). As the side member thickness increases, the transition from initially one (t_2) to two (t_3) plastic hinges per shear plane can be observed. The BoF model was also used to estimate the load-bearing capacity F_{est} of the connections, which is required for the loading and evaluation according to EN 26891 [15]. The tests were carried out displacement-controlled.

3.2 GEOMETRY AND MATERIAL

An example of a tensile test specimen parallel to the grain with 1 x 5 fasteners per connection and reinforcement with fully threaded screws is shown in Figure 3. Due to the symmetrical design, there are two sets of data for each specimen for the evaluation of the connection stiffness. The *timber elements* with a grade of GL75 and GL 60Q were prefabricated with a fully automated joinery machine. The slots for the slotted-in steel plates were made with a width of 14 mm. Fastener holes were pre-drilled to the appropriate nominal diameter from both sides of the timber member. ASSYplus VG 4 CSMP (countersunk head) type screws according to ETA-11/0190 [16] with diameters of 6 mm and 8 mm were partially used for reinforcement. The fully threaded screws were also pre-drilled with diameters of 5 mm and 7 mm to facilitate insertion. For technical reasons, the diameter of the boreholes was slightly larger than recommended in [16]. In addition to screw reinforcements, some specimens were also reinforced with veneer cross-layers. For this purpose, standard Q-boards in beech LVL were produced with a thickness of 42 mm and a cross-layer content of 14 %. Several Q-boards were glued with melamine to the required cross sections.

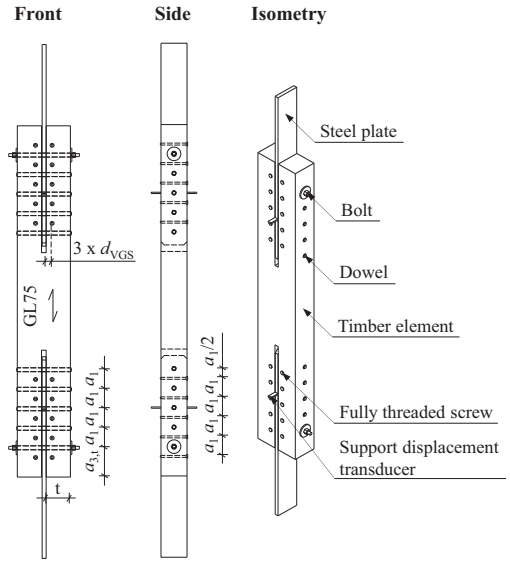

Figure 3: *Example of a tensile test parallel to the grain specimen with 1 x 5 fasteners per connection and screw reinforcement*

The *steel plates* with a grade of S355J2 were manufactured with a thickness of 12 mm. The *fasteners* ordered in S235JR (electrolytically galvanised) steel were made from cold drawn bars. Tensile tests were carried out according to EN ISO 6892-1 [17] on five to six randomly selected samples for each diameter to determine the material properties of the fasteners. The results are summarised in Table 2. Due to the cold forming process of the steel, the technical elastic limit of 0.2 % was taken as yield strength. Compared to the normative values according to EN 1993-1-1 [18], there is a clear overstrength of the steel, where the experimental tensile strength is up to 690 N/mm². This overstrength is also described in the literature (see [4],[5],[19]-[21]).

Table 2: *Mean values of fastener material properties from tensile tests according to EN ISO 6892-1 [17]*

Diameter d [mm]	**Yield strength** $R_{p0.2}$ [N/mm²]	**Tensile strength** R_m [N/mm²]	**MOE** [N/mm²]
8	588.1	627.0	208,540
12	668.6	689.8	210,550
16	568.5	598.0	209,560
20	444.2	500.5	208,500

https://doi.org/10.52202/069179-0160

Table 3: *Experimental programme of tensile tests on steel-timber dowel-type connections in beech LVL*

Fastener	$Ø$ [mm]	$n_\perp$ x $n_\parallel$	α [°]	Reinforcement	Timber grade	Side member thickness
Single, dowel	8 12 16 20	1 x 1	0 90	- Fully threaded screws Veneer cross-layers	GL75 GL 60Q	t_1 t_2 t_3
Single, bolt	8 12 16 20	1 x 1	0	-	GL75	t_1
Group, mixed*	8 12 16 20	1 x 3 1 x 5 2 x 3	0	- Fully threaded screws Veneer cross-layers	GL75 GL 60Q	t_1
Self-drilling dowel*	7	1 x 3	0	-	GL75	t_1

* *Not content of this paper*

4 RESULTS OF THE CONDUCTED TENSILE TESTS

4.1 GENERAL OVERVIEW

Currently (February 2023), 112 out of 172 planned tests have been carried out. The tests of connections with groups of fasteners are planned to be conducted in spring 2023. Table 4 summarises the already experimentally determined initial stiffnesses $K_{ser,test}$ for connections with single fasteners and compares them with the stiffnesses calculated according to Eurocode 5 [2].

4.2 FAILURE MODES

The failure mode of the connections depends, on one hand, on the side member thickness (EYM). On the other hand, the type of fastener (dowel or bolt), the load-to-grain angle α and the timber reinforcement also influence the load-displacement behaviour in the range of the ultimate limit state (ULS).

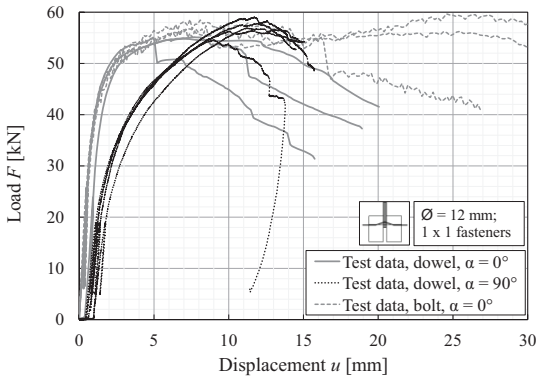

Figure 4: *Load-displacement curves for connections with single fasteners (dowels and bolts) of 12 mm diameter and loading parallel and perpendicular to the grain*

Figure 4 shows the load-displacement curves for connections with single fasteners (dowels and bolts) of 12 mm diameter and loading parallel and perpendicular to the grain. The load-bearing capacity is in a similar range for all of the connections. However, there is a pronounced plastic plateau for connections loaded parallel to the grain rather than perpendicular to the grain. This applies in particular to connections using bolts due to the rope effect.

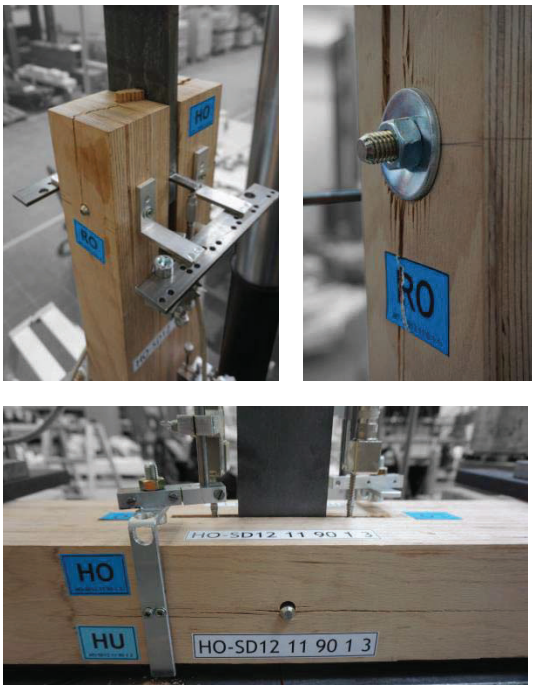

Figure 5: *Top left: Splitting of the timber after ductile deformation of the dowel (α = 0°); Top right: Deformation of a bolt and the washer (α = 0°); Bottom: Lateral splitting of the timber after ductile deformation of the dowel (α = 90°)*

https://doi.org/10.52202/069179-0160

The failure modes associated with the load-displacement curves (Figure 4) are shown in Figure 5. The washer of the bolt is deformed and slightly pressed into the timber (Figure 5, top right). Compared to the failure of bolted connections in spruce glulam due to head pull-through (see [22]), the deformations at the washer in beech LVL are significantly smaller. The splitting and partial block shear failure of the timber occurs after the formation of plastic hinges in the dowel (Figure 5, top left) as well as in the bolt for large side member thicknesses and loading parallel to the grain. Figure 6 shows the deformation figure of a dowel after these tests. Two plastic hinges occured per shear plane. There is also a clear indentation in the area of the steel plate. Shearing-off of the dowels, as observed by Franke & Franke [11], did not occur in any of the tests. In contrast, the connections loaded perpendicular to the grain showed lateral splitting of the timber (Figure 5, bottom). This results in a relatively brittle failure after about 11 mm of deformation at the dowel. The splitting of the timber can be prevented by reinforcing the timber with screws or veneer cross-layers. Often no cracks were externally visible, especially on specimens with cross-layers. Plastic deformations of up to 18 mm were achieved in these tests with a 12 mm diameter fastener.

Table 4: *Initial stiffness $K_{ser,test}$ and comparison with Eurocode 5 [2] for connections with single fasteners*

Series	**Mean** [kN/mm] ($K_{ser,test}$ / K_{EC5})	**SD** [kN/mm]	**COV** [%]
HO-SD8 11 0 1	26.9 (85 %)	6.3	23.4
HO-B8 11 0 1	30.8 (98 %)	7.4	24.2
HO-SD8 11 0 1 t2	22.8 (72 %)	4.4	19.5
HO-SD8 11 0 1 t3	19.5 (62 %)	4.6	23.5
HO-SD8 11 0 1 2	22.0 (70 %)	6.0	27.2
HO-SD8 11 0 Q	17.0 (54 %)	3.3	19.1
HO-SD8 11 90 1	12.9 (41 %)	2.5	19.3
HO-SD8 11 90 Q	12.5 (40 %)	2.1	16.6
HO-SD12 11 0 1	48.2 (102 %)	3.7	7.7
HO-B12 11 0 1	49.9 (106 %)	4.0	8.0
HO-SD12 11 0 1 t2	52.3 (111 %)	9.5	18.2
HO-SD12 11 0 1 t3	45.5 (96 %)	7.6	16.6
HO-SD12 11 0 1 2	40.6 (86 %)	3.4	8.5
HO-SD12 11 0 Q	49.0 (104 %)	8.5	17.4
HO-SD12 11 90 1	24.9 (53 %)	1.8	7.1
HO-SD12 11 90 Q	26.4 (56 %)	2.8	10.6
HO-SD16 11 0 1	76.0 (121 %)	3.4	4.5
HO-B16 11 0 1	74.7 (119 %)	4.7	6.3
HO-SD16 11 0 1 t2	84.9 (135 %)	7.7	9.1
HO-SD16 11 0 1 t3	71.3 (113 %)	4.9	6.9
HO-SD16 11 0 1 2	68.8 (109 %)	10.4	15.2
HO-SD16 11 0 Q	70.7 (112 %)	2.5	3.5
HO-SD16 11 90 1	32.8 (52 %)	8.6	26.1
HO-SD16 11 90 Q	37.0 (59 %)	6.3	17.1
HO-SD20 11 0 1	74.8 (95 %)	7.1	9.4
HO-B20 11 0 1	83.4 (106 %)	12.2	14.7
HO-SD20 11 0 1 t2	104.1 (132 %)	6.3	6.0
HO-SD20 11 0 1 t3	89.6 (114 %)	9.0	10.0
HO-SD20 11 0 1 2	81.3 (103 %)	7.6	9.3
HO-SD20 11 0 Q	121.1 (154 %)	5.1	4.2
HO-SD20 11 90 1	46.9 (60 %)	3.0	6.3
HO-SD20 11 90 Q	62.4 (79 %)	7.7	12.4

Figure 6: *Deformation figure of a dowel after testing (specimen HO-SD20 11 0 Q 3 Top)*

4.3 FACTORS INFLUENCING THE INITIAL STIFFNESS

4.3.1 Diameter

The diameter of the fasteners is already included as an important parameter in the Equations for determining the slip modulus according to Eurocode 5 [2] as well as to SIA 265 [3]. Figure 7 shows the initial stiffness K_{ser} plotted against the fastener diameter d. The test data of the connections loaded parallel to the grain and for all three different types of reinforcement are represented by black crosses (test series for connections with single fasteners). It is worth noting that the connections using fasteners of 20 mm diameter and reinforced with cross-layers achieved significantly higher stiffnesses compared to the other tests. While the dashed black trend line is derived from the data points of all the tests mentioned, the solid trend line is derived by neglecting the circled data points of the connections reinforced with cross-layers. These trend lines are compared with the results obtained from

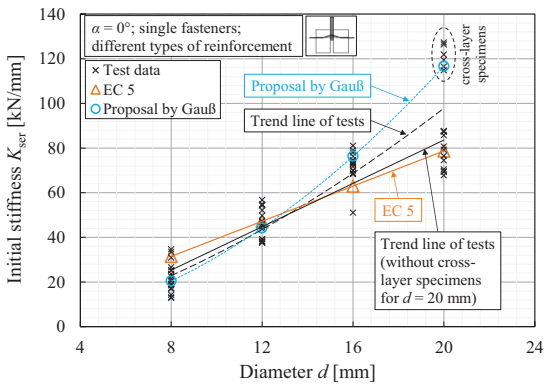

Figure 7: *Influence of the fastener diameter d on the initial stiffness K_{ser} and comparison of the test data with stiffnesses according to Eurocode 5 and to a proposal by Gauß [5],[6]*

https://doi.org/10.52202/069179-0160

the calculated stiffness values according to Eurocode 5 [2] for the corresponding diameters (orange line). The results of Eurocode 5 [2] agree relatively well with the solid trend line of the test data without the circled data points. However, if these data points are included in the trend line, the initial stiffness K_{ser} is underestimated for the tests with a fastener diameter of 16 mm and 20 mm. For this reason, a second comparison with the Equation according to Eurocode 5 [2] modified by Gauß [5],[6] (blue dotted line) is shown. In tests on steel-timber dowel-type connections in spruce glulam, Gauß [5],[6] showed that there is more a quadratic rather than a linear effect of fastener diameter on initial stiffness. For this context, the following proposal for the calculation of the stiffness of steel-timber dowel-type connections based on the Equation according to Eurocode 5 [2] is given by Gauß in [5],[6]:

$$K_{ser,proposal,Gauß} = \frac{2}{230} \cdot \rho_m^{1.5} \cdot d^{1.9} \quad (4)$$

For this approach, the increase in stiffness as the diameter increases can be better described by a trend line which is a power law of the form $y = cx^b$ (blue dotted line). A comparison of the stiffnesses calculated by this approach for the corresponding diameters with the test data in Figure 7 (incl. circled data points) shows, that the curve progression fits well for fastener diameters smaller than or equal to 12 mm. For larger diameters, the proposal according to Gauß [5],[6] overestimates the mean values of the stiffnesses derived from the tests. Maybe an independent treatment of cross-layer specimen should be considered.

4.3.2 Load-to-grain angle

The load-to-grain angle α is not yet considered in the calculation of the slip modulus K_{ser} according to Eurocode 5 [2]. However, tests on steel-timber dowel-type connections in spruce glulam carried out by Kuhlmann & Gauß [5] have shown that there is a non-negligible influence on the stiffness of the connection. For a load perpendicular to the grain, these results suggest that the stiffness is only half of that for a load parallel to the grain, as already considered in the SIA 265 [3]. This relationship is now to be verified for the connections in beech LVL as well. Table 5 indicates the ratios of the initial stiffness K_{ser} for load-to-grain angles of 90° and 0° for all the diameters investigated. A distinction is made between unreinforced connections and connections reinforced with cross-layers. It becomes apparent that for most of the test series the stiffness decreases by about 50 % for a load perpendicular to the grain as compared to a parallel loading. The higher ratios of the 8 mm diameter reinforced series and the 20 mm diameter unreinforced series can be explained by the fact that the mean stiffness values of the respective tests with a load-to-grain angle of 0° are lower than expected. It is also worth mentioning that the decrease in stiffness applies equally to both the unreinforced series as well as the series reinforced with cross-layers. Therefore, a reduction of the initial stiffness by 50 % for a load perpendicular to the grain should also be discussed for connections in hardwood.

Table 5: *Ratios of initial stiffness K_{ser} for load-to-grain angles $\alpha = 90°$ and $\alpha = 0°$ for unreinforced connections and connections with cross-layers*

Diameter	Unreinforced	Cross-layers
d [mm]	$K_{ser,90}/K_{ser,0}$	$K_{ser,90}/K_{ser,0}$
8	0.48	0.74
12	0.52	0.54
16	0.43	0.52
20	0.63	0.52

4.3.3 Side member thickness

Figure 8 illustrates the load-displacement curves of connections with a single dowel of 8 mm diameter and a load parallel to the grain for all three side member thicknesses $t_{1\text{-}3}$ tested. The three different failure modes for steel-timber dowel-type connections can be clearly identified in the load-deformation behaviour. There is a brittle behaviour due to embedment failure and splitting in timber with small side member thicknesses. As the side member thickness increases and plastic hinges are formed in the dowel, a plastic plateau developed and a ductile load-bearing behaviour was achieved. It is noticeable that especially for the large side member thickness t_1 the load can be increased even further in the area of the plastic plateau. This is a typical behaviour for dowel-type connections in hardwood and was also observed by Kuhlmann & Gauß [4].

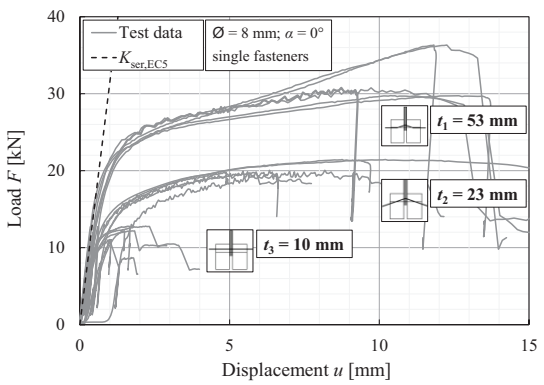

Figure 8: *Load-displacement curves of connections with a single fastener of 8 mm diameter and a load-to-grain angle α of 0° for various side member thicknesses $t_{1\text{-}3}$*

The effect of the side member thickness on the load-displacement behaviour in the range of the SLS is significantly smaller. However, as shown in Table 4, there is a tendency for the initial stiffness to decrease with decreasing side member thickness.

4.3.4 Type of fastener

In addition to connections with dowels, connections with bolts were also tested. Table 4 shows that there is a trend towards a slight increase in initial stiffness for connections using bolts. Nevertheless, the effect of the different types of fasteners is almost negligible. Similar to the side member thickness, the type of fastener has a greater effect on the load-displacement behaviour in the area of the plastic plateau due to the rope effect.

https://doi.org/10.52202/069179-0160

4.3.5 Reinforcement

Unreinforced connections, connections reinforced with fully threaded screws as well as with veneer cross-layers were tested. It was expected that the reinforcement methods would lead to an increase in stiffness. However, the results according to Table 4 do not show a clear relationship between the reinforcement and the initial stiffness. In some cases, even higher stiffnesses were achieved for unreinforced connections. There is currently no explanation for this unexpected effect. However, the progression of the load-displacement curve in the service load range for connections with cross-layers differs from that of unreinforced connections. Figure 9 shows the load-displacement curve of one of the specimens with cross-layers.

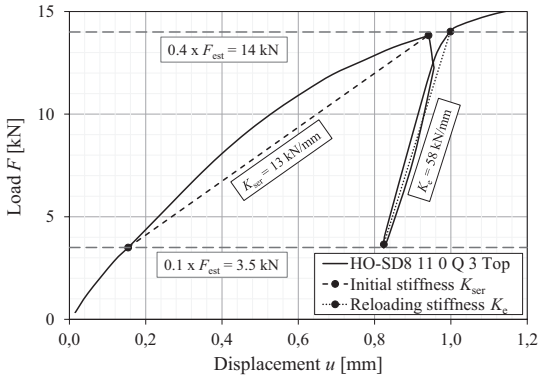

Figure 9: *Load-displacement curve in the service load range and evaluation of the stiffnesses K_{ser} and K_e for the test HO-SD8 11 0 Q 3 Top*

The initial stiffness K_{ser} is evaluated according to EN 26891 [15] by the slope of the curve between 10 % and 40 % of the estimated maximum load F_{est}. It is noticeable that for some connections with cross-layers, the load-displacement curve in this area is not linear but has a convex shape. As a result, the stiffness of these connections is clearly higher in the range between 10 % and 30 % of F_{est} (not shown in Figure 9). However, this cannot be taken into account in the evaluation.

5 CONCLUSIONS

Accurate computational prediction of the load-deformation behaviour of joints in timber is becoming increasingly important for the economic design of complex timber structures. In particular, the connection stiffness is a relevant parameter. Therefore, a detailed knowledge of the parameters influencing the connection stiffness is required, but is currently not available for hardwoods. In this paper, first investigations of a large number of tests on steel-timber dowel-type connections in beech LVL are evaluated and discussed regarding the initial stiffness K_{ser}. An overview of the Equations given in Eurocode 5 [2] and SIA 265 [3] for the calculation of the slip modulus shows that the Equations depend on only a few parameters, such as the timber density and the fastener diameter. In addition, the Swiss standard [3] distinguishes between loading parallel and perpendicular to the grain. This paper summarises several studies indicating that the stiffness calculated according to Eurocode 5 [2] is relatively deficient, even for softwood connections. Recommendations from these studies suggest that additional factors should be considered, such as load-to-grain angle and group effect.

The aim of the investigations presented in this paper is thus to determine the factors influencing the stiffness of connections in beech LVL and to compare the results with the Equation according to Eurocode 5 and with the recommendations given in the literature. The test results indicate, in line with other studies, that there is a large effect of the load-to-grain angle. For most of the test series, the stiffness is reduced by approximately 50 % for a load perpendicular to the grain as compared to a parallel load. Therefore, the implementation of a reduction factor as in SIA 265 [3] of about 0.5 for a load perpendicular to the grain should also be discussed for connections in hardwood. Furthermore, the fastener diameter is an important parameter whose effect on the stiffness tends to be normatively (according to Eurocode 5 [2]) underestimated in the tests, especially for larger diameters. A possibility to better represent the influence of the diameter is to modify the Equation in the Eurocode 5 [2], as proposed by Gauß [5],[6]. The exact value of the exponent implemented in this proposal for the diameter should be investigated in more detail by comparing a large number of experimental data with connections in soft- and hardwoods. For the other parameters investigated, the changes in stiffness did not have a clear trend. For example, there was no clear relationship between the reinforcement and the initial stiffness. In some cases, contrary to expectations, even higher stiffnesses were achieved for unreinforced connections. The type of fastener and the side member thickness have little effect on stiffness, but a greater effect on the development of the plastic plateau and the ductility of the connection.

Within the framework of the current research project, additional tests with groups of fasteners will be carried out in order to be able to estimate the influence of a possible group effect on the stiffness. Furthermore, all test results should also be evaluated in terms of the reloading stiffness K_e, as this may also be relevant for practical applications. The test results will therefore help to increase the data base on the stiffness of dowel-type connections, particularly for hardwoods, and thus enable their efficient use.

ACKNOWLEDGEMENT

This project is supported by the *Ministry of Food, Rural Affairs and Consumer Protection* of the State of Baden-Württemberg as part of the "*Timber Building Initiative*". We would also like to thank Pollmeier Massivholz GmbH & Co. for providing the beech LVL and Adolf Würth GmbH & Co. KG for donating the screws and self-drilling dowels.

REFERENCES

[1] Kuhlmann, U.; Buchholz, L.: *Innovative Holzknoten durch Modellierung der Steifigkeit für leistungsfähige Holztragwerke aus Laub- und Nadelholz (in German).* Research project of the „Timber Building Initiative“ of the Ministry of Food, Rural Affairs and Consumer Protection of Baden-Württemberg, Institute of Structural Design, University of Stuttgart, ongoing research project since 2021.

[2] EN 1995-1-1: *Eurocode 5: Design of timber structures – Part 1-1: General – Common rules and rules for buildings.* European Committee for Standardization (CEN), Brussels, Belgium, 2004 + AC:2006 + A1:2008.

[3] SIA 265: *Timber Structures.* Schweizerischer Ingenieur- und Architektenverein (SIA), Zurich, Switzerland, 2021.

[4] Kuhlmann, U.; Gauß, J.: *Wirtschaftliche Dimensionierung von Holztragwerken durch leistungsfähige Stahl-Holz-Stabdübelverbindungen (in German).* IGF research project No. 20625 N (AiF/iVTH), University of Stuttgart, Final report, Publication of Institute of Structural Design no. 2021-49X, 2019-2021.

[5] Kuhlmann, U.; Gauß, J.: *Stiffness of Steel-Timber Dowel Connections – Experimental and Numerical Research.* In: International Network on Timber Engineering, INTER, 54-7-9, Online-Meeting, Institute for Structural Design, University of Stuttgart, 2021.

[6] Gauß, J.: *Zum Trag- und Verformungsverhalten von Stahl-Holz-Stabdübelverbindungen (in German).* Dissertation, University of Stuttgart, Institute of Structural Design, 2023, in preparation.

[7] Jockwer, R.; Caprio, D.; Jorissen, A.: *Evaluation of parameters influencing the load-deformation behaviour of connections with laterally loaded dowel-type fasteners.* Wood Material Science & Engineering 17 (2022), no. 1, pp. 6-19. DOI: https://doi.org/10.1080/17480272.2021.1955297

[8] Sandhaas, C.; Van de Kuilen, J.-W. G.: *Strength and stiffness of timber joints with very high strength steel dowels.* Engineering Structures 131 (2017), pp. 394-404. DOI: https://doi.org/10.1016/j.engstruct.2016.10.046

[9] Dorn, M.; De Borst, K.; Eberhardsteiner, J.: *Experiments on dowel-type timber connections.* Engineering Structures 47 (2013), pp. 67-80. DOI: http://dx.doi.org/10.1016/j.engstruct.2012.09.010

[10] Franke, S.; Franke, B.: *Steel dowel type connections in beech hardwood.* In: World Conference on Timber Engineering, WCTE, Online-Meeting, 2021.

[11] Franke, S.; Franke, B.: *Bemessung von Stabdübelverbindungen in Buchen-Brettschichtholz (in German).* Bautechnik 97 (2020), special issue „Holzbau“, pp. 35-43. DOI: https://doi.org/10.1002/bate.201900100

[12] Kobel, P.; Frangi, A.; Steiger, R.: *Timber trusses made of European beech LVL.* In: World Conference on Timber Engineering, WCTE, Vienna, 2016.

[13] Buchholz, L.; Kuhlmann, U.: *Experimentelle Untersuchungen an Stahl-Holz-Stabdübelverbindungen in Buchen-Furnierschichtholz (in German).* In: Kuhlmann, et al. (Ed.), Holzbau Forschung und Praxis, pp. 53-60, 2022.

[14] Misconel, A.; Ballerini, M.; Van de Kuilen, J.-W.: *Steel-to-timber joints of beech-LVL with very high strength steel dowels.* In: World Conference on Timber Engineering, WCTE, Wien, 2016.

[15] EN 26891: *Timber structures – Joints made with mechanical fasteners – General principles for the determination of strength and deformation characteristics.* European Committee for Standardization (CEN), Brussels, Belgium, 1991.

[16] ETA-11/0190: *Self-drilling screws as timber fasteners.* Adolf Würth GmbH & Co. KG, Deutsches Institut für Bautechnik (DIBt), Berlin, 2018.

[17] EN ISO 6892-1: *Metallic materials – Tensile testing – Part 1: Method of test at room temperature.* European Committee for Standardization (CEN), Brussels, Belgium, 2020.

[18] EN 1993-1-1: Eurocode 3: Design of steel structures – Part 1-1: General rules and rules for buildings. European Committee for Standardization (CEN), Brussels, Belgium, 2005 + AC:2009.

[19] Brühl, F.: *Ductility in timber structures – possibilities and requirements with regard to dowel type fasteners.* Dissertation, University of Stuttgart, Publication of Institute of Structural Design no. 2020-1, 2020.

[20] Schweigler, M.: *Nonlinear modelling of reinforced dowel joints in timber structures – a combined experimental-numerical study.* Dissertation, TU Wien, 2018.

[21] Sandhaas, C.: *Mechanical behavior of timber joints with slotted-in steel plates.* Dissertation, TU Delft, 2012.

[22] Gauß, J.; Kuhlmann, U.: *Consideration of the connection stiffness in design process – experimental investigations.* In: World Conference on Timber Engineering, WCTE, Seoul, Republic of Korea, 2018.

https://doi.org/10.52202/069179-0160

World Conference on Timber Engineering Oslo 2023

SEISMIC PERFORMANCE OF BOLTED GLULAM TIMBER BRACE CONNECTIONS WITH INTERNAL STEEL PLATES

Zoe Baird[1], Joshua Woods[2], Christian Viau[3], and Ghasan Doudak[4]

ABSTRACT: Mass timber braced frame systems achieve their ductility through the brace connections. Canadian design standards currently lack guidance on how to detail bolted brace connections to achieve a target system-level ductility as defined in the National Building Code of Canada. The objective of this research is to develop guidelines on how to detail bolted glulam timber brace connections to achieve moderate or limited ductility. To accomplish this objective, a 4-storey prototype building was designed to determine realistic brace design forces as well as investigate how different parameters (e.g., fastener diameter and number of slotted-in plates) can impact the design of a timber braced frame. Based on the prototype structure, a connection with two internal steel plates was designed and detailed, which included consideration for the fastener slenderness and spacing to achieve ductile behaviour. To validate the performance of the proposed connection, full-scale testing under monotonic and cyclic loading was conducted. This paper discusses the results of the experimental testing, including connection stiffness, strength, ductility, as well as its energy dissipation capacity.

KEYWORDS: Mass timber, Braced frames, Connections, Ductility, Seismic loading, Experimental test

1 INTRODUCTION

Over the last 10 years, there has been a rapid increase in the number of mass timber buildings constructed in Canada [1], largely due to the environmental benefits of building with wood. Recent national and international climate change initiatives, including the *Canadian Net-Zero Emissions Accountability Act* and the *Paris Agreement*, strive to achieve net-zero emissions in the next three decades and emphasize that a key requirement in that effort is to increase carbon-neutral construction practices [2,3]. The International Panel on Climate Change (IPCC) recently published their list of strategies to reduce emissions by 2030 and "enhanced use of wood products" was one of 5 options in the buildings category [4]. Despite the environmental benefits of building with wood, questions remain surrounding the performance of tall wood structures, particularly under seismic loads.

Modern capacity-based seismic design guidelines allow engineers to detail specific structural elements or connections, commonly referred to as fuses, to dissipate energy during an earthquake in a ductile manner, while protecting brittle elements by designing them to higher seismic load levels through the use of overstrength factors. In the design of mass timber braced frames, steel-timber connections are typically relied upon to act as fuses, providing ductility and energy dissipation capabilities to the system. However, design and detailing considerations ensuring ductile behaviour and capacity-based protection against brittle failures of such connections are required to ensure adequate seismic performance, including the ability to achieve appropriate connection-level ductility to meet system-level demand.

The National Building Code of Canada (NBCC) recognizes both limited and moderate ductility braced frames for multi-storey mass timber structures up to 15 m and 20 m in height, respectively, in areas of high seismicity, and specifies respective system-level ductility modification factors (R_d) of 1.5 and 2.0 [5]. However, no guidance currently exists in the Canadian wood design standards (e.g., CSA O86) on how to design and detail the connections in braced frames to achieve the required system-level ductility [6]. This lack of design guidance can lead to inefficient design, excess material use, and inaccessibility of the structural system to designers [7].

There are several reported studies in the literature focused on bolted timber connections [8-14]. However, few studies have investigated axially-loaded timber brace connections at an appropriate scale for use in mid- and high-rise timber frames under cyclic loading. To address these gaps, the aim of this research is to develop connection design requirements for timber braced frames in taller timber structures, with the long-term goal of providing practical detailing requirements within the CSA O86 framework to achieve the system-level ductility modification factors in the NBCC. The specific objectives of this paper are to: (1) design a prototype mass timber braced frame structure in a Canadian region of moderate seismicity, (2) study the influence of connection design parameters, including bolt diameter, number of slotted-in plates, and bolt spacing, on the design strength and anticipated failure mode for the connection, and (3) evaluate experimentally the behaviour of a full-scale

[1] Zoe Baird, Queen's University, Department of Civil Engineering, Canada, zoe.baird@queensu.ca

[2] Joshua Woods, Queen's University, Department of Civil Engineering, Canada, joshua.woods@queensu.ca

[3] Christian Viau, Carleton University, Dept. of Civil and Env. Engineering, Canada, christian.viau@carleton.ca

[4] Ghasan Doudak, University of Ottawa, Department of Civil Engineering, Canada, gdoudak@uottawa.ca

https://doi.org/10.52202/069179-0161

braced connection from the prototype structure under monotonic and cyclic loads.

2 BACKGROUND

There have been a number of studies that have focused on the behaviour of connections in mass timber structures, most of which involving small-scale connections (capacities ranging from 60 kN – 200 kN) [8-14]. These studies examined the influence of several connection design details, including dowel slenderness, fastener spacing, end distance [8,9], strengthening using self-tapping screws [10-12], effect of bolt pre-tension [13], and dowel material type, including shape-memory alloy [14]. These studies have considered a range of loading conditions to evaluate connection behaviour, including monotonic loads [8,11,12], cyclic loads [9,14,15], blast loads [16], and fire scenarios [17].

Beyond small-scale connection testing, there has been limited experimental research into the performance of large- to full-scale braced frame subassemblies or systems. Chen and Popovski [11] conducted testing on a multi-tier and single-storey braced timber frame with riveted connections, while Popovski et al. [18] conducted shake table testing on a single storey braced frame with bolted and riveted connections. These studies concluded that brace end connections can experience significantly different deformation levels, even if the two connection details are identical, and thus, the deformation capacity of a brace may not be equal to twice the capacity of a single connection [18]. A recent report by FPInnovations highlights the need for continued study into timber braced frames, particularly research on large-scale connections for multi-storey timber frames and their system-level behaviour [19].

2.1 DUCTILE DESIGN OF TIMBER FRAMES

Review of the literature has identified that there is a need to better understand the relationship between system-level behaviour of timber braced frames and the connection ductility demand, as well as the specific connection detailing needed to achieve the required system-level ductility. To address this concern, it is important to identify the hierarchy of ductility used in building design, which has been summarized by Gioncu [20]:

1. *Material ductility:* plastic deformation capacity of the materials (e.g., timber or steel);
2. *Cross-section ductility:* also referred to as curvature ductility, it is the plastic deformation capacity of the cross-section, considering interactions between elements of a cross-section (e.g., flange and web);
3. *Member ductility:* also referred to as rotation or displacement ductility and considers the properties of the member (e.g., length) and the formation of plastic hinges. In an axially loaded element, this could include deformation capacity of the connections; and
4. *System Ductility:* considers the displacement ductility of the entire structure under a lateral load distribution.

In this hierarchy, as one moves from material ductility to system ductility, the overall ductility decreases as it is often difficult to utilize all of the available ductility for complex structures (variability amongst connections and elements) under complex loading. Furthermore, this hierarchy was developed with steel or concrete structures in mind, in which the ductility of the system is typically achieved through yielding of the structural members (e.g., the brace in a steel braced frame or the beam in a reinforced concrete moment frame).

Capacity-based design of timber structures presents a unique challenge when compared with steel structures because of the brittle nature of timber in tension, which means that timber members are typically assumed to remain elastic while the connections are relied upon to act as fuses, providing ductility and energy dissipation capacity to the system. It has been shown by Chen and Popovski [7] that the system-level ductility of a multi-storey braced timber frame is a function of connection ductility, stiffness ratio between the connections and the brace, as well as the number of storeys in the structure. The system-level ductility of a timber frame, assuming all tiers yield simultaneously and that the structure behaves in the first mode, can be computed using Equation (1) [7]:

$$\mu_s = \frac{(\mu_{c1}+\mu_{c2})+k_r}{2+k_r} \quad (1)$$

where μ_{c1} and μ_{c2} are the ductility of the connections at either end of the brace, k_r is the ratio of the stiffness of the connection to the axial stiffness of the diagonal brace, equal to k_c/k_b where k_c is the stiffness of the connection and k_b is the stiffness of the brace.

While Equation (1) assumes that all storeys in a multi-storey braced frame yield simultaneously, this may be difficult to ensure in practice because of the uncertainty and variability surrounding connection capacity, as past tests have shown that there is the potential for only one connection in a brace to yield [7]. At the system-level, complex load distributions and the need to have several different connection designs over the height of a timber frame make it particularly challenging to ensure that all tiers in a braced frame will yield simultaneously. In such cases, a conservative approach to estimate system-level ductility would be to assume that only a single storey yields, and the system-level ductility can be computed using Equation (2) [7]:

$$\mu_s = \frac{(\mu_{c1}+\mu_{c2})-2}{m(2+k_r)} + 1 \quad (2)$$

where m is the number of storeys. To validate these proposed relationships, Chen and Popovski [11] conducted pushover analysis on five building archetypes while varying number of storeys, the ratio of the stiffness of the connection to the stiffness of the diagonal brace, and the connection ductility. In all cases, the braced frames had ductile riveted connections and the results showed that for a moderately ductile braced frame (R_d = 2.0) in which only one of the two brace end connections yield, a connection ductility of 11.5 is required. For situations in which both brace end connections yield, a minimum connection ductility of 6.3 is required. For limited ductility frames, connection ductility of 5.4 and 3.2 are required when one or both connections yield, respectively. An aim of the current research study is to

https://doi.org/10.52202/069179-0161

investigate how to achieve these connection-level ductility requirements for bolted brace connections.

3 PROTOTYPE BUILDING DESIGN

A prototype 4-storey mass timber braced frame structure was designed for a site in Ottawa, Ontario, a region of moderate seismicity in Central Canada, where timber braced frames with moderate or limited ductility would be commonly utilized. The prototype structure was designed to determine realistic design forces and brace connection.

Figure 1 shows a plan and elevation view of the prototype structure, which includes 7 – 6 m bays in each orthogonal direction (42 m × 42 m total building footprint). The dead loads on the roof and floors were 1.88 kPa and 2.64 kPa, respectively, the snow load on the roof was 2.32 kPa for the building location, and the live load for a typical floor was 2.4 kPa for office occupancy, as per the NBCC [5].

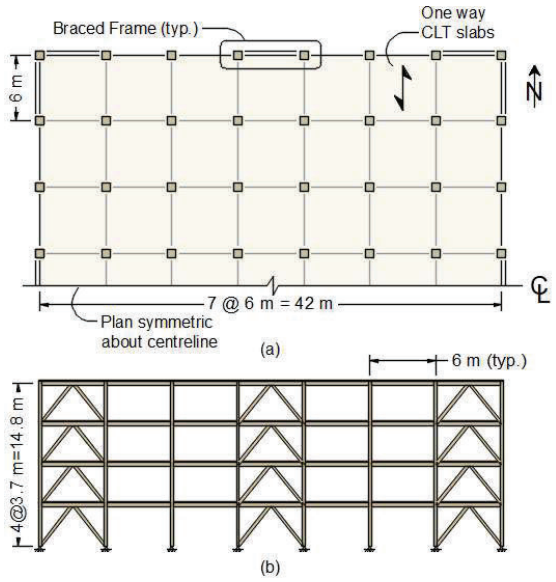

Figure 1: *Prototype structure: (a) plan view; (b) N-S elevation*

The gravity load resisting system in the prototype structure consisted of cross-laminated timber (CLT) slabs with glulam beams and columns. Based on the spans and loads, the selected CLT slabs were 5-layer (35 mm ply) 175 mm thick panels. The glulam beams and columns were grade 20f-E and 12c-E, respectively, and their respective sizes for each storey level are shown in Table 1. All structural members were sized according to the Canadian wood design standard (CSA O86) [6].

Seismic design of the prototype structure was carried out using the equivalent static force procedure outlined in the NBCC [5]. The base shear was determined for Ottawa (City Hall) and the building was assumed to be on a site designated as class C, corresponding to "firm ground". The seismic weight was assumed to be 100% of the dead load plus 25% of the roof snow load. The fundamental period (T) used in the design of the prototype structure was assumed to be $T = 0.1N$, where N is the number of storeys in the structure [5].

Table 1: *Member selection summary (units in mm)*

	Storeys 1-2	Storeys 3-4
Brace	265 × 304	215 × 266
Interior Beam	265 × 456	
Exterior Beam	175 × 380	
Interior Column	265 × 304	
Exterior Column	265 × 266	

The lateral load resisting system for the prototype building consisted of mass timber braced frames in a chevron configuration in both orthogonal directions. For the frame design, the connections between the beams and columns were assumed to be pinned and the columns were continuous over the building height. Slotted-in steel plates were considered for the brace connections. Figure 2 shows an example of the brace connection with two slotted-in steel plates. This type of connection is appealing due to the high connection strength and stiffness while allowing the wood to protect the steel components against fire. This type of connection is used with dowel-type fasteners, such as bolts or tight fit pins. Bolts were used in this research over tight-fit pins because of the beneficial roping effect provided by bolts, which may lead to improved connection performance.

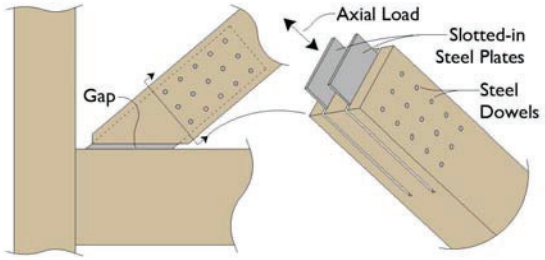

Figure 2: *Timber slotted-in steel plate connection*

One important consideration in the detailing of a timber braced frame is the need to leave a gap between the end of the brace member and the surrounding timber frame (illustrated in Figure 2). The gap allows the connections to deform and yield in both tension and compression, enabling the connection to achieve the required ductility and dissipate the maximum input energy. If no gap is provided, the brace element will be very stiff in compression, which would induce larger forces than expected under earthquake loads leading to less ductility and the potential for bending deformations in the columns which could lead to potential safety concerns [19].

3.1 CONNECTION DESIGN

The brace design forces were determined using the results of the equivalent static force procedure in the NBCC [5]. The resulting brace design force at the first storey of the prototype structure was approximately 250 kN, which was the target design force for the connection. To design the connection, five different failure mechanisms were considered: (1) net tension, (2) row shear, (3) group tear-out, and (4) fastener yielding. Figure 3 illustrates these failure modes.

https://doi.org/10.52202/069179-0161

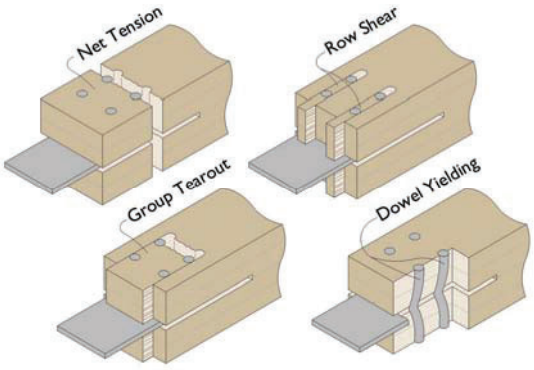

Figure 3: *Connection failure modes*

To initiate the connection design process, the number of fasteners required to achieve a yielding capacity approximately equal to the brace design force was determined, resulting in a 265 mm × 304 mm cross section being chosen. Two internal steel-plates with 10 mm thickness were used, which resulted in timber side member thicknesses of 71 mm [(304 – 2×10)/ 4 = 71 mm]. The fastener diameter was determined by setting a target slenderness ratio of 10 or higher for the connection, which is in line with recommendations from Eurocode 8 [21], which suggests fasteners with a diameter of less than 12.7 mm (1/2") and a slenderness ratio greater than 10 be used for ductile timber connections. The bolts were grade ASTM A307 steel, with a specified yield strength (F_y) of 310 MPa. The yield resistance of the connection was determined according to the provisions of CSA O86 [6]. Ultimately, it was determined that 16 - 9.53 mm (3/8") diameters fasteners were required to carry the factored load, which resulted in a yield capacity of 286 kN.

The capacity of the brittle failure modes (net tension, row shear, and group tear-out) were determined. In the initial design iteration, the minimum fastener spacing according to the Canadian design standard (CSA O86-19) of 4 times the fastener diameter (resulting in a minimum spacing of 38 mm) was used to layout the bolts. Based on this fastener spacing, the resulting row shear, group tear-out, and net tension resistances of the connection were 362 kN, 516 kN, and 1054 kN respectively.

While use of the minimum fastener spacing was satisfactory from a design perspective, it was anticipated that the actual yield resistance of the connection would be higher than the design yield resistance based on the code calculations because of higher yield strength of the bolts. Additionally, the potential for post-yield hardening behaviour in the connection response, could result in premature brittle failure. Consequently, a target minimum overstrength factor of at least 2, computed as the ratio of the resistance of the most critical brittle failure mode (e.g., lowest of the row shear, group tear-out, and net tension resistances) to the yield resistance of the connection was desired. To accomplish this objective, the bolt spacing was increased. Because net tension resistance was found to not govern the brittle failure mode, both row shear and group tear-out resistances could be increased by increasing the fastener spacing. Ultimately, a fastener spacing of 100 mm, which is more than twice the minimum fastener spacing specified in the Canadian wood design standard was selected, which resulted in row shear and group tear-out resistances of 905 kN and 652 kN, respectively, corresponding to an overstrength factor of approximately 2.3.

Finally, compression (i.e., buckling) and gross tension failures were considered in the brace member, which had capacities of 1162 kN and 1054 kN, respectively. Figure 4 shows the connection design proposed for the 4-storey prototype building.

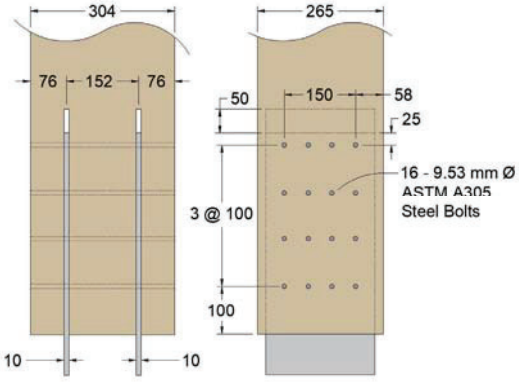

Figure 4: *Prototype connection design*

4 EXPERIMENTAL PROGRAM

To evaluate the ductility of the proposed connection design shown in Figure 4, full-scale connection tests were conducted. The connections were fabricated using grade 24f-E spruce-pine-fir (SPF) glued-laminated (glulam) timber supplied by Nordic Structures (Québec, Canada). The glulam had a density of 560 kg/m^3, a bending strength of 30.7 MPa, a longitudinal shear strength of 2.5 MPa, a compression perpendicular to grain strength of 7.5 MPa, and a modulus of elasticity of 13.1 GPa according to the manufacturer [22]. The bolts were grade ASTM A307, and from testing were found to have an average yield stress of 400 MPa (standard deviation = 16 MPa).

Figure 5 shows a typical specimen in the testing frame. Each specimen included two identical connections (details illustrated in Figure 4), with an overall length of 1350 mm to fit into the experimental testing frame. The holes in the timber were 10.7 mm (27/64") in diameter, which is approximately 1.2 mm larger than the diameter of the bolts. The holes in the steel plates were 12.7 mm (1/2") in diameter to allow for erection tolerance. The results of two specimens are presented in this paper. The first specimen, hereafter referred to as specimen M1, was tested under monotonic load, while the second specimen, referred to as specimen C1, was tested under simulated seismic load using a cyclic loading protocol.

4.1 EXPERIMENTAL TEST SETUP

The connection was tested in a frame with a capacity of 1350 kN in tension and the actuator had a stroke of +/- 250 mm. Figure 5 shows a typical test setup for the connection, which was used for both the monotonic and

https://doi.org/10.52202/069179-0161

cyclic tests. Lateral bracing was installed at the top of member to prevent any out-of-plane deformation during testing. The slotted-in steel plates were attached to the actuator at one end and to a steel assembly at the other end. The steel assembly was fixed to the laboratory strong floor using 8 – 31.8 mm (1-1/4 in.) steel grade B7 rods.

A load cell mounted to the hydraulic actuator was used to measure the force and 12 potentiometers were used to measure the displacement response of the connections, which included two string potentiometers on each connection (top and bottom) to measure their individual displacement response. Linear potentiometers were also mounted across the slots in the timber for the steel plates to measure any potential opening during testing.

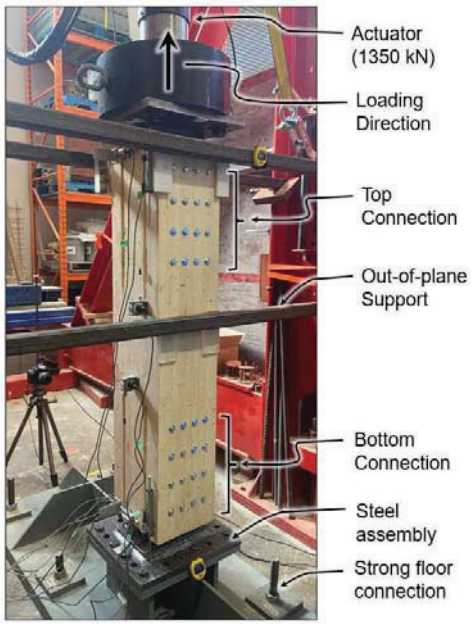

Figure 5: *Test specimens and experimental test setup*

4.2 LOADING PROTOCOL

Monotonic and cyclic loading tests were conducted based on the European Test Standard EN12512 – *Cyclic Testing of Joints made with Mechanical Fasteners* [23]. Monotonic testing was conducted to evaluate the connection strength and failure mechanism, as well as to determine the connection yield displacement (Δ_y) to be used in defining the cyclic loading protocol. The monotonic tensile test was conducted at a constant rate of 2 mm/min, which resulted in a total test time of approximately 20 minutes.

Based on the results of the monotonic test, a cyclic loading protocol was developed to study the connection behaviour under simulated earthquake loads. Figure 6 shows the cyclic loading protocol used in this study. The cyclic tests were executed in displacement control based on increments of the Δ_y of the connection determined from the monotonic test, which included displacement levels of 0.2, 0.4, 0.6, 0.8, 1.0, 1.5, and 2.0 times Δ_y, followed by cycles at increments of Δ_y to failure.

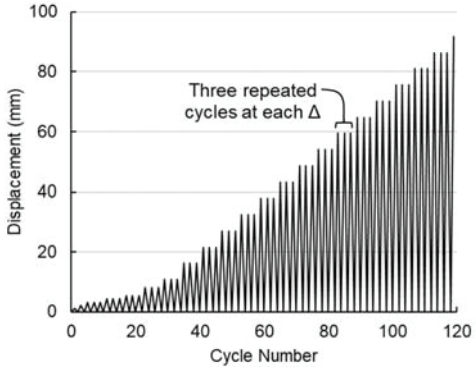

Figure 6: *Tension cyclic loading protocol* [22]

5 EXPERIMENTAL RESULTS

Table 2 summarizes the key structural response parameters for the specimens described in this paper, including the yield load (P_y), peak load (P_{peak}), and ultimate load (P_u) as well as the yield displacement (Δ_y), peak displacement (Δ_{peak}), and ultimate displacement (Δ_u). The yield load and displacement were determined using the method proposed by Yasumura and Kawai [24], which has been shown to produce consistent results for a range of force-displacement behaviours in the past [25]. The peak load was defined as the maximum load achieved during the test. The ultimate load and displacement were defined as the point when the load dropped by 20% from the peak load.

Table 2: *Connection structural response parameters*

	Specimen M1		Specimen C1	
Parameter	Top	Bottom	Top	Bottom
P_y (kN)	557	550	506	506
Δ_y (mm)	3.4	2.4	2.7	3.2
P_{peak} (kN)	1024	1024	775	775
Δ_{peak} (mm)	20.6	16.5	21.3	22.1
P_u (kN)	819	819	620	620
Δ_u (mm)	24.2	16.6	21.4	22.7

5.1 MONOTONIC TEST RESULTS

Figure shows the force-displacement response of the specimen tested under the monotonic load. The results for the top connection show a gradual increase in the load at small displacement levels, which corresponds to the closing of any gaps between the steel plates, timber, and the bolts, which are required for constructability of the connection. After closing any gaps, both top and bottom connections have an elastic behaviour followed by a gradual softening, which results from yielding of the bolts. Following bolt yielding, the connection exhibits post-yield hardening behaviour, which is attributed to embedment stiffness of the timber, which interacts with the bolts even after significant yielding of the fasteners. At a displacement of approximately 23 mm, several bolts in the top connection of the specimen fractured, resulting in a significant drop in load carrying capacity of the specimen.

https://doi.org/10.52202/069179-0161

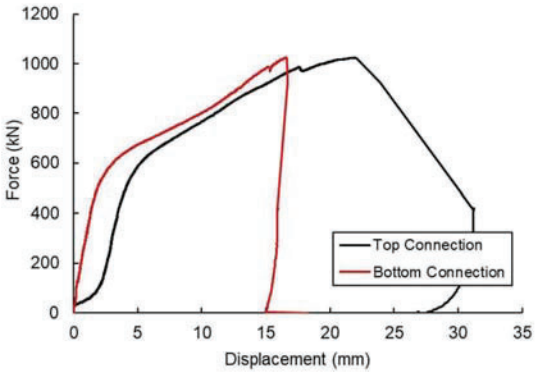

Figure 7: *Connection M1 force-displacement response*

Figure shows sample bolt deformation patterns from the monotonic test and the results show that bolts from both the top and bottom connections had significant plastic deformations and the bolts form six plastic hinges at the locations of the slotted-in plates

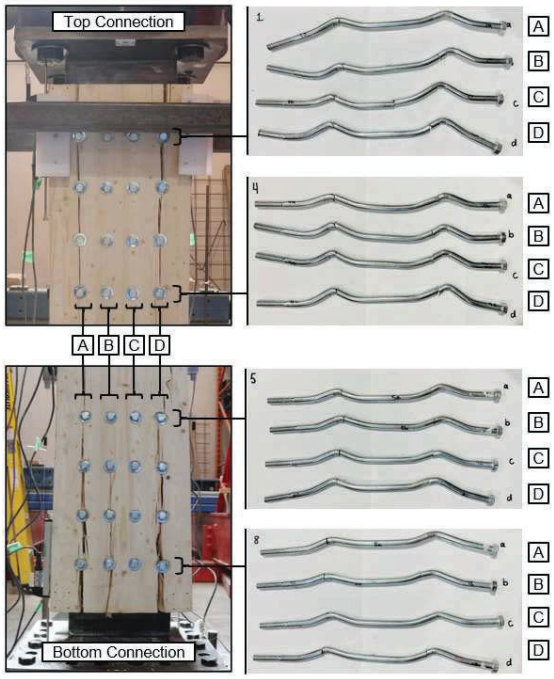

Figure 8: *Connection M1 bolt deformation patterns*

5.2 CYCLIC TEST RESULTS

Figure 9 shows the hysteretic force-displacement response of the bottom and top connections for the second specimen. The results show that the cyclic backbone curve was similar to that of the monotonic test, characterized by an initial gradual increase in stiffness as the bolts engage with the slotted-in plates followed by an elastic and post-yield hardening behaviour up to failure, which occurred due to excessive splitting of the wood. The hysteretic behaviour of the connection shows a highly pinched response, with stiffness degradation under repeated load cycles. This behaviour is attributed to crushing of the wood surrounding the dowel during the initial cycle and on the second cycle the dowel must close a gap before re-engaging the wood, at which point the stiffness of the connection increases. Both connections yield and achieve ductility of 7.1 and 8.1, which is attributed to the post-yield hardening behaviour of the connections. This level of ductility is within the required range suggested by Chen and Popovski [7] to meet the system-level ductility requirements for a moderately ductile timber braced frame according to the NBCC [5].

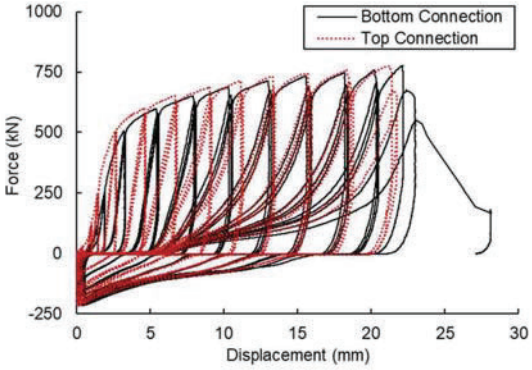

Figure 9: *Connections C1 force-displacement response*

Figure 10 shows the progression of splitting in the connection at various displacement levels throughout the cyclic loading protocol. The results show that no splitting occurred up to a displacement of approximately 13 mm. However, even after the onset of splitting, it did not result in any significant strength degradation and the connection maintained similar hardening behaviour up to failure.

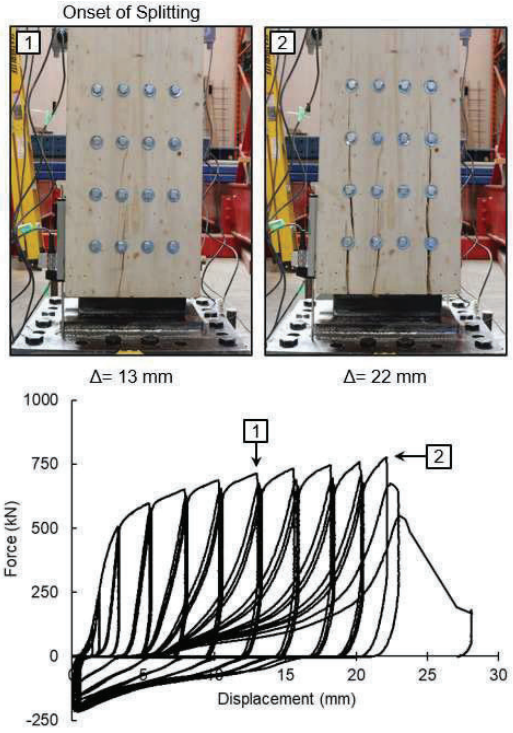

Figure 10: *Specimen C1 bottom connection crack progression*

https://doi.org/10.52202/069179-0161

6 CONCLUSIONS AND FUTURE WORK

The use of mass timber braced frames is rising in Canada, but knowledge gaps remain on how to design timber connections to achieve system-level ductility levels in the NBCC. Through experimental testing of a connection based on the design of a 4-storey prototype structure, the conclusions of this study are as follows:

1. Bolted glulam timber connections with slotted-in steel plates can meet the strength requirements for multi-storey mass timber structures.
2. Emphasis should be placed on the ratio of ductile to brittle failure modes during the connection design phase. In this paper, connections tested with a capacity ratio of 2.3 resulted in high ductility.
3. Connection-level ductility requirements can be achieved to meet the system-level ductility demand for moderate and limited ductility braced timber frames.

The work presented in this paper is part of a larger study focused on the behaviour of bolted glulam timber connections with slotted-in steel plates. Future work includes experimental testing of connections with varying fastener diameter, bolt spacing, and number of slotted-in steel plates. The goal is to better understand the key factors that contribute to the design of a ductile timber connections so that design guidance can be provided in CSA O86 on how to detail timber connections to achieve the required system-level ductility levels in the NBCC.

REFERENCES

[1] MacLennan, R. (2021). "Introducing Mass Timber - The new construction technique that is key for Ontario's economy and greener future." *Ontario Construction News.*

[2] Government of Canada. (2021). "Canadian Net-Zero Emissions Accountability Act."

[3] United Nations. (2021). "The Paris Agreement | UNFCCC." *United Nations Climate Change*,

[4] IPCC (2022). "Climate Change 2022: Mitigation of climate change." *International Panel on Climate Change.*

[5] NRC (2015). "National Building Code of Canada." *National Research Council of Canada.*

[6] CSA (2019). "Engineering Design in Wood." *Canadian Standards Association CSA O86-19.*

[7] Chen, Z. and Popovski, M. (2020). "Connection and System Ductility Relationship for Braced Timber Frames." *Journal of Structural Engineering*, American Society of Civil Engineers, 146(12), 04020257.

[8] Jorissen, A. J. M. (1998). Double shear timber connections with dowel type fasteners. Delft University Press, Delft.

[9] Popovski, M., Prion, HG, and Karacabeyli, E. (2002). Seismic performance of connections in heavy timber construction. Canadian Journal of Civil Engineering, 29 (3), 389-399.

[10] Bejtka, I. and Blaß, H. J. (2005). Self-tapping screws as reinforcements in connections with dowel-type fasteners. In Proc. of CIB-W18 Meeting (Vol. 38).

[11] Chen, Z. and Popovski, M. (2020). "Expanding Wood Use Towards 2025: Seismic Performance of Braced Mass Timber Frames - Year 2," FPInnovations.

[12] Dorn, M., de Borst, K., & Eberhardsteiner, J. (2013). Experiments on dowel-type timber connections. Engineering structures, 47, 67-80.

[13] Awaludin, A., Hirai, T., Hayashikawa, T., and Sasaki, Y. (2008). Load-carrying capacity of steel-to-timber joints with a pretensioned bolt. Journal of Wood Science, 54, 362-368.

[14] Cleroux, M. (2022). Novel SMA dowel connections for seismically resilient timber buildings. University of Waterloo, Waterloo, Canada.

[15] Piazza, M., Polastri, A., and Tomasi, R. (2011). Ductility of timber joints under static and cyclic loads. Proceedings of the Institution of Civil Engineers-Structures and Buildings, 164(2), 79-90.

[16] Viau, C., & Doudak, G. (2021). Behavior and modeling of glulam beams with bolted connections subjected to shock tube–simulated blast loads. Journal of Structural Engineering, 147(1), 04020305.

[17] Maraveas, C., Miamis, K., & Matthaiou, C. E. (2015). Performance of timber connections exposed to fire: a review. Fire Technology, 51(6), 1401-1432.

[18] Popovski, M., Prion, H. G., & Karacabeyli, E. (2003). Shake table tests on single-storey braced timber frames. Canadian Journal of Civil Engineering, 30(6), 1089-1100.

[19] Karacabeyli, E., & Lum, C. (2022). Technical guide for the design and construction of tall wood buildings in Canada. FPInnovations.

[20] Gioncu, V. (2000). Framed structures. Ductility and seismic response: General Report. Journal of Constructional Steel Research, 55(1-3), 125-154.

[21] "Eurocode 8: Design of Structures for Earthquake Resistance." European Standard, 1998.

[22] Nordic Structures. (2022). Mass Timber Construction: Nordic LAM+ Technical Guide, Nordic Structures, Montreal.

[23] CEN, "Timber structures - Test methods - Cycling testing of joints made with mechanical fasteners." European Committee for Standardization, Nov. 2001.

[24] Yasumura, M., and N. Kawai. 1998. Estimating seismic performance of wood-framed structures. *Proceedings of 1998 I.W.E.C*. Switzerland. Vol.2. pp. 564-571.

[25] W. Munoz, M. Mohammad, A. Salenikovich, and P. Quenneville, "Determination of Yield Point and Ductility of Timber Assemblies: In Search for a Harmonised Approach".

World Conference on Timber Engineering Oslo 2023

DEVELOPMENT OF A NOVEL JOINT SYSTEM FOR MID-TO-HIGH-RISE CLT WALL BUILDINGS IN SEISMIC REGIONS

Ahmad Ghazi Aljuhmani[1], Eito Atsuzawa[2], Arata Minegishi[3], Kazuki Tsuda[4], Yutaka Goto[5], Masaki Maeda[6]

ABSTRACT: In Japan, the possibility of multi-story timber buildings is not yet practiced at a large scale due to the complex structural design process and construction cost. In conventional CLT buildings in Japan, a high number of complex steel connections are required. In this practice, complex processing of CLTs panel is also required. The objective of this paper is to propose easy-to-apply and easy-to-design steel joints. The proposed joint is designed to resist both shear and tensile forces to reduce complex steel parts. Single-bolt element tension tests were conducted to investigate the effect of the fibre direction, bolt diameter, and bolt embedded length. Cyclic loading for single and coupled CLT walls with the proposed joints was also conducted. The failure characteristics and strength of single-bolt connections could be predicted by the ratio of bolt embedded length and diameter. The fibre direction was found to have a minor effect on the connection strength. The proposed joint system showed high strength and ductility as found by the cyclic loading. The lateral strength of a wall with two panels was double the single wall case, indicating the lack of interaction between the two panels.

KEYWORDS: Cross-laminated Timber, Hybrid structure, Steel plate-bolt connections, Shear walls, Rocking walls

1 INTRODUCTION

Timber, as a construction material with its carbon-storing capability and renewability, can play an essential role in reducing GHGs emissions related to the construction sector. In Japan, although 66% of the total land area is covered by forests (Japanese Forestry Agency (JFA)), these renewable resources are not being used to their full potential. Buildings higher than three stories (mid-to-high-rise buildings) are mainly non-wooden structures [1], with a share of only 0.06% for timber buildings. This is attributed to the strict seismic and fire protection requirements. To overcome these challenges, Cross-laminated Timber (CLT) is considered a promising engineered wood product (EWP). When compared to sawn timber, CLT can secure the structural and fire safety requirements more efficiently. The laminated structure of CLT helps control the strength, reduces the effect of defects, and increases the dimensional stability of the element [2]. In Japan, the self-sufficiency rate of wood is only about 41%. The commonly used wood in Japan is cedar, which has relatively lower strength and larger number of knots and defects compared to other species. In addition, due to the high cost of timber production and inefficient forest management, imported timbers are more competitive in terms of cost and quality. Therefore, recently, the Japanese government has been putting many efforts to increase the use of domestic forest resources. For example, a law for promoting the use of timber in public buildings was enacted in 2010. By using CLT as a construction material, it is believed that we can ensure utilizing the domestic wood resources, as high strength of the CLT members can be achieved with relatively low-strength wood raw material.

In Japan, in order to fulfil the seismic requirements for the CLT walls, connections with high shear and tensile strength are generally required. However, in the common design practice for CLT buildings, an unreasonable amount of CLT walls (i.e., to compensate for the low strength and stiffness connections), and a large number of complex connections and CLT processing are needed.

In light of these problems, and in order to promote mid-to-high-rise CLT buildings, CLT-steel hybrid structures can be a possible solution. Combining CLT as a low carbon footprint material with a high strength-to-weight ratio with steel which has high ductility and recycling potential would result in a superior structural system in terms of structural performance (i.e., stiffness, strength, ductility, and energy dissipation) and environmental impact. The seismic behaviour of the structure using innovative CLT-steel hybrid systems was investigated by several researchers in the past years [3][7]. Kanazawa et al. [8] experimentally investigated the structural

[1] Ahmad Ghazi Aljuhmani, Tohoku University, Japan, aljehmani@rcl.archi.tohoku.ac.jp
[2] Eito Atsuzawa, Taisei Corporation, Japan, atzeit00@pub.taisei.co.jp
[3] Arata Minegishi, Tohoku University, Japan, minegishi@rcl.archi.tohoku.ac.jp
[4] Kazuki Tsuda, Tohoku University, Japan, tsuda@rcl.archi.tohoku.ac.jp
[5] Yutaka Goto, Chalmers University of Technology/Tohoku University, Sweden/Japan, yutaka@chalmers.se
[6] Masaki Maeda, Tohoku University, Japan, maeda@archi.tohoku.ac.jp

https://doi.org/10.52202/069179-0162

performance of several steel frames with CLT infill using small-diameter drift pin connections. They found that the use of CLT walls can increase the stiffness and strength by 1.5 to 2.3 times and 1.2 to 1.4 times, respectively, compared to the bare steel frame. In the previous studies, existing connection detail, such as tensile bolts, have been considered and the high strength and stiffness of CLT panels have not been fully utilized. Therefore, the objectives of this study are 1. Development of an easy-to-apply bolt-type steel joint system for CLT-steel hybrid buildings that can utilize the strength of CLT. 2. Experimentally investigate the structural performance of the bolted connection (i.e., strength, failure mechanism, and effect of fibre direction). 3. Experimentally investigate the structural performance of the proposed joint system by full-scale CLT wall-steel beam tests.

2 OUTLINE OF PROPOSED JOINT

In this research, a CLT wall-steel frame hybrid structural system was proposed, as shown in Figure 1. In this system, CLT walls are inserted into the steel frame to increase their seismic capacity. To connect the CLT wall with the steel beams of the structure, a joint system using bolted CLT connections was proposed and developed. The proposed joint system consists of four connections which are located at the four corners of the CLT panel, as shown in Figure 2.a. For each connection, a steel plate is connected to only one side of the CLT wall panel by large-diameter high-tensile bolts (HTBs), that work under shear (i.e., the HTBs resist the forces applied on them mainly by shear stresses only and not with friction stresses). Large-diameter bolts were used to achieve high strength and stiffness of the joint in order to utilize the structural advantages of CLT. The panels are then connected to the steel beam with these connections. Compared to the conventional connections (e.g., tensile bolts, Figure 2.b) the proposed joint system has the following advantages: 1. Relatively high stiffness and strength with a ductile behaviour are expected. 2. Resisting of bidirectional force that is resulted from shear and tension (uplift) forces induced by the horizontal load applied on the wall. 3. Simple connections with less complex CLT processing, such as cutting work, with high repairability of the damaged walls.

Under horizontal shear forces (Q) a moment is generated at the bottom of the wall ($M_{W\text{-}B}$). As shown in Figure 3, on the compression side of the wall, the bolts are assumed to resist only shear forces while the compression forces are resisted by the CLT wall. On the tension side of the wall, the bolts resist bidirectional forces of vertical forces (tension) and horizontal forces (shear). For each bolt, the resistance force of the bolt (P_θ, grey arrow in Figure 3) is a combination of vertical and horizontal forces, and thus it is tilted with an angle (θ). The shear and tensile strength of the connections are calculated by taking the result of P_θ on the vertical and horizontal axis multiplied by the number of bolts (n), as shown in Equations (*1*) and (*2*).

$$T_y = n \times P_\theta \times cos\theta \quad (1)$$

$$Q_y = n \times P_\theta \times sin\theta \quad (2)$$

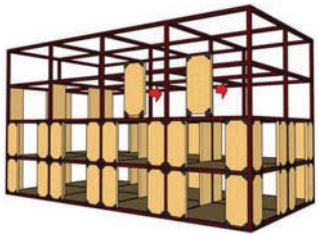

Figure 1: *Basic concept of the proposed CLT-steel hybrid structure*

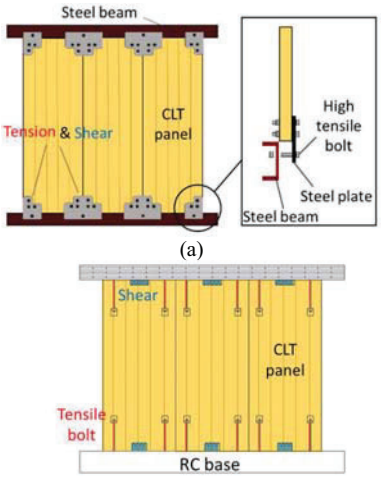

Figure 2: *Comparison between (a) the proposed joint system, and (b) the conventional connections system of CLT panels*

In the case of one-bolt connections, shear brittle failure or ductile embedment failure are considered possible failure modes, as shown in Figure 4. The type of failure can be controlled by changing the embedment length of the bolt (L_n) and the bolt diameter (Φ). The strength (P_θ) for each bolt is calculated as the minimum of CLT shear strength (Q_s) and CLT embedment strength (Q_{cv}), as (Equations (3)-(5)). The (L_n/Φ) ratio for the proposed joint is designed to have ductile embedment failure.

$$P_\theta = \min(Q_s, Q_{cv}) \quad (3)$$

$$Q_s = \tau \times 2 \times L_n \times t \quad (4)$$

$$Q_{cv} = \sigma_{cv} \times \phi \times t \quad (5)$$

Where τ and σ_{cv} (N/mm^2) are the shear and embedment strength of CLT, respectively. t (mm) is the thickness of CLT.

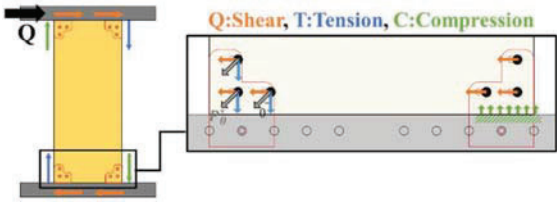

Figure 3: *Load transfer mechanism of the proposed joint system*

https://doi.org/10.52202/069179-0162

To calculate the yielding flexural moment capacity and rotation angle of the CLT wall, the following approach is used. In Japan, in CLT-panel system design practice, in order to ensure ductility, the strength of the wall is generally determined by the yielding of the tensile connections of the CLT wall panel. Minegishi et al. [9] proposed a method to calculate the bending moment capacity of the CLT wall in the same approach as calculating the bending moment of reinforced concrete columns. The calculation approach is illustrated in ***Figure 5***.a. The flexural yielding moment of the wall (M_y) is calculated by Equation (*6*). The shear strength of the wall at flexural yielding (Q_y) is calculated by Equation (7) using M_y. The yielding rotational angle of the wall (θ_y) and rotational stiffness (K_θ) is calculated by Equation (8) and (9), respectively. The neutral axial distance (x_n) is calculated using Equation (10) by taking the equilibrium of the compressive force of the CLT wall (C), the axial force (N), and the tensile yield force (T_y) (***Figure 5***.a.)

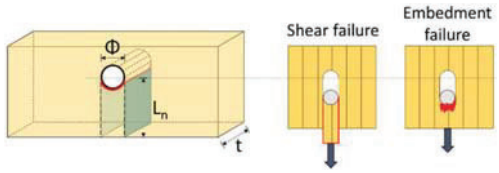

Figure 4: *Expected failure modes for one-bolt connection*

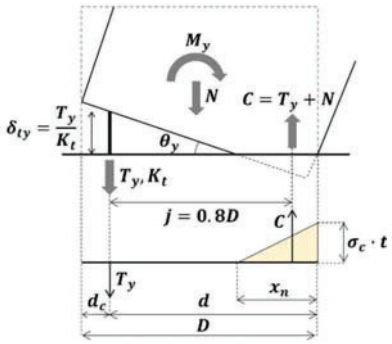

(a) allowable stress condition

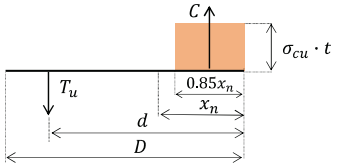

(b) ultimate state

Figure 5: *Stress condition of CLT wall, based on [9]*

$$M_y = T_y \times 0.8D + N \times 0.4D \quad (6)$$

$$Q_y = M_y/h \quad (7)$$

$$\theta_y = \delta_{ty}/(d - x_n) \quad (8)$$

$$K_\theta = M_y/\theta_y \quad (9)$$

$$x_n = 2(N + T_y)/\sigma_c t \quad (10)$$

Where D and t (mm) are the width and thickness of the wall, respectively. h (mm) is the inflection point height, and δ_{ty} (mm) is the deformation of the tensile connection. d (mm) and x_n (mm) are the distance from the tensile connection and neutral axis to the compression edge of the wall, respectively. σ_c (N/mm^2) is the allowable compressive strength of the CLT and it is equal to two-thirds of the compressive strength of CLT.

3 SINGLE-BOLT CONNECTION TEST

3.1 MATERIAL PROPERTIES

Material tests were conducted to get the embedment and shear strength of CLT based on the testing procedures mentioned in [10]. The tested CLT panels were five-layer 150 mm thick, made from Japanese cedar with Mx-60-5-5 (5-ply 5-layer) grade and composition [11]. The average CLT density was 400 kg/m^3, and the average moisture content was 12.0%. Three identical specimens were used for each material test, and the results are summarized in Table 1.

Table 1: *Results of the CLT material tests for single-bolt connection specimens*

Strength (MPa)	Shear		Embedment	
	Major	Minor	Major	Minor
	3.2	2.9	18.6	15.9

3.2 TEST MATRIX

In this study, component-level tests on double plate one-bolt connections were conducted (i.e., two steel plates on both sides of the CLT panel were fixed with a HTB). All the tested specimens have the same dimensions as shown in Figure 6 and were tested under monotonic loading. the tested specimens are summarised in Table 2. In order to investigate the effect of the embedment length (L_n) on the failure mode (as explained in section 2), the experimental parameter was the (L_n/Φ) ratio. In addition, to investigate the effect of fibre angle (i.e., loading direction) on the load-bearing capacity, the outer layer fibre direction (θ) was taken as another parameter. A bolt with a diameter of Φ=40 mm was installed into the specimens. For each type of specimen, three replicates were tested.

3.3 LOADING SET-UP

The loading set-up of the tested specimens is shown in Figure 7. The CLT panel was fixed on top of two steel bases with two threaded rods at each side to prevent out-of-plane deformation. A single 300 kN jack was used to apply a monotonic downward force on the connection's steel bolt, and the loading rate was in the range of 0.15–0.2 mm/s. The vertical displacement of the bolt was taken as the average value of two LVDTs that were attached on both sides of the specimen.

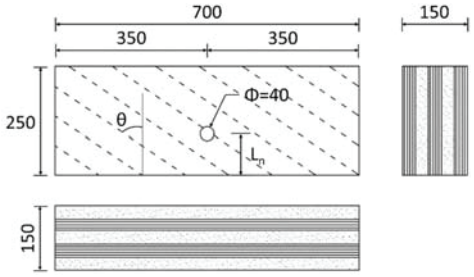

Figure 6: *Dimensions of the tested specimens (mm)*

https://doi.org/10.52202/069179-0162

Table 2: *Test matrix of the CLT panels*

Specimen name	Panel thickness [t] (mm)	Bolt diameter [Φ] (mm)	Embedment length [L_n] (mm)	Fiber angle [θ] (°)	$L_n/Φ$	No. of specimens
40-0-50				0		
40-30-50				30		
40-45-50	150	40	150	45	1.3	3
40-60-50				60		
40-90-50				90		
40-0-100				0		
40-30-100				30		
40-45-100	150	40	150	45	1.3	3
40-60-100				60		
40-90-100				90		
40-0-150				0		
40-30-150				30		
40-45-150	150	40	150	45	1.3	3
40-60-150				60		
40-90-150				90		

3.4 TEST RESULTS

The relation between $L_n/Φ$ ratio and the load-bearing capacity of the tested specimens and fibre direction angle (θ=0° and θ=90°) is shown in Figure 8. All specimens with $L_n/Φ$=1.3 had a shear failure with the lowest load-carrying capacity. Most of the specimens with $L_n/Φ$=3.8 showed ductile embedment failure. For specimens with $L_n/Φ$=2.5, about half of the specimens showed bearing failure, and shear failure was observed for the other half. A comparison between the experimental results and the calculation methods explained in section 2 is shown in Figure 8. The calculated values have a similar tendency to the experimental values and are generally conservative (lower) than experimental values. The failure mechanism can be predicted, and the connection can be designed to have ductile embedment failure by designing $L_n/Φ$ ratio. The load-bearing capacity of a one-bolt connection can be roughly estimated by equations (4) and (5). As shown in Figure 9, the maximum strength obtained from the tests is almost the same regardless of the fibre direction angle (θ). It can be said that the influence of (θ) is almost negligible.

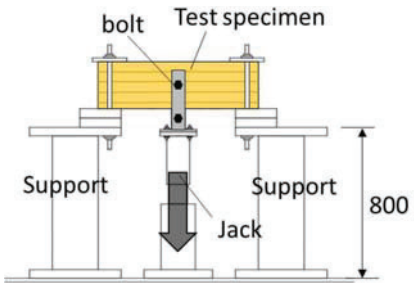

Figure 7: *Loading set-up for single drift pin test*

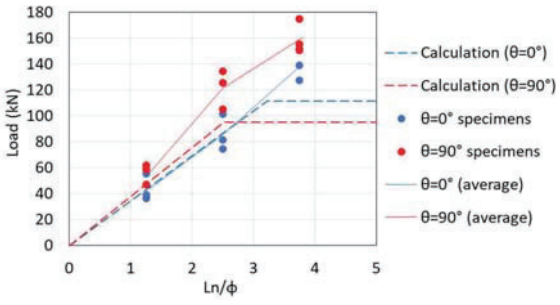

Figure 8: *Effect of Ln/Φ ratio on the load-carrying capacity*

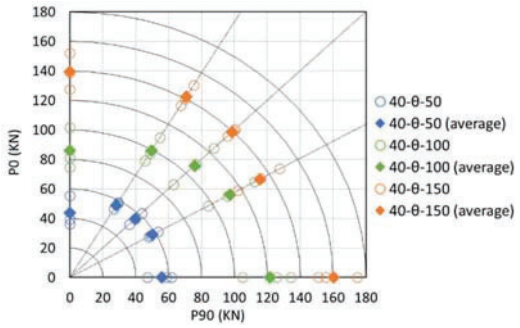

Figure 9: *Effect of loading angle relative to CLT fibre direction on the strength of the drift pin*

4 SHEAR WALLS TESTS

4.1 MATERIAL PROPERTIES

In order to investigate the structural performance of the proposed hybrid structural system, quasi-static cyclic loading tests on three different CLT wall-steel beam specimens were conducted. 90 mm thick CLT panels made from Japanese cedar with Mx-60-3-3 (3-ply 3-layer) grade and composition [11] were used for shear wall tests. The average CLT density was 393 kg/m^3, and the average moisture content was 12.2%. Material tests were conducted to obtain compression, embedment, and shear strength of CLT based on the testing procedures mentioned in [10]. Three identical specimens were used for each material test, and the results are summarized in Table 3.

Table 3: *Results of the CLT material tests for CLT wall tests*

	Compression		Shear		Embedment	
Strength (MPa)	Major	Minor	Major	Minor	Major	Minor
	23.7	10.9	3.8	2.6	21.6	15.5
	Compression [E]		Shear [G]		Embedment stiffness	
Modulus (MPa)	Major	Minor	Major	Minor	Major	Minor
	5926.9	2322.5	299.5	199.2	1767.2	1188.9

4.2 TEST MATRIX

Three CLT wall-steel beam specimens with different connections and wall configurations were tested. The details of the specimens are shown in Table 4. For all tests, 90-mm thick, 1000 mm by 2400 mm CLT wall panels were used. For the steel beams, two-meter C-section steel beams (200 × 90 × 8 × 13.5 in the Japanese Industrial Standards (JIS G 3192)) were attached to the top and bottom of the wall. One of the specimens contained a single CLT wall with the proposed bolt connection (SSB). The second specimen consisted of two CLT wall panels connected in plain using the proposed joint (SCB). SCB wall specimen was tested to investigate the coupled-wall behaviour of the proposed joint system. The third specimen (SSS) is identical to specimen SSB except for the CLT wall-to-beam connections. In the SSS specimen, conventional screw connections were used (i.e., steel plate fixed to one side of the wall using self-tapping screws). The details and dimensions of the connections are shown in Figure 9. 9-mm thick steel plate was used for all the connections. For the bolt connections, three 20-mm HTBs were used, and ($L_n/Φ$) ratio was chosen as $L_n/Φ$=3.5 to

https://doi.org/10.52202/069179-0162

ensure the targeted embedment failure. For screw connections, STS C65 screws with 5.5 kN strength were used, according to the Japanese CLT Design Manual [11]. The number of screws (9) was chosen so that the load-bearing capacity of the conventional connection is equal to that of the bolt connection. The CLT wall was connected to the steel beam using 24-mm HTBs.

4.3 LOADING SET-UP

The CLT wall specimens were tested under quasi-static cyclic loading with the set-up shown in Figure 11. The specimens were loaded by two 200 kN centre-hole jacks at each side of the specimen (pull forces were applied). The two jacks were connected to the steel beams using wire ropes, and a pre-tension force of 10 kN was applied to the two wire ropes in order to prevent the twisting of the specimen in the out-of-plane direction. No axial load was applied to the wall; however, four tie bars were attached to the top steel beam as an uplifting constraint. each tie bar was pre-stressed with a 5 kN tensile force. The lateral load was applied as an incremental cyclic loading based on the loading protocol provided in [12]. Three cycles for each peak drift were adopted.

Table 4: *Test matrix of the CLT wall tests*

Specimen name	SSB	SCB	SSS
Number of panels	1	2	1
Connection type	Bolt (HTB)	Bolt (HTB)	Screws (STS ∘ C65)
Bolts/screws diameter (mm)	20	20	6.5
No. of bolts/screws	3	3x2 (6)	9

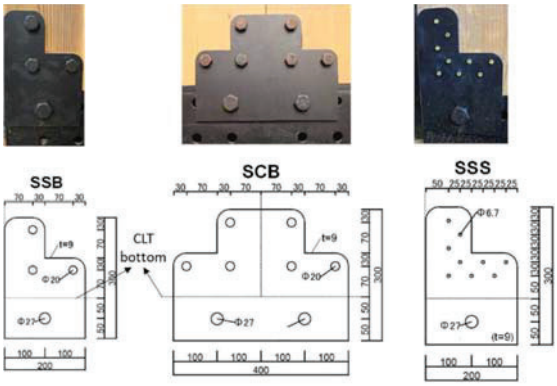

Figure 10: *Details of the steel plates used in the connections*

4.4 INSTRUMENTATION

The applied lateral load was measured using a centre-hole load cell. A typical instrumentation layout for the CLT wall tests is shown in Figure 12. LVDT sensors were attached to the tested specimens to measure story drift, and the story drift angle was calculated by considering the story height between the middle of the top and bottom beam (i.e., calculated by dividing the lateral load by the story height (2600 mm)). Rocking, sliding, shear, and bending deformation of the CLT wall panel were also measured. LVDT sensors to measure the neutral axis of the wall were also attached to the top and bottom of the wall. In addition, to calculate the axial forces in the tie bars, strain gauges were attached to all the bars. The axial force of the tie bar can be calculated as shown in Equation (11). The flexural moment in the bottom of the CLT wall ($M_{W\text{-}B}$) is then calculated using Equation (12) by subtracting the moment caused by the tie bar M_r from the moment of the entire system (M_{total}).

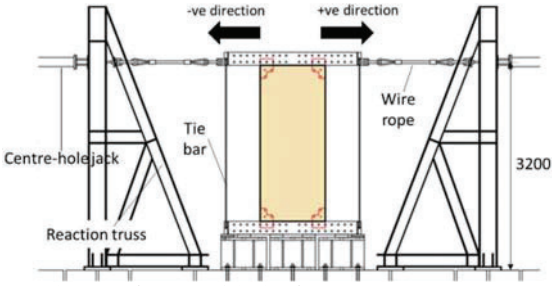

(a) Schematic diagram of the loading set-up

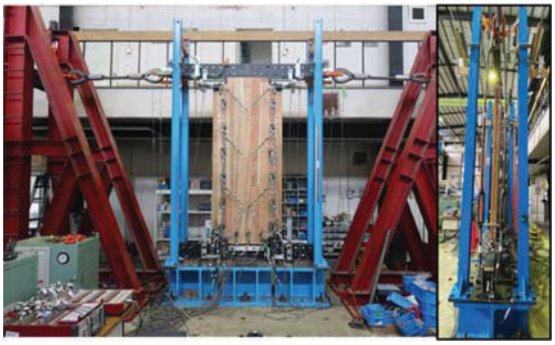

(b) Photo of the loading set-up

Figure 11: Loading set-up of shear wall tests

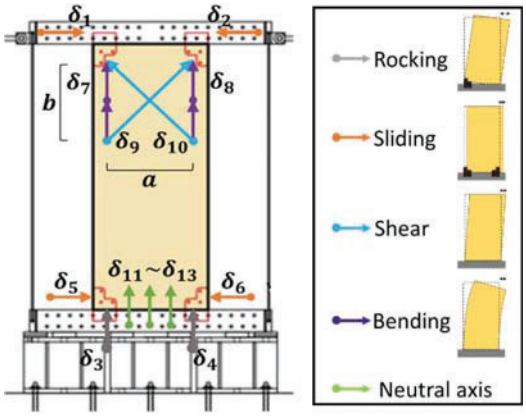

Figure 12: *An example of single wall (SSB) instrumentation*

https://doi.org/10.52202/069179-0162

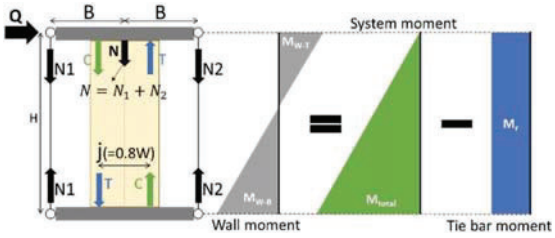

Figure 13: *Calculation method of the wall moment*

$$N_i = \varepsilon \times E \times A \quad (11)$$

Where ε (mm/mm) is the strain of the tie bar as measured, E (N/mm^2) is Young's modulus of the steel bar (2.05×10^5 N/mm^2), and A (mm) is the cross-sectional area of the tie bar (478.8 mm^2).

$$M_{W-B} = M_{total} - M_r \quad (12)$$
$$M_{total} = Q \times H \quad (13)$$
$$M_r = (N_1 - N_2) \times B \quad (14)$$
$$T = M_{wb}/j - 0.5N \quad (15)$$

Where H (mm) is the story height (2600 mm), N_1 and N_2 (kN) are the axial forces in the left and right tie bars, respectively. B (m) is the distance between the tie bar and the centre of the wall (1.025 m). N (kN) is the axial force applied to the wall and is equal to N_1+N_2. j (m) is the distance between the two connections at the bottom of the wall (0.8×D (1.2) =0.96 m), as explained in section 2.

4.5 RESULTS AND DISCUSSION

4.5.1 Failure characteristics

Photos of the failed single wall and coupled wall specimens (SSB and SCB, respectively) are shown in Figure 14. For the SSB specimen, at the bottom tensile connection, the outer layer of the wall (i.e., the outer lamina) failed in plug shear-out failure at 1% story drift angle. After that, a decrease in stiffness was observed; however, the load-bearing capacity of the wall continued to increase. This increase can be attributed to the effect of the compression strut inside the CLT wall, which appears as compression stresses at the compression side of the top and bottom part of the wall. At 5% story drift, the steel beam yielded in flexure (Figure 14.a), and the loading was terminated. For the SCB specimen, the outer lamina of the CLT wall at the tensile connection had a plug shear-out failure at 1.3% story drift. The load-bearing capacity continued to increase after the shear failure. At 4.8% story drift, the tensile connection in the middle of the wall had block shear failure, as shown in Figure 14.b, and the loading was terminated at 5% story drift. For the single wall with screw connections specimen (SSS), at 3% story drift, the screws of the bottom tensile connection started to fracture (2 screws). At 3.7% story drift, a large number of screws in the top and bottom tensile connections were broken and the test was terminated.

Although the expected failure type was supposed to be a uniform embedment failure, the bolt was tilted to the steel plate side of the CLT panel during the experiment. This failure mode was not considered in the design of the connections. In Europe, to calculate the load-bearing capacity of one-bolt connections for ductile failure the European yield model (EYM) is used. Using EYM the strength and failure mode of the connection are mainly governed by the bolt diameter to CLT panel's thickness ratio (Φ/t). When the EYM was applied to the connection used in this test, it was found that the expected failure is bolt-yielding failure (mode 2, Φ/t= 0.22), as shown in Figure 15. The ductile failure strength of the proposed joint was calculated based on the EYM equations provided in [13] and was compared to the experimental results. In order to apply the EYM to CLT, the average embedment strength across the width of the CLT panel was used, instead of lamella-by-lamella calculation. The values of the embedment strength of CLT provided in section 4.1 were used.

(a) SSB specimen

(b) SCB specimen

Figure 14: Failure characteristics of the tested specimens

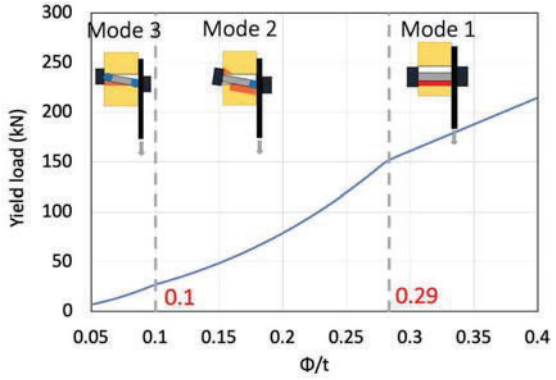

Figure 15: *Failure modes based on the EYM [13]*

4.5.2 Load-deformation response

The shear force-story drift curve for the SSB specimen is shown in Figure 16. The difference between maximum strength in the positive and negative direction was within 8%. When compared to calculation values based on uniform embedment failure (as explained in section 2), the experimental maximum strength (P_{max}) was 38% smaller. However, when compared to strength derived from the EYM, the experimental maximum strength was 18% larger. The EYM model can predict the load-bearing capacity of the proposed joint system with an acceptable accuracy. In addition to that, it was found that high shear strength per wall (τ=0.84 MPa) can be achieved, compared to 0.15 MPa for the wall with a conventional tensile bolt connection. This value (0.15 MPa) is calculated based on the standard strength of the CLT wall used in the simplified design method that is provided in the Japanese CLT Design Manual [11]**.**

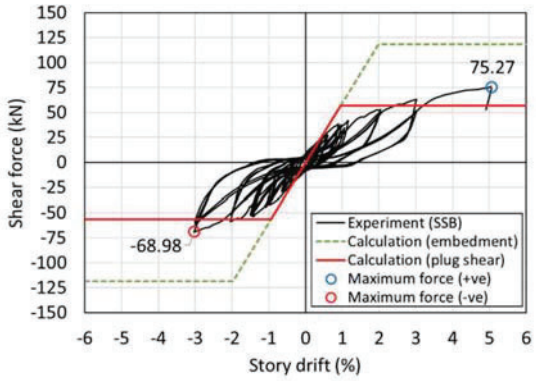

Figure 16: *Shear force-story drift curve for SSB wall specimen*

The shear force-story drift curve for the SSS specimen is shown in Figure 17. The maximum strength in the positive direction was 23% higher than that for the negative direction. Although the screw connection was designed to have a similar strength capacity to the bolt connection, the maximum strength of the SSS specimen was 32% smaller. The shear force-story drift curve for the SCB specimen is shown in Figure 18. The difference between maximum strength in the positive and negative direction was also within 8%. When compared to the single wall specimen (SSB), the maximum strength of the SCB specimen was only two times larger (198%). Therefore, each wall behaved as a separate wall and the proposed connections need to be improved to ensure the single-panel rocking behaviour.

The bilinear curves and the characteristic values (i.e., initial stiffness (K), yield strength (P_y), ultimate strength (P_u), and ductility (μ)) of the tested specimens were calculated based on the standard method described in the Japanese CLT Design Manual [11]. This method is based on the method proposed by Yasumura [14] for framed shear walls subjected to lateral load and is illustrated in Figure 19. The characteristic values of the tested specimens are summarised in Table 5. As a general tendency, for all the characteristic values, the single wall with screws connections specimen (SSS) had smaller values than the single wall with bolted connections specimen (SSB), as shown in Figure 20.a. The SSS specimen had a 60% smaller initial stiffness than the SSB specimen. When compared to the single wall specimen (SSB), the characteristic values of the coupled wall specimen (SCB) were almost two times larger on average. The initial stiffness of the SCB specimen was only 25% larger than the SSB specimen.

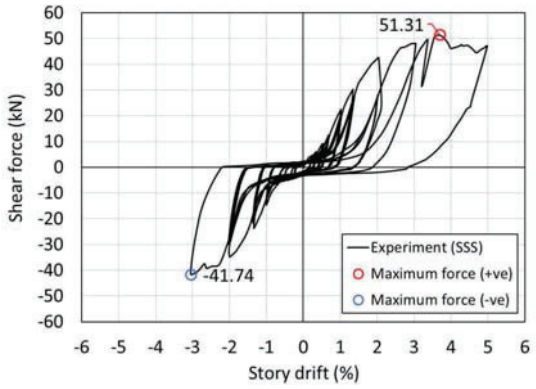

Figure 17: *Shear force-story drift curve for SSS wall specimen*

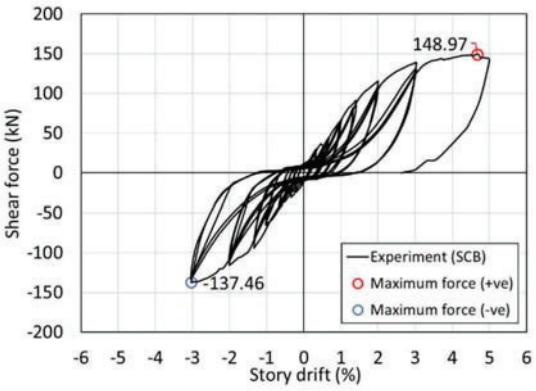

Figure 18: *Shear force-story drift curve for SCB wall specimen*

https://doi.org/10.52202/069179-0162

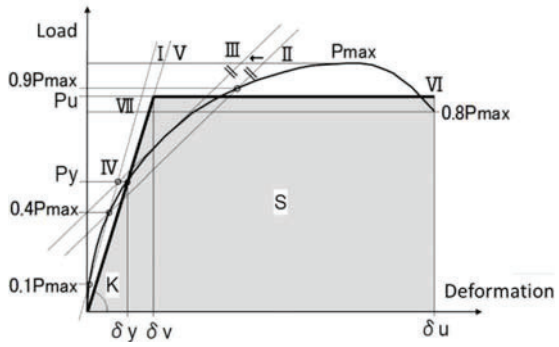

Figure 19: *Calculation method of bilinear of test load-deformation curves, as derived from [11]*

Table 5: *Summary of the characteristic values for specimens*

Specimen	Max. strength P_{max} (kN)	Yield strength P_y (kN)	Ultimate strength Pu (kN)	Initial stiffness K (kN/mm)	Ductility $\mu=\delta u/\delta v$
SSB	75.3	40.6	65.6	1.4	2.7
SCB	149.0	97.1	140.2	2.4	2.2
SSS	51.3	37.7	46.1	0.8	2.3

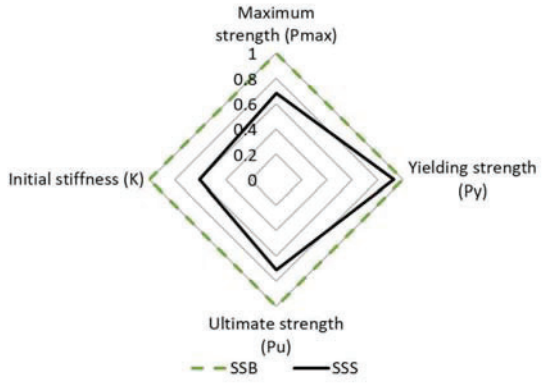

(a) bolts single wall (SSB) vs. screws single wall (SSS)

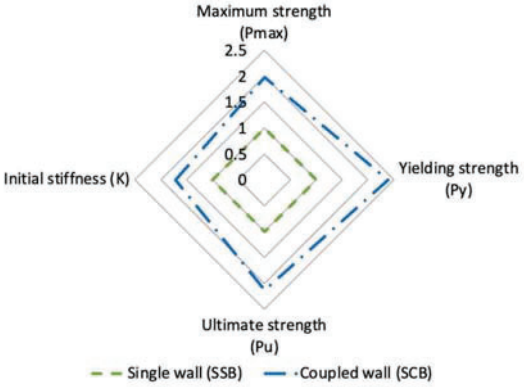

(b) single wall (SSB) vs. coupled wall (SCB)

Figure 20: *Comparison of the characteristic values for the tested wall specimens*

4.5.3 Performance of the proposed joint system

In this section, the performance of the proposed connection, as observed in the single wall specimen (SSB), is discussed. The contribution ratios of the different deformation components for the CLT wall panel at each peak drift in the positive direction are illustrated in Figure 21. In Figure 21, the contribution of the connection to the total deformation, and the bending and shear deformation of the wall panel are compared to the story drift. Deformation at the connection (rocking and sliding) was larger than the deformation of the CLT panel and was dominant from the small to ultimate story drift angle. Rocking deformation had the largest share with a 55.1% ratio on average, compared to the summation of the four components. The sliding deformation ratio was 32.5% on average. The CLT panel bending, and shear deformation ratio was 2.8% and 9.6%, respectively. It was found that the major component in the overall deformation of the wall is the rocking deformation, which represents the vertical deformation of the steel connection. This dominant rocking deformation was further investigated by looking into the relation between the moment at the bottom of the wall and the rocking angle of the wall, as shown in Figure 22.

In Figure 22, for experimental values, the rocking angle was taken as the value of the vertical LVDT sensors attached to the connection (δ_3 in Figure 12), and the flexural moment at the bottom of the wall ($M_{W\text{-}B}$) was calculated using the calculation method explained in section 4.4 (using Equation ((12)). To draw the calculation values curve, the rocking angle was calculated by the calculation method introduced in section 2 (using Equation (8)). Wall moment ($M_{W\text{-}B}$) was also calculated by the calculation method introduced in section 2. The calculated maximum moment was 16% smaller than the experimental result. The same tendency between calculation and experimental results was also found for the overall wall shear force-story drift. It was found that the introduced calculation method can be used to predict the structural behaviour of the proposed connection.

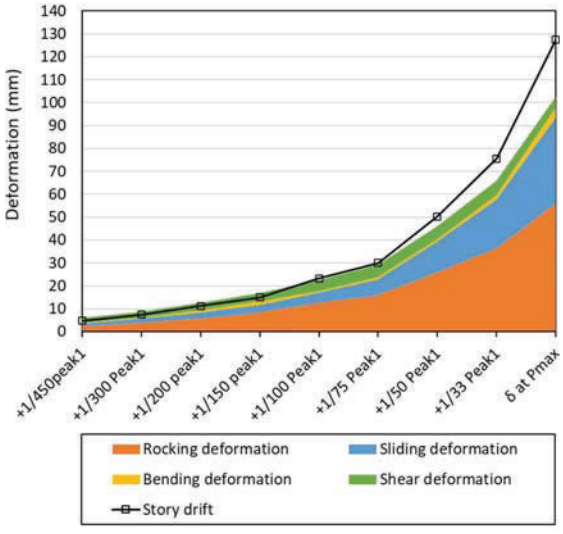

Figure 21: *Deformation components of single wall specimen (SSB) compared to the story drift (in positive direction)*

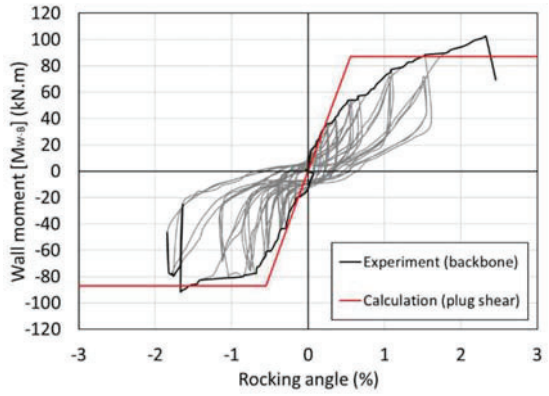

Figure 22: *Moment-rocking deformation curve of (SSB) wall*

5 CONCLUSIONS

In this paper, a novel steel joint system for CLT-steel hybrid structures in seismic regions was proposed. The connections used in this joint system consist of steel bolts and a steel plate and works under bi-directional loading condition. One-bolt connection tests were conducted to investigate the effect of loading direction. Also, full-scale CLT wall-steel beam cyclic tests were conducted to investigate the structural performance of the hybrid structural system. The findings of this research are as follows:

1. Simple and easy-to-install bolted connection that can utilize the actual strength of CLT was developed.
2. Based on the one-bolt connection tests, it was found that maximum strength can be predicted, and the connection can be designed to have ductile embedment failure with the considerable selection of the embedment length over bolt diameter ratio (i.e., L_n/Φ larger than 3.2). Also, for CLT panels with a one-bolt connection, the effect of loading direction on the ultimate strength was not significant (within 16%)
3. For CLT walls tests, the wall with the proposed joint system showed higher average shear strength of 0.83 MPa, compared to 0.15 MPa of conventional tensile bolt connection. The wall also showed ductile behaviour and did not fail until a large story drift angle of 5% (the story drift angle at steel beam yielding). Regarding the coupled wall test, the two walls behaved as separate single walls and the strength was about twice the single wall. Further improvements are required to secure the single-panel rocking behaviour.
4. In the wall-beam system, the deformation of the proposed connection was dominant (i.e., rocking 55.1% and sliding 32.5% of the wall lateral deformation). The proposed calculation method can be used to predict the performance of the joint system.

For future consideration, improvements of the proposed connection to ensure CLT embedment failure is needed. Also, further considerations to improve the rocking behaviour of the coupled walls are desirable.

ACKNOWLEDGEMENT

This research was supported by JSPS Kakenhi Grant Number JP19K22001, and by Miyagi Prefecture CLT Promotion Council. This fund is gratefully acknowledged. The support of Dr. Naoyuki Matsumoto, Assistant Professor, Tohoku University is also appreciated.

REFERENCES

[1] Japanese Forestry Agency, accessed 25 January 2023,<https://www.rinya.maff.go.jp/j/kikaku/hakusyo/r1hakusyo_h/all/chap3_2_2.html>. (In Japanese)
[2] Brandner R., Flatscher G., Ringhofer A., Schickhofer G., Thiel A.: Cross laminated timber (CLT): overview and development. European Journal of Wood and Wood Products, 74:331-351, 2016.
[3] Loss C., Rossi S., Tannert T.: In-plane stiffness of hybrid steel–cross-laminated timber floor diaphragms. Journal of Structural Engineering, 144(8):04018128, 2018.
[4] Khajehpour M., Pan Y., Tannert T.: Seismic Analysis of hybrid steel moment frame CLT shear walls structures. Journal of Performance of Constructed Facilities, 35(5):04021059, 2021.
[5] Dickof C., Stiemer S.F., Bezabeh M.A., Tesfamariam S.: CLT–steel hybrid system: Ductility and overstrength values based on static pushover analysis. Journal of Performance of Constructed Facilities, 28(6):A4014012, 2014.
[6] Bezabeh M.A., Tesfamariam S., Popovski M., Goda K., Stiemer S.F.: Seismic base shear modification factors for timber-steel hybrid structure: collapse risk assessment approach. Journal of Structural Engineering, 143(10):04017136, 2017.
[7] Tesfamariam S., Stiemer S.F., Dickof C., Bezabeh M.A.: Seismic vulnerability assessment of hybrid steel-timber structure: Steel moment-resisting frames with CLT infill. Journal of Earthquake Engineering, 18(6):929-944, 2014.
[8] Kanazawa K., Isoda H., Kitamori A., Usami T., Araki Y.: Structural performance of composite structure with CLT wall infilled in steel frames using drift-pin with steel plate. Journal of Structural and Construction Engineering, 86(788):1430-1439, 2021. (In Japanese)
[9] Minegishi A., Atsuzawa E., Maeda M.: Study on development of a simple and practical analytical model for structural design of CLT buildings. In: Proceedings of Annual Meeting Architectural Institute of Japan (AIJ), No.22246-22247:491-494, 2021. (In Japanese)
[10] Test Manual for Structural Timber Strength. Japan Housing and Wood Technology Center, 2011. (In Japanese)
[11] CLT Building Design Manual. Japan Housing and Wood Technology Centre, 2016. (In Japanese)
[12] JIS A 1414-2: Performance test methods of panel components for building construction. Japanese Standards Association, 2010. (In Japanese)
[13] AIJ Standard for Structural Design of Timber Structures. Architectural Institute of Japan, 2006. (In Japanese)
[14] Yasumura M.: Evaluation of wood framed shear walls subjected to lateral load. In: Proceedings of the 30th CIB-W18, Vancouver, Canada, 1997.

https://doi.org/10.52202/069179-0162

World Conference on Timber Engineering Oslo 2023

A NOVEL LIMITED-DAMAGE 3D-PRINTED INTERLOCKING INTER-MODULE CONNECTION SYSTEM FOR CROSS LAMNINATED TIMBER (CLT) VOLUMETRIC STRUCTURES

Zhengyao Li[1], Konstantinos Daniel Tsavdaridis[2]

ABSTRACT: With both the sustainability of timber and efficiency of modular construction, Cross Laminated Timber (CLT) volumetric construction is considered a potential solution to the severe environmental impact of modern construction. Conventional connection systems of CLT modular structures (angle bracket, hold-down) are mainly designed for panelised and framed construction. Due to their nature, they require careful design while numerous damages have been reported not only on their steel components but also timber fibres. The UK's funded project 3DMBC (https://3dmbc.com) was established to explore new ways of connecting CLT volumetric modules, ideally being damage-free and self-locking onsite during installation, aiming to improve the efficiency, adaptability and reusability of CLT volumetric construction. Damage avoidance philosophy (controlling deformation and damage away from timber and the embedded fasteners) was a key objective in the design of a three-dimensional connector system. A novel inter-locking system was recently proposed, tested experimentally and validated via numerical analysis. The proposed connection design also showcases a new concept of module assembly in CLT volumetric construction with higher efficiency, flexibility and adaptability, meanwhile demonstrates the potential in mitigating (permanent) damage of timber, thus increase service life and enable disassembly and reuse operations. The study shows that the screw-free assembly was provided along with adequate stiffness, strength and ductility by the new connections, and no damage was observed in timber after testing, proving the feasibility of the new connection design.

KEYWORDS: CLT Volumetric Construction, Timber Panel, Interlocking Connection, Damage-controlled Connection

1 INTRODUCTION

Volumetric construction is a modern method of construction (MMC) that is widely applied in buildings with high repeatability such as schools, offices, residential and hotels. Forming buildings with prefabricated flat modules that contain preassembled building accessories such as cladding, internal finishes and MEP services, this construction method is highly efficient with reduced waste production, workspace requirements and reliance on on-site manual work [1-2]. Concrete and steel volumetric construction are now rapidly growing in densely populated regions due to their great efficiency, while the potential of Cross Laminated Timber (CLT) in volumetric construction is also being explored for its additional material sustainability.

In volumetric construction, the connections that joint the adjacent modules (inter-module connections) provide load transferring path and define the overall structural performance, while the installation of them is a widely acknowledged problem due to the limited space (access) between modules for installing and dismantling connections. In CLT volumetric structures, where CLT panels are used as the primary structural elements to form the enclosed flat modules, the space for inter-module connection installation can be even more limited (Figure 1). As a recently developed construction technology, specific connection products have not yet been proposed for CLT volumetric structures. Therefore, flat modules could be left disconnected in low-rise CLT volumetric buildings. Alternatively, conventional timber connections angle brackets and hold-down plates are commonly employed, while the drawbacks are evident, such as the connection accessibility requirements, intensive labour force requirement for installation, insufficient stiffness and strength as well as the unpredictable and unfavourable brittle failure modes [3-5]. To promote the development of multi-storey CLT volumetric structures, the investigations on inter-module connections are crucial.

[1] Zhengyao Li, University of Leeds, United Kingdom, cnzl@leeds.ac.uk
[2] Professor Konstantinos Daniel Tsavdaridis, City, University of London, United Kingdom, konstantinos.tsavdaridis@city.ac.uk

https://doi.org/10.52202/069179-0163

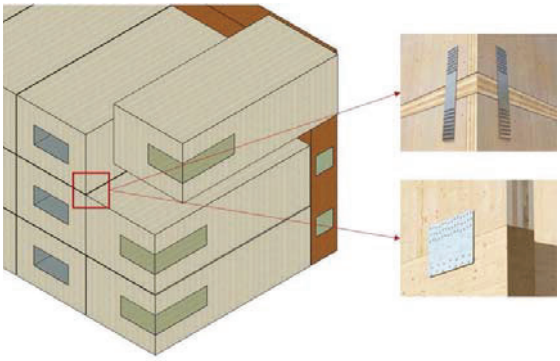

Figure 1: *Illustration of inter-module connection locations and the conventional hold-down (top) and bracket (bottom) that could be used in CLT volumetric structures*

A few bespoke connections (Figure 2) have been proposed recently for bespoke CLT volumetric projects to address the connection accessibility problem. These connections employ slot (groove) and ridge (tongue) designs that have matched shape, which can fit together without additional joining operations, such as adhesive or fasteners. In this way, the needs for access to install fasteners can be eliminated, and thus achieve a more efficient assembly and accurate positioning of modules. However, such connection designs require panel modifications for connection fitting, which may cause cross-sectional loss in structural elements and limit their applicability to other CLT volumetric structures [5]. A universal connection solution was still missing for the ease of design and construction for this structural system. Therefore, a novel interlocking connection system is developed within 3DMBC group, exploring convenient onsite joining methods with enhanced structural performance.

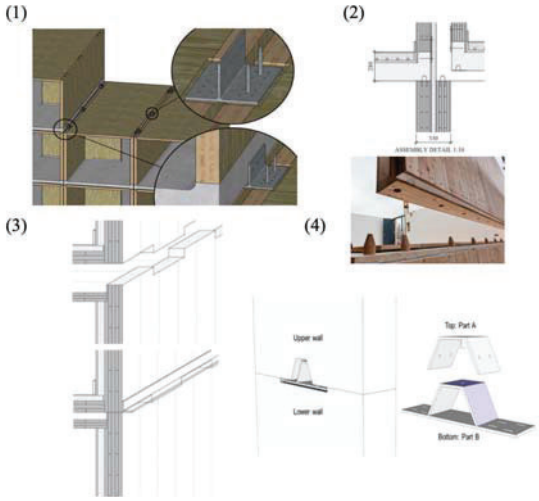

Figure 2: *Novel connection systems for specific CLT volumetric projects: (1) Jakarta Hotel [6]; (2) Heidelberg Student Accommodation [3]; (3) Moxy Modular Hotels (Marriott) [3]; (4) A novel system proposed by the University of British Columbia [7]*

2 CONNECTION DESIGN

2.1 INTERLOCKING CONNECTION SYSTEM

The proposed interlocking connection system consists of a tensile and a shear connection (Figure 3) [8]. Both are strip-like devices that formed by repetitive 3D unit elements. Both shear and tensile connections include two parts, named male connectors and female connectors, which self-lock after assembly, prohibiting module movement on their primary and secondary working directions (Figure 3).

Connection strips are fastened to CLT flat modules in the factories to achieve precise position, proper tightening, as well as improved project efficiency. Utilising this interlocking technique, modules with pre-installed connections can be accurately assembled on-site by simply sliding or stacking them (Figure 3) without additional onsite fastening. The pre-installed sliding connection units (Figure 4) also act as guiding devices to help locate the modules into the right positions and avoid potential construction errors from manual operations advancing the overall construction management tasks. Different from the conventional point-to-point connections, continuous reinforcement is formed along the edges of modules after guided assembly, which is suitable to CLT volumetric structures, where translational forces are important in structural design. The tensile connections provide vertical constraints at the edge of the structure and help resist uplifting. The shear connections provide horizontal constraints at the middle of the structure to resist lateral movement from wind and seismic load (Figure 5).

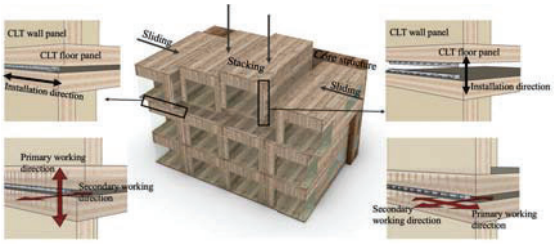

Figure 3: *Interlocking tensile (left) and shear (right) connection and CLT modules assembly (middle) with the pre-installed connections*

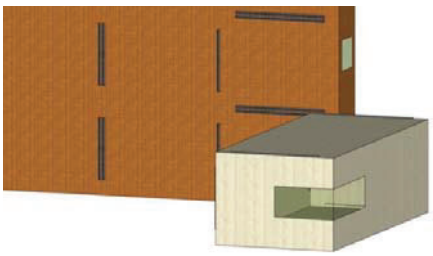

Figure 4: *The preinstalled connections that are used as guiding system to assist modules installation*

https://doi.org/10.52202/069179-0163

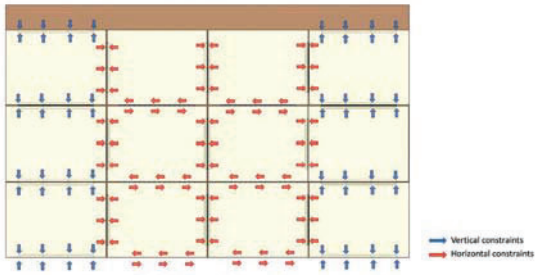

Figure 5: *Continuous reinforcement along CLT modules edges provided by assembled connections [8]*

2.2 CAPACITY DESIGN AND DAMAGE AVOIDANCE PHILOSOPHY

Beyond the advanced installing method, this connection system is also designed with the damage avoidance philosophy to limit the permanent damage in timber that is observed when using the conventional timber connections, hence enable reuse. In timber connection design, fastener deformation is treated as the primary source of ductility, and overstrength method (eq.1) is commonly applied to strengthen the brittle elements and ensure the activation of fastener deformation before the brittle failures happen in timber and metal plates (Figure 6), which is known as "strong plate-weak fastener" behaviour [9].

$$\gamma_{Rd} R_{d,ductile} \leq R_{d,brittle} \quad (1)$$

The application of this method can, however, be problematic due to the inherent defects of timber as natural material, the unclear understanding of the interaction between timber and deformed fasteners, and the insufficient accuracy of currently available analytical models [5]. As the overstrength factor (γ_{Rd}) is calculated by multiplying γ_m (partial factor of material properties), γ_{an} (ratio of estimated value to analytical value of the target strength) and γ_{sc} (scattering of the target strength), the above reasons can lead to unrealistic values of these factors, and then lead to inappropriate overstrength factor, especially when specific overstrength factors are not provided for timber structures in EC8 [10][11]. Such overstrength factor may lead to undesirable failure modes, for example timber splitting and metal plate fracture [12][13]. In addition, the deformed fasteners can crush the timber and create permanent cavities around timber fibres, which lead to degraded stiffness and strength [9], reducing structure's capacity in energy dissipation during seismic events as well as develop large residual displacements that reduce the structure's resistance to aftershocks [14-16]. Consequently, relying on fastener deformation for ductility is not ideal as it imposes difficulties to the design prediction and repair of timber connections (for reuse), and ultimately reduces seismic resistance.

Interlocking connection design benefits from utilising the metal connectors which are treated as the ductile elements (Figure 6). Shifting the ductility source from the timber-fastener interaction to the metal connector deformation (not the screws) can make connection properties dependent on the stable metal material properties, instead of the timber grain orientations and conditions, reducing the risk of brittle failures and providing controlled and easily predicted connection performance.

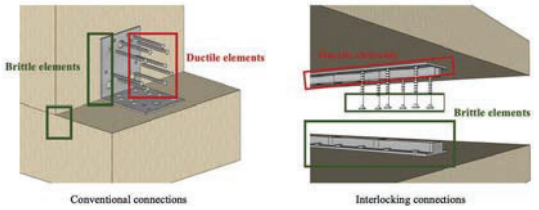

Figure 6: *Capacity design of conventional plate connections (left) and novel interlocking connections with damage avoidance philosophy (right)*

2.3 ADAPTABLE CLT VOLUMETRIC BUILDINGS

In addition, the special functionalities of this proposed connection system, such as the interlocking and damage avoidance effect, can be used for adaptable structures that possess the ability to address changes during construction and meet different functionality requirements during service life, such as partial disposal, change of use, re-usability and extension of buildings, for coping with future building obsolescence and redundancy [17]. The adaptability of such structures is attributed to the design of connections. The below criteria are recognised as crucial factors for developing adaptable connections [17][18]:

Demountability: Adaptable connections should be demountable to comply with the potential modifications in building design, and allow for easy dismantlement without demolition and damage of the structural members at the end-of-service life. The undamaged structural components or even the entire flat modules can be directly reused or recycle at their highest extent, improving the resources scarcity and environmental degradation brought by the building-related activities.

Standardisation: Adaptable connections should be standardised, hence allow for general application without modifications required, facilitating design simplifications.

Size, shape and position tolerance: Adaptable connections should be project-independent products that can fit with structural elements (here CLT panels and volumetrics) with varied dimensions at different positions within the structure. This refers to the connections that need no modification requirements for the fitting of connections.

Individual removability: The structural elements with adaptable connections should be removable without interfering with other elements, in response to external factors.

Direct usability: Adaptable connections should be operational immediately after installation without further modifications, such as fixing, adjusting and controlling to speed up the construction process, eliminate the onsite manual work and ensure safety.

https://doi.org/10.52202/069179-0163

Based on the above criteria, the proposed connections are highly adaptable, as they are demountable, standardised, flexible and can provide immediate reinforcement after self-locking.

3 NUMERICAL AND EXPERIMENTAL ANALYSIS

3.1 EXPERIMENT PREPARATION

To evaluate the realistic performance of the proposed connection design, monotonic and cyclic push-out and pull-out tests were performed on the connection specimens, using loading protocol as prescribed in EN12512 [19]. The unit elements of each connection were tested; first screwed to 5-ply GL24h CLT panels and then assembled together without any fastener (Figure 7). Six LBS7100 and four HBSP12120 from Rothoblaas were used in each of the tensile and shear unit connectors to achieve higher timber-fasteners connection capacity than the estimated interlocking connector capacity, ensuring the successful attainment of damage avoidance effect.

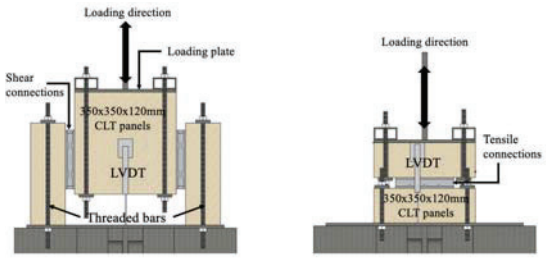

Figure 7: *Experimental set-ups of the push-out (left) and pull-out test (right) on shear and tensile connectors*

Due to the complex geometric design (cantilevering and curvy features) of interlocking connectors and the limited number of specimens needed for testing, 3D printing was used as the manufacturing method to produce the testing specimens using SS420/BR (Figure 8), considering its manufacruting freedom without requesting moulding [20]. All specimens were printed with satisfying accuracy, and both male and female connectors fitted well with 1mm printing tolerance. To determine the actual properties of connection material to be used in the numerical validation, coupons tests were conducted on the specimens from the undeformed female connectors, which confirmed the modulus of elasticity E=130GPa, yield strength σ_y =304MPa, ultimate strength σ_u=638MPa and ultimate strain of ε_u=5.9 % of the 3D printed steel.

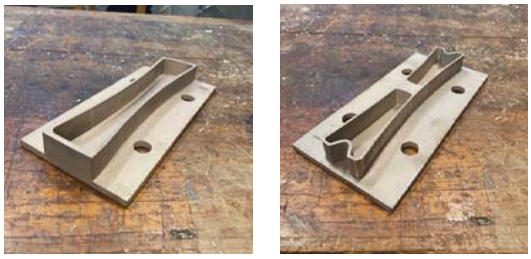

Figure 8: *3D printed specimens of shear (top) and tensile (bottom) connection units*

3.2 EXPERIMENTAL RESULTS

As demonstrated in Figures 5 and 6, the deformation of both connections was localised on part of the connections (the male connectors). After removing the screws, only slight wearing can be observed around the screw holes on the connector plates without visual deformation in the screws and timber, indicating the successful attainment of damage avoidance effect on the structural material.

The primary deformation mode in the shear connection was buckling of the middle of steel plate on both sides. Also, slight close-up at the end suckens can be observed (Figure 9). The primary deformation mode in the tensile connection was bending of the L-shaped elements in the male connector (Figure 10). The female connectors and screws of both connections remained mostly undeformed; only very slight open-up in the bearing walls and slight bending in the bottom plate in the tensile female connector were recorded at the end of testing. Thus, it can be concluded that the deformation of the interlocking connections was well controlled within both male connectors.

Figure 9: *The tested shear connection specimens and screw removal*

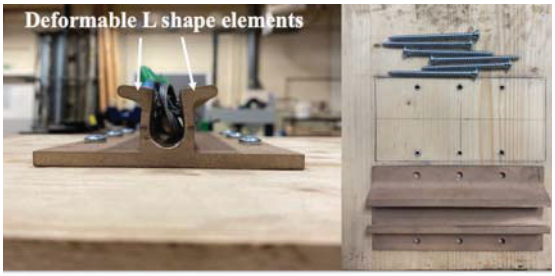

Figure 10: *The tested tensile connection specimens and screw removal*

https://doi.org/10.52202/069179-0163

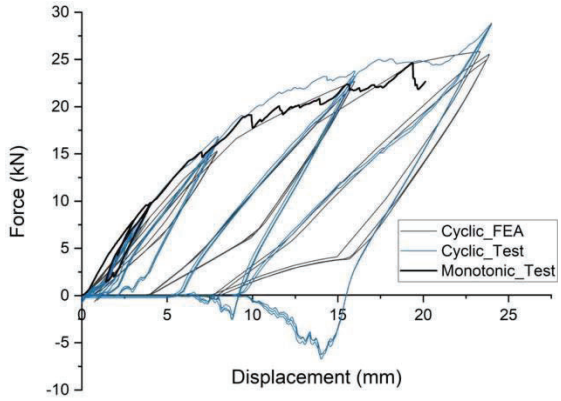

Figure 11: *Force-displacement curve of the tensile connections [8]*

Figure 11 demonstrates the cyclic performance of the tensile connections, and shows adequate strength, stiffness and ductility. The stiffness and maximum strength in the first cycle of each loading step during the cyclic test were well consistent with the monotonic tests, indicating that the plastic deformation in the steel male connector does not affect the maximum capacity in the subsequent loading. On the contrary, conventional timber connections normally demonstrate reduced maximum capacity in cyclic test in comparison to the monotonic test due to the damage of timber in the vicinity of deformed fasteners. However, the plastic deformation causing a gap between the male and female connectors, consequently sliding of the male connector with no reaction force can be identified at the initial phase of each loading cycle.

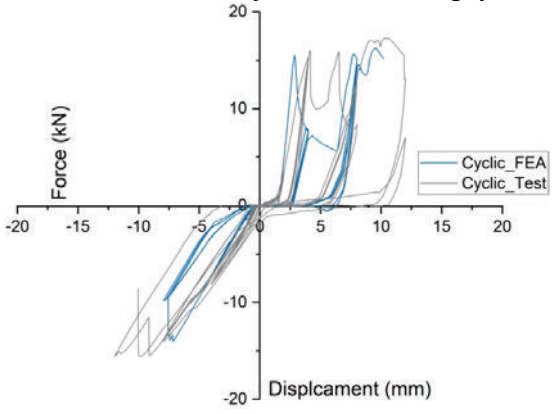

Figure 12: *Force-displacement curve of the shear connection [8]*

As depicted in Figure 12, the shear connections demonstrated higher stiffness but reduced ductility than the tensile connections in the cyclic testing. Three sudden resistance reductions can be identified at the displacement of 4mm, 6.5mm and -8mm, respectively, corresponding to the three buckling points observed in the failed shear specimens. After the buckling, the connection strength continued to develop in the deformed steel band and the end sunken in the male connector, leading to the plump hysteresis loop at large displacement until the breakage happened at the buckling point (Figure 9). Therefore, buckling at the middle of the deformable plate and bending at the sunken design at the end of the steel band are the two major deformation modes identified in the shear connections, and the buckling locations were relatively consistent among all the specimens.

3.3 NUMERICAL ANALYSIS

The numerical models of all experimental models were developed for validation (Figure 13). CLT panels were modelled with an orthotropic elastoplastic material; the properties are summarised in Table 1.

Table 1: *Material properties adopted for CLT panel model (spruce) [21]*

Elastic modulus (MPa)					
E_{11}		E_{22}		E_{33}	
11000		370		370	
Poisson's ratio					
ν_{12}		ν_{13}		ν_{23}	
0.48		0.48		0.22	
Shear modulus (MPa)					
G_{12}		G_{13}		G_{23}	
690		690		50	
Parallel-to-grain (MPa)		Perpendicular-to-grain (MPa)		Shear strength (MPa)	
f_{c11}	f_{t11}	f_{c22}	f_{t22}	f_v	$f_{v,roll}$
36	24	4.3	0.7	6.9	0.5

Grade-300PLUS steel (σ_y= 320MPa and σ_u=440MPa) and Grade 10.9 carbon steel (σ_y=σ_u=940.3MPa) [22] were used for steel fixture devices and screws, respectively, and the material properties of SS420/BR that determined from coupon test were used for the connectors. Different published modelling methods were employed to simulate the screw-timber interactions of screw working in different directions. To model the pull-out behaviours of LBS7100 of the interlocking tensile connectors that rely heavily on the threaded part of screws, an efficient approach presented in the literature was adopted [23] [24]. This method introduces a fictitious layer of 'soft material' that wraps the shank of screws as the simplified threaded part (Figure 13). The 'soft material' is assumed to be perfectly elastic with the same capacity as CLT (Table 1) except for the radial modules (E_{33}). A reduced value of 50MPa was used instead to simulate the weakened compressive capacity of timber around the threads. To model the bending capacity of HBSP12120, only the screws shank was modelled (Figure 13) [25], as it is the primary part that defines the bending behaviours of screws. For all other interfaces, the surface-to-surface discretisation method was adopted with the "Hard Contact" option in the normal direction, and the "penalty friction formulation" option in the tangential direction. The good agreement between the experimental results and numerical output in terms of the maximum strength, initial and reduced stiffness of each loading cycle, as well as the deformation modes, proves the

https://doi.org/10.52202/069179-0163

feasibility of the adopted modelling methods for both interlocking connections (Figure 11&12).

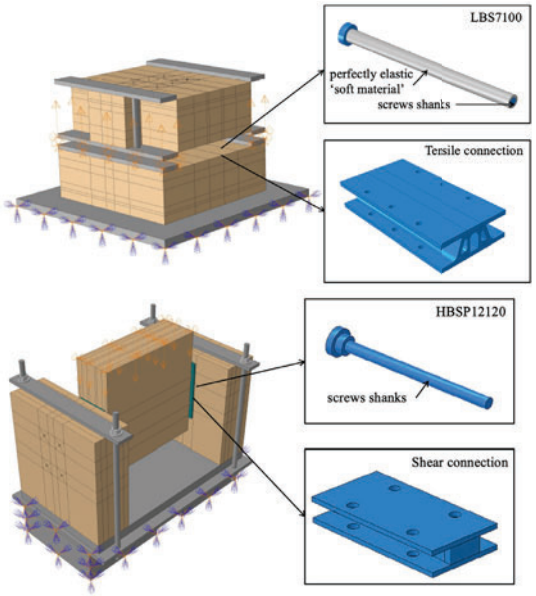

Figure 13: *FE models for tensile connection (top) and shear connection (bottom) validation*

After the validation, complimentary FE analyses were performed to further investigate the performance of the connectors with more common grade of steel S235 (E=210GPa, σ_y =235MPa and σ_u =360MPa) and better understand the deformation progression in the connectors, which are not visual during the testing due to the enclosed connection design.

Both connection models were tested numerically under primary and secondary directions (Figure 3), confirming the adequate stiffness and ductility in both translational directions. In the primary working direction, the damage avoidance effect was attained in both connections with most deformation being localised in male connectors. Negligible strain can be observed in the fasteners and timber. In the secondary working direction, both connections behaved more like conventional connections and all elements deformed including male connectors, female connectors and screws (Figure 14&15).

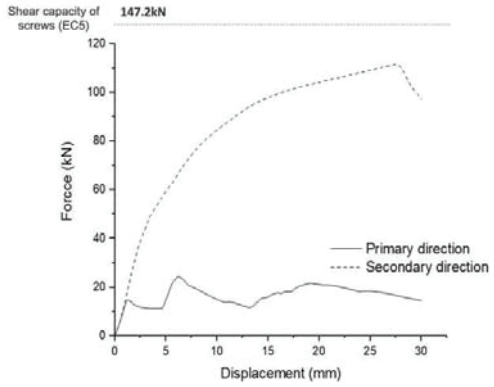

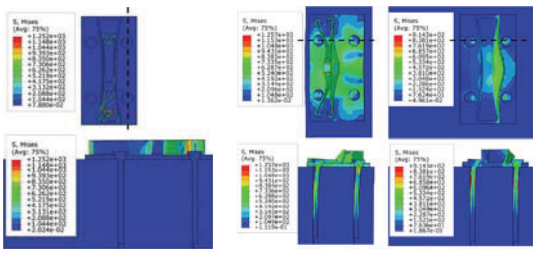

Figure 14: *Force and displacement curve of shear connection with S235 and connection deformation on primary (bottom left) and secondary directions (bottom right) under 15mm displacement [8]*

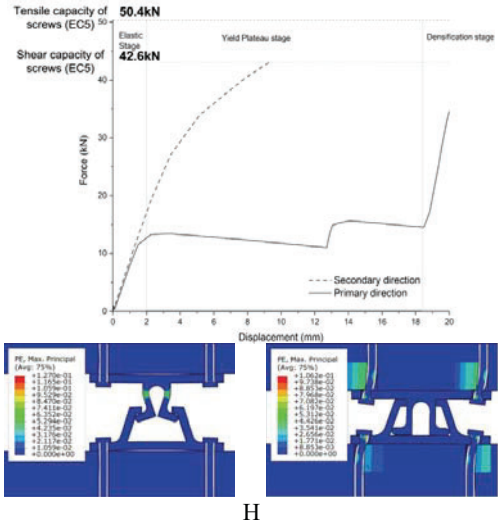

H

Figure 15: *Force and displacement curve of tensile connection with S235 and connection deformation on primary (bottom left) and secondary directions (bottom right) under 15mm displacement [8]*

4 CONCLUSIONS

This research proposed a novel connection system for CLT volumetric construction, as part of the modern methods of construction (MMC), to enable safe and efficient assembly as well as fast erection and dismantling. Without the need of panel modifications, the interlocking connectors can be easily applied to different projects with varied mechanical performance requirements and modules' specifications by simply adjusting the connector strip length. The adoption of unit element design also allows for easy standardisation, as the connections can be directly applied in construction without changes in geometries. Therefore, the proposed connection system can improve the constructability, adaptability and reusability of CLT volumetric structures. The conducted experimental and numerical analyses proved that the proposed connections have adequate translational strength, stiffness and ductility in both primary and secondary directions. The application of plug-and-play connections can enable automation/robotic construction methodologies with accuracy and speed,

https://doi.org/10.52202/069179-0163

resulting to less resources consumption and waste production, thus reduced environmental impact and destruction to the surrounding area. Though construction operations need to be somewhat altered for the sliding operations, this interlocking connection system can be a promising solution to efficient and adaptable multi-storey CLT volumetric construction.

ACKNOWLEDGEMENTS

The authors and the 3DMBC (https://3dmbc.com) group members would like to acknowledge the Royal Academy of Engineering and The Leverhulme Trust funds [LTSRF1819_15_40] as well as The Henry Lester Trust funds for their financial support in 3D printing the connection specimens. The contribution of The George Earle Laboratory staff is also acknowledged for providing technical expertise for the experimental testing. The authors would also like to acknowledge the kind support received from Rothoblaas and Stora Enso with regards to the testing materials (screws and CLT panels).

REFERENCES

[1] Rajanayagam, Pologanathan, K., Gatheeshgar, P., Varelis, G. E., Sherlock, P., Nagaratnam, B., and Hackney, P. A-State-Of-The-Art review on modular building connections. *Structures (Oxford).*, 34:1903–1922, 2021.

[2] Lacey, A.W., Chen, W., Hao, H. and Bi, K. Review of bolted inter-*module connections in modular steel buildings. Journal of Building Engineering*., 23:207-219, 2019.

[3] Carvalho, L.F., Carvalho Jorge, L.F and R. Jerónimo. Plug-and-Play Multistory Mass Timber Buildings. *Achievements and Potentials. Journal of Architectural Engineering.*, 26(2):04020011, 2020.

[4] Stepinac, M., Šušteršič, I., Gavrić, I., Rajčić, V. Seismic Design of Timber Buildings: Highlighted Challenges and Future Trends. *Applied sciences*., 10(4): 1380, 2020.

[5] Li, Z. and Tsavdaridis, K.D. Design for Seismic Resilient Cross Laminated Timber (CLT) Structures: A Review of Research, Novel Connections, Challenges and Opportunities. *Buildings*., 13: 505, 2023.

[6] Gijzen, R. Modular cross-laminated timber buildings, in the faculty of Civil Engineering and Geosciences. Delft University of Technology, 2017.

[7] Zhang, C., Lee, G. and Lam, F. Connections for Stackable Heavy Timber Modules in Midrise to Tall Wood Buildings. 2019, Timber Engineering and Applied Mechanics (TEAM) Laboratory.

[8] Li, Z. and Tsavdaridis, K.D. Limited-damage 3D-printed interlocking connection for timber volumetric structures: Experimental validation and computational modelling. *Journal of Building Engineering.*, 63: 105373, 2023

[9] Latour, M. and Rizzano, G. Cyclic Behavior and Modeling of a Dissipative Connector for Cross-Laminated Timber Panel Buildings. *Journal of earthquake engineering : JEE*., 19(1):137-171, 2015.

[10] EN 1998-1. Eurocode 8-Design of structures for earthquake resistance - part 1: General rules, seismic actions and rules for buildings. European Committee for Standardisation, 2004.

[11] Follesa, Fragiacomo, M., Casagrande, D., Tomasi, R., Piazza, M., Vassallo, D., Canetti, D., & Rossi, S. The new provisions for the seismic design of timber buildings in Europe. *Engineering structures.*, 168: 736-747, 2018.

[12] Izzi, M., Polastri, A. and Fragiacomo, M. Modelling the mechanical behaviour of typical wall-to-floor connection systems for cross-laminated timber structures. *Engineering structures.,* 162:270-282, 2018.

[13] Gavric, I., Fragiacomo, M. and Ceccotti, A. Cyclic behavior of typical screwed connections for cross-laminated (CLT) structures. *European Journal of Wood and Wood Products.,* 73(2): 179-191, 2015.

[14] Ceccotti, A., Sandhaas, C., Okabe, M., Yasumura, M., Minowa, C. and Kwai, N. SOFIE project - 3D shaking table test on a seven-storey full-scale cross-laminated timber., Earthq. Eng. Struct., Dynam. 42 (13):2003–2021, 2013.

[15] Chan, N., Hashemi, A., Zarnani, P., Quenneville, P. Pinching-Free Connector for Timber Structures. *Journal of Structural Engineering (New York, N.Y.).,* 147(5): 4021036, 2021.

[16] Aloisio, A., Pelliciari, M., Berami, A.V., Aloggio, R., Briseghella and B., Fragiaomo, M. Effect of pinching on structural resilience: performance of reinforced concrete and timber structures under repeated cycles. *Structure and infrastructure engineering*., ahead-of-print(ahead-of-print):1-17, 2022.

[17] Rand, A., Bragança, L. and Gervásio, H. Adaptability of Buildings: A Critical Review on the Concept Evolution. *Applied sciences.,* 11(10): 4483, 2021.

[18] Geraedts, R. Upgrading the Adaptability of Buildings. In: International Conference On Adaptable Building Structures. Eindhoven, The Netherlands; 2006.

[19] EN 12512:2001. Timber Structures. Test methods. Cyclic Testing of Joints Made with Mechanical Fasteners. European Committee for Standardisation, 2005

[20] Li, Z., Tsavdaridis, K.D. and Gardner, L. A Review of Optimised Additively Manufactured Steel Connections for Modular Building Systems. In Proceedings of the Additive Manufacturing for Products and Applications, Zurich, Switzerland, 1–3 September 2020.

[21] Sandhaas, C. Mechanical behaviour of timber joints with slotted-in steel platesDelft University of Technology: Netherlands, 2012.

[22] Tomasi, R., Crosatti, A. and Piazza, M. Theoretical and experimental analysis of timber-to-timber joints connected with inclined screws. *Construction & Building Materials.,* 24(9):1560-1571, 2010.

[23] Avez, C., Descamps, T., Serrano, E., Léoskool, L. Finite element modelling of inclined screwed timber to timber connections with a large gap between the elements. *European Journal of Wood and Wood Products.*, 74(3): 467-471, 2016.

[24] Bedon, C. and Fragiacomo, M. Numerical analysis of timber-to-timber joints and composite beams with

inclined self-tapping screws. *Composite Structures*, 207: 13–28, 2019.

[25] Hassanieh, A., Valipour, H.R. and Bradford, M.A., Sandhaas, C. Modelling of steel-timber composite connections: Validation of finite element model and parametric study. *Engineering Structures.,* 138: 35-49, 2017.

https://doi.org/10.52202/069179-0163

World Conference on Timber Engineering Oslo 2023

IMPACT OF MOISTURE CYCLING ON SCREW WITHDRAWAL CAPACITY OF TREATED AND UNTREATED RADIATA PINE

Luis Yermán[1], Zidi Yan[2], Wen Feng[3], Lisa-Mareike Ottenhaus[4]

ABSTRACT: The increased use of wood products for construction has intensified the need to understand how moisture affects the mechanical properties of timber connections. The withdrawal capacity of dowel-type fasteners, such as screws, needs to be measured, or estimated, for the design of timber systems having connections with axially loaded dowel-type fasteners. The influence of the moisture content changes on the timber is often examined, but its effect on the mechanical performance of connections is poorly considered, including the design codes. This work examined changes in the screw withdrawal capacity in light organic solvent preservative-treated and untreated Radiata pine with type 17 screws inserted perpendicular and parallel to the grain and subjected to repeated wetting and drying cycles. A comparison of the screw withdrawal capacities with those predicted from Australian and European codes was performed. The results presented here are part of a larger project that includes the study of embedment strength and lateral resistance in combination with different wood treatments and pine species.

KEYWORDS: Screw withdrawal capacity, Preservative treatment, Moisture content, Radiata pine

1 INTRODUCTION

Wood is a hygroscopic material that easily absorbs and desorbs moisture from the environment, producing swelling or shrinking. Dimensional changes induce stresses in the timber elements that can lead to cracks or failures [1]. Induced stress is even more important in timber connections, as the deformations and movement incompatibilities produced by differential moisture responses create even more stress [2]. For example, the screw withdrawal capacity (SWC) in timber can be affected by moisture/drying exposure conditions that eventually reduce fastener capacity and can also induce metallic corrosion [3].

Most timber buildings are designed to exclude moisture, but some elements may be subjected to wetting and must be supplementally protected with preservatives to provide acceptable service life. Many of these preservatives are water-based products that may accelerate fastener corrosion and eventually the loss of mechanical properties of the timber connection [4]. For this reason, most preservative suppliers recommend the use of either stainless steel or hot-dip-galvanized fasteners.

Despite the potential for preservative treatment to affect fastener performance, there is limited research on the impact of moisture content (MC) changes on treated timber connections. The increased use of wood products in construction has intensified the need to understand how moisture affects the mechanical properties of timber connections, as wetting of these elements can occur due to rain penetration, condensation [5], as well as bathroom or pipe leakages.

Design standards can be used to estimate the strength of a timber connection, and ultimately design safe structures. According to Eurocode 5 (EC5) [6], the withdrawal capacity of dowel-type fasteners is necessary for the design of connections with axially loaded dowel-type fasteners. Nevertheless, the influence of the MC on the mechanical performance of these connections is poorly considered. In the EC5, the design value (X_d) of a strength property of a timber connection is calculated by modifying the characteristic value (X_k) according to Equation 1:

$$X_d = X_k \frac{k_{mod}}{\gamma_M} \quad (1)$$

where k_{mod} accounts for the service class (a function of load duration and expected equilibrium moisture content of the material) and γ_M is the partial factor (a function of the type of material, e.g., solid timber, particleboard). The impact of the MC in the design is considered only through k_{mod} with discreet values ranging from 0.2 to 0.6 in 0.1 intervals. Other design standards, such as the Australian standard AS 1720.1-2010 (AS1720) [7] only consider moisture effects on member strength, but not on the connection strength.

Screws are one of the most used timber fasteners. Nevertheless, little research has been conducted on the effect of MC variations on SWC [8]. Apart from MC, the SWC depends on several factors including connection

[1] Luis Yermán, School of Civil Engineering, The University of Queensland and National Centre for Timber Durability and Design Life, Australia, l.yerman@uq.edu.au
[2] Zidi Yan, School of Civil Engineering, The University of Queensland, Australia, zidi.yan@uq.edu.au
[3] Wen Feng, School of Civil Engineering, The University of Queensland, Australia, w.feng1@uq.net.au
[4] Lisa-Mareike Ottenhaus, School of Civil Engineering, The University of Queensland, Australia, l.ottenhaus@uq.edu.au

https://doi.org/10.52202/069179-0164

geometry (e.g., diameter and penetration depth), tensile screw capacity (which in turn depends on the material and diameter), timber density, and the direction of loading with respect to the grain orientation for larger screws. While this creates an infinite array of possible tests, these can be simplified to several critical factors.

This work examined changes in the SWC in light organic solvent preservative (LOSP) treated and untreated Radiata pine with screws inserted perpendicular and parallel to the grain and subjected to repeated wetting and drying cycles. A comparison of the experimental withdrawal capacity with those predicted from the standards AS1720 [9] and EC5 [6] are presented and discussed. This work is part of a larger project that aims to assess the impact of moisture cycles on the withdrawal capacity, embedment strength and timber joints for a series of Australian timber species and preservative treatments.

2 EXPERIMENTAL

2.1. SPECIMEN CONFIGURATION

Defect-free 272 mm long Radiata pine (*Pinus insignis*) specimens were cut from 5 m long 45 x 90 mm boards with and without LOSP treatment.

LOSP-treated and untreated specimens were conditioned at a temperature of 25 °C and 65 % of relative humidity, using an environmental chamber (Labec F-HWS-250B). The samples were kept inside the chamber until constant mass to ensure moisture equilibrium.

Stainless steel screws with a 4.2 mm outer thread diameter (Table 1) were driven into a lead hole with a 2.94 mm diameter, to a penetration depth of 37.5 mm. Three screws were inserted perpendicular to the grain, and two parallel to the grain (Figure 1). The specimens were designed to meet the minimum requirements according to the testing standards AS 1649 [10] and ASTM D1761 [11]. The screws were weighed before being driven into the wood. After installing the screws, timber samples were checked to ensure that no cracks developed.

Table 1: *Wood and screw specifications for creating the test assemblies, and the number of specimens built for testing.*

Wood type	2	Radiata pine (LOSP treated and untreated)
Screw types	1	Type 17 (8g), SS 304, 4.2 x 50 mm
Screws per specimen	3 + 2 5	Side + end grain TOTAL
Test conditions	5	0, 2, 4, 8 and 12 moisture cycles
Repetitions per condition	15 10	Side grain End grain
TOTAL	**50** **250**	**Wood specimens** **Screws**

The moisture content of the conditioned LOSP-treated and untreated woods was determined using the oven-dry method from 20 smaller samples from the same boards. For the determination of the density, the dimensions (L, W, T) were measured at three different points, using a digital calliper, for each specimen and then averaged (Table 2).

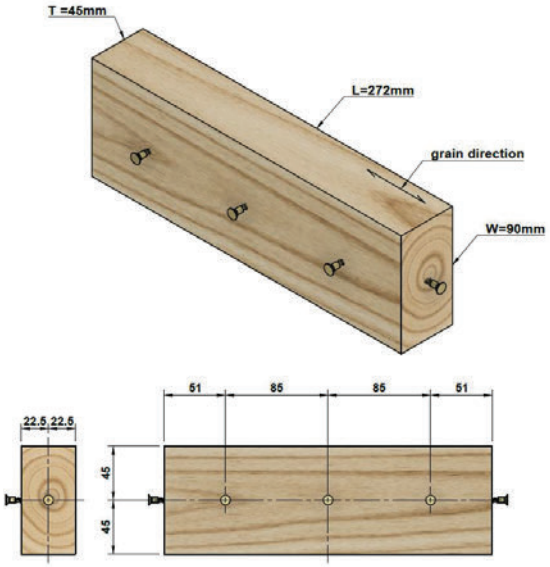

Figure 1: *Specimen dimensions and configuration showing the relative position of the screws and the grain direction. All distances are in mm (L = length, W = width, T = thickness).*

Table 2: *Wood types, mean density, and moisture content of the treated and untreated wood used in the experiments. Values in parenthesis are standard deviations.*

Wood type	*Mean density (kg/m3)*	*MC (%)*
Untreated	485 (49)	11.7 (0.8)
LOSP treated	465 (37)	12.9 (0.9)

2.2. MOISTURE CYCLES

One set of five specimens (controls) was immediately tested, while the remaining specimens were weighed to determine the initial weight and then soaked until their moisture contents had reached 50-60 wt% (between 4 and 6 days). The samples were then dried for 40-50 hours at 50 °C for a slow loss of moisture to a final MC between 10 and 15 wt% before being weighed again. At this point, the specimens were tested or subjected to another wet/dry cycle.

2.3. WITHDRAWAL TESTS

The effects of wetting and drying on withdrawal capacity were assessed after 0 (controls), 4, 8, 12 and 16 moisture cycles. Screw withdrawal tests were carried out according to the standard AS 1649 [10] using an Instron 3400 universal testing machine (Instron, Inc. Norwood, MA, USA). The speciemens were conditioned in the same environmental chamber and conditions mentioned before. The specimens were placed in a specially constructed assembly (Figures 2 and 3) and the screw was withdrawn

https://doi.org/10.52202/069179-0164

at a rate of 2.5 mm per minute. The load required to withdraw the screws was recorded as a function of time.

2.4. COMPARISON WITH DESIGN STANDARDS

The comparison of the experimental SWC with the estimated from the current Australian (AS1720 [9]) and European (EC5 [12]) codes was done based on the following ratio (Equation 2):

$$Ratio = \frac{SWCe}{SWCp} \quad (2)$$

where *SWCe* is the fifth percentile of the experimental SWC values from each series, and *SWCp* is the predicted SWC using Equations 3 and 4, corresponding to the AS1720 and EC5, respectively.

$$N_{k,j} = k_{13} l_p n Q_k \quad (3)$$

In Equation 3, $N_{k,j}$ is the *SWCp*, k_{13} is a modification factor (1.0 for screws on the face grain and 0.6 for screws in the end grain), l_p is the depth of the screw penetration (37.5 mm), n is the number of screws (1 screw), and Q_k is the characteristic capacity (56 N/mm).

$$F_{ax,\alpha,Rk} = \frac{n_{ef}\, f_{ax,k}\, d\, l_{ef}}{1.2cos^2\alpha + sin^2\alpha} \left(\frac{\rho_k}{\rho_a}\right)^{0.8} \quad (4)$$

In Equation 4, $F_{ax,\alpha,Rk}$ is the *SWCp*, n_{ef} is the number of effective screws (1 screw), d is the outer thread diameter of the screw (4.2 mm), l_{ef} is the penetration depth of the threaded part (35 mm), ρ_k is the characteristic density of the wood (considered as the fifth percentile of the density of the batch, in kg/m^3), and ρ_a is the associated density (considered as the 5th percentile of the densities of all the specimens, 418 kg/m^3), $f_{ax,k}$ is the characteristic withdrawal parameter, determined with the 5th percentile of the *SWCe* of the controls (specimens at week 0), and α is the load-grain angle, with screws driven into end grain α = 0º and screws driven into side grain α = 90º.

In practice, *SWCp* values are used to design timber structures. A safe prediction is considered when the ratio is above 1.

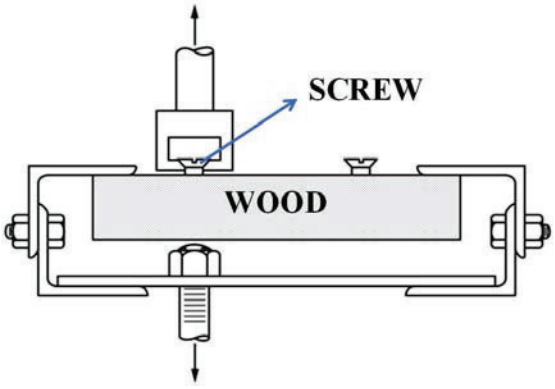

Figure 2: *Diagram of the screw withdrawal test assembly (adapted from* [11]*).*

2.5. STATISTICAL ANALYSIS

The data were subjected to an Analysis of Variance (α = 0.05) to determine the effects of the moisture cycles on the screw withdrawal capacity. Differences between means were examined using T-tests at a confidence interval of 95 %. Normal distribution was verified through Shapiro-Wilk tests.

Figure 3: *Screw withdrawal test setup, showing (a) grip and (b) test rig.*

3 RESULTS AND DISCUSSION

3.1. SCREW WITHDRAWAL TESTS

All withdrawal tests, regardless of load-grain angle, exhibited the same failure mode, as shown in Figure 4. The failure was characterized as a shear failure of the wood spile around the screw's thread.

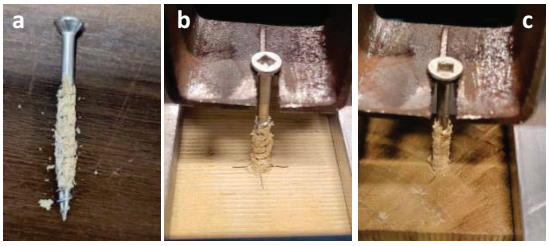

Figure 4: *Failure mode of the specimens, showing the wood spile around the screw's thread (a), the failure on a side-grain test (b) and the failure on an end-grain test (c).*

All load-displacement curves exhibited linear-elastic behaviour up to failure (Figure 5). Screws inserted in the side grain exhibited an initial linear phase, followed by limited 'yielding' (quasi-brittle behaviour) with a significant load drop of about 50 %, after which the load reached an almost constant region, until complete withdrawal from the timber. In contrast, screws inserted in the end grain showed a linear relationship until the maximum load, with a sharp and more significant load drop (about 70-80 %). Furthermore, the curves exhibited half-sine-wave-like shapes during the final withdrawal.

https://doi.org/10.52202/069179-0164

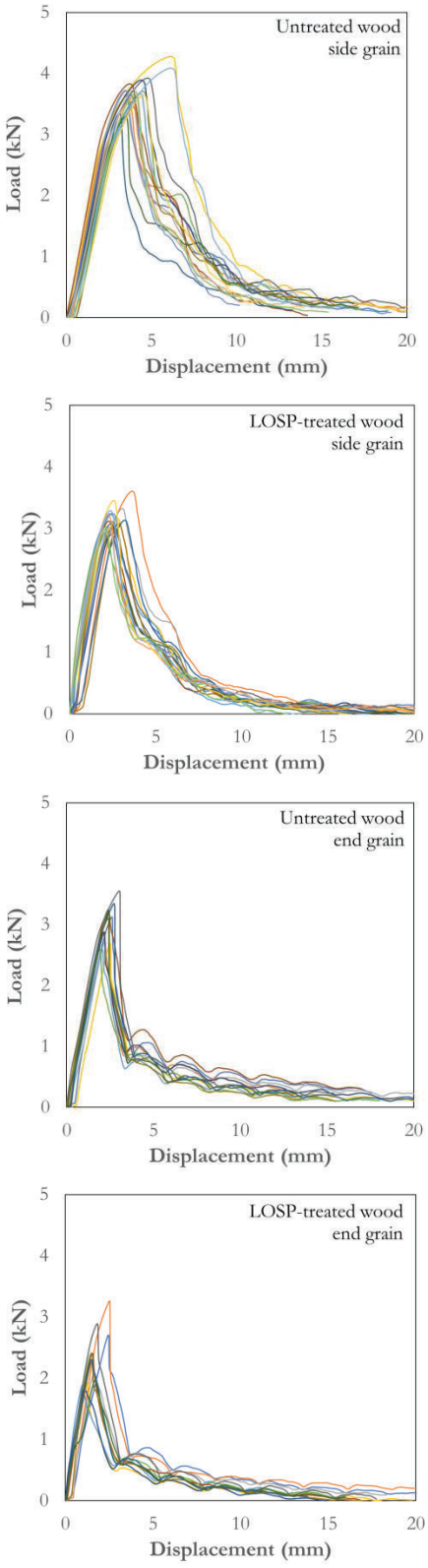

Figure 5: *Examples of load-displacement curves for specimens subjected to 8 moisture cycles.*

Gutknecht and MacDougall [13] observed similar behaviour for screws inserted in the end grain of Douglas fir and eastern white pine. Although they found two different failure modes, they describe this behaviour as a residual strength in the connection after the withdrawal limit is reached due to changes in the friction of the wood spile as it is pulled out. Interestingly, the authors also found that the distance between the minimums of these half-sinus waves coincides with the thread spacing of the screws. The same relationship was found here.

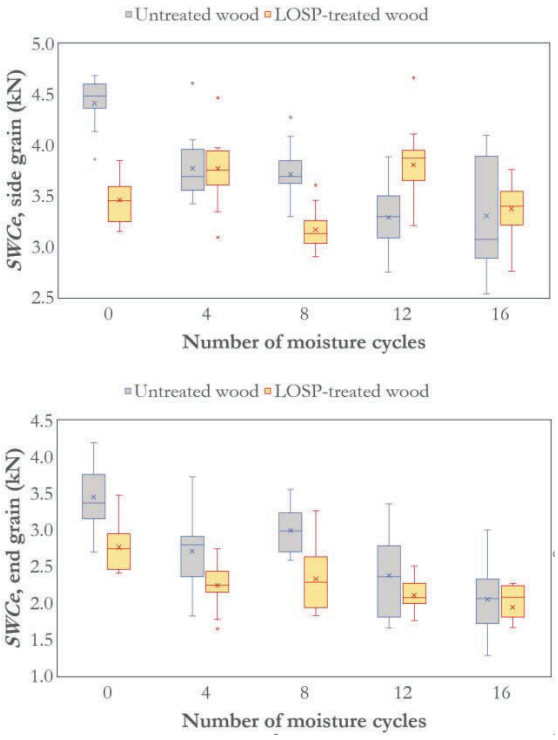

Figure 6: *Experimental withdrawal capacity for screws inserted in the side grain (top) and end grain (bottom) of LOSP-treated and untreated wood. The* X *and line represent the average and median values, respectively. The circles represent the outlier values.*

In terms of maximum withdrawal capacity, results showed that the initial (week 0) *SWCe* in LOSP-treated samples was lower than those in the untreated wood, for both side and end grain. Moreover, the impact of the moisture cycles showed a strong dependence on the timber faces the screws were driven into, only when LOSP-treated wood was tested. To analyse the significance of these differences, independent t-tests for the *SWCe* values in paired moisture cycles were performed (Table 3).

For screws driven in the side grain, the *SWCe* in untreated wood was reduced with increasing moisture cycles (26 % reduction after 16 moisture cycles), whereas the *SWCe* in LOSP-treated wood showed significant fluctuations. Meanwhile, for screws driven in the end grain of untreated

https://doi.org/10.52202/069179-0164

wood, the *SWCe* showed the same behaviour as the side grain, but with a drop of 42 % in this case. Nevertheless, the *SWCe* in LOPS-treated wood showed a 19 % loss after 4 moisture cycles, remaining statistically unchanged afterwards.

The moisture cycling had less effect on the *SWCe* of screws in LOSP-treated samples, possibly due to the protective effects of the residual solvent. LOSP-treated material typically contains up to 50 litres of residual solvent per m^3 of wood and can limit the initial moisture uptake around the connections, although it would eventually evaporate.

Table 3: *P-values results from the T-test performed (the null hypothesis is the SWCs are not significantly different) and the difference of the SWCe averages (Av. diff.) for paired moisture cycles. P-values below 0.05 reject the null hypothesis. Values in bold correspond to SWCe values that are not statistically different.*

Face	Wood	Moisture Cycles	p-value	Av. diff. (%)
Side	Untreated	0 - 4	< 0.001	-15
		4 - 8	**0.526**	**N/A**
		8 - 12	< 0.001	-11
		12 - 16	**0.919**	**N/A**
	LOSP-treated	0 - 4	0.006	+9
		4 - 8	< 0.001	-16
		8 - 12	< 0.001	+20
		12 - 16	< 0.001	-11
End	Untreated	0 - 4	0.002	-21
		4 - 8	**0.098**	**N/A**
		8 - 12	0.007	-21
		12 - 16	**0.160**	**N/A**
	LOSP-treated	0 - 4	< 0.001	-19
		4 - 8	**0.568**	**N/A**
		8 - 12	**0.127**	**N/A**
		12 - 16	**0.269**	**N/A**

3.2. COMPARISON TO DESIGN STANDARDS

The comparison of the 5th percentile of the *SWCe* values with those calculated from the standards AS1720 and EC5 are represented in Figure 7, as per Equation 2.

The results showed a significant overestimation of the *SWC* using the AS1720, with ratios closer to 2, or even above in some cases. This standard was developed about 15 years ago and lacks variables in the prediction. For example, the prediction from the AS1720 does not consider the actual density of the timber, but instead a characteristic density for groups of timber species.

This results in the same predicted value for that group of timber species which needs to be overestimated to compensate for the natural variability in the timber density. On the other hand, the EC5 showed ratios closer to the unit in every case, although in some cases the ratios were below 1. This highlights the importance of considering more specific system characteristics (e.g. wood density, nail diameter) for these predictions.

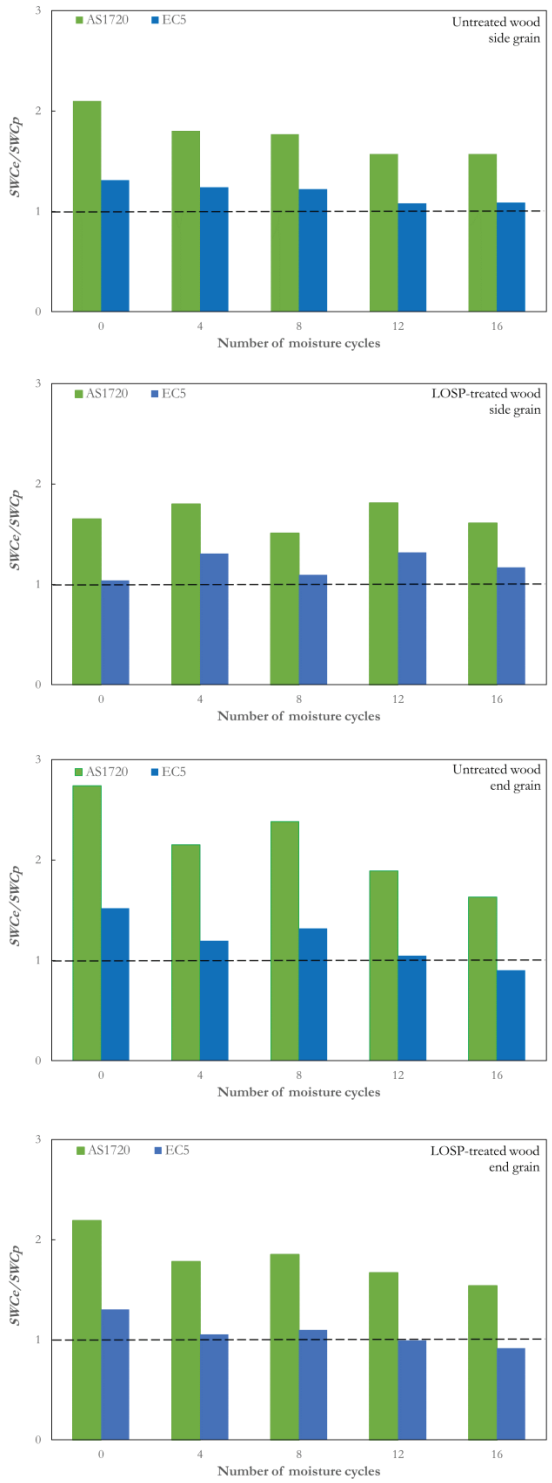

Figure 7: *Ratios of experimental and predicted SWCs for the different series tested (see Equation 2). The dashed line, at ratio =1, marks the limit where the predictions are safe.*

4 CONCLUSION

The main conclusions from this work are as follows:

- The withdrawal capacity for screws driven into the side and end grain of untreated wood after 16 moisture cycles was reduced by 26 and 42 %, respectively.
- The moisture cycling had less effect on the *SWCe* of screws in LOSP-treated samples. For screws driven into the side grain, the *SWCe* fluctuated, having an overall reduction of 2% after 16 moisture cycles. The *SWCe*, in the end, grain showed an initial loss of 19 % after 4 moisture cycles, remaining constant afterwards.
- The Australian standard AS1720 significantly overestimates the SWC value. This would lead to a misuse of resources and also to an over-design and overstrength of the timber connections, which in turn can trigger undesired brittle failures.
- Although in some cases the prediction from EC5 was not safe (ratios below 1), it showed a better prediction than the AS1720. This highlights the importance of considering more system characteristics for these predictions.

5 ACKNOWLEDGEMENT

This research was supported by the National Centre for Timber Durability and Design Life, a collaborative research program at the University of the Sunshine Coast, The University of Queensland, and the Queensland Department of Agriculture and Fisheries. L. Yermán wants to thank Mr Tomas Bravo Tetlak for his useful advice.

REFERENCES

[1] D.T. King, A. Sinha, J.J. Morrell, Effect of wetting on performance of small-scale shear walls, Wood Fiber Sci. 47 (2015) 74–83.

[2] L. Yermán, Y. Zhang, J. He, M. Xiao, L. Ottenhaus, J.J. Morrell, Effect of wetting and fungal degradation on performance of nailed timber connections, 353 (2022). https://doi.org/10.1016/j.conbuildmat.2022.129113.

[3] D.R. Rammer, Chapter 8 - Fastenings, in: Wood Handb. Wood as an Eng. Mater., 2010: pp. 1–28.

[4] L. Yermán, L.-M. Ottenhaus, C. Montoya, J.J. Morrell, Effect of repeated wetting and drying on withdrawal capacity and corrosion of nails in treated and untreated timber, Constr. Build. Mater. in press (2021).

[5] M.Y.L. Chew, N. Silva, S.S. Tan, Maintainability of wet areas of non-residential buildings, Struct. Surv. 22 (2004) 39–52. https://doi.org/10.1108/02630800410530918.

[6] European Committee for Standardization, EN1995-1-1:2004+A2:2014 Eurocode 5: Design of timber structures, 2014. https://doi.org/10.1680/cien.144.6.39.40613.

[7] Standards Australia, AS 1720.1-2010 Timber structures Part 1: Design methods, 2010 (2010).

[8] A. Ringhofer, M. Grabner, C. V Silva, J. Branco, The influence of moisture content variation on the withdrawal capacity of self-tapping screws, Holztechnologie. 55 (2014) 33–40.

[9] Standards Australia, AS 1720.1-2010 Timber structures Part 1: Design methods, (2010).

[10] Standards Australia, AS 1649-2001. Timber — Methods of test for mechanical fasteners and connectors — Basic working loads and characteristic strengths, (2001).

[11] ASTM International, D1761-12. Standard Test Methods for Mechanical Fasteners in Wood, ASTM Stand. (2012). https://doi.org/10.1520/D1761-12.

[12] CEN, Eurocode 5: Design of timber structures - Part 1-1: General - Common rules and rules for buildings, 2004.

[13] M.P. Gutknecht, C. Macdougall, Withdrawal resistance of structural self-tapping screws parallel-to-grain in common canadian timber species, Can. J. Civ. Eng. 46 (2019) 952–962. https://doi.org/10.1139/cjce-2018-0374.

https://doi.org/10.52202/069179-0164

World Conference on Timber Engineering Oslo 2023

ANALYSIS AND DESIGN ASPECTS OF MOMENT-RESISTING, BEAM-TO-COLUMN, TIMBER CONNECTIONS WITH INCLINED THREADED RODS: FROM FASTENER LEVEL TO CONSTRUCTION LEVEL

Haris Stamatopoulos[1], Osama Abdelfattah Hegeir [2], Kjell Arne Malo [3]

ABSTRACT: Moment-resisting timber frames (MRTFs) can be an alternative load-carrying system for mid-rise buildings, compared to systems based on walls or diagonals. The response of MRTFs depends largely on their connections. This paper provides an overview of analysis and design aspects of connections for MRTFs based on inclined threaded rods. Simplified expressions are provided for the properties of such connections and for the properties of threaded rods. Finally, the effects of connection's stiffness variability are explored. It is shown that this variability can result in increased values of actions compared to the values obtained by use of mean connection stiffness.

KEYWORDS: Moment-resisting connections, Moment-resisting frames, Threaded rods, Stiffness variability

1 INTRODUCTION

Moment-resisting timber frames (MRTFs) can reduce the need for bracing by shear walls or diagonal elements and allow for greater architectural flexibility in mid-rise buildings. The response of MRTFs depends on the properties of their connections, especially with respect to the serviceability aspects, see e.g.[1]. Moreover, MRTFs are statically indeterminate structures and the magnitude and distribution of internal forces and moments at the Ultimate Limit State, depend on the stiffness of their connections. The variability of the connections' stiffness can also significantly influence the internal forces and moments as will be shown in Section 4.

A concept for a moment-resisting connection with inclined threaded rods is presented in Figure 1. The rods are inserted with an inclination in pre-drilled holes in the beam and the column and jointed by use of metallic coupling parts. In the prototype tests for this concept [2], beams and columns were made of glued-laminated timber (glulam) and purpose-made steel rings were used as the coupling parts, see Figure 1. To allow fastening of rods to the steel rings, threaded rods with metric thread at their end are used, as shown in Figure 1. The use of steel brackets or plates and friction bolts can be an alternative to steel rings, see for example [3].

As shown in Figure 1, the coupling parts are connected to the column by use of a pair of inclined threaded rods (rods c1-c2 at the top and rods c3-c4 at the bottom). Due to rod inclination and the presence of shear forces, a load situation consisting of both axial and lateral forces occurs in the rods. However, the rods will mainly experience axial forces since their axial stiffness is much greater than the lateral one. The transfer of forces in this configuration resembles the transfer of forces in a truss system where all members are axially loaded. Therefore, the lateral forces in the rods c1, c2, c3 and c4 may be neglected.

The rods in the beam are inserted at a small angle. Rods parallel to the grain are vulnerable to cracks since a single crack along the grain might lead to a considerable loss of strength if the crack occurs in the same plane as the rod. Therefore, the beam is connected to the coupling parts by use of threaded rods (b1 and b2) inserted at a small angle to the grain, i.e. 5°-10°, see Figure 1. Greater angle should be avoided as it would also result in high lateral forces in the threaded rods and therefore smaller stiffness.

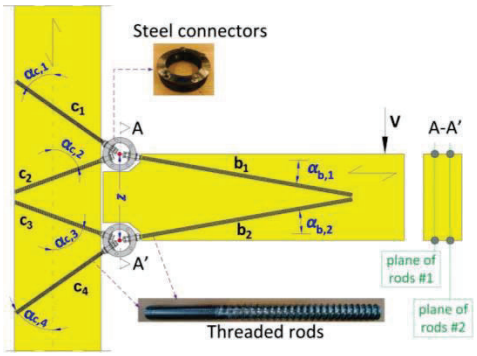

Figure 1: *Moment-resisting connection with inclined rods*

This paper consists of two parts:

- In the first part (Sections 2 and 3), analytical expressions are provided for the estimation of the properties of a connection as shown in Figure 1 and for the rods, based on recent publications;
- In the second part (Section 4) a preliminary study regarding the effects of connection stiffness variability on response of MRTFs is presented.

[1] Haris Stamatopoulos, haris.stamatopoulos@ntnu.no
[2] Osama Abdelfattah Hegeir, osama.a.s.a.hegeir@ntnu.no
[3] Kjell Arne Malo, kjell.malo@ntnu.no
Norwegian University of Science and Technology (NTNU)

https://doi.org/10.52202/069179-0165

2 CONNECTION PROPERTIES

2.1 STIFFNESS

The connection in Figure 1 can be considered as a system of rotational springs in series consisting of: a) the connection of rods c_1-c_4 to the column with spring constant $K_{\theta,c}$, b) the connection of rods b_1-b_2 to the beam with spring constant $K_{\theta,b}$ and c) the connectors with spring constant $K_{\theta,con}$. Therefore, the rotational stiffness of the connection can be determined by Eq.(1). The geometry is given in Figure 2. In [4], Eqs.(2)-(3) were derived by use of the component method and validated by experimental results. The compliance S-terms (Eqs.(4)-(7)) are given as functions of the axial stiffness ($K_{ax,i}$) and lateral stiffness ($K_{v,i}$) of the rods and the rod-to-grain angles (Eq.(8)). In Figure 2 and Eqs.(2)-(3), the lever arm is assumed the same on the beam and the column side ($z_b = z_c = z$). However, Eqs.(2)-(3) can also be applied for different lever arms. Eqs.(2)-(3) depend also on the moment to shear ratio ($L_v = M/V$) which is not known - a priori - in the structural analysis and approximations are needed, see also Eqs.(9)-(12). Eqs.(1)-(8) apply per plane of rods.

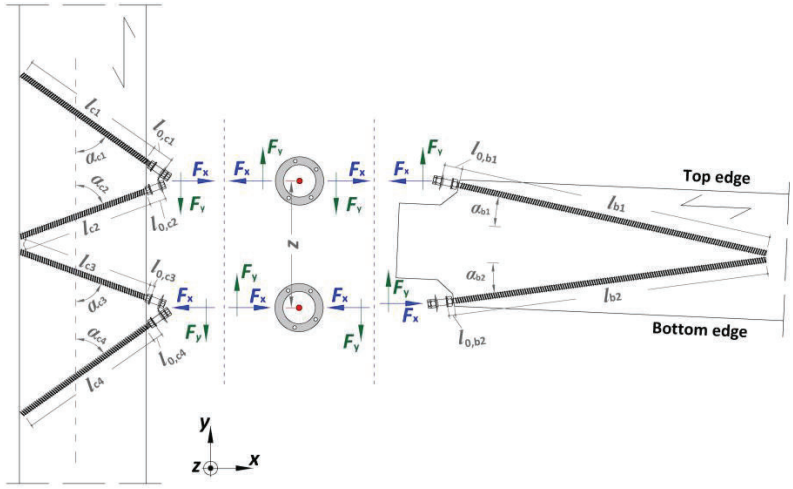

Figure 2: *Forces and geometry of a moment resisting connection with inclined threaded rods*

$$K_\theta = \left(1/K_{\theta,c} + 1/K_{\theta,b} + 1/K_{\theta,con}\right)^{-1} \tag{1}$$

$$K_{\theta,c} = \frac{z^2}{\left(S_{xx,c}{}^{(c1-c2)} + S_{xx,c}{}^{(c3-c4)}\right) + \left(S_{xy,c}{}^{(c3-c4)} - S_{xy,c}{}^{(c1-c2)}\right) \cdot z/(2 \cdot L_v)} \tag{2}$$

$$K_{\theta,b} = \frac{z^2}{\left(S_{xx,b1} + S_{xx,b2}\right) + \left(S_{xy,b2} - S_{xy,b1}\right) \cdot z/(2 \cdot L_v)} \tag{3}$$

$$S_{xx,c}{}^{(c1-c2)} = \frac{{c_{c1}}^2/K_{ax,c2} + {c_{c2}}^2/K_{ax,c1}}{(c_{c1} \cdot s_{c2} + c_{c2} \cdot s_{c1})^2} \; ; \; S_{xx,c}{}^{(c3-c4)} = \frac{{c_{c3}}^2/K_{ax,c4} + {c_{c4}}^2/K_{ax,c3}}{(c_{c3} \cdot s_{c4} + c_{c4} \cdot s_{c3})^2} \tag{4}$$

$$S_{xy,c}{}^{(c1-c2)} = \frac{c_{c1} \cdot s_{c1}/K_{ax,c2} - c_{c2} \cdot s_{c2}/K_{ax,c1}}{(c_{c1} \cdot s_{c2} + c_{c2} \cdot s_{c1})^2} \; ; \; S_{xy,c}{}^{(c3-c4)} = \frac{c_{c3} \cdot s_{c3}/K_{ax,c4} - c_{c4} \cdot s_{c4}/K_{ax,c3}}{(c_{c3} \cdot s_{c4} + c_{c4} \cdot s_{c3})^2} \tag{5}$$

$$S_{xx,b1} = {s_{b1}}^2/K_{v,b1} + {c_{b1}}^2/K_{ax,b1} \; ; \; S_{xx,b2} = {s_{b2}}^2/K_{v,b2} + {c_{b2}}^2/K_{ax,b2} \tag{6}$$

$$S_{xy,b1} = s_{b1} \cdot c_{b1} \cdot \left(1/K_{v,b1} - 1/K_{ax,b1}\right) \; ; \; S_{xy,b2} = s_{b2} \cdot c_{b2} \cdot \left(1/K_{ax,b2} - 1/K_{v,b2}\right) \tag{7}$$

$$c_i = \cos\alpha_i \; ; \; s_i = \sin\alpha_i \; ; \; L_v = M/V \tag{8}$$

Neglecting the shear term in Eqs.(2)-(3) results in the following crude approximations:

$$K_{\theta,c} \approx z^2/\left(S_{xx,c}{}^{(c1-c2)} + S_{xx,c}{}^{(c3-c4)}\right) \tag{9}$$

$$K_{\theta,b} \approx z^2/\left(S_{xx,b1} + S_{xx,b2}\right) \tag{10}$$

Assuming further that the rods are inserted at equal angles in the column ($\alpha_{c,1} = \alpha_{c,2} = \alpha_{c,3} = \alpha_{c,4} = \alpha_c$) and the beam ($\alpha_{b,1} = \alpha_{b,2} = \alpha_b$) and that they approximately have equal stiffness ($K_{ax,c1} = K_{ax,c2} = K_{ax,c3} = K_{ax,c4} = K_{ax,c}, K_{ax,b1} = K_{ax,b2} = K_{ax,b}, \quad K_{v,b1} = K_{v,b2} = K_{v,b}$), Eqs.(9)-(10) can be further simplified as follows:

https://doi.org/10.52202/069179-0165

$$K_{\theta,c} \approx z^2 \cdot K_{ax,c} \cdot {s_c}^2 \tag{11}$$

$$K_{\theta,b} \approx \frac{z^2 \cdot K_{ax,b}/2}{\left(K_{ax,b}/K_{v,b}\right) \cdot {s_b}^2 + {c_b}^2} \tag{12}$$

2.2 FORCES IN THE RODS

The forces in each rod can also be determined by use of the component method [4]. The rods on the column-side are mainly axially loaded and the forces are equal to:

$$\begin{Bmatrix} F_{ax,c1} \\ F_{ax,c2} \end{Bmatrix} = \frac{1}{n} \cdot \begin{Bmatrix} \dfrac{c_{c2} + s_{c2} \cdot z/(2 \cdot L_v)}{c_{c1} \cdot s_{c2} + c_{c2} \cdot s_{c1}} \\ \dfrac{c_{c1} - s_{c1} \cdot z/(2 \cdot L_v)}{c_{c1} \cdot s_{c2} + c_{c2} \cdot s_{c1}} \end{Bmatrix} \cdot \frac{M}{z} \tag{13}$$

$$\begin{Bmatrix} F_{ax,c3} \\ F_{ax,c4} \end{Bmatrix} = -\frac{1}{n} \cdot \begin{Bmatrix} \dfrac{c_{c4} - s_{c4} \cdot z/(2 \cdot L_v)}{c_{c3} \cdot s_{c4} + c_{c4} \cdot s_{c3}} \\ \dfrac{c_{c3} + s_{c3} \cdot z/(2 \cdot L_v)}{c_{c3} \cdot s_{c4} + c_{c4} \cdot s_{c3}} \end{Bmatrix} \cdot \frac{M}{z} \tag{14}$$

On the beam-side, the rods are subjected to combined axial and lateral loading [4]:

$$\begin{Bmatrix} F_{ax,b1} \\ F_{v,b1} \end{Bmatrix} = \frac{1}{n} \cdot \begin{Bmatrix} c_{b1} + s_{b1} \cdot z/(2 \cdot L_v) \\ -s_{b1} + c_{b1} \cdot z/(2 \cdot L_v) \end{Bmatrix} \cdot \frac{M}{z} \tag{15}$$

$$\begin{Bmatrix} F_{ax,b2} \\ F_{v,b2} \end{Bmatrix} = -\frac{1}{n} \cdot \begin{Bmatrix} c_{b2} + s_{b2} \cdot z/(2 \cdot L_v) \\ -s_{b2} + c_{b2} \cdot z/(2 \cdot L_v) \end{Bmatrix} \cdot \frac{M}{z} \tag{16}$$

Eqs.(13)-(16) can be used in the corresponding design checks for the rods, see also Section 3. The parameter n is the number of planes of rods.

2.3 PANEL ZONE

Horizontal forces result in high shear stresses in the panel zone of the column, i.e. the region between rods c1-c2 and c3-c4. Moreover, stresses perpendicular to grain occur around the threaded rods. The combination of tensile stresses perpendicular to grain and shear stresses is unfavourable due to their high degree of interaction [5] and may cause fracture in the panel zone, as shown in Figure 3. Thus, the panel zone must be designed with sufficient strength against combined shear and tension perpendicular to grain. If the rods are long and cross the entire height of the column they act as reinforcements [6], increasing the capacity of the panel zone.

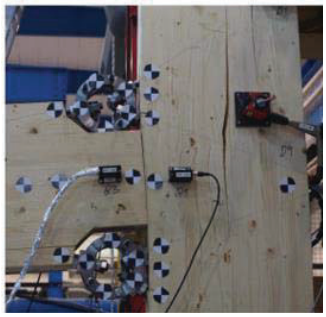

Figure 3: *Fracture in the panel zone due to combined shear and tension perpendicular to grain (Photo: [2])*

3 FASTENER PROPERTIES

The properties of threaded rods are necessary inputs for the properties of the entire connection. The axial stiffness of a threaded rod is given by:

$$K_{ax} = \frac{K_{ser,ax} \cdot K_{ax,l0}}{K_{ser,ax} + K_{ax,l0}} \tag{17}$$

where $K_{ser,ax}$ is the withdrawal stiffness and $K_{ax,l0}$ is the axial stiffness of the non-embedded part of the rod:

$$K_{ax,l0} = A_{net} \cdot E_s / l_0 \tag{18}$$

where $E_s = 210000$ N/mm^2 is the modulus of elasticity of steel, A_{net} is the net cross-sectional area and l_0 is the non-embedded length of the rod. Eq.(19) provides an approximation for $K_{ser,ax}$ (in N/mm) as function of the outer-thread diameter d (in mm), the rod-to-grain angle α, the mean density ρ_m (in kg/m^3) and the embedment length l (in mm). Eq.(19) was derived in [7] by use of non-linear regression on experimental results for threaded rods with diameters 16-20 mm embedded in softwood, see [8-10].

$$K_{ser,ax} \approx \frac{50000 \cdot \left(\frac{d}{20}\right)^2 \cdot \left(\frac{\rho_m}{470}\right)^2 \cdot k_{length,K}}{0.40 \cdot \cos^{2.3}\alpha + \sin^{2.3}\alpha} \tag{19}$$

$$k_{length,K} = \min\left[(l/300)^{3/4}, 1\right] \tag{20}$$

The stiffness of a laterally loaded threaded rod can be determined by Eq.(21). Eq.(21) is derived by modelling the rod as a beam on elastic foundation assuming that rotation is restrained at the loading point, see in detail [7]:

$$K_v = \frac{3 \cdot k_v \cdot l_{ch}}{{\lambda_0}^3 + 3 \cdot {\lambda_0}^2 + 3 \cdot \lambda_0 + 3} \tag{21}$$

$$\lambda_0 = l_0 / l_{ch} \;;\; l_{ch} = \sqrt[4]{4 \cdot E_s \cdot I_s / k_v} \tag{22}$$

The parameter $I_s \approx \pi \cdot {d_1}^4/64$ is the 2nd moment of area and d_1 is the core diameter of the rod. The parameter k_v is the foundation modulus (i.e. stiffness per unit length) of a laterally loaded rod. According to Eqs.(3),(6),(7) and (12) , the lateral stiffness of a rod is an input parameter for the rotational stiffness on the beam-side. There the rods are inserted at small angles to grain and therefore the lateral foundation modulus may be approximately taken as the foundation modulus perpendicular to the grain. Based on an experimental study of laterally loaded rods with $d = 22$ mm embedded in glulam made of pine and spruce [11] an approximate value of $k_v \approx 300$ N/mm^2 may be used.

A power criterion is often used - as an approximation - to determine the capacity of fasteners subjected to combined axial force (F_{ax}) and lateral force (F_v), i.e.:

$$\left(\frac{F_{ax}}{F_{ax,R}}\right)^q + \left(\frac{F_v}{F_{v,R}}\right)^q \leq 1 \tag{23}$$

In Eq.(23), $F_{ax,R}$ and $F_{v,R}$ are the axial and lateral capacity of a fastener respectively. According to EN 1995-1-1 [12], a quadratic failure criterion applies for screws, i.e. $q = 2$. The quadratic criterion has provided safe-sided predictions for long screws (i.e. with steel failure being

https://doi.org/10.52202/069179-0165

more critical than withdrawal) inserted perpendicular to grain [13] and for glued-in rods parallel to grain [14].
The rods on the beam side are subjected to both lateral and axial forces and therefore their capacity should be checked by use of a criterion that considers the interaction of forces, as the one given by Eq.(23). On the other hand, the rods in the column are mainly axially loaded (i.e. $F_{v,ci} \approx 0$) as explained in Section 1 and therefore in this case Eq.(23) reduces to: $|F_{ax,ci}| \leq F_{ax,R}$.

4 STIFFNESS VARIABILITY EFFECTS

MRTFs are statically indeterminate systems, and the distribution of the internal actions depends on the stiffness of their elements and connections. The internal forces and moments are typically determined by use of mean stiffness values in the structural analysis. However, the inherent variability of the connection stiffness can result in variations of internal forces and moments, compared to the expected values obtained by use of mean stiffness values. In this section, the effects of connection stiffness variability are explored by use of a simple beam model with semi-rigid end restrains (Section 4.1) and by linear-elastic Finite Element simulations of MRTFs with semi-rigid moment connections (Section 4.2).

4.1 BEAM MODEL

A beam with semi-rigid end restrains (Figure 4) subjected to uniformly distributed load q is used here -as a simple example- to study the effects of the connections' stiffness variability. The connections are represented by linear-elastic rotational springs with spring constants $K_{\theta,1}$ and $K_{\theta,2}$ which can be expressed in dimensionless form-by dividing by the beam stiffness-as follows:

$$k_1 = \frac{K_{\theta,1}}{(EI/L)} \; ; \; k_2 = \frac{K_{\theta,2}}{(EI/L)} \tag{24}$$

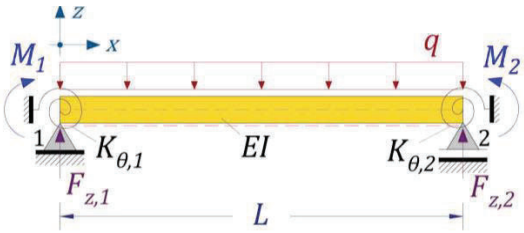

Figure 4: *Simply supported beam with semi-rigid end restrains*

The moments and the vertical forces at the beam ends can be expressed as functions of k_1 and k_2 as follows:

$$M_1 = -\frac{q \cdot L^2}{12} \cdot \frac{k_1 \cdot (k_2 + 6)}{k_1 \cdot k_2 + 4 \cdot (k_1 + k_2) + 12} \tag{25}$$

$$F_{z,1} = \frac{q \cdot L}{2} \cdot \frac{k_1 \cdot k_2 + 5 \cdot k_1 + 3 \cdot k_2 + 12}{k_1 \cdot k_2 + 4 \cdot (k_1 + k_2) + 12} \tag{26}$$

$$M_2 = -\frac{q \cdot L^2}{12} \cdot \frac{k_2 \cdot (k_1 + 6)}{k_1 \cdot k_2 + 4 \cdot (k_1 + k_2) + 12} \tag{27}$$

$$F_{z,2} = \frac{q \cdot L}{2} \cdot \frac{k_1 \cdot k_2 + 3 \cdot k_1 + 5 \cdot k_2 + 12}{k_1 \cdot k_2 + 4 \cdot (k_1 + k_2) + 12} \tag{28}$$

The maximum span moment can be simply written as function of the forces and moments:

$$M_{span} = M_1 + \frac{{F_{z,1}}^2}{2 \cdot q} = M_2 + \frac{{F_{z,2}}^2}{2 \cdot q} \tag{29}$$

By letting $k_1 = k_2 = k_{mean}$, the moments and the reactions at the supports become equal ($M_1 = M_2 = M_{end}$ and $F_{z,1} = F_{z,2} = F_z$):

$$M_{end}(k_1 = k_2 = k_{mean}) = -\frac{q \cdot L^2}{12} \cdot \frac{k_{mean}}{k_{mean} + 2} \tag{30}$$

$$F_z(k_1 = k_2 = k_{mean}) = \frac{q \cdot L}{2} \tag{31}$$

$$M_{span}(k_1 = k_2 = k_{mean}) = \frac{q \cdot L^2}{24} \cdot \frac{k_{mean} + 6}{k_{mean} + 2} \tag{32}$$

For each realization of the connections' stiffness, the ratios between the actual action divided by the corresponding values by use of mean stiffness values were calculated, as specified by Eqs.(33)-(37). These ratios express the deviation between a realization (numerator) and the corresponding value obtained by static analysis by use of mean stiffness (denominator) and they depend only on the normalized stiffness values given by Eq.(24).

$$n_{M,end,1} = \frac{|M_1(k_1, k_2)|}{|M_{end}(k_1 = k_2 = k_{mean})|} \tag{33}$$

$$n_{M,end,2} = \frac{|M_2(k_1, k_2)|}{|M_{end}(k_1 = k_2 = k_{mean})|} \tag{34}$$

$$n_{M,span} = \frac{M_{span}(k_1, k_2)}{M_{span}(k_1 = k_2 = k_{mean})} \tag{35}$$

$$n_{V,end,1} = \frac{F_{z,1}(k_1, k_2)}{F_z(k_1 = k_2 = k_{mean})} \tag{36}$$

$$n_{V,end,2} = \frac{F_{z,2}(k_1, k_2)}{F_z(k_1 = k_2 = k_{mean})} \tag{37}$$

In other words, the ratios by Eqs.(33)-(37) multiplied by the internal forces and moments by use of mean stiffness provide the actual internal forces and moments. Therefore, to get an indication of the unfavourable effect of stiffness variability on the internal forces and moments, it makes sense to consider an upper percentile value of these ratios, e.g. the 95th or 98th percentile. Thus, the variability of the ratios by Eqs.(33)-(37) is important.
To study the effects of stiffness variability, realizations of normalized stiffness values k_1 and k_2 were generated. Note that the variability of parameters k_1 and k_2 results from the variability of the properties of the connection (K_θ) and the material (E). Here, for simplicity k_1 and k_2 were assumed as the random variables instead of K_θ and E separately. Due to the lack of data with respect to the distribution of the connection stiffness K_θ, two different distributions were assumed: namely normal and

https://doi.org/10.52202/069179-0165

lognormal distribution. Figure 6 shows an example of the distribution of the ratio $n_{M,end}$ (Eq.(33) or Eq.(34)) assuming that k_1 and k_2 are either normally or lognormally distributed. The distribution of the output variable $n_{M,end}$ is fairly similar for both assumptions. This observation holds true for relatively small values of k_{mean} and $CoV(k)$ and for the other output variables ($n_{M,span}$ or $n_{V,end}$) with some small deviations.

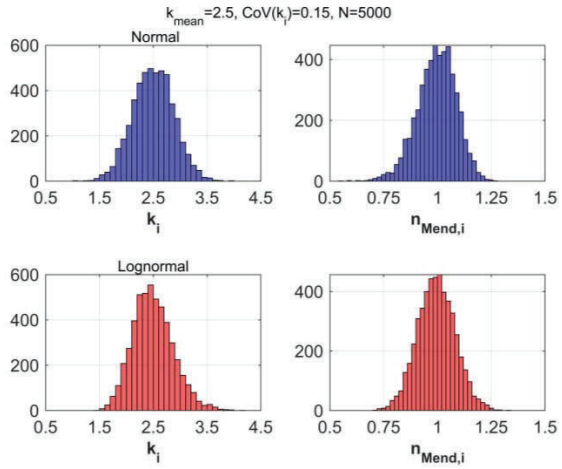

Figure 5: *Distribution of $n_{M,end}$ (right) for normal (up-left) and lognormal (bottom-left) distribution of k_1 and k_2 (example here for $k_{mean} = 2.5$ and $CoV(k) = 0.15$)*

Given that the distribution of the output variables (Eqs.(33)-(37)) is fairly similar for either normal or lognormal distribution of the input variables $k_1$and k_2, only results assuming normal distribution of $k_1$and k_2 are presented further. The mean value is denoted k_{mean} and the coefficient of variation is denoted $\mathrm{CoV}(k)$, thus:

$$k_1 = N\big(k_{mean}, \mathrm{CoV}(k)\big) \tag{38}$$

$$k_2 = N\big(k_{mean}, \mathrm{CoV}(k)\big) \tag{39}$$

Figure 6 shows the ratio $n_{M,end}$ according to Eq.(33) or Eq.(34) for varying values of k_{mean} based on 5000 realizations per k_{mean}-value. Figure 7 shows the corresponding results for $n_{M,span}$ (Eq.(35)) and Figure 8 for $n_{V,end}$ (Eq.(36) or Eq.(37)). All Figures are plotted for $\mathrm{CoV}(k) = 0.15$. Such coefficient of variation has been observed for the rotational stiffness of connections with glulam beams and columns and inclined threaded rods as shown in Figure 1 [15]; however the sample size was small and this number is only used as indicative.
The 95th and the 98th percentiles are also provided in the Figures together with the theoretical estimations that correspond to normal distribution: $X_{95\%} = X_{mean} \cdot (1 + 1.645 \cdot \mathrm{CoV}[X])$ and $X_{98\%} = X_{mean} \cdot (1 + 2.054 \cdot \mathrm{CoV}[X])$. As shown in the Figures, these estimations are in good agreement with the percentiles of each sample.

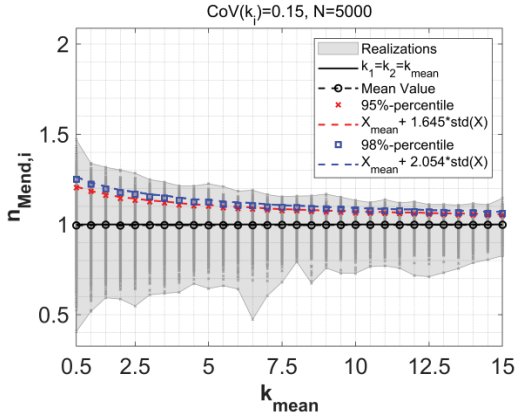

Figure 6: *Ratio $n_{M,end}$ for varying k_{mean} and $CoV(k_i) = 0.15$ (5000 realizations per k_{mean} value, assuming that k_1 and k_2 are normally distributed)*

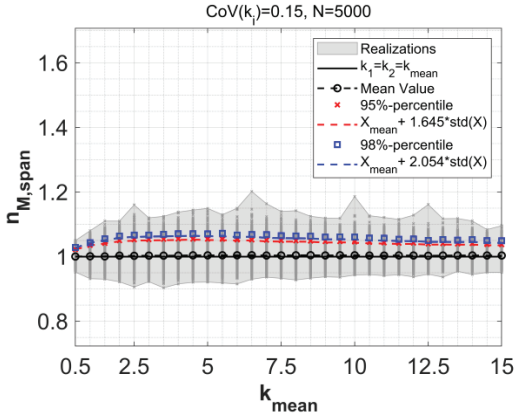

Figure 7: *Ratio $n_{M,span}$ for varying k_{mean} and $CoV(k_i) = 0.15$ (5000 realizations per k_{mean} value, assuming that k_1 and k_2 are normally distributed)*

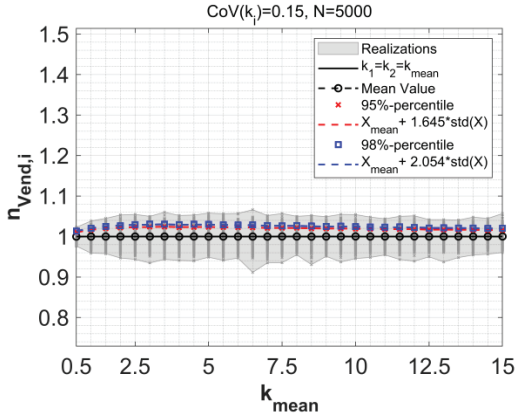

Figure 8: *Ratio $n_{V,end}$ for varying k_{mean} and $CoV(k_i) = 0.15$ (5000 realizations per k_{mean} value, assuming that k_1 and k_2 are normally distributed*

As shown in Figure 6, the end moments are significantly influenced by stiffness variability, especially for low k_{mean}-values. Low mean connection stiffness values result in greater variability of the end moments. Timber moment-resisting connections are typically semi-rigid with k_{mean}-values up to maximum 5-6 and thus such

variability of the end moments is to be expected. For increasing k_{mean}-values (i.e. quasi-rigid connections) the variability and the 95th/98th percentiles of the end moments reduce significantly. On the other hand, the variabilities and the 95th/98th percentiles of the span moment (Figure 7) and the shear forces (Figure 8) are fairly small and not sensitive to k_{mean}-values.

Tables 1-3 provide the coefficient of variation and the 95th/98th percentiles of the ratios $n_{M,end}$ (Eq.(33) or Eq.(34)), $n_{M,span}$ (Eq.(35)) and $n_{V,end}$ (Eq.(36) or Eq.(37)) for varying values of k_{mean} and $\mathrm{CoV}(k)$ based on 5000 realizations.

Table 1: *Coefficient of variation, 95th and 98th percentile of ratio $\boldsymbol{n_{M,end,i}}$ for different mean values and coefficients of variation of the normalized stiffness $\boldsymbol{k}$ (assuming that k is normally distributed, based on 5000 realizations)*

$\mathrm{CoV}(n_{M,end,i})$					
	$\mathrm{CoV}(k)$				
k_{mean}	**0.10**	**0.15**	**0.20**	**0.25**	**0.30**
0.5	0.086	0.130	0.172	0.217	0.261
1	0.076	0.114	0.154	0.194	0.242
1.5	0.069	0.105	0.141	0.184	0.221
2	0.066	0.098	0.131	0.169	0.204
3	0.055	0.086	0.115	0.150	0.183
5	0.044	0.067	0.093	0.120	0.151
10	0.030	0.045	0.065	0.086	0.112
15	0.022	0.036	0.048	0.068	0.091
$n_{M,end,i,95\%}$					
	$\mathrm{CoV}(k)$				
k_{mean}	**0.10**	**0.15**	**0.20**	**0.25**	**0.30**
0.5	1.139	1.208	1.268	1.338	1.404
1	1.118	1.178	1.232	1.283	1.348
1.5	1.110	1.162	1.208	1.259	1.305
2	1.101	1.147	1.188	1.232	1.274
3	1.086	1.127	1.166	1.203	1.241
5	1.067	1.098	1.128	1.153	1.184
10	1.044	1.064	1.087	1.105	1.131
15	1.034	1.050	1.066	1.084	1.101
$n_{M,end,i,98\%}$					
	$\mathrm{CoV}(k)$				
k_{mean}	**0.10**	**0.15**	**0.20**	**0.25**	**0.30**
0.5	1.173	1.259	1.327	1.412	1.505
1	1.151	1.221	1.284	1.345	1.427
1.5	1.134	1.195	1.257	1.316	1.371
2	1.124	1.176	1.224	1.279	1.327
3	1.106	1.156	1.202	1.250	1.289
5	1.082	1.122	1.154	1.194	1.230
10	1.056	1.080	1.106	1.130	1.160
15	1.042	1.063	1.083	1.106	1.135

The 95th/98th percentiles of $n_{M,end}$ can be approximated by the following expressions:

$$n_{M,end,95\%} \approx 1 + 1.15 \cdot {k_{mean}}^{-0.35} \cdot \mathrm{CoV}(k) \qquad (40)$$

$$n_{M,end,98\%} \approx 1 + 1.40 \cdot {k_{mean}}^{-0.35} \cdot \mathrm{CoV}(k) \qquad (41)$$

Table 2: *Coefficient of variation, 95th and 98th percentile of ratio $\boldsymbol{n_{M,span}}$ for different mean values and coefficients of variation of the normalized stiffness $\boldsymbol{k}$ (assuming that k is normally distributed, based on 5000 realizations)*

$\mathrm{CoV}(n_{M,span})$					
	$\mathrm{CoV}(k)$				
k_{mean}	**0.10**	**0.15**	**0.20**	**0.25**	**0.30**
0.5	0.009	0.013	0.018	0.022	0.026
1	0.013	0.020	0.027	0.034	0.042
1.5	0.016	0.024	0.032	0.042	0.051
2	0.018	0.027	0.036	0.046	0.056
3	0.019	0.029	0.039	0.051	0.062
5	0.018	0.028	0.040	0.052	0.064
10	0.015	0.024	0.033	0.045	0.058
15	0.012	0.019	0.026	0.037	0.052
$n_{M,span,95\%}$					
	$\mathrm{CoV}(k)$				
k_{mean}	**0.10**	**0.15**	**0.20**	**0.25**	**0.30**
0.5	1.015	1.022	1.031	1.038	1.045
1	1.024	1.036	1.050	1.061	1.079
1.5	1.028	1.044	1.059	1.080	1.098
2	1.032	1.049	1.068	1.088	1.112
3	1.034	1.053	1.074	1.105	1.130
5	1.033	1.055	1.078	1.109	1.136
10	1.028	1.045	1.067	1.096	1.127
15	1.023	1.038	1.053	1.079	1.109
$n_{M,span,98\%}$					
	$\mathrm{CoV}(k)$				
k_{mean}	**0.10**	**0.15**	**0.20**	**0.25**	**0.30**
0.5	1.019	1.028	1.037	1.050	1.058
1	1.029	1.045	1.063	1.078	1.104
1.5	1.035	1.055	1.075	1.107	1.127
2	1.038	1.061	1.086	1.116	1.148
3	1.044	1.069	1.097	1.133	1.172
5	1.040	1.070	1.103	1.145	1.187
10	1.036	1.060	1.092	1.132	1.188
15	1.030	1.049	1.072	1.106	1.165

The 95th/98th percentiles of $n_{M,span}$ can be approximated by the following expressions:

$$n_{M,span,95\%} \approx 1 + (1 - e^{-k_{mean}}) \cdot \mathrm{CoV}(k)^{1.45} \qquad (42)$$

https://doi.org/10.52202/069179-0165

$$n_{M,span,98\%} \approx 1 + (1 - e^{-k_{mean}}) \cdot \mathrm{CoV}(k)^{1.30} \quad (43)$$

Table 3: *Coefficient of variation, 95th and 98th percentile of ratio $n_{V,end,i}$ for different mean values and coefficients of variation of the normalized stiffness k (assuming that k is normally distributed, based on 5000 realizations)*

$\mathrm{CoV}(n_{V,end,i})$					
	$\mathrm{CoV}(k)$				
k_{mean}	**0.10**	**0.15**	**0.20**	**0.25**	**0.30**
0.5	0.004	0.007	0.009	0.011	0.013
1	0.007	0.010	0.014	0.017	0.021
1.5	0.008	0.012	0.016	0.021	0.025
2	0.009	0.013	0.018	0.023	0.028
3	0.009	0.015	0.020	0.025	0.031
5	0.009	0.014	0.020	0.025	0.031
10	0.007	0.011	0.016	0.022	0.028
15	0.006	0.010	0.013	0.018	0.024
$n_{V,end,i,95\%}$					
	$\mathrm{CoV}(k)$				
k_{mean}	**0.10**	**0.15**	**0.20**	**0.25**	**0.30**
0.5	1.007	1.011	1.014	1.018	1.022
1	1.011	1.017	1.022	1.027	1.035
1.5	1.013	1.020	1.027	1.034	1.042
2	1.015	1.022	1.030	1.038	1.045
3	1.016	1.024	1.032	1.041	1.051
5	1.015	1.023	1.031	1.040	1.051
10	1.012	1.019	1.026	1.034	1.043
15	1.010	1.015	1.022	1.029	1.037
$n_{V,end,i,98\%}$					
	$\mathrm{CoV}(k)$				
k_{mean}	**0.10**	**0.15**	**0.20**	**0.25**	**0.30**
0.5	1.009	1.014	1.018	1.022	1.027
1	1.014	1.020	1.028	1.034	1.043
1.5	1.017	1.026	1.033	1.043	1.052
2	1.018	1.028	1.037	1.049	1.057
3	1.020	1.031	1.042	1.055	1.066
5	1.018	1.030	1.042	1.053	1.067
10	1.016	1.024	1.035	1.046	1.061
15	1.013	1.022	1.029	1.039	1.053

The 95th/98th percentiles of $n_{V,end}$ can be approximated by the following expressions:

$$n_{V,end,95\%} \approx 1 + (0.15 - e^{-5 \cdot k_{mean}}) \cdot \mathrm{CoV}(k) \quad (44)$$

$$n_{V,end,98\%} \approx 1 + (0.20 - e^{-5 \cdot k_{mean}}) \cdot \mathrm{CoV}(k) \quad (45)$$

The relative difference of the 95th/98th percentiles assuming lognormal distribution of the stiffness parameter k is within 6% or less compared to the values in Tables 1-3. This is also indicated by the distribution shape of the output variables, shown in Figure 5.

As shown in the values of Tables 1-3, the ratio $n_{M,end,i}$ (Table 1) is more affected by the variability of the stiffness parameter k. In other words, the end-moments are more sensitive to the stiffness variability compared to the span moment and the shear forces. As expected, the coefficient of variation of the stiffness parameter k results in higher variability of the output variables.

To facilitate comparison, we can consider a connection with $k_{mean} = 1.5$. For $\mathrm{CoV}(k) = 15\%$, the 98th percentile of the end moment, the span moment and the shear force are approx. 20%, 5% and 3% higher than the reference values respectively. The corresponding 98th percentile values for $\mathrm{CoV}(k) = 30\%$ are approx. 37%, 13% and 5%. Especially for the end moments, the 98th percentiles may reach values of the order of 20-40% higher than the reference value for reasonable input ($\mathrm{CoV}(k) \geq 15\%$ and $k_{mean} = 1 - 5$). Such effect should be considered in the design.

4.2 FINITE ELEMENT ANALYSIS OF MOMENT-RESISTING TIMBER FRAMES

The effects of connection stiffness variability are further studied in this Section by use of Finite Element (abbr. FE) analyses of planar MRTFs. The software SAP2000 was used for the structural analysis. An algorithm was developed to perform several analyses with varying properties.

The structural model for the analysis is presented in Figure 9. The frames consisted of glulam columns and beams with cross-sectional dimensions $b_c \times h_c$ and $b_b \times h_b$ respectively. The columns were continuous. The mean modulus of elasticity was $E_{0,\mathrm{mean}} = 13000$ N/mm^2 and the mean shear modulus was $G_{\mathrm{mean}} = 650$ N/mm^2. These values correspond to strength class GL30c [16]. The beams and the columns were modelled as linear elements and the material was modelled as linear-elastic. Shear deformations of timber were taken into account in the model. All frames consisted of 3 bays with 8.0m bay length between the center-lines of the columns. Frames with 4 and 8 storeys were studied. The height of each storey was h =3.0 m.

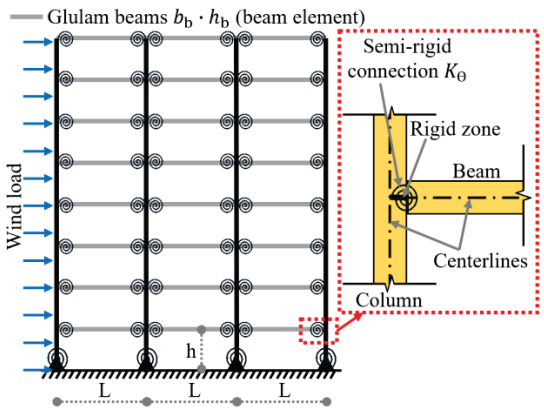

Figure 9: *Structural model for FE analyses*

https://doi.org/10.52202/069179-0165

The connections were modelled as linear-elastic rotational springs with spring constant K_θ (by use of the partial release command of SAP2000). With respect to the translational degrees of freedom, the connections were modelled as rigid. Since the columns were continuous, the connections were placed at the edge of the columns with a rigid offset of $h_c/2$ to the columns' centerline, see the detail in Figure 9. The supports of the frame were assumed rigid with respect to translations while the for the rotational degree of freedom a small rotational stiffness of 5000 kNm/rad was assumed.

Three actions were considered in the analysis: dead load ($G = 2.0$ kN/m^2), live load ($Q = 3.0$ kN/m^2) and the wind action W. The wind load was calculated according to EN 1991-1-4 [17] for a basic wind velocity $v_b = 26$ m/s and terrain category IV (urban environment). For the determination of loads on the frame and wind-induced accelerations it was assumed that the building consists of six frames equally spaced at a distance of 4.0 meters, resulting in a total width of 20 m.

To consider the connection stiffness variability, the stiffness of each beam-to-column connection was selected as a normally distributed random variable (see Eqs.(38)-(39)). Similar to the definition given by Eq.(24), the stiffness can be expressed in dimensionless form by dividing the rotational stiffness by the bending stiffness of the beams, i.e.: $k = K_\theta/(EI_b/L_b)$. Here, L_b is the net bay length. For each frame, analyses with mean dimensionless connection stiffness of $k_{mean} = 1.5$ and $k_{mean} = 2.5$ were performed. These values represent feasible connection stiffness for moment resisting connections with threaded rods (see Section 2). Moreover, they are sufficient, so that the frames fulfil the serviceability requirements with respect to wind-induced deformations and accelerations; see e.g. Figure 10 for accelerations. For each k_{mean}-value, two values of the coefficient of variation were considered: $\mathrm{CoV}(K_\theta) = 15\%$ and 25%.

As a crude simplification, the modulus of elasticity and the shear modulus of glulam were assumed constant and equal to their mean value, i.e. their variability was not taken into account in this analysis. All other parameters (e.g. loads, mass etc.) were also kept constant. Therefore, the results of these analyses should only be considered as indicative; however, they allow for comparison with the results provided in Section 4.1. In total, 8 frames were studied (2 number of storeys × 2 k_{mean}-values × 2 $\mathrm{CoV}(K_\theta)$ values). For each frame type, 3000 realizations were generated and solved by use of FE analysis (in total 24000 analyses were performed).

The following response quantities were quantified by FE analysis, for each frame:

- The internal actions were determined by use of linear-elastic analysis. The envelopes of the internal forces and moments were then determined for the fundamental Ultimate Limit State combinations according to EN1990 [18], with wind load (in both directions) being the leading variable action. The load safety factors were $\gamma_G = 1.2$ for the permanent load, $\gamma_Q = 1.5$ for the live load and $\gamma_W = 1.5$ for the wind load. The ratios between the envelope internal forces and moments for each realization divided by the corresponding values obtained by use of analysis with mean stiffness values were determined for each frame, as specified by Eqs.(33)-(37).
- The horizontal deflections were determined for the characteristic Serviceability Limit State combination according to EN1990 [18], with wind as the leading variable load. The maximum horizontal deflection is denoted Δ and the maximum inter-storey drift is denoted IDR_{max}.
- The fundamental eigenfrequency (f) was quantified by modal analysis. The quasi–permanent load ($G + 0.3 \cdot Q$), according to EN1990 [18] was used to determine the mass.
- The wind-induced accelerations (A) on the top-floor were determined by use of the approximate method given by EN1991-1-4 [17] (Annex B), A damping ratio of $\xi = 2.0$ % was assumed based on measurements of timber buildings [19]. The accelerations were compared to the requirements by ISO10137 [20]. To consider the smaller return period, the basic wind velocity was multiplied by $c_{prob} = 0.73$.

The results of the FE analyses are summarized in Table 4 (4 storey frames) and Table 5 (8 storey frames). The ratios $n_{M,end}, n_{M,span}, n_{V,end}$ (Eqs.(33)-(37)) were determined separately for each connection of the frame and the range is given in the Tables. As indicated by the small ranges the ratios for different connections are quite similar. The FE results can be summarized as follows:

- The end moments are -by far- the action that it is most sensitive to connection stiffness as indicated by the higher $n_{M,end}$-values. On the other hand, the span moments and the shear forces are not very sensitive to connection stiffness as indicated by the low values of $n_{M,span}$ and $n_{V,end}$.
- The ratios $n_{M,end}, n_{M,span}, n_{V,end}$ are quite similar for 4-storey and 8-storey frames. Moreover, they are in very good agreement with the results obtained by the simple beam model in Section 4.1 (Tables 1-3). In fact, the beam model results in slightly higher values of $n_{M,end}$. Therefore, the beam model can be used to provide safe-sided predictions.
- The effect of stiffness variability on deformations, eigenfrequency and top-floor accelerations is quite small as indicated by FE results. Figure 10 shows a plot of the fundamental eigenfrequencies and top floor accelerations for all realizations of MRTFs, compared to ISO10137 **[20]** requirements. As shown by the results, the response of all realizations is quite similar for each frame. Therefore, the effects of the variability of connection stiffness can be neglected in the serviceability limit state.

The aim of the present -preliminary- study was to highlight the effects of connections' stiffness variability. A more detailed reliability analysis considering the variability of the loads and the material stiffness can be used to better quantify the values of ratios $n_{M,end}, n_{M,span}$

https://doi.org/10.52202/069179-0165

and $n_{V,end}$. Moreover, the presented results come solely from linear-elastic analysis; i.e. possible redistribution of moments if the connections are ductile was not considered.

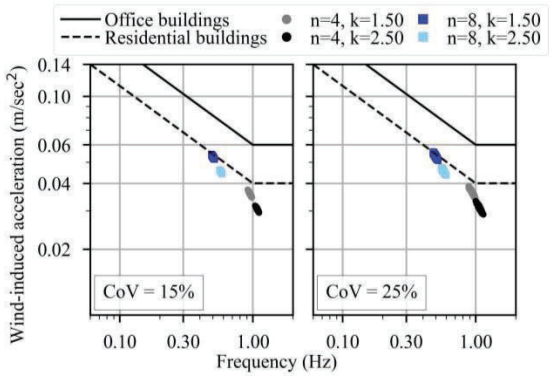

Figure 10: *Fundamental eigenfrequency – top floor acceleration for all realizations of MRTFs, compared to ISO10137 [20] requirements*

Table 4: *FE results of 4-storey MRTFs (3000 realizations per frame)*

Frame datails	N =4 storeys, h = 3.0 m, H = 12.0 m 3 bays, L = 8 m $b_c \times h_c = b_b \times h_b = 430 \times 585$ mm²			
K_θ (kNm/rad)	18866	18866	31443	31443
k_{mean}	1.5	1.5	2.5	2.5
CoV(k)	15%	25%	15%	25%
CoV($n_{M,end}$)	8-9%	14-16%	6-8%	12-14%
$n_{M,end,95\%}$	1.12-1.14	1.19-1.22	1.09-1.11	1.15-1.17
$n_{M,end,98\%}$	1.15-1.17	1.23-1.27	1.11-1.14	1.18-1.21
CoV($n_{M,span}$)	≈2%	3-4%	2-3%	4-5%
$n_{M,span,95\%}$	1.03-1.05	1.06-1.09	1.04-1.05	1.08-1.10
$n_{M,span,98\%}$	1.05-1.06	1.09-1.12	1.05-1.07	1.10-1.13
CoV($n_{V,end}$)	1%	1-2 %	1%	1-2 %
$n_{V,end,95\%}$	1.01-1.02	1.02-1.03	1.01-1.02	1.02-1.03
$n_{V,end,98\%}$	1.02	1.03-1.05	1.02	1.03-1.05
Δ_{mean} (mm)	6.73	6.81	5.13	5.16
CoV(Δ_{max})	9%	15%	9%	16%
mean(IDR_{max}) (mm)	2.71	2.74	2.25	2.26
CoV(IDR_{max})	6%	11%	6%	11%
f_{mean} (Hz)	0.950	0.946	1.080	1.075
CoV(f)	1%	2%	1%	2%
A_{mean} (m/s²)	0.036	0.036	0.030	0.031
CoV(A)	1%	2%	1%	2%

Table 5: *FE results of 8-storey MRTFs (3000 realizations per frame)*

Frame datails	N =8 storeys, h = 3.0 m, H = 24.0 m 3 bays, L = 8 m $b_c \times h_c = b_b \times h_b = 430 \times 585$ mm²			
K_θ (kNm/rad)	18866	18866	31443	31443
k_{mean}	1.5	1.5	2.5	2.5
CoV(k)	15%	25%	15%	25%
CoV($n_{M,end}$)	8-9%	14-16%	6-8%	12-14%
$n_{M,end,95\%}$	1.11-1.14	1.19-1.23	1.09-1.11	1.14-1.18
$n_{M,end,98\%}$	1.14-1.17	1.23-1.27	1.11-1.13	1.17-1.22
CoV($n_{M,span}$)	≈2%	3-5%	2-3%	4-5%
$n_{M,span,95\%}$	1.03-1.06	1.07-1.12	1.04-1.07	1.08-1.13
$n_{M,span,98\%}$	1.04-1.08	1.09-1.15	1.05-1.08	1.10-1.17
CoV($n_{V,end}$)	≈1%	1-2%	≈1%	≈2%
$n_{V,end,95\%}$	1.01-1.02	1.02-1.03	1.01-1.02	1.02-1.03
$n_{V,end,98\%}$	1.02	1.03-1.04	1.02	1.03-1.04
Δ_{mean} (mm)	35.26	35.70	26.39	26.69
CoV(Δ_{max})	3%	5%	3%	5%
mean(IDR_{max}) (mm)	8.49	8.55	6.84	6.92
CoV(IDR_{max})	3%	5%	3%	5%
f_{mean} (Hz)	0.501	0.498	0.577	0.574
CoV(f)	1%	1%	1%	1%
A_{mean} (m/s²)	0.053	0.053	0.045	0.045
CoV(A)	1%	1%	1%	1%

5 CONCLUSIONS AND FUTURE WORK

This paper provides an overview of analysis and design aspects of moment-resisting connections with inclined threaded rods. In the first part of the paper, a series of expressions that estimate the properties of such connections were provided based on recent publications. In the second part of the paper, a preliminary study on the effect of connections' stiffness variability on the structural response of timber frames was presented, based on a simple beam model and Finite Element simulations of planar frames. In common practice, structural analysis of timber structures is performed by use of mean stiffness values. However, in moment-resisting frames the magnitude and distribution of internal forces and moment is highly dependent on the stiffness of their connections. The results of this study have shown that the variability of connections' stiffness can result in great variability of the internal forces and moments. The end moments are more sensitive to this effect with 98th percentiles of the order of 20%-40% higher than the reference values obtained by analysis with mean stiffness values. Such increase should be considered in the design for the Ultimate Limit State. The Finite element results were in good agreement with the predictions obtained by use of a simple beam model

https://doi.org/10.52202/069179-0165

with rotational springs. When it comes to serviceability requirements, the FE models showed that the variability of connections' stiffness has small influence and may be neglected.

REFERENCES

[1] A. Vilguts, H. Stamatopoulos, and K. A. Malo, "Parametric analyses and feasibility study of moment-resisting timber frames under service load," *Engineering Structures,* vol. 228, p. 111583, 2021/02/01/ 2021, doi: https://doi.org/10.1016/j.engstruct.2020.111583.

[2] K. Lied and K. Nordal, "A conceptual study of glulam connections using threaded rods and connecting circular steel profiles," in "Master thesis," NTNU Norwegian University of Science and Technology, Trondheim, Norway, 2016.

[3] A. Vilguts, S. Ø. Nesheim, H. Stamatopoulos, and K. A. Malo, "A study on beam-to-column moment-resisting timber connections under service load, comparing full-scale connection testing and mock-up frame assembly," *European Journal of Wood and Wood Products,* vol. 80, no. 4, pp. 753-770, 2022/08/01 2022, doi: 10.1007/s00107-021-01783-2.

[4] H. Stamatopoulos, K. A. Malo, and A. Vilguts, "Moment-resisting beam-to-column timber connections with inclined threaded rods: Structural concept and analysis by use of the component method," *Construction and Building Materials,* vol. 322, p. 126481, 2022, doi: https://doi.org/10.1016/j.conbuildmat.2022.126481.

[5] R. Steiger and E. Gehri, "Interaction of shear stresses and stresses perpendicular to grain," presented at the Proceedings of the 44th CIB-W18 meeting, Alghero, Italy, 2011.

[6] P. Dietsch, H. Kreuzinger, and S. Winter, "Design of shear reinforcement for timber beams," presented at the Proceedings of the 46th CIB-W18 meeting Vancouver, Canada, 2013.

[7] H. Stamatopoulos and K. A. Malo, "On strength and stiffness of screwed-in threaded rods embedded in softwood," *Construction and Building Materials,* vol. 261, p. 119999, 2020/11/20/ 2020, doi: https://doi.org/10.1016/j.conbuildmat.2020.119999.

[8] H. J. Blaß and O. Krüger, *Schubverstärkung von Holz mit Holzschrauben und Gewindestangen*. Karlsruhe: KIT Scientific Publishing, 2010.

[9] H. Stamatopoulos and K. A. Malo, "Withdrawal stiffness of threaded rods embedded in timber elements," *Construction and Building Materials,* vol. 116, pp. 263-272, 2016, doi: http://dx.doi.org/10.1016/j.conbuildmat.2016.04.144.

[10] H. Stamatopoulos and K. A. Malo, "Withdrawal capacity of threaded rods embedded in timber elements," *Construction and Building Materials,* vol. 94, pp. 387-397, 2015, doi: http://dx.doi.org/10.1016/j.conbuildmat.2015.07.067.

[11] H. Stamatopoulos, F. M. Massaro, and J. Qazi, "Mechanical properties of laterally loaded threaded rods embedded in softwood," *European Journal of Wood and Wood Products,* 2021/09/15 2021, doi: 10.1007/s00107-021-01747-6.

[12] CEN, "NS-EN 1995-1-1:2004+A1:2008+A2:2014+NA:2010," in *Design of timber structures - Part 1-1: General - Common rules and rules for buildings*, ed. Brussels: European committee for standarization, 2004.

[13] T. Laggner, G. Flatscher, and G. Schickhofer, "Combined loading of self-tapping screws," presented at the Proceedings of WCTE 2016 - World Conference on Timber Engineering, Vienna, Austria, 2016.

[14] S. Aicher and K. Simon, "Rigid Glulam Joints with Glued-in Rods subjected to Axial and Lateral Force Action," presented at the Proceedings of the 8th INTER meeting Karlsruher Institut für Technologie (KIT), 2021.

[15] A. Vilguts, "Moment-resisting timber frames with semi-rigid connections," Ph.D. Thesis, Department of Structural Engineering, Norwegian University of Science and Technology, Trondheim, Norway, 2021.

[16] CEN, "EN 14080-2013: Timber structures-Glued laminated timber and glued solid timber - Requirements," ed. Brussels, Belgium: European Committee for Standardization, 2013.

[17] CEN, "NS-EN 1991-1-4:2005+NA:2009," in *Actions on structures - Part 1-4: General actions - Wind actions*, ed. Brussels, Belgium: European Committee for Standardization, 2009.

[18] CEN, "NS-EN 1990:2002+A1:2005+NA:2016," in *Basis of structural design*, ed. Brussels, Belgium: European Committee for Standardization, 2016.

[19] A. Feldmann *et al.*, "Dynamic properties of tall timber structures under wind-induced vibration," presented at the Proceedings of WCTE 2016 - World Conference on Timber Engineering, Vienna, Austria, 2016.

[20] ISO, International Organization for standardization, "ISO10137: Bases for design of Structures - Serviceability of Buildings and Walkways against Vibrations," ed. Geneva, Switzerland: ISO, 2007.

https://doi.org/10.52202/069179-0165

World Conference on Timber Engineering Oslo 2023

APPLICATION OF A TUBE CONNECTOR FOR CATENARY ACTION IN CLT FLOORS

Johannes A. J. Huber[1], Yunbo Huang[2], Sivert Knutsen[3], Alicja Przystup[4], Thomas Tannert[5], Sven Berg[6]

ABSTRACT: Multi-storey buildings require provisions to avoid disproportionate consequences after unexpected events, e.g. explosions or human error during design and construction. To prevent failure progression in the structure after an initial damage (loss of load-carrying elements), alternative load paths, like catenary action, should be provided. Catenary action supports the sagging structure after element loss by transferring the loads horizontally to the adjacent elements; this mechanism requires the connections to remain ductile under high load. Conventional dowel-type connectors in timber structures have limited potential to develop catenary action in beams or floors. A previously developed tube connector exhibited desirable behaviour to develop catenary action in cross-laminated timber floors; however, the tube exhibited and undesirable failure mode. In the present study, the behaviour of a newly designed variant of the tube connector was experimentally investigated under catenary action. The new connector design was tested in varying configurations, at both the component level and full-scale floor level, in Canada and Sweden. The results show that a more desirable behaviour of the adapted connector could be achieved compared to the previous design, with respect to catenary action.

KEYWORDS: Disproportionate collapse, Progressive collapse, Structural robustness, Alternative load paths

1 INTRODUCTION

1.1 BACKGROUND

Multi-storey timber buildings can provide living space for many occupants. The more occupants, the more severe are the possible consequences if unforeseen events lead to a damage and a subsequent collapse. Disproportionately large collapses, in relation to their original cause, e.g. an explosion, a vehicle accident or human errors during design and/or construction, must be avoided. Often, a disproportionate collapse occurs because the progression of an initial component failure cannot be halted, which is then usually referred to as a progressive collapse. Some building codes, e.g. Eurocode 1 [1], require that a progressive collapse shall be avoided for buildings taller than four storeys or with a certain number of occupants.

A building can be designed to resist a progressive collapse by providing alternative load paths (ALPs) after certain components have failed. [2]. Examples of ALPs in floors after the loss of a support include compressive arching action for small deflections, and catenary action or membrane action for large deflections [3]. In catenary action, the beams or floors support the sagging structure by acting like a chain and transferring the loads mainly by in-plane tension to the surrounding undamaged structure.

1.2 FLOOR CONNECTORS AND CATENARY ACTION

In timber structures, catenary action can be developed in beams in post-and beam systems, or in cross-laminated timber (CLT) floor panels. Currently available dowel-type connectors do not allow for large deformations of beam or floors, e.g. tests of timber post-and-beam systems found that conventional connectors failed prematurely and could not develop catenary action; however, a double slotted-in steel plate connector, with elongated holes to allow joint rotation, was able to develop catenary action [4]. Support-removal tests in [5] on lap-jointed solid timber floors and walls in platform-type construction, including CLT floors, found that conventional screw connections were not able to develop catenary action.

In contrast, tube connectors [6] were able to support substantial catenary forces under large displacements in CLT floors [5]. In a numerical optimisation of the original design [7], the most influential parameters were found to be the tube diameter, the tube thickness, and the coupler diameter. The original tube design used a welded coupling nut on the inside of the tube; this was a weak spot where brittle rupture occurred, as shown in Figure 1.

[1] Johannes A. J. Huber, Luleå University of Technology, Skellefteå Sweden, johannes.huber@ltu.se
[2] Yunbo Huang, Luleå University of Technology, Skellefteå Sweden, yunhua-0@student.ltu.se
[3] Sivert Knutsen, Luleå University of Technology, Skellefteå Sweden, sivknu-0@student.ltu.se
[4] Alicja Przystup, University of Edinburgh, Edinburgh, Scotland, a.c.przystup@sms.ed.ac.uk
[5] Thomas Tannert, University of Northern British Columbia, Prince George, BC, Canada, thomas.tannert@unbc.ca
[6] Sven Berg, Luleå University of Technology, Skellefteå Sweden, sven.berg@ltu.se

https://doi.org/10.52202/069179-0166

***Figure 1**: Original tube connector with welded coupler*

In a numerical study [8], 3D finite element (FE) models were developed, and parameter variations were conducted reflecting a building situation to study both traditional screw connections and the tube connector in a support-removal scenario. The study found that catenary action was the dominant ALP and confirmed the suitability of the tube connector for catenary action.

1.3 OBJECTIVE

Given the simplicity of the tube connector regarding manufacturing and installation, and its suitability to develop catenary action under large floor rotations, it was deemed worthwhile to investigate further adaptations to improve its performance. The goal of the present study was to investigate the behaviour of a newly designed variant of the tube connector with a hammerhead under catenary action in CLT floors.

2 MATERIAL & METHODS

Tests were conducted at the Wood Innovation Research Lab in Prince George, Canada, and the lab of the Research Institutes of Sweden (RISE) in Skellefteå, Sweden.

2.1 MATERIALS

In Canada, 100 mm thick 5-ply CLT panels with 20 mm thick layers made of Norway Spruce (*Picea abies*) of strength class C24 [9] were used. The boards were edgewise bonded. All cutting and milling was done in the test lab. In Sweden, 200 mm deep 5-ply CLT panels with 40 mm thick layers of Norway Spruce of strength class C24 [9] were used. The edges of the boards were not glued. The panel geometry including the cut-outs for the tube was cut and milled at the manufacturing site.

The outer diameter of the tubes was 3'' (76,2 mm). The steel for the Canadian tubes was A/SA 106 Grade B (minimum yield strength 240 MPa) and for the Swedish tubes was S355 (minimum yield strength 355 MPa). In Canada, the length of the tube was 100 mm and the thickness was 3 mm, and in Sweden, the length was 140 mm and thicknesses of 4 mm and 5 mm. Two holes on opposing sides were cut at mid-length of the tube for passing through the rod. In Canada, two circular holes were cut, but in Sweden one of the holes was cut as an elongated slot to not restrict the rod movement in certain test variations.

Instead of the welded coupler used in [5], a conically shaped steel part with a cylindrical base was used, herein referred to as the *hammerhead*, and it was held in place by a standard nut. The hammerhead pushed onto the outside of the tube instead of pulling on the inside. In Canada, a hammerhead with an outer diameter (D_1) of was 1,5'' (38,1 mm) and a height (h) of 0,5'' (12,7 mm) was used, with the conical base facing away from the tube, see Figure 2b. The hammerhead was mild steel grade ASTM A36, while for the threaded 5/8" (19,9 mm) rod, grade ASTM A193 Grade B7 was used (minimum yield strength 720 MPa). In Sweden, a hammerhead with $D_1 = 50$ mm and $h = 20$ mm was used and it was positioned with the cylindrical base towards the tube, see Figure 2a. A standard M20 threaded rod with strength class 8.8 (minimum yield strength 640 MPa) was used together with a class 12.9 nut.

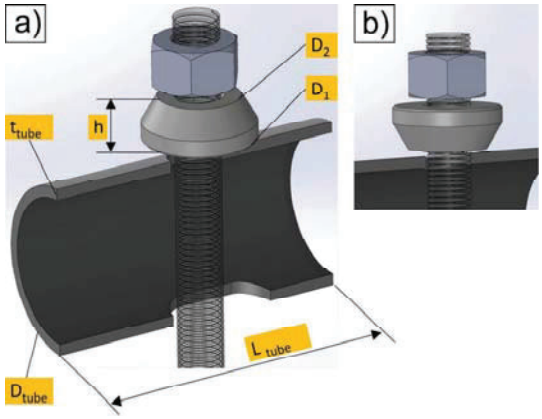

***Figure 2:** Tube connector with hammerhead; a) Swedish and b) Canadian version*

2.2 TUBE PRE-TESTS

Tensile tests on the tube connector, embedded in CLT, were performed by applying a displacement-controlled, quasi-static load along the axis of the rod. The insights gathered during the pre-tests were used for final adjustments of the connector designs to be used on tests in full floor elements.

For the Canadian tests, the CLT samples were 350 mm wide and 800 mm long, see Figure 3. The cut-out to embed the tubes was machined through the full depth of the panel and the part for embedding the rod was machined to a depth of 60 mm (3 layers). A symmetric loading setup with two tubes being tested simultaneously was chosen. The relative displacement between CLT panel and tube edge was measured by two linear variable differential transformers (LVDT) positioned on a thin metal plate locked by nuts to the end of the rod. The load was applied displacement-controlled at 10 mm/min.

https://doi.org/10.52202/069179-0166

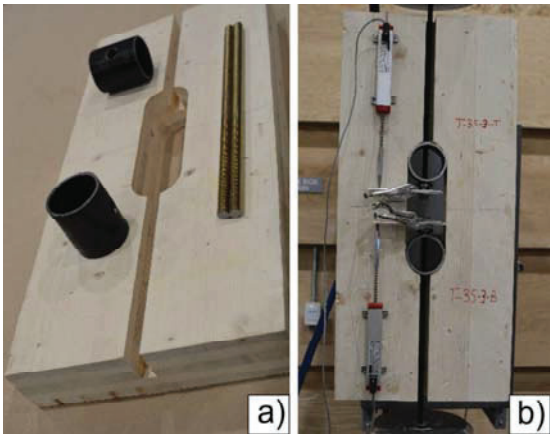

***Figure 3**: Canadian pre-tests of the tube connector*

For the Swedish pre-tests, the CLT samples were 400 mm wide and 600 mm long, see Figure 4. The circular part to embed the tube was machined to a depth of 170 mm and the part to embed the rod was machined to 130 mm depth, see Figure 4a. Only a single tube was used in each test repetition, while the rod was fixed at approximately half its length to a rigid steel frame. The other side of the CLT sample was fixed by nine fully-threaded self-tapping screws (STS) with diameter 13 mm and length 200 mm [10] to customised steel parts which provided a rotation-free connection to the pulling hydraulic cylinder, see Figure 4b. The STSs were inserted using a 45-degree angled washer of type VGU [10]. The displacement in the hydraulic cylinder was increased by 6 mm/min and the resulting load was recorded. The total displacement was measured at the edge of the panel facing the fixed point of the rod using a LVDT. Additionally, the relative displacement between the CLT panel and the customised steel parts was measured to control for slippage.

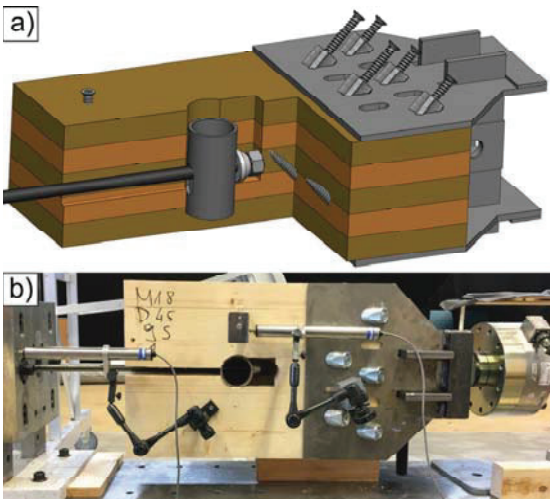

***Figure 4:** Swedish tube pre-test; a) tube placement and b) test setup*

2.3 FLOOR ELEMENT TESTS

To evaluate the performance of the tube connector under catenary action in the lengthwise direction of the floor panels, pushdown tests were conducted with full-length CLT panels over a removed wall support, as shown in Figure 5 for the Canadian tests.

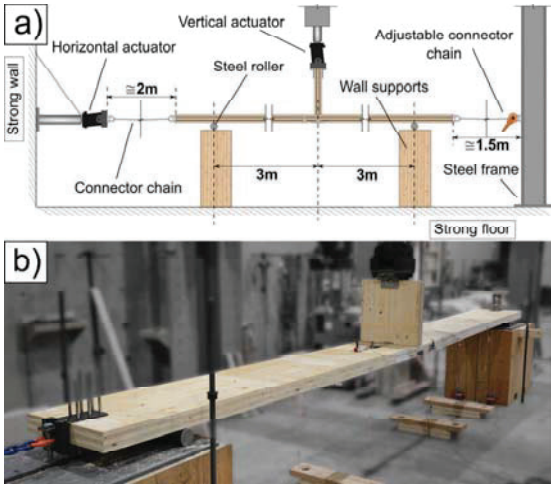

***Figure 5:** Canadian floor element tests; a) idealised and b) lab setup*

For the Canadian tests, a single span of 3 m was assumed, i.e. the nominal length between the supports in the tests was 6 m. The CLT panels were 600 mm wide and butt-jointed lengthwise (Figure 6). The tube connector was inserted in pre-milled cut-outs in the panels. The screws used for the butt connection were 140 mm SWG fully threaded STS [11] installed at 45° angle. To prevent the rod of the tube connector from rising above the surface of the CLT panels, the loading was applied via a CLT wall section on the centre of the joint. A steel stopper was manufactured to fit underneath the load application wall to prevent the rising rod from compromising the wall-to-floor contact. Since the pushdown actuator had a maximum stroke of 500 mm, the test was conducted in two stages to fully deform the tubes; firstly, a 600 mm tall wall section was used up to approximately 300 mm extension of the actuator, and after unloading and exchanging the wall with an 800 mm section, the loading was continued. The vertical supports were long steel rollers, and the horizontal displacement was fixed by running chains from strong wall to the sample on both sides. These were fixed onto steel C-clamps with 6 steel ¾" (19,1 mm) bolts. One of the chains ran to a horizontal actuator which allowed for pre-tensioning of the chains to take out slack while acting as a load cell. Thanks to this setup, compressive arching was omitted as only tensile forces could be transferred through the chain and the friction of the rollers was negligible.

https://doi.org/10.52202/069179-0166

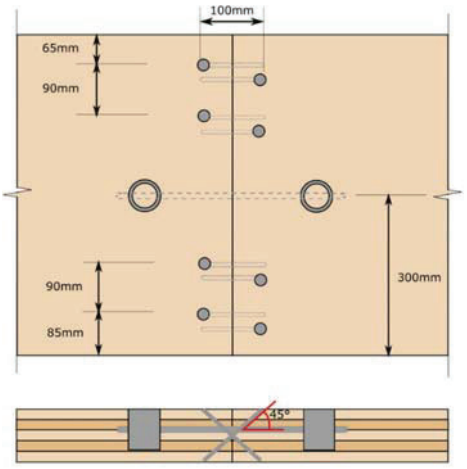

***Figure 6**: Butt joint and tube connector alignment in Canadian floor tests*

For the Swedish tests, the test setup was adapted for an inverted load application, see Figure 7, to allow the use of the full hydraulic cylinder stroke. The panels were flipped, and the tubes were thus inserted from below to connect the panels. The custom steel plate connectors from the pre-tests were slightly adapted and used for rigidly fixing the panels horizontally. Rotation was free at the ends which was achieved by a pinned connection between the end connection and the rigid frame. Effectively, the span was 200 mm larger due to the connector. An additional hydraulic cylinder with a load cell was attached to one of the end connections to measure the horizontal tie force and to apply a 0.5 kN pre-load on the tube connector to prevent it from slipping out of the cut-out.

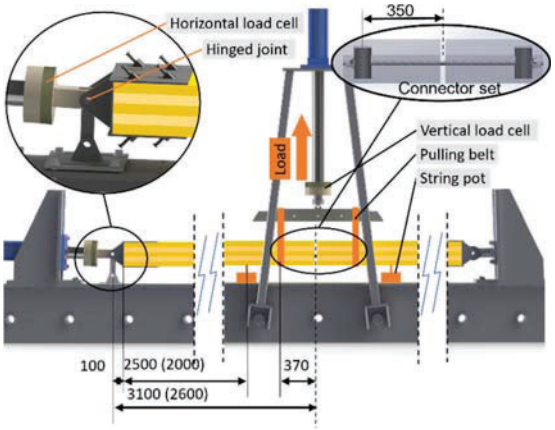

***Figure 7:** Swedish test setup for the floor element tests (mm)*

The panels used were machined symmetrically such that a cut-out for the tube was provided in both ends. After initial tests with a length of 3 m, 500 mm were cut off from the end used in the experiment and the remaining panel was reused at a length of 2.5 m, i.e. a length of 5 m between the supports. For the 2.5 m panels, the tube was inserted as indicated in Figure 4a, i.e. with the slot hole restricting the motion of the rod during rotation, and for the 3 m panels, the tube was inserted in a flipped orientation to allow rod movement during pushdown. For reference, floor elements without a tube connector, but with four angled double-threaded 8.2 mm × 280 mm STS [10] were tested.

The floor system was pushed down (i.e. pulled up) by applying a displacement-controlled quasi-static load via a spreader beam and straps, see Figure 7. The vertical pushdown force and the horizontal tie force were recorded. The pushdown displacement was recorded using string potentiometers. Since the horizontal fixture of the floor was unable to provide noticeable compliance, compressive arching action as in [8] was expected to occur between the panels. Since this resistance mechanism was not of interest for this study, and to single out the effects of catenary action, an initial 20 mm gap was provided between the panels. For the tests with STSs only, no initial gap was provided since a gap was expected to disproportionately affect the performance of the screw connection negatively.

3 RESULTS & DISCUSSION

3.1 PRE-TESTS

A typical development of the tube deformation during the Canadian pre-tests is shown in Figure 8 and the corresponding force-displacement curves in Figure 9. After an initial elastic phase (Figure 8a), tube yielding (8b) and hardening occurred until the ultimate load was reached (8c) and subsequent yielding led to softening (8d). The tubes predominantly engaged in a folding mechanism along a line along the tube length during yielding.

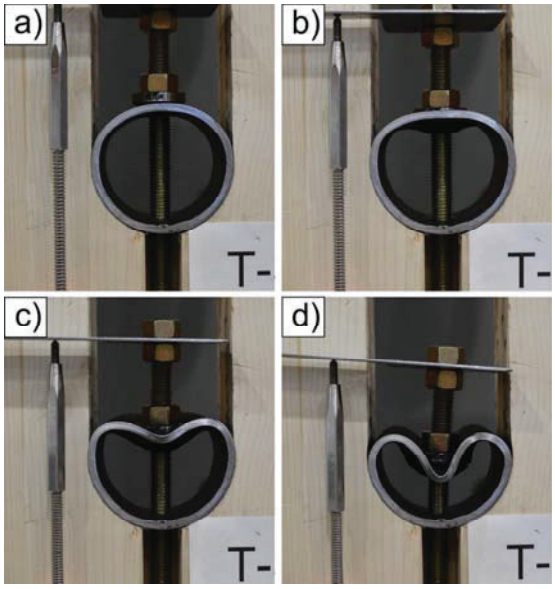

***Figure 8**: Pre-test of the Canadian tubes showing the tube deformation from unloaded to loaded state (a-d)*

https://doi.org/10.52202/069179-0166

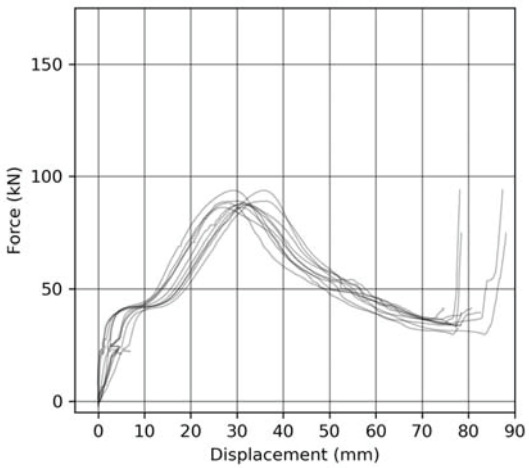

***Figure 9**: Force-displacement curves of 10 Canadian pre-tests.*

The Swedish pre-tests showed that the folding mechanism of the tubes during yielding was dominated by the more point-wise circular impression of the hammerhead (see Figure 10) than the Canadian tests due to the increased tube length. It was observed that the 5 mm tubes induced timber failure before the ultimate load of the tube could be reached. The 4 mm tubes reached their ultimate load consistently without timber failure if hammerheads with $D_1 = 50$ mm were used, see Figure 11. Additional tests with hammerheads of $D_1 = 45$ mm resulted in the hammerhead being pulled through the hole of the tube during yielding before tube folding was completed.

***Figure 10**: Deformed tube from the Swedish pre-tests*

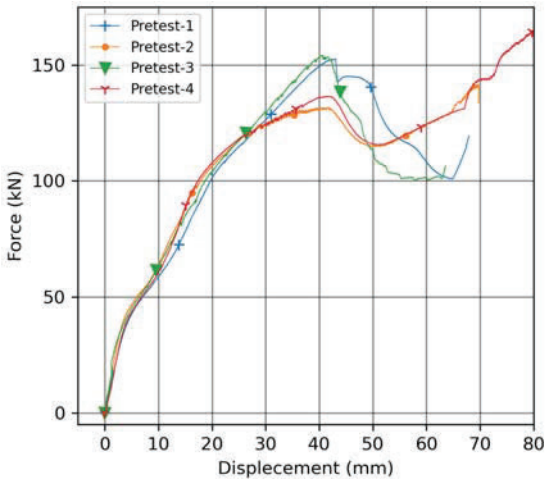

***Figure 11**: Force-displacement curves of the Swedish pre-tests for 4 mm tubes with hammerheads with 50 mm diameter.*

3.2 FLOOR ELEMENT TESTS

Figure 12 shows the pushdown and tie force curves of the Canadian floor element tests. The initial gradual increase in slope proves to be proportional to the geometrical deformation as expected of the steadily increasing catenary response with no compressive arching present. The failure of the butt joint is indicated by load plateau at approximately 350 mm pushdown, after which all load is transferred to the tube connector. Two clear peaks at approximately 10° and 13° floor rotation and subsequent load drops represent both tubes buckling at separate times.

The three-point testing may have affected the redistribution of forces in the connector as the metal stopper (Figure 13b) under the wall forced the deformation in the tubes on both sides to be in line with the panels. This setup might also have caused tube buckling to occur at corresponding lower pushdown distance than in the Swedish four-point tests (see below) because the displacement of the hammerhead was larger in order to conform with the enforced bent shape of the rod. The benefit of this wall configuration however is that the rod alignment remains normal to the tube walls, which could make the tube behaviour more predictable as it can be correlated more directly to the pure tension tests. This may furthermore reduce the risk of punching failure through the tube wall.

Despite the additionally provided actuator stroke, none of the specimen failed completely, after having deformed both tubes fully, see Figure 13c. Given the results of the Swedish tests (see below), it seems likely that the tube connectors in the Canadian tests reached their maximum load at the second buckle peak and that failure would occur not long after.

https://doi.org/10.52202/069179-0166

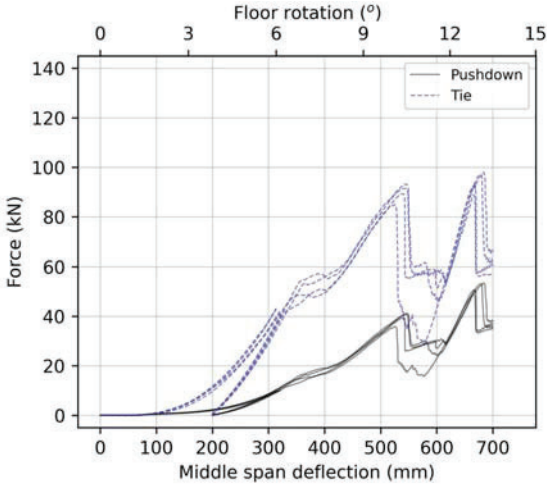

***Figure 12**: Force-displacement curves of the four Canadian floor element tests*

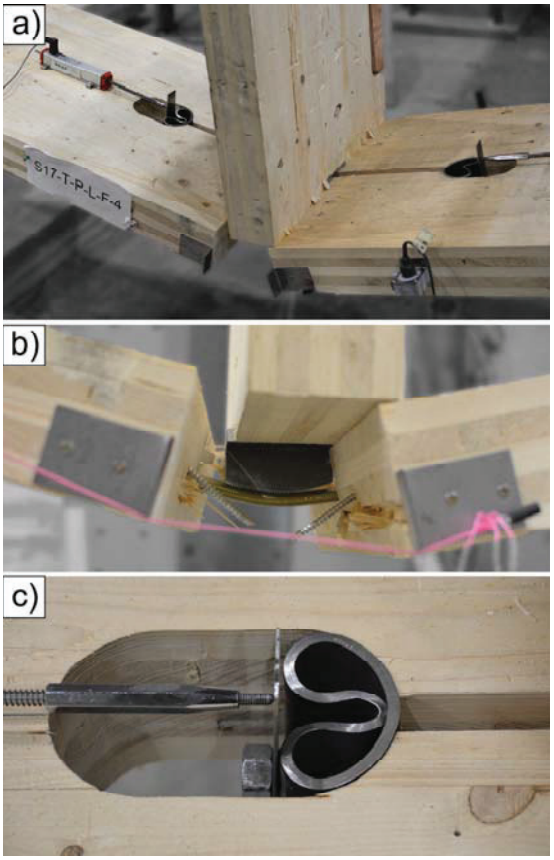

***Figure 13**: Canadian floor level tests during large floor rotations; a) wall section pushing on the floor panels, b) metal plate bending the rod of the tube connector and c) deformed tube connector*

The pushdown and tie force curves for the Swedish floor element tests with tube connectors in 3 m panels are shown in Figure 14 and for the 2.5 m panels in Figure 15.

After an initial dead phase caused by the gap between the panels, catenary action developed and could be sustained up to at least 10° of floor rotation. The dip in force at approximately 570 mm of pushdown deflection in Figure 14 was due to shear failure in the tube since the large rotation led to a load concentration at the hammerhead, see Figure 16a, which was aggravated by the slot hole. This effect was not as pronounced for the 2.5 m panels, because the flipped orientation of the slot kept a straighter pushing direction of the hammerhead onto the tube.

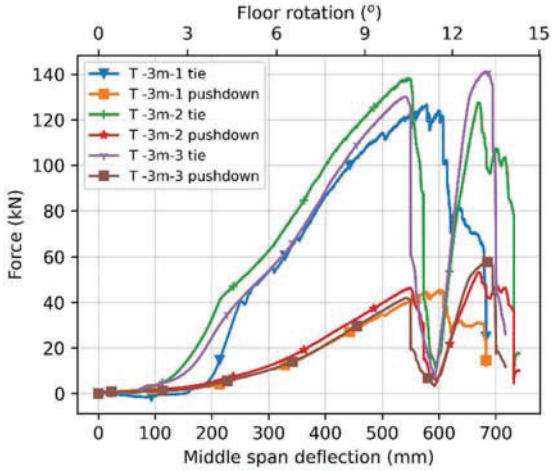

***Figure 14**: Force-displacement curves of the Swedish 3 m floor element tests with tube connectors*

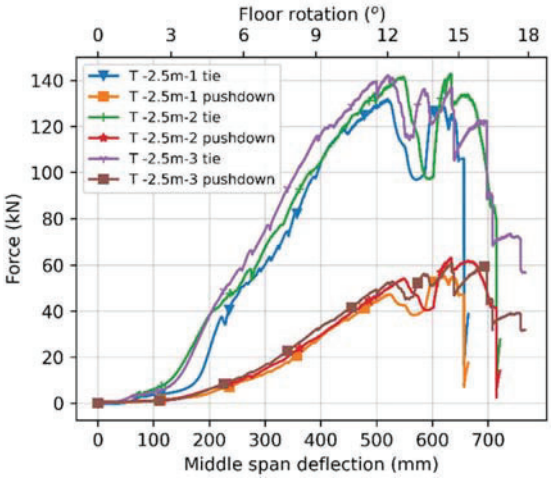

***Figure 15**: Force-displacement curves of the Swedish 2.5 m floor element tests with tube connectors*

https://doi.org/10.52202/069179-0166

***Figure 16**: Swedish floor element test; a) load concentration in the tubes and b) pushed-down floors*

Figure 17 shows the mean pushdown and tie curves of three Swedish floor element tests each with the screw connection. Since no gap existed between the panels, no dead phase occurred and instead, compressive arching action developed below 200 mm of pushdown deflection. Catenary action could not be sustained as the screws were bent and extracted from the CLT, see Figure 18.

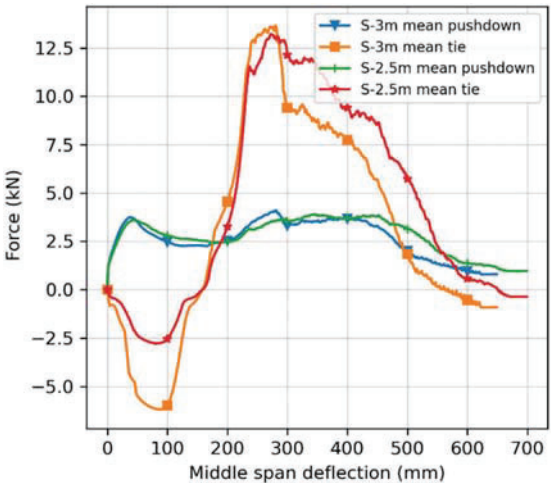

***Figure 17**: Force-displacement curves (means) of the Swedish floor element tests with screw connections*

***Figure 18**: Screw failure during pushdown in the Swedish tests*

3.3 COMPARISON TO PREVIOUS RESULTS

Previously conducted tests of the original tube connector design in [6] tested 3'' diameter tubes (variant T3) of 3 mm thickness in CLT in a similar loading configuration as the pre-tests in the present study. The used steel grade of the tubes had a yield strength of approximately 400 MPa. The results for the monotonic tests in [6] showed an ultimate load of approximately 50 kN at 24 mm displacement in the tube, which are both lower than the corresponding results in the present study. The development of the tube deformation and the characteristic shape of the load-displacement curves were similar in both studies.

The previous tests in [5] used the original tube connector design, as specified above, in similar pushdown tests as in the present study. Two connectors were used in CLT panels of a single span of approximately 2 m. The ultimate load of the tubes was not reached due to limited pushdown displacement and the maximum pushdown force for a single tube connector was approximately 15 kN at a floor rotation of approximately 7.2°. The models in [8] simulated larger pushdown displacements at slightly different boundary conditions for the tests in [5] and predicted an ultimate pushdown force of approximately 24 kN at a floor rotation of 12° for a single connector. The results of the present study indicate higher pushdown forces at corresponding floor rotations.

4 CONCLUSION

A new design of a tube connector for sustaining catenary action after a support removal in CLT was explored. Instead of using an internally welded coupler which may exhibit brittle weld failure, an external hammer pushed onto the tube and plastically deformed it during large joint rotations. The new connector design was tested in varying configurations, at both the component level and full-scale floor level, in Canada and Sweden.

The results indicate that the adapted tube connector could sustain higher catenary forces than the previous design at similar joint rotations. While variants with 4 mm tubes and slot holes which allow a changing direction of load application in the hammerhead could lead to abrupt load decreases due to shear failure, the new design did not exhibit a tendency for brittle failure. The conducted tests provided consistent results although slight variations existed in the material and test setups.

Compared to the initial design, a larger cut-out in the CLT was required to embed the connector. Nevertheless, the new design provides a more independent separation of the design components of the tube connector. The hammerhead geometry may further be adapted to produce a desired plastic deformation mode of the tube under load. With this design flexibility, alternative load paths in a damaged structure may be customised as desired.

https://doi.org/10.52202/069179-0166

ACKNOWLEDGEMENTS

The authors thank for the financial support of the "Tallwood" project as part of the European Union Interreg Nord program, and the project "Främja ökat byggande av flerfamiljshus i trä", funded by the Swedish Agency for Economic and Regional Growth (Tillväxtverket) as part of the European Regional Development Fund. The authors thank Urban Häggström at RISE for his help with the experiments.

The work in Canada was funded by the government of British Columbia through a BC Leadership Chair. The support by the UNBC technicians Michael Billups, James Andal, and Ryan Stern is greatly appreciated.

REFERENCES

[1] European Committee for Standardization: EN 1991: 2006. Eurocode 1 - Actions on structures - Part 7: General actions - Accidental actions. Brussels, 2006.

[2] Ellingwood B. R. et al.: Best practices for reducing the potential for progressive collapse in buildings. National Institute of Standards and Technology – U.S. Department of Commerce, 2007.

[3] Huber J. A. J. et al.: Structural robustness and timber buildings - a review. *Wood Material Science & Engineering*, 14(2):107-128, 2019.

[4] Lyu C. H. et al.: Experimental collapse response of post-and-beam mass timber frames under a quasi-static column removal scenario. *Engineering Structures*, 213:110562, 2020.

[5] Mpidi Bita H. and Tannert T.: Experimental Study of Disproportionate Collapse Prevention Mechanisms for Mass-Timber Floor Systems. *Journal of Structural Engineering*, 146(2):04019199, 2019.

[6] Schneider J. et al.: Experimental assessment of a novel steel tube connector in cross-laminated timber. *Engineering Structures*, 177:283-290, 2018.

[7] Mpidi Bita H. and Tannert T.: Numerical optimisation of novel connection for cross-laminated timber buildings. *Engineering Structures*, 175:273-283, 2018.

[8] Huber J. A. J. et al.: Finite element analysis of alternative load paths to prevent disproportionate collapse in platform-type CLT floor systems. *Engineering Structures*, 240:112362, 2021.

[9] European Committee for Standardization. EN 338:2016, Structural timber - Strength classes.

[10] ETA-Danmark AS: European Technical Assessment ETA-11/0030, Nordhavn, Denmark, 2022.

[11] CCMC 13677-R: Evaluation report SWG ASSY® VG Plus and SWG ASSY® 3.0 Self-Tapping Wood Screws. Canadian Construction Materials Centre, Ottawa, Canada, 2020.

https://doi.org/10.52202/069179-0166

World Conference on Timber Engineering Oslo 2023

EXPERIMENTAL VALIDATION OF PROPOSED CAPACITY-BASED DESIGN APPROACHES FOR MULTI-PANEL CLT SHEARWALLS

Mohammad Masroor[1], Ghasan Doudak[2], Daniele Casagrande[3]

ABSTRACT: Several research studies have proposed capacity-based design (CD) approaches for multi-story buildings containing cross-laminated timber (CLT) shearwalls. The current study contributes to the state of knowledge by evaluating experimental tests and numerical models on multi-panel CLT shearwalls in context of a proposed CD method available in the literature. The evaluation includes the yield hierarchy among energy dissipative elements and requirements to ensure sufficient energy dissipation is achieved in the shearwall. The results from the experimental tests on conventional connections used in CLT shearwalls are presented, as they are used as inputs in the numerical model and CD expressions. Reasonable correlation was found between the results obtained from experimental tests and numerical models. The walls' shear resistance obtained from the CD expressions represented a load level lower than the maximum resistance obtained from the experimental tests and numerical modes. This additional strength could be attributed to the contribution of angle brackets after the yielding of the hold-down, which is represented in the tests and numerical models but not in the CD equations. It was demonstrated that satisfying the proposed equations would lead to the desired lateral behaviour and energy dissipation in CLT shearwalls.

KEYWORDS: Cross-Laminated Timber (CLT); Capacity-based Design (CD); experimental tests; connections; seismic load

1 INTRODUCTION

The performance of cross-laminated timber (CLT) shearwalls subjected to seismic loads is mainly dominated by behaviour of the mechanical connections, which provide resistance and energy dissipation in the system, while the CLT panels can be reasonably assumed to behave like rigid bodies. Experimental tests have demonstrated that multi-panel CLT shearwalls possess better seismic performance than shearwalls consisting of a single panel, since joints connecting the panels together provide significant ductility (e.g., [1], [2]). This is also emphasized in the current version of the Canadian Engineering Design in Wood standard, CSA O86-19 [3], where panel-to-panel connections are defined as one of the main energy-dissipative elements in CLT shearwalls. A typical multi-panel CLT shearwall consists of panels attached together using panel-to-panel connections, and mechanical anchors, such as hold-down and angle brackets, which connect the wall to the foundation or floors, as shown in Figure 1.

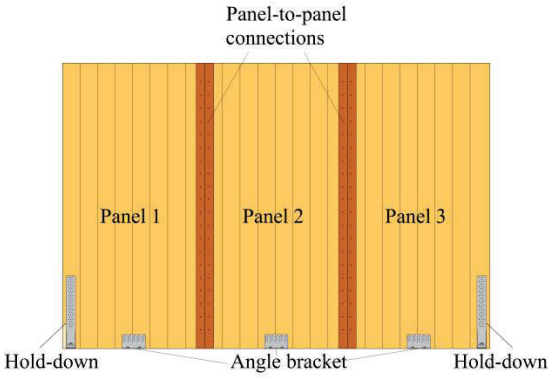

Figure 1: *Example of a multi-panel CLT shearwall*

Recent research has developed and proposed capacity-based design (CD) approaches for multi-story buildings containing CLT shearwalls, with the aim of preventing the occurrence of brittle failure and ensuring adequate energy dissipation under seismic loads. Gavric et al. [4] indicated dissipative connections, such as fasteners (nails and screws) used in panel-to-panel connections, hold-downs and angle brackets, in which plastic hinges are developed, and non-dissipating elements, such as CLT panels and brackets and anchoring bolts attached to the base. The

[1] Mohammad Masroor, Department of Civil Engineering, University of Ottawa, Canada, mmasr100@uottawa.ca
[2] Ghasan Doudak, Department of Civil Engineering, University of Ottawa, Canada, gdoudak@uottawa.ca
[3] Daniele Casagrande, Institute of Bioeconomy - National Research Council of Italy (CNR-IBE), Italy, daniele.casagrande@ibe.cnr.it

https://doi.org/10.52202/069179-0167

authors extended the proposal to multi-storey buildings, identifying panel-to-panel connections and hold-downs as dissipative connections, while requiring angle brackets to remain elastic. As a result of research efforts in Europe, a comprehensive CD approach was developed and proposed for inclusion in the next generation of Eurocode 8 [5]–[8]. Based on the proposal, CLT shearwall buildings can be classified into two levels of ductility, namely: medium ductility, which refers to buildings constructed from single panel or multi-panel CLT shearwalls that behave monolithically, and high ductility, which refers to multi-panel CLT shearwalls behaving in coupled-panel (CP) kinematic mode and where the panel-to-panel connections are designed to dissipate energy.

Casagrande et al. [9] proposed a CD approach for multi-panel CLT shearwalls using minimum potential energy method based on the developed analytical approach presented in [10]. Masroor et al. [11] extended the CD approach to include the bi-directional contribution of angle brackets, which was considered as a circular domain, as presented and investigated in [12]–[14]. A yield hierarchy was introduced for the dissipative connections, while ensuring that non-dissipative elements and those with limited-dissipative capability remain elastic. To achieve the proposed hierarchy and provide protection for non-dissipative elements, the concept of introducing over-strength factors were proposed and discussed.

The current study aims to validate the proposal developed in [11] by means of comparing the procedure to experimental test results and numerical models for multi-panel CLT shearwalls with conventional connections. The results of the experimental tests on connections are also presented, as they were used as inputs in the design equations and numerical models.

2 The CD design approach

2.1 General

This section reviews the CD approaches for multi-panel CLT shearwalls developed and reported in [11]. To ensure the proper sequence of the yield hierarchy, a CP kinematic mode is required, in which panel-to-panel connections yield before hold-downs. This behaviour implies that all panels have individual centers of rotation, which remain in contact with the ground. Figure 2 illustrates the investigated shearwall, consisting of m panels, subjected to gravity load, q, factored bending moment, M_f, and shear, V_f, at the base of the shearwall, and achieving CP kinematic behaviour. The figure also indicates the vertical (uplift) stiffnesses of the hold-down and shear stiffness in each panel-to-panel connection, $k_{h,z}$ and k_f, respectively, horizontal (shear) and vertical (uplift) stiffnesses of the angle bracket, $k_{a,x}$ and $k_{a,z}$, respectively, and the number of panel-to-panel connections and angle brackets used in each panel, n_f and n_a, respectively. The width and height of each panel are denoted as b and h, respectively.

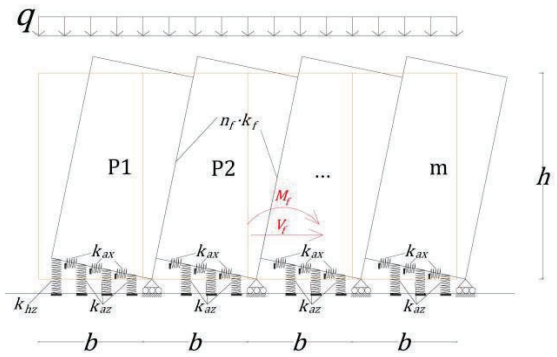

Figure 2: *The CP lateral behaviour of a multi-panel CLT shearwalls*

The proposal defines four categories of structural elements, as presented in Table 1: (1) Primary energy dissipative connections, which refers to panel-to-panel connections, considered to yield prior to other elements; (2) Other energy dissipative connections, which refers to hold-down connections, considered to yield after panel-to-panel connections; (3) Limited energy dissipative connections, which refers to angle brackets, considered elastic when panel-to-panel connections and hold-down have yielded; and (4) Non-energy dissipative elements, which refers to brittle structural elements such as CLT panels, which are expected to remain elastic until the energy dissipative connections reach a given load or displacement. Three over-strength factors were proposed to ensure such yield sequence is achieved and confirm that angle brackets and non-dissipative elements remain elastic. $\gamma_{r,h}$ is proposed to ensure that panel-to-panel connections yield prior to the hold-down, $\gamma_{r,a}$ ensures that angle brackets remain elastic when dissipative connections have yielded, and $\gamma_{r,ND}$ is meant to overprotect non-dissipative connections and ensure they remain elastic.

Table 1: *Proposed framework for the over-strength factors* [11]

Category	Element	Behaviour	Over-strength factor
Primary energy dissipative	Panel-to-panel connections	Yield	-
Other energy dissipative	Hold-down	Yield	$\gamma_{r,h}$
Limited energy dissipative	Angle brackets	Elastic	$\gamma_{r,a}$
Non-energy dissipative	E.g., CLT panels	Elastic	$\gamma_{r,ND}$

https://doi.org/10.52202/069179-0167

2.2 Capacity-based design requirements

The first step to establish requirements for the CD approach involves achieving CP kinematic mode. This is ensured by satisfying the requirement presented in Equation (1), which is a function of the connections' stiffness contributing to rocking behaviour, wall geometry, gravity load, and bending moment acting at the base of the shearwall.

$$\frac{k_{h,z}}{n_f \cdot k_f} \geq \frac{1-\frac{\widetilde{M}\cdot[3\cdot m-2]}{m^2}}{\left(1+\frac{\beta\cdot n_a}{2}\right)-\frac{\widetilde{M}\cdot\left\{m\cdot\left(1+\frac{\beta\cdot n_a}{2}\right)-2\cdot\left[1+\frac{n_a\cdot(2\cdot n_a+1)\cdot\beta\cdot m}{6\cdot(n_a+1)}\right]\right\}}{m^2}} \quad (1)$$

where, $\widetilde{M}$ and β are the dimensionless bending moment and vertical stiffness (uplift) ratio of mechanical anchors, presented in Equations (2) and (3), respectively.

$$\widetilde{M} = \frac{q\cdot m^2\cdot b^2}{2\cdot M_f} \quad (2)$$

$$\varphi = \frac{k_{a,z}}{k_{h,z}} \quad (3)$$

The requirement associated with the panel-to-panel connections yielding prior to the hold-down can be satisfied by ensuring the requirement outlined in Equation (4).

$$r_{h,z} \geq \gamma_{r,h} \cdot r_f \cdot \frac{k_{h,z}}{k_f} \quad (4)$$

where $r_{h,z}$ and r_f are the yield resistance of the hold-down in the vertical direction (uplift) and the yield resistance of one panel-to-panel connection, respectively.

The angle brackets are required to remain elastic when energy-dissipative connections have yielded, which ensures that sliding is minimised. This can be done by satisfying the requirement in Equation (5).

$$\left[\frac{\gamma_{r,a}\cdot n_a\cdot\beta\cdot r_{h,z}}{r_{a,z}\cdot(n_a+1)}\right]^2 + \left(\frac{C_h\cdot V_f}{r_{a,x}\cdot m\cdot n_a}\right)^2 < 1 \quad (5)$$

where, $r_{a,x}$ and $r_{a,z}$ are the yield resistance of one angle bracket in the horizontal (shear) and vertical (uplift) directions. V_f refers to applied shear acting at the base of the shearwall. C_h represents the ratio of the wall's bending moment resistance when hold-down yields to the bending moment acting at the base of the shearwall, and it can be obtained using Equation (6)

$$C_h = \frac{M^c_{r,h}}{M_f} \quad (6)$$

The wall's bending moment resistance when hold-down yields can also be calculated using Equation (7)

$$M^c_{r,h} = b \cdot \left\{r_{h,z} \cdot \frac{[1+n_a\cdot(2\cdot n_a+1)\cdot\beta\cdot m]}{6\cdot(n_a+1)} + r_f \cdot n_f \cdot (m-1) + \frac{q\cdot m\cdot b}{2}\right\} \quad (7)$$

The bending moment resistance of the shearwall, $M_{r,w}$, can be expressed as the wall's bending moment resistance when hold-down yields, $M^c_{r,h}$, which is required to be equal to or greater than the bending moment acting at the base of the shearwall due to the applied lateral loads.

$$M_{r,w} = M^c_{r,h} \geq M_f \quad (8)$$

Finally, the non-dissipative elements are required to be capacity-protected. For example, the resistance of the CLT panels, $V_{r,CLT}$ is required to be equal to or greater than the applied shear load at the base of the shearwall when hold-down yields, considering the appropriate over-strength factor, as shown in Equation (9)

$$V_{f,CLT} = \gamma_{r,ND} \cdot C_h \cdot V_f \leq V_{r,CLT} \quad (9)$$

3 EXPERIMENTAL TESTS RESULTS OF CONNECTIONS

The experimental tests were conducted on conventional connections used for CLT shearwalls. The average results of two tests on fully nailed WHT620 hold-downs [15] under uplift load and two tests on panel-to-panel connections consisting of partially threaded self-taping screws HBS 6x70 mm [16] are obtained from [17]. Figures 3 and 4 illustrate the load-displacement curves of the hold-down connections (HD-1 and HD-2) and panel-to-panel connections (PP-1 and PP-2), respectively. The average mechanical properties of each connection are presented in Table 2, based on the Equivalent Energy Elasto-Plastic (EEEP) curve, according to ASTM E2126-16 [18], including yield load, r_y, and corresponding displacement, d_y, elastic stiffness, k, and ultimate displacement, d_u.

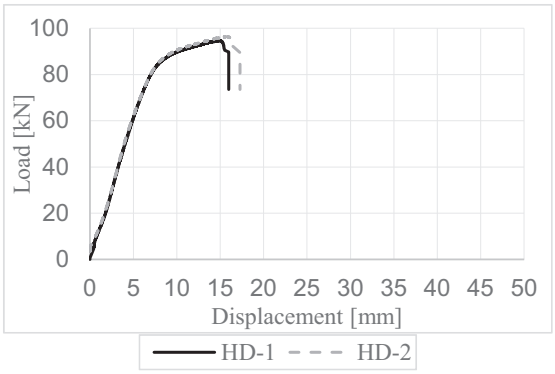

Figure 3: *Load-displacement curves of two tests on fully nailed WHT620 hold-down under uplift* [17]

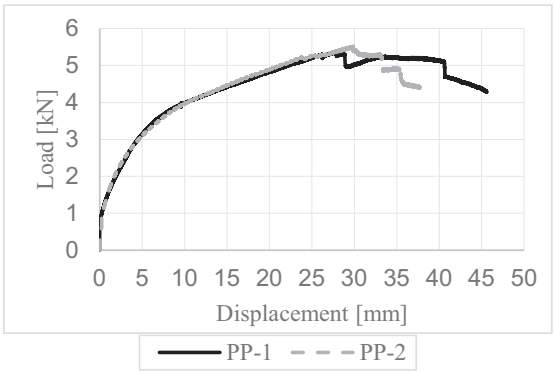

Figure 4: *Load-displacement curves of two tests on spline-joint panel-to-panel connections under shear* [17]

https://doi.org/10.52202/069179-0167

Table 2: *The average of EEEP simulated mechanical properties of hold-down and panel-to-panel connections* [17]

Connection	r_y [kN]	d_y [mm]	k [kN/mm]	d_u [mm]
Hold-down	90.80	7.30	12.44	16.60
Panel-to-panel	4.60	5.50	0.84	41.60

The results of monotonic shear and uplift experimental tests on fully nailed TCN200 angle brackets without washers [19], are presented here in the following and shown in Figure 5. Two repeats were conducted for each loading. A displacement rate of 3 mm/min was selected, consistent with the rates used in tests on the hold-downs and panel-to-panel connections.

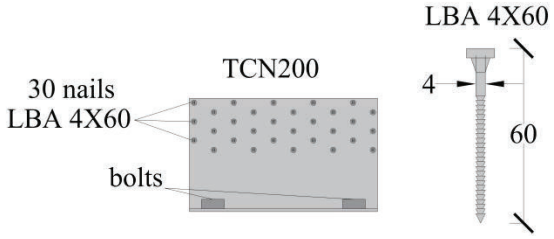

Figure 5: *Fully nailed TCN200 angle bracket*

Figures 6 and 7 illustrate the test setups for the angle bracket under monotonic uplift and shear loads, respectively. The CLT panels were composed of three layers, E1 grade, manufactured according to ANSI/APA (2020) [20]. Panel thickness was 105 mm (35-35-35), and the width of each board was 89 mm.

Figure 6: *Test set-up of angle bracket connection under uplift*

Figure 7: *Test set-up of angle bracket connection under uplift*

Figures 8 and 9 illustrate the load-displacement curves of the angle bracket connections under uplift (AU-1 and AU-2) and shear (AS-1 and AS-2), respectively. The average mechanical properties of the angle brackets are presented in Table 2, based on the EEEP curve.

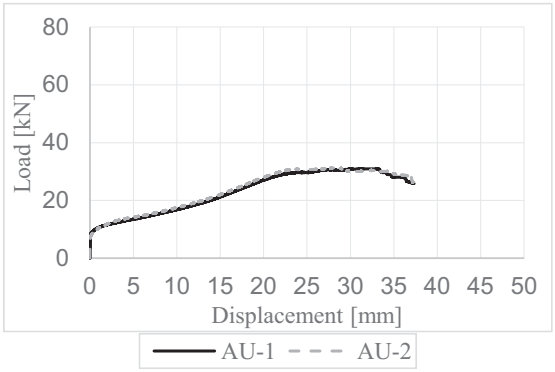

Figure 8: *Load-displacement curves of two tests on fully nailed TCN200 angle brackets under uplift*

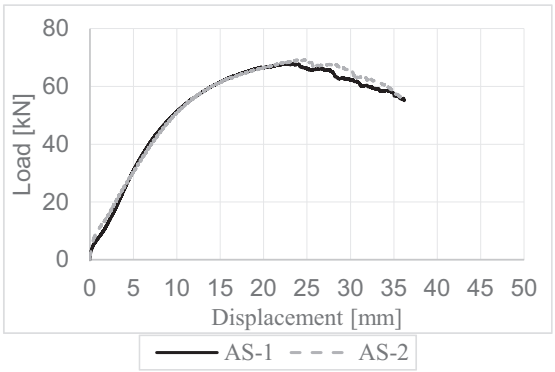

Figure 9: *Load-displacement curves of two tests on fully nailed TCN200 angle brackets under shear*

Table 3: *The average of EEEP simulated mechanical properties of TCN200 angle brackets under uplift and shear*

https://doi.org/10.52202/069179-0167

Load	r_y [kN]	d_y [mm]	k [kN/mm]	d_u [mm]
Uplift	25.4	6.8	3.7	37.5
Shear	62.5	11.0	5.7	36.2

4 EVALUATION OF THE CD PROCEDURE FOR MULTI-PANEL CLT SHEARWALLS

Experimental tests were conducted on two CLT shearwalls (W-1 and W-2), with the configurations shown in Figure 10, to investigate the CD approach proposed in [11] and presented in section 2. Walls W-1 and W-2 were subjected to equivalent uniform gravity loads, q, of 1.45 kN/m and 6.67 kN/m, respectively. The shearwalls consisted of three panels with height and length of 2438 mm and 1219 mm, respectively. The walls were anchored to the steel base and to the CLT panel by means of fully nailed hold-down and angle brackets, (i.e., WHT620 and TCN200). Two hold-downs were used on each face of the wall, while two angle brackets were used in each panel attached only to one face. Panel-to-panel joints consisted of nine HBS 6x70 mm screws.

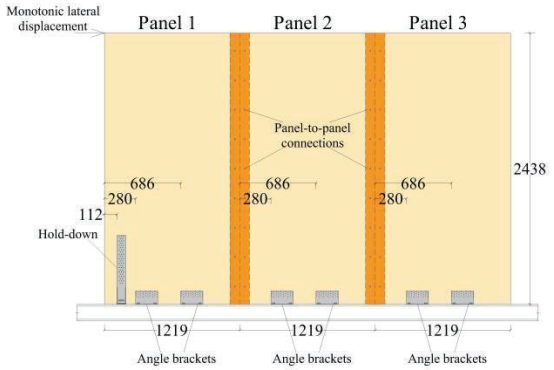

Figure 10: *Test set-up of CLT shearwalls*

Numerical models were developed using SAP2000 software [21], as illustrated in Figure 11. Multilinear link elements were used to model the connections based on the curves obtained from the connection tests. The interaction between uplift and shear in angle brackets were modelled using macro element, as presented in [22]. A concentrated lateral load, F, was applied at the top of the shear-wall consistently with the position of the loading actuator in the experimental tests, while the gravity loads were applied on top of the panels. Rigid gap elements acting only in compression were modelled at the bottom of the walls to simulate the contact between the steel base and the CLT panels. At the top and bottom of each panel, diaphragm constraints were applied. Orthotropic material properties were used for the CLT panels. The input values of $E_{eff,1}$, $E_{eff,2}$, and G_{eff} were equal to 4100 MPa, 7900 MPa, and 361 MPa, respectively [17].

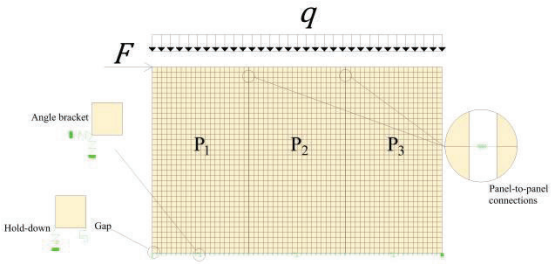

Figure 11: *SAP2000 numerical models of a three-panel CLT shearwalls*

Figure 12 demonstrates the load-displacement curves obtained from experimental tests and numerical models. Also presented in the figure is the wall's shear resistance at the point of hold-down yielding, obtained by dividing the wall's bending moment resistance when hold-down yields (Equation (7)) by the wall height, h. For both walls, reasonable matches can be observed between the results obtained from experimental tests and numerical models. The calculated shear resistance obtained from Equation (7) appears to be lower than the peak resistance obtained from the experimental tests and numerical models. This additional strength could be attributed to the contribution of angle brackets after the yielding of the hold-down, which is represented in the tests and numerical models but not in the CD equations.

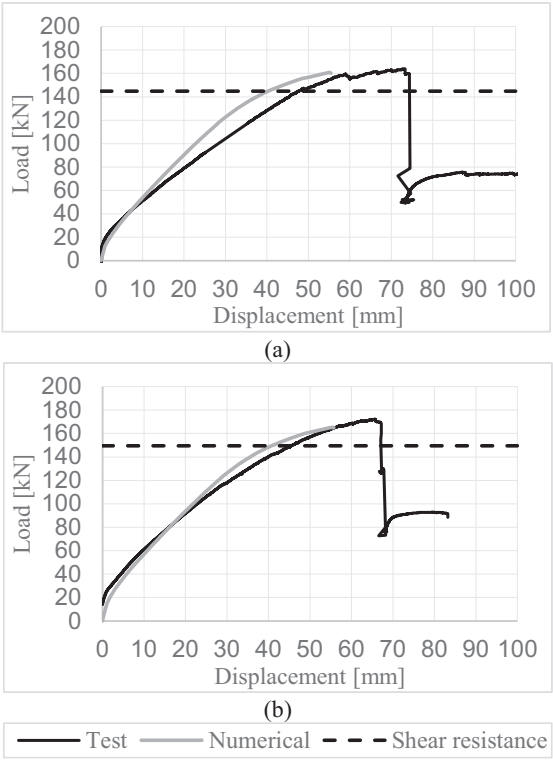

Figure 12: *Load-displacement curves of investigated CLT shearwalls: (a) wall W-1 and (b) wall W-2*

Evaluating the validity of the CD requirements, presented in Section 2.1, it can be noted that the CP kinematic mode was achieved in both experimental tests and numerical models, as shown in Figure 13(a) and (b), respectively. This satisfied the requirement outlined in Equation (1). The panel-to-panel connections yielded before hold-downs, which satisfied the requirement in Equation (4). The angle brackets remained elastic when hold-down yielded, satisfying the requirement in Equation (5), and the requirement related to the CLT panels remaining elastic was clearly also met.

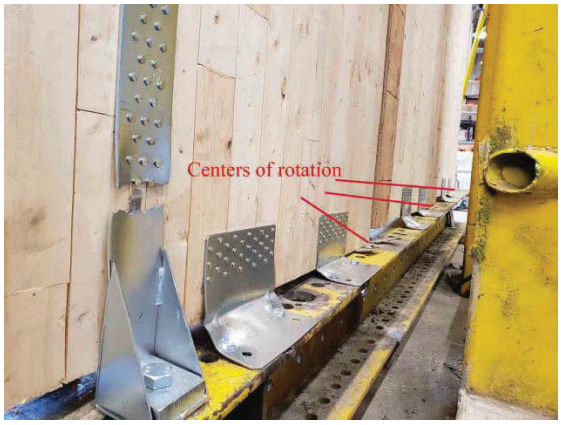

(a)

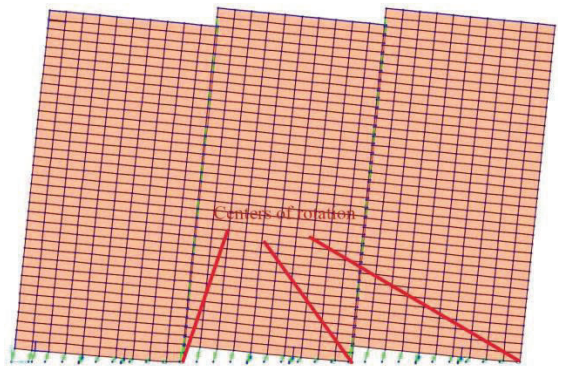

(b)

Figure 12: *Load-displacement curves of investigated CLT shearwalls: (a) wall W-1 and (b) wall W-2*

Table 4 presents the results obtained from the CD expressions for each requirement, as outlined in Section 2.1. Due to the deterministic nature of these examples, overstrength factors of unity were employed for the hold-down, $\gamma_{r,h}$, and the angle brackets, $\gamma_{r,a}$. A value of 1.6 was set for non-dissipative elements, $\gamma_{r,ND}$, such as CLT panels, based on [4]. For each wall, the requirements outlined in Equations (1), (4), (5) and (9) were calculated with inputs obtained from table 2 and 3. As can be observed in the table, all requirements were satisfied for both walls. This demonstrates that satisfying the proposed equations could lead to the desired lateral behaviour in CLT shearwalls. It is also noteworthy to mention that calculating the shear resistance of CLT panels in order to compare it with the value obtained from Equation (9) is out of the scope of this research, however, observations from the experimental study clearly shows that the shear strength of the CLT panels far exceeded the shear forces induced by the lateral load.

Table 4: *CD requirements' values for walls W-1 and W-2*

Eq.	Values		Satisfied
	W-1	W-2	
(1)	3.28>0.85	$3.28 > 0.80$	Yes
(4)	181.60>135.81	181.60>135.81	Yes
(5)	0.65<1.00	0.66<1.00	Yes
(9)	231.62	239.24	-

5 CONCLUSIONS

The current study investigates the validity of a proposed capacity-based design procedure with the help of experimental tests and numerical models on multi-panel CLT shearwalls. The results of experimental tests of fully nailed TCN200 angle brackets without washers under uplift and shear loads were also presented. The mechanical properties of connections obtained from literature and those presented in the current study were used as inputs to the CD equations and numerical models. Experimental tests and numerical models from two CLT shearwalls comprised of the tested connections were evaluated. reasonable match was observed between the results obtained from experimental tests and numerical models, while wall shear resistance obtained from the capacity-based design equations was observed to be relatively lower. All the requirements from the capacity-based design approach were met in experimental tests, numerical modes and the results demonstrated that satisfying the proposed equations would lead to the desired lateral behaviour.

ACKNOWLEDGEMENT

The authors wish to acknowledge Rothoblaas Srl (Italy) and Nordic Structures (Canada) for providing the connections and CLT panels that were used in this study.

REFERENCES

[1] M. Popovski and I. Gavric, "Performance of a 2-Story CLT House Subjected to Lateral Loads," *Journal of Structural Engineering*, vol. 142, no. 4, Apr. 2016, doi: 10.1061/(ASCE)ST.1943-541X.0001315.

[2] A. Polastri and D. Casagrande, "Mechanical behaviour of multi-panel cross laminated timber shear-walls with stiff connectors," *Constr Build Mater*, vol. 332, p. 127275, May 2022, doi: 10.1016/j.conbuildmat.2022.127275.

[3] CSA O86-19, *Engineering design in wood. CSAO86:19*. Mississauga, ON, Canada: CSA Group, 2019.

[4] I. Gavric, M. Fragiacomo, and A. Ceccotti, "Capacity seismic design of x-lam wall systems based on connection mechanical properties," in

https://doi.org/10.52202/069179-0167

International council for research and innovation in building and construction, CIB-W18/46-15-2, 2013.

[5] M. Follesa *et al.*, "A proposal for a new background document of Chapter 8 of Eurocode 8," in *2nd. International Network on Timber Engeneering - INTER*, 2015.

[6] M. Follesa *et al.*, "The new provisions for the seismic design of timber buildings in Europe," *Eng Struct*, vol. 168, pp. 736–747, Aug. 2018, doi: 10.1016/j.engstruct.2018.04.090.

[7] M. Fragiacomo, M. Follesa, D. Casagrande, and M. Piazza, "The revision of the timber chapter of the Eurocode 8," in *In Proc., 5th Int. Conf. on Structural Health Assessment of Timber Structures*, 2019.

[8] V. Rinaldi, D. Casagrande, and M. Fragiacomo, "Verification of the behaviour factors proposed in the second generation of Eurocode 8 for cross-laminated timber buildings," *Earthq Eng Struct Dyn*, Dec. 2022, doi: 10.1002/eqe.3792.

[9] D. Casagrande, G. Doudak, and A. Polastri, "A proposal for the capacity-design at wall- and building-level in light-frame and cross-laminated timber buildings," *Bulletin of Earthquake Engineering*, vol. 17, no. 6, pp. 3139–3167, Jun. 2019, doi: 10.1007/s10518-019-00578-4.

[10] D. Casagrande, G. Doudak, L. Mauro, and A. Polastri, "Analytical Approach to Establishing the Elastic Behavior of Multipanel CLT Shear Walls Subjected to Lateral Loads," *Journal of Structural Engineering*, vol. 144, no. 2, p. 04017193, Feb. 2018, doi: 10.1061/(ASCE)ST.1943-541X.0001948.

[11] M. Masroor, G. Doudak, and D. Casagrande, "Design of Multipanel CLT Shear Walls with Bidirectional Mechanical Anchors following Capacity-Based Design Principle," *Journal of Performance of Constructed Facilities*, vol. 36, no. 1, 2022, doi: 10.1061/(ASCE)CF.1943-5509.0001693.

[12] M. Masroor, G. Doudak, and D. Casagrande, "The effect of bi-axial behaviour of mechanical anchors on the lateral response of multi-panel CLT shearwalls," *Eng Struct*, vol. 224, 2020, doi: 10.1016/j.engstruct.2020.111202.

[13] M. Masroor, D. Casagrande, and G. Doudak, "An analytical approach for multi-panel CLT shearwalls attached to the base with equally spaced anchors," in *World Conference on Timber Engineering 2021, WCTE 2021*, 2021.

[14] G. D'Arenzo, W. Seim, and M. Fossetti, "Experimental characterization of a biaxial behaviour connector for CLT wall-to-floor connections under different load directions," *Constr Build Mater*, vol. 295, p. 123666, Aug. 2021, doi: 10.1016/j.conbuildmat.2021.123666.

[15] *European Technical Approval ETA-11/0086*. Denmark: European Organization for Technical approval, 2018.

[16] *European Technical Assessment ETA-11/0030*. Denmark: European Organization for Technical approval, 2019.

[17] M. Masroor, G. Doudak, and D. Casagrande, "Validation of proposed analytical model and design procedures for multi-panel CLT shearwalls through experimental investigation," in *Canadian Society for Civil Engineering annual conference*, 2022.

[18] ASTM E2126, "Standard test methods for cyclic (reversed) load test for shear resistance of vertical elements of the lateral force resisting systems for buildings," West Conshohocken, PA, 2019.

[19] "European Technical Assessment ETA 11/0496," Denmark, 2014.

[20] ANSI/APA, "ANSI/APA PRG 320:2019 Standard for Performance-Rated Cross-Laminated Timber," *APA- The Engineered Wood Association*, 2020.

[21] CSI, "SAP2000 Integrated Software for Structural Analysis and Design." Computers and Structures Inc., Berkeley, California, 2018.

[22] G. D'Arenzo, D. Casagrande, A. Polastri, M. Fossetti, M. Fragiacomo, and W. Seim, "CLT Shear Walls Anchored with Shear-Tension Angle Brackets: Experimental Tests and Finite-Element Modeling," *Journal of Structural Engineering*, vol. 147, no. 7, Jul. 2021, doi: 10.1061/(ASCE)ST.1943-541X.0003008.

World Conference on Timber Engineering Oslo 2023

GLUED-IN ROD CLT CONNECTIONS WITH FLEXIBLE POLYMER ADHESIVE

Boris Azinović[1], Václav Sebera[2], Meta Kržan[1], Andreja Pondelak[1], Jaka Gašper Pečnik[3], Arkadiusz Kwiecień[4]

ABSTRACT: This paper explores the possibility of using flexible adhesives for glued-in rods in cross laminated timber (CLT). In the first series of tests, a rod glued in a CLT panel with flexible adhesive was investigated for its mechanical resistance. The connection was tested in pull-pull configuration using monotonic and cyclic, tensile-only loading. Different glued-in lengths were tested, for which the rod diameter and glue-line thickness were constant. The tests have shown that the adhesive can resist large elastic deformations, while it does not exhibit large energy dissipation capacity. Based on the test results the numerical analyses were performed to study the behaviour of the connection where other parameters were considered. Existing constitutive models available in Ansys software were used to simulate the specific mechanical behaviour of the connection under monotonic loading. The results of the FE model exposed an optimal glue-line thickness and glued-in length in relation to the engineering design parameters. The second series of tests were material emission tests, which were carried out in a Micro-Chamber (μ-CTE) with the intention to further explore the feasibility of such connections in terms of volatile organic compound (VOC) emissions.

KEYWORDS: CLT connections, glued-in rods, flexible adhesive, polyurethane, cyclic tests, environmental aspects

1 INTRODUCTION

The glued-in rod connections are commonly used also in structures and are constructed from: i. rod, ii. adhesive and iii. structural element (e.g. structural timber, CLT etc.). In most cases such connections consist of brittle adhesive with thin bondline and a steel threaded rod. This combination of materials usually leads to a brittle failure of the connection (see e.g. [1]), where the ductile response could be reached by yielding of the rod.

In this paper, the possibility to reach a more controlled response within the adhesive layer is explored. For this purpose, a thicker bondline and a flexible polyurethane adhesive were selected for investigation. Such "flexible" glued-in rods could be used at the connection between the panel and the wall at the top and/or bottom of the wall (e.g. as hold-down connections – HD). During the seismic loading the panels are exposed to rocking, which causes the rods to be pulled out of the panels. One possible improvement by using "flexible glued-in rods" would be an increase of deformation capacity in the elastic range. Furthermore, while pulling the rod, the energy could be dissipated through the shear deformation of the adhesive layer, making the connection more ductile in comparison with brittle adhesive connections.

The prospect of building larger and taller timber buildings creates new structural design challenges due to wind and seismic actions, such as higher demands on HDs in CLT shear wall buildings: strength to resist loads, lateral stiffness to minimize deflections and damage, as well as deformation compatibility to accommodate the desired system rocking behaviour during an earthquake [2]. While in the proposal for the new Eurocode 8, the plastic deformations in HD connections are allowed [3], [4], the Canadian standard CSA 086 interprets HDs as non-dissipative connections which shall be capacity protected by designing them to remain elastic under the force and displacement demands that are induced in them when the energy-dissipative connections reach the 95th percentile of their ultimate resistance [5]. Therefore, there is also a need to develop HD solutions with high load-bearing and deformation capacities while remaining elastic. In this respect, the flexible glued-in rods could possibly meet these requirements for CLT shear walls without yielding in the (steel) rod itself.

To account for high elasticity and load-bearing capacity, recently, a hyperelastic HD solution for CLT shear walls was developed [6]. These HDs include an elastomeric bearing layer and steel plates, which were fixed inside the CLT panel by steel rods. All steel and CLT members were designed to have no inelastic deformation for a given

[1] Boris Azinović, Meta Kržan & Andreja Pondelak, Slovenian National Building and Civil Engineering Institute (ZAG Ljubljana), Slovenia, boris.azinovic@zag.si, meta.krzan@zag.si & andreja.pondelak@zag.si
[2] Václav Sebera, Mendel University in Brno (MENDELU), Czech Republic, vaclav.sebera@mendelu.cz
[3] Jaka Gašper Pečnik, InnoRenew CoE, Slovenia, jaka.pecnik@innorenew.eu
[4] Arkadiusz Kwiecień, Cracow University of Technology, Poland, akwiecie@pk.edu.pl

https://doi.org/10.52202/069179-0168

target load and therefore the HD deformations result from the rubber layers' deformation. Additionally, the overstrength factor to design the rubber layer needs to prevent the brittle failure of the CLT panel [7]. Depending on the assembly of the hyperelastic HD, the mean load bearing capacity in the study ranged from 100-150 kN, while reaching the corresponding displacements from 3-12 mm [6].

The solution presented in this paper could offer an alternative solution to the hyperelastic HD, where instead of in the rubber layer, the elastic deformation occurs in the adhesive of the glued-in rod connection. This could be achieved in a single glued-in rod connection or a combination of several glued-in rods to increase the load bearing capacity. One of the possible benefits compared to the hyperelastic HD is to retain a visible outer layer of the CLT and protect the connection in case of fire load, since it is hidden within the inner CLT layers. The paper explores the mechanical resistance of such glued-in rod connections on monotonic and cyclic axial load, while also some information on the emission tests is provided.

2 EXPERIMENTS

2.1 TENSILE RESISTANCE

The pull-pull experiments were performed on Zwick Z2500Y testing machine at the Slovenian National Building and Civil Engineering Institute (ZAG). The specimens were cut out of a 5-layer CLT (layers: 33-20-34-20-33 mm, produced according to ETA-12/0281), where the dimensions of the CLT were cca. 25 cm × 100 cm × 14 cm. For inserting the threaded rods, holes of 28 mm diameter were drilled on the tested end and 24 mm at the supported end of the CLT prisms. The rods were oriented parallel to the grain of the laminations in the middle and outer CLT layers. The test setup of the "pull-pull" test is presented in Figure 1.

At the supported end of CLT, a large diameter rod (Φ20 mm) was inserted in the 300 mm deep hole. The rod was glued to the CLT with an epoxy adhesive (HILTI RE 500) of 4 mm thickness. This ensured a large rigidity and large resistance of the fixed support. Behaviour of the rigid supporting connection was not considered in this test, since it has a negligible effect At the tested end, considered for investigation, a threaded rod with smaller diameter (Φ12 mm) was glued in the holes of 28 mm diameter (specimens' description: dh28) with an elastic polyurethane adhesive PST of 8 mm thickness, where two glued-in lengths were tested: 160 mm and 320 mm (La160 and La320). The properties of the adhesive and the timber adhesive bondline were previously determined [8]. At least three samples with the same characteristics were tested for monotonic (M) as well as for cyclic (C) tests to verify the scattering of the results. The configuration of the tested specimens is shown in Table 1.

The glued-in rods were tested under monotonic and cyclic loading in the tensile direction only. The loading was applied to the samples using a constant displacement rate of 70 mm/min. The induced displacements approximately followed the ISO 16670 displacement protocol [10]. According to ISO protocol, the small-amplitude cycles with single repetition are followed by large-amplitude cycles with three repetitions until the failure occurs. The protocol was adapted, since the connection is asymmetric, and it does not deform significantly under compression. Therefore the displacement was induced only in tension and the displacement at failure was estimated as 20 mm, what corresponds to the shear deformation angle (shear strain) of the adhesive layer equal to 250%. The real relative displacement of the connection between the rod and the CLT panel was measured with an optical extensometer which is built into the Zwick test device. The displacement was measured near the tested surface at the distance of 18 cm (Figure 1). In addition, the behaviour of the connection at the tested end was recorded with a HD camera.

Table 1: *The configuration of tests*

Specimen	α [°]	l_a [mm]	Φ_a [mm]	$\Phi_{a,r}$ [mm]	t [mm]	n
La160/M/dh28	0	160	28	12	8	4
La160/C/dh28	0	160	28	12	8	3
La320/M/dh28	0	320	28	12	8	4
La320/C/dh28	0	320	28	12	8	3

α …rod to grain angle
l_a …glued-in length
Φ_a …diameter of the hole at the tested end
$\Phi_{a,r}$ …diameter of the rod at the tested end
t …thickness of the adhesive
n …number of samples
M, C …Monotonic or Cyclic tests

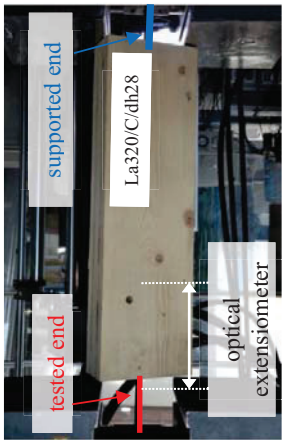

Figure 1: *Test set-up*

All deformations took place in an adhesive joint and the failure (rod pull-out) mainly occurred within the glue line (cohesive failure of the adhesive), see Figure 2. As expected, the behaviour of the connection during the monotonic loading was highly elastic, until maximum

https://doi.org/10.52202/069179-0168

load bearing capacity was reached (Figure 3). The connection resisted large deformations, while it did not prove to fail in ductile manner. The ductility values (D_f) of all tested connections were less than 1.5. The ductility value was calculated for monotonic tests as the quotient of the displacement at failure (u_f) and the displacement at the elastic load limit (u_y). The displacement u_f was determined at the 80% drop of the maximum force (F_{max}), where the displacement u_y was defined according to the method defined in EN 12512 [11].

The results (mean values with Coefficient of Variation – CoV) of monotonic loading showed elastic behaviour up to the displacement of 6.8 mm and 7.1 mm, giving ultimate shear strain of 85% and 89% (calculated for 8 mm adhesive thickness), for glued-in lengths of 160 mm and 320 mm respectively. Load-bearing capacity of the connection is approximately proportional to the glued-in length assuming all other properties are the same; mean value reaches 23.9 kN and 44.3 kN for glued-in length 160 and 320 mm respectively. Mean nominal shear strength values of the polyurethane PST adhesive (cohesive failure), calculated for the cylindrical area at the contact between the steel rod and adhesive ($\pi \times 12 \times La$) are 4.0 MPa and 3.7 MPa, respectively. Similarly, the mean stiffness values also increase by the glued-in length from 4.0 kN/mm to 6.5 kN/mm (Table 2).

Figure 2: *Rod pull-out*

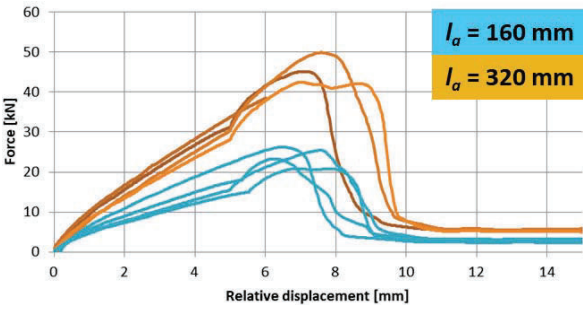

Figure 3: *Results of monotonic experiments for tested glued-in lengths 160 and 320 mm*

Table 2: *The mean results from the monotonic tests: load-bearing capacity (F_{max}), stiffness ($K_{0.1–0.4}$) and displacement at F_{max} (d_u)*

	La160/M/dh28			La320/M/dh28		
sp. no.	F_{max} [kN]	d_u [mm]	$K_{0.1–0.4}$ [kN/mm]	F_{max} [kN]	d_u [mm]	$K_{0.1–0.4}$ [kN/mm]
1	26.25	6.5	5.20	45.11	7.1	6.70
2	20.79	6.9	3.87	42.51	7.0	5.71
3	23.30	6.3	3.93	49.87	7.6	6.13
4	25.43	7.6	3.04	39.51	6.5	7.43
mn.	**23.94**	**6.8**	**4.01**	**44.25**	**7.1**	**6.49**
CoV	10.2%	8.4%	22.6%	10.0%	6.4%	11.4%

The cyclic response of the connections in terms of actuator force versus relative displacement of the joint is shown in Figure 4. The hysteretic curves for the connections with glued-in length of 160 and 320 mm showed a similar response, so only the hysteretic curves for glued-in length of 160 mm are shown, while Figure 5 shows hysteresis envelope curves for the tensile part of the cyclic test. The hysteretic curves show a typical hyperbolic strain hardening up to the maximum load capacity. This is followed by an exponential decrease in strength until failure (minimum residual load).

To characterize the performance of the connections during earthquake loading the amount of dissipated energy was evaluated in terms of equivalent viscous damping for the first cycle. The equivalent viscous damping coefficient (ξ) was evaluated from the hysteretic response as the ratio of dissipated energy (E_{DIS}) to potential energy (E_{INP}) as suggested by Chopra [12]:

$$\xi = \frac{E_{DIS}}{2\pi\, E_{INP}} \qquad (1)$$

The equivalent viscous damping coefficient was calculated for the first loading cycle and is provided in Table 3. The values for moderate amplitudes (up to the maximum load) ranged from 1% to 4.5% for glued-in length of 160 and 320 mm, respectively. The results indicate that the response is mainly elastic with little input energy dissipated.

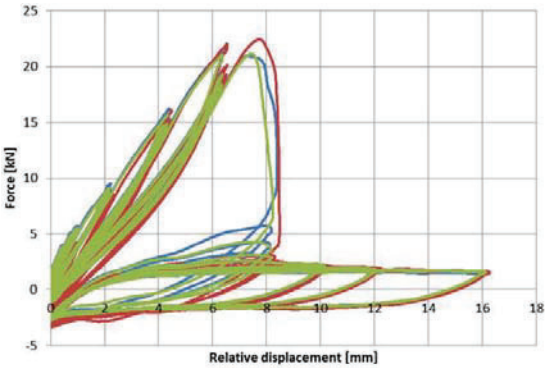

Figure 4: *Results of cyclic experiments for glued-in length 160mm*

https://doi.org/10.52202/069179-0168

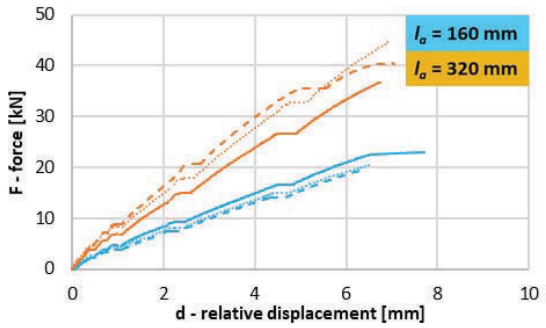

Figure 5: *Hysteresis envelopes of the cyclic tensile tests for glued-in lengths 160 and 320 mm*

Table 3: *Dissipated E_{DIS} and input energy E_{INP} of one loading cycle considered for the calculation of coefficient ξ*

	La160/C/dh28			La320/C/dh28		
sp. no.	E_{INP} [kNmm]	E_{DIS} [kNmm]	ξ [%]	E_{INP} [kNmm]	E_{DIS} [kNmm]	ξ [%]
1	33.4	2.0	0.96	113.5	29.8	4.2
2	21.4	1.3	0.94	155.0	46.4	4.8
3	22.6	1.3	0.91	140.9	35.6	4.0
mn.	**25.8**	**1.5**	**0.94**	**136.5**	**37.3**	**4.3**
CoV	25.6%	26.4%	2.7%	15.5%	22.6%	9.2%

2.2 EMISSIONS TESTS

The investigation of the connection feasibility in practise included emission tests on a CLT panel and on adhesive samples carried out in a Micro-Chamber (µ-CTE) at the Fraunhofer Institute for Wood Research WKI [13]. The purpose of the tests was to obtain general information about the emission strength of the samples and the spectrum of the emitted substances.

Sample preparation

The CLT was cut into small cubes (3 cm x 3 cm x 1 cm). The specimen contained one adhesive joint. The primer (ZP Primer) and adhesive (PS A + B) were applied in a small petri dish. The CLTs were conditioned for 15 minutes, the primer and adhesive for 30 minutes. The adhesive PS differs from the PST adhesive in terms of its mechanical response, but similarities in VOC spectra was assumed due to its source of origin.

Testing

CLT sampling was performed over 30 minutes, corresponding to a volume of about 3 litres. The primer and adhesive were tested for 10 minutes with a sampling volume of 1 litre. The difference in sampling volume was chosen because primer and adhesive are considered high emitting materials to avoid overloading the adsorbent tube. Adhesive and primer were tested in fresh – uncured state. A piece of the sample was mounted in the Micro-Chamber for emission testing (µ-CTE) in cell mode. The test was performed at 23 °C with dry synthetic air. The µ-CTE effluent was collected on a sorbent tube (Tenax TA) and analysed on a thermal desorption GC-MS system. Compounds were analysed using MS-Spectra libraries. Surface area for CLT was 27 cm^2 and the flow rate was 106.5 ml/min, while the surface area for primer and adhesive was 7 cm^2 and the flow rate was 112.8 ml/min.

Results

The Table 4 shows substances emitted from CLT, ZP Primer and adhesive PS A + B. In the case of the CLT panel, more than 30 substrates were detected with the highest concentrations of acetic acid, hexanal, formic acid, acetone, pentanal, pentanol, butanal, furaldehyde, and terpineol. Most of the substances emitted from CLT panels (organic acids, aldehydes and terpenoids) are substances characteristic of wood-based materials [14]. The highest concentrations emitted from the primer were 1-Methoxy-2-propyl acetate, Ethylbenzene and Xylene and formylmorpholine and Xylene in the case of adhesive (Table 4).

The µ-CTE emission tests were performed to obtain general information about the emitted substances from the CLT panel, the flexible adhesive, and the primer. The CLT emitted organic acids, aldehydes and terpenes, which are characteristic of wood-based materials. The primer (ZP) released a range of solvents, with 1-methoxy-2-propyl- acetate, xylene- isomers and C3-benzenes being the most abundant substances. Emissions from adhesive (PS A +B) were much lower, with N-formylmorpholine being released at higher concentrations. As mentioned above, the aim was to assess which volatile compounds were emitted by selected materials. The measurements were made on small samples (27 cm^2 or 7 cm^2) with different sampling volumes (one or three litres) and different result delivery (µg/h*m^2 or µg/h*g), so the measurements cannot be compared with each other.

3 NUMERICAL ANALYSIS

The numerical simulations using the finite element method consisted of three different analyses with the objectives: 1) to study whether it is possible to model a threaded rod without threads; 2) to simulate the real size problem and validate it through conducted experiments; and 3) to perform parametric studies for different glued-in lengths and adhesive thicknesses.

The finite element package Ansys [15] was used for all analyses. All solids were modelled using SOLID185 finite elements. All models were symmetrical, so only a quarter of the problem was modelled to reduce computational effort. Wood was modelled as a linear orthotropic material with the following properties: E_L = 14850, E_R = 352, E_T = 289, E_{LR} = 573, E_{RT} = 53, E_{LT} = 474 [MPa], μ_{LR} = 0.023, μ_{RT} = 0.557, μ_{LT} = 0.014 [-], where L, R, and T stand for longitudinal, radial and tangential anatomical directions, respectively. Steel rod was modelled as linear isotropic material with E = 200 GPa and µ = 0.3. The PST adhesive was modelled as hyperelastic material with Yeoh 3 parametric model given as c_{10} = 1.6641, c_{20} = -0.49288, c_{30} = 0.14807, $d_{1,2,3}$ = 0 that was curve-fitted to following experimental stress/strain data: 0/0.0173, 0.1/0.933, 0.2/1.541, 0.3/2.025, 0.4/2.392, 0.5/2.645, 0.6/2.838, 0.7/3.001 [MPa/-].

https://doi.org/10.52202/069179-0168

Table 4: *Results of the chamber emission test of CLT panel, ZP Primer and adhesive PS A + B*

CLT panel		**ZP Primer**		**PS A + B**	
Substance	**SER_A / µg/h*m²** (V=3L)	**Substance**	**SER_m / µg/h*g** (V=1L)	**Substance**	**SER_m / µg/h*g** (V=1L)
acetone	130	acetone	0.059	2-Butanone (MEK)	0.079
2-propanol	24	2-Butanone (MEK)	0.088	Acetic acid	0.482
Formic acid	159	Acetic acid	0.324	Toluene	0.037
Butanal	28	Toluene	0.088	2,4-Pentanedione	0.226
2-Butanone (MEK)	9	Phenol	<0.029	n-Hexanal	0.037
Acetic acid	2468	Carbon disulfide	0.029	n-Buthyl acetate	0.11
n-Butanol	12	Ethylbenzene	8.386	1-(2-Propenyloxy)-2-propanol	0.045
Propanoic acid	7	1-Methoxy-2-propyl acetate	57.705	Ethylbenzene	0.684
Pentanal	85	m,p-Xylene	23.865	1-Methoxy-2-propyl acetate	7.298
Toluene	2	2-Methoxy-1propyl acetate	0.235	m,p-Xylene	3.151
n-Pentanol	47	o-Xylene	15.537	o-Xylene	1.166
n-Hexanal	282	C9 (nonane)	0.056	n-Heptanal	0.037
2-Furaldehyde	57	Glykolester	0.088	Ethoxypropyl acetate	0.305
2-Heptanone	2	Methylstyren	0.235	Phenol	0.037
n-Heptanal	2	Propylene glycol diacetate	0.118	Octanal	0.037
Alpha-Pinene	57	p-Cymene	0.088	Methylstyren	0.605
Camphene	5	Indane	4.323	1,4-Diazabicyclo[2.2.2]octane (DABCO)	0.666
trans-2-Heptenal	5	Dimethystyren	0.177	n-Nonanal	0.098
Benzaldehyde	5	Naphtalene	<0.029	N-Formylmorpholine	18.236
Hexanoic acid	7	1-Dodecanol	0.029	n-Decanal	0.067
Phenol	2	Sum of C3 benzenes	69.916		
Beta-Pinene	14				
2,2,4,6,6-Pentamethylheptane	5				
Octanal	2				
3-Carene	5				
Limonele	9				
trans-2-Octenal	5				
n-Nonanal	5				
alpha-Terpineol	33				
C14 /tetradecane)	2				
Longifolene	9				
Carbon disulfide	7				

SER_A = Surface area-specific emission rate; SER_m = mass-specific emission rate

https://doi.org/10.52202/069179-0168

Boundary conditions (BC) consisted of: 1) fixing two sides of the block against movement; 2) symmetrical BC's were applied on two other sides; 3) pulling the rod in its axis by 6 mm in a monotonic way. At each step of the rod displacement, the force was read to generate force-displacement diagrams.

3.1 THREADING ANALYSIS

To determine if threading is important to be included in the analysis, the analysis was performed with and without threading. The model (Figure 6) was reduced to a length of 11 mm to reduce computational complexity, and a sensitivity study of mesh density was also performed.

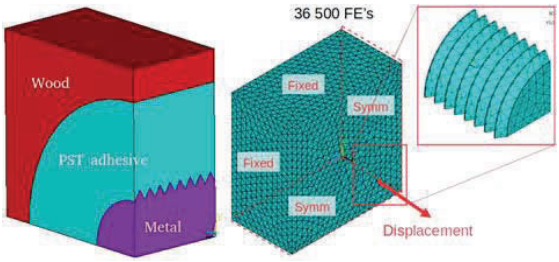

Figure 6: *Symmetrical geometry (left) and FE mesh and BC's (right) of model for thread analysis*

The model resulted in three data series as a function of mesh density (Figure 7). It is clear that the model with M11 thread (red line) behaves according to the same pattern as the models without thread with 10 and 12 mm diameter, and it is between them. This is an important finding because we can omit the thread in the full-scale models without losing the correct overall force-deflection response.

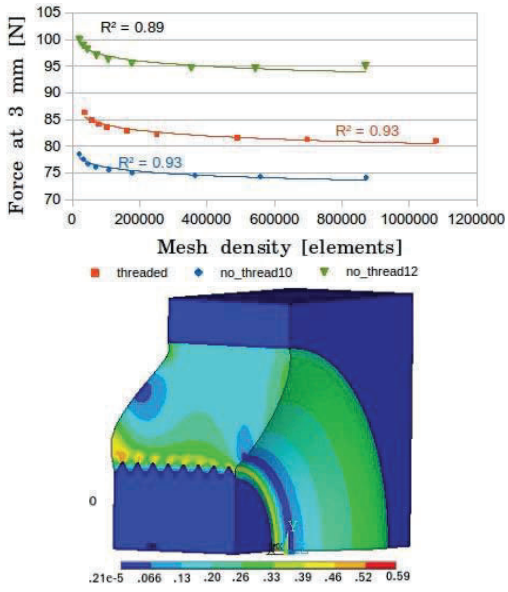

Figure 7: *Threaded vs. non-threaded models depending on mesh density (left) and von Mises Strain around threading*

Figure 7 (right) also shows that the highest strain occurs at the tips of the threads, which could indicate the position of failure initiation.

3.2 VALIDATION WITH EXPERIMENTS

A full-size 3D FE model was made in two lengths reflecting the physical experiments. The comparison of the FE models (blue and red lines) with the experiments (grey and black lines) is shown in Figure 8. The FE models of both lengths predict well the behaviour found in the experiments in terms of stiffness and hyperelastic progression of the force versus displacement. The FE models predict the behaviour up to a displacement of 6 mm, not taking into account the strength limit of the PST adhesive.

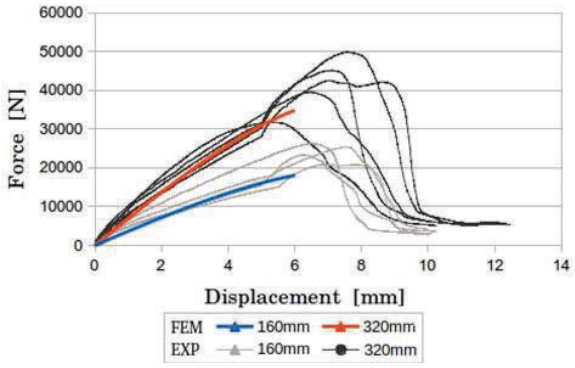

Figure 8: *Comparison of FE models (blue and red line) with experiments (grey and black lines) for both rod lengths*

3.3 PARAMETRIC STUDY

The parametric studies investigated the influence of the glued-in rod length and bondline thickness (Figure 9).

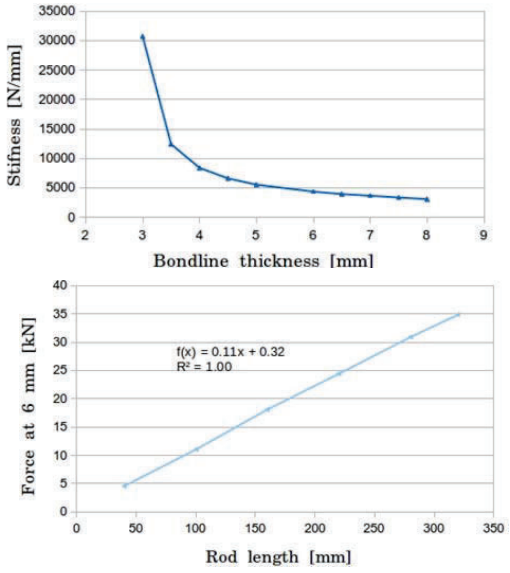

Figure 9: *Influence of bondline thickness on stiffness (top) and influence of glued-in rod length on force (bottom)*

https://doi.org/10.52202/069179-0168

These studies were performed on a full-size model (quarter-symmetrical) and did not include threads. The effect of rod length on force shows a linear trend. The effect of bondline thickness on connection stiffness, on the other hand, shows a hyperbolic trend with a decreasing tendency. Both parametric studies allow the glued-in rod connection with the CLT panel to be designed as required for the given conditions - for specific structural design. Future FE studies should focus on extending the hyperelasticity to include the range of plastic strains, so that the failure of the bonded PST connection can also be predicted, as this is the predominant failure observed in experiments.

4 CONCLUSIONS

Monotonic and cyclic tensile tests were performed on rods bonded with a flexible adhesive in CLT. The tests showed promising behaviour of such connections in terms of their elastic deformability under cyclic loading. On the other hand, a rather brittle failure with limited ductility occurred. Also, the energy dissipation capacity at larger amplitudes was not significant. The tests have also shown that the load-bearing resistance of the connection is proportional to the rod length.

To test the behaviour of the "flexible" glued-in rods when applied in CLT buildings, a series of numerical analyses were performed. First, the numerical model of the connection was calibrated based on the experimental results. The material model was able to simulate the linear part (stiffness) of the connection and provided a relatively good agreement with the experimental results. In the next phase, the model of the connection was used for the parametric study of the glued-in length and bondline thickness. The results showed that the effect of the rod length on the force exhibited a linear trend, while the bondline thickness showed a hyperbolic trend on connection stiffness with decreasing pattern. Both parametric studies demonstrate that the glued-in rod connections in CLT panels can be designed to meet the required boundary conditions in CLT walls.

Additionally, the Micro-Chamber emission tests were carried out in order to obtain general information about the emitted substances from the CLT panel, flexible adhesive and primer. The CLT panel showed the release of organic acids, aldehydes and terpenes characteristic for wood-based materials. The Primer (ZP) released a range of solvents with 1-methoxy-2-propyl-acetate, xylene-isomers and C3-benzenes as most abundant substances. Emissions of adhesive (PS A +B) were much lower with emission of N-formylmorpholine in higher concentrations.

The results of the study show a potential of using CLT wall system with “flexible” glued-in rods in seismic areas. However, future studies are necessary to investigate the long-term behaviour and performance of such connections at elevated temperatures. Also, an improvement of the performance in the nonlinear part of the connection would be essential for its actual applications.

ACKNOWLEDGEMENTS

The authors gratefully acknowledge the European Cooperation in Science and Technology for funding the InnoRenew CoE project [grant agreement #739574] under the H2020 Spreading Excellence and Widening Participation Horizon2020 Widespread-Teaming program, and Slovenian research programs P2-0273 and P4-0430; Javna Agencija za Raziskovalno Dejavnost RS. The financial support by the National Science Centre, Poland under the OPUS call in the Weave programme, No. 2021/43/I/ST8/00554 is also gratefully acknowledged.

REFERENCES

[1] B. Azinović, E. Serrano, M. Kramar, and T. Pazlar. Experimental investigation of the axial strength of glued-in rods in cross laminated timber. *Mater. and Struct*., 51(6), 2018.

[2] T. Tannert and C. Loss. Contemporary and Novel Hold-Down Solutions for Mass Timber Shear Walls. *Buildings*. 12(2):202, 2022.

[3] M. Follesa et al. The new provisions for the seismic design of timber buildings in Europe. *Eng. Struct.*, 168:736–747, 2018.

[4] M. Follesa et al. A proposal for a new Background Document of Chapter 8 of Eurocode 8. In: *INTER,* Šibenik, Croatia, 2015.

[5] CSA Standard O86-09 Engineering design in wood, Mississauga, Ontario, Canada, 2009.

[6] H. Asgari, T. Tannert, M. M. Ebadi, C. Loss, and M. Popovski. Hyperelastic hold-down solution for CLT shear walls. *Constr. Build. Mater.*, 289:123173, 2021.

[7] H. Asgari, T. Tannert, and C. Loss. Block tear-out resistance of CLT panels with single large-diameter connectors. *Eur. J. Wood Prod*., 80(4):805–816, 2022.

[8] J. G. Pečnik et al. Mechanical performance of timber connections made of thick flexible polyurethane adhesives. *Eng. Struct*., 257:113125, 2021.

[9] ISO 21581:2010 Timber structures - Static and cyclic lateral load test methods for shear walls.

[10] ISO 16670:2003 Timber structures - Joints made with mechanical fasteners - Quasi-static reversed-cyclic test method.

[11] EN 12512:2005 Timber structures - Test methods - Cyclic testing of joints made with mechanical fasteners. *Brussels:* CEN, 2005.

[12] Chopra A. K.: Dynamics of structures, 3rd Edition. Pearson Prentice Hall Hoboken, 2006.

[13] Schieweck A.: Test report No. MAIC-2019-4014: Emission test of a CLT panel and an adhesive sample. Fraunhofer WKI, Braunschweig, 2019.

[14] G. Kain et al. Qualitative investigation on VOC-emissions from spruce (Picea abies) and larch (Larix decidua) loose bark and bark panels. *Eur. J. Wood Prod.* 78(2): 403–412, 2020.

[15] ANSYS R19.2. *Ansys Inc, USA*, 2019.

https://doi.org/10.52202/069179-0168

World Conference on Timber Engineering Oslo 2023

EVALUATION OF BEARING STRENGTH PERFORMANCE OF STS CONNECTION ACCORDING TO BEARING SECTION ON LOADING DIRECTION

Keonho Kim[1], In-Hwan Lee[2], Gwang-Mo Kim[3]

ABSTRACT: Since self-tapping screws (STS) are widely used for structural cross-laminated timber(CLT) connections, the bearing performance according to the shape information of fasteners is required to design connections for CLT. In this study, to evaluate the bearing strength of STS connection using the lamina of domestic softwoods, the half-holed bearing test was conducted according to the bearing section on loading direction. The species of lamina were japanese larch, korean pine and japanese cedar. The specimen was prepared according to the thread part (thread + tip) and shank part (shank + shank cutter) of STS and three types of diameters (8, 10, 12 mm) in the bearing section (cross section, radial section, tangential section). The 5 % offset yield bearing load of cross section of japanese larch was the highest value according to the specific gravity of laminas. As the diameter of STS increased, the bearing load showed a tendency to decrease. Even STS with same diameter, the bearing strength of thread part was higher than shank part due to the difference of effective bearing area.

KEYWORDS: Self tapping screw, Bearing strength, Connection, Domestic softwood, Half-holed test

1 INTRODUCTION

The use of engineered wood, known as a carbon storage, has expanded the scale of wooden buildings. The cross laminated timber (CLT), which is generally used in high-rise wooden buildings, is one of the engineered woods and is widely used for shear walls and floors. The lateral resistance of a wooden structure is an important design value to secure its seismic performance. The strength performance of the CLT itself and the lateral strength performance of the connection are important factors for the lateral resistance capacity of the CLT structure. The self-tapping screw (STS) are mainly used for CLT connections. The lateral strength design of the connection can be predicted by the bending performance of the fastener and the bearing strength of members of connection by Korean Design Standard (KDS). In this study, to evaluate on the bearing strength performance of STS connection, the bearing test of CLT using the domestic species was conducted according to the shape of STS and loading direction to the grain.

2 EXPERIMENTAL

2.1 MATERIAL

As the lamina for the CLT, japanese larch (*Larix kaempferi* Carr.), korean pine (*Pinus koraiensis*) and japanese cedar (*Cryptomeria japonica*) were used, which are structural materials for softwoods in Korea (KS F 2020). The cross section of specimens was 50 × 50 mm. The fasteners used in the bearing strength test were the self-tapping screw (galvanized carbon steel) from Rothoblaas (Italia) shown in Figure 2. The type of STS ccording to the diameter is divided into 3 types (8, 10, 12 mm), and their length is 120 mm. The diameter (ds) of the shank was 5.8 mm, 7.0 mm and 8 mm, and the diameter (dc) of the shank cutter was 6.8 mm, 8.4 mm and 9 mm, which is larger than the diameter of the shank. The diameter of the thread is divided into an inner diameter (d2) and an outer diameter (d1).

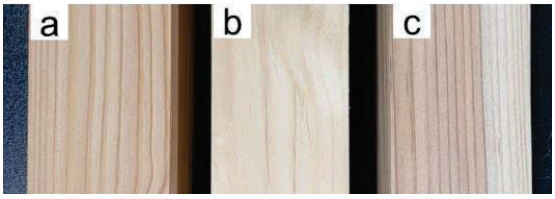

Figure 1: *Photographs of timber (a- Japanese larch, b- Korea pine, c- Japanese cedar)*

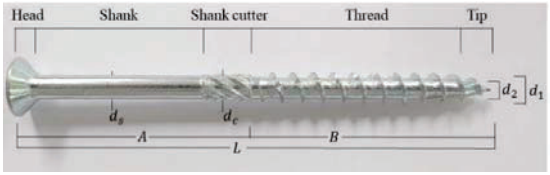

Figure 2: *Photographs and details of self-tapping screw*

The bearing strength test specimens is classified and manufactured according to the shape of STS fastener in bearing section. The bearing part of STS fastener was divided into T-series for bearing with the thread of STS and the S-series for bearing with a shank. The nomenclature of specimens was named according to the species and species cross-section, 8, 10, and 12 mm of the

[1] Keonho Kim, Div. Wood engineering, National Institute of Froest Science, Republic of Korea, keon@korea.kr
[2] In-Hwan Lee, Div. Wood engineering, National Institute of Froest Science, Republic of Korea, ih1990@korea.kr
[3] Gwang-Mo Kim, Div. Wood engineering, National Institute of Froest Science, Republic of Korea, lovewood@korea.kr

https://doi.org/10.52202/069179-0169

Table 1: *Dimension information of Self-tapping screw on diameters*

CODE	L	A	B	d_1	d_2	d_s	d_c
HBS8120	120	60	60	8	5.4	5.8	6.8
HBS10120	120	60	60	10	6.4	7	8.4
HBS12120	120	40	80	12	6.8	8	9

L: Total length of self-tapping screw
A: Length of shank and shank cutter part in the self-tapping screw
B: Length of thread part in the self-tapping screw
d_1: Inner diameter of thread part in the self-tapping screw
d_2: Outer diameter of thread part in the self-tapping screw
d_s: Diameter of the shank part in the self-tapping screw
d_c: Diameter of the shank cutter part in the self-tapping screw

Table 2: *Types of Specimens and Nomenclature*

Species	Gain Directions	Nomenclature On diameter and shape information of STS				
		Thread + Tip			Shank + Shank Cutter	
		8 mm	10 mm	12 mm	8 mm	10 mm
Japanese larch *(Larix kaempferi Car.)*	Longitudinal section	LC8T	LC10T	LC12T	LC8S	LC10S
	Radial section	LR8T	LR10T	LR12T	LR8S	LR10S
	Tangential section	LT8T	LT10T	LT12T	LT8S	LT10S
Korean pine *(Pinus koraiensis)*	Longitudinal section	KC8T	KC10T	KC12T	KC8S	KC10S
	Radial section	KR8T	KR10T	KR12T	KR8S	KR10S
	Tangential section	KT8T	KT10T	KT12T	KT8S	KT10S
Japanese cedar *(Cryptomeria japonica)*	Longitudinal section	CC8T	CC10T	CC12T	CC8S	CC10S
	Radial section	CR8T	CR10T	CR12T	CR8S	CR10S
	Tangential section	CT8T	CT10T	CT12T	CT8S	CT10S

STS standard diameter (d1), and the location of the bearing STS (thread part and sank part). The STS with a diameter of 12 mm was not tested due to the fact that the length of the shank was 40 mm shorter than the length of the specimen. A total of 450 specimens were produced, 10 specimens for each type.

2.2 METHODS

The half-holed bearing test of STS connections was conducted in accordance with KS F 2156. The bearing test specimens was drilled with the diameter of STS fastener. The T-series was tested by inserting it into the groove so that only the thread part, excluding the tip part, was in contact. S-series included both shank and shank cutter, and tested after inserting STS into the groove. A bearing load and an embedment were measured by the universal testing machine (Instron 5585) with the 30 ton load capacity. The loading speed was 0.5 mm/min.

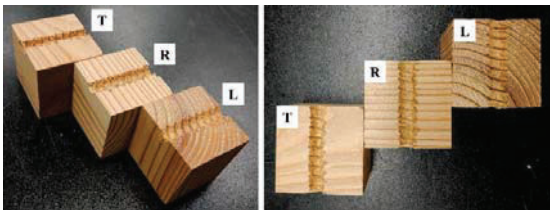

Figure 3: *Configuration of bearing test specimen (note : C, R and T means the cross, radial and tangential section of specimens respectively.)*

https://doi.org/10.52202/069179-0169

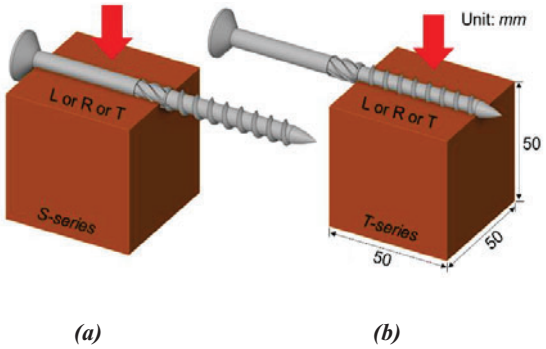

(a) *(b)*

Figure 4: *Direction of bearing loading on types (a : S-series, b : T-series).*

3 RESULTS AND DISCUSSION

3.1 5% OFFSET YIELD LOAD ACCORDING TO SPECIES AND BEARING SECTION

The maximum load of the specimens in longitudinal section is easy to measure because of the clear load drop, but the maximum load of the radial and tangential sections specimens is difficult to measure because the load drop is not clear. Therefore, the bearing strength was calculated jointly as the yield strength, and the results were compared and analyzed.

The yield strength was calculated by the 5% offset of the thread diameter of the STS fastener. The yield strength was calculated according to KS F 2156 (2017). First, the initial straight line of the load-deformation curve obtained in the experiment was shifted 5% of the STS diameter in parallel, as shown in Fig. 6. Then, the yield load way was calculated at the intersection of the moved straight line and the load-deformation curve.

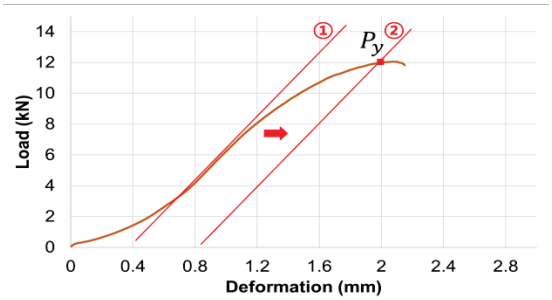

Figure 6*: Load-deformation curve at 5% offset yield load*

Figure 8 shows the average yield load of softwood with STS. The average yield load by tree species was calculated as 6.01 kN for Japanese larch, 5.47 kN for Korean pine, and 4.15 kN for Japanese cedar, with the yield load in the order of Japanese larch, Korean pine, and cedar. It appears that a higher specific gravity of the species resulted in a higher yield load.

The average yield load of the longitudinal section was the highest in all directions at 7.93 kN, the radial section was 3.69 kN, and the tangential section had the lowest yield load at 4.01 kN. The average coefficient of variation was 0.18, 0.14, and 0.18, respectively, and the reliability of the value was high.

For the longitudinal section, the loading direction and the grain direction are parallel, so it can be assumed that the resistance to the bearing load is large. This phenomenon shows a similar trend in structural glulam (Kim and Hong 2008). According to STS type, the average yield load tended to increase with increasing diameter, and the T-series had a higher average yield load than the S-series.

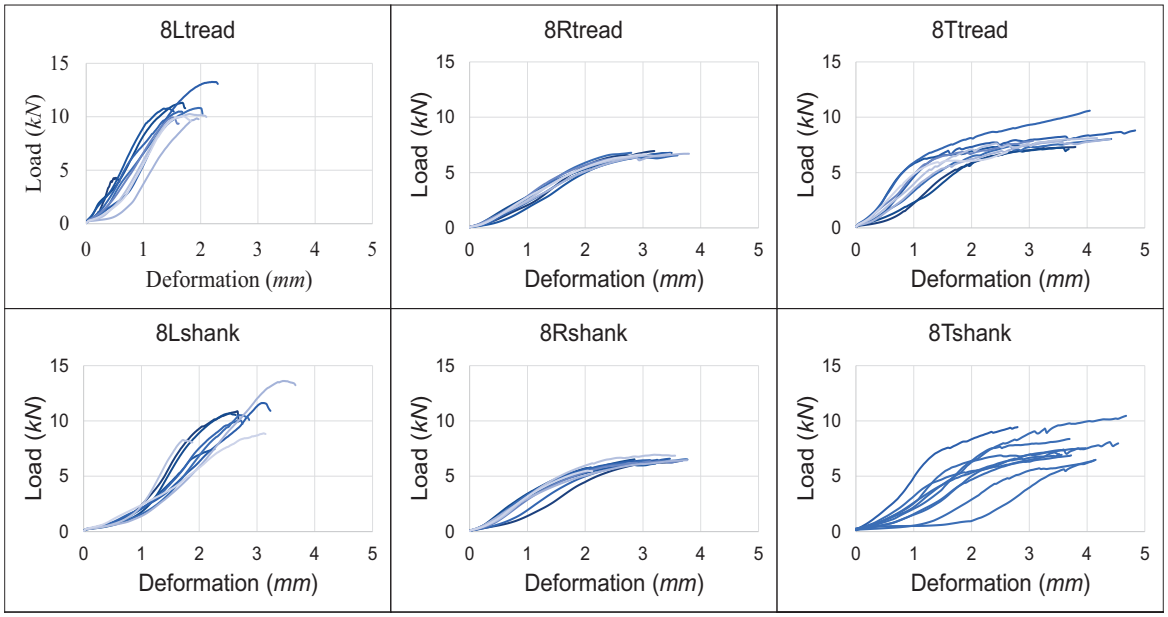

Figure 5: *Load—deformation curves of Japanese larch specimens with 8mm diameter of STS*

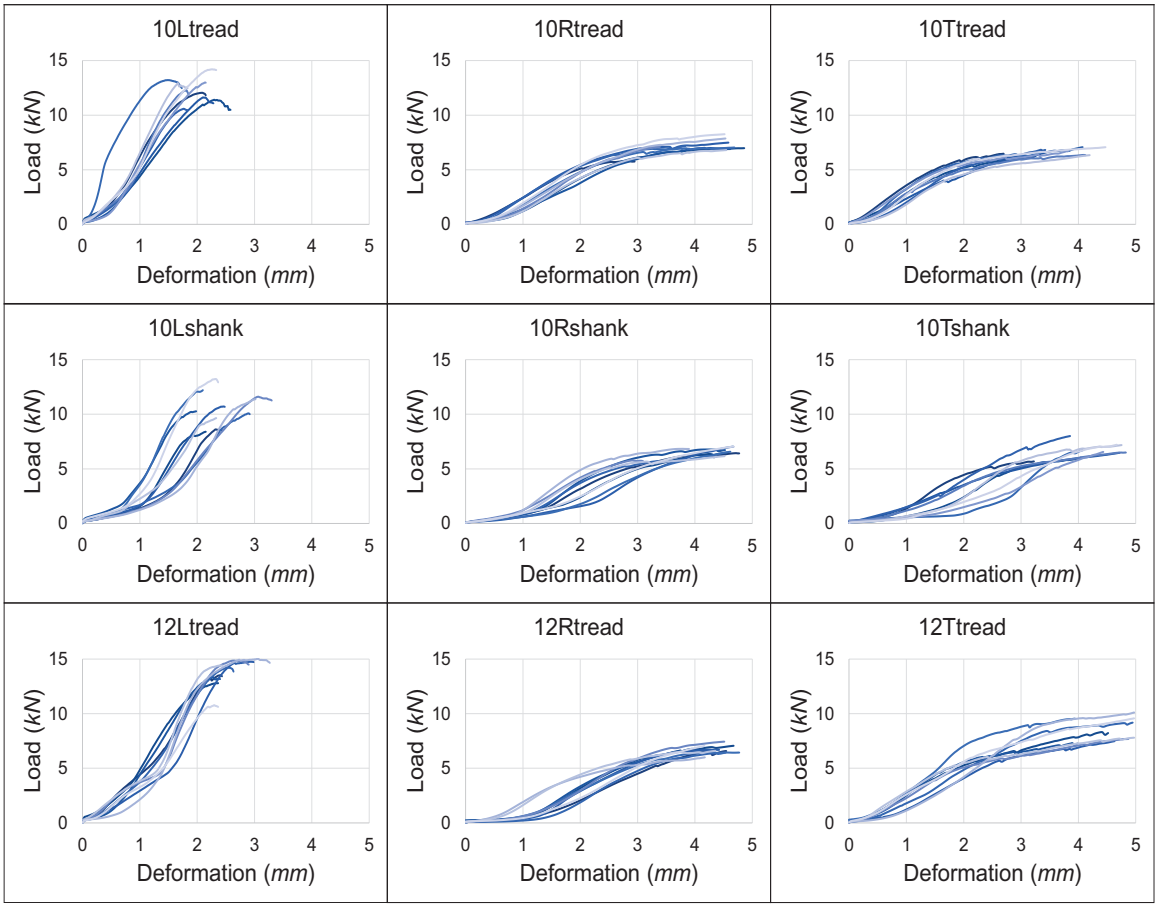

Figure 7: *Load—deformation curves of Japanese larch specimens with 10mm and 12mm diameter of STS*

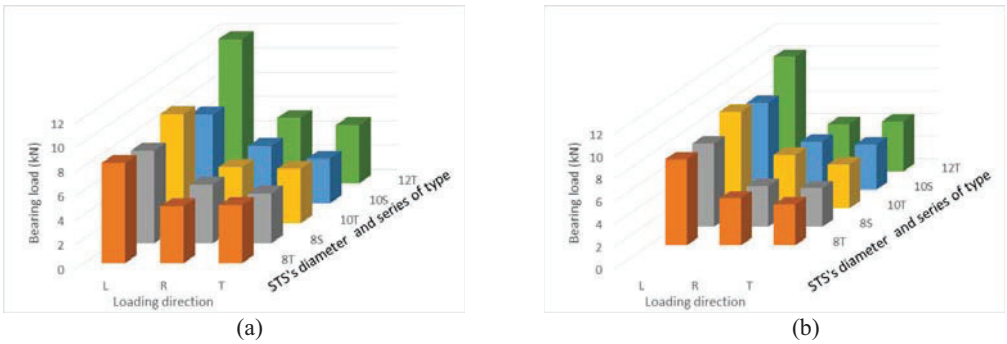

(a) (b)

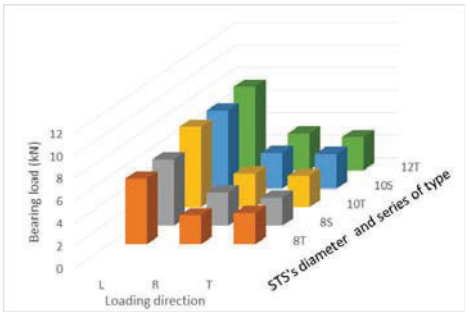

(C)

Figure 8: *Relationship of 5% offset bearing load on loading direction and STS's diameter types(a-Japanese larch, b-Korean pine, c-Japanese cedar*

https://doi.org/10.52202/069179-0169

In case of the series of STS, the average yield load of the T-series specimens with 8mm STS was measured 0.87 ~ 1.17 times than the S-series. The average yield load of the T-series specimens with 10mm STS was measured 0.90 ~ 1.23 times than the S-series. It is considered to because the bearing area of the S-series is smaller than that of the T-series.

3.2 FAILURE MODE UNDER BEARING LOAD

Most of the failure modes of the specimens on the longitudinal section showed that the wood split slightly along the direction of the grain in parallel to the loading direction by STS.

In case of the specimens on radial and tangential secion, the failure mode of bearing area showed that the bearing load at the shank or thread part of STS were concentrated the wood in perpendicular to the grain, resulting in short cleavage. This is the same result as the failure mode for each direction of the pine wood in a previous study (Lee *et. al.* 2022).

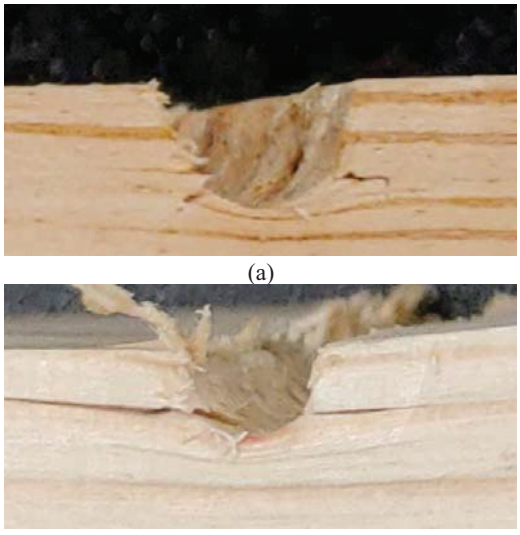

(a)

(b)

Figure 9: *Failure mode of the radial specimens on T-series(a-Japanese larch, b-Korean pine)*

4 CONCLUSIONS

To evaluate the bearing strength performance of STS connection using domestic species, the bearing test on the loading direction to the grain was conducted. The conclusions can be drawn as follows :

1. The bearing load showed a proportional relationship with the specific gravity of the species and the STS diameter.

2. Since the effective bearing area of shank and thread parts of STS is different according to the shape's characteristics of STS, it is necessary to reflect this in the prediction formula of the bearing strength for the connection design.

REFERENCES

[1] Aloisio, A., Pasca, D., Tomasi, R., and Fragiacomo, M. (2020). "Dynamic identification and model updating of an eight-storey CLT building," *Eng. Struct.* 213, Article ID 110593. DOI: 10.1016/j.engstruct. 2020.110593

[2] Brandner, R., Ringhofer, A., and Reichinger, T. (2019). "Performance of axially-loaded self-tapping screws in hardwood: Properties and design," *Eng. Struct.* 188, 677-699. DOI: 10.1016/j.engstruct. 2019.03.018

[3] Brown, J. R., Li, M., Tannert, T., and Moroder, D. (2021). "Experimental study on orthogonal joints in cross-laminated timber with self-tapping screws installed with mixed angles," *Eng. Struct.* 228, Article ID 111560. DOI: 10.1016/j.engstruct. 2020.111560

[4] Dietsch, P., and Brandner, R. (2015). "Self-tapping screws and threaded rods as reinforcement for structural timber elements–A state-of-the-art report," *Constr. Build. Mater.* 97, 78-89. DOI: 10.1016/j.conbuildmat.2015.04.028

[5] Fitzgerald, D., Sinha, A., Miller, T. H., and Nairn, J. A. (2021). "Axial slip-friction connections for cross-laminated timber," *Eng. Struct.* 228, Article ID 111478. DOI: 10.1016/j.engstruct.2020.111478

[6] Hossain, A., Popovski, M., and Tannert, T. (2019). "Group effects for shear connections with self-tapping screws in CLT," *J. Struct. Eng.* 145(8), Article ID 04019068. DOI: 10.1061/(ASCE)ST. 1943-541X.0002357

[7] Kim, K. H., Hong, S. I. (2008). "Bearing properties of domestic *Larix glulam*," *J. Korean Wood Sci. Tech.* 36(4), 93-101.

[8] Korea Forest Service 3020 (2018). *Statistical Yearbook of Forestry*, Daejeon, Republic of Korea

[9] Lee, I. H., Kim, K., and Shim, K. B. (2022). "Evaluation of bearing strength of self-tapping screws according to the grain direction of domestic *Pinus densiflora*," *J. Korean Wood Sci. Tech.* 50(1), 1-11.

[10] Li, X., Ashraf, M., Subhani, M., Ghabraie, K., Li, H., and Kremer, P. (2021). "Withdrawal resistance of self-tapping screws inserted on the narrow face of cross laminated timber made from Radiata Pine," *Structures* 31, 1130-1140. DOI: 10.1016/j.istruc. 2021.02.042

[11] Market Survey of Timber Products (2020). *Korea Forest Service*, Daejeon, Republic of Korea

[12] Mohammad, M., Blass, H., Salenikovich, A., Ringhofer, A., Line, P., Rammer, D., and Li, M. (2018). "Design approaches for CLT connections," *Wood Fiber Sci.* 27-47. DOI: 10.22382/wfs-2018-038

[13] Nguyen, T. T., Dao, T. N., Aaleti, S., van de Lindt, J. W., and Fridley, K. J. (2018). "Seismic assessment of a three-story wood building with an integrated CLT-lightframe system using RTHS," *Eng. Struct.* 167, 695-704. DOI: 10.1016/j.engstruct. 2018. 01. 025

[14] Van de Lindt, J. W., Furley, J., Amini, M. O., Pei, S., Tamagnone, G., Barbosa, A. R., Rammer, D., Line, P., Fragiacomo, M., Popovski, M. (2019). "Experimental seismic behavior of a two-story CLT platform building," *Eng. Struct.* 183, 408-422. DOI: 10.1016/j.engstruct.2018.12.079

[15] Xu, J., Zhang, S., Wu, G., Gong, Y., and Ren, H. (2021). "Withdrawal properties of self-tapping screws in Japanese larch (*Larix kaempferi* (Lamb.) Carr.) cross laminated timber," *Forests* 12, Article Number 524. DOI: 10.3390/f12050524

https://doi.org/10.52202/069179-0169

World Conference on Timber Engineering Oslo 2023

INCLINED SCREW CONNECTIONS WITH INTERLAYERS: BEAM ON FOUNDATION NON-LINEAR MODELLING

Yuri De Santis[1], Angelo Aloisio[2], Dag Pasquale Pasca[3], Igor Gavrić[4], Iztok Šušteršič[5], Massimo Fragiacomo[6]

ABSTRACT: Self-tapping screws, thanks to the speed and ease of installation have become more and more popular in the last 25 years. Slip modulus and strength increase when the screw axis is inclined with respect to the normal to the sliding plane, however, in this configuration screw is subjected to axial and shear force, together with bending moment. Moreover, interlayers having poor mechanical properties are often inserted between main connected members to ensure human comfort in the buildings or because it is required by the structural system. The complex interaction between axial and transversal behaviour of inclined screws may not be fully considered by some of the simplified models in literature and codes, in this paper the behaviour of steel-to-timber connection is experimentally assessed and a finite element model of non-linear beam on foundation is validated. Experimental results are compared with the results of finite element analysis and the with Eurocode 5 model results.

KEYWORDS: Inclined screws, Load-bearing capacity, Timber-to-timber connection, Eurocode 5, Friction.

1 INTRODUCTION

Self-tapping screws are commonly used in timber-to-timber, timber-to-concrete, and timber-to-steel connections and are well suited for use in composite floors and beams. They can be easily inserted at an angle with respect to the normal to the sliding plane. In this configuration their axial resisting mechanisms can be exploited. Stiffness and strength of inclined screws can be 5 to 10 times the stiffness and strength of screws perpendicular to the sliding plane. While for screws perpendicular to the sliding plane the ultimate force is usually reached at the conventional displacement of 15 mm with a ductile behaviour, for inclined screws the failure displacement is between 1 mm and 5 mm depending mainly on the inclination angle of the screw and the connection fails mainly due to screw withdrawal or due to screw failure. However, when the screw is inclined, it is simultaneously subjected to axial force, shear force and bending moment. This strong coupling between the axial and the transversal behaviour of the screw makes difficult to predict the actual connection behaviour by means of simplified models.

The connection mechanical behaviour becomes even more difficult to model when an interlayer having structural or non-structural role is present. Often polyurethane interlayers are used for soundproofing and OSB interlayers are common in light-frame buildings.

The interlayer can be considered rigidly connected when it is glued to the main timber member. The interlayer is weakly connected when the secondary connection between the interlayer and the main timber member has negligible strength and stiffness compared to the main connection. It is the case of staples, nails and small diameter and length screws. Examples of interlayers not connected are soundproofing interlayers.

It is known that the interlayer affects the slip modulus of connections as highlighted in [1], however less studies have been conducted on the capacity of connections with interlayers.

Eurocode 5 design method for strength calculation of dowel type fastener connections is based on the Johansen's work [2]. According to European standards, the load-bearing capacity of a screw simultaneously subjected to shear and axial stress, as in the case of inclined screws connections, is given by a quadratic combination of the stress-strengths ratios for transversal and axial directions [3]. This design model might highly underestimate the strength of connections with inclined screws as highlighted by Tomasi et al. in [4].

Bejtka I. and Blaß H.J. in [5] extended the Johansen's yield theory accounting for the withdrawal behaviour of the screws. However, the complex interaction between axial and transversal stresses of inclined screws may not be fully considered in determining the plastic properties of the screws.

[1] Yuri De Santis, Università degli Studi dell'Aquila, Italy, yuri.desantis@univaq.it
[2] Angelo Aloisio, Università degli Studi dell'Aquila, Italy
[3] Dag Pasquale Pasca, Norsk Treteknisk Institutt (Norwegian Institute of Wood Technology), Børrestuveien 3, 0373 Oslo, Norway
[4] Igor Gavrić, InnoRenew CoE, Slovenia
[5] Iztok Šušteršič, InnoRenew CoE & University of Primorska, Slovenia
[6] Massimo Fragiacomo, Università degli Studi dell'Aquila, Italy

https://doi.org/10.52202/069179-0170

In recent years, several advanced three-dimensional numerical models have been proposed to study the behaviour of connections made of threaded fasteners embedded in timber. The complex screw-timber interaction, due to the presence of thread, has been modelled using various techniques ranging from the reproduction of the actual thread geometry [6] to the use of cohesive contact with damage evolution in conjunction with a fictitious material that wraps the screw and models a complex medium where steel and timber interact [7].
In order to avoid the detailed three-dimensional modelling of the screw using solid elements, some authors developed an approach based on beam to-solid coupling [8].
Also, empirical models for capturing load-slip behaviour joints with dowel-type fasteners were proposed [9, 10].
Another approach to the problem is represented by Beam-On-Foundation (BOF) modelling. According to this method, fasteners are numerically modelled as elastoplastic beams on a nonlinear foundation. BOF modelling has been used to reproduce the hysteretic behaviour and failure mechanisms of timber joints with dowel-type fasteners perpendicular to the sliding plane [11, 12].
In this paper, a BOF model capable of taking into account of the interaction between moment, shear and normal force which may lead to metal fastener yielding at loads below those predicted by the EYM is proposed. The model is able to reproduce the following mode of failure: timber crushing, screw withdrawal and screw yielding. The model also accounts for friction on the sliding plane and interlayer.
The outcomes of an experimental investigation conducted on various inclined screws timber-to-steel connection configurations with or without soundproofing and OSB interlayers are herein described and discussed. These results have been used to validate a finite element modelling approach suitable for describing the ultimate conditions.
The experimental results are also compared with the Eurocode 5 model results.

2 EXPERIMENTAL INVESTIGATION

The experimental campaign involves timber-to-steel connections with screw inclined at 45° inserted in glue laminated timber of strength class GL24h and UPN 100 steel profiles (Figure 1). The screws are self-tapping fully-threaded screws with a diameter of 9 mm and length of 240 mm or 140 mm. The characteristic ultimate stress of the screw is $f_{u,k}$ = 1000 N/mm^2. A special washer is used to restrain the screw head in the tight-fitting oval shape hole in the UPN 100 profile (Figure 2). Washers with an insertion angle α = 45◦ are common for inclined positioned screws in steel-to-timber joints. In this case the washer has the role of replacing the countersunk drill holes in the steel plate by more economically producible slots. However, due to their particular geometry, a part of the screw near the sliding plane is left free of bending. The soundproofing interlayers are made of polyurethane and are 6 mm thick and 100 mm wide whilst OSB interlayers are 22 mm thick.
Four different configurations have been considered:

- C-45-R: reference configuration
- C-45-S35: with soundproofing interlayer
- C-45-O: with OSB interlayer
- C-45-RL: reduced length of the screw

The materials and the geometries of the configurations are summarised in Table 1.

Table 1: *Configurations details*

Configuration	Interlayer	Thickness (mm)
C-45-R	-	-
C-45-S35	Polyurethane	6
C-45-O	OSB	22
C-45-RL	-	-

A detail of sliding plane between the UPN profile and the glulam member with a soundproofing intermediate layer is showed in Figure 1.

Figure 1: *Test setup detail: shear plane with soundproofing interlayer*

2.1 TEST METHODS

The typical test consisted in a standard symmetric push-out test. The specimen, consisting of 3 members and therefore 2 shear planes with a single screw per shear plane, is brought to failure by pushing the central member. The relative displacement between members has been measured through a LVDT (Linear Variable Differential Transformer). Due to the eccentricity between the load applied to the central member and the reaction that the test plane exerts on the lateral members, in the standard configuration for push-out tests the members tend to

https://doi.org/10.52202/069179-0170

separate during the test. For this reason, side members were clamped with support not able to induce pre-stress. No predrilling was applied.
The general principles for the determination of strength and deformation characteristics of joints made with mechanical fasteners are described in the European standard EN-26891 [13]. The procedure requires the knowledge of an estimated maximum load F_{est} to be determined on the basis of experience, calculation or preliminary tests, and should be adjusted if, during the execution of the tests, the mean value of the maximum load of the tests already carried out deviates by more than 20% from the estimated value.
The chosen loading procedure is divided into the following phases:

- force controlled loading from 0.0 F_{est} to 0.4 F_{est};
- force controlled holding at 0.4 F_{est} for 30 s;
- force controlled unloading from 0.4 F_{est} to 0.1 F_{est};
- force controlled holding at 0.1 F_{est} for 30 s;
- force controlled loading from 0.1 F_{est} to 0.7 F_{est};
- displacement controlled until failure or 15 mm.

The speed in the displacement-controlled phase has been set equal to 0.06 mm/s and the loading speed in all other phases has been calculated to achieve 15 mm of relative displacement in 12 min resulting in a loading speed comprised between 0.03 kN/s and 0.20 kN/s depending on the estimated maximum load.

Figure 2: *Washer for timber-to-steel connections*

2.2 RESULTS AND DISCUSSION

From the recorded measurements, the initial slip modulus, the slip modulus, the ultimate slip modulus and the maximum load have been determined.
To calculate the stiffness and ultimate displacement values net of displacement components related to local crushing at the member ends, the LVDT displacement measurements were used.
The initial slip modulus has been determined with the following definition:

$$k_i = \frac{0.4F_{max}}{\nu_{04}} \quad (1)$$

Where F_{max} is the maximum force measured up to a relative slip of 15 mm and ν_{04} is the relative slip in the first loading phase corresponding to the considered load.
The slip modulus has been determined with the following definition:

$$k_s = \frac{0.4F_{max} - 0.1F_{max}}{\nu_{04} - \nu_{01}} \quad (2)$$

Where ν_{04} and ν_{01} are the relative slip in the loading phase corresponding to the considered loads.

Figure 3: *Experimental failure modes: tensile-bending combined failure and withdrawal failure.*

The initial slip modulus and the slip modulus are summarized in Table 2. Significant reductions in slip modulus were observed for both the soundproofing interlayer and OSB interlayer.
The reference configuration C-45-R, the configuration with soundproofing interlayer C-45-S35 and the configuration with the OSB interlayer C-45-O showed a failure due to the screw failure (Figure 3) or due to screw withdrawal. The configuration with reduced length screws showed failure due to the screw withdrawal.
The average of the maximum load registered for each configuration are showed in the plot of Figure 5.
The insertion of the interlayer led to a reduction of 10% and 17% in strength in the cases of soundproofing interlayer and OSB respectively (Figure 5).
The configuration with screws with reduced length has 51% less strength than the reference connection (Figure 5).

https://doi.org/10.52202/069179-0170

Table 2: *Results in terms of stiffness referred to a single screw.*

Configuration	$k_{i,m}$ (kN/mm)	$k_{s,m}$ (kN/mm)
C-45-R	9,1	10,5
C-45-S35	9,1	8,1
C-45-O	4,6	5,8
C-45-RL	10,6	14,5

3 FINITE ELEMENT MODEL

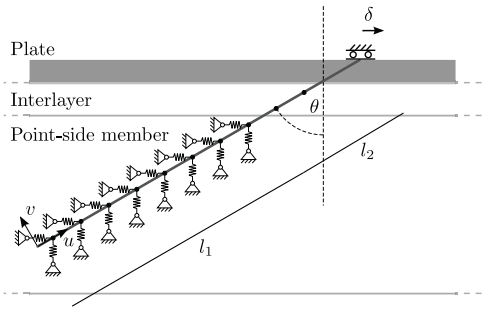

Figure 4: *Finite element model*

3.1 DESCRIPTION

The problem of the determination of the capacity of connections with inclined screws is reduced assuming a beam behaviour for the screw and describing its interaction with timber by 2-node connector elements (Figure 4).

Common screw types have negligible section variations over the screw length. Small section increments are usually made in areas without threads thus causing a partial compensation of the geometric properties. In determining the section properties, the circular section is assumed of diameter equal to 1.1 times the screw core diameter d_c as suggested for transversal capacity calculation in Eurocode 5 [3].

The beam elements used to model the screw are mono-dimensional and linear with section properties integrated during the analysis to account for the steel non-linear behaviour. An elastic-perfectly plastic isotropic behaviour is assumed for the screw steel. The Young's elasticity modulus is E_s = 210000 N/mm^2 and the mean yielding strength is f_y = 1200 N/mm^2. The reaching of high failure stress is granted by the cold forming during the production process.

The interaction between the screw and the surrounding timber along l_1 is modelled through a system of discrete connectors:

- A series of springs parallel to the sliding plane having elastic-perfectly plastic behaviour [14, 15];
- A series of springs perpendicular to the sliding plane having elastic-hardening behaviour and friction parallel to the sliding plane [14, 15];
- A rigid contact with damage between the common node between parallel and perpendicular springs and the node on the beam schematizing the screw (black dots in Figure 4).

The series of springs parallel and perpendicular are non-linear springs which schematize the embedment interaction in the grain direction and in the perpendicular to the grain direction.

Embedment is one of the fundamental load transfer mechanisms in a dowel-type connection. Due to the scale effect, the timber mechanical properties in embedment are significantly different from the mechanical properties that describe the macroscopic behaviour of a timber element. Therefore, proper tests had to be defined in order to provide suitable parameters for mechanical modelling. For a dowel-type fastener, the foundation modulus and the embedment strength can be experimentally determined via test according to EN 383.

In the model, the stiffness of each connector element parallel and perpendicular to the sliding plane has been assumed as:

$$\mathrm{K_{pa}} = \mathrm{k_h d l_m} \cos\theta \tag{3}$$

$$\mathrm{K_{pe}} = \beta \mathrm{k_h d l_m} \sin\theta \tag{4}$$

where $\mathrm{k_h}$ is the stiffness per unit of length of the beam and have been assumed as for the regression formula provided in [1] derived by interpolation of embedment test:

$$\mathrm{k_h} = (-147.8 + 30.9\rho^{0.46}\mathrm{d}^{-0.32})d \tag{5}$$

$\beta = 0.5$, ρ is the timber density, d is the screw thread outer diameter and $\mathrm{l_m}$ the length of the element between two connectors.

The yielding force of parallel to grain connector has been assumed as:

$$\mathrm{F_{y,pa}} = \mathrm{f_{h,0} d l_m} \cos\theta \tag{6}$$

$$\mathrm{F_{y,pe}} = \mathrm{f_{h,90} d l_m} \sin\theta \tag{7}$$

and the ultimate force in the direction perpendicular to the grain at a displacement equal to 2d has been assumed as:

$$\mathrm{F_{u,pe}} = \Omega \mathrm{F_{y,pe}} \tag{8}$$

where Ω has been assumed 1.72 as found by Schweigler et al. in [14, 15] where a strong hardening behaviour in the direction perpendicular to the grain is observed.

In connections with inclined screws in tension, a compression in the direction perpendicular to the sliding plane develops. This compression force generates a friction force parallel to the sliding surface. According to literature this contribution leads to an increase in slip

https://doi.org/10.52202/069179-0170

modulus and strength. To account for this effect connectors perpendicular to the sliding plane are defined as to develop a transversal force proportional to the axial force by means of the friction coefficient. The friction coefficient has been set to $\mu = 0.5$ for connections without interlayer or with OSB interlayer, while $\mu = 0.7$ has been chosen to reproduce the timber-polyurethane frictional behaviour.
The embedment strengths have been assumed as in the Eurocode 5 [3]:

$$f_{h,\alpha} = \frac{f_{h,0}}{k_{90,e} \sin^2 \alpha + \cos^2 \alpha} \quad (9)$$

where $f_{h,0}$:

$$f_{h,0} = 0.082(1 - 0.01 d_{ef}) \quad (10)$$

and where d_{ef} is the effective screw diameter and according to Eurocode 5 [3] can be assumed as 1.1 the screw core diameter d_c. α is the force to the grain angle and $k_{90,e}$ can be assumed as $1.35+0.015d_{ef}$.
The mechanical behaviour of axially loaded screws, and specifically the withdrawal behaviour depends on the interaction along the axial screw direction between the screw thread and the surrounding timber. The withdrawal failure has to be regarded as a local failure of the timber surrounding the screw.
The withdrawal behaviour is modelled through rigid-plastic connectors whose properties are defined according to the findings of Blaß et al. [16] and [17]. According to the formulation proposed by Blaß et al., the withdrawal failure stress can be estimated as follows:

$$f_{w,\alpha} = \frac{f_{w,0}}{k_{90,w} \sin^2 \alpha + \cos^2 \alpha} \quad (11)$$

where $f_{w,0}$:

$$f_{w,0} = 0.6 d^{-0.5} l_{ef}^{-0.1} \rho_m^{0.8} \quad (12)$$

and where d is the screw thread outer diameter, α is the force to the grain angle and $k_{90,w}$ is 1.2.
The associated withdrawal failure force per-connector is:

$$F_{u,E_{tr}} = f_{w,\alpha} \pi d l_m \quad (13)$$

A linear damage evolution with ultimate displacement of 4 mm is assumed to reproduce the withdrawal failure according to the findings of Bedon et al. [7] based on detailed three-dimensional finite element models and experimental outcomes of [17].
The connectors are restrained to external hinges capable of preventing translations only.
Along l_2, that is the length of the part of the screw embedded into the interlayer and the part of the screw free of bending near the sliding plane, no connectors has been considered. The part of the screw free of bending is the section comprised in the UPN web thickness. Therefore, the l_2 of the experimental case C-45-R is greater than zero, despite the absence of interlayer.
The translation perpendicular to the sliding plane and the rotation of the head-end of the screw are restrained to reproduce the clamping effect of the washer (Figure 2). At failure, contact between components is established and the washer behaves as a rotation restraint.
The relative displacement between the UPN profile and the timber members is reproduced by an imposed displacement applied to the screw head, parallel to the sliding plane (Figure 4). Therefore, a typical simulation consisted of a static incremental, displacement-controlled analysis.

3.2 VALIDATION

As highlighted in Figure 5 the finite element model tends to slightly underestimate the failure load, but it is overall quantitatively accurate. Percentage scatters are between -17% and -3%.

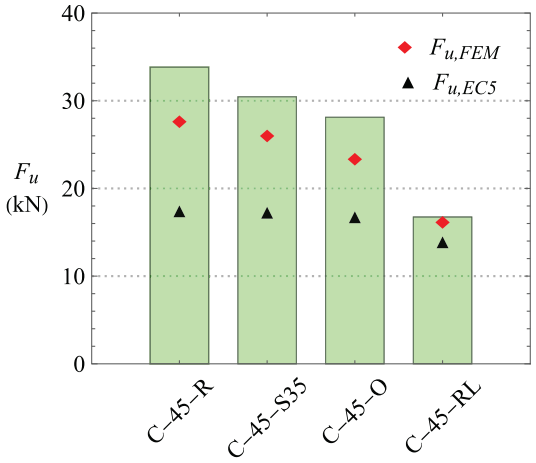

Figure 5: *Experimental (bars) and predicted failure loads with finite element model and Eurocode 5 model (markers).*

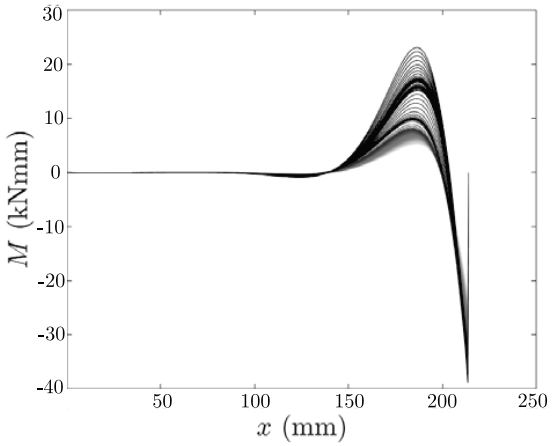

Figure 6: *Bending moment evolution in configuration C-45-R. Darker colour for higher connection slip.*

https://doi.org/10.52202/069179-0170

The plot in Figure 6 shows the bending moment diagram evolution for increasing applied displacement. When the maximum load is achieved, a plastic hinge forms in the head-end of the screw. The bending moment becomes null due to full plasticization of the section caused by the combination of axial force and bending moment.

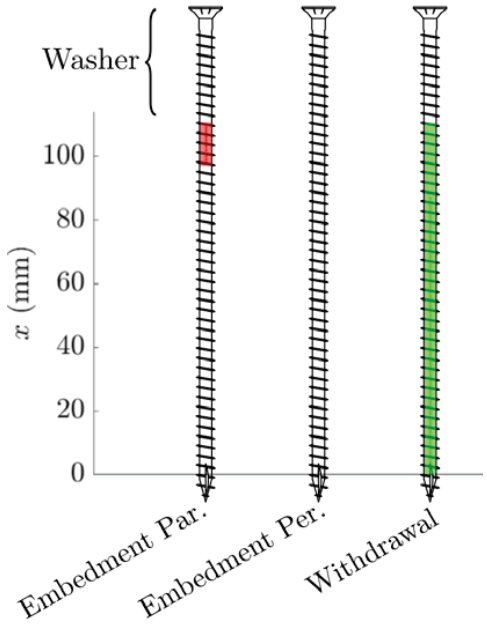

Figure 7: *Failure mode of configuration C-45-RL. Connectors in plastic range position.*

In Figure 7 the connector elements parallel to the sliding plane and the withdrawal connectors that reached plasticization at connection failure are highlighted. No connectors perpendicular to the sliding plane are found to be in plastic range at failure. For the reduced length configuration, a clear withdrawal failure is observed in the finite element model as well as in the experimental investigation. Embedment failure is confined to a zone of negligible extent.

3.3 PARAMETRIC STUDIES

The finite element model has been used to perform parametric studies. The influence of soundproofing interlayer is investigated ($\mu = 0.7$).

The first parametric study is conducted by varying l_2, the length of penetration of the screw into the interlayer plus the part of the screw free of bending, while maintaining the screw length constant (l = 200 mm and l = 100 mm). It can be observed from the plot in Figure 8 that the strength of the connection remains almost unvaried until l_2 reaches 20 mm and 10 mm in the case of 200 mm and 100 mm screw respectively. A small increase in strength is registered between the case of no-interlayer and interlayer length of penetration equal to 5 mm. This is due to the increased friction coefficient granted by the soundproofing interlayer. Moreover, the reduction in strength is more pronounced for shorter screw than for longer screw (-59% and -31% respectively).

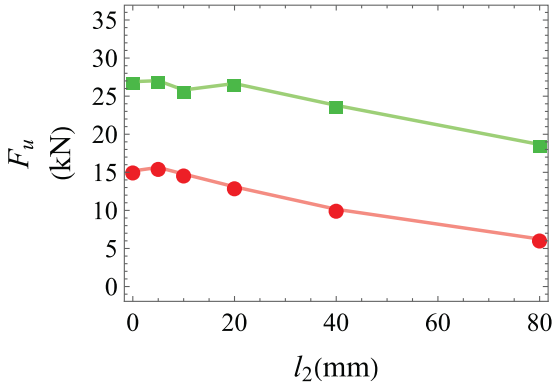

Figure 8: *Interlayer influence on FEM predicted strength for constant screw length: l = 200 mm (green) and l = 100 mm (red).*

The second parametric study is conducted varying the length l_2 while maintaining the screw length constant (l_1 = 200 mm and l_1 = 100 mm). It can be observed from the plot in Figure 9 that the strength of the connection remains almost constant. A small increase in the ultimate force can be observed for increasing l_2. This increase is caused by the increase of the friction component.

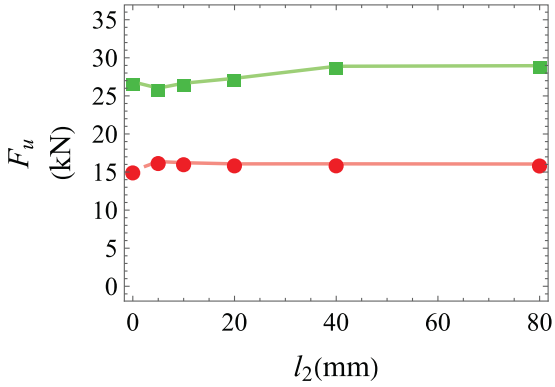

Figure 9: *Interlayer influence on FEM predicted strength for constant length of penetration into the main timber member: l_1 = 200 mm (green) and l_1 = 100 mm (red).*

4 EUROCODE 5 MODEL

The European Yield Model (EYM) is a commonly accepted procedure to calculate the capacity of laterally loaded connections with dowel type fasteners. The EYM is described in the Eurocode 5 [3] and it is based on the Johansen yield theory [2]. According to Johansen yield theory it is assumed that steel and timber exhibit a rigid-plastic behaviour. Different failure modes are identified depending on the degree of restraint that the steel plate has

https://doi.org/10.52202/069179-0170

on the fastener. According to Johansen theory [2] the transversal strength of dowel-type fastener connecting a thick plate to a timber member is given by:

$$R_{tr} = \min \begin{cases} f_h\, l_1\, d_{ef} \;\; Embedment \\ f_h l_1 d_{ef}\left(\sqrt{2 + \frac{M_y}{f_h d_{ef} l_1^2}} - 1\right) 1\ hin. \\ 2.3\sqrt{M_y f_h d_{ef}}\ 2\ hin. \end{cases} \quad (14)$$

In the EYM the rope effect can also be considered to account for the friction contribution induced by the force normal to the sliding plane generated by the deformation of the fastener.
Regarding the axial behaviour, two more failure mechanisms must be considered:

$$R_{ax} = \min \begin{cases} f_w l_1 d \min\left(\frac{d}{8}, 1\right) \;\; Withdrawal \\ f_u \pi \frac{d_{ef}^2}{4} \;\; Tensile \end{cases} \quad (15)$$

According to the current Eurocode 5 [3], a quadratic interaction between transversal and axial capacity should be considered irrespective to the combined failure modes:

$$\left(\frac{F_{tr}}{R_{tr}}\right)^2 + \left(\frac{F_{ax}}{R_{ax}}\right)^2 \leq 1 \quad (16)$$

4.1 RESULTS COMPARISON

Eurocode 5 model underestimates the capacity of all experimental configuration, despite the mean values of input parameters has been considered (Figure 5). EYM shows slightly more accurate in the configuration characterized by a lower penetration length. The scatters between EYM prediction and experimental results are between -48% and -16%.

5 CONCLUSIONS

The connection with inclined screws and interlayer exhibits a more pronounced reduction in stiffness (23% to 45%) than in strength (10% to 17%).
The quadratic combination approach prescribed by Eurocode 5 proved to be too conservative leading to an underestimation of the strength up to 48% while the proposed numerical model can predict the failure load considerably more accurately for the tested configurations (percentage scatters between 17% and -3%).
The proposed finite element model represents a valid alternative to complex three-dimensional models for the study of connections with inclined screws as it accurately describes the experimentally assessed behaviour in terms of both failure mode and failure loads. The reduced computational cost, which is associated with the reduced number of degrees of freedom, makes it suitable for carrying out comparisons and parametric analyses.
Sensitivity studies had demonstrated that the insertion of an interlayer can appreciably affect the failure load of the connection only if the sum of the length of penetration of the screw into the interlayer and the length of the screw free of bending is at least 1/10 of the screw length. Increasing the screw length to compensate for the loss of effective length into the timber member can completely compensate for the interlayer presence.

ACKNOWLEDGEMENT

This article is based upon work from COST Action Helen (CA20139), supported by COST (European Cooperation in Science and Technology).
The authors thank all the people involved in the execution of the experimental campaign.

REFERENCES

[1] De Santis Y., & Fragiacomo M.: Timber-to-timber and steel-to-timber screw connections : Derivation of the slip modulus via beam on elastic foundation model. Engineering Structures, 244(April), 112798, 2021. https://doi.org/10.1016/j.engstruct.2021.112798
[2] Johansen K.W.: Theory of Timber Connectors. Publications of the International Association of Bridge and Structural Engineering. Bern, General Secretariat, No. 9: 249-262, 1949.
[3] European Committe for Standardization (CEN). EN 1995-1-1:2004 (E). Eurocode 5 - Design of timber structures: CEN; 2004.
[4] Tomasi R., Crosatti A., & Piazza, M.: Theoretical and experimental analysis of timber-to-timber joints connected with inclined screws. Construction and Building Materials, 24(9), 1560–1571, 2010. https://doi.org/10.1016/j.conbuildmat.2010.03.007
[5] Bejttka I., & Blaß H.: Joints with Inclined Screws. Proceedings of CIB-W18 Timber Structures, Meeting 35, September, 35-7–4, 2002. http://cib-w18.com/sites/default/files/proceedings/no._35_kyoto_japan_september_2002.pdf
[6] Stamatopoulos H., & Malo K. A.: Withdrawal stiffness of threaded rods embedded in timber elements. Construction and Building Materials, 116, 263–272, 2016. https://doi.org/10.1016/j.conbuildmat.2016.04.144
[7] Bedon C., & Fragiacomo M.: Numerical analysis of timber-to-timber joints and composite beams with inclined self-tapping screws. Composite Structures, 207(September 2018), 13–28. https://doi.org/10.1016/j.compstruct.2018.09.008
[8] Oudjene M., Meghlat E. M., Ait-Aider H., Lardeur, P. Khelifa M., & Batoz J. L.: Finite element modelling of the nonlinear load-slip behaviour of full-scale timber-to-concrete composite T-shaped beams. Composite Structures, 196(March), 117–126,

2018.
https://doi.org/10.1016/j.compstruct.2018.04.079
[9] Hassanieh A., Valipour H. R., & Bradford M. A.: Load-slip behaviour of steel-cross laminated timber (CLT) composite connections. Journal of Constructional Steel Research, 122, 110–121, 2016. https://doi.org/10.1016/j.jcsr.2016.03.008
[10] Schweigler M., Bader T. K., Hochreiner G., & Lemaître R.: Parameterization equations for the nonlinear connection slip applied to the anisotropic embedment behavior of wood. Composites Part B: Engineering, 142(November 2017), 142–158. https://doi.org/10.1016/j.compositesb.2018.01.003
[11] Izzi M., Rinaldin G., Polastri A., & Fragiacomo M.: A hysteresis model for timber joints with dowel-type fasteners. Engineering Structures, 157(July 2017), 170–178.
https://doi.org/10.1016/j.engstruct.2017.12.011
[12] Lemaitre R., Bocquet J.-F., Schweigler M., & Bader T. K.: Beam-on-foundation modelling as an alternative design method for timber joints with dowel-type fasteners – Part 1: Strength and stiffness per shear plane of single-fastener joints. Inter / 54-7-8, 2019.
http://urn.kb.se/resolve?urn=urn:nbn:se:lnu:diva-89340
[13] EN-26891, “Timber structures - Joints made with mechanical fasteners - General principles for the determination of strength and deformation characteristics,” CEN, 1991
[14] Schweigler M., Bader T. K., Vessby J., & Eberhardsteiner J.: Constrained displacement boundary condition in embedment testing of dowel-type fasteners in LVL. Strain, 53(6), 1–18, 2017. https://doi.org/10.1111/str.12238
[15] Schweigler M., Bader T. K., Hochreiner G., Unger G., and Eberhardsteiner J.: Load-to-grain angle dependence of the embedment behavior of dowel-type fasteners in laminated veneer lumber. Construction and Building Materials, vol. 126, pp. 1020–1033, 2016. https://doi.org/10.1016/j.conbuildmat.2016.09.051
[16] Blaß H. J., Bejtka I., and Uibel T.: Tragfähigkeit von Verbindungen mit selbstbohrenden Holzschrauben mit Vollgewinde, vol. 4. 2006.
[17] Ringhofer A., Brandner R., & Schickhofer G.: Withdrawal resistance of self-tapping screws in unidirectional and orthogonal layered timber products. Materials and Structures/Materiaux et Constructions, 48(5), 1435–1447, 2015. https://doi.org/10.1617/s11527-013-0244-9

https://doi.org/10.52202/069179-0170

World Conference on Timber Engineering Oslo 2023

A FRACTURE MECHANICAL AND ANISOTROPIC FEM MODEL OF THE "RECONWOOD JOINT" AND EXPERIMENTAL VERIFICATION

Jesper Kierkegaard Hansen[1], Mads Friborg Nielsen[2], Søren Gustenhoff Hansen[3], Anja Kunic[4], Roberto Naboni[5]

ABSTRACT: Contemporary capabilities in timber fabrication have encouraged the advancement of robotic manufacturing and assembly. In this paper, the *ReconWood joint*, a new type of reversible joint conceived for robotic timber assembly is investigated. The joint use CNC milled shear-keys to ensure enhanced shear capacity and more ductile behaviour over the conventional dowel-type connection. More specifically, we here establish a method for the modelling and structural analysis of such joint where the complex nature of timber is tackled by using material laws which are readily available in most commercial FE software. The paper presents a hybrid material model using the Hill Criterion in combination with fracture mechanics (CZM) to appropriately describe these behaviours. The material model is implemented in a three-dimensional FEM model to simulate the joint's mechanical behaviour, and a test series is presented to validate the modelling approach. The results show that the model is able to predict the mechanical response with great precision, both in relation to the stiffness, ultimate strength, and failure mode.

KEYWORDS: Timber joint, Solid 3D FEM, Experiments, Fracture mechanics, Anisotropy

1 INTRODUCTION

Timber is considered one of the most promising construction materials of the future due to its carbon sequestration capability, its relatively rapid circles of regrowth, and its re-use and adaptation potential while offering great mechanical performance and lightweightness [1].

The structural capacity of timber structures is often governed by the load-carrying capacity or deformations of the bolted joints. However, the past decade's development of contemporary fabrication technologies within timber engineering has led to the advancement of novel, refined, joint typologies. This paper presents a second generation of a shear-key-based bolted joint [2], specifically the *ReconWood joint,* a part of the *ReconWood construction system*. The construction system has been developed by the CREATE Group at the University of Southern Denmark (SDU CREATE), envisioning building components that are robotically assembled, dis-assembled and re-assembled, can be reconfigured into various structural and functional formations and are structurally optimised for re-use [3-5].

The *ReconWood joint* improves the stiffness and load-carrying capacity over conventional bolted joints [2]. To ensure its reusability within multiple structural configurations over time and provide a viable design and engineering tool for the reconfigurable wood architecture of the future, a reliable structural model that encompasses the complex nature of timber's strength and stiffness is crucial. As the capacity and stiffness of the joint are governed by very complex mechanisms and nonlinear material properties, a reliable model must be based on the finite element method, FEM. This paper aims to showcase a reliable model for structural analysis of the *ReconWood joint* using widely available commercial FEM software and perform an experimental verification.

This paper first introduces the *ReconWood joint* before presenting a detailed description of an appropriate material model for structural analysis of the joint. Hereafter, a *ReconWood joint* is analysed, first via FEM and afterwards experimentally. The results are compared before the paper rounds off with a conclusion.

[1] Jesper Kierkegaard Hansen, COWI, Denmark, jshs@cowi.com
[2] Mads Friborg Nielsen, COWI, Denmark, mdnl@cowi.com
[3] Søren Gustenhoff Hansen, COWI, Denmark & Section for Civil and Architectural Engineering, University of Southern Denmark, Denmark, sohn@cowi.com
[4] Anja Kunic, CREATE - Section for Civil and Architectural Engineering, University of Southern Denmark, Denmark, kunic@iti.sdu.dk
[5] Roberto Naboni, CREATE - Section for Civil and Architectural Engineering, University of Southern Denmark, Denmark, ron@iti.sdu.dk

https://doi.org/10.52202/069179-0171

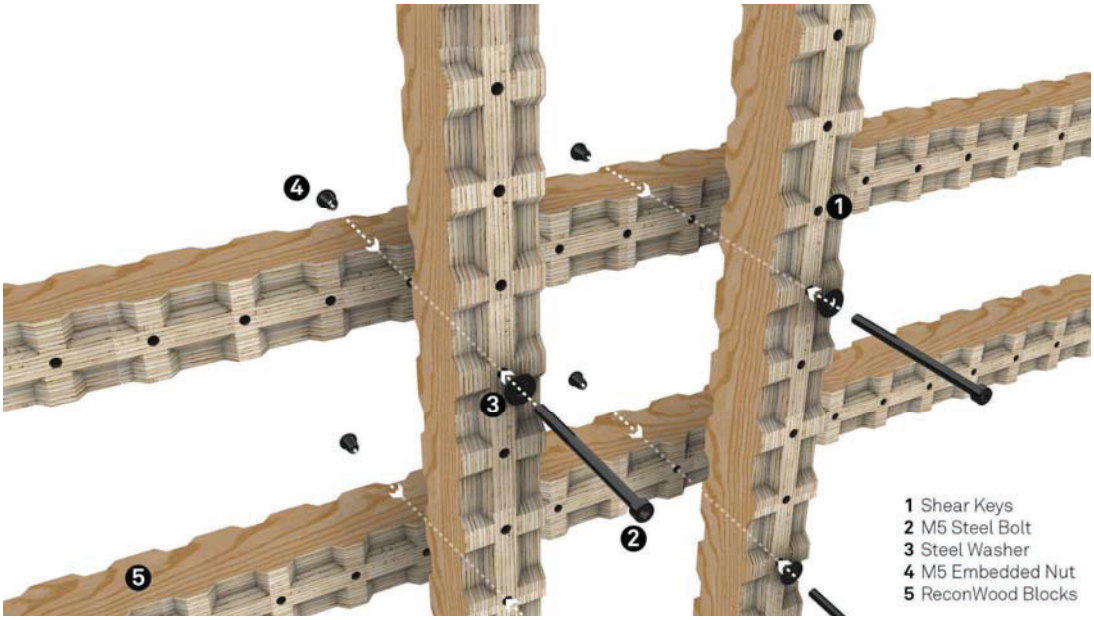

Figure 2: *Exploded view of the ReconWood joints and the construction system*

2 THE *RECONWOOD JOINT*

The *ReconWood joint* is a part of the *ReconWood construction system* [3,4] conceived as a reusable and reconfigurable construction kit made out of discrete building blocks with reversible joints. The blocks and the joints are designed to facilitate robotic assembly and re-assembly of various structural formations as seen in Figure 1. [5]

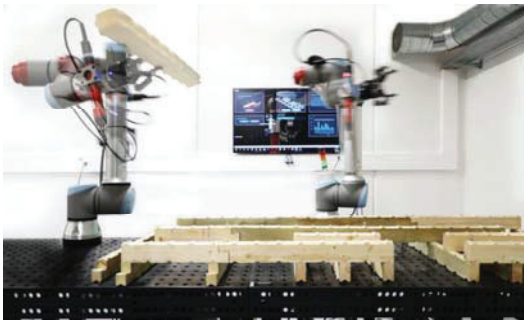

Figure 1: *Collaborative robot assembly of a ReconWood construction system*

The *ReconWood joints* are characterised by robotically milled cross-shaped male/female interlocking features, connected by a steel bolt with insert nut fasteners (Figure 2). The interlocking three-dimensional geometry of the joints assures precision and rigidity during the assembly process.

In the assembled structure, these joints ensure an increased stiffness and capacity when subjected to shear due to the shear key effect facilitated by the milled features [2], instead of activating dowel and rope actions as for the conventional bolted joints. The increased capacity results in a one-bolt joint which (*i*) eases the robotic assembly, and (*ii*) the edge distance does not govern the block dimensions. The increased stiffness of the joints is highly beneficial for the *ReconWood construction system* due to the large number of connections within such a structure, where the global stiffness is significantly affected by the joint stiffness.

3 MATERIAL MODEL FOR NUMERICAL ANALYSIS

The aim of the FEM model is to evaluate the stiffness, load-carrying capacity, and reusability of the *ReconWood joint*. To establish this, the material model must account for the complex mechanisms and nonlinear material properties of timber.

3.1 TIMBER'S MECHANICAL PROPERTIES

Timber is a complex anisotropic material due to its structure. Comprised of tube-shaped cells in a lignin matrix, the strength, stiffness, and post-peak behaviour of timber depend on the direction and the type of stress applied. [6]

The anisotropy of timber is often defined by a cylindrical coordinate system with three axes denoted longitudinal (L), radial (R), and tangential (T), see Figure 3. A common practice in timber engineering is a simplification of using the same mechanical properties for radial and tangential direction resulting in two distinctive directions: parallel-to and perpendicular-to the grain direction. [7,8]

https://doi.org/10.52202/069179-0171

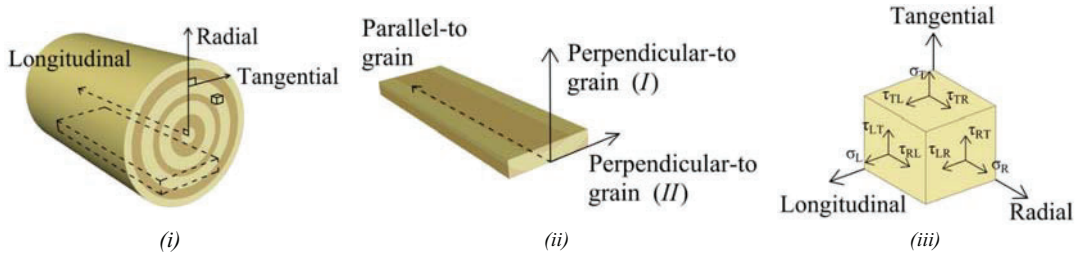

Figure 3: *Material directions of timber and 3D stress components.*

Typically, timber's properties are described for compression, tension, and shear, individually. When subjected to tension, timber can be described by linear elastic and brittle behaviour regardless of the grain orientation. However, the stiffness and strength are highly anisotropic parallel to the grain. In compression, timber has ductile behaviour with anisotropic post-peak behaviour in all directions. Compression parallel to grain direction is characterised by strain softening, while compression perpendicular to grain direction shows strain hardening. [6]

The six shear stress components, referring to the cylindric coordinate system (see Figure 3) are due to equilibrium pairwise equal ($\tau_{\mathrm{TL}} = \tau_{\mathrm{LT}}, \tau_{\mathrm{RL}} = \tau_{\mathrm{LR}}, \tau_{\mathrm{RT}} = \tau_{\mathrm{TR}}$). Each of the three pairs of stress components has an individual shear strength. The shear strength for the four parallel-to stress components ($\tau_{\mathrm{TL}}, \tau_{\mathrm{LT}}, \tau_{\mathrm{RL}}, \tau_{\mathrm{LR}}$) are almost identical and due to convenience, the lowest strength τ_{TL} is used. However, the strength for the perpendicular-to shear stress components, also known as rolling shear, is significantly lower[6,7]. The application of this is further discussed in Section 4.4.

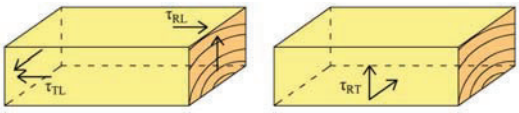

Figure 4: *Shear directions in timber*

This paper proposes a hybrid modelling approach as no available model exists that *(i)* addresses the anisotropic strength and stiffness of timber in combination with simultaneous brittle and ductile behaviour, and *(ii)* is readily implementable in commercial software. Therefore, the material model presented is divided in two - one for the brittle behaviour and one for the ductile behaviour.

3.2 MODELLING THE BRITTLE BEHAVIOUR

For the modelling of brittle failure within solid wood, three main approaches are found in the literature: *Cohesive Zone Model* (CZM) [10-12], *Continuum Damage Mechanics* (CDM) [8-9,13-14], and *lattice models* [15]. Both CZM and CDM are well-researched in the field of advanced numerical analysis of timber structures, while analysis with lattice models is mostly used in mesoscopic and microscopic fields of timber study.

While many studies have employed CDM to model the brittle behaviour of timber e.g. [8-9,13-14], the method has the disadvantage of not being able to show permanent deformations in the analysis as well as being mesh dependent with convergence problems when used in implicit code [7, 14]. As permanent deformations are essential for the analysis of the reusability of the joint, the material model presented has utilised fracture mechanics with cohesive zone modelling (CZM) to model the brittle behaviour of timber. Using CZM has the disadvantage of requiring predefined fracture surfaces, but as these fracture planes are predictable for the *ReconWood* joint, the method fits well.

Two different modes can initiate a fracture in a Cohesive Zone Model: tensile stresses acting perpendicular to the fracture plane (mode I); and tangential stresses acting parallel to the fracture plane (mode II) [16]. In this study the fracture has been restricted to mode II as only this type of failure is expected in the fracture plane. Despite it being possible to define both failure modes, including mixed-mode fracture, it is undesirable unless necessary as CZM requires substantial computational time.

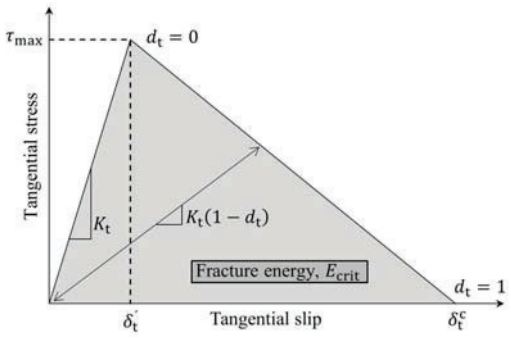

Figure 5: *Cohesive Zone Modelling, CZM, for mode II*

The progressive failure of a Cohesive Zone Model is expressed by a bilinear stress-slip law as shown in Figure 5. Damage is initiated at δ_t' ($d_t = 0$) and is completed at δ_t^c ($d_t = 1$) when the stress reaches zero value. Any further tangential slip occurs without any tangential stress.

https://doi.org/10.52202/069179-0171

3.3 MODELLING THE DUCTILE BEHAVIOUR

In the literature, the compressive behaviour of timber is often modelled as an anisotropic plastic behaviour using a single surface yield function, such as the *Hill Criterion* [10,17], the *Hoffman Criterion* [18], or the *Tsai-Wu Criterion* [19]. A popular alternative is to implement these yield functions as failure criteria within continuum damage mechanics (CDM) [8,9]. This enables the modelling of both strain hardening and softening by modifying the stiffness matrix. However, utilising CDM shows some drawbacks as mentioned in Section 3.2.

Both the Hoffman Criterion and the Tsai-Wu Criterion are modifications of the Hill Criterion introducing separate yield stresses for tension and compression. The Hoffmann Criterion obtains the capability of differentiating yield stresses in tension and compression by including terms that are linear on the stress. The Tsai-Wu Criterion extends this further by the addition of a parameter that accounts for interactions of normal stresses. [7,20] However, as each criterion expands in complexity, so does the application in commercial FE software. The *ReconWood joint* analysed in this paper is not expected to be subjected to noteworthy tensile stresses so applicability is prioritised and the Hill Criterion is utilised. The post-peak behaviour in compression is thus simplified to being ideally plastic, neglecting the direction-dependent hardening and softening.

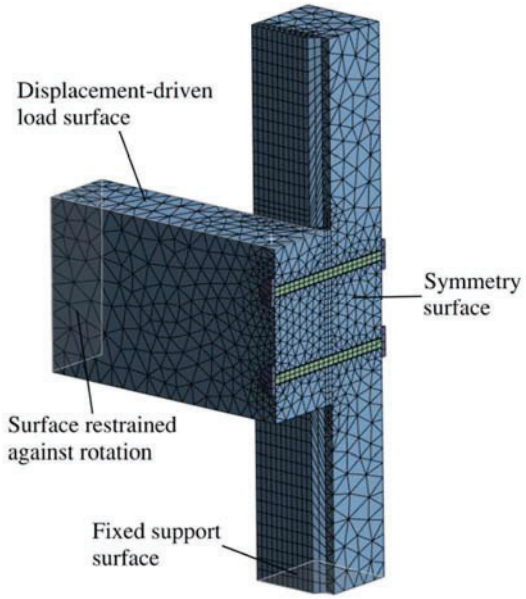

Figure 6: *FEM model with boundary conditions.*

4 FINITE ELEMENT MODEL

The aim of the FEM model is to predict the load-carrying capacity, stiffness, failure mechanism, and reusability of a *ReconWood joint*. The proposed material model is implemented in *Ansys Mechanical* for FEM analysis of the joint.

4.1 GEOMETRY

The joint in question connects two orthogonal timber blocks as used when constructing lattice structures such as that shown in Figure 2. The FEM model, Figure 6, comprises a horizontal timber block containing the male shear key part and a vertical timber block containing the female part. Dimensions of the horizontal block can be seen in Figure 7, while the vertical block is modelled as a perfect negative of the horizontal. The blocks are held together by M5 steel bolts.

4.2 BOUNDARY CONDITIONS, CONTACT DEFINITION, AND MESHING

The model is intended to represent a subpart of a larger lattice structure consisting of multiple *ReconWood joints.* When used in this manner the joints will solely transfer shear forces. Hence the FEM model is designed to investigate the joint in a state of pure shear. This is done by applying the boundary conditions shown in Figure 6.

Interaction between both the timber elements and the bolts and timber are defined by a frictional surface contact with a friction coefficient of 0.2.

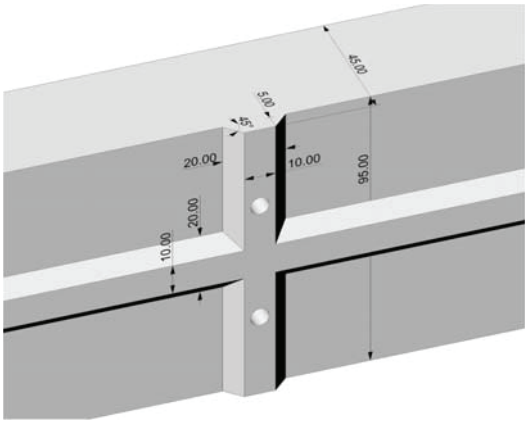

Figure 7: *Geometry of the shear key in the considered ReconWood joint*

The model is discretised with a combination of *tetrahedral* and *hex-dominant* meshes as seen in Figure 6. Generally, the parts are meshed with a size of 8 mm, while the contact surfaces are reduced to 4 mm with a fast transition. A mesh sensitivity study was carried out to balance accuracy and computing resources satisfactorily.

To decrease computational time, a vertical plane of symmetry is used.

https://doi.org/10.52202/069179-0171

Property	Reference	Mean value
Bending strength	Material testing	46.9 MPa
Bending modulus of elasticity, ∥	Material testing	16.3 GPa
Density	Material testing	431 kg m^{-3}
Compressive strength, ∥	[21]	29 MPa
Compressive strength, ⊥	[21]	3.0 MPa
Shear strength	[21]	6.3 MPa
Shear strength, rolling	[26]	1.2 MPa
Bending modulus of elasticity, ⊥	[21,22]	0.54 GPa
Shear modulus	[21,2]	1.0 GPa
Shear modulus, rolling	[28]	0.05 GPa
Poisson's ratio, LR	[8]	0.45
Poisson's ratio, LT	[8]	0.45
Poisson's ratio, RT	[8]	0.50
Tangential fracture energy	[29]	1200 J m^{-2}
Tangential fracture energy, rolling	[29]	600 J m^{-2}

Table 1: *Mechanical properties of C24 determined by material testing and literature. ⊥ denotes properties perpendicular to the fibre direction. ∥ denotes properties parallel to the fibre direction. L, R, and T denote longitudinal, radial, and tangential respectively.*

4.3 IMPLEMENTING THE MATERIAL MODEL

The material model is implemented by utilising the built-in material laws provided by Ansys' *Engineering Data.* This is done in two steps. (*i*) The timber blocks are assigned a material defined by *Hill Yield Criterion;* (*ii*) CZM is included by defining a fracture surface on the back of the shear key as seen in Figure 8. This surface is assigned a *Fracture Energy Debonding* material for mode II debonding.

This two-step implementation enables a distinguishment between two possible failure modes and gives the option to evaluate the level of damage to the joint by analysing both the plastic strains from compression and the damage evolution on the CZM surface from shear.

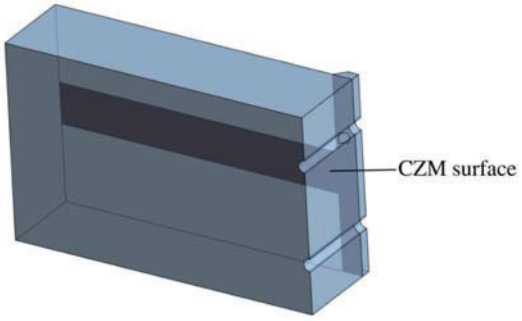

Figure 8: *Predefined fracture surface in FEM model*

4.4 MATERIAL PROPERTIES

The material properties of the timber blocks are based on the verification experiments presented in Section 5. Where applicable, the material properties are determined based on the procedure outlined in EN 384 [21] and JCSS Probabilistic Model Code Part 3 [22], while the remaining properties are based on values found in the literature. The bending strength, the bending modulus of elasticity, and the density are determined experimentally in accordance with EN 408 [23], whereupon these three properties are used to estimate the majority of the remaining properties.

The material properties used in the FEM model are given in Table 1 along with a reference to how the properties were determined. For properties determined using EN384 [21], mean reference properties are used as input in the formulas given in the standard. This is in accordance with the procedure presented in [7]. Using this method also proves to yield reasonable results by comparison with experimental data found in literature e.g. [24].

Neither EN 384 [21] nor JCSS Probabilistic Model Code Part 3 [22] give an estimate of the rolling shear strength, rolling shear modulus or Poisson's ratios. The rolling shear strength is highly discussed in the literature [7,25,26]. EN1995 [26] specifies the rolling shear strength to be approximately twice the tensile strength perpendicular to the fibre direction. This yields a mean strength of 1.2 MPa. This lies well inside the range of values that is normally suggested in other literature, therefore this value is used. Most literature suggests a rolling shear modulus of 50 MPa [7]. Hence, this is the value adopted for this model. The Poisson's ratios are often set in the range of 0.3-0.5 [7,8,27]. Values of $\nu_{LR} = 0.45$, $\nu_{LT} = 0.45$ $\nu_{RT} = 0.50$ are used in this analysis, as suggested in [8].

The bolts are assigned an isotropic linear-elastic material with Young's modulus = 210 GPa and Poisson's ratio = 0.3.

5 EXPERIMENTS

In order to verify the FEM model presented in Section 4, a test series with the same *ReconWood joint* was conducted. The test series consisted of three identical joints with the same material properties and geometry as implemented in the FEM model.

5.1 PRODUCTION OF THE TEST SPECIMENS

The specimens were fabricated using a KUKA KR240 R3330 industrial robot arm equipped with a 12 kW rotary spindle. The employed robot arm has an additional "absolute accuracy" feature, which assures precise

https://doi.org/10.52202/069179-0171

dimensions and geometry of the milled specimen, and therefore a desired tight fit of the male and female parts of the joints.

Three milling tools were exchanged during the fabrication process to produce the cross-shaped joints, utilising automatic tool change. Firstly, the 6 mm holes were drilled, generating some extra space around the M5 bolts. This was desired both for facilitating the automated robotic assembly process as well as for the performance of the joints. Secondly, a V-shaped tool with a 45° inclination blade was used to achieve the inclined sides of the cross geometry in a single cut, and finally, a flat end mill was to clear out the left material and even out all the horizontal sides of the joint.

5.2 TEST SETUP

The experiments were performed with a Zwick/Roell Z050 testing machine, applying a deformation-controlled load at 1.2 mm/min.

The test setup is shown in Figures 9 and 10. To obtain shear in an orthogonal joint, three timber elements were used. The vertical element of the joint was installed in a specially designed steel shoe and connected to the horizontal element by the *Reconwood joint* with M5 bolts. A vertical load-transferring element was likewise installed in a steel shoe and placed on top of the horizontal element. To ensure that the tests were performed in pure shear the load was applied on two knobs located directly in the joint's shear plane.

To eliminate the effects of bending and torsional moments in the joint, two bolts were used instead of one and the horizontal element was restrained against rotation by using two nail plates.

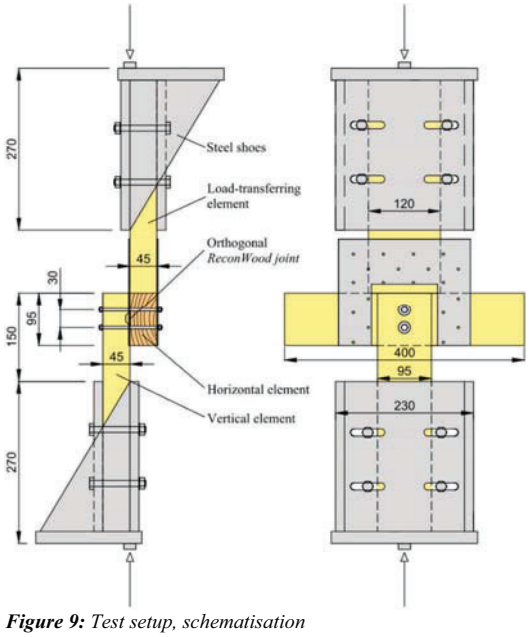

Figure 9: *Test setup, schematisation*

Figure 10: *Test setup, photo*

6 RESULTS AND COMPARISON

The FEM model is evaluated by comparison with the experimental findings, namely by: (*i*) the observed failure mechanism and (*ii*) the force-displacement response.

Additionally, the FEM model presents the option to analyse the reusability. As no evaluation of the reusability was done in the experiments, no comparison can be made. However, an assessment of the joint's reusability is made based on the FEM model and previous studies of the *Reconwood joint*.

6.1 FAILURE MECHANISM

Despite the similarity of the test specimens, two failure mechanisms are observed. The failure mechanisms are *FM1* - local compressive failure; *FM2* - shear cut-off. FM1 corresponds to a situation where the compressive strength is insufficient to carry the load without introducing irreversible deformations. FM2 corresponds to a situation where the shear strength of the keys is insufficient to carry the load, and thus the shear keys are (partly) cut off.

In the FEM model, the failure mechanism is evaluated based on the damage level at the fracture surface. FM1 is defined as the situation where the damage coefficient, d_t, has reached a value of 1 acc. Figure 5. All other situations are interpreted as FM2.

https://doi.org/10.52202/069179-0171

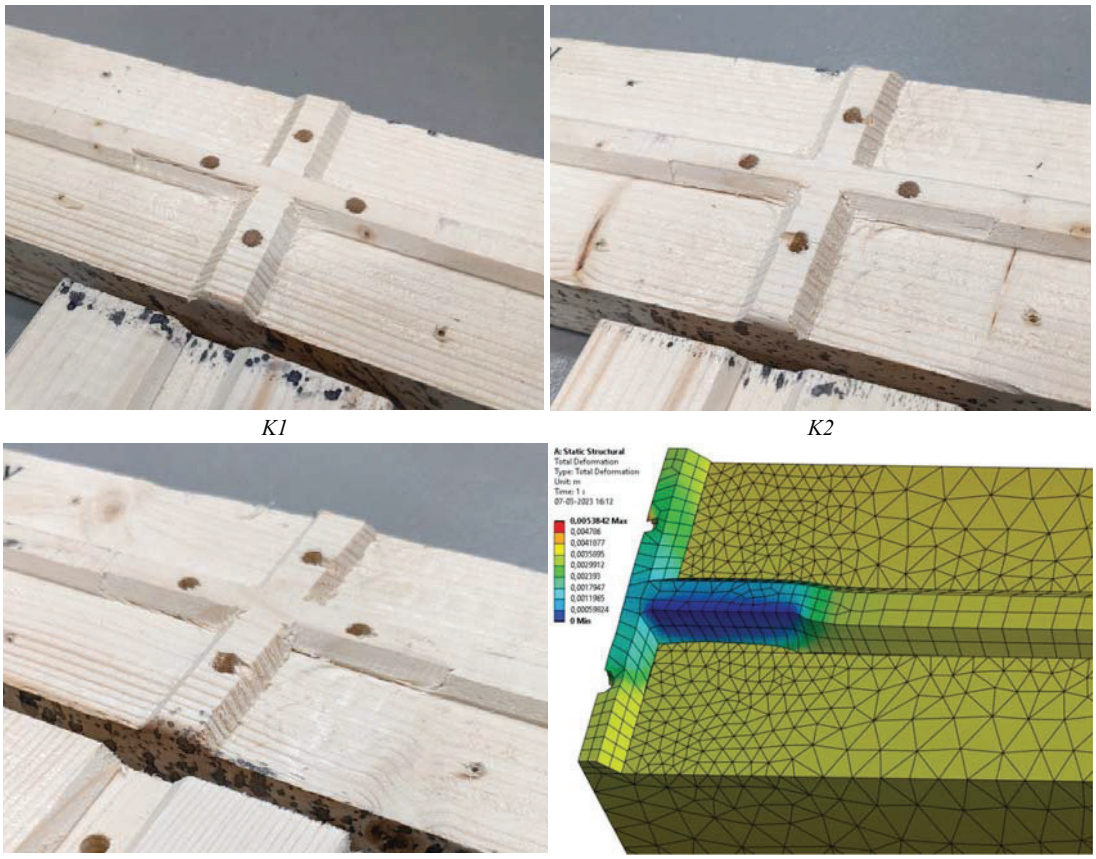

Figure 11: *Failure mechanisms found in the experimental testing and FE analysis*

For the tests, the failure mechanisms are evaluated qualitatively by visual inspection. The failure is classified as FM2 when apparent failure cracks are visible.

The observed failure mechanisms for both the FEM model and the experiments are listed in Table 2 and shown in Figure 11.

Test	FEM model	Experiments
K1		FM1/FM2
K2	FM2	FM2
K3		FM2

Table 2: *Failure mechanisms in FEM model and experiments*

6.2 FORCE-DISPLACEMENT RESPONSE

The force-displacement response curves of the numerical analysis along with the results from the experiments are shown in Figure 12. In this comparison, the weight of the test setup is included in the response of the experiments, which results in an initial load at $d = 0$ mm.

It is seen that the FEM model shows great accuracy in predicting the response of the *ReconWood joint*.

The force-displacement response curves in Figure 12 show that this type of timber joint displays a large degree of nonlinear behaviour when subjected to shear. This corresponds well with the findings in [2] which analysed an earlier generation of the *ReconWood joint*.

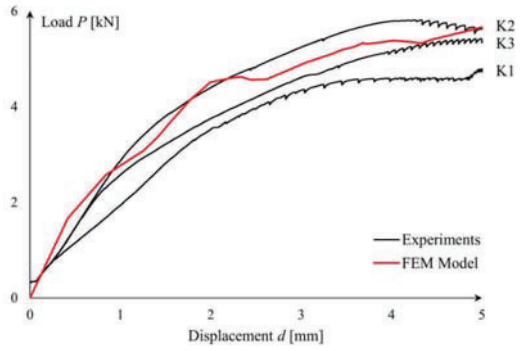

Figure 12: *Force-displacement response curves for the FEM model and the experiments*

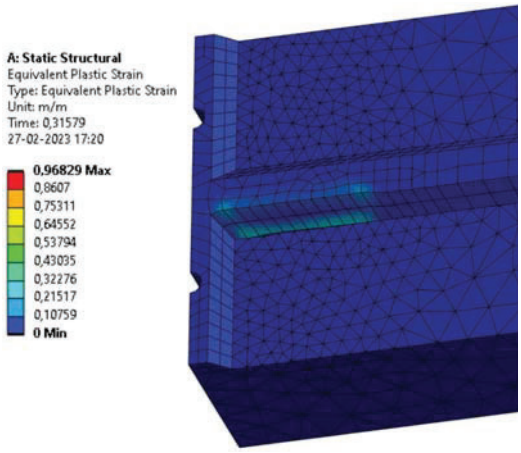

Figure 13: *Plastic strains at 3.4 kN load*

6.3 REUSABILITY

The FEM model presents the option to analyse the reusability in two ways: by permanent deformations of the timber material due to compression and by damage initiation and evolution of the CZM material due to shear.

A qualitative assessment of the reusability of the joint is presented. In Figure 13, the maximum plastic strains at 3.1 kN load are shown as the point of acceptable permanent deformations. Figure 14 shows the damage evolution of the CZM material at 4.4 kN and 5.0 kN, respectively showing the brittle failure from shear. It is seen that approximately no damage is seen at 4.4 kN before a fast escalation of damage. The threshold for reusability of the joint is set at 3.1 kN.

In earlier studies of the first generation of the *ReconWood joint,* a recommendation of 50%-60% of the ultimate capacity was proposed as a threshold for reusability [30]. By studying the FEM model it is found that this threshold gives a good indication of the reusability. The average ultimate capacity of the experiments was found to be 5.48 kN, setting the threshold for reusability at 57%.

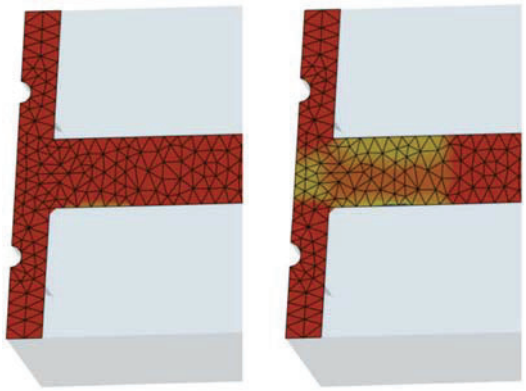

Figure 14: *Damage evolution on CZM material at (i) 4.4 kN and (ii) 5.0 kN load. Damage under* $d_t = 1$ *is marked in red; damage at* $d_t = 1$ *is marked in orange and yellow*

7 CONCLUSIONS

The present paper outlines a method for performing structural analysis of a complex timber joint using FEM along with an experimental verification. Focus has been given to developing a reliable model that can predict the mechanical response while being easily implementable in widely available FE software. This is achieved through a hybrid material model which combines two methods for capturing the complex anisotropy of timber. The ductile behaviour seen in compression is modelled as a single yield surface using the Hill Criterion, and the brittle behaviour from shear by fracture mechanics is modelled with Cohesive Zone Modelling (CZM).

The FEM model is able to predict the failure mechanism observed in the experiments satisfactorily, capturing the failure of the shear keys seen in experiments. Moreover, the model depicts the force-displacement response highly satisfactorily, capturing the stiffness degradation and nonlinear behaviour seen in experiments. The proposed model is highly implementable in conventional FEM software, which sets it apart from more advanced methods, making it accessible and useful for practical engineering applications. The simplicity in the material modelling ensures furthermore a low computational time which facilitates the modelling approach can be upscaled to an analysis of a larger structure with multiple joints.

The present study has been limited to one specific joint, and further experimental and analytical studies are necessary to investigate the applicability and validity of the proposed method to different joint configurations. Additionally, the reusability of the joints was not assessed during the tests; thus, a more comprehensive experimental program is required to expand the scope of the study and investigate the threshold for reusability of the proposed model.

REFERENCES

[1] Ibañez D, Hutton J, Moe K: Wood Urbanism. From the Molecular to the Territorial. Actar Publishers, 2019.

[2] Hansen S, Kunic A, Naboni R: A reversible connection for robotic assembly of timber structures. *Eng Struct 245:*0141-0296, 2021.

[3] Kunic A, Naboni R, Cognoli R: Re:Thinking Timber Architecture. Enhancing Design and Construction Circularity through Material Digital Twin. UIA World Congress of Architects in Copenhagen 2023, 2022.

[4] Kunic A and Naboni R: Collaborative design and construction of reconfigurable wood structures in a Mixed Reality environment. *Proceedings of the SIGraDi 2022 - Critical Appropriations. XXVI International Conference of the Ibero-American Society of Digital Graphics*. Lima, Peru, 2022.

[5] Kunic A, Kramberger A, Naboni R: Cyber-Physical Robotic Process for Re-Configurable Wood

https://doi.org/10.52202/069179-0171

Architecture Closing the circular loop in wood architecture. *Proceedings of the 39th eCAADe Conference - Towards a new, configurable architecture.* Novi Sad, Serbia, 2022.
[6] Borgström E.: Design of timber structures – Structural aspects of timber construction. Volume 1, Edition 2. Swedish Wood; 2016.
[7] Sandhaas, C.: Mechanical behaviour of timber joints with slotted-in steel plates. Dissertation, Universität Karlsruhe, 2012
[8] Eslami H, Jayasinghe L, Waldmann D: Nonlinear three-dimensional anisotropic material model for failure analysis of timber. *Eng Fail Anal 130, 2021*
[9] Sandhaas, C., & Van de Kuilen, J. W. G.: Material model for wood. *Heron*, *58*(2–3), 171-91, 2013.
[10] Gečys, T., Daniūnas, A., Bader, T. K., Wagner, L., & Eberhardsteiner, J.: 3D finite element analysis and experimental investigations of a new type of timber beam-to-beam connection. *Engineering structures*, *86*, 134-145, 2015.
[11] Danielsson, H., & Gustafsson, P. J.: Fracture analysis of perpendicular to grain loaded dowel-type connections using a 3D cohesive zone model. *Wood Material Science & Engineering*, *11*(5), 261-273, 2016.
[12] Franke, B., Franke, S., & Quenneville, P.: Numerical Modelling and Analysis of the Failure Behaviour of Dowel-Type Connections in Wood. In *European Congress Computational Methods in Applied Sciences Enginering (ECCOMAS 2012). Eberhardstenier. J. Vienna, Austria*, 2012.
[13] Xu, B. H., Bouchaïr, A., & Racher, P.. Appropriate wood constitutive law for simulation of nonlinear behavior of timber joints. *Journal of materials in civil engineering*, *26*(6), 04014004, 2014.
[14] Gharib, M., Hassanieh, A., Valipour, H., & Bradford, M. A.: Three-dimensional constitutive modelling of arbitrarily orientated timber based on continuum damage mechanics. *Finite Elements in Analysis and Design*, *135*, 79-90, 2017.
[15] Wittel, F. K., Dill-Langer, G., & Kröplin, B. H.: Modeling of damage evolution in soft-wood perpendicular to grain by means of a discrete element approach. *Computational Materials Science*, *32*(3-4), 594-603, 2005.
[16] Conrad, M. P., Smith, G. D., & Fernlund, G.: Fracture of solid wood: A review of structure and properties at different length scales. *Wood and fiber science*, 570-584, 2003.
[17] Oudjene, M., & Khelifa, M.: Elasto-plastic constitutive law for wood behaviour under compressive loadings. *Construction and Building Materials*, *23*(11), 3359-3366, 2009.
[18] Xu, B. H., Taazount, M., Bouchaïr, A., & Racher, P.: Numerical 3D finite element modelling and experimental tests for dowel-type timber joints. *Construction and Building Materials*, *23*(9), 3043-3052, 2009.
[19] Lee, H.: Damage modelling for composite structures. Dissertation, University of Manchester, 2015.
[20] Schellekens, J. C. J., & De Borst, R.: The use of the Hoffman yield criterion in finite element analysis of anisotropic composites. *Computers & Structures*, *37*(6), 1087-1096, 1990.
[21] CEN European Committee for Standardization: EN 384 Structural Timber - Determination of characteristic values of mechanical properties and density, 2018.
[22] Joint Committee on Structural Safety: JCSS PROBABILISTIC MODEL CODE Part III. 2006.
[23] CEN European Committee for Standardization: EN 408 - Timber structures - Structural timber and glued laminated timber - Determination of some physical and mechanical properties, 2012.
[24] Brandner, R., Gatternig, W., & Schickhofer, G.: Determination of shear strength of structural and glued laminated timber. In *Proc. of the CIB-W18 Meeting* (Vol. 45), 2012.
[25] CEN European Committee for Standardization: EN 16351 - Timber structures - Cross laminated timber - requirements, 2021.
[26] CEN European Committee for Standardization: Eurocode 5: Design of timber structures -Part 1-1: General - Common rules and rules for buildings, 2007.
[27] Sjödin, J., Serrano, E., & Enquist, B.: An experimental and numerical study of the effect of friction in single dowel joints. *European Journal of Wood and Wood Products*, *66*(5), 363-372, 2008.
[28] Sandhaas C, Sarnaghi, A.K. & van de Kuilen, JW. Numerical modelling of timber and timber joints: computational aspects. *Wood Sci Technol* 54, 2020.
[29] Franke, S., Franke, B., Schober, K., Rautenstrauch, K.: The strength behavior of wood in experiment and simulations, 2008.
[30] Kristensen, M. H., Sørensen, M. H.: Shear model and structural integration of a shear-resistant timber connection for reversible robotic assembly. MA thesis, University of Southern Denmark, 2021.

World Conference on Timber Engineering Oslo 2023

NUMERICAL AND EXPERIMENTAL STUDY OF GLULAM BEAMS JOINTED WITH SLOTTED-IN STEEL PLATE CONNECTION

Sigurdur Ormarsson[1], Le Kuai[2], Musaab Ahmed Mahjoub[3], Simon Aicher[4]

ABSTRACT: The present work focuses on analysis of deformation and strength behaviour of slotted-in steel plate connections in glued laminated timber (GLT). In Eurocode 5 (EC5), the design of metal dowel-type timber joints is based on the yield theory presented by Johansen [1]. It consists of analytical expressions to calculate the lateral load-carrying capacity of single fastener joints that exhibit different (plastic) failure modes. When designing optimised multiple fastener connections that are exposed to dominating moment action, the calculation of fastener forces and their directions during progressive plasticization of the dowel group is difficult to perform manually. Therefore, a simple numerical model to simulate progressive elasto-plastic force development for every individual dowel is needed. This study presents new and simple models to analyse the bending deformations of glulam beams jointed with mechanical slotted-in steel plate connections. The proposed models were experimentally verified using results obtained from a joint project with the Material Testing Institute (MPA) at University of Stuttgart.

KEYWORDS: Jointed timber beams, steel-to-timber joints, failure modes, FE-modelling, experiments

1 INTRODUCTION

This investigation arises from the increased usage of large timber trusses jointed with slotted-in steel plate connections in bridges, long-span roofs, and high-rise buildings. For these types of structures, deformation and strength behaviour of the connections are often critical elements in the design, especially if exposed to significant in-plane moment action during varying environmental conditions. The load-carrying capacity calculations of single and double shear joints, according to EC5, are based on the Johansen theory in [1]. According to this theory the joints fail in several plastic failure modes depending on the thickness of the wood members. The shear load carrying capacity for these failure modes differs significantly in size, depending on various parameters such as wood thickness, embedding strengths, dowel diameter and yield moment of the dowel. The embedding strengths are also highly influenced by the angles between the fastener forces and fibre directions of the wood members. In design of multi-dowel connections exposed to significant moment action, a typical hand calculation of the fastener forces and their directions is too simple since the slip modulus does not consider the angle between the fastener force and the fibre direction. To study how fastener forces and their directions vary during progressive plasticization in different dowel groups, simple finite element models need to be developed. Some 3D numerical models to simulate the mechanical behaviour of multiple fastener connections have been published in recent decades, see e.g. [2–5]. These models allow for detailed analyses of the connections in terms of local slip deformations, dowel force distributions and timber failures. They are good for understanding and they can obtain results that are impossible to obtain from experiments. For example, they can show the difference in dowel force size and directions compared to the simple analytical approach used in EC5. As for disadvantage, these models are computationally costly and sometimes numerically unstable. However, the detailed results provided help us to limit the number of expensive experiments and develop more optimized and simpler analytical or numerical models. Some researchers have developed more efficient models to tackle the drawbacks of using 3D models. In [6], a two-dimensional finite element model was developed to simulate multi-dowel timber-to-timber moment-resisting connections. The timber was modelled as an elastic orthotropic material and each fastener was modelled with two nonlinear springs. A semi-analytical model based on kinematic compatibility and equilibrium considerations was presented in [7]. The disadvantage of this model is that it neglects the elastic timber deformations between the dowels. The beam on foundation modelling approach to calculate the slip displacements and load carrying capacity of the connection using nonlinear springs to simulate the embedment behaviour was also used in [8].

This study is based on the master thesis work presented in [9], where three simplified FE-models using structural elements were created to study the bending behaviour of jointed glulam beams using mechanical slotted-in steel plates. To verify the models, extensive experimental tests were performed at MPA, University of Stuttgart. The aim

[1] Sigurdur Ormarsson, Linnaeus University, Sweden, sigurdur.ormarsson@lnu.se
[2] Le Kuai, Linnaeus University, Sweden, le.kuai@lnu.se
[3] Musaab Ahmed Mahjoub, University of Navarra, Spain, mahmedmahjo@unav.es
[4] Simon Aicher, MPA University of Stuttgart, Germany, Simon.Aicher@mpa.uni-stuttgart.de

https://doi.org/10.52202/069179-0172

of this work was to develop effective and flexible engineering models useful when designing jointed glulam beams.

2 MODELLING

To study the slotted-in steel plate connection behaviour in the studied glulam beams, three different finite element models were created. The first was a parameterized single-dowel model for double shear joints; the second was a simple beam model to simulate the global bending deformations and (ideal plastic) load carrying capacity of glulam beams jointed with a slotted-in steel plate. The connection was modelled with two nonlinear connector elements for each dowel group. The final model was a combined beam-shell model of the same glulam member using a few connector elements to simulate each dowel in the dowel groups. This work focuses on developing simple and efficient models by using effective structural elements (beams, shells, and spring-based connector elements) to simulate both global bending deformations and local dowel force distributions in glulam members jointed with slotted-in steel plate connections.

2.1 MODELING OF SINGLE DOWEL JOINTS

For single dowel (slotted-in steel plate) joints loaded to failure, EC5 shows three (plastic) failure modes for different thickness ranges. In Figure 1, these failure modes together with curves (based on Eq. 1) illustrate how the shear load carrying capacity of the joint varies with increasing wood thickness. According to EC5 the shear load carrying capacity of the (slotted-in steel plate) joint is the minimum value obtained from the three following expressions in Eq. (1), where t is the thickness

$$\begin{bmatrix} F_{v,\alpha,Rk,I} \\ F_{v,\alpha,Rk,II} \\ F_{v,\alpha,Rk,III} \end{bmatrix} = \begin{bmatrix} f_{h,\alpha,k} t d \\ f_{h,\alpha,k} d \left[\sqrt{(t+2e)^2 + t^2 + \frac{4M_{y,Rk}}{f_{h,\alpha,k} d}} - (t+2e) \right] \\ f_{h,\alpha,k} d \left[\sqrt{e^2 + \frac{4M_{y,Rk}}{f_{h,\alpha,k} d}} - e \right] \end{bmatrix} \quad (1)$$

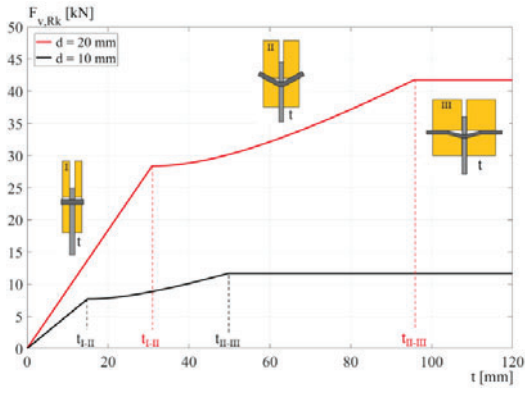

Figure 1: *Three failure modes for single dowel slotted-in steel plate joints together with two curves showing how the shear load carrying capacity varies with increasing wood thickness when* $\rho_k = 350\ [\frac{kg}{m^3}]$, $f_{u,k} = 400\ [MPa]$ *and* $\alpha = 0$.

of the wood members and d is the diameter of the dowel. The characteristic embedding strength of the wood material in the dowel force direction $f_{h,\alpha,k}$ and the characteristic yield moment of the steel fastener $M_{y,Rk}$ are given by

$$M_{y,Rk} = 0.3 f_{u,k} d^{2.6} \quad (2)$$

$$f_{h,\alpha,k} = \frac{0.082(1 - 0.01d)\rho_k}{k_{90} sin^2\alpha + cos^2\alpha} \quad (3)$$

$$k_{90} = 1.35 + 0.015d \quad (4)$$

where the characteristic wood density is ρ_k, the characteristic tensile strength of the steel material is $f_{u,k}$ and the angel between the fibre direction and the dowel force direction is α. The two limit-thicknesses t_{I-II}, and t_{II-III} shown in Figure 1 are given by

$$\begin{bmatrix} t_{I-II} \\ t_{II-III} \end{bmatrix} = \begin{bmatrix} \sqrt{e^2 + \frac{2M_{y,Rk}}{f_{h,\alpha,k} d}} - e \\ \sqrt{\frac{4M_{y,Rk}}{f_{h,\alpha,k} d}} + \sqrt{e^2 + \frac{4M_{y,Rk}}{f_{h,\alpha,k} d}} - e \end{bmatrix} \quad (5)$$

Failure mode *I* is a pure compressional failure of the wood material caused by a constant plastic embedment deformation over the cross-sectional thickness. This failure mode arises for small wood thicknesses ($t < t_{I-II}$), where the maximum moment in the dowel does not reach the yield moment of the dowel. Failure mode *II* is a mixed steel/wood failure caused by varying embedment deformation over the wood thickness. It occurs for larger wood thicknesses ($t_{I-II} \leq t < t_{II-III}$), when a yield hinge in the shear plane has developed together with plastic compressional failure of the wood material caused by combined translational and rotational embedment deformations. Failure mode *III* is also a mixed steel/wood failure caused by varying embedment deformation over a part of the wood thickness. This occurs for large thickness

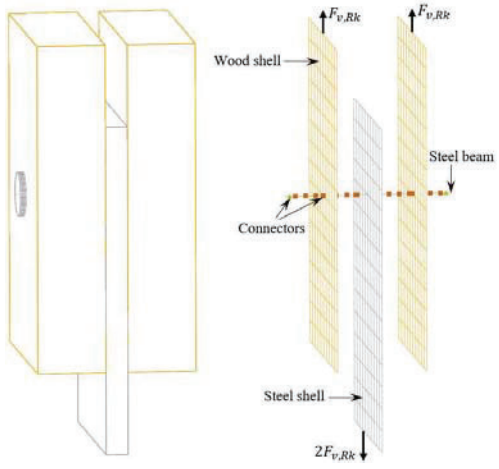

Figure 2: *Illustration of the beam and shell elements used to simulate the single dowel double shear joint.*

values ($t_{II-III} \leq t$), where the plastic clamping moment of the wood member is equal or larger than the yield moment of the dowel. Note that the expressions in Eq. (1) have no criterion concerning maximum embedment deformation related to the risk of crack initiation. The challenge here is to develop an effective FE-model (in a 3D-space) that can simulate both the different failure modes and realistic (slip-driven) elastic and plastic embedment deformations. To achieve model efficiency, the wood members and steel plate were modelled with shell elements and the fastener with beam elements; see Figure 2. Special nonlinear connector elements were also used to connect the different joint members. Both translational and rotational springs were used to model the constantly respective linearly varying elastic and plastic embedment deformations over the wood thickness. This allows us to simulate both the generation of yield hinges in the steel dowel (beam elements) and plastic embedding failure in the wood material (connector elements). The static dowel models for the three different failure modes are shown in Figure 3. The two yellow springs (translational and rotational) in Figure 3 show the two wood-to-dowel connectors used to simulate the embedment deformation of the wood. The yellow strokes parallel to the dowels represent the mechanical contacts

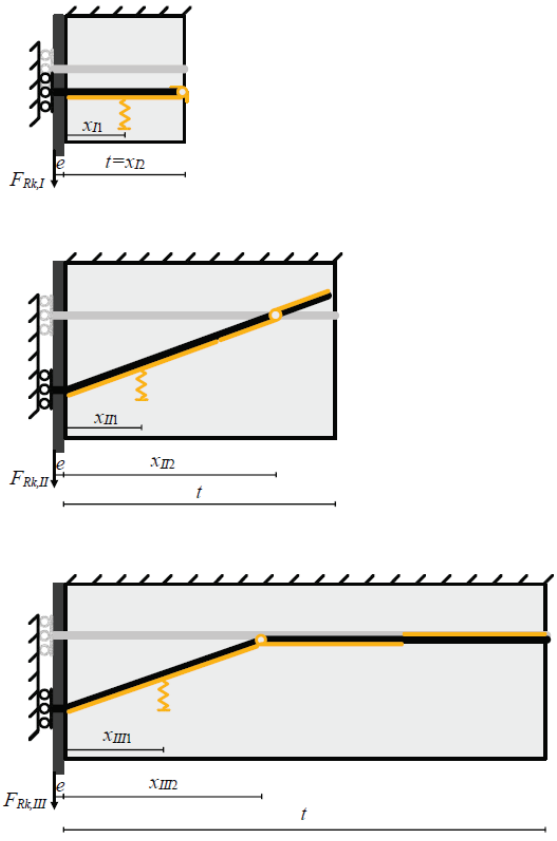

Figure 3: *Static beam-connector models used for the dowels at failure (i.e., failure modes I, II and III).*

between the wood and the dowels. Therefore, the three translational springs represent springs distributed along the lengths ($2x_{I1}$, $2x_{II1}$ and $2x_{III1}$). The translational and rotational spring stiffnesses ($k_{Iu}, k_{IIu}, k_{IIIu}$) and ($k_{I\theta}$, $k_{II\theta}$, $k_{III\theta}$) as well as the yield force ($P_{Iy,w}, P_{IIy,w}$, $P_{IIIy,w}$) and clamping moments ($M_{Iy,w}$, $M_{IIy,w}$, $M_{IIIy,w}$) for the different failure modes are calculated as

$$\begin{bmatrix} k_{Iu} \\ k_{I\theta} \\ k_{IIu} \\ k_{II\theta} \\ k_{IIIu} \\ k_{III\theta} \end{bmatrix} = \begin{bmatrix} \frac{E_{\alpha,k} x_{I1} d}{l_{\alpha,t,I}} \\ 0 \\ \frac{2E_{\alpha,k} x_{II1} d}{l_{\alpha,t,II}} \\ \frac{2E_{\alpha,k} x_{II1} d}{l_{\alpha,t,II}} (t - x_{II2})^2 \\ \frac{2E_{\alpha,k} x_{III1} d}{l_{\alpha,t,III}} \\ \frac{2E_{\alpha,k} x_{III1} d}{l_{\alpha,t,III}} \left(\frac{3(t - x_{III2})}{4}\right)^2 \end{bmatrix} \tag{6}$$

$$\begin{bmatrix} P_{Iy,w} \\ M_{Iy,w} \\ P_{IIy,w} \\ M_{IIy,w} \\ P_{IIIy,w} \\ M_{IIIy,w} \end{bmatrix} = \begin{bmatrix} 2f_{h,\alpha,k} d x_{I1} \\ 0 \\ 2f_{h,\alpha,k} d x_{II1} \\ f_{h,\alpha,k} d (t - x_{II2})^2 \\ 2f_{h,\alpha,k} d x_{III1} \\ f_{h,\alpha,k} d \left(\frac{(t - x_{III2})}{2}\right)^2 \end{bmatrix} \tag{7}$$

where $E_{\alpha,k}$ is the effective modulus of elasticity in the dowel force direction and ($l_{\alpha,t,I}$, $l_{\alpha,t,II}$, $l_{\alpha,t,III}$) are the effective lengths for the embedment deformations in the dowel force direction. Finally, the lengths shown in Figure 3 are defined as

$$\begin{bmatrix} x_{I1} \\ x_{I2} \\ x_{II1} \\ x_{II2} \\ x_{III1} \\ x_{III2} \end{bmatrix} = \begin{bmatrix} \frac{1}{2}t \\ t \\ \frac{\sqrt{(t+2e)^2 + t^2 + \frac{4M_{yRk}}{f_{h,\alpha,k} d}} - t - 2e}{2} \\ \frac{1}{2}\sqrt{(t+2e)^2 + t^2 + \frac{4M_{yRk}}{f_{h,\alpha,k} d}} - e \\ \frac{1}{2}\left(\sqrt{e^2 + \frac{4M_{yRk}}{f_{h,\alpha,k} d}} - e\right) \\ \sqrt{e^2 + \frac{4M_{yRk}}{f_{h,\alpha,k} d}} - e \end{bmatrix} \tag{8}$$

2.2 A BEAM MODEL USING TWO CONNECTORS FOR EACH DOWEL GROUP

Deflection of mechanically jointed timber beams is difficult to calculate manually, especially if the beams are unsymmetric and the connections are exposed to both

https://doi.org/10.52202/069179-0172

shear and moment action. To simulate bending of a jointed glulam with a slotted-in steel plate connection, a simple beam model in a 3D-space was created. To reduce the model size, the mechanical connections between the steel plate and wooden members were modelled with two nonlinear connector elements for each dowel group. The model geometry and locations of beams, connectors and coupling constraints for cross sections are shown in Figure 4.

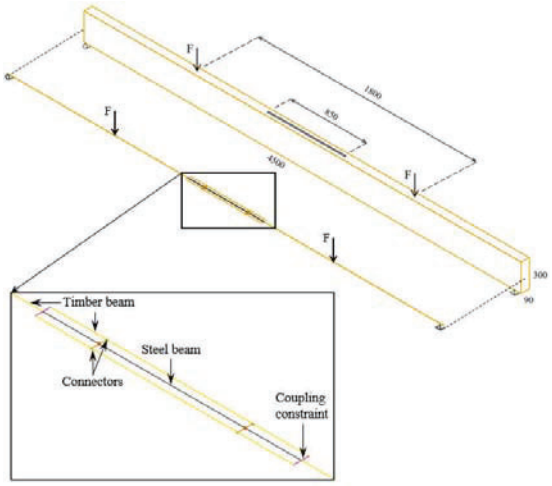

Figure 4: *A beam model of the jointed glulam which also visualizes a 3D-sketch of the beam and a close-up picture showing the most important elements in the connection part.*

Figure 4 shows how beam elements are used for the wooden members and the steel plate. To ensure that each half of the glulam will work as a single member, the two wood beams beside the steel plate are coupled (with a kinematic constraint) to the end-beams. For each shear plane between the steel plate and the wood members the joint behaviour of each dowel group was modelled with only one nonlinear connector. The connectors are placed in the centre of gravity of the dowel group and consist of three uncoupled springs to model the relative in-plane slip deformations caused by normal, shear and moment action in the joint. The stiffness values of the springs are calculated according to Eq. (9), where $E_{m,0}$, $E_{m,90}$ and $E_{m,\alpha i}$ are the mean modulus of elasticity for varying dowel force directions, l_0, l_{90} and $l_{\alpha i}$ are effective lengths for the local embedding deformation, r_i is the radii from the centre of gravity of the dowel group to the different dowels and n is number of dowels in each dowel group. To model the (ideal plastic) dowel group failure at the ultimate load, a failure moment for the rotational spring

$$\begin{bmatrix} k_N \\ k_V \\ k_M \end{bmatrix} = \begin{bmatrix} n\dfrac{E_{m,0}td}{l_0} \\ n\dfrac{E_{m,90}td}{l_{90}} \\ td\displaystyle\sum_{i=1}^{n}\dfrac{E_{m,\alpha i}}{l_{\alpha i}}r_i^2 \end{bmatrix} \quad (9)$$

was defined based on the experimental results in [10], briefly described in Section 3. This model is parametrized, i.e., it can easily be used to study how different joint configurations will influence the bending deformations of the mechanically jointed glulam beams.

2.3 A BEAM-SHELL MODEL USING A FEW CONNECTORS FOR EACH DOWEL

To simulate global bending deformations, failure modes and progressive development of the elasto-plastic force distributions in all dowels, a combined beam-shell model was created, see Figure 5.

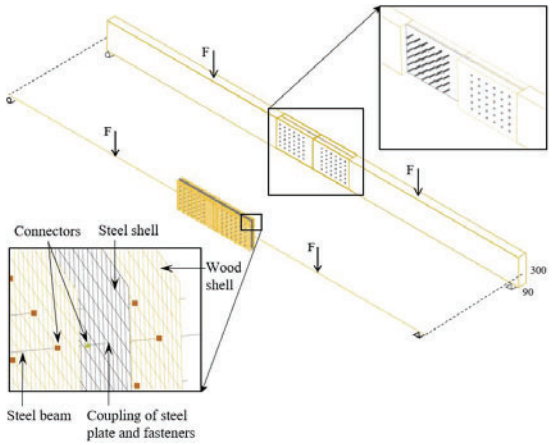

Figure 5: *A beam-shell model of the jointed glulam which also visualises a 3D-sketch of the beam and two close-up pictures showing a dowel group and the most important elements in the connection part.*

For the connection part, the wooden side members and the steel plate are modelled with shell elements, while all the steel dowels are modelled with small beam elements. The two wood shells are coupled (with kinematic constraints) to the beam elements used to model the remaining part of the glulam. The beams for the steel dowels are used as fastener elements between the steel plate and the wooden side members. Interaction between these beams and the steel and wood shells are modelled with nonlinear connector elements. Both elastic and plastic properties of the connectors are defined as for the single joint model.

3 EXPERIMENTAL STUDY

To verify the numerical model, several full-sized glulam beams with a mid-span slotted-in steel plate connection were tested in four-point bending until failure. The tests were performed at an ambient climate, with a temperature range of 20-25 °C. In total, six beams with cross-sectional dimensions of 90x300 mm were tested. Each specimen was constructed of eight stress graded wood lamellae from Norway spruce. The beams were divided into two groups, A with 10 mm dowels and B with 20 mm dowels. Beam assembly resulted in three density classes (DL, DM and DH) for each group. The average moduli of elasticity were 14.3, 15.1 and 15.7 GPa for group A and 14.2, 15.1

https://doi.org/10.52202/069179-0172

and 16.1 GPa for group B. The beams were cut into two equal parts and then re-jointed with a mechanical slotted-in steel plate connection, as shown in Figure 6.

Figure 6: *Glulam beams jointed with mechanical slotted-in steel plate connections.*

The dowel length was 100 mm, and the total number of dowels were 72 for group A and 24 for group B; see the detailed drawings of the connections in Figure 7. The dowel groups are quite different, but the rotational stiffness of group A is only 22% larger than of group B. Throughout the entire experiment, the force-displacement relationship was measured for the maximum mid-span deflection. Figure 8 shows this relationship for all the tested beams. The test results show almost similar linear relationships all the way up to the first crack initiation, when the force significantly drops followed by a jagged curve that on average is quite horizontal under a certain increase of the deflection.

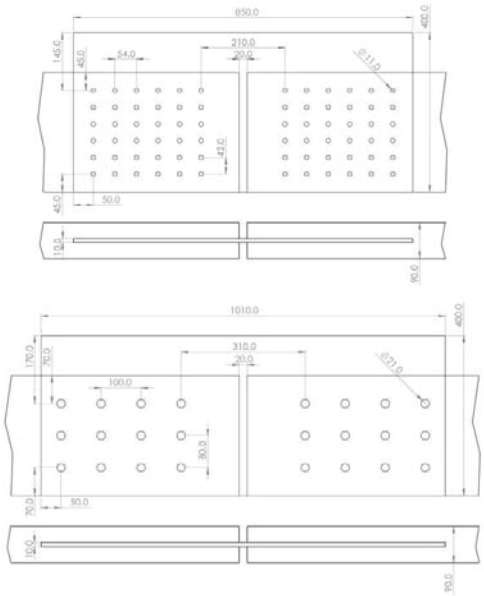

Figure 7: *Connection drawings showing the most important geometrical measures for dowel groups A and B.*

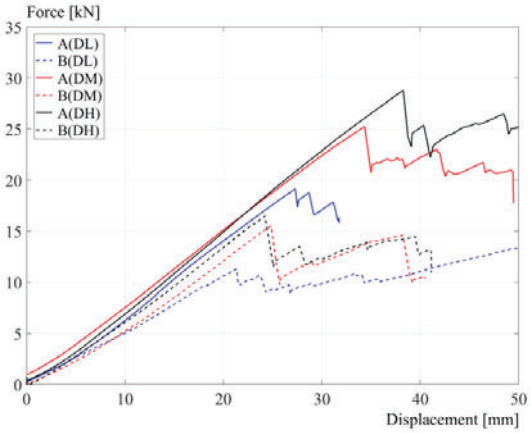

Figure 8: *Experimentally obtained force-displacement relationship for all the beams studied.*

Most of the connection failures show cracks that propagated between the bottom dowels and occasionally between the top dowels. Figure 9 shows two pictures of typical failure appearances for dowel groups A and B.

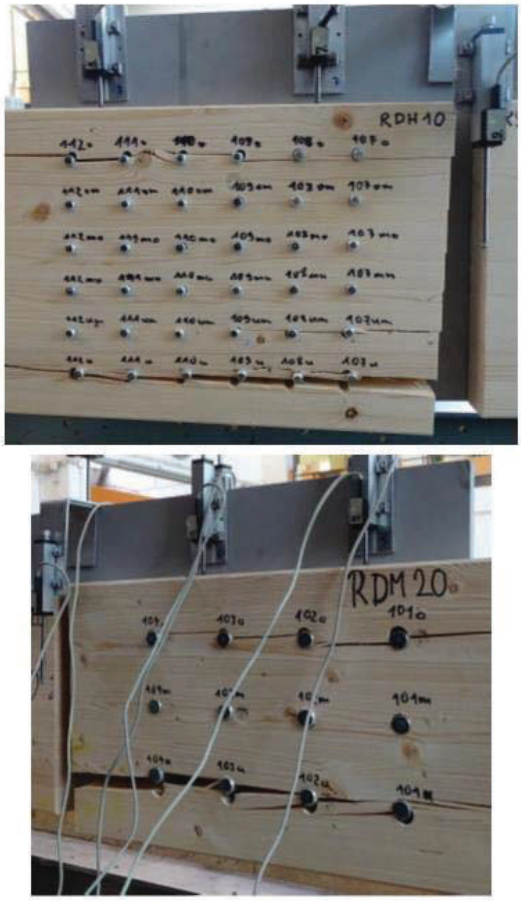

Figure 9: *Typical failure appearances of the slotted-in steel plate connections for groups A and B.*

https://doi.org/10.52202/069179-0172

4 RESULTS AND DISCUSSION

Simulation results are here presented and discussed to show certain outputs from the models.

4.1 SINGLE DOWEL MODEL

The single dowel model was used to simulate deformations and dowel forces in slotted-in steel plate joints of different thicknesses. Figure 10 shows simulated failure modes of three different single dowel joints together with simulated and manually calculated curves that show how the shear load carrying capacity of the joint varies with increasing wood thickness.

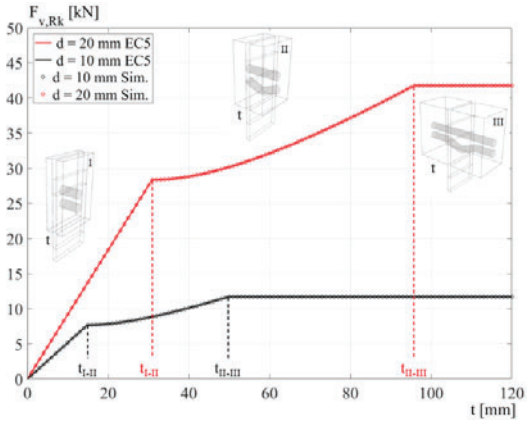

Figure 10: *Comparison of simulated and manually calculated curves showing variation in shear load carrying capacity with increasing wood thickness together with simulated failure modes of the joints.*

Figure 10 shows exact match between simulated and manually calculated load carrying capacity curves as the expected failure modes develop. However, to obtain good results, properly defining the location of the connectors and how to calculate the clamping moment of the dowels are essential. This also allowed us to consider the eccentricity of the fastener forces in the shear joint.

4.2 A BEAM MODEL USING TWO CONNECTORS FOR EACH DOWEL GROUP

This simple model was used to simulate the global bending deformations and (ideal plastic) load carrying capacity of the two tested beam types A and B. The beams had the same geometry, though they had different dowel groups; see Figure 7. The material data used in the model was mainly obtained from the test results. To illustrate some of the model outputs, Figure 11 shows typical bending deformation of beam A together with a close-up figure of the connection part. For a load of $F = 15$ kN, the maximum deflection became $u_{max} = 20.8$ mm. A similar deflection value for beam B is approximately 4% larger than for beam A. The connection of beam A thus reduces the bending stiffness by 19.2% compared with a continuous beam of the same dimensions. This could also be seen as 16.7% reduction of the cross-sectional height in the connection area.

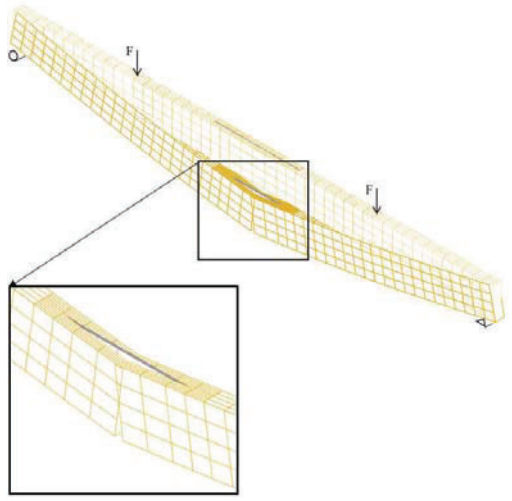

Figure 11: *Magnified bending deformation of the glulam beam A for F = 25 kN.*

The experimental results in Section 3 show a linear relationship between the external load and the deflection all the way up to failure. A typical failure occurs when cracking propagates between the bottom dowels. When cracking starts, the force drops slightly and then maintains a constant or slightly decreasing value under a certain increase of deflection. These test results were used to calibrate the model regarding stiffness and yield moment of the rotational spring. Figure 12 shows the simulated results with the experimentally obtained curves for the three glulam beams of type A. To illustrate the flexibility of the model, Figure 13 shows the bending deformation of the unsymmetric glulam beam jointed with a similar connection that is subjected to both shear and moment loading. The close-up figure in Figure 13 shows clearly the unsymmetric deformation in the connection due to the varying moment and shear forces over the length of the connection.

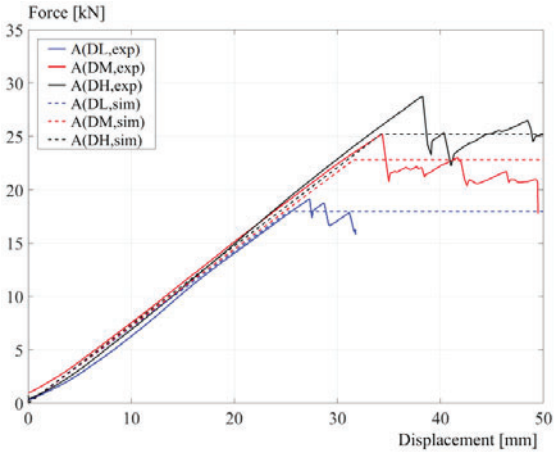

Figure 12: *Simulated and experimentally obtained force-displacement curves for the three beams of type A.*

https://doi.org/10.52202/069179-0172

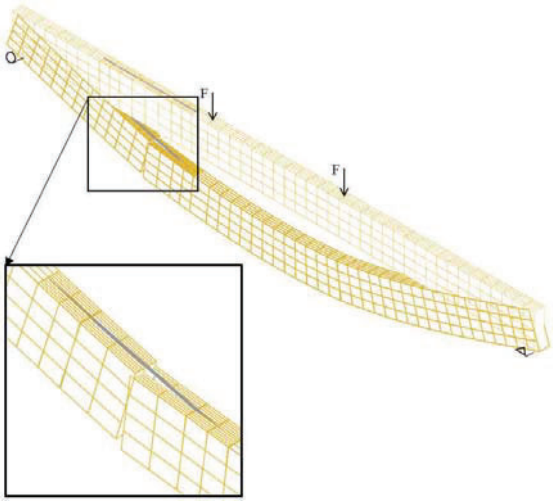

Figure 13: *Magnified bending deformation of an unsymmetric glulam beam with a mechanical connection exposed to both shear and moment action.*

4.3 BEAM-SHELL MODEL WITH A FEW CONNECTORS FOR EACH FASTENER

This model was used to simulate the experimental beams A and B to study how bending deformation and fastener force distribution develop in multiple fastener connections during progressive plasticization of the dowels.

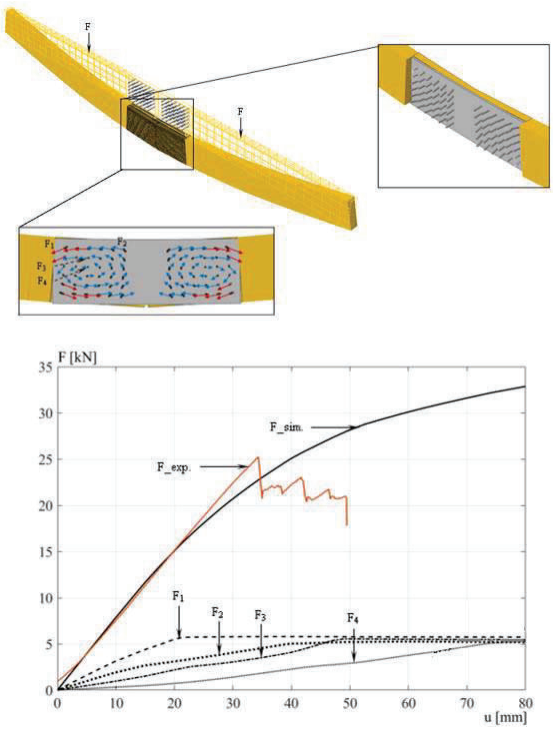

Figure 14: *Simulated bending deformation and fastener force vectors at F = 22 kN as well as simulated and experimentally obtained force-deflection relationships.*

Figures 14*(a)* and 15*(a)* show simulated bending deformations and fastener force distributions when the beams are loaded with F = 22 kN. The bending of the beams is quite similar, though beam B is slightly more curved. The fastener force distribution in beam A shows several plasticized dowels (red arrows), whereas beam B shows none (only blue arrows). The largest forces arose at the corners of the dowel groups, and their directions deviated somewhat from those used in manual calculations. Figures 14*(b)* and 15*(b)* show that the numerical force-deflection curve for beam A fit well with the test results up to a certain force value. However, the conformity was not as good for beam B. To better illustrate the dowel plasticization, the subfigure 14(*b)* also shows elasto-plastic shear force development of some selected fasteners in the dowel groups. The results show clearly how these dowels progressively plasticize during increased loading. The numerical modelling of these beams is based on stiffness data from the experimental study.

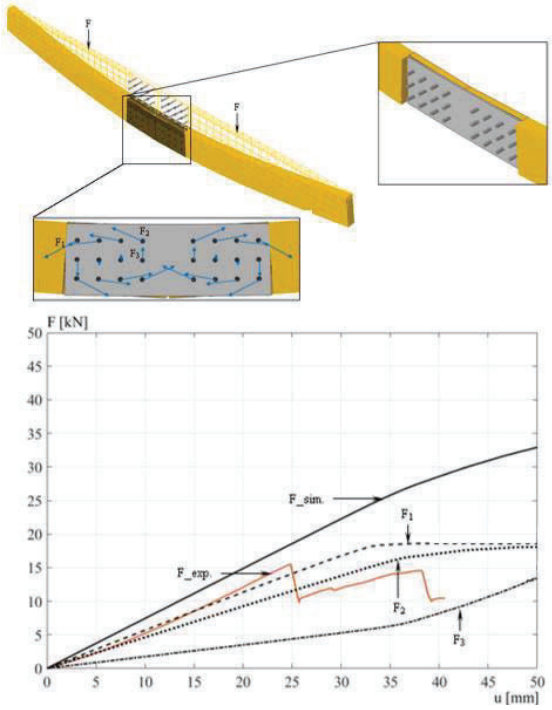

Figure 15: *Simulated bending deformation and fastener force vectors at F = 22 kN as well as simulated and experimentally obtained force-deflection relationships.*

5 CONCLUSION

This work focuses on simple and effective modelling of mechanically jointed glulam beams with slotted-in steel plate connections. The simulation models use beam, shell, and connector elements together with analytical expressions and failure modes from EC5. The single dowel model can simulate both elastic and plastic embedment behaviour of the joints in the form of

https://doi.org/10.52202/069179-0172

deformations and different failure modes. As well, the model was directly implemented when simulating multiple fastener connections where progressive plasticization of the dowel groups was studied during increased loading. Based on the experimental verification, it can be concluded that this model is useful to simulate bending behaviour and failure modes of mechanically jointed timber beams in a constant climate condition. Most numerical results agreed well with the experimental findings up to a certain level of deformation. All experimental results confirmed that these types of connections have low plastic utilization of the dowels, and instead failed in relativity brittle cracking of the wood material. An interesting fact is that beams A have slightly higher bending stiffness but almost double the load carrying capacity of beams B. This indicates that the dowels diameter has a significant impact on the load carrying capacity of jointed glulam beams exposed to dominating moment loading. Based on the experimental observation, a simple beam model was created and used to simulate both global bending deformations and (ideal plastic) load carrying capacity of the two tested glulam beams. It also turned out that the elastic load carrying capacity (with only plasticization in the corner dowels) according to manual EC5 calculations was ca 17% lower than the experimental failure value for beam A(DL) and ca 60% higher for beam B(DL).

A major advantage of the models presented are their short computational time compared to 3D models. It is concluded that these models are useful to simulate bending deformations, fastener forces and failure modes of mechanically jointed timber beams. As well, they have good potential for further development regarding large deformations to simulate rope effect in bolts and screws and moisture related dowel forces.

REFERENCES

[1] K. W. Johansen, “Theory of timber connections,” *Int Assoc Bridge Struct Eng*, vol. 9, pp. 249–262, 1949, doi: 10.5169/seals-9703.

[2] B. H. Xu, M. Taazount, A. Bouchaïr, and P. Racher, “Numerical 3D finite element modelling and experimental tests for dowel-type timber joints,” *Constr Build Mater*, vol. 23, no. 9, pp. 3043–3052, Sep. 2009, doi: 10.1016/j.conbuildmat.2009.04.006.

[3] B. H. Xu, A. Bouchaïr, M. Taazount, and E. J. Vega, “Numerical and experimental analyses of multiple-dowel steel-to-timber joints in tension perpendicular to grain,” *Eng Struct*, vol. 31, no. 10, pp. 2357–2367, Oct. 2009, doi: 10.1016/j.engstruct.2009.05.013.

[4] M. Basterrechea-Arévalo, J. M. Cabrero, B. Iraola, and R. Goñi, “Modelling of moment transmitting beam-to-column timber connections accounting for frictional transmission,” *Eng Struct*, vol. 247, Nov. 2021, doi: 10.1016/j.engstruct.2021.113122.

[5] S. Ormarsson, O. Dahlblom, M. J. Nygaard, “Finite Element Simulation of Mechanical and Moisture-Related Stresses in Laterally Loaded Multi-Dowel Timber Connections,” *In* WCTE 2010 World Conference on Timber Engineering, June 20-24, 2010, Riva del Garda, Trentino, Italy.

[6] A. Bouchaïr, P. Racher, and J. F. Bocquet, “Analysis of dowelled timber to timber moment-resisting joints,” *Materials and Structures/Materiaux et Constructions*, vol. 40, no. 10, pp. 1127–1141, Dec. 2007, doi: 10.1617/s11527-006-9210-0.

[7] M. Schweigler, T. K. Bader, and G. Hochreiner, “Engineering modeling of semi-rigid joints with dowel-type fasteners for nonlinear analysis of timber structures,” *Eng Struct*, vol. 171, pp. 123–139, Sep. 2018, doi: 10.1016/j.engstruct.2018.05.063.

[8] R. and B. J.-F. and S. M. and B. T. K. Lemaitre, “Beam-on-Foundation Modelling as an Alternative Design Method for Timber Joints with Dowel-Type Fasteners: Part 2: Modelling Techniques for Multiple Fastener Connections,” in *6th meeting of INTER (International Network on Timber Engineering Research*, 2019.

[9] M. Mahjoub, “FE modeling of glulam beams with mechanical slotted-in steel plate connections,” Master thesis, Linnaeus University, Växjö, 2021.

[10] K. Simon, S. Aicher, S. Ormarsson and J. Vessby, “Report 1: Materials, specimen manufacture and ramp load reference tests,” MPA University of Stuttgart, 2021.

World Conference on Timber Engineering Oslo 2023

PERFORMANCE OF GLUED-IN RODS IN GLULAM AND MPP IN TENSION AND COMPRESSION

Alexander Salenikovich[1], Étienne Lapointe[2], Bruno Zumbrunn-Maurer[3], Thomas Brotschi[4], Anthonie Kramer[5]

ABSTRACT: This paper is focused on evaluation of the performance of glued-in rods (GIR) in Douglas-fir glulam timber and Mass Ply Panels (MPP) produced in the USA for structural applications. One of the objectives of the study was to compare the performance of GIR joints with and without recess of the bond length in tension and compression. High-strength steel threaded rods of 15.9 mm in diameter were bonded into wood members of 70 mm × 70 mm in cross-section in three configurations. In one configuration, the bond length was 20 times the stress diameter (d_s) of the rod. In another configuration, the embedded length of the rod included a machined portion (constriction zone) near the end of the wood member, which created a recess (not bonded length) of 4d, while the bond length remained the same (20d_s). In the third configuration, the bond length was 24d_s without a recess. Test results clearly demonstrated the benefits of a recess in GIR joints to increase the structural efficiency of timber connections. No GIR buckling was observed in compression tests.

KEYWORDS: Bonded-in threaded rods, GSA Technology, Mass Ply Panel (MPP), splitting, stiffness of GIR joints

1 INTRODUCTION

With growing demand in multistorey mass timber construction, there is a critical need in efficient, reliable, fire-resistant, and aesthetically pleasing connections. Joints with glued-in rods (GIR), if properly designed and executed, meet these requirements. Glued connections are strong and rigid, but due to inherent weaknesses of wood in shear and low splitting resistance, they may provoke undesirable premature brittle wood failures leading to a catastrophic collapse if not taken into account in design. It is desirable to optimize the joints to achieve an equivalent strength and stiffness with the wood structural elements while minimizing the risk of brittle wood failures [1].

Connections with GIR connections have been successfully applied in large-span timber structures in Russia since the 1980s [2], which resulted in the design provisions for GIR [3]. During the last decade, several adhesives for use with GIR systems in timber structures have been developed and approved in Europe [4],[5],[6],[7],[8],[9],[10]. Common rules for the assessment of GIR have been adopted in EU in 2019 [11]. Testing requirements for GIR in glued structural timber products have been adopted in 2021 [12]. Basic provisions for design of GIR for timber connections are now given in EOTA TR 070 [13], and considered in the Eurocode 5 draft [14]. Nowadays, developers seek approval of GIR technologies in North America.

One of the main objectives of this project was to facilitate the development of acceptance criteria for factory installed glued-in rods in wood structural elements to be evaluated for the use in mass timber construction in North America [15]. In addition, the test program was undertaken to compare the performance of GIR in static tension and compression and to demonstrate the advantages of the special rod design used in the GSA Technology.

2 METHODOLOGY

The experimental study was conducted on high-strength steel threaded rods of the class B7 [16] of 15.9 mm (d = 5/8 in.) in diameter bonded at the ends of wood members using the GSA adhesive, a two-component epoxy resin. The high-strength steel was used to minimize the chance of the rod yielding and to force the failure of the bond line or of the wood. The wood members were Douglas-fir glulam timber (GLM) and Mass Ply Panel (MPP) [17] of 70 mm × 70 mm in cross-section. In the first configuration (Series "20d"), the bond length was 267 mm, approximately 20 times the stress diameter (d_s) of the rod. In the second configuration (Series "20d-c"), the embedded length of the rod included a machined portion (constriction zone) near the end of the wood member, which created an additional recess (not bonded length) of 51 mm (14+51 ≈ 4d), while the bond length remained the same (≈ 20d_s). This configuration was representative of the GSA Technology [4]. In the third

[1] Université Laval, Canada, alsal10@ulaval.ca
[2] Université Laval, Canada, etlap6@ulaval.ca
[3] GSA Technology AG, Switzerland, brm@gsa-technology.ch
[4] ASPECT Structural Engineers, thomas@aspectengineers.com
[5] anthoniekramer@gmail.com

https://doi.org/10.52202/069179-0173

configuration (Series "24d"), the bond length was 317 mm (≈ 24d_s) without a recess. Five specimens were fabricated and tested for each configuration and wood material. The dimensions of steel rods are illustrated in Figure 1. The definitions of the variables are depicted in Figure 3. The values of the variables in each test series are summarized in Table 1.

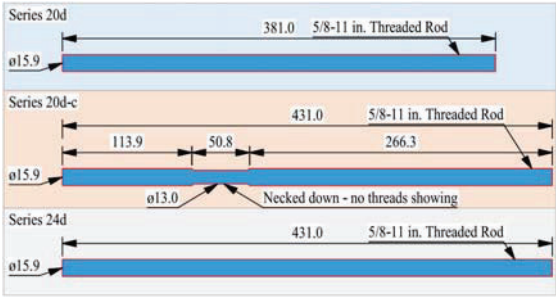

Figure 1: *Dimensions of steel rods*

At first, the specimens were tested in tension by static loading using self-centering pinned fixtures in accordance with ISO 6891 [18] loading procedure until failure at one end. The speed of testing was chosen so to achieve failure within (5 ± 2) minutes. The slip of the joints was measured using three laser-displacement sensors at each end (see Figure 2). The reference plates were glued at the ends of the wood member and the mounting platform for the laser sensors was attached to the ends of the rods with nuts and Belleville washers. The distance between the member end and the mounting platform of the laser sensors was 46 mm in the tension and 26 mm in the compression setup. After the tensile test, the wood member was cut in half, and the surviving joint was tested in compression with a ramp load at the same speed. The load was applied until failure or until the load head reached 15 mm displacement. The maximum load, the slip, the elastic stiffness (slip modulus), and the failure mode were determined for each test. The specific gravity and moisture content of wood members were measured in accordance with ASTM D2395 [19] using full cross-section samples cut near mid-length of each specimen.

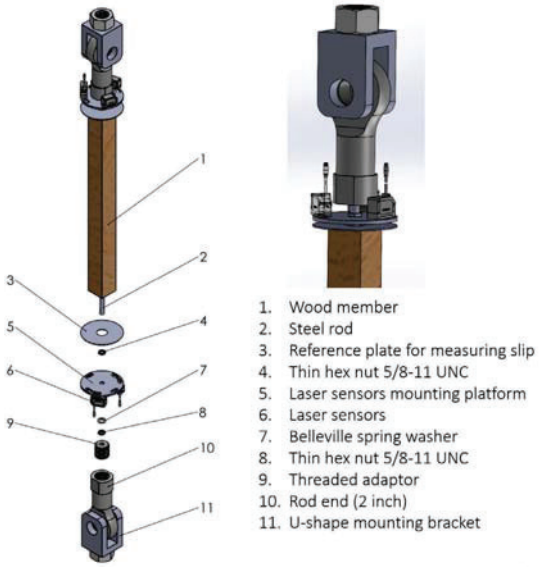

Figure 2: *Tensile load test setup*

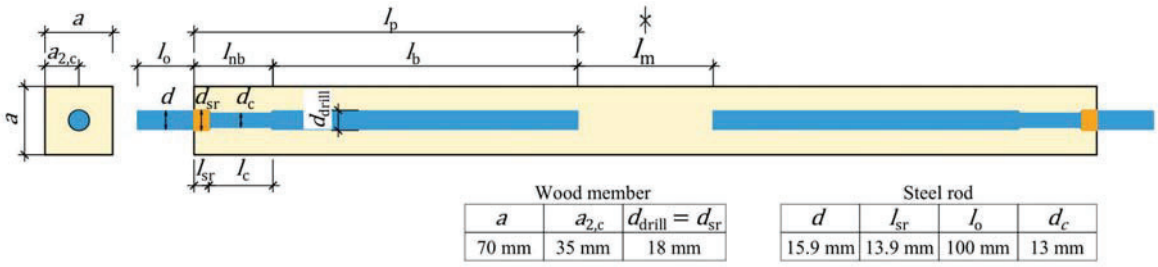

Wood member

a	$a_{2,c}$	$d_{drill} = d_{sr}$
70 mm	35 mm	18 mm

Steel rod

d	l_{sr}	l_o	d_c
15.9 mm	13.9 mm	100 mm	13 mm

Figure 3: *Definition of GIR parameters*

Table 1: *Variable parameters of GIR joints*

Series[1)]	**Load**	d_s	**Bond length (ℓ_b)**		ℓ_c	ℓ_p	ℓ_m
		[mm]	[×d_s]*	[mm]	[mm]	[mm]	[mm]
T-20d	Tension	13.6	20	267	0	281	238
T-20d-c	Tension	13.0	20	266	51	331	138
T-24d	Tension	13.6	24	317	0	331	138
C-20d	Compression	13.6	20	267	0	281	119
C-20d-c	Compression	13.0	20	266	51	331	69
C-24d	Compression	13.6	24	317	0	331	69

* Approximately

[1)] Each configuration was produced with Douglas-fir glulam (GLM) and with Mass Ply Panel (MPP).

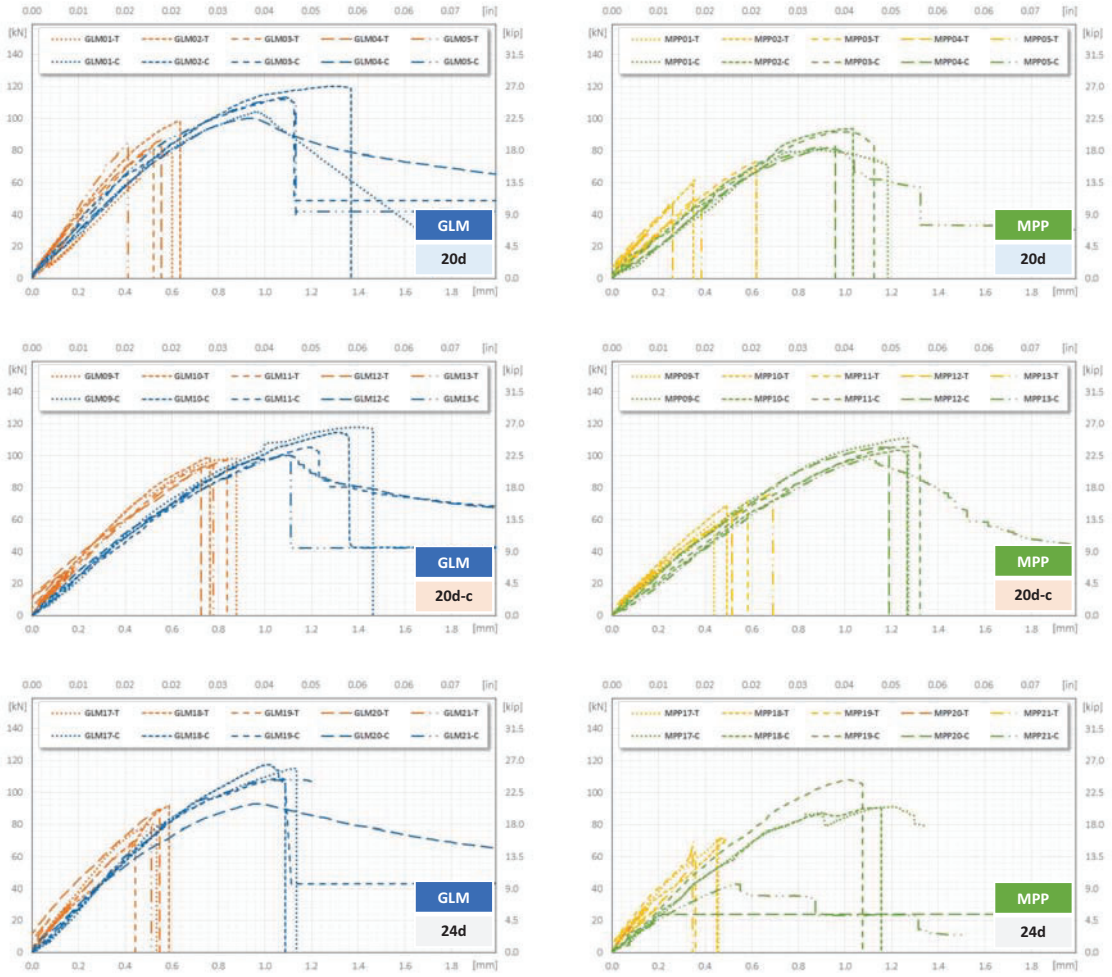

Figure 4: *Load-slip graphs*

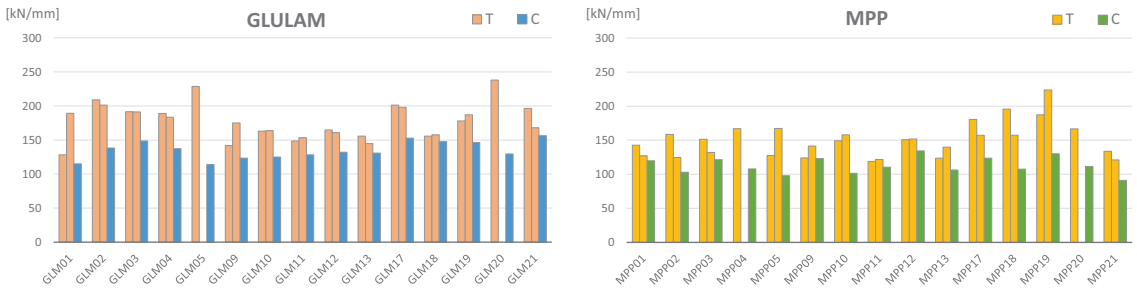

Figure 5: *Slip modulus*

3 RESULTS AND DISCUSSION

A total of sixty tests have been performed in this campaign. Load-slip graphs for each specimen are depicted in Figure 4. For the tensile tests, only the graphs of the failed end are shown. Based on the load-slip data, the slip modulus (k_s) was calculated in the range between 7 kN and 14 kN, which represented 10% and 40% of F_{est} = 70kN. For the tensile tests, the slip modulus was determined for both ends. The values of k_s for each specimen are illustrated in Figure 5.

https://doi.org/10.52202/069179-0173

The statistics for each test series, including the maximum load (F_{max}), the slip modulus (k_s), and predominant failure modes are shown in Table 2 for glulam and in Table 3 for MPP. The mean values and CoV in parentheses are shown for F_{max} and k_s. The moisture content at test and the specific gravity (oven dry mass / oven dry volume) of the specimens are given in Table 4. Typical failure modes of GIR in glulam and in MPP are illustrated, respectively, in Figures 6 and 7, where the top row shows the failures in tension and the bottom shows the failures in compression.

Table 2: *Summary of test results for GIR in DF glulam*

Series	Load direction	F_{max} [kN]	k_s [kN/mm]	Predominant failure mode
20d	Tension	86.4 (8.4%)	190 (14%)	Splitting
	Compression	110 (7.2%)	131 (12%)	Splitting
20d-c	Tension	96.3 (2.9%)	157 (6.6%)	Pull out
	Compression	108 (7.4%)	128 (2.9%)	Push in
24d	Tension	83.7 (13%)	187 (14%)	Splitting
	Compression	109 (8.9%)	146 (7.1%)	Splitting

Table 3: *Summary of test results for GIR in MPP*

Series	Load direction	F_{max} [kN]	k_s [kN/mm]	Predominant failure mode
20d	Tension	60.8 (18%)	144 (12%)	Splitting
	Compression	86.3 (7.0%)	110 (9.5%)	Splitting
20d-c	Tension	67.8 (11%)	138 (11%)	Splitting
	Compression	105 (4.5%)	115 (12%)	Splitting
24d	Tension	68.7 (4.9%)	169 (19%)	Splitting
	Compression	96.7 (29%)	115 (12%)	Splitting

Table 4: *Moisture content and specific gravity (mean and SD)*

Series	Glulam		MPP	
	MC	SG	MC	SG
20d	13.2% (0.6%)	0.519 (0.049)	9.0% (0.5%)	0.531 (0.020)
20d-c	13.1% (0.5%)	0.504 (0.021)	9.4% (0.4%)	0.549 (0.012)
24d	12.8% (0.3%)	0.528 (0.018)	8.6% (0.5%)	0.511 (0.017)

From the test results on GIR in glulam (Series GLM), the following observations were made. The GSA GIR joints (Series 20d-c) showed the highest strength, with the least variability and, most importantly, predominantly favourable failure modes – pull out in tension and push in – in compression. The strength of joints appeared to be independent of the specific gravity of wood. The GIR joints without the constriction zone were somewhat stiffer, but they were weaker and all, but one specimen, failed by wood splitting when loaded in tension. When loaded in compression, all GIR joints in glulam showed a higher resistance than in tension; the maximum load and the variability were independent on the configuration. No buckling of rods was observed, although the maximum loads approached or exceeded the minimum specified yield load of steel.

GIR joints in MPP failed by splitting in 100% of the tests, which led to a lower resistance than expected. The resistance and the stiffness of these joints in tension and in compression were lower than in glulam.

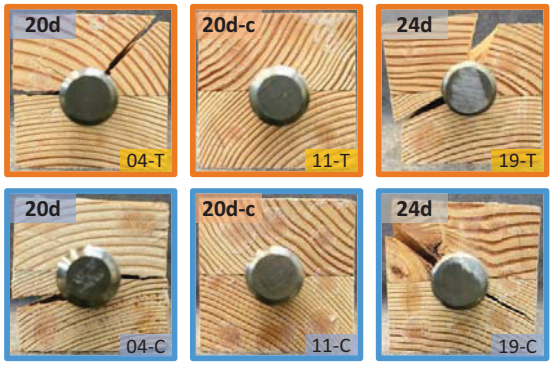

Figure 6: *Typical failure modes of GIR in glulam*

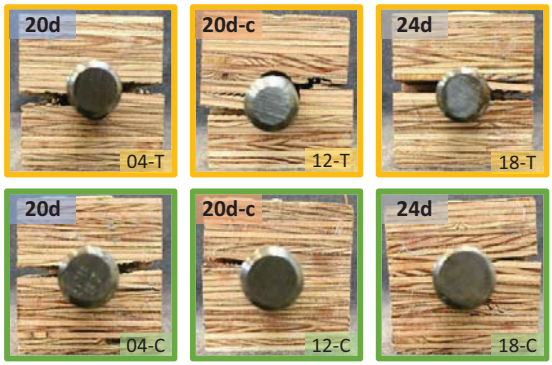

Figure 7: *Typical failure modes of GIR in MPP*

After the tests, each specimen was cut open along the rod to inspect the quality of the manufacturing and further investigate the failure modes and potential reasons for the splitting. It was established that in many cases rods were installed with an inclination of the axis up to 1.6° from the axis of the wood member. Not optimal drilling technology (Auger Bit) is considered as a reason for this misalignment of some predrilled holes in the wood member. Examples are shown in Figure 8. The deviations of the axis were especially frequent in the MPP specimens. These deviations resulted in the eccentricity of the load application, which may have exacerbated the propensity of wood for splitting. However, the investigation showed that the GIR with the largest inclination between the two rods in the specimen did not always fail first in the tension test.

https://doi.org/10.52202/069179-0173

Figure 8: *Inclination of rods in the specimens*

4 CONCLUSIONS

The presented test campaign served for the development and validation of the first edition of the acceptance criteria ICC-ES AC526 for factory installed glued-in rods in wood structural elements for the use in mass timber construction in North America [15]. The developed test procedure and setup with three displacement sensors allowed evaluating the strength and stiffness of GIR in mass timber with high precision. The static test results clearly demonstrated the benefits of recessing the effective bond length in GIR joints to increase the structural efficiency of timber connections. It was demonstrated that resistance in compression was not compromised, and the GIR joints reached the maximum loads without lateral buckling of the rods. It was also observed that the deviation of the rod from the axis of the wood member during fabrication exacerbates the propensity of wood for splitting. Lastly, it was evident that the tested MPP specimens were undersized and were susceptible to splitting; therefore, aiming for a similar resistance per rod, GIR joints in MPP would require larger spacing and edge distances in real structural applications.

ACKNOWLEDGEMENT

Jean Ouellet and Félix Pedneault, technicians at the Renewable Materials Research Centre (CRMR) at Laval University, developed the test setup. Étienne Lapointe conducted the tests at FPInnovations laboratory in Québec City.

REFERENCES

[1] E. Gehri. Glued-in anchors – requirements and applications. In: Internationales Holzbau Forum, Garmisch-Partenkirchen, Germany, 2009.

[2] С. Б. Турковский, А. А. Погорельцев, И. П. Преображенская. Клееные деревянные конструкции с узлами на вклеенных стержнях в современном строительстве (система ЦНИИСК). Москва, РИФ «Стройматериалы». 2013. (in Russian)

[3] CP382. Glued laminated timber structures with glued-in rods. Design Methods. Moscow, RF, 2018.

[4] ETA-19/0752. GSA Technologie. Glued-in rods for timber connections. Austrian Institute for Construction Engineering. 2020.

[5] Avis Technique 3.3/19-986_V1. Goujons collés RBF. CSTB. 2019.

[6] ETA-19/0194. Hilti HIT-RE 500 V3. Glued-in rods for timber connections. Austrian Institute of Construction Engineering. 2019.

[7] ETA-Z-9.1-705. 2K-EP-Klebstoff WEVO-Spezialharz EP 32 S mit WEVO-Härter B 22 TS zum Einkleben von Stahlstäben in Holzbaustoffe. Deutsches Institut für Bautechnik. 2021.

[8] ETA-Z-9.1-778. 2K-EP-Klebstoff GSA-Harz und GSA-Härter für das Einkleben von Stahlstäben in Holzbaustoffe. Deutsches Institut für Bautechnik. 2017.

[9] ETA-9.1-791. Verbindungen mit faserparallel in Brettschichtholz eingeklebten Gewindestangen für den Holzbau. Deutsches Institut für Bautechnik. 2021.

[10] ETA-Z-9.1-896. 2K-PUR Klebstoff LOCTITE CR 821 PURBOND zum Einkleben von Stahlstäben in tragende Holzbauteile. Deutsches Institut für Bautechnik. 2020.

[11] EOTA EAD 130006-00-0304. Glued-in rods for timber connections. European Assessment Document. European Organisation for technical assessment. 2019.

[12] CEN-EN 17334. Glued-in rods in glued structural timber products - Testing, requirements and bond shear strength classification. European Committee for Standardization. 2021.

[13] EOTA TR 070:2019-10. Design of glued-in rods for timber connections. Technical Report. European Organisation for technical assessment. 2019.

[14] CEN/TC 250/SC 5 prEN 1995-1-1:20XX. Eurocode 5: Design of timber structures — Common rules and rules for buildings — Part 1-1: General. 2022.

[15] ICC-ES AC526. Acceptance criteria for factory installed glued-in rods in wood structural elements. June 2022.

[16] ASTM F1554-18. Standard Specification for Anchor Bolts, Steel, 36, 55, and 105-ksi Yield Strength. ASTM International, West Conshohocken, PA, United States. 2018.

https://doi.org/10.52202/069179-0173

[17] APA PR-L325. FRERES Mass Ply Panel (MPP) and Mass Ply Lam (MPL) Beams and Columns. Freres Lumber Co., Inc. APA – The Engineered Wood Association, Tacoma, WA. 2021.
[18] ISO 6891:1983. Timber structures — Joints made with mechanical fasteners — General principles for the determination of strength and deformation characteristics. Reapproved in 2021.
[19] ASTM D2395-17. Standard Test Methods for Density and Specific Gravity (Relative Density) of Wood and Wood-Based Materials. ASTM International, West Conshohocken, PA, United States. 2017.

World Conference on Timber Engineering Oslo 2023

QUASI-STATIC CYCLIC TESTS OF NOVEL HIGH-PERFORMANCE SHEAR-CONNECTORS FOR MASS-TIMBER PANELS

Blériot V. Feujofack K.[1], Cristiano Loss[2]

ABSTRACT: In this work, the results from quasi-static cyclic tests on a novel hybrid steel-grout shear connector for cross-laminated timber (CLT) panels is presented. These tests are part of a set of experimental, analytical, and numerical studies aiming at developing a reliable and resilient hold-down connection for CLT panels in mass-timber construction. The cyclic tests have been done based on monotonic-test results, and all cyclic loading was done below the yield point of each connector. From cyclic-test results, mechanical characteristics, namely, the secant loading stiffness and the residual slip were evaluated and are discussed in this paper. Furthermore, analyses using a Gaussian process regression machine learning algorithm were conducted in order to predict the mechanical characteristics of connectors in function of a vast number of inputs, including geometrical properties of connectors, mechanical properties of each material used, and physical parameters such as the position of lumber laminates in the CLT. It was shown that the steel rod diameter, the grout diameter, and the curing time of the grout are the most influencing parameters regarding the secant loading stiffness of connectors. As for the residual slip, it was found that the grout diameter, the steel rod grade, and the position of face-laminate joints in the CLT are the most influencing parameters. In overall, the results of this work contribute to an improved understanding of the connection under development and confirms the resilience of individual connectors under cyclic loads.

KEYWORDS: CLT, Hybrid steel-grout connector, Quasi-static cyclic, Hysteresis, Secant loading stiffness, Residual slip, Gaussian process regression algorithm, machine learning

1 INTRODUCTION

Mass timber construction is increasingly growing attention among architects, engineers, and other practitioners. Factors such as ease of hybridization, high sustainability potential, along with the better performance of mass timber products under fire motivate building regulators to relax timber buildings' height limitations around the world. For instance, timber buildings can now reach up to 25 m in Australia; 12 stories in Canada; and 18 stories in the USA [1]. Although the development of novel mass-timber products and hybrid timber-based systems can result in high-performance solutions for tall buildings, the structural efficiency of those buildings heavily depends on the connection technologies employed. Various connection technologies have to be reinvented in order to suit the needs of mass-timber construction, among which dowelled hold-downs connections. Research has already been initiated for such connection technologies [2]. The few solutions proposed remain very embryonic, and the observed performance are not always satisfactory, as brittle failure in wood is engaged before developing yielding in the connectors. Therefore, the need for reliable, resilient, and high-performance dowel-type connection technologies for mass timber components is becoming increasingly critical. In this work, the results of quasi-static cyclic tests on a novel hybrid steel-grout shear connector for cross-laminated timber (CLT) panels are presented. Precisely, this work is part of a research program aiming at developing a reliable and resilient hold-down connection for CLT panels in mass timber construction.

2 METHODS

2.1 Description of the hybrid connector

The hybrid shear connector developed and tested in this work consists of a threaded steel rod embedded into cross-laminated timber (CLT) through a thick layer of epoxy-based grout mixture. With specific reference to Figure 1, each connector unit includes:

- A steel threaded rod, which ensures the transfer of shear forces from side members to the connector and conversely. In this study, three steel rod diameters were used and tested, namely 20 mm, 24 mm, and 30 mm. Additionally, two steel rod grades were accounted for, namely 4.8 strength class and 8.8 strength class.

[1] Blériot V. Feujofack K., Ph.D. Candidate, Sustainable Engineered Structural Solutions Laboratory, Department of Wood Science, The University of British Columbia, Canada; bleriotvincent.feujofackkemda@ubc.ca

[2] Cristiano Loss, Assistant Professor, Sustainable Engineered Structural Solutions Laboratory, Department of Wood Science, The University of British Columbia, Canada; cristiano.loss@ubc.ca

https://doi.org/10.52202/069179-0174

• An intermediary thick layer of epoxy-based grout, which enables to embed the threaded rod into the CLT panel (wood). More importantly, this intermediary layer of epoxy-based grout enables to reduce stress and strain on wood, delaying crushing and failure in wood to a great extent. In the current study, the diameter of the grout was varied in function of the diameter of steel threaded rods. The grout-to-rod diameter ratio was set to 2, 3, and 4.

• A CLT block, into which the steel rod and the grout layer are embedded. A 3-ply CLT with fixed thickness of 105 mm was studied. Two CLT grades were used, namely machine graded CLT (E), and visually graded CLT (V). In addition, the CLT block size was varied from 280 mm to 340 mm, to 420 mm, in function of the diameter of steel threaded rods used.

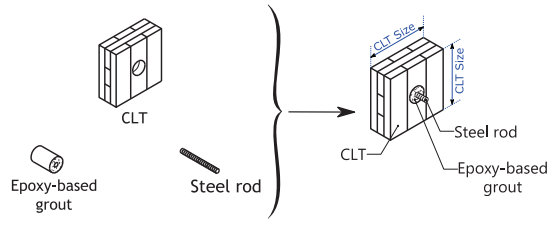

Figure 1: *Individual components (left); the hybrid steel-grout connector (right) for CLT panels*

Shulman and Loss [3], [4] conducted an extensive experimental campaign on this connector and provided insights on the actual structural performance of such connectors under monotonic loading.

2.2 Rationale for conduction of cyclic testing

The shear connector presented in this work is expected to be wood-damage-free and de-constructable. For such goals to be attained, it is important for the connector to remain elastic throughout the building lifespan. For static loading, the connector has been proven to display a high slip modulus and a clearly identifiable yield point [5]. However, repeated cyclic loads can lead to permanent deformation into the connector, even for small load amplitudes. Given that buildings are often subjected to recurrent cyclic loading such as regular winds or gusts, and sometimes earthquakes, it is important to determine the behaviour of the connector under repeated cyclic loading.

In the aim of determining the mechanical properties of the connector when subjected to cyclic loads, load-controlled quasi-static cyclic non-reversed tests were conducted on connectors. The tests were non-reversed, because in the scenario where connectors are used in hold-down connections, each connector is loaded in one direction only: the full reverse of loads does not occur for individual connectors. Three replicates of all the variants tested by Shulman and Loss [3], [4] were fabricated under the same condition and stored for at least seven days, before proceeding to testing. The testing campaign was set to evaluate to what extent cyclic loading, below the connector's yield strength, negatively impacts the connector strength, stiffness, and overall integrity.

2.3 Testing program

2.3.1 Design of experiments

The size of specimens and testing method were set based on monotonic-test results conducted in early 2021 by Shulman and Loss [3], [4]. Cyclic tests were load-controlled, and the amplitude of cycling was kept below the yield point for each connector. As shown in Figure 2, experimental variables include the grade of the CLT panel, the diameter of the steel threaded rod, the strength class of the steel threaded rod, and the ratio between the grout diameter and the steel rod diameter. The combination of all experimental variables yielded a total of 30 connector variants. Each test was replicated thrice, leading to a total of 90 tests for this study.

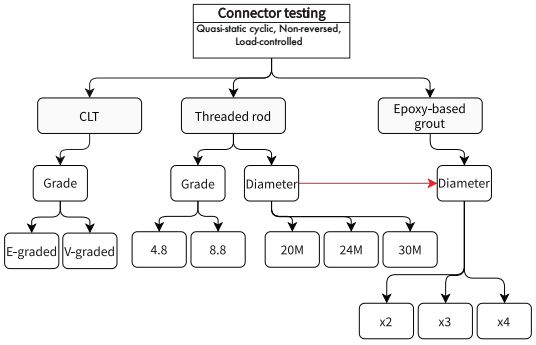

Figure 2: *Experimental variables and their associated levels*

2.3.2 Loading protocol for cyclic testing

The loading protocol was crafted from European [6] and American [7] standards. For each connector variant, the reference maximum load ($\boldsymbol{F_{max-cyclic}}$) was set as the average yield load ($F_{y,mean}$) obtained from monotonic tests by S. Shulman and C. Loss [3], [4]. Then, cyclic loads were applied on connectors by steps, at 5%, 20%, 40%, 60%, 80%, 90%, and 100% of $F_{y,mean}$. Figure 3 shows a graphic of that loading protocol. Specifically, only one cycle was applied at the first load step. For each subsequent load step, five non-reversed loading cycles were applied. The loading speed was set at one cycle per two minutes, for a total of 62 minutes per test. Figure 3 presents the loading protocol of the connector variant 280–E–20M–4.8–2d. Table 1 shows the characteristics of this connector variant such as the CLT block size and grade, the steel rod diameter and grade and the grout diameter; each load step, as well as number of cycles per steps are also provided.

https://doi.org/10.52202/069179-0174

***Table 1**: Loading protocol sample*

Specimen: 280 – E – 20M – 4.8 – 2d				
CLT size	CLT grade	Rod diameter (d)	Steel class (rod)	Grout diameter
280 mm	E	20M	4.8	2d

$$F_{max-cyclic} = F_y = 74.58\ kN$$

Loading schedule					
Steps	Number of cycles	Load percentage (%)	Actual load (kN)	Loading speed (kN/min)	Total time (min)
1	1	5	3.73	3.73	2
2	5	20	14.92	14.92	10
3	5	40	29.83	29.83	10
4	5	60	44.71	44.71	10
5	5	80	59.67	59.67	10
6	5	90	67.13	67.13	10
7	5	100	74.58	74.58	10
Total					62

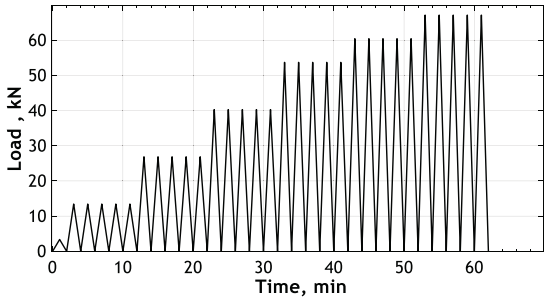

***Figure 3:** Graphic representation of the loading protocol*

All tests were conducted in the Timber Structural and Mechanical Lab at the University of British Columbia, using a custom-made test apparatus, as shown in Figure 4. Throughout the tests, the load was measured and recorded using the built-in load cell of the MTS machine. The slip of the connector was measured with two linear voltage displacement transducers and recorded using a standard data acquisition system. The load and slip data were acquired with a frequency of 4 Hz. Furthermore, physical and environmental variables such as moisture content of the CLT were duly recorded during the tests. In addition to the geometry and mechanical properties of the steel threaded rod, the layer of epoxy-based grout, and the CLT block, parameters such as the number of knots in the loaded end of the CLT and the position of the connector with respect to edge joints in the CLT face lamellae (Figure 5) were recorded as covariate for the predictive models to be developed. The parameter d_1 represents the horizontal eccentricity: it was measured as the perpendicular distance between the vertical axis of the steel threaded rod and the closest face lamination (major) joint of the CLT block. As for d_2, it represents the vertical eccentricity: it is the perpendicular distance between the horizontal axis of the steel threaded rod and the closest lower internal-laminate (minor) joint.

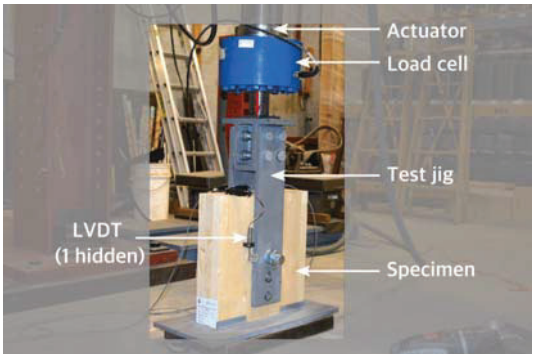

***Figure 4:** Experimental test apparatus*

***Figure 5:** Characterization of the location of the connector in the CLT panel, and defects in the panel*

2.4 Evaluation of structural performance parameters

Based on the experimental tests conducted, a set of parameters have been selected to characterize the structural performance of connectors, namely, the secant loading stiffness (k_{sl}), and the residual slip of the connector and the end of the cycling process ($\delta_{res-slip}$). These structural performance parameters are represented in an idealized hysteresis plot in Figure 6.

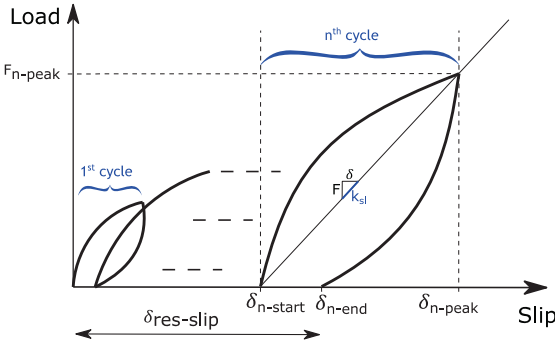

***Figure 6:** Idealised hysteresis curves of the connector and identification of performance parameters.*

https://doi.org/10.52202/069179-0174

With specific reference to Figure 6, the secant loading stiffness for a given cycle n was determined using equation 1 [8], [9].

$$k_{sl} = \frac{F_{n-peak} - F_{n-start}}{\delta_{n-peak} - \delta_{n-start}} \quad (1)$$

Where $\delta_{n-start}$ and δ_{n-peak} correspond to the recorded connector slip at the starting and ending of the load cycle n, respectively. $F_{n-start}$ and F_{n-peak} correspond to the recorded load at the starting and ending of the load cycle n, respectively. In this study, the final value of k_{sl} considered was obtained by averaging the secant loading stiffness of the last five cycles of each test-run. For what ensues, k_{sl} will be referred to as loading stiffness.

2.5 Machine learning regression analyses

Machine learning methods are increasingly used in predicting the mechanical parameters of materials based on experimental data sets. A Gaussian process is a generalization of the Gaussian probability distribution and can be used as basis for sophisticated machine learning algorithms for classification and regression. In machine learning, Gaussian process regression (GPR) was developed out of neural networks research and is a Bayesian method for data regression or classification. Gaussian process models have become very popular for solving non-linear regression problems. They are known to be expressive, interpretable, avoid over-fitting, and to yield a high predictive performance in many thorough empirical comparisons [10], [11]. In this study, a GPR algorithm was used to perform a regression analysis on inputs and output results obtained from cyclic tests on hybrid connectors. Figure 7 features a schematic of the Gaussian process regression network. Squares represent observed variables and circles represent unknowns. x is a general input (predictor) variable, y is target output, and w are weights functions. Often a bias weight or offset is included to avoid over fitting. This noise assumption together with the model directly gives rise to the likelihood, the probability density of the observations given the parameters, which is factored over cases in the training set. Because of the marginalization property of GPR addition of further inputs, x, latent variables, f, and unobserved targets, $y*$, does not change the distribution of any other variables.

In the Bayesian formalism there is a need to specify a prior over the parameters, expressing the beliefs about the prior parameters before looking at the observations. In GPR, a zero mean Gaussian prior is used. Also, a shape of the function is set for the prior; in the case of this work, and exponential shape was used. Inference in the Bayesian linear model is based on the posterior distribution over the weights. The posterior combines the likelihood and the prior and captures everything known about the parameters. To make predictions for a test case, all possible parameter predictive distribution values are averaged and weighted by their posterior probability. Thus, the predictive distribution is given by averaging the output of all possible models regarding the Gaussian posterior. An inherent advantage of GPR processes is that the predicted output is a distribution, and not a number.

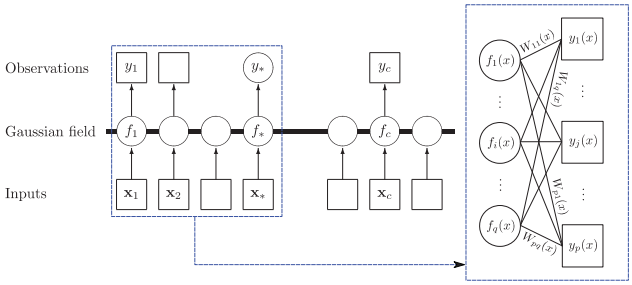

Figure 7: *The Gaussian process regression network. Adapted from [10], [12]*

In this work, the GPR was conducted under the software MATLAB, using the Regression Learner application. Two models were developed: one for the secant loading stiffness, and the other for the residual slip of the connector. The models were trained with normalized input parameters, as presented in Table 2.

Table 2*: Normalization of input parameters for the GPR learning algorithm*

	Actual values	**Normalized values**
	variables	
CLT size (mm)	280, 340, 480	280, 340, 480
CLT grade	E, V	0, 1
Steel rod grade (strength class)	4.8, 8.8	0, 1
Rod diameter	20M, 24M, 30M	20, 24, 30
Grout-to-rod diameter ration	2x, 3x,4x	2, 3, 4
	Covariates	
Horizontal eccentricity, d_1 (mm)	To be measured	Idem.
vertical eccentricity, d_2 (mm)		
Curing time for the grout (days)		

3 RESULTS

In this section, the mechanical characteristics evaluated based on the experiments are presented first; then, outputs from the Gaussian process regression ensue.

3.1 Cyclic performance of the connector

3.1.1 Secant loading stiffness and residual slip of the connectors

The box plots in Figure 8 provide a visualization of statistical information for two output data under consideration, namely the average secant loading stiffness at the last cycle of loading and the residual slip of the connector. The bottom and top of each box are the 25th and 75th percentiles of the data, respectively. Each box covers the interquartile interval, where 50% of the data is

found. The horizontal line in the middle of each box is the sample median. The thinner lines extending above and below each box represents whiskers, which go from the end of the interquartile range to the furthest observation within the whisker length [13]. This variation of the box and whisker plot restricts the length of the whiskers to a maximum of 1.5 times the interquartile range [14]. Data points that are outside this interval are represented as red points on the graph and considered potential outliers.

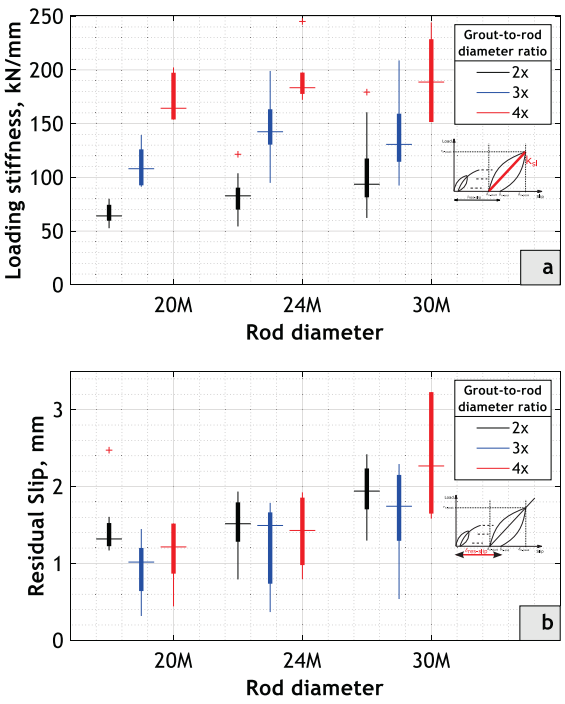

Figure 8: *Box plots of performance parameters. (a) loading stiffness, (b) residual slip. In black – grout to rod diameter ratio is 2; blue - grout to rod diameter ratio is 3; red - grout to rod diameter ratio is 4.*

A general trend is that the variability in loading stiffness increases with the grout diameter. The loading stiffness itself increases with both the rod diameter and grout diameter. As for the residual slip, once again, it is observed that the variability grows with the gout diameter. The effects of the rod and grout diameter on the residual slip are, however, less pronounced.

3.1.2 Hysteresis of connectors

The typical hysteresis of the connector is shown in Figure 9. This hysteresis corresponds to the connector tested with the loading diagram presented in Table 1 and Figure 3. In this plot, the load slip curves from monotonic tests are presented (Shulman and Loss [3], [4]). The hysteresis is represented by bold black, red, and blue lines. A switch in color in the hysteresis means a change of loading step. It was observed that the connector conserves it stiffness during cyclic loading (Figure 9). Additionally, the residual slip was observed to remain in moderate ranges. The premise that the hysteresis of the hybrid connector is contained within the monotonic load-slip curve is also validated. There appears to be a larger loop at the first cycle of the fourth load step: this was observed for all the connector variants tested. Lastly, a slight pinching is observed at the last load step. All tested connectors displayed a similar hysteresis pattern, with an observed residual slip between 40% and 60% of the maximum slip reached during the testing.

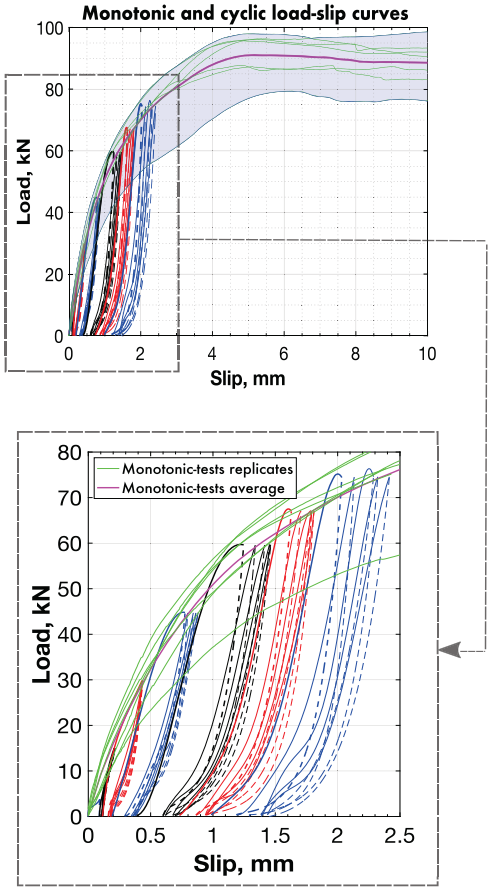

Figure 9: *Hysteresis of a specific tested connector arrangement (280–E–20M–4.8–2d)*

3.2 Gaussian process regression

Gaussian process regression (GPR) machine learning algorithm was used to develop predictive models for the secant loading stiffness and the residual slip of the connectors.

3.2.1 Variables importance scores

First, an F-test was used to determine the importance of each feature variable on the outputs. Figure 10 shows the feature importance scores.

https://doi.org/10.52202/069179-0174

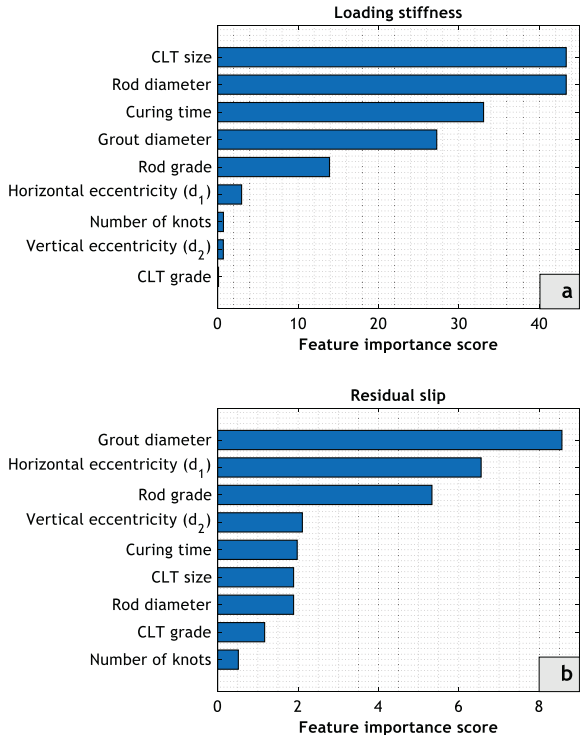

Figure 10: *Feature importance score obtained through the F-Test algorithm. (a) loading stiffness, (b) residual slip.*

It can be observed that the CLT size and the rod diameter have an equal importance score as far as the loading stiffness is concerned (Figure 10.a). This is because these two variables are perfectly correlated. 20M, 24M, and 30M rods were used on 280 mm, 340 mm, and 420 mm CLT blocks respectively. Because of this correlation, only the rod diameter was used for subsequent analyses. The curing time of the epoxy-based grout is third in the ranking of importance factors. Conversely, the CLT grade, the vertical eccentricity, and the number of knots in the face laminations of CLT were found to have very little effect on the secant loading stiffness of connectors.

As for the residual slip, it is observed that the grout diameter, the horizontal eccentricity, d_1, and the steel rod grade are the most significant parameters, with importance scores above 8, 6, and 5, respectively (Figure 10.b). The number of knots and CLT grade were found to have little effect on the residual slip of connectors

3.2.2 Training of GPR models

The GPR was executed twice: once for the secant loading stiffness, and the second time, the residual slip, leading to two trained models. In order to minimize the overfitting, 75% of the ninety data sets were randomly selected and used to train each model. Each model was then validated using the 25% remaining data. The root mean-square error as well as other parameters describing the performance of the algorithm are presented in Table 3. The scatter plots for predicted vs experimental data are presented in Figure 11.

Table 3: *Performance of the GPR learning algorithm*

	Secant Loading stiffness [kN/mm]	**Residual slip [mm]**
RMSE - *Validation*	26.007	0.5734
R-squared	0.70	0.57
Training time (obs/sec)	5700	6800
Prediction speed (sec)	3.353	2.2493

As can be seen from Table 3, the model for the secant loading stiffness presents a good validation root mean square error (RMSE), with a determination coefficient R-squared of 0.7 (this can be observed on Figure 11.a). The prediction speed for the 25% validation data was observed to be below the 3.50s.

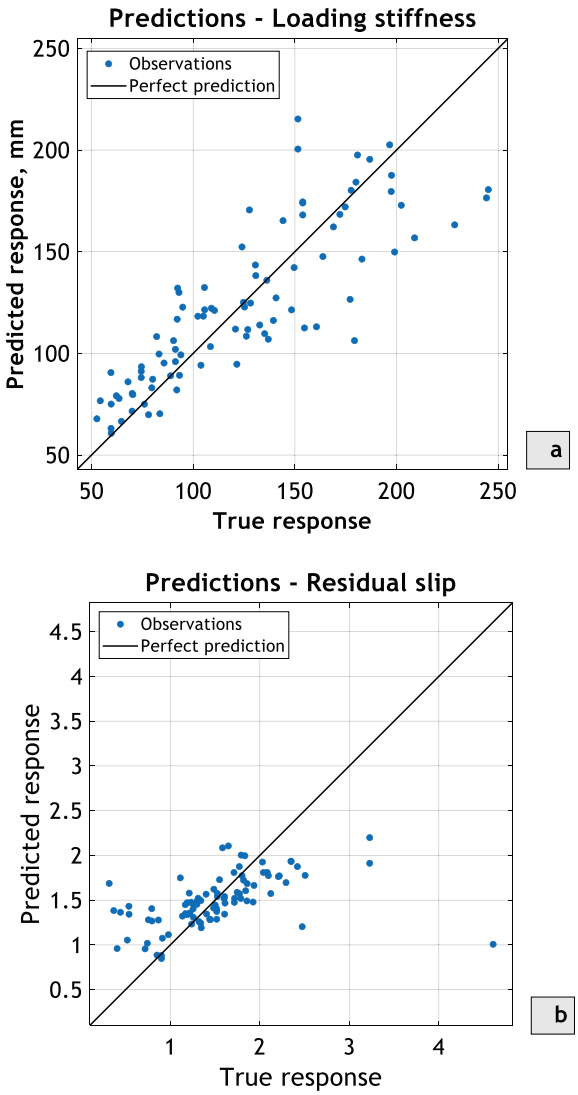

Figure 11: *Scatter plots of the predicted vs experimental data. (a) secant loading stiffness, (b) residual slip.*

The residual slip on the other hand was a little more complex to predict. The coefficient of determination for this model was obtained to be only 0.57 (this can be observed on Figure 11.b, with a few outliers on the lower

right corner of the plot). This can be due to the fact that other non-controlled variables may have a significant effect on the slip of connectors. For instance, the friction between the test apparatus and the specimens was not measured. In addition, the testing apparatus may have not stayed perfectly vertical all along the cycling process (Figure 4). In overall, the prediction speed was higher for the residual slip, with a prediction time of 2.25 s.

3.2.3 Response surface representations of trained GPR models

Using the developed models from the GPR learning algorithm, response surfaces were plotted in order to assess the overall effects of the most significant variables on the outputs.

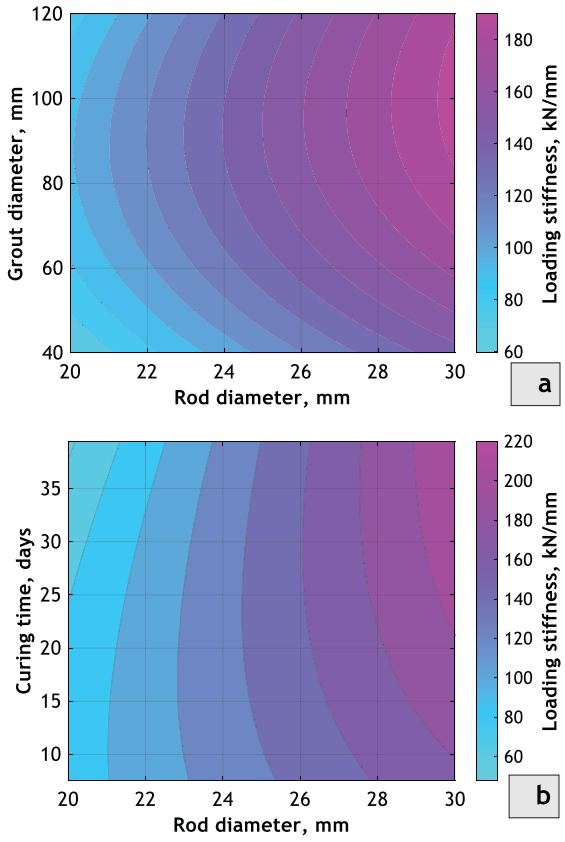

Figure 12: *Response surface of the predicted secant loading stiffness (units in kN/mm). (a) secant loading stiffness vs rod diameter & grout diameter, (b) secant loading stiffness vs rod diameter & curing time.*

First, the secant loading stiffness model was plotted, with variable parameters including diameters of rods and grout. With reference to Figure 12.a, it can be observed that the secant stiffness model captures the effects of the rod and grout diameters. Besides, it is shown that the grout diameter gradually has less impact on the secant loading stiffness as the rod diameter reaches larger values. In Figure 12.b, plots were drawn using the rod diameter and the curing time of the grout as variables. As a result, it can be seen that the curing time of the grout has larger effect on the secant loading stiffness as the rod diameter reaches extreme upper values.

Similarly, the residual slip was plotted, with variable parameters including the grout diameter and the horizontal eccentricity, d_1 (Figure 13.a). The residual slip appears to be lower with lower grout diameters. However, the value of horizontal eccentricity that minimizes the residual slip appears to be between 20 mm and 50 mm, and this value increases with the grout diameter. Results based on the grout diameter and the steel rod grade as variables are plotted in Figure 13.b. From these latter, it can be seen that there is a linear relation between inputs and outputs. The residual slip is minimized as the grout diameter decreases and the steel rod grade is kept at 1 (corresponding to 8.8 strength class).

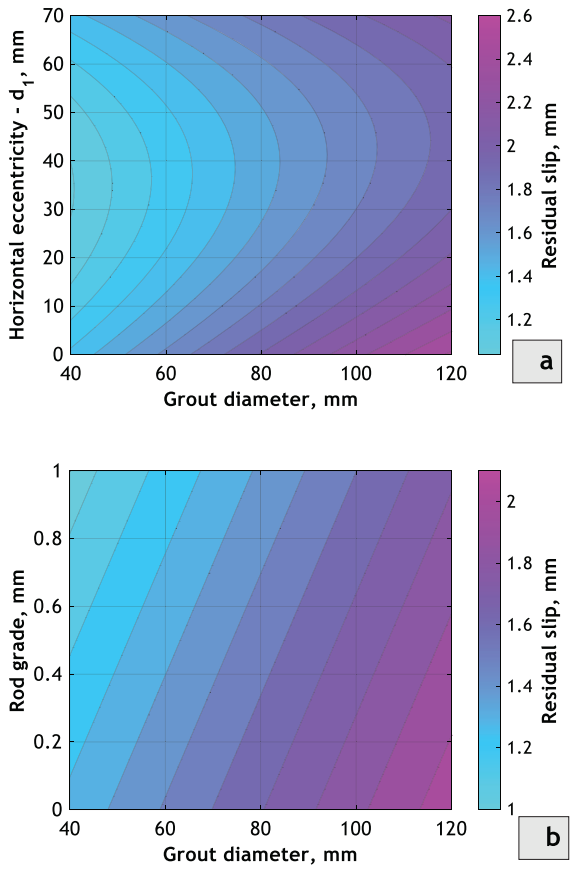

Figure 13: *Response surface of the predicted residual slip (units in mm). (a) residual slip vs & grout diameter & horizontal eccentricity, (b) residual slip vs grout diameter & steel rod grade.*

4 CONCLUSION

This work focused on the performance of a novel high-performance shear connector for mass-timber panels under quasi-static cyclic loading. In addition to assessing the experimental results, two models were developed using a Gaussian process regression machine learning

https://doi.org/10.52202/069179-0174

algorithm to determine the final secant loading stiffness and the residual slip of the connector. Based on the tests performed and analyses conducted, the following conclusions are at the forefront:

- The connector maintains its initial stiffness throughout the cyclic loading history
- The connector displays a relative residual deformation in the order of 50% at the end of the test.
- The most significant parameters influencing the secant loading stiffness are the rod diameter, curing time of the grout, and grout diameter. Whereas the most significant parameters for the residual slip are the grout diameter, the horizontal eccentricity and the steel rod grade.
- The Gaussian process regression algorithm yielded acceptable models for the prediction of the secant loading stiffness and the residual slip, with an r-squared value of 0.70 for the secant loading stiffness and 0.57 for the total residual slip.
- In overall, the results of this work contribute to an improved understanding of the connection under development and confirms the resilience of individual connectors under cyclic loads.

ACKNOWLEDGMENT

The research was funded by the Government of British Columbia through a FII Wood First grant and by the Natural Sciences and Engineering Research Council (NSERC) of Canada through the Discover Program grant number RGPIN-2019-04530, and Discovery Launch Supplement, grant number DGECR-2019-00265. Financial support from the Faculty of Forestry of the University of British Columbia through the Donald S. McPhee Fellowship and Dr. J. David Barrett Memorial Scholarship in Wood Science granted to Blériot Feujofack is gratefully acknowledged.

REFERENCES

[1] S. Breneman, T. Timmers, and D. Richardson, 'Tall wood buildings and the 2021 IBC: Up to 18 stories of mass timber', *American Wood Council*, no. 2019, p. 13, 2019.

[2] M. Geiser, M. Bergmann, and M. Follesa, 'Influence of steel properties on the ductility of doweled timber connections', *Construction and Building Materials*, p. 121152, Oct. 2020, doi: 10.1016/j.conbuildmat.2020.121152.

[3] Shulman, S., Loss, C., 2023, 'Performance of a Grout-Reinforced Hybrid Steel-Timber Shear Connection for Mass Timber Buildings', in: Walbridge, S., Nik-Bakht, M., Ng, K.T.W., Shome, M., Alam, M.S., El Damatty, A., Lovegrove, G. (Eds.), *Proceedings of the Canadian Society of Civil Engineering Annual Conference 2021*, Lecture Notes in Civil Engineering. Springer Nature Singapore, Singapore, pp. 341–352. https://doi.org/10.1007/978-981-19-0511-7_29.

[4] S. Shulman and C. Loss, 'High-performance grout-reinforced shear connectors for hybrid steel-cross-laminated timber building systems: Experimental study', *Journal of Building Engineering*, p. 106014, Feb. 2023, doi: 10.1016/j.jobe.2023.106014.

[5] S. Shulman, 'A deconstructable grout-reinforced hybrid shear connector for tall cross-laminated timber buildings', 2021.

[6] EN 12512, '12512: Timber structures-Test methods-Cyclic testing of joints made with mechanical fasteners', *English version of DIN EN*, no. 2001, p. A1, 2005.

[7] ASTM E2126, 'Standard test methods for cyclic (reversed) load test for shear resistance of vertical elements of the lateral force resisting systems for buildings', *ASTM E2126*, 2011.

[8] T. J. Sullivan, G. M. Calvi, and M. J. N. Priestley, 'Initial stiffness versus secant stiffness in displacement based design', in *13th World Conference of Earthquake Engineering (WCEE)*, 2004, no. 2888.

[9] R. Jockwer, D. Caprio, and A. Jorissen, 'Evaluation of parameters influencing the load-deformation behaviour of connections with laterally loaded dowel-type fasteners', *Wood Material Science & Engineering*, vol. 17, no. 1, pp. 6–19, 2022.

[10] C. E. Rasmussen and C. K. Williams, *Gaussian processes for machine learning*, vol. 1. Springer, 2006.

[11] M. Kuss, C. E. Rasmussen, and R. Herbrich, 'Assessing Approximate Inference for Binary Gaussian Process Classification.', *Journal of machine learning research*, vol. 6, no. 10, 2005.

[12] A. G. Wilson, D. A. Knowles, and Z. Ghahramani, 'Gaussian process regression networks', *arXiv preprint arXiv:1110.4411*, 2011.

[13] D. C. Montgomery and G. C. Runger, *Applied statistics and probability for engineers*. John wiley & sons, 2010.

[14] R. McGill, J. W. Tukey, and W. A. Larsen, 'Variations of box plots', *The american statistician*, vol. 32, no. 1, pp. 12–16, 1978.

World Conference on Timber Engineering Oslo 2023

JOINT PERFORMANCE TESTING OF A CLAMPED JOINT FOR TIMBER STRUCTURES AND APPLICATION TO STRUCTURAL DESIGN

Yoshisato Esaka[1], Tatsuki Ishizaki[2], Tsubasa Seguchi[3], Tokuma Azemi[4]

ABSTRACT: The authors developed a clamped joint system, which they called *Tsunagi-clamp*, to assemble and reassemble timber structures easily without complex wood manufacturing. The purpose of this study is to make clear the performance of joints using *Tsunagi-clamp* and effective method of reinforcement, as well as to predict the horizontal resistance performance of a timber cubic frame structure that used this claimed joint system, in which the analysis was performed on the stiffness of the clamped joints during application. By testing the clamped joints under torsion loading and moment loading, it was confirmed that the stiffness of damaged joints reinforced with screw or wood putty were larger than that of undamaged joint. The assumed deformation by analyzing the cubic frame model, in which the stiffness of the joints deformed 1/100 radians, closely fitted the results of the horizontal resistance test. This result suggests that it is possible to verify the performance of other structures with *Tsunagi-clamp* by using the same analyzing method.

KEYWORDS: Clamped joint, Joint performance, Temporary structure, Structural design

1 INTRODUCTION

From a carbon emission point of view, the demand for medium to large-scale timber buildings is increasing. However, the specialization of the forest industry makes timber distribution complex, especially in Japan. This circumstance disturbs not only normal market principles but also the normal circulation of forests. The authors propose that providing consumers with the opportunity to directly construct human-scale timber buildings will help promote its widespread use. This goal is achieved by suggesting various structures that can be built, transformed, disassembled, and easily relocated. The authors call this structure *Tsunagi*, which means "connect" and "connecting wood" in Japanese.

The authors developed a simple clamped joint system, known as *Tsunagi-clamp*, so to assemble and reassemble the structures easily without complex wood manufacturing.

Figure 1: *Example of transforming "Tsunagi"*

The purpose of this study is to evaluate the performance of joints using *Tsunagi-clamp* and the horizontal resistance performance of a timber cubic frame structure using this clamped joint system and to apply the clamps to structural design.

2 DETAIL OF CLAMPED JOINT

Tsunagi-clamp has been developed based on scaffolding clamps [1], connecting orthogonal members as shown in Figure 2. This clamp is able to clasp a 45 mm squared cross-sectional timber by fastening the bolt at the tip of the clamp as shown in Figure 3.

Figure 2: *Detail of Tsunagi-clamp*

Figure 3: *How to use Tsunagi-clamp.*

One of the characteristic features of *Tsunagi-clamp* is the jagged teeth shape plate. Even if the timber shrinks upon

[1] Yoshisato Esaka, NIKKEN SEKKEI LTD, Structural Engineer, Japan, esakay@nikken.jp
[2] Tatsuki Ishizaki, NIKKEN SEKKEI LTD, Structural Engineer, Japan, ishizaki.tatsuki@nikken.jp
[3] Tsubasa Seguchi, NIKKEN SEKKEI LTD, Structural Engineer, Japan, seguchi.tsubasa@nikken.jp
[4] Tokuma Azemi, NIKKEN SEKKEI LTD, Structural Engineer, Japan, azemi.tokuma@nikken.jp

https://doi.org/10.52202/069179-0175

drying, the clamp can grab the timber firmly using these jagged plates.

There are 5 holes in each plate to reinforce the joint by screws and to connect other components to the clamp. For example, braces can add to *Tsunagi* easily by connecting the eye bolts, or it becomes possible to fix the structure by grabbing poles by connecting to the scaffolding clamp as shown in Figure 4.

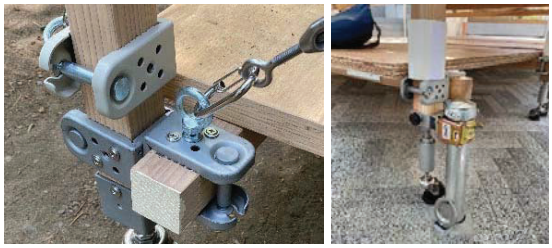

Figure 4: *Example of connecting Tsunagi-clamp and eye bolt or scaffolding clamp*

3 CLAMPED JOINT TESTING

To evaluate the performance of clamped joints, three types of tests were conducted. In all tests, the timber cross-sectional dimension was 45 mm squared, and the timber species was the Japanese Cedar (*Cryptomeria japonica*) with a Young's Modulus of 6000 N/mm^2.

3.1 Torsion tests

The torsion test used a T-shaped joint consisting of two 300 mm long members, connected by *Tsunagi-clamps*. There were five types of specimens as shown in Table 1.

To test the effect of the damage to the area of timber grabbed by the clamp, specimens T3 to T5 were cut down 2 mm in depth before the test. Specimen T2 and specimen T4 were reinforced by four screws, and specimen T5 was reinforced by filling the trimmed area with wood putty (main component was lacquer resin).

Figure 5 shows details of the experimental setup. Static monotonic loading was applied to the vertical member. Vertical force, vertical displacement, slip displacement, and angle of rotation of the vertical member were measured.

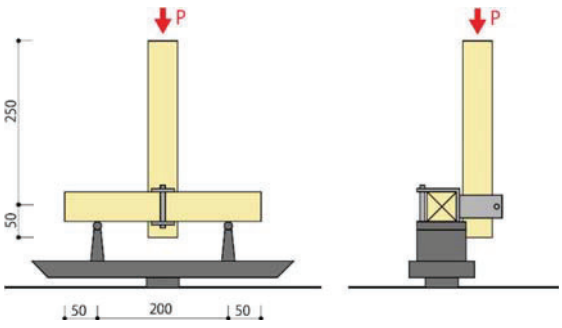

Figure 5: *Test setup of clamped joint torsion tests (units in mm)*

Table 1: *Specimens of the torsion tests*

Testing type	No.	Surface of timber	Reinforcement	Number of specimens
Torsion tests	T1	normal	—	3
	T2	normal	screw	3
	T3	damaged	—	3
	T4	damaged	screw	3
	T5	damaged	putty	3

By adding the vertical force, the nails of *Tsunagi-clump* caved into the horizontal members as shown in Figure 6. These fractures were less detected in Specimen T2 and T4.

Figure 7 shows the relationship between the vertical load and the vertical deformation of the specimens. In each graph, the line of average initial stiffness of T1 was drawn, which was calculated as the slope of the line from the point of $0.1 \times P_{max}$ to that of $0.4 \times P_{max}$, a method based on the structure design guide for framed wall construction houses [2]. This calculation method of initial stiffness was defined as Case 1 in this paper. The average initial stiffness of T4 was 2 times larger and and that of T5 was 4 times larger than that of specimen T1. These results suggest that both ways of reinforcement were effective even if the surface of the timber was damaged.

Figure 6: *Fracture of timber in the area grabbed by timber*

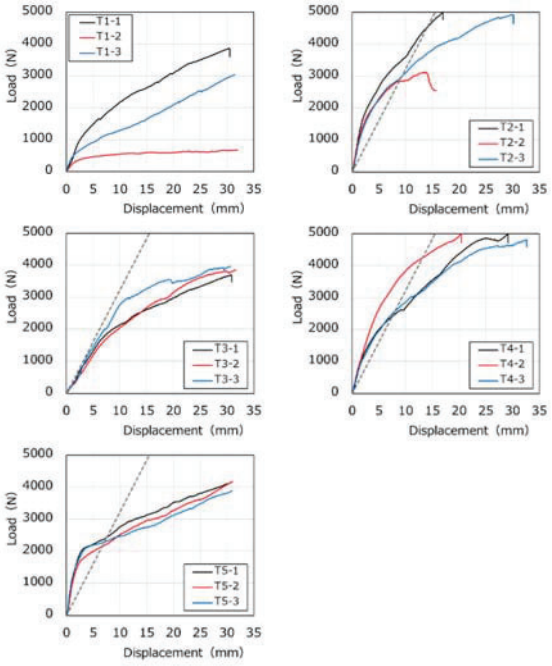

Figure 7: *Load (N) vs. vertical displacement (mm)*

https://doi.org/10.52202/069179-0175

It can be seen that by comparing T4 and T5, the stiffness of the reinforced specimen by screw became smaller gradually, but that by putty had a clear yield point. From this difference, it was assumed that the performance of wood putty method decreased above the initial deformation area.

Vertical displacement was divided into 2 types of displacements, rotate displacement ($= \delta_r$) and slip displacement ($= \delta_s$), both shown in Figure 8 and calculated by Equations (1) and (2). In the initial deformation area, the summation of δ_r and δ_s was closely equivalent to the measured vertical deformation ($= \delta_v$) shown in Figure 9

$$\delta_r = l_1 \times \theta_a \quad (1)$$

$$\delta_s = \delta_{ms} - l_2 \times (\theta_a - \theta_b) \quad (2)$$

Where δ_{ms}= measured slip displacement.

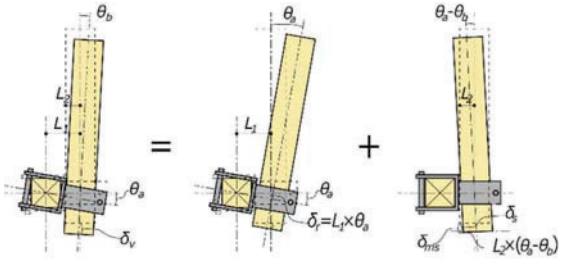

Figure 8: *Model of the deformation in the torsion test*

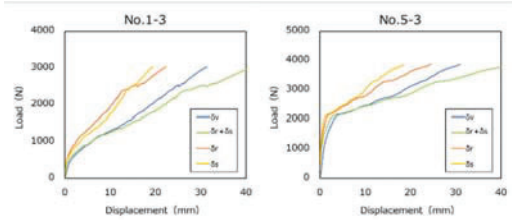

Figure 9: *Load vs. displacement (mm)*

The average stiffness K_r and K_s, calculated by δ_r and δ_s, are shown in Figure 10. In addition to Case 1, the slope of the line, from the starting point to point $\theta_a = \frac{1}{100}$ radians, was calculated as Case 2.

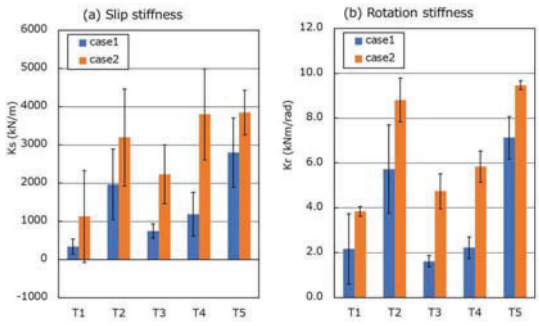

Figure 10: *Average slip stiffness and rotation stiffness.*

The stiffness in Case 1 were smaller than that of Case 2. In Case 1, the average stiffness while slip displacement occurred for T4 was about 1.6 times larger than T3 and T5 was 3.5 times larger than T3. When rotation displacement occurred in Case 1, the average stiffness of T4 was 1.4 times larger than T3 and T5 was 4.4 times larger than T3. From these results, it was assumed that putty was a more effective reinforcement than screws in both displacement cases.

3.2 Moment tests

The specimens for the moment tests consisted of two units of L-shaped joints, arranged to avoid any torsion effects. The lengths of the timber were 300 mm for monotonic loading tests and 450 mm for cyclic loading tests. The 5 types of specimens are shown in Table 2. The condition of the timber surfaces and reinforcement were similar to that of torsion tests, M3 to M5 were damaged and M2 and M4 were reinforced by screws, and M5 was reinforced by wood putty. Monotonic loading was applied to specimens M2 and M5, and cyclic loading was applied to specimens M1, M3, and M4).

Figure 11 shows the details of the test setup. Static monotonic loading was applied to both units. Vertical force, vertical displacement, and rotation angle between each member were measured.

Table 2: *Specimens of the moment tests*

Testing type	No.	Surface of timber	Reinforcement	Number of specimens
Moment tests	M1*	normal	—	6
	M2	normal	screw	3
	M3*	damaged	—	6
	M4*	damaged	screw	6
	M5	damaged	putty	3

*3 speciments were applied cyclic loading

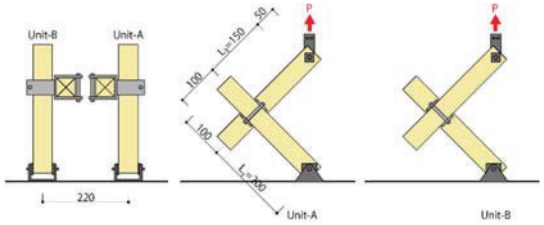

Figure 11: *Test setup of the clamped joint moment tests (mm)*

To analyze the relationship between the moment and angle of rotation, the moment of each unit was calculated by Equations (3) and (4).

$$M = PL \quad (3)$$

$$L = \frac{l_3 l_4 \sin\left(\frac{\pi}{2} + \theta\right)}{\sqrt{l_3^2 + l_4^2 - 2 l_3 l_4 \cos\left(\frac{\pi}{2} + \theta\right)}} \quad (4)$$

Figure 12 shows the relationship between the vertical load and the vertical deformation, and Figure 13 shows the comparison of the average rotational stiffness for the two cases. The initial stiffness of specimen M3 was 25% smaller than the average stiffness of specimen M1. The initial stiffness of specimen M4 was closely equal to that of specimen M3, and M5 was 35% larger than specimen

https://doi.org/10.52202/069179-0175

M1. These results suggested that putty was a more effective reinforcement than screws, similar to the results for torsion loading.

On the other hand, it was assumed that both screw and putty cannot prevent fracture by moment strength effectively since the maximum moment was about 230 Nm for all specimen cases.

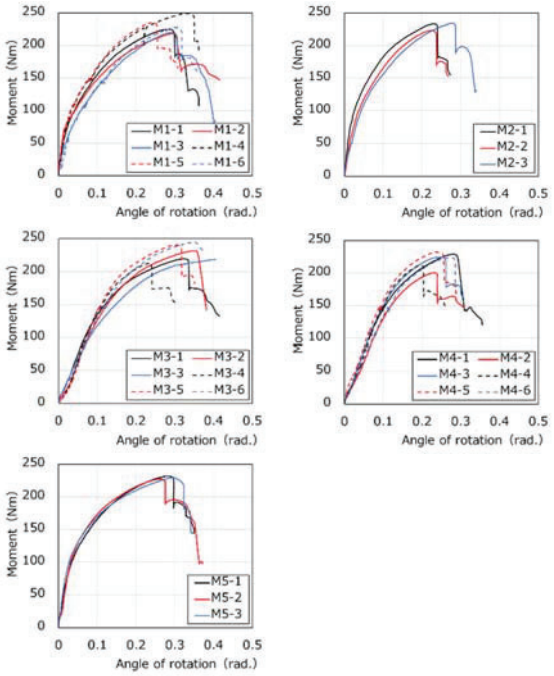

Figure 12: *Moment (Nm) vs. angle of rotation (rad)*

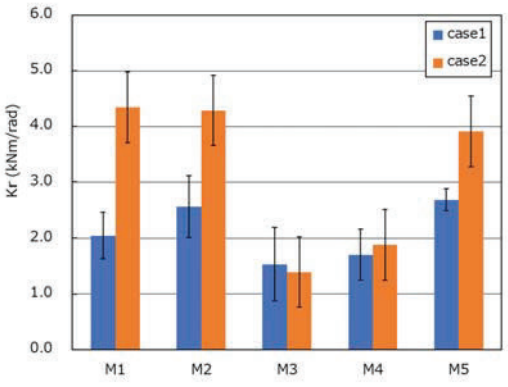

Figure 13: *Average rotational stiffness (kNm/rad)*

3.3 Long-term loading tests

To analyze the behavior of clamped joints under described two types of loading conditions, Long-term loading tests had been conducted for 300 days long. There were 3 types of specimens in each type of loading as shown in Table 3. Specimen LT2 and LT3 were conducted in outdoor conditions. The surface of LT3 was reinforced by filling the trimmed area with wood putty. Specimen LM2 was tested under the same condition as LT2, and LM3 was the same as LT3.

Figure 14 and Figure 15 show the details of the test setup. Static loading was applied to each specimen by hanging mass blocks. Vertical displacement and rotation angle between each member were measured.

Table 3: *Specimens of long-term tests*

Testing type	No.	Surface of timber	Reinforcement	Location	Number of specimen	Loading (N)
Tosion test	LT-1	normal	-	indoor	1	1,000
	LT-2	normal	-	outdoor	1	1,000
	LT-3	damaged	putty	outdoor	1	1,000
Moment test	LM-1	normal	-	indoor	1	100
	LM-2	normal	-	outdoor	1	100
	LM-3	damaged	putty	outdoor	1	100

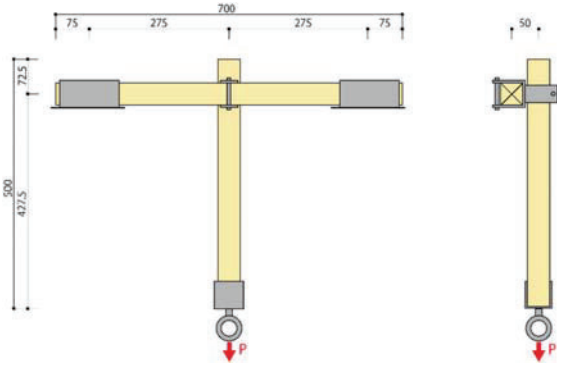

Figure 14: *Test setup of long-term torsion tests (mm)*

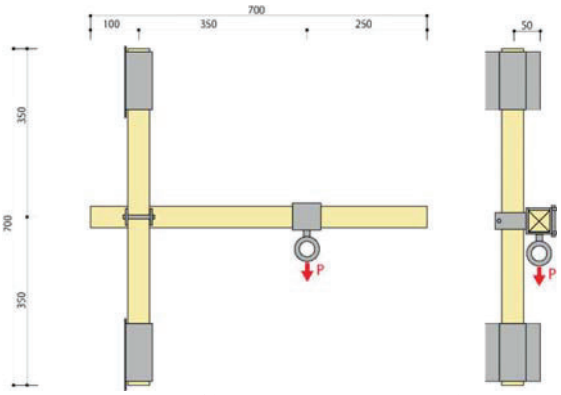

Figure 15: *Test setup of long-term moment tests (mm)*

Figure 16 shows the relationship between the time and angle of rotation. In both tests, the angle of rotation of LT1 increased slower than LT2 and LT3. In the torsion test, the angle of rotation of LT2 was 2 times larger than LT1, and LT3 was 5 times larger than LT1. In the moment test, the angle of rotation of LT2 and LT3 were 2.5 times larger than LT1. The results suggest that under outdoor conditions, filled putty tend to lose the performance of reinforcement, especially for the torsion loading condition.

Table 4 shows the creep coefficient in one week and one month, analyzed with power-law creep [3]. For the moment test, the coefficient ranged from 2.5 to 3.5 regardless of condition. On the other hand, for the torsion test, the factor ranged from 2.3 to 4.4 during normal surface conditions and ranged from 4.7 to 9.3 during wood putty reinforcement. These results suggested that reinforcement by wood putty were not suitable for outdoor usage.

https://doi.org/10.52202/069179-0175

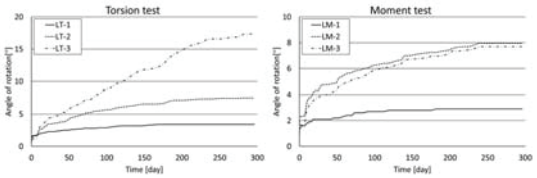

Figure 16: *Angle of rotation (°) vs. Time (day)*

Figure 17: *The nail of the clamp caved into specimens LT-3 and LM-3*

Table 4: *Increasing coefficent of deformation*

	LT-1	LM-1	LT-2	LM-2	LT-3	LM-3
a week	2.32	2.50	3.06	2.32	4.66	2.62
a month	2.72	2.86	4.41	2.91	9.32	3.51

4 ANALYSIS OF CUBIC FRAME STRUCTURE

To confirm the horizontal resistance performance of *Tsunagi* with *Tsunagi-clamp*, an analysis of the cubic frame structure was performed. The model of the cubic frame structure is shown in Figure 19. The model had dimensions of 2.8 m × 2.8 m× 2.1 m and was designed to be used as a medical booth, as shown in Figure 18.

Figure 18: *Modeling of Tsunagi used as a medical booth*

Each lumber was replaced with beam elements (drawn as red lines in Figure 19), each joint was replaced with elastic springs (drawn as black short lines in Figure 19), and the stiffness of clamp joints are listed on Table 5. These stiffnesses of y and z direction were the slip stiffness of T1 shown in Figure 10, these of rotation x direction was the rotational stiffness of T1 shown in Figure 10 and these of rotation y and z direction were the rotational stiffness of M1 shown in Figure 13. These stiffnesses of x direction were set by other joint tests.

The boundary conditions were the 8 pin supports at the base of the columns on both the left and right sides of the booth and the 5 roller supports at the base of columns on both the front and back sides of the booth as shown in Figure 19. Monotonic loadings were applied horizontally at Points A and B.

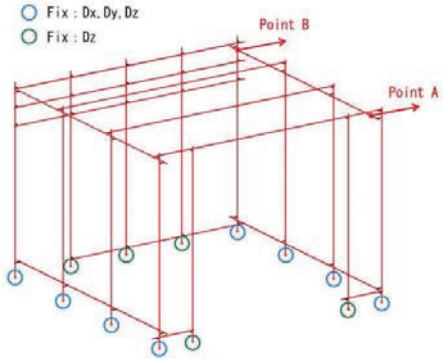

Figure 19: *Model of the cubic frame structure*

Table 5: *Stiffness of the clamp joints*

	Direction (kN/m)		Rotation (kNm/rad)		
Case1	x	420	x	2.2	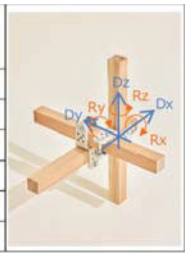
	y	340	y	2.0	
	z	340	z	2.0	
Case2	x	420	x	3.8	
	y	1100	y	4.3	
	z	1100	z	4.3	

5 CUBIC FRAME STRUCTURE TESTING

To confirm the horizontal resistance performance of the cubic frame structure, the authors conducted a full-scale horizontal load experiment as shown in Figure 20. The composition of the frame structure was the same as the analysis model. In order to replicate the boundary conditions used in the analysis, the bottom of each vertical member was fixed by setting the weights.

Monotonic loading of 100 N each was applied step by step to the top of the structure in the horizontal direction. Horizontal force and horizontal displacement at the top of the structure were measured.

The displacements of the frame structure by experiment and by analysis in former section are shown in Figure 21. Due to the difference in the number of joints, displacement at point A was bigger than that at point B. The displacement by case 1 analysis was smaller than the displacement by the experiment in the initial displacement area. But the results of case 2 analysis were closely matched the experimental results in the initial displacement area. Since *Tsunagi* was generally used only when the interlaminar deformation angle was under 1/100 radians, it was assumed more appropriate to use the

https://doi.org/10.52202/069179-0175

stiffness of case 2 in the analysis of *Tsunagi*. In addition, these results support this analysis method can adopt to other types of *Tsunagi* consisted with timber and clamped joint.

Figure 20: *Exsample of specimen of the horizontal loading tests*

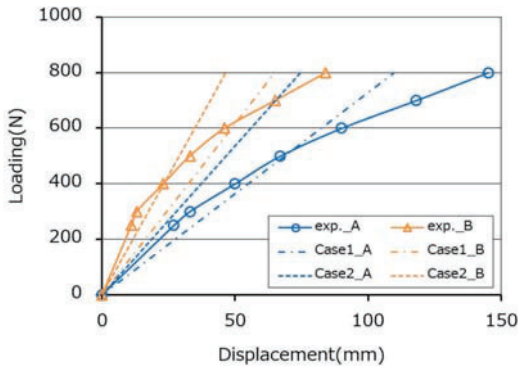

Figure 21: *Displacement of frame structure by analysis and by experiment*

6 EXAMPLE OF STRUCTURE WITH CLAMPED JOINT

The authors used *Tsunagi-clamp* to build cubic frame structures at KITAYA PARK, Shibuya. The overall structure consisted of three cubic structures and the dimensions each structure was 0.9 m × 1.8 m× 1.95 m. Each structure consisted of 13 timbers members and 22 *Tsunagi-clamps* and was built by 2 people in about an hour. To move them easily, these structures had wheels at the bottom of each vertical member. By changing the combination of each structure, the overall structure can be adapted for various usage as shown in Figure 22.

In this park, there is a building that used removable timber for exterior materials. It is envisioned that these *Tsunagi* could be built as temporary tents for emergency support by using this exterior timber in case of disaster.

7 SUMMARY AND CONCLUSION

By testing the clamped joints with *Tsunagi-clamp* in two types of loading conditions, the performance of this joint was analysed. It was confirmed that the reinforcements with screws or putty were effective for the improvement of the stiffness of joints even the surface of timber was damaged. On the other hand, considering long-term use, reinforcement with putty is not effective enough to prevent an increase in joint deformation.

The deformation by analysis of the cubic frame model with the stiffness of clamped joint tests in Case 2 was almost equivalent to that of the horizontal loading test. By analyzing with that stiffness, this clamped joint system can be applied to structural design and the prediction of other types of structure with this joint system are possible.

The authors have designed and constructed a structure as *Tsunagi* and plan to continue this activity to promote wood utilization.

Figure 22: *Tsunagi in KITAYA PARK*

ACKNOWLEDGEMENT

The authors are grateful to Sanshin Metal Working Co., Ltd. for producing *Tsunagi-clamp,* and thank Emachu Mokuzai Co., Ltd. and Shinohara Shoten Co., Ltd. for supplying timber, and thank Miyazaki Prefectural Wood Utilization Research Center for conducting the clamped joint tests.

REFERENCE

[1] Architectural Institute of Japan. Japanese Architectural Standard Specification 2 temporary construction. *Scaffold,* pages 79-121. Tokyo, 2006.

[2] Japan 2x4 Home Builders Association. Frame Wall Construction Method Building Design Guide. Tokyo, 2018.

[3] Japan Housing and Wood Technology Center. Strength Test Manual of Structural Timber. Tokyo, 2013.

World Conference on Timber Engineering Oslo 2023

EXPERIMENTAL STUDY ON CONTROL PARAMETERS FOR AUTOMATED APPLICATION AND IN- SITU PERFORMANCE ASSESSMENT OF JOINTS WITH SELF-TAPPING TIMBER SCREWS

Alexandra Eckert[1], Reinhard Brandner[2], David Glasner[3]

ABSTRACT: The paper in hand presents findings from experimental insertion tests with the purpose of establishing and quantifying necessary parameters for an automated application of the investigated self-tapping timber screws. The effects of input parameters such as contact force and revolutions per minute are examined and control parameters such as insertion moment and insertion length are recorded continuously. The biting-behaviour of screws is highly influenced by the contact force and the material parameters such as screw-diameter, screw-tip as well as the density and growth characteristics of the timber. With continuous control of insertion length and insertion moment a tight fit of the screw can be ensured, without damaging the screw or the surrounding timber. Given automatically applied screws with continuous recording of insertion moment and insertion length, the insertion energy can be calculated easily. As an in-situ performance assessment of automatically applied screws the hypothesis of estimating withdrawal characteristics on the basis of insertion energy is made. To validate this hypothesis, given experimental data of combined insertion and withdrawal tests is re-evaluated. A remarkable potential of predicting withdrawal properties with the insertion energy is found. This allows to thoroughly re-consider the design-to-execution process and the implementation of a research informed design process.

KEYWORDS: Automated application, insertion tests, withdrawal tests, self-tapping screws, in-situ performance assessment, research informed design

1 INTRODUCTION

The following studies were obtained as parts of the FFG BRIDGE project "CLT_joint" (project no. 883672), with the aim of developing an efficient, systematized and quality-assured connection solution for solid timber constructions with cross laminated timber (CLT). The solution is envisaged as a combination of timber-connection (application on CLT-components with self-tapping screws in course of joinery in the factory) and assembly-joint (joining of CLT-components on site). Due to the dominating quasi-brittle properties of timber components, it is intended that the timber-connection is designed with a sufficient over-strength to achieve the required ductility and energy dissipation specifically in the assembly-joint. Considering the prefabrication of the timber-connection this solution promises shorter assembly times and higher reliability and thus enhanced quality and cost-effectiveness in comparison to the current state of manually and completely on-site applied fasteners.

Known and already established, industrially implemented possibilities for an automated application of fasteners (e.g. automotive or aviation industry) motivate the integration of such processes supplemented by continuous quality control measures also within the timber industry, e.g. during the joinery of the CLT-elements. Required process steps for such, in the prefabrication integrated, application-units include separation, feeding and positioning, as well as the insertion of the screws and metal fittings. Common existing application units are limited to screws with small dimensions and correspondingly low max. insertion moments and primarily vertical insertion. For the expected screw dimensions used in timber construction (nominal diameter $d = 6$ to 12 mm, lengths up to 500 mm), the required flexibility to apply such screws at different angles (in and out of plane), together with higher insertion moments must be considered and necessary parameters for a controlled insertion need to be established.

Regarding performance-assessment, the hypothesis is made that the individual information on the insertion-energy, which can be calculated very easily assuming a continuous control of the insertion moment and insertion length, is more suitable for estimating the withdrawal capacity and the slip modulus than the information on the individual maximum insertion moment or the global product density (please note: density is currently the only timber-specific property for estimating the stiffnesses and strengths of fasteners anchored in timber in the course of the design). The background for the made hypothesis is that by recording the insertion energy, the interaction

[1] Alexandra Eckert, TU Graz, Institute of Timber Engineering and Wood Technology, Austria, alexandra.eckert@tugraz.at
[2] Reinhard Brandner, TU Graz, Institute of Timber Engineering and Wood Technology, Austria, reinhard.brandner@tugraz.at
[3] David Glasner, TU Graz, Institute of Timber Engineering and Wood Technology, Austria, david.glasner@tugraz.at

https://doi.org/10.52202/069179-0176

between the material and the fastener, influenced by local growth characteristics such as knots, is considered along the entire screw channel, whereas the single knowledge of the maximum insertion moment, although also considered as individual property, only represents a punctual information. The idea to estimate the withdrawal properties of self-tapping screws based on the insertion energy came up in frame of a previous research project, see [1]. A similar approach was already successfully applied for screws inserted in bones; see [2].

2 INSERTION TESTS

2.1 GENERAL INFORMATION

With the purpose of establishing and quantifying necessary control parameters, insertion tests were carried out. Special attention was set on the two critical phases of an automated insertion process: the biting of the screw-tip and the tightening of the screw-head.

2.2 MATERIALS AND METHODS

2.2.1 Materials and test overview

Insertion tests were carried out with self-tapping screws with countersunk heads, varying nominal diameters d = {8; 10; 12} mm, total lengths l = {180; 300; 400} mm and screw-tips {C; D; F; H}, see Figure 1 and Table 1.

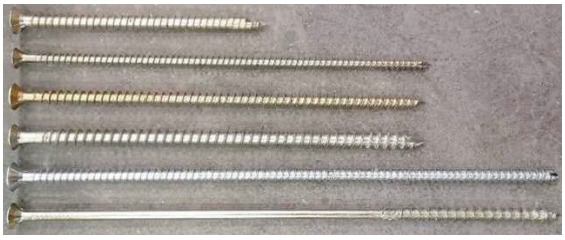

Figure 1: *Investigated self-tapping screws – from top to bottom: 10/180 mm with tip H, 8, 10, 12/300 mm with tip C, 10/400 mm with tip D and 10/400/120 mm with tip F.*

The screws were inserted in the middle layer of five-layer CLT-elements (layup 40 | 20 | 40 | 20 | 40 mm) made of Norway spruce (*Picea abies*). The angle between the axis of the screw and the fiber-orientation of the middle layer (short: load-grain angle α) varied between α = {0; 45; 90} °, see Table 1. In order to adequately represent the characteristics of timber used in construction practice, screws were also applied in finger joints, knots and other typical growth and product characteristics.

Table 1: *Matrix of investigated parameters, such as: screw-tip, nominal screw diameter d, screw length l and load-grain angle α.*

screw-tip	d [mm]			l [mm]	α [°]		
type H	–	10	–	180	0	45	90
type C	8	10	12	300	–	–	90
type D	–	10	–	400	0	45	90
type F	–	10	–	–	0	45	90

Twelve series (three series per screw-tip) with 20 replications each and thus a total of 240 screws were tested. The fully-threaded screws where inserted completely; partially-threaded screws with tip F were only tested in respect to their biting behaviour.

2.2.2 Test configuration

The insertion tests were carried out as illustrated in Figure 2. An electric drive on a fixed support drives the screw while a standard pneumatic cylinder applies pressure between the timber specimen on the moving support and the screw. Both, revolutions per minute (RPM) of the electric drive and contact pressure of the standard pneumatic cylinder, are controlled manually. A cable extensometer between the fixed and the moving support is measuring the displacement. The insertion moment is recorded by a torque transducer, which is placed between the screw and the electric drive. In order to measure the screw force (force between wood specimen and screw head while tightening the screw) a load cell is placed between two steel plates in front of the timber specimen, mirroring a steel-timber joint with outer steel plate. The inserted length of the screws is reduced by 80 mm (height of the load cell plus thickness of steel plates). During insertion testing the parameters time (t), insertion length (l_i)*, insertion moment (M), rotation angle (φ) and screw force (F) were recorded continuously (measurement rate 5 Hz).

* possible small angular deviations might cause differences between insertion length and measured displacement; these are neglected

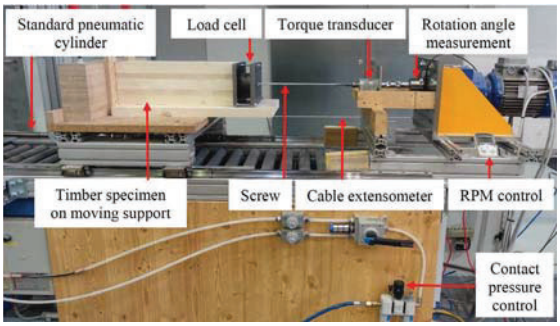

Figure 2: *Test setup and measuring devices of insertion tests.*

2.2.3 Input parameters

To determine optimal conditions for rapid biting of the screw, the effects of input parameters, such as revolutions per minute (RPM) and contact force (CF) between the wood specimen and the application device were investigated. The input parameters RPM and CF were chosen with {50; 100} Hz and by setting the contact pressure to {0.5*; 1.0; 2.0; 4.0; 6.0} bar, respectively. After a small test series and by using the load cell, the according results of the CF are {0.11; 0.14; 0.29; 0.61; 0.95} kN. These results are lower than the calculated force of the standard pneumatic cylinder (contact pressure times cylinder area), which attributes to frictional loss.

* due to inaccuracy of the pressure-control in the lower range the value 0.5 is assumed to be approx. 0.7 bar (corresponds with resulting CF)

https://doi.org/10.52202/069179-0176

2.2.4 Test procedure

The recording of said parameters started after placing the screw tip through the load cell onto the timber specimen. CP and RPM started simultaneously. While the set CP was reached immediately, the acceleration of RPM took a view seconds to reach its set value.

Special attention was set on the critical phase of the insertion: the biting of the screw-tip. In case of no biting after 20 revolutions, the biting process was considered as failed and the CP was raised until biting occurred which enabled the continuation of the insertion test. After reaching a specific insertion length during the insertion (depending on the pitch of the screw and the set RPM), the RPM was decelerated to 5 Hz for better observation of the other critical phase: the tightening of the screw. The testing finished after failure due to torsion of the screw or overturning of the screw.

2.2.5 Evaluation of biting behaviour

To evaluate the biting behavior, the continuous recording of insertion length (l_i), rotation angle (φ) and insertion moment (M) was examined. The biting behaviour was assesed with the amount of revolutions until the screw-tip bite. The evaluation is limited to 20 revolutions, because during testing at this point the biting was classified as failed. When biting occurred the gradient of the insertion length-revolution graph corresponded with the respective pitch (p) of the screw and the insertion moment increased, as exemplarily illustrated in Figure 3.

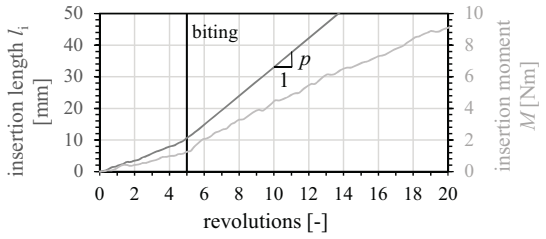

Figure 3: *Example of biting evaluation on insertion length (l_i) and insertion moment (M) plotted over revolutions.*

2.3 RESULTS AND DISCUSSIONS

2.3.1 Density and moisture content

There is only a slight variability in the density between the series and the ranges are quite comparable. The average density ($\rho_{12,mean}$) is 461 kg/m³ with a range from 408 to 515 kg/m³ (CV = 4.7 %). The average wood moisture content is 11.7 %. Further details can be found in the accompanying test report, see [3].

2.3.2 Biting behaviour

To investigate the influence of parameters on the biting behaviour, different sets of test data with equal boundary conditions are compared. Figure 4 shows different load-grain angles and contact forces with equal boundary conditions d = 10 mm and screw tips H, D and F. Wood specimens with knots or other growth or product characteristics are excluded in this diagram to concentrate on the influence of α. The results only differ noticeably in the low CF-range for α = 0°. In the higher range of CF, the influence of the load-grain angle seems to diminish.

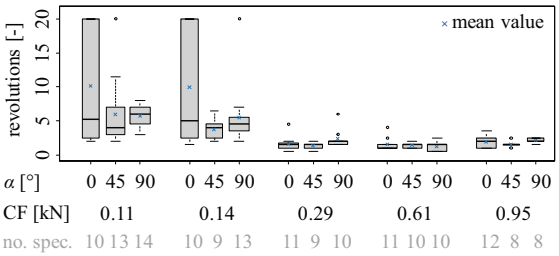

Figure 4: *Biting behaviour vs. load-grain angle α and contact force CF (please note: statistical values of groups exceeding the evaluation-limit of 20 revolutions represent lower estimates).*

In Figure 5 the biting behaviour is shown for different screw diameters and contact forces with equal boundary conditions α = 90° and screw-tip C. In this diagram data from screw insertion in knots and other growth and product characteristics are included. The influence of the screw diameter on the biting-behaviour is evident, but an overall more perceivable effect is again reached by the CF. Setting the CF to approx. 0.3 kN already achieved successful biting for those tested boundary conditions.

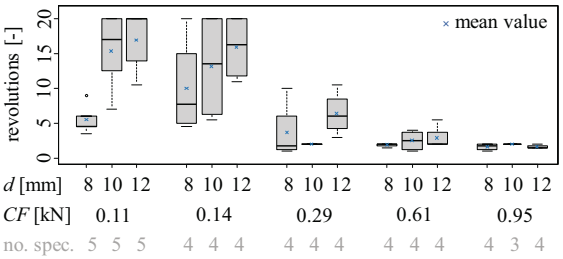

Figure 5: *Biting behaviour vs. diameters d and contact force.*

The required CF for a rapid biting in knots is shown in Figure 6, representing the collected data of screw tips inserted in knots with d = 10 mm regardless of the type of the screw tip {H; C; D; F} and α = {0; 45; 90}°.

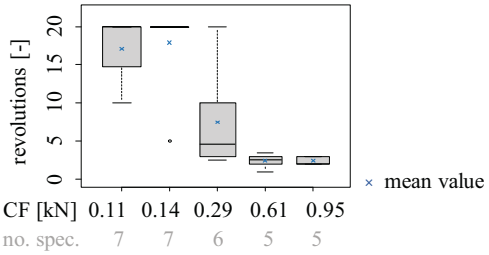

Figure 6: *Biting behaviour of screws applied in knots.*

Regarding RPM no influence on the biting behaviour can be detected due to the fact that the biting often took place

https://doi.org/10.52202/069179-0176

before the set RPM was reached. Yet the observation was made, that in cases of no biting after 20 revolutions where the RPM had reached its set value, the CF needed to be increased even higher at RPM = 100 Hz than at 50 Hz to achieve biting.

2.3.3 Tightening – insertion moment

Beside the biting of the screw, the tightening of the screw represents another critical phase within an automated insertion process. Figure 7 plots the insertion moment of screws with different diameters (d) and the following boundary conditions: $\alpha = 90$ °, $l_i = 220$ mm and screw tip C. The lower box-plots represent the distribution of the max. insertion moment measured from the screw-tip to the beginning of the screw-head and the highest plots represent the max. insertion moment measured from contact of the screw head with the sinking until failure. The full dots in between represent the characteristic values of the torque resistance ($f_{tor,k}$) for each screw diameter according to the European Technical Assessments (ETAs) of these screws. The insertion moment increases with increasing screw diameter, considering the data until head and incl. head.
The max. insertion moment incl. head exceeds the torque resistance by a significant margin. Although the actual resistance of the tested screws is probably higher than the characteristic value, the amount of deviation is most likely a result of the interaction between screw head and steel plate (please note: screws compared in Figure 7 have the same underhead milling ribs).

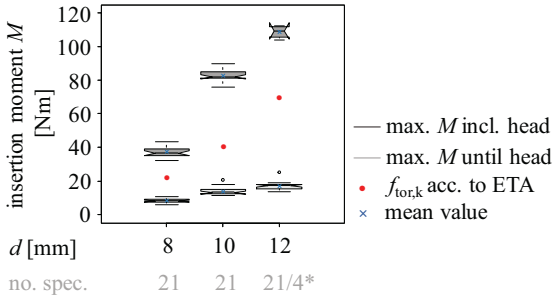

Figure 7: *Diameter vs. max. insertion moment until the beginning of the screw head and max. insertion moment incl. embedment and tightening of the screw head in the sinking of the steel plate (* only 4/21 screws with d = 12 mm failed by torque as the screw drive reached their max. capacity before).*

Figure 8 plots the insertion moment of screws with different insertion lengths and the following boundary conditions: $d = 10$ mm and $\alpha = 90$ °. Whereas screws with $l_i = 100$ and 220 mm had similar underhead milling ribs, screws with $l_i = 320$ mm had a smooth underhead surface. The max. insertion moment until head (lower boxplots) increases with increasing insertion length.
The results of the max. insertion moment incl. head (higher boxplots) of screws with milling ribs ($l_i = 100$ and 220 mm) also increase with increasing insertion length. Between the heads of these screws and the sinkings a high interaction was observed in form of abrasion of the sinking, which is attributed to friction and milling. The investigated screws with a smooth underhead surface ($l_i = 320$ mm) are not reflecting the same effect. This is most likely due to the lower interaction between the head and the sinking which in this case can be attributed solely to friction. Nonetheless, their data incl. head exceeds $f_{tor,k}$ according to the ETA (full dot) by a significant margin.
Screws with insertion lengths $l_i = \{220; 320\}$ mm failed due to torsion of the screw. The screws with the lowest insertion length failed due to overturning of the screw. In combination with a relatively high $f_{tor,k}$ this leads to an overlap of the data incl. head and $f_{tor,k}$ (please note that 10 d represents a low insertion length in timber constructions where high load bearing screwed joints are often designed for screw tension failure).
Speaking for the critical phase of screw tightening, for screws designed for tension failure (where the possibility of overturning principally can be neglected) higher tightening moments are possible and also often required compared to standard screw torsion tests.

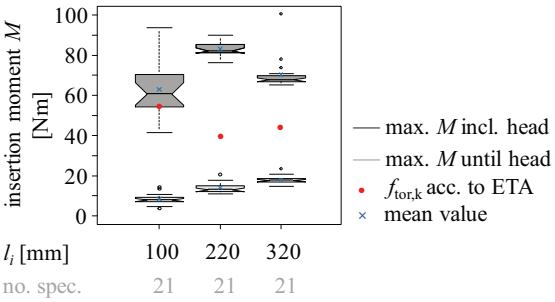

Figure 8: *Insertion length vs. max. insertion moment until the beginning of the screw head and max. insertion moment incl. embedment and tightening of the screw head in the sinking of the steel plate.*

2.3.4 Further results

The insertion energy was calculated with the pitch of the screw and the insertion moment in combination with the insertion length according to Equation (1) in Chapter 3.2. Results show an increase in insertion energy with increasing nominal screw diameter. The same effect is observed, when analysing the maximum screw force of the tested diameters.
The insertion energy and the maximum screw force also increase with increasing insertion lengths, although this effect is limited by the screw capacity itself; the tensile strength ($f_{tens,k}$).
When analysing the influence of input parameters CF and RPM on the maximum insertion moment, the insertion energy and the screw force, no correlation can be determined. For further details see [3].

https://doi.org/10.52202/069179-0176

3 PERFORMANCE-ASSESSMENT AND OPTIONS FOR RESEARCH INFORMED DESIGN (RID)

3.1 SETTING UP THE HYPOTHESIS AND GENERAL COMMENTS

In the following, the hypothesis is analysed, that the total insertion energy, determined along the total insertion length, serves as a better, more reliable predictor for the withdrawal properties (strength and slip modulus) than the maximum insertion moment, as one punctual characteristic, and the density, whether it is available as local or global (product) characteristic.

The background to this consideration is simply the fact, that the total insertion energy, as integral of the measured insertion energy along the insertion length, takes local irregularities into account, such as knots, checks and reaction wood. The prerequisite for this is a quasi-continuous recording and data processing of insertion moment and insertion length together with parameters of thread geometry, as it would be possible during an automated and controlled application of screws. Saying that, the insertion energy provides additional information on screw application but cannot substitute others, e.g. the insertion moment, which still needs to be controlled to prevent overturning and torque failure of the screw.

The following sections analyse the hypothesis in detail. As this is done as a second, widely independent part of the overall paper, the principle structure of a research paper is widely repeated.

3.2 MATERIALS AND METHODS

In total 284 data sets from twelve series, each with 20 to 24 specimens, from insertion tests without predrilling acc. to [5] and withdrawal tests acc. to [6] conducted on the same specimens are used. The tests, made in Norway spruce (*Picea abies*), comprised three different density classes {A; B; C}, two different screw types {RF; P1}, each with a nominal diameter d = 8 mm, and two different load-grain angles $\alpha = \{0°; 90°\}$. Series of the same density class were organised as matched samples, i.e. as series with similar density distributions. To test solely the thread, all screws were screwed through the specimens with a nominal thickness in loading direction of 50 mm, so that the tip and compressor left the opposite side. This boundary condition should be kept in mind as it represents a rather uncommon practical condition. The specimens were conditioned at 20 °C and 65 % rel. humidity before testing. Details on the determination of the moisture content u [%], the local density ρ_{12} [kg/m³], the insertion moment M [Nm], the withdrawal strength f_{ax} [MPa] and the slip modulus K_{ser} [kN/mm] are provided in [3] and [4]. The insertion tests were re-evaluated to determine not only the maximum insertion moment but also the insertion energy W [Nm] calculated acc. to Equation (1):

$$W = \frac{2\pi}{p} \int M \, \partial l_i \qquad (1)$$

where l_i is the insertion length [mm] and p the pitch of the screw [mm].

Three different conditions were investigated for the completion of the summation: (1) the final insertion length, (2) the point of the maximum insertion moment, and (3) 50 mm insertion length. In the following, the insertion energy acc. to (3) is used as it is the most representative for practical applications; it is also rather close to (2); see [3].

3.3 RESULTS AND DISCUSSIONS

3.3.1 General statistics and regression analyses

Table 2 summarizes the main statistics per test series for the most important properties. Statistics for the moisture content are provided in [3] (average moisture contents per series within 12.5 and 13.2 %).

The average densities confirm the successful creation of matched samples within each density class and clearly different densities between the classes. The total bandwidth of 330 to 620 kg/m³ covers a typical range for Norway spruce. The maximum insertion moments for P1 are on average slightly higher than for RF. The difference between both screw types is even higher for the slip modulus, irrespective of the load-grain angle. In contrast, the withdrawal strengths are similar at 90° and slightly lower for P1 at 0°, due to the thicker core of P1; see [7]. Compared to P1, for RF the average values for the insertion energy are in trend clearly higher in case of $\alpha = 0°$ and slightly lower in case of $\alpha = 90°$. The coefficients of variation (CV) for the insertion energy are widely within 15 and 20 % and similar as for M; see [3].

***Table 2**: Main statistics of analysed series of insertion and withdrawal tests.*

Series	n [–]	$\rho_{12,mean}$ [kg/m³]	$f_{ax,mean}$ [MPa]	$K_{ser,mean}$ [kN/mm]	M_{mean} [Nm]	W_{mean} [Nm] | CV [%]
A_P10	24	362	4.5	23.0	2.9	139 | 17
A_RF0	24	358	4.9	18.0	2.8	150 | 10
A_P190	24	368	5.0	13.1	3.2	160 | 12
A_RF90	24	373	5.1	11.3	2.8	155 | 17
B_P10	24	442	3.9	21.3	3.4	163 | 8
B_RF0	24	441	4.4	18.3	3.3	181 | 10
B_P190	23	448	6.3	16.1	4.6	218 | 11
B_RF90	24	450	6.2	14.3	4.0	210 | 13
C_P10	24	536	5.6	30.8	4.9	237 | 25
C_RF0	24	539	6.4	26.4	4.8	265 | 22
C_P190	21	539	7.7	22.5	6.1	290 | 17
C_RF90	24	543	7.8	18.1	5.4	286 | 18

For the statistical analyses of the relationships between the withdrawal properties $\boldsymbol{Y} = \{f_{ax}; K_{ser}\}$ and the indicating properties $\boldsymbol{X} = \{\rho_{12}; W\}$ power regression models are applied which consequence from assumed lognormal variables; see Equation (2):

$$Y_j = \beta_0 X_j^{\beta_1} \varepsilon_j \quad \Leftrightarrow \quad \ln(Y_j) = \ln(\beta_0) + \beta_1 \ln(X_j) + \varepsilon_j \qquad (2)$$

where $\{\beta_0; \beta_1\}$ are the regression coefficients and ε is the standard error. Regression models are calculated for each

https://doi.org/10.52202/069179-0176

screw type {RF; P1} and load-grain angle α = {0°; 90°} whereby the density groups {A; B; C} are combined. The outcomes for the estimated regression coefficients, standard errors (s_e) and adjusted coefficients of determination (r^2_{adj}) are summarized in Table 3.

***Table 3**: Regression coefficients and main statistics of power regression models per screw type and load-grain angle.*

Group	Model	$\hat{\beta}_0$	$\hat{\beta}_1$	s_e	r^2_{adj}
RF0	$f_{ax} \sim \rho_{12}$	0.062	0.724	0.225	0.23
	$f_{ax} \sim W$	0.138	0.686	0.176	0.53
	$K_{ser} \sim \rho_{12}$	49.77	0.990	0.179	0.48
	$K_{ser} \sim W$	366.9	0.763	0.133	0.71
RF90	$f_{ax} \sim \rho_{12}$	0.005	1.164	0.071	0.88
	$f_{ax} \sim W$	0.216	0.631	0.081	0.84
	$K_{ser} \sim \rho_{12}$	5.885	1.275	0.123	0.74
	$K_{ser} \sim W$	365.7	0.685	0.133	0.70
P10	$f_{ax} \sim \rho_{12}$	0.063	0.702	0.225	0.21
	$f_{ax} \sim W$	0.140	0.673	0.172	0.54
	$K_{ser} \sim \rho_{12}$	194.6	0.793	0.216	0.27
	$K_{ser} \sim W$	837.1	0.653	0.178	0.50
P190	$f_{ax} \sim \rho_{12}$	0.004	1.200	0.093	0.82
	$f_{ax} \sim W$	0.112	0.750	0.080	0.87
	$K_{ser} \sim \rho_{12}$	2.557	1.441	0.138	0.75
	$K_{ser} \sim W$	145.8	0.883	0.135	0.76

These power regression analyses are illustrated exemplarily for the screw type RF and α = 0° in Figure 9 and Figure 11 and for α = 90° in Figure 10 and Figure 12.

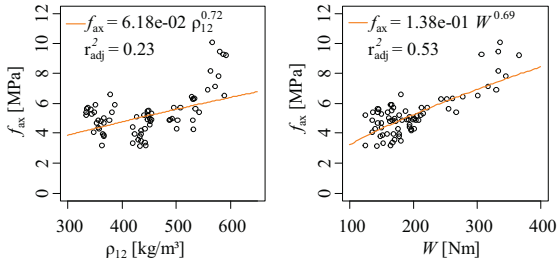

***Figure 9:** Power regression analysis for f_{ax} vs. ρ_{12} (left) and f_{ax} vs. W (right) exemplarily for RF and α = 0°.*

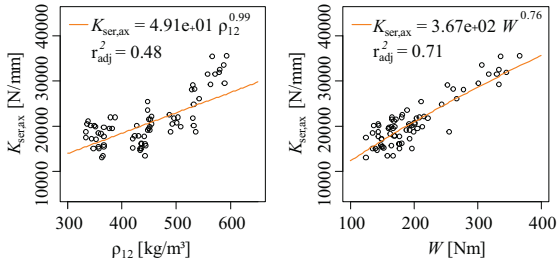

***Figure 10:** Power regression analysis for $K_{ser,ax}$ vs. ρ_{12} (left) and $K_{ser,ax}$ vs. W (right) exemplarily for RF and α = 0°.*

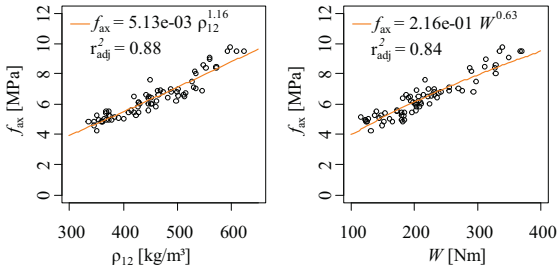

***Figure 11:** Power regression analysis for f_{ax} vs. ρ_{12} (left) and f_{ax} vs. W (right) exemplarily for RF and α = 90°.*

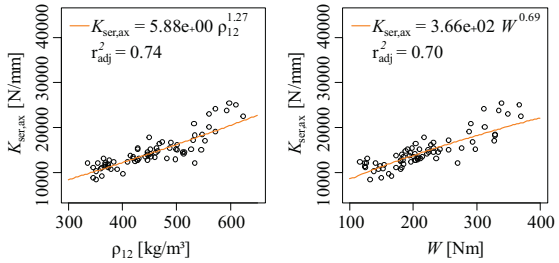

***Figure 12:** Power regression analysis for $K_{ser,ax}$ vs. ρ_{12} (left) and $K_{ser,ax}$ vs. W (right) exemplarily for RF and α = 90°.*

With ρ_{12} as indicating property, the regression coefficients for α = {0°; 90°} are clearly different whereas in case of W the coefficients are rather close. The values for r^2_{adj} confirm previous findings of the very limited capability of ρ_{12} to predict withdrawal properties at α = 0°; see [8] and [9]. This circumstance is usually of less importance as the reference properties normally refer to α = 90° and properties at deviating conditions are adapted accordingly by means of corresponding relationships. W is rather able to reliably predict the withdrawal properties which is clearly demonstrated by overall higher degrees of determination. The total insertion energy also adapts more individually to the insertion conditions which is also visible in Figure 9 to Figure 12 where for the same withdrawal data the ratio $\rho_{12,max}$ / $\rho_{12,min}$ is approximately two whereas it is four for W_{max} / W_{min}. To conclude: based on this analysis there is a clear indication that the total insertion energy serves overall as better and more reliable predictor of the withdrawal strength and slip modulus than the local density.

In order to benefit accordingly from this finding, the acquisition of the data required for this in the course of an automated, controlled screw application process is indispensable. It should be mentioned that the insertion energy is influenced by certain screw features (e.g. cutters and compactors, tip geometry, slide coating, screw length in the case of partially-threaded screws, etc.) which do not (or only to a minor extent) affect f_{ax}. As a result, more general models to describe f_{ax} by means of the insertion energy might need to consider these parameters and thus the individual screw type. In the following it is assumed that this will take place.

3.3.2 Analysis of the current design process and the potential benefits of the new findings

Within the current design process and with focus on the resistance part, the engineer doing the design usually follows design standards and applies characteristic properties, which are tabulated in referenced product standards or can be easily calculated from standardized relationships. The standardized characteristic properties and relationships need to account for all the uncertainties associated with the assumed product, strength class, production, producer and execution; see e.g. [10]. As long as the structure is not realised, these uncertainties belong to the aleatoric part; only the timber product and the nominal strength class are determined by the designer who assumes that it will also be executed that way. By erecting the structure, the aleatoric part becomes epistemic; the properties are fixed but usually still remain unknown.

In the current design of joints in timber, the properties of fasteners determined from their interaction with timber are only related to one timber property, the characteristic (5 %-quantile) of the density of the specific timber product and the nominal strength class. This value has to be distinguished from the local density which is usually determined in tests and used as indicating property in regression analyses to derive the before mentioned standardized relationships. The product density itself is usually not representative for the individual fastener properties as homogenisation effects, caused by the composition of products out of components (e.g. glulam composed of laminations) are considered in setting the characteristic values, whereas fasteners often penetrate only one or a limited number of components and therefore do not realize the same homogenisation effects ([11], [12]).

An automated controlled screw application system combined with the possibility to receive direct information on the local insertion properties, a set of models for a reliable estimation of the individual fastener withdrawal properties and newly created opportunities to adapt the joint execution, e.g. by adaptation of the insertion length, the number of fasteners within a joint and/or the spacing between joints in discretely equipped connection lines, provides a set of new possibilities to thoroughly re-consider the design-to-execution process by implementing research informed design (RID; see [13]). In doing so, a number of uncertainties inherently associated with the current design process would be eliminated. Designers could compensate this by setting higher characteristic properties, referring to higher quantile values, and/or by lower partial safety factors. During the automated screw and joint application, the fulfilment of the requirements set by the designer is individually controlled and adapted if necessary. This way, the determined but in current design-to-execution processes usually remaining unknown properties become known to a significant extend. Thereby, the model uncertainties associated with the estimated withdrawal properties and all uncertainties associated with the execution and quality assurance process, including the uncertainty associated with the measurement itself, shall be considered, e.g. by using lower quantile values of the estimates. For example, under the made assumption of lognormal variables the regression models in Table 3, which lead to average estimates for Y_j given a specific value of X_j, could be easily transformed to calculate quantile values, e.g. acc. to Equation (3):

$$y_{p,j} = \exp\left(\left(\ln(\beta_0) + \beta_1 \ln\left(X_j\right)\right) + z_p \sigma_{\ln(Y_j)}\right) \qquad (3)$$

where $y_{p,j}$ is the p-quantile value of Y for the j-th screw, z_p is the p-quantile value of the standard normal distribution and $\sigma_{\ln(Y_j)}$ is the standard deviation of Y for the j-th screw in the logarithmic domain.

The benefit of this approach is exemplarily demonstrated for the series C_RF90. The reason for selecting this series is its representativeness in respect to CV[f_{ax}] = 14.6 % and CV[ρ_{12}] = 7.0 %; see e.g. [7], [8], [14]. Please note: this demonstration is not intended to validate any of previously presented models. To ensure equal conditions for the following comparisons, all statistics and models are taken directly from series C_RF90.

The characteristic values for the density and the withdrawal strength, as 5 %-quantiles of assumed lognormal variables, are $\rho_{12,05}$ = 484 kg/m³ and $f_{ax,05}$ = 6.1 MPa, respectively. Following the current version of prEN 1995-1-1 [15] and [14], the characteristic withdrawal strength for a material featuring a similar characteristic density as series C_RF90 would be $f_{ax,k}$ = 5.9 MPa. By considering that $f_{ax,k}$ acc. to [15] has to account for all the additional uncertainties related to product, batch and many more (see e.g. [10]), the values appear as too close in this case.

The power regression model $f_{ax} \sim W$ for series C_RF90 reads $f_{ax,j} = 0.1075 \cdot W_j^{0.7583}$, with $r^2 = 0.89$, so 89 % of the variance in f_{ax} can be explained by the regression model; thus, only 11 % uncertainty remain in the individually estimated $f_{ax,j}$. To be in line with current design procedures, by means of Equation (3) 5 %-quantile values $f_{ax,j,05}$ are calculated for each individually estimated $f_{ax,j} \mid W_j$. The average value of these 5 %-quantiles is $f_{ax,j,05,mean}$ = 6.63 MPa. By considering the individual potentials, in comparison to $f_{ax,05}$ for series C_RF90 and $f_{ax,k}$ acc. to [15], the characteristic value is on average 9 % and 13 % higher, respectively. The bandwidth of the ratio $f_{ax,j,05,est} / f_{ax,j,test}$ is 0.77 to 0.92, the average value 0.85, which means that the applied approach is conservative; theoretically the capacity of 1 / 24 specimens could be overestimated.

Acc. to the load and resistance factor design (LRFD) approach, as implemented in the Eurocode, the reduced uncertainty not only consequence in higher characteristic values but also in lower partial safety factors γ_M. Acc. to [16], for simple cases and lognormal variables the design value can be calculated acc. to Equation (4):

$$y_d = \mu_Y \exp\left(-\frac{1}{2}\ln(1 + CV_Y^2) - \alpha_s \beta \sqrt{\ln(1 + CV_Y^2)}\right) \qquad (4)$$

https://doi.org/10.52202/069179-0176

where α_s is the sensitivity factor and β the target reliability index. In the following a 50-year reference period with $\alpha_s = 0.8$ and $\beta = 3.8$ for buildings in consequence class CC2 are applied. Acc. to [15] the reference partial safety factor for connections is $\gamma_M = 1.30$. Considering the significantly reduced uncertainty associated with the individually estimated withdrawal strengths $f_{ax,j}$, the partial safety factor can be adapted accordingly by reformulating Equation (4). In this special and simplified case $\gamma_M = 1.05$ would be sufficient to reach the same reliability (please note: $\gamma_M = 1.30$ is already higher than required for the reference case with CV[f_{ax}] = 15 %).
Although this demonstration example is rather simplified and could be also further elaborated by means of a Baysian approach, it clearly shows the advantages of RID in the sense of applying regression equations with high prediction quality for an individual estimation of withdrawal properties by means of in-situ acquisition of indicating properties. The reduced uncertainty allows to apply higher characteristic values and lower partial safety factors. Apart from that, knowing more about the individual screw properties in combination with a controlled screw application also raises the knowledge on the group behaviour. This enables to increase the effective number of screws accountable in the design, i.e. to apply a higher n_{ef}.

4 CONCLUSIONS

Within this contribution the potentials of an automated and controlled screw application are exemplarily analysed. The first part discusses the basic setting, parameters and requirements to secure a controlled automated screw application for the investigated screws. The second part outlines the power of the insertion energy as indicator for the withdrawal properties and demonstrates exemplarily the advantages of an individual estimation of the screw properties instead of using characteristic values of the population as common in the current design. In the following, the main conclusions of both parts are given.

4.1 AUTOMATED APPLICATION – CONTROL PARAMETERS

The automated application process is divided into its phases: (feeding and) positioning, biting, insertion and tightening (see Figure 13).
In the following paragraphs the established control parameters and their influences are summarized for each application phase. Furthermore, quantified suggestions for an automated application of the investigated self-tapping screws with countersunk heads connecting steel components with timber specimens of a typical density according to Norway spruce, diameters of $d = \{8; 10; 12\}$ mm and insertion lengths designed for screw tension failure, are made.

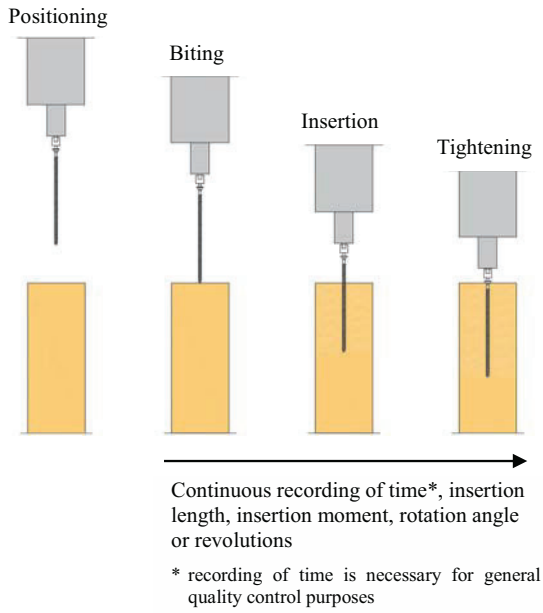

Figure 13: *Principle phases of an automated screw application process.*

- For feeding and positioning information on the screw (type, diameter, length and head), the screw drive, the application angles (in and out of plane) and position on the timber specimen are necessary.
- Strong influences on the biting behavior can be traced back on the contact pressure, the screw characteristics (diameter, tip-type) and on the local properties of the anchoring timber (e.g. density, growth characteristics). Overall, the load-grain angle α was found to have only a minor influence, althought the test results show that biting of screws inserted in grain ($\alpha = 0°$) is slightly more difficult than at $\alpha = 45°$ or 90°. Knowledge of the above mentioned boundary conditions is necessary to define a sufficient contact pressure. In general, a higher contact force is required for larger screw diameters and/or higher densities (including growth characteristics). Within the tested boundary conditions a contact force between 0.5 and 1.0 kN is suggested for rapid biting. The upper limit is set to prevent bending of the screw and damage of the timber specimen in the area of the tip. It is suggested to set the RPM to approx. 20 Hz for rapid biting of the screw.
- As for the insertion of the thread, control of the insertion length and the insertion moment is necessary to prevent failure due to torsion. RPM can be accelerated after biting. To prevent the screw from overturning a limitation of the insertion moment of 70 % of the respective torque resistance is advised.
  Before the tightening of the screw the RPM has to be decelerated in time at a certain insertion length, depending on the pitch of the screw, the RPM during insertion and the deceleration rate of the RPM. Furthermore, angular deviations of the screw must be

taken in account when setting the insertion length for deceleration.

- It is advised to decelerate the RPM asymptotically to 5 Hz (or less) to tighten the screw in a controlled manner, as the insertion moment increases very rapidly when the screw head contacts the sinking. To achieve a tight fit of the screw without failure, limiting the tightening torque with 80-90 % of the torque resistance (depending on underhead features) is advised.

4.2 IN-SITU PERFORMANCE ASSESSMENT – INSERTION ENERGY

- The insertion energy, which can be measured continuously in the course of a controlled automated screw application, has been identified as an extremely powerful predictor for the withdrawal properties of the investigated screw types.
- The high degrees of determination of presented power regression models $f_{ax} \sim W$ and $K_{ser} \sim W$ based on the investigated data sets demonstrate exemplarily the possibility for a significant reduction of the uncertainty in individually estimated withdrawal properties. As consequence, on average higher characteristic withdrawal properties and overall lower partial safety factors for the controlled failure modes could be applied.
- Overall better controlled and research informed executed joints might also be designed for higher capacities which is in addition supported by a higher accountable effective number of fasteners (n_{ef}) for the controlled failure modes. In order to react appropriately on differences between designed and in-situ estimated withdrawal properties, opportunities to adapt the joint execution are required, e.g. by adaptation of the insertion length, the number of fasteners within a joint and/or the spacing between joints in discretely equipped connection lines. This together provides a set of new possibilities to thoroughly re-consider the design-to-execution process by implementing research informed design (RID).
- This new process would have positive effects not only on the overall efficiency of prefabricated timber constructions but in particular on the over-strength-design for the brittle failing connection components since the existing potential could be better exploited. The resulting lower ratio between the properties of ductile and brittle failure mechanisms consequently would yield an economically more viable solution in particular for the design in case of characteristic load scenarios.
- Nevertheless, it needs to be considered that the investigations on the total insertion energy to date are limited to Norway spruce, screw types {RF; P1}, nominal screw diameter $d = 8$ mm, insertion length 50 mm, self-tapping insertion, load-grain angles $\alpha = \{0°; 90°\}$ and screwing through the specimen. Additional investigations are needed to further validate the applicability of the presented approach, in particular under variation of the nominal screw diameter, insertion length, additional load-grain angles and without screwing through the specimen. In addition, certain parameters need to be considered which have an effect on the insertion energy but not on the withdrawal properties. Consequently, structural reliability investigations need to be intensified for a fundamental quantification of expectable gains.

ACKNOWLEDGEMENT

The publication was written in frame of the research project FFG BRIDGE 1 “CLT_joint” (no. 883672) and received public funding by the Austrian Research Promotion Agency (FFG). Their support and the support by the commercial partners, Schmid Schrauben Hainfeld GmbH (Hainfeld, Austria) and TechnoWood AG (Alt St. Johann, Switzerland) are thankfully acknowledged.

REFERENCES

[1] Glasner D., Ringhofer A., Braun W., Hubmann G.: Energy demand for the driving in of self-tapping timber screws and its applicability. WTCE’23, Oslo, Norway, 2023.

[2] Gilmer B., Lang S.: Dual Motor Drill Continuously Measures Drilling Energy to Calculate Bone Density and Screw Pull-out Force in Real Time. *Wolters Kluwer Health, Inc.*, California, USA, 2018.

[3] Eckert A., Brandner R.: Anbisstests und Eindrehversuche im Rahmen des Arbeitspaketes 5 – MOUNT. *Research Report*, Graz University of Technology, Graz, Austria, 2022 (in German).

[4] Reichinger T.: Ausgewählte Untersuchungen zum Tragverhalten einer für Hartlaubholz optimierten Holzbauschraube (in German). *Master Thesis*, Graz University of Technology, 2017.

[5] EN 15737 Timber Structures – Test methods – Torsional resistance of driving in screws. CEN, 2009.

[6] EN 1382 Timber structures – Test methods – Withdrawal capacity of timber fasteners. CEN, 1999.

[7] Brandner R., Ringhofer A., Reichinger T.: Performance of Axially-Loaded Self-Tapping Screws in Hardwood: Properties and Design. *Engineering Structures*, 188:677–699, 2019.

[8] Ringhofer A., Brandner R., Schickhofer G.: A Universal Approach for Withdrawal Properties of Self-Tapping Screws in Solid Timber and Laminated Timber Products. INTER/48-7-1, Sibenik, Croatia, 2015.

[9] Brandner R., Ringhofer A., Grabner M.: Probabilistic Models for the Withdrawal Behavior of Single Self-Tapping Screws in the Narrow Face of Cross Laminated Timber (CLT). *European Journal of Wood and Wood Products*, 76(1):13–30, 2017.

[10] Fink G., Kohler J., Brandner R.: Application of European design principles to cross laminated timber. *Engineering Structures*, 171:934–943, 2018.

[11] Ringhofer A., Brandner R., Schickhofer G.: Withdrawal resistance of self-tapping screws in unidirectional and orthogonal layered timber

https://doi.org/10.52202/069179-0176

products. *Materials and Structures*, 48(5):1435–1447, 2015.
[12] Brandner R., Bratulic K., Ringhofer A.: Serial Correlation of Withdrawal Properties from Axially-Loaded Self-Tapping Screws. ICASP12, Vancouver, Canada, 2015.
[13] Peavey E., Vander Wyst K.B.: Evidence-Based Design and Research-Informed Design: What's the Difference? Conceptual Definitions and Comparative Analysis. *HERD: Health Environments Research & Design Journal*, 10(5):143–156, 2017.
[14] Westermayr M., Brandner R., Ringhofer A., Mahlknecht U., van de Kuilen J.W.G.: Performance, design and execution of screwed steel-timber end-grain connections. INTER/55-7-2, Bad Aibling, Germany.
[15] prEN 1995-1-1: Eurocode 5 Design of timber structures – Part 1-1: General rules and rules for buildings. CEN, 2022.
[16] prEN 1990: Eurocode 0: Basis of structural design. CEN, 2022.

World Conference on Timber Engineering Oslo 2023

INFLUENCE OF LOW CURING TEMPERATURES ON THE STRENGTH DEVELOPMENT OF END-GRAIN BONDED TIMBER

Dio Lins[1], Steffen Franke[2]

ABSTRACT: The end-grain bonding of timber components with the Timber Structures 3.0 technology (TS3) is an emerging construction method in timber engineering for which various research projects are being conducted. For onsite applications, among other things, it is being investigated how low temperatures during the curing process affect the bonding. The current research results show that low curing temperatures have a negative impact on the mechanical properties of the bond. However, it also shows that low temperatures have a different effect on the pure casting resin strength (cohesion) than on the bonding strength (adhesion). It has turned out that the pure casting resin is neither the decisive factor for the tensile strength of the end-grain bonding nor for the curing time. Based on these findings, compensation measures for bonding at low temperatures can be determined and further research can be carried out.

KEYWORDS: Cross Laminated Timber, end-grain bonded timber, tensile strength, temperature effect

1 INTRODUCTION

With the TS3 technology, timber components are bonded together at the end-grain surfaces in a statically load-bearing manner. In particular, this offers the possibility of creating biaxial load-bearing flat slabs made of Cross Laminated Timber (CLT) in any geometry and size. For this purpose, CLT elements with pre-treated side surfaces are mounted next to each other with a 4 mm gap between. This gap is then filled with a casting resin so that a bonding takes place without lateral pressure necessary. A two-component polyurethane casting resin is used, like that used for bonding steel rods into load-bearing timber components.

However, in order to establish this technology internationally and thus create a high-quality climate-neutral substitute for reinforced concrete slabs, the required processing or curing temperature of at least 17 °C according to the approval for bonded-in steel rods in load-bearing timber components [1] is currently still a challenge for construction site application. The reason for this is that this temperature is hardly or only rarely reached during the colder season in parts of the European sales market, especially in Scandinavia, which has a high affinity for timber constructions, but also in the Baltic States and Central Europe. Therefore, practicable solutions must be found to extend the applicability geographically without being limited to the summer season. For bonded-in steel rods, there have already been studies on the temperature dependence of the bonding and experiments on bonding at low temperatures have been carried out, for example using inductive heating (see [2]). The experiments described in this paper also address the question of temperature influence to be able to embed the TS3 technology as soon as possible in quality assuring design standards, as for universal finger joints [3].

2 MATERIAL AND METHODS

2.1 GENERAL

The curing process depends not only on the curing temperature but also on the curing time [1]. According to the approval, this is 14 days at 17 °C until the final strength is reached [1]. To determine whether the specified final strength is only achieved after a longer curing time at lower curing temperatures, or whether this remains significantly lower, the curing process is investigated experimentally as a function of the two parameters temperature and time.

In order to determine the curing characteristics of the casting resin, test specimens are cast at about 20 °C and then allowed to cure at different (lower) temperatures (20 °C, 15 °C, 10 °C, 5 °C, 0 °C) and tensile tests are carried out at different times. These tensile tests take place on the 1. / 2. / 3. / 6. / 10. / 15. / 20. / 30. day after casting. In addition, it is checked whether and, if so, to what extent post-curing takes place during post-storage at 20 °C. For this purpose, after 20 days of curing at low temperature, test specimens are subsequently stored at 20 °C for a further 7 or 14 days (see Figure 1) and then subjected to a tensile test.

According to the manufacturer's data, the tensile strength of the pure casting resin is approx. 45 N/mm^2, which is significantly higher than the previously determined strength of bonded timber (end-grain bonding).

[1] Dio Lins, Bern University of Applied Sciences, Switzerland, dio.lins@bfh.ch
[2] Steffen Franke, Bern University of Applied Sciences, Switzerland, steffen.franke@bfh.ch

https://doi.org/10.52202/069179-0177

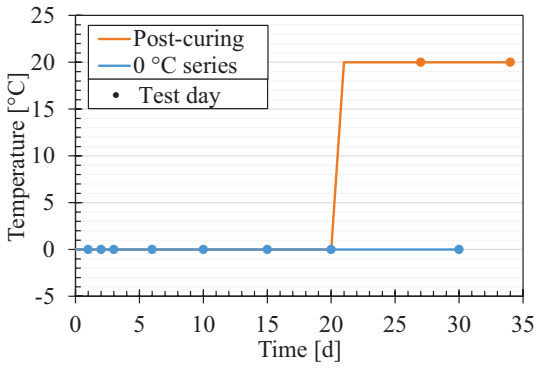

Figure 1: *Exemplary representation of the curing temperature for the 0 °C series incl. post-curing*

Furthermore, low curing temperatures may have a different effect on the curing characteristics of the bonding strength, than of the pure casting resin. Therefore, timber bonding specimens are additionally tested. The development of hardness for similarly stored casting resin samples was also investigated to derive a possible correlation between hardness and strength. This correlation could be used to introduce an additional option for quality monitoring. In this way, the simple and quick handling of the hardness test can be conducted on the construction site and thus conclusions can be drawn about possible curing deficits.

2.2 DETERMINATION OF THE CASTING RESIN STRENGTH

The casting resin strength is tested according to SN EN ISO 527 (Plastics - Determination of tensile properties) [4]. To produce the test specimens, TS3's own 2K-PUR casting resin "TS3 PTS CR192" is poured into a template to obtain the geometry according to Figure 3. This template is fixed in a casting device (see Figure 2). Immediately after casting, the test specimens together with the casting device are stored in a climate chamber at the respective low temperature. On the first test day, all test specimens of a series are taken out of the template and

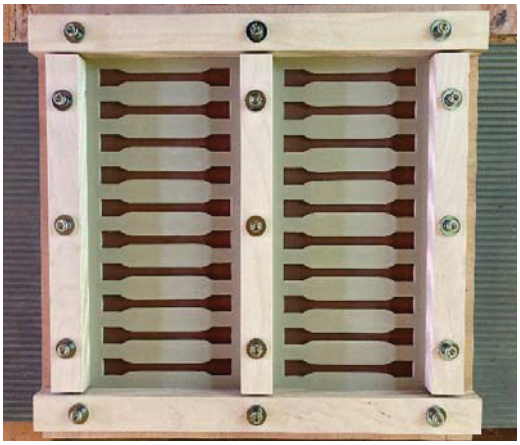

Figure 2: *Casting device*

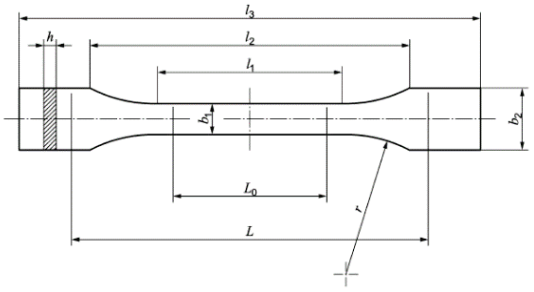

	Specimen type	1A	1B
l_3	Overall length[a]	170	≥150
l_1	Length of narrow parallel-sided portion	80 ± 2	60,0 ± 0,5
r	Radius	24 ± 1	60 ± 0,5
l_2	Distance between broad parallel-sided portions [b]	109,3 ± 3,2	108 ± 1,6
b_2	Width at ends	20,0 ± 0,2	
b_1	Width at narrow portion	10,0 ± 0,2	
h	Preferred thickness	4,0 ± 0,2	
L_0	Gauge length (preferred)	75,0 ± 0,5	50,0 ± 0,5
	Gauge length (acceptable if required for quality control or when specified)	50,0 ± 0,5	
L	Initial distance between grips	115 ± 1	115 ± 1

[a] The recommended overall length of 170 mm of the type 1A is consistent with ISO 294-1 and ISO 10724-1. For some materials, the length of the tabs may need to be extended (e.g. l_3 = 200 mm) to prevent breakage or slippage in the jaws of the testing machine.

[b] $l_2 = l_1 + [4r(b_2 - b_1) - (b_2 - b_1)^2]^{1/2}$, resulting from l_1, r, b_1 and b_2, but within the indicated tolerances.

Figure 3: *SN EN ISO 527-2:2012: Dimensions of type 1A and 1B test specimens [4]*

the thickness is calibrated on a wide belt sander (grit 100) to the specified 4 mm ± 0.2 mm (see Figure 3). Subsequently, the test specimens are again stored at the respective low temperature and removed from the climate chamber at the planned times and subjected to a tensile test. The tensile test also takes place according to EN ISO 527 and is displacement-controlled with a test speed of 2 mm/min. The test is carried out in a constant climate of 20 °C and 65 % r. h. Since the casting resin is a homogeneous material after mixing the two components and thus a low scatter is to be expected, only three test specimens are tested per test day and temperature.

2.3 DETERMINATION OF THE BONDING STRENGTH

The bonding strength of the end-grain bonding at low temperatures is determined following the TS3 approval tests of the MPA University of Stuttgart [5]. These in turn were carried out in close accordance with DIN EN 301 [6] and DIN EN 302-1 [7]. Just like the tensile tests of the pure casting resin, the timber bonding test specimens are also tested at 20 °C and 65 % r. h. with a displacement-controlled test speed of 2 mm/min.

To be able to consider the temperature influence in isolation, all other parameters are excluded as possible influencing factors on the tensile strength as far as possible. For this purpose, spruce timber with a low scattering gross density of 350 kg/m^3 ± 25 kg/m^3 is defined for all test specimens. Secondly, the wood moisture content should be 12 % in all test series. For this purpose, the relative humidity is adjusted according to the respective temperature in such a way that a compensation wood moisture content according to Keylwerth and Noak [8] of 12 % is achieved. For monitoring purposes, the

https://doi.org/10.52202/069179-0177

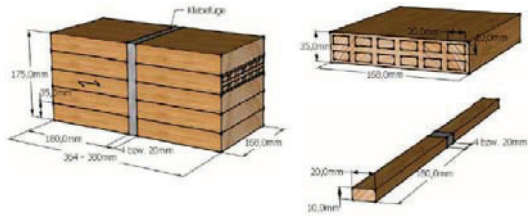

Figure 4: *Schematic representation of the axial composite tensile test specimen [5]*

temperature, the relative humidity as well as the wood moisture content are recorded during the entire test. The wood moisture content is measured in two separate ways on reference test specimens, which are also located in the climate chamber. On the one hand, the wood moisture content is continuously recorded using the resistance method, and on the other hand, several test specimens are weighed regularly, and oven dried at the end of the test series to determine the wood moisture content at the respective measurement times. Since wood defects, such as knots in particular, have a great influence on the tensile strength of the small, end-grain bonded test specimens, these are also excluded in order to be able to determine the temperature influence as accurately as possible.

To produce the timber bonding test specimens, glulam elements are first made from board lamellas, see Figure 4, left. These are then cast together on the end-grain surface according to the TS3 technology and stored in a climate chamber at the intended temperature. Analogous to the determination of the casting resin strength, the glulam elements are cut apart after the first day, so that the test specimens are produced with the dimensions 10 mm x 20 mm, see Figure 4. These are then stored again in the climate chamber and tested on the corresponding days. The aim of this complex test specimen production is to eliminate possible edge influences such as bubble formation or incomplete casting, because although these are negligible on the component scale, they can result in significant deviations in the small test specimen geometry. Since the timber and thus the bonding test specimens, despite the homogenisation approaches mentioned above, give rise to the assumption of greater scattering compared to the casting resin, five test specimens are tested per test day and temperature.

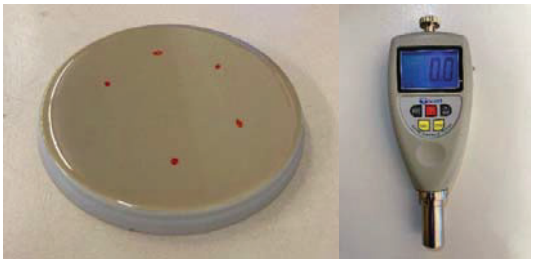

(a) Test specimen *(b) Durometer*

Figure 5: *Test specimen (a) and measuring device (b) for determining the casting resin hardness*

2.4 DETERMINATION OF THE CASTING RESIN HARDNESS

The hardness is determined according to EN ISO 868 [9]. According to the standard, the Shore-D hardness of the "TS3 PTS CR192" casting resin is tested with a corresponding durometer (see Figure 5). The test specimens are small round plates (see Figure 5), which are cast in corresponding templates and then stored with the tensile test specimens in the climate chamber. Five hardness measurements are conducted on different samples for each test day and temperature.

3 RESULTS

3.1 GENERAL

In Figure 7 to Figure 9, the mean value curves of the three measured variables (casting resin strength, bonding strength, casting resin hardness) including standard deviation are plotted against time and compared with each other for the different curing temperatures. This is shown individually for each measurand. In addition, a comparison of the curves of the three measured variables is shown as an example for 10 °C curing temperature in order to recognise the correlation between the casting resin hardness and strength. Furthermore, a proposal is made for a design concept that considers the influence of low curing temperatures on the tensile strength of end-grain bonded timber components.

3.2 CASTING RESIN STRENGTH

Figure 7 shows the development of the tensile strength of the casting resin at the five different curing temperatures. It can be seen that lower curing temperatures result in significantly lower initial strengths. It can also be seen that the strength development is completed more quickly at higher temperatures than at lower ones. It can also be seen that the post-curing effect has a greater impact at lower curing temperatures and is no longer noticeable at 15 °C. The difference between the final strengths after post-curing is exceedingly small and the overall scatter is relatively low, as expected.

3.3 BONDING STRENGTH

Since knots were removed from the composite test specimens to isolate the influence of temperature, the absolute strength values are not directly representative for

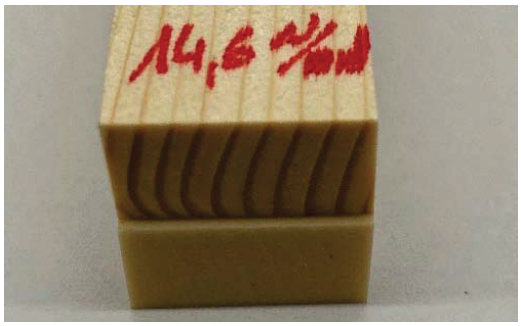

Figure 6*: Fracture pattern of timber bonding test specimen*

https://doi.org/10.52202/069179-0177

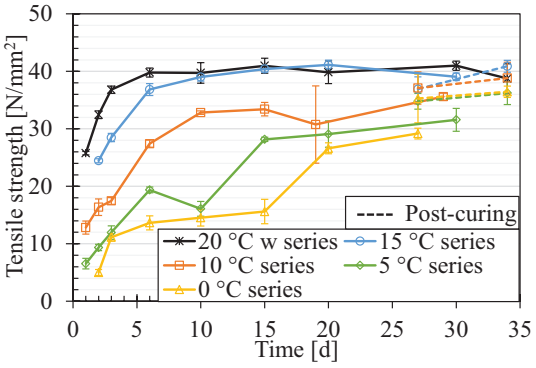

Figure 7: *Temperature comparison of the casting resin strength (mean values)*

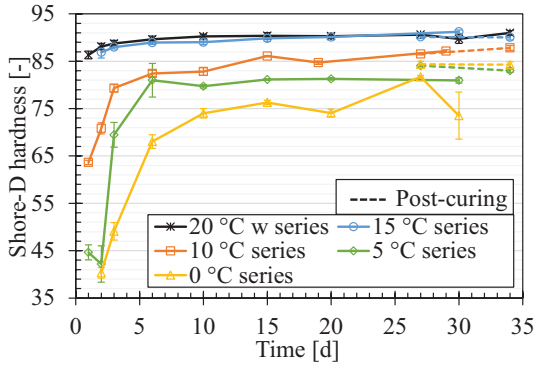

Figure 9: *Temperature comparison of the casting resin hardness (Shore-D hardness; mean values)*

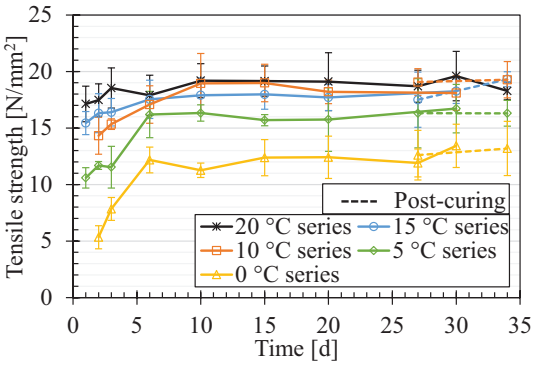

Figure 8: *Temperature comparison of the bonding strength (mean values)*

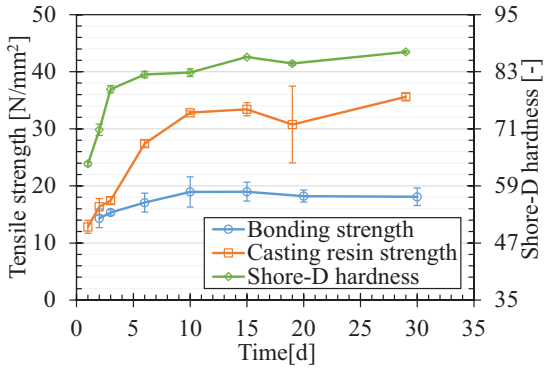

Figure 10: *Comparison of the casting resin strength, the bonding strength, and the casting resin hardness at 10 °C (mean values)*

design; however, the temperature comparison provides an elevated level of information. Figure 8 shows, analogous to Figure 7, the development of the tensile strength of the timber bonding specimens at the different curing temperatures. Here, too, lower temperatures during curing result in lower initial strengths. However, regardless of the curing temperature, the final strength is reached earlier than with the pure casting resin, i.e., at the latest approx. 6 days after casting. Furthermore, there is no further increase in strength during post-curing, so that low curing temperatures also result in lower final strengths. It is also clear that the scatter in the bonding strength is, as expected, higher than with the pure casting resin. Furthermore, it is noticeable that in most cases the fracture appears to occur exactly in the area between the pre-treatment and the casting resin (see Figure 6).

3.4 CASTING RESIN HARDNESS

Figure 9 shows the development of the casting resin hardness at the different curing temperatures. As in the two previous diagrams, it can be seen that a lower curing temperature results in a significantly lower initial hardness. Analogous to the casting resin strength, it can also be seen with the casting resin hardness that curing proceeds more slowly at lower temperatures, since the final hardness is reached significantly later than at higher temperatures. As with the casting resin strength, the post-hardening effect is also greater at lower temperatures than at higher temperatures. Here, however, this effect is no longer significant at 10 °C. Accordingly, the final hardness after post-curing is at a similar level despite the different curing temperatures, but with greater differences than for the casting resin strength. The scatter of the casting resin hardness is also very low, analogous to the casting resin strength.

3.5 COMPARISON CASTING RESIN STRENGTH – BONDING STRENGTH – CASTING RESIN HARDNESS

The comparison between the casting resin strength, the bonding strength, and the casting resin hardness in Figure 10, shown exemplarily for 10 °C curing temperature and without the post-curing, shows that the three measured variables basically correlate with each other over the period of 30 days. However, this fundamental correlation is not very surprising, as all the measured variables mentioned inevitably increase due to the chemical reaction after casting. However, a closer look at the graphs reveals that the casting resin strength and hardness in particular show approximately parallel curves. This can also be confirmed by the correlation coefficient according to Pearson [10] of 0.91 (r above 0.8: "high to perfect correlation"). Compared to the bonding strength, the

https://doi.org/10.52202/069179-0177

deviations of the curves are significantly greater since the bonding strength increases less strongly between initial and final values and also reaches its final values considerably faster.

3.6 DESIGN CONCEPT

In the following, based on the findings on the curing characteristics of the bonding strength, a proposal for a design concept is developed which considers the temperature influence on the tensile strength of the TS3 joint. For this purpose, the results of the timber bonding series are first presented in a different form. The final tensile strengths of the individual series, i.e., the respective values from the 10th day after casting, are summarised and evaluated for each series. The mean value is formed, and the standard deviation is calculated. Then the tensile strength is plotted against temperature instead of time (see Figure 11). As already described in chapter "3.3 BONDING STRENGTH" it can be seen that the tensile strength also increases with increasing curing temperature. However, this relationship is not linear. The additionally drawn green dotted trend line corresponds to a third-degree polynomial.

The design concept is conceived based on DIN EN 1995-1-1 [11] so that it can be integrated as well as possible into the existing standardisation. Accordingly, the design value of the tensile strength of timber in fibre direction is calculated as in equation (1):

$$f_{t,0,d} = k_{mod} * \frac{f_{t,0,k}}{\gamma_M} \quad (1)$$

The following condition must then be fulfilled for the dimensioning (equation (2)):

$$\sigma_{t,0,d} \leq f_{t,0,d} \quad (2)$$

To take into account the temperature influence on the tensile strength of the TS3 joint, a coefficient k_t is proposed, which is included in the design specification as follows (equation (3)):

$$\sigma_{t,0,d} \leq k_t * f_{t,0,d} \quad (3)$$

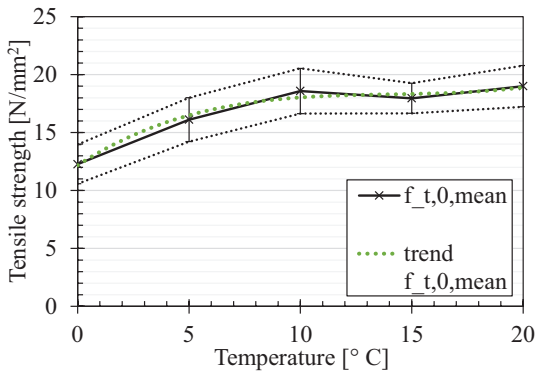

Figure 11: *Temperature comparison of the bonding strength (mean values)*

This coefficient must be dimensionless, lie between 0 and 1 and describe the temperature range between 0 °C and 20 °C to which its application is initially restricted. For the dimensionless determination of the coefficient k_t the ultimate tensile strengths of the different temperatures are normalised so that the tensile strength at 20 °C corresponds to 100 %, i.e., 1.0 (see Figure 12).

In contrast to the cubic trend line in Figure 11, the following bilinear approach for k_t (equation (4) and (5)) is chosen for simpler calculation in engineering practice (see Figure 12):

$$0\,°C \leq t < 10\,°C\colon\ k_t = 0.65 + 0.033 * t \quad (4)$$

$$10\,°C \leq t < 20\,°C\colon\ k_t = 0.98 + 0.002 * t \quad (5)$$

The concept presented is only a first proposal for the consideration of the temperature influence on the tensile strength of the TS3 joint in the design. Apart from the fact that the concept in its described form is on the unsafe side in the range of 15 °C, the introduced coefficient refers to the mean values of very small samples where timber features such as knots were sorted out. For the actual applicability, it is indispensable to generate a representative sample length with a commercially available timber sorting as a basis for the coefficient k_t and to define the ratios of the characteristic tensile strengths as a basis.

4 DISCUSSION AND CONCLUSION

The test results presented provide important findings for TS3 bonding at curing temperatures below the 17 °C specified by the manufacturer. The investigated properties (casting resin strength, bonding strength, casting resin hardness) initially show lower values at lower curing temperatures. However, the curing characteristics of the bonding strength and the casting resin strength differ significantly in some cases. Worth mentioning here is the fact that the final strengths of the timber bonding specimens are achieved significantly faster than those of the pure casting resin, regardless of the temperature. In addition, in contrast to the casting resin strength, there is no discernible post-curing effect in the timber bonding specimens, which means that the final strengths after post-

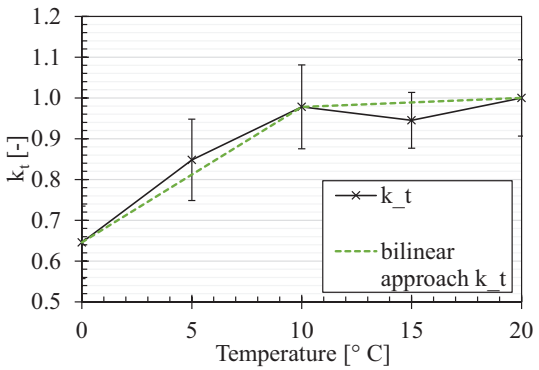

Figure 12: *Coefficient k_t*

https://doi.org/10.52202/069179-0177

curing of the timber bonding specimens differ significantly as a function of temperature, whereas they are at a similar level with the pure casting resin. These observations can be justified based on the bond fracture pattern: Since the fracture apparently occurs in the area between the pre-treatment and the casting resin, it can be assumed that the adhesion between the pre-treatment and the casting resin is the decisive factor for the bonding strength and reaches its final strength approx. 6 days after casting. The further curing of the casting resin therefore no longer has any influence. The following conclusions can be drawn from this:

- An extension of the curing time does not result in a higher bonding strength.

- Possible additional measures for tempering the TS3 joint are only required over a relatively brief period of time.

Furthermore, the assumption that there is a strong correlation between casting resin strength and hardness has been confirmed. This can be used to enable additional quality monitoring by means of on-site hardness tests. However, this can only be used to monitor the properties of the pure casting resin and thus detect possible negative influences (mixing ratio, curing temperature). However, it is not possible to draw a direct conclusion on the bonding strength without further ado, as the timber results in further influencing factors (wood moisture content, raw density, knottiness) that cannot be recorded by the curing characteristics of the pure casting resin.

5 OUTLOOK

To validate the previous findings on the curing characteristics of the bonding strength as a function of temperature, further test series are being carried out. For this purpose, a larger number of samples with larger timber cross-sections are evaluated, which already have the respective low temperature when casting, in order to represent the "worst case" that can occur on the construction site. The timber used corresponds to a commercially available sorting to be able to generate representative absolute tensile strength values. In addition to the distribution function, both the mean values and the characteristic values of the respective tensile strength must be determined. In particular, this is intended to further elaborate the design concept, because up to now this has been based on the mean values of relatively small samples. To be able to actually apply the concept in practice, it must refer to the characteristic values of representative samples. Furthermore, within the framework of these test series, random samples of the fracture patterns are analysed microscopically. In addition, the possibility of casting the resin at a temperature of 35 °C to obtain higher tensile strengths is being investigated.

Another approach to be able to conduct the end-grain bonding in the future even at low outside temperatures without loss of strength is the local tempering of the casting resin joint during the curing time with a heating wire. This possibility is also currently being researched at BFH so that it can be used as soon as possible.

ACKNOWLEDGEMENT

The project is a collaboration of Timber Structures 3.0 AG, Schilliger Holz AG, Henkel & Cie. AG, ETH Zürich and BFH. Gratefully acknowledged by the authors is the intense cooperation among the partners of this project, as well as Innosuisse, which is funding the ongoing project to a greater part.

REFERENCES

[1] DIBt: 2K-PUR Klebstoff LOCTITE CR 821 PURBOND zum Einkleben von Stahlstäben in tragende Holzbauteile. Allgemeine bauaufsichtliche Zulassung Z-9.1-896, 2020-05
[2] Voss, M.; Evers, T.; Vallée, T.: Low-temperature curing of adhesives – Large-scale experiments. The Journal of Adhesion, 2022
[3] SN EN 14080: Holzbauwerke – Brettschichtholz und Balkenschichtholz – Anforderungen. SIA, 2013
[4] SN EN ISO 527-2: Kunststoffe – Bestimmung der Zugeigenschaften – Teil 2: Prüfbedingungen für Form und Extrusionsmassen (ISO 527-2:2012). SNV, 2012-06
[5] Aicher, S: TS3 Arbeitsplan 3 vom 18.09.2018. MPA Universität Stuttgart, 2018-09
[6] SN EN 301: Klebstoffe, Phenoplaste und Aminoplaste, für tragende Holzbauteile – Klassifizierung und Leistungsanforderungen. SNV, 2018-04
[7] SN EN 302-1: Klebstoffe für tragende Holzbauteile – Prüfverfahren – Teil 1: Bestimmungen der Längszugscherfestigkeit. SNV, 2013-05
[8] Keylwerth, R.; Noak, D.: Die Kammertrocknung von Schnittholz. Holz als Roh- und Werkstoff, 1964
[9] SN EN ISO 868: Kunststoffe und Hartgummi – Bestimmung der Eindruckhärte mit einem Durometer (Shore-Härte) (ISO 868:2003). SNV, 2003-09
[10] Sachs, L.: Angewandte Statistik. Springer Verlag, 2002
[11] DIN EN 1995-1-1: Eurocode 5: Bemessung und Konstruktion von Holzbauten - Teil 1-1: Allgemeine Regeln für den Hochbau. Beuth Verlag, 2016

World Conference on Timber Engineering Oslo 2023

EXPERIMENTAL CHARACTERIZATION OF THE MULTI-DIRECTIONAL BEHAVIOUR OF ANGLE BRACKETS AND HOLD-DOWNS

Riccardo Fanti[1], Andrea Polastri[2], Daniele Casagrande[3], Ernesto Callegari[4], Alvise Ramazzini[5], Luca Sestigiani[6], Peter Lang[7]

ABSTRACT: The multi-directional mechanical behaviour of angle brackets and hold-downs (i.e. NINO and WKR) is investigated in this study by means of monotonic tests in tensile (F1), in-plane shear (F2/3) and out-of-plane (F4) load configurations. The values of resistance and stiffness for each angle bracket were determined. For WKR hold-downs the load acting on anchor bolt were measured through a load cell. The analyses of results showed that the tested connectors are characterized by significant strength and stiffness for different load configurations, as reported in other experimental campaign for similar connectors where the multi-directional behaviour was investigated.

KEYWORDS: angle bracket, hold down, CLT connections, multi-directional behaviour, monotonic tests.

1 INTRODUCTION

The mechanical behaviour of Cross Laminated Timber (CLT) and Light-Frame Timber (LTF) shearwalls is typically governed by the connections used to either connect the timber elements each other or anchor the wall to either the foundation or the floor below [1,2]. Hold-downs are usually placed on the two vertical edges of the shearwalls in order to limit the rigid body rotation of the wall while angle brackets are uniformly distributed along the entire length of the shearwall to limit sliding. Angle brackets and hold-downs are typically composed with cold-formed steel plate (2-3mm thick) connected to timber elements by means of nails or screws and to the foundation with a threated steel bar. A uni-directional behaviour of hold-down and angle brackets is typically assumed by the designers [3], so that hold-downs are designed to resist a tensile-vertical load (uplift), due to the rocking, while angle-brackets are primarily designed to resist the shear-horizontal actions: interaction between tensile (F1) and in-plane shear (F2/3) loads is neglected.

Recent experimental campaigns show both traditional [4,5,6] and innovative [7] typologies of angle brackets can be characterized by significant strength and stiffness along multiple directions. The results at connection level are confirmed in shearwalls experimental tests where panels were anchored to the foundation through traditional [8] and innovative [9] angle brackets without using any hold-downs. As a result, the bi-directional behaviour of such types of connectors cannot be neglected in design calculations and experimental testing should be conducted by considering multiple direction load configurations. This paper presents the results obtained from an experimental campaign conducted with the aim to characterize the multi-directional behaviour of the new Rothoblass NINO angle bracket (Figure 1a) and WKR hold-down (Figure 1b). The influence on the mechanical behaviour due to different load configurations, fastener patterns, eccentricity between the fasteners in vertical and horizontal flanges, application of washer and geometry of steel plates were analysed. For tested WKR hold-downs, the load acting on the steel bar used to anchor the hold-down to the foundation was measured in order to determine the load amplification factor on the steel bar.

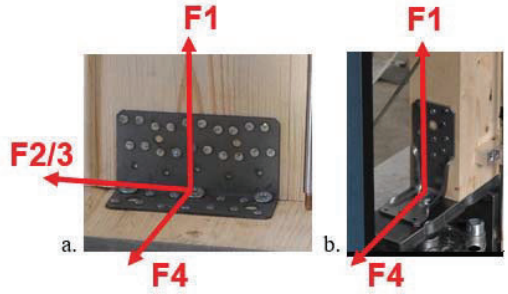

***Figure 1**: a. NINO150100 and b. WKR135 angle bracket*

2. MATERIALS AND METHODS

Rothoblaas NINO angle brackets and WKR hold-downs are obtained from a S235 or S250GD steel plate with different thickness (t) depending on the model. The geometry of each connector (Figure 2) is reported in Table 1. The number and the diameter (d) of holes in vertical flange (Side A) and horizontal flange (Side B) are specified. Holes with d equal to 5mm were used for nails

[1] R. Fanti, Institute for Bioeconomy-National Research Council of Italy (CNR-IBE), Italy, riccardo.fanti@ibe.cnr.it
[2] D. Casagrande, Institute for Bioeconomy-National Research Council of Italy (CNR-IBE), Italy, daniele.casagrande@ibe.cnr.it
[3] A. Polastri, Institute for Bioeconomy-National Research Council of Italy (CNR-IBE), Italy, andrea.polastri@ibe.cnr.it
[4] E. Callegari, Rothoblaas, Italy, ernesto.callegari@rothoblaas.com
[5] A. Ramazzini, Rothoblaas, Italy, alvise.ramazzini@rothoblaas.com
[6] L. Sestigiani, Rothoblaas, Italy, luca.sestigiani@rothoblaas.com
[7] P. Lang, Rothoblaas, Italy, peter.lang@rothoblaas.com

https://doi.org/10.52202/069179-0178

while holes with d equal to 10mm and 14mm were used for screws and bolts, respectively. According to ETA-22/0089 [10], in timber-to-foundation (T-F) connection, NINO15080 and NINO100200 can be installed with specific 6mm thick and 8mm thick washer, respectively.

Table 1: *Geometry of NINO and WKR.*

Con.	b [mm]	h [mm]	p [mm]	t [mm]	Φ5 A	Φ5 B	Φ10 B	Φ14 B
NINO 100 100	104	100	78	2,5	25	13	2	2
NINO 150 80	146	77	55	2,5	25	11	3	2
NINO 100 200	104	197	122	3	49	13	3	4
WKR 095	65	95	85	3	8	-	-	1
WKR 135	65	135	85	3,5	13	-	-	1
WKR 285	65	287	85	3,5	29	-	-	1
WKR 530	65	530	85	3,5	59	-	-	1

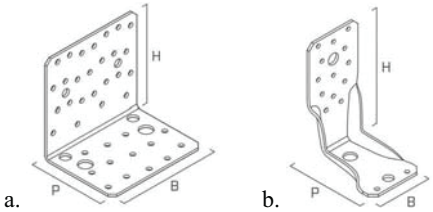

a. b.

Figure 2: *Geometry of: a. NINO and b. WKR.*

In timber-to-timber (T-T) connections NINO angle brackets can be installed in two different configurations: with or without screws VGS 9x140mm in the horizontal flange (screwed with an inclination of 15° close to the bend line as for TTV angle bracket [7] in addition to the 4x60mm ring shank nails. The tension loads are transferred from the threaded shank of these screws into the CLT floor panel, avoiding large deformations of horizontal flange. WKR hold-downs have to be anchored in T-T and T-F connection through screw (HBS, TBS or VGS) and M12 threaded rod (in horizontal plate), respectively. Both NINO and WKR connector can be installed with different fasteners patterns in vertical and horizontal flanges, according to [10].

All three different NINO angle brackets were tested along F1, F2/3 and out-of-plane compression (F4) load directions, see Table 2. The WKR hold-downs were conversely tested along F1 and F4 configurations, see Table 3. In some cases of T-F connection an interlayer was interposed to simulate the mortar layer or the concrete curb under the wall panel. The WKR285 was also tested with 10mm gap under the horizontal flange in order to characterized the behaviour of hold-down for particular applications, when there is no contact between the base of connection and the foundation/floor panel.

Sixty-nine monotonic tests were carried out (three tests for each angle bracket or hold-downs for different fasteners patterns and load configuration). Tests were performed according to EN26891:1991 [11]. The load rate was not greater than 0,2 mm/s and the maximum load was reached in 300 ± 120 s in all tests.

In T-T and T-F connections loaded in F1 direction one NINO angle bracket was fastened at each side of CLT wall panel (two angle brackets on each panel) in symmetric configuration and the specimens were tested as shown in Figure 3a and Figure 3b, respectively, while in the specimens loaded in F2/3 direction two NINO angle brackets were fastened at each side of CLT wall panel (four angle brackets on each panel) in symmetric configuration as shown in Figure 3c and Figure 3d, respectively. In T-T connections along F4 direction one NINO100100 angle bracket was fastened at each end of CLT panel, (two angle brackets on each panel), as shown in Figure 3e. For all load directions tested, NINO angle bracket's horizontal flange in T-T connection was nailed (or nailed and screwed) to the CLT floor panel while in T-F connection was bolted to the steel setup.

Table 2: *NINO test configurations*

AB	ID	Load	Type	Fast. Side A	n°	Fast. Side B	n°
NINO 100 100	1	F1	T-T	LBA 4x60mm	14	LBA 4x60mm	13
	2	F1	T-F	LBA 4x60mm	14	M12 bolt	2
	3	F2/3	T-T	LBA 4x60mm	14	LBA 4x60mm	13
	4	F2/3	T-F	LBA 4x60mm	14	M12 bolt	2
	5	F4	T-T	LBA 4x60mm	14	LBA 4x60mm VGS 9x140mm	13 2
NINO 150 80	6	F1	T-T	LBA 4x60mm	20	LBA 4x60mm VGS 9x140mm	11 3
	7	F1	T-F	LBA 4x60mm	10	M12 bolt	2
	8*	F1	T-F	LBA 4x60mm	10	M12 bolt 6 mm thick washer	2 1
	9	F2/3	T-T	LBA 4x60mm	20	LBA 4x60mm VGS 9x140mm	11 3
	10	F2/3	T-F	LBA 4x60mm	10	M12 bolt	2
	11*	F2/3	T-F	LBA 4x60mm	10	M12 bolt 6 mm thick washer	2 1
NINO 100 200	12	F1	T-T	LBA 4x60mm	21	LBA 4x60mm VGS 9x140mm	13 3
	13	F1	T-F	LBA 4x60mm	21	M12 bolt	2
	14*	F1	T-F	LBA 4x60mm	14	M12 bolt 8 mm thick washer	4 1
	15	F2/3	T-T	LBA 4x60mm	21	LBA 4x60mm VGS 9x140mm	13 3
	16	F2/3	T-F	LBA 4x60mm	21	M12 bolt	4
	17*	F2/3	T-F	LBA 4x60mm	14	M12 bolt 8 mm thick washer	4 1

* angle brackets tested with WASHER

Table 3: *WKR test configurations*

HD	ID	Load	Type	Fast. Side A	n°	Fast. Side B	n°
WKR 095	18	F1	T-T	LBA 4x60mm	6	M12 bolt	1
WKR 095	19	F4	T-F	LBA 4x60mm	6	M12 bolt	1
WKR 135	20	F1	T-F	LBA 4x60mm	11	M12 bolt	1
WKR 285	21	F1	T-T	LBA 4x60mm	22	M12 bolt	1
WKR 285	22*	F1	T-F	LBA 4x60mm	22	M12 bolt	1
WKR 530	23**	F1	T-F	M5 bolt	18	M12 bolt	1

* hold-downs tested with gap (10mm)
** vertical flange was also nailed to stud (see Figure 4b)

https://doi.org/10.52202/069179-0178

3-layer 100 (33-34-33) mm thick CLT panel and 5-layer 140 (30-30-20-30-30) mm thick CLT panel are used in NINO angle brackets experimental tests to represent wall and floor panel, respectively, while a 80mmx160mm C24 solid wood stud is used in WKR hold-downs experimental tests to represent external vertical element of a timber frame.

The vertical flange (Side A) of each connector is fastened to the CLT panel or to the solid wood stud through Rothoblaas LBA 4x60mm ring shank nails (ETA-22/0002 [12]); horizontal flange (Side B) of each connector is fastened to either the CLT panel (T-T configuration) or to the steel base (T-F configuration) by means of Rothoblaas LBA 4x60mm ring shank nails [12] and Rothoblaas VGS 9x140mm screws (ETA-11/0030 [13]) or M12 8.8 steel bolts.

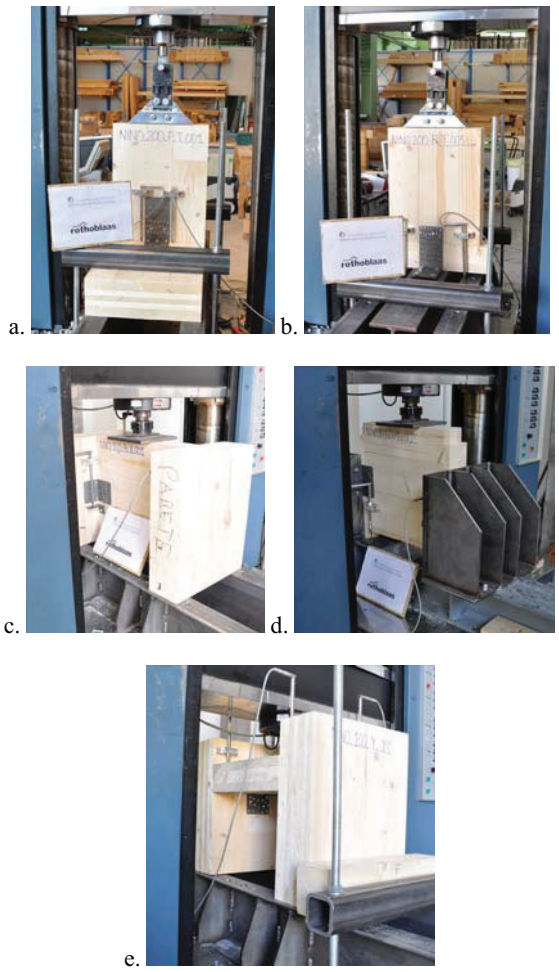

Figure 3: *Setup for: tensile force F1 (a. T-T, b. T-F), shear force F2/3 (c. T-T, d. T-F) and out-of-plane force F4 (e. T-T).*

In WKR hold-down connections loaded in F1 direction (except WKR530) one WKR hold-down was fastened at each side of solid wood vertical stud element in symmetric configuration (two hold-downs on each stud) and tested as shown in Figure 4a (WKR can be noted in the bottom part of the picture). The WKR530 hold-down was bolted directly to the testing machine through M5 bolts and the load was applied directly to the steel plate, as shown in Figure 4b. The vertical flange was nailed to the solid wood stud through twenty-two 4x60mm ring shank nails. In both cases the horizontal flange of hold-down was bolted to the load cell in order to measure the load acting on bolt. Along F4 direction two WKR095 hold-downs were fastened at each end of CLT panel, (four hold-downs on each panel), as shown in Figure 4c.

For each connector the maximum load F_m and corresponding displacement v_m, the load at 15mm F_{15}, the displacements $v_{0,1Fm}$ and $v_{0,4Fm}$ at $0,1F_m$ and $0,4F_m$ were determined from the load-displacement curves. The tri-linear relationship is determined from the mean force-displacement curve obtained from the three tests in each configuration. The value of yielding load F_y, yielding displacement v_y, ultimate load F_u and ultimate displacement v_u are calculated according to EN12512:2005 [14].

For WKR hold-downs tested in F1 configuration, the load acting on each M12 bolt F_{bolt} that anchored the WKR to the foundation was measured through a load cell. The amplification coefficient k_t, defined as the ratio between the tensile load on the anchoring bolt F_{bolt} and the hold-down F_{WKR}, was calculated according to Equation 1. F_{WKR} for WKR530 is equal to the force F_{app}, measured by the testing machine, while for other WKR hold-downs tested in symmetric configuration F_{WKR} is equal to $F_{app}/2$.

$$k_t = F_{bolt}/F_{WKR} \quad (1)$$

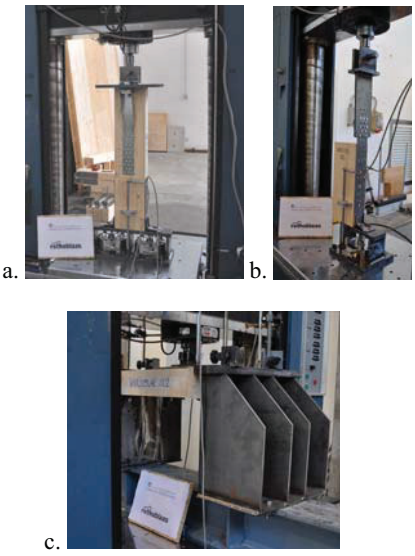

Figure 4: *Setup: a. F1 symmetric, b. F1 WKR530, c. F4.*

3 RESULTS AND DISCUSSION

The results of the experimental campaign on NINO angle brackets and WKR hold-downs are presented in this section. The force-displacement curves, failure modes (Figure 5 and Figure 6 for NINO and WKR connectors, respectively) and tri-linear relationships are reported and discussed.

https://doi.org/10.52202/069179-0178

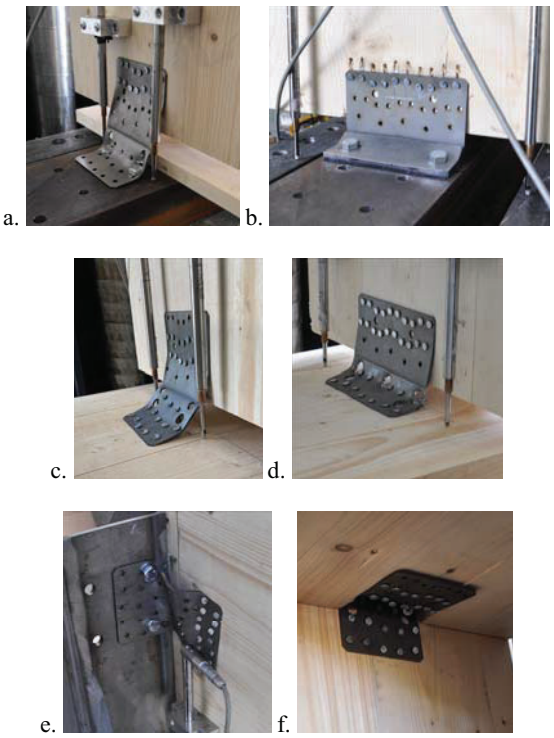

Figure 5: *NINO angle brackets failure modes: a. pull-through of bolt head (F1), b. nails shear failure (F1), c. nails withdrawal (F1), d. pull-through of screw head (F1), e. buckling (F2/3) and f. compression perpendicular to the grain (F4).*

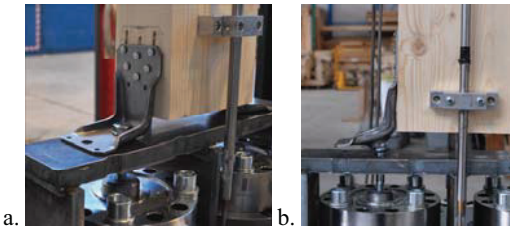

Figure 6: *WKR hold-downs failure modes: a. nails shear failure and b. pull-through of bolt head.*

3.1 NINO ANGLE BRACKETS

Force displacement curves for F1 and F2/3 load directions are reported in Figure 7 (T-F), Figure 8 (T-T) and Figure 9 (T-F), Figure 10 (T-T), respectively.

As shown in Figure 7, in case of T-F connection for F1 load direction, NINO angle brackets equipped with NINO washer showed higher stiffness and strength and a different failure mode compared to the angle brackets without washer: for angle brackets without washer, the failure mode is associated to the pull-through of bolts heads (Figure 5a) in the horizontal flange with large deformation of the steel plate, at the opposite in the angle brackets equipped with washer a ductile failure of nails was observed (Figure 5b).

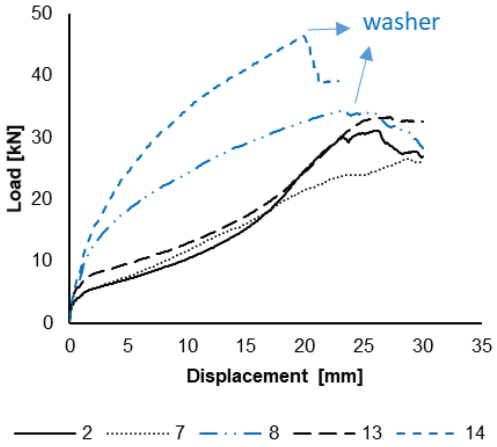

Figure 7: *NINO angle brackets for T-F connection (F1)*

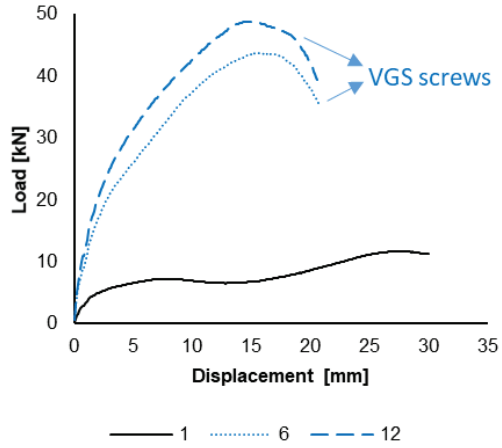

Figure 8: *NINO angle brackets for T-T connection (F1)*

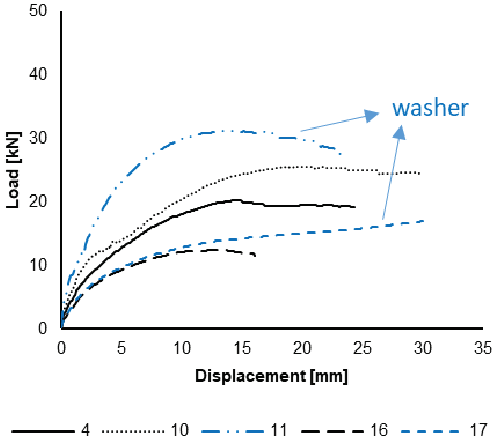

Figure 9: *NINO angle brackets for T-F connection (F2/3)*

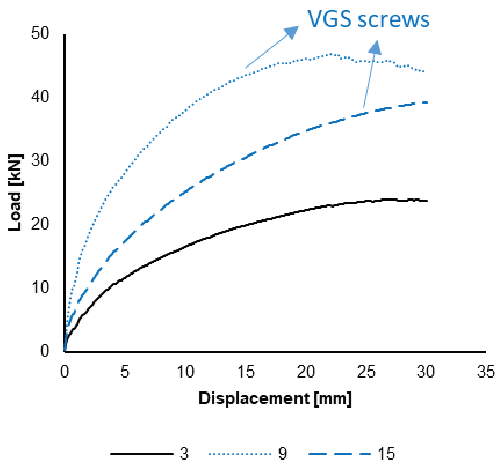

Figure 10: *NINO angle brackets for T-T connection (F2/3)*

As shown in Figure 8, in case of T-T connection for F1 load direction, the NINO angle brackets with VGS screws exhibit a completely different behaviour compared to the NINO without screws when subjected to a F1 load direction. Fully threaded screws installed adjacently to the bend line reduce the eccentricity between the fasteners in the two flanges and significantly increase the strength and stiffness of connections. In NINO angle brackets without VGS screws failure occurs due to the withdrawal of nails in horizontal plate (Figure 5c) while pull-through of screws heads (Figure 5d) or nails shear failure was observed in other cases (depending on the number of nails in vertical flange).

Table 4: *NINO tri-linear curves.*

Con.	ID	k [kN/mm]	vy [mm]	Fy [kN]	vm [mm]	Fm [kN]	vu [mm]	Fu [mm]
NINO 100 100	1	3,6	1,1	4,5	27,8	11,6	30,0	11,2
	2	1,5	17,7	28,5	26,1	31,1	29,8	26,8
	3	2,6	5,6	16,1	27,2	24,0	30,0	23,9
	4	3,0	4,6	15,6	14,6	20,2	24,3	19,1
	5	5,2	5,1	24,2	30,0	44,7	-	-
NINO 150 80	6	6,9	4,2	31,8	16,1	43,6	20,8	34,9
	7	1,5	14,6	23,1	28,7	26,5	30,0	26,0
	8	5,8	2,7	17,7	23,3	34,4	30,0	28,1
	9	8,2	3,1	28,7	22,6	46,9	30,0	43,9
	10	4,3	3,3	16,4	20,8	25,6	30,0	24,6
	11	5,2	4,3	24,9	13,4	31,2	23,3	26,9
NINO 100 200	12	8,6	3,5	34,0	14,8	48,8	20,6	39,0
	13	4,3	3,5	17,1	27,2	33,2	30,0	32,6
	14	5,9	4,9	31,8	19,9	46,4	22,8	39,1
	15	3,7	6,6	26,8	30,0	39,2	-	-
	16	2,7	3,1	9,2	13,1	12,4	16,0	11,5
	17	2,7	3,3	10,0	30,0	16,9	-	-

As for the load direction F1, the angle brackets were tested in F2/3 in different configurations: with and without washer and VSG screws in T-F (Figure 9) and T-T (Figure 10) configurations, respectively. Application of NINO washer or VGS screws allowed to increase the strength and stiffness also in F2/3 load direction, avoiding undesirable failure modes related to large deformations like buckling (Figure 5e) that occurred in some tested NINO angle brackets.

The NINO1001000 angle bracket was also tested in F4 load direction. It was observed remarkable values of strength and stiffness for out-of-plane compression, comparable to the highest values observed in other directions. The connection failed due to the compression perpendicular to the grain (Figure 5f). The tri-linear force-displacement curves parameters were reported in Table 4. The results confirm the marked multi-directional behaviour of NINO angle brackets.

3.2 WKR HOLD-DOWNS

A comparison in terms of force-displacement relationship in F1 load direction is reported in Figure 11 for different WKR hold-downs. The tri-linear force-displacement curve parameters were reported in Table 5.

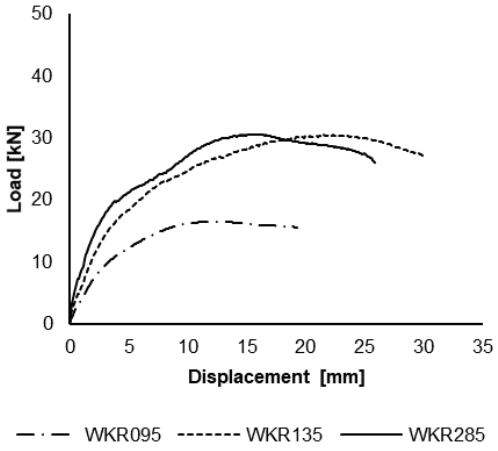

Figure 11: *WKR hold-downs for T-F connection (F1)*

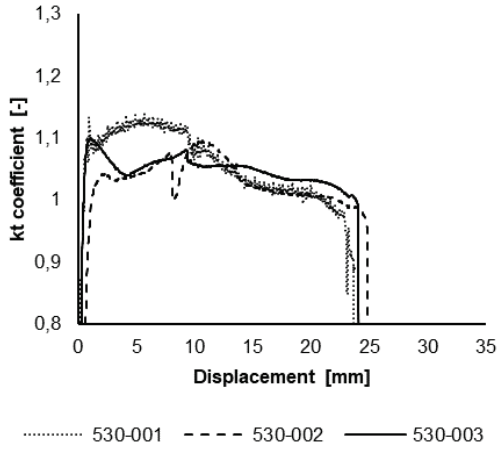

Figure 12*: Coefficient kt for WKR530 hold-down specimens*

In WKR095 hold-downs a shear failure of nails (Figure 6a) was observed while other hold-downs failed due the

https://doi.org/10.52202/069179-0178

pull-through of bolt head (Figure 6b) in the horizontal flange for a value of the load approximately equal to 30 kN (the geometry of the horizontal flange is the same for all WKR hold-downs): for each WKR size greater than WKR095 the pull-through failure was reached (the shear resistance of nails is greater compared to that of the horizontal steel flange).

For all the WKR specimens in F1 load direction the value of k_t factor was calculated for each hold-down and the maximum values are reported in Table 5. In Figure 12 the values of k_t factors calculated according to Eq.1 for the three tested specimens of WKR530 were showed. The values of k_t coefficient never exceed 1,13, for all specimens. The observed values indicate a slightly difference between the load applied to the hold-down and the load acting on anchor bolt. Moreover, the load amplification on anchor system results lower than that obtained from the formulation proposed in several European Technical Assessment [12] (approximately equal to 1,40). As reported in Table 5, the values of coefficient k_t for WKR285 with 10mm of gap are close to one, that means no amplification of load on anchor system are observed for the hold-downs installed with gap. The WKR095 hold-down was also tested in F4 load direction in order to characterized the out-of-plane behaviour: tests showed good results in terms of strength and stiffness (see Table 5).

Table 5: *WKR tri-linear curves.*

Con.	ID	k [kN/mm]	vy [mm]	Fy [kN]	vm [mm]	Fm [kN]	vu [mm]	Fu [mm]	kt [-]
WKR 095	18	3,5	3,5	12,7	11,9	16,4	19,2	15,6	1,05
WKR 095	19	3,3	2,6	8,9	30,0	15,1	-	-	-
WKR 135	20	5,0	3,7	19,7	22,3	30,4	30,0	27,1	1,04
WKR 285	21	6,5	2,6	19,4	15,4	30,6	25,8	26,1	1,11
WKR 285	22	6,1	2,0	13,9	14,4	20,6	20,6	16,5	1,00
WKR 530	23	-	-	-	16,0	30,5	-	-	1,13

4 CONCLUSIONS

The mechanical behaviour of NINO angle brackets and WKR hold-downs was investigated by means of monotonic experimental tests. Several setup configurations were specifically developed in order to test the connectors in different load directions. The main novelties of NINO angle brackets are the use of fully threaded screws and washer in horizontal flange in T-T and T-F connections, respectively. The two devices were never used before for small size angle brackets and significantly increase the strength and stiffness in F1 and F2/3 load direction of connectors. F4 tests confirmed a remarkable multi-directional behaviour for all the tested specimens of NINO angle brackets. WKR hold-downs were studied taking into account the possibility to install the connector with a gap between the horizontal flange and the foundation/floor panel. Proper investigations were conducted in order to measure and calculate the coefficient k_t. Tests showed similar results for installation with or without gap for WKR285 hold-down. The amplification of loads on anchor bolts was measured through load cells and can be taken into account by the designers through the coefficient k_t, which results always lower than 1,13. The tests highlight that the value of this coefficient is close to the unit and is smaller than the value obtained from analytical calculation, reducing the design tensile load on anchor system. No amplification was registered on anchor bolts of WKR285 with gap.

5 ACKNOWLEDGMENTS

The authors would like to acknowledge the CNR-IBE (San Michele all'Adige) mechanical test laboratory staff: Mario Pinna, Diego Magnago and Massimiliano Natale.

REFERENCES

[1] Tomasi R. Casagrande D. Grossi P. Sartori T. Shaking table tests on a three-storey timber building. Proceedings of the Institution of Civil Engineers: Structures and Buildings, 2015. 168(11), pp. 853–867.

[2] Casagrande D. Grossi P. Tomasi R. Shake table tests on a full-scale timber-frame building with gypsum fibre boards. European Journal of Wood and Wood Products, 2016. 74(3), pp. 425–442.

[3] Casagrande D. Rossi S. Sartori T. Tomasi R. Analytical and numerical analysis of timber framed shear walls. World Conference on Timber Engineering 2012. WCTE 2012, 2012. 5, pp. 497–503.

[4] Gavric I. Fragiacomo M. Ceccotti A. Cyclic behaviour of typical metal connectors for cross-laminated (CLT) structures. Materials and Structures (2015), 48:1841-1857.

[5] Shen Y. Schneider J. Tesfamariam S. Stiemer S. Chen Z. Cyclic behavior of bracket connections for cross-laminated timber (CLT): Assessment and comparison of experimental and numerical models studies. Journal of Building Engineering (2021), 39:102-197.

[6] Liu J. Lam F. Experimental test of coupling effect on CLT angle bracket connections. Engineering Structures, 171 (2018), 862-873.

[7] D'Arenzo G. Seim W. Fossetti M. Experimental characterization of a biaxial behaviour connector for CLT wall-to-floor connections under different load directions. Construction and Building Materials, 2021, 295, 123666.

[8] Popovski M. Schneider J. Schweinsteiger M. Lateral load resistance of cross-laminated wood panels. 11th World Conference on Timber Engineering 2010. WCTE 2010. 4, pp. 3394-3403. ISBN: 978-162276175-3.

[9] D'Arenzo G. Casagrande D. Polastri A. Fossetti M. Fragiacomo M. Seim W. CLT shearwalls anchored with shear-tension angle brackets: experimental tests and finite element modelling. J. Struct. Eng. (2021).

[10] ETA-Denmark, ETA-22/0089. European technical assessment. Three-dimensional nailing plate (Angle Bracket or Hold Down for timber-to-timber or timber-to-concrete or steel connections), (2022).

[11] EN26891:1991. Timber structures - Joints made with mechanical fasteners - General principles for the

determination of strength and deformation characteristics (ISO 6891:1983).

[12] ETA-Denmark, ETA-22/0002. European technical assessment. Nails and screws for use in nailing plates in timber structures, (2022).

[13] ETA-Denmark, ETA-11/0030. European technical assessment. Screws for use in timber construction, (2016).

[14] EN12512:2005. EN12512, Timber structures. Test methods. Cyclic testing of joints made with mechanical fasteners. Brussels, Belgium: CEN, (2005).

[15] ETA-Denmark, ETA-11/0086. European technical assessment. Three-dimensional nailing plate (Angle Bracket or Hold Down for timber-to-timber or timber-to-concrete or steel connections), (2015).

https://doi.org/10.52202/069179-0178

World Conference on Timber Engineering Oslo 2023

ASSESSMENT OF COMBINED EFFECTS OF AXIAL AND LATERAL LOADING OF GLUED-IN ROD CONNECTIONS IN LVL

Daniel Fawcett[1], Eleni Toumpanaki[2]

ABSTRACT: Glued-in rod connections for timber offer improved strength, stiffness, aesthetics and fire performance compared to bolts and dowels. Extensive investigations have been done into the pull-out capacity of rods under pure axial load, however the capacity and stiffness of laterally loaded rods, particularly when combined with axial loading, is under-researched, with further investigation being crucial as nearly all connections are subject to this combination. The provision of an unbonded length has been shown to increase pull-out capacity, but its effect on laterally loaded rods has not been investigated. Investigations also often use softwoods over hardwoods. As a result, design codes lack informed guidance for laterally loaded rods and underestimate the capacity of rods in hardwood. In this study, 15 Beech LVL specimens with steel rods glued in with epoxy adhesive were subjected to varying ratios of axial to lateral load, to study the combined effects. The introduction of lateral load had no effect on axial capacity with a governing failure mode of rod yielding. The lateral capacity exceeded the design code prediction by 92%, and alternative parameters and equations were presented and discussed for more accurate estimation.

KEYWORDS: Glued-in rods, timber, LVL, Eurocode 5, moment rotation, epoxy

1 INTRODUCTION

1.1 GENERAL OVERVIEW OF GLUED-IN RODS

Glued-in rods (GiRs) offer a desirable alternative to bolts and dowels for timber connections [1]. By inserting rods into pre-drilled holes in timber and filling the surrounding void with adhesive to bond them together [2], a very strong and stiff connection is achieved. Multiple rods glued-in at a distance apart provide efficient moment resistance due to the couple of axial forces created [3]. Greater aesthetic appearance and fire resistance is achieved with the timber cover provided, obscuring the rods [4], whereas conventional connections are often exposed or covered with limited wood sheathing.

It is common for steel to be used as the rod material due to its strength and, crucially, ductility. Carbon and glass FRPs [5] and basalt FRP [6] are sometimes used, though despite being very strong and stiff, they lack high ductility.

The adhesives that have been studied for glued-in rods are epoxy, polyurethane and fibre-reinforced phenol-resorcinol, in descending order of strength (determined by the GIROD project in the late 90s [4]). The first two are used most frequently [2].

There are numerous potential modes of failure with this connection type, including longitudinal shear failure in the adhesive, timber-adhesive interface, steel-adhesive interface or in the timber surrounding the adhesive; timber splitting due to short rod-edge or rod-rod distances (particularly with lateral rod loading); or tensile yield failure of the rod or the timber cross-section [2]. The ductile failure mode of steel rod yielding is always preferred over the other brittle failure modes [7]. As a result, all relevant failure modes should be assessed during design, and rod yielding must be the critical one. This requires a detailed understanding of all the failure modes, and how variation of the multitude of parameters involved, including the effect of lateral loading, affects the failure load for each mode.

1.2 RESEARCH INTO GLUED-IN RODS

Many studies have focused just on the 'pull-out' capacity of glued-in rods by conduction of tests with the pull-pull test setup (rods glued into both ends of a timber element gripped and pulled apart), as studies can be easily compared if they follow the same experimental programme [8]. Softwoods are often the timber type used for tests, meaning that the current design equations,

[1] Daniel Fawcett, University of Bristol, Department of Civil Engineering, Queen's Building, University Walk, BS8 1TR, UK, tc19705@bristol.ac.uk
[2] Eleni Toumpanaki, University of Bristol, Department of Civil Engineering, Queen's Building, University Walk, BS8 1TR, UK, eleni.toumpanaki@bristol.ac.uk

https://doi.org/10.52202/069179-0179

informed by such tests, often under-predict the pull-out strength of rods glued into hardwoods [9]. In addition, comparatively little research has been done on laterally loaded glued-in rods, let alone combined axial and lateral action. Further research in this area is important as nearly all connections are subject to both axial and lateral force.
The provision of an unbonded length close to the loaded end of the rod has been shown to increase the axial pull-out capacity by shifting the longitudinal shear stress distribution in the timber-adhesive interface away from the end grain, where there would otherwise be a local concentration, decreasing the likelihood of timber splitting [2]. Franke et al. [7] showed that an unbonded length of 2d prevented timber splitting and reduced experimental scatter, and a greater unbonded length of 5d markedly increased the pull-out capacity on top of this.
The recently published EN 17334:2021 [10] provides specific guidance for glued-in rod connections regarding universal testing, design, and manufacturing of glued-in rods. Design guidelines for glued-in rods are included in Annex A of [10], which specifies that lateral rod capacity should be estimated using equations for dowel-type fasteners from EC5 [11], which do not have a glue-line. The presence of glue-line can affect the embedment strength of the rods and there is limited research addressing this aspect.
Due the current lack of design standards for glued-in rods in EC5 [11], there is still much hesitation in the construction industry over use of glued-in rod connections: a survey [12] found that of the 56 European scientists, timber industrialists and structural designers who took part, 9% use glued-in rods frequently, 68% have never or very rarely used them, 60% are not confident in using them, and 89% are not satisfied with current standards. The second generation of EC5 to be released in 2025 will include design guidelines for bonded-in rods.

1.3 EXISTING STUDIES ON COMBINED AXIAL & LATERAL LOADING

There are limited studies investigating the interaction of axial and lateral rod force in glued-in rods, and these have addressed the brittle failure modes (shear failure in the timber or adhesive, or interfacial shear failure). Aicher and Simon [3] performed tests in spruce glulam GL30h with steel rods of class 8.8 and 16 mm nominal diameter, glued-in with 2 mm thick epoxy resin and parallel to grain. Pull-out tests assessed the axial rod capacities, shear tests assessed the lateral capacities, and cantilever tests assessed the combined axial and lateral interaction, with two different beam lengths tested for different ratios of axial to lateral force. The results, shown in Figure 1, strongly support an elliptic relationship which is given by the current governing equation (Equation (8) in this paper). This study also confirmed that providing greater edge distance between the top rod and top of the timber beam results in a significant increase in the lateral capacity, which is currently not accounted for in design code: rather a minimum edge distance of 4*d* (from the centre of the rod of diameter *d*) is specified.

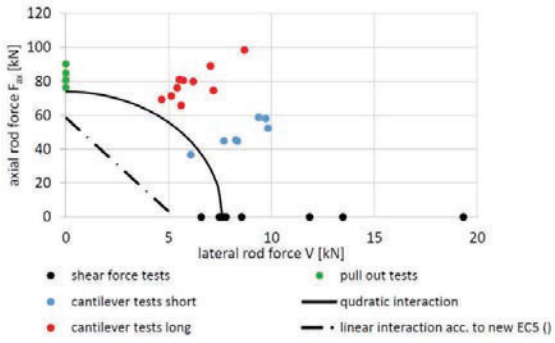

Figure 1: *The plotted ultimate rod axial and lateral loads compared to trend lines for Aicher's and Simon's study [3].*

This minimum edge distance was used for some specimens and the results were close to the EC5 [11] prediction.
Walker and Xiao [13] performed tests with a different setup, whereby rods were glued-in at differing angles to the timber surface but still parallel to grain, as indicated by Figure 2, and pulled out with force normal to the timber surface, inducing a lateral force component in the rotated section of the rod. The timber was LVL, and the bent rods were class 8.8 steel of 12 mm nominal diameter, bonded with 4 mm glue-line thickness. Contrary to the previous study, this yielded a decreasing linear interaction between the axial and lateral rod force, as depicted in Figure 3. Reasons could include the different test method or the different materials.

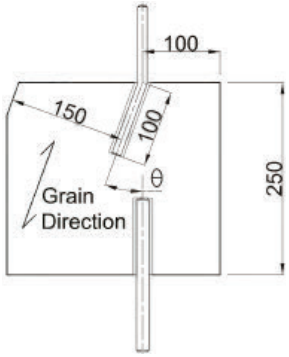

Figure 2: *The setup of Walker's and Xiao's study [13].*

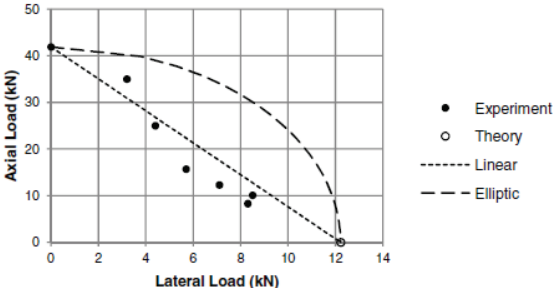

Figure 3: *The plotted ultimate rod axial and lateral loads compared to trend lines for Walker's and Xiao's study [13].*

https://doi.org/10.52202/069179-0179

2 DESIGN EQUATIONS & CRITICISMS

2.1 AXIAL CAPACITY

EN 17334 A.2.4 [10] specifies the axial capacity of glued-in steel rods as given by Equation (1):

$$F_{ax,Rd} = min\begin{cases} f_{y,d}A_{ef} \\ \pi d l_a f_{vr,d} \end{cases} \quad (1)$$

where $F_{ax,Rd}$ is the rod axial capacity (N), $f_{y,d}$ is the design yield strength of the steel rod (N/mm^2), A_{ef} is the effective stress area of the rod (mm^2, equal to the nominal stress area $A_{s,nom}$ specified in [14]), d is the nominal rod diameter (mm), l_a is the bond length (mm), and $f_{vr,d}$ is the design adhesive bond strength (N/mm^2). The two expressions are for the rod yield and adhesive ('pull-out') capacity respectively. Equation (1) is widely used and included in other design codes. However, it does not account for the fact that increasing bond length provides diminishing (not linear) returns for increased capacity, which has been shown by many studies [2].

2.2 LATERAL CAPACITY

For calculation of rod lateral capacity, EN 17334 A.3.1 and A.3.2 [10] specify referral to sections 8.2 and 8.5 of EC5 [11] respectively, which give design equations for the lateral capacity of metal dowel-type fasteners. The lateral capacity of a metal dowel-type fastener (or in this case the glued-in rod) connected to a thin plate in single shear is given by Equation (2):

$$F_{v,Rk} = min\begin{cases} 0.4 f_{h,k} t_1 d & (a) \\ 1.15\sqrt{2M_{y,Rk} f_{h,k} d} + \dfrac{F_{ax,Rk}}{4} & (b) \end{cases} \quad (2)$$

where $F_{v,Rk}$ is the characteristic fastener (rod) lateral capacity (N), $f_{h,k}$ is the characteristic timber embedment strength (N/mm^2), t_1 is equal to the bond length l_a (mm) for glued-in rods, d is the nominal fastener (rod) diameter (mm), $M_{y,Rk}$ is the characteristic fastener (rod) yield moment (Nmm), and $F_{ax,Rk}$ is the fastener (rod) axial capacity (N). Alternatively, the lateral capacity for connections to a thick plate in single shear is given by Equation (3):

$$F_{v,Rk} = min\begin{cases} f_{h,k} t_1 d & (c) \\ f_{h,k} t_1 d\left(\sqrt{2 + \dfrac{4M_{y,Rk}}{f_{h,k} d t_1^2}} - 1\right) + \dfrac{F_{ax,Rk}}{4} & (d) \\ 2.3\sqrt{M_{y,Rk} f_{h,k} d} + \dfrac{F_{ax,Rk}}{4} & (e) \end{cases} \quad (3)$$

Each expression within Equations (2) and (3) is for a different failure mode, with Figure 4 illustrating them. The first terms are the capacities according to Johansen yield theory, and the second term $F_{ax,Rk}/4$ included in some of the expressions is an estimation of the beneficial contribution from the rope effect. EC5 [11] section 8.2.2(2) specifies different limits for the contribution of this effect, as a percentage of the Johansen part, for different fastener types. A 25% limit for bolts was applied for estimated lateral rod capacities in this study, and the appropriateness of this value for glued-in rods was discussed upon analysis of the experimental results.

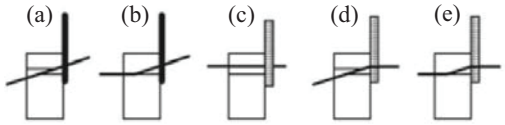

Figure 4: *Depicted failure modes from Equations (2) and (3), in the same order the expressions are in (from Figure 8.3 of EN 1995-1-1:2004).*

The embedment strength parallel to grain is given by equation 8.32 in section 8.5.1.1 of EC5 [11]. EN 17334 A.3.4 and A.3.5 [10] combined specify a factor of 0.125 on this to give the embedment strength perpendicular to grain, $f_{h,90,k}$, given in Equation (4), which is applicable for laterally loaded rods glued-in parallel to grain:

$$f_{h,90,k} = 0.125 \cdot 0.082(1 - 0.01d)\rho_k \quad (4)$$

where ρ_k is the characteristic timber density (kg/m^3). Equation (4) doesn't account for the use of an EWP (e.g. glulam or LVL) over sawn timber, or for the presence of adhesive. The embedment strength of the adhesive and timber in combination and the glue-line thickness are not considered. An effective density equal to the geometric mean of the timber and adhesive densities, given in Equation (5), could be used in place of ρ_k in Equation (4) to calculate the embedment strength required for Equations (2) or (3):

$$\rho_{ef} = \sqrt{\rho_{timber} \cdot \rho_{adhesive}} \quad (5)$$

Furthermore, none of the previous discussion accounts for the presence of an unbonded zone. The absence of adhesive near the shear plane results in a gap around the rod, causing the rod to bend and embed directly into the above timber, affecting the failure mode and capacity. Moreover, the bearing zone is lower than the theoretical one including part of the unbonded length due to the local restrictive effect of the fully bonded length (see Figure 5).

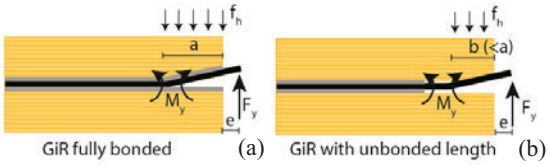

Figure 5: *Embedment stresses in (a) a fully bonded glued-in rod and in (b) a glued-in rod with an unbonded length.*

Riberholt [15] proposed equations to estimate the timber embedment strength and lateral capacity for laterally loaded glued-in bolts, with consideration of the bolt and

hole diameters (the maximum of which is d (mm)), bolt yield moment M_y (Nmm), embedment strength f_h (N/mm^2) and eccentricity, e, of the applied lateral load with respect to the timber loaded face (mm) where there is absence of bearing stresses. The maximum lateral force F (N) acting at distance e is given by Equation (6):

$$F = \left(\sqrt{e^2 + \frac{2M_y}{df_h}} - e \right) df_h \tag{6}$$

with embedment strength f_h given by Equation (7):

$$f_h = (2.3 + 750d^{-1.5})\rho \tag{7}$$

where ρ is the relative timber density (dimensionless, normalised by ρ_{water} = 1000 kg/m^3). Equation (6) accounts for both bolt (rod) yielding and embedment failure. It may appear sensible at first to assign the unbonded length as the load eccentricity, e, as the rod is not supported over this length. However, it will likely not take much rod deformation until the rod contacts with the timber at the end of the unbonded zone, i.e. yield failure in the rod won't yet have occurred. This contact then means more support to resist rod yielding due to bending, and likely embedment failure here instead of at the end of the bonded zone, not predicted by Equations (6) and (7). Furthermore, the equations do not account for thick glue-lines and are derived for glulam, whereas LVL is likely to have greater embedment strength (discussed later). Clearly a new and more comprehensive set of equations is needed. Nevertheless, Equations (6) and (7) were also used to give a prediction of the lateral load capacity.

2.3 AXIAL & LATERAL COMBINED CAPACITY

EN 17334 A.4 [10] recommends an elliptic relationship between the axial and lateral rod forces, given in Equation (8), to be satisfied:

$$\left(\frac{F_{lat,Ed}}{F_{lat,Rd}}\right)^2 + \left(\frac{F_{ax,Ed}}{F_{ax,Rd}}\right)^2 \leq 1 \tag{8}$$

This equation is found in other design codes such as DIN EN 1995-1-1/NA [16], in addition to a linear version (the quotient terms not squared) given in the Final draft *Connections* SC5.T5 to the new DIN EN 1995-1-1:2020 [3]. The results of Aicher and Simon [3] support the elliptic relationship, whereas the results of Walker and Xiao [13] support the linear relationship.

2.4 ROTATIONAL STIFFNESS

There are no standards for the estimation of the rotational stiffness of timber connections [17], but such calculations are important for serviceability checks. As such, analytical models are proposed in literature, and they are verified with experiments. This study makes use of the proposal by [18]: a component method for moment-resisting glued-in steel rod connections in glulam, analogous to that used for steel moment connections. It is recommended to refer to their paper for the full set of equations involved and the supporting diagrams, though an equation of interest is the stiffness of the timber compression zone k_c (N/mm), given by Equation (9):

$$k_c = \frac{E_{w,0}\sqrt{A_c}}{4} \tag{9}$$

where $E_{w,0}$ is the timber elastic modulus parallel to grain (N/mm^2) and A_c is the area of timber in compression (mm^2). Equation (9), as derived from equation 17 in [18], has been modified here so that it is applicable to the specimens in this study, due to differences in the type of support. Note how there is no inclusion of the timber beam length: this is discussed in section 4.4.

To calculate the rod axial stiffness, required for the above model, Xu et al. [1] proposes using the axial rigidity E_sA_s (N) divided by the bond length l_a (mm), but with the addition of a coefficient 0.3 to account for mechanical interlocking and the bond stress distribution along the bonded length, hence providing an effective stiffness. This coefficient value was determined by comparison between FE analysis and an experiment on the same specimen. Deviations due different materials (e.g., glulam versus LVL) and adhesive types may lie between studies. The steel rod stiffness k_s (N/mm) is hence given by Equation (10):

$$k_s = \frac{E_sA_s}{0.3l_a} \tag{10}$$

2.5 OUTLINE OF THIS STUDY

The purpose of this study was to investigate the effects of combined axial and lateral force in the axial withdrawal capacity of glued-in rods in LVL. The study addresses the ductile failure mode for glued-in rods (rod steel yielding) as opposed to the brittle failure modes that have been investigated in other studies. This is because the steel yielding failure mode is the expected design failure mode, to increase ductility and energy dissipation, and favour load re-distribution and non-catastrophic sudden failures. For the evaluation of the axial and lateral load capacities, pull-pull and shear tests were conducted respectively. The combined effects of axial and lateral loading were investigated with cantilever tests of varying length, similar to the test methodology in [3]. The EN 17334 [10] design rules were adhered to, and its design capacity equations were used as the baseline comparison for the results of the study. A fixed unbonded length was provided for all specimens to investigate the resulting effect on the rod capacities when compared to predictions. The axial and rotational stiffnesses of the connections were also measured experimentally and compared to predictions using the analytical models discussed in previous section. Characteristic values (rather than design values) were used.

https://doi.org/10.52202/069179-0179

3 EXPERIMENT PROGRAMME

3.1 MATERIALS

Steel rods with a metric thread, a nominal diameter of 12 mm and of property class 8.8 were used, hence they had characteristic yield strength $f_{y,k}$ = 640 N/mm^2, tensile strength $f_{u,k}$ = 800 N/mm^2 and nominal stress area $A_{s,nom}$ = 84.3 mm^2 [14]. The yield and tensile strengths of the three steel rods were verified by tensile tests. The results were a mean 0.2% proof stress of 613.0 N/mm^2 (standard deviation 14.3 N/mm^2) and a mean tensile strength of 783.0 N/mm^2 (standard deviation 9.2 N/mm^2), respectively 4.2% and 2.1% lower than the respective characteristic strengths. The experimental values were used in the design equations for rod capacities rather than the characteristic strengths given in [14]. An elastic modulus of 200 kN/mm^2 was assumed for the rods. The timber was Beech LVL (BauBuche GL70). An average moisture content of 13.5% was recorded after testing with a Protimeter Surveymaster Moisture Meter using the non-invasive method. Tests on the same timber in [19] yielded a flexural elastic modulus of 15.7 kN/mm^2 and a compressive yield stress of 43 N/mm^2. The adhesive used was a 2-component thixotropic epoxy adhesive (Rotafix Timberset Adhesive), especially suited to bonding metal to timber, with a bond strength of 6-10 N/mm^2 according to the manufacturer, with >6 N/mm^2 specified for UK structural softwoods and >9 N/mm^2 for Jarrah hardwood [20].

3.2 SPECIMEN GEOMETRIES & SETUPS

The specimen geometries and test arrangements are summarised in Figure 6, with the actual specimens shown in Figure 7. The nomenclature adopted is S for shear tests, A for axial pull-pull tests and C for cantilever tests with 1, 2 and 3 referring to a specimen length of 500, 750 and 1000 mm respectively. Three specimens were tested for each test configuration, hence a total of 15. The bond length was fixed at 240 mm, with an unbonded length of 50 mm (the maximum according to [10]) provided for all specimens by wrapping duct tape around the rods in this region to stop adhesive flow encroaching in the unbonded length during manufacturing of the specimens. The rod hole diameters were 16 mm, yielding a 2 mm glue-line thickness. The adhesive was applied by injection and exit through 2 respective pre-drilled holes of 8 mm diameter perpendicular to the rod hole, with the rods inserted beforehand and aligned with acrylic rings. This method of adhesive application ensures minimal skew in rod alignment and good filling of voids with adhesive, providing some quality assurance [2]. Rod lengths, separations and edge distances all complied with rules in [10], such as the minimum top rod edge distance of 4*d* provided for all tests (except the axial tests which had greater edge distance).

3.3 AXIAL (PULL-PULL) TESTS

The axial specimens were subjected to 'pull-pull' tests to study axial behaviour without the influence of lateral load. The test setup is shown in Figure 8(a). The axial

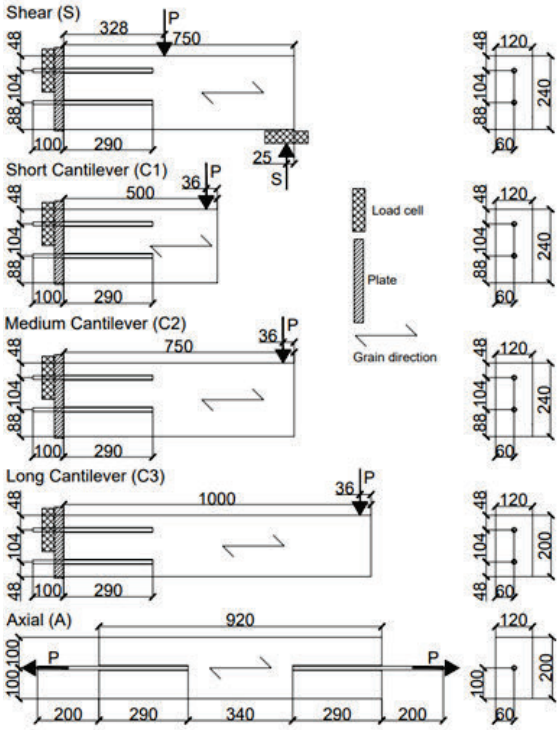

Figure 6: *Summary of the specimen geometries and test setups.*

Figure 7: *Specimens following the application of the adhesive.*

displacement of the rods was tracked by 2 LVDTs on either side (for the mean average). The test was conducted at a displacement control mode of 1 mm/min.

3.4 CANTILEVER TESTS

The setup for the cantilever tests is shown in Figure 8(b). The large supporting plate was 30 mm thick (>d hence thick according to [11]). No separation was provided between the timber face and supporting plate for these tests, to mimic the realistic situation of a timber beam connected to a steel connector plate. As a result, a compressive distribution was to be introduced into the timber. Analytical equations derived in [21] were used to

estimate the position of the neutral axis of bending, which was found to be below the bottom rod for all cantilever specimens. As a result, the bottom rod was predicted to also experience tension, though much less than the top rod. For the cantilever (and shear) tests, a pancake load cell tracked the tension force in the top rod (the expected failure region). Even distribution of lateral force between the rods was assumed, as verified with a FE model in the linear elastic range, so the individual lateral rod forces were taken to be half of the total (equal to the specimen weight plus the applied load *P*).

Axial displacements of the rods were again tracked by 2 LVDTs either side of each rod (for the mean average). The load, *P,* was applied at 3-7 mm/min downward displacement (the longer the cantilever the higher the displacement rate).

Figure 8: *(a) The axial, (b) cantilever and (c) shear test setups.*

3.5 SHEAR TESTS

The setup for the shear tests is shown in Figure 8(c). The shear test setup involved a slight adaptation to the cantilever test setup, with a support provided under the (previously) free end (of which the load taken, *S*, was tracked with a pancake load cell), and with load *P* applied just beyond the end of the bond zone of the rods: a compromise between applying load close to the support to minimise moment hence axial rod load in that region (as these tests are an investigation of the lateral capacity), and applying load away from the end of the rods to avoid interfering with their failure. Separation was provided between the timber and supporting plate with washers in these tests to eliminate steel-timber friction, for accurate tracking of the total lateral rod loads, equal to the specimen weight plus the applied load, *P,* minus the support load, *S*. The load, *P,* was applied at 2 mm/min downward displacement.

4 RESULTS AND DISCUSSION

4.1 AXIAL & CANTILEVER SPECIMEN RESULTS (AXIAL CAPACITY & STIFFNESS)

The results for the rod forces and slippages are summarised in Table 1. Only results for the top rods are shown as failure always occurred here. Note that the 'failure' yield point is top rod yielding for the A and C1-3 specimens, and first crack for the S specimens; and the 'ultimate' load point is the maximum top rod load reached for the A and C1-3 specimens, and the first significant split for the S specimens. One of the C1 specimens failed prematurely (short of top rod yielding) due to a connection issue, hence data from this test was only used for rotational stiffness assessment. One test from the C2 and C3 group stopped prematurely at the ultimate load due to a hydraulics issue.

Examples of the observed failures are shown in Figure 9. The failure mode for all tests, except the shear tests, was yielding of the steel rods at 51.7 kN according to the experimental yield strength value. The predicted failure loads according to Equation (1) range from 54.3-90.5 kN (for adhesive bond strength 6-10 N/mm^2, see section 3) with the lowest value corresponding to steel yielding based on the nominal yield strength. Most specimens reached ultimate load followed by fracture, with a mean ultimate load reached at 64.2 kN for the axial and cantilever specimen top rods (4.7% lower than the nominal value of 67.4 kN). The yield (and consequently fracture) points often occurred in the unbonded zone within the timber. The mean ultimate load value suggests an adhesive bond strength of >7.1 N/mm^2, as no signs of failure of the adhesive were observed.

The LVDT data confirmed tension in the bottom rods for the cantilever tests, with its value estimated by subtracting the measured top rod force from the timber compressive force, which was estimated with Euler-Bernoulli theory. The timber compression was very large, commonly reaching around 112 kN for the C1 and C2 tests, and the resulting extreme fibre compressive stress reached around 35 N/mm^2, below the compressive yield stress of 43 N/mm^2 [19].

Table 1: *Mean average values for load and slip at failure for top rods, and axial stiffness (outliers excluded; bracketed values are ultimate; non-bracketed values are at yield or first crack for S specimens)*

Specimen	Axial Load (kN)	Lateral Load (kN)	Axial Slip (mm)	Axial Stiffness (kN/mm)
S	14.1 (14.6)	18.4 (18.7)	-	-
C1	51.7 (62.5)	14.4 (18.6)	1.1	13.4 (17.3)
C2	51.7 (64.5)	9.0 (12.2)	1.2	12.8 (17.4)
C3	51.7 (64.2)	4.4 (6.1)	1.1	8.4 (11.7)
A	51.7 (65.1)	0.0 (0.0)	0.7	-

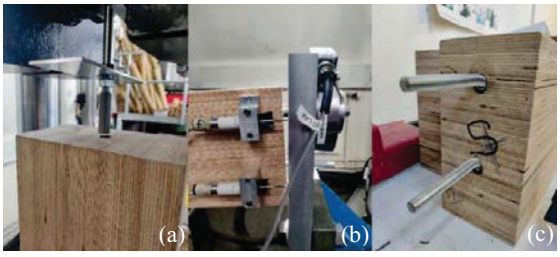

Figure 9: *Typical failures: (a) tensile failure after steel yielding in axial specimens, (b) tensile failure after steel yielding in cantilever specimens, and (c) rod deformation, embedment failure and LVL splitting in shear specimens.*

https://doi.org/10.52202/069179-0179

Figures 10-13 are the graphs of the top rod axial load against rod axial displacement for the axial and cantilever tests. The graphs each show 2 series of results: one corrected for the elastic rod strain (between the end of the bond zone and the nuts used to secure them behind the steel plate) up to the yield load, hence giving the relationship between rod load and rod slippage; and the other showing the full displacements including the region of plastic behaviour (elastic, plastic and slippage displacements; grey plots).

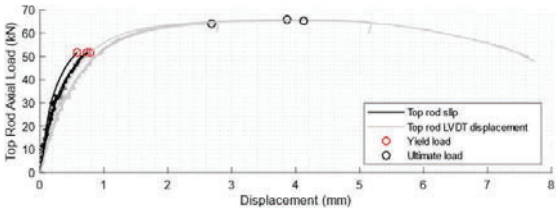

Figure 10: *Top rod axial force-slip and full axial force-displacement curves for the axial (A) tests.*

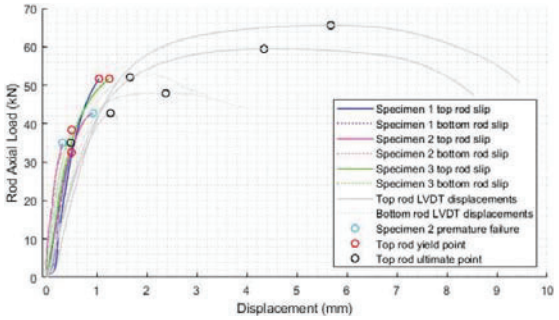

Figure 11: *Top and bottom rod axial force-slip and full axial force-displacement curves for the short cantilever (C1) tests.*

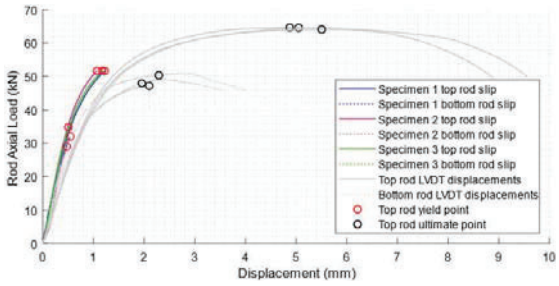

Figure 12: *Top and bottom rod axial force-slip and full axial force-displacement curves for the medium cantilever (C2) tests.*

The axial stiffnesses of the top rods were calculated using the linear elastic range of the load-slip relationship, assumed to be between 10-40% of the ultimate rod load, with the values given in Table 1, as well as the slippage values at yield failure. The cantilever specimen top rod stiffnesses (which were very similar despite differing lateral load) were an average of 43% lower than the axial specimen rod stiffnesses (79.0 kN/mm compared to 138.6 kN/mm), indicating that a small addition of lateral load due to cantilever action markedly decreases the axial stiffness, though internal timber strain differences due

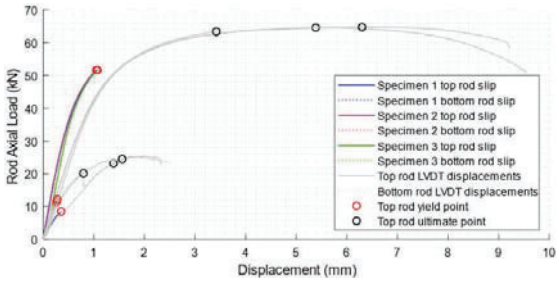

Figure 13: *Top and bottom rod axial force-slip and full axial force-displacement curves for the long cantilever (C3) tests.*

to different rod edge distances and timber areas could also contribute to this.

An interesting observation is how the total lateral forces in the short cantilever tests were only slightly less than those in the shear tests, but no signs of splitting or embedment failure were observed. A reason could be the yielding of the top rod combined with increased embedment stresses leading to load redistribution to the bottom rod, causing neither to quite reach the lateral load capacity. Another likely reason could be a vertical frictional resistance introduced due to the timber-steel contact which, if accounted for (assuming a friction coefficient of 0.2 [22]), is found to be dominant, given the large timber compression force. However, this friction force is expected to be limited given the small hole clearance in the steel plate, and the main bearing action between the rods and the plate. The friction force was not included in the results due to its uncertain value and variation, but its presence can represent a real scenario of a moment resisting connection.

4.2 SHEAR SPECIMEN RESULTS (LATERAL CAPACITY)

The shear specimens failed by splitting of the LVL in lamination plane interfaces around the top rod, as shown in Figure 9 (c). Embedment failure was observed at the end of the unbonded zone as predicted, due to the upward rod deformation which the zone allowed for. The rod deformations and embedment failures were greater in the bottom rods, though this could be due to a transfer of much of the lateral load to the bottom rod upon splitting failure around the top rod, rather than an uneven force distribution between the rods throughout the test within the linear elastic range.

Calculations using the measured *P* and *S* forces confirmed an increasing sagging moment at the rod support for the duration of all 3 shear tests, likely as this end displaced downwards due to rod deformation and embedment failure, but the other end was vertically restrained due to the rigid vertical support provided by the pancake load cell. Such behaviour is expected with plastic hinge formation at the rod support. The top rods experienced axial tension of 23-34% of the yield load, as measured by the pancake load cell, with loads shown in Figure 14. A likely reason could be a significant axial force due to the rope effect, evidenced by the large deformation of the rods observed, causing them to be 'pulled through' the plate.

https://doi.org/10.52202/069179-0179

Such a force would significantly exceed the 25% limit prescribed for the contribution to the lateral capacity of bolts, used to estimate the rod lateral capacities in this study, indicating that a higher limit (the determination of which requires further investigation) may be more suitable for glued-in rods.

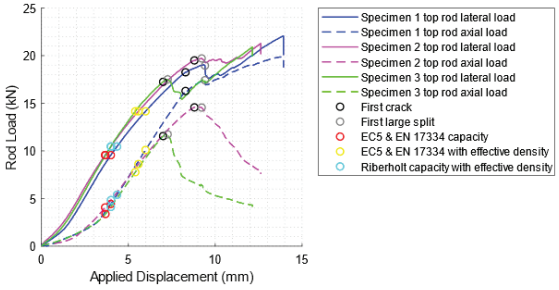

Figure 14: *Graph of top rod loads against the vertical displacement at the point of load application for the shear (S) tests, with predicted and observed failure loads indicated.*

Table 1 includes the lateral force values at failure, with a mean of 18.4 kN observed. Referring back to section 2.2, use of EC5 [11] equations yield an embedment strength of 6.1 N/mm^2 (Equation (4)), and hence a lateral capacity of 9.6 kN according to the failure mode (c) of Equation (3) (as the plate used was thick), which is 92% less than the observed lateral capacity. This disparity is attributed to the use of LVL causing an under-prediction of the embedment strength, and the provision of an unbonded length, which shifts the lateral force distribution away from the timber surface, hence increasing the resistance to splitting. Equation (4) does not account for use of an EWP over sawn timber, with LVL being particularly neglected due to the thinner laminations (as opposed to glulam). Schweigler et al. [23] found an embedment strength of 27.5 N/mm^2 for dowels in LVL (of the same 12mm diameter of the rods used in this study), which is 351% greater than the EC5 [11] predicted value; similarly, Bader et al. [24] found 24.9 N/mm^2. Using $f_{h,k}$ = 27.5 N/mm^2 for Equation (3) yields a much greater capacity of 19.5 kN (again from the bottom expression), which is close to the observed capacity, but does not account for the presence of the adhesive or unbonded length. Alternatively, using an effective density according to Equation (5), with ρ_{timber} = 680 kg/m^3 for GL70 BauBuche LVL [25], and $\rho_{adhesive}$ = 3125 kg/m^3 [20], ρ_{ef} = 1458 kg/m^3 is yielded, hence an increased embedment strength of 13.2 N/mm^2 and an increased capacity of 14.1 kN. Riberholt's [15] proposal yields a lateral capacity of 2.6 kN if Equation (7) is adopted in Equation (6) based on the timber density. This results in a vast underprediction. If the effective density, $\rho_{ef,}$ (converted to relative for Equation (7)) is adopted, this yields a high embedment strength of 29.7 N/mm^2, thus a lateral capacity of 10.5 kN. This is slightly greater than the EC5 [11] and EN 17334 [10] prediction, but it is still only 57% of the experimental lateral capacity. In the previous calculations, e is set to equal 0, such that the embedment strength at the end of the bond zone is estimated. It should be noted that Equations (6) and (7) were derived from fully bonded rods and some deviations are expected due to the non-uniform embedment stresses when an unbonded length is provided.

4.3 COMBINED AXIAL & LATERAL FORCE INTERACTION

Figure 15 shows the experimental data of axial and lateral loads for all specimens (top rods only), compared to the elliptic design capacity relationships (Equation (8)) using the various lateral capacities discussed previously. For the Riberholt capacity using Equation (6), only the effective density was considered. It is evident that there is no relationship between axial load capacities and lateral loads when rod yielding is the dominant failure mode, as the elliptic trend is not followed (as opposed to pull-out failure, for which Aicher and Simon [3] confirmed suitability of the elliptic relationship). This is particularly evident for the short cantilever tests, where the failure loads far exceed the EC5 [11] and EN 17334 [10] design capacity line. The experimental lateral load capacities (from the shear tests) agreed well with the EN 17334 [10] design prediction when a higher embedment strength of 27.5 N/mm^2 was used. The effect of lateral loads in ductile failure modes of glued-in rods should be directly addressed in the current design guidelines.

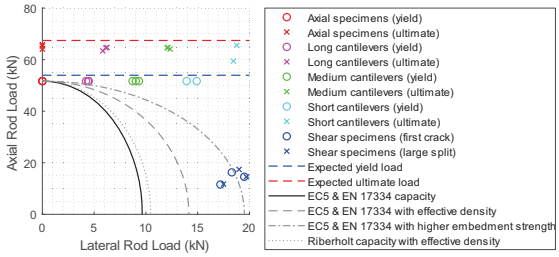

Figure 15: *Graph of axial load against lateral load for the failure and ultimate points for all specimens, with prescribed and suggested elliptic trend lines for load limits also plotted.*

4.4 MOMENT-ROTATION RESULTS

The cantilever specimen support moment and rotation results are summarised in Table 2, in addition to theoretical stiffnesses calculated using the model discussed in section 2.4. The support rotations were derived from the LVDT data for the top rod (combined rod strain and slip) and the predicted strain of the extreme timber compression fibre. In the calculations the weight of the beam was also considered. The moment-rotation relationships are plotted in Figure 16, along with the theoretical predictions. The rotational stiffnesses were calculated using the linear range of the moment-rotation relationships, ranging from 10-40% of the ultimate moment. The mean experimental rotational stiffness of the C1 specimens was 10.7% higher than that of the C2 specimens despite the same predicted stiffness, attributed potentially to an influence of the beam length that is not accounted for by the analytical model used (the C1 specimen length being 33.3% shorter than the C2 length),

https://doi.org/10.52202/069179-0179

though this difference could be insignificant considering experimental scatter.

Table 2: *Mean average values for support moment and rotation at failure (bracketed values are ultimate; non-bracketed values are at yield); and rotational stiffnesses.*

Spec-imen	Support Moment (kNm)	Support Rotation (mrad)	Experiment Rotational Stiffness (kNm/rad)	Theoretical Rotational Stiffness (kNm/rad)
C1	13.4 (17.3)	9.56	1870	1980
C2	12.8 (17.4)	9.55	1690	1980
C3	8.4 (11.7)	11.15	950	1120

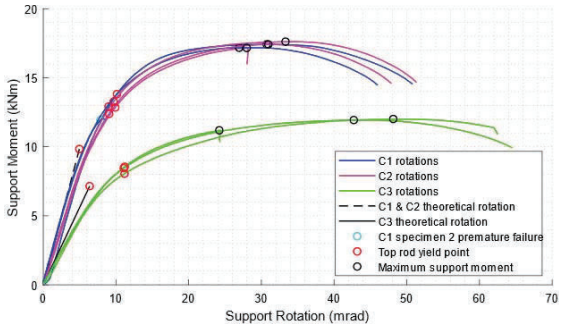

Figure 16: *Moment-rotation curves for the cantilever specimens, with theoretical rotations also plotted.*

The experimental rotational stiffnesses are always lower than the theoretical ones: for a two-tailed t-test with 5% significance, the results for the C1 tests are not statistically significant, but the results for the C2 and C3 tests are. A higher coefficient on the bond length for a greater effective stiffness length (as opposed to 0.3 as discussed in section 3.4) may be more appropriate, given that different timber and adhesive is used here than in [1], where glulam and a different epoxy adhesive were investigated. A coefficient of 0.9 is found to result in a similar axial stiffness to those observed in the cantilever tests. It is also observed that top rod yielding occurs at greater support moment and rotation than predicted.

5 CONCLUSIONS

The application of lateral load to the rods had no effect on their axial capacities with a governing failure mode of rod yielding: this should be addressed in the design guidelines. The lateral capacities of the shear specimens exceeded the design code prediction by 92%, and the use of an effective density accounting for the presence of adhesive in calculation of the embedment strength was shown to give a better prediction. The use of a higher embedment strength for LVL found from literature (27.5 N/mm^2 as opposed to just 6.1 N/mm^2 as predicted by EC5 [11], which is a staggering 351% lower) was shown to predict the lateral capacity very accurately, but it did not account for the adhesive or unbonded length. An unexpectedly significant axial force due to the rope effect was observed for the shear specimens, exceeding the 25% design limit, hence a higher limit for glued-in rods may be appropriate. Axial rod stiffnesses decreased by 43% with a small addition of lateral load due to cantilever action, with the quantity of load not having a notable further effect. Cantilever rotational stiffness was always slightly lower than the theoretical prediction, and a lower stiffness was observed for longer beams but of the same cross-section, which the analytical model used did not account for.

It is of interest to investigate the effect of lateral load on the axial load capacities of steel rods glued into LVL for the brittle failure modes, and understand in depth the lateral load distribution between rods when yielding or first failure occurs in the top rod. A comparison between fully bonded glued-in rods and glued-in rods with an unbonded length will shed more light on the effect of the unbonded length in the embedment stress distribution of GiRs when subjected to lateral loads. This can lead to updates regarding design equations for the lateral load capacity of of GiRs with the presence of a glue-line and an unbonded length.

ACKNOWLEDGEMENT

Acknowledgement is given to Joshua Mudie who sourced the LVL for their project [19] and who's supervisor, James Norman, gave permission for the use of the left-over LVL for this project; and to the staff at the University of Bristol's Mechanical Workshop and Heavy & Light Structures Lab for their assistance with the manufacture and testing (respectively) of the specimens.

REFERENCES

[1] Xu B. H., Bouchair A., Racher P.: Analytical study and finite element modelling of timber connections with glued-in rods in bending. *Construction and Building Materials*, 34:337-345, 2012.

[2] Steiger R., Serrano E., Stepinac M., Rajcic V., O'Neill C., McPolin D., Widmann R.: Strengthening of timber structures with glued-in rods. *Construction and Building Materials*, 97:90-105, 2015.

[3] Aicher S., Simon K.: Rigid Glulam Joints with Glued-in Rods subjected to Axial and Lateral Force Action. In *Proceedings of INTER 2021: The 8th Meeting of the International Network on Timber Engineering Research,* 2021. Timber Scientific Publishing, KIT Holzbau und Baukonstruktionen, Reinhard-Baumeister-Platz 1, 76131 Karlsruhe, Germany, 113-128.

[4] Tlustochowicz G., Serrano E., and Steiger R.: State-of-the-art review on timber connections with glued-in steel rods. *Materials and Structures*, 44(5):997-1020, 2011.

[5] Toumpanaki E., Ramage M. H.: Glued-in CFRP and GFRP rods in block laminated timber subjected to monotonic and cyclic loading: *Composite Structures*, 272:114201,2021.

[6] O'Neill C., McPolin D., Taylor S. E., Martin T., Harte A. M.: Glued-in basalt FRP rods under combined axial force and bending moment: An experimental study. *Composite Structures,* 186:267-273, 2018.
[7] Franke S., Heubuch S., Franke B.: Glued-in Rods in Beech GLT - Investigation of Pull-Out Resistance and Design Proposal. In *Proceedings of WCTE 2020: World Conference on Timber Engineering*, Santiago, Chile, 2020.
[8] Steiger R., Gehri E., Widmann R.: Pull-out strength of axially loaded steel rods bonded in glulam parallel to the grain. *Materials and Structures*, 40(1):69-78, 2007.
[9] Ogrizovic J., Wanninger F., Frangi A.: Experimental and analytical analysis of moment-resisting connections with glued-in rods. *Engineering Structures*, 145:322-332, 2017.
[10] BSI: EN 17334. Glued-in rods in glued structural timber products. Testing, requirements and bond shear strength classification. British Standards Institute, London, United Kingdom, 2021.
[11] BSI: EN 1995-1-1. Eurocode 5: Design of timber structures. General. Common rules and rules for buildings. British Standards Institute, London, United Kingdom, 2004.
[12] Stepinac M., Rajcic V., Hunger F., van de Kuilen J. W. G.: Glued-in rods in beech laminated veneer lumber. *European Journal of Wood and Wood Products*, 74(3):463-466, 2016.
[13] Walker J., Xiao R.: Experimental Testing of a Portal Frame Connection Using Glued-In Steel Rods. In *Proceedings of the RILEM International Symposium on Materials and Joints in Timber Structures,* Stuttgart, Germany, 2013 (Aicher S, Reinhardt HW and Garrecht H (eds)). RILEM Bookseries, vol. 9, pp. 555-566, 2014.
[14] BSI: EN ISO 898-1. Mechanical properties of fasteners made of carbon steel and alloy steel. Bolts, screws and studs with specified property classes. Coarse thread and fine pitch thread. British Standards Institute, London, United Kingdom, 2013.
[15] Riberholt H.: Glued Bolts in Glulam - Proposals for CIB Code. In *Proceedings of the CIB-W18 Meeting 21,* paper 21-7-2**,** Parksville, Vancouver Island, Canada, 1988.
[16] DIN: EN 1995-1-1/NA. National Annex - Nationally determined parameters - Eurocode 5: Design of timber structures - Part **1-1**: General - Common rules and rules for buildings. Deutsches Institut für Normung, Berlin, Germany, 2013.
[17] Johanides M., Mikolasek D., Lokaj A., Mynarcik P., Marcalikova Z., Sucharda O.: Rotational Stiffness and Carrying Capacity of Timber Frame Corners with Dowel Type Connections. *Materials*, 14(23): Article No. 7429, 2021.
[18] Yang H., Liu W., Ren X.: A component method for moment-resistant glulam beam-column connections with glued-in steel rods. *Engineering Structures*, 115:42-54, 2016.
[19] Sebastian W. M., Mudie J., Cox G., Piazza M., Tomasi R., Giongo I.: Insight into mechanics of externally indeterminate hardwood–concrete composite beams. *Construction and Building Materials*, 102:1029-1048, 2016.
[20] Rotafix: Rotafix Timberset Adhesive*,* n.d. See: http://rotafix.co.uk/products/timber-engineering/rotafix-timberset-adhesive/ (accessed 10/04/2022).
[21] Fragiacomo M., Batchelar M.: Timber Frame Moment Joints with Glued-In Steel Rods. I: Design. *Journal of Structural Engineering,* 138(6):789-801, 2012.
[22] McKenzie W. M., Karpovich H.: The frictional behaviour of wood. *Wood Science and Technology*, 2:139-152, 1968.
[23] Schweigler M., Bader T. K., Hochreiner G., Unger G., Eberhardsteiner J.: Load-to-grain angle dependence of the embedment behavior of dowel-type fasteners in laminated veneer lumber. *Construction and Building Materials*, 126:1020-1033, 2016.
[24] Bader T. K., Schweigler M., Serrano E., Dorn M., Enquist B., Hochreiner G.: Integrative experimental characterization and engineering modeling of single-dowel connections in LVL. *Construction and Building Materials,* 107:235-246, 2016.
[25] Pollmeir: Declaration of performance, 2015. See: https://www.pollmeier.com/dam/jcr:98e30343-0ab1-4b41-999f-dd04d3bda04b/EN_Declaration%20of%20performance_beam%20GL70_PM-004-2015.pdf (accessed 14/04/2022).

https://doi.org/10.52202/069179-0179

World Conference on Timber Engineering Oslo 2023

SOLUTIONS FOR EDGE CONNECTIONS TO BUILD TWO-WAY SPANNING CROSS LAMINATED TIMBER SLABS

Thomas Stieb[1], Bernhard Maurer[2], Maximilian Bestler[3], Philipp Dietsch[4], Roland Maderebner[5]

ABSTRACT: Two-way spanning slabs made of cross laminated timber (CLT) require a rigid connection of the single elements. In particular for point-supported flat slabs this connection is necessary to enable spans that exceed the transport-related width of the single CLT-elements. The paper shows solutions how this connection could be designed and realized. In addition to the load-bearing capacity, especially the rotational stiffness is a crucial factor for the edge connection. A certain stiffness is needed to meet the requirements of a floor in terms of serviceability. To determine the load-bearing capacity and stiffness, four-point bending tests were performed on different types of possible edge connection solutions. The investigations revealed two connection types that meet the specified criteria without on-site gluing. One approach consists of a timber-concrete-composite system. Here, reinforcing bars are glued into the narrow surface of the CLT-element and the gap between the adjacent CLT-elements is then casted on-site. A second, completely dry application is to use a system connector with serrated steel plates. This serration ensures the force transmission between the CLT-elements by the connector. In addition to the results of these two types, also further options for the edge connection are presented.

KEYWORDS: Cross laminated timber, two-way spanning slab, flat slab, joints, edge connection, rotational stiffness

1 INTRODUCTION

The Unit of Timber Engineering at the University of Innsbruck has been intensively investigating point-supported flat slabs within the last few years [1-3]. This construction method has its architectonical charm, because it avoids walls and joists, enabling a much more flexible floor plan and increasing the effective living space. An essential structural characteristic of this construction method is the biaxial load carrying capacity of the flat slab. Cross laminated timber (CLT) could be a very suitable material for point supported flat slabs due to its bonded, crosswise layers. However, if the column grid of the floor exceeds the transport and production related maximum width and length of the CLT panels (width: 2.5 – 3.5 m, length ≤ 22 m), a supporting system with joists is still used by the designers most of the time, see Figure 1. The CLT is thereby only loaded in one direction. Nevertheless, the aim is to build flat slabs with a column grid of 5.0 to 7.0 m without any joists to compete with conventional concrete construction. This poses two major challenges from a structural point of view. One of them is the high load concentration in the area of the point support. This topic is treated very comprehensively in the works of [4-6], for example. Secondly, due to the limited width and length, the panels need to be connected on the construction site, so that a flat slab made of CLT can perform a biaxial load-bearing behaviour at all. This joint has to transfer mainly bending moments and shear forces. It should be easy to assemble, as rigid as possible and show ductile failure for reasons of robustness. This paper focuses on the edge connection of such CLT panels. Beginning with an overview of existing solutions for the joint, alternative approaches are shown and new systems are presented. For point supported flat slabs, requirements for the edge connection are defined and the experimental results for selected solutions are analysed in this respect. The findings about structural behaviour of CLT edge connections is not restricted to the use in a flat slab. The connection can also be applied for line supported CLT slabs in order to improve the system's stiffness (e.g. for a better dynamic behaviour), also rigid edge connections can increase the advantageous load-bearing behaviour of CLT near openings, see Figure 2.

Figure 1: *Types of point supported slab constructions with spans of 5 – 7 m*

[1] Thomas Stieb, Unit of Timber Engineering, Universität Innsbruck, Austria, thomas.stieb@uibk.ac.at
[2] Bernhard Maurer, Unit of Timber Engineering, Universität Innsbruck, Austria, bernhard.maurer@uibk.ac.at
[3] Maximilian Bestler, Haug & Partner – Beratende Ingenieure mbB, Germany, mab@haug-wertach.de
[4] Philipp Dietsch, Chair of Timber Structures and Building Construction, Karlsruhe Institute of Technology, Germany, dietsch@kit.edu
[5] Roland Maderebner (Project leader), Unit of Timber Engineering, Universität Innsbruck, Austria, roland.maderebner@uibk.ac.at

https://doi.org/10.52202/069179-0180

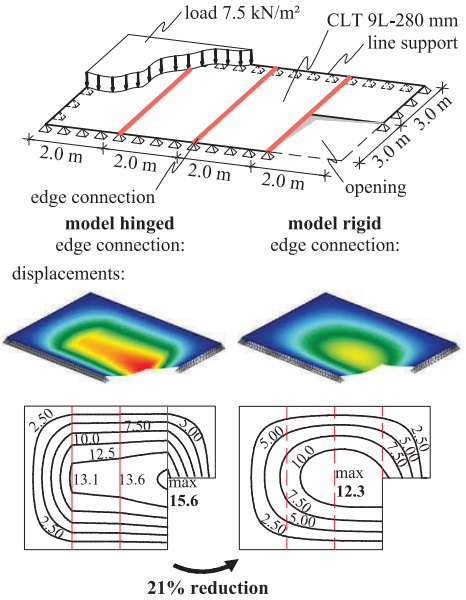

Figure 2: *Benefit of rigid edge connection for a CLT slab with opening (exemplary)*

2 SOLUTIONS FOR THE DESIGN OF THE CLT EDGE CONNECTION

2.1 OVERVIEW OF STATE OF KNOWLEDGE

For the construction of edge connections which enable the transmission of bending moments in addition to shear forces, approaches with splice plates are frequently found in the literature. The plates are usually made of wood-based panels. These are connected to the CLT either by means of screw press gluing [7] or by inclined screws [8]. The force transmission between the two elements takes place via the loading of either the screws or the adhesive joint and the plates. Tests on these types of connections have also been carried out at the University of Innsbruck [9]. A similar approach to enable a rigid connection in the secondary load-bearing direction of the CLT is presented in [10]. Here, the screw press gluing plates made of laminated veneer lumber (LVL) are additionally milled in with finger-joint like profiles.

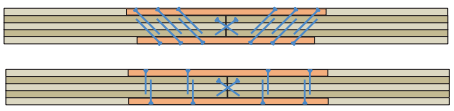

Figure 3: *Solutions with wood-based panels and inclined screws or screw press gluing*

In [11] a special two-component polyurethane adhesive is used for butt gluing of the full narrow surface of the CLT. The approach of glued-in perforated steel plates presented in [12] may also be used for the edge connection. A similar solution is also presented in [5], where sandblasted steel plates are applied. Apart from connections based mainly on adhesives, [2] presented a concept of a dovetail joint combined with a synthetic reaction resin. This solution adds a form closure to the chemical bonding.

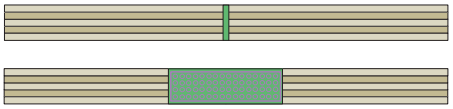

Figure 4: *Solutions with adhesives (butt gluing and glued-in-perforated steel plates)*

These investigations in the literature show a wide variety of solutions with different quality in terms of rigidity and load-carrying capacity. A comparison between different studies is difficult, because the authors didn´t use the same raw material or test setups.

2.2 CONCEPTS WITH CONVENTIONAL MATERIALS

In the work of [13], several solutions for the edge connection were investigated with tests in the laboratory using the same general conditions in each series (CLT dimensions and quality as well as the test setup). Therefore, four-point bending tests were carried out in order to determine the rotational stiffness and load carrying capacity of the edge connection. One solution was similar to the method presented in [8]. However, steel plates are used and fully threaded screws with angled washers were arranged inclined in the tension and compression zone of the edge connection. [13] used for another series self-tapping screws within a planar scarf joint. They should enable the transmission of bending moments and reinforce the CLT panel at once.
A further concept involves a butt joint where a post-tensioning system is installed to compress the joint and therefore enable the application of bending moments before a gap on the tension side of the element occurs.

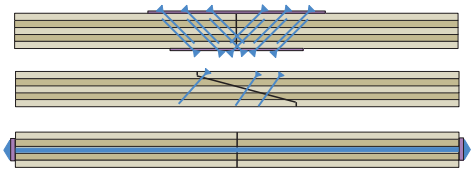

Figure 5: *"Dry" solutions with conventional construction materials*

Another approach in [13] was the use of glued-in reinforcing bars for realising the joint by a timber concrete composite (TCC) system. Here, a lap splice of the reinforcement was created between the two narrow surfaces. The resulting gap is further reinforced acc. to EN 1992-1-1 and then casted with standard concrete. A comparable method was suggested in [14] for the construction of two-way spanning TCC slabs.

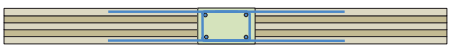

Figure 6: *Timber concrete composite solution [13]*

https://doi.org/10.52202/069179-0180

The results from [13] give the opportunity to compare several construction types in terms of the rotational stiffness of the joint solutions and also the load-carrying capacities. Hence, the next chapters will refer to this work more often.

2.3 CONCEPT WITH SERRATED STEEL PLATES

The Unit of Timber Engineering at the University of Innsbruck is currently developing a new connector for edge connections, which is based on steel plates with micro-teeth [15]. The principle function of this system is illustrated in Figure 7. With the help of pre-tensioned threaded rods, wedges are used to press micro teeth of steel plates into the milled slot surfaces of the CLT. The force is transmitted via the connectors steel plates and the interlocking between the CLT panel and the numerous small teeth.

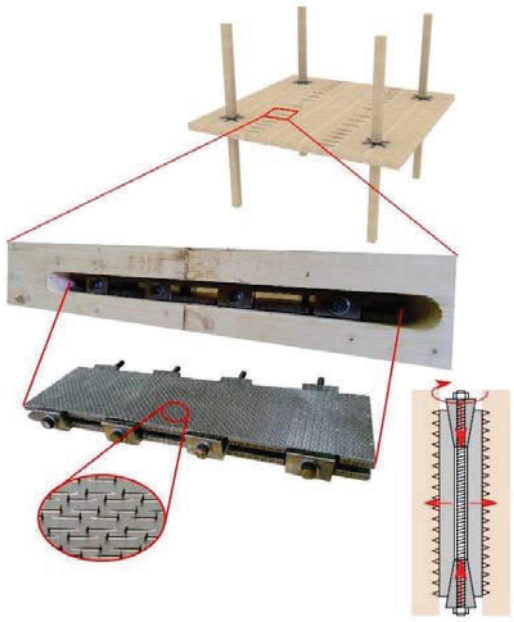

Figure 7: *System connector with serrated steel plates – operating principle [16]*

The major advantage using this type of connection is the mechanical interlocking between the serrations and the timber. As shown later, high stiffnesses with ductile failure can be achieved with this method. Due to the small teeth, the insertion resistance can be reduced compared to punched metal plate fasteners. The pre-tensioning of the threaded rods is intended to ensure the permanent insertion of the teeth over time.

3 INFLUENCE ON VIBRATIONS AND BENDING MOMENTS

Connections are often simplified as rigid or hinged. This section will show how important it is to take the real stiffness into account when designing point supported flat slabs. The focus is on the impact of the stiffness of the edge connections on the vibrational behaviour and the bending moments, even though the impact on deflections, the fire safety, the load carrying capacity or the robustness of the total structure are important aspects, too.

The edge connection between two CLT elements can be simplified to a rotational spring stiffness k_φ (see Figure 8). It´s actually obvious, that this spring has to be rigid and strong enough to prevent the formation of a kinematic chain in point supported flat slabs.

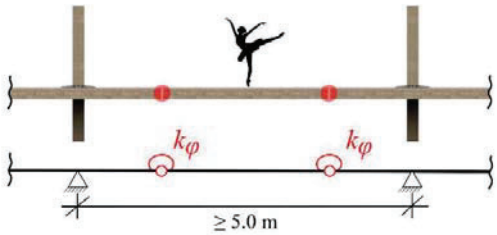

Figure 8: *Panel joints in point supported flat slab*

Within a parameter study of a simple floor system, the effect of the rotational stiffness of the edge connection is shown. The spans of a slab system with 3 x 3 fields are varied between spans of 5.0 and 7.0 m for different CLT element thicknesses (see Table 1). Figure 9 illustrates the model which was used for the parameter study. In general, this construction method requires the use of CLT with a layer structure that generates a balanced bending stiffness ratio ($EI_{ef,x}$ / $EI_{ef,y}$) between the main and secondary load-bearing direction, as shown in Table 1.

Table 1: *CLT used for the parameter study*

CLT depth	Layer	$EI_{ef,y}$ / $EI_{ef,x}$	Layup
200 mm	7	0.838	20-40-20-40-20-40-20
240 mm	9	0.946	20-40-20-20-40-20-20-40-20
280 mm	9	1.079	20-40-20-40-40-40-20-40-20
320 mm	9	0.910	20-40-40-40-40-40-40-40-20

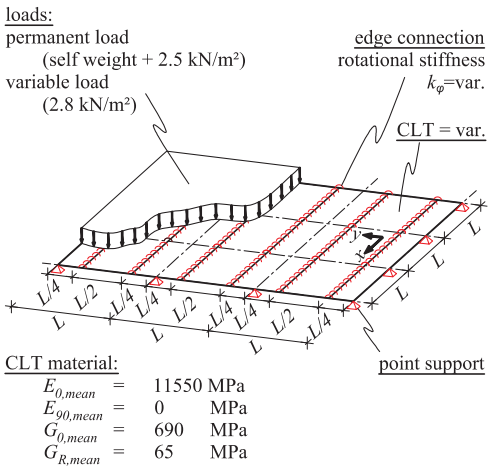

Figure 9: *Parameter study of a point supported flat slab*

https://doi.org/10.52202/069179-0180

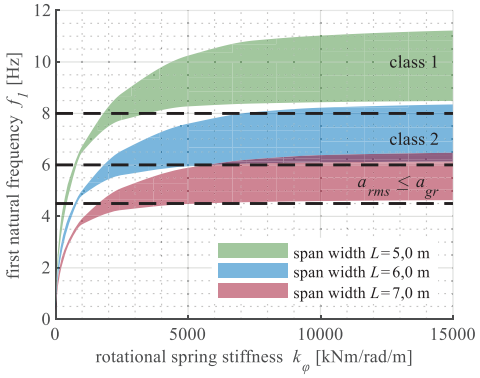

Figure 10: *Influence of rotational spring stiffness on first natural frequency (classification acc. frequency criterion in Eurocode 5)*

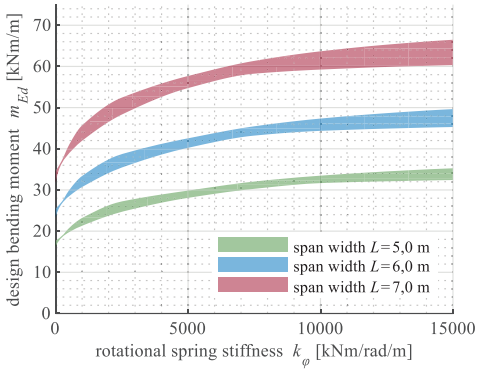

Figure 11: *Influence of rotational spring stiffness on maximum design moment*

The rotational stiffness of the edge connection significantly influences the floor's vibration behaviour. This is shown in Figure 10 by the relation of the first natural frequency of the slab and the rotational stiffness considered. However, it can also be seen that this influence is decreasing as the rigidity is increasing. This influence can also be observed for the maximum bending moment occurring in the edge connection. In the slab considered, this maximum moment occurs in the outmost connection of the end spans.

An important finding of this study is that completely rigid connections are not necessary for the application of the edge connection in point-supported flat slabs. Since connections with stiffness above 5000 kNm/rad/m only improve the investigated system to a minor extent.

4 DETERMINATION OF STIFFNESS AND LOAD CARRYING CAPACITY

The parameter study underlined the relevance of the bending load bearing capacity of the connection as well as the corresponding rotational spring stiffness.

4.1 EXPERIMENTAL APPROACH

Four-point bending tests can be carried out according to the specifications given in [17] in order to gather findings about stiffness and load-carrying capacity of different types of edge connections. By comparing the stiffness of the joined panel with a continuous one, the rotational spring stiffness of the connection can be determined from this test. This was already shown by [5] and described with Equation (1). Where a is the distance from the load to the bearing, l the static length of the specimen, F the full load of the hydraulic cylinder. The displacements w_{ref} and w_{con} are described in Figure 5. At best, the stiffness of a continuous panel is first determined non-destructively. Then the panel is cut, reconnected and finally tested again. However, the stiffness of the continuous CLT panel can be determined analytically too. An advantage of this approach is in general, that the rotation don´t have to be measured.

$$K_\varphi = \frac{a\,l}{8 \cdot \left(\frac{w_{con}}{F_{con}} - \frac{w_{ref}}{F_{ref}}\right)} \tag{1}$$

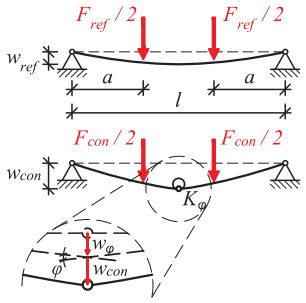

Figure 12: *determination of rotational stiffness of the edge connection*

4.2 INVESTIGATED SOLUTIONS

Seven different solutions of the edge connection were investigated by four-point bending tests. The detailed description can be found in Table 2 and in Figures 13 to 19. Series A, B, C, D, F and G were taken from [13].

Table 2: *Investigated solutions (n – number of tests, l & a acc. to Figure 12)*

Series	Solution	n [-]	l [m]	a [m]
A	butt joint	2	4.80	1.60
B	glued-in steel plates	3	4.80	1.60
C	inclined screws	3	4.80	1.60
D	scarf joint	3	4.50	1.50
E	post-tension system	3	4.75	1.58
F	TCC-system	3	4.80	1.60
G	system connector	3	4.20	1.40

For the tests, 240 mm thick, CLT elements with 7 layers were chosen with a layup of 30-40-30-40-30-40-30. Series A was also used as a reference test to determine the stiffness of a continuous panel. A two-component epoxy resin was used as adhesive. The same resin was used in Series B to glue in the perforated steel plates. The screws

https://doi.org/10.52202/069179-0180

applied in the test complied with the European Technical Approval (ETA) [18]. For Series F, the used concrete quality was C30/37 with reinforcement steel B550. The post-tension system applied in Series E may be taken from ETA [19].

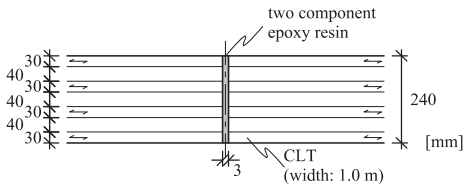

Figure 13: *Series A - butt joint - connection detail*

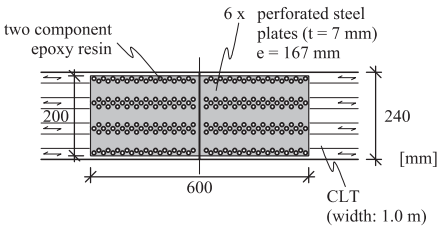

Figure 14: *Series B - glued-in steel plates - connection detail*

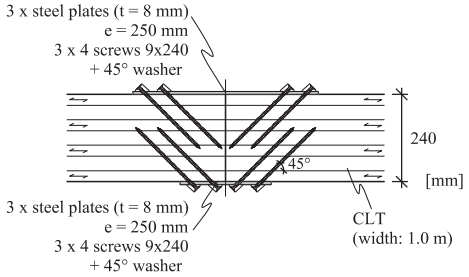

Figure 15: *Series C - inclined screws - connection detail*

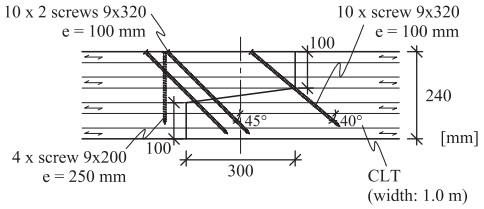

Figure 16: *Series D - scarf joint - connection detail*

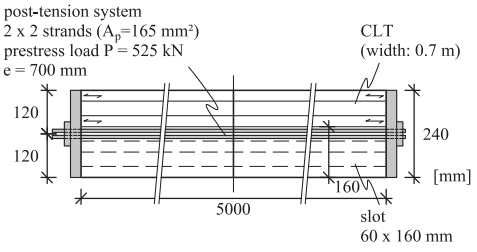

Figure 17: *Series E - post-tension system - connection detail*

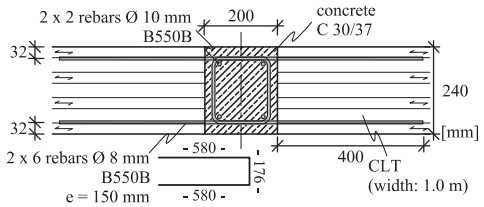

Figure 18: *Series F - TCC-system - connection detail*

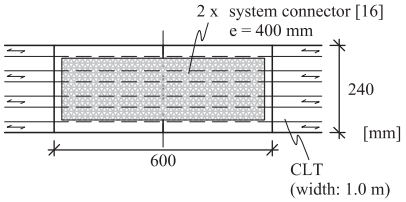

Figure 19: *Series G - system connector - connection detail*

5 RESULTS AND DISCUSSION

The main results of the investigations can be found in Table 3. In addition to the load bearing capacity, an overview of the rotational spring stiffnesses for each series is given. Due to the small number of tests, characteristic values are not stated.

Table 3: *Main results of the experimental study*

Series	F_{max} [kN]	m_{mean} [kNm/m]	$k_{\varphi,mean}$ [kNm/rad/m]
A	44.4 83.4	51.1	∞
B	169.3 167.3 164.4	133.6	∞
C	88.4 79.5 99.1	71.2	2170
D	64.9 73.6 64.3	50.7	2760
E	51.3 50.2 49.1	56.7	3840
F	39.8 46.9 47.5	35.8	14120
G	66.0 75.0 46.1	42.4	6170[1)]

[1)] Only tests 2 and 3 were considered. No global displacement transducers were used in test 1. For all 3 tests the same two system connectors were used.

Series A using the butt joint provided a reference stiffness of a continuous panel to determine the rotational stiffness of the remaining series. The specimens failed in a brittle manner on very different load levels.

https://doi.org/10.52202/069179-0180

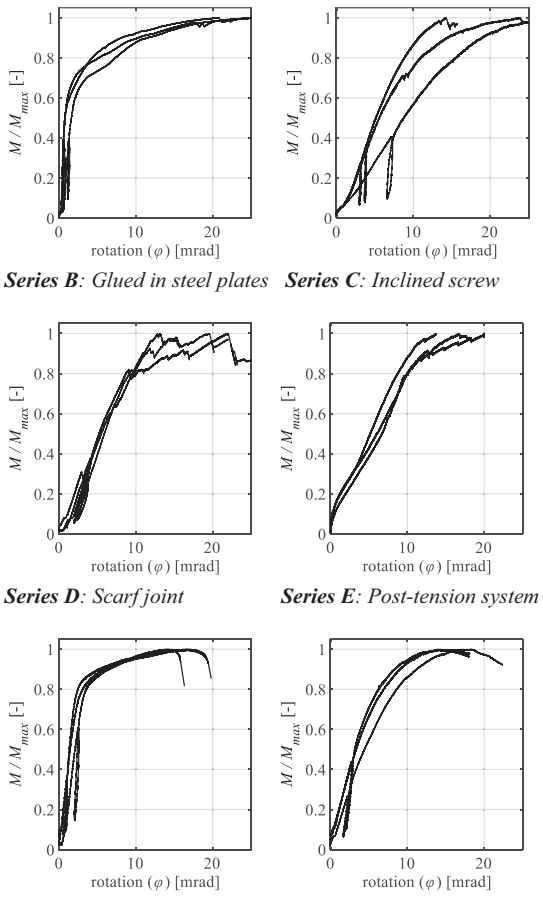

Figure 20: *Moment-rotation diagrams of experimental study*

The series with the glued-in perforated steel plates (Series B) failed in a much more ductile way. Here, very high load-bearing capacities were observed. The load-bearing capacity of the joint may be aligned to the load of the edge connection via the spacing of the glued-in plates. The failure of the test specimens was announced by an opening of the gap between the panels. This is due to yielding of the steel plates in this area. However, there was no difference in the initial stiffness between the reference tests (Series A) and the glued-in perforated steel plates. Therefore, both solutions may be classified as rotationally stiff connections. As presented in Figure 10 an absolutely rotationally stiff connection is not necessary for the use of an edge connection in a point supported flat slab.

The Series C using inclined fully threaded screws resulted in a clearly lower rotational spring stiffness. The initial spring stiffness is only about 2200 kNm/rad/m, although there is a clear increase in stiffness while unloading and reloading the specimens. The tests revealed tensile failure as well as withdrawal failure of the screws. The equivalent rotational spring stiffness of the planar scarf joint (Series D) is only insignificantly higher at around 2800 kNm/rad/m. The specimens failed in a more brittle manner than the series with inclined screws (Series C). Although screws perpendicular to grain were installed to avoid this failure, when reaching the load-bearing capacity, a failure combination of rolling shear and tension perpendicular to grain occurred. A corresponding image of the resulting cracks is presented in Figure 21.

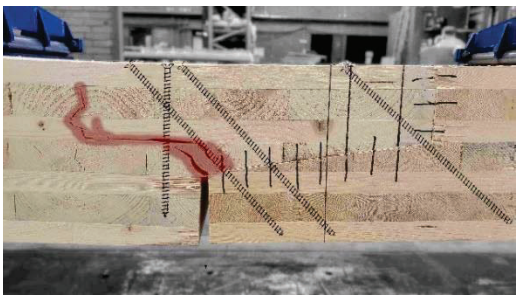

Figure 21: *Failure of Series D - scarf joint (cracks coloured)*

The results of the rotational stiffness for the Series E using the post-tensioning system are also within this range. A stiffness of approx. 3800 kNm/rad/m is obtained here. The load was stopped when a clear decrease of the system stiffness occurred.

For the application in point supported flat slabs, the solutions for the edge connection of Series C, D and E do not meet the requirements stated in section 3. This is mainly caused by the insufficient rotational spring stiffness. However, Figure 22 shows the application of such a stiffness for a flat slab supported on all four sides. The numerical solution for the first natural frequency of a continuous slab corresponds well to the analytical solution according to [20].
Considering the individual CLT elements with a hinged connection reduces the eigenfrequency of the system significantly. Here, even the use of small spring stiffnesses can contribute to a system improvement.

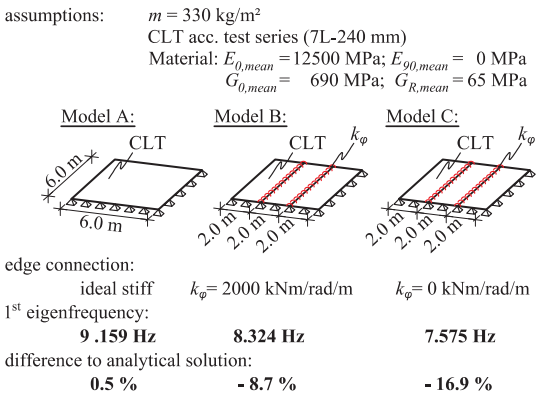

Figure 22: *Influence of rotational spring stiffness on the first natural frequency for a flat slab supported on all four sides*

A much higher rotational spring stiffness was reached in Series F, using the TCC system. On average, a value of about 14100 kNm/rad/m could be achieved. In these tests the glued-in rebars started yielding before failure. This failure was announced by an opening of the gap between the concrete and the CLT panel.

https://doi.org/10.52202/069179-0180

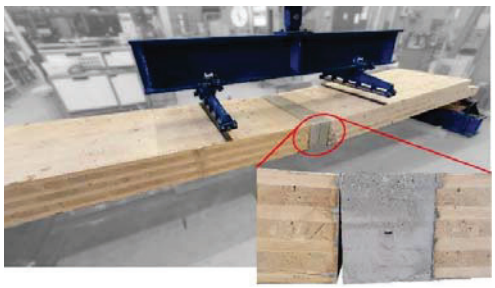

Figure 23: *Failed specimen of Series F - TCC system - opened gap between CLT and concrete*

The force occurring in the rebar may be determined with a similar analytical model as for concrete constructions. However, for CLT the compressed zone should be only assumed at the stiffer longitudinal layers. The stress in the reinforcement may then be calculated over the height of the compressed zone (x) and the inner lever arm (z).

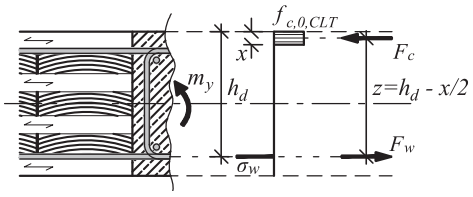

Figure 24: *Analytical model for Series F – TCC system*

$$x = h_d - \sqrt{\frac{f_{c,0,CLT} \cdot h_d^2 - 2 \cdot m_y}{f_{c,0,CLT}}} \qquad (2)$$

$$F_w = \frac{m_y}{z}$$

This analytical model already represents the tests quite well. The results of this model are shown in Figure 25 by comparison with the experimental results once for reaching the yield stress (f_y = 550 MPa) in the rebar as well as the tensile strength (F_{tens} = 33.3 kN acc. to tensile tests).

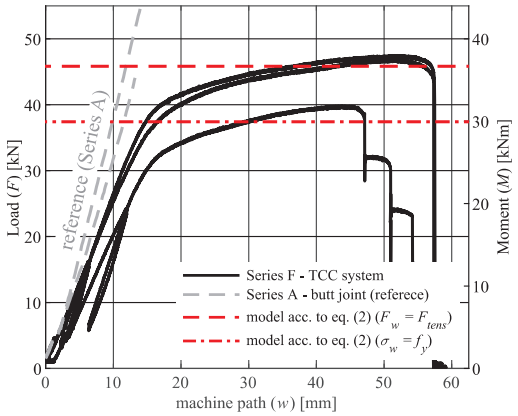

Figure 25: *Results Series F - TCC-system comparison with analytical model acc. to Equation (2)*

Notably, one of the tests showed a significantly lower load-bearing capacity. A possible explanation is that the gluing of one rebar was inaccurate there. To avoid the risks of non-properly fabricated gluing, in the next step the rebars were replaced by fully threaded screws. The force is again transmitted via a lap splice of the screws in the concrete. For this system, comprehensive investigations have been carried out which led to the ETA [21] and will be published in more detail in the future [22].

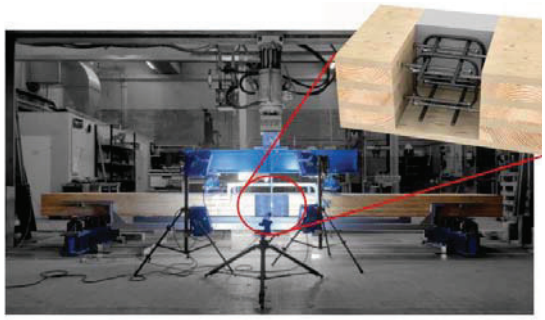

Figure 26: *Ongoing investigations on a TCC-system with self-tapping fully threaded screws [22]*

A completely "dry" solution for the edge connection was carried out using the system connector shown in Figure 7. This connector enables a significant reduction in construction time, for instance by eliminating curing times. With an average of approximately 6200 kNm/rad/m, this system also achieves a rather high rotational spring stiffness.

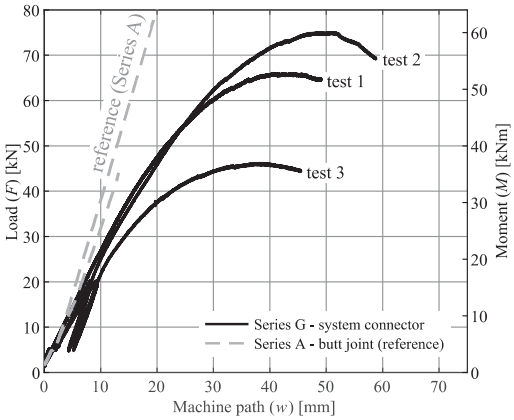

Figure 27: *Result Series G - system connector in four-point bending tests*

These were tests with first prototypes of the connector. There was only one set of two connectors available. So, these two connectors were used three times in a row. While the initial stiffness remained relatively constant, the load bearing capacity decreased significantly in the third test. This may be due to the reuse of the connectors. However, ductile failure behaviour was always observed.

https://doi.org/10.52202/069179-0180

6 CONCLUSIONS AND OUTLOOK

The edge connection between two elements in cross laminated timber slabs has a major influence on the behaviour of the entire system. In an experimental study, solutions for this joint were investigated with regard to the application in point-supported flat slabs. Based on a parameter study, the rotational spring stiffness of the connection is determined as an essential parameter for the suitability. Four-point bending tests are an appropriate test for determining the load-carrying capacity as well as the rotational spring stiffness. It showed that some of the solutions may be more appropriate to improve other slab systems than point supported flat slabs.

Two connection types were identified that meet the mechanical requirements for edge connections used in point supported flat slabs without any on-site gluing. One is the TCC system with glued-in rebars and the other the use of a system connector with micro-teeth. Both connection types are characterised by a distinct ductile failure behaviour and can easily be adapted to the load by variation of the spacing between the fasteners. However, questions regarding the long-term behaviour and the performance of the connection under biaxial loading still remain for both connection types.

The results presented for the TCC system were the initial impulse for further studies. A system where self-tapping, fully threaded screws are used instead of glued-in rebars is the subject of ongoing research.

A major benefit of the system connector compared to the remaining connection types is the quick assembly and the lack of any curing time. The possibilities of using micro-teeth as a new type of joining technique in timber constructions reach far beyond the application at the panel joint. Hence, the University of Innsbruck is currently carrying out extensive research on this topic.

ACKNOWLEDGEMENT

Special thanks are extended to the partners of the research project “STS - Slab to Slab” – the research funding association of Austria (FFG) and the company ROTHOBLAAS SRL from Cortaccia, Italy.

REFERENCES

[1] Zingerle P., Maderebner R., Flach M.: System Solutions for point supported wooden flat slabs. In *Proc. 14th World Conference on Timber Engineering (WCTE 2016),* Vienna, Austria, 2016.

[2] Maurer B., Maderebner R., Zingerle P., Färberböck I., Flach M.: Point-supported flat slabs with CLT panels. In *Proc. 15th World Conference on Timber Engineering (WCTE 2018),* Seoul, Korea, 2016.

[3] Maurer B., Maderebner R.: Cross Laminated Timber under Concentrated Compression Loads - Methods of Reinforcement, Engineering Structures 245, 2021.

[4] Mestek, P.: Punktgestützte Flächentragwerke aus Brettsperrholz (BSP) – Schubbemessung unter Berücksichtigung von Schubverstärkungen, PhD. Thesis, Technical University of Munich, 2011.

[5] Maurer, B.: Lösungsansätze für punktgestützte Flachdecken aus Brettsperrholz, PhD. Thesis, University of Innsbruck, 2020.

[6] Muster, M.: Column-Slab Connection In Timber Flat Slabs, PhD. Thesis, ETH Zurich, 2020.

[7] Wallner-Novak M., Koppelhuber J., Pock K.: Brettsperrholz Bemessung: Grundlagen für Statik und Konstruktion nach Eurocode, proHolz Austria, 2013.

[8] Asselstine J., Lam F., Zhang C.: New edge connection technology for cross laminated timber (CLT) floor slabs promoting two-way action, Engineering Structures 233, 2021.

[9] Stufferin, A.: Biegesteifer Plattenstoß von Brettsperrholzplatten, Master Thesis, University of Innsbruck, 2017.

[10] Tapia C., Claus M., Aicher S.: A finger-joint based edge connection for the weak direction of CLT plates, Construction and Building Materials, 340, 2022.

[11] Zöllig S., Frangi A., Franke S., Muster, M.: Timber structures 3.0–new technology for multi-axial, slim, high performance timber structures. In *Proc. 14th World Conference on Timber Engineering (WCTE 2016),* Vienna, Austria, 2016.

[12] Bathon L., Bletz-Mühldorfer O., Diehl F., Schmidt J., Wagner A., Weil M.: Anwendungen von eingeklebten Lochblechen unter statischen sowie ermüdenden Einwirkungen. In *20. Internationales Holzbau-Forum IHF 2014,* Garmisch, Germany, 2014.

[13] Bestler, M.: Plattenstoßausführungen von Brettsperrholz: ein Beitrag für punktgestützte Flachdecken aus Brettsperrholz, Master Thesis, University of Innsbruck, 2021.

[14] Loebus, S., Dietsch, P., Winter, S.: Two-way Spanning CLT-Concrete-Composite-Slabs. In *International Network on Timber Engineering Research INTER, Meeting 4*, Kyoto, Japan, 2017.

[15] Maderebner, R.: Flächenhafte mechanische Verbindungsmittel. In *25. Internatinales Holzbau-Forum IHF 2019,* Innsbruck, Austria, 2019.

[16] Maderebner, R. (2021): Mezzo di collegamento per collegare componenti in legno, Patent application 04.10.2021.

[17] EN 408:2012-09-01: Timber structures - Structural timber and glued laminated timber - Determination of some physical and mechanical properties

[18] ETA-11/0030:2022-01-18: Rotho Blaas Self-tapping screws and threaded rod, ETA-Danmark A/S

[19] ETA-10/0065:2016-02-19: BBR VT CONA CMB SP – Unbonded Band Post – tensioning System with 01 to 16 Strands, Österreichisches Institut für Bautechnik (OIB)

[20] ÖNORM B 1995:2019-06-01: Eurocode 5: Design of timber structures - Part 1-1: General - Common rules and rules for buildings - Consolidated version with national specifications, national comments and national supplements for the implementation of ÖNORM EN 1995-1-1

[21] ETA-22/0806: Rotho Blaas Timber-Concrete Fusion System, ETA-Danmark A/S (Draft)

[22] Stieb, T.: Biegesteife Verbindungen von Brettsperrholzelementen (working title), PhD. Thesis, University of Innsbruck (manuscript under preperation)

https://doi.org/10.52202/069179-0180

World Conference on Timber Engineering Oslo 2023

EXPERIMENTAL AND ANALYTICAL ANALYSIS OF TIMBER CONNECTIONS WITH INTERPOSED ACOUSTIC RESILIENT STRIP

Luca Pozza[1], Giulia D'Amato[2], Paola Brugnara[3], Ernesto Callegari[3], Luca Sestigiani[3]

ABSTRACT: The load-carrying capacity and stiffness of timber-to-timber or steel-to-timber connections with an interlayer is a topic of great interest, as it is increasingly required to acoustically insulate, by means of resilient strip, the connections used to assemble timber buildings. The effects of the interposed resilient strip on the stiffness and load-carrying capacity of connections have not yet been studied effectively from experimental and theoretical point of view. This paper reports the main outcomes of an ongoing research, supported by Rotho Blaas S.r.l. company, aimed at the characterization of timber connections with interposed an acoustic resilient strip for flanking noise reduction. The research is developed on two levels: experimental and analytical. An experimental campaign conducted on steel-to-timber nailed connections was carried out and analysed. Experimental results were used to validate analytical models available in literature and specialized to account for the effect of acoustic interlayer on both elastic behaviour and failure mechanism.

KEYWORDS: Acoustic layer, Load-carrying capacity, Resilient soundproofing, Sound insulation, Timber joints

1 INTRODUCTION

Timber structures are particularly sensitive to low frequencies and require appropriate sound insulation strategies to comply with critical acoustic performance levels. This problem is significant in light structures such as traditional ceilings or frame walls because of reduced mass and acoustic damping. Cross Laminated Timber (CLT) structures are more soundproof performing thanks to their massiveness and the continuity of the panels. However, the structural connections can cause acoustic bridges which negatively affect the acoustic performance of the system [1]. A valid constructive strategy to limit the acoustic transmission through the connections consists in the insertion of resilient strips between the connected elements (Figure 1).

The effects of the interposed resilient strip on the stiffness and load-carrying capacity of connection have not yet been studied adequately from experimental and theoretical point of view. Calculation is therefore approximatively based on the models developed for standard connections without considering accurately the effects of the interposed layer or gap.

In this work results of an experimental campaign are used to assess the effects of an interposed resilient strip on the mechanical behaviour of timber-to-steel nailed connections. Experimental results are finally used to validate robust analytical models, available in literature and developed for different applications [2-3], to account for the effect of resilient strip on the mechanical response of timber connections.

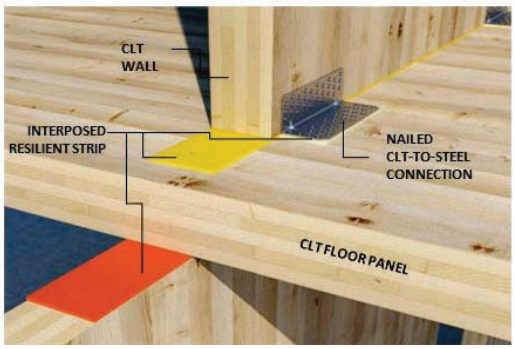

Figure 1: *Example of wall-to-floor CLT joint with interposed acoustic layer.*

2 EXPERIMENTAL CAMPAIGN

The experimental campaign was aimed to investigate the effects of the interposition of a resilient acoustic strip on the mechanical response of a timber-to-steel nailed connections. Four types of timber-to-steel connection were tested varying: the type of timber elements (GluLam or CLT) and the gap between the timber elements (in contact or with 6mm thick resilient acoustic strip). The tested nails are "LBA" type according to ETA-22/0002 [4] while the resilient acoustic strip is "XYLOFON 35" type according to ETA-23/0061 [5]. The experimental program, carried out according to EN 1380 [6] provisions, is summarized in Table 1.

Table 1: *Detail of the experimental campaign*

Sample ID	*Timber element*	*Interposed strip*	*N. of test*
GL-NX	GluLam	*none*	3
GL-X35	GluLam	*Xylofon 35*	3
CLT-NX	CLT	*none*	3
CLT-X35	CLT	*Xylofon 35*	3

[1] Department of Civil, Chemical, Environmental and Materials Engineering (DICAM), University of Bologna, Viale Risorgimento 2, Bologna, Italy

[2] CIRI Buildings and Construction (CIRI-EC), University of Bologna, Via del Lazzaretto 15/5, Bologna, Italy

[3] Rotho Blaas srl - Via Dell'Adige 2/1 Cortaccia (BZ), Italy

https://doi.org/10.52202/069179-0181

The tested sample is geometrically represented in Figure 2 and is composed by the following components:

(a) timber element (GluLam or CLT). The rectangular cross section dimension is 120x80mm while the length is 200mm;
(b) couple of U-shaped 4mm thick steel profiles;
(c) 2 x 5 nails LBA type with a diameter of 4mm and length of 60mm;
(d) 6mm thick XYLOFON 35 resilient acoustic strip (only for X35 configuration).

As prescribed by EN 1380 [6], the timber specimens were conditioned at (20 ± 2)°C temperature and (65 ± 5)% relative humidity for 15 days before performing the tests. The resulting mean density of the samples was equal to 458kg/m^3 for GluLam specimens and to 472 kg/m^3 for CLT specimens.

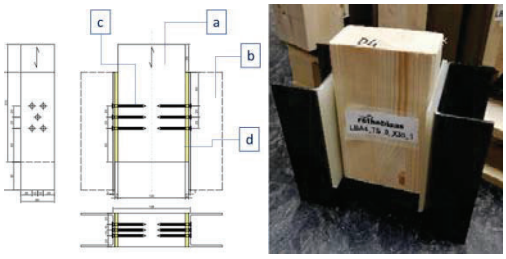

Figure 2: *Geometry of the tested samples*

The samples were tested using a universal testing machine in displacement control. The upper face of the timber element was loaded while the U-shaped steel profiles contrasted against the basement. The nailed connections were therefore monotonically loaded parallel to grain direction. Figure 3 reports a photo of the adopted setup.

During the test the applied force and the timber-to-steel relative displacement were recorded.

Figure 3: *View of the experimental setup.*

3 EXPERIMENTAL RESULTS

This section reports the test results in terms of load-displacement curves and observed failure modes.

It is worth noting that the experimental capacity curve of a steel-to-timber connection generally does not show a well-defined yielding limit [7-10]. Two different criteria can then be adopted for the definition of the yielding condition starting from experimental results [11]: the first one is based on EN 12512 [12] provisions, while the second one is based on an energetic approach (the so-called Equivalent Energy Hardening method [13]).

For traditional steel-to-timber connections, the well know Method "b" of EN 12512 is typically adopted since load-displacement curves are not characterized by a marked variation of the gradient at the level of yielding condition. In this work, in order to better capture the features of the experimental curves, an alternative approach for the definition of the yielding point was adopted referring to the Equivalent Energy Hardening method [12]: the slope of the second branch of the bi-linear curve is defined by forcing the passage through the peak force point and the equivalence of strain energy between the experimental envelope curve and the piecewise linear approximation. In the following, Method "b" of EN 12512 will be labelled as EN12512-b, whereas the Equivalent Energy Hardening method as EEH. Experimental load-displacement curves superimposed to the mean tri-linear backbone curve obtained according to the EN12512-b and EEH methods are reported in Figure 4 and Figure 5 respectively.

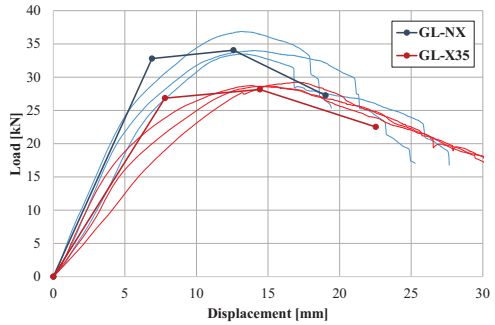

a)

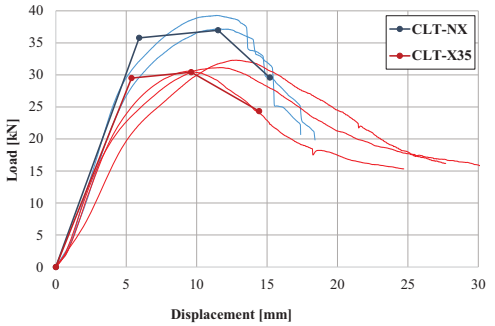

b)

Figure 4: *Experimental load displacement curves superimposed on mean trilinear backbone curve obtained applying the EN12512-b method: a) GluLam and b) CLT configurations.*

https://doi.org/10.52202/069179-0181

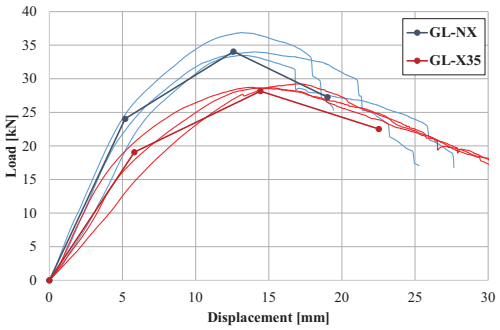

a)

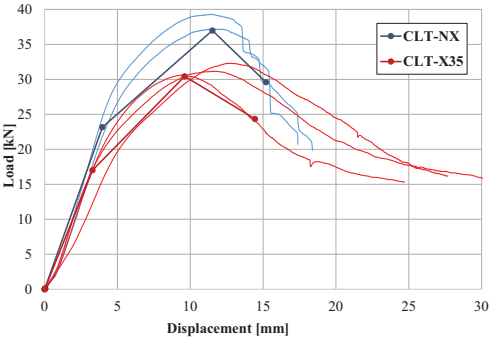

b)

Figure 5: *Experimental load displacement curves superimposed on mean trilinear backbone curve obtained applying the EEH method: a) GluLam and b) CLT configurations.*

The failure mode observed at the end of all experimental tests principally involved the nails used to connect the steel plate to the timber element. Two plastic hinges can be typically recognized in the nails, one under the cap and another one in the shank (about 20–25 mm below the cap). In addition, localized crushing of wood around the nail shank, oriented in the axial load direction, can be observed, see Figure 6-a. For large displacement, the failure of the head of the nails occurred, see Figure 6-b.

a)

b)

Figure 6: *Samples GL-X35_02 at the end of test: a) local crashing of the timber along the grain direction and b) failure of the head of nails.*

The detailed analyses of the experimental results conducted according to method EN12512-b and EEH are reported in Table 2 and Table 3 respectively. More specifically, the tables report: the yielding and peak point parameters; the elastic and post elastic stiffnesses. Analyses were performed separately for each sample and then the averaged values were computed in order to perform a direct comparison between the configuration without and with interlayer.

Table 2: *Analyses of experimental results according to EN12512b method. Label "A" stands for averaged values.*

EN 12512-b GLULAM		GL-NX_1	GL-NX_2	GL-NX_3	**GL-NX_A**	GL-X35_1	GL-X35_2	GL-X35_3	**GL-X35_A**
k1	[kN/m]	3.62	4.73	5.07	**4.47**	4.50	3.28	2.52	**3.43**
k_ult	[kN/m]	0.20	0.21	0.23	**0.22**	0.22	0.17	0.19	**0.19**
dy	[mm]	9.01	6.87	6.98	**7.62**	6.00	8.40	11.17	**8.52**
dFmax	[mm]	13.49	13.94	13.15	**13.52**	13.79	15.21	17.07	**15.36**
du	[mm]	26.77	25.27	19.41	**23.82**	22.97	22.92	23.40	**23.82**
Fy	[kN]	32.60	32.50	35.43	**33.51**	26.98	27.52	28.16	**27.55**
Fmax	[kN]	33.48	34.01	36.87	**34.79**	28.74	28.68	29.26	**28.89**
Fu (0.8 Fmax)	[kN]	26.79	27.21	29.50	**27.83**	22.99	22.94	23.41	**23.11**

EN 12512-b CLT		CLT-NX_1	CLT-NX_2	CLT-NX_3	**CLT-NX_A**	CLT-X35_1	CLT-X35_2	CLT-X35_3	**CLT-X35_A**
k1	[kN/m]	5.94	6.53	5.70	**6.06**	3.96	5.79	5.60	**5.12**
k_ult	[kN/m]	0.19	0.23	0.22	**0.21**	0.21	0.23	0.23	**0.22**
dy	[mm]	6.05	5.82	6.32	**6.06**	7.89	5.13	5.30	**6.11**
dFmax	[mm]	12.25	11.45	11.69	**11.80**	12.84	9.40	9.40	**10.55**
du	[mm]	19.26	18.40	17.39	**18.35**	25.84	24.46	24.47	**23.82**
Fy	[kN]	35.94	38.02	36.01	**36.66**	31.28	29.73	29.67	**30.23**
Fmax	[kN]	37.15	39.30	37.18	**37.88**	32.30	30.59	30.59	**31.16**
Fu (0.8 Fmax)	[kN]	29.72	31.44	29.75	**30.30**	25.84	24.47	24.47	**24.93**

https://doi.org/10.52202/069179-0181

Table 3: *Analyses of experimental results according to EEH method. Label "A" stands for averaged values.*

EEH GLULAM		GL-NX_1	GL-NX_2	GL-NX_3	**GL-NX_A**	GL-X35_1	GL-X35_2	GL-X35_3	**GL-X35_A**
k1	[kN/m]	3.62	4.73	5.07	**4.47**	4.50	3.28	2.52	**3.43**
k_ult	[kN/m]	2.48	2.44	2.80	**2.58**	1.71	2.08	1.88	**1.89**
dy	[mm]	6.88	4.94	5.54	**5.79**	4.15	6.16	8.92	**6.41**
dFmax	[mm]	13.49	13.94	13.15	**13.52**	13.79	15.21	17.07	**15.36**
du	[mm]	26.77	25.27	19.41	**23.82**	22.97	22.92	23.40	**23.82**
Fy	[kN]	24.61	23.01	28.11	**25.24**	18.36	20.03	22.44	**20.28**
Fmax	[kN]	33.48	34.01	36.87	**34.79**	28.74	28.68	29.26	**28.89**
Fu (0.8 Fmax)	[kN]	26.79	27.21	29.50	**27.83**	22.99	22.94	23.41	**23.11**

EEH CLT		CLT-NX_1	CLT-NX_2	CLT-NX_3	**CLT-NX_A**	CLT-X35_1	CLT-X35_2	CLT-X35_3	**CLT-X35_A**
k1	[kN/m]	5.94	6.53	5.70	**6.06**	3.96	5.79	5.60	**5.12**
k_ult	[kN/m]	3.03	3.43	3.18	**3.22**	2.52	2.66	3.25	**2.81**
dy	[mm]	4.89	3.62	4.26	**4.26**	5.35	3.27	3.02	**3.88**
dFmax	[mm]	12.25	11.45	11.69	**11.80**	12.84	9.40	9.40	**10.55**
du	[mm]	19.26	18.40	17.39	**18.35**	25.84	24.46	24.47	**23.82**
Fy	[kN]	28.99	22.15	23.48	**24.87**	20.83	18.12	15.70	**18.22**
Fmax	[kN]	37.15	39.30	37.18	**37.88**	32.30	30.59	30.59	**31.16**
Fu (0.8 Fmax)	[kN]	29.72	31.44	29.75	**30.30**	25.84	24.47	24.47	**24.93**

Data reported in Table 2 and Table 3 are plotted in the graph of Figure 7-9 and Figure 10-12 for GluLam and CLT specimens respectively.

Analysing the results, it is possible to observe that the interposition of a resilient layer strongly affects the global response of the connection. In detail obtained results demonstrate that, regardless of the linearization criterion used, the interposed resilient layer induces:

i) a negligible effect on the yielding and peak displacements and therefore on the ductility values;

ii) a reduction of the yielding force of about 20% for GluLam samples and of about 25% for CLT samples and a reduction of the peak force of about 15% for both Glulam and CLT samples;

iii) a reduction of the elastic stiffness of about 28% for GluLam samples and of about 17% for CLT samples;

vi) a negligible effect on post elastic and ultimate stiffness.

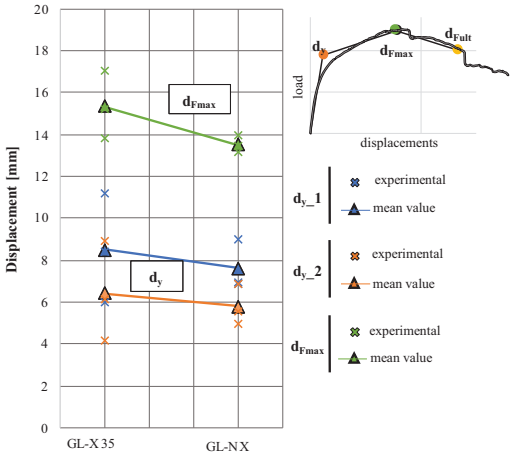

Figure 7: *Effects of interposition of a resilient acoustic strip on the yielding and peak displacement of GluLam samples.*

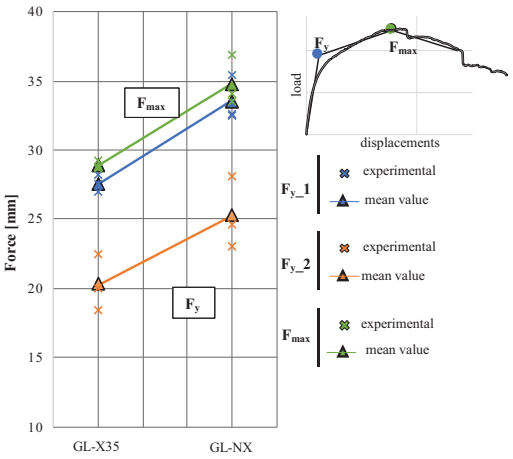

Figure 8: *Effects of interposition of a resilient acoustic strip on the yielding and peak force of GluLam samples.*

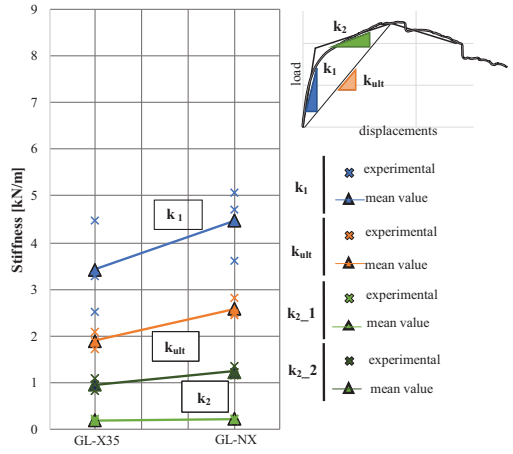

Figure 9: *Effects of interposition of a resilient acoustic strip on the elastic and post-elastic stiffness of GluLam samples.*

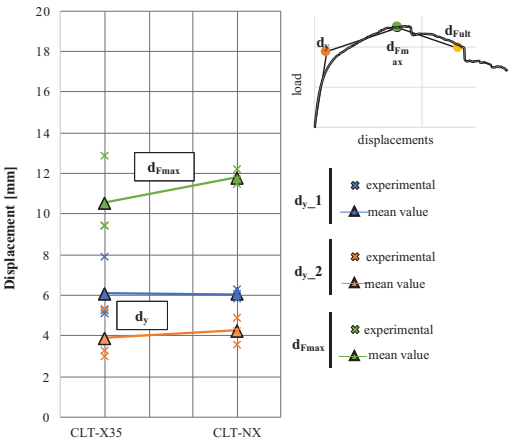

Figure 10: *Effects of interposition of a resilient acoustic strip on the yielding and peak displacement of CLT samples.*

https://doi.org/10.52202/069179-0181

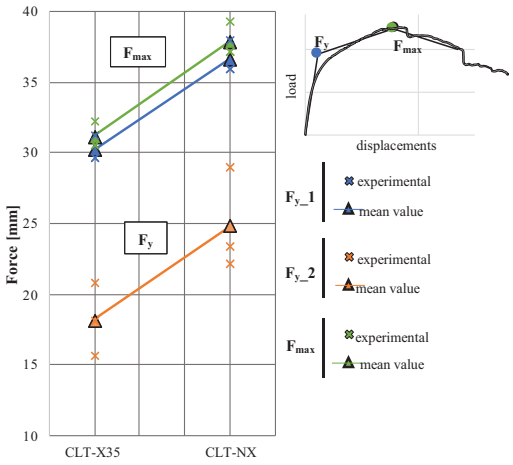

Figure 11: *Effects of interposition of a resilient acoustic strip on the yielding and peak force of CLT samples.*

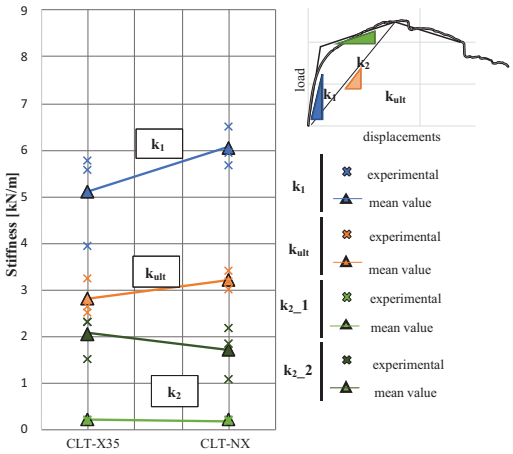

Figure 12: *Effects of interposition of a resilient acoustic strip on the elastic and post-elastic stiffness of CLT samples.*

It is worth noting that the above-described effects of the interlayer on the strength and stiffness of the nailed steel-to-timber connection is relative to the case of an infinitely stiff metal plate.

In the case of connections typically used to transfer shear forces in real GluLam or CLT structures, the geometry of the brackets is three-dimensional with a consequent significant deformative contribution of the steel plates.

When the bracket is used with an acoustic interlayer, the strength and stiffens reduction of the nailing system might not be significant as recorded in the tests exposed in this work as the deformability of the bracket itself could prevail (see for example [13]).

4 ANALYTICAL MODELS

The general formulations proposed in Johansen's theory and reported in the codes [15-16] or product technical sheet [4] are not applicable in the case of an interposed layer in the shear plane. Alternative methods accounting for the gap due to the interlayer are therefore necessary to define the strength and stiffness of the connection.

In this work, two different literature models were analysed and applied to account for the effects of an acoustic interlayer on the behaviour of a timber-to-steel connection.

The first model is based on the universally recognized Johansen theory as specified by Blass et al. [2] to account for the effects of an interlayer on the load-carrying capacity of the timber connection. This model was firstly developed to account for the effects of a OSB panel interposed into single shear timber-to-timber and timber-to-steel joint considering also the interlocking effect due to the stapled OSB-stud connection. This method provides the estimation of the connection strength while does not deal with the aspects related to connection stiffness.

An alternative model, developed for timber-to-concrete connection of composite floor beam, is the one proposed by Gelfi et al. [3]. This model assimilates the connector to a beam on an elastic support considering the connector free to deform in the interlayer. Hence, the effect of the interlayer is accounted both in terms of elastic stiffness and load-carrying capacity.

Despite the different basic formulations, for both models the key parameter governing the effect of the interlayer on the stiffness and strength is the ratio between the thickness of the interlayer and the diameter of the connector.

For the sake of brevity, only the results obtained with the two considered models are reported below; for the complete formulations, see the cited literature.

The geometric parameters of the specimens and the average density values were considered in the calculations. The cases without interlayer were considered as limit condition of zero gap.

The results obtained with the two models are reported in Table 4 and Table 5 for the strength and stiffens respectively.

Table 4: *Strength estimation obtained with the Blaas and Gelfi-Giurinai analytical models. Analytical values include the rope-effect contribution according to ETA-22/0002 [4].*

	F_{y_Enb} [kN]	F_{y_EEH} [kN]	F_{max} [kN]	F_{v_Blass} [kN]	$F_{v\_Gelfi-Giuriani}$ [kN]
GL-NX	33.51	25.24	34.79	28.66	28.66
CLT-NX	36.66	24.87	37.88	28.92	28.92
GL-X35	27.55	20.28	28.89	24.00	22.48
CLT-X35	30.23	18.22	31.16	24.1	22.6

Table 5: *Stiffness estimation obtained with the EC5 and Gelfi-Giuriani models.*

	$K_{1\_exp.}$ [kN/m]	$K_{ser\ (EC5)}$ [kN/m]	$K_{1\_Gelfi-Giuriani}$ [kN/m]
GL-NX	6.06	9.9	5.67
CLT-NX	4.47	10.36	5.79
GL-X35	5.12	-	4.31
CLT-X35	3.43	-	4.4

Results shows that both the analytical models capture the strength reduction due to the interlayer. Analytical

strength values are in the range F_{y_EEH} and F_{max} providing a good estimation of the expected load bearing capacity.
As far as stiffness is concerned, it can be observed that the Gelfi-Giuriani model is able to capture, with excellent approximation, the stiffness reduction due to the interlayer.

5 CONCLUSIONS

Results obtained in this work demonstrate that the mechanical behaviour of a nailed timber-to-steel connections is strongly affected by the interposition of a resilient acoustic strip. Experimental tests conducted on different connection configurations highlight a quite relevant stiffness reduction due to the resilient strip interposition. Otherwise, the strength seems less affected by the presence of the interlayer. Failure modes are not affected by the presence of the interlayer.
Analytical models provide an accurate estimation of the stiffens and strength reduction due to the interposition of resilient strip even if, as far as strength is concerned, they seem to be calibrated on the yield condition and not on the peak force.
Finally, in the case of tri-dimensional bracket used with an acoustic interlayer, the strength and stiffens reduction of the nailing system might not be significant as recorded in this work as the deformability of the bracket itself could prevail.
An extension of the experimental campaign is ongoing with the aim of characterizing the effects of the interposition of an interlayer for the different types of connection typically used in Glulam and CLT structures.

ACKNOWLEDGEMENTS

The Authors would like to thank the company Rotho Blaas S.r.l for the support in the experimental campaign.

REFERENCES

[1] A. Speranza, L. Barbaresi and F. Morandi, «Experimental analysis of flanking transmission of different connection systems for CLT panels,» in World Conference on Timber Engineering, Vienna, Austria, 2016.
[2] H. J. Blaß e B. Laskewitz, «Load-carryiing capacity of joints with dowel-type fasteners and interlayers,» in International Council for Research and Innovation in Building and Construction, Delft , Olanda, 2000.
[3] P. Gelfi, E. Giuriani e A. Marini, «Comportamento della connessione a piolo nelle travi miste in legno e calcestruzzo: modellazione teorica e confronti sperimentali,» in III Workshop Italiano sulle Costruzioni Composte, Ancona, Italia, 1998.
[4] European Technical Assessment ETA-22/0002 of 2022/01/24 - Nails and screws for use in nailing plates in timber structures
[5] European Technical Assessment ETA-23/0061 of 2023/02/24 - Flexible interlayer to be used for the reduction of flanking sound transmission and/or vibration transmission in construction works
[6] UNI EN 1380, Timber structures - Test methods - Load bearing nails, screws, dowels and bolts, 2009.
[7] Trutalli D, Marchi L, Scotta R, Pozza L. Capacity design of traditional and innovative ductile connections for earthquake-resistant CLT structures. Bull Earthq Eng 2019;17:2115–36. https://doi.org/10.1007/s10518-018-00536-6.
[8] Gavric I, Fragiacomo M, Ceccotti A. Cyclic behaviour of typical metal connectors for cross-laminated (CLT) structures. Mater Struct 2014:1–17.
[9] Pozza L, Saetta A, Savoia M, Talledo D. Coupled axial-shear numerical model for CLT connections. Constr Build Mater 2017;150:568–82. https://doi.org/10.1016/j. conbuildmat.2017.05.141.
[10] Piazza M, Polastri A, Tomasi R. Ductility of timber joints under static and cyclic loads. Proc Inst Civ Eng – Struct Build 2011;164:79–90. http://dx.doi.org/10.1680/ stbu.10.00017.
[11] Muñoz PQW, Salenikovich A, Mohammad M. Determination of yield point and ductility of timber assemblies: in search for a harmonised approach. In: Int. counc. res. innov. build. constr., CIB; 2008. p. W18/42–12–2.
[12] EN 12512. Timber structures. Test methods. Cyclic testing of joints made with mechanical fasteners. Brussels, Belgium: CEN; 2011.
[13] Pozza L, Scotta R, Trutalli D, Polastri A, Ceccotti A. Concrete-plated wooden shear walls: structural details, testing, and seismic characterization. J Struct Eng 2016;142:E4015003.
[14] European Technical Assessment ETA-22/0089 of 2022/08/25 - Three-dimensional nailing plate (Angle Bracket or Hold Down for timber-to-timber or timber-to-concrete or steel connections)
[15] CEN European Committee for Standardization. (2009) Design of timber structures—Part 1-1: General—Common rules and rules for buildings. Eurocode 5, CEN, Brussels, Belgium, 2009.
[16] CEN European Committee for Standardization. (2013). “Design of structures for earthquake resistance—Part 1: General rules, seismic actions and rules for buildings.” Eurocode 8, CEN, Brussels, Belgium.

https://doi.org/10.52202/069179-0181

World Conference on Timber Engineering Oslo 2023

ON-SITE GLUING AND WEATHER EFFECTS ON TALL WOODEN WIND TURBINE TOWERS

Viktor Norbäck[1], Pierre Landel[2], Erik Dölerud[3], Anders Wickström[4]

ABSTRACT: Modvion develops modular wind turbine towers made of wood. The application requires strong and stiff connections and to achieve the desired performance, a hybrid connection with perforated steel plates slotted into LVL modules is used. The parts will be glued together on site, using a polyurethane adhesive (PUR), providing high strength and stiffness to the connection. This paper presents a preliminary screening on how temperature and relative humidity of the surrounding air during assembly and curing will influence the strength of the bond glued on-site. Static tests were performed on the hybrid connections which were glued and cured in different climates. Tests were also performed at different hardening times to evaluate strength growth in the studied climates. The test results show that at cold temperatures of 9 °C to 12 °C there is a breakpoint where the rate of strength growth starts to decline. The experiments show also that the relative humidity may influence the final strength of the bond. However, the low number of tested specimens brings uncertainties to this observation. High temperatures up to 27 ºC and dry climates down to 20% RH did not impact the strength of the tested hybrid connections.

KEYWORDS: Hybrid connection, Polyurethane adhesive, On-site gluing, LVL, Glued-in plates connection type

1 INTRODUCTION

The Swedish company Modvion AB is developing modular wind turbine towers made of wood [1]. To be competitive, the production method must be both fast and reliable, following specific standards [2]. To achieve this a recently developed joining technique is used, where the LVL wall-modules are assembled on-site, combining adhesive and perforated steel plates. Thin plates made of high-strength steel are inserted into slots in the wall-modules and bonded using a two-component polyurethane (PUR) adhesive. The method results in strong and stiff connections with glue-dowels through the holes of the plate. This hybrid type of glued-in plate joints has been used in different timber building applications to elegantly assemble CLT, LVL, and GLT elements. Research and development works have been performed in central Europe [3] and in Germany, where the commercial and certified HSK-system from the company TiComTec is available [4]. This technology is similar to glued-in rods in glued structural timber products, which adhesively bond steel rods and timber members. Standardized testing methods and requirements for glued-in rods are defined in the European standard EN 17334:2021 [5]. Some experimental studies on the gluing procedures of glued-in rod joints have shown important outcomes concerning the mechanical effects of elevated moisture contents [6] and temperatures [7].

Connections with glued-in plates provide a strong and stiff joint compared to more traditional mechanical connections for timber structures, e.g., screws and dowels. It can be applied with high precision and keeps the steel elements encapsulated in the timber structure, which protects the steel and allows for additional architectural possibilities. However, the mechanical properties of glues are affected by the temperature and relative humidity of the surrounding air when gluing. As a result, the application process of adhesives for structural timber products is recommended for controlled conditions that are mostly offered in factories. Gluing processes applied on building sites, with uncontrolled and variable weather conditions, are not common.

To be competitive the assembly of tall modular wind turbine towers must be fast without compromising the safety of the workers. To maximize the efficiency of assembly, it is important to have better knowledge on the strength growth of the glued hybrid joints and how it is affected by the temperature and the moisture content of the surrounding air.

This study focuses on how the strength and the rate of strength growth of the hybrid joints used in Modvion's towers vary depending on weather conditions during gluing and curing. Temperature, humidity and curing time are investigated experimentally to determine the impact on the capacity of the joints at different curing times. This screening is aimed to identify suitable weather conditions

[1] Viktor Norbäck, RISE Research Institutes of Sweden, Sweden, viktor.norback@ri.se
[2] Pierre Landel, RISE Research Institutes of Sweden, pierre.landel@ri.se
[3] Erik Dölerud, Modvion AB, Sweden, erik@modvion.com
[4] Anders Wickström, RISE Research Institutes of Sweden, Sweden, anders.wickstrom@ri.se

https://doi.org/10.52202/069179-0182

when assembling the tower and which environmental parameters require further investigation to ensure that the joints perform as desired.

Uni-axial, destructive compression tests were performed on small-scale hybrid joint test specimens. Tests were performed in a reference climate of 20 ºC and 65% RH, which is to resemble good weather conditions. The same test procedure was performed on test specimens, glued and cured in different extreme climates. The studied climates are high and low temperatures and high and low relative humidity.

2 TEST PROCEDURE

Small-scale tests of the hybrid joint were performed at RISE's lab in Borås by Viktor Norbäck and Pierre Landel. The procedure involves destructive compression tests on specimens glued and cured in climates with different temperatures and relative humidity.

2.1 TESTED MATERIAL

The test specimens were assembled from an LVL block with a cut slot in which the steel plate was later slotted. A two-component PUR adhesive was used to glue the two parts together. The glue used was Loctite PURBOND CR821, manufactured by Henkel. Both the timber blocks and the steel plates are shown in Figure 1 with a pen for size reference.

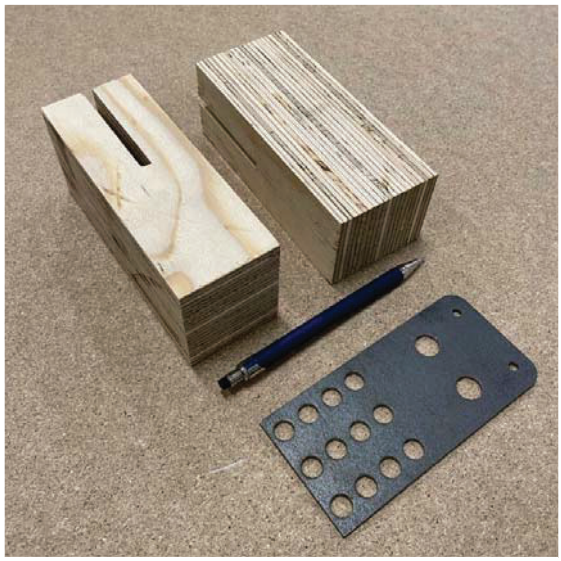

Figure 1: *Test specimen parts. LVL blocks with a cut slit from two different sides and the perforated steel plate. The pen acts as size reference.*

The perforated steel plates were 3 mm thick and had 16 holes. On the side that was slotted into the LVL block, there were 12 holes of diameter 10 mm. It was in these holes where the glue was cast, forming glue dowels connecting the steel plate to the timber part. On the other side of the plate, there were two pairs of holes of diameter 5 and 13 mm. These holes were not used in the compression tests and are meant for another series of tests where the fatigue strength of the hybrid joints is investigated [8]. The perforated steel plate and its holes were cut with a laser cutter with a tolerance of 0.03 mm. Figure 2 shows a blueprint of the perforated steel plates.

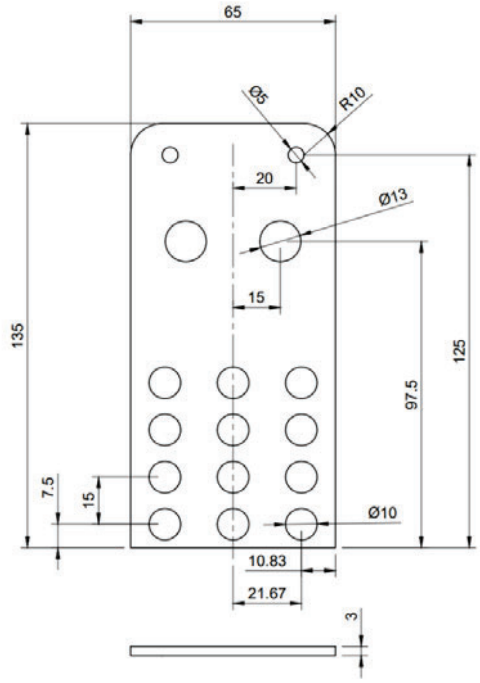

Figure 2: *Blueprint of the perforated steel plate which is slotted into the LVL blocks.*

The LVL blocks were cut from a larger LVL plate manufactured my Metsä wood. The plate consisted of a cross-layup with 21 veneers and a total thickness of 65 mm. The lay-up sequence was [2L/T/7L/T/7L/T/2L] where L denotes longitudinal veneers and T denotes transversal veneers. The direction of the longitudinal and transversal veneers in relation to the LVL block as well as the dimensions of the blocks are shown in Figure 3. Prior to testing, the components and the glue were conditioned until equilibrium in a constant climate of 20ºC and 60% RH.

https://doi.org/10.52202/069179-0182

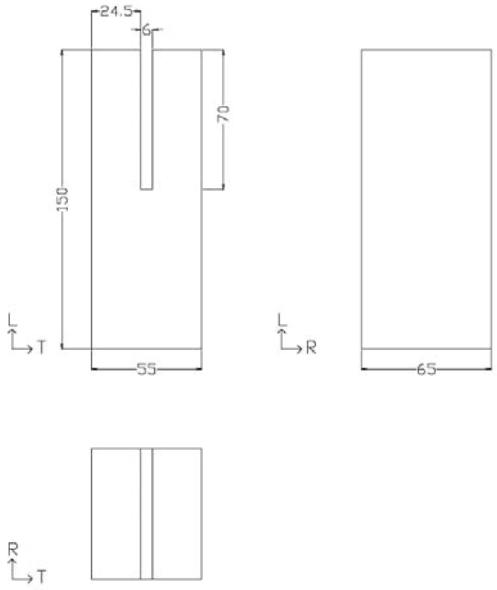

Figure 3: *Blueprint of the LVL blocks with a cut slot.*

2.2 TEST PROCEDURE

From the conditioned climate of 20°C and 60% RH, the specimens were moved and conditioned in a new climate for 48 hours. When two days had passed, the steel and the timber were glued together using the two-component PUR adhesive, which reaches full strength after 7 days and 75% after 2 days according to the manufacturer Henkel [9]. When gluing, 3D-printed plastic holders were clamped onto the timber blocks as shown in Figure 4. In the holders, there was a slot where the steel plate was inserted to be kept in the correct position when gluing. Before inserting the steel plate, a soft foam material was inserted at the bottom of the slot in the timber block to avoid glue from hardening beneath the steel plate. The foam material's stiffness was much lower compared to

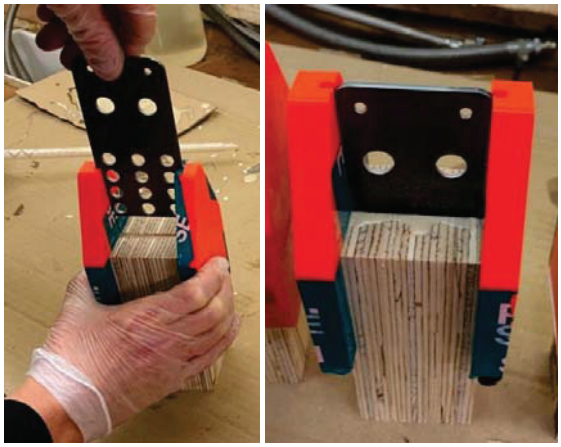

Figure 4: *The perforated steel plates slotted into the slit in the LVL using plastic holders.*

steel and timber. Thereafter, the slot in the LVL block was partly filled with adhesive, leaving room for the steel plate.

Immediately after applying the glue and inserting the steel plates the test specimens were put back in the same climate as before assembly to harden for a certain time. The number of tests in different climates and at different curing times are shown in Table 1. Note that the curing climate is a target climate. There is a variability of up to 0.1°C and 1.2% RH from the target climate.

Table 1. *The number of tests in different climates and for different curing times. Before curing the parts were conditioned for 2 days in the corresponding climate.*

Curing climate	Number of tests	Curing time
20°C 65% RH	1	3.17 h
	1	4.25 h
	1	5.17 h
	1	18.55 h
	1	1 day
	1	3 days
	1	4 days
	1	5 days
12°C 60% RH	3	1 day
	3	5 days
9.1°C 60% RH	3	1 day
	3	5 days
20°C 25% RH	3	1 day
	3	5 days
20°C 95% RH	3	1 day
	3	5 days
27°C 60% RH	3	1 day
	3	5 days

After a certain time, which varies for different test series, the specimens were loaded until failure in a hydraulic press. Two different hydraulic presses were used, both manufactured by Instron, one model 1253 and the other model Satec. 11 tests were performed with model 1253 and 27 tests with model Satec. Two machines were used due to logistic reasons. The setup for both machines was the same; a steel adapter was pushed onto the perforated

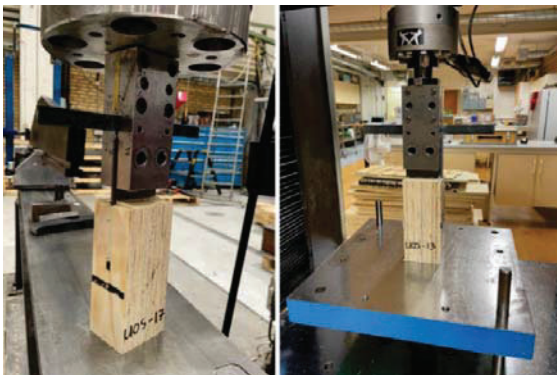

Figure 5: *Compression test setup in both machines. To the left: Instron model Satec. To the right: Instron model 1253.*

steel plate from above, compressing the specimen against

a fixed surface beneath it. The tests were deformation controlled with a constant deformation increment over time. Figure 5 and Figure 6 show examples of the test setup for both hydraulic presses. The foam material was considered to not take any significant loads because of its low stiffness in comparison to steel and LVL.

3 RESULTS, ANALYSIS, AND DISCUSSION

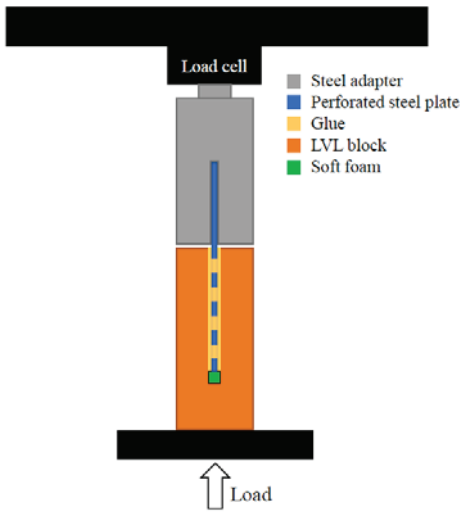

Figure 6: *Principal image of the test setup and the different materials.*

Figure 7 shows a scatter plot including all tested specimens with maximum load in kilonewtons on the vertical axis and curing time in hours on the horizontal axis. The circular data points correspond to the test series studying hardening time in the reference climate of 20°C and 65% RH. The triangular data points correspond to the different assembly and hardening climates at times 27 and 120 hours.

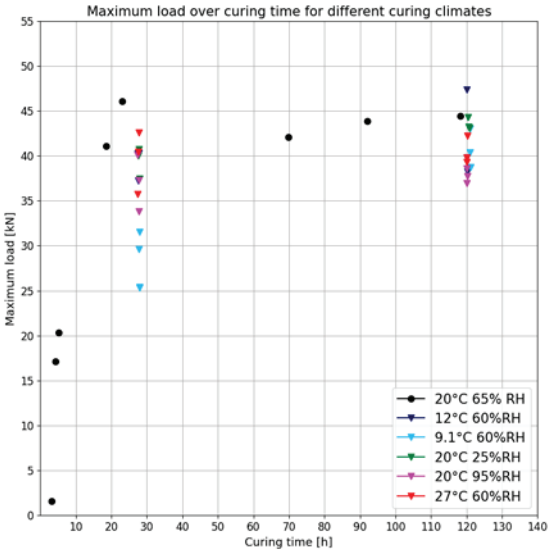

Figure 7: *Maximum load over curing time for different curing climates. On the horizontal axis: Curing time in hours. On the vertical axis: Maximum load in kilonewtons.*

From interpretation of the scatter plot, the strength of the joint starts to build up somewhere between three and four hours at the reference climate. The specimen tested after 3.17 hours demonstrated close to no strength and the specimens tested after 4.25 and 5.17 hours show a strength closer to 20 kN. In addition, for the specimen tested after 3.17 hours the glue was still more or less liquid. To investigate the strength growth of that particular test specimen, the steel plate was slotted back into the LVL block to be tested again after another hour of curing. This time the capacity was much higher similar to the other specimens tested after four to six hours and that had a strength of around 20 kN. The results from the two loadings of the same test specimen are presented in Table 2.

Table 2: *Test results for the same specimen first loaded after 3.17 hours and then loaded once more after a total curing time of 4.50 hours.*

Curing climate	Curing time	Maximum load
20°C 65% RH	3.17 h	1.55 kN
	4.50 h	18.71 kN

During the first day, the strength increased at a high rate up to a level that corresponds to the strength of specimens cured for three, four and five days. This indicates that full strength is reached after the first day of curing in the reference climate. For test specimens cured in other climates, the same trend was observed. Thus, no significant strength growth was noticed after the first day of hardening. However, the specimens cured at 9.1°C and 60% RH were an exception, with lower strength after one day of curing compared to the other specimens cured in other climates. This shows that low temperatures of 9.1°C will influence the curing time of the hybrid joints. The specimens cured at 12°C showed no trend of slower curing time, which suggests a breakpoint for the strength growth between 9.1°C and 12°C at 60% RH.

After 5 days, the specimens cured at 9.1°C and 60% RH had strength in the same range as the other curing climates. This is an indication that the final strength is unaffected by temperatures down to 9.1°C.

Humid climates of 95% RH did not affect the strength growth but may influence the final strength of the specimen. All three specimens tested at 20°C and 95% RH had lower strength compared to the other specimens. However, the number of data points in each climate is low which brings uncertainties as to whether this assumption would be valid if more tests were made in the same climate.

https://doi.org/10.52202/069179-0182

The static loading tests in compression showed two different types of failures. The displacement-to-loading diagrams from the tests exhibit either a brittle failure (Figure 8) or a ductile failure (Figure 9).

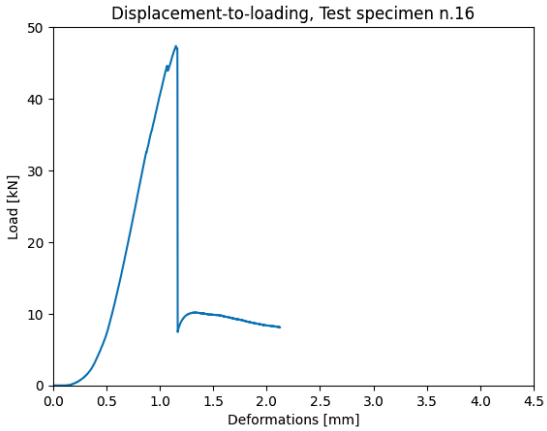

Figure 8: *Displacement-to-loading diagram for a specimen exhibiting a brittle failure.*

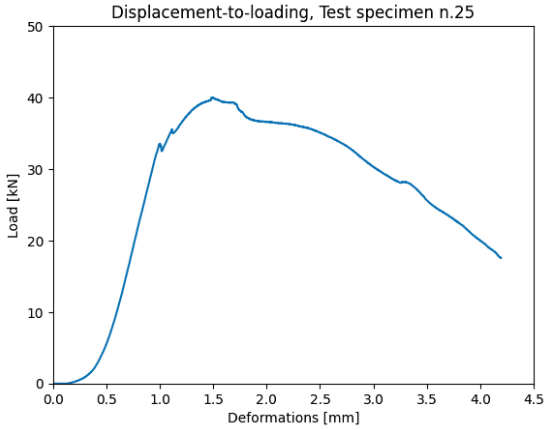

Figure 9: *Displacement-to-loading diagram for a specimen exhibiting a ductile failure.*

After testing, the samples were cut and split to inspect the quality of the gluing inside the joints and possibly reject the samples with lack of glue. Further analysis of the correlation between the failure modes and types would require a larger number of test replicates. Figure 9 and Figure 10 shows pictures of different tested samples and the types of failure modes.

The manufacturing process of gluing the test specimens resulted in specimens of varying quality, according to the testing operators own reflections. This may influence the results, e.g., some specimens had excess glue on top of the timber block and some had a string of glue between the steel plate and the soft foam. The extra glue can influence the joints' ability to transfer loads between the steel plate and the timber part and thus, increase the strength of the test specimen.
In contrast, some specimens had a lack of glue when hardened due to leakage inside or outside the timber

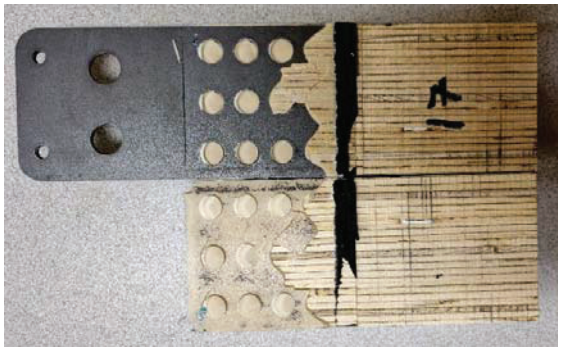

Figure 10: *Combined failure in the glue dowels, the steel-to-glue interface and in the wood-to-glue interface.*

Figure 11: *Failure solely in the glue dowels and in the steel-to-wood interface.*

block. This resulted in a gap at the top of the timber slot of a few millimetres which can lead to lower strength.

Two test machines were used, Instron model Satec and Instron 1253. From the calibration of the machines there is an error of 190 N for model Satec and 330 N for model 1253 for loads in the magnitude of the tests. The measurement uncertainties from the load cells are considered negligible in relation to the spread of quality from assembling the connections in combination with the spread of the material properties of timber.

4 CONCLUSIONS

In this preliminary study, the influences of curing time, ambient temperature and relative humidity when gluing an innovative hybrid connection type are investigated. The experimental results contribute to identifying the critical ambient parameters of such connections glued on-site. Moreover, they bring new knowledge on how to increase the construction speed of larger timber structures without jeopardizing the construction workers' safety or the structural properties of modular towers.

From the results presented in this paper the following conclusions are made:

- High temperatures up to 27 °C and a low relative humidity down to 25% do not influence the strength growth nor the final strength of the tested specimens.
- Strength growth is initially slow when the glue is more liquid. After 3-4.5 hours the curing starts

https://doi.org/10.52202/069179-0182

and strength grows more rapidly, reaching close to full strength after 24 hours of curing.

- Low temperatures down to 9.1°C of the materials and the surrounding air will slow down the rate of strength growth. It does not impact the final strength of the joints.
- There is a possibility that high moisture content in the materials and the surrounding air will influence the final strength of the joint. More test data are recommended to support this outcome.

ACKNOWLEDGEMENT

This project is funded by Energimyndigheten (Swedish Energy Agency) through SWPTC (Swedish Wind Power Technology Centre at Chalmers University). SWPTC aims to develop the Swedish wind turbine industry and promote its expansion.

REFERENCES

[1] Steen, P., P. Landel, E. Dölerud, and O. Lundman. "Structural Design Methods for Tall Timber Towers with Large Wind Turbine." In Proc. of CompWood 2019 Conference, 27–27. Växjö, Sweden, 2019.

[2] IEC 61400-1: Wind turbines – Part 1: Design requirements, International Electrotechnical Commission, 2019.

[3] Bathon, L., O. Bletz-Mühldorfer, F. Diehl, J. Schmidt, A. Wagner, and M. Weil. "Anwendungen von eingeklebten Lochblechen unter statischen sowie ermüdenden Einwirkungen." In Proc. of 29th IHF, 14. Garmisch-Partenkirchen, Germany, 2014.

[4] Deutshes Institut für Bauteknik DIBt, Z-9.1-770 – TiComTec GmbH – HSK-Verbinder und vorgefertigte Holz-Stahl-Klebeverbindungen (HSK-System) für Bauarten unter Verwendung des HSK-Systems, 2020.

[5] EN 17334:2021. Glued-in rods in glued structural timber products – Testing, requirements and bond shear strength classification. European Committee for Standardization, 2021.

[6] Barbalic, J.; Rajcic, V.; Bedon, C.; Budzik, M.K. Short-Term Analysis of Adhesive Types and Bonding Mistakes on Bonded-in-Rod (BiR) Connections for Timber Structures. Appl. Sci. 2021. 11. 2665. https://doi.org/10.3390/app11062665

[7] Verdet, M., Salenikovich, A., Cointe, A., Coureau, J.L., Galimard, P., Toro, W.M., Blanchet, P. and Delisee, C., 2016. Mechanical Performance of Polyurethane and Epoxy Adhesives in Connections with Glued-in Rods at Elevated Temperatures. BioResources, 11(4).

[8] Jockwer, R., Landel, P., Norbäck, V., Ziethén, R., Dölerud, E., Naveda, L.A., Öhman, R. Fatigue resistance of adhesive bonded connections with steel plates in large timber structures. In World Conference on Timber Engineering, Oslo. WCTE 2023.

[9] Deutshes Institut für Bauteknik DIBt, Z-9.1-896 – Henkel & Cie. AG – 2K-PUR Klebstoff LOCTITE CR 821 PURBOND zum Einkleben von Stahlstäben in tragende Holzbauteile, 2020.

https://doi.org/10.52202/069179-0182

World Conference on Timber Engineering Oslo 2023

INFLUENCE OF DENSITY AND PREDRILL IN THE EMBEDMENT STRENGTH OF TWO HARDWOOD SPECIES

Gonzalo Cabrera[1], Gonzalo Moltini[2], Vanesa Baño*[3]

ABSTRACT: The embedment strength is a key parameter in the design of timber connections with metal fasteners. It can be determined by the equations given by Eurocode 5 from the density value. Since those equations were mainly developed for softwood species, the objective of this work is to evaluate the influence of the density in the embedment strength of two high- and low-density hardwood species (beech – *Fagus sylvatica*- and poplar – *Populus x euroamericana*- , respectively) in the parallel- and perpendicular-to-grain direction. Four different experimental test configurations were carried out according to EN 383 for each species using a 5-mm nominal diameter and considering the influence of predrilling in the wood specimens. Results showed a good correlation between density and embedment strength for all the test types. In addition, predrilling showed no significant influence on the value of embedment strength, contrary to what is considered in the equations provided by the current version of the structural design codes. Both, current and new equations proposed by the new draft of Eurocode underestimate the values of embedment strength in both species, thus being on the safe side for the structural design of connections.

KEYWORDS: Embedment strength, density, predrilling, hardwood species, beech, poplar.

1 INTRODUCTION

Timber has been consolidated as a common material in short and large-span ceilings and roofs, and the current tendency is leaning toward mid- and high-rise buildings, where cross-laminated timber panels (CLT) become a key product in the design. In a bibliometric analysis of the research trends related to CLT between 2006 and 2018, the seismic performance of the structures and behaviour of connections resulted in the most relevant topics [1]. In structural design, the good execution and design of connections are vital for adequate behavior and stability of the structure.

Design codes of timber connections are based on the "European Yield Model" proposed by Johansen, whose equations for defining the strength capacity and stiffness of connections depend on the embedment strength of the wood and the yield moment of the fastener. Eurocode 5 [2], currently under review, regulates timber structural design in Europe; however, the Spanish Building Technical Code -CTE- [3] is mandatory in Spain for building design. The CTE got the connections design equations from EC5, but without taking into consideration the rope effect ($F_{ax,Rk}$). In both cases, the equations to determine embedment strength are based on experimental results and fit mostly for softwood species [4,5].

Several authors have studied the embedment strength in solid timber and Engineered Wood Products (EWPs) of softwood and/or hardwood species in different directions with respect to the grain and with different types and geometries of connectors, although most of the studies involve nails, bolts, or dowels, and not screws. For designing connections with smooth shank screws with a diameter greater than 6 mm, EC5 and CTE refer to bolts' equations. Otherwise, the requirements for nails apply. In the latest consolidated draft of Eurocode 5 (prEC5) [6] new equations are included for the specific case of screws in solid structural timber and to cover connections in other EWPs.

The current equations provided by the design codes to determine timber embedment strength are derived from two studies, Whale and Smith [7] and Ehlbeck and Werner [8], which included tests in both softwood and hardwood species. Nonetheless, the number of tests performed in softwood species was considerably higher than in hardwood ones. More studies were performed in the coming years, and some of them such as Sawata and Yasamura [9], Sandhaas et al. [10], and Yurrita et al. [5]found results not aligned with the equations proposed by previous works. In addition, Hubner [11], Sosa Zitto et al. [12], and Franke and Magniere [4], reached the conclusion that the current equations should be reviewed when considering hardwood species, and some of them proposed modifications to the equations based on their results. Since timber´s physical and mechanical properties depend not only on species but also on origin, it becomes necessary to know these parameters for the hardwood species from Spain.

[1] Gonzalo Cabrera, MEng Student, Cesefor, Spain, and Universidad Politécnica de Madrid (UPM), Spain, gonzalo.cabrera@cesefor.com
[2] Gonzalo Moltini, PhD Student, Cesefor, Spain, and Universidad Politécnica de Madrid (UPM), Spain, gonzalo.moltini@cesefor.com
[3] *Vanesa Baño, Dr. Forest Eng., Innovawood, Belgium, and Cesefor, Spain, vanesa.bano@innovawood.eu

https://doi.org/10.52202/069179-0183

The experimental methods that are more extensively used to determine the embedment strength are the ones from the European standard EN 383:2007[13], the American standard ASTM D 5764-97a [14], and the International Standard ISO 10984-2:2009 [15]. These methods have differences from each other, regarding test method, test setup, sample sizes, loading procedures, and evaluation methods. The most important difference is the determination of the maximum load, F_{max}, which leads to different results depending on the method and, therefore, to the difficulty of comparison.

Hardwood species currently visually- [16,17] or machine-graded [18] in Spain for structural use are southern blue gum (*Eucalyptus globulus*), shining gum (*Eucalyptus nitens*), and sweet chestnut (*Castanea sativa*). Since there are not yet harmonized European standards for the manufacturing of EWPs from hardwood species, some Spanish timber industries have obtained the European Technical Assessment (ETA) to commercialize specific certified products, such as glulam beams from oak by Grupo Gámiz and sweet chestnut by Sierolam, or Parallel Strand Lumber (PSL) from poplar by Tabsal.

The increasing demand for wood is leading the industry to look for alternative species for structural uses, both fast-growing with lower mechanical properties, such as poplar, and slow-growing with higher mechanical properties, such as beech. The rotation of poplar varies between 9 years in the south of Spain and up to 18 years in the north, depending not only on the origin but also on the subspecies and hybrid, and in 2016 the cuts represented 1.6% of the total cuts and 3.1% of hardwoods in Spain [19]. Characteristic values of the structural properties of the 18-year-old *Populus x euroamericana, hybrid I-214*, from the North of Spain were $f_{m,k} = 36.5$ N/mm^2, $E_{0,m} = 7746$ N/mm^2, and $\rho_k = 338$ kg/m^3 [20], which fit with the strength class C14 of EN 338:2016 [21]. The values of modulus of elasticity increased to 8800 N/mm^2 for the same hybrid from Central Spain (Guadalajara) [19] and to 9907 N/mm^2 for Portuguese poplar (*Populus alba* and *Populus nigra*) [22], showing in all the cases structural properties like softwood species. Until 2003, poplar was included in the Spanish timber grading standard [16], but it was removed due to the lack of updated data on new species and hybrids. The rotation of beech varies between 90 and 100 years old approximately [23], and occupies 2% of the total forest extension in Spain [24]. Sawmills classify solid wood in two qualities based on the wood color, first quality with white color destined for aesthetic, and second quality with red color and not industrial uses. In other countries of Europe, it is of interest for structural use due to its high mechanical properties [25–27], which reach the strength class D40 ($f_{m,k} = 40$ N/mm^2, $E_{0,m} = 13$ kN/mm^2, $\rho_k = 550$ kg/m^3) in Germany, Switzerland, and Austria [28,29] and D50 ($f_{m,k} = 50$ N/mm^2, $E_{0,m} = 14$ kN/mm^2, $\rho_k = 620$ kg/m^3) in France [27].

Previous experimental studies in these species [30], using 9 mm diameter screws and 12 mm diameter bolts (Fig. 1), showed that current equations of EC5 overestimated perpendicular to grain embedment strength. However, the equation proposed in prEC5 for screws fitted best perpendicular-to-grain embedment strength and underestimated the parallel-to-grain one.

This work aims to study the influence of the density in the embedment strength of poplar and beech from Spain in the parallel- and perpendicular-to-grain direction using a 5 mm diameter screw and considering the influence of predrilling.

2 EXPERIMENTAL CAMPAIGN

An experimental campaign was carried out to determine the embedment strength of two different low- and high-density hardwood species from Spain, poplar, and beech, in two different directions with respect to grain, parallel and perpendicular, using the following screw provided by Rothoblaas®: 5 mm diameter and 50 mm long screw (LBS550), Fig. 1. Specimens of poplar were between 12 and 15 years old, graded as ME-1 according to UNE 56.544:2003, and beech was around 90 years old classified as first quality according to the aesthetic criteria of the sawmill. Specimens were obtained from different boards and then conditioned until constant mass under conditions of relative humidity (65 ± 5) % and temperature (20 ± 2) °C, in a humidity chamber Memmert HCP240, before and after placing the fasteners (Fig. 2).

Figure 1: *5 mm ø screw, 9 mm ø screw, and 12 mm ø bolt provided by Rothoblaas®*

Figure 2: *Conditioning of the test specimens*

Four different test types were carried out for each species, following the specifications of EN 383:2007 [13], as summarized in Table 1, depending on the grain direction, and the predrilling of the wood. Since both CTE and EC5 propose a different formulation of the timber embedment

https://doi.org/10.52202/069179-0183

strength for each case (Eq. 1 and 2), specimens with and without a predrilled hole were tested.

Without predrilled hole:

$$f_{h,k} = 0.082\ \rho_k\ d - 0.3\ (N/mm^2) \quad (1)$$

With predrilled hole:

$$f_{h,k} = 0.082\ (1 - 0.01\ d)\ \rho_k\ (N/mm^2) \quad (2)$$

where, $f_{h,k}$ is the characteristic timber embedment strength, ρ_k is the characteristic timber density (kg/m³), and d is the nail (or screw) diameter (mm).

Table 1: *Test types per species*

	Test	N	Mean MC (%)	ϕ (mm)	Pre-drill	Cross-section (mm³)	Grain direct.
Poplar	T1	9	12.0 (5%)	5	No	17 × 50	∥
	T2	10	12.0 (5%)	5	No	17 × 50	⊥
	T3	10	11.8 (5%)	5	3 mm	17 × 50	∥
	T4	10	11.6 (5%)	5	3 mm	17 × 50	⊥
Beech	T1	7	12.5 (5%)	5	No	17 × 50	∥
	T2	10	12.1 (7%)	5	No	17 × 50	⊥
	T3	9	12.1 (5%)	5	3 mm	17 × 50	∥
	T4	9	12.2 (5%)	5	3 mm	17 × 50	⊥

* Note: MC is the moisture content and the coefficient of variation, CoV, is presented between ( ), and ϕ is the diameter of the screw.

2.1 METHODOLOGY

The specimens were tested in compression through a loading steel device, as shown in Figure 3. Figures 4 and 5 show the experimental tests in parallel- and perpendicular-to-grain compression in poplar and beech, respectively. The loading procedure was defined in terms of the maximum estimated load $F_{max,est}$ for each test. It consisted of two cycles: a preload cycle up to $0{,}4F_{max,est}$, and a final loading until failure. The loading procedure is presented in Figure 6. After testing, a slice of the specimen was extracted to determine its density and moisture content according to EN 13183-1:2002 [31]. Density was later adjusted to a reference moisture content of 12 %.

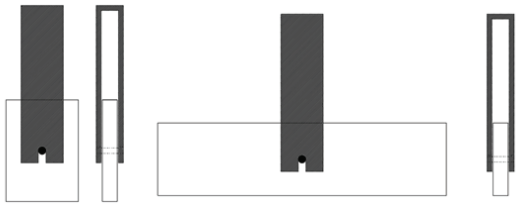

Figure 3: *Parallel- (left) and perpendicular-to-grain (right) tests*

Figure 4: *Experimental tests T1 (left) and T2 (right) performed in poplar.*

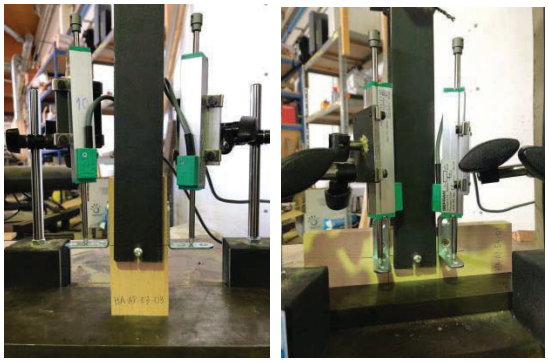

Figure 5: *Experimental tests T3 (left) and T4 (right) performed in beech.*

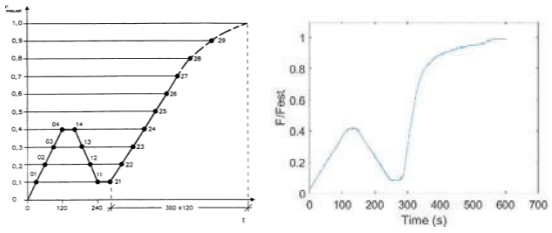

Figure 6: *Loading procedure provided by EN 383 (left) and experimental loading procedure (right)*

https://doi.org/10.52202/069179-0183

3 RESULTS AND DISCUSSION

3.1 LOAD-DISPLACEMENT CURVES

Load-displacement curves of both species tested in the parallel- and perpendicular-to-grain direction, with and without predrilling, are shown in Figures 7-10.

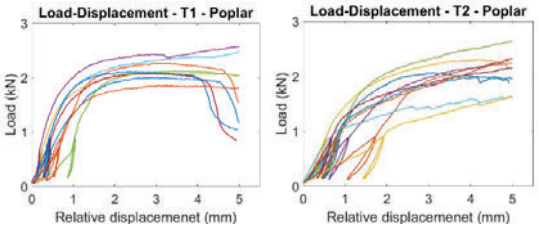

Figure 7: *Load–displacement curves of poplar without predrilling*

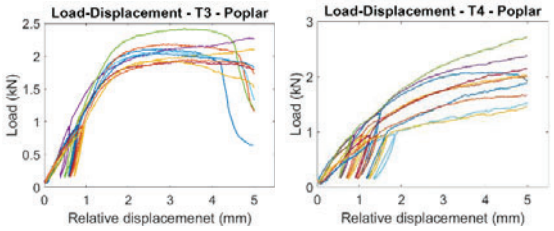

Figure 8: *Load–displacement curves of poplar with predrilling*

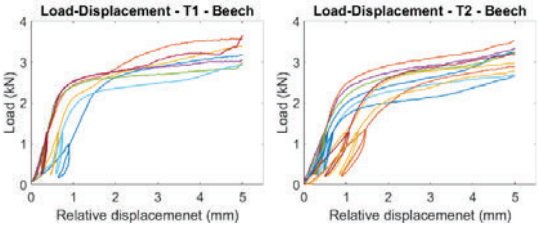

Figure 9: *Load–displacement curves of beech without predrilling*

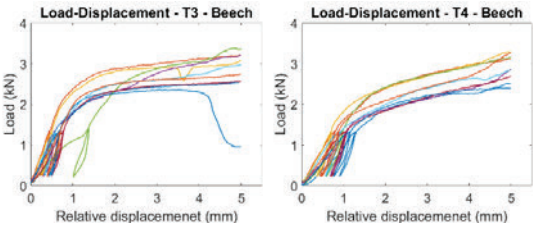

Figure 10: *Load–displacement curves of poplar with predrilling*

As expected, and observed previously by Cabrera et al. [30], beech presents higher values of embedment strength than poplar, and a difference in behavior is observed when comparing parallel- with perpendicular-to-grain tests. A plateau in the diagram is observed after the yield point in the parallel-to-grain tests, while the load increases with relative displacement in the perpendicular-to-grain tests, showing a hardening behavior of wood, but lower than that observed for greater fastener diameters.

Figures 11 and 12 show the comparison of the load–displacement diagrams of tests with and without predrilled holes within the same species. Load–displacement diagram of a particular test specimen representative of the mean behavior of the sample was selected in each case. Through this comparison, it can be directly observed that there are no important differences in behavior due to the execution of the predrilled hole. The shape of the curves in general terms are similar within the same test type for each species.

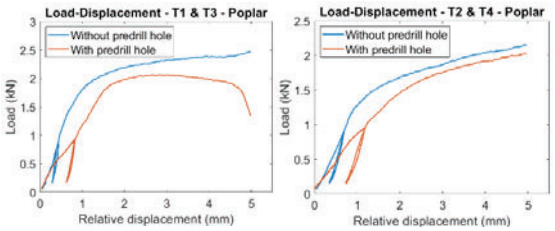

Figure 11: *Load-displacement diagram of poplar with and without predrilling in parallel and perpendicular to the grain tests*

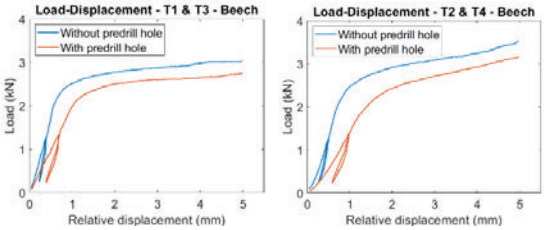

Figure 12: *Load-displacement diagram of beech with and without predrilling in parallel and perpendicular to the grain tests.*

3.2 EMBEDMENT STRENGTH

The embedment strength f_h was determined according to Equation (3), and characteristic values were obtained according to EN 14358:2016 [32] assuming a lognormal distribution.

$$f_h = \frac{F_{max}}{dt} \tag{3}$$

where F_{max} is the maximum load; d is the effective diameter of the screw, taken as 1.1 times the thread root diameter, which resulted in 3.3 mm for LBS550 screws; and t is the thickness of the test specimen.

Results from Cabrera et al. [30] showed that the method provided by EN 383 for the determination of embedment strength could overestimate that value for the perpendicular-to-grain direction. So, the embedment strength obtained from EN 383 was compared with that obtained from ASTM D 5764-97a and EN 408:2010 [33] according to the following criteria:

https://doi.org/10.52202/069179-0183

(i) F_{max} corresponding to a relative displacement of the fastener of 5 mm, or the maximum force in case it was reached at a lower deformation, as specified in EN 383.
(ii) F_{max} as the yield point defined in the load-deformation diagram by a straight line parallel to the elastic slope offset by deformation of 5% of the fastener diameter, as it is defined in ASTM D 5764-97a.
(iii) F_{max} determined according to the method defined in the EN 408 for the perpendicular-to-grain compression strength, like that described in (ii) but with a straight line offset by 0.01 h_t, where h_t is the loaded length, i.e., the distance below the fastener.
Results of mean and characteristic values of embedment strength -obtained from EN 383- and density, with their coefficient of variation, are presented in Table 2 for both species.

Table 2: *Results of the experimental tests according to EN 383*

	Poplar				Beech			
Test	$f_{h,m}$ (N/mm^2)	$f_{h,k}$ (N/mm^2)	ρ_m (kg/m^3)	ρ_k (kg/m^3)	$f_{h,m}$ (N/mm^2)	$f_{h,k}$ (N/mm^2)	ρ_m (kg/m^3)	ρ_k (kg/m^3)
T1	38.3 (11%)	30.6	414 (18%)	253	57.8 (9%)	46.9	670 (11%)	503
T2	37.6 (15%)	26.9	419 (19%)	252	54.6 (9%)	44.9	645 (7%)	549
T3	37.1 (8%)	31.6	424 (21%)	241	52.1 (12%)	39.8	692 (12%)	519
T4	35.1 (20%)	23.0	420 (21%)	239	51.8 (11%)	40.6	685 (10%)	542

Note: The value between brackets shows the coefficient of variation (%); ρ_k is the density adjusted to 12% of moisture content according to EN 384

Figures 13 and 14 show the characteristic values of the embedment strength depending on the standard method for both species and the four test types.
In poplar, experimental values obtained through the three different methods are more even between each other for the two parallel-to-grain tests performed than for the perpendicular-to-grain ones (Fig. 13). Values of perpendicular-to-grain embedment strength evaluated according to EN 383 standard were higher compared with those of the other two methods, especially in tests without predrilling (T2). In addition, perpendicular-to-grain embedment strength is rather lower than parallel-to-grain one, contrary to what the standard states according to its equations.

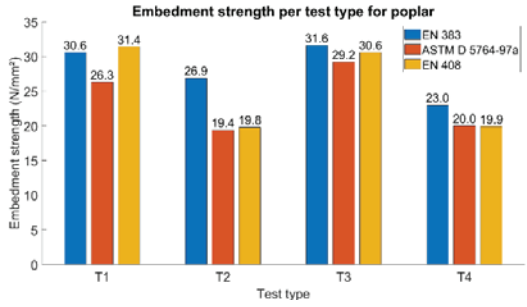

Figure 13: *Experimental characteristic values of embedment strength depending on the standard and test type in poplar.*

In beech (Fig. 14), higher values of embedment strength are obtained according to the EN 383 method for both with and without predrilling and parallel- and perpendicular-to-grain tests, with significant differences with respect to the other methods according to an ANOVA analysis. The small diameter of the screw and the cross-section of the wood specimen could lead to evaluate the embedment strength before the yield point of the load-displacement diagram for the ASTM and EN 408 methods, which could result in an underestimation of the embedment strength parallel to the grain.

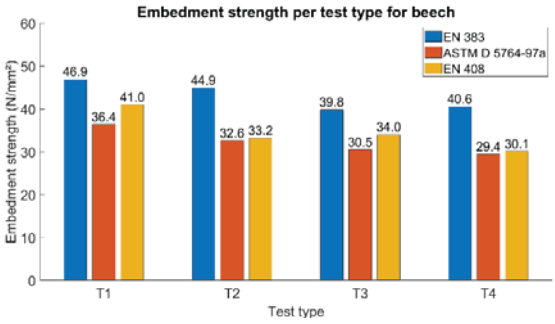

Figure 14: *Experimental characteristic values of embedment strength depending on the standard and test type in beech.*

3.3 FAILURE MODE

Most of the specimens from T1 to T4 tests showed a failure mode that combines the timber embedment with plastic deformation of the screw (Fig. 15), which differs from the failure mode of the fasteners with greater diameter, in which the plastic deformation of the fastener did not occur [30]. As in the case of the greater diameter of fasteners, a combination of embedment and splitting was observed in the perpendicular-to-grain tests especially performed in poplar.

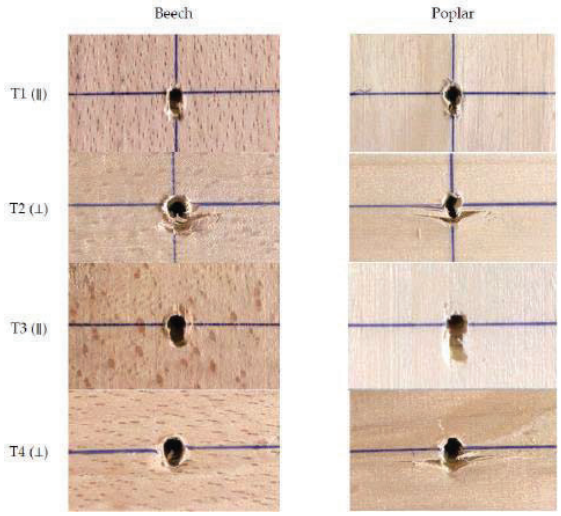

Figure 15: *Failure modes*

3.4 COMPARISON WITH THE THEORETICAL VALUES OF THE DESIGN CODES

For comparing experimental values with theoretical ones, the experimental values obtained according to the method of the EN 383 standard will be considered because of the two main reasons that follow. The first is that experimental values of embedment strength obtained according to the methods of ASTM D 5764-97a and EN 408 tend to underestimate embedment strength since as it was mentioned before, the small diameter of the fastener and geometry of test specimens lead to obtaining a failure point located before the yielding phase of the load-displacement diagram, which does not make any sense. The second reason is that the correlation obtained between density and embedment strength according to the methods of ASTM D 5764-97a and EN 408 was much lower than the one obtained with the results of the EN 383 standard.
Thus, the experimental values of the embedment strength obtained from EN 383 were compared with those obtained from the equations provided by the EC5 and prEC5. The equations that are applicable for each studied case depend on the existence or not of a predrilled hole as a determining factor in the embedment strength according to EC5, but not according to prEC5, which proposes only one equation for both cases, but considers the influence of the angle between the fastener axis and the grain direction, as shown in Table 3. Neither EC5 nor prEC5 considers load-to-grain angle as a determining factor for obtaining embedment strength.
Results are shown in Figures 16 and 17 and the ratios between theoretical values obtained from EC5 and prEC5 and the experimental values are presented in Table 4. It is not clear that a predrilled hole in the wood improves the embedment strength, as EC5 considers, resulting in an underestimation of embedment strength for the studied cases T1 and T2.

Table 3: *Equations provided by EC5 and prEC5 to determine the embedment strength of small-diameter screws.*

Test		Equation of EC5	Equation of prEC5
Nails without predrilling (EC5) Screws (prEC5)	T1 (∥) T2 (⊥)	$f_{h,k} = 0.082\rho_k d^{-0.3}$	$f_{h,k} = \frac{0.019\rho_k^{1.24} d^{-0.3}}{2.5\cos^2\varepsilon + \sin^2\varepsilon}$
Nails without predrilling (EC5) Screws (prEC5)	T3 (∥) T4 (⊥)	$f_{h,k} = 0.082(1 - 0.01d)\rho_k$	

ε is the angle between the fastener axis and the grain direction. $\varepsilon = 90°$ for all tests.

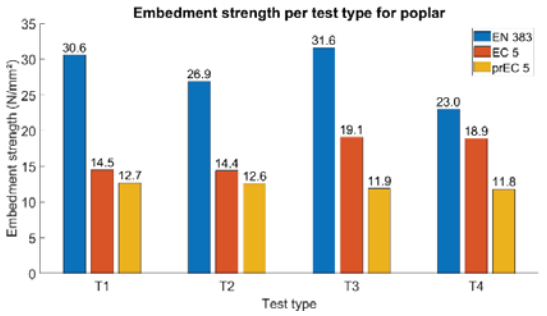

Figure 16: *Experimental vs. theoretical characteristic embedment strength in poplar*

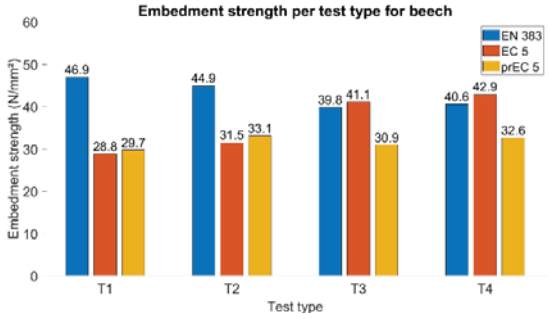

Figure 17: *Experimental vs. theoretical characteristic embedment strength in beech*

Table 4: *Ratios between theoretical and experimental values of embedment strength*

Test	Poplar		Beech	
	$\frac{f_{h,k\_EC5}}{f_{h,k\_exp}}$ (N/mm²)	$\frac{f_{h,k\_prEC5}}{f_{h,k\_exp}}$ (N/mm²)	$\frac{f_{h,k\_EC5}}{f_{h,k\_exp}}$ (N/mm²)	$\frac{f_{h,k\_prEC5}}{f_{h,k\_exp}}$ (N/mm²)
T1	0.47	0.41	0.61	0.63
T2	0.54	0.47	0.70	0.74
T3	0.60	0.38	1.03	0.78
T4	0.83	0.51	1.06	0.80

Results show that the execution of a predrill in the wood does not have a significant influence on the embedment strength for screws of 5 mm of diameter for both species according to an ANOVA analysis with a confidence level of 95%, which was also stated by Sosa Zitto et al. [12]and differs from the current EC5 approach. In addition, the equations provided by the EC5 underestimate the

https://doi.org/10.52202/069179-0183

experimental values for both parallel- and perpendicular-to-grain embedment strength of poplar. When it comes to beech, it is observed that EC5 equations predict appropriately the embedment strength in wood specimens with predrilling and underestimate embedment strength for the cases without predrilling. In terms of structural design, equations could lead to oversizing, but in any case are on the safe side.

New equations proposed by prEC5 showed similar values to those obtained from EC5 without predrilling, which implies that they also underestimate the embedment strength for both species with small-diameter screws.

In addition, no significant influence of the load-to-grain direction was observed for all the studied cases according to an ANOVA analysis with a confidence level of 95%, which goes along with the fact that the formulations proposed are independent of the load-to-grain angle.

3.5 CORRELATION BETWEEN DENSITY AND EMBEDMENT STRENGTH

The correlation between experimental embedment strength and density adjusted to 12% of MC was studied for both species and the different tests performed. Results are presented in Figures 17 and 18.

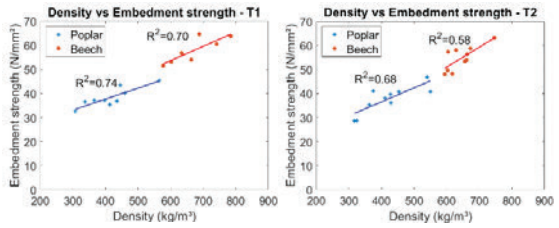

Figure 17: *Correlation between density (ρ_{12}) and embedment strength ($f_{h,exp}$) for wood specimens without predrilling.*

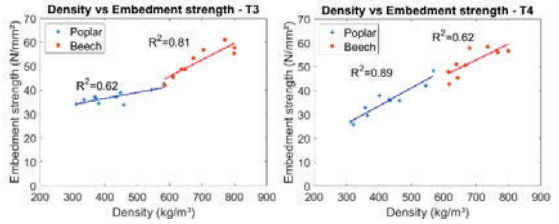

Figure 18: *Correlation between density (ρ_{12}) and embedment strength ($f_{h,exp}$) for wood specimens with predrilling.*

The correlation coefficient between density and embedment strength was higher than 0.62 for all the cases, except for beech without predrilling compression perpendicular to the grain (R^2=0.58) which indicates that density is a good predictor of embedment strength for these species.

4 CONCLUSIONS

Beech showed higher values of embedment strength than poplar for all the cases studied. Embedment failure was observed in parallel-to-grain tests, while a combined failure of embedment and splitting took place in some of the perpendicular-to-grain tests, especially in poplar.

When testing nails or screws with small diameters, the method provided by ASTM D 5764-97a or the one proposed based on EN 408, could lead to underestimation of embedment strength, thus being not appropriate.

Results showed that there is no significant influence of the predrilled hole in the embedment strength of the species studied with the small-diameter screw tested, contrary to what EC5 considers, thus penalizing embedment strength for the case without predrilled holes. New equations provided by prEC5 showed similar values to those obtained from EC5 without predrilling, therefore, a better prediction of embedment strength is obtained in the cases studied if the equation for nails with predrilled holes of EC5 is used in every case.

In addition, results also showed that there is no significant influence of the load-to-grain direction in the embedment strength for the studied cases, a fact that is aligned with the current proposal of EC5.

Density becomes a good predictor of embedment strength for these species and screws studied.

ACKNOWLEDGEMENT

Research project CCTT3/20/SO/0001 funded by the ERD through Junta de Castilla y León, and EUFORE HE No.101081788 by the European Union

REFERENCES

1. Abejón, R.; Moya, L. Cross-Laminated Timber: Perspectives from a Bibliometric Analysis (2006–2018). *Wood Mater Sci Eng* **2022**, *17*, 429–450, doi:10.1080/17480272.2021.1955295.
2. CEN EN 1995-1-1: Eurocode 5: Design of Timber Structures - Part 1-1: General - Common Rules and Rules for Buildings 2004.
3. Ministerio de Fomento Código Técnico de La Edificación Documento BásicoSE-M Seguridad Estructural Madera 2019.
4. Franke, S.; Magnière, N. The Embedment Failure of European Beech Compared to Spruce Wood and Standards. In Proceedings of the Materials and Joints in Timber Structures; Aicher Simon and Reinhardt, H.-W. and G.H., Ed.; Springer Netherlands: Dordrecht, 2014; pp. 221–229.
5. Yurrita, M. New Criteria for the Determination of the Parallel-to-Grain Embedment Strength of Wood. *Constr Build Mater* **2018**, *173*, 238–250.
6. CEN PrEN 1995-1-1:20XX; Design of Timber Structures-Common Rules and Rules for Buildings-Part 1-1: General 2021.
7. Whale, L.R.J.; Smith, I. The Derivation of Design Clauses for Nailed and Bolted Joints in Eurocode 5. *CIB-W18 Meeting 19* **1986**, *1*, 446–472.
8. Ehlbeck, J.; Werner, H. Softwood and Hardwood Embedding Strength for Dowel-Type Fasteners. *CIB-W18 Meeting 25* **1992**, 555–568.

9. Sawata, K.; Yasumura, M. Determination of Embedding Strength of Wood for Dowel-Type Fasteners. *Wood Science* **2002**, *48*, 138–146.
10. Sandhaas, C.; Ravenshorst, G.J.P.; Blass, H.J.; van de Kuilen, J.W.G. Embedment Tests Parallel-to-Grain and Ductility Aspects Using Various Wood Species. *European Journal of Wood and Wood Products* **2013**, *71*, 599–608, doi:10.1007/s00107-013-0718-z.
11. Hübner, U. Embedding Strength of European Hardwoods. *CIB-W18 Meeting 41* **2008**, 203–219.
12. Sosa Zitto, M.A.; Köhler, J.; Piter, J.C. Embedding Strength in Joints of Fast-Growing Argentinean Eucalyptus Grandis with Dowel-Type Fasteners. Analysis According to the Criterion Adopted by European Standards. *European Journal of Wood and Wood Products* **2011**, *70*, 433–440, doi:10.1007/s00107-011-0572-9.
13. CEN EN 383: Timber Structures-Test Methods-Determination of Embedment Strength and Foundation Values for Dowel Type Fasteners 2007.
14. ASTM ASTM D 5764-97a: Standard Test Method for Evaluating Dowel-Bearing Strength of Wood and Wood-Based Products 2002.
15. ISO ISO 10984-2:2009 Timber Structures — Dowel-Type Fasteners — Part 2: Determination of Embedding Strength 2020.
16. AENOR UNE 56544 - Clasificación Visual de La Madera Aserrada Para Uso Estructural. Madera de Coníferas 2022.
17. AENOR UNE 56546 - Clasificación Visual de La Madera Aserrada Para Uso Estructural. Madera de Frondosas 2022.
18. CEN EN 14081-2:2019. Timber Structures. Strength Graded Structural Timber with Rectangular Cross-Section. Part 2: Machine Grading; Additional Requirements for Type Testing. Brussels, Belgium 2018.
19. Gallego, A.; Ripoll, M.A.; Timbolmas, C.; Rescalvo, F.; Suarez, E.; Valverde, I.; Rodríguez, M.; Navarro, F.B.; Merlo, E. Modulus of Elasticity of I-214 Young Poplar Wood from Standing Trees to Sawn Timber: Influence of the Age and Stand Density. *European Journal of Wood and Wood Products* **2021**, *79*, 1225–1239, doi:10.1007/s00107-021-01675-5.
20. Basterra, L.A.; Acuña, L.; Casado, M.; López, G.; Bueno, A. Strength Testing of Poplar Duo Beams, Populus x Euramericana (Dode) Guinier Cv. I-214, with Fibre Reinforcement. *Constr Build Mater* **2012**, *36*, 90–96, doi:10.1016/j.conbuildmat.2012.05.001.
21. AENOR UNE-EN 338:2016 - Madera Estructural. Clases Resistentes. 2016.
22. Monteiro, S.; Martins, C.; Dias, A.; Cruz, H. Mechanical Characterization of Clear Wood from Portuguese Poplar. *Bioresources* **2019**, *14*, 9677–9685, doi:10.15376/biores.14.4.9677-9685.
23. García-Robredo, F. Effect of Species Complementarity on Financial Return in Mixed Stands of European Beech and Scots Pine in Northern Spain. *Forests* **2018**, *9*, doi:10.3390/f9090559.
24. MITECO *Anuario de Estadística Forestal 2019*; Ministerio para la Transición Ecológica y el Reto Demográfico: Madrid, Spain, 2021; ISBN 9788418508493.
25. Hu, W.; Wan, H.; Guan, H. Size Effect on the Elastic Mechanical Properties of Beech and Its Application in Finite Element Analysis of Wood Structures. *Forests* **2019**, *10*, doi:10.3390/f10090783.
26. Brunetti, M.; Nocetti, M.; Pizzo, B.; Aminti, G.; Cremonini, C.; Negro, F.; Zanuttini, R.; Romagnoli, M.; Mugnozza, G.S.; Biologici, S.; et al. Glued Structural Products Made of Beech Wood: Quality of the Raw Material and Gluing Issues. In Proceedings of the International Scientific Conference on Hardwood Processing; 2019.
27. Lanvin, J.D.; Reuling, D.; Legrand, G. French Beech-a New Opportunity in Wood Housing. In Proceedings of the 7th - International Scientific Conference on Hardwood Processing; 2019; pp. 129–137.
28. CEN EN 1912 Structural Timber - Strength Classes - Assignment of Visual Grades and Species 2012.
29. Kovryga, A.; Stapel, P.; van de Kuilen, J.W.G. Mechanical Properties and Their Interrelationships for Medium-Density European Hardwoods, Focusing on Ash and Beech. *Wood Mater Sci Eng* **2020**, *15*, 289–302, doi:10.1080/17480272.2019.1596158.
30. Cabrera, G.; Moltini, G.; Baño, V. Embedment Strength of Low- and Medium-Density Hardwood Species from Spain. *Forests* **2022**, *13*, 1154, doi:10.3390/f13081154.
31. CEN EN 13183-1:2002. Moisture Content of a Piece of Sawn Timber - Part 1: Determination by Oven Dry Method 2002.
32. CEN EN 14358: Timber Structures - Calculation and Verification of Characteristic Values 2016.
33. CEN EN 408:2011+A1: Timber Structures - Structural Timber and Glued Laminated Timber - Determination of Some Physical and Mechanical Properties 2019.

https://doi.org/10.52202/069179-0183

World Conference on Timber Engineering Oslo 2023

STRUCTURAL PERFORMANCE OF HIGH CAPACITY GLULAM MOMENT CONNECTIONS

Ryan Guay [1], Christopher Pitt [2], Reid B. Zimmerman [3], Ignace Mugabo [4], Peter Dusicka [5]

ABSTRACT: Moment connections in glulam members are desirable over simple connections to increase load-carrying capacity and reduce deflections for the same glulam cross section. However, moment connections in glulam members often result in a large tension-compression couple. To achieve high tension capacity, a large number of fasteners acting in dowel shear are often utilized. Brittle failure modes such as block shear and group tear-out can dominate such connections.

This study evaluates the structural performance of high capacity glulam moment and tension connections in two configurations based on the results of physical testing: (1) Steel plates installed with 90-degree screws on both of the outer, side faces of a glulam member, and (2) two steel plates nested into a glulam member and installed with self-drilling dowels. Calculation-based results and physical load test results are compared. The results from this study show that block shear capacity estimations as adopted in design standards may be unconservative for high capacity moment or tension connections. A potential modification through perpendicular-to-grain reinforcing screws to help mitigate the block shear failure is presented. Further research on high capacity moment and tension connections is needed to provide better agreement between design versus actual capacity, especially for block shear type failure modes.

KEYWORDS: Glulam Connections, Self-Drilling Dowels, Wood Screws, Block Shear Failure, Reinforcing Screws

1 INTRODUCTION

Glulam connections commonly used in buildings in North America are configured as simple shear connections with negligible capacity to resist bending moments. Glulam moment connections are uncommon, particularly in cases where high capacities are required. In order to achieve the long-span glulam beams, cantilevers, and wood-steel hybrid structure desired for the new Portland International Airport Terminal Core Redevelopment (TCORE) roof located in Portland, Oregon, USA, high capacity moment connections were developed for deep glulam beams. This paper evaluates dowel-type glulam moment connections using a multi-scale approach and a comparison between test and analytical results. The paper also presents a solution for mitigating premature block shear failures in such connections.

1.1 Background for timber connection testing

The Port of Portland's TCORE project is a roughly $2 billion terminal redevelopment project, including an approximately 300 m x 120 m mass timber hybrid roof with approximately 6 m wide x 2 m deep paired steel plate girder sections spaced at 30 m. Approximately 170 mm wide x 2 m deep x 24 m long Douglas-fir glulam beams span perpendicular to the steel plate girders at 3 m spacing. The roof structure is seismically isolated with curved surface slider (friction pendulum) isolators located at the top of the Y-column connections to the bottom of the steel plate girders [1]. This requires that the glulam beams transmit seismic loading from the roof diaphragm above to the isolation plane below through strong-axis bending. Additionally, glulam beams support roof edge cantilevers of over 10 m and are optimized by functioning as continuous beams with moment connections to the plate girders. Due to the large demands and unique nature of these connections, an effort was made early in design to perform physical load testing of various connection configurations to develop a thorough understanding of their capacities and failure mechanisms.

Allowing for expansion and shrinkage in the glulam beams due to variations in moisture content (MC) during construction and service was a critical consideration. Excessive moisture content change and/or excessive restraint introduced by the dowel-connected steel plate connections could have resulted in wood splitting, compromising the capacity of the connection. Design to prevent splitting pursued limiting the perpendicular-to-

[1] Ryan Guay, KPFF Consulting Engineers, United States, Ryan.Guay@kpff.com
[2] Christopher Pitt, KPFF Consulting Engineers, United States, Christopher.Pitt@kpff.com
[3] Reid B. Zimmerman, KPFF Consulting Engineers, United States, Reid.Zimmerman@kpff.com
[4] Ignace Mugabo, Formerly of KPFF Consulting Engineers, United States
[5] Peter Dusicka, Portland State University, United States, dusicka@pdx.edu

https://doi.org/10.52202/069179-0184

grain distance between outer rows of fasteners connecting steel and glulam to a maximum of 150 mm, and separating the beam end tension/compression connections so they can each move independently in the vertical (perpendicular to grain) direction with the glulam beam end. Due to the critical nature of these connections, moisture cycling was performed on selected specimen followed by load testing, to verify that no significant reduction in capacity occurred due to moisture cycling.

1.2 Brief introduction to general testing approach

To develop the proposed connection configurations, the roof structure was analysed to determine the various levels of tension/compression demand required near the top and bottom of glulam beams to provide bending moment resistance at the beam ends. A data binning approach was used to group various levels of glulam demands to minimize the number of different connections required on the project, while also achieving efficiency in the design. Beam vertical shear demands are resisted by direct bearing of bottom of glulam beams on steel plate girder, not through dowel fasteners.

Analyses determined that (3) connection capacity levels were needed to efficiently meet the loading requirements for this project. Two proposed connection configuration options were explored. Both connection configurations were tested at all capacity levels, equalling (6) connection types, with (2) additional sub-types tested, for a total of (8) unique tested configurations.

Both beam bending specimen tests and smaller axial tension specimen tests were performed on the connection types, with the connections tested at full scale in both cases. The as-constructed connections in the TCORE roof are shown in photo 1 below.

Photo 1: As constructed glulam beam end moment connections

2 MATERIALS, METHODS, AND DATA PROCESSING

2.1 Description of timber connections

Two connection configuration design concepts were included in the testing program for the glulam beam end top/bottom moment connections; one consisted of a connection composed of exposed 6 mm thick steel side plates with 6 mm x 90 mm wood screws installed each side, loaded in single shear. The other consisted of a connection composed of a pair of 6 mm thick steel plates slotted into and concealed within the width of the glulam beam, with 6 mm diameter self-drilling dowels (SDDs) installed through the glulam thickness and both steel plates, loaded on 4-shear planes. See figure 1 below for a graphical representation of the two concepts, along with the various sizes for the connection test configurations and fastener quantity. The left side of figure 1 indicates the external steel side plates with screws connection; the right side of figure 1 indicates the internal steel plates with self-drilling dowels connection.

All glulam specimens were made of Douglas-Fir (*Pseudotsuga menziesii*) timber with a 16.5 MPa tension lam bending stress grade. Specimens were kept at moisture content of 12% +/- 4% during fabrication and load testing of the connections. Four specimens were moisture cycled prior to load testing to study the effects that weather exposure and drying may have on the capacity of the connections. The steel side and thru-plates consisted of 6 mm thick ASTM A572 Grade 50 steel.

The larger type C3 and C6 connection test specimens differed from the connections used in the project in that the test specimens had a single large plate, whereas the project connections used two separate plates to prevent restraint during moisture shrinkage/expansion.

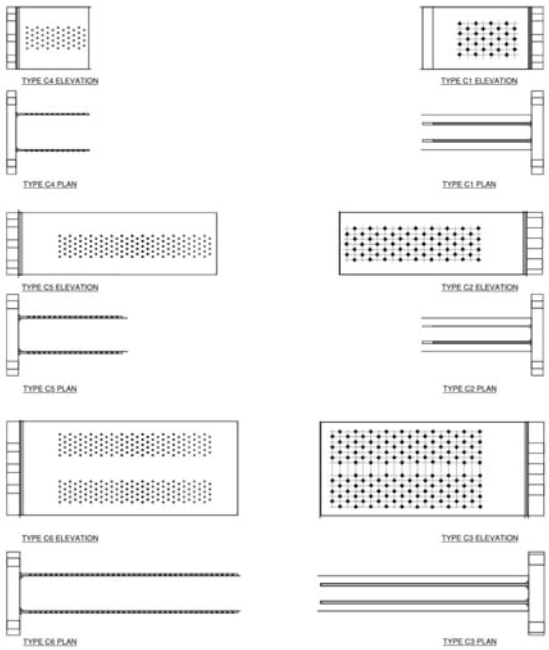

Figure 1: Summary of Connection Types Tested

2.2 Methods of testing

KPFF worked directly with Portland State University to utilize the infrastructure Testing and Applied Research

https://doi.org/10.52202/069179-0184

(iSTAR) Laboratory to perform the specimen load testing, which included both axial tension connection tests and beam bending tests. The specimens were fabricated off site by the same wood subcontractor as would be fabricating the project connections and shipped to the iSTAR Laboratory. A minimum of (8) connection tests were performed for each of the connection types. This number of tests was selected to balance cost/time of testing with the need to collect an adequate data set for performing limited statistical analysis.

Moisture content (MC) cycling testing followed by load testing on an additional (4) axial tension specimens was also performed. MC cycling was conducted in an environmental chamber at Oregon State University after which specimens were shipped to the iSTAR Laboratory for identical load testing to non-MC cycled specimens.

2.2.1 Physical Testing

A total of (28) axial tension specimen tests were performed, (12) tests using the 6 mm SDDs and (16) with the 6 mm x 90 mm wood screws. Following the completion of the axial tension specimen tests, (12) full scale bending specimen tests were performed, (6) using the 6 mm SDDs and (6) with the 6 mm x 90 mm wood screws. Douglas-fir glulam beams were used with the fasteners installed in laminations of equal or lower grade from those present at end connection locations in the project final condition. Steel test rig frames were fabricated to enable hydraulic jacks to apply loading to the specimens, with pressure/load and movements continuously monitored. The tension specimen tests were subjected to direct, concentric axial tension by pulling the two ends of the glulam specimen apart. The beam bending test specimens were subjected to shear and flexure by securing one end of the beam to the stationary test rig with a vertical shear bearing and horizontal compression connection bucket at the top and horizontal tension connection at the bottom, with a vertical upward load applied to the far end of the beam to induce shear and bending proportional with the actual roof demands. The beam bending specimens were each tested twice, with a tension connection installed at diagonally opposite corners to allow them to be flipped and rotated for testing after failure of the initially tested connection.

The connections were instrumented by the iSTAR Laboratory staff with load cells and deformation sensors. Deformation sensors measured deformation across the connection, rather than the entire specimen, directly. As a backup to the load cells for measuring force, pressure sensors for the hydraulic jacks were also present.

The axial tension specimen tests were performed first, which helped direct the path for the remaining tests by revealing which failure mechanisms should be more closely investigated. The axial tension specimen tests were quasi-statically loaded up to the approximate allowable stress design (ASD/service level) loads estimated from preliminary roof structure analyses, the load was held for 10 minutes, and then the connections were quasi-statically loaded to failure. The loading to failure procedure was based on ASTM D1761-12 [2], which is typically used for determining the lateral load resistance for wood screws in the U.S. For each of the axial tension specimen tests, the same connection configuration was installed on each end of the glulam. The measured capacity of whichever end connection failed first was conservatively used as the capacity for both end connections and treated as two equal data points in the data analysis.

The beam bending specimen tests were loaded in a similar manner to the axial tension specimen tests with the exception of one full beam specimen that was loaded and held for a full 24 hour period at the ASD/service load. The objective of this test was to determine if any additional creep occurred during the hold period. See figure 2 for the test setup for representative specimens.

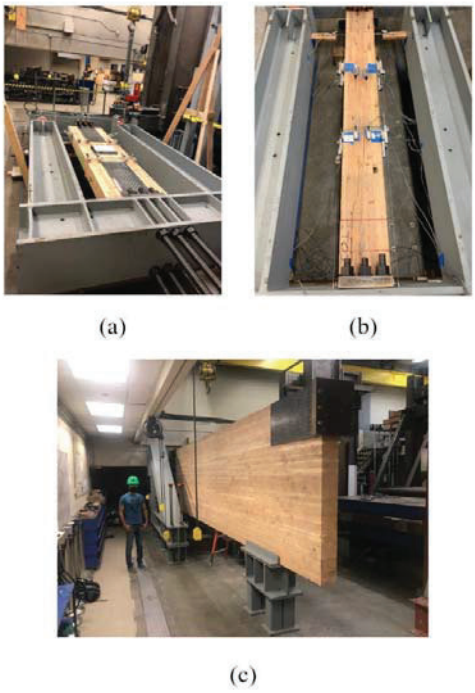

Figure 2: Connection testing setup (a) tension specimen with external steel plates and wood screws, (b) tension specimen with internal steel plates and self-drilling dowels, and (c) bending specimen.

2.2.2 Moisture Testing

To determine whether the proposed connection types were sensitive to wetting/drying (and associated wood shrinkage/expansion) after installation, moisture content (MC) cycling was applied to (4) axial tension test specimens prior to load testing. This was considered important because, in the actual project, the glulam beams would be exposed to weather during some phases of

https://doi.org/10.52202/069179-0184

construction despite best efforts to minimize such exposure through a detailed weather protection plan. For this testing, the connections were installed in glulam beams with industry standard 15%-16% MC, which aligned with the maximum MC allowed by project specifications. Pinned moisture monitors were installed to approximately 75 mm depth to measure internal MC before the glulam beam test specimens were placed in an environmental chamber at Oregon State University. Within the chamber, the temperature and humidity were controlled to cause expedited MC variations. The specimens were periodically sprayed with water for several days under low temperature and high humidity conditions until they increased to 22-27% MC (an increase of 6-12% MC). Then the chamber was set to higher temperature and low relative humidity to induce rapid drying. These conditions were maintained for over 4 weeks until the specimens reduced to 8-13% MC (a decrease of up to 16% MC from peak after wetting). See figure 3.

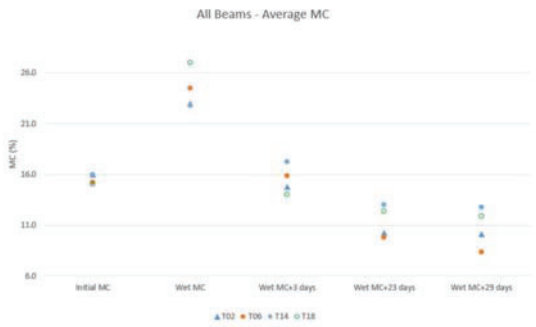

Figure 3: Moisture content (MC) cycling data of glulam specimens

Project specifications included requirements for moisture control and monitoring, which were calibrated to the MC testing performed. These included a maximum MC at time of connection installation, periodic monitoring of glulam beam MC after installation, and a maximum MC allowed at any point in construction. This ensured that the maximum variations in MC for in-situ project conditions were within those evaluated by testing. Final long-term minimum MC in the occupied building is estimated as 8% MC or above based on conservative assumptions of service temperature and relative humidity inside the conditioned building.

2.3 Statistical analysis of test results

To establish design capacities of the load tested connections, KPFF worked with the permitting authority for the project (The City of Portland, Oregon, Bureau of Development Services). Statistical analysis of the load test results following ASTM D2915-17 [3] established a nominal capacity for design on the basis that the physical testing methods for the connections were aligned with those of ASTM D1761-12 [2] and ASTM D5764-97a [4]. These latter ASTM standards are both typically used for testing of mechanical fasteners and dowel-bearing strength in wood products in the U.S.

With the data that was collected from the tests, a 75% confidence level, one-sided tolerance limit, and population content of 95% were chosen (indicating that 95% of the population lies above the tolerance limit, 75% of the time through sampling). This confidence level, tolerance limit, and population content are the traditional approach for establishing structural capacities of wood products in the U.S. (i.e., 5% exclusion of lower capacities).

See Section 3.1 for a summary of the results. A graphical representation of the design capacity compared with the test data for each of the different types of connections is shown in figure 6.

2.4 NDS and Eurocode Calculations

In advance of performing the physical tests, calculations were made utilizing fastener manufacturer listed capacities, the design provisions of Appendix E of the American Wood Council's National Design Specification (NDS) for Wood Construction [5], and Annex A of Eurocode 5 [6] to determine expected design capacities. For block shear calculations (named as group tear-out in the NDS), the NDS equations consider the sum of the resistance from both the shear and tension portions of a potential failure perimeter. In contrast, Eurocode only takes the larger of the shear or tension portion capacity. See figure 4. This represents a fundamental difference in philosophy between the NDS and Eurocode. Where the NDS appears to assume load-sharing between the shear and tension portions of a block shear perimeter up to ultimate failure, Eurocode appears to assume that failure will occur on either the shear or tension portion but not both simultaneously. In other words, Eurocode appears to consider the differing deformations at failure between the shear and tensions portions whereas the NDS either neglects this or assumes some ductility in the portion which reaches capacity first.

Figure 4 below excerpts the relevant equations from NDS and Eurocode for comparison. See Section 3.2 for a comparison of load test results to calculations from both codes.

https://doi.org/10.52202/069179-0184

E.4 Group Tear-Out Capacity

The adjusted tear-out capacity of a group of "n" rows of fasteners can be estimated as:

$$Z_{GT}' = \frac{Z_{RT-1}'}{2} + \frac{Z_{RT-n}'}{2} + F_t' A_{group-net} \qquad \text{(E.4-1)}$$

where:

Z_{GT}' = adjusted group tear-out capacity

Z_{RT-1}' = adjusted row tear-out capacity of row 1 of fasteners bounding the critical group area

Z_{RT-n}' = adjusted row tear-out capacity of row n of fasteners bounding the critical group area

$A_{group-net}$ = critical group net section area between row 1 and row n

(a)

Annex A (Informative): Block shear and plug shear failure at multiple dowel-type steel-to-timber connections

(1) For steel-to-timber connections comprising multiple dowel-type fasteners subjected to a force component parallel to grain near the end of the timber member, the characteristic load-carrying capacity of fracture along the perimeter of the fastener area, as shown in Figure A.1 (block shear failure) and Figure A.2 (plug shear failure), should be taken as:

$$F_{Bs,Rk} = \max \begin{cases} 1{,}5\, A_{net,t} f_{t,0,k} \\ 0{,}7\, A_{net,v} f_{v,k} \end{cases} \qquad \text{(A.1}$$

with

$$A_{net,t} = L_{net,t}\, t_1 \qquad \text{(A.2}$$

$$A_{net,v} = \begin{cases} L_{net,v}\, t_1 & \text{failure modes (c,f, j/l, k, m)} \\ \frac{L_{net,v}}{2}\left(L_{net,t} + 2t_{el}\right) & \text{all other failure modes} \end{cases} \qquad \text{(A.3}$$

(b)

Figure 4: (a) NDS Appendix E block shear (group tear-out) equations. (b) Eurocode 5 Annex A block shear equations.

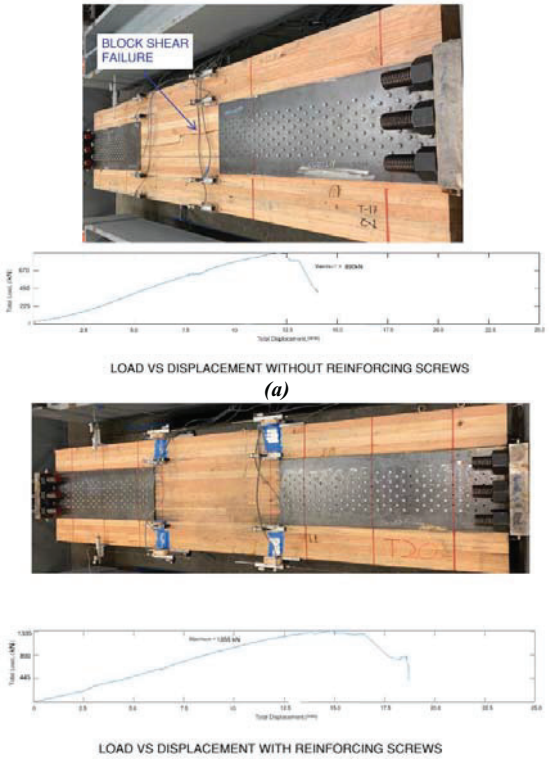

(a)

(b)

Figure 5: (a) tension specimen without reinforcing screws, showing load displacement curve (b) tension specimen with reinforcing screws, showing load displacement curve.

3 RESULTS AND DISCUSSION

3.1 Summary of Results

The axial tension specimen test results for the smaller side-plated wood screw connections (type C4 per figure 1) aligned quite closely with calculated connection capacities based on the manufacturer published values, with load-displacement data indicating that ductile screw flexure was the dominant failure mode in those connections. However, the initial axial tension specimen tests for the medium and large connections (types C2, C3, C5, and C6 per figure 1) demonstrated block shear failures in the glulam beams at load levels significantly below calculations based on manufacturer published fastener shear capacity. After review of preliminary results, groups of (2) 10 mm diameter perpendicular-to-grain reinforcing screws were added at 150 mm spacing along the length of the larger side plate connections (C5 and C6) through the glulam beam, with the spacing of the wood screws in the side plates re-spaced to provide a 50 mm gap at reinforcing screw pair location. These reinforcing screws extended a minimum of 75 mm past rows of connection wood screws, as shown in figure 5 below, to increase resistance to glulam splitting and block shear.

Subsequent tests of reinforced connection types C5 and C6 achieved significantly higher capacities more in-line with the capacities needed for the design and estimated by calculations. See figure 5 showing load vs deformation for the reinforced vs unreinforced connections. It was not feasible to add reinforcing screws for the specimens with the double plates slotted into the glulams (C2 and C3) due to inadequate width of the roughly 50 mm wide glulam sections each side of the plates.

Upon completion of physical load testing, the data was compiled and analysed, and the project team selected the double side plate connections with wood screws for use on the project due to their higher capacity, improved constructability, and lower cost. The test failure loads and calculated nominal design capacity for these connections is shown in figure 6. For design, the LRFD resistance factor of 0.65 was applied to these nominal capacities per NDS [5], and compared against factored loads from ASCE 7-16 [7]. The capacity for the wood portion of the wood connections was based upon the statistical analysis completed per ASTM D2915-17 [3], with the following equation: Avg Load – (Std. Dev. x K). The K factor is based on the one-sided tolerance limit for a normal distribution (with a 75% confidence level and a population content of 95%) which varies depending on the number of tests completed. This is the standard procedure

https://doi.org/10.52202/069179-0184

used for statistical analysis of wood connections in the US. Specimen failure loads and calculated nominal capacities for the connection types used in the project (types C4, C5 & C6) are illustrated in figure 6.

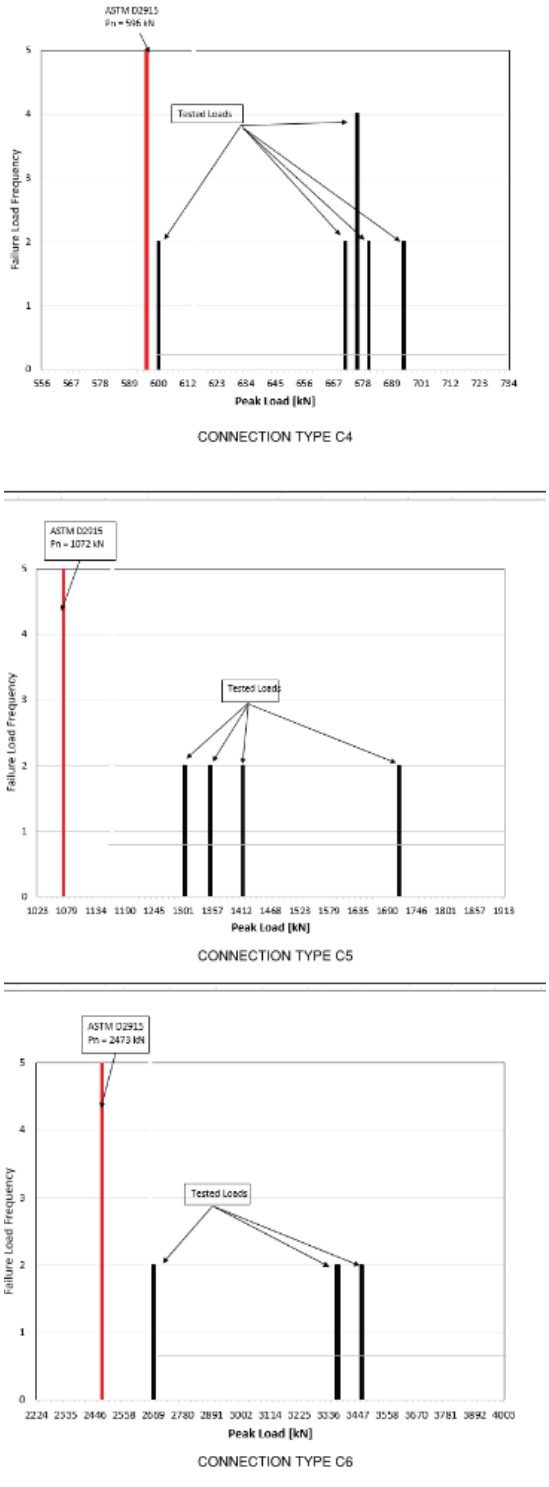

Figure 6: ASTM D2915-17 [3] test data and capacities

The failure loads indicated on figure 6 represent two data points since each tension specimen included two connections, one on each end. It should be noted that two vertical bars representing two specimens with very similar failure loads sometimes appear as a single, wider bar in figure 6. The majority of the tested failure loads are significantly larger than the nominal design capacity per ASTM D2915-17 [3]. However, for connection type C4 and C6, one outlier occurred with a failure load that was closer to the calculated nominal capacity.

The connection testing proved to be valuable in that it proved the connections could safely be used with a justifiable design capacity, with appropriate reinforcing. Additionally, for the actual project design conditions, where possible, the design was optimized such that bending of ductile steel plates in the connection assembly would be the controlling capacity, effectively limiting the load applied to the wood fasteners, to further ensure good behaviour in the event of an unforeseen overload.

3.2 Comparison of Test Data with NDS and Eurocode

For the smallest connection types, the failure mode appeared to be NDS [5] Mode IV fastener yielding, and the test results closely matched the calculated values utilizing the NDS equations (test values were approximately 10-20% higher than calculated values using NDS equations). The capacities utilizing the NDS equations were calibrated to the nominal LRFD capacity using a K_f of 3.32 and a λ of 1.0 (for short term, 10 min loading). None of the smallest connection types exhibited block shear or splitting failures, thus no reinforcing screws were added to the connections.

For the mid-size connection types utilizing the double plates slotted into the glulam with SDDs, the NDS greatly overpredicted the capacity of the connection, whereas Eurocode [6] only slightly overpredicted the capacity. The failure modes in these connection types were predominantly wood block-shear failures. If the Eurocode equation is used and only the shear portion is considered, the calculation closely predicts the tested values (less than 5% difference). However, if the tension portion of the equation is also considered, which in the mid-size connections results in a larger calculated capacity, the calculation moderately overpredicts the tested values (approximately 30%). The NDS equations overpredicted the capacity by approximately 80%. The initial mid-size connections utilizing the double side plates with wood screws similarly initially underperformed relative to calculated capacities, but after adding fully threaded reinforcing screws, the tested capacity more closely matched the calculated capacity.

For the largest connections utilizing the double plates slotted into the glulam with SDDs, the tested capacities were very closely predicted by both the NDS equations and the Eurocode equations. However, due to one outlier (that was significantly stronger than expected), the

https://doi.org/10.52202/069179-0184

capacity using the statistical analysis per ASTM D2915-17 [3] resulted in a capacity 30% lower than the equations predicted due to the increase in standard deviation. For the large connections using the double side plates and wood screws, with reinforcing screws, test capacities exceeded the capacity predicted by both the NDS and the Eurocode calculations. However, one outlier (which was significantly lower than the others), resulted in the capacity using the statistical analysis per ASTM D2915-17 being nearly equal to the code equation predictions.

See figure 7 below for a comparison of the calculated capacities and test values of specimen types.

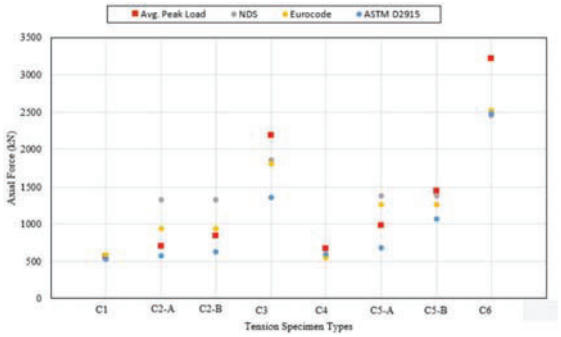

Figure 7: Comparison of calculated versus tested capacities. Connection type C2-A and C2-B indicate connection type C2 with different distances from the last row of fasteners to the end of the glulam. Connection type C5-A and C5-B are both connection type C5 (with C5-A having no reinforcing screws and C5-B with reinforcing screws)

3.3 Discussion

3.3.1. Effect of reinforcing screws

Reinforcing screws passing through the connection area perpendicular to grain significantly improved the performance of the mid-size and larger connections by resisting block shear/splitting across the glulam wood grain. In the cases of the mid-size side plate connection, the capacity of the connections improved by approximately 50% after adding the reinforcing screws.

3.3.2. Effect of moisture testing

See Section 2.2.2 for additional discussion on the specific moisture testing and cycling that was performed. The failure modes and capacities for moisture-cycled specimens were determined to not be statistically different from non-moisture-cycled specimens. As discussed in Section 1.1, the connection geometry was developed per the NDS [5] recommendation of 150 mm maximum dimension of outer rows of fasteners perpendicular to grain to prevent perpendicular to grain splitting due to shrinkage restraint. Tests of the moisture cycled specimens showed no indication of a reduction in capacity with the tested configurations, indicating the NDS recommendations appear to be appropriate for the MC variations considered.

4 CONCLUSIONS

4.1 Summary

Load testing of the initial design of the medium- and large-size connections exhibited brittle block shear/group tear-out failure modes which were not adequately predicted by calculations using the National Design Specification (NDS) for Wood Construction [5]. Calculations using Eurocode 5 [6] provided better predictions. This is a result of the NDS equations considering the sum of the resistance from both the shear and tension portions of a potential failure perimeter whereas the Eurocode equations only taking the larger of the shear or tension portion capacity.

The addition of reinforcing screws perpendicular to grain prevented block shear/group tear-out failure modes and allowed the medium- and large-size connections to realize the ultimate capacity and ductility of the dowel-type fasteners. That ultimate capacity of reinforced connections was reasonably well predicted by NDS equations.

Moisture cycling of connection specimens prior to load testing did not discernibly change the failure modes or capacities compared to connection specimens which were load tested without prior moisture cycling. This may support the conclusion that NDS recommendations for limiting the maximum distance perpendicular to grain between outer rows of fasteners in a given connection are sufficient for the moisture content variations considered in this research. Furthermore, moisture cycle testing on connection specimens provided specific criteria for moisture content management and control of the project connections throughout construction.

Successful physical testing of the glulam moment connections for the TCORE project made possible the long spans/cantilever conditions and resulting large axial tension/compression force couple demands. Although calculation-based approaches were available in the U.S. codes and standards, load testing was pursued by the project team to provide greater assurance and economy of the design. It also resulted in streamlined jurisdictional approval of these connections. As of the end of 2022, all connections had been installed in the over 400 glulam beams present in the roof, and the majority of the roof structure had been erected over the terminal.

4.2 Impact on Future Research and Codes

Based on the results of the connection load testing for this project, it is suggested that a thorough literature review be performed to specifically investigate block shear/group tear-out failure modes, particularly in large connection geometries. If the available literature is lacking or inconclusive, additional load testing may be necessary to determine the capacity of these failure modes. Ultimately, the available literature and any supplemental testing could inform changes to the block shear/group tear-out equations in the NDS [5] and Eurocode [6], especially if,

as identified in this research, the existing equations are not conservative. Finally, in this research, reinforcing screws installed perpendicular to grain were shown to prevent the development of block shear/group tear-out failure modes. However, little to no guidance exists in NDS or Eurocode for the appropriate design (e.g., diameter, length and spacing) of such reinforcing screws.

ACKNOWLEDGEMENT

The authors would like to thank the many individuals at ZGF Architecture (Architect of Record), Swinerton Mass Timber (mass timber subcontractor), and the Port of Portland (owner) who contributed to the glulam connection testing and the TCORE project in general. The authors would also like to thank the laboratory staff at the iSTAR Laboratory at Portland State University and at the environmental chamber at Oregon State University. Finally, the authors would like to acknowledge the significant, sometimes herculean, contributions of our colleagues at KPFF in making this research and project a success.

REFERENCES

[1] Zimmerman, R.B. and Pitt, C. (2022). Seismic Isolation of the Terminal Core Roof at the Portland International Airport. In *Proceedings of the 17th World Conference on Seismic Isolation, Energy Dissipation and Active Vibration Control of Structures*, Anti-Seismic Systems International Society (ASSISi), Turin, Italy, September 11-16, 2022.

[2] ASTM International. (2020). *Standard Test Methods for Mechanical Fasteners in Wood, ASTM D1761-12*. West Conshohocken, PA.

[3] ASTM International. (2022). *Standard Practice for Sampling and Data-Analysis for Structural Wood and Wood Based Products, ASTM D2915-17*. West Conshohocken, PA.

[4] ASTM International. (2018). *Standard Test Method for Evaluating Dowel-Bearing Strength of Wood and Wood Based Products, ASTM D5764-97a*. West Conshohocken, PA.

[5] American Wood Council. (2018). *National Design Specification for Wood Construction*. Leesburg, VA.

[6] European Committee for Standardization. (2008). *Eurocode 5: Design of Timber Structures – Part 1-1: General – Common Rules and Rules for Buildings*. Rue De Stassart, 36 B-1050 Brussels.

[7] American Society of Civil Engineers/Structural Engineers Institute. (2016). *Minimum Design Loads and Associated Criteria for Buildings and Other Structures*. Reston, VA.

https://doi.org/10.52202/069179-0184

World Conference on Timber Engineering Oslo 2023

THE IMPACTS OF SCREW TIP, INCLINATION ANGLES AND NUMBER OF PENETRATION LAYERS ON SCREW WITHDRAWAL CAPACITY IN AUSTRALIAN MACHINE GRADED PINE

Zidi Yan[1], Lisa-Mareike Ottenhaus[2], Jingyuan Lin[2], Robert Jockwer[3], Andreas Ringhofer[4]

ABSTRACT: Connections play an important role in timber structures as they govern the overall stiffness, load-carrying capacity, and most of the ductility in a timber structure. Due to the high axial load-carrying capacity and ease of installation, self-tapping screws are nowadays one of the most widely used fasteners in timber construction. However, variations in national standards, regulations, or even timber species might lead to incorrect predictions for the screw's load-carrying capacity. The current Australian Timber Standard AS 1720.1-2010 has some fundamental limitations since it was primarily derived from old North American research and supplemented in the 1970s with empirical data on Australian hardwoods and a few softwoods. Modern European fasteners are increasingly employed in the Australian building industry, making it critical to examine their performance consistency in the context of Australian timber products. This research work, therefore, aimed to a) evaluate the interactions of numbers of penetration layers, screw tip, and screw characteristic withdrawal strength, b) evaluate the influence of inclination angles on characteristic withdrawal strength, and c) compare experimental results with existing models and provide recommendations.

KEYWORDS: axially loaded self-tapping screws, withdrawal strength, sawn timber

1 INTRODUCTION

McLain stated that 'a structure is a constructed assembly of joints separated by members' [1] and this is especially accurate to describe timber structures. Connections govern the overall structural performance, such as stiffness, strength, and most of the ductility in a timber structure. Due to their high axial performance, flexible geometry, cost efficiency, and quick installation, self-tapping timber screws are nowadays one of the most popular fasteners in global timber construction.

In recent years, European connectors and fasteners are increasingly employed in the Australian market due to the rapid development of the Australian timber building industry and the lack of local suppliers and experiences. In such a case, a performance solution allows the engineer to use the manufacturer's technical approval. However, an inappropriate capacity estimation can cause overstrength and brittle failure of European fasteners in Australian timber species [2,3]. Since the Australian timber standard (AS 1720.1 [4]) was originally derived from North American research and supplemented by Australian empirical data in the 1970s, it is lacking consistent analytical equations to adapt to various modern screws. It is, therefore, of great importance to carefully assess the suitability and performance consistency of European screws in the context of the Australian market.

Withdrawal strength is one of the most critical parameters that govern the performance of axially and laterally loaded screws (i.e., the rope effect that was introduced in Eurocode 5). The geometry of the screw (e.g., diameter, thread, tip), the number of penetrated layers/studs, and screw thread-to-grain angle affect the withdrawal resistance of screws. These potential influences are rarely considered in most of the existing design codes in Australia.

1.1 SCREW PENETRATED LAYERS

Light timber framing is commonly constructed with double studs in Australia, and fasteners penetrate both timber members (i.e., without glue) in most cases. AS 1720.1 [4] does not specify a minimum/maximum penetration length in the second member for withdrawal, yet it stipulates l_{ef} >17d for laterally loaded connections. Hence, the conservativeness of AS 1720.1 needs to be re-evaluated regarding the minimum effective screw penetration length in one or two non-glued timber layers. Moreover, Ringhofer et al. [5–7] studied the influence of the number of penetration layers on screw withdrawal parameter in cross-laminated and glue-laminated timber. They suggested system factors, $k_{sys,}$ for up to 10-layer laminated timber products. As part of this study, the feasibility of applying k_{sys} to non-glued double-layered Australian sawn timber was evaluated.

1.2 SCREW THREAD-TO-GRAIN ANGLE

As inclined screws provide greater strength under lateral loading than orthogonal screws, they are now widely used in timber construction [8]. Pirnbacher et al. [9] adapted Hankinson's relation and developed a modified model to fit the screw thread-to-grain angles (α) between 0° and 72.5°. In contrast, Ringhofer et al. [6] propose a bilinear model to predict the relationship between screw thread-

[1] Zidi Yan, The University of Queensland, Australia, zidi.yan@uq.edu.au
[2] Lisa-Mareike Ottenhaus, The University of Queensland, Australia, l.ottenhaus@uq.edu.au
[2] Jingyuan Lin, The University of Queensland, Australia, jingyuan.lin@uq.net.au
[3] Robert Jockwer, Chalmers University of Technology, Sweden, robert.jockwer@chalmers.se
[4] Andreas Ringhofer, Graz University of Technology, Austria andreas.ringhofer@tugraz.at

https://doi.org/10.52202/069179-0185

to-grain angle and withdrawal performance. According to their research, the withdrawal performance of the screw did not change for $\alpha > 30°$ [6,10]. This study compared the inclined screw withdrawal performance in Australian sawn timber with previous studies.

1.3 SCREW EFFECTIVE LENGTH

Eurocode 5 [11] states that the effective penetration length of the screw (l_{ef}) is limited to the threaded part. However, it is unclear whether the tip should be considered since modern screws commonly have fully threaded tips. The Canadian standard CSA O86 [12] requires l_{ef} to be the threaded length minus the tip length (typically equal to one nominal thread diameter, d). In contrast, AS 1720.1 [4] does not consider the potential influence of the tip and states that l_{ef} is equal to the entire length of a fastener's penetration, which includes the unthreaded shank and tip. Nevertheless, European scientists conventionally agreed that the screw tip should be deducted from the profiled length [13], and a length correction factor should be applied. From this, several questions arise: (1) Defining the length of the tip - should it be the exact length of the tip or include a certain length of regular thread? (2) While some European literature and experimental tests concluded that the tip length should be equal to $1.11d$ [13] or $1.17d$ [9], it is still uncertain whether this applies to Australian timber species due to their relatively higher density compared to European species.

Consequently, this work examined the interactions of numbers of penetration layers, screw thread-to-grain angle, screw tip, and screw characteristic withdrawal strength; evaluated the influence of inclination angles on characteristic withdrawal strength; compared and verified existing models and provided recommendations.

2 MATERIAL AND METHODS

2.1 SPECIMEN CONFIGURATION

This study was separated into three phases: (1) examine the effects of the penetrated layers (single or double stud); (2) assess the effects of different screw-to-grain angles, and (3) evaluate the contribution of screw tip during withdrawal.

2.1.1 TIMBER SAMPLES

Machine grade pine (MGP) specimens with orthogonal or inclined screws were tested according to the Australian Standard AS 1649 [14]. Clear 170 mm long specimens were cut from 3 m long 45×90 mm MGP10 boards. Timber densities were measured according to the weight and dimensions of each specimen. Timber densities were assumed as normal distributed, and the characteristic timber densities, ρ_k were calculated based on EN 14358:2016 [15]. Knotty specimens were removed to obtain more consistent results [5–7]. It is worth mentioning that AS1720.1 gives a mean density $\rho_m = 500$ kg/m^3 for MGP10, however, the timber density is not directly related to connection strength prediction which is based on joint groups that depend on species. Thus, a regression prediction model established by Pirnbacher et al [5] was also compared and verified in this study for the mean value of the screw withdrawal strength.

2.1.2 SCREW SAMPLES

A total of 330 8×120 mm Schmid Rapid screws (ETA-12/0373 [10]) were tested in single stud, double stud, and different inclination angles. All screws were manually installed in the timber specimens using a cordless handheld drill. To ensure the accuracy of inclination angles, a screw installation guide was used. The edge and end spacing of each test were checked according to the requirements of the ETA-12/0373 [10], Australian Standard AS 1649 [14] and EN 1382 [16].

In this study, the effects of the screw penetrated layers (Phase 1) were tested by inserting screws in both single and double layers of 45×90 mm MGP10 boards. The effects of the screw tip and penetrated layers (Phase 2) were examined by installing screw with the tip inside and outside timber specimens, respectively (Table 1). Axial withdrawal tests for inclined screws were carried out, and three load-to-grain angles were tested (Phase 3). In specimen designations, the first letter relates to layers (S = single, D = double) and the second letter relates to the tip position (W = within, O = outside). L is the nominal thread length that penetrated the timber specimen, and n is the replication of each test. The number (i.e., 90, 75, 60, 45 and 30°) attached to the letters indicates the inclination angle of the screws. A schematic diagram of all test series is shown in Figure 1.

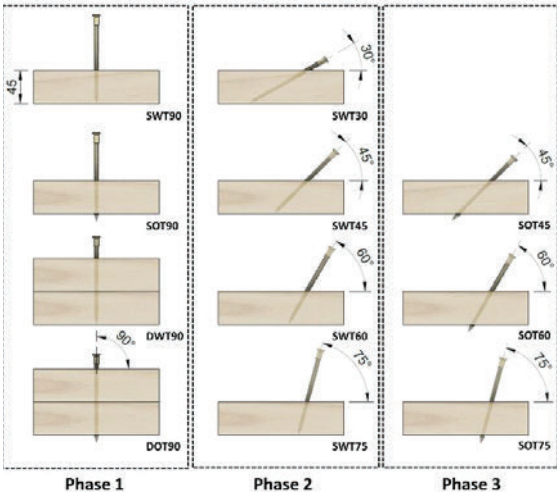

Figure 1. *Illustration of the configurations of all test series*

https://doi.org/10.52202/069179-0185

Table 1: *Test specimen specifications for test assemblies, and number of repetitions.*

Test series	Test name	α [°]	L [mm]	n [-]
Phase 1	SWT90	90	45	30
	SOT90	90	45	30
	DWT90	90	90	30
	DOT90	90	90	30
Phase 2	SWT75	75	47	30
	SWT60	60	52	30
	SWT45	45	64	30
	SWT30	30	90	30
Phase 3	SOT75	75	47	30
	SOT60	60	52	30
	SOT45	45	64	30

2.2 WITHDRAWAL TESTS

Withdrawal tests were carried out according to AS 1649 (with the addition of inclined screw tests) using an Instron universal testing machine with a test rig that was specially made for inclined screw withdrawal (Figure 2). The screws were withdrawn at a constant rate of 2.5 mm/min. The moisture content was determined according to AS 1080.1 [17] (oven drying at 103°C) immediately after withdrawal testing as 12.9±1.1%.

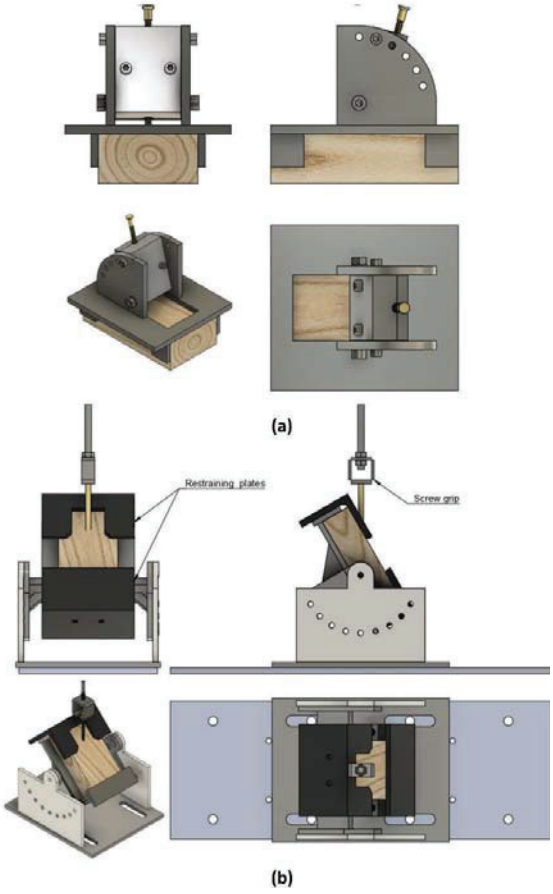

Figure 2*: (a) Screw installation guide and (b) withdrawal test setup.*

2.3 STATISTICAL DATA ANALYSIS

The statistical analysis of the test data was performed using SPSS. The Shapiro-Wilk test, Levene's test, ANOVA, student's T-test, and post-hoc test were used as statistical analysis methods in this study.

3 THEORY

The experimentally determined screw withdrawal parameter $f_{ax,exp}$ was modified from EN1382:2016 [16] as

$$f_{ax,exp} = \frac{F_{ax,exp}}{l_{ef} \cdot d} \quad (1)$$

where $F_{ax,exp}$ is the maximum force recorded from the individual screw withdrawal tests, and l_{ef} is the effective penetration length of the screw, where the penetration length is reduced by the tip length, l_{tp}. In ETA-12/0373 [10] l_{tp} is 11.0 mm for 8×120 mm Schmid Rapid screws. The experimentally determined screw withdrawal parameters were assumed as lognormal distributed, and the characteristic withdrawal parameter, $f_{ax,k,exp}$ was calculated according to EN 14358:2016 [15].

The screw's characteristic withdrawal parameter, $f_{ax,k,ETA}$ given in Schmid's ETA-12/0373 [10] is 13.1 N/mm^2. An equation that considers timber density, species, material, and screw installation angle is proposed by ETA-12/0373 [10] and calculated as

$$f_{ax,k,pre} = \cdot f_{ax,k,ETA} \cdot k_{ax} \cdot k_{sys} \cdot \left(\frac{\rho_k}{\rho_{k,ref}}\right)^{k_\rho} \quad (2)$$

where k_{ax} is the angle factor (k_{ax} = 1 for 30°≤ α ≤ 90°), k_{sys} is the system factor (k_{sys} = 1 for solid timber, however, k_{sys} =1.06 was additionally considered and assumed for DWT and DOT series for this research only), k_ρ is the density factor (k_ρ = 1.1 for softwood and 15°≤ α ≤ 90°), and $\rho_{k,ref}$ is the reference characteristic density ($\rho_{k,ref}$ = 350 kg/m^3). It is important to note that all factors were determined based on the previous study by Ringhofer et al. [5–7].

Apart from the characteristic value, a regression model established by Pirnbacher et al. [9] for predicting mean orthogonal screw withdrawal parameter, $f_{ax,mean,pre}$ is adapted as:

$$f_{ax,mean,pre} = (0.01353 \cdot \rho_m - 0.68679 \cdot d^{0.572} + 2.18888) \cdot \pi \quad (3)$$

Eq (3) was first derived by Pirnbacher et al. [9] after conducting a series of screw withdrawal tests for d = 6 to 12 mm and timber density ρ = 300 to 600 kg/m^3. This Equation was then further verified by Ringhofer et al [5] using screw diameters ranging from 6 to 12 mm and timber density ranging from 375 to 475 kg/m^3. The premise of this equation considered the effective length of screw penetration equals to $l_{ef} = L - 1.17d$.

4 RESULTS AND DISCUSSION

Test results are summarised and compared graphically in notched boxplots and in the following tables. All outliers presented in boxplots were removed from the statistical analysis and were considered as extreme values. Table 2 lists the mean density, ρ_m, coefficient of variation (COV), characteristic density, ρ_k and the number of timber

samples for each test series, n. SWT90 and SOT90 were carried out as the control group since $f_{ax,k,exp}$ were in good agreement with the prediction value $f_{ax,k,ETA}$. All screws failed in screw axial withdrawal and no other failure modes were observed during the tests. It is worth mentioning that after conducting the ANOVA and post-hoc tests, the mean densities of all tested samples presented statistically non-significant differences to each other. Thus, in most instances, the mean withdrawal parameter, $f_{ax,m}$ can be directly compared after applying the student t-test to access the influence parameters.

Table 2: *Sample densities and number of samples*

Test series	Test name	ρ_m [kg/m^3]	COV [%]	ρ_k [kg/m^3]	n [-]
Phase 1	SWT90	405.1	6.3	357.0	30
	SOT90	423.7	5.3	381.9	30
	DWT90	401.2	4.7	365.8	60
	DOT90	401.3	4.0	371.1	60
Phase 2	SWT75	428.4	8.6	359.4	30
	SWT60	448.9	7.7	384.0	30
	SWT45	446.0	4.8	405.7	30
	SWT30	442.2	7.8	377.7	30
Phase 3	SOT75	424.9	7.9	362.0	30
	SOT60	420.6	9.2	348.7	30
	SOT45	425.7	8.0	361.7	30

4.1 Phase 1 – Screw penetrated layers

The effective penetration length, l_{ef} for Phase 1, was considered as L - l_{tp}. In Figure 3, $f_{ax,mean,pre}$ values were calculated according to ρ_m from Table 2. Considering the sample size, the experimental results agreed well with the predictions by Eq (2) and (3) and were only slightly non-conservative for SOT and DOT series.

After conducting the statistical analysis, the mean withdrawal parameter between SWT90 and DWT90 groups showed a non-significant difference, thus, this finding indicates that the multiple penetration layers did not influence screw withdrawal strength when the full length of the screw tip was deducted. In the DOT series, L in the second timber layer is 4.4d, indicating that a penetration length of 4.4d can still provide conservative withdrawal strength. The notched boxplot in Figure 3 shows that the difference between the SOT90 and DOT90 median values is about 1. The notch areas for SOT90 and DOT90 do not overlap, and a p-value < 0.05 indicates that the median and mean values differ significantly. The screw withdrawal parameter was thereby reduced by multiple studs when the screw tip stuck out of the timber specimen, and no glue was applied to the middle of the double boards. This finding was contrary to previous results by Ringhofer et al. [5]. In Table 3, the experimental results for SWT and DWT series are slightly higher than the prediction value. It is suggested to quantify the contribution of the screw tip in future studies. As of this section, it is concluded that the screw tip has a slightly positive effect on the withdrawal parameter, and therefore the accuracy of the deduction length should be re-verified.

Table 3: *Result comparisons - Single/double penetration layer with tip inside/outside of the timber specimen*

		With tip		Without tip	
		SWT90	DWT90	SOT90	DOT90
$f_{ax,m}$	[N/mm^2]	18.1	17.3	17.2	16.3
COV	[%]	15.5	7.7	9.3	6.5
P^1	[-]	0.31		0.00	
$f_{ax,mean,pre}$	[N/mm^2]	17.0	16.8	17.8	16.8
$f_{ax,m,exp}/f_{ax,m,pre}$	[-]	1.06	1.03	0.97	0.97
$f_{ax,k,exp}$	[N/mm^2]	13.7	15.0	14.4	14.5
$f_{ax,k,pre}$	[N/mm^2]	13.4	14.6	14.4	14.8
$f_{ax,k,exp}/f_{ax,k,pre}$	[-]	1.02	1.03	1.00	0.98
		Single layer		**Double layer**	
		SOT90	SWT90	DOT90	DWT90
P^1	[-]	0.32		0.00	

[1] ***P-value for ln(f_{ax})***

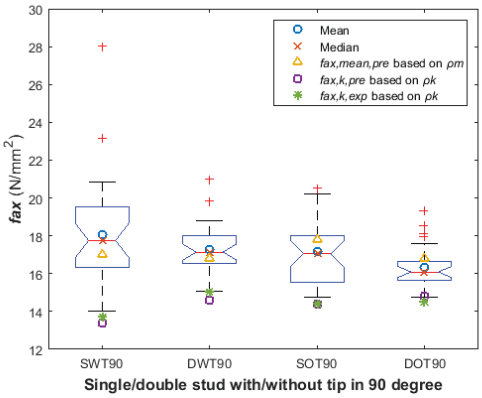

Figure 3: *Single/double penetration layer with tip inside/outside of the timber specimen*

4.2 Phase 2 – Screw inclination angles

SWT and SOT inclined screw withdrawal tests are summarised and compared in Table 4, Figure 4, Table 5, and Figure 5. As previously mentioned in Section 4.1, the effective penetration length for Phase 2 was also calculated as $l_{ef} = L - l_{tp}$.

The results for both SWT and SOT were generally consistent with the previous literature by Ringhofer et al. [6], in which the f_{ax} exhibited a bilinear behaviour (i.e., screw withdrawal strength is constant for $\alpha > 30°$ then a gradual decrease can be observed). Based on statistical analysis, no significant f_{ax} deviations were detected for α = 45, 60 and 75°.

In the SWT series, the screw withdrawal strength gradually increased with decreasing inclination angle (α from 90° to 45°). The boxplots in Figure 4 also suggest that the median values did not show statistical differences for $\alpha > 30°$. However, for $\alpha = 30°$, the ETA prediction equation overpredicted the withdrawal strength, and a dramatic decrease was observed. The strength reduction

https://doi.org/10.52202/069179-0185

for $\alpha = 30°$ might be explained by the orientation of the screw axis approaching the fibre grain direction.
Due to the limitation of the test rig, SOT30 was not conducted. Thus, only 90° to 45° screw withdrawal tests were achieved and evaluated. Future research should confirm whether the strength reduction observed for SWT30 applies to SOT30. In general, Eq. (2) works conservatively in the SOT series and the screw withdrawal strength increased when α decreased to 75°. Since the notched area for SOT90 and SOT75 were not overlapped, the result indicates that the medians differ significantly.

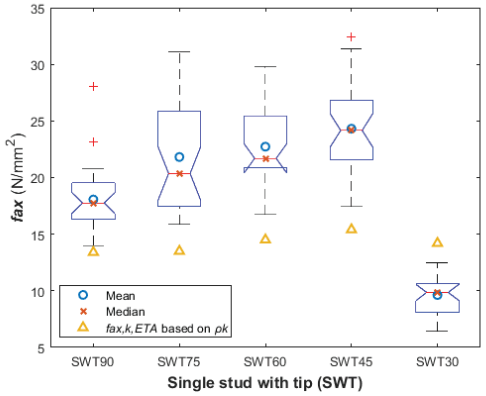

Figure 4: *Different inclination angles in single stud (with tip)*

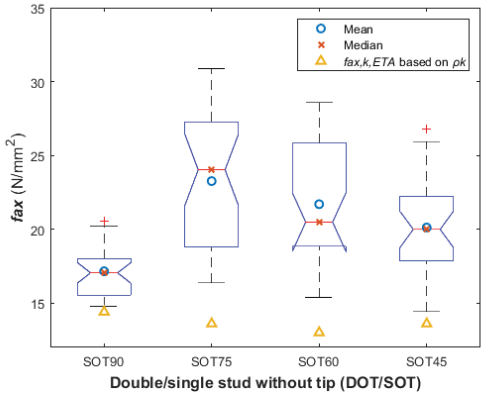

Figure 5: *Different inclination angles in single/double stud (tip outside of the timber specimen)*

Table 4: Result comparisons - Single penetration layer with tip inside of the timber specimen and different inclination angles

		SWT				
		90	75	60	45	30
$f_{ax,m}$	[N/mm²]	18.1	21.8	22.7	24.3	9.6
COV	[%]	15.5	22.4	14.2	15.8	18.1
$f_{ax,k,exp}$	[N/mm²]	13.7	14.2	17.3	17.8	6.7
$f_{ax,k,pre}$	[N/mm²]	13.4	13.5	14.5	15.4	14.2
$f_{ax,k,exp}/f_{ax,k,pre}$	[-]	1.02	1.05	1.19	1.16	0.47

Table 5: *Result comparisons - Single penetration layer with tip outside of the timber specimen and different inclination angles*

		SOT			
		90	75	60	45
$f_{ax,m}$	[N/mm²]	17.2	23.3	21.7	20.1
COV	[%]	9.3	20.2	18.4	15.8
$f_{ax,k,exp}$	[N/mm²]	14.4	15.4	15.2	14.7
$f_{ax,k,pre}$	[N/mm²]	14.4	13.6	13.0	13.6
$f_{ax,k,exp}/f_{ax,k,pre}$	[-]	1.00	1.13	1.17	1.08

4.3 Phase 3 – Screw tip lengths

Figure 6 illustrates the ratio between $f_{ax,k,exp}$ and $f_{ax,k,ETA,}$ and confirms the conservativeness of selected calculation methods for l_{ef} (i.e., (a) $l_{ef} = L$, (b) $l_{ef} = L - 1.11d$, (c) $l_{ef} = L - 1.17d$ and (d) $l_{ef} = L - l_{tp}$). Table 6 lists the results from the student t-tests. Since no differences were observed for timber mean densities after statistical analysis, $f_{ax,m}$ was chosen to be compared directly. The SOT series was considered as the control group in this test campaign. From Table 6, student t-test p-values indicate that the tip length, l_{tp} should not be considered in the full threaded length, except when $\alpha = 45°$ and $L = 8d$. This finding was consistent with the results of a previous study by Pirnbacher et al. [5] in which the tip effect decreased with increasing penetration length.
As stated in Eurocode 5 [11] and ETA-12/0373 [10], l_{ef} must include l_{tp}. As shown in Figure 6, however, the results indicate that $f_{ax,k,pre}$ was overestimated for $l_{ef} = L$. This suggests that the screw tip should not be treated as a fully threaded element, and a length correction parameter should be considered.
Following the statistical analysis, p-values in Table 6 indicate the tip length should be fully subtracted from the penetration length, i.e., $l_{ef} = L - l_{tp}$ when $\alpha \geq 75°$ with $l_{tp} = 1.38d$. However, when $45° > \alpha > 75°$, $l_{tp} = 1.11d$ seems more appropriate for Australian timber species.
Generally, $l_{tp} = 1.17d$ [9] versus $l_{tp} = 1.38d$ only resulted in minor differences in withdrawal strength (i.e., the purple-square, green-cross, and blue-circle lines are positioned closely together) with little feasibility at different inclination angles.

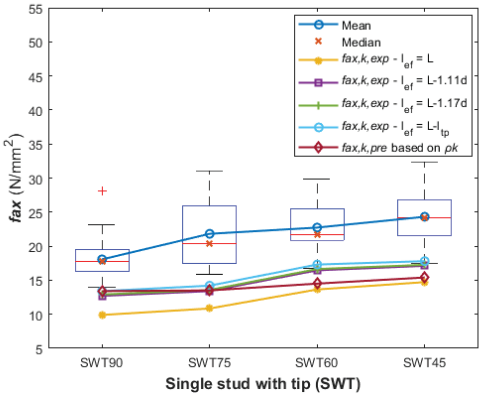

Figure 6: *Comparison of using different lef to calculate withdrawal strength over different inclination angles.*

Table 6: *Sample densities and number of samples.*

Comparison group		***T-test *p-values***			
		$l_{ef} = L$	$l_{ef} = L - 1.11d$	$l_{ef} = L - 1.17d$	$l_{ef} = L - l_{tp}$
SWT90	SOT90	0.00	0.09	0.26	0.31
SWT75	SOT75	0.00	0.03	0.04	0.23
SWT60	SOT60	0.00	0.95	0.74	0.21
SWT45	SOT45	0.60	0.00	0.00	0.00

***p-value for $\ln(f_{ax})$**

5 CONCLUSION

This paper presented an experimental study on the effects of screw tip, inclination angles, and the number of penetration layers on screw withdrawal capacity of Australian machine graded pine. A total number of 330 Schmid screws according to ETA-12/0373 [10] were tested in double or single layers of Australian MGP10 board with inclination angles of 90, 75, 60, 45 and 30 degrees.

Overall, the key findings are:

- When the screw is installed perpendicular to the grain, prediction models based on previous literature and manufacturers' ETA are appropriate for Australian MGP10 and generally give conservative results. However, the tip length should not be fully considered in the screw effective penetration length, l_{ef}, and the ETA model should be re-evaluated when the thread-to-grain angle, α, is equal to 30°.
- Consistent with previous research, the thread-to-grain angle is negatively correlated with axial withdrawal strength in the range between $90° \geq \alpha > 30°$.
- The inclination angle factor k_{ax} in ETA-12/0373 [10] should be re-evaluated for $\alpha = 30°$ in Australian timber species. A deduction factor/equation should be further studied and applied to k_{ax}. To optimise k_{ax}, a regression model is recommended to consider all configurations.
- The tip length, l_{tp} (1.11d) suggested by Pirnbacher et al. [9] is generally conservative and acceptable except when $\alpha > 75°$. In contrast, l_{tp} (1.38d) is generally more versatile as it can be easily adapted for all inclination angles. However, to further evaluate this finding, more experimental tests should be conducted.
- Further research is suggested to develop a more versatile length correction factor. The length correction factor (length of screw tip, l_{tp}) should be optimised and verified using a regression model.
- Using screws in double timber layers (without adhesive) reduced the screw withdrawal parameter, likely due to insufficient local stiffness on layered timber. If no adhesive is applied between layered timber, the k_{sys} factor could likely be conservatively ignored for sawn timber. More experimental tests are suggested to determine the reduction factor.
- Further regression model analysis should be established to obtain an optimized analytical equation for the interactions of the screw tip, numbers of penetration layers, and screw characteristic withdrawal strength in Australian timber species.

In conclusion, the results of this study provide some insights into the withdrawal capacity of modern European screws in Australian machine graded pine. The study highlights the need for further research in this field, particularly in relation to the development of more accurate predictive models for Australian timber products.

ACKNOWLEDGEMENT

This research was jointly funded by the Faculty of Engineering, Architecture, and Information Technology and the School of Civil Engineering of the University of Queensland. Schmid Schrauben Hainfeld GmbH is gratefully acknowledged for providing the screws.

REFERENCES

[1] McLain T. Connectors and fasteners: research needs and goals. Wood Eng 21st Century Res Needs Goals 1998:56–69 n.d.

[2] Ottenhaus L-M, Li M, Smith T, Quenneville P. Mode Cross-Over and Ductility of Dowelled LVL and CLT Connections under Monotonic and Cyclic Loading. J Struct Eng 2018;144:04018074-1–10. https://doi.org/10.1061/(asce)st.1943-541x.0002074.

[3] Yan Z, Ottenhaus L-M, Leardini P, Jockwer R. Performance of reversible timber connections in Australian light timber framed panelised construction. J Build Eng 2022;61:105244. https://doi.org/10.1016/J.JOBE.2022.105244.

[4] Standards Australia. Australian Standard 1720.1-2010 Timber structures Part 1: Design methods. vol. 2010. Sydney, NSW 2001, Australia: SAI Global & Standards Australia; 2010.

[5] Ringhofer A, Brandner R, Schickhofer G. Withdrawal resistance of self-tapping screws in unidirectional and orthogonal layered timber products. Mater Struct Constr 2015;48:1435–47. https://doi.org/10.1617/s11527-013-0244-9.

[6] Ringhofer A, Brandner R, Schickhofer G. A universal approach for withdrawal properties of self-tapping screws in solid timber and laminated timber products. 2nd Work. "COST Action FP1402 - State-of-the-Art", Pamplona, Spain., Pamplona, Spain: 2015.

[7] Ringhofer A, Brandner R, Blaß HJ. Cross laminated timber (CLT): Design approaches for dowel-type fasteners and connections. Eng Struct 2018;171:849–61. https://doi.org/10.1016/j.engstruct.2018.05.032.

[8] Brown JR, Li M, Tannert T, Moroder D. Experimental study on orthogonal joints in cross-laminated timber with self-tapping screws installed with mixed angles. Eng Struct 2021;228:111560.

https://doi.org/10.52202/069179-0185

https://doi.org/10.1016/j.engstruct.2020.111560.
[9] Pirnbacher, G., Brandner, R. and Schickhofer G. Base parameters of self-tapping screws, in 'Proceedings of the 42nd CIB W18 Meeting', Dübendorf (Switzerland). paper CIB-W18/42-7-1 2009.
[10] ETA-12/0373 - Screws for use in timber constructions n.d.
[11] CEN (European Committee for Standardisation). Eurocode 5 - Design of timber structures. Brussels, Belgium: CEN: CEN; 2014.
[12] Canadian Standards Association (CSA). Engineeringdesign in wood, CSA O86-14, Update # 1. Toronto, ON,Canada: 2014.
[13] Hübner U. Withdrawal strength of self-tapping screws in hardwoods, in 'Proceedings of the 46th CIB W18 Meeting', Vancouver (Canada). paper CIB-W18/46-7-4 2013.
[14] Standards Australia. Australian Standard AS 1649:2001 - Timber - Methods of test for mechanical fasteners and connectors - Basic working loads and characteristic strengths 2001.
[15] British Standards Institution. BS EN 14358:2016 Timber structures — Calculation and verification of characteristic values. 2016.
[16] BS EN 1382 : 2016 BSI Standards Publication Timber Structures — Test methods — Withdrawal capacity of timber fasteners 2016.
[17] Standards Australia. Australian Standard 1080.1:2012 — Methods of test Method 1 : Moisture content 2012:1–21.

World Conference on Timber Engineering Oslo 2023

DESIGNING AND TESTING OF A WOOD-ONLY TIMBER FRAME CONNECTION INSPIRED BY THE GROWTH FORMATION OF TREES' STEM-BRANCH JUNCTION

Firas Hawasly[1], Naoyuki Matsumoto[2], Mikio Koshihara[3], and Koji Adachi[4]

ABSTRACT: This paper presents the design approach and testing of a new column-beam connection utilising wood as the sole structural material for application in multi-storey timber frames. This connection was inspired by the all-wood natural formation of trees' stem branch junction model. The growth model features were explored and approached in a simplified application of glued-laminated column-beam members joined through a conical mortise-tenon interface with bent laminated veneer plies flowing seamlessly across the connection. The tested connection was compared to steel-added conventional joint systems resulting in a comparable bending performance with desirable ductile behaviour and presenting the inclusion of seamless bent timber members as a possible reinforcement against bending for timber connections.

KEYWORDS: Bio-inspired, Tree growth, Seamless fibres flow, Bentwood reinforcement

1 INTRODUCTION

The current application of steel and concrete in rigid frame structures is an appealing canvas for architectural applications, providing flexibility, uniformity, and safety; it is an evolved form of the long and rich history of timber framing, overcoming the span limitations and the inherent material combustibility.

The reappreciated potentiality of wood as a construction material following the shortages of iron through the world wars, combined with the awareness of the environmental impact of the construction field, facilitated an expedited shift in timber engineering research [1, 2] to maximise the utilisation of timber products in structural applications. However, and to a certain extent, it was applied by simply substituting the less sustainably sourced and widely utilised concrete and steel members with timber, using the same structural vocabulary, theory, and detailing, and expecting structural behaviour similar to that of the designed and manufactured materials.

In contrast, trees grow wood through 'Morphogenesis' [3], a form generation, adaptive growth process where the material properties are manipulated whilst waste and energy are optimised to ensure maximum functionality and efficiency and create a fully localised functional and structural system. Nevertheless, the adaptive growth processes of a tree, being complicated and ingenious natural systems (e.g., deviation of grain patterns, shedding of branches, encasing of knots), are, however, considered defects when the wood is used as a structural material. The techniques used in modern timber engineering depend on segregating these tree-specific, homogeneous structural tissues. Contrary to the early building traditions, wood was fitted to the desired location based on its form in the tree and guaranteed structural performance, e.g., shipbuilding.

The limitations imposed by the structural capabilities of the segregated, reused, linear, natural material and the limitation in the sourcing processes introduced a myriad of engineered timber products with enhanced structural properties; and have constantly been challenged by the feasibility of achieving an efficient joining system. As a result, a broad spectrum of innovative connections for timber was developed utilising processes and materials foreign to the organic wood. They fulfilled the sought structural requirements while gradually shifting the naturally grown material into a normalised product to suit our growing understanding of timber structures away from the systems and analytical tools initially developed for the designed concrete and steel materials.

While sharing a similar morphology to a timber frame connection, the trees' stem-branch junctions are inherently moment resistant; these cantilevered protrusions resist moments generated at their junctions by self-weight and wind loads [4]. This growth formation is nature's manifestation of wood as a constructional material, an intricately generated form that contributes to the tailored structural behaviour in resisting bending, shear, and fatigue induced by static and dynamic loads. Hence, investigating and mimicking its distinct and specific growth processes is sought to introduce a further befitting constructional language of timber at frame connections.

[1] Firas Hawasly, Institute of Wood Technology, Akita Prefectural University, hawasly_firas@iwt.akita-pu.ac.jp
[2] Naoyuki Matsumoto, Department of Architecture and Building Science, Graduate School of Engineering, Tohoku University, nmatsu@rcl.archi.tohoku.ac.jp
[3] Mikio Koshihara, Institute of Industrial Science, The University of Tokyo, kos@iis.u-tokyo.ac.jp
[4] Koji Adachi, Institute of Wood Technology, Akita Prefectural University, kadachi@iwt.akita-pu.ac.jp

https://doi.org/10.52202/069179-0186

In this paper, biomimetic investigations of load paths and fibre assemblies of stem-branch junctions in trees inspired an approach towards a wood-only utilisation of a structural entity capable of transferring bending loads safely within a timber frame joint.

2 GROWTH FORMATIONS AT TREE BRANCH JUNCTIONS

The secondary growth of trees occurs at the vascular cambium, a thin, active layer of cells that forms a continuous sheath beneath the plant's surface. It increases the thickness of the plant seasonally in concentric layers by division outwards and inwards, creating phloem and xylem tissues, respectively. Xylem tissues, which make the whole woody material from longitudinal tube-like fibrous cells, are responsible for the tree's stability and the transfer of sap in one direction between the roots and leaves; given the energy and waste optimisation, there is no functional requirement, nor structural, for the fibres to flow from the branch up the stem or to other branches.
A single growth layer in a branch can be modelled as a unidirectional, fibrous, double-bent surface; hence, the growth model of a tree is interpreted as a stack of concentric, fibrous, unidirectional, double-bent surfaces. (Figure 1-1). Geometrically, the interface between the surfaces of the stem and the branch is conical and, depending on the branch's growth vigour, is partially or fully encased within the flow of the stem's fibres [5].
At the ridge point, the branch's fibres exhibit a sharp turn with small radii whilst maintaining their conductive functionality and gradually easing towards the junction's lower section in alignment with the stem. Similarly, the upper stem's fibres flow around the branch collar and exhibit similar radii above the branch ridge. Trees utilise the unidirectional flow of the branching fibres to create tissues with interlocking geometric assemblies at the top portion of the branch's collar to prevent failure and damage. These tissues are stiffer and mechanically superior to normal wood, albeit with constricted conductive functionality as a "structural trade-off" to support this critical location.[5, 6]. Furthermore, the naturally optimised form of the stem combined with the residual tensile stresses of its natural growth (preloading) significantly improve the tree's strength [7] and, consequently, the transfer of loads across the junction. [8]
In this paper, the explored growth model features of a branch junction are:

- the uninterrupted, seamless flow of fibres across the junction,
- the complicated compressed fibre formations within the conical interface of the junction, and
- the variable mechanical properties of localised wood cell types across the junction.

2.1 Hypothetical growth model

As the flow of forces in biological materials is governed by the direction of the fibres [9], trees transfer gravity and wind loads along the fibres from the leaves to the roots; additionally, the tree acquires an adequate resistance of uplift loads through the geometric fibres' assembly across the junction.
However, the frame structural connections demand substantial horizontal resistance. Hence, a hypothetical growth model was developed, assuming trees were designed to resist uplift and gravity loads equally by alternating the fibres' flow direction every other growing season, resulting in an equal cross-sectional area of the stem below and above the branching point. (Figure 1-2) (Contrary to Leonardo da Vinci's rule stating that the sum of the cross-sectional area of fibres above the branching point is equal to that below it)However, although this loading pattern contradicts the wood's natural growth and function, it is expected to provide the sought performance in resisting loads in both directions.

2.2 Simplification process

The current limitations in wood sourcing and machining technologies hinder the ability to produce a double-bent unidirectional surface similar to the interpreted model of a growth layer from wooden veneer material, especially with the localisation of different cell types (reaction, opposite and normal wood). Therefore, to utilise simple

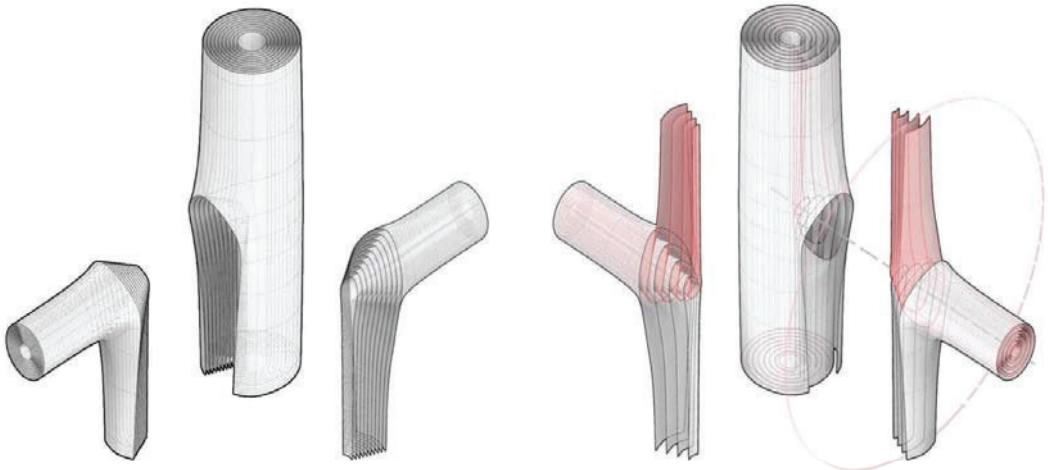

Figure 1: *Interpreted and hypothetical growth models of Stem-branch junction; (left) a detached branch showing the conical interface of the successive growth layers; (right) a detached view of the hypothesized branch through flipping every other growth*

https://doi.org/10.52202/069179-0186

techniques and available wood products, the proposed approach oversimplified the hypothetical growth model into two applicable connection patterns:
- Bent fibre continuity as a stack of one-way bent veneers in a T-formation, where the fibres are seamlessly flowing from the stem to one half of the branch (Figure 1-2), and
- Concentric fibre connectivity as a stack of concentric tubular veneers, where the fibres of corresponding tubes are butt-jointed, resulting in a stepped conical mortise-tenon integration (Figure 1-3).

3 MATERIALS AND METHODS

The approached connection combines both simplified interpretations of the hypothetical model, utilising the conical interface of a glued, stepped mortise-tenon beam integration within the column (Figure 1-6), with a set of symmetrical bent plies flowing seamlessly from the beam across the interface and into both directions of the column (Figure 1-5).
For this application, the dimensions were based on a selected prototype of a generic medium-sized office building with a simple and flexible structural system developed by 'KI' "www.ki-ki.info" (a Japanese timber structural study group and database) to promote and provide technical information for one-way timber frame structures using standardised glued-laminated timber sections for columns and beams at 600x210mm E65-F225 JAS (Japanese Agricultural Standards) in Japanese Cedar (*Cryptomeria japonica)*. In addition, two steel-added

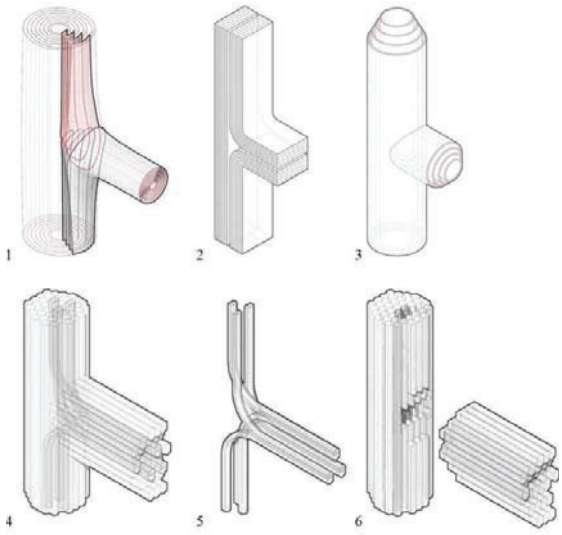

Figure 2: *Simplification and proposed connection typology; 1. hypothetical branch model; 2. bent fibre continuity; 3. concentric fibre connectivity; 4. connection morphology; 5. seamless bent plies; and 6. conical interface*

conventional joint systems were experimentally and numerically tested for this prototype in Japanese Cedar at half width (600x105mm), namely the glued-in rod (GIR) [10] and the lag-screw bolts (LSB) [11].

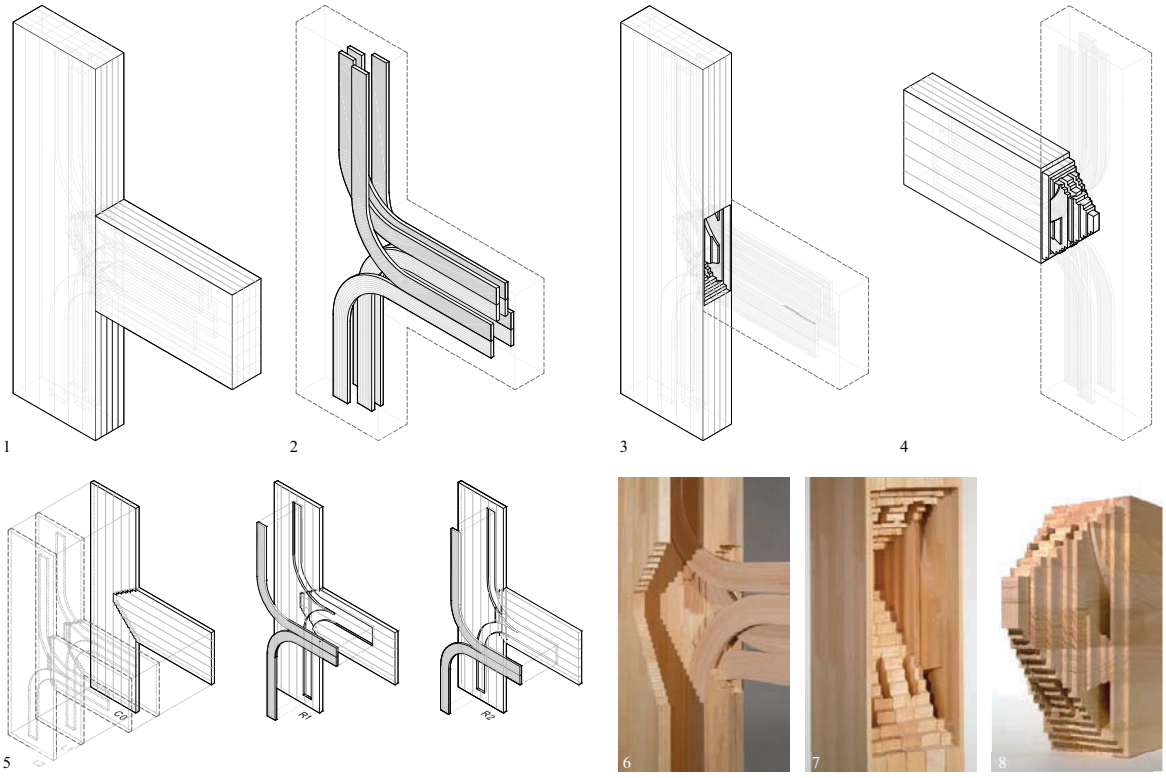

Figure 3: *The proposed connection (1); exploded isometric view of the constituting elements: bent plies (2), column (3), and beam(4); placement of the bent plies within the carved channels in the glue-laminated column-beam lamellae (5), a dry fit of the Pine column with the bent plies in their corresponding channels (6); and the conical interface in the column (7) and the beam (8)*

https://doi.org/10.52202/069179-0186

3.1 DESIGN DEVELOPMENT

Given the symmetrical and volumetric features of the multi-member integration, the size of the tested connection was opted to maintain the original proportions at half scale (300x105mm). Through the lamination process of the five laminated column-beam pairs, eight bent plies were fitted within corresponding channels placed symmetrically along the horizontal and vertical axes of the pair C0 (which contains no channels), flowing seamlessly from the beam and into both directions of the column. (Figure 3). The column-beam members were manufactured in Japanese Cedar (*Cryptomeria japonica)* and Merkusii Pine (*Pinus merkusii*), whereas the included seamless plies were manufactured from bent-laminated veneers in Beech (*Fagus crenata*).

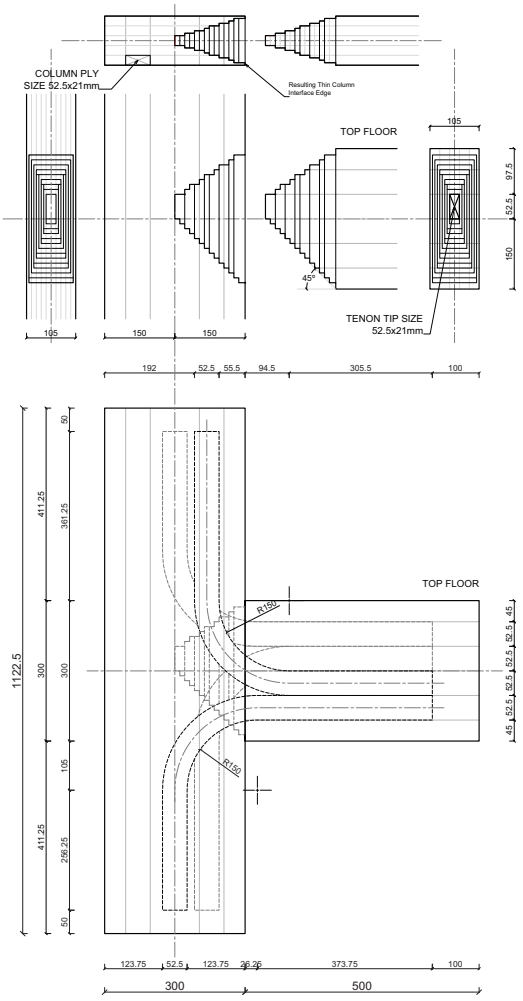

Figure 4: *Sizing of the conical interface without channels (above) and the column-beam assembly with the placement of the included bent plies (bottom) (units in mm)*

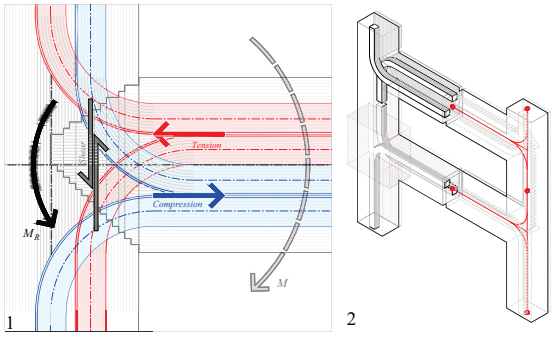

Figure 5: *The schematic structural dynamics of the proposed connection in response to an applied bending moment (1) in the proposed pinned portal frame system typology (2)*

The detailed sizing of the connection was based on a 10.5mm module per half the thickness of a single laminated column-beam pair at 300x21mm; the boards were made from edge-glueing six 52.5x21mm plies and were cut to a finished length of 1122.5mm and 650mm, for the column and beam, respectively.

The conical interface initiated above the column-beam axes' intersection with a single ply (at 52.5x21mm) and stepped towards the entire cross-section of the beam on a 10.5mm cubic grid. (Figure 4 - the asymmetrical interface mimics the shifted axis of the branch integration, a geometric growth feature of the flow of fibres)

Both sides of the column-beam members were processed with a CNC machine to shape the conical interface and carve the 52.5x10.5mm channels for the bent plies. The 90º fit at the edges of the conical interface and channels were processed with relief cuts at the inner corners using a Ø6mm bit. (Refer to Figure 9-left)

The bent plies were made from 90x1x1200mm Beech veneers, and they were bent-laminated with an inner radius of 150mm to a 54mm nominal thickness with aqueous polymer isocyanate adhesive (Koyo-Bond KR-134 at 150gm-2 spread) in block forms and cured under a press at 0.65MPa for 4 hours. Next, eight plies were rip-cut on a bandsaw at 10.5mm width and re-fitted to the desired channel (due to glue-bending spring-back) with ±1.5mm tolerance on a CN machine to a final section of 52.5x10.5mm; and a 3mm radius fillet was added to the edges facing the channels for glue distribution. Finally, the assembly of the connection members in Cedar and Pine was performed using resorcinol formaldehyde resin (Dianol 33N at 150gm-2 spread) and cured under a press at 1.0MPa for 6 hours. Moreover, a column-beam assembly without the channels for the included Beech plies was manufactured in Cedar and Pine to isolate the reinforcement effect of including the bent plies on the bending performance.

3.2 PROPOSED STRUCTURAL DYNAMICS

The modern applications of timber frame joints utilise adding foreign elements (to wood) at joint locations to provide the required resistance against specific loads. (primarily steel, e.g., plates and pins for shear, bolts and tie-rods for tension, and lags and threaded rods for bending) In contrast, the developed system approaches the features of the all-wood natural formation at branch locations through the above-mentioned simplified models in response to the hypothesised loading conditions.

Like the conical branch integration within the stem, the column-beam conical interface distributes shear loads evenly across its faces and reduces concentrated embedment damages. At the same time, the axial transfer

https://doi.org/10.52202/069179-0186

of compressive and tensile loads through the seamless bent plies reinforces the bending and shear performances due to their integration within the conical interface. as illustrated in (Figure 5-1).
Furthermore, the members are manufactured from species with different initial properties that, combined with the resulting multi-directional fibre assemblies, contribute to the approached distribution of mechanical properties; however, unlike trees, it is non-homogenous.
The proposed typology of the structural system utilises a one-way pinned-portal frame, similar to the monopodial nature of trees. [4, 12] (Figure 5-2)

4 TEST SETUPS AND RESULTS

The tests in this study focused on the static bending performance of the used materials and components.

4.1 THREE-POINT BENDING TEST

The bending performance of the Cedar, Pine, and laminated Beech plies was evaluated with a three-point bending test spanning 350mm. Table 1 lists the averaged dimensions, moduli of elasticity and rupture, with the initial stiffness derived from the tests and the initial modulus of elasticity acquired through a stress wave velocity measurement (utilising a *Fakopp* microsecond timer).

4.2 BENDING TEST OF BENT PLIES

The bending performance of six bent-ply specimens was tested in the setup displayed in Figure 6. The plies were laid horizontally and through-pinned on equal distances from the arched portion to the test base at one end and to an actuator at the other; given their slender sections, Teflon sheets separated the plies from the sandwiching steel plates with rollers to suppress the out-of-plane deformations.
Four specimens were loaded cyclically in the push (close) and the pull (open) directions, and two were loaded monotonously in either direction. The setup mimics the loading condition of the plies within the column-beam members in push (close) and pull (open) strokes. The cyclic deformation values were 1, 2, 3.5, 5, 7.5, 10, 15, and 20mm with 5mm increments till failure at a rate of 1mm per minute, corresponding to 750, 375, 200, 150, 100, 75, and 50 rad^{-1} of deformation angle as derived by equation (1):

$$\Theta = 2\,tan^{-1}\left[d \,/\, 2a\sqrt{2} - d\right] \qquad (1)$$

Where Θ is the deformation angle, d *is* the linear displacement between pins, and a is the 45º projection of the distance between the pins (refer to Figure 6).
Table 2 lists the averaged initial stiffness K_0, the maximum load P_{max} in the push (close) and the pull (open) directions, and the resulting bending moment mid-span of the arched section [$M_{max}=P_{max}\,(H + h/2)$], with the corresponding linear displacement d_{max} and the deformation angle Θ_{max}.
As illustrated in the load-displacement curves of four samples loaded till failure in the push (close) and pull (open) cycles (Figure 7), the bent plies exhibited higher ductility in the cyclic push direction and failed with

Table 1: *Three-point bending test results (values in paratheses are the standard deviation)*

Material	n	*b* mm	*h* mm	*l* mm	E_{Fakopp} kN/mm^2	*MoE* kN/mm^2	*MoR* N/mm^2	K_0 N/mm
Cedar Single Ply	6	28.0	29.0	640.8	7.2 (1.4)	8.2 (1.1)	58.3 (6.9)	158.3 (23.6)
Pine Single ply	3	27.0	30.0	832.5	11.9 (1.9)	12.0 (2.8)	58.1 (14.2)	218.4 (62.8)
Beech Laminated Ply	6	24.5	10.5	445.5	10.7 (0.7)	10.2 (0.4)	83.5 (3.3)	140.9 (6.6)

where *b and h are the section dimensions; l, the length of the specimen; E_{Fakopp}, Initial modulus of elasticity; MoE, modulus of elasticity in; MoR, modulus of rupture; K_0 initial stiffness*

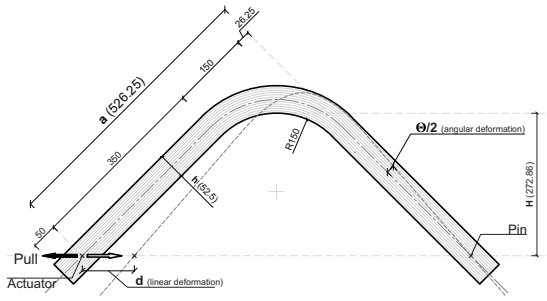

Figure 6: *Bending test setup for Beech bent plies (units in mm)*

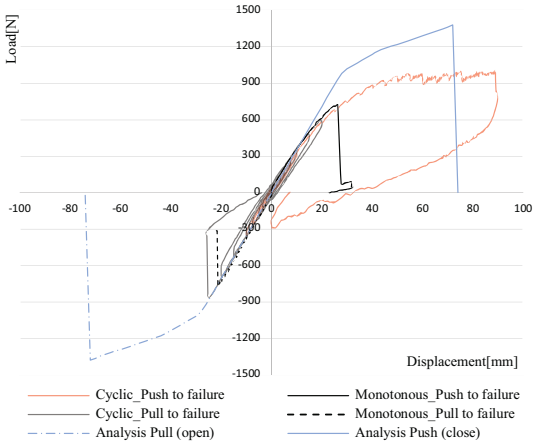

Figure 7: *Load-displacement curves in four tested bent plies in the push (close) and pull (open) directions and the analysed approximation*

Table 2*: Bent plies bending test results*

Stroke	n	K_0 N/mm	P_{max} N	d_{max} mm	Θ_{max} 10^{-3} rad	M_{max} kN.m
Push close	5	33.7 (1.0)	770.5 (210.0)	40.6 (27.4)	56.8 (39.5)	0.23 0.063
Pull pull	5	35.6 (0.9)	584.4 (208.3)	16.2 (6.1)	21.5 (8.0)	0.17 0.062

where *K_0, initial stiffness; P_{max} maximum load and its corresponding d_{max} linear displacement, Θ_{max} angular deformation, and M_{max} bending moment at the middle of the arched portion*

https://doi.org/10.52202/069179-0186

gradual crack development, while they failed in brittle behaviour when loaded in the pull direction.
The concentrated axial forces in the pull (open) cycles initiated failures near the centroidal axis with fibrous fracture patterns; these cracks gradually grew through the glue lines towards the pins, whereas the concentrated compressive forces excreted by the push (close) cycles were translated to fibre kinks on the concave side and tensile fracture on the concave side with out-of-plane deformations (twisting). However, the bent plies included in the full joint assembly will be glued within carved channels, effectively acting as a clamping feature and minimising the lateral deformation while maximising the tensile and shear strengths of the laminated material.

4.3 BENDING TEST OF THE COLUMN-BEAM ASSEMBLIES

The bending performance of the column-beam members with the included bent plies and without the channels for the bent plies (only the conical interface) was evaluated under a cyclic displacement-based loading protocol with values derived from the total frame drift. Table 3 lists the variations of the ten tested connections regarding the column-face support, the inclusion of bent plies, and material, in addition to an assembly in Cedar with a modified conical interface as a characteristic value. [CBRc with rigid column-face support had the central pair C0 of the column-beam lamella flipped, providing a larger glueing surface area and an extended tenon - Figure 9]
The loading was applied once per cycle till failure through an actuator pinned to a steel plate fixed at the upper side (top floor) of the vertical beam; the column face was laid on the test base with rigid or pin supports at its face and rigid supports at the ends, as shown in Figure 8. The different face support conditions were tested to investigate the performance of the second half of the column, given the placement of the bent plies along its centroidal axis.
Additionally, two horizontal supports with spherical rollers were added near the centre of the beam's surface to suppress out-of-plane deformations.
The cyclic angular deformation values in the push and pull directions were 300, 200, 150, 75, 50, 30, and 20 rad^{-1} at a rate of 1mm per minute. The loading was maintained until the load was reduced to 70% of the maximum load or till failure. The moment-rotation angle envelopes of the cyclic hysteresis loops in the push (compression) and pull (tension) directions for the Pine and Cedar variations are illustrated in Figure 10 and Figure 11, respectively. The data and derived evaluation items from the performed tests are listed in Table 3.

4.4 SIMPLIFIED ANALYTICAL MODEL

The comprising members of the connection, i.e., the eight bent plies and the five pairs of column-beam lamellae, were approximated analytically as a combination of individual models of beam-elements (Figure 13), simulating the support and loading conditions of the rigidly supported connection assemblies of PBR and CBR using Midas-iGen. (a general-purpose structural analysis and optimal design system)

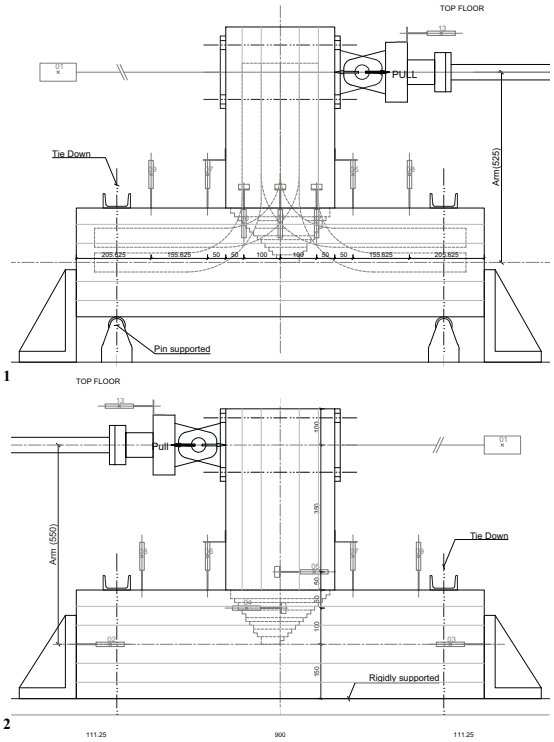

Figure 8: *Column-beam assemblies test setups. 1. Front side of the pin-supported full connection, and 2. Back sided of the rigidly supported column-beam assembly. Both setups share the same placement of transducers (1~13) (units in mm)*

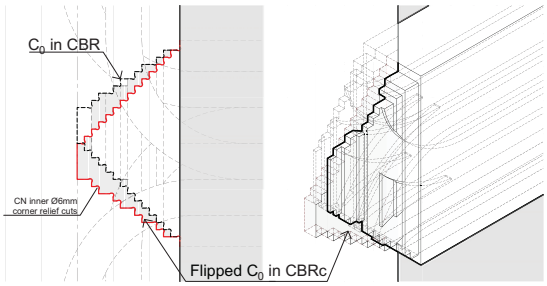

Figure 9 *Details of the flipped C0 in the conical interface of CBRc; hatched areas represent the added gluing surface of the extended tenon (left: illustrates the CN Ø6mm relief cuts)*

The arched portion of the bent ply was modelled in five rigidly connected linear beam-elements (Figure 12-1) with isotropic material properties derived from the three-point bending tests. Each segment had an elastic performance with a plastic hinge (equal to the material's yield strength P_y) near its rigid connections. The simulation followed the bent plies bending tests in support and loading conditions (results are illustrated in Figure 7, noting that the included bent plies were loaded within the plastic region in the column-beam assemblies)
Similarly, the centre-lines of the column-beam members were modelled as two linear beam-elements joined with a rotational spring (Figure 12-2). The spring properties were derived from the sole performance of the conical interface in the column-beam assembly without the bent plies PWR and CWR.

https://doi.org/10.52202/069179-0186

Table 3: *Results of bending tests of column-beam and full connection assemblies*

Material	Name	Bent Plies	Column-face	Number		M_{max} kNm	M_y kNm	M_u kNm	$M_{1/150rad.}$ kNm	δ_{max} 10^{-3}rad	δ_y 10^{-3}rad	δ_v 10^{-3}rad	K_0 kNm/rad	K_s kNm/rad	μ -	D_s -
Merkusii Pine	PWR	Without	Rigid	1	Push	16.5	8.6	14.8	16.1	7.0	4.33	4.04	4146.6	3675.6	3.12	0.44
					Pull	14.4	10.1	13.5	13.6	9.0	4.07	3.57	4118.4	3786.9	2.85	0.46
					Ave.	15.5	9.4	14.2	14.9	8.2	4.20	3.80	4132.5	3731.2	2.98	0.45
	PBR	With	Rigid	1	Push	35.1	18.0	29.0	21.8	12.0	2.34	8.33	3699.9	3475.0	1.42	0.74
					Pull	31.2	19.3	31.7	22.2	14.0	2.68	8.62	3381.9	3671.3	1.96	0.59
					Ave.	33.2	18.6	30.3	22.0	13.1	2.51	8.48	3540.9	3573.1	1.69	0.66
	PBP	With	Primed	2	Push	25.9	15.6	22.7	15.59	16.19	6.61	9.67	2494.1	2349.4	2.77	0.47
					Pull	26.0	16.6	24.0	15.33	16.21	7.58	10.90	2329.4	2210.0	2.01	0.58
					Ave.	26.0	16.1	23.4	15.46	16.20	7.10	10.28	2411.7	2279.7	2.37	0.53
Japanese Cedar	CWR	Without	Rigid	1	Push	10.3	6.2	9.6	9.8	11.0	3.03	4.68	2361.7	2047.8	2.82	0.46
					Pull	9.2	5.8	8.1	8.5	8.0	2.26	3.18	2574.2	2550.1	4.26	0.36
					Ave.	9.7	6.0	8.8	9.1	9.8	2.60	3.93	2467.9	2299.0	3.54	0.41
	CBR	With	Rigid	2	Push	16.0	10.0	14.2	11.3	11.7	5.12	7.32	2079.2	1944.2	4.11	0.37
					Pull	14.3	11.5	13.2	10.9	10.5	7.24	8.35	1663.1	1582.8	2.44	0.52
					Ave.	15.1	10.7	13.7	11.1	11.1	6.18	7.84	1871.2	1763.5	3.22	0.45
	CBRc*	With	Rigid	1	Push	19 .5	10.5	18.2	15.0	14.0	5.17	7.49	2607.9	2430.1	2.34	0.52
					Pull	19.7	10.2	17.9	14.7	13.9	5.26	7.15	2549.9	2505.6	2.25	0.54
					Ave.	19.6	10.4	18.1	14.9	13.9	5.22	7.32	2578.9	2467.9	2.29	0.53
	CBP	With	Primed	2	Push	15.6	10.5	15.3	11.3	13.9	5.58	8.14	1860.1	1888.8	3.21	0.43
					Pull	16.4	9.6	14.8	10.9	15.7	5.62	8.71	1694.8	1700.5	3.14	0.47
					Ave.	16.0	10.1	15.1	11.1	14.8	5.60	8.42	1777.5	1794.6	3.17	0.45

* CBRc with a modified conical interface (refer to Figure 9)

where *M, moment; δ, angular deformation; K, stiffness; μ, Ductility factor; Ds, structural characteristic factor; subscripts; max, Maximum; y, Yield; u, Ultimate; v, yield point; 0, Initial; s, Secant; 1/150, Load corresponding to the angular deformation angle of 1/150 radian.*

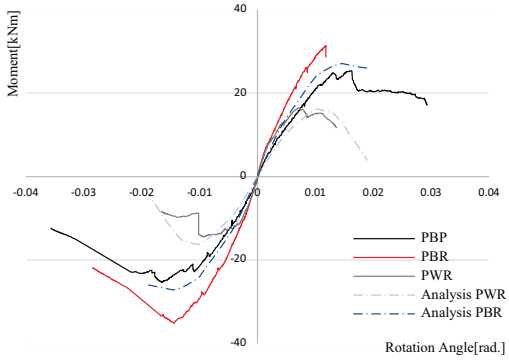

Figure 10: *Moment-rotation angle envelope curves in tested and analysed Pine variations*

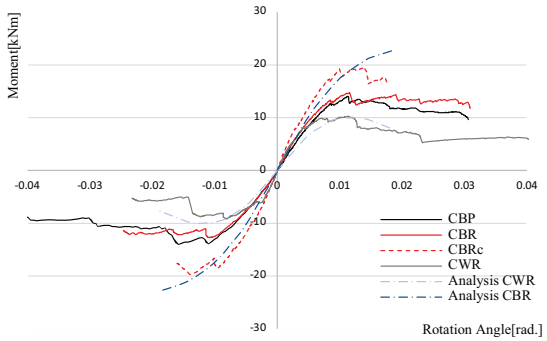

Figure 11: *Moment-rotation angle envelopes curves in tested and analysed Cedar variations*

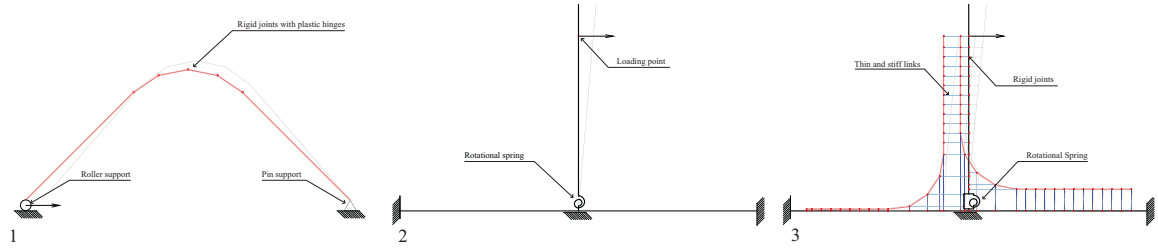

Figure 12: *Analytical beam models of the connection members, 1. bent ply model (in push/close), 2. C0 with a rotational spring (in push), 3. R1\|L1(in push) and R2\|L2 (in pull) combining both models with stiff and thin links accounting for the captive channels*

https://doi.org/10.52202/069179-0186

The conical integration of the beam within the column changes in size across its section, where the central lamina (C0) has the maximum integration. Ideally, the rotational spring should be weighted according to its integration when included in the model of each lamina; however, for simplification, the spring capacity was divided equally across the five laminae, given that the whole connection's analytical result is the sum of its members.

On the other hand, the linear segments of the bent plies were rigidly connected to the nearest column-beam element with thin and stiff links at 30mm intervals, whereas the segmented arched portion was connected to the column and beam elements. (Figure 12-3)

Accordingly, and given the connection's symmetry (where L1|R1 and L2|R2 are mirrored copies), the simplified analytical model of the connection in the push direction is the sum of $[C0_{push}+2L1_{push}+2L1_{pull}]$

The analytical models' performance of the column-beam assembly (without the channels for the bent plies) and the whole connection are illustrated in Pine and Cedar in Figure 10 and Figure 11, respectively.

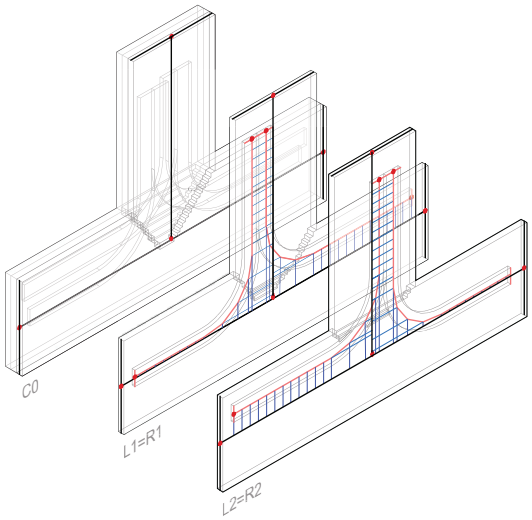

Figure 13: *Beam element models of the whole connection as the sum of the performance of the individual laminae models* $[C0_{push}+ 2L1_{push} + 2L1_{pull}]$

5 DISCUSSION

In all tested variations, early cracks were observed at the finger-joined plies of the glue-laminated boards at the thin edge of the column interface. Additionally, dissecting the connection's conical interface showed that the butt-jointed glue faces perpendicular to the loading plane were weakened by the CN machining corner relief cuts (Figure 14); moreover, the failure of the included bent plies was limited to splitting failure at the centroidal axis.

In the column-beam assemblies (without the bent plies, CWR and PWR), the distributed shear loads across the faces of the conical interface reduced the embedment of the tenon; however, the separation at the relief cuts and the conical geometrical slope caused the beam to pull out due to the cyclic loading, at which the connection was secured by the shear performance of the glue in the stepped surfaces parallel to the loading plane. (Figure 14)

Compared to the sole performance of the conical interface in PWR, including the bent plies in the Pine variations, PBR and PBP achieved a 114% and 68% increase in the maximum moment and a 14% and 42% decrease in the initial stiffness, respectively.

Similarly, the Cedar variations CBR and CBP achieved a 56% and 65% increase in the maximum moment and a 24% and 28% decrease in the initial stiffness compared to CWR, respectively.

However, CBRc with the modified conical interface exhibited the best performance, increasing the maximum moment by 102%, 23%, and 18% and the initial stiffness by 4%, 27%, and 31% compared to CWR, CBR, and CBP, respectively. Since the middle lamella of the conical interface (C0) does not contain any channels and is immediately glued to neighbouring bent plies, flipping its direction in BRc created an extended tenon. It increased the total glueing surface area by 20%, reinforcing the initial stiffness and moment capacity of the whole assembly while reducing the ductility factor; nonetheless, it failed in a similar pattern.

Furthermore, the bent plies acted as shear keys due to their integration within the asymmetrical conical interface, reduced the initial stiffness, prevented the beam from pulling out, and concentrated splintering and interlaminar failures along the vicinity of the conical interface and transverse tensile failure at the central region of the column along their linear axes (Figure 15).

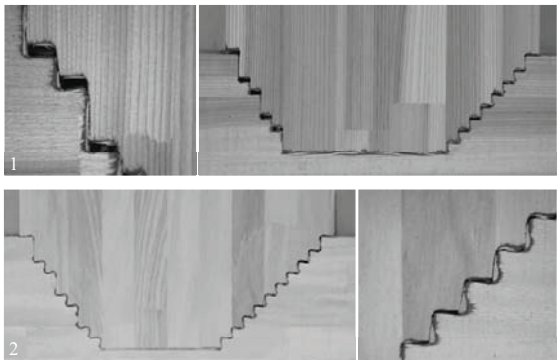

Figure 14: *Pull-out and relief cut separation in a dissected conical-interface in Cedar (1) and Pine (2)*

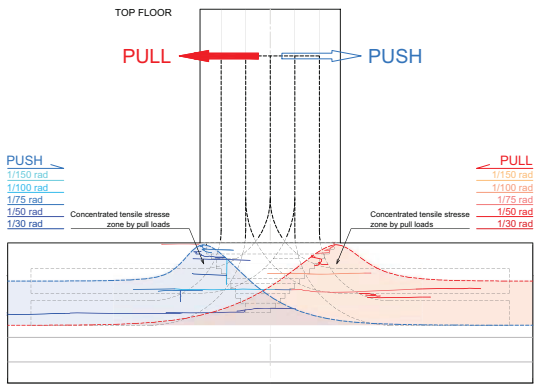

Figure 15: *Zone of the concentrated tensile stresses due to the included bent plies (cracks shown are from a CBR variation)*

https://doi.org/10.52202/069179-0186

However, due to the termination of the beam and bent plies integrations at the column's axis, the lower half was not fully incorporated in resisting the increased tensile stresses of the combined performance of the included bent plies and their captive channels. As a result, the performance of the pinned and rigidly supported connections was comparable in the Cedar variations; however, it was pronounced in the Pine variations (due to its higher MoE); additionally, vertical cracks in the PBP's beam were observed.

5.1 COMPARISON WITH STEEL-ADDED CONNECTIONS

Based on the calculation methods provided for the glued-in rod (GIR) [10, 13] and the lag-screw bolt (LSB) [11] at 105x600mm, the initial stiffness and ultimate loads were derived for a 105x300mm GLT section. Table 4 lists the ultimate moment and the initial stiffness of the compared connections. Figure 16 illustrates the equivalent energy elastic-plastic (EEEP) bilinear models averaged in the push and pull directions, the moment-rotation angle envelopes of tested variations, and the projected performance of GIR and LSB.

Accordingly, CBRc achieved a similar moment capacity to GIR with a reduced initial stiffness and an increased ductility (given the brittle failure pattern of GIR); on the other hand, it exceeded LSB's initial stiffness with a reduced moment capacity. Additionally, it has a joint efficiency of 30%, a practical value for a moment resisting joints in timber structures [14], calculated by Equation(2):

$$\alpha = M_{max}/F_b \times Z \quad (\times 100\%) \qquad (2)$$

Where α, joint efficiency; Mmax, maximum moment; Fb, bending strength of the glue-laminated member (= 27.5 N.mm^{-2} based on the "Japanese Agricultural Standard for Glued laminated timber 2007"); and Z, section modulus of the glulam member at 105x300mm.

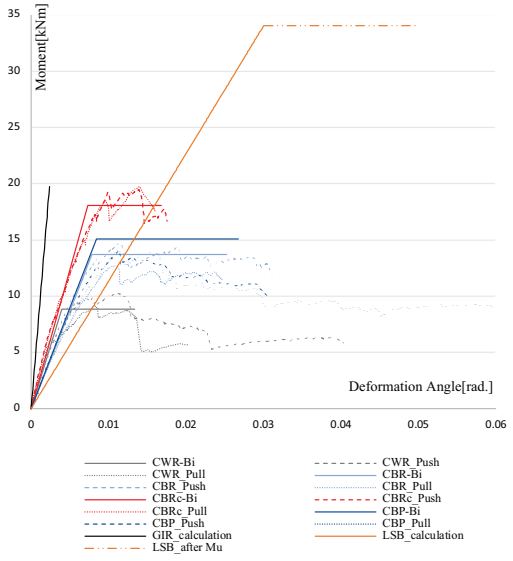

Figure 16 *Moment-Rotation envelopes and the averaged bilinear models of all tested variations in comparison to the calculations of LSB & GIR in Cedar (at 105x300mm)*

Table 4 *Comparison with GIR and LSB [values in brackets are relative to CBRc]*

Theme	Name	K_0 Initial Stiffness kNm.rad^{-1}	-	M_u Ultimate Moment kNm	-
Wood-only Bio-inspired	CWR	2467.9	[96%]	8.8	[49%]
	CBR_{ave}	1871.1	[73%]	13.7	[76%]
	CBRc	2578.9	[100%]	18.1	[100%]
	CBP_{ave}	1777.5	[69%]	15.1	[83%]
Steel-added Conventional	GIR	8325.6	**[323%]**	19.8	[109%]
	LSB	1134.4	[44%]	34.0	**[188%]**

5.2 PARAMETRIC INVESTIGATION

Further investigation in the material combinations was analysed in Cedar in CWR and CBR variations with enhanced material properties as parameters, as follows:

- Column-beam materials: modulus of elasticity *MoE.*
- Conical interface: rotational spring capacity in stiffness *K*, maximum load P_{max}, and yielding load P_y.
- Bent plies: modulus of elasticity *MoE* and yielding load P_y at the hinges.

Table 5 lists the analysed parametric variations, and Table 6 lists the correlations of the maximum moment and stiffness in the parametric and tested variations.

The enhanced material and rotational spring in the column-beam assembly without the bent plies in C2B0R achieved a similar maximum moment and a 57% increase in stiffness in CBRc, whereas C2B1R doubled the initial stiffness and maximum moment in CBR. On the other hand, the enhanced bent plies in C1B2R approached the effect of the elongated conical interface in CBRc, which complies with the tested impact of the bent plies on the shear performance of the conical interface.

Table 5: *Analysed parametric variations*

		Beech (Bent Plies) B0	B1 *1 x MoE, Py*	B2 *2 x MoE, Py*
Cedar (Column-Beam)	C1 *1xMoE, Pmax, Py, K*	C1B0R *(=CWR)*	C1B1R *(=CBR)*	C**B2**R
	C2 *2xMoE, Pmax, Py, K*	C2B0R	**C2**B1R	**C2B2**R

Table 6: *Correlations of the maximum moment [above the diagonal] and stiffness [below the diagonal] in the analysed parametric variations*

			M_{max} [kNm]			Moment at 0.015 rad[kNm]			
			CWR	CBR	CBRc	**C2**B0R	C1**B2**R	**C2**B1R	**C2B2**R
			9.7	15.1	19.6	20.19	22.61	34.39	41.95
Stiffness [kNm.rad^{-1}]	CWR	2299	1	1.56	2.02	2.08	2.33	3.55	4.32
	CBR	1763.5	0.77	1	1.30	1.34	1.50	2.28	2.78
	CBRc	2467.9	1.07	1.00	1	1.03	1.15	1.75	2.14
	C2B0R	2769.3	1.20	1.57	1.12	1	1.12	1.70	2.08
	C1**B2**R	2693.2	1.17	1.53	1.09	0.97	1	1.52	1.86
	C2B1R	3681.2	1.60	2.09	1.49	1.33	1.37	1	1.22
	C2B2R	4144.4	1.80	2.35	1.68	1.50	1.54	1.13	1

https://doi.org/10.52202/069179-0186

6 CONCLUSION

Given that the proposed structural system was based on and limited by the dimensions of the case study and the currently available simple manufacturing technologies, the performance achieved by the bio-inspired, only-wood connection competed with the conventional steel-added joints and presented the utilisation of bent timber members within the frame joints as a possible application for reinforcement against bending moments, inviting further explorations and inspirations from tree structures. The parametric analysis (approximated from the material perspective) provided insights into the different material effects; however, further investigations into the adhesive properties and the geometric design in terms of configuration, size and dimensions are equally important. Furthermore, the proposed system had a long and complicated manufacturing process in controlled factory conditions compared to the simple in-situ application of the steel-added joint systems. Hence, further developments and simplifications for integrating and manufacturing these approaches are required, especially considering the design and assembly of multi-directional seamless members within two-way frame systems.

Although this research presented a valid proposal for the application of wood connections in timber frames in light of its performance in static bending and judging by the failure patterns, it can be argued whether the only-wood applications are supposed to seek a rigid performance comparable or similar to the steel-added ones. Regarding the projected shortcomings and limitations of the wood material in the current structural and constructional applications compared to its superiority and suitability in its natural formation, addressing the concept of damping in timber frames instead of rigidity is expected to provide further insights into timber structures towards a befitting constructional language in structural applications.

ACKNOWLEDGEMENT

- This work was partially supported by 'The Ministry of Education, Culture, Sports, Science and Technology (MEXT) Scholarship' and the 'Japan Society for the Promotion of Science - JSPS KAKENHI Grant number: JP22K20463'.
- Part of this work was submitted to the 'AIJ Journal of Technology and Design (Architectural Institute of Japan)" and was presented at the '73rd Annual Meeting of the 'Japan Wood Research Society (JWRS)'.

REFERENCES

[1] Bell P. W. R.: Wooden Structures by G. G. Karlsen and the Derevyagin beam. In: *History of Construction Cultures*, London, 734–740, 2021

[2] Arlet J. L.: Innovative Carpentry and Hybrid Joints in Contemporary Wooden Architecture. Arts, 10(3):64, 2021

[3] Thompson D. W.: On growth and form. Cambridge University Press, 2014

[4] Grigorian M.: Biomimicry and theory of structures-design methodology transfer from trees to moment frames. Journal of Bionic Engineering, 11(4):638-648, 2014

[5] Slater D.: An argument against the axiom of uniform stress being applicable to trees. Arboricultural Journal, 38(3):143-164, 2016

[6] Hu M., Olsson A., Hall S., and Seifert T.: Fibre directions at a branch-stem junction in Norway spruce: a microscale investigation using X-ray computed tomography. Wood Science and Technology, 56(1):147–169, 2022

[7] Pasini D. and Burgess S. C.: Optimal structural features in trees and their application in engineering. In C.A. Brebbia and L.J. Sucharov, editors, *Design and Nature*, pages 3–15. WIT Press, United Kingdom 2002

[8] Burns L. A.: Bio-Inspired Design of Aerospace Composite Joints. RMIT University, 2012

[9] Mattheck C.: Design in Nature. Springer Berlin Heidelberg, Germany, 1998

[10] K. Tanaka et al.: Study on Strength Mechanism of Joint System Using Metal Connector and Adhesive in Timber Structures Part.23 Consideration of Calculating Method for Bending Performance of Beam-Column Joint Using GIR Joint. (in Japanese), In *Summaries of the 2021 AIJ Annual Convention,* 421–422, 2021

[11] K. Tsuboi et al.: Basic Study on Lag-screw-bolt Connection Performance for Mid-rise Timber Construction. (in Japanese), In *Summaries of the 2021 AIJ Annual Convention*, 413–414, 2021

[12] Hawasly F., Matsumoto N., and Koshihara M.: Bio-Inspired Wood-Only Timber Frame Joint Typologies Based on the Seamless Fiber Continuities of a Tree's Stem-Branch Junction. In *Summaries of the 2021 AIJ Annual Convention*, 873–876, 2021

[13] Sato K. et al.: Study on Strength Mechanism of Joint System: Using Metal Connector and Adhesive in Timber Structures Part.21 Horizontal Loading Test for Moment Resisting Performance of Beam-Column Joint with Shear Key Considering Ease of Construction. (in Japanese) In *Summaries of the 2021 AIJ Annual Convention*, 417-418, 2021

[14] Nakata K. and Komatsu K.: Development of Timber Portal Frames Composed of Compressed LVL Plates and Pins II. Strength properties of compressed LVL joints as moment resisting joints. (in Japanese), Mokuzai Gakkaishi (Journal of the Japan Wood Research Society), 55(3):155-162, 2009

World Conference on Timber Engineering Oslo 2023

EXPERIMENTAL STUDY OF A TYPICAL EXTERNAL WALL-FLOOR-WALL CONNECTION IN A CLT PLATFORM TYPE CONSTRUCTION

Luka Vojnovic[1], Eleni Toumpanaki[2], James Norman[3]

ABSTRACT: This paper presents experimental studies of a typical external wall-to-floor-to-wall connection in a cross laminated timber (CLT) platform type construction in context of disproportionate collapse resistance. The studied connection mimics the finite element models developed by other authors in the international timber robustness research community. The assembled specimens were tested with aim of staying in the linear elastic range and understand how the rate of loading affects CLT and its connections. This study presents data of the observed behaviour of CLT, steel brackets and screws subjected to different rates of loading. Obtained results and observations will inform future testing programmes and experimental analyses whereby aim is to test the specimens beyond the linear elastic range and to failure.

KEYWORDS: CLT buildings, disproportionate collapse, experimental analyses, rate of loading, wall-to-floor-to-wall

1 INTRODUCTION

Cross laminated timber (CLT) is a relatively new construction material and both CLT balloon type and platform type [1, 2] construction methods have been increasingly popular in the building industry in the past three decades to build multi-storey buildings.

Some of the reasons are the advantages of using CLT over traditional materials such as concrete, steel and even timber used in timber frame construction method. For example, CLT panels of various sizes are manufactured and cut with high accuracy off-site in a factory. Assembly of CLT structure on site is usually shorter compared with building with concrete and/or steel, depending on the project size and complexity, requiring less person hours and produces less waste [3]. CLT structures could be lighter than steel and are lighter than equivalent concrete structures thus require less concrete for foundation. CLT has high strength to weight ratio compared to steel, concrete and masonry. In addition, CLT offers good quality and healthy living spaces and has a pleasant feel, should it be exposed inside of a building.

Many schools, hospitals and other commercial buildings have been built with CLT. Furthermore, the shortage in residential sector still exist and a portion of residential buildings could be built with the CLT. The United Nations (UN) projections are that quite a significant number of residential units will be required in the near future, a 2.3 billion new urban dwellers by 2050 – and entail the production of an enormous volume of housing and infrastructure [4].

Along with many other already available and newly emerging engineering solutions, using CLT to build some of the buildings could contribute to a more sustainable construction industry and to reaching the net zero commitment.

As any other building and structure, multi-storey buildings designed as a CLT platform type construction ought to be sufficiently robust to overcome any loads which may result in disproportionate collapse.

Experimental study presented in this paper considered the external wall-to-floor-to-wall (WFW) CLT connection which can be found in a multi-storey platform type building. Widely used construction practices for connecting CLT WFW were researched and a typical connection detail with a single bracket and floor-to-wall screw system was used to assemble the testing specimens.

The effect of different rates of loading (ROL) on the WFW connection and stiffness in the linear elastic range were studied which should inform future testing whereby specimens will be tested beyond linear elastic range including until failure.

Design for disproportionate collapse resistance requires consideration of stiffness and rotational capacity of structure's details, such as vertical and horizontal element connections and fixings. Sufficient tie forces should be present to develop catenary action in beams and membrane action in floors when an alternative load path is being developed at the time of sudden loss of a key structural element. Should stiffness be too high the catenary and/or membrane action cannot develop.

[1] Luka Vojnovic, IEng MICE, Doctoral Candidate at Universityof Bristol, UK, nf21539@bristol.ac.uk
[2] Dr. Eleni Toumpanaki, University of Bristol, UK, eleni.toumpanaki@bristol.ac.uk
[3] Prof. James Norman, University of Bristol, UK, james.norman@bristol.ac.uk

https://doi.org/10.52202/069179-0187

2 LITERATURE REVIEW

Current UK based legislation, codes and guidelines account for disproportionate collapse resistance in a prescriptive manner by relying on expertise acquired through previous research and construction practices mainly based on concrete and steel structures.

The UK Building Regulations have changed since Ronan Point disproportionate and progressive collapse incident occurred in 1968, whereby now the Approved Document, Part A defines disproportionate collapse as: "The building shall be constructed so that in the event of an accident the building will not suffer collapse to an extent disproportionate to the cause." [5]. It is worth noting that disproportionate collapse can lead to progressive collapse and progressive collapse can be disproportionate.

Design codes reference the term robustness which shall account for design to resist disproportionate collapse [6]. For the case of mid-rise timber structures, design to avoid disproportionate collapse is often left solely to engineering judgement [7] although guidance such as Practical guide to structural robustness and disproportionate collapse in buildings is available [8]. One strategy is that each element of a structure shall develop a resistance mechanism – an alternative load path to ensure sufficient robustness against accidental loading cases applied to a structure in the design process.

A thorough review of international research on structural robustness and disproportionate collapse up to 2011 has been undertaken by Arup and published by the UK's Department for communities and local government [9]. It can be highlighted that limitations such as lack of guidance on CLT and behaviour of walls with openings are identified. These can be attributed to lack of disproportionate collapse resistance and robustness of CLT specific research at the time. Nevertheless, Recommendation 19 proposes to undertake a review of the robustness of timber construction and connection including research is urgently undertaken to investigate methods by which effective horizontal tying can be achieved in timber.

Byfield et al. [10] review of progressive collapse research and regulations highlighted guidelines, procedures and methods which are mostly grounded in concrete and steel. Nevertheless, Byfield et al.'s [10] comment that despite tying force method is easiest to implement, it does not require additional structural analysis. Furthermore, constraint of the alternative load path method is being underlined whereby requirement that only one key element at a time is to be removed to check the ability of the structure to redistribute loads without leading to a disproportionate collapse.

Experimental testing to mimic key element removal is related to rate of loading and load removal. Gerhards' [11] study reports observations from a large number and broad range of timber products subjected to different load durations and rates of loading. Gerhards concluded that both do affect timber products. ROL affects ultimate stresses namely tension and compression perpendicular to the grain. Furthermore, further research is suggested too.

More recent reviews of timber robustness were undertaken by Huber et al. [12], Voulpiotis et al. [13] and Cost Action FP1004 [14]. Currently active are CA20139 [15] and CEN/TC250 N3288 [16]. Latest research for example by Bita et al. [7,17], Huber et al. [18, 19], Przystup et al. [20] offers insights to their vast experimental studies for mostly floor-to-floor CLT connections to better understand development of catenary action and horizontal tie forces. These studies are also complemented with numerical finite element modelling.

Akter et al. [2] and Huber et al. [18, 19] study WFW CLT connection in a platform type construction. They undertook multiparametric finite elements analyses of numerical models exploring joint stiffness and Akter et al. [2] studied the impact of wall height, floor length and wall and floor thickness on joint stiffness. Their model predicted a stronger influence of the wall thickness over the floor thickness on the floor connection's rotational stiffness [2]. It is worth noting that floor to wall connection is usually modelled with conservative assumption that the rotational stiffness is negligible due to hinged connection in structural model and calculation [2].

Bruehl et al. [21] studied moment-rotation behaviour in a semi-rigid GL24h timber doweled joint and its ductility to determine the joint stiffness. Evidently the main principle is that should joint be too stiff without any rotational capacity then the timber element would fail in a brittle manner next to the joint without any benefit.

Furthermore, insurance specialists in the UK are currently preparing a framework document which should result in reviewing models to progress and account for new materials and construction methods, such as CLT. Therefore, understanding the risks and mitigation measures when using CLT is important and would support assessing the relevant insurance metrics so that the premiums would be commensurate with risks and therefore making CLT structures more feasible to insure for all involved stakeholders [22].

Authors are not aware of a CLT specific report that would highlight failure of CLT identifying disproportionate collapse and investigation of root causes. Nevertheless, failure of balcony due to moisture was highlighted in oral presentation by the author Nocetti [23] at Rothoschool event in London in 2019.

More timber expertise generally and CLT specifically is required, through research and experimental analyses. These should include studying different typologies and connections between structural timber elements. Inherent material properties of timber prevent formation of plastic hinges hence indicate brittle failure. Research of dynamic response to adverse loading, rate of load within instantaneous load duration capturing joint's stiffness and its ability to plastically deform is required. This research responds to calls by the international robustness community for more experimental studies [2, 10, 11, 13].

3 THE EXPERIMENTAL PROGRAMME

Rate of loading (ROL) within instantaneous load duration on CLT is relatively unknown variable and this is an exploratory study to understand better the impact of changing ROL to inform future testing of the WFW connection. Furthermore, consideration to observe any available rotational stiffness and how it is affected by the ROL in the considered WFW CLT connection.

A series of non-destructive experiments have been performed with intention to stay inside the linear elastic range. Specimen arrangement was focused on the WFW connection level and considered the effect of ROL on the WFW setup at the WFW connection level arrangement. A typical multi-storey platform type CLT building, which would be a class 2B was considered in this study [5, 8]. Three approaches are suggested as levels of robustness commensurate with routine risks, i.e. provision of vertical and horizontal ties, alternative load path(s) to be available upon removal of elements, which is adopted for disproportionate collapse resistance, and specific load resistance method (the provision of key elements) [8].

This paper highlights experimental programme of a WFW connection adopting testing methodologies previously prepared and used as comparison whilst developing finite element modelling. The latter were developed by Akter et al. [2], Huber et al. [10] and Bita et al. [11, 13].

Furthermore, this experimental programme is part of a wider research programme which will study disproportionate collapse resistance of CLT buildings at connection and system level.

3.1 TESTING SET UP ARRANGEMENT

The testing arrangement in this research programme as shown in Figure 1 comprises vertical metal block (1) holding the hydraulic actuators (2 and 3), the horizontal metal blocks (1T and 1B) and metal brackets (4T and 4B).

The hydraulic actuator (2) was connected to a manually operated hydraulic single-acting cylinder-pump and a stop valve (not shown in the drawing).

The hydraulic actuator (3) used in testing had a 25 kN load capacity and piston rod with 260 mm (+/-130 mm) stroke length capabilities.

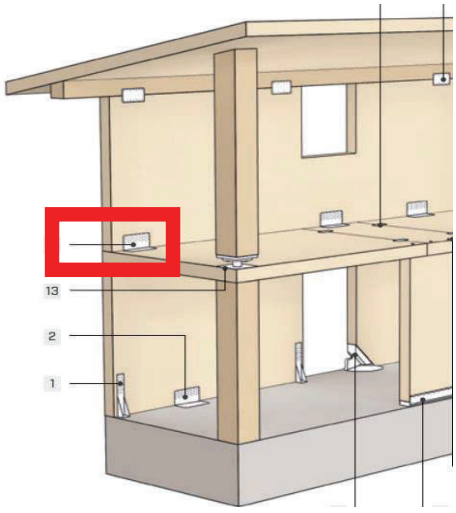

Figure 2: *The WFW connection addressed in the testing [24]*

The testing set up was arranged to mimic a cut at connection as shown in Figure 2, comprising ground floor wall, first floor panel and the first floor wall. Similar experimental arrangement was used elsewhere [2, 18].

The hydraulic actuator (3) was articulated at its rear. At its front a ball-and-cup arrangement was created. The ball part is attached at the end of the load cell which is screwed at the tip of the actuator's piston rod. The ball part is aligned and positioned at the centre of the cup part, which is attached to the floor element of the CLT specimen allowing the hydraulic actuator's piston rod to progress horizontally and upwards when the CLT floor element starts to rotate when subjected to the applied load.

Instrumentation used in this experimental programme were Linear Variable Displacement Transducers (LVDTs) and load cells (LCs) to detect displacements and loads as displayed in Figure 1.

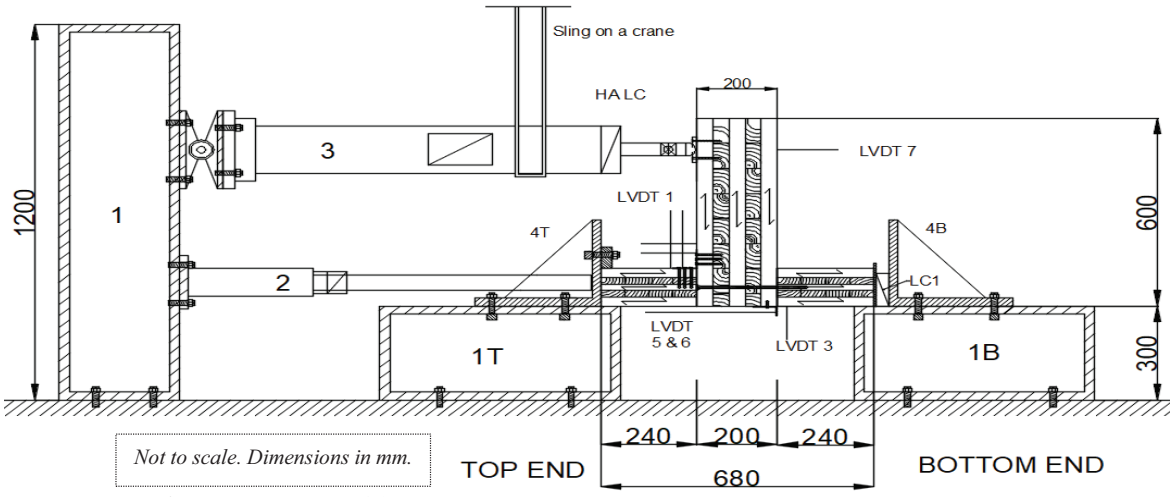

Figure 1: *Near side (NS) cross-section of the testing set up*

https://doi.org/10.52202/069179-0187

3.2 MATERIALS AND TESTING SPECIMENS

Materials used in testing were a combination of widely available commercial products and also generic products to consider their behaviour beyond a single manufacturer.

Self-tapping screws were obtained by Reisser and Spax, mechanical fixings (brackets) and fasteners (screws) were supplied by Rothoblaas and CLT was supplied by StoraEnso, both industry partners to this research.

Generic product, angle brackets made of mild steel were produced at University of Bristol. Rothoblaas brackets are made of zinc plated carbon steel. Rothoblaas screws are made of galvanized carbon steel and fully threaded [24]. Reisser screws are made of carbon steel rod according to EN10268 [25] and are fully threaded. Spax screws are made of carbon steel and are partially threaded [26, 27]. Dimensions are tabulated in Table 1.

Table 1: *List of material variables used in the testing, where A indicates type of timber, B type of bracket, WS wall screw and FWS floor-to-wall screw*

Item	Description
A1	CLT 5ply floor, 200 mm thick
A2	CLT 5ply wall, 120 mm thick
B1	Generic, 200x60x60x2 mm thick
B2	Rothoblaas, Nino15080, 2.5mm thick
WS1	Reisser, R2 Pan, 5.0x60 mm
WS2	Rothoblaas, LBS560, 5.0x60 mm
FWS1	Spax, wirox, 6.0x280 mm
FWS2	Rothoblaas, HBS6280, 6.0x280 mm

The specimens were assembled in combination of either:

UoB = 1x A1 + 2x A2 + 1x B1 + 60x WS1 + 1x FWS1
or
RO = 1x A1 + 2x A2 + 1x B2 + 36x WS2 + 1x FWS2

Where UoB means specimen with generic bracket (B1) and RO means specimen with Rothoblaas bracket (B2).

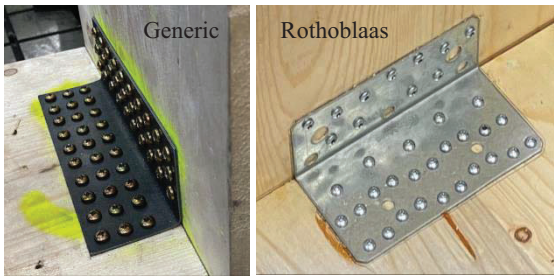

Figure 3: *Generic and Rothoblaas bracket used in testing (figures are not to scale)*

CLT was supplied and delivered cut-to-measure, then assembled in the laboratory to widely accepted and currently used CLT construction practice as per manufacturer's recommendations and as referenced in Swedish Wood CLT Handbook [24-28]. CLT elements and assembled specimens were kept dry at all times.

The humidity and temperature of the air in the large storage space was monitored over several weeks. Average temperature being 21.0°C and relative humidity 37.41%. The moisture content of the CLT was measured with a handheld moisture meter.

Testing specimen arrangement at connection level as shown in Figure 3 shows a typical connection in a multi-storey platform type CLT building. It comprises two wall elements and one floor element, each made of a C24, 5-ply CLT panel, connected with mechanical fixings tabulated in Table 1.

The floor and the bottom wall are fixed with a floor-to-wall screw while the top wall and the floor are connected with an angle bracket which is fixed with a number of self-tapping screws to both the top wall and the floor element.

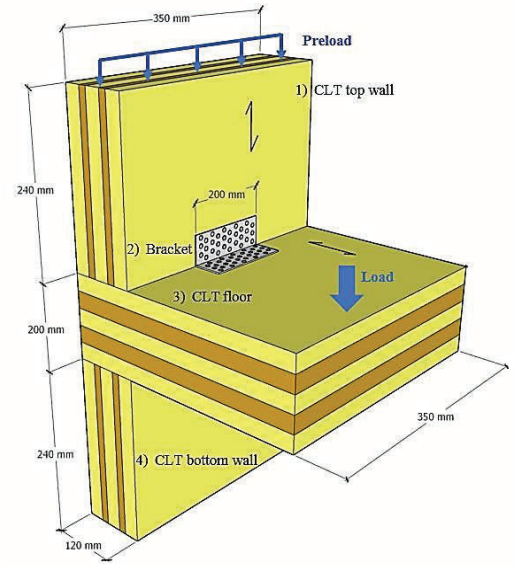

Figure 4: *Schematic of WFW testing specimen (not to scale)*

3.3 TESTING REGIME

Testing programme commenced with numerous preliminary trials to verify appropriateness and workability of the testing set up arrangement and instrumentation set up.

As supply of the CLT was limited, it was appropriate for the preliminary trials to be conducted using timber frame like specimens composed of C24 timber studs and oriented strand board (OSB) panels, fixed with self-tapping screws.

Following the preliminary trials the main experiments were performed with CLT specimens as displayed in Figure 5.

They were placed on the horizontal metal blocks in-between the metal brackets and preloaded with gravity loads of 18 kN induced by the hydraulic actuator (2).

https://doi.org/10.52202/069179-0187

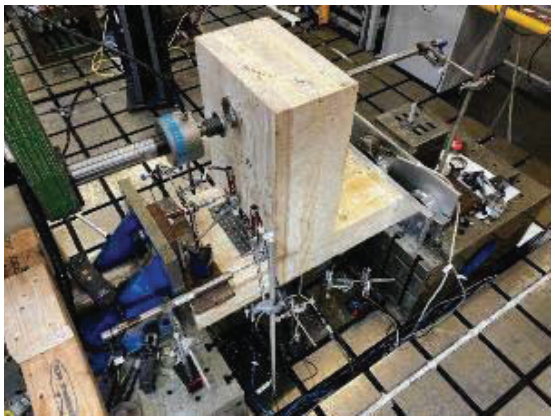

Figure 5: *Example of CLT specimen and the testing set up*

Gravity loads were combined as an accidental loading combination, based on an 8-storey CLT residential building with 6 m spans and 1.5 kN/m^2 live loading as per [29].

Then the metal brackets were bolted and fixed to hold the specimen in position which was restrained and rigidly fixed to mimic real conditions of fixing.

The hydraulic actuator loading operation comprised hold stage, load stage and load release stage.

The load from the hydraulic actuator was applied to the floor element at a predefined rate as tabulated in Table 2, to understand the impact of the ROL application.

ROL was one variable considered in this set of experiments. The load was removed immediately after reaching the predefined displacement.

Table 2: *Loading cases used in the testing, where C indicates the rate of loading (ROL)*

Item	Loading case	Abbreviation
C1	ROL = 6 mm/min	ROL6
C2	ROL = 600 mm/min	ROL600
C3	ROL = 3,600 mm/min	ROL3.6k
C4	ROL = 6,000 mm/min	ROL6k

C1 represents quasi-static load while C2, C3 and C4 represent an accidental loading to account for a scenario of disproportionate collapse modelled by a removal of a key element. In this testing this would be an internal wall in the ground floor.

Displacement controlled loading was used in all loading cases. Data collection frequency when using load scenario C1 and C2 was 1 kHz while using load scenario C3 and C4 it was set to 5 kHz.

4 RESULTS AND OBSERVATIONS

4.1 RESULTS

The results and observations of experiments are presented with series of graphs and tables below. Results obtained at C4 are not representative since they appear to be beyond the linear elastic state yet are still presented. The studied WFW connection is identified as a semi-rigid connection.

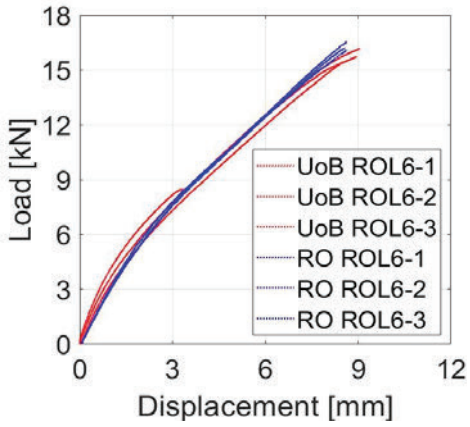

Figure 6: *Load – displacement for ROL 6 mm/min*

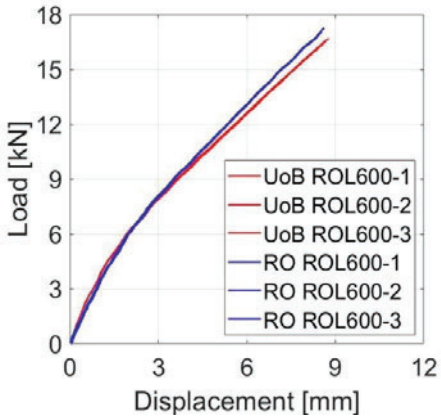

Figure 7: *Load – displacement for ROL 600 mm/min*

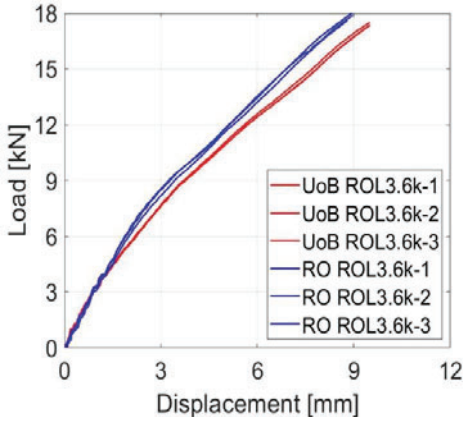

Figure 8: *Load – displacement for ROL 3,600 mm/min*

https://doi.org/10.52202/069179-0187

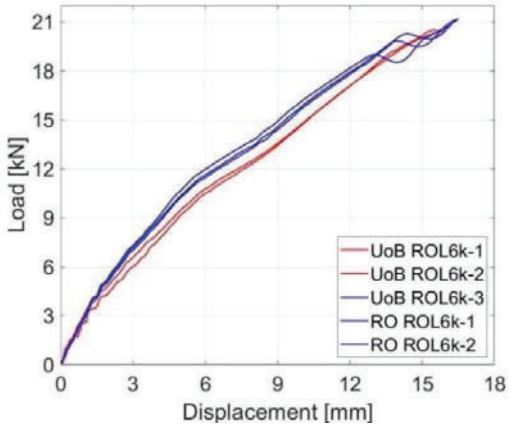

Figure 9: *Load – displacement for ROL 6,000 mm/min*

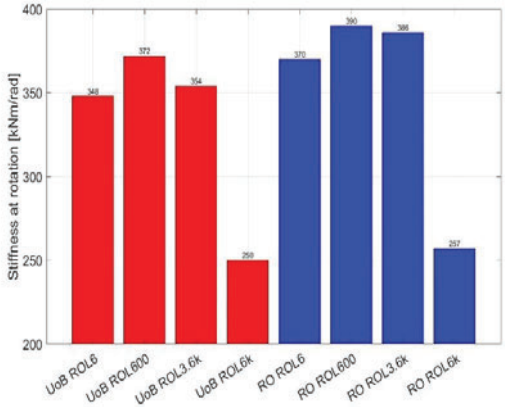

Figure 10: *Stiffnesses at rotation for rates of loads C1-C4*

Stiffness at rotation is calculated using engineering mechanics equations.

$$M = F \times L \quad (1)$$

$$\varphi = tan^{-1}(\frac{u}{L}) \quad (2)$$

$$K = (\frac{M}{\varphi}) \quad (3)$$

Where,

M = moment [kNm], F = force [kN], L = length from point of loading to wall is constant 440 mm (0.44 m),
u = displacement of app. 9 mm (0.09 m) for C1-C3 and app.16 mm (0.016 m) for ROL C4,
φ = rotation and is constant 0.02 rad and 0.036 rad,
K = rotational stiffness [kNm/rad].

Table 3 below tabulates the stiffness values for at the achieved rotations. Moreover, there is certain stiffness available in contrast to analytical approach of having hinged floor-to-wall joint where rotation is not considered.

Table 3: *Stiffness values for tests with generic bracket B1 UoB*

ROL	F	M	K
UoB ROL6	15.809	6.956	348
UoB ROL600	16.519	7.268	372
UoB ROL3.6k	17.431	7.670	354
UoB ROL6k	20.487	9.014	242

Table 4: *Stiffness values for tests with Rothoblaas bracket B2 RO*

ROL	F	M	K
RO ROL6	16.313	7.178	370
RO ROL600	17.177	7.558	390
RO ROL3.6k	17.924	7.886	386
RO ROL6k	21.054	9.264	246

Experimental values do not directly correlate to the models presented by Akter et al. [2] due to differences, such as wall and floor dimensions, fastener type, load on walls and the displacement induced, which resulted in a greater rotation of 0.05 rad.

4.2 OBSERVATIONS

General visual observation is that specimens do globally stay intact after being subjected to C1-C3. C4 however caused specimens to locally reach beyond elastic range. The plastic deformation is attributed to the increased displacement to achieve C4, which was governed by the software and hardware of the hydraulic actuator (3). In order to achieve C4 the displacement had to be greater than displacement at ROL C1-C3.

4.2.1 CLT

Most evident and immediately visible deformation was deflection of the floor, however no damage was identified visually as expected since the testing was planned to remain in the linear elastic range. Displacements of top and bottom walls, the lift and the drop under different ROLs are tabulated in Table 5 and Table 6 below.

Table 5: *Mean values of top wall vertical displacement (lift) LVDT1, where B1 indicates generic bracket (UoB) and B2 Rothoblaas (RO) bracket*

ROL	Mean (UoB)	Mean (RO)
C1	0.400	0.381
C2	0.484	0.423
C3	0.572	0.485
C4	0.722	0.690

Table 6: *Mean values of bottom wall displacement (drop) LVDT3*

ROL	Mean (UoB)	Mean (RO)
C1	3.870	3.926
C2	3.711	3.977
C3	4.107	4.169
C4	7.646	7.951

The bottom wall drops under the subjected loads. This results in opening between the floor element and the bottom wall as displayed in Figure 11. Consequently at C4 the strength perpendicular to the grain in the outer lamellas of the floor element was overreached and local crushing of the CLT occurred, because displacement was greater than in C1-C3. Figure 12 and Figure 13 display local crushing to the CLT.

https://doi.org/10.52202/069179-0187

Figure 11: *Reversible opening for all ROLs when B2*

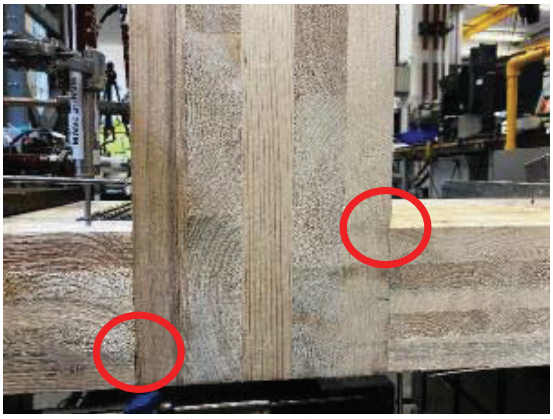

Figure 12: *Localised crushing to floor at both walls (specimen with generic bracket B1 UoB at C4)*

Figure 13: *Localised crushing to floor at the bottom wall (specimen with Rothoblaas bracket B2 RO at C4)*

4.2.2 Screws and brackets

No measurement on screws was undertaken but upon removal of the screws after the test no permanent deformation was observed.

No permanent deformation was anticipated and observed in metal brackets for ROL C1-C4, however generic bracket B1 plastically deformed under C4 as displayed in Figure 14.

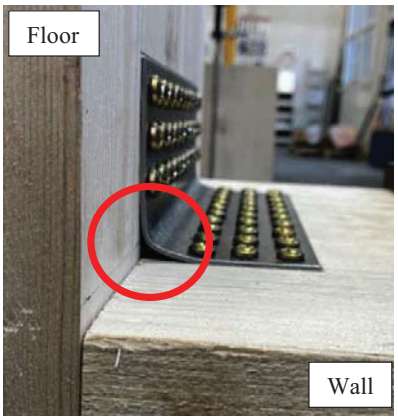

Figure 14: *Plastically deformed generic bracket (B1 UoB) when subjected to C4 and associated displacement*

5 CONCLUSIONS

Experimental studies of a typical wall-to-floor-to-wall (WFW) connection that can be found in a multi-storey building built in the platform type CLT construction were performed. Aim was to keep the specimens in the linear elastic range and to study how various rates of loading (ROLs) affect the CLT WFW connection.

Four different ROLs were used on two varied specimens. Most of the inherent material properties of timber, except the behaviour in compression, require designing in elastic range. When ROL C4 and associated displacement were applied to the specimens plastic deformation was confirmed as visible local crushing of outer lamellas of the floor element when in contact to the wall upon loading due to overreaching compressive strength perpendicular to the grain. Increase in stiffness at the achieved rotations might not be attributed to the ROL but to statistical error.

The outcomes of the performed tests will help with future testing scenarios where specimens will be tested beyond the elastic range and to failure and inform the development of future large scale system level study of the disproportionate collapse resistance of CLT platform type buildings. These are currently based on concrete and steel structures whereas slightly different behaviour is anticipated by CLT.

ACKNOWLEDGEMENT

This work is dedicated in memory of John Macdonald who passed away on 5th March 2022. Authors acknowledge invaluable partnership with EPSRC UK, Rothoblaas and StoraEnso who are supporting this research. Authors acknowledge Waugh Thistleton Architects who shared context information to support this study.

https://doi.org/10.52202/069179-0187

REFERENCES

[1] Chen Z, Tung D., Karacebeyli E., Modelling Guide for Timber Structures (2022), FPInnovations, Special Publication SP-544, Chapter 7.2, Page 5, Section 7.2.3.1.1, Figure 5 and Page 17, Section 7.2.3.2.1, Figure 22; Quebec 2022.

[2] Akter S. T., Bader T. K., Serrano E., Stiffness of cross-laminated timber (CLT) wall-to-floor-to-wall connections in platform-type structures (2020). In: WPC0232 Santiago, Chile: World Conference on Timber Engineering, WCTE 2020.

[3] Trada UK, Case study Stadthaus, Murray grove London, 2009.

[4] Churkina G., Organschi A., Reyer C.P.O. et al. Buildings as a global carbon sink (2020. Nat Sustain 3, 269–276. https://doi.org/10.1038/s41893-019-0462-4.

[5] UK Building Regulations. Approved document A – Structure, Section A3, page 41-45. HM Government by the NBS, part of RIBA Enterprises Ltd, UK, 2010.

[6] BS EN European Committee for Standardization, Eurocode 1: Actions on structures - Part 1-7 : General actions – accidental actions, BS EN 1991-1-1-7: 2006+A1:2014, BSI, 2006.

[7] Bita M. H., Currie N., Tannert T., Disproportionate collapse analysis of mid-rise cross-laminated timber buildings (2018), Structure and Infrastructure Engineering, 14:11, 1547-1560, DOI: 10.1080/15732479. 2018. 1456553.

[8] Dr. Mann A. P. et al. Practical guide to structural robustness and disproportionate collapse in buildings (2010). The Institution of Structural Engineers (IStructE), London, UK. Available at www.istructe.org.

[9] ARUP, Review of international research on structural robustness and disproportionate collapse (2011), Department for communities and local government, UK. Available at Structural robustness and disproportionate collapse of buildings: international research - GOV.UK (www.gov.uk).

[10] Byfield M., Mudalige W., Morison C., Stoddart E., A review of progressive collapse research and regulations (2014). Proceedings of the Institution of Civil Engineers – Structures and Buildings, Volume 167, Issue SB8, August 2014, Pages 447-456, http://dx.doi.org/10.1680/stbu.12.00023

[11] Gerhards C. C., Effect of duration and rate of loading on strength of wood and wood-based materials (1977), Forest Products Laboratory, Forest Service, U.S. Department of Agriculture.

[12] Huber J. A. J., Ekevad M., Girhammar A. U., Berg S., Structural robustness and timber buildings – a review (2019), Wood Material Science & Engineering, 14:2, 107-128, DOI: 10.1080/17480272.2018.1446052

[13] Voulpiotis K., Koechler J., Jockwer R., Frangi A., Quantifying Robustness in tall timber buildings (2020), International Network of Timber Engineering Research (INTER) 2020, online, pp.53-22-1, August 17-20, 2020.

[14] Schober U. K., Experimental research with timber (2014), Cost action FP1004, May 2014.

[15] Palma P., Fink G., Holistic design of taller timber buildings (2022), Cost action CA20139, star report, working group 1 robustness, December 2022.

[16] CEN-CENELEC (ed.): CEN/TC 250 N 3288 - Updated JRC technical report Guidance on the design for structural robustness (2022). Brussels, Belgium.

[17] Bita M. H., Tannert T., Disproportionate collapse prevention analysis for a mid-rise flat-plate cross laminated timber building (2019). Elsevier Engineering Structures 178 (2019) 460–471.

[18] Huber JAJ, Ekevad M, Girhammar UA and Berg S., Finite element analysis of alternative load paths in a platform-framed CLT building (2020). Proceedings of the Institution of Civil Engineers – Structures and Buildings 173(5): 379–390, https://doi.org/10.1680/jstbu.19.00136

[19] Huber J. A. J., Numerical modelling of timber building components to prevent disproportionate collapse (2021), Doctoral thesis, Luleå University of Technology, Skellefteå, Sweden.

[20] Przystup C. A., Lu Y., Reynolds T., Are current robustness design strategies appropriate for large timber structures? (2020), World Conference on Timber Engineering (WCTE) 2020.

[21] Bruehl F., Kuhlmann U., Jorissen A.,Consideration of plasticity within the design of timber structures due to connection ductility (2011), Engineering Structures, Volume 33, Issue 11, 2011, Pages 3007-3017, ISSN0141-0296, https://doi.org/10.1016/j.engstruct.2011.08.013.

[22] Callow P., Glockling J., Mass Timber Insurance Playbook (MTIP) V10 (not published draft), The Alliance for Sustainable Products (ASBP), Built by nature, Obtained with permission and by the authors and ASBP.

[23] Nocetti M., Diagnosis and monitoring of CLT/GLT and solid wood structures (2019), Talk delivered at Rothoschool, seminar on mass timber, London, 2019.

[24] Product catalogue Rothoblaas, page 26-45 (floor-to-wall screw HBS), 102-105 (bracket screws LBS), 2020 and addendum for angle bracket NINO (2022).

[25] Declaration of performance, CE certificate, CE-DOP-005, Reisser R2 screws. June 2013.

[26] European Technical Approval, ETA-12/0114, Spax self-tapping screws, September 2012.

[27] Product catalogue Spax wirox, page 109, 2021.

[28] Gustafsson A. et al. CLT Handbook, Swedish Wood, Föreningen Sveriges Skogsindustrier, Skelleftea, Sweden, 2019. Available at www.swedishwood.com.

[29] BS EN European Committee for Standardization, Eurocode 0 and Eurocode 1: Basis of structural design and Actions on structures, Part 1-1: General actions – densities, self-weight, imposed loads for buildings and Part 1-7: Accidental actions, BS EN 1990: 2002+A1, BS EN 1991-1-1 and BS EN 1991-1-7: 2006+A1:2014.

World Conference on Timber Engineering Oslo 2023

AN EXPERIMENTAL STUDY ON SHEAR PERFORMANCE OF CLT DOWEL JOINTS WITH SHEAR PLATES

Tsuyoshi Akutagawa[1], Hiroya Hanaoka[2], Masamichi Sasatani[3],

ABSTRACT: Cross Laminated Timber (CLT) is often used in mid and high rise timber buildings, and there has been much research into its joints. In this paper, a dowel-type joint with a steel plate and shear plate between two CLTs are proposed, and experiments are carried out to gain knowledge of the shear capacity and stiffness of the joint. The variables in the experiment were the composition of a CLT, shear plate way of insertion, and end distances. The experimental results and Johansen's theory were used to study the stress transfer mechanism and to obtain equations for estimating the stiffness and shear capacity of the joints. The experimental results confirm the superiority of shear plates in terms of shear capacity and other factors.

KEYWORDS: Cross Laminated Timber, Shear plate, drift pins, Shear performance of dowel joint

1 INTRODUCTION

Due to global environmental issues, there is an active movement to develop timber architectures, and Cross Laminated Timber (CLT) is often used, especially in mid and high rise timber architectures. In this case, the performance of the building hinges on the performance of its joints, given the high rigidity of CLT panels. Various techniques are employed to enhance joint strength, including augmenting the diameter or quantity of connectors. In this study, our emphasis was on the use of shear plates as a means of enhancing the performance of single joints.

Shear plates are one type of joint employed in timber architectures, but not enough knowledge is available on combining them with CLT. A design of shear plate connections in CLT is beyond scope of NDS and AIJ [1-2].

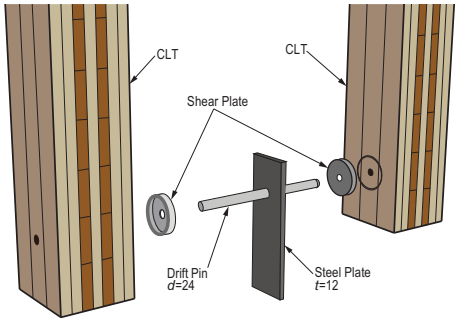

Figure1: *Image of the joint.*

In this study, we conducted experiments on joints that combined drift pins and shear plates, as shown in Fig. 1, and confirmed their shear capacity and stiffness properties. In addition, experimental results and Johansen's theory were used to estimate the load-bearing capacity using a simple equation.

2 TENSILE TESTING OF JOINTS

2.1 EXPERIMENT OVERVIEW

A list of specimens is in Table 1 and experimental variables are shown in Fig. 2.

Experimental variables were a composition of CLT (JAS standard grades: S90-5-7, S90-5-5, S60-3-4, and S60-3-3), way of insertion of shear plates, and end distance. The diameter of drift pins (d = 24 mm) and outer diameter of shear plates (D = 110 mm) used to join specimens were standardized for all variables. By CLT composition, four lengths were used, 417 mm, 297 mm, 237 mm, and 177 mm. Steel plates used for the joints were 12 mm thick, and holes for drift pins (φ=25 mm) were provided with a clearance of 1 mm. Between two CLTs, a plywood plate of a thickness equal to a steel plate was inserted.

A specimen is shown in Fig. 3.

Loading conditions were static monotonic loading and an application rate of 0.05 mm/sec. Displacement transducers were used to measure relative vertical displacement between each CLTs and steel plate at four locations, and mean values were used to evaluate results. An experiment was terminated when a load was reduced to 80% of a maximum load (Pmax) or when a displacement exceeded 25 mm.

[1] suyoshi Akutagawa, Graduate School of Tokyo Denki Univ., M.Eng., Japan, 21uda01@ms.dendai.ac.jp
[2] Hiroya Hanaoka, Graduate School of Tokyo Denki Univ., Japan, 22fma28@ms.dendai.ac.jp
[3] Masamichi Sasatani, Prof., Tokyo Denki University, Dr. Eng., Japan, sasatani@maill.dendai.ac.jp

https://doi.org/10.52202/069179-0188

Table 1: *Experimental variables*

Specimen name	Grade ※1	Composition	Insertion Type	End distance (mm)	Number carried out
J1-(i)-168	S90 5-7	7layer (t=210mm) Cypress	(i)	168	3
J1-(iii)-168			(iii)		3
J2-(i)-168	S90 5-5	5layer (t=150mm) Cypress	(i)	168	6
J2-(ii)-168			(ii)		6
J2-(iii)-168			(iii)		6
J2-(i)-240			(i)	240	6
J3-(i)-168	S60 3-4	4layer (t=120mm) Cedar	(i)	168	3
J3-(iii)-168			(iii)		3
J4-(i)-168	S60 3-3	3layer (t=90mm) Cedar	(i)	168	3
J4-(iii)-168			(iii)		3

※1 Conforms to the standards to the JAS (Japanese Agricultural Standards)

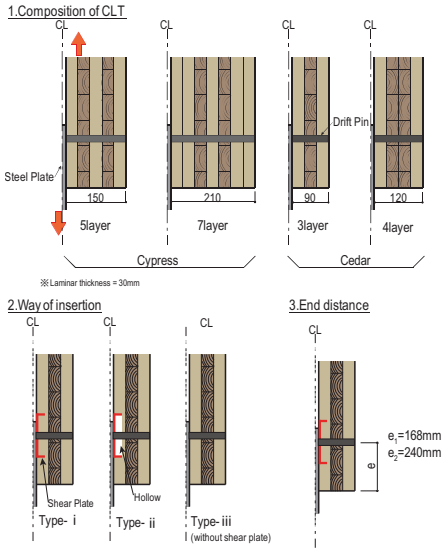

Figure2: *Experimental variables.*

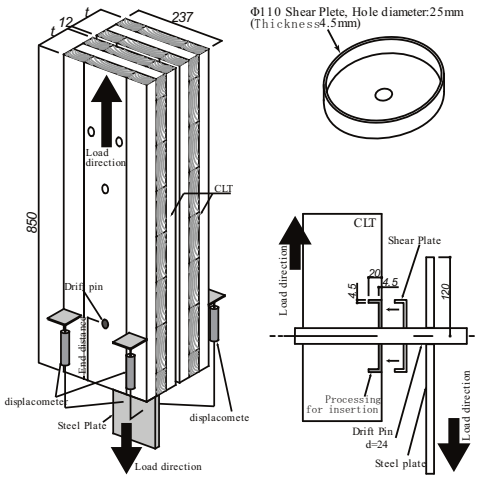

Figure3: *Shape of the test piece and test method.*

2.2 CATEGORIES OF FAILURE

The typical failure modes of CLTs identified at the end of experiments are shown in Fig. 5, the typical drift pin deformation states are shown in Fig. 6, and the categories of failure modes for all variables are shown in Table 2.

In both variables, out-of-plane deformation occurred in the two CLTs due to bending deformation of the drift pins because the CLTs were not constrained to open in the out-of-plane direction.

Four failure modes were observed at the end of experiments when specimens were disassembled as follows.

Mode [a]: embedded drift pin deformation only.

Mode [b]: Shear failure at the end of CLTs.

Mode [c]: Tensile failure of the orthotropic layers and shear failure to laminate surfaces.

Mode[d]: Tensile fracture near a finger joint of laminae on steel plate side.

A Comparison of the failure status of each variable confirms that the insertion of shear plates suppresses the deformation of a drift pin and that the thinner the CLT, the more likely it is to fail in the orthogonal layers.

Mode [a] failure was observed only in the Type-(iii) specimens. Failure of mode [b] was observed in Type-(i) and (ii) but not in Type-(iii). Modes [c] and [d] were observed at J3 and J4, possibly due to the thin CLT thickness, which resulted in large out-of-plane deformations. In particular, mode [d] could be attributed to the stress concentration at the bottom of the shear plate when the CLT was deformed out-of-plane and to the smaller edge distance due to the insertion of a shear plate.

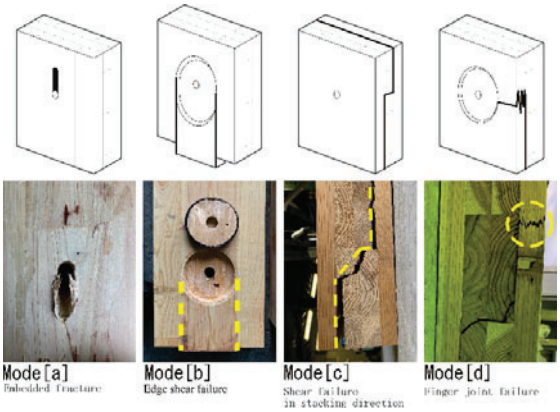

Figure5: *Final failure modes of CLTs.*

Figure6: *drift pin deformations.*

https://doi.org/10.52202/069179-0188

Table 2: *failures of all specimens.*

Specimen	No.					
	(1)	(2)	(3)	(4)	(5)	(6)
J1-(i)-168	b ③	b ③	b ③			
J1-(iii)-168	b ①	b ①	b ①			
J2-(i)-168	b ③	b ③	b ③	b + c ③	b ③	b ③
J2-(ii)-168	b ③	b ③	b ③	b ③	b ③	b ③
J2-(iii)-168	a ②	a ②	a ②	a ②	b ②	b ②
J2-(i)-240	b ③	b ③	b ③	b ③	b ③	b ③
J3-(i)-168	b +d ③	b + d ③	b + d ③			
J3-(iii)-168	b + c ②	c ②	b + c ②			
J4-(i)-168	b ③	b ③	b + c ③			
J4-(iii)-168	a ②	a ②	b + c ②			

2.3 EVALUATION OF JOINT TESTS

A typical load(P)-displacement(δ) curve is shown in Fig. 7, a yield load evaluation method is shown in Fig. 8, bearing capacity and stiffness for each variable are shown in Table 3, and a comparison of experimental results is shown in Fig. 9.

All variables showed initial slip (δ=1mm) for a clearance with a steel plate. After that, stiffness began to decrease when displacement was about 3 mm. Type-(iii) specimens showed increased displacement at a nearly constant load without significantly decreasing load. Type-(i) and Type-(ii) specimens continued to increase in load at about 50-60% of their initial stiffness after the stiffness drop was observed, and the load dropped abruptly at maximum load.

Table 3: *Results of tensile test of joints*

Specimen	Pmax [kN]		K[kN/mm]		Py ①		Py ②	
	mean	C.V. [%]	mean	C.V. [%]	mean	C.V. [%]	mean	C.V. [%]
J1-(i)-168	186.0	9.8	50.66	11.9	119.0	28.4	153.4	12.0
J1-(iii)-168	135.0	3.7	43.05	14.6	97.2	13.4	112.8	5.0
J2-(i)-168	178.0	6.7	53.04	23.6	93.0	11.5	155.5	9.5
J2-(ii)-168	187.6	8.1	54.8	10.9	108.1	19.3	172.2	7.8
J2-(iii)-168	145.2	4.9	59.1	44.8	103.0	10.8	112.5	11.1
J2-(i)-240	213.5	6.7	64.7	14.9	113.7	13.9	183.3	9.4
J3-(i)-168	141.0	9.9	30.42	5.4	97.6	8.2	129.2	1.8
J3-(iii)-168	95.9	9.2	35.51	17.5	71.1	7.1	78.3	8.8
J4-(i)-168	141.7	8.1	39.61	9.6	75.3	21.1	125.0	12.0
J4-(iii)-168	108.5	10.3	40.20	15.8	75.5	12.9	93.6	9.2

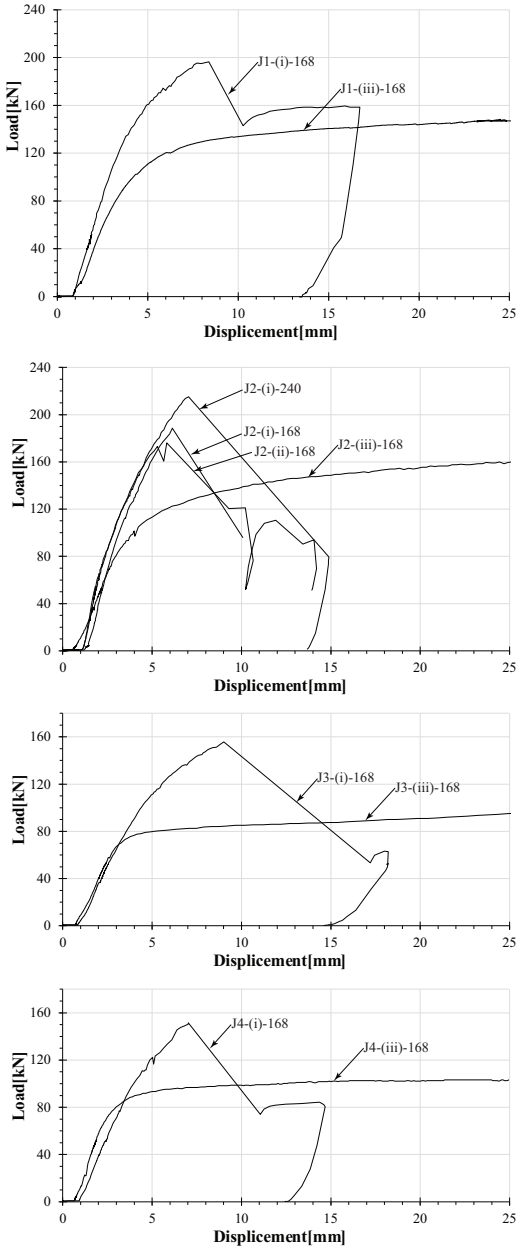

Figure7: *Relations between load and displacement*

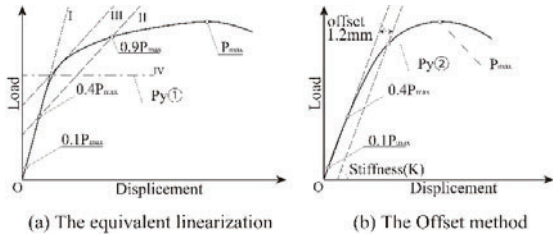

Figure8: *Yield load evaluation method*

Obtained stiffness and strength values are compared. For the maximum load, specimens of Type-(i) and (ii) were increased by 20-50% when compared to Type-(i). There

https://doi.org/10.52202/069179-0188

was no apparent difference in bearing capacity between Type-(i) and (ii), suggesting that the contribution of lumber inside a shear plate to the maximum load is small. No apparent increase or decrease in the stiffness was observed with a way insertion of a shear plate. It was considered that the clearance of holes for shear plate joints meant that a shear plate did not contribute to the stiffness. Yield loads differed significantly depending on the evaluation method. When the offset method(Py②) was used for evaluation, a 25-40% increase was observed for Type-(i) versus Type-(iii), and a 20% increase was observed for e=240mm versus e=168mm for the edge clearance distance e=240mm. On the other hand, when the equivalent linearization method[1] (Py①) was used for evaluation, the increase in bearing capacity was not as significant as the offset method. Depending on the variables, Type-(iii) showed higher results than Type-(i).

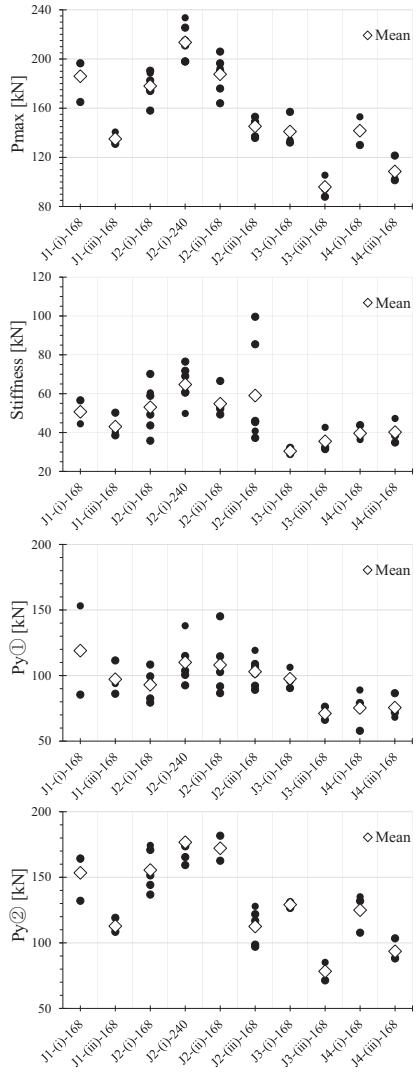

Figure9: *comparison of various property values.*

3 ESTIMATION OF LOAD CARRYING CAPACITY

3.1 EMBEDDING STRENGTH

Before estimating a joint's bearing capacity, an experiment was conducted to confirm CLTs' embedding strength (Fe). Experimental variables are shown in Table 4 and experimental results and specimen densities are shown in Table 5.

This study employed mean values of embedding strength to estimate yield capacities.

CLTs used in experiments were cut from the same panels as those used in Chapter 2, and four variables (S90-5-7, S90-5-5, S60-3-4, and S60-3-3) were conducted. The Dowel diameter (d) used for force application was 24 mm, and embedding strength was checked using the offset method (offset value was 1.2 mm) [3].

In this study, mean values of embedding strength were employed to estimate yield capacities.

Table 4: *Experimental variables (embedding test)*

Specimen	Grade	Composition	Thicness t [mm]	Specimen size
A-1	S90	5-7 (Cypress)	210	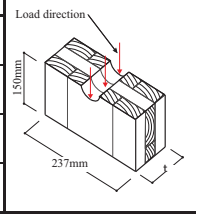
A-2		5-5 (Cypress)	150	
A-3	S60	3-4 (Cedar)	120	
A-4		3-3 (Cedar)	90	

Table 5: *Results of embedding test*

Specimen	Number Carried out	Density Mean [g/cm^3]	Embedding Stress [N/mm^2]
A-1	6	0.476	34.68
A-2	6	0.485	30.04
A-3	6	0.438	22.17
A-4	6	0.36	18.27

3.2 CALCULATION MODEL

Although previous studies have proposed evaluation formulas that consider the ratio of bearing strength for each lamina [4-6], in this study, the yield load was evaluated using equation (1) to simplify the formulas.

$$P_y = C \cdot d \cdot l \cdot F_e \quad (1)$$

Where *Py*: yield strength (kN), *C*: coefficient of joints type, *d*: pin diameter (mm), *l*: effective length of drift pin (mm), and *Fe*: embedding strength of lumber (N/mm2).

C in equation (1) assumes the case of a joint with a steel plate inserted. The equations for calculating *C* in 3 failure modes shown in Fig. 10 are below. The following minimum values are used in equation (1).

https://doi.org/10.52202/069179-0188

$$Mode1: C = 1.0 \tag{2}$$

$$Mode2: C = \sqrt{2 + \frac{8}{3}\gamma\left(\frac{d}{l}\right)^2} - 1 \tag{3}$$

$$Mode3: C = \frac{d}{l}\sqrt{\frac{8}{3}\gamma} \tag{4}$$

Where γ: ratio of material strength (F) of the drift pin to the reference bearing strength of the main material (F/Fe).

For joints with shear plates, *C* is similarly calculated for three failure modes. An assumed stress state is shown in Figure 10. In this case, the stress transmitted through a shear plate ($Fe \cdot D$) is not considered because this stress has a smaller shear span ratio than other stresses. The following equations express formulas for the forces and moments applied to the drift pins in each mode.

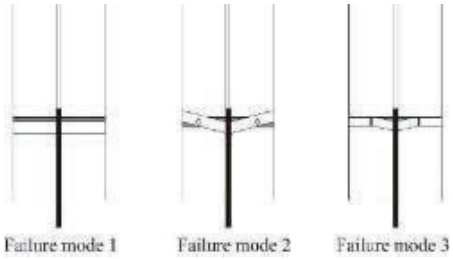

Figure10: *Failure modes.*

$Mode1$

$$\frac{P_y}{2} - F_e \cdot D \cdot h - F_e \cdot d \cdot \frac{l}{2} = 0 \tag{5}$$

$Mode2$:

$$\begin{cases} \dfrac{P_y}{2} - F_e \cdot D \cdot h - F_e \cdot d \cdot (x-h) + F_e \cdot d \cdot \left(\dfrac{l}{2} - x\right) = 0 \\ M_y - F_e \cdot d \cdot \dfrac{(x^2 - h^2)}{2} + F_e \cdot d \cdot \dfrac{\left(\left(\frac{l}{2}\right)^2 - x^2\right)}{2} = 0 \end{cases} \tag{6}$$

$Mode3$:

$$\begin{cases} \dfrac{P_y}{2} - F_e \cdot D \cdot h - F_e \cdot d \cdot (x-h) + F_e \cdot d \cdot \left(\dfrac{l}{2} - x\right) = 0 \\ M_y - F_e \cdot d \cdot \dfrac{(x^2 - h^2)}{2} + F_e \cdot d \cdot \dfrac{\left(\left(\frac{l}{2}\right)^2 - x^2\right)}{2} = 0 \end{cases} \tag{7}$$

Solving each simultaneous equation yields *C* for a joint with a shear plate, expressed by the following equation.

$Mode1$:

$$C = 1 - \alpha + \alpha\beta \tag{8}$$

$Mode2$:

$$C = \sqrt{2(\alpha^2 + 1) + \frac{8}{3}\gamma\left(\frac{d}{l}\right)^2} - 1 - \alpha + \alpha\beta \tag{9}$$

$Mode3$:

$$C = \sqrt{\alpha^2 + \frac{8}{3}\gamma\left(\frac{d}{l}\right)^2} - \alpha + \alpha\beta \tag{10}$$

Where *D* = outer diameter of shear plates (mm), h = depth of shear plate (mm), *My* = plastic moment of drift pin ($F \cdot d^3/6$ (N/mm)), α = ($2h/l$), β = (D/d), *x* = variable representing drift pin rotation center or plastic hinge position (mm).

For the embedded strength (Fe) in Equations (1), (2) through (4) and (8) through (10), the diameter of drift pins and shear plates were not distinguished, and the results in Section 3.1 were used to examine the applicability of a yield load. The calculation model for Type-(ii) was performed without distinction within this study since no difference in bearing capacity due to different ways of insertion was experimentally observed.

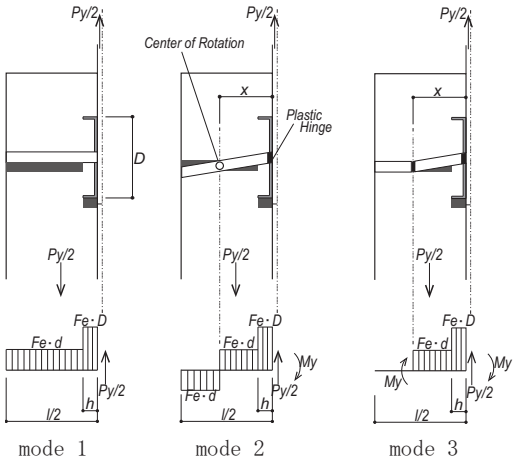

Figure11: *stress condition of joints with shear plates.*

3.3 ESTIMATED FAILURE MODE AND LOAD CAPACITY

Results of the calculation of *C* and estimated failure modes for each variable are shown in Table 6, and a comparison of calculation values and two experimentally obtained yield loads (Py① and Py②) is shown in Table 7. Colorized areas in Table 6 are the minimum values of *C*.

https://doi.org/10.52202/069179-0188

The deformation state of drift pins was generally similar to failure modes assumed from the calculated *C*. On the other hand, specimens Type-(i) and (ii) showed a sudden drop in load due to shear failure at the edge of CLT. A detailed study including shear failure is considered necessary in the following study.

Comparing two experimentally obtained yield loads with calculated values, evaluations using an equivalent linear replacement method tended to be slightly lower than calculated. Conversely, using the offset method, evaluation tends to be larger than calculated values. In addition to the fact that the embedding strength of each lamina was not considered to simplify this calculation, it is necessary to further examine experimental evaluation methods to improve calculation accuracy.

Table 6: *Calculation result for C*

Specimen	*d* [mm]	*l* [mm]	*h* [mm]	*D* [mm]	*F* [N/mm²]	F_e [N/mm²]	*C* mode1	mode 2	mode 3
J1-(i)-168	24	405	18	110	300	34.68	1.32	0.40	0.62
J1-(iii)-168	24	405	-	-			1.00	0.44	0.28
J2-(i)-168 J2-(ii)-168 J2-(i)-240	24	285	18	110	300	30.04	1.45	0.60	0.91
J2-(iii)-168	24	285	-	-			1.00	0.48	0.43
J3-(i)-168	24	225	18	110	300	22.17	1.57	0.83	1.23
J3-(iii)-168	24	225	-	-			1.00	0.55	0.64
J4-(i)-168	24	165	18	110	300	18.27	1.72	1.12	1.62
J4-(iii)-168	24	165	-	-			1.00	0.71	0.96

Table 7: *Comparison of calculation results*

Specimen	$_{(cal)}Py$ [kN]	$_{(mean)}Py$① [kN]	$_{(mean)}Py$② [kN]	$_{(mean)}Py$①/$_{(cal)}Py$	$_{(mean)}Py$②/$_{(cal)}Py$
J1-(i)-168	138.88	119.05	153.45	0.86	1.10
J1-(iii)-168	98.78	97.22	112.76	0.98	1.14
J2-(i)-168	128.36	93.00	155.51	0.72	1.21
J2-(ii)-168	128.36	113.74	183.30	0.89	1.43
J2-(iii)-168	128.36	108.09	172.17	0.84	1.34
J2-(i)-240	93.05	102.98	112.51	1.11	1.21
J3-(i)-168	104.23	97.62	129.17	0.94	1.24
J3-(iii)-168	69.68	71.12	78.33	1.02	1.12
J4-(i)-168	87.18	75.33	124.96	0.86	1.43
J4-(iii)-168	55.16	75.55	93.57	1.37	1.70

4 CONCLUSIONS

The following conclusions can be drawn from this study.

(1) Four types of wood fracture properties and three types of drift pin deformation states were identified. Shear failure at the CLT edge is more pronounced when shear plates are used.
(2) The deformation state of the drift pins indicates that yielding is dominated by the drift pins and the penetration stress.
(3) The use of shear plates is expected to increase the maximum load by 20-50%. On the other hand, the contribution to stiffness was not so great.
(4) The calculation of the joint type of coefficient C used in the proposed equation showed that the failure conditions of the drift pins in the experiment and the assumed yielding mode were in general agreement.

In the future, more detailed studies will be required, such as evaluation methods of the experiments and consideration of the embedded strength of each lamina that constitutes the CLT.

REFERENCES

[1] AIJ:Standard for Structural Design of Timber Strucures, 2018

[2] National Design Specification for Wood Construction, American Forest & Paper Association ANSI/AF & PA、pp.120、2018.

[3] K. Sawata, M. Yasumura：Determination of embedding strength of wood for dowel-type fasteners 、*Journal of Wood Science*, Vol.48, pp138-146, 2002.

[4] T.Uibel, H.J.Blaß:Load Carrying Capacity of Joints with Dowel Type fasteners in Solid Wood Panels, CIB-W18/39-7-5, 2006

[5] S. Nakashima, A. Kitamori, K. Komatsu: Evaluation of tensile performance of drift pinned joints with steel plate on cross laminated timber (in Japanese). *Journal of Structural and Construction Engineering*, 78(687):969-975, 2013.

[6] S. Nakashima, N. Miki, N. Akiyama, Y. Araki: Estimation of initial stiffness, yield load, and ultimate load for the clt drift pinned connection with steel inserted plate and experimental verification (in Japanese). *Journal of Structural and Construction Engineering*, 86(783):793-803,2021

[7] R. Tomitaka, M. Toda: Application of European Yield Theory to Laminated Timber composed of Lumber with any Thickness and Bearing Strength (in Japanese). *Summaries of Technical Papers of Annual Meeting, Architectural Institute of Japan*, Structures III, pp.555-556, 2018

[8] N. Suzuki, Y.Yamazaki, H.Sakata, N.Toba, Y.Nonaka: A study on yield strength of CLT connection using LSB and shear-ring (in Japanese). *Summaries of Technical Papers of Annual Meeting, Architectural Institute of Japan*, Structures III, pp.549-550, 2012

https://doi.org/10.52202/069179-0188

World Conference on Timber Engineering Oslo 2023

EXPERIMENTAL AND NUMERICAL INVESTIGATION OF CROSS-LAMINATED TIMBER JOINTS WITH MULTIPLE GLUED-IN RODS

Younes Shirmohammadli[1], Ashkan Hashemi[2], Reza Masoudnia[3], Pierre Quenneville[4]

ABSTRACT: Glued-in rod connections are highly efficient joints in timber structures, with many advantages, including high strength and stiffness, good fire performance, and architectural design advantages. They have been used for many years, mainly for glulam members and, to a limited degree for laminated veneer lumber (LVL) members in new timber structures or reinforcing existing timber buildings. This research covers glued-in rods in Cross-Laminated Timber (CLT) panels to address the growing interest in constructing mid-to high-rise buildings, where hybrid structural systems are frequently used. Therefore, a combined experimental and numerical investigation has been designed to apply such connections in CLT, and full-scale monotonic and cyclic tests have been performed. For the experimental tests, the specimens vary in embedment length and the location of the rods. Moreover, numerical simulations and parametric studies of glued-in rod connections in CLT have been performed to further extend the scope of the study and make conclusions. The simulations are based on a 3D finite element analysis, using a cohesive surface model for the interaction between the epoxy adhesives and the inner surface of the holes. The parametric studies investigated the influence of the anchorage length, the rod diameter, and the rod-to-grain angle on the load-bearing capacity and stiffness of the glued-in rod connections in CLT. The results of this study demonstrates a high potential of these connections in CLT construction with savings on space and cost when compared to conventional timber connections.

KEYWORDS: Glued-in rods, Timber connections, Cross Laminated Timber, Timber Engineering, Numerical Modeling.

1 INTRODUCTION

In timber structures, connections can take up to 70% of the design effort, and the capacity of the structures is generally governed by the strength and stiffness of the connections and joints [1]. Glued-in rods are high-capacity hybrid connections that are largely used for new timber structures and reinforcement of existing timber buildings. They present high strength and stiffness, good resistance against corrosion and fire, present ductile performance, and provide aesthetic benefits [2]. The efficient design and construction of such high-strength connections often determine the level of success of timber structures compared to concrete and steel.

Glued-in rods have been used in New Zealand and other countries for over thirty years for glulam and LVL members, and well-designed timber structures with appropriate materials have shown good structural performance [3]. With the advent of CLT construction, glued-in rod connections demonstrated the potential to be widely implemented. Because the arrangement of layers and manufacturing process of CLT is different from other engineered wood products, the stress distribution and strength of connections in these products can also be different, which requires more detailed studies [4]. Moreover, depending on the CLT member size and structural design, the rods need to be located on the parallel, perpendicular, or on the boundary of two cross-wised layers.

Most of the studies regarding glued-in rods are focused on the single rod investigation, while in real applications, glued-in rods are used in groups. Plastic deformation of connections is frequently used in timber constructions to achieve ductility. Therefore, the behaviour of those crucial connections in terms of ductility and energy dissipation under cyclic loads must be thoroughly understood.

This research looks into monotonic loading and numerical modeling of glued-in rods embedded in various configurations on the edge of CLT panels. Moreover, the cyclic loading performance of glued-in rods is also investigated. The results of the cyclic loading will illustrate the effect of loading on the stiffness and strength of glued-in rod connections to be designed for high seismic regions.

2 Materials and Methods

CLT panels made of New Zealand-grown Radiata pine bonded with one-component polyurethane adhesive were used as the timber part of the connection. The CLT panels consisted of MSG8-grade laminations for longitudinal

[1] Younes Shirmohammadli, The University of Auckland, New Zealand, yshi829@aucklanduni.ac.nz
[2] Ashkan Hashemi, The University of Auckland, New Zealand, a.hashemi@auckland.ac.nz
[3] Reza Masoudnia, University of Waikato, New Zealand, rm667@students.waikato.ac.nz
[4] Pierre Quenneville, The University of Auckland, New Zealand, p.quenneville@auckland.ac.nz

https://doi.org/10.52202/069179-0189

layers and MSG6-grade laminations for transverse layers. In the experimental tests, for CLT specimens with rods embedded perpendicular to the lamination and rods on the boundary of two cross-wised layers, 5-layer CLT panels were used, while for the rods embedded parallel to the grain, 7-layer CLT panels were used, so the outer layers of the CLT specimens were lengthwise for all of the specimens. The panels were cut into specimens with 240 mm width to provide a 3.5*d* edge distance and a 3*d* rod distance. Four M24 threaded rods (8.8 grade) were placed in holes with 30 mm diameter in the parallel, perpendicular, and on the boundary of two cross-wised layers of the CLT panels at two different embedment lengths (250 and 350mm). The dimensions of the CLT specimens holding the glued-in rods are shown in Figure 1.

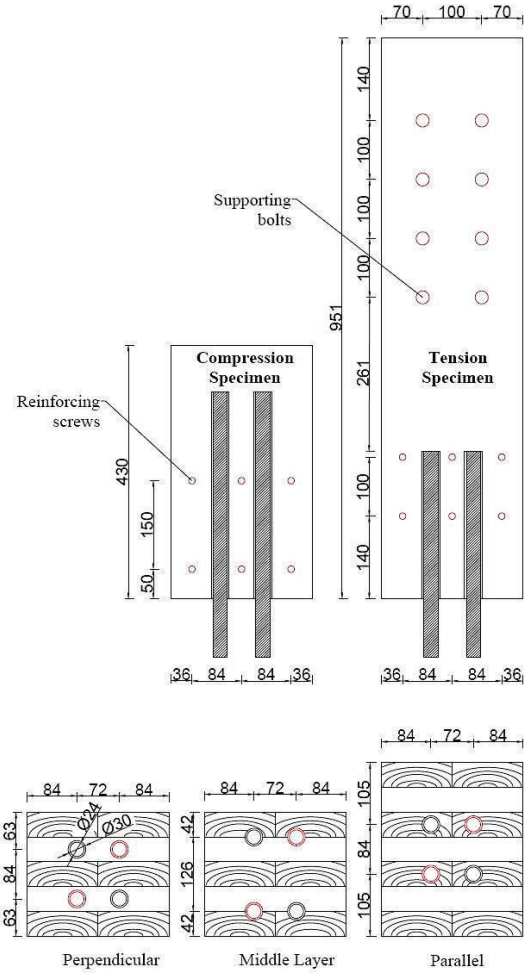

Figure 1. Dimensions of CLT specimens containing rods on the cross section. Rods drawn in red on the cross sections represent two diagonally tested rods.

The epoxy adhesive was injected into the bleeding holes located along each rod's length on the surface of CLT. The adhesive injected from one end of the rod's length travelled the length of the rod and exited from the other end after filling the gap by preventing the air bubble trap.

The properties of the applied epoxy adhesive are provided in Table 1.

Table 1. Typical properties of the cured epoxy adhesive.

	Typical cured properties			
Adhesive	Tensile strength (MPa)	Compressive strength (MPa)	Flexural strength (MPa)	Maximum operating temp (°C)
Epoxy	200-300	300-400	350-450	65-75

2.1 Experimental Tests

For the monotonic and cyclic tests, two diagonal rods were tested. The specimens containing rods with 250 mm embedment length were tested in tension, while specimens with 350 mm embedment length were tested in compression for both monotonic and cyclic tests. The 1000 kN Avery machine at the University of Auckland test hall was used for the monotonic loading, and a 500 kN MTS was used for the cyclic loading of the glued-in rod connections. The test setup of the cyclic tests is shown in Figure 2.

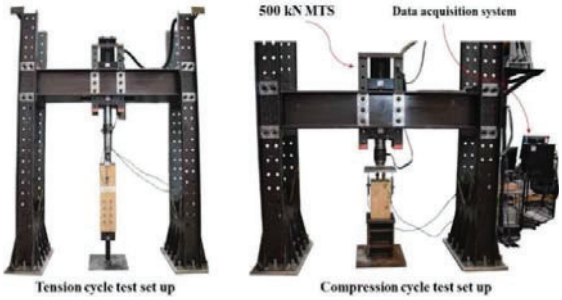

Figure 2. Cyclic loading test set-up.

For the tension tests, the CLT specimens were fixed using two knife plates inserted into the pre-cut slots in the transverse layers of CLT and held by eight M20 bolts. At the other end, a pulling steel member was designed and used to pull out two diagonal glued-in rods at the same time. Figure 3 shows the components of the CLT specimen with rods embedded perpendicular to the lamination to be tested in tension. The monotonic loading was applied at a constant displacement rate of 2 mm/min throughout the loading process. The average displacement/slip of the rods was measured using two LVDTs.

https://doi.org/10.52202/069179-0189

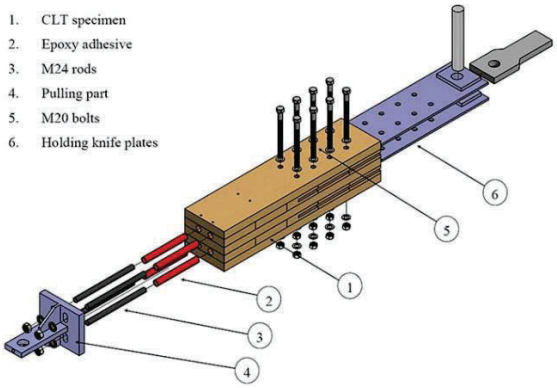

Figure 3. Exploded view of 5-layer CLT specimen with rods embedded perpendicular to the grain.

A loading procedure from BS EN 12512:2001 [7] was modified for cyclic loading. Due to the stiffness of the glued-in rod connections with failure occurring within 1-2 mm displacement of the rods, the rods were loaded in a force-control manner at a rate of 5 kN/s. The force reference for the cyclic loading was determined from the monotonic loading. For testing under cyclic loads, CLT specimens with 250 mm embedded length rods were subjected to tension-only cycles, while specimens with 350 mm embedment length rods were subjected to compression-only cycles. The specimens were put through a tension/compression load in the first cycle that applied 25% of the maximum load. Then, the load was released until zero force. The initial cycle was repeated in the second cycle, but this time 50% of the force was applied. In the third round, three cycles are completed at 75% of the maximum load. For the CLT specimens containing rods with 250 mm embedment length, the load was then increased until failure occurred, and for the specimens containing rods with 350 mm embedment length, three more cycles at the maximum load were established. Glued-in rods with embedment lengths of 250 mm were tested until they failed on the last cycle. However, specimens with embedment length of 350 mm did not fail within the standard range by the machine capacity. The loading cycles of specimens with 250 and 350 mm embedment lengths are shown in Figure 4.

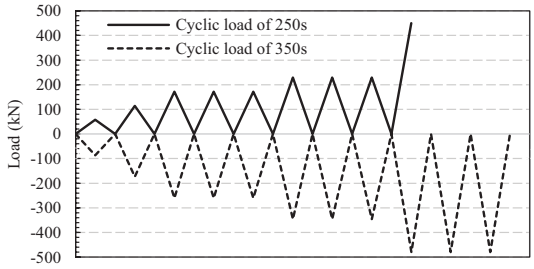

Figure 4. Cyclic loading protocols.

2.2 Numerical Modeling

The numerical analysis is performed using the Abaqus software package (finite element analysis software) [8] to investigate the effect of the rod diameter and embedment length on the pull-out strength and to study the stress distribution along the rods. The 3D model of the CLT panel was designed with cross-wised laminations with orthotropic properties (E_1= 10400 MPa, E_2-E_3= 347 MPa, ν_{12}= ν_{13}= ν_{23}= 0.2, G_{12}=G_{13}= 692, and G_{23}= 69) and tied interaction between the laminations and no edge bonding as in the tested CLT panel. While the properties of the rods (E=210000 MPa and ν=0.3) and epoxy adhesive (E= 2193 MPa and ν= 0.3) were defined as an isotropic material. The interaction between the rod's surface and the inner surface of the epoxy adhesive is defined as a 'tie' since in the experimental tests, no failure was observed (due to the excellent interaction of the threads of the rods and epoxy adhesive). The experimental test data was used to validate the numerical models. The load was applied to the rods with a displacement-based approach, and a rigid body was defined at the end of the CLT specimen and fixed as a boundary condition in the Z-direction to measure the reaction force. The numerical model of the glued-in rod connection is shown in Figure 5.

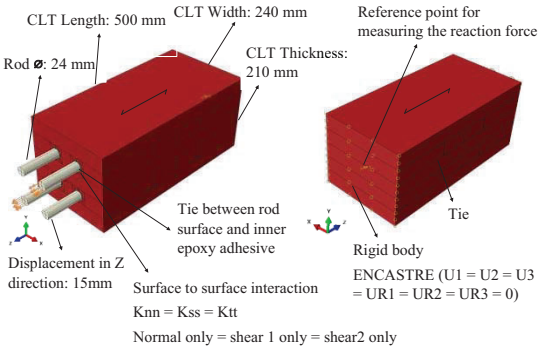

Figure 5. FE modeling of the glued-in rods connection with rods located on the perpendicular layers of CLT.

For each rod to grain configuration, different interaction properties are defined between the outer surface of the epoxy adhesive and the inner surface of the hole, which are shown in Table 2.

Table 2. Interaction properties of embedded rods regarding the rod to lamination angle.

Rod to grain orientation	*Knn* (N/mm^3)	*Kss* (N/mm^3)	*Ktt* (N/mm^3)	*Normal (MPa)*	*Shear-1 (MPa)*	*Shear-2 (MPa)*
Parallel	160	160	160	14.2	14.2	14.2
Perpendicular	225	225	225	14.5	14.5	14.5
Boundary	320	320	320	14.7	14.7	14.7

3 RESULTS AND DISCUSSIONS

3.1 Experimental tests

3.1.1 Monotonic loading

The average pull-out strength of glued-in rods with 250 mm embedment length is shown in Figure 6. For the rods embedded on the perpendicular, parallel, and boundary of

https://doi.org/10.52202/069179-0189

two cross-wised layers, the average pull-out strength of glued-in rods with 250 mm embedment length was 343 kN, 333 kN, and 305 kN, respectively. The shorter distance between the rods and the CLT surface led to a lower pull-out strength of the rods embedded on the boundary of two cross-wised layers. As a result, the stress reached the surface of the CLT specimen and formed a premature crack, subsequently leading to a lower pull-out strength. The glued-in rods with 350 mm embedment length at the perpendicular, parallel, and boundary of two cross-wised layers had average compression strengths of 506, 493, and 482 kN, respectively. The connection strength also decreased as a result of the lower surface distance of the rods embedded on the boundary of two cross-wised layers. The average compression strength of rods with 350 mm of embedment is displayed in Figure 6.

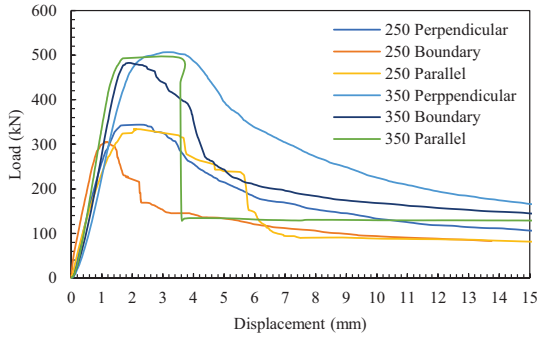

Figure 6. Average values for strength of glued-in rods with 250 and 350 mm embedment length.

The yielding of the steel rods in glued-in rod connections is intended to produce a ductile failure mode. To obtain the tolerance threshold of brittle failure and other types of failures of the connection components, this research was set up so that the steel rods' strength was greater than that of the other connection components. Given the characteristics of CLT, the specimen's failure mode can be influenced by its specifications, including laminations dimension, laminations grade, bonding, etc. For instance, not edge-bonded laminations, weak finger joints, and knots can initiate the failure and reduce the strength of the connection. Common failure modes of CLT specimens with rods embedment at the edge of CLT is shown in Figure 7.

Various potential failures have been reported in the literature for rods embedded perpendicular to the lamination. Most common failure types for rods implanted perpendicular to the grain is the separation of the entire transverse layer or rolling shear [5, 6]. Rolling shear failure in the transverse layers was the observed mode of failure for the rods embedded perpendicular to the lamination, as illustrated in Figure 7a. This is due to the lower tangential and radial strength of the wood. When glued-in rods are used as a connection, the failure in thetransverse layer caused by rolling shear revealed the need for reinforcing the CLT. Rolling shear still seems inevitable despite increasing the edge distance, and it is unaffected by the geometrical characteristics of the connection. This progressive rolling shear failure resulted in a smooth force-displacement curve. However, when the rods were put perpendicular to the grain, the stress did not reach the surface of the CLT. The epoxy adhesive was also crushed along the length of the rods.

The parallel to the grain rods were pulled out in the shape of plugs that held parallel lamination segments, as seen in Figure 7b. Therefore, whether it happened close to the wood-adhesive contact or by removing a block of wood, block shear of wood caused the connections to fail and resulted in a sharp strength reduction. The surface and edge of CLT specimens for the rods embedded parallel to the grain showed no signs of damage. The amount of plugged-out wood close to the rods could potentially be impacted by the non-edge bonded laminations. Similar plug-out failures have been recorded for rods inserted parallel to the lamination in the literature [9].

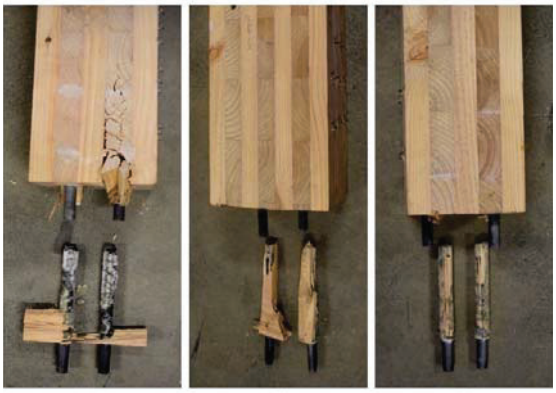

Figure 7. Failure modes on the edge of CLT specimens under tension test, (a) rods perpendicular to the lamination, (b) rods parallel to the lamination, and (c) rods embedded on the boundary of two cross-wised layers.

Rods inserted in the boundary of two cross-wised layers were entirely pulled out in the shape of a cylinder gripping the epoxy that had wood fibres on its surface, as shown in Figure 7c. Moreover, Figure 8 illustrates the influence of the rod's close proximity to the CLT surface by showing the failure mode of rods embedded on the boundary of two cross-wised layers while stress reaching the specimen's surfaces for both tension and compression specimens. When two lengthwise laminations that are not edge-bonded are situated close to the rod's length, this issue gets worse. Regarding the crack spreading to the CLT's surface, the edges of the specimens revealed no signs of damage. This crack formation has also been noticed in glulam specimens with glued-in rods due to the close edge distance, reaching the specimens' surface along the embedment length [10].

https://doi.org/10.52202/069179-0189

Figure 8. Surface crack of specimens containing rods on the boundary of two cross-wised layers.

3.1.2 Cyclic loading

Figure 9 provides an overview of the hysteresis response of the cyclic tests conducted on the glued-in rods embedded in CLT. All curves for the specimens with a 250 mm embedment length displayed a nearly linear trend at cycles until failure. Glued-in rods with 250 mm embedment length that were located perpendicular, parallel, and on the boundary of two cross-wised layers failed at 331, 317, and 297 kN, respectively. The connections for the rods with 350 mm embedment length demonstrated stiff and elastic performance, but there was a slight plastic deformation at each cycle in the last three cycles of the tests.

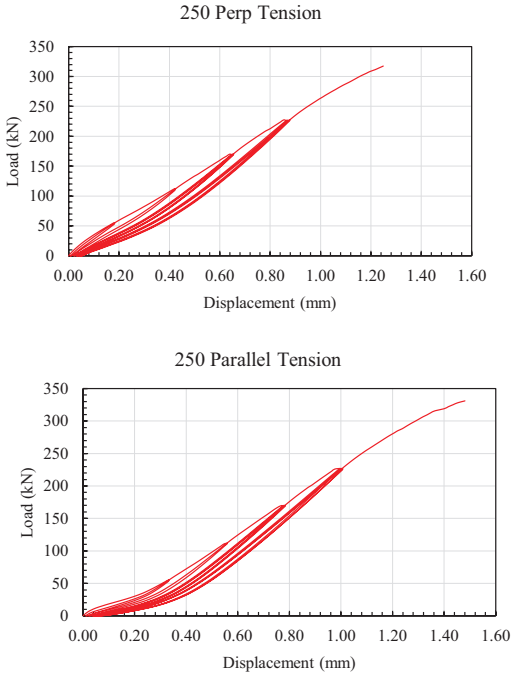

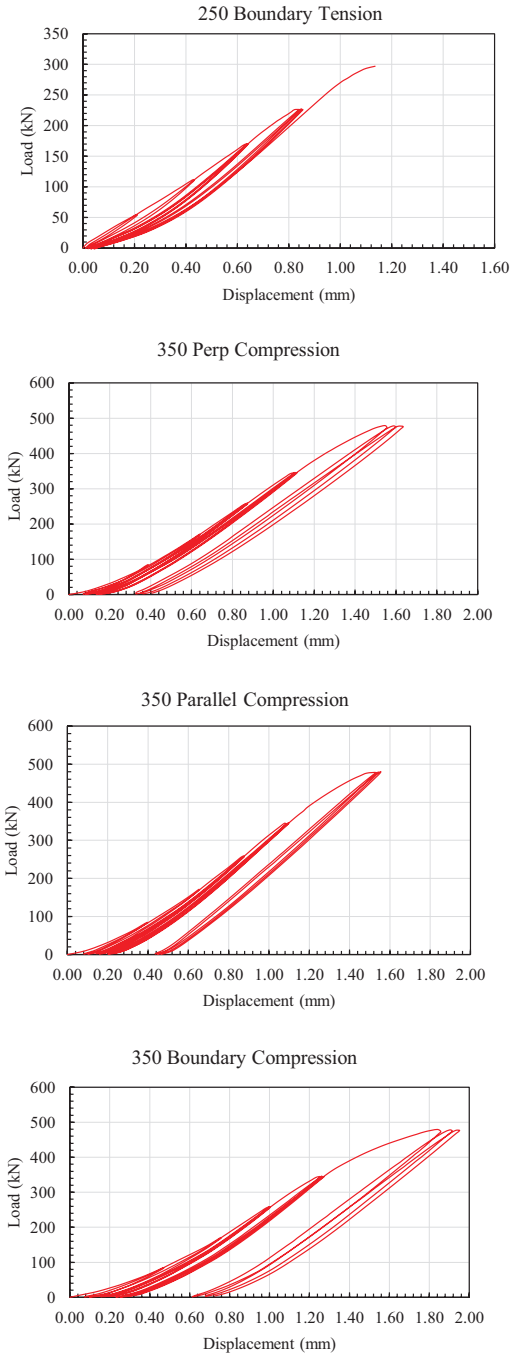

Figure 9. Hysteresis loops of glued-in rods under cyclic loading.

In contrast to glued-in rods with 250 mm embedment length, specimens with 350 mm anchorage length did not fail during the final cyclic tests. The specimens with 250 mm embedment length showed failure modes similar to monotonic tests.

https://doi.org/10.52202/069179-0189

3.2 Numerical modeling

3.2.1 Numerical modeling validation

Experimental tests were used to validate the numerical models. For every embedded rod that was parallel, perpendicular, or in the boundary of two cross-wised layers, high-precision validations were prepared. Maximum failure load, connections stiffness, and failure mode were the three characteristics used to evaluate the accuracy of the numerical modeling validations.

Table 3 compares the maximum loads of numerical models with the outcomes of experimental tests. The numerical models of rods with 250 mm embedment length at different locations were able to predict the pull-out strength with an average of 2% difference.

When the numerical models had been validated for rods with an embedment length of 250 mm, the prediction accuracy of the models was evaluated using experimental test results for rods with an embedment length of 350 mm. For the rods with 350 mm length which were modelled in tension, the numerical models estimated the pull-out strength of the rods with an average of 4% difference. The numerical models predicted the strength of glued-in rods with an overall P_{Test}/P_{FE} of 0.992 and a standard deviation of 0.028, as shown in Table 3. The higher discrepancy between the numerical modeling and experimental tests of rods with 350 mm embedment length was because rods were tested experimentally in compression while they were analysed in tension for the numerical modeling.

Table 3 Comparison of maximum strength of rods between experimental tests (P_{TEST}) and numerical modeling (P_{FE})

Rod to grain orientation	Embedment length (mm)	P_{Test}	P_{FE}	P_{Test}/P_{FE}
	L_a	(kN)	(kN)	
Perpendicular	250	344.0	346.7	0.99
Perpendicular	350	506.6	525.8	0.96
Boundary	250	305.2	310.0	0.98
Boundary	350	482.5	464.1	1.04
Parallel	250	333.9	331.8	1.01
Parallel	350	493.0	510.3	0.97
Average				0.992
Standard Deviation				0.028

The stiffness of the connections was also used to validate the numerical models. Figure 10 exhibits the strong conformity in stiffness between the numerical simulation and experimental tests of the M24 rods embedded perpendicular to the lamination of CLT and the experimental tests. Regarding the specified interaction properties in the numerical models, after following the stiffness and reaching the maximum load, it loses strength, although for the experimental tests, a gradual force reduction was obtained.

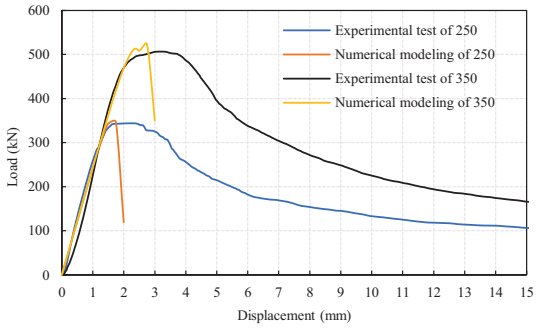

Figure 10. The force vs. displacement curves of numerical modeling and experimental tests for rods with 24 mm diameter and 250 mm anchorage length embedded perpendicular to the lamination.

In the experimental tests of rods embedded on the boundary of two-cross-wised layers, a crack appeared along the length of the rods on the surface of the CLT specimens. The numerical modeling of rods embedded on the boundary of two cross-wised layers revealed the same stress distribution that reached the surface of the CLT specimens, as shown in Figure 11.

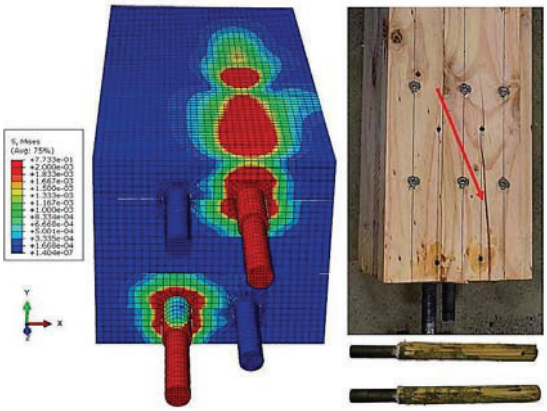

Figure 11. Numerical modeling and experimentally tested specimens of rods embedded on the boundary of two cross-wised layers.

Moreover, experimental tests of the rods embedded perpendicular to the lamination demonstrated rolling shear failure in the transverse layers. The stress distribution and displacement indicated by the numerical modeling of rods embedded perpendicular to the grain were predicted to reach the edge of the CLT specimen and cause rolling shear, as illustrated in Figure 12.

https://doi.org/10.52202/069179-0189

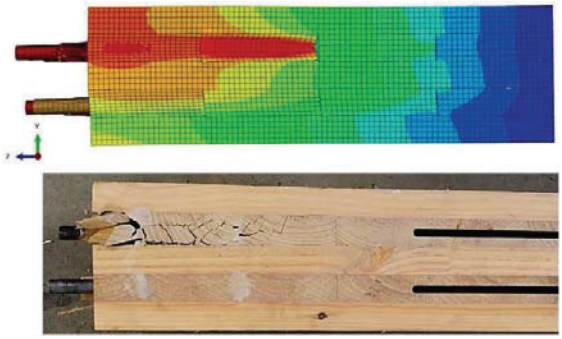

Figure 12. Numerical modeling and experimentally tested specimens of rods embedded perpendicular to the laminations.

3.2.2 Parametric investigation

The parametric study of two rods embedded perpendicular to the laminations and tested diagonally revealed that the pull-out strength increased with increasing the rod diameter and embedment length, as shown in Figure 13. Two rods with 30 mm diameter and embedment lengths of 450 mm reached a pull-out strength of 961 kN.

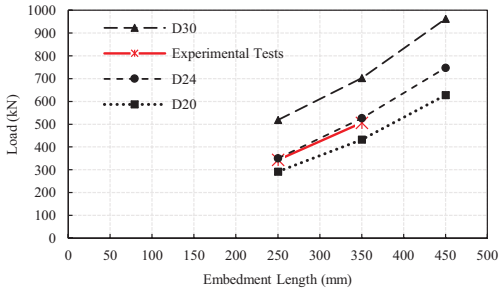

Figure 13. Numerical modeling and experimental test results of rods embedded perpendicular to the grain.

The pull-out strength of the numerical model of the two diagonal rods embedded parallel to the grain increased as the rod diameter, and embedment length increased. The pull-out strength of the rods reached 836 kN for two rods with 30 mm diameter and an embedment length of 450 mm, as shown in Figure 14.

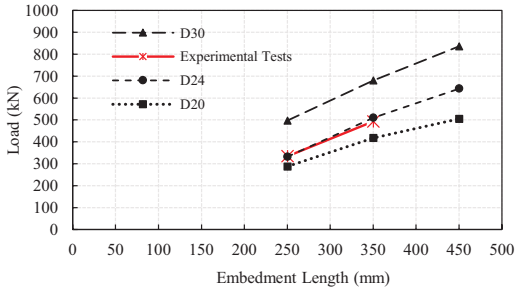

Figure 14. Numerical modeling and experimental test results of rods embedded parallel to the grain.

The pull-out strength of rods with 20- and 24-mm diameters embedded on the boundary of two cross-wised layers showed an increasing trend by increasing the rod diameter and embedment length. On the other hand, when the rod diameter was increased to 30 mm, they did not demonstrate a noticeably higher pull-out strength (as illustrated in Figure 15). This could be as a result of the rods being closer to the surface, which has been demonstrated to develop an early crack failure in experimental tests and numerical models.

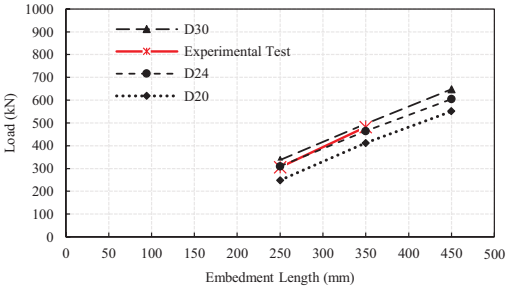

Figure 15. Numerical modeling and experimental test results of 5-layer CLT with rods embedded on the boundary of two cross-wised layers.

Using a new set of numerical models with a 7-layer CLT with rods on the boundary of two cross-wised layers, it was possible to overcome the stress distribution that reached the surface of CLTs, as illustrated in Figure 16. In this numerical model, the rod distance from the surface was extended to 84 mm while keeping the edge distance and rod distance at 84 mm and 72 mm, respectively. The interaction characteristics of this model were obtained from the characteristics of a 5-layer CLT with rods embedded on the boundary of two cross-wised layers.

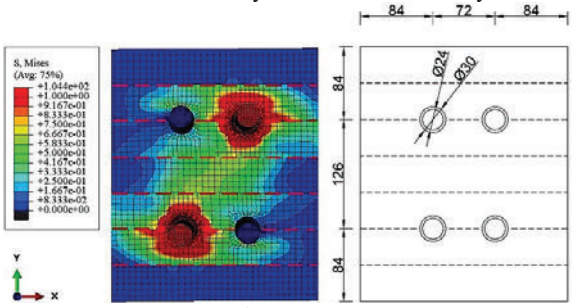

Figure 16. Numerical modeling of a 7-layer CLT containing rods embedded on the boundary of two cross-wised layers.

The numerical modeling of a 7-layer CLT with rods on the boundary of two cross-wised layers showed a proportional increase in the pull-out strength of rods with increasing the rod diameter and embedment length, as shown in Figure 17. By increasing the rod diameter from 24 to 30 mm when embedded on the boundary of two-cross-wised layers of a 5-layer CLT, the capacity of the connections increased by 9%, whereas for rods embedded on the boundary of a 7-layer CLT, the strength of the rods increased by 50%. The pull-out strength of rods with a diameter of 30 mm and embedment length of 450 mm was 738 kN. This occurrence demonstrated the negative impact of the rods' short surface distances for 5-layer CLTs. The pull-out strength of glued-in rods embedded

https://doi.org/10.52202/069179-0189

on the boundary of two cross-wised layers is lower compared to rods embedded perpendicular and parallel to the grain, even when the surface distance between the rods increased. This is because the surface cracking affected the rods' initial contact characteristics, and in practice, it is anticipated that the rods embedded on the boundary of two cross-wised layers of a 7-layer CLT to exhibit higher pull-out strength.

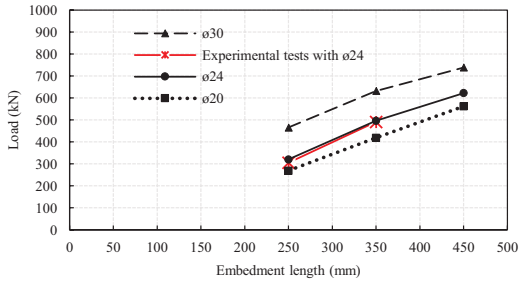

Figure 17. Numerical modeling and experimental test results of 7-layer CLT containing rods on the boundary of two-cross-wised layers.

4 CONCLUSIONS

High-capacity connections are required in designing high-rise buildings, and glued-in rods are one of the solutions to achieve this goal. Current full-scale monotonic and cyclic experimental tests are providing valuable results on the pull-out strength and seismic performance of CLT connections with multiple glued-in rods. The effect of the rods location regarding the laminations orientation is investigated, and stress distribution along the rods at various rod to lamination angles is provided.

According to the results of the experimental tests, the rod's failure mode and failure load were greatly influenced by the rod to lamination angle. Rods embedded perpendicular to the lamination led to the transverse layers rolling shear failure and crushed epoxy adhesive with a smooth force vs. displacement curve with maximum strength among tested configurations. If glued-in rods are used in CLT connections, it is recommended to embed them perpendicular to the grain. Due to the plug-out failure mode, rods embedded parallel to the grain demonstrated lower strength and a sharp strength reduction. Rods embedded on the boundary of two cross-wised layers demonstrated the lowest strength due to their closer distance to the surface of CLT, and rods containing epoxy adhesive were pulled out in a cylindrical shape. The results of the monotonic tests demonstrated that glued-in rod connections could only act ductile and fail when appropriately designed. Moreover, according to the cyclic loadings, glued-in rod connections maintain their elastic properties up until failure. The results of this investigation showed that glued-in rod connection technique could provide a solid connection for CLT construction. But it should be remembered that this investigation only looked at a certain kind of wood, adhesive, and rod. The increased list of parameters needs to be supplemented by more studies, such as using different glued-in rod connection details (rod sizes, adhesive types, spacings, and edge distance). In order to better understand the behaviour of glued-in rod connections, a wide range of test data with multiple failure mechanisms needs to be generated. Overall, this study demonstrated the high potential for this type of connection in CLT construction and showed that with glued-in rod connections, high capacities could be achieved.

ACKNOWLEDGEMENT

The first author wishes to express his gratitude to The University of Auckland for providing him with a Doctoral Scholarship to pursue his Ph.D. programme. The New Zealand Timber Design Society and WIDE Trust's financial help is also gratefully acknowledged.

REFERENCES

[1] Batchelar, M. L., & Mcintosh, K. A. (1998). Structural joints in glulam. In Proceedings of the 5th World conference in Timber Engineering, Montreux (pp. 17-20).

[2] Fragiacomo, M., Batchelar, M., Wallington, C., & Buchanan, A. (2010, June). Moment Joints in Timber Frames Using Glued-In Steel Rods: Experimental Investigation of Long-Term Performance. In World Conference on Timber Engineering, Riva del Garda, Trentino, Italy.

[3] Buchanan A. H.: Timber design guide. Third Edition. New Zealand Timber Industry Federation Inc., Wellington, New Zealand, 2007.

[4] Karacabeyli, E., & Douglas, B. (Eds.). (2013). CLT handbook: Cross-laminated timber. FPInnovations.

[5] Ayansola, G. S., Tannert, T., & Vallee, T. (2022). Experimental investigations of glued-in rod connections in CLT. Construction and Building Materials, 324, 126680.

[6] Azinović, B., Serrano, E., Kramar, M., & Pazlar, T. (2018). Experimental investigation of the axial strength of glued-in rods in cross laminated timber. Materials and Structures, 51(6), 1-16.

[7] European Committee for Standardization (CEN), EN 12512:2001, Timber Structures-Test Methods-Cycling Testing of Joints Made with Mechanical Fasteners, CEN, Brusells, 2001.

[8] Abaqus/CAE User's Manual, Version 6.23, USA, 2021.

[9] Muciaccia, G. (2019). An experimental approach to determine pull-out strength of single and multiple axially loaded steel rods bonded in glulam parallel to the grain. Wood Material Science & Engineering, 14(2), 88-98.

[10] Rossignon, A., & Espion, B. (2008). Experimental assessment of the pull-out strength of single rods bonded in glulam parallel to the grain. Holz als Roh- und Werkstoff, 66(6), 419-432.

World Conference on Timber Engineering Oslo 2023

BEAM-ON-ELASTIC FOUNDATION MODEL OF MECHANICAL PROPERTIES OF RING NAILS AND HEAVY-DUTY SCREWS

Petr Sejkot[1], Asif Iqbal[2]

ABSTRACT: Beam-on-foundation modelling shows huge potential to substitute the limit analysis and empirical stiffness formulas used to calculate the load bearing capacity of timber connections with dowel-type fasteners like nails and screws. It takes into the account the non-linear behaviour of fastener's shank subjected to bending as well as the elastic-plastic behaviour of contact between the fastener and surrounding wood. Its another advantage is the capability to calculate both capacity and stiffness of complex connections commonly used in cross-laminated timber structures. This paper describes numerical models of axially and laterally loaded fasteners in wood. Results from modelling are thereafter compared to the experimentally obtained data.

KEYWORDS: Timber connections, heavy-duty screws, threaded nails, numerical simulation, Python scripting.

1 INTRODUCTION

During the late twentieth century, the limit analysis proposed by Johansen [1] replaced the empirical formulas used to determine the load bearing capacity of dowel-type timber connections. However, Johansen's simple design equations are becoming insufficient to cope with present-day challenges, which are e.g. related to the design of high-rise wooden buildings [2]. Former developments in computational mechanics made it possible to develop both simple [3,4] and advanced [5-9] numerical methods which take into the account the nonlinear phenomena. These approaches have remained unused in practical design due to their complex implementation and their high running time, at the time of their invention, while nowadays computational resources would allow fast and efficient numerical methods-based design. The aim of this paper is to test the applicability of these numerical methods to calculate the capacity and stiffness of various fasteners like ring nails and screws in steel-to-CLT connections.

2 EXPERIMENTAL TESTING

Mechanical properties of four types of fasteners (listed in Table 1) in CLT panels were the scope of the experimental testing.

Table 1: *Overview of used fasteners in connections.*

Fastener	Length	Shank diameter
CNA4-60	60 mm	4.0 mm
SDS10212	63.5 mm (2.5 in)	4.1 mm
SDS25112	38.1 mm (1.5 in)	4.7 mm
SDS25300	76.2 mm (3.0 in)	4.7 mm

For each fastener, two types of test-setups were assembled: to test fastener in the axial direction for withdrawal (Figure 1) and to test fastener in the lateral direction for shear (Figure 2). During each test, load magnitude applied to the fastener's head was recorded. Displacement from its original position was measured only at the fastener's head and its magnitude was related to the adjacent surface of the CLT panel. In addition, observed failure modes were noted down for each tested specimen.

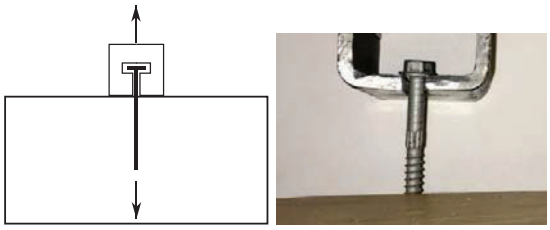

Figure 1: *Illustration of the experimental setup of axially loaded fasteners: schematic (left) and during tests (right).*

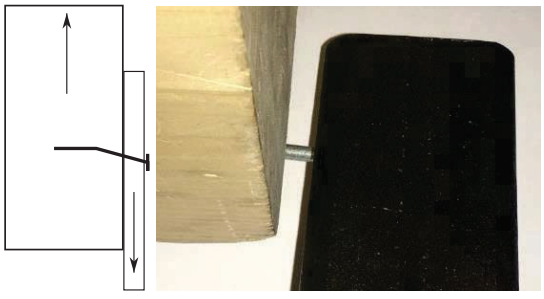

Figure 2: *Illustration of the experimental setups of laterally loaded fastener: schematic (left) and during tests (right).*

[1] Petr Sejkot, Czech Technical University in Prague, Klokner Institute, Czech Republic, petr.sejkot@cvut.cz
[2] Asif Iqbal, University of Northern British Columbia, Canada, Asif.Iqbal@unbc.ca

https://doi.org/10.52202/069179-0190

The aim of the experimental testing was to find the stiffness and load bearing capacity in order to compare it to the results from the simultaneously made numerical simulations.

3 NUMERICAL SIMULATIONS

The numerical models assembled in the Abaqus® software consist of beam elements representing fasteners, surrounding timber volume serving as a foundation and a number of nonlinear spring elements connecting nodes of beam elements to nodes of the surrounding volume made of timber. These nonlinear springs act both, in the axial and in the lateral direction of the fastener. Both the axial and the lateral properties are discretized according to the experimentally based data from the fastener withdrawal and shear tests. A similar approach has been previously successfully used by Izzi in [8] and Gikonyo in [10].

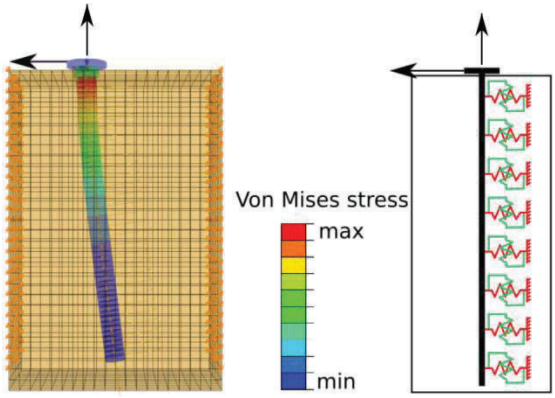

Figure 3: *Illustration of numerical model of single fastener used to simulate both test (lateral shear and axial withdrawal).*

The model presented in Figure 3 shows the single fastener after the simulation of the shear test (in the lateral direction of the fastener). The visualisation of the numerical simulation results shows von Mises stress over the shank of the fastener. The symbolic sketch outlines the way how the nonlinear spring connectors connect timber mesh to the shank of the fastener. The use of the sufficient number of spring element prevents the overloading of nodes of the mesh. The influence of the timber grain direction to the simulation results is neglected since the wood material model has unified properties in radial and tangential direction.

4 RESULTS AND DISCUSSION

The presented meshes obtained by the numerical models in Abaqus (figures 4 a nd 5) illustrate that 2 mm distance between the nonlinear springs placed at the shank of the fastener is a good compromise between the detailed model and reasonable computational cost.

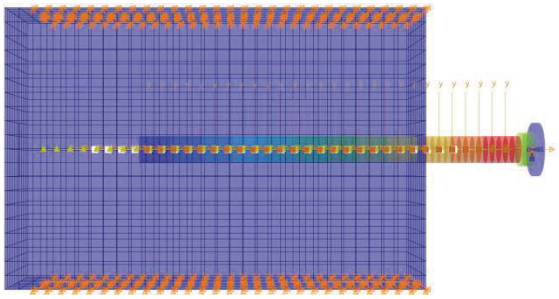

Figure 4: *Von Mises stress from numerical simulation of withdrawal of the CNA 4.0x60 nail from CLT.*

Since the withdrawal stiffness of the nonlinear springs used in the model is just the division of the overall axial stiffness of the fastener, the maximum of von Mises stress occurs at the location of the first spring (see Figure 4). This might be changed in order to get the result of the simulation closer to the real behaviour when the pulled-out fastener loses the contact with the surrounding timber.

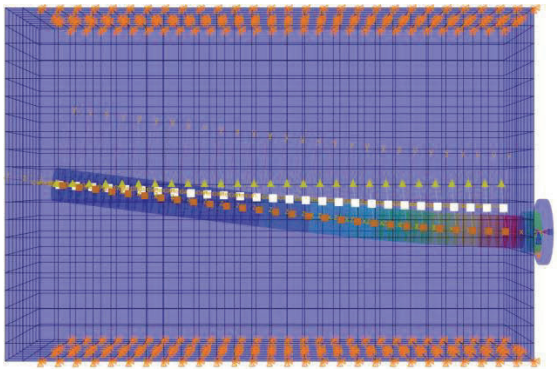

Figure 5: *Von Mises stress from numerical simulation of lateral shear slip of the CNA 4.0x60 nail in CLT.*

The stiffness of the nonlinear spring acting in the lateral direction of the shank of the fastener represents the embedment stiffness of the CLT material. The transfer of load between the fastener and the timber material is simplified by assigning the steel material properties to the parts of the mesh in the close vicinity (not exceeding the diameter of the fastener) of the beam representing the shank of the fastener. The important parameter influencing the behaviour of the model is the bending stiffness of the nail shank.
The following presented load-displacement curves for the individual fasteners in CLT bring a direct comparison between the experimentally and numerically obtained results as well as between the nails and screws.

https://doi.org/10.52202/069179-0190

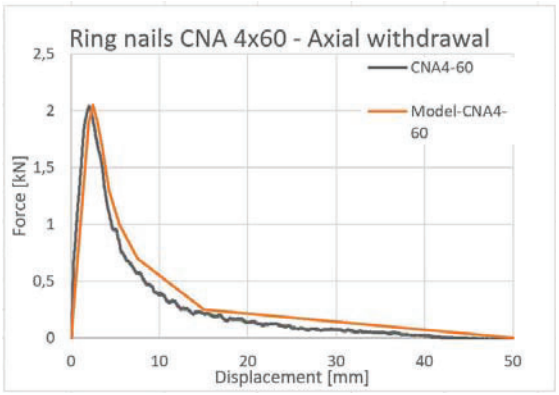

Figure 6: *Results of numerical simulation of CNA 4.0x60 NAIL in CLT connection compared to the numerical simulation.*

One representative specimen from the tested annular ring nails was chosen to be compared to the mechanical parameters used in the model (see Figure 6). It is the one which is closest to the mean behaviour of the tested sample. The spring model of the nail uses the elastic stiffness equal to 2333 N/mm. The rest of the curve is defined by nonlinear plasticity.

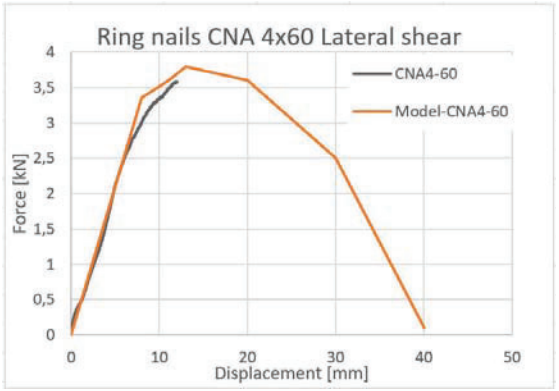

Figure 7: *Results of numerical simulation of CNA 4.0x60 NAIL in CLT connection compared to the numerical simulation.*

One representative specimen from the tested annular ring nails was chosen to be compared to the mechanical parameters used in the model (Figure 7). It is the one which is closest to the mean behaviour of the tested sample. The spring model of the nail uses the elastic stiffness equal to 1014 N/mm. The rest of the curve is defined by nonlinear plasticity. The part of the curve which was not found by the test was extrapolated by using the knowledge of the behaviour of similar nails in a similar material.

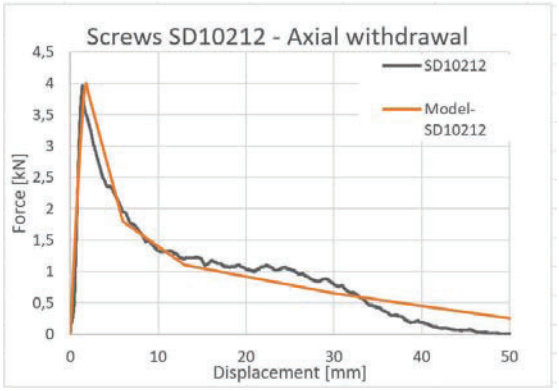

Figure 8: *Results of numerical simulation of SD10212 screw in CLT connection compared to the numerical simulation.*

One representative specimen from the tested screws was chosen to be compared to the mechanical parameters used in the model (see Figure 8). It is the one which is closest to the mean behaviour of the tested sample. The spring model of the nail uses the elastic stiffness equal to 2750 N/mm. The rest of the curve is defined by nonlinear plasticity.

Figure 9: *Results of numerical simulation of SD10212 screw in CLT connection compared to the numerical simulation.*

One representative specimen from the tested screws was chosen to be compared to the mechanical parameters used in the model (see Figure 9). It is the one which is closest to the mean behaviour of the tested sample. The spring model of the nail uses the elastic stiffness equal to 1000 N/mm. The rest of the curve is defined by nonlinear plasticity. The part of the curve which was not found by the test was extrapolated by using the knowledge of the behaviour of similar nails in a similar material.

https://doi.org/10.52202/069179-0190

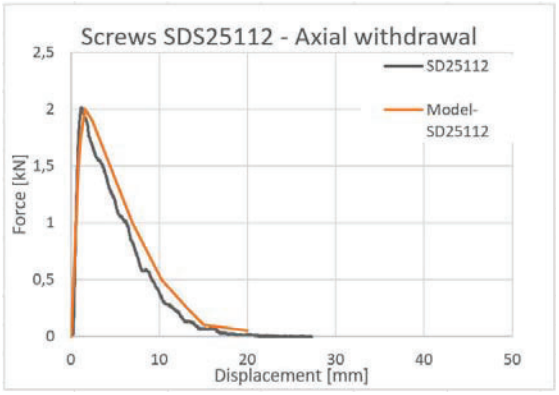

Figure 10: *Results of numerical simulation of SDS25112 screw in CLT connection compared to the numerical simulation.*

One representative specimen from the tested screws was chosen to be compared to the mechanical parameters used in the model (see Figure 10). It is the one which is closest to the mean behaviour of the tested sample. The spring model of the nail uses the elastic stiffness equal to 2000 N/mm. The rest of the curve is defined by nonlinear plasticity.

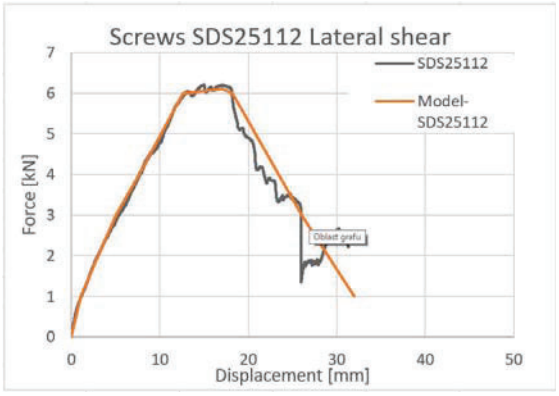

Figure 11: *Results of numerical simulation of SDS25112 screw in CLT connection compared to the numerical simulation.*

One representative specimen from the tested screws was chosen to be compared to the mechanical parameters used in the model (see Figure 11). It is the one which is closest to the mean behaviour of the tested sample. The spring model of the nail uses the elastic stiffness equal to 2000 N/mm. The rest of the curve is defined by nonlinear plasticity.

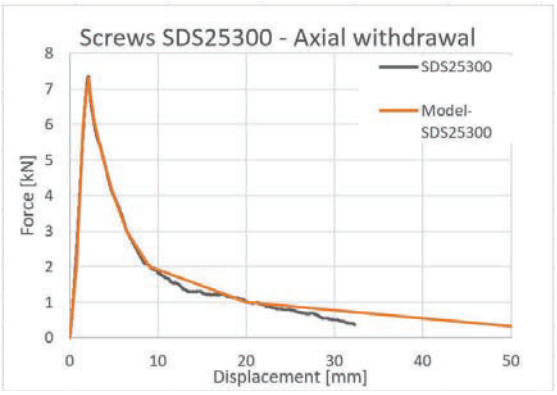

Figure 12: *Results of numerical simulation of SDS25300 screw in CLT connection compared to the numerical simulation.*

One representative specimen from the tested screws was chosen to be compared to the mechanical parameters used in the model (see Figure 12). It is the one which is closest to the mean behaviour of the tested sample. The spring model of the nail uses the elastic stiffness equal to 8000 N/mm. The rest of the curve is defined by nonlinear plasticity.

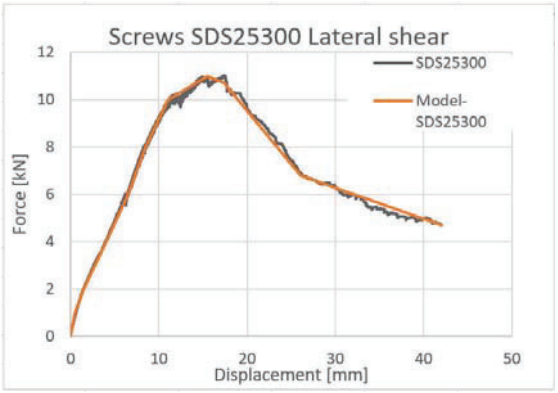

Figure 13: *Results of numerical simulation of SDS25300 screw in CLT connection compared to the numerical simulation.*

One representative specimen from the tested screws was chosen to be compared to the mechanical parameters used in the model (see Figure 13). It is the one which is closest to the mean behaviour of the tested sample. The spring model of the nail uses the elastic stiffness equal to 2000 N/mm. The rest of the curve is defined by nonlinear plasticity.
In addition, the overall comparison of tested fasteners is presented in following two figures.

https://doi.org/10.52202/069179-0190

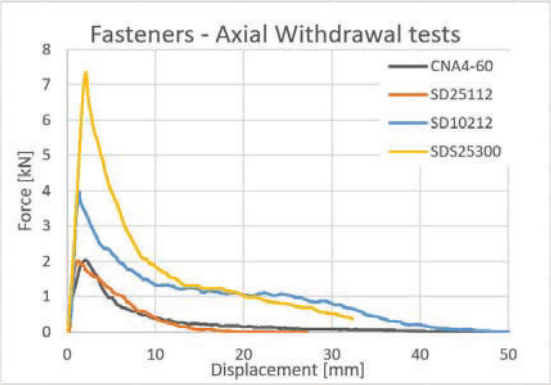

Figure 14: *Representative mechanical behaviour of three types of screws and one type of nail subjected to the withdrawal test.*

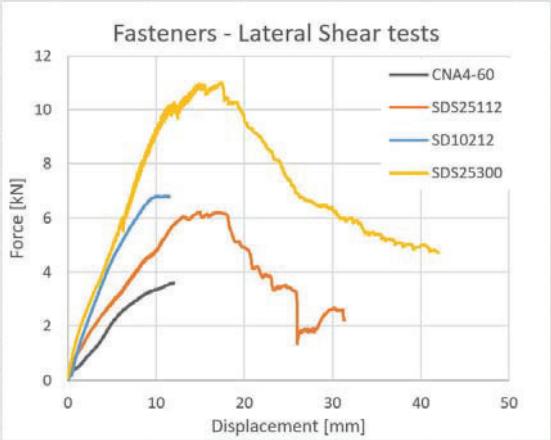

Figure 15: *Representative mechanical behaviour of three types of screws and one type of nail subjected to lateral shear test.*

5 CONCLUSIONS

The modelling approach by beam elements whose nodes are attached to the nodes in the volume of timber by nonlinear springs is relatively lightweight compared to the modelling approach using volume elements and friction for modelling fasteners in wood material. On the other hand, the approach with springs distributed over the shank of the fasteners has an advantage to the single-spring modelling approach of whole fasteners, because using the appropriate number of nonlinear springs allow to allocate the damage of the timber material to the top part of the fastener's shank whereas the properties of connectors placed deep in the timber volume may rest unaffected. Another advantage is a better simulation of coupling since the springs which are close to surface can resist to the shear and the rest of the springs can resist to the withdrawal.

Using multiple connectors over the shank of the screw also allows to simulate relatively easily a complex phenomenon of the cyclic mechanical loading of the fasteners. In this case, damage of wood material close to the surface of the CLT panels occurs, which affects both the axial and lateral resistance.

Another useful application of the proposed model of the presented fasteners can be the case when the connection is subjected to the combination of the axial and lateral loading (as shown in Figure 16). This has not been tested yet. Therefore, it is a scope of the further research to subject the screws and nails to this type of loading and compare the experimental results to the data obtained by numerical simulations.

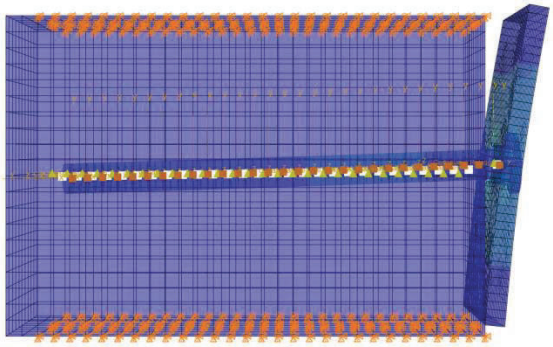

Figure 16: *Von Mises stress from numerical simulation of CNA 4.0x60 nail in CLT subjected to the combination of lateral (shear) and axial (withdrawal) load.*

The combination of the axial and lateral loading is a typical for connections of CLT elements by angle brackets (see Figure 17). It is a topic of an ongoing research to apply the fastener model in a simulation of mechanical loading of a more complex connection and compare the experimental results to the data obtained by numerical simulations (see Figure 18).

Figure 17: *Experimental setup of CLT connection made of angle bracket ABR9020 and screws.*

https://doi.org/10.52202/069179-0190

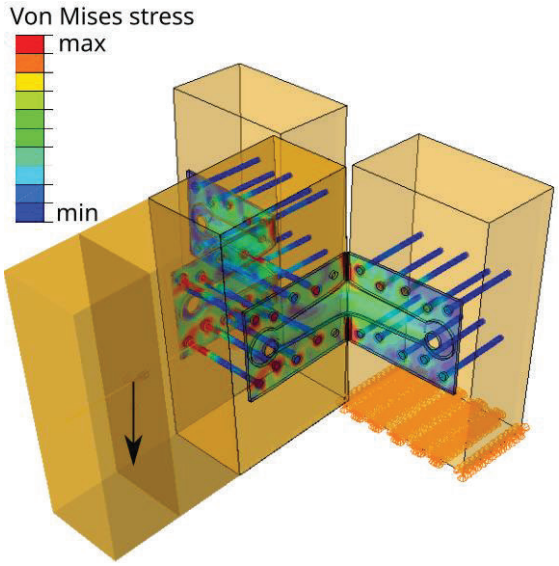

Figure 18: *Von Mises stress from numerical simulation of loaded CLT connection with ABR9020 angle brackets with CNA 4.0x60 nails in CLT.*

ACKNOWLEDGEMENT

This work has been supported by the Ministry of Culture of the Czech Republic, research grant NAKI II DG18P02OVV012 - Sustainable Management of Historical Buildings. The experimental work was supported by Forestry Innovation Investment fund of British Columbia, Canada. The brackets and connectors were supplied by Simpson Strong-Tie Canada.

REFERENCES

[1] Johansen K.W., Theory of timber connections. *International Association for Bridge and Structural Engineering* (ABSE) Pub. 9, 249-262., 1949.

[2] Lemaître, R., Epinal, F., Bocquet, J. F., Schweigler, M., & Bader, T. K., Beam-on-foundation modelling as an alternative design method for single fastener connections. *Design of Connections in Timber Structures*, 207, 2018.

[3] Foschi R.O., Load-slip characteristics of nails. *Wood Science* 17:69-77. 1974.

[4] Hirai T., Non-linear load-slip relationship of bolted wood-joints with steel side members –II – Application of the generalised theory of beam on elastic foundation. *Makusu Gakkaishi* 29 (12): 839-844. 1983.

[5] Bedon C, Fragiacomo M.: Numerical analysis of timber-to-timber joints and composite beams with inclined self-tapping screws. *Composite Structures*. 207:13-28, 2019.

[6] Bedon C, Sciomenta M, Fragiacomo M, Correlation approach for the Push-Out and full-size bending short-term performances of timber-to-timber slabs with Self-Tapping Screws. *Engineering Structures*. 238:112232. 2021.

[7] Bedon C, Sciomenta M, Fragiacomo M. Mechanical characterization of timber-to-timber composite (TTC) joints with self-tapping screws in a standard push-out setup. *Applied Sciences*. 10(18):6534. 2020.

[8] Izzi M, Rinaldin G, Polastri A, Fragiacomo M. A hysteresis model for timber joints with dowel-type fasteners. *Engineering Structures*. 157:170-8. 2018.

[9] Izzi M, Rinaldin G, Fragiacomo M, Polastri A. Numerical modelling of steel-to-timber joints and connectors for CLT structures. *World Conference on Timber Engineering (2016)* (pp. 1-9). 2016.

[10] Gikonyo, J, Schweigler M, Bader T K. A spring model for prediction of the nonlinear embedment load-displacement behaviour of dowel-type fasteners in cross-laminated timber. *World Conference on Timber Engineering (2021)*, WCTE 2021, 2021.

World Conference on Timber Engineering Oslo 2023

DUCTILITY OF WOOD CONNECTIONS WITH SDS SCREWS OR RING NAILS AND ANGLE BRACKETS

Petr Sejkot[1], Asif Iqbal[2]

ABSTRACT: Mechanical connections in wood structures typically consist of structural members connected with combination of cold-formed thin-walled steel angle brackets and fasteners in forms of nails or screws. Design of these steel connectors is typically based on short-term monotonic load bearing capacities. Observations from experimental testing indicate that their failure modes and resistance to a cyclic loading should be checked carefully to prevent the thread of sudden collapse of structures using these connections. This paper presents the experimental results of connections of CLT elements connected together by angle brackets and subjected to the external cyclic loading. Special focus is made on connections using heavy duty screws as fasteners. Results of experimental testing are compared to results of testing of similar connections using ring nails as fasteners. In addition, numerical simulations are made with aim to predict the failure modes and the load bearing capacities of experimentally tested connections.

KEYWORDS: Timber connections, angle brackets, screws, numerical simulation, full-scale tests, Python scripting.

1 INTRODUCTION

Since its invention in Europe, cross-laminated timber (CLT) has become a widely used construction material which has started to attract the global attention [1]. Due to the brittle nature of wood, CLT structures rely on metal connections to achieve required ductility and energy dissipation [2]. When designed properly with steel connectors and CLT elements, the structure can exhibit superior seismic performance by leveraging the high strength-to-weight ratio of wood members and the high ductility of steel components [3]. A good understanding of connections in CLT structures is needed to better predict the performance of the structures and avoid unexpected failures, e.g., caused by the out-of-plane movements under wind and seismic loads [4]. Some scholars [5-10] already used advanced modelling techniques in Abaqus® to predict the performance of structures connected by the steel components, ring nails or screws. Therefore, it is the aim of this paper to continue developing similar numerical models and try to use them to predict the performance of the experimentally tested connections of CLT structures.

2 EXPERIMENTAL TESTING

A number of CLT connections made of steel angle bracket connectors and screws has been extensively tested. Three test setups were made to achieve mechanical loading of the connections in pull-out, shear, and rocking (see Figure 1). Applied force as well as displacement at chosen locations of tested connections was recorded too. In each test-setup, various connections differing by used type of Simpson Strong-Tie® angle brackets (HGA10KT, ABR9020, ABR105) were used. As fasteners, Simpson Strong-Tie® heavy duty SDS screws were used.

Figure 1: *Experimental setup of CLT connection made of ABR9020 bracket and SDS screws subjected to rocking.*

These test-setups are identical to those previously used in [11]. However, the type of used fasteners varies between these two studies. Therefore, the influence of using screws instead of ring nails on the obtained mechanical properties of the tested connections, could be compared. The special attention was paid on load bearing capacity, measured

[1] Petr Sejkot, Czech Technical University in Prague, Klokner Institute, Czech Republic, petr.sejkot@cvut.cz
[2] Asif Iqbal, University of Northern British Columbia, Canada, Asif.Iqbal@unbc.ca

https://doi.org/10.52202/069179-0191

deformations (at the location of the red dot in figures 4-6), ductility and energy dissipations.

Table 1: *Overview of used fasteners in connections.*

Connector	Screw/Nail Type
HGA10KT	SDS25112 + SDS25300
HGA10KT	CNA4-60
ABR 105	SD10212
ABR 105	CNA4-60
ABR 9020	SD10212
ABR 9020	CNA4-60

CNA4-60 is an angular ring shank nail with 60 mm in length and 4.0 mm in diameter.

SD10212 is a screw with 63.5 mm (2.5 inch) in length, 25.4 mm (1.0 inch) long threaded part with 4.10 mm (0.161 inch) shank size.

SDS25112 is a screw with 38.1 mm (1.5 inch) in length, 25.4 mm (1.0 inch) long threaded part with 6.35 mm (0.25 inch) of outer diameter and 4.70 mm (0,185 inch) inner diameter.

SDS25300 is a screw with 76.2 mm (3.0 inch) in length, 50.8 mm (2.0 inch) long threaded part with 6.35 mm (0.25 inch) of outer diameter and 4.70 mm (0,185 inch) inner diameter.

All four types of listed fasteners were tested both in the axial (withdrawal) direction, as shown in Figure 2 and lateral (shear) direction (as shown in Figure 3). These experimentally obtained mechanical properties (force to displacement curves) of the fasteners were used later during the numerical modelling.

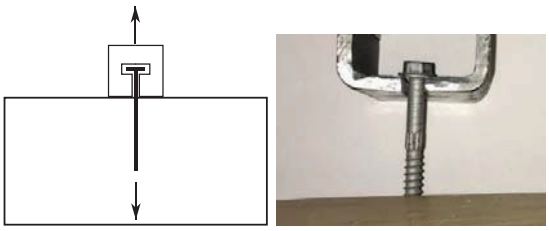

Figure 2: *Experimental setup of axially loaded fastener: schematic (left) and during tests (right).*

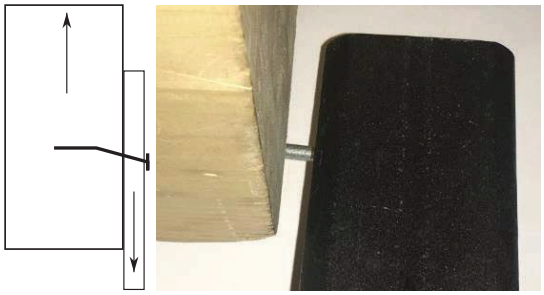

Figure 3: *Experimental setup of laterally loaded fastener: schematic (left) and during tests (right).*

The rocking test-setup consists of two CLT blocks (200x135x300 mm^3) fixed to the floor and one CLT block (105x300x150 mm^3) placed between them. A 3 mm gap between the blocks is designed to avoid friction between the CLT members. The load is applied at the top of the intermediate CLT panel at a distance of 205 mm from the shear plane, as shown in Figure 4. This eccentricity was chosen to ensure large bending load on the connection together with limited shear force action in relation to its shear load carrying capacity. A loading protocol with the maximal magnitude of displacement equal to 50 mm was used.

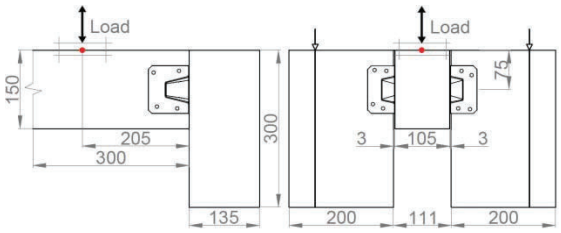

Figure 4: *Side and front view of the experimental setup of HGA10KT brackets for rocking test.*

The shear test setup consists of two CLT blocks (200x135x300 mm^3) fixed to the floor and one CLT block between them (105x320x300 mm^3). A 3 mm gap between the blocks is designed to avoid friction when the external load is applied.
The load is applied at the top of the intermediate CLT panel to act in the shear plane of the connection as shown in Figure 5. A loading protocol was used with a maximum displacement of 35 mm.

https://doi.org/10.52202/069179-0191

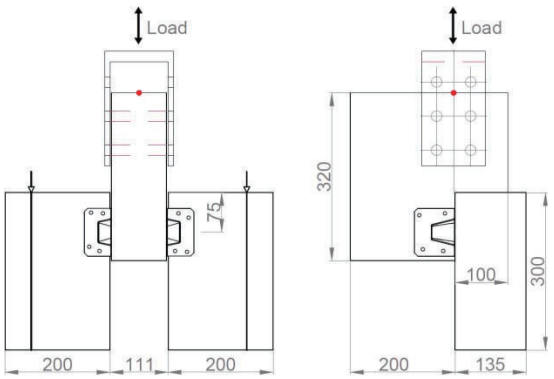

Figure 5: *Front and side view of the experimental setup of HGA10KT brackets for shear test.*

Pull-out test setup was made of one horizontal CLT block (105x150x600 mm^3) fixed to the floor and one vertical CLT block (105x320x150 mm^3). The load is applied at the top of the vertical CLT block as shown in Figure 6. A loading protocol was used with a maximum displacement of 50 mm.

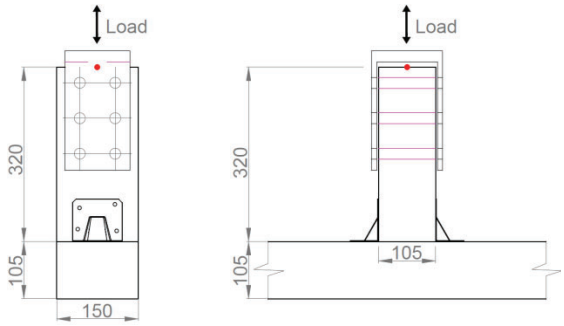

Figure 6: *Front and side view of the experimental setup HGA10KT brackets for pull-out test.*

3 NUMERICAL SIMULATIONS

Realistic numerical models (Figure 7) were assembled in the Abaqus® software, by using the same scripts as were used in [11]. Timber beams, where no contact occurred between the angle brackets and the wood, were simulated with beam elements. Some parts of the timber beams in close vicinity of angle brackets were simulated with shell elements. Shell elements were also used for the angle brackets. The Abaqus® wire elements connecting one point of mesh of beam part and one point of mesh in angle bracket part with assigned "uniaxial behaviour" represented each fastener in the model. This approach was chosen because it allows to define the re-loading path of the wires simulating fasteners in the Abaqus® software.

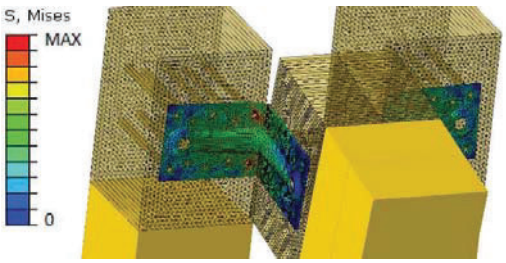

Figure 7: *Numerical simulation of CLT connection made of ABR9020 bracket and SDS screws subjected to rocking.*

Parametric modelling with Python scripting was used to create the model geometry and properties of the connections. This approach allows fast modification of beam dimensions, fastener properties and type of angle brackets, needed to cover a large number of possible combinations of possibly used angle brackets and fasteners. In addition, it allows to define the "uniaxial behaviour" directly to Abaqus® keywords.

4 RESULTS AND DISCUSSION

The presented load-displacement curves for both individual fastener joints and angle bracket connections bring a direct comparison between the nails and screws as well as between the experimentally and numerically obtained results.

4.1 FASTENERS

The presented force to displacement curves in Figure 8 show that the 60 mm long ring nails have very similar withdrawal resistance as only 38.1 mm long screws. In addition, screws are stiffer but less ductile. Other two tested screws (76.2 and 63.5 milometers long) have the same initial stiffness like the 38.1 mm long ones but they vary significantly in their strength.

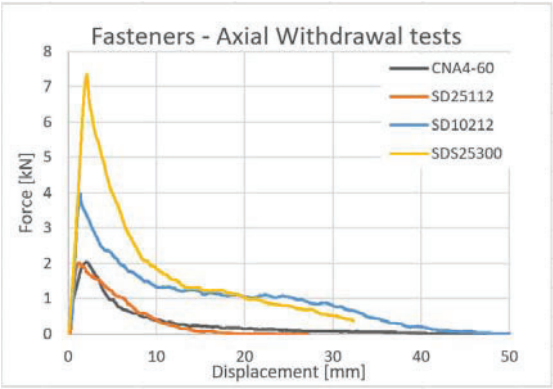

Figure 8: *Representative mechanical behaviour of three types of screws and one type of nail subjected to the withdrawal test.*

https://doi.org/10.52202/069179-0191

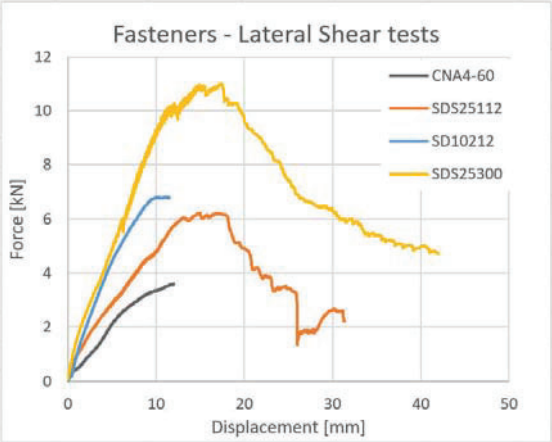

Figure 9: *Representative mechanical behaviour of three types of screws and one type of nail subjected to lateral shear test.*

The presented force to displacement curves in Figure 9 show that ring nails are both less stiff and weaker in term of the lateral resistance. 38.1 mm long screws have similar lateral resistance as 63.5 mm long screws because the shorter ones have thicker shank compared to the longer ones (4.1 mm compared to 4.7 mm). As expected, the longest screws with the thickest shank are both the stiffest and strongest.

4.2 CLT CONNECTIONS

The presented force to displacement curves in Figure 10 show that bigger angle brackets have higher load bearing capacity. In addition, connections with screws (dashed lines) have higher capacity than the similar ones with ring nails (full lines). The same colour is used for the same types of connectors (HGA10KT - blue, ABR9020 - orange, ABR105 - green) which were used in the tested CLT connections.

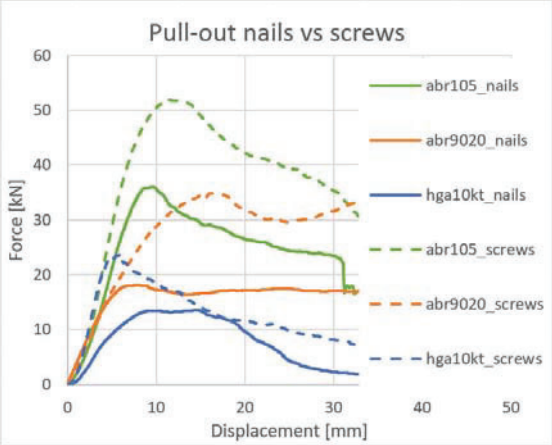

Figure 10: *Representative mechanical behaviour of three types of connections with nails and screws subjected to pull-out.*

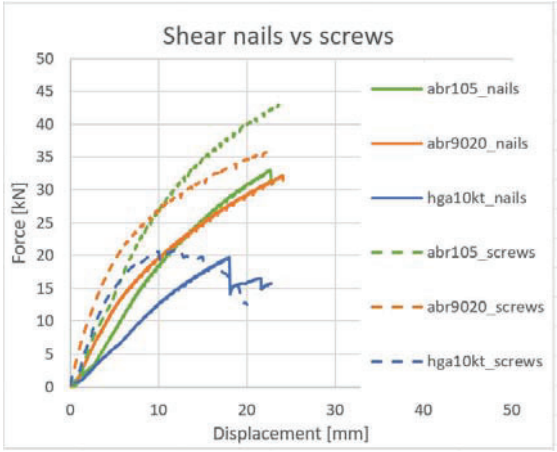

Figure 11: *Representative mechanical behaviour of three types of connections with nails and screws subjected to shear.*

The presented force to displacement curves in Figure 11 show that the size of the bracket does not have as significant influence on the load bearing capacity in shear as in case of the pull-out. Connections with screws (dashed lines) are generally stiffer than those with ring nails (full lines) but they do not have significantly higher capacity than the similar ones with ring nails. This indicates that not only fastener type contributes to the overall stiffness of the tested connections.

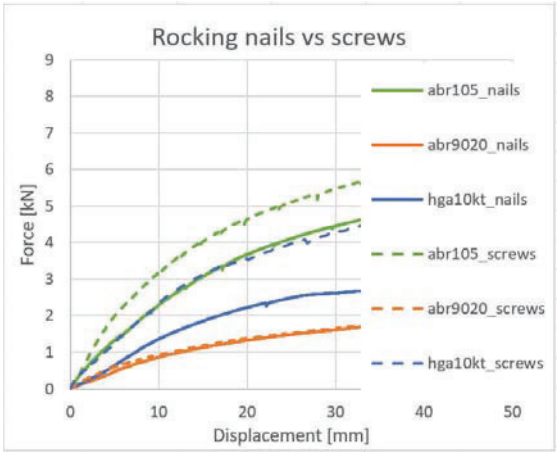

Figure 12: *Representative mechanical behaviour of three types of connections with nails and screws subjected to rocking.*

The presented force to displacement curves in Figure 12 show that the connections with the smallest bracket (HGA10kt) is stronger and stiffer that the medium size one (ABR9020). This might be caused by the influence of its relatively massive rib (compared to the one at the bigger angle bracket) on its stiffness. There is also no significant difference in stiffness nor capacity related to the used type of the fastener in case of the connection with ABR9020 bracket. Other two types of the brackets are stiffer and stronger with screws than with nails.

https://doi.org/10.52202/069179-0191

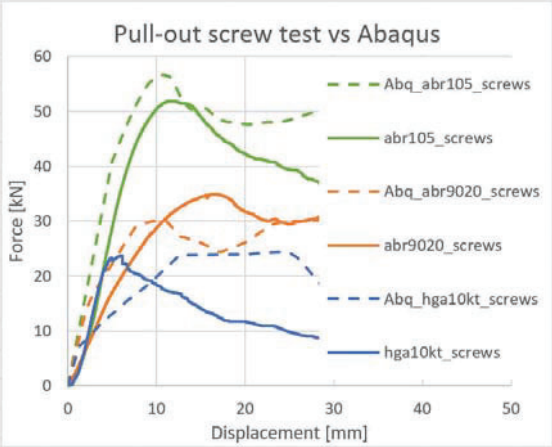

Figure 13: *Representative mechanical behaviour of three types of connections with screws subjected to pull-out compared to the results from simulations assembled in Abaqus (FEA).*

The presented force to displacement curves in Figure 13 show that there is the best agreement in case of the connection with the biggest (ABR105) angle bracket. The other simulations were relatively successful in predicting the stiffness of the connections in case of relatively small deformations and also in predicting of the load bearing capacities of the connections.

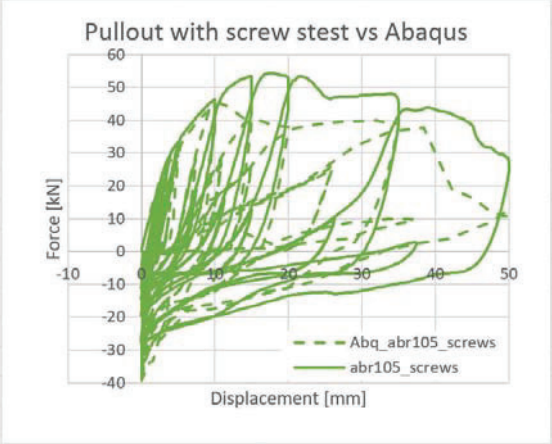

Figure 14: *Representative cyclic mechanical response of connection with angle bracket ABR105 and screws compared to the results from simulations assembled in Abaqus subjected to pull-out.*

The presented force to displacement curves Figure 14 shows the result of the most successful simulation of the mechanical response of the connection using ABR105 angle brackets and screws to the cyclic loading. There is better agreement between the numerical model and the results from the tests in case of the loading and unloading parts of the diagrams than in case of the re-loading ones.

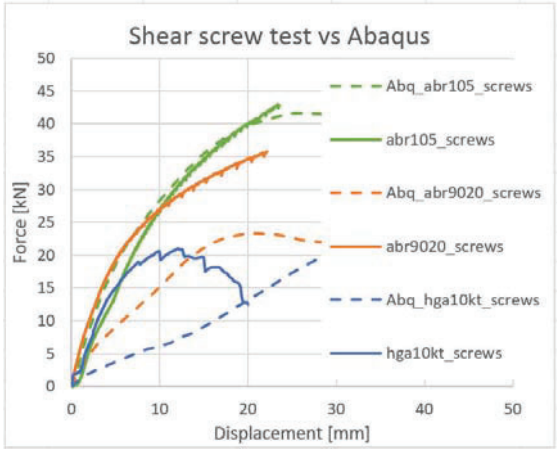

Figure 15: *Representative mechanical behaviour of three types of connections with screws subjected to shear compared to the results from simulations assembled in Abaqus (FEA).*

The presented force to displacement curves in Figure 15 show that there is the best agreement in case of the connection with the biggest (ABR105) angle bracket. The other simulations were relatively poor in predicting the mechanical behaviour of the tested connections.

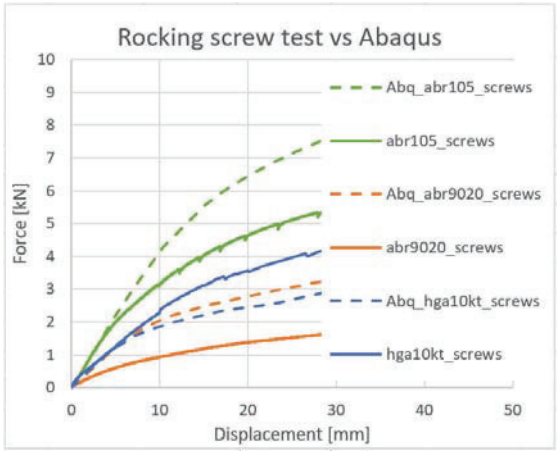

Figure 16: *Representative mechanical behaviour of three types of connections with screws subjected to shear compared to the results from simulations assembled in Abaqus (FEA).*

The presented force to displacement curves in Figure 16 show that there is the best agreement in case of the connection with the biggest (ABR105) angle bracket. However, all the simulations were relatively poor in predicting the mechanical behaviour of the tested connections.

5 CONCLUSIONS

Generally speaking, using screws instead of nails in studied connections lead to stiffer and stronger connections. On the other hand, using too strong screws

https://doi.org/10.52202/069179-0191

may lead to a brittle failure of the connections subjected to the external loading.

The relatively simple numerical models which were quite successful in predicting the deformed shape and the load to displacement curves of the experimentally tested connections of all three studied types of angle brackets and setups, i.e.: pull-out, shear and rocking with ring nails were not so successful in case of screws. This might be caused by failure modes which include cracking the timber during testing, particularly in pull-out (Figure 17) and shear (Figure 18).

Figure 17: *Test specimen with HGA10kt angle bracket and screws after pull-out test.*

Figure 18: Test specimen with HGA10kt angle bracket and screws after shear test

Another factor which seems to be relatively important and is not included in the numerical model is the friction between the steel plate of the angle bracket and the surface of the timber. Therefore, it is the scope of the further research to develop the numerical model further to be able to predict the mechanical response of all the tested connections more accurately.

ACKNOWLEDGEMENT

This work has been supported by the Ministry of Culture of the Czech Republic, research grant NAKI II DG18P02OVV012 - Sustainable Management of Historical Buildings. The experimental work was supported by Forestry Innovation Investment fund of British Columbia, Canada. The brackets and connectors were supplied by Simpson Strong-Tie Canada.

REFERENCES

[1] Espinoza, O., Trujillo, V. R., Mallo, M. F. L., and Buehlmann, U.: Cross-laminated timber: Status and research needs in Europe. *BioResources*, 11(1), 281-295, 2016.

[2] G. D'Arenzo, G. Rinaldin, M. Fossetti, M. Fragiacomo: An innovative shear-tension angle bracket for Cross-Laminated Timber structures: Experimental tests and numerical modelling. *Eng Struct*, 197, p. 109434., 2019.

[3] M. Latour, G. Rizzano: Seismic behavior of cross-laminated timber panel buildings equipped with traditional and innovative connectors. *Arch Civ Mech Eng*, 17 (2) (2017), pp. 382-399, 2017.

[4] Rezvani, S., Zhou, L., & Ni, C.: Numerical analysis of in-and out-of-plane coupling effects on angle bracket connections in CLT structures. *Engineering Structures*, 250, 113494. 2022.

[5] Bedon C, Fragiacomo M.: Numerical analysis of timber-to-timber joints and composite beams with inclined self-tapping screws. *Composite Structures*. 207:13-28, 2019.

[6] Bedon C, Sciomenta M, Fragiacomo M. Correlation approach for the Push-Out and full-size bending short-term performances of timber-to-timber slabs with Self-Tapping Screws. *Engineering Structures*. 238:112232. 2021.

[7] Bedon C, Sciomenta M, Fragiacomo M. Mechanical characterization of timber-to-timber composite (TTC) joints with self-tapping screws in a standard push-out setup. *Applied Sciences*. 10(18):6534. 2020.

[8] Izzi M, Rinaldin G, Polastri A, Fragiacomo M. A hysteresis model for timber joints with dowel-type fasteners. *Engineering Structures*. 157:170-8. 2018.

[9] Izzi M, Rinaldin G, Fragiacomo M, Polastri A. Numerical modelling of steel-to-timber joints and connectors for CLT structures. *World Conference on Timber Engineering (2016)* (pp. 1-9). 2016

[10] Krawinkler, H., Parisi, F., Ibarra, L., Ayoub, A. and Medina, R.: Development of a Testing Protocol for Woodframe Structures, CUREE Publication No. W-02, 2001.

[11] Sejkot, P., A. Iqbal a S. Ormarsson. Finite-element modelling of connectors to achieve ductile connections in wood structures. *World Conference on Timber Engineering (WCTE 2021) Proceedings*. 3026-3032, 2021.

World Conference on Timber Engineering Oslo 2023

EXPERIMENTAL INVESTIGATIONS ON TIMBER STEP JOINTS DETERMINING THE INFLUENCE OF INTENTIONALLY PLACED INACCURACIES ON THE LOAD-BEARING BEHAVIOUR

Matthias Braun[1], Benjamin Kromoser[2]

ABSTRACT: Various circumstances can lead to inaccuracies in timber step joints. Deviations from the desired geometry can be found for example due to inaccuracies within production or changes in the ambient humidity. The predominant question when considering step joints is, to what extent the load-bearing behaviour is influenced by these inaccuracies. To answer this question, the influence of purposefully placed inaccuracies on the load-bearing behaviour was investigated. The determined stiffnesses of the joint design with the intentionally placed inaccuracies were subsequently used within a numerical investigation in order to assess the influence on the deflection of an entire truss system.

KEYWORDS: Timber Joints, Step Joints, Carpentry Joints, Structural Engineering

1 INTRODUCTION

Large-scale prefabrication of components up to entire building sections plays an increasingly important role in the current timber construction industry. This manufacturing approach considerably reduces the on-site construction time. In order to ensure an efficient process on the construction site, a high fitting and dimensional accuracy of the elements is essential. Various methods exist for the connection of the truss components, with the most common being slotted-in steel plates in combination with steel dowels or glued-in threaded rods. In addition to these, carpentry joints can be used as a more environmentally friendly alternative. Step joints are, for example, often used in carpenter-based timber constructions or can be found in historical roof structures. They are characterised by their ability to reliably transfer compressive forces from one component to the next at different angles (between 30 and 60°) via contact surfaces [1,2]. When using timber as a building material, however, inaccuracies can occur for various reasons. Whereas in the past the carpenter's craftmanship was decisive for the production of a precisely fitting joint, nowadays, with modern CNC systems, work preparation including modelling, the creation of machining data and the conscientious work of the machinist play the most important role. Due to the permissible tolerances (-2 to +4 mm for cross-sectional dimension of > 100 and < 300 mm) according to ÖNORM EN 336:2013 11 15 [3], deviations in the cross-sectional dimensions between design and execution may occur when structural timber is used. This deviation from the nominal geometry requires a well-considered positioning of the components in the joinery process in order to ensure the best possible fitting accuracy of the connection. This is illustrated in Figure 1 in case of a double-step joint, with the inaccuracies cumulating when the positioning of the joint member is not considered during production.

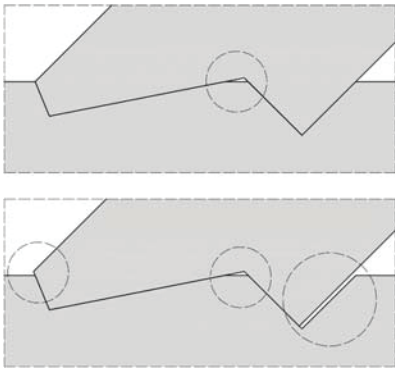

Figure 1: *Influence of the positioning of the joint's components in the joinery process on inaccuracies in case of deviation between nominal and actual cross sections using the example of the double step joint. Expected cross-sectional dimensions 120/120 mm, real cross-sectional dimensions 118/118 mm. Top: favourable positioning, bottom: unfavourable positioning.*

Apart from the dimensional inaccuracies due to the permissible tolerances, adjustments in the moisture content often lead to changes in geometry, which also result in gaps in the joints due to the different degrees of tangential and radial (regarding the annual rings) shrinkage. In order to prevent inaccuracies due to swelling and shrinkage, Blaß et al. [4] recommends that the moisture content of the components during the joining process corresponds to that in the final state.

Connections with mechanical fasteners, such as slotted-in plates and dowels show a slip at the beginning of the

[1] Institute of Green Civil Engineering, University of Natural Resources and Life Sciences, Vienna (BOKU), Austria, m.braun@boku.ac.at
[2] Institute of Green Civil Engineering, BOKU, Austria, benjamin.kromoser@boku.ac.at

https://doi.org/10.52202/069179-0192

force-displacement curve due to the required hole clearance, with the standardised calculation approach for the stiffness found in [5]. According to Seim [6], the slip at the beginning is also usually seen in carpentry joints resulting from inaccuracies, elastic and plastic deformations under load as well as creep and shrinkage deformations. The schematic load-bearing behaviour of a resilient joint is depicted in Figure 2. Initially, the joint cannot transmit any load until it transforms into a perfect fitting connection. After overcoming the initial phase, a linear-elastic behaviour is observed, defined by the stiffness C in N/mm, followed by the non-linear range with decreasing stiffness.

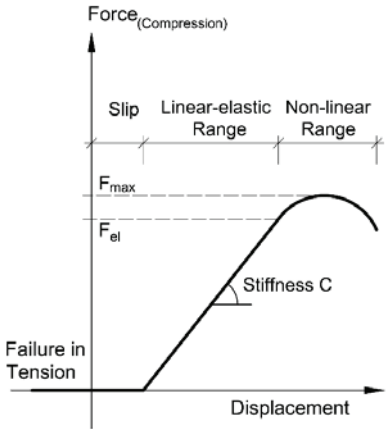

Figure 2: *Schematic force-displacement behaviour of timber step joint with diminished stiffness following [6].*

When modelling timber step joints, it should be noted that only compressive forces can be transmitted. directly under tension as timber steps are not able to transfer any tensile loads. Seim [6] states that the value for the step joints stiffness C defined at 20-25 kN/mm and the simplification of the force-displacement relationship, by disregarding slip and assuming linear-elastic behaviour until failure (see Figure 2), provide sufficiently accurate results for an implementation in practice. This statement will be assessed within this paper.

Numerous publications deal with the load-bearing behaviour of carpentry joints [7–10]. Villar-Garcia et al. [11] suggest adding a gap in the front notch of a double-step joint to improve the load-bearing behaviour. In order to achieve an efficient load transfer when using step joints, a high fitting accuracy is generally assumed as a predisposition, an assumption that has however not yet been quantified in detail. This paper therefore deals with experimental investigations of timber joints with intentionally placed gaps in step joints to determine the influence of inaccuracies on the load-bearing behaviour. The results of the experimental investigations are discussed based on recalculations of realistic truss structures.

2 Experimental Investigations

The load-bearing behaviour of traditional and newly developed step joints with a perfect fit was investigated and compared in a previous publication of the authors [2]. The most relevant geometries for practical application, as depicted in Figure 3, were selected from [2] for the investigations presented within this paper and in [12] in order to determine the influence of inaccuracies on the load-bearing behaviour. Configuration A represents a classic carpentry joint, the double-step joint. For Configuration B a third step was added to the double step joint. Geometry C is a multi-step joint with increasing cutting depth t_v from the front to the rear notch resulting in multiple shear planes. A multi-step joint with seven steps and a single shear plane was also considered within Configuration D. The reference configurations were designed and fabricated with an ideal fit between the joint members to ensure comparability with their related inaccurate versions.

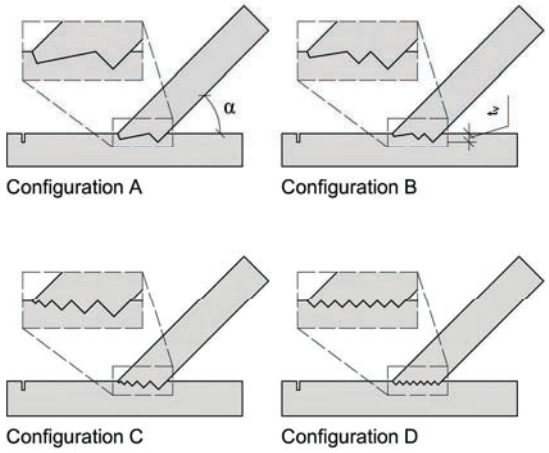

Figure 3: *Illustration of the reference configurations with a perfect fit based on the findings of [2].*

2.1 Test Specimens and Inaccuracy Placement

The investigated configurations, including the placement of the gaps, are pictured in Figure 4. While five different placements of inaccuracies were investigated for Configuration A, only one or two different variations of Configurations B, C and D were assessed. As was the case for the reference configurations and described in more detail in [2,12] the specimens were made from glue laminated timber made from spruce (GL24h) with an intended cross section of 120/120 mm (the actual cross section being 118 L3s configuration (39 l-40 w-39 l) according to ÖNorm EN 14080:2013 [13]) with the joining interfaces milled using the industrial robot at the BOKU robot laboratory [14]. All test specimens were stored in the same environment to ensure comparability of the results. The moisture content was determined using a GANN Hydromette BL H40/HT70 and lied in the required range of 12%.

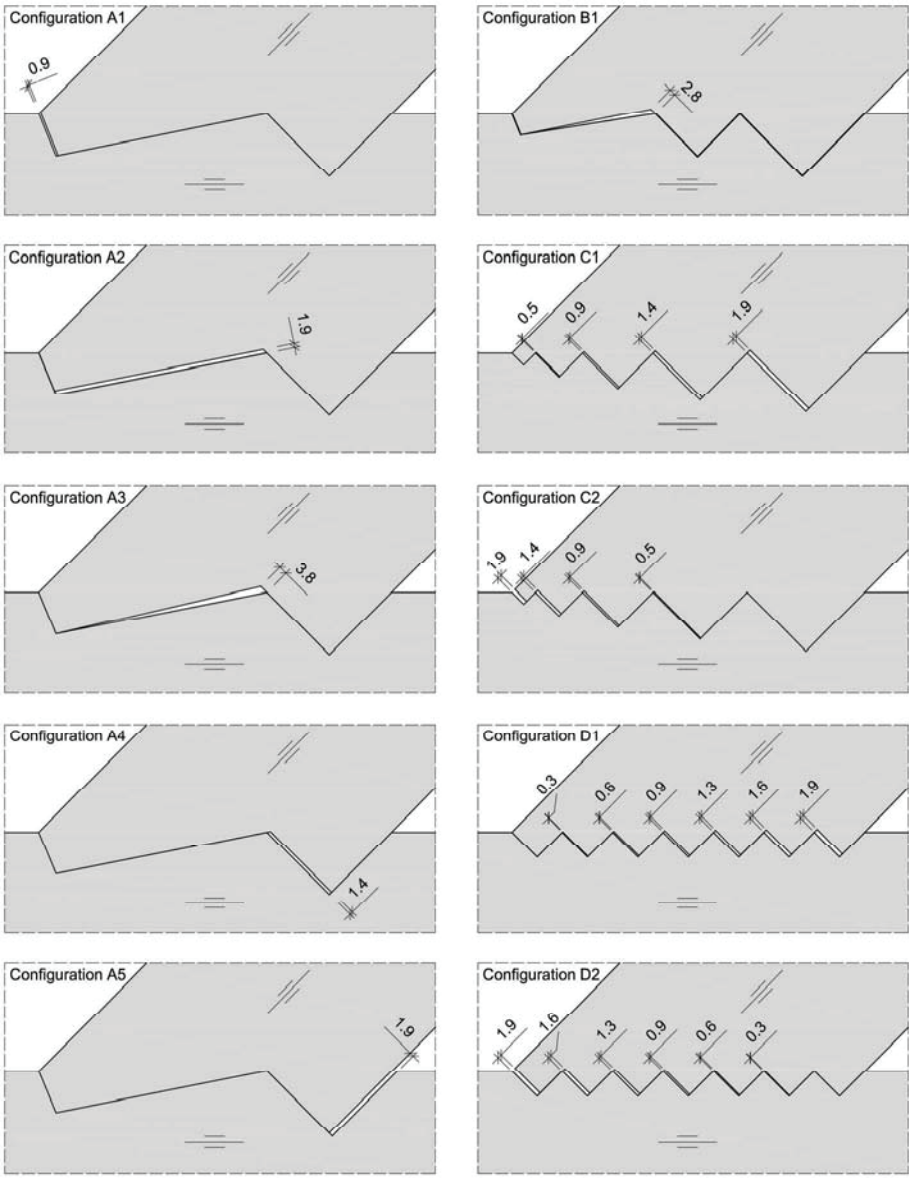

Figure 4*: *Placement of the internally manufactured gaps in the geometries selected from [2] [mm]. ***Configuration A1*: *Inaccuracy at the front of the front notch; ***Configuration A2****: *Inaccuracy at the back of the front notch; ***Configuration A3****: *Inclined inaccuracy at the back of the front notch; ***Configuration A4****: *Inaccuracy at the front of the second step; ***Configuration A5****: *Inaccuracy at the back of the second step ; ***Configuration B1***: *Inclined inaccuracy at the back of the front notch; ***Configuration C1****: *Increasing gap sizes from the front to the rear notch; ***Configuration C2****: *Decreasing gap sizes from the front to the rear notch; ***Configuration D1****: *Increasing gap size from the front to the rear notch; ***Configuration D2****: *Decreasing gap size from the front to the rear notch. [12]*

2.2 Test Setup

The test setup, described in more detail in [2,12], consisted of three steel profiles, welded together at an angle of 45°, as presented in Figure 5, allowing a vertical load application to the specimens. The length of the fore wood was set to 315 mm to achieve compression instead of brittle failure due to shearing of the tie-end.

The load, measured by a load cell, was applied using a servo-hydraulic testing machine in a monotonic, displacement-controlled manner with 1mm/min. During the tests the deformations on the surface of the specimens were recorded using digital image correlation (DIC). In postprocessing a virtual inspect extensometer, as depicted in Figure 5**Fehler! Verweisquelle konnte nicht gefunden werden.**, was used to determine the deformations between two reference points. By linking the measurement data of the load cell to the evaluated changes in length, the load-bearing behaviour was

https://doi.org/10.52202/069179-0192

visualised by means of the subsequently presented force-deformation diagrams.

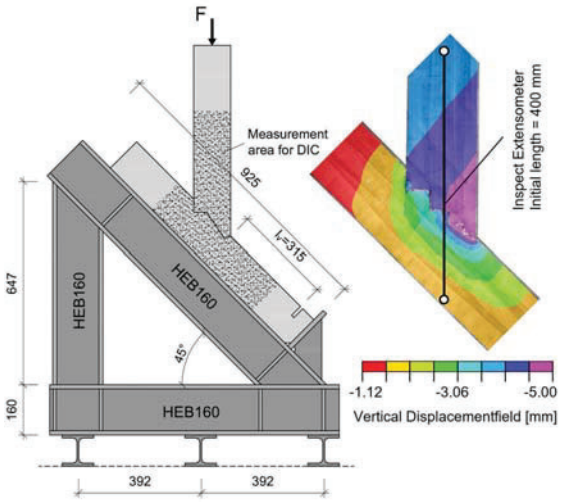

Figure 5: *Test setup including a visualisation of the virtual inspect extensometer in postprocessing. [12]*

2.3 Results and Discussion

The results of the experimental investigation of the in total 42 specimens, which were all carried out until failure, are presented in detail in [12] and illustrated in Figure 6. Within this paper the results are briefly discussed with a focus set on the stiffness C of the investigated joints. Within [12] the stiffness C is referred to as k_{lin}, which is calculated within the linear-elastic range. Apart from the mean values (MV) out of three specimens of the resulting stiffness C, Table 1 lists the mean ultimate load F_{max} for all configurations.

Table 1: *Mean stiffness C and ultimate load F_{max} values with the results of the reference geometries highlighted in bold and the lowest stiffnesses of each configuration underlined. [12]*

Configuration	F_{max} [kN]	C [kN/mm]
A1_MV	175.30	90.4
A2_MV	154.37	89.1
A3_MV	148.27	96.7
A4_MV	143.40	62.2
A5_MV	133.16	74.6
A6_MV	**165.40**	**87.0**
B1_MV	151.39	92.5
B2_MV	**171.26**	**93.9**
C1_MV	160.36	70.2
C2_MV	164.36	62.7
C3_MV	**175.30**	**93.8**
D1_MV	157.16	57.7
D2_MV	160.45	53.5
D3_MV	**176.83**	**107.5**

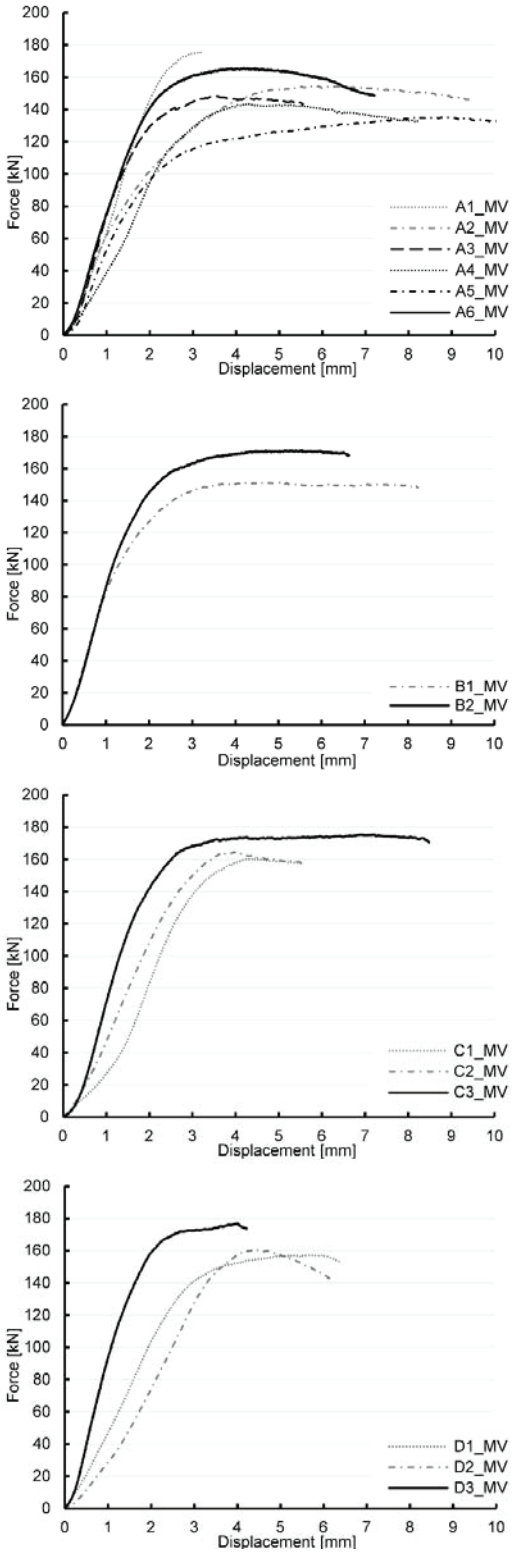

Figure 6: *Force-displacement diagrams of the mean values MV (consisting of three specimens per configuration, except for Configuration B1 with two specimens due to technical problems in postprocessing) of the individual configurations, the solid line represents the reference geometry. [12]*

The results show that, apart from Configuration B1, the intentionally manufactured gaps lead to a significantly lower stiffness C. Even though Configuration C2 shows smaller displacements, the ultimate stiffness C is lower than that of Configuration C1 and is therefore considered within the further investigations.

It could be shown that in all cases inaccuracies reduce the range of the linear-elastic phase, which starts at the end of the initial non-linear phase and ends with the beginning of failure and is characterised by a decrease in stiffness. A detailed description how these points are determined can be found [2,12]. As the linear-elastic range is reduced, the serviceability of a timber structure is negatively influenced for individual configurations if a load level above the linear-elastic range is reached in the static proof in the ULS. In only one out of ten configurations, the load-bearing capacity was increased compared to the reference geometry without gaps. Figure 7 illustrates the individual ranges according to Figure 2 and shows that the reference configurations (highlighted in bold) provide the widest range of the linear-elastic phase.

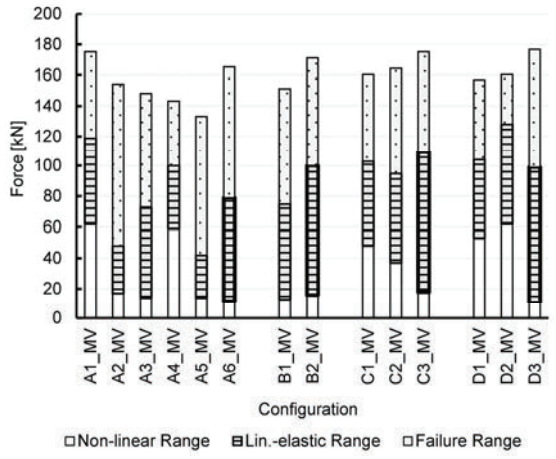

Figure 7: *Observed ranges of the mean values MV of the individual configurations. [12]*

In postprocessing, no damage was detected on the surface of the specimens at the end of the linear phase as determined in [12], so that a hypothesis of a local compression failure of the fibres leading to the stiffness decrease was made. The stiffness C of a single-step joint investigated in [2] was calculated to be 24.84 kN/mm according to [15], lying within the previously mentioned specified range of 20-25 kN/mm according to [6]. The results of the experimental investigations, however, show a stiffness C in the linear-elastic range of 53.5-107.5 kN/mm, as listed in Table 1. Even though the slip and initial non-linear range is not considered in the stiffness according to [6,15] it is still significantly lower than the determined values. This shows that the assumption of a purely linear-elastic response of a step joint with the stiffness according to [6] lying in a rage of 20-25 kN/mm should be seen as rather conservative with the authors advising to at least consider the initial non-linear range in a bi-linear approach.

In regard to the failure modes, a detailed discussion can be found in [12], where the DIC measurements and the thorough documentation of all surfaces allowed for a definition of seven predominant failure modes. Summarising the results, no general valid statement can be made on the relation of the force at the onset of the individual failure modes and the end of the linear-elastic range with the intentionally placed gaps not resulting in the avoidance of specific failure modes.

3 Practical Application

A typical application of step joints is the connection of the compression struts to the chords in trusses. In order to investigate the influence of the previously determined stiffness decreases within the joint areas caused by the inaccuracies in the connections on the overall deflection behaviour of an actual structure, the behaviour of a symmetrical parallel chord truss, as pictured in Figure 8, was determined for various joint stiffnesses using the Software RStab by Dlubal [16]. This study focuses exclusively on the analysis of the influence of inaccuracies within the joint between the connected truss members. Other parameters that additionally influence the deflection behaviour, such as deviations in strut length or joints position, were not considered.

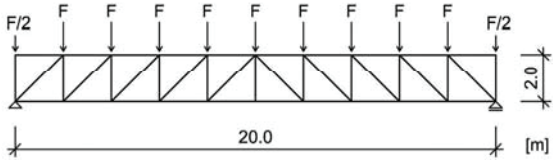

Figure 8: *Illustration of the investigated parallel chord truss.*

The truss was designed with a span of 20 m and an overall height of 2.0 m with a declared strength class of GL24h for all chord and strut elements. As would be the case within the actual construction, the top and bottom chords were modelled as continuous beams with a cross section of 120/200 mm. The vertical truss members were modelled as two 60/120 mm cross sections placed at the outer sides of the chords, while the diagonal struts, subjected to compression, were chosen as in the experimental investigations with a cross section of 120/120 mm.

The considered load cases were the dead weight, a load from a possible superstructure (permanent) and snow (variable). The loads of 7.0 kN and 4.8 kN, respectively, were applied to each node of the top chord and resulted in the maximum utilisation (0.99) of the structure (in particular the diagonal strut near the support) within the ultimate limit state (ULS) according to [5]. The normal forces under the serviceability limit state (SLS) characteristic load combination are presented in Figure 9.

https://doi.org/10.52202/069179-0192

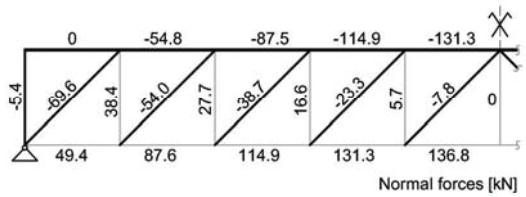

Figure 9: *Normal forces [kN] in the individual truss members (characteristic serviceability limit state SLS load combination).*

In order to make a statement in regard to the influence of inaccuracies of the step joints on the deflection of the entire truss system, the determined load-bearing behaviour from the experimental investigations was implemented within the RStab model. The stiffest and the most ductile connections of each configuration were chosen for a direct comparison, with the reference geometries always being the former and the latter being the configuration underlined in Table 1, resulting in a comparison of Configurations A6 and A4, B2 and B1, C3 and C1 as well as D3 and D2. In addition, the deformations of a truss structure with pin-joints (rigid joints with frictionless nodes) was calculated. The mechanical joint-properties of the compression struts based on the experiments were approximated within the model based on the determined load-bearing behaviour using a multi-linear modelling approach as presented in Figure 10. The kinks within the approximation were set at the end of the non-linear range, at the end of the linear-elastic range and at the point of the maximum force with their corresponding deformation followed by a constant plateau. The calculation was rounded off with the evaluation of a system with a compression joint stiffness C of 20 kN/mm, as defined by Seim [6], and a tensile joint stiffness C of 25 kN/mm using ring connectors for two shear planes with a diameter of 65 mm according to [17].

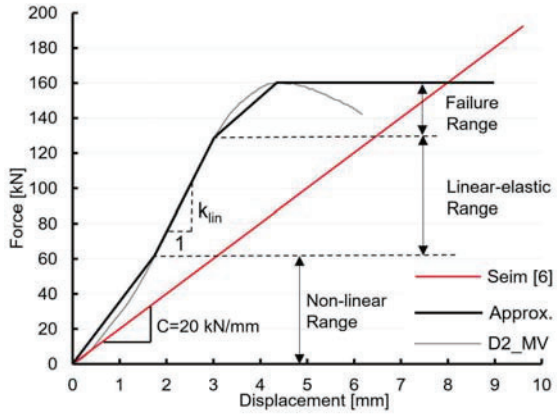

Figure 10: *Illustration of the multi-linear approximation of the load-bearing behaviour in the modelling process of Configuration D2_MV and the linear-elastic behaviour according to Seim [6].*

The results of the numerical investigations are presented in Table 2. It must be mentioned, that within the calculations only the instantaneous deformations w_{inst} were considered and the additional deflections caused by creep where neglected.

Table 2: *Maximum deflection in mid span for the serviceability limit state SLS with the reference geometries highlighted in bold.*

Configuration of compression strut	Maximum deflection in mid span [mm]
Pin-joints	32.9
With C=20 kN/mm according to Seim [6] (compression) and C=25 kN/mm (tension)	66.8
A4_MV	52.5
A6_MV	**48.3**
B1_MV	46.7
B2_MV	**47.3**
C1_MV	55.5
C3_MV	**49.2**
D2_MV	55.3
D3_MV	**46.5**

The results show that the stiffness C of the joints has a significant influence on the deformations when cumulating them over an entire truss structure. As expected, the system with pin-joints and the system with the stiffness defined by Seim [6] represent the upper and lower limits of the assessed systems, with the rigid system showing less than half of the deflection of the other. When considering the deflection w_{inst} without consideration of creep, a limit of l/300 according to [5] is set at 66.7 mm, which is slightly exceeded by the conservative assumptions of Seim [6].

It must be noted that the present study did not use variable cross sections for the compression struts, as this is also often not the case in practice (higher effort in design and execution). The chosen design, however, leads to various load levels within the struts, with the highest being - 69.6 kN at the supports, with a maximal utilisation, and the lowest being in the middle with -7.8 kN and low utilisation. By prestressing the connection, by for example a superelevation of the truss [18], the load level in the minimally utilised struts can be raised resulting in a load-bearing behaviour with a maximum stiffness. The prestressing would also eradicate the effects of the undesirable inaccuracies by counteracting the initial non-linear range, before any external load is even applied.

The present numerical investigation further shows that the most unfavourable positioning of inaccuracies (Configuration A4) within the double-step joint entails a 9% increase of the total deflections of the structure compared to the reference geometry (Configuration A6) and a 60% increase compared to the truss model implementing pin-joints. The investigated load level was not sufficient to use the potential in terms of the linear-

elastic range of the more efficient reference geometry B2. The required load within the joint should lie between 75 (end of linear-elastic range B1) and 100 kN (end of linear-elastic range B2) to exploit the potential of B2 compared to B1 in terms of minimising the deflections. It has to be mentioned, however, that this load level cannot be reached for the given cross section within the static proof in the ULS according to [5] for the given cross section and thus represents a theoretical approach. A noticeable increase in deflection is noticed for both Configurations C3 and D3 compared to their reference geometries with 13% and 16%, respectively.

4 CONCLUSION

With the deflection of timber constructions, especially trusses, essentially depending on the stiffness of the joints, the presented investigations are of high scientific value. Within this paper the influence of intentionally placed inaccuracies on the load-bearing behaviour of step joints is presented. The initial goal of this study was to investigate if specific placements of gaps within joint could influence the failure mechanisms or harbour benefits in regard to the load-bearing behaviour. Four different configurations of multi-step joints were produced and tested in experimental investigations with various inaccuracies and compared to perfect fit reference geometries. The results show that the load-bearing behaviour is negatively affected by inaccuracies with stiffness and load-bearing capacity decreases of up to 16% and 19%, respectively. Furthermore, the individual ranges of the load-bearing behaviour depend on the position of the gaps and show a predominantly negative influence, with a perfect fit critical for the highest possible stiffness in the connection and smallest possible deflection of an entire truss structure. If pin-joints are considered within dimensioning for example by using a FE software the deflection is significantly underestimated, while stiffness estimations from literature, e.g. Seim [6], show rather conservative results with higher deflections than can be expected in reality (without a consideration of creep).

As an endnote it should be mentioned that the use of multi-step joints does not provide any significant advantages considering the deflection of entire systems when compared to the traditional double-step joint.

ACKNOWLEDGEMENT

This research did not receive any specific grant from funding agencies in the public, commercial, or non-profit sectors.

REFERENCES

[1] Neuhaus H. Ingenieurholzbau: Grundlagen - Bemessung - Nachweise - Beispiele. 4. Auflage. Wiesbaden: Springer Vieweg; 2017.

[2] Braun M, Pantscharowitsch M, Kromoser B. Experimental investigations on the load-bearing behaviour of traditional and newly developed step joints for timber structures. Construction and Building Materials 2022;323:126557. https://doi.org/10.1016/j.conbuildmat.2022.126557.

[3] CEN. ÖNORM EN 336:2013 11 15: Bauholz für tragende Zwecke - Maße, zulässige Abweichungen. Brussels: European Committee for Standardization; 2013.

[4] Blaß HJ, Enders-Comberg M. Fachwerkträger für den industriellen Holzbau 2012:176. https://doi.org/10.5445/KSP/1000028217.

[5] CEN. ÖNORM EN 1995-1-1:2019 06 01: Eurocode 5: Bemessung und Konstruktion von Holzbauten - Teil 1-1: Allgemeines - Allgemeine Regeln und Regeln für den Hochbau (konsolidierte Fassung). Brussels: European Committee for Standardization; 2019.

[6] Seim W. Ingenieurholzbau: Vertiefung: Tragwerke und Berechnungsmethoden. Berlin: Ernst & Sohn; 2022.

[7] Enders-Comberg M. Leistungsfähige Verbindungen des Ingenieurholzbaus - Einsatzmöglichkeiten für Nadel- und Laubholz 2015:304.

[8] Markus Enders-Comberg, Hans Joachim Blaß. Treppenversatz - Leistungsfähiger Kontaktanschluss für Druckstäbe. Bauingenieur 2014;89.

[9] Palma P, Cruz H. Mechanical Behaviour of Traditional Timber Carpentry Joints in Service Conditions - Results of Monotonic Tests. From Material to Tructure, Florence, Venice and Vicenza: 2007.

[10] Siem J. The single-step joint – a traditional carpentry joint with new possibilities. International Wood Products Journal 2017;8:45–9. https://doi.org/10.1080/20426445.2017.1302148.

[11] Villar-García JR, Vidal-López P, Crespo J, Guaita M. Analysis of the stress state at the double-step joint in heavy timber structures. Mater Construcc 2019;69:196. https://doi.org/10.3989/mc.2019.00319.

[12] Braun M, Kromoser B. The influence of inaccuracies in the production process on the load-bearing behaviour of timber step joints. Construction and Building Materials 2022;330:127285. https://doi.org/10.1016/j.conbuildmat.2022.127285.

[13] CEN. ÖNORM EN 14080: 2013 08 01: Timber structures - Glued laminated timber and glued solid timber - Requirements. Brussels: European Committee for Standardization; 2013.

[14] Kromoser B, Braun M, Ortner M. Construction of All-Wood Trusses with Plywood Nodes and Wooden Pegs: A Strategy towards Resource-Efficient Timber Construction. Applied Sciences 2021;11:2568. https://doi.org/10.3390/app11062568.

[15] Heimeshoff B, Köhler N. Untersuchung über das Tragverhalten von zimmermannsmäßigen Holzverbindungen. München: IRB Verlag; 1989.

[16] RStab, Ingenieur - Software Dlubal GmbH 2006.

[17] CEN. ÖNORM EN 912: 2011 08 15 Holzverbindungsmittel - Spezifikation für Dübel besonderer Bauart für Holz. Brussels: European Committee for Standardization; 2019.

[18] Matthias Braun. Superelevated wooden truss - increase of load bearing capacity and stiffness, IASS Symposium Form and Force Barcelona: 2019.

https://doi.org/10.52202/069179-0192

World Conference on Timber Engineering Oslo 2023

PREFABRICATED FOUNDATION SYSTEMS FOR TIMBER BUILDINGS

Davide Canetti[1], Francesca Paoloni[2], Riccardo Fanti[3], Alessandro Setti[4], Andrea Polastri[5], Fabrizio Tamburini[6]

ABSTRACT: Wall-to-foundation constructive detail represent a critical issue for timber constructions due to the risk of decay of wooden components, for this reason the designer has to propose solutions aimed to enhance the durability; furthermore, has to consider several aspects such as mechanical connection, thermal insulation, electrical and plumbing systems. This paper presents an innovative concrete prefabricated beam-foundation element, aimed to solve the issues related to durability avoiding unexpected capillary rise of water creating a physical barrier between the ground and the wooden elements. Experimental tests were conducted to characterized the mechanical properties of the analyzed system: results of the experimental campaign are presented and discussed.

KEYWORDS: timber structures, experimental test, CLT-foundation connection, prefabricated beam foundations

1 INTRODUCTION

In the last decades one of the main issue of timber construction is represented by the timber wall-to-foundation details. The design of this construction detail has to deal with mechanical connection, thermal insulation, electrical and plumbing systems and finally durability. The foundation systems have the fundamental task of transfer loads from the structure to the ground: proper connections to anchor the upper structure to the foundations have to be designed. The shape and type of foundations determined the distributions of loads and deformations, conditioning the bearing capacity of the ground and the behaviour of upper structure. For timber buildings, traditional foundation system consists in a slab at the base of entire structure or foundation beams located below the structural wall, in both cases obtained with reinforced concrete casted in situ. These foundation systems, in case of low-mid rising timber buildings, often results be overdesigned and the high stiffness of traditional reinforced concrete foundations compared to the stiffness of timber structures allows to neglect differential vertical settlements and their effects on upper structure. This characteristic simplifies the design of timber elements and connections. Non-structural requirements have an important role in design phase of foundation system. Practitioners have to pay particular attention in the design of details, in particular for wall-to-foundation node [1]. They have to adopt some expedients reported in the state of the art to avoid any kind of issue related to durability that can be occurred during the service-life of a timber structure [2,3,4,5,6,7]. In order to avoid unexpected capillary rise of water from the ground, the foundations system has to be design as a waterproof barrier between the ground and the wooden wall. Usually, concrete beams were casted in situ above the foundation slab along perimeter wall panels. Levelling and alignment of the beam elements are the most critical issue due to imprecision of casted concrete slab and to the presence of the steel rebars protruding from the slab. Recently, several companies proposed different timber-to-foundation systems made with aluminium [8], or reinforced concrete [9,10], aimed to solve those critical aspects. This paper present results of an experimental campaign conducted on an innovative "beam type" foundation system (Figure 1) proposed by Canetti et al. [10]. Tests were performed in order to characterize the mechanical behaviour of the foundation system for different configurations of loads. Different widely used typology of timber walls, like Light Frame Timber (LFT) and Cross Laminated Timber (CLT) are suitable for this foundation system. The wide range of width of concrete beams make eligible the use of bio-based material walls that exhibit a large thickness compared to traditional systems or wall with diagonal boards that combined traditional technology and circular economy.

Figure 1: *Prefabricated concrete beam-foundation element example of use on construction-site (CLT and LFT walls)*

[1] Davide Canetti, Alpeas, Italy, davide.canetti@alpeas.it
[2] Francesca Paoloni, Architect, Italy, fra.paoloni@gmail.com
[3] Riccardo Fanti, Institute of Bioeconomy - National Research Council of Italy (CNR-IBE), Italy, riccardo.fanti@ibe.cnr.it
[4] Alessandro Setti, Institute of Bioeconomy - National Research Council of Italy (CNR-IBE), Italy, alessandro.setti@ibe.cnr.it
[5] Andrea Polastri, Institute of Bioeconomy - National Research Council of Italy (CNR-IBE), Italy, andrea.polastri@ibe.cnr.it
[6] Fabrizio Tamburini, Tamburini Prefabbricati, Italy, info@tamburiniprefabbricati.it

https://doi.org/10.52202/069179-0193

2 PREFABRICATED CONRETE BEAM FOUNDATION SYSTEM

The system here illustrated is composed by reinforced SCC concrete (Self Compacting Concrete) linear elements with rectangular section. The prefabricated beam is intended to be used as a base for structural/non-structural timber walls; in particular, the foundation was optimized for LFT and CLT structures.

The foundation elements are made in a prefabrication plant following specific production controls, proper formworks were designed in order to obtain the required rectangular sections, with a width from 120mm to 200mm and a depth up to 380mm; the maximum length is equal to 4000mm. Thanks to the special adjustable metal formwork and the use of self-compacting concrete, it is possible to create linear elements almost totally free of geometric defects (the expected production tolerances are +/- 6 mm on nominal dimensions) so to guarantee an excellent result during the assembly at the construction site.

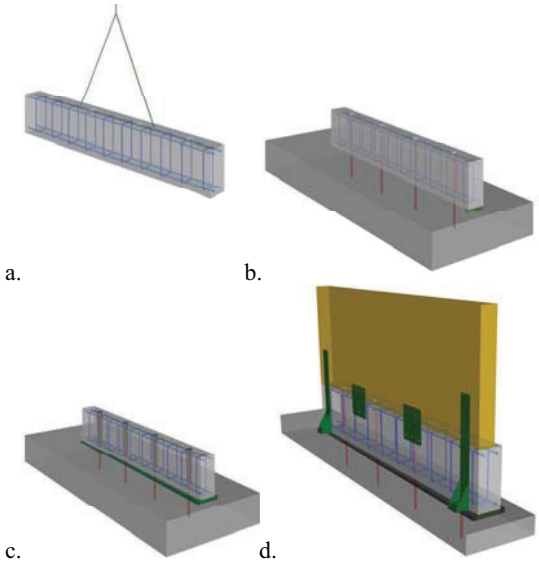

Figure 2: *on site construction phases: a) lifting; b) levelling and anchoring; c) filling vertical cones and horizontal gap with repair mortar; d) connecting timber wall to the prefabricated system*

The design, production and on site operations takes place according to the following procedures: typically, the design phase starts with the executive structural design plant; in particular, it is necessary to properly define the ground floor walls of the timber building and the associated maximum vertical forces per unit length and the maximum horizontal shear forces per unit length along the shear-wall. The designer develops a detailed executive plan of the foundation, standard prefabricated beam modules with a length equal to 2000mm are adopted; where is not possible sub-modules and non-standard elements are designed.

Afterwards, designers perform a structural verification of the anchor bar that connect the prefabricated modules to the foundation slab, a minimum longitudinal reinforcement have to be provided.

Last step is the development of production drawings and a clear assembly diagram to be use on construction site. All the indications needed for handling and storage on site are given through installation tables.

The production of the elements at the concrete prefabrication plant has to consider the installation of the bushings for lifting them. Concrete cubes for product quality control have to be stored and tested.

Once the prefabricated concrete beam modules are on the construction site have to be positioned through the appropriate lifting points, which are already set up in each element (Figure 2a).

Foundation beams are then levelled using proper metal plates and anchored (glued with proper epoxy resin) to the foundation slab with B450C (16mm diameter) reinforcing bar (Figure 2b).

The final operation consists in casting special repair mortar in order to fill all the gap between the prefabricated elements and the foundation, followed by the filling of the upper cones (Figure 2c) using high compressive strength and anti-shrinkage pourable mortar. When the prefabricated elements are properly fixed to foundation timber walls can be installed above the concrete beams and anchored with steel plates to the beam against shear loads and directly to the foundation slab with hold-downs to prevent the rigid rotation (Figure 2d). Steel plates and hold-downs are nailed or screwed to the timber walls and connected to beams and slab by means of threaded rods.

The structural elements are made according to EN13225:2013 [11]. The concrete beam presents several holes with conical shape along its length centred at the middle of the element's width for insertion of vertical anchor bars: lower diameter of 25mm and a flaring with an inclination of 1° towards the outside of the hole. The number of holes has to be designed by the practitioner: equally spaced holes at 500mm are typically adopted.

The concrete cover to be used is 30mm for an ordinary carbonation class XC2, with concrete cover factory control and a nominal life of 50 years. The main geometrical and mechanical properties of prefabricated concrete beam are reported in Table 1.

Table 1: *Geometrical/mechanical properties of concrete beam*

Prefabricated concrete beam	
Concrete	C30/37
Consistency class	SCC
Exposure class	XC2
w/c ratio	0,40
Calcareous filler [kg/m^3]	148
Sand 0-4 [kg/m^3]	245
Gravel 5,6-16 [kg/m^3]	1311

Figure 3 reports some technical details of the prefabricated concrete beam, construction site views in order to show the technological aspects and the construction phases showed in Figure 2, of the proposed systems, that were developed to ease a simple and precise assembling of the foundation beam and consequently of the timber walls placed on it.

https://doi.org/10.52202/069179-0193

Figure 3: *on site construction phases: levelling and anchoring (top picture); placing the CLT walls on the top of the prefabricated beams (central picture); connecting timber wall to the prefabricated system (bottom picture)*

3 EXPERIMENTAL CAMPAIGN

An experimental campaign with three series of monotonic tests for a total number of 10 test typologies were carried out in order to completely characterized the mechanical behaviour of the prefabricated concrete foundation system. The prefabricated concrete beam tested specimens are characterized by a depth equal to 350mm, width from 120 to 160mm and length from 560 to 1300mm. The concrete elements are reinforced either with steel bars and hoops or with steel fibers.
Different configurations were studied by means of specific tests. The experimental tests were designed and performed on: anchor system of the beam element in tensile configuration (Figure 4a), beam-to-slab connection in shear configuration (Figure 4b) and panel-to-beam (CLT-to-concrete) connection (Figure 4c).

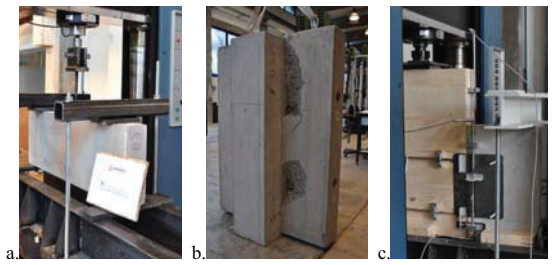

Figure 4: *Prefabricated beam foundation element: a) tensile test; b) specimen after the shear test; c) wall panel-to-beam connection test.*

The tensile tests on anchor system of beam element were carried out according to setup in Figure 4a. Beam elements are characterized by a depth equal to 350mm, width equal to 120mm and a length equal to 1000mm. The single rebar that protrude from the upper surface of the concrete element is fixed to the testing machine in order to transfer the tensile load (Figure 5a).

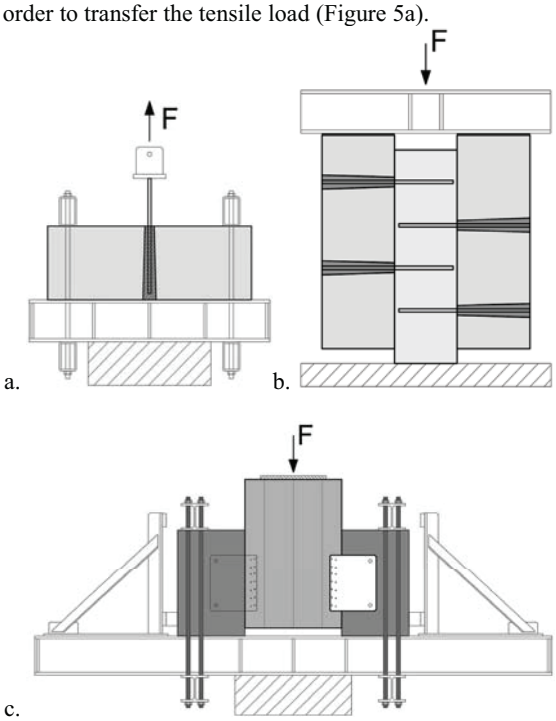

Figure 5: *Test setup: a) anchor system of beam element tensile test; b) beam-to-slab connection shear test; c) panel-to-beam connection shear test*

The element is held down through two rectangular steel profiles. Two different typologies of specimens were tested: beam element reinforced either with steel bars or with steel fibers, according to Table 2. Two tests for each configuration were carried out.

Table 2: *Configurations of anchor system specimens*

ID	test	width [mm]	anchor	d [mm]	reinforcement	n° [-]
1	tensile	120	rebar	16	rebars/hoops	2
2	tensile	120	rebar	16	fibers	2

The beam-to-slab connection specimens were tested according to setup in Figure 4b: two beam elements are fixed (one at each side) of the central concrete element

https://doi.org/10.52202/069179-0193

(slab) through two rebars with a spacing equal to 500mm. Beam elements are characterized by a depth equal to 350mm, width from 120 to 160mm and a length equal to 1300mm. The compression load is applied to the two beam elements by a hydraulic jack through a rigid steel beam, as shown in Figure 5b. The tested configurations are reported in Table 3.

Table 3: *Configurations of beam-to-slab connection specimens*

ID	test	width [mm]	anchor	d [mm]	reinforcement	n° [-]
3	shear	120	rebar	16	rebars/hoops	2
4	shear	120	rebar	16	fibers	2
5	shear	160	rebar	16	rebars/hoops	2
6	shear	160	rebar	16	fibers	2

The panel-to-beam (CLT-to-concrete) connection specimens were tested according to setup in Figure 4c. A compression load is applied by the testing machine to a 5-layer 120mm thick CLT panel (Figure 5c). Two steel plates connect the CLT panel to the two concrete beam elements: the connection plates are placed at the opposite face of the central element. Steel plates are nailed to the panel through fourteen 4x60mm Anker nails and anchored with two 8.8 threaded bars in concrete beam (in this case study the concrete elements are reinforced with fibers). The bars are fixed to the concrete beam with epoxy resin or screwed in special threaded bushing placed during the casting phase (at the production site). The tested configurations details are reported in Table 4. One test for each configuration is carried out.

Table 4: *Configurations of wall panel-to-beam connection specimens*

ID	test	width [mm]	reinforcement	threaded bar fixed system	n° [-]
7	shear	120	fibers	steel bushing	1
8	shear	120	fibers	epoxy resin	1
9	shear	160	fibers	epoxy resin	1
10	shear	160	fibers	steel bushing	1

Tests were performed according to EN26891:1991 [12]. The load rate was not greater than 0,2 mm/s and the maximum load was reached in 300 ± 120 s in all tests.

Results of the three series of monotonic test are reported in Table 5 in terms of mode of failure, stiffness k, maximum force F_{max} and corresponding displacement v_{max}.

Table 5: *Mechanical parameters and mode of failure of the tested specimens*

ID	test	k [kN/mm]	F_{max} [kN]	v_{max} [mm]	mode of failure
1	tensile	-*	59,6	-*	concrete cone combined to pull-out failure
2	tensile	-*	96,9	-*	concrete cone combined to pull-out failure
3	shear	32,7	127,4	29,2	large deformations**
4	shear	52,6	177,5	22,1	limit load***
5	shear	49,9	162,9	28,7	large deformations**
6	shear	43,4	172,1	15,4	limit load***
7	shear	9,6	50,9	14,6	steel-to-timber connection
8	shear	6,9	46,2	13,5	steel-to-timber connection
9	shear	9,7	54,2	14,3	steel-to-timber connection
10	shear	6,5	57,2	15,7	steel-to-timber connection

*displacements were not measured in this test configuration
**test was interrupted due to large deformations (>30mm)
***test was interrupted due to limit load of the hydraulic jack (>400kN)

For the shear tests the mechanical parameters are referred to a single shear plane (i.e. for single concrete beam in beam-to-slab tests and for a single steel plate in panel-to-beam tests). In the cases where two tests are carried out in the same configuration, the average values are reported.

The tensile tests show the same failure mode: the pull-out of rebar combined with the formation of a concrete cone is observed (Figure 6a). In tensile tests the displacement is measured through the testing machine.

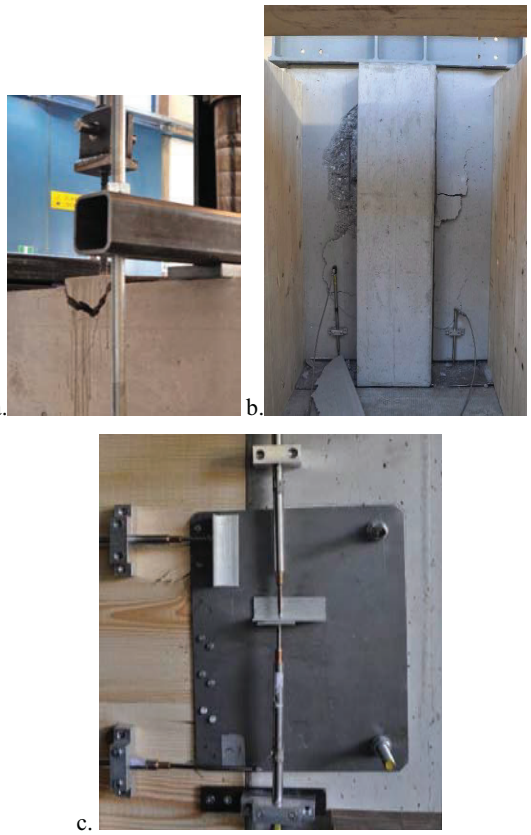

Figure 6: *Failure modes: a) tensile test; b) beam-to-slab connection shear test; c) panel-to-beam connection shear test*

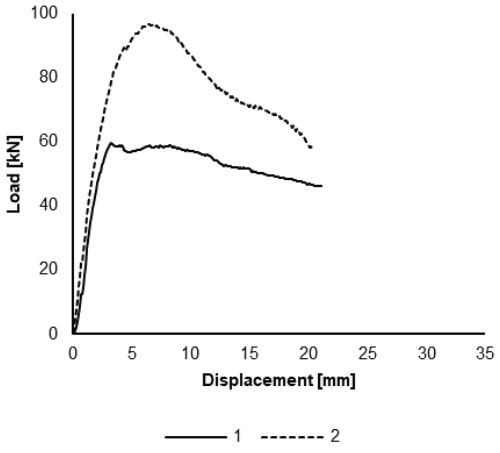

Figure 7: *Tensile tests results*

https://doi.org/10.52202/069179-0193

The fiber-reinforcement beam specimens showed a higher strength and similar value of stiffness compared to rebar reinforcement. The load-displacement curves for both configurations are reported in Figure 7: as mentioned above, the mean values were obtained from two specimens of the same typology.

The shear tests on beam-to-slab connection are interrupted for two different reasons: in case of concrete beam reinforced with rebars tests are interrupted at 30mm of displacement (consistent with the provisions reported in EN12512:2005 [13]), whereas, in case of fiber-reinforcement tests are interrupted due to the reaching of load limit of the hydraulic jack (applied load shouldn't exceed 400 kN). At the end of the tests, in both cases, cracks and spalling of concrete near connections are observed, as shown in Figure 4b. A comparison in terms of load-displacement curves is reported in Figure 8 (mean displacements were obtained from the four LVDTs measurements). After reaching the yielding point (approximately at 5mm of displacement for all specimens) the load in fiber-reinforced specimens rapidly increase until the load limit of the hydraulic jack while slowly increase in other specimens (reinforced with steel bars) until 30 mm of displacement.

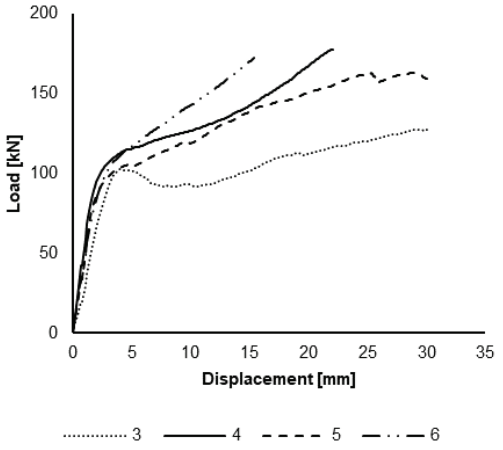

Figure 8: *Shear tests results: beam-to-slab connection*

The shear test on panel-to-beam (CLT-to-concrete) connection failed due to reaching the steel-to-timber connection (nails) strength, as shown in Figure 6c. Rotation of the steel plate and cracks in CLT panels in the nailed areas are observed. The experimental values of maximum strength F_{max} and corresponding displacement v_{max} are approximately the same for each specimen, due to the same failure mode registered in the tests. The values of stiffness of steel-to-timber connection are similar to the values obtained in other experimental campaigns. The width of the beam element (120mm or 160mm) and the different fixing systems, used to anchor the steel threaded bars, seems have no influence on the mechanical behaviour of the tested specimens. No failures are observed in the beam elements. A comparison between the load-displacement curves of the four tested specimens is reported in Figure 9.

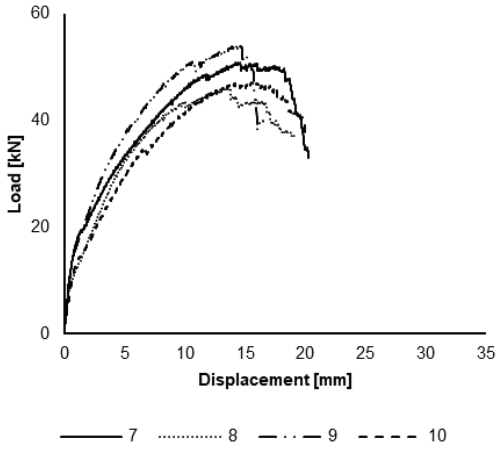

Figure 9: *Shear tests results: wall panel-to-beam connection*

4 CONCLUSION

The paper presents an innovative concrete prefabricated beam foundation system aimed to mitigate the risk of durability issues in timber elements and to ease the on-site building procedure. In particular, results obtained from an experimental campaign are presented and discussed. Tensile tests on anchor system, shear test on beam-to-slab (concrete-to-concrete) and on panel-to-beam (CLT-to-concrete) connection are reported in this paper. The tensile tests on anchor system showed a mode of failure due to the pull-out of rebar combined with the formation of a concrete cone. Beams reinforced with fibers exhibited higher strength than beams reinforced with rebars. The shear tests on beam-to-slab connection show significant strength and stiffness; no failures were observed in case of beams reinforced with steel fibers (the limit load of hydraulic jack is 400kN). Beams reinforced with rebars also exhibited high level of strength and stiffness but less than beams with steel fibers, due to the local cracks and large zone of spalling of concrete cover; after the yielding point, the load slowly increase until the limit displacement, equal to 30mm, where tests were interrupted. The panel-to-beam connection specimens were characterized by a steel-to-timber nail failure mode. Yielding of nails allowed to reach a ductile failure mode. No cracks near the threated bars were observed. Regardless of the width of concrete element no failures were observed in beams. The prefabricated concrete beam presented in this paper can be considered a valuable foundation system developed to guarantee the durability of timber structures. A simple and fast assembling system for timber walls on the construction site, at the foundation level, is ensured through these elements.

https://doi.org/10.52202/069179-0193

REFERENCES

[1] Gasparri A., Canetti D., Sartori T., Giongo I., (2020) Valutare analiticamente la durabilità delle strutture in legno: il caso dell'attacco a terra, Structural, doi: 10.12917/STRU227.05

[2] Frühwald Hansson E., Brischke C., Meyer L., Isaksson T., Thelandersson S., Kavurmaci D., (2012), Durability of timber outdoor structures - modelling performance and climate impacts, World Conf. Timber Eng.

[3] Paoloni F., Ferrante T., Villani T. Maintenance systems and costs for Wooden Façades, WCTE 2018 - World Conference on Timber Engineering (2018).

[4] Paoloni F., Ferrante T., Villani T., (2017) Maintenance systems for wooden façades, Final COST FP1303 meeting: Building with Bio-based materials: Best practice and performance specification.

[5] Daniotti B. and Spagnolo S. L., (2007) Service life prediction for buildings' design to plan a sustainable building maintenance, Port. Sb07 - Sustain. Constr. Mater. Pract. Chall. Ind. New Millenn. Pts 1 2.

[6] Brischke E., Meyer C., Suttie L., (2015) Towards performance based durability standards for wood in construction – part 2: considering moisture risks in wooden components, in XIII Conference on Durability of Building Materials and Components.

[7] Hazleden D. G. and Morris P. I., (1999) Designing for Durable Wood Construction: The 4 Ds, 8th International Conference on Durability of Building Materials and Components

[8] Pozza L., Comunian M., Scotta R., (2019) Soluzione innovativa per prevenire il deterioramento delle pareti in legno all'attacco con la fondazione, Ingenio.

[9] Maines M., Pacchioli S., Polastri A., (2021) Come garantire un corretto ancoraggio tra pareti in CLT e cordoli in c.a.: stato dell'arte e soluzione innovativa, Ingenio

[10] Canetti D., Sartori T., Polastri A., (2020) Timber buildings, a prefabricated solution for the connection to the foundation, Structural, doi: 10.12917/STRU230.19

[11] EN 13225:2013. Precast concrete products - Linear structural elements.

[12] EN26891:1991. Timber structures - Joints made with mechanical fasteners - General principles for the determination of strength and deformation characteristics (ISO 6891:1983).

[13] EN12512:2005. EN12512, Timber structures. Test methods. Cyclic testing of joints made with mechanical fasteners. Brussels, Belgium: CEN, (2005).

https://doi.org/10.52202/069179-0193

World Conference on Timber Engineering Oslo 2023

UPPER AND LOWER RESISTANCE OF SMALL STEEL-TO-TIMBER CONNECTIONS AND COMPARISON WITH REVISED EYM

Jørgen Munch-Andersen[1]

ABSTRACT: The European Yield Model for lateral resistance of connections is revised in the draft for a new Eurocode 5, EN 1995-1-1, for timber structures. In the future there will be only one formula, applying to both timber-to-timber and steel-to-timber connections as well as one or more shear planes. Results from testing of small steel-to-timber connections is compared to estimates using the revised EYM with strength parameters taken from the code as well as the actual values. There is a significant reserve that complicates the estimate of the upper value of the resistance, which is of interest for designing for robustness (against progressive collapse) and against brittle failure during earthquake. The ratio between the upper and lower characteristic resistances is investigated, and methods to reduce the ratio are discussed.

KEYWORDS: EYM, steel to timber, lateral resistance, upper characteristic resistance, lower characteristic resistance

1 INTRODUCTION

The revised version of the European Yield Model (EYM) - to appear in the coming revision of Eurocode 5 part 1-1 for timber structures [1] - is applied to laterally loaded connections with steel plates connected to structural timber using strength parameters determined for the actual timber and fasteners used.

The results are compared to the lateral resistance determined by testing according to in EN 1380 [5]. Investigations at mean value level are carried out, from which the actual rope-effect [16],[17] is determined for the various combinations of fasteners and steel plates used.

The coefficient of variation (CoV) for the different combinations is estimated, which enables to determine the 'true' lower and upper characteristic resistances. The lower value is further compared to lower value obtained using the EYM [1], [2].

The upper value is used to estimate an 'overstrength' factors as the ratio between the 'true' upper and the lower characteristic resistance obtained using the EYM in Eurocode 5.

The overstrength factor is of interest when designing for robustness using the principle of segmentation, where fuse-elements with a known upper value of resistance are needed to halt progressive collapse [1],[4]. It is also needed when designing for seismic loads to ensure the formation of hinges in the fasteners before the timber around the connection fails in a brittle manner.

2 REVISED EYM

The revised EYM is basically the traditional formula for timber-to-timber connections with one shear plane [2], having an equation for each of the six possible failure modes (a)-(f), see Figure 1.

$$F_{D,k}(\mathrm{i}) = \begin{cases} f_{h,k1}\, t_{h1}\, d & \text{(a)} \\ f_{h,k2}\, t_{h2}\, d & \text{(b)} \\ \dfrac{f_{h,k1}\, t_{h1}\, d}{1+\beta}\left(\sqrt{\beta + 2\beta^2\left(1+\dfrac{t_{h2}}{t_{h1}}+\left(\dfrac{t_{h2}}{t_{h1}}\right)^2\right)+\beta^3\left(\dfrac{t_{h2}}{t_{h1}}\right)^2}-\beta\left(1+\dfrac{t_{h2}}{t_{h1}}\right)\right) & \text{(c)} \\ 1{,}05\,\dfrac{f_{h,k1}\, t_{h1}\, d}{2+\beta}\left(\sqrt{2\beta(1+\beta)+\dfrac{4\beta(2+\beta)M_{y,k}}{f_{h,k1}\, d\, t_{h1}^{\,2}}}-\beta\right) & \text{(d)} \\ 1{,}05\,\dfrac{f_{h,k1}\, t_{h2}\, d}{1+2\beta}\left(\sqrt{2\beta^2(1+\beta)+\dfrac{4\beta(1+2\beta)M_{y,k}}{f_{hk,1}\, d\, t_{h2}^{\,2}}}-\beta\right) & \text{(e)} \\ 1{,}15\cdot 2\sqrt{\dfrac{\beta}{1+\beta}}\sqrt{M_{y,k}\, f_{h,k1}\, d} & \text{(f)} \end{cases}$$

where $\beta = f_{h,k2} / f_{h,k1}$

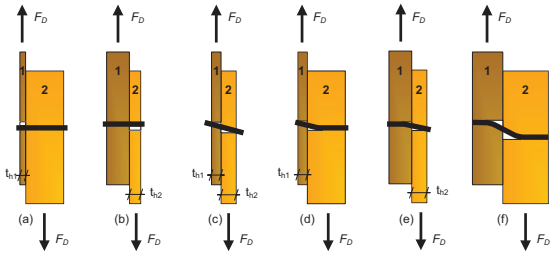

Figure 1: *The dowel contribution F_D to the lateral resistance F_v in EYM. d is the fastener diameter, M_y is the yield moment, t_{h1} and t_{h2} are the embedment depths and f_{h1} and f_{h2} the embedment strengths of member 1 and 2.*

[1] Jørgen Munch-Andersen, BUILD, Aalborg University - Copenhagen, jcma@build.aau.dk

https://doi.org/10.52202/069179-0194

The EYM estimates the lateral resistance as

$$F_{v,k} = \text{Min}\,[F_{D,k}(i) + F_{T,k}(i)]$$

where $F_{D,k}(i)$ is the dowel (or Johansen) contribution and $F_{T,k}(i)$ is the rope-effect contribution, which normally is taken as a fraction of the axial tension resistance, $F_{ax,k}$, but for failure modes (a) and (b) there is no rotation of the fastener so there is no rope-effect).

Multiple shear planes are dealt with by specifying which of the six failure modes that cannot exist and therefore shall be disregarded in the general EYM-formula. For two shear-planes that is mode (c) and (e), when member 1 is the outer members.

Metal-to-timber connections are dealt with by using the actual embedment strength for the metal – which for e.g. steel is called the bearing strength and can be determined according to EN 1993-1-7. It is at least 600 MPa for steel plates. For e.g. aluminium, the actual value should be used, which is considerably smaller.

A further advantage of using the actual embedment strength and thickness of the metal plate is that there is no need for the definition of thick and thin steel plates in [2], the revised EYM-formula will identify the relevant failure mode just like it does for timber-to-timber connections.

It should be noted that the present formulas for steel-to-timber [2] are based on the timber-to-timber formula, just assuming infinite embedment strength and zero thickness of the steel plates. Failure modes (b), (e) and (f) are then associated with 'thick' steel plates which are defined as $d \geq t_1$ and ´thin' as $d \leq 0{,}5\ t_1$. For intermediate values the above-mentioned interpolation is used.

The definition of 'thick' is about the plate thickness needed to clamp a fastener that fits into the holes in a normal steel plate, if the fasteners yield stress is about 600 N/mm^2, so it was a fair approach at the time it was developed. Nowadays, it can be much higher, so the old approach is unsafe. Likewise, it is unsafe if the formula is used for aluminium plates.

'Thin' steel plates were defined as $d \leq 0{,}5\ t_1$, most likely as an 'engineering judgement'.

It is often forgotten that the strength of the metal plate around the fasteners should be checked according to the relevant rules (steel, aluminium, ...). In [2] the failure mode that equals (a) in Figure 1 is left out in the formulas for steel plates, so for e.g. two shear planes with a metal plate as the inner member, to the present Eurocode 5 gives no requirement to the steel plate thickness.

The corrections factors 1,15 and 1,05 in failure modes (d)-(f) partly accounts for the smaller uncertainty of the properties of steel parts than for timber, partly that $k_{\text{mod}} = 1$ for the metal parts. The higher factor applies to mode (f) with two hinges in the fastener and the smaller one hinges. The factors are kept in the draft [1] because the disadvantages of introducing a physically more correct methods by far outweighs the advantages, including that applying results from testing according to EN 1380 [5] is possible without special rules. (There are some mistakes in [2] regarding the use of the correction factors and where the rope-effect exists).

3 TEST PROGRAM

The test program is summarized in Table 1. Test according to EN 1380 to determine the lateral resistance F_v are carried out with four makes of ring shank nails (ID 1 to 4), one makes of smooth nail (ID 5) and two makes of screws (ID 6 and 7). The fasteners are all designed to fit into steel plates with 5 mm holes. Nominal lengths are ranging from 25 to 60 mm. Examples are shown in Figure 3. The resulting $F_{v,obs}$ for each test is taken as the smaller of the maximum load and the load at 15 mm displacement.

Table 1: *Test program, geometry, and mean values of strength parameters. The total number of tests is n = 160.*

Test		**Fastener**									**Steel plate**	
Series	n_i	**ID**	**Nominal length** L_{nom} **mm**	**Diam.** d **mm**	**Yield m.** $M_{y,mean}$ **Nmm**	**L incl head** L **mm**	**Head thic.** t_{head} **mm**	**Profiled** L_g **mm**	**Point** L_p **mm**	**Withdr.** $f_{ax,420}$ **MPa**	**Thickn.** t_1 **mm**	**Holes ø mm**
10	16	1	35 40 50	4,0	14300	L_{nom}+2,5	1,5	L-9,2	8,2	15,0	0,9 2,0	5,0
40	16	1	35 50	4,0	14300	L_{nom}+2,5	1,5	L-9,2	8,2	15,0	1,5 4,0	5,06,5
10	12	2	40 60	4,0	9100	L_{nom}+2,5	1,5	L-9,2	5,8	15,0	0,9 2,0	5,0
10	20	3	35 40 50 60	4,0	8600	L_{nom}+2,5	1,5	L-9,2	5,8	15,0	0,9 2,0	5,0
20	8	3	35 50	4,0	8600	L_{nom}+2,5	1,5	L-9,2	5,8	15,0	2,0	5,0
40	16	3	35 50	4,0	8600	L_{nom}+2,5	1,5	L-9,2	5,8	15,0	1,5 4,0	5,06,5
10	8	4	40	4,0	13700	L_{nom}+2,5	1,5	L-9,2	4,8	15,0	0,9 2,0	5,0
40	16	5	35 50	4,0	8700	L_{nom}+2,5	1,5	L-4.0	6,1	3,3	1,5 4,0	5,06,5
20	16	6	25 35 40 50	5,0	7200	L_{nom}+1,8	2,5	L-7,4	5,0	22,0	2,0	5,0
40	16	6	40 50	5,0	7200	L_{nom}+1,8	2,5	L-7,4	5,0	22,0	1,5 4,0	5,06,5
20	16	7	25 35 40 50	5,0	5100	L_{nom}+1,8	2,5	L-7,4	5,0	22,0	2,0	5,0
L_g is the length of the profiled (threaded) length, including the point The penetration depth for withdrawal resistance F_{ax} is $L_w = L_g - L_p$ (since the whole profiled length is embedded in the timber)								Embedment depth $t_{h2} = L - t_{head} - t_1$ For screws: d_{ef} = 1,1 d_{core} = 3,7 mm For steel plates: f_{h1} = 700 MPa				

https://doi.org/10.52202/069179-0194

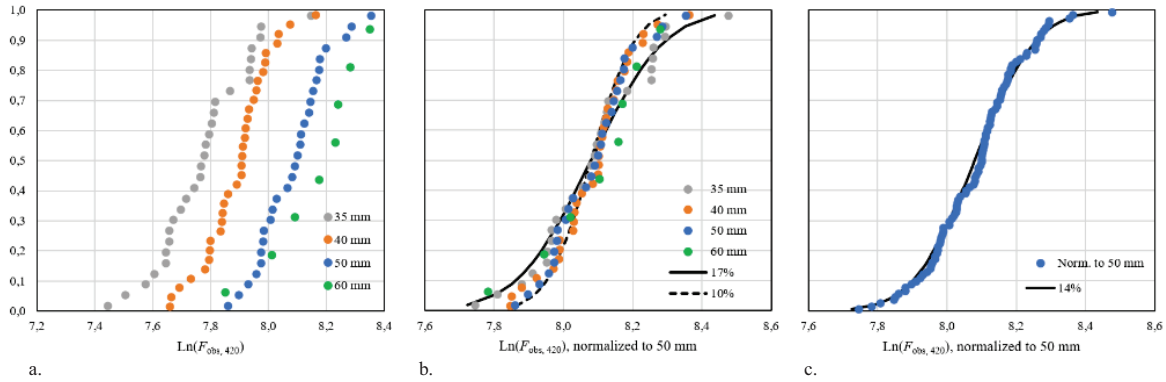

Figure 2: *The distribution function for ln($F_{v,420}$) for all four makes of ring shank nails.*
a. Per length. b. Normalized to the mean value for length 50 mm. c. All lengths considered as one population.

Figure 3: *Examples of fasteners used.*

Tests are carried out in three series named 10, 20 and 40. Test results for Series 10 and 20 originates from[10], for Series 40 from [11]. The timber batches are different for each series. Tests to determine the withdrawal strength f_{ax} for each fastener and batch are also carried out, the results are shown in Table 1.

For Series 10 is used timber with densities fulfilling the requirements to both methods given in EN ISO 8970:2010 [8], where the focus was on limiting the density variation, see [19].

For Series 20 and 40 is used timber with 'low' and 'high' density centred around 350 kg/m^3 and 500 kg/m^3 respectively, representing the extreme values for structural soft wood timber of European strength class C24 with characteristic density 350 kg/m^3 and mean density 420 kg/m^3. The mean density in all series is close to 420 kg/m^3.

The latest edition, EN ISO 8970:2020 [9], focuses on a natural variation of the density of the test specimens and includes methods to correct available data to the natural density variation. Where relevant, all test results are normalized to represent the density 420 kg/m^3 using these methods.

Actual values of yield moments and withdrawal strengths are determined according to EN 409 [6] and 1382 [7] Steel plates with four different thicknesses ranging from 0,9 mm to 4,0 mm has been used. For some thicknesses also test with 6,5 mm holes was carried out as a supplement to the normal 5,0 mm.

4 ACTUAL DISTRIBUTION

In this section only the influence of the nominal length and the density is considered, the rest is considered as residuals. Apart from the yield moment there is little difference between the four makes of ring shank nails (ID 1 to 4). A study of the observed values of F_v does not reveal any dependency on the hole diameter and only a very limited dependency on the yield moment and the steel plate thickness. This is further discussed in section 5.

Since the density distribution is not fulfilling the requirement to a natural variation in the new EN/ISO 8970 [9], i.e. a normal distribution with a coefficient of variation, CoV ~ 10 %, it is necessary to normalize the observations to a reference density, here taken as 420 kg/m^3. The contribution from the density variation to the total CoV is then added as defined in [9].

The observed values are normalized to $F_{v,420}$ by multiplying by $(420/\rho)^c$, where ρ is the actual density. It is found that $c = 1{,}3$ ensures a good fit to the expected LogN-distribution. This value of c is within the expected range, but estimation of c according to Annex B in [9] is not possible since the densities does not follow the normal distribution.

In the following is used ln($F_{v,420}$) as the dependent variable since it is expected to be normally distributed, as al resistances are. Table 2 shows the statistical characteristics of ln($F_{v,420}$) for each nail length and Figure 2a the corresponding distribution functions. Note that e.g. $F = 2000$ N => ln(F) = 7,6 and $F = 4000$ N => ln(F) = 8,3.

https://doi.org/10.52202/069179-0194

Table 2: *Statistical characteristics of ln($F_{v,420}$) for nails, which is assumed to be normally distributed.*

Nail length	35 mm	40 mm	50 mm	60 mm	All
Mean ln(F_v)	7,77	7,89	8,08	8,15	8,08
Std.dev.	0,16	0,10	0,12	0,16	0,13

When adjusting so the mean value for each length becomes equal to the mean value for 50 mm length, the curves shift as shown in Figure 2b, where normal distributions with std.dev. 10% and 17% are seen to include most of the observations. When all date after the shifting are considered as one population the distribution becomes the one shown in Figure 2c, closely following a standard distribution with std.dev. 14 % (meaning that $F_{v,420}$ has CoV_{420} = 14%, see e.g. Annex D.7 in Eurocode 0, [3]). According to e.g. [9] the contribution from the natural density variation, which for strength class C24 is CoV_ρ = 10%, increases the total variation to

$$CoV_{tot} = \sqrt{CoV_{420}^2 + CoV_\rho^2} = \sqrt{0{,}14^2 + 0{,}10^2} = 17\%$$

The lower characteristic value then becomes

$$F_{v,0,05} = \exp(\text{mean } \ln(F_{v,420}) - 1{,}65 \cdot 0{,}17) = \exp(7{,}80) = 2440 \text{ N}$$

and the upper

$$F_{v,0,95} = \exp(\text{mean } \ln(F_{v,420}) + 1{,}65 \cdot 0{,}17) = \exp(8{,}36) = 4280 \text{ N}$$

The ratio is then 4280/2440 = 1,75. This can be generalized to the values in Table 3.

Table 3: *Ratio between upper and lower characteristic value of a LogN-distributed variable X as function of the standard deviation of ln(X).)*

	Characteristic /mean value		
Std.dev.	Low (5%)	High (95%)	Ratio
5%	0,921	1,086	1,18
8%	0,876	1,141	1,30
11 %	0,834	1,199	1,44
14 %	0,794	1,260	1,59
17 %	0,755	1,324	1,75
20 %	0,719	1,391	1,93
23 %	0,684	1,462	2,14
26 %	0,651	1,536	2,36
29 %	0,620	1,614	2,60
32 %	0,590	1,696	2,87
35 %	0,561	1,782	3,17
38 %	0,534	1,872	3,50

For the two makes of screws the same procedure leads to the final distribution for length 50 mm shown in Figure 4, with the mean value ln($F_{v,420}$) = 8,17 and std.dev. = 11 %. According to Table 3 this gives a ratio of 1,44. The total variation for screws becomes CoV_{tot} = 15%.
There are too few observations for smooth nails to make a meaningful analysis for these on their own. Further, the influence of the conditioning is severe [15], so many more tests are required.

5 OBSERVATIONS COMPARED TO EYM USING MEAN VALUES

In this section the observed lateral resistances F_v are compared to an estimate based on EYM, replacing the characteristic values of the strength parameters with the best available estimate for their mean values.
The EYM is used for estimating the mean lateral resistance in the form

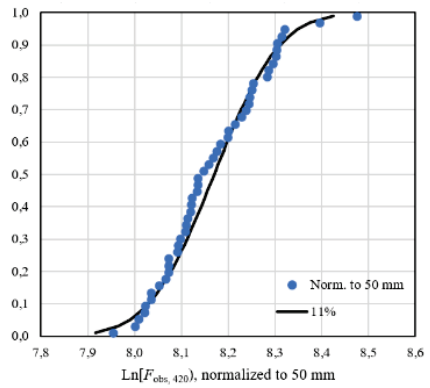

Figure 4: *The distribution function for ln(F_v) for the two makes of screws when normalized to the mean value for length 50 mm and all lengths then considered as one population.*

$$F_v = F_D + F_T \text{ with } F_T = \alpha F_{ax} \quad (1)$$

For F_D is used the formula in Figure 1 setting the correction factors 1,05 and 1,15 equal to 1 because there are no partial factors and k_{mod} adjustment involved.
The measured mean values for the yield moments M_y are given in Table 1. The CoV is about 5%.
For the embedment strength the formula in Eurocode 5 (without predrilling) is used, just replacing the characteristic density by the actual density, thus using

$$f_h = 0{,}082\, \rho\, d^{-0{,}3} \quad (2)$$

The embedment depth t_{h2} is taken as L_g, Table 1. This length includes the point length because the range of lengths used for the tests clearly shows this to be the best estimate. This is demonstrated below, compare Figure 6a and Figure 7.
The withdrawal strength f_{ax} is used for estimating the rope-effect contribution F_T. The rope-effect is taken as a fraction α of the tension resistance F_{ax}. The 'best' value of α is discussed below.
$f_{ax,420}$ given in Table 1 is the withdrawal strength for density 420 kg/m^3 and is determined to apply to the profiled length excluding the point length. The value for the different makes of ring shank nails respectively screws are very similar, so the same values are assumed as seen in Table 1. The withdrawal strength used in the EYM is adjusted to the actual density as

$$f_{ax} = f_{ax,420}\, (\rho/420)^{c\_ax} \quad (3)$$

where ρ is the actual density and c_{ax} is the exponent that gives the best estimate (smallest CoV) when estimating $f_{ax,420}$. The value of the exponent might be different for the

https://doi.org/10.52202/069179-0194

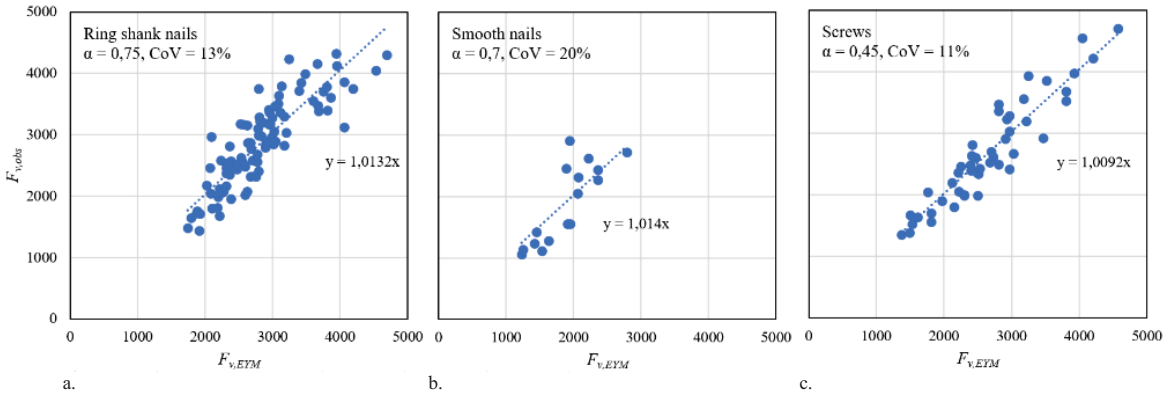

Figure 5: *Observed lateral resistance versus estimate using EYM with mean value of strength parameters. α is the rope-effect factor that ensure a slope just above 1. CoV is the variance of EYM regarded as a model of the resistance in accordance with Annex D.7 in EN 1990 [3].*

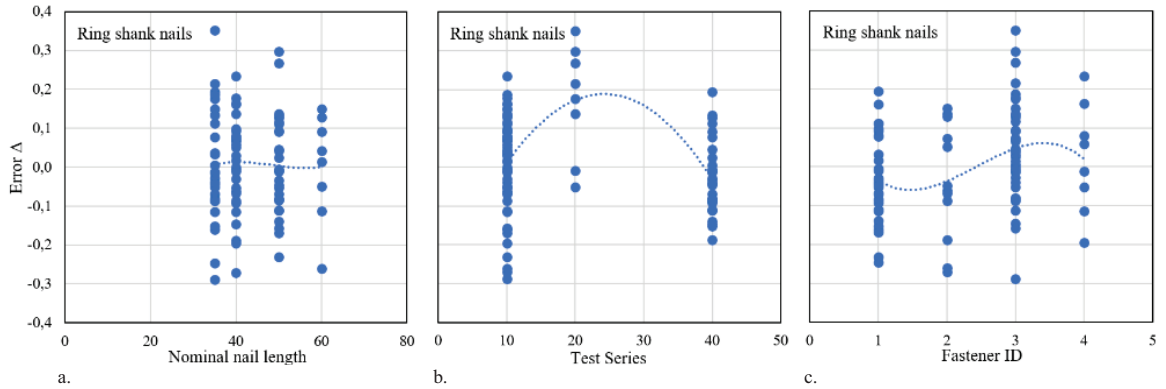

Figure 6: *The error Δ as dependent on the nail length, test series and fastener ID, see Table 1.*

different fastener types. For ring shank nails it was 1,5 and for smooth nails 2,0. For screws any value between 1,0 and 1,5 was about equally good. Henceforth, 1,5 is used for ring shank nails and screws, but the influence is small. For screws is used the effective diameter $d_{ef} = 1{,}1d_{core}$, where d_{core} is the diameter of the core of the thread, both for estimating f_{h2} and in the formula for F_D in Figure 1. For the withdrawal resistance F_{ax} is used the outer thread diameter. These definitions are in accordance with amendment A2 to EN 1995-1-1 [2].

Figure 5 shows plots for each type of fastener of the observed values of F_v against the estimated value using EYM with mean values of strength parameters. The rope-effect factor α given is the one that ensure a slope of the trend line slightly above 1. A slope above 1 means that the mean value model is conservative.

Assuming again that F_v is logN-distributed the CoV of the EYM-model can be estimated from annex D.7 i EN 1990 [3] as the standard deviation of the error Δ, where

$$\Delta = \ln(F_{v,obs}/F_{v,EYM})$$

The CoV's in Figure 5 are determined this way. If a change to the model reduces this CoV, the model is better. A tool to get ideas on how to improve a model is to plot the relation between the error Δ and one of the input parameters.

As an example, Figure 6 shows such plots for the error versus the length of ring shank nails, the test series, and the fastener ID. A polynomial trend line is shown, which has sufficient terms to pass through the weighted average for each variation, so attention should only be made to where the trend line crosses the vertical lines with the determined errors.

Figure 6a illustrates that the influence of the nail length seems to be modelled very well. Figure 6b indicates that the observations in Series 20 are higher than expected from the strength parameters, about 20 %. It is not unexpected that other properties of the timber than the density influences the resistance, see e.g. [18], so the 'error' is in part caused by the natural variation. Finally, Figure 6c indicates that faster ID 2 causes somewhat smaller resistance than average and ID 3 higher, but it is hardly significant, less than 5%. Further, it is part of the natural variation of fastener properties.

Figure 7 is similar to Figure 6a, except that the embedment depth t_{h2} is reduced by the point length. It is obvious that this introduces a systematic error in the model, even the CoV is hardly increased.

https://doi.org/10.52202/069179-0194

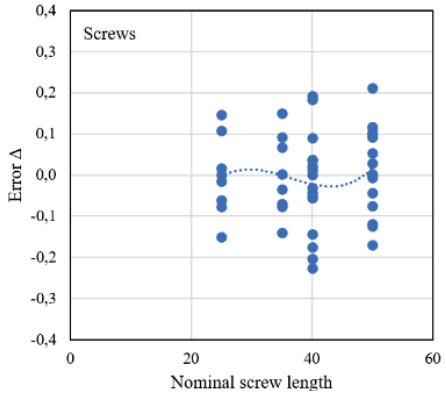

Figure 8 is equal to Figure 6a, but for screws. Again, the influence of the nail length seems to be modelled very well. The dependency on test series and fastener ID is not shown, it is at the same level as for ring shank nails.

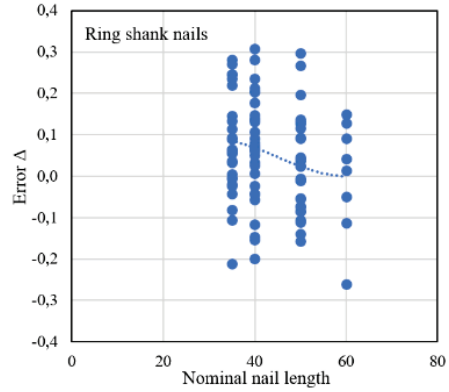

Figure 7: *The error Δ as dependent on the nail length when t_{h2} is reduced by the point length.*

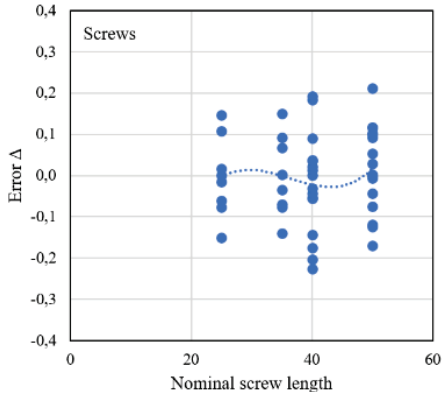

Figure 8: *The error Δ as dependent on the screw length.*

Similar plots for the steel plate thickness and the oversized holes compared to the normal 5 mm holes shows no trends that cannot be attributed to the general variation, mostly related to those combinations tested in Series 20.
As stated above, the rope-effect factor α given in Figure 5 was just chosen to make the EYM fit to the observed resistances. It could be that the dowel contribution F_D was under- or overestimated, e.g. if the formula for the embedment strength is incorrect. This can be investigated by using

$$F_v = \delta F_D + \alpha F_{ax} \quad (4)$$

and then find the combination of δ and α that minimize the CoV of the model keeping the slope just above 1, see Table 4. The values in bold are those used for Figure 5a and c. The table shows that by decreasing δ from 1 to 0,8 or 0,9 the CoV is slightly reduced, but it is a very flat minimum, so there is no evidence for not using $\delta = 1$. The flat minimum is of course related to the fact that the density is decisive for both F_D and F_{ax}.
In the next section it is shown that the sensitivity to the value of M_y is much smaller than to the density. Due to the limited amount of data, it should be regarded as a coincidence that the optimal value for δ seems to be 0,85 for both nails and screws.

Table 4: *Weighing of dowel contribution F_D by δ and axial resistance F_{ax} by α to minimise the CoV of the estimated lateral resistance F_v. The bold values are used in Figure 5 and henceforth.*

δ	0,7	0,8	0,9	**1,0**	1,1
Ring shank nails					
α	0,99	0,91	0,83	**0,75**	0,67
CoV	0,129	0,127	0,127	0,129	0,132
Screws					
α	0,56	0,52	0,48	**0,45**	0,41
CoV	0,106	0,105	0,105	0,107	0,111

It can be deducted from the estimated CoV's that the additional parameters taken into account in EYM do not really improve the accuracy because the CoV's found in Figure 2 for nails and Figure 4 for screws are almost identical to those given in Figure 5. In Figure 4 only a simple adjustment for density and the length of the fastener is applied, whereas in Figure 5 also the influence of the actual values of the yield moment and the steel plate thickness are taken into account by the EYM. So, the CoV should be smaller, but it is 11% for screws in both cases and only drops from 14 % to 13 % for nails. This means that other circumstances than those included in the EYM has a significant influence.

6 CHARACTERISTIC RESISTANCE FROM TESTS AND EYM

The mean value model for the lateral resistance F_v represented by Formula (1) appears from Figure 5 to be a reasonable model for the real resistance when using the strength parameters given in Table 1 and the rope-effect factor α given in Figure 5, i.e. 0,75 for ring shank nails and 0,45 for screws.
The CoV of the model is in section 4 estimated as 17 % for ring shank nails and 15 % for screws for connections using timber C24. According to Table 3, the lover characteristic resistance should then be 0,76 respectively 0,78 of the mean measured value for a certain set of conditions.

https://doi.org/10.52202/069179-0194

6.1 EVM ESTIMATE OF RESISTANCE

In this section mean values of $F_{v,EYM}$ has been estimated for a range of parameters representing the conditions for the tests where F_v were observed. The geometry and properties of the fasteners used is generally as in Table 1. All steel plate thicknesses 0,9, 1,5, 2,0 and 4,0 mm are used for all parameter combinations.

For nails the point length is taken as 6,0 mm in all cases and all the nominal lengths 35, 40, 50 and 60 mm are included. Two yield moments are used, 7500 Nmm and 15000 Nmm.

For screws all the nominal lengths 25, 35, 40 and 50 mm are included. Two yield moments are used, 5000 Nmm and 7500 Nmm.

These 128 estimates are compared to estimates using the same geometries, but inserting characteristic values of the strength parameters M_y, f_h, and f_{ax} in the model, as intended in Eurocode 5.

The characteristic yield moment is determined assuming a CoV of 5%, which means that the characteristic value is 92% of the mean value. For f_h, and f_{ax} is simply used the mean density ρ_m = 420 kg/m^3 for determining the mean value and ρ_k = 350 kg/m^3 for determining the characteristic value in Formula (2) and (3). The aforementioned factors 1,05 and 1,15 are also applied as they are meaningful for the characteristic values.

Hereby is determined pairs of $F_{v,EYM,mean}$ and $F_{v,EYM,charac}$, the relation for ring shank nails is shown in Figure 9 as the blue points. Not surprisingly, the ratio is fairly constant. For screws the relation is shown as the blue point in Figure 10, the slope is seen to be the same as for nails. The slope 0,83 for both nails and screws reflects mainly the ratio between the characteristic and mean value of the density which is 350/420 = 0,833, see 6.4.

6.2 LIMITS TO ROPE-EFFECT

Eurocode 5 has some limitations on the rope-effect, which reduce the characteristic resistance significantly. In the present issue [2] the rope-effect factor, here called α, is limited to 0,25, in the draft it is increased to 0,4 for nails. In both versions, the rope effect contribution F_T is limited

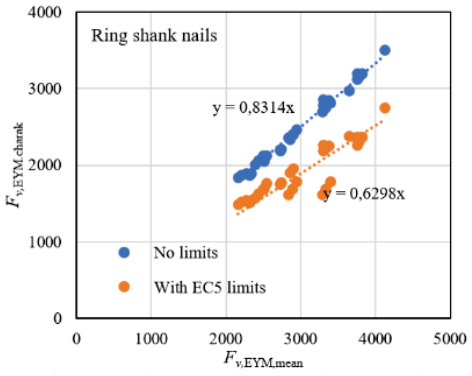

Figure 9: *The characteristic lateral load resistance for nails versus the mean resistance, without and with limits given in Eurocode 5 [2].*

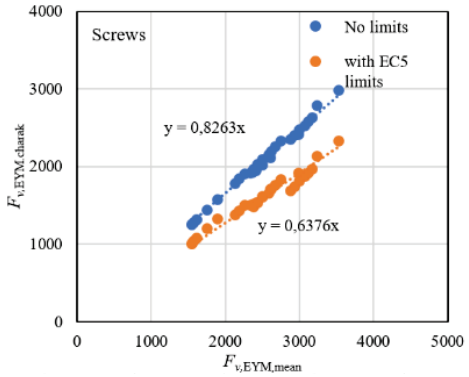

Figure 10: *The characteristic lateral load resistance for screws versus the mean resistance, without and with limits given in Eurocode 5 [2].*

to 0,5 F_D for nails and 1,0 F_D for screws, where F_D is the dowel contribution given in Figure 1. The latter limit is thought to prevent the need for large displacements to reach the estimated resistance but appears rather conservative here since the observed values of F_v used are already limited to 15 mm displacement.

Applying the limitations given in [2]causes a drop as illustrated by the orange points in Figure 9 and Figure 10. The characteristic resistance obtained from Eurocode 5 is seen to end up around 63 % of the mean value.

6.3 OVERSTRENGTH

By overstrength is as stated above understood the factor to arrive from the lower characteristic resistance determined from Eurocode 5 to the real upper characteristic resistance.

In 6.2 is found a factor of 1/0,63 = 1,58 from the characteristic resistance determined form Eurocode 5 to the real mean value and from Table 3 is found that the upper characteristic value is 1,39 times the mean value for a connection if the resistance has a real CoV of up to 20 %. An basic overstrength factor of about 1,58 · 1,39 = 2,2 should therefore be assumed in design.

It is obvious that if the EYM in Eurocode 5 estimate a more accurate (higher) characteristic resistance, the overstrength factor will be smaller.

6.4 SENSITIVITY TO PARAMETERS

The significance of an accurate value of the strength parameters is investigated, assuming the EYM is 'correct'.

For the yield moment the significance is limited. Comparing the EYM results for the two values used for nails, 7500 Nmm and 15000 Nmm, shows that this halving of the yield moment only reduced $F_{v,EYM}$ by 10%.

The steel plate thicknesses ranges from 0,9 mm to 4 mm. The thicker one increases $F_{v,EYM}$ by 7 % compared to the thinner, so again a limited significance.

But if the density is changed by 10%, $F_{v,EYM}$ also change by about 10 %. This is mainly because f_h, is assumed proportional to the density in (2) and f_{ax} is increasing a little more than proportional when $c_{ax} > 1$, see (3).

https://doi.org/10.52202/069179-0194

The low sensitivity to the yield moment and the plate thickness contributes to explains why the CoV in Section 5 does not decrease when using the EYM rather than just correcting for density and length as in Section 4.

6.5 IMPROVEMENT OF THE EYM

Any good model should give a close estimate of the mean value and have a low CoV. The EYM is giving a too low estimate for the mean value and there might be physical phenomenon not taken into account, resulting in a high CoV.

It is obvious that an increase of the rope-effect factor α, will improve the estimate of the mean value, but at the same time a likely source to variability not accounted for by the EYM, is the rope-effect factor α, which might depend on other properties in a more complicated way than assumed now. This is important to understand before the full rope-effect contribution should be used for design. There might also be time dependent issues, even these are more prone to significant impact for larger fasteners.

It is likely that the rope-effect factor will depend on the yield moment and the thickness of the steel plate and the ratios between fastener og plate properties. The rope-effect could, e.g., be higher for thin steel plates than for thick, so the small gain from a thick plate in the dowel contribution is lost again in the rope-effect contribution.

Sørensen [11] noted that the rope-effect consists of two contributions, the component of the axial load in the fastener in the direction of the external load and the friction between the members as they are pressed together by the axial load. The photos in Figure 11 illustrates that the withdrawal resistance might not be the correct measure for the axial load in the fastener when approaching the ultimate load since there are gaps between the fastener and the timber. Sørensen suggested that the axial load could depend on friction between the fastener and the timber rather than the withdrawal resistance. These phenomena were dealt with already by Johansen [12] and Meyer [13], and further by Svensson & Munch-Andersen [16], [17].

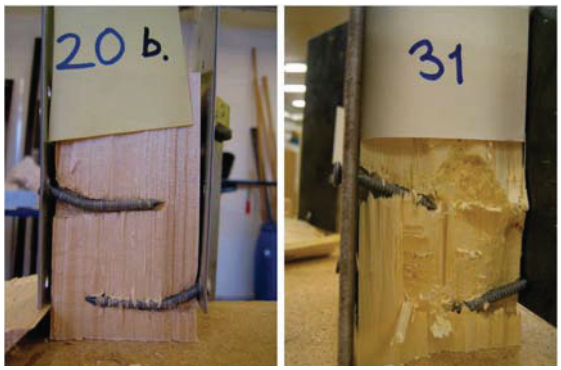

Figure 11: *Observed failure modes. Left, a normal nail, where a hinge is formed in the timber. Right, a hardened nail, where no hinges are formed, even the steel plate is 4 mm thick. [11].*

7 CONCLUSIONS AND FUTURE WORK

The EYM (Euorpean Yield Model) as intended in Eurocode 5 [1] seems to give a good estimate for the dowel-effect contribution F_D to the lateral resistance F_v, but there is a significant reserve when estimating the characteristic lateral load resistance $F_{v,k}$ using the EYM (European Yield Model) as intended in Eurocode 5 [1], [2]. The main reason is that the rope-effect contribution revealed by tests is significantly higher than considered in the code, also in the draft for a new Eurocode 5 [1].

This reserve is to some extent needed to account for e.g. shrinkage and to limit displacements, but it seems larger than necessary. Besides the unnecessary costs and uses of resources it complicates the design when the upper value of the resistance is needed for design, typically when designing for earthquake, where failure need to occur as hinges in the fasteners, and for robustness when the segmentation principle is used and the connection should act as a fuse, halting the collapse.

The overstrength factor – the gap from the lower characteristic resistance estimated from Eurocode and up to the real upper characteristic resistance determined from tests – is estimated to be about 2,2 for the investigated steel to timber connections with small diameter fasteners. This provides that the timber used is not stronger than anticipated. If, e.g., the densities are as for C30 and not as for C24 as assumed in the design, the overstrength factor will increase about 8 % to 2,4. A general factor probably needs to take such a possibility into account.

The rope-effect contribution is limited by fractions of both axial tension resistance and the dowel resistance, see 6.2. Both limits need to be increased if a higher utility of the real resistance of should be allowed. As mentioned, a purpose of the limit seems to be to limit the deformations, which might be reasonable, but the observed resistances used for this study is already limited to 15 mm in accordance with EN 1380 [5], so further limitations should not be necessary to ensure an acceptable deformation at the characteristic resistance.

It should also be noted that when using tests according to EN 1380, e.g. via an EAD and ETA, the 15 mm limit is the only one applying, thus making it quite unattractive to uses the EYM compared to testing.

In further studies focus should be on correct estimate for the rope-effect. One tool would be to examine the displacements during loading more closely – data are available for the tests this study is based on, but not yet used. For Series 40 [11] the actual failure mode is also registered, which should be compared to the prediction from the EYM. Figure 11 might indicate that a fastener with a high yield moment (so it does not form hinges) might need larger displacement to reach its maximum resistance than if the yield moment is lower.

https://doi.org/10.52202/069179-0194

ACKNOWLEDGEMENT

This paper is based on the MSc-thesis by Ane Louise Sørensen[11], who did an outstanding job (which I had the pleasure to co-supervise together with Sigurdur Ormarsson), and test reports from VHT [10], kindly made available by ITW Construction Products, Middelfart, Denmark.

REFERENCES

[1] CEN: Draft prEN 1995-1-1 Eurocode 5: Design of timber structures – Common rules and rules for buildings. 2022.
[2] CEN: EN 1995-1-1 Eurocode 5: Design of timber structures – Part 1-1: General – Common rules and rules for buildings. 2007 +A1:2008 + A2:2014.
[3] CEN: EN 1990 Eurocode – Basis of structural design. 2002 + A1:2005.
[4] P. Palma, J. Munch-Andersen, P. Dietsch: Updating Eurocode 5 – Design guidance for increasing the robustness of timber structures. Paper submitted for WCTE. Oslo. 2023.
[5] CEN: EN 1380: Timber structures - Test methods – Load bearing nails, screws, dowels and bolts. 2009.
[6] CEN: EN 409: Timber structures – Test methods – Determination of the yield moment of dowel type fasteners. 2009.
[7] CEN: EN 1382: Timber Structures – Test methods – Withdrawal capacity of timber fasteners. 2003.
[8] CEN: EN ISO 8970: Timber structures – Testing of joints made with mechanical fasteners – Requirements for wood density. 2010.
[9] CEN: EN ISO 8970: Timber structures – Testing of joints made with mechanical fasteners – Requirements for timber density. 2020.
[10] VHT: Test reports (Prüfbericht) commissioned by ITW Construction Products. 2011.
[11] A.L. Sørensen: Experimental study of laterally loaded nail and screw connections. Master Thesis. Civil Engineering, Technical University of Denmark. 2011.
[12] K.W Johansen: Theory of timber connections. IABSE publications. Vol. 7. 1949.
[13] A. Meyer: Die Tragfähigkeit von Nagelverbindungen bei statischer Belastung, Holz als Roh- und Werkstoff 15. 1957.
[14] H.J. Larsen: K.W. Johansen's nail tests. Bygningsstatiske Meddelelser. 1976.
[15] Munch-Andersen, J.: Withdrawal strength dependency on timber conditioning. In: Proc. of 1st INTER meeting. Bath, UK. 2014.
[16] Svensson, S., Munch-Andersen, J.: Study on the Rope-effect on the Load-carrying Capacity of Nailed Connections. In: Proc. of 1st INTER meeting. Bath, UK. 2014.
[17] Svensson, S., Munch-Andersen, J.: Theory of timber connections with slender dowel type fasteners. Wood Material Science & Engineering. 2016.
[18] Munch-Andersen, J.: Impact of standards and EAD's on the Determination of single fastener properties. In: Proc. of International Conference on Connections in Timber Engineering – From Research to Standards. Graz, Austria. 2017.
[19] Munch-Andersen, J., Sørensen, J. D., Sørensen, F.: Estimation of load-bearing capacity of timber connections. In: Proc. of CIB W18 meeting 43. Nelson, New Zealand. 2010.
[20] Munch-Andersen, J., Svensson, S.: The withdrawal strength of 8 threaded nails types. In: Proc. of CIB W18 meeting 45. Alghero, Växjö, Sweden. 2012.
[21] Munch-Andersen, J., Svensson, S.: Accurate strength parameters for fasteners with examples for ring shank nails. In: Proc. of WCTE 2016. Vienna, Austria. 2016.

World Conference on Timber Engineering Oslo 2023

STRENGTH CHARACTERIZATION OF OVERLAPPED TIMBER SCREWS

Luca Marchi[1], Davide Trutalli[1], Luca Pozza[2], Roberto Scotta[1]

ABSTRACT: The possibility of transmission of axial forces between self-tapping screws fastened in the opposite faces of a timber element and loaded contrariwise is analysed. The screws are intended to be placed sufficiently close one to another and the threaded shanks overlapped by a suitable length. Experimental tests are conducted, varying type, penetration depth and overlapping length of the screws, to evaluate the actual strength and the type of failure of this fastening technique.

KEYWORDS: Self-tapping screws, Withdrawal capacity, Overlapping length, Withdrawal tests

1 INTRODUCTION

The choice of type and arrangement of steel connections to realize timber joints plays a key-role in the capacity of timber structures.

Full-threaded Self-Tapping Screws (STS) are generally used to strengthen a timber element or to connect two or more timber components of a structure, taking advantage of their high axial strength [1]. The increasing interest in such technique is due to its effectiveness since these screws are fast to be installed and do not always require pre-drilling of the timber element. Examples are available in [2–5].

Recent works confirmed that particular attention must be paid to the design of spacing and edge distance to avoid anticipated brittle failures in the timber element, either for solid wood or laminated timber products (e.g., block shear failure, tension orthogonal to the grain) [6].

The ongoing revision of Eurocode 5 [7], based on detailed works recently published in the literature, aims to provide a design toolbox for the practitioners, which helps them in dealing with the design of modern fasteners with different anchoring materials [8].

To this aim, this work analyses the transmission of axial forces across a glued laminated timber element by means of pairs of STS fastened on the opposite faces, placed sufficiently close one to another and with a suitable overlapping length. The screws are installed with a spacing lower than the one required by current European Code [7]. The aim is to analyse, by means of experimental tests, the increased/decreased capability of transmitting axial forces between the screws through the timber member with such particular arrangement.

2 MATERIALS AND METHODS

Experimental tests were performed at the laboratory of Material testing of the University of Padova exploiting a universal testing machine.

2.1 TEST SETUP

Two couples of the same type of screws (four screws in total per single test) were simultaneously pulled contrarywise by means of a proper symmetric pulling configuration, designed, and realized to avoid possible eccentricities of loads (Figure 1). Two steel C-beams reinforced on both webs and flanges with 100-mm steel plates accommodated specifically designed millings that were able to provide a sufficiently rigid pulling force on the screw's head. Specific washers were designed to fit with the screw's countersunk heads avoiding local damages during the pulling tests. Tests were performed according to the load protocol of EN 26891:1991 [9]. Displacements were measured by placing one potentiometer place in proximity to each of the four screws.

Insertion of the screws close to verticality was assured by predrilling the wooden sample with a 5-mm drill bit up to a depth of 60 mm. Then, STS were pre-installed on the glulam samples, leaving a gap between the head and the surface to allow the positioning of the sample between the supporting U-shape beams. Once in place, a torque wrench was used to tighten the screws and provide direct contact between each of the four screws heads with the tensioning steel frame. Pretension on the STS was avoided through real-time reading of the load cell installed on the testing machine.

In addition, withdrawal tests of single STS according to EN 1382:2016 [10] were taken as reference for comparative purposes (Figure 2).

[1] Department of Civil, Environmental and Architectural Engineering, University of Padova, via Marzolo 9 - Padova, 35131, Italy. davide.trutalli@dicea.unipd.it; luca.marchi@unipd.it; roberto.scotta@unipd.it.

[2] Department of Civil, Chemical, Environmental and Materials Engineering, University of Bologna, viale Risorgimento 2 - Bologna, 40136, Italy. luca.pozza2@unibo.it

https://doi.org/10.52202/069179-0195

A total of 35 tests were performed, 30 of which for testing the overlapping conditions and 5 as reference for the withdrawal capacity. Average and characteristic values of all the main mechanical parameters were calculated according to EN 14358:2016 [11].

Figure 1: *Test setup: load transfer*

Figure 2: *Test setup: withdrawal capacity*

2.2 SPECIMEN CHARACTERISTICS AND MATERIALS

Specimen design aimed to obtained a balanced solution between observing a failure governed by the screws withdrawal and failure due to excessive tension orthogonal to the grain. By varying the overlapping length failure should occur between the two possibilities.
Tests involved the use of carbon steel fully-threaded STS fastened to glulam timber samples. Three key parameters were considered in the definition of the test campaign, namely:

- dependency on the overlapping length of the STSs l_o: reference values were 60, 100 and 140 mm or *6d*, *10d* and *14d*;
- dependency on the total penetration length of the STSs l_{eff}: reference values were 130, 150 and 170 mm;
- Alignment between each couple of STS: parallel or perpendicular to the grain direction.

Although the screw's nominal diameter *d* should was potentially an essential variable to be analysed, it was not included in the parametric test: a fixed nominal diameter equal to 10 mm was considered as a good compromise to investigate the load transmission phenomenon while keeping the dimensions of the timber specimens sufficiently small to be manipulated in the testing machine while respecting the provisions on minimum edge distances reported in Eurocode 5 [7]. In detail, dimensions equal to 32x10x20 cm and 28x20x20 cm were chosen for the test in the parallel and perpendicular to grain screws layout (Figure 3). Spacing between the two opposite facing screws was set at a constant value of $2d = 20$ mm. All glulam specimens were cut from two beams having a cross-section of 20 x 28 cm and a certified strength class equal to GL24h [12]. At the age of the tests, all specimens were correctly dried, and each wood sample was assessed with a pin-type digital hygrometer; an average moisture content of 13.97% was measured, thus slightly above the reference value of 12.00%. Wood density was also extrapolated by weighting and measuring each sample, resulting in an average value equal to 431.59 Kg/m³.
Details on specimen nomenclature and relative characteristics are reported in Table 1.

Table 1: *Specimen characteristics*

Specimen ID	140-0	140-90	100-0	100-90	60-0	60-90	W
Number of tested samples	5	5	5	5	5	5	5
Wood element dimensions (cm)	9x32x20h	20x28x20h	9x32x20h	20x28x20h	9x32x20h	20x28x20h	20x20x20h
STS alignment (°)	0	90	0	90	0	90	-
Total length L (mm)	200	200	180	180	160	160	180
Effective length L_{eff} (mm)	170	170	150	150	130	130	150
Overlapping length L_{ov} (mm)	140	140	100	100	60	60	-
Mean density (Kg/m³)	441.39	434.17	424.46	415.22	434.39	444.62	426.88
Moisture content (%)	15.41	12.69	14.75	12.97	15.36	13.68	12.93

https://doi.org/10.52202/069179-0195

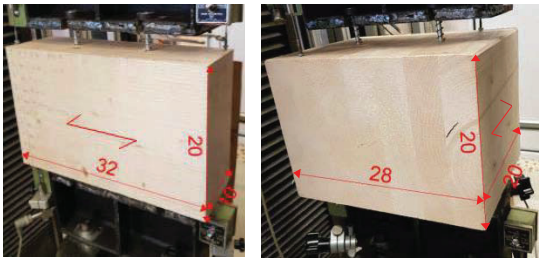

(a) (b)

Figure 3: *Geometry of the Glulam samples for overlapping parallel (a) and perpendicular to grain (b)*

2.3 ANALYTHICAL CALCULATION

Values of the experimental resistance were compared with the analytical load bearing capacity. For the comparison, both the equation reported in the homologation document of the producer [13]:

$$F_{ax,\alpha,Rk} = n_{ef} \cdot k_{ax} \cdot f_{ax,k} \cdot d \cdot l_{ef} \cdot (\frac{\rho_k}{350})^{0,8} \qquad (1)$$

and the one included in Eurocode 5 [7] were used:

$$F_{ax,\alpha,Rk} = \frac{n_{ef} \cdot f_{ax,k} \cdot d \cdot l_{ef}}{1,2cos^2\alpha + sin^2\alpha} \cdot (\frac{\rho_k}{\rho_s})^{0,8} \qquad (2)$$

In the computation, the characteristic withdrawal parameter $f_{ax,k}$ and the factor k_{ax} were respectively set equal to 10.5 N/mm² and 1.0 according to [13]. The characteristic tensile load bearing capacity of the steel $f_{tens,k}$ was equal to 25kN [13].
Finally, the characteristic strength orthogonal to the grain $f_{i90,k}$ for the timber necessary to compute the load capacity $F_{t,90,k}$ of the specimen was set equal to 0.5N/mm².

3 RESULTS AND DISCUSSION

Table 2 reports in summary the maximum pulling load F_{max} obtained from each test as well as average and characteristic values $F_{test,m}$ and $F_{test,k}$.
Three failure modes were evidenced during the experimental tests: screw withdrawal, wood failure for tension orthogonal to the grain or rolling shear. Results shows that for both l_{ov} equal to 100 and 140 mm, when STS were arranged parallel to the grain, force transmission could be mostly ensured thus avoiding the premature splitting of wood. In both configurations, in eight out of ten trials failure was governed by the withdrawal of the STS. The only difference observed was was that for the higher l_{ov}, failure was due to rolling shear rather than tension orthogonal to the grain.
For the lowest l_{ov} of 60 mm, failure on the timber side was mostly happening. This explains why tests on configuration 60-90, namely the ones with the smallest transfer capability, were interrupted before the completion of the series (Table 2).

3.1 LOAD VS. DISPLACEMENT CURVES

Figure 4 reports the curves obtained from the withdrawal tests of the STS according to EN 1382:2016 [10].
Figure 5, Figure 6 and Figure 7 show the load vs. displacement curves obtained from the tests of specimens with l_{ov} equal to 60, 100 and 140 mm respectively. Load refers to a couple of STS, i.e., the total load measured from the load cell divided by two. Displacement is the average displacement calculated from the four potentiometers.

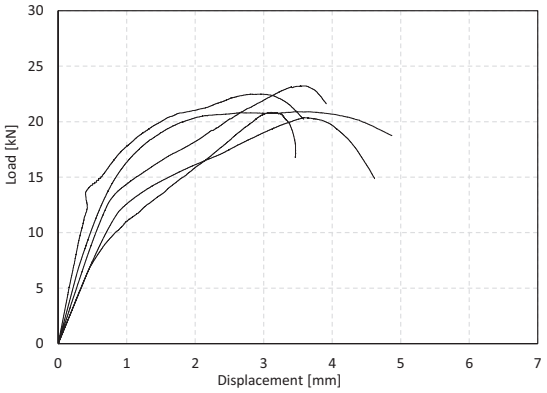

Figure 4: *Load vs. displacement curves of the withdrawal tests according to EN 1382:2016 [10]*

The seldom presence of a red cross at the end of a curve indicates that failure ended with premature failure of the

Table 2: *Values of F_{max} and corresponding failure mode obtained from each test: W = withdrawal failure, T = tension orthogonal to the grain failure, R = rolling shear failure*

		l_{ov} = 60 mm			l_{ov} = 100 mm			l_{ov} = 140 mm		
		F_{max} [kN]	Failure Mode	$F_{test,m}$ [kN]	$F_{test,m}$ [kN]	Failure Mode	F_{max} [kN]	F_{max} [kN]	Failure Mode	$F_{test,m}$ [kN]
	Test 1	18,57	W	17,62 kN	21,25 kN	W	20,27	25,56	W	27,96 kN
	Test 2	16,74	T			W	21,07	29,23	W	
0°	Test 3	18,91	T	$F_{test,k}$	$F_{test,k}$	W	20,38	29,23	W	$F_{test,k}$
	Test 4	14,44	T	12,57 kN	17,65 kN	W	23,80	29,59	W	23,52 kN
	Test 5	19,46	T			W	20,70	26,18	W	
	Test 1	19,04	T	$F_{test,m}$	$F_{test,m}$	T	23,14	26,74	R	$F_{test,m}$
	Test 2	20,08	T	19,56 kN	21,94 kN	W	18,73	24,97	W	26,10 kN
90°	Test 3	-	-			T	24,34	25,49	W	
	Test 4	-	-		$F_{test,k}$	W	20,73	27,22	W	$F_{test,k}$
	Test 5	-	-		16,49 kN	W	22,79	27,20	R	23,52 kN

https://doi.org/10.52202/069179-0195

wood. As a reference, theoretical limits computed for the withdrawal capacity $F_{ax,Rk}$ of the STS and the resistance of timber orthogonal to the grain $F_{t,90,k}$ are also plotted. Additionally, By observing the curves, it emerges the sudden brittle behaviour of wood failure which clearly anticipates the withdrawal of the STS, and that opposes to the typical smooth curve that characterizes failure due to withdrawal.

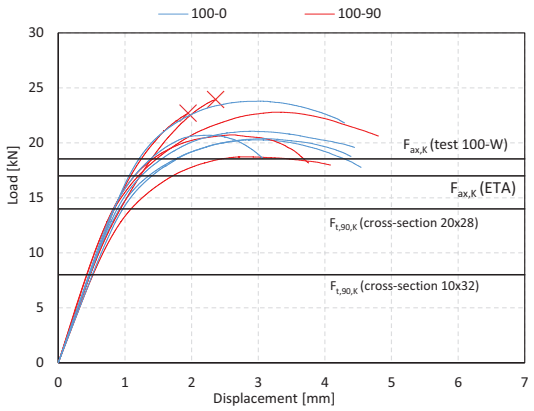

Figure 5: *Load vs. displacement curves with l_{ov} = 60mm*

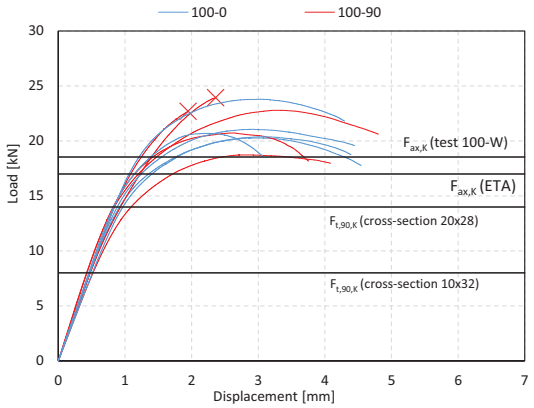

Figure 6: *Load vs. displacement curves with l_{ov} = 100mm*

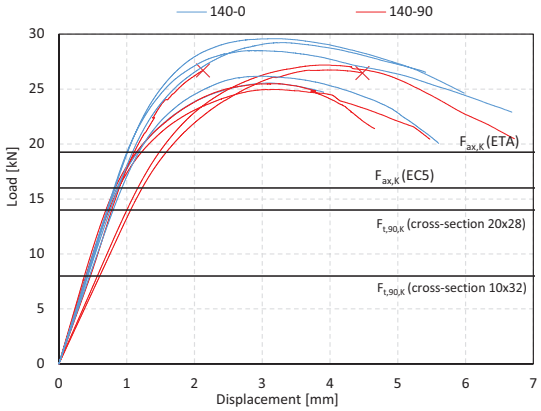

Figure 7: *Load vs. displacement curves with l_{ov} = 140mm*

3.2 FORCE COMPARISON

Figure 8 summarizes the results in terms of characteristic load bearing capacity between analytical and experimental values extrapolated for the three different values of l_{ov}.

The intermediate overlapping length (l_{ov} = 100 mm) can be retained the reference point from where to start comparing the data as the comparison includes also the reference values of $F_{ax,Rk}$ *(test W)* obtained from the withdrawal tests. In this configuration, the joint was almost able to completely exploit the capacity of the STS without incurring into premature brittle failure of the wooden medium. Comparable values of $F_{test,k}$, $F_{ax,Rk}$ (ETA) and $F_{ax,Rk}$ (Test) demonstrates it.

This phenomenon gains more evidence for the configuration analysing the maximum overlapping length (l_{ov} = 140 mm) were $F_{test,k}$ was consistently higher the $F_{ax,Rk}$ calculated from the homologation document (+22.1%). On the opposite, the lowest overlapping length (l_{ov} = 60 mm), did not allow a sufficient load transmission between the couple of STSs, as can be seen by comparing the $F_{test,k}$ with the $F_{ax,Rk}$ calculated from the homologation document (-14.7%).

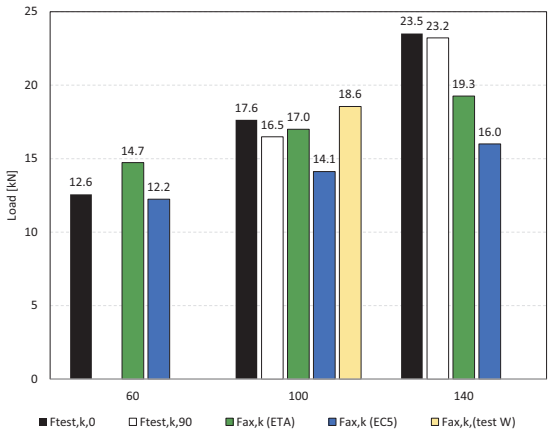

Figure 8: *Comparison of the analytical and experimental load bearing capacity for different l_{ov}*

3.3 FORCE TRANSMISSION IN WOOD

Specimens involving a withdrawal failure were cut along the vertical plane containing the couple of STSs for a detailed visual inspection. Figure 9 and Figure 10 shows the different behaviour of the wood grain in case of STS arrangement parallel and perpendicular to the grain respectively. In the first case, it can be observed how the couple of screws involve the wood fibres between them which, given the short distance, worked in predominant shear. Observing the wood fibres near the screws but on the opposite direction it is also clear the length of the fibres involved in the resisting model during the screws withdrawal.

In the second case, it is clear how no transfer between the overlapping length is visible. The orthogonal alignment of the wood fibres does not allow any interaction between the screws and force transmission is given only by the wooden medium, leading to frequent premature of the

https://doi.org/10.52202/069179-0195

timber element when splitting resistance is lower than the screws withdrawal capacity.

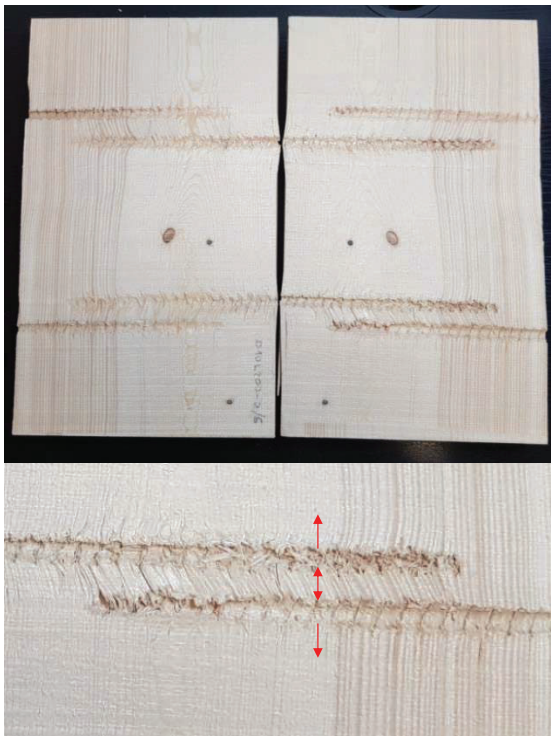

Figure 9: *Inspection of wood grain deformation on specimen 140-0/5 after withdrawal failure*

Figure 10: *Inspection of wood grain deformation on specimen 100-90/5 after withdrawal failure*

4 CONCLUSIONS

In this work, the possibility of transmitting axial forces between screws through the timber element, by partially overlapping the threaded parts was analysed.
Results from experimental tests, varying both the penetration and the overlapping length, showed that only a balanced configuration between effective penetration length (i.e., withdrawal capacity) and overlapping length allowed to transmit high axial forces without incurring into brittle failures of the wooden medium.
Future works may extend the studied configurations to different screws nominal diameters, different spacing between the opposed screws and possibly different screws as well.

ACKNOWLEDGEMENT

The authors would like to thank Eng. Alessandro Rubini for the help in performing the experimental tests during the development of his master thesis.

REFERENCES

1. Ringhofer A, Brandner R, Schickhofer G (2015) Withdrawal resistance of self-tapping screws in unidirectional and orthogonal layered timber products. Mater Struct 48:1435–1447. https://doi.org/10.1617/s11527-013-0244-9
2. D'Arenzo G, Rinaldin G, Fossetti M, Fragiacomo M (2019) An innovative shear-tension angle bracket for Cross-Laminated Timber structures: Experimental tests and numerical modelling. Eng Struct 197:109434. https://doi.org/10.1016/J.ENGSTRUCT.2019.109434
3. Polastri A, Giongo I, Angeli A, Brandner R (2018) Mechanical characterization of a pre-fabricated connection system for cross laminated timber structures in seismic regions. Eng Struct 167:705–715. https://doi.org/10.1016/j.engstruct.2017.12.022
4. Marchi L, Pozza L (2021) Timber-concrete composite connections using GFRP notches fastened with self-tapping screws: Conceiving, numerical modelling and testing. Constr Build Mater 294:. https://doi.org/10.1016/j.conbuildmat.2021.123579
5. Marchi L, Ferretti F, Pozza L, Scotta R (2023) Role of fastenings in modifying the hysteretic response of panel-to-panel joints for CLT structures. Constr Build Mater 364:129856. https://doi.org/10.1016/J.CONBUILDMAT.2022.129856
6. Mahlknecht U, Brandner R (2019) Block shear failure mechanism of axially-loaded groups of screws. Eng Struct 183:220–242. https://doi.org/10.1016/j.engstruct.2018.12.057
7. CEN (2009) EN 1995-1-1 Eurocode 5: Design of timber structures - Part 1-1 : General - Common rules and rules for buildings. CEN, Brussels, Belgium

https://doi.org/10.52202/069179-0195

8. Ringhofer A, Brandner R, Blaß HJ (2018) Cross laminated timber (CLT): Design approaches for dowel-type fasteners and connections. Eng Struct 171:849–861. https://doi.org/10.1016/J.ENGSTRUCT.2018.05.032
9. CEN (1991) EN 26891 - Joints made with mechanical fasteners. General principle for the determination of strength and deformation characteristics. Brussels, Belgium
10. CEN (2016) EN 1382 Timber Structures — Test methods — Withdrawal capacity of timber fasteners. Brussels, Belgium
11. CEN (2016) EN 14358 Timber structures — Calculation and verification of characteristic values. Brussels, Belgium
12. CEN (2014) EN 14080 Timber structures — Glued laminated timber and glued solid timber — Requirements. Brussels, Belgium
13. DIBt (2016) ETA-11/0284 Screws for use in timber constructions

World Conference on Timber Engineering Oslo 2023

MEASUREMENT OF AXIAL FORCE OF SCREWS FOR SPLIT REINFORCEMENT AT TIMBER-STEEL-TIMBER DOWEL JOINT

Kenji Kobayashi[1], Keita Ogawa[2]

ABSTRACT: In this study, joint shear test of timber-steel-timber dowel joint was performed by changing the cross-sectional dimensions of the member, the position and the number of the self-tapping screws for reinforcement. The axial force of the screw was measured using a strain gauge which is placed in the centre of the screw, and the influence of the position and the number of the screws in lateral tensile force was confirmed.

Ultimate displacement became higher by using screws for reinforcement. In Pre-Divided (PD) test specimens, the ultimate displacement was equivalent to that of SR specimen by using two screws per shear plane. It was confirmed that the measured axial force in PD test specimen corresponds to the load axial force after the split occurs. When using two screws, closer screw to the dowel mainly resist to lateral tensile force. The ratio of lateral tensile force changes as the displacement progresses. Total lateral tensile load exceeded 30% of joint shear load in PD specimens.

KEYWORDS: Split reinforcement, Dowel joint, Axial force

1 INTRODUCTION

Timber-steel-timber dowel joint is generally used in large scale timber structures. Ductile behaviour can be ensured by bending deformation of a dowel and embedment at timber member under lateral loading. On the other hand, depending on the conditions of the joint, timber member easily splits due to the lateral tensile stress caused by the dowel, and sufficient ductility cannot be obtained. To prevent splitting failure, it is effective method to insert full-threaded self-tapping screws near the dowel.

Schmid [1] and Bejtka [2] proposed the theoretical models to calculate the force generated in the reinforcing screw. It is proposed that reinforcement elements should be designed to resist 30% of the load transferred by each dowel-type fastener and shear plane [3]. But it is still uncertain how much axial force occurs to reinforcement screws.

Wolfthaler et al. [4] tried to measure the axial force generated in the screw for splitting reinforcement by implementing a strain gauge in the screw. As a result, depending on the conditions, an axial force larger than 30% is generated, and it is pointed out that the load on the screw located at the end of the multiple dowel joint was particularly large. However, the measured axial force is not the same as the transverse tensile force generated at the joint because it is considered that not only the screw but also the wood transfers the lateral tensile force. Furthermore, the effects of the cross-sectional dimensions of the member and the driving position of the screw are also unknown.

In this study, joint shear test of timber-steel-timber dowel joint was performed by changing the cross-sectional dimensions of the member, the position and the number of the self-tapping screws for reinforcement. The axial force of the screw was measured using a strain gauge which is placed in the centre of the screw, and the influence of the position and the number of the screws in lateral tensile force was confirmed.

2 MATERIALS AND METHODS

2.1 Materials

Sugi glulam of strength grade E65-F255 [5] was used for side member. The dimensions of the specimen were 582 mm in length and 105 mm in width, and the thickness t was 45, 75, and 105 mm on each side. A steel plate with thickness of 9mm was used for central member. A steel dowel was used to connect timber and steel plates and the diameter was 16mm. Full-thread screws (pane-lead X, Synegic co. ltd.) were used for split reinforcement. A picture of the screw is shown in Figure 1. A strain gauge (BTM-6C, Tokyo Measuring Instruments Lab.) was implemented in the centre of the screw to obtain the axial force during the joint shear test. The relationship between strain and axial force in each screw was obtained in advance.

[1] Kenji Kobayashi, College of Agriculture, Academic Institute, Shizuoka University, Japan, kobayashi.kenji.b@shizuoka.ac.jp
[2] Keita Ogawa, College of Agriculture, Academic Institute, Shizuoka University, Japan, ogawa.keita@shizuoka.ac.jp

https://doi.org/10.52202/069179-0196

2.2 Test setup

The list of test conditions is shown in Table 1. The first number in each type name indicates the thickness of one side of the specimen. Three thicknesses of 45mm, 75mm, and 105mm were selected. The following symbols represent the reinforcement conditions. Test setup of each reinforcement condition is shown in Figure 2. There were three types of test specimens. Non-reinforced test specimens (hereinafter referred to as NR) has no reinforcement screws and only timber resists to lateral tensile forces. Screw reinforcement test specimens (hereinafter referred to as SR) has one or two reinforcement screws around dowel joint part. At pre-divided test specimens (hereinafter referred to as PD), the glulam was divided into two in the width direction at the center of the dowel, and they were connected by screws so that the lateral tensile stress generated by the dowel during the test is transferred only by the screw. One or two screws were inserted on each side, which is the same as that of SR specimens. The position of the screw is shown in Figure 3. The screws were placed symmetrically on each member. At the test specimen with one screw, self-tapping screw was driven into the position A in the figure. Distances between dowel centre and the position A was 3*d* (*d*: diameter of the dowel). This value was determined to avoid touching the dowel to the screw during the test. Distances between shear plane and the position A was 1.5*d*. At the test specimens with two screws, self-tapping screws were driven into the positions of AB, AC, and AD, respectively. Distances between dowel centre and the position B was 5*d* and two screws are located parallel to the grain. Distances between shear plane and the position B was 3*d* and two screws are located perpendicular to the grain. Position D was located on the unloaded side and the distance was 1*d* to get as close as possible to the dowel.

The upper part of the specimen was fixed to a steel plate with a thickness of 12 mm using a bolt with a diameter of 24 mm A steel plate with a thickness of 9 mm was connected to the lower part of the specimen by a dowel with a diameter of 16 mm. Therefore, there is a total gap of about 3 mm in the lower part of the specimen. Arrangement of the dowel was determined based on the standard of Architectural Institute of Japan [6].

The relative displacement between the main material and the side material was measured with a displacement transducer SDP-

Table 1: *Test series*

Type	Thickness (mm)	Pre-division of member	Screw pos. (see Fig. 2)	*n*
45-NR	45	No	-	9
45-SR-A			A	4
45-SR-AB			AB	7
45-PD-A		Yes	A	6
45-PD-AB			AB	6
45-PD-AD			AD	7
75-NR	75	No	-	9
75-SR-A			A	6
75-SR-AC			AC	6
75-PD-A		Yes	A	6
75-PD-AC			AC	6
75-PD-AD			AD	5
105-NR	105	No	-	9
105-SR-A			A	6
105-SR-AC			AC	5
105-PD-A		Yes	A	6
105-PD-AC			AC	6
105-PD-AD			AD	6

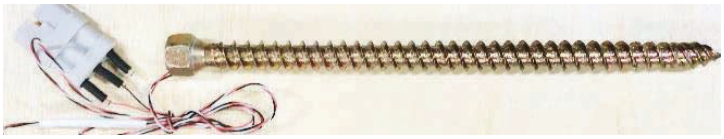

Figure 1: *Self tapping screw with strain gauge*

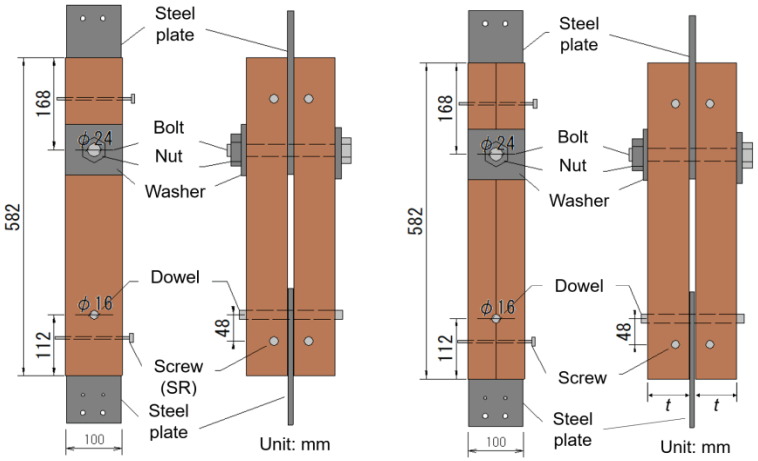

(a) NR and SR specimens ***(b) PD specimens***

Figure 2: *Test setup (an example of SR specimen)*

https://doi.org/10.52202/069179-0196

100C (Tokyo Measuring Instruments Lab.). The axial force was obtained from the strain measured during the joint shear test. In the test, a monotonous load was applied in the tensile direction, and the test was stopped when the load dropped to 80% or less of the maximum load after the maximum load was applied, or when the displacement reached 30 mm.

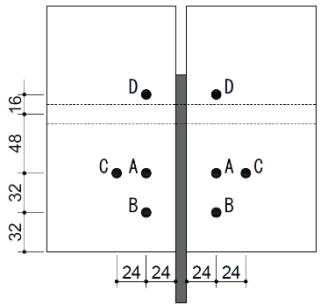

Figure 3: *Position of reinforcement screws*

3 RESULTS AND DISCUSSION

3.1 Failure pattern

Figures 4-5 show examples of failure patterns of NR and SR specimen after the test. In the NR specimen, failure due to row shear and splitting was observed. In the SR specimens reinforced with a single screw, the rate of failure due to splitting and row shear decreased, and the shear displacement of the joints until failure increased. In the SR specimen using two screws, no shear failure or splitting failure occurred in the wood even when the displacement exceeded 30 mm.

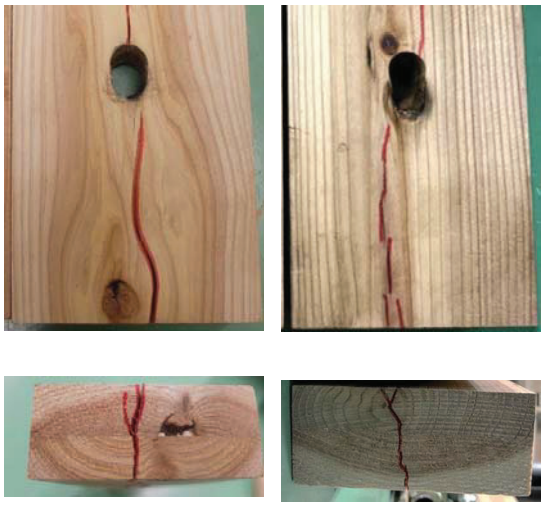

45-NR *45-SR-A*

Figure 4: *Failure of specimens with the thickness of 45mm*

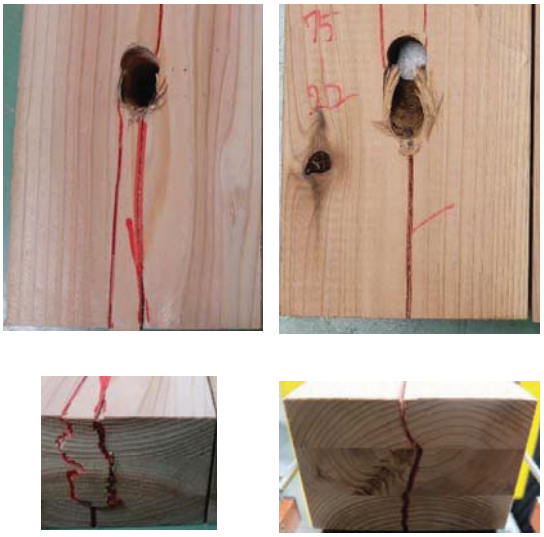

75-NR *75-SR-A*

Figure 5: *Failure of specimens with the thickness of 75mm*

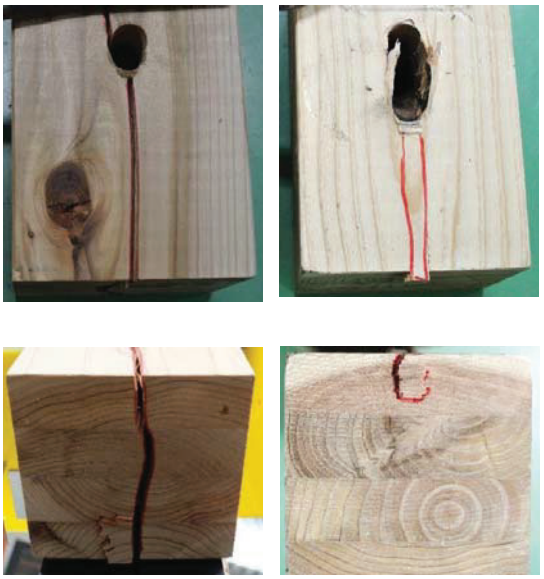

105-NR *105-SR-A*

Figure 6: *Failure of specimens with the thickness of 105mm*

3.2 Ultimate displacement

Figure 7 shows a comparison of the ultimate displacements under each condition. By screw reinforcement, the average value of ultimate displacement increased by 37 to 60% in the SR test specimen with a thickness of 45 mm, 188 to 190% in the test with a

https://doi.org/10.52202/069179-0196

thickness of 75 mm, and 98 to 112% in the test with a thickness of 105 mm compared to NR test specimens. At thicknesses of 75 mm and 105 mm, the ultimate displacement was 30 mm or more. Most of the specimens were not failed and the loading was stopped.
In PD test specimens, the ultimate displacement was not improved by one screw in the test specimens with thickness of 75 mm and 105 mm. The deformation performance equivalent to that of SR specimen was obtained by using two screws.

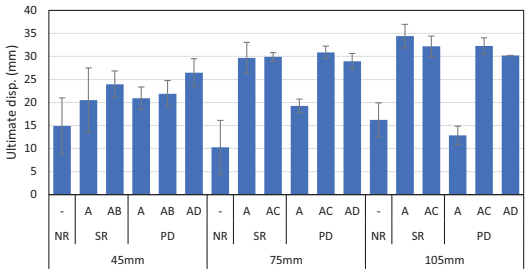

c

Figure 7: *Comparison of ultimate displacement*

3.3 Axial forces measured by screws

As an example of the measurement result of the axial force acting on the screw, the result of the matching test specimen of 45-SR-A and 45-PD-A is shown in Figure 8. PD specimens showed slightly lower load-bearing capacity than SR specimens. At the moment of cracking, the shear load decreased slightly, while the axial force on the screw increased immediately. Similar behaviour was also reported by Wolfthaler et al [3]. In 45-SR-A test specimen, it was confirmed that the axial force increased with the occurrence of splitting.
On the other hand, in 45-PD-A test specimen, the axial force increased immediately after the load was applied. Since the axial force is almost the same after the split occurs in the main materials on both sides, it can be said that the measured axial force in PD test specimen corresponds to the load axial force after the split occurs.

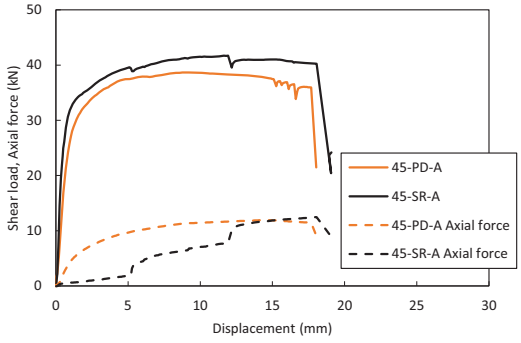

Figure 8: *Load-displacement relationship of 45-SR-A and 45-PD-A*

Ratio of average total axial force of screw on each type to shear force is shown in Figure 9. Axial loads decrease at 45-SR-A and PD-A specimens with all thickness. In these specimens, the number of screws was not enough and withdrawal of screw was observed. At PD specimens with two screws, total axial force finally reached around 30~40% of joint shear load in PD specimens. On the other hand, final axial load was about 10% at SR specimens with two reinforcement screws. This tendency was similar between specimens with different thickness.

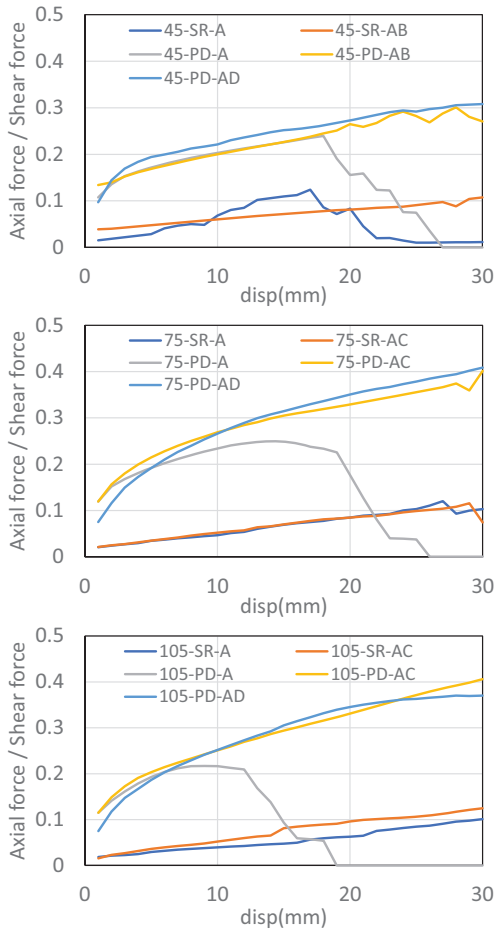

Figure 9: *Ratio of average total axial force of screw on each type to shear force*

Ratio of axial force of screw at each position to shear force is shown in Figure 10. In the reinforced type with one screw, both the shear load and the axial force decreased in the 75mm and 105mm thickness series. This is because the strength of the reinforcing screw was insufficient, and the screw was pulled out, leading to destruction. In the reinforcement type with two screws, no fracture accompanied by a decrease in axial force was observed. In the test type with a thickness of 45 mm, when the driving position was AB, the axial force of B was slightly higher at the initial stage of deformation, but as the

https://doi.org/10.52202/069179-0196

deformation progressed, the screw of A showed higher axial force. Ultimately, the A screw bears a lateral tensile force that is 1.5 times greater than that of the B screw. On the other hand, when the driving position is AD, most of the lateral tensile force was borne by screw A at the initial stage of deformation, but in the end, screw D also borne nearly half of the lateral tensile force.

In the test type with a thickness of 105 mm, when the driving position is AC, although the axial force of screw A, which is closer to the sheared surface, showed a slightly higher axial force, there is a difference from screw C and the axial force tends to increase as deformation progresses. It was mostly the same.

A common point in all measurement results is that the load ratio and distribution of the axial force are nonlinear, and it is difficult to determine a single value with a simple dynamic model. It suggests the need for a model that considers the nonlinear behaviour of wood due to Dowel's local bearing pressure and changes in stress distribution.

Fig. 5 shows the ratio of axial force of screw at each position to shear force in PD test specimens. It was confirmed that the screw position A mainly bears the axial force. The axial force at position C was slightly smaller than the axial force at position A, and a screw at position D initially showed a negative axial force in 105-PD-AD specimen.

Total axial force finally reached about 30-40% of the shear force in PD specimens. Axial force of 30% of shear force was sufficient to ensure the deformation performance of the joint even if the contribution of tensile stress perpendicular to the grain was ignored.

4 CONCLUSION

- Ultimate displacement became higher by using screws for reinforcement. In Pre-Divided (PD) test specimens, the ultimate displacement was equivalent to that of SR specimen by using two screws per shear plane.
- It was confirmed that the measured axial force in PD test specimen corresponds to the load axial force after the split occurs.
- When using two screws, the closer screw to dowel mainly resist to lateral tensile force. The ratio of lateral tensile force burden changes as the displacement progresses.
- Total lateral tensile load exceeded 30% of joint shear load in PD specimens.

ACKNOWLEDGEMENT

This research was supported by LIXIL foundation 2017.
The experiment was conducted by Daiki Matsunaga.

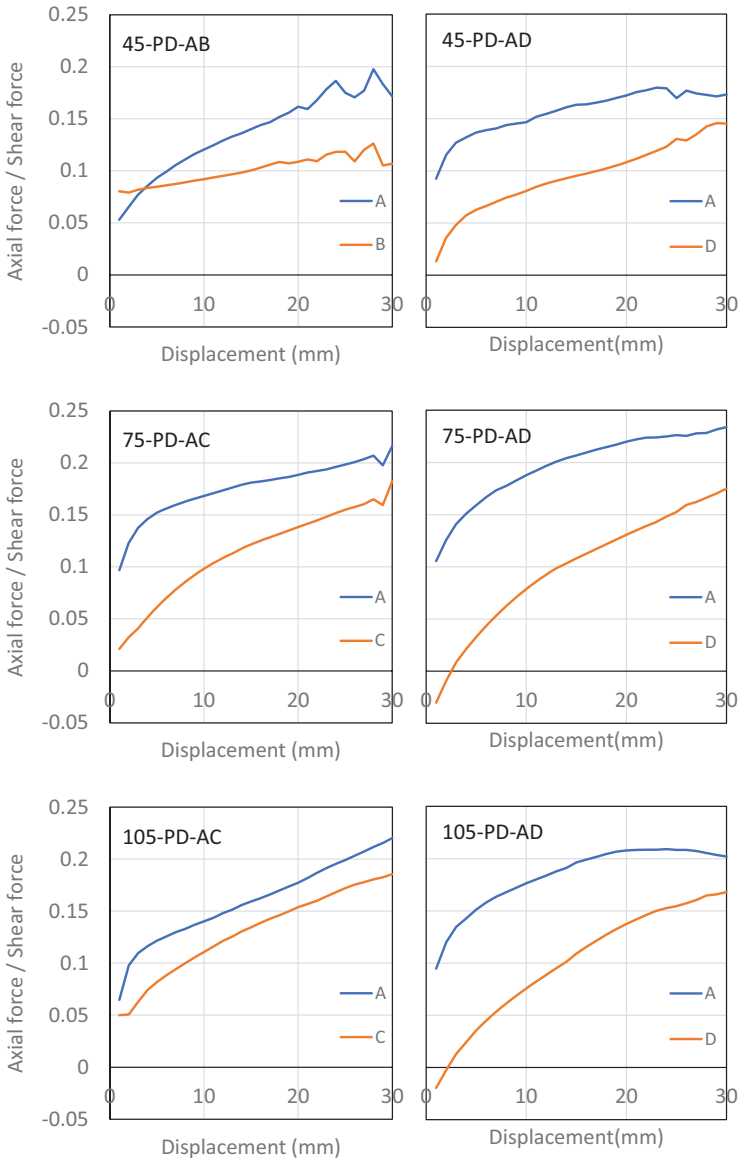

Figure 10: *Ratio of axial force of screw at each position to shear force*

https://doi.org/10.52202/069179-0196

REFERENCES

[1] Schmid M.: Anwendung der Bruchmechanik auf Verbindungen mit Holz. Dissertation, Karlsruhe Institute of Technology, 2002.

[2] Bejtka I.: Verstärkung von Bauteilen aus Holz mit Vollgewindeschrauben. Dissertation, Karlsruhe Institute of Technology, 2005.

[3] Wolfthaler F., Augustin M.: Development of a measurement screw and application for laboratory tests and building monitoring. Proceedings of World Conference on Timber Engineering, Austria, 2016.

[4] Dietsch P., Brandner R.: Self-tapping screws and threaded rods as reinforcement for structural timber elements – A state-of-the-art report. Construction and Building Materials 97, 78–89, 2015.

[5] JAS1152: Japanese Agricultural Standard for glued laminated timber, Ministry of Agriculture, Forestry and Fisheries of Japan, 2007

[6] Standard for Structural Design of Timber Structures. Architectural Institute of Japan, 2006

https://doi.org/10.52202/069179-0196

World Conference on Timber Engineering Oslo 2023

RIGID GLULAM JOINTS TO CONCRETE ABUTMENTS WITH GLUED-IN STEEL RODS

Kai Simon[1], Simon Aicher[2]

ABSTRACT: It is reported on rigid moment and shear force resistant connections of glulam to concrete or steel abutments based on glued-in steel rods. The connections are especially meant for clamped columns and integral bridge decks and wide-span end-clamped floors. In order to prevent premature splitting failure of the joint and to enforce a rather even shear force distribution on spaced rods the issue of lateral joint reinforcement by self-tapping screws or/and glued-on plywood panels is emphasized. The proposed design equations are calibrated by results of an extensive experimental campaign, revealing that the new Eurocode EC5-1-1 is overly conservative regarding lateral forces and respective normal force interaction. It is revealed case study-wise that the investigated rigid joint configurations present superior rotational stiffness and load capacities vs. today´s primarily employed mechanical fastener solutions with slotted-in steel plates or grout embedment of the GLT column in bucket foundations. The study demonstrates a technically competitive and environmentally advantageous timber solution vs. precast concrete columns. It offers new options for hybrid timber-concrete applications for timber bridge decks and clamped wide-span floors.

KEYWORDS: rigid glulam connections, moment and shear force resistant joints vs. concrete abutments, lateral joint reinforcement, self-tapping screws, glued-on plywood panels, clamped columns, bridge decks and floors, hybrid timber-concrete joints

1 INTRODUCTION

Today moment and shear force resistant connections of glulam (GLT) beams to concrete abutments, mainly occurring with columns, are realized by slotted-in steel plates fixed by dowel type fasteners. In order to achieve a high rotational stiffness, the steel "swords" have to be rather long altogether with a high number of dowels (Fig. 1a). Alternatively, the GLT column foot can be directly grouted in bucket foundations (Figure 1b). Both alternatives do not represent a practical construction method in case of rigidly jointing horizontally oriented beams for a timber bridge deck or a wide-span timber floor slab (Figure 1d). Rigid joints based on glued-in steel rods cast-in or screwed to RC abutments present a powerful tool to solve this connection task. Assets beyond high load capacity and stiffness consist in high fire resistance due to the hidden steel bars, minimized corrosion potential and less/no timber durability hazard of the joint due to protection from free or condensation water. A further asset of rigidly clamped column bearings consists in the creation of frame-type construction solutions, leading to reduced efforts in bracing especially at irregular spacings of columns in open space wide-span timber floor systems.

2 TECHNICAL CHALLENGE

The potential of rigid joints in glulam and LVL by glued-in rods is evident from numerous research work, increasing numbers of use in timber construction works and hence its consideration in the presently drafted new Eurocode 5-1-1 [1]. Today such joints are mostly used for timber to timber connections. Hybrid timber to steel joints based on glued-in rods exist (e.g. Figure 2) however are rare (e.g. [4; 5]). The assets of axially loaded steel rods glued-in parallel or inclined to wood fiber direction is widely acknowledged and sufficiently covered by commonly agreed-on design rules. However, in moment-rigid joints, e.g. at a clamped column basis lateral rod

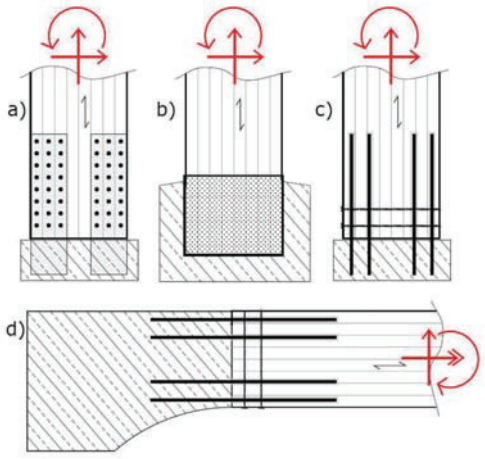

Figure 1: *Rigid glulam to concrete connection alternatives a) dowelled timber steel plate joint b) joint grouted in bucket foundation c), d) glued-in steel rods with lateral reinforcement for columns (c) and bridge decks/floors (d)*

[1] Kai Simon, Materials Testing Institute University of Stuttgart, kai.simon@mpa.uni-stuttgart.de
[2] Simon Aicher, Materials Testing Institute University of Stuttgart, Head of Department

https://doi.org/10.52202/069179-0197

forces resulting from shear force and torsional moment and their interaction with axial forces has to be considered, too. Lateral rod forces induce tensile stresses perpendicular to grain in the end grain area, which can lead to crack formation parallel to the rod axis at low load levels in case the rod distance to the loaded edge $a_{4,t}$ is small. The lateral force resistance of glued-in rods, as addressed now in [1], clearly represents a rather worst-case scenario of a rod positioned very close to the loaded edge. A previous more plausible and economically advantageous design approach has been dropped ([2] and [3]).

In order to prevent premature crack formation by lateral forces the joint has to be adequately reinforced perpendicular to grain. At present it is unknown which type of reinforcement is the best option and to what extent it increases the load capacity and stiffness of the joint. These questions set the frame for the reported research work which aims to provide ready to use joint construction and design solutions.

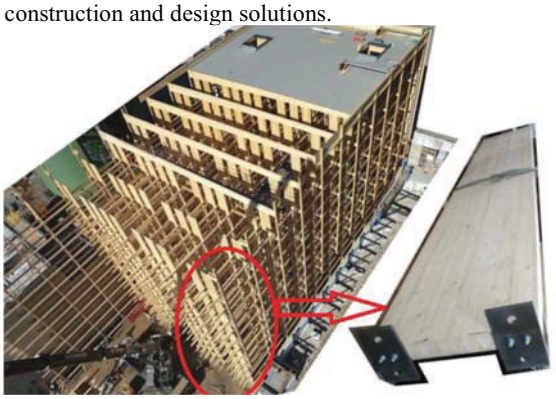

Figure 2: *Example of a timber high bay racking built by Kaufmann Bausysteme GmbH, Reuthe, Austria, in 2007 consisting of clamped columns connected by glued-in steel rods [4]; the joint behaviour and capacity were verified at MPA Stuttgart.*

3 GLUED-IN RODS: STATE OF THE ART

3.1 GENERAL

Research on glued-in steel rods dates back to the 1970ies [5; 6]. The investigations focussed on load capacity of the joints subjected to different loading modes and apt adhesives to enable strong and durable joints. Compilations of previous research, although not exhaustive can be found in [7]. Execution and design of glued-in rods was firstly standardized in DIN 1052:2004 [8] and DIN EN 1995-1-1/NA [9] in conjunction with nationally approved adhesives [10-13]. Based on increased knowledge and built heritage glued-in rod connections have now been incorporated in the draft of Eurocode 5-1-1 [1] referencing EN 17334 [14] with regard to testing and qualification of 2-component adhesives for glued-in rod applications.

3.2 AXIAL LOADING

The literature on axially loaded rods glued in glulam parallel to fiber is vast, e.g. [2; 6; 7; 15-17]. The latest European design proposal for axially loaded rods stated in prEN 1995-1-1 [1] is closely related to specifications given in DIN EN 1995-1-1/NA [9]. The European design equation for the characteristic axial capacity $F_{ax,Rk}$ of a single glued-in steel rod parallel to fiber with bonded-in length l_w reads

$$F_{ax,Rk} = min\begin{Bmatrix}\pi \cdot d \cdot l_{w,ef} \cdot f_{w,k} \\ E_s \cdot A_s \cdot \varepsilon_{u,timber}\end{Bmatrix} \leq F_{t,k} \qquad (1)$$

where

d	nominal diameter of the rod
$l_{w,ef}$	effective withdrawal length as minimum of: l_w; 40·d; 1000 mm
$f_{w,k}$	characteristic withdrawal (shear) strength of the bond line acc. to [1; 9] or e.g. Z-9.1-705 [10]
E_s	modulus of elasticity of the steel rod
A_s	nominal stress area acc. to EN ISO 898-1 for threaded rods and acc. to EN 10080 for ribbed steel bars
$\varepsilon_{u,timber}$	failure strain of timber parallel to grain (= 2,4 ‰ for softwood)
$F_{t,k}$	characteristic tensile resistance of the steel rod (see [1])

Figure 3 depicts the relationship of $f_{w,k}$ with bond / withdrawal length l_w for configurations of rods bonded parallel to fiber as specified in [1; 9]. Further, test results with various slenderness rod ratios and different adhesives presented in [7] are shown.

Spacings and edge distances of axially glued-in rods are specified in [1] as $a_2 = 5 \cdot d$ and $a_{4,c} = 2.5 \cdot d$, see Figure 4.

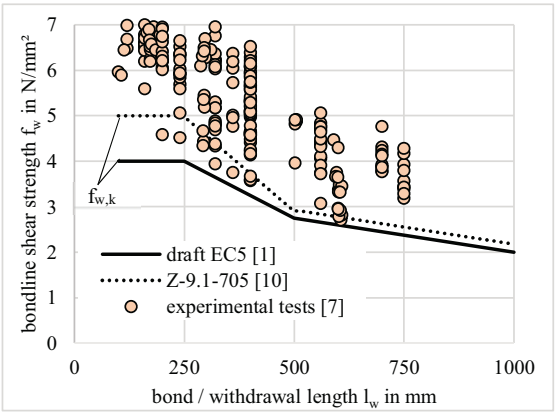

Figure 3*: Bond line withdrawal / shear strength of axially loaded steel rods glued-in parallel to fiber in softwood GLT depending on withdrawal i.e. bond length l_w from test results [7] and design rules acc. to draft EC5 [1] and Technical approval [10]*

https://doi.org/10.52202/069179-0197

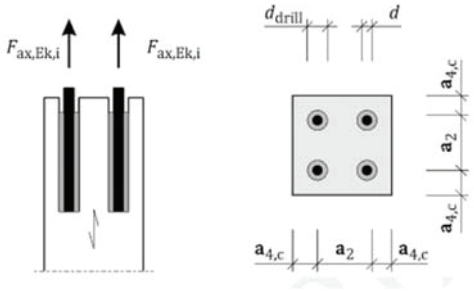

Figure 4: *Notations of spacings and edge distances of axially loaded steel rods glued-in parallel to GLT fiber*

3.3 LATERAL LOADING

Figure 5 shows the basic lateral force resistance behaviour as dependent on the distance to the loaded edge $a_{4,t}$ (see Figure 6) as obtained in former tests by Riberholt in 1977 [15], Möhler and Hemmer in 1981 [16] and then by Blaß and Laskewitz in 2001 [2]. The depicted results represent a test configuration of GLT with metrically threaded glued-in steel rods with a diameter d and bond length l_w of 16 mm and 320 mm (= 20 · d), respectively. A design model by Blaß and Laskewitz [2] based on a calculation model for splitting perpendicular to grain by Ehlbeck et al. [3] which describes the increasing load carrying capacity for larger distances $a_{4,t}$ quite well (see dotted line in Figure 5), was not considered in a standard. Instead the design model presented by Riberholt in 1988 [17] was established in DIN 1052:2004 [8] and later in the German Annex of Eurocode 5 [9]. The design model is based on the Johansen yield model [18] for dowel-type steel fasteners. With regard to splitting perpendicular to grain the model stipulates a minimum distance $a_{4,t} = 4 \cdot d$ to the loaded edge but doesn´t consider any capacity increase for larger edge distances. The most recent European design equations for the lateral load carrying capacity of rods glued-in GLT parallel to grain acc. to prEN 1995-1-1 are

$$F_{lat,Rk} = min \begin{cases} d \cdot f_{h,k} \left(\sqrt{(l_h + 2e)^2 + {l_h}^2} - l_h - 2e \right) & \text{(2a)} \\ d \cdot f_{h,k} \cdot \left(\sqrt{e^2 + \frac{2M_{y,k}}{d \cdot f_{h,k}}} - e \right) & \text{(2b)} \end{cases}$$

where

d	nominal diameter of the glued-in rod
l_h	embedment depth ($l_h = l_w$)
e	distance between load and bond line ($e = l_{can}$)
$M_{y,k}$	the characteristic yield moment of the rod specified as

$$M_{y,k} = 0{,}3 \cdot f_{u,k} \cdot {d_e}^{2,6} \quad (3)$$

where

d_e	the equivalent tensile stress diameter for rods with metric thread
$f_{u,k}$	characteristic tensile strength of steel rod

and the characteristic embedment strength

$$f_{h,k} = 0{,}1 \cdot \frac{0{,}082 \cdot (1 - 0{,}01 \cdot d_{drill}) \cdot \rho_k}{k_{mat}} \quad (4)$$

where

d_{drill}	the drill diameter of the hole in the timber part
k_{mat}	$= k_{90} \cdot \sin^2\alpha + \cos^2\alpha$
k_{90}	$= 1{,}35 + 0{,}015 \cdot d$
ρ_k	characteristic density of the timber

Acc. to [1] the embedment strength for a laterally loaded bonded-in rod inserted parallel to grain should be taken as 10% of the embedment strength of a laterally loaded bonded-in rod inserted perpendicular to grain. Hence as angle α between load and fiber direction is 0° in the here considered configuration, $k_{mat} = 1$ in Eq. (4). It should be mentioned that the embedment strength $f_{h,k}$ for dowels inserted parallel to grain given in [1] is specified extremely conservative and has been significantly lowered as compared to the previous EC5 draft [19] and German Annex of EC5 [9], see below (chapter 6.1).

Spacing a_2 and edge distance $a_{4,c}$ in [1] conform to the provisions of axially loaded steel rods; $a_{4,t}$ is prescribed as 4·d as previously in [8], see Figure 6.

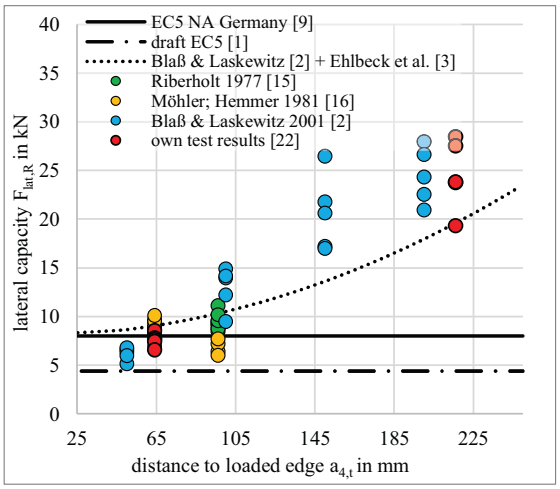

Figure 5: *Lateral resistance capacity of a single rod configuration (d_{rod} = 16 mm, metrically threaded) glued-in parallel to grain acc. to literature [2 - 3; 15 - 16], codes [1; 9] and own experimental tests*

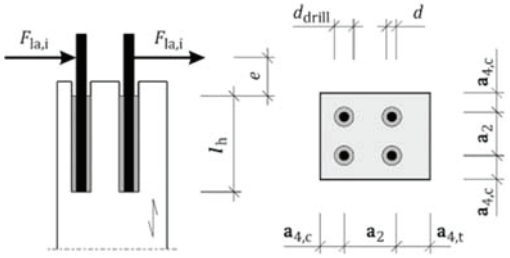

Figure 6: *Spacings and distances of laterally loaded steel rods glued-in parallel to GLT fiber*

https://doi.org/10.52202/069179-0197

4 COMBINED AXIAL AND LATERAL LOADING

For combined lateral and axial loadings acting on glued-in rods prEN1995-1-1 [1] specifies the interaction relationship:

$$\left(\frac{F_{ax,Ek}}{F_{ax,Rk}}\right)^n + \left(\frac{F_{lat,Ek}}{F_{lat,Rk}}\right)^n \leq 1{,}0 \qquad (5)$$

where n = 2. It should be mentioned that the exponent n in Eq. (5) has been changed from formerly n = 1 in [19] to n = 2, as firstly proposed by Riberholt [15] and specified previously in the German Annex of EC5 [9]. The exponent of n = 2 was also substantiated by tests of the authors.

5 RESEARCH PROGRAM AND TEST SET-UPS

Extensive research on rigid joints of GLT to concrete foundations or steel beams / sockets by means of glued-in steel rods started at MPA in 2014 in conjunction with the development of the Stuttgart timber model bridge (STMB) (see e.g. [20; 21]).

Figure 7: *Test specimen of Stuttgart Timber Model Bridge with rigid GLT to concrete connection with glued-in rebars [24]*

Based on the very successful use of the rigid concrete - glulam joint in the STMB project a comprehensive research program was initiated to clarify remaining open questions of this jointing technology. Hereby especially effects of different reinforcement alternatives intended to prevent premature splitting parallel to fiber in the joint area and respective design methods were of prime interest. It is obvious that a transparent validation of the reinforcement gains necessitates as basis knowledge about the load carrying capacity of unreinforced joints inevitably, too. In the same sense it is further important to understand the reinforcement mechanisms and gains firstly at pure axial and lateral rod loading before addressing a combined loading situation as existent in any rigidly clamped reinforced connection.
The load capacities of different actions were identified via: axial tests, predominant shear force tests realized as bending tests and cantilever tests with combined axial and lateral force action. The loading principles of the shear and cantilever tests are shown in Figure 8. It can be seen that the cantilever tests were performed with two different moment – shear force ratios of M/V = 0,55 and 1,15, respectively. All mentioned loading configurations were tested unreinforced and with three different reinforcement alternatives, shown in Figure 9.

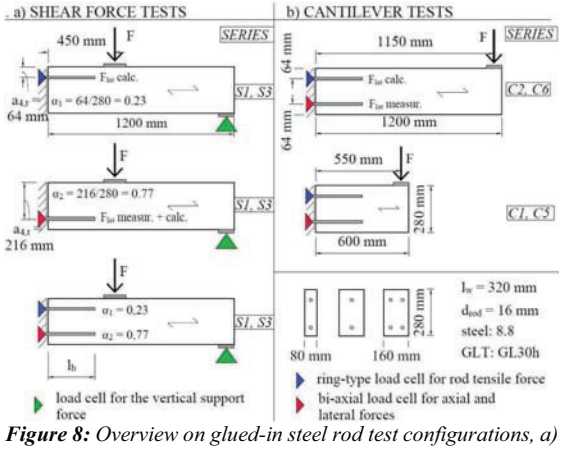

Figure 8: *Overview on glued-in steel rod test configurations, a) quasi pure lateral loading; b) combined axial and lateral loading in cantilever tests*

The investigated reinforcements were i) self-tapping screws (d_{screw} = 8 mm), ii) laterally and iii) end-grain bonded beech plywood panels with a thickness of 20 mm. Tables 1 and 2 give a condensed overview on the test program (see also [22] and [23]). In all cases the glulam (GLT) specimens were of strength class GL30h. The cross-sectional height was throughout 280 mm and widths were 80 mm and 160 mm being 5 or 10 times the steel rod diameter of d = 16 mm, respectively. The spacings of the steel rods were set as the minimally possible acc. to [1] and [9], being $a_{4,t}$ = 4·16 mm = 64 mm. The withdrawal length and the diameter of the drill hole in the GLT were throughout l_w = 320 mm (20·d) and d_{drill} = 20 mm, respectively, representing a practically relevant configuration. The distances of the screws from the end-grain face, from the width edge and from the rod were chosen (closest possible) as $a_{3,CG}$ = 28 mm, $a_{4,CG}$ = 20 mm and a_5 = 20 mm.

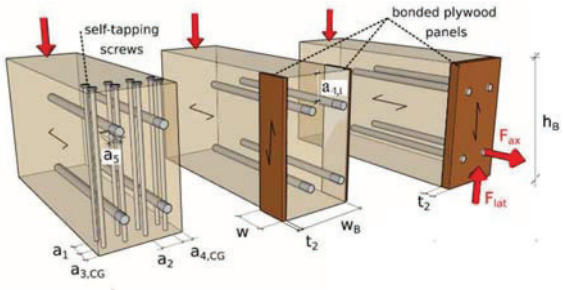

Figure 9: *View of investigated reinforcement alternatives for rigid glued-in rod joints being self-tapping screws, laterally and end-grain bonded beech plywood plates*

https://doi.org/10.52202/069179-0197

In order to grasp the load sharing between the rods with regard to both, lateral and axial forces, specifically designed test set-ups were used to measure both rod loadings with uni- and bi-axial load cells. The axial forces were measured at all rods: Bound to the size of the load cells the lateral force was however measured exclusively at the rod(s) located further from the loaded edge. The lateral force at the rod(s) placed at $a_{4,t}$ (Figure 6) was then derived from the difference of the applied and measured forces. For details see also [23]. To realize a clamped connection of the steel rods to a steel frame, comparable to a concrete connection with in-between positioned load cells, the glued-in rods were either screwed directly to the frame or connected via fitting parts. Figure 10 shows the realized test-set up for the cantilever configuration with M/V = 1,15. The tests were performed either in monotonic or multiple reversed loading, the latter not discussed here. The horizontal and vertical displacements at the clamped and free end of the specimens were measured, too.

Table 1: *Compilation of test program for the shear force tests*

designation of test	type of reinforcement	GLT width and height	position of rod along beam height	number of tests
S1	none		near (α_1)	4
			far (α_2)	3
			near + far (α_1=0,23)	3
S1_screw	screws	80 mm x 280 mm	near (α_1)	2
			far (α_2)	1
			near + far (α_1=0,23)	1
S1_end	end-grain plate		near (α_1)	3
			far (α_2)	2
			near + far (α_1=0,23)	3
S3	none	160 mm x 280 mm	near (α_1)	2
			far (α_2)	2
			near + far (α_1=0,23)	2
S3_end	end-grain plate		near (α_1)	1
			far (α_2)	1

Table 2: *Compilation of test program for the cantilever tests*

designation of test and M/V ratio	type of reinforcement	length of GLT in cm	GLT width and height	position of rod along beam height	number of tests
C1 (0,55)	none	60	80 mm x 280 mm	near + far (α_1 and α_2)	6
C2 (1,15)		120			7
C1_screw (0,55)	screws	60			3
C2_screw (1,15)		120			3
C1_lateral (0,55)	lateral panel	60			3
C2_lateral (1,15)		120			3
C1_end (0,55)	end-grain panel	60			2
C2_end (1,15)		120			3
C5 (0,55)	none	60	160 mm x 280 mm	near + far (α_1 and α_2)	5
C6 (1,15)		120			5
C5_screw (0,55)	screws	60			3
C6_screw (1,15)		120			2
C5_lateral (0,55)	lateral panel	60			2
C5_lateral (1,15)		120			2
C5_end (0,55)	end-grain panel	60			2
C6_end (1,15)		120			2
C7 (1,95)	none	200	80 x 280	near + far (α_1 and α_2)	4
C8 (1,95)			160 x 280		3

Additional to the full-scale beam and cantilever tests small scale tests were performed with regard to determination of the embedment strength of steel dowels of 16 mm and 20 mm diameter oriented parallel to grain in order to verify Eq. (4). These tests were aligned with EN 383 [25]. Further, the bond strength of the bond line between end-grain face of the glulam and the wide plywood panel face, so far unknown, was investigated with block shear specimens. These specimens were tested either in dry condition or after treatment in boiling water acc. to EN 14374, Annex B [26], followed by re-drying at 60°C. The tests were aligned with EN 14080 [27] but shear length had to be reduced due to excessive indentation in the GLT subjected to compression perpendicular to grain when applying the shear force.

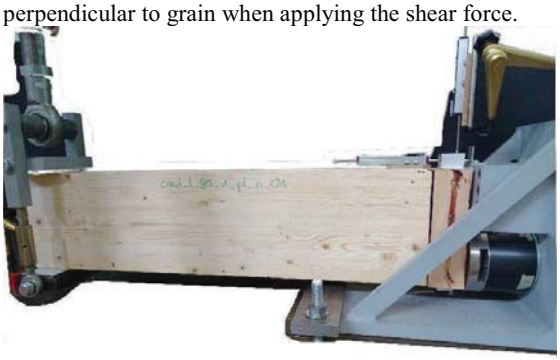

Figure 10: *Test set-up of a cantilever type GLT specimen (b = 80 mm) with two glued-in rods and lateral reinforcement at the clamped end by bonded beech plywood strips*

6 TEST RESULTS

6.1 EMBEDMENT STRENGTH

The results of the embedment strength tests are shown in Figure 11. Despite the rather low number of specimens it is evident that the strength-density relationship given in the EC5-1-1 draft [1] is too conservative especially in the usual density range of softwood glulam. At a density of about 350 kg/m³ the minimum experimentally obtained f_h values are about 5,5 N/mm² as compared to a characteristic value of about 2,5 - 3 N/mm² derived standard-wise from Eq. (4).

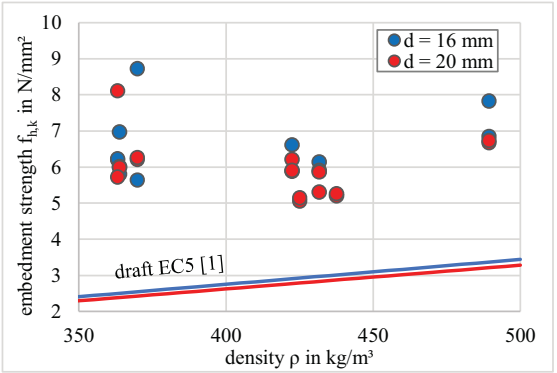

Figure 11: *Test results of GLT embedment strength tests of dowels oriented parallel to grain*

https://doi.org/10.52202/069179-0197

6.2 STRENGTH OF GLT-PLYWOOD END-GRAIN BOND LINES

Up to today end-grain bonding is considered being ineffective and of very low strength and bond line integrity. The only known approach to end-grain bonding then however of two CLT end-grain faces is pursued in the Swiss TS3 technology [28]. For bond lines between end-grain faces of GLT and plywood surfaces no shear strength values can be found in literature. Figure 12 shows the test results and further the requirement acc. to EN 14080 for fiber-parallel face bonded spruce laminations is shown. It can be seen that most of the results fulfil the requirement acc. to [27]. The obtained shear strengths varied from 3,5 - 6 N/mm² with a very high wood failure percentage of almost 100%. The difference between the higher strengths of the untreated specimens vs. the treated ones was about 20% on the mean level. So, the effect of the boiling water treatment revealed to be unexpectedly very low.

For a design of an end-grain reinforced joint (see chapt. 7) mean and minimum values of the shear strength $f_{v,b,end\text{-}grain}$ of 4,6 N/mm² and 3,5 N/mm², respectively, can be proposed tentatively.

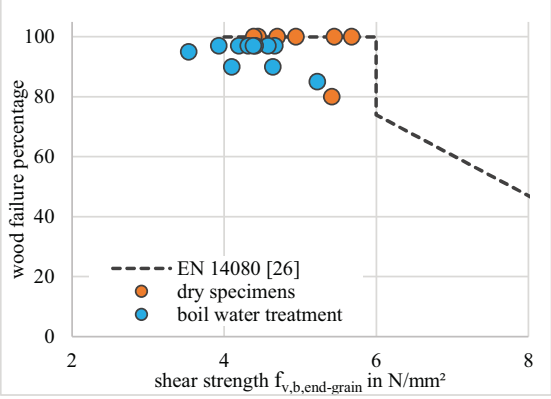

Figure 12: *Bond line shear strength test results of bond lines between GLT end-grain and beech plywood panels*

6.3 SHEAR FORCE TESTS

Figure 13 shows in condensed manner the results of the shear force tests for the unreinforced case (see also Figure 5) and the two reinforcement alternatives being screws and end-grain bonded plywood panels. Firstly, it can be seen that the new tests on the unreinforced joints fully confirm the former findings in literature [2; 15] that the shear force capacity increases significantly with larger distances from the loaded edge. However, most important is the finding that the reinforcement leads to extreme capacity increases vs. corresponding unreinforced configurations. Further, a significant difference between reinforcement with screws and end-grain bonded plates can be seen, whereby the latter method results throughout in higher values. It is sensible that the highest reinforcement increase is obtained for the most inconvenient rod placement with a small $a_{4,t}$ value. Here screws and end-grain plates deliver capacity increases at the mean level by factors of 3,0 and 5,2. These capacity increases, then still large, are reduced to factors of 1,7 and 2,1 in case of a favourable high distance $a_{4,t}$. For the general joint situation with two opposite rods reinforced by screws and end-grain plates mean capacity increases by factors of 1,8 and 2,6 were observed.

Both reinforcement alternatives produce extremely differing stiffnesses and damage evolutions as shown in Figure 14. At very low loads the unreinforced and both reinforced joint configurations reveal comparable stiffnesses in lateral direction. In case of screw reinforcement the stiffness gets highly nonlinear at very low loads. Contrary, the stiffness of the end-grain reinforced joint remains strictly linear up to about 50% of ultimate load and beyond this threshold a progressive nonlinear stiffness evolution starts. The failure mechanisms differ as follows. In case of screw reinforcement similar as with unreinforced joints splitting parallel to fiber occurs starting at the end-grain face at the rod positions closer to the loaded edge. However, the crack propagation is strongly delayed by the screw forces normal to the crack faces. At ultimate load and very large deformations in the rod embedment area a sudden load drop due to cracking of the GLT parallel to grain at the screw reinforcement occurs. Contrary in case of end-grain plate reinforced joints the nonlinearity without any crack formation is induced by deformations of the rod embedment area in the plywood. At ultimate load finally also splitting in combination with either a tensile failure in the net cross-section of the panel (see Figure 17) or a failure of the bond line between the GLT end-grain and reinforcement panel occurs. Details of reinforcements with laterally bonded plywood stripes which delivered comparable capacity gains as the screw reinforcements are not discussed here, as their range of application is limited to rather slender beams because of an expressed decline of the reinforcement effect with increasing width of the GLT.

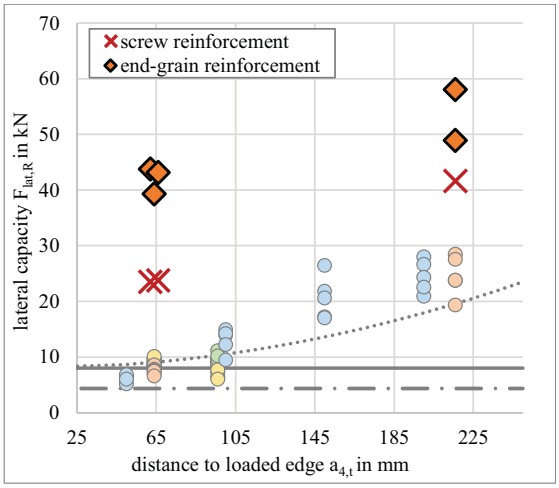

Figure 13: *Test results of quasi pure laterally loaded steel rods glued in GLT parallel to fiber without and with reinforcements by i) self-tapping screws or ii) end-grain bonded plywood*

https://doi.org/10.52202/069179-0197

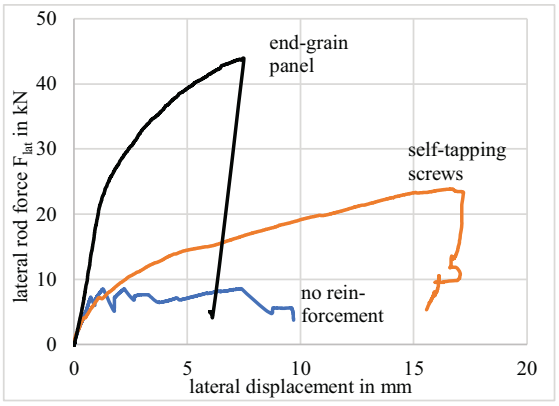

Figure 14: *Stiffness evolution of quasi pure laterally loaded steel rods glued in GLT parallel to grain without and with reinforcement of self-tapping screws or an end-grain bonded plywood panel*

6.4 CANTILEVER TESTS

A brief compilation of the empiric ultimate axial ($F_{ax,u}$) and lateral ($F_{lat,u}$) forces on the mean level is shown in Figure 15. On the left side the results of the shorter (M/V = 0,55) and on the right side the results of the longer (M/V = 1,15) cantilever beams are given. It can be seen, that the capacity gain of reinforced vs. unreinforced joints is decreasing with higher moment to shear force ratios. For a quantification in rough manner the capacities of the different reinforcement alternatives are lumped. At the short cantilevers the capacity gains at $F_{ax,u}$ and $F_{lat,u}$ closely resembling are denoted by factors of 1,7 – 1,8. At the long cantilevers the reinforcement gain of $F_{ax,u}$ and $F_{lat,u}$ decreases to an equal factor of about 1,3. This fact results from the already very high axial force capacity of the unreinforced joints at the higher M/V-ratio resulting in a mean withdrawal strength of f_w = 5,2 N/mm². This narrows the potential for a capacity increase as i) f_w is limited to maximally about 7 N/mm² in pure axial loading and ii) the yield capacity of the steel rod itself is 100,4 kN for the given configuration.

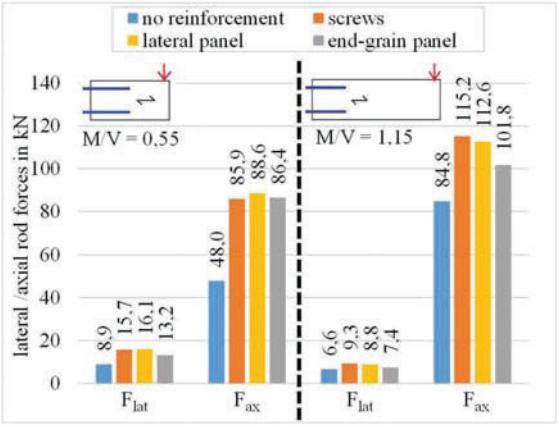

Figure 15: *Test results of cantilever type specimens with clamped glued-in steel rod connections without or with reinforcement*

Figure 16 shows the ultimate capacities of all tests with pure axial, pure lateral and combined moment and shear loading. For comparison the interaction line for the characteristic forces of unreinforced joints acc. to draft EC5-1-1 [1] as derived from Eqs. (1) to (5) is given, too. Similarly, as in case of lateral loading (see Figure 13) the enormous capacity gains throughout all possible $F_{ax} - F_{lat}$ force combinations enabled by the investigated joint reinforcements are evident.

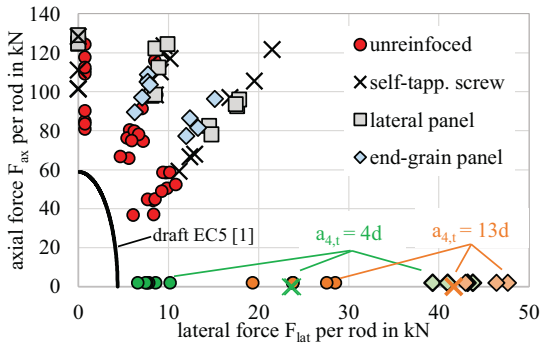

Figure 16: *Compilation of test results from pure axial, pure lateral and combined loaded glued-in rod joint configurations without and with reinforcements*

7 DESIGN PROPOSAL FOR END GRAIN REINFORCED RIGID JOINTS

Riberholt [15], [17] holds the merit for firstly presenting experimental tests with rods glued-in parallel to grain and loaded laterally as well as by combined moment and shear force action. He observed splitting as a weakness of the joints when either the beams were very slim or the rod was close to the loaded beam edge. Based on the test results the lateral rod capacity of unreinforced joints and for an eccentricity of e = 0 mm was then proposed as

$$F_{lat,unreinf,Rk} = f_{h1,k} \cdot d \cdot \sqrt{\frac{2 \cdot M_{y,Rk}}{f_{h1,k} \cdot d}} = \sqrt{2} \cdot \sqrt{f_{h1,k} \cdot d \cdot M_{y,Rk}} \,. \quad (6)$$

Eq. (6) conforms to draft EC5-1-1 [1], here Eq. (2b), and mirrors the case of a single plastic hinge in the timber dowel-jointed to a thin steel plate (Note: Eq. (6) differes from Eq. 8.9 in EC5-1-1 [29] by the prefactor of 1,15 and the missing rope effect consideration.

To overcome the joint splitting deficiency, Riberholt investigated a reinforcement by a 9 mm birch plywood panel glued-on the GLT end-grain. Based hereon Eq. (6) was then extended [17] to the case of an end-grain reinforcement as (see [23])

https://doi.org/10.52202/069179-0197

$$F_{lat,reinf,Rk} = \left[\left(\sqrt{\left(\frac{2 \cdot M_{y,Rk}}{f_{h1,k} \cdot d}\right) - {t_p}^2 \cdot \left(\frac{f_{h2,k}}{f_{h1,k}} - 1\right)} - t_p\right) \cdot f_{h1,k} + t_p \cdot f_{h2,k}\right] \cdot d \quad (7)$$

where

$f_{h1,k}$ embedment strength of spruce (rod parallel to grain and loaded laterally) similar to Eq. (4)

$f_{h2,k}$ embedment strength of the plywood panel as $f_{h2,k} = 0{,}11 \cdot (1 - 0{,}01 \cdot d_{drill}) \cdot \rho_{k,ply}$ [1]

$M_{y,Rk}$ yield moment of the steel rod similar to Eq. (3)

t_p thickness of the plywood panel

d steel rod diameter

d_{drill} the drill diameter of the hole in the timber part

Equation (7) describes a failure mode of a single plastic hinge in the GLT or of two yield hinges in case the glued-on end-grain panel is thick. If the embedment strength of the GLT parallel to grain is neglected ($f_{h1,k} = 0$) in a conservative design approach as being roughly 20 times smaller as compared to $f_{h2,k}$, the lateral capacity acc. to Eq. (7) results in

$$F_{lat,emb,reinf,Rk} = f_{h2,k} \cdot d \cdot t_p \quad (8)$$

and mirrors a pure dependency of the joint capacity with the panels embedment strength.

For the investigated specimen configuration, the lateral force resistances acc. to Eqs. (6) to (8) result in

$F_{lat,Rk,unreinf} = 4{,}4$ kN,

$F_{lat,reinf,Rk} = 19{,}9$ kN and

$F_{lat,emb,reinf,Rk} = 19{,}2$ kN

where $f_{h1,k} = 2{,}8$ N/mm², $\rho_{k,GLT} = 430$ kg/m³, $d_{drill} = 20$ mm, $f_{h2,k} = 60$ N/mm² ($\rho_{k,panel} = 680$ kg/m³); $M_{y,Rk} = 210$ kNmm (with $f_{u,k} = 800$ N/mm², $d_e = 13{,}54$ mm); $d = 16$ mm; $t_p = 20$ mm, e is assumed to be 0.

In addition to the embedment / plastic hinge resistance capacity of the end-grain panel the shear force transfer of the plate bonded to the GLT end-grain face has to be verified for the bond line interface (Figure 17a). Although the panel is bonded over the entire end-grain face area an uneven shear stress distribution has to be considered. In a first approach a roughly triangular distribution can be assumed or as proposed here in conservative manner an effective shearing length of

$h_{b,eff} = 2 \cdot a_{4,t}$

is chosen. The width of the effective bond area is assumed to be

$w_{b,eff} = 5 \cdot d_{rod}$,

which is the minimum spacing between rods acc. to [1].

The characteristic lateral capacity of the bonded GLT-panel interface is then given by

$$F_{lat,bond,Rk} = h_{b,eff} \cdot w_{b,eff} \cdot f_{v,b,end-grain,k} \quad (9)$$

where

$f_{v,b,end-grai\ ,k}$ characteristic bond line shear strength of GLT vs. plywood panel

According to the test results given above for the shear strength with $f_{v,b,end-grain,k} = 3{,}5$ N/mm², the joint bond capacity for a single rod in the given case is

$F_{lat,bond,Rk} = 2 \cdot 64$ mm $\cdot 5 \cdot 16$ mm$\cdot 3{,}5$ N/mm² $= 35{,}8$ kN.

Further the tension capacity of the panel net cross-section in direction of the shear force, being in general parallel to beam height, has to be verified as (see Figure 17b)

$$F_{lat,panel,t,Rk} = t_p \cdot (w_{b,eff} - d_{drill}) \cdot f_{t,plate,k} \quad (10)$$

where

$f_{t,plate}$ characteristic tensile capacity of the plywood panel, assumed as $f_{t,plate,k} = 30$ N/mm² acc. to [8].

Eq. (10) then results for the plywood plate used in the tests in a tensile capacity of

$F_{lat,panel,t,Rk} = 20$ mm$\cdot (80$mm$ - 20$ mm$) \cdot 30$N/mm² $= 36{,}0$ kN

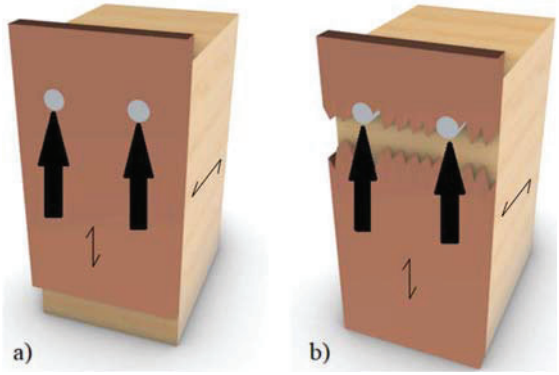

Figure 17: *Failure mechanisms of the end-grain bonded plywood reinforcement a) bond line shear failure b) tensile failure*

Summarizing: for the design of a glued-in rod joint with an end-grain reinforcement the following conditions of the lateral force resistance have to be satisfied:

$$F_{lat,Ek} \leq F_{lat,Rk} = min \begin{cases} F_{lat,emb,reinf,Rk} & Eq.\,(8) \\ F_{lat,bond,Rk} & Eq.\,(9) \\ F_{lat,panel,t,Rk} & Eq.\,(10) \end{cases} \quad (11)$$

Eq. (11) results as outlined in capacities of 19,2 kN, 35,8 kN and 360 kN, respectively. The minimum resistance of 192 kN results from the embedment failure (Eq.(8)) of the glued-on plywood panel. It is apparent that the above derived characteristic design resistance of the joint is significantly lower as compared to the test results. The minimum test result of a laterally loaded end-grain reinforced joint with $a_{4,t} = 4 \cdot 16$ mm $= 64$ mm is by a factor of 2 higher than the result of the embedment design equation. The reason therefore can be explained from the load displacement curve (see Figure 14), which shows that the stiffness develops increasingly non-linear beyond a shear force of about 20 kN which conforms roughly to the characteristic embedment capacity of the bonded plywood panel. A more profound discussion of this altogether with an improved design equation for the

https://doi.org/10.52202/069179-0197

lateral joint capacity resulting from plate embedment and rod yielding is given separately.

8 CONCLUSIONS

In rigidly clamped unreinforced glulam joints made with glued-in rods the connection capacity is widely determined by the lateral loads resulting from the shear force. The lateral rod force leads to tensile stresses perpendicular to grain and hence to premature splitting which undermines the activation of the axial rod capacity potential. Reinforcements of glued-in rod joints are not considered in the draft of the new Eurocode 5 [1]. The presented research on glued-in rods subjected to pure lateral and combined moment-shear-force loading proved that reinforcements by self-tapping screws as well as by laterally and end-grain bonded plywood panel(s) enable the full utilization of the axial rod withdrawal capacity.

End-grain reinforcements of the GLT beam by bonding a plywood panel with a resorcinol adhesive so far not used in timber engineering at all seems to be superior as compared to self-tapping screws because of a lower result scatter. It further provides the potential to reduce the edge distances of the glued-in rods. On the other hand, self-tapping screws which enable high capacity gains, too, are very easy to install and highly apt for reinforcements of existing unreinforced joints.

Laterally bonded plywood strips are comparably efficient as self-tapping screws and end-grain bonded plates but are confined to rather narrow GLT cross-sections due to the limited reinforcement spread.

Auxiliary investigations related to derivation of design equations revealed that the embedment strength of dowel-type-fasteners, here rods, oriented parallel to grain is specified much too conservative in the new draft of Eurocode 5 [1]. Similarly, the missing consideration of the distance to the loaded edge in the draft EC5 design equations for the lateral rod capacity lead in most cases to overly conservative resistances of unreinforced joints. Regarding end-grain reinforcements by plywood made from hardwoods the test results exceed a formerly literature proposed design equation by a factor of two. A new design approach in order to represent the true potential of this promising jointing technology is presently being developed.

ACKNOWLEDGEMENT

The partial support of this work by Deutsche Forschungsgemeinschaft (DFG, German Research Foundation) to project RP3 of IntCDC (Integrative Computational Design and Construction for Architecture) and Germany´s Excellence Strategy is gratefully acknowledged.

REFERENCES

[1] prEN 1995-1-1 (2022) working draft (formal enquiry): Design of timber structures - Part 1-1: General and rules for buildings (CEN/TC 250/SC 5, N 1650). CEN, Brussels, Belgium, 2022.

[2] Blaß H.J.; Laskewitz B.: Glued-in Rods for Timber Structures – Effect of distance between rods and between rods and timber edge on the axial strength; Versuchsanstalt für Stahl, Holz und Steine – Abteilung Ingenieurholzbau; University Fridericiana Karlsruhe, 2001.

[3] Ehlbeck J., Görlacher R., Werner H.: Determination of perpendicular-to-grain tensile stresses in joints with dowel-type fasteners; a draft proposal for design rules, *CIB-W18A proceedings*, Berlin, Germany, 1989.

[4] Wirth C.: High-bay warehouse in wood – new application for wood. In: Conference Proceedings of 13. *Internationales Holzbau-Forum IHF*, Garmisch Partenkirchen, Germany, 2007.

[5] Aicher S, Herr J: Investigations on high strength glulam frame corners with glued-in steel connectors. In: Proceedings of 5th World Conference on Timber Engineering, pp. 273-280, Montreux, Switzerland, 1998.

[6] Edlund G.: I limträ inlimmad skruer. Svenska Träforskningsinstututet, Serie B nr. 333, STFI Svenska Träforskningsinst, 1975.

[7] Aicher S.; Stapf G.: Glued-in rods – state of the art – influencing factors, test results, approvals, adhesive standardisation, dimensioning and design rules (in German). In: Conference Proceedings of 23. *Internationales Holzbau-Forum IHF*, Garmisch Partenkirchen, Germany, 2017.

[8] DIN 1052:2004: Design of timber structures - General rules and rules for buildings. German Institute for Standardization, Berlin, Germany, 2004.

[9] DIN EN 1995-1-1/NA:2013: National Annex - Nationally determined parameters - Eurocode 5: Design of timber structures - Part 1-1: General - Common rules and rules for buildings. German Institute for Standardization, Berlin, Germany, 2013.

[10] German Technical Approval Z-9.1-705: 2K-EP-adhesive WEVO special resin EP 32 S with hardener B22 TS, WEVO-Chemie GmbH Ostfildern-Kemnat. DIBt, Berlin, Germany, 2022.

[11] German Technical Approval Z-9.1-707: 2K-PUR-adhesive LOCTITE CR421 PURBOND for bonding steel rods into timber structures, Henkel & Cie. AG, Sempach Station, Switzerland. DIBt, Berlin, Germany, 2021.

German Technical Approval Z-9.1-778: 2K-EP-adhesive GSA-resin and GSA-hardener for bonding of steel rods into wooden parts, neue Holzbau AG, Lungern, Switzerland. DIBt, Berlin, Germany, 2021

https://doi.org/10.52202/069179-0197

[13] German Technical Approval Z-9.1-902: Connections with glued-in steel rods into timber parts with 2K-EP-adhesive (injection mortar) Hilti HIT-RE 500 V4, Hilti Germany, Kaufering. DIBt, Berlin, Germany, 2021
[14] EN 17334:2021: Glued-in rods in glued structural timber products - Testing, requirements and bond shear strength classification. CEN, Brussels, Belgium, 2021.
[15] Riberholt, H.: Bolte Indlimet I Limtrae; Technical University of Denmark; Structural Research Laboratory, Rapport Nr. R 83; 1977.
[16] Möhler, K; Hemmer, K: Tests with glued-in threaded steel rods; Lehrstuhl für Ingenieurholzbau und Baukonstruktionen, University Fridericiana Karlsruhe, Germany, 1981.
[17] Riberholt, H: Glued bolts in glulam – proposal for CIB code; *International Council for Building Research Studies and Documentation – Working Commission W18A/21-7-2* – Timber Structures; Meeting 21; Vancouver Island, Canada, 1988.
[18] Johansen K.W.: Theory of Timber Connections. *International Association for Bridge and Structural Engineering*, Vol. 9, pp. 249-262, 1949.
[19] Eurocode 5 draft (2021). informal enquiry: prEN 1995-1-1: Design of timber structures - Part 1-1: General and rules for buildings (CEN/TC 250/SC 5 N 1488). Brussels, Belgium: CEN.
[20] Aicher S.; Leitschuh N. und Hezel J.: „Stuttgarter Holzbrücke“, Research Report EFRE research project, Nr. 051203. MPA University of Stuttgart, 2015.
[21] Hezel J., Aicher S.: Die Stuttgarter Brücke – ein neuer Robustheitsansatz. Proceedings 4. International Days on Timber Bridges, IHB Ostfildern, Germany, 2016.
[22] Aicher S., Simon K.: Rigid glulam joints with glued-in rods subjected to axial and lateral force action. In: Proceedings International Network on Timber Engineering and Research (INTER), Meeting 54, pp. 113-128, Karlsruhe, Germany, 2021.
[23] Simon K., Aicher S.: Reinforced rigid glulam joints with glued-in rods subjected to axial and lateral force action. In: Proceedings *International Network on Timber Engineering Research (INTER)*, Meeting 55, pp. 185-201, Bad Aibling, Germany, 2022.
[24] Hezel J, Aicher S, Helbig T: Integral, bonded Timber-Concrete-Abutment-Connection (in German), In Proceedings of 3rd Stuttgarter Holzbau-Symposium, pp. 97-107, Stuttgart, Germany, 2015.
[25] EN 383:2007: Timber Structures –Test methods – Determination of embedment strength and foundation values for dowel type fasteners. CEN, Brussels, Belgium, 2007.
[26] EN 14374:2004: Timber structures - Structural laminated veneer lumber – Requirements. CEN, Brussels, Belgium, 2004.
[27] EN 14080:2013: Timber structures - Glued laminated timber and glued solid timber – Requirements. CEN, Brussels, Belgium, 2013.
[28] Franke S., Zöllig S.: TS3 – A New Technology for Efficient Timber Structures. In: *Current Trends for Civil & Structural Engineering* 4(4): 2020.
[29] EN 1995-1-1 (2010): Design of timber structures - Part 1-1: General - Common rules and rules for buildings, CEN, Brussels, Belgium, 2010.

World Conference on Timber Engineering Oslo 2023

GLULAM FRAMES ADHESIVELY BONDED BY MEANS OF BIRCH PLYWOOD PLATES: PRELIMINARY INVESTIGATIONS

Tianxiang Wang[1], Yue Wang[2], Roberto Crocetti[3], Magnus Wålinder[4], Pontus Persson[5], Patrik Hedlund[6]

ABSTRACT: The design of timber connections is of great importance since their performance is decisive for timber structures. The widely adopted technique utilizing the slotted-in steel plates could possibly be replaced by using timber-based gusset plates due to the significant advantages in terms of the environmental impact, economy, ease of prefabrication, and fire resistance of the latter one. Among the timber-based panels, plywood made of birch was chosen in the study due to the combined benefits of the cross laminated configuration of plywood and the superior mechanical properties of birch compared to most softwoods. In this paper, a preliminary experimental investigation was carried out to study the structural performance of the glulam trusses connected by means of bonded birch plywood gusset plates. Tests were performed on ad-hoc designed frame-like specimens. The plywood gusset plates were under-designed to be the weakest link in the structure, so as to study their load-bearing capacity. The knowledge obtained in this study is the first step towards the establishment of a model for the design of truss nodes with bonded plywood gusset plates. In the study, the face grain orientation of birch plywood was varied (0°, 5°, and 15° to the horizontal axis) in three test series. Test results show that the influence of the face grain angle from 0 to 15 degrees on the global stiffness of the frame structure is insignificant and it can be well predicted by a simplified planar 2D numerical models. Two analytical models, namely, the classic so-called 'Whitmore model' along with a more accurate analytical model, were utilized to illustrate the failure mechanism of birch plywood gusset plates with the concept of the effective width and the spreading angle.

KEYWORDS: Glue connection, Birch plywood, Glulam frame, Face grain angle, Effective width, Spreading angle

1 INTRODUCTION

Timber, as a building material, is paid more attention in the field of civil engineering, due to its low carbon footprint and lightweight. The design of timber connections is of great significance since their performance is decisive for timber structures. In high-rise timber buildings as well as long-span timber applications, slotted-in steel plates are widely used in joints [1].

Nevertheless, plywood plates could be an alternative to slotted-in steel plates. Timber-based gusset plates are more environmental-friendly and cost-effective, with less prefabrication demand and better fire resistance.

Essentially, two types of connections, namely connections with mechanical fasteners and bonded connections, can be adopted between plywood and other timber elements. Bonded connections are generally stronger, stiffer, and cheaper than mechanical connections. However, bonded connections have more severe requirements during assembly, e.g., the surrounding environment, applied pressure, curing time, etc., [2].

Bonded connections between plywood and other timber elements have been studied for a long time. Crutis [3] performed a number of tests on rigid lumber frames in 1960. Douglas fir plywood plates were nailed and glued to the Douglas fir lumber framing members. Three types of failures were summarized: (1) stud or rafter failed due to combined bending and axial load, (2) gusset plates failed due to combined bending and axial load, and (3) gusset plates failed in rolling shear. The effect of the face grain angle of plywood gusset plates was also investigated. It was indicated that the orientation of the face grain has a significant effect on the joint capacities. Wilkinson [4] and Josefsson and Larsson [5] compared different connection systems of the structural applications using (1) nailed plywood plate, (2) nailed steel plate, and (3) nailed and glued plywood plate. Their studies found that the third one with nailed and glued plywood plates delivered the highest stiffness and capacities for the structure.

Although connections using plywood gusset plates seem competitive, slotted-in steel plates are still dominant in the marketplace [6]. One reason of that, is the fact that there are still uncertainties - mainly due to lack of experimental data - concerning the load-bearing capacity of plywood under off-axis loading. The load-bearing capacity of the

[1] Tianxiang Wang, KTH Royal Institute of Technology, Sweden, tiawan@kth.se
[2] Yue Wang, KTH Royal Institute of Technology, Sweden, yue4@kth.se
[3] Roberto Crocetti, KTH Royal Institute of Technology, Sweden, crocetti@kth.se
[4] Magnus Wålinder, KTH Royal Institute of Technology, Sweden, magnus.walinder@byv.kth.se
[5] Pontus Persson, Kvarteret Konstruktörer, Sweden, pontus.persson@kvarteretk.se
[6] Patrik Hedlund, KTH Royal Institute of Technology, Sweden, phedlu@kth.se

https://doi.org/10.52202/069179-0198

steel plates used in timber connections is, on the other hand, easy to calculate by means of well-proven models.
Studies on the structural behavior of birch plywood gusset plates in connections with mechanical fasteners have been initiated recently [7]. This paper aims to gain more knowledge regarding the failure mechanism of bonded birch plywood plates in truss structures. For this purpose, frame-like specimens consisting of glulam elements and laterally bonded birch plywood gusset plates were laboratory tested. Plywood made of birch (*Betula pendula*) was chosen as the material for the gusset plates. The choice of birch is both because it is a wood specie widely available in Scandinavia [8,9] and because it has outstanding mechanical properties. The failure mechanism of the birch plywood plates with varying face grain angles was studied both experimentally and numerically.

2 MATERIALS AND METHODS

2.1 DESCRIPTIONS OF STRUCTURES AND MATERIALS

The structure presented in Figure 1 is composed of inclined members, horizontal members, and birch plywood plates. Inclined and horizontal members made of spruce (Picea abies) glulam GL 28cs were adhesively connected by means of birch plywood gusset plates. Inclined members have an angle of 30° to the horizontal members. The width (direction 1 in Figure 1) and the height (direction 2 in Figure 1) of the frame structure are approximately 1536 mm and 760 mm, respectively. There are three plywood plates at the top and bottom, connected with inclined members, creating four glue lines, annotated as 'Birch plywood A'. Only one gusset plate was glued to the glulam elements on the left and right sides of the frame, connecting the inclined and horizontal glulam elements. This gusset plate, annotated as 'Birch plywood B', was designed to be the weakest link in this structure. Thus, failure in birch plywood B was expected after the destructive test, which is in line with the aim of this paper. The detailed configuration of both birch plywood A and B is shown in Figure 1. The face grain of birch plywood A is parallel to direction 1, while the face grain angle of birch plywood B is varied to investigate its effect on the global behavior of the frame.
All the glulam elements have the same cross-section of 56 mm × 110 mm. These elements were produced from a number of 4 m-long glulam beams GL28cs with a cross-section of 56 mm × 225 mm by using a miter saw and format saw. The weight was measured on each element before the test in order to deduce the density. The mean density was 463 kg/m^3 with a standard deviation (STDV) of 17 kg/m^3. Moisture content (MC) was measured on each glulam element prior to the test by a resistance-based moisture meter (HT 85, GANN, Germany). The mean MC was determined to be 12.6% with a STDV of 1.1%. Five samples were measured by using both HT 85 moisture meter and oven-drying methods [10]. No significant difference between these two methods was observed on glulam elements at a 95% confidence interval. Hence, MC measured from this resistance-based measuring device is considered valid.

Birch plywood plates have a nominal thickness of 9 mm consisting of 7 veneers. The mean density was 714 kg/m^3 (STDV=29 kg/m^3). MC was measured on ten samples cut from the frame specimens after the tests using the oven-drying method. The mean MC was 8.4% (STDV=0.4%). Melamine-urea-formaldehyde (MUF) adhesive (Prefere 4546/5022) was chosen for the tests. The liquid melamine urea adhesive (Prefere 4546) and the liquid hardener (Prefere 5022) were mixed with 100:10 parts-by-weight (pbw). This adhesive system fulfills the requirements according to EN 301 [11] and is classified as a general purpose, gap-filling, and finger-jointing adhesive. However, the applicability of this type of adhesive in this case, i.e., surface bonding between spruce glulam and birch plywood for connection purposes is still uncertain. Therefore, choosing the proper adhesive and the related parameters during assembly is also one of the crucial parts of the investigation for this type of bonded connection.

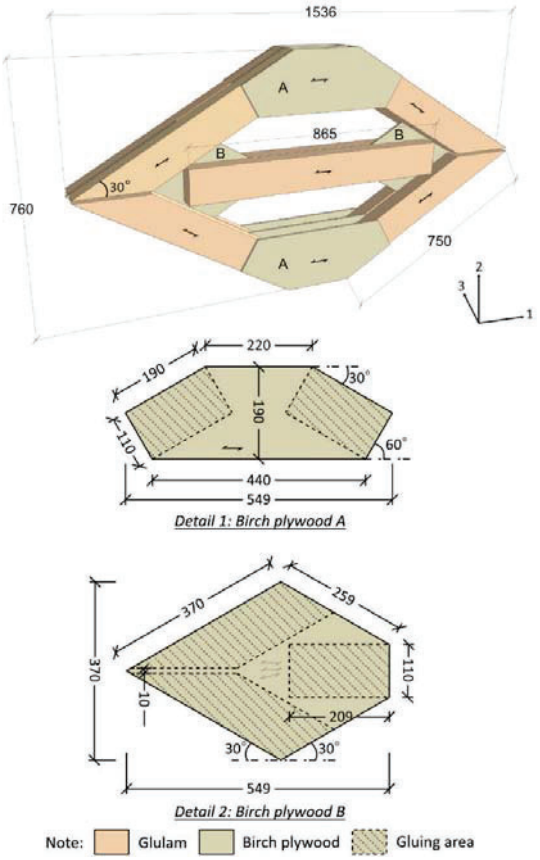

Figure 1: *Configuration of the studied frame (Length unit: mm).*

2.2 ASSEMBLY PROCESS

The assembly process is illustrated in Figure 2. Firstly, the glued areas were sanded by a sanding machine. The adhesive was spread on both surfaces of birch plywood plates and glulam elements. As shown in Figure 2(b), glulam elements were predrilled with 4 mm holes about 2 cm deep. Clamps were utilized to tighten plywood plates

and glulam together for inserting screws. Two screws with an outer diameter of 3.5 mm and a length of 50 mm were inserted into each glulam element. Then, clamps were removed so that new adhesive layers could be applied (Figure 2(c)). Similar to the previous processes, both glulam element and plywood plates were sanded, spread with adhesive, and pressed by screws (Figure 2(d)). By repeating the aforementioned procedures, all the timber elements were assembled as a whole. Lastly, screws with an outer diameter of 5.6 mm and a length of 140 mm were inserted. The positions of these screws are displayed in Figure 2(e), which are along the center axis of the inclined and horizontal members. It is noted that screws utilized in the frame are only considered for assembly purposes. The influence of the screw on the load-bearing capacity of the joints can be neglected because of their significantly lower shear stiffness, as compared to the shear stiffness of the adhesive.

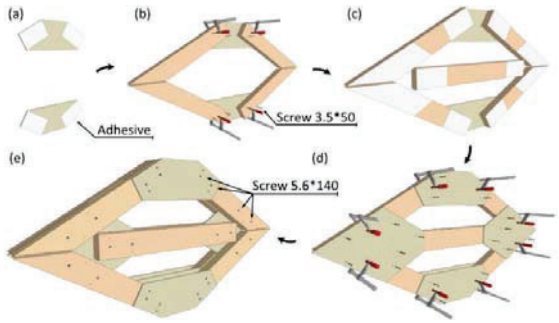

Figure 2: *Assembly process of the studied frame.*

The adhesive spreading mass per square meter was roughly 400 g/m^2. The assembled frames were cured for around 1-2 weeks before testing. The indoor temperature during bonding of the specimens was in the range10-15 °C.

2.3 TEST PROCEDURE

Three test series were performed in the presented study. As displayed in Figure 3(a), the face grain of birch plywood plate B was varied. In test series 1, three frame specimens were tested with the face grain direction of birch plywood B parallel to the horizontal axis. In test series 2 and 3, the face grain angle of birch plywood B was 5° and 15° to the horizontal axis, respectively, with four repetitions.

The test setup is shown in Figure 3(b). Tests were conducted on the MTS810 universal testing machine. All specimens were loaded in compression. During the tests, the loading head motion was constant, with a rate of 1 mm/min. The load signal and the piston movement were recorded simultaneously. In order to avoid applying load directly on birch plywood plates, wedges made of glulam were inserted between the inclined members and birch plywood plates A. The load-bearing capacity was defined as the maximum load attained during the tests. Machine compliance was measured by pressing the loading head to the support, and then it was excluded from the piston movement to derive the vertical displacement of the frame. The stiffness of the tested structure was defined as the slope of the load-vertical displacement curve in the linear portion.

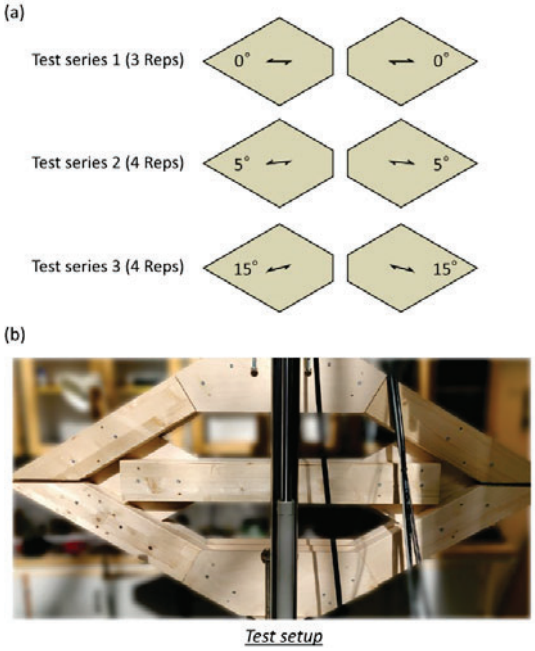

Figure 3: *Test series and setup.*

2.4 NUMERICAL ANALYSIS

Numerical analyses were performed with commercial finite element software Abaqus (Simulia, USA). A planar 2D numerical model was developed to investigate the structural behavior of the studied frame in the linear elastic stage. Both the stiffness on the global level and the section forces on the component level were checked when the face grain orientation of birch plywood plate B changed from 0° to 5° and 15°.

Ideally, structures of this type can be analyzed as 2D trusses with hinges at each joint [12]. Yet in this study, as can be seen in Figure 1-3, glue connections were adopted, and the proportion of the gluing area to the size of the frame is relatively large. Hence, all the glulam components were modeled as beam-type elements.

Glue-laminated timber is usually characterized as an orthotropic material. It can be further simplified to be transversally isotropic, with identical elastic properties in the radial and tangential directions [13]. The physical and elastic mechanical properties of glulam beam GL28cs assigned in the numerical model are listed in Table 1. The properties include the density ρ, the elastic modulus E_{ij}, the Poisson's ratios ν_{ij}, and the shear modulus G_{ij} $(i, j = 1,2,3)$. Axis 1 is along the grain direction, while axes 2 and 3 are in the transversal directions.

https://doi.org/10.52202/069179-0198

Table 1: *Physical and elastic mechanical properties of glulam GL28cs assigned for numerical analyses.*

ρ (kg/m^3)	E_{11} (MPa)	E_{22} (MPa)	E_{33} (MPa)	ν_{12}
463	12500	300	300	0.219

ν_{13}	ν_{23}	G_{12} (MPa)	G_{13} (MPa)	G_{23} (MPa)
0.219	0.582	650	650	65

The input density in Table 1 is the mean value measured in this study and reported in Section 2.1. The elastic properties have been derived according to [14] for the mean values of the elastic modulus and shear modulus and [15] for the Poisson's ratios. Further, the rolling shear modulus G_{23} was assumed to be one-tenth of the shear modulus G_{12} and G_{13} according to [16].

The inclined glulam elements were tied together. For the connection between the inclined and horizontal glulam elements, a spring with the axial stiffness defined in the horizontal direction was assigned in the numerical model. This is due to the fact that there is only one birch plywood plate transferring the axial forces and the potential bending moment between the inclined and horizontal glulam elements. Moreover, the thickness of this plywood plate was under-designed so as to study its failure mechanism after the tests. Therefore, the contribution of this single gusset plate to the global stiffness should be taken into account. It is noticed in Figure 4 that the marked triangular area would take most of the tensile force from the horizontal glulam beams considering that the frame structure was loaded in compression. This marked area was converted into a rectangular shape with the equivalent area. The axial stiffness of the spring can be calculated according to Equation (1).

$$k = \frac{EA}{L} \tag{1}$$

where k is the axial stiffness of the spring; E is the elastic modulus of birch plywood; A is the cross-sectional area of the converted rectangular shape; and L is the length of the same region. It is worth mentioning that the elastic modulus of birch plywood is angle-dependent. When the face grain orientation of the plywood plate varied from 0° to 15°, the assigned elastic modulus should also be different. The elastic modulus of birch plywood at 0° has been experimentally characterized in previous studies [8], with a mean value of 9.4 GPa. It is also found that one theoretical model can predict the off-axis (between 0° and 90°) elastic modulus fairly well [8]. By employing this theoretical model, the elastic modulus at 5° and 15° could be predicted, which is 8.6 GPa and 5.2 GPa, respectively. See Equation (2) for the calculated axial stiffness for the three tested angles.

$$k = \begin{cases} 5.7 \times 10^7\ N/m & (\alpha = 0°) \\ 5.2 \times 10^7\ N/m & (\alpha = 5°) \\ 3.2 \times 10^7\ N/m & (\alpha = 15°) \end{cases} \tag{2}$$

where α is the face grain angle of birch plywood plates B to the horizontal axis.

Moreover, the failure load obtained from the test data was applied in the numerical model to check the internal force of each glulam element at failure, especially the horizontal one that would transfer the tensile force to the birch plywood plate B. The numerical stiffness of the global frame structure was derived as the ratio of the input external load to the corresponding vertical displacement at the top of the frame. It would be further compared with the experimental ones in Section 3.1. Glulam elements were meshed with the beam element type (B21 in ABAQUS/CAE 6.14) and the size of 0.02 m.

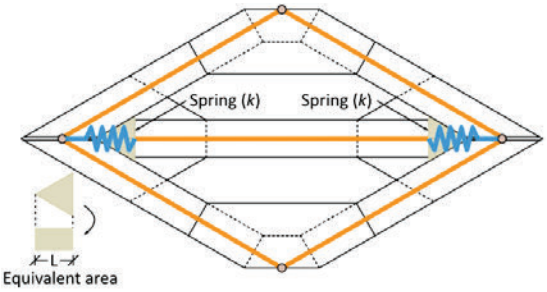

Figure 4: *Illustration of the planar 2D numerical model.*

3 RESULTS AND DISCUSSION

3.1 EXPERIMENTAL RESULTS

The failure load, the stiffness, and the failure mode of each tested frame structure are summarized in Table 2. The experimental load-vertical displacement curves are displayed in Figure 5.

Table 2: *Experimental results*

Test series	Specimen	Failure load (kN)		Stiffness (kN/mm)		Failure mode
01 (0°)	01	72.8	77.6	11.2	10.5	a
	02	81.1		9.8		a
	03	78.8		10.5		a
02 (5°)	01	86.8	80.6	10.0	10.1	a
	02	81.8		10.5		b
	03	74.5		9.7		b
	04	79.3		10.1		a
03 (15°)	01	68.2	75.2	8.0	8.9	b
	02	76.2		9.4		b
	03	79.5		9.0		b
	04	77.0		9.2		b

Note: failure mode 'a' means the bond line failure between birch plywood B and the horizontal glulam while failure mode 'b' represents the failure in birch plywood B.

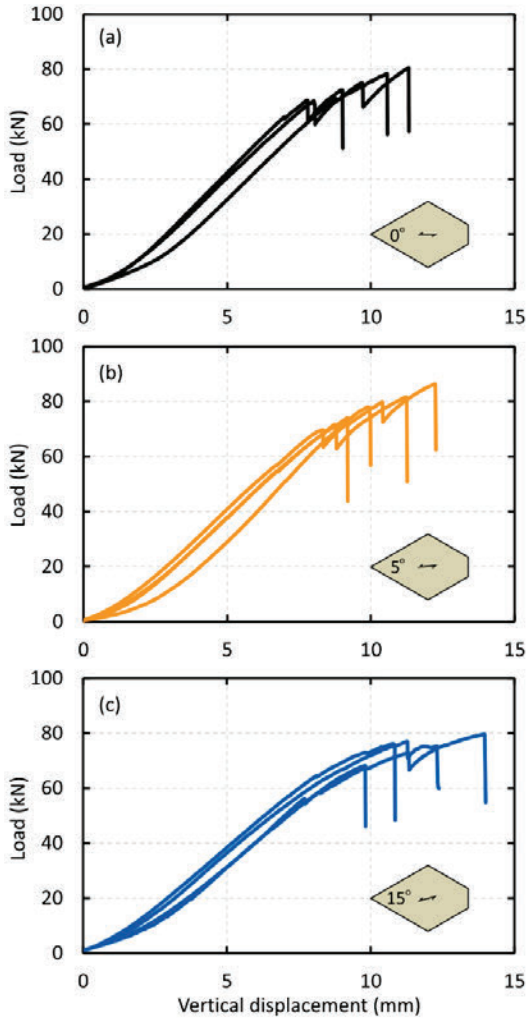

Figure 5: *Experimental load-vertical displacement curves: (a) test series 01 (0°); (b) test series 02 (5°); and (c) test series 03 (15°).*

As noticed in Table 2, test series 02 (5°) has the highest mean failure load, followed by test series 01 (0°) and 03 (15°), which could be explained by the different failure modes. As aforementioned, the birch plywood plate B was designed as the weakest part in the frame. However, for the specimens in the test series 01 (0°), the bond line failure took place prior to the birch plywood failure. The same failure mode was also observed in the first and the fourth specimens in the test series 02 (5°). For the other specimens with the failure occurred in birch plywood, the average failure load of the second and the third specimens in the test series 02 (5°) is 78.2 kN, slightly higher than the average failure load (75.2 kN) of the test series 03 (15°). The stiffness is independent on the failure load and failure mode as it indicates the structural performance in the linear elastic stage. Test series 01 (0°) possesses the highest stiffness, followed by test series 02 (5°) and 03 (15°). It was mentioned in Section 2.4 that the elastic modulus of birch plywood drops rapidly from 9.4 GPa to 5.2 GPa when the face grain angle varies from 0° to 15° to the loading axis. Nevertheless, the influence of the birch plywood face grain orientation on the global stiffness of the frame is not so dramatic, which can also be observed in Figure 5.

The difference in the load-displacement behavior of each test series is not noticeable, with a slight difference in the failure load and the stiffness as presented in Table 2. All the curves grew slowly in the initial stage, which might be because that the wedges inserted at the top and the bottom of the frame were trying to get full contact with the inclined glulam elements. After this initial consolidation stage, the load increased almost linearly with the vertical displacement in the elastic stage. It is interesting to see that, in some specimens, there was a slight reduction of the load. Then, the load increased again until the final failure of the structure. The slight reduction of the load was owing to the premature 'failure' in a certain part of the bonded area and it was more likely to be seen in the specimens with the final failure also in the bond line. To be more specific, only one specimen in test series 03 showed the load reduction before the final failure (see Figure 5(c)), while in other test series, this phenomenon took place more frequently.

Typical failure modes are presented in Figure 6. As can be seen in Figure 6(a) and Figure 6(b), for the specimens that failed in the bond line, only a small part of glulam failure was observed in the bonded area. It is evident that the strength of the timber material has not been fully exploited, and the bonding quality might have been improved. However, it does not necessarily mean that the MUF adhesives did not work for spruce-birch gluing. In fact, many factors influence the bonding quality, e.g., the surrounding environment (temperature and relative humidity), mixing ratio, assembly time, and pressing methods, etc. It is not a trivial task to determine the influence of each factor on the bonding strength between spruce glulam and birch plywood. Systematic studies should be conducted in the future to propose a proper workflow when manufacturing bonded connections made of birch plywood plates and spruce glulam beams.

Although the bonding quality was not ideal, some specimens showed failure in birch plywood gusset plates (see Figure 6(c) and Figure (d)). The plywood plates failed in tension due to the tensile force transferred from the horizontal glulam beams. The cracks are, in general, perpendicular to the horizontal direction and close to the end of the horizontal glulam beams except for a small part along the face grain direction, as shown in the upper part of Figure 6(c). The axial forces in the glulam elements were not measured during the tests. However, these forces can be estimated with reasonable accuracy by means of a numerical model calibrated with data from experimental results. The failure mechanism of the birch plywood plates can then be discussed with the knowledge of the axial forces reported in Section 3.2 by means of the analytical models proposed in Section 3.3.

https://doi.org/10.52202/069179-0198

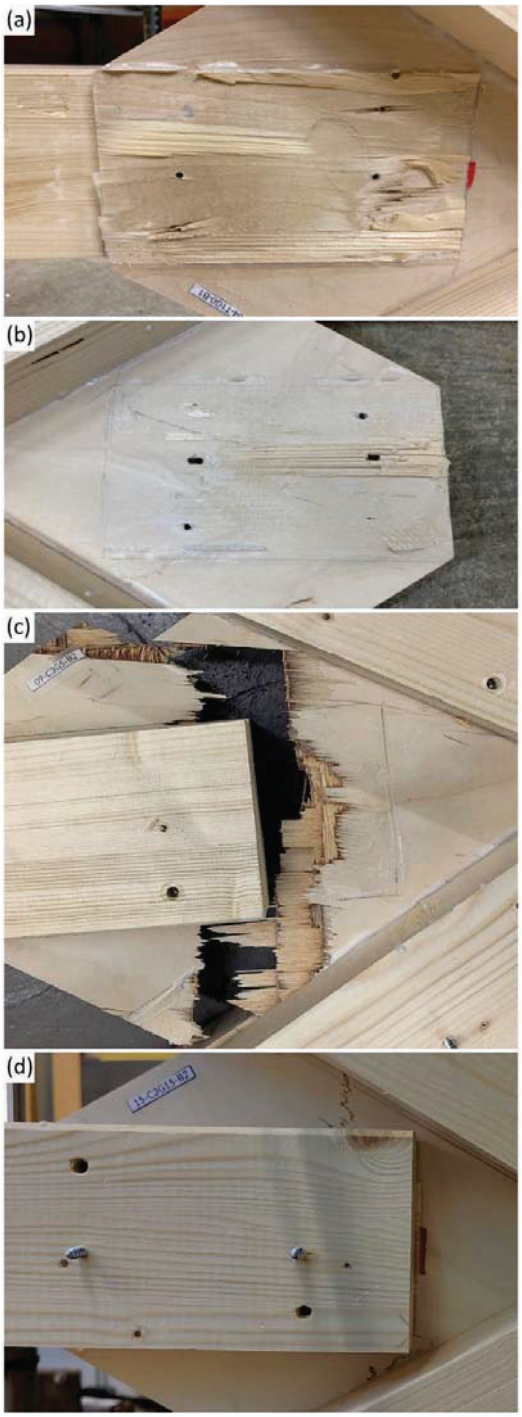

Figure 6: *Typical failure modes: (a) bond line failure in test series 01; (b) bond line failure in test series 02; (c) plywood failure in test series 02; and (d) plywood failure in test series 03.*

Similar studies regarding this frame structure but in mechanical connections have been presented in [7], where the plywood gusset plate B had the face grain orientation parallel to the horizontal axis. Thus, the structural behavior of this timber frame in mechanical connection [7] and glue connection (test series 01 in this study) can be compared (see Figure 7). Not surprisingly, the adhesively connected one possessed both higher load-bearing capacity and global stiffness.

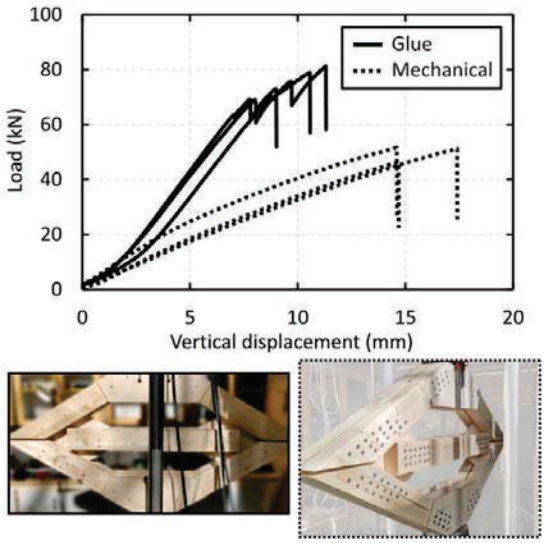

Figure 7: *Load-vertical displacement curves of the frame structures in glue connection (test series 01) and mechanical connection [7].*

3.2 NUMERICAL PREDICTION

Table 3 compares the experimental stiffness with the numerically predicted ones for each test series. The axial forces in the horizontal glulam beams are also listed in Table 3. The underlined numbers indicate that these specimens failed in the bonded area.

Table 3: *Comparison between experimental and numerical results*

Test series	Specimen	Stiffness (kN/mm)		Axial force in horizontal glulam beams at failure (kN)
		Exp. (Mean)	Num.	
01 (0°)	01	10.5	10.1	81.7
	02			91.0
	03			88.4
02 (5°)	01	10.1	9.9	95.0
	02			89.5
	03			81.5
	04			86.8
03 (15°)	01	8.9	8.0	63.4
	02			70.9
	03			73.9
	04			71.6

The stiffness of the frame structure predicted by the planar 2D numerical model showed good agreement with the experimental results. The numerically predicted stiffness was slightly lower than the experimental stiffness. This might be due to that, in this simplified 2D numerical

model, only the cross sections of glulam elements were defined and the additional thickness of the plywood plates in the glued connection regions was neglected.
Despite the slight difference, this numerical model was considered to be valid and the axial forces in the horizontal glulam beams were checked. The horizontal glulam beams were in tension during loading and the tensile forces were taken by the single birch plywood plate B, leading to the tensile failure of the plywood in some specimens. Two specimens in test series 02 (5°) showed plywood failure. The average tensile force at failure is 85.5 kN. In test series 03 (15°), the average tensile force taken by the plywood plate at failure is lower, which is 70.0 kN.

3.3 ANALYTICAL MODELS

In order to predict the failure load of the gusset plate in timber connections, one design model should be put forward. The first step is to gain knowledge with regard to the strength of the birch plywood plate. In this study, the plywood plates failed in tension with the face grain angle of 5° (in test series 02) and 15° (in test series 03) to the horizontal direction. Hence, the tensile strength of birch plywood at 5° and 15° load-to-face grain angle should be obtained. Wang et al. [8] characterized the off-axis tensile properties of 21 mm birch plywood at around 12% MC and found that the empirical Norris failure criterion predicts the closest results to the experimental data among the investigated linear and quadratic failure criteria (see Figure 8).

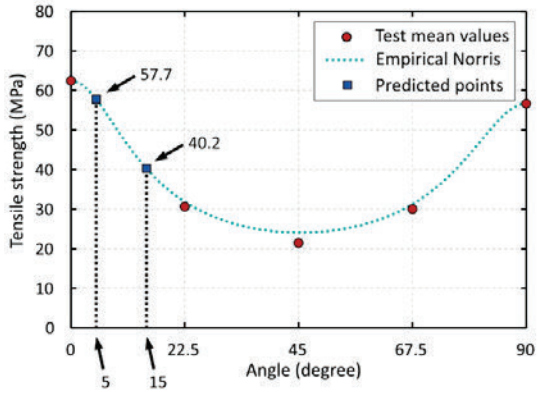

Figure 8: *Tensile strength of birch plywood at any face grain angle to the loading axis predicted by empirical Norris failure criterion.*

It is noticed in Figure 8 that the predicted tensile strength of birch plywood at 5° and 15° are 57.7 MPa and 40.2 MPa, respectively.
Having the tensile force, tensile strength, and the thickness of birch plywood plate at hand, it is possible to derive the width of plywood that was involved in resisting the load, namely, the effective width (see Equation (3)).

$$w_{eff} = \frac{F_t}{f_t \cdot t} = \begin{cases} 164.6\ mm & (\alpha = 5°) \\ 193.5\ mm & (\alpha = 15°) \end{cases} \quad (3)$$

where w_{eff} is the effective width of the birch plywood plate; F_t is the tensile force at failure; f_t is the tensile strength of birch plywood; and t is the plywood thickness. It is evident that the effective width should not be simply assumed as the width of the bonded region, i.e., 110 mm, or the entire crack length, i.e., over 200 mm in Figure 6(c). Besides, the effective width varies at varying load-to-face grain angles. It is worth noting that although the tensile strength of birch plywood decreases roughly 30% when α changes from 5° to 15°, the reduction in the load-bearing capacity of the birch plywood gusset plate in connection is less severe (less than 20%) thanks to the wider w_{eff} at 15°.
The concept of the effective width was first proposed by Whitmore [17] in the last century for the design of the steel gusset plate to mechanically connect other steel members. To define the 'Whitmore effective width' in steel gusset plate, two lines with a spread angle of 30 degrees were drawn from the outer fasteners of the first row to intersect with the line through the bottom row of fasteners. The width between the intersection points is known as the 'Whitmore effective width' [18].
The 'Whitmore effective width' could also be employed in this study for plywood gusset plates in glue connection while the spreading angle should be redefined. See Equation (4) for the derived spreading angle and Figure 9 for the illustration of the adopted 'Whitmore effective width' theory.

$$\theta = \arctan\left(\frac{w_{eff} - w}{2l}\right) = \begin{cases} 7.4° & (\alpha = 5°) \\ 11.3° & (\alpha = 15°) \end{cases} \quad (4)$$

where θ is the spreading angle for birch plywood gusset plate; w is the width of the boned area (110 mm); and l is the length of the bonded area (209 mm).

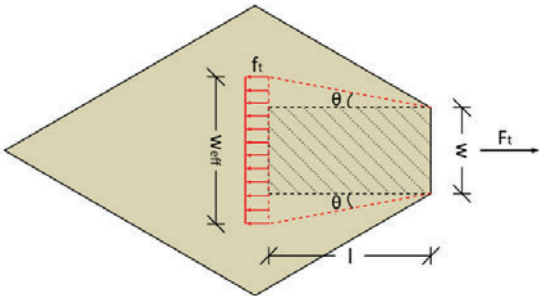

Figure 9: *Illustration of the adopted 'Whitmore effective width' theory.*

As shown in Figure 9, the spreading angle in this classic analytical model starts from the outmost line of the bonded area, resulting in a uniformly distributed tensile stress within the 'Whitmore effective width'.
A modification of the classic analytical model is proposed in the study with the assumption that the tensile force is evenly taken by each part of the bonded area. The bonded area in Figure 10(a) with a width of w and a length of dx could take the tensile force ΔF_t and the tensile stress $\Delta\sigma$ as expressed in Equation (5-7).

https://doi.org/10.52202/069179-0198

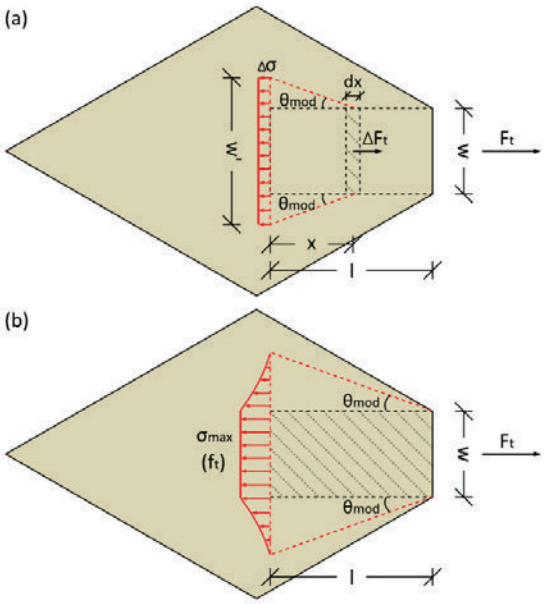

Figure 10: *Illustration of the modified analytical model: (a) the contribution from a calculated bonded region; and (b) the stress distribution.*

$$\Delta F_t = \frac{F_t}{l} dx \tag{5}$$

$$\Delta\sigma = \frac{\Delta F_t}{w' \cdot t} \tag{6}$$

$$w' = w + 2\tan(\theta_{mod}) \cdot x \tag{7}$$

where θ_{mod} is the spreading angle in the modified analytical model; x is the distance of the calculated bonded region to the end of the bonded area; and w' is the effective width of this calculated region. The effective width of the calculated bonded region decreases when it moves from the outmost to the end of the bonded area, leading to a more realistic non-uniform stress distribution. The maximum tensile stress takes place within the width of the bonded area and can be calculated by performing the integral in Equation (8).

$$\sigma_{max} = \int \Delta\sigma = \frac{F_t}{l \cdot t} \int_0^l \frac{dx}{w + 2\tan(\theta_{mod}) \cdot x} \tag{8}$$

By solving Equation (8), σ_{max} is expressed in Equation (9).

$$\sigma_{max} = \frac{F_t(\ln(w + 2\tan(\theta_{mod}) \cdot l) - \ln w)}{2l \cdot t \cdot \tan(\theta_{mod})} \tag{9}$$

Imposing that the failure occurs when the maximum tensile stress reaches the tensile strength of birch plywood:

$$\sigma_{max} = f_t \tag{10}$$

θ_{mod} can be determined (see Equation (11)).

$$\theta_{mod} = \begin{cases} 16.6° & (\alpha = 5°) \\ 25.7° & (\alpha = 15°) \end{cases} \tag{11}$$

4 CONCLUSIONS

In this paper, glulam frames were adhesively connected by means of birch plywood plates and tested monotonically in compression. The face grain of the birch plywood connecting the inclined and horizontal glulam elements was 0°, 5°, and 15° to the horizontal direction in three test series. These plywood gusset plates were designed as the weakest part so as to study their failure mechanism. Nevertheless, some specimens failed in the bonded region with little glulam fiber remaining on the bonded surface. Reasons for the failure in the bonded area have been discussed in the paper; however, more studies regarding the adhesive types and process-related parameters should be conducted in the future to enhance the bonding quality for the formation of a reliable bonded connection between spruce glulam and birch plywood. More than half of the tested specimens showed failure in birch plywood plates as expected. Moreover, a comparison between the adhesively bonded and mechanically connected glulam frames confirms the higher load-bearing capacity and global stiffness of the former one. The main findings with regard to the influence of the birch plywood face grain orientation on the global stiffness and load-bearing capacities are as follows:

Global stiffness: despite the anisotropic elastic properties of the birch plywood plate, the influence of its face grain orientation (0° to 15°) on the global stiffness of the tested frame was limited. The global stiffness was also well predicted by the simplified planar 2D numerical model developed in this paper.

Failure mechanism: for the specimens that failed in birch plywood, tensile failure was observed. With the tensile force of the glulam beams at failure load output from the numerical model and the angle-dependent tensile strength of birch plywood characterized in the previous studies, two analytical models, namely, the classic 'Whitmore' and modified analytical models, were utilized to illustrate the failure mechanism with the concept of the effective width and the spreading angle. It is found that, although the tensile strength of birch plywood at 15° is 30% lower than the one at 5°, the effective width and thus the spreading angle is larger at 15°, leading to the smaller difference in load-bearing capacities, which is beneficial for plywood gusset plates in potential structural applications where they are likely to be subjected to the forces in multiple directions.

The spreading angles derived from these two analytical models were determined from the specific frame structure tested in this study. The magnitude of the spreading angle should be further verified by performing uniaxial tests with a wider range of load-to-face grain angles involved, e.g., from 0 to 45 degrees. Moreover, research questions regarding whether the spreading angle theory is robust for birch plywood with different thicknesses and different bonded areas may also need to be considered in the future.

ACKNOWLEDGEMENT

The authors would like to gratefully acknowledge Vinnova project 2017-02712 "Bärande utomhusträ" within the BioInnovation program as well as the Kamprad

Family Foundation (reference number: 20200013) and from Produktion2030, a strategic innovation program supported by Vinnova [reference number: 2021-03681], Swedish Energy Agency and Formas. China Scholarship Council and Svenskt Trä are thanked for the financial support. Moelven is thanked for supplying the glulam materials. Koskisen is acknowledged for supplying birch plywood panels. Dynea is thanked for supplying the adhesive.

REFERENCES

[1] R. Crocetti. Large-span timber structures. In *Proceedings of the World Congress on Civil, Structural, and Environmental Engineering*, pages 1-23, 2016.

[2] S. Thelandersson, H. J. Larsen. (Eds.). Timber engineering. John Wiley & Sons, 2003.

[3] J. O. Curtis. Design of nailed and glued plywood gussets for lumber rigid frames. *Bulletin (University of Illinois (Urbana-Champaign campus). Agricultural Experiment Station)*, no. 654, 1960.

[4] T. L. Wilkinson. Longtime performance of trussed rafters with different connection systems. US Department of Agriculture, Forest Service, Forest Products Laboratory, 1984.

[5] A. Josefsson, K. Larsson. Ramkonstruktioner av fanerträ, 1991.

[6] T. Wang, Y. Wang, R. Crocetti, and M. Wålinder. Multiple shear plane timber connections with birch plywood and dowel-type fasteners. In *Proceedings of the 17th Annual Meeting of the Northern European Network for Wood Science and Engineering*, pages 131-133, 2021.

[7] Y. Wang, T. Wang, P. Persson, P. Hedlund, R. Crocetti, and M. Wålinder. Birch plywood as gusset plates in glulam frame via mechanical connectors: A combined experimental and numerical study. *J. Build. Eng.*, 105744, 2022.

[8] T. Wang, Y. Wang, R. Crocetti, and M. Wålinder. In-plane mechanical properties of birch plywood. *Constr. Build. Mater.*,340:127852, 2022.

[9] J. Hynynen, P. Niemistö, A. Viherä-Aarnio, A. Brunner, S. Hein, and P. Velling. Silviculture of birch (Betula pendula Roth and Betula pubescens Ehrh.) in northern Europe. *Forestry*, 83(1):103-119, 2010.

[10] BS EN 322: 1993. Wood-based panels – Determination of moisture content. European Committee for Standardization (CEN), 1993.

[11] SS EN 301: 2017. Adhesives, phenolic and aminoplastic, for load-bearing timber structures - Classification and performance requirements. European Committee for Standardization (CEN), 2017.

[12] Z. Chen, D. Tung, and E. Karacabeyli. (Eds.). Modelling Guide for Timber Structures. FPInnovations, 2022.

[13] J. F. Davalos, J. R. Loferski, S. M. Holzer, and V. Yadama. Transverse isotropy modeling of 3-D glulam timber beams. *J. Mater. Civ. Eng.*, 3(2):125-139, 1991.

[14] R. Crocetti, M. Johansson, H. Johnsson, R. Kliger, A. Mårtensson, B. Norlin, A. Pousette, and S. Thelandersson. Design of Timber Structures. Swedish Wood, 2011.

[15] M. Dorn. Investigations on the Serviceability Limit State of Dowel-type Timber Connections [PhD thesis]. Vienna University of Technology, 2012.

[16] H. J. Larsen, J. Munch-Andersen. (Eds.). CIB-W18 Timber Structures - A review of meetings 1-43, 2011.

[17] R. E. Whitmore. Experimental investigation of stresses in gusset plates [Master's Thesis]. University of Tennessee, 1950.

[18] S. J. Chen, C. C. Chang. Experimental study of low yield point steel gusset plate connections. *Thin-Walled Struct.*, 57:62-69, 2012.

https://doi.org/10.52202/069179-0198

World Conference on Timber Engineering Oslo 2023

STRUCTURAL CHARACTERISTICS AND DEFORMATION BEHAVIOUR OF AN ADVANCED CARPENTRY CONNECTION IN TIMBER CONSTRUCTION

Katrin Vögele[1], Moritz Tronnier[2], Yannick Plüss[3], Mike Sieder[4]

ABSTRACT: The following paper addresses the experimental examination of the micro-offset-node, used in an innovative roof structure "ReFlexRoof" developed in the public funded project TimberPlan+ (research consortium led by HTWK Leipzig, Team FLEX). The structural form of the micro-offset-node, called MVK, leads back to a carpentry connection by Friedrich Zollinger. The characteristics of the MVK are described in more detail. In order to represent the load-bearing and deformation behaviour of the roof structure realistic input values for the nodal stiffness in the existing three-dimensional design model are needed. Therefore, laboratory tests on the micro-offset-node are executed at the Institute of Building Construction and Timber Structures (iBHolz, Technische Universität Braunschweig). The experimental methodology as well as observations during the experiments are presented. Based on load-deformation curves, resulting values for the strength and stiffness of the node are calculated. Apart from that, the methodical and manufacturing procedure is examined and discussed.

KEYWORDS: carpentry connections, glued laminated timber, connection stiffness, experimental results

1 INTRODUCTION

Carpenter connections are not part of the static and engineering calculation methods commonly used today. They usually form hyperstatic spatial trusses or frames and are mainly found in historical constructions. Due to the traditional origin of these connections and the associated lack of knowledge about realistic stiffness values of such timber connections, it is difficult for civil engineers to determine the load-bearing capacity and the deformation behaviour of these structures. [1] Today's building codes do not provide sufficient calculation methods to evaluate the connection stiffness and determine the values for numerical or analytical calculations. Therefore, such constructions are calculated on the basis of statically determined simplified models.
However, this approach no longer fits the state of the art. For numerical computational methods and simulations, the nodal stiffness values of these structures are required in order to calculate the internal force distribution. An estimation of the stiffness is not sufficient for hyperstatic structures with multiple nodes. Incorrect and unrealistic assumptions can lead to underestimation of the internal forces and, in the worst case to structural failure.
Regarding the micro-offset-node as an advanced carpentry connection and the ReFlexRoof as a hyperstatic structure, this problem became apparent in the research studies of the TimberPlan+ project.

2 STRUCTURAL DESIGN

The micro-offset-node, described in the following as MVK (German translation "**M**ikro**v**ersatz**k**noten"), is an advanced carpentry connection in the timber roof structure called ReFlexRoof. The structure of the roof can be described as a lamella roof and is shaped as an arch.

2.1 ORIGIN

The first evidence of lamella roofs can be found in the middle of the 16th century. Philibert de l'Orme had cut planks into arch shapes, joined them with wooden nails and wedged them lengthwise. [2] Friedrich Zollinger adopted this construction method in 1921 and formed the planks into a rhombic construction of lamellae instead of a layered connection [3], as shown in Figure 1.

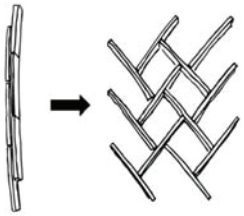

Figure 1: *Adaption of the structure from l'Orme (left) to Zollinger (right) [4]*

This formation of the lamellae generates a reciprocal framework.

[1] Katrin Vögele, iBHolz Technische Universität Braunschweig, German, k.voegele@tu-braunschweig.de
[2] Moritz Tronnier, iBHolz Technische Universität Braunschweig, German, m.tronnier@tu-braunschweig.de
[3] Yannick Plüss, iBHolz Technische Universität Braunschweig, Germany, y.pluess@tu-braunschweig.de
[4] Mike Sieder, iBHolz Technische Universität Braunschweig, Germany, m.sieder@tu-braunschweig.de

https://doi.org/10.52202/069179-0199

Nodes of the Zollinger structure are characterized by a continuous lamella, to which another lamella is butted from both sides. The connection of the node and thus the lamellae is ensured by a bolt that is guided through an oblong shaped hole in the continuous lamella. On the upper side, the lamellae are curved due to the arch shape of the roof construction. On the bottom side the lamellae are straight.
For the completion of the roof boarding planks are attached which are assumed to figure as secondary structure. [3] Zollinger patented this system in 1923. [5]
Although the advantages in the standardization of components formed a fundamental prerequisite for economic efficiency, the weak points of this system became apparent over the years: The ductility of the connection due to the difference in materiality of timber and steel and the arrangement of the bolt generate forces transverse and at an angle to the fibre. This leads to local deformations at the node. In the global structure, these deformations are amplified in association with the redundancy and the creep of timber under external load. All these interactions lead to settling of the structure and thus to change of the internal load distribution. This effect amplifies as the spans become longer. For this reason, the MVK (Figure 2) was developed, which offers the following advantages: [6]

- Precise joinery methods
- Use of kiln-dried timber
- Use of form-fit principle without a bolt

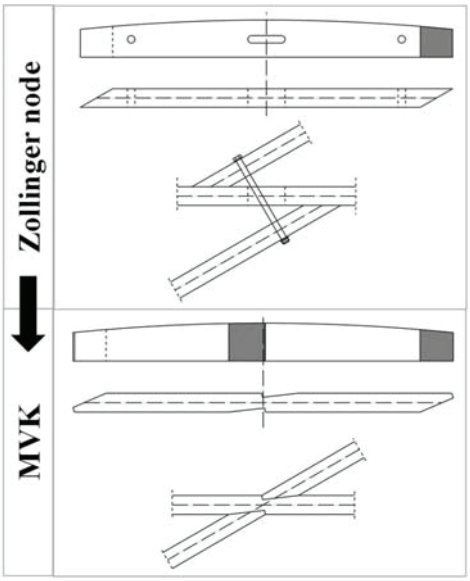

Figure 2: *Illustration of the Zollinger node in comparison to the MVK*

2.2 CURRENT LOCAL AND GLOBAL STRUCTURE

As described, the MVK is an attempt to optimise the traditional Zollinger joint and aims to reduce the creep deformations that can be observed in the construction.
The MVK consists of a step joint with two-sided incision shown in Figure 2. This ensures that the normal forces are transmitted via contact pressure. [6] In contrary to the construction of Zollinger the lamellae are not attached or connected to each other using fasteners. Similar to the original approach is that the lamellae are spanned in a rhombic shape which creates a framework of reciprocal even modules.

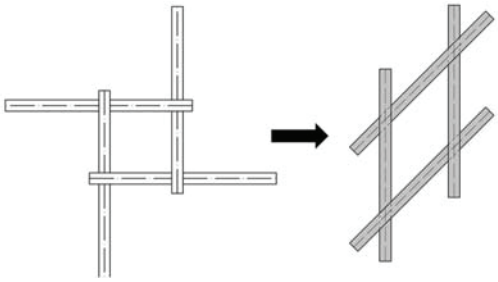

Figure 3: *An example of a reciprocal framework (left) that can be converted into a rhombic shape module (right)*

Several of these reciprocal modules then build an arch shaped roof. The construction is bordered by planks at the gable and by an edge beam the eaves as shown below.

Figure 4: *Construction of the arch shaped roof*

To form the roof structure and to ensure the global load-bearing behaviour, the construction of the lamellae is sheathed with a panel. The connection between the panel and the lamellae is made by staples.
In the global view, the structure forms a highly hyperstatic system due to the great number of reciprocal modules. The consequence is, that the stiffness values of the nodes are highly important for the structural design.
In addition, the construction of the arch shaped roof is segmented. Several MVK-connected lamellae are bonded via a standardized panel element in the factory and are transported to the construction site. At the site the elements are combined to form the final structure.
During building of the prototype construction in the research project, it is discovered that the segments could not always be joined properly. This results in gaps between the lamellae at the node points (Figure 5, right).

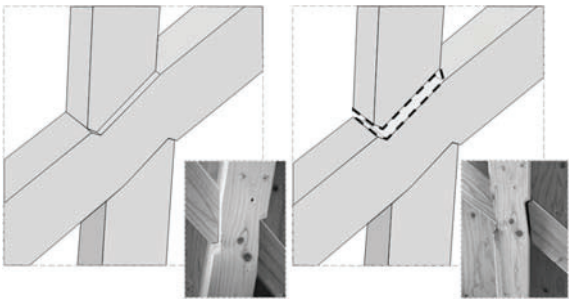

Figure 5: *Local node properties in the quasi-perfect (left) state and in the pre-deformed state (right)*

https://doi.org/10.52202/069179-0199

On one hand, these occur due to material and manufacturing inaccuracies, which are significantly more demanding to implement on the construction site because of the spatial geometry and assembly. On the other hand, the pre-curved planking causes recoil forces, which lead to pre-deformations.
In the research project these aspects have to be examined more closely.

3 MATERIAL AND METHODS

Although the basic local characteristics are approximately known from tests on preliminary models of the MVK [6], the MVK itself and its local load-bearing and deformation behaviour has not yet been extensively examined. Particularly the stiffness of the node has to be evaluated in more detail.

3.1 EXPERIMENTAL INVESTIGATION

With the aim to provide stiffness properties for the use in a computation design model, experimental investigations are carried out at iBHolz.

3.1.1 SETUP

All test specimens are made of two half-lamellae, which are butted on a continuous lamella. The loads are restricted to a compressive force acting axially on the upper lamella. This based on the assumption of an arched roof structure, which follows the line of thrust in the most optimal form. The geometric properties are selected based on the prototype. In order to contain the estimated load within the maximal capacity of the testing machine, the geometric dimensions of the prototype are scaled to the following dimensions:

$$h_S = 14\ cm \qquad t_v = 1.33\ cm$$
$$h_D = 12\ cm \qquad \gamma = 49.5°$$
$$b_D = b_S = 8\ cm$$

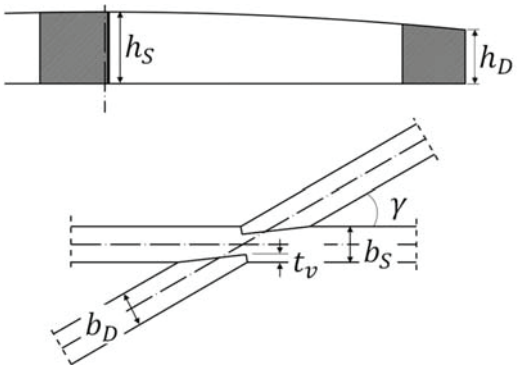

Figure 6: *Definition of the geometric variables at the lamella (top) and at the node (bottom)*

All lamellae are made of GL24h graded glulam timber. The average density of the timber used in the specimens is about 450 kg/m³.
The test concept consists of three test series with five test specimens each. The test series differs as shown in Table 1:

Table 1: *Description and over-view of the test series*

Series	Panel	Screws	Gap
A	x	-	-
B	x	-	x
C	-	x	-
***C4 / C5**	-	-	-

*the screws were removed after an applied load of 5 kN

The panel has a stapled connection (1.53x50 mm) to the lamellae. The spacing of the staples is 120 mm. 12 mm pine multiplex plywood is used as panel. The connection is ensured by three (6x120 mm) screws per half lamella. These are inserted as suggested in the patent for the MVK. In series B, a gap of 1 cm to the front-notch surface and 1 cm to the bottom-notch surface is created as shown in Figure 5 (on the right).

The tests are conducted on a walter+bai LFM 125 testing machine with a maximum capacity of 125 kN. The machine force as well as the displacement of the top pressure plate are recorded. The specimens are tested between two pressure plates which are connected to the testing machine via hinges. This assures that no bending moments are introduced by the compression plates. Before the load is applied the specimens have to be held in place by a supporting frame. The test frame is made of aluminium as shown below.

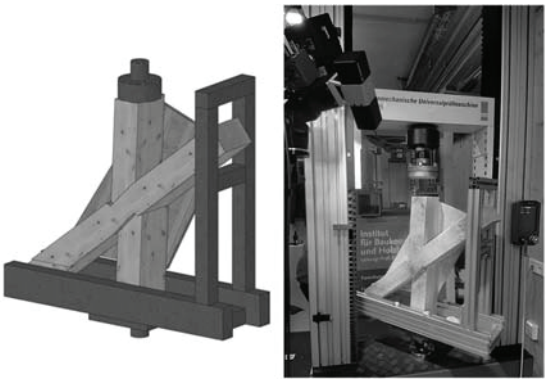

Figure 7: *Model of the test setup (left) and realization (right)*

It is ensured that no forces are transferred from the specimens to the testing frame during the experiment. The tests are accompanied by a photogrammetric measuring system, which takes 200 to 800 pictures per specimen and can be recalled at any time. In addition to the data from the testing machine this system allows further investigation of the load bearing behaviour of the node. The strain at the surface of the timber members can be measured and visualized by the software. The system replaces otherwise used strain gauges. In order to track the deformations, the specimens are painted white with a random black pattern to create better contrast for the measurements.

https://doi.org/10.52202/069179-0199

3.1.2 EXECUTION

The specimens are conditioned at 20°C and at a relative humidity of 65 % prior to the experiments. The average moisture content during the experiments is 11.5 %.
The tests are performed along the lines of DIN 26891. A preload is applied to clamp the specimen between the pressure plates before the hinges are untightened and the rotation of the pressure plates is made possible. A stress-controlled hysteresis cycle is performed between 40 % and 10 % of the expected maximum load. This eliminates any slip and ensures good contact between the lamellae. During the second cycle, the load is increased up to 60 % of the estimated load before switching to deformation control at 0.05 mm/s.
The experiments are terminated when the specimen fails and the load decreases rapidly or when the free movement of the specimen is limited by the testing frame. This happens at different piston displacement values for any specimen and is therefore monitored manually. In most cases the latter condition occurs first, due to the highly ductile behavior of the connection.

3.2 ANALYSIS

Currently, the computational model consists of a combination of beam and shell elements designed as a spatial frame model. The beam elements represent the lamellae and the panels are implemented as shell elements. For simple joints it is sufficient to consider the connection either as rigid or hinged. For more complex timber structures, the nodal stiffness needs to be characterized to provide a realistic internal force distribution.
The experimental investigation is designed to obtain stiffness values in axial direction of the lamella. Based on the load-deformation curves, an axial node stiffness C_x for the beam element (illustrated in Figure 8) can be determined.

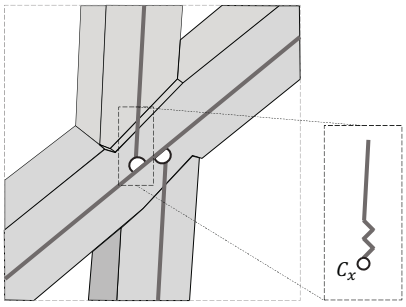

Figure 8: *Extraction of the lamella into a beam element with the node stiffness* $\boldsymbol{C_x}$ *at the joint to the continuous lamella*

Due to the pre-deformed conditions on the node, the specification of the node stiffness must include not only the stiffness in the quasi-perfect state but also the pre-deformed state (Figure 5). These two states represent the two static limit values for the stiffness of the structure.

Therefore, two methods are adopted to evaluate the characteristic mean stiffness C_x in the limit states:

- Heimeshoff and Köhler method (= HaK) [8]
- DIN EN 26891:1991 (= DIN) [9]

For the evaluation of the stiffness, the longitudinal deformation in direction of fibre of the lamella is neglected. The reason for choosing this method is that the longitudinal deformation compared to the total measured displacement does not exceed 2.5 %. The determination of the node stiffness is then simplified to half of the measured displacement regardless for both methods. In addition, for each test series only the measured values of the deformation from the second ascending branch of the hysteresis is taken into account. This excludes the initial slip. In test series B, which has significantly more slip due to the gap, the mean value of the measured slip of the setup from A and C ($u_{slip,set}$) is subtracted in order to be able to represent the effect of the gap at maximum load.

The following description summarizes the approach for the HaK and DIN method. Each load-deformation curve is analysed using both methods.

HaK method (compare to Figure 9):

1) Determination of the 95% fractile of the strengths for $f_{c,\alpha}$ and f_v according to [11] and [12]
2) Estimation of the expected loads $R_{dim,i}$ (equations based on the EC5/NA verifications for carpenter connections [13], [14])

$$R_{dim,compression} = t_v \cdot h_D \cdot \frac{f_{c,\alpha}}{\cos^2 \frac{\gamma}{2}} \quad (1)$$

$$R_{dim,shear} = 8 \cdot t_v \cdot k_{cr} \cdot h_S \cdot \frac{f_v}{\cos \gamma} \quad (2)$$

3) Formation of the mean value $R_{dim,mean}$ from the two proofs (shear force, contact pressure) of EC5/NA
4) Determination of the deformation $u_{R,dim}$ at the load $R_{dim,mean}$
5) Composition of the node stiffness C_x

$$C_x = \frac{R_{dim,mean}}{u_{R,dim}} \quad (3)$$

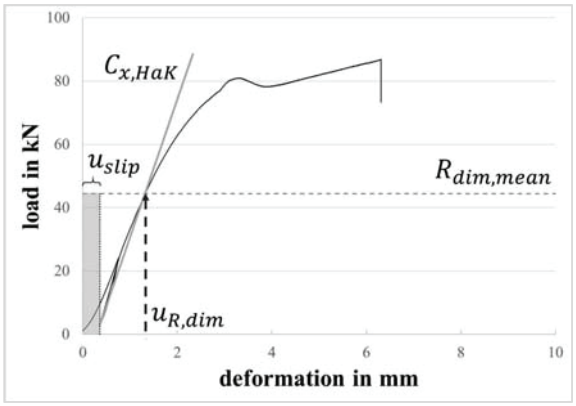

Figure 9: *Illustration of the approach based on the HaK method*

https://doi.org/10.52202/069179-0199

DIN method (compare to Figure 10):

1) Definition of the assumed elastic limit $R_{max,el}$
2) Determination of deformations u based on 0.4 $R_{max,el}$ and 0.1 $R_{max,el}$
3) Composition of the node stiffness C_x

$$C_x = \frac{0.4\ R_{max,el} - 0.1\ R_{max,el}}{u_{0.4\ R_{max,el}} - u_{0.1\ R_{max,el}}} \quad (4)$$

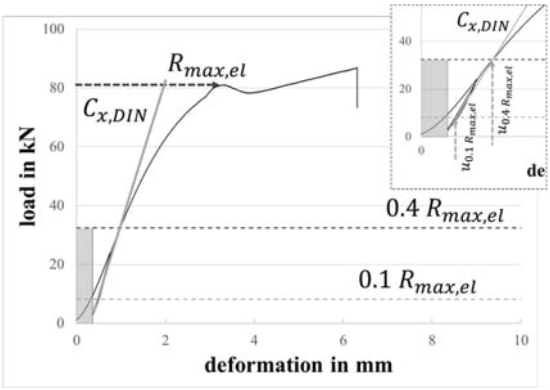

Figure 10: *Illustration of the approach based on the DIN method*

For the evaluation of test series B, a few minor adjustments are made. For the HaK method, the load-bearing capacity of the staple connection is considered to determine $R_{dim,mean}$. The determination of the initial deformation $u_{R,dim}$, the $u_{slip,set}$ is subtracted.

In the DIN method, a slightly different procedure is chosen in step 3. In equation (4), the stiffness is calculated with the consideration of u_{gap} following equation (5) and Figure 11:

$$C_x = \frac{0.4\ R_{max,el} - 0.1\ R_{max,el}}{(u_{0.4\ R_{max,el}} - u_{0.1\ R_{max,el}}) + \frac{3}{4} \cdot u_{gap}} \quad (5)$$

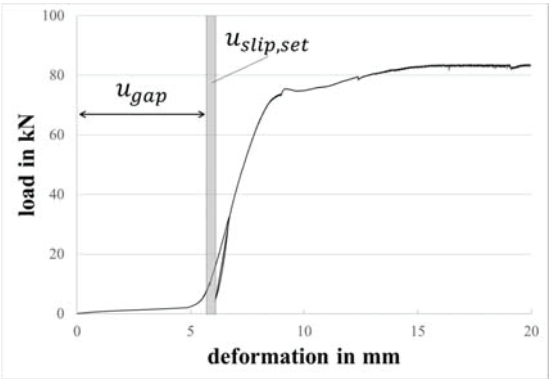

Figure 11: *Representation for the different deformations from the gap and the slip of the setup on one of the test specimen B*

The calculation of the characteristic values of the load-bearing capacity and stiffness is performed according to DIN EN 14358 Section 3 [14]. For the load-bearing capacity, a normal distribution is assumed according to $R_{c,90}$ in [11]. For the stiffness, the characterized mean value is calculated using the given equation 14 in [14].

4 RESULTS

The obtained node stiffness can be used in the numerical model to perform a sensitivity analysis for the evaluation of the internal force distribution. The following results are averages based on an evaluation of all test specimen.

4.1 ELASTIC LOAD-BEARING CAPACITY

For the value of the load-bearing capacity, the first maximum point of the load-deformation is used to determine the elastic limit $R_{max,el}$. To characterize this value to a 5%-quantile, [14] states a factor for a sample size of 5 specimens with

$$k_s(5) = 2.46$$

for the standard deviation.

The calculated standard deviation is applied to the mean values leading to the following characteristic load-bearing capacities $F_{k,el}$:

Table 2: *Average and characteristic values for the load-bearing capacity in the elastic limit state with sample size 5*

Test Series	$R_{max,el,mean}$ [kN]	s_y [-]	$F_{k,el}$ [kN]
A	73.3	7.045	56.0
B	68.1	6.101	53.1
C	66.1	8.384	45.5

It can be seen that the panel has an influence on the load-bearing properties of the node. Thus, A and B show up to 15% to 20% greater values than C at the characteristic value. The screws (in series C) that hold the step joint in position have only little influence on the elastic load-bearing capacity. By excluding C4 and C5 (MVK under preload without screws) from the evaluation of test series C, the values both of the mean and characteristic value differ by less than 4 %. However, it can be clearly noticed that the tests in C have a lower load-bearing capacity than A and B. It is assumed that the panel has a load-bearing effect, which is missing in test series C. In addition to that, the panel prevents the middle lamella from rotating and therefore loosing of form-fit.

The nodes in the overall structure are a combination of the cases A through C, A and B are randomly distributed whereas case C only occurs in planned matter. Therefore, the evaluation can be conducted over a larger sample size. The factor for the sample size decreases with the number of specimens. For the node states A, B the factor is

$$k_s(10) = 2.10$$

and for the node states A, B, C the factor is reduced to

$$k_s(15) = 1.99.$$

This allows to calculate the characteristic load-bearing capacity $F_{k,el}$ according to the Table 3.

Table 3: *Average and characteristic values for the load-bearing capacity in the elastic limit state with sample size 10 or 15*

Test	$R_{max,el,mean}$	s_y	$F_{k,el}$
Series	**[kN]**	**[-]**	**[kN]**
A, B, C	69.2	8.264	52.7
A, B	70.7	6.927	56.5

The difference in the load-bearing capacity of the node is about 7% larger for a composed case of A and B in comparison to the composed case A, B and C.
In order to compare the values with the state of art, the load-bearing capacity is determined according to the equations (1) and (2) which are derived from EC5 NDP [10]. The input strength properties are based on the 5%-fractile and on the 95%-fractile on EC5 [15]. The strength properties from NDP [10] are not used, because k_{cr} which reduces the width in order to limit the shear strength to an admissible value of 2.5 N/mm². $F_{dim,shear}$ would therefore be equal on the characteristic and on the 95 %-fractile level.
The evaluated values are shown in the following table.

Table 4: *5 %-fractile and 95 %-fractile for the load-bearing capacity according to [10] and [15]*

	$F_{5\%,DIN}$	$F_{95\%,DIN}$
	[kN]	**[kN]**
$F_{dim,compression}$	26.4	42.4
$F_{dim,shear}$	53.8	120.9

The characteristic result values of the experiments are close to the 5 %-fractile of $F_{dim,shear}$ as well as in the range of the 95 %-fractile of $F_{dim,compression}$. This shows that higher compressive forces can be transmitted via the step joint of the MVK than assumed by the design model in [10].

4.2 NODE STIFFNESS

Based on the presented methods in section 3.2 the following results for the axial stiffness C_x can be made as shown in the table below. For the analysis another evaluation is performed in test series B. It is listed as B' and shows the stiffness that results after the closure of the gap. The pre-deformation up to the point of contact in the step-joint is on average 5.27 mm based on measurements within the load deformation curve.

Table 5: *Average values for the node stiffness in the elastic limit state with sample size 5*

Test	$C_{x,DIN}$	$C_{x,HaK}$	u_{slip}
Series	**[N/mm]**	**[N/mm]**	**[mm]**
A	53453	49027	0.39
B	4682	5718	0.40*
B'	45608	53580	0.40*
C	48977	45972	0.41

*$u_{slip} = u_{slip,set}$; mean value out of u_{slip} from A and C

Comparing the two methods in each test series, differences in percentages can be observed: For A and C the differences are rather small and less than 10 %. For test series B, the percentage value increases up to 18 %. In case of the additional study B' the deviations are up to 15 %. A comparison of all lines (with exception of B) show, that the stiffnesses for a quasi-perfect node range from 45 kN/mm up to 53 kN/mm.
Considering Table 6, showing the composed test series, it is noticeable that the methods are converging and deviating by a maximum of 3,5 %.

Table 6: *Average values for the node stiffness in the elastic limit state with sample size 10 or 15*

Test	$C_{x,DIN}$	$C_{x,HaK}$
Series	**[N/mm]**	**[N/mm]**
A, B', C	49346	49526
A, B'	49531	51304

4.3 GENERAL OBSERVATIONS

Most of the deformation can be observed at the front-notch and bottom-notch surface (Figure 12) of the MVK.

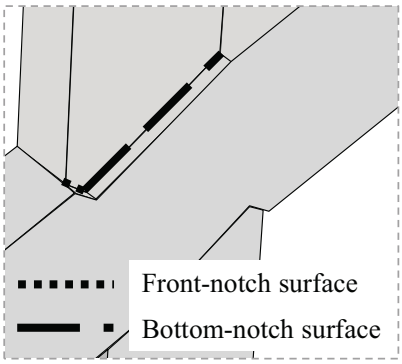

Figure 12: *Illustration of the position of the two surfaces*

At the beginning of the load application, the deformation shifts from the top lamella towards the front-notch surface. With further displacement, the bottom-notch surface is also compressed. As a result, a gap opens at the bottom-notch surface and remains as plastic deformation (Figure 13). Furthermore, it can be identified that the fibres of the abutting lamella protrude beyond the front surface. In addition, the abutting lamella rotates clockwise. Due to the compression on the front, the lamella tends to lose its optimal position. Thus, it is pushed out of the front-notch surface. This leads to an eccentricity of the resulting force and the lamella rotates. This rotation occurs especially in the test series B. Presumably, this is due to the lack of rotational support of the staple connection beyond its elastic limit. The displacement between the panel and the lamellae remains a plastic deformation after unloading.

https://doi.org/10.52202/069179-0199

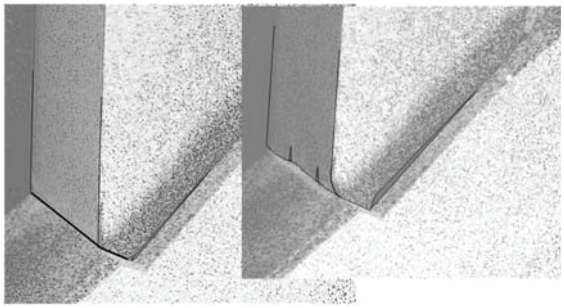

Figure 13:*Illustration of the deformations during the test phase (left) and after the test phase (right), which shows the permanent plastic deformation*

Furthermore, in test series B it is observed that the gap does not always close optimally. This means that a force- and form-fit connection cannot be guaranteed. These effects that occur at the quasi-perfect MVK are intensified in test series B. The tests in series C do not show a significantly different behaviour. In test C4 and C5 the screws are removed after applying a preload. This results in a complete failure by the abutting lamella popping out of the connection at the front-notch.
In general, the failure state of the MVK is determined by the deformations at the front-notch. The stresses in the bottom-notch surface are not decisive for the MVK.

4.4 APPROACH FOR DESIGN

For the determination of internal forces with FE-models, a limit value consideration for the stiffness for specific node states should be attempted. Therefore, three methods can be generated:

1) Design in the ultimate limit state
Historical research [16] shows that it can be assumed that the gaps are closing over time.
As long as it is ensured that the staples and quasi-perfect MVK provide enough plastic deformations capacity to close gaps, the stiffness for determining forces in the lamellae can be considered as the stiffness determined in series A and B':

$$C_x = 49000\ N/mm$$

2) Robustness estimation
In case of insufficient plastic deformation capacity of the quasi-perfect MVKs in an area next to a concentration of pre-deformed MVKs the risk of brittle failure must be addressed. An estimation for the robustness allows to find areas in the structure with a higher risk of failure due to load redistribution from softer node points. Therefore, two stiffness values have to be defined for the numerical model. The lower limit should be applied to nodes within the structure with open gaps.

- **Upper limit for quasi-perfect nodes** (test series A):
$$C_x = 53000\ N/mm$$
- **Lower limit for pre-deformed nodes** (test series B):
$$C_x = 4600\ N/mm$$

If it is considered to use screws to ensure the form-fit of the MVK, variant C can be adapted to the methods shown above.

5 DISCUSSION

Since there is no agreement in the literature ([8], [16], [17], [18], [19]) on how to evaluate the stiffness on carpenter-type connections in modern constructions, the following provides some views on the methodology, results and optimisation.

5.1 ANALYSIS METHOD

For the analysis up to the elastic limit state the linear elastic material law is observed and applied for further calculations.

Hysteresis effect is left out of the evaluation, since the MVK with gap is used to examine the effects of slip in the connection. In addition, the quasi-perfect MVK is manufactured with an accurate fit. For the investigation of the effects of repeated loads applied after closing of the gaps, cyclic tests shall be carried out.

In test series B (pre-deformed node), the nodal stiffness is very low if the closure of the gap is included in the determination of the linear elastic section. The method as proposed by HaK assumes this. The method proposed by DIN excludes this effect by default, as the stiffness value for the linear-elastic section is determined between 10 % and 40 % of the maximum load. The HaK method is therefore modified in B', and the DIN method in B in order to compare the stiffness values obtained in both methods.

If the stiffness is set as a gradient in comparison to the load-deformation curve, two areas between load-deformation curve and gradient are created (Figure 14): In the first one, the load-deformation curve is lower than the gradient. This leads to an overestimation of the internal load in the connected members and the node. In the second area there is an underestimation, because the gap of the MVK is closed. For the ultimate limit state, the overestimation of the stiffness is on the safe side, whereas an underestimation of the stiffness is on the unsafe side. In the serviceability limit state, this issue is inversed. However, a realistic description of the deformation cannot be depicted. A bilinear curve considering the slip and the closed MVK would be more suitable. It is assumed that this increases the computational effort for complex models beyond a reasonable level.

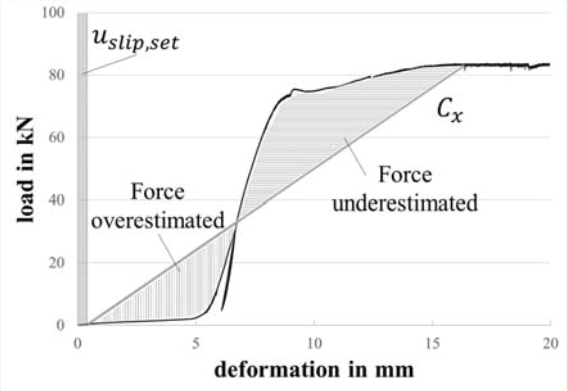

Figure 14: *Gradient of C_x from test series B and one load-deformation curve of a specimen of test series B*

The stiffness values are compared on the mean level, since no other regulations are specified for this purpose. [11]
Properties that could be applied from [11] are the distribution functions for the load-bearing capacity $R_{c,0}$ and $R_{c,90}$. However, these distribution functions differ in their nature. Thus, $R_{c,0}$ is defined as lognormally and $R_{c,90}$ as normally distributed. In order to be able to give a statement about this, an increase in the number of samples is necessary. Current evaluations show an inclination to the lognormal distributed function. This assumption has not yet been statistically tested.

5.2 VERIFICATION OF THE LOAD-BEARING BEHAVIOUR

The elastic results $R_{max,el,mean}$ are in the range of the results published in [8]. Due to the fact that the failure of the MVK is generated by the deformation of the front-notch, the values for the ultimate limit state must be defined at a set deformation limit. This may not represent the maximum elastic limit $R_{max,el,mean}$, which is given in section 4.1. It can be expected that the characteristic values will then approach the state of art for compression $F_{dim,compression}$.

Due to the experimental setup, only few results could be archived at loads above the elastic limit. Most of the tests had to be aborted because the specimen touched the testing frame or the loadcell was tilted. Therefore, only little reliable information about the plastic behavior was gained and no results can be presented.

5.3 VERIFICATION OF THE NODE STIFFNESS

The assumptions in the literature [16] for the stiffness of step joints, mainly rely on historical studies.

Different types of models of the displacement springs are used. In [17] the stiffness is given in two directions: parallel and perpendicular to the fibre – shown below for the MVK at the continuous lamella:

$$C_{\parallel} \approx C_{\perp} \approx 1 \cdot 10^5\ N/mm$$

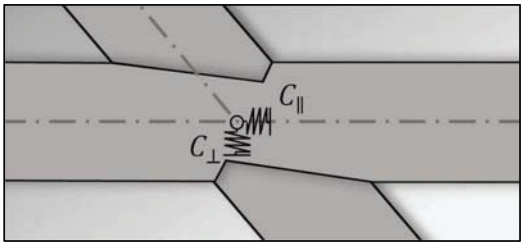

Figure 15: *Arrangement of the deformation springs in adaptation to the MVK*

This value significantly exceeds the resulting values for the MVK obtained in the current study. Another source [18] describes that the step joint can primarily transmit normal forces. This means that an elastic spring should be applied in the direction of the abutting lamella [19]. As a result, the node is designed to be hinged.

Forces perpendicular to the lamella only have a minor influence on the global load transfer. This allows for a rigid modelling regarding the shear forces.
In the mentioned literature[18], a value of the following stiffness has been assumed:

$$C_x \approx 45\ kN/mm$$

This stiffness results from a deformation of 15 mm at the elastic maximum compressive force in the direction of the abutting lamella.
This assumption fits to the result values of the tests.
In [8], another formulation for the stiffness of a step joint, is given by the following equation:

$$C_x[kN/mm] = (45.2 - 42.1 \cdot sin^2\gamma) \cdot \frac{b}{12} \cdot 1 + \frac{t_v - 2.34}{2.34} \cdot 0.1 \quad (6)$$

where b and t_v have the dimension cm

For the dimensions of the tested MVK, the resulting value is:

$$C_x \approx 20\ kN/mm$$

This value is below the load-bearing capacity of the node stiffness of the MVK, which is approximately 50 kN/mm. One possible explanation for the different results is the fact that the wood anisotropy causes very significant scattering. Especially the values from the historical investigation can be affected, because the regulation for sorting, wood moisture and assembly were not strictly specified at that time. Furthermore, different methods of measuring can lead to varying values. Regardless of these aspects, it is also assumed that the connection is strongly influenced by the stiffness perpendicular to the grain which varies considerably. [20] Therefore, there are no provisions for the distribution functions.

6 CONCLUSIONS

During experiments at the TU Braunschweig the load bearing behaviour and capacity as well as the stiffness of the MVK was evaluated. If a load is applied, deformations are primarily observed at the front-notch and bottom-notch surfaces of the MVK. Therefore, the load

https://doi.org/10.52202/069179-0199

deformation curve shows an almost linear elastic area followed by a large plastic area. Multiple test series allowed for the evaluation of the MVK in a pre-deformed and a quasi-perfect state. It was observed that a gap between the lamellae decreases the stiffness significantly while also reducing the load carrying capacity. The difference between the stiffnesses of these pre-deformed nodes and quasi-perfect nodes has to be considered in design.

The determined stiffness values can serve as the basis for a design concept that takes the stiffness distribution into account when determining the internal forces. In the lack of precise knowledge or predominant scattering effects, conservative approaches are usually adopted. In the case of internal force distributions, this does not mean to "lower" the stiffness values, as these lead to an underestimation of the internal forces. Therefore, a method shall be developed, which allows for a safe estimation of internal forces in ULS. Regarding the SLS on the other hand, the slip occurring in some connections can have a major influence on the deformation behaviour and needs to be considered. Further investigations are planned to be conducted on a prototype building located in a testing facility in Leipzig.

One goal in the development of the MVK was to improve the long-term behaviour compared to the Zollinger system. This aspect needs further investigation. Especially considering the load redistribution after closing of the gaps observed in the MVK in proximity to segment joints.

Due to the limitations of the testing equipment, notably the maximum movement during which the specimen could freely deform, no systematic valuation of the plastic deformation capacity could be made. However, qualitatively big plastic deformations can be observed. In order to exploit the full potential of the MVK, the plastic deformation capacity should be taken into consideration and included in the determination of C_u.

The curvature of the structure and therefore the needed bending of the board results in recoil forces that must be absorbed by the staples. However, it can be assumed that these forces decrease over time, so does the resistance of the stapled connection. This needs further investigation.

ACKNOWLEDGEMENT

These investigations were only possible due to project funding from Fachagentur Nachwachsende Rohstoffe e. V. (FNR, project no. 2220HV003C, funding period 2020-2023). A great thank you is given to the FLEX Team of the HTWK Leipzig as well as to the company STRAB GmbH and J. Bengel for the support in the organization, the setting and the delivery of the test specimens.

REFERENCES

[1] Wallner B. et al.: Holz-Holz-Verbindungen. Institut für Holzbau und Holztechnologie Technische Universität Graz. holz.bau forschungs gmbh, 2014.

[2] Erler K.: Kuppeln und Bogendächer aus Holz. Von arabischen Kuppeln bis zum Zollinger-Dach. Fraunhofer IRB Verlag Stuttgart, 2013.

[3] Tutsch J. F.: Weitgespannte Lamellendächer der frühen Moderne. Konstruktionsgeschichte, Geometrie und Tragverhalten. Technische Universität München, 2020.

[4] Zimmermann F., Bairstow C.: Das Dach der Zukunft. Zollinger Lamellendächer der 20er Jahre. Konstruktion, Statik, Ästhetik, Verbreitung, Nachfolge, Beispiele in Bayern. Fachhochschule München, 2003.

[5] Zollinger F.: Raumabschließende, ebene oder gekrümmte Bauteile. Patent Nr. 387469.

[6] Stahr A. et al.: Der Mikroversatzknoten – eine innovative Holzverbindung. *bmH bauen mit Holz,* 3.2019:22-29, 2019.

[7] Stahr A. et al.: Brettrippendächer in elementierter Bauweise. *bmH bauen mit Holz,* 7-8.2019:20-27, 2019.

[8] Heimeshoff B., Köhler N.: Untersuchung über das Tragverhalten von zimmermannsmäßigen Holzverbindungen. Im Auftrag der Entwicklungsgemeinschaft Holzbau (EGH) in der Deutschen Gesellschaft für Holzforschung e. V. (DGfH). Lehrstuhl für Baukonstruktion und Holzbau. Technische Universität München, 1989.

[9] *Timber structures; joints made with mechanical fasteners; General principles for the determination of strength and deformation characteristics*. DIN EN 26891:1991. CEN, July 1991.

[10] *National Annex – Nationally determined parameters – Eurocode 5: Design of timber structures – Part 1-1: General – Common rules and rules for buildings*. DIN EN 1995-1-1/NA. CEN, August 2013.

[11] *JSCC probabilistic model code Part 3: Resistance models.* Joint Committee on Structural Safety. August, 2006.

[12] Loebjinski M.: Bewertung der Tragfähigkeit von Holzkonstruktionen beim Bauen im Bestand – Ein Beitrag zur substanzschonenden Erhaltung von bestehenden Gebäuden. Lehrstuhl für Stahl- und Holzbau. Brandenburgische Technische Universität Cottbus – Senftenberg, July 2021.

[13] Colling F.: Holzbau Grundlagen und Bemessung nach EC 5. Springer-Verlag GmbH Wiesbaden, 2021.

[14] *Timber structures – Calculation and verification of characteristic values.* DIN EN 14358:2016. CEN, November 2016.

[15] *Eurocode 5: Design of timber structures – Part 1-1: General – Common rules and rules for buildings.* DIN EN 1995-1-1:2004. CEN, December 2010.

[16] Görlacher R., Falk V. C., Eckert H.: Historische Holztragwerke – Untersuchen, Berechnen und Instandsetzen. In Wenzel F., Kleinmanns J., editor, *Sonderforschungsbereich 315 „Erhalten historisch bedeutsamer Bauwerke", Karlsruhe. Jahrbuch 1996,* pages 219-245. Ernst & Sohn, Berlin, Germany, 1999.

[17] Blaß H. J., Falk V. C., Görlacher R.: Statische Modellierung der Nachgiebigkeiten historischer

Holzverbindungen. In Wenzel F., Kleinmanns J., editor, *Sonderforschungsbereich 315 „Erhalten historisch bedeutsamer Bauwerke“, Karlsruhe. Jahrbuch 1996,* pages 219-245. Ernst & Sohn, Berlin, Germany, 1999.

[18] Holzer S. M.: Statische Beurteilung historischer Tragwerke Band 2 Holzkonstruktionen. Ernst & Sohn Verlag, Berlin, 2016.

[19] Palma P., Cruz H.: Mechanical behaviour of traditional timber carpentry joints in service conditions – results of monotonic tests. In: From material to structure: Mechanical behaviour of the timber structures, Online Proceedings, 14.ICOMOS IWC Kolloquium, 2007.

[20] Kollmann F.: Technologie des Holzes und der Holzwerkstoffe Erster Band Anatomie und Pathologie, Chemie, Physik, Elastizität und Festigkeit. Springer-Verlag Berlin Heidelberg GmbH, 1951.

https://doi.org/10.52202/069179-0199

World Conference on Timber Engineering Oslo 2023

REPAIR CONNECTION WITH WOODEN WEDGED DOWELS: AXIAL TENSILE AND SHEAR VERIFICATIONS.

Elena Perria[1], Mike Sieder[2], Svenja Siegert[3], Cordula Reulecke[4]

ABSTRACT:. The present paper describes the final results of the research project by the title "Repair connection with wooden wedged dowels. New and alternative repair method that meets the demands of Monument Protection of built substance's gentle care and material fairness". The project aims to develop guidelines for static-constructive use of wood-wood (carpentry) repair connections with wooden wedged dowels as mechanical fasteners. In this paper the boundary conditions and the axial tensile and shear verifications are presented.

KEYWORDS: carpentry connections, mechanical fasteners, wooden wedged dowels, axial tensile verification, shear verification

1 INTRODUCTION

In case of repair or replacement of damaged cross sections in historical timber buildings, metal fasteners like screws and bolts are very often used, especially if the fasteners have to be designed for planned shear or tensile stress, or a clamping effect in the wood-wood connection is required. Another common solution is bonding of steel or plastic rods that realize the connection with the existing structural members by means of synthetic resin grouting, glue, etc. e.g. the so-called Beta-system [1], among others. However, these repair methods and techniques are not to be favored from the point of view of monument preservation [2, 3]. Material conformity and appropriate, durable, repair methods according to the ICOMOS principles [2, 3] play a crescent role as a requirement in the future. In the Charter of Mexico [4] is stated that (a) *traditional wood-wood connections as repair connections are prioritized, while globally recognized as effective, and part of global competences in heritage conservation*. (b) *Non-material conforming techniques have not proven themselves in practice, and their long-term effects on historic wood structures are not sufficiently known; therefore, they are not to be favorized*. This latter statement (b) was mitigated in the 1999´s *Principles for the conservation of wooden built heritage* [5], presented as revision of the Charter of Mexico [4]. Nevertheless, long-term damages can occur when non-conform repair techniques are used [1, 6–8]. The most common damages are chemical effects (e.g. corrosion) on metal fasteners that transfer the oxidation on wood [6], and water condensation in the contact area between plastic or steel fasteners with the cross section, that promotes rot in wood [8]. Comprehensive challenges in the preservation of monuments are increasingly appearing because of improperly carried out renovations in the past decades. This represents a considerable economic factor that greatly increases the expenses for the care and preservation of our architectural heritage [6].

For all these reasons, since two decades, the monument preservation office in southern Lower Saxony, Germany have been made many attempts to reduce the use of metal fasteners/ bonding rods in the repair of wooden structures, and to foster wood-wood connections as repair connections. On the other side, structural engineers are oft unable - due to the lack of calculation basis - to provide a verification for many traditional wood-wood connections; therefore, they are oft not realized.

The aim the research presented in this paper is the development of some necessary engineering tools to perform the verification of carpentry repair connections with wooden wedged dowels as mechanical fasteners (Figure 4) under axial tensile and shear load.

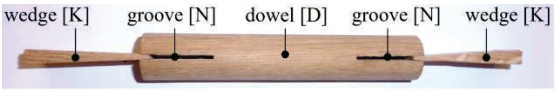

Figure 1: *Components of a wooden wedged dowel (WWD)*

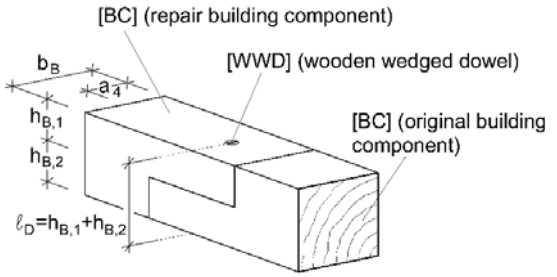

Figure 2: *Illustration of the repair connection with wooden wedged dowel (example of use in a single-shear connection)*

[1] Elena Perria, iBHolz Technische Universität Braunschweig, Germany, e.perria@tu-braunschweig.de
[2] Mike Sieder, iBHolz Technische Universität Braunschweig, Germany, m.sieder@tu-braunschweig.de
[3] Svenja Siegert, IGP Gockel PartGmbB - Ingenieure und Architektin, Germany, siegert.svenja@gockel-ingenieure.de
[4] Cordula Reulecke, Niedersächsisches Landesamt für Denkmalpflege, Regionalreferat Braunschweig, Germany, Cordula.Reulecke@nld.niedersachsen.de

https://doi.org/10.52202/069179-0200

2 METHODOLOGY

In the performed research project [9], the hypothesis about the use of the wooden wedged dowels in the load cases shear and axial tensile load was pursued experimentally, numerically and analytically. With reference to existing theories and verification methods on wooden fasteners [10–14], systematic first-approach tests TV1 [15] were developed. The aim was to define geometric-constructive parameters like crack formation, edge distances and penetration depth. In a second step, the investigated geometric-constructive parameters were classified according to their influence on the mechanical behaviour and on load-carrying capacity, in order to define the geometric-constructive framework for a static verification of the repair connection under axial tensile and shear loading. The firstly assumed hypotheses about the geometric-constructive parameters of the wooden wedged dowels [15] were adapted to the new findings and boundary conditions were defined (tests TV2 in [9]). The results generated so far were confirmed numerically, basing on the finite element method, and experimentally. Carpentry connections with wooden wedged dowels were tested under axial tensile (tests V1 [9]) and double shear loading (tests SV1 [9]), and the characteristic values of the load-bearing capacity were further used for the development of following verifications.

3 GEOMETRY

In order to obtain the expected results in terms of characteristic values of strength and remain in the average of the tested failure modes, general manufacturing rules and geometry features are defined. In the following Table 1, Figure 3 are explained the geometric/constructive parameters and boundary conditions in the repair connection. More information about these parameters is contained in [15].

Table 1: *Parameters of the wooden wedged dowel*

Symbol		Description of the parameter
H		Wood species combination: Dowel / Building Component (BC)
H	H1	Dowel: *Quercus*/ BC: *Picea abies*
	H2	Dowel: *Quercus*/ BC: *Quercus*
	H3	Dowel: *Fraxinus excelsior*/ BC: *Picea abies*
T1		Angle θ between groove´s orientation and direction of the annual rings on dowel´s cross section
		T1-0 → θ = 0°
T2		Angle φ between groove´s orientation on Side 1 [N,1] and fibers´ direction on building component´s surface
		T2-90 → φ = 90°
G		Angle β between groove´s orientation on Side 1 [N,1] and on Side 2 [N,2]
		Orientation of the groove on S1 parallel to orientation on S2 [G//]

As explained in Figure 2 and Table 1 the repair connection is composed by the original and repair building components and one or more mechanical fasteners, the wooden wedged dowels. The tested combinations are reported in the Table 1. More general rules are (a) the wood species for the wedge is always oak (*Quercus*) or the wedge must have a minimum strength of D30 [16] (b) the dowel must have a higher bulk density than the one of both original and repair building components $\rho_D \geq \rho_{BC}$.

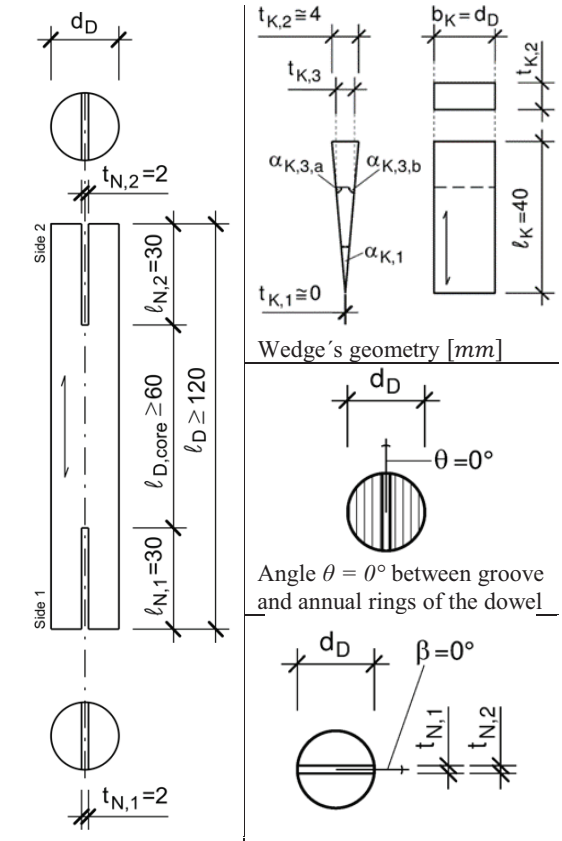

Dowel geometry $[mm]$

Wedge´s geometry $[mm]$

Angle $\theta = 0°$ between groove and annual rings of the dowel

Angle $\beta = 0°$ between groove on side 1 and groove on side 2

Angle φ = 90° between groove on Side 1 and fiber direction of the building component

Margin distances:
$a_1 = a_2 = a_4 \geq 2.5 \cdot d_D$
$a_3 \geq 3 \cdot d_D$
$a_r \geq 2.5 \cdot d_D$

Figure 3: *Geometric boundary conditions for the connection with wooden wedged dowels*

https://doi.org/10.52202/069179-0200

3.1 BOUNDARY CONDITIONS AND WORKING PRINCIPLES OF THE FASTENER

The prerequisite for the transmission of load between fastener and cross section is a contact surface. A distinction is made between two types of contact surfaces for load transfer (Figure 4): A) Load-transfer effect due to wedging (spreading effect) area; B) Load-transfer effect due to skin friction area.

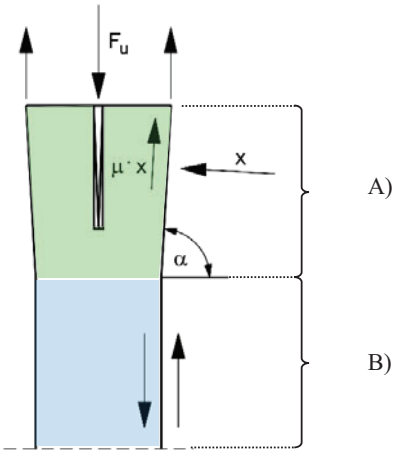

Figure 4: *Mechanical model of the wooden wedged dowel under tensile stress. A) In green, load transfer area activated due to the wedging. B) In light blue, area of action of the skin friction.*

The presented models consider a connection with wooden wedged dowel with idealized load-transfer areas. The load transfer in (A) is independent from manufacturing of connection, but dependent on the type of wood (or better, the wood combination) and the spreading angle α. The load transfer in (B) depends on the manufacturing process and can only be guaranteed if the manufacturing is carried out without deviations from the required geometry (imperfections). As this latter cannot be guaranteed in case of hand-made connections, the skin friction area (B) is neglected in the proposed verification and is considered that the load-carrying capacity of the wooden wedged dowel is determined by the two wedged extremities with the load transfer type (A) (see Figure 4).

4 Results

4.1 VERIFICATION FOR THE REPAIR CONNECTION WITH WOOD WEDGED DOWELS UNDER AXIAL TENSILE LOAD

Starting point for the development of a mechanical model for repair connections with WWD under axial tensile load was the verification model for pile foundations. The relationship between pile displacement y and the horizontal stress σ_h applies here to $\sigma_h = k_S \cdot y$ [17]. From experimental results V1 [9] is defined that the maximum displacement of the system is at the top of the wedging, on BC´s surface, and it is defined as $v(z = 0) \neq 0$. The displacement is reducing to zero along z-axis, in the direction of the center of the wedge. According to numerical simulations the displacement of the system is zero at a depth t_W, defined as $v(z \geq t_W) = 0$. This value defines the depth of load transfer area (A) as in Figure 4. The distribution of the displacement causes a stress distribution that is maximum on BC´s surface. Here, the real and idealized stress distribution is assumed as by Spörk in [18, 19] (see Figure 6, above). The maximum stress value on BC´s surface is defined as $\sigma_N(z = 0) \neq 0$ (see Figure 6, below). The stress has a linear course and is reducing along the z-axis until the maximum depth of the wedging effect t_W. At a depth $z \geq t_W$ the stress is zero $\sigma_N(z \geq t_W) = 0$ an there is no more load transfer between the fastener and the BC´s cross section (see Figure 5). Considering $(x, y, z) \leftrightarrow (u, v, w)$, the stress value $\sigma_N(z)$ in the dowel is the one defined in the eq. (1).

$$\sigma_N(z) = k_S \cdot v(z) \qquad \left[\frac{\mathrm{N}}{\mathrm{mm}^2}\right] \quad (1)$$

with:
$\sigma_N(z)$ = stress value in the system along z-axis
k_S = foundation modulus

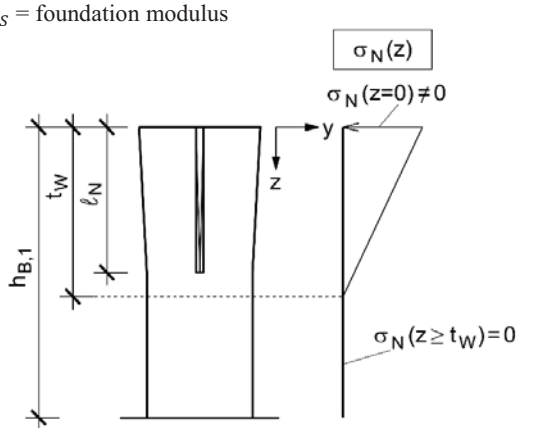

Figure 5: *Mechanical model of the wooden wedged dowel. Distribution of stress along the z-axis due to wedging.*

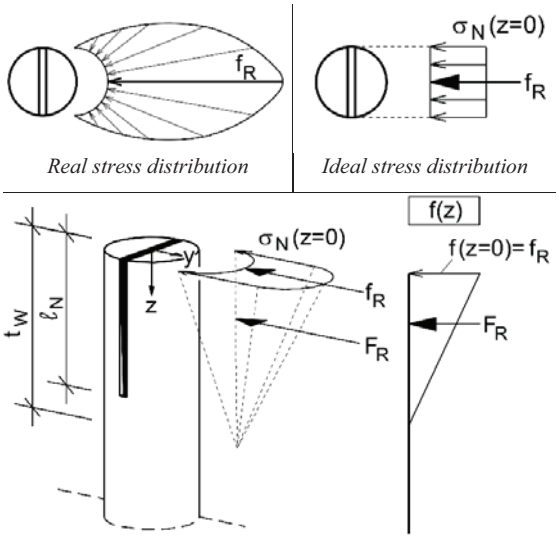

Figure 6: *Mechanical model of the WWD. Above: Two-dimensional representation of the real (left) and ideal (right) stress distribution on BC´s surface $\sigma_N(z = 0) \neq 0$ and linear load distribution f_R. Below: stress distribution along z-axis up to $\sigma_N(z \geq t_W) = 0$ in three-dimensional representation.*

https://doi.org/10.52202/069179-0200

Considering the distribution of the stress on BC´s surface $\sigma_N(z = 0) \neq 0$ constant along the diameter d_D of the dowel and the resultant linear load distribution f_R (2), (3) and taking into account along the z-axis the triangular distribution of the stress up to the maximum depth of load transfer t_W it is possible to calculate the force F_R (4) transferred from the wooden wedge´s spreading surface to the BC (see Figure 6, below). Considering the force F_R is applied on the spreading surface with an angle α, the forces acting perpendicular and parallel to the spreading surface can be calculated from it. Furthermore, the force F_R activates friction according to Coulomb's law of friction (see Figure 7). The static friction plays a decisive role for the tensile load-bearing capacity of the wooden wedged dowel. In fact, the achievement of the sliding friction is defined as the failure point of the fastener.

$$f(z = 0) = f_R \qquad \left[\frac{N}{mm}\right] \qquad (2)$$

$$f_R = \sigma_N(z = 0) \cdot d_D \qquad \left[\frac{N}{mm}\right] \qquad (3)$$

$$F_R = 0.5 \cdot t_W \cdot f_R \qquad [N] \qquad (4)$$

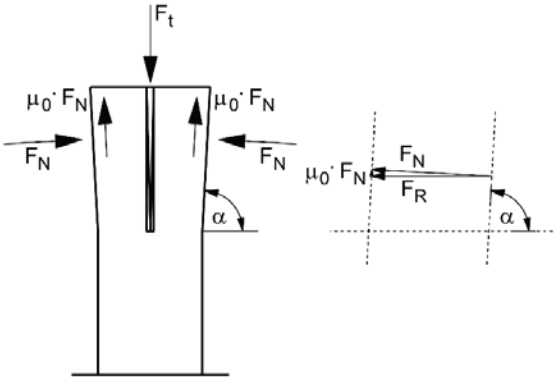

Figure 7: *Mechanical model of the wooden wedged dowel under tensile stress. Equilibrium of forces due to wedging and tensile stress.*

Since the angle α is very small and it can be considered as approximatively a right angle $\alpha \cong 90°$, it is defined that $F_R \cong F_N$ and $F_N \cdot \mu_0 \cong F_R \cdot \mu_0$. Therefore, it can be considered that the value of the tensile force F_t is the one contained in the equation (5)

$$F_t \cong 2 \cdot \mu_0 \cdot F_R \qquad [N] \qquad (5)$$

It is therefore concluded that, the verification for the repair connection with wood wedged dowels under axial tensile load is the one in following equation (6):

$$F_{t,Rk} = \mu_0 \cdot t_W \cdot k_S \cdot v(z = 0) \cdot d_D \qquad [N] \qquad (6)$$

With:
μ_0= friction coefficient between dowel and BC;
t_W = depth of the wedge action;
k_S = foundation modulus;
$v(z = 0)$ = maximum displacement of groove on BC´s surface;
d_D = dowel´s diameter.

The values to be assigned to the parameters contained in the verification (6) can be found in Table 2.

Table 2: *Value of the parameters contained in the verification for the repair connection with wooden wedged dowels under axial tensile load.*

parameter	condition	parameter description, value	unity
μ_0	H1	$\mu_{0,H1} = 0.5$	[-]
	H2	$\mu_{0,H2} = 0.6$	
	H3	$\mu_{0,H3} = 0.4$	
t_W		$t_W = 37.5$	$[mm]$
k_S	H1	$k_{s,H1} = 6.28$	$\left[\frac{N}{mm^3}\right]$
	H2	$k_{s,H2} = 46.40$	
	H3	$k_{s,H3} = 6.28$	
$v(z = 0)$	$d_D = 20$		$[mm]$
	H1	$v(z = 0) = 0.8$	$[mm]$
	H2	$v(z = 0) = 0.2$	
	H3	$v(z = 0) = 0.8$	
	$d_D = 30$		$[mm]$
	H1	$v(z = 0) = 0.59$	$[mm]$
	H2	$v(z = 0) = 0.12$	
	H3	$v(z = 0) = 0.64$	
d_D		$d_D = 20$	$[mm]$
		$d_D = 30$	

The model verification for the wooden wedged dowel under axial tensile stress is carried out taking into account the results from the test series V1 [9]. The parameters contained in the Table 2 are the result of observations in the experimental campaigns TV1 [15], and V1, literature and numerical or mathematical calculations in [9]. The parameters are following explained.
The coefficient of static friction wood-wood μ_0 is found in the literature in the range $\mu_0 = 0.4 \div 0.6$. The static friction coefficients for the verification (6) have been defined basing on the test observations for each wood combination. The definition bases on deductions from studies about the dependence of the embedment strength of fasteners from the surface roughness of drift bolts from Sjödin [20].
The depth of the wedge action t_W was determined from FE-Simulations. The depth of the wedge action defines the depth of load transfer area (A) between the building components and the WWD as in Figure 4. This value is fixed as constant for fasteners with groove´s depth $l_N = 30\ mm$, independently from the wood combination.
The displacement values on BC´s surface $v(z = 0)$ are measured in the experimental campaign V1 [9] for the dowel´s diameter $d_D = 20$ mm, and are result of observations and calculations for dowel´s diameter $d_D = 30$ mm.
The foundation modulus k_S is the resistance of the wood volume to an applied force. In the literature, only studies on embedment strength by Spörk and Hübner [18, 19, 21]

https://doi.org/10.52202/069179-0200

(for hardwoods) and Blaß [22] (for softwoods) were found. Therefore, the foundation modulus for oak (*Quercus*) and ash (*Fraxinus excelsior*) wedges was experimentally determined according to DIN EN 383:2007 [23] The dowels are loaded perpendicular to the grains, parallel to the annual rings. The results are in following (7) and (8).

$$k_{S,quercus,90,EN383} = 48{,}11 \quad \left[\frac{N}{mm^3}\right] \quad (7)$$

$$k_{S,frax.ex,90,EN383} = 35{,}31 \quad \left[\frac{N}{mm^3}\right] \quad (8)$$

The k_S-value in (7) should be valid for dowels in oak (*Quercus)* for the combination H1, H2, and the k_S-value in (8) should be valid for dowels in ash (*Fraxinus excelsior*) for the combination H3. Nevertheless, these tests only served to have first values of k_S. In fact, the k_S-value from (7) is correct to the large order for the wood combination H2 but not for the H1 so far (see Table 2), although both wood combinations have an oak dowel. Similarly, the k_S- value from (8) does not agree with the value of k_S from Table 2 for the wood combination H3. The cause of this incongruities is to be found in the EN 383:2007 [23] itself. Here, the test piece is a rectangular prism of wood loaded by a metallic fastener placed with its axis perpendicular to the surface of the test piece. On the contrary, the foundation modulus in the repair connection with wood wedged dowels is determined, not only by the k_S- value of one wooden species (the test piece), but especially by the interaction between the foundation moduli of the two encountering wood species, in the dowel and in the building component. These two components are stressing each other at a variable stress angle derived by Spörk in [18, 19] (Figure 8), and the angle and wood species with the lower foundation modulus, or reverse, the higher elasticity, determines the final k_S-value for the wood combination.

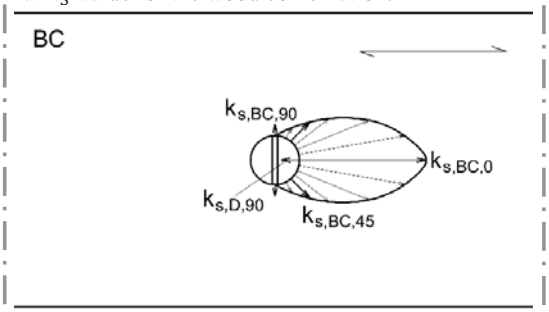

Figure 8: *Assumptions on elastic behaviour of the dowel and building component in the contact area between the building component and the dowel (wedging interaction area).*

Thus, following hypotheses about the stress behavior of the timber combinations are formulated (referring to Figure 8). Assumption for H1 and H3: The elasticity of the BC made of spruce stressed in compression parallel to the grains is greater than the one of the dowel made of oak (in H1) or ash (in H3) stressed in compression perpendicular to the grains (9):

$$k_{S,BC(spruce),0} < k_{S,BC(spruce),45} < k_{S,D(oak/ash),90} \quad (9)$$

Therefore, for the timber combinations H1 and H3, the building component made of spruce determines the properties for the foundation modulus as $k_{S,BC(spruce),0}$. Assumption for H2: The elasticity of the oak dowel, stressed in compression perpendicular to the grain, is bigger than that one of the oak building component, stressed in compression parallel to the grain (10):

$$k_{S,D(oak),90} < k_{S,BC(oak),45} < k_{S,BC(oak),0} \quad (10)$$

Therefore, for the timber combination H2, the dowel made of oak, loaded perpendicular to the grains, determines the properties for the foundation modulus as $k_{S,D(oak),90}$.

4.2 EXPECTED LOAD -BEARING CAPACITY OF WOOD WEDGED DOWELS UNDER AXIAL TENSILE LOAD

In the following Table 3 are reported the load-bearing capacities for one wooden wedged dowel under axial tensile load as fasteners for a carpentry repair connection, in dependence from the wood combination. The expected characteristic values $R_{k,WWD,mod}$ after the presented model are compared with the the 5% quantile of the characteristic values $R_{k,WWD,\exp}$ from the tests V1 [9].

Table 3: *Characteristic values of load-bearing capacity for wooden wedged dowels under axial tensile load in dependence fro the wood combination. Characteristic values of the tests V1 ($R_{k,WWD,exp}$) and the ones after the presented model ($R_{k,WWD,mod}$).*

Parameter	condition	parameter description	unity	deviation
$d_D = 20mm$				
$R_{k,WWD,\exp}$	H1	1.67	[kN]	
	H2	3.58		
	H3	1.93		
$R_{k,WWD,\mathrm{mod}}$	H1	1.88		12.6 %
	H2	4.18		16.8 %
	H3	1.51		-21.8 %
$d_D = 30mm$				
$R_{k,WWD,\exp}$	H1	2.49	[kN]	
	H2	3.14		
	H3	2.40		
$R_{k,WWD,\mathrm{mod}}$	H1	2.08		-16.5 %
	H2	3.76		19.7 %
	H3	1.81		-24.6 %

In the last column of Table 3 the deviations between the characteristic values of load-carrying capacity from the proposed model and the ones of the experimental results are shown. On one side, the load-carrying capacity for the WWD with smaller diameter $d_D = 20mm$ is a little overestimated and the one for the bigger diameter $d_D = 30mm$ is underestimated. The overestimation remains in the tolerance of +20% and the underestimation is on the safe side up to -25%. On the other side, the

experimental results [9] presents a big statistical scatter and the obtained deviation remains in the tolerance of the test results.
Concluding, from the comparison between the results of the proposed model and the experimental results, can be inferred that the proposed model predicts very good the values of load-carrying capacity for the wooden wedged dowel under axial tensile load.

4.3 VERIFICATION FOR THE REPAIR CONNECTION WITH WOOD WEDGED DOWELS UNDER SHEAR LOAD

The verification for the repair connection with wooden wedged dowels under single and double shear loading (with one or two shear planes), bases on existing mechanical models and verifications norms [11–13]. More specific, the here proposed verification model bases on the model from Blaß [12] and norm SIA 269/5:2011 [13].
In the experimental campaign SV [9] experimental tests on a mortise and tenon joint with wooden wedged dowels (WWD), and wooden dowels (WD) as mechanical fasteners under double shear have been carried out. The proposed geometric parameters for the tests are wood combination H1 (refer to Table 1) and dowel´s cross-section $d_D = 20mm$.
In the Table 4 are reported the characteristic values (5% quantile) of the tests SV carried out in [9] for the WWD and WD. The results show that the load-carrying capacity of the wooden wedged dowels is lower than the one for wooden dowels. Furthermore, in the Table 4 are reported the expected characteristic values of load carrying capacity for the WD and WWD calculated after the model from Blaß in [12]. From the comparison among these values it is clear that, on one side, the model [12] describes very well the test results for the wooden dowels, and on the other side, the results of load carrying capacity for the wooden wedged dowels calculated after [12] are too high in comparison with the test results.

Table 4: *Characteristic values of strength for repair connection mortise and tenon joint (double shear) with wooden dowels and wooden dowel under shear load: results after model in [12] and experimental test results.*

Parameter	condition	parameter value	unity
$R_{k,WWD}$	experimental	6.61	[kN]
	After [12, 13]	8.57	
$R_{k,WD}$	experimental	7.62	[kN]
	After [12, 13]	8.67	

In the verification of wooden dowels from [12, 13] the reduction coefficient δ, takes into account the effects of non-linear stress distribution along the borehole, the non-utilization of the embedding strength and rope effects due to friction in the borehole. From the observation of the tests SV [9] was revealed that these side effects are not only evident in wood dowels, but also magnified in wood wedged dowels under shear stress. The presence of the reduction coefficient δ from [12, 13] is therefore particularly interesting for the further development of the verification model for the wood wedged dowels.
In order to update the reduction coefficient δ, some explanations about the causes of reduction of the load-carrying capacity in the WWD were given: the reason may lie in the geometry of fasteners´ components. The geometry causes firstly a change in the distribution of forces along fasteners´ neutral axis and secondly causes a change in the contact area between the building component and the dowel. These phenomena may cause wooden wedged dowels experience earlier shear failure than the wooden dowels. These two hypotheses are following explained.
Hypothesis 1) (refer to Figure 9). During loading the fasteners are generally subjected between the shear joints to bending in the borehole. One half of the fastener´s cross section is loaded in compression and the other half in tension; the shear forces are maximum along the neutral axis.
On one side, the WD has a constant cross-section along the entire length and it distributes the shear forces equally along the whole neutral axis' length. On the other side, in the WWD the grooves at two far ends, exactly cut the cross-section in the ending part of the neutral axis into two half cross-sections. Therefore, the WWD presents a shorter neutral axis' length for absorbing the maximum shear force.

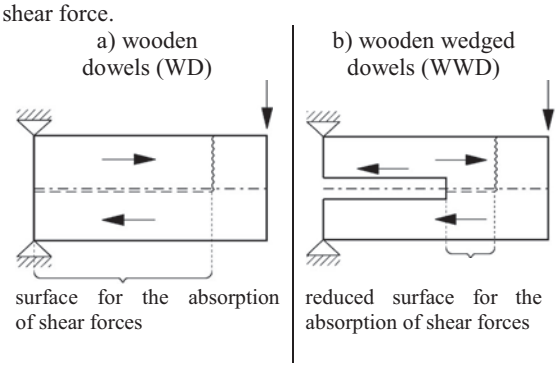

Figure 9: *Representation of hypothesis 1): assumptions on the absorption of shear forces in the two far ends of the fastener in a) WD and b) WWD.*

Hypothesis 2) (refer to Figure 10). During loading the fasteners are generally subjected between the shear joints to bending in the borehole.
On one side, the wooden dowel has no restraints in the borehole except than the skin friction as in the surface (B) described in Figure 4. Therefore, once subjected to bending it can axially shift in the borehole, depending from the contact surface and the presence of imperfections in the geometry. The WD is - mechanically speaking - a displaceable beam in axial direction (see Figure 10a). Referring to the middle wood, the cross-sections of the fasteners are subjected along the neutral axis on the lower half to tensile stress and on the upper half to compression from the bending. On the other side, the wooden wedged dowel (WWD) activates a further load transfer area due to

https://doi.org/10.52202/069179-0200

the wedging; here, the fastener is able to absorb axial tensile forces during loading, as explained in Figure 4. Therefore, once subjected to bending, the WWD cannot axially free shift in the borehole as the WD. The WWD is - mechanically speaking - a non-displaceable beam in axial direction (see Figure 10b). This causes an additional axial tensile stress in the fastener´s cross-sections. Referring to the middle wood, the cross sections are here on the lower half not only subjected to tensile stress from bending, but also to additional tensile stress from the wedging and its clamping effect. As a consequence, the neutral axis shifts from fastener´s main axis to the upper half of the cross-section. Earlier failure in this zone is expected. In experimental tests SV [9] an additional failure in this area was also observed.

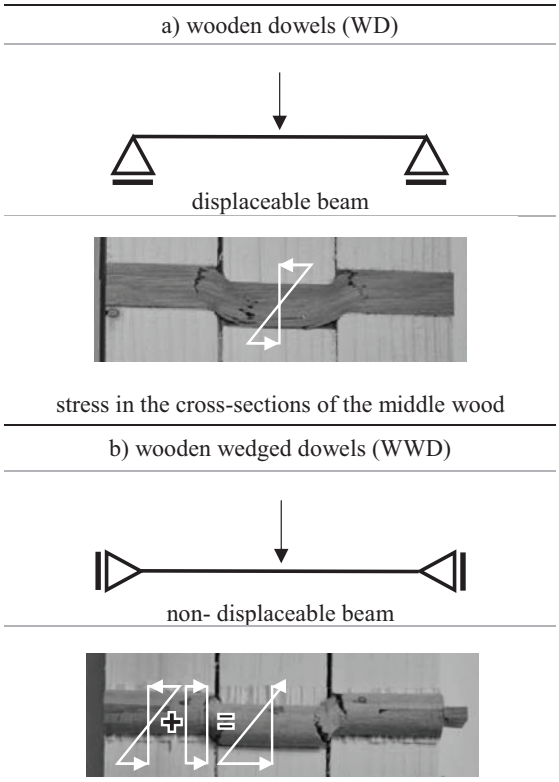

Figure 10: *Representation of hypothesis 2): mechanical interpretation, and stress in the cross-sections of the middle wood after shear loading in the a) WD and b) WWD.*

According to the hypothesis 1 and hypothesis 2, a new reduction coefficient δ', is defined. The reduction coefficient δ' considers the effects of non-linear stress distribution along the borehole, the non-utilization of the embedment strength, rope effects due to friction in the borehole, and the additional clamping effect due to the wedging in the WWD. The updating of the reduction coefficient δ' is calculated back from the characteristic values (5% quantile) of load-carrying capacity of the experimental tests SV [9] and the known variables from the equation of Blaß [11]. The new value for the reduction coefficient is determined as: $\delta' = 0.45$. The verification model for the wooden wedged dowels under shear load is defined in the following equation (11).

$$R_k = \sqrt{\frac{2 \cdot \beta}{1+\beta}} \cdot \sqrt{2 \cdot M_{u,k} \cdot \delta' \cdot f_{h,1,k} \cdot d_D} \quad [N] \quad (11)$$

With:

$$\delta' = 0{,}45 \quad [-] \quad (12)$$

$$\beta = \frac{f_{h,1,k}}{f_{h,2,k}} \quad [-] \quad (13)$$

$$M_{u,k} = \frac{f_{m,k} \cdot \pi \cdot {d_D}^3}{32} \quad [N \cdot mm] \quad (14)$$

$$f_{h,1,k} = 0{,}082 * (1 - 0{,}01 * d_D) * \rho_k \quad \left[\frac{N}{mm^2}\right] \quad (15)$$

The verification (11) describes the maximum calculated characteristic load-carrying capacity for one fastener and per shear joint. The verification is directly connected with the one from [12, 13]. In (13) β describes the ratio of the embedment strength of the side wood to the middle wood (from SIA 265:2012 [24]); here, $f_{h,1,k}$ represents the characteristic embedment strength of the side wood and $f_{h,2,k}$ of the middle wood. In (14) $M_{u,k}$ describes the characteristic value of bending moment of the cylindric wooden fasteners; here, the value $f_{m,k}$ is the value of characteristic bending strength of the wooden fasteners from DIN EN 338 [16]. Finally, the diameter of the wooden wedged dowel is described by d_D and the bulk density of the side wood by ρ_k.

As well as for the verification in [12, 13], the value of load-carrying capacity calculated by (11) is valid if the minimum wood thickness of the side wood ($t_{1,req}$) and the one of the middle wood ($t_{2,req}$) are achieved. For a single shear joint the thickness of the side wood 1 and the side wood 2 is determined in the eq. (16) and eq. (17) respectively. For a double shear joint the thickness of the middle wood is further described in the equation (18).

$$t_{1,req} = \left(2 \cdot \sqrt{\frac{\beta}{1+\beta}} + 2\right) \cdot \sqrt{\frac{M_{u,k}}{\delta \cdot f_{h,1,k} \cdot d}} \quad [mm] \quad (16)$$

$$t_{2,req} = \left(2 \cdot \sqrt{\frac{\beta}{1+\beta}} + 2\right) \cdot \sqrt{\frac{M_{u,k}}{\delta \cdot f_{h,2,k} \cdot d}} \quad [mm] \quad (17)$$

$$t_{2,req} = 4 \cdot \sqrt{\frac{\beta}{1+\beta}} \cdot \sqrt{\frac{M_{u,k}}{\delta \cdot f_{h,2,k} \cdot d}} \quad [mm] \quad (18)$$

If the middle or side woods are thinner than the required minimum timber thicknesses $t_{i,req}$, the characteristic load-bearing capacity according to eq. (11) is reduced according to eq. (19)

$$R_{k,red} = R_k \cdot min \begin{cases} \frac{t_1}{t_{1,req}} \\ \frac{t_2}{t_{2,req}} \end{cases} \qquad [mm] \quad (19)$$

4.4 EXPECTED LOAD -BEARING CAPACITY OF WOOD WEDGED DOWELS UNDER DOUBLE SHEAR LOAD

In the Table 5 the estimated maximum load carrying capacity for the wooden dowels $R_{k,WD,mod}$ is calculated after the model of Blaß [11] and the estimated load-carrying capacity for the wooden wedged dowels $R_{k,WWD,mod}$ is calculated after the proposed model [9].

Table 5: *Characteristic values of load-carrying capacity for WWD and WD under double shear load: results after model in [12], after the proposed model and experimental test results. Slip moduli after experimental results.*

	Parameter	condition	value	unity
WWD	$R_{k,WWD,exp}$	experimental	6.61	[kN]
	$R_{k,WWD,mod}$	after model [9]	6.61	
	$k_{ser,mean,WWD}$	experimental	12.57	$\left[\frac{\text{kN}}{mm}\right]$
WD	$R_{k,WD,exp}$	experimental	7.62	[kN]
	$R_{k,WD,mod}$	After model [12]	8.67	
	$k_{ser,mean,WD}$	experimental	13.21	$\left[\frac{\text{kN}}{mm}\right]$

The values of the maximum load can be used for the calculation of the slip modulus $k_{ser,mean}$ for both the repair connection with wooden wedged dowels according to the proposed verification [9], as well as for the repair connection with wooden dowels according to the model in [12]. The slip moduli $k_{ser,mean}$ presented in the Table 5 are therefore calculated for both the repair connections with WWD and WD according to the norm DIN EN 26891:1991-07 [25].

5 CONCLUSION

Concluding, this paper and the related research project [9] introduce the use of the wooden wedged dowels as mechanical fasteners for carpentry connections and clarify manufacturing rules, geometric boundary conditions, working principles, as well as develop a verification for the prediction of load-carrying capacity for the fasteners under axial tensile and shear load.

Regarding geometric boundary conditions, the definition of manufacturing rules and construction parameters, was fundamental. In fact, different load-carrying capacities are expected in dependence from wood combination and fastener´s diameter. Therefore, changing the geometric boundary conditions, divergent results than the presented ones are expected. For this reason, the presented verification models and expected characteristic load-carrying capacities are valid only under the presented boundary conditions.

Regarding peculiar properties of the fastener wooden wedged dowel, it shows, differently to a normal wooden dowel, an improved contact surface in the borehole given by the clamping effect of the wedge, that always guarantees the load transfer between the fastener and the building component. The clamping effect confers to the fastener a rope effect during the loading. This property of the wooden wedge dowels is advantageous in the case of axial load; however, in case of shear load, the wedging contributes to a reduction of the load-bearing capacity, compared to the load-bearing capacity of an equivalent connection with wooden wedges.

The developed verifications open up for engineers the possibility to apply carpentry repair connections with wooden wedged dowels as fasteners in relevant load cases, for example for hanging ceiling coffer beams (wooden wedged dowels in tensile load), or for ceiling beams and roof rafters (wooden wedged dowels in shear load).

The research project is designed as a long-term project to re-learn and understand historical techniques and carpentry connections in order to promote the "best practice" under static-constructive, economic, culturally oriented aspects in heritage conservation.

6 ACKNOWLEDGEMENT

The research was financed with funds from the research initiative Zukunft Bau of German Federal Institute for Research on Building, Urban Affairs and Spatial Development (BBSR, BMI) (SWD-10.08.18.7-18.16), and of Niedersächsisches Landesamt für Denkmalpflege (NLD).

7 REFERENCES

[1] G. Schickhofer and U. Hübner, Eds., *Bestandsanalyse und Instandhaltung von Holzkonstruktionen,* 8th ed. Graz, 2009.

[2] M. Petzet, Ed., *Grundsätze der Denkmalpflege: 1. ICOMOS, Heft des Deutschen Nationalkomitees*. München, 1992.

[3] ICOMOS and ISCARSAH, Eds., *Grundsätzen zur Erhaltung historischer Holzstrukturen.*, 1999.

[4] ICOMOS and ISCARSAH, Eds., *Principles for the preservation of historic timber structures*, 1999.

[5] ICOMOS and ISCARSAH, Eds., *Principles for the conservation of wooden built heritage*, 2017.

[6] J. Egle, Ed., *Dauerhaftigkeit von Holz bei chemisch- aggressiver Beanspruchung*, 2003.

[7] Forest Products Laboratory, Ed., *Wood Handbook—Wood as an engineering material. General Technical Report FPL-GTR-190.* Madison, WI.

[8] Informationsdienst Holz, “Korrosion metallischer Verbindungsmittel in Holz und Holzwerkstoffen,” Spezial Februar 2003, 2003.

[9] E. Perria, S. Siegert, M. Sieder, and Reulecke C., “Holzkeildolle als Reparaturverbindung: Einsatz

https://doi.org/10.52202/069179-0200

der Holzkeildolle als Möglichkeit neuer Reparaturverbindungen für die Denkmalschutzanforderungen des schonenden Substanzumgangs und der Materialgerechtigkeit," BBSR, Bonn, (in publication) 2022.
[10] M. Kessel and R. Augustin, "Untersuchung der Tragfähigkeit von Holzverbindungen mit Holznägeln für Sanierung und Rekonstruktion von alter Bausubstanz, Forschungsbericht," FH Hildesheim/Holzminden, Fachbereich Bauingenieurwesen, 1992.
[11] M. Kessel and R. Augustin, "Untersuchung der Tragfähigkeit von Holzverbindungen mit Holznägeln," *Bauen mit Holz*, no. 96, pp. 484–487, 1994.
[12] H. J. Blaß, H. Ernst, and H. Werner, "Verbindungen mit Holzstiften - Untersuchungen über die Tragfähigkeit," *Bauen mit Holz*, vol. 10, pp. 45–52, 1999.
[13] *Erhaltung von Tragwerken – Holzbau*, SIA 269/5:2011, SIA Schweizerischer Ingenieur und Architektenverein, Zürich, 2011.
[14] A. Müller, M. Vogel, S. Lang, and F. Sauser, *Historische Holzverbindungen. Untersuchung des Trag- und Verformungsverhaltens von Historischen Holzverbindungen und Erstellung eines Leitfadens für die Baupraxis*: Fachhochschule Biel, 2016.
[15] Perria E., Siegert S., Li X., Sieder M., "Repair connection with wooden wedged dowels: preliminary experimental laboratory tests and fem model for the description of the mechanical behavior.," in *12th International Conference on Structural Analysis of Historical Constructions SAHC 2020*.
[16] *Structural timber - Strength classes*, DIN EN 338:2016-07, DIN Deutsches Institut für Normung e.V.
[17] K. J. Witt, Ed., *Teil 3: Gründungen und geotechnische Bauwerke,* 7th ed.: Ernst & Sohn.
[18] J. Hohenwarter, *Vergleich der Lochleibungsfestigkeit in Folge von Zug- und Druckbelastung*. Graz, 2014.
[19] a. Spörk, "Einflussfkatoren auf die Lochleibungsfestigkeit für die Nadelholzart Fichte," TU Graz, Internes Paper holz.bau forschungs gmbh, Mar. 2007.
[20] J. Sjödin, E. Serrano, and Enquist, Bertil (2008), "An experimental and numerical study of the effect of friction in single dowel joints," in *Holz als Roh und Werkstoff*, pp. 363–372.
[21] U. Hübner, Ed., *Mechanische Kenngrößen von Buchen-, Eschen- und Robinienholz für lastabtragende Bauteile*. Graz: Verlag der Technischen Universität Graz, 2013.
[22] H. J. Blaß, O. Eberhart, and B. Wagner, "Zum rechnerischen Nachweis von Winkelverbindern," *Bauen mit Holz*, no. 102, pp. 42–46, 2000.
[23] *Timber Structures — Test methods — Determination of embedment strength and foundation values for dowel type fasteners*, EN 383:2007, DIN Deutsches Institut für Normung e.V., Berlin, 2007.
[24] *Holzbau*, SIA 265:2012, SIA Schweizerischer Ingenieur- und Architektenverein, Zürich, 2012.
[25] *Timber structures; joints made with mechanical fasteners; general principles for the determination of strength and deformation characteristics (ISO 6891:1983)*, DIN EN 26891:1991-07, DIN Deutsches Institut für Normung e. V., Jul. 1991.

World Conference on Timber Engineering Oslo 2023

Performance Verification and Trial Design for High-rise Timber Frame Buildings with Buckling-Restrained Braces
Part.1 Connection and Frame Testing

Kazuki Tachibana[1], Hiroki Nakashima[2], Taisuke Nagashima[3], Ryota Minami[4], Toshio Maegawa[5], Nobuhiko Akiyama[6], Yoshihiro Yamazaki[7] and Takahiro Tsuchimoto[8]

ABSTRACT: A 10-story apartment building was designed with (1) multi-knife plate steel dowel connections for the joints, (2) BRBs as megastructural−columns for the seismic elements, and (3) GIR joints for the column bases. Tests were conducted to verify that these three types of high-strength connections performed as required. This paper describes the results of these tests and a discussion of the analysis method.

KEYWORDS: High-rise timber structure, Multiple Shear steel-to-timber joints, Buckling-restrained braces

1 INTRODUCTION

While demand for mid-rise and high-rise timber buildings has been increasing in recent years, non-timber structures are still dominate the market for mid-rise and high-rise buildings in Japan. One of the challenges in promoting the use of mid-rise and high-rise timber buildings is to ensure their seismic performance. In order to create a good role model, this study was designed to test a 10-story apartment building with mega-structural columns and Buckling-Restrained Braces (hereinafter referred to as "BRB"). [Fig. 1]

Part 1 describes the tests conducted for the trial design and their results. An analytical model is proposed and compared with test results to verify the validity of the analytical model.

2 CONNECTION TEST

2.1 INTRODUCTION

The Japanese standard [1] describe how to calculate the allowable shear capacity of steel dowel joints with steel inserted plate and with steel side plates, but they do not describe the case where multiple steel plates are inserted or the scope of application, for example, whether it is possible to use large-section glued laminated wood or large diameter drift pins. Here, shear tests were conducted to verify whether the shear strength could be obtained by a simple calculation. Specifically, as shown in Fig. 2, we verified whether the ratio of the number of steel dowels and the addition on the burden area (dowel length) were valid.

2.2 MATERIALS AND SPECIMEN

Fig. 3 shows an overview of the specimens: the A1 has 27 steel dowels inserted; the B1 and B3 have 5 steel dowels inserted; the A1 and B1 have 1 steel plates inserted; the

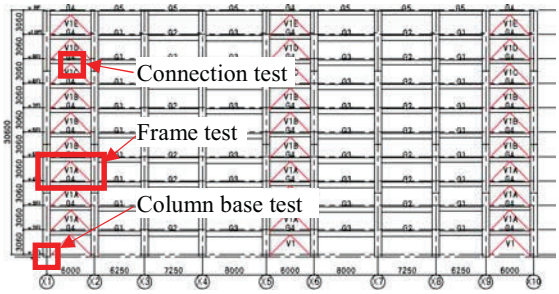

Fig. 1 10-story timber apartment (trial design)

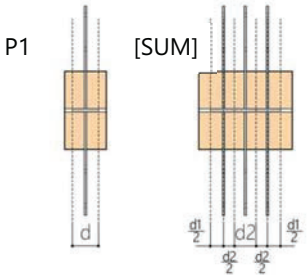

$$[\text{sum}] = \frac{d1}{d}P_1 + \frac{d2}{d}P_1 + \frac{d2}{d}P_1 \qquad \textit{Eq. 1}$$

Fig. 2 Length of steel dowel to bear the load

[1] Kazuki Tachibana, M. Eng., Sumitomo Forestry, Japan, tachibana_ kazuki @sfc.co.jp
[2] Hiroki Nakashima, M. Eng., Sumitomo Forestry, Japan, nakashima_ hiroki @sfc.co.jp
[3] Taisuke Nagashima, Ph. D Eng., Chief Researcher, Sumitomo Forestry, Japan, tsk-naga@sfc.co.jp
[4] Ryota Minami, M. Eng., Kumagai Gumi, Japan, ryota.minami@ku.kumagaigumi.co.jp
[5] Toshio Maegawa, Chief Researcher, Kumagai Gumi, Japan, tmaegawa@ku.kumagaigumi.co.jp
[6] Nobuhiko Akiyama, Dr. Agr., Senior Researcher, Building Dept., NILIM, MLIT, Japan akiyama-n92rg@mlit.go.jp
[7] Yoshihiro Yamazaki, Dr. Eng., Senior Research Engineer, Building Research Institute, Japan, y_ymzk@kenken.go.jp
[8] Takahiro Tsuchimoto, Dr. Agr., Chief Research Engineer, Building Research Institute, Japan, tutti@kenken.go.jp

https://doi.org/10.52202/069179-0201

B3 has 3 steel plates inserted. The timber was laminated Japanese larch E95-F270 with secondary gluing in the width direction, the steel plate was SS400 with a thickness of 12mm, and the steel dowels were SNR490B with a diameter of 20mm. The hole diameter for the steel dowel s was 20mm for the timber and 21mm for the steel plate. Steel dowels were 150mm long for A1 and B1, and 350mm long for B3, with tapered end. A slit of □-16 × 1,180 was cut out in the timber for steel plate insertion. The number of specimens was one for B1 and three each for A1 and B3

2.3 METHODS

Fig. 4 shows the testing machine performance and the test setup of specimen. The test specimen and jig were fixed by frictionally joining the left and right sides of the inserted steel plate. For displacement, the relative displacement of each steel plate to the timber was measured, and the average value was used as the deformation. The load was applied monotonically from the top of the column using a hydraulic jack while measuring the load, and was applied until the load dropped to 80% of the maximum load or until the joint was deformed more than 30 mm and lost its function as a joint.

2.4 RESULTS AND DISCUSSIONS

The experimental results are shown in Fig. 5. From the obtained displacements and loads, the yield capacity P_y and ultimate capacity P_u were obtained in accordance with "How to Obtain Yield Capacity and Ultimate Capacity Using Full Elastic-Plastic Model "[2].

2.4.1 NUMBER OF STEEL DOWELS

Fig. 6 compares the history curves of the A1 specimen with those of the B1 specimen, corrected for a steel dowel count ratio of 27/5 times. Fig. 6 shows that there is a proportional relationship between the number of steel dowels and shear strength.

2.4.2 NUMBER OF INSERTED STEEL PLATES

[Sum]B1 is the prediction of the B3 result from the B1 result based on Fig. 1. The [Sum]B1 and B3 results are compared in Fig. 7, which shows that [Sum]B1 is evaluated on the safe side with respect to B3.

Fig. 8 compares [Sum]A1 obtained from the A1 test result with the results of the B3 specimen multiplied by 27/5. This result also shows that [Sum]A1 is evaluated to be on the safe side compared to 27/5 of the B3 specimen.

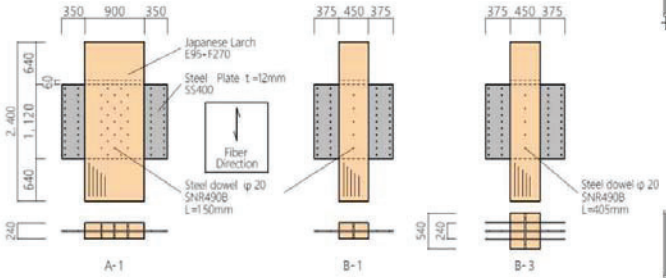

Fig. 3 Specimen detail

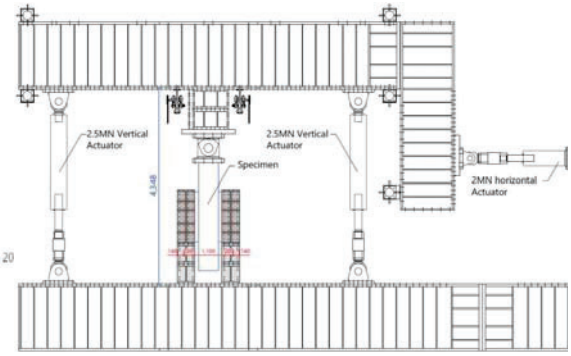

Fig. 4 Test setup of specimen

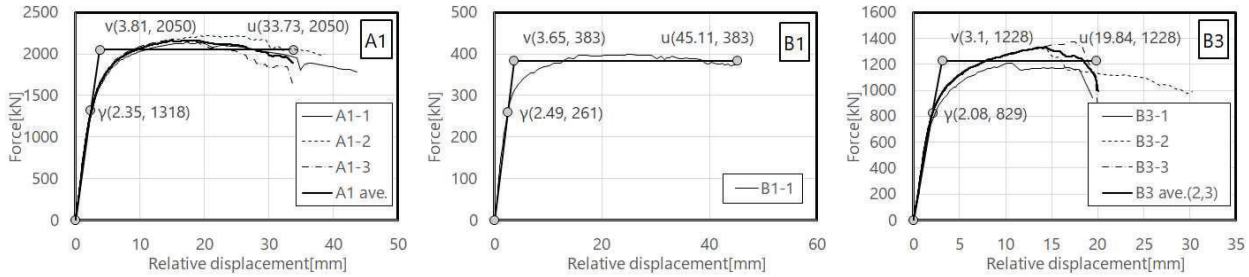

Fig. 5 Load-deformation relationships and Bi-liner carve

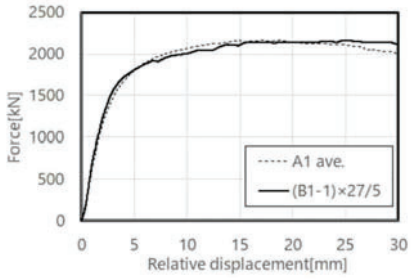

Fig. 6 Analyze impact of number of steel dowel

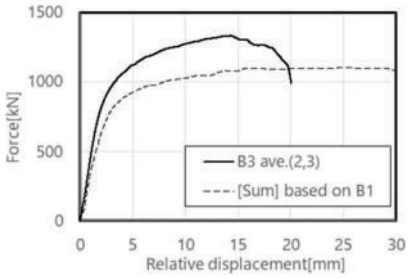

Fig. 7 Analyze impact of number of steel dowel

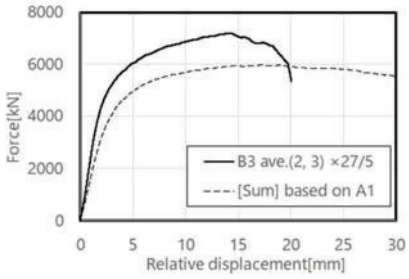

Fig. 8 Analyze impact of number of steel dowel

https://doi.org/10.52202/069179-0201

3 FRAME TEST

3.1 INTRODUCTION

Our trial design of a high-rise timber frame building has BRBs as the main seismic element. The design assumed that the BRBs yield first during deformation, and then the toughness of the BRBs is expected until the safety limit is reached. However, each joint of the frame is not a pin joint but a semi-rigid joint with rotational stiffness, and the frame bears a part of the seismic force after the BRB yields. The frame is designed so that the deformation of the frame is within the elastic range even at the safety limit, but it was confirmed experimentally that the load borne by the frame is as calculated and that the joints do not fail in bending under large deformation. (hereinafter referred to as "Frame test")

In order to estimate the axial force acting on the BRB joint during the frame test and to control the applied force, a cyclic test of the BRB alone (hereinafter referred to as "BRB test") was conducted in advance, and the load deformation of the BRB alone was confirmed up to the ultimate region.

3.2 BRB TEST

3.2.1 MATERIALS AND SPECIMEN

The BRB used for the test specimen was a BRB manufactured by Nippon steel engineering Co., Ltd. The specimen specifications are shown in Table. 1 and the design specifications are shown in Table. 2. Yield stress and strength are based on mill test report. The post-yield stiffness degradation rate was taken from the manufacturer's technical data [3]. The BRBs were custom-ordered with a yield capacity of 113kN and an ultimate capacity of 205kN, and end plates were added to the ends and bolted to the load jig and end plates.

3.2.2 METHODS

Fig. 9 shows the performance of the testing machine, the specimen setup, and the position of instrumentation. The polarity of the load and displacement was set to be positive on the tensile side. The loading method was cyclic loading with hydraulic jacks, which was repeated three times per a cycle. The loading schedule is shown in Table. 3, and the average value of the vertical displacement (7) and (8) of the jig column was considered to be equivalent to the displacement of the plasticized part and was used as the displacement for control.

Overall disp. $\delta_0 = (③ + ④ + ⑤ + ⑥) / 2$ ***Eq. 2***

Control disp. $\delta_1 = (⑦ + ⑧) / 2$ ***Eq. 3***

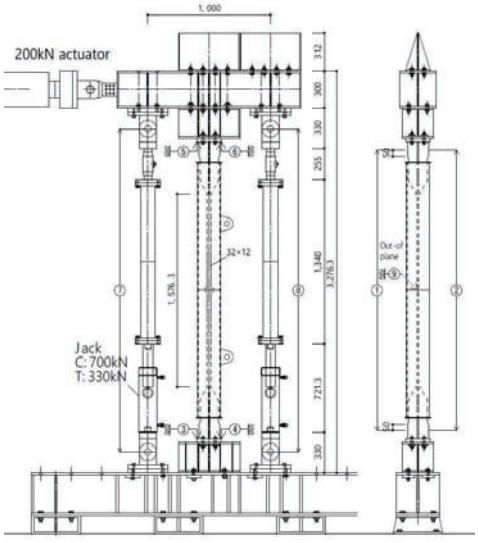

Fig. 9 Test setup of specimen

3.2.3 RESULTS AND DISCUSSIONS

Based on test result, the yield point and the 3%-L_p deformation point were read from the envelope curve and a bilinear (test) was created. The 3%-L_p deformation point was set at the maximum deformation at the first loading. The bilinear model obtained from the design values was designated as bilinear (design), and this graph was used in the analysis. These two bilinears are shown together in Fig. 10. The bilinear model based on theoretical values does not take into account the load rise, but we believe that this model is sufficient for the frame analysis, which is mainly

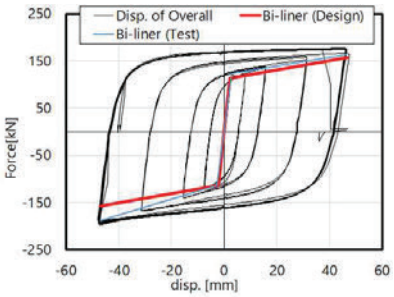

Fig. 10 Load-deformation relationships

Table. 1 Specimen specifications

Parts	Material	Size[mm]	Grade	Standard
Core	Steel plate	12×32	SN400B	JIS G 3136
Cover	Round steel pipe	φ191×4.5	STK400	JIS G 3444

Table. 2 Design specifications

Overall Length	L_0	2,476.3	mm
Yield (Core) Length	L_p	1,576.3	mm
Yield (Core) Area	A	384	mm^2
Young Modulus	E	205,000	N/mm^2
Elastic Stiffness	K_1	49.9	kN/mm
Stiffness reduction ratio	α	0.02	
Yield Stress	σ_y	294	N/mm^2
Strength	σ_u	534	N/mm^2
Yield strain	ε_y	0.00144	

Table. 3 Loading schedule

Target deformation			Cycle
0.5 δ_y	1.13	mm	3
δ_y	2.26	mm	3
L_p -0.5%	7.88	mm	3
L_p -1%	15.76	mm	3
L_p -2%	31.53	mm	3
L_p -3%	47.29	mm	1

https://doi.org/10.52202/069179-0201

Table. 4 The specifications of the members used for the frame specimen

Parts	Classification	Size[mm]	Grade	Standard
BRB (Core)	Rolled steels for building structure	12×32	SN400B	JIS G 3136
BRB (Core)	Carbon steel tubes for general structure	φ190.7×4.5	STK400	JIS G 3444
BRB (Joint)	Torshear type high strength bolt set	M16	S10T	JSS II-09
Beam	Structural glulam (Japanese Larch)	250×480	E95-F275	JAS
Column	Structural glulam (Japanese Larch)	375×720	E95-F275	JAS
Joint (side plate)	Rolled steels for general structure	t=12, 19	SS400	JIS G 3101
Joint (insert plate)	Rolled steels for general structure	t=12, 32	SS400	JIS G 3101
Steel dowel	Rolled steels for building structure	φ20	SNR490B	JIS G 3138

Table. 5 scale factor of the specimen

Length	Floor height	4/5
Section	Width	4/5
	Height	5/12
	Section(stress)	1/3

concerned with the first loading. The bilinear (test) model showed a difference from the bilinear (design) model in that the yield load was larger on the tensile side and the second-order slope was larger on the compressive side.

3.3 FRAME TEST

3.3.1 MATERIALS AND SPECIMEN

The BRB used in the frame tests were the same as those used in 3.2. The specifications of the members used for the frame specimen are shown in Table. 4 and the names of the parts are shown in Fig. 11. The ends of the BRBs were friction-bolted with high-strength bolts friction joints, accompanied by joint hardware and splice plates. Although frame tests were considered at full scale, the largest specimen was set up to match the testing laboratory's frame testing machine. The scale factor of the specimen scaled down from full-scale is shown in Table. 5. The specimen was also rotated 90°, so that the columns and beams were inverted as shown in Fig. 11. There are three types of connections between the beam-column hardware and the timber: C is the connection to the column, G is the connection to the beam, and B is the connection between the BRB and the beam. Joints C and G are drift pin joints with two steel plates inserted into the timber, and joint B is a bolted joint with steel plates on both sides of the timber. The reaction force fulcrums of the test specimens were made by extending the joint hardware steel plates and connecting them to a pin bearing and a roller bearing, respectively. Each joint must have sufficient bearing capacity and deformation capacity to allow the BRBs to withstand the ultimate load. The number of steel dowels was determined so that the short-term shear capacity of joints C, G, and B of the specimen would be sufficient for the axial force of the frame generated when the BRB restoring force was at its maximum, and the arrangement of the steel dowels was determined so that the rotational stiffness would be as small as possible. For joint B, a steel dowel joint with the steel-plate-insertion was planned, but since there was a possibility that the BRB would twist the beam due to the stress of the BRB during loading, bolt joint with the steel side plate was used in the hope that the torsional resistance

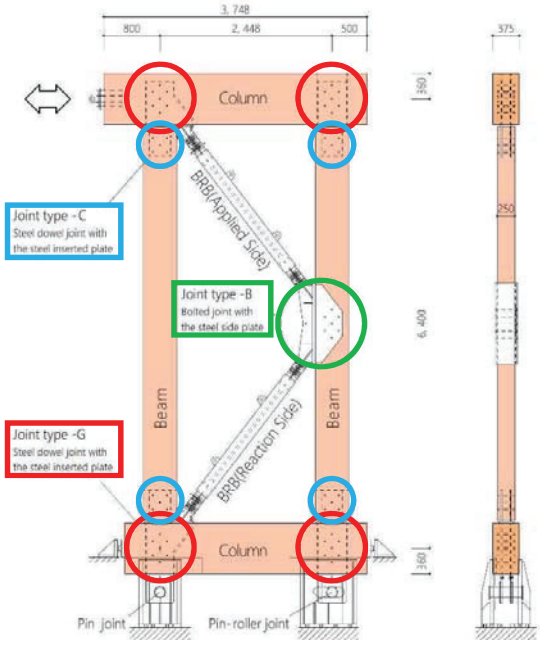

Fig. 11 Test setup of specimen

of the beam would be effectively transmitted. The short-term shear capacity of joint B is smaller than the maximum axial force of the frame and is 1.2 times the frame axial force at yield. The diameter of the holes drilled in the steel plate and timber for each joint was the same as in "2. CONNECTION TEST" for steel dowel joints with the steel-plate-insertion, and 22mm holes were drilled in both the plate and timber for the bolted joint for steel side plate, and φ20 bolts were used.

3.3.2 METHODS

The loading schedule for the tests is shown in Table. 6. Based on the results of the BRB stand-alone tests, the loading was controlled using the value of axial deformation δ_{b1} of the BRB up to the yield displacement δ_y of the BRB at the structure surface, and was repeated 3 times each at $\pm \delta_y \times 0.5$ and $\pm \delta_y$ in alternating cycles. The load was then repeated 3 times alternately at ±1/300, ±1/200, ±1/150, ±1/100, ±1/75, and ±1/50 of the deformation angle of the specimen, respectively, and after 1/50, the load was monotonically applied in the tensile direction until failure. The test was not conducted from 7C to 9C because the target interlaminar deformation angles of 7C to 9C were reached in the first cycle up to

https://doi.org/10.52202/069179-0201

6C. In the frame tests, applied loads, overall displacements, rotation angle and shear deformation of each joint element, and axial displacement of the BRB were measured. The horizontal displacement of the specimen δ was determined by the relative displacement of columns

3.3.3 RESULTS AND DISCUSSIONS

The load-deformation relationship and envelope are shown in Fig. 12. 1C to 6C, the deformations are significantly different on the positive and negative sides. This is partly because the displacement was controlled by the axial displacement of the BRB, but the main reasons for this are the clearance of the bolted joints in the Joint B hardware and the one-sided effect of the hardware, which resulted in a large slip on the tensile side. In each of the subsequent cycles, the load on the compression side was slightly higher than that on the tension side.

Table. 6 Loading schedule

	Target	
	BRB disp. [mm]	Angle of deformation [rad]
1C ～ 3C	1.13	-
4C ～ 6C	2.26	-
(7C ～ 9C)	-	1/300
10C ～ 12C	-	1/200
13C ～ 15C	-	1/150
16C ～ 18C	-	1/100
19C ～ 21C	-	1/75
22C ～ 24C	-	1/50
25C	-	Pull

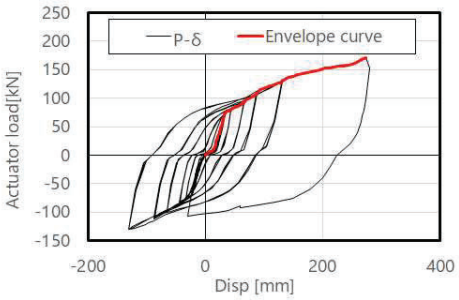

Fig. 12 Test result (P-d carve)

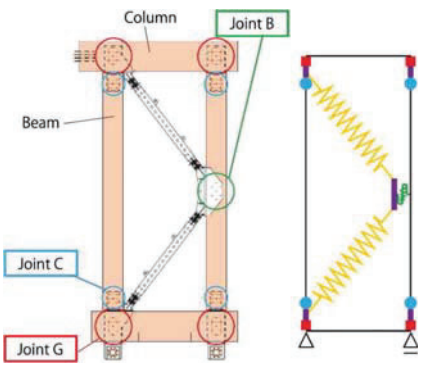

Fig. 13 Analysis model

3.4 ANALYSIS MODEL

3.4.1 JOINT

An overview of the modeling is shown in Fig. 13. The timber is modeled as a beam element, and each joint and BRB are modeled with the nonlinear springs shown in Fig. 14. The beam elements (▬) between joint C (■) and joint G (●), between BRB and joint B (●), were input as rigid bodies. Joint C (■) was modeled with rotational and shear springs, and joint G (●) with rotational and axial springs. For joint B, only the shear spring acting in the vertical direction was input, assuming no rotation. The stiffness and bearing capacity of the joints were determined by the European Yield Theory [1, 4] for performance per a steel dowel and corrected by the burden area based on the results obtained in 2. After confirming that the mode of failure did not change with the difference in burden area, these results were added together.

3.4.2 BRB

The BRB was assumed to be a nonlinear spring of an axial spring. For the modeling of BRBs evaluated as axial springs, BRBs were synthesized from the stiffness of the centrally buckling-constrained core section and the stiffness of the cross section at the ends. If the stiffness of the core section is k_{B1} and the stiffness of the end cross section is k_{B2}, the composite stiffness $k_{BRB}=1/(1/k_{B1}+1/k_{B2})$. From the cross-section of the plasticized section of 12mm x 32mm and the yield point strength of 294 MPa, the yield capacity is 113kN and the axial stiffness k_{B1} is 49.9kN/mm. The stiffness k_{B2} of the cross section was determined to be 300kN/mm for the axial stiffness except for the plasticized section. The ultimate strength of the plasticized section is 400 MPa and the stiffness reduction ratio $\alpha = 0.02$, and the stiffness is obtained by synthesizing the secondary slope in the same manner, assuming that the ends do not yield. The obtained bilinear curve of BRB is shown in Fig. 15.

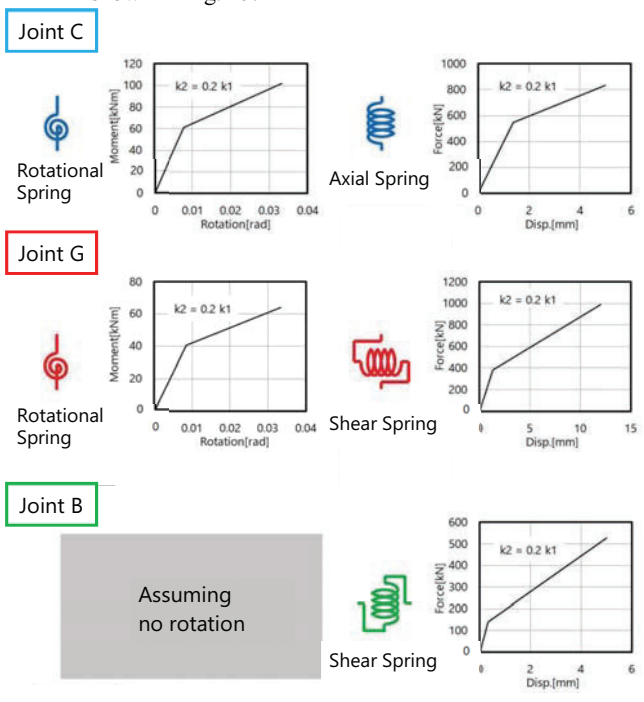

Fig. 14 Analysis model (each joint)

https://doi.org/10.52202/069179-0201

3.4.3 ANALYSIS RESULTS

For the orange graph in Fig. 16, the solid line shows the test results and the dotted line shows the analytical model applied up to 1/20 rad by pushover analysis. The solid line is a graph of the load P and displacement δ extracted at the first deformation experienced in the positive (tensile) direction from the start of the test and when the load value is greater than or equal to the load value recorded previously. The timing of the yielding of the joints during the analysis is noted in the figure. The shear and axial springs were elastic, and the rotational springs yielded at joints G and B, in that order. At these two timings, the four joints yielded almost at the same time. A comparison of the experimental and analytical jack load-deformation relationships for each joint is shown in Fig. 17.

(A) Joint C - Rotation angle

At all locations below 125kN where failure occurs, the analytical and experimental results agree well. The calculated yield rotation angle was 1/130 rad, and yield deformation was not reached.

(B) Joint G - rotation angle

Experimental and analytical values are in good agreement up to a cycle of 100kN and 1/75 rad of the specimen in terms of load value; above 100kN, the experimental value exceeds the analytical value in the large deformation region.

(C) Joint C - horizontal shear deformation

For the applied force side (U), the rotational component was subtracted from the displacement measured on the underside of the timber to obtain a value, so there is some variation in the trajectory of the graph, but the displacement is within about 1mm, which is the clearance of the joint. In North-D_C-S_H, the joint hardware is directly connected to the pin joint but there is some movement, and there is slip until the column member resists. (There are restraints at both ends of the below column to prevent horizontal movement.)

(D) Joint G Load - Vertical shear deformation

Slip of 1mm or less is observed at load 0 in general, which may be due to the effect of the gap around the steel dowel. In the analysis, the joint did not yield up to about 170kN, but in the experiment, plastic deformation occurred around 150kN on the South side at 1/50 rad or later when the joint was pulled apart; when the displacement of South- D_G-S reached 4.4mm, the joint cracked and the displacement increased to 8.8mm at once.

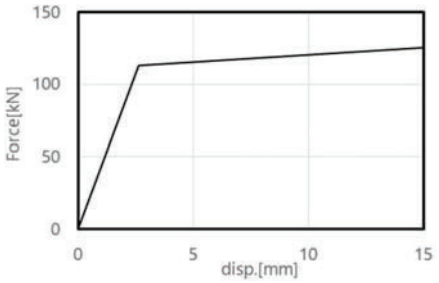

Fig. 15 P-d carve (BRB, bi-liner)

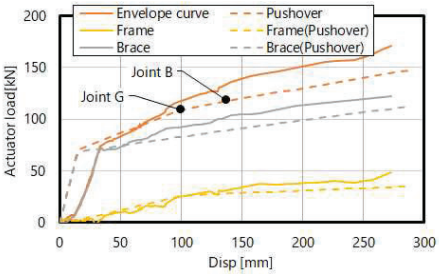

Fig. 16 P-d carve (Envelop curve and Analysis)

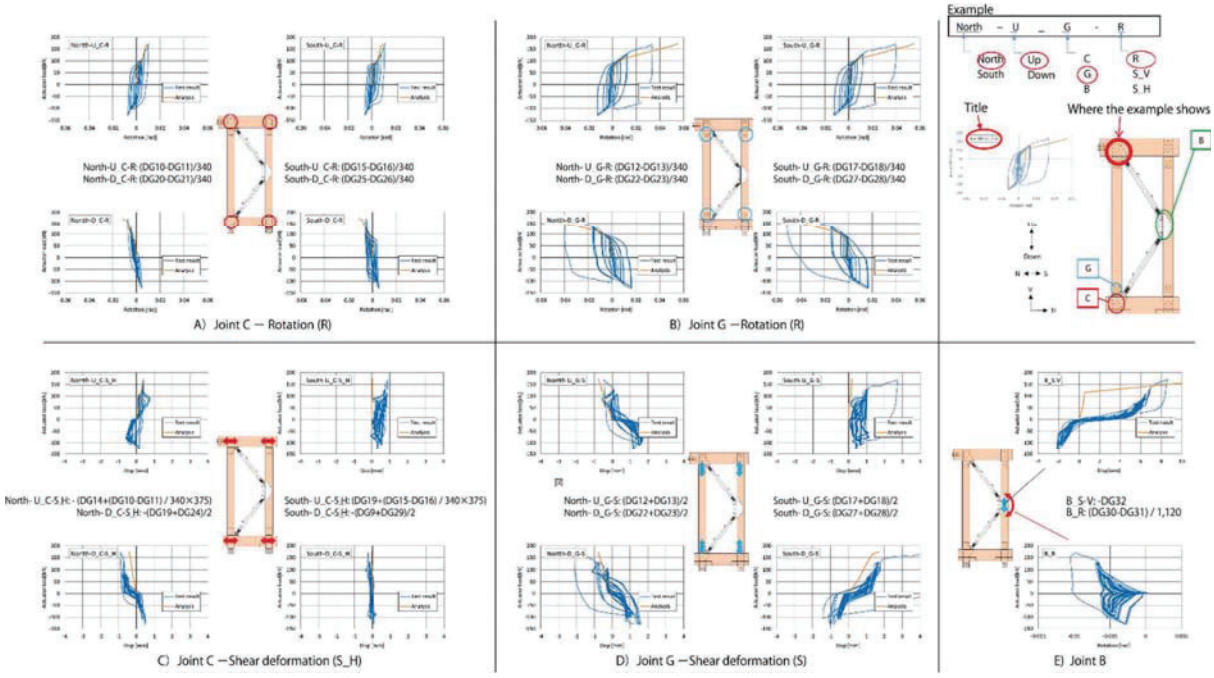

Fig. 17 Comparison of experimental and analytical results (each joint)

https://doi.org/10.52202/069179-0201

Table. 7 The specifications of the members used for the column-base joint specimen

Parts	Classification	Size[mm]	Grade	Standard
Column	Structural glulam (Japanese Larch)	300×900	E105-F300	JAS
GIR	Deformed steel bar (threaded section rebar)	D29	SD345	JIS G 3112
Steel shoe	Rolled steels for building structure	t=16, 22, 32	SN400B	JIS G 3136
Glue	Epoxy	—	—	—

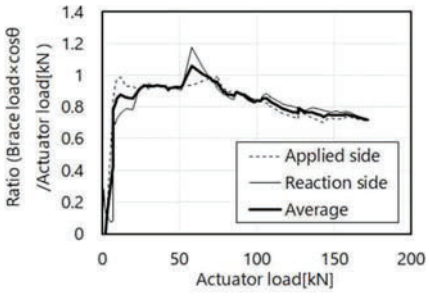

Fig. 19 Ratio of force borne by the brace

E) Joint B

In the experiment, the joint slipped about 4mm in the vertical direction. This is thought to be due to the effect of the gap of the hole on the diameter of the joint B joint. This is also evident in the initial slip of the overall deformation. The reason for the rotation of joint B is thought to be that the deformation of the frame created a hinge in the cruciform steel portion of the brace end, and because of the distance between the attachment points of the connection hardware B, the expansion and contraction of the brace created an angle in the connection hardware.

3.4.4 ESTIMATION OF HORIZONTAL LOADS TO BE BORNED BY THE BRB

In creating the orange lines in Fig. 16, the deformations δ_{b1} and δ_{b2} of the two BRBs were recorded at the same time. The axial force of the brace is estimated from these deformations and the envelope in Fig. 10, BRB test result. The load borne by the BRB during the frame test can be assumed to be the horizontal component of the estimated axial force of the BRB. (Horizontal load borne by BRB = BRB estimated axial force × cosθ [where cosθ = 2,448mm / 4,028mm]). The load-bearing ratio is the ratio of the BRB load divided by the actuator load P. The obtained load-bearing ratio of the BRB is shown in Fig. 19. Initially, the value is small due to slip, but it soon approaches 1.0 and remains at about 1.0 when a force of about 10kN is applied, and after P reaches the yield capacity, the burden ratio decreases to about 0.8. This result indicates that the forces acting on the upper and lower BRBs were almost the same. As a result, there was almost no bending moment of the beams due to the disproportionate force of the braces.

Grey line in Fig. 16 shows the average of the loads on the upper and lower BRBs and yellow line in Fig. 16 shows the load on the frame (the envelope curve of the solid orange line in Fig. 16 minus the load applied to the BRB [Grey line]). From these results, it can be confirmed that up to the yield load, the brace alone resists the load. After the yield load, the frame bears about 20% of the load, but no damage was observed up to 1/50 rad, confirming the integrity of the frame.

4 COLUMN-BASE JOINT

4.1 INTRODUCTION

As buildings rise in height, axial forces (e.g. dead weight) acting on columns increase, and it is known that axial forces affect the moment capacity of column base. Therefore, in order to model the first-floor column bases of a 10-story timber-frame apartment building and to create an *M-N* interaction curve showing this effect, bending tests were conducted using the column axial force as a parameter while applying a vertical load. The test results were used to validate the modeling and the method used to model the first-floor column bases.

4.2 MATERIALS AND SPECIMEN

Fig. 18 shows an overview of the test specimen. Table. 7 shows the specimen specs. The lumber used was E105 F300 laminated larch of symmetrical mixed-grade. The steel shoe was made of SN400B and SN400C, which were used to connect the timber to the slab. The first-floor columns were assumed to be 900mm x 900mm in cross section, but the cross section of the specimen was 300mm × 900mm with the cross section multiplied by 1/3 in the depth direction due to the capacity of the jacks to apply vertical loads and horizontal forces. A maximum axial force of 5,400kN is considered to act on the assumed first-floor columns in the design. The axial force parameters were 1,800kN (test symbol N1800), which is 1/3 of the assumed load, 900kN (test symbol N0900), which is 1/6 of the assumed load, and no axial force (test symbol N0000), and one of each was tested. The specimen setup is shown in Fig. 20 and Fig. 21. The height of the force point was set to 2,500mm, the height of point of contraflexure obtained from the analysis. The height of N0900 and N1800 timber was set to 1,925mm, subtracting

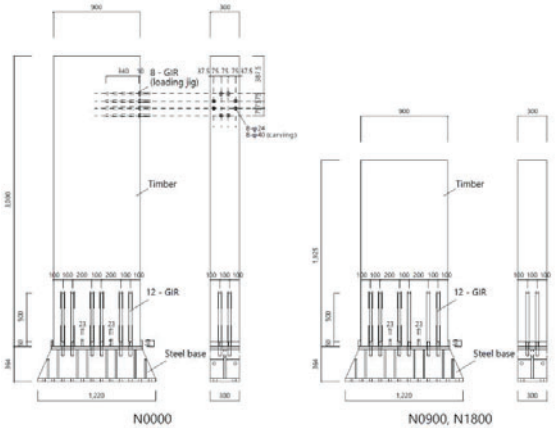

Fig. 18 Specimen detail

https://doi.org/10.52202/069179-0201

the height of the jig. The height of the N0000 timber was assumed to be 3,000mm, including the extra length. The steel shoe was also multiplied by 1/3 in the depth direction. For shear forces acting on the timber column ends, SN400B steel plates, 22mm thick and 50mm high, welded to the top of the steel shoe was designed to act as shear keys and bear the shear forces. Four shear keys were placed at the locations that divide the timber into three equal parts in the width direction and at both ends. Shear keys were inserted into grooves 23mm wide and 60mm deep on the timber side. The Glued in rods (hereinafter referred to as "GIR") for column bases were machined from SD345 D29. The gluing section was 500mm long, with a plasticized section 22mm in diameter and 50mm long, and an M27 screw machined into the end. The GIR used can be considered to have three possible failure modes: (1) failure of the plasticized section, (2) failure of the adhesive section, and (3) collective shear failure of the timber section. The upper limit of the maximum bearing capacity of the plasticized section was assumed to be lower than the lower limit of the maximum bearing capacity of the adhesive section, and it was judged that (2) would not occur. In addition, for the collective shear failure of timber, since the perimeter area surrounded by four GIRs is larger than the perimeter area of one GIR × 4 GIRs, it was judged that (3) collective shear failure of timber would not occur.

From the above, it was confirmed by manual calculations that the joints of GIR fail prior to the plasticized part during pull-out. To control the strength of the plasticized section, an upper strength limit of 550N/mm^2 (=210kN) was ordered, and the actual value (mill test report) was 554 N/mm^2 The JIS standard values and mill test report values are shown in Table. 8. Epoxy resin adhesive (Home Connector Co., Ltd.: AHC-E) was used as the adhesive. After the adhesive had cured, the threaded portion of the GIR was fixed with a double nut while measuring the strain gage value so that the initial tension of the GIR was approximately 10kN. For the specimens with axial force, the nuts were fastened after the axial force was applied.

4.3 METHOD

The specimen with axial force was loaded vertically by vertical jacks at both ends through a pin jig at the top. The pin jig was in contact with the upper timber face and the sides were clamped by brackets with a clamping mechanism. The tightening mechanism was adjusted at the maximum deformation of each cycle because a gap was created on the sides due to the pin fixture when a horizontal force was applied. The distance from the top of the steel frame trestle to the center of the pin was assumed to be 2,500mm at the height of point of contraflexure. For the specimen without axial force, a 3,000mm-high timber was used and eight GIRs were joined so that the force point was at 2,500mm. In this test, deformation was controlled by the angle of rotation between the timber and the steel shoes. The axial force of the GIRs was calculated from the average of the axial strains of the two GIRs. Two strain gauges were placed at the axisymmetric position of the plasticized GIR for the purpose of measuring the axial force of each GIR.

The loading schedule was as follows: three cycles of positive/negative alternating loading at angles of rotation θ of 1/900, 1/450, 1/300, 1/200, 1/150, 1/100, 1/75, and 1/50 rad for the column bases between timber and steel shoes; 1/30 rad of positive/negative alternating loading; and then monotonous loading until failure. For N0000 and N1800, the deformation was controlled by the rotation angle θ. For N0900, it was determined that the rotation angle θ could not be used to control the deformation due to cracking and separation of the timber observed in the N1800 test. The corrected rotation angle θ' used for control is shown in Eq. 4. The corrected rotation angle θ' was corrected using the displacement $\delta_{1/100}$ at 1/100 rad, assuming that the horizontal displacement δ is proportional to the actual rotation angle.

$$\theta = \begin{cases} \theta & (\theta < 1/100\,rad) \\ 0.01 \cdot \delta/\delta_{1/100} & (\theta \geq 1/100\,rad) \end{cases} \qquad \textit{Eq. 4}$$

4.4 RESULT

Fig. 22 through Fig. 24 show the M-θ relationships obtained from the tests. The GIR plasticized section yielded first at the moments shown in each figure, and the bearing capacity decreased with rupture. However, in the case of N0000 and N0900, cracking occurred near the joints before the GIR plasticized section ruptured, and in the case of N0900 and N1800, cracking and separation of

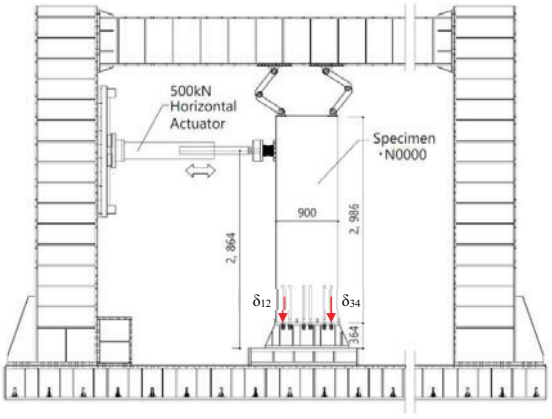

Fig. 20 Test setup of specimen (N0000)

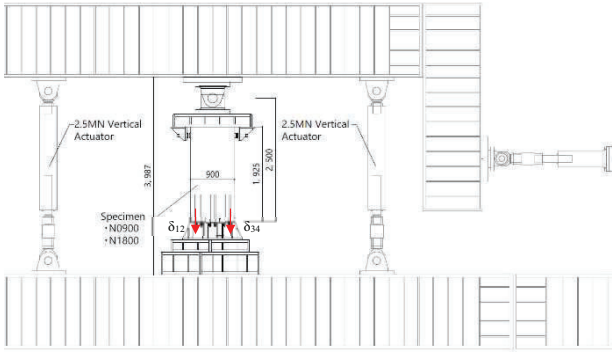

Fig. 21 Test setup of specimen (N0900, N1800)

Table. 8 the value of standard and mill test report

	σ_y N/mm^2	σ_u N/mm^2	YR %	Elongation %
Standard	345~440	Over 490	Over 80	Over 19
Report value	392	554	71	23

https://doi.org/10.52202/069179-0201

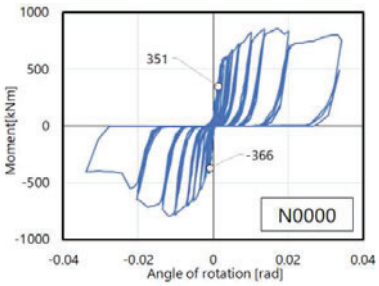

Fig. 22 Moment-rotation relationships(N0000)

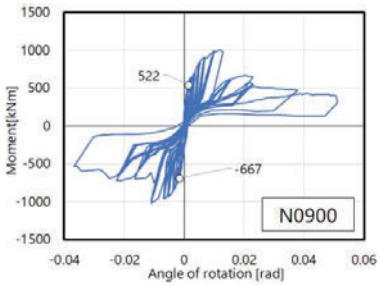

Fig. 23 Moment-rotation relationships(N0900)

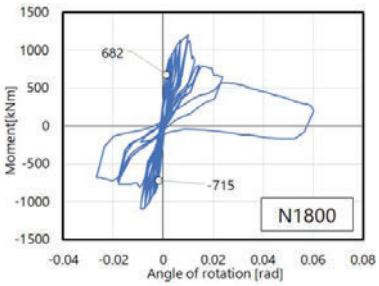

Fig. 24 Moment-rotation relationships(N1800)

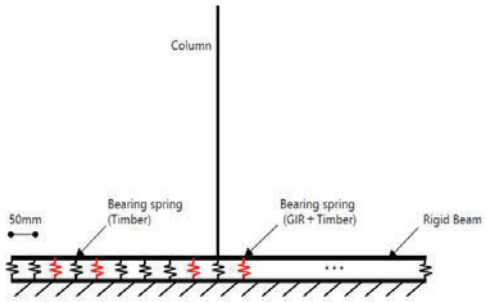

Fig. 25 Multi-spring model

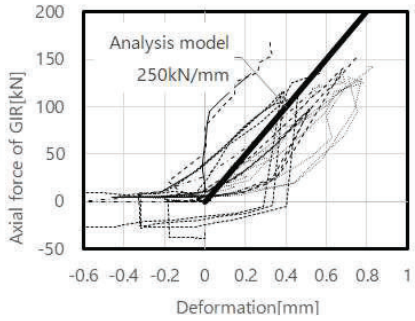

Fig. 26 P- δ curve (GIR)

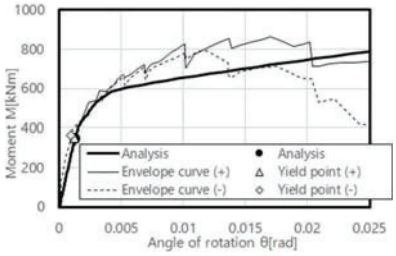

Fig. 27 Moment-rotation relationships(N0000)

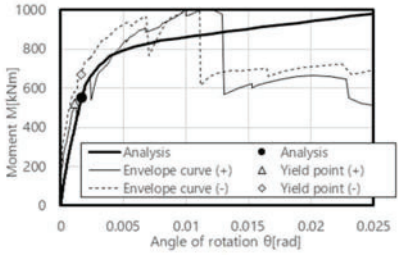

Fig. 28 Moment-rotation relationships(N0900)

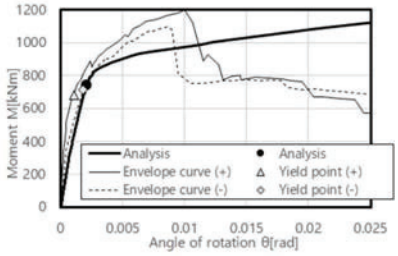

Fig. 29 Moment-rotation relationships(N1800)

the timber occurred as described above. Based on the above, the performance of this column-base joint was allowed up to the yield of the GIR plasticized section.

4.5 ANALYSIS MODELS

4.5.1 MULTI SPRING MODEL

The specimen was modeled with a multi-spring model using beam elements shown in Fig. 25. The analytical model consisted of rigid beams placed parallel to the ground plane and timber beam elements with a cross section of 300 x 900. The rigid beams were split at 50mm pitch, and GIR springs were placed at the same locations as the specimen. The ground plane was input with a surface pressure stiffness spring with stiffness acting only in compression.

4.5.2 EMBEDMENT STIFFNESS

For the embedment stiffness of the multi-spring model, k_{0c}=25N/mm^3[5] was used. For both ends of the rigid beams, 187.5kN/mm was used because the burden area is 1/2 that of other contact points. For yield capacity, a reference bearing capacity of 25.4MPa [1] was used.

4.5.3 GLUED IN RODS

The relationship between axial force and lifting (δ_{12}, δ_{34}) of GIRs obtained from all test results is shown in Fig. 26. The lifting displacement was the average of the vertical relative displacements of the front and back of the timber. From these results, the GIR stiffness k_{GIR} was read as 250 kN/mm, indicated by the thick red line in the figure, and used in this study. k_{GIR} is the composite stiffness obtained by connecting the stiffness k_f of the GIR anchorage section and the stiffness k_y of the plasticized section in series. k_f is obtained as 298kN/mm from k_y = 1,158kN/mm. Based on these results, a value of 500kN/mm was entered for the two GIR springs in the analytical model. α = 0.0088 was used for the GIR stiffness reduction rate, assuming that the elongation reaches the tensile strength at 12%.

4.6 DISCUSSIONS

4.6.1 COMPARISON OF ANARITICAL AND TEST RESULTS

To validate the analytical model proposed in 4.5, the moment-rotation angle relationship of the test results and the analytical results were compared in Fig. 27 through Fig. 29. The analytical results tended to be closer to the less stiff envelope of each positive and negative envelope of the test results. For the analysis results shown in Fig.

https://doi.org/10.52202/069179-0201

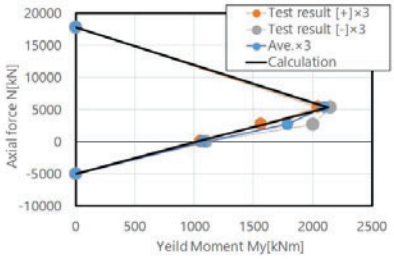

Fig. 30 M-N interaction curve (Section: 300×900)

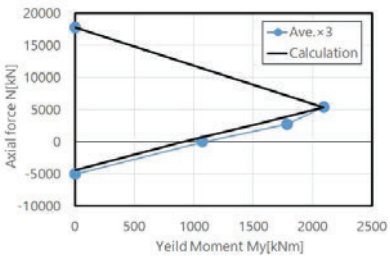

Fig. 31 M-N interaction curve (Section: 900× 900)

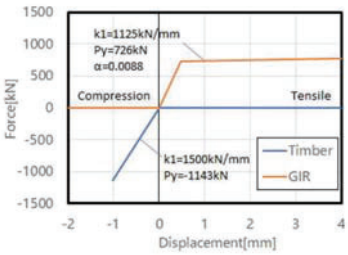

Fig. 32 Springs used for analysis

27 to Fig. 29, the yield point of GIR was taken from the mill test report value (f_y=392 MPa). The *M-N* interaction curve was prepared from the yield moment obtained and is shown in Fig. 30. It was confirmed that the analytical and experimental values were generally consistent.

4.6.2 M-N INTERACTION CURVE FOR ANALYSIS, AND VERIFICATION

The first-floor column cross section of the building under study is 900mm x 900mm. The column cross section is square. This means that in the width direction, the columns have the same configuration as the 300mm x 900mm columns used in the experiment (GIR and shear key locations), and the column cross section on the first floor is the same as three 300mm x 900mm columns in the depth direction. Here, the tripled test results are compared with the results of the analysis on the 900mm x 900mm cross section. In Fig. 31, the test results multiplied by 3 are compared with the analytical results (design specifications) using the lower limit of the reference value for yield strength of deformed bars (f_y = 345 MPa). Fig. 32 shows the parameters of each spring used as analysis conditions. It was confirmed that the values of the design specifications obtained from the reference values were inside the experimental values, i.e., on the safe side. The test ratio of the base metal at *N*=5,400kN was 0.97. The validity of the break point position was confirmed because the failure mode would change if the axial force increased beyond this point.

5 CONCLUSIONS

Multi knife-plates steel dowel connections

1. If the distance between dowels is sufficient, shear performance is proportional to the number of dowels.
2. As a simple calculation method, Multi knife-plates steel dowel connection was confirmed that the addition rule based on the burden area can evaluate.

Frame-testing

1. Using the simplified calculation method obtained in Section 2, the experimental results could be simulated with accuracy.
2. We checked the stress sharing ratio between the brace and the frame, and confirmed that almost no bending moment is applied to the beam ends until the brace yields.
3. Slip of about 4mm was observed at the connection covered by the steel plate. This was due to the clearance of the specimen. (2mm timber + 2mm steel plate) This slip deformation may have contributed to the slip in load de formation relationship.

Column-base joint

1. The performance of the column-base joints with GIR was verified through experiments to develop an *M-N* interaction curve that evaluated the effect of axial forces.
2. It was found that a multi-spring model using embedment stiffness k_{0c}=25N/mm^3 and the lower limit of the reference value for the yield strength of deformed steel bars could be used to model joint performance considering the effect of axial forces.

ACKNOWLEDGEMENT

This research was conducted as part of “Innovative technology for maintenance and management of construction and infrastructure and for disaster prevention and mitigation” in Public/Private R&D Investment Strategic Expansion PrograM (PRISM) add-on item “R&D Project for tall wood building for saving construction site of recovery housing “under the leadership of Japanese Cabinet Office.

REFERENCES

[1] Architectural Institute of Japan: Standards for Structural Design of Timber Structures, 2006.12F
[2] Japan Housing and Wood Technology Center, Allowable Stress Design of Wooden Houses with Post and Beam Construction System (2017 ed.)., 2017.3, p. 301
[3] Nippon steel engineering Co., Ltd., Unbonded Technical Data Design Edition, p3-3, 2019.4.
[4] Johansen K W: Theory of Timber Connections, International Association of Bridge and Structural Engineering, Publication No. 9, Bern, Switzerland, pp. 249-262, 1949.9
[5] Nagashima, T., Tachibana, K., Yano, M. and Ohashi, Y.: Design methods for post-tensioned timber shear walls (Part 1). Triangular embedment stiffness and behavior in the elastic range, Journal of Structural and Construction Engineering, Vol. 85, No.770, pp. 539-549, 2020.4

NOTE

・Regarding to 2, 3.3, 4, these tests were conducted at the Central Testing Laboratory of the Japan Testing Center for Construction Materials.
・Regarding to 3.4, this test was conducted at the Structural Laboratory of Sumitomo Forestry Tsukuba Research Institute.
・Midas iGen Ver.900 was used for the analysis study.

World Conference on Timber Engineering Oslo 2023

HASLE TRE: NORWAY'S FIRST TIMBER OFFICE BUILDING DESIGNED FOR DISASSEMBLY AND REUSE

Ona Flindall[1], Jørgen Tycho[2], Moritz Groba[3]

ABSTRACT: Design for disassembly is a key strategy for ushering the building industry into the age of circular economy. Timber offers an efficient structural solution to meet growing environmental challenges. Yet the timber material lifecycle has primarily remained linear. Design for disassembly and reuse can close timbers material loop and build a circular value chain. The HasleTre project is Norway's first timber office building designed and constructed explicitly with the intention of future disassembly and reuse. In this paper, the architects at Oslotre presents the key design solutions that have been developed for the project. Timber-to-timber connections have been central to the project's design and offers interesting solutions for the circular future of timber architecture and engineering.

KEYWORDS: disassembly, demount ability, reuse, recycle, energy, carbon impact, timber-to-timber joints, carpentry joints

1 INTRODUCTION

Rising prices of timber and other building materials have put an economic incentive on material efficiency, reinforcing the moral imperative in the face of climate change to reduce overall material usage [1]. The C40 report on Building and Infrastructure consumption emissions, highlights that over 60% of the building industry's emissions are associated with the production and delivery of building materials [1].

Timber's ability to sequester carbon gives it significant environmental advantages and offers an efficient method for removing CO2 from the atmosphere and mitigate against the effects of climate change. Yet this equation is only valid for the lifetime of the relevant building components. Once decommissioned timber components are today primarily chipped and used for energy production, releasing the stored CO2 back into the carbon cycle. In 2019, it was estimated of the 815 thousand tons of wood waste produced in Norway, only 6% went to material recovery [1].

In 2021 more than half of all timber waste generated by the Norwegian building industry resulted from demolition and rehabilitation [1]. Office buildings are a typology especially prone to generation of waste materials due to the frequency of tenancy rotation and shifting interior preferences. Depending on tenancy rotation the overall emission cost of refurbishment can ultimately outstrip the emission costs of the building's material production [1].

One key strategy for reducing the environmental impact of refurbishment and end of life demolition, is to design for disassembly and reuse. Ensuring that the lifetime of individual building components are prolonged beyond the lifetime of the buildings they temporarily inhabit. It offers a way of closing material loops, reducing material consumption and waste, prolonging components service life and increasing both on- and off-site reuse.

In this paper, we present Norway's first all-timber office building designed and built to be disassembled and reused; HasleTre.

2 THE PROJECT

2.1 BUILDING, SITE AND SITUATION

HasleTre is situated at the outer edge of the central city of Oslo, Norway. The project is a 3000m2 office building split over 5 floors including basement and roof-terraces. The project is part of a larger city development, HasleLinje, which includes a range of commercial and residential properties. The site is situated as one of two gatehouse plots and frames the square in front of the 1933 Norwegian government wine monopoly distillery, Vinslottet - "the wine castle", see figure 1.

The project was initiated in December 2019 and was completed in 2022.

[1] Ona Flindall, Oslotre AS, Norway, ona@oslotre.no
[2] Jørgen Tycho, Oslotre AS, Norway, jorgen@oslotre.no
[3] Moritz Groba, Oslotre AS, Norway, moritz@oslotre.no

https://doi.org/10.52202/069179-0202

Figure 1: *Historic Vinslottet, refurbished into commercial facilities and housing in 2020.*

2.2 THE BRIEF

The initial brief given by the property developers; Höegh Eiendom and AF Eiendom, was the design and development of an environmentally friendly, flexible, and innovative commercial build.

During the early concept phase of the design process the ambitions of the project were developed in collaboration with the architects and key advisors. Resulting in a revised and ambitious brief for an all-timber building designed for disassembly and reuse. The project should also reduce overall GHG emissions with a minimum of 50% and be certified to BREEAM NOR Excellent standard.

2.3 THE CHALLENGE

Allowing for effective reuse of buildings, both during its lifetime and at the end of service life, offers several separate design challenges and requires a number of different solutions, at different levels of design and development. As a designer you are facing the challenge of designing for a second-hand market whose preferences and needs are yet unknown and in large part unpredictable.

Two key design strategies have been central to the design for disassembly solution for HasleTre. Firstly, the development of timber-to-timber joints and connections allow for reduced use of steel and ease of disassembly. Secondly, the development of technical and structural solutions that allow for flexibility in use during life, simplified separation at end of life, all the while retaining a second-hand value of components and materials.

In combination, these two key design strategies aim to retain the structure's second-hand reuse potential, flexibility and financial value.

2.4 ACKNOWLEDGEMENT

This paper will focus on the architectural and structural design solutions developed for and realised in the HasleTre project. However, the authors of this paper wish to recognise at the outset that the realisation of HasleTre has required a collaborative effort from all actors involved, including developers, contractors, and planning authorities.

HasleTre is a result of a well-established cooperation between ambitious property developers and a visionary design team, with a mutual goal of realising something extraordinary. Without the work and collaboration of Seltor as building contractors, the project would not have been realised. The collaboration and mutual goals of the entire team have been an underpinning prerequisit and requirement for realising a project of this magnitude and ambition.

3 DESIGN

3.1 DESIGN FOR LONGEVITY

3.1.1 Architectural quality and durability

Design for disassembly will mitigate against the emission costs of demolition at end of life. But the most effective climate measure is to prevent, or delay, demolition by extending the buildings service life. [1] In a social and cultural context that values the immediate and transitory extending, a buildings lifetime requires architectural design for aesthetic and material longevity.

Groba has shown how timber as a construction and surface material can increasing the lovability of buildings, and how buildings that are loved last longer and thus contribute to both ecological and social sustainability. [1]

By prioritising quality and simplicity in both structure and interiors HasleTre is designed for durability. The overall design and facades mirror the historic and 'timeless' character of the neighbouring heritage building. The high quality all timber surfaces both interior and exterior are hard wearing and will age with grace and character building on the emotional connection that encourages occupants to care for and remain in the building.

Figure 2: *Designed for longevity and lovability. Designed for enduring taste.*

3.1.2 Planed for flexibility

To extend a building's life expectancy it is important to consider and facilitate for changing needs and requirements. HasleTre embraces flexibility in use as well as reuse. The building is designed to facilitate for shifting spatial needs, technical requirements, and preferences. Organised around a central core the two wings of the plan offer a variety of available areas and a potential for division of the building and individual floors among one or multiple tenants. The floor plans are further subdivided by a 5x5m grid system which can easily subdivide the open spaces into smaller enclosed working spaces, see figure 2. The flexibilities in plan and grid allows occupants to reconfigure plans and internal elements without having to make structural and exterior changes.

Figure 3: *Typical floor plan, divided into two main segments and further subdivided by structural grid.*

Flexibility in structure and plan is facilitated further by use of a Granab subfloor system and open technical infrastructure for ventilation and sprinkling in the ceiling. The technical infrastructure needs of the future may be difficult to predict, but by giving ease of access, HasleTre ensures the building can be adapted for a variety of uses during its lifetime and handle larger societal changes and changing technical infrastructure.

Figure 4: *Subfloor system and open central ventilation system allows for swift and easy changes to interior arrangement.*

3.1.3 Design for production, effective material use and ease of assembly and disassembly

The building is a CLT slab and glulam post and beam structural system. Designed for disassembly and reuse, all components are carefully planned and designed to enable an easy assembly and disassembly process.

All of the timber components are designed to minimize cut-offs in production and designed for standard production dimensions. Designed for the Master Element production in the CLT factory each floor slab utilises the standard three by fifteen meter elements. This reduces the need for cut offs, maximise the space on the lorry and gives a fast assembly.

To retain reuse potential, all permanent fusing joints and sealants had to be avoided wherever possible. A full disassembly manual follows the building at completion.

3.2 DESIGN WITH REUSE

HasleTre was built to be dismantled and reused, but also built to include the reuse of material components where possible. The project reuses the ventilation aggregate, acoustic ceiling plates, sanitary installations like sinks and toilets, flooring in secondary rooms such as basement and technical rooms. Designing with reuse requires an attention to details to handle the overall material pallet and relies on an availability of components.

https://doi.org/10.52202/069179-0202

Figure 4: *Second-hand acoustic panels for use above ceiling battens.*

HasleTre was let to the charity Save The Children from December 2022. As tenants, the reuse approach was further adopted and incorporated in their own interior design. Ensuring that the majority of all furniture and inventory brought into the building was either reused, recycled or upcycled.

3.3 DESIGN FOR REUSE

3.3.1 Second-hand value of standard dimensions

The project aims to be the standard to beat in new circular builds. By utilising standard production formats and dimensions, the timber structure actively aims to retain value of the component for second-hand use. By limiting perforation of structural components the overall material use is reduced in the project, while the potential for second hand adaptations is secured. The CLT floor slabs are utilised as master elements in full. To facilitate for technical facilities the inherent strength of the CLT slabs is utilised to 'carry' the extension between the beam structures. Resulting from this strategy the glulam beams are not perforated to facilitate technical services and the material use and cost is reduced while the beams remain versatile and adaptable for future use.

Figure 5: *Glulam and CLT timber-structure. Note cantilevered beams give space for ventilation and fire systems.*

3.3.2 Timber-to-timber joints

The building structure is an optimised timber structure that aims to reduce the use of steel and other metals to a minimum. Replacing conventional steel joints between timber components with timber-to-timber alternatives. This is done both to reduce the overall use of steel, but also to ensure that the timber component can be reworked and remodelled using industrial tools to facilitate for future reuse without facing limitations due to the danger of steel embedded within the components.

Two key joints have been utilised in the project; Firstly the use of hardwood dowls in post-beam nodes and the use of x-fix joints between CLT slabs. In addition, all interior cladding is assembled with hardwood nails.

Through careful structural design, the tension loads on the joints have been reduced and enabled a simplified dowel joint. Using only two hardwood dowls in beech, the joint is not only materially efficient, but also labour efficient. Significantly reducing the assembly time on site. The dowels are dried to 6% before insertion. Once inserted the wood will adjust to surrounding moisture and lock the components in place. At disassembly the dowel can be drilled through and the connection released.

https://doi.org/10.52202/069179-0202

Figure 6: *Hardwood dowels during assembly of timber structure.*

CLT slabs in the building walls and floors are connected using X-Fix plywood connectors that replace the traditional use of metal screws. This is the first time the X-Fix connectors are used in Norway. This significantly reduces the overall use of steel and increases the reuse potential and value. The X-fix system has also proved to be an incredibly timesaving process in assembly on site.

Figure 7: *X-Fix dove-tail connection between CLT slabs.*

Furthering the timber-to-timber joints to its final conclusion, both interior and exterior cladding is assembled using wooden nails as fasteners. As with the structural components the use of timber joiners enables an easy remodelling or furnishment at the end of life.

Figure 8: *See the heads of the small timber nails to the left in the photo.*

4 LESSONS LEARNT

The HasleTre project has been a valuable learning experience for all parties involved and there is a desire to inspire others to think reuse, both today and for the future. The development and use of innovative and demountable structures require discipline and desire from developers, designers, and contractors. Developing a mutual understanding of collective goals and aims has been essential to the successful application and realisation from development stage to completion.

In all innovative projects the division of responsibilities will be challenging. Uncertainty and insecurity in realising untried approaches and solutions can quickly lead to conflicts and difficulties within the project teams. In the HasleTre project the architects were able to take on the responsibility for the structural engineering and mitigate against insecurities with suppliers unfamiliar with the solution.

The commercial reuse sector is growing and developing quickly, but it is still facing a number of challenges with regards to availability, lack of storage and cataloguing, just in time logistics and certification. This is reflected in the processes around HasleTre where the ambitions for reuse of materials restricted predictability and required selection and ad-hoc choices throughout the process.

Collectively, the timber-to-timber joints and solutions offer an adaptation of traditional building practices to industrial and prefabricated timber structures. Offering financial rewards in terms of reduced assembly time and a retained second-hand value of both interior and structural components.

5 DISCUSSION AND CONCLUSIONS

In 2022, the national building codes TEK17 were updated to include requirements for design and construction for disassembly. There is a political desire to increase circularity in the building sector. The attention HasleTre has drawn both nationally and internationally points to the

https://doi.org/10.52202/069179-0202

need for built projects and examples that can lead the way for implementation of these principles, and showcase the architectural potential in disassembly and reuse.

Vandervaeren, et al., have shown how current calculations methods for LCA fall short on adequately modelling material flows and stocks in demountable buildings. Failing to capture the potential benefit of designing a building for easy disassembly and reuse [1]. They go on to call for a method that captures the effects of demountable design principles in the input and output material flows during the replacement and end-of-life stages of built assemblies, and on the reusability of disassembled building parts.

As design for disassembly and reuse is developed as a design strategy, it is important to be able to show and quantify the benefits for the environment. The authors of this paper hope the HasleTre project will incentivise both the public and private sector to call for greater application and development.

The project showcases a number of key challenges faced when wanting to design, both when utilising and facilitating for future reuse of building components. It also offers a critical view to the choice of hybrid solutions for increased strength and meeting acoustic and fire demands, which if not carefully designed, will potentially limit reuse and recycle potential.

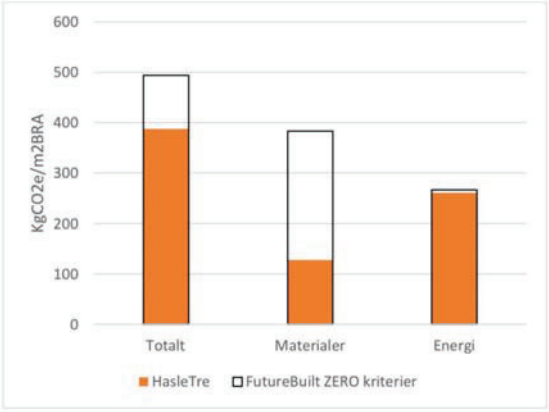

Figure 9: *GHG emissions compared with FutureBuilt ZERO cirteria.*

As built calculations show an overall 59% reduction in emissions from materials and energy use over a lifecycle of 60 years. Use of timber in post and beam structure, slabs and timber-to-timber joints have reduced the steel use in the building by 70% compared to a conventional office building [1].

REFERENCES

[1] Dempsey H., Financial Times, https://www.ft.com/content/53ffd3fc-8c7b-40ba-a29a-7a31cdd933e4, 06.march 2022

[2] C40 Cities, Arup and University of Leeds: Building and Infrastructure Consumption Emissions, 2019.

[3] SSB, www.ssb.no/en/natur-og-miljo/statistikker/avfregno, 2021

[4] SSB, https://www.ssb.no/natur-og-miljo/avfall/statistikk/avfall-fra-byggeaktivitet, 2022

[5] Solem, B., Eggen Arkitekter AS, Bærekraftig materialbruk, 4.november 2019

[6] EEA, Building renovation: where circular economy and climate meet, https://www.eea.europa.eu/publications/building-renovation-where-circular-economy, 2022

[7] Groba, U., The Oslo School of Architecture, Timber Tales: A Qualitative Study of Timber and Martilaity in Housin Projects, 2021

[8] Vandervaeren C., Galle W., Stephan A., Temmerman N.D.: More than the sum of its parts: Considering interdependencies in the life cycle material flow and environmental assessment of demountable buildings. Resources Conservation and Recycling. 2022

[9] Multiconsult, Rapport: Hasletre: Klimagassberegning – BREEAM og FutureBuilt ZERO. 2022

World Conference on Timber Engineering Oslo 2023

TOWARDS ADAPTABILITY AND CIRCULARITY OF TIMBER BUILDINGS

Robert Jockwer[1], Vera Öberg[2], Lisa-Mareike Ottenhaus[3], Paola Leardini[4], Yutaka Goto[5]

ABSTRACT: The construction industry has been a major contributor to resource consumption and global greenhouse gas (GHG) emissions, owed to high demand for building construction and the rapid urbanization trend. Timber construction has gained traction globally due to environmental advantages, such as renewability and carbon sequestration. However, sustainably available wood resources are limited. Extension of service life of timber structures is key to prolong their carbon stock. This paper showcases research projects carried out in Australia and Sweden that aim to design adaptable timber buildings capable of accommodating functional and spatial changes over time, thereby extending the service life of buildings and their components, as well as optimising their life cycles through spatial variations and repair of local damages to structural elements. This approach, known as Design for Adaptation (DfA) is an important step of the roadmap towards circular design solutions for timber buildings, which provide many economic, social and environmental benefits to all stakeholders and key players related to the building process, including manufacturers, engineers, architects, end-users, municipalities, and others.

KEYWORDS: Timber Buildings, Circularity, Adaptability, Sustainability

1 INTRODUCTION

Urban population has dramatically increased since the 1950s, driving the need for more buildings in densely populated areas globally [1]. As the construction industry has been a major contributor to greenhouse gas (GHG) emissions and resource consumption [2], the recent global attempt to decarbonise the construction industry has boosted interest in timber buildings due to their inherent environmental benefits.

For example, the Swedish construction market has seen a rapid growth of multi-storey timber construction for both residential and commercial buildings. The share of wood in newly built multi-storey constructions grew to approx. 20% in 2020, while it was 0% until the legislative change in 1994 [3], which was made possible by advances in fire safety engineering and allows to build more than 2 storeys in timber. Likewise, the Australian government is encouraging timber buildings as a pathway to emission reduction through policies and incentives, which has led to a nationwide timber shortage [4]. Although Sweden currently has a sufficient supply of timber for the domestic market, the export of sawn timber may increase from 70% of the current production to a much higher share in the coming decades, as it is expected that the timber construction industry will continue to grow globally [3].

Wood shortage is aggravated by its use in other sectors; wood is an attractive alternative as a renewable energy source and has applications in the chemical industry and for packaging. It is obvious that there must be a more rational and efficient use of raw materials in the overall wood-consuming industry; therefore, it becomes crucial to maintain the value of wood-based products and building components for an extended time. The best way is to utilize larger elements made of solid timber or engineered wood products (EWPs) as long as possible before letting them be transformed (cascaded) into other less valuable products, such as wood chip, pellets or pulps, which are the most common options. By reusing timber building components, the material is kept at the highest levels of the value chain, also assuring the continued storage of carbon in wood products [5].

In practice, when damages and deterioration of timber elements occur in critical parts of a structure, the whole building might need to be demolished if local repairs are not feasible for technical and/or economic reasons. Often though, other reasons may lead to building demolition and replacement. Regardless of the construction material (wood, concrete etc.), buildings might face the end of their service life due to the functional changes and different user needs over time. According to Thormark [6], there is a tendency for buildings in Sweden to be demolished far too early in terms of their technical service life; approximately 25% of buildings which have been demolished after 1980 were 30 years old or younger. If the construction system of those buildings, had allowed for easy removal or replacement of structural elements and enclosure components, their service life could have been significantly extended.

[1] Robert Jockwer, Chalmers University of Technology, Gothenburg, Sweden, robert.jockwer@chalmers.se
[2] Vera Öberg, Chalmers University of Technology, Gothenburg, Sweden, vera.oberg@chalmers.se
[3] Lisa-Mareike Ottenhaus, The University of Queensland, Brisbane, Australia, l.ottenhaus@uq.edu.au
[4] Paola Leardini, The University of Queensland, Brisbane, Australia, p.leardini@uq.edu.au
[5] Yutaka Goto, Chalmers University of Technology, Gothenburg, Sweden, yutaka@chalmers.se

https://doi.org/10.52202/069179-0203

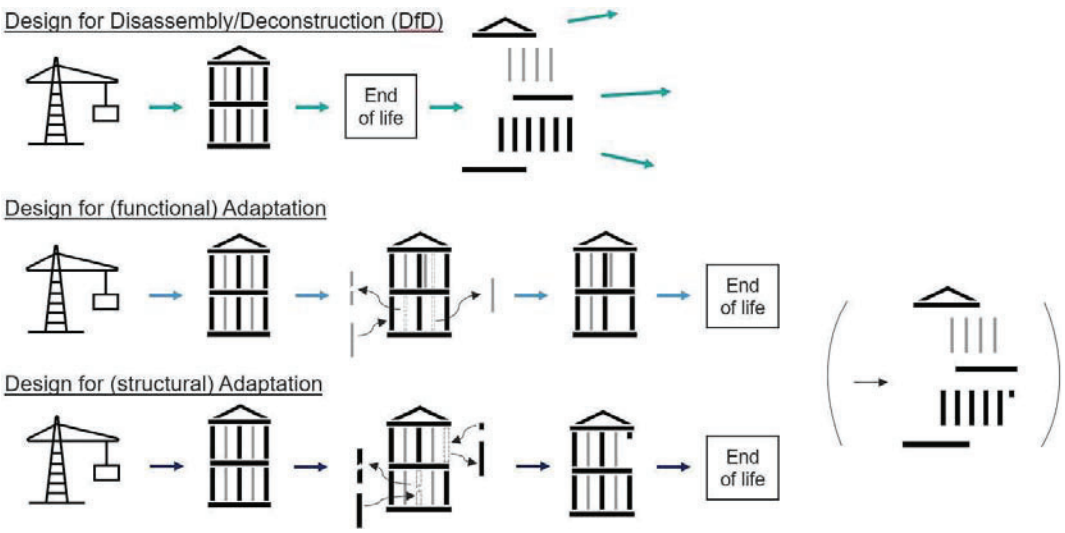

Figure 1: *Definitions and illustration of the concepts of DfD and DfA.*

To explore this potential, projects researching aspects related to adaptability and circular design of timber buildings have been initiated in parallel at Chalmers University of Technology (Chalmers) [7] in 2021 and at the University of Queensland (UQ) in 2022. They both focus on the numerous challenges still to be addressed in the circular design realm, such as a lack of adequate legal frameworks including standards, procurement requirements, regulations, and quality assurance, but also a lack of technical solutions for planners, engineers, and architects as well as a general lack of knowledge regarding the benefits of considering circularity and adaptability already in the design stage. Addressing these gaps requires the definition of a detailed and concrete roadmap towards the implementation of circularity and adaptability in timber buildings.

In this paper, we will critically present and discuss the concept and theory of design for adaptation (DfA), review the status of the timber and construction sector in Australia and propose the next steps to be taken for an effective implementation of DfA in timber construction.

2 CONCEPT AND THEORY

2.1 DfA and related concepts

Existing research on building adaptability has, to a large extent, focused on architectural and spatial changes. Definitions vary, but a common thread is the building's capacity to change in some way to meet new functional requirements or user demands, with the goal of extending its *useful life* [8]-[11] (for engineering aspects the term *service life* is used instead). DfA, in turn, has been described by Graham [12] as "a strategy used to avoid building obsolescence, and the associated environmental and cost impacts of resource consumption and material waste". While this could refer to the design for adaptability of both a building's structure and its non-load-bearing parts, this paper makes a distinction between the two, as designing adaptable non-load-bearing parts is dissimilar, both in execution and desired outcome, to doing the same for load-bearing parts. For example, designing non-load-bearing partition walls to be movable, removable, or replaceable enables the *functional* adaptation of indoor spaces without changing building structure and envelope, while designing parts of the structure, e.g., floors or load-bearing exterior walls, to be moveable, removable, or replaceable could instead defined as *structural* adaptation.

The concept Design for Disassembly or Deconstruction (DfD) is, in many ways, related to DfA, as it is a prerequisite for adaptability. DfD aims to limit waste production and raw material consumption by designing building elements (and the uncontaminated materials they are made of) to be disassembled and reused at the building's end of life [13],[14]. An important aspect of applying this concept to timber structures is the design of reversible connections [15], which are also crucial for designing timber structures for adaptation. It is indeed assumed that a timber structure designed for adaptation would also enable, or at least facilitate, deconstruction and reuse of its parts at its end of life. It should, however, be noted that the deconstruction and reuse of separate elements and materials at a building's end of life is not inherently a part of the DfA concept.

The concepts Design for Disassembly/Deconstruction, Design for (functional) Adaptation and Design for (structural) Adaptation are demonstrated in Figure 1.

2.2 Why do we demolish buildings?

If the purpose of implementing DfA is to prolong the service life of buildings, one should first consider why buildings are typically demolished. Any building, whether it is a single-family house or a multi-storey office building, is presumably at a low risk of demolition while it is considered useful and functional, i.e. if there is a need

https://doi.org/10.52202/069179-0203

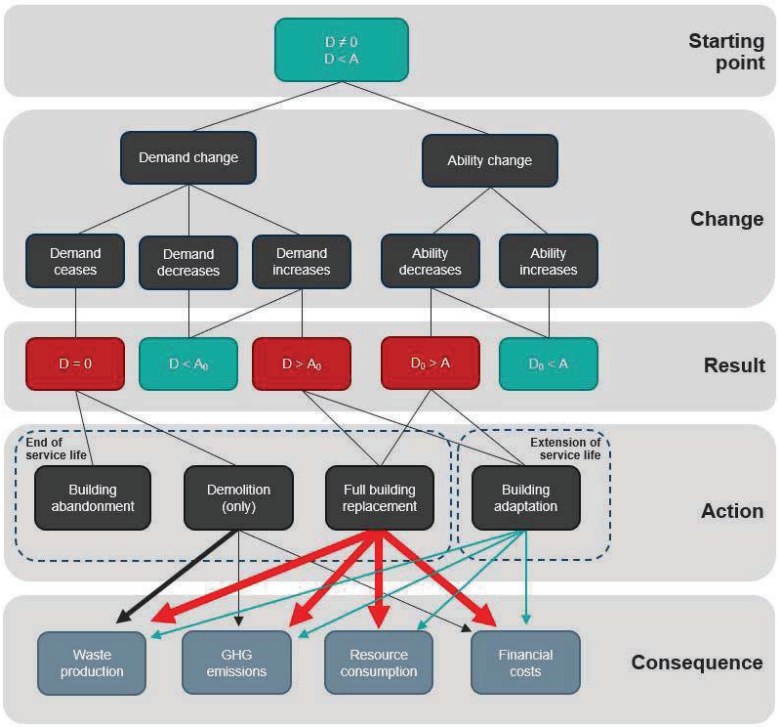

Figure 2: *Why do we demolish buildings?*

for the building in question and the building sufficiently fulfils specific functional and performance requirements. Consider the market **demand (D)** for a building type and its associated performance and functional requirements, versus its **ability (A)** to satisfy those requirements. This is illustrated in Figure 2. The demand is external; for example, the demand for office space at a given location and with its associated imposed structural loads. The ability, instead, is internal; for example, the building's ability to provide office space and carry certain loads. In a simplified model, one could set up two criteria for any given building. The first criterion is that there is a demand ($D \neq 0$), e.g., the demand for office space in the building's location. The second criterion is that the ability is greater than the demand ($D < A$); e.g., the building can sufficiently provide the demanded office space for its location.

If a building meets both criteria, it could be considered useful, which is normally the starting point for a newly constructed building. After some time, however, a change might occur – see Figure 2. In case of an external change, the demand could either cease, decrease, or increase. A complete cease of all demands would render the building in that specific location useless, and logically the owner could choose between abandoning the building or demolishing it. An example of this is a remote building connected to a mining operation, where a complete depletion of the mine might cease the operation and render the building useless. A decrease in demand, however, would still imply that both criteria are being met (economic implications of a significantly decreased demand could, however, still cause a decision to demolish or abandon the building). Lastly, when the demand increases, it might exceed the building's ability, in which case an action needs to be taken. Assuming no additional space is available on site for new construction, a whole building replacement or a building adaptation would be the relevant options. For example, a three-story multi-residential building in a city centre (where land value is high) might be replaced by a taller building as the area becomes more densely populated and the demand for housing is increased.

Regarding internal changes as defined above, the 'ability' of the building, as referred to its performance, typically decreases over time. An ability decrease could be caused by, for example, deterioration, long-term structural effects, or local damage. If the ability decrease falls below the demand, the relevant actions are yet again either fully replacing the building or adapting it to again meet the demand. In structural terms, a building's ability increase might be observed, e.g., if assessment is performed, and more beneficial member properties can be utilized through updated information; an example would be increased strength of concrete beams over time that exceeds 28-day strength used in design.

This model though, is clearly simplified; for example, a change might not be isolated, or a building might have a simultaneous demand and ability change. Furthermore, one demand could simply be replaced by another demand, e.g., a demand for office space being replaced by a demand for housing. In this case, the requirements for span length or floor height might decrease while those for

https://doi.org/10.52202/069179-0203

acoustics and fire safety might increase. Hence, the building might need to be adapted or even replaced to meet the demand for housing along with its associated performance and functional requirements. If some requirements exceed the building's ability, owners may need to consider building adaptation (retrofit) or replacement.

The detailed consequences of these four actions – building abandonment, demolition, replacement, and adaptation – vary on a case-by-case basis. Focusing on waste production, GHG emissions, resource consumption and financial costs, one could compare the assumed effect of each action to identify the most effective (overall or for specific targets). Building abandonment might be an option only if the economic loss of no longer using the building is negligible. Therefore, it is assumed to not cause any of the four consequences in a significant way. After some time and inevitable degradation, however, building abandonment could also lead to demolition. Demolition would presumably mainly cause waste production, along with related GHG emissions and financial costs for demolition and disposal. A whole building replacement, however, would cause all four of these consequences in a substantial way. Finally, a building adaptation would also cause all four consequences, but presumably to a much lesser extent than a building replacement, which must be evaluated on a case-by-case basis; different cases require different levels and intensities of adaptations in terms of cost and technical difficulty. When are the required alterations too complicated and costly, to justify building replacements as the more economical alternative? This is where design for adaptability and disassembly may shift owners' choices. Key to this approach is conceiving a building as an assembly of systems.

A popular way to illustrate a building's separate systems is Brand's [16] concept of 'shearing layers' of change. In this model, Brand identifies six building systems as layers, where the systems' varying lifespans causes shear between them. If relatively isolated, one system with a short lifespan can be changed without affecting the more 'permanent' layers [16]. The load-bearing structure, however, is the system layer with the longest planned lifespan; changes in the structure will likely affect some, or all, other building systems. Furthermore, altering a building's structure can be considered more technically complicated than altering its non-load-bearing parts. While lighter repairs are often favoured over demolition due to economic advantages, severe structural damages often cause a decision to demolish due to technical challenges and the repair costs exceeding the cost of a whole building replacement [17]. In the decision to demolish or rehabilitate a building, Bullen and Love [18] concluded that the leading determinant was the financial criterion, followed by asset condition and regulation. Economic, environmental, and social sustainability were all deemed important factors but given a lower priority in the decision [18],[19]. It is clear that, to make building adaptations a favourable alternative to demolition, it needs to be a cheaper and more technically feasible option, also supported by building regulations.

2.3 Expected benefits

So far, DfA has not been the prevalent concept neither for the design and conception of new buildings nor for the rehabilitation and adaption of existing buildings. It can be stated that the construction sector and building industry still follow a predominantly linear system, with a focus on the construction and development of new buildings. In previous years, the maintenance and rehabilitation of existing structures have contributed only minimally to the revenue of the actors involved in the construction process. Nevertheless, they are gaining importance (not least also in the infrastructure sector), and there is a clear trend to shift from a linear construction process to a more circular approach for the construction, use, and re-use of buildings and structures. In this process prefabrication is a natural way to implement DfA.

Amongst others, the following specific benefits are expected in the construction sector from a successful implementation of DfA for timber buildings:

- Contractors. Improved workflows on the construction site due to an increased use of standardized assemblies and the shift from on-site labour to offsite facilities, with associated benefits in terms of quality, cost, efficiency, and occupational health and safety.
- Manufacturers. Higher added value of building components will strengthen the producers' market position and create new business opportunities, e.g., leasing of components.
- Consultants, engineers, and architects. Best practice detailing and solutions that guarantee compatibility will allow to create more long-lasting solutions instead of individualized compromises.
- Developers. Buildings start to act as material banks, where the building retains a considerable material value. The value is retained after conventional 'end-of-life' through disassembly and reuse. At the same time benefits can be gained from the experience, repetition, and scaling effect of the successful circular concept and building system, hence, making the project development more cost-effective.
- Property owners. Long lasting, sustainable, and smart buildings that can react to changes in use and context conditions, thus maximising their value; this reduces maintenance costs and increases attractiveness of the property on the market.
- Users. Buildings that match user needs. For instance, tenants no longer need to adapt to the individual building; instead, the building adapts to their needs, requirements and wishes.
- Municipalities and society. Long lasting building stock that is able to adapt to changes in societal structure, such as demography or age distribution, to tackle new planning and building regulations, but also that can be used as a whole more effectively as buildings become material banks.

https://doi.org/10.52202/069179-0203

- Financers. Better estimation of economic risks and opportunities due to more sustainable buildings that can adapt to climate change; Thus, inherently lower risk in the light of an uncertain future, e.g., waterfront properties can be disassembled and relocated to respond to sea level rise.

3 REVIEW OF STAKEHOLDER STATUS AND DEMANDS

3.1 Overview

As part of the collaborative investigation carried out by UQ and Chalmers on DfA of timber buildings, the current stakeholder status, demands, and their development potential were evaluated in a study tour in Australia in October and November 2022. This tour was part of a project funded by the Swedish Research Council for Sustainable Development with the aim to establish a strong collaboration between the European and Australasian region with the focus on making timber buildings ever more sustainable by implementing the concepts of adaptability and circularity in their design.

The overall aim of the study tour comprised the following three objectives:

- Mapping the differences in use between new and reclaimed/reused wood-based building materials and elements from the perspectives of all stakeholders, such as producers, contractors, consultants, architects, engineers, and end-users.
- Analysing production, fabrication, design, use and re-use of timber building elements to identify opportunities and barriers to the transition to adaptability and circularity.
- Summarising barriers, challenges, and drivers, as well as possible means and technologies to overcome the differences between scales of applications, from construction products to building design.

By understanding the challenges and opportunities, it is possible to define the necessary steps for adaptability and circularity of timber buildings to be further developed, implemented, and utilised in Sweden and Australia, but also internationally. The following section presents the findings of the study tour, grouped by stakeholder type.

3.2 Stakeholder status, demands and development potential

3.2.1 Wood sector in Australia

Australia has a great diversity of wood species, however, only few softwood species are used to larger extent in the construction industry. In order to create sustainable development while maintaining and developing ecological diversity of forests, the utilisation of a more diverse range of wood species should be considered. Timber Queensland [20] is an association of wood industries in Queensland, which maintains an online tool to purchase Queensland timbers [21]. Finding a suitable application for each of the wood species in different applications will help enable a more sustainable utilisation of resources.

3.2.2 Forestry

Sustainable forestry is a prerequisite for achieving a thriving timber sector and implementing DfA. Timber plantations are a common solution for sustainable forestry and wood production in many parts of the world. For example, in Southern Queensland (Wide Bay Burnett, South East Queensland - SEQ, and Darling Downs South West) HQPlantations [22] manages 310,000 hectares of plantation forest in a 99-year lease contract; HQPlantations is both Forest Stewardship Council (FSC) and Responsible Wood (PEFC) certified, and their softwood supply is used to build 25,000 homes/year, covering most of the demand in the SEQ region.

Different wood species are grown in different locations, depending on the local climate and geographic conditions. For example, the hills around Imbil show great diversity in plantation and natural forests, with a variety of different hard- and softwood species. Natural hardwood forests cover the hilltops whereas diverse plantations stretch across the valleys. In contrast, the flat sandy landscape around Toolara provides soil conditions for large monocultural forests, from which the logs are directly transported to the nearby sawmills [23]. The different wood species at the various locations may offer different benefits for specific applications.

There are two important Southern Queensland wood species. Araucaria (Hoop Pine) is an endemic rainforest species mostly grown for visual grade veneers, baby cots (food grade timber) and musical instruments; its harvesting age is 50 years. The second one is Southern Pine, which is a hybrid of Slash and Caribbean Pine, harvested at 28 years, which supplies SEQ's structural timber demand, including engineered wood products.

Fire management is a crucial part of HQPlantations' activities: fire observation towers are installed in different locations to detect smoke plumes, all vehicles are equipped with firefighting equipment, and the staff consists of trained fire fighters. The active fire management of the forest, through prescribed burning and controlled burns in collaboration with adjacent landowners, is an effective means to control the fuel load.

The direct connection and vertical integration between the forest and the further processing steps in the wood value chain are important to create a more resource efficient wood value chain. An example of this efficiency is linking the growth data from the forest, including stem dimensions and qualities, to the production demands and capabilities of the sawmills, in order to manufacture higher value products and avoid unnecessary waste during production. Such an integration provides benefits both for forest and plantation owners, supplying higher value-added products to sawmills, which can then meet their customers' demands more efficiently. An important first step in this process is, for example, the delivery of full size (untrimmed) logs of Southern Pine from the Toolara plantations by HQPlantations to the Hyne sawmill in Tuan, Queensland [24]. For the plantation owners, this vertical integration includes selecting the most appropriate genetic resources and breeding seedlings in nurseries.

https://doi.org/10.52202/069179-0203

3.2.3 Producers and Sawmills

A variety of structural products are manufactured in different sawmills and production plants across Australia. As part of the study tour, a total of 6 sawmill, glulam, and CLT plants were visited. Depending on the location and the local raw material supply, the sawmills are specialized in different raw materials, timber products, production processes. Despite their individual differences, some commonalities and challenges can be identified:

- Grading and strength classes. The strength class system of machine graded pine (MGP) is rather strict and allows only for a limited range of adaptation to the feedstock. Almost all sawmills use machine grading to produce MGP10 lumber and partly higher qualities. Lower qualities than MGP10 result in F-grade timber, which is assessed based on bending strength rather than stiffness. Over the time, the market demand has adapted to these qualities. However, this strict and limited system of strength classes does not allow for a better and more efficient utilisation of the raw resources in the future. Vertical integration between the sawmill and the users in the construction industry can provide a solution here.
- Timber treatment against termite attack. Most of the timber products used in Australia require chemical treatment against termite attack. The effective and sustainable use of chemicals is a general challenge for the re-use of timber elements and circularisation of resources. Reliable and long-term specification of the treatment type is important. At the same time (private) users are familiar with certain colour codes for different applications and demand these colours without further questioning the performance.
- Optimisation of sawing patterns. The yield of the sawmill depends, to a large extent, on an optimal choice of the sawing pattern for the feedstock. Depending on locations and species of the feedstock, the log's cross-section, length, and straightness can vary quite considerably. E.g., Radiata and Southern Pine used by Associated Kiln Driers Pty Ltd (AKD) Softwood Mill Caboolture, Queensland [25] have a considerably smaller diameter compared to Radiata Pine used by TimberLink, Bell Bay, Tasmania [26]. Good interaction and communication between the forest owners, harvesters, sawmills, and consumers are crucial to achieve an efficient utilisation of resources. The vertical integration enables also to track the product Chain of Custody.
- Hardwood species are used to a much smaller extent in the construction industry compared to softwood. Several manufacturers work with hardwood in Australia and produce glulam or CLT. However, hardwood has not yet fully penetrated the market; some of the challenges of working with hardwoods are the different gluing requirements compared to softwoods and the more careful and slower drying processes to avoid wood matrix damages.
- Automation can help to upscale the production volume compared to elaborate production by hand. Automated glulam production from softwood of standardized sizes in the Hyne timber Glulam factory [24] (Maryborough, Queensland) is a good example. However, individual and customised timber members of other dimensions or bespoke shapes still require manual production.

  The trimming of full size CLT panels on CNC machines at XLam Australia, Wodonga [27][26], offers the possibility to prefabricate entire wall and floor elements and integrate the connection details in factory. This enables to integrate DfA solutions as standardized detailing solutions in the process.

Excellent examples of small innovative producers are CLTP and CUSP Building Solutions [28], in Wynyard, Tasmania, which have developed hardwood CLT and glulam for a better utilisation of local resources: they produce Eucalyptus Nitens and Eucalyptus Grandis composite Glulam beams and Eucalyptus Nitens CLT panels. At the same time, they utilise the finger jointing lines to re-use MGP10 cut-offs to produce structural finger jointed lumber of a similar quality. This is an excellent example of efficient resource utilisation and reuse, well aligned with circularity principles.

3.2.4 Architecture and Engineering

Common challenges for engineers and architects for the development of the mass timber industry where discussed with NexTimber [29], which is the Melbourne-based mass timber (Glulam and CLT) division of Timberlink [30]. These are the reuse of CLT panels, lack of a standardised connection details, repairability of structures, and classified material properties. These gaps impact the ability of engineers and architects to design for deconstruction, reuse, and recertification of timber components, as well as the carbon credits system, as it cannot be assured that timber remains in use and is well maintained.

Advancing education around the use of timber in architecture is in the focus of the Centre for Future Timber Structures at the University of Queensland's St Lucia campus, as well as the Centre for Sustainable Architecture (CSAW) at the University of Tasmania's Newnham campus. UQ projects include, amongst others, research on adaptable timber structures and innovative reversible connections [31][32], and hygrothermal performance of CLT in hot and humid climates [33]. UTas projects include, amongst others, the use of salvaged timber materials for innovative structures, and research on local hardwoods [34]-[36].

Innovative construction concepts are offered by ArKit, Sunshine, Victoria [37]. ArKit's projects range from bespoke architectural designs using volumetric and panelised offsite construction, to Passivhaus standard projects, and volumetric social housing. The use of modular, panelised, and volumetric prefabrication in their factory enables high-performance and quality solutions also for low budget social housing funded by the Australian government. The modularity enables the

refurbishment of existing modules in the factory after their initial lifetime for a second cycle.

3.2.5 Exemplar timber buildings

Structural timber is a common building material used in residential buildings and there are many historic examples of mid-rise timber buildings in Australia, such as the oldest surviving building in Albert Street, Brisbane [38]. The development of modern structural engineered wood products (EWP), namely glued laminated timber (GLT), laminated veneer lumber (LVL), and cross laminated timber (CLT) enabled to build also larger high-performance structures in timber instead of the other prevailing building materials steel and concrete.

One of the most celebrated modern, multi-storey buildings made of EWPs in Australia is the office building at 25 King Street in Brisbane [39]. Lendlease is the developer, Aurecon is the engineering consultant and Bates Smart the architecture firm who designed the building of the 9-storey mass timber office building using Stora Enso CLT. Despite attracting a 'timber premium', the lease worked out much cheaper than Aurecon's previous offices in the CBD. Furthermore, employees enjoy the timber feel of the building with the building winning design and wellbeing awards.

The following structural design features of this showcase building can be highlighted:

- Slotted in steel plates, concealed with timber covers, and timber plugs for bolts and screws to enhance fire performance also enable potential deconstruction.
- 5-layer CLT in the staircase, with the first two layers running vertically to improve load bearing resistance - the staircase has no lateral bracing function. This solution also improves fire resistance rating.
- Hardwood LVL banded Glulam beams to reinforce the beam around services penetrations.
- Large open floor plans offer functional and spatial flexibility.
- Durability and repairability of exposed timber elements improved by adequate protection from wetting and weathering; UV protection is crucial to avoid colour variations in different exposed members.

The timber building at 25 King Street is exemplar towards implementing DfA as, in principle, much of the building is deconstructable due to the fasteners and brackets chosen, and due to a clear and open member design, which applies circular design principles for.

Another exemplar building is the recently opened extension of the Maryborough Fire Station [40], designed by Baber Studio (architecture) [41] and Bligh Tanner (structural engineering), and realised by Hutchinson Builders. While the old brick façade of the existing fire station building was preserved, the whole new extension is made from Glulam and CLT supplied by Hyne Timber and XLam - manufactured from local softwoods from their Tuan mill. Design features of the fire station extension include CLT band beams and concrete ring beams in the fire engine area, to kept timber off the ground while fire engines are being washed down or when leaking water. This building is particularly relevant as it shows the potential of timber also in non-conventional applications.

Finally, the Inveresk UTas Library, in Tasmania, is an exemplar hardwood structure made of local Tasmanian Oak. Tasmanian oak is the name used for three eucalypt hardwoods: Eucalyptus delegatensis (alpine ash) can be found at higher altitudes, while E. regnans (mountain ash) is found in wetter sites; and Eucalyptus obliqua (messmate) has a wide distribution, growing in wet forests but also extending into drier areas. The timber members are used in bespoke roof trusses offering large open spaces and appealing architectural design, which is an excellent example for the use of local resources in a performant structure. The efficient large span truss structure offers a flexible usage of the building.

3.2.6 Research

Circularity of wood products

The circular use of wood requires strategies to maintain wood products at their highest value and then provide efficient solutions for a cascading application, at a lower value. This is one of the focus areas of the Advance Timber Hub, an Industrial Transformation Hub funded by the Australian Research Council (ARC) to advance timber in Australia's future built environment. Furthermore, researchers at Queensland's Department of Agriculture and Fisheries (QDAF) facilities at Salisbury are looking at engineered wood-based composites, kiln drying and sawmilling technology, timber grading,
wood product design, and performance testing, which all enhance timber recovery and durability throughout the value chain. Particularly significant towards the implementation of a circular timber construction sector is research led by A/Prof Benoit Gilbert, which addresses: high quality products from the raw material in form of sawn boards or veneers from different wood species [42] to be used in LVL, glulam, or CLT; recycling and reuse of different waste materials in value-added products, such as tyres and wood fibres in composite particle boards; and product durability to ensure a long and safe service life. Durability of EWPs is also at the centre of a collaborative research project by PhD candidate Marcus Strang, under the supervision of Dr Paola Leardini (UQ) and Dr Maryam Shirmohammadi (QDAF); the study investigates the hygrothermal performance of high-performance CLT construction in hot and humid climates, providing design guidance that, ultimately, also ensures structural durability across different Australian climates [43].

Construction strategies and solutions

Technical solutions for the application of DfA in construction are investigated by the research group of A/Prof Hamid Valipour at the University of New South Wales (UNSW), Sydney. Hybrid steel timber elements are being developed that offer a variety of benefits [44]; the combination of low-grade timber elements with steel rods in hybrid elements can provide high quality usage for low quality timber in standardized components, such as columns or beams. Standardisation facilitates the use and

https://doi.org/10.52202/069179-0203

re-use of these components in different applications. Constructing with standardized components instead of members with individualized geometry is common already e.g., in the steel or prefab-concrete industry and offers high circularity potential also in the timber field. The combination of these hybrid elements with conventional structural solutions in steel or concrete offers the easy implementation of more resource efficient components in the construction sector. Further implementation of specialized connections will facilitate construction and deconstruction, and it enables the implementation of fuse elements to achieve ductility for robustness or seismic purposes.

3.3 Necessary steps towards DfA

While significant research is currently carried out, further steps are necessary to ensure the transition of timber construction to circularity and the implementation of DfA, including:

- Vertical integration of processes, from the forest to the end-user.
- Utilisation of a wider range of wood resources.
- Effective use of all by- and side products of the wood value chain (e.g. structural finger jointed timber, scrimber)
- Production of standardized components instead of materials.
- Design and construction of flexible structures in terms of both floor plans and re-use and deconstruction.
- Use of offsite prefabrication and modularisation as mainstream practice.
- Mapping of differences in use between new and reclaimed/reused wood-based building materials and elements, from the perspective of all relevant stakeholders, such as manufacturers, contractors, consultants, architects, engineers, and end-users.
- Development of business concepts including the re-use of material, members, components, and entire structures for transitioning to adaptability and circularity.
- Translation and commercialisation of circularity and adaptability research in collaboration with industry stakeholders and research providers.
- Education of architecture, engineering and building professionals with respect to durable and circular design, better interdisciplinary networking, and collaboration between industry stakeholder to achieve common goals.

4 CONCLUSIONS

The results of the research and built projects described in this paper provide a greater understanding of the challenges and opportunities of DfA and, more broadly, circularity of timber buildings, with a special focus on the Australian and Swedish market. The concept and general benefits of DfA were explained. Then the current status and ongoing development of the stakeholders in the Australian timber construction industry and research environment were analysed. Following this evidence-based analysis of the Australian timber sector, the paper proposes some first but necessary steps for adaptability and circularity in the timber sector to be further developed, implemented, and utilised. This paper leverages results of government funded research projects on DfA currently being conducted at UQ and Chalmers, thus significant findings are expected in the future.

ACKNOWLEDGEMENT

The paper is based on the following research projects: “Roadmap towards adaptability of timber buildings” (project number 2021-02711) and “Design for adaption for resource efficient timber structures” (project number 2021-02499), both funded by FORMAS, the Swedish research council for sustainable development; and Linkage Project “Offsite manufacture reimagined for high-performance adaptable housing” (LP200301402), funded by the Australian Research Council. The researchers would like to thank Timber Queensland, HQPlantations, AKD, Hyne timber and XLam Australia, Timberlink and NexTimber, CLTP and CUSP, UTas, UNSW, QDAF, Baber Studio, ArKit and Aurecon for their input.

REFERENCES

[1] European Environmental Agency. (2006). Urban sprawl in Europe: The ignored challenge. Office for Official Publications of the European Communities, Luxembourg.
[2] Directorate-general Environment. (2014). Resource efficiency in the building sector – final report.
[3] Svensk Trä: www.svenskttra.se
[4] Building Design Association of Australia. (2021) Timber Shortage Hits Australia. https://bdaa.com.au/timber-shortage-hits-australia/ 12 Dec 2021. Viewed 25 March 2022
[5] Churkina, G. et al. (2020). Buildings as a Global Carbon Sink. Nature Sustainability 3, no. 4, 269–76.
[6] Thormark, C. (2008). Projektera för demontering & återvinning. Svensk byggtjänst, Stockholm.
[7] Jockwer R, and Goto Y. (2021) Design for Adaption - Making Timber Buildings Ready for Circular Use and Extended Service Life. Proceedings of the World Conference on Timber Engineering (WCTE 2021).
[8] Douglas, J. (2006). Building Adaption. 2nd ed. Butterworth-Heinemann, Oxford.
[9] Bullen, P.A. (2007). Adaptive reuse and sustainability of commercial buildings. Facilities, 25(1/2), 20–31.
[10] Schmidt, R., Associate, R., Eguchi, T., Austin, S., & Gibb, A. (2010). What is the meaning of adaptability in the building industry? Paper presented at the 16th International Conference O&SB20210 “Open and Sustainable Building”. Bilbao, Spain.
[11] Wilkinson, S. J., Remøy, H. & Langston, C. (2014). Sustainable Building Adaptation – Innovations in Decision-making. John Wiley & Sons Ltd, West Sussex.
[12] Graham, P. (2005). DESIGN FOR ADAPTABILITY — AN INTRODUCTION TO THE PRINCIPLES AND BASIC STRATEGIES. Environment Design Guide, GEN 66, 1-9.

[13] Durmisevic E. (2006). Transformable building structures – Design for dissassembly as a way to introduce sustainable engineering to building design & construction (Doctoral dissertation, TU Delft, Delft, the Netherlands).
[14] Rios, F.C., Chong, W.K. and Grau, D. (2015). Design for Disassembly and Deconstruction - Challenges and Opportunities. Procedia Engineering, no. 118, 1296–1304.
[15] Sandin, Y. et al. (2022). Design of Timber Buildings for Deconstruction and Reuse —Three methods and five case studies. RISE report 2022:52.
[16] Brand, S. (1995). How buildings learn: What happens after they're built. 2nd ed. Viking, New York.
[17] Alba-Rodríguez, M.D. et al. (2017). Building rehabilitation versus demolition and new construction: Economic and environmental assessment. Environmental Impact Assessment Review, no. 66, 115–126.
[18] Bullen, P. and Love, P. (2011). A new future for the past: a model for adaptive reuse decision-making. Built Environment Project and Asset Management, 1(1), 32–44.
[19] Bullen, P.A. and Love, P.E.D. (2010). The rhetoric of adaptive reuse or reality of demolition: Views from the field. Cities, 27(4), 215–224.
[20] Timber Queensland http://www.timberqueensland.com.au/ , accessed 11/03/2023.
[21] The Accredited Queensland Timber Merchant Network (AQTMN) http://www.buyqldtimber.com.au/ , accessed 11/03/2023.
[22] HQPlantations: https://www.hqplantations.com.au/ , accessed 11/03/2023.
[23] https://gympietoday.com.au/news/2021/12/05/hq-managing-timber-in-region/ , accessed 11/03/2023.
[24] Hyne Timber https://www.hyne.com.au/ , acc. 11/03/2023.
[25] AKD: https://www.akd.com.au/ , accessed 11/03/2023.
[26] Timberlink: https://timberlinkaustralia.com.au/ , accessed 11/03/2023.
[27] XLAM: https://xlam.co/ , accessed 11/03/2023.
[28] CLTP https://www.cltptasmania.com/ , acc. 11/03/2023.
[29] NexTimber: https://nextimber.com.au/ , acc. 11/03/2023.
[30] https://architectureau.com/articles/timberlink-announces-new-clt-and-glt-brand-nextimber/ , accessed 11/03/2023.
[31] Yan, Z., Ottenhaus, L.-M., Leardini, P., & Jockwer, R. (2022). Performance of reversible timber connections in Australian light timber framed panelised construction. Journal of Building Engineering, 61(September), 105244. https://doi.org/10.1016/J.JOBE.2022.105244
[32] Kuiri, L., & Leardini, P. (2022). Design for Adaptability and Disassembly: Towards Zero Construction Waste in the Australian Housing Sector. 1ST International E-Conference on Green & Safe Cities (IeGRESAFE).
[33] Strang, M.; Leardini, P.; Brambilla, A.; Gasparri, E. (2021). Mass Timber Envelopes in Passivhaus Buildings: Designing for Moisture Safety in Hot and Humid Australian Climates. Buildings, 11, 478. https://doi.org/10.3390/buildings11100478
[34] Wood, K., Morrell, J., and Leggate, W. "Enhancing the Durability of Low Durability Eucalyptus Plantation Species: A Review of Strategies." In Proceedings IRG Annual Meeting (ISSN 2000-8953), IRG/WP 20-40910. online: The International Research Group on Wood Protection, 2020.
[35] Chen, Xudong, Yingyao Cheng, Andrew Chan, Damien Holloway, and Gregory Nolan. "Aniso-tropic Tensile Characterisation of Eucalyptus Nitens Timber above Its Fibre Saturation Point, and Its Application." Polymers 14, no. 12 (January 2022): 2390. https://doi.org/10.3390/polym14122390.
[36] Liang, Yingwei, Assaad Taoum, Nathan Kotlarewski, Andrew Chan, and Damien Holloway. "Behavior of Cross-Laminated Timber Panels Made from Fibre-Managed Eucalyptus Nitens under Short-Term Serviceability Loads." Buildings 13, no. 1 (January 2023): 245. https://doi.org/10.3390/buildings13010245.
[37] ARKit: https://arkit.com.au/ , accessed 11/03/2023.
[38] https://heritage.brisbane.qld.gov.au/heritage-places/1987#:~:text=This%20building%2C%20constructed%20circa%201865,Brisbane%20between%201861%20and%201884 , accessed 11/03/2023.
[39] Aurecon: https://www.aurecongroup.com/projects/property/25-king , accessed 11/03/2023.
[40] https://www.abc.net.au/news/2022-11-22/mass-engineered-timber-fire-station-officially-operational-qld/101683446 , accessed 11/03/2023.
[41] Baber Studio: http://www.baberstudio.com.au/maryborough-fire-and-rescue-station/ , accessed 11/03/2023.
[42] Leggate, W., McGavin, R., Outhwaite, A., Gilbert, B., and Gunalan, S. "Barriers to the Effective Adhesion of High-Density Hardwood Timbers for Glue-Laminated Beams in Australia." Forests 13, no. 7 (2022): 1038. https://doi.org/10.3390/f13071038.
[43] Strang, M., Leardini, P., Brambilla, A., and Gasparri, E. "Mass Timber Envelopes in Passivhaus Buildings: Designing for Moisture Safety in Hot and Humid Australian Cli-mates." Buildings 11, no. 10 (2021): 478. https://doi.org/10.3390/buildings11100478 .
[44] Kia, L., and Valipour, H. R. "Radiata Pine and Douglas Fir Timber Steel Encased Columns Subjected to Concentric and Eccentric Loading." Journal of Structural Engineering 148, no. 2 (2022): 04021272. https://doi.org/10.1061/(ASCE)ST.1943-541X.0003266.

https://doi.org/10.52202/069179-0203

World Conference on Timber Engineering Oslo 2023

INVESTIGATION OF STRUCTURAL BEHAVIOR OF WOODEN TRADITIONAL JOINTS VIA FINITE ELEMENT ANALYSIS

Hafshah Salamah[1], Seung Heon Lee[2], and Thomas Kang[3]*

ABSTRACT: With timber buildings becoming increasingly popular, the study of timber structures and joints has gained great attention. As the weakest part of the building, it is fundamental to investigate joints, especially traditional ones. In this research, the structural behaviors of longitudinal joints from Korea and Indonesia were investigated using finite element modeling. *Maettugijjangbu* (Joint 1) and *jumeokangbu* (Joint 2) as Korean traditional joints and *sambungan bibir miring* (Joint 3) and *sambungan bibir lurus* (Joint 4) as Indonesian ones were analyzed. The four types of joints were compared in terms of deformation capacity, and the procedure for investigating their structural behaviors was thoroughly explained. Finite element analysis was performed using linear elastic analysis for orthotropic material. The boundary conditions, loads, and contact surface conditions were input based on design setup. From displacement analysis, it was found that Joint 1 has the smallest deformation in terms of tension and compression load than other joints. Meanwhile, Joint 4 and Joint 3 have the highest deformation under tension load and compression load, respectively. Even though the maximum stress at all joints might be higher than the strength factor (C_f), it is feasible to conclude that Joint 1 performs better than other joints.

KEYWORDS: Structural behavior, wooden traditional joint, finite element modeling

1 INTRODUCTION

Timber buildings have garnered large interest in recent years, due to their advantages of good carbon storage, heat preservation, and sustainability. Modern timber buildings started from the legacy of traditional wooden buildings. As a proven precedent of timber buildings, traditional wooden buildings have good earthquake resistance because of their unique architectural style and structural system. The Korean traditional building, Hanok, uses *ieum* and *machoom* construction method to create solid and durable house [1]. This method allows for wood joints to be assembled without nails. Similarly, Indonesian traditional buildings called Rumah Gadang use mortise tenon joints without metal fasteners [2].

Timber joints are usually the weakest point in timber structures [3]. Although joints or member connections are unavoidable in building structure, timber joints need extra consideration. As structural material, timber has limited size and length which require more joints than other materials. One of the most important traditional joints is in member along with the member direction to extend the length (post to post, beam to beam) or *ieum* in Korean joint classification. This joint is crucial to fulfil the required span of the timber structure. Thus, many studies of these joints have been conducted, especially its mechanical behavior.

Currently, finite element analysis (FEA) is one of the preferred methods to investigate timber joints due to its wide range of applications and type of elements. Even though the resulting capacity of the finite element method is usually lower than the actual value, the result is typically considered to be reliable compared to experimental results [3][4]. Typically, FEA could provide displacement and stress distributions of the structures which are enough to understand the mechanical behavior of joints in preliminary stage.

In this study, traditional joints from Korea and Indonesia were investigated to find their structural behavior using the finite element method. *Maettugijangbu* and *jumeokjangbu* from Korean traditional joints and *sambungan bibir miring* and *sambungan bibir lurus* from Indonesia were analyzed under tension and compression loads. Due to the complex shape of those traditional joints, finite element modeling was used via computer software. Friction and compressive strengths are the most influential factors in the flexural capacity of the joints [5] that are also used in modeling. Friction factor was used in the model setup and compressive strength was used for failure criteria. From the simulation result, the performance of the joints was compared based on joint

[1] Hafshah Salamah, Department of Architecture and Architectural Engineering, Seoul National University, Seoul, hafshah.salamah@snu.ac.kr
[2]* Seung Heon Lee, Department of Architecture and Architectural Engineering, Seoul National University, Seoul, shlee93robin@snu.ac.kr
[3]* Thomas Kang, Department of Architecture and Architectural Engineering, Seoul National University, Seoul, tkang@snu.ac.kr

https://doi.org/10.52202/069179-0204

properties and deformation shape. In this study, stress distributions were not elaborated and expected to be further analysis in the future. Thus, only prediction of general failure of the joints was discussed.

2 FINITE ELEMENT MODELING

Four types of joints were examined within the same factors: material properties, boundary conditions, and forces. FEA was conducted using Dlubal RFEM software. Before starting the simulation, mechanics of material, joint models, and design setup are required to be inputted to the software. Then, after the simulation, the results are analyzed using failure criteria of wooden material.

2.1 MECHANICS OF MATERIALS

As an orthotropic material, wood exhibits a variety of mechanical characteristics along three mutually perpendicular axes (natural axes): longitudinal, radial, and tangential. The longitudinal axis X is parallel to wood grain (fiber); the radial axis Z is normal to the growth rings (perpendicular to grain in radial direction); and the tangential axis Y is perpendicular to grain but tangent to the growth rings (Figure 1).

Since this investigation is not directly performed in the experiment, the wood mechanical properties were chosen based on the availability of material library in Dlubal RFEM. Originally, Korean traditional buildings use softwood material while Indonesian traditional buildings use hardwood material. In this study, the material properties are generated to be the same as hardwood grade D30 (DIN 1052:2008-12) (Table 1).

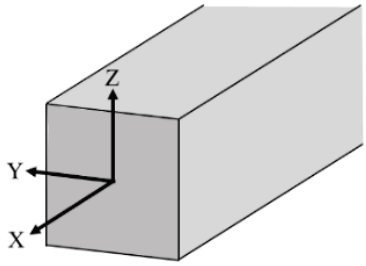

Figure 1: *Wood axis in finite element model*

Table 1: *Wood anisotropy parameters in finite element model*

E_x	$E_y = E_z$	v_{yz}	$v_{xz} = v_{xy}$	G_{yz}	$G_{xz} = G_{xz}$
10000	640	0.1	0.045	60	600

Note: E = modulus of Elasticity (MPa), v = Poisson's ratio, and G = shear modulus (MPa) are mean values. Subscripts xyz in the formula represent the direction of the properties.

The wood material is set as 'Orthotropic Elastic 3D'. This setting is for linear elastic analysis for 3-dimensional models. Following Hooke's law, the elasticity matrix of wood in the software is expressed as:

$$\begin{bmatrix} \varepsilon_x \\ \varepsilon_y \\ \varepsilon_z \\ \gamma_{yz} \\ \gamma_{xz} \\ \gamma_{xy} \end{bmatrix} = \begin{bmatrix} \frac{1}{E_x} & -\frac{v_{yx}}{E_y} & -\frac{v_{zx}}{E_z} & 0 & 0 & 0 \\ -\frac{v_{xy}}{E_x} & \frac{1}{E_y} & -\frac{v_{zy}}{E_z} & 0 & 0 & 0 \\ -\frac{v_{xz}}{E_x} & -\frac{v_{xz}}{E_y} & \frac{1}{E_z} & 0 & 0 & 0 \\ 0 & 0 & 0 & \frac{1}{G_{yz}} & 0 & 0 \\ 0 & 0 & 0 & 0 & \frac{1}{G_{xz}} & 0 \\ 0 & 0 & 0 & 0 & 0 & \frac{1}{G_{xy}} \end{bmatrix} \begin{bmatrix} \sigma_x \\ \sigma_y \\ \sigma_z \\ \tau_{yz} \\ \tau_{xz} \\ \tau_{xy} \end{bmatrix} \quad (1)$$

The following correlation exists between principal Poisson's ratio v_{xy} and secondary Poisson's ratio v_{yx}:

$$\frac{v_{zy}}{E_z} = \frac{v_{yz}}{E_y}; \frac{v_{zx}}{E_z} = \frac{v_{xz}}{E_x}; \frac{v_{yx}}{E_y} = \frac{v_{xy}}{E_x} \quad (2)$$

2.2 JOINT MODELS

Two Korean and two Indonesian traditional joints were chosen from actual traditional buildings: *maettugijangbu* (Korean), *jumeokjangbu* (Korean), *sambungan bibir miring* (Indonesia), and *sambungan bibir lurus* (Indonesia). These joints were analyzed under tension and compression loads. The joints originally come in different sizes and proportions but are adjusted to the same beam size for this investigation. The cross-section size of the beam is 120 x 120 mm. Details of the joints are shown in Figure 2.

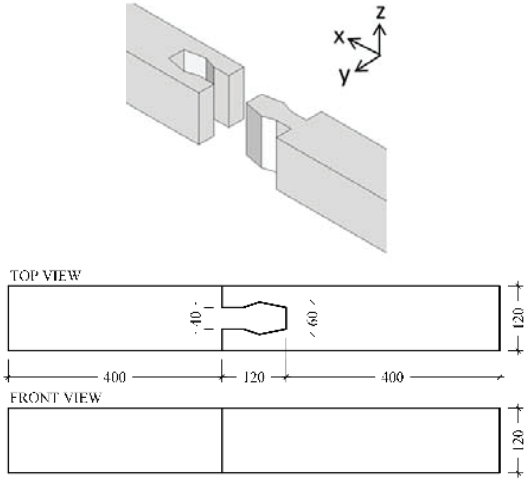

(a) Joint 1. *Maettugijangbu* (Korea)

Figure 2-1: *Details of joints (size in millimeters)*

https://doi.org/10.52202/069179-0204

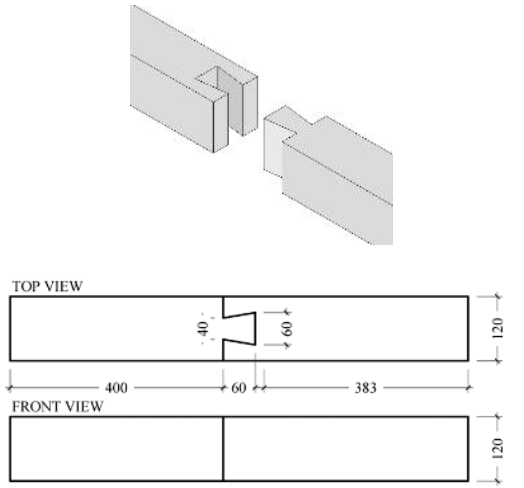

(b) Joint 2. *Jumeokjangbu* (Korea)

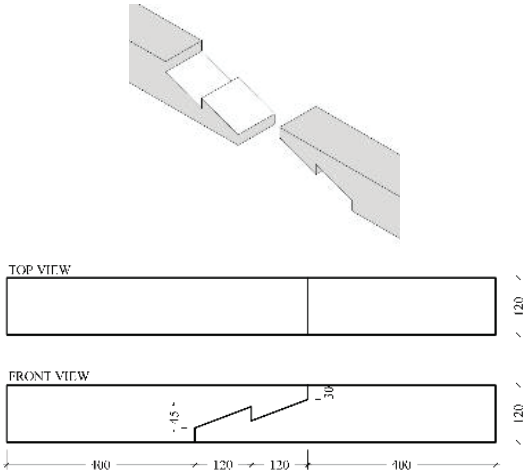

(c) Joint 3. *Sambungan Bibir Miring Berkait* (Indonesia)

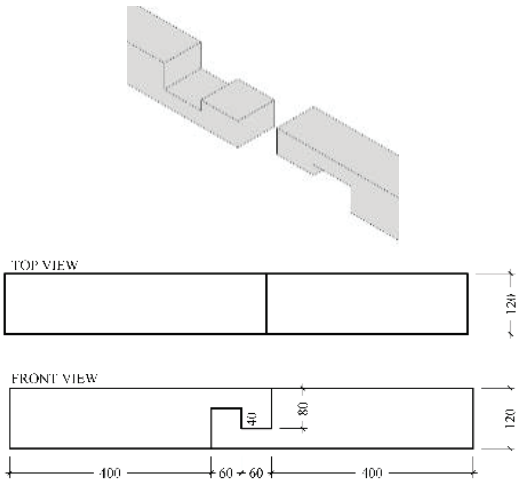

(d) Joint 4. *Sambungan Bibir Lurus Berkait* (Indonesia)

Figure 2-2: *Details of joints (size in millimeters)*

2.3 DESIGN SETUP

After modeling the joint shapes, the next step is to set up the boundary conditions, loads, and surface conditions. The boundary condition is set as a fixed joint on the yz-direction at Point A, and a roll joint at the base on Point D. Then, the joints were applied with nodal loads on the yz-surface of Point D with two conditions: 5 kN tensile force and 5 kN compression force. The length of Points A-B and C-D are 400 mm, whereas Point B-C varies depending on the type of joint (Figure 3a).

Each joint has two solid members, member 1 attached at Point A and member 2 with a roll joint at Point D. Because each member has contact with the other, the 'surface release' setting was used to create separation between the members. The contact surface can be released in this configuration based on the direction and the relationship between the surfaces. The shear between timber members is related to friction force. Based on the wood properties, the friction factor for the D30 wood grade is 0.1875. The finite element was set to 20 mm with a triangular shape element (Figure 3b).

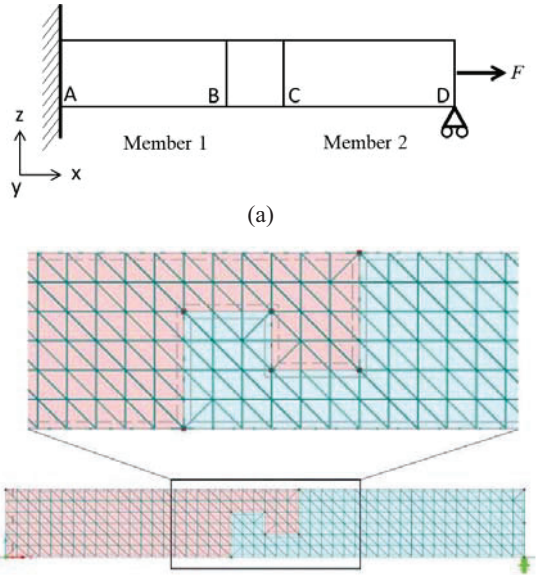

(a)

(b)

Figure 3: *(a) Design setup and (b) FE mesh on Joint 3 from xy-plane*

2.4 FAILURE CRITERIA

Failure at wood connections is typically categorized as either ductile or brittle. The only type of ductile failure is a bearing failure, which occurs before brittle failure or fracture. Meanwhile, brittle failure has three types: splitting, shear failure, and tension failure. However, it is not easy to determine the type of failure in a computer analysis. Thus, the failure analysis of joints is commonly based on evaluating the stress distribution at the joint surface.

https://doi.org/10.52202/069179-0204

Failure criteria in plane stress [6] are adopted to this investigation. The criterion can be written as follows:

$$\left(\frac{\sigma_x}{X_1}\right)^2+\left(\frac{\sigma_y}{Y_1}\right)^2+\left(\frac{\tau_{xy}}{S}\right)^2 \le C_f \quad (3)$$

where σ_x is the limit stress parallel to wood grains, σ_y represents the limit stress perpendicular to wood grains, τ_{xy} is shear stress parallel to wood grains, X_1 represents the limit strength parallel to wood grains, Y_1 is the limit strength perpendicular to wood grains, S is the shear strength parallel to wood grains, and C_f is the strength factor. The limit stress can be a compressive or tension stress.

Failure occurs when the total strength exceeds the strength factor (C_f =1.0). Based on material properties in Dlubal RFEM, D30 wood grade has compressive strength parallel to wood grains, compressive strength perpendicular to wood grains, and shear strength parallel to wood grains of 23 N/mm^2, 8 N/mm^2, and 3 N/mm^2, respectively. Moreover, D30 wood grade has 18 N/mm^2 for tension stress parallel to wood grain and 0.5 N/mm^2 for tension stress perpendicular to wood grain.

3 RESULTS AND DISCUSSION

The performance of four traditional joints was analyzed in terms of joint properties and deformation. Joint properties were analyzed based on the joint shape and its impact on the structure. Deformation was analyzed based on the maximum value obtained from FEA.

3.1 JOINT PROPERTIES

In this study, the chosen joints are the joint between the timber members in the same direction which usually extends the beam or column length. This type of joint has many subtypes with various joint properties. The joint properties are divided into three aspects: orientation shape, shape complexity, and joint length.

Orientation shape is the direction where the unique shape of joints is created. Joints 1 and 2 have the orientation shape on the xy-plane while Joint 3 and 4 have the main joint shapes on the xz-plane. Despite not being covered in this study, this factor affects gravity loads and when wood properties of tangential (y-direction) and radial (z-direction) to wood grain have different values.

The number of formed contact surfaces between timber members determines the complexity of joint shapes. The joint surface in Joints 2, 3, and 4 have five surfaces, while Joint 1 has seven surfaces. The surface direction angle in the contact surface is another element of form complexity. Joints 1, 2, and 3 have diagonal surfaces besides horizontal and vertical contact surfaces. Meanwhile, Joint 4 has only horizontal and vertical contact surfaces. The diagonal surface creates more impacts on the friction force which increases the joint strength. The analysis of the joint is seen on Figure 4.

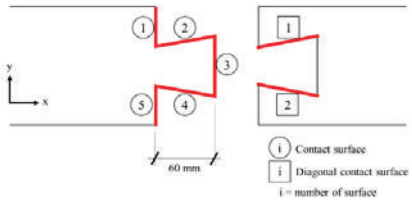

Figure 4: *Joint properties of Joint 2*

According to design setup, the length of the joints in Points A-B and C-D are the same, but the length of B-C depends on the length requirement of the joints. Carpentry joints are made by crafting the edge of the timber members into male and female shape. This process is related to material waste because crafting the joint reduces the beam length to the specified size of the joint. The length of Point B-C in Joint 1 must be the same as the beam width (120 mm), while Joint 2 is only half of the beam (60 mm). For Joint 3 and 4, the length of Point B-C is originally twice of the beam width (240 mm). However, only on Joint 4, the length of Point B-C is reduced to 120 mm. Thus, in terms of material waste, Joint 2 has less waste than Joints 1, 3, and 4.

Table 2: *Joint properties*

Criteria	**Joint 1**	**Joint 2**	**Joint 3**	**Joint 4**
Shape orientation	x-y	x-y	x-z	x-z
Complexity				
Total contact surface	7	5	5	5
Diagonal surface	4	2	2	0
Joint's length (mm)	120	60	240	120

3.2 DEFORMATION

Deformation on joints under tension and compression load are analyzed using global displacement. Joint 1 exhibits the smallest displacement (0.7 mm) of the four joints under tension load, and the maximum displacement on Joint 2 is close to Joint 1 (0.8 mm). The largest displacement occurred in Joint 4 (5.0 mm), while Joint 3 has a max displacement of 1.9 mm (Figure 7a)

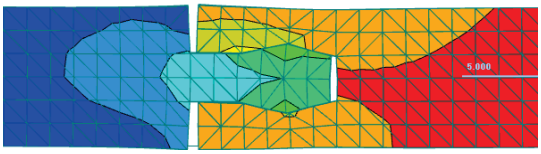

(a) Joint 1 (xy-plane)

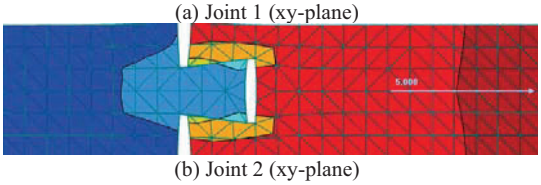

(b) Joint 2 (xy-plane)

Figure 5-1: *Deformation shape on joints under tension load*

https://doi.org/10.52202/069179-0204

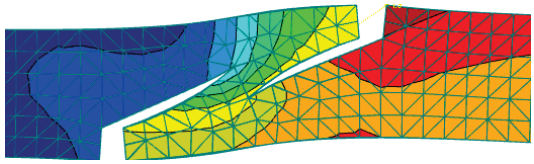

(c) Joint 3 (xz-plane)

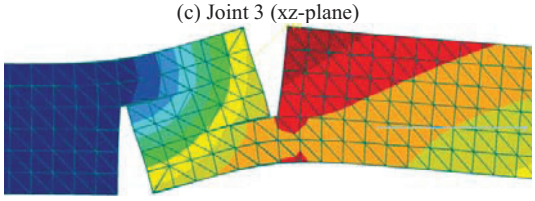

(d) Joint 4 (xz-plane)

Figure 5-2: *Deformation shape on joints under tension load*

The maximum displacements on Joints 1 and 2 are located at point D, which indicates the higher probability of bearing or shear failure. However, the maximum displacements on Joints 3 and 4 are located at point C, which indicates a high probability of brittle failure such as tear-out failure (Figure 5).

The joints under compression load exhibit unexpected results. Joints 1, 2, and 4 have the same maximum displacement (0.3 mm), as opposed to Joint 3 which has larger displacement (0.4 mm) (Figure 7b). From the deformation shape in Figure 6c, it can be seen that Point B-C on the Joint 3 is bending and shows a gap on the middle of the joint. Meanwhile, the rest of the joints look the same as the initial shape.

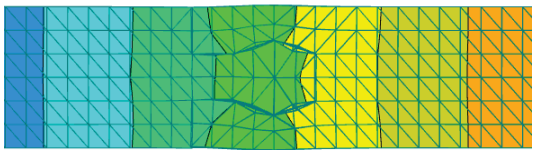

(a) Joint 1 (xy-plane)

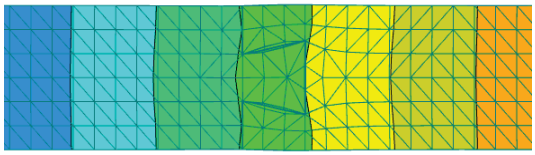

(b) Joint 2 (xy-plane)

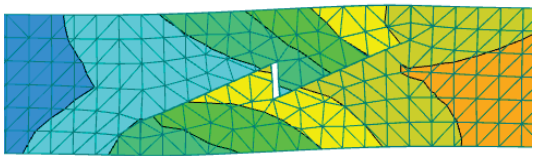

(c) Joint 3 (xz-plane)

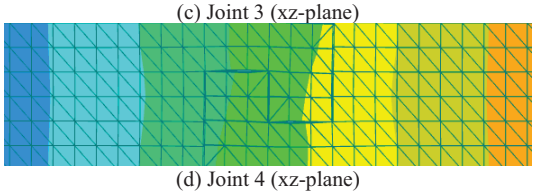

(d) Joint 4 (xz-plane)

Figure 6: *Deformation shape on the joints under compression load*

From the global displacement, it can be concluded that all joints have smaller deformation under compression load than tension load, which alludes to the fact that wood has a higher compressive strength than tension strength. Meanwhile, the joint shape is the most important parameter for a timber joint's structural response under tension load. Yet, there are not many studies on the relationship between joint performance and its shape.

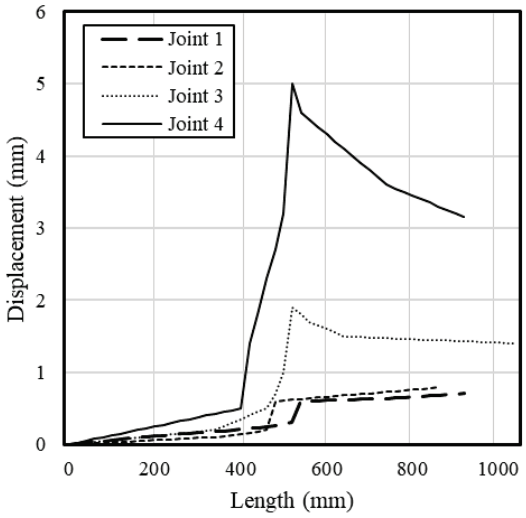

(a)

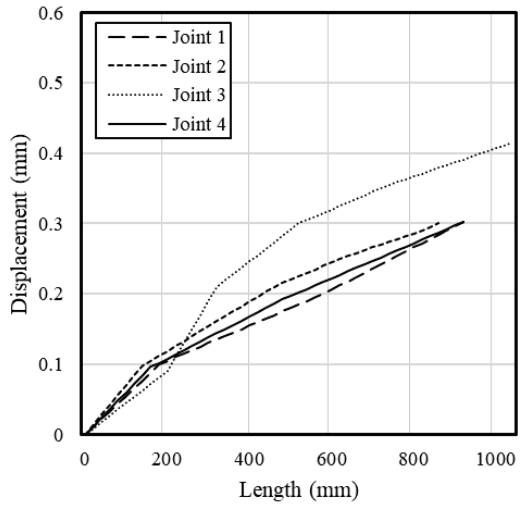

(b)

Figure 7: *Displacement on beam from Point A-D in (a) tension force and (b) compressive force.*

4 CONCLUSIONS

In this study, the four joints of traditional joints have been investigated using finite element analysis. Deformation capacity was obtained from simulation results using Dlubal RFEM software. For modeling and simulation,

https://doi.org/10.52202/069179-0204

several setups were adjusted to the capability of the software.

Based on simulation, Joint 1 and 2 have the smallest displacement compared to the other joints under tension load. It appears that the larger displacement occurred in Joint 4 under tension load while under compression load the larger displacement occurred in Joint 3. Meanwhile, under compression load, Joint 1, 2, and 4 have the same displacement.

Deformation is correlated to stress distribution on the joints. Large displacement has a higher possibility of member failure. Joint failure can be examined by validating the maximum stress on stress distribution to the strength factor (C_f) equation. Thus, the failure occurrence can be checked when the result is above C_f. The inadequate beam size in comparison to the assigned loads is one potential cause of joint failure. Thus, nonlinear analysis is expected in future studies. If the deformation and stress distribution result is connected to the joint properties, a joint with shorter joint length has better compromise than other joints. However, these results still need to be validated for further simulation and experiment.

REFERENCES

[1] Kim, G-C., Matsumura, J. A study on the bending properties of traditional Korean joints. 2011.

[2] Department of Architecture ITB, Minangkabau Architecture. West Sumatra Field Work Lecture Report I. Institut Teknologi Bandung. 1979.

[3] Chen, C.J., Lee, T.L., Jeng, D.S. Finite element modeling for the mechanical behavior of dowel-type timber joints. Computer & Structures. 2003.

[4] Li, S., Zhou, Z., Luo, H., Milani, G., Abruzzese, D. Behavior of traditional Chinese mortise-tenon joints: experimental and numerical insight for coupled vertical and reversed cyclic horizontal loads. Journal of Building Engineering. 2020.

[5] Xue, J., Song, D., Wu, C. Precise finite element analysis of full-scale straight-tenon joints in ancient timber buildings. International Journal of Architectural Heritage. 2021.

[6] Makhlouf, A. S. H., Aliofkhazraei, M. (Eds.). Handbook of materials failure analysis with case studies from the construction industries. Elsevier Science & Technology. 2018.

https://doi.org/10.52202/069179-0204

World Conference on Timber Engineering Oslo 2023

BONDED-IN RODS IN BEECH GLULAM – EFFICIENCY OF A RECESS IN THE BONDLINE

Steffen Franke[1], Bettina Franke[2], Alexander Salenikovich[3]

ABSTRACT: The load-bearing behaviour of bonded-in steel threaded rods (BiR) in hardwood was investigated with special focus on the prevention of the splitting behaviour using a recess (not bonded zone) in the bondline. The main objective was to analyse the influence of the not-bonded length and the rod edge distance on the distribution of longitudinal shear and transverse tensile stresses in joints with bonded-in rods in beech glulam. Several BiR joint configurations were tested experimentally and a wide range of joint configurations with various combinations of recess and bonded lengths and edge distances were numerically investigated. According to the experimental and numerical analyses, a recess length of 2*d* (two times rod diameter) produced a significant positive effect on the stress distribution reducing the risk of splitting of beech glulam in the studied joint configurations.

KEYWORDS: Bonded-in rods, beech, splitting, not bonded length, numerical simulations, shear and tension interaction

1 INTRODUCTION

Discussions and ambition about the use of hardwood as construction material are currently present in Europe. On the one hand, hardwood provides excellent mechanical strength properties, but on the other hand, the strength parameters are less investigated and standardized for the design of connections with mechanical fasteners or bonded-in rods (BiR). The performance of connections in hardwood timber structures must be determined with high reliability to benefit from the naturally higher strength potential of hardwood. In Switzerland, 31 % of the entire wood stock is hardwood, where the biggest part with 18 % counts for beech wood [1]. Therefore, the research work concentrates on the European beech wood.

To use high-performing glued-laminated timber (glulam) from beech wood efficiently, high-performing connection systems must be available too. BiR connections are one of those. However, neither the Swiss standard SIA 265:2012 [2] nor the Eurocode 5 (EC 5) [3] currently include the design of BiR in softwood or hardwood glulam. The German national annex of EC 5 (DIN EN 1995-1-1/NA:2013-08) [4] provides a design method for axially loaded threaded steel rods glued in softwood. Research papers and publications have publicly discussed and proposed methods and approaches for the design of BiR, e.g., [5]. In EU, common rules for the assessment of BiR have been adopted in 2019 [6] and testing requirements for BiR in glued structural timber products have been adopted in 2021 [7]. Basic design provisions for GIR in timber connections are now given in EOTA TR 070 [8], and included in the Eurocode 5 draft [9].

The load-bearing capacity of BiR depends on the following main parameters [10]:

- Geometry; size and proportion of timber, adhesive and rod; slenderness; number and placement of rods (edge/end distances)
- Material stiffness and strength
- Fracture behaviour of timber and adhesive
- Variability of all properties
- Imperfections (quality control)
- Loading situation (forces, moisture, temperature)

For the best performance and robustness, it is preferable to prevent brittle failure modes, such as splitting, like shown in Figure 1, or bondline failures, and to target ductile steel failure. The maximum utilisation of timber (ratio of the connection capacity to the member cross-section capacity in tension) can be achieved by increasing the number of rods per unit area, which leads to smaller spacing and edge distances [11] and, in turn, may provoke

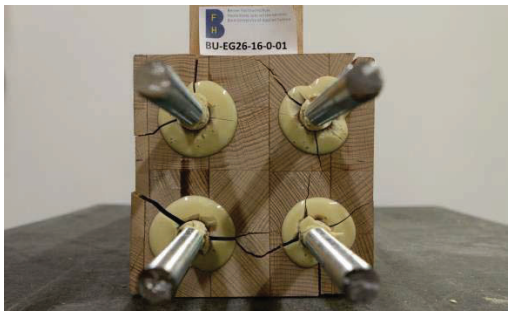

Figure 1: *Typical BiR failure in beech glulam – wood splitting due to transverse tension without a recess in the bondline*

[1] Steffen Franke, Bern University of Applied Sciences, Switzerland, steffen.franke@bfh.ch
[2] Bettina Franke, Bern University of Applied Sciences, Switzerland, bettina.franke@bfh.ch
[3] Alexander Salenikovich, Université Laval, Canada, alsal10@ulaval.ca

https://doi.org/10.52202/069179-0205

the undesirable wood splitting unless special preventive measures are undertaken.

This study is focused on achieving an efficient and robust connection configuration with small edge distances $a_{2,c}$ by using a recess l_{recess} in the bondline, i.e., not-bonded zone in front of the bondline, as shown in Figure 2. Therefore, the load-bearing behaviour depending on the interaction of the longitudinal shear and transverse tensile stresses around the bondline is investigated numerically and experimentally for beech wood glulam.

2 STATE OF THE ART

2.1 EFFECT OF BIR PLACEMENT

The placement, i.e., spacing and edge distance, have a great impact on the load-bearing capacity and performance of BiR connections [12], [13], [14]. By using the standardized spacing of 5d and steel with the tensile strength of 800 MPa results in an equivalent timber stress of 19.6 MPa which is about 60 % utilization for a timber grade GL40, as shown in Figure 3. The maximum utilisation up to 100 % can be achieved with a much smaller wood cross-section a_2 per rod between 3.61 and 3.85 times the rod diameter (d) for the timber grades GL 48 and GL 40 respectively. However, BiR connections with these small spacing and edge distances are not permitted in standards, because of their propensity for wood splitting and reduced pull-out strength even in laboratory tests.

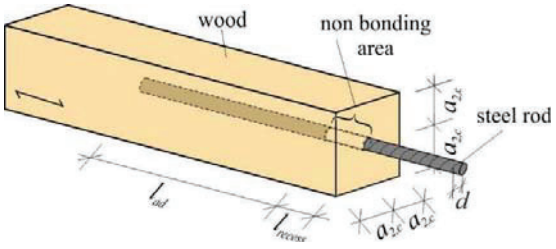

Figure 2: *Principal sketch of BiR and notation of variables and components*

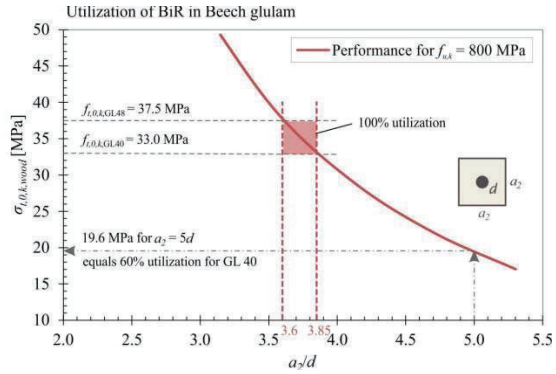

Figure 3: *Utilization of BiR in beech glulam for steel strength of 800 MPa and different timber grades*

For example, Figure 4 illustrates the influence of the edge distance on the pull-out resistance and failure mode of BiR connections in beech wood studied by Franke et al. [15]. Three levels of failure behaviour and capacity can be observed. At the edge distance $a_{2,c}$ (half of a_2) of 1.5d, the pull-out strength of rods, affected by the premature splitting, was about 20 % less than that of rods with 2.5d and 3.5d edge distance, for the same rod diameter, bonded length, and adhesive. Nevertheless, most of the joints with 2.5d edge distance experienced splitting and bondline failures at almost the same breaking loads. At 3.5d edge distance, there was no splitting observed and the strength of BiR joints reached the highest values with minimum variation. However, the cross-section utilisation of only less than 50 % can be achieved. All these tests were conducted on the BiR joints without a recess in the bondline.

2.2 EFFECT OF RECESS IN THE BONDLINE

It is well known that the stress distribution along the length of the BiR is not uniform, with stress concentrations near the ends of the bondline. Recently, Vallée et al. [16] studied the distribution of shear (τ_{RL}) and radial (σ_R) stresses along the bondline via numerical modelling of single BiR in CLT and glulam. Figure 5 illustrates the results for four different bonded lengths of a 12.7 mm (1/2-in) rod. The highest peaks of both shear and radial stresses are seen at the outer end of the bondline. These numerical simulations confirm that the longer the bondline, the greater is the difference between the peak stress and the mean stress, the less stress is transferred into the depth of the wood member, and, hence, the lower is the strength of the bondline.

The peaks of the shear and transverse tensile stresses near the end of the wood member negatively affect the pull-out resistance of BiR due to splitting. Fabris [12] studied the interaction of the stresses on the BiR performance and suggested that a recess of the bondline into the wood creating an unbonded zone near the outer end increases the stressed wood volume around the rod and hence improves the resistance to splitting, as shown in Figure 6.

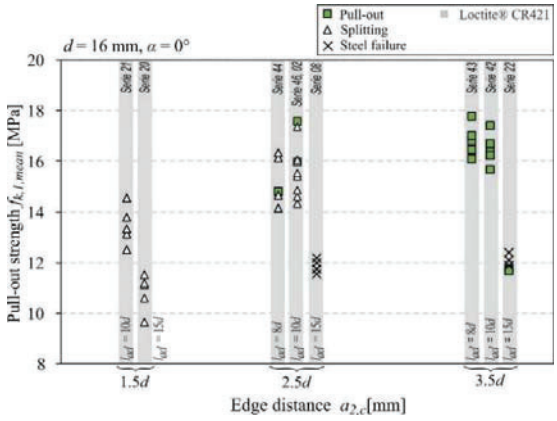

Figure 4: *Pull-out strength and failure modes of BiR in beech glulam for different edge distances [15]*

https://doi.org/10.52202/069179-0205

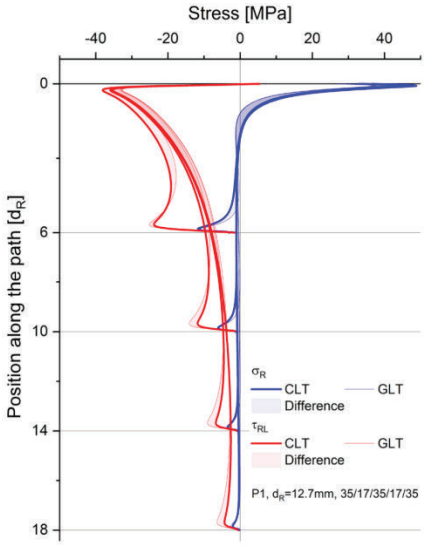

Figure 5: *Shear stresses, τ_{RL}, and radial stresses, σ_R, along the adhesive-wood interface, reference load F_0= 100 kN, from [16]*

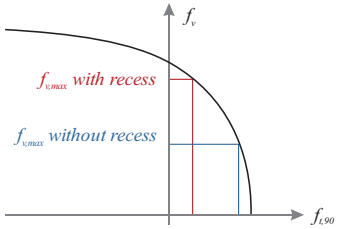

Figure 6: *Interaction of shear and transverse tensile stresses, modified from [12]*

The beneficial effects of a recess in the bondline on the pull-out resistance has been demonstrated experimentally by Salenikovich et al. for BiR in CLT [17] and in glulam [18]. It allowed achieving a higher load capacity and minimizing the risk of splitting and other brittle failure modes, such as plug shear in CLT for rods bonded perpendicular to the grain.

The effect of different recess lengths in beech glulam has not been investigated so far. Besides the increase of the stressed wood volume around the rod, it is assumed that a recess in bondline also changes the interaction of shear and transverse tensile stresses as indicated in Figure 6 and leads to higher capacities. Less transverse stress will exist at much higher shear stress for the case with a recess.

3 INVESTIGATION OF THE RECESS LENGTH

3.1 MATERIALS

All specimens for the investigation have been produced from Glulam GL 40h of European Beech (*Fagus sylvatica*) from Swiss forests with an average density of 710 kg/m³ and moisture content of 10.5 %. Threaded steel rods of M16 with a strength class of 8.8 and 10.9 were bonded-in using a two-component PUR adhesive

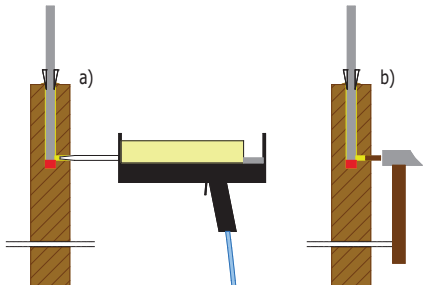

Figure 7: *Preparation of test samples, a) gluing injection from the bottom of the bondline, b) closing of the injection hole with wood dowel*

Loctite® CR421 or its newer version Loctite® CR821. Centering aids and upright position gluing was used, see Figure 7.

3.2 EXPERIMENTAL PROGRAMME

The investigation was carried out in two stages. The first stage started within a research project on efficient connections in hardwood [15], see Table 2. It focused on testing of known connection systems in hardwood to determine their performances. Within the test period from 2019 to 2021, the adhesive was changed from Loctite® CR421 to CR821 in line with current market developments at Henkel & Cie AG and the borehole diameter d_{hole} was reduced by half, from d_{BiR} + 4 mm to d_{BiR} + 2 mm. The experimental programme included a variation of the edge distance $a_{2,c}$ and the bonded length l_{ad} in combination with a recess length of 0d, 2d or 5d which reflected the known practice for softwood glulam.

The second stage stemmed from the first one and focused specifically on the influence of the recess length on the performance and comprised test series S0 to S5 with the recess length between 0d and 5d in increments of 1d. A constant edge distance of 1.75d and bonded length of 13d were used to provoke splitting failure and prevent pull out failure. In the second stage all rods were bonded-in with Loctite® CR821. Table 2 summarizes the configurations and variations of the experimental test programme.

3.3 NUMERICAL SIMULATIONS

The influence of the not-bonded length on the resistance of a BiR joint was also studied using numerical linear elastic simulations of the joint as shown in Figure 2, with a single rod with a varying bonded length l_{ad}, recess length l_{recess} and edge distance $a_{2,c}$. The numerical investigation focused on the analysis of the stress distributions along the bondline and especially at the beginning of the bondline of a single rod connection in beech glulam. A quarter of the specimen was modelled benefiting from the double symmetric conditions, as shown in Figure 8 for a connection with a bonded length of 13d, recess length of 1d and edge distance $a_{2,c}$ of 2.5d. The elastic material properties are summarized in Table 1. The rod was loaded in tension by 100 MPa for all simulations and presented results.

https://doi.org/10.52202/069179-0205

Table 2: Experimental programme of BiR with the rod diameter of M16

Stage	Series	Number of tests	Adhesive Loctite®	d_{hole} [mm]	$l_{ad} + l_{recess}$ [-]	$a_{2,c}$ [-]	Failure		
							Splitting	*Pull-out*	*Steel rupture*
1	02, 46	9	CR421	20	$10d + 0d$	$2.5d$	7	2	-
	07	5	CR421	20	$10d + 2d$	$2.5d$	-	4	-
	08	5	CR421	20	$15d + 0d$	$2.5d$	-	-	5
	20	5	CR421	20	$15d + 0d$	$2.5d$	5	-	-
	21	5	CR421	20	$10d + 0d$	$1.5d$	5	-	-
	22	5	CR421	20	$15d + 0d$	$3.5d$	-	2	3
	42	5	CR421	20	$10d + 0d$	$3.5d$	-	5	-
	43	5	CR421	20	$8d + 0d$	$3.5d$	-	5	-
	44	5	CR421	20	$8d + 0d$	$2.5d$	4	1	-
	M15	3	CR421	18	$10d + 5d$	$2.5d$	-	3	-
	M09, M16	8	CR821	18	$10d + 0d$	$2.5d$	-	8	-
	M13, M17	7	CR821	18	$10d + 5d$	$2.5d$	-	7	-
	M22	3	CR821	18	$10d + 5d$	$1.5d$	-	3	-
2	S0	4	CR821	18	$13d + 0d$	$1.75d$	2	-	2
	S1	4	CR821	18	$13d + 1d$	$1.75d$	1	3	-
	S2	4	CR821	18	$13d + 2d$	$1.75d$	-	3	-
	S3	4	CR821	18	$13d + 3d$	$1.75d$	-	1	3
	S4	4	CR821	18	$13d + 4d$	$1.75d$	-	-	4
	S5	4	CR821	18	$13d + 5d$	$1.75d$	-	-	4

Table 1: Elastic material properties

Component	Young's modulus [MPa]	Poisson ratio [-]	Shear modulus [MPa]
Beech, longitudinal	14'500	0.04	1'000
Beech, transverse	1'100	0.61	380
Adhesive, CR821	2'850	0.37	1'040
Steel rod	210'000	0.30	81'000

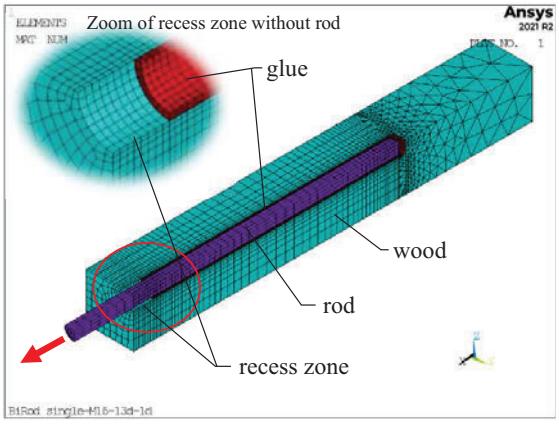

Figure 8: *FE model of a BiR joint, l_{ad} =13d, l_{recess} = 1d*

3.4 EXPERIMENTAL RESULTS

All failure modes, steel rupture (yielding of the rods), wood splitting and rod pull-out (bond rupture), were observed. The failure modes and pull-out strength values calculated from the maximum load divided by the circumference with the nominal rod diameter and the bonded length are summarised in Figure 9.

In general, the BiR joints glued with Loctite®CR821 demonstrated a lower pull-out strength compared to Loctite®CR421. Therefore, the results are analysed separately.

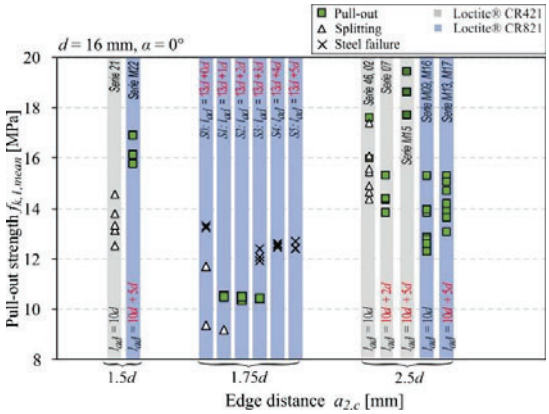

Figure 9: *Pull-out strength results depending on the edge distance, bonded length and recess length for two glues*

Focusing on Loctite®CR421 (columns highlighted in grey):

- Splitting was not observed in joints with the recess length of $2d$ (series 07) and $5d$ (series M15) and the edge distance of $2.5d$ as opposed to joints without a recess (series 46 and 02); the joints with the recess of $5d$ showed higher strength.

Focusing on Loctite®CR821 (columns highlighted in blue):

- Splitting was not observed in joints with the edge distance of $2.5d$ without a recess (series M09 and M16) and with a recess of $5d$ (series M13 and M17); however, less variation and higher mean values were observed for the series with recess.
- No splitting was observed even for the joints with the edge distance of $1.5d$ with the recess of $5d$ (series M22).
- All joints with the bonded length of $13d$ and the edge distance of $1.75d$ (series S0 to S5) showed lower pull-out strength values than those with the bonded length of $10d$ and the edge distance of $2.5d$ (due to the larger bondline circumference).

https://doi.org/10.52202/069179-0205

- Three distinct levels of pull-out strength and failure mode transition can be observed depending on the length of the recess:
  - Although two specimens without a recess (series S0) showed steel failure, two specimens failed by splitting, one of which occurred at a low load level; one specimen with the recess of 1*d* (series S1), failed by splitting at a similar load level.
  - Specimens with the recess length of 1*d*, 2*d* and 3*d* (Series S1, S2, S3) that failed by pull-out (bond failure) showed equal pull-out strength, which was higher than that due to splitting but less than that due to the rod rupture.
  - Starting with the recess length of 2*d* (Series S2), no splitting failures were observed.
  - Three specimens with the recess length of 3*d* (Series S3) reached the steel rod resistance.
  - All specimens with a recess length of 4*d* (Series S4) and 5*d* (Series S5) failed due to steel rod rupture.

3.5 NUMERICAL RESULTS

Figure 10 shows a BiR joint FE model in a deformed state and the deformation gradient in the longitudinal direction for the bonded length of 13*d* and the recess length of 1*d*. The resulting shear and transverse stress distributions along the bondline at the wood/glue interface are plotted for the same joint configuration in Figure 11 and Figure 12, respectively. The stress distributions for the recess length between 0*d* and 4*d* (no visible difference was observed for 5*d*) are summarized in Figure 13 and Figure 14.

The numerical simulations show a 19% increase of the longitudinal shear stress from 0*d* to 2*d* recess length and then a gradual increase up to 26.3% at 5*d* (see Figure 14 and Figure 15). At the same time, the transverse tensile stress at the beginning of the bondline drops down rapidly to 47.5% from 0*d* to 2*d*, and to 46.5% at 3*d* (see Figure 13 and Figure 15). No further reduction of the peak transverse stress is observed beyond $l_{recess} = 3d$.

Similar results were observed in simulations with a bonded length of 10*d* and for connections in softwood.

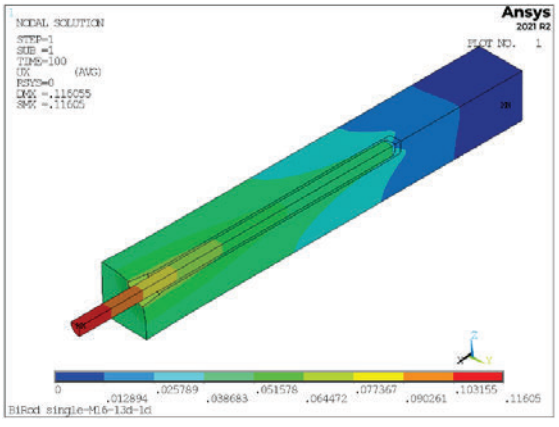

Figure 10: *Deformations of a BiR joint, l_{ad} =13d, l_{recess} = 1d*

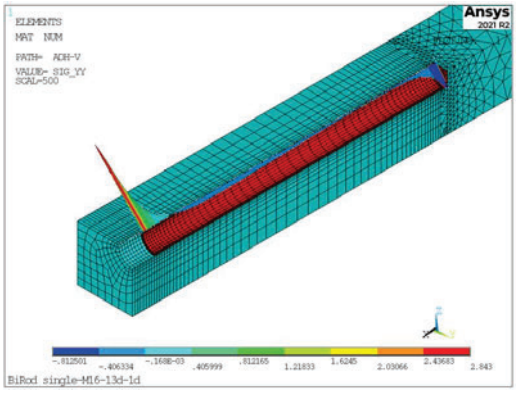

Figure 11: *Transverse stress distribution along the bondline, l_{ad} = 13d, l_{recess} = 1d*

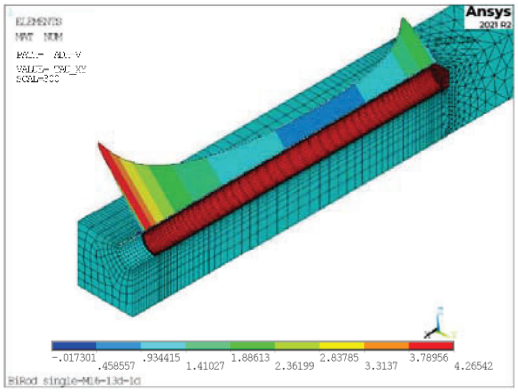

Figure 12: *Shear stress distribution along the bondline, l_{ad} = 13d, l_{recess} = 1d*

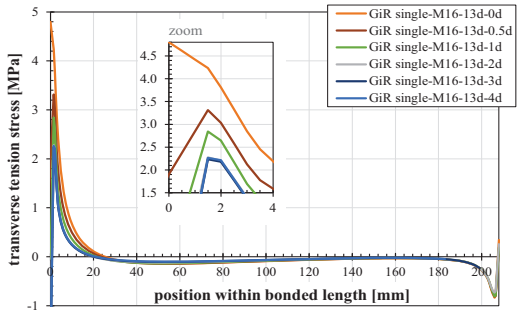

Figure 13: *Transverse stress distribution along the bondline depending on the recess length*

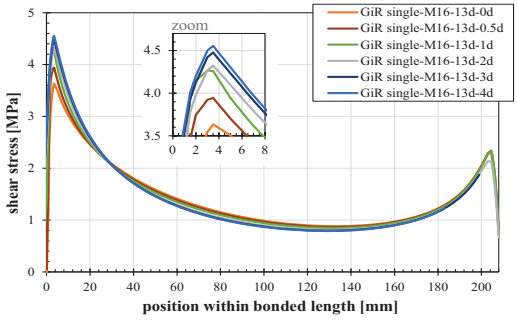

Figure 14: *Shear stress distribution along the bondline depending on the recess length*

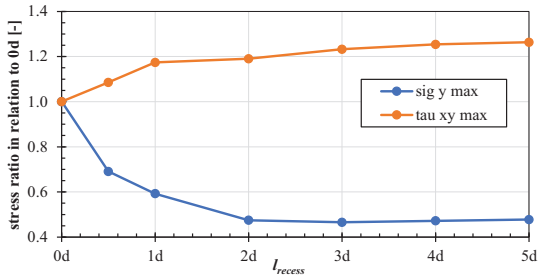

Figure 15: *Increase and decrease of the maximum transverse tensile and shear stresses at the beginning of bondline depending on the recess length*

4 DISCUSSION AND CONCLUSION

From the experimental results it can be concluded that without a recess or with a recess less than 2*d*, the risk of wood splitting in BiR joints with reduced spacing is very high. With a recess of 3*d* and more, the bondline strength increases to the extent that allows reaching the steel rod rupture, which is a preferred failure mode for BiR connections.

These experimental observations are well aligned and explained by the numerical simulations, which show a significant reduction of the peak transverse tensile stress at the recess length of 2*d*. It can also be concluded that no further gain in the splitting resistance is expected when the recess length is beyond 3*d*.

The relation assumed in Figure 6 can be confirmed by summarizing the stress relationship/interaction of shear and transverse tension depending on the recess length in Figure 16. The mean shear strength of 12 MPa and mean transverse tension strength of 7 MPa were assumed for beech wood according to [19]. Up to the recess length of 2*d*, higher shear stresses in combination with lower transverse tensile stresses can be achieved before failure with the increasing recess length. Therefore, the propensity for splitting is reduced and a higher axial load can be applied on the bonded-in rod. No further significant change is observed beyond $l_{recess} = 2d$.

These observations can be confirmed by using equation (1) for the stress verification, which is illustrated in Figure 17 for the GiR joint with bonded length of 13*d* under the same stress of 100 MPa. An optimal utilization starts at a recess length of 2*d*. However, a recess length of 3*d* is recommended for the safety reason before further confirmation with more experimental and numerical results including long-term load and moisture fluctuation effects.

$$\left(\frac{\tau_{yz}}{f_v}\right)^m + \left(\frac{\sigma_y}{f_{t,90}}\right)^n \leq 1 \qquad (1)$$

where

τ_{yz}	shear stress [MPa]
f_v	shear strength [MPa]
σ_y	transverse tensile stress [MPa]
$f_{t,90}$	transverse tension strength [MPa]
m	interaction parameter [-]
n	interaction parameter [-]

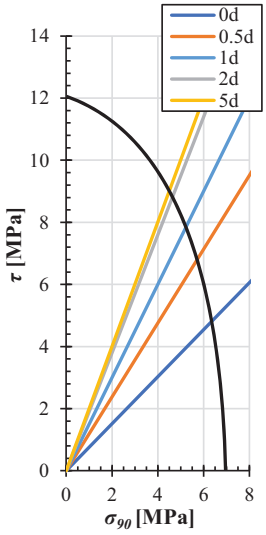

Figure 16: *Stress interaction development curves at the beginning of the bonline in relation to the recess length and in comparison with the failure criteria considering the interaction of shear and transverse tensile stresses*

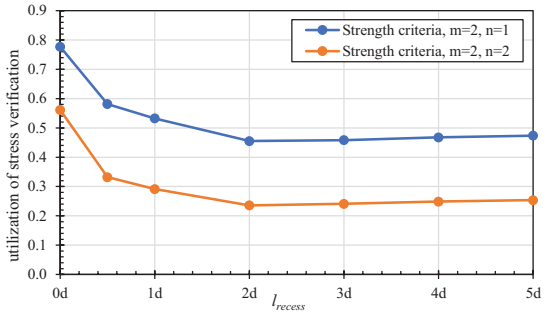

Figure 17: *Utilization of the shear and transverse tensile stress verification for two failure criterias curves (steel rod rupture is not included)*

Further investigations will be done towards

- Probabilistic verification of the timber stress interaction near the beginning of the bondline to analyse the contribution of the wood volume in front of the bondline;
- Implementation of fracture mechanics into the numerical simulations;
- Variations of material parameters as well as geometric parameters; and
- Experimental testing for more statistical values and validation.

ACKNOWLEDGEMENT

Thanks for the SNF-Grant for a research exchange of B. Franke to the Université Laval, Quebec, Canada where part of the research has been conducted and Milos Asenov for his work within the master thesis.

https://doi.org/10.52202/069179-0205

REFERENCES

[1] Eid. Forschungsanstalt für Wald Schnee u. Landschaft, 2018. (in German) Schweizerisches Landesforstinventar, 4. Landesforstinventar 2009 –2013, Switzerland.

[2] SIA265:2021, Holzbau. (in German) Schweizerischer Ingenieur- und Architektenverein, Zürich, Switzerland.

[3] EN 1995-1-1:2014 Eurocode 5: Design of timber structures - Part 1-1: General and rules for buildings. European Committee for Standardization, Brussels, Belgium.

[4] DIN EN 1995-1-1/NA:2013-08 (in German) Nationaler Anhang – National festgelegte Parameter – Eurocode 5: Bemessung und Konstruktion von Holzbauten – Teil 1-1: Allgemeines – Allgemeine Regeln und Regeln für den Hochbau, Deutsches Institut für Normung e.V., Berlin, Germany.

[5] S. Aicher, G. Stapf. (in German) Eingeklebte Stahlstäbe – state of art – Einflussparameter, Versuchsergebnisse, Zulassungen, Klebstoffnormung, Bemessungs- und Ausführungsregeln. Internationales Holzbau Forum IHF, Garmisch Partenkirchen, Germany, 2017.

[6] EOTA EAD 130006-00-0304. Glued-in rods for timber connections. European Assessment Document. European Organisation for technical assessment. 2019.

[7] CEN-EN 17334. Glued-in rods in glued structural timber products - Testing, requirements and bond shear strength classification. European Committee for Standardization. 2021.

[8] EOTA TR 070:2019-10. Design of glued-in rods for timber connections. Technical Report. European Organisation for technical assessment. 2019.

[9] CEN/TC 250/SC 5 prEN 1995-1-1:20XX. Eurocode 5: Design of timber structures — Common rules and rules for buildings — Part 1-1: General. European Committee for Standardization, Brussels, Belgium, 2022.

[10] R. Steiger, E. Serrano, M. Stepinac, V. Rajčić, C. O'Neill, D. McPolin, R. Widmann. Strengthening of timber structures with glued-in rods. Construction and Building Materials (97), 90-105, 2015.

[11] E. Gehri. High performing jointing technique using glued in rods. In: WCTE Conference proceedings, Riva del Garda, Italy, 2010.

[12] A.F. Fabris. (in German) Verbesserung der Zugeigenschaften von Bauholz parallel zur Faser mittels Verbund mit profilierten Stahlstangen. Doctoral Thesis, ETH Zürich, Switzerland, 2001.

[13] E. Gehri. (in German) Eingeklebte Anker – Anforderungen und Umsetzungen. 15. Internationales Holzbau Forum IHF, Garmisch-Partenkirchen, Germany, 2009.

[14] H. J. Blaß, B. Laskewitz. Effect of spacing and edge distance on the axial strength of glued-in rods *In: Proceedings-International Council for Research and Innovation in Building and Construction (CIB W18), August,* Graz, Austria, 1999.

[15] S. Franke, B. Franke, S. Heubuch, A. Frangi, R. Jockwer (in German), Anschlüsse in Buchenholz - Ermittlung von Grundlagen zur Bemessung von Anschlüssen für die Marktimplementierung in der Schweiz, Forschungsbericht, Berner Fachhochschule, Biel, Switzerland, 2019.

[16] T. Vallée, H.R. Rakesh, T. Tannert. Load-carrying capacity prediction of single rods glued into cross-laminated timber. EJWWP. https://doi.org/10.1007/s00107-022-01835-1. 2022.

[17] A. Salenikovich, M-È. Laverdure, R. Bouchard, T. Lefort. A study of the structural performance of glued-in rods in CLT. In: *Proceedings of WCTE 2021*, Santiago, Chile, 2021.

[18] A. Salenikovich, É. Lapointe, B. Zumbrunn-Maurer, T. Brotschi, A. Kramer. Performance of glued-in rods in glulam and MPP in tension and compression. In: *Proceedings of WCTE 2023*, Oslo, Norway. 2023.

[19] Grosser D., Zimmer B., Einheimische Nutzhölzer, holzhandbuch Reihe 4, Teil 2, Folge 2, DGfH, München, Germany, 1989.

World Conference on Timber Engineering Oslo 2023

USING X-RAY COMPUTED TOMOGRAPHY TO MEASURE FIRE DEGRADATION OF A TIMBER CONNECTION

Quentin Rodrigues[1], Johannes A. J. Huber[2], Lars Hansson[3], Rhoda Afriyie Mensah[4], Rostand Moutou Pitti[5]

ABSTRACT: The charring behaviour of timber elements under fire is well understood, however, the effects of fire and heat on connections are not equally well known. Timber connections often use steel fasteners, like screws or angle brackets, which conduct heat much better than wood. Moreover, these fasteners lose their mechanical resistance and capacity under elevated temperatures. X-ray computed tomography (CT) can be used to reconstruct the internal structure of wood non-destructively. It should therefore be possible to use this technology to also study the progressive degradation due to fire of a timber connection. The goal of the present study is to investigate how CT can be used to analyse the degradation of a timber connection due to fire. Samples of Norway spruce with self-tapping screws were scanned before and after a fire exposure, and mechanical tests were performed. The results indicate that the degradation due to fire in a timber connection can be observed in CT scans, but that certain measures need to be taken to minimise the effects of image artefacts due to X-ray scattering and photon starvation.

KEYWORDS: Steel-to-timber fastener, CT, Image artefacts, Image analysis, Density, Charring

1 INTRODUCTION

1.1 BACKGROUND

Connections are often the critical part of a building, since they establish structural continuity among the elements. Timber connections often use steel fasteners, like dowels or screws. The behaviour of timber elements under fire is well understood; charring occurs at a certain speed and the mechanical properties of unburnt timber close to the charring front remain unaffected [1]. Steel, however, behaves very differently under fire, due to its higher thermal conductivity and the tendency to soften under elevated temperatures. Timber connections using steel screws may therefore behave differently under fire than under normal conditions.

The Eurocode provides some recommendation to quantify timber resistance under fire and to passively improve the fire resistance of the connections [2]. It also provides us estimates about charring depth and the charring speed on fire exposed surfaces.

1.2 TIMBER CONNECTIONS UNDER FIRE EXPOSURE

Some studies have been conducted to investigate the mechanical resistance of timber connections using steel fasteners under a fire exposure. These experiments mainly focused on loaded samples. They provided insight on the impact of different parameters, like the position, dimension, and number of fasteners [3][4][5]. However, the conducted studies were only able to observe changes at the surfaces of the timber samples.

X-ray computed tomography (CT) enables non-destructive measurements of the internal density distribution of a scanned object. CT scanning has been used previously to investigate wood, e.g. to study density [6], shrinkage due to moisture changes [7] or for developing simulation models [8]. Since degradation of wood due to fire entails local reductions of density, CT scanning could provide insight on the evolution of this degradation. Furthermore, it could be used to study the degradation of wood in the proximity of a fastener *in situ*, from which the connection resistance could be estimated.

[1] Quentin Rodrigues, Université Clermont Auvergne, Clermont Auvergne INP, Institut Pascal,F-63000 Clermont-Ferrand, France, quentin.rodrigues.pro@gmail.com

[2] Johannes A. J. Huber, Luleå University of Technology, Skellefteå, Sweden, johannes.huber@ltu.se

[3] Lars Hansson, Luleå University of Technology, Skellefteå, Sweden, lars.hansson@ltu.se

[4] Rhoda Afriyie Mensah, Luleå University of Technology, Luleå, Sweden, rhoda.afriyie.mensah@ltu.se

[5] Rostand Moutou Pitti, IRT, Libreville Gabon, Rostand.moutou_pitti@uca.fr

https://doi.org/10.52202/069179-0206

1.3 OBJECTIVE

The aim of the present study is to investigate how X-ray CT can be used to analyse the degradation of a timber connection due to a fire exposure. The results of this study provide insight in the possibilities and limitation of using CT to detect fire propagation in wood. The results can be used to prepare future studies using a designated combustions chamber, where timber charring will be studied *in situ* using a CT scanner.

2 CT SCANS AND ARTEFACTS

All CT scans in this study were acquired by a laboratory-adapted medical CT scanner (Siemens Somatom Emotion Duo) at the facilities of Luleå University of Technology in Skellefteå, Sweden. The images were acquired at locations spaced 1 mm apart and each slice contained a grid of 512 × 512 pixels, at a resolution of 0.68 × 0.68 mm^2.

An initial pre-study was conducted to evaluate the effects of metal connectors on the quality of the reconstructed images from CT scans.

2.1 METAL INDUCED ARTEFACTS

As shown in **Erreur ! Source du renvoi introuvable.**Figure 1, the quality of an image obtained from the scan of a sample made of a piece of wood and a metal fastener is deteriorated by artefacts.

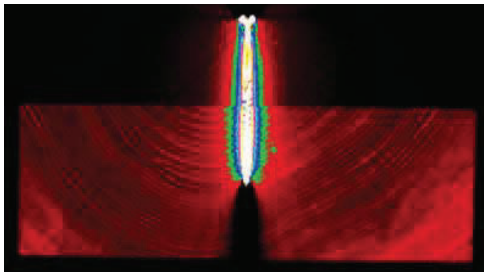

Figure 1: *CT image from of a piece of wooden piece with a screw inserted parallel to the scanning plane.*

We identified two main types of image artefacts. The first one causes the black part in **Figure 1** at the bottom of the screw and is due to photon starvation. It occurs when X-ray beams are attenuated after passing through material of too high density. The second artefact is visible in the proximity of the screw (blue and green on the figure) and is caused by photon deviation by the metal.

2.2 SETUP OPTIMIZATION TO REDUCE ARTEFACTS

Since photon starvation was caused by too large paths of metal in the emitter-sensor plane of the scanner, a first step to reduce artefacts without post-scan image correction was to scan the sample in a plane perpendicular to the screw axis. This way, the X-ray beams only need to pass through at most the diameter of the screw instead of its full length.

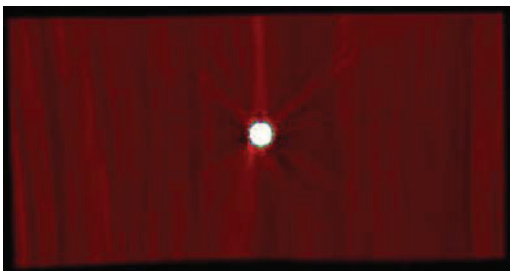

Figure 2: *CT image from a wooden piece with a screw perpendicular to the scanning plane.*

In Figure 2, much of the artefacts could be removed by a perpendicular screw orientation. Some bright streaks are still visible, but it does not affect the image quality substantially. In the proximity of the screw surface, some noise is also still visible, but substantially reduced compared to Figure 1.

2.3 SCAN WITH MORE METAL FASTENERS

Subsequently, scans have been performed on samples with a larger quantity of metal in the wooden sample to investigate the evolution of artefacts. In Figure 3 the effects of two screws in the sample are shown. It was found that both type of artefacts were more visible in both sample orientations. Again it was found, that having the screw axes aligned with the scanning plane deteriorated the image quality more than having the screw axis oriented perpendicular to the scanning plane.

It becomes obvious that “tilting” the sample for better image quality has its limitations with more fasteners involved. Furthermore, it seems difficult to investigate setups with larger metal connectors, e.g. angle brackets.

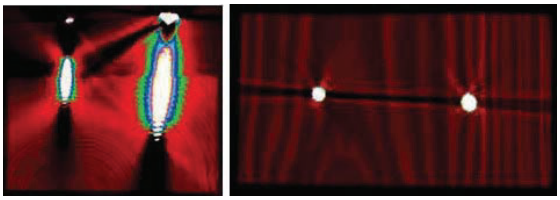

Figure 3**:** *Comparison of the influence of the screw’s positioning with two screws.*

3 SAMPLE PREPARATION AND TESTS

3.1 SAMPLE GEOMETRY AND CT SCANS

Two types of samples have been used for our experiments, as illustrated in Figure 4 one for tests in compression on a wood screw (5 × 120 mm²) perpendicular to the fibres (tagged C- in the text), and one for tests in tension on a wood screw (5 × 70 mm²) parallel to the fibres (T-).

Twelve samples were produced for both sample types; 4 pieces were used as a reference (tagged T-0 and C-0), 4 were fire exposed for 5 minutes (tagged T- or C-5), and 4 were fire exposed for 10 minutes (tagged T- or C-10).

All samples were CT scanned before and after an eventual fire exposure with the screw inserted in the wood. The screws were positioned perpendicular to the scanning

https://doi.org/10.52202/069179-0206

plane, following the reasoning of the pre-study. For those burnt samples where it was possible to remove the screw easily without disintegrating the sample, additional CT scans were conducted without the screw.

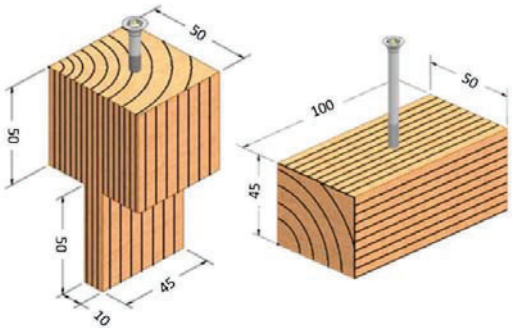

Figure 4: *Sample dimensions for tension (left) and compression (right)*

3.2 BURNING PROCESS

The samples were burnt in a cone calorimeter, according to the ISO 5660 standard [9]. The cone calorimeter is the most commonly used device to study small samples fire behaviour and is illustrated schematically in Figure 5. Samples are exposed to a one-dimensional radiative heat flux from a conical heater, with a constant surface heat flux of 35 kW/m² and a temperature of 722°C. These values have been chosen according to the fire exposition estimated in a real building fire.

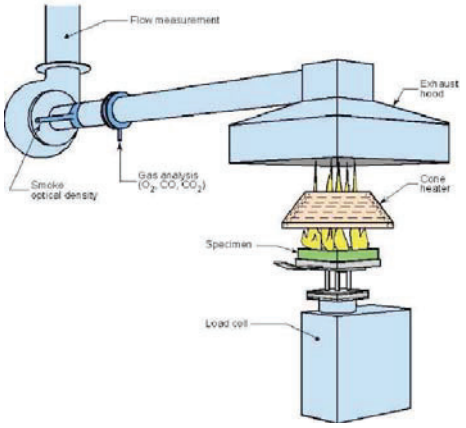

Figure 5: *Cone calorimeter*

To achieve a one-dimensional fire exposure, insulation layers of type Kaowool Blanket with a density of 64 kg/m^3 were wrapped around the wooden samples and fixed with staples, leaving only one surface exposed to the heat.

3.3 MECHANICAL TESTS

The samples were tested with a universal testing machine (MTS Criterion Series 40) for both compression and tension. A loading speed of 0.2 mm/s and a maximum load limit of 10 kN were applied. The setup is shown in Figure 6. For analysis, the mean values of respectively the tension and compression test series were used.

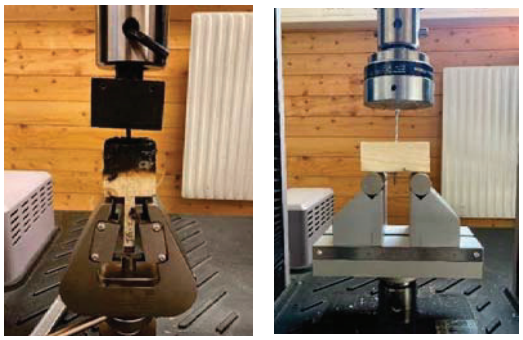

Figure 6: *Mechanical test setup for tension (left) and compression (right)*

4 IMAGE ANALYSIS

The CT images were analysed using Python code. Images of the same samples before and after the fire exposure were compared. The analyses were confined to 20 CT slices from the top of each sample, i.e. from the surface intended to be exposed to fire, which corresponded to 20 mm due to the 1 mm spacing between scans.

4.1 SINGLE IMAGE HISTOGRAMS

At first, the greyscale histograms of single image slices were analysed. Histograms from the same slice of a same sample before and after fire exposure were compared. For illustration, images of the same slice of a representative sample before and after a 10-minute heat exposure are shown in Figure 7.

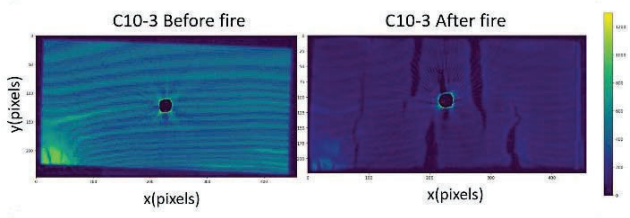

Figure 7: *CT images of the same slice of the same sample before (left) and after (right) a 10-minute fire exposure*

Figure 8 shows the histogram of the unburnt sample in Figure 7. The histogram was truncated at 1000 kg/m^3 for a better readability, but there was also an additional peak at 4000 kg/m^3 caused by the metal of the screw. The histogram was separated into four distinct zones (vertical lines in the figure). We can distinguish two density peaks in Figure 8, which were characteristic for unburnt wood: the first in zone 1 around 50 kg/m^3 representing air around the sample and covering approximately 13 % of the image, and the second in zone 3 between 400 and 550 kg/m^3 representing wood and covering approximately 73 % of the image. The flat area in zone 2 represents approximately 5 % of the image.

https://doi.org/10.52202/069179-0206

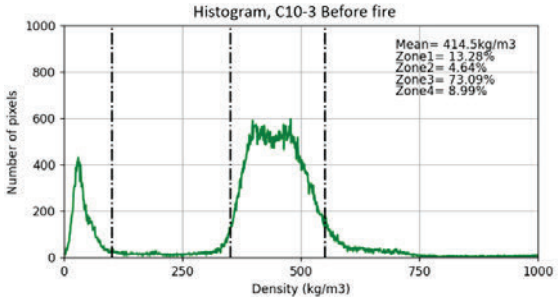

Figure 8: *Histogram of the image before fire exposition*

Figure 9 shows the histogram of the sample in Figure 7 that has been fire exposed for 10 minutes, again truncated for density. We are still able to distinguish two main peaks, however, they are now located in zone 1 (26 %) and zone 2 (73 %). The peak around 500 kg/m^3 in Figure 8 thus shifted to lower values due to the charring process and the resulting lower density of charcoal. The greyscale histogram can therefore be used to detect and quantify fire degradation.

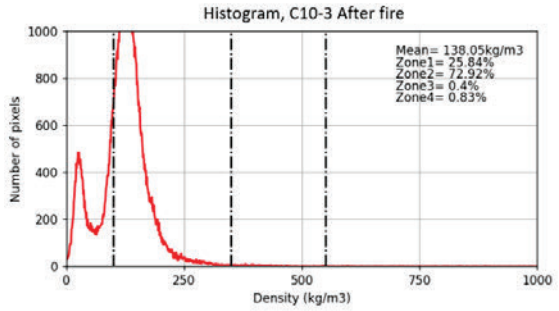

Figure 9: *Histogram of the image after a 10-minute fire exposure*

4.2 HISTOGRAM EVOLUTION THROUGH THE SAMPLE

The classification of the pixels according to the four density zones defined above can be used to study the evolution of the distribution in each class in consecutive slices along the CT scan of each sample.

Figure 10 shows this evolution for one representative sample before and after fire exposure along the top 20 mm from the surface exposed to fire. The figure clearly shows a shifting of the density from zone 3 (350-550 kg/m^3) to zones 1 and 2 (0-350 kg/m^3) when approaching the exposed surface. For the same sample before the fire exposition, we can notice that the zone classification remains constant when traversing the sample. Note also the rise of zone 1 (0-100 kg/m3) close to the top of the sample, which was due crack opening during the burning.

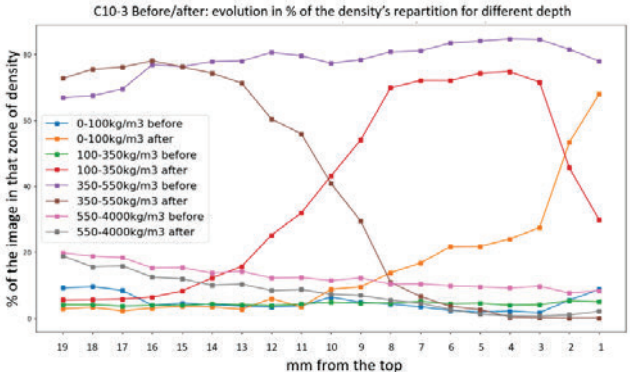

Figure 10: *Evolution of density zones on the top 20 mm of the sample, before and after fire exposure*

4.3 EVOLUTION OF DENSITY CLOSE TO THE SCREW

To study whether any particular degradation occurred due to increased heat conductivity of metal compared to wood, the following method was applied. For each CT slice, concentric circles with radii between 6-30 mm were created around the centre of the screw (Figure 11). Along the perimeter of each circle, the density was integrated, and average density was calculated.

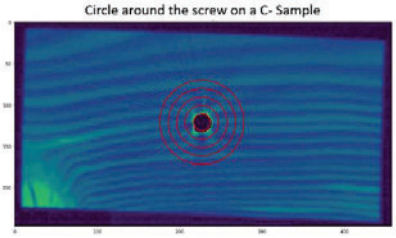

Figure 11: *Concentric circles around the screw for studying wood degradation in the proximity of the screw.*

The procedure was repeated for the CT slices representing the first 20 mm along the sample starting from the surface exposed to fire. The average density along each circle was then plotted for each slice to study its evolution at fixed distances from the centre of the screw.

In the subsequent figures, the density evolution profiles in the proximity of the screw are shown for representative compression and tension samples at 0, 5 and 10 minutes of fire exposure.

In Figure 12, we can see the mean density values on the circles before any fire degradation. The circle with the smallest radius is affected by the density of the screw and fluctuates due to noise from the metal. All the other values are approximately constant over the initial 20 mm from the top of the sample.

https://doi.org/10.52202/069179-0206

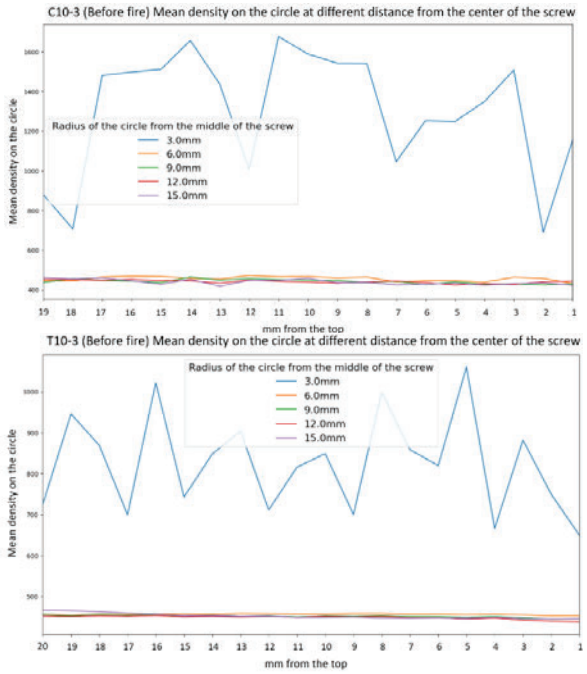

Figure 12: *Graph of density measured on circles for samples without fire exposure*

Figure 13 shows the evolution of the degradation around the screw on samples after a fire exposure of 5 minutes. The average density on all circles started to decrease approximately 7 mm from the top, which indicated the charring front, and it reached a lower constant value, indicating burnt wood. Although the density on the innermost circle again fluctuated due to noise, it followed the same decreasing trend.

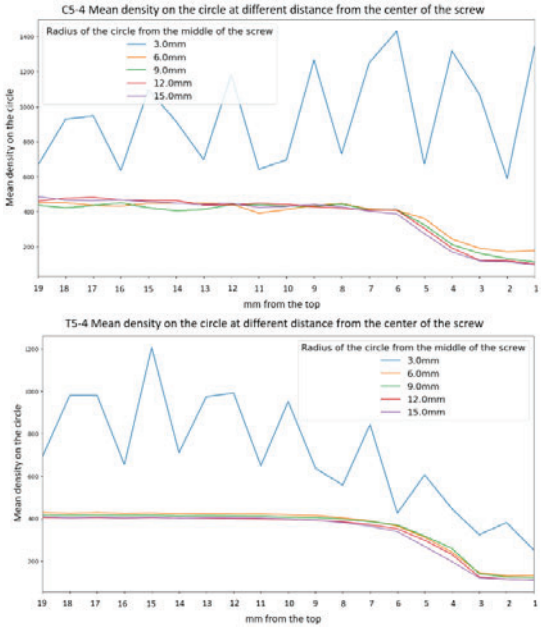

Figure 13: *Graph of density measured on circles for samples after 5 minutes fire exposure*

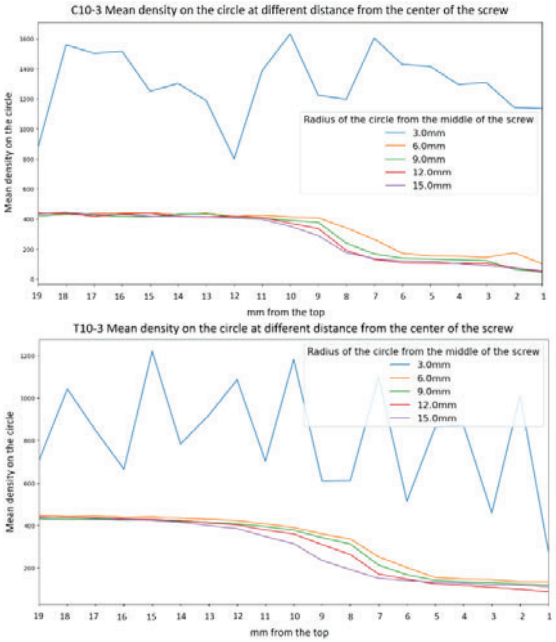

Figure 14: *Graph of density measured on circles for samples after 10 minutes fire exposure*

Figure 14 shows the evolution of the degradation around the screw on samples after a fire exposure of 10 minutes. Similarly to Figure 13, the density dropped to a lower constant value over a certain distance, but starting from a greater distance from the top of the samples due to increased charring.

In general, for all evolution graphs above, the mean density decreased for increasing circle radius, which was probably an effect of artefacts and noise around the screw which artificially increased the apparent density. With the screw still attached during the scans, we could therefore not observe a significant density loss close to the screw, which could have resulted from heat conduction

4.4 EVOLUTION OF DENSITY AFTER SCREW REMOVAL

The degradation of wood in the proximity of the screw was difficult to interpret in scans where the screws were present. The analysis procedure using concentric circles described above was thus repeated for CT scans of four fire-exposed samples in which the screws were carefully removed, instead of conducting destructive mechanical tests.

Figure 15 shows the evolution of the degradation around the screw hole on a representative sample after a fire exposure of 10 minutes and where the screw axis was perpendicular to the fibre direction. All curves follow the similar trend as with the screw inserted, and the noise affecting the innermost circle disappeared. Interestingly, the average density on the innermost circle was considerably higher than on circles further away from the hole. This higher density in the immediate proximity of the hole edge can be explained by compression of the wood during screw insertion, which can also be seen in the corresponding scan of the graph in Figure 16.

https://doi.org/10.52202/069179-0206

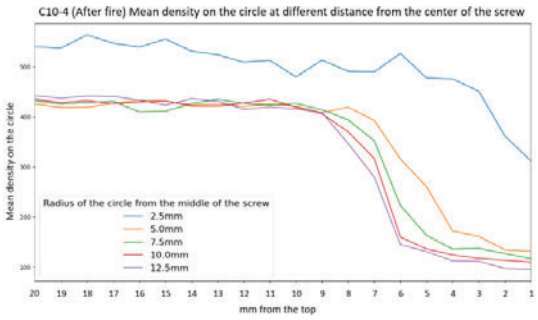

Figure 15: *Graph of density measured on circles around the screw hole for samples after 10 minutes fire exposure and where the screw axis was perpendicular to the fibre direction*

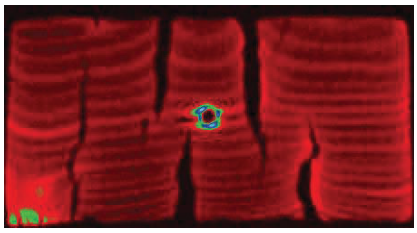

Figure 16: *CT image of the sample used for calculating the graph in Figure 15, blue and green colour indicate elevated and red lower density values.*

Figure 17**Erreur ! Source du renvoi introuvable.** shows the evolution of the degradation around the screw hole on a representative sample after a fire exposure of 10 minutes and where the screw axis was parallel to the fibre direction.

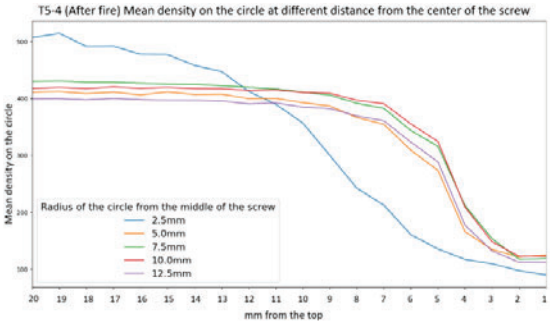

Figure 17: *Graph of density measured on circles around the screw hole for samples after 10 minutes fire exposure and where the screw axis was parallel to the fibre direction*

In contrast to the perpendicular case, the average density of the innermost circle clearly drops below the density of the areas further away from the hole when approaching the top (burnt) surface, which happens at around 10 mm from the top. This indicates that heat degradation in the screw hole has occurred. The lower density in the hole can also be observed in the corresponding scan in Figure 18.

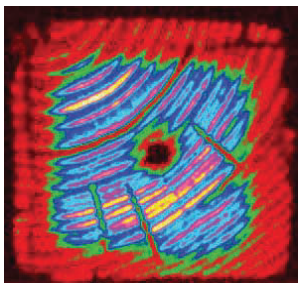

Figure 18: *CT image of the sample used for calculating the graph in* ***Figure 17****, blue and green colour indicate elevated and red lower density values.*

The observations indicate that the insertion direction of the screw with regards to the fibres could affect the fire resistance of the connection. When the screw is inserted, it densifies the wood around this as such should have a protective effect against charring in the hole. However, for the tests in this study, the charring progressed into the hole more easily if the screw was inserted parallel to the fibre directions. The effect could, however, also have been a result of the different sample geometries for the different insertion directions.

5 RESULTS OF MECHANICAL TESTS

Figure 19 shows box plots for the compression and tension tests on the samples. For both, loading parallel and perpendicular to the fibres, the load capacity reacts similarly to increasing length of fire exposure. There was almost no degradation of the load capacity during the five first minutes of fire exposure, but a noticeable degradation after 10 minutes exposure.

The degradation could be clearly linked to the observed charring depth in the image analysis of the CT images. The higher the indicated charring depth from the images, the lower the capacity of the connection.

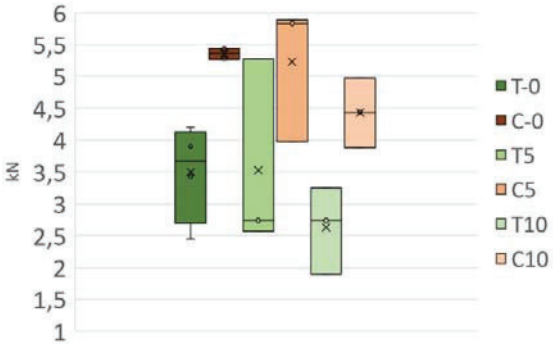

Figure 19: *Load capacity box plots of the tested samples*

Figure 20 shows the evolution of the load capacity of the connection as a function of the charring depth along the screw. Mean values were used for the figure. Compression and tension samples followed the same trend. Linear regression lines in the figure indicate a negative correlation between charring depth and load capacity.

https://doi.org/10.52202/069179-0206

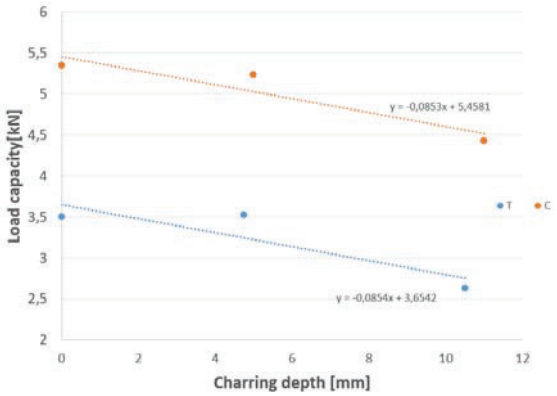

Figure 20: *Evolution of load capacity as a function of the charring depth*

6 CONCLUSIONS

This study has shown that it is possible to use CT images to observe fire degradation in wood with one fastener installed. It was concluded that

- the greyscale histogram of a CT image can be used to separate between wood, burnt wood and metal,
- the evolution of the histogram over increasing depth from a burnt surface can yield information about the charring depth,
- the evolution of the average density in the proximity of the screw hole can yield information about the degradation of the connection, and
- it is difficult to fully avoid artefacts due to metal, but the effect can be mitigated by minimising the amount of metal in the scanning plane, or potentially by using higher energy X-rays.

We developed a first approach to investigate wood degradation close to the screw using the average density of concentric circles around the screw. Noise and artefacts generated by the screw make measurements close to the screw surface difficult in CT images, however, if the screw is removed, the edge of the hole can be investigated more easily. The results indicate that the charring behaviour in the proximity of the screw differs, depending on the insertion direction with respect to the fibres.

In the future, it could be interesting to focus analyses on the charring around the hole after removal of the screw to clarify whether the insertion direction indeed affects the charring.

REFERENCES

[1] Laplanche K.: Etude du comportement au feu des assemblages de structures bois: approche expérimentale et modélisation. PhD Thesis, Université Blaise Pascal – Clermont-Ferrand, 2006.

[2] European Committee for Standardization (CEN): EN 1995-1-2:2004, Eurocode 5: Design of Timber structures – Part 1-2: General - Structural fire design. 2009.

[3] Palma P.: Fire behaviour of timber connections. PhD Thesis, ETH Zürich Research Collection, 2016.

[4] Palma P., Frangi A., Hugi E., Cachim P., Cruz H.: Fire resistance tests on steel-to-timber dowelled connections reinforced with self-drilling screws. In: Proceedings of the 2nd Ibero-Latin-American Congress on Fire Safety, Coimbra, Portugal, 2013.

[5] Palma P., Frangi A., Cachim P., Cruz H.: Fire resistance tests on beam-to-column shear connections. In: 8th International Conference on Structures in Fire, Shangai, China, 2014.

[6] Freyburger, C. et al.: Measuring wood density by means of X-ray computer tomography. Ann. For. Sci. 66, 804, 2009.

[7] Hansson L., Couceiro J. and Fjellner B.A.: Estimation of shrinkage coefficients in radial and tangential directions from CT-images. Wood Mater. Sci. Eng. 12(4):251-256, 2016.

[8] Huber J. A. J. et al.: A method for generating finite element models of wood boards from X-ray computed tomography scans. Comput. Struct., 260:106702, 2022.

[9] Swedish Standards Institute: SS-ISO 5660-1:2019, Reaction-to-fire tests – Heat release, smoke production and mass loss rate – Part 1: Heat release rate (cone colorimeter method) and smoke production rate (dynamic measurement). 2019.

https://doi.org/10.52202/069179-0206

World Conference on Timber Engineering Oslo 2023

ANALYTICAL MODELLING OF POST-TENSIONED TIMBER BEAM-COLUMN CONNECTIONS IN FIRE

Paul D Horne[1], Anthony K Abu[2], Alessandro G Palermo[3]

ABSTRACT: Post-Tensioned Timber (PTT) is a structural system that has many advantages over conventional timber frames, particularly in high-seismic areas such as New Zealand. These include a low-damage, re-centring system and fast construction. Although PTT systems have been shown to perform well in ambient conditions, concerns remain about the performance of beam-column connections in fire. As part of a larger project to address these concerns, a full-scale loaded PTT beam-column subassembly was exposed to a Standard Fire. Connection moment resistance was lost when thread stripping at the anchorage nut. An analytical model was compared to the experimental results. The decompression moment decreased due to the reduced tendon force from heating, the tendon acting eccentrically and the reduced effective cross-section. The analytical connection rotation after decompression was a third of experimental rotation until thread stripping began. This analytical model can be improved by including more complex aspects such as softening of a heated rocking interface and determining the beam stiffness based on the reduced material properties beneath the char layer. A follow up study is being undertaken to address these improvements and to provide a method for designers to evaluate the performance of these connections in fire.

KEYWORDS: Post-Tensioned Timber, Frame, Connections, Fire

1 INTRODUCTION

In high-seismic areas such as New Zealand, building owners and occupiers are also becoming more aware of the downtime and costs of repair or demolition of a building after an earthquake. Instead of conventionally designed structures, they seek low-damage structures which can be reinstated more easily, faster and cheaper. In contrast to conventionally designed structures, where seismic energy is dissipated by plastic hinges in primary structural elements, the primary structure of a low-damage system responds elastically and seismic energy is absorbed by specially designed components, which can be replaced after an earthquake.

Post-Tensioned Timber (PTT) is a technology that meets the demands for both a low-damage structure and timber as the primary structural material. PTT frames utilise prestressed unbonded steel strands or high strength bars inside timber elements, running the length of the frame, with replaceable energy dissipaters at the top and bottom of each beam-column connection (see Figure 1a). Under a lateral load, a gap opens at the rocking beam-column interface and the dissipaters are stretched or compressed, dissipating the seismic energy (see Figure 1b). Moment resistance at the connections is provided by force-couples from the dissipaters in tension and compression and from the tendon and compression of the beam against the column. The stressed tendon re-centres the structure after the conclusion of the lateral action. This technology can also be applied in low seismic areas to achieve longer spans than typically possible with timber elements alone, by using draped tendons and omitting the energy dissipaters (see Figure 1c). The advantageous performance of this structural system is due to the ductile rocking connections which contain the rocking interface and energy dissipation devices (see Figure 1d). The performance of PTT structures under seismic and gravity actions at ambient temperature has been extensively researched at the University of Canterbury [1–7] [1, 2] and a design guide has been published [8]. Several PTT frame buildings have been built in New Zealand and overseas, for example, Trimble Building [9], Young Hunter House and Von Haast [10] in New Zealand and ETH Zurich House of Natural Resources, Zurich, Switzerland [11] (Figure 1e shows a PTT frame during construction).

Although the behaviour of Post-Tensioned Timber box beams in fire has been investigated [12–14], the response of PTT frames and their beam-column connections in fire has not been investigated. Design guidance [8], therefore, proposes two design approaches for PTT structures in fire: the protected and unprotected approach. In the protected approach (see Figure 2a) the tendon is protected from the effects of fire so that the tendon force is maintained. Even though the cross-sections of the timber elements are reduced by charring, the moment resisting connections and moment-frame are preserved. In the unprotected approach (see Figure 2b), the tendon is not explicitly

[1] Paul D Horne, University of Canterbury, New Zealand, paul.horne@pg.canterbury.ac.nz
[2] Anthony K Abu, University of Canterbury, New Zealand, anthony.abu@canterbury.ac.nz
[3] Alessandro G Palermo, University of Canterbury, New Zealand, alessandro.palermo@canterbury.ac.nz

https://doi.org/10.52202/069179-0207

protected from the fire. On this basis, it is assumed the tendon force is zero and the beams are designed as simply supported with reduced cross-sections. All PTT buildings built in New Zealand so far have used the unprotected approach, because there is no additional costs to install protection and the design check is simple [12].

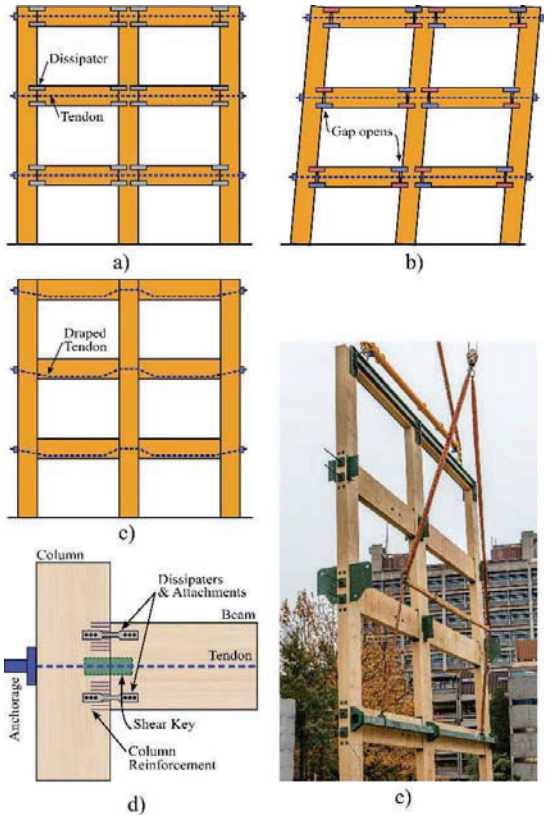

Figure 1. *Illustration of PTT frames a) in a high seismic area at rest and b) under a lateral load and c) in a low seismic area, d) a schematic of a PTT beam-column connection and e) a PTT frame during construction*

While these two design approaches are easily implemented by designers, they do not evaluate the actual response of the connection or structure in a fire. Even in the unprotected case, the tendon will take some time to be heated through an exposed tendon anchorage and for the force in the tendon to decrease. Furthermore, in structures designed for seismic loads, features may already be present that also provide advantageous performance in fire; e.g. larger column sizes for increased lateral stiffness can withstand greater charring in a fire. Although harnessing this advantageous fire performance is an opportunity for increased economy, increased performance in fire is not guaranteed by seismic design and detailing. A previous study has shown that PTT beam-column connections detailed for beneficial seismic performance does not necessarily also improve the connection performance in fire [15].

Previous study [16,17] modified the analytical model for PTT beam-column connections at ambient to the fire scenario and compared results from the analytical model to an experiment of a simple reduced-scale PTT beam-column connection (i.e. had a tendon, anchorage and internal corbel only). The analytical results compared favourably with those from the experiment; the studied connection did not have all the detailing features of a beam-column connection in a multi-storey PTT frame structure (e.g. interface stiffening, creep prevention or an external corbel which is more common) and was also at a reduced-scale. Therefore, questions remain about how representative the analytical model is of "fully" detailed PTT connections.

To address these questions, an experiment of a full-scale PTT beam-column connection is required given the complex thermal and mechanical response of PTT beam-column connections in fire. This paper presents the experimental results from a full-scale PTT connection that was detailed to current design practice in New Zealand and a comparison with an analytical model. Firstly, the components of a PTT beam-column connection and the analytical model are summarised. Secondly, the key results and observations from this experiment are reported and thirdly, the analytical and experimental results are compared.

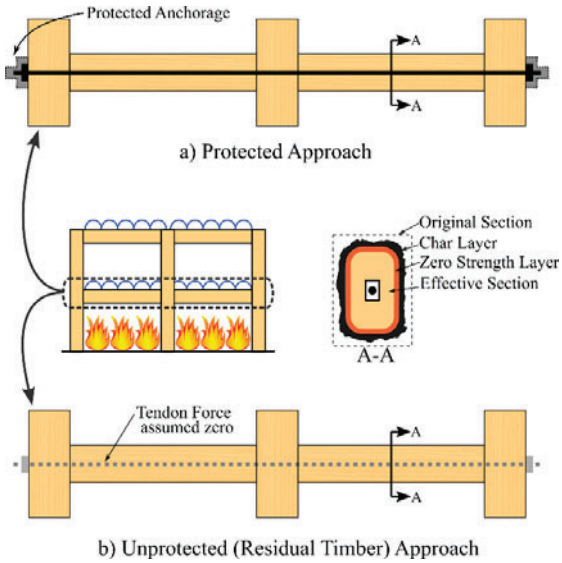

Figure 2. *Illustration of the a) Protected and b) Unprotected approaches to the design of PTT frames*

2 PTT BEAM-COLUMN CONNECTIONS

The advantageous response of PTT structures is directly attributable to the ductile rocking behaviour of the connections while the timber elements remain within their elastic limits. For a beam-column connection in a frame to have this beneficial behaviour, it must contain (see Figure 1d):

1. A tendon passing through ducts in the beam and column.
2. A tendon anchorage at the beam-column connections at each end of the frame.

https://doi.org/10.52202/069179-0207

3. Dissipaters and their attachments to the timber elements. Dissipaters can take several forms from buckling restrained necked bars to reduced cross-section angles.
4. Corbel or shear key to transfer shear from the beam to the column, which can be external or internal.

However, further detailing of the connection must be considered to ensure the desired stiffness and long-term performance is achieved:

1. The rocking interface must be sufficiently stiff so that drift limits under Serviceability Limit State (SLS) lateral actions are achieved. The interface stiffness depends on the material properties and size of the timber elements, and whether there is a steel interface plate.
2. Perpendicular-to-grain crushing of the timber column must be avoided under large gap angles when the bearing area is small.
3. Creep deformations from the compression of timber column perpendicular-to-grain must be limited so the required tendon force is maintained over the life of the building.

Connection detailing to address these considerations includes screw reinforcement in the column, a steel jacket around the column, steel compression elements inside the column or the column being fabricated with rotated timber blocks at the beam-column zone so the grain is parallel to the compressive forces (see [8]).

The mechanical behaviour of PTT beam-column connections in fire strongly depends on the thermal field established in the joint and the complex interaction between the many connection components. Therefore, the behaviour of PTT connections in fire will depend on their configuration and detailing choices by the designer. While different detailing options to achieve the same objective may result in similar ambient temperature performance, e.g. stiffening the interface with reinforcing screws or rotated timber blocks, they may perform differently in fire. This is particularly true where steel components are introduced which conduct much more than the surrounding timber.

3 ANALYTICAL MODELLING OF PTT CONNECTIONS

The presence of a gap at the beam-column interface violates the assumptions of the Euler-Bernoulli beam theory; therefore, it cannot be applied. The Monolithic Beam Analogy was developed to overcome the same limitation in controlled rocking joints from precast concrete elements during the Precast Seismic Structural Systems (PRESSS) project [18,19]. It was extended to timber elements and called the Modified Monolithic Beam Analogy) several additional complexities had to be addressed including initial joint stiffness and compression block [2,4,5,8]. The MMBA establishes a displacement equivalence between the rocking element and a "monolithic" analogue to determine the equivalent curvature in terms of the gap angle. This additional displacement compatibility equation combined with the two equations of equilibrium allows the calculation of the moment for each given rotation or gap angle. The extension of the MMBA into the fire case is summarised here but explained in more depth in [16] and [17].

The MMBA for an element exposed to fire, is derived by establishing displacement equivalence between the fire-exposed rocking and monolithic cantilever elements of length, ℓ, under axial load, N, (which is the tendon force including the additional force from stretching) and external horizontal load, P, as shown in Figure 3. When the element is exposed to fire on three sides, the centroid moves towards the unexposed side, and so the tendon force acts eccentrically (e), producing a uniform moment (Ne) along the element. This moment contributes to decompress the beam, so less external horizontal force is required to decompression the interface. At decompression, the stress at the extreme tension fibre is zero, so it can be expressed as:

$$\frac{N}{A} - \frac{M_{dec}}{Z} = \frac{N}{A} - \frac{Ne + P_{dec}\ell}{Z} = 0 \quad (1)$$

where P_{dec} is the external horizontal force required for decompression. The curvature at the base of the rocking element at decompression is ϕ_{dec}. From the two moments Ne and $P_{dec}\ell$, the sum of the curvatures produced by these moments is: $\phi_{dec} = \phi_{Ne} + \phi_{P_{dec}\ell}$.

The displacement at the top of the rocking and monolithic cantilever elements in terms of the curvature at the base of the element is (i.e., applying Equation 1):

$$\frac{\phi_{Ne}\ell}{2} + \frac{\phi_{P_{dec}\ell}\ell^2}{3} + \theta_{gap}\ell = \frac{\phi_{Ne}\ell}{2} + \frac{\phi_{P\ell}\ell^2}{3} \quad (2)$$

$$\frac{\phi_{P_{dec}\ell}\ell^2}{3} + \theta_{gap}\ell = \frac{\phi_{P\ell}\ell^2}{3} \quad (3)$$

$$\left(\frac{3\theta_{gap}}{\ell} + \phi_{P_{dec}\ell}\right) = \phi_{P\ell} \quad (4)$$

This is the same form as the ambient-temperature seismic MMBA formulation except the curvature required for decompression is reduced by the tendon acting eccentrically.

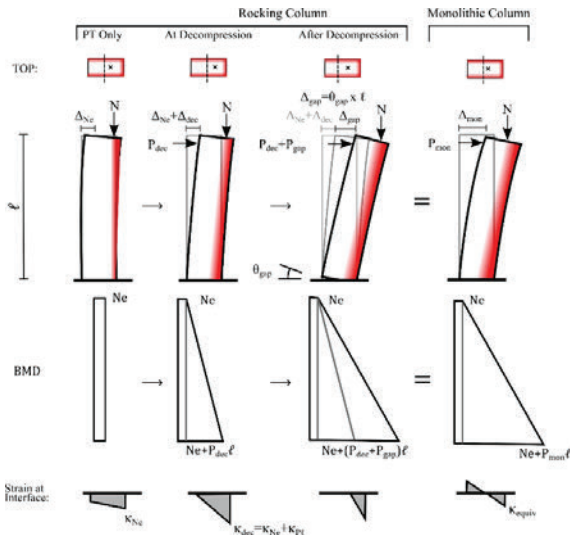

Figure 3: *MMBA for a cantilever element exposed to fire*

4 EXPERIMENT

4.1 SETUP

A 1:1 scale PTT beam-column subassembly, based on the connection detailing of recently constructed PTT framed structures [10] and published design guidance [8], was constructed, loaded and exposed to fire. The tested sub-assembly (shown in Figure 4) was constructed from LVL13 (E=13.2 GPa [20]) 700x310 mm beam and 800x310 mm column with two 75 mm square ducts for the tendons. These timber elements were fabricated from seven 45 mm thick LVL laminations glued to form the 310 mm thick elements. Bare wire K-Type thermocouples were laid in small grooves on the surface of the seven laminations prior to gluing. The two tendons were 26.5 mm diameter high-strength Macalloy 1030 bars [21] tensioned to 160 kN (28% of UTS) with 200 mm square, 40 mm thick anchorage plates. Two 75 mm square hollow steel sections (5 mm wall thickness) were installed inside the ducts to prevent long-term creep perpendicular to the grain of the column. Reinforcing screws were installed in the column at the top and bottom of the beam-column contact area to prevent crushing of the column perpendicular to the grain under large gap angles in seismic events. Vertical support of the beam at the connection was provided by a steel bracket with central stiffener fixed to the column with 10x M20 coach screws. Thermocouples were placed at the interface between the bracket and the beam and column.

The beam-column sub-assembly was placed in a purpose-built enclosure, so that the beam was exposed on three sides and the column was exposed on four sides below a floor level. The enclosure was made from 13 mm calcium silicate board lined internally with an alkaline earth silicate fibre blanket. The effect of a floor was simulated with a 100 mm thick slab of concrete on the beam. Two viewing windows were installed in the enclosure for visual observations. This enclosure was placed on a 3 x 4 m standard fire resistance testing furnace in its vertical orientation (see Figure 5). A point load of 16 kN was applied to the end of the beam to achieve a total connection moment of 29.6 kNm (90% of the decompression moment). An axial force of 50 kN was applied to the top of the column (limited by hydraulic jack capacity). The furnace was controlled to follow the ISO 834 Standard Fire [22] time-temperature curve (according to AS 1530.4 [23]) until failure of the connection.

4.2 OBSERVATIONS

Photos of the connection and the residual cross-section of the timber elements are shown in Figure 6. Corner rounding at the bottom of the beam had occurred and the contoured shape of the column near the connection zone indicates the thermal field was not the same as in the timber elements away from the connection, and charring of the bottom of the column interface which was promoted by conduction through the steel bracket.

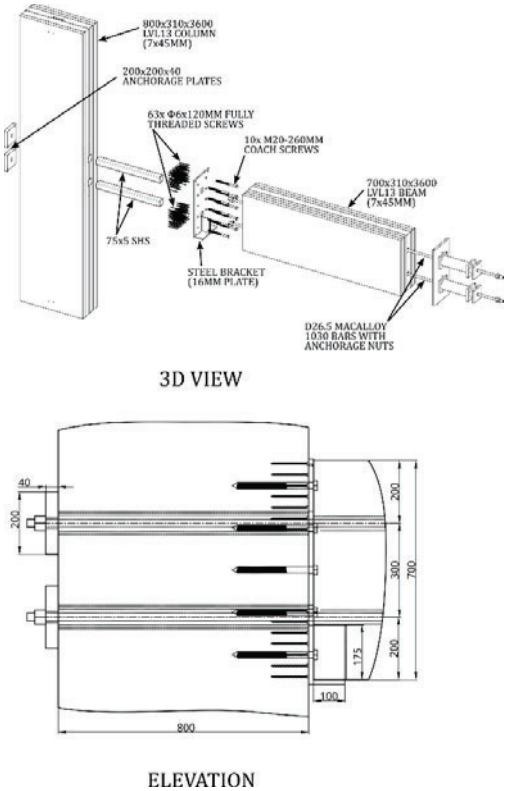

Figure 4: *3D and elevation views of the tested beam-column sub-assembly*

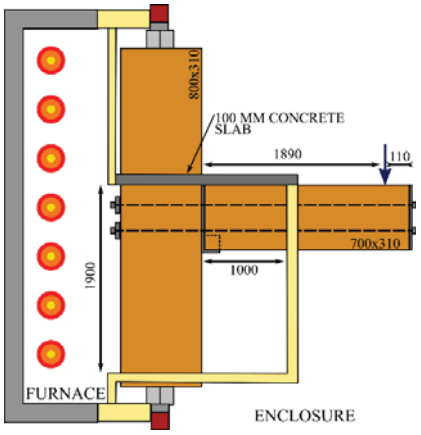

Figure 5: *Schematic of beam-column subassembly in enclosure on furnace*

Also evident in Figure 12 is the effect of anchorage reinforcement; in this case, the anchorage plates are held off the char surface. Although the 40 mm thick anchorage plates did delay the onset of charring underneath by approximately 15 minutes, without reinforcement under anchorage, the large bearing stress would result in crushing of the timber column perpendicular-to-grain at low temperatures. In this connection, the detailing to prevent long-term creep (the SHS tubes inside the column) formed an alternative load path and supported the anchorage plates as the timber underneath charred. Without anchorage reinforcement to resist the high

https://doi.org/10.52202/069179-0207

bearing stress from the anchorage, hot wood/char underneath and anchorage plates would be crushed, and the tendon force would decrease from shortening of the tendon. Therefore, if the moment resistance of connections and the frame is to be maintained, the exterior frame connections should be detailed to avoid this failure mechanism.

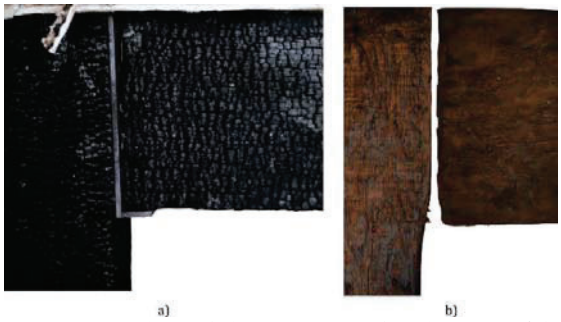

Figure 6: *a) Photo of the connection after the test and b) residual cross-sections*

4.3 TEMPERATURE RESULTS

The temperature of the furnace control thermocouple probes is shown in Figure 7. Char rates, determined from thermocouples in the beam and column away from the connection (using a 300 °C isotherm), ranged from 0.62 to 0.78 mm/min with a mean of 0.70 mm/min. A previous study of the charring of LVL elements in the Standard Fire reported a mean charring rate of 0.72 mm/min [24]. Only a selection of key thermal results are presented here.

The steel bracket, which supported the beam, was exposed to the fire on three sides and conducted heat through the interface. At 21 minutes, the temperature at the interface between the beam the bearing plate of the bracket exceeded 300 °C. Temperatures measured at the interface between the steel bracket and the column are shown in Figure 8. The temperature developments at locations A-D show that a 2D thermal field was established in the lower third of the interface. Heat was conducted up the interface from the exposed bearing plate and from the exposed sides of the interface plate. In the top two-thirds of the interface plate the thermal field was one-dimensional, decreasing in temperature from the exposed edges to the centre of the bracket.

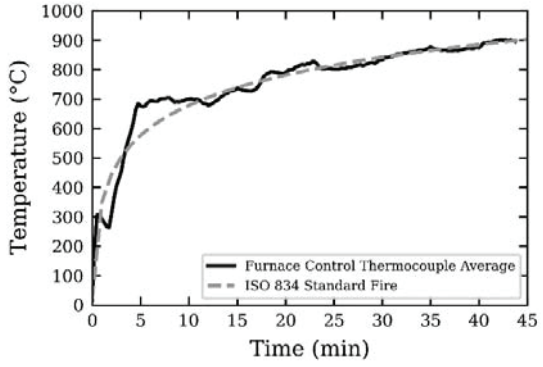

Figure 7: *Temperature of furnace control thermocouple probe*

A large thermal gradient was recorded along the tendon (see Figure 9). The temperature of the tendon underneath the anchorage nut increased quickly and reached a maximum temperature of over 700 °C at the end of the experiment. However, at the same time the temperature 100 mm into the column the tendon was 270 °C and less than 100 °C at 300 mm.

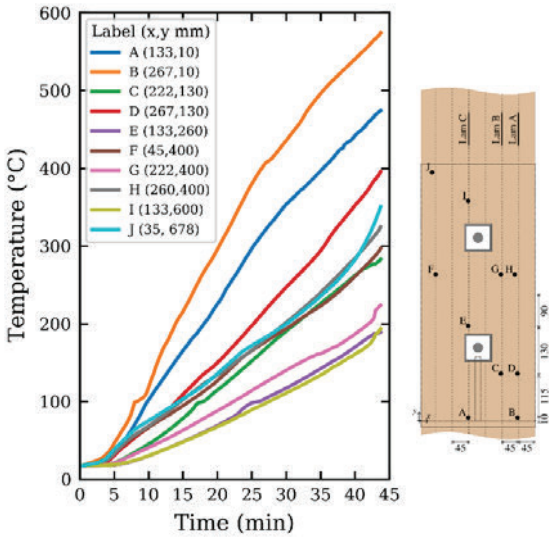

Figure 8. *Temperatures at the interface between the timber column and steel bracket*

The temperature of the tendon was also monitored at the beam-column interface to determine if the tendon was heated by the opening at the interface. The temperature of the bottom tendon did increase slightly (less than 100 °C) as it was heated from the hot steel bracket. The temperature of the top tendon was the same as the bottom tendon except for the final five minutes, when the temperature increased rapidly to 200 °C as hot gases penetrated the gap at the beam-column interface.

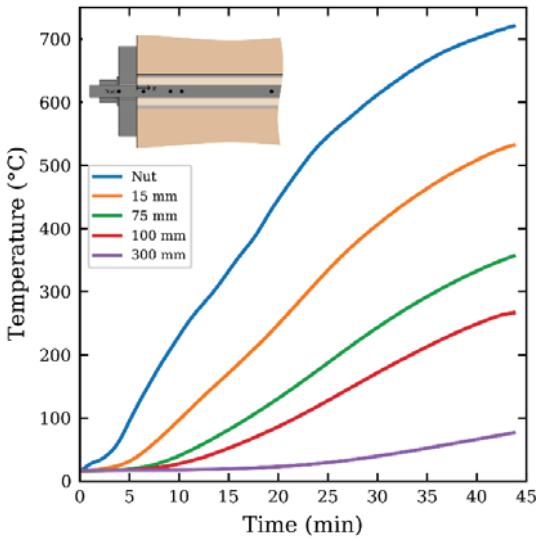

Figure 9: *Temperature of tendon*

https://doi.org/10.52202/069179-0207

4.4 MECHANICAL RESULTS

The connection decompressed after 5 minutes of fire exposure and increased linearly (approximately 0.0014 rad/min) until 37 minutes (a rotation of 0.005 rad). The connection rotation then increased rapidly, and the test was terminated at 44 minutes at a rotation of more than 0.05 rad.

The tendons were initially stressed to 160 kN each although the force in the top tendon increased by around 5 kN and the force in the bottom tendon decreased by the same amount as the beam was loaded. Between 5 and 10 minutes the tendon force in the top and bottom tendons decreased by 13% and 7% respectively. The force in the bottom tendon remained slightly greater than the top tendon until 27 minutes, at which time the force had decreased to 75% of its initial value. After this time, the forces in the tendons reduced at a greater rate. The force in the bottom tendon decreased to 25% of the initial force. The force in the top tendon decreased to 52% at 37 minutes and remained roughly constant for five minutes. In the final minutes of the test the top tendon was unable to sustain the applied force and the interface gap opened to the extent that the bottom tendon was stretched to provide additional moment resistance.

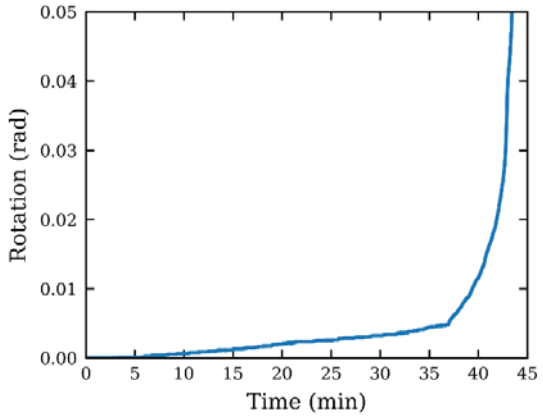

Figure 10: *Connection rotation*

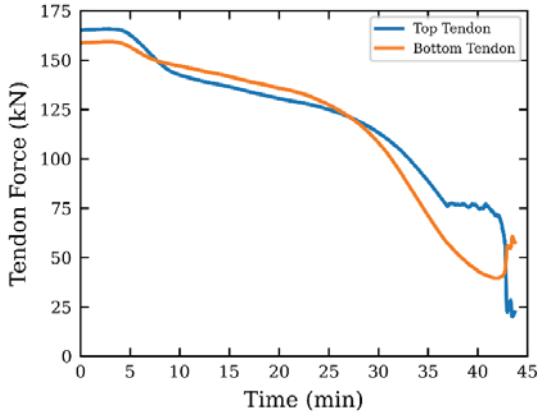

Figure 11: *Forces in the tendons*

The rapid increase in connection rotation (see Figure 10), that began at 37 minutes, coincided with the plateau in the force in the top tendon (see Figure 11). At the conclusion of the experiment, the top tendon had pulled through the anchorage nut (see Figure 12).

For a bar to be pulled a bar through a nut, the threads undergo large plastic deformations, which would explain the constant tendon force and the rapid increase in rotation.

Figure 12: *Tendon anchorages after test*

5 ANALYTICAL MODELLING

The response of the connection in the experiment was modelled using the MMBA procedure that has been modified for fire (see section 3). The effective cross-section of the timber elements was determined using two different implementations of Residual Cross-Section Methods because they are already familiar to practitioners. The two methods were:

1. Char rate of 0.65 mm/min with corner rounding explicitly calculated (radius equal to char depth). This is based on the residual cross-section method in NZS 3603 [25].
2. Char rate of 0.65 mm/min and a 7 mm zero-strength layer. This is based on AS/NZS 1720.4 [26] but the zero-strength layer is considered to develop over 20 minutes [13].

The cross-section was then transformed into an equivalent section with ambient elastic modulus (using modulus ratios) to be used in the MMBA procedure.

The tendon force was reduced by thermal expansion and reduced elastic modulus in the heated portion. For this analysis the temperature profile along the tendon was obtained by fitting a piece-wise linear curve to the tendon temperatures measured in the experiment (Figure 9). Thermal expansion and reduced material properties of prestressing steel were adopted from EN 1992-1-2. The ambient elastic modulus of the tendons was 170 GPa, the secant value provided by the manufacturer [21].

5.1 Decompression Response

The decompression moment is the moment at the connection that corresponds to the point of

https://doi.org/10.52202/069179-0207

decompression; i.e. stress at the extreme fibre is zero. The decompression moment decreases as the effective cross-section of the timber element and the tendon force reduce. The decrease in decompression moment as the connection was exposed to the Standard Fire is shown in Figure 13 for a constant tendon force case and a tendon relaxation case (thermal expansion and reduced elastic modulus as it is heated). After the first five minutes the decompression moment decreased in an almost linear manner. Following 45 minutes of Standard Fire exposure, a 5% reduction in decompression moment was attributable to the loss of cross-section area and approximately 18% was the result of the reduction in tendon force.

The decompression curvature (in the beam and at the interface) is an important parameter in the MMBA as it relates to the displacement prior to decompression. The reductions in decompression curvature for both the constant and relaxed tendon cases are shown in Figure 14. In the case of the constant tendon force, the decompression curvature continues to increase throughout the exposure, by a factor of 1.34 for Method 1 and 1.44 for Method 2 (at 45 minutes). However, when relaxation of the tendon was considered the decompression curvature increased for the first 30 minutes of the exposure, after which it remained relatively constant. The decompression curvature had increased by roughly half the amount, as in the constant tendon force case, to 1.10 for Method 1 and 1.19 for Method 2 (at 45 minutes).

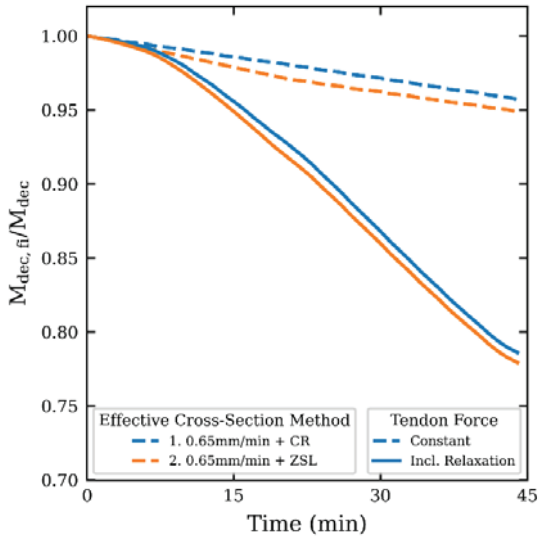

Figure 13: *Decompression Moment when exposed to a Standard Fire*

In seismic resisting PTT applications, the tendons are located so that the centroid of the tendon force and the neutral axis align. However, when the rocking element in a PTT system is exposed to fire on three sides, such as a beam supporting a floor, the neutral axis moves towards the unexposed face as the element is heated and chars. The tendon force then acts eccentrically so an additional moment acts to decompress the connection. Consequently, the moment required to decompress the connection decreases. The additional moment from the tendon acting eccentrically is shown in Figure 15 for both the constant and relaxed tendon cases. The additional moment reached 12-15% of the initial decompression moment after 45 minutes of exposure for the relaxed tendon case, which was about 80% of the additional moment from the constant tendon case.

Figure 16 shows the moment that must be applied to the connection to cause decompression (accounting for the additional moment from the tendon eccentricity and the decreasing decompression moment) as a proportion of the ambient decompression moment. This applied moment for decompression decreases by 17-20% of the ambient decompression moment for the constant tendon case and by a third for the relaxed tendon case.

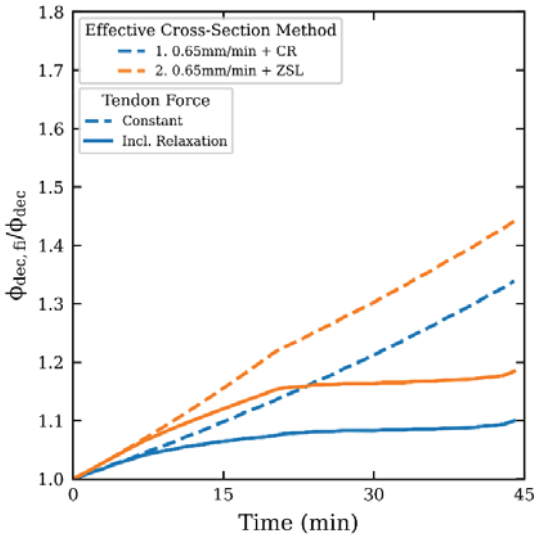

Figure 14: *Decompression Curvature when exposed to a Standard Fire*

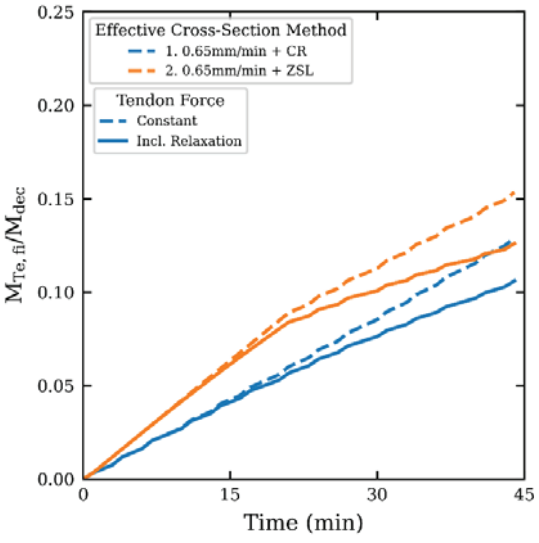

Figure 15: *Additional moment on the connection from the tendon eccentricity when exposed to a Standard Fire*

https://doi.org/10.52202/069179-0207

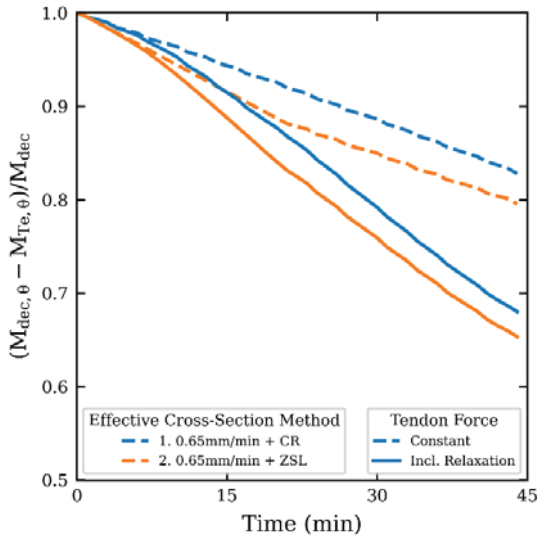

Figure 16: *Moment applied for connection to decompress when exposed to a Standard Fire*

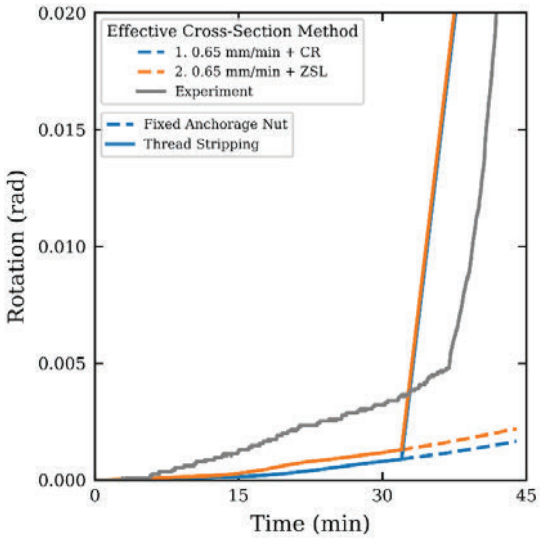

Figure 17: *Analytical and experimental connection rotation*

5.2 Post-Decompression Response

The softening of the interface from the heated interface plate was accounted for by taking the interface stiffness modification factor, k_{gap}, as 0.1 (the value for an unreinforced interface) [9]. Thread stripping of the anchorage nut that was observed in the experiment was included in the model by displacing the anchorage at a constant rate after the strength of the nut was exceeded (32 minutes). This rate assumed the anchorage nut deformation (measured at the end of the experiment) occurred at a constant rate.

Figure 17 compares the analytical connection rotation, with and without thread stripping at the anchorage nut, with the experimental rotation. The connection decompressed at similar times in the experiment and in the analytical models. Like the experimental response, the analytical response had two distinct stages – before and after thread stripping starts. The analytical model predicts only 30% of the experimental rotation before thread-stripping of the anchorage nut began. Thread stripping occurred a few minutes earlier in the analytical model than in the experiment. The thread stripping of the anchorage nut effectively lengthens the tendon and additional connection rotation is required to maintain the tendon force and moment resistance. The different responses of the analytical results with and without thread stripping at the anchorage nut shows that thread stripping dominated the connection response.

6 DISCUSSION

The 1:1 scale experiment of PTT beam-column sub-assembly showed that even when the tendon anchorage is not protected from the fire, the moment-resisting connection has some inherent fire resistance. The unprotected design approach neglects this beneficial performance. The edges and bottom of the steel bracket were exposed to the fire and conducted heat into the connection interface. The elastic modulus and strength of the adjacent wood decreased, softening the connection response. At 37 minutes the top tendon pulled through the anchorage nut. Insulating the anchorage and tendon from the fire will reduce the relaxation of the tendon and delay failure of the anchorage. The internal steel tubes resisted the force from the anchorage when the adjacent timber had charred. Without these tubes, the char and heated layers would have been crushed and the tendon force would have been lost earlier. Similarly, the screw reinforcing in the interface supported the steel bracket when the surrounding timber had charred. Without this screw reinforcement the connection response would have been a lot softer as this timber was crushed and the analytical model would have to be modified to take this into account.

The analytical modelling prior to decompression shows that the pre-decompression behaviour was reduced more by the decreased tendon force (due to thermal expansion and reduced elastic modulus) than the decrease in effective cross-section. Of the two Reduced Cross-Section Methods used to determine the effective cross-section, the method that considered a zero-strength layer always resulted in a softer connection response.

The response of the analytical models compared to the experimental results after decompression indicate that there is a softening phenomenon between 5 and 30 minutes that is missing from the analytical model. This is likely a result of the 3D thermal field in the bottom corner of the beam (due to the heated steel bracket), which is also

https://doi.org/10.52202/069179-0207

where the greatest bearing stresses would normally occur. Any additional deformation of the interface timber would also reduce the tendon force, so the analytical models would better represent the experimental tendon forces. To examine this further, the 3D thermal field at the connection and heat transfer between adjacent parts should be investigated then the analytical model can be modified to include these effects.

The MMBA is based on an additional displacement condition, so the stiffness of the rocking element (i.e. beam) is a key parameter. The stiffness of a timber element exposed to fire depends on the effective cross-section area, due to charring, and the reduced material properties in the heated layer underneath the char layer. Reduced Cross-Section Methods, such as those used in this analysis, are commonly used by designers to predict the failure times of loaded timber elements exposed to a Standard Fire. However, these methods are developed for a strength criterion, so may not be directly applicable to calculating the reduced stiffness. To alternative methods would be to consider a parabolic temperature distribution in the heated layer or determine the temperature distribution using a numerical technique e.g. finite element analysis. Reduced mechanical properties through the heated layer can be explicitly considered, e.g. using the reduced mechanical properties in EN 1995-1-2.

The thread stripping of the anchorage nut on the threaded bar tendon was not considered adequately in this analysis. Further study is required to develop an appropriate sub-model for this plastic deformation. One option would be to limit the tendon force to the shear yield strength of the threads reduced by the temperature-strength relationships of EN 1992-1-2 [27].

The analytical model presented here captured some of the response of realistically detailed PTT beam-column connections, however, the response is much softer than in the experiment and some important aspects are missing. While some detailing features can improve performance in fire (e.g. interface reinforcement screws), other features degrade connection performance (e.g. partially exposed steel bracket). Further study is required to modify the analytical method to account for the softer response of these connections and to refine how different types of detailing change the connection behaviour.

7 CONCLUSIONS

The performance of Post-Tensioned Timber frames is governed by the behaviour of the beam-column connections and their detailing. A loaded 1:1 scale PTT beam-column sub-assembly, with current seismic detailing, was exposed to the Standard Fire. The connection maintained its moment resistance for 40 minutes despite the tendon anchorages being exposed directly to the fire. This was in opposed to the Unprotected design approach, which neglects the tendon contribution from the start of the fire exposure. The internal SHS tubes in the column and the screw reinforcing at the interface, installed for long-term and seismic considerations, were important to obtaining this performance.

An analytical model for PTT beam-column connections in fire, previously used with medium-scale simple PTT connections, was used to evaluate the response of the connection that was tested. Reduced performance of the connection before decompression was primarily due to a reduced tendon force (thermal expansion and lower elastic modulus in the heated portion) and to a lesser extent, the reduced effective cross-section. The analytical model only rotated approximately a third of the experiment before thread stripping occurred. Once it began, thread stripping of the anchorage nut on the bar tendon dominated the connection behaviour.

The analytical model did not capture some behaviour that was observed in the experiments which this study has shown to be important to the connection response, e.g. softening of the rocking interface as it was heated. To address these shortcomings and improve the analytical model, a follow-up numerical study is being undertaken to investigate the connection's thermal field and the resulting structural response. This analytical model will enable designers to assess the actual response of PTT beam-column connections in fire.

ACKNOWLEDGEMENT

Logan Cooper and George Hare provided assistance in constructing the experimental specimen.

Prestressed Timber Limited holds NZ patent 549029 "An engineered wood construction system for high performance structures."

REFERENCES

1. Palermo A, Pampanin S, Buchanan A, Newcombe M. Seismic design of multi-storey buildings using Laminated Veneer Lumber (LVL). In: Proceedings of the NZSEE Conference 2005. Taupo, New Zealand: NZSEE; 2005.
2. Buchanan A, Deam B, Fragiacomo M, Pampanin S, Palermo A. Multi-Storey Prestressed Timber Buildings in New Zealand. Structural Engineering International. 2008 May;18(2):166–73.
3. Granello G, Palermo A, Pampanin S, Pei S, van de Lindt J. Pres-Lam Buildings: State-of-the-Art. J Struct Eng. 2020 Jun;146(6):04020085.
4. Smith T. Post-tensioned Timber Frames with Supplemental Damping Devices [PhD]. [Christchurch, New Zealand]: University of Canterbury; 2014.
5. van Beerschoten W. Structural Performance of Post-tensioned Timber Frames under Gravity Loading [PhD Thesis]. [Christchurch, New Zealand]: University of Canterbury; 2013.
6. Sarti F. Seismic Design of Low-Damage Post-Tensioned Timber Wall Systems [PhD]. [Christchurch, New Zealand]: University of Canterbury; 2015.

7. Moroder D. Floor Diaphragms in Multi-Storey Timber Buildings [PhD]. [Christchurch, New Zealand]: University of Canterbury; 2016.
8. Pampanin S, Palermo A, Buchanan A. Design Guide Australia and New Zealand: Post-tensioned Timber Buildings. Structural Timber Innovations Company; 2013.
9. Brown A, Lester J, Pampanin S. Re-building Trimble Navigation's offices using a damage-limiting seismic system. In: Proceedings of the World Conference on Timber Engineering 2014. Quebec City, Canada: World Conference on Timber Engineering 2014; 2014.
10. Kirstein A, Siracusa J, Smith T. The new timber von Haast replacement building in Christchurch. In: Proceedings of the NZSEE Conference 2018. Auckland, New Zealand: NZSEE; 2018.
11. Leyder C, Wanninger F, Frangi A, Chatzi E. Dynamic response of an innovative hybrid structure in hardwood. Proceedings of the Institution of Civil Engineers - Construction Materials. 2015 Jun;168(3):132–43.
12. Spellman PM. The Fire Performance of Post-Tensioned Timber Beams [Master's Thesis]. [Christchurch, New Zealand]: University of Canterbury, New Zealand; 2012.
13. Costello RS. The Fire Performance of Post-Tensioned Timber Buildings [Master's Thesis]. [Christchurch, New Zealand]: University of Canterbury; 2013.
14. Quiquero H, Gales J, Abu A, Al Hamd R. Finite Element Modelling of Post-tensioned Timber Beams at Ambient and Fire Conditions. Fire Technol. 2020 Mar;56(2):737–67.
15. Horne P, Palermo A, Abu A, Moss P. Implications of seismic design detailing on the fire performance of Post-Tensioned Timber frames. In: Proceedings of the Pacific Conference on Earthquake Engineering 2019. Auckland, New Zealand; 2019. p. 12.
16. Horne P, Abu A, Palermo A. Moment Response of Post-Tensioned Timber Beam-Column Connections in Fire – Part 1: Experimental Behaviour (Submitted). In: Proceedings of the 14th International Symposium on Fire Safety Science. Japan; 2023.
17. Horne P, Abu A, Palermo A. Moment Response of Post-Tensioned Timber Beam-Column Connections in Fire – Part 2: Analytical Modelling (Submitted). In: Proceedings of the 14th International Symposium on Fire Safety Science. 2023.
18. Pampanin S, Nigel Priestley MJ, Sritharan S. Analytical Modelling of the Seismic Behaviour of Precast Concrete Frames Designed with Ductile Connections. Journal of Earthquake Engineering. 2001 Jul;5(3):329–67.
19. Priestley MJN, Sritharan S (Sri), Conley JR, Stefano Pampanin S. Preliminary Results and Conclusions From the PRESSS Five-Story Precast Concrete Test Building. pcij. 1999 Nov 1;44(6):42–67.
20. Nelson Pine. Nelson Pine LVL - Specific Engineering Design Guide. 2016.
21. Macalloy. Macalloy Post Tensioning System. 2017.
22. ISO. ISO 834-1:1999 Fire Resistance Tests - Elements of Building Construction - Part 1: General Requirements. International Standards Organisation; 1999.
23. Standards Australia. AS 1530 Methods for fire tests on building materials, components and structures Part 4: Fire-resistance tests for elements of construction. SAI Global; 2014.
24. Lane W. Ignition, Charring and Structural Performance of Laminated Veneer Lumber [Master's Thesis]. [Christchurch, New Zealand]: University of Canterbury; 2005.
25. Standards New Zealand. NZS 3603: Timber Structures Standard. Standards New Zealand, Wellington, New Zealand; 1993.
26. Standards New Zealand, Standards Australia. AS/NZS 1720.4 Timber Structures Part 4: Fire resistance of timber elements. SAI Global; 2019.
27. CEN. Eurocode 2—Design of concrete structures Part 1-2: General—Structural fire design. European Committee for Standardization. Brussels; 2004.

https://doi.org/10.52202/069179-0207

World Conference on Timber Engineering Oslo 2023

MECHANICAL PERFORMANCE AT ELEVATED TEMPERATURES OF NON-METALLIC DOWELS FOR MASS TIMBER STRUCTURES

Alexandra Boloux[1], Rafik Nizarali[2], Luke Bisby[3]

ABSTRACT: Connections between timber structural elements are normally accomplished using metallic bolts, pins, and rods whose high thermal conductivity typically generates undesirable in-depth heating and charring of timber in fire. Despite existing studies on the fire performance of non-metallic shear connections, knowledge of the isolated mechanical performance of non-metallic dowels at elevated temperatures is scarce. To address this knowledge gap, a bespoke experimental rig was developed to evaluate the performance of circular glass fibre reinforced polymer (GFRP) and oak dowels at elevated temperatures. A comparison between GFRP (E-glass with vinyl ester) and oak dowel strength and deformation with temperature is presented, with GFRP displaying superior performance given its higher strength at all temperatures considered. However, oak maintained its strength better than the E-glass vinyl ester dowels when normalised against ambient temperature capacity.

KEYWORDS: timber connections, elevated temperatures, non-metallic dowels, glass fibre reinforced polymer, oak.

1 INTRODUCTION

A major challenge in building taller and more complex mass timber buildings is the high-level consequences that may manifest in case of fire. In modern mass timber buildings, structural connections are commonly made using metallic plates and fasteners. However, this increases risks in fire due to the high thermal conductivity of metals, and in particular, steel.

If left unprotected in a building fire, steel connections will readily conduct heat into timber elements and may char the surrounding in-depth timber, possibly resulting in structural failure. Non-metallic connections may present possible solutions, due to the drastically lower thermal conductivity of some such fasteners. Despite limited existing research on the structural performance of non-metallic dowelled connections in timber, there is a paucity of literature on the performance of such connections at elevated temperatures. Additionally, there is a lack of data on the isolated mechanical performance of non-metallic shear fasteners at elevated temperatures. The project presented in this paper therefore investigated the mechanical performance (in shear) of non-metallic dowels, namely GFRP and oak, at elevated temperatures.

2 PREVIOUS RESEARCH

2.1 GFRP DOWELS

There is an existing body of literature on performance of non-metallic timber connections, which was pioneered by Drake and other colleagues [1]. Their aim was to show that non-metallic (GFRP) based timber connections can provide suitable alternatives to steel-based connections. Initial experimental programs conducted double-shear tests using GFRP and steel dowels embedded in a laminated veneer lumber (LVL) member [2]. Despite the GFRP dowel yielding at a lower load than its steel counterpart, it "absorbed at least two or three times more energy" [2]. This can typically be considered beneficial in the context of designing mechanical connections, as structural engineers tend to prefer connections that fail in a ductile manner. In addition, the high strength-to-weight ratio, compatible stiffness between GFRP and timber, and a relatively high resistance to corrosion make GFRP-based connections a compelling replacement to steel-based connections in timber structures [2].

GFRP also has a much lower thermal conductivity than steel, which is a key factor influencing the heat transfer and mechanical performance of a dowelled connection in a fire scenario.

Despite experiments and existing literature suggesting that GFRP can be a suitable alternative to steel mechanical fasteners, no design guidance for their application currently exists. Pedersen [3] proposed changes to timber connection design rules when using GFRP connectors, however Thomson et al. [4] argued that there is a discrepancy between Pedersen's proposed yield equations and the available experimental data.

Additionally, the behaviour of GFRP at elevated temperatures has been previously studied in the context of replacing steel bars in reinforced concrete. Despite having a low thermal conductivity compared to steel, most

[1] Alexandra Boloux, University of Edinburgh, United Kingdom, Alex.Boloux@ed.ac.uk
[2] Rafik Nizarali, Arup, United Kingdom, rafik.nizarali@arup.com
[3] Luke Bisby, University of Edinburgh, United Kingdom, Luke.Bisby@ed.ac.uk

https://doi.org/10.52202/069179-0208

polymers burn readily [5] and lose their mechanical properties (i.e., strength, stiffness, and bond) at much lower temperatures than steel, with some GFRP materials softening at temperatures below 100 °C [6].

As the polymer matrix resin in a GFRP softens with an increase in temperature, loss of bond with surrounding materials is typically observed; this has potential consequences where bond integrity is important, as in applications of reinforcing concrete with GFRP bars [7].

Kumahara et al. [8] and Hajiloo et al. [7] tested vinyl ester GFRP rods in tension at elevated temperature. Kumahara et al [8] tested GFRP rods in tension at 240 °C and 400 °C and reported losses of 40% and 60% of tensile strength, respectively. Hajiloo et al. [7] also observed a loss of 25% tensile strength at a temperature of about 150°C. In both cases, the loss in tensile strength was observed at temperatures near the glass transition temperature of the polymer matrix, which for vinyl esters is typically between 55 °C-145 °C [9]. Glass transition temperature may be highly variable within any class of polymers and corresponds to the temperature at which the polymer matrix enters a soft rubbery state and the stiffness and strength rapidly decrease [10].

Brandon [11] tested GFRP bars in torsion to measure shear properties at different temperatures; he observed a decrease in shear strength and modulus of specific GFRP bars with temperature. However, in full-scale testing of dowelled connections under a transient thermal regime, the time to failure of dowelled double shear timber connections was shorter for metallic connections as compared with non-metallic connections [11].

Another important factor to consider for GFRP dowel behaviour at elevated temperatures is creep, which can be expected to accelerate at elevated temperatures.

2.2 TIMBER DOWELS

Given its comparatively poor shear strength relative to either steel or GFRP, softwood timber has not been widely considered as a potential alternative mechanical fastener. Additionally, like GFRP, timber also loses its mechanical properties at relatively low temperatures in comparison to steel; this is potentially important in the context of fire performance. Given its limited shear strength, timber dowelling has mainly been used in furniture applications – with much lower loads than structural applications – and in mortice and tenon joints – which rely on a large section of timber to transfer loads.

Despite existing guidance on timber's thermomechanical properties in the Structural Eurocodes, the existing literature on such matters is comparatively scarce and inconsistent [12-14]. BS EN 1995-1, the Eurocode for Timber Structures, suggests a 60% loss of transverse shear strength at 100 °C.

Despite comparatively poor thermomechanical performance, the experimental program included mechanical tests on oak dowels in addition to GFRP dowels. This is in the interest of advancing understanding of the mechanical behaviour of fully timber connections at elevated temperature.

3 MATERIAL CHARACTERISTATION

Thermogravimetric analysis (TGA), Dynamic mechanical analysis (DMA) and moisture content tests were performed to assess the fundamental properties of the dowels, including the glass transition temperature, T_g, of the GFRP. The results from those characterisation tests were used to decide the testing temperatures in the double-shear tests.

3.1 MATERIAL PROPERTIES

The GFRP rods were manufactured by pultrusion from unidirectional E-glass fibres in a vinyl-ester polymer matrix. The diameter of the rods was 12 mm, so as to be representative of dowel sizes likely to be used in practice. The GFRP rods had a nominal tensile strength of 1000 MPa and a nominal fibre content of 80% by mass.

The timber dowels were made of hardwood oak, chosen for its increased strength, stiffness, and durability compared to typical softwoods [2]. Oak dowel rods were sourced from a local commercial supplier with a nominal diameter of 12 mm; no technical information could be obtained from the supplier on their mechanical properties.

3.2 THERMOGRAVIMETRIC ANALYSIS

Thermogravimetric analysis (TGA) was performed on the GFRP dowels to validate the fibre mass fraction provided by the manufacturer, and to determine the decomposition temperature, T_d, of the polymer matrix. The TGA tests were performed using a Mettler-Toledo TGA/DSC1. Two samples were tested in an oxidative (air) atmosphere, and two in an inert (nitrogen) atmosphere to assess the potential role of oxidation in accelerating decomposition. A temperature range between 25 °C and 800 °C, with a heating rate of 10 °C/min, was used for all samples in accordance with BS EN ISO 11358-1 [15].

The average fibre mass content, determined from a mass loss curve, from the 4 tests, was 79.4% which is in accordance with the value provided by the manufacturer (80%). The mass derivative (MLR) curves for all four samples are presented in Figure 1. These data suggest that no significant decomposition of the GFRP bars occurs below about 225 °C, as should be expected for a glass/vinyl ester polymer composite product. In addition, the mass derivative curves indicate decomposition temperatures of 371 °C and 386 °C in oxidative and inert atmospheres, respectively.

https://doi.org/10.52202/069179-0208

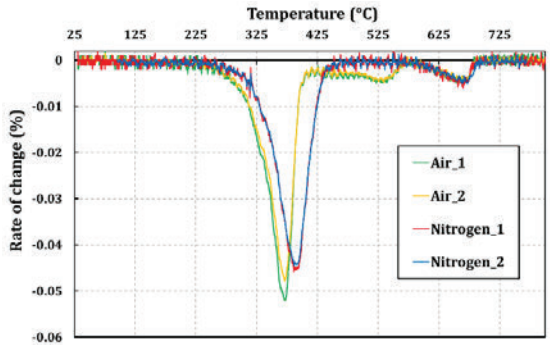

Figure 1: *Differential Thermogravimetry (DTG) results from TGA tests on GFRP dowels.*

3.3 DYNAMIC MECHANICAL ANALYSIS

Dynamic mechanical analysis (DMA) was used to define the glass transition temperature T_g of the polymer matrix and to characterise the elastic and viscous behaviour of the GFRP bars. Even though DMA is generally used to characterise polymers, analysis of oak from the timber dowels used in this study can also indicate changes in the behaviour of this material as temperature increases. The DMA tests were performed using a DMA850 testing device manufactured by TA Instruments. Samples of dimensions 50 mm x 12 mm x 2 mm were tested in three point bending mode and were subject to sinusoidal loading at 1 Hz. They were heated from 25 °C to 180 °C or 200 °C, for the GFRP and oak, respectively; at a heating rate of 3 °C/min.

The results from the DMA were analysed according to BS ISO 6721-11 [16] (see Figure 2). The glass transition temperature of the GFRP was obtained from the peak in the loss factor. From two tests, the T_g of the GFRP was determined to be 154 °C. In addition, the onset temperature, T_{onset}, was graphically determined from tangents to the storage modulus curve as can be seen in Figure 2. The mean onset temperature of the three tests was 130 °C. These TGA data suggest that considerable reductions in polymer matrix dominated mechanical properties (including shear strength and stiffness) can be expected in the temperature range of 130-154 °C.

The DMA results for the oak were not taken to a high enough temperature to determine a classical T_g value, but suggest that oak is less sensitive to elevated temperatures than GFRP (in terms of reductions in elastic modulus under cyclic flexural loading). This is shown in Figure 2, where the modulus values for oak decrease only mildly at temperatures below 180 °C. These TGA data suggest only minor reductions in flexural stiffness of oak at temperatures as high as 200 °C.

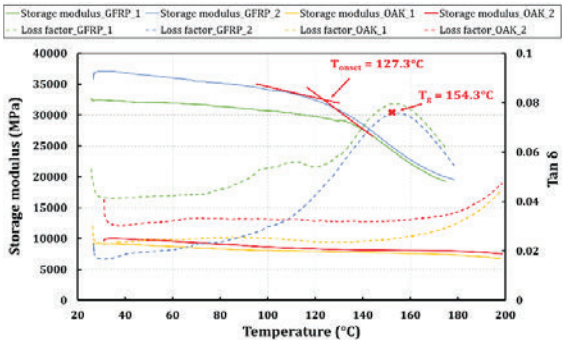

Figure 2: *Storage modulus and loss factor of GFRP and oak dowel materials.*

3.4 OAK MOISTURE CONTENT

Two 60 mm long oak samples were each enclosed in a metal container and dried in an oven at 60 °C for 48 hours. Their mass was measured every 24 hours using a high precision balance, until the change in weight measured was less than 5%. From the two samples, the moisture content of the oak was determined as about 9.0%.

4 MATERIALS AND METHOD

4.1 RIG DESIGN AND FABRICATION

The aim of the rig in this experiment was to load the dowel in shear, up until failure, whilst simulating the embedment of the dowel in timber (Figure 3). The rig was made from steel, due to its superior thermo-mechanical properties in comparison to timber and GFRP and loaded the dowels in double shear. The steel rig provides an embedding constraint and forces the dowel to fail at each of two interfaces [2].

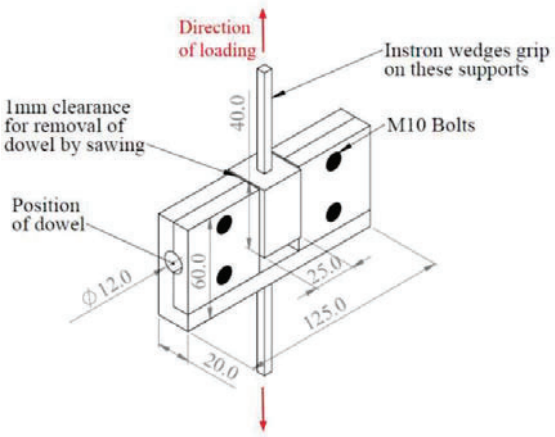

Figure 3: *Isometric view of the double shear steel rig. All dimensions are in millimetres.*

The rig was loaded in tension to help with alignment of the steel elements and dowels during loading. The hole in which the dowels placed was made 12 mm in diameter (later enlarged to fit the timber dowels), for a tight fit around the GFRP dowels.

4.2 TESTING PROCEDURE

The shear tests were performed using an Instron 600LX loading frame with a capacity of 600 kN (Figure 4 a.). The loading frame measures the crosshead displacement of the rig as opposed to the absolute displacement of the dowel. However, given a minimal stress is applied to the steel elements compared to the yield strength of the steel, the deformation of the steel rig and testing frame are assumed to be negligible (aside from seating effects). All results in this paper are presented in terms of displacement measured by crosshead stroke of the testing machine.

GFRP and oak rods were cut into 130 mm long dowels to fit within the rig with their ends protruding to allow observations during testing. All dowels tested at elevated temperature had a 3 mm diameter hole drilled 50 mm into them centroidally along their length so as to fit a T-type thermocouple to measure the dowel internal temperature. For ambient and steady-state tests, a vertical crosshead displacement rate of 2 mm/min was used based on similar experimental programs available within the literature [7,17].

For transient temperature tests, a heating rate of 5 °C/min was used; this facilitated comparatively homogeneous heating of the samples without leading to very long exposure times which may overestimate strength degradation [17]. Two temperatures were recorded (Figure 4 b.) during each test: first, a thermocouple was placed inside the oven to measure air temperature, while a second thermocouple measured the temperature inside the dowel adjacent to the shear failure plane. The second measurement was used to assess critical temperatures for the dowels themselves.

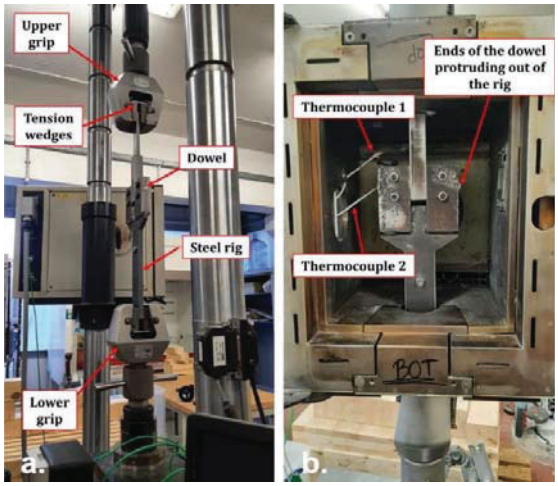

Figure 4: *Experimental set-up: a. rig in Instron frame without oven, b. close-up of the oven.*

4.2.1 Steady state tests

Steady state tests heated the sample to a target temperature before loading it to failure at constant temperature. Four steady state temperatures were selected for each material. For the GFRP, the aim was to study the behaviour of the dowel around the glass transition temperature, since there is a significant drop in mechanical properties around that temperature. A range of temperatures was chosen to observe how this physical change in the material could be correlated to a change in its shear properties at elevated temperatures. A temperature of 120 °C was selected to assess the behaviour just prior to the onset temperature, and a temperature of 140 °C was selected to assess the behaviour just prior to the glass transition temperature. Temperatures of 100 °C and 200 °C were selected since they were respectively well below and well above the glass transition temperature.

For the oak, the aim was to explore the behaviour of the dowel as it loses its moisture content, near to 100 °C. Thus, temperatures of 90 °C and 110 °C were selected. An additional two temperatures, at 140 °C and 200 °C were (semi-arbitrarily) selected to allow comparison between the oak and the GFRP.

4.2.2 Transient state tests

The transient tests loaded the specimens to a target sustained level, and then heated them up while the load remained constant. The critical temperature at failure, under sustained load, was recorded by a thermocouple inside the dowel (as already discussed).

The transient loads were taken (again, semi-arbitrarily) as 20% and 50% of the dowel capacity at ambient temperature. The lower load value was selected from literature as the suggested value to avoid creep-rupture failure in GFRP [18]. The higher loading value was set to allow for meaningful comparisons of the effects of applied stress at credible upper limit in-service levels. From the results presented in the next section, these loads translated to 9.6 kN and 23.9 kN for the GFRP, and 2.2 kN and 5.6 kN for the oak dowels, respectively.

Table 1: *Summary of testing programme.*

		Number of tests	
		Oak	GFRP
Ancillary tests	TGA (air/nitrogen)	-	2/2
	DMA	3	4
	Moisture Content	2	-
Ambient tests	25°C	2	2
Steady state tests	90°C	2	-
	100°C	-	2
	110°C	2	-
	120°C	-	2
	140°C	2	2
	200°C	2	2
Transient state tests	20%	2	2
	50%	2	2

https://doi.org/10.52202/069179-0208

5 RESULTS

5.1 AMBIENT TESTS

Tests were performed at ambient temperature (i.e. approximately 20 °C) to establish a comparison baseline for the mechanical properties and behaviour of the dowels within the loading rig used in this study. Tensile load versus crosshead displacement curves are presented in Figures 5 and 6. The **GFRP dowels** (see Figure 5) exhibited a comparatively higher initial stiffness. A first drop load was observed at a crosshead displacement of around 5 mm, followed by a second shorter drop at around 9.5 mm. These drops, as suggested in previous experiments [19], can be attributed to sequential failures of shear planes within the GFRP material. The mean maximum load reached for the GFRP samples was 48.9 kN. To find the average shear strength of the dowel (within this loading rig), the maximum load was divided by two and then by the cross-sectional area of the dowel; this gave a mean shear strength of 219.6 MPa. Despite loading the dowels in shear, in the next section it is explained that that the calculated strength does not actually correspond to pure shear.

The **oak dowels** (see Figure 6) were much less stiff and much weaker and exhibited a more ductile failure. In both tests, the dowels failed at around 8 mm of crosshead stroke, as indicated by the sharp decrease in load. Compared to GFRP dowels, the oak dowels were much weaker. The mean peak load of oak dowels was 11.15 kN which represents only 23% of the peak shear load carried by the GFRP dowels of similar diameters.

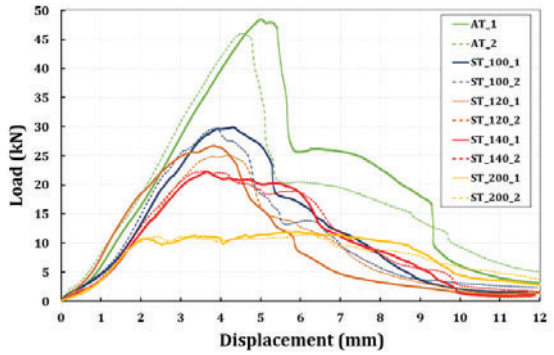

***Figure 5**: GFRP load-displacement curves for steady state tests.*

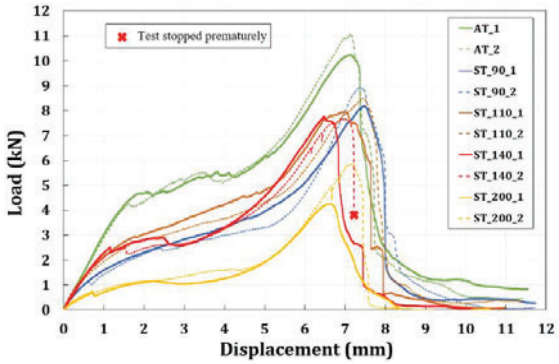

***Figure 6:** Oak load-displacement curves for steady state tests.*

5.2 STEADY STATE TESTS

Figure 5 shows the load versus crosshead displacement curves for GFRP dowels at different steady state temperatures. The reproducibility of the tests was generally reasonable, hence only 2 tests were performed under each condition. Up until 120 °C, and hence before entering the glass transition, the GFRP dowels showed an essentially elastic behaviour until failure, similar to their behaviour at ambient temperature. Furthermore, it can be seen from the slope of the load displacement curves, that the initial stiffness of the dowels remained relatively constant. At 140 °C and 200 °C, the dowels' stiffness drops and the ductility of the response increases. The GFRP dowels change from a comparatively high strength, high stiffness material at ambient temperatures to a lower strength, more ductile material at elevated temperatures.

The general trends for the load versus crosshead displacement curves for oak dowels did not significantly change with increasing temperature (Figure 6). Increases in temperature result in decreases of initial stiffness of the dowels. Failure displacements of the samples however remained unchanged, at around 8 mm at all temperatures.

The loss of strength for both GFRP and oak dowels is presented in Figure 7. Despite the smaller percentage loss of strength of oak dowels at elevated temperatures, comparison of absolute strengths shows that the oak dowels remained considerably weaker than the GFRP dowels for all steady state temperature conditions.

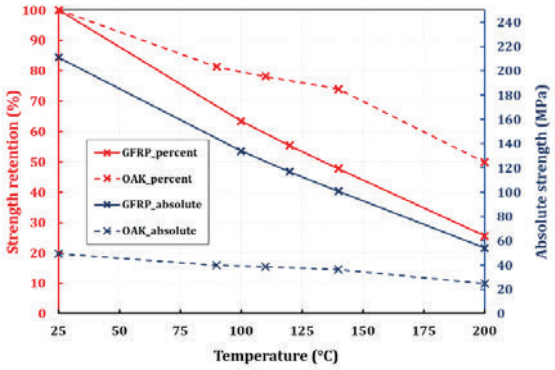

***Figure 7**: Absolute and relative strength of GFRP and oak dowels.*

5.3 TRANSIENT STATE TESTS

For each loading case, Figure 8 shows that the failure temperature was similar between the oak and GFRP dowels. Thus, dowels loaded at 20% of ambient peak strength failed on average at 224 °C. Dowels loaded at 50% failed on average at 105 °C. Despite this similarity, the temperature at failure of oak dowels was on average 14 °C higher than for GFRP dowels. This seems to corroborate findings from the steady state tests, which showed that oak dowels were better at retaining their strength at elevated temperature.

https://doi.org/10.52202/069179-0208

In the 20% loading case, the displacement rate of GFRP dowels increases from 0.13 mm/10°C, until 170 °C, to 1.28 mm/10°C in the rubbery phase of the material, after its glass transition. The oak dowels exhibit a relatively constant increase in displacement until failure, however, they both experience a jump in displacement at 100 °C, which is presumed to reflect the loss of moisture at these temperatures.

In the 50% loading case, the displacement rate of the GFRP dowels is maintained relatively constant until a sudden failure around 100 °C. The oak dowels exhibit a more progressive behaviour to failure. Indeed, between 30 °C and the failure temperature, the oak dowels show a crosshead displacement of 4.4 mm; this is versus a 2 mm displacement for the GFRP dowels.

In addition, between 30 °C and 80 °C, all dowels have similar displacement versus temperature traces, except the oak dowels in the 50% loading case which showed significantly higher deflections at temperatures well below 100 °C.

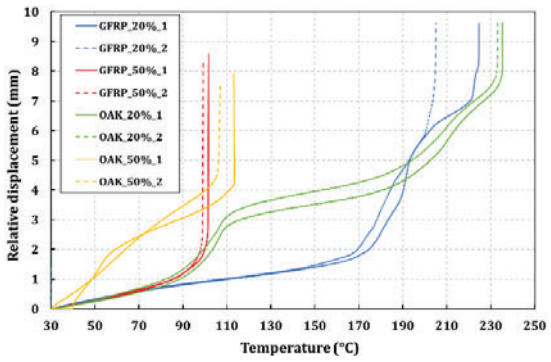

Figure 8: *Transient state analysis for oak and GFRP dowels.*

5.4 SAMPLE OBSERVATION

The GFRP and oak dowels tested in steady state conditions at 140 °C, are presented in Figure 9. The GFRP dowels exhibited signs of delamination at their edges, which is attributed to interlaminar shear failure. On the failure planes, on each side element, it can be seen that the fibres on the top half of the dowel were severed in the transverse axis, whilst the fibres in the bottom half were bent upwards. This behaviour suggests that, during loading, the dowels experienced both transverse shear and bending. Since GFRP is weaker in shear than in tension, it can be assumed that the top fibres in the dowel failed in shear, whilst the bottom fibres, loaded in tension, continued to carry some of the load until fibre failure. This test setup therefore fails to capture "pure" shear, and the true loading condition of the dowels is much more complex as the crosshead displacements grow.

The oak dowels also exhibited signs of a shear/bending behaviour: curvature of the central element, cracks in the bottom part of the side element, cracking of the top fibres and compression of the bottom fibres in the central element. In addition, oak dowels showed strong discolouring at 200 °C, possibly indicating the onset of pyrolysis reactions (Figure 9), as should be expected at these temperatures.

Figure 9: *Failed samples, from top to bottom: GFRP in steady state at 140 °C, oak in steady state at 140 °C, oak in steady state at 200 °C.*

6 DISCUSSION

6.1 INCREASE IN DUCTILITY AT ELEVATED TEMPERATURES

The steady state and transient results show a ductile failure mode at elevated temperatures for both the GFRP and oak dowels. For the GFRP dowels, this represents a net change of behaviour from ambient conditions, characterised by a high stiffness. Indeed, at 200 °C, the dowels maintained their peak load capacity until a crosshead displacement of 9 mm, which represents 3/4 of their nominal diameter. Ambient shear tests from the literature [20], report a maximum test load carried between a fibre displacement of 1/4 and 1/3 of the rebar diameter for GFRP dowels. This difference in deformations is evidence of the increased ductility (and reduced stiffness) of the GFRP at elevated temperatures.

Furthermore, due to the polymeric nature of the GFRP's matrix, the mechanical behaviour of the dowel is greatly influenced by its glass transition. However, the comparison of DMA and steady state results, suggests that the onset temperature is a better indicator of behaviour change than the glass transition temperature determined via peak loss factor. Figure 5 shows that, at 140 °C, the GFRP dowels had already transitioned to a more ductile failure mode at temperatures 14 °C below the glass transition temperature.

The oak dowels exhibited no significant change in their behavioural trends between 25 °C and 200 °C. However, the peak shear strength is notably reduced at 200 °C. In addition, at 200 °C, the oak dowels experienced a sharp increase in loss factor (see Figure 2). Further research is required to fully understand and explain the changes in properties of oak dowels at 200 °C.

https://doi.org/10.52202/069179-0208

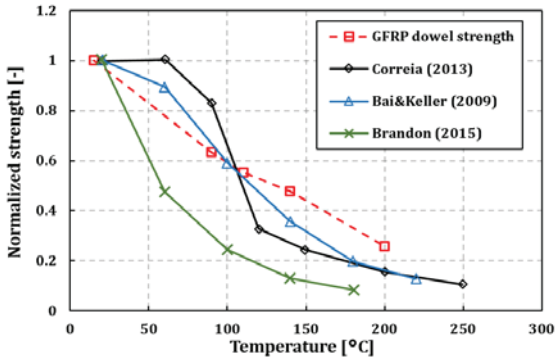

Figure 10: *GFRP dowel strength against literature values of interlaminar shear strength with temperature [17,21,11].*

6.2 SIGNIFICANCE OF BENDING IN DOWEL FAILURE

The study of the failed dowels, for both GFRP and oak, highlighted the significance of bending in their failure. In particular, curving of the fibres in the central oak element, and delamination of the top layers of the GFRP dowel are signs of a combined shear and bending mechanism. As such, results from this study are not in complete agreement with findings from the literature which test dowels in pure shear or pure bending.

From Figure 10, at higher temperatures, the GFRP dowels used in the current study appear to retain more of their strength at higher temperatures than values of interlaminar shear strength obtained for GFRP in studies found in the literature. It is considered likely that, upon loading at elevated temperatures, the dowels – both GFRP *and* oak – first failed essentially in shear, with fibres in the bottom part of the dowel on the tension side continuing to carry the load at larger crosshead displacements up until failure (i.e., a combined shear and flexural mechanism). The choice of testing rig is hence a determining parameter as it influences the amplitude of bending experienced by the fastener. Further, embedding tests of the dowel in a timber element are necessary to assess the degree of bending which non-metallic dowels are able to achieve. Indeed, the current study has not addressed whatsoever the interactions between dowels and timber elements that would undoubtedly be relevant in the elevated temperature performance of a dowelled timber connection (involving the use of any type of dowel, whether oak, GFRP, or indeed steel). Additional research is required to study such issues before GFRP dowels can be confidently applied in connections in timber structures requiring fire resistance.

6.3 COMPARISON OF METALLIC AND NON-METALLIC DOWELS

Figures 7 shows that both types of dowels experienced a loss of strength at elevated temperatures. At 200 °C, the GFRP and oak dowels retain 25% and 50% of their ambient strength, respectively. In comparison, steel shows no reduction of its effective yield strength until about 400 °C, according to EN 1991-1-5 [22]. However, the increased ductility of non-metallic fasteners, which leads to the more progressive failure of the dowel, may present significant advantages in timber connections.
In addition, at elevated temperature steel fasteners, which have a comparatively high thermal conductivity as compared with either oak or GFRP, will conduct heat into a connection and may lead to a loss in strength due to accelerated in depth heating and/or charring of the surrounding timber.

In a ductile failure, the fastener externalises strain energy by means of cracking or displacement, and transfers the energy to the surrounding timber. Since the stiffness of the non-metallic dowel is more compatible with timber than steel [2], the surrounding timber can absorb the energy released by the fastener and experience ductile deformations. Since the stiffness mismatch is reduced between the fastener and the timber, the likelihood of a brittle failure of the connection is thus reduced. It can thus be suggested that, with non-metallic dowels, the failure of the connection at elevated temperatures is a combined failure of the fastener and embedding timber instead of an inefficient and ultimately disadvantageous use of the strength of the metallic fastener.

6.4 DESIGN CONSIDERATIONS

Current timber fire protection strategies typically rely on encapsulation [23]; this aims to protect a connection by ensuring that heat does not reach the fasteners too quickly. However, this strategy leads to an increase in material and weight of the connection, as well as being aesthetically undesirable in many cases. Non-metallic connections, due to the low thermal conductivity of the fasteners, are less susceptible to elevated temperatures. By quantifying the performance of non-metallic dowels at elevated temperatures, design of connections using non-metallic dowels can become a more realistic option.

For GFRP dowels, if adequate protection is provided to the connection to minimise heat exposure of the fastener and ensure that the temperature in the dowel remains below the glass transition temperature of the material, conventional elastic design can perhaps be used, taking the strength of the dowel obtained at 120 °C, or before the onset of glass transition. This strength value represents 55% of the strength of the dowel at ambient temperature.

6.5 FUTURE WORK

The aim of the research presented in this paper was to study the shear behaviour of oak and GFRP dowels. However, in this process, the influence of the embedding timber on the failure of the connection was removed. Further embedding tests, including a direct measurement of the strain of the fastener within embedding timber should be conducted to assess the behaviour of full dowelled connections.

The steady state study should be complemented with more temperatures, especially between 150 °C and 180 °C for the GFRP, to observe the behaviour of the dowel just after its glass transition. In addition, different loading and heating rates should be explored. Finally, extensive modelling research is required to translate the behavioural observations presented in this thesis, into adequate design rules to improve the fire performance of non-metallic dowelled connections in timber structures.

7 CONCLUSION

This paper has explored the behaviour of GFRP and oak dowels at elevated temperatures to initially assess their potential as a replacement for steel in timber connections. The dowels were tested in a steel rig which was designed to simulate the behaviour of a connection. Through a series of steady state and transient state elevated temperature tests, the following preliminary conclusions were obtained:

- The failure of both oak and GFRP dowels was by a combination of bending and shear failure at elevated temperatures. This led to the loss of interlaminar shear strength for GFRP dowels, and failure of fibres in tension for oak dowels.
- At 200 °C, GFRP dowels retained only 25% of their ambient temperature shear strength, whereas oak dowels retained 50%. Despite this less severe loss in strength, oak dowels were significantly weaker than GFRP for all tested temperatures.
- Even though GFRP and oak dowels are significantly weaker than steel dowels, their progressive failure at elevated temperatures – as well as their lower stiffness even at ambient temperatures – increases their compatibility with embedding timber; this may lead to a beneficial more ductile failure of non-metallic dowelled connections.

The non-metallic dowels tested in this study appear to represent feasible alternatives to metallic dowels for some timber connections, and in particular appear to provide compelling advantages for architecturally expressed connections in mass timber structures (subject to considerable additional research).

REFERENCES

[1] Drake R, Ansell M.P., Mettem C & Bainbridge R.J.: Performance of GFRP pultruded dowels versus steel dowels. In 'Advancement of structural connection techniques for timber buildings', International COST 508 Wood Mechanics Conference, Stuttgart, pages 353−364, 1996.

[2] Drake, R. D., The advancement of Structural Connection techniques for timber buildings. PhD thesis, University of Bath, 2003.

[3] Pedersen, M., Dowel Type Timber Connections. PhD thesis, Technical University of Denmark, 2001.

[4] Thomson, A., Harris, R., Walker, P. & Ansell, M., Development of non-metallic timber connections for contemporary applications. In: 11th World Conference on Timber Engineering, 2010.

[5] Sorathia, U., Dapp, T. & Beck, C., 'Fire performance of composites'. In Materials Engineering 109(9), pages 10−12, 1992.

[6] Bank, L. C.: Properties of FRP Reinforcements for Concrete. In 'Fiber-Reinforced-Plastic (FRP) Reinforcement for Concrete Structures', Developments in Civil Engineering, Elsevier, Oxford, pages 59−86, 1993.

[7] Hajiloo, H., Green, M. F. & Gales, J.: Mechanical properties of GFRP reinforcing bars at high temperatures. In Construction and Building Materials 162, pages 142−154, 2018.

[8] Kumahara, S., Masuda, Y., Tanano, H. & Shimizu, A., Tensile strength of continuous fiber bar under high temperature. In SP-138: Fiber-Reinforced Plastic Reinforcement for Concrete Structures International Symposium, 1993.

[9] Wypych, G.: VE-vinyl ester resin, Handbook of polymers 2nd edition, pages 702−703, ChemTec Publishing, Toronto, 2016.

[10] Young, R. J. & Lovell, P. A.: Introduction to Polymers, CRC Press, 2011.

[11] Brandon, D., Fire and structural performance of non-metallic timber connections. PhD thesis, University of Bath, 2015.

[12] British Standards Institution: BS EN 1995-1-2: Eurocode 5: Design of timber structures, Part 1-2: General: structural fire design, 2009.

[13] Adewopo, J. B. & Patterson, D. W.: Effects of Heat Treatment on the Mechanical Properties of Loblolly Pine, Sweetgum, and Red Oak. In Forest Products Journal 61, pages 526-535, 2011.

[14] Balkis, B. F., Hiziroglu, S. & Md Tahir, P.: Properties of some thermally modified wood species. In Materials and Design 43, pages 348−355, 2013.

[15] British Standards Institution: BS EN ISO 11358-1: Plastics - Thermogravimetry (TG) of polymers. Part1: General principles, 2014.

[16] British Standards Institution: BS ISO 6721-11: Plastics — Determination of dynamic mechanical properties. Part 11: Glass transition temperature, 2012.

[17] Correia, J. R., Gomes, M. M., Pires, J. M. & Branco, F. A.: Mechanical behaviour of pultruded glass fibre reinforced polymer composites at elevated temperature: Experiments and model assessment. In Composite Structures 98, pages 303–313, 2013.

[18] Benmokrane, B., Brown, V. L., Mohamed, K., Nanni, A., Rossini, M. & Shield, C.: Creep-Rupture Limit for GFRP Bars Subjected to Sustained Loads. In Journal of Composites for Construction 23(6), 2019.

[19] Genikomsou, A. S., Balomenos, G. P., Arczewska, P. & Polak, M. A.: Transverse Shear Testing of GFRP Bars with Reduced Cross Sections. In Journal of Composites for Construction 22(5), 2018.

https://doi.org/10.52202/069179-0208

[20] Knight, C. C., Manager, P., Kampmann, R., De Caso, F., Roddenberry, M., Ruiz Emparanza Candidate, A. & Assistant, R.: Performance Evaluation of Glass Fiber Reinforced Polymer (GFRP) Reinforcing Bars Embedded in Concrete Under Aggressive Environments, 2018.
[21] Bai, Y. & Keller, T.: Modeling of strength degradation for Fiber-reinforced polymer composites in fire. In Journal of Composite Materials 43(21), 2009.
[22] British Standards Institution: EN 1991-1-5, Eurocode 1: Actions on structures - Part 1-5: General actions - Thermal actions, 2003.
[23] Structural Timber Association: Structural timber buildings fire safety in use guidance. Volume 6 - Mass timber structures. Building Regulation compliance B3, 2020.

World Conference on Timber Engineering Oslo 2023

FIRE PERFORMANCE OF PENETRATIONS IN GLULAM BEAMS: A PRELIMINARY STUDY

Laura Hasburgh[1], Keith Bourne[2], David Barber[3]

ABSTRACT: Glue laminated timber (glulam) is an engineered wood product composed of wood laminations bonded together with durable adhesives. Glulam is versatile ranging from simple, straight beams to complex, curved structural members and are used in a variety of applications including residential and commercial construction where they are often exposed due to the timeless aesthetic of wood. Glulam beams are also resource-efficient and offer designers highly predictable structural and fire performance when used in accordance with design specifications. However, factory-cut or field modifications to glulam beams, such as notching and drilling for routing piping and ductwork, has become common practice, which has the potential to impact structural integrity. There are prescriptive recommendations for these unplanned penetrations to ensure structural capacity remains intact but, in the event of a fire, the field modifications may enlarge and further reduce the beam's cross-section. Here, we present an experimental method to evaluate the char rate and growth of various standard-fire exposed penetrations in glulam beams.

KEYWORDS: Glulam, penetration, char depth, fire performance

1 INTRODUCTION

Structural glue-laminated timber (glulam) beams are engineered building components manufactured from specially identified and placed lumber laminations of varying strength and stiffness. Because of their strength and ability to be specified for unique situations, glulam beams are often highly stressed under design loads and alterations to the beams could result in failure to carry these loads.

Prior to or during construction and installation of glulam beams, it has become common practice to drill horizontal penetrations, also known as horizontal holes, to allow building services (e.g., pipes, ducts, cable trays, etc.) to run through glulam beams such as those shown in Figure 1. Whether factory-cut or field-modified, these penetrations remove wood fibre, reducing the cross-sectional area of the beam at that location. This results in strength reductions and localized stress concentrations [1]. Because of these potential issues, prescriptive recommendations based on a combination of practical experience and engineering analysis for in-field penetrations can be found in a Technical Note S560J published by APA – The Engineered Wood Association [2]. Several investigations have evaluated the fracture behaviour and design of glulam beams with both round and rectangular penetrations that support the recommendations by APA including [3 – 6]. Non-critical zones for simply supported beams are identified in Technical Note S560J as portions of a glulam beam where the stresses are less than 50% of the design bending stress and design shear stress. Additional design guidelines for penetrations that exceed the guidance provided in S560J, Technical Note V700B [7] provides an analytical tool and engineering equations to ensure the structural integrity is not compromised.

Methods for calculating the fire resistance ratings of structural building members are specified by building codes and require the member to endure a specified fire without loss of its loadbearing capabilities. The codified procedure to calculate the fire-resistance ratings for exposed mass timber, such as glulam beams have allowed their use in fire-rated buildings. This mechanistic approach, found within the National Design Specification for Wood Construction (NDS) [8] and the Fire Design Specification for Wood Construction [9], applies to all wood structural members designed per NDS including structural composite materials such as glulam. In this method, the engineering calculations of the ultimate load capacity are adjusted to take into consideration the reduced dimensions with time due to the formation of char. Nominally, a char depth of 38 mm at 1 hour is used for exposed (i.e., no fire protection applied) solid-sawn and structural glued-laminated softwood members with a 20% increase to account for rounding at the corners and loss of strength in the preheated zone located just beyond the char layer.

[1] Laura Hasburgh, USDA Forest Products Laboratory, United States, laura.e.hasburgh@usda.gov
[2] Keith Bourne, USDA Forest Products Laboratory, United States, keith.j.bourne@usda.gov
[3] David Barber, ARUP, Australia, David.Barber@arup.com

https://doi.org/10.52202/069179-0209

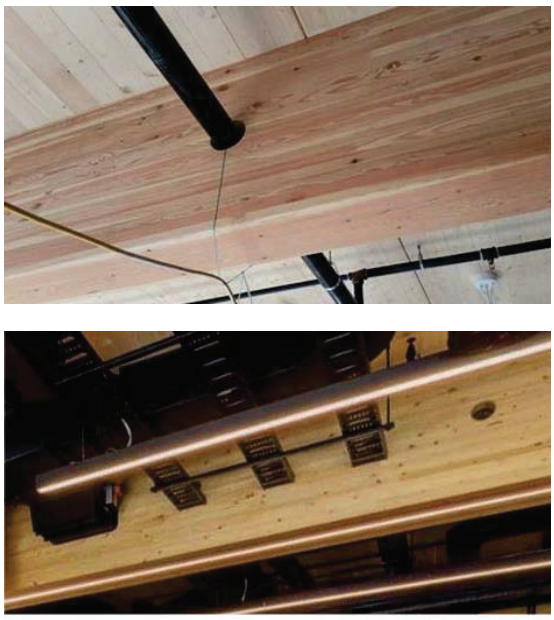

Figure 1: *Glulam beam with field penetrations for a pipe (top) and cable trays (bottom). Photos provided by Barber.*

Firestopping for through-systems do exist, but these systems are applicable to penetrations through fire-rated wall and floor assemblies and the fire testing is conducted from a single direction [10]. This fire testing is not applicable for glulam beams, which are typically exposed on three sides.

While the fire resistance of non-modified beams is well documented and the structural implications of penetrations in glulam beams have been addressed, the intersection of these issues has not been evaluated. The char rates used to calculate fire resistance are typically only applied to the exposed sides of a beam and do not account for penetrations through a beam that may widen due to charring during a fire event.

Here, the method used to expose glulam beams with various penetrations sizes and shapes to a standard fire is presented along with char depth analysis techniques. Additionally, preliminary results pertaining to the increase in penetration size due to charring are provided.

2 MATERIALS AND METHODS

2.1 MATERIALS

A total of six Douglas-fir (*Pseudotsuga menziesii*) glulam beams with dimensions of 343 mm deep (10-ply) by 175 mm wide and 3.66 m long were used. Two of the beams were laminated with a phenol-resorcinol-formaldehyde (PRF) adhesive while the other four were manufactured with a polyurethane (PUR) adhesive. Because the beams were unloaded, the differences in adhesives did not affect the charring around the top and sides of the penetrations.

Three beam configurations (A, B, and C) were designed with a range of penetration sizes and shapes. The dimensions and type of the penetrations for each beam configuration are provided in Table 1 and illustrated in Figure 2. There were three types of round penetrations (small, medium, and large pipes) and two rectangular penetrations (small cable tray and large duct) tested. These penetrations were cut along the centreline of the depth of the beam (x-y plane). It is important to note that the penetration configurations for these beams do not conform to the design guidelines for holes/notches for the beams used and, as such, this study focused on the expansion of the penetrations due to fire exposure and not structural integrity. The penetrations were strictly sized and placed such that the expansion of the holes would not interfere with each other and associated thermocouples. Additionally, the penetration configuration optimized the experimental space in the furnace while allowing replicates of each penetration type.

Table 1: *Beam penetration configurations*

Beam ID	Penetration Shape	Penetration Size (mm)	Insert or empty
A1	large round	Ø168	empty
A1	medium round	Ø 139.7	empty
A1	small rectangular	76 x 177.8	empty
A1	small round	Ø 88.9	empty
A2	large round	Ø 168	insert
A2	medium round	Ø 139.7	insert
A2	small rectangular	76 x 177.8	insert
A2	small round	Ø 88.9	insert
B1	large rectangular	127 x 330	insert
B1	large round	Ø 168	insert
B1	small round	Ø 88.9	insert
B2	large rectangular	127 x 330	empty
B2	large round	Ø 168	empty
B2	small round	Ø 88.9	empty
C1	large rectangular	127 x 330	insert
C1	medium round	Ø 139.7	insert
C1	small rectangular	76 x 177.8	insert
C2	large rectangular	127 x 330	empty
C2	medium round	Ø 139.7	empty
C2	small rectangular	76 x 177.8	empty

Each penetration type was separated by at least 305 mm (12 inches) to reduce potential interactions during the fire exposure, allowing for up to four penetrations per beam.

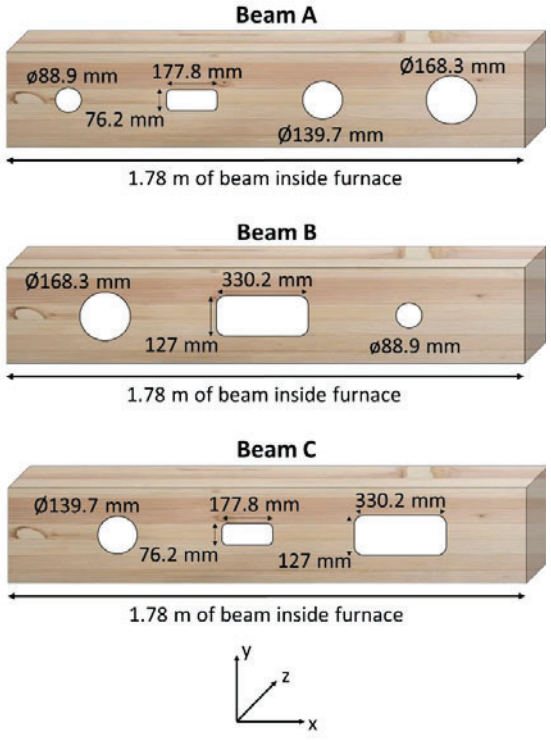

Figure 2: *Glulam beam types with penetration layout: A (top), B (middle) and C (bottom).*

To evaluate the effect of a penetration with equipment through it, two of each beam configuration were run: one with building service components inserted through the penetrations during the fire test and the second with empty penetrations. For the tests with building service components in-place the components were secured with chains as shown in Figure 3. When an insert was included through the beam, a gap of at least 12.7 mm (1/2 inch) around the insert was maintained with sizes of inserts provided in Table 2.

Figure 3: *Glulam beam (Type C) with penetrations for a pipe, cable tray and duct (left to right).*

Table 2: *Building service component details*

Hole Shape	Hole Size (mm)	Insert details	
		Material	Size
large round	Ø168	schedule 40 steel pipe	141 mm diameter with 6.5 mm wall (nominally 5-inch)
medium round	Ø 139.7	schedule 40 steel pipe	114 mm diameter by 6 mm wall (nominally 4-inch)
small round	Ø 88.9	schedule 40 steel pipe	60 mm diameter by 4 mm wall (nominally 2-inch)
large rectangular	127 x 330	galvanized steel duct	102 mm by 305 mm (4 by 12 inches) wall thickness of 0.4 mm (0.02 inches)
small rectangular	76 x 177.8	Cable tray with 5 mm (0.2 inch) steel wire on a 50 mm by 100 mm (2 by 4 inch) with an electro zinc finish	150 mm x 50 mm (6 by 2 inches)

2.2 METHODS

2.2.1 Instrumentation

To obtain the temperature profile around a penetration, 28 thermocouples made in-house from 30-gauge type K wire (Omega GG-K-30-SLE) were embedded in the glulam both above and on each side of every penetration. To install the thermocouples, 2.4 mm (3/32 inch) diameter holes were drilled from the top of the glulam beam to known depths and set distances from each penetration.

For the thermocouples installed on the side of a penetration, arrays of four thermocouples starting at 25.4 mm (1 in) from the penetration edge and spaced at 12.7 mm (1/2 inch) were installed along the centreline of the beam in the x-direction (Figure 4). Above the penetration, four thermocouples were installed along the centreline of the penetration in the z-direction. These four thermocouples started at the top edge of the penetration and were spaced at either 25.4 mm (1 inch) or 12.7 mm

https://doi.org/10.52202/069179-0209

(1/2 inch) in the y-direction and 12.7 mm (1/2 inch) in the z-direction. This installation pattern ensured that the thermocouples were parallel to the isotherm/char front for the side arrays, which has been shown to provide more accurate measurements of temperature. However, the thermocouples arrays above the penetrations were perpendicular to the isotherm. To reduce the impact of this on the data, the holes were filled with fire caulk after the thermocouples were inserted. In addition to the thermocouple data, after the specimens were exposed and cooled, they were sawn and physical measurements of the remaining cross-section were taken to determine the final char depth at 90 minutes.

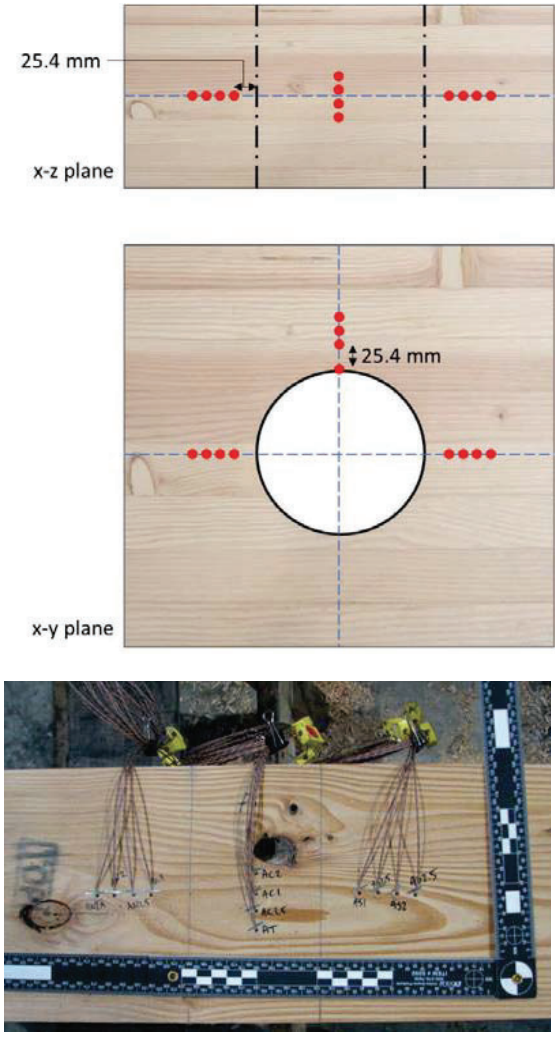

Figure 4: *Top: Schematic of thermocouple placement for a round penetration (not to scale) and Bottom: top of glulam specimen with thermocouples installed.*

2.2.2 Test Furnace

The glulam beams were tested in an intermediate-scale horizontal furnace and subjected to the standard time-temperature curve specified in ASTM E119 [11]. The furnace at the Forest Products Laboratory (FPL) has interior dimensions of 1.8 m long, 1.1 m wide, and 1.3 m high. The furnace has eight diffusion-flame natural gas burners on the floor and all air for combustion was provided by natural draft through vents at the bottom of the furnace. The furnace was controlled via six capped furnace thermocouples located 305 mm from the furnace lid. Approximately 1.78 m of the beam length was exposed to fire within the furnace with 0.94 m on each side of the beam not exposed to the fire. To avoid uneven exposure near the furnace walls, all penetrations were located within the middle 1.5 m of a beam as illustrated in Figure 3. A non-combustible lid was designed such that the top of the beam was not exposed to the fire (Figure 5).

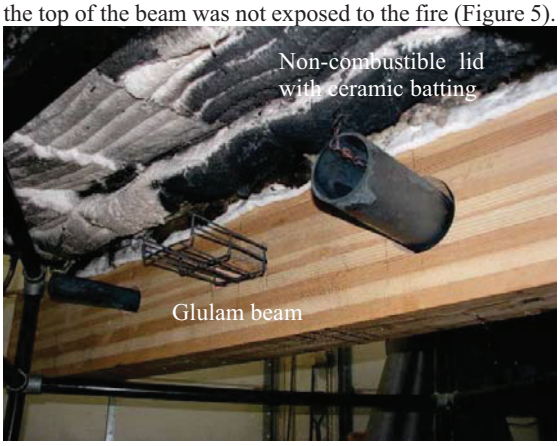

Figure 5: *Glulam beam with non-combustible lid protecting the top of the specimen prior to being placed in the furnace.*

Each beam was exposed for a duration of 90 minutes. The tests were terminated by removing the specimen, extinguishing the fire with water, and scraping all char off to halt smouldering combustion. Figure 6 illustrates these steps through the removal of a burning glulam beam from the furnace, an extinguished beam, and a beam with the char removed for a 127 mm by 330 mm rectangular penetration in beam B that had a duct in place during the fire test.

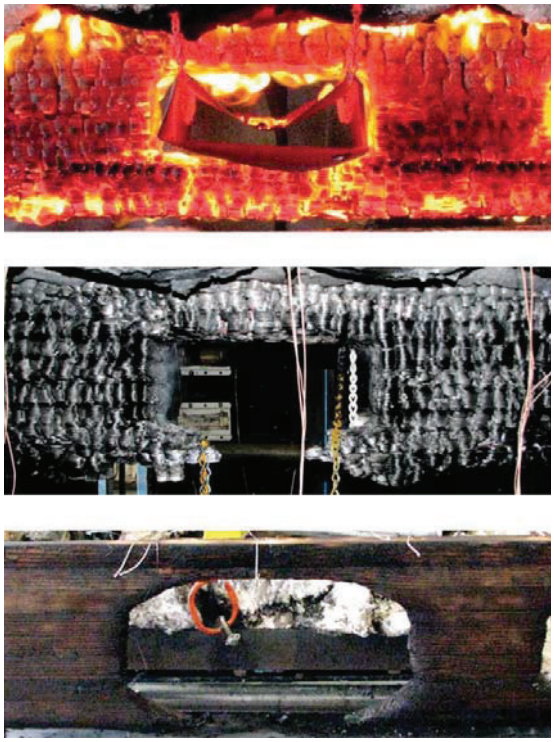

Figure 6: *Image of duct penetration immediately after removal from the furnace (top), once extinguished/cooled (middle), and with the char layer scrapped off (bottom).*

3 RESULTS

During the experiments, the thermocouple data allowed the char front to be monitored by using the commonly-accepted 300°C isotherm as the temperature when wood converts to char [12]. The thermal profile in the glulam beam around a penetration will increase in both temperature and depth with time. As an example, the results collected around one of the penetrations in beam C2 (no building services installed) are provided in Figure 7 with the ASTM E119 standard time-temperature curve provided for reference. The alpha characters identify the penetration type (D = 139.7 mm (5.5 inch) diameter penetration). The side thermocouple arrays are denoted with either N for North or S for South while C indicates the thermocouple array centred above the penetration. The numbers indicate the depth (in mm) of the thermocouple from the exposed interior surface of the penetration.

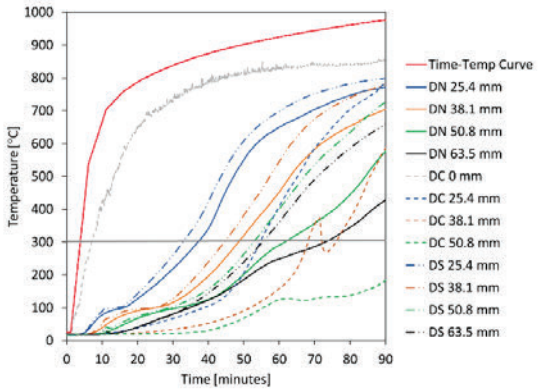

Figure 7: *Thermocouple data around a penetration with a diameter of 139.7 mm (5.5 inch) in beam C2.*

The data in Figure 8 shows that the increase in temperature and the increase in depth at which higher temperatures are measured occurred slightly faster on the side of a penetration versus above the penetration for the specific specimen/penetration configuration. This same trend appears to hold true when evaluating the linear char rates, taken as depth over time (mm/min), for each type of penetration, both with and without pipes/ducts/cable trays in place. Table 3 provides the linear char rates around the perimeter of the various penetrations and with or without a pipe or duct in the penetration. These char rates were calculated for each individual beam/penetration and then averaged for each penetration type at 60 minutes.

Table 3: *Average linear char rates in mm/min for each penetration type.*

Penetration Type	Insert or empty	Char rate at 60 minutes (mm/min)	
		Side	Top[a]
large rectangular	insert	0.65	-
large rectangular	empty	0.92	0.92
large round	insert	0.68	-
large round	empty	0.74	0.47
medium round	insert	0.58	-
medium round	empty	0.99	0.54
small rectangular	insert	0.66	0.48
small rectangular	empty	0.67	0.62
small round	insert	0.51	-
small round	empty	0.69	-

[a] For five tests, the thermocouples above the penetration did not reach a temperature of 300°C at 60 minutes. As such, no data is available.

The results in Table 2 can be compared to the standard nominal char rate of 0.635 mm/min at 60 minutes. Most

https://doi.org/10.52202/069179-0209

of the penetrations were comparable to the standard char rate. However, the medium to large penetrations without building component inserts have much faster char rates between 0.74 mm/min and 0.99 mm/min.

4 CONCLUSIONS

The perimeter of horizontal glulam beam penetrations will increase during a fire, further reducing the effective cross-section of the member. These preliminary results show the char rate at and around penetrations with building services components installed are near the standard nominal char rate of 0.635 mm/min for glulam beams. Therefore, when designing a structural member, in addition to reducing the overall cross section, an effective penetration size that includes an increase for charring should be considered. The results also indicate that if a horizontal penetration is made for a building service component that is later abandoned, the penetration should be filled with a non-combustible material to avoid rapid increase of the penetration during a fire.

ACKNOWLEDGEMENT

The authors would thank Eleanor Q. Lazarcik for her assistance with conducting the experiments.

REFERENCES

[1] B.Yeh. A guide to field notching and drilling LVL and glulam. Construction Specification Institute. November 26, 2021.

[2] "A guide to field notching and drilling LVL and glulam." *American Plywood Association (APA)–The Engineered Wood Association, Tacoma, WA.* Form S560J. 2020.

[3] Aicher, Simon, and Lillian Höfflin. "Fracture behavior and design of glulam beams with round holes." Proceedings of 10th World Conference on Timber Engineering. Vol. 1. 2008.

[4] Lilian Höfflin and Simon Aicher "Design of rectangular holes in glulam beams." Otto-Graf-Journal 14 (2003): 211.F

[5] Okamoto, Shigefumi, et al. "Study on the strength of glued laminated timber beams with round holes: difference in structural performance between homogeneous-grade and heterogeneous-grade timber." Journal of Wood Science 67.1 (2021): 1-25.

[6] Danielsson, H. E. N. R. I. K. "The strength of glulam beams with holes." A survey of tests and calculation methods. Report of Structural Mechanics Department of Construction Sciences, Lund, Sweden (2007).

[7] "Effect of large diameter horizontal holes on the bending and shear properties of structural glue laminated timber." *American Plywood Association (APA)–The Engineered Wood Association, Tacoma, WA.* Form V700B. 2020.

[8] National Design Specification for Wood Construction. American Wood Council. Leesburg, VA USA, 2018.

[9] Fire Design Specification for Wood Construction. American Wood Council. Leesburg, VA USA, 2022.

[10] Ackerman, E. (1998). Firestopping Through-Penetrations. ASTM International.

[11] "ASTM E119 Standard test methods for fire tests of building construction and materials," *ASTM International, West Conshohocken, PA*, 2018.

[12] E. L. Schaffer, *Review of information related to the charring rate of wood* vol. 145: Forest Products Laboratory, 1966.

World Conference on Timber Engineering Oslo 2023

CALCULATION METHOD OF COLLAPSE TIME OF WOOD MEMBERS EXPOSED TO FIRE HEATING WITH HEAT AND WATER TRANSFER ANALYSIS: INFLUENCE OF INITIAL MOISTURE CONTENT ON CHARRING RATE AND MECHANICAL PROPERTIES OF REMAINING SECTION OF WOOD MEMBERS

Tatsuro Suzuki[1], Yuji Hasemi[2]

ABSTRACT: This study formulates a method to calculate the collapse time of wood members exposed to fire heating by considering the influence of temperature and moisture content. Moisture content affects the mechanical properties of wood members adversely during fire heating because of an increase in moisture content by water transfer and thermal softening at high temperature; however, the impact on mechanical properties of wood members during fire heating has been previously evaluated with respect to temperature alone. Consequently, this study formulates the calculation of the buckling time of a Japanese zelkova column under two conditions of initial moisture content (13.4% and 30.4%) and compares it with previous experimental results. This study showed that moisture content increased from 13.4% to 20.0% and from 30.4% to 39.1% at most for the two conditions, respectively, during fire heating. The buckling time could be predicted with good accuracy considering the moisture content dependence of Young's modulus. Although the moment of inertia was 1.67 times at 82 minutes when the column buckled in the experiment when the moisture content was high, the buckling time was only 3.5 min later than at low moisture content. Therefore, this calculation results show high initial moisture content increased in the remaining cross-sectional area and decreased Young's modulus significantly.

KEYWORDS: Fire Heating, Wood Members, Moisture Content, Mechanical Properties, Heat and Water Transfer

1 INTRODUCTION

In recent years, large wooden buildings have been constructed worldwide for the purpose of low-carbon construction or utilisation of forest resources. In Japan, high-rise and large-scale wooden buildings have been constructed due to supportive legislation and technological development. Therefore, the prediction of fire resistance of wood members exposed to fire heating has gained importance to improve the credibility of wooden buildings during fire and design appropriately sized members.

Regarding parameters affecting the mechanical properties of wood members during fire heating, not only temperature but also moisture content is important. Moisture content is significant because an increase in moisture content caused by vapourisation, transfer, and re-condensation of water in the remaining cross-sectional area required to bear load. The experiments in [1-3] showed that fire heating caused an increase in the moisture content of the specimens. Such an increase decreases the mechanical properties of wood members even at room temperature. Second, temperature dependence of mechanical properties of wood members increases significantly under the condition of high moisture content due to the thermal softening of lignin and hemicellulose, as shown in [4,5]. Hence, water transfer and moisture content increase by re-condensation, causing a probable decrease in mechanical properties.

Consequently, this study formulates a method to calculate the mechanical properties of wood members exposed to fire heating by considering the influence of temperature and moisture content. First, this study conducts heat and water transfer analysis, which calculates heat conduction and mass transfer. Second, the mechanical properties of wood members were calculated with distributions of temperature and moisture content given by heat and water transfer. Finally, the validity of the calculation was verified by comparing the calculation results and previous experiments' results.

2 METHOD

2.1 OUTLINE

Fig.1 shows the outline of the calculation method of the mechanical properties of wood members with heat and water transfer analysis.

[1] Tatsuro Suzuki, Adjunct Researcher, Waseda University, Japan, tatsuro@suzukikoumuten.com
[2]Yuji Hasemi, Professor Emeritus, Waseda University, Japan, hasemi@waseda.jp

https://doi.org/10.52202/069179-0210

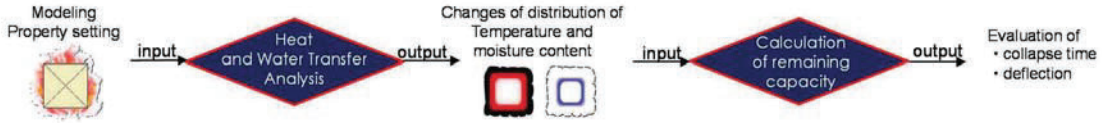

***Figure 1**: The outline of the evaluation method of the mechanical properties of wood members with heat and water transfer analysis*

First, the cross-sectional area of a wood member is divided into finite elements. Moreover, the time variation of the distribution of temperature and moisture content are calculated with heat and water transfer analysis. Second, the remaining ratio of mechanical properties of each element is calculated with those temperature and moisture content. Finally, collapse time or deflection is calculated by adding all remaining

2.2 CALCULATION OBJECT

2.2.1 EXPERIMENTS TO COMPARE

In this study, we compare calculation results with the experimental results in [6] to clarify the influence of initial moisture content on the charring rate and mechanical properties of wood members during fire heating. If the initial moisture content is high, On the on hand, the increase in the latent heat of water causes a decrease in the charring rate. On the other hand, the mechanical properties of wood members decrease under conditions of high moisture content and high temperature. Thereby, high initial moisture content has both positive and negative influences as it causes a decrease in the charring rate and decrease in the mechanical properties of wood members, respectively. In the experiments in [6], specimens in an air-dry state and with high moisture content were heated. Therefore, in this study, we use the initial moisture content as a parameter to calculate the collapse time of wood members due to fire heating and compare the results with the experiments in [6].

Table 1 shows the results of the two experiments in [6]. The buckling time of a full-scale Japanese zelkova cylindrical column was measured during the load heating experiment under the ISO 834 fire heating curve conditions. Before the load heating experiment, the charring rate of a short column was measured during the non-load heating experiment to predict the buckling time in the load heating experiment. Meanwhile, the difference in the initial moisture content levels between the two experiments caused a difference in the charring rate of specimens. Japanese zelkova (Zelkova serrata) is hardwood often used for constructing Japanese shrines and temples.

If the cross-section of a wooden member is large, the interior may continue to remain with a high moisture content because of the difficulty of drying the interior.

2.2.2 CALCULATION CONDITONS

Table 1 shows the calculation conditions with experimental conditions. The initial moisture content in the calculation was set to the same value for each experiment. In the two cases, the mechanical properties of the specimen were calculated by considering and not-considering moisture content dependence, respectively. The diameter of the wood member used in the calculation was the same in both cases, despite the difference in the experiments.

2.3 CALCULATION METHOD

2.3.1 MODEL

Fig.2 shows the calculation model. Heat and water transfer analysis was conducted with a one-dimensional model because the section in the experiment was a circle. The length of the calculation model was half of the experimental diameter since the side of the centre was under adiabatic conditions. Mechanical properties of the specimen were calculated with the assumption that each element has a doughnut-shaped cross-sectional area.

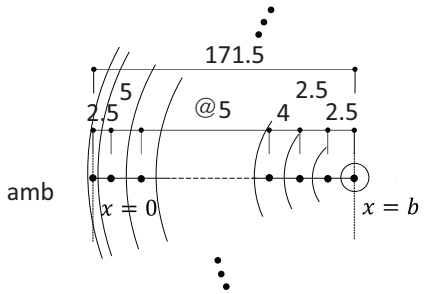

***Figure 2:** Calculation model (Unit: mm)*

***Table 1:** The experimental condition and the calculation results*

Case		Initial moisture content [%]	Experiment [6] Diameter [mm]	Experiment [6] Charring rate [mm/min]	Experiment [6] Buckling time [min]	Calculation Diameter [mm]	Calculation Charring rate [mm/min]	Calculation Moisture content dependence of mechanical properties	Calculation Buckling time [min]
A	A-1	13.7	354	0.77	– (Not Loaded)	343	0.78	valid	78.0
	A-2							invalid	89.5
B	B-1	30.4	343	0.54	82	343	0.56	valid	81.5
	B-2							invaid	116.5

https://doi.org/10.52202/069179-0210

2.3.2 HEAT AND WATER TRANSFER ANALYSIS

Time variation of temperature and moisture content are calculated with heat and water transfer analysis developed in [9]. In the calculation method in [9], temperature, moisture content, vapour pressure, and total pressure are assumed to be the four main variables, and their time variations are calculated.

Equations (1) ~ (4) show the basic formulas for calculating the four variables.

Temperature is calculated by considering the influences of latent heat of water evaporation, thermal decomposition, water adsorption/desorption, and heat generation by oxidation. In this study, heat generation is restricted to 0.4 times the volume to represent the time variation of temperature in the experiment. Consequently, this calculation method has the task of accurate temperature prediction.

Moisture content is calculated with the transfer of liquid water and adsorption/desorption. As a matter of fact, the influence of liquid water transfer is insignificant because the transfer speed of liquid water is slow as compared to gas transfer.

The basic formula of vapour and total gas represents mass conservation. Transfer speeds of gases depend on Darcy's row. In Darcy's row, specific permeability differs for each tree species.

(a) Heat transfer

$$\rho_{wood} c \frac{\partial T}{\partial t} = \frac{\partial}{\partial x}\left(\lambda \frac{\partial T}{\partial x}\right) - Q_{desorp} - Q_{evap} - Q_{decomp} + Q_{ox} \quad (1)$$

(b) Water transfer

$$\rho_{wood\ dry} \frac{\partial M}{\partial t} = \frac{\partial}{\partial x}\left(\rho_{wood\ dry} D_w \frac{\partial M}{\partial x}\right) - R_{desorp} - R_{evap} \quad (2)$$

(c) Mixture gas conservation

$$\frac{\partial \varepsilon \rho_g}{\partial t} + \frac{\partial \rho_g u}{\partial x} = R_{desorp} + R_{evap} \quad (3)$$

(d) Vapour conservation

$$\frac{\partial \varepsilon \rho_v}{\partial t} + \frac{\partial \rho_v u}{\partial x} = \frac{\partial}{\partial x}\left(D_v \frac{\partial \rho_v}{\partial x}\right) + R_{desorp} + R_{evap} \quad (4)$$

An increase in the moisture content is represented by the following algorisms: water evaporation in a higher temperature area, vapour transfer, increase in vapour pressure in a lower temperature area, increase in relative humidity, increase in equilibrium moisture content, and increase in adsorption rate. Thereby, moisture content does not increase above the equilibrium moisture content with the calculation method in [9]. However, if the initial moisture content is higher than the equilibrium moisture content, moisture content increases above the equilibrium moisture content possibly.

In this study, the algorism of water condensation was changed based on Equations (5,6).

(i) Adsorption ($P_v \geq P_{v,max}$)

$$R_{desorp} = \frac{\rho_v - \rho_{v,max}}{\Delta t} = \frac{M_v (P_v - P_{v,max})}{R\bar{T}\,\Delta t} \quad (5)$$

(ii) Desorption ($P_v < P_{v,max}$)

$$R_{desorp} = 0 \quad (6)$$

Table 2 shows the boundary conditions. Boundary conditions of every four variables on the unheated surface were set to adiabatic. On the heated surface, the temperature was calculated by considering conduction and radiation. The boundary condition of moisture content was adiabatic because liquid water was not exchanged. For total pressure, ambient total pressure was set to constant. The exchange of vapour pressure was calculated with the vapour transfer coefficient and the difference in vapour pressure via conductive heat transfer.

Table 3 shows the setting of properties for the calculation. Specific humidity was set to 3.96 [10^{-17} m^2/(Pa・sec)], which is the value of Japanese Elm in [16]. This is hardwood and rings porous wood similar to Japanese zelkova.

2.3.3 CALCULATION OF MECHANICAL PROPERTIES

Buckling time was calculated and compared with previous experimental results because the column collapsed due to buckling in the experiment. Buckling time was regarded as the period after which the load-bearing capacity fell below the load. Load-bearing capacity was calculated with Equation (7), and the load was 640 [kN].

$$P_k = \frac{\pi E I}{L_k^2} \quad (7)$$

Young's modulus is calculated with initial moisture content and Young's modulus remaining ratio. Young's modulus remaining ratio is calculated via the equation in

Table 2: *The boundary condition of the calculation (Words in [ ] mean types of boundary conditions)*

Boundary	Temperature	Moisutre content	Total pressure	Vapour pressure
Heated surface	$-\lambda \frac{\partial T}{\partial x}\Big\|_{x=0} = h_c (T_{amb} - T) + q_{rad}$	$-D_w \frac{\partial M}{\partial x}\Big\|_{x=0} = 0$	$P_g\Big\|_{x=0} = P_{g\ amb}$	$-D_v \frac{\partial P_v}{\partial x}\Big\|_{x=0} = h_v (P_{v\,amb} - P_v)$
	[mixed : convection and radiation]	[2nd : adiabatic]	[1st]	[3rd]
Unheated surface	$-\lambda \frac{\partial T}{\partial x}\Big\|_{x=b} = 0$	$-D_w \frac{\partial M}{\partial x}\Big\|_{x=b} = 0$	$-\frac{\partial u \rho_g}{\partial x}\Big\|_{x=b} = 0$	$-D_v \frac{\partial P_v}{\partial x}\Big\|_{x=b} = 0$
	[2nd : adiabatic]	[2nd : adiabatic]	[2nd : adiabatic]	[2nd : adiabatic]

https://doi.org/10.52202/069179-0210

Table 3: *Setting of properties for the calculation*

Symbol	Parameters		Values	Unit
T_{amb}	ambient temperature		20	°C
$h_{c\,amb}$	convective factor of heat surface		0.04	kW/(m²·K)
$\varepsilon_{r\,amb1}$	emissivity of heat surface		0.9	-
h_v	vapour transfer coef.		0.002	kW/(m·K)
T_0	initial temperature		20	°C
U_0	initial relative humidity		0.40	-
$\rho_{wood\,0}$	bone-dry density		580 *1	kg/m³
c_{wood}	heat capacity of	wood	1.236 [12]	kJ/(kg·K)
c_w		water	4.186	kJ/(kg·K)
c_{char}		char	0.883 [13]	kJ/(kg·K)
λ	conductivity of wood and char		1.39×10^{-4} [14]	kW/(m·K)
L_{decomp}	heat of decomposition		2000	kJ/kg
$T_{decomp1}$	decompositon temperature	start	250	°C
$T_{decomp2}$		finish	400	°C
L_w	heat of adsorption and evaporation		2257	kJ/kg
D_w	diffusivity of water		1.94×10^{-10} [15]	m²/s
K_{wood}	specific permeability of	wood	3.96×10^{-17} [16]	m²/(Pa·sec)
K_{char}		char	3.96×10^{-15} *2	m²/(Pa·sec)
$D_{v\,0}$	diffusivity of vapour		3.8×10^{-5} [17]	m²/s

*1 The value of the specimen was aplied.

*2 The value was set to 0.01 times of wood[2].

[5], which considers the decrease caused by both temperature and moisture content. For instance, Young's modulus remaining ratio of Cryptomeria japonica at 95°C and high moisture content was 0.59, equivalent to that at 200°C and bone-dried state.

Initial Young's modulus was set to 9500 N/mm², which is the same value as the experiments in Case A, and 11020 N/mm², which is calculated by considering the increase by drying as 2% at 1% moisture content increase.

3 RESULTS

3.1 HEAT AND WATER TRANSFER ANALYSIS

3.1.1 TEMPERATURE AND MOISTURE CONTENT

Figs.3,4 show the calculation results of temperature and moisture content at the initial moisture content of 13.7% and 30.4%, respectively.

Regarding temperature, temperature rise stagnates due to the latent heat of water evaporation and thermal decomposition. The temperature fluctuations at high temperatures result from temperature falls when the heat generation of each element stops. In other words, the fluctuation results from the discretisation of the space. Thus, the temperature transition is smooth if the elements are made finer, or in reality.

The influence of the initial moisture content on the charring rate of wooden members due to fire heating can be represented in the calculation. Comparing the temperature transitions under the two cases, the temperature increase was fast at low initial moisture content. Fig.5 shows that the charring rate calculated with temperature reached 260° C. The charring rate was determined as the gradient of the charring depth with respect to the time to reach 260°C when the intercept was set to 0. These values of the charring rate are also shown in Table 1. The difference in the charring rate was caused by the difference in the latent heat of water evaporation. Comparing the charring rate derived from the calculation

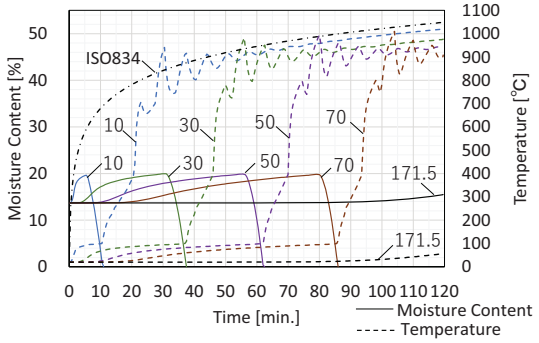

Figure 3: *Results of the calculation of temperature and moisture content at the initial moisture content of 13.7%*
(The values indicate distance from the heated surface)

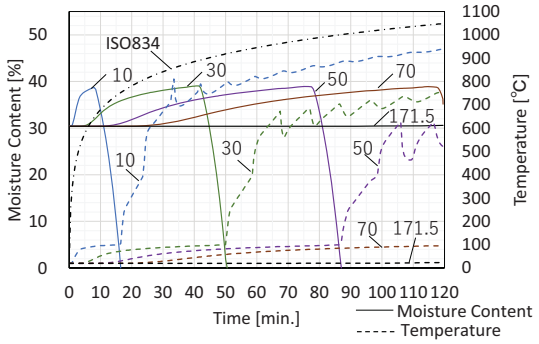

Figure 4: *Results of the calculation of temperature and moisture content at the initial moisture content of 30.4%*
(The values indicate distance from the heated surface)

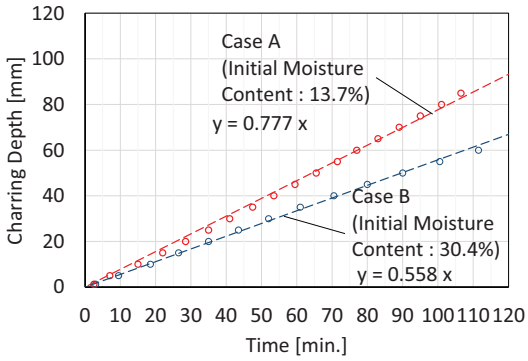

Figure 5: *Calculation results of the charring rates*

and the experiments, the agreement of the results was good. In the two cases, the charring rate was a little higher than the value of the charring rate in the experiments. However, this calculation method should be improved in the future because limits of the heat oxidation made agreement of the charring rate.

Moisture content was increased with temperature increase in the two cases. Maximum moisture content was 20.0% and 39.1%, for the initial moisture content of 13.7% and 30.4%, respectively.

Moisture content of the elements 10, 30, 50, and 70mm from the heated surface increased once and subsequently decreased due to evaporation. Moisture content increased of the elements near the heated surface and, with a

https://doi.org/10.52202/069179-0210

relatively large moment of inertia, decreased the overall bending stiffness. Conversely, the moisture content of the element closest to the non-heated surface also increased gently. Moisture content increased in the area away from the heated surface and at a relatively low temperature, indicating a decrease in the mechanical properties due to moisture content in the areas bearing the load during and after fire heating.

In the calculation method formulated in this study, the maximum moisture content of each element immediately before evaporation was almost constant for each initial moisture content. The amount of increase in moisture content was 19.6 ~ 20.0% and 38.6 ~ 39.1% by the end of evaporation for initial moisture content of 13.7% and 30.4%, respectively. These upper limits of moisture content increase were determined by water adsorption, temperature increase, vapour pressure increase, and difference in vapour pressure decrease. Specifically, when water adsorbs, the latent heat gradually increases the temperature until just before evaporation. Vapour does not flow into the element itself when vapour pressure becomes higher just before evaporation. Moisture content increases only by a small extent at the temperature just before evaporation. As evaporation begins, moisture content starts decreasing. Since it takes a long time for evaporation to start, the amount of increase in moisture content was greater with higher initial moisture content.

These time variations of moisture content should be compared and verified with experimental results. However, the method that can measure local moisture content with electric resistance cannot accurately measure at conditions of high moisture content. For instance, the upper measurement limit in [2] is shown as 30%. Thus, the measurement method at high moisture content conditions should be developed in the future.

3.1.2 TOTAL PRESSURE AND VAPOUR PRESSURE

Figs.6,7 show the calculation results of total pressure and vapour pressure at the initial moisture content of 13.7% and 30.4%, respectively. The stepped transitions resulted from sudden falls of vapour pressure when evaporation in each element was over. Since these discontinuous behaviours are due to the discretisation of the space, vapour transitions are smooth if the elements are made finer or in reality.

Vapour pressure is the highest in the element where evaporation occurs, and the vapour transfer is caused by the difference in vapour pressure. Vapour transferring to a heated surface is released to ambient air. Vapour transferring to an unheated surface causes an increase in the relative humidity to 100% and water adsorption.

Total pressure is the same as the atmospheric pressure at initial moisture content conditions and increases with vapour pressure. Total pressure of the element closest to the unheated surface gradually increases because the boundary condition of the unheated surface was similar to the adiabatic condition.

Comparing the two cases, the maximum values of vapour pressure are almost equal because vapour pressure is limited by saturated vapour pressure, and saturated vapour pressure is calculated with temperature and evaporation

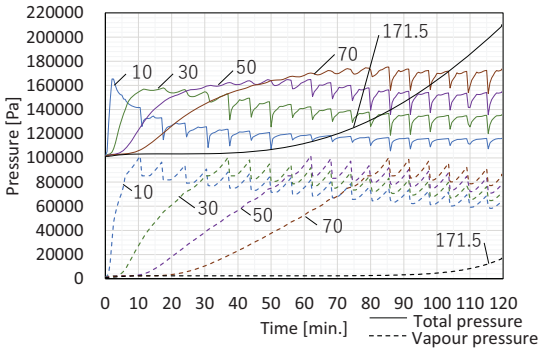

Figure 6: *Results of the calculation of total pressure and vapour pressure at the initial moisture content of 13.7%*
(The values indicate distance from the heated surface)

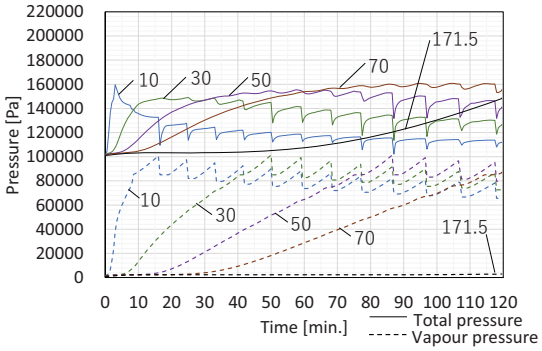

Figure 7: *Results of the calculation of total pressure and vapour pressure at the initial moisture content of 30.4%*
(The values indicate distance from the heated surface)

temperature, which is the same in the two cases. Total pressure of the element closest to the unheated surface at the initial moisture content of 13.7% is higher because temperature and saturated vapour pressure are higher.

3.2 MECHANICAL PROPERTIES

3.2.1 MOMENT OF INERTIA

Fig.8 shows the time variation of the moment of inertia in the two cases. Sudden falls of the moment of inertia occur because mechanical properties are considered 0 when the temperature of each element reaches 260°C.

The moment of inertia remains low as the initial moisture content is low. Comparing the moment of inertia at 82 minutes when the column buckled in the experiment, Case

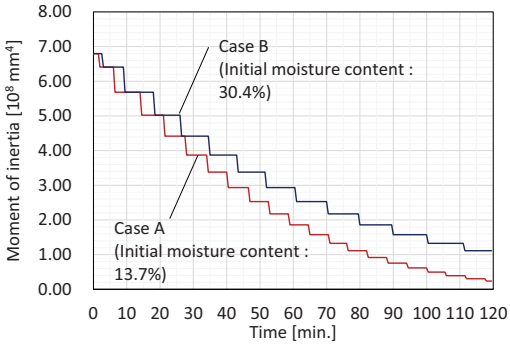

Figure 8: *Calculation Results of time variation of the moment of inertia*

https://doi.org/10.52202/069179-0210

B has 1.67 times more remaining than Case A.

3.2.2 BUCKLING TIME

Figs.9,10 shows the calculation results of buckling time at the initial moisture content of 13.7% and 30.4%, respectively. Buckling time is also shown in Table 1. Buckling time in the calculation was regarded as the period after which the smoothed curves of the load-bearing capacity fell below the load. The smoothed curves were drawn in order to estimate buckling time accurately. The smoothed curves were the result of averaging the calculation results of a total of 11 points every 30 seconds, adding 5 points before and after. Not-smoothed calculation results fell suddenly with changes in the moment of inertia. Additionally, elements close to the heated surface may temporarily recover Young's modulus due to evaporation. If the space is not discretised, the load-bearing capacity of the entire cross-section will not recover temporarily but will gradually decline.

There are two calculation results in Figs.9,10. The blue plots were calculated by considering temperature and moisture content dependence on Young's modulus.

Conversely, the red plots considered only temperature dependence in such a way as to evaluate the influences of moisture content. These temperature and moisture content are derived from the calculations of heat and water transfer in Section 3.1.

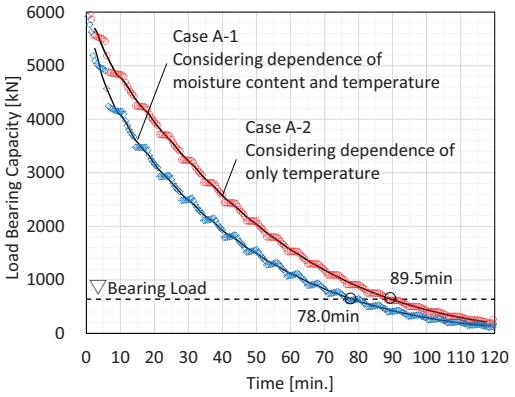

Figure 9: *Calculation results of buckling time at the initial moisture content of 13.7%*
(The plots indicate calculation results every 30 seconds, and the solid lines indicate calculation results after smoothing)

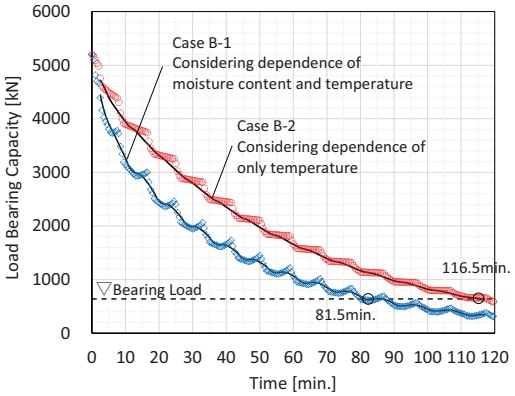

Figure 10: *Calculation results of buckling time at the initial moisture content of 30.4%*
(The plots indicate calculation results every 30 seconds, and the solid lines indicate calculation results after smoothing)

In both cases, the load-bearing capacity decreased when moisture content dependence was considered. The longest buckling time was 116.5 min in Case B-2 because the moment of inertia was greater, and moisture content dependence was not considered. Comparing the case with and without consideration of moisture content (Cases A-1 vs A-2 and B-1 vs B-2), the difference in the buckling time was 11.5 min and 35 min at the initial moisture content of 13.7% and 30.4%, respectively. The load-bearing capacity was further reduced at a high temperature and high moisture content; hence the difference in the buckling time was larger when the initial water content was higher.

In Table 1, comparing the buckling time derived from the experimental results and the calculation in this study (Cases B-1,2 vs the experiment), the buckling time was estimated to be almost the same or slightly earlier with consideration of moisture content. Conversely, for the condition of no consideration of moisture content, the buckling time was evaluated much to be later than that derived from the previous experiments. Therefore, when the initial moisture content is high, the buckling time is assumed to be long except for the condition of consideration of moisture content dependence.

In Fig.10, comparing the buckling time in the case with and without consideration of moisture content (Cases B-1 vs B-2), the difference in buckling time was 35 minutes, and both evaluated the buckling time to be earlier than that derived from previous experiments. The load-bearing capacity was 562kN and 627kN at 82 minutes when the column buckled in the experiment in Cases B-1 and B-2, respectively. This difference is insignificant compared to the difference in the moment of inertia (1.67 times). Although the cross-section remains large due to the high initial moisture content, the decrease in Young's modulus due to the high moisture content is large. Therefore, buckling time does not change significantly.

In conclusion, buckling time can be predicted with heat and water transfer analysis and consideration for moisture content dependence of Young's modulus. Moreover, as a result of the calculation considering the positive and negative influence of moisture content on charring rate and Young's modulus, both effects largely cancelled out in these cases. However, the balance of both effects will change if the calculation conditions change. Considering that Young's modulus decreases as the moisture content increases at room temperature, we conclude that initial moisture content is desired to be controlled in an air-dry state as before.

In the future, the study of other tree species is desired because the behaviour of heat and water transfer and the influence of moisture content differ among tree species. Furthermore, the study of collapse for reasons other than buckling is important to predict the collapse time of wood members other than columns.

https://doi.org/10.52202/069179-0210

4 CONCLUSIONS

This study predicted the buckling time of a Japanese zelkova column exposed to fire heating using heat and water transfer analysis. The results were compared with those of a previous study [6]. The calculations were conducted under two conditions, at the initial moisture content of 13.7% and 30.4%, to evaluate the following positive and negative effects of high initial moisture content: decrease in the charring rate and decreasing of the mechanical properties at a high temperature and high moisture content.

(1) An increase in the moisture content caused by water evaporation, transfer, and re-condensation was represented. Moisture content increased from 13.4% to 20.0% and from 30.4% to 39.1% at most, respectively.

(2) The phenomenon that the higher the initial moisture content, the slower the carbonisation rate was represented by calculation. The agreement between the calculated charring rate and that derived from the previous experiment was good; however, the heat oxidation was intentionally limited so as to reproduce the remaining sectional area.

(3) The buckling time was predicted by considering the dependence of mechanical properties not only on temperature but also on moisture content. Considering the dependence of the mechanical properties of wood members on temperature and moisture content, the calculated buckling times were similar to or slightly faster than the experimental results. Conversely, considering the dependence of the mechanical properties of wood members on temperature alone, the calculated buckling times were longer. Thus, the buckling time should be calculated by considering the moisture content dependence at high initial moisture content.

(4) Under this calculation condition, the effect of the high initial moisture content on slowing down the charring rate and decrease in the mechanical properties of the remaining cross-sectional area of wood members were largely cancelled out by the following results: although the moment of inertia was 1.67 times at 82 minutes when the column buckled in the experiment, buckling time changed by only 3.5 minutes.

In the future, the behaviour of water transfer at high initial moisture content should be measured, compared, and verified after the development of the measurement method. Furthermore, there is a need to conduct this study by considering other tree species; additionally, researchers should also study the collapse of wood members due to reasons other than buckling.

Symbols and Greeks

c	heat capacity [kJ/(kg·K)]
D	diffusion coefficient [m^2/s]
E	Young's modulus[N/mm^2]
e_r	emissivity [-]
h_c	convective heat transfer coefficient [$kW/(m^2 \cdot K)$]
h_v	vapour transfer coefficient [m/s]
I	moment of inertia
K	specific permeability [m^2]
L	latent heat [kJ/kg]
L_k	buckling length
M	moisture content [-]
M'	molecular weight [kg/kmol]
P	pressure [Pa]
P_k	load
q_{rad}	radiant heat [kW/m^2]
Q	heat generation [kW/m^3]
R	rate of water desorption [$kg/(m^3 \cdot s)$]
T	temperature [°C]
$\overline{T}$	absolute temperature [K]
t	time [s]
u	apparent velocity of gas filtration [m/s]
ε	void fraction [-]
κ	Darcy's permeability [$m^2/(Pa \cdot s)$]
λ	thermal conductivity [W/(m·K)]
ρ	density [kg/m^3]
ρ_{ture}	true density [kg/m^3]

Subscripts

amb	ambient air on heated surface
char	char
decomp	decomposition
desorp	desorption
dry	bone-dry state
evap	evaporation
g	gaseous mixture
max	maximum value
ox	char oxidation
v	vapour
w	water
wood	wood
0	initial

REFERENCES

[1] Namiki J., Hasemi Y., Suzuki T., Watanabe S. and Takase R. : Measurement of Time Variation of Moisture Content within Timbers under Steady and Unsteady Heating Conditions In *World Conference on Timber Engineering*, Santiago, Chile, 2021.8.

[2] Fredlund B.：A Model for Heat and Mass Transfer in Timber Structures During Fire. Lund University Sweden, 1985, Ph.D. thesis

[3] Suzuki T., Hasemi Y., Kamikawa D., Yasui N. and Kaku C. : Developmet of Moisture Content Sensor for Wooden Members Exposed to Fire Heating and Measurement of Moisture Content Distribution during Fire Heating. In *World Conference on Timber Engineering*, Santiago, Chile, 2021.8.

[4] Forest Products Laboratory：Wood Handbook，Capter 5，pages5-34 ~ 5-37，2021.3.

[5] Suzuki T., Hasemi Y., Kamikawa D., Yasui N., Kaku C. and Watanabe S. : Development of an Equation Calculating Young's Modulus Remaining Ratio with Temperature and Moisture Content within Wooden Members Exposed to Fire Heating. Journal of Structural and Construction Engineering

https://doi.org/10.52202/069179-0210

(Transactions of AIJ), 85(770):651-661, 2020.4 (in Japanese)
[6] Yasukawa M., Yasui N., Suzuki A., Hasemi Y., Kameyama N., Toyoda K., Kadooka, N., Kamilawa D., Koshihara M. and Ono T.: Experiments for the Verification of the Predict Ability of Structural Fire Resistance of Heavy Hard Wood (Zelkova) Columns. Journal of Structural and Construction Engineering (Transactions of AIJ), 685:633-638, 2013.3 (in Japanese)
[7] Forest Products Laboratory：Wood Handbook，Capter 18，pages18-15 ~ 18-16，2021.3.
[8] Suzuki T. and Hasemi Y. :Heat and Water Transfer Analysis for Influence of Moisture Content on Buckling Capacity in Wooden Column during Fire Heating. In *Annual Meeting of Japan Association for Fire Science and Engineering*, pages126-127, Japan, 2021.5. (in Japanese)
[9] Suzuki T., Namiki J., Hasemi Y., Takase R., Kamikawa D., Yasui N. and Kaku C. : Measurement of Distribution of Temperature and Moisture Content within Wooden Plate under Steady Heating and Numerical Reproduction with Heat and Water Transfer Analysis. Journal of Environmental Engineering (Transactions of AIJ), 85(778):891-901, 2020.12 (in Japanese)
[10] Suzuki T. and Hasemi Y. : Improvement of the Model for Heat and Water Transfer in Wooden Member Exposed to Fire Heating (Part1) Problems of the Model and Improvements on Adsorption/Desorption Rate. In *Annual Meeting of Architectural Institute of Japan*, pages239-240, Japan, 2021.9. (in Japanese)
[11] Chatani, Y. et al. : Measurements of Char Oxidation Rate of Glued Laminated Larch Timber Materials during post Fire Heat Exposure Period, Journal of Environmental Engineering (Transactions of AIJ), 82(736):491-499, 2017.6 (in Japanese)
[12] Forest Products Laboratory：Wood Handbook，Capter 4，page4-14，2021.3.
[13] Forestry and Forest Products Research Institute : Wood Industrials handbook, p834, Maruzen, 1958.12. (in Japanese)
[14] Kollman, F. : Technologie des Holzes und der Holzwerkstoffe, Springer, Berlin, Heidelberg,1955.8. (in Germany)
[15] Yokota, T. : Calculation of Diffusion Coefficient of Moisture Through Cr.miferous Woods, Bulletin of the Forestry and Forest Products Research Institute, Vol.173, pages167-175, 1965.2. (in Japanese)
[16] Kawabe J. and Mori M. : Transverse Air Permeability in Fifteen Wood Species, Journal of the Society of Materials Science, The Society of Materials Science, Japan, pages918-924, 1985.8. (in Japanese)
[17] Harada K., Kajiyama K., Yusa S., Uesugi S. and Namiki K. :Numerical Analysis of Charring Behavior of Wood-based Constructions, Summaries of technical papers of AIJ Kinki Chapter research meeting, pages209-212, 2004.5. (in Japanese)
[18] Forestry and Forest Products Research Institute : Wood Industrials handbook (the revised 4th edition), p85, 2004.3. (in Japanese)

World Conference on Timber Engineering Oslo 2023

HEAT DELAMINATION IN CROSS LAMINATED TIMBER: INTERMEDIATE SCALE TEST BASED UPON THE NORTH AMERICAN STANDARDS

Samuel L. Zelinka[1], Keith J. Bourne[2], Laura E. Hasburgh[3], Kara Yedinak[4]

ABSTRACT: Currently, the North American standard, ANSI/APA PRG 320: *Standard for Performance-Rated Cross-Laminated Timber*, requires a full-scale compartment fire test to qualify adhesives for use in cross laminated timber (CLT) for structural applications. This test is necessary to determine whether the adhesives will experience heat delamination - a premature adhesive failure during fire that can lead to sudden fire regrowth during the decay phase of a fire commonly referred to as a secondary flashover.

The required full-scale test is cost-prohibitive to adhesive manufacturers when developing new adhesive formulations. This paper presents work performed at the Forest Products Laboratory (FPL) focused on developing a low-cost intermediate scale test used to predict if a new adhesive formulation is likely to delaminate and, therefore, fail the full-scale PRG 320 test. In the FPL method, a 2.44 m long by 610 mm wide CLT panel is exposed to a time-temperature profile in a furnace designed to match the PRG 320 test. Additionally, the mechanical loads are scaled to target the bending moment in the PRG 320 test standard. New findings presented in this conference paper include measurements of the oxygen concentration within the furnace during the test.

KEYWORDS: fire performance of CLT, adhesives for CLT, PRG 320

1 INTRODUCTION

Cross laminated timber (CLT) is being rapidly adopted in North American buildings [1-3]. Changes to the International Building Code (IBC) have allowed increases to the height and area limits for CLT buildings [4-6]. The IBC requires that the CLT complies with the ANSI/APA PRG 320: *Standard for Performance-Rated Cross-Laminated Timber* [7] (hereafter referred to as PRG 320) which specifies test methods and minimum performance requirements for CLT panels.

One unique aspect of the PRG 320 standard that was added in the 2018 Edition is the requirement for a full-scale compartment fire test to demonstrate that the adhesive between laminations does not fail during a fire scenario.

Heat delamination, hereafter shortened to delamination, occurs when the adhesive fails as the bond line is exposed to higher temperatures prior to the char front reaching the adhesive bond line during a fire scenario. In 2017, a series of full-scale fire tests on CLT compartments was conducted. During this test series, delamination occurred in unprotected (exposed) CLT surfaces in four of the 6 tests [8-11]. Based on data from thermocouples embedded in the CLT walls, delamination occurred prior to the char front reaching the bond line. In these tests, delamination resulted in a "second flashover"; a rapid increase in temperature that occurred during the decay phase of the fire after delamination exposed fresh, uncharred wood.

Since a second flashover creates unpredictable conditions during a compartment fire, it was decided that North American CLT must not delaminate during fire scenarios [12]. A test to evaluate adhesive performance at elevated temperatures was developed and adopted as Annex B test of the PRG 320 standard. The Annex B fire test involves a full-scale, non-combustible room with a CLT ceiling in which a natural gas burner creates conditions such that the ceiling temperatures closely match those observed in early CLT compartment fires where delamination was observed [8]. An external mechanical load is applied to the CLT ceiling and an adhesive is considered to pass the Annex B test if delamination is not observed during the 4-hour test. Following the development of the Annex B test, more large-scale fire testing has been conducted with adhesives that passed the Annex B test and delamination resulting in secondary flashover was not observed[13,14].

Despite the straightforward nature of the PRG 320 Annex B test, the test method does have some drawbacks. The biggest drawback of the method is the cost. The test is costly to run because it requires a full-scale compartment

[1] Samuel L. Zelinka, Forest Products Laboratory, United States, Samuel.L.Zelinka@usda.gov
[2] Keith J. Bourne, Forest Products Laboratory, United States, Keith.J.Bourne@usda.gov
[3] Laura E. Hasburgh, Forest Products Laboratory, United States, Laura.E.Hasburgh@usda.gov

[4] Kara Yedinak, Forest Products Laboratory, United States, Kara.Yedinak@usda.gov

https://doi.org/10.52202/069179-0211

to be constructed for each test. Furthermore, since the test geometry is different from ASTM/ISO standards, it requires laboratories to build a unique set up prior to testing. These costs have made it difficult to screen new adhesive formulations.

Previous work by the authors introduced an intermediate furnace scale test that could be used to screen new adhesives or CLT panel layouts [15]. (See Section 2 for more details on this method). The previous work evaluated CLT panels constructed with identical adhesives and layups at two scales (intermediate- and full-scale). The intermediate-scale tests had approximately 1 m^2 of exposed CLT whereas the full-scale tests conducted in accordance with PRG 320 has approximately 12 m^2 of exposed CLT [16]. In these tests, panels that delaminated at the full-scale were also observed to delaminate at the intermediate-scale. Likewise, no delamination events were observed in intermediate-scale panels that passed the full-scale test. Finally, temperatures measured within the furnace closely followed temperature profiles measured in the full-scale PRG 320 compartment fire tests.

While the previous work of Zelinka and Bourne [15] showed comparable results between the intermediate- and full-scale tests, several important questions remain regarding the utility of the method and its correlation to full-scale tests. In this paper, we examine the oxygen concentration within the furnace during the intermediate-scale tests and compare it to data collected in full scale compartment fire testing. It is part of a larger effort to develop a low-cost intermediate scale test used to predict if a new adhesive formulation is likely to fail the full-scale PRG 320 test.

2 MATERIALS AND METHODS

2.1 Materials

Several different types of CLT were tested. The adhesives used, lumber species, lumber grade, and performance in the full-scale test are included in Table 1. All specimens were 5-ply with a nominal thickness of 175 mm. The specimens were cut to 610 mm wide by 2.44 m long. Specimens were placed on top of a 1.83 m long furnace such that approximately 1.11 m^2 of mass timber was exposed to the fire in the test. Three replicates were tested for each panel configuration.

Table 1: *Panel information for the mass timber panels tested in both the intermediate and full-scale delamination test.*

Adhesive[1]	Species/grade[2]	Pass full-scale test?
MF	Douglas fir/larch V1	Y
PUR-1	SPF/E1	N
PUR-2	SPF/E1	Y
PUR-3	SPF/V2	Y

[1]MF= melamine formaldehyde, PUR=polyurethane
[2]SPF=spruce, pine, fir species group. Grades E1 and V2 are defined in the PRG 320 standard [7].

2.2 Specimen Instrumentation

Thermocouples were installed in most of the specimens to monitor the thermal profile during the exposure. From the fire-exposed side of the specimen, thermocouples were typically installed halfway through the first ply, at the first bond line, halfway through the second ply, and at the third bond line. Similar arrays were located near the center of the specimen and on each side approximately 0.61 m from the center.

Because many of the CLT specimens were commercially produced, installation of thermocouples during layup was not possible, so they were installed through 2.4-mm-diameter holes drilled from the unexposed side of the CLT. These thermocouples were made in-house from 30-gauge type K thermocouple wire (Omega Engineering GG-K-30-SLE) with welded junctions.

2.3 Panel mechanical loading

According to PRG 320 Annex B, section B9, 'The superimposed load on the CLT floor-ceiling slab shall result in 25% of the effective Allowable Stress Design (ASD) reference flatwise bending moment.' To achieve this, a scenario with two symmetrical and equal load points 0.813 m apart was implemented. For that loading scenario, the maximum bending moment occurs at the point of application of each load and the maximum shear stress is equal to the load at each actuator. With the end supports located just outside the furnace the clear span is 2.34 m with a heated length of 0.99 m. The overall specimen length of 2.44 m allows for a bearing area beyond the contact point.

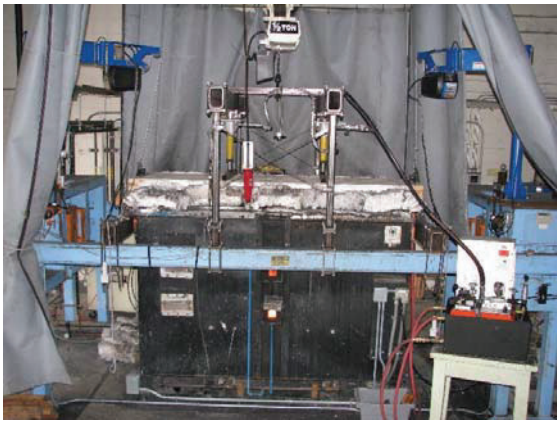

Figure 1: *Photograph of a panel being tested with the Forest Products Laboratory (FPL) intermediate-scale test method. The panel is loaded on a test frame built around a furnace. Two hydraulic actuators apply a mechanical load to match the bending moment prescribed in the standard.*

2.4 Thermal profile

An intermediate scale furnace located at FPL was used to conduct the experiments (Figure 1). The furnace is a metal box lined with ceramic fiber batting and has interior dimensions of 1.83 m long, 1.09 m wide and 1.27 m high.

Eight diffusion flame burners are located on the floor of the furnace and the top of the furnace is open to accommodate a variety of specimen and lid configurations. Suspended 102 mm below the bottom of the specimen face are 3 thermocouples made from 20-gauge type K thermocouple wire (Omega Engineering GG-K-20-SLE). The thermocouples are insulated with ceramic beads with the junction left exposed. These thermocouples approximate the measurement taken by the 5 ceiling thermocouples in the full scale PRG-320 test. Additional furnace details can be found in [13].

In the PRG 320 fire test, a calibration to determine the fuel flow rate necessary to achieve a specified hot gas layer temperature in the compartment is conducted prior to the qualification test. The calibration is run using a diffusion burner in the test compartment and the CLT ceiling is covered with 3-layers of gypsum wall board to create an essentially non-combustible room. While recording the gas flow rate, the burner is used to achieve an average ceiling temperature that matches the ceiling temperature profile measured in the 2017 compartment fire test series where delamination occurred. Upon completion of this 4-hour calibration run, the gypsum wallboard is removed to expose the CLT ceiling and the qualification test is conducted by running the diffusion burner with the same gas flow rate as the calibration run.

The thermal profile for the FPL intermediate scale test method was created using the same approach as the full-scale PRG fire test. First, for the calibration run, a non-combustible lid was placed on the furnace and was controlled so that the thermocouple temperatures within the furnace matched the temperature profile within the PRG 320 standard. Subsequent tests, with CLT samples were run by controlling the gas flow to match the gas consumed in the non-combustible control test. Figure 2 compares the temperatures measured in the intermediate scale furnace against the specified temperatures in the PRG-320 standard.

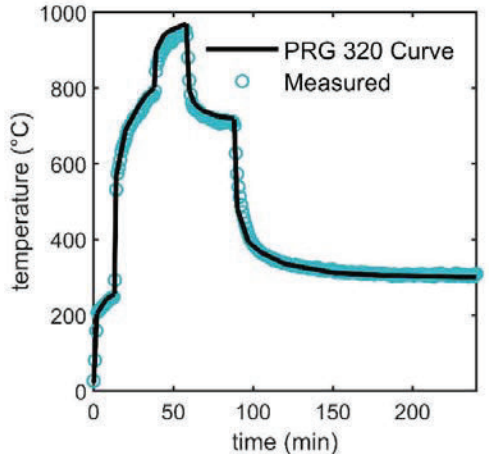

Figure 2: *PRG 320 specified temperature profile plotted against the measured temperature within the furnace with an inert lid.*

2.5 Oxygen measurements

To learn how oxygen concentrations may be affecting combustion within the furnace, measurements were taken in two locations: the exhaust duct and at 100 mm below the centre of the CLT specimen, location A and B in Figure 3, respectively. It is cost-prohibitive to sample multiple points simultaneously, so samples were taken in repeated experiments.

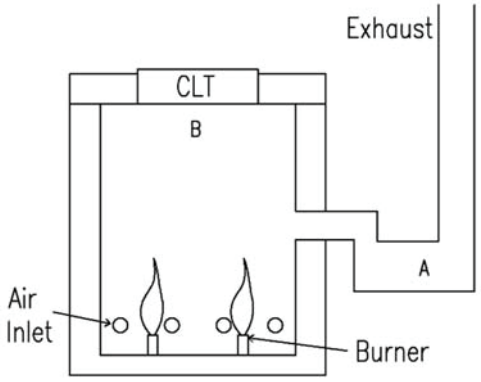

Figure 3: *Schematic of cross section of furnace showing oxygen sample location in exhaust stream (A) and 100 mm below CLT sample (B).*

A sample is continuously drawn from the sample point, either below the CLT specimen or in the exhaust stream. The sample is then passed through a glass wool pre-filter, a heat exchanger, a filter and a drier (Sable Systems ND2 Gas Sample Drier) before being measured. Oxygen measurements were made using a paramagnetic oxygen analyser (Sable Systems PA-10). A pump is located downstream of the oxygen analyser driving the flow. The flow rate is less than 200 ml/min, which is not expected to have significant effect on the temperature or flow inside the furnace.

3 RESULTS

3.1 Temperature Results

Figure 4 shows how the temperature within the furnace during each test compares against the full-scale PRG 320 test results. In Figure 4, the full-scale results are plotted as a blue line, and the intermediate-scale results are shown as a dashed grey line. Three replicates were tested for each adhesive type; all three replicates are plotted as separate grey dashed lines. The solid black curve is the time-temperature curve from the calibration with no-exposed CLT. The figure illustrates the increase in temperature in the furnace due to the fuel contribution from the exposed CLT.

https://doi.org/10.52202/069179-0211

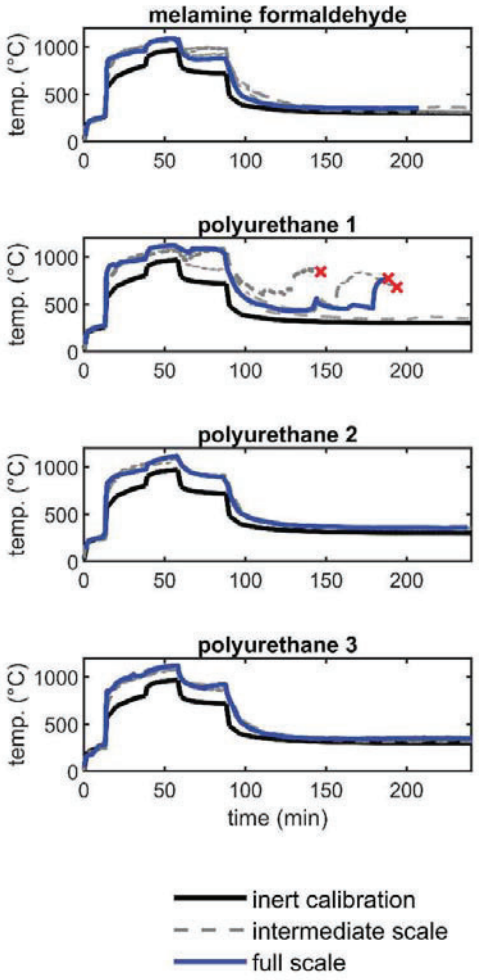

Figure 4: *Comparison of the furnace/compartment ceiling temperatures in the full-scale PRG 320 testing (blue) and intermediate scale test (dashed grey line). The black curve represents the temperature curve with no exposed CLT. The red "x" represents a test terminated due to failure.*

Delamination was observed for the panels constructed with PUR-1 in both the intermediate- and full-scale tests. In these tests, the temperature exhibits an increase during the final phase of the test when the furnace/compartment is cooling. Further evidence of delamination was visually observed from the camera pointed at the furnace floor (Figure 5). For the panels with PUR-1, a significant amount of charred wood material was observed on the furnace floor at 90 and 120 minutes when compared to the other panels types. The furnace tests on CLT with PUR-1 were terminated before the full 240-minute limit to avoid flame through the CLT panel that could cause damage to the loading actuators.

Good correlation was observed between the intermediate- and full-scale temperature results, especially for the panels made with PUR-2 and PUR-3. In two of the three panels with PUR-1 tested at the intermediate-scale, delamination occurred which caused a rapid rise in temperature between 120 and 200 minutes. In the third replicate, the temperature in the furnace increased after 200 minutes, but did was not a full delamination event.

The correlation between the intermediate- and full-scale tests can be most easily seen in Figure 6, which plots the residual of the temperature between the intermediate- and full-scale tests. The data show that the furnace temperature was very close to the compartment temperature for the panels made with PUR-2 and PUR-3. However, for the MF panels, the temperature in the furnace test was higher than in the compartment which was most prominent between 50-120 minutes.

3.2 Oxygen Results

Initial oxygen measurements were taken with inert insulation blocks in place of the CLT specimen. The reduction of oxygen, illustrated in Figure 7, compared to atmospheric levels corresponds to the amount of gas being consumed by the burners. In both measurement locations the lowest concentration is measured during the high temperature portion of the curve between 48 and 58 minutes. It is during this portion of the test that the biggest difference between the measurement locations is observed as well. In location A in the exhaust, the oxygen concentration went as low as 10.5%. At location B near the center of the exposed specimen surface the oxygen concentration was briefly observed to go below 1%. The oxygen concentration curves between each location are very similar before 15 minutes into the test and again after 58 minutes.

https://doi.org/10.52202/069179-0211

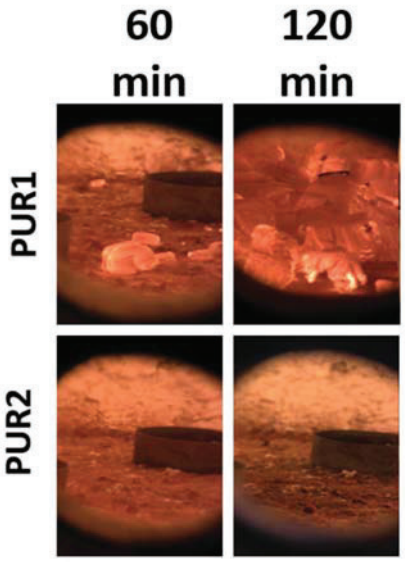

Figure 5: *Images of the furnace floor at 60 and 120 minutes into the test for polyurethane 1 (PUR1) and polyurethane 2 (PUR2).*

The low oxygen concentrations measured in the furnace are expected. Brandon and Dagenais [17] reported that it is important to match the oxygen concentrations within a furnace and compartment when developing a furnace test. They reported that in the 2017 compartment fire tests where delamination was observed, the oxygen concentration was nearly zero during the peak heat release period of the test and worked to mimic that in their furnace test by limiting the oxygen concentration between 15-80 minutes of their 180 minute test [8,17].

This data suggests that there may be adequate oxygen supply in the furnace to support combustion of wood specimens in all but the hottest portions of the test. Furthermore, it shows that there is a large difference in oxygen concentration throughout the furnace. It is measured quite low near the sample surface, the exhaust measurement is essentially an average, so the concentration must be higher somewhere else in the furnace.

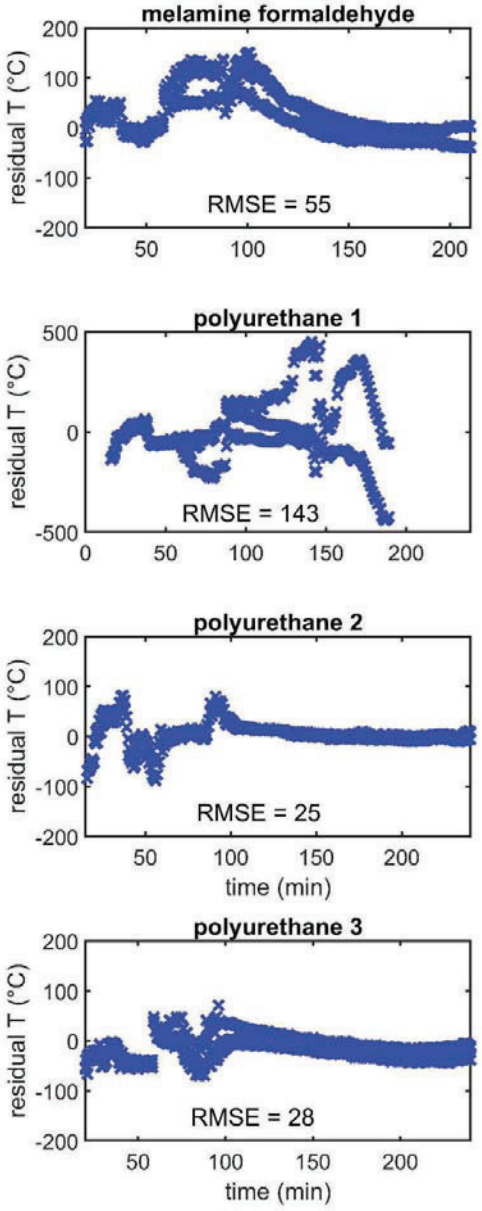

Figure 6: Plots of the temperature residuals calculated by subtracting the *full-scale* test temperature from the intermediate scale test temperature. RMSE = root mean square error calculated from the entirety of the test.

https://doi.org/10.52202/069179-0211

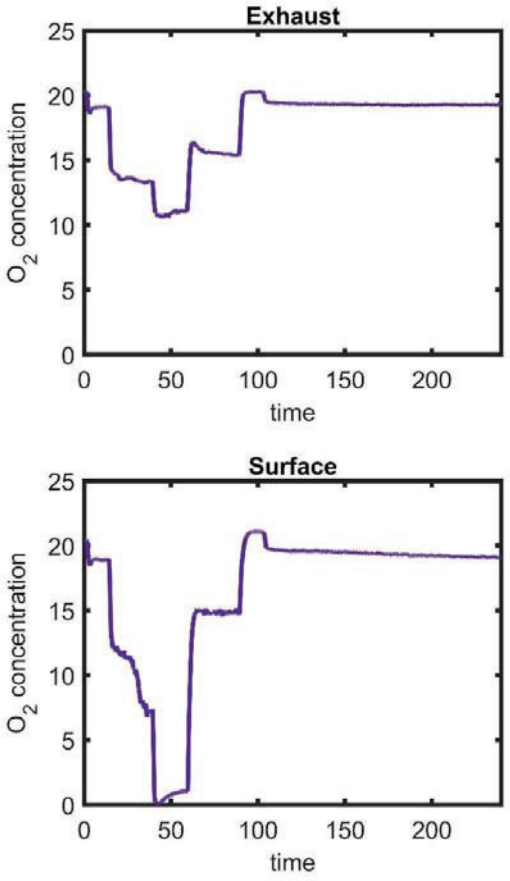

Figure 7: *Comparison of oxygen concentration in exhaust (labelled "Exhaust") versus 100 mm below specimen (labelled "Surface") when experiment is run with inert specimen in place of CLT specimen.*

The low oxygen concentrations measured in the furnace are expected. Brandon and Dagenais [17] reported that it is important to match the oxygen concentrations within a furnace and compartment when developing a furnace test. They reported that in the 2017 compartment fire tests where delamination was observed, the oxygen concentration was nearly zero during the peak heat release period of the test and worked to mimic that in their furnace test by limiting the oxygen concentration between 15-80 minutes of their 180 minute test [8,17].

This data suggests that there may be adequate oxygen supply in the furnace to support combustion of wood specimens in all but the hottest portions of the test. Furthermore, it shows that there is a large difference in oxygen concentration throughout the furnace. It is measured quite low near the sample surface, the exhaust measurement is essentially an average, so the concentration must be higher somewhere else in the furnace.

It is useful to compare the oxygen concentrations measured in this experiment to previous work where oxygen concentrations were measured in furnace tests. Schmid et al. [18] also examined the oxygen concentrations within a furnace during the testing of a CLT panel, although with a standard fire curve [19] rather than the PRG 320 fire curve. Schmid et al. also noted differences between the concentration of oxygen near the panel surface (which was near zero) and the exhaust of the furnace, which was found to vary between 5 and 10% [18]. Future work (See Section 4) will examine how these measured oxygen concentrations change when a wood panel is exposed to the PRG 320 time-temperature curve and how delamination affects the oxygen concentration both near the panel surface and in the furnace exhaust.

4 FUTURE WORK

In the future we intend to repeat the oxygen measurements with CLT specimens made with two different adhesives; one that we have previously observed to delaminate and one that has not. We will then be able to observe what effect the presence of a wood specimen has on the oxygen environment as well as the effect delamination has on the oxygen concentration.

5 CONCLUSIONS

This research aims to develop an intermediate scale test method that can be used to predict adhesive delamination under fire scenarios. The results demonstrate a good correlation between measured furnace temperatures and temperature measured near the ceiling in the full-scale PRG 320 tests that have been conducted.

Additionally, panels made with adhesives that passed the full-scale test also passed the intermediate scale test. Panels made with adhesives that failed the full-scale tests also failed in the intermediate-scale test with the exception of one replicate.

Oxygen measurements taken during the intermediate scale test show very low oxygen concentrations near the burning CLT specimen, which is similar to the oxygen concentrations measured in full-scale CLT compartment fire tests.

ACKNOWLEDGEMENTS

The authors acknowledge funding from Bostik, Inc. and experimental assistance from John Minter and Eleanor Q. Daniels. The findings and conclusions in this report are those of the author(s) and should not be construed to represent any official United State Department of Agriculture (USDA) or U.S. Government determination or policy.

REFERENCES

1. Jakes, J.E.; Arzola, X.; Bergman, R.; Ciesielski, P.; Hunt, C.G.; Rahbar, N.; Tshabalala, M.;

Wiedenhoeft, A.C.; Zelinka, S.L. Not Just Lumber—Using Wood in the Sustainable Future of Materials, Chemicals, and Fuels. *JOM* **2016**, *68*, 2395-2404.
2. Lehmann, S. Sustainable construction for urban infill development using engineered massive wood panel systems. *Sustainability* **2012**, *4*, 2707-2742.
3. Green, M.; Karsh, J. *TALL WOOD- The case for tall wood buildings*; Report prepared for the Canadian Wood Council on behalf of the Wood Enterprise Coalition and Forest Innovation Investment.: Vancouver, BC, 2012.
4. Anon. *International Building Code*; Delmar Cengage Learning: Florence, KY, 2021.
5. Zelinka, S.L.; Hasburgh, L.E.; Bourne, K.J.; Tucholski, D.T.; Ouellette, J.P. *Compartment fire testing of a two-story mass timber building. General Technical Report FPL-GTR-247*; U.S. Department of Agriculture, Forest Service, Forest Products Laboratory: Madison, WI, 2018; pp. 60.
6. Zelinka, S.L.; Hasburgh, L.E.; Bourne, K.J. Overview of North American CLT Fire Testing and Code Adoption. In *Wood & Fire Safety. Proceedings of the 9th International Conference on Wood & Fire Safety 2020*, Osvaldova, L.M., Markert, F., Zelinka, S.L., Eds. Springer International Publishing: 2020; 10.1007/978-3-030-41235-7_35pp. 232-237.
7. Anon. *ANSI/APA PRG 320: Standard for Performance Rated Cross-Laminated Timber.*; APA- The Engineered Wood Association.: Tacoma, WA, 2018.
8. Su, J.; Lafrance, P.-S.; Hoehler, M.; Bundy, M. *Fire Safety Challenges of Tall Wood Buildings – Phase 2: Task 2 & 3 Cross Laminated Timber Compartment Fire Tests*; Fire Protection Research Foundation: Quincy, MA, 2018.
9. Mitchell, H.; Kotsovinos, P.; Richter, F.; Thomson, D.; Barber, D.; Rein, G. Review of fire experiments in mass timber compartments: Current understanding, limitations, and research gaps. *Fire and Materials* **2023**, *n/a*, doi:https://doi.org/10.1002/fam.3121.
10. Pettersson, C. Fire Safety in Timber Buildings- A review of existing knowledge. *BRANDFORSK* **2020**, *10*.
11. Brandon, D.; Östman, B. *Fire Safety Challenges of Tall Wood Buildings – Phase 2: Task 1 - Literature Review*; Fire Protection Research Foundation: Quincy, MA, 2016.
12. Barber, D.; Craft, S.T. Proposed testing methodology to determine CLT heat delamination. An open letter to the PRG-320 committee. (unpublished). 2017.
13. Su, J.; Leroux, P.; Lafrance, P.-S.; Berzins, R.; Gratton, K.; Gibbs, E.; Weinfurter, M. *Fire testing of rooms with exposed wood surfaces in encapsulated mass timber construction*; National Research Council of Canada. Construction: 2021/10/07, 2021.
14. Dagenais, C.; Ranger, L.; Benichou, N. Improved fire performance of cross-laminated timber. In Proceedings of Proceedings of the 2021 World Conference on Timber Engineering, Santaigo, Chile, August 9-12, 2021.
15. Zelinka, S.L.; Bourne, K.J. Intermediate-Scale Laboratory Method to Qualify Heat-Delaminating Adhesives for Use in Cross-Laminated Timber. *Forest Products Journal* **2022**, *72*, 216-225, doi:10.13073/fpj-d-22-00031.
16. Janssens, M. *Development of a fire performance assesment methodology for qualifying cross-laminated timber adhesives. SwRI Project No.01.23086.01.001a*; Southwest Research Institute: San Antonio, TX, 2017.
17. Brandon, D.; Dagenais, C. *Fire safety challenges of tall wood buildings- Phase 2: Task 5- Experimental study of delamination of cross laminated timber (CLT) in Fire*; National Fire Protection Research Foundation: Qunicy, MA, 2018.
18. Schmid, J.; Lange, D.; Sjostrom, J.; Brandon, D.; Klippel, M.; Frangi, A. The use of furnace tests to describe real fire of timber structures. In Proceedings of World Conference on Timber Engineering, Seoul, South Korea, August 20-23, 2018.
19. Anon. *ASTM E119 Standard Test Methods for Fire Tests of Building and Construction Materials*; American Society for Testing and Materials: West Conshohocken, PA, 2014.

https://doi.org/10.52202/069179-0211

World Conference on Timber Engineering Oslo 2023

A NEW METHOD FOR MODELLING TEMPERATURE WITHIN STEEL BAR - TIMBER COMPOSITE BEAM USING DATA BY BURNING TEST

Shizuka Matsushita[1], Shinichi Shioya[2]

ABSTRACT: In light of the current climate crisis, there has been much recent interest in using timber structural members in large buildings, since timber is as renewable natural resource, and moreover, in severe earthquake prone zones, such as Japan, they are more desired on the grounds of light weight of timber members. We are developing a frame system formed by hybrid timber members reinforced with deformed steel bars (i.e. rebars) using epoxy resin adhesive. In order to practice the system, it is necessary to investigate fire resistance performance of the members. We conducted a 60-minute burning test of one specimen of the composite beam. The results will be reported in this WCTE2023[1]. This paper proposes a method for modelling temperature within beam specimen by using finite data obtained by the burning test.

KEYWORDS: Fire, Burning margin, Hybrid timber, Deformed steel bar, Beam

1 INTRODUCTION [3 4 5]

S.Shioya, (author [2]), has proposed a structural system for building construction, adopting Hybrid Glulam Timber members using Steel bars (HGTSB, nicknamed "Samurai" in Japan) [2]. Three-buildings were built with the system. One of them adapted two HGTSB beams, for a trial, at 11th floor of high-rise building, with a refractory coating authorized as two-hour fireproof timber for HGTSB beam, constructed in Tokyo, Japan, in February 2020.

On the other hand, semi-fireproof design method using burning marginal layer (charring layer) for HGTSB is strongly desired for low-rise and middle-rise buildings. In Japan, HGTSB member is defined as a new kind of structural member; Japan Building Standards Law does not allow application of general semi-fireproof design method using burning marginal layer to HGTSB member; several burning tests of beam and column, which are loaded with maximum weight of long-term design, are requested. However, difficulties of practice of the burning test pose at the point of test machine capacity and selection of failure mode of beam during its burning, because bending capacity of HGTSB beam is approximately 3-4 times as much as that of conventional Glulam beam.

The key to the solution of the difficulties is to develop new method for modelling temperature distribution within beam using several finite data of temperature measured during the burning test. The position and the number of the measuring points need to be selected so as to prevent bending capacity and shearing capacity of the beam from deteriorating. Thus, the new method is need. Moreover, verification of the capacity calculated using the modelled temperature distribution and reduction ratio of strength and elasticity of wood of beam is necessary to be conducted by using capacities obtained by loading during the beam burning test.

We conducted 60-minute-burning test of a timber-steel rebar composite beam and will report its outline and experimental results in WCTE2023[1]. This paper reports results of temperature variation inside the glulam timber and a new concept of modelling of temperature within the beam with finite measured temperature data.

2 OUTLINE OF BURNNING TEST

Details of burning test will be described in Literature 2 in this WCTE2023. Please refer to it. Outline of the test is described below.

2.1 SPECIMEN

Figure 1 illustrates measured cross-sections of specimen and a resisting area in the section expected after 60-minute burning. Figure 2 (in next page) illustrates a side view of the specimen and positions of foil strain gauge and thermocouple. Figure 3 illustrates 4 cross-sections of the specimen and positions of thermocouples in each cross-section. Main cross-section of beam is section II-IV with

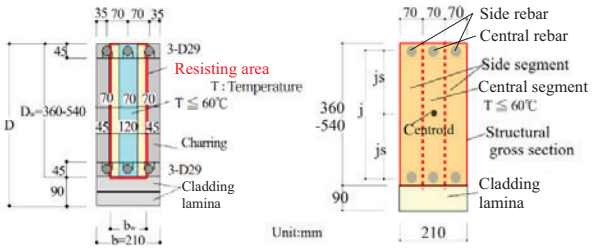

(a) Cross-Section (b) Resisting portion

Figure 1: *Cross-section and resisting segment and area after 60 - minute burning*

[1] Shizuka Matsushita, Department of Architecture, Kagoshima University, Japan, k7422990@kadai.jp
[2] Shinichi Shioya, Department of Architecture, Kagoshima University, Japan, k7347039@kadai.jp

https://doi.org/10.52202/069179-0212

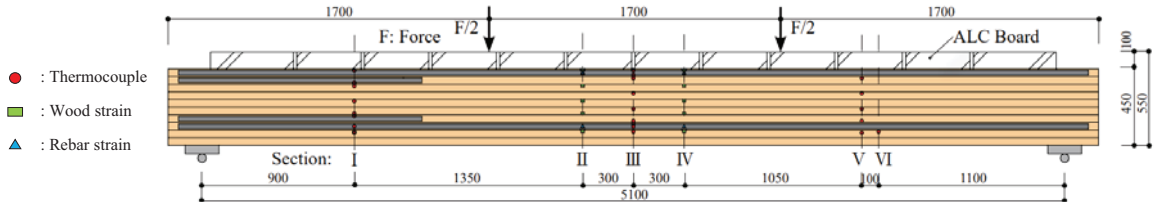

Figure 2: *Side view of specimen and positions of strain gauge and thermocouple*

one tier rebar lamina, in which 3 rebars were embedded, on upper and lower of beam cross-section. The left-hand section I was prepared to investigate effects of the amount and the number of rebars on elevated temperature of wood during burning. The lamina is Cryptomeria Japonica; lamina composition of beam is adhered to Japanese Agricultural Standard E65-F225. Rebar diameter is D29(diameter=29mm) and its grade is SD390(Nominal yielding strength: 390N/mm^2). Adhesive is typical resorcinol resin adhesive for laminating laminas.

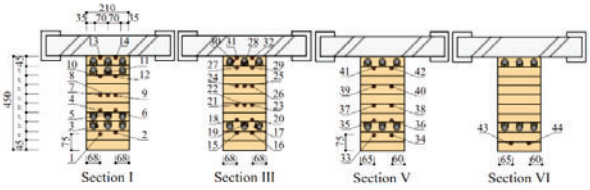

Figure 3 : *Cross-section measured in specimen and positions of thermocouple*

2.2 STRAIN AND TEMPERATURE MEASUREMENT

In Figure 2, locations of thermocouples are shown. Strain in wood and temperature of rebar were measured. Numbering of mark "No." is for thermocouple.

2.3 LOADING

Loading employed four-point bending such as the side view of specimen shown in Figure 2; magnitude of bending moment at mid-span of the specimen was selected to be value of allowable moment for long-term selected to be value under long-term loading design. Value of shearing force of both side shear spans was 10% higher than its allowable shear force for long-term loading design. Force/F.

2.4 HISTORY OF TEMPERATURE

The burning test was conducted on September 28, 2021 at 13:00 (its room temperature: 25.6℃) in a combustion furnace (ISO843-1 compliant furnace) at the Japan Testing Center for Construction Materials. During introducing initial force, deflections and strains in the elastic range were measured. Temperature during 60-minute burning test was controlled to adhere to ISO-fire exposure temperature curve. To capture capacity of the specimen by loading to fracture, a burning time of 5 minutes and 20 seconds after 60-minute burning passed was added; temperature of furnace was maintained at a constant temperature (945℃) by combustion.

3 CHANGE IN TEMPERATURE OF WOOD AND REBAR WITHIN GLULAM TIMBER DURING BURNING

Figure 4, Figure 5, and Figure 6 in the next page show the temperature variation of each measuring point. Figure 6(g) shows the variations of all measuring points for each section; Figure 4 shows that of section I and Figure 5 shows that of section III. The number on curves refers to the number of the measuring point in Figure 6(g); RC refers to the center rebar; RS dose to the side rebar; Va dose to a measured point at which temperature was presumed to increase due to water vapor generated by burning of wood.

Cal.1, Cal.2, and Cal.3 are curves based on an estimation method proposed in Chapter 4. Timber is a natural material, and thicknesses and densities of spring woods and autumn wood are not the same. Timber is not a uniform material to begin with. As the temperatures were measured at one point, it is necessary to analyse trend of temperature variation based on the assumption that the conditions of the material around the measuring point will be slightly different even at same depth from surface of timber, and that there will be some variation in the measured data.

3.1 UPPER LAMINA ENBEDDED WITH REBAR

Figure 4 (b) and Figure 5(b) show temperature variation of the upper lamina.

31V_a and 32V_a in Figure 5(b) show that the temperatures increased rapidly in 20-30 min, maintained about 90°C for 30-50 min, and increased slowly thereafter.

The cause is assumed to be that deflection at mid-span increased space between the upper surface of beam and the ALC board over beam, allowing hot air and flame to penetrate, causing the temperature there to rise quickly and water vapor from the burning of the timber to be suspended. Although RC28V_a was in the same lamina, the temperature rise was extremely slow, but according to Figure 5(f), the rate of rise was faster than that of RC19, i.e., the central rebar at the lower. That time was almost the same as the time when 31Va and 32Va rose rapidly and reached about 90°C.

https://doi.org/10.52202/069179-0212

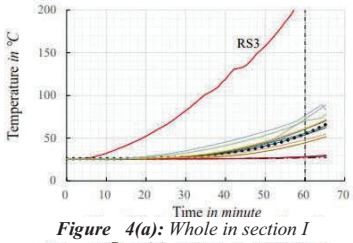

Figure 4(a): *Whole in section I*

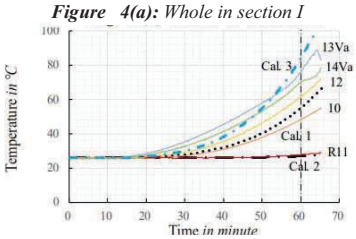

Figure 4(b): *Upper in section I*

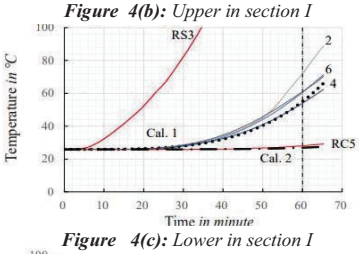

Figure 4(c): *Lower in section I*

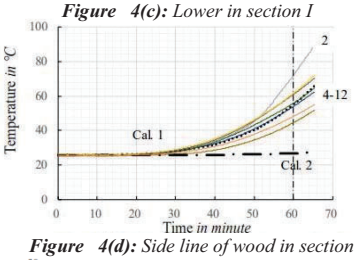

Figure 4(d): *Side line of wood in section I*

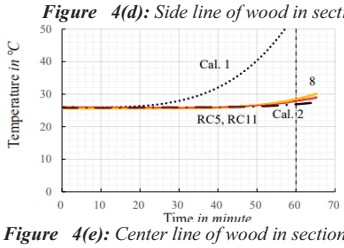

Figure 4(e): *Center line of wood in section I*

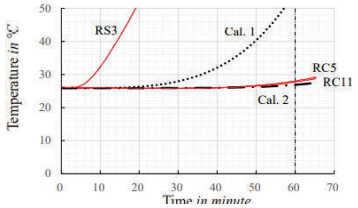

Figure 4(f): *Rebar in Section I*

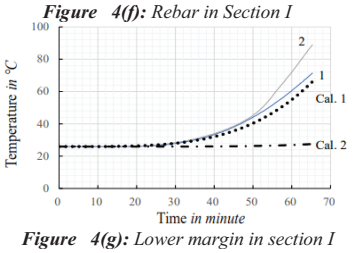

Figure 4(g): *Lower margin in section I*

Figure 4: *Variations of temperatures in section I*

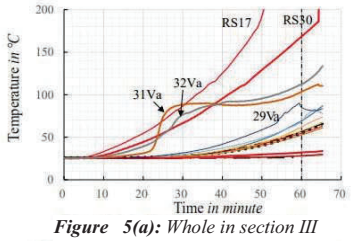

Figure 5(a): *Whole in section III*

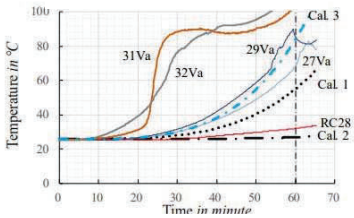

Figure 5(b): *Upper in section III*

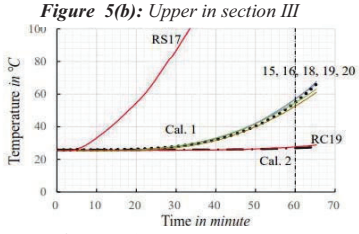

Figure 5(c): *Lower in section III*

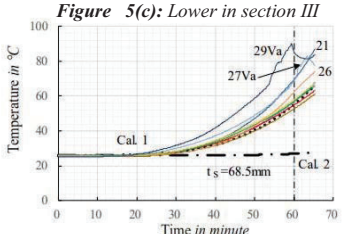

Figure 5(d): *Side line of wood in section III*

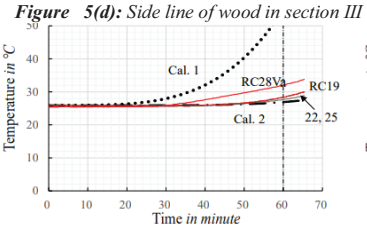

Figure 5(e): *Center line of wood in section III*

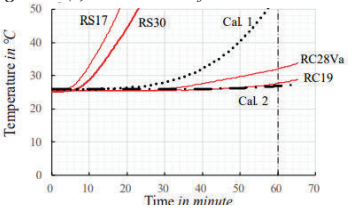

Figure 5(f): *Rebar in Section III*

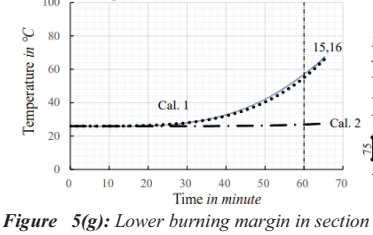

Figure 5(g): *Lower burning margin in section III*

Figure 5: *Variation of temperatures in section III*

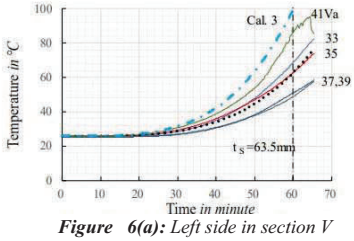

Figure 6(a): *Left side in section V*

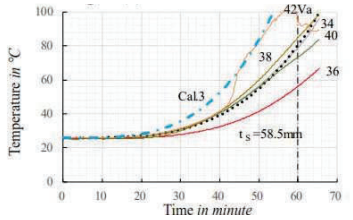

Figure 6(b): *Right side in section V*

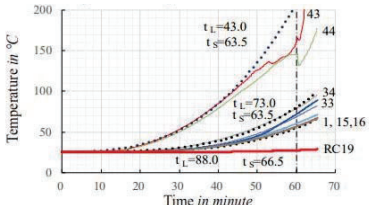

Figure 6(c): *Lower burning in section I, III, V, and VI*

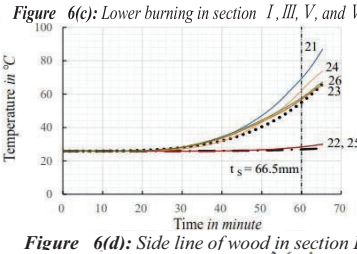

Figure 6(d): *Side line of wood in section III*

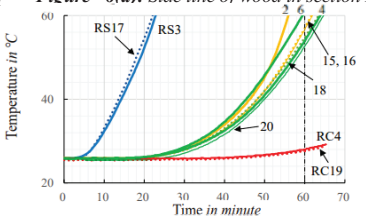

Figure 6(e): *Lower in section V*

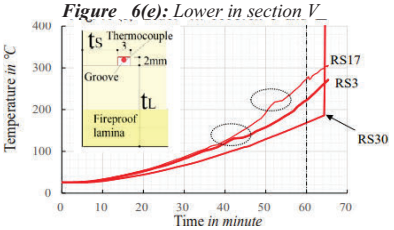

Figure 6(f): *Rebar in section V*

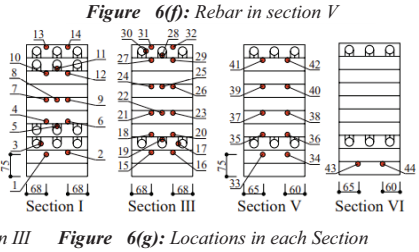

Figure 6(g): *Locations in each Section*

Figure 6: *Variations of temperatures in Section in V, etc.*

https://doi.org/10.52202/069179-0212

A similar trend was observed for $13V_a$ and $14V_a$ in Figure 4(b), but it is less pronounced than for $31V_a$ and $32V_a$ in Figure 5(b). The reason may be that section I had a resulting in a slower rate of temperature increase. $27V_a$ and $29V_a$ in Figure 5(d), 41Va in Figure 6(a), and $42V_a$ in Figure 6(b) are also considered to be affected by the same effect.

3.2 LOWER REBAR LAMINA

Figure 4(c) and Figure 5(c) show temperature variation of the lower rebar lamina. Temperatures of the side rebars/RS3 and RS17 increased rapidly after 6 minutes. In Figure 4(g), temperature of 2 at section I was 72°C at 60 minutes. In Figure 6(e), temperatures of wood (4,6,15,16,18,20) at border of lower rebar lamina of the central segment of except for the 2 were below 60°C. This demonstrates that the lower border of the central column segment in Figure 1(b) is almost suppressed below 60°C.

3.3 WEB

The points have a horizontal depth/t_s (see Figure 6(f)) of 68.5 mm. t_s is horizontal depth from the side surface of beam to the width of the groove (3 mm) where the thermocouple is placed. Figure 6(a) shows the temperature variation at the border with t_s of 63.5 mm in cross-section V and Figure 6(b) shows the temperature variation at the border with t_s of 58.5 mm in the same cross-section. As t_s decreased, temperature increased in 60 minutes, and except for 36 at 58.5 mm in Fig. 6(b), the temperatures were above 70°C. Figure 5(d) shows temperature variation from 21 to 26 in cross- section III. In contrast to the temperatures at t_s of 68.5 mm (21, 23, 24, 26), temperature at center of the width (22, 25) in Figure 5(e) hardly increases at all. Even if there is some difference in the temperature variation at the border of the central segment width 70 mm, temperature near the center of the width decreases rapidly, and effect of the variation on the center rebar is considered to be small.

From the above discussion, it can be judged acceptable to calculate the capacity of the center segment as less than 60°C, except for upper surface of the rebar lamina at top of beam as mentioned in Section 3.1.

3.4 EFFECT OF THICKNESS OF CLADDING LAMINAS TO THE LOWER PORTION

Figure 6(c) shows temperature variation of the cladding lamina. The vertical depth /t_L (Figure 6(f)) of 43 and 44 in cross-section VI from the lower surface was 43.0 mm, thus reaching 150°C in 60 min; t_L of 33 and 34 in cross-section V was 73.0 mm, thus 69 ° C and 79°C, respectively; t_L of 15 and 16 in section III was 88.0 mm, thus both were 57°C. The t_L of 15 and 16 in cross-section III was 88.0 mm, so they were both suppressed to 57°C. RC19, the central rebar near the lower of cross-section III, was 27.6°C, hardly increasing from the initial 25.6°C. The center of the rebar in RC19 was almost 105 mm deep from both the lower surface and side surface of beam, and it can be concluded that that depth suppressed the temperature increase.

Figure 6(d) shows temperature variation of 21-26 of web of the cross-section III. 21, 23, 24, and 26 at the boundaries of the central segment were 56-68°C in 60-minute, while 22 and 25 in the middle of the beam width were both 28 ° C, hardly any increase in temperature. Considering this, the same depth from the lower at the width-middle position may be also quite low, close to 28°C, because 33 and 34 in cross-section V were 69°C and 79°C, respectively as mentioned above. These results suggest that even with a thickness of 75 mm of cladding laminas, the increase in temperature of the central rebar at the bottom of beam is suppressed in a 60-minute burn. However, from the viewpoint of providing extra strength for 60-minute burning, it is desirable to keep the depth from the lower surface to the central rebar close to 105 mm, which is the same depth from the side surfaces.

3.5 EFFECT OF HEAT CAPACITY OF TWO-TIER REBAR

Because the large heat capacity of the two-tier rebar in cross-section I, 10 and 12 in Figure 4(b) were less affected by water vapor than $31V_a$, $32V_a$ in cross-section III in Figure 5(b), and the temperature of 10 and 12 is considered to have remained below 60°C after 60 minutes. On the other hand, the rebar lamina at the lower is not affected by water vapor, and Figure 6(e) shows the temperature variation of the lower lamina, comparing the two-tier/RS3 and one-tier rebar/RS17. The data for the two-tier rebar are shown as blue thick solid lines, while the data for the one-tier rebar are shown as blue dotted lines. The positions close to each other in both cross-sections are shown in the same colour. In some cases, the temperature increase is slightly slower in the cross-section of the two-tier rebar. In the side rebar shown in Figure 6(f), RS3 of the two-tier rebars rose more slowly than RS17 of the one-tier rebars, but the effect of the two-tier rebar in suppressing the temperature was not very promising.

4 CONCEPT FOR MODELLING TEMPERATURE WITHIN BEAM

The portion of wood contributing to bending capacity and shearing capacity of beam is uncharred portion. In this study, the scope limits the uncharred portion and the aim is to formulate the amount of variation in wood temperature/T from room temperature/T_r before the burning test to wood char temperature/T_c, using data of temperature measured during the burning on test.

https://doi.org/10.52202/069179-0212

4.1 FORMULATION OF TEMPERATURE-RELATIVE DISTANCE CURVE FROM CHARRING-BORDER TO A MEASURING POINT

As shown in Figure 7(a), we assume that charring border is proceeding at a constant charring rate/v_c and that measuring point/m is in the direction of the border progressing. In reality, the charring border approaches the point/m, but from the perspective of the charring border, the point/m can be considered to be approaching with a relative velocity/v_c toward. The distance/S between the point/m and the charring border is expressed by Equation (1).

$$S=d_m-v_c\cdot t \tag{1}$$

where d_m is distance between surface of beam and the measuring point/m *in mm*; v_c is charring rate *in mm/minute*; t is time of fire exposure *in minute*.

Figure 7(b) illustrates schematically relationship between temperature/T and distance/S at the measuring point/m after burning time/t passing. The distance/S decreases with the time/t, and the distance/S and the temperature/T can be plotted, yielding a T-S curve. Temperature/T of wood at the start of burning is assumed to be room temperature/T_r, which increases with the progress of charring and reaches charring temperature/T_c. The distance/S is equal to distance/d_m, at the start of burning and to zero, at reaching the charring temperature/T_c.

These two points are designated as x= d_m, y= T_r and x=0, y= T_c in Figure 7(b). These points are to be boundary points at both ends of the T-S curve, which rises linearly with decreasing S for the measuring point closer to the charring border, and rises more slowly at the beginning of burning and rises more rapidly as the charring border approaches for the more apart points.

The T-S curve can be approximated by normalizing the distance/$v_c\cdot t$ of charring progression by the distance d_m of each measuring point and by normalizing the temperature increase/ (T- T_r) by (T_c - T_r); normalizing the coordinate axes as shown in Figure 8. As results, the T-S curve is represented by Equation (2). Substituting x and y in Equation (3) into Equation (2), T is represented by Equation (4).

$$y=x^n \tag{2}$$

$$\text{where, } x=(v_c\cdot t/d_m),\quad y=(T-T_r)/(T_c-T_r) \tag{3}$$

$$T=T_r+(T_c-T_r)\cdot(v_c\cdot t/d_m)^n \tag{4}$$

4.2 EXPONENT/*n* BASED ON HARADA'S DATA

Harada et al. [3] reported a 45-minute loaded burning test on Abies sachalinensis Glulam timber beam to investigate the fire resistance performance of them, and measured temperature of the beam in detail. The model proposed above is applied to the temperature-time curves measured on the beam specimen PRF-b in the literature [3].

Specimen/PRF-b was glued with the same phenol-resorcinol resin adhesive. Figure 10(a) in the next page shows the temperature-time curve measured on PRF-b. The beam cross section and temperature measuring points

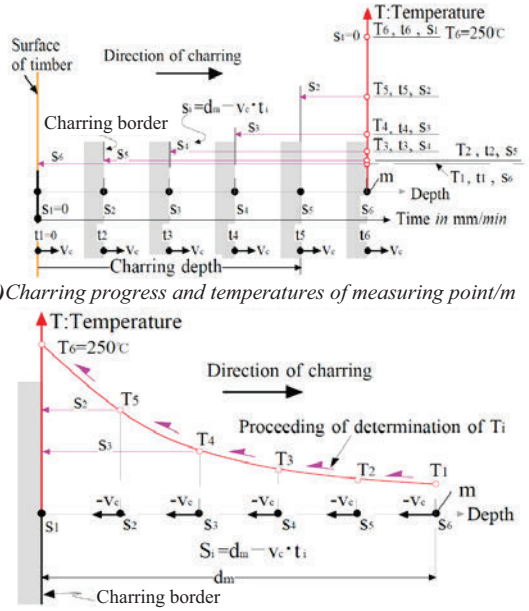

(a)Charring progress and temperatures of measuring point/m

(b)T-S curve of measuring point 'm'

Figure 7: *A new concept for estimation of temperature distribution in uncharred region of wood in timber*

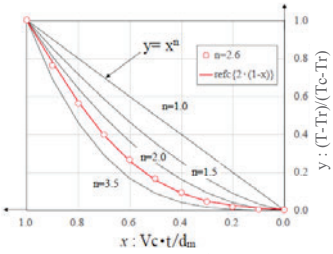

Figure 8: *Curves by Eq.(2)*

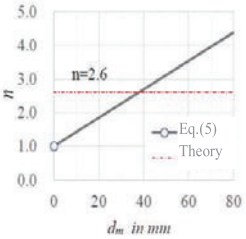

Figure 9: *Changing by Eq.(5)*

are shown in the upper left corner of Figure 10(a). The dotted line in the Figure represents experimentally measured temperature curve.

The T-S curve drawn using S by Equation (1) is shown by coloured thin solid line in Figure 10 (a)and(b). The exponent/n was determined so that the calculated value of temperature in Equation (4) conforms to the experimental curve. The charring temperature/T_c was assumed to be 300°C and the charring rate/v_c was set at 0.65 mm/min. The results are shown as ○ in Figure 10(c).

The y-axis is the exponent/n, and the horizontal axis is the depth/d_m. The exponent/n approaches 1.0 at zero for d_m and tends to change linearly with increasing d_m. Approximating the change with Equation (5), the coefficient/k was 0.0323.

$$n=1.0+k\cdot d_m \tag{5}$$

where k is assumed to be 0.0425 in 1/ mm

As dimensions of beam cross-section increase, exponent/n may differ from the straight line in Equation (5). It is expected to converge to a coefficient based on

https://doi.org/10.52202/069179-0212

temperature distribution during combustion of semi-infinite solid.

However, as the burning test for performance evaluation constrains cross-section dimension to be safe for burning and focus on the measured temperature data, it is out of the scope of this study to identify the convergence value.

In this study, it is enough if the exponent/n can be estimated in a form that allows the change in temperature measured in the burning test to be estimated. The T-S curve calculated with the coefficient/k in Equation (5) as 0.0323 as described above is shown in Figure 10(b) as a thin solid curve. The temperature/T - time/t curve is also shown in Figure 10(a) as a thin solid curve. The curves are coloured by the same colour for each measuring point. The rate of increase of the dotted curve was slower than the rate of the calculated curve at the temperature of 100℃, because moisture in wood becomes water vapour. In the temperature range above 120-140 °C and up to a charring temperature of 300 °C, the temperature of the calculated curves is on the safe side in terms of evaluating beam's resistance during burning, although in some ranges they are estimated to be higher than the experimental temperatures. The correspondence between measured and calculated T-S curves in Figure 10(b) is similar to that in Figure 10(a). The same study also reported the measured data of the test specimen PRF-a, which was glued together using the same adhesive with a lamina thickness of 22 mm in the cross-section in Figure 10(a), and the calculated curve for that was also confirmed to be a similar correspondence with the measured curve.

Although the coefficient/k is likely to depend on dimensions of specimen and its wood species, it can be concluded that the proposed method can be applied to historical data of temperature of burning test to model its temperature variation.

4.3 EXPONENT "*n*" BASED ON THE TEST

Figure 11 shows T-S curves based on data from each measuring point in this test. It is shown up to the end of the burning test; Figure 11(e1) shows the T-S curve for rebars. In this study, amount of loading was selected for the cross-section of the one-tier rebar at the middle of the span, so the exponent/n in Equation (4) was determined to fit the temperature data for cross-sections III, V and VI. The result adopted 0.0425 (1/mm) of n.

The charring temperature/T_c was assumed to be 250°C, T_r was assumed to be 25.6°C, the internal temperature before the burning test, and the charring rate v_c was assumed to be 0.65 mm/min with reference to Eurocode 5.

On the basis of the above approach, various constants were specified.

Figure 8 in the previous page shows the curves for varying n in Equation (2). Symbol '○' indicates the calculated value when n was assumed to be constant value of 2.6. Red curve in Figure 8 is the curve of the complementary error function (y=erfc(2-(1-x)) of the equation for the theoretical solution of temperature inside the semi-infinite solid during burning.

The ○ and red curves are almost identical, which means that Equation (2) can also approximate the curve of the equation of its theoretical solution, within the range of application. Figure 9 shows the variation of the exponent n according to Equation (5) with k of 0.0425. When d_m is close to zero, the shape of the T-S curve becomes steeper as surface of timber charrs at the initial burning, so approximating temperature with a straight line is not a major problem.

4.4 TEMPERATURE VARIATION AND COEFFICIENT/ *k*

Value of the coefficient k in Equation (5) was selected to minimize the standard error between the temperature measured at each position and the value calculated using Equation (4) for Figure 11 (b1), (c1), (c2) and (d1) of the cross section of the one-tier rebar during 60-minute burning.

In this case, the value that minimizes the standard error for the data of cross-section III where the temperature closest to the border of the central segment in Figure 1(b) was measured, was found to be 0.0425.

The d_m of each measuring point in wood was assumed to be the smaller distance between the horizontal depth/t_s and the vertical depth/t_L shown in Figure 11(a1), taking into account dimensions of the thermocouple groove.

Table 1 in the next page lists measured temperatures, their standard deviation/SD, calculated values, and their standard error/SE of the calculated values relative to the measured values for Figure 11 (b1), (c1), and (c2), where t_s (here equal to d_m) is the same for each position.

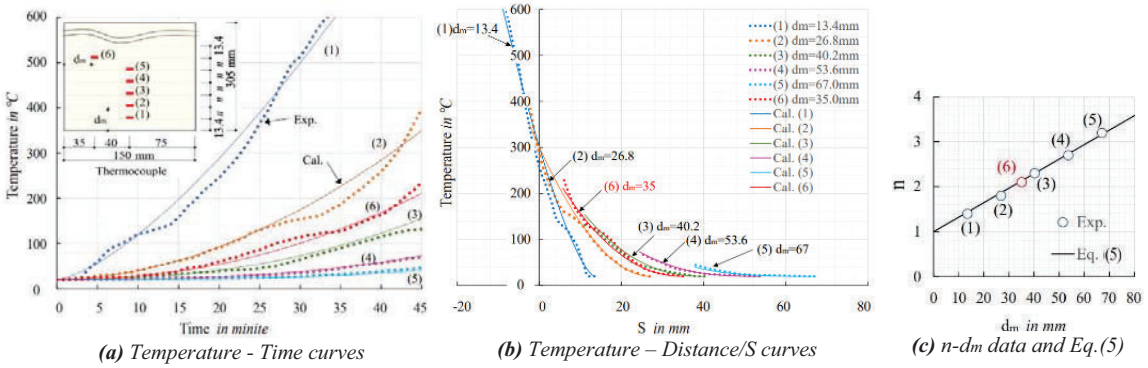

(a) *Temperature - Time curves* ***(b)*** *Temperature – Distance/S curves* ***(c)*** *n-dm data and Eq.(5)*

Figure 10: *Temperature – Time relationship of specimen/PRF-b of Harada's burning test for Japanese Abies* [3]

https://doi.org/10.52202/069179-0212

The position closest to the border of the central segment is Figure 11(b1), i.e., t_s=66.5mm, and the calculation error/SE for Equation (4) is 2.21°C. As temperature within the central segment is lower, its standard error is small.

Figure 11(d1) shows two positions (t_s=58.5, 63.5mm, t_L=75mm) of the cladding lamina in cross-section V. The measured values are almost the same change, which is almost estimated by the red calculated curve. Figure 11(d2) shows a cross-section VI with a depth t_L of 43 mm from the bottom surface, which is the position where charring will take place and where the temperature becomes high, as can be seen in Figure 12(b). Above 100°C, the temperature calculated by the curve is higher than the measured value. However, above 100°C, the reduction in the strength of wood is extremely large [4], and estimating the capacity of beam on the safe side is not a problem.

4.5 TEMPERATURE OF UPPER LAMINAS

Figure 11(a3), (b3) and (c3) show variation of temperature of upper surface of beam and wood on the underside of the rebar lamina immediately below it. Temperatures at the upper surface of beam/13V_a, 14V_a, 31V_a, 32V_a, indicate the temperature affected by water vapor, as thermocouples at the measuring points were in direct contact with the water vapor that might be stayed as mentioned above. Wood temperatures are estimated to be close to the temperature directly below the rebar lamina, i.e., 27V_a, 28V_a, 29V_a, 41V_a, 42V_a. Red one-dot curve in the Figures is curve of the calculated value according to Equation (4). The curve underestimates temperature of the wood directly below the rebar lamina (e.g., 27V_a as

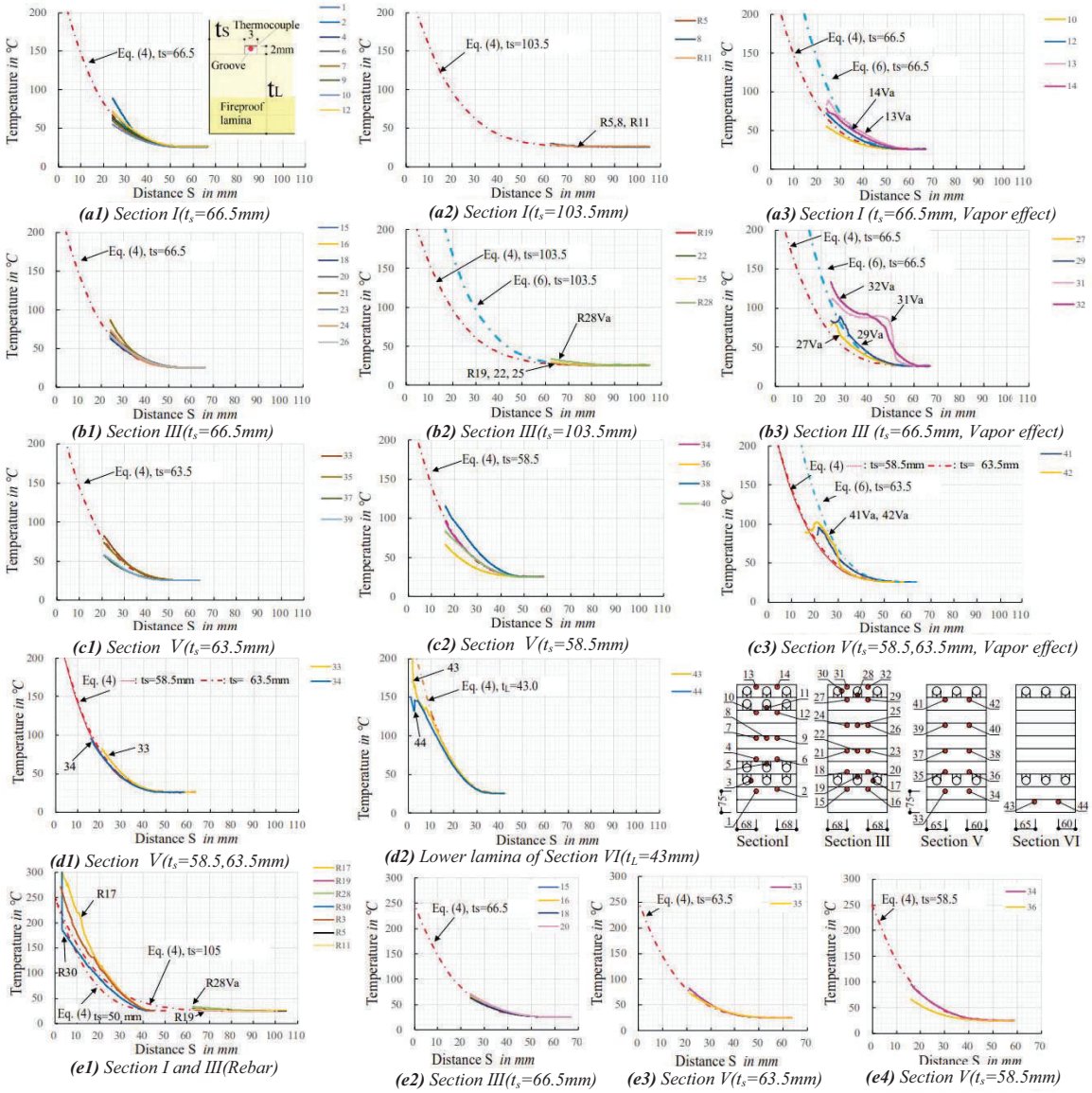

(a1) Section I(t_s=66.5mm) (a2) Section I(t_s=103.5mm) (a3) Section I (t_s=66.5mm, Vapor effect)

(b1) Section III(t_s=66.5mm) (b2) Section III(t_s=103.5mm) (b3) Section III (t_s=66.5mm, Vapor effect)

(c1) Section V(t_s=63.5mm) (c2) Section V(t_s=58.5mm) (c3) Section V(t_s=58.5,63.5mm, Vapor effect)

(d1) Section V(t_s=58.5,63.5mm) (d2) Lower lamina of Section VI(t_L=43mm)

(e1) Section I and III(Rebar) (e2) Section III(t_s=66.5mm) (e3) Section V(t_s=63.5mm) (e4) Section V(t_s=58.5mm)

Figure 11: *Temperature/T-Distance/S relationship in wood by experiment and curves calculated by Eq.(4) and Eq.(6)*

https://doi.org/10.52202/069179-0212

described above). In this study, it was assumed to approximate the temperature variations in the upper rebar lamina with the following Equation (6), in which the temperature increase in the second term on the right side of Equation (4) is multiplied by 2.0 to obtain a relatively accurate estimate of the temperature variations.

$$T=T_r+2.0\cdot(T_c-T_r)\cdot(V_c\cdot t/d_m)^n \quad (6)$$

Curve based on Equation (6) is shown as light blue dotted line. In Figure 11(a3), (b3), and (c3), the light blue curves roughly estimate the variation in temperature, i.e., $27V_a$, $29V_a$, $41V_a$, $42V_a$ of wood below the upper rebar lamina. In Figure 11(b3), temperatures of $31V_a$ and $32V_a$ on the upper surface of beam approach the temperature in the light blue curve after 60-minute burning. In terms of estimating the temperatures of this 60-minute burn, it is seemed that they can be estimated using Equation (6). The value of 2.0 needs to be verified by adding data from other burning tests in the future.

4.6 TEMPERATURE OF WOOD AROUND SIDE REBAR

Figure 11(e1) shows curves of rebars in cross-sections I and III. The curves by red one dot line were calculated by Equation (4), where d_m was assumed to be 50 mm (=35+15) for the side rebar as the side position near the central rebar, and d_m was assumed to be 105 mm for the central rebar as the center of the rebar. As temperature of the central rebar hardly rises, the difference of the calculated value to experimental value is almost negligible. However, temperature of the side rebar reached the charring temperature early because wood cover thickness on the side of the side rebar was 20 mm, and measured temperature of the rebar was larger than the calculated temperature because the thermal conductivity of rebar is larger than that of wood.

Figure 11(e2), (e3), and (e4) show variations of temperature of wood around the rebar lamina at the lower. Figure 13(a) and (b) show positions of thermocouples around the lower rebar lamina. Except for thermocouple 36 in Figure 11(e4), all positions follow the curve of the calculation. In Figure 12(b), wood around the side rebar was deeply charred, but as seen in Figure 11(e2), no increase up to the charring temperature was measured at the location near central side of the side rebar. However, considering charring condition in Figure 12(b), it is safe to assume that wood around the side rebar which is surrounded by pink line in Figure 13(c), cannot resist in burning for 60 minutes.

Table 1: *Depth/t_s of measurement point, distance/S and temperature after 60-minute burning, and temperature/T calculated by Eq.(4)*

Section	Fig.25	n	t_{so}	t_s	S	Temperature *in* ℃			
						Experiment		Calculation	
				in mm		Ave.	SD	Cal.	SE
III	(b1)	8	68.0	66.5	27.5	59.4	4.4	55.0	2.21
V	(c1)	4	65.0	63.5	24.5	57.8	8.2	62.8	4.81
V	(c2)	4	60.0	58.5	19.5	76.6	15.0	80.4	7.72

n: The number of data, t_{so}: Depth of wood from side surface of beam to measure point, t_s: T_{so}-3/2, SD: Standard deviation, SE: Standard error

4.7 RELATIONSHIP BETWEEN TEMPERATURE AND BURNING TIME AT EACH MEASURING POINT

Given the charring rate/v_c and the time of burning/t, the temperature at each point can be calculated using Equation (4) or Equation (6) to obtain a T-t curve of relationship between temperature and burning time. Here, the coefficient/k was assumed to be 0.0425 as mentioned above, charring temperature T_c of cedar wood was assumed to be 250°C [5], T_r was assumed to be room temperature of 25.6°C before the burning test, and the charring rate v_c was assumed to be 0.65 mm/min. d_m follows Section 4.4. The calculation results are shown as curves as Cal.1-Cal.3 in Figure 4-Figure 6. Cal.1 is the curve calculated for the measuring points close to the border of the central segment and Cal.2 is the curve calculated for the central position of beam width, i.e., the central rebar position. Cal. 3 is the curve calculated using Equation (6), which takes into account the effect of water vapor on the upper rebar lamina. The variation of calculated temperature is in good agreement with the experimental variation.

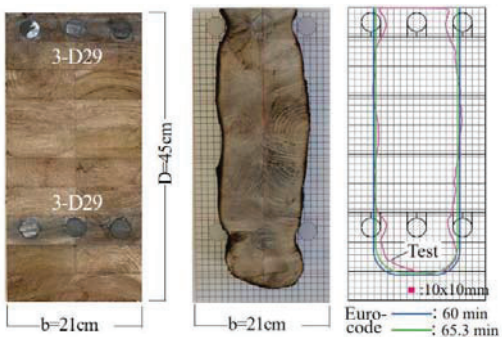

(a)For specimen *(b) Specimen after 65.3-minute burning test*

Figure 12: *A cut cross-section and an uncharred wood in the cross-section and curves calculated by Eurocord 5*

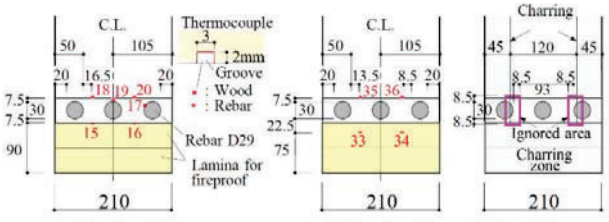

(a) Section III *(b) Section V* *(c) Invalid area*

Figure13: *Portion of thermocouples and ignored area*

https://doi.org/10.52202/069179-0212

5 TEMPERATURE DISTRIBUTION OF UNCARBONIZED CROSS-SECTION WITHIN GLULAM TIMBER DURING 60-MINUTE BURNING

The beam section is divided into charred area and uncharred area as shown in Figure 14; the shortest depth of dy, dx_1, dx_2 is assumed to be d_m, where dy is depth from the lower surface and dx_1 and dx_2 are depth both sides of the beam respectively. The charring border of the outward corner of the lower surface of the beam is circular as shown in Figure 12(b), due to the burning of the lower surface and the side faces; in Eurocord 5[4], a point O is assumed to be inside from those faces at a distance twice the charring depth/$v_c \cdot t$, as shown in Figure 14, and the arc was assumed to be as 1/4 of a circle with the charring depth/$v_c \cdot t$ as radius. Here, in the uncharred area at its outward corner, temperature/T of wood at the position of the arc of concentric circles of radius/r_o centred at point O was assumed to be isothermal and equal to temperature due to burning in one direction on the bottom or side surface. Figure 15 shows temperature distribution in the uncharred area within the cross-section of this beam calculated for a 60-minute burning. The cross-section was divided into 84 sections in the beam width direction and 180 sections in the beam height direction. In future calculations of capacity of beam, it is assumed that wood in the pink range in Figure 13(c) do not resist, and effect of the rebar on temperature of the wood area is ignored.

Figure 15(a) shows the 3-dimensional distribution of isotherms in the right half of the beam cross-section in Figure 15(b). It is shown in the view from the top surface of the beam to the bottom surface. Temperature in the charred area is shown as 250°C. The temperature decreases rapidly as its position moves toward the interior. The x-y co-ordinate axes in the cross-section are indicated in Figure 15(b). The origin of x and y is assumed to be the centre of the beam width at the border between the lower surface of the structural section and the cladding lamina. The y is positive upwards, whereas the negative range of y means the range of the cladding lamina.

Figure 15(c) shows curves of temperature along the beam height. The curves indicate the center of the beam width (x=0 mm), the 50°C border (x=±36 mm), the 60°C border (x=±40.5 mm) and the centre of the side rebar (x=±70 mm). The temperature at the center of the width (x=0mm), where the central rebar is located, is 26.9°C, almost

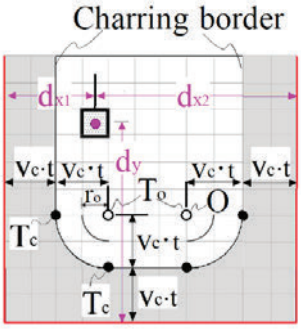

Figure14: *Distance /$d_{x1,x2,y}$ and T at the corner*

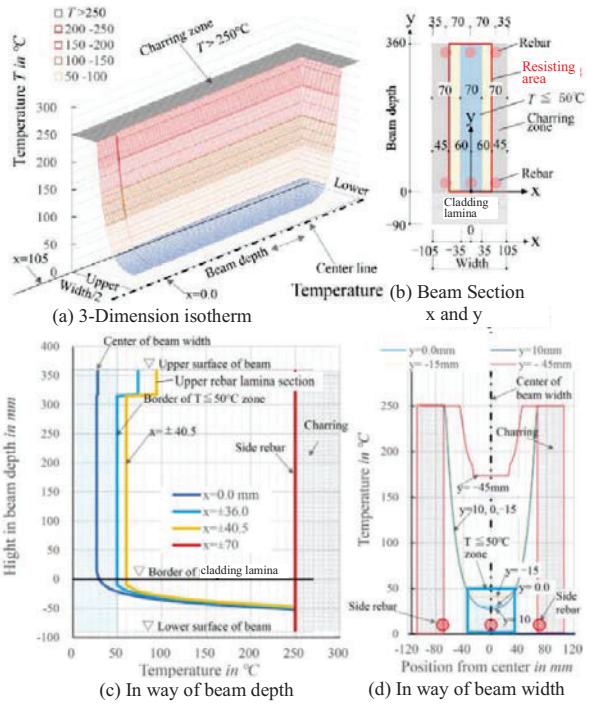

Figure 15: Temperature distribution of wood in beam cross-section after 60-minute burning calculated by the new concept

unaffected by the 60-minute burning in the structural section area ($0 \leq y$), whereas the temperature increases rapidly in the cladding lamina range ($-90 \leq y \leq 0$). This temperature distribution confirms the importance of the 90 mm thickness of cladding lamina.

Figure 15(d) shows curves of temperature in the beam width direction. The curves are for y=-15 mm in the cladding lamina, y=0 mm on the underside of the structural section area and y=10 mm in the structural section area. x=±35 mm is the width border of the central segment. Temperature in the area of the central segment within the structural section area enclosed by the blue line, i.e., $-35 \leq x \leq 35$ and $0 \leq y$, is below 50 °C, of which the area $-25 \leq x \leq 25$ is below 30 °C, resulting in the vicinity of the central rebar D29 being unaffected by burning.

From the above, it can be expected that in the case of a beam width of 210 mm, the central segment will be less than 50 °C and the temperature of the central rebar will hardly increase, even after 60-minute burning, if the thickness of the cladding lamina is 90 mm, and that the central rebar will demonstrate capacity as steel bar - timber composite beam resisting at room temperature.

https://doi.org/10.52202/069179-0212

6 SUMMARY

A method was proposed for estimating the temperature distribution inside steel bar - timber composite beam from experimental data by analysing the historical data of temperatures obtained during a 60-minute-burning test of the beam. The results are summarized as the followings:

i) A method was proposed to estimate temperature distribution in uncharred area of wood in glulam timber for any burning time within 60 minutes from the measured data of wood temperatures at limited locations in glulam timber, which reproduces the curve of the relationship between temperature at measuring point and burning time, showing temperature distribution in the cross-section during 60-minute burning.

ii) Based on the temperature distribution, beam width of 210 mm was divided into three equal sections, and the central segment of them was less than 50 °C even after 60 minutes burning, while central rebar and its vicinity were less than 30 °C (at room temperature of 25.6 °C) and were hardly affected by burning. The central segment can be expected to exhibit resistance as steel bar - timber composite beam. However, this assumes that 90-mm-thick cladding lamina are bonded to the underside of the beam.

iii) Around the side rebar, charring progresses quickly inwards in 60-minute burning, thus effect of this should be taken into account in the calculation of the capacity of beam.

iv) In 60-minute burning, the large heat capacity of the two-tier rebar in the cross-section had a small effect on the suppression of the temperature rise of wood in the glulam timber.

Note that to generalize the proposed modelling of the temperature distribution, it is necessary to generalize the method of setting the value of k for the coefficient in Equation (5).

ACKNOWLEDGEMENT

This project was funded as Grants-in-Aid for Scientific Research-B by Japan Society for the Promotion of Science.

REFERENCES

[1] S. Matsushita, S. Shioya: Burning test of steel bar - timber composite beam, Oslo, WCTE 2023

[2] S. Shioya, et al.: An innovative hybrid timber structure in Japan: performance of column and beam, Wein,WCTE 2016

[3] H. Toshiro, et al.: Temperature Dependence of Adhesive Strength and Fire Resistance of Structure Glued Laminated Timber Beams, Journal of the Japan Wood Research Society, Vol.59, No.4, pp.219-226, 2013(in Japanese)

[4] Eurocode 5, Design of timber structures - Part 1-2 General -Structural fire design, EN 1995-1-2, EUROPEAN COMMITTEE FOR STANDARD-IZATION, 2004

[5] S. Kikuchi, et al.: Internal Temperature Change of Wood by Radiation Heating, J. Hokkaido For. Prod. Res. Inst. Vol.9, No.5, 1995 (in Japanese)

https://doi.org/10.52202/069179-0212

TRAVELLING FIRES IN COMPARTMENTS WITH EXPOSED CROSS-LAMINATED TIMBER SURFACES

Andreas Sæter Bøe[1], Kathinka Leikanger Friquin[2]

ABSTRACT: This paper presents results from two large-scale experiments where the fire spread in large open-plan compartments with exposed cross-laminated timber (CLT) was studied. In the first experiment, #FRIC-01, the ceiling was exposed, and in the second, #FRIC-02, both the ceiling and the back wall was exposed. The charring rates of the CLT, the mass loss rates and heat release rates of the CLT and wood crib were measured. In addition, the fire spread was studied visually by recording the development of the fire with several cameras. The experiments provide unique information about how exposed surfaces affects the fire dynamics and fire spread in a modern wooden compartment. Both experiments showed that the presence of exposed CLT surfaces significantly affect the fire spread rate and fire dynamics of a compartment fire.

KEYWORDS: Cross-Laminated Timber, Compartment fire, Fire spread, Travelling fire

1 INTRODUCTION

Cross-laminated timber (CLT) has in recent years become very popular due to its many advantages; possibility of prefabrication, low carbon footprint, easy handling and mounting of wood, it's aesthetic look, and high strength and stiffness properties. With the increased popularity, CLT is now used in large apartment buildings, public buildings and office buildings.

Through a number of experiments, it has been found that the fire dynamics of a compartment is significantly changed when exposed surfaces of CLT are present. Examples of such changes are: higher heat release rate (HRR), increased duration of the fire, higher temperatures, and larger external flames [1, 2].

However, most experiments with CLT have been conducted in small compartments with nearly quadratic floor areas, and with small window openings, resulting mainly in ventilation-controlled fires [3-5]. Modern buildings, on the other hand, have large open-plan spaces and large window openings to allow for natural light. Fire dynamics of large, and sometimes long, open-plan spaces with large window openings is often characterized as travelling fires [6]. Travelling fires are recognized with a clear leading and trailing edge which propagates through the space.

Several full-scale experiments with travelling fires have been conducted over the last years, but mostly in compartments with non-combustible surroundings [7]. However, recently experiments have also been carried out with an exposed CLT ceiling. These experiments have provided new knowledge about how an exposed CLT surface affects the fire dynamic and fire spread rate.

In a small scale test, Nothard et al.[8] studied the effect of exposing CLT in the ceiling, and reported a more rapid fire spread with an exposed ceiling. In the Malveira fire experiments, the fire spread slowly for ~4 hours, until the fire spread to a location of the compartment where the ceiling was combustible. The burning ceiling significantly increased the fire spread in the rest of the compartment.

In the CodeRed-experiments [9, 10], the fire spread across a ~380 m^2 compartment with an exposed CLT-ceiling in 5 and 8 minutes. After ignition of the exposed CLT in the ceiling, the fire spread rapidly across the ceiling. This triggered the spread across the wood crib due to the strong radiation heat flux from the ceiling towards the wood crib. The impact of the exposed ceiling could clearly be demonstrated when compared against the X-ONE [11] and X-TWO [12] fire experiments, which were almost identical to the CodeRed-tests [10], but without exposed CLT in the ceiling. In these tests, the fire spread across the room in 25 and 32 minutes, respectively.

Through the few tests performed with a combustible ceiling, it is evident that there is a need for more knowledge on how different exposed CLT surfaces affects the fire spread and fire safety in large compartments. The rate at which a fire spreads is highly relevant for several aspects within fire safety, for example available time for people in the compartment to evacuate safely or be rescued, and efforts needed to contain and

[1] Andreas Sæter Bøe, Department of Civil and Environmental Engineering, Norwegian University of Science and Technology NTNU, Norway, andreas.s.boe@ntnu.no
[2] Kathinka Leikanger Friquin, Dept. of Architecture, Materials and Structures, SINTEF Community, Norway, kathinka.friquin@sintef.no

https://doi.org/10.52202/069179-0213

suppress the fire, extinguishing tactics, spread to other parts of the building, etc.

To better understand how an exposed CLT-surface affects the fire spread in a large open-plan compartment with large window openings, two large-scale experiments have been conducted. This paper is a short summary of some of the results. Additional results will be published in separate articles.

2 METHOD

Two experiments were conducted. The first, #FRIC-01, had an exposed CLT ceiling, while in the second, #FRIC-02, the CLT was exposed in both the ceiling and the back wall. The compartment is shown in Figure 1-Figure 3.

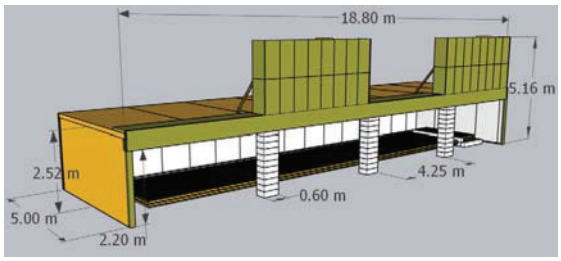

Figure 1 Sketch of compartment with dimensions.

Compartment

The compartment was built of a CLT roof and three CLT walls, while the front wall with large openings was made of a glue-laminated timber beam and three Siporex columns. The CLT in the roof and back wall was 140 mm thick, with 5 layers (40-20-20-20-40 mm), made of Norwegian spruce, and glued together with a regular polyurethane (PUR) adhesive. The CLT in the end walls were 80 mm thick with 3 layers (30-20-30 mm).

The inner geometry of the compartment was 18.8 m x 5.0 m x 2.52 m (l x w x h). The compartment was well ventilated with four large window openings in the front wall, with a total opening of 17.0 m x 2.2 m (l x h). This corresponds to an opening factor of 0.18 $m^{1/2}$. A 2.45 m high inert façade wall was mounted above two of the windows to study the external flame. The beam in the front wall protruded 350 mm below the ceiling.

The unexposed CLT surfaces were protected with 2 layers of 15 mm fire rated gypsum boards (type F) [13] to prevent any contribution from them. The edges of the CLT and the beam in the front wall were protected with a ceramic insulation.

Fuel load

The fuel load density was 373 MJ/m^2 per floor area and was chosen to represent a typical office building. The fuel load was represented by a 2.8 m x 15.5 x 0.2 m continuous wood crib and a 2.8 m x 1.0 m x 0.2 m wood crib positioned on a scale. The wood crib was made of four alternating layers with wood sticks with a 50 mm x 50 mm cross-section. The wood crib is shown in Figure 2 and Figure 3.

Figure 2 Compartment with exposed ceiling and back wall in #FRIC-02.

Figure 3 Inside compartment before ignition in #FRIC-02, with exposed CLT in ceiling and on back wall. Wood crib on the floor, TC-trees hanging from the ceiling. #FRIC-01 was identical except for gypsum boards covering the CLT back wall.

The fire was ignited at one end of the wood crib, the left end. Ten aluminium trays with heptane were evenly distributed under the end of the wood crib. In #FRIC-01 a total of 5.0 litres of heptane was used, and in #FRIC-02 a total of 9.8 litres.

Instrumentation

The compartment was instrumented with thermocouples (TC) and plate thermometers (PT) distributed inside and outside the compartment. The sensors measured the temperature and heat fluxes, and gave valuable data on fire spread rate, temperature distributions, charring rates, and heat flux towards the façade.

Charring rates of the CLT were determined based on temperature measurements. Embedded TCs were installed into the CLT elements from the sides, parallel to the isotherm, at depths 0, 10, 20, 30 and 40 mm into the CLT (Figure 4), at three different locations in the compartment.

https://doi.org/10.52202/069179-0213

Figure 4 TCs were embedded into the CLT from the rebate joint.

Determination of heat release rate

The determination of the heat release rate (HRR) of the wood crib was inspired by the method of Rackausakaite et al. [11], which determined the HRR per unit (here: 50 mm of crib length) and then integrated over the entire wood crib. In contrast to the method of Rackausakaite et al., the HRR per unit was determined from the mass loss rate (MLR) of the small wood crib positioned on a scale, instead of just an average value between start and end of burning.

The HRR contribution from the CLT was derived based on the charring rates, the density, and the area of the exposed CLT. Charring rates of the CLT were determined based on the development of the 300°C isotherm inside the timber [14].

3 RESULTS AND DISCUSSION

3.1 Fire development

In #FRIC-01, the heptane fire did not cause the ceiling to ignite, and the wood crib fire almost extinguished when the heptane burned out after 4 minutes. After ca. 20 minutes the wood crib fire had developed to cover an area of about 1 m x 2.8 m of the crib. The flame height was 0.5-2.2 m above the floor, i.e. not impinging the ceiling. During the next 13 minutes the flames travelled 0.5 m of the wood crib, but the base area and flame height was almost unchanged as the flames at the left end of the crib were dying out.

After ca. 33 minutes the CLT in the ceiling ignited. This occurred from a combination of radiation and convection, as the flames did not impinge the ceiling After this the fire spread across the entire room in approximately 12 minutes. Within these 12 minutes, the fire travelled back and forth in four distinct waves or cycles (Figure 5). We have chosen to call them *flashing waves* in this article.

The flashing waves were recognized by a rapid flash fire along the ceiling, followed by a spread along the top layer of the wood crib, triggered by the radiation from the ceiling. Each wave caused external flaming from the window openings. After a short intense fire of 30-60 seconds, the flames gradually reduced in the ceiling, and the radiation-controlled fire in the top layer of the wood crib was reduced or even extinguished. The wood crib fire grew in size after each wave, and spread to the right end of the compartment in the the 3rd and 4th wave, in which the full flashover occurred at the end of the 4th wave at 45:30 (mm:ss).

Figure 5 #FRIC-01: Fire spread and retraction of 3rd flashing wave. Time (hh:mm:ss).

https://doi.org/10.52202/069179-0213

Figure 6 #FRIC-01: Most intense phase of burning shortly after flashover.

After the flashover, the fire burned intensely for about a minute (Figure 6), and then gradually decreased in intensity. From 49 minutes, the fire was clearly most intense at the far end from ignition, and external flames were only present from the far end window. Self-extinguishment of flames in the CLT ceiling started at around 50 minutes, from the left end of the compartment towards the right end over the next 10 minutes. The wood crib fire was continuous until about 60 minutes into the fire. From 60 to 95 minutes, the wood crib fire became increasingly discontinuous, starting from the left end of the compartment and moving towards the right end. Visible flames in the wood crib self-extinguished at 95 minutes. The compartment was observed for a total of 4 hours. At this point, very little of the wood crib was left. A few lamellae of the outer layer of the CLT in the centre of the compartment were hanging down from the ceiling. Hot spots were present around these loose lamellae. Manual extinguishing was then conducted. No reignition occurred after the manual extinguishment.

In #FRIC-02, the amount of heptane used to ignite the wood crib was increased to avoid the risk of self-extinguishment, based on the experience from #FRIC-01. The extra heptane caused both the ceiling and the wall to ignite at 2 minutes. From this point on, the fire spread extremely fast, and flashover occurred at 3 minutes and 15 seconds (Figure 7).

After flashover, the fire burned intensely with large external flames for about 8 minutes. The flames in the CLT wall and ceiling gradually extinguished from the left end of the compartment after ca. 14 minutes. At around 16 minutes all flames in the wall and ceiling had self-extinguished, and only the wood crib was still burning.

From around 25 minutes, the crib was burning with discontinuous flames, and the last flames extinguished after 40 minutes. However, after 75 minutes a 2nd flashover was seen with flames on the entire back wall and the ceiling (Figure 8). The fire continued until 175 minutes (Figure 9), when it was manually extinguished.

3.2 Mass loss rate and heat release rate

#FRIC-01

The HRR of the CLT was estimated to be 21 MW at maximum, while the estimated HRR of the wood crib was 20 MW. Combined the total HRR was estimated to 41 MW, see Figure 10.

#FRIC-02

The HRR of the CLT was at maximum 24.5 MW for the ceiling, and 13 MW for the wall. The estimated HRR of the wood crib was 35 MW at maximum. The total HRR was at maximum approximately 73 MW. This is 32 MW (78 %) higher than in #FRIC-01.

However, the contribution from the CLT wall was only 13 MW. The additional 19 MW, compared to #FRIC-01, is due to an increased HRR from the wood crib, which was 15 MW higher than in #FRIC-01, and from the CLT ceiling, which was ca. 4 MW higher.

https://doi.org/10.52202/069179-0213

Figure 7 #FRIC-02: Most intense phase of burning shortly after flashover. Time (hh:mm:ss).

Figure 8 #FRIC-02: A 2nd flashover developed about an hour after the flames in the CLT had self-extinguished. Time (hh:mm:ss).

Figure 9 #FRIC-02: The fire was still burning strongly just before it was manually extinguished.

https://doi.org/10.52202/069179-0213

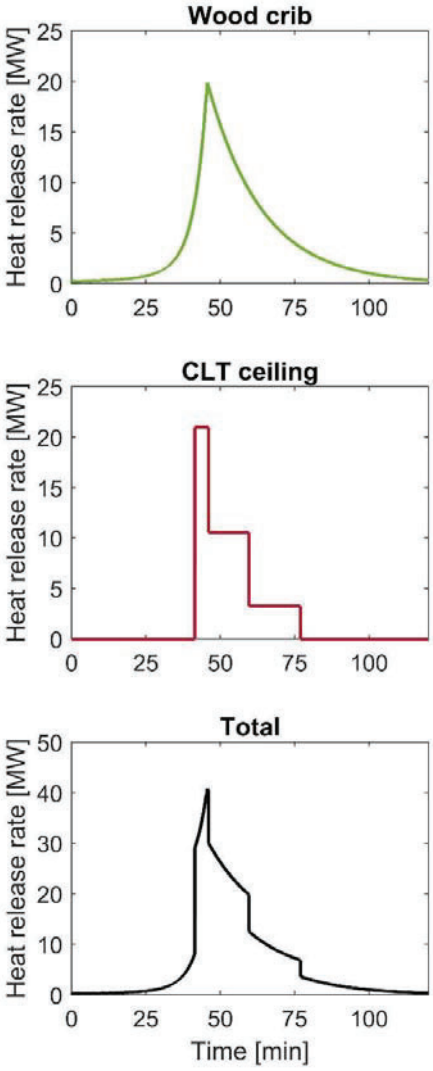

Figure 10 #FRIC-01: Estimated heat release rates of the wood crib and the CLT ceiling

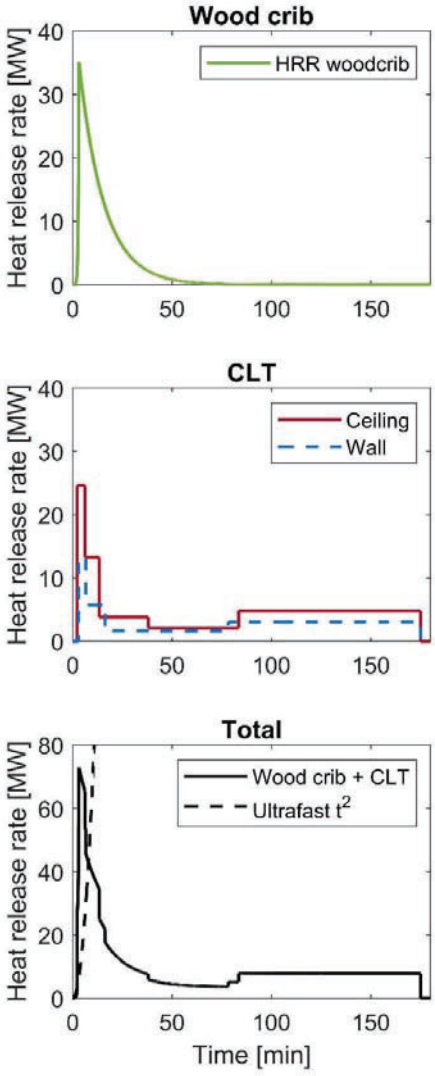

Figure 11 #FRIC-02: Heat release rate of wood crib and CLT in the ceiling and on the back wall

4 CONCLUSIONS

The experiments #FRIC-01 and -02 were conducted to increase the knowledge about fire spread and fire dynamics in large open-plan compartments with large ventilation openings. Both #FRIC-01 and -02 showed, in line with previous experiments, that the presence of exposed CLT surfaces significantly affect the fire spread rate and fire dynamics of a compartment fire.

In #FRIC-01, however, the time until ignition of the CLT ceiling occurred later than in previous experiments. This can be explained by the flame height of the wood crib fire, which were not impinging the ceiling.

In #FRIC-02 the ignition of the ceiling occurred earlier due to the increased amount of heptane in the start fire. However, the flame spread after ignition of the ceiling was much faster in #FRIC-01, which can be explained by the additional exposed surfaces on the CLT wall.

Both tests, but in particular #FRIC-02, show clearly that the presence of exposed CLT could cause a rapid fire development. A rapid fire development affects fire safety in several ways, for example available time for safe evacuation and rescue, and the size of the fire when the fire brigade enters the building.

https://doi.org/10.52202/069179-0213

REFERENCES

[1] J. Su, P.-S. Lafrance, M. S. Hoehler, and M. F. Bundy, "Fire Safety Challenges of Tall Wood Buildings–Phase 2: Task 3-Cross Laminated Timber Compartment Fire Tests. Report no. FPRF-2018-01-REV," NFPA, 2018.

[2] R. Emberley *et al.*, "Description of small and large-scale cross laminated timber fire tests," *Fire Safety Journal,* vol. 91, pp. .

[3] D. Brandon, J. Sjöström, E. Hallberg, A. Temple, and F. Kahl, "RISE report - Summary report - Fire Safe implementation of visible mass timber in tall buildings - compartment fire testing (2020:94)," 2020.

[4] D. Brandon and B. Östman, "Fire Safety Challenges of Tall Wood Buildings – Phase 2: Task 1 - Literature Review," NFPA, 2016.

[5] G. Ronquillo, D. Hopkin, and M. Spearpoint, "Review of large-scale fire tests on cross-laminated timber," *Journal of Fire Sciences,* vol. 39, no. 5, pp. 327-369, 2021, doi: 10.1177/07349041211034460.

[6] J. Stern-Gottfried and G. Rein, "Travelling fires for structural design–Part I: Literature review," *Fire Safety Journal,* vol. 54, pp. .

[7] V. Gupta, J. P. Hidalgo, D. Lange, A. Cowlard, C. Abecassis-Empis, and J. L. Torero, "A Review and Analysis of the Thermal Exposure in Large Compartment Fire Experiments," *International Journal of High-Rise Buildings,* vol. 10, no. 4, pp. 345-364, 2021.

[8] S. Nothard, D. Lange, J. P. Hidalgo, V. Gupta, and M. S. McLaggan, "The response of exposed timber in open plan compartment fires and its impact on the fire dynamics," presented at the Proceedings of the 11th International Conference on Structures in Fire (SiF2020), 2020.

[9] P. Kotsovinos *et al.*, "Fire dynamics inside a large and open-plan compartment with exposed timber ceiling and columns: CodeRed #01," *Fire and Materials,* vol. n/a, no. .

[10] P. Kotsovinos *et al.*, "Impact of ventilation on the fire dynamics of an open-plan compartment with exposed timber ceiling and columns: CodeRed #02," *Fire and Materials,* 2022, doi: 10.1002/fam.3082.

[11] E. Rackauskaite *et al.*, "Fire Experiment Inside a Very Large and Open-Plan Compartment: x-ONE," *Fire Technology,* 2021, doi: 10.1007/s10694-021-01162-6.

[12] M. Heidari *et al.*, "Fire experiments inside a very large and open-plan compartment: x-TWO," presented at the Proceedings of the 11th International Conference on Structures in Fire (SiF2020), 2020.

[13] *EN 520:2004+A1:2009. Gypsum plasterboards - Definitions, requirements and test methods*, CEN, Brussels, Belgium, 2004.

World Conference on Timber Engineering Oslo 2023

CHARACTERIZING THE FIRE PERFORMANCE OF ADHESIVES USED IN GLUED-IN RODS CONNECTIONS

Diego Flores[1], Christian Dagenais[2], Pierre Blanchet[3]

ABSTRACT: Glued-in rods are an aesthetically and performant type of connection that has seen its usage increase in the last few years. However, there is still a lack of data concerning the fire performance of glued-in rods, limiting its integration in standards. Recent studies suggest that the adhesive is critical to the fire performance of glued-in rods, since its capacity is greatly reduced when the temperature exceeds its glass transition temperature (T_g), ranging between 45-65 °C for most structural adhesives. To validate these findings, dynamic mechanical analysis (DMA) tests were performed to better assess the T_g and other thermomechanical properties of the adhesives used in this research. Axial tension tests at stabilized temperature were performed on 67 glued-in rods specimens using five different adhesives (three epoxies and two polyurethanes) and various sets of temperatures at the glue line interface. Most of these specimens have shown a ductile failure mode for temperatures below the T_g of the adhesive and a brittle failure mode for temperatures above the T_g. This research helps determine guidelines for the fire design of glued-in rods and related testing, and ultimately leading to a design method for providing fire resistance to connections made of glued-in rods.

KEYWORDS: Girods, Fire behaviour, Adhesive, Glass transition temperature, Thermal resistance

1 INTRODUCTION

Glued-in rods, a connection system in which a metal rod is glued inside a wood element by means of a structural adhesive, are gaining in popularity in the construction industry due to their high bearing capacity, good slip stiffness, and great aesthetic. Since the metal rod is concealed inside the wood element, the connection is naturally protected in a fire situation. Wood has a predictable behavior under high temperatures, with a char depth given by Equation 1 [1] where $x_{c,n}$ is the notional char depth (mm), β_n is the notional char rate (0.70 mm/min for glulam) and t is the time (min). Wood also has a high thermal gradient that can be determined through Equation 2 [2], where T is the temperature (°C), T_o is the initial temperature (typically taken as 20°C), T_p is the temperature at the base of the char layer (300°C), x is the position within the thermal penetration depth (mm) and α is the thermal penetration depth (35 mm).

$$x_{c,n} = \beta_n \times t \quad (1)$$

$$T = T_0 + (T_p - T_0)(1 - \frac{x}{\alpha})^2 \quad (2)$$

However, in North America there is no consensus between experts on the design of glued-in rods, and existing standards does not cover all adhesive types, limiting its use in the construction industry [3]. While glued-in rod connections have been well characterized at ambient temperature, their thermomechanical behavior at elevated temperatures using different adhesives has been understudied.

Previous research suggests that the adhesive is the critical element in glued-in rod connections when exposed to elevated temperatures since its capacity decreases drastically when the glass transition temperature (T_g) is exceeded [4-7]. The latter is defined as the temperature where permanent modifications occur in the molecular structure of the polymer, leading to a transition of a solid to rubberlike state of the adhesive [8-11]. At temperatures above the T_g, this results in a considerable loss of adhesion and cohesion in the adhesive layer, translating to a poor performance of the connection with an undesirable brittle failure mode [7, 12-15].

The T_g of an adhesive strongly depends on its type, formulation, curing time, curing temperatures and thermal history [16, 17]. The latter refers to the effect of post-cure, which can increase the T_g by creating additional crosslinks in the adhesive. Furthermore, the T_g is not a fixed temperature, but is rather a range of temperatures that can vary between different test methods, and even within the same test method [16]. For this reason, it is a difficult task to accurately assess the temperature at which the thermomechanical performance of glued-in rods starts to deteriorate. The Dynamic Mechanical Analysis (DMA) is a sensitive method commonly used to determine the range of the T_g for all adhesives tested according to three curves: 1) storage modulus, 2) loss modulus and 3) tan δ. The storage modulus, which is a quantification of the

[1] Diego Flores, Université Laval, Canada, diego.flores.1@ulaval.ca
[2] Christian Dagenais, Université Laval/FPInnovations, Canada, christian.dagenais@sbf.ulaval.ca
[3] Pierre Blanchet, Université Laval, Canada, pierre.blanchet@sbf.ulaval.ca

https://doi.org/10.52202/069179-0214

adhesive's stored energy [18], is an indication that the mechanical properties of the adhesive start decreasing at this temperature [19]. The thermomechanical behavior of glued-in rods can be determined through axial tension tests at stabilized temperatures [20], which informs the researcher on the stiffness, capacity, and failure modes of the connections at specific temperatures.

This research aims to characterize the performance of adhesives used in glued-in rods connections at elevated temperature. To do so, the effect of temperatures below the storage modulus, above the storage modulus and above the loss modulus on the resistance, stiffness and failure mode of the connection have been evaluated. The only variables in this research were the nature of the adhesive and the temperature of exposure. The findings will help determine guidelines for the fire design of glued-in rods and related testing.

2 EXPERIMENTAL

2.1 MATERIALS AND DIMENSIONS

Glued-laminated timber (glulam) made from Spruce-Pine of grade 12c-E per CSA O122 [21] provided by Art Massif were used in the fabrication of all glued-in rod specimens. The timber was conditioned at a temperature of 20°C and 65% relative humidity (RH) until their masses were at a constant value, meaning an equilibrium moisture content of ±12%. Each glulam specimen had dimensions of 80 x 104 x 686 mm (length of 1372 mm when fully assembled), with holes of 19 mm in diameter and 402 mm in length drilled in the middle lamella by a computer numerical control (CNC). Threaded steel rods of 16 mm nominal diameter and 800 mm length of grade ASTM A307 [22] with minimal strength of 414 MPa were used. An example of a glued-in rod specimen is shown in Figure 1.

A total of five structural adhesives were used in the fabrication of glued-in rods connections: three epoxies (EPX1, EPX2 and EPX3) and two polyurethanes (PUR1 and PUR2) which were deemed, per the adhesive suppliers, suitable for glued-in rods application. The identity of each adhesive is not provided due to non-disclosure agreements. Once injected into the connection, the adhesive had a 1.5 mm thickness around the steel rod.

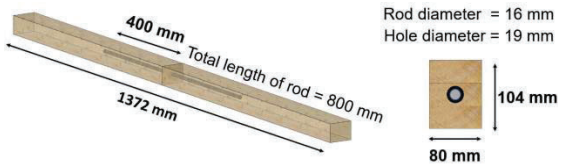

Figure 1: *Glued-in rod specimen*

2.2 FABRICATION OF GLUED-IN RODS

Two 9.5 mm diameter injection/ejection holes were drilled perpendicular to grain at 380 mm from the middle of the glued-in rod specimen. A threaded steel rod was inserted inside the 19 mm drilled hole of a glulam specimen. Prior to concealing the connection with a second glulam, butyl tape was added between both timber elements to limit the spread of the adhesive at this butt joint and have a preliminary bonding. A tight contact between the connection was ensured by two clamps. The adhesive was then continuously inserted through the injection hole until it ejected through the ejection hole. Both holes were closed by 9.5 mm diameter timber dowels to seal the assembly and limit heat flow during the heating of the specimens. The fabrication process is shown in Figure 2. Once fabricated, the glued-in rod specimens were untouched for 48h to allow the cure of adhesive at room temperature. The latter were then transferred to a conditioning room at 20°C and 65% RH for a minimum of 10 days, ensuring the same conditions for all specimens. A total of 67 glued-in rod specimens, consisting of 13 specimens per adhesive plus two additional samples for the EPX3 adhesive, with final dimensions of 80 x 104 x 1372 mm was fabricated.

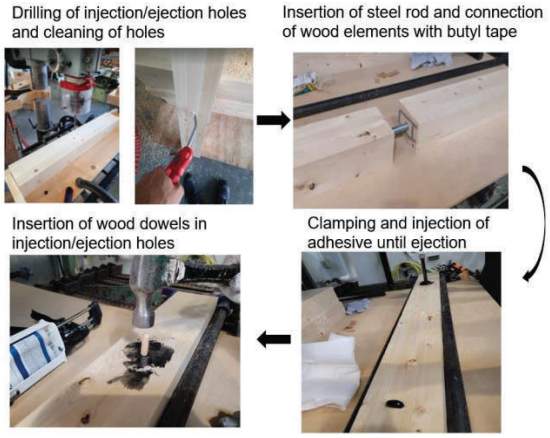

Figure 2: *Fabrication process of glued-in rods*

2.3 CHARACTERIZING ADHESIVES

To better assess the T_g and other thermomechanical properties of the adhesives used in this experimentation, DMA tests were performed. A DMA Q800 machine from TA Instruments was used, with a heating rate of 3ºC/min until 150ºC and a strain of 0.1%. The T_g obtained from these tests were used to determine the various sets of target temperature at which the glued-in rods were exposed for the mechanical testing. A total of 30 DMA tests were performed, meaning each adhesive was tested six times.

A second DMA run was performed on all adhesive samples previously tested, therefore fully crosslinked, to evaluate the effect of post-cure on the T_g from the storage modulus and loss modulus.

2.4 EXPERIMENTAL SET-UP AND INSTRUMENTATION

Four steel plates were fastened to the glued-in rod specimens using 16 self-tapping screws of 120 mm in length fixed at a 45° angle of the longitudinal direction at

https://doi.org/10.52202/069179-0214

each extremity. The number, length and angle of screws were determined to offer a greater resistance than the steel rod at ambient conditions. They have been calculated according to the withdrawal resistance equation from the Canadian Construction Materials Centre (CCMC) Evaluation report 13677-R [23]. To limit the heat transfer at both ends from the high thermal conductivity of the steel plates, the latter were wrapped into ceramic fiber blankets, as shown in Figure 3a.

A total of 8 type K thermocouples (TC) were positioned inside and outside the specimen to monitor the temperature in real time: two TC at the glue line interface (1 and 4), four TC at 15 mm around the glue line interface (2, 3, 5 and 6), one TC on the surface (7) and one TC in the oven (8), as shown in Figure 3b and 3c. A firestop caulking was used to seal the holes drilled for the insertion of each TC.

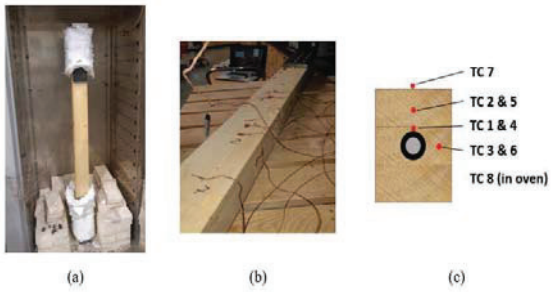

Figure 3: *Heating experimental set-up*

2.4 AXIAL TENSION TEST AT STABILIZED TEMPERATURE

The glued-in rod specimen was inserted inside an oven preheated at 200°C, regardless of the target temperature, to expose each specimen to the same heating conditions. The oven temperature was set to be below the auto-ignition temperature of the glulam, while being sufficiently high for an adequate heat transfer. The target temperatures used in this research were: 1) 21°C (ambient), 2) just below the T_g found through the storage modulus, 3) between the storage and loss modulus, and 4) above the loss modulus specific to each adhesive. Once the average of both TC at the glue line interface (1 and 4) reached the predetermined target temperatures, the specimen was transferred and fixed to the axial tension test bench within 10 minutes.

Four 25 mm Linear Variable Differential Transformer (LVDT) lasers were installed (two on each side of the large face) at 12.5 mm from the center of the specimen, as shown in Figure 4a. The LVDT lasers allowed to adequately measure the slip of the connection from all sides when axially loaded. Each specimen was subjected to an axial displacement rate of 0.5 mm/min until failure of the connection. Pin-pin end conditions were used to connect the specimen to minimize additional bending moment applied on the glued-in rod (Figure 4b). The temperature within the specimens was constantly monitored throughout the entire duration of the axial tension test to ensure that the glue line's temperature remained near the target.

Upon the failure of the specimen during the axial tension test, the failure mode was determined, and load-slip curves were generated, giving information on the strength of the connection (F_{max}), i.e. the peak of the load slip curves, and the stiffness of the connection (k_i). The latter was calculated following Equation (3) provided by EN 26891 [24] standard, where v_i is the slip at $0.4F_{max}$.

$$k_i = \frac{0.4F_{max}}{v_i} \tag{3}$$

Two additional tests were performed on the EPX3 specimen (EPX3-14 and EPX3-15) to determine the effect, if any, of post-cure on the thermomechanical behavior of glued-in rods. The latter were previously heated at the T_g of the fully crosslink adhesive (65°C) for three hours. These specimens rested for 12 hours at ambient conditions before heating in the oven for a second time and performing the axial tension test.

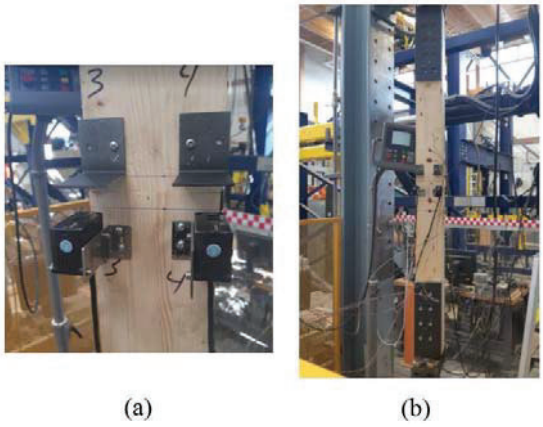

Figure 4: *Axial tension test set-up*

3 RESULTS

3.1 DMA TESTS

A total of six DMA tests were performed for each adhesive to determine the T_g through the storage modulus, loss modulus and tan δ. The former was identified by the intersecting the tangent at the top of the curve and at its inflection point, while the loss modulus and tan δ were valued at the peak of their respective curves, as show in Figure 5.

https://doi.org/10.52202/069179-0214

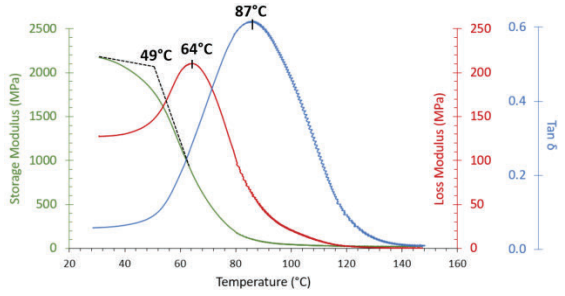

Figure 5: *DMA test of EPX1-3 specimen*

Table 1 displays the average T_g values of the storage modulus and loss modulus of each adhesive tested. Since the mechanical and physical properties of adhesives are already significantly affected at temperatures above the loss modulus, results for the T_g found through the tan δ are not displayed and will not be considered hereafter.

Table 1*: T_g values based on storage and loss modulus*

Specimen	Storage modulus (°C)	Loss modulus (°C)
EPX1	52	67
EPX2	48	59
EPX3	51	60
PUR1	56	71
PUR2	24	34

Table 1 shows that the storage modulus of all epoxies (EPX) samples was similar, with a difference of less than 4°C between each other. A greater dissimilarity was found for the loss modulus of the latter, with an 8°C difference at most. The polyurethane (PUR) specimen 1 had the highest Tg found through the storage modulus and loss modulus, while the PUR2 specimen demonstrated the poorest values of all adhesives. In addition to the reference specimen tested at ambient conditions, these results were used to determine the target temperatures each glued-in rod specimen was exposed during the axial tension test at stabilized temperature.

The post-cure effect did not have the same influence on the T_g of all adhesives. The EPX1, PUR1 and PUR2 adhesive specimens showed a decrease in the average T_g found through the storage modulus compared to the first heating cycle. The EPX2 and EPX3 adhesives demonstrated a considerable positive impact in their storage modulus, with an increase of +7°C and +15°C, respectively. As for the T_g found through the loss modulus, the EPX1 specimen showed a reduction while the EPX2, EPX3, PUR1 and PUR2 specimen had an increase ranging from +5°C to +19°C. Figure 6 displays the difference in the T_g between the first and second heating cycle for all adhesives. Since the EPX3 was the most positively affected by the post-cure, it was chosen to determine the effect on the thermomechanical properties of previously heated glued-in rod connections.

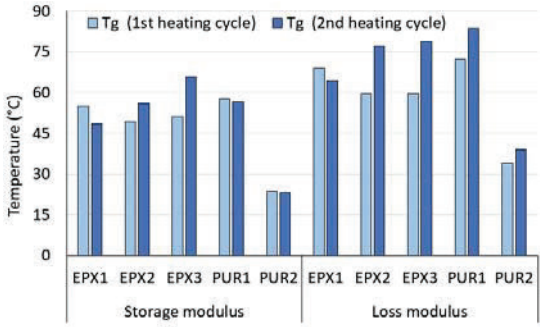

Figure 6: *Influence of post-cure on T_g*

3.2 MECHANICAL BEHAVIOR OF GLUED-IN RODS AT DIFFERENT TEMPERATURES

The reference values and failure mode for each glued-in rod specimens fabricated with a different adhesive were determined from an average of three specimens per adhesive tested at ambient temperatures. The average resistance and stiffness at 21°C for the EPX1, EPX2 and EPX3 specimen were respectively 75 kN and 177 kN/mm, 72 kN and 161 kN/mm, as well as 74 kN and 180 kN/mm. While the PUR1 specimen had a similar average resistance and stiffness than the EPX specimens, i.e. 74 kN and 178 kN/mm respectively, the PUR2 specimen had average values of 73 kN and 62 kN/mm. Most specimens had a ductile failure mode in the steel rod (Figure 7a), except for the PUR2 specimens which all failed in a brittle manner in the adhesive layer (Figure 7b).

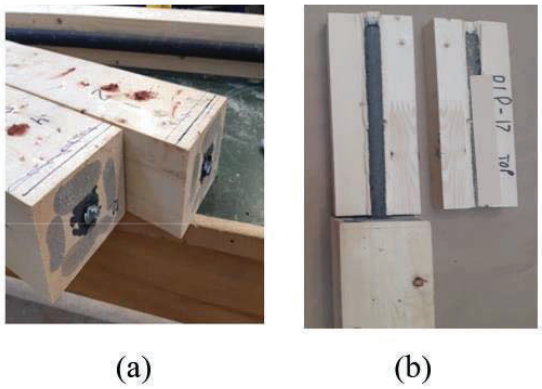

Figure 7: *(a) Ductile failure and (b) brittle failure mode*

When tested at temperatures just below the storage modulus specific to each adhesive, the resistance of almost all specimens dropped by less than 4%, regardless of the adhesive. However, the specimens tested closest to the storage modulus showed a decrease of between 23% and 29% for the EPX1, EPX3 and PUR1 adhesive, while the EPX2 adhesive demonstrated a reduction of 17%. At this temperature the failure mode remained ductile in most cases, while a brittle failure mode in the wood component

https://doi.org/10.52202/069179-0214

occurred for in the EPX2 specimen. Given that the T_g found through the storage modulus of the PUR2 was relatively low, no tests were performed at this temperature for the latter.

When tested at temperatures just above the storage modulus, the capacity of the glued-in rod specimens remained similar than the reference values, with a reduction of less than 5%. As for the stiffness, a reduction of between 59% and 70% was observed in the EPX1, EPX2, EPX3 and PUR1 specimen when compared to their respective reference value. The PUR2 specimens showed a stiffness reduction of 23%. A ductile failure mode occurred for all EPX1 and EPX3 specimen, while the adhesive failed in all EPX2, PUR1 and PUR2 specimens.

As the temperature increased closer to the T_g based on the loss modulus, the capacity of the EPX1, EPX2 and EPX3 decreased by 28%, 22% and 4%, respectively when compared to the reference values. The PUR1 specimen showed the largest decrease with 41%. The stiffness of those specimens decreased by between 66% and 77%. The PUR2 specimen had a reduction in its capacity and stiffness by 14% and 36%, respectively. All specimens demonstrated a brittle failure mode in the adhesive layer.

The mechanical properties of all specimens further decreased when tested at temperatures above the loss modulus, which was around 79°C. Almost all specimens had lost more than 50% of their initial strength, and more than 74% of their initial stiffness. In the case of the PUR2 specimens, it lost 65% of its initial strength and 57% of its initial stiffness. A brittle failure in the adhesive layer occurred in all specimens. The temperature (T) in °C, capacity (cap) in kN and stiffness (stiff) in kN/mm are displayed in Table 2 and 3 for the EPX and PUR, respectively. Figures 8 to 12 shows the evolution of the capacity, stiffness and failure modes of all specimens as the temperature increases.

***Table 2**: Test temperature, capacity and stiffness of EPX specimens*

#	EPX1			EPX2			EPX3		
	T	cap	stiff	T	cap	stiff	T	cap	stiff
1	21	74	192	21	72	157	21	75	160
2	21	75	156	21	73	163	21	75	194
3	21	75	184	21	72	162	21	73	187
10	47	71	126	42	71	144	43	74	162
11	45	72	150	43	63	133	45	72	133
4	55	72	68	51	71	144	54	70	76
5	55	73	60	57	64	40	52	73	82
6	53	72	63	54	68	49	54	72	74
12	62	66	41	59	61	55	60	71	61
13	68	54	29	60	56	44	65	63	38
7	73	42	34	86	32	38	78	41	42
8	77	48	31	73	33	38	77	38	44
9	79	36	33	79	37	42	77	44	37

***Table 3**: Test temperature, capacity and stiffness of PUR specimens*

#	PUR1			PUR2		
	T	cap	stiff	T	cap	stiff
1	21	75	174	21	73	63
2	21	75	203	21	74	58
3	21	73	157	21	74	65
10	47	73	134	28	72	48
11	58	71	64	29	72	56
4	56	73	76	54	36	27
5	54	73	88	53	41	28
6	56	73	64	50	41	27
12	65	64	45	36	63	40
13	68	44	23	40	51	39
7	80	34	27	77	25	27
8	80	34	28	76	28	26
9	77	32	29	77	26	24

When evaluating the effect of post-cure, i.e. the thermomechanical behavior of a glued-in rod specimen with a fully crosslinked adhesive, the EPX3-14 specimen had an increase of 14% in the resistance and an increase of 99% in the stiffness compared to the EPX3-13 specimen which did not go through two heating cycles. Both specimens were tested with a glueline temperature of 65°C. The EPX3-15 specimen also demonstrated an increase in the capacity and stiffness even when compared to specimens tested with a lower glueline temperature, as shown in Figure 13.

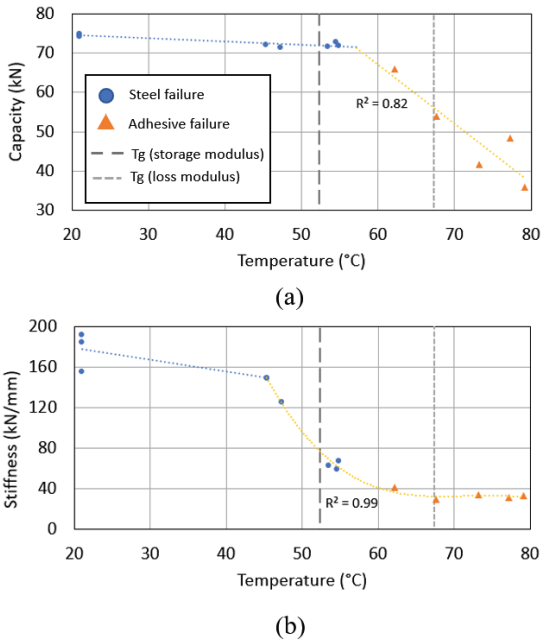

***Figure 8:** (a) Capacity and (b) stiffness evolution of EPX1*

https://doi.org/10.52202/069179-0214

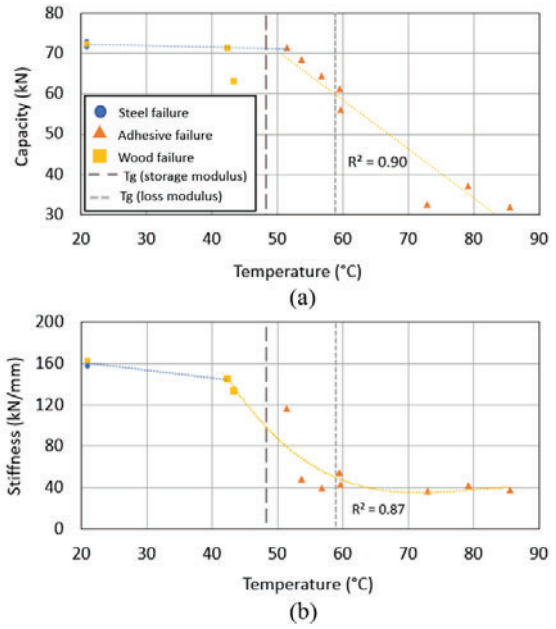

Figure 9: *(a) Capacity and (b) stiffness evolution of EPX2*

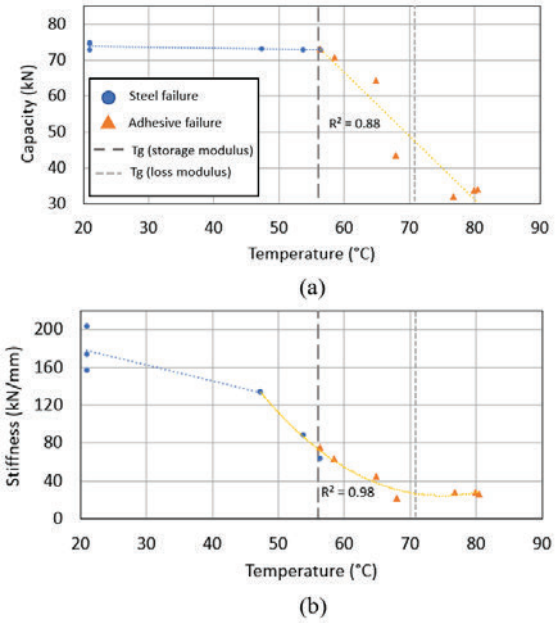

Figure 11: *(a) Capacity and (b) stiffness evolution of PUR1*

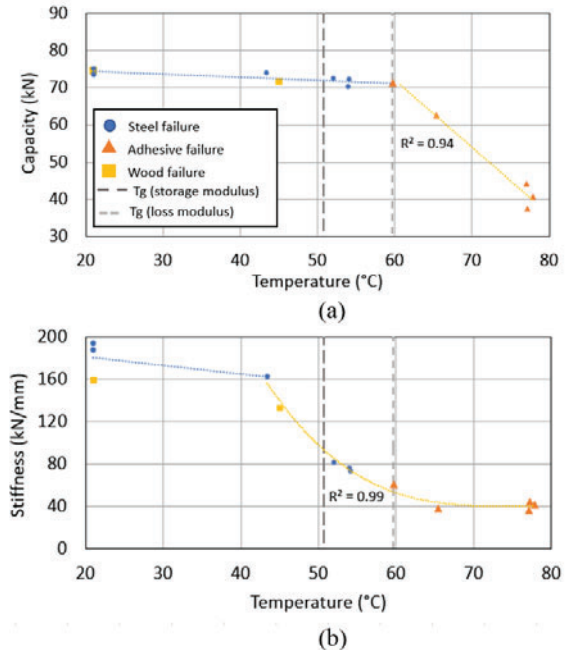

Figure 10: *(a) Capacity and (b) stiffness evolution of EPX3*

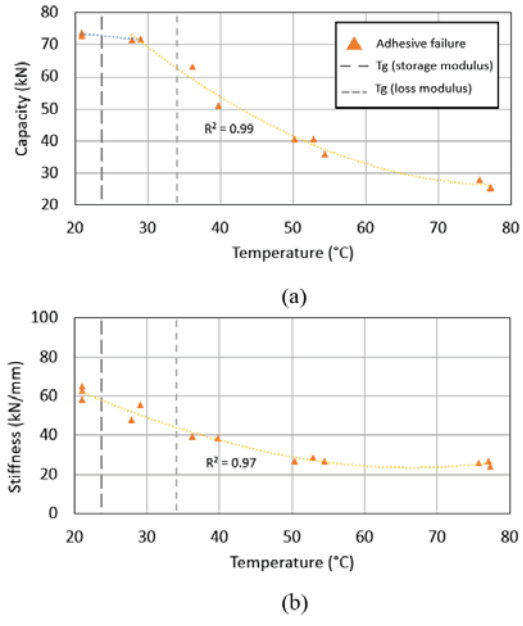

Figure 12: *(a) Capacity and (b) stiffness evolution of PUR2*

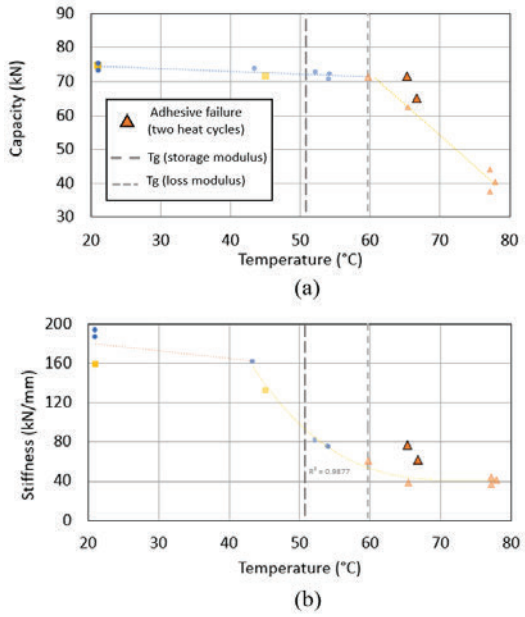

Figure 13: *Effect of post-cure on the (a) capacity and (b) stiffness of glued-in rods with EPX3*

4 DISCUSSION

The DMA tests revealed that the T_g of all adhesives, except that of the PUR2, was similar. Therefore, the thermomechanical behavior of each glued-in rod specimens could be easily compared, and correlations can be drawn. A significant increase in the capacity and stiffness occurred in both specimens that were exposed to two heating cycles, i.e. where a post-cure effect was intentionally evaluated. The latter suggest that the method chosen to evaluate the thermomechanical properties of the glued-in rods did not enable the adhesive to fully crosslink, leading to representative results.

The results of the axial tension test suggest that the mechanical properties of the adhesive, thus the glued-in rod connections, are considerably affected when the glueline interface is exposed to elevated temperatures. As it can be observed in this research, the Tg found through the storage modulus of a DMA test is a good indication that the connection will not have the same mechanical behavior, regardless of the adhesive. In fact, all specimens have shown that when exposed to temperatures below the storage modulus, only a small decrease of the capacity occurred (≤4%) while a more noticeable decrease in the stiffness was observed (≤29%). However, the failure mode remained ductile in most specimens.

When the glueline temperature exceeded its T_g found through the storage modulus, the stiffness of all adhesives dropped by up to 70% compared to their initial stiffness. The failure mode occurred in the adhesive layer rather than the steel rod in three adhesive specimens, while it remained ductile in the other two adhesives tested. As the temperature at the glueline interface increased closer to the Tg of the loss modulus specific to each adhesive, all specimens had a brittle failure mode in the adhesive layer. This suggests that the thermomechanical behavior glued-in rods at this temperature is dependent on the nature of the adhesive.

The loss of capacity and stiffness of glued-in rods at elevated temperatures can be attributed to the increased mobility of molecules in the internal structure of the adhesive, leading to a rubbery state of the latter. This also translated into an undesired failure in the adhesive layer.

These observations align with the results of Verdet *et al.* [7], Lahouar *et al.* [8], Lartigau *et al.* [9], Di Maria *et al.* [12] and Luo *et al.* [15]. However, the findings of this research have determined that the Tg found through the storage modulus of a DMA test would be a reliable limit to impose for the temperature at the adhesive interface. These observations could pave the way for provisions and guidelines for the fire design of glued-in rods.

For example, to design a glued-in rod with the EPX1 adhesive (i.e. with a Tg from storage modulus of 52°C) required to provide a fire resistance rating of 1h without using protective materials, the designer would:

1. Determine the depth of the char layer from Eq.1:

$$x_{c,n} = 0.7 \times 60 = 42\ mm$$

2. Determine the position at which the temperature would reach the Tg from the storage modulus after 1h of fire from an adaptation of Eq.2:

$$x = \frac{35}{\sqrt{\frac{52-20}{300-20}}} = 103.5\ mm$$

3. Add both values:

$$Min.dimension = 42 + 103.5 = 145.5\ mm$$

Therefore, a glued-in rod fabricated with the EPX1 and a cross-sectional dimension greater than 146 x 146 mm would be adequate to resist a 1h fire scenario. This would assume that the butt-joint between the glulam elements would be properly fire-stopped to prevent fire penetrating and directly affect the steel rod.

5 CONCLUSION

Even though glued-in rods are a type of connection that is gaining in popularity, their thermomechanical behavior has been understudied, thus limiting its inclusion in standards around the world. Many researchers have suggested that the Tg of the adhesive used was the critical temperature at which the mechanical properties of the glued-in rods will deteriorate. Yet, the Tg is a range of temperature that can vary according to the method of determination chosen or the parameters used within a method. The results suggest that a Dynamic Mechanical

https://doi.org/10.52202/069179-0214

Analysis is an accurate method to inform on the properties of adhesives at different temperatures by determining the Tg through the storage modulus, loss modulus and tan δ. The objective of this research was to characterize the performance of adhesives used in glued-in rod connections at elevated temperatures. The following key observations have been found throughout this research for different temperatures at the connection's glueline interface:

1. All glued-in rod specimens had over 95% of their initial load-carrying capacity when the temperature at the bondline was lower than their respective Tg found through the storage modulus of a DMA test;
2. Except for the PUR2 specimen, no failure occurred in the adhesive layer below their respective storage modulus, while 3/5 adhesive specimens failed at temperatures just above the storage modulus;
3. All glued-in rod specimens had a brittle failure in the adhesive layer when the latter reached temperatures close to their respective loss modulus;
4. The stiffness of glued-in rods is most affected by elevated temperatures, with a decrease of up to 70% at temperatures just above the storage modulus;
5. The axial tension test at stabilized temperature did not enable a considerable post-cure effect, thus providing representative results on the thermomechanical properties of glued-in rods.

Therefore, the Tg determined through the storage modulus of a DMA test would be a reliable limit to impose for the temperature at the adhesive layer. Above the latter, the thermomechanical behavior of the connection is dependent on the nature of the adhesive, which could lead to unsafe connections. It is recommended to take precautions, i.e. protect with gypsum board, fire protective coatings or increase the section dimension, to limit a temperature rise above the Tg found through the storage modulus of a DMA test at the bondline.

Future research on the fire performance of glued-in rods should include an exposure to a standard fire curve, more repeatability at temperatures between the storage modulus and loss modulus, and/or evaluate the fire performance of glued-in rods subjected to a bending moment.

Some limits of this research include the grade of the ASTM A307 rod, since only a minimal tensile strength of 414 MPa is required by the standard. Furthermore, the charring at the butt joint of the connection, which could expose the steel rod to high temperature and increase the heat conductivity along the rod was not considered.

REFERENCES

[1] CSA (2019). "Engineering design in wood (CAN/CSA Standard No.O86-19)." *Standard*, Canadian Standards Association., Toronto, Canada. 566 p.

[2] Buchanan, A. H. and Abu, H. (2016). "Structural Design for Fire Safety." John Wiley & Sons Ltd, 440p.

[3] Bengtsson, C., Johansson, C-J. (2002). *GIROD – Glued In Rods for Timber Structures.* Swedish National Testing and Research Institute.

[4] Lahouar, M. A., Caron, J.-F., Foret, G., Benzarti, K., and Mege, R. (2018). "Temperature effect on the mechanical behavior of glued-in rods intended for the connection of timber elements." *Construction and Building Materials*, 186, 438–453.

[5] Lartigau, J., Coureau, J.-L., Morel, S., Galimard, P., and Maurin, E. (2015). "Effect of temperature on the mechanical performance of glued-in rods in timber structures." *International Journal of Adhesion and Adhesives*, 57, 79–84.

[6] Park, J.-S., Buchanan, A. H., and Lee, J.-J. (2006). "[this article has been retracted] fire performance of laminated veneer lumber (LVL) with glued-in steel rod connections." *Journal of Fire Sciences*, 24(1), 27–46.

[7] Verdet, M., Salenikovich, A., Cointe, A., Coureau, J.-L., Galimard, P., Munoz Toro, W., … Christine Delisée. (2016). *Mechanical performance of polyurethane and epoxy adhesives in connections with glued-in rods at elevated temperatures.* Biosources, 11(4), 8200-8214.

[8] Lahouar, M. A., Caron, J.-F., Pinoteau, N., Forêt, G., and Benzarti, K. (2017). "Mechanical behavior of adhesive anchors under high temperature exposure: Experimental investigation." *International Journal of Adhesion and Adhesives*, 78, 200–211.

[9] Lartigau, J., Coureau,. Lartigau, J., Coureau, J.-L., Morel, S., Galimard, P., & Maurin, E. (2015). *Effect of temperature on the mechanical performance of glued-in rods in timber structures*. International Journal of Adhesion and Adhesives, *57*, 79–84.

[10] Kotynia, R., Adamczewska, K., Strąkowska, A., Masłowski, M., and Strzelec, K. (2017). "Effect of accelerated curing conditions on shear strength and glass transition temperature of epoxy adhesives." *Procedia Engineering*, 193, 423–430.

[11] Yang, T.-H., Wang, S.-Y., Tsai, M.-J., Lin, C.-Y., and Chuang, Y.-J. (2009). "Effect of fire exposure on the mechanical properties of glued laminated timber." *Materials &amp Design*, 30(3), 698–703.

[12] Di Maria, V., D'Andria, L., Muciaccia, G., and Ianakiev, A. (2017). "Influence of elevated temperature on glued-in steel rods for timber elements." *Construction and Building Materials*, 147, 457–465.

[13] Harris, S. (2004). “Fire resistance of epoxy-grouted steel rod connections in laminated veneer lumber (LVL),<https://ir.canterbury.ac.nz/handle/10092/14749>.

[14] Jahani, Y., Baena, M., Barris, C., Perera, R., and Torres, L. (2022). “Influence of curing, post-curing and testing temperatures on mechanical properties of a structural adhesive.” *Construction and Building Materials*, 324, 126698.

[15] Luo, L., Shi, B., Liu, W., Yang, H., and Ling, Z. (2020). “Experimental investigation on the fire resistance of glued-in rod timber joints with heat resistant modified epoxy resin.” *Materials*, 13(12), 2731.

[16] Carbas, R., da Silva, L., Marques, E., and Lopes, A. (2013). “Effect of post-cure on the glass transition temperature and mechanical properties of epoxy adhesives.” *Journal of Adhesion Science and Technology*, 27(23), 2542–2557.

[17] Custódio, J., Broughton, J., and Cruz, H. (2009). “A review of factors influencing the durability of structural bonded timber joints.” *International Journal of Adhesion and Adhesives*, 29(2), 173–185.

[18] Park, B.-D., & Kim, J.-W. (2008). *Dynamic mechanical analysis of urea–formaldehyde resin adhesives with different formaldehyde-to-urea molar ratios. Journal of Applied Polymer Science, 108(3), 2045–2051.* doi:10.1002/app.27595

[19] Mazzeo, F. (n.d.). “Characterization of pressure sensitive adhesives by rheology.” *TA Instruments, 8 p. USA*,<https://www.tainstruments.com/pdf/literature/RH082.pdf>.

[20] Lahouar, M. A., Caron, J.-F., Foret, G., Benzarti, K., and Mege, R. (2018). “Temperature effect on the mechanical behavior of glued-in rods intended for the connection of timber elements.” *Construction and Building Materials*, 186, 438–453.

[21] CSA (2021). “Structural glued-laminated timber (CAN/CSA Standard No.O122-21).” Standard, Canadian Standards Association, Toronto, Canada.

[22] ASTM (2021). “Standard specification for carbon steel bolts, studs, and threaded rod 60 000 psi tensile strength.” *Standard ASTM A307-21*, ASTM International, West Conshohocken, PA, USA. 6 p.

[23] CCMC (2021). “Swg assy® vg plus and swg assy® 3.0 self-tapping wood screws.” *Evaluation Report CCMC 13677-R*. National Research Council. 23 p.

[24] EN 26891 (1991). “Timber structures - joinst made with mechanical fasteners - general principles for the determination of strength and deformation characteristics.” *Standard*, European Committee for Standardization, BSI, Brussels. 6p.

https://doi.org/10.52202/069179-0214

World Conference on Timber Engineering Oslo 2023

NUMERICAL MODELLING OF CONTEMPORARY MASS TIMBER CONNECTIONS IN FIRE

Bronwyn Chorlton[1], Mathieu Létourneau-Gagnon[2], Christian Dagenais[3], Marc-André Langevin[4]

ABSTRACT: Timber buildings are becoming increasingly popular due to their sustainability and aesthetic appeal. There remains however, a need to fully understand the fire performance of mass timber construction, including the fire performance of the connection. Beam-column connections can be complex to assess in fire, due to the proprietary and custom nature of many connection designs. The purpose of this study is to create a numerical model that can assess the residual fire resistance capacity of mass timber connections exposed to fire. This endeavour was completed using finite element modelling considering heat transfer of mass timber connections. Two approaches were taken, first, the heat flux through the fastener's shank establishes the reduction factors that predict the residual thermal capacity of fasteners, and the second establishes the residual length of penetration that provide adequate structural capacity into timber elements. These thermal analyses work towards developing a simplified design method for evaluating mass timber connections exposed up to two hours of standard fire exposures. By providing additional information related to the expected temperatures and strengths of timber connections in fire, novel designs become more accessible for innovative timber structures.

KEYWORDS: fire, connections, mass timber, numerical modelling

1 INTRODUCTION

Fire design of connections in timber buildings faces unique challenges due to the interaction of combustible structural elements and noncombustible metallic fasteners that perform differently in fire conditions. Given that there are a multitude of possibilities for how mass timber connections might be designed, with trends for connection configurations continuing to be developed, design tools are needed for timber connections to understand the effect of parameters such as the number and size of fasteners used, as well as the spacing in between fasteners. While standard fire tests are always an option, this type of testing can be costly and time consuming when only a small change is made to a design in attempt to optimize either the thermal or the thermomechanical performance of the mass timber connection.

Traditionally, heavy timber construction used steel or iron caps, as well as large metallic hangers and plates (Figure 1). These were used on buildings where little to no fire-resistance rating was prescribed in building codes. When such a connection is used, the metallic cap directly transfers the gravity loads to the column below and the beams are directly supported on top of that column. As such, even if this cap heats and loses strength, it will most likely not result in structural collapse. Based on their good historical performance, it is usually agreed that this type of construction provides an acceptable level of fire safety.

Figure 1: *Traditional heavy timber construction using iron/steel connections.*

With the recent advances in mass timber construction and products, construction and design techniques have also evolved. Taller buildings are also typically required to provide greater fire-resistance ratings, up to 2 and 3-hours, which is much beyond the deemed performance of traditional timber construction. Innovative fasteners such as self-tapping screws are gaining lots of popularity due to their ease of use and high capacity, while being aesthetically pleasant. While there has been a shift towards shear-type connection (i.e., similar to steel

[1] Bronwyn Chorlton, Queen's University (formerly FPInnovations), bronwynchorlton@gmail.com
[2] Mathieu Létourneau-Gagnon, Technorm, mletourneau@technorm.ca
[3] Christian Dagenais, FPInnovations, christian.dagenais@fpinnovations.ca
[4] Marc-André Langevin, Technorm, malangevin@technorm.ca

https://doi.org/10.52202/069179-0215

construction), modern connection design is going back to traditional timber engineering method – that is to use as much of the timber embedment and compression strength and conceal all metallic components. Figure 2 shows a modern version of the same type of connection shown in Figure 1. Gravity loads are being transferred directly to the column underneath and beams are also supported by that column. Little to no forces are being transferred in the metallic (concealed) fasteners. While the engineering behind these designs are sound, there is a need to better understand the underlying thermomechanical properties and performance of modern mass timber connections.

Figure 2: *Modern timber construction using concealed connection.*

The objective of this study is to develop a numerical model using finite element analysis software that can predict the thermomechanical behaviour of contemporary mass timber connection configurations, for exposure durations longer than one hour. The development of these models will provide information to designers regarding the distribution of the temperatures in different connection configurations, allowing for an understanding of the heating rate through the fastener's shank into timber element for a standard fire exposure. The results will ultimately be used to validate an analytical model to predict the structural fire resistance of connections in design standards.

2 BOLTED CONNECTIONS

Herein, a series of experimental studies will be discussed to assess the developed numerical model. Many of these tests consider the timber assembly loaded in tension parallel to grain, and for a relatively short duration.

From the University of Canterbury, Chuo [1] considered the fire performance of Hyspan laminated veneer lumber connections. The connections were loaded to either a factor of the characteristic strength of the bolts used, and exposed to the ISO 834 [2] standard fire. The fire resistance of the connections was found to be less than 25 minutes.

In 2010 from Carleton University, Peng [3] published an experimental test series looking at the performance of wood-steel-wood and steel-wood-steel bolted connections using 20f-EX S-P glulam (test groups 2 through 5) and No. 2 SPF dimensional lumber (test group 1), loaded in axial tension and exposed to the CAN/ULC-S101 [4] standard fire, where it was found that the fire resistance of the bolted connections was less than 45 minutes. The tests were loaded to a fraction of their calculated ultimate load capacity. The experimental component of the study was followed by the creation of a finite element model which agreed well with the experimental data.

Also from Carleton University were test series completed by Alam [5] and Ali [6]. Alam tested four wood-steel-wood connections in tension, exposed to the CAN/ULC-S101 standard fire. The wood members in Alam's study were 24F/NPG glulam while Ali used 24F/ES12 glulam. Alam's assemblies were loaded to their calculated faxtored axial tensile strengths, and times to failure ranged from 12 to 32 minutes. Ali performed bending tests of beam-to-column timber connections, with either concealed, seated, or exposed steel plates. The glulam beams were 140 × 191 × 1 900 mm, and were loaded using third point loading configuration. The specimens were exposed to the CAN/ULC-S101 standard fire. Only Tests 1.1 and 1.2 by Ali are considered herein, both concealed steel connections (e.g., knifeplate connections).

Select connections from the above experimental tests from literature are considered in analysing the model results in Section 2.2 of this study. The connections considered herein are outlined in Table 1.

2.1 METHOD

A numerical model was created using ABAQUS to carry out transient heat transfer modelling of metallic fasteners into the timber. The purpose of this model was to determine the temperature profiles of the metallic fasteners, in order to understand how much strength could potentially be lost during heating that occurs during the thermal exposure. Bolted connections were considered due to experimental data regarding these connection types being widely available in literature.

In developing the ABAQUS model, bolts were assumed to have a hole 2 mm greater than the diameter of the bolt, as per CSA O86 [7]. Thus for this analysis, a 1 mm air space was assumed to be evenly surrounding the bolt. In reality, a portion of the bolt would be in contact with the surrounding wood, and a portion will have an air gap larger than 1 mm, however, previous studies have found that the size of air gap has little effect on heat transfer when the size of the gap is less than 4 mm [3]. Washers were assumed to be located between the bolt head and the top surface of the timber, and were taken as the maximum washer size as permitted by CSA O86. Fastener threads have been neglected in this model, as previous studies have found that neglecting threads can reduce computational time without significantly affecting the heat transfer of the model [8].

https://doi.org/10.52202/069179-0215

Table 1: *Summary of parameters of experimental tests from literature considering bolted connections.*

Test	t_1[1] (mm)	t_2[2] (mm)	d_f[3] (mm)	n_R[4]	n_c[5]	Load (kN)
Chuo – 1	45 × 150	63	12	1	1	23
Chuo – 2	45 × 150	63	12	3	1; 2[6]	4.9
Peng – 1	2@38 × 140	9.5	12.7	1	2	17.4
Peng – 2	130 × 190	9.5	12.7	2	2	34.5
Peng – 3	130 × 190	9.5	19.1	1	1	19.5
Peng – 4	130 × 190	9.5	19.1	2	2	68.1
Peng - 5	2@80 × 190	9.5	19.1	2	2	72.9
Alam – 1	137 × 178	9.5	12.7	2	2	72
Alam – 2	2@86 × 178	9.5	12.7	2	2	80
Alam – 3	228 × 267	9.5	19.1	2	2	162
Alam – 4	2@137 × 267	9.5	19.1	2	2	175
Ali – 1[7]	140×191 ×1900	9.5	19.1	2	2	21.5
Ali - 2[7]	140×191 ×1900	9.5	12.7	2	2	21.5

1 – Side member thickness
2 – Centre member thickness – all steel; except Chuo 1 and 2
3 - Fastener diameter
4 – Row number
5 - Number of fasteners in a row
6 – Two rows of 2 fasteners, 1 row of 1 fastener
7 – Concealed beam-column connection

Connections were subjected to the CAN/ULC-S101 from one side, and the distribution of temperatures through the fastener's shank into timber element were observed. A schematic of the ABAQUS model is seen in Figure 3. The transient heat transfer modelling was compared to temperatures as reported in existing literature.

Based on the interaction of timber and steel, the residual capacity of the connections exposed to the CAN/ULC-S101 standard fire was estimated. This was done by assessing the temperature at the interface of the shank of the bolt with the timber, and reducing the strength of the bolt according to temperature, as per the steel reductions outlined in CSA S16 [9]. Though the temperature on the outside of the bolt may not be quite as hot as at the centre of the bolt, assessing temperature along the side will allow for comparison with any future experimental testing in which a thermocouple could be placed at the interface of the timber and the bolt. The degradation of the timber followed the reduced cross section method as outlined by Annex B of CSA O86. A schematic of the ABAQUS model for a 12.7 mm bolt after 15 minutes of standard fire exposure is seen in Figure 4.

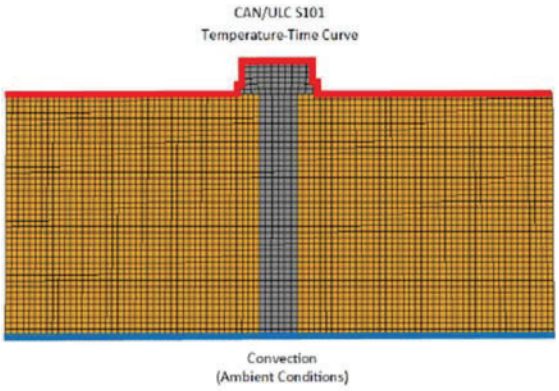

Figure 3: *Schematic of ABAQUS model (15 min exposure).*

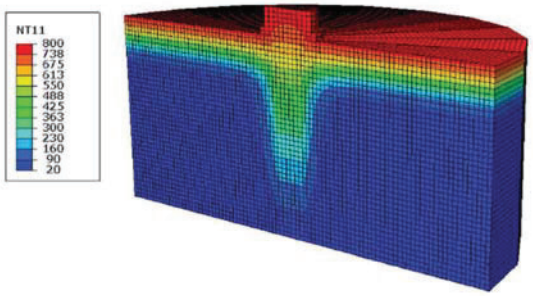

Figure 4 : *Schematic of ABAQUS model (15 min exposure).*

It is noted that only thermal degradation of the timber and the metallic bolt are considered herein. Strength loss of any steel plates used in the connection is not considered. This assumption was made as the ABAQUS model only considers heat transfer in one dimension. Thus, the steel plates largely remained at ambient temperature throughout the duration of the thermal exposure. However, for longer thermal exposures and more severe thermal exposures, strength loss of the steel plate due to fire should be explicitly considered.

2.2 RESULTS

Figure 5 presents a comparison of the experimental fire resistance as reported in the literature, the calculated fire resistance time considering only the degradation of the timber (the bolt is considered to retain full strength), and the calculated failure resistance time considering both the degradation of the timber, as well as a reduction of strength of the bolt using temperatures extracted from the ABAQUS model and reduced per Annex K of CSA S16. The temperature of the bolt was taken at the intersection of the bolt and the timber, along the top surface of the timber (immediately below the washer). Through the analysis, temperature of the bolt was taken at other locations along the shank for consideration and analysis into the optimal depth to read bolt temperature – these

depths included at set depths (e.g., 10 mm from the face of the timber), and as a function of the final char depth (e.g, 10% the depth of the char). It was found that using the temperature directly beneath the washer resulted in greater temperature (thus greater steel strength reduction), and ultimately better predictions of the failure times.

For the most part, the calculated results were more closely aligned with the experimental results when considering a strength reduction for the steel bolt, correlated with temperature. The exception to this would be the experiments performed by Alam [5], where the specimens were loaded to the CSA O86 predicted ambient factored failure load. Thus, any additional reduction in strength, either via the charring of the timber cross-section or the reduction in steel strengths only shortened the calculated fire resistance time. The experimental fire resistance time was therefore much greater than predicted.

The test series by Ali [6] considering beam-column connections in bending were also analysed using the method outlined above. It can be seen in Figure 5, in the case of Ali, that the modelling used to reduce the strength of the fastener did not affect the predicted fire resistance of the assembly. This is because the failure mode, considering only the timber's reduction in cross-sectional area, was found to be bending at the connection, which is not dependant on the strength of the fastener. Nevertheless, considering the degradation of the timber only, the calculated results had relatively good agreement with the experimental tests (with a calculated failure at 38 min, compared to 33 min for Test 1.1, and 40.3 for Test 2.1).

The calculated results, as seen in Figure 5, still had some deviation from the experimental results. However, considering the reduction in steel fastener strength at high temperature in addition to reduction of timber cross section did make a considerable difference in more closely aligning the experimental and calculated fire resistance times. Considering the degradation of the timber only, the average percent difference between the experimental and calculated fire resistances was 87%, whereas considering the degradation of the timber in addition to the strength reduction of the bolt, the average percent difference between experimental and calculated fire resistances was 37%.

2.3 DEVELOPMENT OF REDUCTION FACTORS FOR BOLTS

As it was found that the calculated fire resistance times were better aligned to the experimental results when the strength reduction of the bolts at high temperatures are considered, a series of reduction factors are proposed herein. From the temperature of the bolt at a given time – either 15 or 30 mins – a reduction factor was determined per the reduction factors outlined in CSA S16-19 Annex K [9] which is applied to the ultimate and yield strengths of the steel fastener. The reduction factors are in relation to the initial strength of the material (i.e., the strength at 20 °C). The resulting reductions for each fastener type are summarized in Table 2. It should be noted that the results of this study are, at this point in time, limited to the tests available in literature. Thus, the results are limited to 12.7 and 19.1 mm bolts, tested for up to a maximum of 31 minutes. Model development also relied on experimental tests of tension connections, with a bending test also considered as a point of comparison (however the calculated failure mode of the bending test was independent of bolt temperature). Thus, the results of Table 2 apply to short duration fires where the members are loaded in tension.

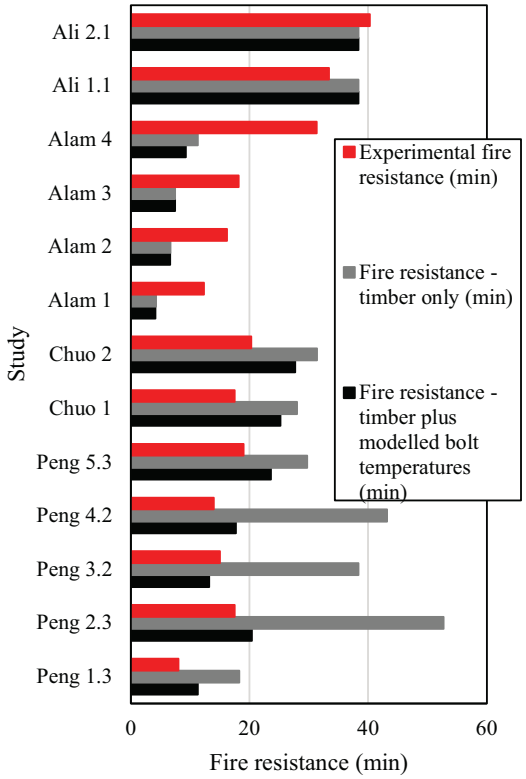

Figure 5: *Experimental and calculated fire resistance times for the tensile tests.*

The reduction factors were applied to the steel strengths within the connection equations of CSA O86-19. In essence, the reduction factors would be applied to the steel fastener strengths, and the capacity evaluation of the connection would be combined with a reduced cross-section approach for the timber portion of the connection (i.e., the dimensions of the timber will reduce with the time of fire duration, accounting for the charring rate and zero-strength layer set out by Annex B of CSA O86-19 [7]).

While the outcomes detailed herein provide a basis towards a calculation method in which the connection of timber structures can be considered at high temperature, further research and testing are needed to expand the applicability of these results. With additional testing of longer durations and testing of other connection configurations, the method presented in this study of deducing a reduction factor from the expected thermal

https://doi.org/10.52202/069179-0215

profile of a fastener can be extended to scenarios beyond short duration fires on tension connections.

Table 2: *Proposed reduction factors*

Bolt size (mm)	Standard Fire Exposure (min)	Steel Reduction Factor
12.7	15	0.22
	30	0.13
19.1	15	0.26
	30	0.15

3 SELF-TAPPING SCREWS

The fire performance of the self-tapping screw (STS) is mainly influenced by the residual capacity of the wood surrounding the fastener, i.e., the residual penetration length. This residual penetration length is affected by the heat conduction through the fastener shank which depend on its thermal capacity and fire exposure [10].

To evaluate the conductive heating rate of different mass timber fasteners, another transient heat transfer model using the finite element (FEM) method was developed to compare the effects of geometric parameters on the thermal behaviour of the fastener, such as the length, the size of the head, and the shank diameter.

3.1 MATERIALS AND METHODS

Six full-thread screws with self-drilling tip and countersunk head (SWG ASSY®3.0 VG CSK) and one full-thread screw with self-drilling tip and cylinder head (SWG ASSY®3.0 VG CYL) were examined with the head exposed to CAN/ULC-S101 standard fire. The STS are made of carbon steel and have a bending yield strength of 1015 to 1147 MPa and a shear strength of 341 to 533 MPa, depending on the types of STS [11]. Three high-strength structural bolt diameters (Ø12.7 mm, Ø19.1 mm and Ø25.4 mm) were examined. A length of penetration of 200 mm was assumed for all bolt-type fasteners. In attempt to evaluate the impact of bolt head, one dowel diameter of Ø12.7 mm were also examined. The dimensions of fasteners are presented in Table 3 and Table 4.

Table 3 : *Dimensions of self-tapping screws in accordance with CCMC 13377-R [11]*

Outside Thread Diameter (d_F) (mm)	Head Diameter (d_{head}) (mm)	Shank Diameter (d_{min}) (mm)	Length (L)/ Threaded length (L_F) (mm)	Penetration (mm)
10[1]	13.4	6.2	200/185	200
8	14.8	5	200/183	200
10	19.6	6.2	100/77	100
10	19.6	6.2	200/185	200
10	19.6	6.2	400/385	400
10	19.6	6.2	800/782	800
12	22.1	7.1	200/185	200

[1] Full-thread screw with self-drilling tip and cylinder head

Table 4 : *Dimensions of dowel and bolts.*

Fastener Head Diameter (d_F) (mm)	Shank diameter (d_{min}) (mm)	Length (L)/Threaded Length (L_F) (mm)	Lead Hole Diameter (mm)	Penetration (mm)
12.7[1]	12.7	177.8/25.4	12.7	200
22.23	12.7	177.8/25.4	12.7	200
31.75	19.05	177.8/34.9	19.1	200
41.28	25.4	177.8/44.5	25.4	200

[1] Dowel

Each fastener was inserted in a glulam of the 20f-EX spruce-pine stress grade conforming to CSA O122 [12]. The exposed top surface of timber element was 100 mm diameter with 8-ply of 35 mm, as shown in Figure 6. For the STS with a length of 400 mm and 800 mm, the STS was inserted in a 17-ply glulam and a 24-ply glulam to fully surrounding the STS with wood fibres.

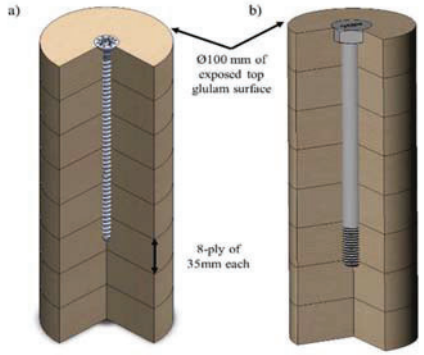

Figure 6 : *Geometrical configurations: a) Ø10 × 200 mm SWG ASSY®3.0 VG CSK inserted in 8-ply glulam; b) Ø12.7 × 179 mm A325 bolt inserted in 8-ply glulam.*

The three-dimensional transient heat transfer model through a solid timber using ANSYS was developed with a fastener inserted at the geometric center of the glulam element in attempt to characterize the thermal penetration depth of fasteners. The top surface of the glulam specimen and the head of the fastener were exposed to the CAN/ULC S101 standard fire for two hours. Eleven (11) heat transfer models were developed, i.e. one for each fastener type. The same boundary conditions were applied, as previously discussed in Section 2.1. Due to symmetry, the transient thermal model was performed only for one quarter of the specimen and cylindrical shank of the fastener (i.e., no threads), as shown in Figure 7a). The 3D temperature fields were also divided into elements with a length of 3 mm using 3D hexahedral elements.

To compare the temperature distribution between the simulation and the fire tests, five (5) coordinate systems and five (5) thermocouples were created in the heat transfer model at the exposed surface (0 mm), 1st glueline (35 mm), 2nd glueline (70 mm), Mid-length of the fastener, 3rd glueline (105 mm), and the tip of the fastener as presented in Figure 7b).

https://doi.org/10.52202/069179-0215

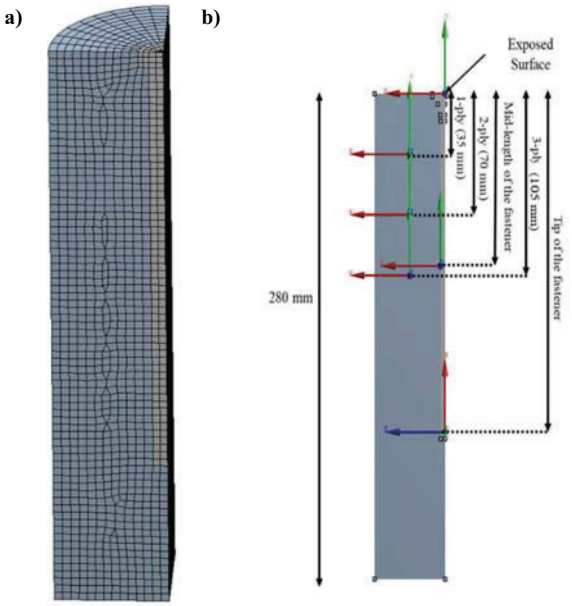

Figure 7 : *Geometrical parameters used for heat transfer modelling of 8-ply glulam.: (a) Meshing; (b) Distance of thermocouples from the exposed surface along Ø10 × 200 mm SWG ASSY®3.0 VG CSK.*

3.2 RESULTS

3.2.1 Influence of STS fastener diameter

Exposing the cylinder head (CYL) and the countersunk head (CSK) of Ø10 × 200 mm STS had some influence on the temperature distribution along the fastener. For similar temperatures at the fasteners' head, the thermocouples at the mid-length (100 mm), and at the tip (200 mm) of the STS estimated temperatures of 402 °C and 143 °C for CYL, whereas the temperatures reached 413 °C and 151 °C for CSK after two hours of fire exposure, as shows in Figure 8. The variation of temperatures between the two STS was due to the larger head diameter at the exposed surface, which was 19.6 mm for the CSK compared to 13.4 mm for the CYL. While little differences were observed, the results suggest that the larger heated area of CSK increases the amount of heat conduction along the shank inside the timber.

Moreover, the shank diameter of the fastener was also influencing the temperature distribution along the fastener when comparing the different diameter shank of CSK fastener. For instance, the temperature of the Ø8 mm CSK at the tip (200 mm) was around 110 °C, compared to 133 °C at the tip (200 mm) of the Ø12 mm CSK after two hours, as shown in Figure 8.

The same results are being observed with bolts and dowel where the temperature through the fastener increases with the diameter of the head and shank. Figure 9 shows the measured temperatures of the bolts and dowels analyzed. As expected, the bolt and dowel fasteners reached much higher temperatures along the fastener shank due to the larger thermal capacity.

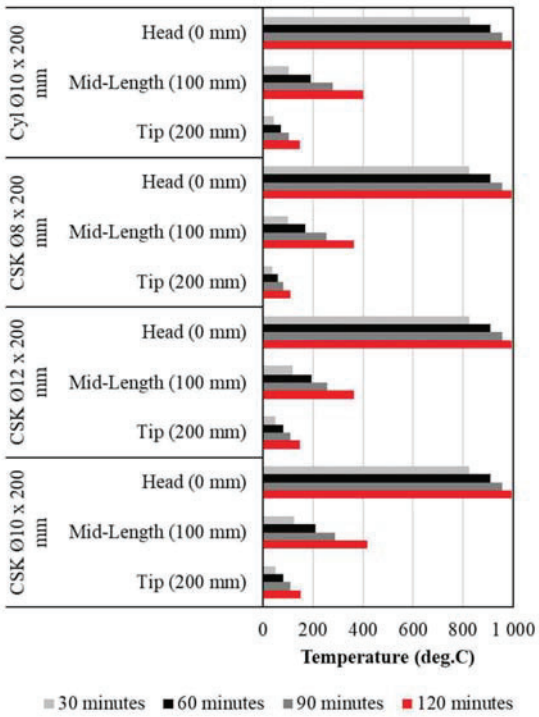

Figure 8 : *Distribution of temperatures on unprotected STS head using three (3) various STS outside diameters under the CAN/ULC-S101 [4] standard fire .*

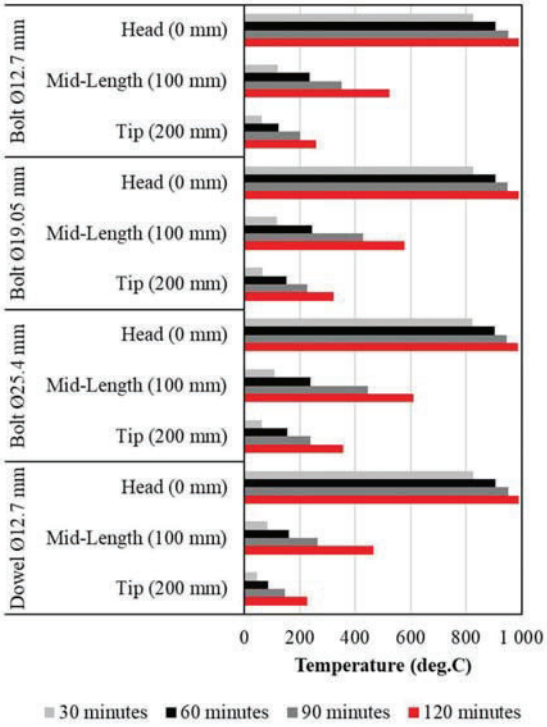

Figure 9 : *Distribution of temperatures on unprotected bolt and dowel head using (3) various shank diameters under the CAN/ULC-S101 [4] standard fire .*

https://doi.org/10.52202/069179-0215

In attempt to evaluate the impact of the shank diameter on the temperature distribution along the fastener, Figure 10 presents the temperatures at the mid-length (i.e., depth of 100 mm) of the screw-type and bolt-type of 200 mm long fasteners when exposed to the standard fire of CAN/ULC S101 for one and two hours. Three (3) shank diameter of screw-type fasteners (i.e., Ø5 mm, Ø6.2 mm, and Ø7.1 mm) and three (3) shank diameter of bolt-type fasteners (i.e., Ø12.7 mm, Ø19.05 mm, and Ø25.4 mm) were analyzed to compare the heat transfer through the fastener's shank.

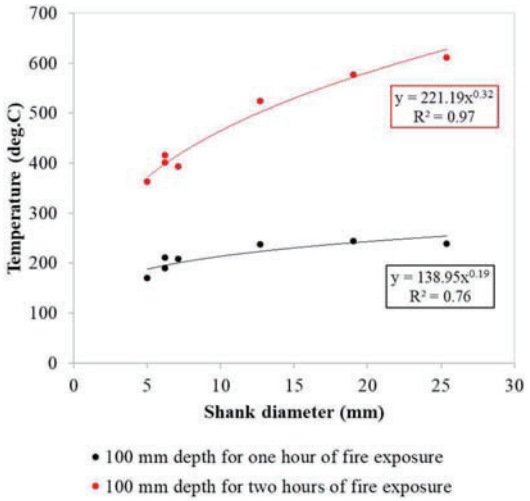

Figure 10 : *Temperatures on different fastener shanks exposed to the CAN/ULC-S101 [4] standard fire .*

The temperature distribution seems to increase as a power function with the shank diameter of the fastener, as illustrated in Figure 10. Influenced by the duration of fire exposure with higher temperatures for longer exposure, the power functions generated from the temperature data predicted by the FEM model shows high coefficients of determination R^2, suggesting that the natural power fitting curve is adequate (which is somewhat expected given that the standard fire exposure is characterized using a power curve). This effect demonstrates that the temperature along the fastener seems to increase as a power function with the shank diameter of the fastener, regardless of fastener types. Therefore, the results support the assumption that the conductive heating rate through the fastener shank is proportional to the amount of exposed area and thereby increasing as a power form with the shank diameter of the fastener, regardless of fastener types.

3.2.2 Influence of fastener length

The length of fasteners showed the greatest influence on the temperature distribution along the fastener shank. The ability of STS to penetrate the timber further away from the exposed surface allows the timber thermal capacity to limit heat transfer along the fastener. This effect was observed by increasing the length of Ø10 mm STS exposed to two hours of fire exposures, as shown in Figure 11.

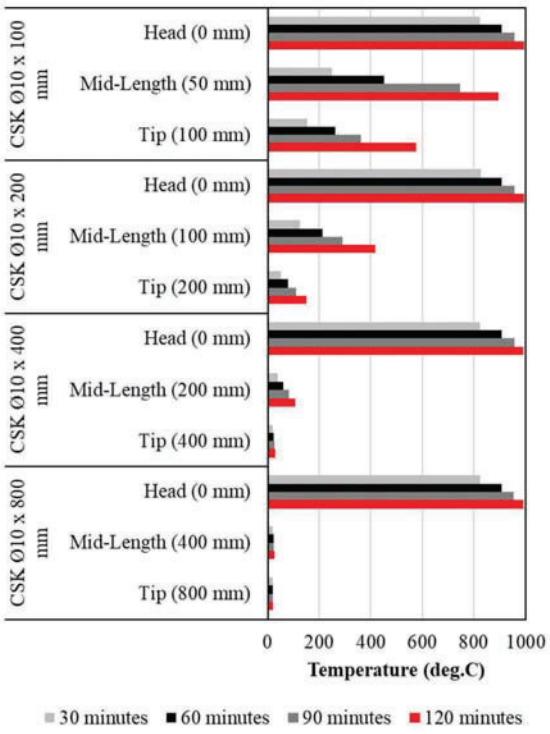

Figure 11 : *Distribution of temperatures on unprotected STS head using three (3) various STS lengths exposed to under the CAN/ULC-S101 [4] standard fire.*

For similar diameter at the head and the shank, using longer STS decreases the temperature along the fastener. For instance, the tip temperature of a 100 mm long STS (i.e., depth of 100 mm) is 154 °C, while a mid-length temperature of 200 mm long STS reached of 124 °C at the same distance from the exposed surface after 30 min, as shows in Figure 11. In addition, the 400 mm and 800 mm long STS maintain temperatures under 100°C along the screw at its mid-length and tip for up to two hours of fire exposure.

In attempt to evaluate the impact of the length of the fastener on the temperature distribution along the fastener, Figure 12 presents the temperatures at a depth of 100 mm and at a depth of 200 mm for a Ø10 mm STS by increasing the length of STS between 100 mm to 800 mm. The temperature distribution by increasing the length of fastener did not have a substantial influence on the heat transfer through the fastener, as similar temperatures were noted at the same depth from the exposed surface under one and two hour of fire exposures. Although the temperatures were very high for the screw length of 100 mm, the temperatures were similar for all screws at a depth of 100 mm and 200 mm, as illustrated in Figure 12. This effect demonstrates that longer STS did not substantially influence the temperatures through the fastener shank under longer fire exposure. The insulation effect of timber limits the thermal penetration along the fastener by the high slenderness of the STS (i.e., the ratio of their diameter to their length). It should be noted that higher temperatures for the screw length of 100 mm are

likely because the tip of the STS was not deep enough to limit the thermal penetration than those at a depth of 200 mm. Therefore, the temperature profiles through fasteners depend mainly on the diameter of the fastener rather than its length.

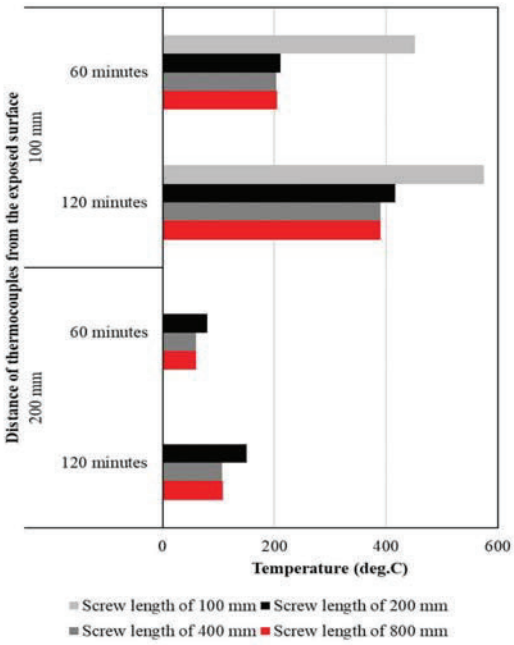

Figure 12 : *Temperatures on different lengths of Ø10 mm STS exposed to the CAN/ULC-S101 [4] standard fire.*

3.2.3 Effect of Fasteners on the Timber Charring Rate

The heat transfer model after two hours of standard fire exposure is presented in Figure 13 and Figure 14. These results were obtained by applying the 300 °C isotherm of the heat transfer model and measuring the distance between the char line to the exposed surface after one and two hours of standard fire exposures.

The fastener contributes by increasing the charring depth due to the larger thermal capacity. Due to the high conductivity of the steel, the heat transmitted through the fastener shank leads to higher temperatures into the timber. This effect was observed when comparing the heat transfer model of the bolt and the STS after two hours of fire exposures. For instance, the char depth was limited along the STS shank while the bolt shank created a notable char depth. This difference was caused by the larger heated area of the bolt shank that conducted heat faster and affected the timber surrounding the steel shank, whereas smaller screws had limited the temperature into the timber.

Although the diameter was found to be the major geometric parameter on the heating rate along the STS, longer fastener will increase the STS's effective length of penetration with more threads fully secured in unaltered wood fibers, which are still at ambient conditions (i.e., full capacity). When considering the mechanical properties of the wood fibers at a maximum of 100°C to retain sufficient residual strength, Létourneau-Gagnon et al. [10] demonstrated that the capacity of a STS was not influenced with an increase of fire exposure duration. While CSK Ø10 × 100 mm and CSK Ø10 × 200 mm have wood fibers above 100 °C along the entire shanks, CSK Ø10 × 400 mm and CSK Ø10 × 800 mm have wood fibers of 100 °C at a depth of 218 mm from the exposed surface. In fact, the residual penetration length for the 400 mm and 800 mm STS is 182 mm and 582 mm, respectively, after two hours of standard fire exposure, which can be defined as the length of penetration that will provide adequate structural capacity [10]. Therefore, longer screws would provide longer fire-resistance than shorter screws.

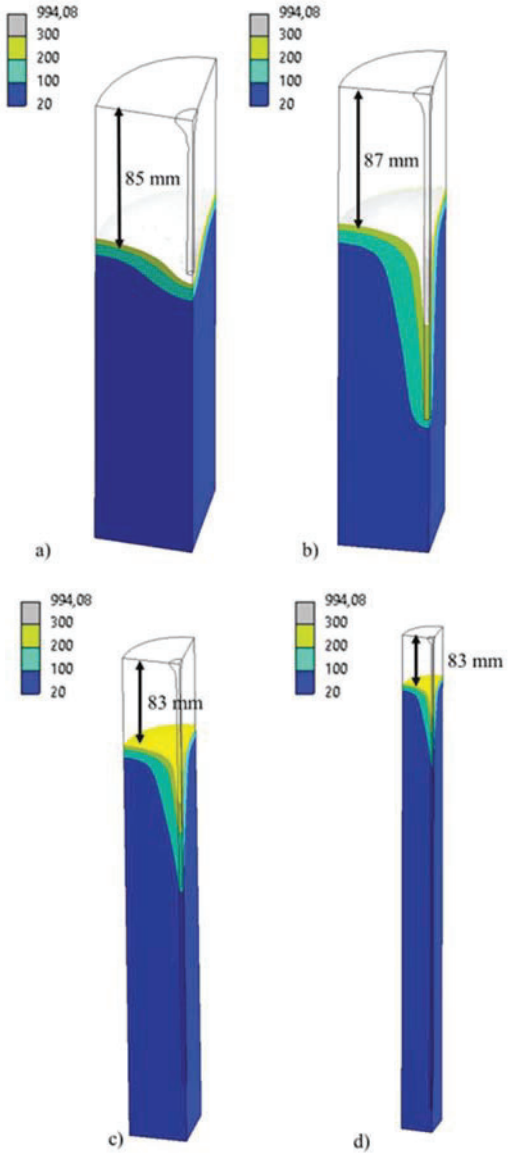

Figure 13 : *Heat transfer model exposed to the CAN/ULC-S101 [4] standard fire curve for two hours: a) Ø10 × 100 mm SWG ASSY®3.0 VG CSK; b) Ø10 × 200 mm SWG ASSY®3.0 VG CSK; c) Ø10 × 400 mm SWG ASSY®3.0 VG CSK; d) Ø10 × 800 mm SWG ASSY®3.0 VG CSK (Temperature in °C)*

https://doi.org/10.52202/069179-0215

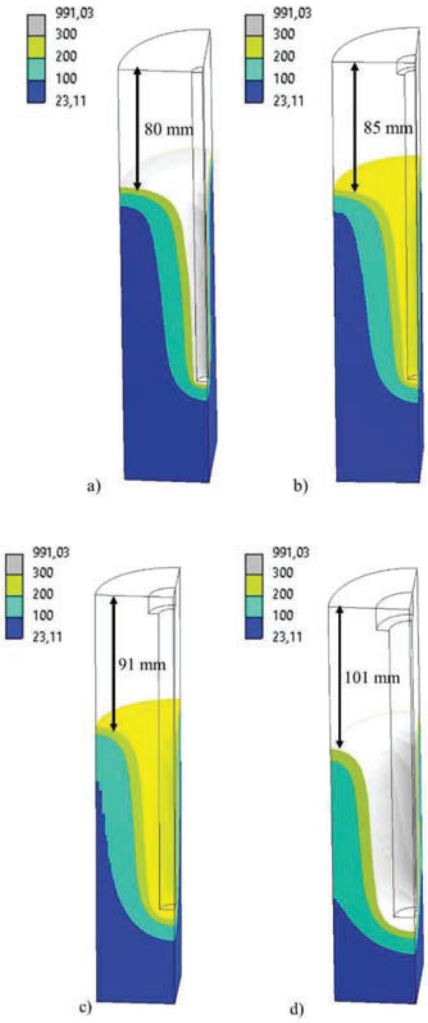

Figure 14 : *Heat transfer model exposed to the CAN/ULC-S101 [4] standard fire curve for two hours: a) Dowel Ø12.7 mm ; b) Bolt Ø12.7 mm; c) Bolt Ø19.05 mm; d) Bolt Ø25.4 mm (Temperature in °C)*

4 CONCLUSION

With the recent advances in mass timber construction and products, construction and design techniques have also evolved. Taller buildings are also typically required to provide greater fire-resistance rating, up to 2 and 3-hours, which is much beyond the deemed performance of traditional heavy timber construction. There is a need to better understand the underlying thermomechanical performance of the mass timber connection.

This study continues the development of a numerical model that aims to comprehensively simulate the thermal-structural performance of mass timber connections. The results of the novel developments towards this endeavour include the determination of reduction factors reflective of a simplified method for calculating the strength of a connection subject to a standard fire (e.g., CAN/ULC S101). The existing model was also expanded to consider contemporary connection types including those that use self-tapping screws.

Results from the numerical modelling suggest that for connections using bolts, using the steel strength reduction factors from CSA S16 as a function of the fastener temperature at the surface of the timber (i.e., underneath the washer) combined to the reduced cross-section of the timber components, provides reasonable agreements when compared to actual fire test data.

For connections using self-tapping screws (STS), the modelling predictions suggest that the STS shank diameter has an impact on the heat transfer, although minimal. Head of STS seems to have more impact on the heat conduction along the shank than the STS length. However, the length allows to slower heat conduction along the shank, and thus prevent undesired charring of the wood fibres surrounding the STS. Using longer STS will allow to maintain the connection capacity longer in fire conditions, when compared to using shorter screws.

Although this study provides valuable insight on the thermal performance of modern timber connections, their structural fire-resistance has not yet been evaluated through full-scale fire tests. Additional fire testing are currently planned at FPInnovations to further validate these assumptions and develop design guidelines for future implementation in CSA O86 wood design standard.

REFERENCES

[1] T. Chuo. Fire Performance of Connections in Laminated Veneer Lumber. University of Canterbury, 2007.

[2] International Organization for Standardization. ISO 834-11: Fire resistance tests -Elements of building construction - Part 11: Specific requirements for the assessment of fire protection to structural steel elements 2014.

[3] L. Peng. Performance of Heavy Timber Connections in Fire. Carleton University, 2010.

[4] Standards Council of Canada. CAN/ULC-S101-14: Fire Endurance Tests of Construction and Materials 2014.

[5] Alam M, Hadjisophocleous G, Erochko J: Performance of Timber-to-Steel Bolted Connections Exposed to Fire. In: WCTE 2016 - World Conf. Timber Eng., Vienna, Austria: 2016.

[6] S. Ali. Fire Performance of Hybrid Timber Connections. Carleton University, 2016.

[7] CSA Group. CSA O86-19: Engineering Design in Wood 2019.

[8] C. Dagenais. Assessing the Fire Integrity Performance of Cross-Laminated Timber Floor Panel-to-Panel Joints. Carleton University, 2016.

[9] CSA Group. CSA S16-19 Design of Steel Structures 2019.

[10] M. Létourneau-Gagnon, C. Dagenais, and P. Blanchet. Fire Performance of Self-Tapping Screws in Tall Mass-Timber Buildings. *Appl. Sci.* , 11, pp. 3579, 2021. https://doi.org/10.3390/app11083579.

[11] Canadian Construction Materials Centre. Evaluation Report CCMC 13677-R SWG Assy

VG Plus and SWG ASSY 3.0 Self Tapping Wood Screws", Canadian Construction Materials Centre: Ottawa, ON, Canada. 2013.
[12] Canadian Standards Association. CSA 0122-16 Structural Glued-Laminated Timber", Canadian Standards Association: Mississauga, ON, Canada. 2016.

https://doi.org/10.52202/069179-0215

World Conference on Timber Engineering Oslo 2023

BURNING TEST OF STEEL BAR - TIMBER COMPOSITE BEAM

Shizuka Matsushita[1], Shinichi Shioya[2]

ABSTRACT: From a viewpoint of the current climate crisis, there has been much recent interest in using timber structural members in large buildings because timber can be used as renewable natural resource, and moreover, in severe earthquake prone zones, such as Japan, they are more desired on the grounds of light weight of timber members. We are developing a frame system consisting of hybrid timber members reinforced with deformed steel bar using epoxy resin adhesive. In order to practice the system, it is necessary to investigate fire resistance performance of the members. This paper reports a burning test of a beam burned for 60-minute semi-fireproof using burning marginal layer ,i.e., charring layer.

KEYWORDS: Fire, Burning marginal layer, Hybrid timber, Deformed steel bar, Beam

1 INTRODUCTION [3][4][5]

When constructing a large rigid-frame building with timber construction, the low bending stiffness and the low bending strength of timber become a serious problem.
S.Shioya, (author[2]) proposed a structural system for building construction, adopting Hybrid Glulam Timber members using Steel bar (HGTSB, nicknamed as "Samurai" in Japan) and has developed the structural design methodology, and constructed the first prototype building, a two-way frame structure using the structural system as seen in Figure 1 [1]. Three buildings were built with the system. One of them adapted two HGTSB beams, for a trial, at the 11th floor of a high-rise building, with a refractory coating authorized as two-hour fireproof timber for HGTSB, constructed in Tokyo, Japan, in February 2020. On the other hand, fireproof design method for using burning marginal layer (i.e. charring layer) for HGTSB is strongly desired for low-rise and middle-rise buildings. We scheduled to establish the semi-fireproof design method for HGTSB and conducted a fire resistance test of a beam.
The purpose of this study is to propose a method for estimating capacity of HGTSB beam that follows the semi-fireproof design method. A 60-minute burning test of a real-size beam was conducted. The safety factor, ratio of residual capacity of the beam after 60-minute burning divided by the loading expected under long-term loading, has not been sufficiently clarified. The safety factor is very important in the development of a new timber composite beam such as HGTSB. In the case of HGTSB, its bending strength is 3.0 to 4.0 times greater than that of timber beams, which means that the larger the cross-section, the greater the load on the beam, making it impossible to load the beam with Japanese burning test equipment. In such cases, if a method is established to estimate the safety factor of bearing resistance of the beam on the safe side, the burning test of the beam with its maximum cross-section is possibly eliminated.
Several studies [2,3] on fireproofing of carbon fibre-timber composite beam in which wood is used as main material, were conducted but there are no studies on fireproofing of steel bar-timber composite beam that use steel bar (i.e., rebar) as reinforcement against bending.
This paper reports the calculation concept for capacity of the beam during its burning, and the test to testify the concept and its results. Also, in another paper in WCTE2023, a new concept of modelling of temperature within beam with temperature data of only several measurement points is proposed [4].

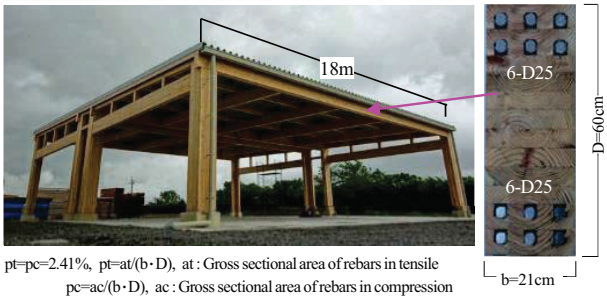

Figure 1: *Prototype building utilizing the hybrid beam and column proposed in this study, designed by S. Shioya with approval from authorities and constructed in July 2014*

[1] Shizuka Matsushita, Department of Architecture, Kagoshima University, Japan, k7422990@kadai.jp
[2] Shinichi Shioya, Department of Architecture, Kagoshima University, Japan, k7347039@kadai.jp

https://doi.org/10.52202/069179-0216

2 CALCULATION CONCEPT FOR BEAM CAPACITY

Resisting portion expected within a beam cross-section after 60-minute burning is illustrated in Figure 2(a).

1) Additional wood laminas of 90mm thickness are to be bonded to lower surface of the beam as fireproof for lower rebar within HGTSB beam.

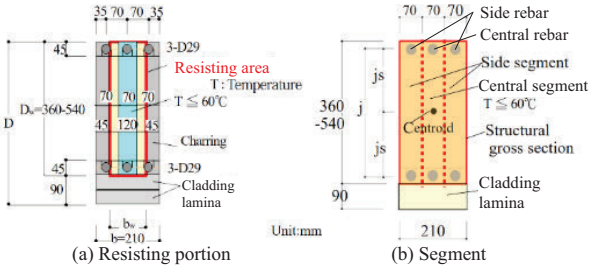

(a) Resisting portion (b) Segment

Figure 2: *An expected cross-section after 60 - minute burning and segments defined*

Table 1: *Rebar tensile properties*

Rebar	Er	σ_y	σ_t
D29	1.99×10^5	413	609

E_r:Young's modulus,
σ_y:Yielding modulus,
σ_{ty}:Tensile brealing strength (N/mm^2)

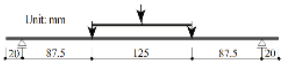

Figure 3: *Force for bending test*

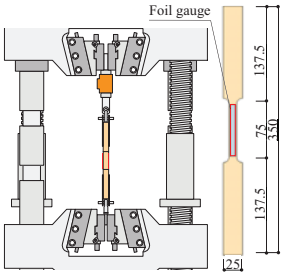

Figure 4: *Tensile test*

Table 2: *Mechanical properties of laminas*

No.	The number of pieces	Grade of Lamina	Bending test			Compression test		Moisture content	Block shearing test		
			Pure lamina		with joint	Pure lamina			n	Pure lamina	
			E_{wb}	σ_m	σ_m	E_{wc}	σ_m	%		τ_m	SD
L10	3	L80	8300	62.7	37.5	4026	30.3	12.3	-	N/A	
L9	3	L70	9000	66.9	N/A	6574	30.9	11.9	10	9.54	0.45
L8	3	L60	10700	61.7	45.0	3048	28.9	13.3	10	11.35	1.31
L7	3	L60	9400	62.7	N/A	5285	31.4	12.3	10	8.76	0.88
L6	3	L60	9100	57.2	N/A	5211	32.2	12.6	10	7.79	1.41
L5	3	L60	9700	54.8	N/A	3696	26.5	12.5	10	10.52	0.62
L4	3	L70	9400	65.6	51.0	4676	34.6	12.0	10	8.49	0.92
L3	3	L80	7400	46.5	49.7	3612	32.4	11.4	-	N/A	
L2	3	L60	7400	59.8	N/A	2682	29.7	11.9	10	12.50	2.86
L1	3	L60	9300	73.2	N/A	2715	35.4	12.3	10	11.78	2.19
Total	30	Average	8970	61.1	45.8	4152	31.2	12.2	80	10.22	1.33

E_{wb},E_{wc}: Young's modulus σ_w,τ_m: Strength SD:Standard deviation
n: The number of pieces

Table 3: *Assumed values and results for calculation of deflection under the initial cross-section before burning test*

D	b	E_{wba}	Er	Er/E_{wba}	I_o	I_c	I_c/I_o	κ_d	G_w
in mm		*in N/mm^2*			*$x10^9$*	*in mm^4*			*in N/mm^2*
450	210	8970	2.05×10^5	22.9	1.59	3.71	2.32	1.23	824
360					0.82	2.87	3.51	1.08	

E_{wba}: Average of E_{wb} in Table 2 $I_0 = b \cdot D^3/12$
κ_d: Shape factor for share deformation G_w: Modulus of shear elasticity

2) The resistance of the bonded laminas is not expected in the structural design.
3) Depth of charring layer is assumed to be 45mm after 60-minute burning.
4) Portion of area ($b_w \cdot D_w$) enveloped by red line is assumed to resist as wood.
5) The residual wood portion is assumed to resist at the allowable stress level for short-term loading.
6) Central segment of three segments equally divided in beam width as Figure 2(b) is assumed to resist as HGTSB because of its being cooler than allowable limit temperature (60°C) for HGTSB.

3 EXPERIMENT

3.1 SPECIMEN

Figure 6 in the next page illustrates cross-sections of specimen. Main cross section of the beam is Section II-IV with one-tier rebar lamina, which 3-rebars were embedded on the upper and the lower lamina of beam cross-section. Figure 5 illustrates a side view of the specimen and positions of strain gauge and thermocouple. The left-hand Section I is prepared to investigate effects of the amount and the numbers of rebars on elevated temperature of wood during burning.

The rebar laminas were prepared in the same way as in our previous paper [5]. The lamina was Cryptomeria Japonica; lamina composition of beam was adhered to Japanese Agricultural Standard E65-F225. Rebar diameter is D29(29mm) and its grade is SD390(Nominal yielding strength: $390N/mm^2$). Adhesive was typical resorcinol resin adhesive for laminating the laminas and epoxy resin adhesive for rebar, of which allowable upper limit temperature is 110°C.

3.2 YOUNG'S MODULUS, STRENGTH, AND MOISTURE CONTENT OF LAMINA

Table 2 lists mechanical properties of laminas by bending test, compression test, tensile test and block shear tests. Figure 3 shows applied force of the bending test. Compression tests were performed using specimens with cross section of 25 x 25 mm and height of 100 mm. Figure 4 shows configuration of the tensile test. The center length of 75mm was shaved down to 10 mm in width. Table 2 lists moisture content of lamina testpiece (45 x 210 x 20 mm), of which the numbers was three for each lamina. The shear plane for the block shear test were 26 x 36 mm. The numbers of specimens for these tests were 10 for each lamina.

Table 4: *Assumed values and results for calculation of bending moment capacity/Mu and shear capacity/Qws after burning, applied force/F and shear force/Q*

bw	Dw	Fw	fws	awt, awc	js	yt, yc	Iwo	Iw	Zw	Mwu	at, ac	fry	j	Mry	Mu	L/3	F/2	→	F	Q	fws	κs	Qws	Q/Qws
in mm		*in N/mm^2*		*in mm^2*		*in mm*	*$x10^8$*	*in mm^4*	*$x10^6$*	*in mm^3*	*in kN·m*	*in mm^2*	*in N/mm^2*	*in mm*	*in kN·m*		*in m*		*in kN*		*in kN*	*in N/mm^2*		*in kN*	
120	360	22.5	15.0	1054	158	180	4.67	4.14	2.30	51.8	642.4	390	315	78.9	130.7	1.70	65.3	→	132	66.0	1.8	1.25	63.2	1.06

$M_u = M_{wu} + M_{ry}$ $M_{wu} = k_z \cdot Z_w \cdot f_{ws}$ $M_{ry} = a_t \cdot f_y \cdot j$ $Q_{ws} = f_{ws} \cdot b_w \cdot D_w \cdot / \kappa_s$ $Q = M_u/(L/3)$ j_s,j: See Figure 2 y_t,$y_c = D_w/2$ $I_{wo} = b_w^3/12$ $I_w = I_{wo} - (A_{wt} + A_{we}) \cdot (j/2)^2$

Table 5: *Results of calculation of stress of wood and rebar, and shear capacity under the initial cross-section before burning test*

D	b	M	Fw	rσy	kz	Mu	M/Mu	yt	yc	Zwt	Zwc	σ wbt	σ wbc	σ rt	σ rc	Q	κ s	τ m	fLa	τ m/fLa
in mm		*in kN·m*	*in N/mm^2*			*in kN·m*		*in mm*		*$x10^6$*	*in mm^3*		*in N/mm^2*			*in kN*		*in N/mm^2*		
450	210	112.2	22.5	390	0.96	365	0.31	251	199	14.8	18.6	7.58	6.04	96	122	66.0	1.46	1.02	0.99	1.03
360					0.98	305	0.37	181	179	15.8	16.0	7.09	7.01	142	140		1.25	1.09		1.10

M= F/2·(L/3) = 66.7·1.7= 112.5kN·m $M_{wu} = k_z \cdot Z_w \cdot F_w$ $Z_{wt} = I_c/y_t$ $Z_{we} = I_c/y_c$ $\sigma_{wbt} = M/Z_{wt}$ $\sigma_{wbc} = M/Z_{wc}$ k_z: Size factor for bending strength of timber
y_t,y_c: Depth from centroid to upper fringe and lower fringe over beam σ_{rt},σ_{rc}: Stress of upper rebar and lower rebar

https://doi.org/10.52202/069179-0216

3.3 THE CENTER OF GRAVITY OF THE CROSS-SECTION AND SECTIONAL SECONDARY MOMENT OF BEAM

Using Young's modulus in bending for each lamina, distance/y_o from lower surface to the center of gravity of the cross-section and the cross-sectional secondary moment/I_e were calculated using Equation (1) and Equation (2) below.

$$y_o=(\Sigma n_{wi}\cdot a_{wi}\cdot y_{woi}+\Sigma(n_r-1)\cdot a_{ri}\cdot y_{roi}) /(\Sigma n_{wi}\cdot a_{wi}+\Sigma(n_r-1)\cdot a_{ri}) \quad (1)$$

$$I=\Sigma n_{wi}\cdot a_{wi}\cdot y_{woi}^2+\Sigma n_i\cdot I_{wi}+\Sigma(n_r-1)\cdot a_{ri}\cdot y_{roi}^2+\Sigma(n_r-1)\cdot I_{ri} \quad (2)$$

where, $n_{wi}=E_{wi}/E_{wo}$, $n_r=E_r/E_{wo}$, E_{wi} : Young's modulus in bending for each lamina, E_{wo}: Average value of all laminas, E_r: Young's modulus for rebar, a_{wi}, y_{woi} : Cross-sectional area of each lamina and distance from lower surface to the center of cross-section area of each lamina to origin, a_{ri}, y_{roi}: Cross-section area of each rebar and distance from lower surface to the center of cross-section of each rebar, I_{wi}: cross-sectional secondary moment of each lamina only ($=b\cdot t^3/12$), b: Lamina width, t: Lamina thickness, I_{ri}: Cross-sectional secondary moment of rebar ($Pi\text{-}d^4/64$), d: Diameter of rebar

Table 3 lists calculated values of the cross-sectional secondary moment/I_e, with and without considering fireproof laminas. I_e was 2.32 times greater than I_0 in the former case and 3.51 times greater in the latter case. Young's modulus/E_r and cross-sectional area/a_{r0} of the rebar were set to standard value ($E_r=2.05\text{x}10^5$ N/mm^2).

3.4 STRAIN AND TEMPERATURE MEASUREMENT

Figure 5(b) illustrates a side view of the beam specimen and positions of foil strain gauges and thermocouples. Figure 5(a) illustrates locations and names of the measured cross sections. It shows the locations where strain of wood and strain of rebar were measured. Numbering of mark "No." is for thermocouple; "W" is for uniaxial strain of wood in direction of beam axis, "R" is strain for rebar in the same direction. Figure 7(a) illustrates the gluing of foil gauge for wood. Before gluing laminas as beam, grooves were processed into laminas and the foil gauges were attached with adhesive for long-term measurement. The surface of the gauges was then coated with wax and was overwrapped with vinyl tape. Foil gauges were 3-wire type with lead wire temperature compensation. Thermocouples were used to measure temperature. Lead wire of the foil gauge and the thermocouple was pulled out from left or right end of the beam.

3.5 LOADING

Loading employed the four-point bending in Figure 8; magnitude of bending moment at mid-span of the specimen was selected to be value of allowable moment under long-term loading design. Value of shearing force of both side shear spans was 10% higher than its allowable shear force for long-term loading design. Force/F, vertical displacement, temperature, and strains of wood and rebar were measured. Deflections were measured for mid-span, two loading points, and both support points.

4 RESULT

4.1 HISTORY OF FORCE, TEMPERATURE, AND FRACTURES

The burning test was conducted on September 28, 2021 at 13:00 (its room temperature: 25.6°C) in a combustion furnace (ISO843-1 compliant furnace) at the Japan

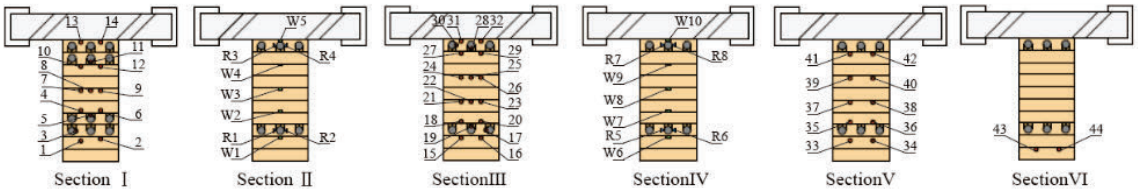

(a) *Locations of strain gauge and thermocouple*

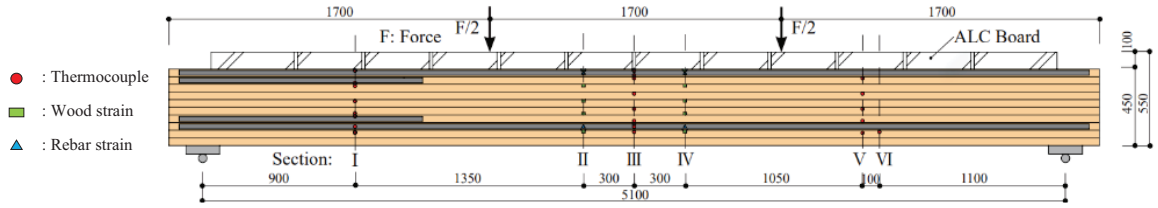

(b) *Side view of specimen*

Figure 5: *Side view of specimen and Locations of strain gauge and thermocouple*

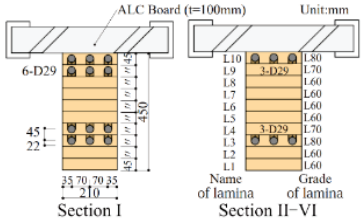

Figure 6: *Cross-sections of beam specimen*

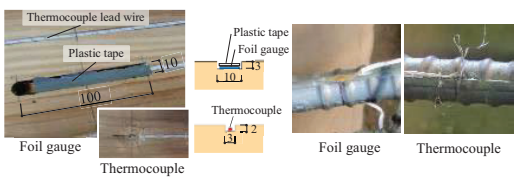

(a) *For wood* (b) *For rebar*

Figure 7: *Settlement of strain gauges and thermocouple*

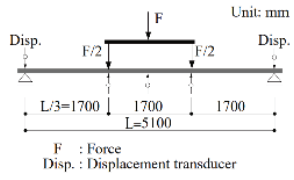

Figure 8: *The applied force and locations of deflection measurement*

https://doi.org/10.52202/069179-0216

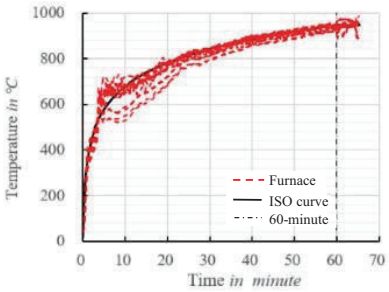

Figure 9: Temperature in furnace

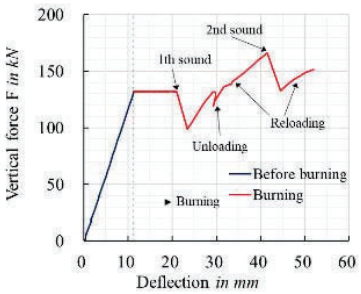

Figure 10: Force-deflection relationship

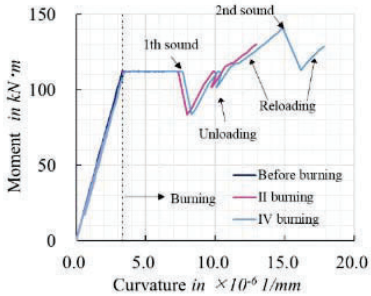

Figure 11: Bending moment-curvature relationship

Testing Center for Construction Materials. During introducing initial force, deflections and strains in the elastic range were measured. Figure 9 shows the heating temperature history of the air inside the furnace. After five minutes after completion of the loading, burning test was initiated. Temperature during 60-minute burning test was controlled to adhere to ISO-fire exposure temperature curve. Figure 12 shows changing of deflection at mid-span until the end of additional loading to investigate capacity after the burning. As burning proceeding, the deflection increases gradually, but an impact sound occurred suddenly just before 60-minutes passed, degrading the deflection stiffness, and ALC board over top of the specimen was found to be leaning.

At this time, it was confirmed that the capacity calculated by the concept mentioned in Chapter 2 was supported and the deflection of the mid-span was less than several thresholds for deflection required as semi-fireproof construction of the beam in Japan.

By reloading to the specimen at time of the impact sound before 60-minutes passed, the force F could again recover the initial applied force value, and then the additional loading was continued to be conducted. When the second impact sound occurred, the test was terminated because of the ALC board leaning largely. This additional time after the 60-minute burning passed was 5 minutes and 20 seconds; Temperature of the furnace was maintained at a constant temperature (945°C) by burning.

4.2 DEFLECTION - LOAD RELATIONSHIP DURING THE BURNING TEST

Figure 10 shows force-deflection relationship and Figure 11 shows bending moment–curvature relationship until the end of the burning test. The curvature is the same as that of the cross-section II and IV of Figure 15 mentioned later. Immediately after the first impact sound, the force decreased by 33.5kN; the deflection and curvature increased. The force increased to 166.2kN after 60-minute burning and decreased by 29.6kN at the second impact sound. The maximum force was 166.2kN, which was 26% higher than the initial force(F=132kN). The similar magnitude of the load drop immediately after the impact sounds is part of the evidence supporting the buckling of the upper two side rebar, which will be discussed in Section 4.6.

4.3 PERFORMANCE IN ELASTIC RANGE DURING INTRODUCTING INITIAL LOAD

Figure 13 shows strain distribution of wood and rebar of cross sections of II and IV during introduction the initial

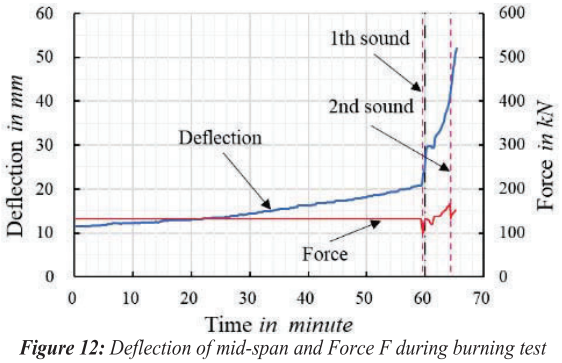

Figure 12: Deflection of mid-span and Force F during burning test

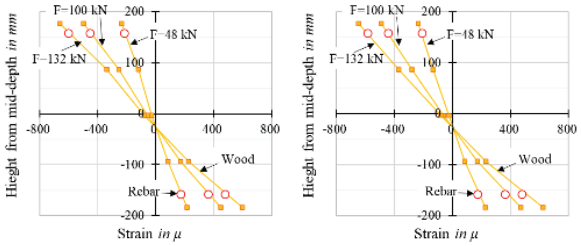

(a) Section II (b) Section IV

Figure 13: Bending strain profiles while introducing load

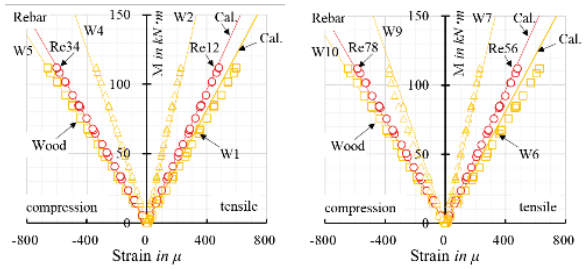

(a) Section II (b) Section IV

Experiment : □, △ : Stain of wood ○ : Strain of rebar
Calculation: — : Stain of wood — : Strain of rebar

Figure 14: Comprision of calculation to experiment of bending moment-strain curves of timber surface and rebar

load. Strains of rebar are seen to be located on the line connecting the strain of wood, proving that rebar and wood in the same position within beam distort with same strain value. Figure 14 shows changing in the strain of the wood and rebar near lower or upper surface of beam, which are compared to those calculated using the plane section assumption in response to bending moment. The calculated values have approximately estimated the experimental values. Therefore, the assumption of the

https://doi.org/10.52202/069179-0216

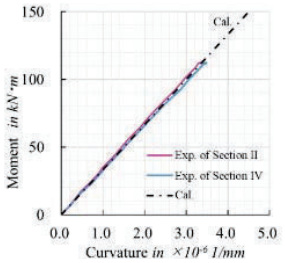

Figure 15: *Bending moment – curvature relationship*

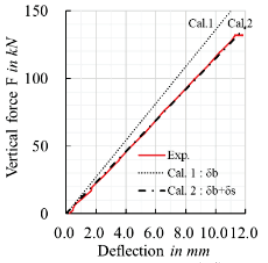

Figure 16: *Force-deflection relationship*

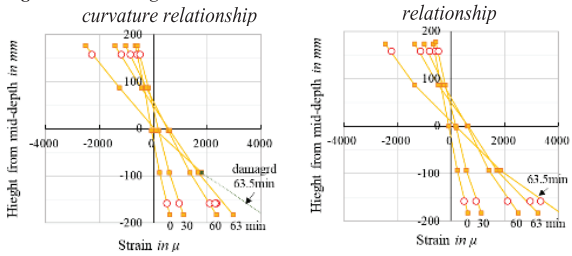

(a) Section II (b) Section IV

Figure 17: *Bending strain profiles during burning*

plane section is, also for RGTSB beam, confirmed to be allowed.

Figure 15 shows bending moment-curvature relationship for the cross-section II and IV. The curvature was assumed to be equal to average slope of strain distribution of wood cross section. The calculated bending stiffness is represented by a black one-dot chain line. The stiffness was calculated by I_e and E_{wba} in Table 3. Young's modulus of rebar was assumed to be its standard value. The bending moment-curvature relationships are almost same to the calculation line.

Figure 16 shows force-deflection relationship (red line) at the mid-span and relationships calculated using elastic stiffness. In the calculations, the fire cladding lamina was taken into account. Cal. 1 is deflection taking only bending deformation component/δ_b into account; Cal. 2 includes shear deformation component/δ_s. The coefficient of shear deformation /κ_d was assumed to be the value of 1.23 calculated by Eq. (10) in Reference [6]. The shear modulus of elasticity was not measured in this experiment, so the average value (824 N/mm^2) of the average value (15 pieces) of the center height of the beam web in Figure 24 of Reference [5]. In Figure 16, Cal. 2, which considers bending and shear deformation components, estimates the experimental relationship with high accuracy.

4.4 STRAIN DISTRIBUTION OF WOOD AND REBAR WITHIN BEAM DURING BURNING

Figure 17 shows strain distribution of wood and rebar at the cross section II and IV during burning. Amounts of strain increased with combustion proceeding resulted from decrease in resistance area within the beam as the combustion proceeding. In the Section II, at 63.5 min, strain value of rebar near the lower at 63.5min is small against wood strain distribution, i.e., black dotted line which was estimated on the basis of the trend of change up to that point because the wooden gauge at the lower could no longer be used for measurement. At the point of yielding in rebar, mill scale of rebar surface locally peels off and the adhesive around the rebar delaminates, resulting in stress relaxation in the rebar. This leads to variation in the strain of the rebar after the start of yielding. Excluding the variation of the effect, even after 60-minute burning, these results suggest that the assumption of plane in the cross section within the beam is reasonable.

4.5 DAMAGES AND CHARRING CONFIGURATION AFTER BURNING TEST

Photo 1(b) shows the specimen immediately after the burning test. The side rebars were supposed to be curved because of their buckling caused by thermal expansion in its axial direction during burning. When water was then poured on the specimen, temperature of the rebars decreased to room temperature and the rebars approached a straight line due to decay of thermal expansion, as shown in Photo 1(c). The specimen was applied to reveal capacity of the burnt specimen as mentioned later in Chapter 4. Figure 18(b), (c) shows cross-sections of residual wood portion over which its charring layer was removed after the additional loading test. Figure 18(d) shows lines of charring border of experiment and according to Eurocode 5 with a charring rate of 0.65 mm/min: red line is one of experimental results; blue line is line calculated assuming the combustion time reaching 60 minutes, and green line is line calculated assuming the combustion time reaching 65 minutes and 20 seconds.

(a) *Specimen before the burning test*

(b) *Specimen immediately after burning test*

(c) *Specimen cooled with water*

Photo 1: *Specimen*

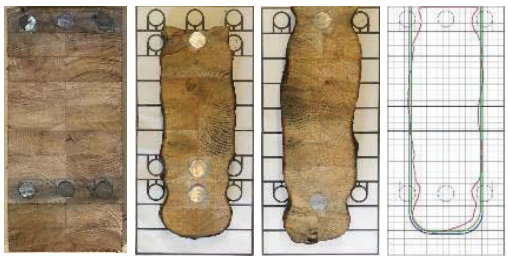

(a) (b) (c) (d)

(a)Cross-section of unburned portion
(b)Cross-section of Section I
(c)Cross-section of Section II-VI
(d)Curve of charring border
Red curve: experiment of (c),
Blue curve: Calculation by Eurocode with 60-min burning,
Green curve: Calculation by Eurocode with 65.3-min burning

Figure 18: *Cross-section of specimen after 65.3-minute burning*

https://doi.org/10.52202/069179-0216

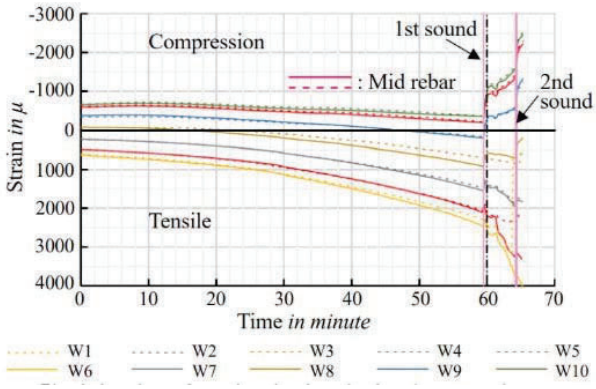

Figure 19: *Strains of wood and rebar Section II and IV*

Charring depth around the side rebar is larger than that of portion apart from the rebar. The reason may be that the side rebars buckled and some space generated between the rebar and wood by its curving. The side rebar is found to accelerate charring of wood in the case of 60-minute burning. The wood portion around the side rebar is necessary to be assumed not to contribute the capacity of beam at 60-minite burning on the safe side.

4.6 INFERENCE OF MECHANISM FOR THE IMPACT SOUND

Figure 19 shows changing in strains of wood and central rebar in the Section II and IV during burning: the dotted line indicates that of the Section II; the solid line indicates that of the Section IV; red line indicates that of the rebar. At the first impact sound, strain of the lower central rebar suddenly exceeded yielding strain (2075μ) of rebar, while the upper mid rebar reversed its trend of decreasing in compression and suddenly increased, exceeding the yielding strain (-2075μ) at the second impact sound. These suggest buckling of the upper side rebar, which is accompanied by impact sound.

Figure 20(a) shows schematically change in resistance of the upper rebars during burning. The upper rebar resists a greater compressive force due to bending moment of beam than that of the lower side rebar because it tries to extend axially during burning, whereas compressive force of the upper central rebar, which is lower in temperature than the side rebar, decreases. At the stage before the first impact sound, as seen in Figure 19, the strain of the upper central rebar (red solid and dotted lines) decreases in compression. Immediately after the first impact sound, the upper central rebar suddenly increased in compression strain and the reversal of velocity of strain changing can be seen to have occurred. These phenomena can be reasonably explained by the buckling of the side rebar. The reversal of strain velocity implies that the acceleration is great, which can be interpreted as a greater movement resulting in the impact sound; the similar amount of load drop after the two impact sounds, as discussed in Section 4.2, suggests that the load drop due to buckling of those two bars was of the same magnitude.

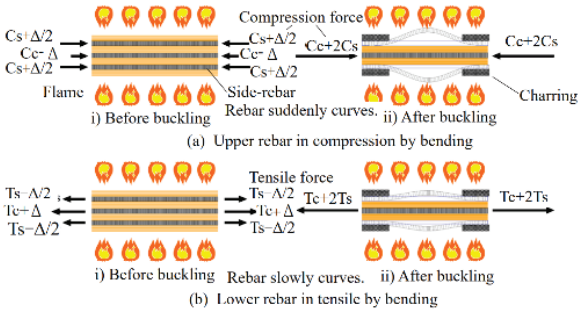

Figure 20: *Behavior of side-rebar curved during burning test*

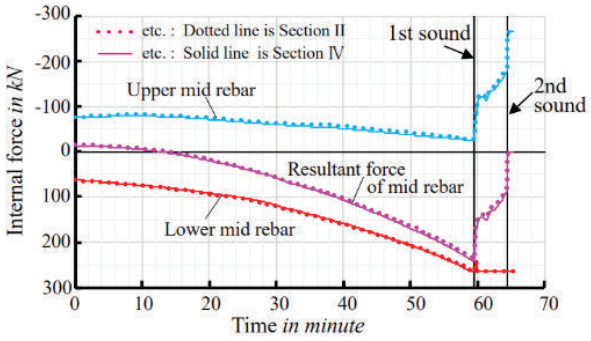

Figure 21: *Internal forces of mid rebar in Section II and IV*

On the other hand, as the lower side rebar was subjected to tensile strain by bending, tensile force of the side rebar was gradually transferred to the lower central rebar from the start of burning, and even if the lower side rebar buckled due to axial extension, the velocity of movement of buckling is supposed to have been slow to the extend such that its acceleration was slow and did not lead to the motion that produced the impact sound.

4.7 EXTINCTION OF TEMPERATURE STRESS IN REBAR

Figure 21 shows changing of axial force of the upper (light blue line) and lower (red line) central rebar and resultant force (pink line) by sum of the axial forces. Dotted line indicates that of the Section II and thin line indicates that of the Section IV. The axial force was calculated by multiplying value of axial strain of the central rebar by nominal Young's modulus and cross-section. The resultant force (pink line) increases in tension from the start of burning but decreases at the first impact sound and reaches zero immediately after the second impact sound.

The reason for its becoming zero is that the lower central rebar yields in tension and the upper central rebar yields in compression, cross-section area of the rebars is identical, and the forces cancel each other. Because the side rebars have already buckled and are not resisting, the resultant force by rebars on the cross section of the timber will be zero at the section that fractures in bending. In other words, the component of bending moment resisted by the timber can be estimated using the properties of only wood taking into account the temperature increase,

https://doi.org/10.52202/069179-0216

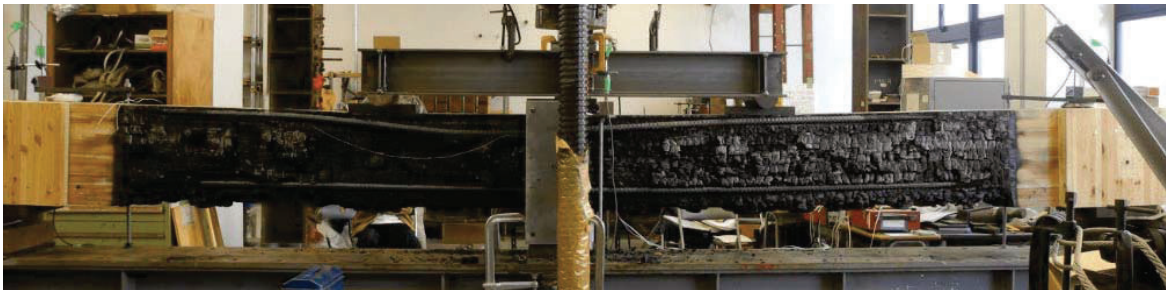

Photo 2: *Specimen before additional loading test burning test*

without the effect of the rebar. On the other hand, the component of bending moment resisted by the central rebar can also be estimated using on yield stress and sectional-area of rebar.

Bending capacity of the composite beam can be considered as the sum of these components. Rebar yields at approximately 0.2% of strain; then plastic flow occurs; the yield stress level is constant up to the start of strain hardening (about 2.0%). Assuming that the timber will fracture in bending, bending capacity of the beam can be estimated as the sum of both.

As can be seen in Figure 19, the rebars (red solid and dashed lines) almost strains in unison with wood portion (W1, W5, W6, and W10) around rebar until the rebar yielding. If yielding strain of rebar is smaller than rupture strain of wood at lower surface of beam and rebar is placed close to the surface, the assumption is satisfied. In this respect, HGSTB meets the requirements.

On the other hand, yield strain of rebar is about 0.2%, and fracture strain of wood in tensile by bending is expected to be approximately 0.4%, even if the wood ruptures at the finger joint of lamina.

However, the rupture strain is the value at room temperature. It may decrease at high temperatures. It is necessary to discuss the estimation of capacity at high temperature by considering the rupture strain of wood at high temperature.

4.8 LOADING TEST AFTER BURNING TEST

Because the additional loading immediately after the burning test did not reveal capacity of the specimen owing to the limitation of the loading apparatus, loading test was conducted to reveal the capacity as shown Photo 2 at Kagoshima University laboratory on February 15, 2022, i.e., 4.5 months after the burning test.

The force was the same as those of the burning test. Figure 22 shows the force-deflection relationship with a black curve. Figure 23 shows the bending moment-curvature relationship at the mid-span as yellow and black curves.

Those are overlaid on Figure10 and Figure 11. Yellow curve is with curvature by strain of wood; black curve is curvature by strain of rebar. In Figure 23, the stiffness of the curvature of rebar was reduced at the point indicated by '○'. In Figure 22, the point is also indicated with the same symbol, where the deflection stiffness also decreases.

Photo 3 shows failure of the upper of beam. When the capacity of beam decreased, wood portion at the force

Photo 3: *Partial compressive deformation around loading plat*

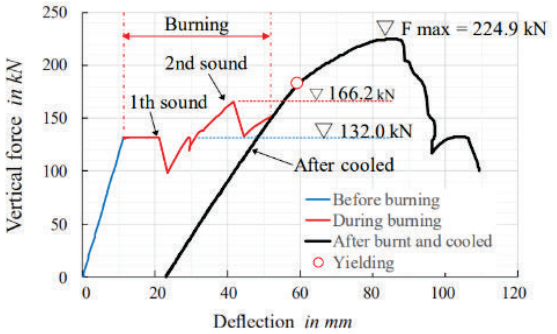

Figure 22: *Force-deflection relationship after cooled*

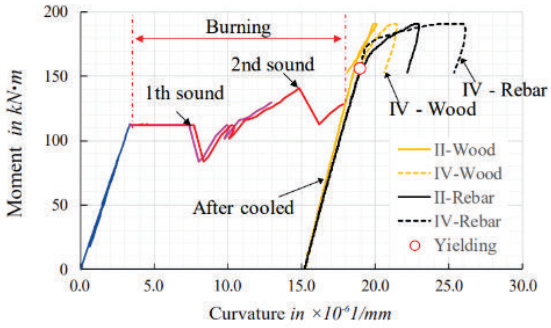

Figure 23: *Bending moment-curvature relationship after cooled*

position became more dented, causing the left side of the upper portion to bounce up.

In Figure 22, the maximum force of 166.2kN in the burning test is indicated with red dotted horizontal line. The force value was 73.9% of the maximum force in this test (F=224.9kN); this means that bending capacity of the specimen could not have been measured by during additional loading just after the 60-minute burning test.

The maximum capacity was 170.4% of the long-term loading load (132kN); this means that the capacity of specimen was sufficient against the collapse of the specimen in the 60-minute burning test.

https://doi.org/10.52202/069179-0216

These experimental results suggest that the approach for calculation of capacity proposed in Chapter 2 has sufficient potential to estimate bending and shear capacity of steel bar - timber composite beam just after 60-minute burning on the safe side.

5 SUMMARIES

In order to establish a design method for semi-fireproof for steel bar-timber composite beam, a 60-minute burning test was conducted, clarifying temperature [4] and strain behaviour inside the beams. The following i) to ii) were found during loading before the burning test, and iii) to vi) were found by the 60-minute combustion test and additional loading test to its specimen cooled after the burning test.

i) Detailed strain measurements of the wood and rebar within the specimen showed that rebar and wood in the same position within beam subjected bending distort with same strain value, providing a basis for the assumption of plane section within the composite beam's cross-section.

ii) Bending stiffness calculated based on assumption of the plane section within beam subjected to bending and using Young's modulus in bending of each lamina within beam specimen could estimate accurately moment-curvature relationship of the beam and changes in strain of wood and steel bars within the beam. Deflection stiffness of the composite beam was also accurately estimated by adding shear deformation to bending deformation component.

iii) Burning tests confirmed that a steel rebar-timber composite beam specimen bonded with two laminas (sum thickness of 90 mm) at the lower surface of beam exhibited bending and shear capacities calculated using the proposed resistance section model even after 60 minutes of burning.

iv) After 60 minutes of burning, load was increased with continuing the burning, and it was confirmed that the specimen could withstand up to 126% of the long-term allowable load. Furthermore, the specimen was cooled and subjected to loading test, and it was confirmed that load reached a maximum of 170.4% of the allowable long-term load and then collapsed. It was confirmed that the proposed estimation method for capacity of the beam after 60-minute burning is sufficient to estimate load capacity of timber-rebar composite beam on the safe side.

v) Although during 60-minute burning test, a component of elongation was added to upper central rebar and lower central rebar within beam width owing to the difference in temperature between surface portion and interior portion within beam, and with buckling of the upper side-rebar, the addition changed abruptly, causing the central rebars to yield before reaching the bending capacity and the thermal stress in the wood and rebar beam extinct.

vi) Charring depth for 60-minute burning wood was in approximately close agreement with the Eurocord 5 value. However, it should be taken into account that the depth is greater around the side rebar.

ACKNOWLEDGEMENT

This project was funded as Grants-in-Aid for Scientific Research-B by Japan Society for the Promotion of Science.

LITERATURES

[1] S. Shioya: Hybrid timber-steel bar glulam and its building system, JTCCM, JOURNAL Vol. 52, 2-7, 2016.8 (in Japanese)

[2] T G. Williamson, B Yeh: Fire performance of FRP reinforced glulam, MEETING THIRTY-NINE FLORENCE, ITALY, August, 2006

[3] Abdulrahman Zaben, et al. : Residual performance of a prototype hybrid timber-FRP glulam beam after fire, Santiago, Chile, WCTE 2021

[4] S. Matsushita, S. Shioya: A new method for modeling temperature within steel bar - timber composite beam using data by burning test, Oslo, WCTE 2023

[5] Kazuya Mori, Shinichi Shioya: Stiffness and strength of full-scale steel bar-timber composite beams with comparative small-depth, Santiago, WCTE 2021

[6] N. Fukutomi, S. Shioya: Design method to estimate stiffness and strength of hybrid timber-steel bar beams, Seoul, WCTE 2018

https://doi.org/10.52202/069179-0216

World Conference on Timber Engineering Oslo 2023

ADVANCED FIRE MODELLING IN SUPPORT OF PERFORMANCE-BASED FIRE DESIGN OF TIMBER BUILDINGS

Christian Dagenais[1], Zhiyong Chen[2]

ABSTRACT: The wood products industry is growing, as evidenced by the desire to build larger and taller buildings with timber and the start-up of new manufacturers. Despite the benefits of timber, projects are still experiencing approval resistance, namely when performance-based design is proposed to demonstrate code compliance. To gain approval, testing is often required to confirm the performance of a given product or design. While large-scale testing can always be performed, it tends to be very costly and time consuming, and can be argued to be valid only for the scenarios being tested. Fortunately, greater knowledge in fire safety engineering now allows for advanced/sophisticated fire modelling techniques, including models using the computational fluid dynamic and finite element method. This paper presents a number of advanced modelling tools and an ongoing effort to develop and harmonize a material database to be used in these models. Given the complexity of advanced modelling and the variety of input parameters and properties, an initiative is being launched at FPInnovations to generate a centralized material properties database, with the intent of making it available to the design community. Guidance on the proper use of advanced models in support of performance-based design with timber elements is also being developed.

KEYWORDS: Fire safety engineering, modelling, fire dynamics, timber buildings, performance-based design.

1 INTRODUCTION

The wood products industry is growing, as evidenced by the desire to build larger and taller buildings with timber and the start-up of new manufacturers. Some of the benefits that are fuelling renewed interest in timber construction include sustainability, prefabrication, reduced construction times, and the creation of more reliable timber products suitable for larger and taller applications. This has led to a resurgence of wood-based products in markets that have been historically dominated by steel and concrete mainly due to prescriptive limitations for using wood in larger and taller buildings, as well as non-residential construction.

Despite the benefits of timber, projects are still experiencing approval resistance, namely when performance-based design (PBD), i.e., alternative solutions, are proposed to demonstrate code compliance. To gain approval, testing is often required to confirm the performance of a given product or design.

While large-scale testing can always be performed, it tends to be very costly and time consuming, and can be argued to be valid only for the scenarios being tested. Fortunately, greater knowledge in fire safety engineering now allows for much more advanced/sophisticated fire modelling techniques, including models using the computational fluid dynamic and finite element method. These modelling techniques are gaining popularity in lieu of large-scale testing to extrapolate results and support PBD, provided the input parameters and results are verified and validated appropriately.

The purpose of this paper is to outline some available tools and ongoing efforts related to PBD, such that continued developments needed towards PBD can be identified. The need for a centralized material database to be used in these models is also discussed.

2 TIMBER CONTRIBUTION

When conducting a performance-based fire design, the contribution of combustible materials to the fire growth, intensity and duration is an important behaviour that need to be properly assessed. Combustion properties such as heat release rate, ignition temperature and mass loss rate as a function of the incident heat flux, among others, are used to predict the effect of combustible components to the fire dynamics. Charring rate dictates the rate at which timber is converted to char and is typically used to evaluate the structural fire-resistance of building elements. Each of these factors is pertinent in understanding the potential fire dynamics of a compartment in which structural timber is used, essentially for a PBD.

2.1 COMBUSTION PROPERTIES

The hazard related to exposing mass timber surfaces is due to the potential fire contribution of these surfaces.

[1] Christian Dagenais, FPInnovations, Canada, christian.dagenais@fpinnovations.ca
[2] Zhiyong Chen, FPInnovations, Canada, zhiyong.chen@fpinnovations.ca

https://doi.org/10.52202/069179-0217

When exposed to appropriate conditions, mass timber elements will ignite, release heat and flames, and ultimately reach self-extinction, should appropriate conditions be reached. Fire effluents, such as smoke and fractional effective dose, are also hazards to consider, namely as it relates to life safety of occupants and evacuation.

Advances in fire science and engineering have allowed for rapid progression in fire and smoke modelling. As such, the traditional prescriptive design is no longer the only compliance method for designing a fire-safe buildings [1]. Parametric modelling, zone models and field models using computational fluid dynamics (CFD) are among the most used in the fire engineering community. CFD models divide a given space into numerous control volumes where mass, momentum and energy conservation are numerically solved for each control volume.

Fire Dynamics Simulator (FDS), developed by NIST, is a commonly used CFD model. Modelling a fire source or a combustible material in FDS can be done from various methods. The most common methods, as described in FDS User Guide [2], are to use:

1) the pyrolysis model embedded in FDS following an Arrhenius function; or,
2) the use a of defined heat release rate (HRR) curve.

Both approaches require test data as input parameters.

2.1.1 Pyrolysis Kinetic Properties

Pyrolysis kinetic properties can easily and rapidly be obtained through a series of micro-scale thermogravimetric analysis (TGA). The mass change of a material as a function of time or temperature is measurement with high accuracy. The specimen is placed in either an inert environment (e.g. nitrogen) or in an oxidative environment (e.g. air). Through a series of data processing, it is relatively easy to determine the kinetic properties.

Several timber decomposition models can be found in the literature, ranging from simple models to more complex and sophisticated models. The level of accuracy, computational time and intended use of a given model is to be carefully evaluated when selecting the type of decomposition scheme. Using a simpler model helps at minimizing the uncertainties that may arise from each additional input parameter (i.e., level of complexity) to the total model uncertainty [3]. The simplest model consists at converting a solid material (wood) into char, volatiles and residues following an Arrhenius function consecutively, as shown in Equations (1) and (2). FDS User Guide [2] presents a detailed methodology for determining the activation energy (E) and pre-exponential constant (A) for use in the Arrhenius function.

$$Wood(\%MC) \xrightarrow{r_1} Dry\ Wood + Water\ Vapour$$

$$Dry\ Wood \xrightarrow{r_2} Char + Volatiles \quad (1)$$

$$Char \xrightarrow{r_3} Residues + Volatiles$$

$$r_i = Y_i^{n_{s,i}} A_i e^{\left(\frac{-E_i}{R\,T}\right)} \quad (2)$$

Where r is the reaction rate (s^{-1}), $n_{s,i}$ is the reaction order, Y_i is the mass fraction, A is the pre-exponential factor (s^{-1}), E is the activation energy (kJ / mol), R is the universal gas constant (8.314 x 10^3 kJ / mol·K) and T is the temperature (K).

Figure 1 shows the results from a TGA analysis performed at a heating rate of 20 K/min. A first reaction (r_1) is observed between 20 and 100°C, which is the wood at a given moisture content being converted into dry wood. The second reaction (r_2) occurs between 200 and 400°C, which is the wood being converted into char and volatiles and is clearly the most important reaction. The char oxidation (r_3) then occurs up to approximatively 600°C. Beyond 600°C, the specimen is entirely converted to residues. It is noted that Figure 1 shows the reaction rate as a function of temperature rather than as a function of time. This representation is typically used to better understand the effect of temperature on the reaction rates.

It is noted that conducting TGA under an inert environment (nitrogen) or an oxidative environment (air) does not provide the same trend towards the end of the decomposition. As reported and observed in [4, 5, 6], TGA performed in an oxidative environment provides more complex and detailed results than those done in an inert environment. The char oxidation occurring towards the end of the second reaction is not well captured when done in an inert environment, as shown in Figure 1. The maximum reaction rates are also greater when evaluated in an oxidative environment. The heating rate in a TGA is also affecting the decomposition, where a low heating rate typically increases the yield of char and a fast heating rate increases the yield of volatiles. As such, performing TGA in an oxidative environment should be favoured, as well as using a fast heating rate to evaluate the yield of volatiles, which would essentially be the pyrolysis gazes fueling the flaming combustion of wood.

Another method embedded in FDS is to directly enter the TGA test parameters and some data processing. Only, the TGA heating rate (K/min), the reference temperature (°C or K) and the pyrolysis range (°C or K) can be provided and FDS will calculate the E and A. The pyrolysis range can be estimated as the width of the reaction rate curve, assuming it to be of a triangular shape (pyrolysis range would be about ±120°C in Figure 1).

https://doi.org/10.52202/069179-0217

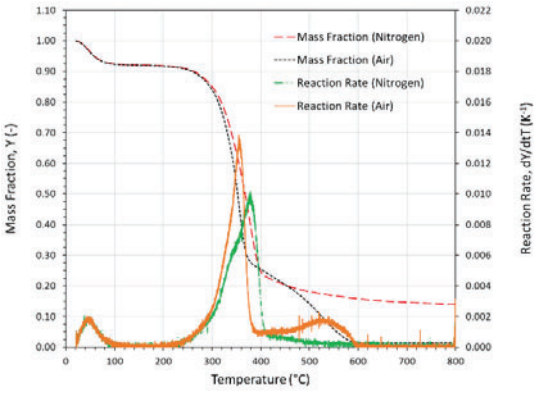

Figure 1: *TGA results conducted in an oxidative environment (air) at 20 K/min*

2.1.2 Heat Release Rate Curve

Heat release rate (HRR) of a material is among the most important combustion parameter to assess its potential contribution to fire growth. Heat release rate of materials or components can be evaluated using oxygen calorimetry, such as a small-scale cone calorimeter conforming to ISO 5660 standard [7], to a large-scale calorimeter, which was used to measure the HRR of mass timber compartments during a study in 2018 [8]. Intermediate-scale calorimeter can also be used to evaluate smaller components and assemblies, such as office cubicles, upholstered furniture, etc.

When the HRR of a given material or component is known, it can be implemented into FDS so that its fire development will follow that of the calorimeter test. The HRR values can be adjusted as a function of time using the RAMP function in FDS. It is noted that the RAMP values are to be determined after ignition occurs (i.e., RAMP time increment starts at the ignition time and not at the test/modelling time – thus once the material ignites). Other parameters can also be used to determine more realistic behaviour, such as ignition and extinction temperatures, as well as the recently implemented FDS function CONE_HEAT_FLUX. This function allows to scale up or down the HRR of a material exposed to a given constant or transient incident heat flux, based on its reference heat flux value (e.g., at 50 kW/m²). As reported by Hernouet *et al.* [9], a combustible material exposed to a radiant heat flux will be subjected to a greater incident heat flux due to flame irradiance generated from the combustion. As such, this increases in incident heat flux should be explicitly considered when determining the RAMP values in FDS.

However, at the time of writing this paper and based on discussion on the online Google FDS-SMV forum, the FDS developers confirmed that the CONE_HEAT_FLUX function is still under development and not yet ready for proper use. As such, the option of using a HRR curve will not be further detailed herein.

2.2 CHARRING RATE

When exposed to an adequate heat source (e.g., fire), timber will experience pyrolysis and ultimately charring. Charring is a fundamental property for timber and is the main parameter used to estimate the structural capacity of timber elements in fire (i.e., residual cross-section method). A thorough review of factors affecting the charring rate of timber was recently done by Bartlett et al. [10]. Among others, charring is influenced by various factors, such as wood density, moisture content, oxygen concentration and exposure conditions (fire severity).

Butler [11] reported charring rates as a function of radiant heat fluxes varying from 20 to 3000 kW/m² using a linear regression. The data were obtained using timber slabs having sufficient thickness to behave as a thermally-thick solid. Babrauskas [12] reported that this linear regression is however arguable given that some of the charring data was indirectly obtained from mass loss data and assumed that the residual char density as being nil. It was also mentioned that the linear regression over-estimates the charring rate when exposed to high levels of heat flux, suggesting that charring rate is not linearly proportional to the heat flux level. White & Tran [13] found a similar relationship whereas the charring rate is proportional to the ratio of external heat flux ($\dot{q}$) over wood density (ρ) based on oven-dry mass and volume, per Equation (3).

$$\beta = 5\left(\frac{\dot{q}_{rad}}{\rho}\right) + 0.374 \quad (3)$$

Mikkola [14] evaluated the parameters affecting charring of timber, such as density, moisture content, external heat flux and oxygen concentration of the surrounding air. Spruce specimens with a density of 490 kg/m³ and a 10% moisture content were subjected to external heat fluxes of 25, 50 and 75 kW/m² and exhibited charring rates of 0.56, 0.80 and 1.02 mm/min, respectively. The author suggested that a linear relationship exists between the charring rate and the external heat flux in the early phase of charring (first 20 minutes after ignition) when the protective char layer is in its growing phase. When the char layer reaches its maximum thickness, the effect of the external heat flux is less pronounced, and the charring rate decreases considerably. Experiments that used white pine specimens exposed to a constant heat flux and oxygen concentrations of 21%, 10.5%, and 0% showed that the mass loss rate decreased by 50% when the oxygen concentration decreased from 21% to 0%. It is noted that typical cone calorimeter tests are conducted in normal oxygen concentration (ambient, thus 21%), while it can drastically reduce to less than 5% in a standard furnace test and in compartment fire tests, as mentioned by Schmid & Frangi [15]. This suggests that as a fire grows within a compartment and the oxygen concentration declines, the charring rate is expected to decrease and should be determined accordingly.

https://doi.org/10.52202/069179-0217

2.3 STRUCTURAL FIRE-RESISTANCE

Modelling structural fire-resistance involves three fundamental components. It includes 1) a fire model, 2) a heat transfer model, and 3) a structural model, as illustrated in Figure 2. The fire model generates a specific fire exposure (temperature boundary conditions) for the thermal simulation using the heat transfer model which in turn develops thermal gradients in the structural components / connections. The structural model will calculate the response of the components / connections under fire and loads (mechanical boundary conditions).

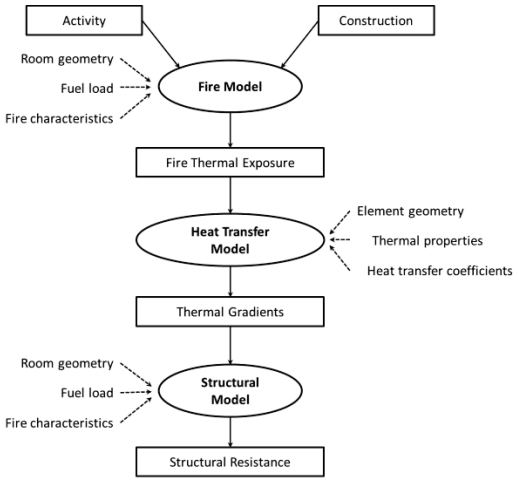

Figure 2: *Flow chart for calculating structural fire-resistance, redrawn from Buchanan & Abu* ***[16]***

The performance of structures exposed to fire can be evaluated from models that are using the finite element method, in which the results of a transient heat transfer are typically sequentially imported into a structural model (i.e., a 1-way coupling). A fully coupled analysis (i.e., 2-way coupling) should however be used when the thermal and mechanical solutions affect each other, as with timber.

A fully-coupled constitutive model, called WoodST, was developed at FPInnovations for assessing the structural fire-resistance of timber elements and connections. "S" means "Structural" and "T" is for "Thermal". This unique finite element model (FEM) combines several mechanics-based submodels, as detailed in Chen et al. [17]. The model has been verified and validated against a number of fire tests. It has also been used in support of PBD for evaluating the performance of timber structures in fire.

Additional guidance for advanced modelling of timber structures can be found in a recently published modelling guide for timber structures [18].

3 ADVANCED FIRE MODELLING

Several validation scenarios are presented herein. Additional information and details of the modelling parameters can be found in [17, 19].

3.1 FIRE DYNAMICS

With the main objective to develop and to validate fire dynamics combustion properties and CFD models in support of performance-based fire design, several verification and validation scenarios were conducted. The modelling properties were implemented in Fire Dynamic Simulator (FDS) version 6.7.9. Simple models (TGA) were easily run on a personal computer with an Intel® Core™ i5-8265U CPU @ 1.60GHz. The more complex models (cone calorimeter, wood cribs and mass timber fires) were run using high-performance computers from the Digital Research Alliance of Canada.

3.1.1 Validation of pyrolysis kinetic properties

With the desire to increase the amount of exposed mass timber in buildings, specimens of commercially-available mass timber products have been used. Specimens from Douglas fir lumber used in the manufacturing of glue-laminated (glulam) timber beams and columns, as well as specimens of the Spruce-Pine-Fir (SPF) species group used in glulam and CLT elements were evaluated. These products have been selected given their wide use in North American mass timber construction and that they are among the two main wood species group used for structural applications.

Thermogravimetric analysis (TGA) was modelled in FDS at the same heating rates as the actual TGA tests, i.e., 5, 10, 20, 50 and 100 K/min. The FDS model used to replicate a TGA analysis was adapted from [20], with the pyrolysis kinetic properties detailed in [19]. The thermal properties from EN1995-1-2 [21] were assumed. The density relationship given in EN1995-1-2 is ignored as it is explicitly being considered by the pyrolysis kinetic properties obtained from TGA. Moreover, the sharp peak in specific heat at a temperature of 100°C is neglected, also due to the explicit consideration of water evaporation through the 1st reaction kinetics.

During the verification and validation of the pyrolysis kinetic properties, it was found that the 1st reaction (moisture evaporation) was best modelled using the alternative method embedded in FDS – that is to input the TGA heating rate, the reference temperature and the pyrolysis range (taken as 100°C) – rather than explicitly using the E and A of that reaction. The 2nd and 3rd reactions were modelled using their respective E and A.

Table 1 summarizes the pyrolysis kinetic properties obtained from TGA performed at 50 K/min. The mass fraction and reaction rate predicted by FDS are shown in Figure 3 and Figure 4 for Douglas fir and SPF, respectively, at a heating rate of 50 K/min and in an oxidative environment (air). It can be observed that the

https://doi.org/10.52202/069179-0217

pyrolysis properties provide reasonable predictions of the mass fraction and reaction rate when compared to test data. Although not shown herein, it was also found that faster heating rate (e.g., TGA at 50 and 100 K/min) provides better predictions in FDS when compared to slower heating rates (e.g., 5, 10 and 20 K/min).

Table 1: *Pyrolysis kinetic properties for Douglas fir and Spruce-Pine-Fir from TGA at 50 K/min*

Property	Douglas fir	Spruce-Pine-Fir
1st reaction (r_1)		
T_{ref} (°C)	54	55
Pyrolysis range (°C)	100	
Heating rate (K/min)	50	
2nd reaction (r_2)		
E_2	1.142×10^5	9.923×10^4
A_2	3.692×10^7	1.479×10^6
3rd reaction (r_3)		
E_3	2.525×10^4	3.042×10^4
A_3	1.344×10^{-1}	3.602×10^{-1}

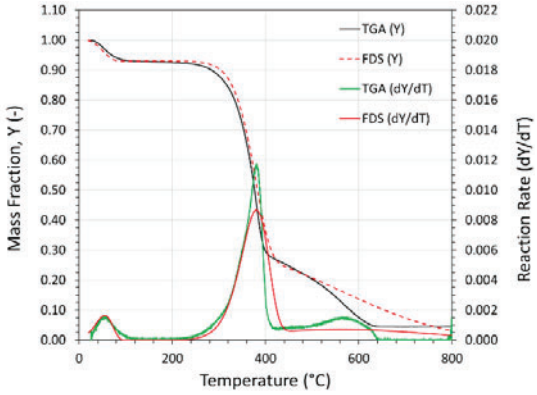

Figure 3: *TGA predictions from FDS compared to test data – Douglas fir at 50 K/min in oxidative environment (air)*

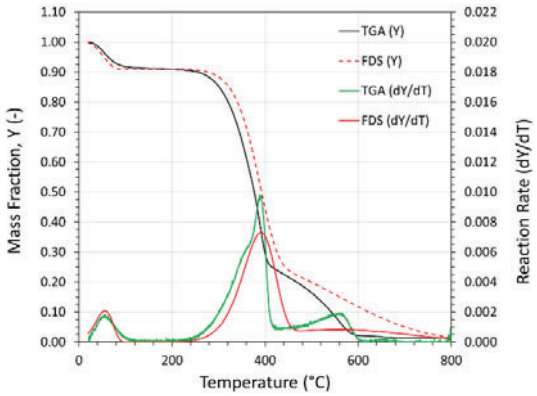

Figure 4: *TGA predictions from FDS compared to test data – Spruce-Pine-Fir at 50 K/min in oxidative environment (air)*

During the verification and validation, it was found that all pyrolysis kinetic properties showed a strong relationship with the heating rate, which was also found by Bakar [20]. Figure 5 shows the relationship for the reaction rate of SPF specimens.

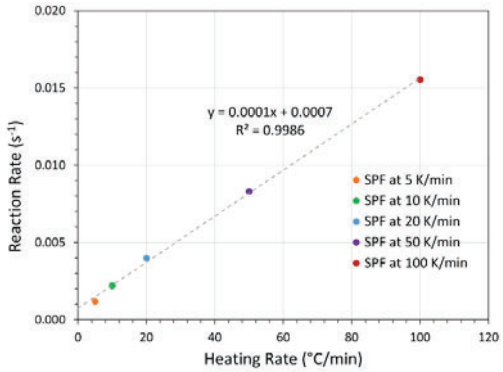

Figure 5: *Reaction rates as a function of the heating rate for Spruce-Pine-Fir specimens (2nd reaction)*

Currently, FDS does not allow to adjust the pyrolysis properties as a function of the heating rate. A single set of properties can only be used (e.g., those from 50 K/min) for modelling. However, given that the pyrolysis properties are sensitive to the thermal conditions, there would be a merit for FDS to allow such adjustments using a specific function (i.e., as with the RAMP function used for HRRPUA). This would be more realistic of a transient exposure from a fire exhibiting a growth, steady-state and decay phases.

3.1.2 Validation of combustion properties

Cone calorimeter conforming to ISO 5660 were also modelled in FDS, using the same radiant heat levels as the actual tests, i.e., 25, 50 and 75 kW/m². The FDS model used to replicate a cone calorimeter consists in a simplified domain where the specimen properties are assigned as a simple surface (called VENT in FDS). The specimen is then subjected to an external heat flux of the required magnitude. The surface properties (specimen) consisted of a fraction of water (moisture content) and dry wood. The specimen surface was 100 x 100 mm with a thickness set to 25 mm, with its back being set to "insulated" to replicate a cone calorimeter test. Due to equipment malfunctioning, the heat of reaction used in this study is taken from the literature [3]. Values of reaction of 355 kJ/kg and 205 kJ/kg were assumed for the Douglas fir and SPF, respectively. Based on cone calorimeter tests, an average effective heat of combustion of 12.35 MJ/kg and 13.30 MJ/kg is used for Douglas fir and SPF, respectively.

Table 2 summarizes the HRR obtained from test data and FDS modelling. It can be observed that FDS provides reasonable HRR when compared to test data (taken over an 1800 s burning period), while being slightly lower. The results suggest that using the properties from TGA tests done at a fast heating rate (e.g., 50 and 100 K/min)

https://doi.org/10.52202/069179-0217

provides better HRR predictions when compared to actual test data. Lastly, it was found that for both wood species, the modelling predictions were in much better agreements with the test data when exposed to greater heat flux levels (50 and 75 kW/m²). At 25 kW/m², the ignition time is always predicted too early.

Table 2: *Heat release rate – Test data compared to FDS for Spruce-Pine-Fire specimens of 25 mm in thickness*

Cone calorimeter tests		FDS Predictions	
Heat flux (kw/m²)	**$HRR_{tig+1800s}$ (kW/m²)**	**Heating Rate (K/min)**	**$HRR_{tig+1800s}$ (kW/m²)**
		5	25.25
	45.23	10	27.46
25	49.92	20	34.45
	52.99	50	32.52
		100	40.94
		5	71.63
	77.76	10	76.94
50	90.56	20	81.33
	77.89	50	78.33
		100	80.30
		5	80.67
	87.05	10	80.64
75	91.25	20	81.83
	93.28	50	80.66
		100	80.61

Figure 6 illustrates the heat release rate (HRR) profile obtained by the numerical modelling for the 25 mm Douglas fir exposed to 50 kW/m². The modelling provides consistent results when compared to actual test results, while being slightly underpredicting.

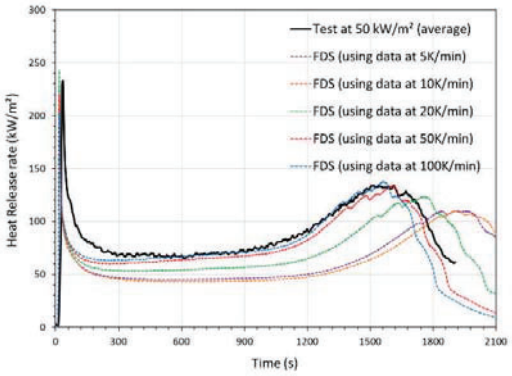

Figure 6: *Heat release rate predictions from FDS compared to test data – Douglas fir at 50 kW/m²*

For all 3 heat flux levels (i.e., 25, 50 and 75 kW/m²), TGA data from heating rates of 50 and 100 K/min provided the best profiles with respect to HRR and THR. These faster heating rates support the assumption where faster heating rates should be favoured in attempt to better predict the yield of volatiles (i.e., pyrolysis gazes). The mass loss was evaluated by calculating the consumed mass of reacting fuel (i.e., dry wood) and water vapor, and compared to actual tests. As shown in Figure 7, the mass losses obtained in FDS are in good agreement when compared to test data.

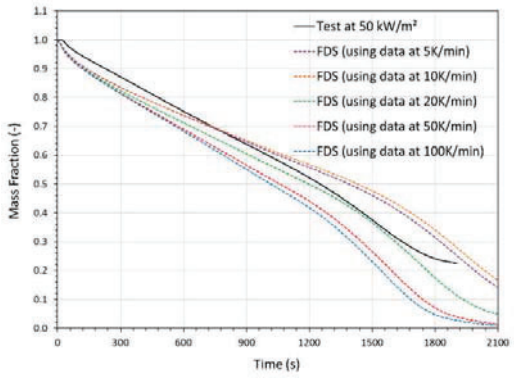

Figure 7: *Mass loss predictions from FDS compared to test data – Douglas fir at 50 kW/m²*

3.1.3 Wood crib packages

In attempt to develop fuel packages for use in advanced modelling in support of performance-based fire design, wood cribs were also modelled in FDS using the pyrolysis kinetic properties presented herein and detailed in [19]. Wood cribs are widely used in large-scale fire tests to simulate moveable fuel load.

HRR and THR were calculated using the analytical model presented in the SFPE Handbook of Fire Protection Engineering [22]. FDS predictions were compared to the calculations as well as test data by Bwalya *et al.* [23]. Figure 8 illustrates the total heat release (THR) for a large wood crib (8 layers). Interestingly, the mesh size used in FDS influenced the HRR and THR. A mesh size of 5 cm was found to provide the best predictions (vs. 10 cm). In addition to the recommendations about mesh resolution in the FDS User Guide [2], it is strongly suggested to conduct a sensitivity analysis when trying to use fuel packages in advanced modelling.

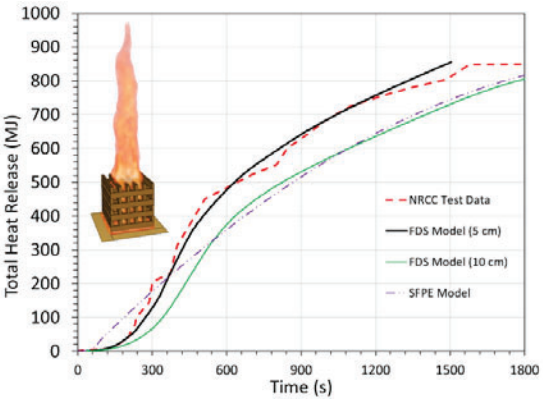

Figure 8: *Total heat release rate of a large wood crib*

https://doi.org/10.52202/069179-0217

3.2 CHARRING AND CHAR DEPTH

During a series of demonstration fires in Canada, large-scale mass timber constructions were subjected to various fire scenarios (https://firetests.cwc.ca/). Among those, pilot-scale tests were conducted in Richmond (BC) in June 2021 to demonstrate the fire performance of mass timber construction during the construction phase, thus when not protected or encapsulated.

3.2.1 Mass timber 1

Mass timber 1 (MT1) was constructed using glulam and CLT elements. The cube was 3 m x 3 m x 3 m (10' x 10' x 10') and subjected to a fire developed by two (2) large wood cribs (8 layers of wood sticks). All timber elements, including the CLT back wall, were fully exposed to fire. A partition protected by gypsum board was installed to simulate a corner effect. Four (4) thermocouples were positioned in each quadrant underneath the ceiling.

Wood cribs and mass timber elements were modelled in FDS using the pyrolysis properties presented herein (Figure 9). In the modelling, in addition to monitoring the temperature underneath the CLT ceiling, devices were added to monitor the oxygen concentration and incident heat flux at each quadrant. Figure 10 shows the temperature profiles obtained from the test data and those from FDS. When combining the charring rate, calculated per Equation (3), to the reduction effect due to the oxygen concentration, a char depth of 13 mm is obtained. When not considering oxygen concentration, a char depth of 17 mm is obtained. A char depth varying between 10 and 15 mm was obtained from hand measurements after the demonstration fire (Figure 12).

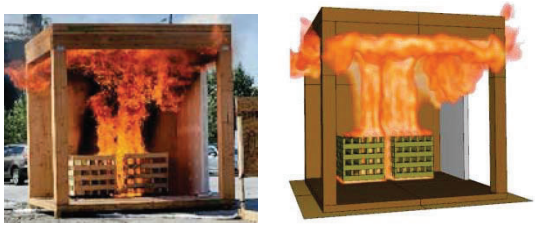

Figure 9: *MT1 – left is the actual test, right is FDS modelling*

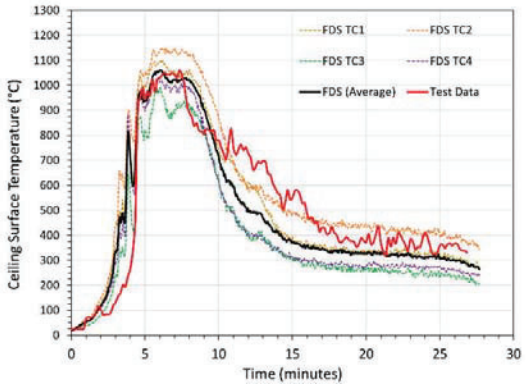

Figure 10: *Temperature at the MT1 ceiling – Test data compared to FDS predictions*

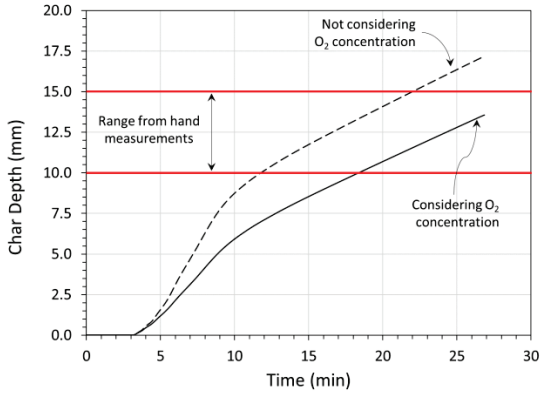

Figure 11: *Char depth of MT1 ceiling as a function of time compared to hand measurements*

Figure 12: *MT1 charred specimens cut for hand measurements*

While the difference between the charring predictions and hand measurements may not be large, it is noted that the fire was left to burn in the open for only 27 min and subjected to a low moveable fuel load (±190 MJ/m²). In an actual compartment scenario where a greater fuel load is present and oxygen may be limited, the difference between considering and neglecting the effect of oxygen concentration will further increase, which would ultimately impact the structural fire-resistance if the char depth is overly estimated.

3.3 STRUCTURAL FIRE RESISTANCE

Structural modelling of timber elements and connections exposed to a standard fire was performed using WoodST. A laminated veneer lumber (LVL) beam and a bolted connection were modelled to assess the time-displacement curve as well as the time to failure and failure mode [17]. The constitutive model was also used to assess the performance of a timber structure in fire, in support of a Technical Report ISO/TR 24679-5 [24] developed by FPInnovations for ISO TC92/SC4/WG12.

https://doi.org/10.52202/069179-0217

3.3.1 Beam

Structural composite lumber (SCL) beams were tested for fire-resistance by the American Wood Council. The beams were exposed to the standard fire on 3 sides. One of them was used to verify and validate WoodST – that is LVL beam #7 of 89 x 241 mm subjected to 50% of its allowable bending strength. It was assumed that SCL has the same thermal properties as timber (i.e., those of EN1995-1-2).

A static stress/displacement analysis was first performed. Under a total load of 16.8 kN, the predicted deformation at mid-span was 15.1 mm, compared to 14.5 mm in the actual test. Then, a transient thermal analysis was carried out to assess the temperature distribution and charring rate. The charring rates for the LVL model were 0.79 mm/min on its side and 0.94 mm/min at the bottom, respectively. The higher charring rate at the bottom is caused due to corner rounding affecting the bottom of the beam. These verifications suggest that the input properties were satisfactory.

Lastly, a coupled thermal-stress analysis was performed. The finite element analysis (FEA) showed that the deformation of LVL beam #7 increased with time and temperature, as shown in Figure 13. Elements of the LVL beam were first charred and then removed once the strain met the criterion. The model predicted a failure time of 28.5 mins, based on the mean properties obtained by converting the allowable stress design values from the LVL evaluation report. The test failure time was recorded as 33.7 min. The prediction would be expected to be closer to the actual test result if the actual material properties of the specimen were known.

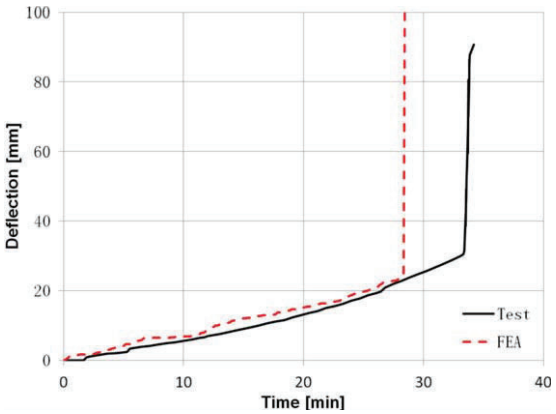

Figure 13: *Deflection as a function of time – LVL beam #7*

3.3.2 Bolted connection

A wood-steel-wood (WSW) bolted assembly was modelled in WoodST. Glue-laminated (glulam) timber elements of 130 x 190 mm were connected axially using 12.7 mm diameter bolts and a 9.5 mm internal steel plate. During the fire-resistance test, a constant axial tension load of 11.5 kN was applied, which represented 10% of the ultimate resistance at ambient conditions [25]. As with the LVL beam modelling, the mechanical properties were soft-converted to their mean values in accordance with CSA O86 standard procedures [26].

The static stress/displacement analysis predicted an ultimate capacity of 111.3 kN, which is within 5% of the test result of 115 kN. The transient heat transfer allowed to assess the temperature profiles of the glulam elements and metallic parts, as well as the charring rate of the glulam with great precision (Figure 14).

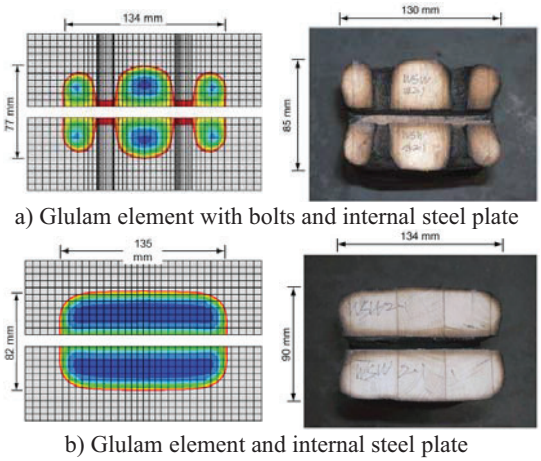

Figure 14: *Residual cross-section*

The coupled thermal-stress analysis showed that the deformation increased in time and temperature (Figure 15). The displacement increased shortly after 10 min, which was caused by the wood crushing in the bolt holes due to the effects of load and fire (Figure 16). The model predicted a failure time of 23.5 min, while it failed at 28.0 min in the test.

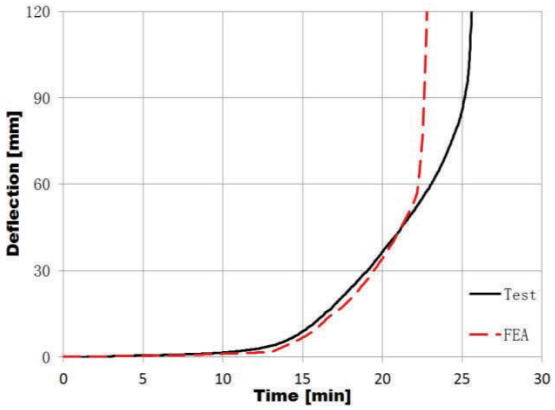

Figure 15: *Deflection as a function of time – Bolted connection*

https://doi.org/10.52202/069179-0217

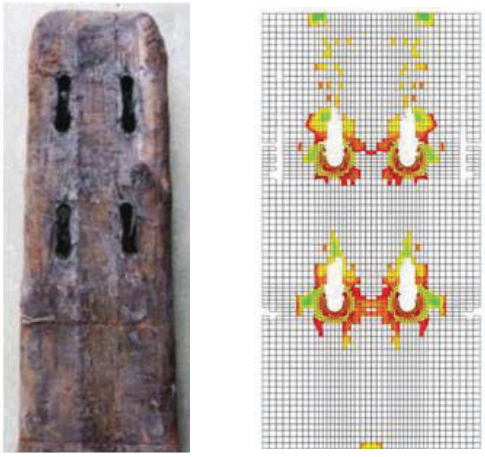

Figure 16: *Bolt elongation in the glulam element*

3.3.3 Performance of structures in fire

The results of design fire scenarios from FDS were used as imposed thermal fields in WoodST, namely the incident heat flux, surface temperature and oxygen concentration at the vicinity of timber elements' surface. This allowed to determine the residual cross-section of elements exposed to a design fire, along with their structural performance. This work was done during the development of a Technical Report (TR) on the performance of structures in fire under the aegis of ISO TC92 SC4 WG12 [24]. ISO/TR 24679-5 should be published during 2023.

The analysis was made for a glulam beam and column, both were partially exposed to fire. The load-displacement curves of both elements were obtained and compared to analytical calculations using CSA O86 [27]. The performance criteria were evaluated accordingly. The incident heat flux and oxygen concentration at the vicinity of the surfaces were explicitly considered for the charring rate. Figure 17 and Figure 18 show the deflection as a function of time (fire exposure) for a beam and column, respectively. Analytical calculations are also presented for comparison between simplified (calculations) and advanced (FEM) methods.

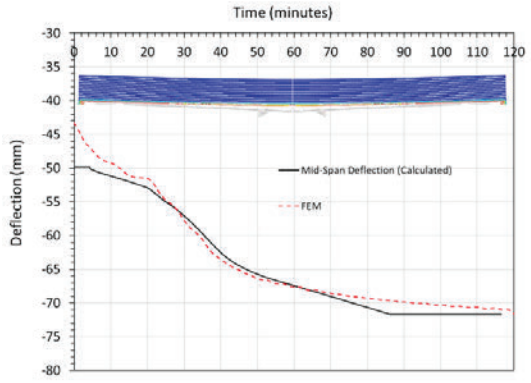

Figure 17: *Assessment of mid-span deflection of beam B1*

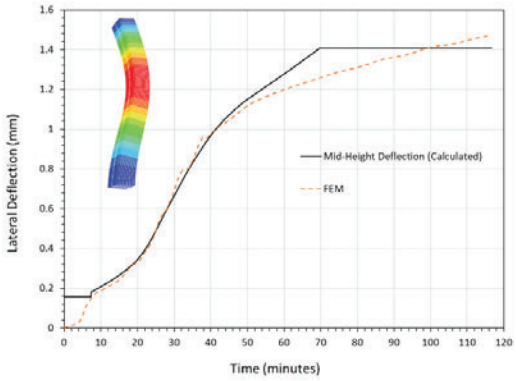

Figure 18: *Assessment of lateral deflection of column C2*

4 DEVELOPMENT OF DATABASE

While all models should be verified and validated appropriately, the quality and accuracy of their results remain at the discretion and knowledge of the users. FDS and models using the FEM require a large number of data entry, including material combustion behaviour and thermo-mechanical properties. Timber is an anisotropic material and therefore its properties vary as a function of the grain orientation between the longitudinal, radial and tangential directions, and should be explicitly considered.

Given the complexity of advanced modelling and the variety of input parameters and properties, the creation of a centralized database becomes relevant. An initiative has been launched at FPInnovations to generate a database of commonly-used products such as those of interior linings and structural elements, with the intent of making it available to the design community. Research organizations members of WoodRise are involved in this initiative, namely FCBA (France) and RISE (Sweden). The material database will be made available through various publications as well as a web platform (host of the platform is yet to be determined).

ACKNOWLEDGEMENT

FPInnovations would like to thank Natural Resources Canada (Canadian Forest Service) for funding this project and supporting our research. The authors would also like to acknowledge and thank Esko Mikkola and Henri Kuronen from KK Consulting (Finland) for their guidance and expertise regarding fire modelling using FDS, as well as guidance by Eric Guillaume from Efectis (France) and Grégoire Pianet from FCBA (France). Technical support provided by FDS developers through the Google forum is also greatly acknowledged. Lastly, we thank Alex Bwalya from National Research Council Canada for sharing test data on wood cribs, as well as Andrew Harmsworth and Claire Yuan from GHL Consultants for the data and observations during the pilot-scale mass timber fire tests.

REFERENCES

[1] Pope N. D. and Bailey C. G.: Quantitative comparison of FDS and parametric fire curves with post-flashover compartment fire test data. Fire Safety Journal (41), pp. 99-110, 2006.

[2] McGrattan K. B., McDermott R. J., Vanella M., Hostikka S. and Floyd J.: Fire Dynamics Simulator User's Guide, Sixth Edition (NIST Special Publication 1019). National Institute of Standards and Technology, USA, 2021.

[3] Rinta-Paavola A. and Hostikka S.: A Model for the Pyrolysis of Two Nordic Structural Timbers. Fire and Materials, vol. 46, pp. 55-68, 2022.

[4] Fateh T.: Étude experimentale et numérique de la cinétique de décomposition thermique de contreplaqués en bois (thèse doctorale). École Nationale Supérieure de Mécanique et d'Aérotechnique, France. 2011.

[5] Richter F. and Rein G.: Heterogeneous Kinetics of Timber Charring at the Microscale. J. Analytical and Applied Pyrolysis, vol. 138, pp. 1-9, 2019.

[6] Brandon D., Sjöström J., Temple A., Hallberg E. and Kahl F.: Fire Safe Implementation of Visible Mass Timber in Tall Buildings - Compartment Fire Testing (RISE Report 2021:40). RISE Research Institute of Sweden, Sweden, 2021.

[7] ISO 5660-1: Reaction-to-fire tests - Heat release, smoke production and mass loss rate - Part 1: Heat release rate (cone calorimeter method). International Organization for Standardization, Swtizerland, 2002.

[8] Su J., Lafrance P. S., Hoehler M. and Bundy M.: Fire Safety Challenges of Tall Wood Buildings - Phase 2: Tasks 2 & 3 - Cross-Laminated Timber Compartment Fire Tests. NFPA Fire Protection Research Foundation, USA, 2018.

[9] Hernouet F., Guillaume E., Rogaume T., Richard F. and El Houssami M.: Experimental Determination of the Evolution of the Incident Heat Flux Received by a Combustible during a Cone Calorimeter Test: Influence of the Flame Irradiance. J. Fire Sciences, pp. 119-141, 2021.

[10] Bartlett A. I., Hadden R. M. and Bisby L. A.: A Review of Factors Affecting the Burning Behaviour of Wood for Application to Tall Timber Construction. Fire Technology (55), pp. https://doi.org/10.1007/s10694-018-0787-y, 2019.

[11] Butler C. P.: Notes on Charring Rates in Wood (Fire Research Note No.896). Department of the Environment and Fire Offices' Committee, 1971.

[12] Babrauskas V.: Charring Rate of Wood as a Tool for Fire Investigations. Fire Safety Journal (40), pp. 528-554, 2005.

[13] White R. H. and Tran H. C.: Charring Rate of Wood Exposed to a Constant Heat Flux. Wood & Fire Safety 3rd International Scientific Conference, Slovak Republic, 1996.

[14] Mikkola E.: Research Report 689 - Charring of Wood. Technical Research Centre of Finland, Finland, 1990.

[15] Schmid J. and Frangi A.: Structural Timber in Compartment Fires - The Timber Charring and Heat Storage Model. Open Engineering, pp. https://doi.org/10.1515/eng-2021-0043, 2021.

[16] Buchanan A. H. and Abu A. K.: Structural Design for Fire Safety - 2nd Edition. John Wiley & Sons, 2017.

[17] Chen Z., Ni C., Dagenais C. and Kuan S.: WoodST: A Temperature-Dependent Plastic-Damage Constitutive Model used for Numerical Simulation of Wood-Based Materials and Connections. J.Struct.Eng., vol. 146(3), pp. https://ascelibrary.org/doi/10.1061/(ASCE)ST.1943-541X.0002524, 2020.

[18] Chen Z., Tung D. and Karacabeyli E.: Modelling Guide for Timber Structures - First Edition (Special Publication SP-544). FPInnovations, Canada, 2022.

[19] Dagenais C.: Expanding Wood Use Towards 2025: Part 1 - Combustion Properties for Advanced Fire Modeling (Report No. 301015176). FPInnovations, Canada, 2023.

[20] Bakar A. S. A.: Characterization of Fire Properties for Coupled Pyrolysis and Combustion Simulation and Their Optimised Use (Doctoral Thesis). Victoria University, Australia, 2015.

[21] EN1995-1-2: Design of timber sructures - Part 1-2: General - Structural fire design. European Committtee for Standardization, Belgium, 2004.

[22] SFPE Handbook of Fire Protection Engineering - 5th Edition. Springer, 2016.

[23] Bwalya A., Lougheed G., Su J., Taber B., Benichou N. and Kashef A.: Development of fuel package for use in the fire performance of houses (NRCC-45582). National Research Council Canada, Canada, 2007.

[24] ISO 24679-5: Fire safety engineering - Performance of structures in fire - Part 5: Example of a multi-storey timber building (DRAFT VERSION). International Organization for Standardization, Switzerland, 2023.

[25] Peng L.: Performance of Heavy Timber Connections in Fire (doctoral thesis). Carleton University, Canada, 2010.

[26] CSA Standard Practice Relating Specified Strengths of Structural Members to Characteristic Structural Properties. CSA Group, Canada, 2001.

[27] CSA O86 Engineering Design in Wood. CSA Group, Canada, 2019.

https://doi.org/10.52202/069179-0217

World Conference on Timber Engineering Oslo 2023

EFFECT OF THE SACRIFICIAL LAYER THICKNESS AND THE BARRIER LAYER TYPE ON SELF-EXTINGUISHING FOR WOODEN FIREPROOF-STRUCTURAL ELEMENTS

Tomoyo Hokibara[1], Yuji Hasemi[2], Daisuke Kamikawa[3], Tsutomu Nagaoka[4]

ABSTRACT: The effects of the thickness of the sacrificial layer and the type of barrier layer on the self-extinguishing performance of wooden fireproof structural elements made from Japanese cedar were clarified. Three series of small fireproof heating tests were conducted. It was clarified that with a wood-based protection layer, there was an optimum thickness of the sacrificial layer regardless of the heating time. The use of gypsum and fire-retardant wood as the barrier layer was then compared in terms of suppressing the temperature rise through the latent heat of the barrier layer, and the effect of the sacrificial layer thickness on the self-extinguishing performance was clarified.

KEYWORDS: Japanese cedar, glowing combustion, Flame die-out, Fire-resistive construction

1 INTRODUCTION

High-rise wooden structures must be fireproof. The fire-resistant performance in Japan, as an earthquake-prone country that does not assume firefighting activities, requires high-rise wooden structures to self-extinguish and become independent after a fire.

In recent years, there have been frequent international examples of fires rapidly spreading to the upper floors of high-rise buildings and causing enormous damage[1]. Fire-resistant structures that self-extinguish in the event of a fire should thus be considered even for high-rise wooden buildings.

The authors have clarified the specifications of fire-resistive structures that achieve 1 and 2-hour fire resistance adopting the concept of the sacrificial layer as shown in **Figure 1** and clarified the self-extinguishing performance of the sacrificial layer[2][3]. They showed that if the sacrificial layer is designed to be thick according to the required fire resistance time, the performance of the barrier layer can be minimized and an efficient member design achieved[2].

Meanwhile, when a long fire resistance time is required in the case of a high-rise building, the actual fire heating time may be shorter than the required fire resistance time. In this case, the sacrificial layer designed to be thick according to the fire resistance time may maintain glowing combustion after the fire. The fire resistance structure must perform even when it is heated by fire for a time shorter than the required fire resistance time. The present study thus examines the optimum thickness of the sacrificial layer regardless of the required fire resistance time.

The optimum thickness of the sacrificial layer depends on the suppression of the temperature rise through the latent heat of the barrier layer, and the appropriate thickness of the sacrificial layer when the barrier layer is gypsum is thus also examined in the present paper.

Three series of tests were conducted to examine the effects of the thickness of the sacrificial layer and the type of barrier layer on the self-extinguishing performance of the sacrificial layer. In all tests, specimens were heated following the ISO834 fire temperature–time curve and then left in a quiescent environment. All specimens were made from Japanese cedar, the wood most used for construction in Japan.

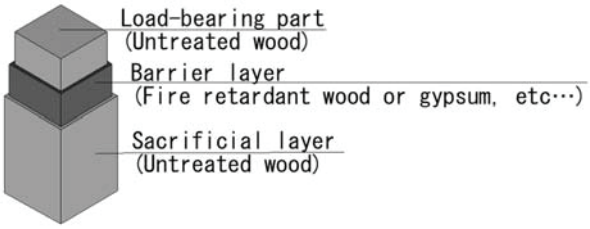

Figure 1: *Wooden fireproof structural elements*

[1] Tomoyo Hokibara, Waseda University, Japan hokibara@waseda.jp
[2] Yuji Hasemi, Waseda University, Japan, hasemi@waseda.jp
[3] Daisuke Kamikawa, Forestry and Forest Products Research Institute, Japan, daikami@affrc.go.jp
[4] Tsutomu Nagaoka, Takenaka Co. Research & Development Institute, Japan, nagaoka.tsutomu@takenaka.co.jp

https://doi.org/10.52202/069179-0218

2 EFFECT OF THE THICKNESS OF THE SACRIFICIAL LAYER ON SELF-EXTINGUISHING WITH A WOOD-BASED PROTECTION LAYER

2.1 THICKNESS AND SELF-EXTINGUISHING OF THE SACRIFICIAL LAYER

2.1.1 Purpose

The first series of tests was conducted to clarify whether fireproof-structural elements with a sacrificial layer thickness designed for the required fire-resistant time will self-extinguish when exposed to heating for a time shorter than the required fire-resistant time.

Specifically, test pieces with sacrificial layers of 50 mm, which were designed to have fire resistance for 120 minutes, were heated for 60 and 120 minutes to verify whether they self-extinguished even after 60 minutes of heating.

2.1.2 Outline of tests

In the first series of tests, using a small furnace at the Forestry and Forest Products Research Institute, test pieces were heated for 1 or 2 hours according to the ISO834 standard heating curve and allowed to cool in the furnace for 6 hours. **Figure 2** is a schematic diagram of the furnace and the layout of the test specimen.

Two specimens were prepared with a sacrificial layer having a thickness of 50 mm and fire-retardant plywood for the barrier having a thickness of 50 mm. The materials of barrier layer, fire-retardant plywood, were rated as quasi-incombustible materials. The fire-retarding agent injected 180 kg/m^3 into the fire-retardant plywood.

The measurement items were the internal temperature of the specimen and the furnace temperature. The temperature measurement points are shown in **Figure 3**.

2.1.3 Test results and discussion

Table 1 shows that the sacrificial layer with the 120-minute heating specification extinguished itself after heating whereas the sacrificial layer with the 60-minute heating specification continued to burn. Previous studies [2] have shown that the self-extinguishing of the sacrificial layer is greatly affected by a rise in the barrier layer temperature to the decomposition temperature of the fire retarding agent (195 °C) during heating. **Figures 4 and 5** show that the temperature within the barrier of self-extinguishing specimen S50-120 exceeded the decomposition temperature 97 minutes after the start of heating, whereas the non-self-extinguishing specimen S50-60 did not even reach 100 °C. This is probably because the sacrificial layer was too thick and the barrier layer did not reach the decomposition temperature of the fire retarding agent during heating and did not self-extinguish.

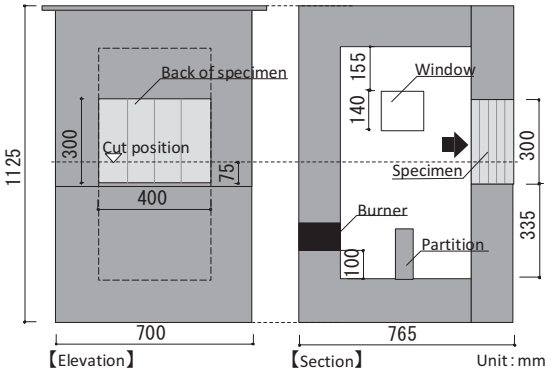

Figure 2: *Specimen layout in the first and second series of tests*

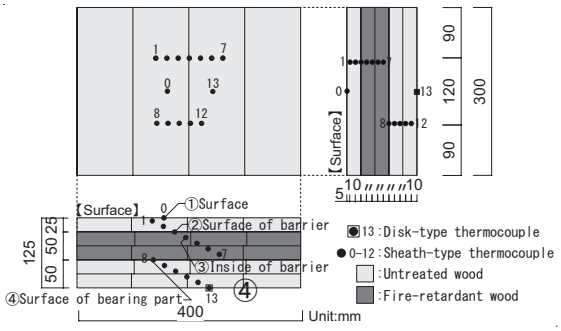

Figure 3: *Specimens in the first series of tests*

Table 1: *Results of the first series of tests*

Specimen	Sacrificial layer thickness [mm]	Heating time [min]	Carbonization [mm]	Results*1
series(1)tests S50-60	50	60	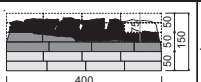	× (Continued to burn)
series(1)tests S50-120		120	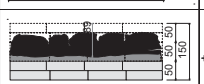	○ (Extinguished)

:Untreated wood : Fire-retardant wood : Char layer

*1: ○:Glowing combustion stopped after end of the test, ×:Glowing combustion continued after end of the test

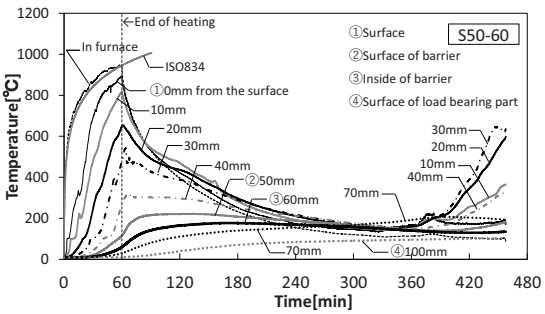

Figure4: *Temperature (S50-60)*

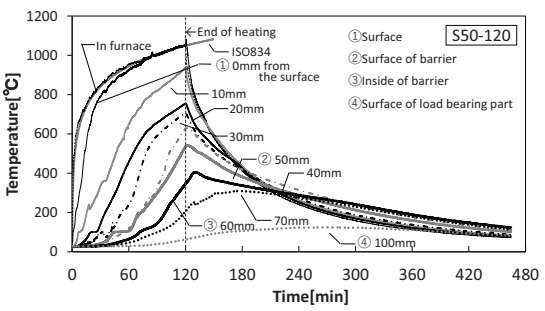

Figure 5: *Temperature (S50-120)*

https://doi.org/10.52202/069179-0218

The results show that for the same thickness of the sacrificial layer, self-extinguishing depends on the heating time. It is considered that there are two reasons for the continuation of combustion in the sacrificial layer.

(1) The barrier layer did not reach the decomposition temperature of the retarding agent during heating and could not contribute to suppressing the temperature rise inside the sacrificial layer.

(2) The carbonized layer on the surface of the specimen suppressed the heat loss to the outside, and the combustion of the uncarbonized part of the sacrificial layer continued.

Therefore, in the next section, the optimum thickness of the self-extinguishing sacrificial layer is examined regardless of the heating time.

2.2 OPTIMUM SACRIFICIAL LAYER THICKNESS REGARDLESS OF THE HEATING TIME

2.2.1 Purpose

The second series of tests was conducted to examine the optimum thickness of the sacrificial layer regardless of the heating time. From the results of past experiments[2], it is thought that if the carbonization depth is under 10–20 mm, a specimen will self-extinguish through heat loss from the surface. The carbonization rate of Japanese cedar is 0.6–0.8 mm/min[4], and it is thus presumed that fire heating for 12.5–33.3 min will result in the specimen self-extinguishing through heat loss from the surface. Additionally, in the case of heating for 30 minutes or longer, the temperature of the barrier layer must reach the decomposition temperature of the retarding agent during heating. **Figure 4** shows that the depth reaching the decomposition temperature of the fire retarding agent (195 °C) after heating for 30 minutes was 20–30 mm, and it is thus estimated that the optimum thickness of the sacrificial layer is 20–30 mm.

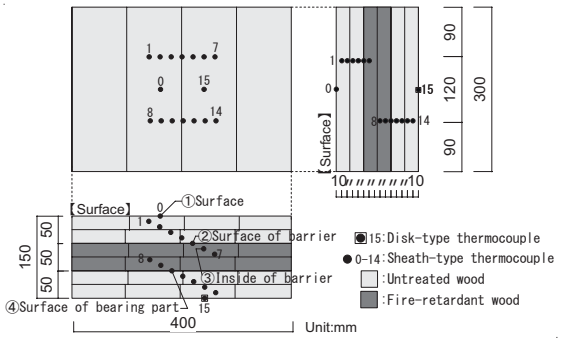

Figure 6: *Specimens in the second series of tests*

Table 2: *Results of the second series of tests*

	Specimen	Sacrificial layer thickness [mm]	Heating time [min]	Carbonization	Char layer depth [mm] Heating end*1	Char layer depth [mm] Test end	Results*2
series(2)tests	S25-30	25	30		22	27 (+5mm)	Succeeded (Non exists)
	S25-45		45		31	35 (+4mm)	Succeeded (Non exists)
	S25-60		60		33	48 (+15mm)	Succeeded (Non exists)
	S25-120		120		58	78 (+20mm)	Succeeded* (Non exists)

:Untreated wood : Fire-retardant wood : Char layer

*1:Char layer depth is calculated linear interpolation of internal tempreture. Carboonization tempreture is 260℃ for untreated wood, 195℃ for fire-retardant wood.

*2: ○:Glowing combustion stopped after end of the test, ×:Glowing combustion continued after end of the test

2.2.2 Outline of the tests

In the second series of tests, four specimens with a sacrificial layer thickness of 25 mm were prepared for self-extinguishing regardless of the heating time. The fire-retarding agent was injected 180 kg/m^3 into the fire-retardant plywood at as in section 2.1. Following the ISO834 standard heating curve, heating tests were conducted with heating times of 30, 45, 60 and 120 minutes.

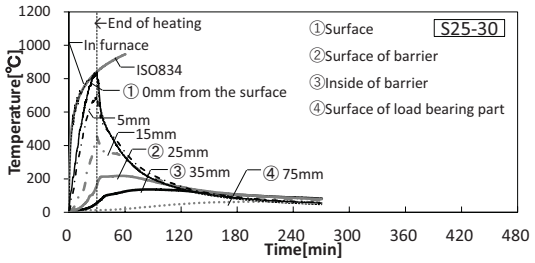

Figure 7: *Temperature (S25-30)*

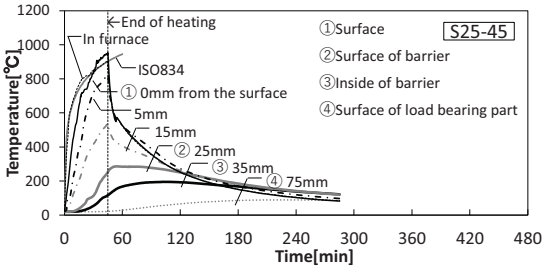

Figure 8: *Temperature (S25-45)*

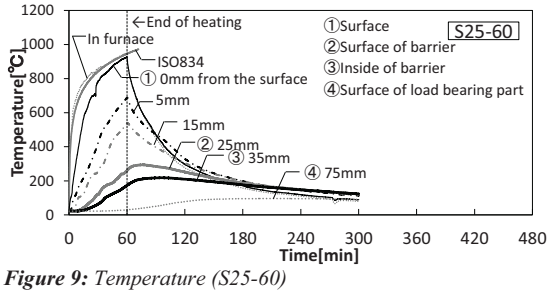

Figure 9: *Temperature (S25-60)*

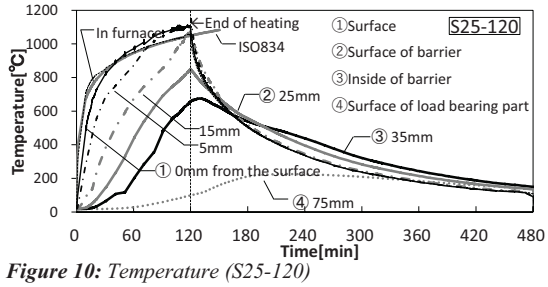

Figure 10: *Temperature (S25-120)*

https://doi.org/10.52202/069179-0218

Specimens were then allowed to cool in the furnace for a time longer than three times the heating time. The layout of the furnace and test specimen and the measurement items were the same as those in section 2.1. The temperature measurement points are shown in **Figure 6**.

2.2.3 Test results and discussion

Table 2 presents the cross section of each specimen, the carbonization depth, and whether glowing combustion continued at the end of the test. There was self-extinguishing for all heating times. **Figures 7** to **10** show the internal temperatures.

Table 2 reveals that carbonization progressed to the load-bearing part after heating for 2 hours. The temperature of the load-bearing part decreased with the temperature inside the furnace, and it is thus considered that the progress of combustion after heating was due not to the glowing combustion of the sacrificial layer but to the insufficient performance of the barrier layer. Additionally, the burning of the ends was due to the poor coating of the ends.

In the specimen heated for 30 minutes, the carbonization depths at the end of heating and at the end of the test were 22 and 27 mm, respectively (**Table 2**). It can be said that the sacrificial layer was generally carbonized entirely during heating and that the barrier layer was hardly carbonized and extinguished by itself after the heating. Meanwhile, because the barrier layer did not reach 100 °C at the end of heating, it is thought that if the sacrificial layer is 25 mm, the sacrificial layer will self-extinguish through heat loss from the surface, regardless of the self-extinguishing effect of the barrier layer.

In the specimen heated for 45 minutes, the sacrificial layer was completely carbonized at the end of heating, and the barrier layer reached the retarding agent decomposition temperature (195 °C) (**Figure 8**). It is thus presumed that an self-extinguishing effect of the barrier layer was exerted.

On the basis of these results, it can be said that the performance of the barrier layer determines whether the specimen can self-extinguish when exposed to fire heating for 45 minutes or longer. Therefore, the thickness of the sacrificial layer that reliably self-extinguishes regardless of the heating time is estimated to be 25 mm from the heat loss from the surface and the effect of the barrier layer.

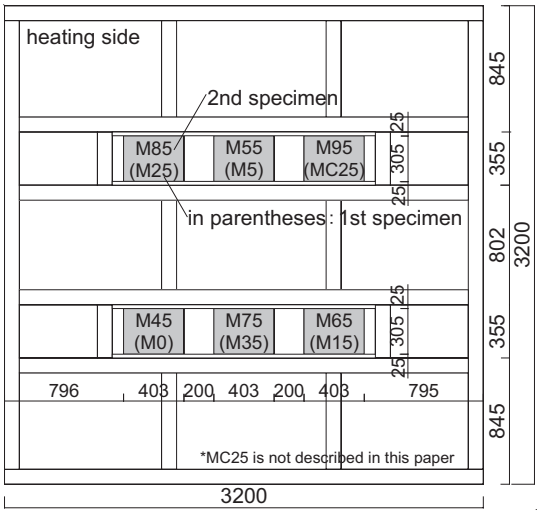

Figure 11: *Specimen layout in the third series of tests*

3 EFFECT OF THE THICKNESS OF THE SACRIFICIAL LAYER ON SELF-EXTINGUISHING IN THE CASE OF A GYPSUM-BASED PROTECTION LAYER

3.1 Purpose

The results obtained in section 2 revealed that the self-extinguishing performance is affected by whether the effect of suppressing the temperature rise due to the latent heat of the barrier layer is exerted during heating.

Gypsum exposed to heat suppresses a temperature rise of the sacrificial layer through the heat of vaporization of the water of crystallization within.

In a third series of tests, with gypsum used as the barrier layer, the thickness of the sacrificial layer was prepared from 0 to 95 mm, to clarify the effect of the thickness of the sacrificial layer on the self-extinguishing performance.

3.2 Outline of tests

In the third series of tests, using a wall furnace (3 m × 3 m) at the Takenaka Co. Research & Development Institute, specimens were heated for 1 hour following the ISO834 standard heating curve and allowed to cool in the furnace for 4 hours. **Figure 11** is a schematic diagram of the furnace and the layout of the test specimen.

Eleven test specimens were prepared with the thickness of the sacrificial layer ranging from 0 to 95 mm in increments of 10 mm. Gypsum-based self-leveling material and Japanese larch were used for the barrier layer. The thickness of the barrier layer was set at 40 mm. The load bearing part and sacrificial layer were integrated, and the gypsum-to-larch length ratio of the barrier layer was set at 2:1 considering the minimum width that could bear the shear force that needs to be borne by a structural member. The measurement items were the internal temperature of the specimen and the furnace temperature. Specimens and the temperature measurement points are shown in **Figure 12**.

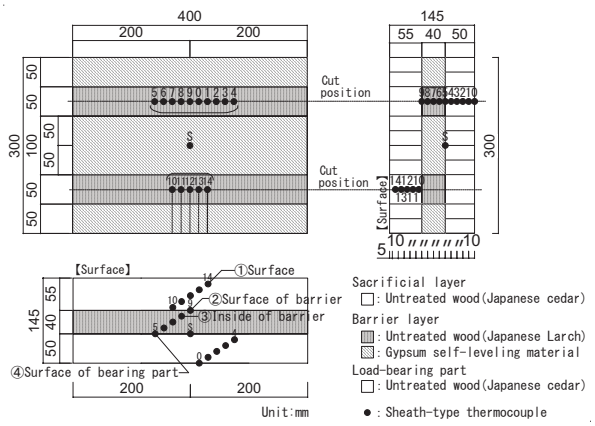

Figure 12: *Specimens in the third series of tests (M55)*

https://doi.org/10.52202/069179-0218

Table 3: *Results of the third series of tests*

	Specimen	Sacrificial layer thickness [mm]	Heating time [min]	Carbonization		Char layer depth Heating end[*1] Test end (upper/under)	Results[*2]
				upper side	underside		
series(3)tests	M0	0	60	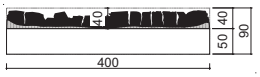	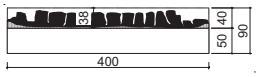	29mm / 40mm / 38mm	○ (Extinguished)
	M5	5		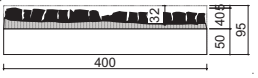	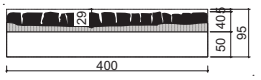	32mm / 32mm / 29mm	○ (Extinguished)
	M15	15		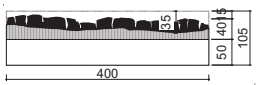	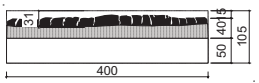	29mm / 35mm / 31mm	○ (Extinguished)
	M25	25		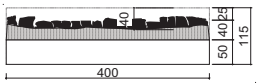	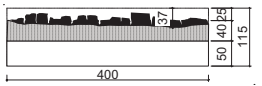	33mm / 40mm / 37mm	○ (Extinguished)
	M35	35		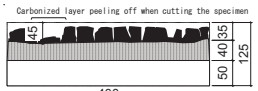	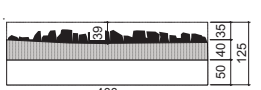	35mm / 45mm / 39mm	○ (Extinguished)
	M45	45		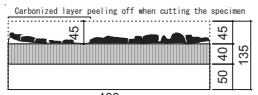	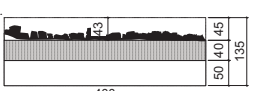	32mm / 45mm / 43mm	○ (Extinguished)
	M55	55		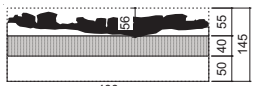	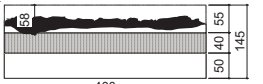	39mm / 56mm / 58mm	○ (Extinguished)
	M65	65		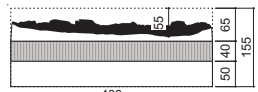	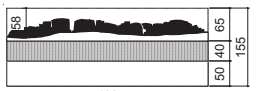	35mm / 55mm / 58mm	× (Continued to burn)
	M75	75		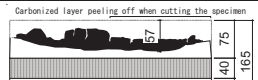		34mm / 57mm / -	× (Continued to burn)
	M75	85		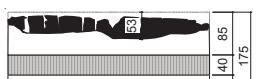	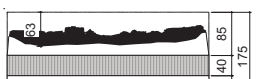	36mm / 53mm / 63mm	× (Continued to burn)
	M75	95		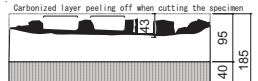	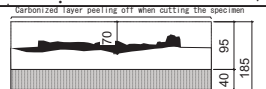	36mm / 43mm / 70mm	× (Continued to burn)

:Untreated wood : Gypsum self-leveling material : Char layer

*1:Char layer depth is calculated linear interpolation of internal tempreture. Carboonization tempreture is 260℃ for untreated wood, 195℃ for fire-retardant wood.

*2: ○:Glowing combustion stopped after end of the test, ×:Glowing combustion continued after end of the test

https://doi.org/10.52202/069179-0218

3.3 Test results and discussion

Table 3 presents the cross section of the specimen, the carbonization depth, and whether glowing combustion continued at the end of the test. No specimen carbonized up to the load-bearing part. Self-extinguishing was confirmed when the thickness of the sacrificial layer was 55 mm or less, but with a sacrificial layer having a thickness of 65 mm or more, glowing combustion continued and the sacrificial layer did not self-extinguish. **Figure 8** shows the temperature of the barrier layer and **Figure 9** shows the temperature of the sacrificial layer for M35 to M85, which became the boundary of self-extinguishing. **Table 3** shows that the sacrificial layers of self-extinguished of M0 to M45 were uniformly carbonized. After heating, the temperature at the inside of the barrier layer (55 to 85 mm deep surface from) of M45 quickly reached 100℃ and was maintained until the end of the test (**Figure 14**). It is thus considered that the carbonization of the sacrificial layer was completed by heat conduction after the end of heating, and the continuation of combustion was suppressed by the heat of vaporization of the barrier layer.

As shown in **Figure 14**, the temperature of M55, which also extinguished itself, gradually increased to a maximum of 150 °C inside the barrier layer more than 1 hour after the end of heating.

In M55, after heating, the temperature of the inside of the sacrificial layer (15 to 35 mm in **Figure 13**) decreased as the temperature inside the furnace decreased, and then increased again to a maximum of approximately 500 °C. Furthermore, **Table 3** shows there were variations in the carbonization depth within the cross section of a specimen. It is thus considered that the temperature of the barrier layer rises owing to glowing combustion in the sacrificial layer after heating, and the heat of vaporization of the moisture present in the gypsum suppresses the continuation of combustion.

Meanwhile, in M65, which continued burning, the temperature of the barrier layer rose owing to heat conduction after heating, but the temperature of the barrier layer deeper than 95 mm from the heating surface did not reach 100 °C. Additionally, **Table 3** shows that an uncarbonized sacrificial layer with thickness of approximately 10 to 20 mm remained after the test was

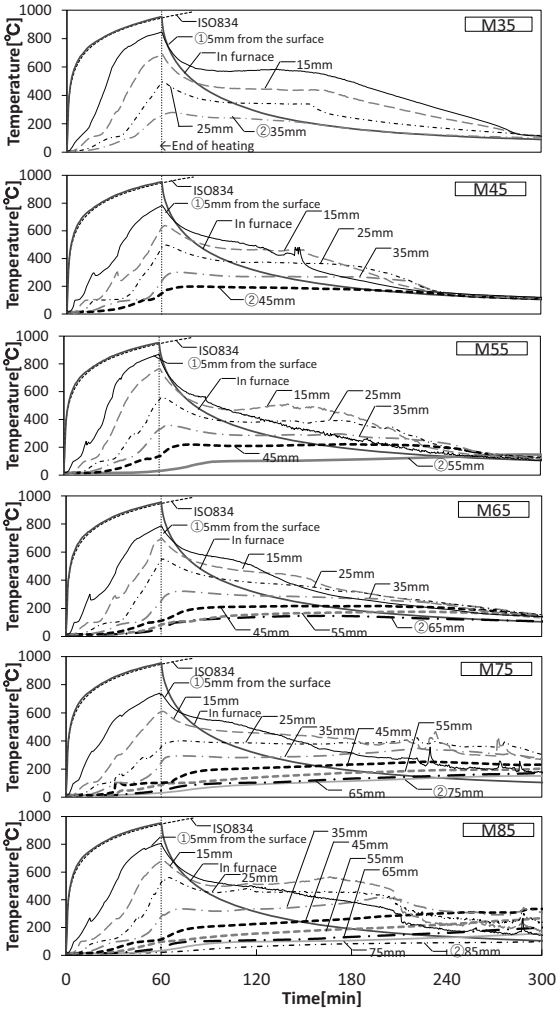

Figure 13: *Temperature of the sacrificial layer (M35, M45, M55, M65, M75, M85)*

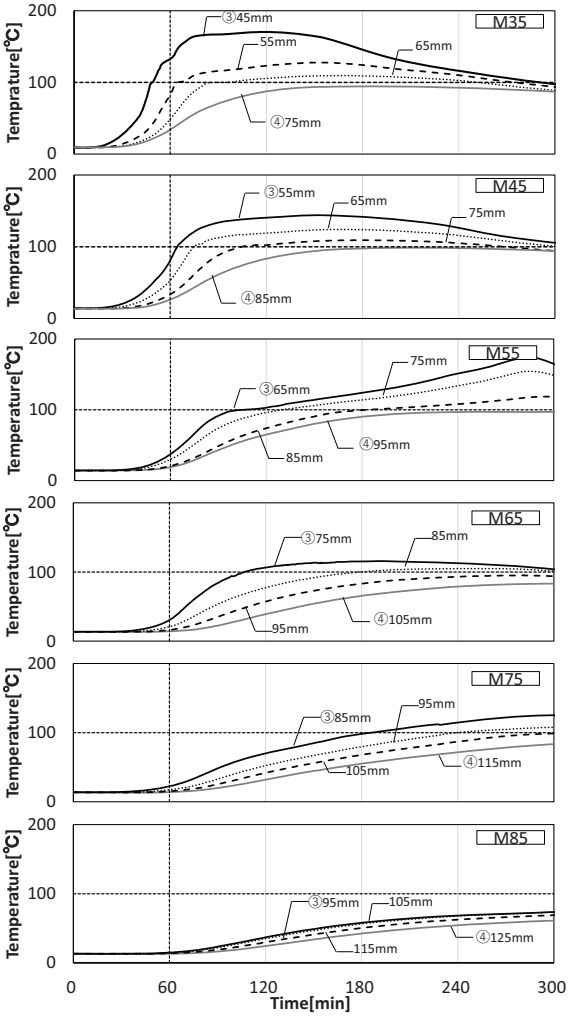

Figure 14: *Temperature of the barrier layer (M35, M45, M55, M65, M75, M85)*

https://doi.org/10.52202/069179-0218

complete. It is thus considered that the sacrificial layer was so thick that the temperature did not rise to the vaporization temperature (100 °C) of the moisture present in the gypsum and did not self-extinguish within the test time.

4 EFFECT OF THE DIFFERENCE IN THE BARRIER LAYER TYPE ON ACHIEVING SELF-EXTINGUISHING

The results presented in sections 2 and 3 reveal that the self-extinguishing performance is determined by whether or not there is latent heat of the barrier layer during heating. In the specimens with a barrier layer made from fire-retardant plywood, the thickness of the sacrificial layer was set at 25 mm or less, and the sacrificial layer extinguished regardless of the heating time.

In the test specimens with a gypsum barrier layer, the sacrificial layer reached the vaporization temperature through refractory heating at a thickness of the sacrificial layer of 45 mm or less and the sacrificial layer extinguished by itself.

With the gypsum barrier layer, the sacrificial layer self-extinguished even if it remained uncarbonized by approximately 20 mm. The water evaporation temperature in gypsum is lower than the decomposition temperature of the fire-retardant wood, and it is thus thought that the temperature control effect appears earlier for gypsum.

Furthermore, from the relationship between the heating time and the carbonization depth in **Tables 2 and 3**, the minimum thickness of the coating layer of the sacrificial layer + the barrier layer can be found with respect to the required fire resistance time. For example, in the case that the fire resistance time is 60 minutes, when the barrier layer is wood (as in the second series of tests), the minimum thickness of the covering layer is 48 mm, whereas when the barrier layer is gypsum (as in the third series of tests), the minimum thickness of the covering layer is approximately 32 to 58 mm, which is not so different.

Therefore, if the required fire resistance time increases, it will be necessary to consider changing the thickness of the sacrificial layer according to the type of barrier layer and improving the performance of the barrier layer.

5 CONCLUSIONS

The following conclusions are drawn from the results of the study.

(1) If the heating time is shorter than the required fire resistance time, it may not be possible to ensure self-extinguishing of the sacrificial layer.

(2) The optimum thickness of the sacrificial layer is 25 mm when using fire-retardant wood as the barrier layer.

(3) The gypsum barrier layer self-extinguished even if the sacrificial layer was about 20 mm thicker compared to the fire retardant wood-based barrier layer in the case of heating for 1 hour. It is thought that the effect of suppressing the temperature rise through the latent heat of water in the gypsum appears earlier.

ACKNOWLEDGEMENT

Part of this study was conducted under a JSPS Grant for "Engineering Approach to the Fire Safety Design of Large Scale Wooden Structural Assemblies". We thank Edanz (https://jp.edanz.com/ac) for editing a draft of this manuscript.

REFERENCES

Yamaguchi T. is the maiden name of the author, Hokibara Tomoyo.

[1] Hasemi Y., Itagaki N., Yamaguchi T., Development of wood-based fireproof buildings in Japan, WCTE2016 (Vienna)

[2] Yamaguchi T., Hasemi Y., Kamikawa D., Suzuki J., Optimization of the wood-based fire protection layer—an engineering approach to the design of fire-resistive building elements based on a sacrifice-layer concept, WCTE2018 (Seoul)

[3] Aoyama G., Hasemi Y., Hokibara T., Saiyoshi T., Kamikawa D., Takase R., Design methodology of total timber 2-hour fire-resistive structural beam on sacrifice layer concept, WCTE2021 (Vienna)

[4] Naruse, T., Nakamura, K., Yusa, S., Masuda, H., Harada, T., Yamada, M., Sato, A., Fire resistance of structural timber. Part 1: charring rate cedar and larch, Summaries of Technical Papers of Annual Meeting, Architectural Institute of Japan, Fire Safety, pp. 11-12, 2004

World Conference on Timber Engineering Oslo 2023

FIRE TESTING EXTERIOR CROSS-LAMINATED TIMBER WALLS TO NFPA 285

David Barber[1], Hans-Erik Blomgren[2]

ABSTRACT

Mass timber buildings are utilizing CLT for floors, walls and if permitted by regulations and codes, as exterior wall elements. In the United States, the IBC allows an exterior (external) wall to be load-bearing and constructed from Cross-Laminated Timber, provided the exterior surface is protected with fire rated gypsum board and if located above 12.2m, passes an NFPA 285 fire test. Supported by a US Forest Service grant, two CLT based exterior wall assemblies have been fire tested to NFPA 285, a global first. This paper presents the design of the exterior walls, summarizes the required code path and provides the results of the fire tests. The fire test assembly includes a 3 ply CLT panel, fire rated gypsum board, a commonly used water resistive barrier and mineral wool. Both of the CLT based exterior wall assemblies successfully passed the NFPA 285 test and will enable greater use of mass timber in future buildings. All data, drawings and test reports will be made public to progress the acceptance of CLT for fire safe use in exterior walls.

KEYWORDS: Mass Timber, Cross-Laminated Timber, Exterior walls, NFPA 285, Tall timber buildings, Fire testing

1 INTRODUCTION

Mass timber construction utilizing glulam and Cross-Laminated Timber (CLT) continues to be popular globally due to the carbon storage it offers, the efficiency in construction and as a differentiator in a competitive leasing market. Within the US, the nationally adopted model code is the International Building Code (IBC) [1] and the 2021 edition includes new provisions that increase the use of mass timber in multi-story office and residential buildings, up to 18 floors in height. As part of this change there are new requirements for exterior (external) walls that allow construction to be based on CLT panels. This change allows building designers to consider differing structural typologies for mass timber high-rise buildings.

1.1 EXTERIOR WALLS UTILIZING CLT – MOTIVATION FOR FIRE TESTING

The 2021 IBC provides a significant step-change for mass timber construction and CLT is permitted to be used as part of an exterior wall assembly for buildings of the new IBC mass timber Construction Types IV-A, B and C. Type IV-A construction allows mass timber up to 18 floors and 82m (270ft) in height. CLT can also continue to be used as an exterior wall in the mid-rise Construction Types IV-HT, V-A and V-B, being limited to a height of 25.9m (85ft) or less. The prescriptive IBC language says CLT can be utilized in a load bearing or non-load bearing exterior wall, provided the CLT is clad on the exterior side with a single layer of fire rated gypsum board of 16mm (5/8in). An exterior wall is made up of a number of different layers and components from the interior to the exterior face, with these components referred to as an assembly. The CLT forms the supporting panel for the exterior wall components (see Figures 1 and 2).

Figure 1: *CLT exterior wall assembly prefabricated off-site being lifted at site. CLT forms the support for the thermal and water barriers to the exterior face (image credit: Blomgren)*

Due to CLT combustibility, the IBC contains multiple conditions for exterior walls that trigger a requirement that the exterior wall assembly pass a fire test to NFPA 285 "*Standard Fire Test Method for Evaluation of Fire Propagation Characteristics of Exterior Wall Assemblies Containing Combustible Components*" [2]. The NPFA 285 testing requirement is most commonly triggered for wall heights greater than 12.2m (40ft).

NFPA 285 is the nationally adopted fire test standard to determine vertical flame spread acceptance for exterior walls. It is the author's understanding that no CLT based exterior wall has ever successfully passed an NFPA 285 fire test. Due to the compliance cost and timing barriers of completing an NFPA 285 test, building designs in the

[1] David Barber, Arup, Melbourne, david.barber@arup.com
[2] Hans-Erik Blomgren, Timberlab, Seattle WA, hanserikblomgren@timberlab.com

https://doi.org/10.52202/069179-0219

US typically avoid using CLT as part of an exterior wall, even though a CLT exterior wall can provide efficiencies in construction, especially for residential buildings. A building project wanting to use CLT as a load bearing, or non-load bearing exterior wall over 12.2m (40 ft) in height will face a technical justification barrier and will need to invest in an NFPA 285 fire test specific to the proposed wall assembly, adding significant project expense and risk.

Figure 2: *Five story building constructed in the US with CLT exterior wall approved without NFPA 285 fire testing (image credit: Blomgren)*

With the lack of substantive fire testing available globally on CLT as part of an exterior wall and given the issues of interpretation and application by building authorities of the IBC requirements, and further, to remove a degree of project risk, a project supported by a 2021 US Forest Service Wood Innovation Grant has been undertaken. The project aims were to determine: 1) The IBC code language requirements for exterior walls; 2) If the IBC approved solution for CLT use in exterior walls above 12.2m (40ft) will pass an NFPA 285 test; and 3) The minimum encapsulation required for the CLT exterior wall to pass an NFPA 285 test. The background to the IBC requirements, exterior wall test set up and results are described in this paper.

1.2 GLOBAL IMPLICATIONS

The use of combustible construction within exterior walls of buildings is of global concern given the number of catastrophic fires that have occurred when highly combustible composite panels have been used. Building Regulations in England have been changed to severely limit the use of timber as part of exterior walls due to fire safety concerns [3]. No fire testing has occurred on mass timber based external / exterior walls to prove or disprove if this change in regulations is appropriate. With few fire tests to any national standards on CLT exterior walls available for designers and regulators to assess, these fire tests to NFPA 285, an internationally recognized standard, will be of significant interest and can assist with decision making regarding the fire-safe implementation of CLT as part of a building's exterior wall.

2 IBC REQUIREMENTS

Where CLT is used as part of an exterior wall above 12.2m (40ft), the exterior wall assembly must be checked for compliance based on a range of code sections. The IBC requirements for exterior walls are included within Chapters 6, 7 and 14 and are open to interpretation, as compliance is based on building construction type, height of the exterior wall, separation to neighbouring buildings, the combustibility of the water resistive barrier (WRB) and the inclusion of CLT or other timber in the assembly.

The IBC requires that where CLT is used for an exterior wall assembly that it be protected from fire by direct fixing a layer of 16mm (5/8in) fire resistant gypsum board to the exterior face, so no timber is exposed and is deemed to protect the timber by 40 minutes. These requirements apply up to 82m (270ft) or 18 floors. The interior face of the CLT may be exposed or covered by non-combustible protection, required by separate IBC requirements not related to exterior walls. The WRB in use has strict flammability limits and when a WRB is combustible, which the majority are for use in modern construction, the IBC then requires an NFPA 285 fire test when used above 12.2m (40ft).

For a non-load bearing CLT based exterior wall assembly within Construction Type IV-A, IV-B, IV-C or IV-HT construction, the code requirements are summarized below and introduce one possible code compliance path. It should be noted that each building situation will differ and may result in outcomes that change the path to code compliance. The type of exterior wall arrangement is also important as to whether the exterior wall is part of a "balloon framing" solution (also referred to as a by-pass or curtain wall); or part of a platform framed solution (also referred to as an in-fill or window wall). The code references below are based on the unmodified 2021 IBC.

Chapter 6

Table 601:	Sets a fire resistance rating requirement for exterior load bearing walls from no requirement for Type V-B to a 3-hour FRR for Type IV-A.
Section 602.4:	Allows mass timber to be used in exterior walls in Type IV construction provided the requirements are met including the following:
Section 602.4.1.1: IV-A **Section 602.4.2.1: IV-B** **Section 602.4.3.1: IV-C**	Requires 40 minutes of non-combustible protection for the exterior face of the CLT determined per section 722.7 and flammability requirements for the WRB. The 40 mins can be provided with one layer of 16mm (5/8in) Type X fire rated gypsum board. Requires all components of the exterior wall covering be non-combustible except WRBs meeting the flammability requirements.

https://doi.org/10.52202/069179-0219

Section 602.4.4.2: IV-HT	Requires exterior protection of CLT in exterior walls in IV-HT of either 11.9mm (15/32in) fire retardant treated sheathing, 12mm (½in) gypsum board, or any non-combustible material.
Chapter 7	
Section 705.5:	Sets a fire resistance rating required of an exterior wall based on fire separation distance if the building is located near a boundary lot line or another building. Also determines if the fire resistance rating is required for fire exposure from the exterior only or both the interior and exterior.
Section 705.6:	Sets the requirements for the supporting construction of the exterior wall with different requirements for interior elements and exterior elements or within the exterior wall. Requires elements that brace the exterior wall but are not located within the plane of the exterior wall, to achieve a fire resistance meeting Table 601. This is relevant where the CLT wall is balloon framed or platform framed.
Section 715.4:	If the CLT is balloon framed (by-pass or curtain wall), the exterior wall intersection to the floor requires an approved fire seal that meets with ASTM E2307, to provide an "F" rating consistent with the floor (for Type IV-B this is 2hrs).
Section 722.7	Where required in Type IV construction, determines the required protection from non-combustible coverings on the exterior of the CLT. Recognizes that 40 mins can be provided with one layer of 16mm (5/8in) Type X fire rated gypsum board.
Chapter 14	
Section 1402.5:	For an exterior wall over 12.2m (40ft) in height in all but Type V construction, if the water-resistive barrier (WRB) is combustible then the exterior wall is required to undergo a fire test to NFPA 285 "*Standard Fire Test Method for Evaluation of Fire Propagation Characteristics of Exterior Wall Assemblies Containing Combustible Components*". There are two exceptions. Both Exceptions are not applicable to CLT framed exterior walls as the exceptions apply when the WRB is the ***only*** combustible component in the exterior wall assembly. Most, if not all, commercially viable WRBs are combustible. The combination of the combustible WRB and with mass timber framing in the exterior wall results in this Section requiring the exterior wall assembly comply with the NFPA 285 acceptance criteria when used above 12.2m (40ft).
Section 1405.1.1:	In all but Type V construction, exterior wall coverings are not permitted to be constructed of fire-retardant-treated wood above 18.3m (60 ft) above the grade plane nor constructed of other combustible materials above 12.2m (40 ft) above grade plane.

2.1 Summary

Where CLT is to be used within an exterior wall assembly, once the wall is above 12.2m (40ft) an NFPA 285 fire test is required, as the WRB will normally always be combustible. This is further clarified within the document "*Mass Timber Buildings and the IBC 2021 Edition*" [4] by the International Code Council and American Wood Council under "Change Significance 602.4.1.1 Exterior Protection" as follows:

> Buildings of Type IV-A, IV-B and IV-C construction will be subject to testing prescribed for exterior walls. Section 1402.5 of the IBC requires these walls to be tested according to NFPA 285. Nothing in this section is intended to preclude that test being applicable to these new types of construction. Even for wall assemblies passing the NFPA 285 test, all construction materials exterior to a mass timber wall, except the water-resistive barrier, must be noncombustible.

The CLT based exterior wall in Type IV-A, B, and C construction differ in required protection to the exterior face compared with Type IV-HT. Type IV-HT has more flexibility in the required non-combustible covering to the exterior face. A higher level of protection by non-combustible materials may also be needed if the exterior wall is load bearing or has a close fire separation distance.

3 DESCRIPTION OF THE NFPA 285 FIRE TEST

NFPA 285 "*Standard Fire Test Method for Evaluation of Fire Propagation Characteristics of Exterior Wall Assemblies Containing Combustible Components"* specifies a fire test for an exterior wall assembly to determine the potential for flame spread vertically up the wall, laterally across the wall and within the wall assembly. The fire test requires a two-story wall, including a window opening, to be constructed. A successful test demonstrates the exterior wall assembly, as a whole, passes the test, not any individual element.

The NFPA fire test uses two separate gas burners, one located within the lower story room that ignites from time zero. This burner provides a simulated fire that replicates the ASTM E119 *Standard Test Methods for Fire Tests of Building Construction and Materials* [5] fire curve which is used to determine fire resistance. After 5 mins of testing, a second gas burner is moved into position in front

https://doi.org/10.52202/069179-0219

of the window to simulate large external flames for a fire, replicating a fire that starts internally, then breaches a window or wall and then grows on the exterior face of the building (See Figure 3). This method of fire testing was developed from testing in the 1980's to assess combustible exterior cladding materials.

There are several different pass or fail criteria for the wall, with temperatures checked at various heights above the window and laterally away from the window. Temperatures are also checked within the wall. Flame spread height above the window is also visually observed and measured (see Figure 3). A wall needs to meet all test criteria to have been deemed to have passed.

Figure 3: *NFPA 285 test showing window burner in position for testing (image credit: Barber)*

4 EXTERIOR WALL ASSEMBLY DESIGN AND FIRE TEST SET-UP

Two CLT based exterior wall assemblies were designed, constructed and tested. The assemblies were selected based on a typical wall that would be constructed for locations with a mild temperature and humidity range in the U.S. The aim of the design was to make the exterior wall applicable and extendible to a broad range of mass timber projects (see Figures 4 to 12).

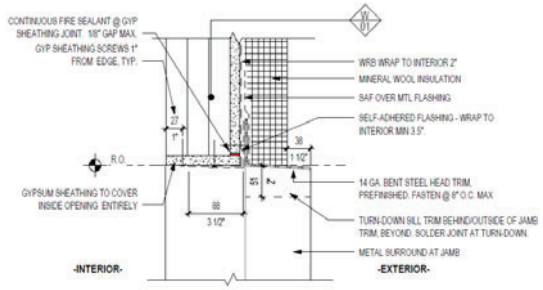

Figure 4: *Details at window head (image credit: Mithun Architects)*

The exterior wall assemblies included:

- A 3 ply 105mm (4.1in) CLT panel manufactured to ANSI/APA PRG 320-2019. Given this is the minimal CLT thickness expected for any exterior wall.
- The WRB was specified to have a reasonable performance for moisture control. The WRB did not meet the flammability classification criteria within IBC Sections 602.4.1.1, 602.4.2.1, 602.4.3.1 or 1402.5 Exception 2, being more flammable. This was based on understanding how limited the supply is for a very low flammability WRB and their high cost. A WRB typically used for mid and high-rise construction was chosen.
- The mineral wool batts were non-combustible and of a high-density given their better insulative performance with a minimal thickness included. A typical building in most USA climate regions will have a thicker depth of mineral wool.
- The window opening jambs, sill, and header were highly detailed given this is an area of likely failure. A window frame product was not included in the tests. For actual projects the expectation is the window will positively fasten to the CLT edges at the opening.
- The interior face of the CLT was left exposed given this may be the architectural solution desired. In having the interior face of the CLT exposed, there was additional combustible fuel added to the test as the CLT interior face combusted and charred.
- The CLT based exterior wall assemblies were tested with no exterior facing rain screen or wall covering. This allows additional non-combustible coverings to be directly fixed on the exterior face of the assembly. By not including a rainscreen, the exterior face of wall was exposed to worst-credible fire conditions, as a rainscreen would beneficially shield the wall.
- For Test 1 the exterior side of the CLT is clad with 16mm (5/8in) fire rated gypsum board, a combustible water resistive barrier and 50mm (2in) of mineral wool insulation.
- For Test 2 the wall assembly is similar to Test 1, but the fire rated gypsum board was removed, with only the WRB and 50mm (2in) of rockwool in place.
- All details are provided within drawings that will be available for download from www.woodworks.org.

https://doi.org/10.52202/069179-0219

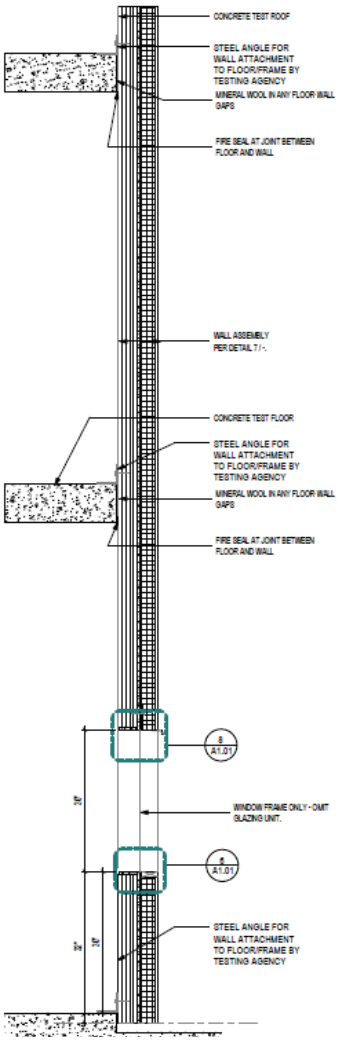

Figure 5: *Section through CLT wall specimen for testing (image credit: Mithun Architects)*

Two fire tests were carried out at Southwest Research Institute in San Antonio, in April and May 2022.

Figure 6: *Detail of C Test 1 set up, showing CLT wall completed in frame (image credit: Barber)*

Figure 7: *Test 1 set up, showing installation of fire rated gypsum board (image credit: Barber)*

https://doi.org/10.52202/069179-0219

Figure 8: *Test 1 set up, showing (left) installation of WRB (image credit: Barber)*

Figure 9: *Test 1 set up, showing installation of mineral wool (image credit: Barber)*

Figure 10: *Test 1 set up, close up of gypsum board to window edge and WRB wrap-around (image credit: Barber)*

Figure 11: *Test 1 set up, showing installation of window frame surround and sealing tape, prior to mineral wool overlay (image credit: Blomgren)*

Figure 12: *Completed wall set up prior to testing (image credit: Barber)*

5 FIRE TEST RESULTS

A brief description of the two fire tests undertaken to NFPA 285 are provided below.

5.1 Test 1 Summary

Test 1 was designed to be near compliant with the 2021 IBC, with a single layer of 5/8in (16mm) Type X fire rated gypsum board located on the exterior side of the CLT face, meeting section 602.4.2.1. As noted above, the WRB did not meet section 602.4.2.1 or section 1402.5 for limited flammability.

https://doi.org/10.52202/069179-0219

The CLT based exterior wall assembly passed the NFPA 285 test with no temperatures exceeding the failure criteria of the standard and the flame extension was limited in height and lateral spread. During the test and on completion of the test and disassembly of the panel, the following was observed:

- Interior face of the CLT was visibly flaming through the whole test, as expected and was charred.
- The mineral wool above the opening was heavily scorched yet still provided protection to the underlying CLT, preventing flame spread.
- The WRB had significant heat damage directly above the window, but this was limited in height to about 600mm (24in)
- The window surround suffered damage and remained in place throughout the test.

The interior face of the CLT based exterior wall assembly was exposed to the gas burner was significantly charred. The combustion of the CLT and resultant charring negatively impacted the performance of the exterior wall by increasing the extent of flames above that prescribed by the NFPA 285 test. By exposing the CLT on the internal face, the worse-case conditions for the CLT exterior wall assembly were tested (see Figures 13 to 18).

Figure 13: *Test 1 underway (image credit: Barber)*

Figure 14: *Test 1 flames impinging on mineral wool above window (image credit: Barber)*

Figure 15: *Test 1 completed, showing window burner extinguished with on-going flaming within test room (image credit: Barber)*

https://doi.org/10.52202/069179-0219

Figure 16: *Test 1 completed, showing damage to assembly layers with mineral wool manually removed (image credit: Barber)*

Figure 17: *Test 1 completed, showing interior side of CLT and extent of charring (image credit: Barber)*

Figure 18: *Close-up of Test 1 charring at top side of window opening. Charring extends into the first lamella only (image credit: Barber)*

5.2 Test 2 Summary

Given the results of Test 1, the CLT based exterior wall assembly was modified and the single layer of 16mm (5/8in) Type X fire rated gypsum board was not included on the exterior face of the panel. The exterior face of the CLT panel relied on the mineral wool to provide the protection against fire spread. This exterior wall assembly also passed the NFPA 285 test. The following was observed:

- Similar charring to the panel as for Test 1.
- Similar damage to the mineral wool and window surrounds as for Test 1.
- More heat damage to the WRB was observed, with damage extending up the face behind the mineral wool approximately 900mm (36in) and across the width of the window opening (see Figure 18).
- Overall temperatures and flame heights were similar to Test 1.

https://doi.org/10.52202/069179-0219

Figure 19: *Test 2 completed, showing extent of damage, with mineral wool manually removed. Damage can be compared with that of Test 1, shown in Figure 16 (image credit: Blomgren)*

5.3 Discussion

Two successful NFPA 285 fire tests were completed for a CLT based exterior wall. Test 1 was closely compliant with the requirements of the IBC as a CLT based exterior wall, with only the WRB being of a higher flammability classification. Test 2 did not include the non-combustible protection of gypsum board to provide 40 minutes of protection to the exterior face, utilizing mineral wool only to provide the non-combustible protection. The WRB was the same as for Test 1. Hence the CLT based exterior wall assembly for Test 2 had two variances with the requirements of IBC Section 602.4.

The test set-up for both walls was based on a design that replicates a typical project, acknowledging that there are many different types of exterior walls that could be designed and constructed. While the tests demonstrated the assembly as tested will pass the NFPA 285 test, an assembly with any of the following changes is also expected to pass the NFPA 285 criteria:

- CLT as a load bearing wall: Using the CLT as a load bearing wall is determined via ASTM E119 testing or similar approved method.
- Change in CLT depth: A thicker CLT panel can be used and would have no detrimental impact on the outcomes of the fire test.
- Addition of an exterior wall covering: A non-combustible wall covering can be included to the exterior face. This exterior covering would need to be direct fixed to the mineral wool insulation and could not include a vertical void or airspace as this could result in accelerated vertical flame spread between the mineral wool and the exterior wall covering.
- Addition of an interior covering to the CLT: The NFPA 285 tests had the CLT exposed on the interior side (facing into the interior or occupied building area). The results would not be changed if the CLT was covered with a non-combustible covering.

Test 2 was successful without the inclusion of a single layer of 16mm (5/8in) Type X fire rated gypsum board, which IBC Table 722.7.1(2) recognizes to provide the required 40 mins of non-combustible protection. For Test 2 the mineral wool insulation provided the CLT the non-combustible protection. For Test 2 to be used in a Type IV A, B or C building, an application to the authority having jurisdiction would be required, such as applying for a code variance or alternative material, design, or method of construction, given the wall assembly did not include the IBC required single layer of Type X fire rated gypsum board.

5.4 Applicability of NFPA 285 Testing to Mass Timber Buildings

NFPA 285 is a standard for assessing fire spread on exterior walls. Like all international fire tests for exterior / external walls and facades, the test methodology may need to be revisited where a building includes a large area of exposed mass timber structure (internal to the building), given that the exterior flaming is extended in length and temperatures are increased, due to the exposed timber structure [6]. NFPA 285 is a referenced standard for the IBC and would be used where an exterior wall is of a height over 12.2m (40ft), hence applicable for mid and high-rise mass timber buildings.

Fire testing of CLT based exterior walls with similar design set-ups is encouraged to occur in other countries to national standards, especially to test standards such as BS 8414 [7] and the proposed harmonised European test [8].

6 CONCLUSIONS

This project has demonstrated that a CLT based exterior wall assembly can pass the NFPA 285 fire test. In doing so, the results provide guidance to building officials, architects, engineers, and contractors as to how they can design and construct a CLT based exterior wall assembly that satisfy IBC requirements. The wall assemblies were designed so that the exterior face of the CLT was not directly exposed to flames and the detailing was well-thought through to prevent vertical flame spread.

With funding from a USFS Wood Innovation Grant, a current market barrier to mass timber construction has been removed by successfully demonstrating that a CLT based exterior wall assembly can pass NFPA 285. By publishing the details of the exterior wall designs and the fire test results, these CLT based exterior wall assemblies can be replicated for future multi-story mass

https://doi.org/10.52202/069179-0219

timber building projects and can be used by building authorities, architects, engineers and contractors, acknowledging the exterior wall design and limitations of the test method.

ACKNOWLEDGEMENTS

The project was led by Timberlab, supported by Arup, Mithun Architects, SmartLam, Rothoblaas, Rockwool and WoodWorks, with funding from the USDA 2021 Wood Innovation Grant # 21-DG-11062765-735.

REFERENCES

[1] International Code Council, 2021: *International Building Code*

[2] NFPA 285:2019 *Standard Fire Test Method for Evaluation of Fire Propagation Characteristics of Exterior Wall Assemblies Containing Combustible Components*

[3] Schulz, J., Kent, D., Crimi, T. Glockling, J., Hull T., *A Critical Appraisal of the UK's Regulatory Regime for Combustible Façades*. Fire Technology 57, 261–290 (2021)

[4] International Code Council and American Wood Council, 2021, *Mass Timber Buildings and the IBC* 2021 Edition

[5] ASTM E119 *Standard Test Methods for Fire Tests of Building Construction and Materials*

[6] Glew, A., Turnbull R., Møller Poulsen F., Amin R., Christensen E., Kotsovinos P., O'Loughlin E., Heidari M., Rein G., Barber D., Schulz J., 2023 *A Design Approach to External Fire Spread from Buildings with Exposed Mass Timber*, Proceedings of World Conference on Timber Engineering, Oslo

[7] BS 8414-1:2020 *Fire performance of external cladding systems - Test method for non-loadbearing external cladding systems fixed to, and supported by, a masonry substrate*

[8] J. Sjöström, J. Anderson, F. Kahl, L. Boström, and E. Hallberg, 2021 *Large scale exposure of fires to facade - Initial testing of proposed European method* RISE Report 2021:85

World Conference on Timber Engineering Oslo 2023

FIRE SAFETY OF MID-RISE BUILDINGS WITH LIGHT TIMBER STRUCTURES – STUDIES OF THE FIRE RESISTANCE OF A NOVEL CONSTRUCTION SYSTEM

Kathinka Leikanger Friquin[1], Johan Kr. Møller[2]

ABSTRACT: A novel construction system with light timber structures is being developed for mid-rise timber buildings. Requirements for the fire resistance of the building elements and structures increase with taller buildings because the consequences of a fire are higher than for small buildings. Mid-rise buildings therefore need fire resistance of 60-90 minutes. Floor elements with light timber structures have been studied with regards to the fire performance. Experimental results for the floor construction designed for large spans are presented here. The experimental results show that it is possible to achieve fire resistance REI 90 or more for the floor. The results indicate that large void cavities in the construction delays the charring of the timber structure. The construction provides fire protection of the main beams throughout the full fire scenario.

KEYWORDS: Light timber frame, construction system, fire resistance, temperature development, void cavity

1 INTRODUCTION

1.1 BACKGROUND

Wood is a renewable resource, light, easily and locally available in most areas, and environmentally friendly. The focus on sustainability therefore makes timber structures attractive and its suitability is now evaluated for all types of buildings. Elements with light timber frames can be prefabricated with a high degree of completion, with insulation, cladding/flooring, etc. Prefabrication ensures high quality, and the work environment is better than outdoors. Installation of the elements is fast, which makes the construction time for a building shorter than with traditional methods, reducing the time-related costs and exposure to wind, rain and frost [1]. An important challenge for mid-rise and tall buildings with light timber structures is the fire safety. The performance-based building regulations developed in Europe and many other countries the 1990s allowed for larger timber buildings than previously. However, the research focus has since mainly been on development of heavy timber structures for large buildings [2].

1.2 A NOVEL CONSTRUCTION SYSTEM

A novel floor construction is developed for spans of approximately 8 m, which is longer than what is possible for traditional light timber floors. The structure is therefore designed to achieve a higher stiffness and strength. A novel solution to enable installation of the noise reducing ceiling in the factory is developed to achieve a higher degree of prefabrication. The construction is also designed to give long fire protection of the main load-bearing structure.

1.3 OBJECTIVES

The main objective of the project is to develop a novel construction system with light timber structures and a high degree of prefabrication, for buildings with 5-8 floors with large open spaces. The main objectives of the experiment presented in this paper were to study; the fire resistance performance of the novel floor construction, whether it is possible to prevent involvement of the main structural members in the full duration of the design fire scenario, if the insulation would fall out during the fire and if the large void cavity would delay the thermal exposure on the timber construction. The fire behaviour during exposure to a "complete" fire development, including the cooling phase, is studied as this is a requirement for mid-rise timber buildings in Norway [3].

2 METHOD

2.1 TEST SETUP

The standard test method described in EN 1365-2 [4] was used. The floor specimen is placed on top of a horizontal furnace with dimensions 3080 mm x 4060 mm, see Figure 1. Siporex elements are used to cover the furnace completely, as the specimen is not wide enough, see pt. 2.2. A few deviations from the test method were made; on the cold side of the floor only the thermocouples for measurements of the average temperature change were installed, external load was not applied on the floor during the test because the span across the furnace is too short to

[1] Kathinka Leikanger Friquin, Department of Architecture, Materials and Structures, SINTEF Community, Norway, kathinka.friquin@sintef.no
[2] Johan Kr. Møller, Department of Architecture, Materials and Structures, SINTEF Community, Norway, johan.moller@sintef.no

https://doi.org/10.52202/069179-0220

test the load bearing capacity for a structure as stiff as this floor. Numerous additional thermocouples were installed inside the construction. The planned temperature-time curve was also different than described in the test method, see pt. 2.4.

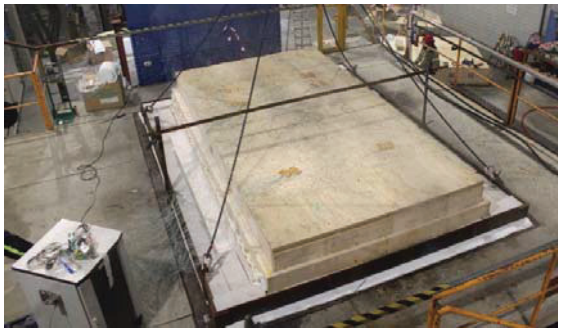

Figure 1: *The floor specimen mounted on the horizontal furnace (Photo: RISE Fire Research AS)*

2.2 TEST SPECIMEN

The novel floor construction is optimized with respect to the strength and stiffness, and to protect the load-bearing structure. The specimen is 2400 mm wide and 4382 mm long, with free span of 4300 mm. Description of the floor, see also Figure 2:
(1) wooden board
(2) structural timber beams
(3) structural timber flange
(4) ceiling system with 2 x 15 mm fire rated gypsum boards, acc. EN 520 [5]
(5) stone wool insulation, acc. EN13162 [6].

The cavity between the gypsum boards and timber structure is larger than 50 mm deep. The three main beams in the specimen are numbered BA1, BA2 and BA3.

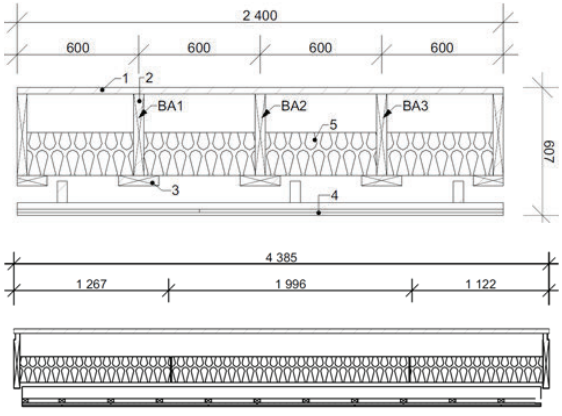

Figure 2: *Floor construction, cross-section (top) and longitudinal section (bottom). Measurements in metre (m) (Ill.: Støren Treindustri AS)*

The gypsum boards in the ceiling, the flanges and the insulation between the beams are, among other factors, designed to maximize the performance during fire. The load-bearing structure is made of structural timber. The specimen was stored inside the lab for 6 days before testing, at approximately 21°C. The moisture content in the components was not measured.

2.3 INSTRUMENTATION

Instrumentation of the floor was partly according to the test standard EN 1365-2 [4], but with additional instrumentation at three locations inside the construction to gain more knowledge and information about the temperature development inside the floor. The three locations are on/near beam BA1 at distance 966 mm from one end of the floor, on/near beam BA2 at distance 2193 mm from one end of the floor, and on/near beam BA3 at distance 1092 mm from the other end of the floor. Thermocouples of the type Quick-Tip were installed on and inside the beams, and at several other positions at the three locations. Figure 3 shows the positions on the surfaces of the flanges and beams, and the positions on/between each layer.

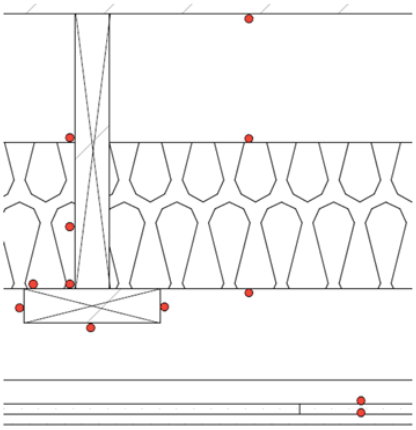

Figure 3: *Instrumentation on the surfaces inside the construction (Ill.: Støren Treindustri AS)*

Thermocouples were also drilled into the flanges from the top, see Figure 4. To measure the temperatures in the vertical direction, thermocouples are positioned at a distance of 10 mm to the side of the beam, see Figure 5. Depths from the underside of the flanges are 8, 18, 28, 38 mm. Horizontal measurements are positioned 10 mm below the top surface of the flange, at depths from the lateral side 10, 20, 30, 40, 50 mm.

https://doi.org/10.52202/069179-0220

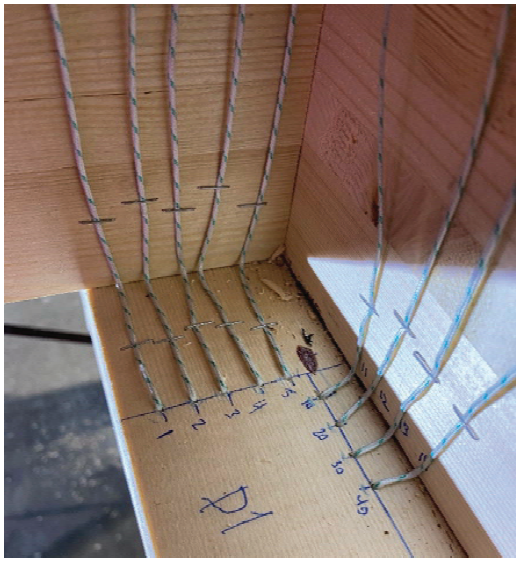

Figure 4: *The TCs inside the flange were drilled into the wood from the top of the flange*

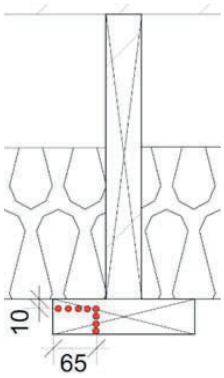

Figure 5: *Instrumentation inside the flange of the main beams (instrumentation group D) (Ill.: Støren Treindustri AS)*

2.4 TEST CONDITIONS

The furnace temperature followed the standard temperature-time curve given in EN 1991-1-2 [7] for 90 minutes. After 90 minutes the temperature was planned to decrease, with a cooling rate of 20°C/minute to represent the cooling phase of a complete fire, see the blue curve in Figure 6. Cooling was planned to be achieved by reducing, and eventually turning off, the gas burners, and removing the Siporex elements on the sides of the specimen.

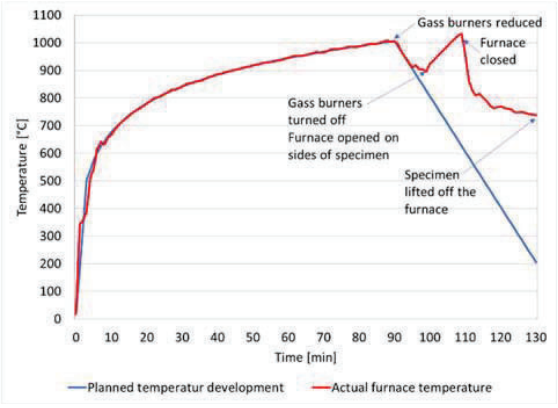

Figure 6: *Planned (blue) and achieved (red) temperature-time development in the furnace*

3 RESULTS AND DISCUSSION

3.1 TEMPERATURE MEASUREMENTS

The temperatures in the furnace and inside the floor were not registered during the time-period 100-109 minutes, because the logging stopped when the gas burners were turned off after 100 minutes. In the figures showing the results, a straight line is drawn between these two points. However, this might not be the actual temperature development. This does not affect the analysis of the results where charring of the wood has started, but can give a few minutes error for the reading of when charring temperatures of 300°C were reached on the top of the flange and inside the flanges. The error is less than 9 minutes.

Before lifting the specimen off the furnace after 130 minutes, the cables for the thermocouples had to be cut because they were too short. The temperatures in the specimen were therefore not measured after this.

The specimen was left outside the furnace until 255 minutes, i.e. 125 minutes after lifting it off the furnace. No flaming combustion was observed during this period, only glowing. It was then cooled with water to stop the combustion.

3.2 FURNACE TEMPERATURE

The planned temperature development in the furnace was difficult to achieve, and the cooling phase became different than planned, see Figure 6. The gas burners were reduced after 90 minutes to decrease the temperature, and turned off after 100 minutes when the cooling no longer followed the planned curve. At the same time, the Siporex elements on the sides of the specimen were removed. However, cooling at the planned rate was still not possible, mainly due to the free surfaces of flanges and other combustible material. After 130 minutes, the floor was therefore lifted off the furnace for continued cooling, but without external extinguishment, see Figure 7. The presence of combustible materials such as the flanges

https://doi.org/10.52202/069179-0220

made it difficult to decrease the temperature in the furnace after the gypsum board fall-off, and removing the Siporex increased the supply of Oxygen. These are the main reasons the planned cooling was not achieved.

Figure 7: *Lifting the floor off the furnace to achieve cooling*

The temperature development inside the cross-section and flanges might be affected by the elevated temperatures during the cooling phase, with a quicker temperature increase than if the cooling had evolved as planned. It is not possible to determine the scale of this.

3.3 TEMPERATURE DEVELOPMENT INSIDE THE FLOOR

Temperatures between all layers and on the surfaces were measured with thermocouples, as described in pt. 2.3. Figure 8 shows the average of the temperature development at each position, based on three measuring points. Observed fall-off of the gypsum boards and measurements of start of charring of the flanges are given in Table 1. The charring temperature of wood is defined to be 300°C in EN 1995-1-2 [8]. Time to start of charring is therefore determined by the time at which the temperature on the surface of the wood reaches 300°C.

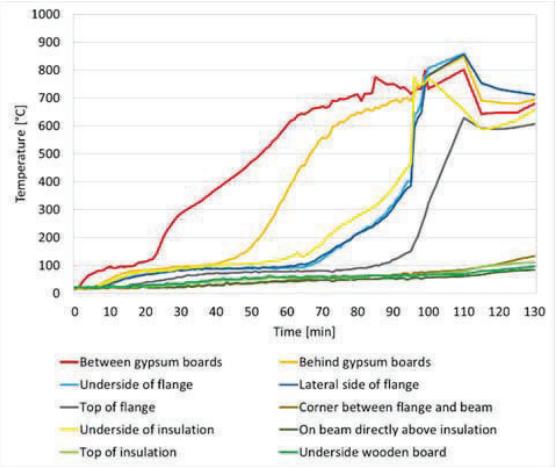

Figure 8: *Temperature development through the floor at different positions, average of the three measuring locations in the floor*

Table 1: *Time until fall-off of gypsum boards and start of charring of wooden battens and flanges*

Measuring point	Results
Temperature behind gypsum boards >300°C	57 min
Temperature on underside of insulation >300°C	83 min
Temperature on underside of flanges >300°C	88 min
Temperature on lateral sides of flanges > 300°C	89 min
Fall-off second gypsum board layer	95 min

Figure 8 shows a considerable difference between the temperature behind the gypsum boards and on the undersides and lateral sides of the flanges. The temperature on the unexposed surface of the gypsum boards increased fast after evaporation of the moisture in the boards, while on the other surfaces the heating rate was considerable slower. At its maximum the difference is approximately 370°C. This is probably caused by the large void cavity, which delays the temperature development considerably.

Charring temperatures behind the gypsum boards were reached after 57 minutes, but on the flanges, charring only started after 88-89 minutes. Charring of the flanges was, in other words, delayed by approximately 31 minutes. As mentioned above, this is probably mainly due to the large void cavity between the gypsum boards and flanges. The positive influence of a void cavity of a certain depth has been reported by Schleifer [9], and is included in design models for determination of the fire resistance of light timber frame assemblies [10]–[12].

3.4 FIRE PROTECTION PROVIDED BY THE GYPSUM BOARDS

Charring temperature 300°C was reached behind the gypsum boards in the ceiling after 57 minutes. Both gypsum board layers had fallen down after 95 minutes. The combination of fire protection provided by the boards and the large void cavity contributed greatly to prevent charring of the wooden structure before 88 minutes into the fire exposure.

The gypsum boards provided fire protection longer than expected based on guidance given in [10], [11], where 2 x 15 mm fire rated gypsum prevents charring for 46 minutes and falls down after 57 minutes. The design methods, developed to calculate the fire resistance of load-bearing timber structures and fire separating building elements, are meant to be conservative to cover most products on the market. Based on the results, the gypsum boards used in this experiment had better fire properties.

https://doi.org/10.52202/069179-0220

3.5 CHARRING

Charring of the timber structure in the floor element started at approximately 88 minutes, when the undersides and lateral sides of the flanges reached 300°C, see Table 1. This is 31 minutes after the temperature behind the gypsum boards in the ceiling reached 300°C. As described in pt. 3.1, this indicates that the large void cavity in the floor element significantly delayed the start of charring behind the gypsum boards in the ceiling. Calculations based on the design methods given in [10], [11] do not account for an effect of this magnitude from void cavities.

The temperature development in the flanges measured by the thermocouples drilled into the wood is shown in Figure 9 for vertical direction, and in Figure 10 for horizontal direction. See Figure 5 for the positions of the thermocouples.

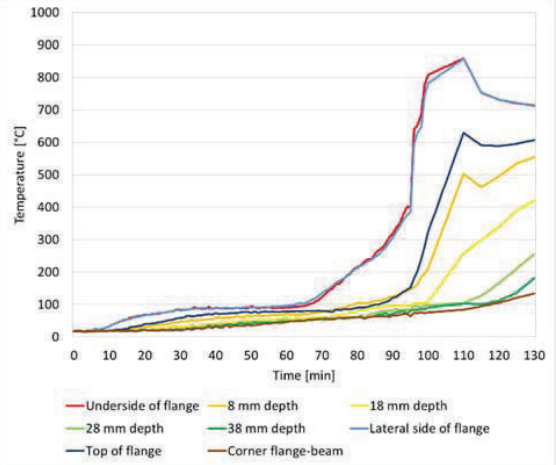

Figure 9: *Temperature development inside the flanges at depths 8, 18, 28, 38 mm from the underside, average of the three measuring locations in the floor*

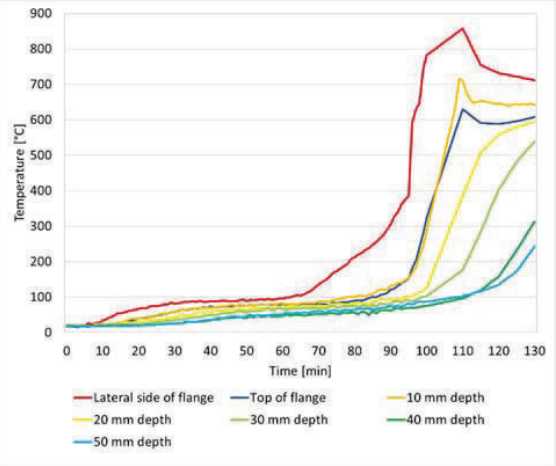

Figure 10: *Temperature development inside the flanges at depths 10, 20, 30, 40, 50 mm from the lateral side, average of the three measuring locations in the floor*

The average char depths of the flanges after 90 and 130 minutes, based on the temperature measurements inside the flanges, are given in Table 2.

On top of the flange the temperature approximately 20 mm in from the corner, see Figure 3, follows the temperature at depth 10 mm in the flange from lateral side. This indicates that there is some air leakage between the flange and the insulation. This leakage is negligible in the corner between the flanges and beams, at distance 75 mm from the lateral side of the flanges.

The residual cross-sections of the flanges were also measured physically after the fire experiment at three positions, see Figure 11 and Table 2. These are not at the same positions as the thermocouples. Residual height and width, plus width of the "shelf" of the flange for insulation to rest on, are similar to the last readings before the thermocouples were disconnected after 130 minutes, see Table 2. The cooling phase continued after this for approximately 125 minutes, but the charring of the timber stopped early in the cooling phase or the charring rate decreased considerably.

Figure 11: *The residual cross-sections of the flanges after the fire experiment. The main load-bearing beam is discoloured but not charred*

Table 2: *Average char depth at 90 minutes, when the specimen was lifted off the furnace at 130 min, and after the experiment*

Measuring point	Char depth at 90 min	Char depth at 130 min	Char depth after experiment
Flange height	5 mm	31 mm	27 mm
Flange width	7 mm	48 mm	49 mm

The char depth varied considerably between the measuring locations, between 2-25 mm, with largest variation for the height of the flange.

https://doi.org/10.52202/069179-0220

Charring after the specimen was lifted off the furnace and the surrounding temperature dropped to around 20°C, during the 2 hours before extinguishment, was negligible.

The charring rates during the different phases of the charring of the flanges are given in Table 3. The phases are:
Phase 2 – before fall-off of gypsum boards
Phase 3 – after fall-off of the gypsum boards
Phase 4 – after the char layer has reached a thickness of 28-30 mm.

Table 3: *Charring rates during different phases*

Charring phase	Vertical direction	Horizontal direction
Phase 2, before fall-off	0.60 mm/min	0.89 mm/min
Phase 3, after fall-off	0.74 mm/min	1.38 mm/min
Phase 4, char layer min. 28-30 mm	0 mm/min	0.70 mm/min

Charring on the lateral sides of the flange is faster than on the underside, with 10 mm larger char depth at 130 minutes. This is due to the simultaneous heating from the underside.

3.6 FIRE PROTECTION OF THE MAIN LOAD-BEARING STRUCTURE

The novel design of the floor, with 2 x 15 mm fire rated gypsum boards, large void cavity and flanges under the beams, protected the main load-bearing beams and prevented charring of them for the duration of the fire experiment. In addition to the fire protection given by the gypsum boards and the cavity reported above, the flanges prevented charring of the beams from below. The flanges also held the insulation in place and prevented charring from of the lateral sides of the beams.

3.7 FIRE RESISTANCE

Fire resistance of the floor is at least 90 minutes for both the load-bearing and fire separating properties. No external loading was applied on the floor in the experiment. This is because the structure has high strength and stiffness, and it would therefore not be possible to apply a sufficiently large load to cause noticeable deflections. The floor will have little deflection also with a span of 8 m. It can therefore be assumed that the fire protection with gypsum boards will remain intact also in a real building.

4 CONCLUSIONS

An experiment has been performed to study the fire behaviour of a novel floor construction with light timber structure during a "complete" fire development, including cooling phase. The main findings are:

- it is possible to achieve fire resistance of 90 minutes or more for the floors load-bearing and fire separating properties,
- the large void cavity between the gypsum boards and wooden surfaces of the structure delays the charring of the timber structure,
- the construction provides fire protection of the main load-bearing beams throughout the fire,
- the experimental results were significantly better than results from design methods, mainly due to longer fire protection provided by the gypsum board and the effect of the large void cavity,
- the insulation is held in place by the flanges throughout the fire experiment,
- the charring stopped when the specimen was lifted off the furnace.

Achieving a cooling phase in the furnace was difficult due to the large surfaces of the combustible elements in the specimen.

The effect of the void cavity should be studied further, and design methods improved to account for this effect.

ACKNOWLEDGEMENT

This project is funded by the Research Council of Norway, Project No. 309363, and Støren Treindustri AS, as part of the innovation project BV2020 Bærekraftige og innovative trebygg opptil 8 etasjer med bindingsverk (Sustainable and innovative buildings with up to 8 floors of light timber structures).

REFERENCES

[1] P. D. Kremer, L. Ritchie. Understanding Costs and Identifying Value in Mass Timber Construction: Calculating the “Total Cost of Project”. *Mass Timber Construction Journal*, 1(1):14-18, 2018.
[2] B. Orta, J. Martínez-Gaya, J. Cervera, J. Aira. Timber high rise, state of the art. *Informes de la Construcción*, 72(558), 2020.
[3] KMD. Forskrift om tekniske krav til byggverk (Byggteknisk forskrift). Kommunal- og moderniseringsdepartementet, Oslo, Norge, 2017.
[4] CEN. EN 1365-2:2014 Fire resistance tests for loadbearing elements - Part 2: Floors and roofs. European Committee for Standardization (CEN), Brussels, Belgium, 2014.
[5] CEN. EN 520:2004+A1:2009 Gypsum plasterboards - Definitions, requirements and test methods. European Committee for Standardization (CEN), Brussels, Belgium, 2004.
[6] CEN. EN 13162:2012+A1:2015 Thermal insulation products for buildings - Factory made mineral wool (MW) products – Specification. European Committee for Standardization (CEN), Brussels, Belgium, 2012.
[7] CEN. EN 1991-1-2:2002 Eurocode 1: Actions on structures - Part 1-2: General actions - Actions on structures exposed to fire. European Committee for Standardization (CEN), Brussels, Belgium, 2002.
[8] CEN. EN 1995-1-2:2004/AC:2009 Eurocode 5: Design of timber structures - Part 1-2: General -

Structural fire design. European Committee for Standardization (CEN), Brussels, Belgium, 2004.
[9] V. Schleifer. Zum Verhalten von raumabschliessenden mehrschichtigen Holzbauteilen im Brandfall. PhD Thesis. ETH Zürich, Zürich, Switzerland, 2009.
[10] B. Östman, Ed., *Fire safety in timber buildings. Technical guideline for Europe*. Stockholm, Sweden: SP Sveriges Tekniska Forskningsinstitut, 2010.
[11] B. Östman, Ed., *Brandsäkra trähus v.3*. Stockholm, Sweden: SP Sveriges Tekniska Forskningsinstitut, 2012.
[12] A. Just, J. Schmid, editors. Improved fire design models for Timber Frame Assemblies - Guidance document. ETH, Zürich, Switzerland, 2018.

https://doi.org/10.52202/069179-0220

World Conference on Timber Engineering Oslo 2023

EXPLORING THE INFLUENCE OF HEATING CONDITIONS IN THE CHARRING PROFILE OF BARE TIMBER AND TIMBER PROTECTED WITH A THIN INTUMESCENT COATING

Stavros Spyridakis[1], Jeronimo Carrascal[2], Felix Wiesner[3], David Barber[4], Cristian Maluk[5]

ABSTRACT: This research examines the influence of a thin intumescent coating applied on mass timber, focusing on how changes in the in-depth charring rate may occur during a fire event. An experimental fire methodology was used whereby the transient in-depth heating conditions were carefully measured during testing. The heating conditions at the exposed surface of each sample were controlled by keeping a constant incident radiant heat flux at the exposed surface of the sample, considering the transient swelling of the intumescent coating – employing the H-TRIS method. Test samples of (200×200) mm^2 were prepared from Cross Laminated Timber (CLT) with a depth of 110 mm. The mean measured DFT amongst the coated samples was 1.19 ± 0.10 mm. Fire experiments were conducted for bare and coated timber samples, with the heated surface exposed at three different heat fluxes of: 25, 50, 75 kW/m^2. The outcomes of this experimental study demonstrated that timber protected with a thin intumescent coating shows a delayed onset of charring and reduced in-depth charring rate for all heating conditions examined. However, the coating underwent considerable thermal degradation and regression at higher heat fluxes. Additionally, the mean measured charring rate was directly proportional to the incident radiant heat flux.

KEYWORDS: Mass timber, Thin intumescent coatings, Timber charring, Fire experiment, H-TRIS

1 INTRODUCTION

1.1 BACKGROUND

Mass timber structures are becoming prominent across the globe as an avenue to a greener and more sustainable building industry, among other benefits such as speed of construction. Advances in the manufacturing of mass timber have led to the mainstream use of Engineered Wood Products (EWPs) – e.g., Cross Laminated Timber (CLT) and Glue Laminated Timber (Glulam) for varied applications (Figure 1) – with more reliable mechanical properties over sawn timber.

The increased aspiration for EWPs to be used in the built environment, especially in applications where fire safety considerations are vitally important (e.g., mid-, and high-rise buildings), has highlighted the need for understanding the fire behaviour of mass timber structures. One key challenge is the flaming combustion (i.e., burning) of exposed mass timber surfaces during a fire, including circumstances where flaming or smouldering (i.e., flameless combustion) of timber continues even after the moveable fuel load in the compartment has burnt out.

Figure 1: *Interior views of exposed mass timber framing (Ascent building, Milwaukee, Wisconsin – USA). Photo © David Barber.*

Consequently, burning of exposed mass timber elements can increase the severity and duration of a fire event [1-4], with potentially detrimental fire safety and structural implications. To date, a common fire engineering solution to mitigate the challenges with mass timber structures burning in a fire event has been the partial or complete

[1] Stavros Spyridakis, School of Civil Engineering, The University of Queensland, Australia, s.spyridakis@uq.edu.au* (Corresponding author)
[2] Jeronimo Carrascal, School of Civil Engineering, The University of Queensland, Australia, j.carrascaltirado@uq.edu.au
[3] Felix Wiesner, Faculty of Forestry – Department of Wood Science, The University of British Columbia, Canada, felix.wiesner@ubc.ca
[4] David Barber, Arup, Australia, david.barber@arup.com
[5] Cristian Maluk, School of Civil Engineering, The University of Queensland, Australia | Semper, UK, c.maluk@sempergrp.com

https://doi.org/10.52202/069179-0221

encapsulation of timber using fire rated plasterboards. In its most basic definition, the purpose of encapsulating mass timber elements is to prevent timber from becoming part of the fuel load during a fire [5], and for load-bearing purposes to prevent or delay timber charring. Charring is usually assumed to occur when timber has reached a temperature of approximately 300 °C [6], with the charred section assumed to have negligible mechanical properties. However, the use of plasterboard does not allow for the expression of mass timber elements and can result in additional construction costs, as plasterboards need to be fitted after EWPs have been erected and installed on-site.

1.2 THIN INTUMESCENT COATINGS

Thin intumescent coatings are extensively used for steel construction in lieu of traditional passive fire protection, due to their proven architectural aesthetics, versatility (on-site or off-site application), and speed of application [7]. They are thermally reactive materials, applied to a coating thickness of a few millimetres – referred to as Dry Film Thickness (DFT). Intumescent coatings can swell multiple times their original thickness when heated [8], forming a thermal barrier that insulates the substrate material during fire, keeping its temperature below critical values, thus preserving its mechanical properties.

Despite the proven fire performance of thin intumescent coatings on steel structures, there is sparse published research available on their effectiveness for mass timber structures [9, 10]. However, exploratory testing to date on their application for mass timber has shown that they do swell during fire exposure, resulting in a delayed onset of charring and a reduced in-depth charring rate [11].

Additionally, recent developments in the production of intumescent paint products have led to the emergence of transparent intumescent coatings – which would make their commercial exploitation for mass timber buildings more likely. In the near future, the mainstream use of thin intumescent coatings on mass timber structures could result in (1) ease of application on-site or even off-site and (2) building aesthetic benefits.

1.3 RESEARCH MOTIVATION

This experimental study aims to demonstrate and provide confidence that thin intumescent coatings can be used for reducing the in-depth charring of mass timber during a fire, and to quantify how sensitive this may be to varied fire scenarios. Additionally, the work presented herein is the first stage of a larger experimental campaign of fire tests, to illuminate the effects of different intumescent paint types and thicknesses on the fire performance of mass timber.

2 EXPERIMENTAL METHODOLOGY

2.1 TESTING APPARATUS

A bench-scale version (Figure 2) of the Heat-Transfer Rate Inducing System (H-TRIS) test method [12] was used to impose fire exposure conditions for this study.

This bench-scale version of H-TRIS is comprised of four radiant panels with a radiative surface of (300x400) mm^2, capable of controlling the incident radiant heat flux at the heated surface of test samples – in the range of 5 and 100 kW/m^2. For this study, H-TRIS was coupled with a sample holder with an integrated spark ignition system providing piloted ignition during testing.

The objective of this testing setup is to control the heating conditions at the target surface of the test sample protected with a intumescent coating or the bare timber sample. The position of the radiant panels is corrected to account for the swelling of the coating. The integrated spark ignition system was kept in a fixed position to the test sample.

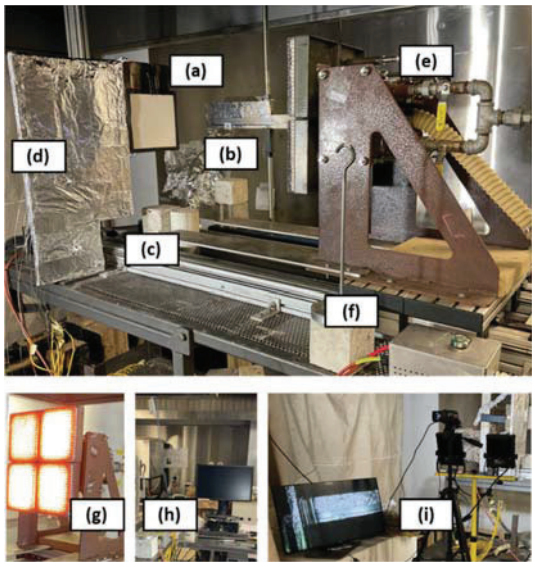

(a) Sample holder with integrated spark igniter
(b) Stand with fixed ruler to track the coating's expansion
(c) Computer-controlled motion system for H-TRIS
(d) Thermocouples with shield protecting them from heat
(e) Gas and air supply for H-TRIS radiant panels
(f) Igniter box to turn on/off the spark igniter
(g) Radiant panels (300 x 400) mm^2 – H-TRIS system
(h) Computer system controlling H-TRIS with data logger
(i) Camera and monitor setup to record coating expansion

Figure 2: *Experimental setup with key components highlighted.*

2.2 TEST METHOD

The samples were tested at constant incident radiant heat fluxes of either 25, 50, or 75 kW/m^2 for 60 min. This time duration has no relation with the Fire Resistance Rating or Level used in Standard fire testing. Instead, it was selected for the purpose of obtaining sufficient data during testing based on the dimensions of the selected samples.

For the bare timber samples, the spark ignition was turned off when sustained flaming at the heated surface of the sample was observed – defined as continuous flaming greater than 30 sec. This is longer than the time required by standard reaction-to-fire tests [13].

For timber samples with intumescent coating, the spark ignition was kept on for the first 5 min of the experiments to capture the expansion of the coating under piloted conditions, also ensuring a consistent testing approach with the bare timber samples. This time was verified by

https://doi.org/10.52202/069179-0221

preliminary testing. Further, the presence of the pilot is considered a more realistic testing approach, as in a real-life fire scenario pilot sources (e.g., flame, spark, embers) will usually be present.

The lowest heating condition (25 kW/m^2) was chosen to assess the burning behaviour of the samples above the critical heat flux for ignition of timber (13-14 kW/m^2) [14], but also near the threshold whereby most cellulosic materials are expected to auto ignite in a real fire (≥ 20 kW/m^2) [15]. The middle heating condition (50 kW/m^2) was selected such that to prevent self-extinction of bare timber [16], thus allowing for the timber's charring to continue. The purpose of the highest heating condition (75 kW/m^2) was to further examine the ability of the thin intumescent coating to reduce timber charring and char depth under more onerous heating conditions.

2.3 INSTRUMENTATION

The swelling of the tested thin intumescent coating was measured using a high-resolution video camera placed perpendicular to the direction of the expanding paint (i.e., on the side of the coated sample).

The internal temperature of timber was measured using thermocouples along the sample's depth and placed near the middle of the exposed surface. The 300 °C isotherm was tracked during post-processing of the experimental data, associated with the timber's char depth. The location of the 300 °C isotherm was calculated from a smoothing spline fit [17, 18] for every time instant.

Prior to testing, the thermocouples were inserted from the side of the sample (i.e., perpendicular to the principal direction of heat inside the sample) – minimising error of temperature readings as described by past researchers [19, 20]. Thermocouples were placed at the following depths from the heated surface: 5, 10, 20, 33, 50, 78, 110 mm.

The interior temperature evolution for both bare timber and timber protected with intumescent coating was recorded along the depth of each sample for the whole duration of heating (60 min) and cooling after the radiant panels were turned off (30 min).

2.4 TEST SAMPLE PREPARATION

Test samples of (200×200) mm^2 were prepared from CLT with a depth of 110 mm. The tested CLT comprised of three lamellas (32.5 mm, 45 mm, 32.5 mm) of Australian radiata pine softwood.

A commercially available solvent-based thin intumescent coating was used. Samples with intumescent coating were sprayed using an airless paint gun by a registered professional contractor, as per the product guidelines. The coating used has an opaque white finish and was originally formulated for structural steel applications, for either on-site or off-site use.

The bulk density of each sample was measured before each test by measuring its mass on a laboratory scale. The mean DFT of the coated timber samples was measured using an electronic gauge with an ultrasonic probe for timber substrates. The mean measured DFT for the six coated samples was 1.19 ± 0.10 mm – see Table 1.

The bulk moisture content of the tested timber was estimated using the oven dry method [21] from four sacrificial samples, which were stored in the same conditions as the test samples – at ambient temperature in a laboratory environment; the moisture content varied between 9.1 % and 9.8 %. Lastly, when placed inside the sample holder, each sample was wrapped on its sides using a ceramic wool and aluminium foil tape before being tested (Figure 3). This was done to minimise heat exchange between the sides of the sample and the metallic sample holder during testing, in order to enforce one dimensional heat transfer conditions akin to those in large, panelised mass timber.

Table 1: *Density and mean DFT for each test sample.*

Sample ID	Density [kg/m^3]	Mean DFT [mm]
BT-25-S1	509.6	-
BT-25-S2	476.9	-
BT-50-S1	501.1	-
BT-50-S2	472.9	-
BT-75-S1	523.6	-
BT-75-S2	495.8	-
IC-25-S1	494.9	1.18
IC-25-S2	519.0	1.20
IC-50-S1	510.6	1.12
IC-50-S2	496.5	1.11
IC-75-S1	509.1	1.26
IC-75-S2	556.2	1.29

Nomenclature:

- *Sample type: BT (Bare Timber), IC (Timber + Intumescent)*
- *Heating Condition: 25, 50, 75 (25, 50, 75 kW/m^2)*
- *Sample repetition: S1, S2, (S1 – first, S2 – second)*

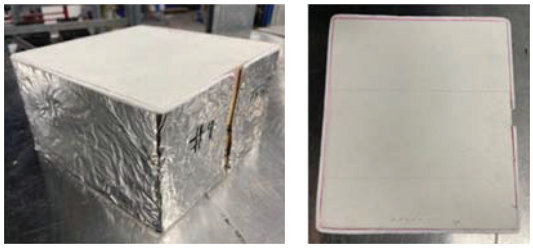

Figure 3: *Typical preparation of a sample prior to testing.*

3 TEST RESULTS

3.1 INTERIOR TIMBER TEMPERATURE

The temperature inside the timber was measured during heating (60 min) and cooling (30 min) of each test sample.

Figure 4 shows the in-depth temperature vs. time data carried for each repeat test – comparing plots without and with intumescent, side-by-side. Figure 5 shows the profile of temperature for each repeat test during heating – i.e., in-depth temperature vs. depth from the heated surface.

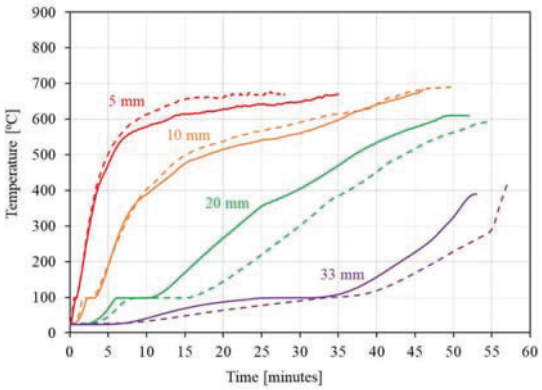

(I): Bare timber samples at 25 kW/m^2

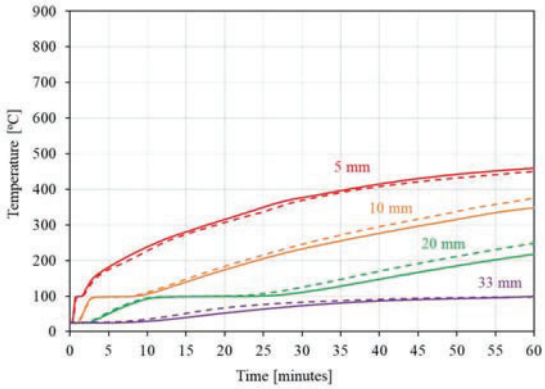

(II): Intumescent-coated timber samples at 25 kW/m^2

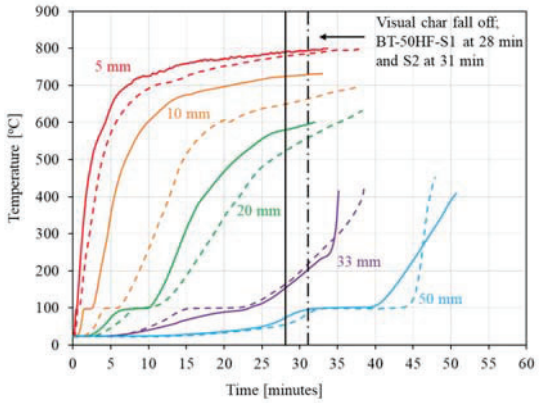

(III): Bare timber samples at 50 kW/m^2

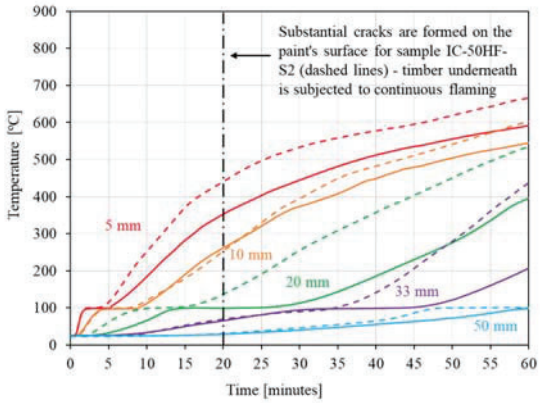

(IV): Intumescent-coated timber samples at 50 kW/m^2

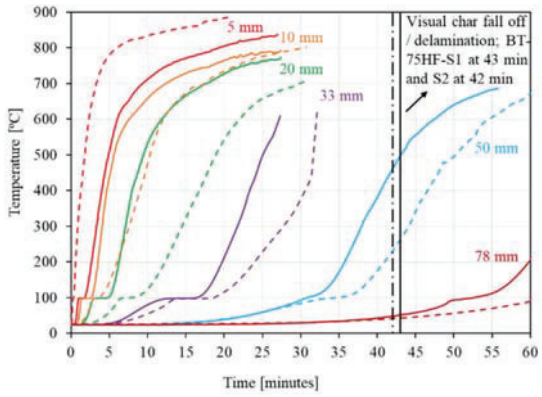

(V): Bare timber samples at 75 kW/m^2

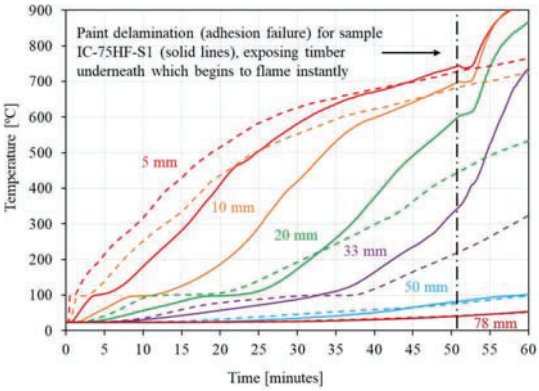

(VI): Intumescent-coated timber samples at 75 kW/m^2

Figure 4: *In-depth temperature vs. time for varied depths from the heated surface. Plots are shown for samples without (left) or with intumescent (right) under different heating conditions. Note: Dashed lines show repeat samples.*

https://doi.org/10.52202/069179-0221

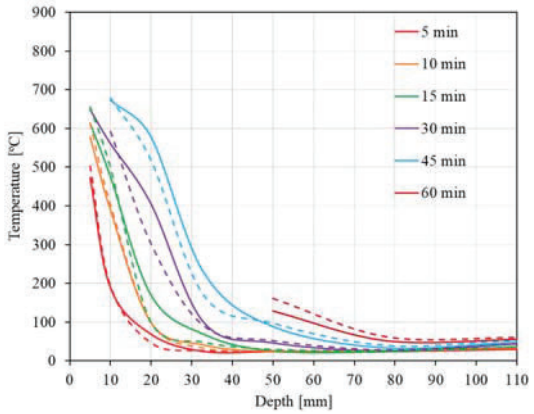

(I): Bare timber samples at 25 kW/m^2

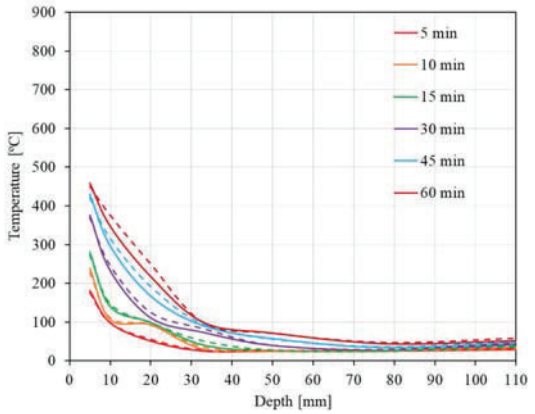

(II): Intumescent-coated timber samples at 25 kW/m^2

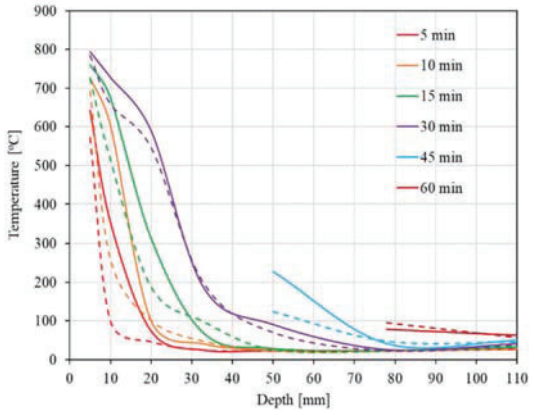

(III): Bare timber samples at 50 kW/m^2

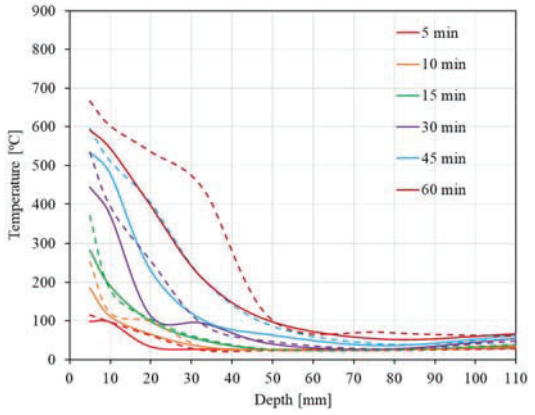

(IV): Intumescent-coated timber samples at 50 kW/m^2

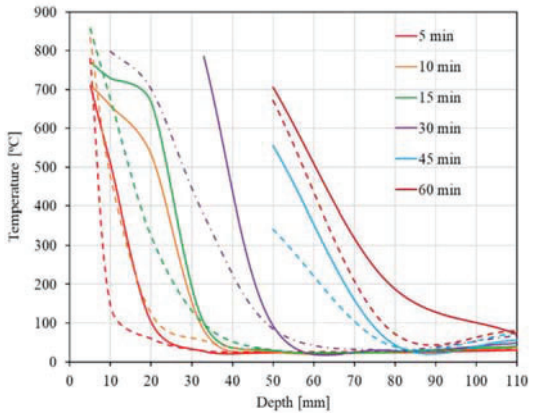

(V): Bare timber samples at 75 kW/m^2

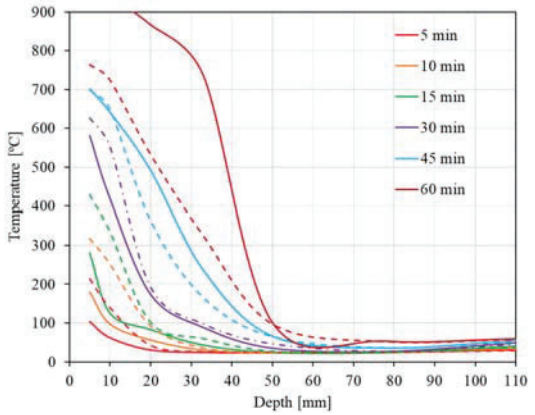

(VI): Intumescent-coated timber samples at 75 kW/m^2

Figure 5: *In-depth temperature vs. depth from the heated surface at discrete times. Plots are shown for samples without (left) or with intumescent (right) under different heating conditions. Note: Dashed lines show repeat samples*

https://doi.org/10.52202/069179-0221

3.2 CHARRING OF TIMBER

Figure 6 shows char depth from the heated surface against time. As noted before, the char front is assumed to be aligned with the 300 °C isotherm. In addition, the mean charring rate is calculated from the char depth data during heating; a summary of this data is provided in Table 2.

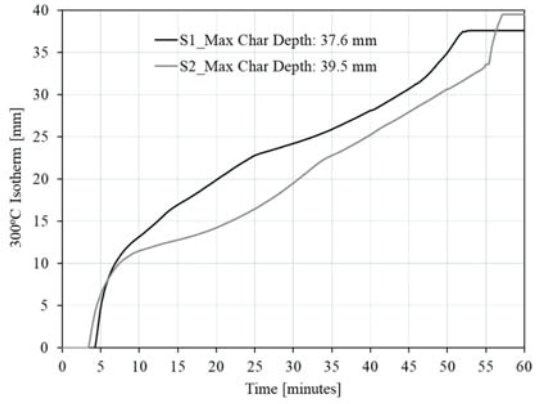

(I): Bare timber samples at 25 kW/m^2

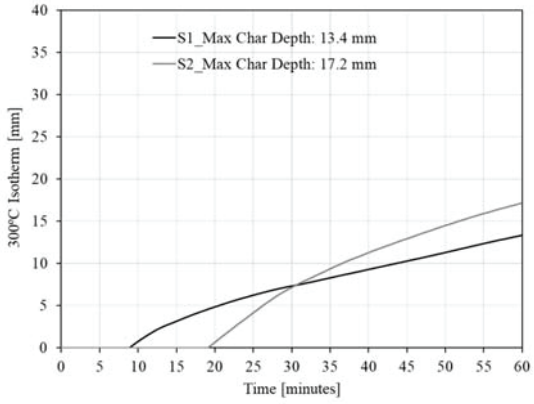

(II): Intumescent-coated timber samples at 25 kW/m^2

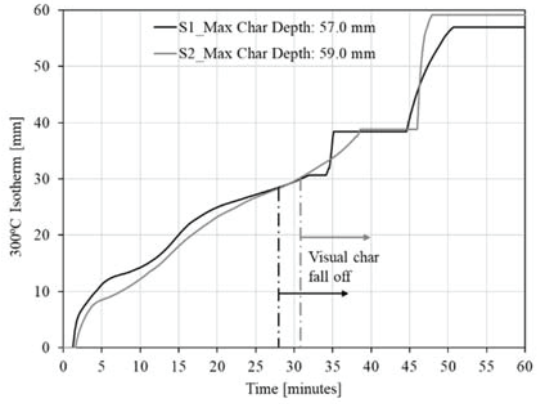

(III): Bare timber samples at 50 kW/m^2

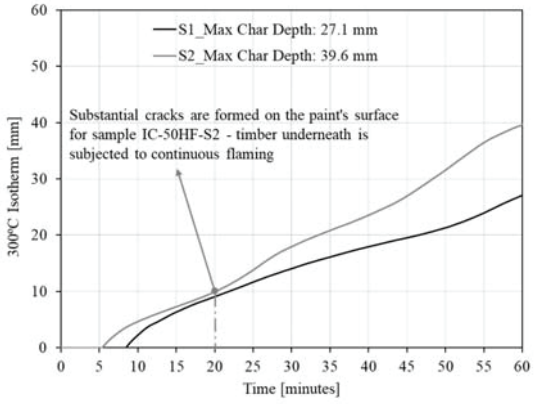

(IV): Intumescent-coated timber samples at 50 kW/m^2

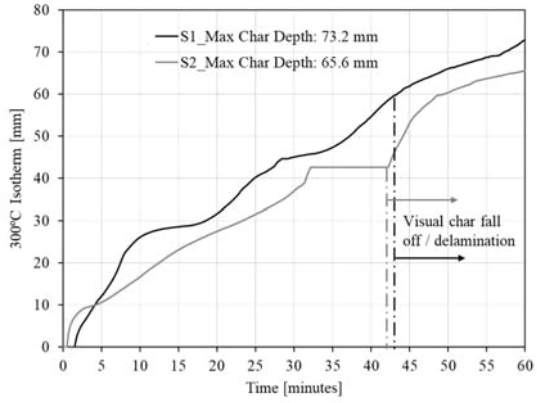

(V): Bare timber samples at 75 kW/m^2

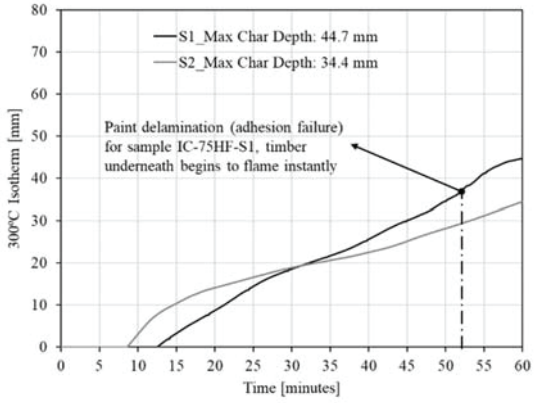

(VI): Intumescent-coated timber samples at 75 kW/m^2

Figure 6: *Char depth from the heated surface vs. time – based on 300 °C isotherm. Plots are shown for samples without (left) or with intumescent (right) under different heating conditions. Note: Vertical axis scale varies per heating condition.*

https://doi.org/10.52202/069179-0221

The condition of a typical test sample during fire testing is shown in Figure 7 for both coated and bare timber samples. Specifically, the exposed sample's surface at the beginning of the test (10 min) and near the end (45 min) under different heating conditions.

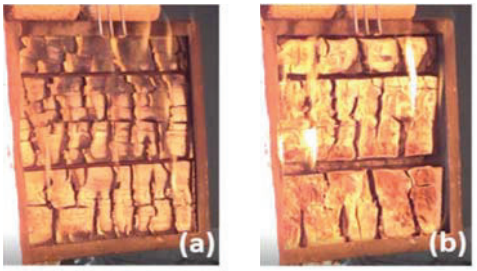

(I): Bare timber samples at 25 kW/m^2

10 min (a); 45 min (b)

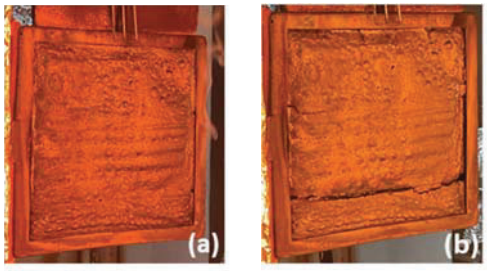

(II): Intumescent-coated timber samples at 25 kW/m^2

10 min (a); 45 min (b)

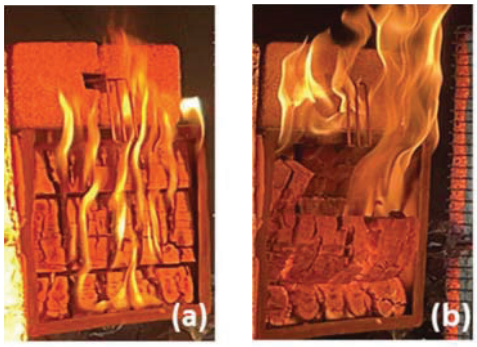

(III): Bare timber samples at 50 kW/m^2

10 min (a); 45 min (b)

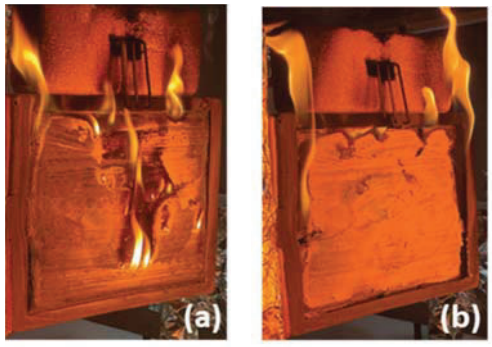

(IV): Intumescent-coated timber samples at 50 kW/m^2

10 min (a); 45 min (b)

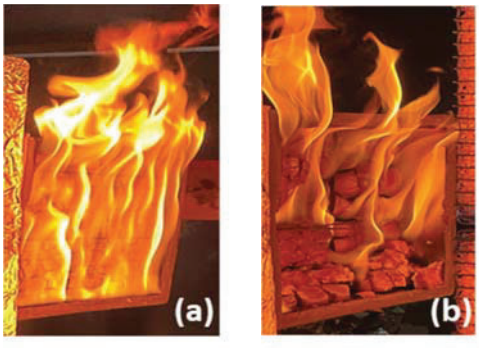

(V): Bare timber samples at 75 kW/m^2

10 min (a); 45 min (b)

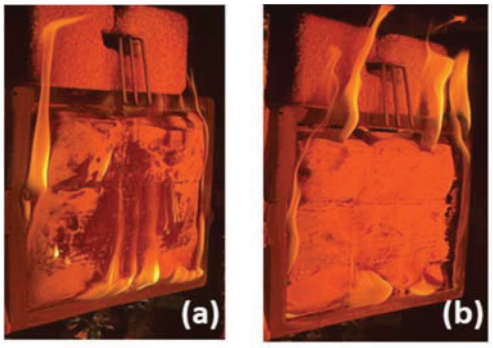

(VI): Intumescent-coated timber samples at 75 kW/m^2

10 min (a); 45 min (b)

Figure 7: *Photographs showing the condition of a typical test sample during fire testing; early in the test (10 min) and towards the end (45 min). These are shown for samples without (left) or with intumescent (right) during varied heating conditions.*

https://doi.org/10.52202/069179-0221

4 ANALYSIS OF RESULTS

4.1 INFLUENCE OF INTUMESCENT COATING

The thin intumescent coating influence in the charring rate of the tested timber samples is summarised as follows:

Onset of charring – As shown from plots in Figure 6, there is at least a 5-min-delay on the onset of charring for timber samples with intumescent coating when compared to bare timber samples, irrespective of the heating condition.

In-depth charring rate – For the lowest heating condition (25 kW/m^2), a ~60 % reduction in the mean measured charring rate was observed for coated timber samples when compared to bare timber, while for the higher incident radiant heat fluxes of 50 and 75 kW/m^2, the mean measured charring rate was reduced by ~40 %.

Further, where periods of plateaus are noticed for the measured char depths presented in Figure 6 (i.e., in-depth temperature at the given location < 300 °C, thus zero charring rate), this reflects periods during testing where the timber samples either didn't start charring (e.g., at the beginning of the experiment), or due to char fall off in bare timber samples exposing the thermocouples to gas phase. The latter results in a delay of the subsequent in-depth solid phase measurements, given the gas phase measurements were removed from the temperature data (see Figure 4 and Figure 5) at the point of thermocouple exposure, as these readings do not represent this study.

4.2 INFLUENCE OF HEATING CONDITION

As seen in Table 2 below, the charring rate is directly proportional to the incident radiant heat flux at the heated surface of timber (without or with intumescent coating). In addition, the coating application significantly delayed the timber's time-to-ignition for samples tested at the higher incident radiant heat fluxes (50 and 75 kW/m^2), and it prevented ignition altogether at 25 kW/m^2.

Table 2: *Mean measured charring rate and time-to-ignition.*

Sample ID	Time-to-ignition [sec]	Charring rate [mm/min]
BT-25	67 ± 5	0.65 ± 0.02
BT-50	14 ± 1	0.95 ± 0.02
BT-75	13 ± 1	1.11 ± 0.04
IC-25	no ignition	0.25 ± 0.04
IC-50	257 ± 62	0.56 ± 0.10
IC-75	229 ± 14	0.66 ± 0.09

Note: *Time-to-ignition and mean measured charring rate values in each row are from two tested samples (bare or with coating) at the specified heat flux condition. The charring rate is taken as the mean of the char depth's first derivative – based on the 300 °C isotherm derived from a smoothing spline fit [17, 18] for every time instant.*

4.3 OBSERVATIONS DURING TESTING

In addition to the above, the following relevant events were observed during testing:

- The intumescent coating generally began to crack first along the edges of the timber boards (85 mm wide). For samples tested at 50 and 75 kW/m^2, the swelled coating underwent considerable thermal degradation (i.e., oxidation) and regression during the fire tests.
- Although at the end (> 60 min) of the 25 kW/m^2 fire tests the coating remained in place and no flaming was observed at the heated surface, edge crack formation propagated causing the swelled coating to regress.
- Flaming combustion (during the 50, 75 kW/m^2 tests) of the coated timber samples was generally observed near the sides of the heated surface due to shrinkage and thermal degradation of the timber and coating, exposing the bare timber edges to direct radiant heat. There were also small pockets of poor paint formation near the centre of the samples – creating small gaps exposing timber to direct radiant heat, resulting to intermittent flaming of the timber underneath.
- Swelled intumescent coating fall off was observed during late stages of the fire tests (during heating or cooling) for samples tested at 50 and 75 kW/m^2 – e.g., IC-50-S2 (> 70 min) and IC-75-S1 (> 50 min). This resulted from adhesion failure of the oxidated coating or delamination of charred timber.

5 CONCLUSIONS

Based on the experimental outcomes described herein, the following can be concluded:

- The onset of timber charring was delayed for at least 5 min for the intumescent-coated samples, regardless of the heating condition.
- The mean measured in-depth charring rate of timber was greatly reduced when using intumescent coating – in the range of ~40 to 60 % depending on the severity of the heating condition.
- Timber ignition was either prevented at the lowest incident radiant heat flux (25 kW/m^2), or significantly delayed at more onerous heating conditions (50 and 75 kW/m^2) when using a thin intumescent coating – for the duration of the 60 min heating period.
- The integrity of the thin intumescent coating was challenged at high heating conditions, experiencing large crack formations, or fall off when tested at an incident radiant heat flux of 50 or 75 kW/m^2.

Future work, being part of this fire research, will include testing and analysis of the following campaigns – under the previously nominated heating conditions:

- Timber test samples with intumescent coating applied at a higher DFT of the same commercially available intumescent product presented herein; and
- Timber test samples with a transparent intumescent paint product, also at different coating thicknesses. This paint product is a water-based thin intumescent coating for timber substrates, generally applied at low DFTs (< 1 mm).

https://doi.org/10.52202/069179-0221

ACKNOWLEDGEMENT

The authors gratefully acknowledge the financial support provided by the Australian Research Council Research Hub to Transform Future Tall Timber Buildings IH150100030. They are also grateful to XLam Australia, for donation of material used in testing. The authors also wish to thank the technical staff at The University of Queensland for their valuable assistance, especially Stewart Matthews, Fraser Reid, and Jason Van der Gevel.

REFERENCES

[1] R. M. Hadden *et al.*, "Effects of exposed cross laminated timber on compartment fire dynamics," *Fire Safety Journal,* vol. 91, pp. 480-489, 2017.

[2] F. Wiesner *et al.*, "Structural capacity of one-way spanning large-scale cross-laminated timber slabs in standard and natural fires," *Fire Technology,* vol. 57, no. 1, pp. 291-311, 2021.

[3] F. Wiesner, R. Hadden, S. Deeny, and L. Bisby, "Structural fire engineering considerations for cross-laminated timber walls," *Construction and Building Materials,* vol. 323, p. 126605, 2022.

[4] T. Gernay, "Fire resistance and burnout resistance of timber columns," *Fire Safety Journal,* vol. 122, p. 103350, 2021.

[5] D. Barber, "Fire Safety and Tall Timber Buildings—What's Next?," in *Structures Congress 2017*, 2017, pp. 556-569.

[6] M. Violette, "Memoire sur les Charbons de Bois," *Ann. Chim. Phys,* vol. 32, p. 304, 1853.

[7] R. G. Puri and A. Khanna, "Intumescent coatings: A review on recent progress," *Journal of Coatings Technology and Research,* vol. 14, no. 1, pp. 1-20, 2017.

[8] T. Mariappan, "Recent developments of intumescent fire protection coatings for structural steel: A review," *Journal of fire sciences,* vol. 34, no. 2, pp. 120-163, 2016.

[9] T. Wakefield, Y. He, and V. Dowling, "An experimental study of solid timber external wall performance under simulated bushfire attack," *Building and Environment,* vol. 44, no. 10, pp. 2150-2157, 2009.

[10] Q. Xu, Y. Wang, L. Chen, R. Gao, and X. Li, "Comparative experimental study of fire-resistance ratings of timber assemblies with different fire protection measures," *Advances in Structural Engineering,* vol. 19, no. 3, pp. 500-512, 2016.

[11] A. Lucherini, Q. S. Razzaque, and C. Maluk, "Exploring the fire behaviour of thin intumescent coatings used on timber," *Fire Safety Journal,* vol. 109, p. 102887, 2019.

[12] C. Maluk, L. Bisby, M. Krajcovic, and J. L. Torero, "A heat-transfer rate inducing system (H-TRIS) test method," *Fire Safety Journal,* vol. 105, pp. 307-319, 2019.

[13] I. O. f. Standardization, "ISO 5660-1: 2015 Reaction-to-Fire Tests—Heat Release, Smoke Production and Mass Loss Rate—Part 1: Heat Release Rate (Cone Calorimeter Method) and Smoke Production Rate (Dynamic Measurement)," ed: International Organization for Standardization Geneva, Switzerland, 2015.

[14] D. Drysdale, *An introduction to fire dynamics*. John wiley & sons, 2011.

[15] R. D. Peacock, P. A. Reneke, R. W. Bukowski, and V. Babrauskas, "Defining flashover for fire hazard calculations," *Fire Safety Journal,* vol. 32, no. 4, pp. 331-345, 1999.

[16] R. Emberley *et al.*, "Description of small and large-scale cross laminated timber fire tests," *Fire Safety Journal,* vol. 91, pp. 327-335, 2017.

[17] MATLAB, *version 9.5.0944444 (R2018b)*. The MathWorks Inc., 2018.

[18] F. Wiesner, R. Hadden, and L. Bisby, "Influence of Adhesive on Decay Phase Temperature Profiles in CLT in Fire," in *Proceedings of the 12th Asia-Oceania Symposium on Fire Science and Technology (AOSFST 2021). Presented at the 12th Asia-Oceania Symposium on Fire Science and Technology (AOSFST 2021), The University of Queensland, Online. https://doi.org/10.14264/a023d21*, 2021.

[19] J. V. Beck, "Thermocouple temperature disturbances in low conductivity materials," 1962.

[20] I. Pope, J. P. Hidalgo, R. M. Hadden, and J. L. Torero, "A simplified correction method for thermocouple disturbance errors in solids," *International Journal of Thermal Sciences,* vol. 172, p. 107324, 2022.

[21] R. Boone and E. Wengert, "Guide for using the oven-dry method for determining the moisture content of wood," *Forestry Facts,* vol. 89, no. 6, pp. 1-4, 1998.

World Conference on Timber Engineering Oslo 2023

MEASUREMENT OF DIRECTIONAL CHARACTERISTICS OF MOISTURE TRANSPORTATION IN WOOD UNDER HEATING

Hirokatsu Kimura[1], Tomoyo Hokibara[2],Yuji Hasemi[3], Soma Suzuki[4], Tatsuro Suzuki[5], Ryo Takase[6]

ABSTRACT: Time variations in moisture content and temperature inside Japanese Cedar *(Cryptomeria Japonica)* specimens exposed to steady heating from three different directions were measured with small resistive sensors, as developed by Suzuki et al [1]. Radial, tangential, and longitudinal heating at 4.5 kW/m^2 with Cone Calorie Meter were conducted to investigate the anisotropy of water transfer and its effect on the rise in temperature under fire heating; specimens were controlled in air-dry or bone-dry conditions. As a result, longitudinal water transfer was large and observed most frequently in the three heating directions, because of which tracheid worked as a path of transporting vapor away from the heating surface. Moreover, the rise in the temperature of Air-Dried specimens was suppressed compared to that of Bone-Dried specimens, especially in longitudinally heated specimens, and the temperature difference was up to 4.6 times larger than that of radially and tangentially heated specimens. It was because the heating caused by re-condensation was the smallest in longitudinally heated specimens, according to the largest water transfer.

KEY WORDS: Moisture Content, Heat and Water Transfer, Sorption, Anisotropy, Cone Calorie Meter, Japanese Cedar

1 INTRODUCTION

With the increasing number of high-rise wooden buildings, the importance of accurate prediction of the mechanical properties of wooden member has increased. Water content in wooden members is a key factor that affects the decrease in the mechanical property of wooden members under fire. Kaku et al. [2] reported that the moisture content and rising temperature reduced the mechanical properties at high temperature; the Young's modulus of Japanese Cedar specimen at high moisture content near 100 ℃ is was found to be as low as that of the dry specimen at 200 ℃. It was confirmed that the water in the wooden members exposed to fire transferred as vapor from high temperature part to low temperature part for recondensation [1]. Considering the rise in moisture content, the Young's modulus of inner part of wooden fireproof beam after heating for 2 h near 100 ℃ was estimated to decrease as low as that of 230 ℃ in dry wood [3].

As for anisotropy of properties of wood, that of thermal conductivity is discussed by Maku [4] that longitudinal thermal conductivity is approximately 2.5 times larger than that of the radial or tangential ones; Kawabe et al. [5] measured longitudinal permeability and found it to be significantly larger than the transverse ones.

Moreover, structural members are heated three dimensionally under fire heating as shown in Figure 1, and there is temperature incline in longitudinal direction, because the wooden thermal conductivity is significantly small. Therefore, it is assumed that the water transfer has anisotropy as thermal and vapor pressure incline as a driving force of water transfer has anisotropy. Furthermore, it can affect the moisture content distribution in wooden structure members. Although, water transfer in wooden members is measured in previous studies, the anisotropy of wood is not considered. In this study, to measure the time variation of local moisture content caused by anisotropy of wood, three directional steady heating tests were conducted on two conditions of Japanese Cedar (*Cryptomeria Japonica*) specimens.

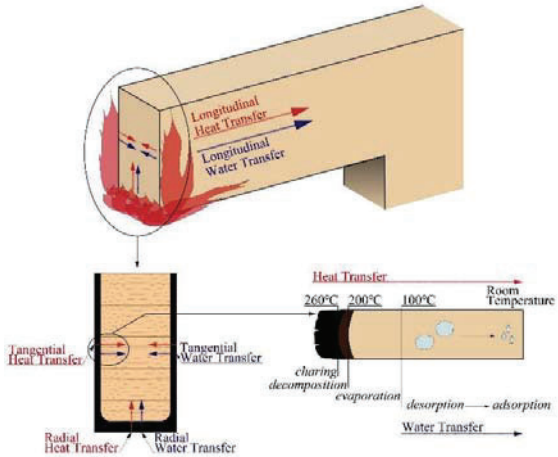

***Figure 1**: Moisture Transfer in a Timber during Fire Heating*

[1] Hirokatsu Kimura, POLUS Co, Ltd (Formerly, Graduate School of Waseda Univ.), Japan, hiro.k_7@ruri.waseda.jp
[2] Tomoyo Hokibara, Assistant Prof., Dept. of Architecture, Waseda Univ., Ph.D., Japan, Hokibara@waseda.jp
[3] Yuji Hasemi, Emeritus Prof., Department of Architecture, Waseda Univ., Ph.D., Japan, hasemi@waseda.jp
[4] Soma Suzuki, Graduate School of Waseda Univ., Japan, somasuzuki7474@moegi.waseda.jp
[5] Tatsuro Suzuki, Visiting Researcher, RISE, Waseda Univ., Ph.D., Japan, tatsuro@suzukikoumuten.com
[6] Ryo Takase, Forest Research and Management Organization, Ph.D., Japan, ryotsmst@gmail.com

https://doi.org/10.52202/069179-0222

2 EXPERIMENTAL METHOD

2.1 METHOD

Each Specimen were heated with Cone Calorie Meter, with heat flux of 4.5 kW/m^2 for 60 min. The incidence of heating flux supposes the heating situation of load-bearing part of fireproof timber which temperature lower 180 ℃. The temperature and moisture content distribution of four points in specimens were measured. Temperature was measured with thermocouples in each 2 s. Moisture content was measured with resistance moisture meter proposed in previous paper [1]. The resistance between the two electrodes installed in the specimens was measured and converted into moisture content by a reported calibration curve. The two electrodes were lined up parallel to the tangent of growth ring with a 10 mm gap between them. A couple of electrodes separated by 2 V were applied to measure resistance in interval of 16 s, because it takes 4 s to measure the resistance of each point.

2.2 SPECIMENS

Specimens are made of heartwood of Japanese Cedar (*Cryptomeria Japonica*). As shown in Figure 2, size of 100×100×45 mm, and the largest surface were heated. Four sets of thermocouples and moisture sensors were inserted from non-heating surface in each specimen, two sets were placed at 20 mm from heating surface, and other two sets were placed at 30 mm from the heating source. Each measuring point was named as below.

Moisture Content or Temperature – Depth – No.
[MC or T] – [20 or 30] – [a or b]

The side surface of specimens was sealed with aluminum foil tape with an aim to stop the water transformation orthogonal to a heating direction.

2.3 EXPERIMENTAL CONDITIONS

Table 1 shows the specimen list. The heating directions and initial moisture content were the parameters. As shown in Figure 2, the heating directions were radial, tangential, and longitudinal, which are referred to as R, T, L, as shown below.

The initial moisture contents were air-dry and bone-dry. Air-dry specimens were stored in a plastic jar. The relative humidity in the plastic jar was controlled by saturated NaCl solutions until the weight became stable. The average moisture content of the R, T, L specimens are in the range of 12.0–13.6%. The initial moisture content of each specimen was obtained by drying a sample, which was cut from as same wood as each specimen and stored in the same condition as the specimen. First, the bone-dry specimens were dried in the drying furnace at 90 ℃ until the weight of specimens became stable, after that the specimens were stored in a tightly sealed plastic bag with silica gel desiccant in room temperature. In Bone-dry condition tests, only the thermal couples were inserted to clarify the anisotropy of heat transfer without the effect of water.

***Table 1**: Condition of specimens*

Condition of Moisture Content	Heating Direction	ID		Bone-Dry Density* [g/cm^3]		Width of Annual Rings [mm]		Initial Moisture Content* [%]	
					Average		Average		Average
Air-Dry	Radial	AR	AR-1	0.260	0.257	2.4	3.7	13.6	13.6
			AR-2	0.252		4.4		13.3	
			AR-3	0.260		4.2		13.9	
	Tangential	AT	AT-1	0.287	0.274	4.1	4.2	13.4	13.5
			AT-2	0.287		3.7		13.4	
			AT-3	0.250		4.8		13.8	
	Longitudinal	AL	AL-1	0.251	0.254	4.9	5.2	11.5	12.0
			AL-2	0.256		5.3		12.2	
			AL-3	0.256		5.3		12.2	
Bone-Dry	Radial	DR		0.260		4.8		-	
	Tangential	DT		0.278		4.5		-	
	Longitudinal	DL		0.251		5.4		-	

* Values of thin samples which were cut from specimen

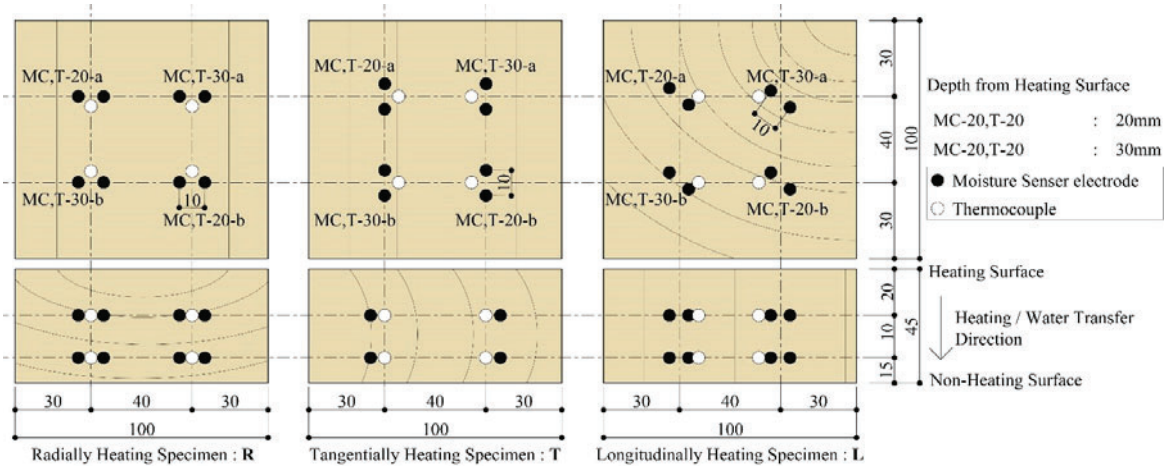

***Figure 2**: Position of Thermocouples and Moisture Sensors*

https://doi.org/10.52202/069179-0222

3 RESULTS

3.1 BONE-DRY SPECIMENS

Figure 3 shows the temperature variation of Bone-Dry specimens in each condition and the difference of the rise in temperature among the longitudinally heated specimens (DR), radially (DR), and tangentially (DT) heated specimens, Figure 4 shows temperature increase rate of Bone-Dry specimens in each condition and the differences as same as those shown in Figure 3. We obtained the rate of temperature rise as a moving average of the two minutes of temperature rise for each specimen and averaging them.

The difference of the rise in temperature of DR and DT were small, that is, 0.2 to 3.6 ℃. The temperature rise of DL was found to be 34.7 ℃ higher than that of DR, and DT after 20 min. The difference was increased 25.5 ℃ on 20 min to 34.7 ℃ on 60 min at 30 mm depth. After 20 min, the difference in the rise in temperature differed in the cases of 20 mm depth 30 mm depth; that is, the temperature rise was 8.4 to 14.7% smaller in the case of 20 mm depth compared to that in the case of 30 mm depth. However, until 20 min, there was a difference between the temperature difference in the case of 20 mm depth and that of 30 mm depth.

Moreover, Figure 4 shows that the rate in temperature increasing of DL was larger and had sharper peak than that of DR and DT. The difference of the rate increased quickly in the maximum rate of 4.0[℃/min] until 8.0min at 20mm depth, and maximum rate of 2.7[℃/min] until 19.8min at 30mm depth, then those differences kept increasing similarly at an average rate of 0.25 [℃/min] for 60 min.

The temperature difference between DL to DR and DT was due to the anisotropy of thermal conductivity; thermal conductivity of longitudinal direction is 1.5 to 2.8 times larger than that of the radial or tangential direction [6]. Moreover, the difference of thermal conductivity caused the difference of temperature increasing rate of 0.25 [℃/min]; therefore, for the cases of 20 mm and 30 mm depths, heating was considered to be steady after 8.0 and 16.8 min, respectively, according to the slope of temperature difference became nearly constant and thermal conductivity is thought to be the critical factor of temperature increasing in materials with equal heat specific heat and density.

3.2 AIR-DRY SPECIMENS

3.2.1 INITIAL MOISTURE CONTENT

Figure 5 shows the relationships of the initial moisture content obtained by sample drying and initial moisture content obtained by moisture sensor.

Initial moisture content obtained by sample drying was distributed in the range of 11.5–13.9%, while the initial moisture content measured by the moisture sensor was in the range 10.9 ─ 19.8%. Although several values obtained by moisture sensor were higher than those obtained by sample drying, a few of them were lower. The difference between the values obtained by sample drying and

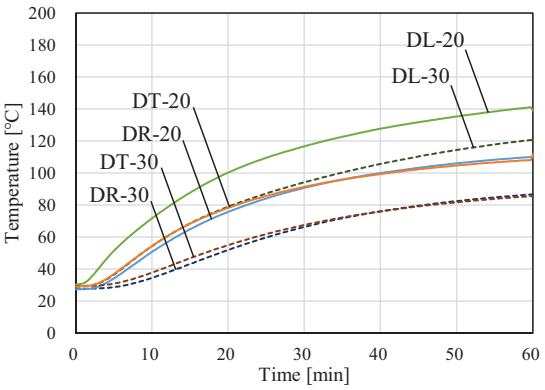

*: Each line shows mean value. “-20”, “-30” indicate values at 20, and 30mm depths, respectably

***Figure 3**: Time Histories of Temperature of Bone-Dry Specimens*

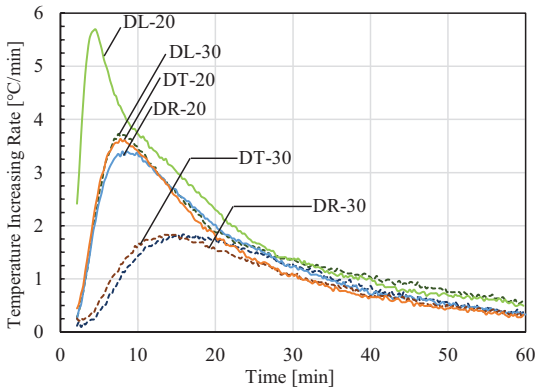

*: Each line shows mean value. “-20”, “-30” indicate values at 20, and 30mm depths, respectably

***Figure 4** Time history of the Rate of Temperature Rise of Bone-Dry Specimens*

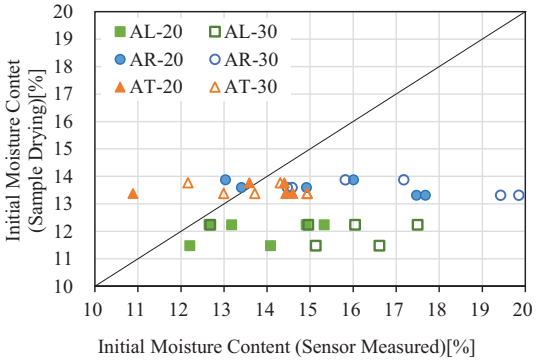

***Figure 5**: Relationships of initial moisture content obtained by sample drying and by moisture sensor*

moisture sensor was in the range 2.5–6.5% in all the specimens and average value of the difference was 1.8%. The factors affecting the initial moisture content remains unclear, and these factors can be categorized into two groups: (1) The factors affect the resistance of moisture sensors, and (2) the factors affect the moisture content in

https://doi.org/10.52202/069179-0222

wood. For instance, the first group includes the amount of adhesive used to fix electrodes in wood and width between the electrodes; lower amount of adhesive or larger width of electrodes causes higher resistance which results in lower moisture content value. The other group includes distribution of moisture content in a wood specimen. In this experiment, we cannot clarify the factors affecting the difference, and identifying the causes is a future issue.

3.2.2 TIME HISTORY OF MOISTURE CONTENT AND TEMPERATURE

Figure 6 shows the time history of temperature and moisture content of typical one specimen of each condition. Figure 7 shows the range of increase of moisture content and range of decrease of moisture content of each condition. We obtained increase and decrease range of moisture content as below Equation (1) and (2). Increase range of moisture content indicates maximum moisture concentration in each specimen. Furthermore, if both the ranges of increase and decrease were large, we considered that both the moisture concentration and transfer to have occurred in the specimen.

$$(Increase\ range) = (Maximum\ value) - (Initial\ value) \quad (1)$$

$$(Decrease\ range) = (Initial\ value) - (Minimum\ value) \quad (2)$$

In AR-1, the moisture content increased or decreased at MC-20-a, b and slowly increased at MC-30-a, b. Some types of moisture content variations were measured at six points of MC-20 in three specimens. In two specimens (AR-1, 3), the moisture content of MC-20-a increased up to 18.4 and 22.3 %, which then decreased. The moisture content of MC-20-b kept decreasing. When the moisture content decreased, the average temperature was 71.5 ℃. In one specimen (AR-2), both of MC-20-a, b kept increasing until 60 min up to 27.8 and 28.2%. Additionally, the rise in the moisture content at MC-30 in AR-2 was significant. The moisture content increased continuously till it reached 39.9 and 87.0% over the valid range (10–30%) of moisture sensor. The moisture content at the other MC-30 measuring points kept increasing slowly for 60 min. The increase in temperature was similar in six measuring points. The average temperatures and coefficient of variation at 60 min were 85.6 ℃, 3.0% at T-20, and 73.5 ℃, 1.9% at T-30.

In AT-1, the moisture content kept decreasing until the heating stopped at almost all the measuring points. As shown in Figure 7, the mean value of the increase range of AT was 0.4% at MC-30, 0.6% at MC-20, and these were smallest in three conditions. Similar to AR, the increase in temperature was similar in six measuring points. The average temperatures and coefficient of variation at 60 min were 91.0 ℃, 3.0% at T-20, 75.7 ℃, 3.5% at T-30.

In AL-1, the moisture content first increased up to 15.7 to 19.4%, and then decreased. Although, MC-20-b in AL-1, MC-20-a, and MC-30-b in AL-2 showed little increase,

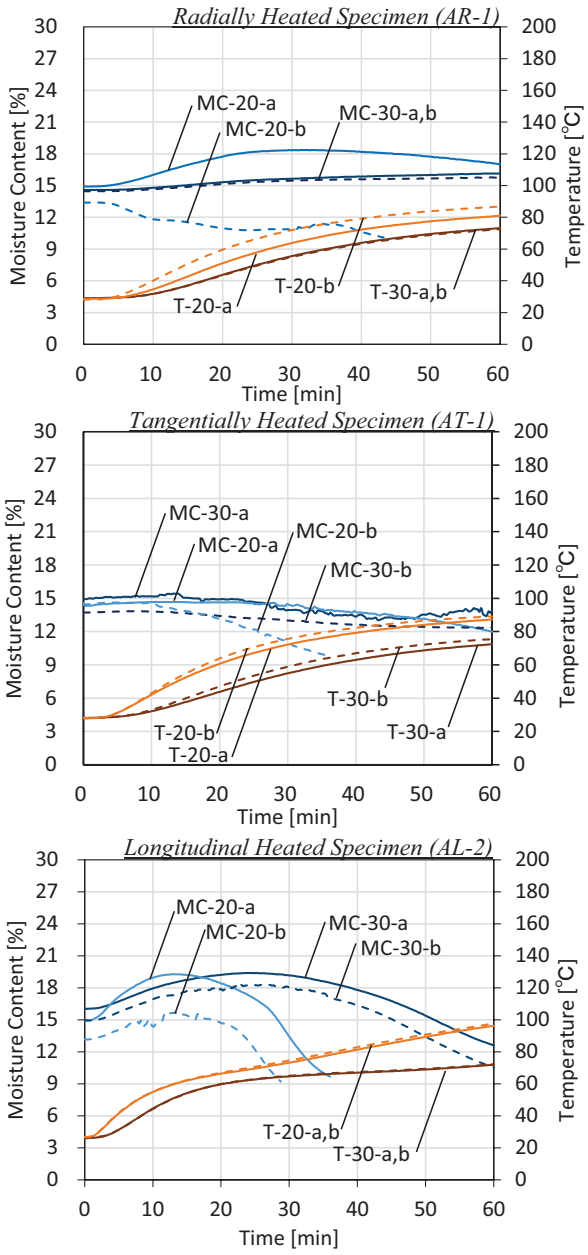

***Figure 6**: Time Histories of Temperature and Moisture Content*

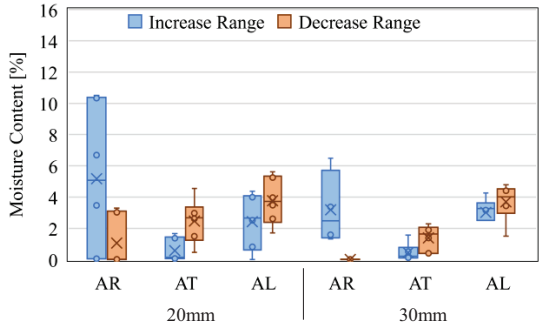

R: Radial heating, T: Tangential heating, L: Longitudinal Heating
20 mm, 30 mm: depth from heating surface
*Values of MC-30-a, b in AR-2 were excepted because maximum value exceeded range of moisture sensor.

***Figure 7**: Increase and Decrease Range of Moisture Content*

https://doi.org/10.52202/069179-0222

other nine measuring points showed the increase and decrease in the moisture content. When the moisture content decreased, the average temperatures of the measuring points were 67.7 ℃ and 65.0 ℃ at T-20 and T-30, respectively. Additionally, the temperature variation was similar in all the specimens. The average temperatures and coefficient of variation at 60 min were 97.6 ℃, 4.3% at T-20, 75.5 ℃, 5.5% at T-30. However, in AL, the increase in temperature was faster than that in the AR or AT for 20 min; furthermore, the increase in the temperature was almost linear until the end of experiment.
As shown in Figure 7, according to the result of each condition, moisture increase range of the longitudinally heated specimens were as large as the radially heated specimens and 4.2–6.8 times larger than that of the tangential heated specimens and decrease range of longitudinal direction was 1.4–3.6 times larger than that of other direction; however, the result of MC-30 in AR was excepted, as moisture content of the condition kept increasing for 60 min and the decrease range of MC-30 in AR was 0.0%.
Increase of moisture content in radial heated specimens indicated that less diffusion or desorption from measuring points occur in radial direction and possibility of significant moisture concentration. As mentioned above, variation of moisture content in AR specimens was apparently different in each specimen. The water concentration in radial direction can be significantly affected by individual difference of each specimen.
Water transfer, especially the decrease in moisture content was fastest in longitudinal direction. Figure 6 showed large variation of moisture content in longitudinal heated specimens. Furthermore, as shown in Figure 7, both the increase and decrease of moisture content were largest in the three conditions. Moreover, Figure 8 showed that the rate of moisture content range was largest in the three conditions.
Considering that the increase of moisture content indicates concentration of water at measuring points and decrease of moisture content indicates vaporing or diffusion or desorption at measuring points, significant increases and decreases of moisture content indicate the occurrences of both water concentration and diffusion or desorption in the longitudinal heated specimens.

3.2.3 CORRELATION BETWEEN MOISTURE CONTENT VARIATION AND TEMPERATURE

Figure 8 shows the relationship between the changing rates of temperature and moisture content. We obtained the ongoing change in the rate of change in moisture content by calculating moving average of the two minutes moisture content change for each specimen and averaging those changes of three specimens. In all the conditions, the rate of change of moisture content generally remained in the range of -0.20–0.20 [%/min] and there was small difference between values of 20 mm depth to 30 mm depth. The rate of change of moisture content in AT generally took negative values; whereas for AL and AR, the rate increased from room temperature to 49.1–53.3 ℃ and then decreased, with negative rates at approximately 65 ℃ in AL and 76 ℃ in AR. AL exhibited a significant decrease in the negative range and took a minimum rate of moisture content change of -0.49 [%/min] in the high temperature range above 70 ℃. The minimum rate of change of moisture content in AL was 2.6 times larger in absolute value.
Figure 8 showed that the rate of moisture content range of longitudinally heated specimens was largest in three conditions and the increase and decrease of moisture content was largest in longitudinally heated specimens as mentioned above. These results clarify higher mobility of water in longitudinally direction.
For several wooden properties, such as permeability, diffusivity of water and diffusivity of vapor higher water mobility in the longitudinal direction (along the grain) was reported compared to that of radial or tangential direction (across the grain). Kawabe [5] reported that the permeability along the grain was 5.6–9.3×10^3 times larger than that across the grain. Yokota [7] reported that diffusivity of water and vapor along the grain were 5–20 and approximately one hundred times larger than those across the grain respectably. According to these reports, the anisotropy on diffusivity of water was near to the anisotropy of increase or decrease of moisture content and

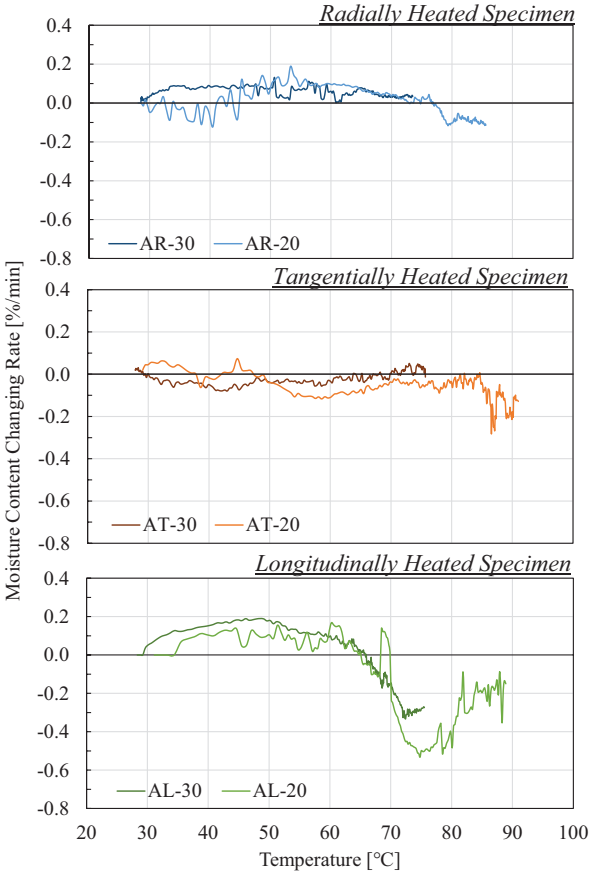

***Figure 8**: Relationship of Temperature and the Rate of Change in Moisture Content*

https://doi.org/10.52202/069179-0222

the rate of change in the moisture content, whereas the anisotropy of the permeability and diffusivity of vapor were ten to hundred times larger than that of the isotropy we measured in this experiment. Considering that the rate of change in the moisture content decreased in the range of 20–30 °C, which is lower than the vaporing temperature, vaporing was considered to be occurring inactively when the rate decrease.

Therefore, we consider that properties affect transfer of vapor do not significantly affect the water transfer and mobility of bound water is dominant or other properties such as desorption rate of water on wood tissues limited the water transfer in wood under fire heating.

3.3 COMPARISON OF AIR-DRY AND BONE-DRY CONDITIONS

Figure 9 shows the maximum temperature of Air-Dry condition and suppression of the rise in temperature between the bone-dry to air-dry conditions. Maximum temperature of each condition was AL>AT>AR at both of 20 mm and 30 mm depths; however, the difference was larger at 30 mm depth. The average maximum temperatures were 82.1 ℃ in AL, 79.6 ℃ in AT, 74.0 in AR at 30 mm depth, and 102.7 ℃ in AL, 95.3 ℃ in AT, 86.1 ℃ in AR at 20 mm depth. The rise in the temperature of air-dry specimens were reduced to be lower than that of bone-dry specimens in all the heating directions. The temperature differences between the air-dry specimens to bone-dry ones on 60 min at 20 mm and 30 mm depth were 9.9, 17.2 ℃ in AR, 12.8, 24.1 ℃ in AT, 45.3, 43.4 ℃ in AL on average, respectively.

The difference at 30 mm depth from the heating surface in AL was 1.8–2.5 times at 20 mm depth and 3.6–4.6 times larger than for the other conditions; suppression of the rise in temperature was the largest in longitudinal direction. Furthermore, the suppression of the rise in temperature in AL at 20 mm depth was as same that of the suppression of 30 mm depth; however, that in AR or AT at 20 mm depth was twice larger than that of the suppression at 30 mm depth.

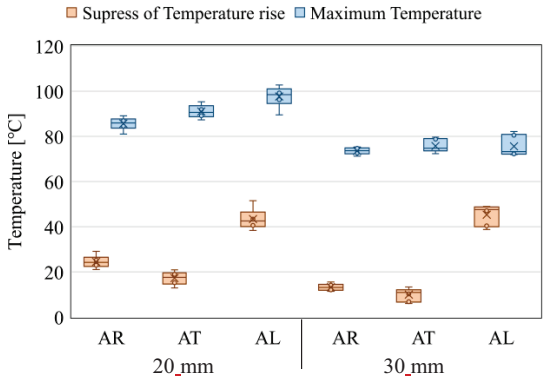

R: Radial heating, T: Tangential heating,
L: Longitudinal Heating
20 mm, 30 mm: depth from heating surface

***Figure 9**: Suppression of Temperature rise and Maximum Temperature at 60 min*

From the result, it is evident that the moisture content can suppress the temperature rise, and the effect is apparently largest in longitudinally heating.

We considered that the suppression of temperature rise was caused by large heat capacity of water. The heat capacity of water is approximately 4.18 [kJ/(kgK)], which is approximately 3.5 times larger than that of heating capacity of Bone-Dry woods [6]. This is the reason for Air-Dry specimens having 1.3 times larger heat capacity that that of Bone-Dry specimens and the difference caused the difference of temperature rise.

Furthermore, anisotropy of suppression of temperature rise is caused by anisotropy of transfer of water. At first, temperature suppression in wood under fire heating was caused by difference of heat capacity as mentioned above, indicating that the moisture is heated instead of wood. Then, the heated moisture is thought to transfer along heating direction as vapor or bound water because of the gradient of vapor pressure or moisture content in wood tissue; furthermore, water can heat wood tissues away from heating surface with lower temperature after the transfer. In this scenario, if moisture transfers quickly and it is released out of wood, temperature rise is further suppressed as moisture does not heat wood tissues. Therefore, the rise in temperature was largely suppressed in the longitudinally heated specimens of which moisture transfer is fastest in three directions.

4 CONCLUSIONS

Following information was obtained measuring time variations of temperature and moisture content in air-dry and Bone-Dry Japanese Cedar specimens under 4.5 [kW/m^2] steady heating for 60 min with Cone Calorie Meter.

(1) Temperature rise of Bone-Dry specimens was larger in longitudinally heated specimens compared to that of the other conditions, and that of the other two conditions were similar. The difference between longitudinally to radially or tangentially heated specimens increased up to 34.7 ℃ at 30 mm depth from heating surface. The difference between longitudinally heated specimens to radially or tangentially heated specimens at 20 mm depth was as same as that of the 30 mm depth.

(2) Increase in the moisture content was 4.2–6.8 times larger in the longitudinally and radially heated specimens compared to that in the tangentially heated specimens and decrease of moisture content in longitudinally heated specimens was 1.4–3.6 times larger than the other two conditions.

(3) The rate of moisture content changing rate of the longitudinally and radially heated specimens increased up to 49.1–53.3 ℃ and then decreased. These rates took zero around 65–76 °C. Moreover, the minimum of the rate of moisture content changing of longitudinally heated specimens was 2.6 times larger in absolute value compared to the other conditions.

https://doi.org/10.52202/069179-0222

(4) In all the conditions, the rise in temperature in air-dry specimens was lower than that of bone-dry specimens. In the longitudinally heated specimens, the temperature rise was 1.8–4.6 times largely reduced compared to radially or tangentially heated specimens, and difference of the suppression between 20 mm depth to 30 mm depth was little in longitudinally heated specimens but twice in the radially or tangentially heated specimens.

In this experiment, we noted some future issues. One is discrepancies of the moisture content between the values obtained by sample drying and by moisture sensor, another is the difference of moisture content variation between each specimen in radially heated specimens. Moreover, experiment under conditions of higher heating intensity is required, which can clarify water transfer around heating surface in wooden structural members.

ACKNOWLEDGEMENT

This study was funded by the JSPS program on "Empirical study on heat and moisture transfer in wooden members under fire heating and its mechanical effects" （The Research Leader was Yuji HASEMI） and Waseda University Grants for Special Research Projects (Tokutei Kadai) No.2021C-535, (The Research Leader was Tomoyo HOKIBARA.)

REFERENCES

[1] Suzuki T., et al: Development of Dynamic Moisture Content Measurement System for Wooden Members Exposed to Fire Heating, Journal of Structural and Construction Engineering (Transactions of AIJ), 762:1123-1133, 2019. (in Japanese)

[2] Kaku C., et al: Influence of Moisture Content on the Structural Properties of Wood under High Temperature −Exposure water content dependence of Young's modulus and bending strength under heating of Cryptomeria Japonica and Zelkova serrata−, World Conference on Timber Engineering, Vienna, Austria, 2018

[3] Saiyoshi T., et al: Time Histories of Moisture and Temperature in Timber Beam with Wooden Fire Protective Layers at Standard Furnace Test: Dynamic Measurement and Implications to Fire Resistance, Journal of Environmental Engineering (Transactions of AIJ), 802, 777-784, 2022, (in Japanese)

[4] Maku T.: Relation between the Specific Gravity and Thermal Conductivity of Wood, Bulletin of the Wood Research Institute, Kyoto University, 9:1-13, 1952, (in Japanese)

[5] Kawabe J., et al: Transverse Air Permeability in Fifteen Wood Species, Journal of the Society of Materials Science, Japan, 34(383):918-924, 1985, (in Japanese)

[6] Forest Products Laboratory, Wood Handbook: Wood as an Engineering Material, Wisconsin, p. 4-13-14, 2021.3

[7] Yokota T.: Wood and Water II, Journal of the Society of Materials Science, Japan, 21(220):58-64, 1971 (in Japanese)

https://doi.org/10.52202/069179-0222

World Conference on Timber Engineering Oslo 2023

FIRE SAFETY ENGINEERING OF BUILDINGS WITH VISIBLE TIMBER CONSTRUCTIONS

Leif Tore Isaksen[1], Martin Hagen[2]

ABSTRACT:

Is it possible to build high rise timber buildings without sacrificing fire safety?

On a global basis, the use of timber as building material is rapidly increasing. Fire safety engineers meet new challenges compared to prevalent design with incombustible building materials. There are several questions and problems which must be addressed for the engineer to design a firesafe building from wooden construction materials.

The ambition of the project Mjøstårnet was to build the tallest wooden building in the world, at the same time being a distinct wooden building allowing visible wooden constructions. These ambitions may come into conflict with Norwegian fire regulations that requires the building to withstand a complete burnout without structural failure of the primary load bearing system. Standard fire safety calculations will not verify neither burnout nor required fire resistance to withstand burnout with combustible construction materials. A common belief, also reflected in the building regulations, is that surviving burnout requires incombustible materials, or incapsulating combustible construction materials, hence disfavoring the choice of timber as a building material. To address these challenges, an innovative approach was established for the design and verification of legal requirements for the tallest wooden building in the world, Mjøstårnet.

KEYWORDS: Fire safety, massive timber, highrise buildings, Mjøstårnet

1 INTRODUCTION

1.1 SUSTAINABLE QUALITIES

Wood is one of the most sustainable and environmentally favorable construction materials available. This is due to its absorption of carbon dioxide while growing. Wood is a renewable material, it lasts a long time, can be recycled and reused, it's great at retaining heat, its waste is 100 percent biodegradable, and it has a positive effect on your physical and mental health[1,2,3].

Pressing environmental concerns and urgent housing needs, urban densification, and the use of existing resources together with otherwise sustainable materials are of key importance for the increasing use of timber.

Besides its many other benefits, timber as a construction material is especially suitable due to its low weight and ample prefabrication possibilities.

1.2 FIRE SAFETY

Working with fire safety in wooden buildings, the fire safety engineers meet new challenges compared to traditional design with incombustible building materials. There are several questions and problems which must be addressed for the engineer to design a firesafe building from wooden construction materials.

- Firstly, can the loadbearing system resist fire when the construction materials themselves burn?
- Secondly, can existing calculation methods and test criteria, often based on incombustible materials, be utilized in the design?

There is an ever-growing base of experimental evidence and related guidance documents that shed light on these questions. Just in the last few years there are a number of review papers that summarizes the experimental work done on fire in timber compartments [4,5,6,7]. These highlight some of the gained knowledge and future challenges. A recent paper [6] reviews 63 compartment fire experiments involving timber constructions, the majority of which use cross laminated timber (CLT). The recent experiments show that timber constructions can survive a full duration [8,9] of a fire deemed "burnout", however the papers also address some challenges. Some of these include significant uncertainty and variability in for instance charring rates. They also highlight the need for more research on a range of compartment configurations, including larger compartment sizes.

[1] Leif Tore Isaksen, Discipline Coordinator – Fire & Safety, Sweco Norway AS, leif.isaksen@sweco.no
[2] Martin Hagen, Senior Engineer - Fire & Safety, Sweco Norway AS, martin.hagen@sweco.no

https://doi.org/10.52202/069179-0223

Although the major focus on recent research effort is CLT elements, it highlights an important difference between CLT and common constructions elements like glue-laminated members (Glulam). CLT elements can be susceptible to delamination of lamellas during fire, giving access to uncharred wood and consequently an increase in fire severity.
Some of these challenges are addressed in guidance documents for fire safety design of timber buildings [10]. However, the constant progression of research dictates a continuous development of guidance documents and legislation that deals with these new challenges including design of tall timber buildings. In the US The International building code [11] is one such example and a guidance document for building compliance of mass timber structures [13] is produced in the UK.

2 FIRE SAFETY DESIGN IN MASSIVE TIMBER BUILDINGS

Sweco has worked with fire safety design in several timber buildings, where the most famous one is Mjøstårnet. Mjøstårnet with a height of 85,4 meters was officially ratified by Council on Tall Buildings and Urban Habitat and Guinness World Records as the tallest timber building in the world (May 2019). The building, located in Brumunddal Norway, is an 18-story mixed-use building, containing offices, apartments and a hotel.
The building is constructed as follows:

- High strength glulam columns, beams and diagonals
- CLT shafts for elevators and stairs
- Wooden decks in the first ten floors (made by Moelven Træ8 floor elements), protected with plasterboards in the ceilings and concrete on the floors
- Concrete slabs in the upper floors for apartments. This improves the dynamic behavior (horizontal accelerations), and the sound insulation between the apartments in the building
- Wooden prefabricated façade elements make up the building's envelope

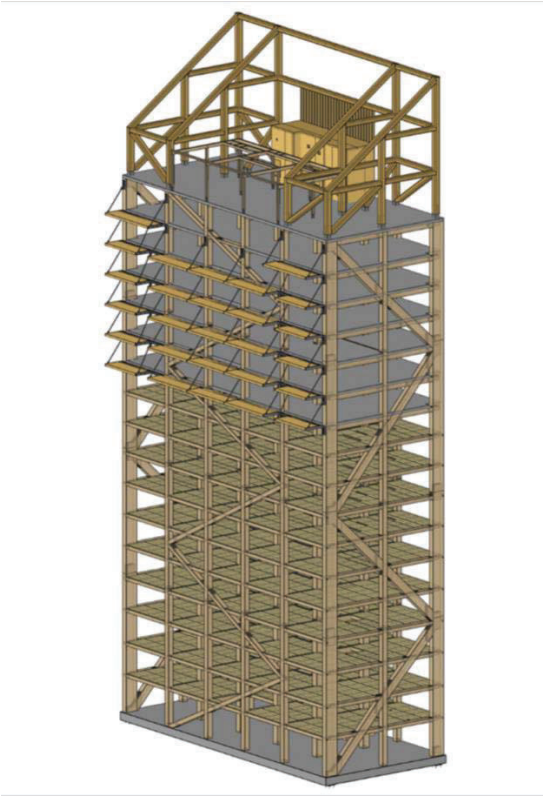

Figure 1: *The structures in Mjøstårnet*

2.1 FIRE SAFETY REQUIREMENT AND APPROACH

The ambition of Mjøstårnet was to build the tallest timber building in the world, with distinct visible timber constructions.
One major hurdle for the project was the fire safety design and its compliance with Norwegian fire regulations.
The regulations require verification that the building will survive a complete burnout without structural failure of the primary load bearing system.
Standard fire safety calculations will not verify neither burnout nor required fire resistance to withstand burnout with combustible construction materials. To address these challenges, an innovative approach was established for the design and verification of legal requirements for Mjøstårnet.

This approach consisted of:

- Prolonged fire testing, including the decay phase, of glulam columns to document the charring rate and the protection of the connections.
- Extending calculation methods for charring rates based on Eurocodes and parametric fire exposure.
- Introducing additional safety measures in the building

https://doi.org/10.52202/069179-0223

2.2 FIRE TESTING OF GLULAM COLUMNS

To support the analytical design of Mjøstårnet, experiments were set up to study the charring and burning behavior of glulam columns throughout the duration of the fire. Emphasis was made on the decay phase of the fire (Figure 2, and whether charring eventually ceases.

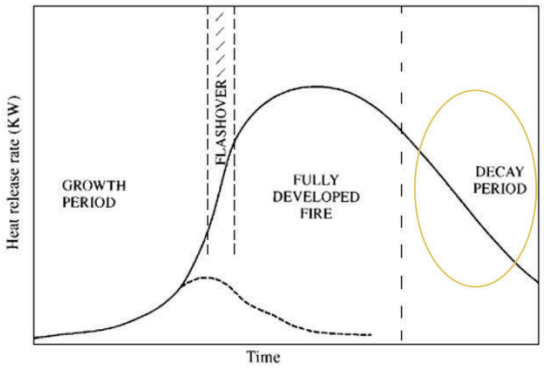

Figure 2: *Heat release including the decay period*

Additionally, the project needed proof that steel connectors were well protected inside the timber. To help answer these questions, full scale testing of three glulam columns was conducted to record the charring behavior of wooden structures with emphasis on the decay period of the fire. The fire tests were conducted by Rise Fire and research AS, together with Moelven and Limtreforeningen.

2.2.1 Findings from the fire tests

3 glulam columns with the measurements of 0,5meter width and depth and a height of 3 meter were used in the fire test:

- 2 identical glulam columns to study the charring and burning behavior throughout the duration of the fire
- 1 glulam column mounted together with steel connectors inside, to study whether steel connectors can be protected inside the timber
- All the samples were mounted with thermocouples inside, measuring the temperature inside the timer construction during the fire test

Figure 3 shows a horizontal cross section of the columns with the thermocouples mounted inside the samples.

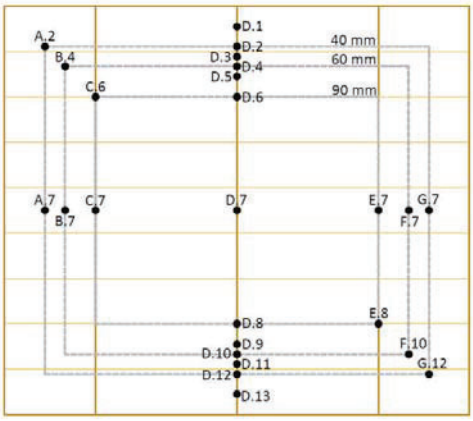

Figure 3: *Thermocouples mounted inside the samples*

The tests were carried out using the ISO 834 temperature curve for 90 minutes. After 90 minutes the burners were turned off. One of the two identical samples (column A) was left inside the furnace to slowly cool for 330 minutes as shown in Figure 4. The other sample (column B) was lifted out of the furnace to cool for 330 minutes in a large laboratory area with natural ventilation from an open door to the outside

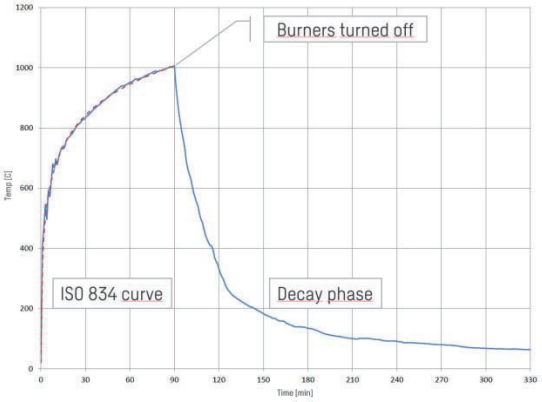

Figure 4: *time/temp curves form the test recorded in the furnace*

These tests showed that the charring rate decreased in the decay period of the fire and eventually stopped. According to Figure 5 the charring reached 40 mm into the columns after 60-70 minutes, 60 mm into the columns after 100-110 minutes, but never reached 90 mm into the columns. In Figure 5 the temperatures 40 and 60 mm into the samples are only shown until the results indicated that the thermocouples begin to loosen (uncertain results when the charring reach the thermocouples). Another interesting result learned from this test is that the temperature in the center of the columns never reached

https://doi.org/10.52202/069179-0223

more than 40 degrees Celsius during the 330 minutes the temperatures were recorded.

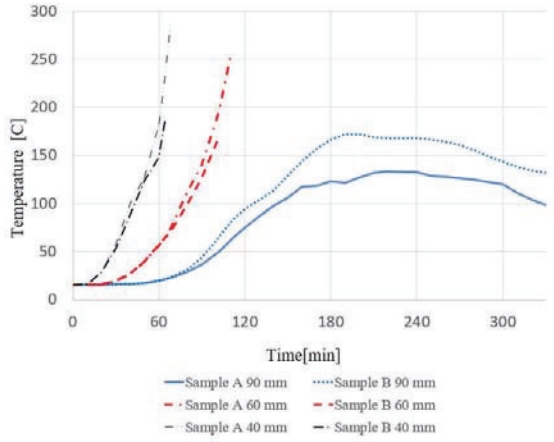

Figure 5: *temperatures inside the columns during the fire test*

At the end of the test (330 minutes with burning and charring) the actual charring depths was measured:

- Column A: 74 mm
- Column B: 71 mm

It was also noted that the actual charring rates in the heating phase were less than notional design charring rates in the Eurocodes. Even though the results might support a less conservative approach the design was made on the safe side according to the Eurocodes.

The steel connectors inside the columns were mounted together with bolts, and the openings were covered using wooden plugs to protect them from high temperatures. In the fire test some of the bolts were left unprotected to study the sensitivity of the solution as well. Figure 6 depicts a vertical arrangement of the bolts and steel plates and the corresponding thermocouples.

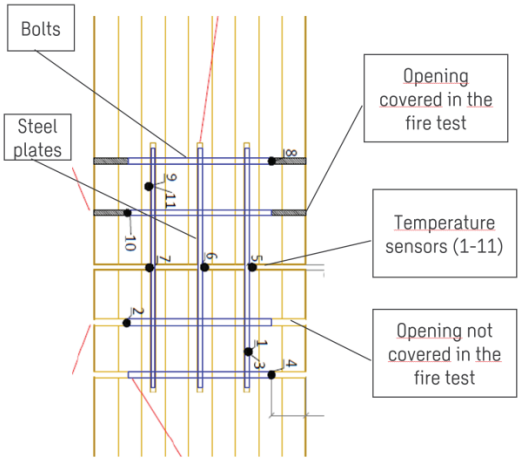

Figure 6: *Steel connectors inside the columns*

The results shown in Figure 7 showed that the steel connectors were well protected inside the timber. The temperatures of the steel connectors never reached more than 270 degrees (C) throughout the duration of the test.

The dotted lines in Figure 7 shows the temperatures of the unprotected bolts (not covered with wooden plugs). It is noted that solid lines, belonging to the temperatures of the protected bolts, did not differ much from the temperatures in the unprotected bolts. In the design of Mjøstårnet, all the bolts were protected. The results from the tests were only used to verify the robustness of detailing, and this indicates that the connectors are well protected, even considering failure in the protection of the steel connectors.

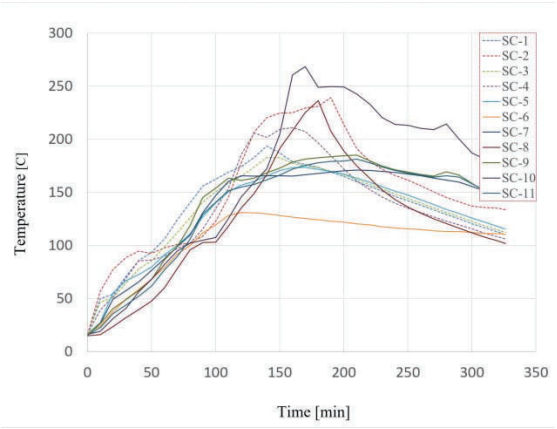

Figure 7: *Temperatures in the steel connectors.*

2.2.2 The heat wave that progresses through the timber

The fire test showed that the charring rate decreased and eventually stopped over the duration of the test. But there is still a heat wave that progresses through the timber after burnout and weakens the uncharred timber to such an extent that failure after burnout is possible. This is an important consideration when designing timber constructions. As structural response of the timber constructions is beyond the scope of this study, only the outlines and conclusion of these considerations are presented here.

Disproportionate collapse due to accident or fire was considered in the structural design of Mjøstårnet. The results from the fire test, measuring temperatures inside timber constructions during a complete fire, was used together with calculation methods from Eurocodes [12] and relevant handbooks[3].

The conclusion is that the timber constructions in Mjøstårnet can withstand a burnout, even considering the heat wave that progresses through the timber after a burnout fire.

https://doi.org/10.52202/069179-0223

2.3 ANALYTICAL DESIGN WITH WOODEN STRUCTURES BASED ON NATURAL FIRES

Parallel to the full-scale tests, calculations for modeling the full duration of a fire in timber structures needed further development and verification.

Standard design charring rates in the Eurocodes are constant values and do not reflect a fire scenario with a decay phase. The charring rate based on the parametric fire exposure, given in annex a of Eurocode 5 [13], on the other hand considers varying fire severity including the decay phase, using actual compartment geometry. However, the model is based on a constant fire load and gives no consideration of the extra fire load form the wooden structures themselves. The altered method used in the design of Mjøstårnet includes the following steps:

- Based on the parametric fire exposure of Annex A of Eurocode 5, the final charring depth can be calculated together with the corresponding mass of wood contributing to the fire.
- This corresponding mass of charred wood produces additional fire load
- The calculation of the parametric fire exposure is repeated, this time, adding the extra fire load.
- This again will make the charring depth increase and add even more energy to the fire.
- These iterations are repeated, and if they converge, they indicate burnout.

Figure 8 shows schematically the iteration of the parametric time-temperature curve and Figure 9 the corresponding charring depth, according to the methodology described above.

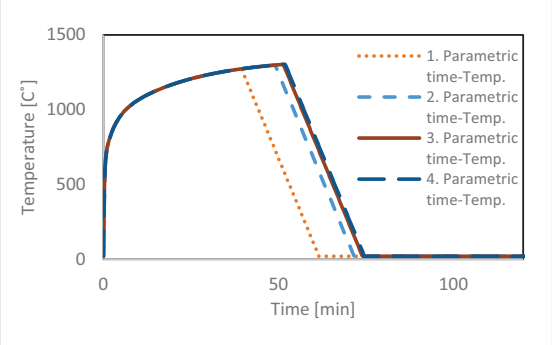

Figure 8: *Parametric time temperature with 4 iterations.*

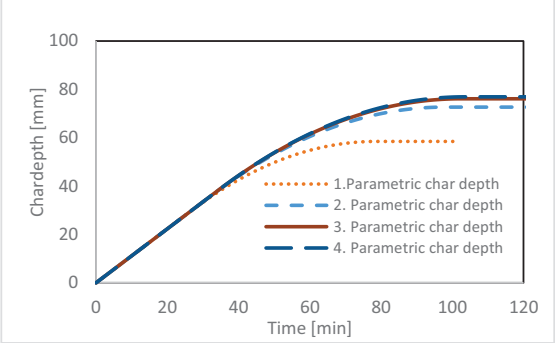

Figure 9: *Parametric charring depths with 4 iterations.*

If the calculations do not converge within reasonable charring depths, they can be repeated reducing the exposed area of wooden surfaces. This makes it possible verifying the acceptable extent of exposed wooden surfaces and at the same time indicating burnout before structural failure.

After the design of Mjøstårnet, similar and improved analytical methodologies are presented by Brandon [14] together with more advanced methodologies that seeks to capture more details of the fire dynamics and material response [8].

2.3.1 Validating the methodology

To validate the analytical methodology used in the design of Mjøstårnet a comparison of experimentally observed charring depths were used. A set of recent experiments where the burning and charring stops after prolonged exposure were selected [9,15-20]. These experiments and their governing parameters are summarized in several recent publications[6,7].

As wood itself is an inhomogeneous material a large scatter of results would be expected. These experiments also contain a broad spectrum of geometries and wooden constructions which would contribute to the uncertainties. Inputs in the calculations are based on values given in the Eurocodes. This means that all wooden constructions area assumed to have a heat of combustion of 17.5 MJ/Kg and a combustion factor of 0,8 with a charring rate of 0,65 mm/min for standard fire exposure. The fire load and geometry are taken from the experiments and the thermal absortivity for the total enclosure is assumed to be 500 $J/s^{1/2}m^2K$. The methodology assumes a one-dimensional charring rate based on the parametric fire exposure over the entire surface of wooden constructions and is iterated as previously explained. Figure 10 shows a plot of measured char depths against calculated char depths. Experiments that significantly exceeds the validation range of relevant parts of the Eurocodes are excluded from the plot. All safety factors in the Eurocode for determining fire load are taken as 1 in these calculations. The calculated results will therefore deviate from the design values.

https://doi.org/10.52202/069179-0223

The grey line constitutes a perfect match between experiments and calculations and points on the right-hand side will be on the safe-side meaning an overprediction of charring depths.

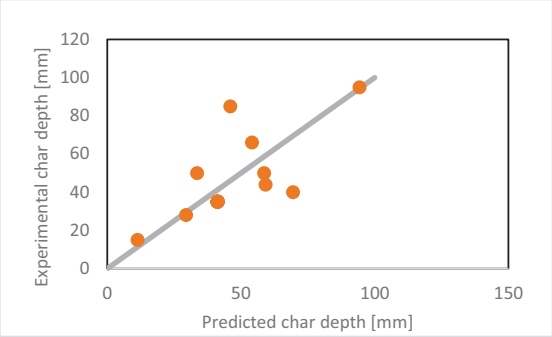

Figure 10 *Predicted vs experimental char depth*

The experiments on the left-hand side which underpredicts the char depths, either experienced delamination of the CLT element or increased charring due to local effects of abutting wooden surfaces. It is also noted that several experiments, all with a large overprediction, are excluded as the time limitations of the parametric charring rate are exceeded.
Considered the validity range of the Eurocodes, the methodology gives a good match between predicted and experimental charring depths.

2.4 ADDITIONAL SAFETY MEASURES IN MJØSTÅRNET

Using an innovative approach for the design and verification of relevant requirements, introduces uncertainties in the results.
To ensure robustness and increase the level of safety for Mjøstårnet, several additional design solutions/fire safety technologies were implemented in the building. Some of them are:

- Loadbearing structures with fire resistance R120 (Designed to resist a burnout with safety margins included)
- Shafts are fire stopped at each floor with fire resistance EI 60
- Sprinklersystem with increased reliability according to EN 12845 Annex F. Hazard class OH3, double water supply, and quick response sprinkler heads
- The water supply to the sprinkler systems is specially designed for Mjøstårnet. In addition to normal water supply, the swimming pool facilities in the building can deliver water to the sprinkler systems. This will secure functionality of the sprinkler, even if the water supply system in the area fail.
- Fire protection of ventilation ducts with incombustible insulation
- No combustible surfaces in voids and technical rooms
- Two pressurized escape stairs
- Automatic fire alarm, which automatically alarms the Fire brigade
- Facilitation for the Fire brigade
  - Firefighting lift
  - Dry risers
  - Control room
- Façade
  - Materials that comply with the requirement B-s1,d0. (Materials that has limited combustibility, low smoke production, no burning droplets)
  - No combustible insulation materials in the building
  - Certain areas of the façade are sprinkler protected (The balconies and façade covered with combustible materials in the two first levels of the building).
  - Firestop in the cavities at each floor. Vertical gaps are thus closed for each floor. In addition, there are fire stops over the windows to further reduce the chance for fire spread in the façade.
  - The risk of fire-spread between different floors in the building is also reduced, introducing balconies and/or vertically distance between windows in different floors

2.4.1 Level of safety in Mjøstårnet

Some of the requirements implemented in this project follows from the Norwegian regulations for buildings of more than 8 floors. These requirements are further combined with additional design solutions/fire safety technologies to ensure robustness and increase the level of safety. Combined with the analytical design methodology used in this project, it's verified that the level of safety in Mjøstårnet meets the requirements following from the Norwegians codes, even when using timber as construction materials.

3 Conclusion

A tall timber building can be designed to resist a complete burnout without failure of the primary loadbearing system at the same time allowing visible timber constructions. Careful considerations of fire behavior, verification methods and additional fire safety measures must build the foundation of such design.

https://doi.org/10.52202/069179-0223

ACKNOWLEDGEMENT

The fire test was conducted by Rise Fire and research AS with assistance and financial support from Moelven and Limtreforeningen

REFERENCES

[1] H. Ikei, C. Song, and Y. Miyazaki, 'Physiological effects of wood on humans: a review', J Wood Sci, vol. 63, no. 1, Art. no. 1, Feb. 2017,

[2] R. Rowell, Ed., Handbook Of Wood Chemistry And Wood Composites. CRC Press, 2005.

[3] R. J. Ross and J. R. Anderson, Eds., Wood handbook: Wood as an engineering material, vol. 282. U.S. Department of Agriculture (USDA), 2021.

[4] J. Liu and E. C. Fischer, 'Review of large-scale CLT compartment fire tests', Construction and Building Materials, vol. 318, p. 126099, Feb. 2022,

[5] C. Kontis, C. Tsichlas, D. I. Kolaitis, and M. A. Founti, 'Fire Performance of CLT Members: A Detailed Review of Experimental Studies Across Multiple Scales', in Wood & Fire Safety, 2020, pp. 251–257.

[6] H. Mitchell, P. Kotsovinos, F. Richter, D. Thomson, D. Barber, and G. Rein, 'Review of fire experiments in mass timber compartments: Current understanding, limitations, and research gaps', Fire and Materials, Dec. 2022.

[7] G. Ronquillo, D. Hopkin, and M. Spearpoint, 'Review of large-scale fire tests on cross-laminated timber', Journal of Fire Sciences, vol. 39, no. 5, pp. 327–369, Sep. 2021.

[8] D. Brandon, A. Temple, and J. Sjöström, 'Predictive method for fires in CLT and glulam structures – A priori modelling versus real scale compartment fire tests & an improved method', RISE. Research Institutes of Sweden, Stockholm, Sweden., RISE Report 2021:63, 2021.

[9] J. Su *et al.*, 'Fire testing of rooms with exposed wood surfaces in encapsulated mass timber construction', National Research Council of Canada. Construction, A1-012710.1, Oct. 2021

[10] J. Schmid, Cross laminated timber - a competitive wood product for visionary and fire safe buildings: proceedings of the Joint Conference of COST Actions FP1402 & FP1404 KTH Building Materials, 10.3.2016. Stockholm: KTH Royal Institute of Technology, Division of Building Materials, 2016.

[11] International Code Council, 2021 International Building Code (IBC). 2021.

[12] Standard Norge, NS-EN 1995-1-1:2004+A1:2008+NA:2010. Eurocode 5: Design of timber structures - Part 1-1: General - Common rules and rules for buildings 2004.

[13] Standard Norge, NS-EN 1995-1-2:2004+NA:2010 Eurocode 5: Design of timber structures - Part 1-2: General - Structural fire design, 2010.

[14] D. Brandon, 'Fire Safety Challenges of Tall Wood Buildings – Phase 2: Task 4 – Engineering Methods', Fire Protection Research Foundation, FPRF-2018-04, 2018.

[15] P. Kotsovinos et al., 'Impact of ventilation on the fire dynamics of an open-plan compartment with exposed timber ceiling and columns: CodeRed #02', Fire and Materials, Jul. 2022,.

[16] D. Brandon and A. Just, 'Fire Safety Design of CLT buildings – an experimental case study. RISE rapport 2018:24', RISE. Research Institutes of Sweden, Stockholm, Sweden., 2018.

[17] J. Su et al., 'Fire testing of rooms with exposed wood surfaces in encapsulated mass timber construction', National Research Council of Canada. Construction, A1-012710.1, Oct. 2021.

[18] A. R. M. Hevia, 'Fire Resistance of Partially Protected Cross-Laminated Timber Rooms', Carleton University, 2014. Accessed: Feb. 01, 2023.

[19] S. Zelinka, L. Hasburgh, K. Bourne, D. Tucholski, and J. Ouellette, 'Compartment Fire Testing of a Two-Story Mass Timber Building', USDA, United States Department of Agriculture, FPL-GTR-247, May 2018.

[20] P. Kotsovinos et al., 'Impact of partial encapsulation on the fire dynamics of an open-plan compartment with exposed timber ceiling and columns: CodeRed #04', Fire and Materials, Jan. 2023.

Su,

World Conference on Timber Engineering Oslo 2023

OBSERVATIONS OF SMOULDERING FIRE IN A LARGE TIMBER COMPARTMENT

Harry Mitchell[1], Rikesh Amin[1], Panagiotis Kotsovinos[2], Mohammad Heidari[3], Daniel Thomson[2], David Barber[4], and Guillermo Rein[1]

ABSTRACT: Understanding the end of the decay phase in a compartment fire is important for safety design, as it can indicate when structural hazards in a compartment have ceased. However, smouldering, a slow, persistent, and flameless form of combustion, can continue for days and hours following flames. Smouldering of mass timber has rarely been reported in timber experiments due to many experiments being stopped shortly after flames. This work presents for the first-time observations following the end of flames in three large compartment experiments with cross-laminated mass timber ceiling and glulam columns, known as CodeRed. The analysis focuses on initiation and growth of smouldering over 48 hours. 0.012–0.58 hotspots per m of timber edge developed in 19 locations, and nine spread through the CLT, forming holes in the ceiling, compartment integrity failure, and collapse of an unloaded column. Visual and infrared imaging was used to track smouldering, extinction, suppression, transition to flaming, and formation of holes. This paper shows that smouldering poses a hazard to mass timber buildings because it is hard to detect and can weaken the structure over days following flames, and transition to flaming, starting new flaming fires. These findings are important for building post-fire recovery.

KEYWORDS: Mass timber, Wood, Fire safety, Smouldering, Tall building

INTRODUCTION

Fire safety is a hazard that continues to be a hot topic in safe mass timber design. As well-acknowledged in previous research [1] and current design standards such as Eurocode 5, timber elements including ceiling slabs and columns will char and degrade during a building fire, reducing their overall structural capacity and posing hazards that need to be addressed in design. However, comparatively less research and recommendations have been made to address the hazards posed to a timber building after flames have become extinct. One key hazard present after a building fire is smouldering.

Smouldering is a phenomenon involving the slow, persistent, flameless combustion of porous media such as timber [8,9]. Timber smouldering has been studied in the context of wildfires, however little research is available on the smouldering in real mass timber compartments. Thick timber elements such as logs and roots can continue to smoulder in the hours and days after a wildfire has passed through a region, known as residual burning [13].

There has been very few observations of smouldering in timber compartment fire experiments (currently <5 cases of smouldering in the 65< experiments in the literature). This can firstly be attributed to firstly to previous experiments not including a large volume of mass timber compared to current building demands – the largest compartment timber experiments prior to 2021 were 84 m^2, resulting in less usage of mass timber, and less complex design requirements (e.g. minimal slab-to-slab timber connections). Secondly, many experiments conclude observations either during or shortly after the end of flames by means of suppression or cessation of data collection, meaning observation bias may impact the perception of the likelihood of smouldering following a timber building fire.

A previous mass timber compartment fire experiment [11] observed structural failure of a mass timber ceiling 29 hours following the onset of heating, which was attributed to unseen smouldering. As only the collapse of the ceiling was observed, smouldering was only highlighted as a possible driving factor. Smouldering of mass timber has been investigated at the small scale [3], which determined that, for CLT in the arrangement specified, smouldering did not self-sustain unless subjected to a threshold heat flux and airflow.

However, very little work has been done to analyse the formation and spread of smouldering in structural mass timber elements following a compartment fire. Despite this concern, smouldering has been highlighted as a hazard in timber design by insurance bodies [10], researchers [1] and fire-safety design [14].

[1] Department of Mechanical Engineering, Imperial College London, UK, g.rein@imperial.ac.uk
[2] Fire Engineering, Arup, London, UK, panos.kotsovinos@arup.com
[3] Fire Testing Centre, CERIB, Épernon, France, m.heidari@cerib.com
[4] Fire Engineering, Arup, Melbourne, Australia, david.barber@arup.com

https://doi.org/10.52202/069179-0224

As a result, this paper outlines for the first time experimental observations and analysis of smouldering following the end of flames in three large open-plan mass timber compartment fire experiments. This paper will overview the Infrared (IR), visual and thermocouple analysis carried out on a smouldering hotspot observed in the CLT over 38 hours following the end of flames in the compartment.

1 METHODOLOGY

The CodeRed experiment series comprised of a 352m^2 compartment with a CLT ceiling and two glulam columns [12], as shown in figure 1. In the three experiments discussed (CodeRed #01 [5], #02 [6], and #04 [7]), the ventilation (50% reduction in CodeRed #02) and level of encapsulation (50% CLT encapsulated in CodeRed #04) were varied to investigate their impact on fire dynamics and charring during and after the end of flames.

Figure 1: *Photo of CodeRed compartment before ignition.*

Following the end of flames, both IR and visual cameras were used to track localised regions of smouldering, known as hotspots, in both the CLT ceiling and Glulam columns. Hotspots were identifiable visually by glowing and the emission of smoke, although not in all cases, particularly for concealed or in-depth smouldering. IR imaging was significantly more effective at identifying hotspots, as they were indicated by regions of high IR intensity, indicating regions of elevated temperature, as depicted in figure 1.

All mass timber elements were studied for the development, progression, and extinction of hotspots over the 48 hours following the end of flames for each experiment. Sixteen smouldering hotspots in total were observed across the three experiments, with nine resulting in holes through the thickness of the CLT ceiling, and one resulting in the collapse of a glulam column. The lateral spread rate of several hotspots were also tracked to further understand the behaviour of smouldering timber hotspots. Using IR, the lateral spread of smouldering hotspots was tracked as shown in figure 2.

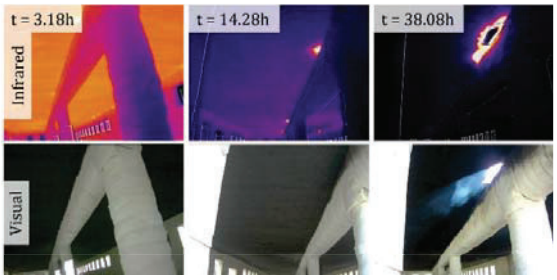

Figure 2: *Initiation and spread of an observed hotspot in CodeRed #01, underneath the concrete beam above the crib ignition line. At 3.18h after flames, the hotspot is only visible in infrared, and not visual observation. The hotspot spreads in-depth until a hole is formed through the ceiling, at which point the smouldering is visible due to the hole and smoke emitted.*

2 RESULTS AND DISCUSSION

2.1 FORMATION OF HOTSPOTS AND HOLES

Table 1: *Summary of observed smouldering behaviour*

CodeRed #	01 [5]	02 [6]	04 [7]
Hotspots	3	7	9
Holes	2	6	2

Immediately after the flames along the timber ceiling and wood crib reached extinction, the entire charred ceiling surface continued to glow, until internal compartment temperatures steadily decayed to ambient conditions within 4 hours, as shown in figure 3. However, over this period of decay and cooling several localised regions in all three experiments continued to glow, both in the ceiling and glulam columns; these regions are known as smouldering hotspots, an example of which is shown in figure 2. A summary of the number of smouldering hotspots in each experiment is given in table 1, which shows that over three experiments 19 hotspots were observed, nine of which resulted in holes through the thickness of the mass timber ceiling, and one resulting in the collapse of a glulam column.

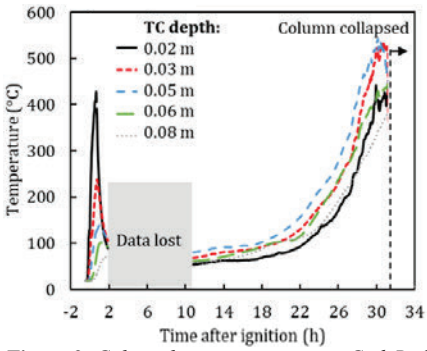

Figure 3: *Column base temperature in CodeRed #02 after ignition. Flames lasted for 27 min before temperatures decayed to ambient levels. In the 32 hours following this, the base column temperatures increased steadily, indicating smouldering.*

Smouldering hotspots in the ceiling initiated exclusively along the edges of each slab, including connection lines between two CLT slabs, connections between the wall and CLT slabs, and the interface between CLT slabs and the insulated concrete column along the compartment length. A summary of the smouldering observed over the three experiments is outlined in table 1.

In CodeRed #01, over the 38 h after flames, a hotspot developed and spread at the ignition end of the compartment (figures 2 and 5), at the midpoint of the CLT

https://doi.org/10.52202/069179-0224

surface near the mineral wool insulated concrete mid-span beam. Infrared imaging was applied to identify the location of the hotspot which immediately after the end of flames were not otherwise identifiable from direct observation. Figures 2 and 5 show that smouldering occurred in the CLT in a small, localised region, which grew in area over the span of 38 h after the end of flames. At 38 h after flames, a 23 min period of rainfall occurred, causing the smouldering to extinguish. Although suppression is an important tool in fire response, without thermal tools such as thermocouples or IR cameras these hotspots can be hard to identify before they begin to alter the structural capacity of the mass timber element.

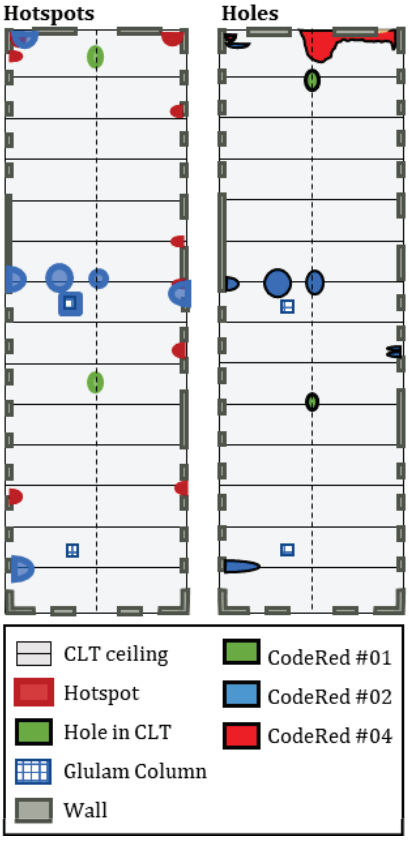

Figure 4: *Sketch of smouldering hotspots in the ceiling and columns from the end of flaming to the end of smouldering (> 48 h) in each experiment. Straight black lines represent edges of timber slabs.*

2.2 SMOULDERING IN COLUMNS AND ENCAPSULATION

Columns are typically structurally loaded elements and can therefore be of increased risk of structural failure during, or after, a fire [4]. However, each glulam column was unloaded and had no in-built connection to the ceiling or floor, partially contributing to one column in CodeRed #02 falling to the ground. This column was observed to smoulder at its base from 0 h after the end of flames. The column reached temperatures of ≤ 400°C during the fire, before steadily cooling below 100°C. However, as can be seen in Fig. 7, temperatures at thermocouple locations

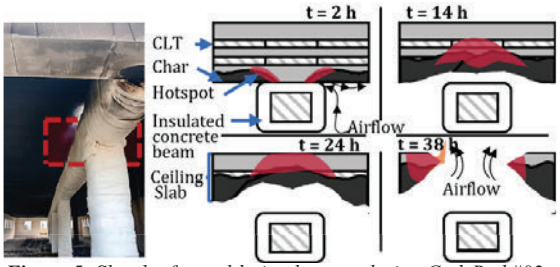

Figure 5: *Sketch of smouldering hotspot during CodeRed #02 progressing through the ceiling thickness, and forming a hole in the ceiling.*

embedded both inside the timber element and along the glue line began to increase above ambient conditions from around 12 h following the end of flames, indicating the spread of smouldering from the base of the column in-depth and upwards along the column length. Smouldering at the base of the column was also observed with IR imaging. The column base smouldered for 31.82 h through the cross-section of the column base until the top of the column was observed to shift from the ceiling connection point. At 32.02 h, as shown in Fig. 6, the column collapsed fully onto the floor. This was attributed to degradation of the column base cross-section due to continued smouldering.

Embedded thermocouples at the base of the column are depicted in Fig. 7, showing the column base reaching up to 500°C at 28 h after the end of flames, above the temperature at which flaming could reoccur. After the column collapse, the side of the column facing the floor continued smouldering, resulting in near-full decay of the column cross-section across the column length, as shown in figure 6.

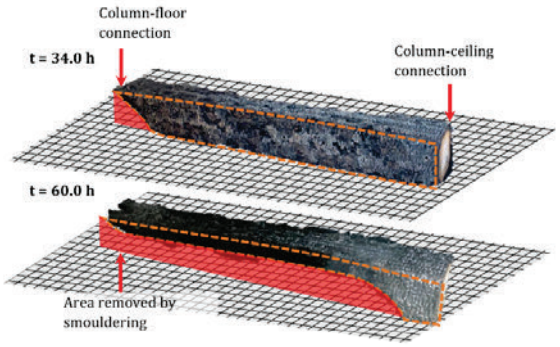

Figure 6: *Smouldering under collapsed Glulam column from CodeRed #02 after collapsing to the concrete floor.*

Encapsulation is used in mass timber design to protect timber elements from fire, therefore limiting their contribution to the fire load, and limiting the impact of the fire on the element's structural integrity. Smouldering not only can still occur in encapsulated timber elements, but this can often make smouldering more challenging to locate even while using IR [2]. The encapsulation used in CodeRed #04 was a commercial encapsulation that covered 48% of the exposed surface of the CLT ceiling, with the goal of reducing the overall contribution of the CLT to the fire load. During the fire, the majority of protected CLT remained uncharred by the flames. Over

https://doi.org/10.52202/069179-0224

48 h of observation, no smouldering was observed underneath the encapsulation.
Two hotspots at the interface between the CLT and the crib ignition-end wall formed holes through the CLT thickness. Further to this, both hotspots continued to spread along the width of the compartment, until the smouldering progressed underneath the encapsulation as shown in Fig. 9. 22 days (528h) following the end of flames, an approximately 1.7 m^2 region of encapsulation collapsed (Fig., directly below a region of smouldering similar in size that had spread through the thickness of the CLT ceiling. This undetected smouldering indicates that although encapsulation can be effective at mitigating the impact of fire on mass timber elements, it is not completely effective at preventing smouldering, particularly when it spreads from the edges of the encapsulation.

2.3 TRANSITION TO FLAMING AND EXTINCTION

Given suitable conditions, smouldering can transition from flameless combustion to flaming combustion. Smouldering to flaming transition is primarily driven by a change in heat flux incident on the smouldering surface, and oxygen supply to the smouldering reaction [20]. Transition to flaming can present a hazard to timber structures following the end of flaming by producing new fires hours after the original fire had ended. This can be particularly hazardous in the case of smouldering that forms penetrations to adjacent compartments or other floors, such as in Fig. 7, as this can lead to unburnt compartments being exposed to a new ignition source.
Smouldering spread and transition to flaming can be more likely to occur with the provision of insulation close to the smouldering surface, while still providing a small gap for air flow. In several smouldering hotspots, transition to flaming was observed following the formation of holes in the ceiling. This is due to an increase in air flow local to the hotspot, providing greater oxygen to the smouldering process, allowing a greater rate of char, leading to flaming.

***Figure** 7: CLT ceiling smouldering hotspot 40 hours after flames, forming a hole in the CLT. Transition to flaming is also observed.*

In a design scenario where a compartment of similar design to CodeRed may represent a single floor in a tall timber structure, transition to flaming in a breach of compartmentation between a unburnt compartment and a burnt-out compartment may lead to a new compartment fire being initiated, presenting all new structural hazards. As a result, this paper recommends that future work continues to understand the conditions under which transition to flaming may occur in smouldering mass timber elements following a compartment fire, and methods of avoiding these conditions to prevent multiple fires in the same structure.
Suppression and subsequent extinction of smouldering hotspots was also observed, both by short 20–40-minute periods of rainfall and direct intervention by firefighters using a firehose. Rainfall was only observed to be partially effective at extinguishing hotspots, whereas after significant intervention a firehose was successfully used to extinguish a smouldering hotspot.

3 DISCUSSION

The end decay phase of a building fire is typically defined as the time at which the entire compartment has cooled to ambient temperatures [12]. Flaming will cease long before much of the compartment has reached ambient conditions, however smouldering, as evidenced by CodeRed, can continue hours and days after the decay phase is assumed to conclude. Following the end of flames of each CodeRed experiment, the entire of the CLT surface smouldered during the decay phase before extinguishing without suppression, known as self-extinction. The definition of "extinction" is typically used by fire safety experts to define when the hazard posed to a building during a fire has ceased. This is typically defined by either when the flames have ended, or shortly afterwards when most of the compartment has cooled to ambient temperatures. However, as evidenced by this paper, smouldering can not only cause localized regions of high temperature within a compartment, but also extend the period over which structural hazards continue to develop over hours and days after flames have ended.
The 9 holes observed in the CLT ceiling posed not only a structural hazard to the building, but also a failure of compartmentation. Further to this, several hotspots were observed to transition to flaming hours after the end of flames, providing pathways to further larger fires forming and further damaging the structure.
The smouldering hotspots that progressed under the encapsulation in CodeRed #04 indicate that encapsulation may not be effective at preventing smouldering of CLT in some situations, particularly when smouldering has initiated in a non-encapsulated area and spreads horizontally to encapsulated parts.
The conditions for self-extinction are important to identify when a mass timber element will cease smouldering, therefore reducing further hazards to the structure. The complex design of timber buildings means that heat losses in certain locations can be low, smouldering surfaces can re-radiate onto each other, and sufficient air flows can occur naturally within a

compartment. Suppression of hotspots occurred either independently or by the addition of water local to the smouldering region, either from a period of rainfall (occurred in both CodeRed #01 and #02), or with a fire hose.

Due to the complex geometries of timber elements observed in the CodeRed experiments, self-sustaining smouldering hotspots were observed over the 48-h following the end of flames. Smouldering timber favours regions which reduce head losses of smouldering, including voids, underneath encapsulation, and near insulating materials such as mineral wool. Smouldering will also spread at a greater rate when subjected to a higher airflow, providing a greater supply of oxygen to the oxidation reaction. In the context of tall timber buildings, the spread of smouldering may be enhanced by regions where airflow exists, such as small gaps between timber connections. Compared to future and current occupied mass timber buildings the design of the CodeRed compartments is low in complexity, meaning that in practice the presence of smouldering in a modern timber building may be more challenging to predict, detect, and suppress than what is discussed in this paper.

Identifying design components and locations where smouldering is likely to occur is key to not only reducing the likelihood of smouldering, but aiding firefighting services in detecting its presence. To that end, self-sustaining smouldering was only observed along the edge of timber elements. Considering the overall edge length of each experiment (154 – 257 m where edges comprise of ceiling slab to wall connections, ceiling slab to ceiling slab connections, and ceiling slab to insulated concrete beam connections), a hotspot occurrence frequency of 0.012 – 0.58 hotspots per meter of edge was found. Scaling this to modern design demands such as office spaces of 5000 m2, 30 – 150 hotspots may occur, each presenting a hazard to the structure.

The prevention of smouldering in timber buildings can be addressed by avoiding designs which promote its initiation. However, in application timber structures have other design components. Therefore, this paper recommends smouldering is studied further in complex timber design elements to determine the hazard that smouldering may pose. These include voids between compartments with combustible elements (e.g. ceiling and wall slabs, voids behind combustible facades), structural connections (e.g. ceiling slab connections, ceiling to column connections, beam and column connections), penetrations in slabs for electrical/plumbing servicing, and any regions where mass timber is insulated by another design component or an air gap (encapsulation, insulation, and other low-conductivity construction materials).

Detection is vital to help firefighting operations identify if smouldering is present in a timber structure, and therefore if structural hazards are present. This paper has shown that in many cases smouldering may not be visible by direct observation, due to it being flameless and occurring in-depth and in hidden areas of in timber elements. Therefore, it is recommended that when investigating a timber building after a compartment fire, infrared imaging is used [2]. However, it should be noted that concealed timber surfaces such as voids, encapsulation, and cavities can cause smouldering to not be immediately observable with infrared either. This paper and previous work [2] show that water mist hoses can extinguish smouldering hotspots when identified. However, it is recommended that work is conducted to understand the most effective methods to apply water to extinguish smouldering hotspots, and how to extinguish smouldering in regions that may be more challenging for firefighters to access.

4 CONCLUSIONS

This paper outlines experimental observations that show that smouldering fire is a structural threat to modern timber buildings. The remaining 19 hotspots observed highlight that structural hazards in a compartment fire continue not only during the decay phase, but in the hours and days afterwards. Smouldering presents a hazard for two reasons: one, the smouldering hotspots after a flaming fire are difficult to detect and suppress, so smouldering can burn through timber elements overnight and lead to partial collapse. Secondly, smouldering can lead to transition to flaming, which creates pathways to further fires hours after both the fire, and decay periods. Also, encapsulation was found to be not completely effective at mitigating smouldering. This is the first study focused on smouldering fires in mass timber, showing that smouldering is proven to be a structural hazard that must be considered and addressed by designers, stakeholders, and firefighters.

ACKNOWLEDGEMENT

This research was funded by EPSRC and Arup. The co-authors would like to acknowledge the CodeRed team, comprising of members of CERIB, Arup, and Imperial College London.

REFERENCES

[1] Mitchell, H., Kotsovinos, P., Richter, F., Thomson, D., Barber, D., & Rein, G. Review of fire experiments in mass timber compartments: Current understanding, limitations, and research gaps, *Fire and Materials*, 1-27, 2022

[2] Brandon, D., Sjöström, J., Temple, A., Hallberg, E., & Kahl, F. Fire Safe implementation of visible mass timber in tall buildings–compartment fire testing, *RISE report*, 2021

[3] Crielaard, R., van de Kuilen, J. W., Terwel, K., Ravenshorst, G., & Steenbakkers, P. Self-extinguishment of cross-laminated timber. *Fire Safety Journal*, 105, 244-260. 2019

[4] Gernay, T., Zehfuß, J., Brunkhorst, S., Robert, F., Bamonte, P., McNamee, R., Mohaine, S., Franssen, J. M. Experimental investigation of structural failure during the cooling phase of a fire: Timber columns. *Fire and Materials*. 2022

[5] Kotsovinos, P., Rackauskaite, E., Christensen, E., Glew, A., O'Loughin, E., Mitchell, H., Amin, R., Robert, F., Heidari, M., Barber, D., Rein, G., Schulz, J. Fire dynamics inside a large and open-plan compartment with exposed timber ceiling and columns: CodeRed #01. *Fire and Materials,* 2022a

https://doi.org/10.52202/069179-0224

[6] Kotsovinos, P., Rackauskaite, E., Christensen, E., Glew, A., O'Loughin, E., Mitchell, H., Amin, R., Robert, F., Heidari, M., Barber, D., Rein, G., Schulz, J. Impact of ventilation on the fire dynamics of an open-plan compartment with exposed CLT ceiling and glulam columns: CodeRed #02. *Fire and Materials*. 2022b.
[7] Kotsovinos, P., Christensen, E., Glew, A., O'Loughin, E., Mitchell, H., Amin, R., Robert, F., Heidari, M., Barber, D., Rein, G., Schulz, J. Impact of partial encapsulation on the fire dynamics of an open-plan compartment with exposed timber ceiling and columns: CodeRed #04. *Fire and Materials*. 2023.
[8] Ohlemiller, T. J. Smoldering combustion propagation on solid wood. *In Fire safety science—proceedings of the third international symposium*, 565-574. Routledge. 2006
[9] Rein, G. "Smoldering combustion," in SFPE Handbook of Fire Protection Engineering, *Springer New York*, 581–603. 2016
[10] RISCAuthority. Insurance Challenges of Massive Timber Construction and a possible way forward. 2022
[11] Wiesner, F., Bartlett, A., Mohaine, S., Robert, F., McNamee, R., Mindeguia, J. C., & Bisby, L. Structural Capacity of One-Way Spanning Large-Scale Cross-Laminated Timber Slabs in Standard and Natural Fires. *Fire Technology*, 1-21. 2020
[12] Mitchell. Fire safety in tall timber buildings, Thesis, Imperial College London 2023
[13] Santoso, M. A., Christensen, E. G., Yang, J., & Rein, G. Review of the transition from smouldering to flaming combustion in wildfires. *Frontiers in Mechanical Engineering*, 5, 49, 2019
[14] Buchanan, A., & Östman, B. Fire Safe Use of Wood in Buildings: Global Design Guide, 432, *Taylor & Francis*. 2022

World Conference on Timber Engineering Oslo 2023

EXPERIMENTAL INVESTIGATION OF THE RELATIONSHIP BETWEEN TIMBER SPECIES AND SMOULDERING

Wenxuan Wu[1], Luis Yermán[2] Juan P Hidalgo[3], Jeffrey Morrell[4], Felix Wiesner[5]

ABSTRACT: Smouldering, the exothermic solid-phase oxidation process of porous char, can damage or destroy timber structures long after a fire has burnt out or its flame front has passed. Reaction kinetic parameters (i.e. activation energy E_a and frequency factor A) of timber oxidation can be determined from thermogravimetric analysis (TGA). These parameters along with timber density could potentially be used to predict the self-sustaining smouldering of timber species. To verify this hypothesis, the relationship between the occurrence of self-sustained smouldering and the properties of different timber species, namely density and activation energies of pyrolysis and oxidation, was determined through bench-scale smouldering tests using Cone Calorimeter and TGA for nine Australian timber species. Less dense timbers with lower activation energies were more prone to initiate and sustain smouldering under extreme laboratory conditions.

KEYWORDS: Timber, Timber Species, Smouldering, Oxidation, Thermogravimetric Analysis, Fire Safety, Combustion, Bushfires

1 INTRODUCTION

As an organic material, timber is combustible and therefore its use in construction poses multiple fire safety challenges. Flaming ignition is usually considered an indicator of the start of a fire, while the extinction of the flame marks the end of the event. Because of the large amounts of energy released by visible flames, and their associated spread and damage, the focus of research and standardised guidance documents often focuses on the flaming combustion process.

Subsequent smouldering combustion is sometimes overlooked for structural fires due to its occurrence at relatively low temperatures, lack of visible indicators (i.e. flames) and slow spread rate [1, 2]. Consequently, smouldering in timber infrastructure often appears only as a footnote to recent primary research outcomes concerned with flaming. Nevertheless, the consequences of timber infrastructure under smouldering combustion can also be catastrophic. For example, a mass timber slab collapsed 29 hours after flame self-extinction, due to the subsequent smouldering combustion in a structure fire [3]. Smouldering spread along bridges via the deck planks and across the bridge via the crossbeams has been reported after bushfires [4].

Smouldering combustion can be observed in timber after it has been pyrolysed [5, 6] and is a leading combustion phenomenon in wildland fires [7, 8], constituting a hazard to assets and a health issue from the smoke (Figure 1). Moreover, the transition from smouldering to flaming can occur under the appropriate conditions [4] and introduces hazards to fire intervention in timber buildings and post-bushfire areas.

Figure 1: *Examples of wood smouldering after a bushfire exposure (photos from cn.depositphotos.com)*

Smouldering combustion of timber involves multiple chemical reactions that can be approximated by a lumped 3-step chemical pathway as described in [2, 9]:

Pyrolysis: **Wood (s)** $\rightarrow$ Pyrolyzate (g) $+$ **Char (s)** $+$ Ash (s) , $\Delta H > 0$ (endothermic) (1)

Gas-phase oxidation: Pyrolyzate $(g) + O_2 \rightarrow CO_2 + H_2O + other\ gases$, $\Delta H < 0$ (exothermic) (2)

Heterogeneous oxidation: **Char (s)** $+ O_2 \rightarrow CO_2 + H_2O + other\ gases +$ **Ash (s)** , $\Delta H < 0$ (exothermic) (3)

[1] Wenxuan Wu, School of Civil Engineering, The University of Queensland, Australia, wenxuan.wu@uq.edu.au
[2] Luis Yermán, National Centre for Timber Durability and Design Life and, School of Civil Engineering, The University of Queensland, , Australia, l.yerman@uq.edu.au
[3] Juan P Hidalgo, School of Civil Engineering, The University of Queensland, Australia, juahime@gmail.com
[4] Jeffrey Morrell, National Centre for Timber Durability and Design Life, University of the Sunshine Coast, Australia jmorrell@usc.edu.au
[5] Felix Wiesner, The University of British Columbia, Canada, f.wiesner@uq.edu.au

https://doi.org/10.52202/069179-0225

When solid timber is exposed to fire, its surface heats up and decomposes (pyrolysis), creating a char layer. This process occurs at around 300 °C [10]. The char comprises a porous reactive matrix with a high surface-to-volume ratio that allows oxygen diffusion [2]. The external heat supply initiates pyrolysis and other endothermic processes, such as evaporation, before oxidation occurs. Self-sustained smouldering will occur after the external heat is removed and progress if the exothermic oxidation reaction (Equations 2 and 3) generates sufficient heat to propagate pyrolysis (Equation 1) and compensate other endothermic processes such as water evaporation, sensible enthalpy increase and heat losses. Smouldering is not sustainable without these attributes and will quench [11, 12].

According to the Arrhenius model (Equation 4), the kinetic parameters that govern a chemical reaction are the activation energy (E_a) and the frequency factor (or pre-exponential factor A).

$$\dot{\omega}''' = Ae^{-E_a/RT} \quad (4)$$

Ea is the energy threshold and must be surpassed to transform reactant molecules into products. A represents the proportion of molecules participating in the reaction if all molecules are beyond the activation energy.

These parameters can be used to predict the reaction rate of the process and can be determined from thermogravimetric analysis (TGA) results, considering the peak temperature at the maximum decomposition rate. Wu et al. [13] found that lower activation energy in preservative-treated pine was more likely to initiate self-sustained smouldering in bench-scale (Cone Calorimeter) tests and caused faster mass loss rates during smouldering combustion. Similarly, lower-density timber also led to faster smouldering combustion. These processes may be linked to porosity of wood, which generally decreases with increased density [14-16]. In addition, high thermal diffusivity caused by low density leads to deeper heat penetration at a given time.

This study explored the influence of the timber species on self-sustained smouldering, evaluated in terms of occurrence and rate. Micro-scale TGA and bench-scale smouldering tests were performed on nine native Australian timbers with a wide range of bulk densities. Determining smouldering occurrence and rate can help assist in the selection of timber species for specific end-use applications, especially in bushfire-prone areas. Ultimately, a better understanding of the smouldering phenomenon can help to develop risk mitigation strategies and optimise trade-offs between availability, durability, design life, and fire resilience.

2 MATERIAL AND METHODS

2.1 MATERIAL PREPARATION

Nine Australian hardwood timber species were used in this study: *Acacia mearnsii* (Black Wattle – BSL), *Erythrophleum chlorostachys* (Cooktown Ironwood – CTI), *Eucalyptus tetrodonta* (Darwin Stingybark – DSB), *Eucalyptus paniculata* (Grey Ironbark – GIB), *Intsia bijuga* (Merbau – MRB), *Cardwellia sublimis* (Northern Silky Oak – NSO), *Flindersia brayleyana* (Queensland Maple – QMP), *Alstonia scholaris* (Queensland Whitewood – QWW), *Elaeocarpus grandis* (Silver Quandong – SLQ).

Australian bushfire standard AS 3959 [17] defines the term bushfire attack level (BAL) as the hazard for bushfire-prone areas. The severity of BAL is measured by potential exposure to ember attack, radiant heat and direct flame contact, using radiant heat flux expressed in kW/m^2 [18, 19]. Among the species used in this work, based on their density, GIB, DSB and CTI are considered suitable timber species for BAL – 19, representing a moderate risk from ember attack and ignition of debris with a heat flux of up to 19 kW/m^2. Merbau is considered a bushfire-resistant timber species according to AS 3959 [17], enabling its use in BAL – 29 areas.

Specimens for TGA were ground to pass through a 0.25mm-mesh screen using a RETSCH Cutting Mill SM 300. The initial moisture content and dry density of all samples (measuring 100 mm by 100 mm by 19 mm) for the bench-scale smouldering tests were determined using the oven-drying method, according to ASTM D4442 [20], in duplicate. The mean density and initial moisture content of the timber species are summarised in Table 1. The oven-dry samples were used in bench-scale testing immediately after removal from the oven, to minimise the effect of different moisture contents across the timber species. This is a conservative boundary condition to assess the smouldering occurrence, where a minimum amount of additional energy is required to evaporate the free water. Ceramic paper was used as insulation around the sample edges to reduce heat losses and allow for oxygen mass transfer.

Table 1: *Dry density and initial moisture content of the nine timber species.*

Sample	Texture	Dry Density (kg/m^3)	Initial Moisture Content (%)
GIB		1048	12
NSO		504	10.3
SLQ		407	11.4
BSL		586	11.6
DSB		1047	8.5
QMP		572	11.5
MRB		769	10.5
QWW		467	10.4
CTI		1213	9.8

2.2 THERMOGRAVIMETRIC ANALYSIS

Thermogravimetric analysis of the nine timber species was conducted in an oxidative (air) environment using a NETZSCH STA449-F3 Thermogravimetric Analyzer using 10 ± 0.5 mg of undried powdered sample in an alumina crucible at 5, 10 and 20 °C/min heating rates, from 50 to 800 °C and using an airflow rate of 100 mL/min. Thermal decomposition reaction rates were assessed by applying the first derivative to the mass-temperature data (DTG).

From Kissinger's model (Equation 5) [21], the activation energy (Ea) and pre-exponential factor (A) can be obtained by identifying the oxidation peak temperature (T_p) from the DTG curves of different heat rates (β).

$$\ln\left(\frac{\beta}{T_p^2}\right) = -\frac{Ea}{RT_p} + \ln\left(\frac{AR}{E}\right) \quad (5)$$

2.3 BENCH-SCALE SMOULDERING TEST

The Bench-scale smouldering method used herein was designed to simulate passing bushfire scenarios. For these experiments, the nine timber species were ignited in a Cone Calorimeter with pilot ignition to establish an initial flaming combustion period where the heat release rate was measured according to AS/NZS 3837 [22]. A heat flux of 20 kW/m^2 was chosen as the fire intensity for this study, which was considered a moderate fire risk.

Heat flux exposures were maintained at 20 kW/m^2 until flaming combustion produced a timber mass loss of 40 %. This mass loss criterion was used as an indication of the degree of physical damage associated with flaming duration. A quasi-steady flaming state before external heat removal was confirmed from stable heat release rate readings and CO_2 yield to substantiate thermal equilibrium within the sample. Once the target mass loss was reached, the external heat supply was removed, the time to ignition and flaming duration were recorded, and the samples were transferred to an Ohaus V-7000 load cell under ambient temperature conditions. From that point onwards, the mass loss over time was measured to determine the smouldering rate. Each species was tested twice to ensure repeatability.

Both optical and infrared cameras were used to record the propagation pattern of the self-sustained smouldering along the sample surface. The airflow from the exhaust hood was measured via a Hot-Wire Anemometer to vary between 0.02 to 0.1 m/s; this was the lowest achievable airflow under our laboratory conditions. Figure 2 shows a schematic representation of the equipment and procedure with the different stages of a self-sustained smouldering test.

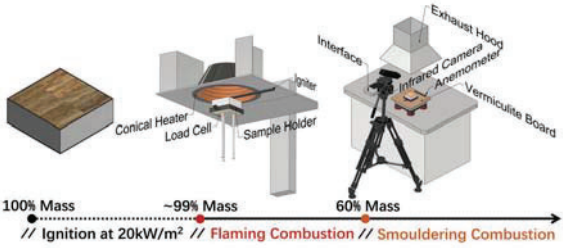

Figure 2: *Schematic representation of the equipment and procedure showing the stages of the bench-scale self-sustained smouldering tests.*

3 RESULTS AND DISCUSSION

3.1 THERMOGRAVIMETRIC ANALYSIS

Figure 3 shows representative DTG results for BSL under 5, 10 and 20 °C/min heating rates. All timber species showed the same pattern. The first small peak from the left, around 80 °C was due to water evaporation. The second peak, around 320 °C, was attributed to endothermic wood pyrolysis (Equation 1). The third peak, between approximately 450 and 485 °C, corresponded to exothermic char oxidation (Equation 3). Both the drying and pyrolysis stages were relatively consistent among species, while more marked differences among species were observed in the onset and maximum temperature of the third peak, at all heating rates. The peak temperatures for the pyrolysis and oxidation stages of nine species are summarised in Tables 2 and 3, respectively.

Linear correlations were established by plotting $\ln(\beta/T_p^2)$ against $1/T_{(\beta,p)}$ **(**Equation 4**)**; the correlation fittings are shown in figures 4 and 5. The E_a for pyrolysis and oxidation stages were calculated based on the slopes from figures 4 and 5, respectively, and are summarised in Table 4.

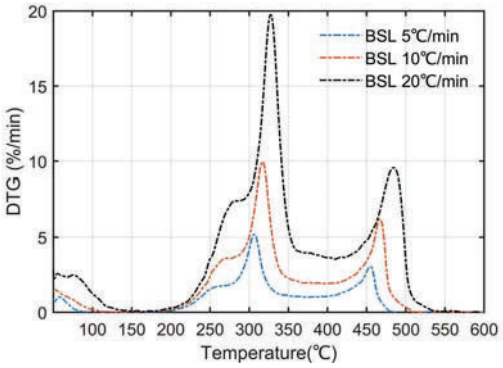

Figure 3: *Representative DTG results from TGA experiments of BSL tested in air atmosphere using heating rates of 5, 10 and 20 °C/min.*

https://doi.org/10.52202/069179-0225

Table 2: *Peak temperatures at the pyrolysis stage (T_{P_β}) using 5, 10 and 20 °C/min heating rates.*

Sample	Heating rate (°C/min)		
	5	10	20
	T_{PP} (°C)		
GIB	307.6	319.4	331.3
NSO	302.4	314.6	325.7
SLQ	306.0	317.4	328.2
BSL	306.5	317.1	327.4
DSB	307.6	319.9	331.3
QMP	307.1	318.0	328.0
MRB	310.0	320.6	331.6
QWW	301.0	311.9	324.1
CTI	308.4	321.1	333.7

Table 3: *Peak temperatures at the oxidation stage (T_{PO_β}) using 5, 10 and 20 °C/min heating rates.*

Sample	Heating rate (°C/min)		
	5	10	20
	T_{PO} (°C)		
GIB	455.9	467.4	480.8
NSO	460.5	471.0	481.2
SLQ	456.8	464.0	471.5
BSL	455.0	467.0	484.2
DSB	473.1	488.2	510.8
QMP	436.7	442.5	448.2
MRB	449.7	460.6	473.0
QWW	435.9	446.0	455.8
CTI	470.0	483.1	498.1

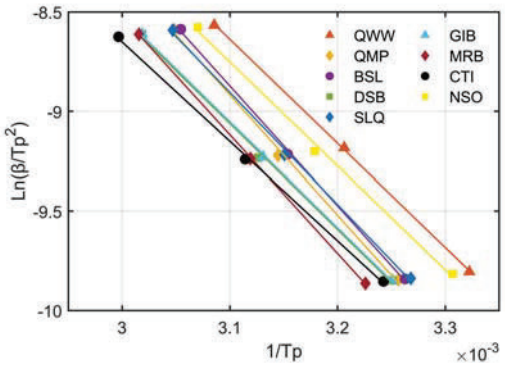

Figure 4: *Plot of $ln(\beta/Tpp^2)$ versus inverse peak pyrolysis temperature $1/T_{(\beta,p)}$ for all species.*

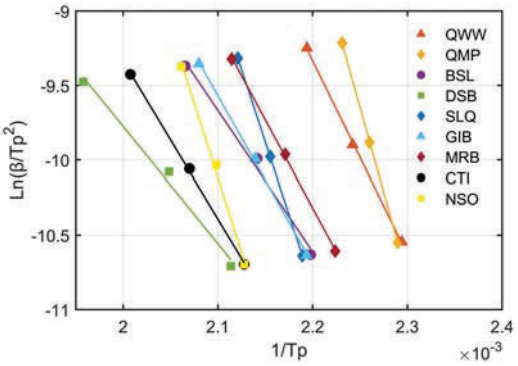

Figure 5: *Plot of $ln(\beta/Tpp^2)$ versus inverse peak oxidation temperature $1/T_{(\beta,p)}$ for all species.*

The Ea of the pyrolysis stage for all nine timber species was approximately 40 to 50 kJ/mole, while the Ea for the oxidation stage varied markedly across species. This indicates that wood species affected the characteristics of the char that was produced during the pyrolysis, which influenced the subsequent oxidation kinetics.

Table 4: *Activation energies of pyrolysis and oxidation stages for nine timber species.*

Reaction	Pyrolysis stage		Oxidation stage	
Sample	Ea_p (kJ/mole)	A (s^{-1})	Ea_o (kJ/mole)	A (s^{-1})
GIB	44.2	9.1E+06	93.6	1.5E+10
NSO	43.4	8.8E+06	115.5	4.0E+12
SLQ	46.8	2.9E+07	161.2	5.0E+08
BSL	50.0	1.1E+08	78.5	2.5E+08
DSB	44.2	8.7E+06	65.1	2.8E+06
QMP	50.2	1.1E+08	188.8	2.3E+22
MRB	49.5	6.8E+07	97.9	7.0E+10
QWW	43.5	1.0E+07	107.6	2.7E+12
CTI	41.5	2.8E+06	87.9	1.4E+09

3.2 BENCH-SCALE SMOULDERING TEST

3.2.1 Duration of heat exposure

Table 5 shows the mean ignition time and flaming duration from the bench-scale tests. Timber species with a higher density require a longer time to ignite and for the flame to consume the same mass percentage. Longer flaming increases heat production and penetration depth and generates more char as an insulator, which can affect subsequent smouldering behaviour.

Timber density was strongly positively correlated with the flaming duration with a Pearson Correlation Coefficient of 0.87 suggesting that these parameters cannot be considered independent towards smouldering performance due to their collinearity (Figure 6).

Table 5: *Density, time to ignition, and flaming duration to reach 40% mass loss for the nine timber species.*

Sample	Density (kg/m^3)	Ignition (minutes)	Flaming to 40 % Mass Loss (minutes)
GIB	1048	4.8	15.7
NSO	504	3	14
SLQ	407	1.5	9.7
BSL	586	2.3	8.4
DSB	1047	5.8	19.3
QMP	572	2.5	11.6
MRB	769	3.5	11.7
QWW	467	2.4	7.8
CTI	1213	22.3	20

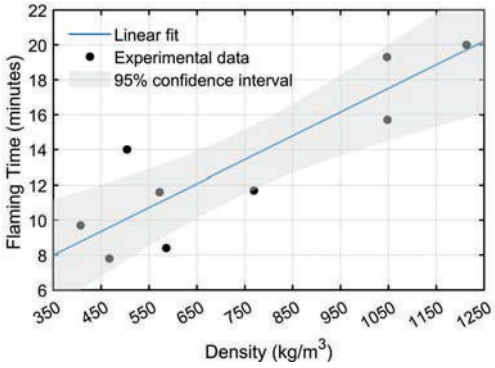

Figure 6: *Linear regression between timber density and the flaming time to reach 40 % mass loss with a Pearson Correlation Coefficient 0.87.*

3.2.2 Propagation pattern

A series of representative infrared and optical images of timber undergoing self-sustained smouldering at different times were used to analyse the smouldering front (Figure 7). A rapid cooling stage occurred on the surface after the external heat supply ceased (Figure 7a to 7b). The smouldering front then propagated from the edges to the centre, generating visible smoke. A transition to flaming only occurred for QWW (Figure 7b) from the insulated edge for around 10 minutes. The smouldering front then progressed deeper into the wood, coinciding with surface regression from char oxidation. At this stage, glowing could be observed (Figure 7c). Eventually, the temperature decreased until less than 1 % mass residual was left after 75 minutes (Figure 7d).

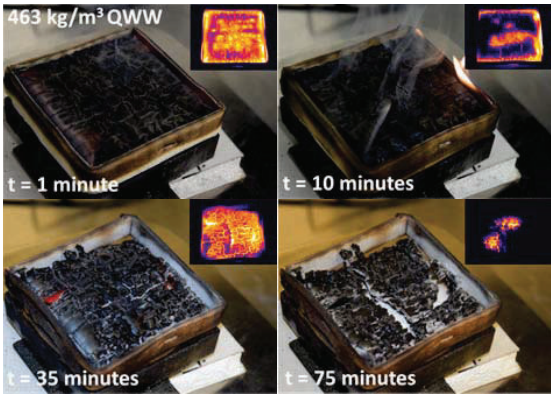

Figure 7: *Photographs of QWW at different times during the smouldering combustion stage. Note the transition to flaming from one side at 10 minutes and the glowing at 35 minutes. Thermal images showing the exposed surface are inserted in the top-right corners of the figures.*

3.2.3 Smouldering Performance

Figure 8 shows the mass percentage evolution during the smouldering stage for all the timber species that exhibited self-sustained smouldering (QWW, MRB, GIB, and BSL). Those samples ultimately lost more than 99 % of their initial mass. In contrast, the smouldering for other species (i.e., NSO, SLQ, DSB, QMP, CTI) either quenched during the smouldering process or never initiated smouldering. An example of QMP smouldering and quenching is shown in Figure 8, with a flat tail at around 30 % mass remaining, indicating the end of the reaction.

Table 6 summarises the density, smouldering occurrence and the time to reach a remaining mass of 1 %. This time can be considered to approximately correspond to the time required to fully complete smouldering, since the asymptotic behaviour in Figure 8 indicates that 0 % mass may never have been reached.

The porosity (which can be deduced from density) of timber and char is crucial as it determines the oxygen availability in the smouldering front through oxygen diffusion.

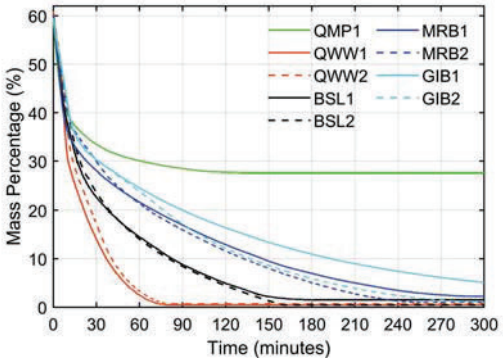

Figure 8: *Mass evolution during the smouldering stage of QWW, QMP, BSL, MRB and GIB*

https://doi.org/10.52202/069179-0225

Table 6: *Density, smouldering occurrence and time to reach less than 1 % mass during smouldering in nine timber species.*

Sample	Density (kg/m^3)	Self-sustained Smouldering? (Y/N)*	Time to <1% of initial mass (minutes)
GIB	1048	Y	299
NSO	504	N	-
SLQ	407	N	-
BSL	586	Y	159
DSB	1047	N	-
QMP	572	N	-
MRB	769	Y	252
QWW	467	Y	77
CTI	1213	N	-

* Y = yes, N = no smouldering initially propagated or quenched.

Table 7 combines the micro-scale measured Ea for oxidation, with the wood density and smouldering occurrence of the nine timber species tested at bench scale. These results show that:

- NSO, SLQ and QMP had the highest Ea_o, which meant they required higher residual heat from flaming combustion to initiate oxidation. This resulted in insufficient energy to initiate the reaction or caused quenching after some time, despite the relatively low densities of these species.
- CTI had the highest density (usually related to lower porosity) among nine species, which may have limited oxygen mass transfer. This would have negatively affected the reaction rate (Equation 5). Thus, despite CTI's relatively low Ea_o , smouldering did not initiate.
- In contrast, GIB with a similar density as CTI has a higher exponential factor A. However, it had the lowest smouldering rate compared to QWW, MRB or BSL, which had low Ea_o and low densities.
- DSB had the lowest Ea_o and similar density to GIB; however, the smouldering did not self-sustain. It suggests the presence of yet unknown underlying factors affecting smouldering. Further tests are required to reduce uncertainties arising in the kinetic parameters in the model.

Figure 9 graphs wood density against activation energy and demarcates the occurrence of self-sustained smouldering. High Ea_o, above a threshold between 120 and 160 kJ/mole, appeared to prevent self-sustained smouldering for species with a relatively low density. Oxidation in this range for those timber species required higher energy to initiate, which was seemingly not compensated by the increased oxygen supply that occurs in lower density (and thus higher porosity) species.

DSB and GIB have a similar density around 1050 kg/m^3; the former did not smoulder while the latter smouldered. At the same time CTI did not self-sustained smoulder, which could be attributed to its high density. Similarly, an activation energy threshold may exist around 110 kJ/mole – where two low density species (i.e., NSO and QWW) exhibited different smouldering performances. A distinction in Ea_o between these species cannot be confirmed with confidence according to the errors arising from the imperfect linear fit. These results suggest that the boundary defining the occurrence of self-sustained smouldering is sensitive to experimental variability at the bench and micro-scale (e.g., limited repetitions, measurement error, imperfect fitting, and apparatus heating non-uniformity). Furthermore, underlying parameters could affect the smouldering behaviour and merit further study. For example, the pre-exponential factor A of oxidation was the lowest for DSB (2.8E+06 s^{-1}, Table 4), which could help to explain why the smouldering quenched midway, as effective collisions for those molecules beyond the Ea_o failed to generate sufficient heat to overcome the heat losses and energy required for further pyrolysis.

Table 7: *Ea_o and A of oxidation, densities and smouldering occurrence for nine timber species.*

Sample	Ea_o (kJ/mole)	A (s^{-1})	Density (kg/m^3)	Smouldering (Y/N)
GIB	93.6	1.5E+10	1048	Y
NSO	115.5	4.0E+12	504	N
SLQ	161.2	5.0E+08	407	N
BSL	78.5	2.5E+08	586	Y
DSB	65.1	2.8E+06	1047	N
QMP	188.8	2.3E+22	572	N
MRB	97.9	7.0E+10	769	Y
QWW	107.6	2.7E+12	467	Y
CTI	87.9	1.4E+09	1213	N

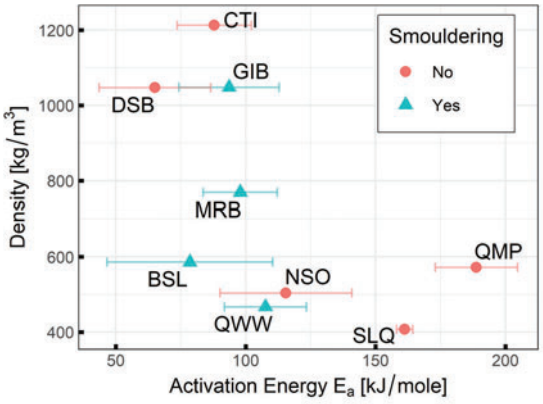

Figure 9: *Scatter plot of occurrence of self-sustained smouldering for nine timber species after 40% mass loss during flaming combustion under 20 kW/m^2 versus activation energy of oxidation stage. Error bar refers to standard error arising from linear fit.*

3.3 Limitations

Some experimental conditions in this study were deliberately conservative in detecting distinct behaviour between species in smouldering. This allowed comparisons between smouldering and activation energy or density, providing fundamental knowledge about the link between self-sustained smouldering and micro-scale parameters or material properties. However, it should be acknowledged that completely dry timber is unlikely to exist in the field, even in wildfire conditions, where mean moisture contents have been reported as ranging between 3 to 6 % [23]. Thus, the results of smouldering for individual species tested herein should not be interpreted to completely account for the smouldering propensity of these species under field conditions.

While the moisture contents were chosen conservatively to be as low as possible to limit variability between species, the ventilation conditions were also chosen as low as possible to reduce their influence on the results and focus on the timber's intrinsic kinetic and physical properties instead of external conditions. The ventilation conditions were non-conservative, and increased airflow may increase the occurrence and rate of smouldering.

Further studies on external effects may help improve our understanding of smouldering factors and develop better selection criteria for bushfire performance that consider performance beyond the flaming period.

4 CONCLUSION

This paper investigated multiple factors that may affect the rate and occurrence of smouldering. Some qualitative conclusions are:

- Grey Ironbark (GIB) is considered a suitable timber species for BAL-19, and MRB is on the list of bushfire-resistant timbers. However, both show propensities to self-sustained smoulder under extreme conditions, indicating the need for more appropriate methods for assessing bushfire performance.
- Activation energy and density combined to affect the rate and occurrence of smouldering. Overall, low density and Ea_o should facilitate self-sustained smouldering.

Future work should be done to reinforce the conclusion:

- More timber species, covering a wider range of densities (i.e. complementary data points).
- More heating rates to increase confidence in linear fitting of the activation energy for each species.
- Other parameters to assess the influence of further factors (e.g., primary elemental composition difference).

ACKNOWLEDGEMENT

This research was supported by the National Centre for Wood Durability and Design Life, a collaborative program between the University of the Sunshine Coast, The University of Queensland, and the Queensland Department of Agriculture and Fisheries and funded by Forest and Wood Products Australia. The authors greatly appreciate technical support from the UQ Fire Laboratory manager, Mr Jeronimo Carrascal, during this work.

REFERENCES

[1] Ohlemiller, T. and W. Shaub, *Products of wood smolder and their relation to wood-burning stoves*. 1988, National Bureau of Standards, Washington, DC (USA). Center for Fire Research.

[2] Rein, G., *Smoldering combustion*, in *SFPE Handbook of Fire Protection Engineering*. 2016, Springer. p. 581-603.

[3] Wiesner, F., et al., *Structural Capacity of One-Way Spanning Large-Scale Cross-Laminated Timber Slabs in Standard and Natural Fires.* Fire Technology, 2021. **57**(1): p. 291-311.

[4] Dowling, V.P., *Ignition of timber bridges in bushfires.* Fire Safety Journal, 1994. **22**(2): p. 145-168.

[5] Ahrens, M., *Home structure fires: National Fire Protection Association*. 2013: Quincy, MA.

[6] Hall, J.R., *The smoking-material fire problem*. 2010: National Fire Protection Association Quincy, MA.

[7] Dale, F.A., *Fence Posts and Fire*, in *Forest Products Newsletter*. 1966: Melbourne, Australia.

[8] Rein, G. and X. Huang, *Smouldering wildfires in peatlands, forests and the arctic: Challenges and perspectives.* Current Opinion in Environmental Science & Health, 2021. **24**: p. 100296.

[9] Torero, J.L., et al., *Processes defining smouldering combustion: Integrated review and synthesis.* Progress in Energy and Combustion Science, 2020. **81**: p. 100869.

[10] Schaffer, E.L., *CHARRING RATE OF SELECTED WOODS--TRANSVERSE TO GRAIN*. 1967, Forest Products Lab Madison Wis.

[11] Yermán, L., *Self-sustaining smouldering combustion as a waste treatment process*, in *Developments in Combustion Technology*. 2016, InTech Rijeka. p. 143-165.

[12] Wyn, H.K., et al., *Self-sustaining smouldering combustion of waste: A review on applications, key parameters and potential resource recovery.* Fuel processing technology, 2020. **205**: p. 106425.

[13] Wu, W., et al., *Experimental Study on smouldering of timber with durability treatment*, in *12th Asia-Oceania Symposium on Fire Science and Technology*. 2021: Brisbane, Australia.

[14] Dunlap, F., *Density of wood substance and porosity of wood.* JOURNAL OF AGRICULTURAL RESEARCH, 1914.

[15] Usta, İ., *Comparative study of wood density by specific amount of void volume (porosity).* Turkish Journal of Agriculture Forestry, 2003. **27**(1): p. 1-6.

[16] Duarte, B.B., et al., *Correlation between density and porosity from ten species of tropical wood.* Duarte Journal of Engineering Research and Application, 2020: p. 30-32.

https://doi.org/10.52202/069179-0225

[17] *AS 3959-2009: Construction of Buildings in Bush Fire Prone Areas*. SAI Global - Australian Standard.
[18] Winandy, J.E., et al., *Fire performance of timber: review for use in wildland-urban interfaces.* Holzforschung, 2022.
[19] Baker, G., A. Webb, and P. Whiting, *Regulatory controls for buildings in wildfire-prone areas of Australia.* Fire technology, 2020. **56**(5): p. 1903-1935.
[20] *ASTM D4442-20, Standard Test Methods for Direct Moisture Content Measurement of Wood and Wood-Based Materials*. 2020, American Society for Testing and Materials.
[21] Kissinger, H.E., *Reaction kinetics in differential thermal analysis.* Analytical Chemistry, 1957. **29**(11): p. 1702-1706.
[22] *AS/NZS 3837 Method of test for heat and smoke release rates for materials and products using an oxygen consumption calorimeter (Reconfirmed 2016)*. 1998, Standards Australia: Melbourne, Victoria.
[23] Macindoe, L. and J. Leonard, *Moisture content in timber decking exposed to bushfire weather conditions.* Fire and Materials, 2012. **36**(1): p. 49-61.

World Conference on Timber Engineering Oslo 2023

PREDICTING THE EFFECTIVE CHAR DEPTH IN TIMBER ELEMENTS EXPOSED TO NATURAL FIRES, INCLUDING THE COOLING PHASE

Andrea Lucherini[1,2], Daniela Šejnová Pitelková[3,4], Vladimír Mózer[5]

ABSTRACT: This paper presents a numerical study on the effect of the heating and cooling phases on the reduction of the effective cross-section of timber elements, in particular on the evolution of the char depth (300°C isotherm) and zero-strength layer. An advanced calculation method based a finite-difference heat transfer model is compared to the simplified approach suggested by Eurocode 5. For the heating phase, defined as the standard fire curve (ISO 834), the simplified Eurocode 5 method generally provides more conservative char depths, while the zero-strength layer is under-predicted. Nevertheless, the values of effective char depth are comparable. Including the cooling phase evidences that, during this phase, the heat wave penetration leads to a significant increase in the char depth and zero-strength layer. Particularly, this increase directly depends on the fire cooling rate: a slower cooling phase further reduces the effective cross-section of timber members. As a result, this research highlights how the heat wave penetration during the fire cooling phase can significantly reduce the load-bearing capacity of timber elements.

KEYWORDS: timber structures, fire safety, heat transfer, charring, zero-strength layer, cooling.

1 INTRODUCTION

Urban densification, sustainability drivers and technological advances are fostering the development of high-rise structures using bio-based materials like engineered wood products. Tall mass timber buildings now represent the fastest growing sector in the construction industry [1]. However, challenges related to their fire safety represent a main barrier for the robustness and the success of these structures. The primary difference from traditional construction materials, like steel, concrete, and masonry, is that timber buildings are mainly composed of wood, which is combustible and can contribute to building fires [2]. From a structural engineering perspective, the wood pyrolysis and combustion reduce the effective cross-section and therefore load-bearing capacity of structural elements. Consequently, they can compromise the structural integrity and stability of individual timber components, as well as the whole structural system [3].

The structural performance of timber elements is typically associated with the concept of charring. Charring, considered as the formation of a residual high-carbon char upon pyrolysis, is generally assumed to undergo for temperatures above 300 ºC. Charred wood is typically characterised by low mechanical properties (strength and stiffness), which are normally assumed null [3]. Accordingly, in structural applications, the penetration speed of the char layer, known as charring rate, plays a key role in the evaluation of the load-bearing capacity of timber elements exposed to fire.

The fire performance of structures, as well as the charring rate, is normally defined in a prescriptive manner relying on the standard fire curve, an unrealistic ever-increasing thermal exposure with time, conceived as the worst-case design scenario [4]. Crucially, although a compartment fire within a building enclosure is typically composed of a growth phase, a fully-developed phase, a decay phase and a cooling phase, the standardised fire tests completely ignore what happens after the fully-developed fire phase, deemed less onerous due to its lower temperatures [5,6].

However, during the fire decay and cooling phases, heat continues to penetrate within structural materials through conduction. Consequently, the structural capacity of load-bearing elements gradually continues to reduce [7]. This phenomenon can be more or less significant for various construction materials and systems. This problem is more critical for timber structures because wood loses its mechanical properties in an irreversible manner at relatively low temperatures, compared to traditional construction materials like steel and concrete. For instance, at 100 ºC typical softwood has a compressive strength reduction of about 75%, compared to the value at ambient temperature [4]. Consequently, after the end of the fully-developed fire phase, the load-bearing capacity of timber element can reduce up to an additional 30%

[1] Dr Andrea Lucherini, Department for Fire-safe Sustainable Built Environment (FRISSBE), Slovenian National Building and Civil Engineering Institute (ZAG), Ljubljana, Slovenia, andrea.lucherini@zag.si.
[2] Dr Andrea Lucherini, Department of Structural Engineering and Building Materials, Ghent University, Belgium, andrea.lucherini@ugent.be.
[3] Mrs Daniela Šejnová Pitelková, Czech Technical University in Prague, University Centre for Energy Efficient Buildings of Czech Technical University in Prague, Fire Laboratory, Czech Republic, daniela.pitelkova@cvut.cz.
[4] Mrs Daniela Šejnová Pitelková, Czech Technical University in Prague, Faculty of Civil Engineering, Department of Architectural Engineering, Czech Republic, daniela.pitelkova@cvut.cz.
[5] Dr Vladimír Mózer, Czech Technical University in Prague, Faculty of Civil Engineering, Department of Architectural Engineering, Czech Republic, vladimir.mozer@cvut.cz.

https://doi.org/10.52202/069179-0226

(compared to the ambient one), and structural failure could occur after fuel burnout, even after a fire seems extinguished [8-12]. The main challenge is related to the fact that, after fire extinction, this hazard cannot be easily detected, and structural collapse may occur with little or no warning. This situation represents a critical scenario for fire brigade interventions.

As a result, this framework leads to an inadequate assessment of timber structures exposed to fire. The precise interaction between fire and structural materials needs to be understood and carefully considered because the temperature propagation through the load-bearing timber can unexpectedly lead to structural collapse [10]. Current regulations simplify the problem by adding a zero-strength layer (ZSL), which is introduced to take into account the reduced mechanical properties of the heated uncharred wood [4,13]. However, the methodology is highly simplified (constant value for ZSL) and typically only carried out for the heating phase of a post-flashover compartment fires. The available literature on the matter is quite limited, but this hazardous issue has been underlined by many researchers [8-12]. Fundamental technical issues still need to be resolved to fundamentally comprehend the heat wave penetration in timber elements during all the fire phases to truly enable the performance-based design of fire-safe tall timber buildings.

This research study investigates the effect of the heating and cooling phases on the reduction of the effective cross-section of timber elements. The study focuses on the evolution of the char layer and zero-strength layer, thus the effective char depth. Simplified (Eurocode 5) and advanced calculation methods (conductive heat transfer model) are employed to estimate their thicknesses and penetration speeds during both the heating and cooling phases. For the cooling phase, the effect of various cooling rates is also investigated.

2 METHODOLOGY

A pure conduction heat transfer model is formulated to investigate the heat penetration within structural timber elements exposed to fire conditions. The finite differences model is based on the numerical method developed by Emmons and Dusinberre, and it explicitly solves a one-dimensional heat conduction problem by resolving energy-balance equations in the main direction of the heat flow [14-16]. The model is discretised into a number of finite elements, associated to nodes.

The heat transfer model is defined in accordance with the Eurocode advanced calculation methods (ACM) [4]. Solid softwood is modelled using the Eurocode 5 effective temperature-dependent material properties, namely mass density ratios, specific heat capacity and thermal conductivity [4]. Common timber density and moisture content are assumed: mass (wet) density equal to 420 kg/m^3 and a moisture content of 12%. The thickness of the timber element is set 200 mm to ensure its thermal thickness (semi-infinite solid), taking into consideration the defined material properties and thermal conditions.

The thermal boundary conditions at the fire-exposed timber surface are also defined according to Eurocode, starting from a defined temperature-time curve: a convective heat transfer coefficient equal to 25 W/m^{2}K and a timber surface emissivity equal to 0.8 [4,17].

The solid space is discretised in finite elements with a thickness of 1 mm, and the time step is set to 0.025 s, following model stability criteria [14-16].

3 RESULTS FOR STANDARD FIRE (ONLY HEATING PHASE)

The heat transfer in structural timber elements is first investigated considering the fire exposure as the standard fire temperature-time curve for a duration of 2 hours.

3.1 THERMAL CHARACTERISATION AND CHAR DEPTH

The modelling results are first analysed in terms of temperature. Figure 1 shows the temporal evolution of the temperatures at various depths within the timber substrate, while Figure 2 reports the various in-depth temperature profiles at various instants.

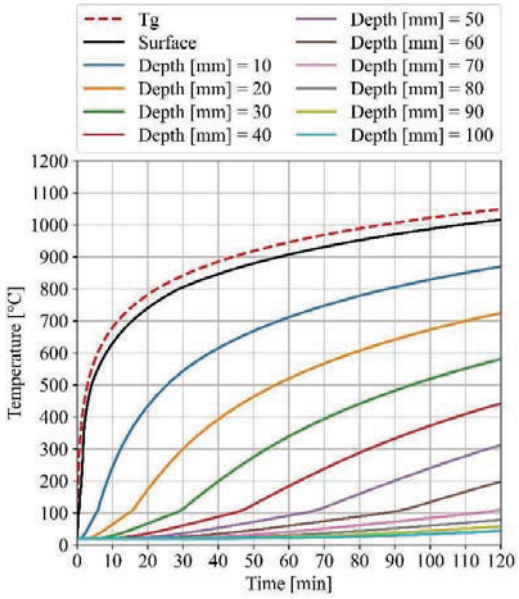

***Figure 1**: Temperature evolution at various depths within the timber substrate.*

The plots highlight how the timber surface closely follows the gas fire temperature and typical thermal gradients within timber elements exposed to fire are shown. These thermal evolutions are directly related to the defined thermo-physical properties of timber at ambient and elevated temperatures (in particular, thermal inertia and thermal diffusivity). It is also important to emphasise that, within the 2 hours of standard fire exposure, the heat wave only slightly penetrates beyond 100 mm in the timber substrate.

https://doi.org/10.52202/069179-0226

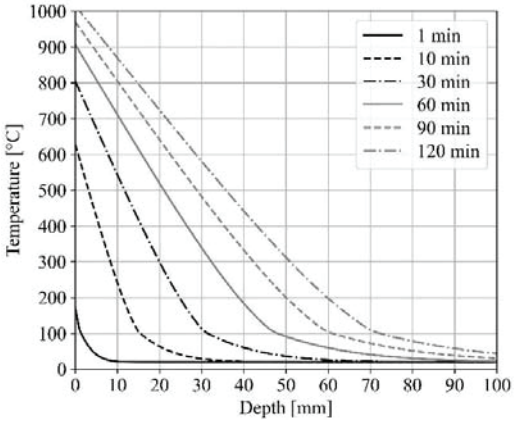

***Figure 2**: Evolution of thermal profiles within the timber substrate at different instants.*

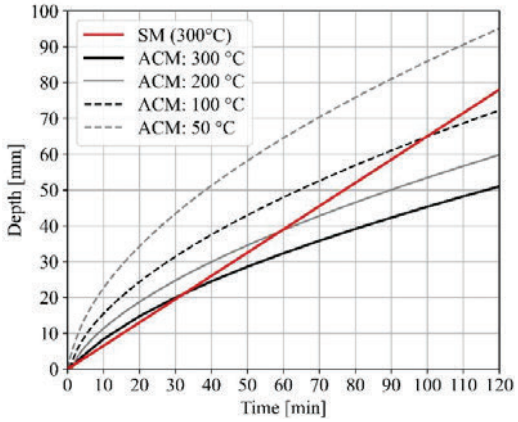

***Figure 3**: Evolution of the isotherms depths (300 ºC, 200 ºC, 100 ºC and 50 ºC) and comparison with EN 1995-1-2 simplified method (SM).*

The temperature fields shown in Figure 1 and Figure 2 are further analysed to study the thermal penetration of various isotherms within the timber substrate. Figure 3 and Figure 4 report the depths and penetration speeds of the 300 ºC, 200 ºC, 100 ºC and 50 ºC isotherms during the fire exposure. These isotherm curves correspond to various levels of reduced timber mechanical properties, and they are fundamental to quantify the structural capacity of load-bearing timber elements. In particular, the 300 ºC isotherm usually represents the location of the char front and, from its evolution, it is possible to estimate the charring rate within the load-bearing timber cross-section. Beyond this temperature, timber pyrolysis process is typically assumed completed and the resulting charred wood has null strength and stiffness [3].

Figure 3 shows how, for the defined case, the various isotherm curves penetrate the timber substrate, while Figure 4 displays their penetration speeds. It is evident how isotherms of lower temperatures typically have a higher speed compared to isotherms of higher temperatures. At identical instants, 50°C has always the highest penetration speed, while 300°C the lowest. Nevertheless, Figure 4 underlines how the penetration speeds gradually decrease during the fire exposure, all tending to values included between 0.2 and 0.5 mm/min. Accordingly, the distance between the various isotherms increases during the fire exposure, hence the thermal gradient becomes less steep (see Figure 2).

Special attention is paid to the 300°C isotherm depths (i.e. char depth) and penetration speed (i.e. charring rate). In particular, this curve evaluated using the described heat transfer model (advanced calculation method – ACM) is compared to the simplified method (SM) which assumes a constant charring rate [4]. For the case of softwood, this value is set equal to 0.65 mm/min (β_0). Figure 3 and Figure 4 show how this value over-estimates the timber charring rate for standard fire exposures above 15 minutes, while the timber char depth is under-estimated only below 15 minutes.

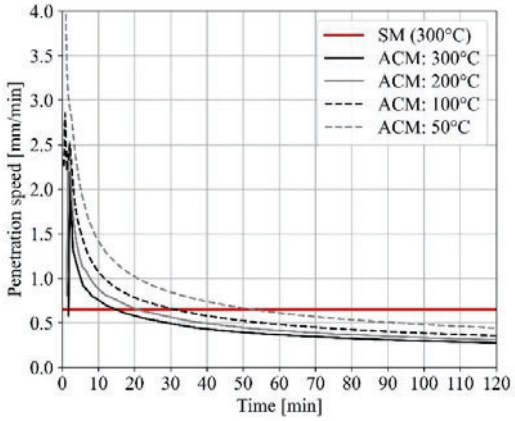

***Figure 4**: Evolution of the isotherms penetration speeds (300 ºC, 200 ºC, 100 ºC and 50 ºC) and comparison with EN 1995-1-2 simplified method (SM).*

3.2 ZERO STRENGHT LAYER

Once estimated the char depth, the effect of the heat penetration within the timber cross-section must be considered to assess the load-bearing capacity of timber structural members exposed to fire. Indeed, timber undergoes significant decomposition processes also for temperatures below charring (300°C) and, consequently, important reductions in the mechanical properties.

The Eurocode reduced-cross section method traditionally introduces a "zero-strength layer" (ZSL) to take into account the reduced mechanical properties in the timber heated below charring temperature [4]. This layer is assumed to have null strength and stiffness as charred wood, and it is summed to the char depth to estimate the residual effective cross-section. Eurocode 5 typically prescribes a zero-strength layer of constant thickness: in the current version, this is equal to 7 mm, for fire exposures beyond 20 minutes [4]. In contrast, the new version suggests various constant thicknesses depending on the member types and stress state.

Since the zero-strength layer is linked to the structural capacity of timber members, it is rarely associated with a temperature interval, given the fact that it should theoretically depend on both the mechanical state of the

https://doi.org/10.52202/069179-0226

cross-section (i.e. stresses) and the thermal gradient within the heated timber. However, using the presented numerical heat transfer model and assuming various constant thicknesses suggested by the Eurocode, it is possible to study the thermal gradient within the zero-strength layer. One edge of the thermal gradient is defined by the charring temperature (300°C), while the other depends on the defined thickness.

Figure 5 shows the evolution of the thermal gradient within zero-strength layers of various thicknesses: 7 mm, 9 mm, 14 mm, and 16 mm. Thicker zero-strength layers have larger thermal gradients and the thermal gradient gradually decreases for longer fire exposures: this is in line with the decreasing thermal gradients observed in Figure 2 and Figure 3. In general, the zero-strength layer extends up to temperatures as low as 70-80°C. This result is in line with what found by Huc *et al.*, who estimated 80-120°C as the edges of the zero-strength layer for timber beams exposed to parametric fire curves [18].

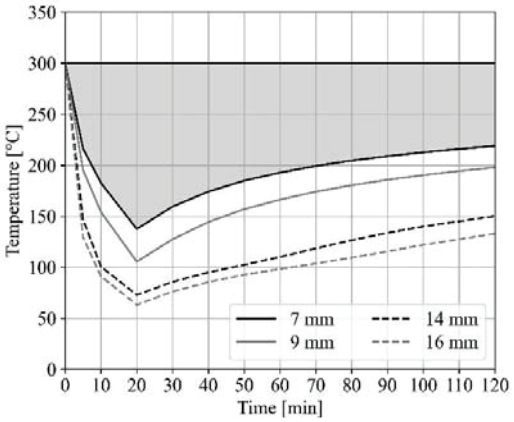

***Figure 5**: Evolution of the thermal gradients within the zero-strength layer for different thicknesses (7mm, 9mm, 14mm, and 16 mm).*

Following these considerations, the zero-strength layer is also estimated for the presented case study using two different approaches. The first approach assesses the zero-strength layer based on the in-depth temperatures. Following the previous analysis, the temperature gradient within the zero-strength layer is set to 80-300°C, 100-300°C, and 120-300°C. The second approach calculates the zero-strength layer considering the reduced mechanical properties of the timber section, as shown in Figure 6. Using the reduction factors prescribed by Eurocode 5 (tension and compression) [4], the in-depth thermal gradient shown in Figure 2 can be associated to a distribution of reduced mechanical properties within the timber section (see Figure 7). Assuming the timber cross-section under a homogenous stress state (tension or compression), once estimated the char depth (d_{char}), the zero-strength layer (d_{ZSL}) can be simply calculated based on an effective area equivalence, as shown in Figure 6.

Figure 8 reports the results related to the estimation of the zero-strength layer according to the two methodologies and compared to the current Eurocode 5 simplified method (7 mm). Since temperature continues to penetrate the timber substrate, the zero-strength layer continuously increases during the whole fire exposure. The highest values are calculated for the reduced mechanical properties approach for compression, which induces the highest reductions in the material strength, while the 120-300°C temperature approach represents the least critical conditions. In general, the estimated values are far beyond the 7 mm prescribed by Eurocode 5, ranging between 17 and 34 mm after 2 hour of standard fire exposure. This result again agrees with the research study carried out by Huc *et al.*, who found out thicknesses of zero-strength layer up to 30.5 mm [18].

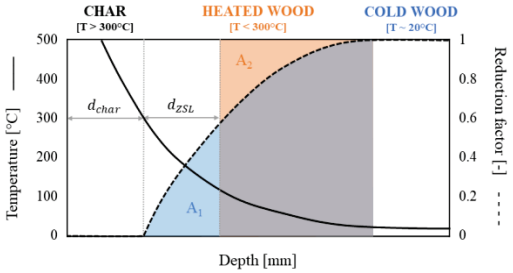

***Figure 6**: Schematisation of the methodology to calculate the zero-strength layer based on the reduced mechanical properties, given an in-depth thermal gradient.*

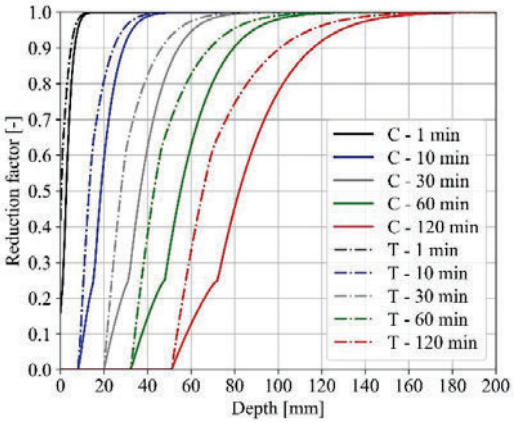

***Figure 7**: Evolution of the reduction factor of timber mechanical properties for compression (C) and tension (T) at different instants.*

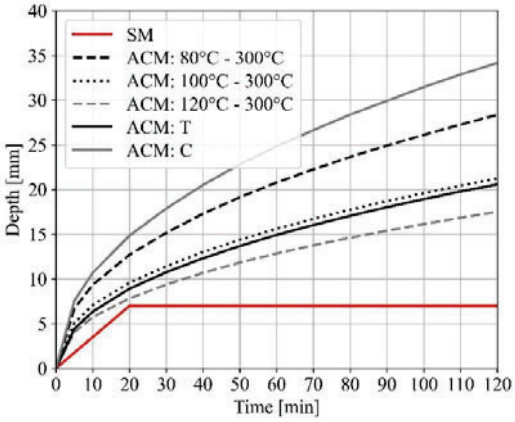

***Figure 8**: Evolution of the zero-strength layer according to temperature and reduced mechanical properties approaches, compared to EN 1995-1-2 simplified method (SM).*

https://doi.org/10.52202/069179-0226

3.3 EFFECTIVE CHAR DEPTH

To finally assess the structural capacity of timber members, the effective load-bearing cross-section is obtained considering both the contribution of the charred wood and the wood heated below charring temperature. Indeed, the effective char depth that is assumed to have null strength and stiffness can be calculated as the sum of the char depth and the zero-strength layer. This process can be carried out according to the above-mentioned methodologies. If the results for the char depth (Figure 3) and the zero-strength layer (Figure 8) are merged together, the effective char depth can be evaluated.

Figure 9 shows the effective char depths obtained following the temperature and reduced mechanical properties approaches, compared to the current Eurocode 5 simplified method. The previous sections have highlighted how the Eurocode 5 simplified method generally over-estimates the timber charring rate (beyond 15 min) and under-estimates the zero-strength layer, compared to the results obtained with the presented advanced calculation method based on heat transfer modelling. However, the values of effective char depths appear comparable, as shown in Figure 9. Nevertheless, for the presented case, these results evidence how the Eurocode 5 simplified method is usually less conservative, at least for standard fire durations below 60 minutes.

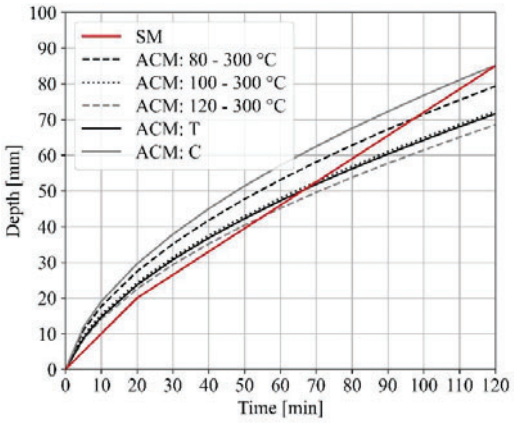

***Figure 9**: Evolution of the effective char depth according to temperature and reduced mechanical properties approaches, compared to EN 1995-1-2 simplified method (SM).*

4 RESULTS FOR NATURAL FIRE (HEATING AND COOLING PHASES)

The previous section has presented the modelling results considering the fire exposure as the standard fire temperature-time curve (ISO 834), hence only analysing the fire heating phase. In this section, a cooling phase is introduced, and the fire exposure is modelled according to the Eurocode parametric fire curves (EPFC) methodology [17]. The case of a squared compartment of 7.5 m × 7.5 m in plan, 3 m in height, with an opening factor of 0.04 $m^{0.5}$, a fuel load density of 720 MJ/m^2 and compartment linings with a thermal inertia of 1160 $J/m^2s^{0.5}K$ is considered. The resulting fire curve is shown in Figure 10. This scenario is chosen to provide a heating phase of 1 hour similar to the standard fire curve (Γ factor equal to 1), followed by a cooling phase from maximum temperature (944°C) to ambient temperature (20°C) of about 2 hours, causing a cooling rate of about 8.3°C/min (linear cooling according to the Eurocode parametric fire curves methodology).

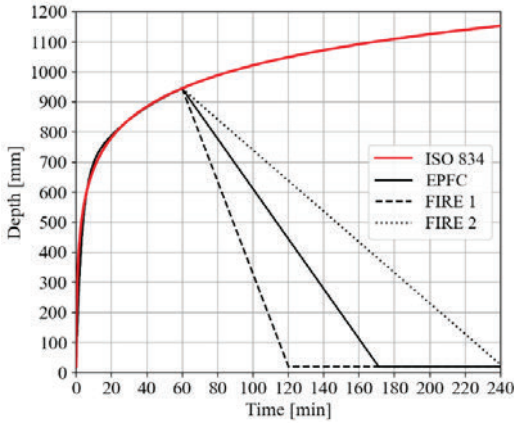

***Figure 10**: Standard fire curve (ISO 834) compared to Eurocode parametric fire curve (EPFC) and other fire curves with different cooling rates (FIRE 1 and FIRE 2, see Section 5).*

The thermal conditions within the timber element are identically calculated using the same heat transfer model in Section 3. Nevertheless, for the cooling phase, various assumptions and simplifications are necessary. The temperature evolution in each investigated node is strongly dependent on material properties, which are temperature-dependent. Once again, the thermo-physical properties of timber at elevated temperature are set according to Eurocode 5 [4]. However, these relationships are relevant and have been validated only for the heating phase, hence it is not known if these material properties can be assumed identical for the cooling phase. This is because certain underlying phenomena are not reversible, for instance water evaporation and thermal decomposition processes. To address this limitation, the timber material properties for the cooling phase are fixed and remain the same depending on the highest temperature reached in each node. This simplification avoids reverse thermal decomposition processes and moisture re-condensation.

4.1 THERMAL CHARACTERISATION AND CHAR DEPTH

The temperature evaluation in the studied material under the exposure of the described Eurocode parametric fire curve (EPFC) is presented in Figure 11. Based on the defined conditions, the heating phase (60 min) is identical to the previous analysis. In contrast, in the cooling phase, the effect of surface cooling on the in-depth temperature and the penetration of the heat wave within the timber element can be observed. The temperature decrease is evident mainly at depths closer to the exposed surface, while this effect decreases with increasing depth. In particular, from 70 mm the temperature evolution almost plateaus within the investigated time period.

The thermal profiles presented in Figure 12 confirm the penetration of the heat wave within the timber cross-section. More specifically, it can be noted the progress of

https://doi.org/10.52202/069179-0226

the char depth (300°C) for 30 minutes into the cooling phase (note 60 min and 90 min thermal gradients). Similarly, the amount of heated wood slowly increases, causing a further reduction of the in-depth timber mechanical properties and therefore an increase of the zero-strength layer.

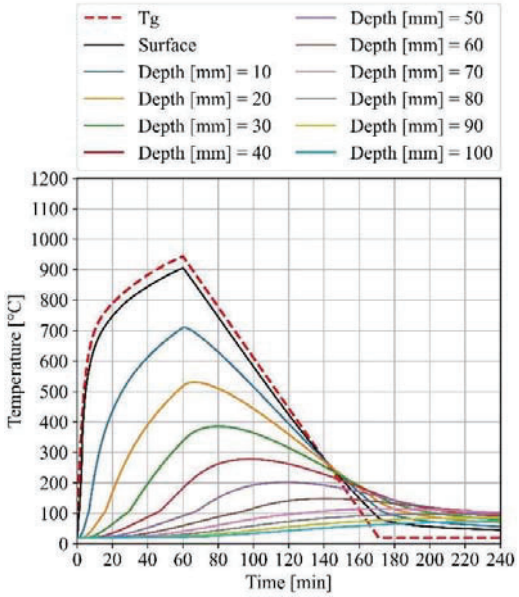

***Figure 11**: Temperature evolution at various depths within the timber substrate.*

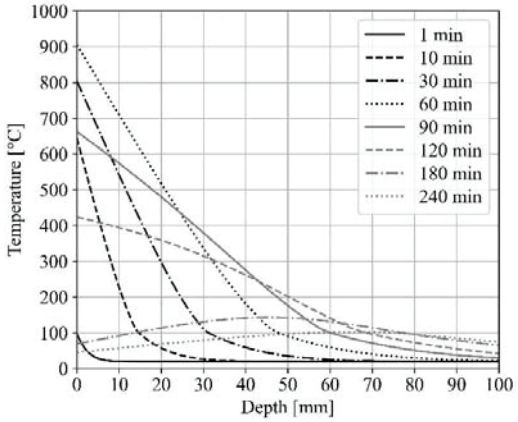

***Figure 12**: Evolution of thermal profiles within the timber substrate at different instants.*

A clearer illustration of this trend is evident through the penetration of the various isotherms (300 ºC, 200 ºC, and 100 ºC) during the fire exposure, presented in Figure 13. The isotherm curves highlight the continuous progression of char front and heat wave into the timber element even during the cooling phase. In particular, the 300°C isotherm evidences how the char front further increase for about 20 minutes during the cooling phase, increasing from 32 mm at the end of the heating phase to the maximum value of 37 mm. Similar conclusions can be drawn for the other isotherm curves, underlying how lower temperatures have a further and longer penetration into the timber cross-section during the cooling phase.

These results are also evident in Figure 14, which displays the penetration speeds of the discussed isotherm curves. Once again, the isotherms of lower temperatures have a higher speed compared to isotherms of higher temperatures, thus the thermal gradients tend to become less steep. In addition, the penetration speeds gradually decrease during the fire exposure. Given the defined thermal boundary conditions, there is a sharp change in the penetration speed of the various isotherm curves a few minutes after the end of the heating phase (note the 300°C isotherm). After this point, the penetration speeds quasi-linearly decrease to zero following specific rates. Consequently, the maximum penetration depths are reached long after the end of the heating phase, causing a further reduction of the timber mechanical properties. For instance, the 100°C isotherm reaches its maximum value about 140 minutes after the end of the heating phase (30 min after the end of cooling phase).

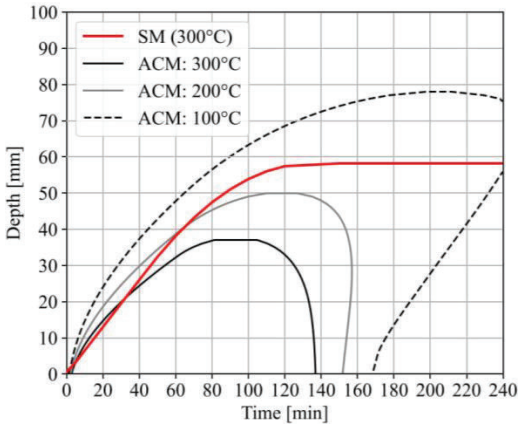

***Figure 13**: Evolution of the isotherms depths (300 ºC, 200 ºC, and 100 ºC) and comparison with EN 1995-1-2 simplified method for parametric fire curves (SM).*

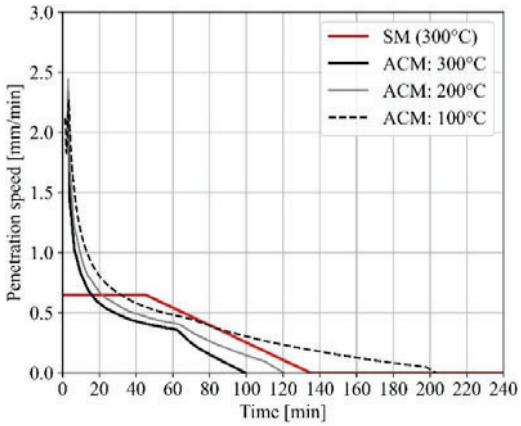

***Figure 14**: Evolution of the isotherms penetration speeds (300 ºC, 200 ºC, and 100 ºC) and comparison with EN 1995-1-2 simplified method for parametric fire curves (SM).*

Special focus is again placed on the 300°C isotherm depths (i.e. char depth) and penetration speed (i.e. charring rate). In particular, in Figure 13, the char depth (300°C isotherm) is compared to the Eurocode 5 simplified method for the parametric fire curve (Annex A) [4]. As in the previous case, the estimation of the char

depth and charring rate according to Eurocode 5 (SM) is a more conservative approach compared to the presented advanced calculation method (ACM).

4.2 ZERO STRENGHT LAYER

Similarly to Section 3.2, once estimated the char depth, it is necessary to analyse the effect of heat penetration within the timber cross-section and the consequent reductions in the mechanical properties. This is done again through the concept of the zero-strength layer (ZSL), which is calculated according to the two previously-described approaches.

As regards to the mechanical properties approach, the reduction factors of the timber mechanical properties are estimated assuming their irreversibility. The reduced mechanical properties are based on the maximum temperature reached in each node, hence the reduction factor remains at the lowest attained value even if the node temperature decreases during the cooling phase. Starting from the thermal gradients shown in Figure 12, the distribution of reduced mechanical properties within the timber section can be obtained for tension and compression. As displayed in Figure 15, the effect of the heat penetration on the timber mechanical is evidenced by the lower reduction factors at higher depths.

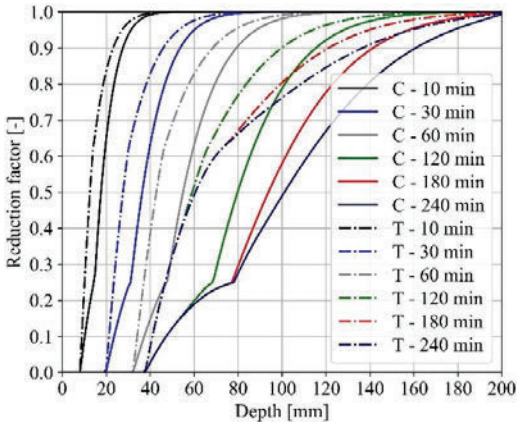

***Figure 15**: Evolution of the reduction factor of timber mechanical properties for compression (C) and tension (T) at different instants*

Figure 16 shows the calculated thicknesses of the zero-strength layer according to the temperature and reduced mechanical properties approaches. As a comparison, the constant value suggested by the Eurocode 5 simplified method (7 mm) is also reported. It is evident how all approaches and assumptions offer different results, with the highest values obtained for the reduced mechanical properties approach for compression and the lowest values for the 120-300°C temperature approach. In general, Figure 16 underlines how the zero-strength layer keeps increasing for a long time after the end of the heating phase and, possibly, the cooling phase. Constant values are achieved for the temperature approaches. In contrast, due to the continuous penetration of the heat wave (and corresponding reduction in the mechanical properties), the zero-strength layer according to the mechanical properties approach does not reach its maximum value even after 1 hour after the end of the cooling phase. Nevertheless, these results evidence how the values of the zero-strength layer at the end of the heating phase are about 2-3 times smaller than the values calculated by including the penetration of the heat wave during and after the cooling phase. When compared to the simplified Eurocode simplified method (SM), it is evident how this approach largely under-estimates the thickness of the zero-strength layer. The presented methodologies predict thickness between 30 and 65 mm, which is up to 10-times greater than the value suggested by the simplified method.

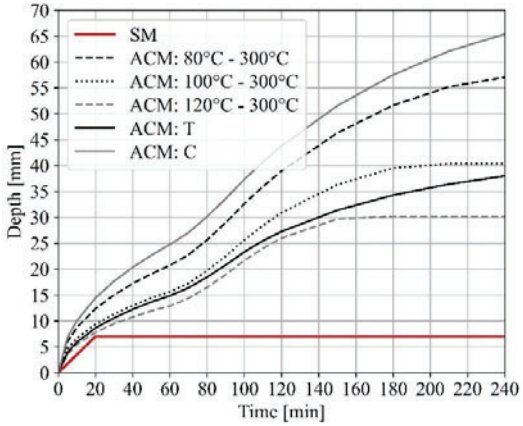

***Figure 16**: Evolution of the zero-strength layer according to temperature and reduced mechanical properties approaches, compared to EN 1995-1-2 simplified method (SM).*

4.3 EFFECTIVE CHAR DEPTH

The results related to the char depth and the zero-strength layer are finally combined to evaluate the structural capacity of timber members. Figure 17 reports the effective char depths obtained following the temperature and reduced mechanical properties approaches, compared to the Eurocode 5 simplified method for parametric fire curves (SM).

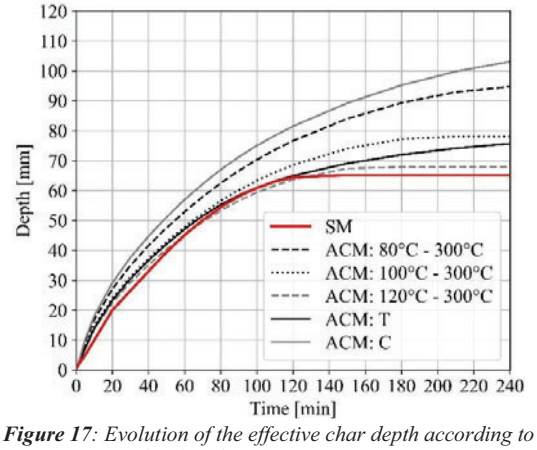

***Figure 17**: Evolution of the effective char depth according to temperature and reduced mechanical properties approaches, compared to EN 1995-1-2 simplified method for parametric fire curves (SM).*

https://doi.org/10.52202/069179-0226

The Eurocode 5 over-estimation of the char depth and important under-estimation of the zero-strength layer lead to a general under-estimation of the effective char depth. The results are only comparable for the 120-300°C temperature approach, which are the lowest values according to the advanced calculation method. Otherwise, the simplified method generally offers less conservative values. For the highest values obtained for the reduced mechanical properties approach (compression), the final effective char depths differ by more than 34 mm (103 mm vs. 68 mm).

5 PARAMETRIC STUDY: COOLING RATE

The previous section has highlighted how the cooling phase of natural fire exposure have a key role in assessment of the heat penetration and the consequent reduction of the mechanical properties of timber structural elements. For this reason, this section investigates the influence of the cooling phase on this problem. Considering the same heating phase defined in Section 3 and Section 4 (standard fire curve for 1 hour), the two additional curves (FIRE 1 and FIRE 2) are introduced, starting from the previous-adopted Eurocode parametric fire curve (EPFC) as the median case. As the EPFC case, the fire curves are characterised by a constant cooling rate. The considered EPFC has a cooling phase from maximum temperature to ambient temperature of about 2 hours, resulting in a cooling rate of about 8.3°C/min. In constant, FIRE 1 has faster cooling (1 hour) and a cooling rate of about 15.4°C/min, while FIRE 2 slower cooling (3 hours) and a cooling rate of about 5.1°C/min. The defined fire curves are shown in Figure 10.

5.1 THERMAL CHARACTERISATION AND CHAR DEPTH

As in the previous cases, the penetration of the heat wave within the timber cross-section can be investigated by analysing the penetration depths and speeds of the various isotherms. In this case, Figure 18 and Figure 19 displays the results for the 300 ºC and 200 ºC isotherms. Similar conclusions to the cases of the standard fire curve and parametric fire curve can be drawn. However, the fire curves characterised by different cooling rates underline the influence of the cooling phase on the penetration of the heat wave. Indeed, even if the thermal boundary conditions defined for the fire exposure are applied at the element surface, these have an evident effect on the distribution of the in-depth temperatures. Both Figure 18 and Figure 19 highlight how lower cooling rates enable higher penetration depths and speeds, and lower temperatures have a further and longer penetration into the timber cross-section during the cooling phase. The penetration speeds quasi-linearly decrease to zero during the cooling phase, after a clear trend change a few minutes after the end of the heating phase.

Focusing on the 300°C isotherm, it can be observed that the final (maximum) char depth is reached much later than the end of the heating phase. In particular, the difference between the char depth at the end of the heating phase and the maximum char depth is directly related to the cooling rate. A slower cooling phase allows a deeper penetration of the char front: 32 mm at the end of the heating phase and a maximum value of 35 mm, 37 mm, and 41 mm for lower cooling rates, respectively. Similar conclusions can be drawn for the other isotherm curves, emphasising the fact that this effect becomes more important for lower temperatures (higher penetration depths and speeds). As a consequence, it can be expected that the cooling phase has an important impact on the reduction of the mechanical properties in heated timber, therefore the zero-strength layer.

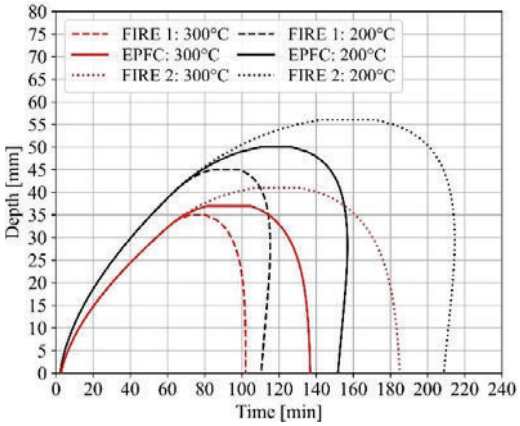

***Figure 18**: Evolution of the isotherms depths (300 ºC and 200 ºC) for different fire exposures.*

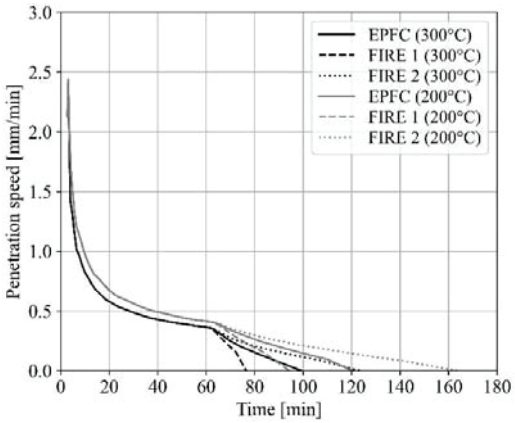

***Figure 19**: Evolution of the 300°C and 200 ºC isotherms penetration speeds for different fire exposures.*

5.2 ZERO STRENGHT LAYER

Starting from the temperature evolutions and in-depth gradients and once estimated the char depth, the zero-strength layer (ZSL) can then be calculated according to the two previous-discussed approaches. Figure 20 displays the calculated thicknesses of the zero-strength layer for the various fire exposures according to the temperature approach, while Figure 21 the ones according to the reduced mechanical properties approach. The results again estimate a large range of thicknesses, from 25 mm to 77 mm), up to more than 10-times the value suggested by the Eurocode 5 simplified method. The numerical results also underline how the zero-strength layer continues to grow for a long duration after the end

https://doi.org/10.52202/069179-0226

of the heating phase and the final value directly depends on the cooling phase. A slower cooling leads to a deeper heat penetration, therefore a higher reduction of the timber mechanical properties and higher zero-strength layer (± 5-10 mm). It was also confirmed that the 120-300°C temperature approach is the least conservative approach and the reduced mechanical properties approach for compression the most conservative. This is again related to the continuous penetration of the heat wave, which proceeds differently according to the investigated temperature: lower temperatures have deeper penetration depths and therefore the zero-strength layer reaches its maximum value at a later instant.

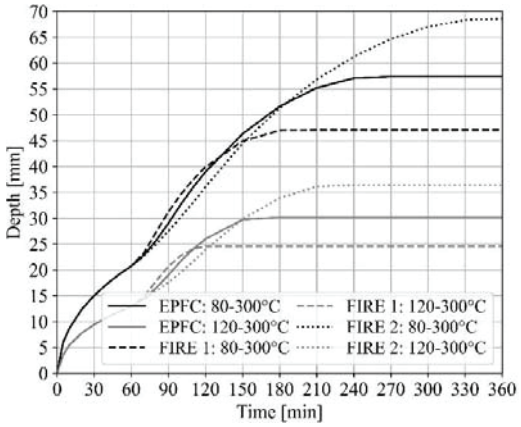

***Figure 20**: Evolution of the zero-strength layer according to the temperature approach (80-300°C and 120-300°C) for different fire exposures.*

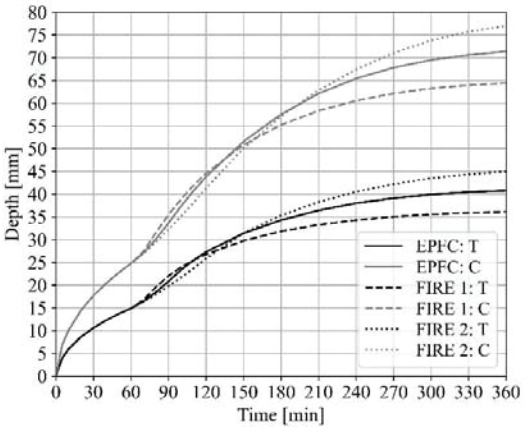

***Figure 21**. Evolution of the zero-strength layer according to the reduced mechanical properties approaches (tension and compression) for different fire exposures.*

5.3 EFFECTIVE CHAR DEPTH

The final effective char depths for the different fire exposures, shown in Figure 22 and Figure 23 and obtained by summing the char depths and the zero-strength layers, offer a similar understanding on the influence of the cooling phase on the structural capacity of timber members. The maximum effective char depths, hence the most critical design conditions, are typically achieved after the end of the fire cooling phase and sit within a wide range of values, from 60 mm to 118 mm.

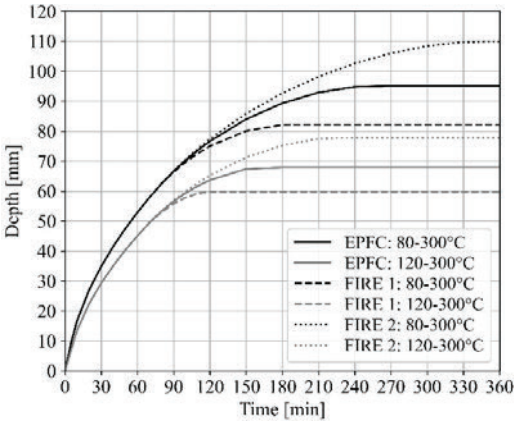

***Figure 22**: Evolution of the effective char depth according to the temperature approach (80-300°C and 120-300°C) for different fire exposures.*

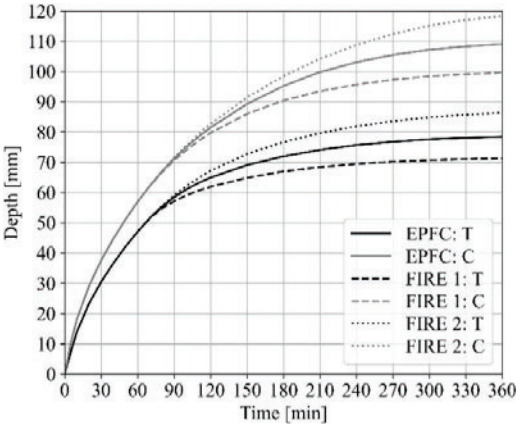

***Figure 23**: Evolution of the effective char depth according to the reduced mechanical properties approaches (tension and compression) for different fire exposures.*

6 CONCLUSIONS

The presented research study focuses on the comparison of the char depth and zero-strength layer determined using the simplified approach suggested by Eurocode 5 and those estimated through an advanced calculation method. The advanced calculation method was based on a finite-difference heat transfer model using effective temperature-dependent material properties. The char depth was calculated as the 300°C isotherm, while the zero-strength layer was determined following two approaches: one based on the timber in-depth temperatures, and one based on the timber reduced mechanical properties (tension and compression).

The first comparison investigated the fire heating phase only, defined according to the standard fire temperature-time curve (120 minutes). For the defined case, it was found that the simplified Eurocode 5 method provides more conservative of char depths from 30 minutes onwards, while the zero-strength layer is generally under-predicted (up to 34 mm, instead of 7 mm). However, the overall comparison revealed that the two methods offer comparable results, with Eurocode 5 being usually less conservative, at least for standard fire durations below 60 minutes.

https://doi.org/10.52202/069179-0226

The influence of the cooling phase on the evolution of the char depth and zero-strength layer was then investigated defining a series of fire exposures: a heating phase of 60 minutes standard fire curve followed by a cooling phase defined according to the Eurocode parametric fire curves, compared to a slower and faster cooling. For all the cooling phases, the heat wave penetration within the timber cross-section led to an increase in the char depth, up to 1 hour after the end of the heating phase. In particular, the difference between the char depth at the end of the heating phase and the maximum char depth is directly related to the cooling rate: a slower cooling phase allowed deeper penetration of the char front. Similar but more pronounced behaviour was also observed for the zero-strength layer. Even for the fastest cooling rate, the zero-strength layer kept increasing for at least 1 hour after the onset of the cooling phase. Accordingly, the maximum effective char depth was typically achieved after the end of the cooling phase.

The research outcomes highlight the importance of including the cooling phase in modern performance-based methodologies for the fire-safe timber structures. It was shown how, during the cooling phase, the load-bearing capacity of timber elements can significantly reduce due to the heat wave penetration and disregarding this phenomenon can lead to important under-estimation, on the unsafe side.

This research study was based on a finite-difference heat transfer model using the effective temperature-dependent material properties suggested by Eurocode 5. Future studies should focus on the effect of various wood species (e.g. density) and wood thermo-physical properties, with various complexities: from various effective material properties for pure conduction heat transfer to the inclusion of models of higher levels of complexity, for instance including the moisture transport and pyrolysis reactions. Also, in this research study, only a few specific heating and cooling phases were investigated, and future studies should cover a broader range of fire exposures to generalise the observed trends. Finally, future research should certainly aim at validating the presented numerical results with experimental data and quantifying the accuracy of the estimated char depth and zero-strength layer approximations, which significantly contribute to the overall effective char depth.

ACKNOWLEDGEMENTS

The authors would like to gratefully acknowledge the financial support for the FRISSBE project within the European Union's Horizon 2020 research and innovation programme (GA 952395).

REFERENCES

[1] Ramage M., Foster R., Smith S., Flanagan K., Bakker R. Super Tall Timber: design research for the next generation of natural structure. *The Journal of Architecture*, 22, 1, 104-122, 2017.

[2] Bartlett A., Hadden RM., Bisby L.A. A Review of Factors Affecting the Burning Behaviour of Wood. *Fire Technology*, 55, 1-49, 2019.

[3] Buchanan A.H., Abu A.K. Structural design for fire safety. *John Wiley & Sons*, 2nd Edition, 2017.

[4] CEN. EN 1995-1-2 Eurocode 5: Design of timber structures – Part 1.2: General – Structural fire design. Brussels, Belgium, 2004.

[5] Drysdale D. An introduction to fire dynamics. John Wiley & Sons Ltd, 3rd Edition, 2011.

[6] Lucherini A., Torero J.L. Defining the fire decay and the cooling phase of post-flashover compartment fires. *Under review*.

[7] Gernay T., Franssen J.M. A performance indicator for structures under natural fire. *Engineering Structures*, 100, 94-103, 2015.

[8] Wiesner F., Bartlett A., Mohaine S., Robert F., McNamee R., Mindeguia J.C., Bisby L. Structural capacity of one-way spanning large-scale Cross-Laminated Timber slabs in standard and natural fires. *Fire Technology*, 57, 291-311, 2021.

[9] Gernay T. Fire resistance and burnout resistance of timber columns. *Fire Safety Journal*, 122, 103350, 2021.

[10] Gernay T., Zehfuß J., Brunkhorst S., Robert F., Bamonte P., McNamee R., Mohaine S., Franssen J.-M. Experimental investigation of structural failure during the cooling phase of a fire: Timber columns. *Fire and Materials*, 1-16, 2022.

[11] Wiesner F., Hadden R., Deemy S., Bisby L. Structural fire engineering considerations for cross-laminated timber walls. *Construction and Building Materials*, 323, 126605, 2022.

[12] Wiesner F., Bisby L.A., Bartlett A.I., Hidalgo J.P., Santamaria S., Deeny S., Hadden R.M. Structural capacity in fire of laminated timber elements in compartments with exposed timber surfaces. *Engineering Structures*, vol. 179, pp. 284-295, 2019.

[13] Schmid J., Just A., Klippel M., Fragiacomo, M. The reduced cross-section method for evaluation of the fire resistance of timber members: discussion and determination of the zero-strength layer. *Fire Technology*, 51, pp.1285-1309, 2015.

[14] Emmons H.W. The numerical solution of heat conduction problems, Transactions of the American Society of Mechanical Engineers, 65(6), 607-615, 1943.

[15] Dusinberre G.M. Heat Transfer Calculations by Finite Differences, International Textbook Company, Pennsylvania, USA, 1961.

[16] Lucherini A. Fundamentals of thin intumescent coatings for the design of fire-safe structures. PhD thesis, School of Civil Engineering, The University of Queensland, 2020.

[17] European Committee for Standardization (CEN). EN 1991-1-2 Eurocode 1: Actions on structures – Part 1.2: General actions – Actions on structures exposed to fire. Brussels, Belgium, 2002.

[18] Huc S., Pečenko R., Hozjan T. Predicting the thickness of zero-strength layer in timber beam exposed to parametric fires. *Engineering Structures*, 229, 111608, 2021.

World Conference on Timber Engineering Oslo 2023

EXPERIMENTAL AND FINITE ELEMENT ANALYSIS OF IRISH SITKA SPRUCE CLT WALL PANELS UNDER EXPOSURE TO STANDARD FIRE CONDITIONS

Muhammad Yasir[1], Conan O'Ceallaigh[2], Kieran Ruane[3], Andrew Macilwraith[4]

ABSTRACT: Cross-laminated timber (CLT) is a sustainable engineered timber product. The fire behaviour of cross-laminated timber (CLT) is a significant concern due to its combustible nature. Currently, there is limited data available on the performance of charring of CLT panels made from C16 grade timber under fire. In this research, an experimental and numerical investigation of CLT floor panels exposed to a standard fire i.e., ISO 834 was performed. The CLT floor panels were manufactured from C16 grade Sitka spruce grown in Ireland. Overall, four CLT floor specimens were tested using standard heating conditions. The charring rate and temperature distribution at different depths from the fire-exposed face of the CLT panel were studied. The test panels were also protected with different protective claddings and the delay in charring of the CLT panel provided by these claddings is presented. Furthermore, a 2D finite element (FE) model was developed and the results from the FE model were compared with experimental results that show a good correlation in terms of the charring rates and temperature distributions.

KEYWORDS: Charring rate, Cross-laminated timber, Finite element analysis, Fire testing, Sitka spruce.

1 INTRODUCTION

Cross-laminated Timber (CLT) consists of at least three layers of timber boards that are glue bonded orthogonally. CLT is gaining popularity due to its enhanced structural capabilities compared to traditional timber construction methods and its simple erection process. The fire behaviour of CLT is an important research aspect and therefore the investigation of fire analysis of timber products has increased in the past few years. For the fire design of timber structures exposed to ISO 834 [1], two simplified methods i.e., the reduced cross-section method and the reduced properties method are presented in Eurocode 5 [2]. The former method measures the charred depth of timber by considering that the char will occur at a uniform charring rate of 0.65 mm/min for solid timber with a density greater than 290 kg/m^3. Furthermore, a section of 7 mm, called the zero-strength layer adjacent to the charred area that is considered to have zero load-bearing capacity, will be added to the char depth.

Timber undergoes thermal degradation upon heating which passes through different stages to reach the decay phase [3]. During the thermal degradation of timber, combustible gases evolve in addition to a mass loss which results in the formation of a char layer. The lower thermal conductivity of the char layer protects the inner section of the timber from heating up rapidly until cracks appear in the char layer causing heat penetration to the unburnt timber [4]. The degradation of timber on heating and fire behaviour can be analysed in terms of charring rate. Various factors that affect the charring rate include the type of wood, density, heat flux and ventilation conditions [4]. Eurocode 5 (EC-5) [2] uses the simplified one-dimensional charring rate β_0 for solid and glue-laminated timber panels with a density of more than 290 kg/m^3 when exposed to standard fire conditions i.e., ISO 834 [1]. A notional charring rate β_n is used to consider the effect of corner rounding in beams and columns which leads to an increase in the charring at the corner of the cross-section. The one-dimensional and notational charring rates for different wood products from EN 1995-1-2 are shown in Table 1.

Both experimental [3, 4] and numerical investigations [5]–[8] have been performed on the fire behaviour of CLT panels. The studies performed by Friquin et al. [3] show that the fire behaviour and charring rates of CLT panels largely depend on the fire curves. High temperatures and fast temperature growth of a fire curve led to a higher charring rate compared to fire curves with slower temperature growth and low peak temperatures. The magnitude and duration of the charring peak of CLT depend on the rate of heating, the test setup, as well as the size of the test sample and its orientation [5]. A series of 5-layer CLT floor panels were tested when exposed to Standard temperature conditions by Fragiacomo et al. [11]. The authors found that the CLT panels which were directly exposed to fire exhibited similar charring rates as given in the Eurocode 5. Furthermore, the finite element

[1] Muhammad Yasir, Munster Technological University, Ireland, muhammad.yasir@mycit.ie
[2] Conan O'Ceallaigh, University of Galway conan.oceallaigh@universityofgalway.ie
[3] Kieran Ruane, Munster Technological University, Ireland, Kieran.Ruane@mtu.ie
[4] Andrew Macilwraith, Munster Technological University, Ireland, Andrew.Macilwraith@mtu.ie

https://doi.org/10.52202/069179-0227

(FE) model showed a good correlation in predicting the charring rates with that of the experimental results [11].

Table 1: *Charring rate as per the EN 1995-1-2 [2]*

Material	β_0 (mm/min)	β_n (mm/min)
Softwood and beech Glued laminated timber with a characteristic density of 290 kg/m^3	0.65	0.70
Solid timber with a characteristic density of 290 kg/m^3	0.65	0.8
Hardwood Solid or glued laminated hardwood with a characteristic density of 450 kg/m^3	0.50	0.55
Panels*		
Wood paneling	0.9	
Plywood	1.0	
* The one-dimensional charring for the panels is applied to a panel thickness of 20 mm or more with a characteristic density of 450 kg/m^3.		

The behaviour of CLT can be different from solid timber in a fire. Experimental tests have been performed to study different factors that affect the fire performance of CLT including the behaviour of the adhesive [12], layer thickness and the number of layers [12]–[14], the effect of protective cladding [11, 15], and calculation of a zero-strength layer [7].

Numerical models are often developed to extend the experimental results and to avoid expensive fire tests [10], [15]–[18]. Validated numerical models can be useful tools to examine the behaviour of CLT in a multitude of different fire-loading situations, ensuring compliance with design standards and can significantly increase the safety associated with CLT in construction. Wong, B.V.Y [10] developed a 2D FE modelling to simulate the thermal behaviour of CLT when exposed to a standard fire and found good agreement with the experimental results.

Similarly, Wang et al. [19] developed a FE model which was validated with experimental fire test results and it was shown to accurately simulate the thermomechanical behaviour of the CLT panel under elevated temperatures. While CLT has been used as an exposed surface in many structures, there are also alternative finishes that are commonly used to protect the CLT from direct exposure to fire which include gypsum plasterboard. Gypsum plasterboard is a protective cladding that is widely used as a fire protection system due to its easy installation, ready availability, and high specific heat capacity [20]. Gypsum plasterboards are non-combustible and are commonly available in two thicknesses i.e., 12.5mm and 15mm. At a temperature of up to 100°C during a fire, the gypsum plasterboard absorbs a significant amount of heat to remove water causing delays in the development of high temperatures until the whole board is dehydrated. Furthermore, the low thermal conductivity of the gypsum plasterboard keeps the unexposed surface of the plasterboard at lower temperatures [21].

For the CLT panels which are initially protected, the following will need to be considered:

- The charring behind the protective cladding is delayed until time t_{ch}, where t_{ch} is the time at which the charring behind the protective layer starts.
- The charring behind the cladding can start before the failure of the protective layer with a lower charring rate until the failure time t_f of the fire protection as shown in Figure 1. After the failure of protective cladding (t_f), the charring rate increases in line with the values shown in Table 1, from the EN 1995-1-2, until time t_a, where t_a is the time at which a char depth of 25 mm has been made.
- The charring rate returns to the value given in Table 1 of EN 1995-1-2 at a time t_a when the charring depth is either 25 mm or equal to the charring depth of the same member without fire protection.

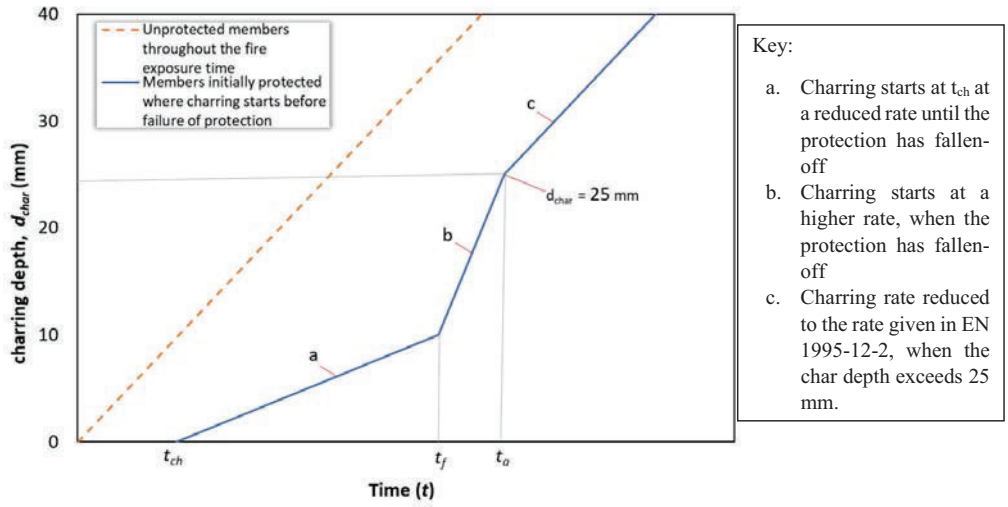

Figure 1*: Variation of the charring depth when for* $t_{ch} < t_f$ [2]

https://doi.org/10.52202/069179-0227

In recent years, considerable efforts have been made to focus on the fire analysis of CLT panels. However, the fire behaviour of CLT can vary for different timber species. Limited research studies have been conducted on the fire analysis of CLT floor panels made of Irish spruce which is characterised as a low-density timber due to the rapid growth conditions in Ireland and typically achieves a C16 structural grade. In this study, Irish spruce CLT floor panels were tested under exposure to standard temperature conditions. Furthermore, an FE analysis was carried out and validated against the experimental results creating an FE tool for CLT elements manufactured from Irish-grown Sitka spruce to be modelled in more significant and severe conditions.

2 EXPERIMENTAL TESTING

2.1 Materials

Boards of C16 grade Irish Sitka spruce were used to produce CLT floor panels that were 970 mm long and 500 mm wide. Boards used in the production of CLT floor panels were conditioned at a relative humidity of 65% ± 5% and a temperature of 20 °C ± 2°C. For the preparation of CLT panels, one-component polyurethane (PUR) adhesive was applied on the surface of the lamellae at a spread rate of 0.0160 microns/cm^2. The pressing of the panels was performed using steel plates to apply a pressure of 60 N/cm^2 for 120 mins. The panels were placed again in the conditioning chamber before the experimental tests to ensure and limit the moisture content of the specimens.

2.2 Test Specimens

The experimental work was carried out at the Structural Engineering laboratory of the Munster Technological University (MTU). A total of four CLT floor panels were tested in the fire-testing kiln under ISO standard heating conditions [1]. Three and five lamellae CLT lay-up configurations were studied having an overall thickness of 110 mm and 140 mm, respectively. All the CLT panels were simply supported and a constant concentrated load of 0.8 kN was applied at the mid-span throughout the fire testing. A deflection gauge was installed to measure and record the deflection at the mid-span during the testing. Specimen details and test setup for both the 3-layer and the 5-layer CLT panels are shown in Figure 2. The tested CLT panels were manufactured from Irish Spruce timber having a measured average density of 381 kg/m^3 at a 12% moisture content (MC). The measured average moisture content was 11.5-12.5% prior to the testing. The details of specimens and test configurations are provided in Table 2. Specimens A-1 and B-1, which comprised 3 layers and 5 layers, respectively received no protective cladding. The exposed surfaces of the remaining 3-layer and 5-layer CLT panels were protected with different protective claddings. The 3-layer CLT panel was protected with two different protective cladding configurations i.e., a combination of 12.5 mm Fireline gypsum plasterboard (FP) and 12.5 mm plywood (PW). The exposed face of the 5-layer CLT panel was protected with a 12.5 mm Fireline gypsum plasterboard.

2.3 Placement of thermocouples

The temperature of the kiln was monitored throughout the test and each CLT panel was instrumented with thermocouples (TC). A plate thermometer was used to record the temperature in the kiln during the test. Type K TCs were inserted in a drilled hole from the side of the CLT panels at different depths, to record the internal temperature distribution and the progression of the char line during fire testing. The thermocouples were strategically placed at the interfaces between different layers of the CLT panels as well as between the fire-protective cladding and the CLT panel. The details of the thermocouple tip location and its depth from the exposed surface are shown in Table 3.

3 RESULTS

Different researchers defined the charred front at different temperatures in timber due to the high-temperature gradient. In this study, the charred front which is a transition between charred wood and pyrolysis layer is considered to be at the 300˚C isotherm as defined in EN

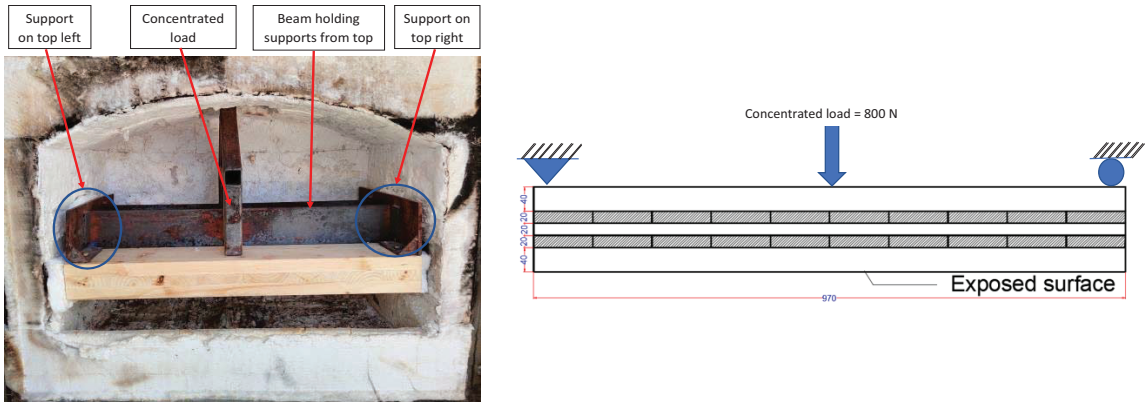

a. b.

Figure 2: *a. 3-layer CLT floor panel in the kiln b. Drawing and layout of 5-layer CLT panel*

https://doi.org/10.52202/069179-0227

Table 2: *Test specimen details*

Specimen	layers	Layers layout (mm)	Panel thickness (mm)	Protection on the exposed side
A-1	3	40-30-40	110	No
A-12.5FP12.5PW	3	40-30-40	110	12.5 mm Fireline gypsum plasterboard and 12.5 mm Plywood
B-1	5	40-20-20-20-40	140	No
B-12.5FP	5	40-20-20-20-40	140	12.5mm Fireline gypsum plasterboard

1991-1-2. The charring rate of CLT panels and their individual layers were measured by considering the temperature measured at various TCs from the exposed surface. For CLT panels which were protected with different protective claddings, the charring rate of the outermost layer is taken when the temperature at the interface between the protective claddings and the CLT panel reaches 300˚C.

3.1 Temperature distribution

The temperatures recorded at different depths of the CLT panels using K-type TCs for all fire tests are shown in Figure 3. Moreover, the kiln temperature was recorded using a plate thermometer, ensuring the experimental fire curve is comparable with the ISO-834 curve heating conditions.

It can be seen from Figure 3 (a-d), the temperature of the kiln closely followed the standard fire curve in all tests. It can also be observed from the temperature-time curves, that the temperature at different depths of the CLT panels plateaus at around 100°C which was then followed by a rapid rise in temperature. This can be attributed to the loss of water at around 100 ˚C to 120˚C which also results in a decrease in the density as well as a decrease in specific heat capacity. In panels which were initially protected with different claddings, the temperature distribution at the interface between the CLT panel and cladding demonstrates the same trend. In all protected panels, the temperature behind the cladding reached the kiln temperature when the interface temperature between the CLT panels and the cladding was around 700°C and 800°C. This quick rise in temperature behind the claddings indicates that the fall-off of the protective cladding occurs when the temperature of the inner face of the cladding reached approximately 700°C and above.

3.2 Charring rate

The charring rate of the CLT panels and their individual layers were measured by considering the temperature measured at various TCs and their respective depths from the exposed surface. The char line which is a transition between charred wood and the pyrolysis layer is taken at the 300°C isotherm as given in the EC-5 (EN 1995-1-2). The temperature recorded by TCs installed at various depths of the CLT panels was used for measurement of the charred depth with time which in turn gives the charring rate. The charring rate calculated from TCs data at different depths of the CLT panels is illustrated for each specimen in the right column of Figure 3. It can be observed that in an unprotected CLT floor panel (Figure 3a (A-1), and Figure 3c (B-1)), the charring rate calculated throughout the cross-section of the CLT panels was close to the one-dimensional charring rate of 0.65 mm/min as defined in the EC-5. The CLT panels which were initially protected with different claddings showed a delay in the charring of the CLT panels as expected. The charring of the CLT panels was then started with a lower rate as shown in the right column of Figure 3 (c) and (d). The lower charring rate was followed by a sudden higher charring rate which is due to the fall-off of the protective cladding on the exposed face of the CLT. The fall-off of the cladding exposes the CLT panel directly to fire and thus the char rate increases. The fall-off of the claddings happens in all tests at around 70 min to 80 min from the start of the fire which can be observed from the sudden increase in temperature between the CLT panel and the exterior cladding. The temperature recorded by the thermocouple placed between the CLT panel and protective cladding is shown by TC0 in Figure 3. (b), and (d).

Table 3: *Location of thermocouples from the exposed face of the CLT panel to fire*

Specimen	Between two claddings	Between cladding & CLT panel	Thermocouples depth from the exposed surface of CLT panels (mm)						
			20	30	40	50	60	80	100
A-1	-	-	-	TC30	TC40	TC50	TC60	TC80	-
A-12.5FP12.5PW	TC-12.5	TC0	TC20	-	TC40	-	TC60	TC80	-
B-1	-	-	-	TC30	TC40	-	TC60	TC80	TC100
B-12.5FP	-	TC0	TC20		TC40	-	TC60	TC80	-

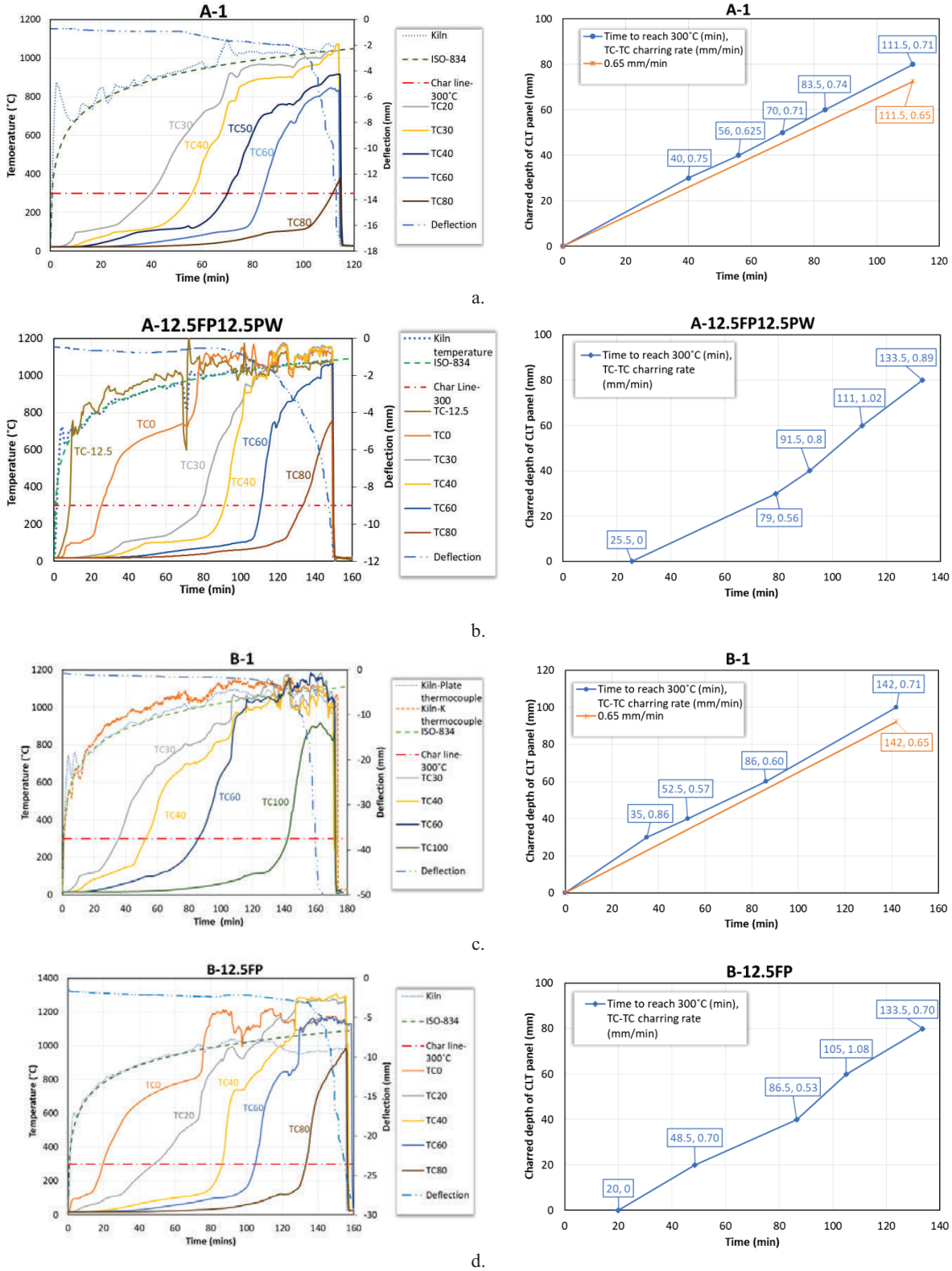

Figure 3: *Left column: Temperature-time curves of test panels, Right column: Charring rate from TC-TC, (a) A-1, (b) A-12.5FP12.5PW, (c) B-1, (d) B-12.5FP*

https://doi.org/10.52202/069179-0227

The charring rate of plywood from EN 1995-1-2 with a thickness of less than 20 mm is given in Equation (1).

$$B_{0,\rho,t} = \beta_0 * k_\rho * k_h \quad (1)$$

Where, $k\rho = \left(\frac{450}{\rho k}\right)^{0.5}$, $kh = \left(\frac{20}{hp}\right)^{0.5}$

h_p is the thickness of the panel in millimetres and ρ_k is the characteristic density in kg/m^3.

The charring rate from Equation (1) for a 12.5 mm plywood layer is 1.10 mm/min while the experimental testing gave a higher charring rate of 1.47 mm/min.

It can be observed from the charred depth-time curves of protected panels as shown in the right column of Figure 3 (b), and (d), that the charring behind the protective cladding is delayed until time t_{ch}. It can also be observed that the charring behind the cladding started at a reduced rate, while the protective layer is still up against the CLT panel. However, an increase in the charring rate was observed after the failure of the protective claddings in all protected test panels. The overall charring rate at the end of the fire tests for all panels is shown in Figure 4 (a). The overall charring rate of both unprotected 3-layer and 5-layer CLT panels were 0.71 mm/min and 0.70 mm/min, respectively, which is slightly higher than the one-dimensional charring rate of 0.65 mm/min as defined in EC-5 for glue laminated or solid timber with densities greater than 290 kg/m^3. The charring rate calculated for initially protected panels after the charring begins was at a similar rate to unprotected panels. This shows that the protective cladding initially delays the charring of the CLT panel. However, after the CLT panel starts charring, the char rate remains similar to the unprotected panel, if it's exposed to fire for a longer duration. This shows that the protective cladding only delays the charring of the CLT panels, and it still chars at a similar rate if it's exposed to fire for a longer duration.

3.3 Effect of protective cladding on the delay of charring

Protective claddings provided at the exposed face of the CLT panel delayed the charring of the test specimens. The delay in charring of the CLT panels provided by different claddings on the exposed face of the CLT panel to fire in terms of time (mins) is given in Figure 4 (b). The 12.5 mm FP gives a protection time of 20 mins when used on the exposed face of a 5-layer CLT floor panel. A combination of 12.5 mm FP and 12.5 mm PW delayed the charring of the CLT panel by 25.5 mins. It was observed that the temperature at the interface between the exterior 12.5 mm PW layer and the inner 12.5 mm FP reached 300˚C in 8.5 mins. EN 1995-1-2 [2] provides the relation as given in Equation 2 to measure the start of charring of the CLT panel behind the gypsum type A or F plasterboards at internal locations or the perimeter adjacent to filled joints. The delay in charring of the CLT panels calculated using Equation 2. for type A and type F plasterboards are 21 mins, which is very close to the experimental values of 20 mins as calculated in this research for 12.5 mm FP.

$$t_{ch} = 2.8h_p - 14 \quad (2)$$

Where h_p is the thickness of the protective cladding.

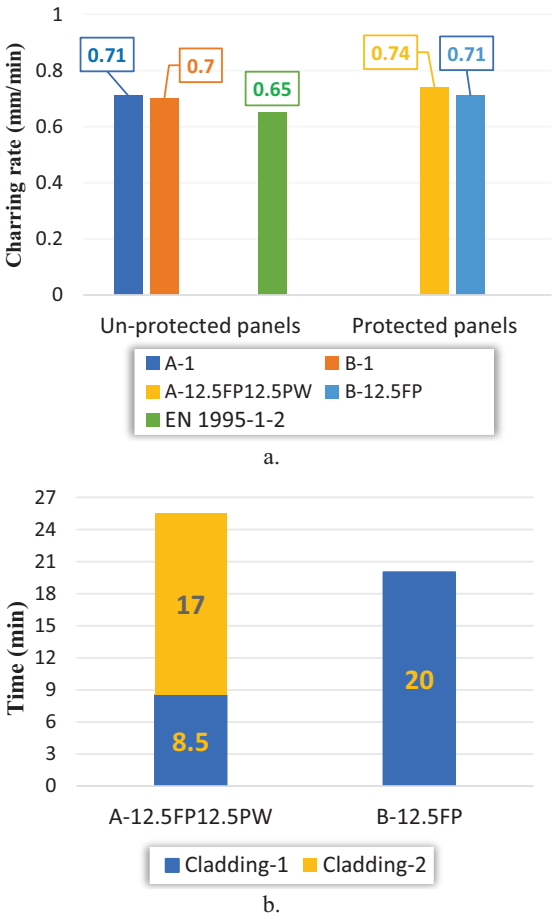

Figure 4: *a) Charring rate for tested CLT panels, b) Fire protection provided by different cladding configurations.*

4 NUMERICAL ANALYSIS

The numerical FE analysis was carried out in Abaqus FE software. The 2D model of the CLT panel was developed in full length with the load and supporting conditions, material properties, and exposure to fire applied. The element type considered for this analysis was CPE4T which is a 4-node plane strain thermally coupled quadrilateral, bilinear displacement and temperature. Thermomechanical analysis which is a sequential thermal stress analysis was performed for all CLT panels. The analysis was performed in 2 steps. In step one, the load was applied to the CLT panel followed by the fire exposure of the CLT panel in the second step.

4.1 Material properties

The mechanical properties of the C16 timber both in parallel and orthogonal orientation were applied to the model. In this research, the EC-5 temperature-dependent modulus of elasticity model was used. The material properties were taken from the research performed on similar wood by O'Ceallaigh et al. [22]. The temperature-dependent thermal properties of the timber including the conductivity, specific heat and density relationships were used as defined in the EN 1995-1-2 [2]. As recommended

by EN 1991 and EN 1995-1-2, the convection coefficient and emissivity were taken as 25 W/(m^2.K) and 0.8, respectively. In addition to the thermal properties provided by EC-5, the FE analysis was also performed using modified values of conductivity at higher temperatures as shown in Table 4. In order to make the analysis simpler, the conductivity values of timber given by EC 5 were adopted to consider the effect of faster charring and quick temperature raise after the layer's fall off.

A mesh sensitivity study was carried out and an element size of 10 mm was used in all CLT panels to ensure adequate accuracy in the results as well as to obtain temperature data for the nodes in a similar location to the location of thermocouples in the experimental testing. For the CLT panel which was initially fire-protected with plywood and plasterboard, the plywood has not been modelled due to the unavailability of its thermal properties at higher temperatures as well as its negligible mechanical resistance.

Table 4: *Temperature-dependent thermal conductivity used in FE analysis*

New Proposal	EC-5	Temperature
W. m^{-1}. K^{-1}		(°C)
0.12	0.12	20
0.15	0.15	200
0.07	0.07	350
0.09	0.09	500
0.35	0.35	800
0.5	-	850
1	-	900
2	-	950
10	1.5	1200

4.2 FE results and comparisons with experimental tests

In all of the experimental tests, the temperature of the kiln closely followed the Standard fire curve [1]. Therefore, the standard heating conditions were applied on the exposed face to fire in the FE analysis of initially unprotected panels. The comparison of experimental and FE results in terms of the overall charring rate from the fire-exposed side of the CLT panels was made and is shown in Table 5. It can be observed from Table 5 that the charring rate predicated using the model proposed in this research gives a closely matching charring rate to that of experimental fire testing. The charring rate predicated using EC-5 thermal properties gives a lower charring rate than the experimental results. This is partially due to the fact that thermal properties in EC-5 are presented for solid or glue-laminated timber which doesn't consider the effect of delamination, which usually happens in horizontal CLT panels. Furthermore, the char layer provides extra protection to timber from direct exposure to fire and thus reduces its overall charring rate. Thus the effect of an increase in the charring rate due to the fall off of sections of charred timber is needed to be considered in the thermal analysis. A simplified procedure to consider a higher charring rate after the layers charred has been included in the FE model which is validated with the experimental results. This is performed by using higher thermal conductivity values for a temperature of more than 800°C to avoid considering the complexity of modelling the char fall-off in the numerical simulation. In Figure 5, the charred depth at 60 mins from the start of the fire test from the FE analysis is shown for B-1 and B-12.5FP panels using the EC-5 thermal properties with the conductivity values taken from the new proposal as shown in Table 4. The charred depth of the CLT panels in Figure 5 is represented by a grey colour while the pyrolysis layer is shown in red.

Furthermore, the temperature distribution at different depths from the exposure of a panel to fire from experimental tests is compared with the FE analysis and is shown in Figure 6. It can be observed that the temperature-time curves for both experimental tests and FE results using the new proposal follow a similar trend to reach the char line temperature (i.e., 300˚C). Overall the temperature distribution from the numerical analysis, which is predicated using thermal properties given in EC-5 gives lower temperature distribution than the experimental results. The temperature-time curves from the FE analysis using EC-5 thermal properties follow a similar trend to that of the experimental results for the first hour of the FE analysis. The difference in the time to reach the char line temperature from FE analysis using EC-5 was higher than the experimental results for a longer duration of tests. On the other hand, the proposed model not only gives a good approximation of the char depth but also closely predicts the time to reach the char line temperature and the charring rate well.

Table 5: *Comparison of experimental and FE results*

Specimen	Overall charring rate (mm/min)		
	Exp	FEM	
		New Proposal	EC-5
A-1	0.72	0.71	0.58
A-12.5FP12.5PW	0.70	0.76	0.68
B-1	0.70	0.71	0.61
B-12.5FP	0.71	0.73	0.71

https://doi.org/10.52202/069179-0227

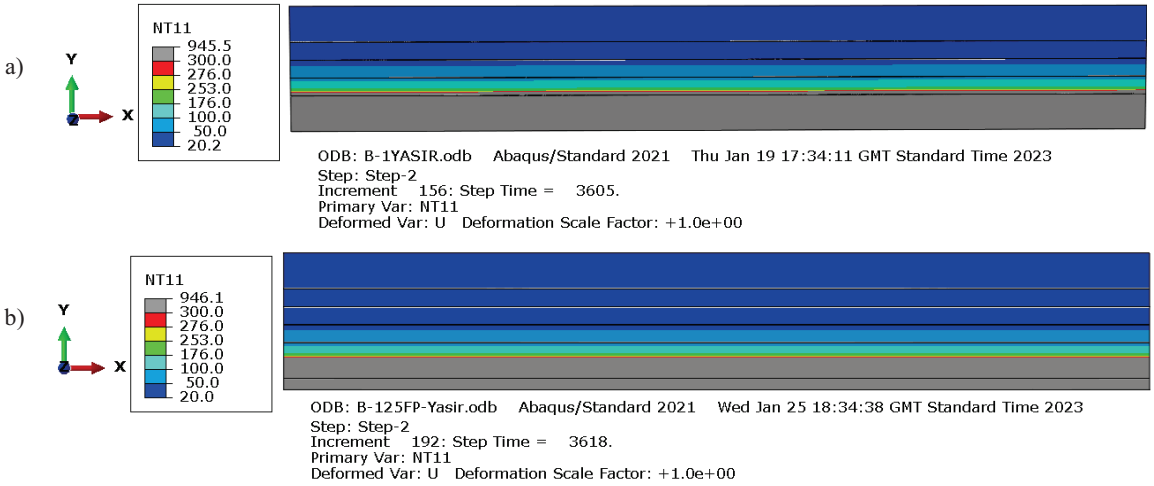

Figure 5: *Visualization of charred depth at 60 mins from FE analysis, a) B-1, b) B-15FP*

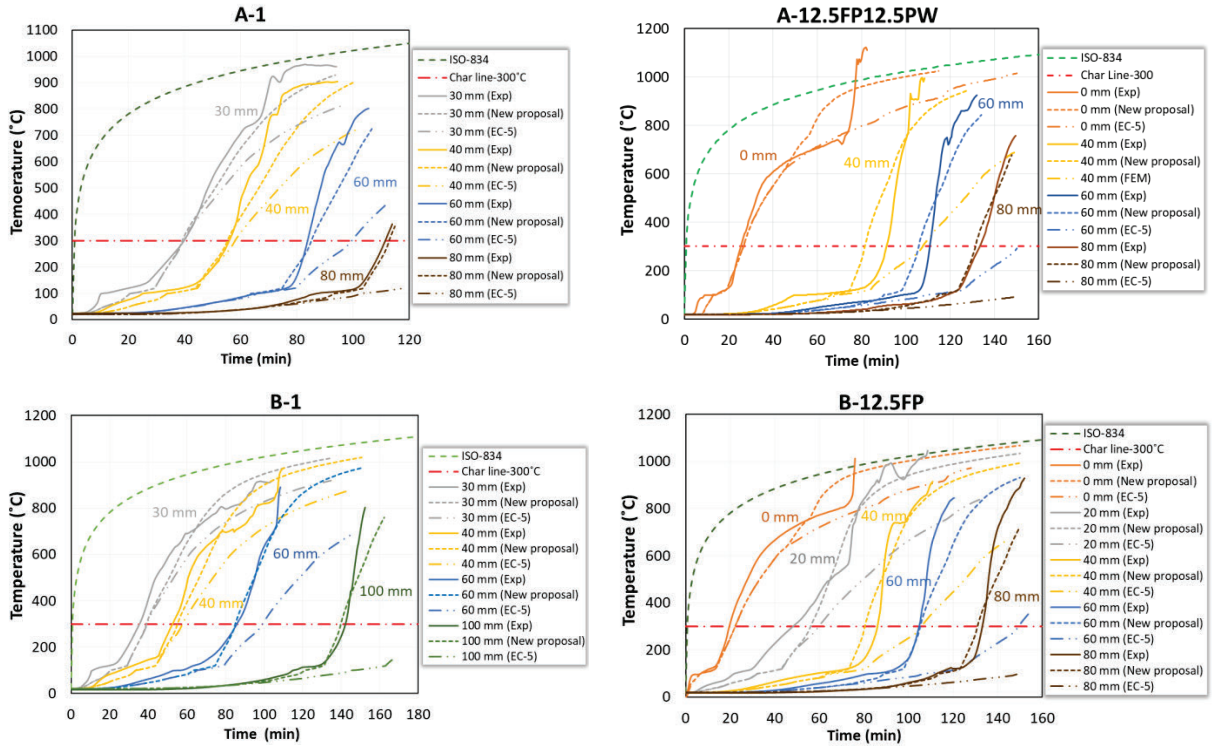

Figure 6: *Comparison of temperature distribution at the interfaces of layers of experimental tests and FE analysis*

5 CONCLUSIONS

The experimental testing of CLT floor panels made from C16 Grade Irish Sitka spruce was performed to measure the charring rate under ISO-834 standard heating conditions. Different protective claddings were used on the fire-exposed side of the CLT panels to determine their effectiveness in delaying the charring of the CLT panels. The main conclusions drawn from the experimental testing and FE analysis are as follows:

- The charring rate of both 3-layer and 5-layer unprotected CLT panels is 0.71 and 0.70 mm/min respectively, which is slightly higher than the one-dimensional charring rate given by the Eurocode 5 (EN 1995-1-2). No significant difference in the effect of the thickness of CLT layers was observed on the charring rate.
- The 12.5 mm Fireline gypsum plasterboard delayed the charring of the CLT panels by 20 minutes. A combination of a 12.5 mm Fireline gypsum

plasterboard with a 12.5 mm plywood protects the CLT panel from charring by 25.5 minutes.

- All CLT panels which were initially protected using different protective claddings give an overall charring rate of 0.70 mm/min to 0.71 mm/min. A higher charring rate was observed after failure and fall off of the fire protective cladding.
- In all of the panels with a protective layer, the charring of the CLT panels started while the protective cladding was still intact with the panels. In all of the panels, the protective claddings fall off around 70 mins to 80 mins from the start of the test.
- It was observed that the protective layer on the fire-exposed face of the CLT panels delayed the start of charring of the CLT panels. However, there is no significant difference in the overall charring rate of both unprotected and initially protected CLT panels at the end of the fire test.
- A 2D FE model was developed in Abaqus with a new proposal to consider higher values of conductivity than that defined in EC-5 for temperatures more than 800°C. The results from the FE analysis using the new proposal were shown to be in good agreement with the temperature distribution and charring rate of the experimental testing of the CLT panels. The FE analysis using the new proposal demonstrated good agreement with the experimental results in terms of charring rate and time to reach the charring temperature compared to the FE analysis performed using EC-5 thermal properties.
- The validated FE model may now be used to analyse a series of different fire loading conditions, panel lay-ups and protective measures for C16 Grade material and will serve as a useful tool to improve the safety and reliability of timber structures subject to fire loading.

ACKNOWLEDGEMENTS

The MODCONS Project is a joint project between the Timber Engineering Research Group at the University of Galway and Munster Technological University focused on increasing the knowledge and use of timber in modular construction. The MODCONS Project is funded by the Irish Department of Agriculture, Food and the Marine Competitive Research Funding Programmes (Project Ref: 2019R471).

REFERENCES

[1] ISO 834-1, Fire Resistance Test - Elements of Building Construction, Part 1: General Requirements, International Organization for Standardization ISO 834, Geneva, Switzerland, 1999.

[2] 'European Committee for Standardisation (CEN). Eurocode 5. Design of timber structures. Part 1-2: General – Structural fire design; EN1995-1-2. Brussels, Belgium, 2004.'

[3] K. L. Friquin, M. Grimsbu, and P. J. Hovde, 'Charring rates for cross-laminated timber panels exposed to standard and parametric fires', presented at the World Conference on Timber Engineering, 2010, p. 9.

[4] A. Frangi and M. Fontana, 'Charring rates and temperature profiles of wood sections', Fire Mater., vol. 27, no. 2, pp. 91–102, Mar. 2003, doi: 10.1002/fam.819.

[5] A. I. Bartlett, R. M. Hadden, L. A. Bisby, and A. Law, 'Analysis of Cross-Laminated Timber Charring Rates upon Exposure to Non-standard Heating Conditions', presented at the Fire and Materials, San Francisco, USA, 2015, p. 16.

[6] S. van der Westhuyzen, R. Walls, and N. de Koker, 'Fire tests of South African cross-laminated timber wall panels: fire ratings, charring rates, and delamination', J. S. Afr. Inst. Civ. Eng., vol. 62, no. 1, 2020, doi: 10.17159/2309-8775/2020/v62n1a4.

[7] R. Dârmon and O. Lalu, 'The fire performance of Cross Laminated Timber beams', Procedia Manufacturing, vol. 32, pp. 121–128, 2019, doi: 10.1016/j.promfg.2019.02.192.

[8] T. T. Tran, M. Khelifa, A. Nadjai, M. Oudjene, and Y. Rogaume, 'Modelling of fire performance of Cross Laminated Timber (CLT) panels', J. Phys.: Conf. Ser., vol. 1107, p. 032002, Nov. 2018, doi: 10.1088/1742-6596/1107/3/032002.

[9] M. Aguanno, 'Fire resistance tests on cross-laminated timber floor panels: an experimental and numerical analysis.', Master of Applied Science thesis, Ottawa-Carketon Institute of Civil and Environmental Engineering, 2014.

[10] B. V. Y. Wong, K. F. Tee, and T. M. Yau, 'Numerical Study of Cross-Laminated Timber Under Fire', presented at the Ninth International Seminar on Fire and Explosion Hazards (ISFEH9), 2019, pp. 1088–1096. doi: 10.18720/spbpu/2/k19-101.

[11] M. Fragiacomo1, A. Menis, I. Clemente, G. Bochicchio, and A. Ceccotti, 'Fire Resistance of Cross-Laminated Timber Panels Loaded Out of Plane', J. Struct. Eng., vol. 139, no. 12, p. 11, 2013, doi: 10.1061/(ASCE)ST.1943-541X.0000787.

[12] A. Frangi, M. Fontana, E. Hugi, and R. Jübstl, 'Experimental analysis of cross-laminated timber panels in fire', Fire Safety Journal, vol. 44, no. 8, pp. 1078–1087, Nov. 2009, doi: 10.1016/j.firesaf.2009.07.007.

[13] A. Frangi, M. Fontana, M. Knobloch, and G. Bochicchio, 'Fire behaviour of cross-laminated solid timber panels', Fire Saf. Sci., vol. 9, pp. 1279–1290, 2008, doi: 10.3801/IAFSS.FSS.9-1279.

[14] M. Kippel, C. Leyder, A. Frangi, and M. Fontana, 'Fire Tests on Loaded Cross-laminated Timber Wall and Floor Elements', Fire Saf. Sci., vol. 11, pp. 626–639, 2014, doi: 10.3801/IAFSS.FSS.11-626.

[15] M. Fragiacomo, A. Menis, I. Clemente, G. Bochicchio, and B. Tessadri, 'Experimental and numerical behaviour of cross- Laminated timber floors in fire conditions', presented at the World Conference on Timber Engineering, 2012, p. 9.

[16] M. Shahnewaz, T. Tannert, M. S. Alam, and M. Popovski, 'Experimental and finite element analysis of cross laminated timber (CLT) panels', in First

https://doi.org/10.52202/069179-0227

International Conference on Advances in Civil Infrastructure and Construction Materials, 2015, pp. 560–567.
[17] J. Schmid, M. Klippel, A. Just, A. Frangi, and M. Tiso, ‘Simulation of the Fire Resistance of Cross-laminated Timber (CLT)’, Fire Technology, vol. 54, no. 5, pp. 1113–1148, May 2018, doi: 10.1007/s10694-018-0728-9.
[18] M. Fragiacomo, A. Menis, P. Moss, A. Buchanan, and I. Clemente, ‘Numerical and Experimental Evaluation of the Temperature Distribution Within Laminated Veneer Lumber (LVL) Exposed to Fire’, Journal of Structural Fire Engineering, vol. 1, no. 3, pp. 145–159, Sep. 2010, doi: 10.1260/2040-2317.1.3.145.
[19] Y. Wang et al., ‘Experimental and numerical analysis on fire behaviour of loaded cross-laminated timber panels’:, Advances in Structural Engineering, vol. 23, no. 1, pp. 22–36, Jan. 2020, doi: 10.1177/1369433219864459.
[20] A. Frangi, V. Schleifer, M. Fontana, and E. Hugi, ‘Experimental and Numerical Analysis of Gypsum Plasterboards in Fire’, Fire Technol, vol. 46, no. 1, pp. 149–167, Jan. 2010, doi: 10.1007/s10694-009-0097-5.
[21] R. IMA, Thermal and mechanical properties of gypsum boards and their influences on fire resistance of gypsum board based systems. PhD thesis, School of Mechanical, Aerospace and Civil Engineering, University of Manchester, 2011.
[22] C. O’Ceallaigh, K. Sikora, D. McPolin, and A. M. Harte, ‘Modelling the hygro-mechanical creep behaviour of FRP reinforced timber elements’, Construction and Building Materials, vol. 259, p. 119899, Oct. 2020, doi: 10.1016/j.conbuildmat.2020.119899.

World Conference on Timber Engineering Oslo 2023

A DESIGN APPROACH TO EXTERNAL FIRE SPREAD FROM BUILDINGS WITH EXPOSED MASS TIMBER

Adam Glew[1*], Rory Turnbull[2], Frederik Møller Poulsen[3], Eirik Christensen[3], Panagiotis Kotsovinos[4], Eoin O'Loughlin[3], David Barber[5], Judith Schulz[3]

ABSTRACT: Engineered wood products (EWPs) are relatively new, innovative construction materials which, if used correctly, can serve as sustainable alternatives to more common construction types. They provide an opportunity for designers to reduce the embodied carbon of proposals. Given the climate crisis, it is vital that the sector decarbonises.
However, lessons must be learnt from previous sustainability-driven design decisions that did not sufficiently consider safety implications. Often there is a desire from building owners, occupiers and/or designers to expose mass timber. Doing so can provide aesthetic, wellbeing, cost and carbon benefits over encapsulation. However, exposing large areas of mass timber introduces an additional fuel load to the compartment – the structural fuel load, and compartment fire experiments to date have shown that this can lead to larger external flaming.
This paper aims to investigate potential implications of this phenomenon on: (i) large-scale 'standard' façade tests, and (ii) radiation assessments to neighbouring buildings.
First, temperature data recorded outside the opening(s) of seven mass timber compartment fire experiments is compared to temperatures in front of the façade recorded during three 'standard' industry façade fire tests. It is found that BS 8414 and the proposed harmonised European test generally expose the façade to more/as severe temperatures than observed during mass timber compartment fire experiments. Therefore, these tests are considered applicable to exposed mass timber buildings. The NFPA 285 test, which was designed for traditional buildings, is less severe than the mass timber experiments reviewed.
Heat fluxes recorded opposite openings in three mass timber compartment fire experimental series are then compared to heat flux predictions made following first principles-based radiation calculations following the enclosing rectangles and configuration factor method (as in BR 187). Using the "low" and "high" fire load assumptions in BR 187 leads to underpredictions of heat flux received. Modelling the external flame as an emitter (of the same temperature as the opening) has little impact on results. Therefore, a higher emitter temperature is recommended when carrying out radiation calculations from exposed mass timber compartments.

KEYWORDS: timber, external flaming, external fire spread, standard façade tests, radiation, compartment experiments

1 INTRODUCTION

1.1 THE CLIMATE CRISIS AND TIMBER

Buildings are responsible for approximately 40% of global CO_2 emissions, with embodied carbon accounting for around a quarter of that. Unlike operational carbon emissions, which can be reduced over time, embodied carbon is 'locked in' once an asset is constructed. As the global building stock is expected to double in terms of floor area by 2060, there is an urgent need for architects and engineers to use sustainable construction materials, such as engineered wood products (EWPs) [1], [2].
Innovations in EWPs (or 'mass timber') have presented opportunities for designers to use timber for larger structures. Timber sequesters carbon during its growth, and when it is sustainably sourced, used efficiently, and designed with the end-of-life scenario considered from the outset, can result in buildings with lower embodied carbon than those predominantly using steel and/or concrete [3], [4]. In addition, EWPs are aesthetically desirable, can have wellbeing benefits for building users [5], and may command higher rental rates [6].

1.2 EXPOSED MASS TIMBER AND EXTERNAL FLAMING

Exposing large areas of mass timber introduces additional fuel load to a compartment. The majority of small- and medium-scale compartment fire experiments conducted to date have shown that this can result in larger external flames [7], [8] and increased heat flux to both the building of fire origin and opposite [9] than from an otherwise identical compartment constructed from non-combustible materials. One experimental series, with a very high movable fuel load (of 1085 MJ/m^2), did not observe a significant increase in flame height when mass timber was

[1] Arup, Level 5, 151 Clarence Street, Sydney, Australia *Adam.Glew@arup.com
[2] Arup, 63 Thomas Street, Bristol, UK
[3] Arup, 8 Fitzroy Street, London, UK
[4] Arup, 6th Floor, Three Piccadilly Place, Manchester, UK
[5] Arup, Sky Park, One Melbourne Quarter, 699 Collins Street, Melbourne, Australia

https://doi.org/10.52202/069179-0228

introduced, but did report higher temperatures [10]. Significant external flaming was also observed during the large-scale *CodeRed* experimental series [11]–[13].
These observations highlight the need for existing fire safety design methods to be revisited, scrutinised and, if necessary, adjusted before they are applied to buildings with large areas of exposed mass timber. Larger external flaming may have an impact on:
(i) applicability of 'standard' large-scale façade tests,
(ii) radiation assessments to neighbouring buildings,
(iii) heat transfer analyses to external loadbearing structure.
The latter has been studied in separate work [14] so is not covered in this paper.

1.3 FIRE SAFETY OBJECTIVES

Broadly speaking, buildings are legally required to limit the risk of external fire spread:
- over the façade of the building of fire origin, and
- from one building to another,

to an 'acceptable level'. An 'acceptable level' may be determined based on a number of parameters, such as the type and scale of the building, occupancy characteristics, proximity to other buildings, etc.
Building regulations typically consider life safety. Clients and insurers may have additional objectives to limit damage to property, contents and/or business operations.
Different guidance documents exist as reference to enable designers to demonstrate compliance with fire safety objectives. In England, statutory guidance in the form of the approved documents "provide guidance for common building situations". "Compliance with the guidance set out in the approved documents does not provide a guarantee of compliance with the requirements of the regulations because the approved documents cannot cater for all circumstances, variations and innovations" [15].
Mass timber is a recent innovation within the construction industry that has not yet been widely adopted in the UK, so its use does not yet represent a "common building situation" [16].
Whilst there will always be some knowledge gaps, and "satisfactory engineering solutions may be achieved with partial information" [17], research is needed so that built environment professionals can understand mass timber further, and design, construct and maintain safe, sustainable buildings.

1.3.1 Limiting fire spread over external walls

Designers typically have two options for limiting fire spread over the façade of the building of fire origin:
(i) selecting materials which meet prescriptive reaction-to-fire performance requirements, or
(ii) conducting a large-scale 'standard' façade fire test and passing specified performance criteria.
This paper focuses on the latter. Large-scale façade tests submit a multi-storey test sample of the façade to a large fire, represented by wooden cribs or a gas burner. The 350kg wood crib specified in BS 8414 as part of the large-scale test, for example, gives a total energy output of ~4500 MJ over a 30 minute period, with a peak heat release rate of 3 ± 0.5 MW [18]. The intent of these tests is to simulate a realistic worst-case fire scenario, such as the flame projecting from a compartment fire post-flashover, or from a burning skip positioned close to the façade [19]. NFPA85 uses gas burners.
Data has been sourced by the authors from the proposed harmonised European test, the NFPA 285 test and the BS 8414 test for comparison with data from seven large-scale timber compartment experiments.

1.3.2 Limiting fire spread from one building to another

It is generally acknowledged that the risk of fire spread between buildings should be limited, however there is no internationally agreed method for doing so. Most national building codes (e.g., National Construction Code (NCC) [Australia], NFPA 5000 [USA], International Building Code (IBC) [USA], The Model Building Code [Germany], etc.) set out prescriptive separation distances based on building type. However, there is little scientific reasoning provided in support of these methods, which are often based on historical observations [20], [21]. The national building codes of some countries permit a calculation-based methodology to be used by designers to quantitatively assess the emitted radiation from a severe post-flashover fire onto an adjacent building/boundary such that they can ensure a maximum heat flux is not exceeded. BR 187 – *External fire spread – Building separation and boundary distances* [22] is one such method, which is the focus of this paper. The BR 187 method is based on research carried out by Margaret Law in the 1960s [23], [24]. The fire compartment is assumed to be a radiating emitter with a uniform temperature of either 830 °C (low fire load) or 1040 °C (high fire load). The typical acceptance criteria for incident radiation on an exposed building is 12.6 kW/m^2, the threshold for piloted ignition of wood.
The 2014 revision of BR 187 notes that some compartments, such as those that are well insulated, can result in higher temperatures. A document released as part of The Grenfell Tower Public Inquiry highlighted the need for further guidance on higher compartment temperatures and external flaming from well insulated compartments [25]. However, no guidance is currently provided on this topic, and it is therefore often not considered by designers. Similarly, no guidance currently exists on whether the assumptions within BR 187 are suitable for compartments with large areas of exposed mass timber.

1.4 STRUCTURE AND CONTENT OF THIS PAPER

This paper presents novel data from *CodeRed*, supplemented by data from the RISE [26] and Épernon experiments [27]. Temperatures recorded above and heat fluxes recorded opposite the openings in the experiments are used to understand the impact of exposed mass timber on externally venting flames and radiation from the compartments. First, temperature data is compared to temperatures from a selection of 'standard' façade fire tests (the proposed harmonised European test, NFPA 285 and BS 8414), to evaluate whether the tests are sufficiently severe. Then, the heat fluxes recorded opposite the openings are compared to heat fluxes

https://doi.org/10.52202/069179-0228

calculated following a common radiation calculation method (BR 187).

2 THE *CODERED* EXPERIMENTS

Arup designed and commissioned a purpose-built facility for the *CodeRed* experimental series which took place at CERIB's Centre d'Essais au Feu (Fire Testing Centre).

The experiments aimed to study the fire dynamics in large, open-plan compartments with an exposed timber surface. The test geometry is shown in Figure 1.

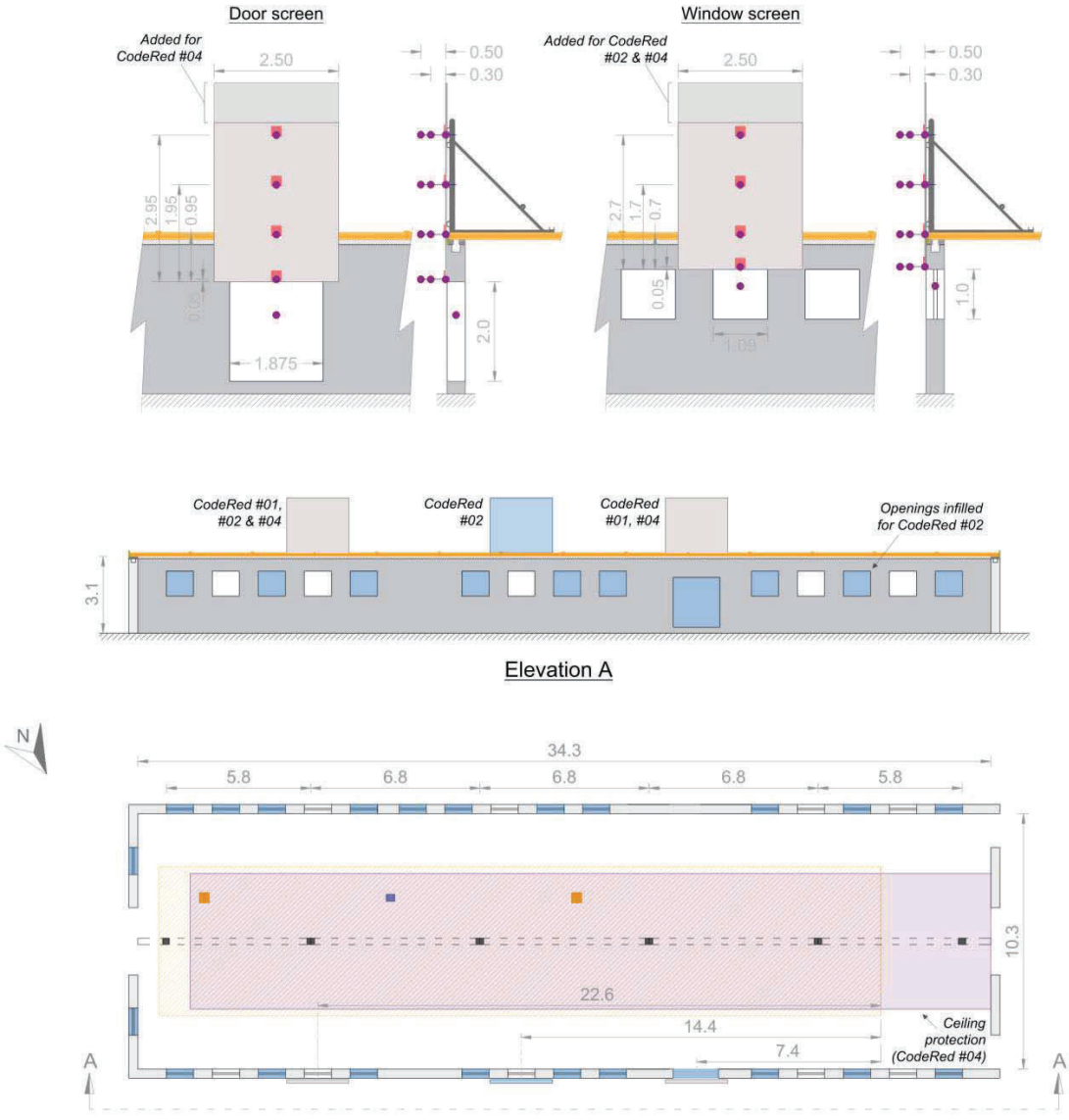

Figure 1: *Plan of CodeRed compartment, with elevations showing instrumented doors and windows. Openings coloured blue were infilled during CodeRed #02. Purple shading on plan indicates the area of encapsulation on the CLT ceiling in CodeRed #04.*

The compartment had an internal floor area of 352 m^2. The fuel bed was identical in all experiments and consisted of continuous wood cribs with a fuel load density of ~380 MJ/m^2 over a floor area of 174 m^2. The fuel load was chosen to enable comparison with earlier experiments studying travelling fire dynamics in equivalent non-combustible compartments *x-ONE* [28], *x-TWO* [29]. Table 1 summarises the key parameters of the *CodeRed* experiments without suppression.

2.1 INSTRUMENTATION

The fire development in the *CodeRed* experiments, both inside and outside the compartment, was captured via an extensive arrangement of instrumentation. A brief overview of the instrumentation used to capture the data presented within this paper is presented in this section. A more detailed description of the instrumentation used for each experiment can be found in the literature [11]–[13].

https://doi.org/10.52202/069179-0228

Table 1: *Summary of the key parameters of the three CodeRed experiments without suppression.*

Experiment		*CodeRed #01*	*CodeRed #02*	*CodeRed #04*
Date		09 Mar 2021	01 Jun 2021	14 Dec 2021
Internal floor area, A_F	[m^2]	352	352	352
Total area of openings, A_w	[m^2]	56.6	**28.3**	56.6
Exposed CLT area, A_{CLT}	[m^2]	352	352	**176.7**
Total internal surface area of compartment (floor, ceiling and walls), **inc. opening area**, A_t	[m^2]	980	980	980
Total internal surface area **exc. opening area**, A_T	[m^2]	923	952	923
Area-weighted average window height, h_{eq}	[m]	1.488	1.818	1.488
Opening factor as per Eurocode [30] $A_t/(A_w h_{eq}^{1/2})$	[m$^{-1/2}$]	14.2	25.6	14.2
Opening factor as per L&O'B [31] $A_T/(A_w h_{eq}^{1/2})$	[m$^{-1/2}$]	13.4	24.9	13.4
Modified opening factor as per [32] $(A_T-A_{CLT})/(A_w h_{eq}^{1/2})$	[m$^{-1/2}$]	8.3	15.7	10.8
Instrumented openings		W1, D1	W1, **W2**	W1, D1
TC in openings?		No	**Yes**	**Yes**
HFG opposite openings?		No	**6m, 8m**	**6m, 8m**

2.1.1 Internal instrumentation

To measure the gas temperature distribution within the compartment, 57 thermocouples (TCs) were distributed across the compartment, organised into 17 thermocouple trees. To account for the radiative heat flux from the fire, the recorded temperatures were corrected using a methodology referred to as the *β-method*, which was consistent across *x-ONE* [28], *x-TWO* [29] and *CodeRed*.

2.1.2 External instrumentation

Outside the compartment, non-combustible screens were installed above two openings as shown in Figure 1. The screens were annotated to allow approximation of flame geometry. Thermocouples and plate thermometers were installed on each façade screen. In *CodeRed #02* and *#04*, thermocouples were also positioned within the openings.
The thermocouples recorded data every 10 seconds (i.e., a frequency of 0.1 Hz) for *CodeRed #01* and every 5 seconds for *CodeRed #02* and *#04* (i.e., a frequency of 0.2 Hz). To reduce noise, all data from the thermocouples was smoothed using the Savitzky-Golay filter [33] available within SciPy, with a time frame of 60 s.

CodeRed #02

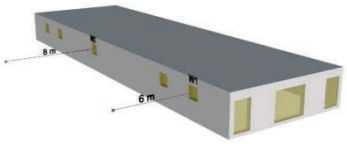

CodeRed #04

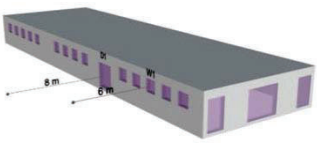

Figure 2: *Isometric models of CodeRed #02 and #04 showing instrumented openings.*

Unlike the internal thermocouple data, the temperatures recorded by the external thermocouples were not corrected to account for radiation received from the compartment fire, because the radiation received is expected to be small.
Heat flux gauges (HFGs) were installed opposite the centroid of the instrumented openings in both *CodeRed #02* and *#04*, as shown in Figure 2.
Two cameras were positioned opposite each instrumented opening to observe the external flame extension above the openings. Various other stationary cameras were placed around the compartment. Drones and handheld cameras were also used to give a dynamic view of the fire.

3 EXPERIMENTAL DATA

Papers covering the *CodeRed* experiments have been published which include detailed plots of internal and external temperature and heat flux data [11]–[13]. The following section presents additional data which has not yet been published.

3.1 HEAT FLUX OPPOSITE THE OPENINGS

Heat fluxes measured opposite the instrumented openings for *CodeRed #02* and *#04* are plotted in Figure 3. As expected, the heat flux measured by the HFG positioned 6 m opposite opening W1 recorded slightly higher heat fluxes in both experiments than the HFGs placed 8 m away from openings W2 / D1.
The peak heat flux recorded opposite W1 in *CodeRed #04* was 11.6 kW/m^2, compared with 7.9 kW/m^2 in *CodeRed #02* – an increase of 47 %. Despite the ceiling in *CodeRed #04* being partially encapsulated ceiling, it caused a higher heat flux opposite the same W1 opening. This is thought to be due to the greater number of openings in *CodeRed #04* radiating to the HFG.
The heat flux reading opposite the larger D1 opening was lower than the measurement opposite the window, contrary to expectations when considering the openings as uniform temperature emitters (i.e., ignoring external flames). The D1 opening had smaller external flames than the window openings which suggests the external flames were responsible for the higher measurement opposite the window opening W1 [13].

https://doi.org/10.52202/069179-0228

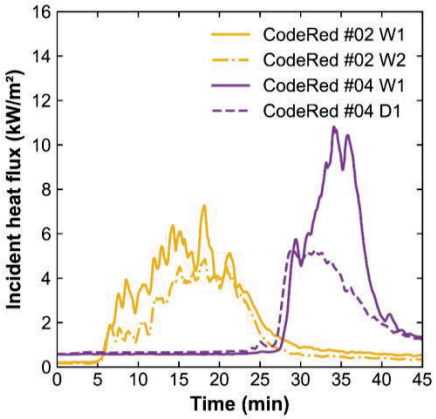

Figure 3: *Heat fluxes recorded at 6 m opposite opening W1 and 8 m opposite openings W2/D2 in CodeRed #02 and #04.*

Figure 3 also shows that peak heat fluxes occur later in *CodeRed #04* compared to *CodeRed #02*, due to the encapsulation slowing the growth phase and delaying the involvement of the CLT ceiling in the fire.

The fire duration in *CodeRed #02* was longer due to the reduced ventilation [12]. This is reflected in Figure 3, where an incident heat flux was registered opposite the openings for a period of around 20 minutes, compared to 10-15 minutes for *CodeRed #04*.

3.2 GAS TEMPERATURE IN THE OPENINGS

The temperatures recorded in the openings (shown in Figure 4) largely mirror the heat fluxes recorded opposite. Peak temperatures in the openings during both *CodeRed #02* and *#04* are very close to the 1040 °C that BR 187 assumes for "high fire load" compartments.

The temperatures in the window openings were broadly similar in each experiment. The door opening in *CodeRed #04* had a lower peak temperature, nearer 830 °C. This may be because the thermocouple for this opening was positioned lower in the opening (see Figure 1).

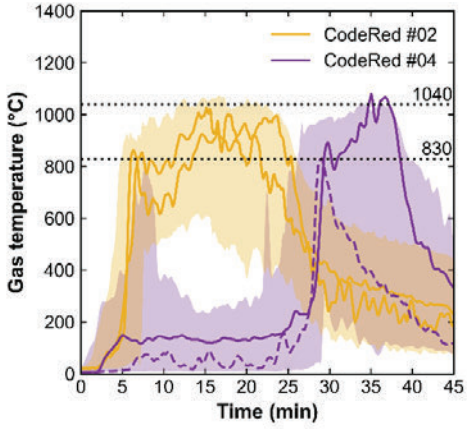

Figure 4: *Gas temperatures recorded during CodeRed #02 and #04. Lines show temperatures recorded within the windows (solid lines) and door (dashed line). Clouds show the range of corrected gas temperatures recorded inside the compartment.*

4 ANALYSIS

4.1 COMPARISON WITH 'STANDARD' LARGE-SCALE FAÇADE FIRE TESTS

As discussed in Section 1.3.1, large-scale testing of façade systems containing combustible materials (such as insulation or cladding) is a route to compliance for limiting external fire spread on the building of fire origin.

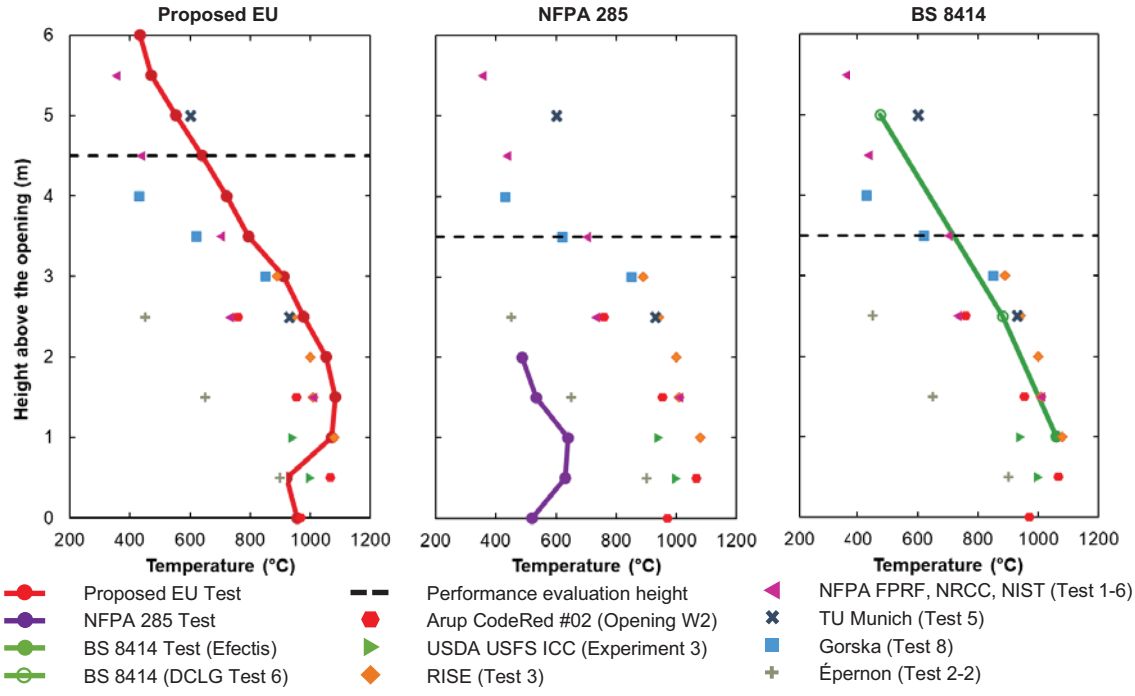

Figure 5: *Temperatures recorded outside timber experiments compared with those experienced during 'standard' large-scale tests.*

https://doi.org/10.52202/069179-0228

To understand whether the existing 'standard' test fires are severe enough to represent the external flaming observed in large scale experiments with exposed timber, the external temperature data from *CodeRed* and other notable mass timber experiments with external instrumentation has been compared to available data from large-scale industry 'standard' façade fire tests. Namely:

- the BS 8414 test.
- the NFPA 285 test, and,
- the proposed large-scale harmonised European (EU) test, which is broadly based on the BS 8414 test [34].

These tests were chosen as they are widely applicable, and data was available from tests which had either no façade system installed [34]–[36] or a limited combustibility façade installation only [37], such that the façade system itself did not contribute to the temperature data.

Figure 5 plots the 'standard' façade fire test data on top of maximum temperatures recorded at different heights outside the openings of a range of small- to large-scale mass timber compartment fire experiments.

The proposed EU test represents a relatively accurate upper bound of the external temperature data recorded during the mass timber compartment fire experiments. The only minor inaccuracy is at around 0.5 m above the top of the opening, which may be due to the thermocouple being placed outside the flaming region (e.g., if the flame did not adhere to the façade).

The BS 8414 test performs similarly, however has slightly lower temperatures than the proposed EU test. Some timber compartment fire external flame temperatures slightly exceed the BS 8414 test temperatures, by approximately 50-100 °C.

The NFPA 285 test, on the other hand, exposes the façade to much lower temperatures than those seen during timber compartment fire experiments. This is not surprising given the room gas burner follows the ASTM E119 *Standard Test Methods for Fire Tests of Building Construction and Materials* time-temperature curve. The temperatures recorded during calibration of the NFPA 285 test are lower than all external temperatures recorded during the mass timber compartment experiments chosen for this analysis. These findings are similar to those reported by [38].

4.2 COMPARISON WITH THE BR 187 RADIATION ASSESSMENT METHOD

As discussed in Section 1.3.2, one route for demonstrating compliance in terms of limiting fire spread from one building to another is completing a quantitative assessment of the expected incident radiation on a neighbouring building or boundary in case of a post-flashover fire. BR 187 describes one such method.

4.2.1 Temperature of emitter

BR 187 recommends adopting 830 °C for "low fire load" spaces (office, residential) and 1040 °C for "high fire load" spaces (industrial, retail) when selecting the emitter temperature. It also notes that "further work is required to investigate whether a higher temperature should be used for … buildings with higher levels of insulation" [22].

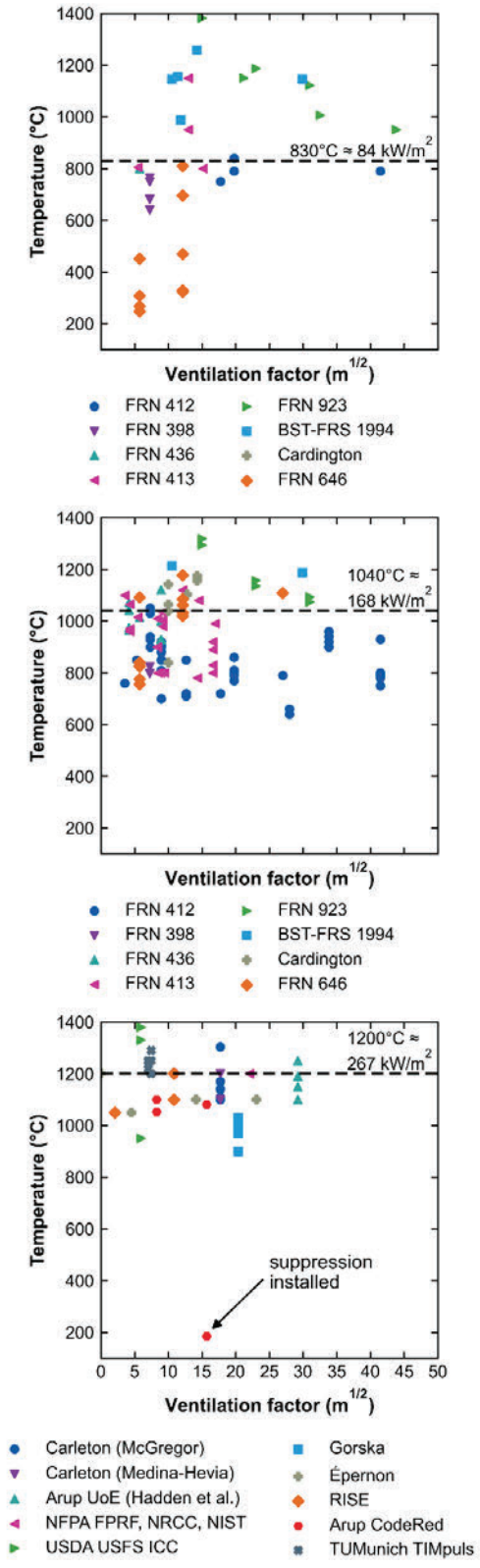

***Figure 6**: Maximum internal temperature versus ventilation factor for compartment experiments with (i) low fire load, (ii) high fire load, and (iii) exposed mass timber structure.*

https://doi.org/10.52202/069179-0228

Figure 6 presents the original data that the 830 °C and 1040 °C values within BR 187 are based on. A wide scatter of the underlying data from various small- and medium-scale compartment fire experiments is notable.
To determine a more suitable emitter temperature for mass timber compartments, a similar plot has been made for ten mass timber compartment fire experimental programmes. A general shift towards higher temperatures is evident through the three subplots. This suggests that a higher emitter temperature may be appropriate when conducting BR 187 assessments for buildings with exposed mass timber which do not benefit from e.g., sprinkler protection. 1200 °C has been chosen as a representative temperature for the analysis in this paper.

4.2.2 Geometry and emissivity of emitter(s)

BR 187 presents three methods to evaluate fire spread risk between buildings, namely, in BR 187 Section:
2.2.1. Enclosing rectangles,
2.2.2. Aggregate notional areas (or protractor method),
2.2.3. An alternative approach using look-up tables.
The enclosing rectangles method is typically used for modern buildings with a majority glazed façade whereby the entire glazed façade is modelled as an emitter.
Appendix A of BR 187 outlines the radiation calculation which is then made following configuration factor theory. Appendix B of BR 187 summarises Law and O'Brien's seminal work on external flaming [31], though in the experience of the authors, this is rarely applied in practice. BR 187 states that, when Appendix B is followed, the results are very similar to the 'conventional' analysis [22].

4.2.3 Parametric study of radiation to other buildings

A parametric study has been completed to evaluate various emitter temperatures, geometries and emissivities.

4.2.3.1 Scenarios modelled

Scenario 1 (BR 187 Appendix A)
In this scenario, all openings are modelled as radiating emitters, following BR 187 Section 2.2.1 and Appendix A. All other construction is assumed to be 'protected' i.e., constructed from fire resisting construction and not emitting radiation to the nearby building. The temperature of the emitters was taken as 830 / 1040 / 1200 °C.

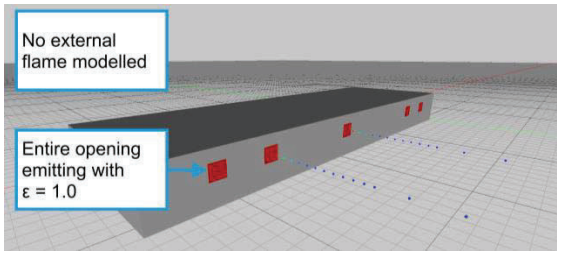

Figure 7: *Scenario 1 modelling parameters for CodeRed #02.*

Scenario 2 (BR 187 Appendix B)
Following BR 187 Appendix B, whereby the upper ⅔ of the opening(s) and an external flame are modelled as radiating emitters, both with the same emitting temperature. The emissivity of the opening, $\varepsilon_o = 1.0$. The emissivity of the flame, ε_f, calculated as per BR 187 / Law and O'Brien using $\varepsilon_f = 1.0 - exp(-0.3X_{ef})$, where X_{ef} is the thickness (depth) of the flame. Flame height was calculated based on the crib fuel load only (i.e., no CLT contribution was considered), as no generally agreed analysis method currently exists that determines the impact of the structural (CLT) fuel load on external flame height. Temperature of emitters is also varied as per (1).

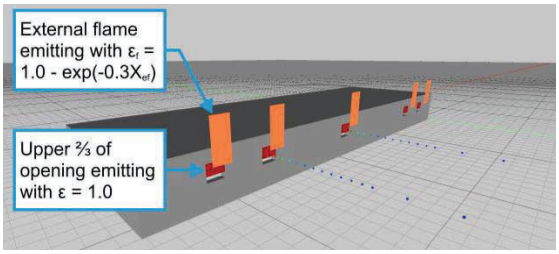

Figure 8: *Scenario 2 modelling parameters for CodeRed #02.*

Scenario 3 (BR 187 App. B, with $\varepsilon_f = 1.0$)
The same as (2), but with an assumed worst-case emissivity of the external flame, $\varepsilon_f = 1.0$, used.

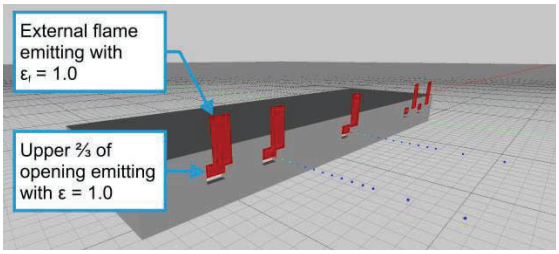

Figure 9: *Scenario 3 modelling parameters for CodeRed #02.*

Only Scenarios 1 and 3 are presented in this paper, due to the quantity of data and because the predictions in Scenario 2 were very similar to Scenario 1. This aligns with BR 187 Figure B4, which also shows very similar predictions between the two methods.

4.2.3.2 A note on flame emissivity, ε_f

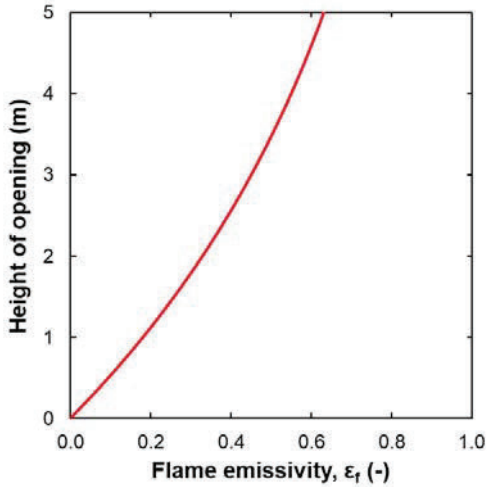

Figure 10: *Relationship between opening height and ε_f.*

Figure 10 shows the BR 187 correlation between the emissivity of the flame and the height of the opening (which determines the flame thickness (depth), X_{ef}).

https://doi.org/10.52202/069179-0228

In *CodeRed*, the window openings were 1.0 m tall, which results in a calculated flame emissivity of 0.18, meaning the contribution of the external flames to the incident heat flux calculated opposite is minimal when following BR 187 Appendix B. This is also the case for most real-world design scenarios. For example, a fire in a single-storey compartment with 3.0 m tall floor-to-ceiling glazing (assuming full glass breakage) would result in flames with an emissivity of 0.45. This would reduce the heat flux calculated from the flame emitter by over half.

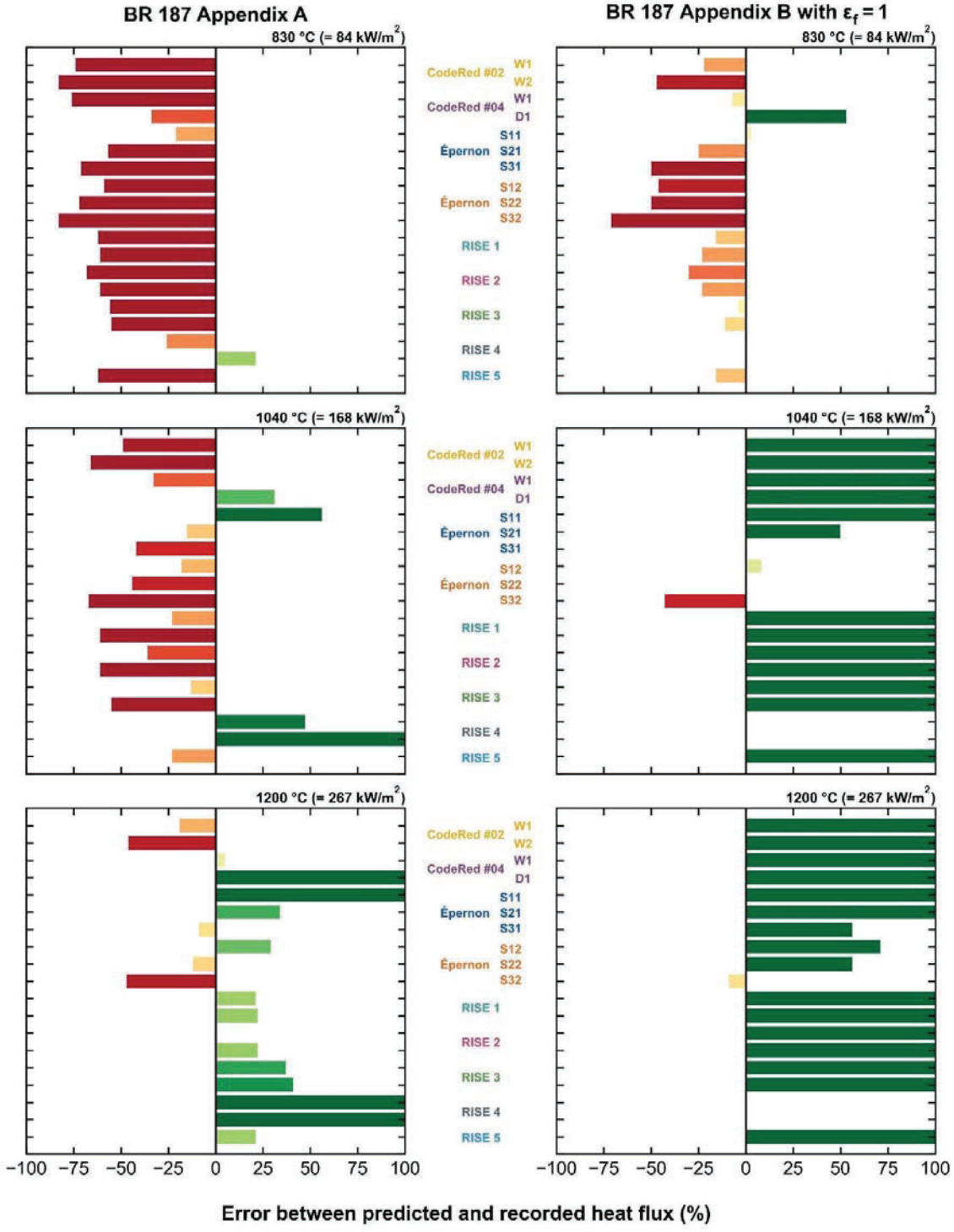

Figure 11: *Bar charts showing percentage error between predicted heat fluxes and the peak heat fluxes recorded during a range of timber compartment fire experiments. An error of +100% represents a heat flux prediction which is twice the recorded heat flux.*

https://doi.org/10.52202/069179-0228

4.2.3.3 *Compartment experiments analysed*

The parametric study was applied and compared to:

- Large-scale experiments *CodeRed #02* and *#04*, which had external HFGs as per Section 2.1.2.
- Medium-scale timber compartment fire experimental programmes by RISE and Épernon, which also had external HFGs as per [26], [27].

RISE Test 4 was not modelled following BR 187 Appendix B because the flame height calculated was so low as to be negligible. Sprinklers are not considered in this work as none of the compartment experiments analysed had them installed.

4.2.3.4 *Comments on results*

Figure 11 presents the results from the parametric analyses using bar charts. The plots visualise the performance of the predictions made following BR 187 compared to the actual heat fluxes recorded during the experiments, as percentage error between predicted heat fluxes and the peak heat fluxes recorded during a range of timber compartment fire.

Figure 11 shows:

- Using an emitter temperature of 830 °C resulted in significant underpredictions of heat flux across the experiments analysed. 18 out of 19 predictions were low when modelling the opening only as an emitter. 15 out of 17 predications were low when following BR 187 Appendix B (i.e., modelling the external flame) and conservatively assuming the flame emissivity is 1.
- Using an emitter temperature of 1040 °C made only a small improvement to the predictions. When modelling only the opening, three predictions were satisfactory (i.e., overpredicted with a reasonable factor of safety). However, one prediction largely overpredicted, and the other 15 predictions were low.
- When the modelled geometry was adjusted following Appendix B (i.e., with a flame at the same temperature as the opening (1040 °C) and with an emissivity of 1), the predictions swung the other way. 12 predictions overpredicted significantly. The same observation (albeit slightly worse) is made for the 1200 °C emitters following Appendix B.

The best predictions for heat flux received opposite the mass timber compartments analysed were from the models which assumed emitters representing the opening geometry only (i.e., without external flames) at a temperature of 1200 °C. 10 out of 19 of these predictions (i.e., more than 50%) were satisfactory (made overpredictions by a reasonable factor of safety). In four cases, significant overpredictions were made while underpredictions were made in only five cases.

5 DISCUSSION

5.1 APPLICABILITY OF EXISTING LARGE-SCALE 'STANDARD' FAÇADE TESTS

External temperature data recorded during seven mass timber compartment fire experiments has been gathered and presented. This data has been compared to temperatures recorded in front of the façade during three 'standard' industry façade fire tests – namely BS 8414, NFPA 285 and the proposed harmonised European test – to evaluate if the existing tests subject façade system to an appropriate fire severity where a building contains exposed mass timber.

The comparison showed that the proposed harmonised European test has the most severe external flame, which envelopes the data from mass timber compartment experiment well: 89% of the data points from mass timber compartment experiments were exceeded by the test.

The BS 8414 test also showed relatively good enveloping of the data: 65% of the data points from mass timber compartment experiments were exceeded by the test.

However, it should be noted that the BS 8414 data was more limited than the proposed European test data. Only three data points were available, from two different sources. Therefore, the observations are less robust than those made when comparing to the proposed European test. The proposed European test is based on BS 8414, and broadly represents that test, so similar observations should be expected (as was evident in this work).

The NFPA 285 test was shown to have a lower external flame severity than all the mass timber compartment experiments reviewed (i.e., it didn't envelope any of the data points). NFPA 285 is referenced in the IBC and NFPA 5000, for use with buildings that include combustibles as part of the exterior wall, located over 18m in height. The applicability of the NFPA 285 test for analysing the performance of façades of buildings that include large areas of exposed mass timber structure (interior to the building) is therefore questionable and future editions of this standard will need to address the available experimental data.

5.2 APPLICABILITY OF EXISTING RADIATION CALCULATION METHODS

The underlying data behind the "low fire load" and "high fire load" assumptions within BR 187 for compartment temperature has been presented. This has been compared to a new dataset, of the peak internal compartment temperatures recorded during a selection of ten mass timber compartment fire experimental programmes. The general upward shift indicates a hotter emitter temperature may be appropriate for buildings with large areas of exposed mass timber and no beneficial fire protection measures such as sprinkler protection. 1200 °C was chosen as a "very high fire load" compartment temperature. This enveloped most of the timber compartment experiments reviewed, with a scatter no greater than seen in the underlying data for non-combustible compartment experiments.

Based on this, a parametric analysis has been undertaken to evaluate the accuracy of existing BR 187 calculation methods when applied to mass timber compartment fire experiments. The analysis evaluated three different emitter temperatures (830 °C, 1040 °C and 1200 °C), two geometry combinations (openings only, openings and flame) and three emissivity combinations ($\varepsilon_o = 1.0$, $\varepsilon_o = 1.0$ and $\varepsilon_f = 1.0 - exp(-0.3X_{ef})$, and $\varepsilon_o = 1.0$ and $\varepsilon_f = 1.0$). A total of 53 calculations were made across three different mass timber compartment fire experimental series.

https://doi.org/10.52202/069179-0228

The analysis showed that, if the existing assumptions within BR 187 for temperatures of "low fire load" and "high fire load" compartments were applied to spaces with large areas of exposed mass timber, underpredictions can be expected, even when modelling the external flaming following Appendix B. Adjusting the Appendix B external flaming method to include a flame emissivity of 1.0 was found to be overly conservative.

The best predictions for heat flux were made following the existing BR 187 enclosing rectangles method using a "very high fire load" compartment emitter temperature of 1200 °C. Whilst the authors recognise the 'crudeness' of the BR 187 method, it has been the focus of this paper because it is a popular method for assessing the risk of external fire spread between buildings in the UK. The findings are based on first principles radiation analyses, so could be adopted elsewhere where similar quantitative design methods are permitted [21].

Other more sophisticated approaches, such as the probabilistic method outlined in BR 187 IP 3-16 [39], will require further investigation to determine if these methods are appropriate on timber buildings, or if further amendments are needed.

It is noteworthy that the current draft of EN 1995-1-2 [40] proposes a modified version of the existing external flame correlation in EN 1991-1-2 [30] and BR 187 Appendix B to account for the structural fuel load present in timber buildings. This method has not been assessed as part of this study though further review against the available datasets are recommended.

6 CONCLUSIONS

Many timber compartment fire experiments, including *CodeRed*, have shown that large external flames and higher compartment temperatures can be expected from compartments with exposed mass timber where there is no automatic fire suppression installed. This paper investigates the impact of this phenomenon on: (i) the applicability of large-scale 'standard' façade tests, and (ii) radiation assessments to neighbouring buildings.

Firstly, novel external temperature and heat flux data from the *CodeRed* experiments is presented. Then, this data is supplemented with temperature data from a collection of ten medium- and large-scale compartment fire experiments with varying areas of exposed mass timber, and compared to temperatures recorded outside three industry 'standard' large-scale façade fire tests. Two of the large-scale tests, the proposed large scale harmonised European test and the BS 8414 test, generally enveloped the timber data points well. These large-scale tests therefore are reasonable tests to use for façade systems on buildings with large areas of exposed mass timber. NFPA 285 did not envelope any of the timber compartment fire data points.

The second focus of the paper is existing radiation calculation methods for assessing the heat flux that may be expected on neighbouring buildings/boundaries. When carrying out such a calculation, the temperature of the emitter is a key parameter. Temperature data which underlies existing assumptions within BR 187 is presented and compared with temperature data from a selection of 10 mass timber compartment fire experiments. An obvious trend towards higher peak internal temperatures is observed, which indicates that a higher emitter temperature may be appropriate for buildings with large areas of exposed mass timber.

Based on this, a parametric analysis has been completed to assess the performance of the BR 187 calculation method (the current design method in the UK for evaluating the external fire spread risk between buildings). Heat flux data recorded opposite three mass timber compartment fire experimental programmes is compared to predictions made following BR 187. It was found that simply increasing the emitter temperature to 1200 °C yielded the best results based on the test data available to the authors. Should further data come to light that contradicts the findings of this analysis, then this temperature may need to be revaluated.

Whilst this paper has focused on the BR 187 method, the findings are based on first principles, therefore will apply to other countries which have similar quantitative analysis methods.

ACKNOWLEDGEMENT

This research has been fully funded by Arup and was undertaken in partnership with Imperial College London. The experiments were carried out at CERIB's Centre d'Essais au Feu (Fire Testing Centre) in France throughout 2021. All CERIB staff and PhD students from Imperial College London that were fundamental in the successful completion of the experiments are gratefully acknowledged. Clara Bermejo Bordons (Engineer at Arup) was fundamental in the production of Figures 1 and 2 in this paper. The authors would also like to acknowledge Gary Walker (now retired fire safety engineer at Arup) for the preliminary analysis into BR 187 and the collation of the underlying data sources. We would also like to extend our heartfelt thanks to the steering group guiding the project, which includes Dr Susan Lamont, Andrew Lawrence, and Dr Clare Perkins. The contribution of Dr Eglė Račkauskaitė in the design of the experiment is also acknowledged.

REFERENCES

[1] Architecture 2030, "Why The Building Sector?," 2022. https://architecture2030.org/why-the-building-sector/ (accessed Mar. 26, 2022).

[2] WBCSD and Arup, "Net-zero buildings - Halving construction emissions today," 2023.

[3] W. Hawkins, "Timber and carbon sequestration," *Struct. Eng.*, vol. 99, no. 1, pp. 18–20, 2021.

[4] Arup, "Net Zero Carbon Buildings: Three Steps to Take Now," 2020.

[5] D. R. Fell, "Wood in the human environment: restorative properties of wood in the built indoor environment," University of British Columbia, 2010. doi: 10.14288/1.0071305.

[6] L. Wingo, "The obstacles and opportunities of mass timber construction in the US," *Arup Perspectives*, 2021. https://www.arup.com/perspectives/the-obstacles-and-opportunities-of-mass-timber-construction-in-the-us (accessed Mar. 26, 2022).

[7] J. Sjöström, A. Temple, D. Brandon, E. Hallberg, and F. Kahl, "Exposure from mass timber compartment fires to facades," Brandforsk, 2021.

[8] C. Gorska, “Fire Dynamics in Multi-Scale Timber Compartments,” University of Queensland, 2019. [Online]. Available: https://espace.library.uq.edu.au/view/UQ:ec263ab/s4408332_final_thesis.pdf

[9] A. Bartlett *et al.*, “Heat fluxes to a facade resulting from compartment fires with combustible and non-combustible ceilings,” in *FSF 2019 – 3nd International Symposium on Fire Safety of Facades*, 2019, pp. 62–69.

[10] T. Engel and N. Wether, “Impact of Mass Timber Compartment Fires on Faade Fire Exposure,” *Fire Technol.*, 2022, doi: 10.1007/s10694-022-01346-8.

[11] P. Kotsovinos *et al.*, “Fire dynamics inside a large and open-plan compartment with exposed timber ceiling and columns: CodeRed #01,” *Fire Mater.*, pp. 1–27, 2022, doi: 10.1002/fam.3049.

[12] P. Kotsovinos *et al.*, “Impact of ventilation on the fire dynamics of an open-plan compartment with exposed timber ceiling and columns: CodeRed #02,” *Fire Mater.*, pp. 1–28, 2022, doi: 10.1002/fam.3082.

[13] P. Kotsovinos *et al.*, “Impact of partial encapsulation on the fire dynamics of an open-plan compartment with exposed timber ceiling and columns: CodeRed #04,” *Fire Mater.*, pp. 1–30, 2023, doi: 10.1002/fam.3112.

[14] A. Glew, E. O’Loughlin, P. Kotsovinos, D. Barber, and J. Schulz, “Application of the Law and O’Brien correlation for external flames to mass timber compartments,” in *SiF 2022 - The 12th International Conference on Structures in Fire*, 2022.

[15] HM Government, *Fire safety: Approved Document B. Volume 2: Buildings other than dwellings*, vol. (inc. 2020. 2019.

[16] HM Government, “Approved Document B: Fire safety - frequently asked questions - GOV.UK.” https://www.gov.uk/guidance/approved-document-b-fire-safety-frequently-asked-questions (accessed Sep. 21, 2022).

[17] M. Law and P. Beever, “Magic numbers and golden rules,” in *Proceedings of the Fourth International Symposium on Fire Safety Science, Ottawa, Canada, 13-17 June 1994*, 1994, pp. 78–84.

[18] S. Colwell and T. Baker, *BR 135: Fire performance of external thermal insulation for walls of multistorey buildings*, Third. Watford: BRE, 2013.

[19] J. Schulz, D. Kent, T. Crimi, J. L. D. Glockling, and T. R. Hull, “A Critical Appraisal of the UK’s Regulatory Regime for Combustible Façades,” *Fire Technol.*, vol. 57, no. 1, pp. 261–290, 2021, doi: 10.1007/s10694-020-00993-z.

[20] E. Carlsson, “External Fire Spread To Adjoining Buildings - A review of fire safety design guidance and related research,” Lund University, 1999.

[21] D. Thomson, P. Currie, and J. Mai, “A Comparative Analysis of the Use of Different External Fire Spread Calculation Methods,” in *Proceedings of the 11th conference on performance-based codes and fire safety design methods*, 2016, no. 22-25 May.

[22] R. Chitty, *BR 187 External fire spread: building separation and boundary distances*, Second. Watford: BRE, 2014.

[23] M. Law, “Fire Research Technical Paper No. 5 - Heat Radiation from Fires and Building Separation,” 1963.

[24] P. H. Thomas, A. J. M. Heselden, and M. Law, “Fully-developed compartment fires - two kinds of behaviour,” Borehamwood, 1967.

[25] R. Chitty and T. Lennon, “Department for Communities and Local Government Final Work Stream Report: BD 2887 - Compartment sizes, resistance to fire and fire safety project,” Watford, 2015. [Online]. Available: https://assets.grenfelltowerinquiry.org.uk/CLG00006271_BRE_ DCLG Final Work Stream Report - Compartment sizes%2C resistance to fire and fire safety project - Work stream 6 - Space Separation dated 3 March 2015_4.pdf

[26] D. Brandon, J. Sjöström, E. Hallberg, A. Temple, and F. Kahl, “Fire Safe implementation of visible mass timber in tall buildings – compartment fire testing,” 2020.

[27] The University of Edinburgh and CERIB, “Épernon Fire Tests Programme,” 2020.

[28] E. Rackauskaite *et al.*, “Fire Experiment Inside a Very Large and Open-Plan Compartment: x-ONE,” *Fire Technol.*, 2021, doi: 10.1007/s10694-021-01162-6.

[29] M. Heidari *et al.*, “Fire experiments inside a very large and open-plan compartment: x-TWO,” in *SiF 2020 – The 11th International Conference on Structures in Fire*, 2020, no. November, pp. 479–491. doi: 10.14264/b666dc1.

[30] The British Standards Institution, *Eurocode 1: Actions on structures Part 1-2: General actions – Actions on structures exposed to fire*. 2013.

[31] M. Law and T. O’Brien, “Fire Safety of Bare External Structural Steel,” *Constrado*, 1981.

[32] C. Gorska, J. Hidalgo, and J. Torero, “Fire dynamics in mass timber compartments,” *Fire Saf. J.*, 2020, doi: 10.1016/j.firesaf.2020.103098.

[33] A. Savitzky and M. J. E. Golay, “Smoothing and Differentiation of Data by Simplified Least Squares Procedures,” *Anal. Chem.*, vol. 36, no. 8, pp. 1627–1639, Jul. 1964, doi: 10.1021/ac60214a047.

[34] J. Sjöström, J. Anderson, F. Kahl, L. Boström, and E. Hallberg, “Large scale exposure of fires to facade - Initial testing of proposed European method,” 2021.

[35] Thomas Bell-Wright, “NFPA 285 - 2019 calibration data.” Thomas Bell-Wright, Dubai, 2019.

[36] Efectis, “FIRE TESTS REPORT n° EUI-20-000358, Regarding: The characterization of: Large exposure cribs,” 2020. doi: 10.1002/fam2667.

[37] BRE Global Ltd, “BRE Global Client Report - BS 8414-1:2015 + A1:2017 test referred to as DCLG test 6,” Watford, 2017.

[38] J. Sjöström, R. Mcnamee, and A. Temple, “External fire plumes from mass timber compartment fires — Comparison to test methods for regulatory compliance of façades,” no. January, pp. 1–12, 2023, doi: 10.1002/fam.3129.

[39] S. Koo, *BR 187 IP 3/16 External fire spread - Supplementary guidance to BR 187 incorporating probabilistic and time-based approaches*. Watford: BRE, 2016.

[40] Comité européen de normalisation, *prEN 1995-1-2:2025 (Final Draft). Eurocode 5: Design of timber structures Part 1-2: General — Structural fire design*. 2021.

https://doi.org/10.52202/069179-0228

World Conference on Timber Engineering Oslo 2023

NUMERICAL ANALYSIS ON THE FLEXURAL PERFORMANCE OF COMPOSITE STEEL-TIMBER BEAMS UNDER FIRE CONDITIONS

Zhiyuan Liu[1,2], Binsheng Zhang[1,*], Huijuan Jia[2] and Tony Kilpatrick[1]

ABSTRACT: Recently, a novel type of composite structure, composite steel-timber (CST) structure, has attracted much attention by connecting steel and timber in an effective way to form composite structural components. However, the relevant research is lacking, especially in structural fire design and analysis. In this study, based on the sequentially coupled method, commercial finite element software ABAQUS was used to numerically simulate the dynamic performances in the temperature field and the flexural behaviours in the displacement field of a novel CST beam with steel element embedded within the Glulam and connected by adhesives and bolts under standard fire for two hours. During the numerical simulations, the temperature distributions within the CST beam were explored, and the flexural performances of the beam in the displacement field were examined. Through the comparative analysis, the temperature distributions of the embedded steel beam and the surrounding Glulam beam under one-hour standard fire verified the advantages of this type of CST beam in structural fire design. Parametric studies on the fire resistance of the CST beam were also conducted by adjusting the bolt spacing and the protection thickness of Glulam. The obtained results indicated that reducing the bolt spacing and thickness of the Glulam protection layer would have an adverse effect on the temperature distributions in the embedded steel element to a large extent.

KEYWORDS: composite steel-timber (CST) structure; structural fire design and analysis; numerical simulation and analysis; bearing capacity; refractory limit

1 INTRODUCTION

Since enhanced structural effectiveness and combined material properties, composite structures, especially composite concrete-steel structures have been thoroughly researched and form relatively complete structural systems. Recently, composite steel-timber (CST) structures have attracted more attention from researchers and gained initial engineering applications in Japan [1,2]. This innovative composition mainly combines advantages of high strength and excellent ductility of steel and decent sustainability and fire resistance of timber while potentially helping overcome the instability and fire susceptibility of steel members and brittle behaviour of timber components [3-6].

Based on the literature review, it is found that current researches are focusing on the structural performance, bearing capacity, initial stiffness and failure modes of various CST structural components, i.e. beams [7-9], columns [10-13], shear walls [14], flooring systems [15] and their connections [16,17] under static or cyclic loading conditions by experiments and/or numerical simulations and parametric studies to investigate the potential impacts brought by the adjustment of steel/ timber members' geometry and shear connectors' spacing on their ultimate load-bearing capacity. However, there are few investigations and analyses related to structural fire design and analysis of the CST structure.

Considering potential structural and economic losses brought by fire accidents in buildings, therefore, during structural design, fire safety has been regarded as a basic requirement and should be equally treated as the load carrying capacities [18]. Two methods are recommended for structural fire design and analysis based on Eurocodes. In practice, prescriptive approach is one of the commonly approaches recommended by Eurocodes and can be further divided into two categories, i.e. standard fire test method and simplified calculation method. Both methods for timber and steel materials are described in Parts 1-2 of Eurocodes 3 and 5 in details [19,20].

In this study, comprehensive numerical simulations were conducted by using ABAQUS to investigate the flexural performances and fire resistances of a novel CST beam under fire conditions with different bolt connection spacings and timber protection thicknesses by following general approaches indicated in Eurocodes 3 and 5.

2 PROFILES OF THE CST, GLULAM AND STEEL BEAMS

CST beams for simulations in this study were assumed to be used in Canada, where the annual average temperature

[1,2] Zhiyuan Liu, Glasgow Caledonian University (GCU), Glasgow, Scotland, UK & Jinling Institute of Technology (JIT), Nanjing, Jiangsu, China, ZLIU206@caledonian.ac.uk
[1*] Binsheng Zhang, Glasgow Caledonian University (GCU), Glasgow, UK, Ben.Zhang@gcu.ac.uk
[2] Huijuan Jia, Jinling Institute of Technology (JIT), Nanjing, Jiangsu, China, Jiahuijuan@jit.edu.cn
[1] Tony Kilpatrick, Glasgow Caledonian University (GCU), Glasgow, UK, A.R.Kilpatrick@gcu.ac.uk

https://doi.org/10.52202/069179-0229

is relatively low. Thus, the ambient temperature could reach 0℃. In addition, the composite beam could be integrated with timber or concrete floor slabs to form composite flooring systems and hence the CST beam could be seen as three sides directly exposed to fire in the structural fire analysis [21]. For simplification, each type of beam specimens was modelled and analysed for a unit length.

2.1 STANDARD CST BEAM

In Figure 1, the proposed standard CST beam was mainly composed of three parts: Glulam beam, steel beam and bolts. The Glulam beam was assumed to be formed by bonding ten Glulam blocks made of Canadian beech [22] with epoxy ethane adhesives. The steel beam was the steel I-beam section, with the dimensions of length × height × width × flange thickness × web thickness = 1000 mm × 150 mm × 100 mm × 8 mm × 6 mm, embedded in the middle of the Glulam beam with adhesives, and the outer edges of the steel beam flanges had a 50 mm distance to the outer edges of the Glulam beam. Common M20 bolts were selected to strengthen the composition, and the bolts had a 200 mm spacing in the longitudinal direction and penetrated into the composite beam.

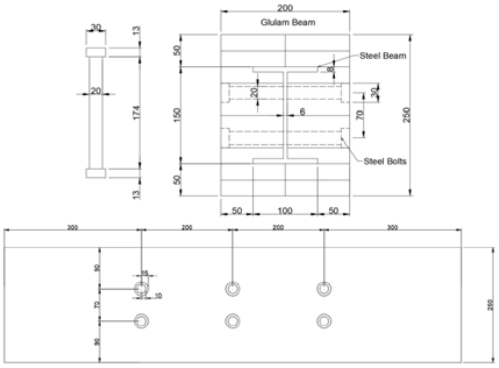

Figure 1: *Profiles of the CST beam model and M20 steel bolts for the standard CST beam*

2.2 COMPARED GLULAM AND STEEL BEAMS

As indicated in Figure 1, the Glulam and steel beams for comparison had the same sizes as the standard CST beam.

2.3 CST BEAMS FOR PARAMETRIC STUDY

As to the CST beams for the parametric study, illustrated in Figure 2, the bolt spacing was reduced from 200 mm to 150 mm or the protection thicknesses of the outer Glulam layer for the steel beam along the height and width were reduced from the original 50 mm to 30 mm.

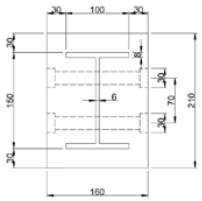

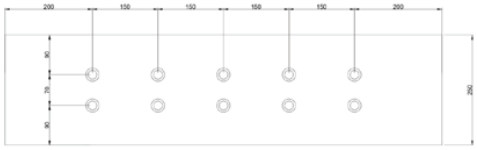

Figure 2: *The profiles of the parametric CST beam models*

3 FINITE ELEMENT ANALYSIS (FEA)

From the experimental test results, Tsai [13] and Zhang [26] indicated that the CST specimens did not have large structural deformations and damages that affected the heat transfer and temperature field distributions in the process of fire. Considering the accuracy in the thermal-solid coupling simulations and analyses on this kind of CST beam model and computational costs, the commercial finite element software ABAQUS and the sequentially coupled analysis method recommended by some previous researchers [26,27] was adopted.

Therefore, the temperature field would be first operated and analysed based on the ISO standard fire curve [28], and then the calculated temperature results were imported into the displacement field as the predefined field to calculate the final bending performances of the CST beams after being exposed to fire for 2 hours.

3.1 THE ESTIMATION METHOD

The material properties, including thermal and mechanical properties of steel and timber, show variations in response to elevated temperatures and their specific relationships would be input into ABAQUS in the tabular form based on the relevant specifications and the existing research data.

For steel, indicated by BS EN 1993-1-2 [19], its density ρ could be seen as a constant value when the surrounding temperature rises, i.e. ρ = 7850 kg/m^3, and the specific heat and thermal conductivity are shown as functions of temperature, respectively. Similarly, BS EN 1995-1-2 [20] also gives the suggested thermal parameter values for timber materials after fully considering water evaporation, wood carbonisation decomposition and material composition changes during combustion.

As for the mechanical properties, steel was regarded as an isotropic material and an elastic-linear – perfectly plastic model was adopted [27]. Generally, timber materials for Glulam have different properties in normal, radial and tangential directions and can be regarded as an ideal anisotropic elastoplastic body with suggested engineering data [22] for simulations.

3.2 SETUP OF THE NUMERICAL MODELS

During the modelling, the influence of adhesives on the temperature field was not considered. It was assumed that there was no air layer between the components. Because the thickness of the adhesives layer was small, and the heat from the external fire site would be quickly transferred to the interior components. The 3 mm fine mesh around the bolt holes and the 15 mm loose mesh for other areas were applied according to the configuration

https://doi.org/10.52202/069179-0229

characteristics of the parts. The final assembled model is shown in Figure 3.

Transient heat transfer and general static steps are defined for the thermal and mechanical models, respectively. Besides, the external fire site should be applied in the temperature field by defining an amplitude based on the standard fire curve, and in the displacement, the uniformly distributed load should also be directly applied on the top surface of the composite beam in the pressure form of 100 kN/m^2. As to the boundary conditions, the absolute zero temperature, the Steve-Boltzmann constant (5.678×10^{-8} W/m^{2}K^4) and the ambient temperature, the emissivity values (0.7 and 0.8 for steel and timber) and convection coefficient (25 W/m^2°C) [27] should be defined in advance to facilitate the calculations and analyses of heat conduction, radiation and convection in the temperature field. As to the contact definitions, in the normal direction, hard contact was defined to apply no restrictions to the pressures transferred between timber and steel and the Coulomb's friction model [26] with the friction coefficients of 0.3 and 0.001 for steel-timber and steel-steel contacts. During the flexural performance analysis, both ends of the composite beam in two directions shall be restricted, for the simulation requirement of a simply supported beam. More modelling details can be found from the ABAQUS User Manual [24].

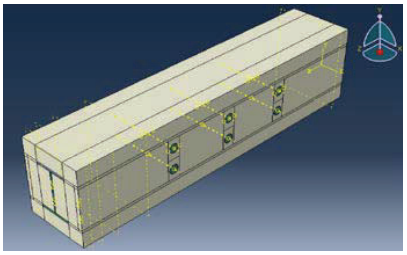

Figure 3: *The final assembled CST beam model in ABAQUS*

4 NUMERICAL SIMULATION RESULTS AND ANALYSES

4.1 TEMPERATURE FIELD ANALYSES

4.1.1 Temperature distributions

As shown in Figure 4, the temperature distributions for the Glulam, steel beam and steel bolts are presented and analysed.

The Glulam serving as the protection layer, firstly carried out heat transfer between itself and the surrounding fire environment. Therefore, the calculated node temperatures of the outermost layer of the Glulam quickly reached a high value, up to 1000°C, while the top surface of the Glulam beam was not directly affected because it directly contacted with the floor slab. The overall temperature distribution presented a trend that node temperatures would decline from the outside towards the centre, where they had the lowest values, which is consistent with the test results in the literature [26].

The web and lower flange of the steel beam were the parts with the highest temperatures in the whole beam, namely 350°C ~ 420°C. The bolt holes in the middle of the web, where steel bolts were through the beam and carried out the heat transferred from the external fire field, induced the rises in the node temperatures near the bolt holes of the steel webs, especially around the bolt holes near the bottom of the CST beam, which bear the double heat penetration from all three heat transfer directions of the fire field and from the external bolts. The upper flange at both ends of the steel beam was far away from the thermal penetration of the bolt holes and was insulated by the outer Glulam beam. Therefore, the node temperature did not increase significantly and remained at around 150°C.

All six bolts show the characteristics of high temperatures at both ends and lower temperatures in the middle. The reason for this is that both heads and nuts of the bolts were exposed first to fire conditions, and were surrounded by the Glulam beam, so the heat would mainly extend along the bolt direction, which was in line with the engineering practice. Furthermore, the temperature distributions of the lower bolts were slightly different from the upper ones and more unfavourable, which were consistent with the differences in the temperature distributions of the bolt hole areas adjacent to the lower and upper flanges of the steel beam, due to the uneven heat transfer from the fire field onto three sides of the CST beam. However, the temperatures of the central bolts at the mid-span were higher than those of the bolts near the supports, which may be due to the superposition effect of the temperature penetrations from the bolts on the left and right sides.

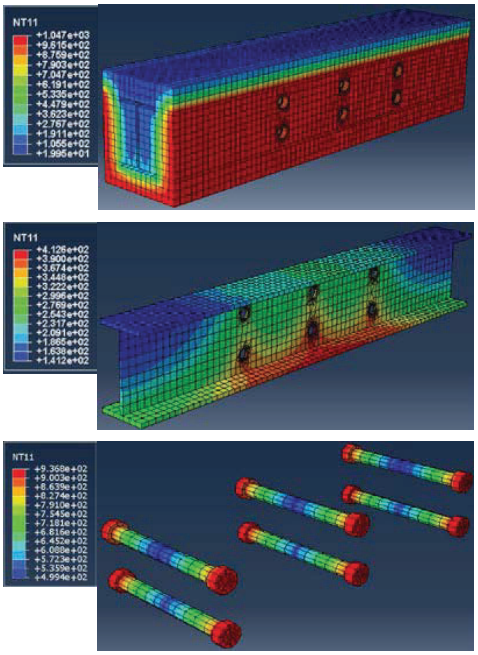

Figure 4: *Node temperature contours of the Glulam beam, steel beam and steel bolts at t = 120 min*

4.1.2 Assessment of the protection ability of Glulam

In Figures 5 and 6, the temperature distribution results at t = 15 and 60 min are presented and further analysed, combined with results illustrated in Figure 4, in terms of the protection effects brought by the external Glulam beam.

When *t* is equal to 15 min, according to the standard fire curve, the ambient temperature had completed nearly 70% of the final temperature loading, and the heads and nuts of the steel bolts had reached around 260°C. However, the overall temperature of the steel beam was no higher than 30°C because the outer Glulam beam provided good insulation, which was highly consistent with the Tsai's test results [13], and the protection effect of the outer Glulam was reliable and effective within the first 15 minutes under the fire conditions. In addition, due to the heat conduction of the bolts through the CST beam, the temperature growth of the steel beam started from the bolt holes in the steel web and gradually extended to the flanges and both ends of the steel beam.

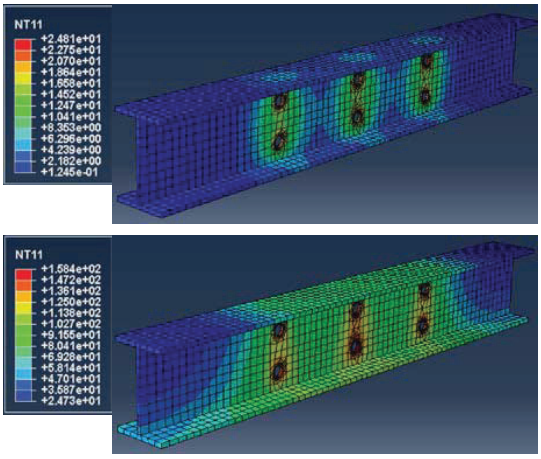

Figure 5: *Node temperature contours of the steel beam at t = 15 min and 60 min.*

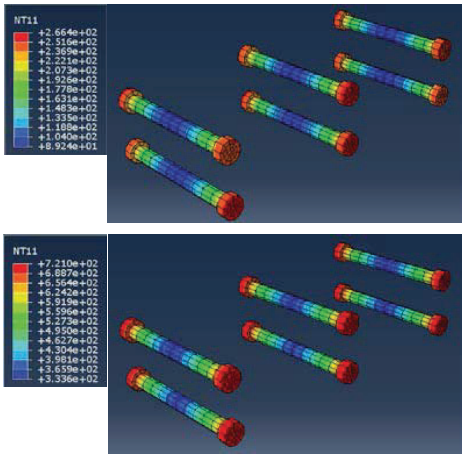

Figure 6: *Node temperature contours of the steel bolts at t = 15 min and 60 min.*

When the standard fire was applied for 60 minutes, the ambient temperature gradually increased to 945.3°C. At this point, the temperature field near the areas of the bolt holes in the middle of the steel beam became significantly superposed, and the temperatures in the areas at the mid-span were the highest, which was presented by the software with the large red block. In addition, the mid-span temperature "diffusion" increased further and extended to the lower flanges at both ends of the beam, but the temperatures in the upper flanges at both ends remained below 50°C. Combined with the temperature field distributions of the bolts at this time, the node temperatures in the middle of the bolts had reached the temperature range of 330°C ~ 400°C, while the maximum temperature in the middle of the steel beam was only about 160°C, presenting a "gap" of heat transfer. This may be because when the bolts temperature rose rapidly, part of the heat was absorbed by the surrounding Glulam beam, while the rest was absorbed by the steel beam. In other words, the internal Glulam played a vital role in absorbing and blocking the fire heat transferred from the bolts.

After the 2-hour burning, the temperature increment of the external fire site levelled off, reaching 1049°C, and the heat transfer lasted for quite a long time. However, from Figure 5, the highest temperature zone of the steel beam occurred in the web and lower flange of the mid-span, reaching about 410°C, while the temperatures in most areas were in the range of 200°C ~ 300°C. This distribution characteristic was similar to that in the 60-minute stage where the temperatures at both ends were low and those at the mid-span were high. According to the typical stress-strain curves [29] of the steel (see Figure 7) at elevated temperatures, the mid-span of the inner steel beam could retain most of its yield strength, and more strains could be spared for deformations, showing stronger plasticity even in the 120-minute fire stage.

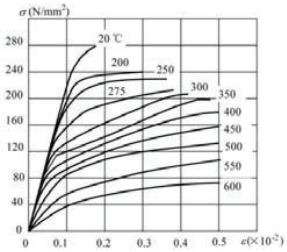

Figure 7: *Typical stress-strain curves of steel at elevated temperatures [29].*

4.1.3 Analysis of the charring results of the Glulam

For the ABAQUS simulations, the timber elements with temperatures exceeding 300°C should be regarded as the carbonised layers. Charring rate, referring to the ratio of the depth of the charring layer to the fire exposure time, is an important index to verify the accuracy of the numerical model. However, the charring rate is not constant [26], and the formation of the charring layer hinders the heat transfer to the interior. Therefore, with the increase of the heating time, the charring rate decreases.

The charring depths and charring rates were roughly calculated (based on the bottom surface) by analysing the temperature distributions in the CST beam section in four time points (see Table 1). According to the calculated data in the table, it can be found that the charring depth increased with the increase of the acting duration of the standard fire curve, while the charring rate decreased as the process continued, which would basically conform to

https://doi.org/10.52202/069179-0229

the law mentioned above. Besides, with the increase of the charring depth, the outer Glulam gradually lost its ability to protect the steel, and Figure 8 shows that a 50 mm outer Glulam protection layer for the steel beam was basically burned out completely. If the fire temperature kept rising, the temperatures in the steel beam would quickly increase, eventually causing the complete strength loss of the steel.

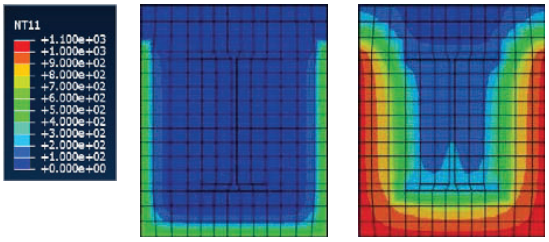

Figure 8: *Temperature field distributions of the CST beam section at t = 15 min and 120 min.*

Table 1: *Summary of the charring depth and rate results at the selected four time points*

Time duration (min)	Charring depth (mm)	Charring rate (mm/min)
15	13.3	0.89
30	20.2	0.67
60	30.1	0.50
120	49.8	0.42

4.2 DISPLACEMENT FIELD ANALYSES

4.2.1 Analysis of the simulation results

Figure 9 illustrates the 3D displacement and von Mises stress contours of the embedded steel beam. For the simulated displacement results, the maximum displacement appeared in the mid-span region and decreased from that region toward both ends. This was consistent with the displacement distribution of a simply supported steel beam under bending actions at room temperature. Under the uniformly distributed load of 100 kN/m^2, i.e. 10 kN/m line load, the maximum displacement was 9.65 × 10^{-5} m. According to the linear relationship between the maximum mid-span displacement and bending loads applied onto the steel beam, combined with the generally recognised deflection limit of L/360 under service loading, the maximum load capacity could be estimated to be close to 300 kN/m, which also matches the engineering practice. Therefore, this served as an initial validation for the established model and based on this, reflected a good deformation capacity for the embedded steel beam subjected to the 2-hour fire conditions.

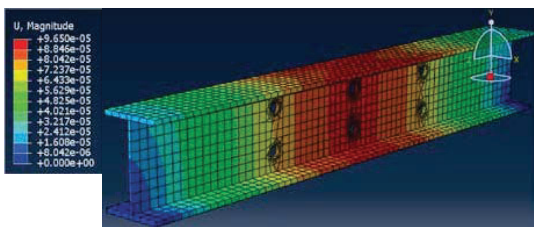

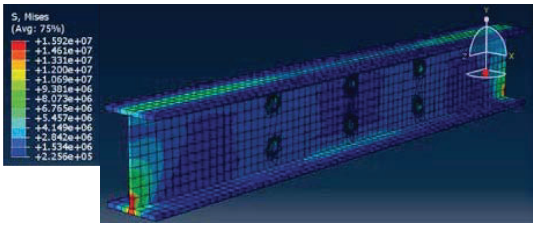

Figure 9: *Simulated 3D displacement and von Mises stress of the embedded steel beam in the displacement field.*

The 3D von Mises stress contour shows that lower flange at the two ends and the upper flange in the middle span region of the steel beam sustained unfavourable stress distributions. This may be because the steel beam at this moment had a tendency of buckling on both sides of the upper flange under the applied uniformly distributed load, and the lower flange in the middle span, subjected to the highest bending moment and tensile stress, was weakened by the bolt holes in the web, resulting in strong stress concentrations. The general trends matched the original expectations and were similar to the generally recognised stress distributions of the steel beam under the bending action. However, due to the restrictions of the outer residual timber beam, the stress distributions of the embedded steel beam were not obvious.

4.2.2 Manual estimation calculations

Figure 10 illustrates the simplified calculation diagram of the steel beam and the geometrical parameters of its cross-section by ignoring the imperfection effect caused by the bolt holes in the steel web. Therefore, the second moment of area and the sectional modulus of the steel beam could be calculated as 9277185 mm^4 and 123696 mm^3. It was also assumed that the UDL acting on the steel beam was w in kN/m, including the self-weight of the steel beam and the variable loads on the upper flange.

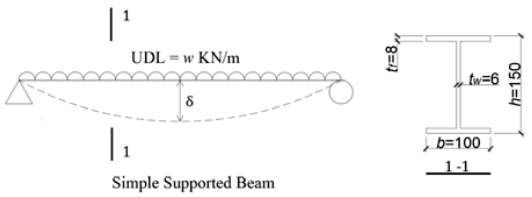

Figure 10: *Illustration of the simply supported embedded steel beam under the UDL.*

Under fire conditions, the maximum temperature of the embedded steel appeared in the lower flange at the mid-span, which coincided with the maximum bending moment and deflection point of the steel beam under the static loading at room temperature. In this case, the load bearing capacity calculation would mainly be focused on the mid-span location. The temperature at the mid-span of the steel beam reached 416°C after a two-hour standard fire. According to BS EN 1993-1-2 [19], both the elastic modulus and yield strength of steel would drop at this temperature and the reduction coefficients could be applied as 0.685 and 0.97, respectively, i.e. E = 0.685 ×

210000 = 143850 N/mm^2 and f_y = 0.97 × 400 = 388 N/mm^2.
According to BS EN 1993-1-1 [30], the bending moment capacity could be related to the UDL as

$$M_{c,Rd} = \frac{W_{pl} f_y}{\gamma_{M0}} = \frac{123695.80 \times 388 \times 10^{-6}}{1.0} = M_{Ed} = \frac{w L^2}{8}$$

i.e. $M_{c,Rd}$ = 47.99 kNm and w = 383.95 kN/m.
Under the UDL w = 383.95 kN/m, the mid-span deflection δ_{max} would be:

$$\delta_{max} = \frac{5 w L^4}{384 E I} = 3.75 \text{ mm} > \delta_{limit} = \frac{L}{360} = 2.78 \text{ mm}$$

The steel beam failed due to the exceeded deflection under the UDL w = 383.95 kN/m. Thus, letting the maximum deflection at the mid-span be equal to its limit would yield the maximum UDL the steel beam could support, that is, w = 284.70 N/mm = 284.70 kN/m.
At this time, although the bearing capacity could reach up to 383.95 kN/m, the deflection would exceed its design limit. Therefore, if the deflection requirements were met, the final bearing capacity would still need to be further reduced. However, in practice, since the outer Glulam beam had not completely burned out, it serves as a T-shape coating outside the steel beam to limit its excessive deflection and the buckling failure of its upper flange and web. Thus, the ultimate bearing capacity would still be governed by the bending moment capacity.

4.3 COMPARATIVE ANALYSES

4.3.1 Steel Beam

A steel beam model with the same size as the embedded steel section in the standard CST beam was created in ABAQUS (without bolt holes), with the similar step, amplitudes and interactions assigned as well. The calculation results for t = 15 min were selected and are shown in Figure 11 below.
It can be seen from the figure that, without the protection of the outer Glulam, the temperature of the steel beam rapidly reached above 600°C within only 15 min, and the highest temperature in the web was nearly 700°C. The steel beam exhibited "thermo-plastic" phenomenon, and most of the strength was lost. At this moment, even a small load was applied on the steel beam, its web would quickly buckle due to insufficient strength and stiffness, leading to the failure of the steel beam.

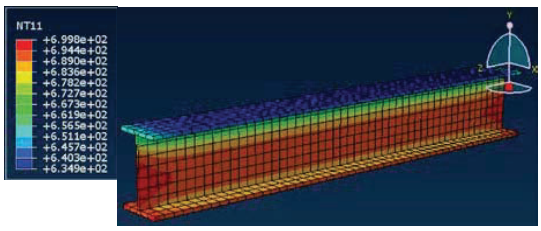

Figure 11: *Node temperature contour of the pure steel beam at t = 15 min.*

4.3.2 Glulam beam

The Glulam beam model without embedded steel and through bolts was created in ABAQUS with the same size as the external Glulam beam of the standard CST at t = 15 min and 60 min.
It is apparent that the overall temperature distributions and charring depth of the Glulam beam, which was about 16.7 mm, were similar to those of the CST beam. This means that the steel bolts, which brought the heat from the outside fire environment, did not have a critical effect on the overall temperature distributions of the Glulam beam during the first heating hour. As for its bending capacity, it could be estimated by using the reduced cross-section method, as described in BS EN 1995-1-2 [20]. In this case, the effective cross-sectional dimensions of the Glulam beam were smaller than 160 mm × 230 mm under the external loads. However, with the introduction of the steel beam, the overall bearing capacity can be a sum of the individual capacities of both Glulam and steel beams [13], which was greatly improved. Moreover, with the increase of the fire exposure time to one hour, the external Glulam gradually lost most of its strength, with the charring depth to 45.2 mm, while the steel beam material strength reduction was relatively small. Thus, the overall combined value would still show a good bearing capacity or resistance to the external loads.

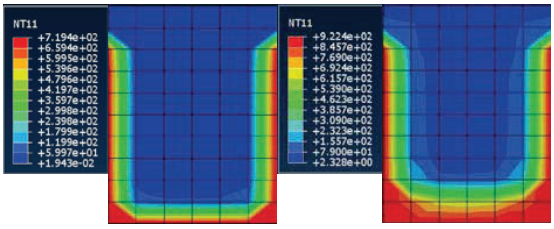

Figure 12: *Temperature distribution contours of the pure Glulam beam section at t =15 min and 60 min.*

5 PARAMETRIC STUDY

To improve the simulation efficiency in ABAQUS, parametric models were symmetrically established as the quarter of an entire beam by creating appropriate symmetry boundary conditions in ABAQUS.

5.1 EFFECT OF REDUCING BOLT SPACING

5.1.1 Charring characteristics

The charring depth was basically the same as that of the standard beam without significant difference for up to one-hour fire exposure (see Figure 13). However, when the fire action extended to 2 hours, the node temperatures of the bottom of the Glulam beam reached 400°C, and thus it was considered that all the protection layers of Glulam failed by then.

5.1.2 Temperature field of the embedded steel beam

By comparing Figures 4 and 14, it can be found that in terms of the overall temperature distributions, due to the decrease in the bolt spacing, more heat from the external fire field penetrated into the internal steel beam through the bolts, specifically through the bolt hole areas in the

https://doi.org/10.52202/069179-0229

web, which resulted in the heat conduction to the surrounding area and eventually the overall temperature distributions in the steel. For instance, for t = 60 min, the average temperature in the steel web exceeded 130°C, while the average temperature in the standard beam was only 110°C. In addition, the smaller bolt spacing made it easier to connect and superimpose the temperature fields around adjacent bolt holes. This could be verified by the fact that the temperature field near the areas of the bolt holes of the standard beam for t = 15 min only had a tendency, while the current beam model completed most of the temperature field connections. Consequently, due to this strengthened superimposition impact, after burning in the fire field for 120 min, the lower flange of the embedded steel beam had reached 462°C. Compared with that of the standard CST beam, namely 416°C, the temperature rose significantly.

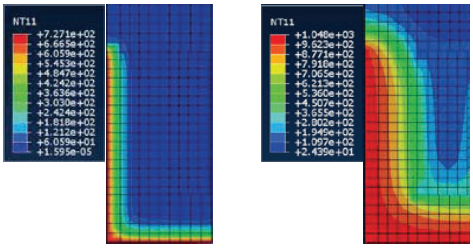

Figure 13: *Node temperature contours of the Glulam section of an adjusted CST beam with the reduced bolt spacing at t = 15 min and 120 min.*

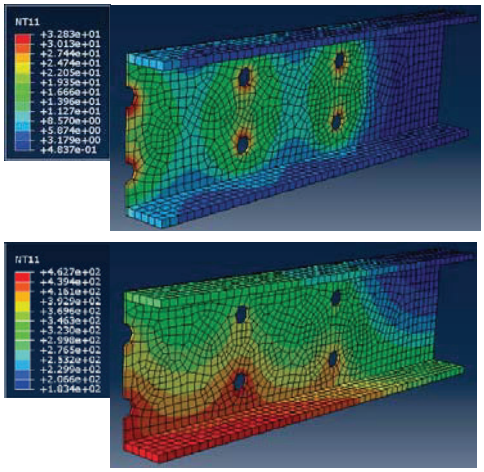

Figure 14: *Temperature contours of the quarter steel beam with the reduced bolt spacing at t = 15 min and 120 min.*

5.1.3 Estimated consequent displacement field

The reduction in the bolt spacing and the increase in the number of bolts per unit length could improve the composition robustness of the Glulam and steel beams, and additionally better the bending performances under room temperature. For structural fire design and analysis, this adjustment would pump more external heat into the internal steel beam, making the temperatures in its web rise faster. Especially after the structure was exposed to the fire for 2 hours, the Glulam at this moment was completely burnt out, and the lower flange of the embedded steel beam would be fully exposed to the fire. If a continuous fire field was applied, the steel beam would be heated up quickly and largely lose its strength. In other words, this would finally weaken the protection ability of Glulam, and the steel beam would lose its bearing capacity faster than the standard CST beam.

5.2 EFFECT OF REDUCING GLULAM PROTECTION THICKNESS

5.2.1 Charring characteristics

By comparing Figures 8 and 15, it can be found that there was a big difference in the charring depth of the adjusted model at t = 2 hour, but there was not much difference between the corresponding charring depths at t = 15 min. This could be because when the protection layer thickness of the Glulam decreased with the increase of the fire duration, the protection layer was burned off and heat gradually came into contact with the bottom flange of the steel beam. Thus, the steel beam could well transfer the heat evenly to other areas of the beam for a better thermal conductivity. This would help absorb some heat from the Glulam. When the action time was small, the protection effect of Glulam still played a governing role, and thus the charring depth difference was not so big.

5.2.2 Temperature field of the embedded steel beam

By comparing Figures 5 and 16, it can be found that because of the reduced protection layer thickness of the Glulam, heat from the fire environment would be able to penetrate the bottom flange of the embedded steel beam more quickly, and this led to the quicker rises in the overall temperatures in the steel beam. Especially, at t = 60 min, the average temperature of the lower flange had exceeded 230°C, while the average temperature of the standard beam was only 120°C. This huge difference became more obvious in the 120-min temperature field. At this moment, the maximum node temperature occurred at the mid-span of the lower flange and reached almost 670°C, which was much higher than that of the standard CST beam model, namely 416°C, and would cause excessive reductions in the material properties. Hence, reducing the thickness of the Glulam protection layer would greatly increase the heating rate of the embedded steel beam.

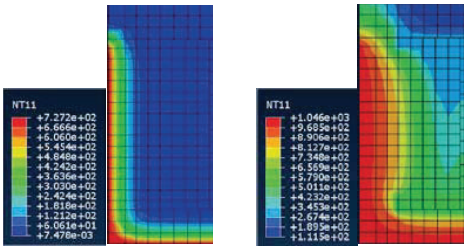

Figure 15: *Node temperature contours of the Glulam section of an adjusted CST beam with the reduced Glulam protection layer at t = 15 min and 120 min.*

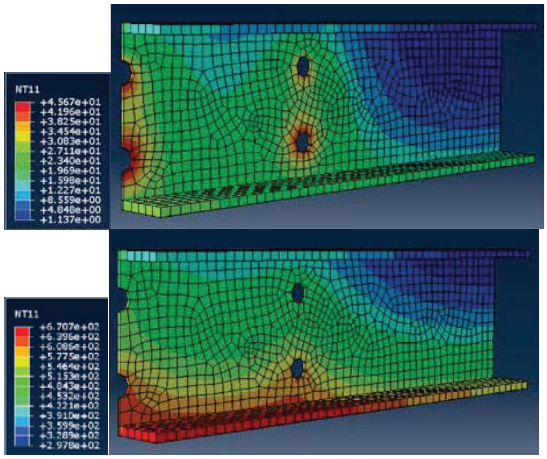

Figure 16: *Node temperature contours of the quarter steel beam with the reduced Glulam protection thickness at t = 15 min and 120 min.*

5.2.3 Estimated consequent displacement field

Although the thickness of the protection layer of the Glulam is reduced, the self-weight of the composite beam decreases as well, and thus the structural efficiency under room temperature will be improved to a certain extent which eventually reduces the costs. However, in terms of structural fire design and analysis, such adjustment will make the heating rate of the embedded steel accelerate because its lower flange prematurely participates in the heat transfer of the temperature field of the whole structure, and the refractory limit will be greatly reduced. If the requirements of structural efficiency and fire resistance are considered at the same time, the optimal protection layer thickness can be determined through subsequent experiments and analysis for achieving the double benefits of economy and structural safety.

6 Conclusions

In this research, based on the commercial finite element analysis software ABAQUS, numerical simulations and analyses of the temperature field and displacement field of the standard CST beam were conducted in a sequential coupling way. Through the analyses on the temperature field results, the validity of the calculation model was verified, and the heat transfer process and distribution characteristics of this type of CST beam under fire conditions were summarised. By analysing the results of the displacement field, the flexural performances of the embedded steel beam after the fire were determined. Additionally, the corresponding steel beam and Glulam beam models were simulated for comparison, and the advantages of this type of CST beam in the structural fire design were verified. Finally, by adjusting the parameters of the standard CST beam model, the effects of reducing the bolt spacing and the Glulam protection layer thickness on the temperature fields of the CST beam were analysed, respectively.

Based on the obtained numerical results, the following conclusions on the research results can be drawn.

- After the 120-min standard fire, the 50 mm external Glulam protection layer was almost burned out and charred completely. However, this could effectively protect the embedded steel beam, except the areas of the bolt holes at the mid-span, from experiencing excessive temperature rises and help maintain most of its mechanical properties and structural performances.
- Under the uniformly distributed load, the embedded steel beam showed fairly good flexural resistance, and the stress and displacement distributions were not largely different from those at normal temperature.
- Pure steel beams and Glulam beams compared with the CST beams, presents the inferior loading bearing capacity due to the strength loss induced by “thermos-plasticity” or the excessively reduced effective cross-section area.
- Although reducing the bolt spacing, i.e. increasing the number of bolts per unit length, could improve the composition integrity of the two materials, but under fire conditions, it reversely promoted the temperature field superposition of the bolt hole areas in the steel beam web and accelerated the heating rate in the embedded steel beam, and thus the ultimate load bearing capacity and refractory limit could be reduced.
- Although reducing the thickness of the Glulam protection layer, i.e. reducing the self-weight of the CST beam, and improving the structural and economic efficiencies, the distributions of the composite structure in the temperature field were largely affected. After the 60-minute standard fire, the Glulam protection layer was completely burned out, and the continuous heating would lead to a rapid rise in the temperature in the embedded steel, and finally the overall failure of the composite steel-timber beam structure would happen.

In general, the structural fire analysis of the new type of CST beam, carried out through the numerical simulations in this study, was relatively abundant, after verifying its potential advantages in fire engineering, evaluating its flexural performance under the two-hour standard fire, and assessing the impacts of the variations in the bolt spacing and Glulam protection thickness on the structural performances of the CST beam under fire conditions. In the future, the comparative explorations between laboratory combustion data and numerical simulation results as well as the parameter optimisation analyses based on the secondary development of finite element software will be the focus of subsequent research.

ACKNOWLEDGEMENTS

This project is supported by both the School of Computing, Engineering and Built Environment at Glasgow Caledonian University, Scotland, UK, and the Department of Civil Engineering, School of Architectural Engineering, Jinling Institute of Technology, Jiangsu Province, China. The project is also supported by the MDPI journal Buildings, together with its Special Issues

https://doi.org/10.52202/069179-0229

"Advanced Concrete Structures in Civil Engineering" and "Dynamic Performances of Building Structures".

REFERENCES

[1] Fujita, M., Sakai, J., Oda, H. and Iwata, M. Building system for a composite steel-timber structure. *Steel Construction*, 2014, 7(3), 183-187.

[2] Japan Association of Building Construction Technicians (JABCT): 100 Selected Typical Examples of Structural Technology in Japan. China Building Industry Press, Beijing, China, 2005.

[3] Liu, Z., Jia, H., Wu, C., Li, M. and Chen, X. Research on the life cycle management method of 3D visualized fabricated steel structure based on BIM technology. In *Proceedings of Jiangsu Steel Structure Conference*, Oct 2019, Nanjing, China, 238-242.

[4] Zhang, Y. and Zhou, X: Design Principle of Steel Structure (2nd Ed). Higher Education Press, Beijing, China, 2004.

[5] Bai, R., Jiang, Z. Research on steel-timber composite structure. *Journal of Hebei Institute of Architecture and Civil Engineering*, 2016, 34(3), 75-78.

[6] Wang, X., Chen, Z., Bai, J., Li, S. and An, Q. Research status and development prospect of timber-steel composite structure. In *Proceedings of National Steel Structure Academic Annual Conference*, Apr 2011, Kunming, China.

[7] Chiniforush, A.A., Valipour, H., Akbarnezhad, A. and Bradford, M. Steel-timber composite (STC) beams: Numerical simulation of long-term behaviours. *Eurosteel*, 2017, 1(2-3), 2051-2059.

[8] Fujita, M. and Iwata, M. Bending test of the composite steel-timber beam. *Applied Mechanics and Material*, 2013, 351-352, 415-421.

[9] Luo, J., Li, Q. and Deng, R. Numerical analysis on flexural performance of a new kind timber-steel composite beams. *Low Temperature Architecture Technology*, 2017, 39, 46-48.

[10] Pan, F. *Experimental Research and Finite Element Analysis on Steel-Timber Combined Members*. Master's Thesis, Southeast University, Nanjing, China, 2008.

[11] Wang, J. and Duan, S. Experimental analysis of eccentric pressure behaviour of steel-timber composite columns. *Building Technology*, 2019, 46(9), 16-17.

[12] Hua, Q., Gao, Y., Meng, X. and Diao, Y. Axial compression of steel-timber composite column consisting of H-shaped steel and Glulam. *Engineering Structures*, 2020, 216, 1-12.

[13] Le, T. and Tsai, M. Behaviour of timber-steel composite with dowel connection under fire. *Key Engineering Materials*, 2019, 803, 195-199.

[14] Liu, Y., Chen, Z., An, Q. and Chen, B. Experimental investigation on lateral resistance performance of light timber-steel hybrid shear wall. *Journal of Tianjin University (Science and Technology)*, 2017, 50, 78-83.

[15] Zhou, X., Li, Z., Wang, R. and Shi, Y. Study on load-carrying capacity of the cold-formed steel joists-OSB composite floor. *China Civil Engineering Journal*, 2013, 46(9), 1-11.

[16] Keipour, N., Valipour, H.R. and Bradford, MA. Steel-timber composite beam-to-column joints: Effect of connections between timber slabs. *Journal of Constructional Steel Research*, 2018, 151, 132-145.

[17] Hassanieh, A., Valipour, H.R., Bradford, M.A. and Sandhaas, C. Modelling of steel-timber composite connections: Validation of finite element model and parametric study. *Engineering Structures*, 2017, 138, 35-49.

[18] Knobloch, M. Structural fire design - developments in research and assessment of fire in steel and composite structures. *Eurosteel*, 2017, 1(2), 133-142.

[19] BSI. *BS EN 1993-1-2:2005 Eurocode 3: Design of Steel Structures - Part 1-2: General Rules - Structural Fire Design*. The British Standards Institution (BSI), London, UK, 2005.

[20] BSI. *BS EN 1995-1-2:2004 Eurocode 5: Design of Timber Structures - Part 1- 2: General - Structural Fire Design*. The British Standards Institution (BSI), London, UK, 2004.

[21] Zhang, J., Liu, Z., Xu, Y., Ma, S. and Xu, Q. Experimental and numerical study on the charring rate of timber beams exposed to three-side fire. *Science China: Technological Sciences*, 2012, 55 (12), 3434-3444, 10.1007/s11431-012-4996-1.

[22] Product Guide: Glulam. Available online: https://www.apawood.org/publication-search?q=X440&tid=1 (Accessed on 10 November 2020).

[23] 3D EXPERIENCE, ABAQUS; Version 2020 [Computer software]; Dassault Systèmes Simulia Corp., Providence, RI, USA. 2019.

[24] ABAQUS 6.14: Analysis User's Guide. Available online: https://www.academia.edu/28334906/ Abaqus_Analysis_Users_Guide/ (accessed on 20 May 2021).

[25] Zhu, Y. and Cai, W. *Introduction to ABAQUS/ Standard Finite Element Software - ABAQUS/CAE Edition*. Tsinghua University Press, Beijing, China, 2003.

[26] Zhang, Y. *Experimental Study on the Fire Performance of Post-and-Beam Timber Structure with Bolted Steel-Timber Connection.* Master's Thesis, Southeast University, Nanjing, China, 2016.

[27] Ohene, A.A. *Modelling the Fire Performance of Hybrid Steel-Timber Connections*. Master's Thesis, Carleton University, Ottawa, Canada, 2014.

[28] ISO. *ISO 834-1: Fire Resistance Tests - Elements of Buildings Construction - Part-1: General Requirement*, International Organization for Standardization (ISO), Switzerland, 1999.

[29] Li, G. and Wang, W. State-of-the-art and development trend of fire safety research on steel structures. *China Civil Engineering Journal*, 2017, 50(12), 1-8.

[30] BSI. *BS EN 1993-1-1:2005 + A1:2014 Eurocode 3: Design of Steel Structures −Part 1-1: General Rules and Rules for Buildings*. The British Standards Institution (BSI), London, UK, 2005.

World Conference on Timber Engineering Oslo 2023

FIRE-PROTECTED TIMBER ELEMENTS OF CONSTRUCTION – RESPONSE DURING FIRE DECAY AND COOLING PHASE

Paul England[1], Boris Iskra[2]

ABSTRACT: The Building Code of Australia now permits the use of Fire-protected Timber in all classes of buildings up to an effective height of 25 metres (typically 8-storeys). Fire-protected Timber elements of construction consist of lightweight structural timber-frame or massive timber elements protected by fire-protective grade linings to reduce the risk of ignition of timber members and achieve the required fire-resistance level in addition to other criteria such as the acoustic and thermal performance appropriate to the class of building.

In support of this Code change, research was undertaken to investigate the post-fire decay and cooling phase behaviour of lightweight structural timber-frame or massive Fire-protected Timber elements for which there is currently limited research and publicly available data. As with all structural building materials, this post-fire behaviour can lead to failure of structural building elements if not adequately addressed. The research demonstrated that on-going combustion of Fire-protected Timber elements could be prevented using encapsulation provided by an appropriate layer of fire-protective grade coverings.

KEYWORDS: Lightweight timber-frame, CLT, fire, decay phase, cooling phase

1 INTRODUCTION

Changes to the Building Code of Australia Volume One (BCA) in 2016[1] and 2019[2] introduced Deemed-to-Satisfy (DTS) provisions as a means of demonstrating compliance for mid-rise timber buildings based on the concept of Fire-protected Timber.

These changes now permit lightweight structural timber-frame or massive timber elements protected by fire-protective grade linings, installed in conjunction with automatic sprinkler systems, to be used in all classes of building up to 25 metres in effective height (vertical distance from the ground floor storey to the floor of the topmost storey - typically up to 8-storeys); where previously non-combustible building elements were required.

In support of this Code change, a risk-based approach was adopted, incorporating multi-scenario analyses requiring evaluation of scenarios where the ignition criteria of protected timber were exceeded. Conservative assumptions were made including the assumption that if fire brigade intervention was unsuccessful, and the protected timber element was ignited, the element would fail (i.e., self-extinguishment would not occur).

Subsequently, additional research has been undertaken to investigate the potential for exposed and Fire-protected Timber to self-extinguish or, if sustained combustion continues, to evaluate the rate of deterioration of the timber elements during the post-fire decay and cooling phase to further extend applications for timber construction. The post-fire behaviour of both lightweight structural timber-frame and massive Fire-protected Timber construction elements are being investigated.

Detailed analyses undertaken in support of the Australian Code change were made with several conservative assumptions; including that if the surface temperature of timber exceeded 250°C for lightweight timber framing, or 300°C for massive timber elements, combustion would continue until failure occurred; unless fire brigade intervention occurred prior to the temperatures being exceeded.

This paper describes subsequent research undertaken investigating the post-fire behaviour of these timber building elements when exposed to the standard heating regime in accordance AS 1530.4[3] and more severe fire scenarios. This post fire behaviour can lead to failure of structural building elements if not adequately addressed which is not unique to timber.

Further details of the research and analysis is provided in the WoodSolutions Technical Design Guides #18[4] and #38[5].

[1] Paul England, EFT Consulting, Australia, paul.england@eftconsult.net
[2] Boris Iskra, Forest and Wood Products Australia (FWPA), Australia, boris.iskra@fwpa.com.au

https://doi.org/10.52202/069179-0230

2 DECAY AND COOLING PHASE RESPONSE

Building enclosure fires are typically categorised into four stages – (1) incipient/initiation, (2) growth, (3) fully developed and (4) decay. In some applications, it may be necessary to extend the analysis and consider a cooling phase if the behaviour of elements of construction after extinction of the contents (i.e., the moveable fire load) and combustible elements is to be considered – refer Figure 1. Typically, this may be necessary where degradation of elements of construction occurs after extinction of the contents due to thermal inertia, degradation on cooling (Dimia *et al*[6]) and/or localised smouldering combustion of elements of construction (McGregor[7]).

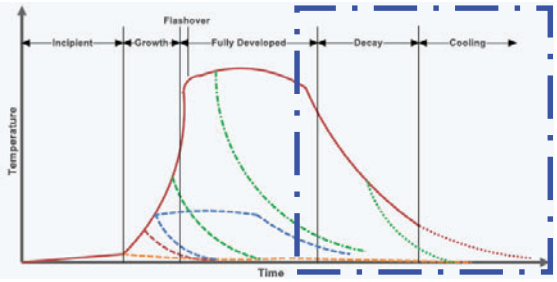

Figure 1: *Building enclosure fire stages*

The response of elements of construction during the decay and cooling phase can be an important consideration; particularly in applications such as high-rise buildings where fire brigade intervention and evacuation of occupants may be difficult during some fire scenarios.

Once the majority of the fire load is consumed, the burning rate will reduce significantly leading to reduced enclosure temperatures. However, there may still be potential for a thermal wave to spread through an element due to its thermal inertia and/or for smouldering combustion of timber structural elements to continue.

Under some circumstances, a thermal wave can subsequently lead to structural collapse of common building structural materials used such as timber, concrete and steel. The risks of smouldering combustion or of incipient fire spread is specific to combustible materials and can also eventually lead to structural collapse or reignition of flaming combustion.

In most instances, both natural and furnace fire-resistance tests are terminated at the end of a nominated exposure time so there is relatively limited data on their behaviour during the decay and cooling phases; which can last for extended periods varying from several hours to 24 or more hours in extreme cases. Recent studies, such as the Epernon Series[8] and Fire Safe Implementation of Visible Mass Timber[9], have monitored conditions at the end of tests to evaluate performance during the decay phase.

2.1 PREMATURE STRUCTURAL FAILURE

Premature structural failure of building elements may occur as a result of failure of automatic sprinkler systems, fire-protective coverings, and detection and alarm systems as well as a relatively slow fire brigade response. However, structural failures can also occur sometime after fire exposure due to several causes, including:

- temperatures of structural elements continue to increase during the decay period of a fire due to the thermal inertia of the enclosure fabric and fire protection systems
- stresses may be induced on cooling
- material properties may change on cooling, and
- smouldering combustion and incipient spread of fire may continue.

Some fire-resistance tests performed for FWPA have included monitoring of simulated decay phases in conditions with normal atmospheric concentrations of oxygen by removing specimens from the furnace and continuing exposure of the specimen to heat as described below.

3 TESTED SYSTEMS

3.1 ENCAPSULATED LIGHTWEIGHT ENGINEERED FLOOR-CEILING SYSTEM

A full-scale, loadbearing fire-resistance test was undertaken on a lightweight engineered timber floor-ceiling system to determine the fire resistance of various types of lightweight engineered beams (e.g., timber and metal webbed parallel chord floor trusses, timber and metal webbed I-joists) protected by a plasterboard ceiling system. The specimen was subjected to the AS 1530.4 standard heating regime for 122 minutes.

The ceiling system comprised three layers of fire-protective grade plasterboard, each 16 mm thick, fixed to metal furring channels that were supported from the floor joists by direct fixing metal brackets using typical industry installation practices. The test was terminated after two hours without failure under the criteria of structural adequacy, integrity and insulation and achieved a 2-hour fire-resistance (FRL 120/120/120).

In addition, a 120-minute Resistance to the Incipient Spread of Fire (RISF) level was also achieved. RISF is a criterion within AS 1530.4 which was originally introduced for ceiling membranes to ensure that the space between a ceiling and roof, or ceiling and floor above, is insulated so as to limit the temperature rise of materials in this cavity space to a level that will not permit the rapid and general spread of fire throughout the space to adjoining compartments. Failure under the criterion of RISF is deemed to have occurred when the maximum temperatures at the nominated positions on the ceiling system exceed 250°C. Application of the RISF criteria was extended to other light-weight Fire-protected Timber elements such as partition wall systems by the BCA in 2016.

https://doi.org/10.52202/069179-0230

After 120 minutes, the heating was terminated and the specimen was raised 600 mm above the furnace allowing free access to the laboratory atmosphere while being exposed to heat from the furnace floor and walls to simulate the decay and cooling phases under natural convection. The floor-ceiling specimen was then monitored for a further 17 hours without intervention – refer Figure 2.

Figure 2: *Exposed face of specimen at the end of the monitoring period.*

The temperatures measured below the ceiling during the fire test exposure and for the first two hours of the cooling phase are shown in Figure 3. The specimen then continued to support the full test load while cooling to ambient temperatures over the remaining 15 hours of the monitoring period.

There was no evidence of combustion of the timber elements during the test and throughout the monitoring period. The temperatures on the upper surface of the plasterboard sheeting peaked after approximately 150 minutes (30 minutes after termination of heating) but temperatures did not exceed 250°C as shown in Figure 4.

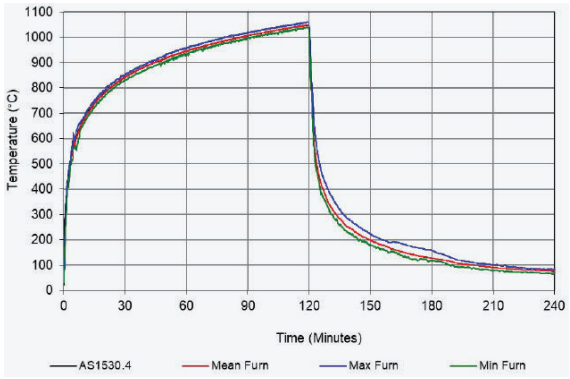

Figure 3: *Complete heating and first two hours of cooling exposure measured by exposed thermocouples*

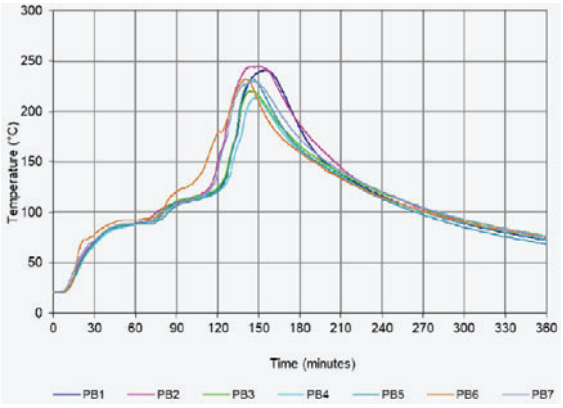

Figure 4: *Temperatures of upper surface of the plasterboard*

3.2 PROTECTED CROSS-LAMINATED TIMBER PANEL

3.2.1 Section within encapsulated lightweight engineered floor system test

A section of cross-laminated timber (CLT) was included within the encapsulated lightweight engineered floor system cavity (described in Section 3.1) and temperatures were measured at various positions within and adjacent to the CLT element. These temperatures are summarised in Table 1 which illustrates that a thermal wave passed through the CLT with temperatures at depths of 20 mm and 55 mm peaking at 94°C and 84°C respectively more than 120 minutes after the end of the heating period.

Table 1: *Peak CLT specimen temperatures and temperatures after 120 minutes*

Ref	Description	Temp. °C @ 120 minutes	Max. Temp. °C
CL-1	Plasterboard-CLT interface temperature	120	226
CL-2	19 mm below CLT soffit (air temp)	109	161
CL-3	CLT soffit	96	151
CL-4	10 mm depth	77	105
CL-5	20 mm depth *(lower glue line)*	52	94
CL-6	55 mm depth *(upper glue line)*	58	84

3.2.2 One layer of 16 mm fire-protective grade plasterboard – Shorter test duration

Two standard fire-resistance tests, in accordance with AS 1530.4, were performed on 105 mm thick CLT panels protected by one layer of 16 mm fire-protective grade plasterboard. The first test was of 45 min duration and the second of 60 min duration. Prior to the tests, the time for the CLT plasterboard interface to reach 300°C was estimated to be approx. 30 minutes and this was confirmed in both tests. Also in both tests, volatiles from the CLT panels ignited at joint positions in the plasterboard but self-extinguished during the monitoring period.

https://doi.org/10.52202/069179-0230

The following is a more detailed review of the 60-minute test.

The specified and measured furnace temperatures for the 60-minute test are shown in Figure 5 for the heating period. At the end of the 60-minute heating period, the area under the mean furnace temperature/time plot exceeded the prescribed standard heating regime by approximately 1.5%.

At the end of the heating period the interface temperatures between the plasterboard and CLT were approximately 500°C and as the specimen was raised above the furnace to allow natural airflow across the surface of the specimen, flaming at the joint between the plasterboard sheets was observed as shown in Figure 6.

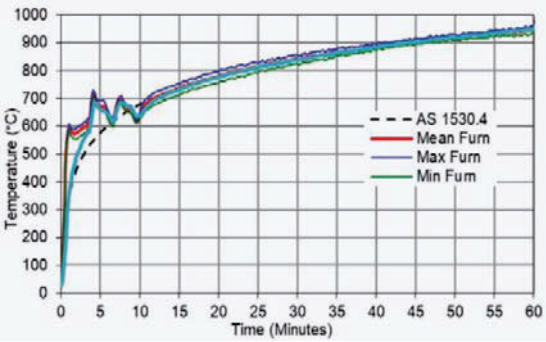

Figure 5: *Furnace temperatures during the 60-minute heating period*

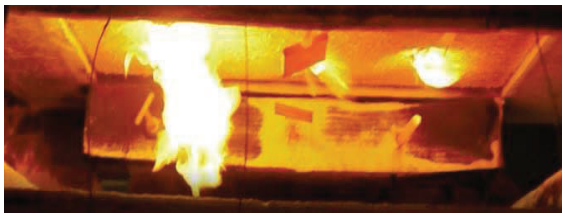

Figure 6: *Flaming from joint between plasterboard 30 seconds after the end of the heating period.*

The flaming gradually reduced and ceased after approximately 11 minutes.

Data monitoring continued for 23 hours and during this period, the CLT panel temperatures had effectively reduced to ambient temperatures with no evidence of continuing flaming or smouldering combustion – refer Figure 7 for interface temperatures between the plasterboard and CLT, and Figure 8 for the temperatures of the CLT panel at varying depths.

This data indicates that the charring was restricted to a depth of approximately 6 mm and that self-extinguishment of smouldering combustion had occurred as well as any flaming combustion.

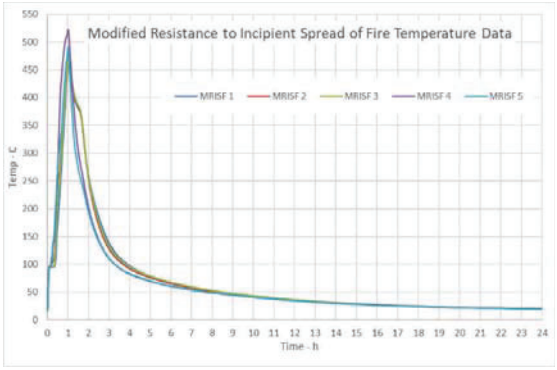

Figure 7: *Thermocouple temperatures at the interface between plasterboard and CLT*

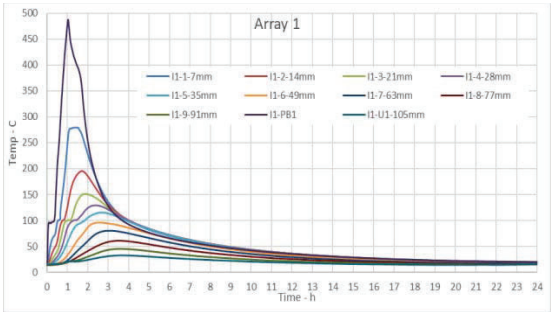

Figure 8: *Thermocouple temperatures across the CLT section*

The incident heat flux to which the underside of the specimen was exposed is shown for the 180 minutes of the monitoring period in Figure 9. Approximately 11 min after completion of heating, the measured heat flux had reduced to approximately 10 kW/m^2; at 42 min after completion of heating, it had reduced to approximately 4 kW/m^2 and 108 min after completion of heating, it had reduced to approximately 2 kW/m^2.

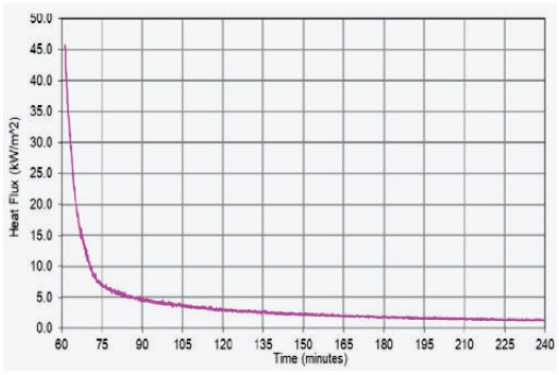

Figure 9: *Heat flux from furnace and specimen for 180 min after heating*

Figure 10 shows the CLT panel with the plasterboard removed clearly highlighting the surface charring to the lower lamella layer. No significant delamination had occurred, but the individual lamella had shrunk in dimension opening the edge joints between the lamella which were not bonded, i.e., no adhesive applied, during the CLT manufacturing process.

https://doi.org/10.52202/069179-0230

Figure 10: *Underside of CLT panel with plasterboard removed after 23-hour monitoring period.*

3.2.3 One layer of 16 mm fire-protective grade plasterboard – Longer test duration

A 225 mm thick CLT panel protected by a single layer of 16 mm plasterboard was subjected to the standard heating regime as a comparative test to the shorter test durations described in 3.2.2.

The CLT panel width was constructed with a central half-lap joint with two joint treatments – half the length of joint sealed with two beads of sealant between the bearing surfaces, and the other half with a plasterboard cover on the non-fire-exposed side.

The test was terminated after approximately 171 min when failure at the joints position was imminent. The conditions were subsequently monitored for a relatively short period of 59 min since the element showed evidence of continuing char oxidation; albeit at a reduced rate. A comparison of the shorter and longer duration CLT tests with one layer of 16mm plasterboard is provided in Table 2.

Table 2: *CLT comparison tests – Single layer of 16 mm fire-grade plasterboard protection*

Test	CLT depth (mm)	Furnace Heating (h:min)	Monitoring period (h:min)	Time CLT-PB interface > 300ºC (min)	PB Fall-off (min)
6	105	0:45	15:00	34	No
8	105	1:00	23:00	32	No
2	225	2:51	0.59	32	115

Heat flux measurements from Test 2 during the decay period are presented in Figure 11. It is noteworthy that, despite evidence of some ongoing combustion, the decay of measured heat flux from the specimen (thin line) reduced to approximately 11 kW/m^2 after 60 min and the measured heat flux received by the specimen from the furnace walls and floor (thicker line) is comparable.

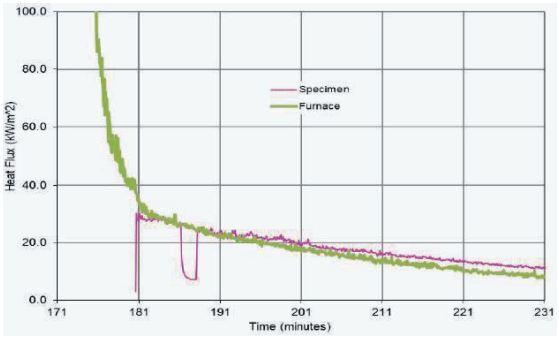

Figure 11: *Heat flux from the furnace and specimen for 60 minutes after heating*

Combustion of the specimen was ongoing at the joint positions and the exposed perimeter of the specimen at the end of the 60-minute monitoring period. Significant delamination occurred such that 90 mm or more of the specimen face had been lost over the heated area, creating a detail at the perimeter where a horizontal face meets a vertical face of timber, facilitating radiative feedback as shown in Figure 12.

Figure 12: *Fire side after the 59-minute monitoring period showing continued edge combustion.*

These observations indicate that as heat penetration into timber elements increases, intersections and joint details will become more critical if self-extinguishment is an objective. It may also be important to maintain fire-protective coverings in place to reduce radiant heat interchanges at intersections of elements.

3.3 TIMBER-FRAME STUD WALL SYSTEM

3.3.1 System construction

A fire-resistance test was undertaken on a loadbearing timber-frame wall system comprising three layers of 16 mm thick fire-protective grade plasterboard applied to each face of 140 mm x 45 mm studs with cavities filled with non-combustible stone wool.

The stone wool insulation was installed, in lamella form, to provide a practical way to reliably install the insulation to be in intimate contact with the timber studs with a controlled level of compression. The high-temperature performance specification and compression was intended to maintain one-directional heating of the timber studs by

https://doi.org/10.52202/069179-0230

avoiding heat transfer through the cavity. The temperature data from the test indicated this was effectively achieved. Figure 13 shows the internal structure of the timber-frame wall system comprising vertical timber studs, horizontal timber noggings and fitted stone wool insulation.

Figure 13: *Internal structure and non-fire side of the high-performance timber-frame wall system*

Laminating screws were used to secure the outer third layer of plasterboard which facilitated the positioning of screw fixings 38 mm from board edges and a reduction of fixing centres over the board area which was expected to significantly improve the retention time for the outer board layer.

3.3.2 Fire performance

The specimen was subjected to the AS 1530.4 standard heating regime for 227 min, after which the specimen was removed from the furnace and conditions were monitored for a further 30 min. The specimen achieved an FRL in excess of 180/180/180 and the Resistance to the Incipient Spread of Fire (RISF) criteria were satisfied for in excess of 120 min.

A total load of 12.3 kN/stud was applied to the specimen; equivalent to a load ratio of 0.5 (i.e., ultimate fire limit state design load to ultimate (ambient) limit states design load). The full test load was applied until 198 min and then progressively reduced until heating was terminated after 227 minutes due to the potential risk of damage to the loading equipment; with no failures under the criteria for insulation and integrity.

Measurements taken during the test included interface temperatures of each plasterboard layer using thermocouples soldered to copper discs at the centre and centre of each quarter section of the wall. Thermocouples were also fitted at approximately these locations on the inner surface of the base plasterboard layer on the fire-exposed side of the specimen to determine the RISF performance.

The RISF results are plotted in Figure 14 and the temperature of the RISF thermocouples after 120 min of the test was approximately 130°C before exceeding the 250°C limit after 136 min.

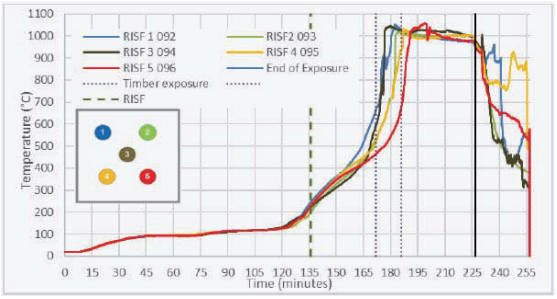

Figure 14: *Resistance to the Incipient Spread of Fire (RISF) temperature data and estimated time of direct exposure of the timber frame to furnace heating*

At the end of the heating period the specimen was removed from the furnace. To enable observation and the fitting of a heat flux meter to measure radiant heat released from the specimen, the specimen was rotated at an angle to the furnace as shown in Figure 15.

(i) Approx. 4 mins post-test *(ii) Approx. 26 mins post-test*

Figure 15: *Exposed face of partition during monitoring period*

Visual observations confirmed continuing combustion and char oxidation with a slight reduction in intensity further away from the furnace, which can be explained by the lower incident radiant heat from the adjacent furnace. Temperatures measured within the char were generally in the range of 500°C to 600°C throughout this period, indicating continued combustion within the char.

Due to the test being of a loadbearing timber-frame, temperature data was obtained from three internal horizontal noggings containing thermocouples and is plotted against time in Figure 16.

Figure 16: *Char depth versus time along nogging centreline*

https://doi.org/10.52202/069179-0230

Char rates obtained during the test were substantially higher than those recommended in EN 1995-1-2:2004 Eurocode 5[10] and AS/NZS 1720.4:2019[11]. For example, the notional char rate in accordance with AS/NZS 1720.4, assuming a nominal density of 550 kg/m^3, would be 0.66 mm/min and for protected systems is increased by a factor of 1.1 yielding an increased char rate of approximately 0.73 mm/min. Whereas the average calculated char rate from commencement of charring (at approx. 158 minutes) to a char depth of 90 mm (at approx. 221 minutes) was 1.43 mm/min.

This may be explained by the longer pre-heating period and higher heat fluxes due to the longer fire-resistance test period and would highlight the need for an upper bound fire resistance time to be specified for the notional char rates currently specified in design codes or additional char rates specified for long durations and different heating regimes.

4 CONCLUSIONS

The overview of the results of extended fire resistance tests performed on Fire-protected Timber elements has been presented. The specimens were monitored at the end of the heating period to determine if the elements self-extinguish, or sustained combustion continued.

The tests demonstrate that on-going combustion can be prevented using encapsulation provided by appropriate fire-protective grade covering systems that maintain the temperature of the protected timber elements below critical values.

The results so far demonstrate that for timber-framed construction, a temperature limit of 250°C is appropriate but above this limit, ignition and sustained combustion is likely to occur.

The results from tests on fire-protected massive timber construction, such as CLT, indicate that at interface temperatures above 300°C, the CLT member may ignite particularly at the position of joints in plasterboard coverings but self-extinguishment is still possible provided (1) the protective coverings remain in place, (2) the exposure is one-dimensional, (3) solid massive timber elements are used and, (4) detailing of joints between panels and at the perimeter of elements prevents increased heating of the timber.

Further work is being undertaken to evaluate the behaviour of Fire-protected Timber and unprotected timber under different heating conditions.

ACKNOWLEDGEMENT

The authors gratefully acknowledge the support provided by FWPA in undertaking this research and the knowledge and dedication of the fire resistance testing team at Warringtonfire Australia's Melbourne testing facility.

REFERENCES

[1] ABCB: National Construction Code 2016 Volume One, Building Code of Australia Class 2 to 9 Buildings. Australian Building Codes Board Canberra, 2016

[2] ABCB: National Construction Code 2019 Volume One, Building Code of Australia Class 2 to 9 Buildings. Australian Building Codes Board Canberra, 2019.

[3] Standards Australia: AS 1530.4 Methods for fire tests on building materials, components and structures Part 4: Fire-resistance tests for elements of construction. Standards Australia Sydney 2014.

[4] England, P., Iskra, B.: Technical Design Guide 18 Fire Safe Design of Timber Structures – Methods of Analysis and Supporting Data. WoodSolutions Melbourne 2022.

[5] England, P.: Technical Design Guide 38 Fire Safety Design of Mid-rise Timber Buildings – Basis for the 2016 changes to the National Construction Code (Supplementary Notes included). WoodSolutions Melbourne 2021.

[6] Salah Dimia, M., et al., Collapse of concrete columns during and after the cooling phase of a fire. Journal of Fire Protection Engineering, 2011. 21(4): p. 245-263

[7] McGregor, C.J., Contribution of cross laminated timber panels to room fires. 2013, Carleton University Ottawa.

[8] Collignon C., Tessier C.: Epernon *(test 1 and 5)* Fire Resistance Test of a Loadbearing CLT Slab according to Standard EN 1365-2. CERIB Fire Testing Centre France 2019.

[9] Brandon, D., et al.: Final Project Report Fire Safe implementation of visible mass timber in tall buildings – compartment fire testing. RISE Research Institutes of Sweden AB Sweden, 2021.

[10] EN 1995-1-2:2004 Eurocode 5: Design of timber structures - Part 1-2: General - Structural fire design. European Committee for Standardisation (CEN) 2004.

[11] Standards Australia: AS/NZS 1720.4:2019 Timber structures: Part 4 Fire resistance of timber elements. Standards Australia Sydney 2019.

https://doi.org/10.52202/069179-0230

World Conference on Timber Engineering Oslo 2023

NUMERICAL SIMULATION OF FIRES WITH EXPOSED TIMBER

Sabrina Spörri [1], Chamith Karannagodage [2], Joachim Schmid [3], Andrea Frangi [4]

ABSTRACT:

The burning of timber is a complex process because of its inhomogeneous structure and the interlinked processes of material decomposition and gas-phase combustion. One approach to predict the burning behaviour of timber in fire is through simulations. This work studies the charring properties of the timber with the complex pyrolysis model in the Fire Dynamic Simulator (FDS). A timber specimen of 260 mm × 225 mm × 120 mm exposed to an external heat flux in a non-standard experimental environment has been simulated with the FDS using the appropriate input parameters for the pyrolysis and gas phase combustion. The simulations also investigated the influence of the moisture and temperature-dependent specific heat on the simulation results. When the simulation results were compared to the experimental results, there was a good agreement for the charring rates, with a maximum deviation of 0.06 mm/min. The results showed the importance of moisture in the pyrolysis model to obtain accurate results. The findings suggest that the FDS can be used to study and predict the char depth of timber to calculate the residual cross-section for building designs.

KEYWORDS: Fire dynamics, Numerical simulations, Exposed timber, Timber pyrolysis

1 INTRODUCTION

Fires are a dynamic process with their intensities being dependent on the prevalent boundary conditions. An important factor influencing the behaviour of fires is whether the fire is burning openly or enclosed in a compartment. In open fires, there is an unlimited supply of oxygen for the combustion reaction and the resultant smoke plume can rise unimpeded depending on the stability of the atmosphere. In contrast, when a fire occurs in a compartment, the oxygen supply to the combustion reaction is limited by the size of the opening(s) and the smoke plume is trapped within the enclosure. In these types of fires, all the enclosing components are heated up in a fire, especially in the upper part of the compartment, where the hot combustion products are trapped beneath the ceiling and form a hot layer.

The flames above the fire, the heated surfaces of enclosing components, and the layer of hot combustion products accumulated under the ceiling can all be considered sources of radiant heat flux. These radiating sources potentially contribute to further heating the burning and non-burning fuel. To summarise, the main aspects influencing the compartment fire dynamics are the distribution and the type of fuel load, the compartment geometry, the ventilation configuration and the material of the compartment boundaries [1].

Nowadays, the traditional construction material timber is experiencing a renaissance as it is an environmentally-friendly material which contributes to a sustainable construction, but also satisfies the architectural need for new designs and aesthetics [2–4]. When the boundary surfaces consist of combustible material like timber, this will significantly impact the compartment fire dynamics by adding an additional fuel load to the fire. Studies have shown that the additional fuel will increase the severity of the external flaming and the thermal load that must be resisted by the structure to ensure that safety criteria are satisfied [5,6].

Recent trends have increased the market demand for the larger floor spaces (fire compartments), increased quantities of visible (unprotected) timber and taller buildings. These trends will not only influence the duration and the intensity of the compartment fires but also the techniques used to fight them [7]. Very recent changes in regulations in UK and Scandinavia require the determination of “physically based design fires”. These design fires must consider the compartment geometry, architectural linings and the potential influence of any combustible structures (timber).

Although proposals for modifying the parametric fire design are available [7], it appears to be challenging to

[1] Sabrina Spörri, ETH Zurich (IMFSE), Switzerland, sabrina.spoerri@gmx.ch
[2] Chamith Karannagodage, ETH Zurich, Switzerland, karannagodage@ibk.baug.ethz.ch
[3] Joachim Schmid, ETH Zurich, Switzerland, schmid@ibk.baug.ethz.ch
[4] Andrea Frangi, ETH Zurich, Switzerland, frangi@ibk.baug.ethz.ch

https://doi.org/10.52202/069179-0231

describe the complex aspects of the fire dynamics in timber structures with the available design frameworks. Consequently, it is expected that a performance-based design allows a greater design flexibility, promoting innovation and a better use of resources allowing for a better fire risk management [8]. When applying a performance-based approach to timber structures, a key input that is missing is the development and the combustion of the char layer in the compartment environment.

Moreover, reliable numerical models could decrease the necessity of full-scale tests, which are costly and require a large amount of resources. That way, fire-design approaches could rely on numerical models to assess the use of innovative and more sustainable building materials and allow maximum freedom in building design while upholding the required level of building safety.

This paper simulates the burning behaviour of a timber specimen using a field model. This simulator couples the gas and solid phase processes that occur in a fire. The gas phase processes are the combustion of flammable gases and the local air flow whilst the solid phase processes include the thermal degradation of fuel (pyrolysis). A summary of the simulating steps and an overview of the most important parameters for the simulations are presented with the comparison of results from the fire experiment.

2 STATE OF THE ART

2.1 BURNING PROCESS OF TIMBER

Timber is a substance with an anisotropic structure [8] and mainly constitute with the cellulose, hemicellulose and lignin [10]. Depending on the wood species, the percentage of these three molecules vary, but a rough approximation for dry wood is 50% of cellulose, 25% of hemicellulose and 25% of lignin [10]. Timber naturally contains moisture. This can exist either as bound water in the cell walls (hygroscopic water) or as free water in the voids of the wood (capillary water) [13].

The burning process of timber can be divided into two main processes. First, when the timber is exposed to heat, at high temperatures it begins to change its cellular structure initiating the pyrolysis process. Pyrolysis is the thermal decomposition of fuel material [14]. At elevated temperatures, timber degrade the constituent natural polymers producing volatile gases, tar and char. Secondly, when the pyrolysis volatile gases mix with ambient air it makes a combustible mixture which can lead to a flaming combustion (fuel oxidation) [15].

2.1.1 Pyrolysis of timber

Timber shows different stages in the pyrolysis process due to its material properties as shown in Figure 1. When heated to 100°C, the moisture within the timber starts to evaporate. Upon further heating, the pyrolysis process begins when the fuel reaches around 200°C producing volatiles. This is initially a relatively slow process until the fuel reaches 300°C after which the production rate of the volatile gases increases. [15].

On a general level, the pyrolysis is an endothermic reaction, and the energy is needed to break the polymers into smaller parts to present in the gaseous phase [12,15]. This process produces inert and combustible gases, liquid tar, solid carbon-rich non-volatile char and inorganic non-burning ashes as shown in Equation (1) [15].

$$wood \rightarrow gases + tar + char + ash \quad (1)$$

The produced gases are mainly CO, CO_2 and H_2O. The combustible gases will further undergo the combustion as explained in the Section 2.1.2. The char contains heavier and larger molecules which stay on the timber surface forming a layer which affects the heat transfer to the virgin timber. The char can further undergo the solid phase oxidation which is visible as smouldering or glowing combustion. This decomposition also creates a surface regression of the timber and makes the cross-section smaller [4]. The char yield of the reaction is influenced by the presence of organic impurities in the wood and for most of the situations, the char formation starts around 300°C [15]. It should be noted that, this is a simplified description of the processes. In reality, several interdependent chemical reactions occur at the same time and the process is further complicated by the inhomogeneity of wood and the influence of the produced char layer [9].

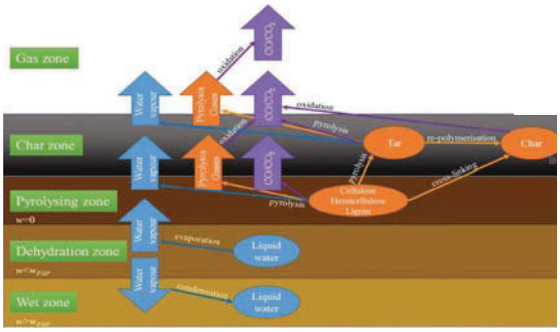

Figure 1: *Chemical and physical processes of a burning timber specimen. Modified from [15].*

2.1.2 Gas phase combustion

The mixing of combustible pyrolysis products with air in the right proportion (flammability limit) and in the right environmental conditions leads to their oxidation. This process is called the gas phase combustion [12,15]. This is an exothermic process producing the energy which could further enhance the production of the pyrolysis gases by transferring heat to the surface of the fuel [15]. If this heat feedback mechanism produces enough heat to release further volatiles within the flammability limit, then the mixture can sustain flaming combustion. The flammability limit or the flammable limit is the amount of combustible gas in an air mixture when the mixture is flammable.

https://doi.org/10.52202/069179-0231

2.2 PYROLYSIS MODELS

As the overall process of pyrolysis is very complex to work with, a lot of models have been proposed to describe the pyrolysis process in a simplified way adapting to desired real-life applications. Moghtaderi [13] gives an overview of the different pyrolysis models and classifies them based on their decomposition reaction as how the conversion from the virgin fuel into the gaseous products and char residues is described.

Distinctions are to be made between simple thermal models and comprehensive models. These two groups differ in the way they define the conversion of the fuel into the products, by the pyrolysis rate. The simplified models derive the rate only from the energy balance and the comprehensive models by a combination of kinetic schemes, mass and energy balances [13].

2.2.1 Simple thermal models

Simple thermal models use the criteria of a critical pyrolysis temperature while ignoring the physical and chemical processes to derive the pyrolysis rate (i.e., mass loss rate) from the energy balance. Depending on the solution method used to solve the equation, the simple thermal models are divided into the Algebraic, Analytical and Integral models. Equation (2) shows an example of an analytical simple thermal modal where the mass loss rate is proportional to the net absorbed heat flux for a thermally thin slab exposed to constant heat flux [13],

$$\dot{m} = \frac{\dot{q}_e^{''} A_s}{\dot{Q}_p} \tag{2}$$

where $\dot{m}$ = Mass loss rate [kg/s], $\dot{q}_e^{''}$ = External heat flux [kW/m^2], A_s = Surface area of solid [m^2], $\dot{Q}_p$ = Heat of pyrolysis [kJ/kg]

These models have the advantage of being relatively simple to use. However, they have the disadvantage of relying on a critical temperature for the ignition and neglecting many chemical processes. The use of a critical temperature simplifies the fact that the chemical processes occur faster than the diffusion processes. This is only true in very high temperatures. However, the chemical kinetics play a big part at the lower temperatures.

2.2.2 Comprehensive models

The comprehensive models incorporate the chemical and diffusion processes that occur during the pyrolysis. They have thus overcome the fundamental nature of a simple thermal model. As a result, these comprehensive models can also include the thermal degradation processes. Furthermore, other processes like heat transfer, morphological changes, expansion, shrinkage, char formation, chemical reactions, and in-depth radiation are also frequently included in the models [16]. The examples of the comprehensive models are Gypro, ThermaKin, Pyropolis, and FiresCones [16]. Because of the complexity of these models, numerical solution methods such as finite difference or finite volume are almost always required to solve the equations.

The comprehensive models are classified as follows by the reaction scheme,

- One-step global reaction schemes
- One-step multi-reaction schemes
- Multi-step semi-global schemes

The simplest one is the one-step global reaction scheme which only considers a primary reaction like the conversion of virgin timber into products as given in Equation (1). In this model, the thermal degradation products are considered as lumped materials. The pyrolysis rate is calculated by the Arrhenius expression given in Equation (5), which is proportional either to the weight residue or the weight loss of the fuel [13]. The input parameters for the equation need to be defined experimentally.

The one-step multi-reaction scheme is a more detailed reaction scheme than the previous one. Here also, each component undergoes only one independent reaction, but this time the timber is not modelled as a lumped material but made out of several components. Each of these components goes through a different reaction that occurs in parallel. In this case, the pyrolysis rate is the sum of the reaction rates of each component weighted by the percentage of each component. The subsequent reaction that some of these products can undergo is the next step in the complexity. These are known as the secondary reactions [10], and one example is the char oxidation. Multi-step semi-global schemes are the models that take such reactions into account.

Some comprehensive models can also consider the effect of moisture presence in the pyrolysis process. However, a disadvantage of these comprehensive models is that many input parameters are needed even with a simple reaction scheme. That number increases drastically if more complex reaction schemes are used.

2.3 FDS PYROLYSIS MODEL

The Fire Dynamics Simulator (FDS) developed by the National Institute of Standards and Technology (NIST) is a Computational Fluid Dynamics (CFD) software package which solves simplified forms of Navier-Stokes equations numerically. The FDS can be used to simulate low-speed thermally driven fluid flow with the smoke plume. FDS is a powerful tool to predict heat generation and transfer from a fire [17]. The main models in FDS are hydrodynamic, combustion, and radiation transport models [18].

The combustion model is mainly used as a single-step, mixing-controlled chemical reaction. The combustion reaction includes air, fuel and products which are treated as lumped species and explicitly tracked in the simulations.

2.3.1 Pyrolysis model

FDS has the option to include different types of pyrolysis models, ranging from simple thermal ones to complex models based on the kinetics [18,19]. This study will use

the complex pyrolysis model from FDS. The complex pyrolysis model needs to define one or several chemical decomposition reactions and input data to calculate the reaction rate as explained in the previous section. The FDS definition of the pyrolysis reaction rate $r_{\alpha\beta}$ is a combination of solid and gas phase conditions and defines the reaction rate depending on the temperature of the solid T_s. The definition in the FDS contains the following sub-terms, Equations (3)–(5) [19]. In this study, only the reactant dependency and the Arrhenius function were used to define the reaction rate.

$$r_{\alpha\beta} = Reactant\ dependency \times Arrhenius\ function \times Oxidation\ function \times Power\ function \quad (3)$$

$$Reactant\ dependency = \left(\frac{\rho_{s,\alpha}}{\rho_{s(0)}}\right)^{n_{s,\alpha\beta}} \quad (4)$$

$$Arrhenius\ function = A_{\alpha\beta} exp\left(-\frac{E_{\alpha\beta}}{RT_s}\right) \quad (5)$$

where α = Material component in material layer, β = Name of reaction, $\rho_{s,\alpha}$ = Solid density of material component α [kg/m^3], $\rho_{s(0)}$ = Initial solid density of material layer [kg/m^3], $n_{s,\alpha\beta}$ = Partial reaction order for material component α in material layer and reaction β, $A_{\alpha\beta}$ Pre-exponential factor [1/s], $E_{\alpha\beta}$ = Activation energy [J/mol], R = Gas constant [J/K·mol], T_s = Temperature of solid [K]

Furthermore, the heat transport through the depth of the solid is calculated by the conduction in FDS. In this study, the heat conduction is only considered as one-dimensional into the solid.

2.3.2 Gas combustion model

The gas combustion model is a single-step mixing controlled combustion based on the Eddy Dissipation Concept where the mixing is approximated as having been burnt [19] and where only one fuel can react [18]. The chemistry model relies on a reaction of the following form as in Equation (6).

$$C_xH_yO_zN_v + v_{O_2}O_2 \rightarrow v_{cO_2}CO_2 + v_{H_2}H_2O + v_{co}CO + v_sSoot + v_{N_2}N_2 \quad (6)$$

Therefore, the user needs to specify the chemical equation of the burning fuel along with the yield of CO, soot and the volume fraction of the hydrogen in the soot. The enthalpy of formation of the gaseous fuel can either be specified directly for each gas or can be calculated from the (specific) heat of combustion of the reaction if the enthalpy of formations of all the other molecules in the reactions are known [19]. This second approach will be chosen in this study for the definition of the enthalpy of formation.

3 PYROLYSIS MODELLING WITH TIMBER IN FDS

3.1 INPUT PARAMETERS FOR THE FDS PYROLYSIS MODEL

The pyrolysis model used in this study was a one-dimensional heat transfer model with a simple, one-step global reaction scheme. To be compatible with the experimental data described in the section 3.4 "Experiment description", spruce was selected as the wood type. As shown in Equation (7), the chemical reaction was defined as the conversion of spruce into char and pyrolyzate.

$$Spruce \rightarrow char + pyrolyzate \quad (7)$$

In the experimental setup, the spruce sample had a moisture content of 12%. However, the simulations were started with dry spruce to keep the reaction scheme simple. Subsequently, the moisture content was added to the simulation. Only the reactant dependency and the Arrhenius function are used to calculate the reaction rate (Equations (3)–(5)). The oxidation function and power function of the FDS pyrolysis model were not studied further during this study. The default FDS values were used for those terms in the analyses.

For estimating the material and kinetic properties of spruce and char, the values were based on the research of Rinta-Paavola and Hostikka [20]. Thermogravimetric analysis (TGA) was used in the aforementioned study to estimate the yield of char and pyrolyzate, as well as the activation energy and pre-exponential factor [20]. This work provided the input parameters for the pyrolysis of spruce for simple and parallel reaction scheme in FDS. Further, these input parameters were validated and optimised against the cone calorimeter experiments at different heat fluxes. The value for the heat of combustion was derived from the micro-combustion calorimetry (MCC) experiments [20].

The heat of combustion is the effective heat of combustion, which is also the default definition in the FDS [18]. The heat of reaction for this simple reaction is defined as endothermic and is the optimised value by model fitting for a heat flux of 35 kW/m^2 in a cone calorimeter test [20]. Table 1 summarises the input parameters that were used for the decomposition process in the FDS simulation.

Table 1: *Input parameter for decomposition process [18,20]*

Parameter	Value
Number of reactions	1
Yield of char	0.16
Yield of pyrolyzate	0.84
Activation energy (J/mol)	190'500.00
Pre-exponential factor (1/s)	4.691×10^{13}
Absorptivity (1/m)	50'000.00
Reaction order	1
Heat of combustion (kJ/kg)	14'000.00
Heat of reaction (kJ/kg)	19

https://doi.org/10.52202/069179-0231

Other material properties for spruce, char, and pyrolyzate should be defined in addition to the pyrolysis parameters. These parameters for the two materials are shown in the Table 2 and in the text following the table. The next section will provide the information on the gaseous product "pyrolyzate".

Table 2: *Material properties for spruce and char [20,21]*

Parameter	Spruce	Char
Density (kg/m^3)	408	59
Emissivity (-)	0.9	0.85
Conductivity (W/m K)	0.09	0.22

The conductivity for spruce was the optimised value by model fitting for a heat flux of 35 kW/m^2 in a cone calorimeter test. The char density of 59 kg/m^3 was in the same range as reported in the literature, where the initial char density is 10–20% of that of the dry wood [22]. The value for the emissivity of char was from Chaos [21].

The last input parameter needed is the specific heat for spruce and char. They were defined as temperature-dependent in the publication of Rinta-Paavola and Hostikka [23]. The specific heat capacity of spruce ($C_{p,spruce}$) was defined as a linear growth from 30°C with 920 J/(kg·K) to 230°C with 1800 J/(kg·K). The specific heat capacity was assumed to be constant below and above that temperature. The specific heat of char ($C_{p,char}$) was defined by Equation (8).

$$C_{p,char} = 1430 + 0.355 \cdot T - \frac{7.32 \times 10^7}{T^2} \qquad (8)$$

where T = Temperature [K]

3.2 INPUT PARAMETERS FOR THE FDS GAS COMBUSTION MODEL

The main fuel for the gas combustion is the gaseous product pyrolyzate produced by the decomposition reaction in Equation (1). The input parameters for the gas combustion in the FDS were defined as follows; the chemical composition of the burning gas of spruce (C:1, H:3.584, O:1.55, N:0), the soot yield (0.015), the effective heat of combustion (14 MJ/kg), the viscosity (0.00059 kg/m·s) and the diffusivity (4.3×10^{-7} m^2/s) [20],[23][24].

For the conductivity, the value for the spruce was used [20], the diffusivity was the axial diffusivity for dry ash [23] and the viscosity was for wood [24]. For the surrogate molecule of the thermal radiation, FDS has a predefined list to choose from [18]. From there, a chemically similar molecule to the gaseous product was chosen, which was 'METHANOL'. Additionally, the default FDS values were used for the other parameters in the gas combustion model.

3.3 ANALYSING METHOD TO DETERMINE THE CHARRING DEPTH AND CHARRING RATE

The temperature profile inside the timber specimen was used to calculate the position of the charring front in the simulations. It was defined as the 300°C isotherm [25]. The distance from the surface of the timber specimen to the position of the charring front at the end of the simulation was then defined as the charring depth. The charring rate was calculated by dividing the charring depth by the simulation time when the charring front reached that depth. An experimental setup was followed to create the simulation environment to model the timber pyrolysis and to evaluate the performance of the simulation.

3.4 EXPERIMENT DESCRIPTION

The Fire Apparatus for Non-standard Heating and Charring Investigation (FANCI) [4] was chosen as the experimental setup. It enables the investigation of the charring behaviour, the char layer surface regression, and the temperature distribution in a timber specimen, among other things. The experimental environment is called non-standard as the application of an airflow from 1 to 6 m/s is possible with a variable incident heat flux up to 120 kW/m^2 from a quick response heat panel to ignite the specimen [4]. Figure 2 and Figure 3 show the experimental setup used for the fire apparatus.

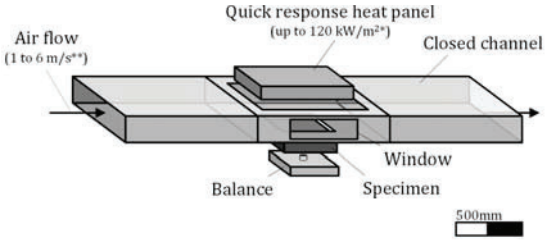

* variable external heat flux

** reference velocity at normal temperature

Figure 2: *Schematic view of the FANCI experiment setup [4]*

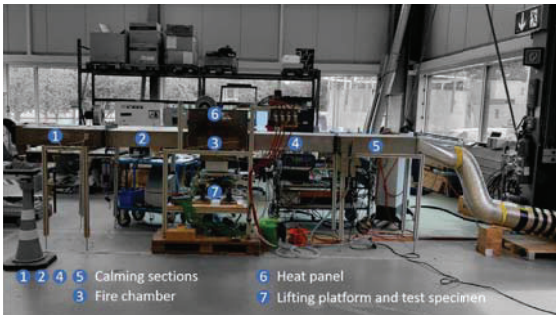

Figure 3: *FANCI test setup with the different components [27]*

The apparatus consisted of a long tunnel made of five sections, each section with a length of approximately 0.9 m, a width of 0.5 m and a height of 0.15 m as shown in Figure 3 [27]. The total length was approximately 4.5 m. Steel plates with a thickness of 1.5–3.0 mm were used to make these sections. The airflow was from the left

to right with respect to Figure 2. The timber specimen was placed in the section 3, called the fire chamber and positioned on the floor opposite a heat panel on the ceiling. The specimen had a length of 260 mm, a width of 225 mm and a thickness of 120 mm. The wood type was spruce, with a moisture content of around 12%.

For the comparison with the simulation results, the test JF00 from the FANCI test series was chosen [26]. In this experiment, a timber specimen was placed in the apparatus at a prevailing velocity of around 2.5 m/s, and the heat flux panel was calibrated to produce an incident heat flux of 96.4 kW/m^2 on the surface of the timber specimen. The specimen was heated by the heat panel for 20.1 min. The ignition occurred after ca. 0.42 min. The reported charring depth was 24 mm which was reached after 20 min. The charring rate for this test was 1.21 mm/min and the surface recession was 0.22 min/mm.

3.5 FDS MODEL

3.5.1 Geometry and mesh

The length of the tunnel for the simulation was shortened to 2.2 m instead of the length of 4.5 m in the actual experiment to reduce the computational time during the simulations. This was chosen after a sensitivity analysis to investigate the influence of the mesh size (1.25 cm, 1.0 cm and 0.625 cm) and the tunnel length on the airflow. Following the mesh sensitivity analysis, a mesh size of 1 cm was selected for the simulation. As there were no significant differences in the flow fields between the two geometries for all the simulations, a shortened geometry of the FANCI tunnel appears to be reasonable and capable of incorporating all the measurements that were measured in the FANCI-test experimental setup. The Figure 4 compares the geometry of the experiment and the simulation.

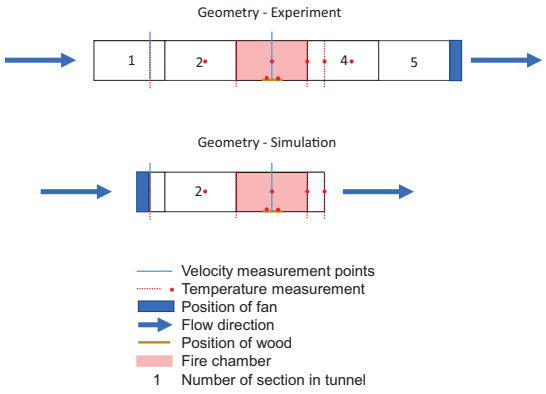

Figure 4: *Comparison of the geometry of the experiment and the simulation*

3.5.2 Temperature measurement

Following the experimental setup, gas temperature values were measured on the centre line of the tunnel. In the simulation, the temperature devices were distributed between the start of the fire chamber and the outlet, as shown in the Figure 4. Similar to the experimental setup, additional temperature measurements were done on the surface of the timber specimen and inside the solid.

3.5.3 Implementation of the mesh inside the timber specimen

For further analysis of the properties inside a solid, FDS has a special output recording option called &PROF [18]. This provides in-depth profiles of physical properties such as inlaid temperature, overall density, or density of different solid material components. The spacing of the solid grid defines the recording positions of these properties, which is done automatically by FDS unless changed manually [18].

Equation (9) defines the size of a solid phase cell or, in the case of one-dimensional heat transfer, the thickness of one layer inside the solid in the FDS. The simulation thickness is less than or equal to the calculated value.

$$\sqrt{\frac{\tau k}{\rho c}} \tag{9}$$

where τ = time constant [s], k = thermal conductivity [W/m·K], ρ = density [kg/m^3] and c = specific heat [J/kg·K].

By default, the distance between layers is smaller at the solid's surfaces and increases towards the middle by doubling their size to reduce the computational resources. They begin to shrink again as they approach the mid-depth. To some extent, the user can modify this solid grid by making the node spacing more uniform or by changing the mesh cells. The code line STRETCH_FACTOR, which is set to 2 by default, is responsible for the non-uniform spacing. This STRETCH_FACTOR was set to 1.0 for all the simulations to achieve a uniform spacing after a solid mesh sensitivity analysis. This resulted in approximately 248 layers inside the solid with a maximum thickness of 0.5 mm.

It should be noted that the spacing in Equation (9) is dependent on the thermal properties of the materials. when one of these changes, the number of layers also changes. Furthermore, if the burning causes the material to shrink or swell, resulting in a change in material thickness, FDS rechecks the total number of layers and adds or removes the layers as necessary.

3.6 OVERVIEW OF THE SIMULATIONS

The information available from the experiment for heating the timber specimen was an estimate of the incident heat flux on the surface of the timber specimen. Two heating methods were tested to achieve a similar incident heat flux on the timber surface in the FDS simulations.

The first option involved simulating an external heat flux with the same intensity as the experimental incident heat flux over the timber specimen. This simulation is named "S1-exHF" in this paper. In this method, the heat flux functions similarly to a perfect radiant panel or conical heating unit [18]. Option two involved defining a heat

https://doi.org/10.52202/069179-0231

panel on the tunnel ceiling above the wood specimen and calibrating it so that the amount of incident heat flux measured on the timber specimen surface has the same intensity as the one estimated in the experiment. This simulation is named "S2-HP". Dry timber specimens were simulated in these simulations using the temperature-dependent specific heat and the other input parameters listed in Section 3.1 and considered as the "standard simulations".

Additional simulations with modified input parameters were run apart from the standard simulations. One modification was introducing the moisture content to the timber specimen into the standard simulations ("S1-exHF-moisture" & "S2-HP-moisture"). This change also agrees with the experimental information, where the spruce had a moisture content of 12%. The goal was to see whether a more complicated pyrolysis model adds additional value to the output.

The other modification was to see the influence of the temperature-dependent input parameters on the simulation results. Instead of a temperature-dependent parameter, constant values were used for the specific heat of spruce and char in the standard simulation. This simulation is called "S1-exHF-cp". The simulation time was similar to the duration of the experiment, which was 20.1 (min).

4 RESULTS

4.1 COMPARISON OF THE IGNITION METHOD

The two methods which were used to ignite the timber specimen, once by a constant external heat flux over the specimen ("S1-exHF") and once by a heat panel ("S2-HP") showed similar results as shown in the Figure 5. The surface temperature measurements are slightly higher for the heat panel than the heat flux.

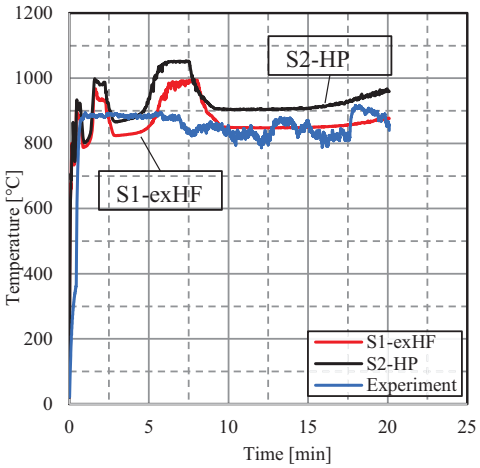

Figure 5: *Comparison of the surface temperature for experimental and modelling results for two ignition methods (S1, S2)*

The comparison of the mean surface temperatures shows temperature measurements of simulation to be very close to the experimental measurements but slightly higher. Taking into account that the measurements in the simulation were done by direct temperature measurements where the higher measurements were expected than those in the experiment where thermocouples have been used with a thermal inertia. Overall, it is visible that the temperature measurements in the simulation are in a good range. The external heat flux over the specimen is the best method to simulate the incidence heat flux on the specimen to compare with the experiment.

4.2 SURFACE TEMPERATURE MEASUREMENTS

The Figure 6 shows the comparison of the surface temperature of the specimen for different simulations compared to the experimental temperature values. The mean surface temperature for the experiment was 834.7°C, and the simulation values for the standard case and modified simulations are within 5% of this experimental mean value. These findings show that the surface temperatures in the experiment and simulations were very similar, indicating that the simulations had a similar fire exposure to the experiment. The modifications to the standard cases in the simulations have no significant effect on the results when compared to the experimental values.

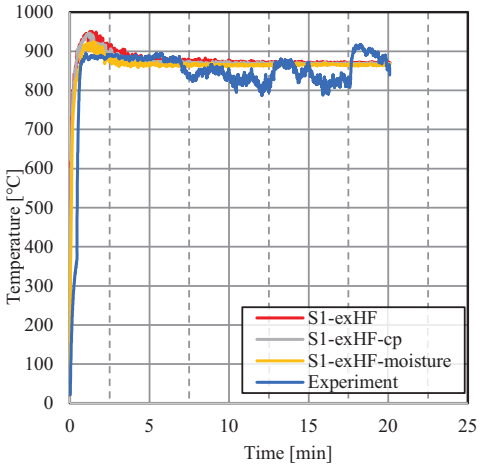

Figure 6: *Comparison of the surface temperature for experimental and modelling results for three specimens: dry, with constant specific heat and moist*

4.3 INLAID TEMPERATURE MEASUREMENTS

The temperatures inside the timber specimen from the experimental data are compared with the simulated results at various depths in the Figure 8. The thermocouple positions correspond to the depths measured in the experiment from the exposed surface as shown in the Figure 8.

Overall, the comparison indicates that the simulation temperatures are generally higher than the experiment. The above-mentioned trend was observed throughout the entire time, particularly at the deeper depths from the exposed surface. On the other hand, at the 6 mm and the

https://doi.org/10.52202/069179-0231

12 mm, the simulation temperatures close to the exposed surface are higher at the beginning of the test, but the experimental values gradually increase and become higher than the simulation values during the tests, as shown in the Figure 8. Further, at a depth of 18 mm, the simulation and experimental results end up in a similar temperature range. The comparison of the experimental and simulation results with ignition by a heat panel revealed the same pattern.

The reasons for the above difference could be diverse and might be related to the simplified definition of the charring process in the simulation or due to the inertia of the thermocouples in the experiment. Furthermore, the reaction parameters that were given as an input need to be optimised to define a realistic heat transfer into the solid for a non-standard fire exposure.

4.4 CHAR PROPERTIES

The graph in the Figure 7 compares the progression of the charring front through the timber specimen using the 300°C isotherm profile, where timber might char for the three simulations where the ignition was simulated by an external heat flux and for the experimental data. The charring rate has calculated using a linear regression in the experimental analysis. The data points in the simulations, on the other hand, show a logarithmic behaviour for the progression of the 300°C isotherm.

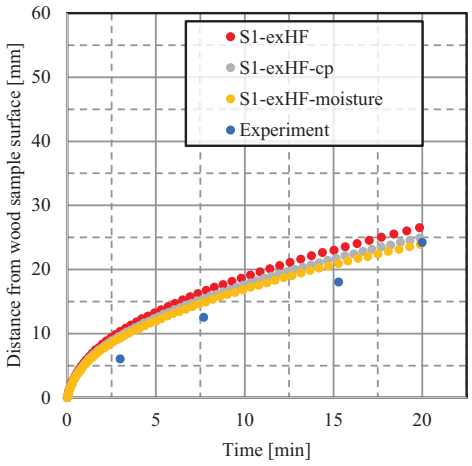

Figure 7: *Comparison of the char layer progression for experimental and modelling results for three specimens: dry, with constant specific heat and moist*

The Table 3 presents the charring depth and calculated charring rates for the simulations and the experiment at the end of the test. The comparison shows higher charring rates for the simulations with the dry specimen. The maximum difference in the charring rate for the simulations with the dry specimen is a 15.7% deviation from the experimental charring rate. On the other hand, the results for the charring rates with the moisture are very close to the experimental value.

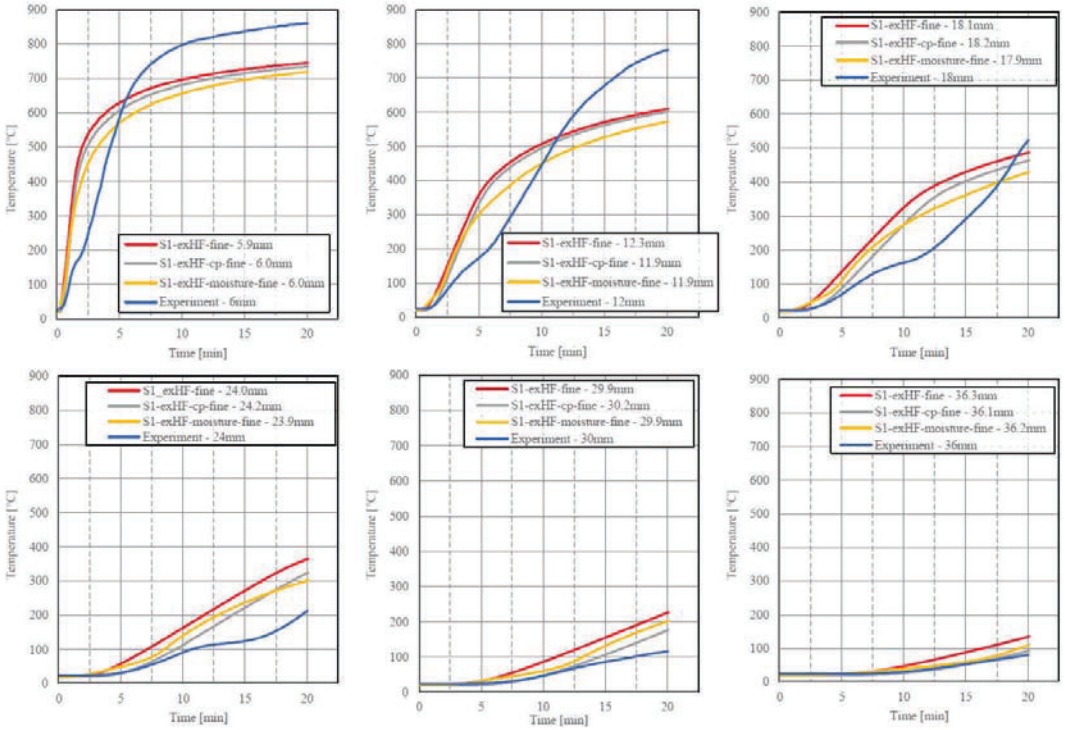

Figure 8: *Comparison of the temperature profile inside the timber specimen for experimental and modelling results at different depths for three specimens: dry, with constant specific heat and moist*

https://doi.org/10.52202/069179-0231

Table 3: *Charring depth and charring rate comparison after 20 minutes*

Parameter	Charring depth (mm)	Charing rate (mm/min)
S1-exHF	26.5	1.33
S1-exHF-moist	23.9	1.20
S1-exHF-cp	24.9	1.25
S2-HP	28.0	1.40
S2-HP-moist	25.4	1.27
Experiment	24.2	1.21

When the moisture is added to the specimen in the simulation, the charring rate decreases. This is because the moisture slows the heat transfer to the solid, resulting in a lower charring depth and rate. The simulation for moist specimen with the external heat flux accurately predicted the charring rate observed in the experiment. The difference is only 0.01 mm/min for the charring rate and 0.3 mm for the charring depth. Moreover, when the heat panel ignites the specimen in the simulation with moisture, the charring depth shows a 4.9% difference from the experimental value and the charring rate has a variation of 0.06 mm/min. Furthermore, it is visible that the simulation with a constant specific heat leads to a lower charring rate compared to the dry specimen and a higher charring rate compared to the moist specimen.

5 CONCLUSIONS

The purpose of the study was to simulate the burning behaviour of a timber specimen using the field model FDS. The simulation coupled the gas and solid phase processes in a fire. The focus was given to predicting the charring depth and the charring rate.

The comparison of the simulation and experimental results revealed a relatively good agreement for the charring rate and surface temperature measurements. The comparison of the temperature profiles inside the timber specimen revealed that the simulation temperatures are generally higher than the experiment temperatures. However, this trend was different close to the exposed timber surface.

The presence of moisture in the pyrolysis model of the timber specimen resulted in lower surface and inlaid temperatures compared to the results with the dry specimen. Further, the moisture influenced the charring rate and it is recommended to include that in the simulation for accurate results. On the other hand, using a constant specific heat instead of a temperature-dependent value also resulted in a slightly smaller charring depth. This shows the dependency of the simulation on the user input data and the importance of selecting accurate inputs for the model. The modified simulations with the constant specific heat showed only a 0.08 mm/min difference in the charring rate compared to the simulation with the temperature-dependent values. Therefore, in the initial simulations it is possible to use a dry specimen with constant specific heat to reduce the computational time while achieving reasonable results for the charring properties. Later, the moisture and temperature-dependent properties can be added to the simulation to achieve a higher level of accuracy.

Even though the simulations showed good agreement with the experiment for the solid phase measurement, there were few variations in the gas phase measurements. Therefore, further research is necessary to improve the simulations and to produce accurate gas phase results. Furthermore, to study the surface regression of the char, a more complex pyrolysis model is needed, including char oxidation.

ACKNOWLEDGEMENT

Authors would like to thank Prof. Dr. Bart Merci and Dr. Andrea Lucherini for the valuable discussions. Furthermore, we are grateful for the support of International Master of Science in Fire Safety Engineering (IMFSE).

REFERENCES

[1] D. Drysdale, An introduction to fire dynamics, 3rd ed. Chichester: Wiley, 2016.

[2] S. Deeny, B. Lane, R. Hadden, and A. Laurence, “Fire Safety Design in Modern Timber Buildings,” *Struct. Eng. J. Inst. Struct. Eng.*, vol. 96, no. 1, pp. 48–53, 2018.

[3] B. Östman, D. Brandon, and H. Frantzich, “Fire safety engineering in timber buildings,” *Fire Saf. J.*, vol. 91, no. May, pp. 11–20, 2017.

[4] J. Schmid and A. Frangi, “Structural timber in compartment fires – the Timber Charring and Heat Storage Model.” *Open Eng.*, vol. 11, no. 1, pp. 435–52, 2021. https://doi.org/10.1515/eng-2021-0043.

[5] C. G. Putynska, A. Law, and J. Torero, “An investigation into the effect of exposed timber on thermal load,” in *Proceedings of the 24th Australasian Conference on the Mec. of Struct. and Mater., ACMSM24*, pp. 939–944, 2016.

[6] J. Schmid, R. Fahrni, A. Frangi, N. Werther, D. Brandon, and A. Just, “Determination of design fires in compartments with combustible structure – modification of existing design equations,” in *Proceedings INTER International Network on Timber Engineering Research 52* , pp. 0–3, 2019.

[7] D. Brandon, C. Dagenais, Fire Safety Challenges of Tall Wood Buildings – Phase 2: Task 5 – Experimental Study of Delamination of Cross Laminated Timber (CLT) in Fire. *National Fire Protection Association*, 2018.

[8] G. De Sanctis, K. Fischer, J. Kohler, M.H. Faber, and M. Fontana, Combining engineering and data-driven approaches: Development of a generic fire risk model facilitating calibration. *Fire Safety Journal*, 70, 23–33, 2014. https://doi.org/10.1016/J.FIRESAF.2014.08.017.

[9] C. Di Blasi, “Modeling and Simulation of Combustion Processes of Charring and Non Charring Solid Fuels,” *Prog. Energy Combust. Sci.*, vol. 19, pp. 71–104, 1993.

[10] S. Sinha, A. Jhalani, M. Ravi, and A. Ray Chaudhury, “Modelling of pyrolysis in wood: a review,” *SESI J.*, vol. 10, no. 1, pp. 41–62, 2000.

[11] L. Shi and M. Y. L. Chew, "A review of thermal properties of timber and char at elevated temperatures," *Indoor Built Environ*., vol. 0, no. 0, pp. 1–16, 2021.
[12] C. Gorska Putynska, "Fire Dynamics in Multi-Scale Timber Compartments," Diss. PHD Thesis, Univ. Queensland., Brisbane, 2019.
[13] B. Moghtaderi, "The state-of-the-art in pyrolysis modelling of lignocellulosic solid fuels," *Fire Mater*., vol. 30, no. 1, pp. 1–34, 2006.
[14] L. Lowden, and T. Hull, Flammability behaviour of wood and a review of the methods for its reduction. *Fire Science Reviews*, 2(1), 4, 2013. https://doi.org/10.1186/2193-0414-2-4.
[15] A. I. Bartlett, R. M. Hadden, and L. A. Bisby, A Review of Factors Affecting the Burning Behaviour of Wood for Application to Tall Timber Construction. *Fire Technology*, 55(1), 1–49, 2019. https://doi.org/10.1007/s10694-018-0787-y.
[16] T. Nyazika, M. Jimenez, F. Samyn, and S. Bourbigot, "Pyrolysis modeling, sensitivity analysis, and optimisation techniques for combustible materials: A review," *J. Fire Sci*., vol. 37, no. 4–6, pp. 377–433, 2019.
[17] N. L. Ryder, J. A. Sutula, C. F., Schemel, A. J. Hamer, and V. Van. Brunt, "Consequence Modeling Using the Fire Dynamics Simulator." *Journal of Hazardous Materials*, vol. 115, no. 1, pp. 149–54, 2004.
[18] K. McGrattan, S. Hostikka, R. McDermott, J. Floyd, C. Weinschenk, and K. Overhold, "Fire Dynamics Simulator User 's Guide (FDS)," *NIST Spec. Publ. 1019*, Sixth Edition, pp. 1-378, 2020.
[19] K. McGrattan, S. Hostikka, R. McDermott, J. Floyd, C. Weinschenk, and K. Overholt, "Fire Dynamics Simulator Technical Reference Guide Volume 1: Mathematical Model," *NIST Spec. Publ. 1019*, Sixth Edition, pp. 1–147, 2015.
[20] A. Rinta-Paavola and S. Hostikka, "A model for the pyrolysis of two Nordic structural timbers," *Fire Mater*., vol. 46, no. 1, pp. 55–68, 2022.
[21] M. Chaos, "Spectral aspects of bench-scale flammability testing: Application to hardwood pyrolysis," *Fire Saf. Sci.*, vol. 11, pp. 165–178, 2014
[22] K. W. Ragland, D. J. Aerts, and A. J. Baker, "Properties of wood for combustion analysis," *Bioresour. Technol.*, vol. 37, no. 2, pp. 161–168, 1991.
[23] M. J. Hurley et al., "SFPE handbook of fire protection engineering, fifth edition," SFPE Handb. Fire Prot. Eng. Fifth Ed., pp. 1–3493, 2016.
[24] J. Faouel, F. Mzali, A. Jemni, and S. Ben Nasrallah, "Thermal conductivity and thermal diffusivity measurements of wood in the three anatomic directions using the transient hot-bridge method," *Spec. Top. Rev. Porous Media*, vol. 3, no. 3, pp. 229–237, 2012.
[25] EN 1995-1-2, Eurocode 5, "Design of timber structures. Part 1-2 General – Structural fire design", European standard, CEN, Brussels, 2004
[26] J. Felder, "Timber Members in Natural Fires - Influencing Parameters in Decay Phase," Master's thesis, ETH Zurich, 2019.
[27] F. Hirzel, "Design Fires for Timber Components - Combustion Behavior, Temperature Profiles and Self-Extinction," Master project thesis, ETH Zurich, 2020

https://doi.org/10.52202/069179-0231

World Conference on Timber Engineering Oslo 2023

EXPLICIT FIRE SAFETY FOR MODERN MASS TIMBER STRUCTURES – FROM THEORY TO PRACTICE

Laura Schmidt[1,2], Ryan Hilditch[1], Adam Ervine[1], Joshua Madden[1]

ABSTRACT: A holistic methodology for explicit fire safety strategies for buildings with mass timber structures has been developed based on theoretical frameworks outlined in the literature and the current state of published research on the fire behaviour and safety of mass timber structures. This paper presents the four main pillars of this methodology: tenability for occupant evacuation; heating of the mass timber structure and loss of loadbearing capacity; external flaming; and assessment of the potential for self-extinction of the mass timber structure after burnout of the movable fuel load. The application of the methodology to three case study buildings showed the need for interdisciplinary collaboration throughout the design and planning of mass timber buildings. Engineering and design decisions including structural design options, the extent of exposure of the timber, façade type and construction and general building layout influence the resultant level of fire safety to an even greater extent for buildings utilising structural mass timber elements than for buildings with non-combustible structures. All practitioners collaborating on design projects with mass timber structural elements require a contemporary understanding of the persisting limitations around timber fire safety strategies and research as anyone whose work affects or limits the fire safety measures on such a project will carry a certain ethical or legal responsibility for the outcomes and consequences of a fire.

KEYWORDS: Mass timber structures, exposed engineered timber, fire safety strategy, holistic fire engineering

1 INTRODUCTION

The construction industry is faced with increasing pressure from different stakeholders to integrate mass timber structures into modern designs. Specifically, fire engineers are expected to support these designs in their many forms. The main hazard of mass timber structures is the potential for the structure itself to contribute to the fuel load in a fire, potentially affecting the fire severity and duration. Exposure to fire and heat will also result in reduced structural capacity of structural mass timber elements. The consequence associated with loss of structural capacity is a local or global structural failure, leading not least to breach of compartmentation, potentially endangering occupants by not providing sufficient time to safely evacuate the building and fire brigade personnel by not providing sound structural conditions for search and rescue operations and intervention.

Fire safety strategies must consider the inherently different fire performance of combustible structures: from the ignition of the timber structure, fuel contribution, and altered fire dynamics to self-extinction. However, traditional frameworks and calculation methods currently available for fire and structural engineering have been originally developed for non-combustible structural materials.

This paper presents a theoretical methodology developed for fire engineering practice. It will discuss the shortcomings and knowledge gaps hindering the application of the developed methodology and report further challenges encountered in the practical realisation of real-life timber building designs.

Fire safety engineers must carefully assess which tools originally developed for non-combustible structures, like reinforced concrete or steel structures, remain applicable and where new frameworks and methodologies are required when materials and geometries change. Historically, most research has been focused on small compartments in the order of 10 m2 [1]. Consequently, most existing frameworks for assessing fire safety have been developed for small compartments. Research into the fire dynamics governing fire evolution in large, open-plan compartments has only begun to receive focus in the last few decades [2]. Until very recently [3], this work again assumed the use of non-combustible structures.

The characteristics of the local temperature profiles and fire dynamics become more complex in fires that involve combustible structures [4]. This complexity is especially due to the in-depth heating affecting both the loss of loadbearing capacity and production of flammable pyrolysis gases for combustible structures: The energy released by the combustion of the movable fuel load causes heat transfer into the timber structure. At elevated temperatures, pyrolysis of the timber structure results in combustible gases adding additional fuel to the combustion reaction. A char layer may form on the timber surface. The production and combustion of combustible gases contributed by the structure itself affect the local and global energy balance, which, in turn, has an impact on the pyrolysis reaction within the timber. In summary, the burning of the movable fuel load and the thermomechanical degradation and burning of the combustible structural elements are coupled [5].

[1]WSP Australia Pty Limited, Australia
[2] WSP UK Limited, United Kingdom,
laura.schmidt@wsp.com

https://doi.org/10.52202/069179-0232

The complexity of assessing combustible timber elements' degradation and fuel contribution is further increased since the degradation is thermomechanical, i.e. it depends on the mechanical and thermal loading. Phenomena like char fall-off have the potential to further weaken the structure [6] [7].

The possible impact of the burning of the timber structure itself on the fire growth is presented in Figure 1, in direct comparison with the fire development expected in a compartment with a non-combustible structure. The fire could grow more rapidly following the onset of pyrolysis and ignition of mass timber elements as they contribute additional fuel to the fire. The additional fuel may lead to higher heat release rates inside the compartment of origin, causing a faster transition to flashover, i.e. a fire involving all available fuel. Moreover, external flaming is expected to become more severe if an increased amount of gaseous fuel burns outside the compartment openings [3].

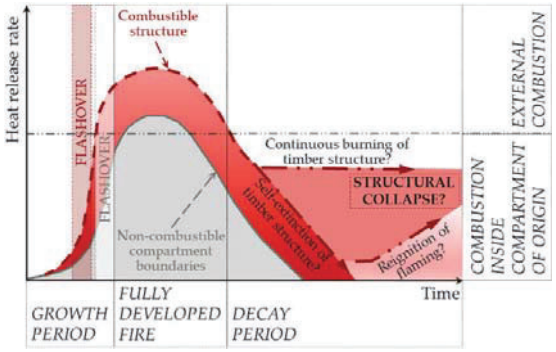

Figure 1: *The expected impact of a combustible structure (dashed red curve) on the fire development following ignition of the structure in comparison to non-combustible compartment boundaries (solid grey curve) in small compartments: increased total heat release and faster transition to flashover, changed heating conditions and thermo-mechanical degradation of the structure, potential for more severe external flaming and the possibilities of continued burning of the structure until collapse or self-extinction (adapted from Drysdale [8] and Hidalgo [9]).*

Fire safety strategies for high-rise buildings generally rely on structural integrity being maintained for longer than the duration of a fire. High-rise buildings require extended evacuation periods, during which occupants must be provided with adequately safe conditions. Moreover, the structural capacity must be sufficient to provide safe conditions for emergency personnel, who may need to enter the building for search-and-rescue operations or internal firefighting. The fire – referring to the combustion of the moveable fuel load (building contents) as well as the combustible structure itself – must eventually cease if sufficient structural capacity is to be retained.

A sound fire engineering methodology must assess if a given design (geometry, ventilation, exposed timber surface area, engineered timber products and other factors) allows for self-extinction to be achieved. In this context, self-extinction refers to the total burnout of the structural fuel. Self-extinction of the mass timber structure shortly after burnout of the movable fuel load is critical to avoid loss of load-bearing capacity until structural collapse [4].

It is important to differentiate between the extinction of flaming combustion and the extinction of smouldering combustion. Smouldering combustion may occur after flaming combustion [10]. While the heat generation of smouldering combustion is generally lower than flaming combustion, smouldering has been seen to continue for hours with prolonged heating leading to structural collapse hours after the extinction of visible flaming combustion [11] [12].

Most existing frameworks, including standard fire resistance tests, were originally developed for non-combustible structural materials, products, and elements. The additional energy generation from exposed combustible members is not accounted for [13]. Standard methods and calculations have been shown to potentially underpredict the loss of structural capacity [11] [14]. Moreover, calculating a Fire Resistance Level (FRL) using the existing frameworks does not allow a holistic assessment of fire safety and in no way supports the prediction of the potential for self-extinction of the combustible structural elements. For timber, some guidance documents describe so-called char depth or zero strength layer calculations to assign FRL to building elements. However, these calculations generally do not consider the fire dynamics and the importance of the incident heat flux. Therefore, existing frameworks are not able to assess the fire safety of mass timber structures to the level of existing knowledge around the complexities and relevance of the critical phenomena.

This paper aims to present the four key areas of fire safety that need to be addressed in the design of any building with combustible structural elements through a holistic fire safety strategy:

1. Influence of the burning of combustible structural elements on fire growth and tenability conditions;
2. Loss of loadbearing capacity of the heated combustible structural elements, considering the impact on the fire intensity and duration;
3. Potential impact on external flaming;
4. Self-extinction of the combustible structure after burnout of the movable fuel load.

The boundary conditions, compartment configuration, ventilation and other design decisions greatly influence the fire behaviour of combustible structures but vary considerably between buildings. Therefore, any fire safety strategy for buildings with mass timber elements needs to be performance-based. However, to the knowledge of the authors, currently, no prescriptive framework exists that addresses all of the above.

A holistic methodology based on concept steps proposed in previous literature [4] has been developed. Through practical application to several real building designs, critical knowledge gaps and limitations around key design variables have been identified and will be discussed in the following. In practice, a collaborative approach between all involved disciplines and stakeholders has proven critical to the development of fire-safe mass timber buildings.

https://doi.org/10.52202/069179-0232

2 PROPOSED METHODOLOGY

A four-part methodology is proposed to enable a holistic review and assessment of mass timber structures (see Figure 2). This methodology addresses the key elements of any fire safety strategy (fire growth and extinction; evacuation and tenability; heating of structural elements and structural stability; smoke spread and external flaming) with a special focus on the hazards introduced by the use of combustible structural timber.

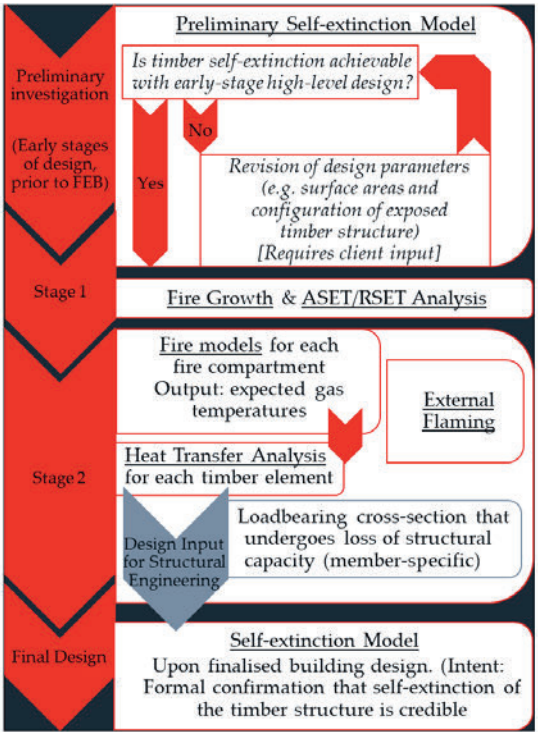

Figure 2: *Proposed fire engineering analysis of mass timber structures in the context of performance-based design.*

The order in which the different assessments are performed is based on the flow of projects encountered in construction practice, involving several stakeholders and interdisciplinary design decisions influencing the fire safety strategy, as well as the outputs of certain frameworks feeding into the calculations performed thereafter. The assessment of self-extinction is performed in the conceptual stage and informs important design decisions. The refined design is then assessed with different design fires regarding evacuation and tenability criteria.

It is not possible to accurately predict the nature of an accidental fire (fire source, spread directions, spread rate, etc.). This is especially true for large, open-plan compartments since the boundary conditions play a significant role in the fire development. Therefore, design fires for the assessments of tenability and heat transfer to the structure (see below) need to be chosen to provide upper and lower bounds, possibly working backwards using a worst-outcome approach.

The evacuation and tenability criteria are mostly identical to those that would be used in a building of the same occupancy and design but with a non-combustible structure. However, for the analysis of a mass timber structure, an additional criterion considering the ignition of the combustible structure needs to be considered. The structure's loss of loadbearing capacity due to heating is then assessed considering the thermal environment inside the compartment during different design fires. The output feeds into the structural design which can then provide sufficient sacrificial depth for the considered design fires on the one hand and optimise the material use on the other hand.

2.1 SELF-EXTINCTION

The potential of a proposed design to achieve self-extinction is the most critical design parameter and hence is suggested as the first step in the early design stages. Structural collapse will occur eventually if extinction of all combustible structural elements is not achieved. Once the continuous heat transfer from self-sustained combustion of the structure has reduced the structural capacity sufficiently to cause local collapse, the loss of compartmentation is a likely consequence, allowing for fire to spread outside the compartment of origin and violating the basic principles of most fire safety strategies. Therefore, the potential for self-extinction must be assessed by any fire safety strategy relying on the integrity of combustible structural elements. The framework for self-extinction of the timber structure is therefore proposed to assess indirectly the potential to retain adequate structural stability after burnout of the movable fuel load, for which self-extinction of the combustible structure is critical.

The term *self-extinction* must refer to the complete cessation of both flaming and smouldering combustion in this context. It is important to note that many publications report *self-extinction* as the cessation of flaming, regardless of smouldering combustion. As such, most of the criteria presented in literature which can be used as a design basis are limited to flaming extinction alone. Only after all combustion and therefore heat generation has stopped, the transfer of additional heat into the structure will cease and the elements can begin to cool down. Therefore, both flaming and smouldering combustion must self-extinguish or be actively extinguished and not continue self-sustained after burnout of the movable fuel load. Continued smouldering can also lead to the reignition of flaming. However, significant knowledge gaps around the smouldering of solid timber persist, especially with regard to its self-extinction.

The period of interest for consideration of timber self-extinction is during the fire decay phase after the flaming combustion of the moveable fuel has ceased within the compartment. Numerous focused studies [5] [15] [16] have observed that self-extinction of exposed timber, i.e. cessation of flaming combustion involving the exposed timber itself, can occur gradually within a compartment if well-ventilated conditions are present after the burnout of the moveable fuel load.

The proposed framework assesses a design fire scenario in which flashover has resulted in the ignition of all

exposed mass timber elements which continue to combust and emit heat simultaneously immediately after the movable fuel load has burned out. At this point, it is critical to understand the energy balance across the compartment, and whether the heat losses from each structural timber element are sufficient to result in the self-extinction of the member in this worst-case scenario in terms of ignition of available combustible structural fuel load. Adequate assumptions regarding the boundary conditions are critical as they impact the global energy balance of the compartment.

If the model shows that the incident heat flux into the timber is lower than the critical heat flux for sustained combustion while all surrounding mass timber elements are radiating, this means that these conditions cannot be self-sustained, i.e. permitting eventual self-extinction. If the received heat feedback results in a local positive energy balance sufficient to promote further pyrolysis beyond the char layer, the timber element can continue to undergo and promote combustion and will eventually lose structural integrity.

Computational Fluid Dynamics (CFD) modelling of each fire compartment can determine the theoretical potential heat feedback between burning timber surfaces. Therefore, each fire compartment is modelled with the proposed dimensions and other relevant characteristics. For the assessment, the surfaces of the remaining timber members are considered to be at elevated temperature and continuously undergoing exothermic reactions transferring heat into the compartment. A burning rate per unit area and temperature are assigned to the surface of each combustible structural element as proposed by Sahoo et al. [17]. Radiation modelling in CFD models is very sensitive to input parameters such as the soot yield, radiative fraction, radiation solid angles and path length. The incident heat received by each exposed mass timber surface as feedback from the other radiating timber surfaces must be below the critical incident heat flux for self-sustained burning. Otherwise, design parameters like the orientation and extent of exposed timber members need to be adjusted. The factors affecting the potential for self-extinction of the mass timber structural elements (geometry, configuration and view factors between timber surfaces, choice of materials, compartmentation, ventilation, etc.) must be considered in major design decisions, which are generally made in the early stages of a project. It is therefore advisable to perform a preliminary self-extinction assessment including a sensibility study in the early conceptual design stage to ascertain the credibility of timber self-extinction. The design limitations posed by the need for self-extinction can then inform the project going forward. The final self-extinction assessment can be carried out as the last step of the holistic fire safety assessment of the refined design.

2.2 EVACUATION AND TENABILITY

Life safety is the underpinning principle of any fire safety engineering effort. Safe conditions must be maintained for the required evacuation duration. Evacuation and tenability are often quantitatively assessed through a comparison of the Available Safe Egress Time (ASET) with the Required Safe Egress Time (RSET) with adequate safety factors for a range of primary and secondary fire scenarios.

The onset of untenable conditions for evacuating occupants, i.e., the end of the ASET, can be defined as and assessed via a range of criteria, e.g. sufficiently low temperatures not endangering human life, visibility levels that allow identification and navigation of evacuation routes, and adequate toxicity levels. These criteria can be applied to buildings with and without combustible structural materials.

In buildings with combustible mass timber structures, the ignition of the mass timber elements must be introduced as a further criterion to mark the potential onset of untenable conditions. The time between the initial onset of the burning of the movable fuel load and the ignition of the mass timber structure will vary between different fire scenarios and fire compartments.

In the context of tenability and evacuation, the expected critical impact of the burning of the timber structure is a potential decrease in the time until the onset of flashover conditions and a potential increase in the heat release rate within the compartment. All these effects can negatively impact the ASET.

Once a timber ceiling has ignited, it is expected that fire spread across the ceiling will occur rapidly [3] [12] [18]. The fire spread across combustible ceilings has been experimentally observed to support a rapid transition to flashover conditions [3] [12] [18], the rate of which is also affected by the ceiling profile. During flashover, all combustible materials within the compartment are on fire and more combustible gases are released than can burn within the compartment, which leads to combustion occurring outside the openings of the compartment. Occupant survival within a flashover compartment is considered impossible. Notably, the fire compartments with timber ceilings in our case studies were up to three times larger than the compartments in the subject experimental studies (see Section 4).

2.3 HEATING OF THE STRUCTURE

The temperature evolution within each structural mass timber element affects its loss of loadbearing capacity throughout the fire growth, fully developed fire, and decay phase. The remaining structural capacity needs to adequately support at least the design loads in the fire case which must be assessed in collaboration with the structural engineer. The selection of temperature criteria for the reduction of loadbearing capacity of heated timber members needs to be well documented to provide transparency and be based on relevant literature.

Heat transfer modelling to theoretically determine the in-depth temperature of the mass timber structure requires knowledge of the boundary conditions, including the incident heat flux or surface temperature of the timber element over time, as well as material properties. Expected maximum timber surface temperatures during the fully developed fire could theoretically be obtained from the modelling of a set of fire scenarios. The burning of the movable fuel load and combustible structural elements are coupled, as

https://doi.org/10.52202/069179-0232

explained previously [5]. Hence estimations of the expected burning duration must consider the coupled burning of the movable fuel load and mass timber structure, the compartment geometry, and ventilation.

If fire-protective layers are installed, it must be assessed when critical temperatures are reached within the timber underneath, causing loss of loadbearing capacity and contribution of combustible gases to the global fuel load (pyrolysis). Passive fire protection like protective non-combustible layers (e.g. plasterboard) are sometimes installed to delay the heating in depth of the timber and prevent involvement of the combustible structure in the fire. It is important to recognise the duration of the protective function provided and to consider the possibility of plasterboard failure as observed in large-scale experiments after which the formerly protected timber surfaces experience significant heat transfer [5] [10].

In the context of structural heating, the potential impact of the burning of the timber structure is firstly to increase the heat release and heat release rate and secondly to extend the burning duration by increasing the total available fuel load. Not only the increased total energy release but also the extended duration of heating can increase the in-depth heating of the timber structure, which is expected to result in increased and prolonged thermal degradation. Given the coupling of the combustible structure's thermal degradation and the fire dynamics, increased in-depth heating of the timber results in increased fuel contribution to the fire, which results in a feedback loop between the structure and the ongoing fire. This process can theoretically continue until all combustibles are consumed, unless sufficient char is formed and retained to allow for self-extinction of the timber, or firefighting intervention occurs.

Numerical models of burning timber must consider complex temperature-dependent processes like drying, pyrolysis and char oxidation. A finite difference model that accounts for the change in properties between virgin timber, dried timber and char was presented by Osorio [19] together with a review of existing models. Models like this can be used to estimate the in-depth temperatures in timber using a simplified energy balance accounting for the incident heat flux at the surface by summing the external heat flux and heat losses based on material properties and the thermal environment [7]. Heat transfer modelling to determine the temperature profiles within the timber complement the calculations performed by the structural engineers.

Due to the laminated nature of engineered timber, parts of the timber product can detach from the underlying structure [5] [6] [7]. In a fire, this phenomenon can add fuel, delay or prevent self-extinction and decrease residual structural capacity.

To account for the possible separation of lamella or loss of charred sections, it is proposed to consider the material properties of the proposed timber type and species, and to define failure, i.e. fall-off of lamellae and subsequent exposure of the underlying timber sections in the heat transfer model.

Prediction of debonding in heated engineered timber would require further research on the combined thermal and mechanical loading, and presents a highly complex problem. Publications that investigate the loss of charred sections from burning timber [6] [7] report no direct correlation between temperatures at the adhesive-timber interface and char fall-off. Therefore, it must be assumed that charring as well as char loss may occur.

A sensitivity study could be employed to assess the potential impact of the volume of charred lamella detaching from the exposed mass timber structure on the heat release within the compartment. Additional heat release from smouldering or flaming combustion of the detached char and partly charred sections needs to be considered as additional fuel load after falling to the compartment floor. The impact of the heat release of these materials on the potential for self-extinction of the mass timber structure after burnout of the movable fuel load must also be analysed as heat generation from smouldering combustion of charred timber has been observed to possibly continue for extended durations [12]. This additional heat release may have the potential to increase the incident heat to the exposed combustible structural elements beyond the critical limits for self-extinction.

For structural purposes, it is proposed to fully discard the depth of the cross-section that heats above a critical temperature. The additional required depth of timber has to be added to the cross-sectional depth of any load-bearing timber member as required for structural purposes.

2.4 EXTERNAL FLAMING

The potential for external flame spread to other floors, fire compartments, and neighbouring buildings must be assessed. External flaming radiates heat back at the façade of the building. Sufficiently high incident radiant heat received by other floors above and below the floor of fire origin can result in glazing breakage and ignite combustible materials within adjacent fire compartments, potentially resulting in uncontrolled vertical fire spread throughout the building, as seen in fires like the Grenfell Tower Fire in 2017 [20].

The potential severity of external flaming is expected to initially increase with increasing fuel load. Governed by the ventilation conditions, the combustible gases will partly burn inside and partly outside the fire compartment after partial or full window glazing failure. Increased heat release within the compartment can result in a larger effective height of the flames external to ventilation-controlled compartments. The assessment of external flaming must therefore consider the contribution of fuel provided by the timber structure itself over time, as well as several other factors such as available ventilation, opening orientation, compartment layout and the like.

Some local boundary conditions are especially difficult to predict and account for, yet could have an impact on the external flaming in a real fire. For example, wind conditions or the burning of a column located at the external compartment boundary are qualitatively understood to influence the intensity of the flame protruding but are difficult to quantify based on existing knowledge. Published scientific literature currently

lacks experiments assessing flame extension from uncontrolled fires in very large compartments of 100 m² or more, especially for buildings with mass timber structures [2] [8]. For example, the experimental work that underpins the Eurocode flame extension calculation was based on compartments with an area of less than 100 m². However, many modern designs aim for compartment areas in the order of 1000 m². This introduces further uncertainty into the external flame length calculation for such complex spaces.

When using the Eurocode calculation method to evaluate the impact of increasing the quantity of available fuel, a fuel load density quantity is reached after which increasing the fuel load density further ceases to increase the external flame height. This is understood to be because once a constant/maximum temperature is reached inside the compartment, the production of pyrolysis gases is then considered limited by the surface area of available fuel, and the combustion by the availability of oxygen based on the size of the compartment openings. These complex mechanisms bound the rate of combustion internally and, to some degree, control the impact of the contribution of the timber fuel to the internal combustion. The complex compartment fire dynamics that the combustible timber contributes to are responsible for affecting the resultant heat fluxes within the compartment and, by extension, the pyrolysis of the timber throughout the fire duration. These complex actions contribute to the resultant quantity of unburnt combustible gases escaping the compartment, and upon reaching fresh oxygen, undergoing flaming combustion externally.

3 CASE STUDIES

The methodology presented above was applied theoretically to three buildings with exposed mass timber structures, following the sequence as presented in Figure 2. Detailed design plans were attained and the buildings were assessed in line with Australian national building codes and regulations. Application of the methodology to the theoretical projects emphasised the limitations of existing guidance documents and persisting knowledge gaps around most of the design variables discussed previously.

3.1 DESCRIPTION OF THE BUILDINGS

The design plans utilised for the case study assessment represented three buildings with varying degrees of open-plan compartmentation; two were office buildings with typical open floor plates in the order of 1,000 m^2, one with seven and the other with three storeys, and an education building with large open areas adjacent to a series of smaller classroom configurations (total floor plate also in the order of 1,000 m^2, four storeys).

The designs of the mass timber structures of each building were seen to be generally similar: glulam columns, cross-laminated timber (CLT) beams and floor slabs, non-combustible internal partition walls (typically stud walls finished with plasterboard), and slab-to-slab height in the order of 3.8 m. Each building included storeys interconnected via an open stair or atrium configuration (never more than two storeys at a time). All buildings were provided with fire-isolated stairs and fire sprinklers. Other safety systems were provided in accordance with the prescriptive requirements of the Australian National Construction Code. The undersides of the CLT floor slabs were exposed in most areas (no suspended ceilings). The floors were provided with non-combustible, raised floor systems. Some exposed timber floors were also proposed in isolated locations.

The extent of glazing in the external walls in the case studies differed substantially from the compartments in studies published to date. Each case study building included 50-70 % glazed curtain wall, generally in a slab-to-slab design, whereas the majority of timber structure fire research to date has utilised external walls with a series of smaller windows, normally occupying the upper half of the wall [2] [3] [10] [12].

3.2 FIRE GROWTH & TENABILITY

The Stage 1 model assessed the onset of untenable conditions during occupant evacuation using CFD fire/smoke modelling and an empirical evacuation model to compare the Available Safe Egress Time (ASET) until untenable conditions were reached with the Required Safe Egress Time (RSET) for occupants to safely evacuate.

The fire scenarios modelled the movable fuel load with an initial t-squared fire growth rate based on the subject project and took account of the impact of the involvement of any of the exposed mass timber by conservatively assuming that rapid fire spread across the ceiling would occur should the timber ceiling reach the critical temperature for ignition (taken as 300°C [8]) in any location. This also accounts for the variable ceiling spread rate observed across experimental works.

Research [3] [12] has shown rapid fire spread horizontally under combustible ceilings where fire sprinklers are generally deemed ineffective and vertically on combustible walls. It is understood that flashover conditions occur soon after ignition of the combustible surfaces where significant or sustained pre-heating has taken place prior. Therefore, ignition of the exposed timber was considered as a failure criterion, meaning occupants must evacuate the fire floor before timber ignition.

It is important to note that the fire sprinkler system was considered to have failed on demand for all fire scenarios. This is considered to be reasonable based on our internal review of the available sprinkler statistics. Broadly speaking, it is prudent to assume that one out of ten fires results in an uncontrolled fire scenario, meaning that sprinkler failure must be considered as part of a holistic fire engineering assessment.

The impact of setting timber ignition as 300°C versus a traditional t-squared fire was significant. The available safe egress time is normally assessed with criteria such as the smoke temperature at a given height and the resultant radiant flux to the floor with the capacity to cause injury to occupants, with the time required for smoke layer build-up being the mechanism of interest. By contrast, the exposed timber ceiling, most likely directly above the fire plume, is at risk of igniting in a

https://doi.org/10.52202/069179-0232

fraction of the time of unacceptable smoke layer build-up. Across our models, this time was in the order of half. However, the time to timber ignition depends on the building layout, structural member configuration and orientation, slab-to-slab height, beam layout and opening location.

3.3 HEAT TRANSFER & CHAR DEPTH

Different design fire scenarios were developed to attain temperature curves near the ceiling that were then used as inputs for the heat transfer model. The aim was to develop temperature curves representative of a fire involving the structural timber in the real space as designed. Different bounding fire growth scenarios were developed, including rapid growth to a high HRR resulting in a shorter burning duration, to assess short hot fires, and slow fire development with extended fully developed and a decay phase. Various opening configurations, building layouts and exposed timber configurations were considered, and could be similarly assessed as part of a collaborative design approach with the architect and structural engineer in real projects.

The finite difference heat transfer model [7] [19] with the estimated heating curves in the subject compartments was then applied to a range of timber members with different lamella layups to estimate the thermal gradients in depth of the CLT or glulam. The model attempted to account for the potential impact of loss of charred section on CLT members by assuming failure at consecutive glue lines, which is understood to be an oversimplification. However, no methodology exists which can account for all relevant coupled causal factors such as mechanical and thermal loads throughout the timber and in particular affecting the bond between lamellae. Thicker outer lamella were generally understood to provide preferable outcomes as the glue lines were seen to receive less heat later. However, failure of heated bonded lamellae and various adhesive types is not well understood (also see Section 4.5) [6].

Uncertainty persists around required input values such as thermal conductivity, specific heat capacity, and heat transfer coefficients that are functions of temperature, species and other factors. Assumptions for these variables were made based on available scientific literature. However, the available data does not support rapid and robust application of this approach to real timber designs.

This theoretical approach assesses the heat transfer for compartment-specific design fire scenarios. The in-depth heating rate depends on a range of variables including the compartment design and ventilation. The incident heat may be less, similarly or significantly more onerous than that from a standard fire curve.

3.4 EXTERNAL FLAME HEIGHT

The fully-developed design fire could amount to a ventilation-controlled or fuel-controlled fire, depending on the available ventilation through compartment openings. In a ventilation-controlled fire (A), the expected impact of adding more fuel gas is to prolong or increase the intensity of the external flaming, i.e. the combustion of unburnt fuel gases that exit the compartment. The addition of the mass timber fuel possibly has little impact upon the HRR achieved within the compartment if all of the available oxygen is already consumed by the moveable fuel combustion. If the burning of the moveable fuel load is not ventilation-limited but fuel-controlled (B), some of the additional mass timber fuel is considered to burn within the compartment, up to the limit permitted by the available ventilation, and increase the heat released within the compartment.

While modelling the range of buildings and various compartments, both ventilation-controlled (A) and fuel-controlled (B) cases were observed. During the case studies, a flame extensions review was undertaken in accordance with BS EN1995-1-2 to assess the impact of the additional fuel load provided by the timber structure on external vertical flaming. A range of fuel load densities was assessed and the fuel provided by the mass timber structure was added. The calculation assessed a scenario in which an uncontrolled fire had occurred (sprinkler failure) and enough glazing broke to sustain a post-flashover fire. The external heat release rate increased by 15-17 % when the timber fuel was added to each fire scenario. The ratio of the maximum HRR attributable to the moveable and timber fuel in each scenario varied, as did the number of available openings.

Experiments assessing flame extension from uncontrolled fires in very large compartments are lacking from the scientific literature, especially for the case of a building with a mass timber structure. The experimental work that underpins the Eurocode flame extension calculation studied compartments with an area of less than 100 m^2. Therefore, the case study calculations were run for typical small compartments in the order of 3 x 3 m and also at the limits of applicability of the calculation method (ca. 100 m^2), despite the floor plate of the case study building compartments generally were in the order of 1,000 m^2. The impact of increasing the room size from 9 m^2 to 100 m^2 (i.e. one order of magnitude) was to increase the incident flux by 0.5 kW/m^2 to ca. 16.5 kW/m^2.

Upon review of the range of results, the external flame was evaluated as the radiant flux back to the building at 2.0 m above the opening. In the case studies, the incident radiant flux received by the glazing of the floor two storeys above the fire floor was deemed too low to induce thermal glazing failure. A review of the limited available literature on heat-induced glazing failure determined that laminated glazing is not likely to fail when exposed to an incident flux of up to 25 kW/m^2. The unknowns regarding extrapolation test results with specific designs to real design cases needs to be assessed in future work.

3.5 SELF-EXTINCTION

The assessment involved CFD modelling of fire compartments with dimensions as designed, and varying extent and configuration of exposed mass timber surfaces. The timber surfaces were assigned a burning rate per unit area (heat release rate per unit area) and temperature. The boundary conditions for the

compartment at the point of extinction of the moveable fuel load were defined to assess the scenario of minimum heat losses.

The incident flux received across all exposed timber surfaces calculated by the model was then compared with the critical incident heat flux for self-extinction reported in published research to determine if self-extinction was credible. The critical incident flux for flaming combustion reported in the literature is in the order of 30 to 42 kW/m2 for a series of lab and compartment experiments [15] [21]. However, the critical incident heat flux for self-extinction is a function of the experimental environment and conditions, including the char layer thickness [21]. Consequently, the critical heat flux for self-extinction will vary on a case-by-case basis depending on compartment boundary conditions, such as the available ventilation (quantity and size of openings) or the configuration and orientation of internal surfaces. The unknowns regarding extrapolation of experimental values for a range of compartment sizes and configurations needs to be assessed in future work.

4 DISCUSSION AND LIMITATIONS

The proposed methodology including the finite difference heat transfer model is a fundamental approach to mass timber design for fire safety. However persisting scientific knowledge gaps require to be filled to improve confidence and enable reduced inherent error in this fundamental approach. The key limitation of the proposed methodology relates to data availability and applicability, predominantly in the areas discussed in the following.

4.1 BURNING AND HEAT RELEASE RATES IN OPEN-PLAN COMPARTMENTS

The rate of energy released by the burning movable fuel load changes over time as a function of the thermal environment within the fire compartment. Higher heat feedback to the fuel increases the energy release rate and reduces the fire duration due to energy conservation.

The heat feedback to the fire changes with changing compartment geometries. The assumptions based on ventilation-controlled regimes no longer apply once the compartment becomes sufficiently large and well-ventilated. Spatial and temporal distributions of temperatures and incident heat fluxes on compartment boundaries are determined by the fire spread mode [2]. The heterogenous temperatures throughout a large compartment can lead to longer burning durations of the movable fuel load compared to compartments in which uniform burning of all fuel can be assumed [2]. As a consequence, the duration of thermal exposure to structural members increases.

Both the heat received over time and the burning duration affect the heat transfer into structural elements within the fire compartment. A high HRR over a short duration can be more favourable from a structural perspective than a longer lower HRR.

Different fire scenarios have to be assessed considering the movable fuel load and the burning rates expected for the compartment at hand. However, burning rates for large compartments, especially those with combustible compartment boundaries, form a critical research gap.

4.2 BURNING OF CEILINGS AND WALLS

The fire dynamics in a compartment with combustible boundaries are expected to differ once the compartment boundaries become involved in the fire. In traditional scenarios, all fuel is located on the compartment floor. The impact of burning combustible ceilings and walls on the fire dynamics are currently understudied.

4.3 THERMAL PROPERTIES AND EXTINCTION

The applicability of material properties required as input parameters for fire safety assessments of timber structures is uncertain and has not been sufficiently validated. Therefore, the results which can be obtained with any framework hold high uncertainty. Values determined in bench-scale experiments for a limited number of timber species may not scale up to full-scale applications and likely vary between timber species. The critical heat flux for self-extinction is conditional on the char layer thickness, which may differ substantially between timber species and application scales.

In addition, Sahoo et al. [17] determined best-fit results between a CFD model and an experimental study on small-scale compartments made of Radiata Pine CLT [16]. However, the modelling approach to assess self-extinction by Sahoo et al. [17] was not benchmarked against large-scale experiments. The incident heat flux obtained using fire CFDs are very sensitive to fuel (e.g. radiative fraction) and scale-dependent (e.g. path length) parameters from the radiation solver.

4.4 CONTINUOUS SMOULDERING

Numerous studies [5] [15] [16] have reported gradual self-extinction of flaming of exposed timber after the burnout of the moveable floor fuel load and following cessation of flaming combustion involving the exposed timber within well-ventilated compartments. However, large-scale experiments observed hotspots which continued smouldering for hours or days after flaming combustion was considered to have self-extinguished [12]. This is a fundamental safety problem for the long-term viability of timber building design that cannot be addressed with improved input parameters and calculations. A collective stakeholder approach involving the design team, first responders and other stakeholders must assess the potential consequences of continuous smouldering.

The methodology outlined in Section 2.1 allows qualitative identification of areas likely receiving increased heat feedback or losing insufficient heat critical for total self-extinction. However, the method cannot quantify the phenomenon or predict the consequence of these hotspots potentially undergoing self-sustained smouldering for extended periods of time. Critical heat fluxes and other critical variables (geometry, lamella thickness, air flows, etc.) regarding

https://doi.org/10.52202/069179-0232

the extinction of smouldering combustion of charred solid timber form a critical research gap.

The qualitative consequence of localised hotspots that do not undergo self-extinction can be low but prolonged heat generation, gradually weakening nearby loadbearing elements and eventual re-transition to flaming combustion. Kotsovinos et al. [12] observed the smouldering burn-through of an exposed CLT ceiling over a 40-hour period in a large-scale open-plan compartment after a flaming fire that lasted under 23 minutes. In a real building, this would have resulted in the loss of compartmentation. Kotsovinos et al. observed hotspots primarily at the interface between the CLT ceiling and concrete beams, i.e. where the two surfaces radiated back and forth over a short distance.

The observations of local hot spots suggest that even with conditions that appear generally favourable for self-extinction of exposed mass timber, localised heat generation can continue and spread through the structural timber members. The impacts thereof that need to be considered in structural design in practice is, to date, unknown. Partial evacuation seems unadvisable in buildings with combustible structural elements as delayed structural collapse and compartmentation by smouldering cannot be quantitatively assessed. Furthermore, it emphasises the importance and complexity of fire brigade intervention to ensure the complete extinction of structural timber members. The practical considerations of fire brigade intervention in post-flashover compartments with load-bearing timber are beyond the scope of this paper but must urgently be addressed in an open dialogue between the fire brigade, building authorities, researchers and fire engineers.

4.5 LOSS OF CHARRED CROSS-SECTION

Loss of charred timber section due to fall-off is a complex, currently unpredictable phenomenon that can cause iterative self-enhancing loss of loadbearing cross-section and affect compartment fire dynamics. It can delay or prevent self-extinction and enhance the in-depth heating of the timber structure [7].

The laminated nature of engineered timber products results in a potential for lamellae detaching once the capacity of their bond is exceeded. Temperatures like those expected in compartment fires can negatively affect the bond strength. The loss of charred timber sections through phenomena like delamination or char fall-off exposes the underlying timber and adds additional fuel to the fire. Char fall-off was visually observed to be followed by flaming combustion of the newly exposed, previously protected timber surface in full-scale compartment experiments with mass timber walls, and temperature devices recorded a local temperature increase in local temperatures [22].

A theoretical possibility to account for the loss of load-bearing cross-section to char fall-off is to perform a heat transfer calculation and continuously discount lost cross-section exceeding a critical state. Experimental research has observed char fall-off to occur over a wide range of temperatures as low as 140 ºC [6] and to be a thermomechanical phenomenon, i.e. a function of the local absolute temperature and mechanical loading [7]. Therefore, current knowledge does not support the use of a critical temperature criterion for char fall-off.

4.6 HEAT TRANSFER & COOLING PHASE

Fire curves in real compartment fires do not resemble the standard curve. In fire safety engineering practice, the standard curve is generally assumed to encompass all most reasonably foreseeable fire cases. It is not the scope of this paper to discuss the adequacy of standard furnace testing for non-combustible structural members. However, for designs using combustible structural members, the fundamental difference between furnace tests of combustible versus non-combustible elements becomes problematic and the real timber-involved fire may in fact fall well outside of what was once considered the reasonably foreseeable fire cases, and this occurrence is lost by relying only upon the furnace test to support timber structural member design.

In a standard furnace test, structural members are tested against standard temperature-time curves with gas burners providing heat [13]. Unlike non-combustible members, combustible elements like structural timber members themselves add to the fuel load in a furnace test, leading to reduced heat supply from the gas burners [13]. The timber's energy contribution is effectively deleted by the furnace recalibration procedure.

The peak temperatures in-depth of mass timber elements can be reached later than peak compartment temperatures due to thermal lag. The temperature evolution within a compartment after burnout of the movable fuel load depends on the heat losses from the compartment through compartment boundaries and openings and is influenced by fluid flows and, in the case of mass timber, the additional heat generation from combustible elements and their self-extinction.

4.7 WINDOW GLAZING FAILURE

Currently existing knowledge does not allow prediction of the timing, amount and locations of glazing breakage in compartment fires, especially in open-plan compartments. However, the amount of glass breakage can have critical importance regarding the energy balance in a post-flashover compartment, which can be especially critical for self-extinction of combustible structures. Therefore, the sensitivity of the assessments to varying amounts and configurations of intact and broken glazing must be analysed for the design at hand.

5 CONCLUSIONS

An explicit fire safety strategy for mass timber buildings with different compartment geometries has been developed based on theoretical frameworks proposed in existing literature. The four frameworks address self-extinction, tenability, adequate structural capacity in fire and external flaming. A review presented the applicability of available research as well as the remaining knowledge gaps. This approach highlights the need for research that addresses the fundamental questions including self-extinction, compartment fire dynamics and the material response to fire required for the safe design of modern mass timber structures.

https://doi.org/10.52202/069179-0232

A lot of responsibility lies with fire safety engineers to determine whether the existing knowledge of the profession, the design tools available and their individual knowledge and skills are sufficient to deliver a holistically adequate fire-safe design when faced with the challenge of a project that is proposed to include a mass timber structure. It is critical to clearly communicate limitations and potential consequences related to fire safety in mass timber buildings with all stakeholders as a part of executing due diligence.

REFERENCES

[1] J. P. Hidalgo, A. Cowlard, C. Abecassis-Empis, C. Maluk, A. H. Majdalani, S. Kahrmann, R. Hilditch, M. Krajcovic and J. L. Torero, "An experimental study of full-scale open floor enclosure fires," *Fire Saf J.,* 2017.

[2] V. Gupta, J. P. Hidalgo, D. Lange, A. Cowlard, C. Abecassis-Empis and J. L. Torero, "A review and analysis of the thermal exposure in large compartment fire experiments," *IJHRB,* 2021.

[3] J. P. Hidalgo, T. Goode, V. Gupta, A. Cowlard, C. Abecassis-Empis, J. Maclean, A. I. Bartlett, C. Maluk, J. M. Montalvá, A. F. Osorio and J. L. Torero, "The Malveira Fire Test: Full-Scale Demonstration of Fire Modes in Open-Floor Plan Compartments," *Fire Saf J.,* 2019.

[4] A. Bartlett, F. Wiesner, R. M. Hadden, L. A. Bisby, B. Lane, A. Lawrence, P. Palma and A. Frangi, "Needs for total fire engineering of mass timber buildings," in *WCTE 2016*, 2016.

[5] R. M. Hadden, A. I. Bartlett, J. P. Hidalgo, S. Santamaria, F. Wiesner, L. A. Bisby, S. Deeny and B. Lane, "Effects of exposed cross laminated timber on compartment fire dynamics," *Fire Saf J.,* 2017.

[6] L. Schmidt, D. Fernando and R. M. Hadden, "Observations and impact of char layer formation and loss for engineered timber," *Fire Saf J.,* [Submitted].

[7] L. Schmidt, *Experimental study on the effect of char fall off on the heat transfer within loaded cross-laminated timber columns exposed to radiant heating (Master thesis),* The University of Edinburgh, 2020.

[8] D. Drysdale, An Introduction to Fire Dynamics, 3 ed., John Wiley & Sons, Ltd, 2011.

[9] J. P. Hidalgo, *The need for a fire engineering design framework for mass timber buildings [Presentation],* IFE (CPD Event), 2020.

[10] H. Xu, I. Pope, V. Gupta, J. Cadena, J. Carrascal, D. Lange, M. McLaggan, J. Mendez, A. F. Osorio, A. Solarte, D. Soriguer, J. L. Torero, F. Wiesner, A. Zaben and J. Hidalgo, "Large-scale compartment fires to develop a self-extinction design framework for mass timber-Part 1: Literature review and methodology," *Fire Saf J.,* 2022.

[11] F. Wiesner, A. Bartlett, S. Mohaine, F. Robert, R. McNamee, J. Mindeguia and L. A. Bisby, "Structural Capacity of One-Way Spanning Large-Scale Cross-Laminated Timber Slabs in Standard and Natural Fires," *Fire Technol,* 2021.

[12] P. Kotsovinos, E. Rackauskaite, E. Christensen, A. Glew, E. O'Loughlin, H. Mitchell, R. Amin, F. Robert, M. Heidari, D. Barber, G. Rein and J. Schulz, "Fire dynamics inside a large and open-plan compartment with exposed timber ceiling and columns: CodeRed #01," *Fire Mater,* 2022.

[13] A. I. Bartlett, R. McNamee, F. Robert and L. A. Bisby, "Comparative energy analysis from fire resistance tests on combustible versus noncombustible slabs," *Fire Mater,* 2020.

[14] D. Lange, J. Sjöström, J. Schmid, D. Brandon and J. P. Hidalgo, "A Comparison of the Conditions in a Fire Resistance Furnace When Testing Combustible and Non-combustible Construction," *Fire Technol,* 2020.

[15] R. Emberley, T. Do, J. Yim and J. L. Torero, "Critical heat flux and mass loss rate for extinction of flaming combustion of timber," *Fire Saf J.,* 2017.

[16] C. Gorska, *Fire dynamics in multi-scale timber compartments (Doctoral dissertation),* The University of Queensland, 2020.

[17] S. R. Sahoo, C. Gorska, H. Xu and J. P. Hidalgo, "A Simplified Assessment of Thermal Feedback in CLT Compartments After Burnout," in *AOSFST 2021*, 2021.

[18] S. Nothard, D. Lange, J. P. Hidalgo, V. Gupta and M. McLaggan, "The response of exposed timber in open plan compartment fires and its impact on the fire dynamics," in *SiF2020*, 2020.

[19] A. F. Osorio, J. P. Hidalgo and P. D. Evans, "Enhancing the fire performance of engineered mass timber and its implications to the fire safety strategy," in *WCTE 2018*, 2018.

[20] "Grenfell Tower Inquiry: Phase 1 Report, Volume 1," Crown Copyright, 2019.

[21] J. Cuevas, J. L. Torero and C. Maluk, "Flame extinction and burning behaviour of timber under varied oxygen concentrations," *Fire Saf J.,* 2021.

[22] I. Pope, H. Xu, V. Gupta, J. Carrascal, D. Lange, M. McLaggan, J. Mendez, A. Solarte, D. Soriguer, J. L. Torero, F. Wiesner and J. P. Hidalgo, "Fire Dynamics In Under-Ventilated Mass Timber Room Compartments," in *AOSFST 2021*, 2021.

[23] A. Bartlett, R. M. Hadden, L. Bisby and B. Lane, "Auto-extinction of engineered timber as a design methodology," in *WCTE 2016*, 2016.

[24] R. McNamee, J. Zehfuss, A. Bartlett, M. Heidari, F. Robert and L. Bisby, "Enclosure fire dynamics with a cross-laminated timber ceiling," *Fire Mater,* 2021.

https://doi.org/10.52202/069179-0232

World Conference on Timber Engineering Oslo 2023

FIRE CHARACTERISTICS OF A COMPARTMENT WITH EXPOSED CLT WALLS: AN EXPERIMENTAL INVESTIGATION USING THE STANDARD ISO 834 CURVE

Andrianos E. Koklas[1], Dionysios I. Kolaitis[2], Maria A. Founti[3]

ABSTRACT: Cross Laminated Timber (CLT) panels are increasingly used for building construction; in specific cases, the indoor surface of the CLT panels is required to be "exposed", thus making adequate fire protection of these elements a significant challenge. The main aim of this work is to experimentally determine the impact of an exposed CLT panel, in this case a ceiling, to the characteristics of a compartment fire. Experiments using either fire-resistant panels or a CLT exposed ceiling are performed in a test rig, corresponding to the 1/3 scale of the standard ISO 9705 compartment; a broad sensor network is installed to determine the main characteristics of the developing thermal- and flow-fields inside the compartment. In order to overcome certain limitations associated with achieving adequate levels of repeatability when a "realistic" time-dependent fire curve is used, a PID controller-based gas burner is employed; the ISO 834 standard temperature-time curve is used in all fire tests. The experimental results suggest that, as expected, when a CLT ceiling is used, the total fuel consumption at the burner is significantly lower. The thermal field inside the compartment exhibits certain differences, while the opening velocities were largely unaffected by the installation of the CLT ceiling.

KEYWORDS: Compartment fires, CLT, charring, fire engineering, measurements

1 INTRODUCTION

Wood construction is known to exhibit a range of advantages, compared to "conventional" construction methods (e.g. using concrete), in terms of seismic performance, cost and environmental footprint. However, due to the combustibility of wood, its fire behaviour is a major limiting factor in the development of new wooden buildings. Cross laminated timber (CLT) elements are load bearing elements, used either in vertical walls or slabs. In both of these cases, in order to enhance their fire performance, CLT elements can be encapsulated, i.e. covered by fire-resistant panels (e.g. gypsum plasterboards); however, due to aesthetic reasons, it is commonly required to leave "exposed" as much timber as possible. In the latter case, the adequate fire protection of the CLT elements poses significant challenges.

In order to investigate the fire behaviour of construction products, compartment fire tests are commonly used [1-5]. In these tests, the temporal evolution of the Heat Release Rate (HRR) usually follows either a "constant value" or a "time transient" profile. However, when a timber construction element is involved (e.g. an exposed CLT wall), the HRR inherently varies with time, due to the combustion process occurring in the wood, thus imposing an additional, time-varying fire load [1]. In the majority of fire tests using a "time transient" HRR profile, the fire source used is usually a wooden crib [2, 3, 4] or, in some rare cases, pertinent to large-scale compartments, actual furniture items [5]. However, both these options do not provide adequate levels of controllability and repeatability. In this context, this work presents a novel approach, where a series of fire tests are performed in a medium-scale compartment, equipped with a CLT wall, where the standard ISO 834 [6] time-temperature curve, commonly used in fire resistance furnace tests, is employed, aiming to ensure acceptable levels of repeatability.

This work is mainly aimed at investigating the effects of exposed CLT panels on the thermal characteristics of the fire developing inside a typical compartment. In this frame, two series of fire tests are performed in a medium scale compartment, one using an inert (non-combustible) material and the other using exposed CLT panels; the obtained measurements are then qualitatively and quantitatively compared.

2 EXPERIMENTAL SETUP

2.1 COMPARTMENT GEOMETRY

The fire compartment dimensions correspond to a 1/3 scale of the ISO 9705 [7] standard compartment, representing a typical room. The compartment's internal dimensions are 1200 mm (length) × 900 mm (width) × 900 mm (height); the door-type opening's dimensions are 266 mm (width) × 666 mm (height).

In the first test series, all sides of the compartment envelope (floor, walls, ceiling) were constructed using 20 mm thick fire-resistant ceramic boards; in the second

[1] Andrianos Koklas, National Technical University of Athens, Greece, andrianos.e.koklas@gmail.com
[2] Dionysios Kolaitis, National Technical University of Athens, Greece, dkol@central.ntua.gr
[3] Maria Founti, National Technical University of Athens, Greece, mfou@central.ntua.gr

https://doi.org/10.52202/069179-0233

series, the ceiling was replaced with a 3-layered (30 mm / 20 mm / 30 mm) 80 mm thick CLT panel (Figure 1), corresponding to a "fully exposed" CLT ceiling scenario.

***Figure 1**. Indicative photos of the test compartment with inert (left) and CLT (right) ceiling installed.*

2.2 FIRE SOURCE

In the majority of medium-scale and small-scale laboratory fire tests, the fire source used is either a gas burner, operating in "steady state" conditions, or a pool/crib fire burning freely. Both of these test methods exhibit certain drawbacks, i.e. the first is rather "unrealistic", while the latter is significantly lacking in repeatability. Aiming to investigate the possibility of using a gas burner (thus allowing adequate repeatability) in conjunction with a "realistic" time-temperature profile, a PID controller was developed in-house. In the fire tests presented here, the standard ISO 834 [1] curve was employed in order to comparatively assess the characteristics of the thermal- and flow-field developing inside the compartment, when an "inert" or a "combustible" (CLT) ceiling is used.

***Figure 2**. Indicative photo (top view) of the burner and the installed sensor network inside the compartment.*

A rectangular porous burner was used as the fire source. The burner dimensions were 125 mm (length) × 125 mm (width) × 60 mm (height) and it was positioned at the centre of the compartment's floor. The burner was fed with commercial propane (C_3H_8) (Figure 2). A digital mass-flow controller (Bronkhorst F-203AV-1M0-RGD-55-V) was used to measure and control the propane flow rate. More specifically, the average of the upper gas layer temperature and the ISO 834 standard temperature were estimated every second. The measured average upper gas layer temperature corresponded to the input of the PID controller, while the latter quantity was the set-point of the PID, changing every second; the PID controller's output was the signal to the mass flow controller. In this way, when the compartment temperature was higher than the corresponding ISO 834 value, the mass flow controller was instructed to reduce the fuel flow and vice versa.

2.3 SENSOR NETWORK

A broad network of measurement sensors was installed inside the test compartment to determine the main characteristics of the developing flow and thermal fields. Overall, 81 K-type thermocouples, 4 bi-directional velocity probes, 2 Pitot-static tubes, 4 heat flux meters, 1 continuous gas analyser and 3 digital flow meters were used.

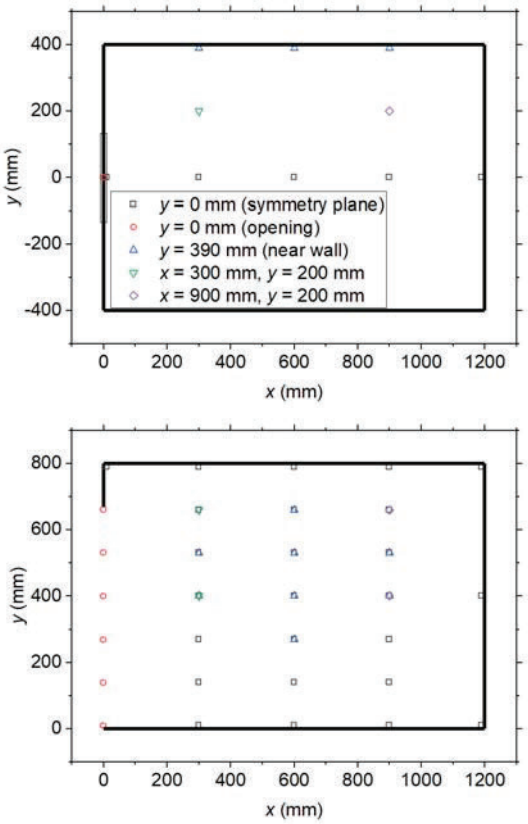

***Figure 3:** Spatial distribution of gas temperature and velocity measurement sensors, top view (top) and side view (bottom).*

The thermocouples were installed both inside the compartment (c.f. Figure 3), thus allowing measurement

https://doi.org/10.52202/069179-0233

of the gas phase temperature, as well as "inside" the ceiling (c.f. Figure 4) and compartment walls (c.f. Figure 5), at various locations across the thickness of the compartment envelope, aiming to record the temporal evolution of the thermal field developing "inside" the solid boundaries. When a CLT ceiling was tested, thermocouples were installed at the back (unexposed) side of each lamella (layer), corresponding to a distance of 30 mm, 50 mm and 80 mm from the exposed side, across the thickness of the CLT panel. The coordinate system used employs an axis origin that is located in the centre-line symmetry axis of the compartment (y = 0 mm), at the opening (x = 0 mm) on the floor level (z = 0 mm) (c.f. Figure 3).

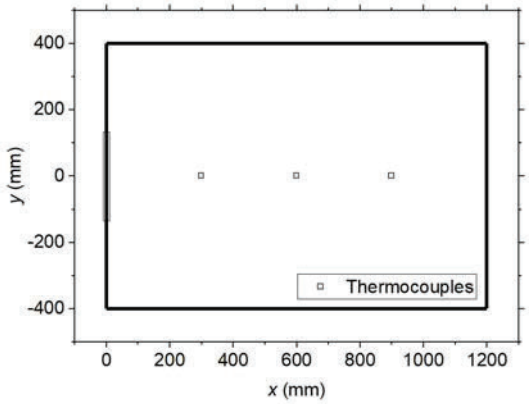

Figure 4: *Spatial distribution of the ceiling temperature measurement sensors.*

The gaseous combustion products were collected and a sample was fed to the gas analyser, where the oxygen, carbon dioxide and carbon monoxide concentrations were recorded. These measurements were later used to estimate the overall heat release rate, using the oxygen consumption calorimetry method (Equation 1) [8], where φ is the oxygen depletion factor, calculated using Equation 2. A brief description of all parameters that appear in Equations 1 and 2 is given in the Nomenclature.

$$\dot{Q} = \left[E_{O_2}\varphi - \left(E_{CO} - E_{O_2}\right)\frac{1-\varphi}{2}\frac{X_{CO}^{A^e}}{X_{O_2}^{A^e}} \right] \times \times \frac{\dot{m}_g}{1+\varphi(\alpha-1)}\frac{M_{o_2}}{M_a}\left(1-X_{H_2O}^{a}\right)X_{O_2}^{A^a} \quad (1)$$

$$\varphi = \frac{X_{O_2}^{A^a}\left(1-X_{CO_2}^{A^e}-X_{CO}^{A^e}\right)-X_{O_2}^{A^e}\left(1-X_{CO_2}^{A^a}\right)}{\left(1-X_{O_2}^{A^e}-X_{CO_2}^{A^e}-X_{CO}^{A^e}\right)X_{O_2}^{A^a}} \quad (2)$$

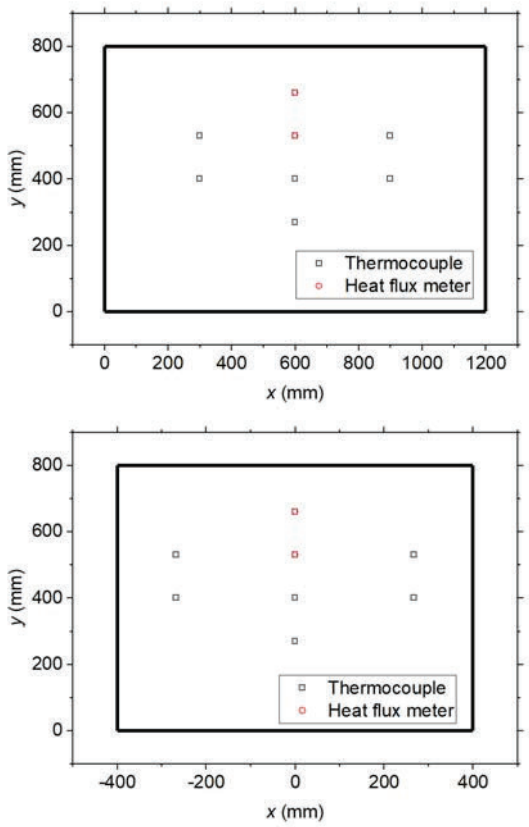

Figure 5: *Spatial distribution of the temperature and heat flux measurement sensors, at the side (top) and back (bottom) wall.*

2.4 MEASUREMENT UNCERTAINTIES

The gas temperatures were measured using K-type thermocouples connected to the signal acquisition system via extension wires. The systematic uncertainties of the thermocouples were a standard calibration uncertainty of ± 2.2°C or ± 0.75% of the measured value (the largest value is taken into account) for a 99% confidence interval (3σ), an uncertainty due to the wires and their extension of ± 2.2°C and a conversion uncertainty of ± 0.5%. The opening velocities were measured using bi-directional velocity probes and Pitot tubes. In terms of the systematic uncertainties, the bi-directional velocity probes exhibited a flow approaching uncertainty of ± 10% [4], a conversion uncertainty of ± 1% of the maximum pressure of the pressure sensor (10 Pa). The heat flux was measured using SBG01 water cooled heat flux meter. The calibration error is ± 3% of the measured value and the non-linearity error is ± 4% of the maximum heat flux (200 kW).

https://doi.org/10.52202/069179-0233

3 EXPERIMENTAL RESULTS

3.1 INERT ENVELOPE - REPEATABILITY

In the first series of fire tests, all sides of the compartment envelope were constructed using 20 mm thick ceramic boards. The standard ISO 834 time-temperature curve was used; the duration of each fire test was 3600 s. Measurements obtained at the upper gas layer of the compartment ($z \geq 660$ mm) were used to estimate the "average" temperature used in the PID controller to determine the required increase or decrease in the fuel flow.

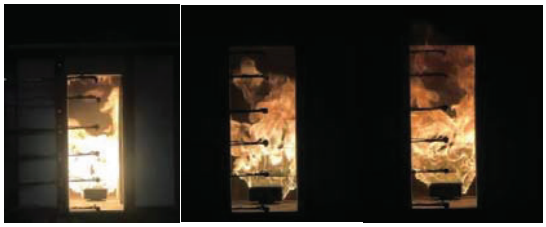

Figure 6: *Photos of a typical "inert" fire test, 600 s (left), 1800 s (middle) and 3600 s (right) after ignition.*

Initially, three identical fire tests have been performed, aiming to assess the "repeatability" of the test setup, based on the obtained measurements. In Figure 6, indicative images of the first "inert" (non-combustible envelope) fire test, using the standard ISO 834 time-temperature curve, are shown for three characteristic time instances, 600, 1800 and 3600 s after ignition. It is evident that the size of the developed flame covers a significant part of the compartment's height; in fact, the fuel mass flow rate at the 3600 s mark corresponds to a HRR value roughly equal to 100 kW.

Figure 7 depicts the temporal evolution of the standard ISO 834 fire curve against the experimentally measured values at the upper gas layer for the three "inert" experiments. It is evident that in all cases, the compartment temperature follows closely the standard ISO 834 curve.

Figure 8 depicts the temporal evolution of the gas temperature measurements obtained at three characteristic height levels, at a distance of x = 300 mm from the opening. The relatively small discrepancies observed among the three tests suggest that the developed test setup is capable of reaching increased levels of "repeatability".

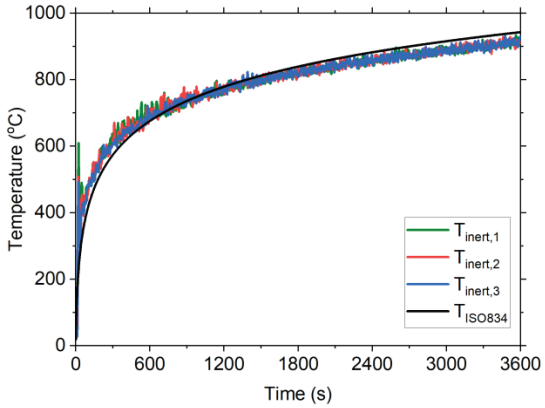

Figure 7*: Temporal evolution of average upper gas layer temperatures compared against the standard ISO 834 fire curve for the three "inert" experiments.*

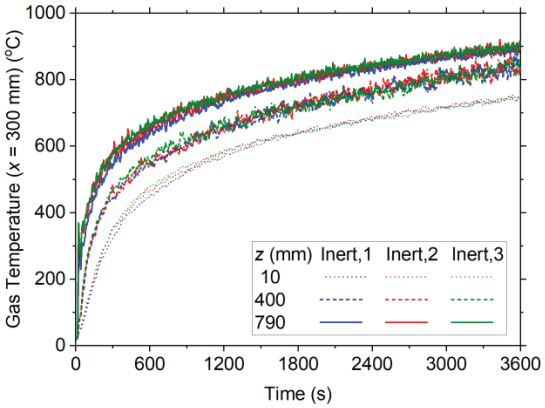

Figure 8*: Temporal evolution of indicative gas temperatures at a distance of x = 300 mm from the opening, for the three "inert" experiments.*

Figure 9 illustrates the spatial distribution of gas temperatures at the central symmetry plane ($y = 0$ mm) of the compartment, at three different time instants ($t = 600$ s, 1800 s and 3600 s). The grey box corresponds to the burner location, whereas the open rectangle (on the left, $x = 0$ mm) depicts the position of the compartment's door-type opening. As expected, the highest temperatures are observed near the centre of the compartment (above the burner) and at the upper gas layer (ceiling jet). Low temperatures close to the bottom part of the opening suggest the inflow of cold ambient air, providing oxygen for the fuel combustion process. Since standard ISO 834 curve imposes a monotonically increasing temperature profile, average compartment temperatures are gradually increasing with the elapse of time.

https://doi.org/10.52202/069179-0233

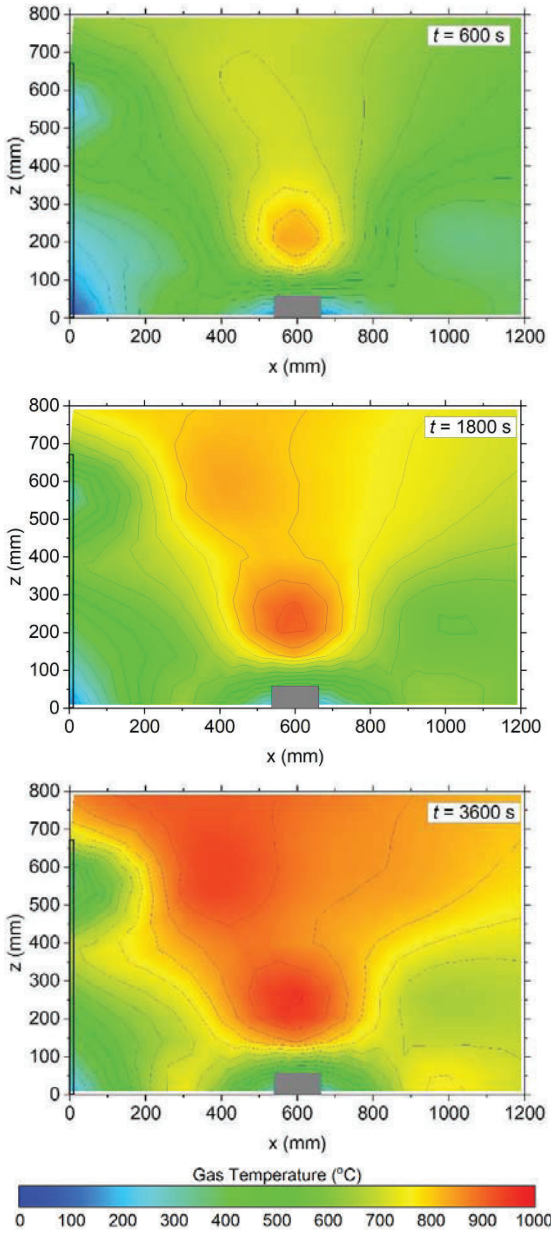

***Figure 9**: Spatial distribution of gas temperatures inside the compartment, 600 s (top), 1800s (middle) and 3600 s (bottom) after ignition.*

3.2 "EXPOSED" CLT CEILING

In the second series of fire tests, a Cross Laminated Timber (CLT) ceiling is installed in the test compartment, aiming to assess the impact on the fire characteristics. An 80 mm thick three-layer (1st layer 30 mm, 2nd layer 20 mm, 3rd layer 30 mm) CLT was used (Figure 10). Thermocouples were installed at the unexposed side of each layer, at two different axial locations (c.f. Figure 5).

The fire test was terminated after 55 minutes, due to the collapse of the ceiling.

***Figure 10**: Inner view of CLT panel, installed at the compartment ceiling.*

Figure 11 shows characteristic views of the compartment where the CLT ceiling is installed, using the ISO 834 fire curve, at three distinct time instances. Although the temperature inside the compartment is similar in both test cases, in the CLT case the flame ejects from the opening faster than the non-combustible ceiling case. This is due to the additional pyrolysate gases released through the CLT ceiling. Since the upper gas layer is oxygen-lean, the pyrolysate gases cannot be burnt promptly; they have to exit the compartment, through the opening, in order for their combustion to be completed in the ambient air. By comparing Figures 6 and 11, it is evident that in the CLT case, flames appear also in the upper part of the compartment, due to the partial combustion of the pyrolysate gases released through the ceiling.

***Figure 11**: Photos of the "exposed CLT ceiling" fire test, 600 s (left), 1800 s (middle) and 3300 s (right) after ignition.*

In Figure 12, the temporal evolution of the average upper gas layer temperature in the two investigated test cases is compared against the standard ISO 834 curve. The "CLT" case exhibits some initial perturbations (due to inertia of the PID system that prevented the rapid adjustment of the fuel controller to the additional heat release due to CLT pyrolysis and combustion); however, after the 900 s mark, both cases follow closely the ISO 834 curve.

https://doi.org/10.52202/069179-0233

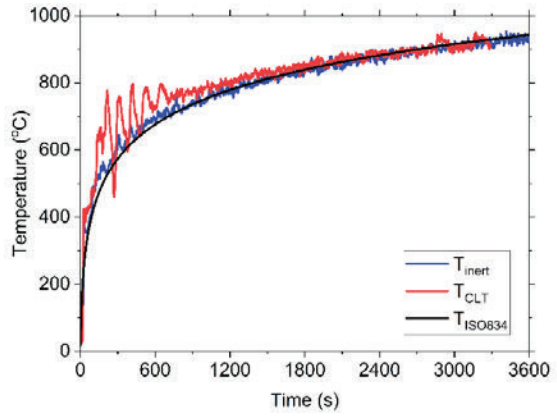

***Figure 12**: Temporal evolution of average upper layer gas temperatures compared against the standard ISO 834 fire curve.*

Figure 13 depicts the temporal evolution of the total fire HRR, corresponding to the sum of the HRR due to propane combustion and the HRR due to timber combustion, which was estimated using the oxygen combustion calorimetry method. After the initial period of fuel flow perturbations (t < 600 s), both cases result in similar HRR values. However, after the 2700 s mark, the total HRR in the CLT case is increased, thus suggesting that the increased HRR due to timber combustion cannot be counterbalanced anymore by the decreasing fuel flow to the burner; in fact, the gradually intensifying combustion of the CLT ceiling resulted in its partial collapse at 3300 s, thus prompting the early termination of the test.

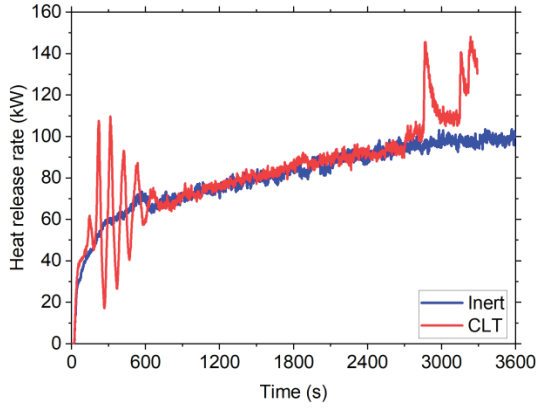

***Figure 13**: Temporal evolution of HRR for the "inert" and "CLT" test cases.*

Figure 14 illustrates the volumetric flow rate of the fuel, which was regulated by the PID controller; in Figure 15, the difference between the fuel flow rate in the "CLT" case, compared to the "inert" case is quantified. As expected, in order to achieve the ISO 834 curve, the "CLT" case requires a reduced fuel flow rate; in general, the reduction in the required fuel flow was more than 50% (Figure 15).

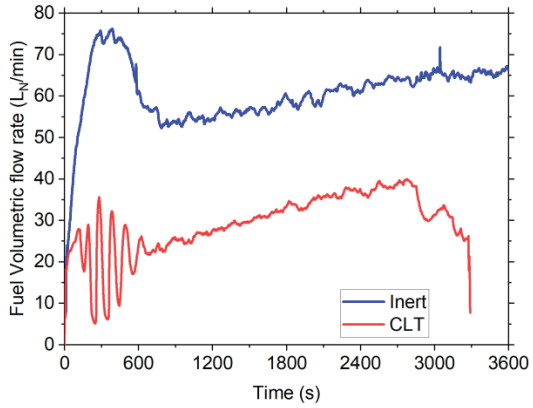

***Figure 14**: Temporal evolution of fuel volumetric flow rate for the "inert" and the "CLT" test cases.*

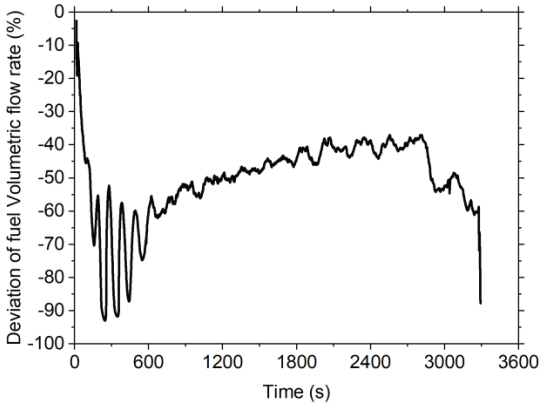

***Figure 15**: Temporal evolution of the deviation between the fuel flow rate between the "inert" and the "CLT" test cases.*

Figure 16 illustrates the spatial distribution of the gas temperature at the central plane of the compartment for three different time instances (t = 600s, 1800s and t = 3300s). Compared to the respective experimental results for the "inert" case (Figure 9), the "CLT" case results in a more "extended" region of higher temperatures close to the ceiling, due to the additional timber combustion processes that occur in this region.

https://doi.org/10.52202/069179-0233

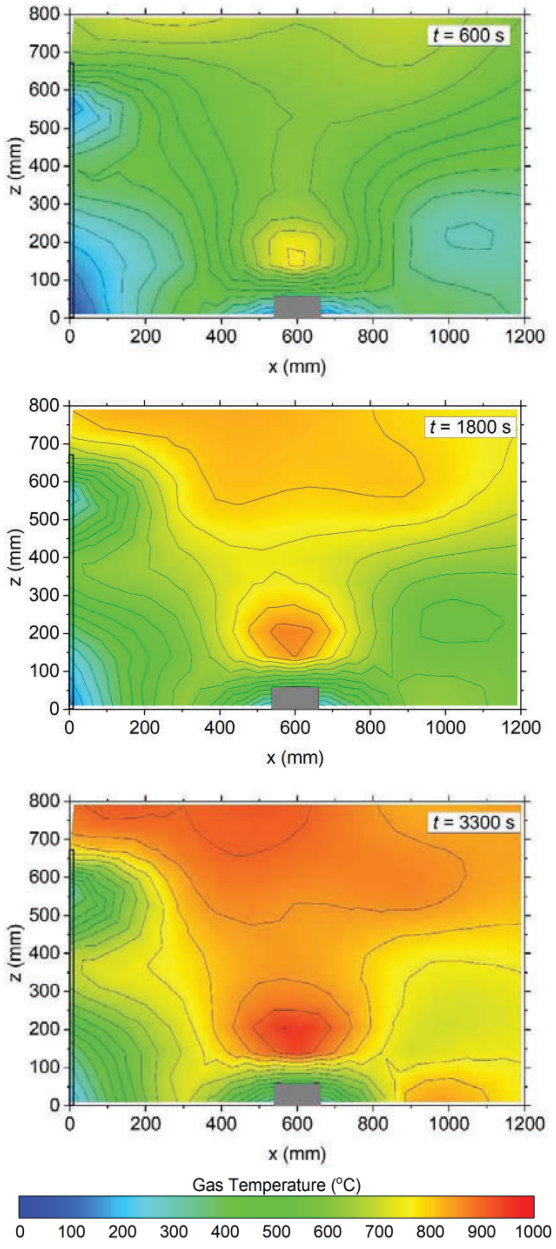

***Figure 16**: Spatial distribution of gas temperatures inside the compartment, 600 s (top), 1800s (middle) and 3600 s (bottom) after ignition.*

Figures 17-19 depict the temporal evolution of the gas temperature inside the compartment at three characteristic height levels (z = 140 mm, 400 mm and 660 mm above the floor); the measurements are provided for three locations across the compartment's symmetry axis, the first (x = 300 mm) close to the opening (Figure 17), the second at the centre (x = 600 mm) of the compartment (Figure 18) and the last close (x = 900 mm) to the back wall (Figure 19).

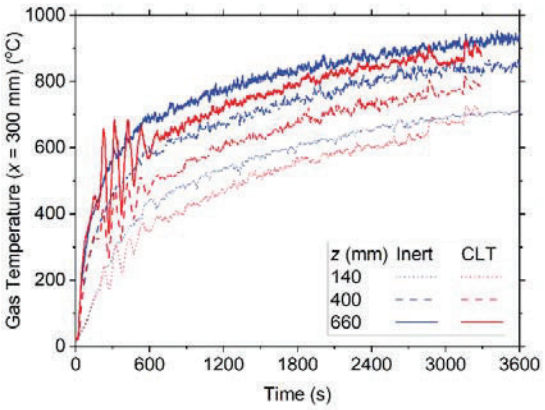

***Figure 17**: Temporal evolution of gas temperatures at three characteristic height levels, near the opening (x = 300 mm).*

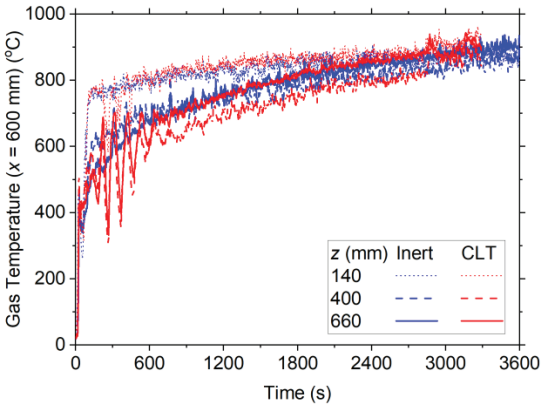

***Figure 18**: Temporal evolution of gas temperatures at three characteristic height levels, at the centre of the compartment (x = 600 mm).*

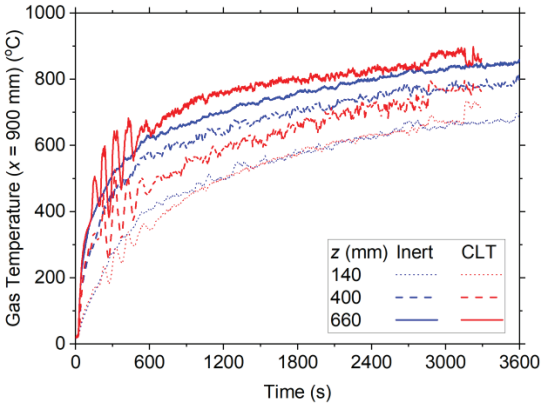

***Figure 19**: Temporal evolution of gas temperatures at three characteristic height levels, near the back wall (x = 900 mm).*

As expected, due to thermal buoyancy, gas temperatures are generally increasing with increasing height, with the

sole exception of gas measurements obtained just above the burner (z = 140 mm, Figure 20) which correspond to the peak temperature values inside the compartment (c.f. Figures 10 and 18). Since the pyrolysate gases close to the opening are ejected to the ambient air before being completely burnt, the average temperatures of the "inert" case are slightly higher than the corresponding values of the "CLT" case (Figure 19). However, at the "back" of the compartment (Figure 21), the thermal feedback from the burning CLT ceiling, in conjunction with the longer residence times of the produced pyrolysate gases allow a more "complete" combustion, thus leading to higher temperatures near the ceiling (z = 660 mm) for the "CLT" case.

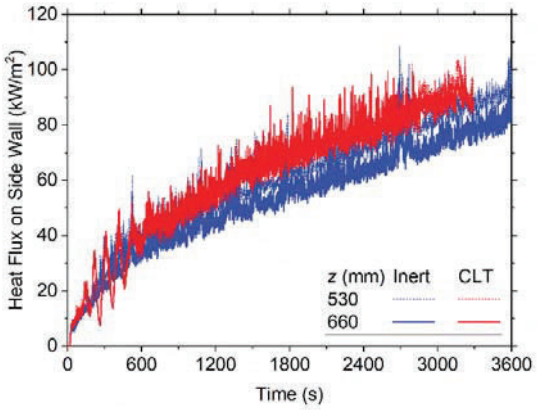

***Figure 20**: Temporal evolution of heat flux at the side wall (y = 400 mm).*

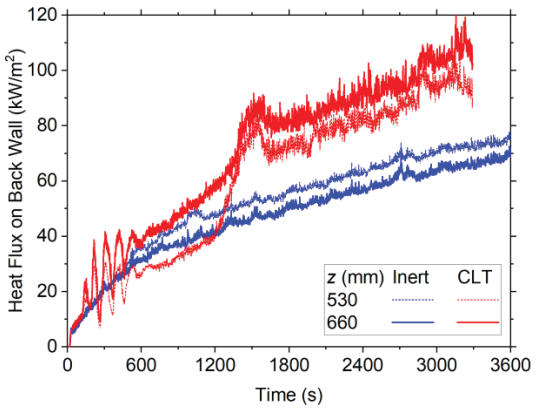

***Figure 21**: Temporal evolution of heat flux at the back wall (x = 1200 mm).*

Figures 20 and 21 show the temporal evolution of the incident heat flux at the side and the back wall, respectively. As expected, in all cases the measured heat flux values are increasing with time. For the "inert" test case, peak heat flux values are observed at a lower height level (z = 530 mm), due to the shorter flame developing in this case (c.f. Figures 6 and 11). However, in the "CLT" case, higher heat flux levels are recorded closer to the ceiling (z = 660 mm), where timber combustion takes place. In general, higher heat flux levels are observed in the "CLT" case compared to the "inert" case, due to the additional radiation from the flames appearing close to the ceiling (c.f. Figure 11).

Figure 22 depicts the effects of the combustible ceiling on the temporal evolution of the flow field developing at the opening plane. Positive velocity values suggest ambient air entering the compartment, whereas negative values signify combustion products exiting through the opening.

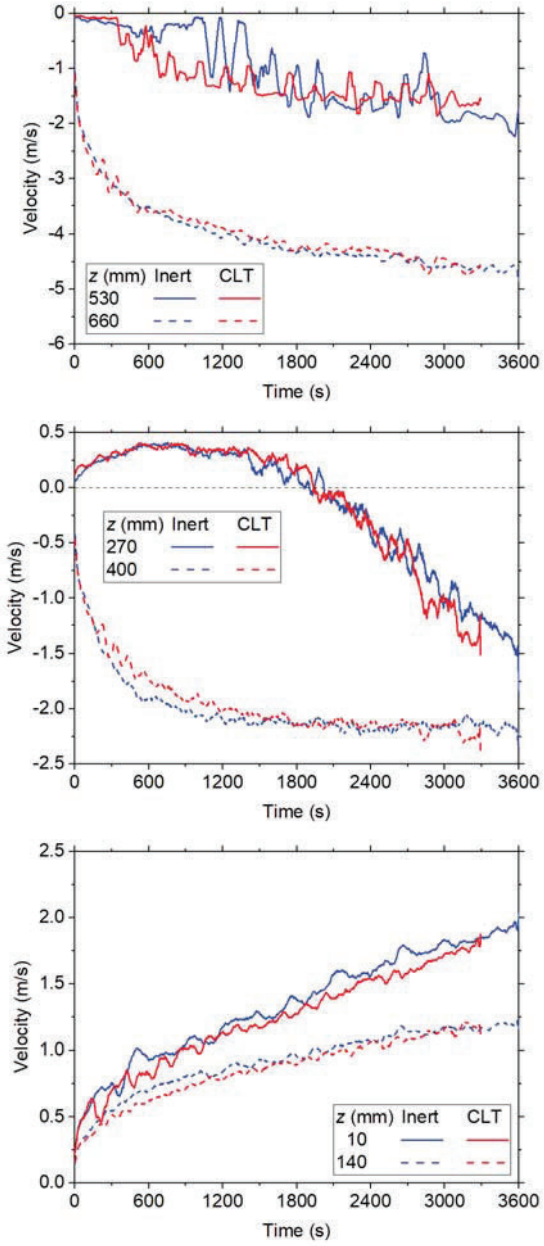

***Figure 22:** Temporal evolution of gas velocities in the upper (top), middle (middle) and lower (bottom) layer of the opening.*

https://doi.org/10.52202/069179-0233

As expected, at the top section of the opening (Figure 22, top), only negative velocity values are recorded, thus suggesting that the hot combustion products, concentrated under the ceiling, escape through the opening's lintel. The gradual increase of the compartment's temperature and, therefore, of the HRR, results in an increasing mass flow rate of the combustion products; as a result, the absolute values of the corresponding velocities are also increasing. Negative velocity values are recorded at the top half of the opening ($z > 300$ mm). During the first half of the fire test ($t < 1800$ s), velocity measurements obtained at a height of $z = 270$ mm (Figure 22, middle) suggest that ambient air is entering the compartment. However, as time goes by and the HRR is increased, the increasing mass flow rate of the hot combustion products results in a "reversal" of the flow direction at this specific height, thus leading to negative velocity values. At the lower part of the opening (Figure 22, bottom), the velocity of the incoming ambient air is monotonically increasing, due to the increasing HRR and, therefore, the need for oxygen.

In general, the CLT ceiling does not seem to significantly affect the measured velocity values. This is also evident in Figure 23, where the vertical velocity profiles at the opening, for three characteristic time instances, are shown. It is interesting to note as time goes by, due to the increasing HRR, the absolute values of both the incoming air and the outgoing combustion products are increased.

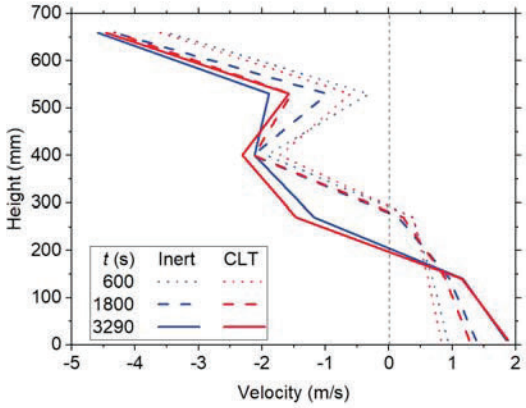

Figure 23: *Gas velocity profile in the opening at 600 s, 1800 s and 3600 s.*

Figure 24 depicts the recorded solid-phase temperatures across the thickness of the CLT ceiling. The distance from the opening ($x = 600$ mm vs. $x = 900$ mm) does not seem to significantly affect the CLT temperatures. According to the recorded temperatures at the unexposed side of the 1st layer, the charring front did not reach the second layer of the CLT ceiling. Near the 3000 s mark, the first CLT layer started to fall-off and the temperatures between the first and second lamella started to rise. The fall-off did not affect significant the temperatures measured between the 2nd and 3rd lamella.

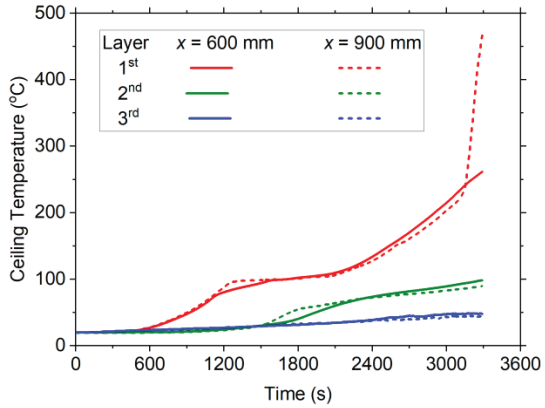

Figure 24*: Temporal evolution of solid-phase temperatures at the unexposed side of each lamella (layer) of the CLT panel.*

4 CONCLUDING REMARKS

In this work, two different series of laboratory experiments were conducted, aiming to assess the impact of installing an exposed CLT panel at the compartment's ceiling, on the characteristics of the thermal- and flow-fields developing inside the compartment, when the ISO 834 standard fire curve is used.

Based on the experimental observations made during the tests, the main effects of installing an exposed CLT ceiling are summarized below:

- The flames eject from the opening quite earlier, a fact that should be taken into account during the building design phase, e.g. suggesting potential additional requirements for the fire protection of façade systems.
- The fuel needed to reproduce the standard ISO 834 fire curve was about 50% less compared to the "inert" case. This fact highlights certain concerns, regarding the use of time-temperature curves for classification purposes, e.g. fire-resistance tests of combustible materials.
- Although the average compartment temperature was kept constant, in the case of the CLT ceiling, higher temperatures were observed at the back of the compartment (and, consequently, lower temperatures near the opening) compared to the respective measurements obtained for the non-combustible ceiling.
- The heat flux levels recorded inside the compartment were significantly higher in the case of the exposed CLT ceiling.
- The addition of the CLT ceiling does not seem to have any significant affect to the exhaust gas and the incoming air velocities.

The presented experimental campaign will be extended in the future, aiming to investigate the effects of alternative exposed CLT panel configurations, i.e. exposed ceiling, one exposed side wall, two exposed side walls, exposed ceiling and one side wall and exposed ceiling and two side

https://doi.org/10.52202/069179-0233

walls, as well as the effects of different fire curves (e.g. temperature-time, HRR-time).

ACKNOWLEDGEMENTS

This work has been financially supported by the E.C. in the frame of the H2020-project "Build-in-Wood: Sustainable Wood Value Chains for Construction of Low-Carbon Multi-Storey Buildings from Renewable Resources" (Grant agreement No. 862820).

REFERENCES

[1] Crielaard, R., Van de Kuilen, J., Terwel, K., Ravenshorst, G., Steenbakkers, P. (2019). Self-extinguishment of cross-laminated timber. *Fire Safety Journal, 105*, 244-260. doi:10.1016/j.firesaf.2019.01.008

[2] Bartlett, A.I., Hadden, R.M., Hidalgo, J.P., Santamaria, S., Wiesner, F., Bisby, L.A., Lane, B. (2017). Auto-extinction of engineered timber: Application to compartment fires with exposed timber surfaces. *Fire Safety Journal, 91*, 407-413. doi:10.1016/j.firesaf.2017.03.050

[3] Hadden, R.M., Bartlett, A.I., Hidalgo, J.P., Santamaria, S., Wiesner, F., Bisby, L.A., Lane, B. (2017). Effects of exposed cross laminated timber on compartment fire dynamics. *Fire Safety Journal, 91*, 480-489. doi:10.1016/j.firesaf.2017.03.074

[4] Wiesner, F., Bisby, L.A., Bartlett, A.I., Hidalgo, J. P., Santamaria, S., Deeny, S., Hadden, R.M. (2019). Structural capacity in fire of laminated timber elements in compartments with exposed timber surfaces. *Engineering Structures, 179*, 284-295. doi:10.1016/j.engstruct.2018.10.084

[5] Li, X., Zhang, X., Hadjisophocleous, G., McGregor, C. (2014). Experimental study of combustible and non-combustible construction in a natural fire. *Fire Technology, 51*(6), 1447-1474. doi:10.1007/s10694-014-0407-4

[6] ISO 834-1, Fire Resistance Test-Elements of Building Construction, Part 1: General Requirements, ISO, Geneva (1999).

[7] ISO 9705-1, Reaction to fire tests - Room corner test for wall and ceiling lining products - Part 1: Test method for a small room configuration, ISO, Geneva (2016).

[8] Janssens, M.L. (1991). Measuring rate of heat release by oxygen consumption. *Fire Technology, 27*(3), 234-249. doi:10.1007/bf01038449

NOMENCLATURE

Symbol	Unit	Description
α	-	Combustion expansion factor
E_{CO}	kJ/kg	Net heat release per unit mass of O_2 consumed for CO
E_{O_2}	kJ/kg	Net heat release per unit mass of O_2 consumed
M_a	kg/kmo1	Molecular weight of air
$\dot{m}_g$	kg/s	Mass flow rate of exhaust gas stream
M_{o_2}	kg/kmo1	Molecular weight of O_2
$\dot{Q}$	kW	Heat release rate
$X_{CO}^{A^e}$	-	CO mole fraction of the exhaust gas stream
$X_{CO_2}^{A^a}$	-	CO_2 mole fraction of ambient air
$X_{CO_2}^{A^e}$	-	CO_2 mole fraction of the exhaust gas stream
$X_{H_2O}^{a}$	-	H_2O mole fraction of ambient air
$X_{O_2}^{A^a}$	-	O_2 mole fraction of ambient air
$X_{O_2}^{A^e}$	-	O_2 mole fraction at the exhaust gas stream
φ	-	Oxygen depletion factor

https://doi.org/10.52202/069179-0233

World Conference on Timber Engineering Oslo 2023

FLAME SPREAD CHARACTERISTICS IN LARGE COMPARTMENTS WITH AN EXPOSED TIMBER CEILING

Panagiotis Kotsovinos[1*], Eirik G Christensen[1] Harry Mitchell[2], Rikesh Amin[2], Mohammad Heidari[3], Guillermo Rein[2], David Barber[4], Judith Schulz[1]

ABSTRACT: In the pursuit of the net-zero agenda set by the global community to fight climate change, more architects and engineers have turned their attention to heavy/mass timber as an alternative structural material to concrete and steel which are the materials predominantly used in building construction. Current evidence from fire experiments is primarily limited to small compartments with an area of 84m^2 or less. To address the lack of knowledge in this area, Arup, CERIB and Imperial College London completed the CodeRed experiments in a 352m^2 open-plan compartment with an exposed CLT ceiling and glulam columns. Four experiments were undertaken in total in 2021, with three of them focusing on fire dynamics. The facility was a replica of the previous largest experiment with a non-combustible ceiling undertaken to date, such that a direct comparison on the impact of the timber ceiling can be made. This paper presents an overview of these experiments, and specifically presents the experimental outcomes relating to flame spread rates observed on the fuel bed, and the influence of the timber ceiling on fire dynamics when compared to experiments completed similar non-combustible compartments. These experiments show that a timber ceiling significantly accelerates the fuel-bed flame spread rates compared to a comparable non-combustible compartment. This has implications for means of escape of occupants, fire-fighting interventions as well as structural response.

KEYWORDS: timber ceiling, large-scale compartment fire experiment, flame spread rates, fire safety

1 INTRODUCTION

In the pursuit of the net-zero agenda set by the global community to fight climate change, more architects and engineers have turned their attention to mass timber as an alternative structural material to concrete and steel which are the materials predominantly used in building construction. Understanding he response of mass timber to fire is critical to delivering safe and sustainable building designs. Two key parameters that must be considered with respect to structural fire protection in mass timber buildings are: a) the size of the fire compartment and b) the materials of construction exposed to the fire compartment.

Our experience indicates that architects are increasingly considering mass timber as the primary structural material for buildings designed for office, retail, and assembly occupancies. These buildings often have large open-plan floor areas (e.g. >1000m^2) with aspirations of maintaining as much timber exposed as possible to meet sustainability goals (reducing use of applied cladding materials) and improve aesthetic appeal for occupants and stakeholders. The exposed timber surfaces in open-plan office buildings are often desired to be in the form of a CLT or glulam ceiling (soffit) supported by a glulam frame.

Traditional fire safety design for structural fire resistance (termed "loadbearing capacity" in UK guidance) is based on small compartments. The 'travelling fire' design concept (see Figure 1) has been developed over the past 10 years, and is increasingly applied to large open-plan compartments. However, existing experimental evidence for travelling fires is based on compartments constructed from largely non-combustible materials. Travelling fires are assumed to cover a limited area of a compartment ("near field") and spread across the floorplate. The burning area is defined by the leading edge (front of the fire) and the trailing edge of the fire, where the fuel has been consumed leading to burn-out of the fire. Both the leading and trailing edges spread until the total available fuel is consumed [1].

A review by Rackauskaite et al. [2] has highlighted previously that compartment fire experiments with exposed timber surfaces published at the time of the authors' review were limited to a compartment area of 84m^2. This limits the understanding of fire regimes that can occur in larger compartments, such as characteristics of flame spread, which are less significant in small compartments. Furthermore, temperatures in large compartments can vary significantly both spatially and temporally. This is important because there is a potential that traditional structural fire protection design may lead to under- or over-provision of protection materials to large compartments. The former is potentially unsafe, while the latter is unwelcome in terms of sustainable development.

https://doi.org/10.52202/069179-0234

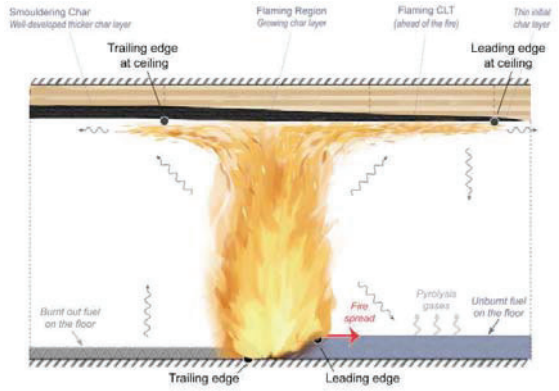

***Figure 1**: The travelling fire dynamics phenomena expected in a large scale open-plan compartment with exposed mass timber ceiling. Arrows indicate radiation from fire and heated surfaces preheating fuel and timber ahead of the flames, and continuing heating of charred timber behind the flames in addition to the heating from smoke (not indicated in this figure for clarity).*[2]

Therefore, there exists an important gap in knowledge around understanding fire dynamics in large timber compartments. This gap must be filled to establish credible design fire scenarios and to inform fire safety design methods for timber buildings that adequately mitigate risks introduced by the timber construction.

To address this knowledge gap, a consortium comprising Arup, Imperial College London and CERIB completed the CodeRed experimental series[3].

This paper presents an overview of the outcomes from the CodeRed experiments. It focusses on the impact of the timber ceiling on fire dynamics, and specifically how this influences flame spread rates within the compartment. Detailed results from each experiments are published separately for each experiment in [4]–[6] &[9].

2 THE EXPERIMENTS

A series of full-scale fire experiments in a purpose-built, compartment of 352m^2 was conducted in 2021. These experiments aimed to capture fire dynamics in large compartments with exposed timber. The experiments examined different parameters such as ventilation, encapsulation and the provision of a water mist system.

The facility used for the CodeRed series was built at CERIB's site in Epernon, France. The CodeRed experiment configuration was constructed to match as closely as possible that of an existing non-combustible building used in a series of experiments, known as *x-ONE* [7] and *x-TWO.1* [8]. These prior experiments studied travelling fire dynamics in open-plan compartments of non-combustible construction. The CodeRed experiments were design to enable, so far as was practicable, direct comparison of the impact of exposed timber on fire dynamics.

2.1 THE NON-COMBUSTIBLE COMPARTMENT EXPERIMENTS (x-ONE and x-TWO.1)

Compartment configuration

x-ONE and xTWO.1 were carried out in an existing building near Warsaw, Poland. The building had one floor that was mostly open plan with thick external masonry walls. The beam and block concrete slab ceiling was supported by reinforced concrete columns, beams, and external masonry walls. The experiments were carried out in the open-plan section of the building which had a floor plan of approximately 384 m^2. The compartment was 10.8m wide, 35.5m in length, and height ranging from 2.93m to 3.19m.

Ventilation was provided via fixed open holes in the concrete perimeter walls of the experimental building. See Table 1 for the % perimeter area of ventilation provided.

Fuel load design

The fuel load used in x-ONE and x-TWO.1 constituted of a continuous wood crib to encourage a natural spatial and temporal fire growth. The fuel load density of was approximately 370 MJ/m^2 (19.4 kg/m^2) and covered a floor area of 174 m^2 (6 m x 29 m).

The fuel bed was not covering the whole length of the compartment, and started approximately 6m from one end. This was the part of the fuel bed that was ignited.

The fuel setup consisted of 11.5 layers of a continuous wood crib (4 sticks each layer). In x-ONE two layers of 4 mm fibreboard were included within the crib build-up and across the whole fuel area to facilitate a faster flame spread. In x-TWO.1 the additional fibreboard was provided only to the first metre of the fuel load.

The previous experimental series had one further case, *x-TWO.2* [8] that had a reduced fuel load density. In this case the flames did not touch the ceiling, and therefore this experiment is not included in the comparisons set out in this paper.

2.2 THE COMBUSTIBLE COMPARTMENT EXPERIMENTS (CODERED)

Compartment configuration

The details of the CodeRed compartments are set out below and in Figure 2 to demonstrate their equivalence to the previous experiments described above.

- 10.27 m wide,
- 34.27 m long and
- 3.1 m high,

The building was constructed from aerated concrete blocks (365 mm thick, 350 kg/m^3). The ceiling was composed of 14 CLT panels supported by hinge connections on the perimeter walls and a central concrete beam. The CLT consisted of 5 ply (40-20-20-20-40 mm) spruce wood with MUF adhesive; the CLT was not treated with any fire retardant. The CLT ceiling been tested by

https://doi.org/10.52202/069179-0234

the manufacturer not to experience char fall-off (no glue line integrity failure in fire) in a long duration fire exposure (120 minutes to the ISO 834 standard fire). As the primary focus of the experiments was to observe the fire dynamics, the structure was supporting self-weight only and was not substantially connected mechanically. Figure 1 describes the building layout and Figure 3 describes typical instrumentation provided.

Ventilation was provided via fixed open holes in the concrete perimeter walls of the experimental building. See Table 1 for the % perimeter area of ventilation provided.

Fuel load design

All three CodeRed experiments reported in this paper matched the x-TWO.1 fuel load design. See the yellow area in Figure 2 for the extent of the fuel bed. This was designed to match the fuel bed of x-TWO.1.

Instrumentation

The fire development in the *CodeRed* experiments, inside and outside the compartment, were captured via thermocouples, plate thermometers, as well as fixed and drone mounted cameras, as seen in Figure 3.

Parameters varied in each experiment

The four experiments comprised:

- *CodeRed #01* – arrangements similar to that of non-combustible experiments, but with an exposed CLT ceiling and glulam columns [4]
- *CodeRed #02* – same as *CodeRed #01* but with 50% of the ventilation [5]
- *CodeRed #03* – looking at the effectiveness of a water mist system with timber ceilings (outside the scope of this paper) [9]
- *CodeRed #04* – same as *CodeRed #01* but with ~50% of the timber encapsulated in fire resisting cladding. The extent of encapsulation is shown in the blue box in Figure 3. [6]

Overview of fire response

CodeRed #01, *#02* and *#04* had no suppression or firefighting intervention, allowing the fires to grow, spread and decay naturally and enabling smouldering to be observed. Combustion of the wood cribs was observed as follows:

- #01 – Flaming ended: 22 min 30 s after ignition. Smouldering observed for 48 hours;
- #02 – Flaming ended 26 min 30 s after ignition, smouldering observed for 60 hours; and
- #04 – Flaming ended 45 mins after ignition, smouldering was observed for 24 days.

As indicated above, after the flames had ceased in the crib, smouldering and intermittent flaming was observed in the CLT of all experiments in multiple locations. In many instances the smouldering spread through the thickness of the CLT panel leading to the formation of holes in the CLT slab.

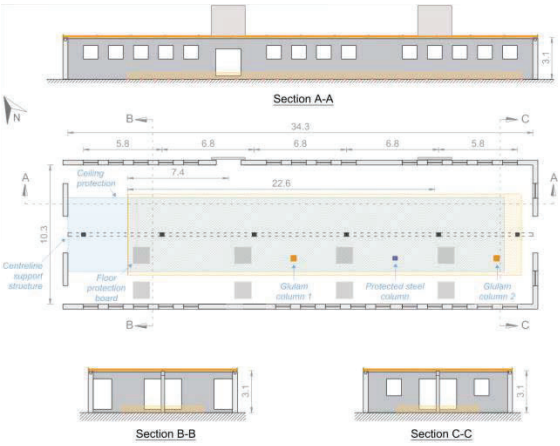

Figure 2: *Floor plan and sections of the compartment used for the CodeRed experiments. Units in metres.*

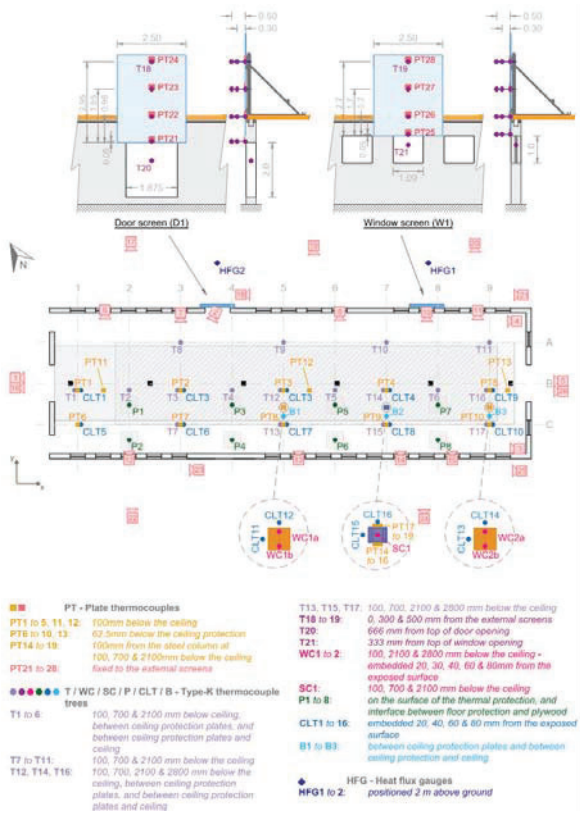

Figure 3: *Typical instrumentation in the CodeRed experiments.*

2.3 COMPARISON OF FEATURES

With regards to the specific objectives of this paper, footage from all recovered cameras were used to measure the locations of the leading (i.e. flame front) and trailing (i.e. burn-out) edges of the fire as in *x-ONE* [7] and x-*TWO.1* [8]. Cameras located inside the compartment and at compartment openings were placed in heat and

https://doi.org/10.52202/069179-0234

radiation-resistant containers to protect the instrumentation and data collected.

See Table 1 for a comparison of the relevant experiments.

Table 1. Summary of the differences in the key parameters of interest between the previous non-combustible travelling fire experiment and the CodeRed experiments. CodeRed #03 is not included in the table as its aim is not related to this study.

Parameter	x-ONE [7], x-TWO.1[8]	*CR#01* [4]	*CR#02* [5]	*CR #04* [6]
Ceiling	Non-combustible	*Fully exposed ceiling (CLT)*	*As CR #01*	*52% exposed*
Ventilation	20%	*21%*	*10%*	*As CR #01*
Width x length	10.8 m x 35.52 m	10.27 m x 34.27 m	*As CR #01*	*As CR #01*
Height	2.93 m to 3.19 m	3.1 m	*As CR #01*	*As CR #01*
Area	384m^2	*352m^2*	*352m^2*	*352m^2*
Type of fuel – wood sticks	Wood sticks 0.03m x 0.03m x 1m	Same as x-ONE and x.TWO.1	Same as x-ONE and x.TWO.1	Same as x-ONE and x.TWO.1
Fibreboard	Wood fibreboard throughout (x-ONE) and only in first meter (x-TWO.1)	Same as x.TWO.1	As x.TWO.1	As x.TWO.1
Size of fuel bed	6 m x 29 m	As x-ONE and x-TWO.1	As x-ONE and x-TWO.1	As x-ONE and x-TWO.1
Fire duration (cessation of flaming of wood cribs)	25 min (x-ONE) 32 min (x-TWO.1)	22.5 min	27 min	46 min

3 IMPACT OF EXPOSED TIMBER ON FLAME SPREAD

The CodeRed experimental set-up mimicked previous "travelling fire dynamics" experiments undertaken in a non-combustible compartment to allow for direct comparison between each experiment series. For reference purposes the extracted locations of the flame and spread rates of the flames for x-TWO.1 are shown in Figure 4 [8].

3.1 FLAME SPREAD IN NON-COMBUSTIBLE COMPARTMENTS

In x-TWO.1 the flame spread rate showed two main conditions. For the first 5m of the fuel bed, flame spread 4.16 mm /s (0.25 m/min). this took approximately 14 minutes. As the flames passed the large ventilation opening that was present in this location, the flame spread rate then increased to an average value of almost 58.3 mm/s (3.5 m/min) until reaching the end of wood crib. After 5 min from the ignition, a clear trailing edge of fire started to move along the compartment, with the spread rate of ~ 4.2 mm /s (0.25 m/min) almost the same as the leading edge. After 13 minutes from ignition of the fuel bed, the spread rate of the trailing edge of the flames accelerated to a maximum value of 41.7 mm/s (2.5 m/min). The spread of the trailing edge stopped at around 25 minutes. In the locations where the trailing edge has passed the fuel had experienced burn out. See [8] for more information on the experimental results.

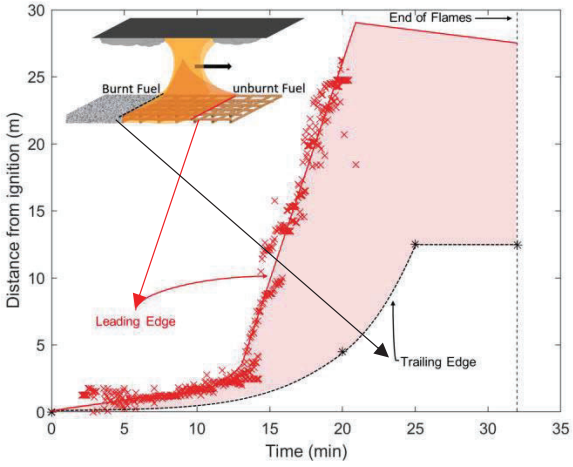

Figure 4: Locations of the leading and trailing edges of flame spread across the compartment for x-TWO.1.[8]

3.2 FLAME SPREAD IN CODERED #01

As shown in **Error! Reference source not found.** in *CodeRed #01*, the flame spread along the crib was observed to follow two main burning regimes. For the first 2.5 minutes of spread, the leading edge spread rate was approximately steady at 11 mm/s, 2.5 times the rate of the x-TWO.1 experiment. The spread rate accelerated substantially at the point the CLT ceiling surface ignited, spreading across the full fuel bed within 5 minutes of ignition. Noting that it took the x.TWO.1 experiment 20 minutes for the leading edge to reach the far end of the fuel bed.

After the leading edge reached the end of the fuel bed, it was also observed to regress into the compartment as the crib was consumed from both ends. This was not observed in the x.TWO.1 experiment.

The trailing edge, was identifiable and began to substantially traverse the compartment at approximately

https://doi.org/10.52202/069179-0234

12 min (comparable to x.TWO.1) and steadily spread across the compartment with an average spread rate of 37 mm/s (2.2 m/min). This is at the higher end of the trailing edge spread rates observed in x.TWO.1.

The distinct and identifiable movements of both the leading and trailing edge are characteristic of a travelling fire. This demonstrates that it is valid to consider travelling fire conditions in compartments of this size.

The average spread rate of flames across the CLT, based on the time between the ignition of the CLT and the flames reaching the far end of the compartment, was 200 mm/s (12 m/min) spreading 30 m in 2 min 29 s. This is approximately 3.5 times faster than the x-TWO.1 test results.

The fire was at its maximum size between 6 and 12 min when the full extent of the crib and CLT were burning simultaneously. This was not observed in the x.TWO.1 experiment, as the trailing edge had spread before the leading edge reached the far end of the fuel bed. This meant that the fuel at the start of the compartment had already burnt out as the fire was travelling.

3.3 FLAME SPREAD IN CODERED #02

As shown in **Error! Reference source not found.**, in *CodeRed #02* as in *CodeRed #01* flame spread across the ceiling was rapid once the CLT ignited. At 7 min 25 s the leading edge of both the crib and the ceiling arrived simultaneously to the far end of the compartment as seen in **Error! Reference source not found.** The crib at the far end of the compartment was observed to quickly burn out, resulting in the leading edge receding back through the compartment at approximately 13 min 30 s after ignition. The trailing edge appeared to progress much slower than the receding leading edge.

Based on the timing of the ignition of the CLT and the arrival of the flames at the end of the compartment the average flame spread rate across the CLT in CodeRed#2 was 153mm/s (9m/s) compared to 200mm/s (12m/s) for *CodeRed #01.* The spread rate across the crib was less impacted than the CLT, with an average spread (after CLT ignition) of ~147 mm/s (0.15 m/s), compared to 161 mm/s (0.16 m/s) in *CodeRed #01*. As such the reduction in ventilation appeared to have a greater overall impact on the spread rate of flame across the CLT (-23%) than the crib (-8%). Similarly to CodeRed #01, in CodeRed #02 the crib was burning simultaneously for the majority of the fire duration unlike x-TWO.1

3.4 FLAME SPREAD IN CODERED #04

Overview of difference with other tests

In *CodeRed #04* ~50% of the ceiling was encapsulated, mostly above the fuel bed. In this experiment there was an initial delay of 20 minutes until the exposed CLT ceiling ignited (see Figure 7. This delay was because of the encapsulation preventing flames and hot gasses impinging on the CLT directly above the fuel bed, where CodeRed #01 and #02 ignited first. Instead of direct flame impingement from the wood crib fire onto the CLT ceiling, the fire in the wood cribs instead heated up the encapsulation instead, driving out the moisture in the board protection. Additionally, the moisture of the wood cribs was higher than the earlier experiments due to environmental conditions during *CodeRed #04* which took place in December. This effect is discussed in detail below.

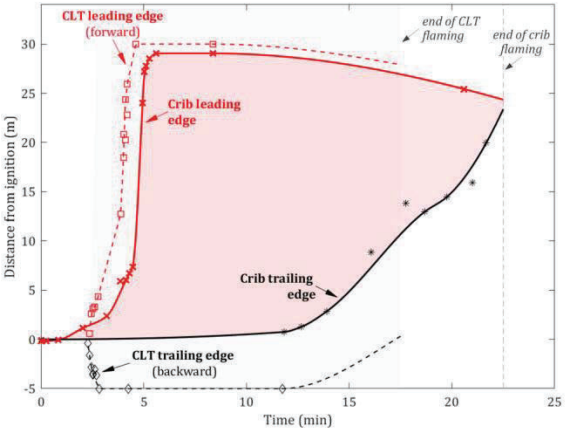

Figure 5*: Locations of the leading and trailing edges of flame spread across the CLT (dashed lines) and the wood crib (solid lines) for CodeRed #01. The time of end of observed flaming combustion of the CLT (17.5 min) and crib (22.5 min) are marked with vertical shaded area and dotted line, respectively.*[4]

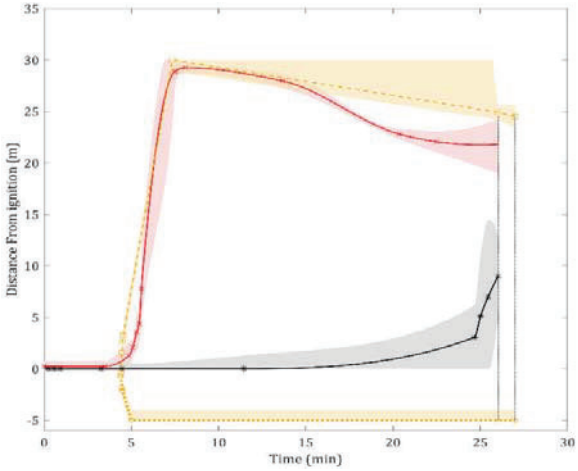

Figure 6: *Leading and trailing edges of flame spread along the wood crib, and leading flame edges both forwards and backwards under the CLT ceiling for CodeRed #02. Error cloud indicates deviations in edge location along the width of the crib, as edges are not constantly parallel to compartment width.* [5]

Fire spread observations

Figure 7 presents the positional data of the leading and trailing edge gathered from image analysis for *CodeRed*

#04. Before the first ignition of the CLT, the leading edge spread linearly with an average spread rate of 3 mm/s (0.18 m/min). By comparison, in *CodeRed #01* this spread was 11 mm/s (0.66 m/min), over a shorter duration, and while the fire was spreading through the section of the crib with fibreboard. When the CLT ignited, the leading and trailing edges had already travelled 4.4 m and 3.0 m respectively. As a result, a smaller extent of the crib was involved during the peak fire period in *CodeRed #04* compared to *CodeRed #01*and *#02*.

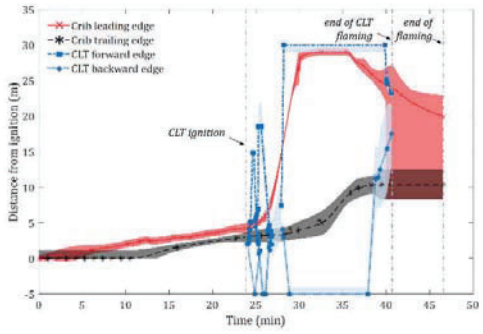

***Figure** 7: Locations of leading and trailing edges of flame spread across the cross-laminated timber (CLT) (dashed lines) and the wood crib (solid lines) for CodeRed #04. The time of end of observed flaming of the CLT (40 min 59 s) and crib (46 min) are marked with vertical dotted lines.* [6]

Following the sustained ignition of the CLT, the spread rate of crib fire grew to an average of ~107 mm/s (6.4 m/min), taken between the time of sustained CLT ignition and when the flame spread was observed to spread the length of the crib. The average spread across the CLT was ~222 mm/s (13.3m/min), measured from the point of sustained ignition of the CLT. In *CodeRed #01,* the spread rates were 161 and 200 mm/s (9.6 and 12m/min) for the crib and CLT, respectively.

Impact of encapsulation

The encapsulating boards were observed to largely remain in place over the whole flaming period, preventing flaming from the surface of the protected CLT ceiling. The last layer failed in some instances during decay but the encapsulation met its objectives in preventing flaming.

The decrease in flame spread rate in *CodeRed #04* across the crib is likely due to the effects of the calcium silicate board protection and different moisture content in the *CodeRed #04* crib. The encapsulation of the CLT delayed ignition of the CLT and instead resulted energy being absorbed in driving out moisture from the board protection [10]. The encapsulation also reduced radiative feedback from the ceiling to the fuel bed. The flame spread across the CLT was broadly within the same range, as in *CodeRed #01* once the CLT ignited.

Impact of moisture content

The greater moisture content within the wood crib of *CodeRed #04* (17.7%) compared to that in *CodeRed #01* (13.5%), and the presence of the board protection is expected to have reduced the spread rate of the leading edge, as greater energy and time are required to dry the wood. This difference in moisture content in the crib equates to an approximately 34% increase in energy required to dry the wood, and an approximately 32% increase in the overall energy required to combust the timber which also includes heating (to 350 ℃, specific heat capacity = 2.3MJ/kgK [11]) and pyrolyzing the timber (1.82 MJ/kg [12]).

Therefore, when comparing the results of *CodeRed #04* with those of *CodeRed #01*, the increased moisture and resulting increase in energy required to heat the timber, needs to be taken into consideration as it a significant influence on the results, particularly in the initial stage of the fire. The energy required to dry the moisture from the encapsulation system may have also played a role.

The results from CodeRed #04 suggest that in partly encapsulated compartments the flame spread over the fuel bed will be slower than fully exposed ceilings but faster than non-combustible compartments. However, when ignited, the exposed CLT ceiling spread flame at the same rate as a fully unprotected CLT ceiling.

3.5 FIRE SIZE OF WOOD CRIBS

The amount of fuel load burning at one time is important to the understanding of how quickly a severe compartment fire may grow and spread. Therefore, the amount of the fuel bed burning simultaneously was compared between all the tests.

As discussed earlier the same wood crib configuration was used in the x-ONE, x-TWO.1 and CodeRed experiments. All experiments had the same number and arrangement of wood sticks. A wood fibreboard throughout the fuel load was also included in x-ONE and but only in first meter for x-TWO.1 and CodeRed.

Figure 8 plots the length of the wood cribs on fire simultaneously as a comparison across all the compared experiments. Comparing the fire length on the fuel bed allows to establish the extent of flaming within the compartment at any given time and be able therefore to compare the relative impact of the timber ceiling in affecting the extent of flaming of the cribs. The crib fire size results are presented for the duration of each test after CLT ignition occurred (CodeRed) or flames touched the ceiling (x-ONE & x-TWO.1) for a more representative comparison over time.

Based on the results it can be seen that the CodeRed #01 and #02 experiments resulted in a larger extent of the cribs burning simultaneously compared to x-TWO.1, even though the fuel load configuration was identical. The fully exposed timber ceilings of CodeRed #01 and #02 also resulted in a larger extent of the wood cribs flaming

https://doi.org/10.52202/069179-0234

simultaneously compared to the presence of the fibreboard in the x-ONE experiment. Comparing CodeRed #04 with x_ONE and x-TWO.1, a similar peak size of flaming was reached between the three experiments but in the case of CodeRed #04 that was reached more quickly than the non-combustible experiments.

Therefore, the CodeRed experiments support a conclusion that exposed CLT ceilings are likely to lead to more severe fire conditions earlier in a fire.

The CLT ceilings also had an influence on external flaming as discussed further by [13].

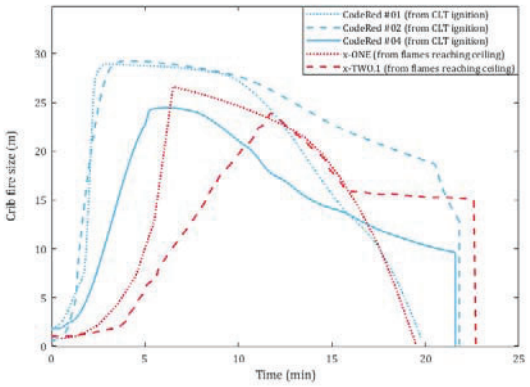

***Figure 8**: Fire size of the wood cribs – comparison of all the experiments.*

4 DISCUSSION

This section discusses the impact of introducing the CLT ceiling on flame spread rates, fire duration and Design fires.

4.1 IMPACT ON FLAME SPREAD RATES

In all CodeRed experiments the leading and trailing edges were observed to initially spread across the compartment, characteristic of travelling fires. However, once the timber ceiling was ignited, the flames spread at a rate much faster compared to the equivalent non-combustible compartments x-ONE & x-TWO.1.

Flame spread rates for the experiments across the wood cribs in the non-combustible compartments, and across the wood cribs and the CLT in the combustible compartments are summarised in *Table 2*.

Table 2. Flame spread rates in [mm/s] for the x-ONE and x-TWO.1 and CodeRed experiments. CodeRed #03 is not relevant to this study.

Parameter	*x-ONE*	*x-TWO.1*	*CodeRed #01*	*CodeRed #02*	*CodeRed #04*
Crib spread rate before flames touch the ceiling (x-ONE and x-TWO) or before CLT ignites (CodeRed)	3.3	1.9	11	2.1	3.3
Crib spread rate after flames touch ceiling / after CLT ignites	67	34	161	147	68 (first ignition) 107.5 (sustained ignition)
CLT spread rate	N/A	N/A	200	153	95 (first ignition) 222.1 (sustained ignition)

For the first two CodeRed experiments the presence of the timber ceiling resulted in a much more rapid flame spread in the wood cribs compared to the equivalent non-combustible structure, and consequently also a relatively shorter fire duration.

This increase in flame spread rate of the wood crib with the presence of the timber ceiling is most likely due to radiative heat transfer from the flaming of the CLT preheating the crib, resulting in a faster fire growth than in previous experiments with the same configuration in a non-combustible enclosure.

As expected, the overall fire dynamics experienced in *CodeRed #04*, fall between the characteristics observed in *CodeRed #01* and the reference non-combustible experiments, *x-TWO.1* that had identical fuel load arrangement. x-ONE that has a different fuel load arrangement with the addition of fibreboard led to similar spread rate with *CodeRed #04* when taking the time for first ignition (but slower when taking the taking the time from second ignition). Despite the initial delay for the protected CLT ceiling to ignite, once the CLT had ignited, flames spread rapidly over the timber ceiling albeit not at the same rate as in the cases with a fully exposed ceiling. The slower spread rate across the CLT ceiling in *CodeRed #04* is substantially influenced by 1) the CLT directly above the wood crib being protected with the encapsulation; and 2) some energy was absorbed in driving out the moisture content of the wood crib and board protection covering half of the CLT.

https://doi.org/10.52202/069179-0234

The observed CLT flaming spread rates in the CodeRed experiments are rapid. It should be considered however that the

4.2 IMPACT ON FIRE DURATION

The impact of the timber ceiling on flame spread and overall fire duration is an important consideration as it informs the fire severity that the structure is expected to withstand.

The experimental results suggest that the presence of substantial CLT linings do not substantially reduce the wood crib flaming period due to the more rapid flame spread across the ceiling. This is unlike experience from small compartments where increased fuel load would be expected to result in an increased flaming duration.

Table 3 presents the comparative results on flaming duration. The fire in *CodeRed #01* was growing more rapidly during its initial stage before flames touched the ceiling (11 mm/s) than x-ONE and X-TWO (3.3 mm/s and 1.9 mm/s respectively). In addition, in *CodeRed #04* there was a delay in sustained CLT ignition. Therefore, time differences in the overall wood crib flaming duration are not solely due to the presence of the timber ceiling. Instead considering the duration after flames have ignited the combustible ceiling or when the flames touched the non-combustible ceiling allows for more direct comparisons of the relevant metrics.

Table 3. Fire durations for each experiment

Parameter	*x-ONE*	*x-TWO.1*	*CodeRed #01*	*CodeRed #02*	*CodeRed #04*
Total fire duration from ignition of the wood cribs	25 min	32 min	22.5 min	27 min	46 min
Fire duration after flames touching the ceiling (x-ONE & x-TWO.1) or CLT ignition (CodeRed)	19 min 30 s	23 min	19 min 43 s	22 min 49 s	22 min 07 s (first ignition) 19 min 30 s (sustained ignition)

4.3 IMPACT ON DESIGN FIRES

The CodeRed experiments showed that an exposed timber ceiling leads to a rapid spread of the fire that exhibits both – rapid - travelling behaviour and simultaneous burning across the entire a compartment. It was shown that the increase of fuel load (and therefore heat release rate) in the compartment through the addition of the timber ceiling did not result in a subsequent increase in overall fire duration.

The flame spread across the cribs was 4.3 to 4.7 times faster in the compartment with a fully exposed timber ceiling compared to the equivalent non-combustible experiment (x-TWO.1), measured from the point of CLT ignition / flame impingement on the ceiling. With 50% encapsulation the flame spread rate across the wood cribs was 2 times faster when taking time from first ignition and 3.2 times faster when taking time from sustained ignition.

While travelling fire characteristics were observed in all experiments, the rapid flame spread rates suggest that uniform flashover conditions may be a good approximate for large compartments with exposed timber ceilings for the characterisation of the internal thermal environment.

Applying such uniform flashover conditions to large compartments for some types of structures that are sensitive to non-uniform compartment temperatures such as steel frames may yield unconservative structural responses [14]. This means it will be necessary to further develop travelling fire analysis models [1] that are suitable to represent fire dynamics in large compartment with exposed timber, and provide adequate design fires for structures under uneven heating conditions.

Barber et al. [15] indicate the importance of assessing thermal penetration in loadbearing timber elements as peak temperatures in mass timber elements occur long after flaming combustion in the compartment has ceased, often several hours later. Columns are particularly vulnerable.

Further analysis is necessary for timber framed structures to investigate the impact of non-uniform burning seen across large compartments with exposed timber surfaces.

It is noted that taking an approach of uniform temperatures across the entire compartment may be overly conservative where heat transfer is evaluated to the floor (i.e. fire exposure from above); this is discussed in more detail in [19]

The presence of the CLT on the ceiling produced more rapid flame spread rates compared to those assumed in the travelling fire methodologies in the literature [16] that assume non-unform burning which have been developed for non-combustible ceilings.

The existing methods do not incorporate the contribution of additional combustible surfaces to the overall energy release inside the compartment, or the role of combustible surfaces in increasing spread rates.

Further research and development is required to incorporate these fire dynamics phenomena into travelling fire design fire methods to make them appropriate for application in large CLT compartments.

Nevertheless, the travelling behaviour occurs so rapidly that further review is also needed to determine under

https://doi.org/10.52202/069179-0234

which scenarios design fires based on simpler flashover assumptions would yield sufficiently conservative results from a fire safety engineering perspective for mass timber structures.

The timber ceiling also affects external flaming outside the compartment that is not captured by current design methodologies [13]. Further research is needed to understand heat release rates in compartments with an exposed timber ceiling and how this additional combustion is influencing fire severities outside and inside the compartment (% of combustion inside vs outside).

4.4 IMPACT ON MEANS OF ESCAPE AND FIRE-FIGHTING ACTIVITIES

The CodeRed research has shown that once a timber ceiling is ignited flame spread can be rapid.

The recorded flame spread rates over the untreated CLT ceiling are high, with up to 200 mm/s (0.2m/s) where there is a fully exposed ceiling, from the point that the ceiling becomes involved in a fire.

It is acknowledged that in practice, untreated timber surface, which would commonly be assigned a reaction to fire classification of Euroclass D, would not be permitted in large open spaces; common fire safety standards used in e.g. the UK, BS9999 [17], and Approved Document B [18], would expect a Class B reaction to fire finish, unless the rooms are very small.

It is important however to consider how close these observed flame spread rates are to evacuation speeds adopted in fire engineering practice (0.5-1.2 m/s), particularly when considering that people may initially move towards the fire to investigate the cause, and attempt to extinguish it.

The ability of surface treatments to improve the reaction to fire performance of timber to slow fire growth and flame spread in more severe fire conditions would benefit from further study.

The observed increase in flame spread rates and subsequent earlier and larger maximum heat release rate reduced the time available for fire-fighting activities in mass-timber buildings to commence while a fire is still growing. Fire fighting tactics also need to take account of risk of ongoing smouldering e.g. in junctions that can continue for multiple days under the right conditions.

Designers need to take these into consideration when determining fire safety strategies for large compartments with exposed timber ceilings.

5 CONCLUSIONS

The CodeRed series of experiments conducted in 2021 had as one of its fundamental objectives to study the impact of timber on fire dynamics in large open-plan compartments.

This paper specifically focuses on flame spread rates within compartments, comparing CodeRed to previous non-combustible compartment experiments that were used as prototype for CodeRed.

Rapid flame spread was observed across the CLT ceiling once the ceiling ignited (~153 to 220 mm/s). Compared to the reference non-combustible enclosure experiments the flame spread across the wood cribs was also significantly faster (3.1 to 4.7 times faster considering the time from sustained ignition of the CLT ceiling).

In all CodeRed experiments, leading and trailing edges observed, characteristic of a travelling fire, transitioning to full flashover fire where the fire was burning across the entire wood crib and CLT ceiling simultaneously.

The rapid flame spread rates suggest that uniform flashover conditions may be a good approximate for larger compartments with exposed timber ceilings.

However for structural systems sensitive to non-uniform compartment temperatures such as steel frames, and very large compartments, such simplified design fires may yield unconservative structural responses.
There may be a range of different design fires that a combustible structure needs to be evaluated against.

Travelling fire analysis models that are suitable to represent fire dynamics in large compartment with exposed timber are therefore necessary to provide adequate design fires for structures sensitive to uneven heating conditions, and for large compartments where uniform flashover conditions may be unconservative.

6 Further work

The observed CLT flaming spread rates in the CodeRed experiments are rapid. It should be considered however that the experimental configuration may have played a role on the observed flame spread rates in the experiments. In particular the availability and position of ventilation compared to the location of ignition of the fire in both the CoreRed and x-ONE and x-TWO.1 experiments may have influenced the early fire growth period and therefore influenced the outcomes.

Future tests should establish if the observed CLT flame spread rates observed in CodeRed would also apply to other compartment and ventilation arrangements.

ACKNOWLEDGEMENT

This research has been fully funded by Arup and was undertaken in partnership with Imperial College London. The experiments were carried out in a bespoke facility built at CERIB's Fire Testing Laboratory site in France.

REFERENCES

1. Stern-Gottfried, J. and Rein, G., (2012), "Travelling fires for structural design–Part I: Literature review," *Fire Safety Journal*, Vol. 54, pp. 74–85.
2. Rackauskaite, E.Kotsovinos, P.and Barber, D., (2021), "Letter to the Editor: Design Fires for Open-Plan Buildings with Exposed Mass-Timber Ceiling," *Fire Technology*, Vol. 57, No. 2, pp. 487–495.
3. Arup, "Large compartment fire experiments: expanding knowledge of building safely with timber," 2022. [Online]. Available: https://www.arup.com/perspectives/large-compartment-fire-experiments-expanding-knowledge-of-building-safely-with-timber.
4. Kotsovinos, P.Rackauskaite, E.Christensen, E.Glew, A.O'Loughlin, E.Mitchell, H.Amin, R.Robert, F.Heidari, M.Barber, D.Rein, G.and Schulz, J., (2022), "Fire dynamics inside an open-plan compartment with an exposed CLT ceiling and glulam columns: CodeRed #01," *Fire and Materials*, Vol. 2022, pp. 1–27.
5. Kotsovinos, P.Christensen, E.G.Rackauskaite, E.Glew, A.Loughlin, E.O.Mitchell, H.Amin, R.Robert, F.Schulz, J.Barber, D.and Rein, G., (2022), "Impact of ventilation on the fire dynamics of an open-plan compartment with exposed timber ceiling and columns : CodeRed #02," No. March, pp. 1–28.
6. Kotsovinos, P.Christensen, E.G.Glew, A.O'Loughlin, E.Mitchell, H.Amin, R.Robert, F.Heidari, M.Barber, D.Rein, G.and Schulz, J., (2022), "Impact of partial encapsulation on the fire dynamics of an open-plan compartment with exposed CLT ceiling and glulam columns: CodeRed #04," *Fire and Materials*.
7. Rackauskaite, E.Bonner, M.Restuccia, F.Fernandez Anez, N.Christensen, E.G.Roenner, N.Wegrzynski, W.Turkowski, P.Tofilo, P.Heidari, M.Kotsovinos, P.Vermesi, I.Richter, F.Hu, Y.Jeanneret, C.Wadhwani, R.and Rein, G., (2021), "Fire Experiment Inside a Very Large and Open-Plan Compartment: x-ONE," *Fire Technology*.
8. Heidari, M., "Travelling fires methodology and probabilistic design of structures," Imperial College London, 2021.
9. Kotsovinos, P., Christensen, E.G., Gale, J., Mitchell, H., Amin, R., Robert, F., Heidari, M., Barber, D., and Rein, G., "The Effectiveness of a Water Mist System in an Open-plan Compartment with an Exposed Timber Ceiling : CodeRed # 03," *FPE eXTRA*, Vol. 74, 2022.
10. Frangi, A.Schleifer, V.Fontana, M.and Hugi, E., (2010), "Experimental and Numerical Analysis of Gypsum Plasterboards in Fire," *Fire Technology*, Vol. 46, pp. 149–167.
11. Richter, F.Atreya, A.Kotsovinos, P.and Rein, G., (2019), "The effect of chemical composition on the charring of wood across scales," *Proceedings of the Combustion Institute*, Vol. 37, No. 3, pp. 4053–4061.
12. Tewarson, A. and Pion, R.F., (1976), "Flammability of plastics—I. Burning intensity," *Combustion and Flame*, Vol. 26, pp. 85–103.
13. Glew, A., Turnbull, R., Poulsen, F.M., Christensen, E.G., Kotsovinos, P., O'Loughlin, E., Barber, D., and Schulz, J., "A design approach to external fire spread from buildings with exposed mass timber," in *World Conference on Timber Engineering 2023, WCTE 2023*, 2023.
14. Rackauskaite, E.Kotsovinos, P.and Rein, G., (2017), "Structural response of a steel-frame building to horizontal and vertical travelling fires in multiple floors," *Fire Safety Journal*, Vol. 91, No. February, pp. 542–552.
15. Barber, D., Christensen, E.G., Kotsovinos, P., Heidari, M., Mitchell, H., and Schulz, J., "Accounting for post-peak compartment temperature thermal degradation of mass timber," in *World Conference on Timber Engineering 2023, WCTE 2023*, 2023.
16. Stern-Gottfried, J. and Rein, G., (2012), "Travelling fires for structural design-Part II: Design methodology," *Fire Safety Journal*, Vol. 54, pp. 96–112.
17. British Standard Institution, *BS 9999: Fire safety in the design , management and use of buildings – Code of practice*, 2nd editio. London: BSI, 2017.
18. Regulations, B., *Approved Document B: Fire Safety*, 2020 Editi. HM Government, 2010.
19. Christensen, E.G., Khoo, B., Kotsovinos, Barber, D., and Schulz, J., "Protection and thermal exposure of CLT ceiling and floor surfaces" in *World Conference on Timber Engineering 2023, WCTE 2023*, 2023.

https://doi.org/10.52202/069179-0234

World Conference on Timber Engineering Oslo 2023

ACCOUNTING FOR POST-PEAK COMPARTMENT TEMPERATURE THERMAL DEGRADATION OF MASS TIMBER

David Barber[1], Eirik Christensen[2], Panos Kotsovinos[3], Mohammad Heidari[4], Judith Schulz[5]

ABSTRACT:

Mass timber load-bearing members need to be assessed for structural adequacy in fire. For high-rise buildings their strength has to be determined once the fire has completely decayed and the timber member is no longer impacted by the heat of the fire. For a decaying fire, the thermal penetration into a timber member continues well after the peak compartment temperature, resulting in timber strength degradation, which is not typically assessed and accounted for. From a review of experimental data sets for exposed mass timber members and using the glulam column data from the CodeRed large scale compartment experiments, an assessment of the issues for thermal penetration and heat diffusion has been carried out. Initial studies have shown that peak temperatures in a timber column will occur well after the end of flaming and that thermal loss from the member in the decay phase of the fire is slowed by the char layer built up. Assessment of structural adequacy of columns has shown that the reduced cross-section needs to account for the compartment post-peak temperature thermal penetration, or the engineering design may be non-conservative.

KEYWORDS: Mass timber, structural fire engineering, heat transfer, fire resistance, columns

1 INTRODUCTION

Buildings constructed with mass timber continue to increase in popularity globally. Low and medium rise buildings with exposed mass timber can generally be designed to meet fire safety goals of local regulations, codes or standards. Where mass timber is exposed within a high-rise building, the structure needs to be able to withstand a range of design fires, that includes both the standard fire and natural (physically based) fires. The structural adequacy of mass timber elements that resist loads in a fire is based on determining an effective cross-section, after exposure to a design fire. Where large areas of mass timber are exposed, design fires are influenced by that exposed timber and changing ventilation, a highly complex assessment. The effective cross-section is determined from a reduced initial cross-section, based on a char layer and the reduced strength of the wood ahead of the char, due to thermal impact. Simple design rules are based on the effective cross section supporting the applied loads for the period of fire exposure, such as EN 1363-1 [1] or ASTM E119 [2].

For a timber member exposed to a natural fire, the heat flux received varies with time and as the external heat flux reduces from a peak, the resultant thermal penetration (thermal wave) will continue to cause timber degradation after the compartment peak temperature has been reached. The resultant strength reduction in-depth after the peak exposure temperature has had limited research, is not normally assessed by engineers and is highly relevant for high-rise mass timber structures exposed to longer duration and decaying fires, and in particular, vertical load-bearing elements such as columns.

This paper presents the initial work carried out in literature reviews, background theory and summary of results from the CodeRed series of large-scale experiments. Work is on-going and further updates are to be published later in 2023 that includes finite element modelling and developing an engineering method to predict the impact of thermal degradation on timber strength for the decay phase of natural fires.

2 BACKGROUND

Timber exposed to a heat flux has three distinct zones, as was first described by Schaffer [3], being a charred layer where the temperature is in excess of 300°C, a transitional zone (pyrolysis zone) between 300°C and ambient temperature, typically called the thermal penetration depth, and ambient temperature timber (assumed to be 20°C). The position of the char front is set by the 300°C isotherm and under standard fire exposure (such as to EN 1363-1 or ATM E119), is predicted using a nominal char rate (β_o) of 0.65mm/min. The structural adequacy (capacity) of an exposed timber member reduces when exposed to fire based on the time of exposure, with the constant char rate (β) and a fixed zone of timber behind the char with no strength (zero strength layer, ZSL), to determine where the cross-section has full strength (effective cross-section). This is based historical fire

[1] Arup Melbourne, david.barber@arup.com
[2] Arup London, eirik.christensen@arup.com
[3] Arup Manchester, panos.kotsovinos@arup.com
[4] Fire Testing Centre, CERIB, Paris, m.heidari@cerib.com
[5] Arup London, Judith.Schulz@arup.com

https://doi.org/10.52202/069179-0235

testing to the standard fire. The fixed char rate and ZSL are only valid for standard fire exposure.

2.1 Relevance of Timber Strength Proportional to Temperature

The strength of timber reduces at relatively low temperatures. The mechanical properties of timber are reversible if temperatures are lower than 100ºC. For timber of temperatures higher than 100ºC, the properties are permanently degraded [4]. Research indicates that wood between 100ºC and 200ºC is considered to be in transition, with thermal breakdown occurring at temperatures past 200ºC. Once fully charred at 300ºC, timber is considered to have lost all strength. The transitional zone between the fully charred and ambient temperature timber therefore has three parts - the timber at a temperature between ambient and 100ºC which has a reversible strength reduction; temperatures of 100ºC and 200ºC where temperature effects are not reversible, though temperatures are not elevated enough to start pyrolysis; and the timber between 200ºC and 300ºC, where pyrolysis occurs and the mechanical properties degrade to zero [4, 5, 6].

From an engineering point of view, the question to be addressed in the design of a timber member is at what point of the thermal penetration of timber between 100ºC and 300ºC does temperature matter? Eurocode 5 (EN 1995-1-2) [7] provides data for the reduction in mechanical properties for timber proportional to temperature. This data is only applicable for standard fire exposure. Schmid et al [8] shows this data for strength and stiffness, with f_c representing compression, f_t for tension and f_v for shear (see Figure 1).

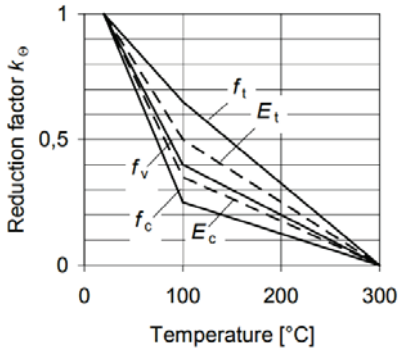

Figure 1: *Reduction factors for strength and stiffness properties from adapted from Eurocode 5, for standard fire exposure [8]*

Of most relevance is how sensitive compressive strength is to temperature. Timber at 140ºC has lost 80% of its compressive strength. At the same temperature timber has lost only 40% of its tensile strength. For columns that are under load and have timber that has reached 140ºC, whether the impact of thermal strength degradation is reversible or not, losing 80% of compressive strength is very significant. The 140ºC isotherm may not need to penetrate too far into a column before the member would lose structural adequacy, typically through buckling. Once structural adequacy has been lost, the reversibility of the timber strength loss is moot.

2.2 Relevance of Zero Strength Layer and Thermal Penetration Depth

The ZSL is an engineering approximation for the thermal penetration depth and is used to account for the area of reduced strength behind the char layer, given the temperature range is between 300ºC (charred wood) and ambient, for standard fire exposure. The thermal penetration depth has been researched for over 40 years with data from fire testing on solid timber and glulam being analysed [9]. Janssens and White [10] summarised test data and provided a method to determine the temperature at any point and showed that temperatures reached ambient at 40mm behind the char layer, for various softwood timber species. Frangi and Fontana [11] estimated 25mm to 50mm (see Figure 2).

These temperature correlations were used to determine the ZSL as 7mm behind the char zone, as an approximation for engineering design, to account for thermal penetration depth. The use of 7mm has been reviewed for many years as not reflecting known mechanical properties of timber and is revised in the current Eurocode 5 update [12], with higher values for the ZSL, depending on the forces being resisted in the timber for compression, tension or shear, reflecting actual timber mechanical properties.

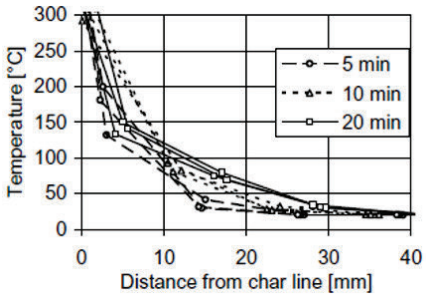

Figure 2: *Temperature profiles in a timber beam, behind the char, for 60min standard fire exposure [11]*

The experimental results above for thermal penetration depth are only accurate for standard fire exposure and not applicable for a natural fire, or the decay phase of a fire. To determine the thermal penetration depth for a natural fire, the temperature through the timber cross-section needs to be assessed, which requires the heat transfer into the timber to be analysed. This can be completed by experimental work or finite element modelling.

2.3 Determination of Thermal Penetration Depth for Natural Fire Exposure

There have been over 40 different compartment experiments with exposed mass timber and a natural fire. Temperature growth and decay curves are shown in Figure 3 from a Canadian experimental series [13], showing the relatively slow decay phase due to the extent of exposed mass timber, with limited ventilation.

https://doi.org/10.52202/069179-0235

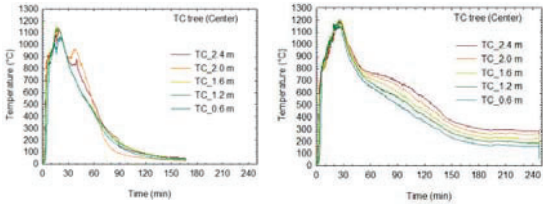

Figure 3: *Temperature profiles from an exposed mass timber compartment fire, with no timber exposed (left) and CLT exposed on one wall (Test 2) (right). The difference in temperatures at 120 mins can be seen. The change in rate of cooling near 700°C can also been seen. The CLT had proven glue line integrity in fire [13]*

A natural fire will decay (ignoring fires that do not decay due to CLT glue line failure or encapsulation failure) and the fire heat release will trend to zero and room temperatures trend to ambient. The lack of fire and thermal exposure will result in the charring of any exposed mass timber to stop. While the charring may stop, the thermal wave from the compartment fire and the glowing and smouldering residual fuel on the floor, will continue to penetrate the mass timber element. A review of experimental data shows that the thermal penetration continues to occur well after the peak compartment temperature has been reached and through the full decay phase of the fire. Determining where the thermal penetration is between 300°C and 100°C behind the char layer in a timber member, during the fire decay phase, becomes essential to determine structural adequacy.

3 REVIEW OF RELEVANT EXPERIMENTAL WORK

To determine the extent of experimental data that shows how thermal waves penetrate timber members in the decay phase of fires, over 60 experimental works were reviewed. The following is brief summary of the most relevant work.

The experimental series "Fire Testing of Rooms with Exposed Wood Surfaces in Encapsulated Mass Timber Construction" [13] was based on natural fire tests with exposed CLT, with in-depth thermocouples in the CLT, recording temperatures during the decay period through to four hours after ignition. Using Test 2 as an example (see Figure 4), the peak compartment temperature occurred at 28 to 31 mins after ignition and did not drop below 200°C. The peak temperatures in the CLT at depths of 35mm and 52.5mm are at initially near 120mins after ignition, then continue to rise through to the test being extinguished at four hours. Char depths of the CLT wall measured after the fire was extinguished ranged from 50mm to 95mm, with high values located near the floor. Ignoring the values at the base of the panel where charring was deeper due to the burning of the residual fuel on the floor, the average char depth was 62mm.

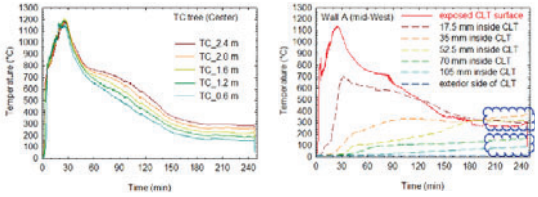

Figure 4: *Temperature profiles from Test 2 with an exposed mass timber wall (left). Temperature profiles within the CLT wall with increasing temperatures in-depth clouded [13]*

When compared with the temperatures recorded in-depth of the CLT wall, at 70mm from the exposed surface the temperature reaches 140°C at approximately 210 mins after ignition. At 105mm depth from the exposed surface the temperature is just over 100°C at 240 mins after ignition and was still increasing. These thermocouple readings indicate that thermal penetration occurred through to 70mm and up to 105mm deep into the CLT, compared to the char depth recorded that was between 50mm and 85mm, with an average of 62mm, with thermal penetration still increasing at 240 mins when the experiment was stopped. The char depth would indicate structural adequacy could be assessed using a reduced cross section in the order of 62mm, whereas the in-depth thermocouples would indicate that thermal degradation impacting timber strength occurs past 70mm and likely 105mm into the CLT.

In the "Compartment Fire Testing of a Two-Story Mass Timber Building" by the US Forest Service [14], natural fire tests with exposed CLT were completed, with temperatures recorded at depth within the CLT. The recorded post-experiment char depth in the panels was measured at approx. 30 to 35mm. For the experiment with CLT walls exposed, the delay in peak temperatures in-depth in the CLT are significant when compared to the time of the temperature peak for the natural fire. Figure 5 shows the peak temperatures in the living room and bedroom were at approx. 15 to 25 mins after ignition.

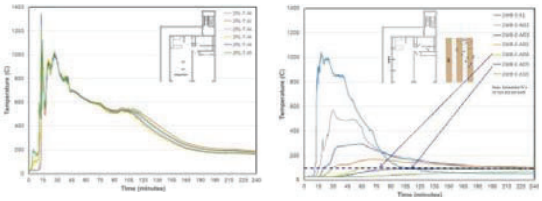

Figure 5: *Temperatures from the USFS Test 3 compartment fire with CLT walls part exposed. Living room temperature profile (left). Temperature profiles within the living room CLT wall, with 100°C line annotated (blue line) (right) [14]*

Within the living room the temperature at 35mm from the exposed surface is between 140°C and 160°C at 75 mins after ignition; and at 58mm depth between 100°C and 120°C between 60 mins and approx. 180 mins. Within the bedroom the temperature at 47mm from the exposed surface is between 120°C and 140°C at 105 mins after ignition; and at 58mm depth between 100°C and 120°C between 105 mins and approx. 180 mins. Hence, the in-depth thermocouples show that thermal penetration in the timber occurs through to a depth of 47mm and up to

https://doi.org/10.52202/069179-0235

58mm in the fire decay phase but measured char depths only record about 35mm. The additional depth of thermally degraded timber (approx. 12 to 23mm) that would have reduced strength, is not accounted for.

Harada's tests on a 100mm thick glulam timber wall [15] were exposed to a 60 min ISO834 fire and allowed to cool within the furnace, while in-depth thermocouple data was recorded. The glulam wall was 800mm by 800mm of exposed area, with thermocouples located at 20mm, 40mm, 60mm, and 80mm from the exposed surface. The exposed surface temperatures decay steadily but slowly due to the furnace enclosure and at 240 mins range from 120ºC to 350ºC (see Figure 6).

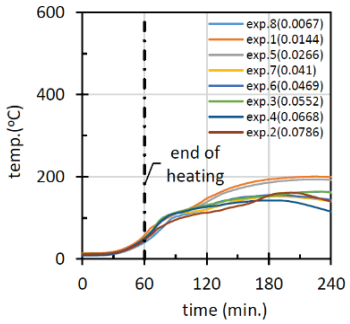

Figure 6: *In-depth temperatures measured at 60mm from the exposed surface [15]*

Based on the 60mm in-depth thermocouples, thermal degradation occurs through to 4 hrs of exposure, with thermocouples measuring between 120ºC to 200ºC. The data indicates the timber strength would be permanently impacted past 70mm depth. Charring post-test was recorded at approx. 52mm, showing the thermal degradation in-depth was deeper than the post-test char measurements.

Zeng et al [16] completed experiments on 3 and 5 ply CLT floors, exposing them to both standard and a simulated natural fire. In-depth CLT temperatures were recorded through the decay period for some of the experiments. The researchers recorded char depths of 37mm to 41mm after the test. Test (F5-20-N) shows thermocouples TC7 at a depth of 49mm and TC8 at a depth of 56mm from the exposed face recorded temperatures greater than 250ºC and 140ºC respectively through the fire decay period, and the temperatures were still increasing at the end of the test (see Figure 7). Thus, the timber at a depth of at least 56mm was thermally degraded, but char depths recorded were only up to 41mm, noting temperatures were still increasing when the experiment was stopped.

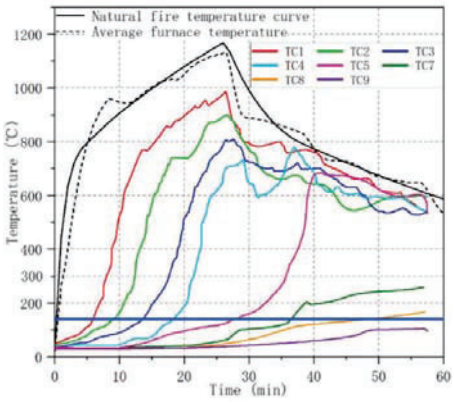

Figure 7: *Temperature profiles in a 5 ply CLT floor exposed to a natural fire (F5-20-N). Blue line indicating 140ºC [16]*

3.1 Summary of Review

A review of experimental work indicates there are only a limited number of useful data sets that provide information on in-depth temperatures during fire decay within timber. There are few experiments that have a decaying fire, where data is recorded for multiple hours without firefighting intervention. Of those experiments, many do not have thermocouples located deep enough to record useful data.

What the above useful data shows is that in the fire decay period, whether that be natural fire or a form of decaying fire within a furnace, that temperatures do not decay quickly in-depth and that temperatures can still be increasing when the experiment stops. The in-depth temperatures are also elevated enough to degrade strength. Where char depths at the end of an experiment are recorded, the in-depth thermocouples indicate that strength degradation occurs to a much greater depth than the recorded char layer.

4 IMPACT OF THERMAL PENTRATION DURING NATURAL FIRE DECAY – APPLICATION

For high-rise buildings with exposed mass timber (timber not encapsulated so exposed to the full heat of a fire), engineers need to determine the strength of a load-bearing timber member for the full duration of a fire. The strength of the timber member has to include the period through fire decay, such that the timber member is no longer impacted by the heat of the fire. In the growing phase of a fire the timber member chars, with the char providing insulative protection, with the char layer typically at temperatures between 300ºC and 600ºC. Once the fire reaches its peak temperature and starts to decay the timber member is exposed to a reducing heat flux. In a compartment with large areas of exposed mass timber, the fire decays more slowly, compared to a non-combustible compartment (see for example experiments from [13], [14]).

The reviewed data has shown that for a decaying fire, the thermal penetration into a timber member behind the

https://doi.org/10.52202/069179-0235

depth of char continues well after the peak compartment temperature and during the fire decay phase. As the compartment cools, the timber member starts to dissipate heat back to the compartment, as the char will be at a higher temperature than the surrounding compartment. This heat dissipation from the member occurs slowly given there are four possible impediments to rapid cooling: (1) thermal waves still penetrating the timber member from the peak heat flux; (2) the received radiative heat flux from the cooling compartment boundaries; (3) the char being a heat source, and (4) the insulative properties of the char preventing heat dissipating from the timber member back to the cooler compartment. The same insulative properties of char that prevent the timber from being damaged by the fire in the growth stage of a fire then become problematic as the char slows the timber member from cooling, as the compartment cools.

Thus, designing timber structures assuming the thermal impact in the timber member ceases when the fire peak temperature is reached, such as for a standard fire; or when the flaming ceases, such as for a natural fire, can be non-conservative. These approaches do not account for the ongoing heat transfer into the timber member and the associated thermo-mechanical degradation to the timber. This is relevant for high-rise timber structures and disproportionally impacts compressive members such as columns and load-bearing walls.

4.1 Implications

Columns are most vulnerable for the assessment of thermal penetration post-peak compartment temperatures, given there are few paths for heat dissipation given the four-sided charring. Their base can also be surrounded by smouldering residual fuel, continuing to conduct heat into the lower part of the column. Beams are normally exposed on three sides with the fourth side fixed to a floor system allowing for heat dissipation to a colder non-fire compartment. Hence, the slow heat dissipation that will occur in columns, and the significant reduction in compressive strength with elevated temperatures above 100°C (see Figure 1), results in columns being highly vulnerable to thermal penetration in the fire decay phase. Given the lack of sufficient data sets, it was determined by the project team in the formation of the CodeRed experimental series that glulam columns were to be included within all experiments to provide a novel data set [17, 18].

5 DATA AND FINDINGS FROM THE CODERED EXPERIMENTAL SERIES

The CodeRed large scale compartment experiments were set up to provide a detailed data set on thermal degradation in-depth of the timber, and data was recorded for a period in excess of 24hrs after fire ignition. The compartment had an internal floor area of 352 m^2. The fuel bed was identical in all experiments and consisted of continuous wood cribs with a fuel load density of ~380 MJ/m^2 over a floor area of 174 m^2. Two glulam columns were included within the CodeRed series of experiments and instrumented with thermocouples to collect in-depth data. The CLT panels located at the ceiling were also instrumented with in-depth thermocouples. The columns were 400mm x 400mm and the CLT panels were 5 ply (40-20-20-20-40 mm) spruce wood with MUF adhesive. Information presented below is from the first two experiments CodeRed #01 and #02 [17, 18]. A full description of the experimental setup, fuel load, ventilation, instrumentation, fire dynamics and charring behaviour in the timber members is within the referenced papers.

Figure 8 shows temperatures in-depth within Column 1, with thermocouples at depths of 20, 30, 40, 60 and 80mm. The variance of temperatures over column height is also shown through three different heights of thermocouple locations. Similar data was obtained for column 2 and also from experiment CodeRed #02, which had 50% less ventilation to the compartment. The data shows a delay to reaching the peak temperatures within Column 1 (centrally located) with peak of just over 300°C at 60 mins after ignition at 30mm depth; and a peak of just over 200°C at ~70 mins at 40mm depth. At 60mm depth, the peak temperature of just over 100°C is not reached until close to 90 mins after ignition (see Figure 9). Column 2 had similar results, though slightly lower temperatures as this column was closer to the building end. The measured char depth at the end of the experiment was 23mm for column 1 and 18mm for column 2 (weighted average).

Based on the temperatures recorded within the columns, thermal degradation occurs at a greater depth than the post-test char recordings show. At a 40mm depth the timber is thermally degraded with temperatures ranging from 139°C to 207°C and average close to 180°C. The peak temperatures occur 43 mins after the end of wood crib flaming. At a depth of 60mm, temperatures are very closely aligned with a range of 92°C to 106°C, with a peak occurring approx. 60 mins after the end of wood crib flaming. Based on the thermocouple data and using a temperature limit of 140°C (as discussed in Section 2.1 above), there is thermal degradation through to 52mm of column depth. This differs significantly from the post test charring with an average of 23mm deep. The data is also shown in Figure 10, represented by plotting at different column heights, the delay to reach peak temperature and the temperature reached. Further data is shown in Table 1. This data shows that the temperatures in the columns continue to increase well after the peak fire temperature (20 mins after ignition) and after the flaming has stopped (27mins after ignition). The additional timber that is thermally impacted behind the char layer needs to be accounted for in engineering design.

https://doi.org/10.52202/069179-0235

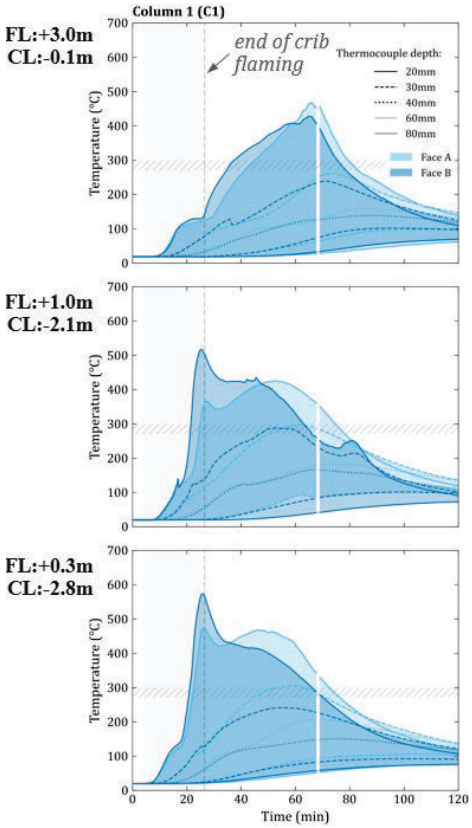

Figure 8: *Column C1 temperatures at various depths from CodeRed #01, at three different heights from ceiling (FL +3.0m) to floor (FL: +0.3m). End of crib flaming is shown. Peak compartment temperature was at 20 mins*

TC depth	Column 1	Column 2	Delay to Peak
20 mm	426 - 574°C	460 - 632°C	25 - 66 mins
30 mm	238 - 304°C	164 - 467°C	42 - 73 mins
40 mm	139 - 207°C	110 - 215°C	61 – 88 mins
60 mm	92 - 106°C	75 - 96°C	76 – 251 mins
80 mm	65 - 80°C	58 - 82°C	124 – 297 mins

Table 1: *Summary of Column 1 and 2 in-depth peak temperatures, based on thermocouple depth. Range shows the difference in peak temperatures depending on thermocouple location. Third column shows range of time to reach peak*

5.1 Relevance of the Delay of In-depth Peak Temperatures

The data from CodeRed illustrates an important factor in the engineering design and assessment of mass timber elements exposed to fires, being the delay in reaching peak temperature in-depth within the timber member. The thermal penetration into a timber member takes significant time to occur, relative to the growing and decaying fire, which has not received discussion in the literature reviewed. The CodeRed data for columns 1 and 2 show delays in peak temperatures that are relevant for thermal degradation of up to 88 mins after ignition (40mm depth), with the end of flaming of all flaming occurring at 27 mins. A graph of the delay to peak temperature is shown in Figure 11, indicating the trend.

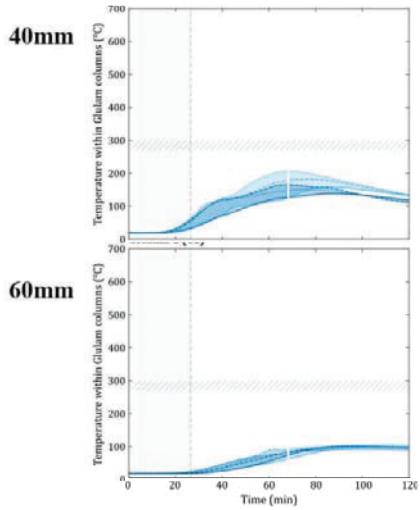

Figure 9: *Column C1 temperatures at 40mm and 60mm deep from CodeRed #01, with vertical dotted line showing the end of crib flaming. Peak compartment temperature was at 20 mins*

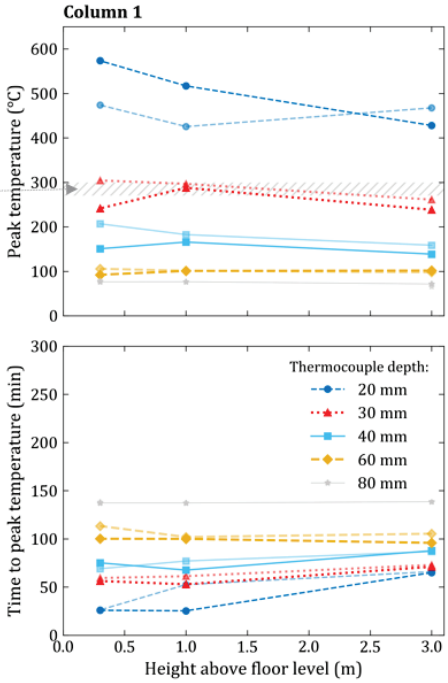

Figure 10: *Column C1 peak temperatures and time to reach that peak temperature at each depth, based on height above floor, for two differing sets of thermocouples at each in-depth location.*

A collated graph of the delay to peak temperature for both the exposed CLT and columns is shown in Figure 12. Whilst there is a range of scatter, the data shows a definite trend that the peak temperatures at the same depth in CLT are lower than in the columns. The time to reach the peak temperature is also slower in the columns.

https://doi.org/10.52202/069179-0235

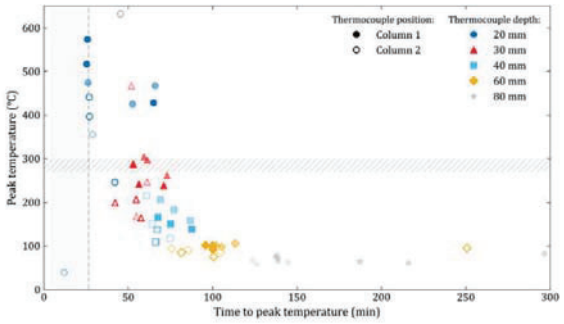

Figure 11: *Columns 1 and 2 from CodeRed #01 showing the peak temperature and time after ignition of that peak temperature, for differing thermocouple depths. Timber with temperatures above 100°C will have reduced strength that is not reversible*

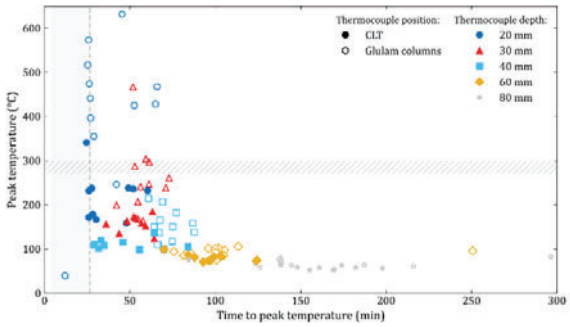

Figure 12: *Column and CLT temperature data from CodeRed #01 showing the peak temperature and time after ignition of that peak temperature, for differing thermocouple depths.*

This data indicates how a CLT floor benefits from having a cool surface on the non-fire surface (topside). This ambient temperature surface assists in reducing the overall temperatures in the CLT and allowing for faster heat dissipation, when compared to columns that are heated on four sides and also have insulative char build-up on all four sides. This difference in time to peak temperature at depth and relative hotter or cooler temperatures between CLT and the columns is undergoing further study, with finite element analysis. It should be also noted that the thermal impact is different to that caused by smouldering, which occurs in a localised area. The thermal penetration occurs throughout the whole column and as the CodeRed data shows, across the whole height of the column.

6 Using Code Red Results - How Is Structural Adequacy Impacted?

A code based approach for the assessment of structural adequacy for a column exposed to a 60 or 120 minute standard fire would be based on a char rate and zero strength layer (as described above in Sections 2.1 and 2.2). Using the EC 5 approach would result in 84mm of charring plus a 7mm zero strength layer, for 120 minutes of standard fire exposure. The cross section would be reduced by this char depth on all four sides to determine structural adequacy.

For engineering design, the CodeRed data (and the other data sets reviewed) shows that the end of flaming for a timber member cannot be taken as the end of the fire. The end of flaming or cessation of flaming is often referred to as "self-extinguishment" of a timber element [see 19, 20 as an example]. Of concern is that engineers and designers are using the end of flaming of a timber member as an indicator that the impact of heating and thermal penetration from the fire has stopped. The data sets reviewed within this paper clearly show that the cessation of flaming or self-extinguishment of timber cannot be used as an indicator for the end of thermal impact on strength for timber members, especially columns. If the cessation of flaming is used as the basis for engineering design of timber members, this will lead to non-conservative results.

Under exposure from a natural fire, the char depth can be calculated by assessing the radiative heat flux from a time-temperature curve and resultant char depth determined, for the growing and decaying fire. From the temperature data presented above, the reduced cross-section where the strength would be adequate for the full duration of the fire exposure is at 60mm depth (for CodeRed #01), given the temperatures are at or just above 100°C and thus thermally impacted strength reduction is reversible. If a limiting temperature of 140°C is used, where 80% of compressive strength parallel to the grain is lost, and this is used to determine effective cross-section, i.e. timber inside this isotherm still has load-carrying capacity, timber outside this does not, this would be at depth of approx. 52mm (based on interpolating average temperatures). If the design was based on the column section having full compressive strength timber, then the depth would be 60mm. As noted above, the CodeRed #01 char depths were 23mm for Column 1 and 18mm for Column 2 (weighted average). Figure 13 shows the percentage reduction in compressive strength for the timber located up to 40mm deep (88% reduction) and 60mm deep (76% reduction) in Column 1 from CodeRed #01.

As a further indication of the impact, column design for a building is highly proportional to the slenderness ratio and cross-sectional area. Using the CodeRed 400mm x 400mm column, with a length of 3.1m, as a design example and following the methodology within Eurocode 5: *Design of Structures. Part 1-1: General – Common Rules and Rules for Building* [21] Section 6.3.2 *Columns subjected to either compression or combined compression and bending*, and choosing typical glulam characteristic compressive strength of the timber parallel to the grain, $f_{c,0,k}$, gives the following comparison (GL30 grade glulam): Using a post-test measured char depth of 23mm + 7mm zero strength layer, could resist an applied load (factored for the fire load combination) of up to 247kN. Using the thermally impacted depth of 52mm, the same column can only resist an applied load (again factored for the fire load combination) of 63kN, i.e. the same column can safely resist only 26% of the load that is estimated from measuring post-test char depth. This indicates that the transient thermal wave has a significant impact on the

https://doi.org/10.52202/069179-0235

reduction in column capacity, even with this conservative assessment. Assuming column capacity based on measured char depth alone overestimates the column capacity to adequacy resist loads and is non-conservative.

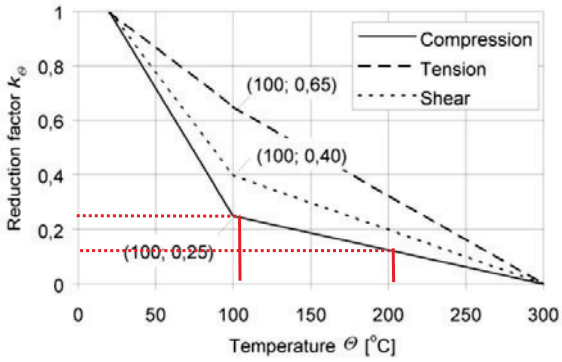

Figure 13: *Reduction factor for strength parallel to grain of softwood from Eurocode 5 [7], with Column 1 peak temperatures at 40mm (207°C) and 60mm (106°C) annotated showing compression strength reduction*

From an engineering viewpoint, the factor of time of thermal exposure is also important. As highlighted earlier in the paper, the in-depth temperatures within the column stay elevated for a relatively long duration, compared with the fire duration. For example, the fire duration in CodeRed #01 to the end of flaming is 27 mins. At 40mm depth, the column is at a temperature of 100°C or more for 90 mins. Experimental data reviewed shows elevated temperatures (above 100°C) can occur in-depth in timber members for three or more hours. This duration of elevated temperature needs to be considered from an engineering design viewpoint, given that fire is seen as an instantaneous load duration condition, and not a short-term loading condition. There is no real guidance available to engineers as to how the duration of exposure to elevated temperatures from a fire should be assessed in the determination of load factors and reduction factors for mechanical properties (impacting k_{mod}). Load duration between short-term and instantaneous is considered the difference between up to a week versus minutes (respectively). As an illustration, the compressive strength parallel to the grain f_c is reduced by 50% at 75°C and in the very short duration CodeRed #01 fire, Column 1 has a temperature at a depth of 40mm higher than 75°C for 2 hours. At 60mm depth the temperature above 75°C occurs for over an hour. Can these elevated temperatures be considered as instantaneous load conditions? Engineers do need to make their own judgements as to whether this thermal degradation duration is important, or not.

6.1 Impact on the assessment of time-equivalence

This information is also important for assessment of time equivalence, an important engineering design analysis needed for building construction. A typical approach would be to equate the 23mm of char depth back to an equivalent fire char depth based on a standard fire exposure, which would be 43 mins (at 0.7mm/min, standard fire exposure plus 7mm). For a heat impacted depth of 52mm, this would equate to 74 mins of standard fire exposure (no zero strength layer would be included). Hence based on the CodeRed data, the column exposure as determined from the post-fire char depth measurement would be adequate to achieve a 60 min fire resistance. But based on the thermocouple data for thermal penetration where (excluding cross-sectional area of timber that has lost 80% of its compressive strength parallel to grain), the column would not achieve 60 mins of fire resistance.

7 DISCUSSION – EXPERIMENTAL DATA

The data reviewed, including the data from the CodeRed series, shows that the peak temperatures in-depth with the timber members are often not recorded within experiments or tests as these occur well after the test has been stopped. In many of the experiments reviewed, the in-depth temperatures are still increasing at the end of the experiment and hence the actual peak temperature at depth are not actually recorded. The data reviewed does not provide suitable sets of data that can be used because thermocouples are not deep enough within the timber, the thermocouples are spaced to far apart and lead to coarse measurements, and the experiments are not being carried out long enough to allow all relevant data to be collected. In hindsight, the CodeRed data also could have benefited from more in-depth thermocouples at locations of 50mm and 70mm.

The review of data shows that more experimental series are required to understand the in-depth temperatures and requires timber members, preferably columns, exposed to a natural fire, with thermocouples embedded in-depth at no more 10mm spacings and the experiment is run to allow temperatures within the timber member to reduce from their peak back to ambient, most likely running the experiment for four to six hours after ignition.

8 NEXT STEPS - ASSESSMENT METHOD

The reviewed and CodeRed data indicates that there are three issues to be considered for the assessment of thermal penetration into a timber column during a natural fire. The first is the depth within a timber member for thermal penetration to occur that results in temperatures that will cause permanently reduced timber strength. The second is the duration of time that the elevated temperature occurs, which can also be measured as the delay until the temperature returns to less than 100°C. The third is whether the reversible strength reduction below 100°C is relevant to the design for the timber column, given that at 75°C, the compressive strength parallel to the grain is reduced by 50% and a column may be exposed to these elevated temperatures in-depth for multiple hours and hence, could actually fail under buckling given this reduction in compressive strength due to the longer-term nature (hours rather than minutes) of the thermal wave. The longer-term nature of this thermal impact is also relevant for fighting actions, which can still be occurring multiple hours after the fire has occurred and been extinguished.

https://doi.org/10.52202/069179-0235

The next steps with the CodeRed data are to carry out detailed finite element analysis of the columns to attempt to accurately model the recorded data and to then be able to determine methods for engineering design, based on a range of natural fires.

To design a timber column within a high-rise building exposed to a natural fire, the engineer needs to assess the impact of the thermal penetration and heat dissipation within the timber member, what should be a relatively straight-forward assessment of heat transfer. A changing external heat flux for compartment fire growth and decay, means the timber only reaches an equilibrium heat transfer state well after the compartment fire has decayed. Heat transfer analysis of the thermal penetration in the timber can be estimated with the timber element considered as a semi-infinite three part solid, with an outer layer of char and an inner layer of ambient temperature timber and a transition layer. Fourier's law for heat transfer through solids is normally adequate for most heat transfer problems in engineering [22], but the assessment becomes more challenging when the properties of the char are changing with temperature and the dissipation of the heat is not straight forward.

The methodology currently being attempted for a column is to determine the thermally impacted effective cross-section by segmenting the column into thin slices, assessing the temperature and residual strength (reduced mechanical properties, based on temperature of each slice). Modelling the physical properties of char is demanding as timber physical properties are not accurately known for natural fires and modelling the dissipation of heat from a heated timber member is also difficult to verify. As the thermal penetration is assessed through the timber member, the reduction in load-carrying capacity can then be determined, through to the full dissipation of the heat.

The engineering design of columns cannot just be based on designing to withstand a fire until flame cessation (self-extinguishment) or even compartment burnout (fire has decayed to less than 1MW or temperatures have returned to ambient). The method for designing columns must be based on assessing thermal degradation in-depth and determining the strength reduction to that depth to determine structural adequacy (maintaining stability).

8.1 Limitations and further work

There are a number of limitations in the current modelling and design approach. This includes the thermomechanical properties of timber being effective properties based on the standard fire temperature-time curve, which have limited accuracy for other thermal exposures or decaying fires.

More research is needed to understand the strength properties of timber at the 100ºC to 200ºC range and how permanent strength reductions are. This temperature range has received little research or attention as wood pyrolysis has not been reached, which is of interest to fire scientists. The thermomechanical properties of wood above 100ºC, where moisture migration determines the impact requires revisiting given the work by researchers such as Schaffer [9] and Gerhards [23] is 40 years old and is not reflective of modern mass timber members.

The relatively slow decay that occurs in fires with large areas of exposed timber and the resultant duration of thermal penetration in the timber member is also worthy of further research. Determining the importance of the slow thermal dissipation of in-depth heat and the depth of impacted timber is important from an engineering design perspective. In standard fire testing the thermal heating is relatively quick in the first 20 mins and then slowly increases, leading to thermal penetration through the timber that is fairly uniform, given the slowly increasing temperature after 30 minutes of exposure. The thermal gradient between the back of the char layer at 300ºC and ambient temperature therefore occurs over a relatively small thickness of approx. 40mm. For an exposed mass timber compartment, the extended fire decay phase leads to a temperature gradient over a much deeper thickness of timber than 40mm, between 300ºC and ambient.

9 CONCLUSIONS

Experimental data from a range of mass timber studies have shown that thermal penetration continues in a timber member after peak temperatures from fire exposure have been reached. This thermal penetration reduces structural capacity of a timber member in-depth. In the decay phase of a natural fire, the built-up char layer also slows heat dissipation from the timber member. Columns are particularly vulnerable given they have four-sided charring and compressive strength parallel to the grain reduces quickly at elevated temperatures above 50ºC.

Analysis of structural adequacy of timber columns in high-rise buildings where a range of natural fires has to be assessed, needs to account for the loss of structural capacity from the thermal penetration and the slow heat dissipation due to the char layer. Using experimental results from the CodeRed series of experiments, the authors have made progress in the understanding of the engineering issues. Further work is currently being undertaken with finite element modelling to develop engineering methods to predict the impact on structural capacity of timber columns for the full duration of a fire.

To address this issue, possible means of mitigation include (1) increasing the member cross-sectional area to account for the thermal wave, based on a heat transfer analysis; (2) including non-combustible protection to the timber member to prevent heating by fire exposure (3) if columns are to be exposed (not encapsulated), these should be located near windows where the compartment temperatures and thermal impact is reduced.

ACKNOWLEDGEMENTS

This research would not have been possible without all the hard work and attention to detail by those involved with the CodeRed experiments at Arup, CERIB and Imperial

College London, especially Fabienne Robert (CERIB) and Guillermo Rein (Imperial College London).

REFERENCES

[1] CEN EN 1363-1:2020 Fire resistance tests. General requirements, European Committee for Standardization, Brussels, Belgium.
[2] ASTM E119 Standard Test Methods for Fire Tests of Building Construction and Materials
[3] Schaffer, E., 1984, "Structural Fire Design: Wood," Research Paper FPL 450, USDA Forest Service, Forest Product Laboratory, Madison, WI.
[4] Ross, R., 2021, "Wood Handbook: Wood as an engineering material", USDA Forest Service, Forest Products Laboratory, General Technical Report FPL-GTR-190
[5] Rowell, R., editor 2005 "Handbook of wood chemistry and wood composites" CRC Press
[6] Schaffer, E.,1966, "Review of Information Related to the Charring Rate of Wood" United States Department of Agriculture, Forest Service, Forest Products Laboratory, Research Note FPL-0145
[7] CEN, 2004a, EN 1995-1-2 Eurocode 5: Design of timber structures - Part 1-2 - General - Structural Fire Design, European Committee for Standardization, Brussels, Belgium.
[8] Schmid, J., König, J., Köhler, J., 2010 "Fire-exposed cross-laminated timber—modelling and tests", Proceedings from World Conference on Timber Engineering
[9] Schaffer, E., Marx, C., Bender, D., Woeste, F., 1980 "Strength validation and fire endurance of glued-laminated timber beams", Research paper No. 467, Forest Products Laboratory
[10] Janssens, M., White, R., 1994, "Short Communication: Temperature Profiles in Wood Members Exposed to Fire," Fire and Materials, 18, p. 263.
[11] Frangi, A., Fontana, M., 2003; "Charring Rates and Temperature Profiles of Wood Sections", Fire and Materials, 27, pp. 91–102.
[12] CEN, 2021, prEN 1995-1-2 Eurocode 5: Design of timber structures - Part 1-2 - General - Structural Fire Design, official draft for revision, European Committee for Standardization, Brussels, Belgium.
[13] Su, J., Leroux, P., Lafrance, P., Berzins, R., Gratton, K., Gibbs, E., Weinfurter, M., 2018b, "Fire Testing of Rooms with Exposed Wood Surfaces in Encapsulated Mass Timber Construction", National Research Council, Canada Report No. A1-012710.1
[14] Zelinka, S., Hasburgh, L., Bourne, K., Tucholski, D., Ouellette, J., 2018, "Compartment Fire Testing of a Two-Story Mass Timber Building", US Forest Service, Forest Products Laboratory, General Technical Report GTR–247
[15] Harada, K., Sun, A., Makino, S., Daisaku, N., 2022 "Burning Behaviour of GLT Walls During Cooling Period After ISO 834 Exposure in a Small Furnace", Proceedings Structures in Fire, Hong Kong
[16] Zeng, X., Yuexiang, W., Jin, Z., Ma, H., 2021, "Comparative study on fire resistance and zero strength layer thickness of CLT floor under natural fire and standard fire", Construction and Building Materials 302, 124368
[17] P. Kotsovinos, E. Rackauskaite, E. Christensen, A. Glew, E. O'Loughlin, H. Mitchell, R. Amin, F. Robert, M. Heidari, D. Barber, G. Rein and J. Schulz, 2022 "Fire dynamics inside an open-plan compartment with an exposed CLT ceiling and glulam columns: CodeRed #01", Fire and Materials.
[18] P. Kotsovinos, E. Christensen, E. Rackauskaite, A. Glew, E. O'Loughlin, H. Mitchell, R. Amin, F. Robert, M. Heidari, D. Barber, G. Rein and J. Schulz, 2022 "Impact of ventilation on the fire dynamics of an open-plan compartment with exposed CLT ceiling and glulam columns: CodeRed #02", Fire and Materials.
[19] Emberley, R., Gorska C., Bolanosa, A., Lucherinia, A., Solartea, A., Soriguera, D., Gutierrez, M., Humphreys, K., Hidalgoa, J., Maluka, C., Law, A., Torero, J., 2017, "Description of Small and Large-scale Cross Laminated Timber Fire Tests", Fire Safety Journal 91, pp 327–335
[20] Bartlett, A., Hadden, M., Hidalgo, J., Santamaria, S., Wiesner, F., Bisby, L., Deeny, S., Lane, B., 2017, "Auto-extinction of engineered timber: Application to compartment fires with exposed timber surfaces" Fire Safety Journal
[21] CEN 2004, Eurocode 5: Design of Structures. Part 1-1: General – Common Rules and Rules for Building, European Committee for Standardization, Brussels, Belgium
[22] Lienhard, IV, J. H., Lienhard, V, J. H., 2019, "A Heat Transfer Textbook", 5th Edition, Dover Publications, Mineola, NY
[23] Gerhards, C., 1982, "Effect of Moisture Content and Temperature on the Mechanical Properties of Wood: An Analysis of Immediate Effects" Wood and Fiber, 14(1), pp 4-36

https://doi.org/10.52202/069179-0235

World Conference on Timber Engineering Oslo 2023

PROTECTION AND THERMAL EXPOSURE OF CLT CEILING AND FLOOR SURFACES

Eirik G. Christensen[1]* , Benjamin Khoo[2], Panagiotis Kotsovinos[3], David Barber[4], Judith Schulz[5]

ABSTRACT: Timber is increasingly used in buildings because of its favourable embodied carbon credentials compared to traditional materials such as steel and concrete. However, due to it combustible nature, encapsulation products are frequently used to prevent or limit the timbers contribution to a fire. These encapsulation products introduce additional weight, cost and carbon to project, which limit the benefit of timber construction. The performance of these products in natural fires and the relative fire severity experienced by products placed near the ceiling and the floor has received little attention. Here we present data on the performance of encapsulation applied to the timber ceiling and floor elements within the *CodeRed* experiments – a series of large-scale timber compartment experiments with varying ventilation and extent of exposed timber. Compartment temperatures were measured at the ceiling and near the floor, indicating a lower temperatures at floor level; the time temperature curve 'seen' by the floor encapsulation is dependent on whether or not there is residual glowing embers on the floor. Both the 25 mm calcium silicate encapsulation to the floor, when located below the wood crib and when adjacent to it, and the three layers of 12.5 mm gypsum fibreboard board applied to the ceiling were shown to be adequate in preventing the ignition of the underlying timber. However, smouldering was observed to sustain remote to encapsulation, but eventually spread beneath the encapsulation which facilitated continued smouldering. This highlights that smoulder can progress behind encapsulation. A 1D Finite Difference Model (FDM) was used to explore the temperature development of timber surfaces beneath simulated encapsulation details using the gas temperatures measured near the ceiling and floor. Converting the modelled peak temperatures to time equivalent times revealed an 23% average reduction in time equivalent fire severity near the floor level for natural fires with a severity equivalent to a 30 min standard fire. When considering greater fire severities, this reduction remained similar, indicating that applying the same fire protecting rating to the floor as to the ceiling is likely overly conservative. The study represents the first step in quantifying a more refined protection required at the floor and to the ceiling; with further research it may be possible to justify a reduction in the required fire protection performance of floor level encapsulation for long duration fires compared to that on the ceiling, taking into account the observed distribution of compartment gas temperatures in large compartments. Ultimately this offers an opportunity to reduce the embodied carbon, costs, and weight of the structural design.

KEYWORDS: encapsulation, timber, *CodeRed*

1 INTRODUCTION

The construction industry is quickly turning to timber as construction material as a solution to achieving the net-zero carbon agenda. However, as the influence of exposed timber on fire dynamics creates new hazards, is complex and subject to extensive research still, timbers surfaces are encapsulated to limit or eliminate the involvement of timber in a fire [1]. This in turn, reintroduces additional embodied carbon, cost, construction time to the project. BS EN 13501-2:2016 defines the performance of an encapsulation system to protect a substrate, with the designation of a K2 classification [2]. The standard requires the encapsulation system to limit the temperature increase at the surface of the substrate to below 250 ℃ on average or 270 ℃ in any location while preventing the pyrolysis of the protected material when exposed to a "standard fire". In addition, there can be no collapse of the covering during the test. However, this standard makes no distinction between the requirements of a floor or ceiling element. The temperature distribution within real fires is such that the thermal severity of a floor may be expected to be less than that of a ceiling in a timber compartment. Studies found that, in a ventilation controlled fire, gas temperature near the floor are on average 100 – 200 °C lower than near the ceiling [3–7], as shown in Figure 1. As such applying the same fire protection for encapsulation on both the ceiling and floor may result in excessive conservative encapsulation, inflating the mass, embodied carbon, and cost of a building. It is valuable to understand not only the performance of encapsulation system in real fire scenarios but also understanding the

[1] Arup London, eirik.christensen@arup.com
[2] Arup London, benjamin.khoo@arup.com
[3] Arup Manchester, panos.kotsovinos@arup.com
[4] Arup Melbourne, david.barber@arup.com
[5] Arup London, judith.schulz@arup.com

https://doi.org/10.52202/069179-0236

extent of protection required for the protection of CLT floor slabs.

This paper presents data from *CodeRed #01*, *#02* and *#04*, experiments from a series of large-scale timber compartment experiments which varied ventilation, and extent of exposed mass timber/encapsulation. We analyse the performance of the encapsulation of the CLT and floorboards to improve the understanding of such measures.

Additionally, this paper presents a first proposal in quantifying relative fire severity experience near the ceiling and floor. This is done in the following way:

- An idealised calcium silicate board protection over CLT is modelled to establish the timber surface temperatures, for both ceiling and floor arrangements, for the respective time- temperature profiles near the floor ceiling observed from the *CodeRed* experiments; this is done using a 1D Finite Difference Model (FDM).
- Using those peak temperatures at the surface of the encapsulated timber, the time equivalent 'fire protection' rating is derived that would deliver the same surface temperature in a standard fire test; this is done to convert the results into a commonly used fire safety performance metric.
- A ratio of those time equivalent values between the ceiling and floor is calculated to quantify the relative fire severity between the ceiling and the floor.
- A simplified design fire is created, informed by the *CodeRed* temperature measurements, to extend the analysis to fires of greater severity.

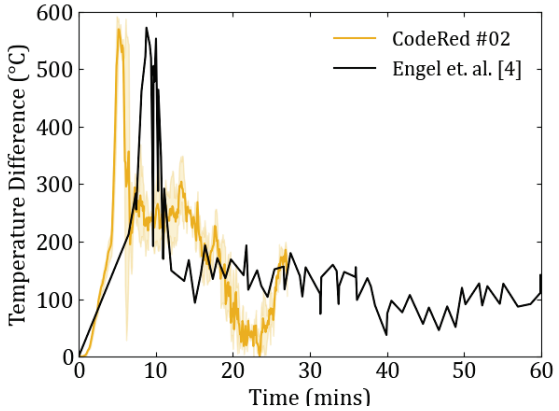

Figure 1: *Gas temperature difference measured near the ceiling and the floor, averaging at around 200 °C while the fire is ventilation controlled. At minute 18, the fire becomes more akin to fuel controlled in CodeRed #02.*

2 *CODERED* EXPERIMENTS

The *CodeRed* experiments were conducted in a purpose-built structure at CERIB's site in Epernon, France. The compartment measured 10.27 m wide, 34.27 m long and 3.1 m tall. The experimental set up is shown in Figure 2. A detailed description of the experimental set up is available in [6–8]. The compartment included a CLT ceiling and continuous wood crib (6 × 29 m) with a fuel load of around 380 MJ/m^2. The crib was ignited along its full width at one end, and the fire then allowed to naturally spread.

Thermocouples were distributed within the compartment at 100 mm, 700 mm, 2100 mm and in limited locations 2800 mm (T12, T14, T16) below the ceiling level to study the fire dynamics. The thermocouple measurements were corrected using the β-method [9] to account for radiative heat flux from the fire. In *CodeRed #02* and *#04*, eight, 18 mm plywood floorboards (P1-P8) where placed within the compartment as indicated in Figure 2, which were then protected with a single layer of 25 mm thick calcium silicate board encapsulation. These were instrumented with thermocouples on the surface of the board and at the interface between the plywood and the encapsulation.

In *CodeRed #04*, just under 50% of the CLT ceiling was encapsulated using a proprietary $K_2$60 protection product comprising 3 layers of each 12.5 mm thick gypsum fibreboard.

Thermocouples were placed between each layer of boarding and at the interface with the CLT. Data from *CodeRed #02* and *#04* are used to study the performance of the encapsulation of the CLT and floorboard.

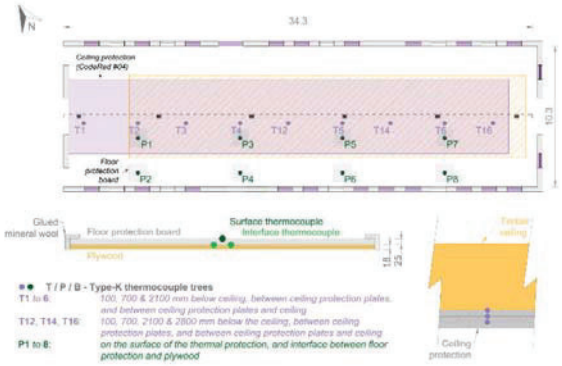

Figure 2: *Floor plan of the CodeRed experiments, sections of the encapsulation build ups, and instrumentation. Ceiling protection was only provided in CodeRed #04. Units in metres.*

The key differences between the *CodeRed* series are summarised in Table 1.

Table 1 *Summary of the differences in the key parameters between the CodeRed series*

Parameter	*CodeRed #01*	*CodeRed #02*	*CodeRed #04*
Ceiling	Fully exposed	Fully exposed	48% encapsulated
Ventilation	20.5%	10%	20.5%

3 NUMERICAL METHODS

A simple 1D heat transfer model was implemented using FDM which used two layers: an encapsulation layer and a timber layer. This model does not consider the contact resistance between the layers. Figure 3 shows a cross section of the floor encapsulation system as an example. The first layer represents encapsulation with a thickness is modified between analysis, while the second layer represents the 140 mm thick timber. The timber thickness was taken as 140 mm (the thickness of the CLT) instead

https://doi.org/10.52202/069179-0236

of 18 mm (the thickness of the plywood floorboards) to avoid modelling additional layers, and to reduce error at the internal boundary.

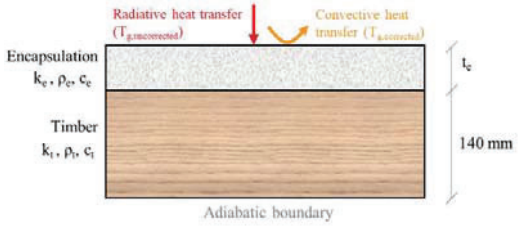

Figure 3 *Cross section of the model build up.*

The thermal model uses a simple finite difference scheme that calculates temperature at each internal nodes using the following equation:

$$T_n^{s+1} = Fo(T_{n-1}^s + T_{n+1}^s) + (1 - 2Fo)T_n^s \quad (1)$$

Where T is the temperature of a given node, n is the space step level, *s* is the time step level and *Fo* is the Fourier number.

For the temperature at the interface between the encapsulation and the timber, the calculation is given by:

$$T_n^{s+1} = Fo_1(T_{n-1}^s - T_n^s) - Fo_2(T_n^s - T_{n+1}^s) + T_n^s \quad (2)$$

Where Fo_1 and Fo_2 is the Fourier number of the encapsulation and CLT respectively. The distribution of grid nodes needs to be arranged accordingly such that Fourier number for both layers are similar. This is to reduce errors, especially at the internal boundaries for multilayer thermal modelling as noted by Waters et al [10].

The boundary condition for the exposed surface is given by:

$$T_0^{n+1} = \frac{2dt}{\rho_1 c_{p_1} dx_1}(h_c(T_g^s - T_0^s) + q_{rad} + 2Fo_1(T_1^s - T_0^s) + T_0^s \quad (3)$$

Where *dt* is the time step, ρ_1, c_{p_1} and dx_1 is the density, heat capacity and node size of the encapsulation respectively, T_g is the gas temperature at the exposed side corrected with the β-method [9] , T_0 is the temperature at the exposed surface, h_c is the convective heat transfer coefficient set at 25 and 35 W m^{-2} K^{-1} , for furnace conditions and natural fires respectively in line with EC1, and q_{rad} is the radiative heat transfer.

The radiative heat transfer is estimated using *eq* 4, and uses the uncorrected thermocouple (T_u) measurement as this captures the influence of radiation so provides a more accurate measure of the radiative temperature.

$$q_{rad} = e\sigma(T_u^{s4} - T_0^{s4}) \quad (4)$$

Where e is the surface emissivity set at 0.8 as recommended by EC1 and σ is the Stefan-Boltzmann constant.

For the back boundary of the CLT is assumed to be adiabatic and the temperature at the boundary is formulated as:

$$T_n^{s+1} = 2Fo_2(T_{n-1}^s - T_n^s) + T_n^s \quad (5)$$

To ensure numerical stability, *Fo* and *Fo*(1+*Bi*) is limited to 0.5 by limiting time step, *dt* to 0.1 s.

3.1 MATERIAL PROPERTIES

The material properties are that are used for the simulations are described in Table 2. These properties are provided by the manufacturer or material handbook and are assumed to be constant with varying temperature. As the thermal property is expected to change with temperature, which is not accounted in this work, some modelling errors are expected to be introduced.

Table 2 *Material thermal properties obtained from the product literature.*

Materials	Thermal conductivity, κ (W m^{-1} K^{-1})	Density, ρ (kg m^{-3})	Specific heat capacity, c_p (J kg^{-1} K^{-1})
Plywood/CLT [11]	0.126	380	2300
Gypsum fibreboard [12]	0.32	1150	1100
Calcium silicate board [13]	0.20	900	960
Light weight concrete [14]	1.00	1600	840
Normal weight concrete [14]	1.60	2300	1000

4 RESULTS

4.1 CLT CEILING ENCAPSULATION

In the *CodeRed* experimental series the encapsulation was generally found to be effective in preventing the ignition of timber both at the ceiling and the floor. The temperature development measured between the layers of encapsulation is presented in Figure 4. The average peak temperature measured at the ceiling encapsulation (across all locations apart from T1) was 106°C, 104°C, and 94°C for thermocouples between layer three and two, two and one, and at the interface of the CLT respectively. The similarity of the peak temperatures at all depths below the exposed surface may be due the formation of gaps between the encapsulation panels preventing heat transfer through the encapsulation, reducing the temperature within the encapsulation system as well as the evaporation of moisture content. However, no rigorous investigation on why such observation was made as it is outside the scope of the *CodeRed* experiments.

https://doi.org/10.52202/069179-0236

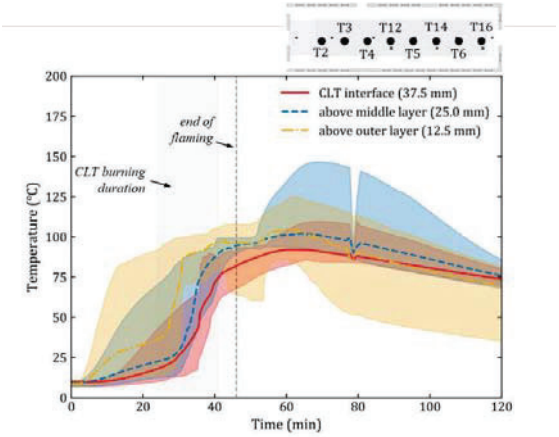

Figure 4: *Temperature development within between the layers of encapsulation. Solid line represents the mean temperature development, while the cloud should the range of measurements.*

The ceiling encapsulation was observed to remain in place until near the end of the fire at which point cracks started to form and portions of the outer layer of the encapsulation began to fall off. However as this occurred during the cooling period, after the cessation of flaming, it never exposed any of the underlying CLT. However, this highlights the benefits of a multilayer encapsulation system whereby the failure of a single layer does not result in the exposure of the underlying timber.

At the perimeter of the ceiling encapsulation some charring was observed beneath the encapsulation, but smouldering did not appear to sustain or spread. The damage was limited to within 40 mm of the end of the encapsulation.

Some smouldering occurred at the junction between one perimeter wall and the ceiling, over the course of several days without any firefighting intervention, which spread approximately 1.3 m beneath the encapsulation. The encapsulation provided a seemingly hospitable environment for the smouldering despite the test being completed in the winter, as it spread and consumed a larger extent than was seen in previous experiments (see Figure 5). This can, in part, be explained by the longer period of time to deconstruct CLT ceiling during without any firefighting intervention.

Hence, encapsulation can potentially hide smouldering; which means that it may be necessary for firefighters to remove encapsulation to identify any residual pockets of smouldering so they can be supressed.

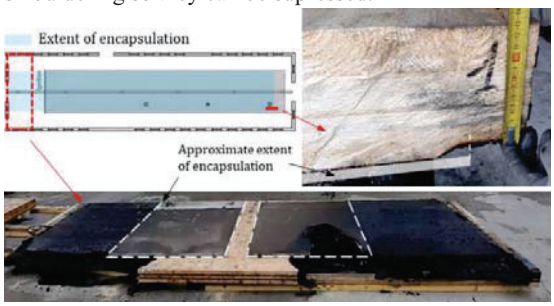

Figure 5: *Char and smouldering beneath encapsulation. figure in the top right shows a cut through the CLT slab, and the extend of charring. bottom image shows the underside of the first CLT panel in the compartment.*

4.2 FLOORBOARD ENCAPSULATION

Floorboards comprising a layer of 18 mm ply protected by 25 mm calcium silicate board were placed below and alongside the wood crib to represent the potential encapsulation of a CLT floor from a fire from above. The average peak temperatures measured at the surface of the encapsulation and the interface with the timber are presented in Table 3 for both *CodeRed #02* and *#04*. No floorboards were used in *CodeRed #01*.

Temperatures at the surface of the plywood below the protective board did not exceed 200°C, and there was no evidence of ignition of charring. Notably, this is greater than the temperature measured beneath the outer layer (12.5 mm) ceiling encapsulation, despite the locally lower measured temperatures. It is unclear why the performance of the ceiling encapsulation appeared to perform better than that on the floor. It may be due to the characteristics of the specific encapsulation product, moisture content within the encapsulation and inclusion of multiple layers which may introduce insulating air gaps.

Table 3: *Peak temperatures measured at the floor protection at the surface and the interface with the timber below.*

Experiment	Position	Peak temperature (°C)	Time to peak (min)
Temperature at surface of protective boards			
CodeRed #02	Below crib	497	28
	Next to crib	576	20
CodeRed #04	Below crib	330	37
	Next to crib	431	44
Temperature at surface of plywood (below protective board)			
CodeRed #02	Below crib	193	59
	Next to crib	187	47
CodeRed #04	Below crib	155	68
	Next to crib	147	60

The experiment showed that 25 mm calcium silicate board provided adequate protection for a fire with similar severity as the *CodeRed* experiments. However, with a more severe fire, it is expected that the same board thickness may not be sufficient.

In all cases the peak temperature occurs after the cessation of flaming, due to the effect of thermal lag, as the thermal wave continues to propagate through the encapsulation. The temperature development of the floorboard in *CodeRed #02* and *#04* is illustrated in Figure 6.

While the peak temperatures measured at the interface with the timber surface are similar for floorboards located below and along the crib, the time at which the peak occurs happens later where the boards are below the wood crib.

The peak temperatures measured at the surface of the encapsulation was, on average, 90°C hotter beside the crib compared to those under the crib. However, for the floorboards under the crib, the surface of the encapsulation remained around 300-500°C for longer,

https://doi.org/10.52202/069179-0236

well after the end of flaming, while beside the crib the temperatures decreased towards the end of flaming. This difference is likely due to the burning wood crib initially shielding the floorboards beneath from some of the radiation within the compartment but, before the remnants of the glowing embers of what is left of the wood crib continued smouldering after the end of flaming, and conducting heat towards the floor.

The similarity in the average peak temperature of the timber floorboard is noted, despite the differences in the temperature profiles measured at the surface of the encapsulation; it may be coincidental. It highlights the importance of considering the impact of smouldering of fuel remnants on the floor in the consideration and design of floor build up and section thickness, as this will contribute to the continued conductive heating through the encapsulation to the timber below.

Further research is needed to understand the heat transfer into floor elements from above, and the significance of a smouldering fuel bed heating the floor slab after the end of flaming.

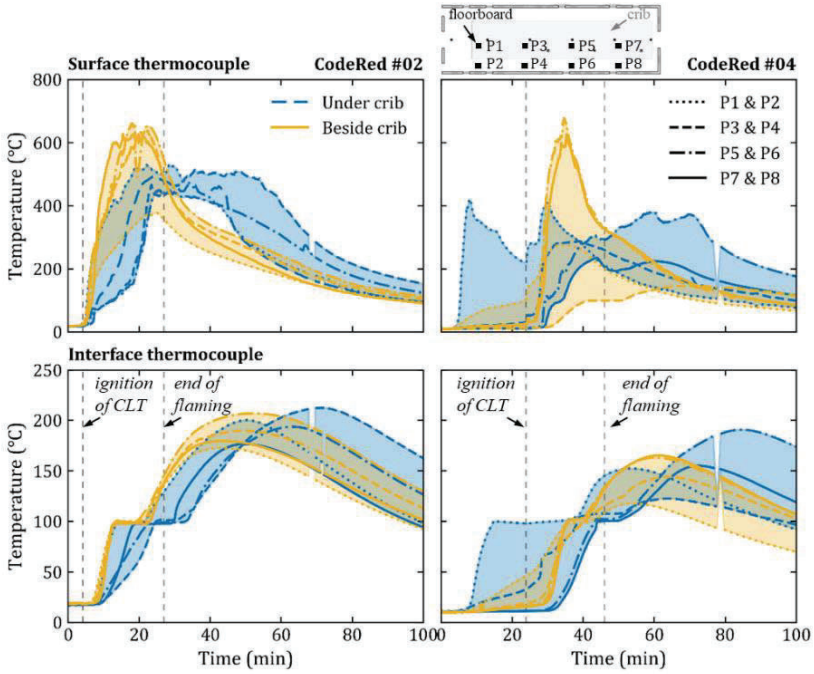

Figure 6: *Temperature development of eight plywood floorboard samples P1 to P8 each protected by a 25mm thick layer of calcium ciliate in CodeRed #04. Gas temperature given for reference.*

4.3 NUMERICAL ANALYSIS

The different encapsulation systems used at the floor and the ceiling makes direct comparison of their thermal response difficult. Therefore, to study the relative fire severity experienced by an encapsulation product fixed the ceiling and floor based on the different temperature distribution observed in *CodeRed*, a 1D FDM model was used to represent the thermal response of a hypothetical single layer encapsulation system fixed to the floor and ceiling. The model output was then compared to the measured results found from the *CodeRed* experiments to assess its performance.

4.3.1 Modelling floor protection vs experimental observations

The floorboard arrangements in *CodeRed #02* and *#04* were modelled, using the temperatures measured by the T12 thermocouple tree as the input for the boundary conditions on the basis that gas temperature were measured both near the ceiling (Ceiling level (CL) -100 mm) and near the floor level (floor level (FL)+300 mm). These locations also represent the worst-case temperature profile as indicated by the deepest char depth measured in *CodeRed #02* and *#04*. The modelled results are then compared against the temperatures measurements at the interface at floorboards P3 and P5 as they are the closest floorboards to T12, located approximately 3.7 m away.

An example model prediction of the floorboard temperature development is presented in Figure 7. The temperature at the interface between the encapsulation and plywood is overestimated in both *CodeRed #02* and *CodeRed #04* by an average of 39.9 % and 19.4 %, respectively.

The interface temperature prediction for *CodeRed #02* shows a larger discrepancy than *CodeRed #04* despite similar average and peak temperatures being recorded in both experiments. The likely explanation for this discrepancy is moisture content in the encapsulation and/or timber. The moisture content the temperatures at the interface between the encapsulation and the plywood stagnates at 100 °C for approximately 10 and 5 min for *CodeRed #02* and *#04*, respectively, which is not captured by the model. Other potential errors include: not

considering varying thermal properties with temperature, contact resistance, and modelling the ply layer as 140mm thick CLT rather than ply on a concrete screed.

Despite these errors, the model is suitable to provide a comparative analysis of the relative fire severity near the ceiling and floor level using the local temperature measurements and considering an idealised and simplified single layer encapsulation product.

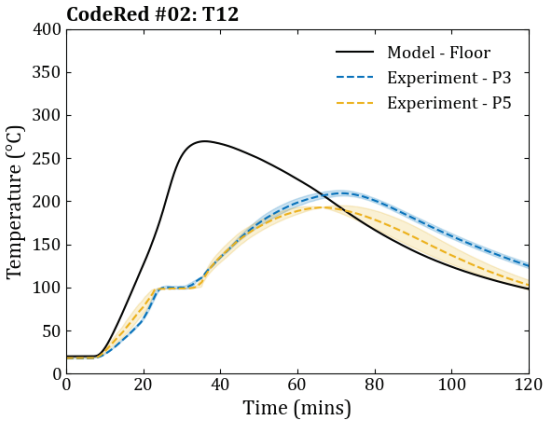

Figure 7: Comparison between the model of the interface temperature and the measured value in the experiment. Temperature over prediction is likely due to not modelling moisture content

5 INVESTIGATING RELATIVE FIRE SEVERITY AT THE CEILING VS AT FLOOR LEVEL

5.1 MODEL CONFIGURATIONS INVESTIGATED

The different encapsulation systems used at the floor and the ceiling makes direct comparison of their thermal response difficult.

Therefore, to study the relative fire severity experienced by an encapsulation product fixed to the ceiling and floor, the thermal response of the following hypothetical scenarios were further studied, comprising:

- a single layer of 25 mm thick encapsulation system fixed to 140 mm thick CLT, exposed to
- the temperature-time curves measured at T12 near the ceiling and floor in the *CodeRed #01*, *#02* and *#04* experiments (to simulate the exposure of encapsulation at the floor and ceiling), and
- The standard fire curve.

The analysis was undertaken using the FDM model and associated input parameters described in section 4.3 above, using calcium silicate boarding as encapsulation product.

The resulting modelled peak timber temperatures using the *CodeRed* time temperature curves were then converted using the time equivalence method. For the purposes of this study it is defined as the modelled exposure duration to a standard fire (in line with Eurocode 1 (EC1)) required to achieve the equivalent peak timber surface temperature found using the *CodeRed* fire curves.

5.2 RESULTS FROM *CODERED* FIRE CURVES

The model predicted timber surface temperatures beneath the ceiling encapsulation to be 75 °C (34 %), 66 °C (24%) and 52 °C (28%) greater compared to the timber surface temperatures below the floor encapsulation, using fire curves of *CodeRed #01*, *#02* and *#04*, respectively.

The simulation results suggest that in terms of fire exposure to the encapsulation system, *CodeRed #02* is experienced the most severe condition (i.e. least reduction out of all three), followed by *CodeRed #01* and *CodeRed #04*, as shown in Figure 8Figure 8.

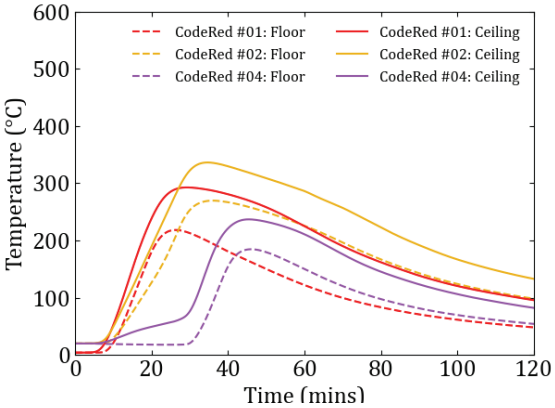

Figure 8: *Comparison of the modelled timber surface temperatures of the hypothetical encapsulation build ups position of the floor and ceiling when exposed to the CodeRed temperature curves. Model comprised of 25 mm calcium silicate encapsulation fixed to 140mm CLT .*

This is likely due to the increased burning duration in the ventilated-controlled fire of *CodeRed #02* which resulted in a more severe fire. As such the simulation results are consistent with previous observation where the average char depth is higher in *CodeRed #02* than *CodeRed #01* [6], suggesting a more severe fire in *CodeRed #02*. The slow temperature increase in *CodeRed #04* is due the gypsum fibreboard encapsulation preventing the CLT ignition until 23 min 53 s after the ignition of the crib compared to 2 min 47 s and 4 min 11 s in *CodeRed #01* and *#02* respectively.

5.3 TRANSLATION TO TIME EQUIVALENT VALUES

These results were then translated to a “time equivalent” value (TE), which is a standard metric used by fire engineers to compare fire severity. Here it is considered to be the time required for the timber surface temperature beneath the encapsulation to reach the peak temperature (modelled using the *CodeRed* fire curves) when exposed to a standard fire test. This is practice is often used for protected steel members.

Table 4 summarises the peak temperature at the timber surface following the *CodeRed* fire curves at each position, the time equivalent value, and the ratio between the time equivalence of the ceiling and floor, calculated as TE_{floor} / $TE_{ceiling}$.

Table 4: *Peak timber surface temperature and associated time equivalence calculated for the three CodeRed fire curves, at the floor and ceiling respectively, and the ratio found between them.*

https://doi.org/10.52202/069179-0236

CodeRed fire curve	Location	Peak timber surface temperature - *CodeRed* (°C)	TE (min)	TE ratio (-)
#01	Floor	218	26	0.74
	Ceiling	293	35	
#02	Floor	270	30	0.79
	Ceiling	336	38	
#04	Floor	185	21	0.78
	Ceiling	237	27	

The predictions shows that the time equivalence is, 26%, 21% , 22% lower at the floor than at the ceiling when using fire curves derived from *CodeRed #01, CodeRed #02* and *CodeRed #04* respectively.

This indicates that a lesser fire protection rating may be sufficient for the floor encapsulation to achieve an equivalent performance to that on the ceiling.

These results are based on a short fire, achieving time equivalences severity of around 30 min. Further analysis was completed to examine how the time equivalence ratio might change in fires with greater durations.

5.4 EXTRAPOLATING TO INVESTIGATE LONGER DURATION FIRES

To understand how more severe fires could affect the time equivalence ratio, a simplified time temperature profile was derived from the *CodeRed* data in the absence of available data for long duration large compartment fires.

To derive the time-temperature profile for longer duration fires at the floor and ceiling, the maximum temperature during the peak flaming period (as defined in [6–8]) in the most severe fire (*CodeRed #02*) was used, namely 912 °C measured near the ceiling and 617 °C near the floor. These temperatures are rounded to 900 °C and 600°C respectively and are applied as fixed boundary conditions to the encapsulation build up.

The time equivalent ratios between encapsulation on the ceiling and floor exposed to fires of greater severity were calculated as follows:

Step 1 - Calculate the minimum thickness of encapsulation necessary to keep the timber surface temperature at or below 270°C (one of the acceptance criteria for the K_2 protection in BS EN 13501-2:2016) for 30, 60, 90 and 120 min of standard fire exposure.

Step 2 - Calculate the equivalent '*CodeRed* fire duration' using the *ceiling temperature* curve (i.e 900°C) to achieve the 270°C at the timber surface temperature (see Figure 9) using the minimum thicknesses calculated in step 1.

Step 3 - Calculate the timber surface temperature of the same encapsulation build up established in Step 1, for the '*CodeRed* fire duration' established in Step 2, using the *floor temperature* curve (i.e 600°C) (see Figure 9).

Step 4 - Calculate the time equivalence for the timber surface temperature established in Step 3 by modelling the same encapsulation thickness found in step 1 exposed to the standard fire.

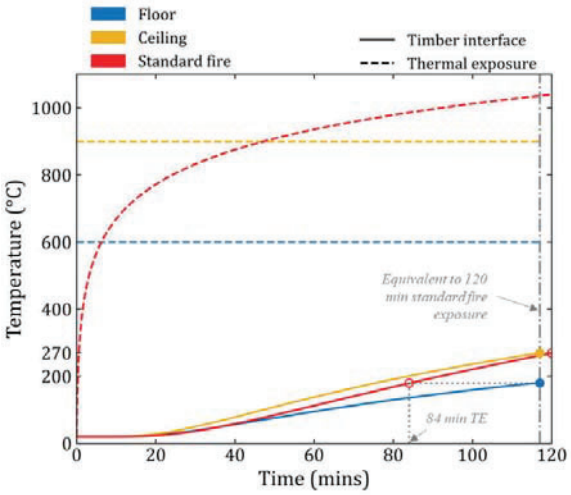

Figure 9: *Simplified time temperature development within modelled ceiling and floor encapsulation to 120 min equivalent exposure based on averaged temperature data from the CodeRed #02 fire curve, and resulting temperatures at the timber interface below the encapsulation.*

5.4.1 Example calculation

For instance, to find the ratio time equivalence ratio for a fire of 120 min fire severity the steps outline above are illustrated in Figure 9 and performed as follows:

Step 1: The minimum thickness of encapsulation necessary to keep the peak temperature of the timber surface protected after 120 min standard fire exposure to 270°C is 60.5 mm of calcium silicate board (noting again that this analysis is simplified with limitations that have been discussed earlier in this paper, and that actual thicknesses must be demonstrated by testing to the relevant standard as the likely failure mechanism will be fixings which cannot be modelled).

Step 2: The duration of exposure to the *ceiling temperature* curve to achieve the same timber surface temperature (270°C) as 120 min standard fire exposure is 117 min.

Step 3: Modelling the temperature development within the build-up using the near floor temperature condition of 600°C for 117 min, yields a predicted peak temperature of 180°C.

Step 4: This, in turn, equates to an 84 min time equivalence value. The time equivalence ratio is 0.7. As such the relative fire severity near the floor is 30% less than near the ceiling for a 120 min fire.

5.4.2 Time equivalent ratios for longer fire durations

The relative fire severity near the floor and ceiling and was similar for 90, 60 and 30 min equivalent exposure, as shown in Table 5. As expected, the ratio calculated for an equivalent 30 min exposure is similar to that calculated using the *CodeRed* temperature profiles which had time equivalent severity between 21-38 min. This may suggest the use of the 900 and 600°C temperature conditions is a reasonable approximation.

To explore this further, the critical thickness calculated for 90 min standard fire exposure is modelled with the floor level thermal condition (600°C) for 117 mins

https://doi.org/10.52202/069179-0236

(equivalent to 120 min fire exposure using the near ceiling condition, 900°C). The peak interface temperature was predicted to be 228°C. Similarly, the predicted interface temperature for a 60 min and 30 min rated floor encapsulation in a 90 and 60 min equivalent standard fire exposure was 248 °C and 298 °C, respectively. This indicates that reducing the floor encapsulating fire rating by one step may be possible for 120 and 90 min fire exposure but not for 60 min fire exposure and as this results in a temperature rise greater than the 270°C required for K_2 protection. On this basis there may be an opportunity to reduce the prescribed protection required to the floor while maintaining the intended performance. However, due to simplification taken in these models, more research must be undertaken before any conclusive guidance can be given.

Table 5: *Summary of extended fire duration exposure of encapsulation on floor and ceiling. Results are modelled using ceiling (900°C) and floor (600°C) temperatures to model peak timber surface temperature, associated time equivalence values and time equivalence ratios.*

Standard fire duration (min) [encapsulation thickness (mm)]	Location	Peak timber surface temperature (°C)	TE (min)	TE ratio (-)
120 [60.5]	Ceiling	892	120	0.70
	Floor	589	84	
90 [51.0]	Ceiling	891	90	0.70
	Floor	587	63	
60 [39.5]	Ceiling	888	60	0.68
	Floor	583	41	
30 [25.0]	Ceiling	882	30	0.70
	Floor	574	21	

5.4.3 Limitations

It is important to emphasise that there are significant uncertainties regarding the temperature development and heat transfer for long duration fires.

Also, the results are modelled based on a primarily ventilation-controlled fire which in CodeRed were observed to have more variation across the vertical temperature profile. Vertical temperatures in a fuel-controlled fire have been found to be more uniform. However, it is expected that a fuel-controlled fire will typically have a shorter duration and is less likely to require significant fire ratings.

The preliminary results presented here indicate that the concept of setting different fire protection levels for the ceiling compared to the floor may be viable, subject to further study.

While the assumptions used here are deliberately simplified to test the viability of the idea of prescribing different fire protection performance for the ceiling compared to the floor, they provide a model which produces reasonable results when applied to both the natural fire as well as the standard fire as an initial study into the relative fire severity near the floor and ceiling.

The idea is promising, however the time equivalence ratios determined here should not be used to justify a reduction in encapsulation specification. However, it does suggest that such reduction may be possible provided further experimentation or more advanced models.

6 DISCUSSION

The current analysis suggests that due to the post flashover temperature gas differences near the ceiling compared to near the floor level it may be possible to reduce the fire protection requirements of the encapsulation provided to the top surface of timber floors to protect them from fire from above, while still achieving a similar performance to the ceiling encapsulation of the mass timber ceiling in case of fire from below. The analysis presented also indicate that this reduction may be more likely and reasonable where greater fire resistance / fire protection is required.

To examine the value such a reduction in fire resistance may bring, the estimated mass and embodied carbon of toppers is summarised in Table 6. The FDM was utilised to approximate the critical thicknesses of typical materials available as floor topping to prevent the surface of the timber igniting, as done previously. The critical thickness was calculated for 30, 60, 90 and 120 min of standard fire exposure (see Table 6). These are conservative thicknesses as the model does not account for such things as moisture, thermal contact resistance, or temperature dependent thermal properties. This was similarly modelled by [15], and has good agreement.

Table 6 emphasises the potential significant contribution of the encapsulation system to the total mass and embodied carbon of the structural system. For instance, the reduction from 120 min to 90 min protection to the topside of the floor slab, with normal weight concrete, would results in a 17.6% decrease in required material. This translates to a reduction of 2074 kg of embodied carbon and a 20.1 tonnes in total mass, for a 500 m^2 compartment. This reduction in mass may also return additional reductions in the section of the structural members.

In the interest of reducing carbon in the construction industry further research is needed to evaluate the relative thermal severity experienced near the floor level compared to near the ceiling in more detail.

Table 6: *Critical thickness of CLT floor toppers to limit the temperature of the timber below 270°C, in line with a K2 classification according to BS EN 13501-6:2016 and using a standard fire. Boundary conditions used are in line with Eurocode 1*

Topper material	Critical thickness (mm) [embodied carbon (kg CO_2e/m^2)]				Embodied Carbon (kg CO_2e/m^3) [Reference]
	120 min exposure	90 min exposure	60 min exposure	30 min exposure	
Calcium Silicate board	60.5 [7.1]	51.0 [6.0]	39.5 [4.6]	25.0 [2.9]	117 [16]

https://doi.org/10.52202/069179-0236

Light weight concrete	105.5 [32.1]	88.0 [26.8]	67.0 [20.4]	40.5 [12.3]	304 [17]
Normal weight concrete	99.5 [23.6]	82.0 [19.4]	62.0 [14.7]	35.5 [8.4]	237 [16]

7 CONCLUSIONS

This paper investigated the performance of encapsulation in protecting the timber floor and ceiling in the *CodeRed* experimental series, a series of large-scale timber compartment fires. Both the 25 mm calcium silicate floorboard encapsulation and the three layers of 12.5 mm gypsum fibre boarding applied to the ceiling was shown to be adequate in preventing the ignition of the underlying timber. However, while smouldering beneath the encapsulation was not sustained immediately after the cessation of flames, smouldering was observed to sustain remote from the encapsulation and beneath the ceiling protection, where it burned an area of timber approximately 3 × 1.3 m in extent in one location. This suggests that while encapsulation may be effective in preventing the ignition of CLT, it is not 100% effective in preventing smouldering which can occur and spread behind the encapsulation.

Gas temperature measurements from the *CodeRed* experiments have showed that the temperatures near the floor are significantly lower (~300 °C) than near the ceiling in ventilation-controlled conditions. The significance of the difference in gas temperature near the ceiling and floor on the fire protection performance of encapsulation products in these positions was studied using a 1D FDM model. A single layer of 25mm calcium silicate encapsulation protecting a 140 mm CLT was modelled, using the measured gas phase temperatures near the ceiling and floor from the *CodeRed* experiments as the boundary condition of this model.

The predicted peak temperature at the surface of the timber was converted to time equivalent values. The ratio between the time equivalent value modelled for the encapsulation positioned on the floor and ceiling revealed, on average, a 23% reduction in the fire severity on to the encapsulation on the floor compared to the ceiling. This suggests that a reduced fire protection performance may be sufficient to protect a CLT floor, compared to the fire protection required for a CLT ceiling.

While the CodeRed experiments are estimated to have the approximate time equivalent fire severity of a 30 min standard fire, fires of greater severity and duration were also modelled to study the influence its influence on the time equivalence ratio.

This was done by developing simplified design fires for near ceiling and floor level exposure based on measurements taken from *CodeRed #02* and applying them to encapsulation thicknesses which were optimised to achieve the K_2 encapsulation standard (270°C at the surface of the encapsulated timber) after 120, 90, 60, and 30 min standard fire exposure. Comparing the standard fire time equivalent values of the encapsulation exposed to the ceiling and floor level design fires revealed a 30% reduction in fire severity to the encapsulation on the floor compared to the ceiling for severities up to 120 min.

Modelling an optimised encapsulation thickness exposed to a fire duration of 120 and 90 minutes standard equivalent fire for the ceiling respectively revealed that 90 and 60 min encapsulation performed adequately when positioned on the floor and exposed to the floor level design fires. However, applying a 30 min optimised encapsulation thickness to a 60 min standard fire equivalent floor level design fire yielded temperatures greater than the 270°C required for K_2 protection.

There may be an opportunity to develop a protection regime for mass timber compartments where the prescribed protection required to the floor is lower than that applied to the ceiling while maintaining the intended performance. This reduction offers an opportunity to reduce, the mass, embodied carbon and cost associated with encapsulation products. It should be noted that the results found here should not be directly applied to justify a reduction in prescribed fire resistance requirements. This study is the first step in quantifying the relative standard fire resistance requirements required at the floor and to the ceiling to help guide practitioners on designing and constructing safe and sustainable buildings and highlight the need for further research to enable better characterisation of fire severities at ground level of large compartments with a timber ceiling.

ACKNOWLEDGEMENT

This research has been fully funded by Arup and was undertaken in partnership with Imperial College London. The experiments were carried out in a bespoke facility built at CERIB's Fire Testing Laboratory site in France.

REFERENCES

[1] E. Rackauskaite, P. Kotsovinos, D. Barber, Letter to the Editor: Design Fires for Open-Plan Buildings with Exposed Mass-Timber Ceiling, Fire Technol. 57 (2021) 487–495. https://doi.org/10.1007/s10694-020-01047-0.

[2] British Standard Institution, BS EN 13501-2: Fire Classification of Construction Products and Building Elements. Part 2: Classification Using Data from Fire Resistance Tests, Excluding Ventilation Services, 2016.

[3] J. Su, P.-S. Lafrance, M. Hoehler, M. Bundy, Fire Safety Challenges of Tall Wood Buildings - Phase 2: Task 2 & 3 - Cross Laminated Timber Compartment Fire Tests NFPA Rep. No. FPRF-2018-01. NRC Rep No. A1-010659.1, 2018.

[4] T. Engel, N. Werther, Impact of Mass Timber Compartment Fires on Façade Fire Exposure, Fire Technol. (2022). https://doi.org/10.1007/s10694-022-01346-8.

[5] P. Kotsovinos, E. Rackauskaite, E. Christensen, A. Glew, E. O'Loughlin, H. Mitchell, R. Amin, F. Robert, M. Heidari, D. Barber, G. Rein, J. Schulz, Fire dynamics inside a large and open-plan compartment with exposed timber ceiling and

columns: CodeRed #01, Fire Mater. (2022). https://doi.org/10.1002/fam.3049.
[6] P. Kotsovinos, E.G. Christensen, E. Rackauskaite, A. Glew, E. O'Loughlin, H. Mitchell, R. Amin, F. Robert, M. Heidari, D. Barber, G. Rein, J. Schulz, Impact of ventilation on the fire dynamics of an open-plan compartment with exposed timber ceiling and columns: CodeRed #02, Fire Mater. (2022). https://doi.org/10.1002/fam.3082.
[7] P. Kotsovinos, E.G. Christensen, A. Glew, E. O'Loughlin, H. Mitchell, R. Amin, F. Robert, M. Heidari, D. Barber, G. Rein, J. Schulz, Impact of partial encapsulation on the fire dynamics of an open-plan compartment with exposed timber ceiling and columns: CodeRed #04, Fire Mater. (2023). https://doi.org/10.1002/fam.3112.
[8] P. Kotsovinos, E. Rackauskaite, E. Christensen, A. Glew, E. O'Loughlin, H. Mitchell, R. Amin, F. Robert, M. Heidari, D. Barber, G. Rein, J. Schulz, Fire dynamics inside an open-plan compartment with an exposed CLT ceiling and glulam columns: CodeRed #01, Fire Mater. 2022 (2022) 1–27. https://doi.org/10.1002/fam.3049.
[9] E. Rackauskaite, M. Bonner, F. Restuccia, N. Fernandez Anez, E.G. Christensen, N. Roenner, W. Wegrzynski, P. Turkowski, P. Tofilo, M. Heidari, P. Kotsovinos, I. Vermesi, F. Richter, Y. Hu, C. Jeanneret, R. Wadhwani, G. Rein, Fire Experiment Inside a Very Large and Open-Plan Compartment: x-ONE, Fire Technol. 58 (2022) 905–939. https://doi.org/10.1007/s10694-021-01162-6.
[10] J.R. Waters, A.J. Wright, Criteria for the distribution of nodes in multilayer walls in finite-difference thermal modelling, Build. Environ. 20 (1985) 151–162. https://doi.org/10.1016/0360-1323(85)90010-1.
[11] F. Richter, G. Rein, Heterogeneous kinetics of timber charring at the microscale, J. Anal. Appl. Pyrolysis. 138 (2019) 1–9. https://doi.org/10.1016/j.jaap.2018.11.019.
[12] Fermacell ® Gypsum Fibreboards Safety Data Sheet, (2019). https://www.fermacell.co.uk/fermacellapi/downloads/file/en-GB/0690J000004BxHIQA0.
[13] Promatect-MST Technical Data Sheet, (2019). https://www.promat.com/siteassets/industry/downloads/technical-data-sheets-tds/calcium-silicates/eng/promat-promatect-mst-product-data-sheet.pdf?v=49cca6/Download.
[14] M. Foley, D.D. Drysdale, Heat transfer from flames between vertical parallel walls, Fire Saf. J. 24 (1995) 53–73. https://doi.org/10.1016/0379-7112(94)00033-C.
[15] M. Rauch, N. Werther, THE CONTRIBUTION OF SCREED FLOOR TOPPINGS TO THE FIRE RESISTANCE, in: World Conf. Timber Eng., 2020. https://doi.org/10.13140/RG.2.2.16032.00004.
[16] C. Jones, Embodied Carbon - The ICE Data Base, (2019). https://circularecology.com/embodied-carbon-footprint-database.html.
[17] F. Kanavaris, O. Gibbons, E. Walport, E. Shearer, A. Abbas, J. Orr, B. Marsh, Reducing the carbon footprint of lightweight aggregate concrete, in: Int. Conf. Low Carbon Cem. Concr., 2020.

https://doi.org/10.52202/069179-0236

World Conference on Timber Engineering Oslo 2023

COMPARATIVE PERFORMANCE OF PROTECTIVE COATINGS FOR MASS TIMBER STRUCTURES

Lorna Johnson[1], David Morrisset[2], Antonela Colic[3], Luke Bisby[4]

ABSTRACT: The use of engineered mass timber in large scale structures is increasing due to the demand for low carbon, sustainable building design. The potential for structural timber to combust and contribute to a fire event adds hazards and complexity to the design of mass timber buildings. To address these issues, various surface treatments are available aiming to protect or alter the reaction to fire behaviour, relevant during early stages of a fire, and charring behaviour of fire exposed timber which is relevant during the developed stage of a fire. The performance of three specific commercially available fire protective coatings for timber was studied by exposing coated 95mm x 95mm x 45mm horizontal softwood samples to radiant heat flux of 35 and 60 kW/m^2 in a cone calorimeter from above, a level of radiation representative of a developing fire. Ignition time, heat release rate, mass loss rate, gas species emissions, in-depth temperatures, and char progression were recorded to study sample performance when compared against uncoated timber. Results indicate that two of the protective coatings used successfully developed a protective intumescent char layer, while one product did not. The former two displayed significantly reduced mass loss and heat release rates, as well as reduced in-depth thermal penetration when compared to uncoated timber. One coating did not intumesce and performed similarly to uncoated timber. These results illustrate the importance of not extrapolating from reaction to fire classifications to make assumptions about improved fire performance outside the scope of such classifications, without substantial further testing and validation of those assumptions.

KEYWORDS: Protective coatings, intumescent coatings, fire performance, mass timber, cone calorimeter

1 MOTIVATION AND BACKGROUND

1.1 INTRODUCTION

The use of engineered mass timber in large scale structures is rising due to the demand for low carbon, sustainable buildings [1]. Mass timber offers benefits such as being lightweight and less constrained by size or shape in comparison to concrete and steel. However, the potential for structural timber to ignite and contribute fuel to a fire, as well as timbers comparatively higher susceptibility to reductions in mechanical properties at elevated temperatures, necessarily adds complexity to the design of mass timber buildings. To address these issues, surface treatments are available aiming to alter the reaction-to-fire [2-4] and/or the charring behaviour of fire exposed timber to achieve a higher fire resistance period than untreated timber. Unlike structural steelwork, with which intumescent coatings are more commonly used, timber structural elements will char and can fail at comparatively low temperatures due to thermal decomposition (i.e., pyrolysis) and timber strength degradation at elevated temperatures when exposed to sufficient heating. Intumescents are passive fire protection coatings that react when exposed to heating and swell to form a protective char layer which can reduce heat transfer to the substrate materials [5] and hence, in the case of a timber substrate, reduce mass flow of pyrolysates from the exposed surface. Intumescent coatings are typically specified to achieve a better reaction to fire classification than untreated timber would achieve, but may also be relied upon to reduce charring rates which would be determined by the relevant standardised testing method. Transparent protective coatings are appealing for mass timber designers, compared with rigid encapsulation alternatives, due to the aesthetics of exposed timber surfaces. However, experimental data (as opposed to compliance classifications) for such coatings are extremely scarce for a range of relevant heating scenarios. A greater understanding of intumescent products for mass timber is therefore required since many such products are already in widespread use in the built environment. The study presented in this paper aims to quantify and compare the behaviour of timber specimens coated with three different commercially available transparent fire

[1] Lorna Johnson, Arup, Arup Fire, lorna.johnson@arup.com
[2] David Morrisset, The University of Edinburgh, School of Engineering, d.morrisset@sms.ed.ac.uk
[3] Antonela Colic, The University of Edinburgh, School of Engineering, a.colic@sms.ed.ac.uk
[4] Luke Bisby, The University of Edinburgh, School of Engineering, luke.bisby@ed.ac.uk

https://doi.org/10.52202/069179-0237

protection coatings, achieving European reaction to fire Class B, under various heating conditions. These coatings have been independently obtained, and the authors make no attempt herein to endorse (or otherwise) any of them; we simply present and discuss experimental outcomes under the scenarios investigated.

1.2 PROTECTION OF WOOD

Key concerns for safe structural design of timber are related to the potential fuel contribution of timber elements in a fire (fire dynamics), in combination with reductions in mechanical properties on heating (fire resistance). In order to specify the dimensions of timber structural components, whilst complying with building stability, integrity, and insulation requirements, multiple forms of passive fire protection are available to designers [6-7]. These passive protection measures may include board/encapsulation products, intumescent coatings, and impregnation treatments, all of which aim to reduce the heat transfer to the underlying timber. Gypsum plasterboards are a common, albeit often architecturally undesirable, passive fire protective measure where the thickness or number of layers of board can be adjusted to provide differing levels of protection. Intumescent coatings have the advantage that they can be applied in thin layers whilst maintaining the aesthetic qualities of the unprotected mass timber; however, may require re-application to maintain their performance, and may not function as intended when combined with other surface treatments.

1.3 INTUMESCENT COATINGS

When sufficiently heated, intumescent coatings swell and form a protective char layer [5]. These coatings commonly incorporate various chemical components which react to ensure intumescence and char formation [5,8] under standardised heating scenarios. The interactions of these components in the "correct" sequence is key to ensuring successful formation of an intumescent char, and therefore to the protection of the substrate from fire [5]. A char begins to form when the intumescent compounds decompose and release gases within the melted substance, forming a 'multi-cellular' char layer [5]. Trapped bubbles provide a low density, protective char layer which reduces heat transfer to the structural member and therefore postpones the conditions (i.e., temperatures) favourable for timber to pyrolyze. The mixture of chemical compounds used in intumescent coatings formulated specifically for wood is likely to be unique to each specific commercially available product. Hence, the speed of intumescent char growth, thickness, density, and porosity distribution within the intumescent char all depends on the specific product formulation (and, critically, on the heating conditions). Due to the different chemical compositions of intumescents, and therefore different activation temperatures of their chemical groups, there is a critical temperature required for an intumescent coating to react, char, and provide altered properties that are relevant to the intended substrate material [9].

Possibilities for transparent or coloured coatings make intumescents aesthetically desirable, and their thin, lightweight nature minimises additional structural loads and structural member sizes. However, care must be taken that coatings are applied appropriately; relevant conditions as specified by the manufacturer are required in order to ensure products perform as intended. Factors such as humidity, moisture, and thickness must be considered to ensure their durability, longevity, and performance in fire.

1.4 INTUMESCENT COATINGS FOR WOOD

Popescu et al. [10] describe that in addition to insulating a timber element, intumescent coatings can enhance fire performance by 'reducing the amount of heat released during the initial stages of fire, by retarding the spread of flame and by limiting the production of smoke and flammable volatiles'. The effectiveness of the intumescent coating also depends on the thermal boundary conditions, including the temperatures of the substrate material. A challenge for intumescent coatings applied to timber is that they must have a lower critical temperature (i.e., the temperature that initiates the expansion of the intumescent) than those used for other materials, such as steel, in order to provide protection before significant pyrolysis occurs. This may mean that intumescents for timber are quickly impaired at a higher temperatures [10].

The performance of intumescent coatings (in terms of reaction-to-fire response) is typically determined using standard test methods such as European reaction to fire 'single burning item test' and 'single flame source test' (BS EN 13501-1, BS EN 13823 and BS EN ISO 11925-2 as described in Section 2.2) [2-4]. However, some variables of potential importance in fire are not directly measured or reported in most standard tests, including gas species generation, char depths and rates, mass loss rates, and toxicity. This limits a holistic understanding of the fire performance of intumescent coatings generally, and specifically for those used to provide fire protection of wood [7].

Experimental studies involving intumescent coatings for wood have been presented by, for example, Wladyka-Przybylak, Hassan et al., Bahrani et al., Hartl et al., Lucherini et al. and Xu et al. [8, 11-15] in relation to different coating formulations, durability and the effects of external weathering, and their performance when compared to other passive fire protection methods (e.g., gypsum plasterboards). However, there remains a need for rigorous fire science data regarding the fire performance of existing timber intumescent coatings under a range of relevant heating conditions. This is in order to better understand the performance of reaction to fire coatings, coatings seeking to impact on the resultant fire dynamics and/or slow char rates to improve fire resistance of timber under more severe fire conditions, and to establish their reliability under natural fire conditions.

This paper aims to characterise the fire performance of different reaction to fire treatments under a range of

https://doi.org/10.52202/069179-0237

relevant heating conditions so as to better understand a broader range of impacts of some commercially available coatings when placed under more onerous heating regimes.

2 METHODS

The performance of three commercially available intumescent fire protection coatings for timber was studied by exposing coated samples of softwood to radiant heating. The coatings were then compared against untreated wood to quantify their influence on ignition and burning behaviour. This was done qualitatively by visual observation and quantitatively in terms of heat release rate (HRR), in-depth temperatures, mass loss rate (MLR), and gas species production.

2.1 TEST SAMPLES

Timber samples tested were cut from solid Norway Spruce and had 95 x 95 mm cross sections with 45mm thickness. Three in-depth 1.5 mm diameter K-type thermocouples were installed from the side of the sample and were positioned at 5mm depth intervals from the exposed surface to allow for in-depth temperature measurements at depths of 5, 10, and 15 mm.
All samples were surrounded by aluminium foil and ceramic fibre paper to mitigate mass transport, reduce pyrolysis gas escape from the sides, and reduce heat transfer to the sides of the sample (see Figure 1).

Figure 1: *Coating A timber sample preparation.*

2.2 INTUMESCENT COATINGS

The three products used in this study are commercially available in the UK and designed for the fire protection of timber; advertising a "reduction of ignitability" and to "insulate against heat", "prevent propagation of fire and spread of flame" and "suppress emission of deadly smoke & gases" whilst providing a reaction to fire classification and/or fire resistance period [16-18].
Each coating system consists of an intumescent base coat and top coat. No primer was used for application of these coatings, as specified by manufacturers for clean softwood. The respective coating systems were applied in thin layers and allowed to dry between each application, as per the respective manufacturers' instructions.

It was noted that despite all coatings being described as transparent, each had a slightly different appearance once all layers had been applied and dried (Figure 2).

Figure 2: *Comparison of intumescent coating appearance. From left to right; Coating B, C, A and uncoated.*

Coating A (sold as HW Envirograf) is a water-based intumescent system which is advertised on their website as achieving European classification B-s1, d0; on the basis of testing to the 'single burning item test' and 'single flame source test' [2-4, 16]. Such tests are designed to measure production of heat, production of smoke, horizontal flame spread, ignition, and the falling of flaming droplets and particles in controlled fire conditions. The product is also advertised for application e.g. on fire doors for fire resistance periods using standard furnace tests, for 30 and 60 minute fire resistance ratings based on BS 476-20 and BS 476-22 tests for non-/load-bearing elements, and 66 minutes integrity is claimed with reference to a BS EN 1364-1 wall test [16]. No fire classification or fire test reports were available for download from the website to provide further detail and limitations of the fire performance of the product.

Coating B (sold as Sika Pyroplast) is a water-based intumescent system advertised to achieve European classification B-s1, d0 [17]. The manufacturer does not advertise any ability to provide fire resistance with their product.

Coating C (sold as Thermoguard Fire Varnish) is a combined resin-acid catalyst and white spirit based intumescent system. This coating is advertised to achieve European reaction to fire classification B-s2, d0 (thus greater smoke production than coatings A and B) [18]. Coating C's manufacturer also state that fire resistance classifications are possible using their product but that this requires further consultation.

Each of the coatings used in the current study are sold on the basis of improving the fire performance of timber, either in relation to the reaction to fire classification or fire resistance classification.
The proprietary nature of each product likely results in different reactions under heating and therefore different intumescent performance in real fire scenarios.

https://doi.org/10.52202/069179-0237

2.3 APPARATUS AND MEASUREMENTS

Each sample was exposed to a constant radiant heat flux in a cone calorimeter for 30 minutes, since initial investigations determined that this provided sufficient time to develop the protective char layer. Experiments were performed at two nominal incident heat fluxes (35 and 60 kW/m^2) aiming to span a range of heat fluxes that is broadly representative for a compartment fire scenario. Gas species, heat release rate, mass loss rate, and in-depth temperatures were recorded. Measurements of ignition, char thickness (i.e., swelling), and char depth were also recorded so as to further characterise the coating response. Guidance for the testing was taken from BS ISO 5660-1. The surface of the sample was separated from the lowest point of the cone heater by 50 mm to prevent contact between the intumescing coating and the cone heater [19]. However, due to the use of intumescent coatings and their unpredictable behaviour, the samples were not placed in a standard sample holder and instead wrapped (as previously described) and then placed directly onto a load cell [19].

3 RESULTS

3.1 IGNITION

Ignition times for each product are given in Table 1. Both the uncoated and coated samples were observed to ignite under the heat flux conditions used in this work. The uncoated samples experienced continued flaming, after ignition, throughout the experiments, while Coating B and Coating C treated samples experienced extinction shortly after ignition. Later re-ignition was observed for coating B and C samples exposed to 60 kW/m^2; however, this was not observed for 35 kW/m^2. The ignition times for Coating C samples were found to be less than for the uncoated samples at both heat fluxes used. Coating A was found to delay ignition compared to the uncoated sample, however this product displayed continued flaming, after ignition, throughout the experiments.

The earlier ignition of Coating B and Coating C appeared to result in the formation of a protective char *before* the majority of the underlying wood surface reached its pyrolysis temperature, hence protecting the wood substrate once the swollen intumescent layer had formed.

Table 1: *Times to ignition, extinction, and re-ignition of flames for each coating and heat flux tested.*

Coating Type	Heat Flux (kW/m^2)	Time to Ignition (s)	Time to Extinction (s)	Time to Re-Ignition (s)
Coating A	*35*	71	n/a	-
	60	6	n/a	-
Coating B	*35*	39	61	n/a
	60	9	28	152
Coating C	*35*	12	63	n/a
	60	3	37	159
Uncoated	*35*	65	n/a	-
	60	6	n/a	-

3.2 VISUAL OBSERVATIONS

Observation of the intumescent coatings during testing suggested that only two of the three coatings expanded significantly when exposed to the heat flux conditions used in the current study. Coating B and Coating C, both of which swelled, produced insulating char layers with maximum depths of 12 mm from the exposed surface of the sample. Thus, each of these two coatings grew to approximately 10 times the original applied dry film thickness. Coating A did not swell.

Although successful at extinguishing flames shortly after early ignition, both coatings B and C demonstrated different char growth phases (uniform/non-uniform as further explained), presumably due to their unique chemical formulations. Given the proprietary nature of these products, the exact formulations and hence reactions that occur upon exposure to heating are not known.

The differing swelling phases of the intumescents can, however, be visually correlated to phenomena that were observed during the experiments. Phases of intumescent coating thermal resistance correspond to the growth and decay phases of the char layer; thermal resistance being the ratio of expanded thickness to thermal conductivity of the intumescent layer (Li et al. and Lucherini et al.) [14,20].

COATING B

The growth of Coating B slowly developed as an unevenly distributed white char across the sample surface (Figure 3a), which then blackened (Figure 3b). Ignition of the volatiles produced during coating pyrolysis occurred soon after heating (see Section 3.1).

Once ignited (Figure 3c), surface flaming then contributed additional heat feedback to the surface, which increased the rate of pyrolysis (evidenced by the mass loss rate in Section 3.3). This accelerated pyrolysis rate also accelerated the rate at which the intumescent char layer developed. The growing char layer served to reduce the rate of heat transfer to the underlying timber substrate, and thus to a decrease in the pyrolysis rate. The pyrolysis rate then decreased below the critical rate to sustain flaming and the flame extinguished (Figure 3d).

Upon completion of the swelling of the intumescent and the oxidation of its char, its thermal resistance peaked [14]. Hence, this was the upper limit of its insulating capability (Figure 3e). Regression of the intumescent char then slowly occurred, resulting in a reduction in thermal resistance. This coating reached a maximum char thickness of 12mm above the surface of the sample.

https://doi.org/10.52202/069179-0237

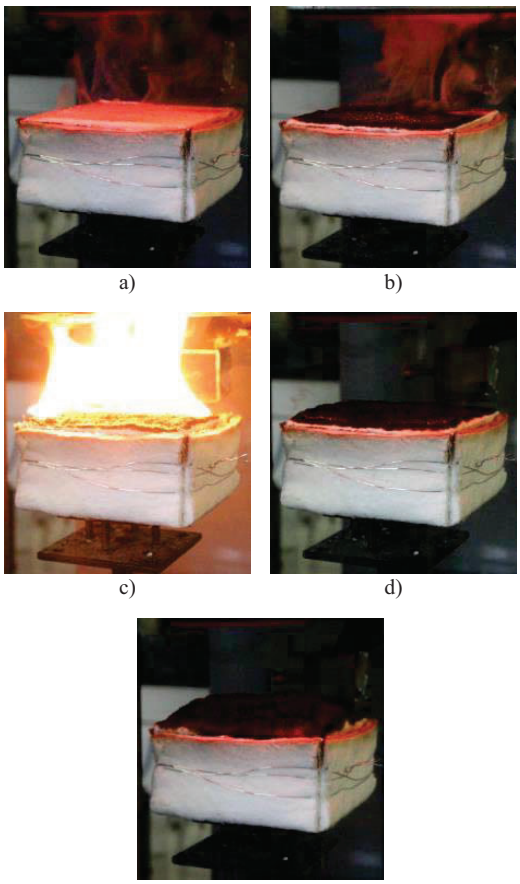

Figure 3: *Phases of Coating B (Sika Pyroplast) intumescent growth at 35 kW/m^2.*

Coating B displayed significant variation in intumescent blister shape and distribution across the surface; this can be seen clearly in Figure 4.

Figure 4: *Intumescent char formations for Coating B (Sika Pyroplast) sample removed from apparatus at 35 kW/m^2.*

COATING C

Coating C did not behave as expected based on the existing literature [7,14]. Before growth of the char bubble matrix, an outermost layer of the coating appeared to trap a portion of intumescent pyrolysis gases and formed a single large (approximately 16mm deep) bubble over the entire surface of the coated sample. Ignition of volatiles released from this bubble caused a large initial flame on ignition, resulting in significant heat feedback to the sample surface. The coating then entered a transient phase by forming a multitude of small bubbles that developed into a protective char layer. This coating reached a maximum char thickness of 8mm, and then – as for Coating B – it gradually regressed.

COATING A

When exposed to heating, Coating A immediately melted, pyrolysed, and changed to a blackened colour. Upon ignition however, this coating appeared to immediately disintegrate, cracking, and peeling away in thin curling leaves to reveal the underlying substrate. Little initial bubbling and no obvious intumescent growth were observed. The timber then began to char and fracture as if uncoated. Flaming of Coating A samples continued until the end of the experiments.

3.3 BURNING BEHAVIOUR

The heat release rate (HRR) for the samples was measured using oxygen consumption calorimetry. The mass loss rate was also determined via cone calorimetry and provides an indication of thermal decomposition of the samples. Mass loss can evidence drying of timber, decay by pyrolysis, or oxidation of the carbon-rich char [21]. The heating process that causes the greatest loss of timber substrate mass is pyrolysis, generating ash and gaseous products. Both the time-resolved HRR data and MLR data are given in Figure 5 to Figure 9.

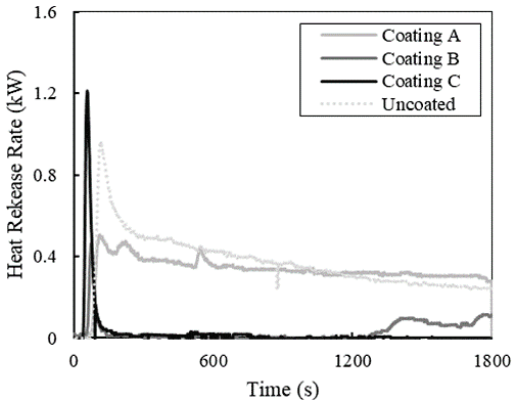

Figure 5: *Stages of intumescent burning at 35 kW/m^2.*

https://doi.org/10.52202/069179-0237

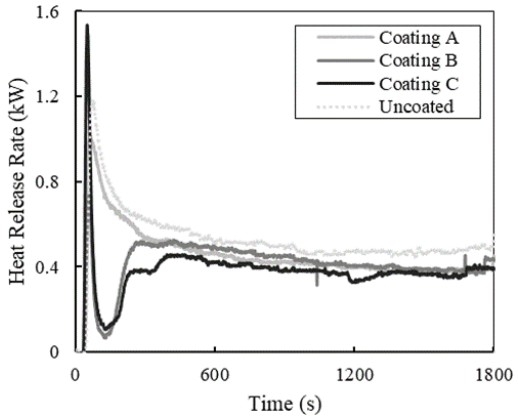

Figure 6: *Stages of intumescent burning at 60 kW/m^2.*

Across the exposure conditions used, the two coatings that swelled (coatings B and C) displayed distinctly different burning behaviour as compared with uncoated wood. The time resolved HRR data for an uncoated sample exposed to 60 kW/m^2 is given in Figure 7. The early stages of the experiment displayed high rates of pyrolysis prior to ignition, then a rapid increase in the HRR after ignition. The HRR then increased to a peak value which gradually decreased as the char layer developed and heat transfer was reduced in-depth in the timber (as expected).

The HRR with time for a typical intumescent coating (Coating C) exposed to 60 kW/m^2 is given in Figure 8. A peak HRR value was observed soon after ignition of the intumescent coating. The HRR then reduced to well below the value recorded for uncoated timber. For trials at 60 kW/m^2, the intumescent char then began to degrade after about 150 seconds; the surface then eventually reignited, with commensurate increase in the HRR (Figure 6).

For experiments conducted at 35 kW/m^2, re-ignition did not occur and HRR did not increase after the initial peak (Figure 5). The discrepancy between the behaviours across the two heat fluxes illustrates the potential importance of the heating conditions when studying the performance of intumescents, as previously suggested in the available literature [13-14]. The heat fluxes to which such coatings are subjected when assessed via regulatory tests is therefore potentially very important in terms of the credibility of assessment for performance in real (rather than regulatory) fire scenarios.

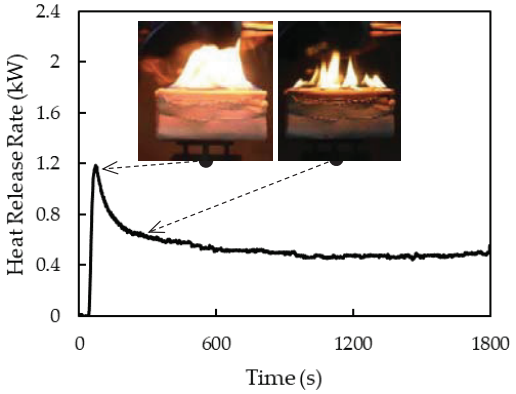

Figure 7: *Phases of flaming and heat release rate at 60 kW/m^2 for uncoated samples.*

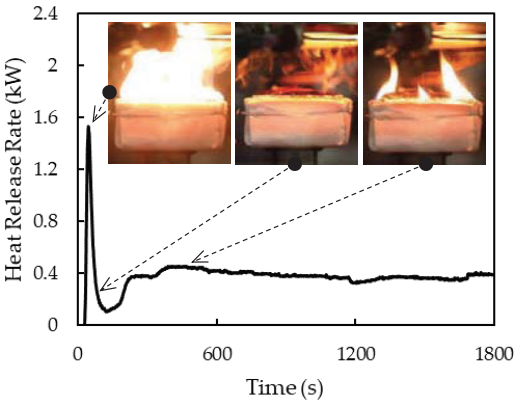

Figure 8: *Phases of flaming and heat release rate at 60 kW/m^2 for Coating C (Thermoguard Fire Varnish) coated samples.*

Figure 5 to Figure 9 show that Coating C had the fastest and largest HRR and MLR peak for all coatings and heat fluxes. This peak occurred in less than 20 seconds at 35 kW/m^2 and less than 10 seconds at 60 kW/m^2. HRR then declined rapidly, suggesting there was a sudden release and then ignition of combustion products – this aligns with the observation of a single large bubble on the surface of the Coating C samples. After this initial growth the intumescent char layer protected the timber and therefore HRR and MLR declined. After approximately five minutes, the HRR behaviour for trials conducted at 60 kW/m^2 was observed to converge to similar general behaviours as the samples transitioned into a regime of predominantly char oxidation. All ignition, extinction, or re-ignitions occurred within the first three minutes of each experiment.

https://doi.org/10.52202/069179-0237

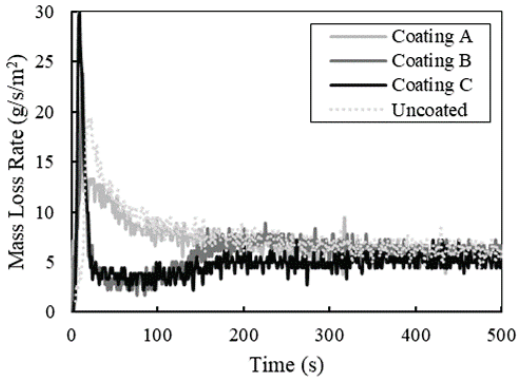

Figure 9: *First 500 seconds of mass loss at 60 kW/m².*

Despite the behaviour of each sample within the first 500 seconds being distinctive, all data began to converge to a mass loss rate of approximately 4 g/s/m² at 35 kW/m² and 5 g/s/m² at 60 kW/m², once 1500 seconds had elapsed.

The results for heat release rate and mass loss rate correlate well, as expected given that both are manifestations of the burning rate. The trends of mass loss therefore correspond to those described for HRR, i.e., the initial mass loss rate is higher due to the added presence of more volatile products.

For coatings B and C which swelled, the peak in mass loss rate occurred as the intumescent blisters were forming. This occurred more quickly than for Coating A or uncoated samples and can likely be attributed to the reduced reactional temperature of the intumescent in comparison to the pyrolysis temperature for timber. The reduced mass loss and heat release rate after the initial peak supports the idea that the intumescent char layer does protect the underlying timber.

3.4 GAS SPECIES

Recorded values of carbon monoxide (CO) and carbon dioxide (CO_2) in the cone calorimeter flue gases provide insight into the emissions from both the timber substrate and each of the protective coatings; the CO results are shown in Figure 10. The pyrolysis and burning of timber can be expected to produce CO, CO_2, and various other products. The intumescent coatings will also contribute combustion products, including CO and CO_2. The rate of CO and CO_2 generation will vary with the presence of a flame or with the presence of solid phase char oxidation. Therefore, the measurement of CO and CO_2 lend insights into the global combustion conditions of the tested specimen. Periods of high CO_2 generation tend to indicate periods of sustained flaming, as a result of the flame sheet rapidly oxidizing CO produced during pyrolysis to CO_2 [22]. The CO values found in this study, however, varied significantly between coatings and heat fluxes, following differing trends throughout the 30 minute exposures.

High generation of CO has been associated with both pyrolysis and solid phase char oxidation [23]. The CO production for samples coated with coatings B and C were significantly higher than for uncoated wood, suggesting that the increased CO yield may be a result of the oxidation of the intumescent char. Intumescent products commonly incorporate carbonising agents, and it is possible that decomposition of these elements leads to the production of CO in the early stages of intumescent growth [8]. It is also likely that char oxidation dominates the production of CO in the later stages of the experiments presented herein [24].

For coatings B and C exposed to 35 kW/m², the CO value grew significantly after an initial peak, peaking for a second time after 20 minutes and 30 minutes, respectively. At 60 kW/m² the initial CO peak was much higher, and production then rapidly decreased. This variation of gas species generation between the two heat fluxes supports the idea that different chemical reactions may occur within the intumescents at different temperatures. It is also noteworthy that production of these gases only occurred after the thermal decomposition of the protective layer had been initiated.

The CO_2 and CO concentrations varied considerably between each Coating B repeat test. This suggests that even with the same application of coating and heat flux, the behaviour of this intumescent may differ in terms of both char formation and reaction products.

As with the previous results, the Coating A samples behaved similarly to uncoated wood in relation to both CO_2 and CO concentrations at both 35 and 60 kW/m².

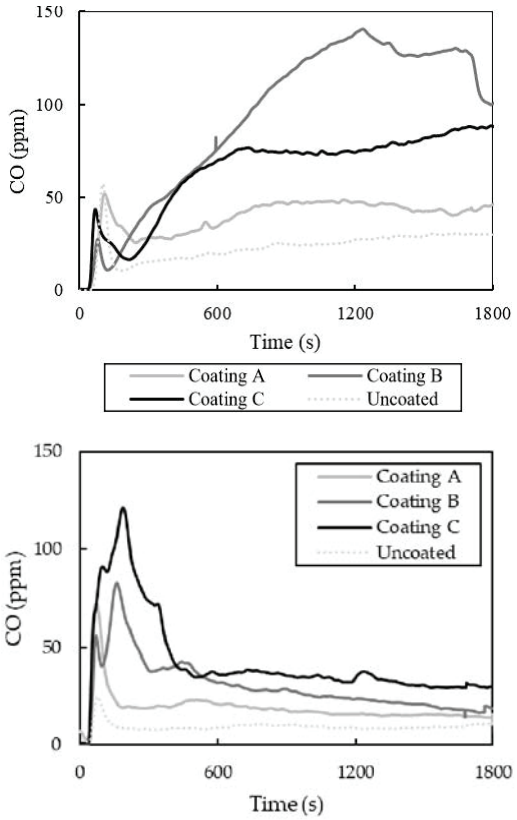

Figure 10: *CO gas concentrations in exhaust gases at 35 kW/m² (top) and 60 kW/m² (bottom), respectively.*

https://doi.org/10.52202/069179-0237

3.5 TEMPERATURE AND CHAR DEPTH

The in-depth temperature gradients in the samples provide indications of the degree of thermal penetration in the timber. Dominating burning regimes correlate with different temperature bounds, therefore, a profile of temperature through the depth of the sample can elucidate the processes occurring at any one time and suggest the degree to which the overall strength of the timber section would have been reduced due to in-depth heating. At approximately 100ºC moisture vaporization and transport will occur variably throughout a timber cross section, causing dehydrated wood to become more brittle and saturated wood layers to soften [21]. At 100ºC, timber is typically assumed to lose 75% of its flexural strength [25]. At about 200ºC, the timber will begin to pyrolyze [26] which not only further reduces the structural capacity of the member but also produces flammable gases which may ignite. At temperatures in the range of 400-600ºC, any char is likely to experience solid phase char oxidation. The 300°C in-depth isotherm is typically assumed to represent the effective depth of the "char layer" (i.e., the position at which timber has lost effectively all of its mechanical strength). However, mechanical properties are also lost in thermally-affected regions at temperatures below 300°C [25].

The samples that most rapidly reached 300°C, both at the surface and at locations in-depth, were the uncoated samples. These were closely followed by samples with Coating A.

Coatings B and C, both of which insulated the timber as already discussed, resulted in consistently lower in-depth temperatures compared against uncoated trials.

At 35 kW/m^2, the surface of the timber protected by Coating C was up to 300°C less than for uncoated timber samples. The char depth after 30 minutes of exposure was reduced by 4-7 mm for coatings B and C.

Figure 11 shows the thermal gradients developed through the depth of exposed uncoated and Coating B specimens. This thermal gradient can then be compared across products to assess the rates and degree of thermal penetration experienced.

In addition to in-depth temperature results, the impact of each coating on final char depth of the timber was evaluated by visual examination of the samples after testing. Samples were cut vertically in half to observe the char depth and unpyrolysed wood, where distinction was made by qualitatively reviewing the colour change of the cross section. By measuring the remaining depth of wood, the loss of material was quantified in thickness (as well as mass from the mass loss readings).

As should be expected, the greatest loss of timber substrate was found for the uncoated timber when tested at 60 kW/m^2.

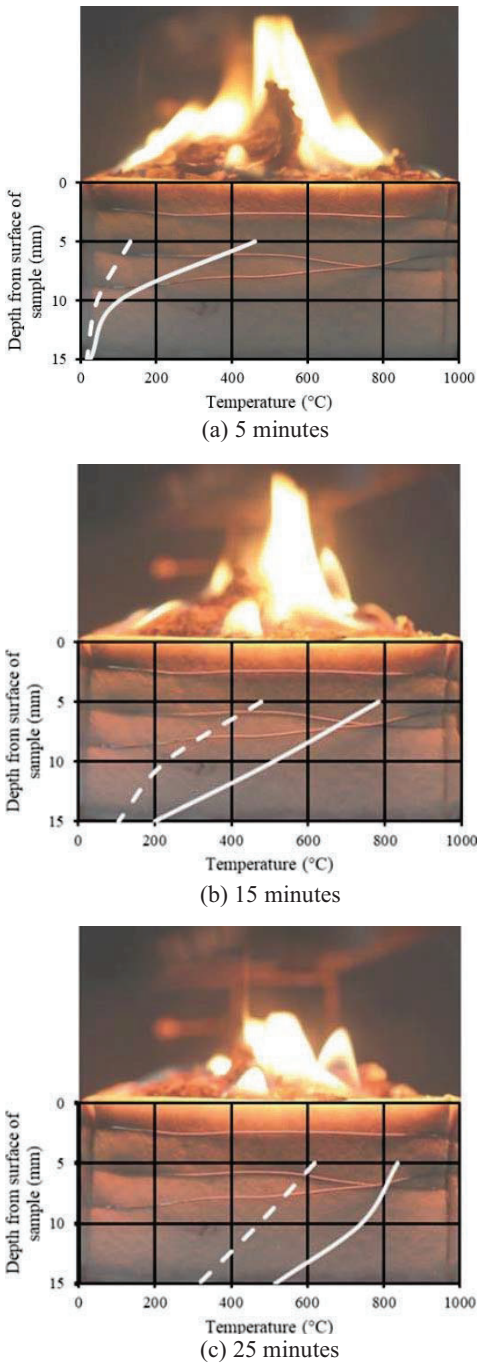

Figure 11: *Temperature distribution through the depth of samples at 60 kW/m^2. Solid line: uncoated sample. Dashed line: Coating B (Sika Pyroplast) (TCs at 5, 10, 15 mm).*

4 DISCUSSION

The data presented in the preceding sections provide insights into timber and intumescent coating response when exposed to radiant heating at small scale. The behaviours observed allow a comparison of the coatings' performance in terms of the intumescent growth phases, burning behaviour, products of combustion, thermal penetration, and char depth. These measurements allow for the evaluation of the product performance alongside

https://doi.org/10.52202/069179-0237

claims made by each product manufacturer, and hence their potential effectiveness in regard to a range of potential applications in mass timber buildings.

4.1 HEAT FLUX

All samples were tested at both 35 kW/m^2 and 60 kW/m^2 and it was confirmed – as expected – that a higher initial incident heat flux consistently resulted in earlier ignition, greater heat release rates, greater mass loss rates, acceleration of in-depth temperature increase, greater in-depth temperature, and greater final char depth. This was seen both in uncoated and coated samples (all other factors being equal).

4.2 COATING A

The data presented consistently suggests that the performance of Coating A samples resembled that of uncoated wood. It was observed that instead of the intumescent layer growing from the surface of the timber when exposed to heating, the coating peeled away to reveal the timber underneath. Albeit time to ignition was mildly extended using this coating.

It is possible that the comparative ineffectiveness of this coating has been caused by the uncontrolled moisture content of samples before application. The manufacturers 14% maximum moisture content, however, is extremely difficult to achieve for existing structural elements which the coating is advertised for, suggesting that successful protection using this intumescent would be very difficult to attain if conditioning is absolutely necessary.

4.3 COATING B

The data for Coating B confirmed that it performed as expected for a typical intumescent coating, forming a cellular char layer that extinguished flames at both heat fluxes tested. The depth of the intumescent char was the greatest of all coatings tested; this resulted in decreased HRR, MLR, flaming, in-depth temperatures, and char depth in comparison with uncoated wood.

The behaviour of this coating during testing confirms that it has beneficial impacts on the HRR and insulation of underlying timber.

The inconsistent performance of Coating B across the surface of the sample and between repeat tests may be an indication that the product protection may be prone to variation in practice. It is suggested that further repeat experiments are completed to ensure the overall performance of Coating B is quantified. Furthermore, large scale and realistic orientation tests should be completed to observe whether the variation of intumescent growth is significant over larger surface areas and whether it maintains intumescent char structure when vertical.

4.4 COATING C

Coating C was successful in reducing HRR, MLR, flaming, in-depth temperatures and char depths in comparison with uncoated wood. Moreover, Coating C samples demonstrated the least amount of flaming after the initial peak in heat release rate, and consistently gave the lowest in-depth temperatures amongst all coatings.

Early ignition in comparison to uncoated wood was observed for Coating C; however, as early ignition then promoted the rapid growth of the intumescent char layer, early ignition is not necessarily in itself a negative result in terms of fire performance. Large scale testing at various orientations is recommended to understand the consequences of ignition and flame spread over an intumescent coated surface and hence fire growth rates for timber surfaces within realistic fire compartments in buildings.

5 CONCLUSIONS

The research presented within this paper serves as a preliminary study investigating the reaction-to-fire performance of three transparent passive fire protective coatings for wood, when exposed to more severe heat flux conditions from above, with the sample in a horizontal orientation. The testing results indicate that Coating A did not swell and therefore performed similarly to that of uncoated samples. The two remaining intumescent coatings (B and C) produced multi-cellular char layers that reduced the heat release rate, mass loss rate, CO_2 concentrations, in-depth temperatures, and char depths under the experimental conditions used in the current study. The potential for these products to improve the reaction-to-fire and burning behaviour and wood is therefore promising. However, their widespread application in mass timber buildings with exposed timber surfaces requires further study to better understand the influence of e.g. scale, orientation and much higher heat fluxes seen in natural fire conditions in large timber-lined compartments [27].

Research and experimentation has highlighted the importance of a range of parameters for evaluating the effectiveness of an intumescent product for wood. Additional research is needed to determine the suitable applied surface treatments across the relevant range of fire safety strategy considerations, where they are intended to improve e.g. char rates, or be used as a justification for slower fire spread rates in large compartments. The current fire classifications of reaction to fire classification and fire resistance derived from standard tests are unlikely to be suitable for that purpose.

To accurately predict the behaviour of an intumescent in a real fire scenario, further experimentation involving the exposure of intumescent coatings to transient heat sources, (e.g., increasing heat flux, interactions within a real compartment, etc.) in a realistic orientation that accounts also for the impact of gravity (as products are usually applied to walls or ceilings) would be necessary to better represent the changing conditions.

ACKNOWLEDGEMENT

The authors gratefully acknowledge the support of the University of Edinburgh School of Engineering, Edinburgh Fire Research Centre, and the supplier of the intumescent coatings (not the manufacturer). The authors

would like to thank and acknowledge Michal Krajcovic for his technical support and advice.

REFERENCES

[1] Abed, J., Rayburg, S., Rodwell, J., Neave, M.: A Review of the Performance and Benefits of Mass Timber as an Alternative to Concrete and Steel for Improving the Sustainability of Structures. *Sustainability* 14(9): 5570, 2022.

[2] BSI: BS EN 13501-1:2018 Fire classification of construction products and building elements. Classification using data from reaction to fire tests. BSI, 2019.

[3] BSI: BS EN 13823:2020 Reaction to fire tests for building products. Building products excluding floorings exposed to the thermal attack by a single burning item. BSI, 2020.

[4] BSI: BS EN ISO 11925-2:2020 Reaction to fire tests. Ignitability of products subjected to direct impingement of flame. Single-flame source test. BSI, 2020.

[5] Puri, R.G., Khanna, A.S.: Intumescent coatings: A review on recent progress. *Journal of Coatings Technology and Research* 14(1): 1-20, 2016.

[6] Schmid, J., Barber, D., Brandon, D., Werther, N.: The Need for Common Terminology for Fire Safe Design of Timber Structures. In *12th Asia-Oceania Symposium on Fire Science and Technology*, 2021.

[7] Gerazimov, N.: The behaviour of intumescent coatings under non-standard heating conditions. The University of Edinburgh, 2020.

[8] Wladyka-Przybylak, M., Kozlowski, R.: The thermal characteristics of different intumescent coatings. *Fire and materials* 23(1): 33–43, 1999.

[9] Hao, J., Chow, W.K.: A Brief Review of Intumescent Fire Retardant Coatings. *Architectural Science Review* 46(1): 89-95, 2003.

[10] Popescu, C.M., Pfriem, A.:Treatments and modification to improve the reaction to fire of wood and wood based products – an overview. *Fire and Materials* 44(1): 100-111, 2020.

[11] Hassan, M.A., Kozlowski, R., Obidzinski, B.: New fire-protective intumescent coatings for wood. *Journal of applied polymer science* 110(1): 83-90, 2008.

[12] Bahrani, B., Hemmati, V., Zhou, A., Quarles, S.L: Effects of natural weathering on the fire properties of intumescent fire-retarding coatings. *Fire and materials* 42(4): 413-423, 2018.

[13] Hartl, A., Razzaque, Q.S., Lucherini, A., Maluk, C.: Comparative Study on the Fire Behaviour of Fire-Rated Gypsum Plasterboard vs Thin Intumescent Coatings Used in Mass Timber Structures. In *SiF 2020 The 11th International Conference on Structures in Fire*, 901– 910, 2020.

[14] Lucherini, A., Giuliani, L., Jomaas, G.: Experimental study of the performance of intumescent coatings exposed to standard and non-standard fire conditions. *Fire Safety Journal* 95:42-50, 2018.

[15] Xu, Q., Wang, Y., Chen, L., Gao, R., Li, X.: Comparative Experimental Study of Fire-Resistance Ratings of Timber Assemblies with Different Fire Protection Measures. *Advances in Structural Engineering* 19(3): 500-512, 2016.

[16] Envirograf: Intumescent paint for wood (HW system). Envirograf, 2022. Accessed via: https://envirograf.com/product/intumescent-paint-and-varnishes-for-wood-etc/.

[17] Sika: Fire Protection for Wood Skia Pyroplast Wood T with topcoat Sika Pyroplast Wood Top T New. Sika, 2022. Accessed via: https://deu.sika.com/en/49680/fire-protection/fire-protection-forwood/sika-pyroplast-woodtwithtopcoatsikapyroplastwoodtoptnew.html.

[18] Thermoguard: Fire Varnish basecoat – Thermoguard UK – Products. Thermoguard, 2022. Accessed via: https://thermoguard.co.uk/portfolio-items/fire-varnish-2k-basecoat/.

[19] BSI: BS ISO 5660-1:2015+A1:2019 Reaction-to-fire tests. Heat release, smoke pro-duction and mass loss rate. Heat release rate (cone calorimeter method) and smokeproduction rate (dynamic measurement). BSI, 2015.

[20] Li, G., Zhang, C., Lou, G., Wang, Y., Wang, L.: Assess the Fire Resistance of Intumescent Coatings by Equivalent Constrant Thermal Resistance. In *Fire Technology* 48: 529-546, 2012.

[21] Law, A., Hadden, R.: We need to talk about timber: fire safety design in tall buildings. *The Structural Engineer* (3), 2020.

[22] Zhang, M., Yu, J., Xu, X.: A new flame sheet model to reflect the influence of the oxidation of CO on the combustion of a carbon particle. *Combustion and Flame* 143(3): 150-158, 2005.

[23] Nyombi, A., Williams, M.R., Wessling, R.: Toxic emissions from smouldering combustion of woody biomass and derived char with a case study of CO build-up in an ISO container. *Energy Sources, Part A: Recovery, Utilisation, and Environmental Effects* 42(24): 2990-3007, 2020.

[24] Morrisset, D., Hadden, R.M., Bartlett, A.I., Law, A., Emberly, R.: Time dependent contribution of char oxidation and flame heat feedback on the mass loss rate of timber. *Fire Safety Journal* (120), 2021.

[25] Weisner, F., Hadden, R., Deeny, S., Bisby, L.: Structural fire engineering considerations for cross-laminated timber walls. *Construction and Building Materials* (323), 2022.

[26] Lowden, L.A., Hull, T.R.: Flammability behaviour of wood and a review of the methods for its reduction. *Fire Science Reviews* 2(4), 2013.

[27] Kotsovinos, P., Christensen, E., Rackauskaite, E., Glew, A., O'Loughlin, E., Mitchell, H., Amin, R., Robert, F., Heidari, M., Barber, D., Rein, G., Schulz, J.: Impact of ventilation on the fire dynamics of an open-plan compartment with exposed timber ceiling and columns: CodeRed #02 *Fire and Materials*: 1-28, 2022.

https://doi.org/10.52202/069179-0237

World Conference on Timber Engineering Oslo 2023

FIRE DESIGN OF GLULAM CONNECTIONS WITH TIMBER-TO-TIMBER BEARING INTERFACES

Hans-Erik Blomgren[1], David Barber[2], Graham Montgomery[3]

ABSTRACT

High-rise mass timber buildings require beam end connections to maintain the fire resistance rating of the beam. Connections where a glulam beam ends bear directly onto a supporting glulam column are commonly utilized because they reduce cost, require only simple CNC fabrication, meet the desired architectural aesthetic, and have high load carrying capacity. In addition, a properly designed bearing connection can achieve a 1hr-to-2hr fire rating. A beam to column bearing connection designed and fire tested for a high-rise building project in the United States is presented in this paper. An assessment of the bearing area required to support the load under fire conditions required detailed review of the scientific literature to understand how the thermally impacted timber ahead of the char front reduces the perpendicular-to-grain mechanical properties at the bearing interface. An estimate of the reduced perpendicular-to-grain stiffness and strength at the bearing area was used to design the connection. Two 2hr fire tests to ASTM E119 were performed to experimentally validate the design assumptions. This paper concludes with a discussion of how engineering guidance for bearing type connections exposed to fire can be further developed.

KEYWORDS: Mass Timber, Connections, Fire Engineering, Structural Engineering, Bearing Behavior, Joints, Intersections, Interfaces

1 INTRODUCTION

The construction of large-scale multi-story mass timber buildings is rapidly expanding across the world as developers, architects, and contractors become more experienced with the new construction type. To market these buildings, there is a strong desire to expose the wood surfaces as the architectural finish. Building Codes require the primary structural frame to be fire rated between 1hr and 2hr depending up on the height and floor area of the structure [1]. The principles of engineering glulam beam and column member cross-sections for fire resistance through a protective charring layer of the timber have been well established in building codes for decades [2]. However, design methods for engineering exposed glulam connections for fire are limited.

This paper provides background, analysis, fire test information and post-test assessment for the fire performance of exposed timber beam-to-column bearing connections. These designs have been employed by the authors on some of the first projects in the US that require up to a 2hr fire resistance rating (Figure 1).

Figure 1: *Washington DC - 2hr fire resistance rated building in the United States with exposed glulam beam to column bearing connections (Credit: Arup).*

2 FIRE RATED BEARING CONNECTION REQUIREMENTS

Bearing connections are commonly used in North American timber construction and many historic heavy timber buildings utilize this connection type. Traditionally, the beams bear onto the column through an external steel metal cap that provides sufficient support for the beam and direct load transfer to the column while also allowing the column load above to transfer to the

[1] Hans-Erik Blomgren, Timberlab, Seattle WA, hanserikblomgren@timberlab.com
[2] David Barber, Arup, Melbourne, david.barber@arup.com
[3] Graham Montgomery, Timberlab, Greenville SC, graham.montgomery@timberlab.com

https://doi.org/10.52202/069179-0238

column below in direct end-grain bearing at the cap plate as shown in Figures 2 and 3.

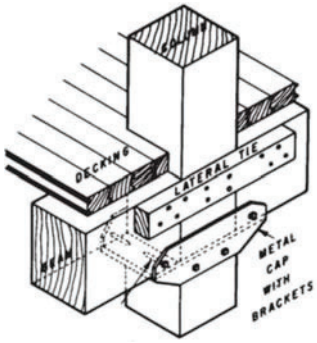

Figure 2: *Heavy Timber beam to column bearing connection with exposed metal cap plate [3].*

Figure 3: *Historic heavy timber beam to column bearing connection with exposed metal cap plate (credit: DeStefano & Chamberlain).*

In modern mass timber construction, beams commonly bear directly on cut-outs or notches in the columns with screws providing the positive fixing as shown in Figure 4. This bearing connection type is utilized because it provides the benefit of reduced cost, simple CNC fabrication, desirable aesthetic, and high load carrying capacity.

When the exposed beam and its end connection are required to have a fire-resistive rating, the use of an external cap plate connection is prohibited because the external steel parts are not protected from the fire exposure temperatures. The bearing capacity of the beam end supported on the column is determined by calculating the reduced bearing area due to char and a zero-strength layer ahead of the char front multiplied by an allowable perpendicular-to-grain bearing stress for fire exposure conditions.

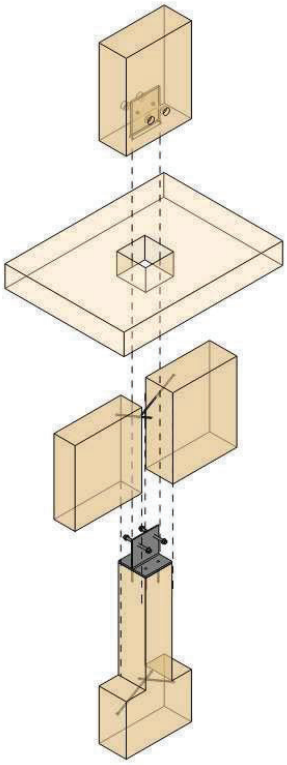

Figure 4: *Exploded view of notched column glulam beam bearing connection (credit: Timberlab).*

3 NOTCHED COLUMN BEARING CONNECTION

A glulam beam end can be designed to bear directly onto a notch fabricated into the column face as shown in Figure 4 to create an efficient connection. The glulam beam end is loaded in perpendicular to grain bearing and the column is loaded parallel to the grain at the contact surfaces. At the vertical abutted interface between the beam end and face of notched column, a small gap is detailed to allow for construction tolerances, and when required by building codes, to accommodate rotations due to the building horizontal seismic design drift [4]. These vertical end gaps are typically in the order of 2 to 6 mm. Fire protection of these interface gaps are discussed in Section 6 of this paper. Note that fire sealing of the fire rated floor assembly (typically CLT panels with a non-combustible topping) around the notched column that penetrates the floor is beyond the scope of this paper.

4 BEARING BEHAVIOR

Before investigating bearing connections under fire exposure, is it warranted to review the behavior of perpendicular-to-grain bearing for the non-fire load case. Perpendicular-to-grain bearing strength is a distinct limit state for timber design because strength is established based on a deformation (serviceability) limit and short

https://doi.org/10.52202/069179-0238

term (time-dependant) loading stress increases are not applicable.

In the United States, the nationally adopted model code is the International Building Code (IBC) [1], with the 2021 edition the current latest publication. The IBC references the National Design Specification for Wood Construction (NDS) [2] which includes the allowable stress design (ASD) values for various species and grades of timber. The perpendicular-to-grain bearing stress in the NDS is determined from ASTM D143 [5] testing that utilizes small 50mm x 50mm x 150mm clear green wood specimens subjected to compressive pressure from a 50mm x 50mm steel block on the top face and uniform support below on the full specimen surface area. The measured stress at 1mm of deformation for each specimen is measured and the resulting 5th percentile strength is calculated. To convert the tested value to the ASD reference design value, the 5th percentile value is divided by 1.5 for a factor of safety and duration of load. This value is then multiplied by a strength ratio of 1.0 and multiplied by 1.5 for and adjustment for dry use.

From time-to-time the validity of using the small-scale ASTM D143 test method for real large scale building structures has been questioned. Testing in the 1990s by Madsen [6] investigated the behavior of full-scale perpendicular-to-grain bearing of dry-use glulam members for a range of bearing plate sizes from 25mm x 25mm to 177mm x177mm. Bearing at the middle and ends of glulam were tested. Figure 5 presents a representative graph from Madsen's work for the average load-deformation relationship of a 125mm x 125mm bearing plate at the end of a dry use Douglas fir glulam beam. This graph exhibits a gradual transition or "proportional limit" between deformations of 1mm and 2mm where the deformation becomes non-linear resulting in permanent indentation (deformations) in the wood. The occurrence of this transition between 1mm and 2mm was found to be consistent across all tests performed by Madsen.

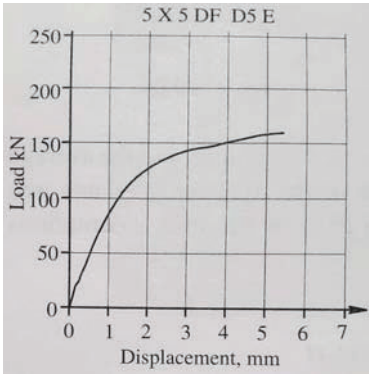

Figure 5: *Perpendicular-to-grain load-deformation plot for a 125mmx125mm plate located at the end of a Douglas Fir glulam, Madsen [6].*

Based on these tests, Madsen proposed a design method that accounted for the effects of i) bearing on the contact surface area ii) the length of bearing edge parallel to grain, and iii) the length of bearing area perpendicular to grain. When the proposed design method is applied to a large bearing plate condition (178mm x 350mm) it is shown that a 2mm indentation in the glulam (deformation) is required to attain the factored design strength calculated using the ASD reference design load multiplied by the LRFD format conversion factors documented in the NDS [2]. This example indicates there is reasonable correlation of strength and deformation between the two design methods for perpendicular-to-grain bearing on large bearing areas.

5 WOOD PROPERTIES AT ELEVATED TEMPERATURE

To properly engineer mass timber elements under the conditions of fire exposure, the change in strength and stiffness of the material as a function of temperature between ambient conditions (20C) and the char temperature (300C) must be quantified. Research in this area has been available for decades and is based on exposing wood samples to a standard fire, such as ASTM E119 [7]. For temperatures in this range, Eurocode 5 [8] provides graphs for parallel to grain tension and compression loads. The reduction of strength and stiffness is characterized by bi-linear lines that exhibit strength losses of 75% (Compression) to 35% (Tension) at 100C and then reducing linearly to zero at 300C. Where timber is heated up to 100C, the strength losses are reversible on cooling. Above 100C, the strength losses are not reversible on cooling [9].

As timber chars due to fire exposure, a thermal penetration depth beyond the char front into the depth of the wood develops. Due to this heating, a portion of the moisture present in the wood is driven ahead of the thermal wave further into the wood. The increase in moisture content and wood temperatures up to 50mm beyond the char font have been experimentally measured by several researchers [10, 11, 12] and found the heat penetration and driven moisture have a combined effect on the immediate mechanical properties of wood. Figure 6 from Schaffer's work [10] plots the temperature and moisture content as a function of the distance from the surface of the charred wood.

https://doi.org/10.52202/069179-0238

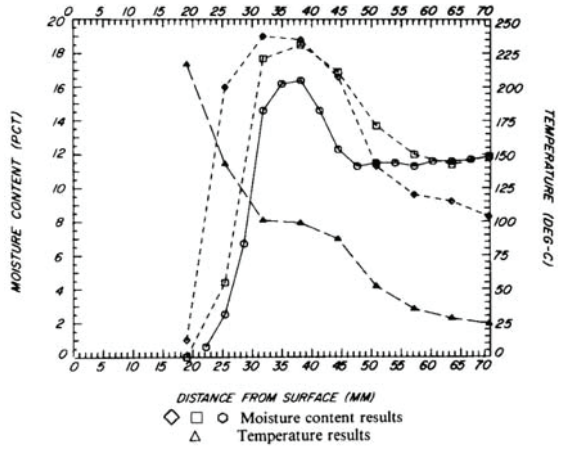

Figure 6: *Measured temperature and moisture content gradients beyond the char front for southern pine specimen with an initial MC of 10%. One face of wood exposed to 538C furnace temperatures for approximately 20mins, Schaffer [10].*

Schaffer's work [10] also experimentally measured the relative parallel-to-grain stiffness and parallel-to-grain compressive and tensile strength beyond the char front, as shown in Figure 7. The lines in this plot show the complexity of the combined effect that increasing temperatures and increasing moisture content have from 0mm to 50mm beyond the char front that need to be accounted for in the structural fire design of exposed timber members.

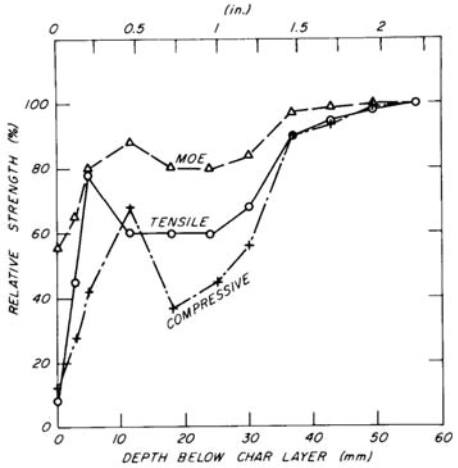

Figure 7: *Measured parallel-to-grain stiffness and compressive and tensile strength of softwood beyond the char front expressed in percent of that at 25C and initial moisture content of 12%. Schaffer [10].*

The strength reduction of wood due to fire exposure discussed so far in this section has only considered parallel-to-grain loading. For the fire design of bearing connections, the strength and stiffness reduction of wood perpendicular-to-grain at elevated temperatures needs to be quantified. The authors of this paper found limited published research on this subject. A report by Gerhards [13] provides a summary of experimental testing that studies the immediate effects on the mechanical properties of wood due to changes in moisture content and temperature. His report includes all mechanical properties for wood including perpendicular-to-grain compressive loading. Gerhards' summary shows that for a relative change in temperature from 20C to 70C the compressive stiffness and strength perpendicular-to-grain decreases by approximately 35%. This reduction is reported at an MC greater than 10% with the trend being clear that a higher MC in combination with higher temperatures increase the reduction in strength and stiffness.

It is noted that Gerhards' report is limited to maximum wood temperatures of 70C creating a gap in knowledge about the mechanical properties of wood in compression perpendicular-to-grain at temperatures from 70C leading up to the 300C char front where strength diminishes to zero. Limited experimental testing on full scale perpendicular-to-grain bearing interface connections have reported large and rapid loss of strength and stiffness due to fire exposure. The publication by Buchanan and Ostman [14] provides a short discussion and photos showing large permanent perpendicular-to-grain deformations in the high stress contact area of test specimens that were dissected after fire testing.

6 JOINTS AND INTERSECTIONS

Notched bearing connection fire performance needs to consider both the horizontal and vertical joints between the beam and column. Figure 8 shows this typical condition where the column is notched on two faces to support beams framing in from each side. The remaining center portion of the column penetrates the CLT floor to support the column above in end-grain bearing. Both of these joints are discussed in the following sections.

Figure 8 *Photo of a beam to notched column bearing connection. This connection creates a horizontal bearing interface and vertical joint at the abutted members (credit: Timberlab).*

https://doi.org/10.52202/069179-0238

6.1 Fire protection of the Vertical Joint

The vertical timber joint requires a gap to be detailed to account, at a minimum, for fabrication and installation tolerances. Using state-of-the-art CNC equipment, a 2mm gap for tolerances is typically found to be satisfactory. For buildings in high seismic regions of the US, the IBC reference standards require the non-participating gravity system to accommodate seismic design story drifts [4]. This results in cyclic beam-column joint rotation deformations being imposed on the connection which means a larger vertical joint gap may be required. As well, wood shrinkage during the building operational life can also result in gaps forming.

IBC requirements for fire protection of timber-timber gaps such as this have only recently begun to be developed. In the US, the Fire Design Specification (FDS) [15] states that all gaps from 0mm up to 3mm have to account for char penetration into the joint that is 2 times the nominal char rate of timber. For gaps larger than 3mm, the FDS states surfaces within the gap are assumed to be fully exposed to fire for the full depth of the gap.

From a connection design standpoint, advanced charring into the vertical gap has to be prevented as any charring in this area rapidly reduces the beam bearing area and thus the load bearing capacity of the connection. As well the cross-section area of the notched portion of the column supporting floor loads from above is reduced. To address this problem, engineers in the US have begun to use intumescent fire tape products that are concealed in the depth of the vertical gap as shown in Figure 9.

Figure 9: *Photo of a glulam beam end with fire tape seal applied in a vertical joint before it is installed onto a supporting glulam column (credit: Blomgren)*

Under fire exposure and temperatures in the order of 200C, the intumescent tape activates and expands across the joint providing an effective and durable seal that slows or prevents fire penetration into the joint that is greater than the advancing char depth of the parent timber material. Manufacturers of these tape products have begun to demonstrate the fire protection performance of these products for these applications by testing to ASTM E1966 [16].

6.2 Fire Protection of the Horizontal Bearing Interface

The bottom of the beam delivers its load in perpendicular-to-grain bearing to the end grain of the supporting column. This interface is in compression and assuming accurate fabrication tolerances, the load is applied as a uniform pressure across the full bearing area. To confirm char penetration into this interface does not occur which would severely undermine the bearing capacity of the connection, the American Wood Council (AWC) managed a testing program of these loaded connection types exposed to ASTM E119 furnace temperatures. The testing applied a relatively low pressure to the bearing interface to represent a lower bound lightly loaded beam connection. The AWC reported that thermocouple data from these tests found no advanced char line penetration into the compression bearing joint [17].

7 ENGINEERING CALCULATION

For a 2hr fire rated mass timber building on the east coast of the US, the authors of this paper, designed and fire tested a large timber beam-to-column bearing connection. To efficiently support the beam end loads to the column, they are directly seated onto the column, with each incoming beam end sharing one-half of the column end area. To support the column load from above in end-grain bearing, a steel post with end plates is located within the timber beam depth. Small notches are formed in each abutted beam end to provide space for the post. Photos of the connection specimen being assembled at the testing laboratory are shown in Figure 10. The joint at the vertically abutted beam ends are protected with fire tape as shown above in Figure 9.

Figure 10: *Photos of the test specimen glulam beam ends to column support test specimen being assembled. A steel post to support the column above was included to replicate the actual project detail (credit: Blomgren).*

https://doi.org/10.52202/069179-0238

The design of a bearing connection is a very simple calculation where the applied bearing pressure is compared to the design bearing resistance pressure that includes an appropriate safety factor. However, for a fire condition, design guidance for the engineer is lacking. To design the first test the authors referenced the NDS [2] for timber that states the char depth at 2hrs of fire exposure is 66mm. Following with the NDS provisions, an effective char depth was determined by increasing the char depth by 20% to 79mm to account for the pyrolysis zone and zero strength layer for parallel to grain loading (i.e. bending, axial tension, and axial compression). Charring was assumed to occur on the three faces of the column under the supported beam end, and concurrently the three faces of the beam. This results in a 66% reduction in bearing area as shown in Figure 11. For this design the steel post and base plate were detailed with a minimum wood cover of 89mm which provides sufficient thermal protection for 2hr.

Continuing with the design, the published allowable perpendicular to grain bearing stress for the glulam product used is 4.13MPa. For fire conditions the NDS [2] allows allowable stresses to be increased to account for short term loading and adjusting the 5th percentile strength to an estimated mean strength. Using this method, the perpendicular-to-grain bearing stress increase adjustment for fire design was calculated to be 1.67 x 4.13=6.9MPa.

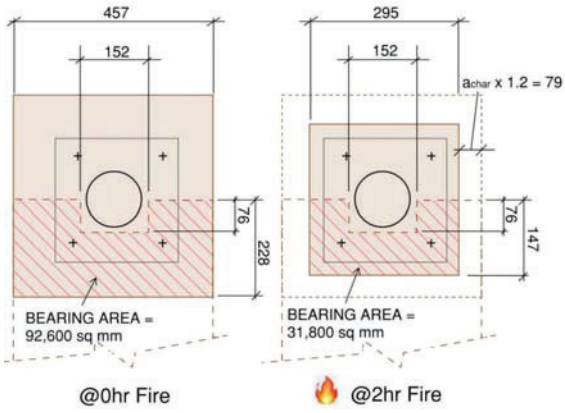

Figure 11: *The calculated bearing area for Test 1 at zero hour and 2hr.*

With the bearing stress design values and bearing area areas calculated, it is evident the fire condition at 2hrs controls the design by limiting the maximum allowable beam end reaction to 6.9MPa x 31,800mm^2 = 219kN.

8 ASTM E119 FIRE TESTING

8.1 Test 1

To justify the use of an exposed 2hr fire rated timber bearing connection for the building project, the mass timber supplier chose to perform full scale testing in general accordance with the ASTM E119 fire test standard. Testing is a specific code compliance pathway provided in the 2021 IBC [1] that has adopted new provisions for mass timber high-rise buildings. Project-specific testing was chosen, rather than analysis methods, due to the lack of existing testing data to justify the timber-timber bearing connection design under large loads. Building permit approvals were also more straightforward and efficient with a successful fire test rather than an analysis approach. It should be noted that ASTM E119 does not have a specific section in the standard for the fire testing of connections. The methodology for testing a connection was therefore based on an approach consistent with the standard, based on advice from the testing facility and consistent with other full-scale fire tested connections (timber and steel).

The specimen was constructed and inserted into a self-reacting test frame with an actuator capable of applying a maximum 204kN load to the specimen as shown in Figure 12. The specimen was carefully designed and detailed to ensure the actuator load imposed compressive forces on the beam to column interface with no secondary load paths. To accomplish this, the CLT panel that forms the lid of the furnace was split into two parts with a shearing joint located over the end of the beam. In addition, the CLT perimeter was supported on the four edges of the furnace with multiply layers of compressible ceramic blankets.

Figure 12: *Glulam bearing connection specimen and test frame prior to being lifted and placed in the furnace (credit: Blomgren).*

Testing commenced by applying a 204kN load to the specimen. An immediate actuator extension of 8mm was measured which can be attributed to elastic compression of the specimen through the CLT and beam depth and some flex in the test frame itself. This measurement was zeroed out and the furnace was ignited. The deformation

https://doi.org/10.52202/069179-0238

grew slowly measuring 10mm at the 60min mark. Soon after this time, the deformation increased exponentially resulting in failure at 86min which was only 72% of the calculated 2hr fire resistance time discussed in Section 7. The actuator extension curve for the test is provided in Figure 13. At the final moment before the actuator force reduced to zero, the recorded actuator extension was 60mm. The actuator briefly extended up to 105mm due to the failed beam end sliding off the supporting column before the test was terminated.

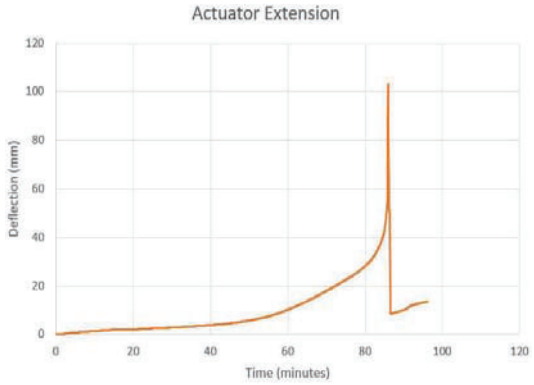

Figure 13: *Plot of the actuator extension vs. time for Test 1 showing test specimen failure at 86m.*

Although the results of the ASTM E119 fire test did not correlate well with the calculated prediction, it did provide a time-to-failure test to learn from. After the test, the data was reviewed, the disassembled specimen was visually observed, and other possible factors that may have caused the early failure time were investigated. After this effort, it was concluded the most likely cause of early failure was due to elevated temperatures in the bearing region that softened and weakened the wood more than anticipated resulting in excessive deformations and loss of strength allowing the beam end to slide off the column support. This result indicated that the 1.2x factor applied to the 2hr char depth to determine the effective bearing area in the engineering calculation discussed in Section 7 was unconservative.

At 86min of ASTM E119 fire exposure the calculated char depth per NDS [2] is 51mm. Using this char depth and the allowable fire design bearing pressure of 6.9MPa and bearing area of 31,800mm^2 derived in Section 7, an approximate 1.5x "zero strength layer" adjustment factor was back calculated.

8.2 Test 2

A second specimen was designed and ASTM E119 fire tested to 2hrs. To successfully pass this test the compression bearing area was increased by using a larger supporting glulam column. However, due to project design constraints on glulam member cross-section sizes, it was not possible to increase the bearing area by the full 1.5x adjustment factor determined from the Test 1 results. Only one edge of the column bearing length was increased from 228mm to 254mm. To account for this, the strength and stiffness of the bearing interface connection was supplemented with fully threaded compression reinforcing screws. Seven screws were installed into the underside of the beam with their countersunk heads installed flush and bearing over the bottom steel post base plate. The location of the screws in the connection area had sufficient wood cover to be thermally protected for the 2hr fire exposure as shown in Figure 14.

At a 2hr fire exposure, the screws were calculated to provide 76kN of supplemental ultimate bearing strength while the strength of the bearing area using a 1.5x adjustment factor was calculated to be 128kN. The resulting total calculated bearing capacity was 204kN. The calculated reduction in bearing area at 2hrs was 74% as show in in Figure 14.

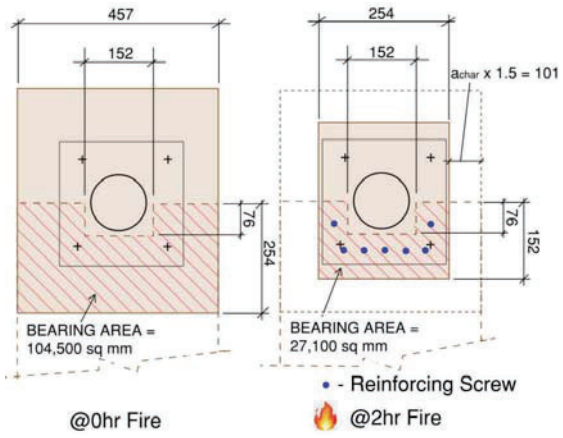

Figure 14: *The calculated bearing area for Test 2 at zero hour and 2hr using a 1.5x adjustment factor on achar.*

The Test 2 specimen successfully carried the applied 204kN actuator load for 2hrs. It is of note that in the last minutes of the test, the actuator extension increased exponentially from 10mm to 35mm indicating the connection was very close to its failure time. The actuator extension curve for Test 2 is provided in Figure 15.

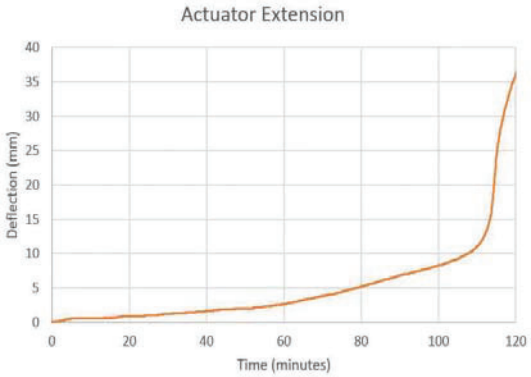

Figure 15: *Plot of the actuator extension vs. time for Test 2. The test was terminated at 120m.*

Figures 16 and 17 show the post-fire test disassembled beam exhibited significant perpendicular-to-grain crushing localized in the high bearing stress contact area. As well, the compression screws were observed to be permanently pushed into beam, providing visual evidence they supported load during the test.

Figure 16: *The disassembled specimen beam bearing area for Test 2. Note the localized permanent compressed wood at the high contact stress region (credit: Blomgren).*

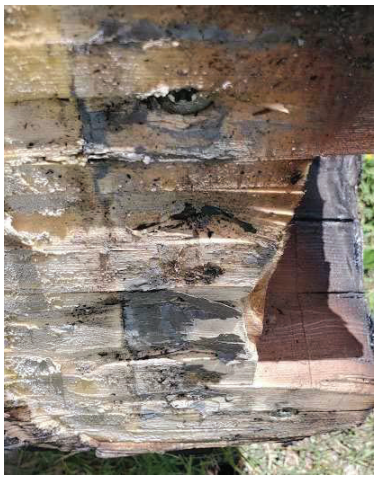

Figure 17: *A close up photo of the Test 2 beam bearing face shows the compression screw heads are permanently pushed into the wood surface (credit: Blomgren).*

9 CONCLUSIONS

Perpendicular-to-grain bearing for glulam beam-to-column connections are an efficient design option for building projects. To achieve a fire resistance rating through charring of the timber members, the bearing area needs to consider the reduced mechanical properties of the timber ahead of the char layer due to elevated temperature and moisture content and detail for construction tolerance gaps at the abutted surfaces. The fire testing in this paper has shown that engineering methods and guidance needs to be improved. A summary of observations and findings from this paper are as follows:

- ASTM D143 test methods and the testing by Madsen for non-fire conditions show that perpendicular-to-grain bearing strength of timber has a consistent transition or "proportional limit" between 1-2mm of indentation of the wood. For fire design, it is generally accepted that serviceability (deformation) limits states are not of concern. The fire tests presented in this paper measured deformations at time of failure that were an order of magnitude larger than for non-fire design conditions.
- Schaffer's research presented in Figure 6 shows temperatures up to 100C for a distance into the timber that is approximately equal to the char depth, when timber members are exposed to a fire temperatures such as ASTM E119. In the same region, the moisture content of the timber can also increase by 1.3x to 2x. Figure 7 from Shaffer's research shows the reduction in parallel-to-grain mechanical properties attributed to these effects.
- The summary report by Gerhards reported middle-trend immediate strength and stiffness loss for compression perpendicular-to-grain as high as 35% at 70C and MC>12%. These reductions are higher than those reported for parallel-to-grain and bending properties. There is a gap in the literature for perpendicular-to-grain mechanical properties greater than 70C.
- Joints and intersections need to be appropriately detailed with gaps to account for installation tolerances, shrinkage, and potentially rotation capacity of the connection due to design seismic drifts. Vertical abutted edges require fire protection products, such as intumescent fire tape to ensure the timber surfaces in the joint are not subject to charring.
- CNC fabrication and construction practices for the horizontal interface needs to assure uniform bearing of this joint. Testing performed by the American Wood Council and the testing presented in this paper found no evidence of accelerated charring at the bearing interface.
- Based on the testing presented in this paper, a 1.2x factor applied to the char depth for bearing strength calculations did not correlate well with Test 1 which failed at 72% of the targeted 2hr mark. Using the results of Test 1, it is possible to back calculate an approximate 1.5x adjustment factor applied to the char depth which correlates with the test outcome. This 1.5x factor has been adopted in the 2022 edition of the FDS for the design of bearing interfaces.
- Test 2 was redesigned based on the results of Test 1. Due to member size constraints for the building project a sufficient bearing area using the 1.5x factor could not be achieved. To provide supplemental connection strength and stiffness, fully threaded compression screws

https://doi.org/10.52202/069179-0238

were installed into the bottom of the supported beam over a steel post base plate. Test 2 successfully passed the ASTM E119 exposure by supporting the applied actuator load for 2hrs.

Engineering a mass timber bearing connection for fire resistance is more complex than just calculating a simple area of bearing based on ambient temperature strength. The area of weakened timber behind the char layer needs to also be addressed, given the reduced strength. A design approach has been recommended within this paper to address the fundamental issues.

REFERENCES

[1] International Buiding Code: International Code Council, Washington, DC, 2021.

[2] National Design Specification for Wood Construction, American Wood Council: American Wood Council, Leesburgh, VA, 2018.

[3] American Wood Council: Heavy Timber Construction, Wood Construction Data 5, Leesburgh, VA, 2003.

[4] American Society of Civil Engineers 7: Minimum Design Loads and Associated Criteria for Buildings and Other Structures, Reston, VA, 2022.

[5] ASTM D143: Standard Test Methods for Small Clear Specimens of Timber, West Conshohocken, PA, USA, 2022.

[6] Madsen B.: Behavior of Timber Connections, Timber Engineering Ltd., British Columbia, Canada, p. 139-157, 2000.

[7] ASTM E119: Standard Test Methods for Fire Tests of Building Construction and Materials, West Conshohocken, PA, USA, 2020.

[8] EN 1995-1-2 Eurocode 5: Design of timber structures - Part 1-2 - General - Structural Fire Design, European Committee for Standardization, Brussels, Belgium, 2004.

[9] Forest Products Laboratory: Wood Handbook—Wood as an Engineering Material. Gen. Tech. Rep. FPL–GTR–113. Madison, WI: U.S. Department of Agriculture, Forest Service, Forest Products Laboratory. 463 p. 1999.

[10] Schaffer E.L.: Structural Fire Design: Wood, Research Paper FPL 450, U.S. Department of Agriculture, Forest Service, Forest Products Laboratory, 1984.

[11] Frangi A., Fontana M.: Charring Rates and Temperature Profiles of Wood Sections, Fire and Materials, 27, pp. 91–102, 2003.

[12] Janssens M., White R.: Short Communication: Temperature Profiles in Wood Members Exposed to Fire, Fire and Materials, 18, p. 263, 1994.

[13] Gerhards C.C.: Effect of Moisture Content and Temperature on the Mechanical Properties of Wood: An Analysis of Immediate Effects, Wood and Fiber, V.14(1), January 1982.

[14] Buchanan A., Ostman B.: Fire Safe Use of Wood in Buildings - Global Design Guide, CRC Press, Boca Raton FL, p. 293-294, 2022.

[15] Fire Design Specification for Wood Construction: American Wood Council, Leesburgh, VA, 2022.

[16] ASTM E1966: Standard Test Method for Fire-Resistive Joint Systems, West Conshohocken, PA, USA, 2015(2019).

[17] Nyseth D.S., Smart, J.: Anatomy of a Mass Timber Bearing Intersection, Structure Magazine, October 2021.

World Conference on Timber Engineering Oslo 2023

FIRE RESISTANCE TESTING OF CLT-CONCRETE COMPOSITE FLOOR SLABS WITH STRIP NOTCH SHEAR CONNECTIONS

Javad Tashakori [1], Osama (Sam) Salem [2]

ABSTRACT: The latest edition of the National Building Code of Canada (NBCC 2020) permits wood products to be used as the primary material in constructing up to twelve-story buildings. This results in an enduring increase in the application of mass timber sections, such as glued-laminated timber (glulam) and cross-laminated timber (CLT). Timber floors in such tall mass timber buildings can be even more robust and span longer by adding a top concrete layer to allow the formation of timber-concrete composite (TCC) floor systems when adequate shear connectors are utilized. In TCC systems, notch connections can allow a gap between the timber and the concrete top layer to have a better floor system in terms of cost saving and acoustic characteristics.

This paper presents the experimental results of two full-size TCC floor slabs that have been examined under service load and standard fire exposure. Each test assembly had a 5300 mm total length with a 5000 mm clear span and 900 mm width. The composite sections were formed of a 5-ply CLT panel of 143 mm thickness and a 65-mm thick concrete layer on a 25-mm thick insulation layer. In those two fire tests, the performance of CLT-concrete composite slabs was achieved due to the nearly full composite action between the CLT panel and the concrete top layer, resulting from the utilization of 150-mm wide rectangular strip notch shear connections. Test results show that the failure of the composite slabs under standard fire exposure depends mainly on the reduction of the CLT section due to charring. However, due to the activation of the composite action, both composite floor slabs sustained the applied service loads for the 90 min duration of standard fire exposure. However, a whole-wide strip notch connection needs to be designed carefully to achieve acceptable fire resistance based on available design equations. In addition, having a whole-wide notch connection would influence the initial deflections of the supporting CLT panels while poured concrete is still wet if no shoring is provided in the middle of the slabs. Thus, to avoid excessive initial mid-span deflections and to meet the design serviceability requirements, intermediate support needs to be provided until concrete is hardened.

KEYWORDS: Timber-concrete composite sections, CLT panels, Strip notch shear connections, Fire performance

1 INTRODUCTION

Advantageously, engineered wood products, such as glued-laminated timber (glulam) sections and cross-laminated timber (CLT), have been utilized in tall wood building construction since they have less carbon footprint and construction costs than concrete and steel materials. Moreover, since mass timber panels, such as CLT panels, have high tensile strength and sufficient fire resistance, to be utilized in TCC floor systems, it is more likely that they provide flexural strength and stiffness comparable to concrete floor slabs. The current edition of the National Building Code of Canada (NBCC 2020) [1] permits wood products to be used as the primary material in constructing up to twelve-story buildings. This results in an enduring increase in the application of mass timber sections, such as glulam for beams and columns and CLT for walls and floors. Over the past few years, mass timber construction has been assembling momentum in North America since wood is an environmentally friendly and sustainable material with lower construction costs.

The CLT panels with structural polyurethane (PUR) adhesive conforming to ANSI/APA PRG 320 (up to its 2012 edition) were tested in several furnace experimental studies with the FPInnovations research programs [1-4]. Based on the outcomes of those studies, there has been one common observation, which is the falling of localized piece of the charred layers when the CLT lamination interface temperature reached 115 to 250 ºC. This phenomenon led the second and subsequent delamination to start earlier, which also was more pronounced for

[1] Javad Tashakori, Ph.D. Candidate, Dept. of Civil Engineering, Lakehead University, Ontario, Canada, jtashako@lakeheadu.ca
[2] Sam Salem, Professor and Chair, Dept. of Civil Engineering, Lakehead University, Ontario, Canada, sam.salem@lakeheadu.ca

https://doi.org/10.52202/069179-0239

thinner lamination. It is claimed that if it was desirable for greater fire resistance for CLT slabs, there should be no adhesive melting up to 300 ºC [5]. However, it was not a compulsory requirement for CLT manufacturers, that CLT products under fire conditions should be able to reach this temperature at the glue line without excessive delamination until the 2017 edition of ANSI/APA-PRG-320 [6] has been published.

TTC systems includes timber components which can be made of solid, glulam, laminated-veneer lumber (LVL), or CLT sections that are supporting and connected to a topping concrete layer (usually around 70 mm in thickness) utilizing a wide range of shear connectors. TCC floor systems own the advantageous characteristics of both materials (i.e., timber and concrete) if their shear connections are robust enough under service and ultimate design limits. In TCC sections, timber is used as the primary tensile load-carrying material due to its high strength-to-weight ratio. In contrast, concrete is used for its high compressive strength and advantages in terms of stiffness and acoustic characteristics.

The primary technique to provide a sufficient shear connection between the timber section and concrete layer in TCC sections is to use shear connections that come in various metal connectors, grooved connections, or adhesive connections. They include mechanical fasteners such as nails, screws, toothed metal plates, glued-in steel plates embedded into the timber, and notches cut from the timber or a combination of them. In order to estimate the composite strength of a TCC system with a well-recognized shear connection (stiffness and strength), Annex B of Eurocode 5 [7] provides the mechanically jointed beam theory (gamma method). In this method, a uniform distribution of shear connectors along the span of the floor is considered. Moreover, the flexural stiffness of both materials and the shear stiffness of the connection provides the composite flexural stiffness as well as the amount of axial and moment demands imposed on each material in such composite action.

The mechanical characteristics of various fasteners and connectors used for timber-to-timber joints are provided in Eurocode 5 [7]. Also, as far as the connection stiffness is concerned, for steel-to-timber or concrete-to-timber connections, the timber-to-timber joint stiffness might be multiplied by a magnifying factor. Salem and Virdi [8] experimented inclined self-tapping screw (STS) connections of CLT-concrete composite section through push-out direct shear tests. Tests results show that the stiffness of their STS shear connections was almost the same as that provided by Eurocode 5 [7].

As for determining the stiffness of notch connections, there has been no available analytical method so far and thus, only experimental evidences are used to predict its stiffness, otherwise the γ method strength predictions would not be accurate enough.

While the design of TCC sections with various mechanical shear connectors is well addressed in different design codes in the EU, there are no provisions in the current Canadian *Engineering design in wood* standard [9]. The only design guide that recently became available in Canada is the Design Guide for Timber-Concrete Composite Floors in Canada [10], which guides the design of TCC systems in ambient and fire conditions. Although several research studies were conducted to investigate the mechanical characteristics and structural behaviour of TCC floor systems under service and ultimate limit state conditions, there are still several uncertainties related to the influence of elevated temperatures on their structural fire performance. In general, TCC sections possess considerable fire resistance due to the large size of the timber cross-sections utilized in them; however, the type and design of the shear connectors in use significantly impact the actual behaviour of those composite systems when subjected to fire.

Van der Linden [11] introduced a relationship based on differential equations to define the more efficient composite action in which designers could avoid too thin concrete topping layer attached to mass timber beams and vice versa. In other words, an efficient composite action would be achieved with a concrete layer thickness that is more than 70 mm, which is common in construction. That ends up using a thicker concrete layer, which makes a TCC floor uneconomical. However, if there is a gap between the concrete top layer and the timber supporting component underneath, this would allow not only stiffer TCC sections but also economical floor systems. However, the fastener stiffness should be decreased by 25, 44 and 50% for gap/d ratio of 2, 3, and 4, respectively [12], where d is the diameter of the fastener based on Table 7.1 of Eurocode 5 CEN [7]. Therefore, it is significantly likely that a notch connection could accommodate this gap if the shear area of concrete at the notch is able to sufficiently transfer the shear forces at the interface between the concrete top layer and the supporting timber component with the existing constructional gap.

This paper presents the experimental results of two full-size, one-way TCC floor slabs that have been examined under service load and standard fire exposure. In the two fire resistance tests conducted as part of this current study, the performance of CLT-concrete composite floor slabs was achieved due to the nearly full composite action between the CLT panel and the concrete top layer resulting from the utilization of 150-mm wide rectangular strip notch shear connections with 25-mm thick gap in between the two materials to provide a more economical TCC floor system yet having considerable strength and stiffness.

2 EXPERIMENTAL PROGRAM

The main objective of the full-size testing of flexural TCC floor slab presented in this paper was to assess the performance of strip notch connections as they could accommodate the gap between the concrete top layer and the supporting CLT panel. Moreover, most tests done on

CLT-concrete composite systems experienced excessive ply fall off due to adhesive melting under fire conditions, while it is now an obligation requirement for CLT manufacturers to produce CLT panels that should be able to reach charring temperature without excessive delamination [6].

Therefore, designers might be able to have a low charring rate of 0.65 mm/min throughout the entire fire exposure time instead of the current design procedure assumption of 0.8 mm/min charring rate after the first major ply has burnt out. This assumption was based on ply fall-off phenomena which used to happen for CLT with polyurethane (PUR) adhesive in the past. The CLT panels utilized in the test specimens of this study were produced by Nordic Structures with the industrial name of Nordic X-Lam. This product is certified by APA (Product Report PR-L306C) per ANSI/APA PRG 320 standard [6].

2.1 TEST SPECIMENS DETAILS AND FABRICATION PROCESS

The fabrication of the two full-size TCC floor assemblies and their fire endurance testing were carried out at Lakehead University Fire Testing and Research Laboratory (LUFTRL). Each test assembly had a 5300 mm total length with a 5000 mm clear span and 900 mm width. The composite sections were formed of a 5-ply CLT panel of 143 mm thickness and a 65-mm thick concrete layer on a 25-mm thick insulation layer. The CLT panel in each test specimen was prepared with six rectangular strip notches each aligned in the transverse direction along the entire width of the panel, Figure 1. The insulation layer was deliberately added to enhance the flexural stiffness and the acoustic characteristics of the TCC floor assemblies and to maintain a reasonable cross-sectional moment of inertia with less weight, Figure 1.

The CLT panels utilized in fabricating the TCC floor assemblies tested in this study were Nordic X-lam cross-laminated timber that is certified E1 CLT stress grade, using 1950 Fb-1.7E Spruce-Pine-fir (S-P-F) MSR lumber in the longitudinal layers and No. 3/Stud S-P-F lumber in the transverse layers. This product is certified by APA (Product Report PR-L306C) per ANSI/APA PRG 320 standard [6] and shall be used in dry service conditions. As per the data published by Nordic Structures, the carbon balance is approximately -590.97 CO_2 of one cubic meter of Nordic X-Lam [13]. The concrete poured for the topping layer had a 28-day strength of 43 MPa and its strength on the fire test day was 46 MPa. Four 12-mm diameter lag screws were installed along each strip notch to allow more ductile performance for the TCC floor slabs in the ambient ultimate state.

The strip notch connections are normally strong enough connections to be implemented just at the far ends of a TCC element. However, such approach might not offer sufficient strength nor stiffness required for the fire resistance design based on the reduction of the structural integrity because of the cross-section loss due to charring. Therefore, with 800 mm spacing between the strip notches prepared in the CLT panels, there were six strip notches along the longitudinal direction of the floor slab to provide sufficient structural integrity during fire exposure, Figure 1. As far as the concrete depth along the span is concerned, in the three middle panels, a 65-mm thick concrete layer on top of a 25-mm thick insulation layer was considered to have sufficient composite action behaviour. However, in the two end panels from each end of the slab specimens, a full thickness (90 mm) of the concrete layer was cast to avoid any shear failure that could happened near the ends of the floor test specimens not during the fire tests but when the burned specimens are removed out of the furnace after fire testing, Figure 1.

2.2 TEST SETUP

Test specimens were loaded under four-point flexure bending using a steel spreader beam connected to the piston of a hydraulic cylinder that is attached above the furnace to the steel loading framed structure that is also supporting the fire testing furnace, as shown in Figure 1.

The load applied on each test specimen throughout the fire test consisted of 2.4 kPa dead load including self-weight and additional 2.4 kPa accounting for service live load. These loads were applied to the floor specimen at least 30 mins before the fire test started in conform to CAN/ULC-S101 [14]. Afterwards, the applied load was maintained constant throughout the entire duration of the fire test.

The vertical deflections of the test specimens were measured using draw-wire displacement transducers installed at three different locations along the length of the floor slabs: the midspan and under each point load (1667 mm apart and cantered along the specimen span).

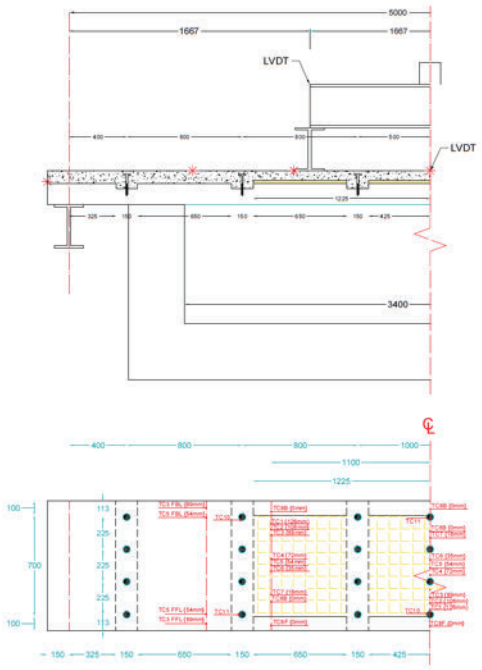

Figure 1: *A general test setup with a typical TCC floor test assembly with strip notch connections and thermocouples layout*

https://doi.org/10.52202/069179-0239

Each floor assembly was instrumented with 45 Type-K thermocouples that were inserted from the top inside pre-drilled tight holes with various depths into the CLT panels. A few thermocouples were placed at the interface between the CLT plys and at the mid-thickness of each ply. Other thermocouples were located at the interface between the concrete top layer and the CLT panel and at the coach screws. Figure 2 illustrates the distribution of thermocouples around one of the strip notches.

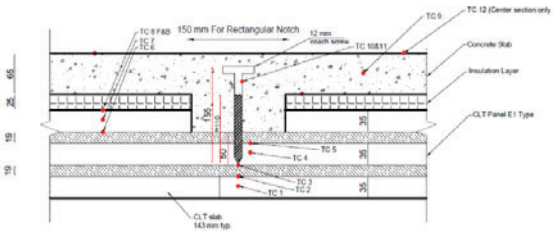

Figure 2: *Distribution of thermocouples around one of the strip notches*

3 DESIGN PROCEDURE

The current design method of timber structures is based on the limit states design (LSD) philosophy in Canada. It takes three design categories into account: Serviceability Limit States (SLS), Ultimate Limit States (ULS), and Fire resistance conditions. The serviceability limit states intend to guarantee the structural components be capable of sustaining the applied loads without any significant defects and/or service disruptions, including excessive deflection, vibration, permanent deformation, and local structural damage such as cracking [15].

3.1 NOTCH CONNECTION DESIGN

Design Guide of Timber Composite Floors in Canada [10] provides concrete crushing and shear failure strength capacity by Equations (1) and (2). These equations are much more conservative than their counterparts in the design guideline provided by Yeoh et al. [16]. Therefore, several strip notch connections need to be designed and implemented along the span of the TCC floor slabs tested in this study to achieve the targeted 2-hour fire resistance. However, cutting into the entire thickness of the utmost longitudinal ply of the CLT panel in the direction of major strength axis to accommodate the strip notch depth can reduce the overall flexural strength of the TCC section in fire conditions once the natural axis of the composite section escalates up and be relocated within the thickness of the concrete top layer. In addition, having a whole-wide notch connection would influence the initial deflections of the supporting CLT panels while poured concrete is still wet if no shoring is provided in the middle of the slabs. Thus, to avoid excessive initial mid-span deflections and to meet the design serviceability requirements, intermediate support needs to be provided until concrete is hardened. Alternatively, two-stage concrete casting procedure shall be followed. First, concrete shall be poured in the strip notch grooves prepared in the CLT panel until it reaches certain strength with rough surface condition and then, concrete could be poured over the entire floor CLT slab as a second stage.

$$V_{\mathrm{r,\,Conc.\ Comp.}} = \alpha_1 \phi_c f'_c d_n b_n, \quad \alpha_1 = 0.85 - .0015 f'_c \tag{1}$$

$$V_{\mathrm{r,\,Conc.\ Shear}} = 0.8P_{r,w} + 2.76\phi_c b_n(2d_n \tan(\theta) + L_n) \leq 0.5\phi_c f'_c b_n(2d_n \tan(\theta) + L_n) \tag{2}$$

Where, d_n is notch depth, b_n is notch width, $P_{r,w}$ is lag screw withdrawal resistance, L_n is notch length, and ϕ_c is the concrete resistance factor, Figure 3.

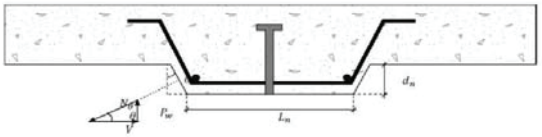

Figure 3: *Force equilibrium at notch connection*

3.2 ELASTIC DESIGN METHOD (γ-method)

As the shear connection performance determines the degree of composite action in a TCC floor systems, such sections shall be designed with this consideration whether the connection yielded before reaching the ultimate limit state condition or not. The γ method can predict the behaviour of TCC floor systems as long as the behaviour of the shear connection is still within the elastic region, such as those utilized nails, HBV steel plates, and notches. Alternatively, the Design Guide for Timber-Concrete Composite Floors in Canada [10] provides an elasto-plastic model (EPM) to capture the behaviour of TCC floor systems at the ultimate state limit with shear connections that can even sustain plastic deformations. However, since notch shear connections normally exhibit elastic behaviour, the γ method is accurate enough to estimate the flexural strength of TCC systems with strip notch shear connections.

4 RESULTS AND DISCUSSION

4.1 DEFLECTIONS

Figures 4 and 5 show the time-deflection curves developed based on deflection values measured at the midspan and left-side loading point for both floor assemblies, Slab 1 and Slab 2, respectively. Due to electronic malfunction in one of the displacement transducers, the floor deflections at the right-side loading point were not recorded. According to the presented time-deflection curves, both slabs experienced gradual increase in their vertical deflection until approximately 25 mins into the fire tests with a slop that is slightly higher than that experienced by both slabs for the next 25 mins (25 to 50 mins into the fire tests). It is worth mentioning that at 25 mins into the fire tests less than half the thickness of the first ply charred in both slabs according to the thermal measurements obtained. While at 50 mins into the fire tests the entire thickness of the first ply charred, which can

https://doi.org/10.52202/069179-0239

be correlated to the bounce back of higher slops exhibited by the time-deflection curves started at that time mark. Both slabs maintained that relatively linearly increased slop until almost the end of the fire tests when both tests were deliberately terminated a few mins after surpassing the targeted 90 mins fire resistance time mark.

At the termination time of the first tests (90 mins), the mid-span recorded deflections were 35 and 30 mm in Slab 1 and Slab 2, respectively, including the initial deflections due to the pilot loading applied before the start of the fire tests, Figures 4 and 5.

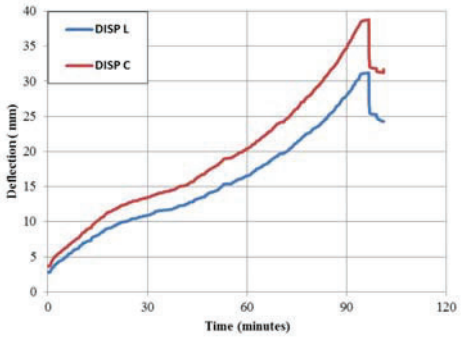

Figure 4: *Time-deflection curves of Slab 1*

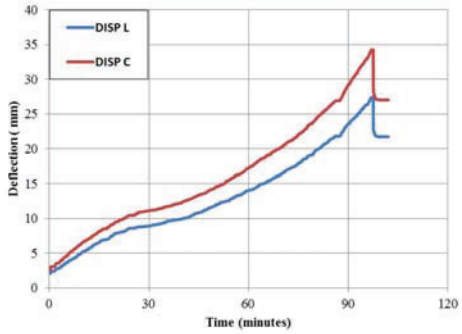

Figure 5: *Time-deflection curves of Slab 2*

Throughout the duration of the fire test, the char front progressed closer to the top plys. In particular, the top three plys in the CLT panel. The bottom of the middle longitudinal ply was the location of the thermocouple labelled TC3. The middle longitudinal ply was deemed critical for the targeted 90-min fire resistance under standard fire exposure if it burned away.

Figure 6 shows the time-temperature curves of the thermal measurements of the critical thermocouple (TC2) installed at the bottom of the first transverse ply and those measured by thermocouple TC3 installed at the bottom of the middle longitudinal ply at three different sections (L, M, and R) along the span of Slab 1. The left and right-side sections were 1100 mm offset from the midspan, as shown in Figure 1. As shown in Figure 6, as per the design of the TCC floor specimens, the bottom transverse ply began to char at approximately 55 mins as the temperature measured by TC2 reached 300 °C at this time mark. While the temperature measured by TC3 was less than 200 °C at the end of the fire test.

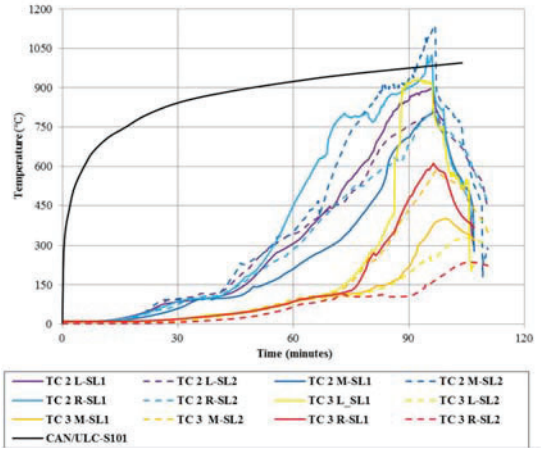

Figure 6: *Time-temperature curves of thermocouples TC2 and TC3 located at the three different sections in both slabs*

Figure 7 shows one of the floor test specimens (Slab 1) still burning right after the termination of the fire test and before extinguishing the specimen by spraying it with pressurized water mist.

Figure 7: *Slab 1 with its CLT panel still burning right after the termination of the fire test*

Table 1 presents the charring rate calculations based on the temperatures measured by the critical thermocouple (TC2) installed at the bottom of the first transverse ply and those measured by thermocouple TC3 installed at the bottom of the middle longitudinal ply at three different sections (L, M, and R) along the span of Slab 1. The average charring rates according to the calculations performed based on the thermal measurements of the selected thermocouples located at the three sections are 0.63 and 0.61 mm/min for Slab 1 and Slab 2, respectively. It is worth mentioning that there was no delamination observed due to adhesive melting in the CLT panel of any of the two test specimens. Thus, the calculated charring rates based on actual thermal measurements meet those rates provided in ANSI/APA-PRG-320 [6] as a requirement of reaching 250 ºC temperature at the glue line without excessive delamination.

https://doi.org/10.52202/069179-0239

Table 1: *Calculated charring rates based on measured temperatures at the three different sections in both slabs*

TC No.	Section along the span	Ply used for the charring rate calculations	Charring rate (mm/min) Slab 1	Slab 2
TC 2	Left	1st long. ply	0.59	0.64
TC 3		1st trans. ply	0.83	0.54
		1st long. & trans. plys	0.66	0.60
TC 2	Middle	1st long. ply	0.50	0.64
TC 3		1st trans. ply	0.85	0.63
		1st long. & trans. plys	0.58	0.64
TC 2	Right	1st long. ply	0.64	0.57
TC 3		1st trans. ply	0.67	0.66
		1st long. & trans. plys	0.65	0.60

5 CONCLUSIONS

Two identical full-size, one-way CLT-concrete composite floor slabs have been fire tested at Lakehead University Fire Testing and Research Laboratory (LUFTRL). Based on the design equations provided in the Design Guide for Timber-Concrete Composite Floors in Canada [14], the strip notch connections of the two test specimens were designed.

As a result of the activation of the composite action between the concrete top layer and CLT panel, both TCC floor slabs sustained the applied service loads for the 90 min duration of standard fire exposure. This show at least 30 mins added to the 1-hr fire resistance that those CLT panels with the same span (5000 mm) can have under the same applied load (4.8 kPa), as per the data provided by their manufacturer.

According to the outcomes of this new experimental research study, it is recommended that for strip notch connections in TCC floor assemblies like the ones examined under standard fire exposure in this study, at least one longitudinal ply in the major strength direction other than the utmost longitudinal ply that was cut due to the implementation of the six rectangular notches along the length of the CLT panel needs to stay unburned and remain in the residual section of the TCC after fire.

Another important observation is that having a whole-wide strip notch connection would influence the initial deflections of the supporting CLT panels while poured concrete is still wet if no shoring is provided in the middle of the slabs. Thus, to avoid excessive initial mid-span deflections and to meet the design serviceability requirements, intermediate support needs to be provided until concrete is hardened.

ACKNOWLEDGEMENT

This research project has been mainly funded using the Discovery Grant awarded to the second author by the Natural Sciences and Engineering Research Council of Canada (NSERC). The authors would like to thank Nordic Structures for their support and generous in-kind contributions in form of providing all CLT panels used to fabricate the large-size TCC floor test assemblies examined in this project. Thanks are extended to Pioneer Construction Inc., Miller Precast Ltd., and Harris Rebar (Thunder Bay) for their in-kind contributions. Thanks are due to lab technologist, Mr. Cory Hubbard for his great assistance during the experimental investigation stage of this project.

REFERENCES

[1] Osborne L., Dagenais C., Bénichou N.: Preliminary CLT Fire Resistance Testing Report. FPInnovations, Québec, QC, 2012.

[2] Osborne L., Dagenais C.: Fire-Resistance Test Report of E1 Stress Grade Cross-Laminated Timber Assemblies. FPInnovations, Québec, QC, 2013.

[3] Osborne L.: Fire Resistance of Long Span Composite Wood-Concrete Floor Systems. FPInnovations, Québec, QC, 2015.

[4] Dagenais C.: Investigation of Fire Performance of CLT Manufactured with Thin Laminates. FPInnovations, Québec, QC, 2016.

[5] Karacabeyli E., Gagnon S.: Canadian CLT Handbook. FPInnovations, Québec, QC, 2019.

[6] ANSI/APA-PRG-320, Standard for Performance-Rated Cross-Laminated Timber (American National Standard). 2017: APA – The Engineered Wood Association, Tacoma, WA.

[7] CEN, European Committee for Standardization Eurocode 5: Design of timber structures. Part 1-1: General–Common rules and rules for buildings. EN 1995-1-1. Brussels, Belgium: CEN., 2004.

[8] Salem O. S. , Virdi V.: Experimental Testing Of The Shear Strength Of CLT-Concrete Composite Sections Utilizing Screws As Shear Connectors, 2022, *Lecture Notes in Civil Engineering* (LNCE), Vol. 244, Springer, Singapore. https://link.springer.com/chapter/10.1007/978-981-19-0656-5_33

[9] CSA O86. 2019. Engineering Design in Wood. Canadian Standards Association (CSA), Toronto, Canada.

[10] Auclair S.C.: Design Guide for Timber-Concrete Composite Floors in Canada. 2020.

[11] Van der Linden M.R.L.: Timber-Concrete Composite Floor Systems. Doctoral dissertation, 1999.

[12] Ceccotti A.: Composite concrete–timber structures. Prog. Struct. Engng Mater, John Wiley & Sons, Ltd., 2002. 4: p. 264-275.

[13] Nordic-Structures, Nordic_X Lam_Technical_Guide. 2022: 100-1100 Canadiens-de-Montréal, Québec H3B 2S2.

[14] CAN/ULC-S101-REV1, Standard Methods of Fire Endurance Tests of Building Construction and

Materials. Underwriter Laboratories Canada, Scarborough, Canada, 2019.
[15] Canadian Commission on Building and Fire Codes. National Building Code of Canada, National Research Council of Canada, Ottawa, ON, Canada, 2020.
[16] Yeoh D., Fragiacomo M., De Franceschi M., Buchanan A.: Experimental Tests of Notched and Plate Connectors for LVL-Concrete Composite Beams. *J. Struct. Eng*., 2011. 137(2): p. 261-269.

https://doi.org/10.52202/069179-0239

World Conference on Timber Engineering Oslo 2023

FIRE RESISTANCE TESTING OF CLT-CONCRETE COMPOSITE FLOOR SLABS UTILIZING GLUED-IN STEEL PLATES AS SHEAR CONNECTORS

Adam Petrycki[1], Osama (Sam) Salem[2]

ABSTRACT: Timber-concrete composite (TCC) sections have shown desirable mechanical characteristics for use in the structural design of mass timber buildings at both ambient and elevated temperatures. TCC sections have advantages over conventional steel-reinforced concrete elements or timber elements on their own. While some recent performance-based design guidelines have been developed to aid in the design of TCC sections, they primarily rely on experimental data from specific TCC arrangements with certain types of shear connectors (e.g., steel plates, metal screws, etc.). The study presented in this paper involves experimental testing of two full-size CLT-concrete composite one-way floor slabs that were exposed to elevated temperatures of the CAN/ULC-S101 standard fire time-temperature curve, while being subjected to four-point flexure bending that is equivalent to the moment developed by a uniformly distributed 4.8 kPa service load. Each TCC slab assembly had a clear, simply supported span of 5000 mm and a width of 900 mm. The CLT panel composition (5 plys) and thickness (143 mm) were chosen to investigate how its one-hour fire resistance under the applied service loads could be increased to two hours by developing the composite action with the added concrete layer (90 mm thick) that otherwise would impose |dead load on the CLT panel without contributing to the overall strength of the floor system. Shear connectors utilized in these two TCC floor assemblies were perforated steel plates installed in prepared longitudinal slots using epoxy.

KEYWORDS: Timber-concrete composite (TCC) sections, Glued-in steel plates, Shear connectors, Fire performance

1 INTRODUCTION

Timber-concrete composite (TCC) systems were initially developed and used before being replaced by reinforced concrete slabs several decades ago. Nowadays, such composite systems are experiencing increased use in new construction and rehabilitating existing timber structures. TCC systems are developed by creating a shear connection between a timber section carrying the tensile forces and a concrete topping layer to carry the compressive forces. The behaviour of a TCC section is defined mainly by the rigidity of the connection between the two materials. Failure in such composite systems can occur as brittle failure in the wood section or a brittle or ductile failure at the interface of the connection between the two materials [1]. While mechanical shear connectors, such as screws and steel plates, are approved for specific composite systems in the EU, there are no provisions in the current Canadian standard for *Engineering design in wood* [2]. The only guidance available for engineers in Canada is the recently developed *Design guide for timber-concrete composite floors in Canada* [3], which provides some guidance for the performance-based design of TCC systems at normal and elevated temperatures with mechanical connectors such as screws, plates, and notches in the timber section.

Recent changes in the National Building Code of Canada [4] have allowed for the construction of timber buildings up to 12 storeys if a solid core is designed for lateral loads, such as the recently completed Brock Commons building at the University of British Columbia [5]. The two-way CLT floor slabs were designed to be point-supported on glulam columns with a concrete layer on top in the said building. However, no composite action was developed between the two materials. Thus, the concrete's compressive strength was not fully utilized to increase the stiffness of the floor system or its fire resistance; both are observed benefits of TCC systems [6]. Due to the non-homogenous nature of timber, extensive testing is required on the shear connectors to determine their stiffness, strength, and ductility ratio. Once those characteristics are defined, large-size samples are tested to validate the small-size experimental results and then evaluate how the characteristics of the examined shear connectors can influence the overall behaviour of TCC systems. Ultimately, TCC systems with certain engineered wood products and selected types of shear connectors/connections undergo standard fire testing. The experimental results of a very limited selection of shear connections in CLT-concrete composite floor systems can be found in the available literature, especially in the context of large-scale specimens. The focus has been primarily on notched connections [7] or dowel type

[1] Adam Petrycki, Ph.D. Candidate, Dept. of Civil Engineering, Lakehead University, Ontario, Canada, apetryck@lakeheadu.ca
[2] Sam Salem, Professor and Chair, Dept. of Civil Engineering, Lakehead University, Ontario, Canada, sam.salem@lakeheadu.ca

https://doi.org/10.52202/069179-0240

fasteners and nailed plates [8-10]. Thus, there is a lack of studies on longitudinal connectors secured by adhesive in CLT floor panels, such as the glued-in steel plates utilized in the floor assemblies tested in the current study.

This paper presents the experimental results of two full-size CLT-concrete composite, one-way floor slabs exposed to elevated temperatures of CAN/ULC-S101 standard fire [11], while being subjected to four-point flexure bending that is equivalent to the moment developed by a uniformly distributed 4.8 kPa service load, are presented. The TCC floor slabs involved in this study utilized glued-in perforated steel plates as shear connectors.

2 EXPERIMENTAL PROGRAM

2.1 SPECIMEN DESIGN AND DESCRIPTION

For the design of the TCC floor test specimens of the present study, the gamma and elastoplastic methods were used to determine their flexure bending strength. Hence, their time to failure under standard fire exposure was determined before conducting the fire endurance experiments. Both test specimens were 5300 mm long x 900 mm wide, with a 5000 mm clear simply supported span. The TCC floor assemblies were composed of 5-plys CLT panels of 143 mm thickness, alternating between 35-mm thick lamina in the major axis direction and 19-mm thick lamina in the minor axis direction. A regular strength concrete layer, with a thickness of 90 mm and a 28-day strength of approximately 40 MPa was cast on top of the CLT panel and reinforced with the minimum required steel reinforcement to prevent shrinkage cracking. According to the design, the shear connectors utilized to develop the composite action in the TCC sections were longitudinal glued-in perforated steel plates that measured 254 mm long x 90 mm high. The plates were embedded inside 40-mm deep longitudinal kerf cuts of approximately 3 mm width prepared in the CLT panel. Steel plates were affixed to the CLT panel using a two-component epoxy. The remaining 50 mm depth of the steel plates was embedded within the concrete layer. It is worth mentioning that the mechanical characteristics of the utilized proprietary glued-in Holz-Beton-Verbund (HBV) steel plates are documented, and those types of shear connectors are already installed in a few mass timber buildings recently constructed in North America. A plan view of the layout of the longitudinal steel plate shear connectors in one of the TCC floor assemblies is shown in Figure 1.

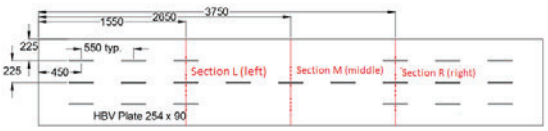

Figure 1: *Plan view of the layout of the steel plate shear connectors in a typical TCC floor assembly*

The relevant design and mechanical properties of the TCC components are summarized in Tables 1 through 3. Based on the listed values, the CLT slabs deflection under simply supported conditions (to mimic the in-site use of the CLT panels as form work) from the curing concrete was calculated and checked against the allowable deflection of *Span/360* and found to be within the allowable design serviceability limits.

Table 1: *Mechanical properties of the utilized CLT panels*

CLT floor panel properties	
M_r	65.0 kN.m
T_r	1780.0 kN
V_r	43.0 kN/m
EA	1480.0 x10^3 kN

Table 2: *Concrete properties*

Concrete slab properties		
	Test 1	Test 2
f'_c	36.94 MPa	40.43 MPa
ρ_c	2477 kg/m^3	2458 kg/m^3
Slump	90 mm	85 mm
Maximum aggregate size	13 mm	13 mm

Table 3: *Mechanical properties of the utilized steel plates*

HBV steel plate shear connector	
V_r	24.4 kN
k_s	209 kN/mm
k_u	139.3 kN/mm

Using the CSA-O86 Standard [2] and the FPI Design Guide for TCC Floors in Canada [3], the design of the TCC floor test assemblies was checked for vibration criteria and SLS and ULS limits under 2.4 kPa dead load (including slab's own weight) and 2.4 kPa live load combinations, and was found to be adequate. Also, based on an assumed notional charring rate of 0.65 mm/min, the TCC test assemblies were determined to safely achieve a 2-hr fire resistance time before failure.

2.2 INSTRUMENTATION

Each specimen had 37 Type-K thermocouples installed at varying depths at three sections (namely Sections L, M and R), as shown in Figure 1. The layout of the thermocouples installed at Section L (near the left side of the specimen within the maximum shear force zone) is shown in Figure 2. While Figure 3 illustrates the distribution of the thermocouples installed at different depths at Section M (at the middle of the specimen within the maximum bending moment zone).

https://doi.org/10.52202/069179-0240

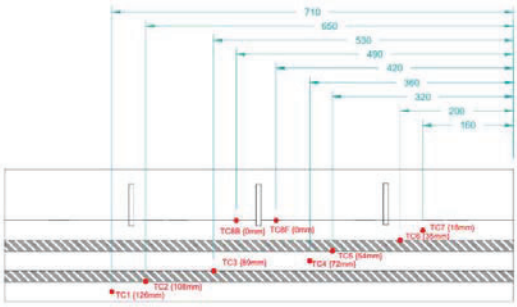

Figure 2: *Thermocouples layout at Section L, where the maximum shear exists (cross-section view)*

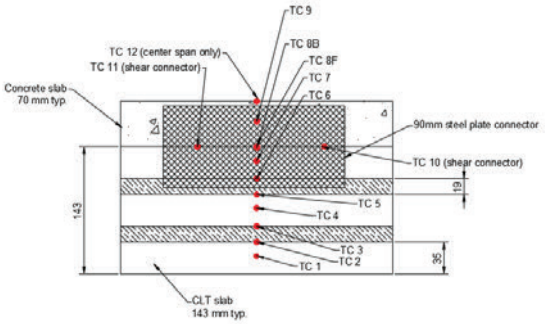

Figure 3: *Thermocouples layout at Section M, where the maximum bending moment exists (sectional-elevation view)*

Thermocouples were distributed to capture a representative sampling of the thermal measurements due to standard fire exposure over the width and along the length of the floor slabs. Also, careful attention was given to ensure that thermocouples were installed in their respective holes drilled to the correct depth, Figure 4.

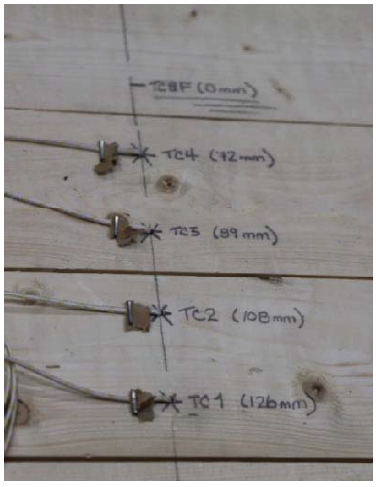

Figure 4: *Thermocouples installed and labelled in one of the two CLT panels*

The temperature readings were used to monitor the test specimens during fire testing and thus, thermal measurements were used to calculate the charring rates which were then compared to the thicknesses of the residual CLT sections measured after the completion of the fire tests.

In addition to the thermal measurements, it was essential to evaluate the mechanical behaviour of the test assemblies by measuring their vertical deflections at three different locations: at the midspan of the specimen and at each of the two applied load points. Thus, three draw-wire displacement transducers were installed above the furnace and safely connected to the top surface of each test specimen.

2.3 TEST SETUP

The two full-size TCC one-way floor slab assemblies were experimentally examined at elevated temperatures following the CAN/ULC-S101 standard fire time-temperature curve. During fire tests, floor assemblies were subjected to four-point flexure bending equivalent to a 4.8 kPa service load (2.4 kPa dead load including the slab's own weight, and 2.4 kPa live load). The loading equals the maximum service load applied to the CLT panels with the same span designed to have a 1-hr fire resistance. The study parameters and matrix of the fire experiments presented in this paper are summarized in Table 4.

Table 4: *Study parameters and matrix of fire experiments*

Test ID.	TCC-HBV-CC
Number of tests	2
Shear connector	254 x 90 mm, HBV steel plates
Wood material	900 mm wide x 143 mm thick x 5000 mm span (5-ply) E1-grade CLT
Concrete material	90 mm conventional concrete, ~ 40 MPa, with 6-mm dia. welded wire mesh
Designed fire resistance time	120 min

A sectional-elevation view of the test set-up applied for the fire experiments of this study is illustrated in Figure 5.

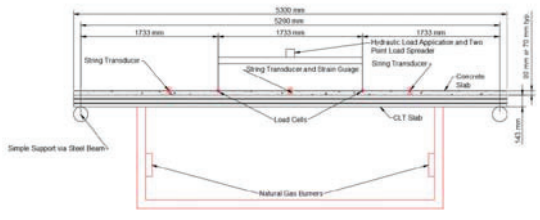

Figure 5: *A typical TCC floor assembly test setup and mechanical instrumentation layout*

https://doi.org/10.52202/069179-0240

TCC floor test assemblies were subjected to monotonic loading throughout the entire duration of the standard fire endurance tests. Shortly after each floor assembly achieved the 2-hr fire resistance time mark, test was deliberately terminated. Figure 6 shows one of the TCC floor test assemblies installed on top of the large-size furnace accommodated at Lakehead University Fire Testing and Research Laboratory (LUFTRL).

Figure 6: *A TCC floor assembly installed on top of the large-size furnace accommodated at LUFTRL*

Throughout the entire duration of each fire test, the applied transverse load was kept constant as the floor slab continued deflecting. Vertical deflections, applied load, and external and internal temperatures were all monitored and logged over the course of each fire test via a data acquisition system connected to a computer. Also, the test specimens were periodically monitored visually through the two observation viewports on the furnace front door. The underside of the first test specimen undergoing fire testing is shown via one of the viewports in Figure 7.

Figure 7: *The underside of a TCC floor assembly undergoing fire testing captured via one of the furnace's viewports*

After the termination of the fire tests, the underneath of the TCC slabs, which were still burning, were sprayed with pressurized water mist. Then, the specimens were removed out of the furnace for examination and visual inspection to determine the thickness of the remaining uncharred CLT section once the char layer was removed.

3 RESULTS

Test specimens were exposed to the CAN/ULC-S101 standard time-temperature curve for a few additional minutes beyond the two hours, exactly 126 minutes, to ensure satisfaction of the designed 2-hr fire resistance rating required by applicable building codes for the construction of tall timber buildings in Canada. Both samples sustained a 28.0 kN.m bending moment applied at their midspans under simply supported end conditions for the entire duration of the 2-hr standard fire exposure with no run-away deflection or any other characteristics of failure. This shows that a significant increase (more than 1 hr) in fire resistance time can be achieved for CLT floor slabs like the ones utilized in this study with the addition of a top layer of concrete that can work in composite action with the supporting mass timber section as a results of the utilization of the HBV glued-in steel plates as shear connectors between the timber and concrete elements in such TCC floor systems.

3.1 MECHANICAL BEHAVIOUR

After casting the concrete layer on top of the CLT slab, the initial mid-span deflections of the prepared test specimens due to the weight of wet concrete were measured and found to be 6.7 mm and 9.3 mm for Slabs 1 and 2, respectively. Afterwards, the test specimens were stored indoors for at least 28 days for full concrete curing, before each TCC floor assembly was installed on top of the furnace. Before the commencement of the fire test, a two-point load causing a maximum bending moment of 28.0 kN.m at the specimen midspan was applied in four increments, each of 25%, with the total applied load maintained stable for at least 30 minutes in conformity with CAN/ULC-S101. Then, the vertical deflections were measured due to the pilot loading prior to the start of the fire test. The applied bending moment maintained relatively constant throughout the entire duration of the fire test, while the gradually increased vertical deflections of the specimens were measured and recorded. The time-deflection curves for both floor slabs are shown in Figure 8.

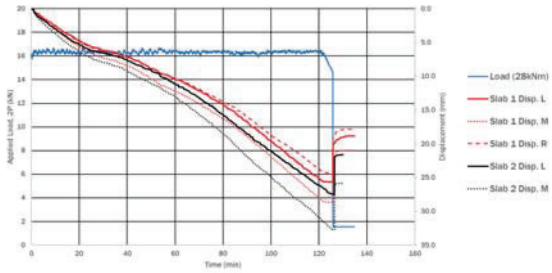

Figure 8: *Time-deflection curves for Slab 1 and Slab 2*

A summary of the maximum vertical deflections measured at the slab midspan and each point-load location is provided in Table 5. Readings for the right-side deflections of Slab 2 were not recoded due to a malfunction that occurred with the displacement transducer prior to the start of the fire test.

https://doi.org/10.52202/069179-0240

Table 5: *Summary of the maximum vertical deflections measured for Slab 1 and Slab 2*

Test specimen	Initial deflections due to weight of wet concrete (mm)		
Slab 1	6.7		
Slab 2	9.3		
	Deflections due to pilot loading (mm)		
	L	M	R
Slab 1	2.9	3.9	3.7
Slab 2	2.6	3.0	Error
	Final deflections right before terminating the fire tests		
Slab 1	29.1	32.1	28.4
Slab 2	32.7	38.7	Error

Generally, the vertical deflection values were found to be in good agreement with each other and consistent over the two slabs. From the time-deflection curves previously shown for both slabs in Figure 8, the floor slab deflection behaviour was more of a linear increase, which is characteristic of the reduction of the CLT cross-section over time due to charring. No exponential trend or run-away deflection was observed for the time-deflection curves for any of the two floor slabs throughout the entire duration of the 2-hr fire tests. It is worth mentioning that the deflection values rebounded a noticeable amount when the load was removed at the termination of the fire test. This behaviour is aligned with the TCC sections still undergoing elastic deformations and not exhibiting any plastic deformations in their shear connectors or brittle failure in the timber nor concrete components.

3.2 THERMAL BEHAVIOUR

Over the course of the 2-hr fire test, 37 thermocouples measured the internal temperatures of each test specimen at different locations with various depths. As the CLT bottom plys burned away, the exposed thermocouples were found to reach and follow the time-temperature profile of the followed standard fire as anticipated.

As the fire test progressed, the charring front moved closer to the more critical plys. These plys were the last two remaining plys in the CLT panel (one transverse with a 19 mm thickness and the very top longitudinal ply with a 35 mm thickness). The bottom of the last transverse ply was the location of the thermocouple labelled TC5. The transverse ply was deemed critical for the 2-hr standard fire exposure, not because the assembly could no longer sustain the load if it burned away, but for two reasons:

1) As per the composition of the utilized CLT panels, the transverse glued layer transfers the load to the remaining longitudinal plys, which were not edge glued. If the said transverse ply burned away, the CLT slab would no longer be in a composite action with the top concrete layer and thus, the behaviour of the remaining very top longitudinal ply solely supporting the concrete layer could no longer be as accurately predicted with either the gamma method or the elastoplastic method;

2) Since the HBV steel plate shear connectors were installed into the CLT panels using an epoxy material that is sensitive to elevated temperatures a minimum wood cover needed to be maintained to ensure the integrity of the adhesive and accuracy of the predicted behaviour of the shear connection with no failure in the adhesive due to fire exposure.

Figure 9 shows the time-temperature curves of the thermal measurements of the critical thermocouple (TC5) installed at the bottom of the top transverse ply and those of the thermocouple installed at the mid thickness of the said ply (namely TC6) in one of the slabs (i.e., Slab 1). As shown in the figure, as per the design of the TCC floor specimens, the top transverse ply began to char near the end of the fire test at approximately 123 minutes as the temperature measured by TC5 reached a temperature of 300 °C at this time mark.

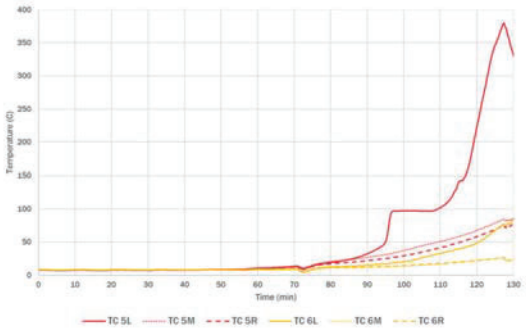

Figure 9: *Time-temperature curves of thermocouples TC5 and TC6 installed in Slab 1*

Generally, it was observed from the thermal results that the internal temperatures measured at the midspan of the floor slabs (Section M) increased with time to reflect a charring rate that is close to the notional rate of 0.65 mm/min that is standard for the utilized CLT panels. However, in the maximum shear zones of the floor slab, near the walls of the furnace, steeper temperature gradients were observed. Due to the non-combustible nature of the furnace insulated walls, fire vortexes formed at the corner where the furnace wall intersects with the underneath surface of the test specimen at each end. While this phenomenon unrealistically increased the charring rates near the left and right-side walls of the furnace, it did not affect the fire resistance of the test specimens or prematurely fracture the remaining longitudinal ply at the midspan where the maximum bending moment exists. This confirmed a continued composite action between the CLT plys remained after charring and the concrete layer until the termination of the fire resistance test at 126 minutes.

3.3 CHARRING RATE

After the TCC floor slabs were taken out of the furnace, they were securely positioned on their back longitudinal edge to allow for the removal of the developed char layer as shown in Figure 10 for Slab 1. The char layer was removed on the entire bottom surface of each test specimen using a wire brush on an electrical drill. Figure 11 shows the residual CLT section at the midspan of Slab 2 after removing the char layer.

Figure 10: *Char layer removed on the entire bottom surface of Slab 1*

Figure 11: *Residual CLT section at the midspan of Slab 2 after removing the char layer*

Once the char layer was removed, small holes were drilled into the CLT residual section at different locations until the drill bit touched the concrete slab. A digital calliper was inserted into the drilled holes to measure the residual thickness of the CLT section. The average thickness of the CLT residual section from various locations near the midspan of the test specimens were found to be 57 mm and 59 mm for Slab 1 and Slab 2, respectively.

The CLT residual thicknesses are reflective of a 2hr and 6-minute standard fire exposure, followed by approximately 5 minutes of a cool down phase before extinguishing of the test specimens started. Therefore, the charring rate was found to be between 0.65 mm/min and 0.68 mm/min assuming a time of either 131 minutes or 126 minutes, respectively. Based on the thermal measurements taken by the thermocouples implemented inside each test specimen (discussed in Section 3.2), the average charring rate was calculated at approximately 0.65 mm/min based on the assumption that the location of the char front in the CLT slab corresponded to a thermocouple reading of 300 °C.

4 DISCUSSION

The new results of the fire resistance tests of the two full-size one-way TCC floor slabs show that both test specimens achieved the targeted two-hour fire resistance time. Neither slab experienced failure while loaded with a total service load equivalent to 4.8 kPa over the course of exposure to two hours of a CAN/ULC-S101 standard fire. The CLT slab itself, under the same loading conditions, which could include a poured concrete layer without composite action with the supporting CLT slab, was only rated for a 60-minute fire resistance. The experimental results were found to be in good agreement with the predicted design calculations and the assumed charring rate used in the design of the CLT residual sections at the 2-hr fire resistance time mark were confirmed to be accurate. In addition, the fire performance of the HBV steel plates as the shear connectors used in the test specimens of the present study can be accurately predicted using the gamma method or the elastoplastic method based on the following two assumptions:

1. A minimum adequate thickness of a wood layer beneath the kerf saw cut in the CLT floor slab is maintained over the duration of the fire and thus, at no point the adhesive securing the steel plate connector into the timber is exposed to direct fire.
2. That the remaining plys of the CLT floor slab maintain its mechanical properties over the course of the fire. In the case of the CLT panels used in the experiments of the present study, the laminas were not edged glued and thus, it had the bottom underlying transverse layer (second ply from the bottom) burned away completely near the end of the 2-hr fire test. Accordingly, there would have been little to no interaction between the individual longitudinal lamina and the shear connectors would only be interacting with the longitudinal lamina they were embedded in and not

https://doi.org/10.52202/069179-0240

any adjacent longitudinal lamina without shear connectors in the wood

5 CONCLUSIONS

Using the HBV glued-in steel plates as effective shear connectors enhanced the fire resistance of the two CLT-concrete composite floor slabs tested in this study by creating a near-complete composite action that achieved a minimum fire resistance of two hours as required by applicable building codes for mid-rise residential buildings. The designed TCC floor slabs satisfied deflection limits during the initial concrete curing stage. Also, the stiff shear connectors increased the degree of composite action between the CLT and concrete layer and thus, reduced the mid-span deflections of the TCC slabs under the applied load, keeping the exhibited deflections within the allowable limits for SLS criteria. The TCC slabs were found to satisfy ULS criteria at both ambient and after a 2-hr standard fire exposure. The ambient and fire design outcomes based on the gamma and elastoplastic methods for the experimentally examined TCC floor slabs were found to be supported by the experimental results and thus, their fire behaviour was proven to be accurately predicted.

ACKNOWLEDGEMENT

This research project has been mainly funded using the Discovery Grant awarded to the second author by the Natural Sciences and Engineering Research Council of Canada (NSERC). The authors would like to thank Nordic Structures for their support and generous in-kind contributions in form of providing all CLT panels used to fabricate the large-size floor test assemblies examined in this project. Thanks are extended to Pioneer Construction Inc., Miller Precast Ltd., and Harris Rebar (Thunder Bay) for their in-kind contributions. Thanks are due to lab technologist, Mr. Cory Hubbard for his great assistance during the experimental investigation stage of this project.

REFERENCES

[1] Fragiacomo M., Lukaszewska E.: Development of prefabricated timber-concrete composite floor wsystems. *Proceedings of the Institution of Civil Engineers-Structures and Buildings*, 164(2): 117-129, 2011.

[2] Canadian Standards Association. CSA O86-19, *Engineering design in wood*, Mississauga, ON, 2019.

[3] Cuerrier-Auclair S.: Design guide for timber-concrete composite floors in Canada. Montréal, FPInnovations, 2020.

[4] Canadian Commission on Building and Fire Codes. National Building Code of Canada, National Research Council of Canada, Ottawa, ON, Canada, 2020.

[5] Staub-French S., Pilon A., Poirier E., Fallahi A., Kasbar M., Calderon F., Teshnizi Z., Froese T.: Construction process innovation on Brock Commons tall wood house. *Construction Innovation*, 22(1), 2021.

[6] Hozjan T., Bedon C., Ogrin A., Cvetkovska M., Klippel M.: Literature review on timber-concrete composite structures in fire. *Journal of Structural Engineering*, 145(11), 04019142, 2019.

[7] Klippel M., Boccadoro L., Klingsch E. W., Frangi A.: Fire tests on timber-concrete composite slabs using beech laminated veneer lumber. *Proceedings of the World Conference on Timber Engineering*, Vienna, Austria, 2016.

[8] Osborne (Ranger) L.: Fire resistance of long span composite wood-concrete floor systems. Vancouver: FPIInnovations, 2015.

[9] Dagenais C., Ranger L., Cuerrier-Auclair S.: Understanding fire performance of wood-concrete composite floor systems. *Proceedings of the world conference on timber engineering.* Austria, Vienna, 2016.

[10] Shephard A. B., Fischer E. C., Barbosa A. R., Sinha A.: Fundamental behavior of timber concrete-composite floors in fire. *Journal of structural engineering*, 147(2), 2021.

[11] CAN/ULC-S101-REV1, Standard Methods of Fire Endurance Tests of Building Construction and Materials. Underwriter Laboratories Canada, Scarborough, Canada, 2019.

World Conference on Timber Engineering Oslo 2023

FIRE RESISTANCE TESTING OF CLT-CONCRETE COMPOSITE FLOOR SLABS UTILIZING SELF-TAPPING SCREWS AS SHEAR CONNECTORS

Sarah Barclay[1], Osama (Sam) Salem[2]

ABSTRACT: In massive production, mass timber sections made of engineered wood, such as cross-laminated timber (CLT) panels, accelerated the pace of the construction of tall wood buildings in North America in the past few years. However, more stringent fire safety measures are applicable to tall timber buildings. Most critically, floor systems in mass timber buildings can be made more robust, span longer distances and exhibit enhanced fire resistance by adding a top layer of concrete to allow a timber-concrete composite (TCC) floor system when adequate shear connections are utilized. This paper presents the experimental results of the fire resistance tests of two full-size, one-way TCC floor slabs that utilized self-tapping screws (STS) as shear connectors. The main objective of this new experimental study is to investigate the enhancement of the fire performance when designing a CLT panel as a TCC floor assembly through achieving the required composite action with a top concrete layer at the interface between the two materials. Test results show that a minimum fire resistance of two hours required by applicable building codes for mid-rise residential buildings has been achieved for CLT floor panel by designing it as a TCC floor assembly, taking advantage of the composite action activated by the utilization of 45-degree inclined STS as shear connectors.

KEYWORDS: Timber-concrete composite sections, Fire resistance, Self-tapping screws, Shear connectors

1 INTRODUCTION

A key aspect of structural engineering research and design is looking at the optimization of sections and finding more efficient solutions to fundamental behaviours. That is the primary motivation and reasoning behind the design of composite structural members. They are maximizing the strengths of materials and compensating for the weaknesses. While many composite members can be designed, timber-concrete composites (TCC) sections are of great interest, with the timber material resists the tensile stresses and concrete resists the compressive stresses.

TCC sections are an excellent solution for both designing new structures and restoring existing timber structures since a fundamental improvement is in service for vibration and drastic change possible for fire resistance rating requirements in current building codes and design standards. Thereby, increasing the possibility of not only building tall with timber but also leaving the material exposed, impacting the architectural concept of the structure, and increasing the use of engineered-wood products (EWPs) as a design solution.

As under current standards, the only possibility to design tall mass timber building is with incorporating a type of construction known as Encapsulated Mass Timber Construction (EMTC). This forms an alternative solution for tall wood buildings to meet the code objectives and functional statements pertinent to the requirements of the combustible construction [1]. EMTC is defined as a type of construction in which a degree of fire safety is attained using encapsulated mass timber elements with an encapsulation rating and minimum dimensions for the structural timber members and other building assemblies [2].

In recent years, there has been a new surge of interest and studies for the introduction of EWP in taller mass timber buildings. Such products include cross-laminated timber (CLT) panels, which has been gaining popularity since they were first introduced in the early 1990s in Europe. Not initially examined in Canada until 2007, and not until 2017 when it was fully implemented into CSA-O86 *Engineering design in wood* standard [3]. CLT panels are mass timber sections made by gluing and pressing wood lamellas with alternating fibre directions (±90°) [4]. The panels shall have an odd number of lamellae (Typ. 3, 5, 7, or 9) arranged symmetrically around the centre layer, with the thickness of each layer ranging from 20 to 45 mm.

It is typical in mass timber construction to pour a concrete layer on top of timber floor slabs to improve their vibration and acoustic characteristics as well as to provide a space for conduits to run electrical and plumbing

[1] Sarah Barclay, Ph.D. Student, Dept. of Civil Engineering, Lakehead University, Ontario, Canada, sbarclay@lakeheadu.ca
[2] Sam Salem, Professor and Chair, Dept. of Civil Engineering, Lakehead University, Ontario, Canada, sam.salem@lakeheadu.ca

https://doi.org/10.52202/069179-0241

utilities. However, this practice is a missed opportunity to improve the overall structural behaviour and fire resistance of such timber floor sections. TCC sections have the involved materials (i.e., timber, concrete, shear connectors, etc.) working together in each respective strength and thus, altering the location of the neutral axis of the composite section to achieve the maximum possible strength and stiffness.

Contrary to popular belief and hesitation when considering mass timber materials for construction, they have excellent fire resistance and perform well under elevated temperature conditions. Although without verified test results, it causes a limitation of the industry's progression and possibilities when considering building tall in timber and options to have structural elements left exposed.

2 LITERATURE REVIEW

2.1 CLT BEHAVIOUR UNDER FIRE

To design TCC sections utilizing CLT panels, it is essential first to understand the expected behaviour and performance of the mass timber panel as a standalone element. More extensive research programs have focused on CLT panels when exposed to fire. Most of the fire testing completed when studying the behaviour of CLT floor slabs followed standard fire testing conditions. It is the most straightforward approach for comparing results with different parameters or materials for equivalent fire severity. However, studying test specimens under natural fire conditions allows a more accurate representation of fire in a realistic setting. The key benefit of natural fire exposure is adjusting for different ventilation conditions. This mainly affects the fire growth rate, as when a fire reaches the point of flashover, this influences the duration of the steady state burning stage of the fire.

The studies conducted by Mindequia et al. [4] and Wiesner et al. [5] were both part of the Epernon Fire Test Programme, a multi-partner collaborative research project launched in 2017 and focussed in its studies on the comparison between natural and standard fires in their effects on buildings. For the studies conducted by Frangi et al. [6] and Wang et al. [7], the primary study parameter was changing the thickness and number of plys used in the composition of the CLT panels, as well as the corresponding changes in the temperature profile and charring rate of their test specimens. In the study conducted by Mindeguia et al. [4], the structural capacity of the CLT panels was investigated, while Wiesner et al. [5] examined the thermo-mechanical behaviour of the CLT panels.

As with studying the fire performance of any construction material, it is crucial to understand the development and progression of heat transfer within the material. It is even more critical with CLT panels and other engineered-wood products. Such products are not homogenous, and their composition involves adhesives, even in relatively small amounts. Having accurate temperature readings throughout the sections is critical, as this information is essential to determine the actual charring rates and depths.

When fire contacts wood, a charred layer on the side of contact is formed, and as the heat continues to grow, the thickness of the char layer increases. Advantageously, this char layer protects the remaining uncharred core of the cross-section that is not yet exposed to fire. However, there is still a reduction in the cross-section area sustaining the applied loads. When studying the fire performance of CLT panels, a significant difference in the cross-section overall fire resistance is whether the charred layer falls off or remains intact. If the charred layer falls off, the protective function it gives is lost; thus, a new char layer starts forming. When a layer falls off, there is an increase in the charring rate as the underlaying layer becomes exposed to elevated temperatures that are higher than its initial temperature at the beginning of the fire test. Falling off of those layers is described as a delamination effect. This can occur locally at isolated locations, or globally when most of a ply falls simultaneously from a CLT slab exposed to fire.

Charring rate is evaluated by determining the thermal progression throughout a fire test and then, comparing temperatures afterward to determine the time each point reached 300°C. In general, the nominal charring rate of solid and glued-laminated timber sections under one-dimensional standard fire exposure is 0.65 mm/min, given by Eurocode 5. While, in general, the values agree reasonably well with the standard value from Eurocode 5, there is still some differences. This suggests that the charring rate alone is insufficient for predicting the residual loading capability of CLT floor slabs.

Thermocouples are essential to monitoring temperature, but they are limited by their placement location and can only determine when that spot reaches the critical temperatures. By removing the charred thickness and measuring the remaining section, a more holistic view of the slab performance and the differences across the slab can be achieved. Therefore, the char layer depth recorded in each experimental study is an important parameter as it influences the residual sections of a CLT slab that remain after fire exposure to sustain the applied loads without collapse.

2.2 DESIGN OF TCC SECTIONS

For TCC sections, two key assembly types of sections can be used: beam-type assembly and slab-type assembly. First, the beam-type system consists of a concrete slab supported by timber beams made of either mass timber or EWPs. A thin wood layer can also be placed between the concrete and beams to act as permanent formwork. The second type is the slab-type assembly which consists of a concrete slab on top of a solid mass timber panel. An important distinction between the two assembly types, besides the timber components being in either the shape of beams or slabs, is the exposure of the concrete to fire.

When designing such TCC sections, there are two methods to follow, the γ-method and the Elasto-Plastic Method (EPM). The former is the more common and original design concept. At the same time, the latter is relatively new and explicitly implemented for ductile connectors as the γ-method assumes elastic behaviour before the point of yielding. When EPM is within the plastic range and afterwards, the shear connectors begin to yield. Both design methodologies need to be checked, but EPM is critical to the design of TCC sections for shear connectors with less stiffness, such as self-tapping screws (STS).

One of the three fundamental aspects of the design of TCC sections is the shear connectors used to connect the two materials, giving the location to transfer stresses between the different materials. This results in many possible connectors that can be used, with their pros and cons in quantity required, level of skilled labour for insulation, cost per unit, availability, and research studied with validated results and behaviour in ambient and fire conditions. Therefore, to advance the understanding of the behaviour of TCC sections more experimental examining of the various shear connectors in full-scale testing setup to capture in-situ conditions and the overall performance of the sections is needed.

STS are a commonly used type of metal fasteners in timber structures, whether used for connections or for strengthening structural elements and connections. They can either be fully or partially threaded; while in TCC sections, the fully threaded screws are the preference. This is mainly due to the more uniform load transfer between the fully threaded screw and the timber material, which results in better withdrawal resistance. Thus, enhancing the strength and stiffness of the shear connections developed by those STS in TCC sections. STS that are fully threaded is hardened to develop a high yield moment and tensile and torsional strengths, while their long threads provide reliable embedment in the timber elements [3]. A benefit of their inherit design is that typically no pre-drilling is required, meaning they are faster to install than their counterpart shear connectors. All that makes them cost-efficient shear connectors for TCC sections, which requiring significantly less quality control measures or skilled labour during installation.

2.3 TCC SECTIONS BEHAVIOUR AT AMBIENT TEMPERATURE

The majority of completed studies are on the behaviour of TCC sections at ambient temperature. However, only a few studies have been completed recently after streamlining to focus on sections utilizing CLT panels and STS as shear connectors. Many factors influence the design and strength of the screw-type shear connections: overall dimensions, embedment length, angle of inclination, and screw spacing. Those parameters alter the strength, stiffness, and overall behaviour of TCC sections.

The study completed by Gerber [8] included an extensive experimental program studying different types of connections used in different timber materials and testing variances of each type of shear connectors. TCC sections experimentally tested in that study included: (a) screws at 30-degree angle of inclination, (b) screw pairs at 45-degree angle of inclination, and (c) screw pairs at 45-degree angle of inclination with an interlayer. The research study also included different screw lengths and diameters. In a relatively recent study completed by Mirdad and Chui [9], three different parameters were investigated in different TCC sections: screw embedment length in the timber; thickness of the insulation layer used; and the screw angle of inclination with the horizontal.

Another experimental study completed by Salem and Virdi [10] examined the influence of three parameters on the shear strength of TCC sections: longitudinal screw spacing; number of screw rows in the transverse direction; and age of concrete. Study parameters involved reducing the longitudinal screw spacing from 200 mm to 150 mm; increasing the quantity per row from two to three screws; and increasing the concrete curing age from 14 to 28 days. Interestingly, results of that study show that reducing the screw longitudinal spacing or increasing the number of screws in the row resulted in a similar increment in the maximum load sustained by the different TCC sections. However, the authors of that study recommended increasing the number of screw rows over decreasing the screw longitudinal spacing as this allows a more uniform distribution of the shear stresses in the transverse direction of the TCC section.

As part of the previously mentioned study conducted by Gerber [8] and after completing the pilot testing phase which included a series of shear tests, four-point flexure bending testing on long TCC slabs was completed. Test specimens involved CLT slabs as the timber component with screws at 30-degree angle of inclination in the shear flow direction. The screw spacing in the longitudinal direction alters, with a spacing of 150 mm in the high shear zone near the supports increased to 300 mm in the low shear zone in the middle of the slab. Higgin et al. [11] also conducted flexure bending tests as a part of their experimental program. However, their samples were tested under three-point flexure bending, and they utilized 45-degree orientated screws in the shear flow direction with two different spacing arrangements. In the first arrangement, the screws were installed at a constant spacing equal to 305 mm along the length of the specimen. While in the second arrangement, screws were widely spaced at 610 mm within the low shear zone in the middle of the slab and spaced at only 305 mm in the high shear zone near the supports.

While each of the parameter investigated in the previously mentioned studies influences the strength and stiffness of the experimentally examined TCC sections, it ultimately affecting their performance in flexure bending and the corresponding flexural rigidity based on the load-

https://doi.org/10.52202/069179-0241

displacement relationships developed for the different TCC sections. Results from Gerber [8]

Typically, TCC sections, especially when considering a timber component that utilizes a CLT panel along with STS as shear connectors, exhibit brittle failure under extreme flexure bending. As observed in tests completed by Gerber [8], all specimens subjected to flexure bending and utilized STS into CLT panels exhibited brittle failure, specifically a timber tensile facture. However, the author of the said study noted that the specimens exhibited brittle failure modes (i.e., concrete crushing or tensile fracture) failed at more significant applied loads compared to those that exhibited ductile failure modes (i.e., connector yielding or screw withdrawal).

2.4 TCC SECTIONS BEHAVIOUR UNDER FIRE

While TCC sections, when under ambient conditions, is more extensivity researched and studied both in terms of experimental and numerical analysis, there is lacking information when the fire conditions are involved. As previously mentioned, the need for further investigation to study CLT panels under fire exposure; the same goes for TCC sections. As for any TCC slab-type assembly, the behaviour of the overall floor is highly dependent on the behaviour of the timber component and the shear connections.

In fire conditions, the material ability to resist forces is affected due to the increased temperature and reduced timber area due to charring. This loss in strength leads to a shift in the location of the cross-section neutral axis and thus, result in loss of the stiffness of the TCC section. Complex thermal and mechanical responses must be considered when examining TCC sections exposed to fire, thereby increasing the challenge to develop both simple analytical methods and advanced numerical procedures to quantify their fire resistance according to the relevant codes [6]. However, to develop such models, there is a demand for more reliable experimental results to run comparative analyses to verify their reliability. Considering the limited research focused on studying of TCC sections using STS as shear connectors and having the timber component made of CLT panels, more large-scale fire experiments on such slab-type TCC floor systems are highly needed [13].

In that regard, an experimental study on long span TCC floor slabs was conducted by Osborne [14]. In that study, three key depths were important to consider, which are the depths at the interfaces between the first three ply's (i.e., 35 mm, 70 mm, and 105 mm). The first ply charred at 60 min, beginning to fall at 90 min, giving a char rate of 0.52 mm/min. The second ply charred at 105 min, falling at 120 min, giving a charring rate of 0.68 mm/min. Then the third ply was charred at 150 min, falling at 180 min, giving a charring rate of 0.68 mm/min. Since the TCC slab reached failure due to mid-span deflection at 187 min, the testing was terminated. Therefore, the charring rate began like that of the accepted European standard of 0.65 mm/min, but as the ply fell and delamination occurred, the charring rate further increased. Another important measurement was the temperatures measured at the interface between the concrete top layer and the CLT panel, where there was only a slight increase of about 20°C and only 5°C at the mid-depth of the concrete layer by the end of the fire tests. Also, the temperature of the screws was important to be monitored, as it increased by 93°C by the end of the fire tests. However, this did not occur until the tip of the screw reached a temperature of 100°C. Afterwards, the heat quickly transferred through the screw from the tip to the head and increased much more rapidly once the wood fell around the tip of the screw and was directly exposed to the fire. It is worth noting that although the temperature in the screw was raised, there was negligible heat transfer to the concrete top layer.

Relatively similar thermal behaviour was seen for the TCC slab assemblies examined by Shephard et al. [13]. In that study, the heat transferred from the exposed side to the interface between the concrete and the timber component and raised the temperature at the interface to 59°C and the temperature at the mid-thickness of the concrete layer to 72°C by the end of the fire tests. Also, the charring rates determined in that study was 0.66 mm/min based on the burning of the first ply. However, it was determined at 0.8 mm/min based on the burning of the subsequent plys. Greater charring rates also lead to a greater loss of timber section with an average depth remaining of 25 mm, which would be only the very top ply of the CLT panel. Unlike the study conducted by Osborne [14], where both the fourth and fifth ply remained uncharred, one reason for the difference could be that the adhesive used in manufacturing the CLT panels utilized in the TCC specimens experimentally examined by Shephard et al. [13] affected the delamination occurrence. Although the placement of the screws and corresponding spacing were different between the TCC slabs of those two studies [13 and 14], this would cause a difference in their mechanical behaviour in terms of strength and stiffness, but not the charring rate of the CLT panels. Another possibility is the influence that the panel-to-panel joint affected the fire performance of the TCC floor assemblies examined by Shephard et al. [13]. This is a much-needed topic for further exploration, as the panel-to-panel connection is a very critical component in a mass timber floor system, especially in fire conditions.

3 EXPERIMENTAL PROGRAM

While TCC sections have been studied for many years across various countries, limited testing and verification are completed in Canada. This shows that the possibility of TCC sections being implemented into the Canadian *Engineering Design in Wood* standard [3] requires more extensive experimental testing, computer modelling, and numerical analyses. Currently, TCC sections have only been designed using performance-based guidelines, as the

prescriptive methods are still lacking in many published wood design standards.

Following typical fire resistance design procedures, TCC floor assemblies were subjected to monotonic loading before being exposed to standard fire. Each floor assembly was exposed to CAN/ULC-S101 standard fire time-temperature curve for the two fire tests of the research study presented in this paper. In Canada, a minimum fire resistance rating of 45 minutes is required for structural timber components. However, considering the new era of erecting tall wood buildings and the introduction of EMTC, the goal has been changed to achieve a minimum fire resistance rating of 2 hours for buildings more than six stories.

3.1 TEST SETUP

Fire endurance testing was carried out at Lakehead University Fire Testing and Research Laboratory (LUFTRL) located on Thunder Bay campus, Ontario. This state-of-the-art facility, accommodates a large custom-designed furnace with two natural-gas fed burners that can raise the furnace's temperature to 1300 °C. The furnace is equipped with a control panel that can be set to follow a programmable fire time-temperature curve.

The roof of the furnace is comprised of three separated strips that are joined together. As for this research, each of the 900-mm wide TCC floor slab was placed instead of the middle roof strip, thereby acting as part of the furnace roof. Thus, test slabs were exposed to standard fire only from underneath, which reflected one-dimensional heat transfer, Figure 1.

Figure 1: *Interior of the testing furnace with one of the TCC floor test assemblies installed*

The overall dimensions of any TCC floor assembly are 5300 mm x 900 mm, with a clear span of 5000 mm. As the furnace itself is not load-bearing, the TCC floor slab rests on simple supports placed on the transverse beams of the exterior loading/supporting steel framed structure. Thereby, not the entire span (5000 mm) of the floor slab was exposed to fire, but rather a middle length equivalent to the interior length of the furnace chamber (3750 mm) was exposed to fire. This allowed 75% of the floor slab length to be exposed to fire and guaranteed to keep the supports outside the furnace. Meanwhile, under the four-point flexure bending applied on the TCC floor slabs, the greatest shear, moment, and deflection locations were always within the furnace chamber.

To accomplish the objectives of this experimental study, measurements and experimental data were required to evaluate and quantify the performance of the TCC floor slabs when exposed to standard fire. It is essential to provide reference and insight to the recorded visual observations of the floor assemblies as they were designed to achieve a fire resistance rating of 2 hours. Thus, fire tests were terminated shortly after reaching this fire resistance time mark. As tests was duplicated, the first specimen (Slab 1) was exposed to fire for 125 min, while the second specimen (Slab 2) was deliberately exposed to fire for extended period (145 min). Thereby being able to show no sudden change or failure occurrence shortly after the 2-hour threshold.

Test assemblies were loaded to the design load, including 2.0 kPa dead load (in addition to self-weight) and 2.4 kPa live load, representing in situ loading for typical residential occupancy loading. Each specimen was designed to achieve a 2-hr fire resistance, thereby doubling the fire resistance of the CLT panel as a standalone element as reported by the manufacturer, Nordic Structures. The design of each TCC specimen and its shear connections was determined by adopting the clauses and equations in the Canadian Wood Design Handbook [2], Design Guide for TCC Floors in Canada [15], and European Design Code for screw capacity.

3.2 MATERIALS

3.2.1 CLT Panels

This research project utilized CLT panels supplied by Nordic Structures, Quebec, Canada. The principal mechanical properties of the sections were provided by the manufacturer and verified by the Canadian Construction Materials Centre (CCMC) in Evaluation Report CCMC 13654-L [16]. A 5-ply CLT panel was chosen when considering the experimental setup, overall specimen dimensions, and applied loading. Nordic Structures manufactures two different 5-ply CLT panels, one with all ply thickness being 35 mm, giving an overall depth of 175 mm; while the other is with the major strength direction plys of 35 mm thickness each and the minor strength direction plys of 19 mm thickness each, giving an overall depth of 143 mm. The slenderer one was chosen to align with the research objectives.

3.2.2 Concrete

The concrete used in this experimental study was normal strength concrete with 28-day compressive strength designed for 30 MPa. Coarse aggregates were dolomite based with a maximum aggregate size of 16 mm and a nominal diameter of 13 mm. Smaller-diameter aggregates are common in TCC sections as it allows for the mix to

https://doi.org/10.52202/069179-0241

flow and bond around the shear connectors adequately. Water-cement ratio used was approximately 0.56 and no additives were used in the concrete mix. Additionally, the minimum reinforcement ratio of 0.002 of the concrete cross-sections was achieved by placing a wire mesh with 150 mm grid of 6-mm diameter steel wires. This is mainly to control tension cracking due to concrete shrinkage.

3.2.3 Self-Tapping Screws (STS)

The type of STS used in this study were SWG ASSY VG plus cylindrical head, Figure 2. The properties of those screws include diameter (8 mm), total length (240 mm), embedment length in CLT (150 mm), insertion angle 45°, longitudinal spacing (150 mm), transverse spacing (350 mm), bending strength (1015 MPa), tensile strength (18.9 kN), and shear strength (641 MPa). The product evaluation report for the utilized STS provides the full technical specifications for the screws [17].

3.2.4 Insulation Layer

The seen benefit of including insulation layer at the interface with respect to increasing the moment arm between the timber and concrete components, decreasing overall weight, and increasing the thermal and vibration characteristics, a layer of insulation was added to both test specimens. However, due to the less desirable effects of placing STS directly through the installation layer with the decrease in strength and stiffness as the screw tends to twist and bend, the insulation was only placed between the rows of screws. Type of insulation was FOAMULAR CodeBord XPS Insulation cut to strips of 200 mm wide and placed intermediate between screw rows, Figure 3.

3.3 FABRICATION OF TEST SPECIMENS

Due to the detailed composition of TCC floor slabs, it is a multi-step process that must be followed to fabricate each test specimen. Special care was taken to ensure accurate measurements of the thermal data during fire testing. This step is vital as it directly reflects results and conclusions drawn.

High-temperature insulated Type-K thermocouples were installed at specific locations in the CLT panel, concrete slab, and on selected STS. In total, there were 37 thermocouples installed in each test specimen at specified depths, Figure 4. The thermal data measured by the installed thermocouples provides information on the transfer of heat through the specimen and the temperature of different components at a given time during the fire test. Thus, can be used to observe the relationship between time, temperature, and the depth into the floor assembly cross-section. As shown in Figure 4, thermocouples TC1 through TC7 were installed in the CLT panel, located at the interface between each ply and at the mid-depth of the major plys. TC8 was installed at the interface between the concrete and the CLT panel, TC9 at the mid-depth of the concrete layer, TC10 and TC11 around one of the STS, and TC12 on the concrete layer top surface.

Figure 2: *Installation of STS in CLT Panel*

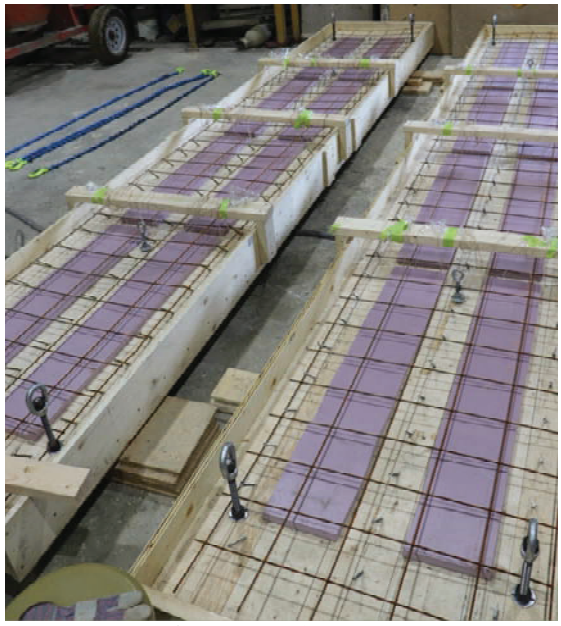

Figure 3: *Prepared CLT slabs before casting concrete*

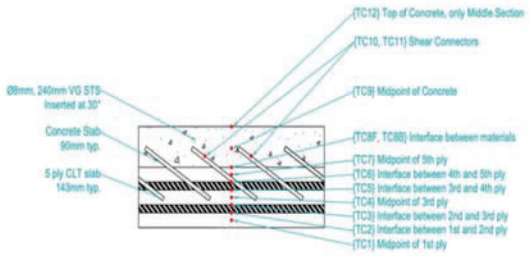

Figure 4:*Thermocouple layout (sectional elevation view)*

Figure 5 shows the final appearance of the two fabricated TCC floor slabs while taking off their formworks after 7-day concrete curing age.

https://doi.org/10.52202/069179-0241

Figure 5: *Removing formwork from TCC floor slabs*

4 RESULTS & DISCUSSION

4.1 MEASURED TEMPERATURES

During any fire testing on structural elements, it is essential to monitor and analyse their thermal behaviour, even more so when considering combustible materials like CLT to understand the rate of heat transferred and charring of the section. Unlike other materials where structural integrity is only diminished, with wood products, this occurs in addition to the loss of cross-section. Thereby, this significantly influences the ultimate strength and stiffness as well as the cross-section loss that is unrecoverable. Examining CLT when exposed to fire conditions is complex but extremely important to designing TCC with slab-type assemblies and providing adequate reliability in fire conditions.

Results were analysed in two distinct ways. First, compared the slabs against themselves by looking at the overall sections and studying the differences with the three separate thermocouple locations: left side, midspan, and right side. The left and right lines are just offset from the location of the point-loading application. Second, is comparing the slab against each other, tracking if duplicate specimens are consistent.

Temperature profiles were developed for each slab and based on the thermal measurements it is confirmed that both TCC floor slabs are in good agreement with each other and very comparative in terms of rate and heat transfer through the slab cross-sections. The first five thermocouples are the most critical, with TC1 being 17.5 mm inward, TC2 being 35 mm, TC3 being 54 mm, TC4 being 71.5 mm, and TC5 being 89 mm, as they are first to experience the effects of fire. Also, the rate at which their temperatures are increased dictates the overall performance of the TCC floor assembly. Additionally, temperature measured by TC5 was used as the test critical temperature where the fire tests were to be terminated if its temperature reached the 300 ˚C (wood charring temperature) to protect the utmost major strength ply of the CLT panel.

4.1.1 Temperature Profiles

Figures 6 and 7 show the entire fire test duration and temperature profiles of data averaged for the thermocouples installed at the same depths at the different three sections along the length of each slab. This is to better examine the overall performance of the slabs and compare them against each other more simply. All presented time-temperature curves show relatively smooth profiles with a more gradual increase in temperature (e.g., no sudden jumps in increased temperature). This is attributed to the minimal delamination the CLT panels experienced during fire tests. As there are no sudden spikes in the thermal behaviour of the fire tested TCC floor slabs, no significant amount of charred timber fell during testing on the furnace floor. Delamination is a critical issue for CLT panels in fire conditions, and

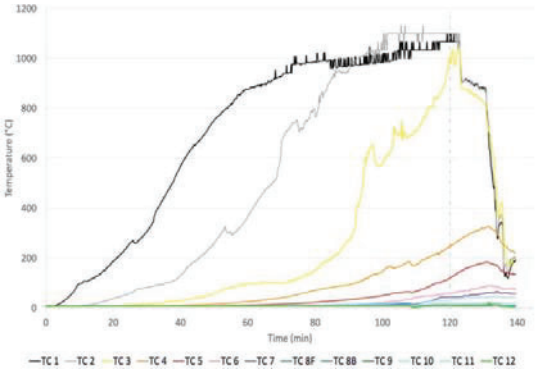

Figure 6: *Slab 1 average temperature readings*

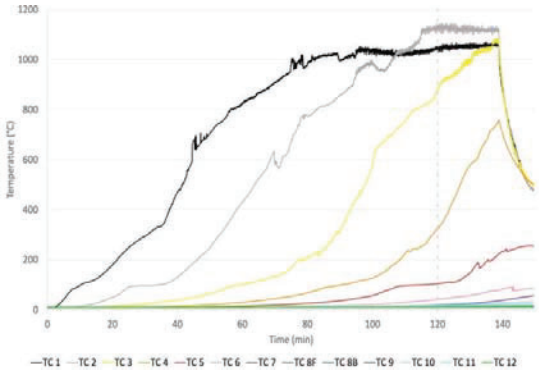

Figure 7: *Slab 2 average temperature readings*

4.1.2 Critical Thermocouple Comparison

The most critical thermocouple (TC5) was carefully monitored throughout fire tests. The measurements of that thermocouple were used to terminate the fire test. The said thermocouple (TC5) is located at the interface between the third and fourth ply of the CLT panel, thereby having this thermocouple not reaching the charring temperature allowed for this minor-strength direction ply to protect the utmost and final major-strength direction ply. Since the examined TCC floor specimens were one-way slabs, only the major-strength direction plys resisted the applied

https://doi.org/10.52202/069179-0241

loading and thus, were used to determine the strength and stiffness of the CLT panels under fire exposure.

After examining the developed time-temperature profiles at the targeted 2-hour fire resistance time mark, the measurements of TC5 reach approximately 100-150°C. Therefore, the location is undoubtedly experiencing the effects of the fire but not at the point where significant strength of the CLT panel was lost.

4.1.3 Heat Transfer Through TCC Sections

Monitoring the fire development and charring progression of the TCC sections throughout the fire testing comes down to evaluating how heat transfers through the floor slabs. Apart from the thermocouples that are exposed initially and others not until near the end of the fire test, it is essential to examine the temperatures measured by the thermocouples that are protected from previous layers of wood and those located in the concrete top layer.

Thus, examining the time-temperature profiles shows that very minimal temperature increase occurred above the temperatures measured by TC5. Meaning a lack of heat transfer to the top of the slab, although the bottom is experiencing a fire temperature of approximately 1000°C. Proving a lack of heat transfer through the slab as most of the installed thermocouples did not reach temperatures higher than 40°C after the 2-hour fire duration. It also should be noted that those thermocouples that measured increased temperatures are mostly TC6 and TC7, which are still located in the CLT panel. Comparatively, the thermocouples found in the concrete and at the interface between materials barely increased (approximately 10°C only) from the initial starting temperature before the fire test began.

4.2 CHARRING BEHAVIOUR

4.2.1 Charring Rates

A crucial aspect in studying the behaviour of timber materials when exposed to fire is the rate and development of the charred front. While compared to contemporary theories and reasons for the hesitation when increasing the construction of tall timber buildings, these combustible products perform very well in fire conditions. Heat transfer through the different plys that form a CLT panel takes a significant amount of time. Proving the insulation properties of the material, and while the temperature threshold of loss of strength is low, it takes an extended period while exposed to an elevated temperature to reach this point.

The nominal charring rate from the European Code is 0.65 mm/min. Additionally, this is the recommendation from the Canadian Wood Council in the Canadian *Engineering Design in Wood* Standards [3] for CLT. The charring rate is 0.65 mm/min when the char depth is within the first ply of a CLT panel and an increased rate of 0.80 mm/min is considered when the charred front progresses beyond the first glue line. The 0.80 mm/min charring rate is exceedingly higher than expected and previously recorded behaviour.

Results from charring rate calculation can be seen in Tables 1 and 2, showing each thermocouple location as well as the averaged results for the entire test specimen. The typical behaviour can be observed from the results where there is initially a lower charring rate as the fire is just beginning and, therefore, not at the hottest temperatures. Then increases while the fire continues as the CLT is ignited and charring starts to develop upward. However, notice that later locations continue to decrease again as although there is a developed char layer, it works as a layer of insulation to the unburned internal plys.

Table 1: *Slab 1 calculated charring rates based on thermal measurements*

Averaged temperature across the slab for TC No.	Charring rate (mm/min)
TC 1	0.59
TC 2	0.67
TC 3	0.59
TC 4	0.56

Table 2: *Slab 2 calculated charring rates based on thermal measurements*

Averaged temperature across the slab for TC No.	Charring rate (mm/min)
TC 1	0.57
TC 2	0.66
TC 3	0.61
TC 4	0.60

The overall average charring rate is approximately 0.60 mm/min with standard deviation of only 0.0396. It also shows the reliability of the European Standard charring rate of 0.65 mm/min and the good agreement with the experimental results of this study.

4.2.2 Residual CLT Thickness

Comparing Figures 8 and 9 shows the difference when the char layer is removed, thereby exposing the remaining wood to resist the applied loads. The apparent difference in appearance makes it easy to differentiate between charred and robust wood.

Only Slab 1 had the char removed as the test had a duration of 125 min where this fire test was terminated shortly after passing the 2-hour fire resistance time mark. Therefore, it was essential to know how much wood was remaining. At the same time, it is understood that more fire exposure for the other slab (Slab 2) would simultaneously lead to a more significant reduction in the residual wood section.

Figure 8: *Slab 1 right after fire testing and before the char layer was removed*

Figure 9: *Slab 1 after 2-hr standard fire exposure and the char layer removed*

It is relatively easy to distinguish between the major and minor plys from Figure 9, with the different ply orientations. However, it is more challenging to know the difference between the middle major ply and the top major ply from the figure alone. Thus, Table 3 presents the residual depth at the three different sections along the first fire tested floor slab. The residual section is more accurate following the centreline of the slab in the longitudinal direction rather than near the edges of the slab.

Table 3: *Residual CLT depths with 2-hr fire exposure in Slab 1*

Location	Residual depth
Left side	54.0
Centreline	68.9
Right side	64.6

It should be noted that the residual depth values greater than 54 mm would indicate that the charring progressed into the third (or middle) ply along the major strength direction. The residual section would be in the fourth ply based on the predicted values using an increased charring rate. While according to the experimental results of this study, with average charring rate calculated based on thermal measurements at 0.60 mm/min, which is very close to the European code nominal charring rate (0.65mm/min), the residual section would be in the third ply.

5 CONCLUSIONS

The new insurgence of structural design involving mass timber elements and increasing the buildings height restrictions under a prescriptive design methodology is tethered to the understanding of the structural fire performance of the main structural systems utilized in such tall timber buildings. Addressing these concerns requires extensive experimental programs to study such mass timber elements and verify their actual fire resistance ratings. Studying TCC sections offers valuable knowledge in expanding their use and design procedures and opening possibilities to further progress the mass timber construction. Both in terms of building taller in timber and having these elements exposed, thereby not limiting design options to EMTC.

Based on the results obtained from the experiments presented in this study to investigate the behaviour of TCC slab-type floor assemblies, the following conclusions can be drawn:

1. TCC floor assemblies can successfully be designed to meet the required 2-hour fire resistance rating. An essential requirement to create tall mass timber buildings and limiting factor in the Canadian *Engineering Design in Wood* standard.

2. The correct design and procedures can enhance the fire resistance of CLT panels by converting the floor systems to TCC sections with the addition of shear connectors and top concrete layer. This successfully takes a CLT panel rated for 1-hour fire resistance and achieve 2-hour fire resistance under the same loading. Thereby doubling the fire resistance time and proving the impact that TCC sections can have on the industry and design recommendations.

3. The thermal behaviour of the two TCC floor assemblies was comparable to each other, providing consistency in results and outcomes while studying time-temperature curves and charring behaviour. Furthermore, it agreed with the standardized charring rate of timber under the European Code nominal value of 0.65 mm/min, and test specimens did not globally delaminate.

4. Even though the exposed CLT was experiencing elevated temperatures of approximately 1000°C near the end of the 2-hr fire tests, there was still minimal heat transfer at the interface between the top concrete layer and the CLT panel or at any depth in the concrete. This demonstrates the benefits of the TCC slab-type floor assembly over the beam-type assembly as it is not needed to consider the thermal effects on the concrete component. Additionally, when the wood charred ply remains intact it acts as an excellent insulator to the inner and yet unexposed plys.

In conclusion, the unique results of the full-size experimental fire tests presented in this paper enhance the current understanding and assist in reducing the knowledge gap on the actual behaviour of TCC floor assemblies utilizing CLT panels when subjected to fire in Canada and globally, especially considering the rarity of large-size fire testing programs. Additionally, providing reliable experimental results for designers to validate the performance-based design and assign appropriate fire resistance times are very beneficial.

ACKNOWLEDGEMENT

This research project has been mainly funded using the Discovery Grant awarded to the second author by the Natural Sciences and Engineering Research Council of

https://doi.org/10.52202/069179-0241

Canada (NSERC). The authors would like to thank Nordic Structures for their support and generous in-kind contributions in form of providing all CLT panels used to fabricate the large-size TCC floor test assemblies examined in this project. Thanks are extended to Pioneer Construction Inc., Miller Precast Ltd., and Harris Rebar (Thunder Bay) for their in-kind contributions. Thanks are due to lab technologist, Mr. Cory Hubbard for his great assistance during the experimental investigation stage of this project.

REFERENCES

[1] Su J.: Fire safety of CLT buildings in Canada, *Wood Fiber Sci.*, vol. 50, no. Special Issue: CLT/Mass Timber, pp. 102–109, 2018.standard and natural fires," *Fire Mater.*, vol. 45, no. 7, pp. 866–884, 2021, doi: 10.1002/fam.2938.

[2] Canadian Wood Council (CWC). Wood Design Manual, 2020: The complete reference for wood design in Canada. Ottawa, Canada.

[3] CSA O86. 2019. Engineering Design in Wood. Canadian Standards Association (CSA), Toronto, Canada.

[4] Mindeguia J.-C., Mohaine S., Bisby L., Robert F., McNamee R., Bartlett A.: Thermo-mechanical behaviour of cross-laminated timber slabs under standard and natural fires, *Fire Mater.*, vol. 45, no. 7, pp. 866–884, 2021, doi: 10.1002/fam.2938

[5] Wiesner F., Siyimane M., Robert F., McNamee R., Christophe M.-J., Bisby L.: Structural Capacity of One-Way Spanning Large-Scale Cross-Laminated Timber Slabs in Standard and Natural Fires, *Fire Technol.*, vol. 57, no. 1, pp. 291–311, Jan. 2020, doi: http://dx.doi.org.ezproxy.lakeheadu.ca/10.1007/s10694-020-01003-y.

[6] Frangi A., Fontana M., Hugi E., Jübstl R.: Experimental analysis of cross-laminated timber panels in fire, *Fire Saf. J.*, vol. 44, no. 8, pp. 1078–1087, Nov. 2009, doi: 10.1016/j.firesaf.2009.07.007.

[7] Wang Y., Zhang J., Mei F., Liao J., Li W.: Experimental and numerical analysis on fire behaviour of loaded cross-laminated timber panels, *Adv. Struct. Eng.*, vol. 23, no. 1, pp. 22–36, Jan. 2020, doi: 10.1177/1369433219864459.

[8] Gerber A. R.: Timber-concrete composite connectors in flat-plate engineered wood products, University of British Columbia, 2016. doi: 10.14288/1.0300229.

[9] Mirdad A. H., Chui Y. H.: Load-slip performance of Mass Timber Panel-Concrete (MTPC) composite connection with Self-tapping screws and insulation layer, *Constr. Build. Mater.*, vol. 213, pp. 696–709, Jul. 2019, doi: 10.1016/j.conbuildmat.2019.04.117.

[10] Salem O. S. , Virdi V.: Experimental Testing Of The Shear Strength Of CLT-Concrete Composite Sections Utilizing Screws As Shear Connectors, 2022, *Lecture Notes in Civil Engineering* (LNCE), Vol. 244, Springer, Singapore. https://link.springer.com/chapter/10.1007/978-981-19-0656-5_33

[11] Higgins C., Barbosa A. R., Blank C.: Structural Tests of Concrete Composite-Cross-Laminated Timber Floors, April. 2017. https://cce.oregonstate.edu/sites/cce.oregonstate.edu/files/pdfs/som_report_osu_1701.pdf

[12] Hozjan T., Bedon C., Ogrin A., Cvetkovska M., Klippel M.: Literature Review on Timber–Concrete Composite Structures in Fire," *J. Struct. Eng.*, vol. 145, no. 11, p. 04019142, Nov. 2019, doi: 10.1061/(ASCE)ST.1943-541X.0002418.

[13] Shephard A. B., Fischer E. C., Barbosa A. R., Sinha A.: Fundamental Behavior of Timber Concrete-Composite Floors in Fire, *J. Struct. Eng.*, vol. 147, no. 2, p. 04020340, Feb. 2021, doi: 10.1061/(ASCE)ST.1943-541X.0002890.

[14] Osborne L.: Fire resistance of long span composite wood-concrete floor systems, Mar. 2015. https://library.fpinnovations.ca/en/permalink/fpipub40130

[15] Auclair S. C.: *Design Guide for Timber-Concrete Composite Floors In Canada.* S.L.: National Library, 2020.

[16] CCMC. 2019. Evaluation Report: Nordic X-Lam. Canadian Construction Materials Centre Report No. CCMC 13654-L.

[17] CCMC. 2020. Evaluation Report: SWG ASSY VG Plus and SWG ASSY 3.0 Self-Tapping Wood Screws. Canadian Construction Materials Centre Report No. CCMC 13677-R.

World Conference on Timber Engineering Oslo 2023

IMPLICATIONS OF A DOWN-STAND BEAM ON THE CEILING FLAME EXTENSION CHARACTERISTICS IN A LARGE-SCALE CLT ENCLOSURE FIRE EXPERIMENT

Danny Hopkin[1], Michael Spearpoint[1], Renaud Blondeau[2], Tim Sleik[3], Harald Krenn[4], Gordian Stapf[5] & Wojciech Węgrzyński[6]

ABSTRACT: This paper provides further understanding of the fire performance of exposed cross-laminated timber (CLT) in large enclosures. An office-type configuration has been represented by a 3.75 by 7.6 by 2.4 m high enclosure constructed of non-combustible blockwork walls, with a large opening on one long face. Two experiments are described in which propane-fuelled burners created a line fire that impinged on CLT ceilings. The first experiment had a smooth CLT soffit, with the CLT formed from 160 mm thick panels (40-20-40-20-40 mm). The second experiment adopted the same CLT but included a 400 mm deep, 200 mm wide glulam beam half-way along the length of the enclosure. In both experiments, the lamella of each CLT were bonded using a standard polyurethane adhesive. The facing lamella of the CLT was not edge bonded. The results indicate the importance of consideration of the impact of ceiling protrusions, such as down-stand beams, with differences in both radiative heat flux to the ceiling and floor observed between the two cases. Considering large contemporary open plan office enclosures, this would likely translate to differences in spread rate within an enclosure and time to auto-extinction of flaming combustion which should be addressed by designers.

KEYWORDS: cross-laminated timber; auto-extinction; flame spread; glulam; ceiling protrusion

1 INTRODUCTION & MOTIVATION

When conceiving of a new office building in the UK, timber is increasingly considered as part of any potential framing solution. This is driven by a combination of embodied carbon, aesthetics, and constructability considerations. Commercial premises, such as offices, often have specific user/client demands, with emphasis placed on high floor-to-ceiling heights, long spans between column members and large areas of glazing. For this reason, the UK market is converging upon hybrid construction solutions where timber, in the form of cross-laminated-timber (CLT), is used in concert with other materials, such as steel and concrete.

Recent guidance has been published [1] which has clarified the design evidence that should be provided by engineers when demonstrating that an adequate level of structural fire performance will be achieved when adopting a combustible structural framing solution. In higher consequence of failure buildings, e.g., medium- to high-rise offices, the structure must be designed in a manner whereby it has a reasonable likelihood of surviving the full duration of a fire. This necessitates that if the structure becomes involved as a source of fuel, combustion must cease and the structure should remain capable of supporting the applied loads both during and beyond a fire. The cessation of combustion is generally taken to be that of flaming, with some expectation that fire service intervention is necessary to stop any subsequent smouldering combustion.

To design a structure to undergo auto-extinction of flaming combustion, there needs to be an understanding of: (a) the fire dynamics in the enclosure, in particular spread rates; and (b) the heat flux to the combustible structural elements. Both are likely to be impacted by the presence of ceiling protrusions, such as beams. To date, limited effort has been committed to understanding the importance of such protrusions, other than at reduced scale [2].

This paper, as part of a larger experimental campaign by the Structural Timber Association (STA) special interest group on CLT enclosure fire dynamics, reports on two large-scale experiments that compare fire behaviour of engineered timber ceilings (comprising CLT and glulam) both with and without a beam protrusion.

2 THE EXPERIMENTS

2.1 The fire enclosure

The geometry of the fire enclosure was chosen to: (a) ensure CLT spans were broadly aligned to that commonly

[1] OFR Consultants, Sevendale House, Lever St, Manchester M1 1JA, UK, danny.hopkin@ofrconsultants.com
[2] Stora Enso Oyj, Wood Product - Building Solutions, PL 309, 00101 Helsinki, Finland
[3] Binder Holz GmbH, Zillertal Straße 39 · A, 6263 Fügen, Austria
[4] KLH Massivholz GmbH, Gewerbestraße 4, 8842 Teufenbach-Katsch, Austria
[5] Henkel & Cie. AG, Industriestrasse 17a, Sempach Station, 6203 Neuenkirch, Switzerland
[6] Instytut Techniki Budowlanej (ITB), Filtrowa 1, 00-611 Warszawa, Poland

https://doi.org/10.52202/069179-0242

adopted in hybrid commercial (office) construction, with the CLT spanning 3.75 m from front to back, and (b) to be as large as feasible within the constraints of the laboratory, considering both footprint and anticipated maximum heat release rate (HRR). This led to an enclosure of internal dimensions of 3.75 m (depth) by 7.6 m (width) by 2.4 m (height). The enclosure of the rig was constructed from exposed lightweight concrete blockwork that was 240 mm thick. Given commercial construction is typically characterised by a large amount of perimeter glazing, one elevation of the rig featured a large permanent opening, measuring 7.6 m wide and 2.0 m high. To allow for the characterisation of potential external flames from the opening, a mock-up façade extension was included. This extended the full width of the enclosure, measuring 2.6 m in height, with a down-stand that extended 0.4 m below the CLT soffit.

Figure 1: *Image of the enclosure with the propane gas burners shown at the quarter point.*

2.2 The mass timber elements

In all cases, the CLT was 160 mm thick, with lay-up 40-20-40-20-40 mm lamellae. At the time of the experiments, the estimated moisture content of the CLT slabs was in the range of 12–14% by mass. Non-edge-bonded CLT was chosen in both experiments with the intent of realising a lower bound of fire performance, i.e., the lack of edge-bonding can permit the rapid development of gaps between CLT facing lamella upon heating and subsequent dehydration, followed by pyrolysis. In both experiments, lamellae were bonded with a standard polyurethane (PUR) adhesive (Henkel Loctite HB S).

The first experiment had a smooth exposed CLT ceiling, i.e., no ceiling protrusions. This is henceforth referred to as the "no beam" case. The second "with beam" experiment included glulam beam measuring 200 mm wide by 400 mm deep. This was fixed to slab 3, such that the beam edge aligned with the joint to slab 2. The glulam beam was fixed to the slab from below, using stirrups. These comprised a universal bracket commonly used for propping ventilation ducts from below, which were supported on threaded tension rods on each side.

Slabs are distinguished in the discussion of instrumentation and loading, see Figure 4.

2.3 Fire source

The ceiling was heated using propane gas burners, elevated to sit 1 m below the soffit. The burner array comprised of 6 burners, each measuring 150 × 300 mm on plan, configured to achieve a rectangle measuring 300 × 900 mm. The burners were located off-centre (at the quarter point), with the aim of inducing flame extension to 50% of the ceiling length in a reference experiment reported elsewhere [3] and a heat flux exceeding 120 kW/m^2 at the plume centreline. The HRR of the fire was controlled via mass flow switches, leading to a HRR that ramped to a maximum of 1250 kW (achieved over an 8 min period in 250 kW steps). The duration of steady heating (at 1250 kW) for the exposed CLT experiments was chosen to induce significant char fall-off in the smooth soffit experiment (above the burner), resulting in a steady phase duration of 80 min. After this phase, the burners ramped down in 250 kW increments every 5 min, before being switched off, see Figure 2. An imagine of the burner impinging on the ceiling is given in Figure 3.

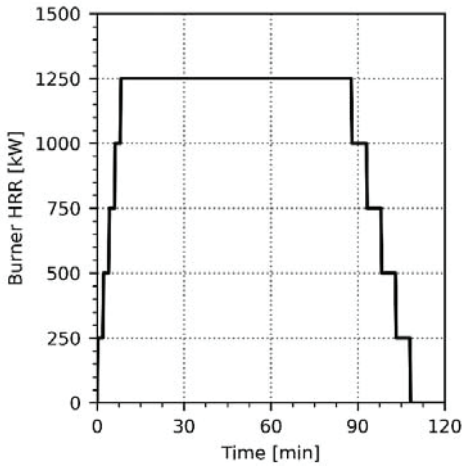

Figure 2: *Burner heat release rate with time.*

Figure 3: *Image of burner and ceiling jet, "no beam" experiment 1.*

2.4 Instrumentation and loading

The enclosures were instrumented using a combination of bead and plate thermocouples and water-cooled heat flux gauges. CLT slabs were loaded to achieve a nominally uniformly distributed load of 153 kg/m^2, or c. 4300 kg in total. Slab displacement was monitored, and CLT mass loss rate (MLR) estimated from load-cells. The experiments were identical, other than the inclusion of a glulam beam in the second experiment. Key dimensions and locations of instrumentation are shown in Figure 4.

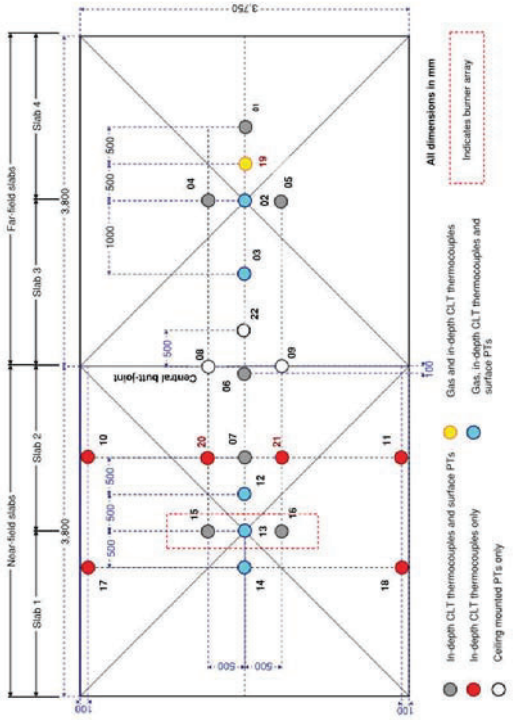

Figure 4: *Enclosure plan showing key enclosure dimensions, measurement locations and references, slab locations and burner array position.*

The CLT support structure comprised a perimeter steel frame, from which each pair of CLT slabs were suspended via tension rods. In line with these tension rods were a load cell to each corner, i.e., eight in total, recording the tensile load acting on the supports. The arrangement is as shown indicatively in Figure 5. The slabs sat within the perimeter of blockwork wall enclosure, ensuring the CLT and supporting structure were not propped by the perimeter wall. Minor gaps at the ceiling edges were fire stopped with mineral wool.

3 RESULTS

The emphasis of the results in this paper are on the fire development characteristics, i.e., no comment is made on the charring rates or mechanical performance associated with the engineered timber ceilings. To this end, results are presented in terms of the ceiling mass loss and heat release rate (HRR), gas temperatures below the ceiling, estimated radiative heat flux to the ceiling and floor, and the heat flux opposing the opening. Each are discussed in the sub-sections that follow.

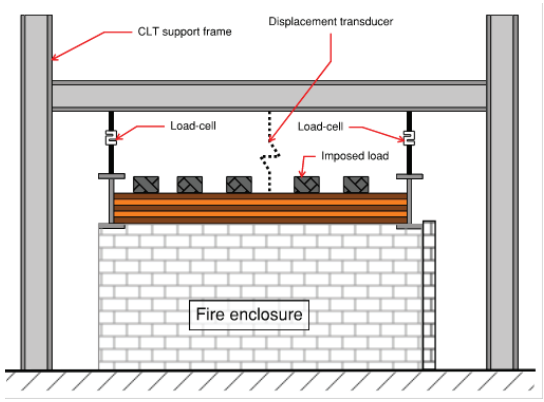

Figure 5: *Illustrative section through the rig showing CLT support mechanism, including load cells and displacement transducers.*

3.1 Timber mass loss and estimated HRR

The eight load-cells were summed and normalised relative to the starting mass on the system upon ignition of burners, with the resulting total mass lost with time for both experiments shown in Figure 6.

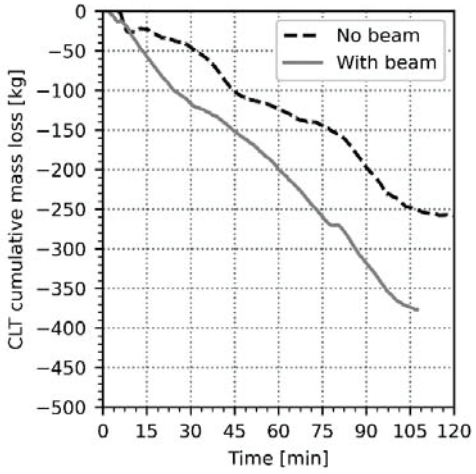

Figure 6: *Comparison of total slab mass lost with time.*

At the onset of the experiment, there was a c. 200 kg difference between the starting mass on the system for the "no beam" vs "with beam" case, which is largely attributable to the glulam beam mass, estimated at c. 40 kg/m.

Differentiating the mass lost with time and applying exponentially weighted smoothing over a 60 s period, gives the MLR, which has been presented per unit area in Figure 7. The MLR has been utilised alongside a net heat

https://doi.org/10.52202/069179-0242

of combustion of the timber of 17.5 +/- 2.5 MJ/kg to estimate the total heat release rate of the enclosure, when summed with the burner contribution given in Figure 2. The results are shown in Figure 8.

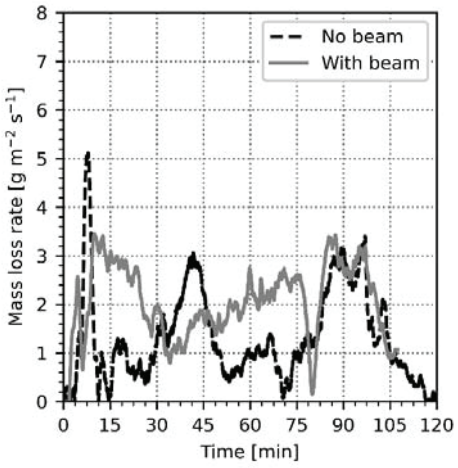

Figure 7: *Comparison of slab mass loss rate with time.*

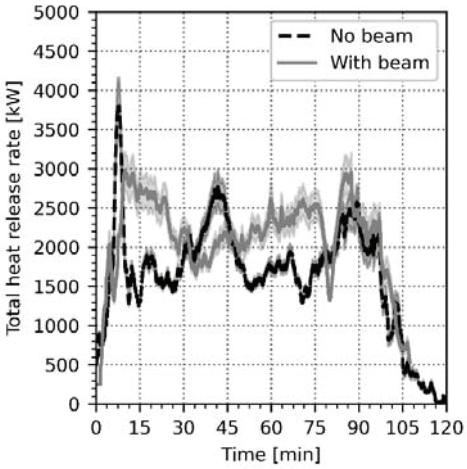

Figure 8: *Comparison of total heat release rate with time, based on mean heat of combustion of 17.5+/- 2.5 MJ/kg (shaded region)*

3.2 Heat flux to the floor and ceiling

Ceiling and floor mounted plate thermometers (PT) were utilised to estimate the radiative heat flux to the surfaces, adopting the correlations presented in Wickstrom et al. [4], as adopted by other researchers for similar applications, e.g., Su et al. [5]. Neglecting the heat storage term of the energy balance of the PT, as per Ingason and Wickstrom [6], the radiative heat flux was derived according to Equation (1) and Table 1.

$$\dot{q}''_{inc} = \frac{\varepsilon_{pt}\sigma T_{pt}^4 + (h + K_{cond})(T_{pt} - T_\infty)}{\varepsilon_{pt}} \quad (1)$$

Resulting profiles of radiative heat flux relative to distance from the burner are shown in Figure 9 and Figure 10.

Table 1: *Terms and constants adopted to estimate radiative heat flux to ceiling and floor, adopted from [7]*

Parameter	Description	Value	Unit
ε_{pt}	Emissivity of the PT	0.9	-
σ	Boltzmann constant	5.67×10^{-8}	$W \cdot m^{-2} \cdot K^{-4}$
h	PT convection coefficient	10	$W/m^2 \cdot K$
K_{cond}	Conduction correction factor	8	$W/m^2 \cdot K$
T_{pt}	PT temperature	Varies	K
T_∞	Ambient temperature	293	K

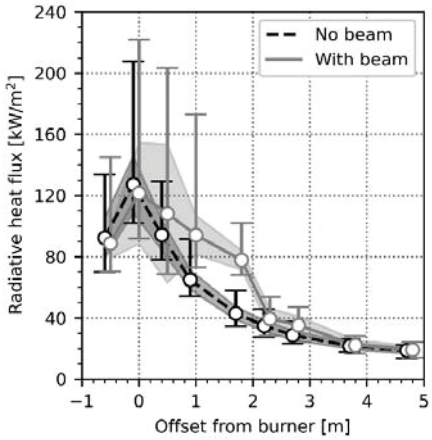

Figure 9: *Radiative heat flux to the ceiling at different burner offsets, comparison of no beam vs. with beam. Burner HRR = 1,250 kW. Shaded envelope shows +/- one standard deviation, error bars show range of values.*

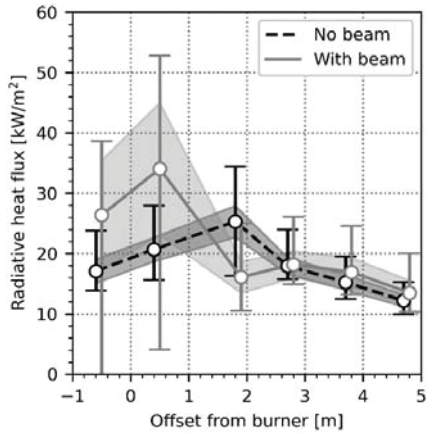

Figure 10: *Radiative heat flux to the floor at different burner offsets, comparison of no beam vs. with beam. Burner HRR = 1,250 kW. Shaded envelope shows +/- one standard deviation, error bars show range of values.*

3.3 Gas temperatures

Figure 11 and Figure 12 show the gas temperatures at ceiling level for the locations given in Figure 4.

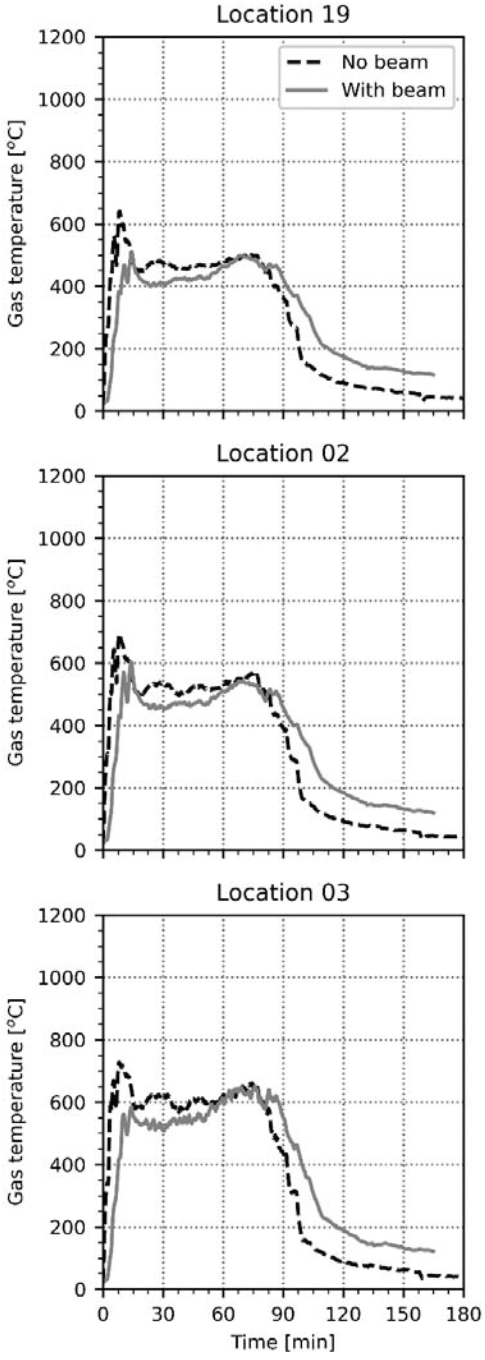

Figure 11: *Ceiling gas temperatures with time for locations 19, 02 and 03 (far field)*

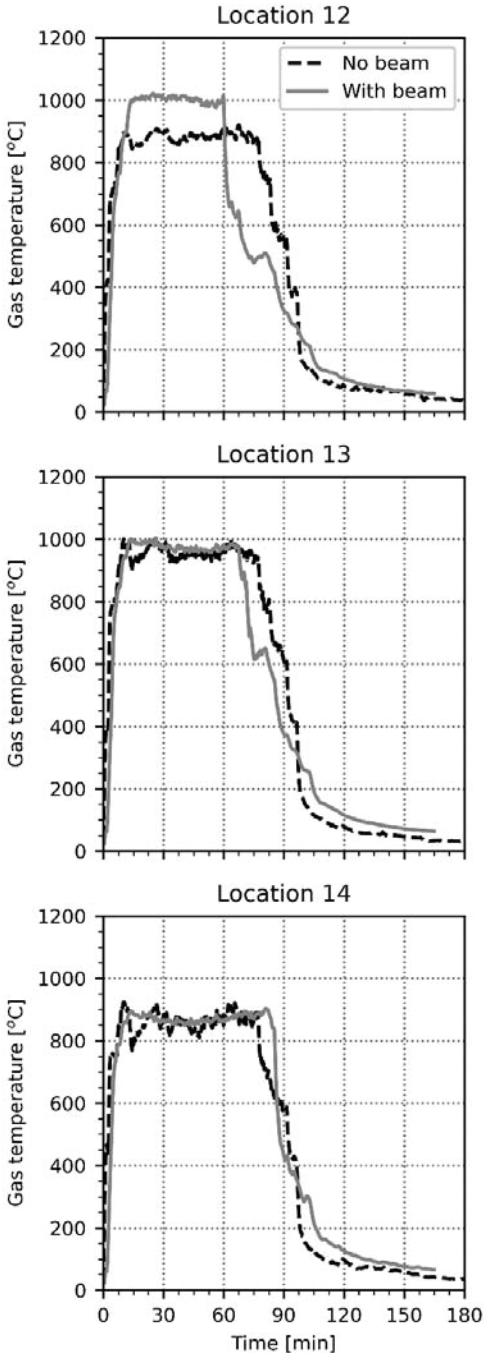

Figure 12: *Ceiling gas temperatures with time for locations 12, 13 and 14 (near field)*

https://doi.org/10.52202/069179-0242

4 DISCUSSION

4.1 Thermal exposure to the CLT soffit

Exposure to the CLT soffit can be distinguished by two zones, the near field and far field. The near field can broadly be taken as the ceiling area where burners impinged or resulted in a ceiling jet. This near field comprised slabs 1 and 2, with the far field slabs 3 and 4. In the case where a beam was included, this separated the near and far field.

In terms of the gas temperatures, Figure 11 showing results for the far field indicate no significant difference regardless of the inclusion of the glulam beam. Figure 12 for the near field shows increased gas temperatures in proximity to the glulam beam. This is likely a combination of (a) the flaming of the beam; and (b) a smoke reservoir effect, containing hot gases beneath slabs 1 and 2.

The increased gas temperatures correspond to increased heat fluxes to the ceiling in the near field, as evident in Figure 9 for the steady phase, where the burner HRR is 1250 kW. On the near field side of the beam, i.e., c. 1.8 m offset from the burner, the radiative heat flux (80 kW/m^2) is circa twice that observed for the flat ceiling case (40 kW/m^2).

Approximating the flame tip to coincide with a heat flux of c. 20 kW/m^2 indicates that the beam did not reduce the flame extension at ceiling level. During the steady phase where the burner HRR is 1250 kW, flames extended over the full length of the ceiling in both cases.

4.2 Thermal exposure to the floor

In the near field, the beam increased the heat flux to the floor. At locations either side of the burner, the heat flux at the floor for the case with a beam was c. 150% of that without a beam, during the steady phase (burner HRR of 1250 kW).

The format of the experiments undertaken, i.e., with a discrete heat source and otherwise fuel load free enclosure, did not permit any direct evaluation of what the combustible ceiling might mean for flame spread rates within a large enclosure. However, the radiative heat flux to the floor provides insight as to what might be expected through benchmarking against complementary studies, such as that by Gupta et al. [8]. In their studies on mechanisms of flame spread in large enclosures, Gupta et al. observe a correlation between the external heat flux to the fuel in advance of the flame front and the flame front velocity. In a proposed phenomenological model, Gupta et al. postulated that as the external heat flux to the fuel in advance of the flame front converges on a critical ignition criterion (taken as 10.5 kW/m^2 therein), the ratio of flame front to burn-out front velocity tends towards infinity, i.e., the flame spread rate is so fast so as to induce a "Mode 1" fire, which implies a fully developed post-flashover fire.

With reference to Figure 10, much of the floor in the far field receives a radiant heat flux significantly above 10.5 kW/m^2, implying that the combustion of the ceiling in either case would induce a change from a Mode 2 (growing fire) or Mode 3 fire (travelling fire) to Mode 1 (i.e., extremely rapid flame spread and transition to flashover). Such a rate of flame spread is supported by recent observations by Kotsovinos et al. [9] in their fire experiment in a 352 m^2 enclosure with exposed CLT ceiling. In Kotsovinos et al.'s "CodeRed #01" experiment, once ignition of the ceiling occurred, flame spread over the cribs covering the full length of the enclosure was observed in under 3 min. The beam had little utility in reducing the heat flux to the floor in the far field, with similar values observed to the case without a beam. It may even be the case that the presence of a protrusion, such as a beam, could lead to more rapid fire spread as heat flux to the floor in vicinity of the flame front (burner in this case) was substantially higher.

4.3 Implications for mass loss and HRR

Revisiting Figure 6, the overall mass lost was greater for the case with the beam versus without. This, in part, is likely a result of an overall greater system mass, including both more combustible material and combustible surface area arising from the glulam beam.

The involvement of the combustible ceiling in both cases can be considered by contrasting the HRR of the burner in isolation (Figure 2) and the estimated total HRR, adopting load-cell data for the engineered timber ceiling (Figure 8). Upon ignition of the timber ceiling, the total HRR is around three times that of the burner in isolation, regardless of the inclusion of a beam. Post-ignition, the HRR for the case with a beam remains higher than without. This corresponds with the observation of generally higher ceiling heat fluxes in the near field attributed to the constraining of the ceiling jet and a marginally deeper smoke layer.

During the steady phase of the burner assault, i.e., from 8 to 88 min, MLR and, correspondingly, HRR, were higher for the case with a beam versus without. With the beam, the HRR was c. twice that of the burner in isolation. Without the beam, the HRR was c. one and a half that of the burner in isolation.

In both experiments, the flaming of the CLT was observed to stop over most of the exposed surface. Owing to the method of fixing of the glulam, i.e., stirrups versus screwing from above, flaming continued in the vicinity of the glulam beam requiring intervention to finally extinguish the combustion. This is reflected in the residual in MLR and HRR towards the end of the experiment, see Figure 7 and Figure 8.

4.4 Bond-line failure

Bond-line failure (BLF) leading to premature char fall-off was observed in both the experiment with and without the

glulam beam. For the case without the beam, this is shown in Figure 13. With the beam, the detached charred lamella is seen on the floor and on top of the burner in Figure 14.

Figure 13: *Bond-line failure leading to premature char fall-off in experiment without beam.*

Figure 14: *Bond-line failure leading to premature char fall-off in experiment with beam. Detached char is apparent on floor and burner.*

Despite the BLF and resulting premature char fall-off, flaming of the CLT ceiling was observed to stop. Due to the limited exposed combustible surface area, i.e., only a ceiling, upon turning off the burners, the heat flux to the engineered timber ceiling quickly dropped below thresholds typically associated with auto-extinction, see Figure 15. This suggests that for hybridised construction formats, where little interaction between combustible surfaces exists and combustible surfaces are generally limited to ceilings, averting BLF through more heat resistant adhesives is not a prerequisite for adequate structural performance in the event of fire. However, it does require the designer to consider BLF in terms of the impact on structural capacity.

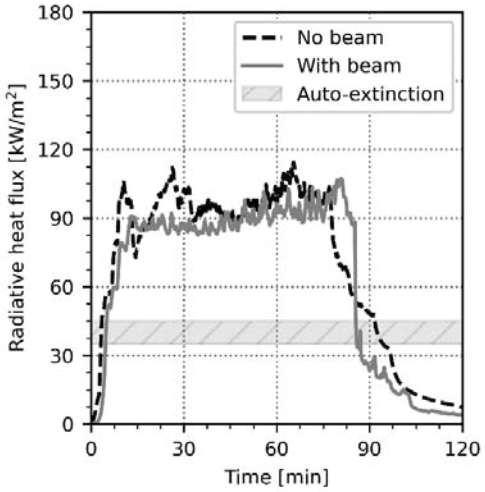

Figure 15: *Radiative heat flux with time to the ceiling at location 14.*

5 CONCLUSIONS

Two experiments are reported herein that are part of a larger body of research work. This paper has focused on the differences between exposed engineered timber ceilings that either include a beam (a glulam beam with CLT slabs) or feature a flat soffit (only CLT). In both experiments, the only variable is the beam which results in a ceiling protrusion. All other parameters, i.e., the CLT type, lay-up and adhesive, burner HRR and instrumentation remained the same. Considering the impact of the down-stand beam, it can be concluded that:

- The presence of the beam locally increased heat fluxes to the ceiling in the near field relative to the case without a beam. In proximity to the beam, this increase was around a factor of two and is attributed to a combination of the constraining of the ceiling jet and a deeper smoke layer.
- The increased heat flux to the ceiling translated to an increase in heat flux to the floor when considered relative to the case without a beam.
- The beam had little impact on reducing the flame lengths at ceiling level, with flaming observed over the full extent of the ceiling in both experiments once the burner HRR reached 1250 kW.
- The increased heat fluxes in the case with a beam present resulted in both a higher overall mass lost by the engineered timber ceiling and total heat release rate.

In more general terms, it is noteworthy that regardless of the presence of a beam, auto-extinction of flaming combustion of the CLT was observed to occur in both experiments. This was despite bond-line failures in both experiments, leading to premature char fall-off. In the

https://doi.org/10.52202/069179-0242

case with a beam, flaming continued in proximity to the glulam beam, which was attributed to the method of fixing, with the beam held in place from below via stirrups. This allowed a gap to develop between the top of the CLT and glulam beam, where flaming persisted, ultimately requiring intervention.

Based upon the findings of other studies conducted as part of the larger STA project, it is expected that the results of these experiments would be applicable to CLT manufactured by different suppliers, subject to consistency in moisture content, adhesive type, edge-bonding condition, CLT thickness and CLT lay-up. Studies reported in Hopkin et al. [10] noted there to be nominal differences in the fire behaviour characteristics of CLT from three different leading suppliers, subject to the same specification parameters. It is expected that such a small-scale testing format/regime could be utilised to inform whether the data developed from the large-scale experiments reported herein could be applicable to a given product/supplier.

ACKNOWLEDGEMENTS

The authors wish to acknowledge the contributions of the wider STA project team, including the discussions and technical contributions made by the Structural Timber Association (STA), BK Structures and Eurban.

REFERENCES

[1] Structural Timber Association, Structural timber buildings fire safety in use guidance. Volume 6 - Mass timber structures; Building Regulation compliance B3(1), V1.1. Structural Timber Association, 2020.

[2] S. Nothard, D. Lange, J. P. Hidalgo, V. Gupta, and M. S. McLaggan, 'The response of exposed timber in open plan compartment fires and its impact on the fire dynamics', in Proceedings of the 11th International Conference on Structures in Fire (SiF2020), Online, Nov. 2020. doi: 10.14264/5d97785.

[3] D. Hopkin et al., 'Large-scale enclosure fire experiments adopting CLT slabs with different types of polyurethane adhesives: Genesis and preliminary findings', Fire, vol. 5, no. 2, Art. no. 2, Apr. 2022, doi: 10.3390/fire5020039.

[4] U. Wickström, J. Anderson, and J. Sjöström, 'Measuring incident heat flux and adiabatic surface temperature with plate thermometers in ambient and high temperatures', Fire and Materials, vol. 43, no. 1, pp. 51–56, Jan. 2019, doi: 10.1002/fam.2667.

[5] J. Su, P.-S. Lafrance, M. Hoehler, and M. Bundy, 'Fire safety challenges of tall wood buildings – Phase 2: Task 2 & 3 – Cross laminated timber compartment fire tests', Fire Protection Research Foundation, Quincy, FPRF-2018-01, 2018.

[6] H. Ingason and U. Wickström, 'Measuring incident radiant heat flux using the plate thermometer', Fire Safety Journal, vol. 42, no. 2, pp. 161–166, Mar. 2007, doi: 10.1016/j.firesaf.2006.08.008.

[7] A. Häggkvist, J. Sjöström, and U. Wickström, 'Using plate thermometer measurements to calculate incident heat radiation', Journal of Fire Sciences, vol. 31, no. 2, pp. 166–177, Mar. 2013, doi: 10.1177/0734904112459264.

[8] V. Gupta, A. F. Osorio, J. L. Torero, and J. P. Hidalgo, 'Mechanisms of flame spread and burnout in large enclosure fires', Proceedings of the Combustion Institute, vol. 38, no. 3, pp. 4525–4533, 2021, doi: 10.1016/j.proci.2020.07.074.

[9] P. Kotsovinos et al., 'Fire dynamics inside a large and open-plan compartment with exposed timber ceiling and columns: CODERED #01 ', Fire and Materials, p. fam.3049, Feb. 2022, doi: 10.1002/fam.3049.

[10] D. Hopkin et al., 'Experimental characterisation of the fire behaviour of CLT ceiling elements from different leading suppliers', in Applications of Structural Fire Engineering, Ljubljana, Slovenia, 2021.

World Conference on Timber Engineering Oslo 2023

PERFORMANCE OF PASSIVE PROTECTION OF CROSS LAMINATED TIMBER DURING STANDARD FURNACE TESTS AND NATURAL FIRES

Siyimane Mohaine[1], Antonela Colic[2], David Morrisset[2], Jean-Christophe Mindeguia[3], Jean-Marc Franssen[4], Jochen Zehfuss[5], Robert McNamee[6], Luke Bisby[2], Fabienne Robert[1]

ABSTRACT: This paper presents the results of an experimental campaign designed to compare and understand the performance of passive protection under exposure to standard furnace tests and natural fires. As part of this campaign, five natural fire experiments were performed with partially protected cross-laminated timber (CLT) compartments under a range of ventilation conditions. In all the tests, only one side wall was left completely unprotected, and all other timber surfaces were protected with either two layers of 18 mm standard gypsum boards (GB) or two layers of 25 mm standard GBs. The structural CLT ceilings were subjected to a superimposed dead load of 1.35 kN/m² during the natural fire tests, and the fire load was (on average) 950 MJ/m²; chosen to represent the Eurocode 1991-1-2 characteristic value for dwellings. The performance of the passive protection was mainly evaluated with regards to the time to reach a protected timber surface temperature of 250°C. The testing confirms that the resulting fire protection performance of a given gypsum board layout depends on the ventilation conditions of the fire compartment, with more severe (and closest to ISO testing) outcomes when testing under ventilation-controlled scenarios. This paper provides data that sheds light on the co-dependency of the passive protection design and compartment fire dynamics and underlines the importance of considering the safety objectives of a building when defining the performance criteria of its structural elements.

KEYWORDS: Fire protection, Gypsum Plasterboard, Mass timber, Cross laminated timber, Natural fire

1 INTRODUCTION

"Too much fire protection is expensive, too little is dangerous" [1]. The use of structural passive fire protection (e.g. plasterboards) is often a key design approach – especially when designing for burnout of a compartment – to limit/prevent structural timber from contributing to a fire event and thus allow for successful compartmentation [2]. The thermal and physical properties of the plasterboards mitigate heat transfer to the structural timber elements in the event of a fire. For mass timber structures, the effectiveness of the protective plasterboards can be quantified in practice by tracking the temperatures at the interface of the plasterboard and the protected timber surfaces. This allows designers to compare the performance of such protective systems under various heating conditions.

Large scale compartment fire tests allow for the investigation of the fire protection instability depending on the natural fire dynamics combined with the application of structural load. Previous studies have demonstrated that flaming extinction in compartments can occur with limited amounts of exposed mass timber, and with the passive fire protection remaining in place. However, this has typically only been demonstrated for the designed fire duration (e.g. 4h [3]), after which experiments are usually terminated using manual suppression. In such prior test series, it has been shown that the total thickness of the necessary passive protection to prevent the contribution of timber to fire (for the constant fire load) varies depending on the ventilation conditions of the compartment. Since plasterboards are sensitive to the high incident heat fluxes (i.e., high heating rates may lead to accelerated deterioration), some natural fire scenarios may result in failure occurring earlier than in standard fire (i.e., furnace testing) conditions [4]. This was also noted by Hartl et al. [5] who tested small scale samples of gypsum plasterboards at heat fluxes of 50 and 100 kW/m².

[1] CERIB Fire Testing Centre, Epernon, France s.mohaine@cerib.com, f.robert@cerib.com
[2] School of Engineering, The University of Edinburgh, Edinburgh, The UK, a.colic@sms.ed.ac.uk, d.morrisset@ed.ac.uk, l.bisby@ed.ac.uk
[3] University of Bordeaux, I2M, France, jean-christophe.mindeguia@u-bordeaux.fr
[4] University of Liège, Belgium, jm.franssen@ulg.ac.be
[5] IBMB, Germany, j.zehfuss@ibmb.tu-bs.de
[6] RISE and Lund University, Sweden, robert.mcnamee@ri.se

https://doi.org/10.52202/069179-0243

The tests presented in the current paper are part of a larger research programme: the Épernon Fire Tests Programme – Phase 2. The project seeks to understand the links between normative fire resistance ratings and real fire performance in buildings for combustible and non-combustible structures [6] [7] [8] [9]. The objective of the second phase presented herein is to investigate the performance of different passive fire protection layouts under both standard furnace testing and compartment fire scenarios. The impacts of various parameters are considered, such as the ventilation conditions and the proportion of exposed mass timber surfaces. The performance of the implemented passive protection solutions is evaluated with regards to *(i)* the surface temperature between the fire protection boards and the timber during the entire duration of the fire (including the decay phase) and *(ii)* the time at which the protection fails (see later).

2 CHOICE OF THE PASSIVE FIRE PROTECTION LAYOUTS

The layouts investigated under standard furnace and natural fire conditions were chosen based on existing French guidelines for a layout associated with a fire resistance time of 60 min ([10] [11]). The proposed layout consisted of two Type A 18 mm thick gypsum boards (GBs). An additional layout with a presumed higher fire protection time was also considered, which consisted of two layers of 25 mm GBs. The same mechanical fixing rules – as presented in Table 1 – were used for both the standard furnace and compartment tests. The joints between the boards were staggered from one layer to the other. Distance of fasteners to edges and joints was 10 mm approximately.

Table 1: *Fixing rules for gypsum boards*

2*18 mm GBs			
GB layer		1st (inner) layer	2nd (outer) layer
Screws (length)		35 mm	55 mm
Spacing *(in both directions)*	Ceiling	300 mm	150 mm
	Walls	600 mm	300 mm
2*25 mm GBs			
GB layer		1st (inner) layer	2nd (outer) layer
Screws (length)		45 mm	70 mm
Spacing *(in both directions)*	Ceiling	300 mm	150 mm
	Walls	600 mm	300 mm

Throughout this work, the temperatures at the interface between the mass timber and the inner GB are identified as "surface temperatures" and the temperatures between two GB layers are identified as "interface temperatures".

3 STANDARD FURNACE TESTS

Intermediate scale furnace testing was performed to evaluate the performance of the chosen passive protection layouts under standard fire conditions. The performance has been assessed based on two parameters:
- the time at which the surface temperature reaches 250°C, and
- the time at which the inner GB layer starts to physically fall-off. This was evaluated through visual observation of the exposed face during the tests and the verification of the time at which the surface temperature differed by less than 50 K from the furnace temperatures.

For the performance of 2*18 mm GBs, three different sourcing of the gypsum boards were tested (S1, S2, S3). For the 25 mm GBs, only one sourcing of the boards was used. The tests were conducted under the ISO 834 standard fire exposure and were run until the GBs on all the timber surfaces started to detach from the timber. The GBs were fixed to horizontal CLT slabs (1,70 x 0,98 m²) and were exposed to fire over a surface of 1,30 x 0,98 m².

Table 2 summarizes the time at which the average surface temperatures reach 200°C (a temperature criterion suggested in the STA fire safety guidance to mitigate the onset of pyrolysis for the full duration of the relevant fire resistance period [12]), 250°C (a rise of 250 K is the temperature criterion according to EN 13501-2 and EN 14135 [13]) and 300°C (the temperature typically considered as representing the charring isotherm for timber [14]). In all cases, these temperatures were reached after 60 minutes, and only small deviations were observed between the three specimens. From the temperature criterion presented in Table 2, the difference between the 200°C and 300° criterion provides on average a difference of 12 minutes. For the remainder of the experimental programme presented in the current paper, all GBs correspond to S2.

Table 2. Inner interface temperature of the three 18mm GBs systems from different suppliers under ISO fire

	Interface temperature			Start of GB fall-off
	200°C	250°C	300°C	
S1	86 min *(±4 min)*	91 min *(±3 min)*	97 min *(±4 min)*	113 min
S2	81 min *(±2 min)*	87 min *(±3 min)*	93 min *(±4 min)*	118 min
S3	87 min *(±3min)*	93 min *(±3 min)*	99 min *(±4 min)*	132 min

An additional test has been performed to assess the performance of a thicker layer system, i.e. 2 x 25 mm GBs from supplier S2. The interface and surface temperatures of both layouts under the ISO exposure are shown in ***Figure 1***. Increasing the thickness of each individual GB layer by 7 mm postpones the time at which an average surface temperature of 250°C is reached by about 55 minutes.

https://doi.org/10.52202/069179-0243

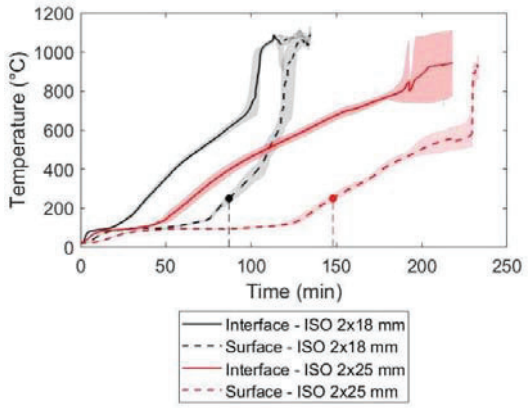

Figure 1. Comparison of ISO exposures with both 2x18 mm and 2x25 mm boards. The symbols indicate the time at which the surface reaches 250°C for each case.

4 NATURAL FIRE TESTS

The natural fire compartments were constructed with an internal area of approximately 21 m² enclosed by mass timber elements which are then surrounded by walls of aerated concrete blocks (Figure 2). Protected walls had two layers of GBs. The inner dimensions of the compartment after the installation of the timber elements and the GBs were 5.6 m (length) x 3.8 m (width) x 2.5 m (height), with small deviations when changing the arrangement of the protected walls (Table 3) or the thickness of the GBs.

The compartment was made of two lateral (i.e. side) loadbearing walls 180 mm thick CLT (40/30/40/30/40) supporting the timber ceiling, and two non-loadbearing longitudinal walls made of 60 mm thick (20/20/20) CLT.

In each test, only one timber surface was left initially exposed to fire. Figure 2 and Table 3 show the distribution of the protected and unprotected surfaces for each test, the passive protection layouts that were used, and the opening factors according to EN 1991-1-2 [15].

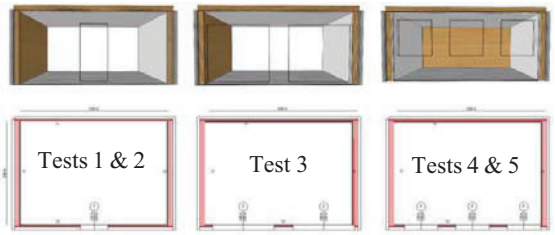

Figure 2: *Compartment plan with 3D view illustrating the opening configurations (W1: left wall, W2: right wall, W3: back wall, W4 : front wall with openings). Tests 1&2 (W1 exposed), Test3 (W1 exposed), and Test 4&5 (W3 exposed).*

The ceiling of the compartment used was a 180 mm thick CLT slab (40/30/40/30/40) for Tests 1 to 4 and a timber frame assembly (TFA) for Test 5 (Figure 3). The joists used in Test 5 were positioned on the spanning length of the ceiling and were spaced every 600 mm on centres. Noggins were also placed every 1,250 mm between the joists to allow additional fixing points for the GBs. The ceilings of the five tests were subjected to an imposed load composed of five dead weights for a total force of 29.5 kN, i.e., an average superimposed dead load of 1.35 kN/m².

Different ventilation openings were arranged in one of the long walls of the compartments to yield different ventilation conditions (i.e., fuel- or ventilation-controlled). Ventilation conditions ranged from an opening factor of 0.032 $m^{1/2}$ to 0.142 $m^{1/2}$.

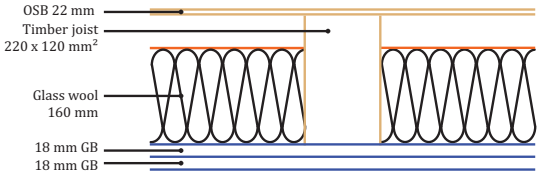

Figure 3: *Composition of the TFA ceiling (Test 5)*

Table 3. Description of the compartments for the 5 natural fire tests

	Test 1	Test 2	Test 3	Test 4	Test 5
Opening factor	0.032 $m^{1/2}$	0.032 $m^{1/2}$	0.142 $m^{1/2}$	0.065 $m^{1/2}$	0.065 $m^{1/2}$
Wall 1	180 mm CLT				
	2*18 GBs	2*25 GBs	2*18 GBs	2*18 GBs	2*18 GBs
Wall 2	180 mm CLT				
	-	-	-	2*18 GBs	2*18 GBs
Wall 3	60 mm CLT				
	2*18 GBs	2*18 GBs	2*18 GBs	-	-
Wall 4	60 mm CLT				
	2*18 GBs	2*18 GBs	2*18 GBs	2*18 GBs	2*18 GBs
Ceiling	180 mm CLT				220 TFA
	2*18 GBs	2*25 GBs	2*18 GBs	2*18 GBs	2*18 GBs

A total moveable fire load of about 950 MJ/m² (related to the floor area), consisting of six wood cribs (and a combination of heptane and gasoline for ignition) was adopted to represent dwellings as per EN1991-1-2 Annex E [4].

Gas phase temperature measurements were made with plate thermometers (PTs) installed 100 mm from the boundary surfaces of the compartment (11 PTs in front of the ceiling and 9 PTs in front of each wall). Surface and interface temperatures were measured with 7 Type K thermocouples (diameter 1.5 mm) per surface.

In the following subsections, the gas phase compartment and surface/interface temperatures are illustrated for a duration of 130 minutes to interpret the growth and decay phases of the fires. Only the temperatures under the

https://doi.org/10.52202/069179-0243

ceiling are presented in this paper; the complementary data will be presented elsewhere.

4.1 VARIATION IN PASSIVE PROTECTION THICKNESS: 2x18 mm | 2x25 mm

Tests 1 and 2 were intended to represent ventilation-controlled fires (opening factor 0.032 $m^{1/2}$), with an exposed load bearing CLT wall positioned on the left from the opening. The two tests employed different thicknesses of the passive fire protection installed on all other surfaces: 2x18 mm for Test 1, and 2x25 mm GBs for Test 2.

Plasterboard Performance

Figure 4 presents the gas phase compartment temperatures at the ceiling for the two thicknesses of GBs tested. The results seen in ***Figure 4*** are also compared against the ISO 834 temperature-time curve. Performance is analysed in three representative stages for Test 1: <80min (growth), 80-100 min (decay) and >100min (re-growth); and two stages for Test 2: <80min (growth), >80min (decay). Visual representation of the stages is also presented in ***Figure 5*** and ***Figure 6***.

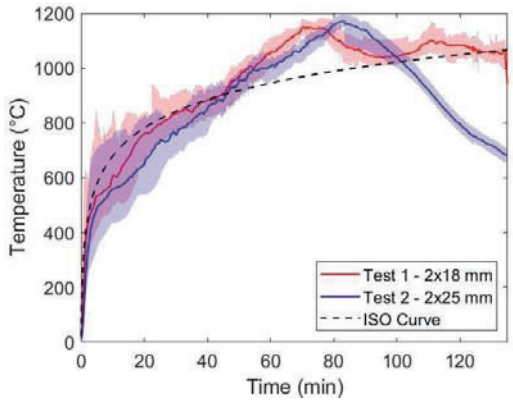

Figure 4: Compartment temperatures (from 11 PTs) under the ceiling for Test 1 (GB 2x18 mm) and Test 2 (GB 2x25 mm) compared to the ISO standard time-temperature curve (shaded areas show the extents of temperature variability).

As indicated in ***Figure 4***, after approximately 40-50 minutes the compartment temperatures in the natural tests 1 and 2 rise above the standardised test curve. The second stage marks the beginning of a decay phase at around 80 min for both natural fire scenarios. However, the onset of mechanical failure of the thinner (18 mm) layer of fire protection boards in Test 1 then led to the third stage, with fire regrowth at around 100 minutes. The temperatures inside the compartment remained approximately steady (at around 1000-1100°C). Conversely, in Test 2, the GBs remained in place for the full duration of the fire, and temperatures decreased in the compartment as a result.

In Test 1, the fire was manually suppressed after 135 minutes due to the severe fire regrowth and safety concerns. In Test 2, the temperatures continued to decay and the fire was manually suppressed after 225 minutes (when average temperatures were about 460°C). Moveable fuel was effectively consumed before the manual suppression in each case. Localised continuous flaming of the exposed load bearing wall was observed independently of the burn-out of the moveable fuel load, as shown in ***Figure 6***-3. This localized flaming continued up until the point of manual suppression (***Figure 6***-4). Continuous burning of the exposed CLT wall, as well as continuous smouldering in the other mass timber elements, were observed in both tests.

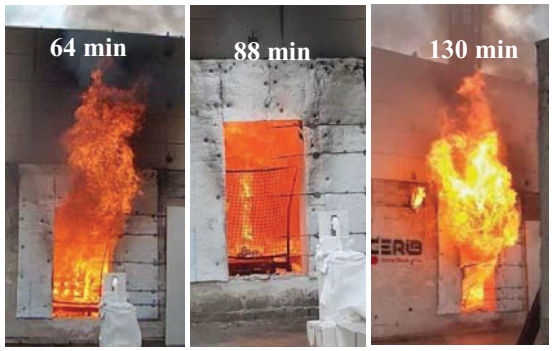

Figure 5. Test 1 stages: growth (l), decay (2), re-growth (3).

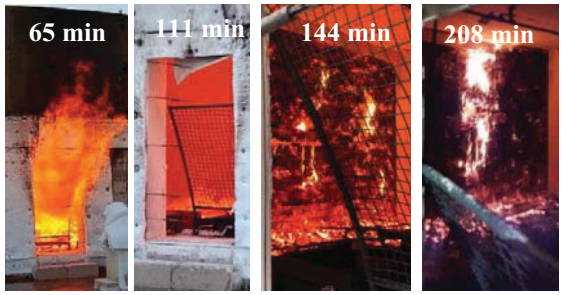

Figure 6. Test 2 stages: growth (l), decay (2); Continuous localised combustion of the exposed wall (3 & 4).

Interface and surface temperatures

Figure 7 shows the ceiling interface (i.e. between two layers of GBs) and surface (i.e. between timber and the inner GB) temperatures in Tests 1 and 2. During the first fire growth stage (<80min), the temperature plateau at 100°C is characteristic of the GB dehydration reaction in both tests, with a notably longer dehydration plateau seen in Test 2. The increased plateau duration was a result of the added thickness (i.e., increased volume of water in the GBs) from the 2*25 mm GBs compared to the 2*18 mm GBs.

https://doi.org/10.52202/069179-0243

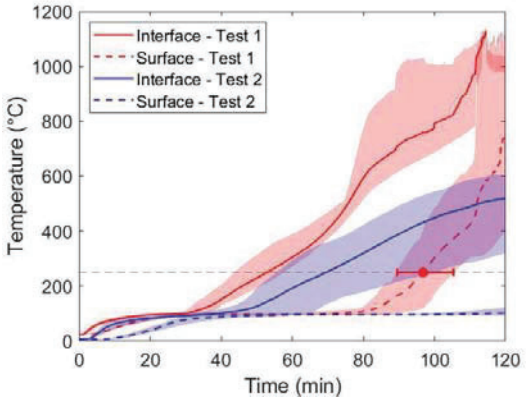

Figure 7. Test 1 and 2 – Ceiling interface and surface temperatures. The symbol indicates the time at which the surface of Test 1 reaches 250°C (error bars indicating the range of times observed).

In Test 1, thermally induced cracks lead to mechanical failure of the boards at about 100 minutes followed by rapid increases in interface temperatures. It should also be noted that after such mechanical failures these temperature measurements may be significantly influenced by gas phase temperatures and may no longer represent the interface temperatures. CLT surface temperatures reach 250°C as early as 90 minutes (an average time of 97 minutes). In Test 2, where thicker GBs are used, interface temperatures between the GBs enter a steady phase from 110 minutes onwards. The surface temperature of the CLT remains below 250°C for the full duration.

4.2 EFFECTS OF VENTILATION CONDITIONS

Tests 1 and 3 include compartments with the same boundary conditions (i.e. applied GBs and orientation of the exposed timber wall) and fuel loads, but a different size of the openings. Two ventilation conditions have been used, whereby an opening factor of 0.032 $m^{1/2}$ leads to ventilation-controlled conditions whereas 0.142 $m^{1/2}$ to fuel-controlled conditions.

Fire development is described in three stages for both experiments. Stages for Test 1 were explained in ***Figure 5***. Test 3's stages are: fire growth (<5minutes), steady state (<30min), and decay (>30minutes) as shown in ***Figure 8*** and ***Figure 9.*** The ventilation conditions resulted in faster fire growth in Test 3, reaching a maximum temperature of 1100°C within 10 minutes. The initial fire growth rate in Test 1 is lower, however it leads eventually to maximum temperatures of approximately 1100°C at 80 minutes.

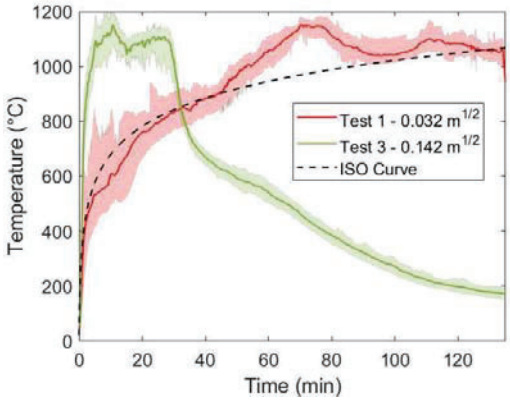

Figure 8: Compartment temperatures for Test 1 (opening factor 0.032 $m^{1/2}$) and Test 3 (opening factor 0.142 $m^{1/2}$) compared to the ISO 834 temperature-time curve.

Figure 9. Test 3 stages: growth (1-upper left), steady-state (2-upper right), decay (3-lower left); Continuous combustion of the exposed wall (4-lower right); Cracks after burnout of the moveable fuel load (5- last).

Rapid fire growth in Test 3 leads to a period of approximate steady temperature conditions where the temperature difference ranges between 200 to 600°C higher than compared to Test 1 or standardised furnace test during the first 30 minutes. The third stage of Test 3 is a decay phase where most of the moveable fuel is consumed; after which localised smouldering and flaming combustion of the combustible wall continues (***Figure 9-4***). All of the GBs remained fixed to the ceiling and walls

https://doi.org/10.52202/069179-0243

in Test 3, however many pronounced cracks were visible (***Figure 9-5***). Manual suppression was *not* performed, and eventually continuous smouldering combustion resulted in collapse of the unprotected wall at some unknown point during the following night.

Interface and surface temperatures

Figure 10 illustrates a more rapid increase in the interface temperatures early into Test 3 compared to Test 1. Test 3 also displays a shorter 100°C temperature plateau due to the more sever heating conditions. Interface temperatures continue to rise 30 minutes into Test 3, after which the compartment temperatures decay (see ***Figure 8***).

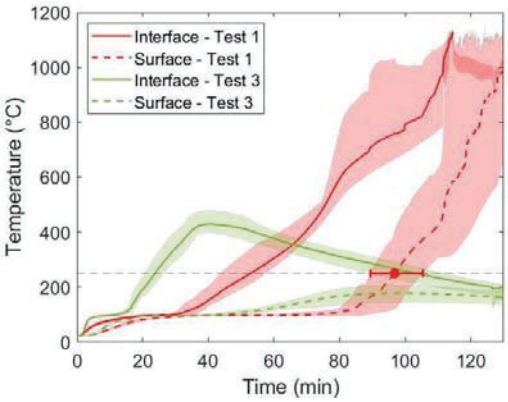

Figure 10. Test 1 and 3 – Ceiling interface and surface temperatures. The symbols indicate the time at which the surface reaches 250°C for each case.

The interface temperature data presented in ***Figure 10*** illustrates an earlier increase in the temperature at the interface compared to Test 1 but the surface temperatures for Test 3 were maintained below 200°C throughout the test. These results suggest that the rapid period of fire growth resulted in an earlier thermal wave through the first plasterboard, but the time scales of burning prevented the thermal penetration to significantly affect the second layer of plasterboard.

In Test 1 both surface and interface temperatures continued to rise at the similar rate once the GBs were dehydrated. Whilst the influence of the heating rate on the performance of the plasterboards was discussed previously [5], premature failure of the front exposed GBs was not observed for the fire conditions in Test 3. This result this confirms the importance of the exposure duration in addition to the heating rate [5].

Interface and surface temperatures: Test 1 and standard furnace fire test

The under-ventilated fire scenario (Test 1) and the ISO 834 furnace test show similar trends in the temperature developments. The average interface temperatures for the standard fire test and Test 1 follow similar heating rates up to 60 min. At about 75 minutes, a local rapid increase of temperatures was observed in Test 1, leading to local temperatures of 1000°C as early as 90 minutes (***Figure 11***).

Surface temperatures for Test 1 are comparable to the ISO 834 standard fire results. An average surface temperature of 250°C was reached at 87 minutes for the ISO 834 test and 97 minutes for Test 1, while this was never reached for Test 3.

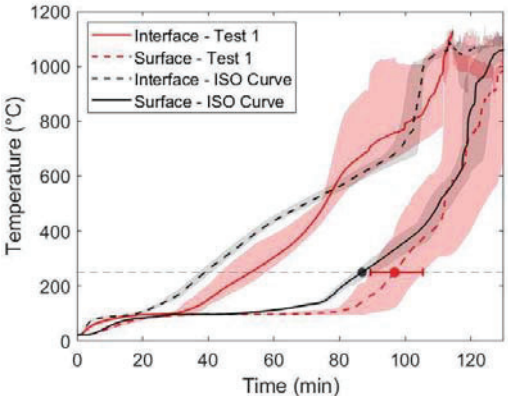

Figure 11. Surface and interface temperatures for Test 1 and furnace test (2*18 mm GBs). The symbols indicate the time at which the surface reaches 250°C for each case.

4.3 CLT VS. TIMBER FRAME CEILINGS

The last two tests of the series differ from Test 1 to Test 3 on two points:
- the use of an "intermediate" opening factor of 0.065 $m^{1/2}$ statistically representative of openings in many residential buildings (see e.g. [16]); and
- the modification of the exposed timber surface. In the first three tests, one lateral 180 mm CLT loadbearing wall was systematically exposed to fire, and continuous smouldering long after the end of the test led to eventual collapse. Thus, in the last two tests, it was decided to expose one long 60 mm CLT non-loadbearing wall (W3, in Figure 2).

Two additional tests were performed with intermediate ventilation conditions in order to compare a CLT and TFA ceiling in natural fire conditions. Test 4 and Test 5 are in all other respects identical except for the nature of the timber ceiling itself. Test 4 consisted of a CLT ceiling (identical to the one used for the previous tests) whilst the latter included a TFA ceiling. Whilst a detailed analysis of these two tests will be provided in a forthcoming paper, the main outcomes are presented here to illustrate differences that can be observed between the performance of mass timber and timber frame under natural fire conditions. Figure 12 shows the compartment temperatures for the two tests, with a reasonable similarity. Test 5 was, however, terminated at 250 minutes due to collapse of the TFA ceiling (see Figure 13).

https://doi.org/10.52202/069179-0243

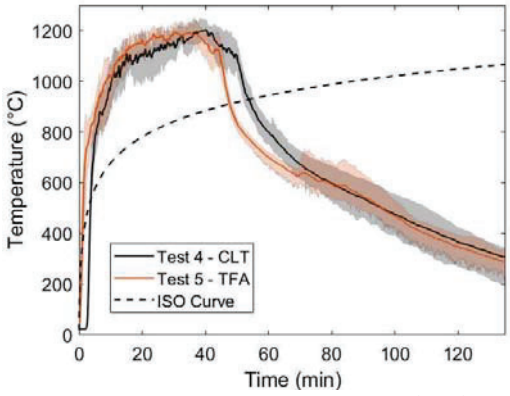

Figure 12. Compartment temperatures under the ceiling (measured with PTs) for tests 4 and 5.

Figure 13. Test 5 failure stages of the protected TFA ceiling.

5 DISCUSSION

Usually standardised pass/fail requirements for surface temperatures are representations of pyrolisis isotherms which indicate that timber is charring or has charred (i.e. 300°C in EN 13381-7 [17], or T_{amb}+250°C in EN 14315 [13] and as a threshold for K classification according to EN 13501-2 [18]). If one considers the *onset* of timber pyrolysis as a timber degradation criterion, this can be considered to occur from about 200°C [19]. The standard tests performed on three different sources of a 2x18 mm GBs layouts have shown that the difference in time to reach these different temperatures is about 10 minutes. Rather than discussing the temperature criteria themselves, an important question to answer is therefore the duration during which this temperature criterion should be delayed or prevented in a standard furnace test in order to limit the contribution of structural timber elements to a real fire – depending on the safety objectives and the fire safety strategy for any given building. If the temperature criterion is reached but the temperatures in the compartment remain high, the degradation of the GBs and the pyrolysis of the protected timber is likely to continue, which could then lead to fire regrowth and the prevention of burnout conditions [2] without fire service intervention. A single fire resistance rating (i.e., R60 or R90) could be associated with different safety objectives or fire safety strategies depending on the type of building (dwellings, offices ...). For some building categories (e.g. dwellings) a common strategy in some European jurisdictions is to limit the immediate evacuation to the floor (or even only the apartment) where the fire has started, while in other jurisdictions the strategy is instead that all people should leave the building alongside an assumption that the fire brigade *will* rapidly intervene. Such complexities warrant further investigation to observe the performance under a range of natural fire conditions.

Five natural fire tests have been performed in timber compartments of 21 m² with one exposed CLT wall and all other surfaces protected by either 2x18 or 2x25 mm GBs. It should be noted that different outcomes could result from exposing more timber surfaces or from changing the orientation of the exposed timber surfaces (e.g., ceiling instead of a wall). Three ventilation conditions were used, ranging from a ventilation-controlled fire (one opening, O=0.032 $m^{1/2}$) to a fuel-controlled fire (two openings, O=0.142 $m^{1/2}$). The variable of the ventilation factor in a realistic fire scenario assumes airflow through an available opening area (e.g., windows). However, toughened and fire rated glazing may not ultimately break, which could lead to a ventilation-limited fire even when large amounts of glazing are present. Hence, this paper analysed performance of the gypsum boards as a product and their influence on the compartment performance (i.e. fire dynamics) assuming all available openings allow for ventilation.

The compartment temperatures leading to manual fire suppression (Tests 1, 2 and 5) or without manual fire suppression (Tests 3 and 4) are given in Figure 14.

In the under-ventilated fire scenarios, the failure of the protection layouts in Test 1 (with 2x18 mm GBs) did not appear for the first 60-80 minutes, but the GBs failure ultimately led to fire regrowth and termination of the test by manual suppression (135 minutes). In Test 2, increasing the thickness of the two GBs by 7 mm each (25 mm layouts instead of 18 mm) significantly reduced the surface temperatures, keeping them below 250°C for the entire duration of the test up to manual suppression. Test 3 was more representative of a fuel-controlled fire and was characterised by a rapid growth and comparatively short fully developed phase. Thus, the interface temperatures in Test 3 were observed to decrease after approximately 40 min and the surface temperatures were found to remain below 250°C for the duration of the experiment. Results for tests 4 and 5, where three openings were used (O=0.065 $m^{1/2}$), are not part of this discussion but are noted to inform that the results obtained on CLT structures cannot strictly be applied to TFA structures. In the performed tests, an earlier failure of the TFA ceiling was observed compared to the CLT ceiling.

https://doi.org/10.52202/069179-0243

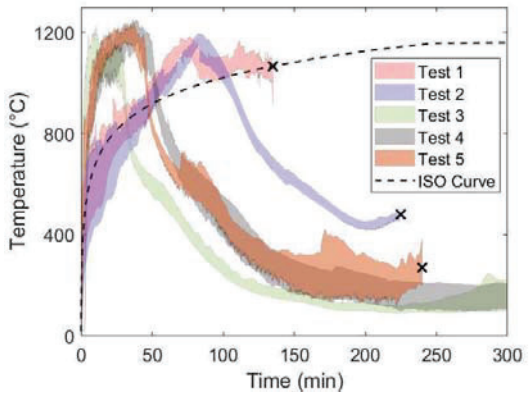

Figure 14. Overview of the compartment temperatures of the five natural fire tests up to 300 minutes with indication of manual suppression times (Tests 1, 2 and 5)

Each compartment was observed to collapse in the night following the experiment. Even the trials in which the CLT surface was measured to remain below the pyrolysis temperature were observed to ultimately fail (e.g., Test 3). In Test 1, following fire suppression at 135 min, the compartment temperatures were observed to steadily increase over a period of approximately 250-500 min. While the time of the structural failure is difficult to predict with certainty from temperature measurements alone, a collapse was observed approximately 6 hours following manual fire suppression. This underlines the importance of properly suppressing continued flaming and smoldering. In-depth heating of the timber may result in ongoing smouldering of mass timber structural elements, and potentially in re-ignition at a later stage. Understanding the mechanisms that may lead to delayed collapse, as observed in these experiments, requires further investigation.

6 CONCLUSIONS

A series of furnace and natural fire tests has been performed to study the performance of two passive fire protection schemes in various standard and natural compartment fire scenarios, and with the presence of one exposed CLT wall. It should be noted that different outcomes may result from exposing more timber surfaces or from changing the orientation of the exposed timber surfaces (e.g., ceiling instead of a wall). The experimental campaign confirmed that the performance of a given GB layout depends on the ventilation conditions of the fire compartment, with more severe outcomes when testing under ventilation-controlled scenarios for the given fuel loads used. This paper and the overall Épernon Fire Tests Programme Phase 2 suggest that GB passive protection applied to CLT appeared to perform about as well as it did in furnace tests (for the chosen performance criteria and the configurations tested). The data confirmed that ongoing smouldering and localised burning, if not fully supressed after the steady burning phase of a severe fire, have the potential to result in reignition and/or structural collapse at some time after the fire *appears* to have been extinguished. The conducted tests provide data that underline the importance of considering the safety objectives of the concerned building when defining performance criteria of a structural element.

REFERENCES

[1] P. H. Thomas et J. M. Heselden, «Fully-developed fires in signle compartments : a co-operative research programme of the conseil international du bâtiment (CIB report n°20),» Fire Research Note n° 923, 1972.

[2] A. Law et R. M. Hadden, «Burnout means burnout,» *SFPE ,* vol. Q1, n° %1Issue 5, 2017.

[3] J. Su, P.-S. Lafrance, M. Hoehler and M. Bundy, "Fire Safety Challenges of Tall Woof Buildings - Phase 2: Task 2 & 3 - Cross Laminated Timber Compartment Fire Tests (FPRF-2018-01)," Research for the NFPA mission, 2018.

[4] B. Chorlton, B. Forrest, J. Gales et B. Weckman, «Performance of type Y gypsum board on timber to non-standard fire exposure,» *Fire and Materials,* pp. 1-16, 2020.

[5] A. Hartl, Q. S. Razzaque, A. Lucherini et C. Maluk, « Comparative study on the fire behaviour of fire-rated gypsum plasterboards vs. thin intumescent coatings used in mass timber structures, in:,» chez *SiF 2020 – 11th International Conference of Structures in Fire*, Queensland , 2020.

[6] F. Wiesner, A. Bartlett, S. Mohaine, F. Robert, R. McNamee, J.-C. Mindeguia et L. Bisby, «Structural Capacity of One-Way Spanning Large-Scale Cross-Laminated Timber Slabs in Standard and Natural Fires,» *Fire Technology,* n° %1https://doi.org/10.1007/s10694-020-01003-y, 2020.

[7] J.-C. Mindeguia, S. Mohaine, L. Bisby, F. Robert, R. McNamee et A. Bartlett, «Thermo-mechanical behaviour of cross-laminated timber slabs under standard and natural fires,» *Fire and Materials,* p. 1–19, 2020.

[8] S. Mohaine, N. Kalaba, J.-M. Franssen, L. Bisby, A. Bartlett, J.-C. Mindeguia, R. McNamee, J. Zehfuss and F. Robert, "Thermal and mechanical response of reinforced concrete slabs under natural and standard fires," in *6th International Workshop on Concrete Spalling due to Fire Exposure*, Sheffield, UK, 2019.

[9] A. Bartlett, R. McNamee, J. Zehfuss, S. Mohaine, C. Tessier et L. Bisby, «Heat fluxes to a façade resulting from compartment fires with combustible and non-combustible ceilings,» chez *3rd International Symposium of Fire Safety of Façades*, Paris, 2019.

[10] AFNOR, *NF EN 1995-1-2/NA - Eurocode 5 : Conception et calcul des structures en bois - Partie 1-2: Généralités - Calcul des structures au feu - Annexe Nationale à la NF EN 1995-1-2:2004,* Avril 2020.

[11] ADIVBOIS, *Bâtiments d'habitation de 8 à 28 m - Préconisations pour la sécurité en cas d'incendie pour les immeubles bois prévus dans le cadre des prochains JOP de Paris 2024,* 10 mars 2020.

[12] STA, «Structural timber buildings fire safety in use guidance - Volume 6 - Mass timber structures; Building Regulation compliance B3(1),» STA fire safety research and guidance project Version v1.1 October 2020.

[13] AFNOR, *NF EN 14135 - Revêtements - Détermination de la capacité de protection contre l'incendie,* 2005.

[14] AFNOR, *NF EN 1995-1-2 : Eurocode 5 - Conception et calcul des structures en bois - Partie 1-2 : généralités - Calcul des structures au feu,* 2005.

[15] AFNOR, *Eurocode 2 : Calcul des structures en béton - Partie 1-2 : règles générales - Calcul du comportement au feu,* 2005.

[16] D. Brandon, «Fire Safe implementation of visible mass timber in tall buildings – compartment fire testing,» RISE Report 2020:94, 2020.

[17] AFNOR, *NF EN 13381-7 - Méthodes d'essai pour déterminer la contribution à la résistance au feu des éléments de construction - Partie 7 : protection appliquée aux éléments en bois,* 2019.

[18] AFNOR, *Classement au feu des produits et éléments de construction - Partie 2 : classement à partir des données d'essais de résistance au feu à l'exclusion des produits utilisés dans les systèmes de ventilation,* 2016.

[19] A. Bartlett, R. Hadden et L. Bisby, «A Review of Factors Affecting the Burning Behaviour of Wood for Application to Tall Timber Construction,» *Fire Technology,* vol. 55, pp. 1-49, 2019.

[20] C. Wade, C. Dagenais, M. Klippel, E. Mikkola et N. Werther, Fire Safe Use of Wood - Global Design Guide, https://doi.org/10.1201/9781003190318: 1st Edition, CRC Press, 2022.

https://doi.org/10.52202/069179-0243

World Conference on Timber Engineering Oslo 2023

NATURAL FIRE TESTS ON GLT COLUMNS INCLUDING THE COOLING DOWN PHASE

Fabienne Robert[1], Jean-Marc Franssen[2], Jochen Zehfuß[3], Sven Brunkhorst[4], Patrick Bamonte[5], Silvio Renard[6], Robert McNamee[7], Thomas Gernay[8]

ABSTRACT: This paper presents the data and the results of seven fire tests performed on glue laminated timber columns in a compartment built especially for the tests and in which timber wood cribs created a so-called natural fire. These tests are part of a research programme titled "burnout resistance" to establish a new methodology to better describe performance of structural elements during the whole duration of a fire. Comparisons with similar tests made in a fire resistance furnace allow comparing charring rates observed in standard conditions and in natural fires.

KEYWORDS: Fire, Column, GLT, timber, cooling

1 INTRODUCTION

The concept that has been used overwhelmingly for nearly one century to characterize and classify the ability of loadbearing members to withstand fire exposure is the concept of *fire resistance*. The element is loaded and then subjected to a standardised heating regime characterised by a time-temperature curve, for example the ISO 834 fire curve mentioned in Eurocode 1 [1] in Europe. If the fire resistance is determined by a test (as opposed to calculation), some prescriptions are also given about the pressure and the oxygen content in the furnace atmosphere [2]. The concept of fire resistance is a grading system. It is known that the duration which is the expression of the result must not be taken as the time during which the member, used in a real structure, would survive to a real fire that would develop in a real building. The underlying hypothesis of using the concept is that there is a monotonically increasing relationship between the fire resistance time and the performance level in a real fire; an element that has a higher fire resistance should perform better in a real fire, whatever the fire may be, than an element with a lower fire resistance. Similarly, if two different elements have the same fire resistance time, their performance in a real fire should be equivalent.

Although the concept of fire resistance has many shortcomings, there is some logic in that as long as the temperature of the fire is constantly increasing, as this will lead to constantly increasing temperatures in the elements and thus presumably to a constantly decreasing load bearing capacity.

Yet not all structures collapse during the heating phase of a fire. Some, if not most of them when the fire design was appropriate, are still standing when the fire temperatures start decreasing, either from firefighting intervention or from a lack of combustible material in the fire compartment. If the structure collapses during the cooling phase of the fire or even after the temperatures in the building compartment have gone back to ambient, this is a serious hazard for occupants that may not yet have evacuated the building but also for firefighters and rescue services who may still be fighting the fire or searching for occupants. There is a need for a new concept to allow evaluating the risk of collapse during or after the peak of the heating phase, as the current concept of fire resistance does not address this phase of the fire.

This paper first explains why the risk of collapse during the cooling phase of the fire may be particularly critical for timber elements, from theoretical considerations, then from some numerical examples and from experimental tests performed in a revised standardised environment. It then presents the results of seven tests performed in a room filled with a timber fuel load to generate a so-called natural fire with the first objective to check whether the observations and the conclusions derived from theoretical considerations, from numerical modelling and from standardised tests would remain valid when timber elements are subjected to a fire development more similar to a real fire. The final objective of the research is to provide appropriate tools to design non-protected timber elements which maintain stability during the whole duration of the fire including the cooling down phase.

2 THEORETICAL CONSIDERATIONS

Timber is a solid material in which heat transfer is predominantly by conduction when subjected to a

[1] Fabienne Robert, CERIB, France, f.robert@cerib.com
[2] Jean-Marc Franssen, Liege University, Belgium, jm.franssen@uliege.be
[3] Jochen Zehfuß, Technische Universität Braunschweig, Germany, J.Zehfuss@ibmb.tu-bs.de
[4] Sven Brunkhorst, Technische Universität Braunschweig, Germany, S.Brunkhorst@ibmb.tu-bs.de
[5] Patrick Bamonte, Politecnico di Milano, Italy. patrick.bamonte@polimi.it
[6] Silvio Renard, CERIB, France, s.renard@cerib.com
[7] Robert McNamee, RISE Research Institutes of Sweden and Lund University, Sweden, robert.mcnamee@ri.se
[8] Thomas Gernay, Johns Hopkins University, USA, tgernay@jhu.edu

https://doi.org/10.52202/069179-0244

temperature gradient. This is the case in a solid timber wall or slab when building physics considerations are at stake, for thermal insulation of a house in the winter, for example. This is also the case in timber or in the charred layer of a timber element subjected to the fire, although many chemico-physical phenomena which are much more complex than conduction occur in this case, such as evaporation of moisture, movement of moisture, pyrolysis, combustion of the char, formation of cracks and shrinkage leading to a change of geometry [3]. The subsequent considerations are based on a simple conductive model, the simplicity of which allows deriving interesting qualitative conclusions.

Starting from an initial condition when a section is at a low quite uniform temperature distribution, the thermal gradient during a fire is from the outside to the inside of the section as long as the fire temperature increases and, in the beginning of the cooling phase, as long as the fire temperature is higher than the surface temperature of the section. The heat transfer is thus also from the outside to the inside of the section and the temperatures are rising everywhere in the section.

When the fire temperature becomes lower than the surface temperature of the section, the heat exchange at the surface is from the section to the environment and the peripheral zones of the section start cooling down. Yet, there is still a positive temperature difference between these peripheral zones and the centre of the section. As a consequence, part of the energy of the peripheral zones does not travel toward the environment, but toward the centre of the section where the temperatures keep on rising for a certain time, to finally decrease when the whole section goes back to ambient temperatures.

Figure 1, for example, shows the temperature profile along the centreline of a 280 x 280 mm² timber section subjected to the parametric fire of Eurocode 1 [1] with a Γ factor equal to 1 (and, thus, a temperature evolution during the heating phase very close to the ISO 834 fire curve) and a heating phase of 60 minutes; see Figure 4 for curves with a Γ factor equal to 1. The curves of Figure 1 result from numerical modelling, see section 3, and the temperatures are given after 1, 2, 3 and 4 hours.

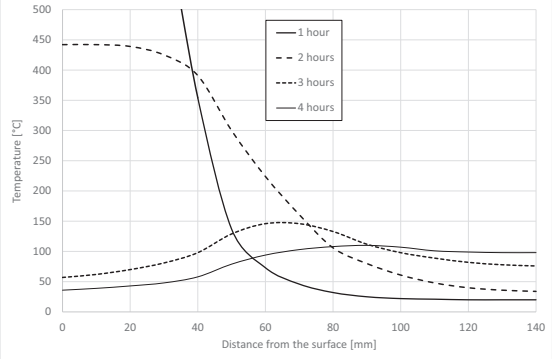

Figure 1: *Temperature evolution in a square timber section*

It can be observed that the temperature continues increasing in the zones of the sections long after the fire has reached its maximum temperature. A similar behaviour occurs in a human body member that has been severely burnt at the surface, hence the recommendation to keep the member under cold water for a long duration. What is specific to timber yet, is that the loss of mechanical properties with temperature is very fast, with all strength being lost at a temperature as low as 300°C according to Eurocode 5 [4]. Figure 2, for example, shows the evolution of the relative compressive strength of timber according to Eurocode 5 [4].

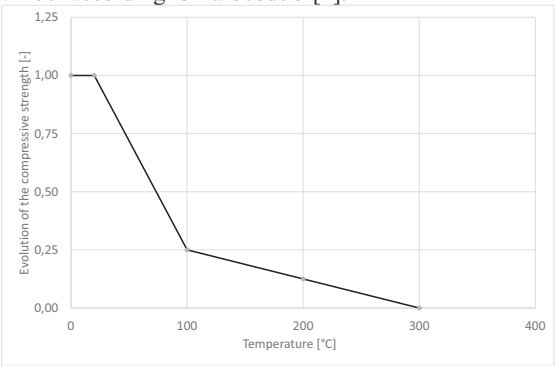

Figure 2: *Decrease of compressive strength according to EC5*

In addition to that, most of the phenomena that develop during heating, such as moisture evaporation, pyrolysis and combustion are irreversible (moisture may re-enter in the section in the long term, but not in the timeframe of a few hours) and it is thus unlikely that the mechanical strength can recover when char or heated timber cool down. Figure 3 shows, as a dotted line, the maximum temperature observed at any time along the centreline under the parametric fire discussed in Figure 1 and, as a full line, the residual compressive strength obtained from the curve of Figure 2 assuming that the residual strength is the same as the one determined at the maximum temperature.

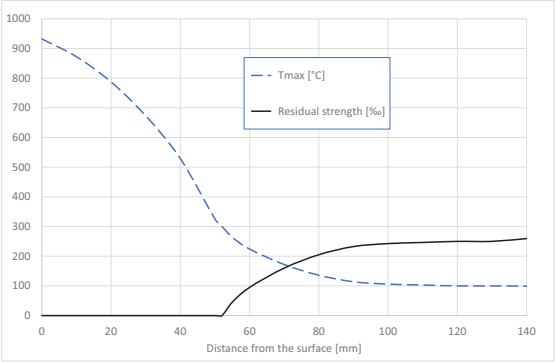

Figure 3: *Maximum temperature computed and corresponding residual compressive strength in a timber square section*

3 NUMERICAL SIMULATIONS

To quantify the theoretical considerations developed in section 2, Gernay made extensive numerical simulations

https://doi.org/10.52202/069179-0244

on timber columns [5], deriving their 'Duration of Heating Phase' (DHP [6]). The DHP quantifies the *longest* duration of exposure to heating according to the standard ISO 834 fire that will guarantee stability of a member throughout the entire fire duration. Figure 4 shows, in addition to the ISO curve on which the fire resistance time R has been noted, four parametric fire curves, each characterized by a different duration of the heating phase. Only one of these curves, the black one, corresponds to the DHP.

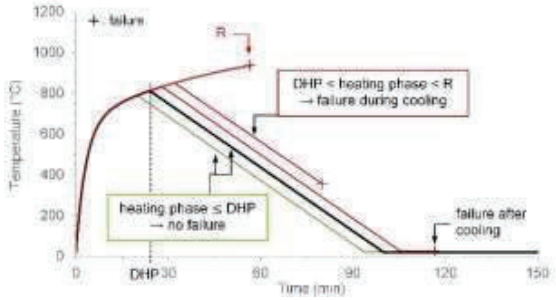

Figure 4: *Principle of the DHP*

In these simulations, the thermal and mechanical properties were taken as recommended by Eurocode 5 and it was assumed that all properties during the cooling phase keep the value they had at maximum temperature.
Gernay concluded that, depending on conditions, the DHP of timber columns varies between 20% and 50% of their standard fire resistance time. In other words, a column that is rated as R60 will collapse during or after the cooling phase if it is heated by the ISO curve for more than 30 minutes, followed by a linear cooling down phase of the fire temperature. In the worst situations, the heating phase of the fire cannot last for more than 12 minutes if stability after full burnout must be ensured.

4 EXPERIMENTAL TESTS IN MODIFIED STANDARD CONDITIONS

The numerical results mentioned in Section 3 are dependent on hypotheses on the material properties that, although they seem reasonable, have not been validated experimentally. The precise determination of all these properties in the cooling phase may be the topic of further fundamental research. In the meantime, researchers rely on experimental tests performed on timber elements to investigate the behaviour of these elements, such as the tests reported by Kinjo et al on GLT beams [7]. An experimental program was launched by CERIB with international partners to see whether the conclusions of the numerical simulations reported in [5] could be confirmed by tests on full scale timber columns.
A series of 8 tests were performed at the Technische Universität Braunschweig glued laminated timber columns with a section of 280 x 280 mm² [8]. The columns were pinned-pinned at the ends with a length between the support of 3,72 m and the load was applied with an eccentricity of 20 mm at each end. The columns were tested in a standard fire resistance furnace in which the heating according to the ISO 834 curve was applied for different durations, followed by a linear cooling down phase with a rate of -10.4°C/min.
The fire resistance of the columns was first determined as 55 and 58 minutes (two specimens). Two specimens were then subjected to a heating phase of 15 minutes and failed after 98 and 153 minutes. Two specimens heated for 10 minutes both survived the defined heating-cooling exposure. These furnace tests showed that timber columns can fail during the cooling phase when exposed to standard ISO 834 fire exposure for a duration significantly shorter than their standard fire resistance. In this particular case, the DHP between 10 and 15 minutes, is in the range of (18% ; 27%) of the average value of the fire resistance time (56.5 minutes), rather on the lower side of the range (20 % ; 50%) observed in the numerical analysis.
Thermocouples inside the columns also confirmed the sustained temperature increases for hours after the end of the heating phase, as shown by the numerical models.

5 EXPERIMENTAL TESTS UNDER NATURAL FIRE CONDITIONS

5.1 INTRODUCTION

Although the tests mentioned in section 4 confirmed the theoretical considerations and the numerical simulations, these tests have some features which are different from those of a real fire such as, for example, the nature of the fuel, the oxygen content, the shape of the cooling phase curve and the procedure that was followed in the tests to control the temperature in the cooling phase.
A series of tests was thus performed in a compartment specifically built at the Fire Testing Centre of CERIB, in France, in condition supposed to represent as closely as possible the conditions which could prevail in a real fire.
.

5.2 THE COMPARTMENT AND THE FIRE LOAD

The compartment was made of 300 mm walls of aerated concrete blocks and the roof was made of 200 mm thick slabs of aerated concrete. The concrete floor was insulated by a layer of mineral fibres, covered by a 20 mm thick layer of plasterboards. The ceiling was made of 200 mm thick slabs of aerated concrete, protected for the tests 11 to 15 by 55 mm of mineral wool.
The distance from the floor to the ceiling was 3.10 m for tests 9 and 10 and 3,05 m thereafter, and the internal dimensions in the plan view were 6.00 m by 4.00 m.
Different openings were made in one of the long walls to create the desired opening factor as mentioned in Table 1.
The fire loads was made of wood cribs of (0.75 m)³ made of 10 layers of 5 sticks with a section of 83 x 83 mm². The fire load was also varied from test to test to create the fire load density mentioned in Table 1. The wood cribs were ignited simultaneously to reach as quickly as possible a post-flashover fire.

https://doi.org/10.52202/069179-0244

The main characteristics of each tests are shown in Table 1, with the shaded cells showing the difference with respect to test 10 which could be seen as a reference from which variations have been made.

Table 1: *Conditions in the fire compartment*

Test	O ($m^{1/2}$)	q (MJ/m^2)	Section (mm^2)
9	0.144	780	280 x 280
10	0.065	780	280 x 280
11	0.065	950	280 x 280
12	0.065	780	340 x 340
13	0.065	780	360 x 360
14	0.065	420	280 x 280
15	0.032	780	280 x 280

5.3 THE COLUMNS

The tested columns were made of GLT with a section of 280 x 280 mm² for most of them, 340 x 340 mm² for test 12 and 360 x 360 mm² for test 13. The length of the timber columns was 3 680 mm. With the steel head plate and base plate, axes of the cylinders that formed the boundary conditions at both ends were at a distance of 3 740 mm.

5.4 THE LOAD

As for the tests made in Braunschweig, a load of 322 kN was applied with an eccentricity of 20 mm in one direction at both ends. The load was maintained for 15 minutes before the fire load was ignited and it was kept constant during the whole fire duration.

5.5 THE FIRE TEMPERATURES

The average temperature recorded in the compartment for all tests can been seen on Figure 5.

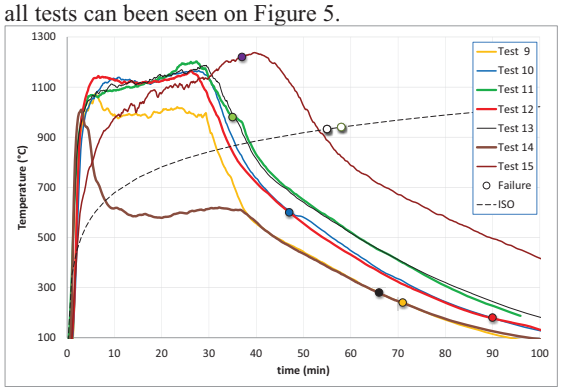

Figure 5: *Temperatures in the fire compartment*

Test 9 had a very large opening factor created by 3 openings of 1,30 x 2,50 m², see Figure 6, which led to the temperatures being limited to 1 000°C during only 30 minutes.

Figure 6: *Test 9 during the cooling phase*

The five subsequent tests were performed with an opening factor reduced by a factor of 2, with 3 openings of dimensions 1,30 x 1,50 m².

A similar situation developed in the compartment during tests 11, 12 and 13 although the fire load has been increased by 22% in test 11.

The fire load was reduced in Test 14 leading to a fuel-controlled fire with a lower power than the previous tests as soon as the heptane used as an ignition source was consumed. Oxygen concentration in the compartment indeed remained around 15% from minute 7 to minute 40 and increased in the cooling phase (oxygen concentration was around 2% for all other tests - except test 9 were it was around 5% - until the cooling phase started). This resulted in the peak temperature of around 1 000°C to be observed only from minute 2 to minute 5, after which a plateau of 600°C lasted for about 40 minutes.

The opening factor was again reduced by a factor of 2 for test 15 which was performed with a single opening of dimensions 0,95 x 2,40 m². The temperature development was more severe in this test with average temperatures reaching 100°C after 10 minutes, increasing steadily up to some 1 250°C after 45 minutes when the cooling down phase started.

5.6 RESULTS

In test 9, the column failed after 71 minutes when the temperatures in the compartment were down to the range from 200 to 300°C. Figure 7 shows the evolution of the temperature measured at different depth from the surface on the centreline of the section, each curve being the average of 6 measurements, 2 in the lower part of the column, 2 at mid height and 2 in the upper part. Although these temperatures have been obtained for a different fire curve and they are presented in a different form, these results confirm the trend presented in Figure 1, with temperatures decreasing very soon after the peak of the gas temperatures in peripheral zones of the section, while they keep on increasing during the cooling down phase in the central zones.

https://doi.org/10.52202/069179-0244

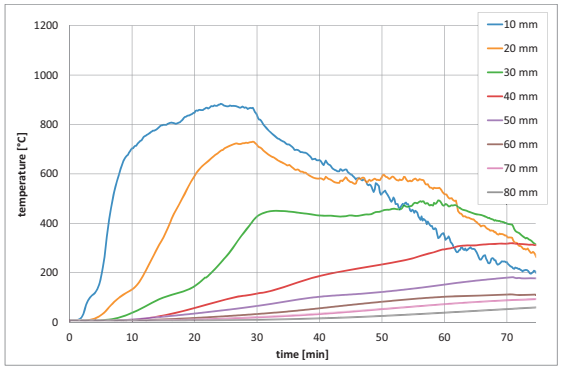

Figure 7: *Evolution of the temperature at different depth in the section for test 9*

At the time of failure, temperatures were at or above 300°C at 42 mm from the surface, 115°C at 60 mm and 55°C at a 80 mm. From the time it took to the 300°C isotherm to reach different depth, the average value of the charring rate can be calculated as 1.41 mm/min for the first 14 minutes, 0.83 mm/min from 14 to 26 minutes, and 0.28 mm/min from 26 to 61 min. These values can be compared to the quasi-constant value of 0.6 mm/min which was observed during tests 1 and 2 made under ISO curve in Braunschweig.

In test 10 where the opening factor had been reduced, the column failed after 47 minutes when the temperatures in the compartment were around 600°C. The temperatures in the peripheral zones increased faster, with average values of the charring rate varying from 1.78 mm/min during 11 min, 1.33 mm/min to 19 min and 1 mm/min up to 27 min. At the time of failure, a layer of 46 mm was at or above 300°C, the temperature was 115°C at 60 mm, but still at ambient at 80 mm.

In test 11 where the fire load had been increased but the compartment temperatures nevertheless followed the same evolution as in test 10, failure occurred after only 35 minutes, early in the cooling down phase with gas temperatures still around 980°C. This result, compared to the result of test 10, gives an idea of the variability inherent to the material.

Test 12 was made in the same conditions as test 10 but with a column that had a section of 340 x 340 mm². The objective was to see whether these additional 30 mm of "protection", together with an initial load level reduced to 68% of the one of test 10, would allow the column to survive to the fire until complete burnout and after. Collapse occurred after 90 minutes when the temperatures in the compartment were down to 180°C.

The section was increased again to 360 x 360 mm² for test 13 made in the same conditions as tests 10 and 12. The column was still supporting the load after 98 minutes, when an instability of the loading system developed at one of the supports due to an imperfect insulation of this support.

For test 14, the 280 x 280 mm² section was used again, but with a reduced fire load and hence, significantly lower temperatures in the compartment, exceeding 600°C for only 7 minutes. Collapse occurred after 66 minutes, with gas temperatures around 280°C.

Test 15 was also made with the 280 x 280 mm² section, with the same fire load as in test 9, 10, 12 and 13 but with a reduced opening factor leading to a longer duration of the heating phase and to higher temperatures in the cooling phase. Collapse occurred after 37 minutes, shortly before the end of the heating phase. It has yet to be mentioned that the temperatures measured differed significantly from one side of the section to the other side. Figure 8 showed that this was observed consistently for all three levels in the compartment where the measurements were made.

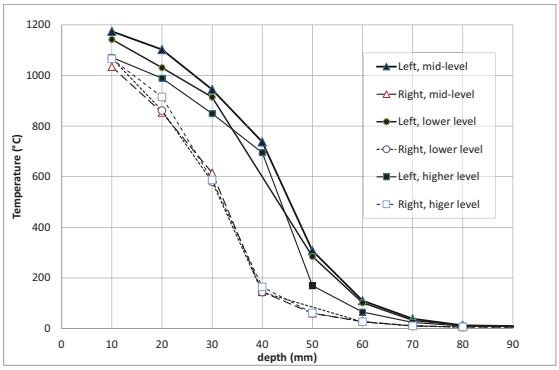

Figure 8: *Temperature distribution in the section at the time of collapse in test 15*

This may be due to the position of the unique opening which was not symmetrically located with respect to the column, as can be seen on Figure 9.

Figure 9: *Position of the opening in test 15*

This non symmetrical temperature development in the section developed although the temperatures measured in

https://doi.org/10.52202/069179-0244

the compartment did not display the same pattern, as can be seen on Figure 10. This may be due to a different oxygen content on the side of the column which was close to the opening compared to the other side.

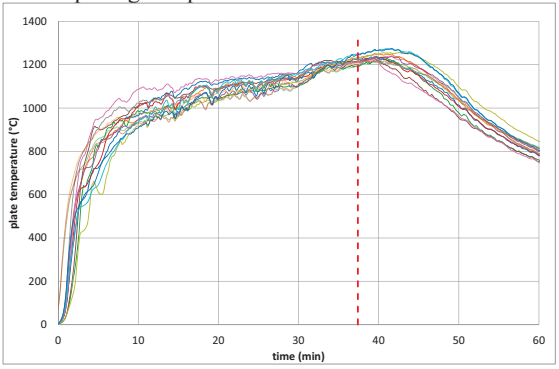

Figure 10: *Temperatures in the compartment in test 15*

Timber is indeed a material in which the physical phenomena that develop in case of fire are driven not only by the temperature but also by oxygen penetration.
This non symmetry in the section has created a structural imperfection that may have influenced the stability of the column. Although this makes it more difficult to compare the results of this test with those of the other tests in this scientific campaign, there is also a lesson to be learnt in the sense that nothing will guarantee a perfectly symmetrical development of the temperatures and of the char penetration in a real fire. Other materials would also be affected by differences in temperatures whereas timber may be the only material affected by differences in oxygen concentration.

5.7 CHARRING RATES

In was not possible, in these destructive tests, to measure the charring rate by direct visual observation. If charring is defined as reaching a temperature of 300°C, temperature measurements at different depth from the exposed surface allowed to observe the time at which each thermocouple reached this temperature and, hence, the average charring rate for the zone between two thermocouples.

Table 2: *Average charring rate for different zones along the depth.*

	0 - 10 mm	10 - 20 mm	20 - 30 mm	30 - 40 mm	40 - 50 mm
Test 1 (ISO)	0,67	0,63	0,55	0,51	
Test 2 (ISO)	0,67	0,70	0,63	0,50	
Test 9	1,71	1,20	0,83	0,28	
Test 10	1,82	1,74	1,33	1,13	
Test 11	1,69	1,82	1,17	0,92	
Test 12	1,74	1,69	1,05	0,78	
Test 13	2,00	2,14	1,05	1,29	1,24
Test 14	1,88	0,47	0,32		
Test 15	1,52	1,48	1,11	0,85	1,11

Table 2 shows the average value of the charring rate for different zones of 10 mm. Results from test 1 and 2 [8] show that the logarithmic increasing character of the ISO curve ensures a charring rate that is more constant than the one produced during the phase of the natural fire where the fire temperature was quasi constant. The charring rate in the natural fire tests decreases constantly during the period of quasi constant gas temperature, to finally drop down to 0 or very low values during the cooling phase.
Another difference is that, in natural fires, there is no zero strength layer of constant depth pushed ahead of the charring front, as assumed in the simple method of Eurocode 5. In the cooling phase of natural fires, the isotherms at 200°C and 100°C continue their progression long in the cooling phase.
This seems to indicate that a simple method to design timber elements under natural fire curves cannot result from a simple adaptation of the two values used for the constant charring rate and constant zero strength layer.

6 FUTURE TESTS AND FUTURE WORK

Two more tests should be performed by the time of the conference. Numerical simulations performed with the code SAFIR® [9] will also supplement the test results and will allow verifying whether the effective thermal properties of timber proposed in Eurocode 5 can be applied for computing temperatures in timber under nonstandard fires.
The last task will be to define a simple calculation method that ensures survival of timber columns during the whole duration of natural fire curves.

7 CONCLUSIONS

Seven tests have been performed under natural fire conditions on glue laminated timber columns for which the reference section of 280 x 280 mm² was shown to have a fire resistance of 55 and 58 minutes in standard testing conditions (two tests made).
In one test (test 15), collapse occurred after 37 minutes of the heating phase, but the temperatures in the compartment were higher than those of the ISO curve and a difference of temperature was observed between one side of the section and the other side, which induced a structural load eccentricity.
In one test made on a column with section increased by 65% (test 13), the columns had survived a heating phase of 30 minutes and was still supporting the load when a problem at one support of the loading system left to the premature termination of the test after 98 minutes, long into the cooling phase but not long enough to have all temperatures in the section back to ambient.
For the other 5 tests, failure occurred during the cooling down phase. For 3 of them with the same section (tests 9, 10 and 11), the temperature in the compartment had been higher than that of the ISO curve for the first 32 to 38 minutes and lower thereafter. For another one (test 12) the

https://doi.org/10.52202/069179-0244

temperature had been higher than that of the ISO curve during the first 35 minutes, but the fact that the section had been increased by 47% did not prevent it from collapsing after 90 minutes, when the temperatures in the compartment had significantly decreased. For one test (test 14) the section also collapsed in the cooling phase although the temperatures in the compartment had been significantly lower than those of the ISO curve for most of the test.

These tests confirm the conclusion of previous numerical and experimental studies that a timber column can fail in a fire long after the fire temperatures started to decrease, and the fact that the structural element displays some "self-extinction" does not mean that its stability is ensured.

Some of the results tend to confirm that the influence from a fire on a timber member is not as directly linked to temperature as could be the case for other inert materials. Oxygen content in the vicinity of the element and other complex exothermic phenomena may probably also play a role. Temperature development and oxygen repartition in the compartment can be influenced by wind velocity and direction and, although the tests were performed with a maximum wind velocity in the order of 2 m/s (maximum gusts at 3 m/s), the direction varied from test to test.

The quantitative results should, with the results of the additional tests planned and with the help of numerical modelling, allow deriving a simple model for computing the behaviour of timber members under real fires including the cooling down phase. Also, using the DHP as a simple metric indicating real fire behaviour including the cooling phase will be further investigated.

ACKNOWLEDGEMENTS

The support from the French Federation of insurers FRANCE ASSUREURS is gratefully acknowledged.

REFERENCES

[1] Eurocode 1: Actions on structure – Part 1-2: General actions – Actions on structures exposed to fire, CEN Brussels, 2002.

[2] EN 1363-1:2020, Fire resistance tests – Part 1: General requirements, CEN, Brussels, 1999.

[3] Bartlett A. I., Hadden R. M. and Bisby L. A.: A Review of Factors Affecting the Burning Behaviour of Wood for Application to Tall Timber Construction. *Fire Technology*, 55:1-49, 2019.

[4] Eurocode 5: Design of timber structures Part 1.2: General – Structural Fire Design, CEN, Brussels, 2004.

[5] Gernay T.: Fire resistance and burnout resistance of timber columns, *Fire Safety Journal*, 122, 103350, 2021.

[6] Gernay T, Franssen J.-M.: A performance indicator for structures under natural fire, *Engineering Structures*, 100, 94–103, 2015.

[7] Kinjo H., Yusa S., Horio T., Hirashima T., Matsumoto T. and Saito K., Fire performance, including the cooling phase, of structural glued laminated timber beams, in: 8th International Conference on Structures in Fire, 593-600, 2014

[8] Gernay T., Zehfuß J., Brunkhorst S., Robert F., Bamonte P., McNamee R., Mohaine S. and Franssen J.-M.: Experimental investigation of structural failure during the cooling phase of a fire: Timber columns, *Fire and Materials*, 1-16, 2022.

[9] Franssen, J.-M., Gernay, T. Modeling structures in fire with SAFIR®: Theoretical background and capabilities. *Journal of Structural Fire Engineering*, 8 (3), 300-323, 2017.

World Conference on Timber Engineering Oslo 2023

FULL SCALE VIBRATION TESTS ON A LONG SPAN TIMBER FLOOR

Patricia Hamm[1], Valentin Knöpfle, Johannes Ruf, Philipp Bacher[2], Tobias Götz

ABSTRACT: Since January 2021, Biberach University of Applied Sciences has been working in cooperation with PIRMIN JUNG Deutschland GmbH, Remagen, on the development of a lightweight, vibration-optimized timber floor system for large spans. There is already research that deals with the vibration behaviour of wooden floors. The new focus in this project is primarily on size. Structures such as schools, administrative and office buildings require floors with very large column spacings and therefore very large spans. Existing approaches to serviceability design of timber floors reach their limits for long-span timber floors with spans over 8 m. Therefore, a physical test bench with an aera of 12.5 by 12.5 m² and the inclusion of flexible bearings was built. Various floor systems with spans of up to 12 m were measured and evaluated. As a result, the cooperation partners have received important input for new design rules for very large timber floor systems.

KEYWORDS: Vibration, Timber Floor, full scale tests, long span,

1 INTRODUCTION

Since 2021, Biberach University of Applied Sciences has been working in cooperation with PIRMIN JUNG Deutschland GmbH, Remagen, on the development of a lightweight, vibration-optimized timber floor system for large spans. There is already research that deals with the vibration behaviour of wooden floors. The new focus in this project is primarily on size. Structures such as schools, administrative and office buildings require floors with very large column spacings and therefore very large spans. Existing approaches to serviceability design of timber floors reach their limits for long-span timber floors with spans over 8 m. Therefore, a physical test bench with an aera of 12.5 by 12.5 m² and the inclusion of flexible bearings was built. Various floor systems with spans of up to 12 m were measured and evaluated. The vibrations are measured when people walk on the test floor, to evaluate the conditions with the best vibration properties.

This research project "Development of a lightweight, vibration-optimized flooring system with beams for large spans over 8 m" includes theoretical and practical considerations on the vibration and damping behaviour of timber floors with large spans and beams.

2 EXISTING DESIGN RULES IN CODES AND LITERATURE

2.1 EUROCODE 5

Eurocode 5 [1] gives a suggestion, how to proof the vibrations of floors.
It is divided in the following **three verifications**:

1. The natural frequency of the floor should be at least 8 Hz, see equation (1).
2. The deflections due to a single force should be less than a varying value a, see equation (2), values for a are given in figure 1.
3. The velocity v due to an impulse of 1 Ns should be less than the value according equation (3) (for b see figure 1).

$$f_{e1} \geq 8\ Hz \tag{1}$$

$$\frac{w}{F} \leq a \quad [mm/kN] \tag{2}$$

$$v \leq b^{(fe1 \cdot D-1)} \quad [m/(Ns^2)] \tag{3}$$

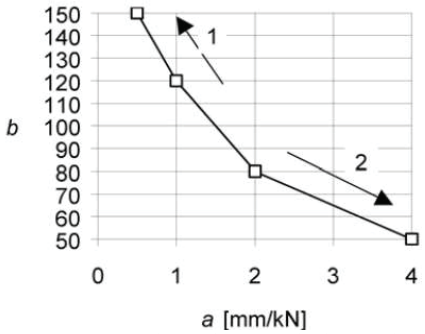

Figure 1: *Interrelation between the limit values a and b taken from Eurocode 5 [1]: Direction 1 means better behaviour, direction 2 means worse behaviour.*

[1] Patricia Hamm, Biberach University of Applied Sciences, Germany, hamm@hochschule-bc.de
[2] Philipp Bacher, Pirmin Jung Deutschland GmbH, Germany, philipp.bacher@pirminjung.de

https://doi.org/10.52202/069179-0245

If equation (1) is neglected and the natural frequency is less than 8 Hz, a more precise investigation should be conducted. However, Eurocode 5 [1] does not provide any further information on this more detailed verification.

2.2 FORMER RESEARCH

To close this gap, a research project was carried out at the Technical University of Munich from 2007 to 2009 and published in [2]. The research project showed that floors with natural frequencies less than the limit frequency work if two conditions are given: The frequency must be greater than the minimum frequency of 4.5 Hz and the acceleration due to walking in resonance with half or third the natural frequency is less than a limit acceleration.
The proof of acceleration is successful only in case of a heavy floor, such as timber-concrete composite systems or systems with wide spans.
The following flowchart (figure 2) shows the proof of vibrations according to [2].

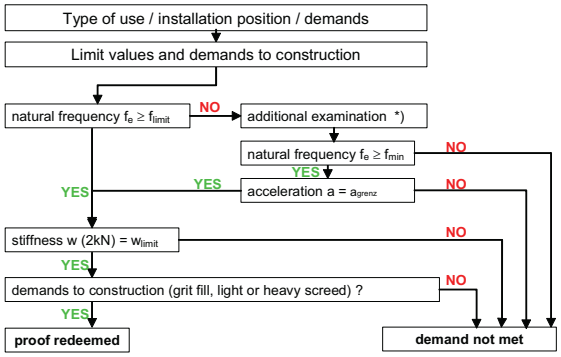

Figure 2: *Chart of rules for design and construction according to [2].*

2.3 DRAFT OF EUROCODE 5

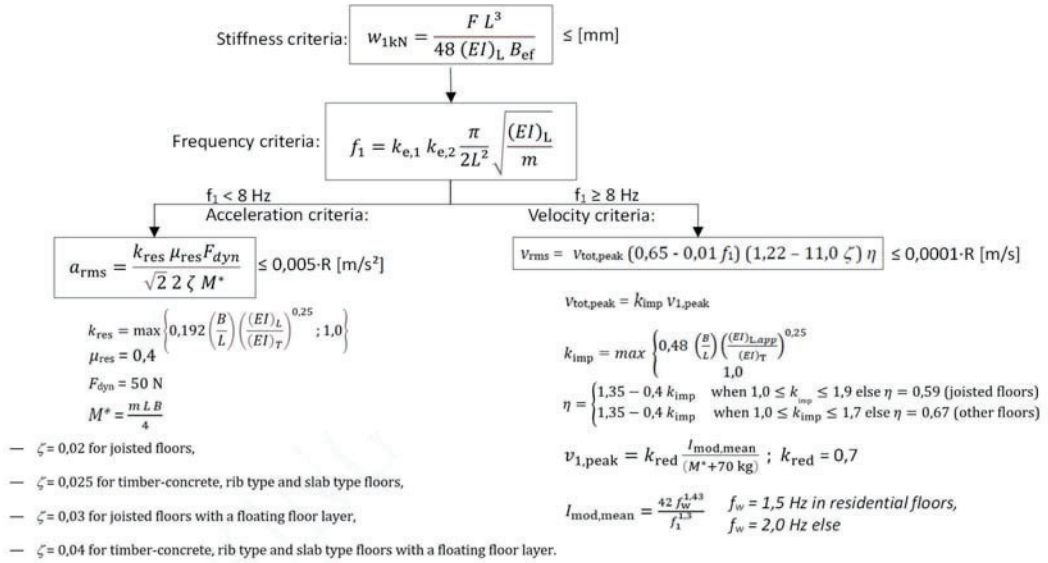

Figure 3. *Flowchart and equations according to [3].*

The basic idea of the new draft of Eurocode 5 [3] was to change the rules in a way, that the perception will be the most important value. Therefore, it was decided to introduce the response factor R. The perception depends on the first natural frequency, as shown below:

a_{rms} < Response factor × $a_{rms,base}$ when $f_1 < 8$ Hz
v_{rms} < Response factor × $v_{rms,base}$ when $f_1 \geq 8$ Hz

Figure 3 shows the principal way and the main equations of the proof, see also [4]. Table 1 contains the limit values of deflection due to point load and the response factors depending on the performance levels, taken from [3].

Table 1: *Limit values and response factor R according to performance level.*

	Floor performance levels					
Criteria	I	II	III	IV	V	VI
Response factor R	4	8	12	24	36	48
Stiffness criteria for all floors w_{1kN} [mm] ≤	0,25		0,5	1,0	1,5	2,0
Frequency criteria for all floors f_1 [Hz] ≥	4,5					
Acceleration criteria for resonant vibration ($f_1 < 8$ [Hz]) a_{rms} [m/s²] ≤	0,005 R					
Velocity criteria for transient vibration ($f_1 \geq 8$ [Hz]) v_{rms} [m/s] ≤	0,0001 R					

https://doi.org/10.52202/069179-0245

3 MOTIVATION

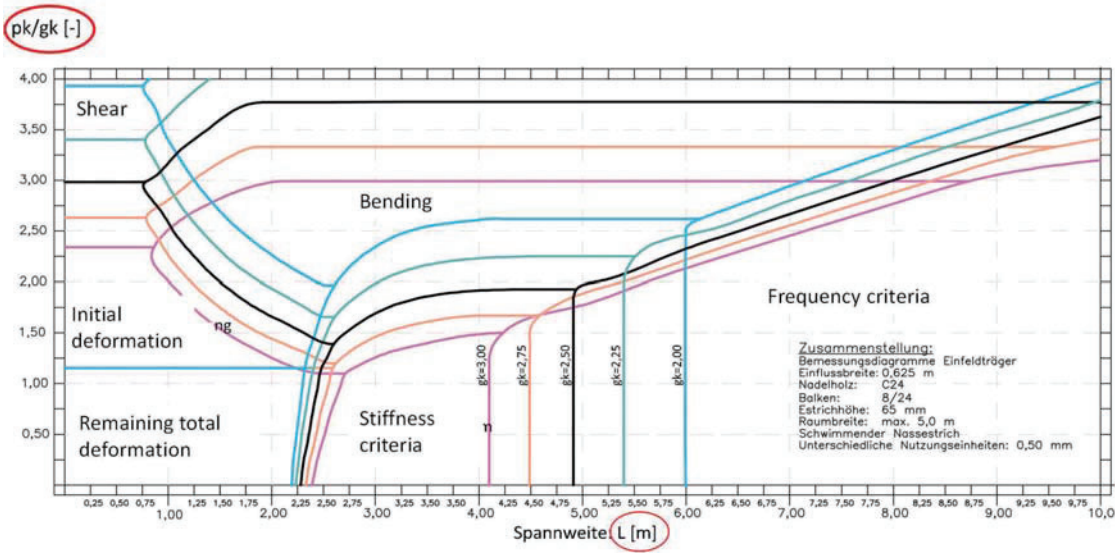

Figure 4. *Design relevant proof for a floor depending on span, based on [2], taken from [5].*

In [2] a possibility to handle low frequency floors is given. This "additional examination" has been adopted to [3] quite similar. Since this proof is based on mechanical laws, it works well.
The background is that low frequency floors are in resonance with one of the higher harmonics of the force that users exert to the floor when walking. Assuming resonance, the resulting acceleration can be calculated and compared to the limit value. To fulfil this proof, very heavy floors are needed.

On the other hand, resonance can be avoided. This means that the natural frequency of the floor must be greater than 8 Hz, see equation (1). In case of large spans, this proof would be relevant for designing the beams of the floor. Figure 4 shows the relevant proof depending on the span L (x-axes) and the relation of live load to steady load (y-axes). It can be seen that the proof of frequency criteria becomes relevant in case the spans are greater than 4-6 m.

For architectural reasons, long span floors are increasingly in demand. These floors would either be very heavy to fulfil the acceleration criteria or designed with very big dimensions to fulfil the frequency criteria.

In order to find out if this is really necessary or if the proofs can be modified and adapted for great spans, the research project mentioned above is carried out.

4 BUILDING UP THE TEST BENCH

The proof of vibration is a proof in the serviceability limit state. The most important thing is that the users of the floor feel safe and comfortable. To find out how people feel on the floor, the structure is built in scale 1:1.

The test bench is set up on a 1: 1 scale, so that all effects can be measured and felt. It has an area of 12.5 m x 12.5m and consists of box elements. The build-up of the test bench is shown in the figures 5 to 11. For detailed information regarding the planning and erection see [6].

Figure 5: *Beams are positioned.*

Figure 6: *Three-layer boards are glued on.*

https://doi.org/10.52202/069179-0245

Figure 7: *Beams are configured to elements.*

Figure 8: *The supporting wall is built.*

Figure 9: *Elements are turned and laid on the wall.*

Figure 10: *Raw floor without top planking.*

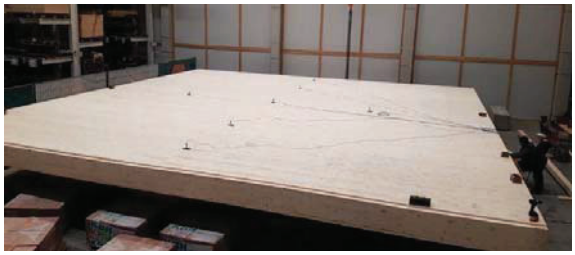

Figure. 11: *Raw floor with top planking, type 1a.*

Figure 12: *Test bench with mass and screed elements, type 3.*

5 MEASUREMENTS ON TEST BENCH

5.1 MODIFICATION IN CONSTRUCTION

Working with the test bench it was possible to build up different types of construction. The following different types were built and measured, see figures 13, 14 and 18:

1. raw floor. The main construction are box elements.
2. raw floor with mass. Mass realized by paving stones.
3. raw floor with mass, sound insulation layer and heavy screed. Screed is made by concrete elements.
4. raw floor, sound insulation layer and screed

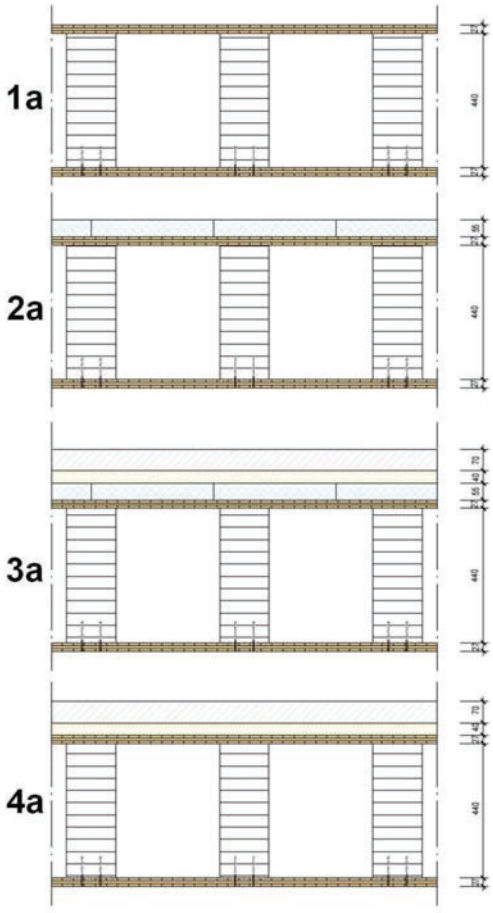

Figure 13: *Different constructions on the floor. Type 1a to 4a.*

https://doi.org/10.52202/069179-0245

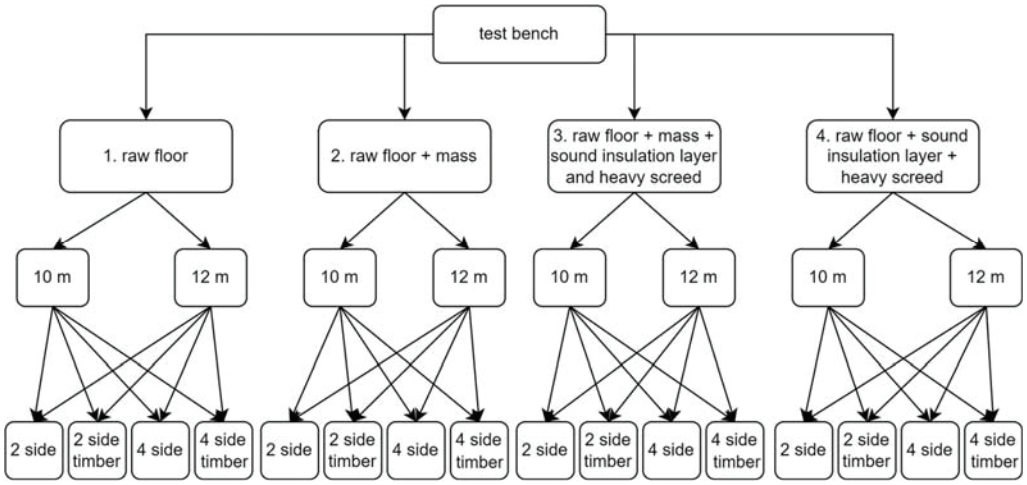

Figure 14: *Modifications in construction, spans and bearings.*

5.2 MODIFICATION IN SPAN AND BEARINGS

By using the test bench, the span could be varied. Spans from 8 m to 12 m were tested.
Another feature was to modify the bearing situation:

- stiff bearings (walls) on two sides
- stiff bearings (walls) on four sides
- elastic bearing (timber beam with two different widths) replacing one stiff bearing
- elastic bearing (steel beam)

Figure 14 shows the tested combinations.

5.3 EXCITATION

The following methods were used to excite the structure:

- heeldrop, to measure the natural frequencies, damping and velocity (see figure 15)
- a person walking around, to simulate the user and measure the velocity (v_rms)
- a group of people walking around
- walking or running in resonance in the centre of the structure, to measure the acceleration
- using a shaker, to have a defined excitation (see figure 16)

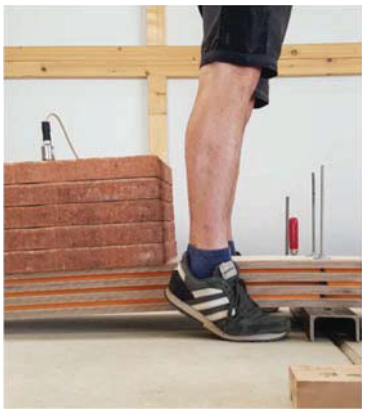

Figure 15: *Person doing a heeldrop.*

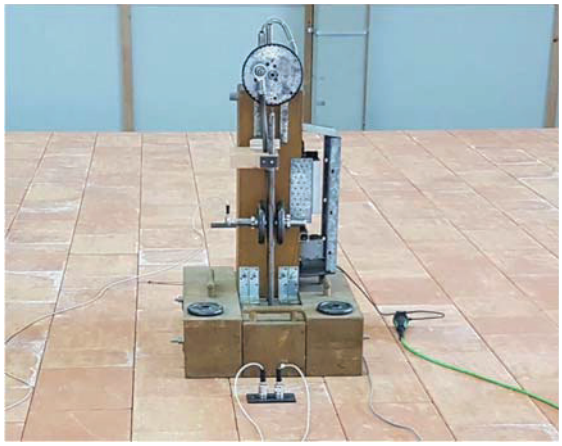

Figure 16: *Mechanical shaker placed on the floor, type 2b.*

5.4 MEASUREMENT DEVICE

The measuring equipment consists of

- 8 accelerometers (MMF Accelerometer KF48C)
- measuring amplifier (MMF Charge Amplifier M68D1 Ver. C)
- measurement card (Geitmann Siconn USB2-basic),

see figure 17.
The measurement, control and simulation tasks were carried out with the software DASYLab 2013.

Figure 17: *Measuring amplifier, accelerometers and measurement card.*

https://doi.org/10.52202/069179-0245

5.5 SUBJECTIVE EVALUATION

One of the most important points is the subjective evaluation of the floor vibration. The floor was evaluated by the test takers Johannes Ruf and Valentin Knöpfle, always in coordination with the other authors. Sometimes groups of students or other interested people visited the test bench. They were asked to evaluate the vibration behaviour, too. The used marks follow the research report [2] and Kreuzinger/Mohr [7]: Rate 1 (no vibration problem) to rate 4 (heavy vibration problem).

6 RESULTS OF MEASUREMENT

The combination of different types of construction and bearing conditions leads to many measurement situations.

Table 2: *Overview of combinations, frequency, damping ratio.*

construction	span [m]	bearings	elastic beam	measured frequency [Hz]	damping ratio incl. person [%]	v_rms [mm/s]
1a	9	2 side	steel	5,4	1,0	2,11
1a	10	4 side		9,3	1,7	1,00
1a	10	4 side	timber	7,5	1,3	1,24
1a	10	2 side		9,1	1,3	1,40
1a	10	2 side	timber	7,4	1,4	1,20
1a	12	4 side		7,2	1,4	1,48
1a	12	4 side	timber	6,1	1,6	1,21
1a	12	2 side	timber	6,0	2,4	1,38
2a	10	4 side		7,2	1,2	1,51
2a	10	4 side	timber	5,7	1,6	1,03
2a	10	2 side		7,0	1,1	2,33
2a	10	2 side	timber	5,5	1,3	1,18
2a	12	4 side		5,3	1,4	2,43
2a	12	2 side		5,1	1,1	2,13
2a	12	2 side	timber	4,4	1,3	1,20
2a	12	2 side	steel	4,0	1,0	1,35
3a	10	4 side		6,2	1,8	0,61
3a	10	4 side	timber	4,9	1,8	0,90
3a	10	2 side		5,8	1,7	0,49
3a	10	2 side	timber	4,8	1,7	0,60
3a	10	2 side	steel	4,1	1,3	0,64
3a	12	4 side		4,6	2,2	0,54
3a	12	4 side	timber	4,1	1,8	0,48
3a	12	2 side		4,4	1,7	0,51
3a	12	2 side	timber	3,9	1,6	0,50
4a	10	4 side		6,8	1,9	1,37
4a	10	4 side	timber	5,2	1,9	2,20
4a	10	2 side		6,6	1,6	1,03
4a	10	2 side	timber	5,2	1,7	2,01
4a	12	4 side		5,2	1,7	2,54
4a	12	4 side	timber	4,3	1,7	0,75
4a	12	2 side		4,9	1,4	1,15
4a	12	2 side	timber	4,2	1,5	0,61

6.1 FREQUENCY, DAMPING, VELOCITY

Table 2 shows some of the combinations, the natural frequency of the first vibration mode, the damping ratio and the velocity v_rms. This v_rms value is measured due to one walking person. It is the average of several steps.

The natural frequency is clearly influenced by the mass of the construction, the span and the elastic bearings.

The damping ratio is measured during the decay curve after excitation in resonance. The measured values are mostly smaller than 2%. Usually, damping ratios for timber floors are taken from [1], [2] or [3] as

- 2% for joisted floors
- 2,5% for rib type floors (type 1a or 1b)
- 3 % for joisted floors with a floating floor layer (type 3 or 4)

As a main result, it can be mentioned that the vibrations are perceptible and sometimes annoying, in spite of the great mass of the test bench (50 – 60 to). One of the reasons may be found in the small damping ratio. Therefore, the possibility to instal tuned mass dampers will be examined.

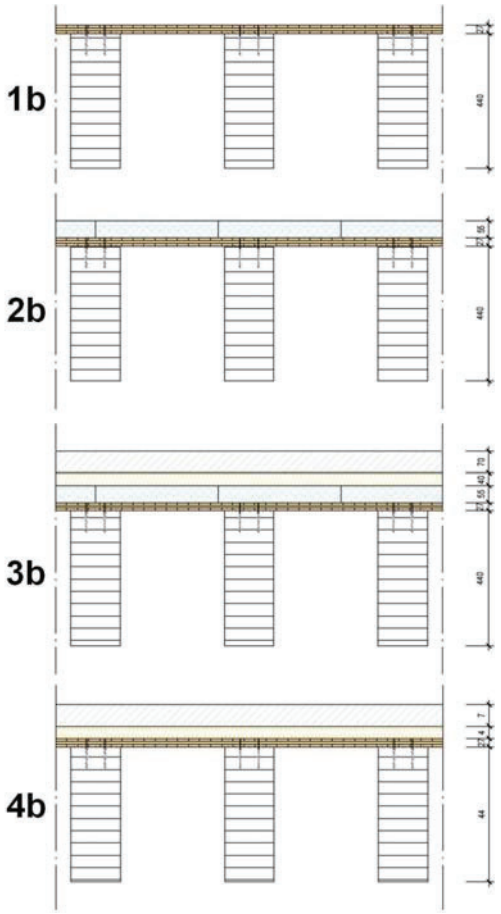

Figure 18: *Different constructions on the floor. Type 1b to 4b.*

https://doi.org/10.52202/069179-0245

6.2 MODIFIED CONSTRUCTION

In addition to the modifications in construction (type 1a to 4a) one of the three-layer panels was removed. This led to the following modifications type 1b to 4b shown in figure 18. Table 3 shows the results of the measurements and a comparison of the damping ratio including a person standing on the floor and no person on the floor. In this case the floor was excited by the shaker.

Comparing table 2 and table 3, one can see the influence of the second three-layer panel on the natural frequency. The construction with one three-layer panel only is less stiff. This results in reduced values of natural frequencies.

Table 3: *Overview of combinations, frequency and damping.*

construction	span [m]	bearings	elastic beam	frequency [Hz] measurement	damping ratio incl. person [%]	damping ratio without person [%]	v_rms [mm/s]
1b	12	2 side		6,20	1,9%		
2b	12	2 side		4,56	1,2%		2,62
3b	12	2 side		4,20	1,5%		0,73
3b	12	4 side		4,0	1,8%	1,3%	0,73
3b	12	4 side	timber	3,6	1,7%	1,2%	1,14
3b	12	2 side		4,0	1,6%	1,2%	0,69
3b	12	2 side	timber	3,6	1,6%	1,2%	1,48

From table 3 one can see the influence of the exciting person on the damping ratio: the damping ratio with one person standing on the floor is always higher.

7 CALCULATIONS WITH FINITE ELEMENT METHOD

To transfer the measurement results to calculations of future long span timber floors, it must be ensured that the measured values agree with the calculation. This was done with the help of a FE model (see figures 19 and 20). The model was built up step by step, analogue to the test bench. By this all the individual conditions like E-modulus, mass etc. could be taken into account.

The modelling was done with the program “Mechanical APDL” of the company “Ansys Inc.”. The advantage of this program is that data can be entered using the company’s own script language. This ensures that the parameters entered are used and not standardizes parameters from a database. At the same time, automation is possible without major effort. All parameters used are stored as variables and linked to each other. When a parameter is changed, most of the values adapt immediately.

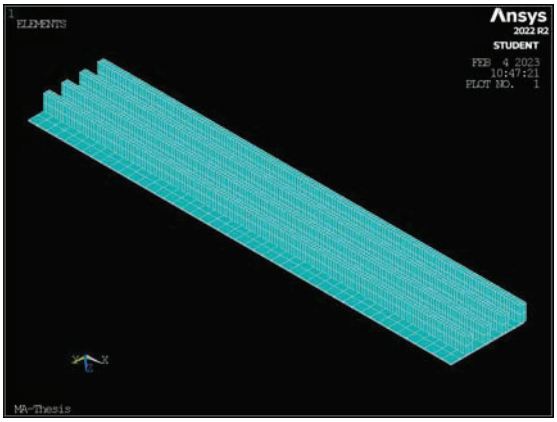

Figure 19: *One element for the step by step construction.*

In order to be able to transfer the subjective behaviour of people to other long span timber floors, the prevailing computational values must be known, at which the sensation of the persons was examined. By calibrating the model based on the measurement results, realistic predictions of new situation are possible through the model.

Table 4: *Comparison measured and calculated frequencies, first 3 modes.*

Construction	measured frequencies [Hz]			calculated frequencies [Hz]		
	mode 1	mode 2	mode 3	mode 1	mode 2	mode 3
one beam	7,32	-	-	7,32	-	-
one element	6,85	14,45	19,42	6,79	14,45	19,44
raw floor type 1b	6,20	7,43	8,62	6,24	7,43	8,65
type 2b	4,56	5,23	6,15	4,07	5,04	5,75
type 3b	4,20	4,95	5,09	4,35	4,64	5,20

It was shown that a simulation of the structural behaviour by using FE models, especially under special boundary conditions, can be carried out very accurately (see table 4). In the first step, the calibration was performed on the natural frequencies (see figure 19). However, to use this model for an assessment of the vibrations of timber floors, further investigations are necessary. For example, the velocities and accelerations due to walking and running persons will be considered, too.

Nevertheless, it is subsequently possible to determine the vibrations behaviour of the timber floor in the model without the need for costly on-site construction or modification of the floor and to subsequently investigate this behaviour by measurements. For detailed information on the FE model and the calibration see [8].

https://doi.org/10.52202/069179-0245

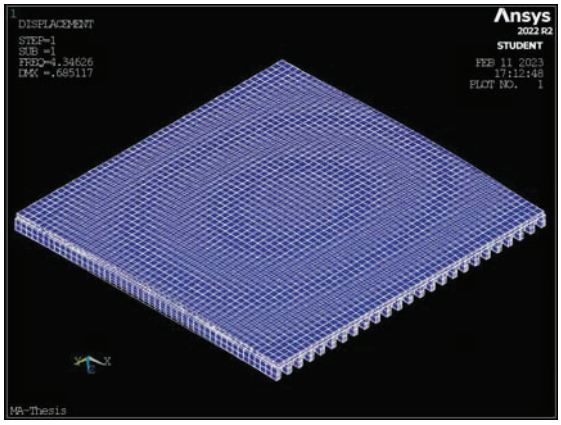

Figure 20: *Finite element model showing the first mode.*

8 RESULTS AND OUTLOOK

The result will be an extended design concept for long span timber floors. As the evaluation of measurement data and further measurements are going on, the concept will be presented during the oral presentation in Oslo.
As an outlook it can be stated that long span timber floors are likely to vibrate in spite of their great mass. The possibility to instal tuned mass dampers will be examined.

CONCLUSIONS: ZIM Research Project Pirmin Jung – Biberach University

A ZIM research project is being carried out in cooperation with Pirmin Jung Deutschland GmbH and the Institute for Timber Construction at Biberach University of Applied Sciences. It is precisely these wide-span floors that are being examined.
The aim of the research project is to develop a standardized and vibration-minimizing design system for wooden floors with beams and large spans of more than 8 m - based on theoretical and practical considerations.
For this purpose, a test stand for a timber floor with approx. 12.5 m x 12.5 m is set up, which is constantly being rebuilt. As a result, the cooperation partners have received important input for new design rules for very large timber floor systems.

ACKNOWLEDGEMENT

The research project has been carried out at Biberach University of Applied Sciences in cooperation with PIRMIN JUNG Deutschland GmbH, Remagen from 01.01.2021 to 30.06.2023. It was financed by ZIM. “ZIM” stands for “Zentrales Innovationsprogramm Mittelstand”, which means “Central Innovation Programme for small and medium-sized enterprises (SMEs)”. It is a funding programme of the Federal Ministry for Economic Affairs and Climate Action.

REFERENCES

[1] Eurocode 5: EN 1995-1-1: Eurocode 5: Bemessung und Konstruktion von Holzbauten - Teil 1-1: Allgemeines – Allgemeine Regeln und Regeln für den Hochbau. Deutsche Fassung. Dezember 2010.
[2] Hamm P., Richter A., Winter S.: Floor vibrations – new results. In: WCTE World Conference in Timber Engineering. 20. – 24. Juni 2010. Riva del Garda, Italy.
[3] Eurocode 5: pr EN 1995-1-1:20XX: Design of timber structures — Common rules and rules for buildings - Part 1-1: General.Not yet published.
[4] Hamm P., Marcroft J., Toratti T.: Vibrations of floors – Comparison of measured data and suggested design. In: INTER - International Network on Timber Engineering Research. 17. – 19. August 2020, Kap. 53-20-1, 14 S. (http://holz.vaka.kit.edu/540.php), Planned to be held in Chile, because of Covid-19 held as an Online meeting. Editor: Karlsruher Institut für Technologie (KIT), Holzbau und Baukonstruktionen, Karlsruhe.
[5] Bender, M.: Bemessungsdiagramme für Holzbalkendecken bei unterschiedlichen Anforderungen an den Schwingungsnachweis. Masterthesis. Biberach University. 2016.
[6] Ruf J.: Planung, Aufbau und Durchführung eines Prüfstandes für weitgespannte Holzdecken zur Untersuchung des Schwingungsverhaltens. Masterthesis. Biberach University of Applied Sciences. 2022.
[7] Kreuzinger H., Mohr B.: Gebrauchstauglichkeit von Wohnungsdecken aus Holz; Abschlussbericht Januar 1999. TU München, Fachgebiet Holzbau. Forschungsvorhaben durchgeführt für die EGH in der DGfH.
[8] Knöpfle V.: Planung, FE-Modellierung und Kalibrierung einer weitgespannten Holzbalkendecke mittels Schwingungsmessungen. Masterthesis. Biberach University of Applied Scienes. 2023.

World Conference on
Timber Engineering
Oslo 2023

ACOUSTIC SENSITIVITY ANALYSIS AND MODELING OF SOUND INSULATION PERFORMANCE OF LIGHTWEIGHT WOODEN FAÇADE STRUCTURES

Mohamad Bader Eddin[1], Sylvain M*é*nard[2], Delphine Bard[3], Jean-Luc Kouyoumji[4].

ABSTRACT: A prediction model is developed based on neural networks approach to estimate the air-borne sound insulation performance of lightweight wooden façade walls. A hundred insulation curves are used to develop the model, and they are lab-based measurements performed on various façades in one-third-octave bands (50 Hz– 5 kHz). For each wall, geometric and physical information (material types, dimensions, thicknesses, densities, and more) are used as input structural parameters. The results are satisfactory, and the model can estimate air-borne sound reduction with acceptable variations. A better estimation is achieved at middle frequencies (250 Hz–1 kHz), while lower and higher frequency bands often depict higher deviations. The weighted air-borne sound reduction index (R_w) can be forecast with a maximum error of 3 dB. In certain cases, the model shows high deviations within fundamental and critical frequencies, which influence the predictive precision. A sensitivity analysis is implemented to investigate on which structural parameters the model relies. The results emphasize the importance of façade thickness and the total density of the clustered exterior layers.

KEYWORDS: Sound insulation, Façades, Artificial neural networks, Sensitivity analysis

1 INTRODUCTION

Wood has been widely used in structural engineering due to its availability in nature and ease of handling [1]. Additionally, it has a remarkably lower carbon footprint than concrete and offers significant thermal insulation. [2, 3]. In Scandinavia and Australia, wooden constructions have become widely popular due to their advantages [4, 5]. Moreover, In North America, wood frame systems were dominant in the building construction industry in the 20th century [6].

Despite the fact that these types of structures reduce both cost and construction time, a disadvantage in these constructions is that the subjective sound isolation quality is considered lower than in concrete or heavy constructions, with the same insulation data [7]. This applies to different lightweight elements, such as floors, roofs, internal walls, and façades. Façade structures are vital to control the indoor acoustic environment by attenuating the outside noise. Inappropriate design may lead to undesirable impact on indoor acoustic comfort for occupants.

However, many façade structures are designed mostly for certain purposes, such as fire safety and thermal insulation, but acoustic aspects are often not considered or misunderstood [8]. The acoustic performance of such structures is derived from standardized measurements, such as

[1]Mohamad Bader Eddin, University of Quebec at Chicoutimi, Canada, Mohamad.Bader-Eddin1@uqac.ca
[2]Sylvain M*é*nard, University of Quebec at Chicoutimi, Canada, Sylvain_Menard@uqac.ca
[3]Delphine Bard Hagberg, University of Quebec at Chicoutimi, Canada, delphine.bard@acouwood.com
[4]Jean-Luc Kouyoumji, Technological Institute FCBA, France, Jean-Luc.Kouyoumji@fcba.fr

https://doi.org/10.52202/069179-0246

ISO and ASTM, but it requires time and cost, and the results cannot be generalized to different structures.

A theory-based analytical expression uses stiffness, mass, and damping is utilized as a direct prediction tool known as the mass law [9]. This can be adapted for single-leaf partition, but it is not appropriate for lightweight multi-layered elements. Accurate estimation of the acoustic performance of multilayer structures remains a challenge [9]. Moreover, the standardized method in ISO 12354 Part 1 [10] is extracted using insulation data for heavy monolithic partitions, which is not applicable to lightweight multi-layered structures [11].

The applications of machine learning have paved the way for complex technological achievements in different fields that were considered challenging, such as image recognition, language translation, and building acoustics [12, 13, 14]. In this approach, large and diverse data is essential to enable the algorithm to learn and to improve its predictive power. Artificial neural networks (ANN) approach was used in building acoustics to predict air-borne sound insulation curves in $1/3$-octave bands for masonry walls [14]. 34 laboratory measurements were used to develop the model. Despite the concordance between the results, the study focused on a single monolithic partition.

To bridge this gap, 252 insulation curves of different lightweight wooden floors were used to develop an ANN model [15]. Structural parameters were used as inputs for the model, such as material thickness, density, depth and type of the joists, and more. The model can predict the weighted sound reduction index R_w and normalized impact sound pressure levels $Ln_{n,w}$ with maximum deviations of 2 and 5 dB, respectively.

The scope of this study is to develop an ANN model to estimate the air-borne sound insulation curves of façades structures. The data comprises lab-based measurements of lightweight wooden façades without considering the presence of windows, doors and small openings in the wall. Finally, sensitivity analysis was performed to shed light on the most important factors that influence the prediction of insulation curves.

2 MATERIALS AND METHODS

2.1 DEFINITION OF ARTIFICIAL NEURAL NETWORKS

The ANN model is a mathematical model which is inspired by the human neural system to simulate its behavior [16]. A simple model comprises layers: input, hidden, and output (see Figure 1). Each layer contains artificial neurons (computational units) and intermediate parameters, called weights, connect adjacent layers. The ANN model propagates information (input values) from the first layer (input layer) to the output layer, where prediction values are calculated [17]. The latter process is referred to as the training phase, in which weights and bias values (features of ANN) are tuned in order to reduce errors and achieve higher predictive accuracy. The output of an artificial neuron can be determined by,

$$y = f(\sum(w_i x_i + b)), \tag{1}$$

where y, w_i, x_i, and b are output, weight, input, and bias values, respectively. The computed output is called activation value, and it is utilized as an input value to the chosen activation function. The most common functions for ANN are tangent, sigmoid, and LeakyReLU [18].

In this study, a multilayer perceptron class of ANN is adapted. The network model comprises two hidden layers. The cross-validation technique is employed to validate the network model and to prevent overfitting issues. As an activation function, LeakyReLU (Leaky Rectified Linear Unit) is chosen for hidden layers [19]. Adam optimizer [20] is employed during the training phase.

Three subsets of measurements are used by splitting the entire curve measurements, namely: training, validation, and test set (Table 1). The root-mean-square error ($RMSE$) function is used as a cost function to evaluate the performance of the network,

$$RMSE = \sqrt{\frac{1}{n}\sum_{i=1}^{n}(\hat{y}_i - y_i)^2}, \tag{2}$$

where n presents the number of observations (measurements) that are used in the training

phase. Output (predicted) and input (measured) values are donated by $\hat{y}_i$ and y_i, respectively. In this study, the network model depicted an overall prediction accuracy of 4.44 dB between the predicted and measured curves. However, for a better evaluation of the results at different frequencies, each estimated curve is analyzed with comparison to the measured one using the *RMSE* function considering values in each one-third-octave band from 50 Hz to 5 kHz.

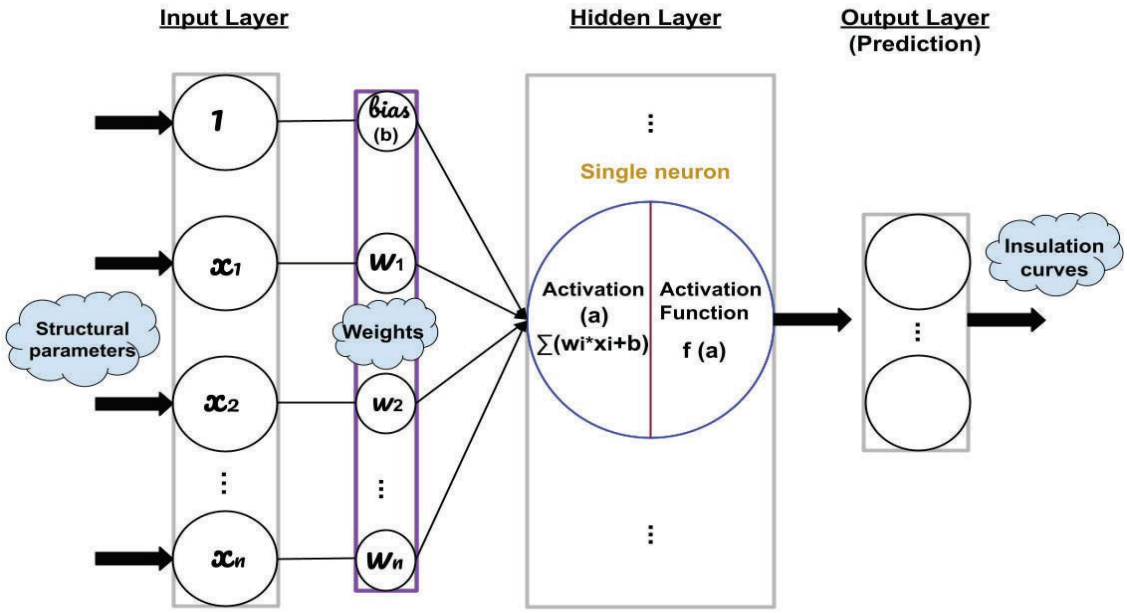

Figure 1: The architecture of an ANN model illustrating input, hidden, and output layers and how the structural parameters propagate through the network model.

2.2 ACOUSTIC DATA

A hundred lab-based measurements were collected from Lund University in Sweden and the National Research Council (NRC-CNRC) [21] in Canada. The data consists of air-borne sound insulation curves that concern various lightweight façade structures in one-third-octave bands (50 Hz to 5 kHz). The measurements were performed respecting ISO 10140-2 (2010) [22] and ASTM E90-09 (2016) [23]. All the insulation data that are performed in compliance with ASTM standards are converted to follow ISO 717-1 (2013) [24] descriptor (the weighted air-borne sound reduction index R_w). This conversion is essential to handle the data and to have a better agreement between them.

The database is organized using different structural parameters (Table 2) that are used as inputs to the network model. Despite the importance of some elastic properties, such as dynamic stiffeners and the modulus of elasticity, they are not considered in the study due to the lack of information provided by the acoustic reports. 10 measurements of different façade walls are used to initiate the features of the ANN model, known as validation set, and another set of 10 curves were selected (randomly from the total number of curves) to test the accuracy of the model (Figure A1 in the Appendix). Each façade configuration is clustered in three parts: interior, main and exterior parts, respecting the installation order of each façade component. The dominant component or material is represented by the main part. Therefore, the interior and exterior sections present components clustered and located alongside the main façade material (Figure 2).

https://doi.org/10.52202/069179-0246

Table 1: A description summary of acoustic measurements that are used to develop the network model.

	Database	ANN model		
Measurements No.	100	100		
	air-borne	training set	validation set	testing set
	100	80	10	100

Table 2: Structural variables that are utilized to organize the measurements to be used by the ANN model.

Parameter	Unit	Class
– type of material	—	i.e., CLT panel, insulation materials, etc.
– Material installation order	—	first/ second/. . .
– Material thickness	mm	—
– Group thickness	mm	interior, main and exterior parts
– Total thickness of a façade	mm	—
– Material density	kg/m^3	—
– Group density	kg/m^3	interior, main and exterior parts
– Total density of a façade	kg/m^3	—
– Façade area S	m^2	—
– Volume of the receiving room V	m^3	—
– Studs depth	mm	—
– Spacing between studs	mm	—
– Resilient channels depth	mm	—
– Spacing between Resilient channels	mm	—

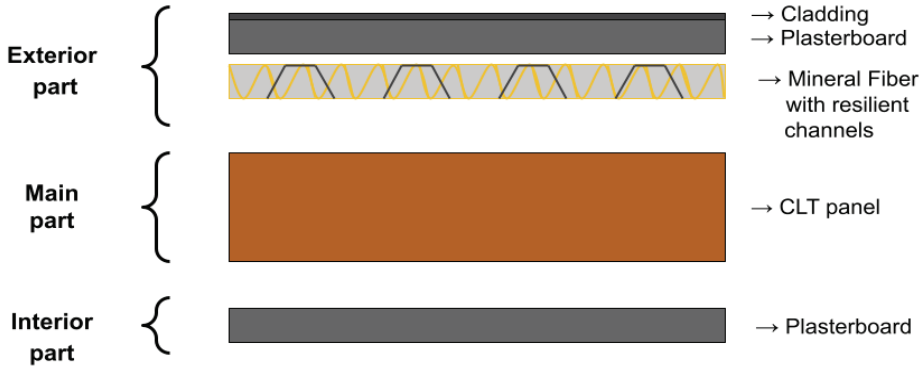

Figure 2: An explanation schematic presenting how façade components are clustered in the database using an example of the test façade #6.

2.3 SENSITIVITY ANALYSIS

Understanding the mechanism of ANN models is cumbersome, especially that they are known as black box prediction tools [25]. To recognize the parameters on which the ANN model relies on,

an axiomatic approach, called integrated gradients (IG) is adapted. The IG method is defined as $IG_i(x)$. Supposing a function $F : R^n \rightarrow [0,1]$ represents a network model. Using $x = (x^1, ..., x^n) \in R^n$ as an input and $z \in R^n$ as a baseline relative to x. Then a vector $A_F(x,z) = (a^1, ..., a^n) \in R^n$ is the attribution of the input x, where a^i is the attribution of x^i of function $F(x)$. IG values can be extracted by calculating the gradients across the straight path between the input x and the baseline z. Hence, IG for ith dimension is donated by [26],

$$IG_i(x) = (x_i - z_i) * \int_{\alpha=0}^{1} \frac{\partial F(z + \alpha * (x - z))}{\partial x_i} d\alpha. \quad (3)$$

3 RESULTS AND DISCUSSION

3.1 AIRBORNE SOUND INSULATION PREDICTIONS

Figure 3 depicts a comparison between predicted and measured curves. It shows that the estimations are close to the measurements with certain deviations in some cases at high or/and low frequencies. The smallest *RMSE* value is 2.19 *dB* for façade #3, and the highest is 5.73 *dB* for slightly complex wall #10.

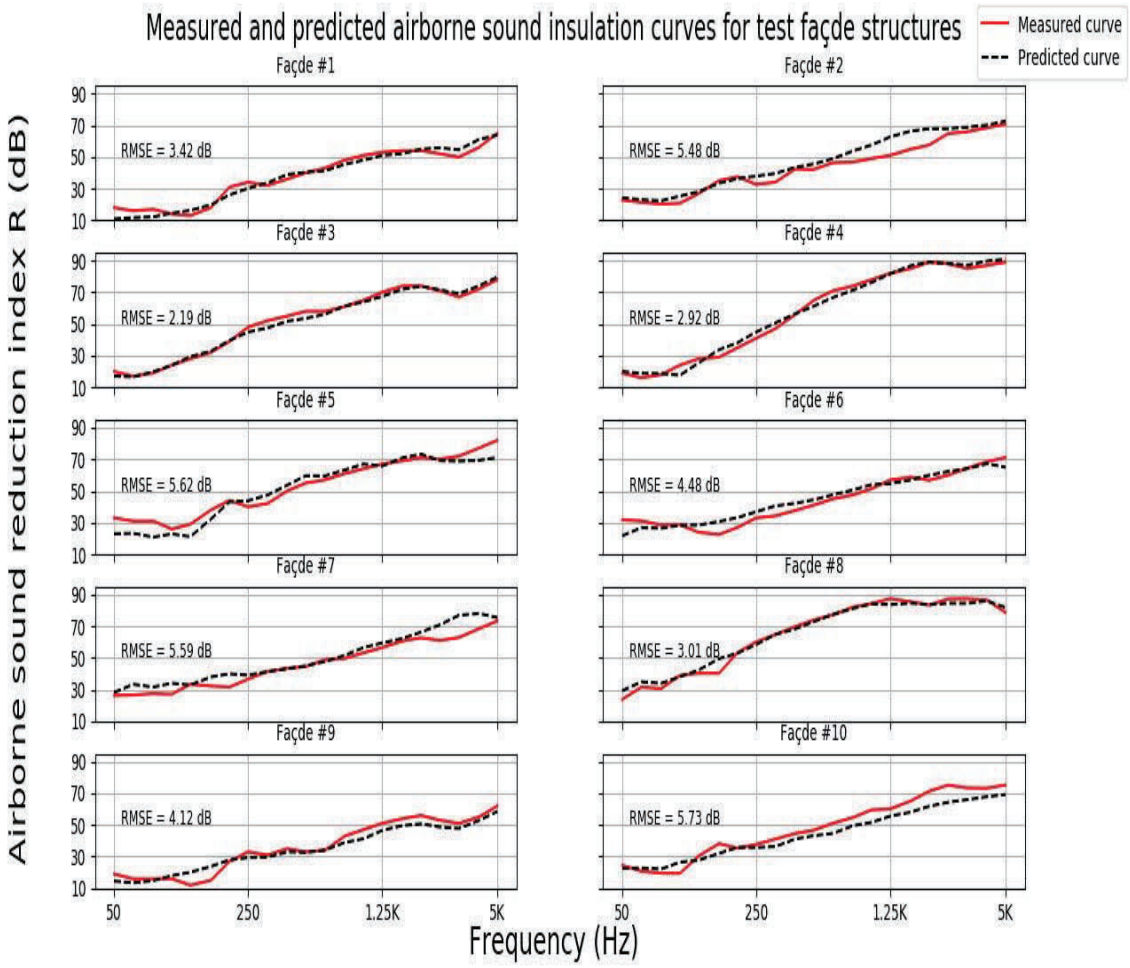

Figure 3: Predicted and measured air-borne reduction index curves for test façades.

https://doi.org/10.52202/069179-0246

In high frequency bands (1.25–3 kHz), a significant gap is notable between the curves. The later range usually includes the critical (coincidence) frequency for lightweight structures. At these frequencies, a match occurs between the incident wavelength that is projected onto the plate and the wavelength of the bending wave in the plate [9]. As a consequence of this matching, the structure will easily and efficiently radiate sound at and above this range [27].

Furthermore, similar deviations are observed at frequencies lower than 200 Hz, e.g. walls #1, #8 and #9. This can be explained due to the presence of fundamental resonances or first eigenfrequencies [9]. This reveals the limitation of the ANN model in the estimation around these frequencies. Similar challenges were also reported for ANN models [15, 14].

Table 3 presents the RMSE values in the prediction of air-borne sound insulation curves. It also shows the calculated single-number quantities (SNQ), R_w and $R_{wPredicted}$, for each curve. Façade #7 has the highest error with 3 dB, while the network model can estimate the same weighted reduction index values (walls #3 and #6). Additionally, the maximum difference in the calculation of correction terms ($C_{100–3150}$ and $C_{50–5000}$) is 4 dB in façade #5.

Table 4 summarizes the distribution of errors in estimation of insulation curves using *RMSE*, and taking three frequency ranges into account: low (50–200 Hz), middle (250 Hz–1 kHz) and high (1.25–5 kHz) frequency. The results showed that the model accuracy is the best in the middle frequency, while higher deviations are found in low and high frequency ranges. Again, this can probably be described due to the presence of resonance and critical frequencies.

Table 3: Predicted and measured weighted sound reduction indices of test walls.

Façade no.	*RMSE* **(dB)**	$\mathbf{R}_w$ **(dB)**	$C_{100–3150}$	$C_{50–5000}$	$\mathbf{R}_{wPred}$ **(dB)**	$C_{Pred\ 100–3150}$	$C_{Pred\ 50–5000}$
1	3.42	39	−4	−3	40	−3	−3
2	5.48	46	−2	−2	48	−1	−1
3	2.19	53	−4	−6	53	−4	−6
4	2.92	50	−3	−4	51	−6	−6
5	5.62	52	−2	−2	51	−6	−6
6	4.48	55	−4	−4	55	−5	−5
7	5.59	48	−1	−1	51	−2	1
8	3.01	65	−5	−7	67	−4	−5
9	4.12	37	−4	−3	38	−1	−1
10	5.73	49	−3	−3	47	−2	−1

Table 4: Error distributions in the prediction of air-borne insulation curves considering three frequency regions.

	Root-Mean-Square Errors in dB		
Frequency Bands	**Low** **50–200 Hz**	**Middle** **250 Hz–1 kHz**	**High** **1.25–5 kHz**
R (air-borne sound)	4.67	3.52	4.99

3.2 SENSITIVITY ANALYSIS OF FAÇADES STRUCTURAL PARAMETERS

A sensitivity analysis is implemented to investigate the influence of the thickness and density of exterior, main and interior parts of each façade on the forecast. In those types of graphs, a user can find out the importance of each parameter considering the magnitude of $y-$ axis. Higher values indicate a larger size effect of the inputs. However,

values close to zero suggest a weaker relationship.

Plots in Figure 4 illustrate the contribution of the thickness and density of interior, main and exterior parts of walls to the prediction of insulation curves. It is noticeable that the density and thickness play a significant role at all frequencies. The density spectrum of the interior part illustrates fluctuation near the fundamental frequencies. In addition, the density of the exterior part is vital and the effects of fundamental and critical frequency are obvious on the attributions. A peak near 150 Hz and a dip near 1.25 kHz are obvious, which is probably due to effects of fundamental and critical frequencies, respectively. This is likely resulting due to coupling between resonant wall components that permits energy to transfer between them [27]. The latter happens when elements are physically connected, and they have sufficiently close natural or critical frequencies. This amplifies the radiations from components and affects the isolation negatively [9].

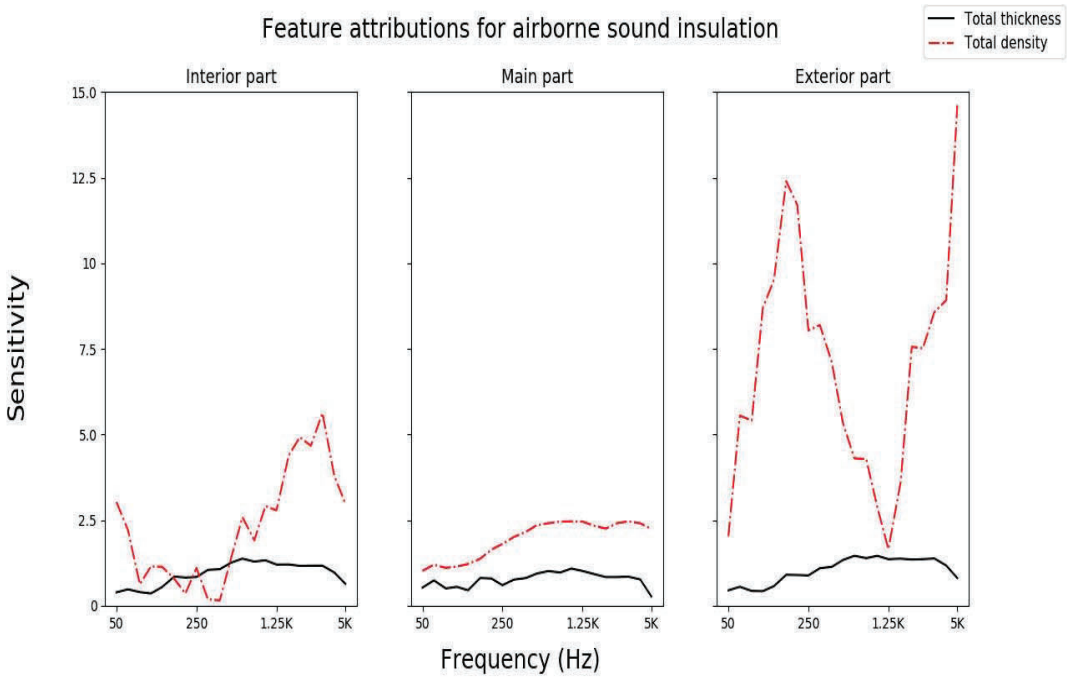

Figure 4: Feature attributions of interior, main and exterior parts façades to the predictions.

4 CONCLUSION

This study reveals the potential of ANN model to predict the air-borne sound insulation curves using 100 lab-based measurements of lightweight façade walls. The results are reasonable, and the model can forecast the sound weighted reduction index R_w with a maximum difference of 3 dB. These results encourage considering the network model in the early design phases, in particular the difference around 2 dB is lower than the noticeable noise differences. Regarding the whole frequency band. The best achieved accuracy is at the middle frequencies (250 Hz – 1 kHz). However, the prediction around fundamental and critical frequency is challenging for the network model and reveals some deviations.

A sensitivity analysis is carried out to explore the attribution of the input parameters to the predictions. The total thickness and total density of interior, main and exterior parts of façades have remarkable effects at all frequencies, and a higher attribution to the total density of the exterior part. The coupling between resonant façade components, resulting from fundamental and critical frequencies of each component, has a significant influence on the prediction.

https://doi.org/10.52202/069179-0246

Further research would be expected on enlarging the sensitivity analysis study to cover different structural parameters, and how these parameters can be optimized to enhance the sound insulation prediction. This would pave the way to explore the importance of certain structural parameters to achieve the desired isolation.

ACKNOWLEDGMENT

The authors are grateful to Natural Sciences and Engineering Research Council (NSERC) of Canada for the financial support through its IRC and CRD programs (IRCPJ 461745-18 and RDCPJ 524504-18), the Region Nouvelle Aquitaine for the financial support (ref. 2017-1R10223), and the industrial partners of the NSERC industrial chair on eco-responsible wood construction (CIRCERB). Special thanks for Lund university and CNRC for providing the acoustic measurement data of sound insulation.

REFERENCES IN THE TEXT

[1] Radkau, J. *Wood: A History*; Polity: Cambridge, UK, 2012.

[2] Ottelin, J.; Amiri, A.; Steubing, B.; Junnila, S. Comparative carbon footprint analysis of residents of wooden and non-wooden houses in Finland. *Environ. Res. Lett.* 2021, *16*, 074006.

[3] Bettarello, F.; Gasparella, A.; Caniato, M. The Influence of Floor Layering on Airborne Sound Insulation and Impact Noise Reduction: A Study on Cross Laminated Timber (CLT) Structures. *Appl. Sci.* 2021, *11*, 5938. https://doi.org/10.3390/app11135938.

[4] Jayalath, A.; Navaratnam, S.; Gunawardena, T.; Mendis, P.; Aye, L. Airborne and impact sound performance of modern lightweight timber buildings in the Australian construction industry. *Case Stud. Constr. Mater.* 2021, *15*, e00632. https://doi.org/10.1016/j.cscm.2021.e00632.

[5] Forss*é*n, J.; Kropp, W.; Brunskog, J.; Ljunggren, S.; Bard, D.; Sandberg, G.; Ljunggren, F.; *Å*gren, A.; Hallström, O.; Dybro, H.; Larsson, K.; Tillberg, K.; Sjökvist, L-G.; Östman, B.; Hagberg, K.; Bolmsvik, *Å*.; Olsson, A.; Ekstrand, CG.; Johansson, M. *Acoustics in Wooden Buildings, State of the Art 2008, Vinnova Project 2007-01653*; Report 2008:16, SP Trätek; Technical Research Institute of Sweden: Stockholm, Sweden, 2008.

[6] Popovski, M.; Ni, C. *Mid-Rise Wood-Frame Construction Handbook*; FPInnovations: Vancouver, BC, Canada, 2015.

[7] Rasmussen, B.; Machimbarrena, M. *Building Acoustics throughout Europe Volume 1: Towards a Common Framework in Building Acoustics throughout Europe*; DiScript Preimpresion, S.L.: Madrid, Spain, 2014.

[8] Secchi, S.; Cellai, G.; Fausti, P.; Santoni, A.; Martello, N. Z. Sound transmission between rooms with curtain wall façades: A case study *Build. Acoust.* 2015, *22*, 193–207. https://doi.org/10.1260/1351-010X.22.3-4.193.

[9] Vigran, T.E. *Building Acoustics*; CRC Press: Boca Raton, FL, USA, 2014. https://doi.org/10.1201/9781482266016.

[10] *ISO.12354-1*; Building Acoustics–Estimation of Acoustic Performance of Buildings from the Performance of Elements—Part 1: Airborne Sound Insulation between Rooms. International Organization for Standardization: Geneva, Switzerland, 2017.

[11] Guigou-Carter, C.; Villot, M.; Wetta, R. Prediction method adapted to wood frame lightweight constructions. *Build. Acoust.* 2018, *13*, 173–188. https://doi.org/10.1260/135101006778605424.

[12] Thai, L.H.; Hai, T.S.; Thuy, N.T. Image classification using support vector machine and artificial neural network. *Int. J.*

Inf. Technol. Comput. Sci. 2012, *4*, 32–38. https://doi.org/10.5815/ijitcs.2012.05.05.

[13] Sign-to-speech translation using machine-learning-assisted stretchable sensor arrays. *Nat. Electron.* 2020, *3*, 571–578. https://doi.org/10.1038/s41928-020-0428-6.

[14] Serpilli, F.; Di Nicola, G.; Pierantozzi, M. Airborne sound insulation prediction of masonry walls using artificial neural networks. *Build. Acoust.* 2021, *28*, 391–409. https://doi.org/10.1177/1351010X21994462.

[15] Bader Eddin, M.; Ménard, S.; Bard Hagberg, D.; Kouyoumji, J.-L.; Vardaxis, N.-G. Prediction of Sound Insulation Using Artificial Neural Networks—Part I: Lightweight Wooden Floor Structures. *Acoustics* 2022, *4*, 203–226. https://doi.org/10.3390/ acoustics4010013.

[16] Svozil, D.; Kvasnicka, V.; Pospichal, J. Introduction to multi-layer feed-forward neural networks. *Chemom. Intell. Lab. Syst.* 1997, *39*, 43–62. https://doi.org/10.1016/S0169-7439(97)00061-0.

[17] Nielsen, M.A. *Neural Networks and Deep Learning*; Determination Press: San Francisco, CA, USA, 2015. https://doi.org/10.4249/ scholarpedia.32832.

[18] Sharma, S.; Sharma, S.; Athaiya, A. Activation functions in neural networks. *Towards Data Sci.* 2017, *6*, 310–316.

[19] Xu, J.; Li, Z.; Du, B.; Zhang, M.; Liu, J. Reluplex made more practical: Leaky ReLU. In Proceedings of the 2020 IEEE Symposium on Computers and Communications (ISCC), Rennes, France, 7–10 July 2020; IEEE: Piscataway, NJ, USA, 2020. https://doi.org/10.1109/ISCC50000.2020.9219587.

[20] Kingma, D.P.; Ba, J. Adam: A method for stochastic optimization. *arXiv* 2014, arXiv:1412.6980. https://doi.org/10.48550/arXiv. 1412.6980.

[21] Bradley, J.S.; Birta, J.A. *Laboratory Measurements of the Sound Insulation of Building Facade Elements*; Institute for Research in Construction, National Research Council Canada: Ottawa, ON, Canada, 2000.

[22] *ISO.140-2*; Acoustics–Laboratory Measurement of Sound Insulation of Building Elements—Part 2: Measurement of Airborne Sound Insulation. International Organization for Standardization: Geneva, Switzerland, 2010.

[23] *ASTM.E90-09*; Standard Test Method for Laboratory Measurement of Airborne Sound Transmission Loss of Building Partitions and Elements. ASTM International: West Conshohocken, PA, USA, 2016.

[24] *ISO.717-1*; Acoustics—Rating of Sound Insulation in Buildings and of Buildings Elements—Part 1: Airborne Sound Insulation. International Organization for Standardization: Geneva, Switzerland, 2013.

[25] Smilkov, D.; Thorat, N.; Kim, B.; Viégas, F.; Wattenberg, M. Smoothgrad: Removing noise by adding noise. *arXiv* 2017, arXiv:1706.03825. https://doi.org/10.48550/arXiv.1706.03825.

[26] Sundararajan, M.; Taly, A.; Yan, Q. Axiomatic attribution for deep networks. In Proceedings of the International Conference on Machine Learning, PMLR, Sydney, Australia, 6–11 August 2017; pp. 3319–3328.

[27] Rindel, J.H. *Sound Insulation in Buildings*; CRC Press: Boca Raton, FL, USA, 2017. https://doi.org/10.1201/9781351228206.

5 APPENDIX

https://doi.org/10.52202/069179-0246

Façade #1

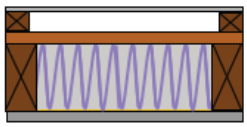

Façade components

1	mm	Vinyl siding cladding
11	mm	OSB board
152	mm	Glass fiber
13	mm	Plasterboard

Façade #2

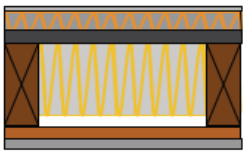

Façade components

6	mm	Mineral plaster
40	mm	Wood fiber insulation
15	mm	Lightweight concrete panel
140	mm	Wood fiber insulation
15	mm	OSB board
9.5	mm	Plasterboard

Façade #3

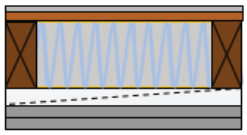

Façade components

1	mm	Vinyl siding cladding
11	mm	OSB board
140	mm	Rock fibre
13	mm	Resilient channels
13	mm	Plasterboard
13	mm	Plasterboard

Façade #4

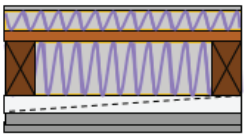

Façade components

1	mm	Vinyl siding cladding
25	mm	Rigid glass fibre
11	mm	OSB board
89	mm	Glass fibre
13	mm	Resilient channels
13	mm	Plasterboard
13	mm	Plasterboard

Façade #5

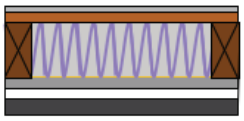

Façade components

13	mm	Cladding plaster
152	mm	Glass fibre
11	mm	OSB board
16	mm	Air gap
89	mm	Thick brick

Façade #6

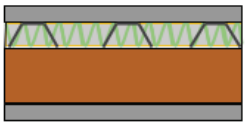

Façade components

18	mm	Cladding plaster
20	mm	Metal studs
20	mm	Rockwool
80	mm	CLT panel
18	mm	Plasterboard

Façade #7

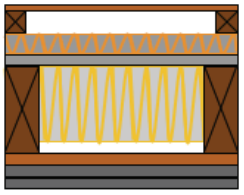

Façade components

20	mm	Wood board
61	mm	Wood fiber insulation
12.5	mm	Plasterboard
140	mm	Wood fiber insulation
15	mm	OSB board
12.5	mm	Gypsum fiber board
12.5	mm	Gypsum fiber board

Façade #8

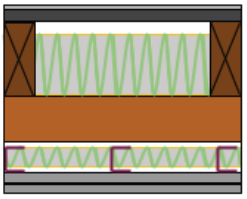

Façade components

5	mm	Mineral plaster
12.5	mm	Lightweight concrete panel
30	mm	Air gap
200	mm	Rockwool
80	mm	CLT panel
10	mm	Air gap
40	mm	Rockwool
10	mm	Air gap
12.5	mm	Plasterboard
10	mm	Plasterboard

Façade #9

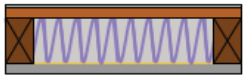

Façade components

1	mm	Vinyl siding cladding
11	mm	OSB board
89	mm	Glass fibre
13	mm	Plasterboard

Façade #10

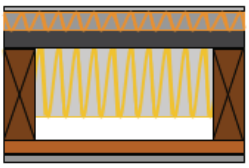

Façade components

7	mm	Miniral plaster
40	mm	Wood fiber insulation
15	mm	Lightweight Concrete panel
140	mm	Wood fiber insulation
15	mm	OSB board
9.5	mm	Plasterboard

Figure A1: Floor configurations that are used to evaluate the network model for air-borne sound predictions.

World Conference on Timber Engineering Oslo 2023

DESIGN OF LONG-SPAN LIGHTWEIGHT TIMBER FLOORS SUBJECT TO WALKING EXCITATIONS: A CASE STUDY

Hassan Karampour[1], Farid Piran[2], Adam Faircloth[3], Chandan Kumar[4], David Zhang[5], Benoit. P. Gilbert[6], Hong Guan[7], Lin Hu[8], Ying Hei Chui[9] and Wen-Shao Chang[10]

ABSTRACT: Lightweight timber construction is popular in buildings with two or more storeys in Australia. The floors are made of a floorboard supported on joists or trusses. Recently, the sector is moving towards multi-storey construction of different building classes with different floor usages and shared tenancy. Thus, a need for high performing lightweight floor systems becomes urgent. The current vibration control criteria in the Australian standard recommends limiting static deflection, which is a coarse method and does not necessarily guarantee satisfactory performance. In the current study, vibration performance of a 6m×6m floor system with particleboard flange and truss webs is investigated under single walker excitations and at different walking frequencies. The vibration responses are compared to the predictions and performance criteria recommended in international standards and guidelines. The results show inconsistencies in the calculated levels of acceptance from different sources using simplified expressions and more rigorous methods of analysis. This highlights the significance of the need for further research to develop a harmonised method of analysis that can be used by manufacturers and engineers in Australia to confidently design floors for vibrations.

KEYWORDS: Floor dynamics, Footfall-induced vibration, Lightweight timber floors, Non-destructive testing.

1 INTRODUCTION

There is an increased global focus on using timber structures due to the availability of timber-based and engineered wood products (EWPs) as well as sustainability and lower carbon footprint of timber compared to other conventional construction materials [1]. In Australia, there is a growing trend in lightweight timber floors to enter the multi-storey market [2], mainly due to the increasing surge in land prices in capital cities. A major restriction in current buildings with timber floors is their close column spacing, while most developments require more open space. For spans longer than 6 meters, the design is governed by serviceability not strength; therefore, accurate assessment of the vibration performance of the floor is essential.

The current work aims to investigate the vibration performance of a 6m×6m lightweight timber floor system typically used in Australian buildings. The investigation is comprised of measurement of natural frequencies and accelerations due to walking of the examined floor as well as numerical modal analyses. The vibration responses are calculated and compared to recommendations in existing standards: CSA 086:2019 [3], EN 5:2004 [4], AS 1170.0:2002 [5] and guidelines of CCIP-016 [6], SCI-P354 [7], AISC DG11 [8], HIVOSS [9], and recommended performance criteria in ISO 10137 [10] and BS 6472.1 [11]. The paper is concluded by an analysis of the aforementioned comparison.

2 FLOOR VIBRATION DESIGN IN CURRENT STANDARDS AND GUIDELINES

Canadian standard CSA 086 [3] and Eurocode 5:2004 [4] provide simple methods for vibration design of timber floors. CSA-086 [3] uses simple T-beam equations and gives vibration-controlled span limit of joisted floors. The approach is based on the comprehensive experimental works of Hu and Chui [12, 13] and offers a limit based on the relation between fundamental frequency of the floor system and static deflection under 1 kN at its centre. More rigorous methods that categorise the floor based on the

[1] Hassan Karampour, Griffith University, Australia, H.Karampour@griffith.edu.au
[2] Farid Piran, Griffith University, Australia, Farid.Piran@griffithuni.edu.au
[3] Adam Faircloth, Queensland Dept. of Agric. and Fisheries, Australia, Adam.Faircloth@daf.qld.gov.au
[4] Chandan Kumar, Queensland Dept. of Agric. and Fisheries, Australia, Chandan.Kumar@daf.qld.gov.au
[5] David Zhang, Multinail, Australia, David.Zhang@multinail.com
[6] Benoit. P. Gilbert, Griffith University, Australia, B.Gilbert@griffith.edu.au
[7] Hong Guan, Griffith University, Australia, H.Guan@griffith.edu.au
[8] Lin Hu, FPInnovations, Canada, Lin.Hu@fpinnovations.ca
[9] Ying Hei Chui, University of Alberta, Canada, Yhc@ualberta.ca
[10] Wen-Shao Chang, The University of Sheffield, UK, W.Chang@sheffield.ac.uk

https://doi.org/10.52202/069179-0247

fundamental frequency and calculate the response from modal analyses are outlined in [6-8]. However, these methods are developed for steel, concrete or steel-concrete composite floors and their appropriateness for timber floors is disputed.

Prediction of vibration in floor systems requires determination of vibration modes, associated frequencies and damping values. In order to assess the floor systems against serviceability criteria, the floors are categorised into (i) low-frequency floors and (ii) high frequency floors. Low frequency floors are associated with a steady-state resonant response under footfall-induced vibrations, whereas in high-frequency floors, the floor response is transient, and is damped out after each footstep. There is no clear quantitative measure that separates the two categories, and different guidelines [6-8] suggest cut-off frequencies ranging from 7 Hz to 10.5 Hz.

3 EXPERIMENTAL AND NUMERICAL RESULTS

3.1 PHYSICAL TESTS

In the present work footfall-induced vibration (FIV) of the 6 m×6 m lightweight timber floor system (shown in Figure 1) comprised of a floorboard (19 mm particleboard) resting on timber chords MGP12 (softwood), 90 mm × 35 mm in cross-section, and steel braced trusses and supported on 200 PFC steel bearer beams on two sides is studied.

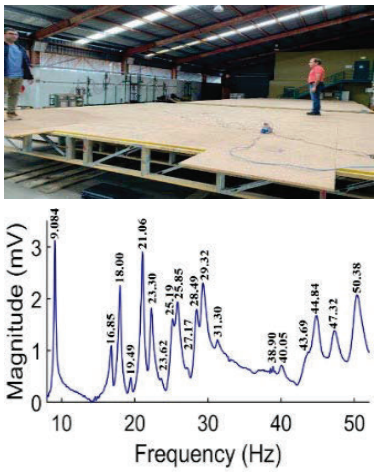

Figure 1: *The tested 6m×6m floor system and the frequency response function (FRF) showing frequency-domain response.*

The floor was excited using a digital hammer at a location close to the accelerometer 'A' shown in Figure 2. The impulsive excitation was repeated 10 times. Using Fast Fourier Transform (FFT) of the acceleration time-history, Frequency Response Functions (FRF) were developed and natural frequencies were calculated as shown in Figure 1. Natural frequencies, f_i measured at accelerometer A, and corresponding critical modal damping values ζ_i, showing average and CoVs are represented in Table 1. Damping values are calculated from the half-bandwidth method according to AS ISO 2631.2 [14]. The deflection of the floor under a static 1 kN load applied at the centre was found to be 1.54 mm.

Table 1: *Measured frequencies and critical damping.*

	Accelerometer A (centre of the floor)		Damping	
Mode, i	$f_{i\,(avg)}$ (Hz)	CoV	ζ	CoV
1	9.08	0.59%	0.90%	0.14%
2	17.05	3.77%	1.08%	0.66%
3	17.84	0.01%	1.03%	0.17%
4	19.41	0.01%	0.84%	0.55%
5	20.98	0.01%	0.91%	0.14%
6	22.01	0.26%	0.89%	0.14%
7	24.86	0.01%	0.95%	0.21%

Then, the floor was excited to dynamic walking forces, and accelerations were measured at three different locations (A, B, and C) on the slab.

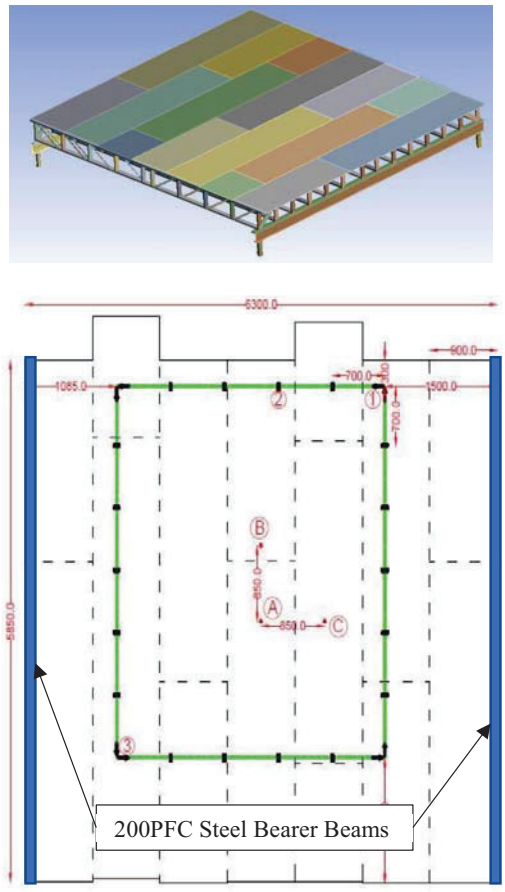

Figure 2: *The floor layout and walking path (in Green).*

Two walking scenarios, with single walker (80kg) in two different walking frequencies f_w of 1.80 Hz (brisk walking) and 2.25 Hz (fast walking), of W1 and W2, respectively, were selected to examine footfall-induced vibration of the floor. The 4th harmonics of walking

frequency of 2.25 Hz and the 5th harmonics of walking frequency of 1.80 Hz, correspond to the fundamental natural frequency (9.08 Hz) of the floor system.

The acceleration time-histories were calculated from each accelerometer and were filtered using the weighting factors outlined in AS 2670.1 (ISO 2631-1) [15]. The vibration responses of each walking scenario were calculated in terms of root-mean-square (rms) and Vibration Dose Value (VDV) defined in Equations (1 & 2):

$$a_w(t_0) = \sqrt{\frac{1}{\tau}\int_{t_0-\tau}^{t_0} [a_w(t)]^2\, dt} \quad (1)$$

$$VDV = \left\{\int_0^{\tau} [a_w(t)]^4\, dt\right\}^{\frac{1}{4}} \quad (2)$$

where τ is the time (integration variable) recommended to be equal to 1 second. The raw and ISO weighted acceleration time histories of W1 and W2 walking configuration tests are plotted in Figure 3. There were some differences between accelerometer results at A, B and C. However, for the sake of comparison against standards and guideline only results of accelerometer, A which is located at the centre of the floor are presented herein.

The acceleration time histories show a steady-state response much more significant than the transient response in both walking configurations, distinguished with a clear resonant excitation in W2.

The frequency content (FFT) of W2 walking test is also shown in Figure 3, and indicates that the fundamental frequency (9.08 Hz), as well as modes with frequencies of 21 Hz and 18 Hz are significantly excited. These frequencies were also shown to have the largest amplitude as displayed in the frequency domain results of Figure 1.

The measured vibration response parameters are represented in Table 2. Following recommendations of ISO 2631-1 [15], the running r.m.s. acceleration, a_w, is calculated using an integration time constant of 1 second. The maximum acceleration, $a_{w,max}$ corresponds to the peak in the time-history.

Table 2: *Measured vibration responses of the floor system.*

	a_w (m/s^2)	$a_{w,max}$ (m/s^2)	VDV (m/s$^{1.75}$)
T1	0.75	1.75	0.92
T2	0.91	2.05	1.10

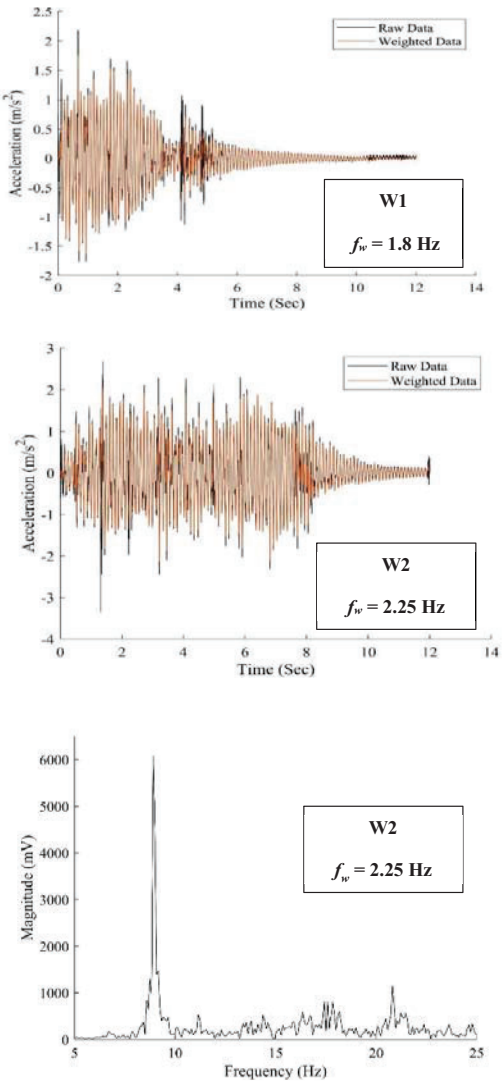

Figure 3: *The raw (black) and weighted (orange) acceleration time-histories of a single person walker, 80 kg at walking frequencies of 1.8 Hz (W1) and 2.25 Hz (W2). The frequency content of W2 is shown in the bottom of the figure.*

3.2 FINITE ELEMENT ANALYSIS (FEA)

Modal analysis of the floor system was carried out in the commercial package, Ansys [16]. Mechanical properties of sawn timber boards (orthotropic) and steel beams were taken from AS 1720.1:2010 [17] and AS 4100:2020 [18], respectively. Particleboard was assumed to be isotropic [19]. In the FEA model (see Figure 4) MGP boards, particleboard, PFCs and the supporting short columns were meshed using 8-noded Shell-181 elements with 5 integration points, and the metal webs were modelled with 2-noded beam elements [16]. The connection between the bearer beam and the PFC, and that between the PFC and the short column was defined a Mohr-Coulomb frictional contact with a coefficient of friction of 0.45 (calculated from a simple sliding test). From a mesh sensitivity analysis (not shown here for the sake of brevity), a mesh

https://doi.org/10.52202/069179-0247

with a total of 182,550 nodes was selected, which has mid-span deflection and fundamental frequency of less than 5% difference from an FEA model with 303,015 nodes. Mid-span deflection of the floor system from the FEA is 1.99 mm and the mode shapes and associated frequencies are shown in Figure 4.

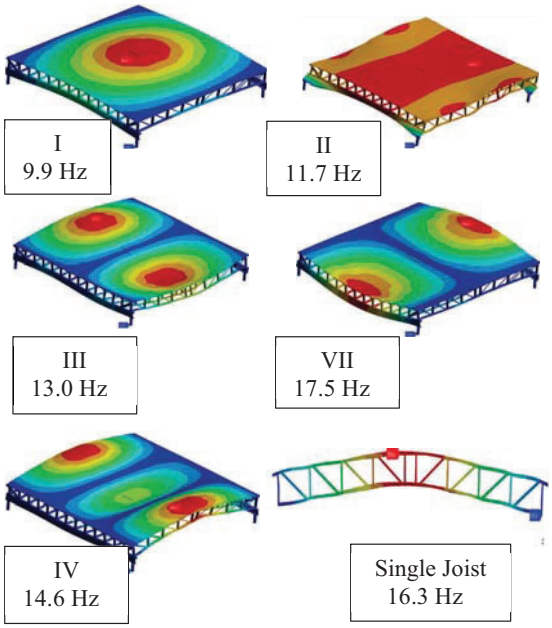

Figure 4: *Mode shapes and frequencies from the FEA ranked based on ascending frequencies.*

There is a relatively reasonable agreement between experimental and numerical frequencies. The fundamental FEA frequency of 9.9 Hz corresponds to a plate-type mode shape. The next frequency (11.7 Hz) is due to minor-axis bending of the PFC (steel) beams. Flexural modes along unsupported edges occur at frequencies below 15 Hz. Bending mode along the supported edge is at 17.5 Hz from FEA, and probably corresponds to the 18 Hz peak in the experimental FFT results of Figure 1.

The fundamental frequency of the floor system can be approximated from deflection under self-weight, δ:

$$f_1 = \frac{17.8}{\sqrt{\delta}} \tag{3}$$

Knowing δ is equal to 4.72 mm (from FEA), a fundamental frequency of 8.2 Hz is calculated using Equation 3, which is 10% lower than the measured frequency.

The other method normally used to calculate fundamental frequency of composite floor systems supported by primary beams and secondary beams of frequencies f_b, and f_j, respectively, is the Dunkerly's modal decomposition method [20] in Equation 4:

$$\frac{1}{f_1^2} = \frac{1}{f_b^2} + \frac{1}{f_j^2} \tag{4}$$

where the frequencies f_b, and f_j in Equation 4 shall be associated with the same mode shape as the fundamental mode shape of the floor system. The major axis flexural mode shape and frequency of the joist (16.3 Hz) is shown in Figure 4. Frequency of the PFC beam in the minor bending mode is 8 Hz (from FEA). Using Equation 4 and knowing the floor system has 2×PFC beams and 14×joists, a fundamental frequency of 15.9 Hz is calculated, which is 75% greater than the measured frequency. If the number of PFC beams and joists are reduced to one in Equation 4, a frequency 7.2 Hz is derived.

4 COMPARISON AGAINST EXISTING STANDARDS AND GUIDELINES

Several methods are available that provide insight into floor vibration. These methods vary from simple rules to more sophisticated methods. Simple methods require less design effort, modelling and analysis, whereas more complicated methods have more room for flexibility, engineering judgement and innovation. Vibration performance of the investigated floor system is discussed from a code-compliancy point of view, here forth.

4.1 AUSTRALIAN STANDARD

Most commonly accepted simple rule to minimise the annoying vibration is a limit on deflection based on the design live load. In the Australian standard AS 1170.1 [21] the design live load is 1.5 kPa for residential buildings and 3 kPa for commercial ones (excluding shopping areas, public assembly areas, dance halls, etc.). The ripple/sag serviceability limit state criterion in AS 1170.0 [5] is $L/300$ for dead load plus 40% live load combination. Moreover, for vibration serviceability, a static mid-span deflection under a 1 kN vertical load, (d_{1kN}) of less than 1 to 2 mm is recommended. The measured and FEA deflections of the floor system are both under 2 mm, which can be interpreted as satisfactory vibration performance according to the Australian standard. Under a self-weight plus 40% live load combination with 1.5 kPa (residential) and 3 kPa (commercial) distributed live loads, floor centre deflections are 13.9 mm and 23.1 mm (from FEA), respectively, compared to the 20 mm limit ($L/300$). Thus, in deflection serviceability, the floor is acceptable for residential usage, but misses the acceptance tolerance of commercial buildings by a margin of 15.5%.

4.2 ISO/TR 21136 [22]

The ISO/TR 21136 method [22] proposes a relation between fundamental frequency and static deflection of the floor as indicated in Equation (5), which is developed from a logistic regression on the database of field light

frame timber floors in across Canada occupants' survey and testing.

$$d_{1kN} \le \frac{f^{2.56}}{1090.31} \quad (5)$$

Knowing the fundamental frequency, *f*, is equal to 9.08 Hz, Equation 5 gives a deflection limit of 0.6 mm, which is 61% smaller than the measured deflection. The floor is "unacceptable" to ISO/TR 21136 [22].

4.3 Eurocode 5:2004 [4]

Eurocode 5:2004 [4] divides the floors into better performance and poorer performance using three criteria for controlling vibration in residential floors: (i) frequency limit, (ii) deflection limit, and (iii) impulse velocity control. These conditions are outlined in Equation 6.

$$(i) f > 8Hz \;;\; (ii)\frac{d}{F_s} \le a \;;\; (iii) v \le b^{(f\,\xi^{-1})} \quad (6)$$

where *v*, is the unit impulse velocity response, calculated as the maximum initial vertical velocity (m/s) caused by an ideal unit impulse (1 Ns) applied at a location on the floor that gives the maximum response. The first condition in Equation 6 is satisfied since the fundamental frequency is larger than 8 Hz. The force (F_s)-defection (a) criterion is also satisfied and places the floor within the better performance region of the curve in EN 5:2004 [4]. However, assuming 1% damping, the calculated unit impulse velocity response is v=23 mm/Ns^2, which is 42% larger than the recommended value of 16.2 mm/Ns^2 calculated using Equation 6.

4.4 CANADIAN STANDARD [3]

CSA 086:2019 [3] has a vibration-controlled span approach for single-span wood joisted floor systems with prefabricated wood I-joists and wood structural panel subfloor. The maximum recommended span l_v (m) is

$$l_v = \frac{0.122(EI_{eff})^{0.284}}{k_{tss}^{0.14} m_L} \quad (5)$$

$$k_{tss} = 0.0294 + 0.536k_1^2 + 0.516k_1^{0.5} + 0.31k_1^{0.75}$$

where EI_{eff} (Nm^2) is the effective flexural stiffness of the floor system in the span direction, k_{tss} is a factor that accounts for the flexural stiffness in the transverse direction, and m_L is the mass per unit length (kg/m) of the composite floor system. Using FEA and calculating k_1 and K_{tss} of 0.15, and 0.49, respectively, and EI_{eff} of 2.35×10^6 Nm^2, a maximum recommended span, l_v of 5.3 m is calculated, which suggests that the floor system is 13% longer than recommended.

4.5 CCIP-016 [6]

In floors with low-frequency (<10 Hz) the guideline [6] recommends prediction of vibration response based on the first four harmonics of the footfall forces for a range of walking frequencies. That requires calculation of the response in all modes to each of these harmonics and then combining them. The method in CCIP-16 [6] is valid for floors with natural frequencies less than 4.2 times the maximum footfall frequency (i.e. about 15 Hz). The calculation method is comprised of several steps to find mode shapes, frequencies, mode shape amplitudes at excitation and response locations, and eventually calculating the response factor by dividing calculated accelerations by the base accelerations in BS 6472-1 [11].

Response factors at the centre of the floor in a range of walking frequencies (1-2.8 Hz) based on CCIP-016 [6] are displayed in Figure 5. Response factors from the measurements are calculated by dividing a_w in Table 2 by the base acceleration of 0.05 m/s^2 recommended in ISO 2631.2 [14]. It should be noted that the CCIP-016 [6] response factors in Figure 5 are based on 3% damping (in all modes) recommended in the guideline, whereas the experimental response factors are based on the measured damping of 1% (see Table 1).

Using the CCIP-016 method, a maximum R of 479 is calculated at walking frequency of 2.48 Hz (the 4th harmonic of the FEA fundamental frequency), which is much greater than R=18.2, from walking measurements at walking frequency equal to the 4th harmonic of the measured fundamental frequency.

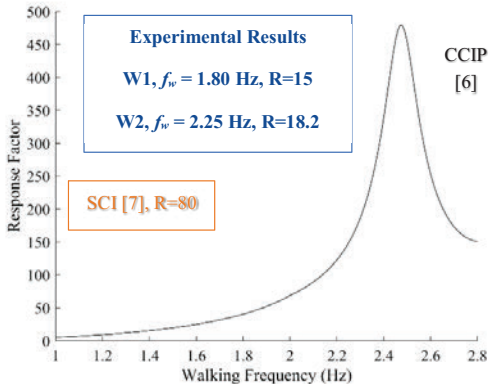

Figure 5: *Response factors from CCIP-016 [6] and SCI-P354 [7] modal approaches and those calculated from the experimental measurements.*

Acceptable response factors for residential and commercial floors are typically below 8. Therefore, assessment based on CCIP-016 [6] indicates that the floor is not acceptable.

4.6 SCI-P354 [7]

The method described in SCI P354 [7] is based on finding peak response (acceleration or VDV) from range of walking frequencies and floor frequencies. The cut-off

https://doi.org/10.52202/069179-0247

frequency (distinction between low- and high-frequency floors) for general floors is 10 Hz in SCI-P354 [7]. In low-frequency floors, both steady-state response and transient responses need to be checked. All modes of vibration with natural frequencies up to 2 Hz higher than the cut-off frequency shall be considered. Initially, the weighted root mean square (RMS) acceleration response of each force harmonic at every mode of the response at the centre of the floor from excitation at designated point on the floor is calculated. Then, the total acceleration response function is found by summing up RMS of each mode of vibration at each harmonic of the forcing function.

Using 1.1% damping for joisted timber floors suggested in [7], an r.m.s. acceleration of 0.4 m/s^2, and a response factor of 80 is calculated and is presented on Figure 5. The calculated response factor is larger than the recommended values (4-8) for residential and office floors, for continuous and intermittent vibrations in BS 6472-1 [11]. However, assuming impulsive vibration, response factors of 60-128 can be acceptable for office and school floors [11].

4.7 HIVOSS [9]

The method is developed by ArcelorMittal (Steel manufacturer) in their design for vibration of timber floors and is based on the statistical distribution of walking frequencies [9]. A design value $OS\text{-}RMS_{90}$ called the "*one step root mean square 90*", is developed which covers the response velocity of the floor filtered using the weighting functions for a significant step with the intensity of 90% of people's walking normally. In this method, the fundamental frequency and corresponding modal mass are calculated from FEA or simple equations. A critical damping value is chosen and from the provided design diagrams, a classification of the floor is derived.

Using a damping of 3% (recommended in [9] for joist timber floors) the floor is classified as 'E' in HIVOSS, which means it is critical for residential and office buildings. However, if used in industrial and sport facilities the floor will have vibration performance at an acceptable level.

5 CONCLUSIONS AND RECOMMENDATIONS

Dynamic properties and vibration response parameters of a lightweight timber floor was studied experimentally. The experimental results were compared to the predictions from simple methods and modal superposition methods, by implementing modal analysis in FEA.

Simplified methods of vibration design, provide a rigid "Yes" or "No" acceptance criterion. The acceptance criterion is based on frequency-deflection equations in which the frequency appears in powers of 2 and larger. Hence, finding the accurate frequency of the floor system is critical. It was understood that a modal analysis in FEA can provide a reasonable approximation of the measured fundamental frequency of the floor system. However, simplified equations fail to provide accurate predictions of natural frequencies. It should be noted that in future work, study of effects of edge supports (4-edge supported floors) on the floor dynamics and vibration performance will be implemented.

The other issue in using simplified methods is calculation of the deflection. The deflection of the floor system under a 1 kN concentrated load is normally smaller than 2 mm and its measurement is a delicate task.

An engineer may decide to use modal superposition methods. The vibration performance in these methods is based on the frequency cut-offs, modal mass, mode shapes and damping. This will provide the engineer more flexibility to make a judgement on the vibration performance of the floor. However, the current study shows that the response factors predicted by modal superposition methods considerably outweigh the experimental observations. The conservative design approach causes oversizing of the floor systems and their structural elements and may result in forsaking a timber design.

Based on the findings of the current study, the following future research directions may be pursued to promote implementation of timber floors in longer spans in buildings of different usages:

- Measure and formulate load functions of continuous and impulsive excitations as well as rhythmic activities, tailored for long-span timber floors.
- Characterise the dynamic properties (natural frequencies, modal mass, mode shape and damping) and response to vibration of floor slabs (i) in the laboratory environment, and (ii) floor systems in selected constructed or completed buildings. This will help understand the difference between a slab design analogy and the actual performance of the floor within the structural system.
- To develop experimentally validated analytical models that can reliably predict the dynamic properties and vibration response of the floor systems.
- To assess occupant comfort with different floor usage and identify acceptance criteria for the investigated floor systems.

In order to establish design criterion in Australia, subjective evaluation of occupants' perception of level of comfort needs to be conducted. There will be enormous benefit in gathering the data from field tests and occupant surveys to establish an international database for researchers and practitioners worldwide for vibration design of long-span floor systems.

REFERENCES

[1] Ramage, M. H., Burridge, H., Busse-Wicher, M., Fereday, G., Reynolds, T., Shah, D. U., ... & Scherman, O. The wood from the trees: The use of

timber in construction. Renewable and Sustainable Energy Reviews, 68, 333-359, 2017.
[2] Carradine, D. Multi-storey light timber-framed buildings in New Zealand–Engineering design. BRANZ, Judgeford, New Zealand, 219.
[3] Canadian Standards Association, CSA 086:19 Engineering Design in Wood. 2019.
[4] Eurocode 5. Design of timber structures-Part 1-1:General Common rules and rules for buildings. European Committee for Standardisation, 2004.
[5] Standards Australia, AS 1170.0: Structural Design Actions–General Principles. Standards Australia (SA), Sydney, Australia, 2002.
[6] Willford, M. R., Young, P., & CEng, M. A design guide for footfall induced vibration of structures. London, UK: Concrete Society for The Concrete Centre, 2006.
[7] Smith, A. L., Hicks, S. J., & Devine, P. J. Design of floors for vibration: A new approach. Ascot, Berkshire, UK: Steel Construction Institute, 2007.
[8] Hechler, O., Feldmann, M., Heinemeyer, C., & Galanti, F. Design guide for floor vibrations. In Proceedings of EuroSteel 2008 Conference, 2008.
[9] HIVOSS. Design of footbridges guideline. Human induced vibrations of steel structures. RFS2-CT-2007-00033, 2009.
[10] International Standards Organisation. Basis for design of structures-serviceability of buildings and walkways against vibrations, ISO 10137:2007.
[11] British Standards Institution. Guide to evaluation of human exposure to vibration in buildings, BS 6472-1:2008.
[12] Hu, L. J., Desjardins, R., & Chui, Y. H. Nature of vibrations induced by footsteps in lightweight and heavyweight floors. In 9th World Conference of Timber Engineering. Portland, USA, 2006.
[13] Hu, L. J., Chui, Y. H., & Onysko, D. M. Vibration serviceability of timber floors in residential construction. Progress in Structural Engineering and Materials, 3(3), 228-237, 2001.
[14] International Standards Organisation. Mechanical vibration and shock - Evaluation of human exposure to wholebody vibration, Part 2: Vibration in buildings (1 Hz to 80 Hz), AS ISO 2631.2:2014.
[15] International Standards Organisation. Evaluation of human exposure to whole-body vibration, Part 1: General requirements, AS 2670.2:2001 (ISO 2631.1).
[16] DeSalvo, G. J., & Swanson, J. A. ANSYS Engineering Analysis System: User's Manual. Swanson Analysis Systems, 1979.
[17] Standards Australia. Timber structures, Part 1: Design methods. AS 1720.1-2010.
[18] Standards Australia. Steel structures. AS 4100:2020.
[19] Nemli, G., & Aydın, A. Evaluation of the physical and mechanical properties of particleboard made from the needle litter of Pinus pinaster Ait. Industrial Crops and products, 26(3), 252-258, 2007.
[20] Ebrahimpour, A., & Sack, R. L. A review of vibration serviceability criteria for floor structures. Computers & Structures, 83(28-30), 2488-2494, 2005.
[21] Standards Australia. Structural design actions, Part 1: Permanent, imposed and other actions. AS 1170.1:2002.
[22] International Standards Organisation. Timber structures — Vibration performance criteria for timber floors. ISO/TR 21136:2021.

https://doi.org/10.52202/069179-0247

World Conference on Timber Engineering Oslo 2023

EXPERIMENTAL STUDY ON THE VIBRATION CHARACTERISTICS OF A PREFABRICATED CROSS-LAMINATED TIMBER-STEEL COMPOSITE FLOOR

David Owolabi[1], Critiano Loss[2]

ABSTRACT:

Prefabricated mass timber-based floors are lightweight flooring alternatives gaining attention in building applications given their ease of erection, low carbon footprint and structural benefits in reducing the overall seismic mass and foundation requirements in buildings. However, in these floor archetypes, serviceability limit state requirements such as deflection and vibration performance often govern member sizing and layout design. In this paper, the vibration properties of one such flooring system – a prefabricated cross-laminated timber (CLT) -steel hybrid floor, are examined at full-scale via modal and walking tests, considering variations in material properties, geometric configurations, support conditions, walking paths and walking frequencies. The test results indicate that the composite floor is a high-frequency system with a transient response. The study also provides valuable insight into the potential vibration performance of CLT-steel composite floors for residential applications. A prediction of its vibration serviceability via the vibration dose value method indicates that it has a low probability of attracting adverse comments from users in residential applications when a continuous slab is created by connecting its fundamental units using self-tapping screws.

KEYWORDS: Floor vibration, CLT-steel composite floor, prefabricated construction; low-carbon structures

1 INTRODUCTION

1.1 DEVELOPMENT OF STEEL-TIMBER COMPOSITE FLOORS

The use of timber-steel composite decks dates back several decades. One of the earliest applications of this system is in bridge construction, notable among which are some bridge projects in Ontario, Canada. They featured prestressed wood and steel girders connected through shear studs welded to the girders and embedded in the timber via fibre-reinforced grout [1]. More recently, there has been a growing application of mass timber in the construction industry. This can be attributed to its low embodied carbon and constructional efficiency which provide a means of achieving sustainability targets in construction and fast-tracking project completion timelines.

To further optimize the performance of mass timber flooring systems, composite solutions are being developed and mass timber-steel composites are one of the promising solutions. In these flooring systems, steel often provides ductility while mass timber's light weight and low-carbon qualities provide for an environmentally friendly, modular, and demountable system. In building applications, one of the foremost studies on mass timber-steel composite floors examined the feasibility of replacing the conventional composite steel-concrete floor with a CLT-steel solution, focusing on the floor performance under lateral loading action (seismic and wind loads) [2]. More investigations into mass timber-steel composite floors wherein mass timber panels such as CLT or LVL are connected to hot-rolled or cold-formed steel beams to achieve superior structural performance and efficiency have since been carried out [3-6]. These flooring systems have the potential as viable alternatives to mainstream steel-concrete composite floors.

1.2 VIBRATION DESIGN OF LIGHTWEIGHT FLOORS

The design of lightweight flooring systems is often governed by their serviceability limit state requirements – i.e., deflection and vibration, which control their allowable spans. Several guidelines on the vibration design of lightweight floors are available in the literature. These include the American Institute of Steel Construction Design Guide 11 [7], Steel Construction Institute Publication 354 [8], European Guideline on Human-Induced Vibration of Steel Structures [9] and Applied Technology Council Design Guide 1 [10]. Prominent vibration assessment methods contained in these guidelines include the baseline curve culled from ISO 10137 [11], the response factor method and peak acceleration criteria which are derivatives of the baseline

[1] David Owolabi, PhD candidate, Sustainable Engineered Structural Solution Laboratory, University of British Columbia, Canada, dowolabi@mail.ubc.ca

[2] Cristiano Loss, Professor (Assistant), Sustainable Engineered Structural Solution Laboratory, University of British Columbia, Canada, cristiano.loss@ubc.ca

https://doi.org/10.52202/069179-0248

curve, and the vibration dose value (VDV) method detailed in ISO 10137 [11] and BS 6472 [12].

Many vibration control criteria have also been proposed for timber-joisted floors. These include deflection control requirements [13-15], fundamental frequency benchmarks [14-16], and thresholds on peak velocity and acceleration [14,15]. Recently, a span-limiting vibration control equation for CLT floors was adopted in CSA O86 [17] based on the Canadian CLT handbook [18] which also has a similar requirement for timber-concrete composite floors. However, the literature on the vibration behaviour of timber-steel composite floors and their specific vibration design guidelines is very limited [19,20].

1.3 STUDY OVERVIEW

This paper presents an investigation into the vibration characteristics of a prefabricated modular CLT-steel composite floor via modal tests and walking-induced acceleration measurements on full-scale specimens. The in- and out-of-plane static performance of analogous prototypes of the floor has been previously studied and found to be highly satisfactory [3, 21], but its vibration attributes have been hitherto untested. The study provides insights essential for the development of provisions for the vibration design of CLT-steel composite floors.

2 STUDIED FLOOR CONFIGURATION

The studied composite floor consists of fundamental modules, as shown in Figure 1, connected along their edges via self-tapping screws (STSs). Each fundamental module features a 3-layer CLT panel coupled to twin cold-formed steel beams having omega-shaped profiles. The beams are spaced such that the maximum transverse bending capacity of the CLT panel is not exceeded. Composite action is achieved by the transmission of shear stresses between the beams and panel via STSs.

In regions of high horizontal shear stresses (i.e., close to the beam ends), the STSs are driven in at 30°, guided by steel tubes welded over slots machined in the flange of the beams. In the middle regions of low shear, the STSs are inserted perpendicularly. The CLT panel, which enables two-way loading, is designed to be capacity protected, while the thin-profile steel beams (4.7mm thick) primarily take on plastic deformation. The dry assembly process enables easy production and decommissioning.

Module assembly

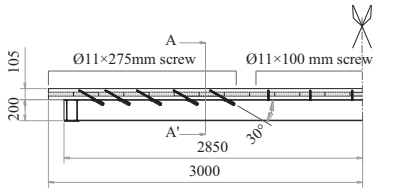

Longitudinal section

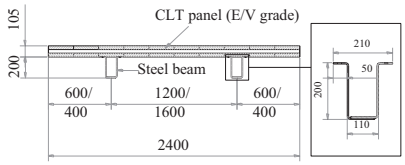

Section A-A'

***Figure 1**: Fundamental unit of tested composite floor: Module assembly (left) and section details (right)*

3 TESTING METHOD

3.1 PARAMETRIC CONSIDERATIONS

Roving hammer modal tests and walking-induced acceleration measurements were systematically carried out on the floor components, fundamental units, and pairs of connected units. The parametric changes considered during the tests are summarized in Figure 2. These include variations in the Canadian CLT panel grades – E and V grades; beam length – 5.7m and 6m; shear connection – full shear connection and partial connection wherein every other screw is omitted; and spacing of the beams – 1.2m and 1.6m. Regarding the beam spacing, 1.2m was adopted in the original design of the fundamental unit, while 1.6m is the maximum spacing for which a symmetric double T section can be maintained and the transverse bending stress in the CLT panels would remain below the permissible threshold. Also, the longitudinal edge conditions of combined modules were varied, considering free edges, and simply supported edges – to imitate panel continuity. At the supports, a simple support condition was maintained for all specimens throughout the testing.

https://doi.org/10.52202/069179-0248

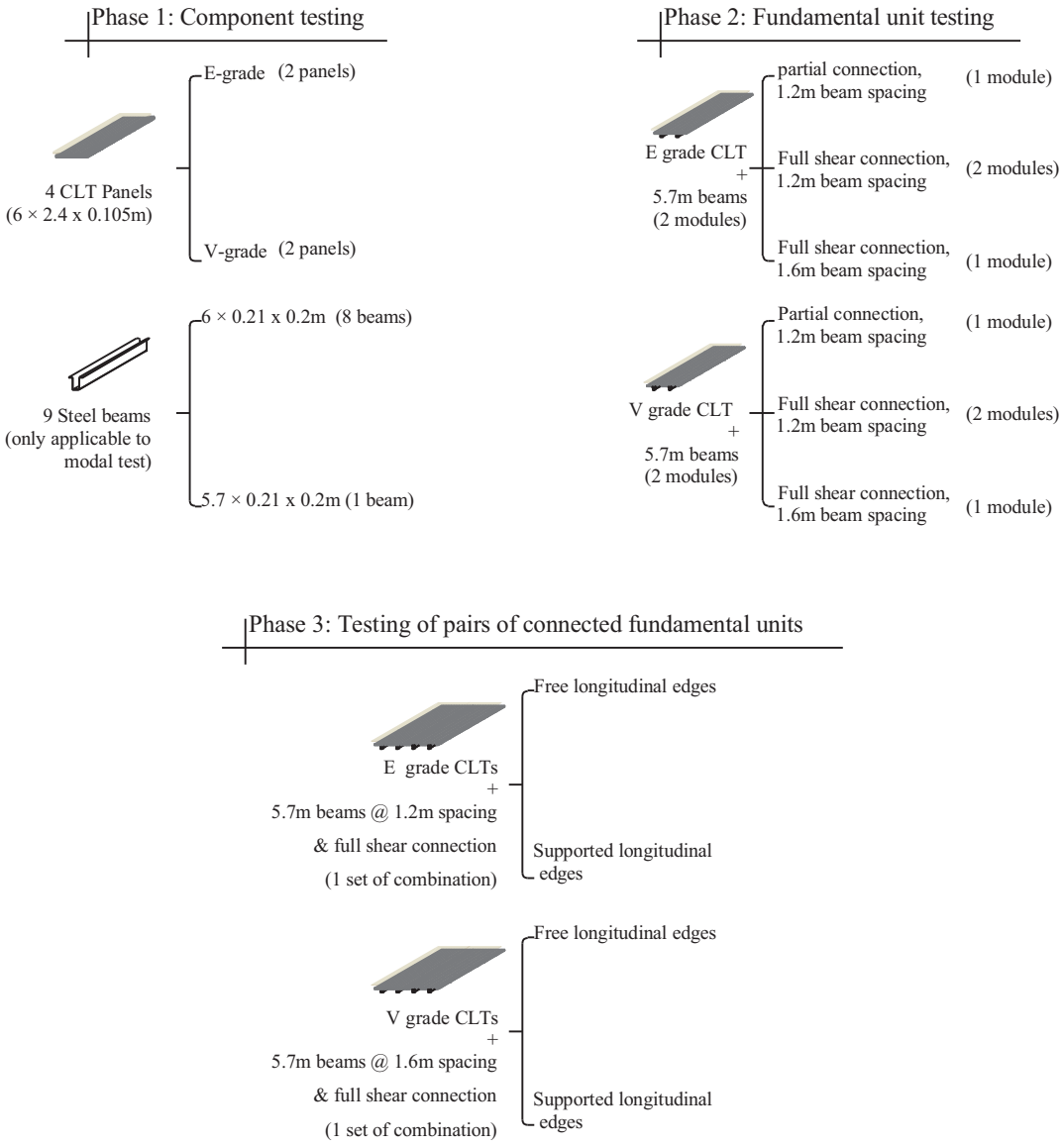

Figure 2: *Parametric variations considered during modal and acceleration measurements in the three testing phases*

3.2 MODAL TESTING AND ANALYSIS

Roving hammer modal tests were carried out in line with ISO 18324 [22] and BS EN 16929 [23]. The testing process and instrumentation are shown in Figure 3. In each tested CLT panel, fundamental unit and combined units, the experiment involved 49 impact locations and five accelerometers placed along the panel diagonal. In testing the beams, seven impact locations were set up along the base of each beam and three accelerometers were installed. The accelerometers employed in the modal test had an average sensitivity of 1mV/m/s^2. A six-channel data acquisition hardware with an input range of DC – 50kHz was used to record the data over eight seconds. Three averages were taken at each impact location of the beams, while two averages were taken for the CLT panels, fundamental units, and combined units, given their greater number of impact points compared to the beams.

Frequency response functions (FRFs) were generated from the excitation forces and frequency-domain accelerations obtained by fast Fourier transformation (FFT). The FRFs were used in the identification of modal parameters (i.e., mode shapes, natural frequencies, and damping ratios) via the rational fraction polynomial method.

https://doi.org/10.52202/069179-0248

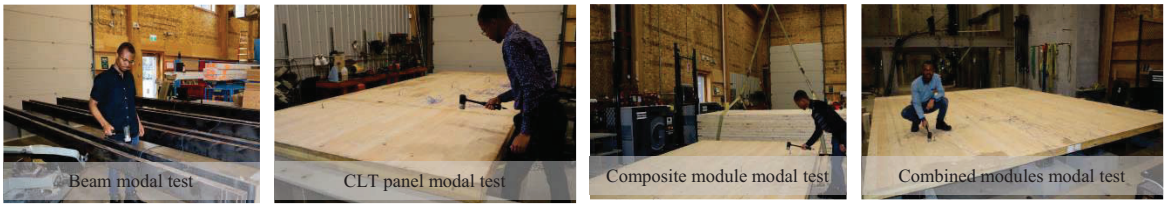

Instrumentation for CLT panel/ single module/ combined modules:

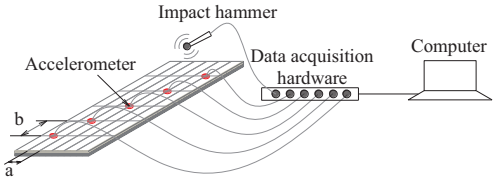

a: spacing of impact points/ accelerometers in the transverse direction (0.4m in single module, 0.8m in combined modules)

b: spacing of impact points/ accelerometers in the longitudinal direction (1m in single and combined modules)

Instrumentation for steel beams:

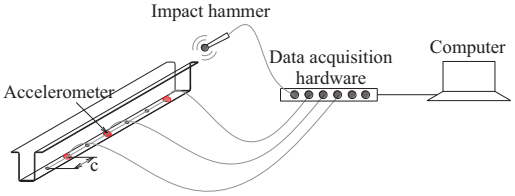

c: spacing of impact points along the beam (0.713m for 5.7m-beams, 0.75m for 6m-beam)

Figure 3: Modal experiment and instrumentation

Pertinent walking paths and accelerometer location for analysis of floor response:

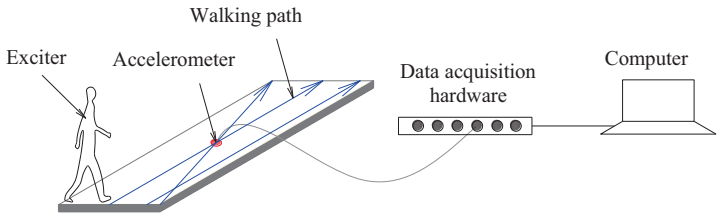

***Figure 4**: Walking-induced acceleration measurement*

3.3 WALKING-INDUCED ACCELERATION MEASUREMENT AND POST-PROCESSING

In this test, a 58kg human exciter aided by a metronome, walked over the specimens at different frequencies (1.2 Hz, 1.6 Hz, 2.0 Hz and 2.4 Hz) in line with ISO 10137-suggested range of forcing frequencies [11]. The acceleration data were obtained through the same set of accelerometers and data acquisition hardware used in the modal test. The pertinent walking events considered in analyzing the response of the specimens were those carried out along the longitudinal edge, diagonal and longitudinally along the middle of the specimens (Figure 4). Also, the acceleration data used in the analysis were those recorded at the centre of the specimens.

The root mean square values of the recorded vertical accelerations (A_{rms}) were computed, and the frequency-weighted acceleration data were obtained following guidance in ISO 2631-1 [24]. These were then used in calculating VDVs – see Equation (1), for predicting the probability of adverse comments by users based on BS 6472 [12].

$$VDV = \left(\sum_{n=1}^{N} \int_{0}^{T} a_n^4(t)dt \right)^{0.25} \quad (1)$$

where a_n is the frequency-weighted acceleration for vibration episode "n" and T is the total duration of the vibration event.

https://doi.org/10.52202/069179-0248

The VDV approach was chosen given its suitability for interpreting intermittent vibration events expected in residential settings. In obtaining the VDVs, a 16-hour day setting was adopted, with the assumption of a 10-minute interval between walking events. The worst value (highest value) of VDV obtained for each tested configuration was selected for drawing inferences about their vibration serviceability.

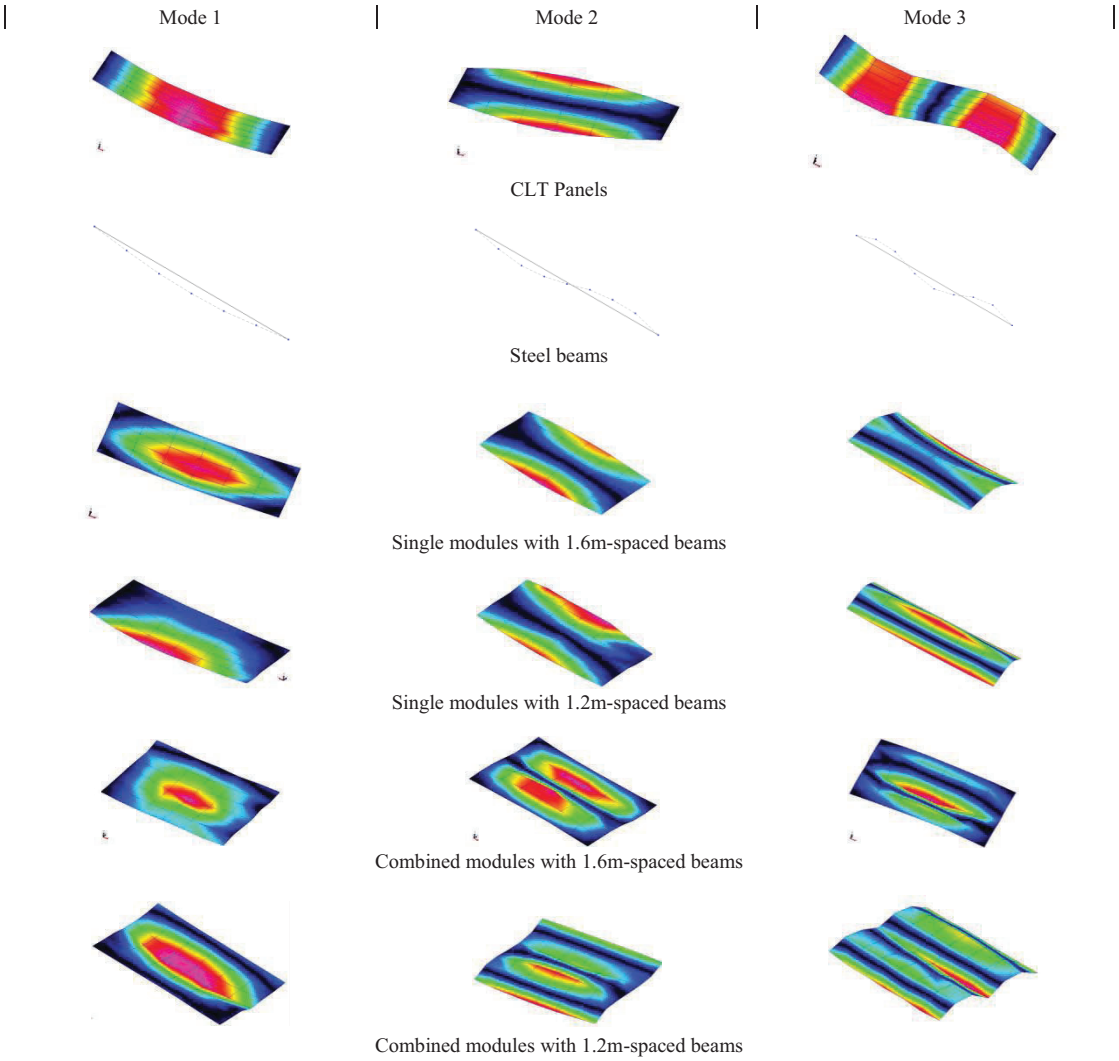

***Figure 5**: First three mode shapes of floor modules and their components*

4 RESULTS AND DISCUSSION

4.1 MODE SHAPES OF FLOOR MODULES AND THEIR COMPONENTS

Figure 5 shows the first three vibration modes of the tested specimens. The observed modes shapes of the steel beams were in conformity with the sinusoidal modes of an ideal simply supported beam. For the CLT panels, the first and third modes were bending modes while the second was torsional as anticipated. The spacing between beams was found to be the main influencer of mode shape discrepancies in the composite modules. As such, the vibration modes for composite modules in Figure 5 have been grouped based on beam spacing. In the fundamental modules, the first bending mode of specimens with 1.2m -spaced beams was partial longitudinal bending, while that of their counterparts with 1.6m-spaced beams was domed-shaped bending. However, their second (torsional) and third (transverse bending) vibration modes were similar. The combined modules had similar domed-shaped fundamental modes, but those with 1.2m-spaced beams experienced transverse bending in their second and third modes while the corresponding modes in specimens with 1.6m-spaced beams were akin to mirrored domes.

4.2 NATURAL FREQUENCIES AND DAMPING RATIOS OF FLOOR MODULES AND THEIR COMPONENTS

Table 1 summarizes the natural frequencies and damping ratios of the tested components and modules. Regardless of material grade, the CLT panels had similar natural frequencies and damping ratios (less than a 10% difference in the observed range of fundamental frequencies and damping values). The same is true of the steel beams where the discrepancy is less than 20%. The fundamental frequencies of the composite floors were heavily influenced by the beams, leading to high fundamental frequency values (greater than 15 Hz) which classified them as high-frequency floors. Other parametric changes did not significantly influence the fundamental frequencies. Also, their fundamental damping ratios (1.8% – 3.2%) were consistent with values suggested in ISO 10137 [11] for bare floors (1.3% – 2%).

The damping ratios of the combined modules were at least a fifth higher than those of the single modules. Also combined modules with supported longitudinal edges (introduced for simulating floor continuity) had about 21% higher damping values than their unsupported counterparts on average. This is suggestive of better vibration performance in on-site settings where there will be floor continuity.

Table 1: *Modal properties, A_{rms} and VDVs of floor modules and their components*

Component	$f_{1\ mean}$ (Hz)	$\xi_{1\ mean}$ (%)	$A_{rms,\ max}$ (m/s^2)	VDV_{max} (m/s$^{-1.75}$)	P (Adverse comment) [a]
Steel beam	18.1 (16.8 – 19.9)	1.5 (1.4 – 1.6)	-	-	-
CLT panels	6.6 (6.4 – 6.8)	4.4 (4.1 – 4.5)	1.3 (0.5 – 1.3)	4.3 (1.6 – 4.3)	Very likely
Single modules (1.2m-spaced beams)	17.9 (17.0 – 19.1)	1.9 (1.8 – 2.1)	0.4 (0.1 – 0.4)	2 (0.4 – 2.0)	Very likely
Single modules (1.6m-spaced beams)	16.8 (15.4 – 18.1)	1.9 (1.8 – 2.0)	0.6 (0.4 – 0.6)	2.8 (1.6 – 2.8)	Very likely
Combined modules (1.2m-spaced beams, free edges)	16.9	2.5	0.1	0.4	Low
Combined modules (1.2m-spaced beams, supported edges)	16.9	3.2	0.1	0.4	Low
Combined modules (1.6m-spaced beams, free edges)	17.4	2.8	0.1	0.4	Low
Combined modules (1.6m-spaced beams, supported edges)	17.9	3.2	0.1	0.4	Low

Note: Values in parentheses are the range of values obtained for the specimens in each category. Entries without values in parentheses have the same values for all tested replicates.

[a] P (adverse comment): the probability of adverse comment. 0.2 to 0.4 – low probability of adverse comment, 0.4 to 0.8 – adverse comment possible, 0.8-1.6 – adverse comment probable, >1.6 – adverse comment very likely [12]

4.3 RESPONSE OF COMPOSITE MODULES AND CLT PANELS TO WALKING

The VDVs and A_{rms} values of the tested specimens are presented in Table 1. Specifically, the values obtained for the CLT panels and fundamental units varied significantly in each category and their VDVs were unsatisfactory for residential applications as implied by the predicted high probability of adverse comments. On the contrary, the results for the combined modules – the form in which the floor system will be installed in practice – were less varied and favourable. Their VDVs translated to a low likelihood of adverse comments by residential building occupants per BS 6472 [12] provisions. Further details on the vibration response of the floor system and its serviceability performance are presented in the paper titled: "Vibration properties and serviceability performance of a modular cross-laminated timber -steel composite floor system" which is currently under review.

5 CONCLUSIONS

The vibration characteristics of a modular CLT-steel composite flooring solution have been examined in this paper. The modal properties, acceleration responses and prediction of its vibration serviceability have been elucidated. The main deductions of the study are as follows:

https://doi.org/10.52202/069179-0248

- The studied composite flooring solution is a high-frequency floor largely due to its beam components
- The floor's damping ratios are in agreement with the provisions in ISO 10137 [11] for the precursory design of bare floors
- The modal properties and acceleration response of the floor were mainly influenced by beam spacing, module combination and edge condition while other parameters – CLT panel grades, and shear connection – were less significant
- The combined floor modules were found to have consistent A_{rms} and VDVs. The VDVs of the combined modules also indicated favourable vibration serviceability. Nonetheless, evaluations involving real humans are required to ascertain the veracity of the vibration serviceability prediction

ACKNOWLEDGEMENT

This research was funded by the Government of British Columbia through the FII Wood First Grant, "Investigating the structural performance of a modular prefabricated dry-assembly mass timber-steel hybrid floor element Phase II," and by the Natural Sciences and Engineering Research Council (NSERC) of Canada through the Discover Program grant number RGPIN-2019-04530, and Discovery Launch Supplement, grant number DGECR-2019-00265. Fruitful discussions with Dr. Jianhui Zhou on vibration testing are gratefully acknowledged. The authors appreciate the assistance rendered by James Andal and Michael Billups of the UNBC Wood Innovation Research Laboratory and the civil engineering students at the University of Northern British Columbia during the experiments. The authors are grateful to Rothoblaas Canada Construction Products Inc. for providing screws used in the floor assembly and for the CLT discount by Structurlam, BC. The scholarships granted to David Owolabi: UBC Four-Year Doctoral Fellowships, Dr. J. David Barrett Memorial Scholarship in Wood Science, Special UBC Graduate Scholarship, and Donald S. McPhee Fellowship are also gratefully acknowledged.

REFERENCES

[1] Krisciunas R.: Ontario's experience with Composite Wood/Steel Bridges. In: National Conference on Wood Transportation Structures, US Forest Service, Forest Products Laboratory; Federal Highway Administration, No. FPL-GTR-94, 1996.

[2] Asiz A., Smith I.: Demands placed on steel frameworks of tall buildings having reinforced concrete or massive wood horizontal slabs. Structural Engineering International, 19(4):395-403, 2009.

[3] Loss C., Davison B.: Innovative composite steel-timber floors with prefabricated modular components. Engineering Structures, 132:695-713, 2017.

[4] Hassanieh A., Valipour H. R., Bradford M.A.: Experimental and numerical investigation of short-term behaviour of CLT-steel composite beams. Engineering Structures, 144:43-57, 2017.

[5] Hassanieh A., Valipour H.R., Bradford M.A.: Experimental and numerical study of steel-timber composite (STC) beams. Journal of Constructional Steel Research, 122:367-78, 2016.

[6] Owolabi D.O., Loss C.: Experimental and numerical study on the bending response of a prefabricated composite CLT-steel floor module. Engineering Structures, 260:114278, 2022.

[7] Murray T.M., Allen D.E., Ungar E.E., Davis B.D.: AISC design guide 11: Vibrations of steel-framed structural systems due to human activity. 2nd ed. American Institute of Steel Construction, Chicago, 2016.

[8] Smith A.L., Hick S.J., Devine P.J.: Design of floors for vibration: A new approach. Ascot: The Steel Construction Institute, 2009.

[9] Feldmann M., Heinemeyer C., Lukic M., Caetano E., Cunha Á., Goldack A., et al. Human-induced vibration of steel structures (HiVoSS). European Commission, Brussels, 2007.

[10] Allen DE, Onysko DM, Murray TM. ATC design guide 1: Minimizing floor vibration. California: Applied Technology Council; 1999.

[11] International Organization for Standardization. ISO 10137: Bases for design of structures – Serviceability of buildings and walkways against vibrations. International Organisation for Standardization, Geneva, 2007.

[12] British Standards Institution. BS 6472-1: Guide to evaluation of human exposure to vibration in buildings. Part 1: Vibration sources other than blasting. BSI Standards Limited, London, 2008.

[13] Canadian Commission on Building and Fire Codes, National Research Council of Canada. User's guide-NBC 2010 structural commentaries (Part 4 of Division B). Canadian Commission on Building and Fire Codes, Canada, 2011.

[14] European Committee for Standardization. EN 1995-1-1: Design of timber structures - Part 1-1: General rules and rules for buildings. European Committee for Standardization, Brussels, 2004.

[15] Hamm P., Richter A., Winter S.: Floor vibrations – New results. In: 2010 World Conference of Timber Engineering Italy, 2010.

[16] Dolan J.D., Murray T.M., Johnson J.R., Runte D., Shue B.C. Preventing annoying wood floor vibrations. Journal of Structural Engineering, 125 (1):19-24, 1999.

[17] Canadian Standard Association (CSA): CSA-O86-19: Engineering design in wood. CSA Group, Toronto, Canada, 2019.

[18] Karacabeyli E., Gagnon S.: CLT handbook 2nd Canadian edition. FPInnovaitons Special Publication SP-532E, Pointe-Claire, Canada, 2019.

[19] Chiniforush, A. A., Makki A.M., Dackermann U., Valipour H. R., and Akbarnezhad A.: Vibration behaviour of steel-timber composite floors, part (1): Experimental & numerical investigation. Journal of Constructional Steel Research 161: 244-257, 2019.

[20] Hassanieh A., Chiniforush A. A., Valipour H. R., & Bradford M. A.: Vibration behaviour of steel-timber composite floors, part (2): Evaluation of human-

induced vibrations. Journal of Constructional Steel Research, 158: 156-170, 2019.
[21] Loss C., Frangi A. Experimental investigation on in-plane stiffness and strength of innovative steel-timber hybrid floor diaphragms. Engineering Structures, 138:229-44, 2017.
[22] International Organization for Standardization. ISO 18324: Timber structures – Test methods – Floor vibration performance. International Organisation for Standardization, Geneva, 2016.
[23] British Standards Institution. BS EN 16929: Test methods – Timber floors – Determination of vibration properties. BSI Standards Limited, London, 2019.
[24] International Organization for Standardization. ISO 2631-1 – Mechanical vibration and shock – Evaluation of human exposure to whole-body vibration – Part 1: General requirements. International Organization for Standardization, Geneva, 1997.

https://doi.org/10.52202/069179-0248

World Conference on Timber Engineering Oslo 2023

EXPERIMENTAL INVESTIGATIONS ON VIBRATION PERFORMANCE OF TIMBER-CONCRETE COMPOSITE BEAMS USING LIGHTWEIGHT AGGREGATE CONCRETE

Bo Wen[1], Benkai Shi[2], Haotian Tao[3], Huifeng Yang[4], Bowen Huang[5]

ABSTRACT: Better structural performances can be obtained by using concrete slabs instead of timber slabs in floor system of timber structures. The use of lightweight aggregate concrete (LWAC) in timber-concrete composite floors can reduce the self-weight of the slab. However, the vibration performance of timber-LWAC composite floors remains need to be studied. In view of this, an experimental programme was conducted to investigate the dynamic properties of the timber-LWAC composite beams. Three test specimens with different types of connections were designed and fabricated. The test results demonstrated that the timber-LWAC composite beams have good vibration performance with the fundamental natural frequency much higher than 8 Hz. Additionally, the vibration frequency of the composite beams with notch-screw connections or glued-steel plate connections is higher than that of the composite beams with crossed inclined screw connections.

KEYWORDS: Timber-concrete composite beams, Lightweight aggregate concrete, Vibration performance, Timber-concrete connections, Experimental investigations

1 INTRODUCTION

Floor system is the component with the closest contact between the human and building, which requires high structural performance both in ultimate limit state and serviceability limit state. The vibration performance is one of the crucial behaviours of floor systems, which significantly affects the comfort and safety of the structure. Due to the lightweight and low elastic modulus of timber, the traditional timber floor is prone to generate large vibration response. Excessive floor vibration will bring negative psychological effects to the occupants, and even affect the structural safety, which will restrict the development of modern timber structures [1].

Stiffness is the key factor affecting the vibration performance of floor system. Industry regulations control the vibration of timber floors by increasing the structural stiffness and limiting the deformation of timber members [2-4]. With the development of timber structures, the dynamic characteristic index is gradually used as an important parameter to evaluate the vibration performance of timber floors, such as the fundamental natural frequency $f_1 > 8$ Hz in the modal parameters of the floor, and the acceleration generated by human-induced load excitation [5-7]. In addition to the continuous development of vibration control methods, with the development of timber processing technology and structural construction, the types of timber floors are also changing. For the research work on the vibration performance of timber floors, the current main research object has changed from the traditional joist timber floor to the new types represented by cross-laminated timber (CLT) and timber-concrete composite (TCC) floor [1]. In recent years, some studies have proven that the timber-concrete composite (TCC) floors can significantly improve the vibration performance of the floor [8,9].

TCC structure has apparent advantages in stiffness, bearing capacity, sound insulation performance, and fire resistance when compared with traditional timber structures. Also, compared with concrete structures, TCC structure can effectively reduce the consumption of traditional building materials and promote the development of sustainable buildings [10,11]. Lightweight aggregate concrete (LWAC) has the characteristics of light self-weight, high stiffness, and good thermal insulation performance, which is more suitable for TCC structures than the traditional normal concrete [12].

However, few studies have been conducted on the vibration performance of timber-LWAC composite beams. In this study, the dynamic properties and vibration performance of the timber-LWAC composite beams were investigated, and the influences of different types of shear connectors on the vibration performances of the composite beams were evaluated.

[1] Bo Wen, Nanjing Tech University/ Sanjiang University, China, 2244548122@qq.com
[2] Benkai Shi, Nanjing Tech University, China, benkaishi@njtech.edu.cn
[3] Haotian Tao, Southeast University, China, 804073159@qq.com
[4] Huifeng Yang, Nanjing Tech University, China, hfyang@njtech.edu.cn
[5] Bowen Huang, Shentong Semiconductor Technology (Nantong) Co. Ltd, China, 1325593844@qq.com

https://doi.org/10.52202/069179-0249

2 TEST SPECIMENS AND METHODS

2.1 SPECIMENS

In this experimental programme, three timber-LWAC composite beams were designed, by considering different types of shear connectors. The connectors adopted in the composite beams include the crossed inclined screws, glued-in steel plates, and notched-screws. The specific component parameters were designed according to the Eurocode 5 [13], and the parameters of the specimens are shown in Table 1.

Table 1: *The parameters of the specimens*

Specimens	Connector		
	Types	Spacing (mm)	Quantity
TLCC-IS	crossed inclined screw	480	10
TLCC-GS	glued-in steel plate	600	8
TLCC-NS(R)	notch-screw (reinforcing bar)	550	8

The dimensions of the timber beam are 4800 mm × 135 mm × 300 mm (length × width × height), while the LWAC slab are 4800 mm × 600mm × 80 mm (length × width × height). The spacings of the crossed inclined screws connections are 480 mm, while those of the glued-in steel plate connections and notch-screw connections are 600 mm and 550mm, respectively, as shown in Fig. 1.

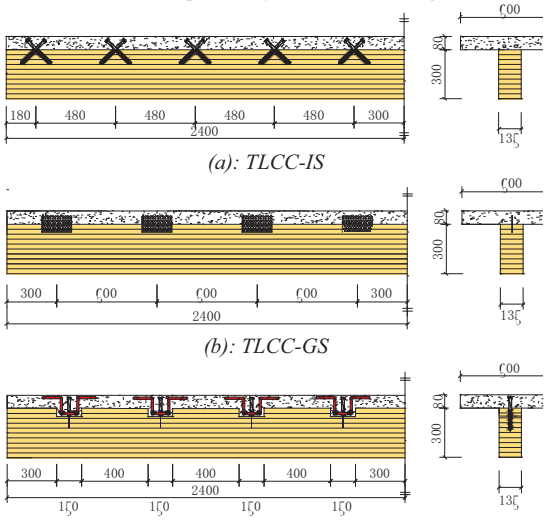

(a): TLCC-IS

(b): TLCC-GS

(c): TLCC-NS(R)

Figure 1: *Configurations of the specimens*

In order to obtain the basic mechanical properties of the connectors, the push-out tests on the connectors were carried out. The parameters of the push-out specimens are shown in Table2.

The push-out specimens adopted the symmetrical configuration, as shown in Fig. 2. For the specimens with crossed inclined screws, the inclination angle of the screw was 45°, and two screws with the diameter 16 mm and length 200 mm (M16L200) were adopted in each shear plane. For the specimens with glued-in steel plates, the length and width of the slots are 190 mm and 10 mm, respectively, and the glued-in depth is 50 mm. For the specimens with notch-screws, the length, width, and depth of the notch are 135 mm, 150 mm, and 50 mm, respectively.

Table 2: *The parameters of the push-out specimens*

Specimens	Connector	Metal Parts and Construction Methods
ISLC	crossed inclined screw	Two M16L200 screws, crossed and inclined at 45°
GSLC	glued-in steel plate	A 180mm×100mm×3.75mm steel plate was glued in the timber
NSLC(R)	notch-screw (reinforcing bar)	Reinforcing steel bars and M16L200 are set in the rectangular notch

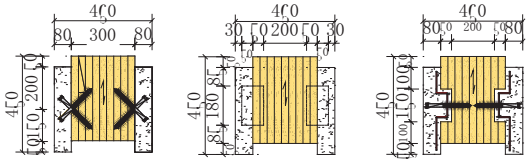

(a): ISLC *(b): GSLC* *(c): NSLC(R)*

Figure 2:*Configurations of the push-out specimens*

2.2 MATERIALS

The glulam beams were made of North American Douglas Fir. The basic mechanical performances of the glulam are shown in Table 3.

Table 3: *The basic mechanical properties of timber*

Properties	Value (MPa)
Tension strength	69.7
Compressive strength	43.3
Shear strength	9.4
Modulus of elasticity	13100

The lightweight aggregate used in the LWAC slab is spherical shale ceramsite. The strength grade of lightweight aggregate concrete is LC30, and the mix design is shown in Table 4.

Table 4: *The mix design of LWAC*

Composition	Mass (kg/m^3)
Portland cement	490
Water	200
Coarse aggregate - shale ceramsite	485
Fine aggregate - sand	750

The standard cubic test blocks with a size of 150 × 150 × 150 mm^3 and standard cylindrical test blocks with a diameter of 150 mm and a height of 300 mm were tested. The test results show that the average compressive

https://doi.org/10.52202/069179-0249

strength of lightweight aggregate concrete is 28.15 MPa, and the elastic modulus is 18800 N/mm^2.

The screw connectors adopted in this experimental programme are galvanized hexagonal head self-tapping screws with a specification of M16L200, and the strength grade is Q235. Referring to ASTM F1575 [14], the yield bending moment of the screws was measured as 206430 N·mm. The strength class of the perforated steel plate in the glued-in steel plate connector is grade Q235, and the dimensions are 180 mm × 100 mm × 3.75 mm (length×width×thickness). The hole diameter is 10 mm, and the distance between the holes is 15 mm.

The adhesive used in the glued-in steel plate connector is a type of two-component epoxy resin, and the performance parameters are provided by the manufacturer, as shown in Table 5.

Table 5: *Basic mechanical properties of adhesive materials*

Properties	Value (MPa)
Tension strength	9.37
Bending strength	63.1
Compressive strength	110.1
Shear strength	16.7

The test specimens were fabricated in Nanjing Tech University. Fig. 3 and Fig. 4 show the fabrication processes of installing the connectors on the timber beam and pouring the concrete, respectively.

Figure 3: *Installed connectors on the timber beams*

Figure 4: *Poured concrete*

2.3 TEST DEVICE AND MEASUREMENT SCHEME

The test mainly attempts to extract the fundamental natural frequency f_i of the vertical bending mode of the specimen [13]. In the modal test, the simply supported boundary conditions were used for the beam specimens. One end of the beam was adopted as fixed hinge, while the other end was set as sliding hinge. The span between the supports is 4500 mm. The beams were stroked by a pulse hammer, and the vibration responses were captured using accelerometers mounted on the beam, as shown in Fig.5. Experimental Modal Analysis (EMA) software was used to identify the fundamental natural frequencies in the modal parameters of the timber-LWAC composite beams. Fourier transform was used to convert the acquired time-domain signals into a frequency-domain signals. The modal parameters of beam specimens were extracted from the frequency response using the post-processing module of the software. In this test, the dynamic signal test system with the model of TST3828E was used for collecting the response signals, and the software with model of DASP was used for analysing the dynamic performance modal. In order to improve the accuracy and reliability of the data, three repeated tests were carried out for each beam specimen, and the dynamic performance was determined according to the average value from the three tests.

Figure 5: *Dynamic test for timber-LWAC composite beam*

3 TEST RESULTS AND ANALYSIS

3.1 INTERFACE PROPERTIES OF COMPOSITE BEAM

The shear performances of interfacial connectors for timber-LWAC composite beams were determined by push-out tests. Based on EN 26891-1991 [15], the test device and loading procedure are shown in Fig. 6 and Fig. 7, respectively. The interfacial slip was recorded by the displacement meters. The slip stiffness value (K_s) of the connector at serviceability limit state can be obtained by Eq.1. The results are shown in Table 6.

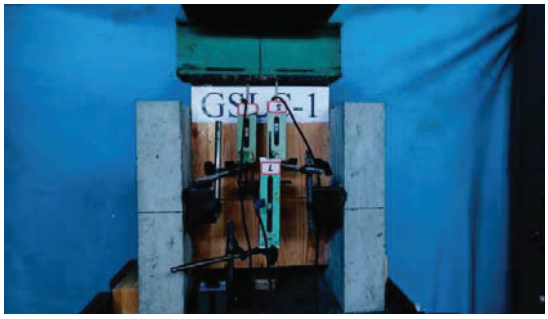

Figure 6: *Test set up of the push-out test*

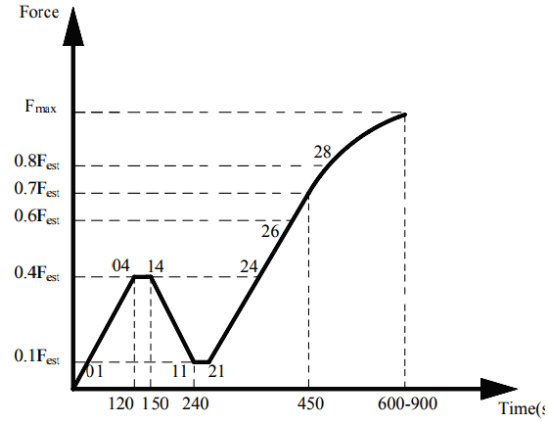

Figure 7: *Loading procedure*

$$K_s = \frac{0.4F_{est}}{4/3(\delta_{04} - \delta_{01})} \quad (1)$$

where F_{est} is the predicted value of the shear bearing capacity of the connector; δ_{01} is the corresponding slip value (mm) at $0.1F_{est}$; δ_{04} is the corresponding slip value (mm) at $0.4F_{est}$.

Table 6: *Push-out test results*

Specimen code	K_s (kN·mm^{-1})
ISLC	79.0
GSLC	220.5
NSLC(R)	264.5

As shown in Table 6, the slip stiffness of the cross inclined screw, glued-in steel plate, and notched-screw connectors at the serviceability limit state are 79.0 kN/mm, 220.5 kN/mm, and 264.5 kN/mm, respectively.

3.2 DYNAMIC PROPERTIES OF THE TIMBER-LWAC COMPOSITE BEAMS

Fig. 8 shows the acceleration response time-domain signals of each timber-LWAC composite beam. The experimental value of the fundamental natural frequency $f_{1(exp)}$ of the timber-LWAC composite beams can be obtained by performing Fast Fourier Transform (FFT) on the time-domain signals through the analysis and processing software. The average values of $f_{1(exp)}$ obtained from 3 repeated excitation tests are listed in Table 7. At the same time, the damping ratios of the beams were calculated by the half-power method [16], and were listed in Table 7.

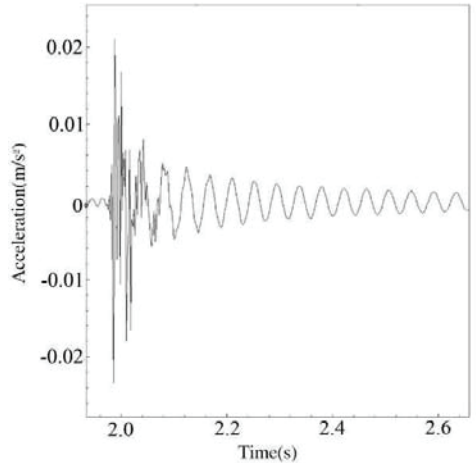

(a): TLCC-IS

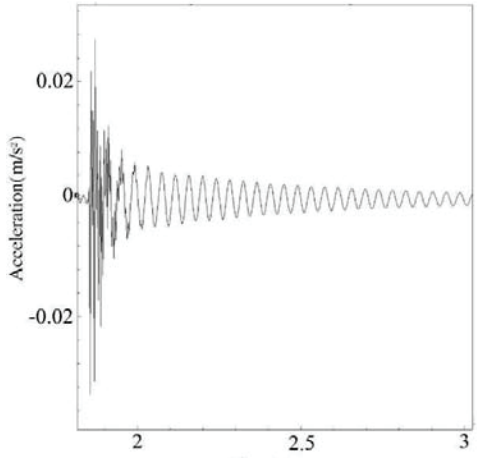

(b): TLCC-GS

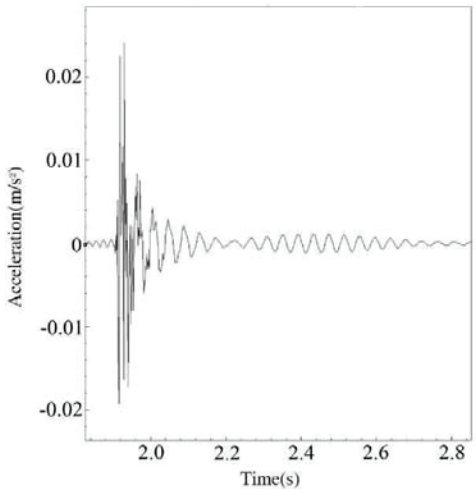

(c): TLCC-NS(R)

Figure 8:*Time-domain signals*

Table 7: *Dynamic properties of timber-LWAC composite beams*

https://doi.org/10.52202/069179-0249

Beam code	$f_{1(exp)}$(Hz)	$f_{1(cal)}$(Hz)	Damping ratio
TLCC-IS	23.68	23.69	3.9%
TLCC-GS	23.93	26.13	1.7%
TLCC-NS(R)	24.17	26.78	3.5%

The timber-LWAC composite beam was used as the one-way slab. Therefore, the fundamental natural frequency of the beam could be considered as that of the floor. The estimation of the fundamental natural frequency of the composite beam mainly refers to the Equation (2) according to Eurocode 5 [13].

$$f_1 = \frac{\pi}{2l^2}\sqrt{\frac{EI}{m}} \quad (2)$$

where l is the span of the floor (m), $(EI)_l$ is the effective bending stiffness of the floor (Nm^2/m), m is the mass per unit area of the floor (kg/m^2).

For timber-LWAC composite beams simply supported at both ends, the effective bending stiffness is calculated using Equation (3).

$$(EI)_{\text{eff}} = E_c I_c + E_t I_t + \gamma_c E_c A_c a_c^2 + \gamma_t E_t A_t a_t^2 \quad (3)$$

where E_cI_c and E_tI_t are the bending stiffness of the concrete slab and the timber beam of the composite beam, respectively; γ_c and γ_t are the reduction coefficients of the beam combination action, respectively; A_c and A_t are the cross-sectional areas of the concrete slab and the timber beam, respectively; a_c and a_t are respectively converts the distance from the section centroid to the concrete slab and timber beam centroid.

The subscripts c and t stand for concrete and timber, respectively. When calculating the value of the γ coefficient, the value of the slip stiffness K_s of the corresponding connectors determined by the push-out test was used.

The theoretically predicted fundamental natural frequency $f_{1(cal)}$ of each beam was calculated by Eq. 2, and were also listed in Table 7.

3.3 DISCUSSION

The theoretically predicted and the measured fundamental natural frequency are listed in the Table 7. It can be found that the fundamental natural frequency values estimated by Eurocode 5 method have a very small difference compared with the measured values, and the accuracy can meet the needs of engineering design.

It can be seen from the test data that if the timber-LWAC composite beams in this test are directly used as a one-way floor, the measured fundamental natural frequency values are all between 23 and 25 Hz, which can meet the general requirement of 8 Hz [13]. At the same time, the frequencies of the timber-LWAC composite beams are far away the frequencies range (1.0-4.0 Hz) of human-induced loads (such as walking, jumping, running, etc.) [17], which can effectively prevent the occurrence of resonance caused by people in the use of the floor.

The differences between the theoretically predicted values of the fundamental natural frequency and the experimentally measured values are 0.04%, 9.2%, and 10.8% for the timber-LWAC composite beams connected by crossed inclined screws, glued-in steel plate, and notch-screw connections, respectively. The calculation method in the Eurocode 5 showed the relatively high prediction results. This phenomenon may be caused by the overestimated values in effective bending stiffness for all beam specimens.

The fundamental natural frequencies of the beam specimens TLCC-NS(R) and TLCC-GS are bigger than that of TLCC-IS. This is because the glued-in steel plate (GSLC) and notched-screw (NSLC(R)) showed higher slip stiffness compared with cross inclined screw connection (ISLC). This result lead to the higher values in effective bending stiffness for beam specimens TLCC-NS(R) and TLCC-GS, compared with the beam specimen TLCC-IS. Investigating the reason, in the case of the same beam span and the same quality, it can be seen from the push-out test results that the slip stiffness value of the crossed inclined screws connector is smaller than that of the glued-in steel plate and notch-screw connector. On the other hand, there are also differences in the number of connectors. The number of crossed inclined screw connectors is 10 groups, while the number of glued-in steel plate and notch-screw connectors is 8 groups. The number of crossed inclined screw connectors is less than the other two, which further shows that the decisive factor is still the slip stiffness value of the connector. From this phenomenon, it can be deduced that the slip stiffness value of the connectors is a very important factor of the vibration performance for timber-LWAC composite beams.

In terms of damping ratio, the specimen TLCC-GS showed the value of 1.9%, which is much smaller than specimens TLCC-IS and TLCC-NS(R). There is no direct relationship between the connector stiffness and the damping ratio. The above results were only preliminary inferences obtained through sample tests, and the influence of sample size and test accuracy cannot be ruled out.

4 CONCLUSIONS

In this study, the dynamic tests were carried out on the timber-LWAC composite beams using three different connectors. The fundamental natural frequencies of beams were predicted by the calculation method suggested in Eurocode 5, and the predicted values were compared with the experimental values. By analyzing the modal parameters, such as the fundamental natural frequency and damping ratio, the basic vibration performances of the timber-LWAC composite beams were obtained. The main conclusions are summarized as follows:

The fundamental natural frequencies of the timber-LWAC composite beams in this study are in the range of 23.68 to 24.17 Hz, which meet the primary requirement in Eurocode 5. The fundamental natural frequency of the timber-LWAC composite beam is much higher than 8 Hz [13], which means the vibration performance meets with the preliminary comfort requirements.

From the test results, it can be preliminarily inferred that the number and slip stiffness of shear connectors can significantly affect the fundamental natural frequency of timber-LWAC composite beams.

The theoretical fundamental natural frequency of the specimens calculated according to Eurocode 5 show good agreement with the test results. However, there is still a certain difference between the predicted and experimental values, which might be caused by the overestimation of the bending stiffness of composite beams.

ACKNOWLEDGEMENT

Financial support was provided by the National Natural Science Foundation of China (51878344), the General Project of Natural Science Research of Higher Education Institutions of Jiangsu Province (20KJB560002), and the Science and Technology Project of Construction System of Jiangsu Province (2019ZD001205).

REFERENCES

[1] Wen B.,Yang H.,Shi B.: Research progress in vibration and its control of modern timber floor (in Chinese). Journal of Nanjing Tech University (Natural Science Edition),44(1):10-19, 2022.

[2] FHA: *Minimum property standards for one and two living units.* Federal Housing Administration (FHA),Washington D.C, USA, 1964.

[3] Onysko D. M.: Serviceability criterion for residential floors based on a field study of consumer Response. Project No. 03-50-10-008 for Canadian Forestry Service (CFS). Forintek Canada Corp, Ottawa, Canada, 1985.

[4] NRCC: *National building code of Canada*. National Research Council of Canada (NRCC), Institute for Research in Construction (IRC), Ottawa, 2015.

[5] Ohlsson S.: Ten years of floor vibration research: a review of aspects and some results. *Proceedings of the Symposium/Workshop on Serviceability of Buildings(movements, deformations, vibrations).* 1988.The University of Ottawa.

[6] Smith I., Chui Y. H.: Design of lightweight wooden floors to avoid human discomfort. Canadian Journal of Civil Engineering, 15(2): 254, 1988.

[7] Dolan J. D., Murray T. M., Johnson J. R., et al.: Preventing annoying wood floor vibrations. Journal of Structural Engineering, 125 (1): 19, 1999.

[8] Skinner J., Martins C., Bregulla J.: Concrete upgrade to improve the vibration response of timber floors. Journal of Structures and Buildings, 167(9): 559-568, 2014.

[9] Santos P., Martins C., Skinner J., et al.: Modal frequencies of a reinforced timber-concrete composite floor: testing and modeling. Journal of Structural Engineering, 141(11): 04015029, 2015.

[10] Ceccotti A.: Composite concrete-timber structures. Progress in Structural Engineering and Materials, 4(3): 264,2002.

[11] F Asdrubali., B Ferracuti., L Lombardi., et al. A review of structural, thermo-physical, acoustical, and environmental properties of wooden materials for building applications. Building and Environment, Vol.114(No.1):307-332, 2017

[12] Chandra S., Berntsson L.: *Lightweight aggregate concrete.* Elsevier Science Ltd, Amsterdam, Netherlands, 2002.

[13] CEN: *Eurocode 5: Design of timber structures – Part 1-1: General - Common rules and rules for buildings.*Comité Européen de Normalization (CEN), EN 1995-1-1. Brussels, 2004.

[14] ASTM: *Standard Test Method for Determining Bending Yield Moment of Nails*.American Society for Testing and Materials(ASTM),ASTM F1575M-21.West Conshohocken, 2022

[15] BSI: *Timber structures - Joints made with mechanical fasteners - General principles for the determination of strength and deformation characteristics.* BS EN 26891 (ISO 6891:1983). BSI, London, UK, 1991.

[16] Chen K.: *An Introduction to mechanical vibration (in Chinese).* China Agricultural University Press, Beijing, China, 2014.

[17] Chen J.: *Human-induced load and structural vibration (in Chinese).* Science Press, Beijing, China, 2016.

https://doi.org/10.52202/069179-0249

World Conference on Timber Engineering Oslo 2023

DEVELOPMENT OF A STAND-ALONE VIBRATION MEASUREMENT SYSTEM FOR BRIDGE MONITORING

Dio Lins[1], Steffen Franke[2], Roger Weber[3], Bettina Franke[4], Joel Karolin[5]

ABSTRACT: The quality assurance of timber bridges is currently ensured mainly manually by regular visual inspections over the entire life cycle. To reduce this (cost) effort, the possibility of continuously recording the condition of bridges through monitoring is being investigated. This would also increase the confidence in the long-term load-bearing capacity of timber bridges among planners and public. In addition to the permanent recording of the wood moisture content, conclusions can also be drawn about the condition and even possible damage by recording the natural frequencies which depends on the stiffness. For this purpose, a stand-alone vibration measurement and evaluation system was developed, which is easy to handle and suitable for long-term monitoring due to its energy efficiency. Beside a first application on a low-traffic timber bridge for several months, the system was validated with investigations on various types of artificial damages on the natural frequency of timber components.

KEYWORDS: Vibration measurement system, timber bridges, natural frequency, damage identification, quality assurance

1 INTRODUCTION

Every structure vibrates due to natural excitation or use in its natural frequency (see Figure 1), which depends on the mass and stiffness. If damage in individual structural members or the complete structural system occurs, the stiffness may change and so does the natural frequency [1]. By continuously recording the natural frequency, possible damage can therefore be detected at an early stage. However, the previous studies on this topic mostly refer to steel or reinforced concrete structures [2]. In timber construction, knowledge is available for the pure vibration assessment of timber ceilings or bridges, e.g. [3], [4]. The application to timber bridge structures for condition assessment is not yet established. Bridges are normally used daily and the slow traffic as well as heavy traffic causes the supporting structure to vibrate. The continuous recording of the changes of the natural frequency of timber bridges therefore not only serves to detect damage, but also to systematically gain knowledge.

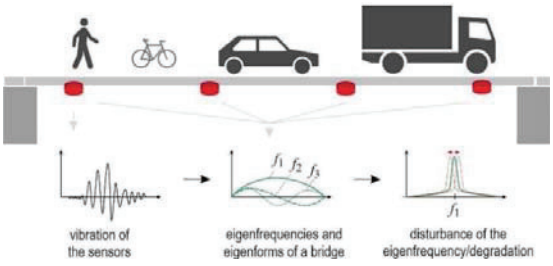

Figure 1: *Daily loading situations of a bridge*

Bridges are indispensable in the traffic area and are subject to regular quality inspections. In Germany for example, bridges must undergo a simple and a main inspection every three years alternately [5]. These are always carried out close to hand and therefore entail a great deal of effort, especially for timber bridges [6], [7], [8]. Efficient digital tools for monitoring purposes are missing in everyday life and are not specifically adapted to the material or purpose of timber bridges.

For the development of a monitoring system of the natural frequencies, the constantly occurring measurement data (accelerations, vibrations) must be digitally recorded, filtered, and analysed so that differences in the vibration behaviour, in the natural frequency, can be recognised. In this way, e.g., as a traffic lights principle, authorities can obtain results about the condition of the timber bridge and at the same time engineers or researchers can obtain general data sets to improve vibration measurement or design. Here, the development of a measurement system of vibration sensors including online analysis for monitoring the vibration behaviour of timber bridges during daily use should support.

[1] Dio Lins, Bern University of Applied Sciences, Switzerland, dio.lins@bfh.ch
[2] Steffen Franke, Bern University of Applied Sciences, Switzerland, steffen.franke@bfh.ch
[3] Roger Weber, Bern University of Applied Sciences, Switzerland, roger.weber@bfh.ch
[4] Bettina Franke, Bern University of Applied Sciences, Switzerland, bettina.franke@bfh.ch
[5] Joel Karolin, Bern University of Applied Sciences, Switzerland, joel.karolin@bfh.ch

https://doi.org/10.52202/069179-0250

2 THE NEW VIBRATION MEASUREMENT SYSTEM

2.1 COMPOSITION OF THE MEASURING SYSTEM

For the development of a standalone, wireless, battery-operated, easy to use and to install vibration measurement system, the requirements for the specific application at timber bridges or timber floor systems were examined, such as the measurand (speed/acceleration), the required accuracy and whether 1- or 3-axis sensors can be used. Focus was also given to the lowest possible energy consumption for the acquisition and transmission of the measurement data (digitisation).

The developed system consists of several sensor nodes and a powered HUB, (see Figure 2). Each sensor node includes an accelerometer (+/- 6g) with a sampling rate of 2 kSamples/s and a bandwidth of 70 Hz, and subsequent downsampling to 100 Samples/s and allows the 3-axial acquisition of the accelerations. They are battery-operated (runtime 0.5 year) and communicate up to 100 m with the HUB via Bluetooth Low Energy 5.2. A nRF52840 from Nordic is used as CPU and BLE transceiver.

The HUB is based on a Linux board from Toradex (Apalis i.MX8), is powered by the network and is located within the 100 m range of the sensor nodes. Raw data is stored locally and sent via LTE to the database on the server (see Figure 3). The HUB controls and monitors the sensor nodes. Problems such as short disconnections to the sensor nodes are detected and handled so that long-term use is ensured.

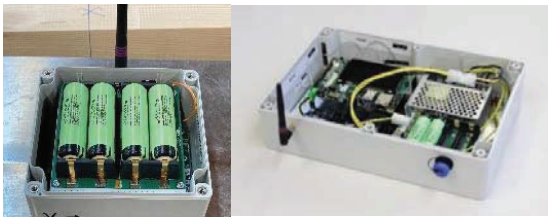

Figure 2: *Sensor node with 3-axis acceleration sensor below the battery pack (left) and HUB (right)*

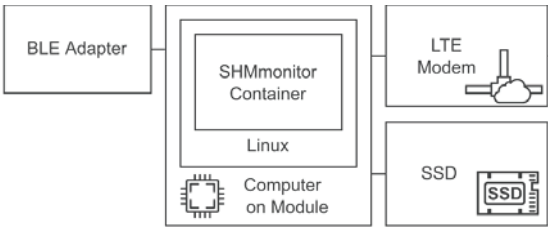

Figure 3: *Details of the HUB*

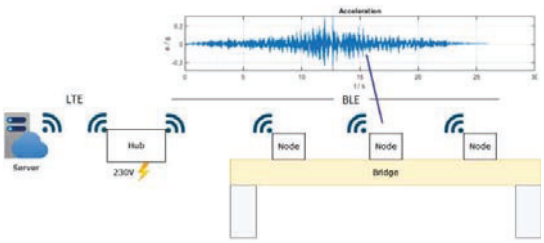

Figure 4: *Schematic diagram of the measuring system as cluster configuration*

2.2 SINGLE AND CLUSTER USE

In cluster use, several nodes can be integrated into one measuring system by the HUB to analyse several vibration frequencies at the same time or to determine the vibration form of the structure. All sensor nodes transmit the raw acceleration data to the HUB, which sends the data on to a server (see schematic diagram in Figure 4). Here, the data is evaluated and visualized offline by the SHMlive software developed in-house. Sensor data can be displayed in the time domain as well as in the frequency domain. Thus, it is possible to display the natural frequencies and to detect a shift/change of the frequencies.

As an alternative to the cluster use with the HUB, an adapter and notebook can be used to create a status recording or single use of one node. In this configuration, the sensor node directly transmits the raw acceleration data to a PC in real time where it can be further analysed. For this purpose, the SHMlive software is directly used to control the sensor nodes and visualise the acceleration data.

2.3 VALIDATION OF THE SYSTEM

The accuracy of the system was tested. To this end, status recordings were carried out on single span beams that were triggered by an impact (see Figure 5). The results of

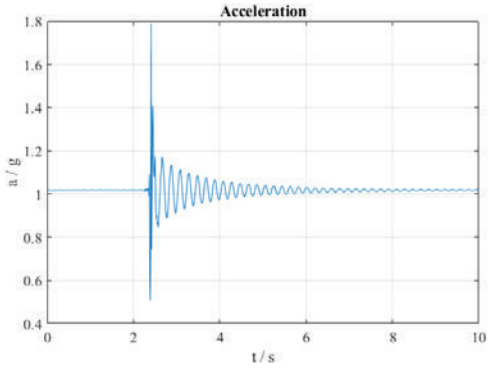

Figure 5: *Time domain: Acceleration over time*

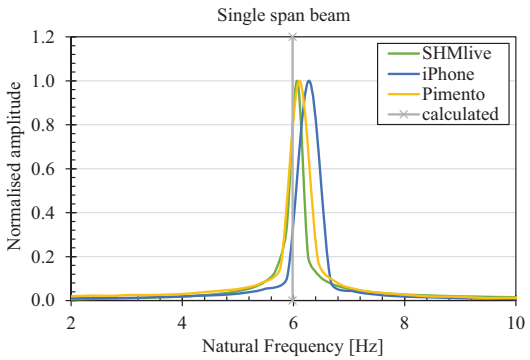

Figure 6: *Comparison of natural frequencies between different measurement systems*

https://doi.org/10.52202/069179-0250

the new system were then compared with existing measurement systems. Those were “Pimento” with one sensor and the application “phyphox” developed by RWTH Aachen University on the mobile phone (IPhone SE). As you can see in Figure 6, there is only a difference of 0.6 % compared to the “Pimento” system in this test. The deviations from “phyphox” are greater with 3.5 %, but this is also not a scientific measuring system as an application for the mobile phone. In addition, the repeatability of the new system was tested in various trials and found to be 0.05 Hz. In all these trials, it was also possible to ensure that the handling of the newly developed system is practicable and easy.

3 INVESTIGATION OF ARTIFICIAL DAMAGES

3.1 METHODOLOGY AND TEST SETUP

Tests were carried out to quantify what influence various types of artificial damage have on the natural frequency of timber components and to what extent these can be detected with the new system. For one of the experiments, a beam with a cross-section of 60 mm x 80 mm was used. This single span beam was separated at half span and a lap joint was created. To reconnect the two parts, side members with the same height and half thickness were screwed on both sides on the beams with 6 screws per connection and shear plane (Figure 7). By means of a 4-point bending test (see Figure 8) the lap joint was stepwise plastically deformed to analyse the influence on the natural frequency. It was loaded and unloaded in 8 cycles, increasing the maximum force for each of them, cp. Figure 9. After the individual cycles, the beam was retested for its natural frequency with an additional weight of 5 kg and 20 kg placed in the middle of the beam to analyse the influence within two different frequency ranges.

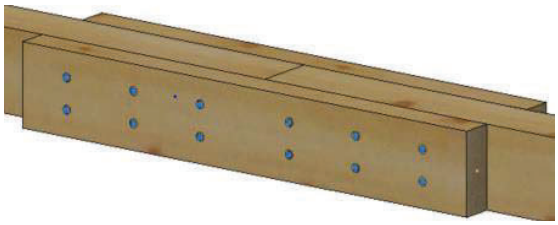

Figure 7: *Lap joint with screws (4.5 mm x 60 mm)*

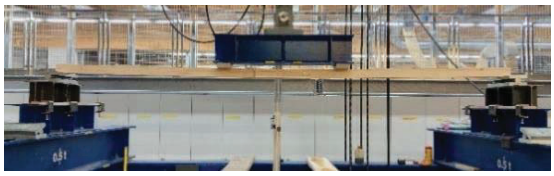

Figure 8: *Test setup*

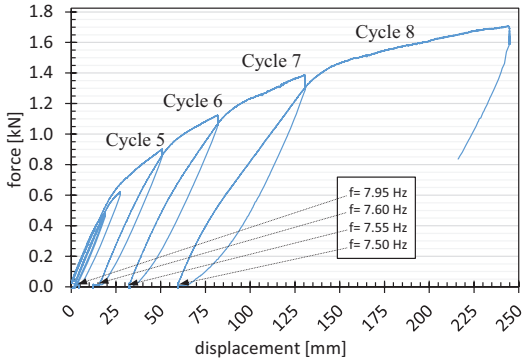

Figure 9: *Force-deformation diagram with associated natural frequencies*

3.2 RESULTS

Figure 10 shows the beam with lap joint at maximum deflection in the test setup (top) and a detail of the deformed joint (bottom). In the last loading cycle a maximum force of 1'684 N and a maximum deformation of 245 mm was achieved.

The force-deformation diagram in Figure 9 shows the load levels considered and the corresponding natural frequencies with an additional weight of 5 kg. The experimental investigation shows that frequencies can be measured with a resolution of 0.05 Hz using the developed system. This results from the FFT analysis and essentially depends on the analysed time duration, which was chosen to be about 15 s. As expected, the natural frequency of the beam tends to decrease with increasing artificial damage. However, the differences are very small, and the observation did not occur consistently across all measurements (see Table 1), so the results are still subject to some uncertainty.

Table 1 shows all the measured natural frequencies with the different additional weights. Even though it tends to decrease with increasing plastic deformation, for 5 kg an

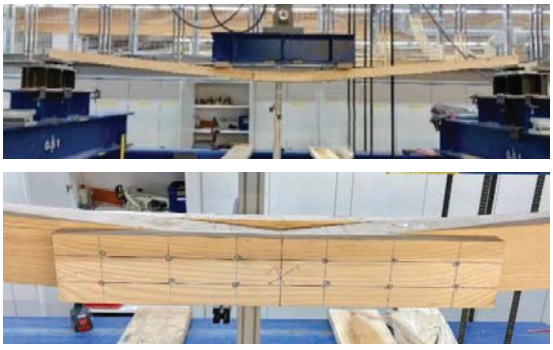

Figure 10: *Test setup (top) and deformed joint (bottom) at maximum displacement*

Table 1: *Natural frequencies [Hz]*

Load-cycle	1	2	3	4	5	6	7	8
5 kg	7.90	7.80	7.85	7.95	7.60	7.55	7.50	7.60
20 kg	5.20	5.20	5.20	5.15	5.10	5.10	5.15	5.10

https://doi.org/10.52202/069179-0250

increase of 0.05 Hz and 0.10 Hz is evident after cycles 3, 4 and 8. For an additional weight of 20 kg, an increase of 0.05 Hz can be observed after cycle 7. To validate these observations, further investigations need to be carried out with larger cross-sections and static systems.

4 MEASUREMENTS AT NEUMATT-BRIDGE AS APPLICATION

4.1 TEST SETUP

The developed vibration measurement system was installed on the Neumatt-Bridge near Burgdorf (Figure 11 and Figure 13). The Neumatt-Bridge is a covered truss system bridge made of soft- and hard wood products. With a span of 59 metres, it is the largest free-span timber truss bridge in Switzerland. It is used for slow traffic (mainly pedestrians and bicycles but also agricultural vehicles). With regard to be used at a Swiss Festival in 2013, four mass dampers adjusted to the natural frequency of the bridge were installed in order to limit the vibration accelerations. The new vibration measuring tool was installed at three positions, and each node measures the accelerations in x-, y-, and z-direction. The positions of the sensor nodes on the bridge were chosen to be at the points of maximum deflection of the first and second eigenform, i.e., two at the midpoint (at both trusses) and one at a quarter point of the bridge (see Figure 12). The sensor nodes were attached to the top chord of the trusses so that direct influences from the roadway planking did not falsify the results and the overall structural behaviour could be analysed.

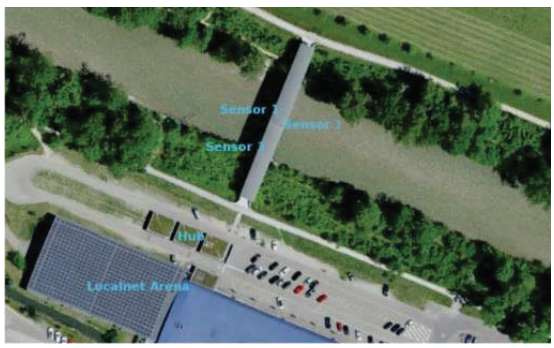

Figure 11: *Neumattbridge Burgdorf, side view of the timber bridge (top) and location of the measuring sensors and data logging station (bottom)*

During the monitoring period from March to June 2022, a data logging of the acceleration was started every 10 minutes for a period of 30 seconds with a sampling rate of 100 Hz. This corresponds to 144 measurements per day (Figure 14), whereby a PSD (Power Spectral Density) analysis was carried out for each measurement to determine the natural frequencies accordingly (Figure 15). The first natural frequency was averaged over one complete day. The data transmission and management are used as described before in chapter 2.1 and 2.2.

4.2 RESULTS

Figure 14 to Figure 16 show the results of the long-term vibration measurement in vertical direction of the timber bridge. Figure 14 shows in example the acceleration over time of one randomly selected single measurement. In Figure 15 the corresponding power spectral density analysis (PSD-analysis) is shown. The peak at a frequency of approx. 2.9 Hz represents the first natural frequency. Figure 16 summarizes the determined first natural frequencies averaged over one day for the complete measuring period. The results of all three sensors are shown for the first month. The results of sensor 3 are shown for all three months. In average, the fluctuations are between 2.5 Hz and 3.0 Hz. The sporadic higher readings are related to the daily analyses of the PSD rather than a change in the condition of the structure.

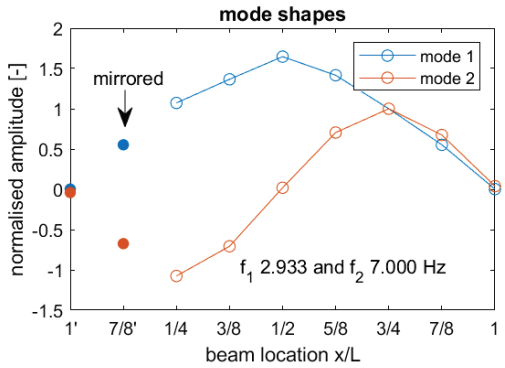

Figure 12: *First and second eigenform measured of the bridge*

Figure 13: *One of the sensor nodes of the new vibration tool*

https://doi.org/10.52202/069179-0250

A visual inspection of the Neumatt-Bridge was carried out before and after the measurement period. No visible defects were found in the supporting structure or in the connection details what is confirmed by the measurement results. Especially the measuring sensor 3 in Figure 16 does not show any trend development from the average level.

The vibration measurement handling and results are satisfying. The measurement sensitivity was sufficient for this first application and in relation to the built-in vibration dampers. Changes in the natural frequency could only be recorded through the daily stimulation by the random slow traffic. The measurement results achieved confirm the generally good condition of the Neumatt-Bridge.

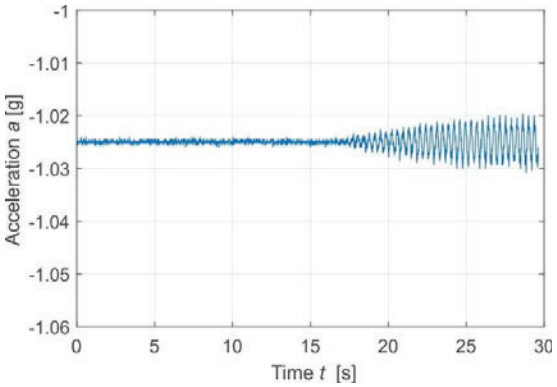

Figure 14: *Time domain: Acceleration over time*

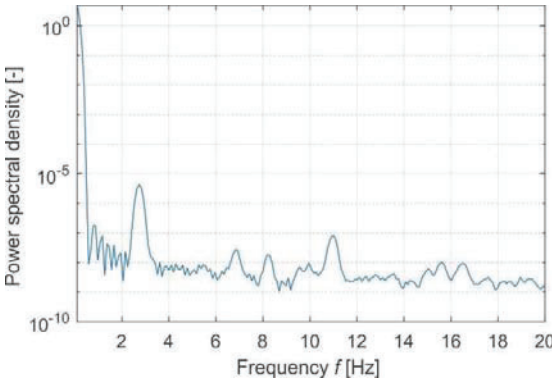

Figure 15: *Frequency domain*

5 CONCLUSIONS AND OUTLOOK

It was possible to develop a new type of vibration measurement system for simplified use, quick measurements, but also for monitoring. In a first step, the developed vibration measuring system was compared with other measuring systems. It shows a comparable accuracy to existing vibration measuring systems. However, the accuracy of the natural frequency measured is not only dependent on the hardware, but also on the evaluation period and the sampling rate of the recording.

The influence of different artificial damages on the natural frequency of timber components was investigated experimentally on a simple system (single span beam) at small scale. The artificial damages considered were investigated regarding their influence on the natural frequency. In general, artificial damage led to a decrease in the natural frequency. Damage to the structure usually leads to a loss of stiffness, which leads to a reduction in natural frequency. The first results reached are plausible but should be further verified on larger cross-sections, and long-term measurements. It was shown that the occurrence of artificial damage to beams can be detected by means of a natural frequency analysis. However, it was realised that a high measurement resolution is required to detect already smallest damages or anomalies.

The 3-month measurement at the Neumatt-Bridge in Burgdorf showed almost constant values of averaged natural frequencies. This confirms the overall good condition of the timber bridge by visually inspections. To be able to distinguish possible damages from seasonal fluctuations in the evaluation, measurements would have to be carried out for longer periods, at least one year. On consideration of the large fluctuations of the natural frequency on individual days it is noticeable that the frequencies are multiples of the most commonly measured frequency in the range of 2.5 Hz to 3.0 Hz and thus represent other natural frequencies of the bridge.

The vibration measurement system achieved is promising for the quality monitoring of timber structures and timber bridges. The wireless connection between the sensors and the HUB makes it possible to measure vibrations in buildings over several floors or rooms, for example. Due to the simple evaluation of the data, the required values

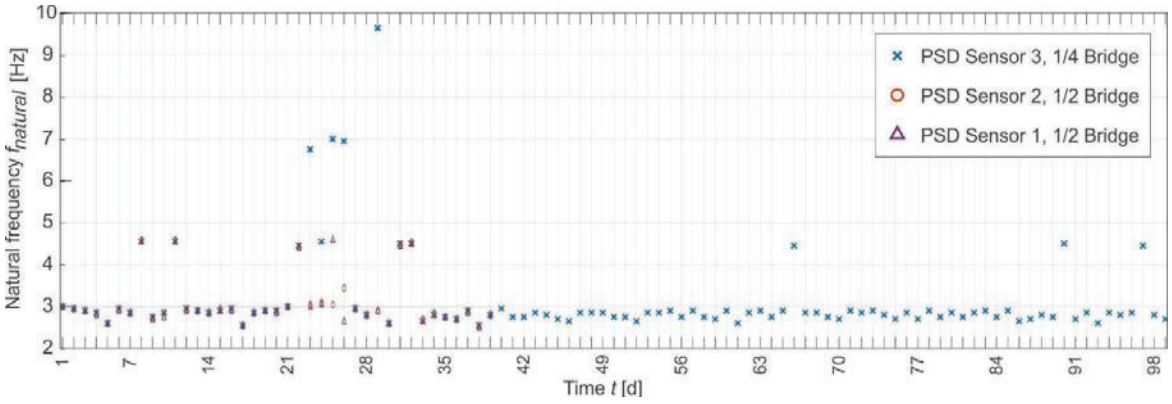

Figure 16: *First natural frequency vs time*

https://doi.org/10.52202/069179-0250

can be determined immediately. In addition, a live output of the intended values is possible by means of the supplied software.

In next steps, further areas of application in the monitoring of supporting structures or other materials could be examined. For long-term vibration monitoring of structures, it is also important to learn about damage-independent fluctuations of the natural frequency due to e.g., data analysing, averaging and climatic changes (temperature, humidity respectively wood moisture content) or seasonal changes. With this results, possible damage could be qualitatively reliably detected. The extent to which changes in load-bearing structures can be diagnosed at an early stage cannot yet be assessed with the experiments currently being carried out. Damages can only be detected so far, but neither localised nor determined in its extent.

The newly developed vibration measurement system can be requested for monitoring timber structures. With these continuing monitoring campaign, open questions can be answered, and possible market entry can be achieved.

ACKNOWLEDGEMENT

The project is a collaboration between the departments Architecture, Wood and Civil Engineering and Engineering and Computer Science of Bern University of Applied Sciences. Gratefully acknowledged by the authors is the intense cooperation among the partners of this project, especially Adrian Ivo Oesch, Stefan Lüthi and Sébastien Bonifacio as well as Bern University of Applied sciences, which made this interesting project possible.

REFERENCES

[1] Blum R., Kerkhof K.: Bestimmung von Steifigkeits-veränderungen bei der Sanierung der Klosterwegbrücke mit Hilfe der Schwingungsanalyse. *Bauingenieur 62*, pp 513-518, 1987.

[2] Mangerig I., Retze U.: *Monitoringmethoden zur Diagnose des Tragwerkszustandes bestehender Brückenbauwerke*. 14. DASt – Forschungskolloquium Stahlbau – Berlin, 2003.

[3] Hamm P.: Schwingungen bei *Holzdecken – Konstruktionsregeln für die Praxis*, 2. Internationales Forum Holzbau, Beaume 2012.

[4] Hamm P., Schänzlin J., Francke W., Schäuble S.: *Monitoring of timber bridges by repeatedly measuring the natural frequency*; WCTE 2016 – World Conference on Timber Engineering; Vienna, Austria, 22-25 August 2016.

[5] DIN 1076: *Ingenieurbauwerke im Zuge von Strassen und Wegen – Überwachung und Prüfung*. Beuth Verlag, 1999-11.

[6] Simon A., Müller A.: Die Bauwerksprüfung geschützter Holzbrücken – handnah und wirtschaftlich? *3. Internationale Holzbrückentage IHB* 2014, Bad Wörishofen, 2014.

[7] Müller A., Franke B.: *Methoden der Zustandserfassung bei Holzbauwerken*, 8. Europäischer Kongress (EBH 2015) Bauen mit Holz im urbanen Raum, Köln, 2015.

[8] Müller A., Brunner M.: *Structural safety thanks to quality: Plan robustness, build with checks, monitor permanently*, World Conference on Timber Engineering, Quebec City, Canada, 2014.

https://doi.org/10.52202/069179-0250

World Conference on Timber Engineering Oslo 2023

ACTIVE MASS DAMPERS FOR TIMBER FLOORS

Thomas Hillberger[1], Thomas Furtmüller[2], Philipp Dietsch[3], Roland Maderebner[4]

ABSTRACT: Extensive modeling of timber slabs with active vibration elements has shown that, compared to passive vibration dampers, a significantly better effect is achieved with a fraction of the required mass. In this respect, it is obvious to intensify research in the field of active vibration control. These active damping systems are intended to positively affect the vibration properties of slender slab structures in particular. Fundamental for this research is that the requirements of the Eurocodes are met and the weight of the active elements is kept low. In the present work, the vibration properties, in particular the vibration response of cross laminated timber are addressed. The dynamic parameters determined for a simply line supported system define the following tests which are carried out with actively controlled damping elements. The tests with the cross laminated timber panel suggest that counteracting at certain times and with predefined levels of intensity causes a considerable reduction of the acceleration values. Based on controlling the acceleration response, tests are performed on a complex timber construction. Different excitation, including the random and dynamic motion of people moving on the slab, increase the difficulty to solve this task for slab systems using common control systems. Therefore, the purpose of this research is to verify the reduction of floor vibrations and to demonstrate its effectiveness in experiments with human-induced excitation. The results show a significant reduction in vibration acceleration for different types of excitation and highlight the possibilities of active vibration control.

KEYWORDS: Timber structures, cross laminated timber, active damper, vibrations, frequency

1 INTRODUCTION

A particular challenge in the design of timber floors are the requirements for the serviceability limit state (SLS). Fundamental research in the field of floor vibrations for different timber constructions was presented in [1]. Since then, the possible span of timber structures has evolved significantly due to improvements in timber products and fasteners.

If considering just the ultimate limit state (ULS), enormous advances in the realisation of slender floor elements are possible with currently executable constructions. However, this is accompanied by the fact that the SLS is becoming more and more relevant for the dimensioning of the components due to the large spans. In order to meet the noise reduction standards, appropriate masses are needed to ensure that the required sound insulations are achieved. This trade-off is solved with so-called heavy floor structures consisting of fillings, impact sound insulation boards and mineral floating screeds. These additional loads make it necessary to increase the structural heights and hence the material use of the timber slab to stay within the required limit value of the natural frequency.

The increasing number of publications regarding human-induced vibrations highlight the relevance of this topic for structural engineering [2,3]. Due to the dynamic properties of timber floors, experiments relating to the vibration behaviour are essential. The modal parameters such as natural frequencies and damping characteristics of floor elements depend on different design assumptions. The influence of support conditions of cross laminated timber (CLT) floors on the vibration properties has already been addressed in [4]. [5] deals with the effects of support conditions respectively plan aspect ratios on the natural frequencies and damping of the floor elements corresponding to the serviceability. By in-situ measurements but also in the laboratory, various research works have additionally examined the vibrational characteristics of the raw floor slab and furthermore differences between different floorings [4,6-8]. The tests presented in the current paper also provide measurement data for the human-induced excitation as well as additional experimental results for different floorings and support conditions. These experimental investigations are currently being performed as part of an ongoing research project at the Universität Innsbruck.

There are various approaches for improving the vibrational behaviour of floors. In [9] implementation examples of active vibration control with focus on seismic excitation are presented. Parallel-connected passive tuned mass dampers for slab elements have been examined [10]. The potential that active control systems can provide for floor constructions are discussed in [11]. Particularly active systems should enable to maintain the required serviceability limits despite the reduction in floor thickness. The effect of active vibration control (AVC) in a reinforced concrete slab is impressively shown in [12]

[1] Thomas Hillberger, Unit of Timber Engineering, Universität Innsbruck, Austria, thomas.hillberger@uibk.ac.at
[2] Thomas Furtmüller, Unit of Applied Mechanics, Universität Innsbruck, Austria, thomas.furtmueller@uibk.ac.at
[3] Philipp Dietsch, Chair of Timber Structures and Building Construction, Karlsruhe Institute of Technology, Germany, dietsch@kit.edu
[4] Roland Maderebner (Project leader), Unit of Timber Engineering, Universität Innsbruck, Austria, roland.maderebner@uibk.ac.at

https://doi.org/10.52202/069179-0251

(acceleration feedback control) and [13] (velocity feedback control). The tests in these publications are based on recorded accelerations of the vibrating structures. The values are converted according to the used method and provide the actuator data for the counteraction. A significant reduction of the acceleration values can be achieved with these methods.
The aim of this research work is to demonstrate, the effect of adaptive, actively controlled vibration dampers on the acceleration values of CLT panels caused by human-induced vibrations. With the current state of research on active mass dampers and the use of this knowledge to reduce vibrations, the possibilities for timber construction are presented in the course of this work.

2 MATERIALS AND METHODS

2.1 GENERAL

Experimental tests are applied to verify the effectiveness of the active vibration elements. The vibration characteristics of the floor elements are essential. The experimental tests focus on CLT elements with different dimensions. The dimensions of the used plates can be found in Table 1. The excitation of the CLT panels is realized by different means, e.g. heel-drop or shaker. This is supplemented by experimental investigations of human-induced vibrations with the same test setup. In the experiments with active vibration control, the excitation is mainly imposed by a shaker, because initially reproducible vibration response is necessary.

Table 1: *Overview of CLT elements used in experimental investigations*

Type	Layer (mm)	Length (mm)	Width (mm)	Depth (mm)
CLT_01	5-Layer 40/20/40/20/40	7000	1222	160
CLT_02	3-Layer 30/30/30	4000	400	90
CLT_03	3-Layer 30/40/30	2000	970	100

2.2 EXPERIMENTS – VIBRATIONAL CHARACTERISTICS

For these tests, the element type CLT_01 from Table 1 is used. I-beams (HEB 300) with steel shaft ensure a hinged support (support distance of 5.80 m). In Figure 1 the test setup is visualized in addition to the two excitation modes (walking person and shaker). To determine the modal parameters, the plate is excited by an impulse hammer. The first natural frequency identified by these tests is 10.33 Hz. Furthermore, response data are recorded, which result from the excitation according to a heel-drop. Figure 2 and Figure 3 show the dynamic behaviour of the centrally placed sensors ACC-Sensor3 and ACC-Sensor4. These two sensors highlight the dominance of the first eigenfrequency. The acceleration values of a walking person are presented in Figure 2. Figure 3 shows the mid-section acceleration values according to the excitation mode heel-drop. All obtained experimental data are compared to results from fundamental literature [4-6] and used as basis to validate the computational models.

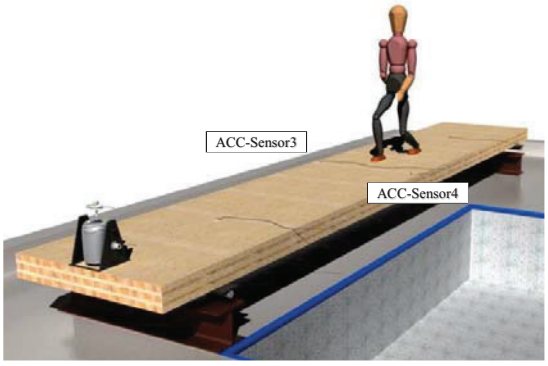

Figure 1: *Test setup for identifying vibrational characteristics with two different excitation (shaker and walking person) [14]*

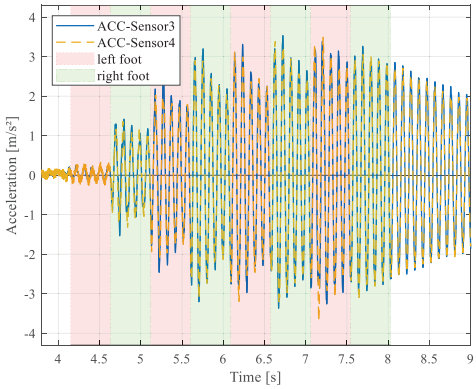

Figure 2: *Recorded response from walking tests*

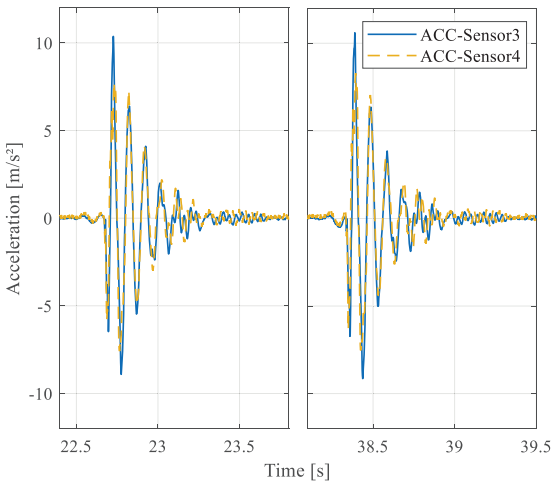

Figure 3: *Recorded response from heel-drop tests*

https://doi.org/10.52202/069179-0251

2.3 EXPERIMENTS – ACTIVE MASS DAMPER

The model of active vibration dampers in combination with slab elements corresponds to vibratory systems with two parts of force excitation. In Equation (1) M, C and K denote the mass, damping and stiffness matrices. The force excitation is on the one hand related to the excitation by a person $F_P(t)$ and on the other hand to the reaction of the active vibration elements $F_{AD}(t)$.

$$M \cdot \ddot{x}(t) + C \cdot \dot{x}(t) + K \cdot x(t) = F_P(t) + F_{AD}(t) \qquad (1)$$

The vibration response of the slab elements is reduced by defined force excitation in opposite direction to the load imposed by a walking person. Figure 4 depicts a possible reaction function of the active vibration elements. In fact, the diagram is an excerpt of an experimental test. It should clarify when the counteracting impulses of the vibration elements are needed and how the principle reaction of the active mass dampers (AMD) looks like.

The first tests for active damping are carried out with the test setup as displayed in Figure 5. The support conditions are defined in the same way as described for the preceding section. Figure 6 is intended to provide a better explanation of the measuring equipment and the entire experimental setup. Included are the input channels from the accelerometers (ACC-Sensor1 - ACC-Sensor6) to the measurement and control unit (MCU) and the output channel from the MCU to the shaker (LDS Shaker V400 Series with amplifier LPA 600). The CLT_02 is used in these test series.

With the previously determined eigenfrequencies, the structure can be excited at its first natural frequency (17.78 Hz). Such a reproducible excitation can be seen in Figure 7. In this diagram, the response recorded with the accelerometers (ACC-Sensor1 to ACC-Sensor4) and the output function for the exciter are displayed. After six periods, the shaker is switched off and the system can freely vibrate. The aim of these experiments is to demonstrate the effects on the vibration behaviour when the acceleration is counteracted by an active element at predefined times and with specified intensities. Figure 8 shows how the active counteraction can be realized in the experiments.

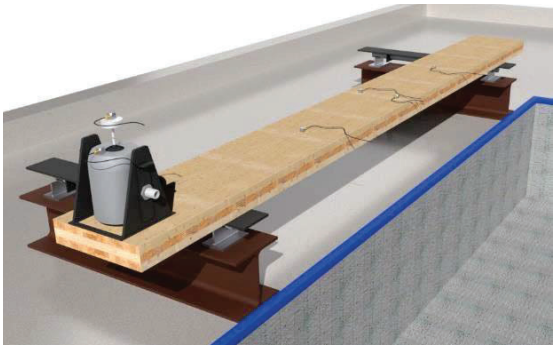

Figure 5: *Test setup for the first active damping tests with the shaker [14]*

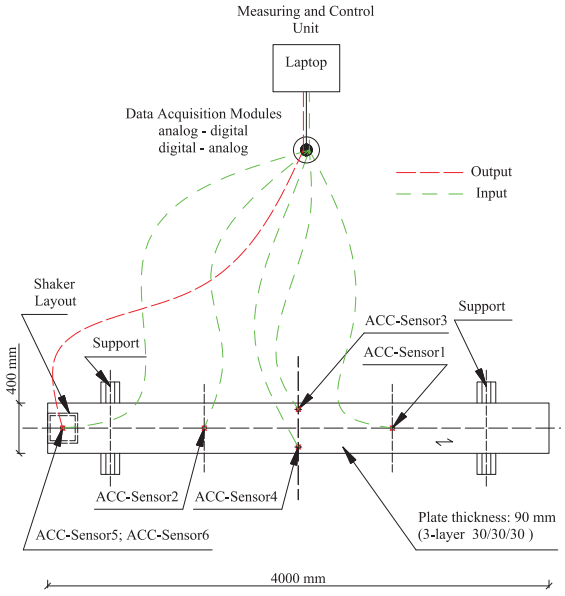

Figure 6: *Visualization of the measurement- and control systems*

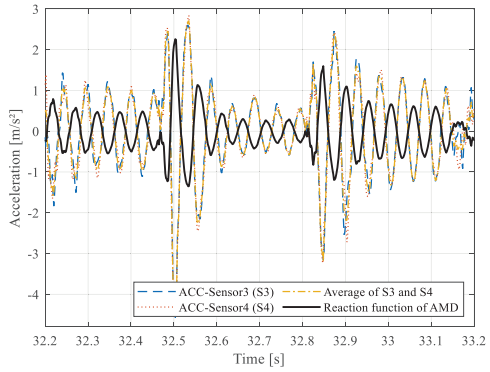

Figure 4: *Acceleration of measurement gauges and active mass damper (AMD) on a CLT element excited by a moving person*

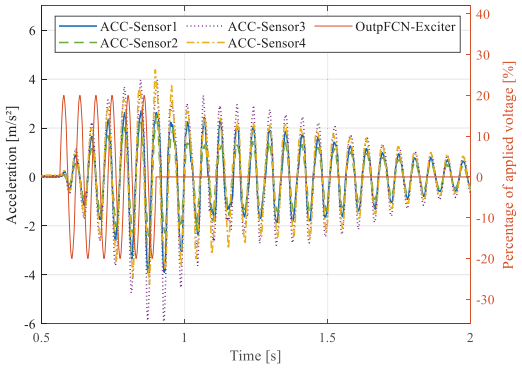

Figure 7: *Measured acceleration values for the reference test – free vibration after excitation by shaker*

https://doi.org/10.52202/069179-0251

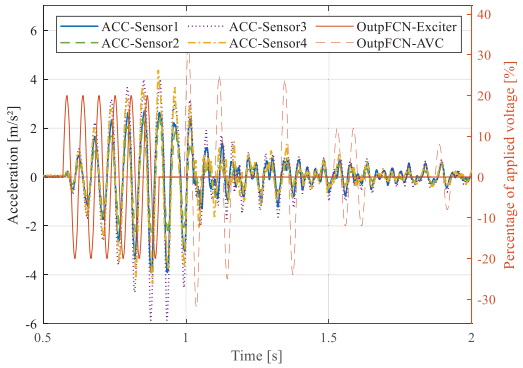

Figure 8: *Measured acceleration values for the active damping – counteracting damper after excitation by shaker*

2.4 EXPERIMENTS – ACCELERATION FEEDBACK

For the tests with active vibration control (AVC), the measured acceleration is used as measure for the intensity during counteraction (according to [12]). The experimental investigations are carried out with the test type CLT_03. A complex setup (see Figure 9 and Figure 10) is planned for this test series. In the lower left area, the CLT element has a fixed support. Due to the defined placement of additional masses (seen upper left and lower right), the first two eigenfrequencies of the system are close to each other (15.5 Hz respectively 18.2 Hz). The used shakers of type APS 400 (Shaker I and Shaker II) act on the system at the corner points. In addition, 800VA amplifiers of type APS 145 are used. Shaker I acts as exciter and Shaker II as active element for vibration control. Accelerometers ACC-Sensor1 and ACC-Sensor2 are placed next to the connection between the shakers and the CLT element. The records from ACC-Sensor2 are used for acceleration feedback.

Three different excitation modes are examined in these tests. On the one hand, as mentioned before, Shaker I serves as exciter (sweep and impulse) and on the other hand, a human-induced excitation by fist drop is performed. The voltage values for the two excitation by Shaker I can be seen in Figure 11. The linear sweep is performed between 5.0 Hz and 35.0 Hz over a duration of 30.0 s. The voltage amplitude is kept constant at a value of 3.7 V. The pulse is generated by a sine half-wave. The voltage amplitude is approx. 13.7 V and the periodicity is 0.5 s. In this test the data are recorded over a period of 10.0 s. The used equipment is from National Instruments. Data is collected and delivered by CompactDAQ and with Field Programmable Gate Array (FPGA) Target from CompactRIO the control of Shaker II is carried out. A Siglent SDG1032X function generator produces the sweep and pulse excitation.

During the tests, the measured acceleration of the plate at ACC-Sensor2 is transferred to the ComactRIO of the Control Unit (CU). Shaker II can also be switched on through this CU. The acceleration value is multiplied by a gain factor and the resulting voltage is sent to the Shaker II via the amplifier.

Figure 9: *Test setup for the active damping tests with acceleration feedback control [14]*

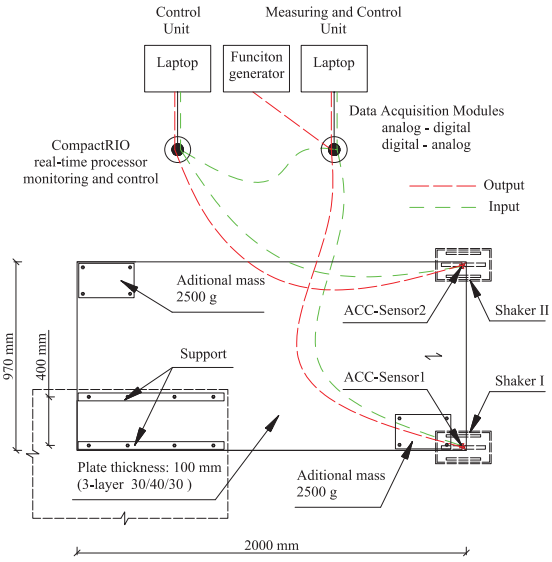

Figure 10: *Visualization of the measurement- and control systems (active damping with acceleration feedback control)*

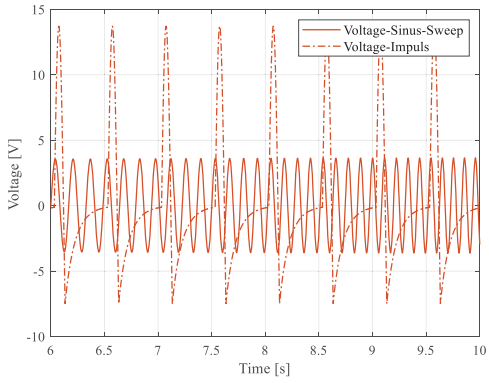

Figure 11: *Measured voltage of the exciters as a result of linear sweep and generated pulse*

https://doi.org/10.52202/069179-0251

2.5 COMPUTATIONAL MODELS

First preliminary calculations are performed with the program *RFEM Release 5.24.01* [15]. The load functions of a moving person on a slab are based on the research work of Bachmann and Baumann [16]. The computational model and the loading method are illustrated in Figure 12. For realistic outcomes different walking paths are simulated.

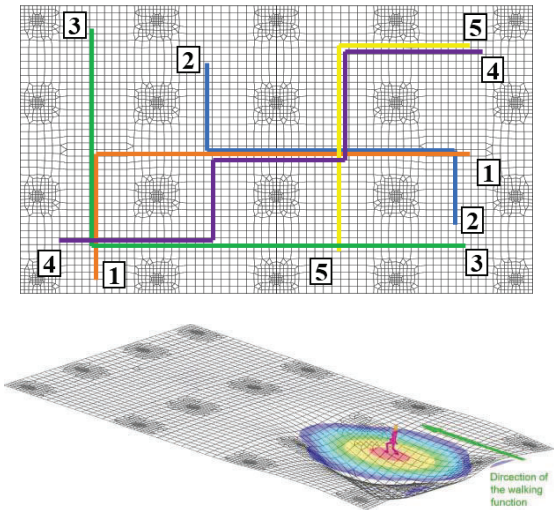

Figure 12: *Computational model of a point supported flat slab with the walking person*

3 RESULTS AND DISCUSSION

3.1 GENERAL

The following section focusses on the results of active damping with counteraction at specific times and control with acceleration feedback. There is always a comparison between reference system and the actively controlled tests. The so-called root-mean-square acceleration (a_{RMS}, see Equation (2)) is used as a reference value for the measurements. a_{RMS} is calculated with the acceleration $a(t)$ over the period T from an initial time T_1 to the end of duration T_2 ($T = T_2 - T_1$). For comparability, these values are shown in the diagrams as constant lines over the calculated period.

$$a_{RMS} = \sqrt{\frac{1}{T} \cdot \left(\int_{T_1}^{T_2} (a(t)^2 \cdot dt) \right)} \tag{2}$$

3.2 ACTIVE MASS DAMPER

In the first tests defined intensities at specific times are used to counteract the vibrating structure. For this purpose, those times are determined at which the lowest value for a_{RMS} is reached over the period T of 1.0 s (Equation (2)) after the excitation phase by means of a given counterimpulse. Due to the programming it is possible to run these tests several times with different time steps t_1 to t_n and the corresponding time increment Δt between the impacts (see Equation (3)). The aim is to identify the extremal values with respect to the minimum of a_{RMS}. In the current experiments, values between 2 and 30 milliseconds are used for Δt (depending on the sampling frequency f_{sample} = 2560 Hz and vibration behaviour of the plate).

$$\begin{aligned} t_1 &= t_0 + \Delta t \\ t_2 &= t_1 + \Delta t \\ &\dots \\ t_n &= t_{n-1} + \Delta t \end{aligned} \tag{3}$$

For each pulse this procedure is performed repeatedly. In the present case, this results in a process with six impacts at different times. Figure 13 shows the acceleration values of the reference measurement and the test with the active element switched on. The data refer to the sensors ACC-Sensor3 and ACC-Sensor4. For ACC-Sensor3, there is a reduction of the a_{RMS} of approx. 58 % and for ACC-Sensor4, the reduction is 62 %.

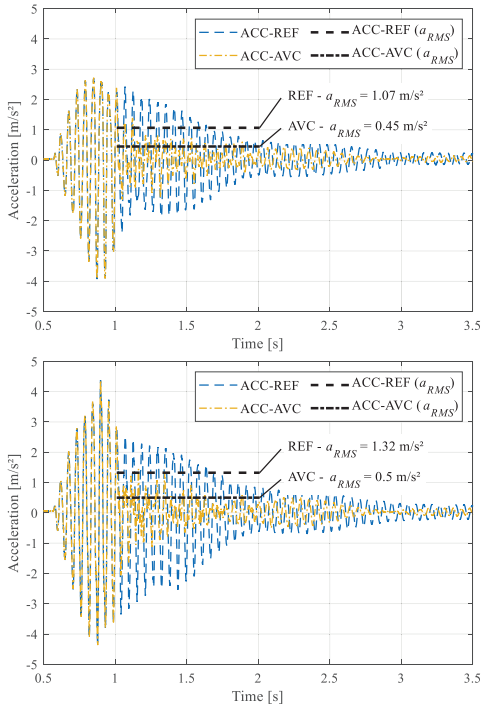

Figure 13: *Acceleration values of sensors ACC-Sensor3 (top) and ACC-Sensor4 (bottom) – reference test ACC-REF and test with active vibration control ACC-AVC*

3.3 ACCELERATION FEEDBACK CONTROL

Figure 14 to Figure 16 display the tests with a linear sweep over a defined frequency band of 30 Hz. Figure 14 shows the reference values (ACC-REF) and the test with active counteraction respectively active vibration control (ACC-AVC). At the local maxima in the area of 15.5 Hz and 18.2 Hz, the first two eigenfrequencies of the system are excited. Especially the response related to the first natural frequency can be controlled very well which is shown in Figure 14.

In the tests which are affected by switching on Shaker II, these two distinct maximum values are no longer visible.

A single peak at about 12.4 s is now clearly apparent. For clarification of this effect and the possible reduction of the vibration acceleration in this section, see also Figure 15 and Figure 16. Displayed are also the measured values of the applied voltages of Shaker I and Shaker II. In the period between 10.0 s (15.0 Hz) and 11.0 s (16.0 Hz), the reduction of a_{RMS} is 77.5 % and between 11.9 s (16.9 Hz) and 12.9 s (17.9 Hz) it is 48.9 %.

The tests excited by the pulses can be seen in Figure 17. With a periodicity of 0.5 s, a pulse with a vibrating duration of the sine half-wave T_{SHW} = 0.1 s is generated. The resulting accelerations are again measured by the reference test and the actively controlled system. The calculation is made with the duration T of 1.0 s (Equation (2)) to get comparative values of acceleration. For the reference system a_{RMS} = 0.39 m/s², with the active vibration control a_{RMS} = 0.26 m/s². This corresponds to a reduction of 33.1 %.

Of great interest, however, are the human-induced excitation. In the tests presented, the interaction between a person and the CLT element always takes place in the same way by a fist drop, but important is the possibility to generate comparable values. Care is taken to ensure that in both the reference system and the actively controlled system, two impacts are compared which have the same maximum value in the first 30 milliseconds. Although it must be considered that this peak is already damped to a certain extent (controlling in real-time). Therefore, the given comparison values are conservative. Figure 18 shows the raw data of both test series. The values from the reference system are compared with the values from actively controlled system. a_{RMS} is calculated over the time span T of 0.5 s (Equation (2)). For clarification, these tests are shown in detail in Figure 19. The time axis is taken from the reference system. The a_{RMS} is reduced by 53.2 % when comparing fist drop 1 (FD1) with fist drop 2 (FD2), and a reduction of 52.4 % is obtained when comparing the tests fist drop 3 (FD3) and fist drop 4 (FD4).

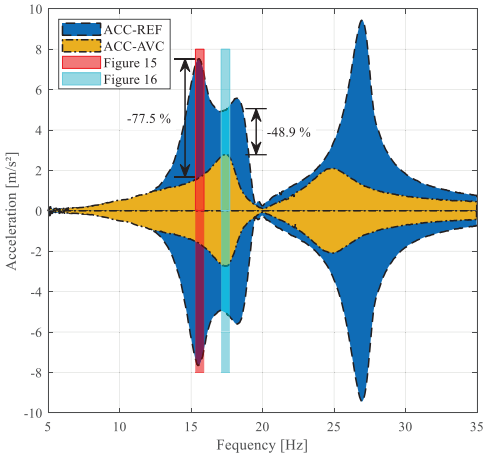

Figure 14: *Measured acceleration values of ACC-Sensor2 as a result of excitation by a linear sweep – reference test ACC-REF and test with active vibration control ACC-AVC*

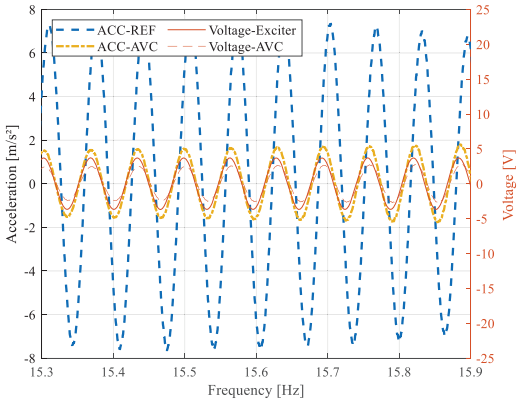

Figure 15: *Measured acceleration and voltage values of the frequency band with included first natural frequency of the reference system*

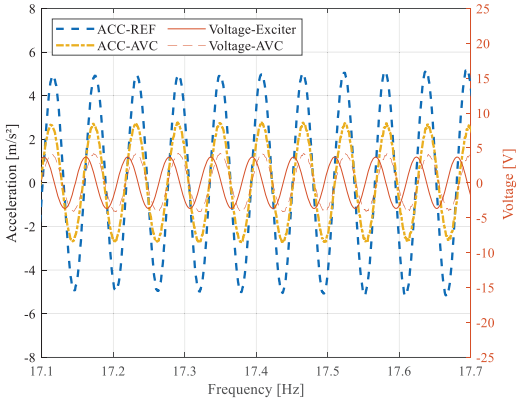

Figure 16: *Measured acceleration and voltage values of the frequency band with included first natural frequency of the active controlled system*

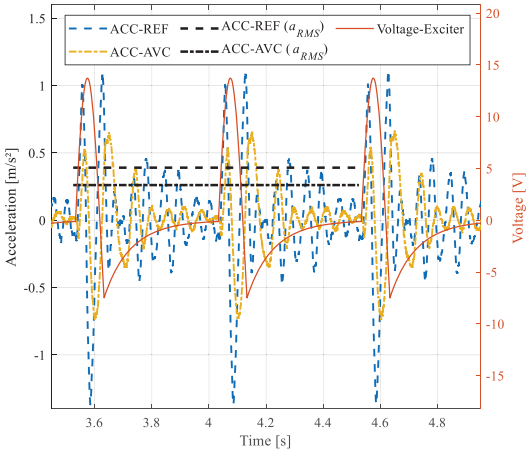

Figure 17: *Measured acceleration, voltage values and a_{RMS} of ACC-Sensor2 as a result of excitation by impulse function – reference test ACC-REF and test with active vibration control ACC-AVC*

https://doi.org/10.52202/069179-0251

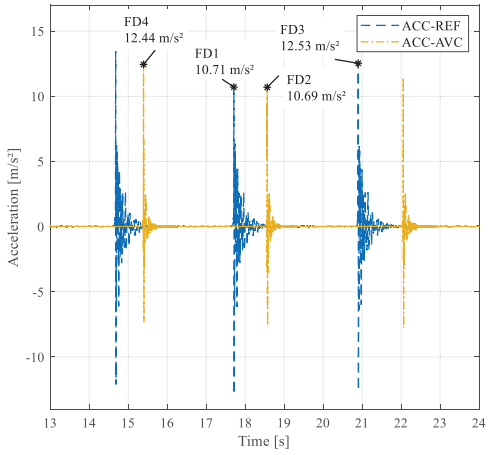

Figure 18: *Measured acceleration values of ACC-Sensor2 as a result of excitation by fist drop – reference test ACC-REF and test with active vibration control ACC-AVC*

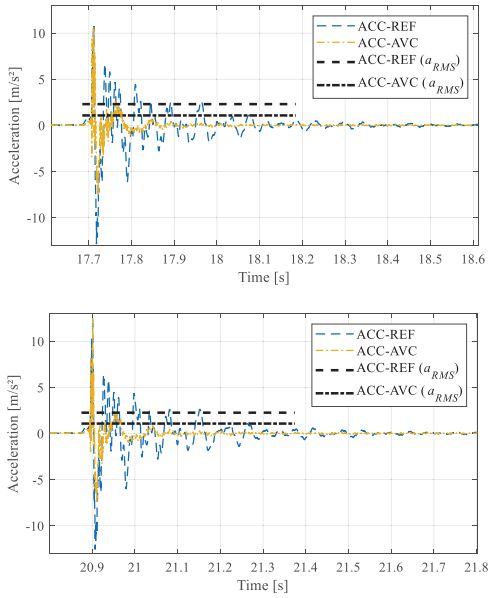

Figure 19: *Measured acceleration and a_{RMS} of the comparable fist drops FD1 and FD2 (top); FD3 and FD4 (bottom) – reference test ACC-REF and test with active vibration control ACC-AVC*

3.4 RESULTS OF CALCULATION MODELS

Research on point supported flat slabs [17] and solutions for edge connections [18] at the Universität Innsbruck highlight the importance of the floor's vibrational characteristics. In the course of these studies, the relevance of investigations in active counteraction, to control the vibrations of such slabs, increased. By using active vibration dampers and intelligent control systems, a considerable improvement of the vibration behaviour based on the slab structure can be achieved. Figure 20 shows the results of the calculation models. Despite the low natural frequency, values in the range of higher demands for floor structures can be achieved. The example of a point supported flat slab in Figure 20 shows that two active mass dampers are sufficient to achieve the vibration verification of the calculated floor construction even for higher demands according to EN 1995-1-1.

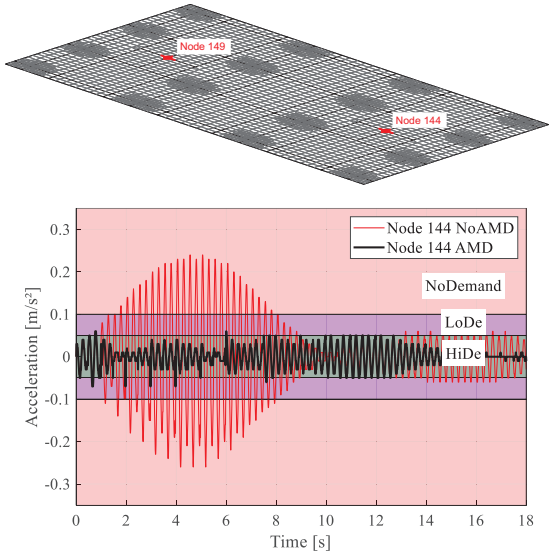

Figure 20: *Results of the calculation models; AMD ... active mass damper, LoDe ... low demands and HiDe ... high demands*

4 CONCLUSION AND OUTLOOK

The results for damping by active elements demonstrate an enormous improvement compared to the reference measurements in terms of the recorded vibration accelerations. Challenges like generating reproducible measurements as well as reacting in real-time could be solved with the available equipment. The reproducibility can be realized by means of shakers. The use of the CompactRIO enables the reaction to accelerations in real-time. Due to the encouraging results by active vibration control both in the area of impulsive counteraction and acceleration feedback control, further tests with the active elements are planned. For this purpose, the measurement and control equipment will be integrated into the experimental setup presented in Section 2.2. Human-induced vibrations, such as those caused by walking occupants, should also be significantly damped despite different setups, support distances and hence varying natural frequencies.

For the determination of modal parameters, further tests are scheduled in addition to the presented ones. The focus is on different support conditions and the variation of flooring. The comparison with existing literature and the possible validation of future calculation models will deliver an important input to the serviceability of timber floors. The calculations show promising results in terms of a better behaviour with regard to the vibrational characteristics and the possibilities in the reduction of construction materials. However, the calculations have to

https://doi.org/10.52202/069179-0251

be confirmed by laboratory tests and parameter studies. Another important issue is the optimization (dimensions, control, etc.) of the active damping systems. Experimental investigations with the AMD's complement the modeling and calculations.

In addition, the possibilities of machine learning to control the AMD's will be tested. Large-scale field experiments are then used to train the AMD's and make them able to react on numerous movement sequences.

5 ACKNOWLEDGEMENT

The authors would like to thank the partners of the research project "Good Vibrations" – the research funding association of Austria (FFG), Technical Laboratory for Research and Testing (TVFA) and the company SIHGA GmbH from Ohlsdorf, Austria.

6 REFERENCES

[1] Hamm P., Richter A., Winter S.: Floor vibrations – new results. In *Proc. World Conference on Timber Engineering (WCTE 2010)*. Riva del Garda, Italy, 2010.

[2] Mohammed A., Pavic A.: Human-structure dynamic interaction between building floors and walking occupants in vertical direction. Mech. Syst. Sig. Process. 147, 107036, 2021.

[3] Ussher E., Arjomandi K., Smith I.: Status of vibration serviceability design methods for lightweight timber floors. J. Build. Eng. 50, 104111, 2022.

[4] Zimmer S. E.: Ein Beitrag zur Aufarbeitung der Schwingungsthematik für die Holz-Massivbauweise in Brettsperrholz. Masterarbeit, Technische Universität Graz, 2013.

[5] Weckendorf J., Ussher E., Smith I.: Dynamic response of CLT plate systems in the context of timber and hybrid construction. Compos. Struct. 157, 412–423, 2016.

[6] Winter S., Hamm P., Richter A.: Schwingungs- und Dämpfungsverhalten von Holz- und Holz-Beton-Verbunddecken. Schlussbericht Juli 2010. TU München, Lehrstuhl für Holzbau und Baukonstruktion, 2010.

[7] Kreuzinger H., Mohr B.: Gebrauchstauglichkeit von Wohnungsdecken aus Holz; Abschlussbericht Januar 1999. TU München, Fachgebiet Holzbau, 1999.

[8] Kawrza M., Furtmüller T., Adam C.: Experimental and numerical modal analysis of a cross laminated timber floor system in different construction states, submitted for publication. Constr. Build. Mater., 344, 128032, 2022.

[9] Meinhardt C.: „Smart Structures" – aktive und passive Schwingungsreduktion von Bauwerken – Stand der Technik und Erfahrungen bei der praktischen Realisierung. Bautechnik 98, H. 12, S. 930–937, 2021.

[10] Billmaier M., Bamer F.: Tilger-Systeme zur Verbesserung des Schwingungsverhaltens von weitgespannten Bauteilen. In *Proc. 16. D-A-CH-Tagung: Erdbebeningenieurwesen und Baudynamik*. Innsbruck, Austria, 2019.

[11] Hudson M.J., Reynolds P.: Implementation considerations for active vibration control in the design of floor structures. Eng. Struct., 44, pp. 334–358, 2012.

[12] Díaz I.M., Reynolds P.: Acceleration feedback control of human induced floor vibrations. Engineering Structures, 32(1): 163–173, 2010.

[13] Nyawako D., Reynolds P.: Response-dependent velocity feedback control for mitigation of human-induced floor vibrations. Smart Mater. Struct. 18 (7), 2009.

[14] Hillberger T.: Schwingungsreduzierung bei Flachdecken aus Brettsperrholz (working title). Dissertation. Universität Innsbruck, manuscript under preparation.

[15] RFEM 5. Finite element program for design of spatial structures. Dlubal Software GmbH. Release 5.24.01

[16] Baumann K., Bachmann H.: Durch Menschen verursachte dynamische Lasten und deren Auswirkungen auf Balkentragwerke. Bericht/Institut für Baustatik und Konstruktion ETH Zürich, 7501(3), 1988.

[17] Maurer B., Maderebner R.: Cross Laminated Timber under concentrated compression Loads – Methods of Reinforcement. Eng. Struct. 245:112534, 2021.

[18] Stieb T., Maurer B., Bestler M., Dietsch P., Maderebner R.: Solutions for edge connections to build two-way spanning cross laminated timber slabs. In *Proc. World Conference on Timber Engineering (WCTE 2023)*. Oslo, Norway, 2023.

https://doi.org/10.52202/069179-0251

World Conference on Timber Engineering Oslo 2023

FIELD MEASUREMENT OF VIBRATION LEVEL DIFFERENCE ACROSS VERTICAL JUNCTIONS IN A TIMBER FRAME BUILDING

Simone Conta[1], Anders Homb[2]

ABSTRACT: Reliable vibration level difference $D_{v,ij}$ data are necessary to accurately predict flanking transmission. In this paper we present the measurement of $D_{v,ij}$ we performed on two timber frame buildings and a selection of the obtained results. The measurements were performed according to ISO10848 with different excitation sources. The analysis focuses on both methodological aspects and constructive solutions. Methodological aspects comprise the comparison of the different excitation sources used (shaker, impact hammer, loudspeaker) and the discussion of the challenges related to mixed wall constructions in field situation. Constructive solutions include the assessment of a party wall compared to an outer wall and the possible mounting options for the inner plasterboard leaves, i.e., directly on the timber frame, on timber laths, on metal Z-profile and on metal resilient bars. Results show that hammer and shaker provide comparable and reliable excitation. The loudspeaker did not provide sufficient excitation. Mixed wall construction will lead to different values of $D_{v,ij}$. Sensor placement can help reducing the mixed effect, but the introduced uncertainty could not be evaluated in the field. Finally, the different mounting options of the inner plasterboard showed a potential improvement of more than 20 dB over a broad frequency range by replacing the direct installation on the timber frame with resilient bars, the other options performing in between.

KEYWORDS: flanking sound transmission, vibration velocity level difference, field measurements, experimental setup.

1 INTRODUCTION

Vibration level differences across a junction are required to predict flanking sound transmission [1, 2]. Several papers present laboratory measurements and the corresponding results, often highlighting the related challenges [3-6]. Measuring vibration level differences in the field is necessary to increase the knowledge and the amount of data set available for reference [7, 8]. However, field measurements must tackle uncertainties in the vibration transmission path. Suitable excitation is also needed, but not straightforward due to practical limitations and the risk of airborne excitation of other transmission paths. In the context of a research project aimed at developing a building system for 8 stories timber frame building, we performed several field measurements of vibration level difference. In this paper, we present a preliminary selection of the obtained results discussing methodological aspects and constructive solutions. We look i) at different excitation sources, ii) at the challenge in the field due to mixed wall assemblies and iii) measured vibration level differences with different solutions for the mounting of the inner plasterboard wall leaf. The paper is structured as follow; in chapter 2, we give a description of the measurement objects with the corresponding constructive details. In chapter 3, we give a brief overview of the measurement setup. In chapter 4, we present and discuss the results; 4.1 is about the comparison of the excitation sources, 4.2 is about the comparison of party wall and outer wall and the effect of mixed construction, 4.3 looks at the effect of resilient bars and metal Z-profiles, 4.4 compare the collected results with data from the literature. In chapter 5, we present our conclusions.

2 MEASUREMENT OBJECTS

We performed measurements at two apartment buildings under construction at two different locations, which we will refer to as location 1 (L1) and location 2 (L2). Figure 1 shows an outer view of location 1. Both buildings are erected using prefabricated timber frame modules. The two buildings have comparable load bearing structure but different wall and floor assemblies.

Figure 1: Outer view of one of the two buildings used for the measurements.

[1] Simone Conta, SINTEF Community, Norway, simone.conta@sintef.no
[2] Anders Homb, SINTEF Community, Norway, anders.homb@sintef.no

https://doi.org/10.52202/069179-0252

At each location, we performed the measurements between two apartments with identical floor plan located above each other and including a party wall (W1) and an outer wall (W2). In this paper, we restrict the analysis to the vertical wall-wall transmission. The floor plans and the considered walls are shown in Figure 2 and Figure 3.

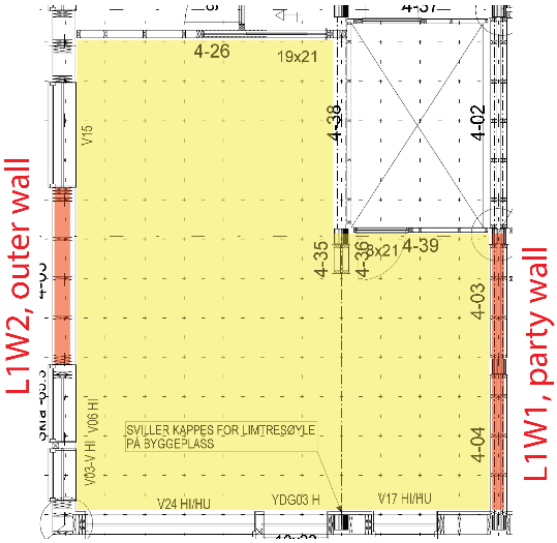

Figure 2: Floor plan of the apartment used for the measurements at location 1. The investigated walls L1W1 and L1W2 are highlighted.

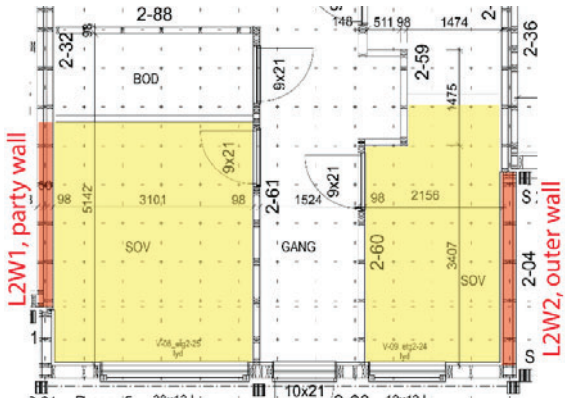

Figure 3: Floor plan of the apartment used for the measurements at location 2. The investigated walls L2W1 and L2W2 are highlighted.

The two locations used the same type of elements but with different solutions for the interior wall cladding and for the floor assembly. The wall assemblies are given in Table 1. The respective cross sections are shown in Figure 4 and Figure 5. The main difference between the two locations is the mounting method chosen for the inner plasterboard. At location 1, metal resilient bars (L1W1) or metal Z-profiles (L1W2) were used. At location 2, the plasterboard was screwed on the timber laths installed on the main wall frame. Figure 6 shows a horizontal section for location 1, where both the party wall and the outer wall are visible and a picture of the party wall with the resilient bars.

Table 1 Wall assemblies at the two locations.

Location 1		Location 2	
Party wall (one side)			
2x 13 mm	plasterboard 9 kg/m^2	2x 13 mm	plasterboard 9 kg/m^2
25 mm	resilient bar	1 x 11 mm	chipboard
98 mm	timber lath	98 mm	timber lath
Outer wall			
2 x 13 mm	plasterboard 9 kg/m2	13 mm	plasterboard 9 kg/m2
50 mm	steel Z-profile	48 mm	timber lath
295 mm	beam / insulation	225 mm	beam / insulation
11 mm	OSB board	11 mm	OSB board
12 mm	bitumen impr. fibreboar exterior cladding	12 mm	bitumen impr. fibreboar exterior cladding

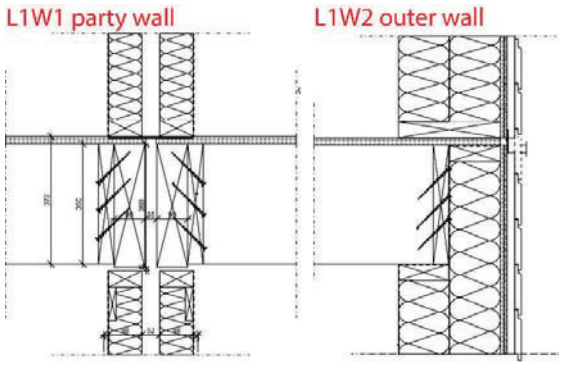

Figure 4: Cross section at the party wall and at the outer wall for location 1. See Table 1 for correct wall assembly.

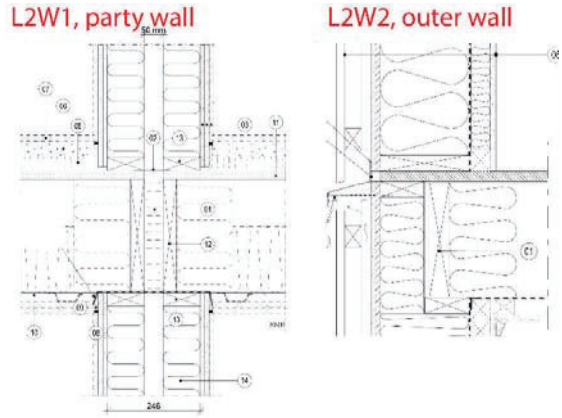

Figure 5: Cross section at the party wall and at the outer wall for location 2. See Table 1 for correct wall assembly.

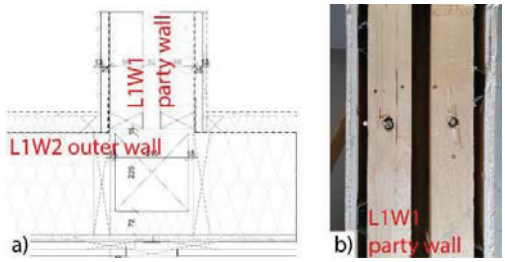

Figure 6:
a) Horizontal section of the walls at location 1. See Table 1 for correct wall assembly.
b) Picture of L1W1 showing the plasterboard installed on the resilient bars.

https://doi.org/10.52202/069179-0252

3 MEASUREMENT SETUP

We designed the measurements with two main objectives; the first was to test and gain experience with the measurement method itself. The second was to collect data for further reference and further development of the constructive solutions. We performed the measurements according to the standard ISO10848 [1]. We defined measurement positions on both wall and floors. We measured the acceleration simultaneously on the sending and receiving side by means of several accelerometers that were moved at different locations. We used at least 9 measurement positions and two excitation positions, totalling at least 18 measurement positions per surface. Excitation and measurement positions were chosen both on wall studs and in between. The velocity was calculated by integration of the acceleration signal. We used different type of excitation; instrumented hammer, electrodynamic shaker driven with white noise, loudspeaker, and standardized tapping machine. The latter will not be discussed further here. Figure 7 gives an overview of the expected transmission paths and the sensor placement and the assignment of the codes D, d, F, f to the building elements. Figure 8 shows the shaker installed in front of the wall at location 1 and the accelerometers distributed on the surface. The yellow circles are excitation positions (5) while the blue circles, solid and dashed are the two groups of measurement positions used (2 x 6), totalling in this case to 60 measurement positions. $D_{v,Ff}$ was calculated from the average over all source and receiver positions according to the procedure described in the standard. In all figures presenting the results, the plotted line represents the vibration level difference and the area above and below the line represent the standard deviation.

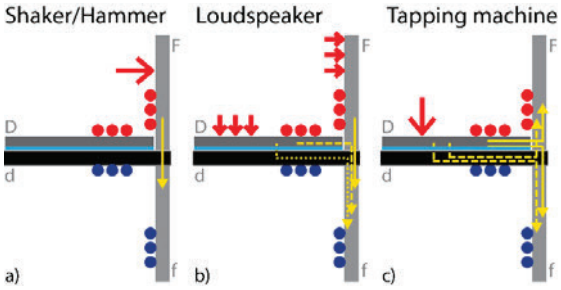

Figure 7: Excitation and expected main transmission paths.

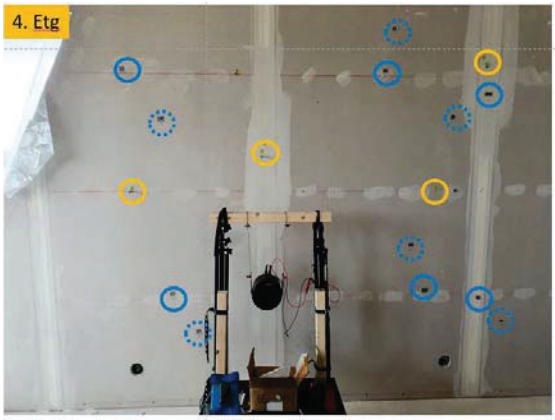

Figure 8: Shaker and accelerometers on the sending side.

4 RESULTS AND DISCUSSION

4.1 EXCITATION SOURCES

Figure 9 shows a comparison of the $D_{v,Ff}$ measured on the same partition with excitation from three different sound sources: hammer, shaker and loudspeaker.

The data show that hammer and shaker excitation provide comparable results, well within the standard deviation range. The measured $D_{v,Ff}$ with loudspeaker excitation clearly deviates from the other two sources. The loudspeaker was driven with typical levels for building acoustics measurements ($L_{A,eq}$ in the order of 95 dB). A closer look at the vibration velocity data on the receiving side revealed that the loudspeaker did not provide sufficient excitation; the generated vibration levels did not exceed the background level on the receiving side. The measured $D_{v,Ff}$ is therefore erroneous and too low. Also not shown, but important to note the measurement in the opposite direction, delivered comparable data for each source type. The results from the measurements performed at location 2, show the same trend: the loudspeaker did not deliver enough energy and the measured $D_{v,Ff}$ is lower than it should as shown in Figure 10.

We can draw two main conclusions; first, suitable excitations are hammer or shaker excitation. Loudspeaker it is not a suitable source. Secondly, a maybe natural remark on the quality check of the data: it is important to measure the background noise levels and plot them along with the excited vibration levels to verify that sufficient excitation was provided. A simple check that the measured values in the two directions are comparable might lead to a wrong assessment.

https://doi.org/10.52202/069179-0252

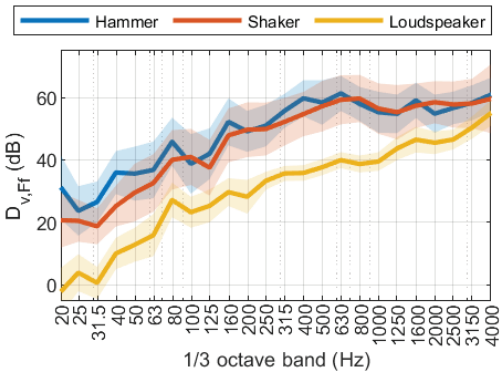

Figure 9: Vibration level difference measured on the L1W1 wall (path Ff) with hammer, shaker and loudspeaker excitation.

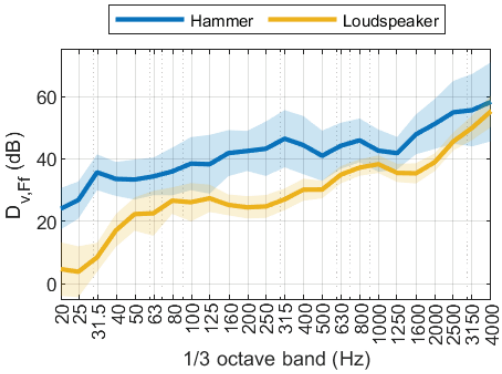

Figure 10: Vibration level difference measured on the L2W1 wall (path Ff) with hammer and loudspeaker excitation.

4.2 DIFFERENT WALL TYPES AND MIXED WALL ASSEMBLIES

When measuring in the field, it rarely happens that conditions are ideal. A challenging example was the situation at location 2. Both the party wall and the outer wall which were available to perform measurements presented mixed constructions as shown in Figure 3. Both walls had a portion that was party wall and a portion that was outer wall, although in different ratios. L2W1 was primarily a party wall and L2W2 was primarily an outer wall. The visible plasterboard layer covered over the two different portions at both walls. We chose to place several measurement positions on the larger portion and have one measurement position on the minor portion as a control point. We excited the wall within the major portion. In Figure 11 and Figure 12, we show the obtained results for L2W1 and L2W2 respectively. The continuous line is obtained from the measurement position on the larger portion and the dashed line from those on the minor portion.

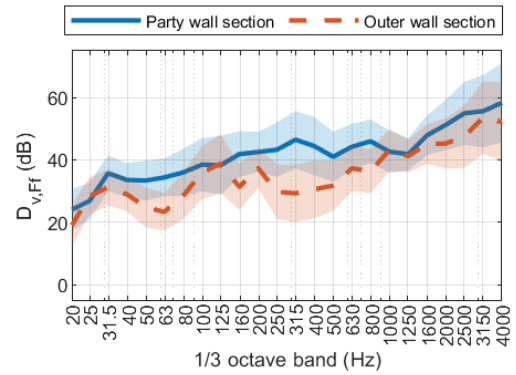

Figure 11: Vibration level difference measured at L2W1. The larger portion of this wall is a party wall.

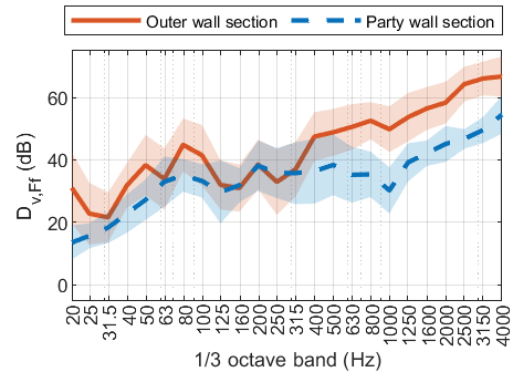

Figure 12: Vibration level difference measured at L2W2. The larger portion of this wall is an outer wall.

The results in Figure 12 show that there are clear differences between the two different portions of the wall. The measured $D_{v,Ff}$ for the outer wall portion above 500 Hz exceeds by more than 20 dB the $D_{v,Ff}$ measured for the party wall portion. Differences between the two portions of the wall are also observed in Figure 11 but the trend is not as clear as on Figure 12; the $D_{v,Ff}$ measured for the two portions fall within the standard deviation range in large part of the frequency range. We observe the larger deviations in the frequency range 200 – 800 Hz.

In Figure 13, we compare $D_{v,Ff}$ for the party wall (main portion of L2W1) and the outer wall (main portion of L2W2). We observe the same trend as in Figure 12: the vibration transmission along the party wall seems to be stronger (lower $D_{v,Ff}$) than along the outer wall. However, the difference is not as strong as observed in Figure 12. An exception is the range 100-350 Hz where the transmission appears to be stronger along the outer wall.

https://doi.org/10.52202/069179-0252

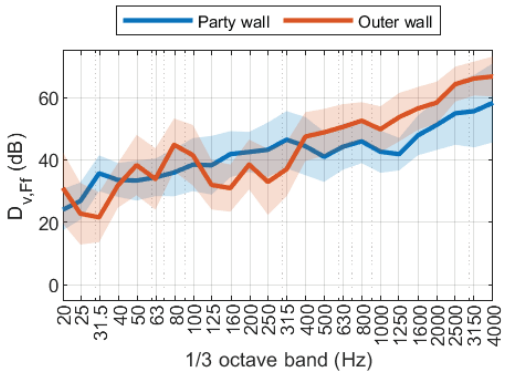

Figure 13: Vibration level difference measured at location 2 for the party wall (L2W1) and the outer wall (L2W2).

In this section, we looked at measurement performed on walls that had different construction on different portions. The results showed that it is possible to observe the differences between the different portions by placing the accelerometers well within the corresponding area. However, with the available data we cannot assess the measurement uncertainty that it is introduced in this kind of situation.

4.3 EFFECT OF RESILIENT BARS AND Z-PROFILES.

We performed the measurements at two locations (L1, L2) on two wall types: party wall (W1) and outer wall (W2). The respective basic wall structure was comparable at the two locations while the installation of the inner plasterboard was different. At location 1, the plasterboard was installed by means of resilient bars on the party wall (L1W1) and Z-profiles on the outer wall (L1W2). At location 2, the plasterboard was screwed directly on the timber framing both on the party wall (L2W1) and the outer wall (L2W2).

Figure 14 shows the comparison between the measured $D_{v,Ff}$ for L1W1 and L2W1, showing the effect of the resilient bars. The results show clearly that the resilient bars increasing effectively $D_{v,Ff}$ in the frequency range 125-2500 Hz by 10 to 20 dB. The resilient bars seem to have no effect at lower and higher frequencies. At frequencies close to 40 Hz, the $D_{v,Ff}$ measured on the wall with resilient bars is lower than that for direct installation; this might have to do with the resonance frequency of the system.

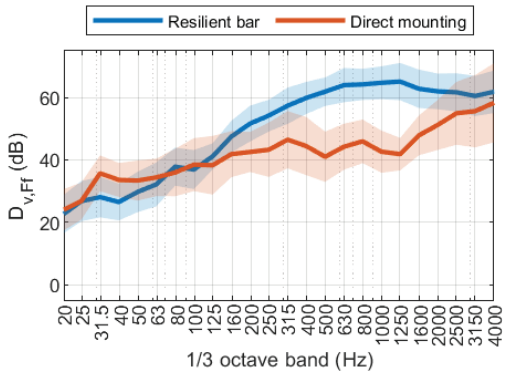

Figure 14: Vibration level difference measured on the party wall the two locations with hammer excitation. With resilient bar: L1W1. Direct installation: L2W1.

Figure 15 shows the comparison between $D_{v,Ff}$ for the outer walls at location 1 and 2 (L1W2, L2W2) and the effect of the Z-profiles. The $D_{v,Ff}$ below 100 Hz are comparable. Between 100 Hz and 1250 Hz, $D_{v,Ff}$ for L1W2 is up to 5 to 20 dB higher than for L2W2. This result shows that the Z-profiles effectively dampen the vibration transmission from the inner plasterboard to the wall structure, but on a reduced frequency range compared with the resilient bars.

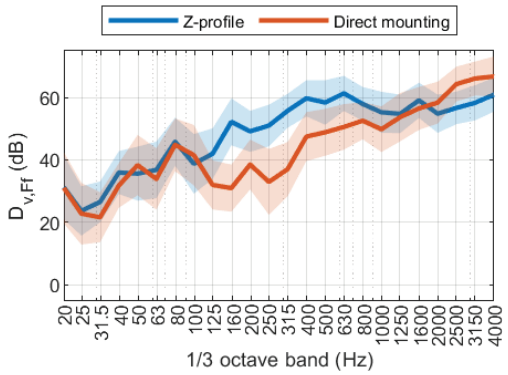

Figure 15: Vibration level difference measured on the party wall the two locations with hammer excitation. With Z-profile: L1W2. Direct installation: L2W2.

https://doi.org/10.52202/069179-0252

4.4 COMPARISON WITH DATA IN THE LITERATURE

Homb in [8] published $D_{v,Ff,n}$ values from an experimental setup and compared with several other published data. In Figure 16 we compare the measurements results from our measurements with a relevant one from the datasets in [8].

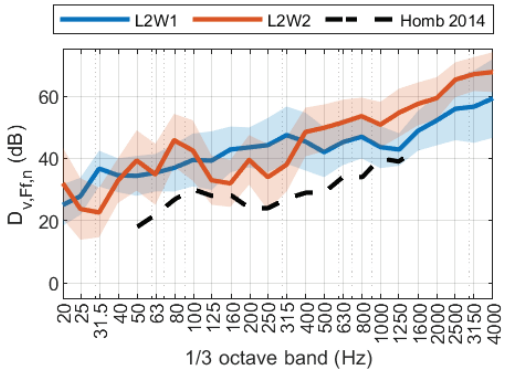

Figure 16: Comparison of the results for L2 with data from the literature [8].

The comparison shows that the measured values at location 2 are 10 – 15 dB higher than those from the referenced paper. The main difference between the measurement objects was the installation of the plasterboard: at location 2 the plasterboard is screwed to horizontal laths which are screwed to the load bearing timber frame. In the reference the plasterboard was screwed directly to the timber frame. This leads to at least two relevant differences; i) the horizontal laths influence the vibration field in the plate and ii) there is an additional vibration transmission reduction at the interface between the laths and the beam of the timber frame due to the connection loss. The combination of the two effects justifies the observed difference in the $D_{v,Ff,n}$ values.

5 CONCLUSIONS

We performed $D_{v,Ff}$ measurements at two different buildings erected as timber frame. The collect data and experiences allow to draw conclusions at two levels; at a methodological level and in terms of reference data for practitioners.

The methodological conclusions we can draw are:

- Hammer or shaker are convenient excitation sources. They deliver comparable results.
- Loudspeaker excitation with typical sound pressure level was not sufficient to measure vibration level differences in the field situation.
- Background noise on the receiving side must be monitored during measurements and included in the analysis to ensure reliable data.
- Mixed wall assemblies in field situation are a challenge that might limit measurement reliability. By choosing appropriate measurements positions, it is possible to observe significant differences. With our measurement setup, we could not quantify the uncertainty that this situation introduces.

The collected data can be used as reference in further projects. The collected data and the comparison with data from the literature showed that, assuming the same wall assembly in the sending and receiving room:

- Installation of plasterboard on horizontal timber laths, gives a broadband vibration transmission reduction in the order of 10 to 15 dB compared to direct installation on the frame.
- Installation of plasterboard using metal Z-profiles, gives a vibration transmission reduction in the range between 100 Hz and 1250 Hz in the order of 5 to 20 dB compared to the installation on the laths.
- Installation of plasterboard using metal resilient bars, gives a vibration transmission reduction in the range between 100 Hz and 2500 Hz in the order of 10 to 20 dB compared to the installation on the laths.

ACKNOWLEDGEMENT

The measurements have been performed within the project BV2020. BV2020 is a project of Støren Treindustri, supported by the Research Council of Norway. SINTEF Community is the research partner.

REFERENCES

1. ISO10848:2017, *Acoustics - Laboratory and field measurement of flanking transmission for airborne, impact and building service equipment sound between adjoining rooms - Part 1: Frame document, Part 3: Application to Type B elements when the junction has a substantial influence.*
2. ISO12354-1:2017, *Building acoustics -- Estimation of acoustic performance of buildings from the performance of elements -- Part 1: Airborne sound insulation between rooms*.
3. Craik, R.J.M. and L. Galbrun, *Vibration transmission through a frame typical of timber-framed buildings.* Journal of Sound and Vibration, 2005. **281**(3): p. 763-782.
4. Crispin, C., et al., *The vibration reduction index K ij: Laboratory measurements for rigid junctions and for junctions with flexible interlayers.* 2006. **13**(2): p. 99-111.
5. Schoenwald, S., et al., *Application of the direct method of ISO 10848 to flanking transmission through double leaf gypsum board walls.* Proceedings of Internoise 2006, 2006.
6. Schöpfer, F., et al., *Measurement of transmission functions in lightweight buildings for the prediction of structure-borne sound transmission from machinery*. 2017. **103**(3): p. 451-464.
7. De Geetere, L., B. Ingelaere, and M. Rychtarikova, *Vibration level difference measurements on a timber frame mock-up.* Proceedings of Internoise 2013, 2013.
8. Homb, A. *Measurements of junction vibration level differences of timber framed constructions*. in *INTER-NOISE and NOISE-CON Congress and Conference Proceedings*. 2014. Institute of Noise Control Engineering.

https://doi.org/10.52202/069179-0252

World Conference on Timber Engineering Oslo 2023

CHARACTERISATION OF RESILIENT INTERLAYERS

Paola Brugnara[1], Alice Speranza[1], Luca Barbaresi[2], Luca Sestigiani[1]

ABSTRACT: In buildings the sound transmission between rooms is characterized not only by direct transmission but also by flanking transmission through the structure. Timber structures, like all lightweight structures, do not have high acoustic performance if they are designed like heavy structures. It is important to take in account the effect of sound propagation through the wall/ceiling structure junctions, because it can significantly reduce the acoustic performance of these elements. Elastic separating layers between rigid junction can prevent the propagation of sound vibrations in the building structure and reduce the contribution of flanking transmission.

This paper provides the guideline to codify the characteristics of flexible interlayer made by a homogeneous viscoelastic material for the reduction of flanking sound transmission for airborne, impact and building service equipment.

To select a correct resilient strips, it is important to consider that acoustic interlayers are working at the level of the structure and the material needs to be extremely stable in long term to guarantee the stability of the building and avoid later deformation that will affect linings and static.

KEYWORDS: Building acoustic, interlayers, flanking transmission, static-acoustic interaction, standardisation

1 INTRODUCTION

The wooden structures are statically assembled with different types of connections. Mainly we talk about screws, angular and hold-down. These connection systems have the task of precisely coupling the different structural elements to form a single large junction structure. While in parallel to overcome the problem of transmission of vibrations, in recent years resilient profiles in polyurethane or EPDM are very often being used which have the task of decoupling and reducing the transmission of vibrations between the different elements.
To date, there are no common standards that describe in detail how to characterize the product and which performance shall be determined to guarantee a proper static and acoustic performance.
Aim of this paper is to analyse the intended use of resilient interlayers and define the values that allow to design a joint with them. Defining a common test procedure allow also to compare products from different manufactures and chose the best product depending on project requirements.

2 EUROPEAN ASSESMENT DOCUMENT (EAD)

Resilient interlayers are used between structural elements, typically between floor and wall, and they become part of the structure. For this reason, not only acoustic performance, but also static stability and durability over the time shall be investigated.
For materials used as elastic interlayers, there are no standards which characterize the mechanical properties in accordance with the use for reducing noise transmission in buildings.
From an acoustic point of view, it is not enough to define dynamic elastic modulus and damping factor. K_{ij} value must be determined for the calculation of airborne sound insulation between rooms according to ISO 12354-1 [1] and impact sound insulation between rooms according to ISO 12354-2 [2].
From a static point of view, it is important to test the compressive behaviour of the material through the determination of elastic modulus, compressive creep, compressive stress and deformation and compression set.
In recent years, resilient interlayers are increasing their presence in buildings for the reduction of flanking transmission and consequently the demand to characterize and compare the different types of products placed on the market has increased.
In order to find a common criterion for the assessment of product's performance, a specific EAD was developed. The EAD is developed by the EOTA network consisting of some 45 highly qualified Technical Assessment Bodies (TABs) mandated by their states to issue ETAs. EOTA also co-operates with external experts and stakeholders to

[1] Paola Brugnara, Rothoblaas, Italy, paola.brugnara@rothoblaas.com
[1] Alice Speranza, Rothoblaas, Italy, alice.speranza@rothoblaas.com
[2] Luca Barbaresi, University of Bologna, Italy, luca.barbaresi@unibo.it
[1] Luca Sestigiani, Rothoblaas, Italy, luca.sestigiani@rothoblaas.com

https://doi.org/10.52202/069179-0253

develop state-of -the-art technical specifications for the construction sector.
EAD provides manufacturers with a way to CE marking for construction products that are not or not fully covered by a harmonised European standard (hEN) under the Construction Products Regulation (EU) 305/2011.
It contains, at least, a general description of the construction product and its intended use, the list of essential characteristics relevant for the intended use, methods and criteria for assessing the performance of the product and principles for the implementation of the system for assessment and verification of constancy of performance.

2.1 DESCRIPTION AND INTENDED USE

The EAD covers flexible interlayers made of a homogeneous viscoelastic layer of monolithic polyurethane or EPDM (ethylene propylene diene monomer rubber) or similar material.
The product is used as flexible interlayer for the reduction of flanking transmission for airborne, impact and building service equipment sound between adjacent rooms and/or vibration transmission. The product is installed between at least two elements (i.e., floor and wall).
Methods and criteria for assessing reaction to fire, compressive creep, compression set, compressive stress and deformation, dynamic elastic modulus, damping factor, flanking transmission for airborne, impact and building service equipment sound between adjacent rooms and compressive modulus are described in the EAD.

2.2 COMPRESSIVE CREEP AND COMPRESSION SET

Resilient interlayers are subjected to constant load during their working life.
It is important to estimate the long-term behaviour for static reasons (to avoid differential failure in the structure) and for acoustic reasons (a crushed interlayer does not have the same elastic response and consequently the acoustic performance decays).
For the same reason it is important to define the ending thickness of the product after compression for a given time and after a given recovery time.
For the determination of the compressive creep ISO 8013 [7] can be used, for the determination of compression set it is recommended ISO 1856 [8].

2.3 COMPRESSIVE STRESS AND DEFORMATION AND COMPRESSIVE MODULUS

Resilient interlayers have been tested with very high compression stress, demonstrating a linear behaviour even with high loads. Despite this behaviour, from a static point of view it is important to provide the compressive stress as a function of the strain (e.g.: 1mm, 2mm and 3mm compression) in order to limit the maximum deformation and possible structural failure.
Compressive stress and compressive modulus have been tested according to EN ISO 844 [9] under different conditions of friction.
Tests show that friction could affect the result and for this reason it is necessary to perform always the measurements with appropriate lubricant to make the effects of surface friction negligible. This ensures the repeatability of the result and without any treatment to have the in situ operating value of elastic modulus and compressive strength [10].

2.4 FLANKING TRANSMISSION

In previous investigations it has been shown that K_{ij} depends on the test setup. Due to the lack of a common standard, each manufacturer provides K_{ij} values tested in a different configuration (choosing the type of joint, the number of fastening system, etc). Many variables can affect the K_{ij} and it is important to make clear the test setup [3, 4, 12].
Considering the variety of possible joints, materials and fastening systems, it was not possible to define a single configuration useful to define the performance of the resilient profile.
Although there is a detailed standard to determine the vibration reduction index (ISO 10848 [5]), there is a need to improve the way results are expressed in order to avoid ambiguities on fastening systems.

3 EUROPEAN TECHNICAL ASSESMENT (ETA)

The European Technical Assessment (ETA) provides an independent Europe-wide procedure for assessing the essential performance characteristics of non-standard construction products.
The ETA offers manufacturers a voluntary route to CE marking, when the product is not or not fully covered by a harmonised standard (hEN) under the Construction Products Regulation (EU) 305/2011.
CE marking based on the ETA allows manufacturers to freely market their product on the entire European internal market and introduce innovative products and new product features with short lead times.
Only independent Technical Assessment Bodies (TABs) may issue ETAs. The independent assessment strengthens the credibility of the product performance information, enhances market transparency and builds customer trust.
ETAs provide reliable product performance information that is comparable across Europe based on harmonised technical specifications, the European Assessment Document (EAD).

3.1 MEASUREMENT OF COMPRESSION CREEP

The samples provided are in the form of cylinder of 13 mm diameter and 6 mm of nominal thickness (tolerance class M4 according to the ISO 3302-1). The test is carried out on 3 specimens of each material.

https://doi.org/10.52202/069179-0253

The method for the determination of the compression creep consists in subjecting the samples to a compression of 10% strain for 6000 seconds.

$$\frac{\Delta\varepsilon}{\varepsilon_1} = \frac{\delta_1 - \delta_2}{\delta_0 - \delta_1} \quad (1)$$

Where:

- δ_0 [mm]: initial thickness of the test piece
- δ_1 [mm]: thickness of the test piece under constant force 10 min after application of the force
- δ_2 [mm]: thickness of the test piece under constant force 6000 s after the application of the force

The test is done at ambient temperature. The compression is made with a hydraulic machine for tensile/compression INSTRON 8032. by mounting a load cell of 1 kN for the transduction of the pressing load. After the compression of 10% strain. the force obtained is held constant and the acquisition of the deformation starts for 6000 s.

Table 1: *Compressive creep*

Product	$\frac{\Delta\varepsilon}{\varepsilon_1}$
XYLOFON 35	0,54
XYLOFON 50	0,53
XYLOFON 70	2,9
XYLOFON 80	10,3
XYLOFON 90	0,28

3.2 COMPRESSION SET

The samples provided are in the form of squares of 50x50mm with 6 mm of nominal thickness (tolerance class M4 according to the ISO 3302-1).
Four samples are overlapped to obtain the minimum thickness of 25 mm. The assembly shall work as a single layer of equivalent thickness.
The method for the determination of the compression set consists in subjecting the samples to a thermal conditioning at ambient temperature and then to a mechanical conditioning. imposing a deformation of 50% for a 22h time interval. At the end of the application of the static load, after a recovery time of 30 minutes, the residual deformation is measured and the compression set (c.s.) is calculated as a percentage variation in the thickness of the sample compared to the pre-test measured thickness.
The compression set $c.s._i$ is defined as:

$$c.s._i = \frac{d_0 - d_r}{d_0} \times 100 \quad [\%] \quad (2)$$

The absolute value of the product after compression and recovery. $t_{c.s.}$. is defined as:

$$t_{c.s.} = t - (c.s. \times t) \quad [mm] \quad (3)$$

Where:

- d_0 [mm]: original thickness of test piece
- d_r [mm]: thickness of the test piece after recovery
- t [mm]: nominal thickness of the product

The thermal conditioning of the specimens is made at ambient temperature, according to EN ISO 1856 [8]. The mechanical conditioning of the specimens runs on a hydraulic machine for tensile/compression INSTRON 1275 (±100 mm stroke) by mounting a load cell of 500 kN for the transduction of the pressing load.
After the mechanical conditioning and the subsequent relaxation time, the thickness of the sample is measured again on 5 points using the bench thickness gauge.

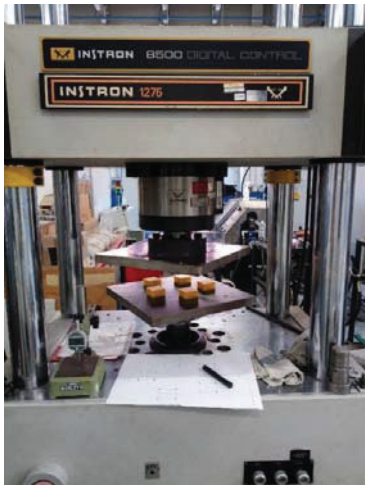

Figure 1: *Measurement equipment mounted on the hydraulic machine INSTRON*

Table 2: *Compression set*

Product	c.s.	t [mm]	$t_{c.s.}$ [mm]
XYLOFON 35	0.72 %	6	5,96
XYLOFON 50	1,25 %	6	5,93
XYLOFON 70	0,71 %	6	5,96
XYLOFON 80	1,31 %	6	5,92
XYLOFON 90	2,02 %	6	5,88

Results of the test show that the tested materials have very good elastic behaviour and the residual deformation is negligible.

https://doi.org/10.52202/069179-0253

3.3 COMPRESSIVE STESS AND DEFORMATION

The samples provided are in the form of squares of 50x50mm with 6 mm of nominal thickness (tolerance class M4 according to the ISO 3302-1).
The test is carried out on 5 specimen and 5 lubricated specimens of each material.
The method for the determination of the compressive stress σ at 1mm, 2mm and 3mm is to correlate the pressure required to obtain the different deformations.
The thermal conditioning of the specimens is made at ambient temperature, according to EN ISO 1856. Also the test is done at ambient temperature. The compression is made with a hydraulic machine for tensile/compression INSTRON 8032 by mounting a load cell of 10 kN for the transduction of the pressing load.

Table 3: *Compressive stress and deformation*

Product	σ_{1mm} [MPa] $\sigma_{1mm,\ lubricant}$ [MPa]	σ_{2mm} [MPa] $\sigma_{2mm,\ lubricant}$ [MPa]	σ_{3mm} [MPa] $\sigma_{3mm,\ lubricant}$ [MPa]
XYLOFON 35	0,5 0,3	1,5 0,7	3,6 1,6
XYLOFON 50	1,1 0,5	3,5 1,2	8,6 2,6
XYLOFON 70	2,4 1,2	5,4 3,0	11,1 6,0
XYLOFON 80	3,9 2,1	9,5 5,2	19,5 9,8
XYLOFON 90	5,8 3,4	14,4 8,0	29,0 14,9

Where:
- σ_{1mm} [MPa]: mean value of compressive stress at 1 mm strain (surfaces not treated with lubricant)
- $\sigma_{1mm,lubricant}$ [MPa]: mean value of compressive stress at 1 mm strain (surfaces treated with appropriate lubricant)
- σ_{2mm} [MPa]: mean value of compressive stress at 2 mm strain (surfaces not treated with lubricant)
- $\sigma_{2mm,lubricant}$ [MPa]: mean value of compressive stress at 2 mm strain (surfaces treated with appropriate lubricant)
- σ_{3mm} [MPa]: mean value of compressive stress at 3 mm strain (surfaces not treated with lubricant)
- $\sigma_{3mm,lubricant}$ [MPa]: mean value of compressive stress at 3 mm strain (surfaces treated with appropriate lubricant)

3.4 COMPRESSIVE MODULUS

The samples provided are in the form of squares of 50x50mm with a 6 mm of nominal thickness (tolerance class M4 according to the ISO 3302-1).
The test is carried out on 5 specimen and 5 lubricated specimens of each material.
The compressive modulus is calculated as following:

$$E_{C.i} = \frac{\boldsymbol{\sigma}_{\mathbf{15.i}} - \boldsymbol{\sigma}_{\mathbf{5.i}}}{\varepsilon_{15} - \varepsilon_{5}} \quad (4)$$

Where:
- $\sigma_{15.i}$ [MPa]: compressive stress at 15% strain (ε_{15})
- $\sigma_{5.i}$ [MPa]: compressive stress at 5% strain (ε_{5})

The thermal conditioning of the specimens is made at ambient temperature according to EN ISO 1856. Also the test is done at ambient temperature. The compression is made with a hydraulic machine for tensile/compression INSTRON 8032 by mounting a load cell of 10 kN for the transduction of the pressing load.

Table 4: *Compressive modulus*

Product	E_c [MPa]	$E_{c,lubricant}$ [MPa]
XYLOFON 35	3,2	1,7
XYLOFON 50	7,1	2,9
XYLOFON 70	14,2	7,3
XYLOFON 80	25,4	13,2
XYLOFON 90	36,6	21,9

3.5 DYNAMIC ELASTIC MODULUS AND DAMPING FACTOR

The samples provided are in the form of a cylinder of 9 mm diameter and a nominal thickness (class M4 according to the ISO 3302-1) of 6 mm. The form factor is h(height) : d(diameter) = 1:1.5.
The test is carried out on 3 specimens of each material.
The thermal conditioning of the specimens is made at ambient temperature, according to EN ISO 1856.
The measurement equipment is made of DMA 242E Artemis NETZSCH.

https://doi.org/10.52202/069179-0253

Figure 2: *DMA apparatus*

Table 5: *Dynamic elastic modulus*

Product	E'_{1Hz}[MPa]	E'_{5Hz}[MPa]	E'_{10Hz}[MPa]	E'_{50Hz}[MPa]
	E''_{1Hz}[MPa]	E''_{5Hz}[MPa]	E''_{10Hz}[MPa]	E''_{50Hz}[MPa]
XYLOFON 35	2,8	3,1	3,3	3,6
	0,8	1,0	1,1	1,4
XYLOFON 50	4,6	3,9	4,1	4,4
	0,6	0,7	0,7	1,0
XYLOFON 70	6,0	6,4	6,9	7,9
	0,5	0,8	1,0	2,2
XYLOFON 80	15,4	16,9	18,0	21,8
	1,5	2,5	3,3	6,9
XYLOFON 90	32,2	39,9	45,4	65,7
	6,9	12,2	16,0	29,8

Where:

- E'_{1Hz} [MPa]: mean value of elastic normal modulus (storage normal modulus) at 1 Hz
- E''_{1Hz} [MPa]: mean value of loss normal modulus at 1 Hz
- E'_{5Hz} [MPa]: mean value of elastic normal modulus (storage normal modulus) at 5 Hz
- E''_{5Hz} [MPa]: mean value of loss normal modulus at 5 Hz
- E'_{10Hz} [MPa]: mean value of elastic normal modulus (storage normal modulus) at 10 Hz
- E"10Hz [MPa]: mean value of loss normal modulus at 10 Hz
- E'50Hz [MPa]: mean value of elastic normal modulus (storage normal modulus) at 50 Hz
- E"50Hz [MPa]: mean value of loss normal modulus at 50 Hz

Table 6: *Damping factor*

Product	$\tan\delta_{1Hz}$ [MPa]	$\tan\delta_{5Hz}$ [MPa]	$\tan\delta_{10Hz}$ [MPa]	$\tan\delta_{50Hz}$ [MPa]
XYLOFON 35	0,28	0,32	0,33	0,38
XYLOFON 50	0,15	0,17	0,18	0,23
XYLOFON 70	0,08	0,12	0,15	0,28
XYLOFON 80	0,10	0,15	0,19	0,32
XYLOFON 90	0,21	0,31	0,35	0,45

Where:

- $\tan\delta_{1Hz}$: mean value of tangent of the loss angle at 1 Hz
- $\tan\delta_{5Hz}$: mean value of tangent of the loss angle at 5 Hz
- $\tan\delta_{10Hz}$: mean value of tangent of the loss angle at 10 Hz
- $\tan\delta_{50Hz}$: mean value of tangent of the loss angle at 50 Hz

3.6 FLANKING TRANSMISSION

The samples provided are in the form of rolled stripes of 6 mm of nominal thickness (tolerance class M4 according to the ISO 3302-1).

The vibration reduction index K_{ij} is a quantity related characterises the transmission of vibrations through the structural elements of a junction. It is calculated according to ISO 10848 [5]:

$$K_{ij} = \frac{D_{v,ij} + D_{v,ji}}{2} + 10\,log\frac{l_{ij}}{\sqrt{a_i \cdot a_j}} \quad dB \tag{5}$$

Where:

- $D_{v.ij}$ [dB]: velocity level difference between element i and j when element i is excited
- $D_{v,ji}$ [dB]: velocity level difference between element j and i when element j is excited
- l_{ij} [m]: common junction length between elements i and j
- a_i [m]: equivalent absorption length of element i
- a_j [m]: equivalent absorption length of element j

The values stated in the ETA refers to transmission path characterized by the presence of the resilient interlayer. For each path shall be defined the vibration reduction index with resilient interlayer in frequency (K_{ij}) and correction of the $\overline{K_{ij}}$ in presence of elastic interlayers in junction (Δ_l).
Δ_l for a specific path is calculated as difference between $\overline{K_{ij}}$ of the same path with and without resilient interlayer. $\overline{K_{ij}}$ is the arithmetic average of K_{ij} within the frequency range 200 Hz to 1 250 Hz (one-third octave bands) according to point 10 of the EN ISO 10848-1 [5].

$$\Delta_l = \overline{K_{ij,with}} - \overline{K_{ij,without}}$$

For the acquisition of the velocity levels the panels were excited using piezoelettrics shaker screwed to panels. Velocity levels were acquired using 4 accelerometers at a time.
Structural reverberation times T_{15} have been extracted from MLS measurements, which were measured in the number of six positions on each panel.
The excitation and measurement points were chosen according to the EN ISO 10848 [5] standard. For each element a minimum of 3 source positions are required and for each excitation position three pairs of measurement positions must be considered randomly over the test element. In the measurement session 6 receivers and 3 source were used.
Two types of junctions were constructed: "T vertical junction" and "X vertical junction".

Tested build up of "T vertical junction" (Figure 1):
- (4) Top wall: 5-ply CLT, 100 mm, (2,4 m x 3 m)
- (1) Floor: 5-ply CLT 100 mm (2,4 m x 3,5 m)
- (2) Bottom wall: 5-ply CLT, 100mm, (2,4 m x 3 m)

Fastening system:
- 6 Partially threaded screws HBS 8x240mm; step 440mm
- 2 Angle brackets NINO15080 (CLT pattern with 31 screws 5x50 mm) + XYLOFON 35 (55x150x6 mm); step 1760mm

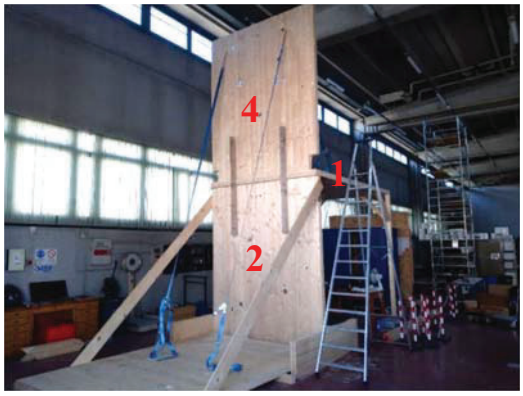

Figure 3: *"T vertical junction" build up*

Tests on this configuration were conducted changing the type of resilient interlayer and the load applied. An example with results follows.

Product: XYLOFON 50
Position: between top wall and floor and between floor and bottom wall.
Dimensions: width=100mm, thickness=6mm, length=2,40m
Contact area: continuous stripe (same width and length of the wall)
Load applied[N/m^2]: 338000

Path 1-4

F (Hz)	100	125	160	200	250	315	400	500
K_{14} (dB)	17,6	17,7	20,5	21,3	18,4	21,9	24,3	16,9

F (Hz)	630	800	1000	1250	1600	2000	2500	3150
K_{14} (dB)	20,5	21,0	18,6	19,7	21,9	16,1	16,3	20,7

$\overline{K_{14}}$=19,9 dB $\overline{K_{14,0}}$=13,3 dB $\Delta_{l,14}$= 6,6 dB

Path 1-2

F (Hz)	100	125	160	200	250	315	400	500
K_{12} (dB)	22,1	19,2	15,9	21,0	20,5	21,5	24,0	21,2

F (Hz)	630	800	1000	1250	1600	2000	2500	3150
K_{12} (dB)	19,8	23,0	23,7	23,6	26,8	23,2	24,3	28,3

$\overline{K_{12}}$=21,8 dB $\overline{K_{12,0}}$=14,5 dB $\Delta_{l,12}$= 7,3 dB

Path 2-4

F (Hz)	100	125	160	200	250	315	400	500
K_{24} (dB)	18,7	26,7	26,6	31,1	24,4	27,8	26,6	25,3

F (Hz)	630	800	1000	1250	1600	2000	2500	3150
K_{24} (dB)	22,5	27,8	28,6	33,2	28,6	33,3	34,0	31,6

$\overline{K_{24}}$=27,9 dB $\overline{K_{24,0}}$=17,3 dB $\Delta_{l,24}$= 10,6 dB

Tested build up of "X vertical junction" (Figure 2):
- (4) Top wall: 5-ply CLT, 100 mm, (2,4 m x 3 m)
- (1+3) Floor: 5-ply CLT 100 mm (2,4 m x 7,1 m)
- (2) Bottom wall: 5-ply CLT, 100mm, (2,4 m x 3 m)

Fastening system:
- 6 Partially threaded screws HBS 8x240mm; step 440mm
- 2 Angle brackets NINO15080 (CLT pattern with 31 screws 5x50 mm) + XYLOFON 35 (55x150x6 mm); step 1760mm

https://doi.org/10.52202/069179-0253

Figure 4: *"X vertical junction" build up*

Tests on this configuration were conducted changing the type of resilient interlayer and the load applied. An example with results follows.

Product: XYLOFON 50
Position: between top wall and floor and between floor and bottom wall.
Dimensions: width=100mm, thickness=6mm, length=2,40m
Contact area: continuous stripe (same width and length of the wall)
Load applied[N/m^2]: self-weight of the structure

Path 1-4

F (Hz)	100	125	160	200	250	315	400	500
K_{14} (dB)	17,4	20,1	18,5	17,8	15,6	17,6	19,8	19,6

F (Hz)	630	800	1000	1250	1600	2000	2500	3150
K_{14} (dB)	21,0	19,2	25,1	23,0	24,1	21,8	18,7	21,6

$\overline{K_{14}}$=20,2 dB $\overline{K_{14,0}}$=17,0 dB $\Delta_{l,14}$= 3,2 dB

Path 1-2

F (Hz)	100	125	160	200	250	315	400	500
K_{12} (dB)	19,6	18,9	14,0	14,9	14,7	17,1	19,7	21,0

F (Hz)	630	800	1000	1250	1600	2000	2500	3150
K_{12} (dB)	23,0	20,9	22,1	21,5	25,3	24,1	23,5	24,2

$\overline{K_{12}}$= 19,8 dB $\overline{K_{12,0}}$= 15,9 dB $\Delta_{l,12}$= 3,9 dB

Path 2-4

F (Hz)	100	125	160	200	250	315	400	500
K_{24} (dB)	14,9	27,3	23,4	25,4	23,0	29,5	28,3	25,4

F (Hz)	630	800	1000	1250	1600	2000	2500	3150
K_{24} (dB)	29,0	28,5	33,3	34,2	33,7	36,4	34,6	32,0

$\overline{K_{24}}$=29,0 dB $\overline{K_{24,0}}$=23,2 dB $\Delta_{l,24}$= 5,8 dB

Other junction types we assessed following the same principles, changing the type od profile and the load applied.

4 CONCLUSIONS

The aim of this work is to demonstrate how a harmonized standard can be produced to uniquely characterize resilient profiles used in flanking transmission, to assess in a harmonized manner the effects of including these profiles in building joints from an acoustic, mechanical and structural point of view.
The project led to the definition of a European Assessment Document (EAD) and to the issue of a European Technical Assessment (ETA), that allows manufacturer to introduce innovative products and new features to the entire European market.

REFERENCES

[1] ISO 12354-1:2017. Building acoustics – Estimation of acoustic performance of buildings from the performance of element. Part 1: Airborne sound insulation between rooms. ISO, Switzerland.
[2] ISO 12354-2:2017. Building acoustics – Estimation of acoustic performance of buildings from the performance of element. Part 2: Impact sound insulation. ISO, Switzerland
[3] Barbaresi L., Morandi F., Garai M., Speranza A. *Experimental measurements of flanking transmission in CLT structures*. Proc. Mtgs. Acoust. **28**, Buenos Aires, 2016
[4] Speranza A., Barbaresi L. and Morandi F. *Experimental analysis of flanking transmission of different connection systems for CLT panels*. Proc. of WCTE 2016, Vienna, 2016.
[5] ISO 10848:2017. Acoustics — Laboratory and field measurement of flanking transmission for airborne, impact and building service equipment sound between adjoining rooms, ISO, Switzerland
[6] ISO 4664-1:2011. Rubber, vulcanized or thermoplastic, Determination of dynamic properties, Part 1: General guidance, ISO, Switzerland
[7] ISO 8013:2019. Rubber, vulcanized, Determination of creep in compression or shear, ISO, Switzerland
[8] ISO 1856:2018. Flexible cellular polymeric materials, Determination of compression set, ISO, Switzerland
[9] ISO 844:2021. Rigid cellular plastics, Determination of compression properties, ISO, Switzerland
[10] Barbaresi, L., Morandi, F., Belcari, J., Zucchelli, A., Speranza, A. *Optimizing the mechanical characterization of a resilient interlayer for the use in timber construction,* 24th International Congress on Sound and Vibration, ICSV 2017, 2017
[11] What is an ETA? | EOT
S. Mecking, T. Kruse, U. Schanda Measurement and calculation of sound transmission across junctions of solid timber building elements EuroNoise, Maastricht, The Netherlands (2015)

World Conference on Timber Engineering Oslo 2023

VIBRATION SERVICEABILITY PERFORMANCE OF MASS TIMBER FLOORS UNDER VARIOUS SUPPORT CONDITIONS

Chenyue Guo[1], Jianhui Zhou[2*]

ABSTRACT: Mass timber floors are prone to human-induced vibration due to their light weight. Vibration serviceability limit design often governs the maximum allowable span of mass timber floors. The current design methods including the vibration-controlled span equation in CSA O86-19 and the design method in EC5 usually assume the mass timber floors are simply supported on rigid walls, which can't be directly applied to floors being supported by beams. In this study, the vibration performance of mass timber floors including nailed laminated timber, dowel laminated timber, and cross-laminated timber floor panels was investigated experimentally. The effect of various support conditions on the dynamic properties of mass timber floors was studied through modal testing, and the vibration acceptability of these floors under normal human walking was assessed by subjective evaluations. The test results indicated that the stiffness of the support significantly impacts the dynamic properties and vibration performance of the entire floor slab. The performance criterion specified in CSA O86 demonstrated potential for accurately predicting the vibration performance of beam-supported mass timber floors. However, both the vibration-controlled span equation and the beam stiffness equation were found to be insufficient for designing such floors. The vibration response-based design methods that utilize the ISO 10137 baseline curve showed inconsistencies across all groups. Dunkerley's system frequency prediction equations yielded overestimated results, while Kollar's method exhibited an average error within 5%, demonstrating promising potential for practical use. Further research is required to develop a reliable design approach for beam-supported mass timber floors.

KEYWORDS: Mass timber floors, vibration performance, support conditions

1 INTRODUCTION

Mass timber panels (MTPs) are a category of large-dimension panelized wood products, including cross-laminated timber (CLT), nailed laminated timber (NLT), dowel laminated timber (DLT), or glued-laminated timber (GLT) panels [1]. They are used mainly as load-bearing floors, walls, and roofs in mid-rise or high-rise wood buildings. In comparison to alternative materials, such as concrete and steel, MTP-constructed floors possess a relatively lighter weight and lower damping ratio, thereby making them susceptible to human-induced vibrations [2].

The vibration performance of mass timber floor is significantly dependent their edge support conditions [3-4]. Beside the rigid wall supports often found in platform CLT buildings, there are a large portion of mass timber building projects that uses post-and-beam combined with mass timber panel floors. It should be noted that the structural design of supporting beams is to meet ultimate limit state (ULS) including moment compacity and shear resistance strength as well as serviceability limit state (SLS) including deflection limits of the beams only. The effect of the beam flexibility on the floor vibration performance is not considered.

Current design methods including the vibration-controlled span equation in Canadian standard CSA O86 [5] and the vibration design method in Eurocode5 [6] are based on the assumption that the mass timber floors are simply supported on rigid walls. Due to the flexibility of beams that support the floor panels, these design equations cannot be applied to such beam-supported floors. Thus, FPInnovation [7] proposed a beam stiffness equation to limit the beam's stiffness to ensure the supporting beams are sufficiently rigid, which enables the applicability of the vibration design method in CSA O86 to beam-supported CLT floors. However, this beam stiffness equation was developed based on the subjective evaluations of a few beams under heel drop excitations in a laboratory condition, without experimental verifications on beam-supported CLT floors.

The current engineering practice also adopts vibration response-based design methods using the ISO 10137 [8] baseline curve and multiplying factors for mass timber floor vibration design [9]. To conduct a response-based vibration serviceability design, it is inevitable to calculate the system's natural frequencies of floors with flexible supports, with the fundamental natural frequency being a key parameter. Dunkerley's method is widely used and adopted in American Institute of Steel Construction (AISC) DG-11 [10] for the prediction of system natural

[1] Chenyue Guo, University of Northern British Columbia, Canada, cguo@unbc.ca
[2] Jianhui Zhou, University of Northern British Columbia, Canada, jianhui.zhou@unbc.ca, corresponding author

https://doi.org/10.52202/069179-0254

frequency, which are being used for mass timber floors with beam supports. However, the validity of such criteria as well as the frequency prediction equations for mass timber floors remains unverified to date. In addition, Kollar [11-13] proposed a model and equations for the calculation of the fundamental natural frequency of plates which considered the deflection of the supporting beams. However, these equations have yet to be verified through experimental studies.

The aim of this study is to examine the dynamic properties of mass timber floors under varying support conditions and evaluate their vibration serviceability performance through both physical parameter measurements and subjective evaluations. Additionally, the study will assess the validity of commonly-used vibration design criteria for mass timber floors with supporting beams, and assess the accuracy of prediction equations for system frequency.

2 THEORETICAL BACKGROUND

2.1 COMMONLY-USED MASS TIMBER FLOOR VIBRATION DESIGN CRITERIA

In an effort to establish standards for acceptable vibrational behavior in mass timber floors, numerous approaches have been proposed. In Canada, Hu [14] first proposed a performance criterion which used the combination of fundamental natural frequency and the deflection under 1 kN point load. This performance criterion was derived through a comprehensive analysis of field floor data and the results of occupant perception surveys, utilizing logistic regression analysis, as shown:

$$\frac{f_1}{d^{0.39}} \geq 15.3 \quad (1)$$

where d is the measured static deflection under 1 kN concentrated load at the center of the floor, and f_1 is the measured fundamental natural frequency of the floor.

The accuracy of the criterion was confirmed through a comparative analysis of 58 lightweight flooring systems, using subjective evaluation ratings as a reference. The results indicated that when the ratio calculated through the equation exceeded 15.3, the flooring system was highly likely to meet the vibrational performance requirements and be deemed acceptable to occupants.

This approach was adopted for the development of the vibration-controlled span equation for CLT floors in accordance with CSA O86-19 [5]. The same form of design criterion which used the calculated parameters is shown in equation (2), the equations to calculate the parameters are also shown as follows:

$$\frac{f_1}{d^{0.7}} \geq 13.0 \quad (2)$$

$$f = \frac{\pi}{2l^2}\sqrt{\frac{EI}{m}} \quad (3)$$

$$d = \frac{1000Pl^3}{48EI} \quad (4)$$

where m is the mass per unit area, kg/m^2; l is the floor span, m; EI is the bending stiffness of the 1-meter-wide floor, N·m^2; P= 1000 N.

The performance criterion equation takes into account the measured results to assess the vibration serviceability performance of a built timber floor. However, the vibration design of CLT flooring systems is achieved through the second equation, referred to as the "design criterion", which was developed based on the lab tests of CLT floors with three different thickness. Both the performance and design criteria will be used to analyze the test data obtained in this study.

The direct method for evaluating floor vibration serviceability takes into account human perception of whole-body vibration and requires appropriate response measurements. According to ISO 10137 "Bases for design of structures—Serviceability of buildings and walkways against vibrations" [8], the baseline curve representing the acceleration in the z-axis provides a limit for human perception of vibration. Within the frequency range of 4 to 8 Hz, vibrations at a level of 0.005 m/s^2 are considered to be negligible. ISO 10137 also provides multiplying factors for different occupancies, suggesting a factor of 2 to 4 for continuous or intermittent vibrations in the case of residential buildings during daytime hours. The AISC DG 11 [10] uses peak acceleration based on the principles outlined in ISO 10137. Although this guide was initially developed for steel-framed floors, it has been widely adopted in the timber engineering community [9] for the design of mass timber flooring systems.

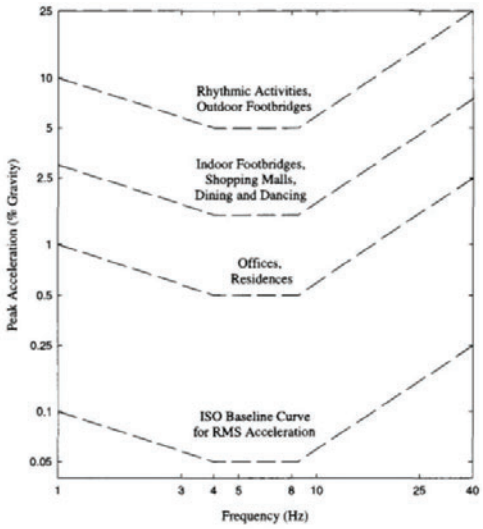

Figure 1: *Recommendation of acceleration for human comfort in AISC 2016*

2.2 SUPPORTING BEAM STIFFNESS LIMITATION

Since Eq. 2 was developed with CLT floors with rigid supporting walls, FPInnovation [7] proposed a beam stiffness equation so that Eq. 2 can be used for beam-supported CLT floors. This equation limits the beam's

https://doi.org/10.52202/069179-0254

stiffness to ensure the supporting beams are sufficiently rigid to avoid negative effect on floor vibration performance.

$$EI \geq F_{span} 132.17 l^{6.55} \quad (5)$$

where EI=the supporting beam apparent stiffness (N/m^2), l=the clear span of supporting beam (m), F_{span} is taken as 1 for simple span beam and 0.7 for multi-span continuous beam.

The evaluation of the rigidity of the beams was conducted by doing a heel drop test on the center of the beam, the specimen can be treated as rigid if the evaluator does not feel any movement after the heel drop. It should be noted that the beam stiffness requirement is not dependent on the mass timber floor thickness and span according to Eq. 5.

2.3 SYSTEM FREQUENCY PREDICTION

In the AISC DG 11 [10] for the vibrations of steel framed structural systems and the revised version of EC5 [15], Dunkerley's method was suggested for the estimation of system frequency:

$$\frac{1}{{f_n}^2} = \frac{1}{{f_j}^2} + \frac{1}{{f_g}^2} \quad (6)$$

where $f_j$is the beam or joist panel mode frequency, f_g is the girder panel mode frequency.

Kollar [11-13] proposed a model and equations using Dunkerley's method and Southwell's method for the calculation of the fundamental natural frequency of orthotropic plates which considered the flexibility of the supporting beams. The equations considered different configurations when the floor was supported by one to four beams on edge, and the equations were applied to timber and timber-concrete floors and verified by numerical models. The equations for floors with two opposite beams are simplified as shown, more details can be found in [13].

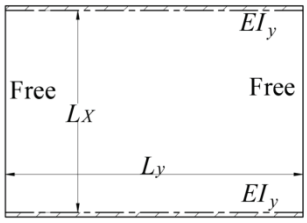

Figure 2: *Floor supported on two opposite beams*

$$D_{11} = \frac{E_x h^3}{12(1-\gamma^2)} \quad (7)$$

$$D_{22} = \frac{E_y h^3}{12(1-\gamma^2)} \quad (8)$$

$$f_x^2 = \frac{\pi^2 D_{11}}{4mL_x^4} \quad (9)$$

$$f_y^2 = \frac{\pi^2 D_{22}}{4mL_y^4} \quad (10)$$

$$f_{EIy}^2 = \frac{\pi^2 EI_y}{2mL_x L_y^4} \quad (11)$$

$$\delta_y = \frac{1}{1 + {f_y}^2/{f_x}^2} \quad (12)$$

$$f^2 = \left(\frac{1}{f_x^2} + \frac{1}{f_{EIy}^2 + \delta_y f_y^2}\right)^{-1} \quad (13)$$

where E_x and E_y is the Young 's modulus, m is the mass over unit area, h is the thickness, γ is the Poisson's ratio, L_x and L_y are the dimensions of the plate in the x and y direction,EI_y is the supporting beams' stiffness.

3 MATERIALS AND METHODS

3.1 MATERIALS

The dowel laminated timber (DLT) panels, nail laminated timber (NLT) panels and cross laminated timber (CLT) panels were investigated. The DLT and NLT panels were assembled with one 11-mm oriented strand board (OSB) panel as the sheathing, in accordance with construction practices.

Three floors with varying dimensions and layouts were constructed in the laboratory at the University of Northern British Columbia for testing purposes. DLT floor and NLT floor were both made by three 4.3 m × 1.8 m panels, CLT floor was made by three 4.0 m × 1.8 m panels. The panels were spanned in the major strength direction at 4.1 m o.c and 3.9 m o.c respectively. The non-destructive test developed by Zhou [16] was used to simultaneously measure the elastic constants of each panel including modulus of elasticity in major and minor strength directions (E_x and E_y) as well as in-plane shear modulus G_{xy}. These parameters are required if the floor plate is modeled as a two-dimensional orthotropic thin plate. The floor dimensions and measured elastic constants are shown in Table 1 and 2. It is important to note that the CLT panels were obtained from prior testing and contained some internal cracks, which led to a lower E_x value than its design value. However, this did not impact the floor's vibration performance with the tested span.

Table 1: *Information of the constructed mass timber floors*

Floor Material	Length (m)	Width (m)	Thickness (m)	Density (kg/m^3)
DLT	4.3	5.4	0.151	448
NLT	4.3	5.4	0.151	446
CLT	4.0	5.4	0.245	470

Table 2: *Measured elastic constants of the constructed mass timber floors*

Floor	E_x (MPa)	E_y(MPa)	G_{xy} (MPa)
DLT	7491	81	58
NLT	7909	29	80
CLT	2900	42	124

https://doi.org/10.52202/069179-0254

In this study, the rigid wall and glulam beams were both selected as floor supports. The design and construction of two beams with varying cross-sectional configurations were carried out to meet both ULS and SLS requirements first with a structural grid of 6×6 meters according to NBCC 2020 [17]. The 20f-E sprue-pine glulam beams with a span of 6 meters and a density of 435 kg/m^3 were selected. In this study, the 175*494 mm supporting glulam beams B1 were designed based on Eq.5 which is expected to has the adequate stiffness to avoid negative effect on floor vibration performance. The 175*608 mm beam B2 was then selected which has a stiffness two times higher than B1. The elastic constants of the two groups of beams were obtained through the methodology established by Chui [18] and are presented in Table 3.

Table 3: *Information of the supporting beams*

Beam	Width (mm)	Thickness (mm)	E (MPa)	G (MPa)
B1	175	494	11705	693
B2	175	608	12090	629

3.2 FLOOR CONSTRUCTION

The floors were sitting on wood walls resting on the ground along the major span direction, which can be treated as rigid supports (Figure 3). Panel-to-panel connections were achieved by installing full-thread self-tapping screws at 45˚ (Holz CLC, 8 mm diameter and 160 mm length,), with a spacing of 400 mm. Panel-to-support connections were also installed by using half-thread self-tapping screws at 90˚ (HBS, 8 mm diameter and 220 mm length,), with a spacing of 450 mm.

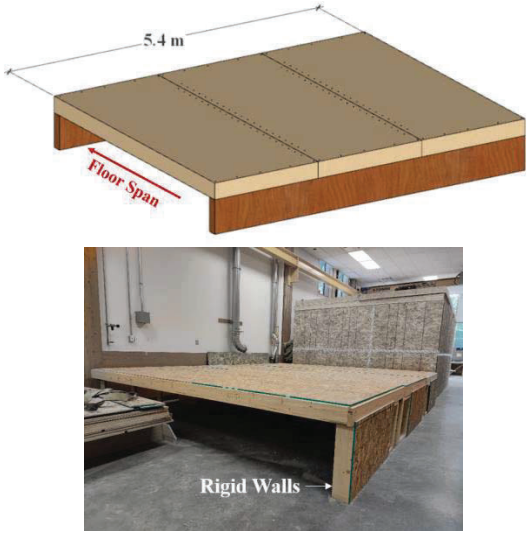

Figure 3: *Floor with rigid supports*

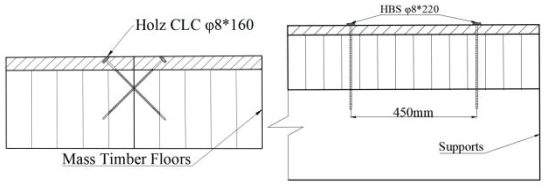

Figure 4: *Panel-to-panel connection and panel-to-support connection*

The floors were then supported on two groups of beams respectively, the beam-to-column connections were achieved by PITZL-HVP connectors with a dimension of 80*220 mm, the screws used are φ 5 mm*100 mm. When the beams were connected with columns on both sides, the floor panels were placed on the two beams along the longitudinal direction with the same panel-to-panel and panel-to-support connections.

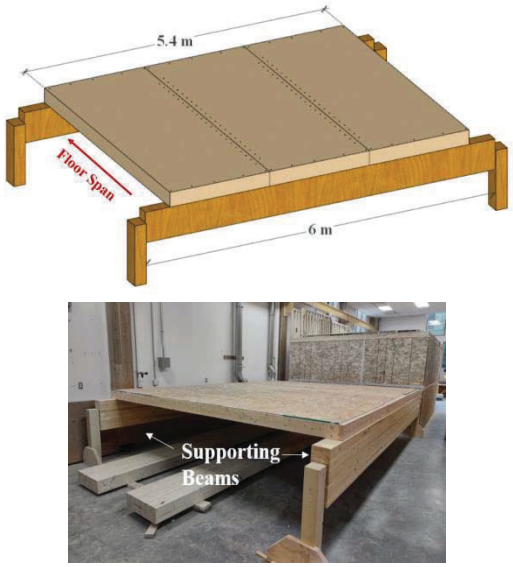

Figure 5: *Floors with supporting beams*

Figure 6: *Beam-column connectors*

3.3 METHODS

3.3.1 Modal tests

Experimental modal test was performed to obtain the dynamic properties including natural frequencies, damping ratios and mode shapes. To accurately capture the corresponding mode shapes, a 7×7 grid was divided on the floor, and each point is impacted by an instrumented impact hammer [PCB Model 086D05] for

three times to obtain an averaged frequency response function (FRF) curve. Five accelerometers [PCB Model 352C04, nominal sensitivity 1.02 mV/(m/s^2)] were installed on the floor with hot melt glue, and the signals from the impact hammer and accelerometers were recorded by a dynamic data analyzer (Brüel & Kjær, LAN-XI 3050) within the frequency range of 100 Hz. BK Connect (Brüel & Kjær) vibration engineering software was used to conduct the modal analysis. The location of accelerometers and test setup is illustrated in Figure 7.

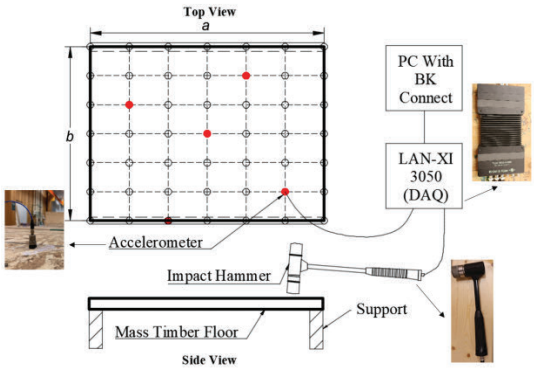

Figure 7: *Schematic drawing of modal test setup with selected accelerometer locations*

3.3.2 Vibration performance tests

After the modal test, a floor vibration performance test was conducted in each group for their acceleration levels under normal human walking. The walking test was performed by a 75 kg evaluator following several walking paths with a gait around 2 Hz. For each floor, four accelerometers were mounted on the left and right midspan (Am-1 and Am-2), and on top and bottom of the floor center (Ac-1 and Ac-2) respectively. The acceleration responses were recorded at various locations that were believed to exhibit the highest possible vibration magnitude and recorded by BK Connect Software. The time-domain acceleration data of the whole walking path was post-processed based on ISO 2631 [19].

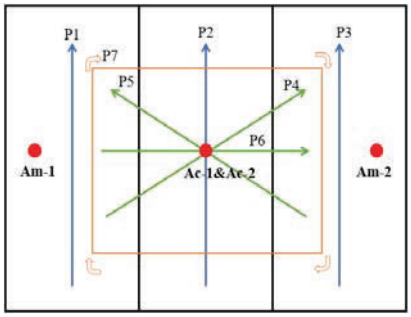

Figure 8: *Human walking paths on the tested floors*

Deflection test was conducted according to ISO 18324 [20] by applying a 1kN point load (a 100 kg concrete block) at the center of the floor, the deflection of the floor was measured by one dial indicator with an accuracy of 0.01 mm at the midspan under the loading point.

Figure 9: *Deflection test (Left: Applied 1 kN concentrated load on the floor, Right: Data collection)*

Subjective evaluations were conducted for the acceptance level of the floors according to ISO 21136 [21], categorizing the floors into levels 1 to 5, i.e. 1 = definitely unacceptable, 2 = unacceptable; 3 = marginal, 4 = acceptable, 5 = definitely acceptable. A survey with 20 evaluators was conducted on each floor. The evaluator first walked on the floor, then stood and sat stationary at the center while a 75kg walker walked on the floor, as shown in Figure 10. Each evaluator completed a questionnaire provided in ISO 21136 to report his/her perception and acceptance regarding vibration levels, all the ratings for each floor were averaged and reported as its final rating.

Figure 10: *Subjective evaluation of tested floors*

4 RESULTS AND DISCUSSION

4.1 DYNAMIC PROPERTIES

Modal tests were performed on the floor panels with different supports. The first three natural frequencies as well as the damping ratios were obtained and presented in Table 4, the corresponding mode shapes with rigid supports and beam supports of NLT and CLT are shown in Figure 11 and 12.

Table 4: *Measured dynamic properties of the floor specimens*

Floor	Supports	f_1 (Hz)	f_2 (Hz)	f_3 (Hz)	Damping (%)
DLT	Rigid	14.88	15.88	19.50	3.6
	B1	11.13	16.25	17.64	3.5
	B2	12.05	16.05	17.97	2.8
NLT	Rigid	14.38	14.88	18.13	4.8
	B1	11.13	16.88	18.08	2.7
	B2	12.13	16.62	20.33	2.9
CLT	Rigid	17.25	18.63	21.98	3.1
	B1	10.63	17.00	21.00	3.7
	B2	12.15	19.75	21.00	3.4

https://doi.org/10.52202/069179-0254

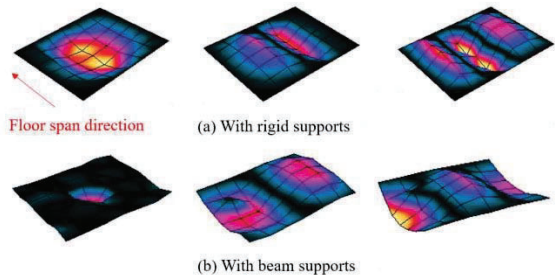

Figure 11: *Corresponding first three mode shapes of NLT floors*

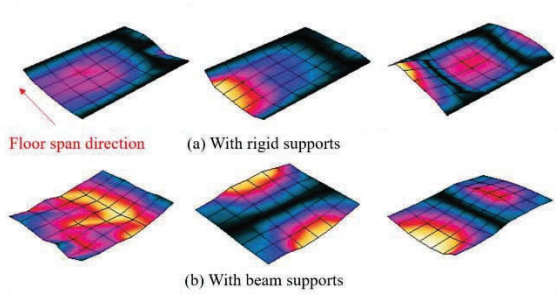

Figure 12: *Corresponding first three mode shapes of CLT floors*

The dynamic properties of the supporting beams were measured prior to their connection with the floor panels. The fundamental natural frequency of beams B1 and B2 was found to be 28.32 Hz and 32.57 Hz respectively, when connected with columns. Table 4 showed that the fundamental natural frequency (f_1) of DLT, NLT, and CLT floor systems decreased over 20% as they were supported from rigid supports to glulam beams, while f_1 increased as the beam stiffness was increased. The damping ratios of each floor system remained relatively unchanged as the support conditions changed, with an average value of 3% to 4%.

Since the composition and material properties of DLT and NLT plates are relatively similar, they had the same mode shapes in the modal test. The corresponding mode shapes of NLT floors are the same under different support conditions, which are the first three bending mode along the longitudinal direction. The CLT also had the first three bending mode shape with rigid supports. Due to the flexibility of supporting beams, the first mode shape of CLT floor is governed by the supporting beams which is the bending mode along the beam direction.

4.2 VIBRATION SERVICEABILITY PERFORMANCE ACCESSMENT

The vibration performance parameters were determined by the experimental tests, subjective evaluations for each floor were also conducted, the results for each floor systems are shown in Table 5-7.

Table 5: *Summary of DLT Floor's vibration performance parameters*

Support	Supporting beams' span (m)	f_1 (Hz)	d_{1kN} (mm)	Rating
Rigid	/	14.88	0.72	3.5
B1	6	11.13	0.74	2.9
	3	13.88	0.67	3.0
	2	14.75	0.66	3.5
B2	6	12.05	0.71	3.0
	3	13.62	0.63	3.5
	2	13.82	0.62	3.5

Table 6: *Summary of NLT Floor's vibration performance parameters*

Support	Supporting beams' span (m)	f_1 (Hz)	d_{1kN} (mm)	Rating
Rigid	/	14.38	0.73	3.5
B1	6	11.13	0.77	2.8
	3	14.00	0.70	3.0
	2	14.25	0.62	3.5
B2	6	12.13	0.80	3.0
	3	13.73	0.71	3.5
	2	14.25	0.73	3.5

Table 7: *Summary of CLT Floor's vibration performance parameters*

Support	Supporting beams' span (m)	f_1 (Hz)	d_{1kN} (mm)	Rating
Rigid	/	17.25	0.15	5.0
B1	6	10.63	0.17	2.9
	3	14.50	0.12	3.5
	2	16.13	0.11	4.0
B2	6	12.15	0.16	4.0
	3	14.92	0.13	4.5
	2	15.67	0.10	5.0

Changing the supports from rigid to supporting beams has a significant influence on the floor's fundamental natural frequencies, while the static deflection increased slightly due to the flexibility of beams. From the occupants' perspective, the NLT and DLT were acceptable for most of them when using the rigid wall supports, but they performed worse with the supporting beam 1 with an average rating lower than 3, which means not acceptable. Even the beam thickness was largely increased from 494 mm to 608 mm, the occupants still gave a marginal rating towards the floor vibration performance. CLT floors with the rigid simple supports can achieve a rating of 5, which is totally acceptable for the evaluators, while the performance changed significantly to not acceptable when connected with B1, and improved slightly with B2.

https://doi.org/10.52202/069179-0254

To address the influence of supporting beams' stiffness to the vibration performance of the whole floor, the multi-supports were installed under the supporting beams to shorten their effective span. The test results showed that the installation of multi-supports under the beams reduced the floor deflection slightly, and increased the fundamental natural frequencies gradually close to the floors with rigid supports, leading to improved floor vibration performance for the occupants.

The results of this study were compared to the performance and design criterion outlined in CSA 086-19, as shown in Figure 13 and 14. When evaluating the results using the performance criterion, a good correlation was observed between the data points and the subjective evaluation results, with a value greater than 15.3 indicating an acceptable level of floor vibration performance. However, the CLT floors in the study had a greater thickness, leading to smaller deflections compared to the DLT and NLT floor systems, but with similar fundamental natural frequencies. This resulted in an $f/d^{0.39}$ value that exceeded the limit, despite subjective evaluations that did not always align with the predictions.

The design criterion was developed using data from three CLT floors with rigid supports, the calculated design parameters (calculated using equation (4) and (13)) and the subjective evaluation results in this study did not correlate well with the curve provided in the design criterion. This suggests that the vibration-controlled span equation may not be suitable for real-world design applications for mass timber floors supported by beams.

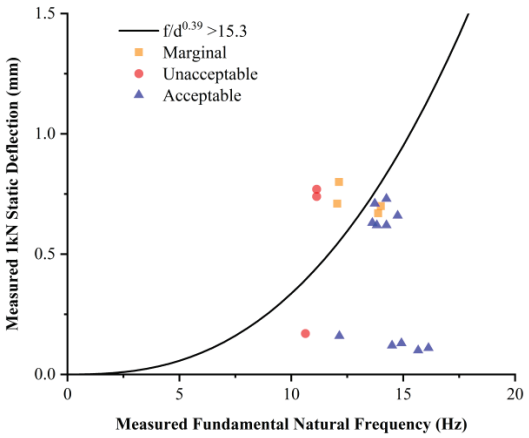

Figure 13: *Comparison between measured result and their subjective rating by performance criterion*

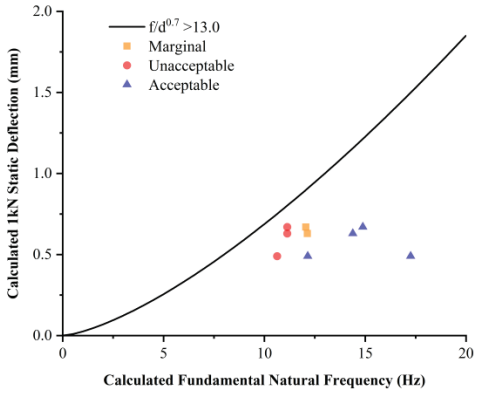

Figure 14: *Comparison between calculated result and their subjective rating by design criterion*

The peak and root-mean-square acceleration under human walking on floors were collected and the maximum value from all the walking paths is shown in Table 8. An example of captured acceleration waveform of CLT floor with B2 under human walking is shown in Figure 15, each peak represents a step on the floor. A transient response of the floor under human walking excitations can be observed, the frequency weighted data is also shown.
The peak acceleration can be greatly affected by the walker, walking path, boundary conditions, and any random disturbance from a single foot pulse excitation, which also showed great differentiation among each group in this study. Despite utilizing the same walking paths and excitation source in every test, the results still showed variation among the groups and all values were found to be higher than the tolerance value as specified by ISO 10137 even after the application of the multiplying factors. The results obtained from the RMS measurement do not align well with the subjective ratings obtained from the evaluators. This highlights the need for further investigation if RMS acceleration levels are to be used as an indicator of floor vibration performance.

Table 8: *Measured maximum frequency-weighted accelerations (m/s^2)*

Floor	Supports	$a_{w,rms}$	$a_{w,peak}$
DLT	Rigid	0.323	5.720
	B1	0.255	2.320
	B2	0.181	0.800
NLT	Rigid	0.375	5.330
	B1	0.077	0.670
	B2	0.111	0.510
CLT	Rigid	0.038	0.259
	B1	0.025	0.119
	B2	0.190	0.639

https://doi.org/10.52202/069179-0254

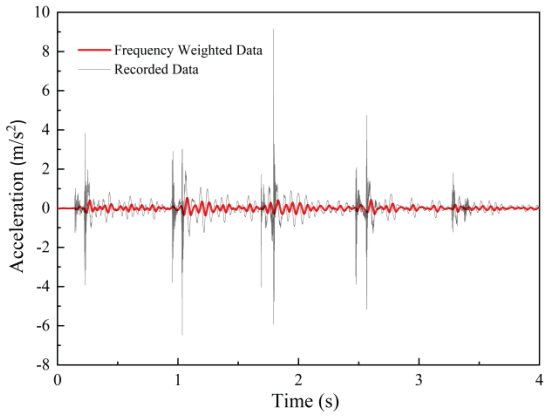

Figure 15: *Time history acceleration data of CLT floor under human walking excitation*

The beam B1 was designed by FPInnovation's beam stiffness equation, however, though the beams' bending stiffness meet the requirement, from the vibration performance tests and the subjective evaluations, all three mass timber floors performed much worse when they were constructed with B1 supporting beams, where the fundamental natural frequencies decreased significantly and the static deflection increased, and the ratings reduced from acceptable to not acceptable. Even with the supporting beam B2, which has twice the stiffness of B1, the floor's vibration performance was still impacted. Since this equation was developed by a few beam test data in the laboratory, further investigation is needed to verify and complete this method.

4.3 VERIFICATION OF SYSTEM FREQUENCY PREDICTION EQUATIONS

Dunkerley's method and Kollar's method were used to calculate the system frequency with the given material properties. The results were compared with the test result, shown in Figure 16:

Table 9: *Calculated f_1 of simple-supported floors and beams*

	Calculated f1(Hz)
DLT	14.87
NLT	15.31
CLT	17.25
B1	32.24
B2	40.42

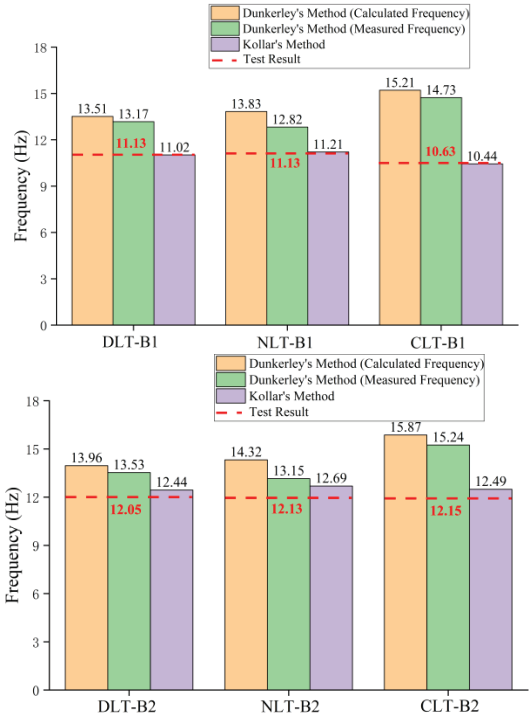

Figure 16: *Comparison of Dunkerley's method and Kollar's method to experimental test result of floor fundamental frequency*

It can be observed from the two figures that the estimated fundamental natural frequencies by Dunkerley's method are overestimate the floor system frequency. Even using the measured value from floors and beams under simple-supported conditions, the estimated value is still higher than the test result with an error of over 10% to 40%. However, the Kollar's method can predict the system' frequency precisely with an average error within 5% in each group.

5 CONCLUSIONS

In this study, modal test, vibration response test and subjective evaluation were conducted on three types of mass timber floors (NLT, DLT and CLT) under various support conditions. The measured dynamic properties of those floor systems were compared among each group and evaluated by the current commonly-used design criteria. The accuracy of prediction equations for beam-supported floor's frequency was also examined. From the study these conclusions can be drawn:

1. The stiffness of the support has a significant effect on the dynamic properties and vibration performance of the mass timber slab floors. When the rigid wall support is replaced with beam supports, the system's fundamental natural frequency is reduced and the subjective feeling becomes much worse. By increasing the thickness of the beam or adding multiple supports under the supporting beams, the frequency gradually returns to a level similar to that of the rigid support and the subjective perception improves.

https://doi.org/10.52202/069179-0254

2. The performance criterion outlined in CSA O86 generally exhibit a high level of correlation with experimental results, demonstrated potential for accurately predicting the vibration performance of beam-supported mass timber floors. However, for the design of such floors, the vibration-controlled span equation and the beam stiffness equation proposed by FPInnovation are both insufficient. The acceleration criterion outlined in ISO 10137 reveals notable discrepancies across all groups, with results consistently surpassing established limits.
3. The Dunkerley's equation overestimate the fundamental frequency of mass timber floor system by up to 40%. While the method proposed by Kollar had an average error within 5%, which demonstrates remarkable potential for practical use.

Future studies aim to extensively explore the feasibility of accurately predicting the dynamic parameters of beam-supported slabs through numerical modeling. The research also seeks to synthesize and develop a practical vibration design method for beam-supported mass timber slabs, based on a comprehensive analysis of current laboratory data and data collected from multiple on-site buildings.

ACKNOWLEDGEMENT

This project was financially supported by NSERC Discovery Grant and BC Forestry Innovation Investment – Wood First program. The authors appreciate the technical support from Wood Innovation Research Laboratory at UNBC and the help of undergraduate research assistant Prakhar Parashar. The authors want to thank all evaluators during the subjective evaluations.

REFERENCES

[1] Niederwestberg, Jan, Jianhui Zhou, and Ying-Hei Chui. "Mechanical properties of innovative, multi-layer composite laminated panels." Buildings 8, no. 10. 2018: 142.

[2] Zhou, Jianhui, and Zijian Zhao. "Apparent impact sound insulation performance of cross laminated timber floors with floating concrete toppings." In INTER-NOISE and NOISE-CON Congress and Conference Proceedings, vol. 263, no. 1, pp. 5203-5215. Institute of Noise Control Engineering, 2021.

[3] Casagrande, Daniele, Ivan Giongo, Federico Pederzolli, Alessandro Franciosi, and Maurizio Piazza. "Analytical, numerical and experimental assessment of vibration performance in timber floors." Engineering Structures 168. 2018: 748-758.

[4] Jarnerö, Kirsi, Anders Brandt, and Anders Olsson. "Vibration properties of a timber floor assessed in laboratory and during construction." Engineering structures 82.2015: 44-54.

[5] CSA (Canadian Standards Association). Engineering design in wood. CSA O86 19. Toronto, ON, Canada: CSA.2019.

[6] European Committee for Normalization (CEN). "Eurocode 5: Design of timber structures–Part 1-1: General–Common rules and rules for buildings." EN 1995–1–1, Brussels, Belgium.2004.

[7] FPInnovations. Advanced Wood-Based Solutions for Mid-Rise and High-Rise Construction: Proposed Vibration-Controlled Design Criterion for Supporting Beams. Natural Resources Canada.2018.

[8] ISO 10137. Bases for design of structures–Serviceability of buildings and walkways against vibrations. International Organization for Standardization, Geneva, Switzerland.2007.

[9] U.S. Mass Timber Floor Vibration Design Guide. Wood Products Council. USA. 2021.

[10] Murray, Thomas M., David E. Allen, Eric E. Ungar, and D. Brad Davis. Vibrations of steel-framed structural systems due to human activity. American Institute of Steel Construction, 2016.

[11] Kollár, László & Kulcsar, Bela. Vibration of floors supported by beams (part 1: Single span floors). Structural Engineer. 91. 34-41. 2013.

[12] Kollár, László & Kulcsar, Bela. Vibration of floors supported by beams (part 2: Multi span floors). Structural Engineer. 91. 43-48. 2013.

[13] Kollár, László P., and Zsuzsa B. Pap. "Modal mass of floors supported by beams." In Structures, vol. 13, pp. 119-130. Elsevier, 2018.

[14] Zhang, Sigong, and Lei Xu. "Vibration serviceability evaluation of lightweight cold-formed steel floor systems." In Structures, vol. 38, pp. 1368-1379. Elsevier, 2022.

[15] Schirén, Whokko, and Trixie Swahn. "Vibrations in residential timber floors: A comparison between the current and the revised Eurocode 5." 2019.

[16] Zhou, J., Chui, Y., Gong, M., & Hu, L. 2017. Elastic properties of full-size mass timber panels: Characterization using modal testing and comparison with model predictions. Composites Part B: Engineering, 112, 203-212. doi: 10.1016/j.compositesb.2016.12.027

[17] National building code of Canada. Ottawa, Ontario: Canadian Commission on Building and Fire Codes.2020.

[18] Chui, Y. H. "Simultaneous evaluation of bending and shear moduli of wood and the influence of knots on these parameters." Wood science and technology 25, no. 2 .1991: 125-134.

[19] ISO (International Organization for Standardization).Mechanical vibration and shock — Evaluation of human exposure to whole-body vibration — Part 2: Vibration in buildings (1 Hz to 80 Hz). ISO 2631-2, Geneva, Switzerland: ISO. 2003.

[20] ISO (International Organization for Standardization). Timber structures— Test methods — Floor vibration performance. ISO 18324, Geneva, Switzerland: ISO. 2016.

[21] ISO (International Organization for Standardization). Timber structures – vibration performance criteria for timber floors. ISO/TR 21136, Geneva, Switzerland: ISO. 2017.

https://doi.org/10.52202/069179-0254

World Conference on Timber Engineering Oslo 2023

DYNAMIC CHARACTERISTICS AND DYNAMIC RESPONSE OF TIMBER FOOTBRIDGES TO DYNAMIC HUMAN ACTIVITIES

Marek Pantak[1], Whokko Schirén[2], Carl Larsson[3], Michael Dorn[4]

ABSTRACT: The dynamic action of footbridge users in different forms of activity (especially during walking and running) may cause an excessive vibration of the footbridge deck and may disturb the comfort of use of the structure. The dynamic susceptibility of the footbridges varies depending on the construction material used to build the footbridge and the typical construction solutions (construction details) resulting from the construction material used. The paper presents the basic dynamic characteristics of timber footbridges of various structural solutions, collected during dynamic field tests of these structures. The obtained results indicate relatively high dynamic resistance of timber footbridges to the dynamic loads generated by users under normal conditions of use. In addition, the results show that in the case of timber footbridges, it is possible to consider changing the requirements of international standards defining the range of natural frequencies sensitive to the dynamic impact of users. In the case of timber footbridges, characterized by a relatively high self-weight (compared to steel footbridges), high stiffness and high damping, it is possible to consider changing the requirements for performing forced vibration analyses only for structures with fundamental vertical vibration frequency $f_v \leq 3.0$ Hz instead of the currently defined $f_v \leq 5.0$ Hz.

KEYWORDS: Timber Footbridges, Vibration, Dynamics, Damping, Walking, Running, Comfort of Use.

1 INTRODUCTION

Footbridges are perceived as lightweight structures. The main features observed in the design of footbridges, i.e., the scale of the structure adapted to the human scale, a relatively small deck width, often a high slenderness of the structure, and the application of new (lightweight and/or high-strength) materials, can lead to a reduction in the stiffness of the structures and an increase in their dynamic susceptibility.

In a situation of dynamic impact of pedestrians on footbridges, in a large number of cases, steel and composite steel and concrete footbridges with a span length $L \geq 25.0$ m exhibit high dynamic susceptibility. For lengths $L \approx 25.0 \div 45.0$ m, the fundamental natural vibration frequency of steel footbridges is often in the range of the steep frequency f_s of a running person $f_s \geq 2.40$ Hz (Figure 1). The vibration acceleration caused by a single running person can significantly exceed the allowable vibration acceleration value for vertical vibrations $a_{max} \approx 0.50 \div 1.0$ m/s^2 (respectively: maximum and minimum comfort level; 1.0 m/s^2 permitted for rarely occurring vibration) [1-4]. For span lengths $L \geq 35.0$ m, these footbridges also become susceptible to dynamic action of walking users.

The high dynamic susceptibility of the footbridge under the influence of people walking or running may contribute to excitation of its vibrations by vandals jumping or doing squats with a frequency equal to the natural vibration frequency of the structure.

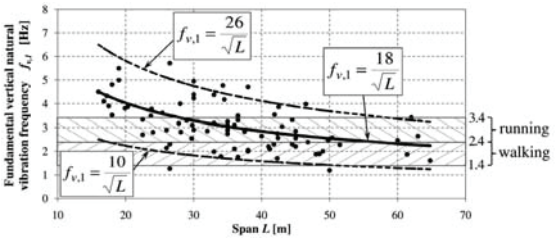

Figure 1: *Fundamental natural vibration frequency $f_{v,1}$ of steel and composite steel and concrete footbridges (own research results).*

As indicated by numerous dynamic field tests of timber footbridges, the dynamic susceptibility of these structures is much lower than steel and composite steel and concrete structures.

The lower dynamic susceptibility of timber footbridges to dynamic impacts of users results from their relatively high stiffness and, thanks to this, high value of their natural vibration frequencies as well as their ability to quickly dissipate energy (high value of the vibration damping coefficient).

It is worth remembering that in the case of resonant vibrations, the vibration amplitude is inversely proportional to the vibration damping coefficient. In other words, a large value of the vibration damping coefficient

[1]Marek Pantak, Cracow University of Technology, Poland, mpantak@pk.edu.pl
[2] Whokko Schirén, Linnaeus University, Sweden, whokko.schiren@lnu.se
[3] Carl Larsson, Linnaeus University, Sweden, carl.larsson@lnu.se
[4] Michael Dorn, Linnaeus University, Sweden, michael.dorn@lnu.se

https://doi.org/10.52202/069179-0255

leads to a decrease in the vibration amplitudes of the structure.
The paper presents the results of numerous dynamic field tests of timber footbridges of various structural solutions. Basic dynamic characteristics of timber footbridges are presented, i.e., basic vibration frequency, damping, and the maximum dynamic response of the structure (maximum vibration acceleration) for various operating conditions.

2 DYNAMIC FIELD TESTS

Dynamic field tests of 25 footbridges were carried out for normal and exceptional operating conditions of the structure. Under normal operating conditions, the vibrations of the tested structure were induced by people walking or running with the step frequency f_s defined as normal for a given type of activity. Normal step frequency for walking was assumed to be f_s = 1.75 Hz [5]. Normal step frequency for running was assumed to be f_s = 2.65 Hz [5].
In exceptional operating conditions, the vibrations of the tested structure were induced by squatting. The frequency of human activity in exceptional operating conditions was assumed to be equal to the natural frequency of the tested structure in order to induce resonant vibrations of the structure.
In the first stage of the research, in order to determine the fundamental vertical natural vibration frequency of the structure, a person positioned in the middle of the footbridge span and in the middle of the footbridge deck made a series of unrestrained (unsynchronized) jumps.
In order to identify the frequency of torsional vibrations, the person jumping was positioned near the edge of the footbridge deck. Identification of the frequency of transverse vibrations was carried out by affecting the structure of the transverse force generated by the lateral displacement of the body by the person inducing the vibrations with the simultaneous impact of the foot on the footbridge deck.
The pre-identified natural frequencies of the structure were then confirmed by subsequent tests involving the excitation of resonant vibrations of the structure through dynamic actions in the form of jumps, running and transverse body swaying. The correct value of the frequency of activity was indicated by an electronic metronome.
The vibrations of the structure (vibration acceleration) were collected using portable data loggers (portable accelerometers) with a sampling frequency of 200 ÷ 1000 Hz.
Based on the collected vibrations of the footbridge deck induced by a person running along the entire length of the footbridge with resonant frequency of steps, the identification of the number of vibration extremes of the footbridge was carried out, and thus the mode shape of the footbridge was identified.

3 CHARACTERISTIC OF TESTED FOOTBRIDGES

Dynamic field tests were carried out on slab, beam, truss, arch, cable-stayed and suspension timber footbridges with a span length of 12.0 ÷ 50.0 m. General views and parameters of the tested footbridges are shown in Figure 2.

a)
Växjö, Sweden
Stress laminated timber
L = 12.0 m
f_v= 7.1 Hz, δ = 37.0%

b)
Växjö, Sweden
Stress laminated timber
L = 16.0 m
f_v= 3.5 Hz, δ = 30.0%

c)
Växjö, Sweden
SLT deck supported by 5 glulam girders
L = 25.0 m
f_v= 4.3 Hz, δ =10.2%

d)
Muszyna, Poland
2 glulam girders
L = 21.6 m
f_v= 5.4 Hz, δ = 13.0%

e)
Muszyna, Poland
2 glulam girders
L = 21.6 m
f_v= 5.6 Hz, δ = 11.0%

f)
Muszyna, Poland
2 glulam girders
L = 32.7 m
f_h= 1.4 Hz, δ = 9.5%
f_v= 2.9 Hz, δ = 7.7%

g)
Karolinka, Czechia
2 glulam girders
L = 37.5 m
f_v= 3.2 Hz, δ = 9.5%

h)
N. Hrozenkov, Czechia
2 glulam girders
L = 24.0 m
f_v= 4.7 Hz, δ = 7.0%

i)
Pardubice, Czechia
2 double glulam girders
L = 43.5 m
f_h= 1.9 Hz, δ = 8.8%
f_v= 4.7 Hz, δ =10.4%

j) 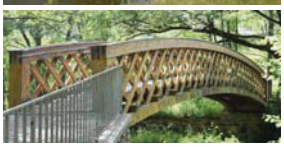
Husinec, Czechia
2 truss girders
L = 19.0 m
f_h= 1.8 Hz, δ =15.5%
f_v= 5.1 Hz, δ = 16.8%

https://doi.org/10.52202/069179-0255

k)
Hovmantorp, Sweden
2 truss girders
L = 19.0 m
f_v= 4.4 Hz, δ =20.6%

l)
Växjö, Sweden
2 truss girders
L = 19.3 m
f_v= 4.2 Hz, δ = 13.8%

m)
Växjö, Sweden
2 truss girders
L = 22.2 m
f_v= 4.2 Hz, δ =13.3%

n)
Växjö, Sweden
2 truss girders, 3 simple supported spans
L = 3 x 26.4 m
f_v= 3.5 Hz, δ = 14.0%

o)
Växjö, Sweden
2 truss girders, 2 simple supported spans
L = 2 x 28.5 m
f_v= 4.5 Hz, δ = 8.4%

p)
Brno, Czechia
2 truss girders
L = 28.5 m
f_v= 4.1 Hz, δ = 7.1%

q)
C. Budějovice. Czechia
2 truss girders
L = 33.0 m
f_v= 6.4 Hz, δ = 24.5%

r)
Muszyna, Poland
2 tied-arch girders
L = 27.5 m
f_v= 3.5 Hz, δ = 7.8%

s) 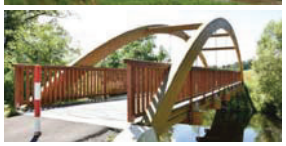
Cheb, Czechia
2 arch girders
L = 28.0 m
f_v= 3.8 Hz, δ =8.2%

t)
Brno, Czechia
2 tied-arch girders
L = 28.0 m
f_v= 5.3 Hz, δ = 8.6%

u)
Stožec, Czechia
2 tied-arch girders
L = 36.0 m
f_v= 3.9 Hz, δ = 10.0%

v)
Val. Meziříč, Czechia
2 tied-arch girders
L = 37.5 m
f_v= 3.8 Hz, δ = 7.0%

w)
Příbor, Czechia
Cable-stayed footbridge
L = 4.0 + 39.0 m
f_v= 3.0 Hz, δ = 3.3%

x)
StaréHutě, Czechia
Cable-stayed footbridge
L = 38.0 m
f_v= 2.5 Hz, δ = 6.8%

y)
Semily, Czechia
Suspension footbridge
L = 50.0 m
f_h= 1.0 Hz, δ = 19.6%
f_v= 3.1 Hz, δ = 2.6%

Figure 2: *General views and parameters of 25 tested footbridges (L – span length, f_v – vertical vibration frequency, f_h – horizontal vibration frequency, δ – mean value of the logarithmic decrement of damping)*

4 TESTS RESULTS

For all tested footbridges, the basic natural frequencies, the maximum vibration accelerations for normal and exceptional conditions of use and the values of the logarithmic decrement of vibration damping were determined.

In Figure 2, the basic natural frequencies and the values of the logarithmic decrement of vibration damping are presented. In most of the tested footbridges, the basic form of vibration was vertical vibration. In the case of four footbridges, the basic form of vibrations was horizontal vibrations transverse to the longitudinal axis of the structure (Figure 2 f, i, j, y).

The value of the logarithmic decrement δ was determined using the free vibration decay method.

a) 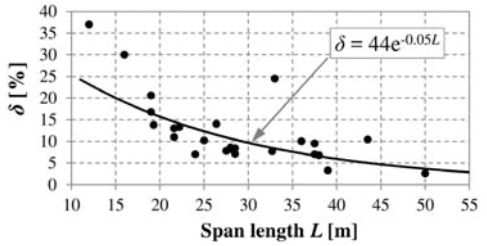

b) 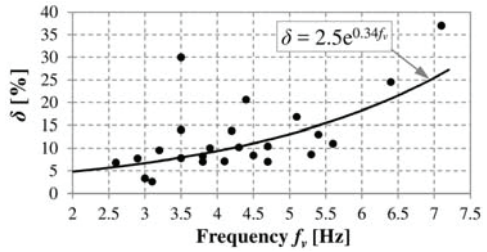

Figure 3: *Variation of the logarithmic decrement of damping δ for vertical vibrations (mean values) with the corresponding regression lines and equations: a) δ as a function of span length L, b) δ as a function of vibration frequency f_v.*

The δ values were determined on the basis of vibration acceleration signals, recorded during excitation of

vibrations by one person running (the person inducing the vibration was leaving the structure, the vibrating structure was loaded only by its self-weight). Parts of the recorded vibration accelerations representing free vibrations of the structure were used to determine δ. Filtered vibration acceleration signals were used in the analyses. The Butterworth low-pass filter of order 4 and a cut-off frequency of 10 Hz was used. The final value of δ was determined as the average of 5 ÷ 8 measurements at each bridge. Figure 3 shows the variability of the logarithmic decrement of damping for vertical vibrations as a function of the span length and vibration frequency for the 25 bridges.

The dynamic responses of all footbridges were tested in normal and exceptional operating conditions.

Figure 4 shows examples of vibrations accelerations of footbridges decks recorded under normal operating conditions, i.e., vibrations induced by people walking with a step frequency f_s = 1.75 Hz and people running with a step frequency of f_s = 2.65 Hz.

Figure 5 shows examples of vibration accelerations of footbridge decks recorded under exceptional operating conditions, i.e., vibrations induced by people doing squats in place with a frequency corresponding to the natural vibration frequency of the structure (resonance).

Figures 4 and 5 show the vibrations of the footbridges presented in Figure 2c and n.

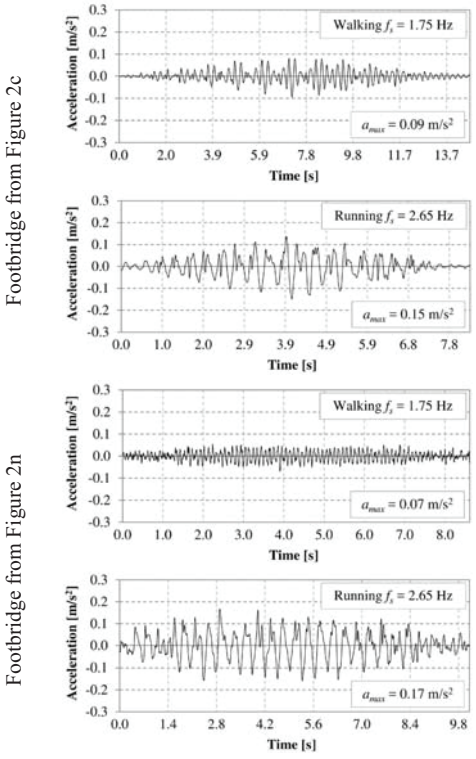

Figure 4: *Examples of vibration acceleration induced by a person walking and running with step frequencies f_s = 1.75 Hz and f_s = 2.65 Hz.*

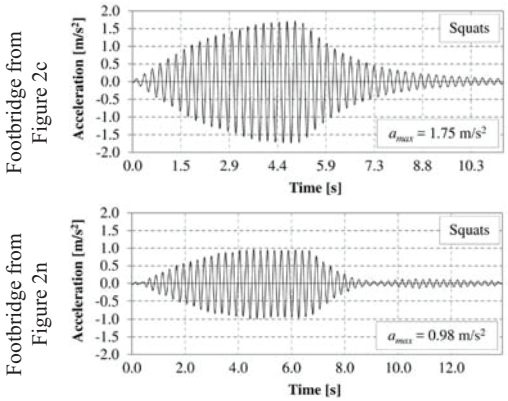

Figure 5: *Examples of vibration accelerations induced by a person doing squats with a frequency corresponding to the natural vibration frequency of the structure.*

Table 1 presents the values of the maximum vibration acceleration obtained on each of the examined footbridges. The given values were read from the filtered vibration acceleration signal.

Figure 6 presents the results from Table 1 in relation to various comfort levels for vertical vibrations [4, 6, 7]:

- $a_{max} \leq 0.5$ m/s^2: maximum comfort –vibrations are imperceptible to users, dotted line in Figure 6;
- $0.5 < a_{max} \leq 1.0$ m/s^2: average (medium) comfort – vibrations are slightly felt by users, dashed line in Figure 6;
- $a_{max} > 1.0$ m/s^2: minimum comfort – vibrations are clearly felt by users, vibrations disturbing walking, acceptable only in case of the occasional occurrence, area above dashed line in Figure 6;
- $a_{max} < 5.0$ m/s^2: structure safety level – maximum acceptable vibration level defined for exceptional events such as acts of vandalism (jumps, squats), vibrations are clearly felt by users, comfort of using the structure is strongly disturbed, free walking is impossible, standing or running is difficult and strongly disturbed, dash-dotted line in Figure 6b.

Table 1: *Dynamic response of the footbridge under normal and exceptional operating condition*

Footbridge from Figure 2	Vibration acceleration [m/s^2]		
	Walking f_s = 1.75 Hz	Running f_s = 2.65 Hz	Squats
a)	0.03	0.07	0.63
b)	0.05	0.11	0.53
c)	0.09	0.15	1.75
d)	0.11	0.27	1.96
e)	0.16	0.39	2.15
f)	0.12	0.53	2.86
g)	0.06	0.14	1.57
h)	0.08	0.41	2.43
i)	0.14	0.34	2.21
j)	0.12	0.28	1.28
k)	0.04	0.15	0.84
l)	0.06	0.21	1.15
m)	0.08	0.23	1.68

https://doi.org/10.52202/069179-0255

n)	0.07	0.19	0.98
o)	0.12	0.32	1.36
p)	0.07	0.47	1.18
q)	0.04	0.12	0.56
r)	0.11	0.41	2.77
s)	0.18	0.55	2.32
t)	0.08	0.43	1.56
u)	0.06	0.23	1.31
v)	0.07	0.53	3.48
w)	0.11	0.48	2.35
x)	0.14	0.87	1.67
y)	0.16	0.51	1.31

a)

b)

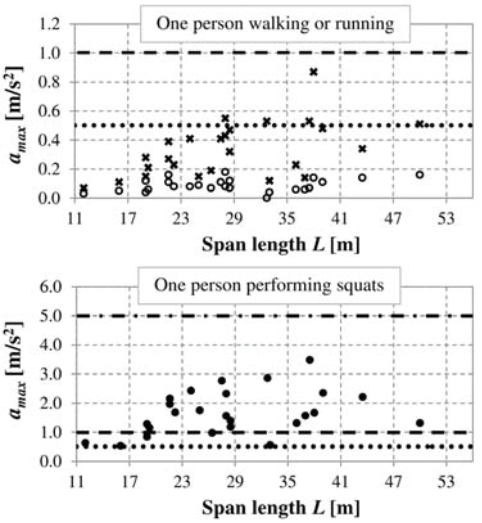

Figure 6: *Vertical vibration accelerations of the tested footbridges in relation to comfort levels for a) vibrations induced during walking (circles) and running (x mark), and b) vibrations induced during squats (comfort levels explained in the text).*

Figure 7 presents vertical vibration accelerations of the tested footbridges for normal operating conditions in relation to the vibration frequency and the level of maximum comfort of using the structures.

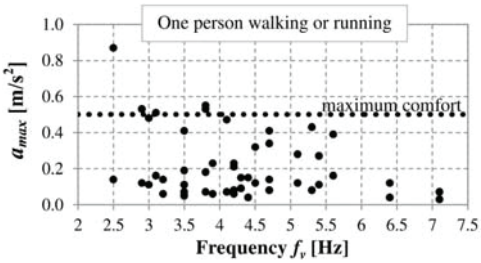

Figure 7: *Vertical vibration accelerations of the tested footbridges for normal operating conditions in relation to the vibration frequency and the level of maximum comfort of using the structures (dotted line).*

5 SUMMARY AND CONCLUSIONS

The tested timber footbridges are characterised by relatively high damping. The logarithmic decrement of damping δ for 70% of the tested footbridges is in the range of 5 ÷ 15%. The obtained results are in accordance with the recommendations of [8] according to which the δ value for wooden bridges is in the range of 6 ÷ 12%.

Regression lines presenting the variability of δ for vertical vibrations, in relation to the footbridge span length as well as vibration frequency (Figure 3), seem to be appropriate to determine the value of logarithmic decrement of damping of timber footbridges. These results can be used in dynamic analyses of timber footbridges.

Two of the tested SLT footbridges showed exceptionally high damping of 30 ÷ 40%. This result is interesting and worth confirming by further research of SLT structures. In the light of the results of field tests, the SLT technology seems to be beneficial from the point of view of the dynamic resistance of footbridges to dynamic impacts of users. The high value of vibration damping ($\delta \approx 30 \div 40\%$) has a positive effect on reducing the vibration amplitudes of the structure. The achieved effect probably results from the presence of many planes of cooperation of elements in the SLT structure that allow for effective energy dissipation. The presented result was obtained for a structure with a short span length. It will be interesting to perform vibration damping analyses in SLT structures with larger spans. However, high self-weight of the SLT structure may lead to a significant reduction in their natural vibration frequency and an increase in their dynamic susceptibility. This subject requires further research and analyses.

The natural frequencies of the presented glulam beam, truss and arch footbridges reached values of $f > 3.0$ Hz and relatively high values of the logarithmic decrement of vibration damping δ = 7% ÷ 20% (about 4 ÷ 10 times higher than δ for welded steel structures $\delta \approx 2.0\%$). This effectively reduces the risk of excitation of their vibrations by users.

In the case of the presented cable-stayed and suspension footbridges, the values of frequency and vibration damping are lower than in other tested objects. Comparison of the results achieved for cable-stayed and suspension footbridges with the results achieved for other tested structures indicates the presence of an increased risk of their dynamic excitation by users. However, the data set is too small to draw clear conclusions about structures of this type. Vibration accelerations induced on the cable-stayed and suspension structures by walking people were within the range of maximum comfort. Vibration accelerations induced on these structures by runners were in the range of average comfort. Also, intentional excitations of vibrations by squats did not cause significant vibrations of the structure. The vibrations induced during squats remained in the range of minimal comfort. In the case of a rare occurrence, they can be considered acceptable. The analysed cable-stayed and suspension structures are either characterised by relatively high frequency and low damping or low frequency and high damping. The high frequency of natural vibrations or the relatively high vibration damping value ensured the appropriate dynamic resistance of these structures.

The obtained results of the dynamic tests indicate relatively high dynamic resistance of timber footbridges to the dynamic loads generated by users under normal

conditions of use. The induced acceleration of vibrations only in rare cases lightly exceed the level of maximum comfort specified for the moving people for vertical vibrations. If the maximum comfort level is exceeded, the structure's vibrations remain in the medium comfort area. This means that under normal conditions of use of the analysed structures, their vibrations are not felt by users.
The amplitudes of vibrations intentionally induced by people doing squats (resonant action) exceed the level of minimum comfort. However, these vibrations do not reach the limit value due to the safety of use of the structure. Compared to the results obtained for steel footbridges (vibration acceleration induced by one squatting person in the range of 3.0 ÷ 8.0 m/s^2), the obtained results prove the relatively high resistance of timber footbridges to intentional excitation of vibrations. The explanation of this situation can be found in two factors: in the high value of the ratio of self-weight of the structure to the value of moving loads (G/Q = self-weigh/pedestrians' weight) and in the relatively high value of structural damping.
In addition, on the basis of the obtained results, in the case of timber footbridges, it seems appropriate to verify the requirements of international standards [1] defining the range of natural frequencies sensitive to the dynamic impact of users. In the case of timber footbridges characterized with relatively high self-weight, stiffness and damping, it seems reasonable that the dynamic analyses should be required for structures with a fundamental vertical vibration frequency $f_v \leq 3.0$ Hz instead of the currently defined $f_v \leq 5.0$ Hz.

ACKNOWLEDGEMENTS

The paper is the result of a PhD seminar on vibration of footbridges held by Marek Pantak in May 2022 at Linnaeus University and his cooperation with the employees of the LNU. The presented research results have been collected by the main author since 2017 during numerous field tests of footbridges with various structural systems.

REFERENCES

[1] EN 1990:2002/A1:2005: Eurocode – Basis of structural design, CEN, 2002 and 2005.
[2] EN 1991-2:2003: Eurocode 1 – Traffic loads on bridges, CEN, 2003.
[3] ISO 10137:2007: Bases for design of structures - Serviceability of buildings and walkways against vibrations, ISO/TC 98/SC 2, 2007.
[4] *SETRA*: Footbridges, Assessment of vibrational behaviour of footbridges under pedestrian loading, *SETRA Technical guide*, Paris, 2006.
[5] Bachmann H.: "Lively" footbridges – a real challenge. In: *Proc. Inter. Conf. "Footbridges 2002"*, Paris, 2002.
[6] Flaga A. Pańtak M.: Vibration comfort criteria for pedestrians on footbridges. In *Proc. Inter. Conf.* "*Footbridges 2008"*, Porto, 2008.
[7] Pańtak M., Marecik K.: Assessment of comfort of use of footbridges. *Technical Sciences*, 21(3): 233-246, 2018.
[8] EN 1991-1-4:2005+A1:2010: Eurocode 1 - Actions on structures - Part 1-4: General actions - Wind actions, CEN, 2010.

https://doi.org/10.52202/069179-0255

World Conference on Timber Engineering Oslo 2023

A comparative study of design standards for assessment of long-span steel-timber composite floors under human-induced vibration

Sardar Malek[1], Najmeh Cheraghi-Shirazi[2], Keith Crews[3], Roger Parra[4], Ariel Creagh[5], Parham Khoshkbari[6]

ABSTRACT: Steel-timber composite (STC) floors are gaining popularity for residential and commercial buildings worldwide. Adding steel joists to wood-based panels is an attractive option for some designers to increase the span of timber floors. However, there is often a serviceability (vibration) concern with timber composite floors. It is well-known from the literature that human comfort due to vibration is subjective, and people's perception of comfort varies. Nevertheless, structural engineers still need to consider vibration in designing composite timber floors according to various standards and guidelines, especially when comparing two alternative designs. This study investigates the vibration behavior of STC floors under footfall force using a numerical model validated by experimental data. Transient finite element (FE) analysis is conducted to simulate human walking on the floor. The study also discusses acceptability of STC floors according to guidelines and building codes (e.g., AISC Design Guide 11, ATC, CLT Handbook, Eurocode 5). Lastly, the effects of various design parameters, such as CLT thickness, damping ratio, and CLT-to-CLT connection, on the vibration behavior of the composite timber floor are assessed.

KEYWORDS: Finite element analysis (FEA), Timber, Steel, Vibration, Standards, Mass timber buildings

1 INTRODUCTION

Over the past 20 years, significant research has been conducted on the vibration behavior of timber and timber-concrete composite (TCC) structures [1–6]. However, limited studies have been done on steel-timber composite (STC) systems [7]. STC flooring systems consist of steel joists and wood-based flooring panels such as cross-laminated timber (CLT) panels and oriented strand boards (OSB). Steel sections provide longer floor spans due to steel's high strength and stiffness. However, human comfort is increasingly considered a vital serviceability requirement for STC floors.

There are different criteria in standards and guidelines to investigate floor vibration based on various parameters, such as frequency, deflection, acceleration and velocity. A finite element (FE) model can accurately determine such parameters. Basaglia et al. [8] employed a numerical model in ANSYS to simulate walking on timber floors. They also used analytical equations in AISC Design Guide 11 [9], CCIP-016 [10], and SCI P354 [11] to find floor responses due to walking. Experimental results showed that the numerical model accurately predicted floor response (RMS acceleration) with an error of less than 3%. Chiniforush et al. [12] and Hassanieh et al. [7] studied the numerical modelling of STC floors under human-induced vibration. Their numerical model was calibrated using 22 variables (i.e., E, G, μ, k) with ABAQUS software [13]. The calibrated model was used for parametric studies to determine influential parameters on the vibration performance of STC floors. Huang et al. [14] generated a numerical model in OPENSEES to simulate running on STC floors. Elastic beam-column elements and springs were used to model CLT panels. All connections were modelled with extremely high stiffness values. Wang et al. [15] used the same numerical model to simulate walking on another steel-timber floor. A review of previous studies suggests more research is needed to create a numerical model for STC floors using characteristic (not calibrated) values of parameters. Moreover, engineers need the ability to model timber composite floors numerically without relying on springs or beam-column members for CLT panels. Further parametric studies are necessary, especially for parameters not studied by researchers, like footfall load functions, damping ratios, CLT panel connections, and loadings.

This study uses numerical modelling to examine the vibration performance of STC floors under footfall forces according to different standards. Similar to Basaglia et al. [8], transient analysis is performed to determine floor velocity and acceleration due to walking. The numerical (FE) model results are compared with estimates from the simplified equation in AISC Design Guide 11 [9] and with limits provided in various standards. Finally, the effect of important design parameters on floor vibration is analyzed.

[1] Sardar Malek, University of Victoria, Canada, smalek@uvic.ca
[2] Najmeh Cheraghi-Shirazi, University of Victoria, Canada, ncheraghishirazi@uvic.ca
[3] Keith Crews, Centre for Future Timber Structures, University of Queensland, Australia
[4] Roger Parra, Degenkolb Engineers, California, USA
[5] Ariel Creagh, Degenkolb Engineers, California, USA
[6] Parham Khoshkbari, Google LLC, California, USA

https://doi.org/10.52202/069179-0256

2 VIBRATION CRITERA

Generally, guidelines and standards use different approaches to assess floor vibration. The behavior of floors under human-induced force may be examined based on simple parameters such as deflection and frequency [16–18]. More complicated parameters, such as Vibration Dose Value (VDV), peak (or RMS) acceleration, or peak velocity, can be used to assess floor vibration according to ISO [19,20], BS 6472-1 [21], CCIP-016 [10], and the AISC Design Guide 11 [9]. Some standards use a combination of two criteria. For example, Eurocode 5 [22] considers deflection and the limit for maximum impulse velocity. All these standards and guidelines may be used for timber composite floors. However, the different results from various references make it challenging for structural engineers to decide whether a floor has adequate serviceability. To showcase the challenge faced by practitioners, the vibration performance of two STC floors is assessed based on design guides such as the AISC Design Guide 11 [9], ATC [23], as well as timber-specific standards like Eurocode 5 [22] and CSA Standard O86-19 [24].

3 NUMERICAL MODELLING

3.1 Geometry

A finite element (FE) model in ETABS software [25] has been developed to understand floor performance. Under static and dynamic loads, the model was employed to inspect floor response, such as the floor mid-span deflection, velocity, or acceleration. The floor geometry and input properties were selected based on the previous work of Wang et al. [15], as shown in Figure 1. The simply supported floor comprised two steel joists (HN 450×200 mm) and five CLT panels (1.2×6×0.105 m) placed on top of the joists. The properties of CLT layers are provided in Table 1. As Wang et al. provided E1 and E2, other parameters have been taken from Hassanieh et al. [7]. A layered shell and beam elements were used in ETABS software [25] to simulate the three layers of CLT panels (with a thickness of 105 mm) and steel beams, respectively.

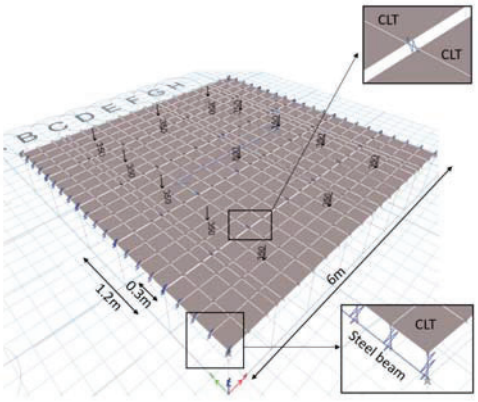

Figure 1: *STC floor considered in Wang et al.* [15] *and selected for this study*

Table 1: *Mechanical properties (MPa) of CLT panels obtained from literature [7, 15]*

Wang et al. [15]		Hassanieh et al. [7]						
E_1	E_2	E_3	G_{12}	G_{13}	G_{23}	υ_{12}	υ_{13}	υ_{23}
10767	979	530	610	860	120	0.59	0.57	0.24

3.2 Connections

As shown in Figure 1, there are six connections between adjacent CLT panels. In the numerical model, the value of 900 N/mm was selected for the shear stiffness of half-lapped connections perpendicular and parallel to CLT panels, according to Ussher et al. [26]. Furthermore, the CLT panels were connected to steel beams at a spacing of 0.3 m. The connection shear stiffness was selected based on the values provided in Hassanieh et al. [7] for Coach Screw 12, Coach Screw 16, and BGP 12 connections. The results varied by less than 3%, and the stiffness of Coach Screw 16 was selected for the results presented in this paper.

3.3 Loading

To define the floor's maximum deflection, a 1 kN static load was applied. For the maximum acceleration of the floor, a walking simulation was conducted according to the experimental study of Wang et al. [15]. In the ETABS software, a 75 kg human walking at 0.789 s/step was considered. Also, concentrated loads (according to the experiment) equal to a constant load of 0.15 kN/m2 were applied on the floor. Figure 2 shows the function employed to model the footfall force according to the experimental data. A transient modal analysis was performed to define the maximum acceleration of the middle point of the floor with a damping ratio of 2% and 3% under the human-induced force.

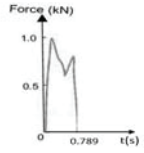

Figure 2: *The single footfall function considered to simulate walking on the floor in Wang et al. [15]*

According to Eurocode 5 [22], an impulsive force of 1 Ns was employed to investigate the velocity of the floor caused by walking. To simulate the impulsive force, the function recommended by Ohlsson [18] and presented in Hassanieh et al. [7] was used, as shown in Figure 3.

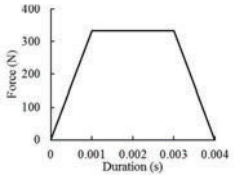

Figure 3: *The force function to simulate the impulsive force of 1 Ns according to Eurocode 5* [22]*, obtained from Hassanieh et al.* [7]

https://doi.org/10.52202/069179-0256

3.4 Convergence study

Mesh convergence was conducted to determine the suitable mesh size. The acceleration and frequency of the floor remained constant with a finer mesh size of 16 cm. Hence, 16 cm mesh size was used in the study.

4 Validation

The current numerical model was validated using the experimental results of Wang et al. [15] in terms of frequency and acceleration. Table 2 shows the comparison of predicted and measured floor frequencies, with a difference less than 3%. Figure 4 compares the measured acceleration and the current model's predictions of the acceleration at the middle of the STC floor, considering two damping assumptions of 2% and 3%. The results demonstrate that the STC floor is a low-frequency floor (frequency below 9 Hz and 10.5 Hz per AISC Design Guide 11 [9] and CCIP-016 [10], respectively) with a resonant response to walking. The figure depicts a good agreement between the results, displaying a similar trend of changing acceleration over time for all cases.

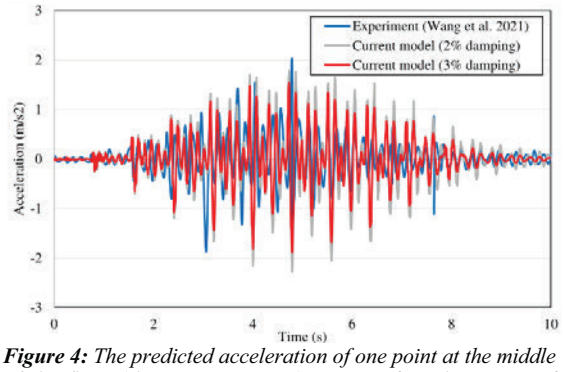

Figure 4: *The predicted acceleration of one point at the middle of the floor (shown in Figure 1) compared to the measured acceleration*

Table 2: *The predicted and measured frequency (Hz) of the STC floor (see Figure 1 for details of the floor)*

Measured frequency (Hz)	Predicted frequency (Hz)	
Wang et al. (2021)	Wang et al. (2021)	Current study (ETABS model)
5.21	5.16	5.15

5 VIBRATION PERFORMANCE

Wang et al. [15] calculated VDV for the floor depicted in Figure 1. The study found that the floor's VDV was about 0.8 m/s$^{1.75}$ with poor vibration performance (likely to receive an adverse comment) as per BS 6472-1 [21] (refer to Table 3). In the current study, the floor vibration is assessed according to other standards and guidelines, such as AISC Design Guide 11 [9], Eurocode 5 [22], ATC [23], and the Canadian CLT Handbook [27].

Table 3: *The VDV values range presented in BS 6472-1* [21]

Place and Time	Low Probability of Adverse Comment (m/s$^{-1.75}$)	Adverse Comment Possible (m/s$^{-1.75}$)	Adverse Comment Probable (m/s$^{-1.75}$)
Residential buildings (16 h daytime)	0.2 to 0.4	0.4 to 0.8	0.8 to 1.6
Residential buildings (8 h night)	0.1 to 0.2	0.2 to 0.4	0.4 to 0.8

5.1 AISC DESIGN GUIDE 11

According to AISC Design Guide 11 [9], the simplified design criterion based on peak acceleration for low-frequency (< 9 Hz) floors is defined by:

$$\frac{a_p}{g} = \frac{P_o e^{-0.35 f_n}}{\beta W} \leq \frac{a_o}{g} \quad (1)$$

where P_o is the constant force (65 lb), W is the effective weight of the floor (lb), β is the damping ratio, a_o is the vibration tolerance acceleration limit according to Figure 5, and a_p is the peak acceleration of the floor.

For high-frequency (>9 Hz) floors, the equivalent sinusoidal peak acceleration (a_{ESPA}) is calculated and compared to the acceleration limit. a_{ESPA} is defined using a calibration factor to adjust the prediction to match the measured data, as:

$$\frac{a_{ESPA}}{g} = \left(\frac{154}{W}\right)\left(\frac{f_{step}^{1.43}}{f_n^{0.3}}\right)\sqrt{\frac{1-e^{-4\pi h\beta}}{h\pi\beta}} \leq \frac{a_o}{g} \quad (2)$$

where W is the effective weight of the floor (lb), f_n is the fundamental natural frequency (Hz), and f_{step} is the step frequency (Hz) while $f_n = hf_{step}$. h is the step frequency harmonic that matches the natural frequency (see Table 4). a_o is the tolerance acceleration limit, according to Figure 5.

Table 4: *Step frequency harmonics matching the natural frequency of high-frequency (>9 Hz) floors adopted from AISC design guide 11* [9]

f_n (Hz)	h
9–11	5
11–13.2	6
13.2–15.4	7

The frequency of the floor presented in Figure 1 was below 9 Hz, making it a low-frequency floor according to AISC design guide 11 [9]. The calculated a_p (from Equation (1)) for the STC floor was around 6.7% g, exceeding the limit shown in Figure 5 for offices and residences.

According to modelling results, the maximum acceleration was 19% g, which exceeds the limit provided in Figure 5 for offices and residences. Therefore, the floor vibration is unacceptable according to AISC Design Guide 11 [9]. It should be noted that there is a considerable discrepancy between the results from Equation (1) and the numerical model for the maximum acceleration of the floor (see the blue and red points in Figure 5). More research is needed to investigate the

accuracy of existing design equations for timber composite floors.

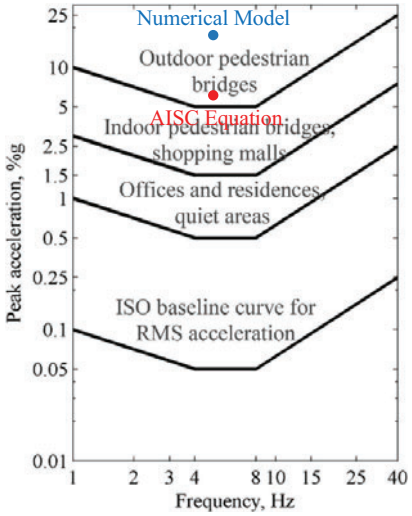

Figure 5: *Vibration performance of the floor showed in Figure 1 according to AISC Design Guide 11* [9]. *Red and blue points highlight the maximum acceleration of the floor estimated from the AISC simplified equation and the numerical model, respectively*

5.2 EUROCODE 5

Eurocode 5 [22] presents simplified equations to evaluate the vibration performance of timber floors with a frequency above 8Hz. This standard limits vertical deflection and unit impulse velocity response (due to an impulsive force of 1Ns) based on the following equations:

$$\frac{w}{F} \leq a \tag{3}$$

$$v \leq b^{(f_1\zeta-1)} \tag{4}$$

where w is the floor maximum instantaneous deflection (mm) under a point load F (kN), v is the unit impulse velocity response (m/(Ns^2)), and ζ is the modal damping ratio. Two constant floor vibration parameters, a and b, and the relation between them are obtained from a graph in Eurocode 5. Their relationship can be formulated [28] as follows:

$$b = 180 - 60a \qquad a \leq 1\ mm \tag{5.a}$$

$$b = 160 - 40a \qquad a > 1\ mm \tag{5.b}$$

According to the UK National Annex (UKNA) to Eurocode 5 [29], the floor deflection, a (mm), due to 1 kN force, should meet the following requirements [28]:

$$a \leq 1.8\ (\text{mm}) \quad ; \quad L \leq 4000\ mm \tag{6.a}$$

$$a \leq 16{,}500/L^{1.1}\ (\text{mm}) \; ; \quad L > 4000\ mm \tag{6.b}$$

where L is the floor span length (mm).
In ETABS software, an impulsive force of 1 Ns was modelled using the function recommended by Ohlsson [18], as presented in Figure 3.

Figure 6 presents the floor velocity diagram due to the impulsive force. Results showed that the maximum velocity of the floor is approximately 5.5 mm/s, which is below the allowable velocity of 18 mm/s. The maximum deflection of the floor under 1kN is 1.5 mm, while the allowable deflection is 1.15 mm. As noted in previous research [30], deflection is a more decisive criterion than velocity. However, the floor does not meet the frequency limit of 8 Hz. Hence, evaluating the floor according to Eurocode 5 may not be appropriate [22].

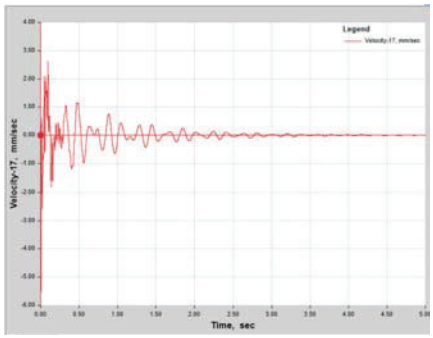

Figure 6: *Floor velocity diagram due to the impulsive force of 1 Ns using the function recommended by Ohlsson [18]*

5.3 ATC DESIGN GUIDE

ATC [23] defines a relation for light-frame floors with a fundamental frequency of more than 8 Hz to limit the maximum floor deflection under a 1 kN load applied at the mid-span. This criterion is defined based on Equation (7):

$$\Delta_p \leq 0.61 + 2.54e^{-0.59(L-1.95)} \leq 2.0\ mm \tag{7}$$

where Δ_p is the maximum floor deflection (mm) and L is the span length (m). Equation (1) is also used by ATC [23] as a resonance criterion. Modelling results showed a maximum floor deflection of 1.5 mm, which is exceeding the allowable deflection of 0.84 mm. Therefore, the vibration performance of the floor is unacceptable according to ATC [23].

5.4 CLT HANDBOOK

The Canadian CLT Handbook [27] presents the following equation to define the deflection of a CLT floor under the uniformly distributed load.

$$\Delta = \frac{5wL^4}{384(EI)_{eff}} + \frac{wL^2}{8(GA)_{eff}} \tag{8}$$

where $(EI)_{eff}$ is the floor's effective bending stiffness (N-mm^2), $(GA)_{eff}$ is the effective shear rigidity (N/mm), L is the span length (mm), and w is the distributed load (N/mm). The FE model predicted the deflection of the floor within 5% of the result of Equation (8). The maximum deflection of the floor under a distributed load of 0.15 kN/m^2 was 2.6 mm, while the result of Equation (8) was around 2.5 mm. According to the Canadian CLT Handbook [27] and the CSA Standard [24], the vibration-

https://doi.org/10.52202/069179-0256

controlled span (m) for a CLT floor (simply supported) can be obtained from the following equation:

$$L \leq 0.11 \frac{\left(\frac{(EI)_{eff}}{10^6}\right)^{0.29}}{m^{0.12}} \quad (9)$$

here m is the mass of CLT for a 1-meter width (kg/m), and $(EI)_{eff}$ is the floor's effective bending stiffness (N-mm^2). The vibration performance of the considered floor (Figure 1) with a span length below 3 m is satisfactory using Equation (9). Hence, the floor with a span length of 6 m as in (Figure 1) is unacceptable according to the CLT Handbook.

In summary, the floor with the configuration presented in Figure 1 showed unsatisfactory vibration performance per AISC Design Guide 11 [9], ATC [23], and Canadian CLT Handbook [27]. The ratio of floor deflection to allowable deflection in Eurocode 5 [22] seems to be very low. Hence, lowering span length or using thicker CLT panels will increase floor frequency and decrease the deflection. Accordingly, the floor can be acceptable according to Eurocode 5, but still unacceptable according to AISC Design Guide 11 [9], ATC [23], and Canadian CLT Handbook [27]. Hence, it might be helpful to look at another example that illustrates the discrepancy between the results of different standards and guidelines, namely the STC floor studied by Hassanieh et al. [7].

Using the data provided by Hassanieh et al. [7], Table 5 presents the vibration performance of the floor according to different standards and guidelines. The maximum acceleration of the floor exceeded the limit provided in Figure 5 (with a ratio of 1.16). Furthermore, the maximum deflection of the floor (0.72 mm) is more than the allowable deflection according to ATC [23] (0.68 mm) and less than that allowed by Eurocode 5 [22] (0.84 mm). In addition, as a result of Equation (9), the floor (with a span length of less than 10 m) was acceptable according to the CLT Handbook [27]. As mentioned before, AISC Design Guide 11 [9] and ATC [23] were more conservative than others.

Table 5: *Acceptability of STC floors according to different standards and guidelines*

	Vibration performance according to			
Floor	AISC DG 11 [9]	Eurocode 5 [22]	ATC [23]	CLT handbook [27]
[15]	×	×	×	×
[7]	×	✓	×	✓
* see Figure 1 for floor details. ** simply supported STC floor consists of two steel beams (310UB32.0) and 160 mm thick (5-layer) CLT panels on top of the joists with a span of 8m.				

6 Parametric studies

Different design parameters can affect the acceleration of the floor due to walking. This study focuses on previously understudied parameters such as force function used to simulate walking. Further research is needed to investigate the effect of various footfall force functions and step frequencies on floor vibrations. Additionally, adding secondary steel beams to CLT panels can change the behavior of the floor from resonant to transient, resulting in a significant reduction of floor acceleration. This study quantifies the impact of CLT thickness, damping ratio, and CLT-to-CLT connections on the acceleration of the floor under footfall force over time, and demonstrates that increasing CLT thickness and damping ratio, as well as improving CLT-to-CLT connections, can effectively decrease floor acceleration.

6.1 CLT thickness

Different thicknesses of CLT panels (105, 160, and 180 mm) with layers at different thicknesses (20, 30, 35, and 40 mm) were used to investigate the effects of the CLT thickness on the acceleration of one point at the middle of the floor. Figure 7 shows that the maximum acceleration of the floor was reduced by almost 65% when the thickness of the CLT panels increased from 105 mm to 180 mm. All models utilized a 3% damping ratio for the floor, with six connections between adjacent CLT panels.

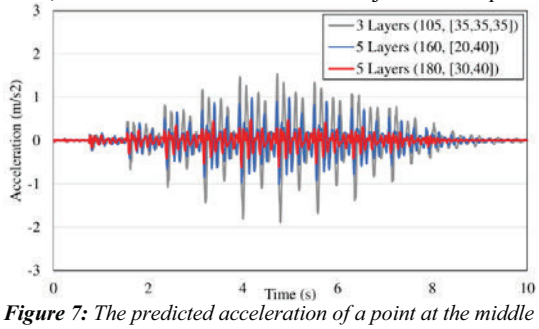

Figure 7: *The predicted acceleration of a point at the middle of the floor (see Figure 1) for different CLT thicknesses*

6.2 Damping ratio

The damping ratio of floors is influenced by multiple factors, such as the floor type and non-structural elements. Figure 8 illustrates that increasing the floor's damping from 1% to 3% reduces the maximum acceleration by approximately 35%. However, further increases in damping have a negligible effect on the floor's maximum acceleration. Despite 3% being suggested as the damping ratio in various sources, further research is needed to assess its impact on the vibration performance of different STC floor types. All models in Figure 8 utilized 105mm thick CLT panels with six connections between them.

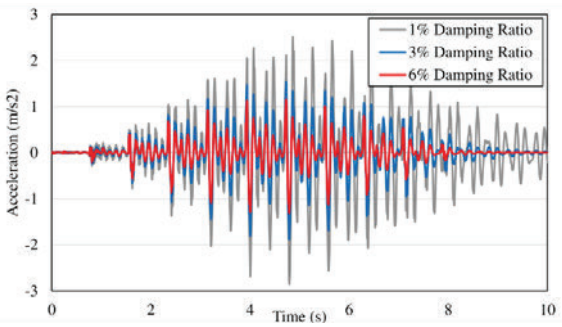

Figure 8: *The predicted acceleration of a point at the middle of the floor (see Figure 1) for different damping ratios*

6.3 CLT-to-CLT connections

Internal spline, single-spline, double-spline, and half-lapped are different methods of connecting adjacent CLT panels. This study used half-lapped connections as described in Section 3.2. To investigate the effect of the number of connections on the acceleration of the floor due to walking, a numerical model was employed using six connections, no connections, and fully bonded connections. The results indicated that increasing the number of connections from 0 to 6 reduced the maximum acceleration by approximately 35% (see Figure 9). However, further increasing connections to fully bond the adjacent CLT panels had little impact on the results. All models utilized a 3% damping ratio for the floor, with 105mm thick CLT panels. The type of CLT-to-CLT connections did not appear to have a significant effect on the floor acceleration under footfall forces. Further research with more detailed information is necessary to validate this finding.

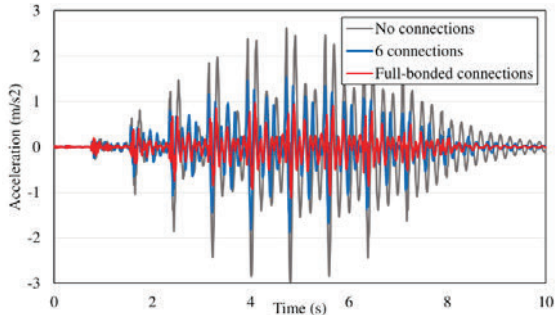

Figure 9: *Predicted acceleration at the mid-floor point (see Figure 1) for different CLT-to-CLT connections*

7 CONCLUSION

The findings of this paper indicate:

- There are various standards and guidelines that may seem applicable to STC floors.
- Different standards may lead to contradictory results based on floor dimensions.
- The AISC Design Guide 11 [9] has an appropriate criterion if the floor's acceleration is predicted accurately.
- The simplified equations in the AISC did not accurately predict the peak acceleration of the floor as compared to the results from the numerical model. Further research is necessary to determine the accuracy of these simplified equations for both high-frequency and low-frequency timber and timber composite floors.
- The deflection limit was found to be a more important criterion than velocity in the Eurocode 5 assessment of floor performance.
- The use of a detailed FE model will enable structural engineers to optimize the design of STC floors according to various standards and assess the impact of different design parameters, such as floor span, damping, and panel-to-beam and panel-to-panel connection systems, on floor vibration.
- Human tests may be necessary to determine the most appropriate standard or guideline for evaluating the vibration performance of composite timber floors.
- Design parameters such as CLT thickness, damping ratio, and CLT-to-CLT connections can affect the maximum acceleration of the floor significantly.

This research suggests the need for further studies to investigate the impact of various single footfall forces with different step frequencies on the acceleration of the composite timber floor. Further research is needed to validate the relevance of the developed numerical model for a real building, taking into account all details including column-to-beam connections, beam-to-beam connections, internal and external walls, and openings.

ACKNOWLEDGEMENT

The authors would like to express their gratitude to Katie Boisseree and Kyle Steuck of Degenkolb Engineers for valuable technical discussions. They also acknowledge the financial supports received from the University of Victoria (through FGS award) and the Charles S. Humphrey Graduate Student award.

References

[1] Ebadi MM, Doudak G, Smith I. Evaluation of floor vibration caused by human walking in a large glulam beam and deck floor. Eng Struct 2019;196:109349. https://doi.org/10.1016/J.ENGSTRUCT.2019.109349.

[2] Casagrande D, Giongo I, Pederzolli F, Franciosi A, Piazza M. Analytical, numerical and experimental assessment of vibration performance in timber floors. Eng Struct 2018;168:748–58. https://doi.org/10.1016/J.ENGSTRUCT.2018.05.020.

[3] Dackermann U, Li J, Rijal R, Crews K. A dynamic-based method for the assessment of connection systems of timber composite structures. Constr Build Mater 2016;102:999–1008. https://doi.org/10.1016/J.CONBUILDMAT.2015.10.009.

[4] Casagrande D, Giongo I, Pederzolli F, Franciosi A, Piazza M. Analytical, numerical and experimental assessment of vibration performance in timber floors. Eng Struct 2018;168:748–58. https://doi.org/10.1016/J.ENGSTRUCT.2018.05.020.

[5] Derikvand M, Jiao H, Kotlarewski N, Lee M, Chan A, Nolan G. Bending performance of nail-laminated timber constructed of fast-grown plantation eucalypt. Eur J Wood Wood Prod 2019;77:421–37. https://doi.org/10.1007/S00107-019-01408-9.

[6] Shahnewaz M, Dickof C, Zhou J, Tannert T.

https://doi.org/10.52202/069179-0256

Vibration and flexural performance of cross-laminated timber – glulam composite floors. Compos Struct 2022;292:115682. https://doi.org/10.1016/J.COMPSTRUCT.2022.115682.
[7] Hassanieh A, Chiniforush AA, Valipour HR, Bradford MA. Vibration behaviour of steel-timber composite floors, part (2): Evaluation of human-induced vibrations. J Constr Steel Res 2019;158:156–70. https://doi.org/10.1016/j.jcsr.2019.03.026.
[8] Basaglia BM, Li J, Shrestha R, Crews K. Response Prediction to Walking-Induced Vibrations of a Long-Span Timber Floor. J Struct Eng 2021;147:4020326.
[9] Murray TM, Allen DE, Ungar EE, Davis DB. Vibrations of steel-framed structural systems due to human activity: AISC Design Guide 11, Second edition. American Institute of Steel Construction; 2016.
[10] Willford MR, Young P. A design guide for footfall induced vibration of structures. CCIP 016 2006.
[11] Wyatt TA. Design guide on the vibration of floors (SCI Publication 076). Ascot, UK 1989.
[12] A. Chiniforush A, Makki Alamdari M, Dackermann U, Valipour HR, Akbarnezhad A. Vibration behaviour of steel-timber composite floors, part (1): Experimental & numerical investigation. J Constr Steel Res 2019;161:244–57. https://doi.org/10.1016/j.jcsr.2019.07.007.
[13] Abaqus. Inc., Dassault Systèmes Simulia Corp., Providence, RI, USA. n.d.
[14] Huang H, Gao Y, Chang WS. Human-induced vibration of cross-laminated timber (CLT) floor under different boundary conditions. Eng Struct 2020;204:110016. https://doi.org/10.1016/j.engstruct.2019.110016.
[15] Wang C, Chang WS, Yan W, Huang H. Predicting the human-induced vibration of cross laminated timber floor under multi-person loadings. Structures 2021;29:65–78. https://doi.org/10.1016/j.istruc.2020.10.074.
[16] Dolan JD, Murray TM, Johnson JR, Runte D, Shue BC. Preventing annoying wood floor vibrations. J Struct Eng 1999;125:19–24.
[17] AS 3623 - Domestic Metal Framing, Standards Association of Australia 1993.
[18] Ohlsson S. Springiness and human-induced floor vibrations: A design guide. Swedish Counc Build Res 1988.
[19] ISO 10137. Bases for design of structures Serviceability of buildings and walkways against vibrations. International Standards Organization; 2007.
[20] ISO 2631-2. Evaluation of human exposure to whole body vibration - Part 2: human exposure to continuous shock-induced vibrations in builidngs (1 to 80 Hz) 1989.
[21] BS 6472-1:2008 - Guide to evaluation of human exposure to vibration in buildings – Part 1: vibration sources other than blasting. Br Stand 2008.
[22] EN 1995-1-1: Eurocode 5: Design of timber structures - Part 1-1: General - Common rules and rules for buildings. 2004.
[23] Guide ATCD. 1, Minimizing Floor Vibration. Appl Technol Counc Redwood, California, USA 1999.
[24] CSA O86-19 Engineering design in wood. Can. Stand. Assoc., Canadian Standards Association; 2019.
[25] ETABS V20.3.0. Computers and Structures, Inc., Berkeley, California, USA.
[26] Ussher E, Arjomandi K, Weckendorf J, Smith I. Predicting effects of design variables on modal responses of CLT floors. Structures 2017;11:40–8. https://doi.org/10.1016/J.ISTRUC.2017.04.006.
[27] Karacabeyli E, Gagnon S. Canadian CLT Handbook 2019 Edition. 2019.
[28] Porteous J, Kermani A. Structural timber design to Eurocode 5. Oxford: Wiley-Blackwell; 2007.
[29] BSI. NA to BS EN 1991-1-1:2002. NA: UK national annex to Eurocode 1: Actions on structures--Part 1-1: General actions--Densities, self-weight, imposed loads for buildings. 2002.
[30] Weckendorf J, Toratti T, Smith I, Tannert T. Vibration serviceability performance of timber floors. Eur J Wood Wood Prod 2016;74:353–67.

World Conference on Timber Engineering Oslo 2023

ASSESSING THE EFFECTS OF BOUNDARY CONDITIONS ON THE VIBRATIONAL COMFORT OF ON-SITE TIMBER-CONCRETE COMPOSITE FLOORS

Francesca Lanata[1], Clement Boudaud[2]

ABSTRACT: The design of timber-concrete composite structures (TCC) is usually governed by the serviceability rather than the strength, particularly for medium to long span floors. In terms of users' comfort, issues can come from vibrations of TCC floors. Indeed, discrepancies are usually observed between the calculations at the design stage and the on-site measurements, due to the gap between design assumptions and in service conditions (boundary conditions, partition walls, floor finishing…). This paper focuses on the comparison between analytical, experimental (on-site and laboratory) and numerical approaches in the assessment of vibration performance of a TCC floor to obtain the frequencies corresponding to different boundary conditions. Results show unexpected differences between analytical models and laboratory experimental measurements for simple boundary conditions. A new equation is being developed to adapt the design of the TCC floors of the full-scale building under study, which presents the specificity of a TCC floor with overhang. A FEM model is developed to assess the validity of the proposed analytical equation.

KEYWORDS: timber-concrete floor, overhang, vibration assessment, multi-approach analysis

1 INTRODUCTION

TCC is known for improving the vibrational comfort for users compared to a timber floor. Nevertheless SLS (vibration) is still a dimensional criterion. The next version of EC5 should include a new design method, modifying both the assessment of the fundamental frequency (proposing an equation for semi-rigid support for example) and the limit criteria ($4 \cdot f_w$, 7 or 8Hz depending on the required performance level) [1]. Yet literature suggests that while analytical models and laboratory experiments fit well together (on dynamical properties), they are too conservative compared to the dynamic properties observed in real buildings [2, 3], and therefore force oversized designs to meet the SLS criteria.

The objective of this work is to assess the influence of boundary conditions (support conditions, overhang, partition walls and floor finishing), by combining modelling (analytical and numerical) and experimentation (laboratory and on-site) on a case study presenting particularities about overhangs. Indeed, TCC floors in the building under study (ESB) have one overhang, and they are supported by a truss structure with an overhang portion itself. The laboratory tests are conducted on two TCC specimens that are as identical as possible as those in the full-scale building (where on-site measurements were conducted in the past [4]). Yet, as dimensions and materials could not be exactly the same, direct comparisons between on-site and laboratory results are not possible. Moreover, due to current limitation in the numerical model (only rigid timber/concrete interface), it cannot be directly compared to laboratory and on-site measurements. For these reasons, and because an evolution of an analytical equation is proposed in this paper, analytical calculations serve as the reference to which numerical, laboratory and on-site are successively compared. In the following, once the case study is described (§2), analytical state of the art and proposed evolution necessary for the case study (overhang combined with 2D behaviour) are detailed in §3. Experimental (§4) and numerical (§5) works are then explained.

2 DESCRIPTION OF STUDIED TCC FLOORS

The case study introduced in this paper is the large-span TCC floor of the ESB building, built in 2011 and presenting some interesting features for the aim of this work. Several experimental campaigns have been performed on the on-site building and parallel laboratory tests have been conducted to better understand the structural response of the floor and propose an analytical and numerical approach to better design such a TCC floor. Two TCC specimens have been built at a smaller scale but as identical as possible as the floors of the full-scale building. The characteristics of both building and specimens are detailed in the following.

[1] Francesca Lanata, Wood and biosourced materials science and technology, LIMBHA, France, Francesca.lanata@esb-campus.fr
[2] Clément Boudaud, Wood and biosourced materials science and technology, LIMBHA, France, Clement.boudaud@esb-campus.fr

https://doi.org/10.52202/069179-0257

2.1 ON-SITE BUILDING

The expansion of the ESB building is constituted by three floors, realized with two parallel trusses in glue-laminated timber (Figure 1). The trusses are around 45m long and 13m height with a one-side overhang of about 9 to 10m. The architectural design of both trusses is the same, but timber cross-sections are different because of the slightly different supported loads.

Figure 2 shows that each truss is simply supported in three points (one is V-shaped): the part between the two vertical columns (Section C) is linked to the existing concrete building, the part with the overhang (Sections A and B) is more flexible because of the lack of a closed ground floor. Some partition walls have a structural function to assure the wind bracing resistance.

Figure 1: *3D representation of the ESB expansion building (overhang on the right)*

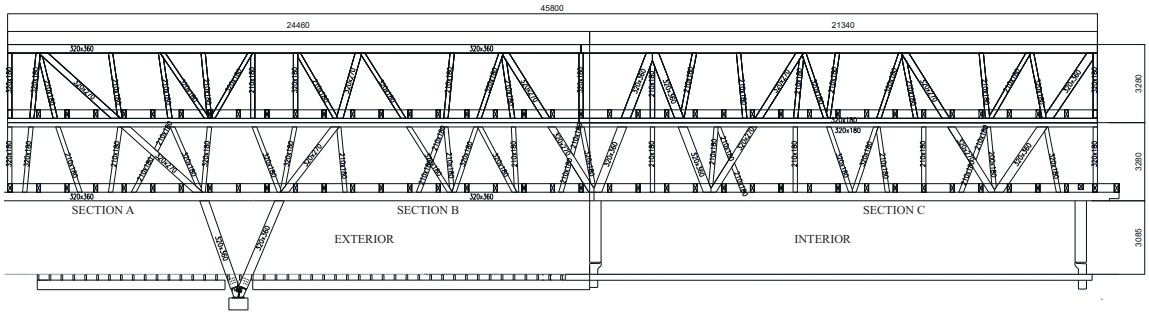

Figure 2: *Geometry of the South truss (overhang on the left side), with the biggest cross-sections and loads*

The South and North trusses are linked together through TCC floors object of the study. The total span of the floor is 9.6m, including a walkway of 2.0m, forming an overhang (Figure 3), also visible in Figure 1.

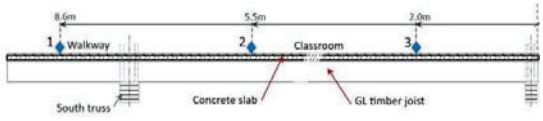

Figure 3: *Geometry of the TCC floor. The two supporting trusses with different cross-sections are visible. 1, 2 and 3 are the sensors positions (§4.2)*

The cross section of the TCC floor is represented in Figure 4 and the main characteristics are detailed in Table 1.

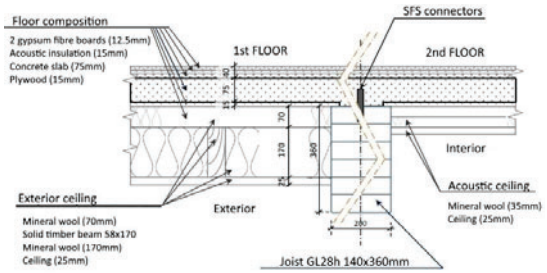

Figure 4: *Cross-section of the TCC floor for the first floor (left) and the second floor (right)*

Table 1: *Geometric and mechanical properties of materials used for the TCC floors (from design papers and Eurocodes)*

Element	Material property	Symbol	Value
GL28h timber joists	Width	b_2	140mm
	Height	h_2	360mm
	Effective width	b_{eff}	1.2m
	Total span	L_{tot}	9.6m
	Overhang span	L_f	2.0m
	Joists spacing	e	1.2m
	Mean density	ρ_{m2}	460kg/m^3
	Young's modulus	E_{m2}	12600N/mm²
Plywood	Thickness	h_3	15mm
	Mean density	ρ_{m3}	580kg/m^3
Concrete slab C20/25	Thickness	h_1	75mm
	Mean density	ρ_{m1}	2200kg/m^3
	Young's modulus	E_{m1}	29962N/mm²
Connector	Diameter	d	7.5mm
	Length	l	165mm
	Mean distance between connectors	s_p	344mm
Non-structural elements	Ceiling and floor finishing	m	514kg

https://doi.org/10.52202/069179-0257

2.2 LABORATORY SPECIMENS

The laboratory tests have been performed on two specimens as similar as possible as the on-site TCC (§2.1). The dimensions of the TCC specimens are represented in Figure 5.

Before assembly, the mass, density, moisture content and longitudinal Young modulus (through vibration method) of each glulam beams have been measured. A 20µm polyethylene protective film between the concrete slab and the timber (beam and plywood) was used to avoid excessive humidification.

Figure 5: *Geometry of the two laboratory TCC specimens*

The mechanical characteristics of the specimens are detailed in Table 2. For the Young's modulus of timber and its density, the mean values from the four timber joists are given.

Table 2: *Geometric and mechanical properties of materials used for the laboratory specimens*

Element	Material properties	Symbol	Value
GL24h timber joists	Width	b_2	80mm
	Height	h_2	220mm
	Effective width	b_{eff}	540mm
	Total span	L_{tot}	6.0m
	Overhang span	L_f	1.0m and 2.0m
	Joists spacing	e	0.6m
	Mean density	ρ_{m2}	473kg/m^3
	Young's modulus	E_{m2}	11224N/mm²
Plywood	Thickness	h_3	21mm
	Mean density	ρ_{m3}	580kg/m^3
Concrete slab C25/30	Thickness	h_1	70mm
	Mean density	ρ_{m1}	2157kg/m^3
	Young's modulus	E_{m1}	31476N/mm²
Connector	Diameter	d	7.5mm
	Length	l	100mm
	Mean distance between connectors	s_p	231mm
Non-structural elements	Floor finishing and partition wall	m	30kg

3 ANALYTICAL APPROACH

3.1 EQUATIONS STATE-OF-THE-ART

The current version of EC5-1-1 [5] suggests to assess the vibrational comfort of a floor following three steps:

1. Calculation of the fundamental frequency f_1 (Hz);
2. Calculation of the maximum deflection w_{1kN} (mm) due to a vertical static point-load F=1kN;
3. Calculation of the velocity v (m/N s²) as a structural response due to a unit impact force

The paper will be only focused on the calculation of the fundamental frequency. The proposed calculation of this parameter is given from Equation (1):

$$f_1 = \frac{\pi}{2L^2}\sqrt{\frac{(EI)_L}{m}} \quad (1)$$

where L is the floor span, in m, $(EI)_L$ is the bending stiffness along the floor span par meter width, in Nm²/m, and m is the floor mass per unit area, in kg/m².

The velocity criterion is used for single span floors having a fundamental frequency exceeding 8Hz, that are approximatively rectangular in plan and are supported by rigid supports [6]. Equation (1) is a simplified version of the flexural behaviour of a rectangular orthotropic plate (LxB) on supported edges, whose equation takes into account the elastic constant D in both directions, along and transverse to the floor span (Equation (2)) [7].

$$f_{m,n} = \frac{\pi}{2L^2\sqrt{\rho}}\sqrt{D_x m^4 + 2D_{xy}m^2n^2\left(\frac{L}{B}\right)^2 + D_y n^4\left(\frac{L}{B}\right)^4} \quad (2)$$

Even if EC5-1-1 does not specify this, Equation (1) can only be used when the transversal bending stiffness $(EI)_B$ is not exceeding 1% of the longitudinal bending stiffness $(EI)_L$. This means that the approximated value of the fundamental frequency from Equation (1) is given for a one-way spanning floor (1D behaviour), having a negligible effect of transversal bending stiffness (low $(EI)_B$ and/or large floor width B). The EC5 National Annex of Finland [8] suggests using the complete equation to better assess the fundamental frequency of a two-way spanning floor (2D behaviour) on supported edges (Equation (3)).

$$f_1 = \frac{\pi}{2L^2}\sqrt{\frac{(EI)_L}{m}}\sqrt{1 + \left[2\left(\frac{L}{B}\right)^2 + \left(\frac{L}{B}\right)^4\right]\frac{(EI)_B}{(EI)_L}} \quad (3)$$

As Equation (1) is based on some strict assumptions and validated on floors having a span not exceeding 4.5m, the calculation of fundamental frequency is usually quite far from the real measured one from experimental results [2, 3]. The provisional version of the future EC5 [1] includes lots of improvements to adapt and generalize Equation (1), as indicated in Equation (4).

https://doi.org/10.52202/069179-0257

$$f_1 = k_{e,1} k_{e,2} \frac{\pi}{2L^2} \sqrt{\frac{(EI)_L}{m}} \quad (4)$$

First of all, the consideration of the two-way spanning (2D) behaviour of a floor to consider the effect of the transverse floor stiffness has been added, through the factor $k_{e,2}$, given in Equation (5).

$$k_{e,2} = \sqrt{1 + \left(\frac{L}{B}\right)^4 \frac{(EI)_B}{(EI)_L}} \quad (5)$$

The equation given for $k_{e,2}$ is a simplification of Equation (3), neglecting the $(L/B)^2$ term. This is similar to the current approach used into the National Annex of Austria [9], to be used when the ratio between transversal and longitudinal bending stiffnesses is higher than 5%. Nevertheless, no specification concerning this ratio is given in the future version of EC5. The presence of a double span floor is also considered in prEN EC5-1-1 [1] through the factor $k_{e,1}$. The Annex K has to be considered if the floor configuration is more complex. Finally, the stiffness of the supports has been introduced to include floors supported by elastic beams. The suggested equation in prEN EC5-1-1 (Equation (6)) is adapted from [10].

$$\frac{1}{{f_1}^2} = \frac{1}{f_{1,rigid}^2} + \frac{1}{f_{1,beam1}^2} + \frac{1}{f_{1,beam2}^2} \quad (6)$$

Considering the boundary conditions, neither the current version of EC5 [5] nor the provisional version of the future EC5 [1], mention the possibility to have other supports than the isostatic ones (pin/roller). In the literature, some coefficients have been proposed to consider the fixed/pinned, the fixed/fixed, the fixed/free (cantilever) conditions [11, 12, 9]. In Equation (1) the coefficient $\pi/2$ is substituted by $\lambda^2/2\pi$, also called C_B. The same approach is suggested into the National Annex of Austria, by multiplying Equation (1) by a coefficient $k_{e,1}$, different from the $k_{e,1}$ of the future EC5.

Table 3: *Comparison between coefficients proposed to adapt Eq. (1) to different ends conditions*

Ends conditions	λ [11]	C_B [12]	$k_{e,1}$ [9]
Pin-roller	π	1.57	1
Fix-pin	3.927	2.45	1.562
Fix-fix	4.730	3.56	2.268
Fix-free	1.875	0.56	0.356

However, the studied boundary conditions do not cover the case of overhangs, as in the case of ESB building. To adapt the fundamental frequency equations to the full-scale ESB floor, an approximated equation proposed by [13] and adapted by [14] from a FEM analysis has been used. Equation (7) is defined for a simply supported beam with one-side overhang of an arbitrary length. The coefficient K_1 is given graphically as a function of the ratio between the span without overhang and the total length of the beam (Figure 6).

$$f_1 = \sqrt{K_1 \frac{(EI)_L}{\rho A L^2}} \quad (7)$$

The calculation of the equivalent bending stiffness $(EI)_{ef}$ for a composite floor is unchanged (EC5 Annex B).

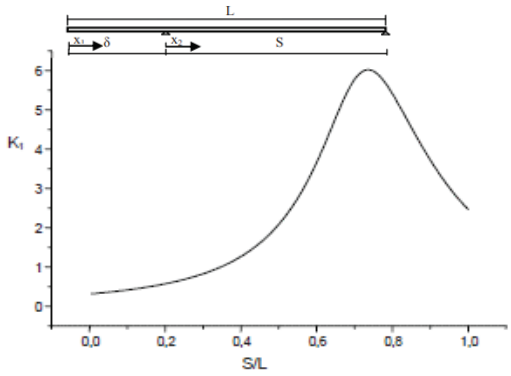

Figure 6: *Representation of the variation of K_1 as a function of the S/L ratio [14]*

3.2 ANALYTICAL RESULTS FOR ON-SITE BUILDING

To assess the fundamental frequency of the ESB floor, Equation (7) has firstly been applied to catch the overhang behaviour. A coefficient K_1 equal to 5.55 has been assessed from Figure 6 entering with the ratio $(L_{tot}-L_f)/L_{tot} = 0.79$. The longitudinal bending stiffness $(EI)_L$ has been computed from the Annex B of EC5. The value for the ESB floor is $2.34 \times 10^7 Nm^2/m$. The floor mass has been computed as the sum of self-weight loads, including supported and suspended layers, but not partition walls. The numerical value of m for the ESB floor is $238 kg/m^2$. L is the total length of the joists L_{tot} (Table 1). A fundamental frequency of 8.09Hz has been determined from Equation (7).

Equation (7) has also been studied with pinned-clamped ends restraints [14]. These conditions approach much more the on-site conditions because of the stiffness of the supporting walls. The fundamental frequency increases to 11.97Hz in this case. However, it seems difficult to justify such a configuration for the ESB floors, as the two supports conditions are very similar.

The current version of EC5 (Equation (1)) has been used for the original design computation of the floor, without considering the overhang and using a span of 9.6m (L_{tot}). A fundamental frequency of 5.39Hz is computed with these assumptions. When the overhang if fully neglected, considering a span of 7.6m, a frequency of 8.62Hz is retrieved (Table 4). It seems therefore very important to consider the presence of the overhang for a better assessment of the fundamental frequency.

https://doi.org/10.52202/069179-0257

In all cases, the 2D behaviour of the floor is not considered yet. The ratio between transversal and longitudinal bending stiffnesses for the ESB floor has been assessed to check if the 2D behaviour is really negligible. The obtained ratio is around 5%, showing the important 2D behaviour of this TCC floor, mainly due to the connected concrete slab. With this assumption, Equation (3) and its simplified version from the National Annex of Austria seems to be more precise in assessing the fundamental frequency of the floor. The results give 5.47Hz and 5.76Hz respectively. A floor width B of 12m (10x1.2m) has been considered for the computation, according to the slab discontinuity joints at each partition wall with wind bracing functions. Indeed, no specification is given in EC5 to clarify the definition of the floor width to consider. Finally, it has to be underlined that the future EC5 approach (Equation (4)) is the same as the Austrian equation, with $k_{e,1} = 1$ for the ESB case. Table 4 summarizes the results when applying the explained equations.

Table 4: *Results of fundamental frequencies f_1 for ESB floor from current available equations*

Configuration	2D floor	f_1 (Hz)	Source
	-	8.09	Eq. (7)
	-	11.97	Eq. (7)
	-	5.39	Eq. (1)
	-	8.62	Eq. (1)
	yes	5.44	Eq. (4)(5)
	yes	5.59	Eq. (3)

The last parameter to consider is the elastic supports. As a matter of fact, the ESB floor is supported by two timber trusses, that cannot be considered as rigid supports. Equation (6) has thus to be used and the natural frequencies of supporting trusses (beams) assessed. For this purpose, a numerical model has been realized for both trusses. The models are slightly different due to the cross-sections and loads, but the truss design is the same. As the stiffness of the truss itself is affected by the overhang, the modal shapes have been observed to retrieve the fundamental frequency for the overhang and the one for the part between the V-shaped column and the first vertical column (Section A and Section B respectively, Figure 2). It has to be underlined that the analysis only focuses on the less stiff part of the trusses (the exterior part, Sections A and B). The results for the fundamental frequencies of the trusses are summarized in Table 5. The difference between South and North trusses can be considered as negligible.

Table 5: *Fundamental frequencies f_1 of the supporting trusses*

Truss	f_1 (Hz) Section A	f_1 (Hz) Section B
South	5.82	8.40
North	5.84	8.42

Equation (6) has been applied to the results of Table 4 (except for the clamped case), giving a frequency value for Section A and another one for Section B (Table 6).

Table 6: *Results for the ESB floor on elastic supports*

Configuration	f_1 (Hz) Section A	f_1 (Hz) Section B
	3.67	4.79
	3.27	4.00
	3.72	4.90
	3.29	4.01
	3.32	4.07

Taking into account the elastic supporting beams have a very strong impact on fundamental frequency, especially for the overhang part, as it will be demonstrated in §4.2.

Existing equations are not fully adapted to such a complex configuration. The authors have decided to combine the different equations to better catch the real structural dynamic response of the ESB floor. The suggested equations from the future version of EC5 (Equations (4), (5) and (6)) have been adapted considering the coefficient K_1 taking into account the overhang configuration. The 2D behaviour is considered too, giving finally Equation (8).

$$f_1 = \sqrt{K_1 \frac{(EI)_L}{m}} \sqrt{1 + \left[2\left(\frac{L}{B}\right)^2 + \left(\frac{L}{B}\right)^4\right] \frac{(EI)_B}{(EI)_L}} \qquad (8)$$

A different width B has been considered for Section A and Section B to take into account the discontinuity joints cutting the concrete slab where the partition walls are (across the V-shaped column). For the overhang (Section A) it has been assumed B = 8.4m (7x1.2m) and for Section B the floor width is assumed as 12m. The results are summarized in Table 7. The results from Equation (3) have also been added for comparison purposes (in italic).

Table 7: *Results of f_1 for the ESB floor with two-way spanning and elastic supports (values from complete equation in italic)*

f_1 (Hz) rigid	f_1 (Hz) Section A	f_1 (Hz) Section B
8.39 (*8.83*) (B = 8.4m)	3.70 (*3.74*)	-
8.16 (*8.61*) (B = 12m)	-	4.81 (*4.89*)

3.3 ANALYTICAL RESULTS FOR LABORATORY SPECIMENS

The analytical equations described in §3 are used to estimate the fundamental frequency of some of the configurations tested in laboratory. The TCC tested are

https://doi.org/10.52202/069179-0257

described in §2.2, calculations are based on the geometry and the material properties given in Table 2. Additional information about these tests (configurations, protocol) can be found in §4.3. Table 8 presents the equation used for each configuration, the value of the coefficient (either λ from Table 3 or K_1) and the fundamental frequency f_1. As the specimens are only 1080mm wide and not supported on their sides, 1D equations (only based on $(EI)_L$) are used. It should be noted that the results for configurations including a fixed support are expected to be quite far from experimental results, as laboratory means were not adapted to generate such a perfect mechanical linkage.

Table 8: *Fundamental frequencies f_1 according to analytical equations for the TCC tested in laboratory*

Configuration	Equation	f_1 (Hz)
	Eq. (1) $\lambda = \pi$	10.04
	Eq. (1) $\lambda = 3.927$	15.68
	Eq. (1) $\lambda = 4.730$	22.75
	Eq. (7) $K_1 = 5.0$	14.29
	Eq. (7) $K_1 = 4.8$	14.00

4 EXPERIMENTAL APPROACH

4.1 EXPERIMENTAL SET-UP

Measurement protocol has been defined according EN 16929 [15], which specifies test methods for the determination of natural frequencies, damping, unit point load deflection and acceleration of floors composed of sawn timber, engineered wood products, mass timber beams or slabs, with or without concrete screeds, as well as for timber-concrete composite floors. Data acquisition was performed with a NI measurement device and a LabVIEW interface, with a packager for accelerometers (8µg resolution, sensitivity 10V/g (± 5%) and a frequency range of 0.15 to 1000Hz (± 5%)). A total of 9 accelerometers was available for the experimental set-up. Double face tape (on-site measurements) and metal plates (laboratory tests) were used to fix the accelerometers to the floor (Figure 7).

Figure 7: *Accelerometers floors fixation for on-site (left) and laboratory (right) measurements*

The approach used for all performed tests was to have an output-only signal, without measuring force. Different excitation sources have been used: weight drop, walking, running, ambient vibrations. The registered signals are accelerations at the measurement points.

Different acquisition frequencies have been tested, assuming finally that 100-150Hz is enough to capture the relevant frequencies of these systems. The acquisition length for each measurement was between 10 to 90 seconds, depending on the time necessary to reach the static equilibrium.

The modal analysis technique used to get the structural response in terms of natural frequencies and modal shapes is the Frequency Domain Decomposition [16].

4.2 EXPERIMENTAL MEASUREMENTS FOR ON-SITE BUILDING

Measurements took place at first and second floor, focusing on the external part only (Sections A and B). Two positions have been tested, one in Section A and the other in Section B. For each position 3 accelerometers have been installed parallel to the joists, at half distance between joists (points 1, 2 and 3 in Figure 3). The building was empty during measurements.

Different types of loading were tested: 5kg weight drop (sandbag) from 80cm height (using a small crane or manually), normal and fast walk, and ambient vibrations. Impact tests and walking are performed in different locations of the floors. For each position, at least 3 measurements have been performed to manage repeatability.

Table 9 presents the results of the fundamental frequency at different measurements points and floor positions. Only the results at 2nd floor are presented, the 1st floor gives globally the same frequencies. The results show that the elastic supports have a strong impact. The fundamental frequency of Section A decreases of about 40% compared to Section B because of the overhang flexibility. Compared to the analytic results based on Equation (8), which is the most complete available (overhang, 2D and elastic supports), experimental measurements show quite different and greater values of f_1. The differences between analytical and on-site frequencies observed by [2, 3] on single span floors are therefore observed again in the case of overhang floors on elastic supports.

Table 9: *Analytical and on-site experimental results for the ESB floor (2nd floor)*

Section	Pos.	Analytic	Exp.	Δ^* (%)
	1		4.33	
A	2	3.70	4.40	18.1
	3		4.37	
	1		7.03	
B	2	4.81	7.00	46.1
	3		7.05	

**Δ is the difference (in %) of the experimental result relatively to the analytical one*

https://doi.org/10.52202/069179-0257

4.3 EXPERIMENTAL MEASUREMENTS ON LABORATORY SPECIMENS

The aim of the laboratory experiments was to measure the dynamic properties for different ends conditions and finishing: roller, pinned or fixed supports, with or without overhang, with or without floor finishing and with partition walls at different locations on the floor. Different preliminary tests have been performed to verify the reliability of the measurements protocol:

- The calibration of the load drop height to assure that accelerometers are not overloaded. A drop height of 50mm has been chosen.
- Checking that the energy given to the floor is enough to induce vibration on the whole specimen: two accelerometers were fixed on the concrete slab and under the joist to ensure having the same response in terms of frequency and damping ratio.
- The fixation of accelerometers to the rough concrete slab: a three-point metal plate has shown to be more adapted to the irregular surface than double face tape, to avoid surface sanding.
- The number of measurements repetitions to have a coefficient of variation lower than 0.5%: 4 measurements prove to get the purpose.
- The definition of measurement positions to catch as much as possible the modal shapes for all boundary conditions: all configurations have been numerically modelled to define the maximum displacement for each modal shape. A set-up of 6 accelerometers has shown to be the better configuration to get all the modal shapes with a good accuracy.
- The specimens were put on small pieces of wood directly on the ground: by applying Equation (6) it has been shown that such supports can be considered as rigid supports.

A sandbag (mass 4636g) was dropped at different locations to excite the TCC. The impact force was applied for all boundary conditions on the top of TCC at mid and third span to excite the first three flexural modes.

Firstly, the geometrical ends conditions presented in Table 8 were tested for both specimens: Pin-roller, Fix-pin, Fix-fix and Pin-roller with one-side overhang of 1 and 2 m (Figure 8, right). The pinned configuration resists both vertical and horizontal movements but not bending moment; as specimens have a huge masse (1076kg), there was no need to put anything to restrain the horizontal and vertical movements. The roller configuration, allowing the horizontal movement, was realized by putting a steel rod under the specimens (Figure 8, left). Finally, the fixed configuration was achieved by putting a concrete block (600 kg) on edges, applying its weight on the slab trough a surface of approximately 30x80cm (Figure 8, middle).

Figure 8: *Tested boundary conditions (roller, fixed, overhang)*

Results are summarized in Table 10 for both specimens. Second and third frequencies and damping ratios have also been assessed through laboratory measurements, but not presented in this paper. The differences between the two specimens are negligible.

Table 10: *Experimental fundamental frequency f_1 (Hz) for laboratory specimens under different ends conditions*

Ends condition	Specimen 1	Specimen 2
	8.33	8.37
	9.05	9.10
	9.24	9.29
1m	11.26	11.28
2m	11.46	11.40

Table 11 presents a comparison between these experimental results and the analytical prediction. The biggest differences appear for fixed configurations, which can be explained by the fact that the experimental means of realizing a fixed support do not increase the rigidity enough. Nevertheless, better fit was expected for isostatic supports, as differences are high (between 9.0 and 13.7%). The assumed values of some material properties might be the cause: compression tests on concrete could not be performed to assess its Young's modulus, data for moisture content of wood were lost for some stages of the whole study, timber properties are the mean values from the two specimens, even if experimentally values from both specimens are very close (Table 10).

Table 11: *Analytical and experimental results for laboratory specimens*

Ends condition	Ana.	Exp.	Δ^*(%)
	9.18	8.35	-9.0
	14.34	9.08	-36.7
	20.80	9.27	-55.4
1m	13.06	11.27	-13.7
2m	12.80	11.43	-10.7

**Δ is the difference (in %) of the experimental result relatively to the analytical one*

Other tests have been realized to consider the effect of finishing and partition walls. The ends conditions are the isostatic ones for all these tests. Only the specimen 2 has been selected for the further measurements. The configuration without any finishing has been tested

https://doi.org/10.52202/069179-0257

again, to have a reference value. Previous tests have been performed during summertime, this second measurement campaign was performed during winter, in a heated building, leading to dryer moisture content of wood. A parquet floor has been put in place over a fibrewood undercoat 5mm thin (Figure 9, left). Frequencies decrease compared to the floor without finishing (Table 12). Finally, the presence of partition walls has been investigated. The wall provides an additional mass of 27kg to the floor. Six configurations have been tested: two positions of the wall perpendicular to the joists (at 2/5 and 3/5 of the span), two positions of the wall parallel to the joists (at 2/5 of the span and at mid-span), one position with two partition walls parallel to the joists and one position with a T-section wall approximatively at mid-span (Figure 9, middle and right).

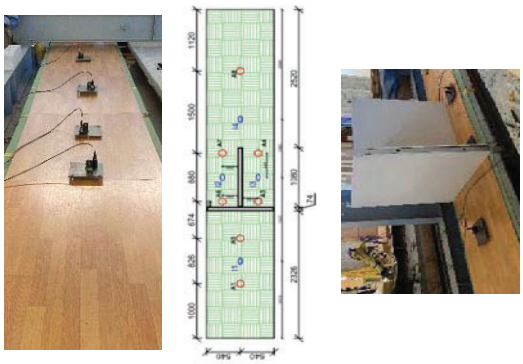

Figure 9: *Tested specimen with finishes (left) and partition walls (T-section)*

Results for this second measurement campaign are summarized in Table 12. Adding a partition wall at mid-span has a negative impact on fundamental frequency, as expected, because in this situation the wall is not connected to other elements of the building, therefore its weight is obviously added to the floor, while the possible increasing floor stiffness is not adequately represented with this setup. The orientation of the wall has a relatively small impact on the structural response. Adding twice the partition wall mass, the frequency decreases, mainly when the wall is positioned near to the mid-span.

Table 12: *Experimental results for laboratory specimen under various finishing (floor and partition walls) conditions*

Finishing condition	f_1 (Hz)
Without finishing	9.63
Parquet floor	9.47
Perpendicular wall at 2/5 span	9.22
Perpendicular wall at 3/5 span	9.25
Parallel wall at 2/5 span	9.33
Parallel wall at mid-span	9.22
Two parallel walls	9.15
T-section wall	9.03

5 NUMERICAL MODEL

The long-term objective of the finite elements model is to predict the rigidity and the modal parameters of TCC for different boundary conditions. In this paper, the focus is to corroborate the analytical equations used in §3, especially the one combining the 2D behaviour with an overhang (Equation (8)). The rest of the numerical study being too extensive and not totally finalized yet, it will be the focus of a future publication.

5.1 COMPARISON TO AVAILABLE ANALYTICAL EQUATIONS

The case study for analytical and numerical comparisons is the geometry and materials described in §2.2. The 6m long floor (L_{tot}) includes two joists and one concrete slab. For the sake of comparing the different analytical equations to FEM results, the aim is not the determination of the equivalent stiffness of the composite section $(EI)_{ef}$, but the effect of boundary conditions on the fundamental frequency. Therefore, the model introduced in this paper uses a perfectly rigid interface between timber and concrete.

Concrete is modelled as an isotropic material and timber as an orthotropic one. The values for modules of rigidity and densities are given in Table 2, except for the timber shear modulus. Indeed, the low G values for timber induce deflections that are significant compared to bending deflections. As this shear deflection is not modelled analytically, it was artificially removed from the model by implementing values ten times greater than normal (G = 6GPa).

The different modelled boundary conditions are: single span floor on isostatic supports, with an embedded support on one and on both ends, a one-side overhang floor on isostatic supports with 1 and 2m overhang, and finally a one-side overhang floor embedded at one end with a 1 and 2m overhang (Table 13). Supports are modelled by defining a surface of 75mm x b_2 (joists width) beneath the joists, where either the 3 translations or just the vertical one are fixed. For embedded supports, the surfaces of the section on the end are fixed.

The meshing is generated using Hex20 50mm length side volumetric meshes. A modal analysis is performed on the aforementioned models, modal shapes are observed (*e.g.* Figure 10) and the fundamental frequencies are extracted (Table 13). These models and calculations are achieved using the software Ansys Mechanical 2023 Release 1.

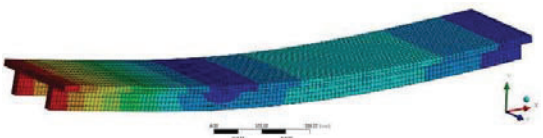

Figure 10: *Modal shape (f_1 = 15.81 Hz) for an isostatic floor with 2m overhang*

Table 13 includes also the analytical fundamental frequencies corresponding to each numerical model.

https://doi.org/10.52202/069179-0257

The difference (Δ) is calculated as a percentage of the analytical value. It can be observed a relatively good accordance between analytical and numerical values with a difference up to 7.3%.

Table 13: *Analytical and numerical comparison of the fundamental frequency (Hz) for different boundary conditions*

Configuration	Analytical	Numerical	Δ^* (%)
	11.84	11.65	-1.6
	18.50	17.97	-2.9
	26.84	25.51	-5.0
1m	16.42	16.08	-2.1
2m	16.59	15.82	-4.6
1m	25.73	24.71	-4.0
2m	19.53	18.11	-7.3

**Δ is the difference (in %) of the numerical result relatively to the analytical one.*

5.2 COMPARISON TO PROPOSED ANALYTICAL EQUATION

As previously showed (§5.1), the numerical model predicts quite well the analytical results of available equations (Equations (1) and (7)). The numerical model can now be used to assess the validity of the proposed Equation (8), the one combining the K_1 factor for overhang configurations and $(EI)_B$ on $(EI)_L$ ratio to include the 2D behaviour. The modelling approach is similar for materials, meshing and boundary conditions. In the longitudinal direction, three configurations are used: single span floor on isostatic supports, 1 and 2m overhang on isostatic supports. In the transversal direction, widths of 1.2, 2.4, 4.8 and 9.6m (Figure 11) are modelled, and a blocked vertical displacement is imposed to the ends of the concrete slabs, therefore modelling the 2D effect on the floor.

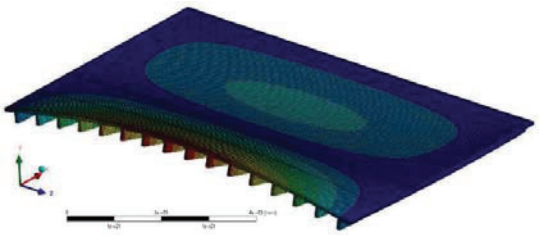

Figure 11: *Modal shape (f_1 = 16.43 Hz) for an isostatic floor with 2m overhang (width B = 9.6m) supported on its longitudinal sides*

Table 14 shows that the numerical model predicts accurately the results of Equation (3) for a single span floor on isostatic supports (Δ_{max} is 5.7%). It should be noted that analytical calculations using the proposed equations of the future EC5 (Equations (4) and (5)), without the $(L/B)^2$ term, provide less satisfactory results, with Δ values between 8 and 19.5%. The equation proposed in this paper (Equation (8)) fits relatively well (Δ_{max} = 4.2%) for lower values of the ratio L/B (B equal to 4.8 and 9.6m), but is much less precise for bigger values of L/B (Δ_{max} = 23.9%) for 1.2 and 2.4m. Additional calculations should be performed to assess more precisely the L/B ratio over which the analytical equation fits. As bigger values of L/B are not very representative of real floors, it is hoped that Equation (8) could be validated for realistic L/B ratios.

Table 14: *Analytical and numerical comparison of the fundamental frequency (Hz) for different widths of floor supported on their longitudinal sides (2D effect)*

Model		1.2m	2.4m	4.8m	9.6m
	Ana	86.80	28.05	14.78	12.10
	Num	86.99	26.46	14.80	12.57
	Δ^* %	0.2	-5.7	0.1	3.9
	Ana	119.20	36.47	19.41	16.73
1m	Num	90.68	30.65	19.55	17.09
	Δ^* %	-23.9	-16.0	0.7	2.2
	Ana	116.79	35.74	19.02	16.40
2m	Num	97.51	35.27	19.82	16.44
	Δ^* %	-16.5	-1.3	4.2	0.2

**Δ is the difference (in %) of the numerical result relatively to the analytical one.*

6 CONCLUSIONS

The first main conclusion of the work presented in this paper is that analytical calculation of the fundamental frequency of a floor is possible via several equations, yet none was strictly adapted to the specific case of TCC floors with overhang. Equations exist to take into account its longitudinal and transversal stiffness and the elasticity of its supports, other ones to take into account an overhang. In this study these equations have been combined to compare the analytical results to on-site measurements. It is observed that same conclusions as in [2, 3] (made for single span floors) can be drown also in the presented case study with overhang. Nevertheless, the validity of the proposed equation is still to be fully justified, a FEM model tends to show that for realistic L/B ratios (when B is greater than 1 or 2m) the proposed equations fits well.

The analytical approach has been used as a reference to compare experimental and numerical results, because experimental on-site and laboratory measurements cannot be directly compared (scaled specimens).

The important differences between analytical and experimental laboratory results are quite surprising, especially for simple boundary conditions. More detailed investigations will be necessary, nevertheless some variations can be already explained by the possibly different moisture content of the specimens during the experimental campaigns. Materials properties (timber and concrete) are also assumed as mean values from both specimens, the analytical approach should add a sensitivity analysis based on varying materials properties. Expected analytical results have to show a

https://doi.org/10.52202/069179-0257

confidence interval to catch the variability from experimental results.

The experimental on-site analyses present a higher stiffness of the ESB floor, even considering the overhang and the elastic supports. The analytical calculations are more conservative because they do not consider the stiffness contribution of secondary elements and partition walls. This means that current equations, including the ones proposed into the future EC5, tend to underassess the fundamental frequency of TCC floors.

The numerical approach has to be fully validated for a rigid connection between timber and concrete. Nevertheless, it allows some interesting comparisons with analytical equations, showing that the two-way spanning behavior cannot be neglected into design.

Further steps of the work should allow the development of a more reliable numerical model, taking into account the real stiffness of the interface. A comparison between on-site and laboratory experiments will finally be possible through the numerical model.

ACKNOWLEDGEMENT

Authors acknowledge the commitment of the following students having worked on the project: Tom Escribano, Alaa Al Fay, Engin Aydeniz and Rita Medlej.

REFERENCES

[1] prEN 1995-1-1:20XX. Eurocode 5: Design of timber structures. CEN-CENELEC/TC250, 2021.

[2] Casagrande D., Giongo I., Pederzolli F., Franciosi A., Piazza M. Analytical, numerical and experimental assessment of vibration performance in timber floors. *Eng. Struct.*, 168:748-758, 2018.

[3] Zimmer S.E., Augustin M. Vibrational behaviour of cross laminated timber floors in residential buildings. In: *WCTE*, 2016.

[4] F. Lanata. Le monitoring de l'extension de l'ESB à Nantes, retour d'expérience. In: *7ème Forum International Bois Construction*, 2017.

[5] EN 1995-1-1:2004. Eurocode 5: Design of timber structures - Part 1-1: General - Common rules and rules for buildings. CEN, 2014.

[6] S. Ohlsson, Floor vibration and human disconfort, Doctoral thesis, UK: Chalmers University of Technology, Division of steel and timber structure, 1982.

[7] A.W. Leissa. Vibration of plates. Pages 250-262. NASA SP-160, 1969.

[8] SFS-EN 1995-1-1. Annex 16 – National Annex to standard SFS EN 1995-1-1, SFS, Finland.

[9] ÖNORM B 1995-1-1. 2013-12, Nationale Festlegungen, nationale Erläuterungen und nationale Ergänzungen zur ÖNORM EN 1995-1-1, Austrian Standard Institute, Austria.

[10] Dolan J., Murray T., Johnson J., Runte D., Shue B. Preventing annoying wood floor vibrations, *ASCE J. Struct. Eng.*, 125(1):19-24, 1999.

[11] I. Ward. Modal Maths Formulas For Structural Dynamics. Issue 2. 2014.

[12] T.A. Wyatt. Design Guide on the Vibration of Floors (SCI Publication 076). Ascot, UK: SCI, 1989.

[13] J. F. Murphy. Transverse Vibration of a Simply Supported Beam with symmetric Overhang of Arbitrary Length. *J. Test. Eval.*, 25(5):522-524, 1997.

[14] Chalah-Rezgui L., Chalah F., Falek K., Bali A., Nechnech A. Transverse Vibration Analysis of Uniform Beams under Various Ends Restraints. In: *APCBEE Procedia*, 9:328-333, 2014.

[15] EN 16929:2019. Test methods - Timber floors - Determination of vibration properties, CEN, 2019.

[16] Brincker R., Zhang L., Andersen P. Modal identification of output-only systems using frequency domain decomposition. *Smart Mater. Struct.*, 10(3):441, 2001.

World Conference on Timber Engineering Oslo 2023

LOCAL DAMAGE ASSESSMENT STRATEGY OF A TWO-STORY CLT WALL THROUGH VIBRATION-BASED NON-DESTRUCTIVE TECHNIQUES

Alexander Opazo-Vega[1], Franco Benedetti[2], Alan Jara-Cisterna[3], Peter Dechent[4]

ABSTRACT: This paper presents a methodology to evaluate the damage in CLT walls by applying non-destructive vibration-based methods. The main contribution is that the methodology allows locating the damage and estimating the severity of damage in the different wall joints, going beyond the typical global damage detections. One of the relevant aspects was the novel combination of Operational Modal Analysis, Finite Element Model Updating, and Regional Sensitivity Analysis. The methodology was successfully applied to a 2-story CLT module built in the laboratory and instrumented with accelerometers. The wall was evaluated in 11 different damage scenarios induced by incremental pseudo-static lateral loads. The results obtained correlated reasonably well with the visually observed damage, so it is estimated that this methodology could be extended to more complex CLT wall configurations.

KEYWORDS: Massive timber, CLT joint damage, Operational Modal Analysis, Model Updating, Sensitivity Analysis.

1 INTRODUCTION

Previous research has shown that earthquake-induced damage tends to be concentrated in the joints of CLT walls [1]. Therefore, it is desirable to assess the condition of these joints after seismic events. However, such an assessment cannot always be made visually because the joints are usually hidden behind non-structural elements.

To face the difficulties mentioned above, some researchers have preferred to instrument this type of buildings with sensors that measure the structural dynamic response induced by ambient or forced vibrations [2-5]. In this way, any relevant change in the measured dynamic properties can be an indicator of damage in its joints and thus justify a complete inspection. The dynamic properties most used as an indicator of damage in CLT buildings have been the natural vibration frequencies. For example, previous investigations have shown that the lateral frequencies can decrease between 15% and 36% depending on the level of lateral solicitation [6-10]. However, these investigations have only focused on detecting global damage without providing information about the localization of the damage in the joints or the associated level of local damage severity.

This work aims to propose a methodology to detect, locate, and evaluate the severity of damage in CLT wall joints. The methodology mentioned above combines Operational Modal Analysis (OMA), Finite Element Model Updating (FEMUP), and Regional Sensitivity Analysis (RSA), applied to a two-story CLT wall of cross-section H. The results obtained are expected to contribute to structural health monitoring of two-story CLT dwellings in developing countries.

2 MATERIAL AND METHODS

2.1 DESCRIPTION OF THE CLT WALL

One 2.6-m-long, 1.2-m-wide, and 4.2-m-high CLT wall was built from the assembly of eight wall panels (2.0-m-high, 1.2-m-wide) and two slab panels (2.6-m-long, 1.2-m-wide) (Figure 1). All CLT panels had a thickness of 100 mm consisting of three layers of C16 Radiata Pine timber bonded with bi-component polyurethane.

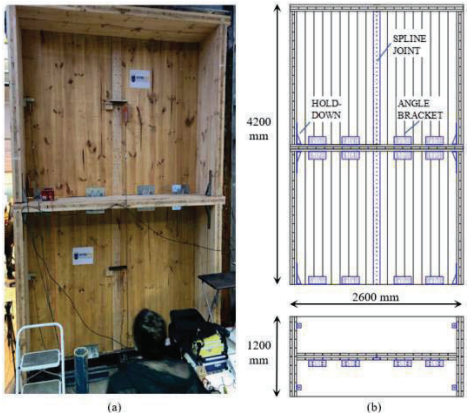

Figure 1: *(a)Laboratory assembly, (b)Dimensions and joints.*

[1] Alexander Opazo-Vega, University of Bío-Bío, Chile, aopazove@ubiobio.cl
Centro Nacional de Excelencia para la Industria de la Madera (CENAMAD), Pontificia Universidad Católica de Chile.
[2] Franco Benedetti, University of Bío-Bío, Chile, fbenedet@ubiobio.cl
Centro Nacional de Excelencia para la Industria de la Madera (CENAMAD), Pontificia Universidad Católica de Chile.
[3] Alan Jara-Cisterna, University of Bío-Bío, Chile, afjara@ubiobio.cl
[4] Peter Dechent, University of Concepción, Chile, pdechen@udec.cl

https://doi.org/10.52202/069179-0258

The CLT panels were joined together through metal hardware, screws, and nails. To prevent the panels from uplifting, metal hardware of the hold-down type (model HTT4) was used. On the other hand, metal hardware of the angle brackets type (model ABR255) was used to avoid the relative horizontal sliding of the panels. Furthermore, the hold-down and angle brackets used ring-shank nails (CNA 4x60mm) and bolts (diameter 13mm) to connect to the different panels. Finally, to avoid relative vertical slippage between panels, spline-type joints were used, with pieces of wood screwed to the panels (2 DSVT3R screws spaced every 100mm). All the connector models mentioned above are shown in Figure 2, while their quantity and distribution are shown in Table 1.

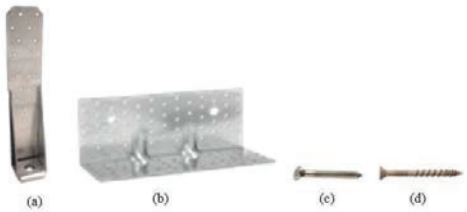

Figure 2:*(a) HTT4 hold-down, (b) ABR255 angle bracket, (c) CNA 4.0x60 nail (HTT4, ABR255), (d) DSVT3R screw (spline joints)*

Table 1: *Quantity and distribution of connectors*

Item	Story 1	Story 2
Number of hold-downs (number of nails)	8(18)	4(9)
Number of angle brackets (number of nails)	8(40)	4(35)
Number of screws in vertical spline joints	2@100mm	2@100mm

2.2 METHODOLOGY FOR ESTIMATING DAMAGE LOCATION AND SEVERITY

The proposed methodology has four stages: 1) induction of initial global damage, 2) measurement of dynamic properties, 3) numerical model simulations, and 4) regional sensitivity analysis.

2.2.1 Induction of initial global damage

In the first stage, initial damage is induced in the structure by applying a pseudo-static lateral load on the second story. The load is applied in the longitudinal direction X, parallel to the web panels, as shown in Figure 3. After maintaining the load for a few minutes, the wall is completely unloaded. This first stage was carried out 11 times with different levels of initial loads to generate different levels of damage to the walls. The first time this stage was performed, a minimal lateral load was applied, close to 0 kN, to adjust the measurement systems. On the other hand, in the following ten times, the lateral loads were increased every 10 kN until reaching 100 kN.

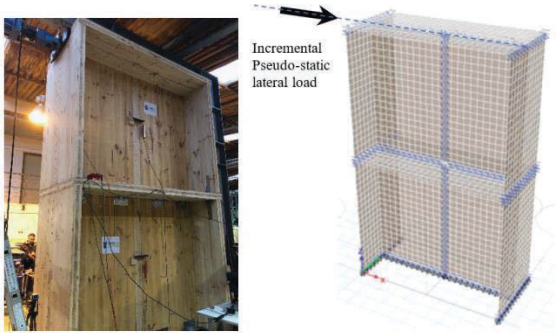

Figure 3: *Incremental pseudo-static test.*

2.2.2 Measurement of dynamic properties

Then, in the second stage, the dynamic properties of the wall (frequencies and modal shapes) are measured using OMA techniques (EFDD and SSI methods) [11]. The wall is excited through a series of low-energy impacts in the X direction. The impacts are applied at the intersection between the left flange panel and the web wall panel but at different heights. On the other hand, the lateral dynamic response is recorded in the right flange panel through six uniaxial accelerometers oriented in the X direction. With this information, it is possible to identify the first two frequencies and modal shapes in the X direction of the wall. It is important to note that this stage is also performed 11 times immediately following each load-unload level applied in the first stage. The experimental setup mentioned above is shown in Figure 4.

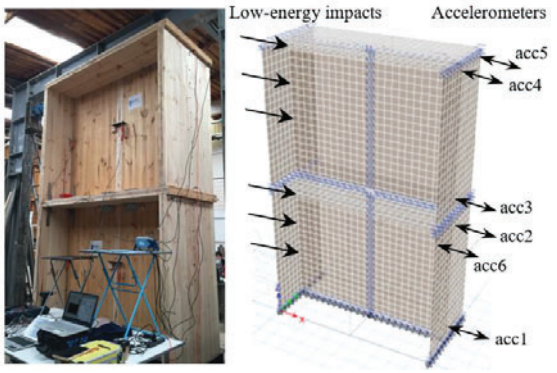

Figure 4: *Dynamic impact testing.*

2.2.3 Numerical model simulations

Next, in the third stage, a 3D finite element model of the wall is generated in the ETABS software to calculate its dynamic properties numerically. The CLT panels were modeled with four-node linear-elastic orthotropic shell elements. Their elastic properties were obtained from previous investigations [12]. On the other hand, the most relevant connections were modeled through link-type elements with uniaxial multilinear-elastic properties, as

https://doi.org/10.52202/069179-0258

shown in Figure 5. In the numerical model, it was assumed that the hold-down connectors only restrict displacements in the vertical direction to avoid the uplift of the wall panels (HD_1 to HD_4). On the other hand, for the angle-bracket connectors, it was assumed that they could restrain both vertical (AB_{t1} to AB_{t8}) and horizontal (AB_{s1} to AB_{s8}) displacements, but in an uncoupled manner. Finally, for the spline connectors, it was assumed that they could only restrain relative vertical displacements between the central wall panels. Therefore, the model considered 22 link-type elements to incorporate the relevant degrees of freedom of the connectors.

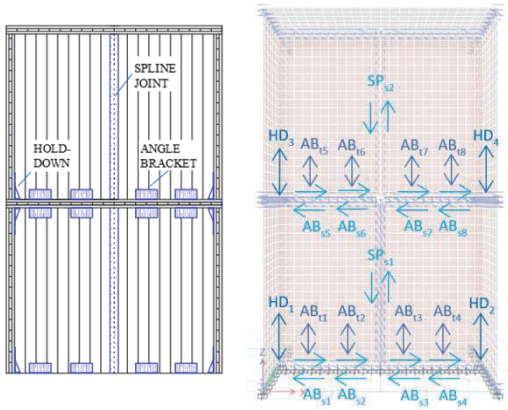

Figure 5: *Numerical model and input parameters.*

Each of the link-type elements of the model was assigned a multilinear-elastic force-deformation curve in their respective degrees of freedom. Specifically, a tri-linear axial force-deformation curve in tension and a linear force-deformation curve in compression were assigned to HD and AB's vertical degrees of freedom (see Figure 6a). These differences in the tensile and compressive behaviors are because these connectors are only susceptible to damage and stiffness degradation in the vertical direction when tensile. At the same time, when compressed, they maintain a high stiffness that is controlled by the crushing in the CLT panels. On the other hand, trilinear-elastic force-deformation curves were assigned to the ABs in the horizontal direction and to the SPs in the vertical direction because in those degrees of freedom, the aforementioned connectors work in shear (see Figure 6b).

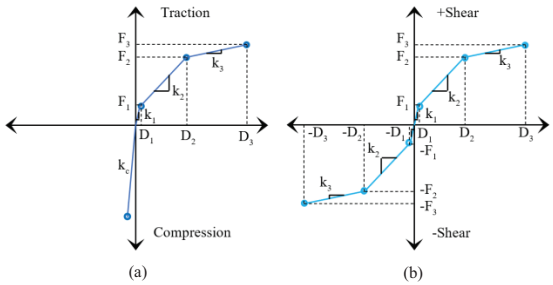

Figure 6: *Force-deformation curves: (a) tension, (b) shear.*

As can be seen in Figure 6, several input parameters are needed to define the force-deformation curves in multilinear-elastic link elements. However, several of these parameters were assumed as constants to simplify the model, considering results from previous experimental tests on similar connectors. For example, the first section of the tri-linear curves mainly represents the joints' friction mechanisms. In that section, the value of D_1 is small and quite close to 0.5 mm. Moreover, the stiffness k_1 of that section is generally very high and four times the stiffness of the second section k_2. The second section is one of the most important since it represents the elastic stiffness of the connectors, which the manufacturers generally report in their catalogs. Finally, the third section represents the degradation of the elastic stiffness of the connector, with deformation values ranging from D_2=4mm to D_3=15mm on average and a stiffness k_3 of the order of half of k_2. Therefore, given the importance of the parameter k_2, it will be assumed as the only input variable and indicator of the eventual damage to each of the connectors. The rest of the parameters will be assumed as constant or as a function of k_2 (D_1=0.5mm, D_2=4mm, D_3=15mm, k_1/k_2=4, k_3/k_2=0.5).

Once the finite element model is defined, running a series of numerical simulations is possible. Each numerical simulation has a different set of values of its 22 relevant input parameters, i.e., the k_2 elastic stiffnesses of the AB, HD, and SP connections. In this way, it is possible to calculate a set of dynamic properties of the wall in each numerical simulation through the solution of a finite element eigenvalue and eigenvector problem. These "simulated" dynamic properties of the wall correspond to the output parameters of the model.

It is essential to consider the possible combinations of the 22 input parameters of the model in the best way. For this purpose, a minimum and maximum value of k_2 must first be defined for each type of connector, representing different levels of damage, from severe to minor, respectively. The values considered are shown in Table 2 and were obtained from previous research [13]. Then, for each k_2 range, 2400 values are sampled with the Latin hypercube technique, assuming a uniform distribution and varying all input parameters at the same time. The execution of the numerical simulations was done by combining the API tools of the ETABS finite element software and the Python programming language.

Table 2: *Minimum and maximum values for k_2 joint stiffnesses.*

Item	Min (kN/mm)	Max (kN/mm)
HD_1 to HD_4	0.18	7.15
AB_{t1} to AB_{t8}	0.15	9.20
AB_{s1} to AB_{s8}	0.94	14.00
SP_{s1} to SP_{s2}	0.02	0.81

2.2.4 Regional sensitivity analysis

Finally, in the fourth stage, a regional sensitivity analysis (RSA) [14] is applied to each of the 11 damage levels induced to the wall in stage one. The objective of RSA is

https://doi.org/10.52202/069179-0258

to identify which joint stiffnesses (22 input parameters) are most influential on the dynamic properties of the wall and in what range of values these stiffnesses are most influential.

A necessary first step in applying RSA is to define an objective function (defined *Y*), which is an estimation of model performance calculated by comparison of measured and simulated variables. In the context of this work, it is convenient to choose the objective function as the differences between the dynamic properties measured in the wall (step two) and the dynamic properties simulated in the models (step three). Furthermore, as the simulated dynamic properties depend on the input parameters (stiffnesses of the joints stored in a vector *k*), the objective functions also depend on these input parameters ($Y_{(k)}$).

The dynamic properties are sometimes scalar (vibration frequencies) and sometimes vectors (modal shapes); therefore, it is advisable to use an objective function that includes both kinds of dynamic properties. Accordingly, Equation 1 shows the expression of $Y_{(k)}$.

$$Y_{(k)} = \alpha \cdot \frac{1}{n}\sum_{i=1}^{n}\left|\frac{\widetilde{f_i} - f_{i(k)}}{\widetilde{f_i}}\right| + \beta \cdot \frac{1}{n}\sum_{i=1}^{n} NMD\left(\widetilde{\phi_i}, \phi_{i(k)}\right) \quad (1)$$

where n is the number of identified dynamic properties (two in this case), $\widetilde{f_i}$ are the measured frequencies, $f_{i(k)}$ are the simulated frequencies, NMD is the normalized modal difference [11], $\widetilde{\phi_i}$ are the measured modal shape vectors, and $\phi_{i(k)}$ are the simulated modal shape vectors. The α and β constants take values between 0 and 1 depending on the relative importance to be given to the differences between frequencies concerning the differences between modal forms. In this case, both were assumed to be equal to 0.5.

After defining the objective functions, RSA requires that the models be separated into two groups. The first group corresponds to all models with objective function values below a specific acceptable threshold. These models are generally referred to as behavioral (B models) and, in this case, are characterized by generating simulated dynamic properties that differ very little from the measured dynamic properties. On the other hand, the rest of the models, which have objective function values higher than the threshold, are called non-behavioral models (NB models). Consequently, the acceptable threshold value was selected as 0.15 for the objective function $Y_{(k)}$.

Once it is known which models belong to groups B and NB, RSA requires the calculation of the cumulative density functions (CDF) of each input parameter for both B and NB models. That information makes it possible to rank which input parameters influence the objective functions most. For example, if, for an input parameter, the CDF of the B models is different from the CDF of the NB models, then that input parameter is very influential on the objective functions. However, this degree of influence is only sometimes possible to distinguish graphically; therefore, it is usual to resort to the Kolmogorov-Smirnov (K-S) statistical test to estimate the degree of influence of the input parameter. According to the suggestions of [13], an input parameter can be grouped into three possible sensitivity classes depending on the p-value obtained in the K-S test: critical (p-value < 0.01), important (0.01< p-value < 0.1), and negligible (p-value > 0.1). This kind of ranking of the influence of the input parameters helps estimate the location of the joints that could suffer more damage, given a variation in the global dynamic properties of the wall.

Finally, with the data associated with the B models, it is possible to know in what range of values the input parameters most influenced the objective functions. These ranges can be quickly visualized through box plots of the input parameters and further analyzed using the ANOVA statistical test. In this way, it is possible to evaluate the severity of the damage in the joints by studying the variation of their stiffnesses.

3 RESULTS AND DISCUSSION

3.1.1 Variation of the wall's dynamic properties

Figure 7 shows the variation of the first two vibration frequencies measured in the wall as the lateral load increased and, therefore, the level of damage. On the other hand, Figure 8 shows the modal shapes measured in the right-flange wall.

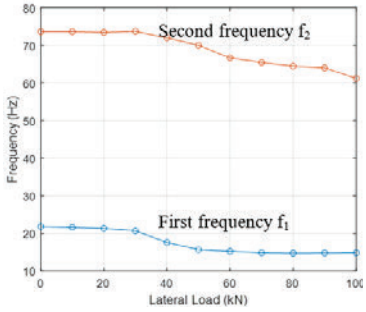

Figure 7: *Measured vibration frequencies.*

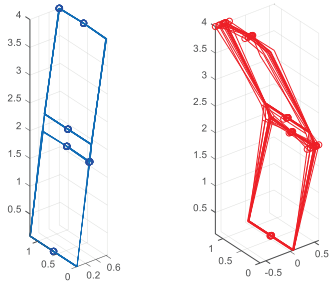

Figure 8: *Measured modal shapes: first vibration mode (left), second vibration mode (right).*

Figure 7 shows that the two vibration frequencies identified were decreasing as the damage caused by lateral loads increased. The decreases of the frequencies between

the undamaged and maximum damage states were 32% and 17% for f_1 and f_2, respectively. These decreases are the first global indicator of damage in the CLT wall joints; however, they do not indicate where the damage may be located or the severity of the joints' stiffness degradation. The measured modal shapes shown in Figure 8 suggest that the first vibration mode experienced almost no variation in the different levels of damage induced. However, the second mode of vibration showed more relevant variations as the lateral load on the wall increased.

3.1.2 Damage location and severity estimation.

The first relevant result of the RSA was ranking the most influential joint rigidities in the *Y* function. At each lateral load level, the value of *Y* was calculated for each simulated combination of input parameters and compared with the threshold value of 0.15. In this way, it was possible to separate the B models from the NB models and to visualize these results in scatter plots and CDF curves. Some examples of the graphs mentioned above are shown in Figures 9 to 12.

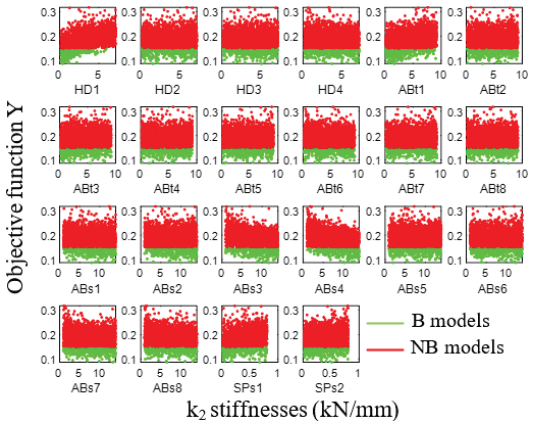

Figure 9: *Dispersion plots for k_2 stiffnesses, after 50kN lateral load.*

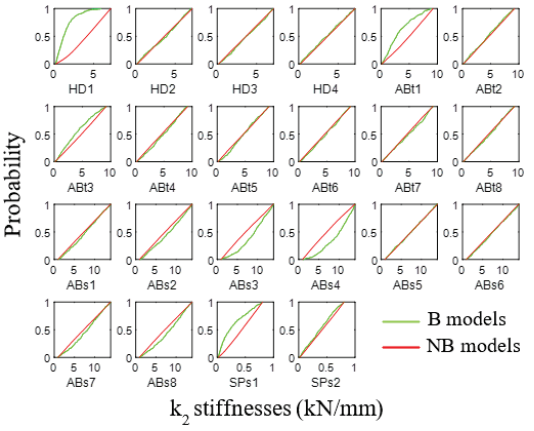

Figure 10: *CDF curves for k_2 stiffnesses, after 50kN lateral load.*

Then, applying the K-S test to the CDF curves, it was possible to obtain the ranking of the most influential stiffnesses of the connectors. Table 3 shows the top 5 ranking for each lateral load level.

Table 3: *Ranking of the most influential k_2 stiffnesses.*

Lateral Load (kN)	1st	2nd	3rd	4th	5th
0	AB_{s4}	AB_{s3}	HD_1	AB_{s8}	AB_{s7}
10	AB_{s4}	AB_{s3}	HD_1	AB_{s8}	AB_{s7}
20	AB_{s4}	AB_{s3}	HD_1	AB_{s8}	AB_{s7}
30	AB_{s4}	AB_{s3}	HD_1	AB_{s8}	AB_{s7}
40	AB_{s4}	AB_{s3}	HD_1	SP_{s1}	AB_{s2}
50	HD_1	AB_{t1}	SP_{s1}	AB_{s4}	AB_{s3}
60	HD_1	AB_{t1}	AB_{s3}	SP_{s1}	AB_{s4}
70	HD_1	AB_{t1}	SP_{s1}	AB_{s3}	SP_{s2}
80	HD_1	AB_{t1}	SP_{s1}	AB_{s4}	AB_{s3}
90	HD_1	AB_{t1}	SP_{s2}	SP_{s1}	AB_{s3}
100	HD_1	SP_{s2}	AB_{t1}	HD_3	SP_{s1}

From Table 3, up to the lateral load of 40kN, the most influential connectors were the angle brackets working in shear on the right side of the wall on the first and second floors (AB_{s4}, AB_{s3}, AB_{s8}, and AB_{s7}). Exceptionally, the tension stiffness of the hold-down on the left side of the first floor (HD_1) also appeared. These results are reasonable since there was practically no damage to the connectors for lateral loads less than 40kN, and most of the deformation was associated with the relative horizontal sliding of the wall panels. However, from a lateral load of 50kN onwards, the influence ranking of the connectors changed radically. The level of damage to the connectors increased, and the deformation mechanisms were those associated with wall rocking. Therefore, the tension stiffness of HD_1, the tension stiffness of AB_{t1}, and the vertical shear stiffness of SP_{s1} took an important role in the first story of the wall. This can also be seen in Figures 9 and 10. For a lateral load of 50kN, the B models tend to concentrate on the lower values of the stiffnesses of HD_1, AB_{t1}, and SP_{s1}, with more severe damage levels expected in these zones. The severity of damage in these connectors can be analyzed by studying the evolution of their stiffnesses in the B models for different lateral load levels. Figures 11 to 13 show this through box plots.

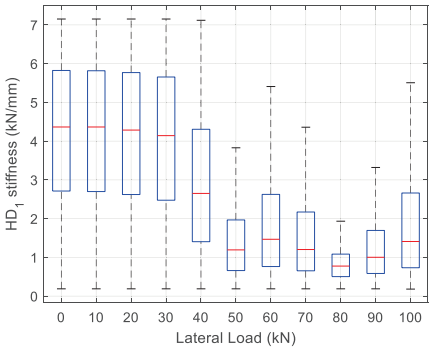

Figure 11: *Boxplot of k_2 stiffnesses for HD_1 connector.*

https://doi.org/10.52202/069179-0258

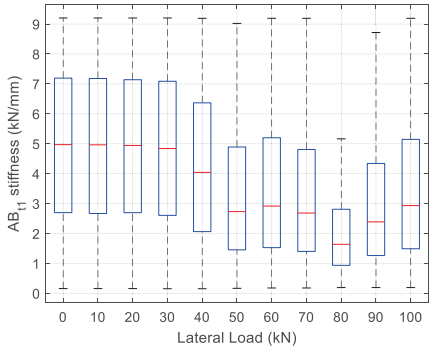

Figure 12: *Boxplot of k_2 stiffnesses for AB_{t1} connector.*

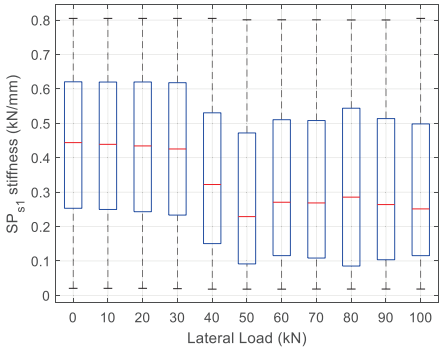

Figure 13: *Boxplot of k_2 stiffnesses for SP_{s1} connector.*

Figures 11 to 13 show that significant degradation of the stiffness of HD_1, AB_{t1}, and SP_{s1} connectors occurred as the lateral load increased. The initial stiffnesses of these connectors decreased by 63%, 36%, and 27%, respectively. These stiffness reductions obtained by the proposed vibration-based non-destructive method closely matched the real damage observed, as shown in Figures 14 to 16 [].

Figure 14: *Damage in HD_1 connector after 100kN lateral load.*

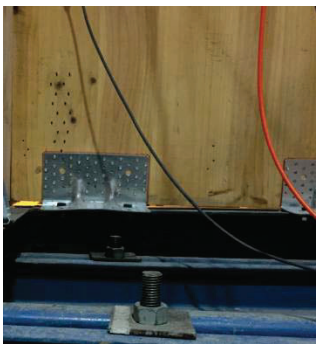

Figure 15: *Damage in AB_{t1} connector after 100kN lateral load.*

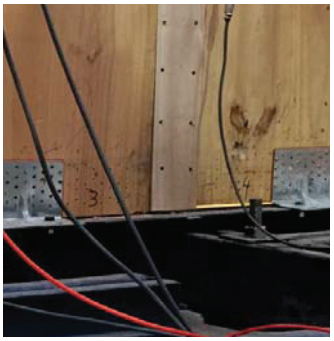

Figure 16: *Damage in SP_{s1} connector after 100kN lateral load.*

4 CONCLUSIONS

In this paper, we have described a new approach to estimate the location and severity of damage in CLT wall joints based on OMA, FEMUP and RSA techniques. We have obtained satisfactory results showing that this non-destructive methodology can be extended to more complicated structural configurations.

REFERENCES

[1] M. Izzi, D. Casagrande, S. Bezzi, D. Pasca, M. Follesa, R. Tomasi.: Seismic behaviour of Cross-Laminated Timber structures: A state-of-the-art review. Engineering Structures, 170: 42–52, 2018.

[2] T. Reynolds, R. Harris, W.-S. Chang, J. Bregulla, & J. Bawcombe.: Ambient vibration tests of a cross-laminated timber building. Proceedings of the Institution of Civil Engineers - Construction Materials, 168(3): 121-131, 2015.

[3] T. Reynolds, D. Casagrande, & R. Tomasi.: Comparison of multi-storey cross-laminated timber and timber frame buildings by in situ modal analysis. Construction and Building Materials, 102: 1009-101, 2016.

[4] A. Aloisio, D. Pasca, R. Tomasi, & M. Fragiacomo.: Dynamic identification and model updating of an eight-storey CLT building. Engineering Structures, 213: 110593, 2020.

[5] B. Kurent, B. Brank, & W. K. Ao.: Model updating of seven-storey cross-laminated timber building designed on frequency-response-functions-based modal testing. Structure and Infrastructure Engineering, 0(0): 1-19, 2021.

[6] A. Ceccotti, C. Sandhaas, M. Okabe, M. Yasumura, C. Minowa, & N. Kawai.: SOFIE project – 3D shaking table test on a seven-storey full-scale cross-laminated timber building. Earthquake Engineering & Structural Dynamics, 42(13): 2003-2021, 2013.
[7] G. Flatscher, & G. Schickhofer.: Shaking-table test of a cross-laminated timber structure. Proceedings of the Institution of Civil Engineers - Structures and Buildings, 168(11): 878-888, 2015.
[8] M. Popovski, & I.Gavric.: Performance of a 2-Story CLT House Subjected to Lateral Loads. Journal of Structural Engineering, 142(4): E4015006, 2016.
[9] F. T. Matos, J. M. Branco, P. Rocha, T. Demschner, & P. B. Lourenço.: Quasi-static tests on a two-story CLT building. Engineering Structures, 201: 109806, 2019.
[10] I. Mugabo, A. R. Barbosa, A. Sinha, C. Higgins, M. Riggio, S. Pei, J. W. van de Lindt, & J. W. Berman.: System Identification of UCSD-NHERI Shake-Table Test of Two-Story Structure with Cross-Laminated Timber Rocking Walls. Journal of Structural Engineering, 147(4): 04021018, 2021.
[11] C. Rainieri, G. Fabbrocino.: Operational Modal Analysis of Civil Engineering Structures. Springer New York, 2014.
[12] A. Opazo-Vega, F. Benedetti, M. Nuñez-Decap, N. Maureira-Carsalade, & C. Oyarzo-Vera.: Non-Destructive Assessment of the Elastic Properties of Low-Grade CLT Panels. Forests, 12(12): 1734, 2021.
[13] F. Benedetti, V. Rosales, A. Opazo-Vega, S. Sepulveda, A. Jara-Cisterna.: Experimental analysis of a two-story three dimensional panelized CLT module. In: Proceedings of the World Conference on Timber Engineering, Chile, 2021.
[14] A. Saltelli, M. Ratto, T. Andres, F. Campolongo, J . Cariboni, D. Gatelli, M. Saisana, S. Tarantola.: Global sensitivity analysis: the primer. John Wiley & Sons, 2008.

https://doi.org/10.52202/069179-0258

World Conference on Timber Engineering Oslo 2023

PREDICTION OF THE ACOUSTIC INSULATION OF A PREFABRICATED WOODEN-BASED SYSTEM FOR COLLECTIVE BUILDINGS

Marina Tenório[1], Sandra M. Silva[2], Jorge M. Branco[3]

ABSTRACT: Using wood, a renewable, carbon sink material with outstanding thermal properties associated with the prefabrication process and its benefits, a construction system for multi-storey multifamily buildings based on prefabricated wooden panels was developed to act as a tool for meeting the national carbon neutrality targets. It will contribute to the promotion of increasingly sustainable cities that optimise the use of materials and rely on highly energy-efficient buildings. This sustainable alternative to conventional construction materials was designed to comply with the Portuguese needs, regulations, and regulatory requirements regarding construction, structural, functional, and logistics demands. As the acoustic behaviour of wooden buildings is a sensitive subject due to the wood's lightweight and poor insulation performance for low-frequency sounds, this work aims to analyse the panels regarding their acoustic behaviour through INSUL software. The predictions showed favourable results for airborne insulation and partially favourable for impact sound insulation.

KEYWORDS: Wooden buildings, Acoustic, INSUL

1 INTRODUCTION

As a growth strategy for a competitive economy, efficient in the use of resources and, consequently, aligned with sustainable development, one of the European Union's priorities is to achieve carbon neutrality by 2050. As a result, Portugal has stipulated a reduction in greenhouse gas (GHG) emissions of between 85-90% [1].

In this context, reviewing the construction sector's conventional models becomes a priority given its impact: 40% of energy demand, 36% of GHG emissions, 40% of raw material consumption, and 33% of waste [2]. Materials processing holds the most significant share of energy consumption and GHG emissions [3], with cement and steel responsible for 4-7% [4] and 5% [5] of CO_2/year global emissions, respectively.

Wood re-emerges as a promising alternative due to its carbon storage capacity and lower embodied energy. Its processing/transport generally emits less carbon than that stored by wood, strengthening the carbon economy through local production. The buildings' operation phase, responsible for 45-80% of their carbon emission [6], benefits from the wood's high insulating capacity: 10 times higher than concrete and 400 than steel [2]. Also, at the end of its life, wood enables reuse to generate new products or energy [7].

Population and urban expansions (230bi m² of new constructions by 2060 [8]) dictate the need for increasingly denser forms and transform cities into opportunities for sustainable development, highlighting the wood sector's potential in offering carbon-neutral solutions for buildings. This modern application of wood was possible through the introduction of Engineered Wood Products, which optimised the timber structural capacity and overcame many of its limitations, reinventing the industry with competitive products to concrete and steel. Withal, the development of CAD/CAM technology, CNC equipment, and integrated design in BIM methodology has raised the degree of precision and quality of wood products that, produced in a factory, have the potential to reduce work times, site costs, noise, pollution, waste, accidents, and deterioration due to moisture exposure [9,10].

However, in the last decades, the diffusion of high-rise timber buildings, mainly in countries with cold climates, has promoted the development of knowledge and the proposal of solutions to this specific scenario, which does not apply to the Portuguese reality. Despite the rich history of using wood on floors and roofs, Portugal did not follow its transition to high performance, so the projects are few and conservative. It represents a missed opportunity for economic, social, and environmental gains, proving fundamental to developing specific knowledge of this typology application in the national context.

To make this typology compatible with the Portuguese context, a construction system for multi-storey buildings using prefabricated panels and 3D modules with a timber

[1] Marina Tenório, Department of Civil Engineering, Institute for Sustainability and Innovation in Structural Engineering (ISISE), University of Minho, Portugal, tenorio.mcu@gmail.com

[2] Sandra M. Silva, Department of Civil Engineering, Institute for Sustainability and Innovation in Structural Engineering (ISISE), University of Minho, Portugal, sms@civil.uminho.pt

[3] Jorge M. Branco, Department of Civil Engineering, Institute for Sustainability and Innovation in Structural Engineering (ISISE), University of Minho, Portugal, jbranco@civil.uminho.pt

https://doi.org/10.52202/069179-0259

structure is proposed, designed to meet local needs and act as a tool to fulfil the national objectives of carbon neutrality.

Besides contributing to the reduction of carbon emissions in the production and operation phases of the buildings from the renewable nature and carbon storage potential of the wood itself, it makes use of the prefabrication process that, optimized to its maximum, contributes to the rationalization of the construction, reducing waste and, consequently, the ecological footprint of the system, besides providing healthy interior environments from the precise and controlled production process.

Based on features designed and validated for successful application in the Portuguese context, the aim was to propose a solution with high replication and sustainable impact potential in Portuguese cities, besides promoting scientific enrichment in the use of wood in multi-storey buildings. The construction system was, then, idealized based on the rules and good practices of design for timber structures identified in the literature, considering the supply and consumption patterns of the national market (species, products, and prefabrication technologies of the sector), the conditions and restrictions of production, transport and construction phases, as well as the applicable normative requirements.

Acoustics is an important performance aspect of wood construction and a prerequisite for the acceptance of wood buildings by the construction industry, owners, and consumers.

The acoustic behaviour of wooden buildings, whether for airborne or impact sounds, differs from that observed in heavy constructions, such as those in concrete. It is because the construction weight is a decisive parameter for its acoustic performance, especially for the lower frequency range (generally 20 – 200 Hz). Therefore, wooden constructions are often associated with poor acoustic insulation, suffering significant vibrations and disturbances, especially in this frequency range [11].

In this context, prediction models become indispensable tools in the wooden structures' design, despite the existing methods being more suitable for predicting the acoustic insulation of heavy and homogeneous structures. Moreover, low-frequency results are often associated with prediction difficulties, which makes them even more uncertain.

The alternative of using a test building is common practice, although it is an expensive process and therefore puts wood at a disadvantage compared to other materials. Furthermore, the results obtained through measurements are mostly exclusive to those specific conditions, so they may not be useful for application in non-similar projects. The variations in sound insulation measurements often imply over-qualifying the construction elements through a high safety margin in the design phase to secure the fulfilment of the appropriate requirements [12].

Aiming at developing a system that provides acoustic comfort to the occupants and that is adequate to the regulatory requirements for building performance in Portugal, in this work, the construction system panels, composed of timber-frame walls and CLT panels floors, are evaluated aiming for its acoustic performance validation regarding their airborne and impact sound insulation.

2 THE CONSTRUCTION SYSTEM

The construction system was developed from the identification of design constraints and strategies, which range from the definition of the concept and design assumptions determining the system's applicability to the detailing of the layers, materials, joints, and finishes. Based on the design objectives, the premises of the system were established:

- Use of timber as the sole structural material, except for the foundation and connections associated with the timber elements (that are metallic);
- Definition of the basic structural unit in 2D panels, whether for walls, floors or roofs;
- Suitability for multifamily building structures;
- Compliance with the structural, functional and logistic requirements and conditions imposed by national regulations, valuing safety, durability, comfort and applicability;
- Maximisation of the prefabrication process and off-site operations;
- Use of complementary materials in line with national consumption and technical-financial accessibility standards to facilitate replication and acceptance of the system;
- High potential for adaptation to various projects due to architectural versatility (dimensions, combinations, and modularity) and the possibility of combining different aesthetic solutions;
- Simple, fast, and precise production, transport, assembly, and installation processes.

The development and application of the construction system (besides the definition of the concept that stipulates its essence and purposes) are also subject to predefinitions that typify and specify the panels and confer the ideal design conditions for the fulfilment of the system's structural and functional objectives. Therefore, it is determined that:

- The wall panels resistant to vertical loads are made of light timber-frame structure, except for the core wall panels, which enclose stairwells and lift shafts and which, due to their function as a central core, can be materialised by CLT or mixed panels (CLT + timber-frame) (Figures 1 a-c);
- The floor panels, in order to produce resistant diaphragms in the structure, are made of CLT panels (Figures 1 d-e);
- The foundation must be made of reinforced concrete.

Besides the structural definitions, the functional layers of the system play a decisive role in guaranteeing its adequate performance and have the potential to ensure, for instance, the durability of the construction, one of the topics of greatest distrust regarding the use of wood in buildings.

https://doi.org/10.52202/069179-0259

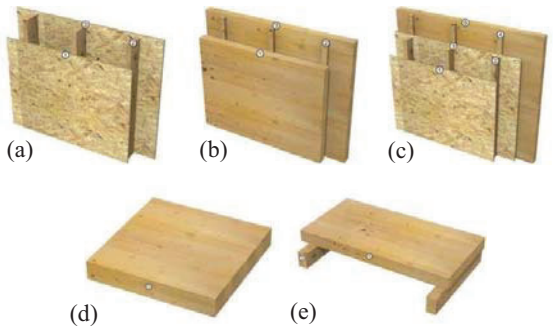

Figure 1: *Design strategies – Structural solutions. (a) Timber-frame; (b) CLT wall panels; (c) Mixed solutions with timber-frame and CLT; (d) CLT floor panels; (e) CLT floor panels with beams*

The critical functions to be performed and the functional layers that directly or indirectly contribute to this end were then identified (Figure 2). It was possible through an in-depth study of the literature, seeking to understand the behaviour of wooden structures and identify the traditional and innovative strategies/design practices specific to this construction typology and the existing solutions available on the market. In the scope of this work, the strategies pertinent to noise control stand out.

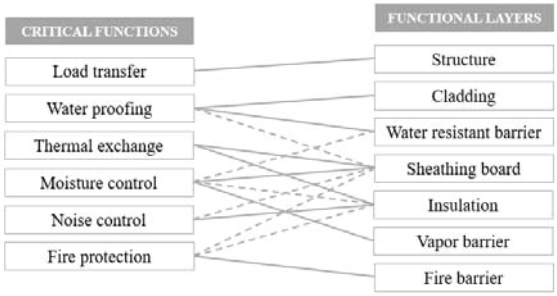

Figure 2: *Critical functions and the correspondent functional layers*

Thus, the noise control strategies adopted are (Figure 3):

- Use of rock wool as a thermal insulation layer and as an acoustic absorbing material to reduce the transmission of airborne sounds;
- Desolidarisation between rigid elements using resilient material layers or flexible connectors to reduce the transmission of impact-generated sounds;
- "Duplication" of elements, such as the construction of suspended ceilings, additional wall panels (such as a service layer, a layer originally conceived for MEP installations that can be filled with insulation to provide thermal and acoustic benefits) and floating floors, which are employed in association with resilient and absorbent materials;
- Double plasterboard internal lining and, for some panels, adoption of acoustic membranes. These solutions increase the system's mass and, consequently, the absorption of sound waves.

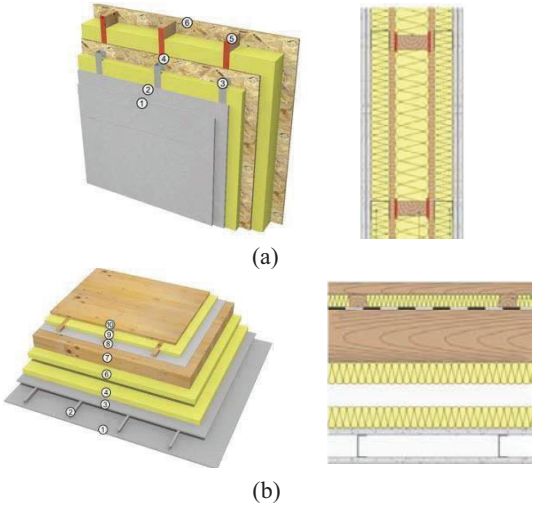

Figure 3: *Design strategies – Noise control. (a) Eg.: Internal walls (Par_Int_Nest_TF); (b) Eg.: Intermediate floors (Pav_Int_CLT)*

The panels developed for the various elements of the buildings, which make up the construction system, are shown in Figure 4. The construction details of each panel can be consulted at [13].

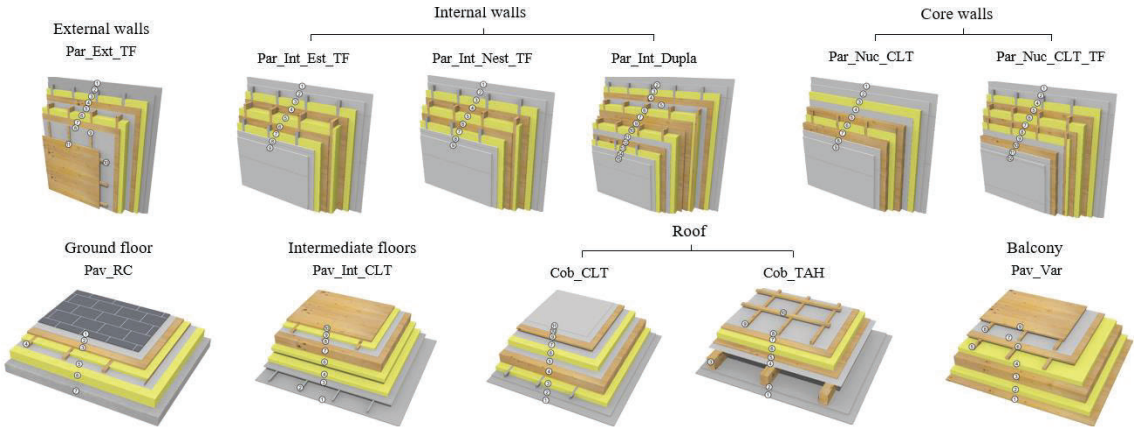

Figure 4: *Overview of the panels' configurations of the construction system*

https://doi.org/10.52202/069179-0259

3 MATERIALS AND METHODS

The Portuguese Regulation on the Acoustic Requirements for Buildings (RRAE) (Decree-Law 129/2002, of 11 May 2002 [14]) regulates acoustic performance within the building regulations, contributing to improving the quality of the acoustic environment and the well-being and health of the population, in articulation with the Legal System on Environmental Noise. RRAE establishes minimum acoustic performance values for both new and existing buildings subject to reconstruction, extension, or alteration of the various building types, including multifamily buildings.

As the acoustic performance criteria are based on indexes dependent on the function of the element in the building (e.g. external wall, walls or floors between dwellings or dwellings and office spaces), the panels are assessed according to all their possible functions to consider the hypotheses that present the most rigorous criteria.

The determination of the sound reduction index for airborne and impact sounds to be compared with the maximum and minimum values established in the Portuguese Building Acoustic Regulation was obtained from the INSUL software [15], a tool for predicting the acoustic insulation in walls, floors, ceilings, and roofs. It models materials using well-known elastic plate theory, including allowances for thick panel effects, as stated by Ljunggren [16], Rindell [17] and others. More complex partitions are modelled using work by Sharp [18-20], Cremer [21,22] and others.

The software estimates transmission loss (TL) and sound insulation to impact sounds (L_n) in 1/3 octave bands. According to the concept of weighted value (single index) and from the comparison of the sound insulation curves with the reference curves contained in EN ISO 717-1 [23] and EN ISO 717-2 [24], it provides the sound reduction index (R_w) or sound insulation index to impact sounds ($L_{n,w}$).

The comparison between the curve described by the predicted values for TL and L_n, by frequency, with the conventional reference curve is performed by superimposing it so that the sum of the unfavourable deviations is as high as possible without exceeding 32 dB for 1/3 octave bands. Once this adjustment has been achieved, the value of R_w or $L_{n,w}$ corresponds to the value of the y-axis of the reference curve for the 500 Hz frequency.

As with any prediction tool, the INSUL software [15] is not a substitute for *in-situ* measurement. However, comparisons with test data indicate that it reliably predicts R_w values within 3 dB for most constructions [25].

As the objectives of the system design, which comprise the development only of the opaque panels and their suitability for various architectures, this study focuses on strategies detached from the architectural and location conditions. Therefore, for the acoustic analysis, aspects related to marginal transmission, interior acoustics, natural ventilation conditions in the façade or mechanical ventilation causing a break in acoustic insulation, and closure elements (such as doors, windows, and shutter boxes) will not be addressed.

4 RESULTS

The acoustic simulation produced in INSUL software [15] resulted in the sound insulation indexes to airborne and impact sounds (R_w and $L_{n,w}$) presented in Tables 1 and 2 for each of the construction elements developed. Tables 1 and 2 also present the minimum values for airborne sounds and the maximum values for impact sounds that each element must comply with, according to the RRAE. To specify these values, the supposed locations and functions that a given building element could assume in a building were considered, requiring the appropriate performance foreseen in the RRAE in terms of acoustic insulation.

It should be noted that the values obtained for the external walls through the simulation in the INSUL software correspond to panels without windows, while the values defined in the RRAE correspond to a wall with windows.

For all simulations, a fixed spacing between laths and studs of 300 mm was considered, although the system accepts spacings of 300 mm up to 600 mm because this represents the worst case since it increases the points of support between the different panels of the construction elements. The construction elements comprising CLT panels were analysed for 72 mm thickness when applied to walls and 120 mm when applied to floors.

Although the software is a practical option for acoustic insulation prediction, limitations were found. The software's student version does not allow the parameterization of new materials, limiting the analysis to the pre-existing materials in its database. Thus, it was necessary to assume materials with similar properties to the original ones. Also, the methods employed by the software support, at most, triple elements, which implies a limitation to the number of cavities between the element's panels (maximum of two). For the proper analysis of the elements presenting more than two cavities, considerations and adaptations were necessary to allow all the layers to be considered in the prediction of their acoustic performance.

The prediction of the acoustic insulation of the external wall panels (Par_Ext_TF) presented a sound reduction index of 55 dB (Figure 5a). Additionally, simulations were made to identify the contribution of each component in ensuring the required and desired acoustic insulation.

If the resilient material used between the rigid elements (studs and OSB) was dismissed, the anticipated sound reduction index would decrease by around 6 dB. In the same way, when considering a stiffer metallic support for the plasterboard than the one originally considered, with a thickness of 0.55 mm, lower insulation levels are achieved: 53 dB with 0.75 mm studs and 49 dB with studs between 1 mm and 1.6 mm.

https://doi.org/10.52202/069179-0259

Table 1: *Verification of the airborne sound reduction index according to RRAE*

Element	Sound emission space	RRAE $D_{2m,nT,w}$ or $D_{nT,w}$ (dB)	INSUL R_w (dB)
Par_Ext_TF	Exterior [1]	28 33	55
Par_Int_Est_TF	Common circulation area or a room [2]	48 50	63
Par_Int_Nest_TF	Common circulation area or a room [2]	48 50	63
Par_Int_Dupla_TF	Common circulation area or a room [2]	48 50	77
Par_Nuc_CLT	Vertical circulation [3]	40 48	63
Par_Nuc_CLT_TF	Vertical circulation [3]	40 48	65
Pav_Int_CLT	Garage or commercial or office areas [4]	50 58	61

[1] The standardised airborne sound insulation index measured two meters from the facade, $D_{2m,nT,w}$, between the outside of the building and bedrooms or living areas of dwellings shall be equal to or above 28 dB in sensitive areas (low noise neighbourhoods, mainly with residential buildings) and 33 dB in mixed areas (areas with residential and non-residential buildings).
[2] The standardised airborne sound insulation index, $D_{nT,w}$, between a room (emission) and bedrooms or living areas of another dwelling (reception) in a building shall be equal to or higher than 50 dB. When the emission comes from common circulation areas of the building, $D_{nT,w}$ should be equal to or higher than 48 dB in general conditions.
[3] The standardised airborne sound insulation index, $D_{nT,w}$, between a vertical circulation path (emission) of a building with lifts and bedrooms or living areas of dwellings (reception) shall be equal to or higher than 40 dB. When the building only has stairs, $D_{nT,w} \geq$ 48 dB applies, according to the previous item.
[4] The standardised airborne sound insulation index, $D_{nT,w}$, between a car parking garage (emission) and bedrooms or living areas of the dwellings (reception) should be equal to or higher than 50 dB. When considering the possibility of having a non-residential space on the ground floor of buildings, the acoustic insulation between commercial, industrial, offices or entertainment zones (emission), $D_{nT,w} \geq$ 58 dB applies.

Table 2: *Verification of the impact sound insulation according to RRAE*

Element	Sound emission space	RRAE $L'_{nT,w}$ (dB)	INSUL $L_{nT,w}$ (dB)
Pav_Int_CLT	Dwelling rooms or building common circulation areas	60	51
	Office spaces [1]	50	
Cob_CLT	Common circulation areas	60	64

[1] Inside the bedrooms or living areas of the dwellings (reception), the sound insulation index to impact sounds, $L'_{nT,w}$, from a standardised impact on floors of other dwellings or common circulation areas of the building (emission), should be equal to or less than 60 dB. When the emission occurs on the floors of the building with commerce, industry, offices or entertainment areas (emission), the sound insulation index to impact sounds, $L'_{nT,w}$, shall be equal to or less than 50 dB.

Instead of two layers of plasterboard, if only one layer is applied, a decrease of the sound reduction index to 52 dB and a worsening performance in low frequencies are observed. Still, when considering the exemption of the service layer keeping the two plasterboard finishing layers, an increase in the sound reduction index of 1 dB (56 dB) was observed. This fact can be justified by the lower stiffness of the gypsum plasterboard when supported on the rock wool compared to the case in which they are supported directly on the OSB, allowing greater oscillation of this layer and, consequently, the propagation of sound waves through its components. If the service layer is dismissed and the finishing is done with just one layer of plasterboard, the sound reduction index would be 52 dB.

Regardless of the variations imposed for simulation purposes, the opaque part of the external wall performs well. Its structural core (timber-frame with a cavity filled with rock wool and resilient material between the uprights and OSB) reaches a sound reduction of 46 dB itself. To meet the acoustic requirements, the external wall must have windows with high acoustic performance and adequate perimeter sealing.

Both interior walls, structural and non-structural timber-frame (Par_Int_Est_TF and Par_Int_Nest_TF), presented a sound reduction index of 63 dB, so the difference in thickness of the timber-frame and, consequently, of the acoustic absorbing material inside the cavities (140 mm and 90 mm, respectively) had no significant influence on the predicted performances. When the two service layers are removed, the sound insulation of both solutions decreases to 60 dB.

https://doi.org/10.52202/069179-0259

The results obtained for the different simulations developed for the external walls and structural and non-structural internal walls show that the greatest contribution to sound insulation comes from the double plasterboard finish, its support conditions in the adjacent layer, and the dissociation between the rigid elements of the panels.

By analysing the double-walled configuration (Par_Int_Dupla_TF), which presented sound insulation of 77 dB, it was possible to quantify the contribution of the acoustic membrane layers. Once removed, the Par_Int_Dupla_TF achieved a sound reduction of 76 dB, a result very close to the original configuration which, because it is so robust and with acoustic insulation significantly higher than the minimum limits defined in the legislation, makes the use of acoustic membranes in the promotion of acoustic comfort unnecessary. A less robust configuration of this wall solution, exempting the service layers, presented a noise insulation prediction of 74 dB.

The same was observed for the core walls, Par_Nuc_CLT and Par_Nuc_CLT_TF, which presented a decrease of 1 dB and 0 dB compared to the original configuration by removing the acoustic membrane. The acoustic membrane use had a more relevant impact on the panels' behaviour for the low-frequency sounds (lower than 125 Hz).

Considering the core wall panels' behaviour, when the remotion of the plasterboard layers was simulated to consider situations where the exposure of the CLT is wanted for aesthetic purposes, the sound reduction index decreased from 63 dB to 57 dB in the Par_Nuc_CLT and from 65 dB to 62 dB in the Par_Nuc_CLT_TF.

Associating the removal of the plasterboard layers on the CLT face with the removal of the service layer, some changes are observed only in the Par_Nuc_CLT, which reduces its sound insulation to 54 dB and significantly worsens the insulation level for the low-frequency range (more evident due to the removal of the service layer). The Par_Nuc_CLT_TF, with an absorbing material inside the timber-frame cavity, didn't present any change with the removal of the service layer, keeping the sound insulation of 62 dB and, in all its configurations (original and alternatives), presented insulation indexes in the low-frequencies higher and more stable than the results presented by Par_Nuc_CLT.

In terms of the airborne sound insulation of Pav_Int_CLT, the element fulfils the acoustic requirement when the emitting space is an office or a commercial area. Knowing that the prediction of acoustic insulation is based on a delicate analysis that can often lead to misunderstandings when compared to the actual acoustic insulation of the element, additional studies are needed to rigorously determine the performance of this element to ensure the minimum required behaviour. However, variations in the original configuration that may increase its acoustic performance were evaluated: the increase of the floating floor cavity to 100 mm and the adherence of continuous acoustic membranes over the CLT, both motivated by the need to include service installations.

For the isolated or associated application of both strategies, the same increase in sound reduction to 62 dB was obtained. It should be noted that this analysis considered spacings between slats and hangers of the suspended ceiling of 300 mm, so for any higher spacing, the acoustic insulation will be favoured. Also, as observed for the walls when simulating the removal of the service layers and, essentially, of its interior acoustic absorbing material, for Pav_Int_CLT it was noted that the adoption of one or two layers of acoustic absorbing material inside the suspended ceiling did not result in variations in the acoustic insulation. However, it was noted an expressive contribution of the acoustic suspended ceiling in the insulation to low-frequency sounds, mainly when in association with the increase of the floating floor cavity to 100 mm. When used over garages, whose requirement is lower, one can consider replacing the suspended ceiling with a 60 mm rock wool layer under the CLT, resulting in an acoustic insulation of 55 dB. This configuration can also be increased by using an acoustic membrane and enlarging the cavity of the floating floor, resulting in an acoustic insulation of 56 dB, although this measure is not necessary.

In terms of impact sound insulation, Pav_Int_CLT has a reasonable performance when it comes from impacts produced in residential or common circulation areas of the building (Figure 5b).

Compliance with the requirements is maintained even when the acoustic suspended ceiling is replaced by the slenderest option for the element, in which a 60 mm layer of rock wool is placed under the CLT and with a double plasterboard layer, with sound insulation to impact sounds of 56 dB. The same was not observed when the emission is from places in the building intended for commerce, industry, offices, or entertainment. However, this work aims essentially to the analysis of the developed construction system when applied in multi-family buildings, so the most stringent requirement ($L'_{nT,w} \leq 50$ dB) does not apply. The evaluation of the construction system for other building programs will be the object of future studies. However, seeking to identify the potential of the solution also for these cases, the application of resilient ceiling suspenders and more efficient damping systems for the floating floor was simulated, with the potential to achieve about 45 dB for the sound insulation to impact sounds.

Furthermore, assuming that the slightly tilted visitable roof is a common circulation area for the building occupants, its impact sound performance was simulated. Although the original Cob_CLT configuration did not meet the requirements imposed on this case, when using resilient materials under the deck slats and acoustic suspenders for the 60 mm suspended ceiling, sufficient sound insulation was achieved, 57 dB.

All the results presented are a prediction based on considerations about the construction elements. Future studies based preferably on laboratory tests on prototypes and *in situ* measurements are required to determine the acoustic performance of the construction elements more reliably, including the effect of the connection between panels and the flanking transmissions.

https://doi.org/10.52202/069179-0259

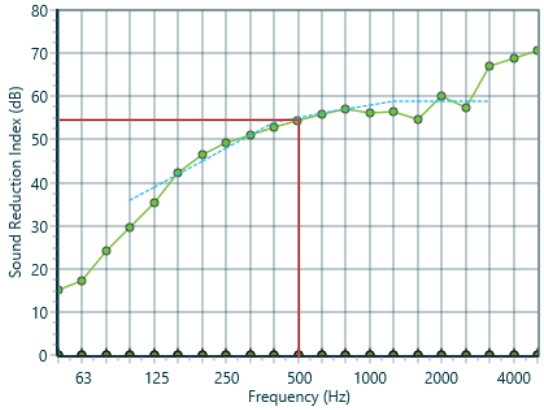

(a)

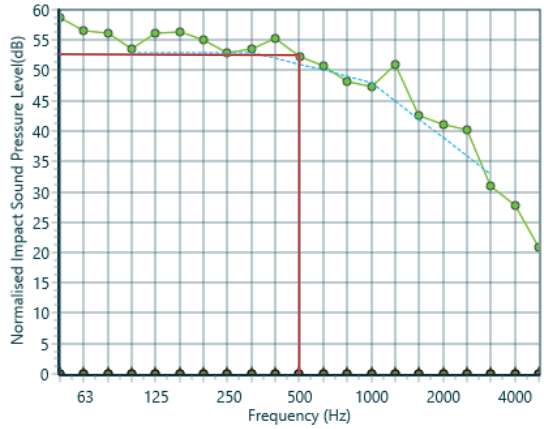

(b)

Figure 5: *Example of sound reduction index curve. (a) Example of predicted airborne sound insulation curve (in green) and reference curve (in blue) - Par_Ext_TF; (b) Example of predicted impact sound insulation curve (in green) and reference curve (in blue) - Pav_Int_CLT*

5 CONCLUSIONS

This paper describes numerical simulations carried out through INSUL software to predict the airborne and impact sound insulation of a construction system based on prefabricated wooden panels developed for the Portuguese market. The results of this investigation contribute to the validation of a construction system in terms of its acoustic performance.

The acoustic performance prediction showed favourable results for airborne sound insulation (Table 1) and partially for impact sound insulation (Table 2), depending on the type of emission space (another dwelling, office, circulation area). Note that all confirmed vulnerabilities have been mitigated.

The acoustic analysis was developed disconnected from a defined and invariable architecture, so it is essential to evaluate aspects such as flanking transmission, interior acoustics, natural ventilation conditions in the façade or mechanical ventilation causing a break in acoustic insulation, and closure elements such as doors, windows and shutter boxes for each project using this construction system.

Future studies based on laboratory tests on prototypes and *in situ* measurements will be carried out.

ACKNOWLEDGEMENT

This work was supported by national funds through FCT – Fundação para a Ciência e a Tecnologia, within the scope of a Ph.D. scholarship (PRT/BD/152841/2021) granted by MIT Portugal Program to the first author.

REFERENCES

[1] Resolução do Conselho de Ministros n.º 107/2019. RNC 2050 – Roteiro para a Neutralidade Carbónica 2050: Estratégia de Longo Prazo para a Neutralidade Carbónica da Economia Portuguesa em 2050. Diário da República, 1ª série, nº 123 (1 de julho de 2019).

[2] Jeffree, M., Wood – Building the bioeconomy, The European Confederation of Woodworking Industries, Brussels, Belgium, Oct. 2019. Available from: https://www.cei-b ois.org/publications

[3] D'Amico, B., Pomponi, F., Hart, J,. Journal Pre-proof Global potential for material substitution in building construction: the case of cross laminated timber, Journal of Cleaner Production, 2021, 279, 123487.

[4] Shanks, W., Dunant,C., Drewniok, M. P., Lupton, R., Serrenho, A., Allwood, J. M., How much cement can we do without? lessons from cement material flows in the UK, Resour. Conserv. Recycl., 2019, 141, 441-454.

[5] Davis, S. J., Lewis, N. S., Shaner, M., Aggarwal, S., Arent, D., Azevedo, I. L., Benson, S. M., Bradley, T., Brouwer, J., Chiang, Y. M., et al., Net-zero emissions energy systems, Science, 2018, 360, 6396.

[6] Chen, Z., Gu, H., Bergman, R., Liang, S., Comparative Life-Cycle Assessment of a HighRise Mass Timber Building with an Equivalent Reinforced Concrete Alternative Using the Athena Impact Estimator for Buildings, Sustainability, 2020, 12, 4708.

[7] Hossain, M. U., Poon, C. S., Comparative LCA of wood waste management strategies generated from building construction activities, Journal of Cleaner Production, 2018, 177, 387-397.

[8] Abergel, T., Dean, B., Dulac, J., Towards a zero-emission, efficient, and resilient buildings and construction sector. Global Status Report 2017, UN Environment and International Energy Agency, Nairobi, Kenya, 2017. Available from: https://www.worldgbc.org/sites/default/files/UNEP%20188_GABC_en%20%28web%29.pdf

[9] Carvalho, L. F., Jorge, C., Jerónimo, R., Plug-and-Play Multistory Mass Timber Buildings: Achievements and Potentials, Journal of Architectural Engineering, 2020, 26, 2.

[10] Smith, R. E., Griffin, G., Rice, T., Hagehofer-Daniell, B., Mass timber: evaluating construction performance, Architectural Engineering and Design Management, 2018, 14, 1- 2, 127-138.

[11] Östman B., Källsner B., National Building Regulations In Relation To Multistorey Wooden Buildings In Europe. In CONCERTO. Växjö University, Sweden, 2011.

[12] Forssén J., Kropp J., et al., Acoustics in wooden buildings: State of the art 2008. Vinnova project 2007, Stockholm, 2008.
[13] Tenório, M., Construction system in modular panels for collective buildings with wooden structure. Master in Sustainable Construction and Rehabilitation at the University of Minho, Guimarães, 2022. *In Portuguese*
[14] Decree-Law nº 129/2002. D.R. n.º 109/2002, Series I-A (11-05-02) 4421-4428 – Regulamento dos Requisitos Acústicos dos Edifícios.
[15] INSUL, Version 9.0.23. Marshall Day, New Zealand, 2021.
[16] Ljunggren, S., Generation of waves in an elastic plate by a vertical force and by a moment in the vertical plane, Journal of Sound and Vibration, 1983, 90(4), 559-584.
[17] Rindel, J. H., Dispersion and absorption of structure-borne sound in acoustically thick plates, Applied Acoustics, 1994, 41(2), 97-111.
[18] Sharp, B. H., A Study of Techniques to Increase the Sound Insulation of Building Elements, Wyle Laboratories Report, WR 73-5, Wyle Laboratories Research Staff, El Segundo, California, 1973. Distributed as PB-222 829, National Technical Information Service, United States Department of Commerce, Springfield, Virginia.
[19] Sharp, B. H., Prediction Methods for the Sound Transmission of Building Elements, Noise Control Engineering, 1978, 11(2), 53-63.
[20] Sharp, B. H., Kasper, P. K., Montroll, M. L., Sound Transmission through Building Structures - Review and Recommendations for Research, NBS-GCR-80-250, National Bureau of Standards, United States Department of Commerce, Washington, D. C., 1980. Distributed as PB81-187072, National Technical Information Service, United States Department of Commerce, Springfield, Virginia.
[21] Cremer, L., Heckl, M., Ungar, E. E., Structure-Borne Sound - Structural Vibrations and Sound Radiation at Audio Frequencies, Springer-Verlag, Berlin, 1973.
[22] Cremer, L., Theorie der Schalldämmung Wände bei schrägem Einfall, Akustische Zeitschrift, 1942, 7, 81–104. Most of this article has been republished with an English language summary, Northwood, T. D., Theory of the Sound Attenuation of Thin Walls with Oblique Incidence, in Northwood, T. D., ed., Architectural Acoustics, Benchmark Papers in Acoustics, 10, Dowden, Hutchinson and Ross, Stroudsburg, Pennsylvania, 1977, 367-399.
[23] CEN, EN ISO 717-1:2013: Acoustics — Rating of sound insulation in buildings and of building elements — Part 1: Airborne sound insulation. Brussels: European Committee for Standardization, 2013.
[24] CEN, EN ISO 717-2:2020: Acoustics — Rating of sound insulation in buildings and of building elements — Part 2: Impact sound insulation. Brussels: European Committee for Standardization, 2020.
[25] INSUL, Features. Marshall Day, New Zealand, 2023. Available at: https://www.insul.co.nz/features/

https://doi.org/10.52202/069179-0259

World Conference on Timber Engineering Oslo 2023

IMPACT SOUND INSULATION PERFORMANCE OF RAISED DISCRETE FLOATING FLOOR ASSEMBLIES ON MASS TIMBER SLABS

Jianui Zhou[1], Zijian Zhao[2], Chenyue Guo[3]

ABSTRACT: Bare mass timber structural slabs have relatively low impact sound insulation performance. Though certain floating floor assemblies on mass timber slabs can provide adequate single number ratings, such assemblies are mainly effective in the middle to high frequency range. This study presents the impact sound insulation performance of raised discrete floating floor assemblies for mass timber slabs. The raised discrete floating floor assemblies were composed of elastomer blocks, insulation materials**,** wood-based sheathing panels and concrete topping or cement boards. Impact sound insulation tests were conducted on a mock-up building under different excitation sources including human walking, ISO tapping machine and ISO rubber ball. The results showed that raised discrete floating floor assemblies tested in this study could improve the impact sound insulation ratings of the bare slabs by up to 41 dBA under ISO tapping machine excitation. Under different excitation sources, the impact sound pressure level spectra obtained from ISO rubber ball had similar frequency characteristics with that from human walking, though the magnitudes were higher at each octave band. The discrete raised floor without any mass topping had similar performance (L_{Fmax}=74.3 dBA) in attenuating low frequency sound to the continuous floating concrete topping of 50 mm thickness. The advantage of the raised discrete floor assemblies with dry solution boards over the continuous floating concrete topping assemblies based on the ISO tapping machine tests did not exist with the ISO rubber ball testing. Higher topping mass resulted in lower L_{Fmax}.

KEYWORDS: Impact sound insulation, Floating floor, Mass timber, Dry construction

1 INTRODUCTION

Mass timber panels including cross laminated timber (CLT), dowel laminated timber (DLT), nail laminated timber (NLT) and other large-dimension engineered wood panels are used largely as floor slabs in mass timber buildings and hybrid timber buildings due to their dry and fast construction. Exposed wood ceiling is appealing to both designers and occupants. However, bare mass timber panels have relatively low impact sound insulation performance [1], especially in the low-frequency range [2]. The common solution is to add a floating mass topping, such as a concrete topping, to improve the impact sound insulation performance [3]. However, continuous floating concrete topping assemblies had limited improvements on mass timber slabs [4]. It was reported that the apparent impact insulation class (AIIC) of CLT slabs with only continuous concrete topping floated on various market available elastic interlayers was difficult to achieve more than 55 dBA [4].

Conventional raised floor system is normally designed to provide an even finishing floor surface and space for ducts and cables, which is not meant for attenuating impact sound or insulating airborne sound. The discrete raised floor system incorporates elastic mounts for vibration isolation between the raised floor assembly and the structural floor for improved sound insulation performance. Homb et. al. reported that the such floor assemblies had high performance in middle to high frequency range on the light wood frame structural floor [6]. Its acoustic performance has not been fully explored compared with the continuous floating floor system, especially on mass timber floors. Previous study showed that raised discrete floating concrete floor had the potential to provide high impact sound insulation performance for CLT slabs according to typical ISO tapping machine testing [7]. However, it is not clear whether the system performs the same under different excitation sources, especially in the low frequency range, which is of great importance to the application in mass timber buildings.

This study aims to further investigate the impact sound insulation performance of raised discrete floating floors on mass timber slab, especially under different excitation sources including ISO tapping machine, ISO rubber ball and human walking. Moreover, the proposed assemblies

[1] Jianhui Zhou, University of Northern British Columbia, Canada, jianhui.zhou@unbc.ca
[2] Zijian Zhao, University of Northern British Columbia, Canada, zhao0@unbc.ca
[3] Chenyue Guo, University of Northern British Columbia, Canada, cguo@unbc.ca

https://doi.org/10.52202/069179-0260

adopt dry construction concepts to minimize cast-in-place concrete toppings.

2 MATERIALS AND METHODS

2.1 MATERIALS

Both CLT and DLT, were selected as the structural floors for testing. The CLT floor was made of 3 pieces of 5-layer (139-mm-thick, 35/17/35/17/35) spruce-pine-fir (SPF) CLT panels (CrossLam CLT 139V). Each CLT panel was 4.0 m long and 1.8 m wide. The DLT floor was made of 2 pieces of 140-mm-thick SPF DLT panels (StructureCraft) with 11 mm oriented strand board (OSB) on the top. Each DLT panel was 5.4 m long and 2.0 m wide. The panel-to-panel and panel-to-wall were connected with ϕ8.5×215 mm fully-thread self tapping screws with spacing of 40 cm. All gaps were sealed by acoustic sealant and tapes.

The raised discrete floating floor assemblies illustrated in Figure 1 were composed of elastomer blocks (AFB (Getzner), AMC25 and AMC40 (AMC Mecanocaucho)), Rockwool insulation material, OSB sheathing panels and mass topping. The AFB had a capacity of 60 kg load per mount, while AMC25 and AMC40 had designed capacity of 25 kg and 40 kg per mount respectively. AFB blocks were glued onto the structural floor with 60 cm spacing. Wood sleepers with a dimension of 19mm × 64mm were glued on the top of AFB blocks by polyurethane glue. 11-mm- thick OSB panels were fastened together with wood sleeper by 38 mm-long wood screws, and the remaining cavity was filled with 89 mm Rockwool insulation. AMC floor block series was made by 50 mm × 50 mm × 25 mm elastomer blocks and AMC innovated metal mounting frame. AMC floor mounts were fixed on structural floor by two 38 mm long wood screws with 50 cm spacing between each mount point. Then, the 50 mm by 50 mm wood sleepers were placed and fixed on the mounts, and 89 mm Rockwool insulation filled the cavity. Finally, 11 mm OSB panel was placed on the top of wood sleepers and fastened by 38 mm in length wood screws.

Four pre-cast 1.6 m × 1.6m normal strength (35 MPa) concrete toppings (38 mm, 50 mm, 70 mm and 100 mm) were floated as mass toppings. The concrete masses were 234, 307, 430 and 614 kg, equivalent to an area density of 91, 120, 168 and 240 kg/m^2, respectively. Besides the pre-cast concrete toppings, two types of cement boards and one type of gypsum board were selected as the dry-solution for floating floor. Fire rated gypsum board is the most commonly used drywall material in residential construction, and it demonstrates fire-resistance property to enhance the fire resistance level of the discrete floating floor. Each floated layer of 11 mm cement board (HardieBacker 500), 11 mm USG cement board and 11 mm gypsum board contributed to 13.4, 11.9 and 7.8 kg/m^2 area density to the system, and two layers of cement boards met the basic requirement of fire resistance [8]**Error! Reference source not found.**. All the cement board and gypsum board toppings were connected with the raised discrete floating floor by 38 mm wood screws.

In the small scale tests, the discrete mount assemblies were about to have a dimension of 1.6 × 1.6 m. Both AMC25 and AMC40 block mounts were assembled as a 5.0 × 3.6 m floor after the impact sound tests on small scale assemblies. In the impact sound test of full size assemblies, double layer USG cement boards and 12.7 mm gypsum boards (7.8 kg/m^2) were installed as mass toppings. Because the raised discrete floating floor has multiple components, each assembly is named as Mass timber_Block type_Insulation_Topping. CLT_AFB_INS_C100 represents that the AFB discrete raised floor with Rockwool insulation in cavity floating 100 mm concrete topping was installed on the CLT structural floor. Moreover, CB and USG represent two types of cement boards while GYP is short for gypsum board. The number after each floating board name indicates the layer of board applied on the discrete raised floor. The full size assembly has "Full" as suffix after the component name.

Figure 1: *(a) schematic diagram for discrete floating floor system, (b) raised discrete floor without mass topping, (c) floating concrete topping, (d) floating triple layer HardieBacker cement boards, (e) full-size floating double layer USG cement boards, (f) AFB floor mounts, and (g) AMC25 and AMC40 floor mounts*

2.2 IMPACT SOUND INSULATION TESTS

The impact sound insulation tests were conducted using a mock-up building as shown in Figure 2. The mock-up room was built with staggered wood stud walls (140 mm thick) with OSB sheathing panels, two layers of gypsum panels with resilience channels and rockwool insulation batts in the cavity. The mock-up has a height of 2.4 m, an outer floor size of 5.4×4 m^2 and an internal volume of 44 m^3. CLT and DLT floors were constructed on the mock-

https://doi.org/10.52202/069179-0260

up room. The apparent impact insulation class (AIIC) was be measured according to ASTM E1007-16 [9] using an ISO tapping machine (Larson Davis BAS004) and sound pressure meter (Larson Davis 831).

The impact tests using ISO rubber ball were conducted according to JIS A 1418 [10]. On the small scale 1.6 × 1.6 m floor assemblies, the rubber ball was dropped at 1.0 m from the floor surface for 4 consecutive times at center of floating floor with fixed location of sound level meter at the geometry center of receiving room. The locations of rubber ball dropping on full size floor assembly was according to Figure 2 (c). The rubber ball was dropped at each location for 4 times, and total of 20 impacts were recorded at the geometry center of receiving room. For real human walking excitation, a 75kg adult was walking on the floor in a random path for 1 minute, and the sound pressure level meter was fixed at receiving room center as well. L_{Fmax} single number rating was used to quantify the performance of floating floor assembly. The SPL of ISO rubber ball dropping was corrected according to [10].

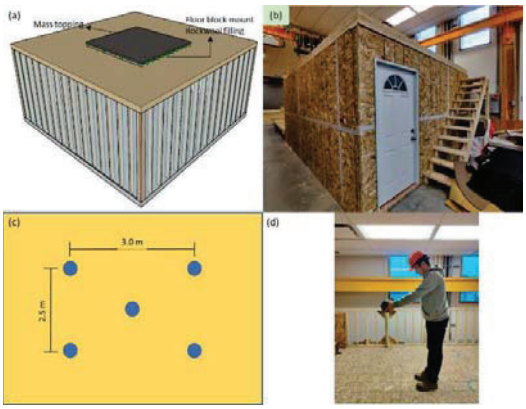

Figure 2: *(a) Sketch of the mock-up room, (b), photo of mock-up room (c) location of dropping rubber ball on full size floating floor and (d) dropping rubber ball*

3 RESULTS & DISCUSSION

3.1 APPARENT IMPACT SOUND INSULATION PERFORMANCE OF SELECTED ASSEMBLIES UNDER ISO TAPPING MACHINE EXCITATION

As listed in Table 1, the AIIC single number ratings for AFB discrete raised floor as well as 3 selected continuous floating floor assemblies on mass timber floor tested in [5]. With only AFB raised discrete floor on the bare CLT floor, AIIC rating increases from 26 to 47 dBA. This basic assembly without a mass topping has higher AIIC rating than that of most of floating concrete assemblies tested on the same CLT floor [4]. The insertion of Rockwool insulation (INS) in the cavity brought AIIC another 3 dBA higher to 50 dBA. The addition of 38 mm concrete topping further improved the AIIC to 58 dBA, which was higher than 55 dBA recommended by [11]. The increasing of concrete topping thickness does not affect much on AIIC rating of discrete floor system. The four concrete mass toppings each brought up single number rating 1 or 2 dBA gradually until 62 dBA with 100 mm concrete topping. The 50 mm mass topping with engineered floor finishing was tested as a potential solution for actual construction with an AIIC of 59 dBA. The overall impact sound insulation performance of AFB discrete raised floor assemblies on CLT and DLT structural floor are similar, which means that the type of structural floor does not affect the impact sound insulation performance of the discrete raised floor system. Furthermore, the concrete thickness did not affect the performance significantly, which indicated that dry construction boards such as cement boards and gypsum boards might be used.

Table 1: *Comparison AIIC ratings between AFB discrete floating assemblies and continuous floating concrete floors*

Structural Floor	AIIC ratings of different floating assemblies (dBA)								
	Bare Floor	AFB	AFB_INS	AFB_INS_C38	AFB_INS_C50	AFB_INS_C70	AFB_INS_C100	AFB_INS_C50 EngFloor	AFB_INS_SF_C50
CLT	21	47	50	58	59	60	62	62	62
DLT	37	43	53	N/A	58	N/A	61	61	60

The apparent normalized impact sound pressure level (ANISPL) curves of the discrete floating floor system on CLT is summarized in Figure 3 (a). As it can be seen, the discrete floating floor assemblies contributed significantly in both frequency regions below 315 Hz and higher than 1000 Hz. Using only AFB mounts covered by OSB, middle to high frequency impact sound pressure level decreased for at least 25 dBA on CLT. The Rockwool filling insulated middle frequency sound more effectively than extreme low or high regions on CLT. Adding a 50 mm concrete topping reduced sound pressure level in the low-to-mid frequency (100 – 400 Hz) up to 20 dBA. As a result, mass topping did not reduce sound pressure level in the high frequency (more than 400 Hz) as significant as it in low frequency range (lower than 400 Hz). A wide peak occurred between 400 and 630 Hz after adding the concrete topping, and that peak was not eliminated with further surface finishing. Still, installing the engineered floor can reduce the negative effect of hard concrete surface in the frequency range higher than 400 Hz. The sound pressure spectra for the assemblies on DLT are shown in Figure 3 (b). The bare DLT floor has much lower peak SPL than bare CLT. The curve for AFB mounts covered by OSB has a major peak at 160 Hz which does not appear in the assembly on CLT. Unlike the plateau below 400 Hz in Figure 3 (a), the spectra in Figure 3 (b) drops linearly right after the occurrence of 160 Hz peak. The filling of Rockwool in the cavity had almost even contribution throughout the entire frequency domain. These differences observed on DLT revealed that the structural floor had noticeable effect on impact sound

https://doi.org/10.52202/069179-0260

insulation according to frequency, despite the AIIC single number ratings did not show strong differences in between. The spectra of floating the 50 mm concrete topping on DLT assembly demonstrates the similar characteristic as that on CLT, with generally flatter shape. The ANISPL spectra characteristics for further layers of toppings beyond the 50 mm concrete are more identical on DLT than CLT. The type of structural floor did not noticeably affect ANISPL spectra of discrete mounts floating concrete topping. In summary, the AFB discrete raised floating floors had high efficiency on impact sound insulation and demonstrated similar performance on both CLT and DLT under ISO tapping machine excitation.

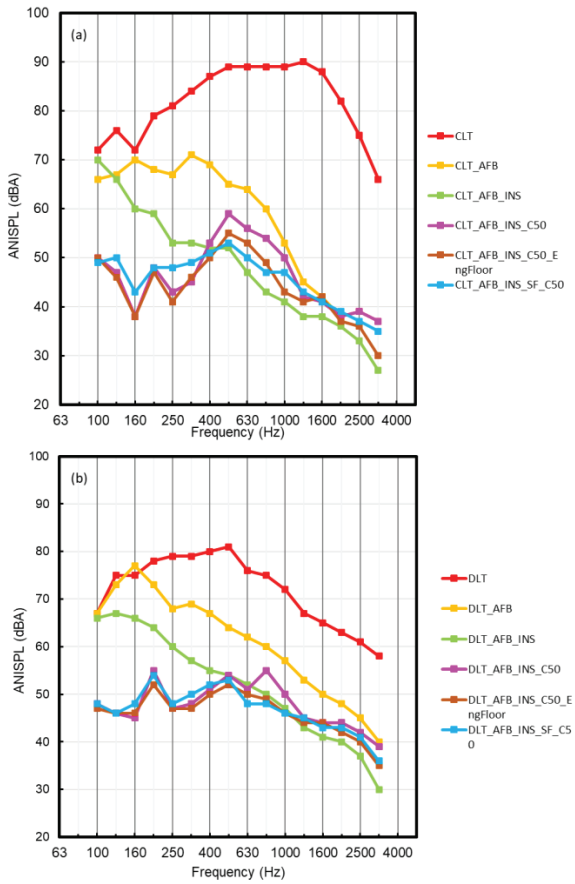

Figure 3: *Impact sound insulation performance of discrete floating floor on (a) CLT and (b) DLT structural floor under ISO tapping machine*

As the discrete raised floor floating concrete toppings have AIIC ratings more than 60 dBA, more types of discrete raised floor with various light-weight dry solutions were tested for pursuing a more environment friendly and lower mass assembly. The results of impact sound test on two types of AMC innovated mounts with various low-mass toppings are discussed below. The maximum allowable load for AMC25 is approximately equal to 38 mm concrete topping, and AMC40 has maximum load capacity for 50 mm normal strength concrete. This is the main reason of only conducting the impact sound test on one concrete topping on each discrete raised floor. The bare DLT floor has AIIC rating of 36 dBA, and the AMC25 floor mounts with OSB surface brought the single number rating 11 dBA higher, which was slightly lower than AFB. With Rockwool insulation, the single number rating increases to 55 dBA. According to Table 2, double layers of cement board (CB2) floating on AMC25 reaches the AIIC rating more than 60 dBA. However, the third layer of cement board (CB3) did not contribute much on impact sound insulation performance, which also indicated that the increase of mass did not contribute much to the performance. Floating double layer of cement boards would fulfil the fire resistance requirement and provided high performance impact sound insulation solution. The finishing layer of engineered wood floor on AMC25 floating CB2 assembly brought the AIIC 1 dBA higher. While this assembly had about only 30% mass of 38 mm concrete topping, the AIIC rating was 62 dBA, which was same as floating a 38 mm concrete topping.

Table 2: *AIIC rating of AMC25 and AMC40 floor block assemblies on DLT*

Floor Block Mount	AIIC ratings of different assemblies (dBA)								
	Bare DLT Floor	DLT_AMC	DLT_AMC_INS	DLT_AMC_INS_CB1	DLT_AMC_INS_CB2	DLT_AMC_INS_CB3	DLT_AMC_INS_CB2_Engfloor	DLT_AMC_INS_C38	DLT_AMC_INS_C50
AMC25	36	47	55	58	61	61	62	62	N/A
AMC40	36	47	52	57	60	60	62	N/A	57

AMC40 has higher allowable load of 40 kg/mount and is able to float 50 mm concrete topping. Floating of 50 mm concrete topping had the same AIIC rating as floating single layer of cement board, with the same single number rating of 57 dBA. Meanwhile, floating CB2 reached the AIIC rating 60 dBA. Similar as AMC25 discrete raised floor, the third layer of CB did not contribute to improving impact sound insulation performance. Comparing the impact sound insulation performance between the AMC25 and AMC40 discrete raised floor floating multiple layers of cement boards, the difference between single number ratings was below 3 dBA benchmark. The increment from single to double layer had slight increase on AIIC, and it kept the same with floating the third layer. Floating 3 layers of CB did not have any noticeable contribution on impact sound insulation. The advantage of higher mass for concrete topping was not favoured in the AMC25 and AMC40 discrete floating floor assemblies, however, the dry solution with cement boards demonstrated high impact sound insulation performance on the discrete raised floor. Choosing adequate floor mount corresponding to topping load is important in

https://doi.org/10.52202/069179-0260

practical applications though the difference was within 3 dBA benchmark.

3.2 IMPACT SOUND PRESSURE LEVEL SPECTRA UNDER DIFFERENT EXCITATION SOURCES

As the correction considering background noise and reverberation time is different in ASTM E1007-16 [9] and JIS A 1418 [10] is different, the directly measured SPL spectra are plotted in Figure 4 for comparison. The two standard impact sources have higher SPL than real human's walking with the steel-toe safety boots on both bare CLT and DLT. It is obvious the ISO tapping machine generated higher SPL on both structural floors. SPL spectra for both rubber ball and human walking demonstrate similar trend on mass timber floors, except the curves for rubber ball are about 20 dBA higher than human walking throughout the entire frequency domain. The SPL of tapping machine increases above 80 Hz, however that decreases for the rubber ball which is more similar to human walking SPL spectra. Human walking generated impact sound between 40 and 50 dBA, with the peak value merely 55 dBA for both SPL curves. The difference between maximum and minimum SPL on human walking is about 15 dBA, which is similar to the trend of rubber ball spectra.

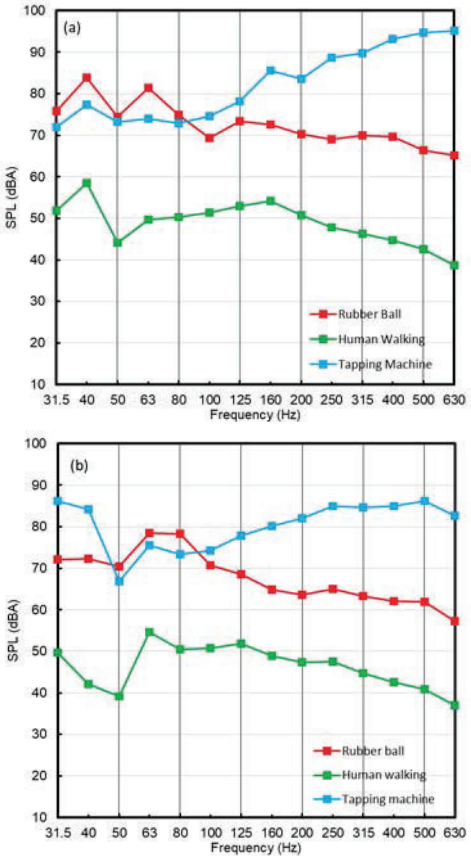

Figure 4: *Sound pressure level curves under different impact sources on bare (a) CLT and (b) DLT*

The SPL curves with three different sound sources on selected (a) continuous and (b) discrete raised floating floors on the DLT floor are shown in Figure 5. The continuous floating concrete assembly consists an elastic interlayer (AFM 35, Getzner) and a 50 mm thick concrete topping. The rubber ball demonstrates the same SPL trend as human walking, and the overall SPL difference between them is within 15 dBA. However, the SPL difference between tapping machine and human walking curve increases up to 30 dBA at 630 Hz. However, the SPL curve characteristics of rubber ball and tapping machine are similar to each other, except the rubber ball generated higher impact sound below 100 Hz. In the frequency range below 125 Hz, all three curves have similar trends with peaks and drops occur at 63 and 50 Hz, respectively. The SPL drop linearly above 125 Hz about 15 dBA for all spectrum, while the total SPL is mainly below 40 dBA.

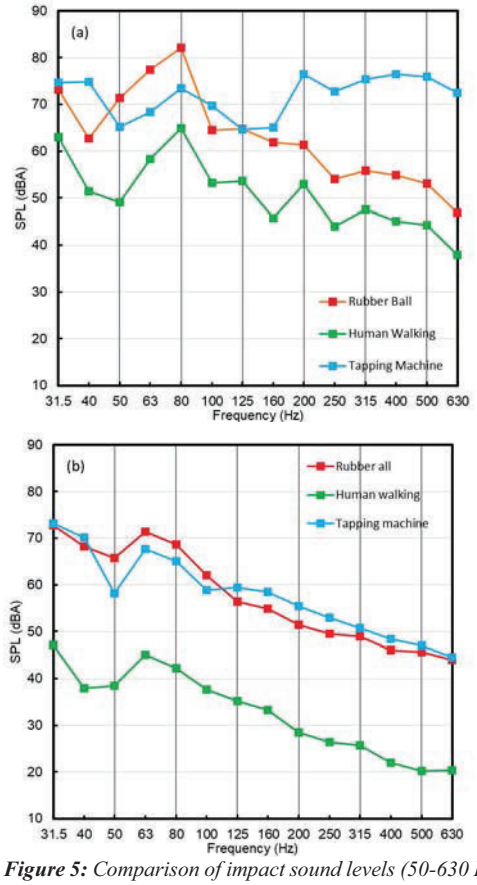

Figure 5: *Comparison of impact sound levels (50-630 Hz) of (a) continuous and (b) discrete floating floor assembly under different excitation sources*

In summary, rubber ball is an excitation source which can generate SPL spectra of similar frequency characteristics with that by human walking on mass timber floors. This is in contradictory to the conclusion that CLT bare floors mimicked the impact sound pressure level values of a bare concrete floor in [12], which was tested using the tapping

https://doi.org/10.52202/069179-0260

machine. ISO rubber ball is more suitable for impact sound testing of mass timber floors in the current study.

3.3 IMPACT SOUND PERFORMANCE UNDER ISO RUBBER BALL EXCITATION

As discussed above, floating double layer cement boards on the base raised floor showed high performance using the tapping machine. Further investigations and modifications are based on this assembly. Two types of cement boards and one gypsum board were selected as the alternative mass topping to concrete topping. According to Table 3: , the AMC40 raised floor floating 50 mm concrete topping is still the best solution with L_{Fmax} of only 64.8 dBA. Among the result of floating dry solution boards above, full size assembly of floating the double layer of USG (USG2) has the best performance. The full size USG2 improved the single number rating for 3 dBA on AMC40 discrete raised floor. However, the single number rating after installing GYP2 was 2 dBA lower than the AMC40 basic assembly. However, at the current stage, there is no performance criteria based the L_{Fmax} single number rating developed for mass timber floors. Future research is required if ISO rubber ball is adopted for standardized testing and evaluation of impact sound insulation performance of mass timber floor assemblies.

Table 3: *L_{Fmax} single number rating for selected discrete floating floor assemblies*

Bare DLT	Bare CLT	DLT+AMC40+INS	DLT+AMC40+INS+ CB2	DLT+AMC40+INS+ CB2 Engfloor	DLT+AMC40+INS+ C50	DLT+AMC40+INS+ USG2 Full	DLT+AMC40+INS+ USG2 Full Engfloor	DLT+AMC40+INS+ GYP2 Full
78.4	81.3	74.3	75.3	71.4	64.8	71.3	71.0	76.5

The impact sound pressure level spectra of two full size assemblies and selected small size floors are summarized in Figure 3.1. Even though JIS 1418 only requires the frequency between 50 and 630 Hz to derive the L_{Fmax} single number rating, the SPL spectra in this figure includes 31.5 to 3150 Hz which beyond the frequency region of both JIS 1418 and ASTM E1007, which shows a wider perspective on rubber ball impact sound test on discrete raised floating floor assemblies. In Figure 3.1 (a), the discrete floating floor assemblies are efficient in higher frequency region. Considering 40 dBA as a benchmark for a quiet room, most assemblies insulate the noise above 1250 Hz very effectively. Floating a 50 mm concrete topping insulates the noise above 200 Hz and makes most noise inaudible, and the assembly with floating 50 mm concrete topping had average 6-10 dBA lower SPL than floating the other dry solution toppings, and the 50 mm concrete topping had about 10 times of unit mass of the cement boards, so adding extra mass further reduced the resonant frequency of the assembly and improved the impact sound insulation performance.

In SPL curves of floating dry solution boards, an obvious peak occurs between 50 and 80 Hz where the L_{Fmax} ratings come from shown in Table 3: . On discrete floating floor system, mass may not be the only factor which affects the impact sound insulation performance, and material selection is critical. The least dense gypsum board (GYP) had better performance than the densest CB between 63 and 200 Hz. Double layer of USG boards brought the SPL below 40 dBA at 630 Hz which was at much lower frequency than 1250 Hz for CB2 and GYP2. Applying 40 dBA cut-off line in the SPL spectra i, floating 50 mm concrete topping dropped below that at 250 Hz. Material property should be considered on selecting the dry solution mass toppings. In summary, the full size USG2 assembly on AMC40 has outstanding performance. The SPL difference between this assembly and floating a small scale 50 mm concrete is within 5 dBA in average.

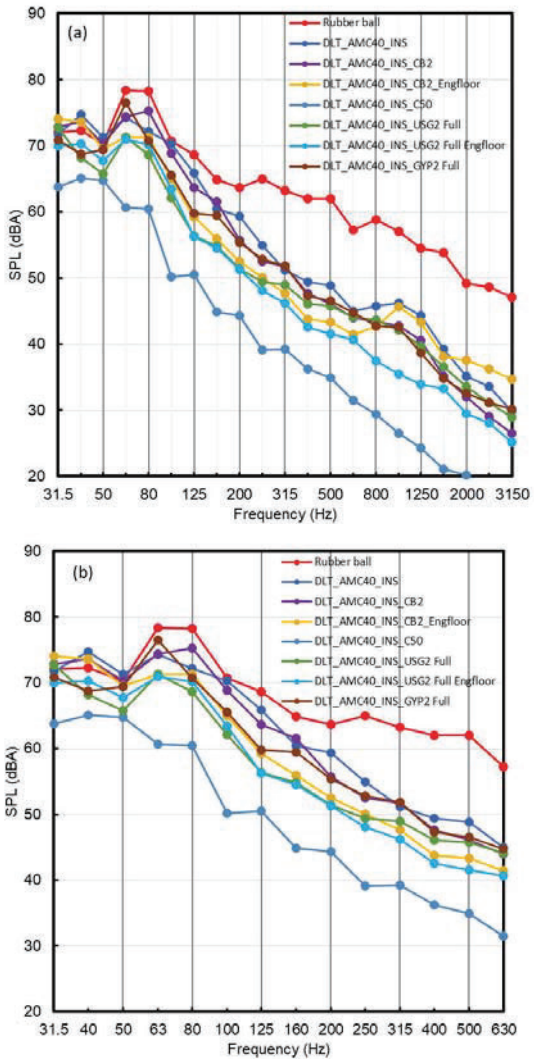

Figure 3.1 (a) The impact sound of discrete floating floor assemblies using the rubber ball (31.5 - 3150 Hz)

https://doi.org/10.52202/069179-0260

4 CONCLUSIONS

The raised discrete floating floor assemblies tested in this study provide high impact sound insulation performance on mass timber slabs. However, the excitation sources are of great importance to the evaluation of the performance.

1. The raised discrete floating floor is an effective method to attenuate impact sound on mass timber floor tested with ISO tapping machine according to ASTM standards. The raised discrete floor system with all three types of floor block mounts were able to reach AIIC higher than 60 dBA. The type of structural floor (CLT and DLT) did not have strong effect on impact sound insulation performance, and the thickness of concrete topping was not critical on improving the AIIC ratings.
2. The comparison between AMC25 and AMC40 floor mounts concluded that the load capacity of floor block mount had minor influence on impact sound insulation performance, and the discrete raised floors had similar SPL curve characteristics. Floating dry solution boards had similar single number rating as floating 38-50mm thick concrete topping, and it can attenuate middle to high frequency sound more effectively.
3. The ISO rubber ball is able to generate impact sound SPL spectra of similar frequency characteristics with that by human walking on bare mass timber floors and both continuous and discrete raised floating floors considering. When tested with the rubber ball, the discrete raised floating floor assembly with dry solution boards has similar single number rating as the selected elastic interlayers floating 50 mm concrete topping. The discrete raised floating floor assembly with 50 mm thick concrete had the lowest L_{Fmax}. However, performance criteria is need for adopting the rubber ball for impact sound insulation performance testing and evaluation of mass timber floors.

ACKNOWLEDGEMENT

The financial support from BC Forest Innovation Invest - Wood First program, the Natural Sciences and Engineering Research Council of Canada (NSERC) and University of Northern British Columbia (UNBC) is greatly acknowledged. We acknowledge the in-kind contributions from StructureCraft, Structurlam, Getzner and AMC Mecanocaucho, as well as the technical supports from Wood Innovation Research Lab at UNBC.

REFERENCES

[1] Caniato M., Schmid C., and Gasperella A. A comprehensive analysis of time influence on floating floors: Effects on acoustic performance and occupant's comfort. Appl. Acou., 166: 107339, 2020.

[2] Andargie MS, Touchie M, O'Brien W. A survey of factors that impact noise exposure and acoustics comfort in multi-unit residential buildings. Canad. Acou., 48:3, 2020.

[3] Bard D., et al. Modelling prerequisites - FEM/ SEA impact and airborne sound (RISE Report 2017:56). RISE Research Institutes of Sweden AB, Sweden, 2017.

[4] Zhao Z., Zhou J., Li G. Efficiency of floating concrete toppings on mass timber floors for impact sound insulation. Proceedings of World Conference on Timber Engineering, 2021

[5] Sabourin I. "Measurement of Airborne Sound Insulation of 8 Wall Assemblies & Measurement of Airborne and Impact Sound Insulation of 29 Floor Assemblies" (Report No. A1-006070.10). National Research Council Canada, Ottawa, Canada, 2015

[6] Homb A., Guigou-Carter C., and Rabold A. Impact sound insulation of cross-laminated timber/massive wood floor constructions: Collection of laboratory measurements and result evaluation. Build. Acou. 2017, 24(1):35-52

[7] Zhou J., Zhao Z. Apparent impact sound insulation performance of cross laminated timber floors with floating concrete toppings. Internoise, 2021

[8] Alberta Provincial Building and Fire Administrators, National Fire Code - 2019 Alberta Edition. 2020

[9] ASTM E1007-16, Standard Test Method for Field Measurement of Tapping Machine Impact Sound Transmission Through Floor-Ceiling Assemblies and Associated Support Structures, ASTM International, West Conshohocken, PA, 2019.

[10] JIS A 1418-2. Acoustics – measurement of floor impact sound insulation of buildings – Part 2: Method using standard heavy impact sources. Japan Standard Association, Tokyo, Japan, 2000

[11] National Research Council (NRC). National Building Code of Canada. 2020, Canada.

[12] Hindman D.P., and Golden M.V. Acoustical properties of southern pine cross-laminated timber panels. J. Archit. Eng. 2020; 26:2

World Conference on Timber Engineering Oslo 2023

SOUND INSULATION IN CROSS LAMINATED TIMBER BUILDINGS AND THE EFFECT OF JUNCTIONS AND FASTENERS

Eli Toftemo[1], Anders Løvstad[2]

ABSTRACT: Sound insulation in cross laminated timber buildings can be challenging and is difficult to predict due to lack of reliable predicting models. Details in either the construction itself or in mounting may cause measurement results to vary significantly. Solutions vary notably between projects. Pre-accepted solutions are sparse and in high demand. Residential buildings are especially challenging and commonly need complementary floors, suspended ceilings and wall linings due to high sound insulation requirements. Clients and consumers in Norway often want the timber to be exposed, which make the flanking sound control essential.

Sound tests on a full scale CLT model have been conducted to identify efficient solutions. Flanking sound paths were tested using various resilient interlayers and fasteners in the junctions, and the vibration level difference across the junctions was measured between rooms. Elastically decoupled angle brackets performed better than ordinary angle brackets and screws that penetrate the vibration protection. Additionally, sound insulation measurements are reported on for various slab constructions, including both light and heavy weight complementary floors.

KEYWORDS: Cross Laminated Timber, junction damping, sound insulation

1 INTRODUCTION

Use of cross laminated timber (CLT) in building constructions has increased rapidly in recent years due to its environmentally sustainable and light weight capacities, rapid and efficient assembly, and other desirable physical parameters as summarized by Di Bella et al. [1]. Consequently, the interest from architects, developers, engineers, and politicians has increased notably. Studies on sustainability such as the overview of life-cycle assessment (LCA) by employing CLT in building constructions presented by Younis et al. [2], finding a possible reduction in greenhouse gas emissions of around 40 % is likely to further enhance the interest in CLT.

Espinoza et al. [3] estimated a growth in annual global CLT production from 2010 to 2015 of 250 %, with most of the growth occurring in new production countries outside Europe. Brandner et al. [4] similarly predicted an accelerated rise in the global production volume towards 2025, and particularly in countries such as Canada, United States and Japan, which is accordance with Plackner [5], who projects a possible annual global production of 3 million m^3 by 2025. Muszyński et al. [6] summarized the above and gives an interesting overview of the global CLT manufacturing plants per 2016. Sandoli et al. [7] reported an increase in CLT production in Europe alone from 650,000 m^3 in 2015 to 1,2 million m^3 in 2020. As the use of CLT has surged, the need for standardization and regulative processes for product, testing, mounting, and requirements of a solid timber construction system with CLT quickly became imminent [4], and is now a continuous ongoing process.

National guidelines and documentation of CLT floor and wall constructions published over the last couple of decades [8,9] give good starting points for dimensioning, where the latter presently is being revised as reported by Mahn et al. [10]. Such guidelines are supplemented by investigations of airborne and impact sound insulation for various floor assemblies and resilient layers with CLT constructions, as done by Verdaxis et al. [11], while Homb et al. [12] collected and compared impact sound insulation for typical floor assemblies in different European countries (and laboratories).

In Norway, CLT constructions in buildings with sound requirements are typically mounted with extensive use of screws, commonly also going through the strategically placed elastic layers, reducing their effect [13]. The dimensions of the CLT slabs and walls vary, but due to airborne and impact sound requirements heavy floating floors, addition of mass directly onto slabs, suspended ceilings and separate wall linings are common measures to ensure sufficient sound insulation quality. The extent of these measures is governed not only by the sound insulation requirements themselves, but in many cases

[1] Eli Toftemo, Brekke & Strand Akustikk, Norway, eto@brekkestrand.no
[2] Anders Løvstad, Brekke & Strand Akustikk, Norway, anl@brekkestrand.no

https://doi.org/10.52202/069179-0261

just as much by which margin the constructors and designers are comfortable with. Experience with directly comparable constructions best enable reduction of such measures, but due to the detailing, vulnerability of construction errors, and variations in junction assembly and in the constructions themselves, such experience is often somewhat limited. Accordingly, Simmons [14] argued that specific experience with the same construction allows for reduced calculation margins with CLT, especially if junctions and lining types are known, while a provisional margin of at least 8 dB is needed for relatively unknown constructions. Such variations are not uncommon when a certain number of presumably identical rooms are included in measurement programs in larger measurement documentation setups, to the authors experience either. When such variations occur, they are usually due to specific construction errors, and not systematic design errors. Systematic deviations from project requirements may also be of such magnitude with limited control of junction design or linings.

CLT is presently considered in buildings with high sound insulation requirements, such as dwellings, cultural centres, and theatres, despite the increased challenges in prediction of sound insulation and vibration compared with heavier materials and constructions. Malo et al. [15] reported on structural design issues with a 14-storey CLT in 2016, and since then even more acoustically complex and higher buildings have been built or are planned in Scandinavia [16].

Additionally, clients and consumers in Norway often want the CLT to be exposed to a large extent, which makes control of flanking sound and junctions essential. Measurements of vibration reduction indices using various elastic interlayers and fasteners have been done by Morandi et. al. [17], who compared junction damping and sound insulation between floors and rooms for a selection of available products with elastic interlayers. Increased knowledge of junction damping and design are essential if wall linings and suspended ceilings should be omitted, the extent of floating floors reduced, and visible timber increased. However, available research results are not always easy to apply in an actual building project.

This paper reports on measurements of flanking sound paths using various resilient interlayers and fasteners in the junctions, and the vibration level difference across the junctions between rooms. Airborne and impact sound insulation measurements are done for various slab constructions, including both light and heavy weight complementary floors. The possible removal of wall linings and suspended ceilings with good junction design is also addressed.

2 THE TEST SETUP

A full-scale CLT mock-up construction was built in an industrial warehouse, with two rooms on the ground floor and one room on the top floor, as shown in Figure 1. The top floor could be lifted from the ground floor by hydraulic jacks, which allows repetitive testing of various resilient interlayers (RI), fasteners, angle brackets or screws commonly used as vibration protection in buildings with sound requirements. The different RI types were applied in the junctions vertically between floors or horizontally between adjacent rooms. These mounting methods were changed and repeated as the rooms were fitted with combinations of suspended ceilings, light or heavy floating floors and wall linings to assess how the mounting method affected the sound insulation and flanking sound transmission.

Figure 1: *Test room set-up.*

A schematic layout of the mock-up is shown in Figure 2, where the room dimensions and thicknesses of the CLT walls and floors are given. Vertical CLT panels were 3-ply of 100 mm thickness throughout. The ground floor and top roof were 3-ply 120 mm thick CLT panels, while the horizontal slabs between the floors and roof of the one-story high part were 5-ply 160 mm CLT. The test rig was delivered from Splitkon AS, element strength classes T15 and T22. The density of the wood is 460 kg/m^3.

Tests of airborne and impact sound insulation were done according to ISO 16283-1 and -2 [18,19], respectively. Variations in damping across building elements were assessed by measurements of velocity level difference across building elements. The velocity level difference is described in ISO 10848-1 [20].

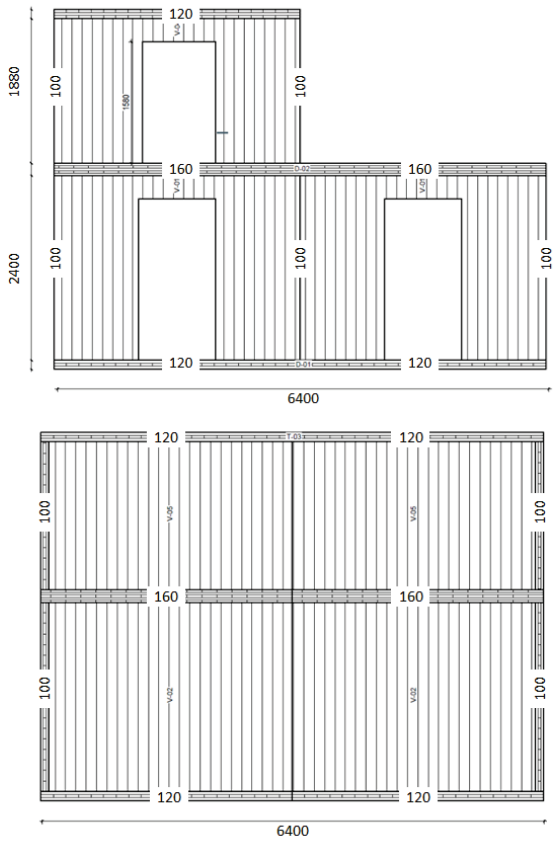

Figure 2: *Vertical section drawings of the test mock-up; a) length section and b) width section. All dimensions are given in mm.*

Four measurement positions were employed on each panel/building element to measure the velocity level difference, as Figure 3 shows. Tests were carried out using three different sound sources; pink noise fed through a loudspeaker, a tapping machine and hammer excitation. The results from hammer excitations have been left out since the excitation proved difficult to control. Results from junction damping shown in this paper have been conducted using a loudspeaker placed on sylomer pads as excitation, with two source positions for each measurement.

Velocity level differences show averaged values of two sets of sensor positions mounted on two corresponding walls, except for horizontal measurements and measurements with the floating floor, where only one set is included. Alltogether eight positions on the slab in the receiving room were used for horizontal measurements of junction damping.

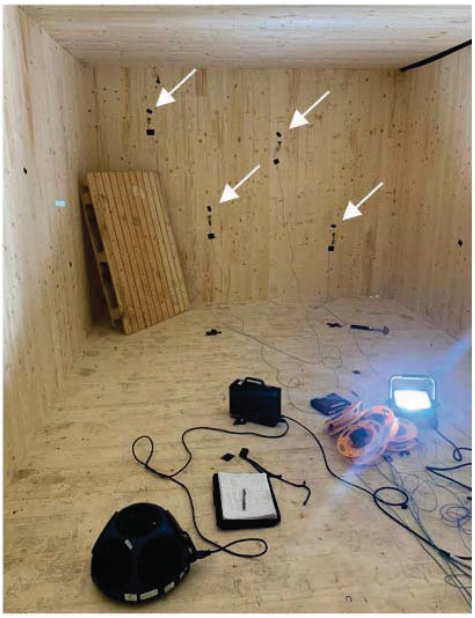

Figure 3: *Photo of sensor setup inside of the test rooms. Sensor positions indicated with white arrows.*

3 MEASUREMENTS RESULTS

3.1 VERTICAL JUNCTION DAMPING

Figure 4 shows the principle vertical junction between floors. The drawing displays a configuration with a RI between the upper wall and the slab and screws connecting the slabs to both the upper and lower wall.

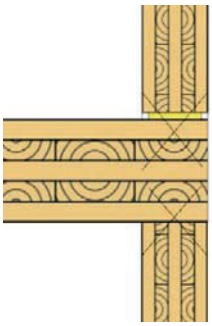

Figure 4: *Drawing of the vertical junction with resilient interlayer and screw fasteners indicated.*

Measurements of velocity level difference between floors using various RI fitted between the floors are shown in Figure 5. The lines show the arithmetic middle value from measurements with each RI type. One measurement (black line) was conducted without using any fastener in the junction between floors.

Measurements using screws and regular angle brackets as fastener resulted in similar results. Angle brackets placed on a RI resulted in marginally better damping above 400 Hz, while elastically decoupled angle brackets gave significantly higher damping.

https://doi.org/10.52202/069179-0261

These tests showed that the type of fastener has a paramount effect on the junction damping between floors.

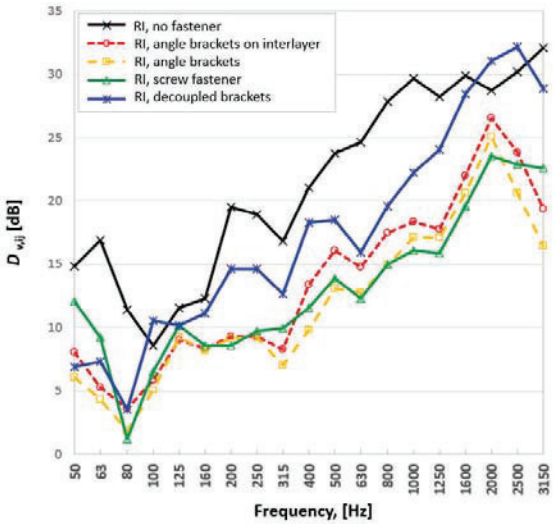

Figure 5: *Measurement results with RI between floors and various fasteners. Blue line shows damping obtained with elastically decoupled angle brackets, red line angle brackets with elastic interlayer between the bracket and the CLT, beige line regular angle brackets, green line screw fasteners and black line without fastener.*

A series of tests were conducted using screws of various thicknesses and centre distance. Both partially threaded (PT) screws, and fully threaded (FT) screws were tested. All screws were mounted diagonally in pairs through the wall-floor junctions between floors. While changing the type of fasteners made an impact on the result, the screw configurations resulted in little variation in junction damping.

An interesting finding is that RI between the floors did not improve the damping around the middle frequencies when screws were inserted through the junction, which corresponds well to results reported by Morandi et al. [17]. This is shown in Figure 6 where a measurement using no RI (black line) is compared to tests conducted with different RIs. This indicates that screws that penetrate the resilient interlayer ruin the effect of the RI and gives limited vibration protection.

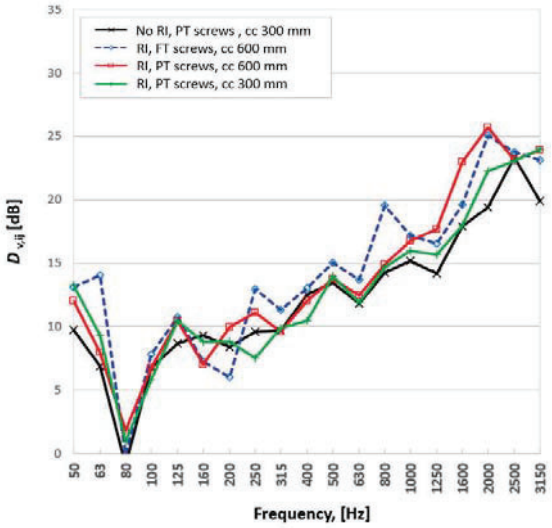

Figure 6: *Measurement results of vertical damping with screw fasteners of various types and spacing. Blue line shows damping obtained with FT screws cc 600 mm, red line PT screws cc 600 mm, green line PT screws cc 300 mm and black PT screws cc 300 mm and no elastic interlayer between the floors.*

3.2 HORIZONTAL JUNCTION DAMPING

Measurements on horizontal junction damping were also conducted. The top floor of the mock-up was removed and the roof slab and connection walls were cut in half, as shown schematically in Figure 7. A floating floor and wall linings were applied in the sending room to control the flanking paths.

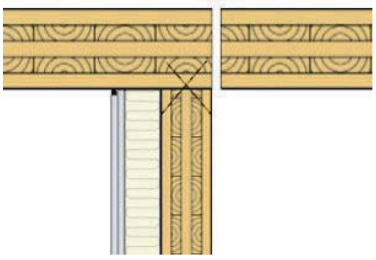

Figure 7: *Drawing of vertical cross section displaying the junction between horizontally adjacent rooms.*

Various fasteners were inserted across the cut between the horizontally adjacent rooms. Sensors were mounted on the roof slab on both sides of the parting wall.

https://doi.org/10.52202/069179-0261

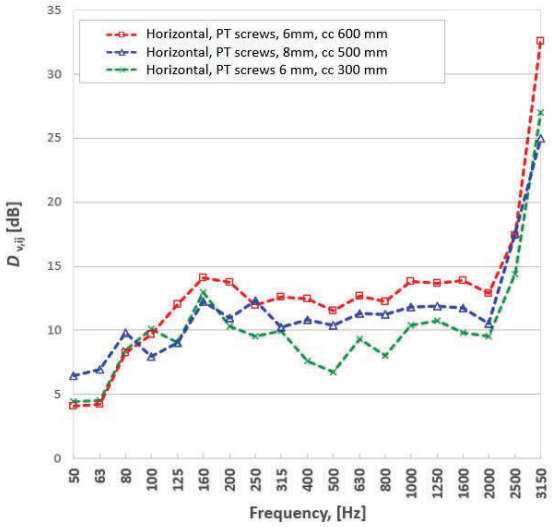

Figure 8: *Measurement results of horizontal damping with screw fasteners.*

Figure 6 and Figure 8 illustrate that screw fasteners measured across horizontal and vertical junctions result in similar damping, around 10 dB, in the middle frequencies. The horizontal damping is higher than in the vertical direction in the low frequencies, while vertical damping is better in the high frequencies.

The results from the horizontal measurements also show improved damping with increased centre distance between screws, as opposed to vertically where the results are the same, as the red and green line in Figure 6 show. Morandi et al. [17] points out that the weight of the overlying structure could cause a connection between the elements that reduces the effect of the type of fastener used.

3.3 VERTICAL JUNCTION DAMPING WITH AND WITHOUT HEAVY FLOOR CONSTRUCTIONS

To add mass to the CLT slab 100 mm gravel was laid directly onto the CLT floor, with a floating floor consisting of 40 mm mineral wool with 70 mm concrete on top.

Measured velocity level differences with and without heavy floating floor are shown in Figure 9. Sylomer is used as elastic interlayer in both measurements, and decoupled angle brackets, GePi 240, as fastener.

Adding the floating floor increased the velocity level difference more than 15 dB from 125-1000 Hz.

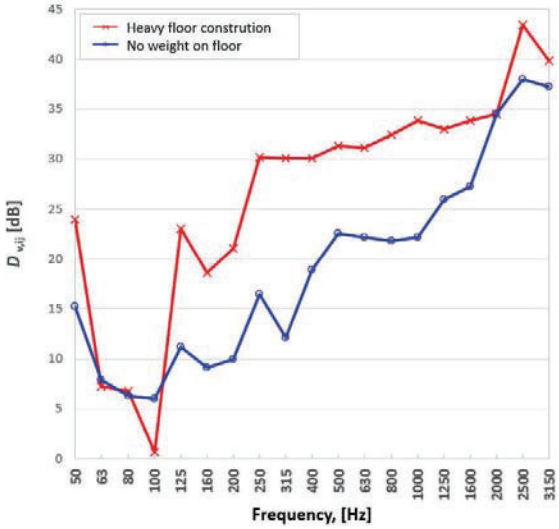

Figure 9: *Measurement results with (red line) and without (blue line) heavy floor construction.*

3.4 SOUND INSULATION WITH FLOATING FLOORS

Airborne and structural sound insulation was measured with different floors constructions, ceilings and linings. Vertical measurements shown below are conducted with various floors as described in Table 1, but without a suspended ceiling to keep the wood exposed in the bottom room. Linings were used to reduce the flanking sound, making the sound travelling directly through the slab would dominant.

Table 1: *Description of floating floor constructions. Exposed CLT ceiling in receiving room.*

Floor type	Floating floor (top to bottom)
A	2x22 mm chipboard, 40 mm mineral wool
B	2x22 mm chipboard, 135 mm joists on 25 mm Sylodyn. Insulated cavity
C	2x22 mm chipboard, 135 mm joists on 25 mm Sylodyn. Insulated cavity. Concrete slabs in cavity covering the majority of the floor area.
D	2x22 mm chip board, 40 mm mineral wool, 100 mm gravel
E	70 mm concrete cast, 40 mm mineral wool, 100 mm gravel

Results for airborne and impact sound insulation with the various floor types described in Table 1 are shown in Figure 10 and summarized in Table 2. As expected, adding weight to the light weight CLT floor construction improves the sound insulation noticeably in the lower frequencies. Gravel added directly to the CLT floor gave considerable improvement, especially for impact sound insulation, as the results with floor types D and E show. The results indicate that the type of the floating floor is not crucial if weight is added directly to the CLT floor.

https://doi.org/10.52202/069179-0261

Measurements C, D and E comply with the current Norwegian minimum requirements for sound insulation between dwellings of $R'_w \geq 55$ dB and $L'_{n,w} \leq 53$ dB.

Table 2: *Results from measurements of airborne and impact sound insulation on various floating floor constructions.*

Floor type	R'_w ($C_{50\text{-}5000}$) [dB]	$L'_{n,w}$ ($C_{I,50\text{-}2500}$) [dB]
A	53 (-2)	57 (6)
B	54 (-2)	55 (5)
C	58 (-1)	52 (3)
D	63 (-3)	44 (9)
E	61 (-2)	43 (7)

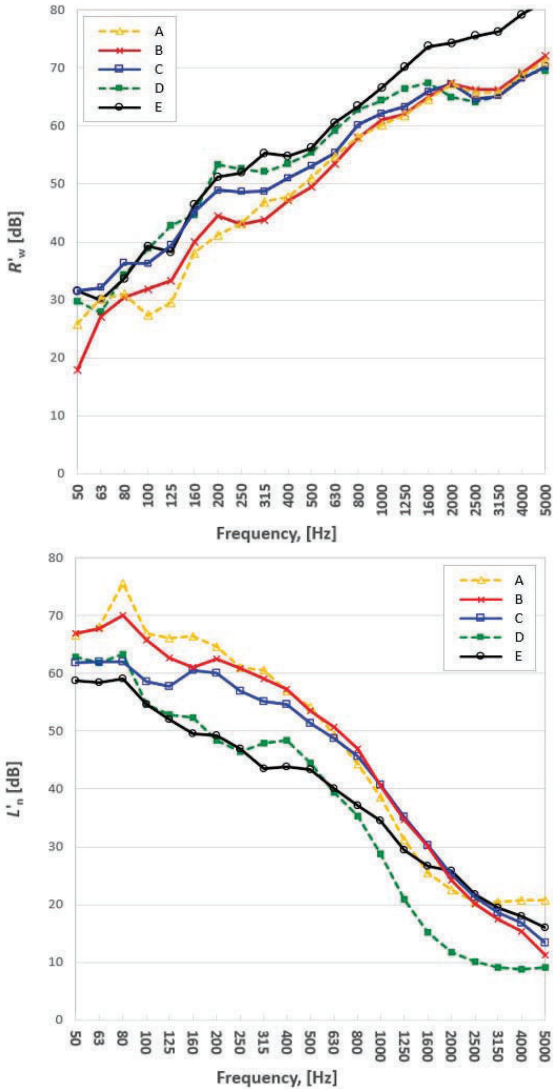

Figure 10: *Vertical airborne (upper) and impact (lower) sound insulation measured between floors with various floor constructions. Slab element was kept exposed in the bottom room, i.e. no suspended ceiling.*

3.5 EFFECTS OF HEAVY FLOOR CONSTRUCTIONS ON SOUND INSULATION WITH EXPOSED CLT

Measurements were performed vertically on a heavy floating floor construction equal to construction E described in Table 1. Elastically decoupled angle brackets were used as fastener in the junction between the floors.

Repetitive tests were done exposing various parts of the CLT construction in the bottom room. All walls and ceiling on the top floor were kept visible throughout the measurements. Results are shown in Figure 11 and summarized in Table 3.

These tests indicate that part of the CLT can be kept visible when using a sufficiently good fastener and applying weight to the floor and still fulfil quite high sound insulation requirements, including the Norwegian minimum requirements for dwellings. Impact sound insulation increased by 6 dB when the suspended ceiling was added. An improvement in the low frequency region from 80-125 Hz can be seen for impact sound insulation with a suspended ceiling, which is especially important to subjective annoyance [21]. Still, the spectrum adaptation terms were equal and smaller without the suspended ceiling for airborne and impact sound insulation, respectively.

The other tests show a up to 3 dB decrease in sound insulation from exposing the wood construction. All three measurements fulfil the minimum sound regulations in Norway between dwellings.

Table 3: *Result table of measurements of airborne and impact sound insulation on heavy top floor and various degree of visible CLT in bottom room.*

Meas. no.	Description	R'_w (+ $C_{50\text{-}5000}$) [dB]	$L'_{n,w}$ ($C_{I,50\text{-}2500}$) [dB]
E	Exposed CLT in ceiling. Linings in bottom room.	61(-2)	43(7)
F	Sound insulated ceiling, exposed wall in bottom room.	62(-2)	39(8)
G	Sound insulated ceiling. Linings in bottom room.	64(-3)	37(10)

https://doi.org/10.52202/069179-0261

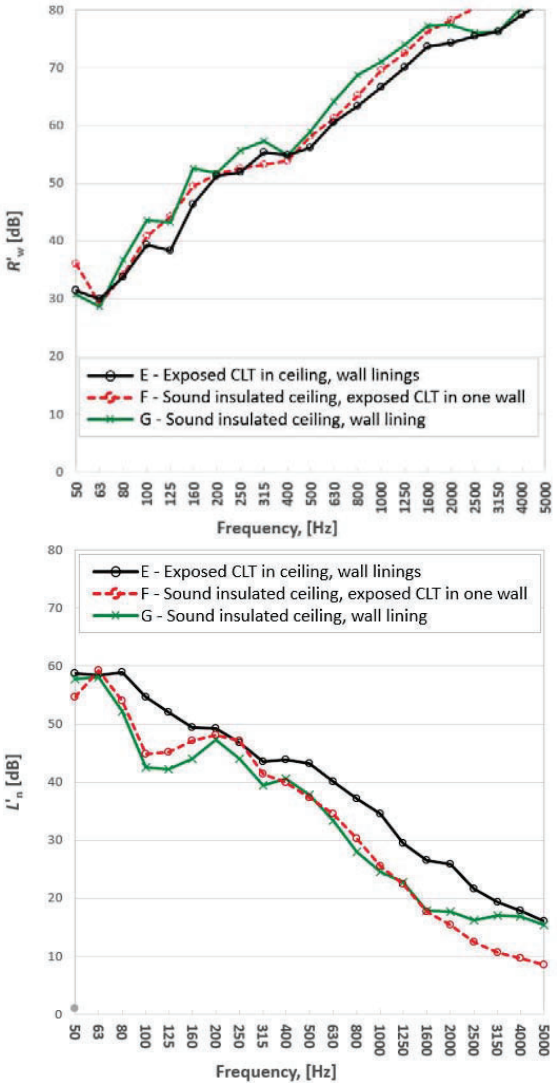

Figure 11: *Vertical airborne (upper) and impact (lower) sound insulation between floors showing effects of visible wall/slab elements.*

4 CONCLUSIONS

The variation in damping between various configurations of elastic interlayers and fasteners in junctions has been assessed by measuring the velocity level difference on a full scale CLT mock-up. Measurements of sound insulation were done in parallel to the measurements of velocity level differences.

Results show that the type of fastener is crucial to the junction damping. The use of elastically decoupled angle brackets proved to increase the damping compared to regular angle brackets and traditional screw fasteners.

Tests conducted on various screw fasteners show low damping effect and little change between various configurations regardless of elastic interlayer. Measurements of horizontal damping proved more sensitive to various configurations of screw fasteners than vertical measurements. As a whole, the test results suggest that the choice of fastener has greater impact on the damping than the type and use of vibration protection.

Heavy floating floors added onto the CLT floor significantly increased the velocity level differences between rooms, as various upper floor constructions were tested. Weight applied directly on to the CLT floor showed a significant increase in low frequency sound insulation.

Three floor constructions using a heavy floor construction were in accordance with the minimum regulations for sound insulation between dwellings in Norway, one of which was measured with exposed CLT in the ceiling. Thus, the measurements of sound insulation reveal that part of the wood can be kept visible when using a favourable fastener and applying weight to the floor.

ACKNOWLEDGEMENTS

This project was initiated by Lars Strand, senior consultant at Brekke & Strand Akustikk AS, along with Splitkon AS. Contributors are Splitkon, Green Advisers, Brekke & Strand Akustikk, Skogtiltakfondet, Innovasjon Norge, Christian Berner, Rothoblaas and others.

REFERENCES

[1] Di Bella et. al.: Acoustic characteristics of Cross-Laminated Timber systems, *Sustainability*, 2020, 12, 5612.

[2] Younis et. al.: Cross-laminated timber for building construction: A life-cycle-assessment overview, *J. Build. Eng.*, 2022, 52, 104482.

[3] Espinoza et. al.: Cross-Laminated Timber: Status and Research Needs in Europe, *BioResources*, 11(1):281-295.

[4] Brandner et. al.: Cross laminated timer (CLT): overview and development, Eur. J. Wood. Prod., 2016, 74: 331-351.

[5] Plackner H: Brettsperrholz wächst global. (https://www.holzkurier.com/schnittholz/2015/02/brettsperrholz_waechstglobal.html), last accessed 27.02.2023.

[6] Muszyński et. al.: Insights into the Global Cross-Laminated Timber Industry, *BioProducts Bus.*, 2017, 2:77-92.

[7] Sandoli et. al.: Sustainable Cross-Laminated Timber Structures in a Seismic Area: Overview and Future Trends, *Appl. Sci.*, 2021, 11(5):2078.

[8] Homb et al.: Lydoverføring i byggesystemer med massivtreelementer, SINTEF Byggforsk, 2011, 80 (In Norwegian).

[9] Mahn et al.: *RR-335: Apparent Sound Insulation in Cross-Laminated Timber Buildings*, Technical Report National Research Council Canada, 2017.

[10] Mahn et al.: Measurement of the Vibration Reduction Index for Cross-laminated Timber Walls in Canada, In: *Proc. 24th International Congress on Acoustics*, 2022, Gyeongju, Korea.

[11] Verdaxis et al.: Evaluating Laboratory Measurements for Sound Insulation in Cross-Laminated Timber

https://doi.org/10.52202/069179-0261

(CLT) Floors: Configurations in Lightweight Buildings, *Appl. Sci.*, 2022, 12, 7642.
[12] Homb et al.: Impact sound insulation of cross-laminated timber/massive wood floor constructions: Collection of laboratory measurements and result evaluation, *Building acoustics*, 2017, 24(1): 35-52.
[13] Toftemo et. al.: Sound insulation in cross laminated timber buildings and the effect of junction damping, In: *Proc. 24th International Congress on Acoustics*, 2022, Gyeongju, Korea.
[14] Simmons C: Can our standard digital tools predict the sound insulation in wooden buildings? A systematic comparison with laboratory and field measurements on various floor constructions, *Proc. Baltic-Nordic Acoustics Meeting 2021*; 3-5 May 2021; Oslo, Norway.
[15] Malo et al.: Some structural design issues of the 14-storey timber framed building "Treet" in Norway, *Eur. J. Wood. Proc.*, 2016, 74:407-424.
[16] https://www.sarakulturhus.se/en/a-climate-smart-house/building-in-wood-has-a-distinguished-past-and-a-bright-future/, last accessed 13.03.2023.
[17] Morandi et. al.: Measurement of flanking transmission for the characterisation and classification of cross laminated timber junctions. *Applied acoustics*, 2018, 141:213-222.
[18] ISO 16283-1: Acoustics – Field measurement of sound insulation in buildings and of building elements – Part 1: Airborne sound insulation, 2014.
[19] ISO 16283-2: Acoustics – Field measurement of sound insulation in buildings and of building elements – Part 2: Impact sound insulation, 2020.
[20] NS-EN ISO 10848-1: Acoustic – Laboratory and field measurements of flanking transmission for airborne, impact and building service equipment sound between adjoining rooms. Part 1: Frame document., 2017.
[21] Løvstad et al.: Perceived sound quality in dwellings in Norway, In: Proc. 12th ICBEN Congress on Noise as a Public Health Problem, 2017.

World Conference on Timber Engineering Oslo 2023

INFLUENCE OF MECHANICAL FASTENER SPACING ON ACOUSTIC PERFORMANCE IN TIMBER COMPOSITE PANELS

Aedan Callaghan[1], Wilson Byrick[2]

ABSTRACT: Mass timber construction is an increasingly common way of building taller and larger wood buildings utilizing renewable building materials with lower embodied carbon. With a lighter mass and higher flexibility relative to concrete, however, a mass timber panel provides relatively poor acoustic separation between adjacent spaces. This poor acoustic performance combined with the desire for exposed mass timber ceilings means that an additional subfloor layer decoupled by an acoustic interlayer, is often used to provide adequate separation between spaces within the building. In some structural systems, screw fasteners through the acoustic interlayer maybe required. This study investigates the deterioration of the airborne and structure borne sound transmission performance due to the addition of metal fasteners through interlayer 304.8 mm, 609.6 mm and 1219.2 mm on centre (o.c.). The change to both the airborne and structure borne sound transmission is directly related to the spacing of the fasteners, with the most significant decrease in performance noted between 200-4000 Hz. This data provides insight into the performance of composite timber floor systems requiring fasteners through the resilient interlayer and will assist with designing these systems with more certainty in regard to the sound transmission that will occur within the building.

KEYWORDS: Acoustics, Resilient Interlayer, Cross Laminated Timber

1 INTRODUCTION

Mass timber has rapidly gained popularity due to the lighter weight of buildings, faster speed of construction, and lower embodied carbon compared to concrete structures. The most common type of mass timber panel is cross laminated timber (CLT), where dimensional lumber is assembled in alternating directions perpendicular to the previous layer. The panels are then adhered with structural adhesive and pressed into panels, typically with an odd number of layers/plies (3-ply, 5-ply, 7-ply, etc.) [1].

However, with this lower mass and stiffness comes worse acoustic performance. A typical bare 3-Ply CLT at 104.8 mm thickness and having a mass of 53.66 kg/m^2 is measured as having a sound transmission class (STC) and impact insulation class (IIC) of 38 and 21 respectively [2]. To put this in context, the International Building Code (IBC) 2021 section 1206 requires STC 50 or higher and IIC 50 or higher to separate any living units with adjacent spaces [3]. This requires a robust assembly that can provide this 12-point improvement to STC and 29 point improvement to IIC.

To accommodate the desire for the mass timber ceiling to remain exposed, a resilient interlayer between the mass timber structural panel and an additional subfloor mass layer is the most common approach to improving the acoustics. This type of floating floor system can drastically improve both the airborne and structure borne acoustic performance of the timber floor panel. The resonance of floating floors (f_0) has been well studied and can be calculated based on spring stiffness (K_F), air stiffness (K_A) and mass sitting on the spring (m) as shown in equation (1) [4].

$$f_0 = \sqrt{\frac{K_A * K_F}{m}} \quad (1)$$

When the CLT or mass timber panel is designed as the full floor structural system, the additional topping can be fully decoupled and act as the mass layer needed for the floating floor. However, the use of timber composite floor systems can sometimes provide the most efficient structural system for a building and requires the timber and topping, typically normal concrete, to be mechanically connected to utilize the strength of both materials (timber typically in tension, concrete in compression) [1]. Given that a resilient interlayer is often the main form of added sound control to improve the acoustic performance, the addition of mechanical fasteners in this location will inhibit the overall acoustic performance. While many projects have utilized these composite systems with fasteners penetrating through the acoustic interlayer, little data is available to quantify the degradation on the airborne and structure borne sound

[1] Aedan Callaghan, Pliteq Inc, Canada, acallaghan@pliteq.com
[2] Wilson Byrick, Pliteq Inc, Canda, wbyrick@pliteq.com

https://doi.org/10.52202/069179-0262

transmission of these composite panels compared to the fully decoupled floating floors.

Rigid or semi rigid penetrations through an acoustic isolation system are often referred to as a short circuit as they provide an unintended path for vibrations to travel and bypass the intended isolation system. Previous research on the effects of short-circuiting resilient channels with improper installation showed that the number of fasteners shorting out the resilient channels had a significant impact on performance [5]. Up to a 6dB decrease to the STC rating and 9 dB decrease to the IIC rating has been observed when the fasteners penetrating though the resilient channel into the joists were spaced at 609.6 mm o.c. by 406.4 mm o.c.

This study aims to provide a similar understanding of short circuiting of the resilient interlayer in mass timber. The effect of these short circuits and the influence of spacing will be analyzed with 3 different spacings of 304.8 mm, 609.6 mm and 1219.2 mm on centre (o.c.) based on some common timber concrete composite designs [6].

2 THE ASSEMBLY

A 3-Ply CLT assembly with resilient interlayer and wood subfloor was assembled at Intertek ATI floor ceiling acoustical test chamber. The test chamber has a top opening of 3023 mm by 3632 mm with the exposed area in the receiving room below of 2896 mm by 3505 mm. A plan view of the assembly is shown in Figure 2. Intertek-ATI is accredited to perform ASTM E90 and E492 by the International Accreditation Service.

A cross section of the assembly is shown in Figure 2. In order to be able to add the self-tapping screws in an iterative fashion, a thinner 3-ply CLT was selected as the subfloor panel. A summary of the components in the assembly with thickness and weight are provided in Table 1.

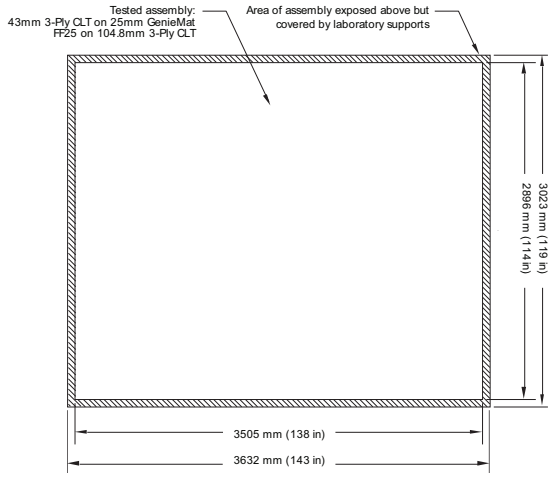

Figure 1: *Plan view of the tested assembly and lab chamber dimensions*

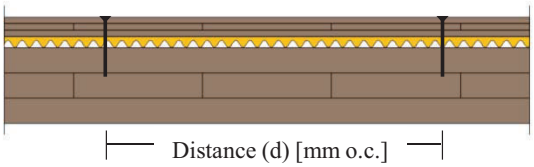

Figure 2: *Section view of the tested floor-ceiling assembly*

2.1 STRUCTURAL PANEL

A 3-ply cross laminated timber was used as the base structural panel for this testing. The panel measured at 104.8 mm thick panel with a mass of 53.66 kg/m^2.

2.2 RESILIENT INTERLAYER

A 25 mm recycled rebounded rubber elastomeric interlayer with a dimpled profile named GenieMat® FF25 was utilized as the decoupling material for this testing. It has an areal mass of 10.2 kg/m^2.

2.3 TOPPING

A thinner 3-ply CLT was used as the topping subfloor layer in this test series. It measured 44 mm in thickness with a mass of 23.43 kg/m2.

2.4 SELF-TAPPING SCREW

Fully threaded self-tapping screw with countersunk head 127 mm length were used for mechanically fastening the subfloor to the structural CLT and penetrate through the resilient interlayer.

Table 1: *Assembly component dimension and weights*

Component	Thickness (mm)	Mass (kg/m^2)
3-Ply CLT (Base)	104.8	53.66
GenieMat FF25	25	10.27
Thin 3-Ply CLT (subfloor)	44	23.43
Total	173.8	87.36

3 TEST PROCEDURES

The assembly was tested according to ASTM E90 and ASTM E492 with 3 different spacings of screws penetrating the resilient interlayer. These short circuits were created by fastening 9, 30 or 99 screws through the 44 mm subfloor panel and 25 mm GenieMat FF25 with 58 mm of embedment into the structural 3-Ply CLT panel. The assembly was tested with no short circuits. The first 9 screws were added at a 1219.2 mm o.c spacing. The assembly was then retested. The number of short circuits was increased to 30 at a 609.6 mm o.c. spacing and retested. Finally, the number of short circuits was

https://doi.org/10.52202/069179-0262

increased to 99 with a 304.8 mm o.c. spacing. The locations of each short circuit are shown in Figure 3A-D.

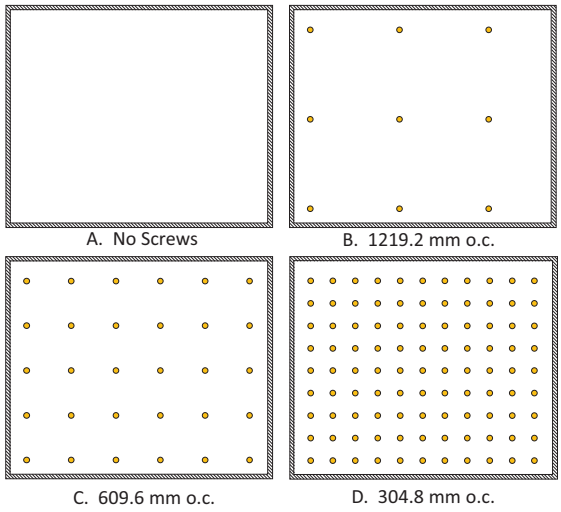

Figure 3: *Location of screws for the various configurations of short circuits. A: baseline case with no short circuits. B: 9 screws spaced 1219.2 mm o.c., C: 30 screws spaced 609.6 mm o.c., D: 99 screws spaced 304.9 mm o.c.*

4 RESULTS AND DISCUSSION

A summary of the STC and IIC single number ratings for each fastener spacing can be seen in Table 2. The STC rating decreased from 47 with no short circuits to 39 with screws at a 304.8 mm o.c. spacing. The IIC decreased from 41 with no short circuits to 35 with the screws at 304.8 mm o.c. for a total change of 6 IIC points. The HIIC was most affected by the increase in short circuits and decreased from 52 to 34 over the test series. Meanwhile the LIIC remained quite stable at 50-51 throughout all 4 tested assemblies.

Table 2: *Summary of STC and IIC performance*

Fastener Spacing (mm o.c.)	STC	IIC	HIIC	LIIC
None	47	41	52	50
1219.2	46	40	42	51
609.6	44	38	38	51
304.8	39	35	34	50

The 1/3 octave band frequency plots of transmission loss (TL) and normalized impact sound pressure levels (NISPL) for each test can be seen in Figure 4. While single number metrics are helpful for high level comparisons, the 1/3 octave band comparison provides further insight into the change in sound transmission at various screw spacings.

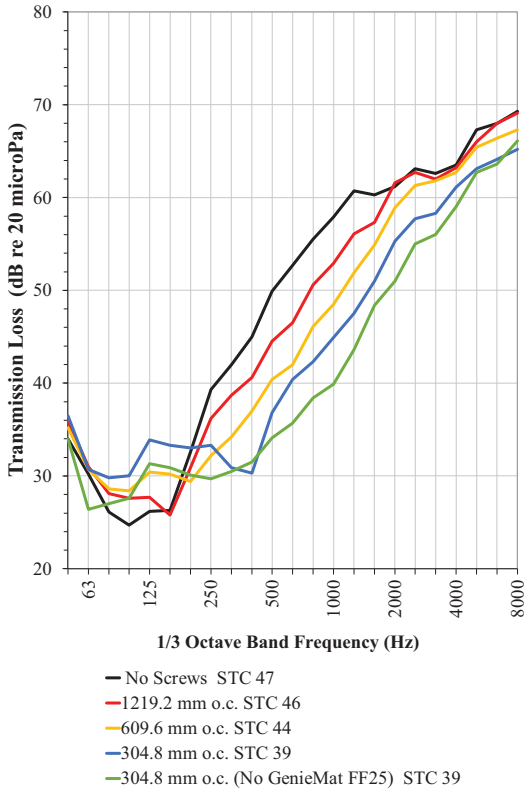

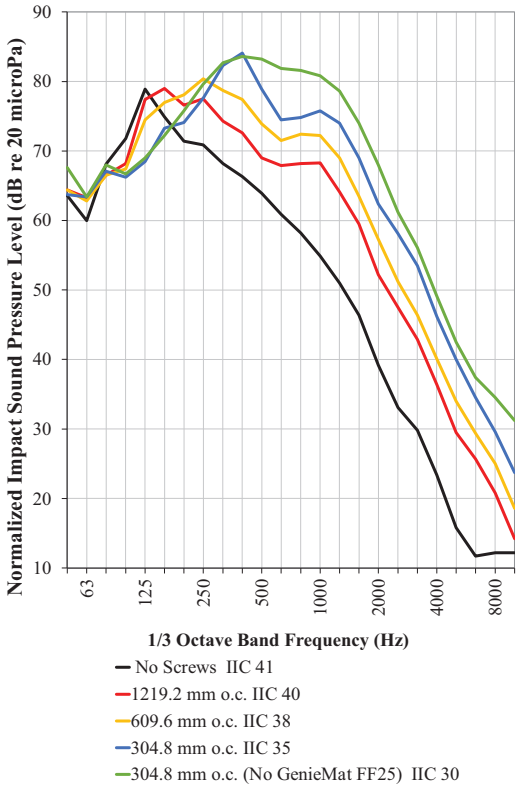

Figure 4: *Transmission loss (Top) and Normalized Impact Sound Pressure Level (Bottom) results of the tested assembly with various screw spacings*

https://doi.org/10.52202/069179-0262

The data shows a relatively consistent shift to the curves with each sequential addition of more screws and reduced spacing. The TLs in the 250-2000Hz range all display a similar slope with an offset in the curves. Table 3 shows the change in TLs across that frequency range for each screw spacing. When the change in each sequential halving of screw spacing is compared, the decreases in TLs were 4 dB, 3.8 dB and 3.4 dB respectively with each increase in fasteners.

Table 3: *Change to TL at each screw spacing from 250-2000Hz*

	Change to TL (relative to no screws)		
1/3 Octave Band (Hz)	1219.2 mm o.c. (dB)	609.6 mm o.c. (dB)	304.8 mm o.c. (dB)
250	-3.1	-7.1	-6.0
315	-3.3	-7.8	-11.1
400	-4.4	-8.0	-14.7
500	-5.4	-9.5	-13.1
630	-6.2	-10.7	-12.3
800	-4.9	-9.4	-13.2
1000	-5.0	-9.4	-13.0
1250	-4.6	-8.8	-13.2
1600	-3.0	-5.4	-9.3
2000	0.4	-2.3	-5.9
Average	-4.0 dB	-7.8 dB	-11.2 dB

When comparing the change in NISPL across the tests, the area with the most consistent shift of the curve appears to be the same frequency range of 250-2000Hz. This data can be seen in Table 4 and shows the average increase to NISPL for each spacing. Across the selected frequency range, the shift is greatest with an average increase in NISPL of 9.4 dB in going from no screw to the 1219.2 mm o.c. spacing with the relative change then 4.2 dB and 3.8 dB respectively for each addition of screws.

Table 4: *Change to NISPL at each screw spacing from 250-2000Hz*

	Change to NISPL (relative to no screws)		
1/3 Octave Band (Hz)	1219.2 mm o.c. (dB)	609.6 mm o.c. (dB)	304.8 mm o.c. (dB)
250	6.6	9.5	6.7
315	6.1	10.5	14.1
400	6.3	11.1	17.8
500	5.1	10.0	15.0
630	7.0	10.6	13.6
800	10.0	14.2	16.6
1000	13.4	17.3	20.9
1250	13.1	18.0	23.0
1600	13.1	17.1	22.6
2000	13.0	18.1	23.2
Average	9.4 dB	13.6 dB	17.4 dB

To better understand the trends across all 1/3 octave bands, the change to TL and NISPL for the 3 different screw spacings (relative to new screws) are plotted in Figure 5.

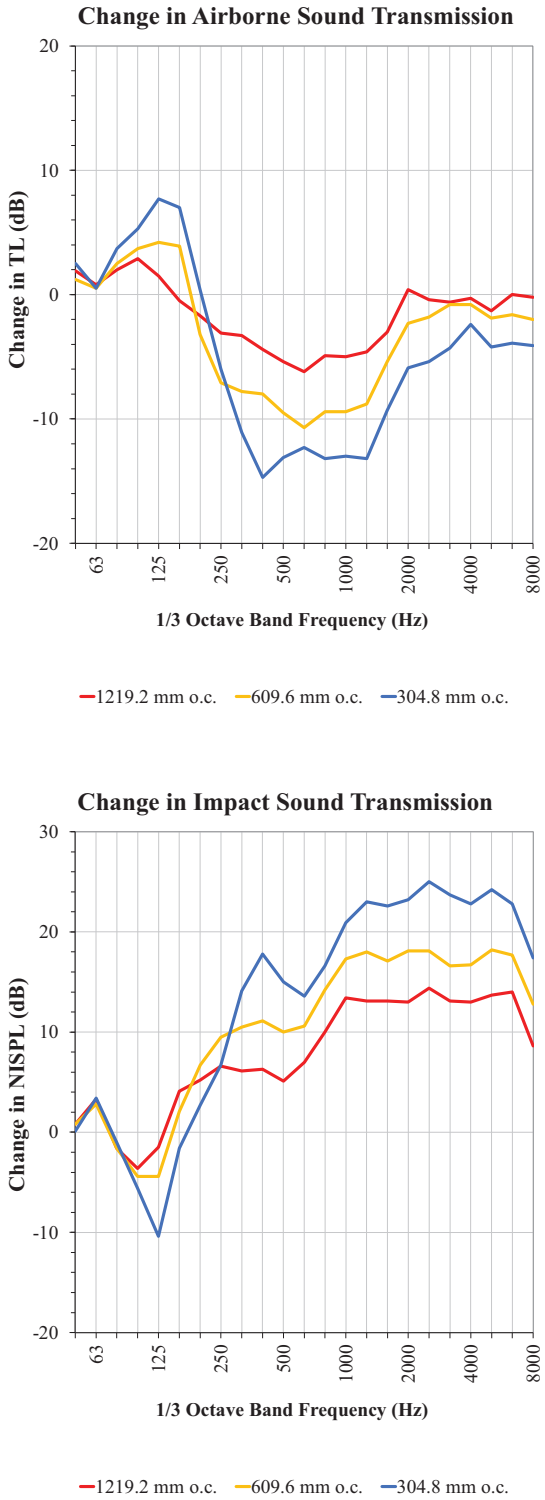

Figure 5: *Change in TL (Top) and NISPL (Bottom) across the 1/3 octave band frequencies.*

https://doi.org/10.52202/069179-0262

When looking at the change in performance in Figure 5, at mid and high frequencies, there is an increase in both airborne and impact sound transmission correlating to the addition of the fasteners through the GenieMat FF25 interlayer. This is in line with the expectation for rigid fasteners acting as short circuits. However, the change across both the TL and NISPL data show an inversion near 200 Hz. In both cases, some improvement from the addition of more fasteners is observed at the low frequencies below 200 Hz. There are no signs of error in the lab testing or issues with background noise at those frequencies, so the improvement is believed to be real. This low frequency range is considered the stiffness-controlled region so the addition of screws stiffening the overall assembly is likely contributing to this improvement.

To evaluate the role of stiffness, the GenieMat FF25 was removed, and the topping panel was reinstalled with fasteners returned at their 304.8 mm spacing. This showed similar low frequency NISPL behaviour, indicating this is fully due to the stiffening effect. However, the TL performance was worse without the resilient interlayer. The resilience and damping properties of the GenieMat FF25 may also be contributing by creating a constrained layer damping system.

Since higher frequency impact sound (400 Hz and up) is more easily rolled off simply by adding a finish floor on a thin recycled rubber underlayment like in concrete construction, a timber composite system that can improve the low frequency impact performance without requiring the addition of concrete could have major benefits. Further research is needed to determine what role the damping properties play and quantify the impact of stiffness compared to a constrained layer damping effect. A prefabricated timber panel. A timber composite system that does not rely on a high embodied carbon material such as concrete would offer a more sustainable system and could allow for further offsite fabrication with the full cassette ready for installation on site. Additionally, a composite panel system that does not incorporate poured concrete is fully de-constructable allowing for all components to be separated, reused and recycled.

5 CONCLUSIONS

The addition of screws penetrating through a resilient interlayer has a significant impact on the acoustic performance and must be considered for adequate STC and IIC performance. Up to a 25 dB increase in NISPL and up to a 14 dB decrease in TL were observed in comparing an assembly with no fasteners through the resilient interlayer to one with screws at 304.8 mm o.c. While very significant to the final performance, the fastener spacing is correlated to a gradual impact on airborne and impact sound transmission and can be taken into consideration during design of the structural system.

ACKNOWLEDGEMENT

I would like to thank the entire Pliteq team for supporting me in this research and providing the resources necessary to carry out the testing. I would also like to thank Vaagen Timbers for providing the CLT panels. Lastly, we are grateful for the opportunity to work collectively to reduce the carbon emissions of new construction and meet Pliteq's goal of ensuring that every scrap tire is recycled

REFERENCES

[1] E Karacabeyli, S Gagnon: *Introduction to Cross-Laminated Timber*. Canadian CLT Handbook 2019 Edition, 1-35, 2019.

[2] Pliteq Intertek Report # k7453.01-113-11-r1

[3] 2021 International Building Code, *Chapter 12 Sound Transmission*, 2(1) Sept 2021

[4] J Bligh: *Quantifying and Reducing Embodied Carbon in the Acoustic Design of Mass Timber Buildings*. In: InterNoise22, Glasgow, Scotland, Pages 5002-5992, pp. 5500-5509(10)

[5] M Golden, A Vaisman.: *Resilient Channel: One Screw Makes a Difference*, InterNoise2018, Chicago, IL.

[6] Mirdad, M. A. H., Khan, R., & Chui, Y. H. (2022, June 22). *Analytical procedure for timber−concrete composite (TCC) system with mechanical connectors*. MDPI. Retrieved March 12, 2023, from https://www.mdpi.com/2075-5309/12/7/885

https://doi.org/10.52202/069179-0262

World Conference on Timber Engineering Oslo 2023

PLASTIC DEFORMATION CONTRIBUTIONS OF CLT AND LTF SHEAR WALLS: DEVELOPMENT OF AN ANALYTICAL CAPACITY MODEL

Angelo Aloisio[1], Yuri De Santis[1], Francesco Boggian[2], Massimo Fragiacomo[1], Roberto Tomasi[3]

ABSTRACT: This paper compares the experimental cyclic response of Cross-Laminated Timber and Light Timber Frame shear walls. The goal is extracting the fractions of the lateral displacement due to sliding, panel's deformation and rocking. The three contributions to the total displacement, expressed in percentage, are then used to develop an analytical capacity model valid for CLT and LTF shear walls. The model is based on the sole equilibrium equations of the hold-down forces, obtained by reducing the pivot length of the hold downs reactions. Additionally, they examine the overstrength of the CLT panel, and LTF sheathing to the shear walls collapse due to the hold-down failure.

KEYWORDS: Experimental cyclic response; timber engineering; shear walls; rocking; Cross Laminated Timber; Light Timber Frame.

1 INTRODUCTION

Currently, the most diffuse timber constructive systems in Europe are based on the use of Light Timber Frame (LTF) and Cross Laminated Timber (CLT) shear walls [1]–[3]. There are numerous and diverse capacity models in the scientific literature for Cross-Laminated Timber (CLT) and Light Timber Frame (LTF) shear walls. Some researches merely attempt to elaborate closed-form models which best seize the observed response. Others, like [4], append to the mentioned efforts, an interpretative framework useful in developing simplified and reliable tools for the prediction of the lateral response. Specifically, [4] developed an analytical procedure and a simplified numerical model for the elastic response of LTF and CLT shear walls. They found that, in the elastic response range of CLT shear walls, 77% of the total displacement is due to rigid-body rotation, 16% to the rigid-body translation and 7% to the panel deformation. Conversely, in LTF shear walls, 45% is expected to the rigid-body rotation, 6% to the rigid body translation, and 45% and 4% to the sheathing-to-framing connection and sheathing panel deformation, respectively. In this paper, the authors investigate CLT and LTF systems in the post-elastic range. The rigor and straightforwardness of elastic analysis vanishes when dissipative phenomena arise. The authors devoted their efforts in interpreting experimental data by clustering the displacement response in rocking, sliding and deformation components. In a second step, based on the observed results, an elementary capacity model based on the sole hold-down experimental response is compared to the experimental results to estimate the related approximation.

2 EXPERIMENTAL TESTS

The results presented in this paper descend from the experimental data on LTF and CLT shear wall tests performed at the University of Trento. [5]–[7]. The first part of this paper focuses on the description of the test setup and the experimental responses. The second part attempts to understand the leading deformation contributes to the shear walls lateral response and proposes a capacity model based on the hold-down contribution. The research novelty of this paper, with respect to [6], [8], derives from the (1) complete report of the cyclic test results on CLT shear walls, (2) comparing CLT and LTF by decomposing the experimental response into rocking, sliding and deformation fractions, (3) the proposal of a novel capacity model driven by hold-down reactions, and (4) the estimation of overstrength factors.
The full description of the test setup of LTF and CLT shear walls is detailed in [5], [9], [10]. Tab.2 summaries the primary outcomes of the cyclic tests. Tab.2 reports only F_u and v_u, F_u measuring the strength capacity, while v_u the displacement capacity. The former expresses ultimate resistance; the latter is related to ductility. The optimum performance of a structural system derives from the optimum balance between resistance and ductility. Therefore, F_u and v_u may be suitable synthetic indicators of the experimental structural performance. Fig.2 presents the results in the form of force-displacement curves.

[1] Department of Civil, Construction-Architectural and Environmental Engineering Università degli Studi dell' Aquila, L'Aquila, 67100, Italy (angelo.aloisio1@univaq.it; yuri.desantis@univaq.it; massimo.fragiacomo@univaq.it)
[2] Department of Civil, Environmental and Mechanical Engineering, University of Trento, Trento , Italy (francesco.boggian@unitn.it)
[3] Faculty of Science and Technology , Norwegian University of Life Sciences, Ås , Norway (roberto.tomasi@nmbu.no)

https://doi.org/10.52202/069179-0263

Table 1: *Cyclic test result of LTF shear walls: Fu, ultimate experimental racking load; vu, slip corresponding to the ultimate load; both evaluated according to EN12512*

	LTF	
Test	F_u [kN]	v_u [mm]
STD-L0	47.6	60.6
STD-L10	58.1	78.4
STD-L20	57.5	74.5
2F-L20	38.9	33.5
150-L20	49.6	70.8
50/RG-L20	97.6	76.0
50-L20	65.5	53.5
SCREW-L20	57.6	74.9
WHD-L10	34.0	54.1

Table 2: *Cyclic test result of CLT shear walls: Fu, ultimate experimental racking load; vu, slip corresponding to the ultimate load; both evaluated according to EN12512*

	CLT	
Test	F_u [kN]	v_u [mm]
STD-L0	55.6	42.2
STD-L20	80.2	43.3
NA620-L0	124.0	29.1
NA620-L20	146.5	28.6
ND620-L0	132.9	30.4
ND620-L20	160.5	32.6
NA340-L20	83.6	57.4
NAWH-L20	66.6	57.7

3 EXTRACTION OF THE PLASTIC DEFORMATION COMPONENTS

The sliding fraction is estimated as the limit of the ratio between the horizontal displacements in points D and B, as illustrated in Fig.1:

$$s := \lim_{u_B \to \infty} \left| \frac{u_D(t)}{u_B(t)} \right| \quad (1)$$

The values of $u_D(t)$ and $u_B(t)$ are direct measures from the experimental campaign, and when plotted, they reveal an hyperbolic behaviour, with a clearly visible asymptote for higher values of the imposed displacement

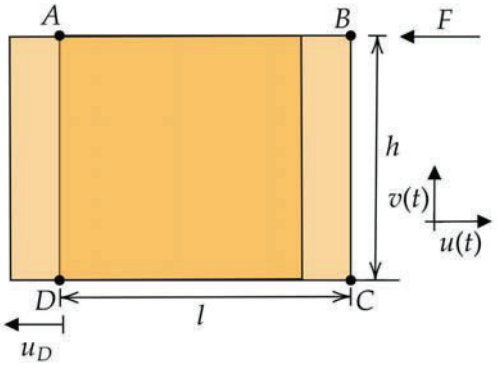

Figure 1*: Illustration of the rigid-body translation of the panel and the adopted notation.*

The relative displacement between the points A-C and B-D is a measure of the diagonal deformations in the East and West directions identified by d_E and d_W respectively. At this stage, the authors assume that the panel manifests a predominant shear deformation, as illustrated in Fig.2.

$$d_{E,W} = r_2 - r_1 \quad (2)$$

The shear displacement δ derives from Eq.(2) by expliciting the two radii r_2 and r_1:

$$\delta = l - \left[(h\sqrt{2} - d_{E,W})^2 - h^2 \right]^{0.5} \quad (3)$$

The ratio between δ and u_B approaches a constant value at higher displacement values. The following definition of the deformation fraction, d, attempts to grasp the approaching asymptot.

$$d := \lim_{u_B \to \infty} \left| \frac{\delta}{u_B} \right| \quad (4)$$

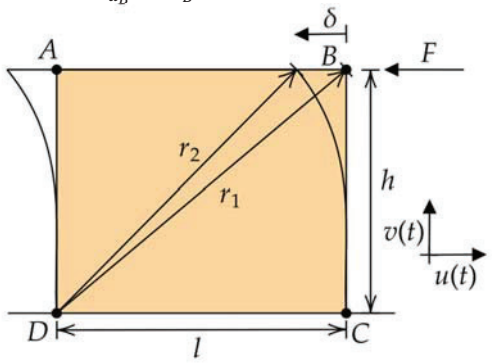

Figure 2*: Illustration of the shear deformation of the panel and the adopted notation.*

The rocking component is estimated as a complement to one of the already estimated sliding and deformation contributions, see Fig.3:

$$r = 1 - (s + d) \quad (5)$$

The whole displacement field of the shear wall is illustrated in Fig.7, where all the contribution to the top displacement u_B are highlighted: u_D represents the sliding contribution while δ represents the deformation contribution, both evaluated in the previous sections. The rocking component can be expressed by θh. By assuming small displacements, the displacements can be written as:

$$u_B - u_D - \delta = \theta h \quad (6)$$

$$v_C = \theta(l - x) \quad (7)$$

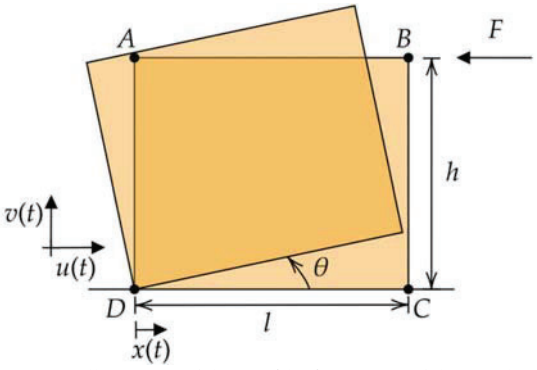

Figure 3 *Illustration of the rigid-body rotation of the panel and the adopted notation.*

https://doi.org/10.52202/069179-0263

4 RESULTS

Tab.3 reports the three displacement contributions in all the tested specimens, expressed as percentages. The displacement components in Tab.3 refer to the post-elastic behaviour. They originate from Eqs.(1),(4),(5) respectively, which present an asymptotic definition of the three displacement fractions. The experimental data reveal that the three displacement components rapidly converge towards a definite value after the elastic phase. The values stationarity proves that the excitation amplitude does not modify the balance between the three contributions after a certain post elastic displacement value.

Table 3: *The table attempts to synthesize the displacement components due to sliding, deformation and rocking, expressed as a fraction of the imposed displacement in point B, estimated using Eqs. (1),(4),(5) respectively.*

Test	s [%]	d [%]	r [%]
LTF STD-L0	9.5	4.7	85.9
LTF STD-L10	2.1	17.8	80.1
LTF STD-L20	5.1	21.7	73.2
LTF 2F-L20	3.8	33.4	62.8
LTF 150-L20	7.6	34.6	57.8
LTF 50/RG-L20	7.7	18.8	73.5
LTF 50-L20	0.8	15.4	83.9
LTF SCREW L20	2.0	34.5	63.5
LTF WHD-L10	1.4	8.1	90.5
CLT STD-L0	5.6	4.2	90.2
CLT STD-L20	5.0	12.8	82.3
CLT NA620-L0	7.7	3.8	88.5
CLT NA620-L20	3.6	7.9	88.6
CLT ND620-L0	4.0	8.6	87.4
CLT ND620-L20	8.5	5.7	85.8
CLT NA340-L20	4.1	2.2	93.7
CLT NAWH-L20	6.8	0.1	93.0

The prevalent contribution to the total displacement comes from the rigid-body rotation. The rocking motion of LTF shear walls is lower than CLT: LTF shear walls are more deformable than CLT. The vertical load has almost the same effects in both the shear walls: the load increment reduces the rocking component. The vertical load acts as a rotation restraint. The reduction of the base connections determines a significant increment of the rocking motion, like in the case without hold-downs (WHD). Interestingly the test LTF SCREW, which uses screws distributed uniformly on the bottom rail as a sliding restraint, shows that the presence of screws may influence the rocking mechanism, by offering an additional uplift restraint, thus limiting the rocking percentage as seen from Tab.3.

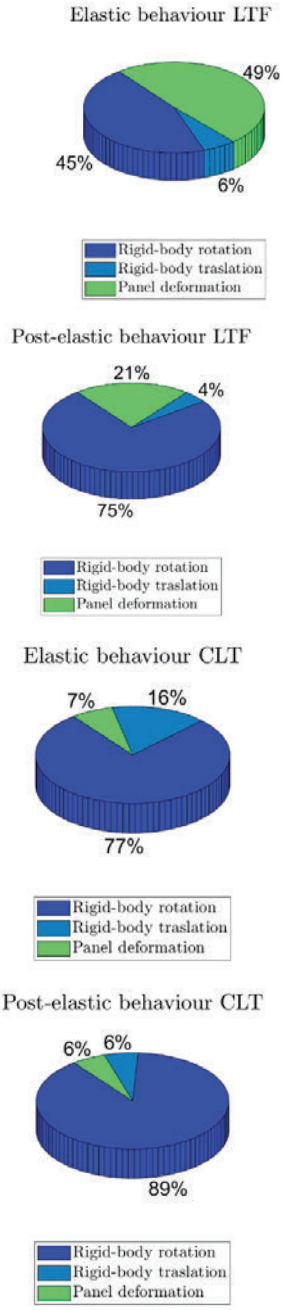

Figure 4*: Percentage of displacement on top of the shear walls due to each single contribution in both the elastic (calculated by* [4]*) and post-elastic range (as calculated from the experimental data. in this paper)..*

The sliding component does not significantly change between LTF and CLT shear walls. The rigid-body translation mainly depends on the transverse resistance of the base connections and does not likely depend on the vertical load. This shred of information conveys some details about the occurring of friction phenomena. The amount of the Coulomb-type friction restraint depends on the vertical load: the substantial independence of the

sliding fraction on the vertical load proves the possible independence of friction in the sliding restraints, primarily provided by the base connections. In the current setup, friction phenomena are then negligible compared to the restraining capacity of the connections.

Additionally, Tab.4 proves the substantial independence of the sliding component on the angle brackets. The CLT shear wall has four angle brackets, while the LTF shear wall has two. Nonetheless, the CLT sliding is lower than LTF. The sliding fractions are quite similar between the two structural typologies and the increment in the number of the angle brackets does not enhance the sliding restraint, likely. The panel deformation changes between LTF and CLT as expected. The impact of deformation on shear walls with low load values and a few base connections (WHD) is shallow and very similar between the two structural typologies. However, as the load increases as well as the base connections, the impact of deformation increases in LTF, while CLT does not deform significantly.

5 CAPACITY MODEL

The dominance of the rocking response due to the hold-downs deformation may inspire the proposal of an elementary capacity model based on the sole hold down reactions. However, the accuracy of the model mostly depends on an accurate estimation of the extension of the compressed area. In contrast with the elastic behaviour, the extension of the compressed area tends towards a sort of plastic asymptote due to the stress redistribution. The definition of the neutral axis is the following:

$$x_p := \lim_{u_B \to \infty} \left| l - \frac{v_C}{\theta} \right| \tag{8}$$

There are no studies about the trend of the stress in the compressed area, which depends on several factors: e.g. the planarity of contact areas, timber grading and the slenderness of the panel.

Tab.4 attests that the extension of the compressed area depends on the vertical load, the in-plane stiffness of the panel and the boundary restraints. The compressed area expands significantly when the vertical load raises, the in-plane stiffness reduces, and there are fewer base connections. An analytical correlation between the x_p variable and the three mentioned variables (vertical load, in-plane stiffness and boundary conditions) is critical for a conservative estimation of forces acting on the base connections. Specifically, the estimation of the pivot point is essential when assessing the force on the hold-downs: the assumption of the pivot point by one edge of the panel would significantly underestimate the hold-down reactions.

Table 4: *Estimate of the asymptotic neutral axis in the considered test configurations.*

Test	$\mathbf{x_p}$ [m]	$\mathbf{x_p/l}$ [%]	**r** [%]
LTF STD-L0	0.01	0.4	85.9
LTF STD-L10	0.43	17.2	80.1
LTF STD-L20	0.71	28.2	73.2
LTF 2F-L20	0.72	28.8	62.8
LTF 150-L20	0.02	0.8	57.8
LTF 50/RG-L20	0.01	0.4	73.5
LTF 50-L20	0.01	0.4	83.9
LTF SCREW L20	0.59	23.7	63.5
LTF WHD-L10	0.09	3.6	90.5
CLT STD-L0	0.19	7.5	90.2
CLT STD-L20	0.88	35.4	82.3
CLT NA620-L0	0.20	8.0	88.5
CLT NA620-L20	0.13	5.3	88.6
CLT ND620-L0	0.05	2.0	87.4
CLT ND620-L20	0.70	27.9	85.8
CLT NA340-L20	0.37	14.9	93.7
CLT NAWH-L20	0.48	19.2	93.0

Tab.4 lists the expected extension of the compressed area. The second column presents the percentage ratio between the estimated x_p value and the base length l. The x_p extension depends on the balance between deformation and rocking components: the increment of the deformation fraction yields an increment of the x_p value. In this paper, the authors do not investigate the compressed area extension based on mechanical analytical models. This step would entail dedicated research efforts based on adequate mechanical models of the shear wall post-elastic response.

As shown in Fig.5, the wall is assumed to pivot around the position P of its neutral axis, characterized by a compression region of extension x_p; no specific assumption is made regarding the shape of the stress distribution in the compression zone. The contribution of angle brackets to the racking mechanism is neglected. Hereafter follows the equilibrium equations:

$$\uparrow \quad -ql - H + k_C \sigma_C x_p t_{\text{eff}} = 0 \tag{9}$$

$$\circlearrowleft \; Fh - ql\left(\frac{l}{2} - x_p\right) - H(l - x_p) + k_C \sigma_C x_p t_{\text{eff}} l_c = 0 \tag{10}$$

where q is the distributed vertical load, l the wall length, F the top horizontal force, h the wall height, H the hold down reaction force, σ_c the averaged compression stress on timber, k_c a modification parameter which accounts for the increment of resistance due to compression hardening and the shape feature of the stress diagram, x_p the extension of the neutral axis, t_{eff} is the thickness of the wall reacting in compression, l_c is the lever arm of the compression region. The k_c and the l_c factors are in fact unknown.

https://doi.org/10.52202/069179-0263

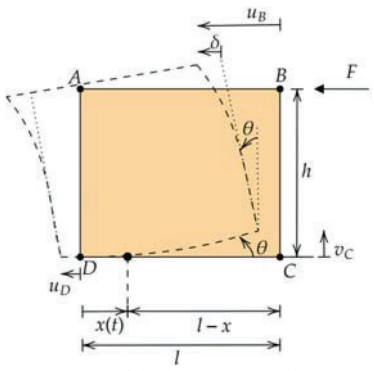

***Figure 5**: Mechanical model of the shear wall.*

The goal of this section is to demonstrate that the cyclic behaviour of the tested shear walls is mainly dependent on the hold-down. The force acting on the wall is then evaluated by considering the sole hold-down contribution to the rotational equilibrium, and neglecting the contribution of the unknown compression stresses in timber:

$$F = H \cdot \frac{\tau \cdot l}{h} + q \cdot \frac{l}{h}\left(\tau \cdot l - \frac{l}{2}\right) \quad | \quad \tau = \frac{l - x_p}{l} \tag{11}$$

Eq.(11) bestows the top horizontal force acting on the wall, given the hold-down force H, the vertical load q and the position of the pivot point x_p. The authors validated this model by comparing, in terms of cyclic curves and maximum force values, the forces measured in point B of the shear wall, with the horizontal force $F(t)$. $F(t)$ is obtained from the simplified model in Eq.(11), using the forces measured on the hold-downs $H(t)$ and the pivot point x_p value estimated in Tab.4. Tab.5 quantifies the discrepancies between the two curves in terms of the maximum forces.

***Table 5:** Comparison between the maximum forces in kN attained by the experimental cyclic tests and the capacity model based on the sole hold-down reactions.*

Test	$F_{max,exp}$	$F_{max,sim}$	Err. [%]
LTF STD-L0	72.8	75.9	-4.3
LTF STD-L10	75.6	82.7	-9.3
LTF STD-L20	75.6	68.1	10.0
LTF 2F-L20	60.0	54.6	9.0
LTF 150-L20	62.7	65.9	-5.2
LTF 50/RG-L20	128.9	116.1	9.9
LTF 50-L20	84.4	89.0	-5.4
LTF SCREW L20	74.2	74.7	-0.6
	Avg |Error|		6.7
CLT STD-L0	81.3	87.9	-8.1
CLT STD-L20	107.6	105.5	1.9
CLT NA620-L0	131.1	144.9	-10.5
CLT NA620-L20	143.6	149.5	-4.2
CLT ND620-L0	138.8	151.6	-9.2
CLT NDS20-L20	165.2	148.7	10.0
CLT NA340-L20	107.5	98.4	8.5
	Avg |Error|		7.5

Tab.5 proves that a capacity model based on the sole hold down reaction is quite faithful, and an elementary formula for the prediction of the hold-down response could descend by taking the 95% percentile of a Gaussian distribution of the τ factor in Eq.(11). Accurately, the 95% percentiles of the τ factor in the LTF and CLT shear walls are:

$$\begin{aligned} \tau_{\mathrm{LTF},95\%} &= 0.81 \\ \tau_{\mathrm{CLT},95\%} &= 0.86 \end{aligned} \tag{12}$$

These values suggest that the estimate of F needs a proper reduction of the pivot point of the hold-downs. The decrease is higher in the case of LTF shear walls due to the higher deformability. Eqs.(11)-(12) represent simplified formulations possibly useful for engineering purposes, which attempts to avoid underestimating the hold-down reaction by reducing the distance of the rotation point. In conclusion, LTF and CLT shear walls do not display significant differences in the considered configurations. This fact is essentially due to the overstrength of the panel to the base resistance derived from the base connections. Fig.6 illustrates the probability distributions of two resisting mechanisms: the failure reached during testing, mainly due to hold-down collapse, and the OSB sheathing/CLT panel collapse.

Fig.6 illustrates the probability distributions of two resisting mechanisms: the failure reached during testing, mainly due to hold-down collapse, and the OSB sheathing/CLT panel collapse.
The experimental probability density functions of the CLT and LTF shear walls are calculated directly from the values of failure of the cyclic tests. The probability density functions related to the capacity of the CLT panel / OSB sheathings derive by assuming the same variance of the corresponding experimental curves, and by assuming the shear failure of the OSB sheathing in LTF walls and the in-plane torsional shear failure in CLT panels (see [11], [12]). The authors used the following values of strength: $f_{vk} = 6.8$ MPa for OSB/3 and $f_{v,\mathrm{tor},k} = 2.5$ MPa for CLT [13], [14]. Fig.6 expresses the true nature of the considered structural systems. The two systems behave likewise due to the similarity of the base connections. Still, the CLT panel is far more resistant than the LTF when different boundary restraints and loads may activate other resisting mechanisms.

$$\gamma_{RD} = \frac{R_{k,b}}{R_{k,d}} \tag{13}$$

The authors reported the overstrength values, estimated as shown in Eq.(13). $R_{k,b}$ is the characteristic load bearing

capacity of the panel assuming the timber failure mode (brittle), while $R_{k,d}$ the characteristic load bearing capacity of the panel assuming the hold-down failure mode (ductile). The characteristic values are set equal to the 5-th percentile of the corresponding strength distributions. In the considered cases, the overstrength of LTF shear walls is almost two times of that of CLT. The obtained overstrength values are not general and depend from the specific structural configurations and the considered failure modes. The extension of these results to different structural arrangements must be the object of devoted efforts by the authors.

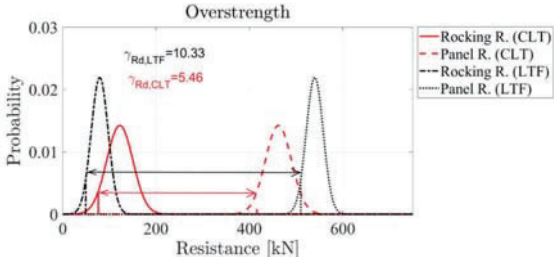

Figure 6: *Comparison between the experimental cyclic response of CLT shear walls and the capacity model based on Hold-Down measured forces.*

6 CONCLUSIONS

Light Timber Frame (LTF) and Cross Laminated Timber (CLT) shear walls exhibit similar response under cyclic loading. The authors compared the experimental test of LTF and CLT wall assemblies characterised by similar geometric features. The rigid-body rotation is the predominant deformation contribution. This contribution, expressed in percentage to the total deformation, is on average 75% and 88% in LTF and CLT specimens, respectively. The rocking response dominance, due to the hold-down deformation contribution, led to an elementary capacity model based on the hold down reactions and the assumption of a pivot point. The 95th percentile of the Gaussian probability distribution of the ratio between the extension of the compressed area and the panel length is about 0.2: the adoption of the panel edge as a rotation point would determine an approximate 20% underestimation of the hold down reactions in the considered capacity model.

ACKNOWLEDGEMENT

The authors acknowledge the research efforts of Paolo Grossi, Paolo Endrizzi, Tiziano Sartori and Ermanno Acler, who carried out the experimental tests with the support of the staff of the University of Trento.

REFERENCES

[1] A. Aloisio, D. Pasca, R. Tomasi, and M. Fragiacomo, Dynamic identification and model updating of an eight-storey CLT building, *Eng. Struct.*, vol. 213, Jun. 2020, doi: 10.1016/j.engstruct.2020.110593.

[2] M. Piazza, R. Tomasi, and R. Modena, Strutture in legno, *Mater. Calc. e Progett. Second. le nuove Norm. Eur. (Wooden Struct. Mater. Calc. Des. Accord. to new Eur. Regul. Bibl. Tec. Hoepli Milano, Milano*, pp. 512–558, 2005.

[3] A. Aloisio, R. Alaggio, and M. Fragiacomo, Equivalent Viscous Damping of Cross-Laminated Timber Structural Archetypes, *J. Struct. Eng.*, vol. 147, no. 4, p. 4021012, 2021.

[4] D. Casagrande, S. Rossi, R. Tomasi, and G. Mischi, A predictive analytical model for the elasto-plastic behaviour of a light timber-frame shear-wall, *Constr. Build. Mater.*, vol. 102, pp. 1113–1126, 2016.

[5] P. Grossi, T. Sartori, and R. Tomasi, Tests on timber frame walls under in-plane forces: part 1, *Proc. Inst. Civ. Eng. Build.*, vol. 168, no. 11, pp. 826–839, 2015.

[6] E. Acler, P. Endrizzi, and R. Tomasi, Monotonic and cyclic in-plane behavior of CLT panels tested by using different types of metal devices, 2012.

[7] M. Andreolli and R. Tomasi, Bemessung von Gebäuden in Brettsperrholzbauweise unter Erdbebenbeanspruchung, *Bautechnik*, 2016.

[8] P. Grossi, PARETI INTELAIATE IN LEGNO: indagine sul comportamento meccanico tramite prove sperimentali a scala reale, University of Trento, 2011.

[9] P. Endrizzi, I sistemi di connessione di base del pannello xlam compensato di tavole indagine sperimentale in scala reale e modellazione numerica della capacità portante globale di parete ottenuta con l'impiego di una nuova tipologia di angolare a taglio, University of Trento, 2011.

[10] A. Aloisio, F. Boggian, T. Roberto, and M. Fragiacomo, The role of the hold-down in the capacity model of CLT andLTF shear walls based on the experimental lateral response, *Constr. Build. Mater.*, vol. In press, 2021.

[11] R. Tomasi, T. Sartori, D. Casagrande, and M. Piazza, Shaking table testing of a full-scale prefabricated three-story timber-frame building, *J. Earthq. Eng.*, vol. 19, no. 3, pp. 505–534, 2015, doi: 10.1080/13632469.2014.974291.

[12] F. Boggian, M. Andreolli, and R. Tomasi, Cross Laminated Timber (CLT) beams loaded in plane: testing stiffness and shear strength, *Front. Built Environ.*, vol. 5, p. 58, 2019.

[13] EN 594:2011 Timber structures, Test methods - Racking strength and stiffness of timber frame wall panels, *BSI, London UK*, 2011.

[14] R. Brandner, G. Flatscher, A. Ringhofer, G. Schickhofer, and A. Thiel, Cross laminated timber (CLT): overview and development, *Eur. J. Wood Wood Prod.*, vol. 74, no. 3, pp. 331–351, 2016.

https://doi.org/10.52202/069179-0263

World Conference on Timber Engineering Oslo 2023

ASEISMIC DESIGN LEVEL USING RESPONSE SPECTRUM FOR WOODEN HOUSES

Koji Yamada[1]

ABSTRACT: Reviewed equations for horizontal resistant force of Japanese wooden houses are discussed in considering both the acceleration response spectrum with sharp peaks and the acceleration response spectrums of observed earthquake motion. This acceleration spectrum with sharp peaks is the sum of Minimum requirement spectrum and the order spectrum. The observed earthquake motions are divided into 2 groups. The one consists of Kobe JMA 1995, the motions distributed by BCJ. The other consists of 592 motions observed from 1996 to 2012 in Japan, their maximum acceleration are over 400 cm/s^2. The new horizontal resistant force is defined as the product of the coefficient of eccentricity ratio, the coefficient of a damping factor, and the coefficient of horizontal resistant force. This coefficient of horizontal resistant force is the function of the ductility factor, the natural period, the period of a response spectrum peak and its acceleration. The verification of the proposed coefficient of horizontal resistant force is checked by the ratio of the ductility factor subjected to input earthquake motions over the set ductility factor. As a result, the response analysis shows that the proposed equations give the safe side of the horizontal resistant force.

KEYWORDS: Acceleration response spectrum, Structural design, Base shear coefficient

1 INTRODUCTION

It is difficult to estimate input earthquake motions accurately in response analysis. Then the response spectra are used to define the input earthquake motions in structural design. In Japan, base shear coefficient is given in structural code. This base shear coefficient is related the acceleration response spectrum in [1]. Therefore, it is useful that the base shear coefficient is calculated from any acceleration response spectrum. In previous paper [2], new equations for base shear coefficient are discussed in considering the acceleration response spectrum with sharp peaks. The new base shear coefficient (Co) is defined as the product of the coefficient of eccentricity ratio(Fes), the coefficient of a damping factor(Fh), and the coefficient of horizontal resistant force(Ds). This coefficient of horizontal resistant force is the function of the ductility factor(μ), the natural period (Ts), the period of a response spectrum peak and its acceleration. This proposed base shear coefficient is discussed by the average of the maximum ductility factors by 10 input motions. In this paper, reviewed equations for horizontal resistant force of Japanese wooden houses are discussed in considering both the acceleration response spectrum with sharp peaks and the acceleration response spectrums of observed earthquake motion. The new horizontal resistant force is defined as the product of the coefficient of eccentricity ratio, the coefficient of a damping factor, and the coefficient of horizontal resistant force. This coefficient of horizontal resistant force is the function of the ductility factor, the natural period, the period of a response spectrum peak and its acceleration.

2 TARGET ACCELERATION SPECTRUM AND ANALYSIS SUPPOSITION

2.1 TARGET ACCELERATION SPECTRUM

The target acceleration spectra are shown in Fig.1. This acceleration spectrum is the sum of Minimum requirement spectrum and the order spectrum. The minimum requirement spectrum has the corner period (Tc), and the order spectrum has the peak periods(Ti).
The input earthquake motions are shown in Fig.2. There 10 input earthquake motions in each spectrum. Each input earthquake motion has random phase and 163.84 sec duration time. The minimum requirement spectrum has the 0.86 sec corner period and 1200gal constant acceleration spectrum region. The target spectrum A has both minimum requirement spectrum and 1400gal peak at 0.4sec natural period. The target spectrum B has both minimum requirement spectrum and 2000gal peak at 0.4sec natural period. The target spectrum C has minimum requirement spectrum, 1400gal peak at 0.4sec natural period and 1400gal peak at 1.2sec natural period. The input earthquake motions are multiplied 0.8 for response analysis of 1 DOF model.

[1] Koji Yamada, N. I. T., Toyota College, Japan, kyamada@toyota-ct.ac.jp

https://doi.org/10.52202/069179-0264

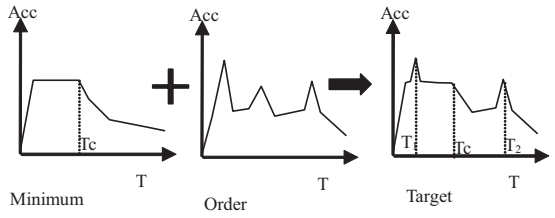

Figure 1: *Acceleration response spectrum for structural design*

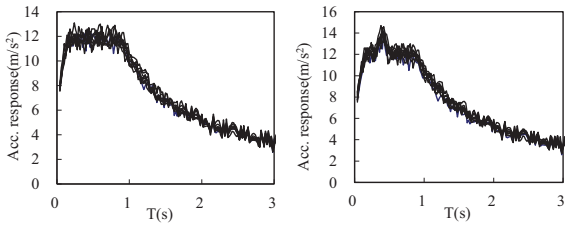

a) Minimum requirement *b) Target spectrum A*

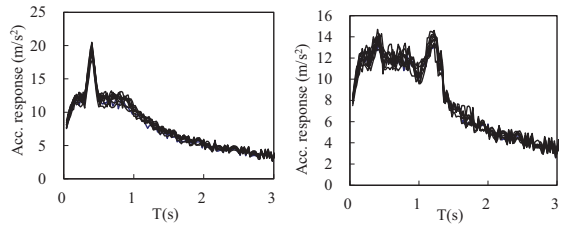

c) Target spectrum B *d) Target spectrum C*

Figure 2: *Acceleration response spectrum of input earthquake motions(h=0.05)*

2.2 OBSERVED EARTHQUAKE MOTIONS

The observed earthquake motions are divided into 2 groups. The one consists of Kobe JMA 1995, the motions distributed by BCJ. The other consists of 592 motions observed from 1996 to 2012 in Japan, their maximum acceleration are over 400 cm/s^2.

2.3 PROPOSED BASE SHEAR COEFFICIENT

The proposed base shear coefficient (Co) in Eq.(1) is defined in [2] as the product of the coefficient of eccentricity ratio(Fes), the coefficient of a damping factor(Fh), and the coefficient of horizontal resistant force(Ds). This coefficient of horizontal resistant force is the function of the ductility factor(μ), the natural period (Ts), the period of a response spectrum peak and its acceleration in Eq.(3) - (7). Three restoring force characteristics are considered in this paper(Fig.3). The coefficient is the bearing force of Bi-linear component over the whole bearing force. The parameters of restoring force characteristic are the natural period(T) and the bearing force(Co). The natural periods are set from 0.2 to 3.0sec. The bearing force is calculated by Eq.(1) - (7). The damping factor(ho) is 0.05 basically, are 0.02 and 0.10 for parameter analysis.

$$C_o = F_{es} F_h \overline{D}_s \tag{1}$$

$$F_h = \sqrt{\frac{1+\alpha h_o}{1+\alpha h_{eq}}} \tag{2}$$

$$\alpha = 25$$

$$\overline{D_s} = D_{si} C_{oi} \tag{3}$$

$$C_{oi} = 0.816 * Acc(T) / 980 \tag{4}$$

For Minimum requirement

$$D_{sc} = \begin{cases} \dfrac{1}{\sqrt{2\mu - 1}} + \beta \dfrac{T_c - T}{T_c} & T \le T_c \\ \dfrac{1}{\sqrt{2\mu - 1}} \dfrac{T_c}{T} & T > T_c \end{cases} \tag{5}$$

For customer order requirwement

$$D_{si} = \begin{cases} \dfrac{1}{\sqrt{2\mu - 1}} + \beta \dfrac{T_i - T}{T_i} & T \le T_i / 0.8 \\ 0 & T > T_i / 0.8 \end{cases} \tag{6}$$

$$\beta = \begin{cases} 0.1 & Bi-linear \\ 0.5 & Slip \\ 0.5 - 0.4\gamma & Composite \end{cases} \tag{7}$$

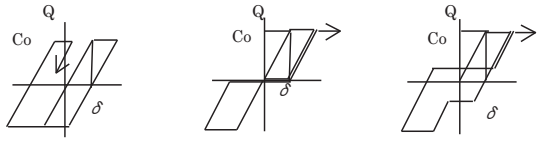

a) Bi-linear b) Slip c) composite

Figure 3: *Restoring force characteristic*

Hence, the restoring force characteristic of a wooden house is shown in Fig.4. It seems like the composite type. The calculation value of β is 0.47, I suppose β as 0.5. The natural period of a wooden house is supposed as 0.4 sec. The adequacy of the proposed base shear coefficient at 1/120 rad is checked up by the ductility factor subjected to input earthquake motions over the set ductility factor (μ). Hereinafter, the ratio of the ductility factor subjected to input earthquake motions over the set ductility factor (μ) is called the ductility factor ratio.

https://doi.org/10.52202/069179-0264

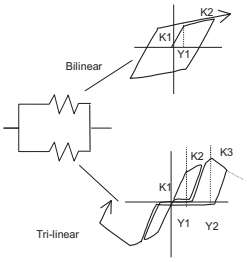

Figure 4: *Restoring force characteristic of a wooden house*

3 VERIFICATION

3.1 VERIFICATION OF PROPOSED BASE SHEAR COEFFICIENT ON TARGET ACCELERATION SPECTRUM

Firstly, the proposed base shear coefficient is checked by input earthquake motions in Fig.2. The ductility factor ratio is shown in Fig.5. The ductility factor ratio is between 0.2 and 0.4. These ductility factor ratios are too small for a design code. The new equations are proposed in Eq.(8) and (9).

For Minimum requirement

$$\begin{aligned} &\overline{D_s} = D_{sc} C_{oc} \\ &C_{oc} = 0.816 * Acc / 980 \\ &D_{sc} = \begin{cases} \dfrac{1}{\sqrt{4\mu - 1}} + \beta \dfrac{T_c - T}{T_c} & T \le T_c \\ \dfrac{1}{\sqrt{4\mu - 1}} \dfrac{T_c}{T} & T > T_c \end{cases} \end{aligned} \tag{8}$$

For customer order requirement

$$\begin{aligned} &\overline{D_s} = D_{si} C_{oi} \\ &C_{oi} = 0.816 * Acc / 980 \\ &D_{si} = \begin{cases} \dfrac{1}{\sqrt{4\mu - 1}} + \beta \dfrac{T_i - T}{T_i} & T \le T_i / 0.8 \\ 0 & T > T_i / 0.8 \end{cases} \end{aligned} \tag{9}$$

The ductility factor ratio in Eq.(8) and (9) is shown in Fig.6. These new equations have an improvement in the range of the ductility factor ratio against in Fig,5.

3.2 VERIFICATION OF PROPOSED BASE SHEAR COEFFICIENT ON OBSERVED EARTHQUAKE MOTIONS

Next, the proposed base shear coefficient is checked by observed earthquake motions. The damping ratios are supposed as h=0.05, 0.10 and 0.20 because of using seismic energy dissipation systems. The ductility factor ratio is shown in Fig.7. The damping ratio is set in proportion to the secant stiffness at 1/120 rad. The ductility factor ratios of some samples are over 1.0. Nevertheless, almost all ductility factors are less than 1.0. proposed equations give the sufficient base shear against earthquakes.

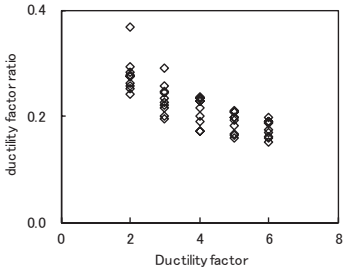

a) Minimum requirement

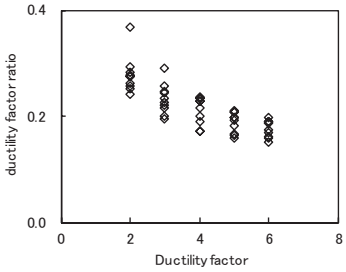

b) Target spectrum A

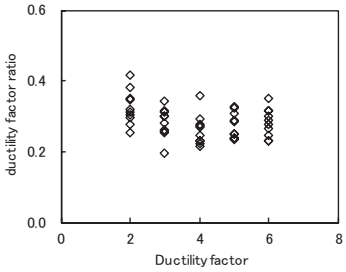

c) Target spectrum B

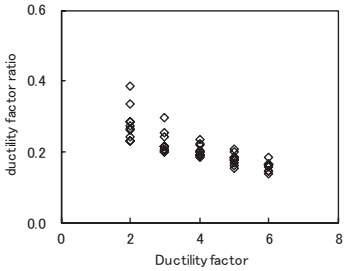

d) Target spectrum C

Figure 5: *Ductility factor ratio subjected to earthquake motions in Fig.2 (h=0.05)*

https://doi.org/10.52202/069179-0264

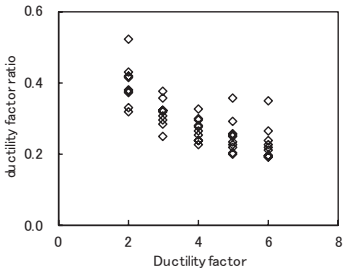

a) Minimum requirement

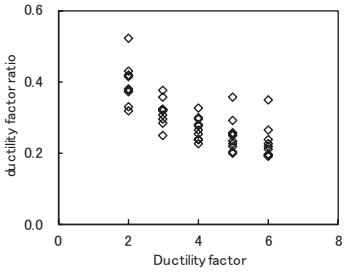

b) Target spectrum A

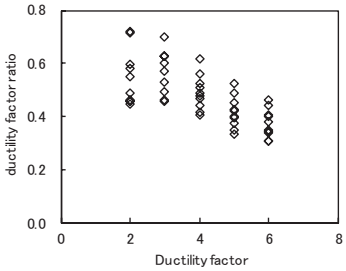

c) Target spectrum B

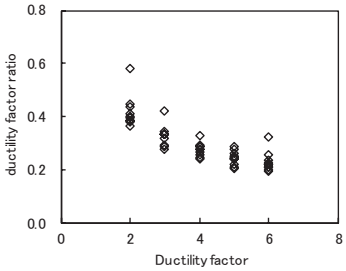

d) Target spectrum C

Figure 6: *Ductility factor ratio subjected to earthquake motions in Fig.2 (h=0.05)*

4 VERIFICATION OF PROPOSED BASE SHEAR COEFFICIENT WITH SEISMIC ENERGY DISSIPATION SYSTEM

The damping ratio in Fig. 7 is a simple supposition. So the result of Fig. 7 is not applied to actual seismic energy dissipation systems. In this section, a hysteresis damping system and a velocity proportional viscous damping system with relief valve are supposed as actual seismic energy dissipation systems. The hysteresis damping system has the bi-linear restoring force characteristic in Fig. 8. Its yield displacement is 0.5cm and its yield strength is 8kN. The viscous damping system is the brace system, whose 1st damping coefficient is 4 kN/(cm/s), whose 2nd damping coefficient is 0.04 kN/(cm/s), whose relief velocity is 0.9sm/s, and whose stiffness is 20kN/cm. These seismic energy dissipation systems are supposed to be set at 1st floor because the almost Japanese wooden houses collapse at their 1st floor. Their demand in a house is calculated from both of the difference between the set damping ratio value and structural damping ratio 5%, and the 1 loop energy dissipation at 1/120 rad of slope by relative storey displacement of the energy dissipation systems.

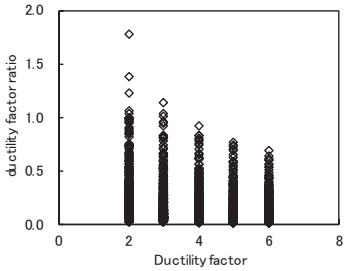

a) h=0.05

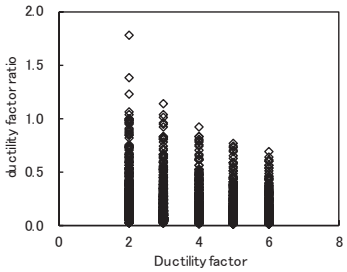

b) h=0.10

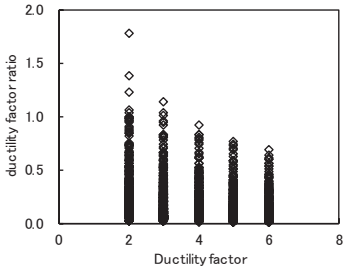

c) h=0.20

Figure 7: *Ductility factor ratio subjected to observed earthquake motions*

https://doi.org/10.52202/069179-0264

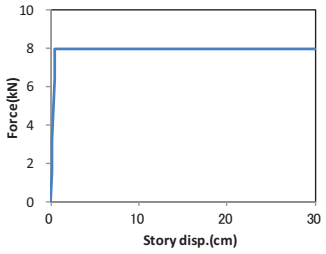

Figure 8: *Characteristic of hysteresis damping system*

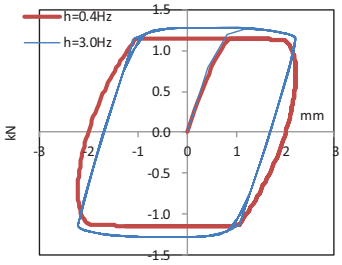

Figure 9: *Characteristic of viscous damping system*

The results are shown in Fig. 10 and Fig. 11. The result on the viscous damping system (Fig.11) is similar to the result in Fig. 7. But the result on the hysteresis damping system (Fig.10) shows that the ductility factor ratio in Fig. 7 is smaller than that in Fig.10.

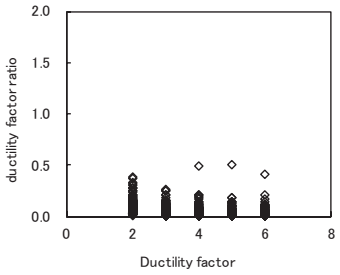

a) h=0.10

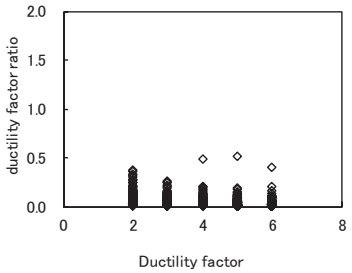

b) h=0.20

Figure 10: *Ductility factor ratio subjected to observed earthquake motions with hysteresis damping system*

The reason is that the consideration of a hysteresis damper is only 1 loop energy dissipation. There is no consideration on its strength. The adequate method to consider the strength of a hysteresis damper is to change β in Eq. (8) and (9). The change of β needs the calculation on the effect of the strength of a hysteresis damper. It is cumbersome procedure. In this paper, a next simple method is proposed. The method is the increase of the 1 loop energy dissipation. The result on double count of 1 loop energy dissipation is shown Fig.12. This figure shows that the ductility factor ratio is a little larger than that in fig.7. But the proposed method is in safe side on structural design.

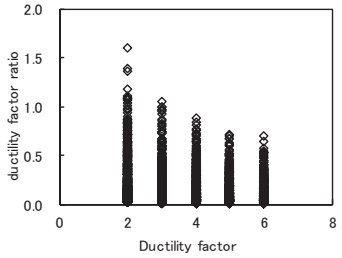

a) h=0.10

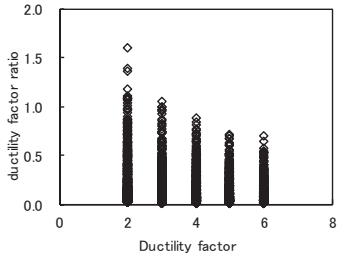

b) h=0.20

Figure 11: *Ductility factor ratio subjected to observed earthquake motions with viscous damping system*

5 CONCLUSIONS

In this paper, new equations for horizontal resistant force of Japanese wooden houses are discussed in considering both the acceleration response spectrum with sharp peaks and the acceleration response spectrums of observed earthquake motion. The new horizontal resistant force is defined as the product of the coefficient of eccentricity ratio, the coefficient of a damping factor, and the coefficient of horizontal resistant force. This coefficient of horizontal resistant force is the function of the ductility factor, the natural period, the period of a response spectrum peak and its acceleration. As a result, the response analysis shows that the proposed equations give the safe side of the horizontal resistant force.

https://doi.org/10.52202/069179-0264

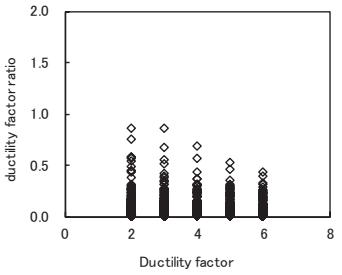

a) h=0.10

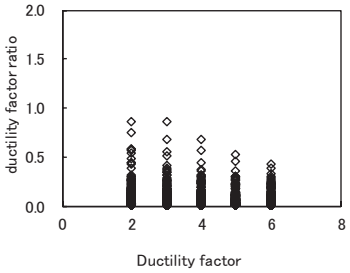

b) h=0.20

Figure 12: *Ductility factor ratio subjected to observed earthquake motions with hysteresis damping system whose energy dissipation is counted double.*

ACKNOWLEDGEMENT

Strong motion data from K-NET, KiK-net, Railway Technical Research Institute, The Building Center of Japan and JMA were used in this study.

REFERENCES

[1] Ministry of Land, Infrastructure: Transport and Tourism: Examples and exposition for Calculation of Response and Limit Strength, 70-71, 2001.

[2] Koji Yamada: ASEISMIC DESIGN LEVEL USING RESPONSE SPECTRUM AND IT'S APPLICATION, 17th World Conference on Earthquake Engineering, 2C-0031, 2021.

[3] Koji Yamada: Aseismic design level using response spectrum and it's application, Journal of Structural Engineering, Vol.61.B, .365-371, 2015.

[4] Koji Yamada: Aseismic design level using response spectrum Cases of observed eathquake motions, Journal of Structural Engineering, Vol.64.B, 71-79, 2018.

[5] Architectural Institute of Japan (1990): Ultimate Strength and Deformation Capacity Buildings in Seismic Design (1990), 1990.

[6] NIED K-NET, KiK-net,National Research Institute for Earth Science and Disaster Resilience, doi:10.17598/NIED.0004

https://doi.org/10.52202/069179-0264

World Conference on Timber Engineering Oslo 2023

MASS TIMBER BRACED FRAMES WITH MASS TIMBER BUCKLING RESTRAINED BRACES

Emily Wiliamson[1], Chris P. Pantelides[2], Hans-Erik Blomgren[3], Douglas Rammer[4]

ABSTRACT: A mass timber lateral force resisting system (LFRS) is proposed using a timber buckling restrained brace (TBRB) for improved seismic performance in high seismic applications. To develop a high-performance braced frame, it is essential to quantify the behaviour of the connections including failure modes and moment-rotation capacities. Cyclic and monotonic tests were conducted on six mass timber beam-column connections to investigate the response of mass timber joints connected with slotted-in steel plates and mild steel dowels. The goal of the subassembly tests was to measure the maximum rotation of such connections for monotonic and cyclic loads; these results were used to optimize the number of mild steel dowels for the TBRB frame design. The tests showed that the connections with three different steel dowel details reached a maximum rotation of 0.11 rad. with no loss of strength. Scaled tests of a full braced timber frame with a TBRB were carried out to verify the LFRS which included the effect of column axial load and out-of-plane displacements.

KEYWORDS: Braced frame, Buckling restrained brace, Lateral Force resisting system, Mass timber, Seismic

1 INTRODUCTION

Mass timber buildings are popular due to their sustainable characteristics, architectural appeal, and high strength-to-weight ratio. Engineered timber products such as glulam, cross laminated timber (CLT) and mass ply panels (MPP) allow engineers to take advantage of these characteristics. Currently, tall timber buildings must be combined with a lateral force resisting system (LFRS) made of steel or reinforced concrete because current building codes lack defined values for a ductile timber LFRS; this can lead to compatibility issues and increase construction cost and time.

A ductile timber (LFRS) is needed for the expanded use of mass timber in new taller buildings. There has been some work to develop and improve the performance of CLT shear walls [1-6], but shear wall systems can limit the flexibility of the building floor plan. Current timber frames have limited hysteretic energy dissipation and ductility capabilities because they rely on the connections for the response to loading [7-8]. To address this issue, researchers have developed a buckling restrained brace with a timber casing (TBRB) [9]; tests showed that a TBRB exceeds the qualification requirements of a conventional BRB [10]. Researchers have also completed a series of TBRB tests to propose new design methods and avoid certain failure modes such as bulging of the timber restraining element [11]. Furthermore, researchers have successfully tested a full-scale glulam frame with two conventional steel and concrete BRBs in a chevron configuration [12].

The overall performance of a complete TBRB frame (TBRBF) also depends on the beam-column and gusset plate connection performance. Researchers have been interested in the performance of moment resisting timber connections for some time [13-16]; however, dowel-type connections often experience premature failure due to tension splitting of the timber under induced beam-column joint rotations. Additional reinforcement perpendicular to the grain is often required to improve connection performance. Joint reinforcement with screws placed perpendicular to grain using glulam connections achieved a maximum rotation of 0.08 radians [17]. Dowels arranged in a circular pattern using plywood as reinforcing for the joints achieved a maximum rotation of 0.03 radians [18].

In this study, six beam-column joints were designed and tested under monotonic and cyclic loads with varying number of dowels. Mass ply lam (MPL) [19] was used for the beams and columns to provide resistance against perpendicular-to-grain tension splitting in the connection regions due to the additional strength and stiffness provided by the cross-ply veneers included the layup of the material. Informed by the results of the beam-column connection tests, an MPL frame with a TBRB was designed and tested. The frame was tested with multiple levels of axial force applied to the columns and with some out-of-plane displacement imposed on the frame. In addition to the TBRBF subassembly tests, the frame was tested on its own to monitor the condition of the connections and provide an improved understanding on the TBRB contribution to the performance of the subassembly.

[1] Res. Assist., Dept. of Civil and Env. Eng., University of Utah, USA, emily.diedrich@utah.edu
[2] Prof., Dept. of Civil and Env. Eng., University of Utah, USA, c.pantelides@utah.edu
[3] Struct. Eng., Timberlab, USA, h.blomgren@timberlab.com
[4] Res. Eng., Forest Products Laboratory, USA, douglas.r.rammer@usda.gov

https://doi.org/10.52202/069179-0265

2 MASS TIMBER CONNECTION TESTS

The initial phase of the research discussed in this paper includes the design and testing of six beam-column connections [20]. These tests were carried out to provide a clearer understanding of the connection performance including failure modes, moment-rotation relationships and rotation capacity.

2.1 CONNECTION EXPERIMENT DESIGN

The connections designed for the experimental program were meant to represent a beam-column-brace connection within a TBRBF with a beam span of 4.27 m and a story height of 2.90 m (Figure 1). The length of the members was based on cutting the joint out at the mid-span of the beam and at half a story height above and below the joint. The beam and column were 381 mm square MPL, a material made of layers of laminated veneer lumber with different cross grain directions of the veneer layers [19]. MPL in the joist orientation (Figure 2a) was chosen to take advantage of the cross-ply layers in the layup which act as self-reinforcing and attempt to avoid the additional joint reinforcing that is typically required to improve the strength and rotation capabilities of timber connections. The members were connected with 248 MPa, 12.7 mm slotted-in steel plates and 12.7 mm diameter smooth-shank mild-steel dowels (Figure 2). In a beam-column-brace connection, the steel connection plates will extend beyond the timber members to form gusset plates for the TBRB connection, but these were not included in the connection tests. The impact of the gusset plates and brace connection on the performance of the connection was studied in more detail during the MTRBF tests described in Section 3.

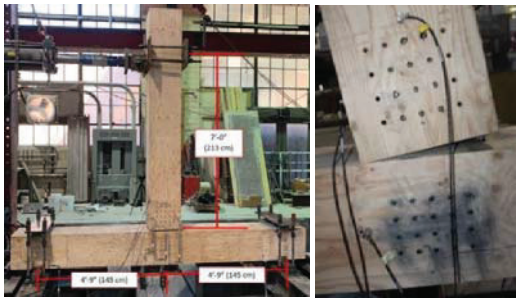

Figure 1: *Beam-column joint setup and maximum rotation for joint with 12 beam dowels*

The connections were designed to resist the overstrength forces from a 267 kN tensile yield strength TBRB using the National Design Specification (NDS) for Wood Construction and the NDS Technical Report 12 for dowel-type connectors [21,22]. The joint was idealized as an equivalent series of three-member connections [23] and the theoretical moment capacity was calculated using the model in [18]. The geometry of the dowel connection was selected to allow yield mode IV to be the limiting yield mode of the design because it is a more ductile yield mode as it is limited by the bending of the steel dowels rather than the crushing of the timber. A 25 mm gap between the end of the beam and the face of the column was built into the connection to allow for large beam rotations without contact with the column.

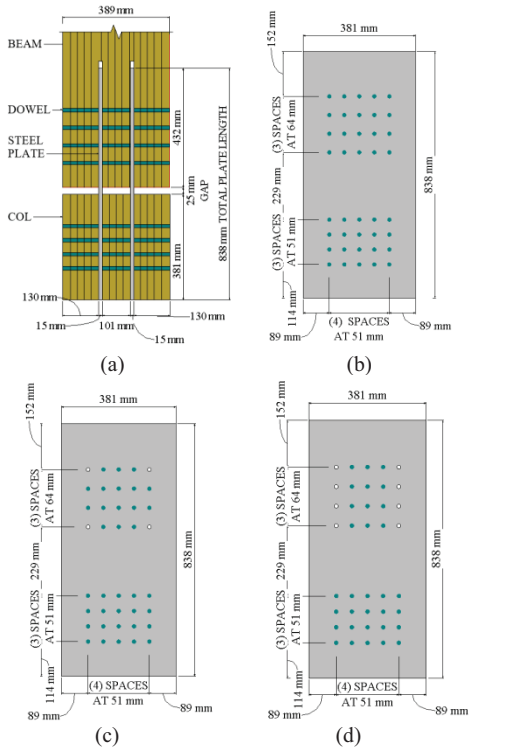

Figure 2: *Connection:(a) section, (b) 20 dowels, (c) 16 dowels, (d) 12 dowels*

Three pairs of connections were tested, each with a different number of dowels in the beam; the first pair had 20 dowels, the second pair 16, and the third pair 12. All connections had 20 column dowels. For each variation, one connection was tested under monotonic loading and one under cyclic loading. The cyclic loading protocol was adopted from ASTM E2126 test method B [24]; the loading protocol was defined with the maximum horizontal displacement imposed on the beam end as 254 mm, which was equivalent to the maximum stroke of the actuator used to apply the load (Figure 3). To facilitate testing, the joint was rotated 90 degrees counter-clockwise so that the 2.13 m beam was vertical; a horizontal load was applied at the beam end (Figure 1).

https://doi.org/10.52202/069179-0265

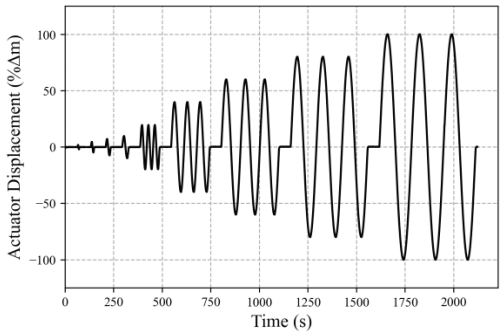

***Figure 3**: ASTM E2126 test method B loading protocol*

2.2 CONNECTION EXPERIMENTAL RESULTS

All six joints reached a maximum rotation of 0.11 radians without any loss of strength or any visible external damage such as timber splitting in the joint region; the only joint that experienced contact between the beam and column was the joint with 12 dowels in the beam under monotonic loading (Figure 2). The tests were stopped at 0.11 radians of rotation because this was the maximum displacement allowed by the length of the actuator. After testing was complete, the joints were dissected to observe the internal damage to the connection. Although most of the deformation observed was small, the most deformation was observed in the joint with 12 dowels in the beam (Figure 4a). In all tests, the dowels yielded in mode IV as expected based on the design; necking of dowels at the steel plate interface and elongation of the holes in the direction of the force in the respective dowel were observed (Figure 4b). Furthermore, most of the damage was observed in the dowels in the perimeter of the connection.

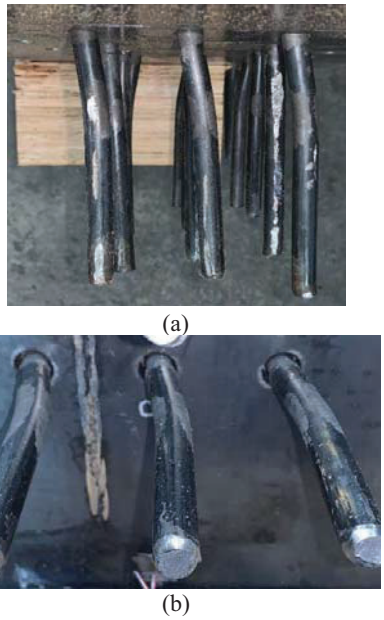

(a)

(b)

***Figure 4:** Post-test connection dissection (a)bending of the dowels and (b) deformation of the holes in the steel plate*

The moment capacity of the beam-column connections appeared to be proportional to the number of dowels in the beam (Figure 5). The envelope response of these connections can be broken down into three main stages (Figure 5a): the slip stage, the elastic stage, and post-yield stage. The second increase in load exhibited in the 12 beam dowel connection's monotonic response was caused by the contact between the beam and column, which occurred at approximately 0.09 radians. The slip stage occurs in the beginning of the loading because some displacement must be imposed on the connection before it is fully engaged. This is largely due to construction tolerances of the holes, which need to be slightly oversized in order to fit the dowel through the three timber and two steel elements. Once the dowel has overcome the gap and fully engaged with the timber, the connection is able to develop more stiffness and it enters the elastic stage. During this stage, the connection continues to develop strength until the steel dowels begin to yield. After the dowels yield and begin to deform, the connection is not able to resist additional load; however, the connection continues to rotate, resulting in a ductile connection response. The Y and K method [25] was used to estimate the yield point of the connection. The displacement ductility of these connections was then determined to range from 1.8 to 4.1 based on the maximum rotation achieve during testing; however, this is a lower bound because the tests were forced to terminate before a loss in strength occurred due to the limited stroke length of the actuator.

The hysteresis of the cyclic tests (Figure 5b) displays some pinching effects. This is common for timber doweled connections because there is some slack in the connection when the load is reversed and the dowel has some distance to recover before it is fully engaged with the timber again since it may have already crushed it in that region during a previous cycle.

https://doi.org/10.52202/069179-0265

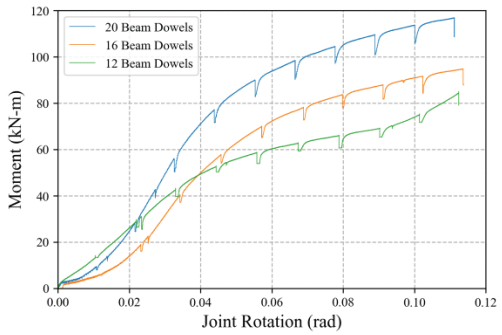

(a)

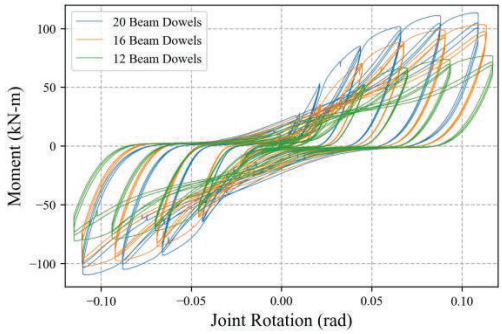

(b)

Figure 5: *Experimental results: (a) monotonic tests and (b) cyclic tests*

3 TBRBF SUBASSEMBLY TESTS

After evaluating the response of the connections during the connection tests, a TBRBF was designed and constructed for performing cyclic, quasi-static subassembly tests (Figure 6).

3.1 TBRBRF SUBASSEMBY EXPERIMENT DESIGN

The frame was designed as an approximately two-thirds scale, single-bay frame with a column spacing of 3.05 m and a story height of 2.29 m. To properly simulate the performance of a frame in an upper story of a building, the columns were extended beyond the bottom beam to the strong floor. Furthermore, the base of the west column was designed to be a roller to drag the horizontal component of the brace force through the bottom beam to the base of the east column, which was fixed by extending the connection plates 25 mm lower than the base of the column and welding it to the steel support structure. The beams and columns are of the same MPL material and same cross-section as the joint tests described in Section 2. The connections in the frame also have two 12.7 mm thick slotted-in steel plates and are connected by 12.7 mm diameter mild steel dowels. All connections were designed using the same approach as described in Section 2.1 of this paper for the expected forces of a TBRB with a tensile yield force of 178 kN. The expected forces were determined with a compression adjustment factor of 1.25 and a strain hardening factor of 1.45, which were the maximum of each value determined in [9]. The gusset plates are formed by extending the connection plates beyond the timber members; they were reinforced with steel stiffeners and steel cheek plates to ensure the TBRB would be the limiting structural element in the frame. The 25 mm gap between the beam end and column face was also implemented for the connections in the frame.

The restraining element of the TBRB is mass plywood panel (MPP) blocks bolted together on either side of the mild steel yielding core. The MPP blocks were 254 mm wide by 152 mm deep; they were placed so that the laminas were perpendicular to the steel yielding core. To achieve a 178 kN TBRB, the yielding portion of the core was specified to be 13 mm thick by 51 mm wide and have a yield stress of 276 MPa. At the ends of the brace, the core width increases to 178 mm for the pin connection to the two gusset plates. In addition, there are stiffeners welded to the ends of the core to ensure that yielding occurs within the intended yielding zone. Finally, there was a 25 mm diameter dowel welded to the steel core at the midpoint of the yielding zone to promote even load distribution and help keep the core in place within the casing. The TBRBs used in this experimental program had a pin to pin length of 2730 mm and a yielding length of 1554 mm.

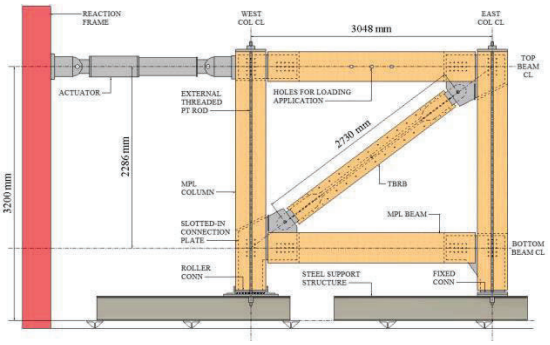

Figure 6: *Experiment of TBRBF*

The same timber frame was used for nine total tests: four TBRBF tests and five bare frame tests. The bare frame tests were done at the beginning of the testing series, at the end of the testing series, and between each TBRBF test. Moreover, the bare frame tests were completed within the elastic range of the frame to provide an understanding of the frame contribution to the subassembly performance and to monitor the condition of the connections after a TBRBF test. Two levels of axial force were applied to the columns during testing: the low-level axial load was equivalent to 5% of the column capacity and the high axial load was equivalent to 12% of the column capacity. The axial force was applied to the columns with two all-thread bars, which were external to the columns and post-tensioned to achieve the desired load level. Each level of axial load was tested once in-plane and once with a 25 mm out-of-plane displacement imposed on the top east connection. A summary of the tests is listed in Table 1.

https://doi.org/10.52202/069179-0265

Similar to the connection tests, the loading protocol adopted for these tests was based on ASTM E2126 test method B [24] (Figure 3). The cycles were defined based on a maximum displacement associated with a drift ratio of approximately 3%. To ensure the connections remained elastic during the bare frame tests, the loading protocol was terminated after the $0.6\Delta_m$ loading step.

Table 1: *Timber Frame Experimental Program*

Test Name	Out-of-plane displacement	Axial Load Level
Bare Frame	None	Low
I-TBRB1	None	Low
I-TBRB2	None	High
O-TBRB3	25 mm	Low
O-TBRB4	25 mm	High

3.2 TBRBF SUBASSEMBLY RESULTS

Frame tests without a TBRB were completed as intermediate steps during the experimental program to monitor the condition of the connections and provide insight into how the TBRBF performance compares to the bare frame performance. The hysteresis in Figure 7 is representative of all the bare frame tests that were conducted throughout the testing series since the connections experienced minimal damage during both the bare frame tests and the TBRBF tests. Because they were carried out as intermediate steps, the tests were concluded earlier in the loading protocol to ensure the connection remained mostly elastic; the slender hysteresis loops and no significant excessive drift at zero force confirm this assumption.

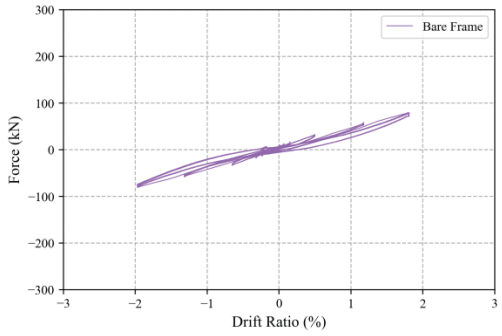

Figure 7: *Bare frame hysteresis*

The hysteresis curves for the TBRBF tests are shown in Figure 8; Figure 8a shows the response of the frames with low axial force applied to the columns and Figure 8b shows the response of the frames with high axial load. Both the level of axial load and the intentional out-of-plane displacement had little impact on the performance of the subassembly. There is a slight decrease in stiffness between the first TBRBF test, I-TBRB1, and the subsequent tests due to the slight crushing of the timber in the dowel regions caused by the first test. Some slip can be observed when the load was reversed; this is due to the movement of the dowels within their respective holes before the dowels are fully engaged. The TBRBF tests were able to achieve similar forces in tension and compression as expected from a BRB system. Furthermore, at the same drift ratio, the TBRBF resisted 3.0 to 3.8 times the amount of lateral load than the bare frame.

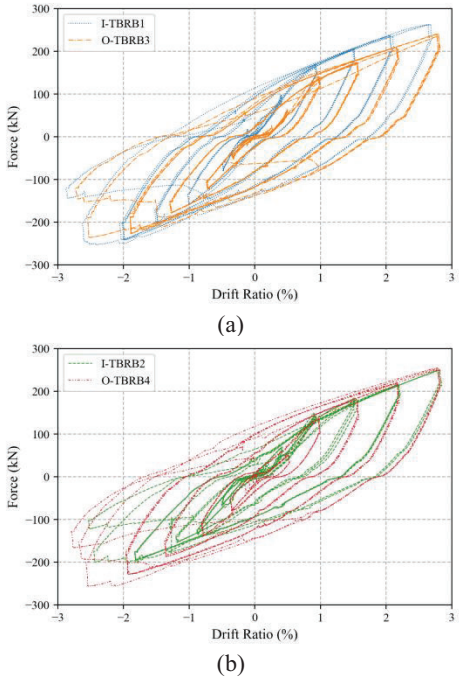

Figure 8: *TBRBF Hysteresis curves (a) low axial load and (b) high axial load*

All four of the hysteresis curves are relatively stable with minimal pinching. This indicates effective hysteretic energy dissipation (Figure 9) from the diagonal TBRB core plate. Test O-TBRB4 shows the most energy dissipation because it was allowed to complete the entire loading protocol despite TBRB failure. This shows that the system is able to continue to dissipate energy even after TBRB failure. Test I-TBRB2 dissipated the least amount of energy of the TBRBF tests because a weld in the support structure fractured during the test which caused the east column to behave as a rocking column and limited the amount of force the system was able to resist when the actuator was pulling the frame to the west (negative drift ratio). Figure 9 demonstrates the impact of the TBRB on the subassembly's ability to dissipate energy effectively. When comparing the energy dissipated by the TBRBF to the energy dissipated by the bare frame after the same number of cycles, the TBRBF dissipates 4.0 to 8.6 times the hysteretic energy dissipated by the bare frame.

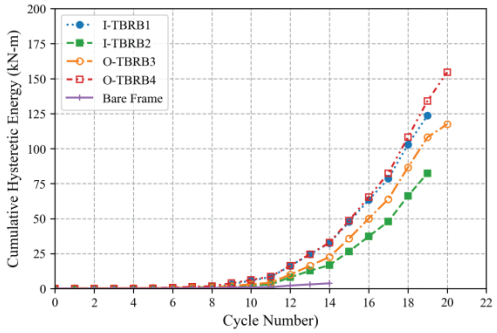

Figure 9: *Cumulative hysteretic energy*

The secant stiffness was calculated for each cycle to show the stiffness degradation of the system throughout the loading protocol. It was calculated based on the peak forces and displacements achieved for each cycle. Figure 10 shows a comparison between the stiffness of test I-TBRB1 and the first bare frame test. Since the connections provide limited moment-resisting capabilities, the stiffness of the bare frame is smaller than the stiffness of the TBRBF.

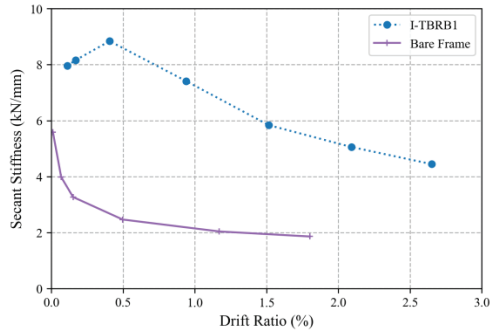

Figure 10: *Stiffness comparison between TBRBF and bare frame*

In addition to the hysteretic energy and the stiffness degradation, the ductility of the TBRBF system was evaluated using the Y and K method [25] because it is able to effectively estimate the yield point of a timber structure even when the connections have a lower initial stiffness consistent with what is observed with the dowel-type connections [26]. The maximum displacement ductility for the TBRBF tests determined by the Y and K method ranged from 3.1 to 3.5. To properly compare to existing research, the yield point and ductility was also estimated using the EEEP method [24]; the maximum displacement ductility determined by this method ranged from 2.1 to 2.9. This is double the ductility found for conventional timber brace frames [27], and comparable to the findings of research in which timber frames were tested with conventional steel-concrete BRBs [12].

All TBRBF tests experienced failure of the TBRB during the compression segment of the second cycle of the 100%Δ_m loading step. The failure was initiated by weak axis buckling of the steel core near the end of the yielding zone (Figure 11a). As the amplitude of the buckled core increased with higher displacement cycles, the casing began to split between the layers at the location of the largest wave; the splitting eventually propagated along the length of the casing (Figure 11b)

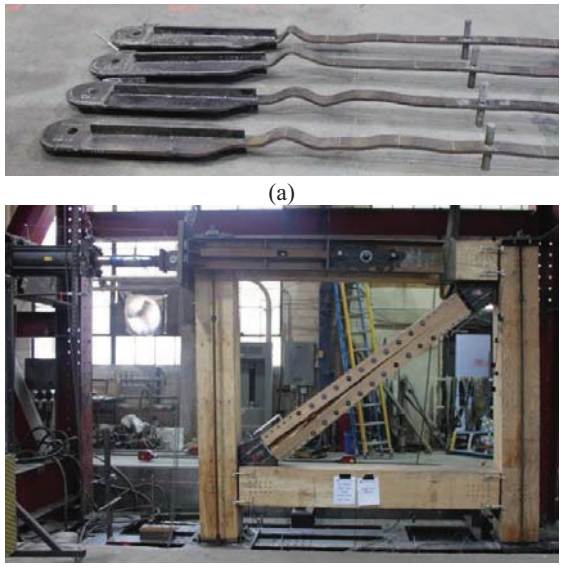

(a)

(b)

Figure 11: *TBRB failure modes (a) weak axis buckling of the steel cores and (b) splitting of the MPP casing*

The connections of the timber frame experienced no visible external damage such as tension splitting or timber crushing. After the testing series was complete, the connections were dissected to investigate if there was any internal damage; there was very slight bending of the dowels, which indicates that the connections may have remained mostly elastic during the TBRBF tests as well as the bare frame tests. Throughout testing, the rotation of the connections was monitored by linear variable displacement transducers (LVDTs); they recorded a maximum rotation of 0.036 radians during the testing series.

4 CONCLUSIONS

Six beam-column joint specimens were tested which achieved a rotation of 0.11 rad. This large rotation shows that the connections behave in a ductile manner, a good characteristic of an element in a LFRS. The MPL material did not experience any perpendicular to grain splitting; this eliminates the need for costly joint reinforcement and confirms the hypothesis that the cross-grain layers would behave as self-reinforcing by providing additional stiffness in the perpendicular-to-grain direction. Additionally, the 25 mm gap helped avoid crushing of the timber by preventing contact between the beam end and column face. The bending moment that the joint was able to resist was proportional to the number of dowels in the beam. The results of these tests showed that the existing

https://doi.org/10.52202/069179-0265

methods for connection design are applicable for this type of connection and result in a ductile response.

After the connection tests, a series of timber frame tests were completed including four tests with a TBRB and five tests with the bare frame. All four TBRBFs achieved similar forces and drifts in both tension and compression; the TBRBs consistently failed during the compression portion of the 100%Δ_m step of the loading protocol. The failure mode was weak axis buckling of the steel core near the end of the yielding zone. The increasing amplitude of the waves eventually caused the MPP casing to split along its length. The TBRB improved the performance of the subassembly by improving the hysteretic energy capabilities by 4.0 to 8.6 times and increasing the lateral load capacity by a factor of 3.0 to 3.8. The ductility of the TBRBF was evaluated using two methods and was found to be comparable with other timber frames using conventional BRBs and double the ductility of conventional timber braced frames.

The same frame was used for all nine tests with no visible damage to the connections. This demonstrates the resilience of this TBRBF system where the TBRB can be removed and replaced following a seismic event, without the need to replace the bare timber frame. Further testing including full-scale dynamic tests is suggested to confirm the findings of this study.

ACKNOWLEDGEMENT

The authors acknowledge the financial support provided by Wood Innovations, USDA Grant 20-DG-11046000-615, the donation of materials by Freres Lumber Co., Inc., and the in-kind CNC fabrication assistance provided by the Timberlab. The authors acknowledge the assistance of M. Bryant, D. Tran, I. Dangol, D. Briggs, S. Neupane and S. Shrestha of the University of Utah for their assistance in carrying out the experiments.

REFERENCES

[1] Morrell I., Soti R., Miyamoto B. and Sinha A.: Experimental Investigation of Base Conditions Affecting Seismic Performance of Mass Plywood Panel Shear Walls. *J. Struct. Eng*. 146(8), 2020.

[2] Lo Ricco M., Rammer D.R., Amini M.O., Ghorbanpoor A., Shiling P. and Zimmerman, R.B.: Equivalent lateral force procedure for a building with a self-centering rocking story of cross-laminated timber (CLT) walls." *Proceedings of the World Conference on Timber Engineering 2020*, 2021. Santiago, Chile.

[3] Pei, S., van de Lindt, J.W., Barbosa, A.R., Berman, J.W., McDonnell, E., Dolan, J.D., Blomgren, H.-E., Zimmerman, R.B., Huang, D., and Wichman, S.: Experimental seismic response of a resilient 2-story mass-timber building with post-tensioned rocking walls. *J. Struct. Eng*., 145(11): 04019120, 2019.

[4] van de Lindt J., Amini, O.M., Rammer D.; Line P.; Pei S., Popovski M.: Determination of seismic performance factors for cross-laminated timber shear walls based on FEMA P695 methodology. *General Technical Report FPL-GTR-281*, 2022.

[5] Ganey R., Berman J., Akbas T., Loftus S., Dolan J.D., Sause R., Ricles J., Pei S., van de Lindt J. and Blomgren H.-E.: Experimental investigation of self-centering cross-laminated timber walls. *Journal of Structural Engineering,* 2017.

[6] Busch, A., Zimmerman, R.B., Pei, S., McDonnell, E., Line, P., and Huang, D.: Prescriptive seismic design procedure for post-tensioned mass timber rocking walls. *Journal of Structural Engineering*, 148(3): 04021289, 2022.

[7] Cao J., Xiong H. and Cui Y.: Seismic performance analysis of timber frames based on a calibrated simplified model. *Journal of Building Engineering* 46, 2021.

[8] Popovski M., Prion H. G.L. and Karacabeyli E.: Shake table tests on single-storey braced timber frames. *Canadian Journal of Civil Engineering* 30:1089-1100, 2003.

[9] Murphy, C., Pantelides, C.P., Blomgren, H., Rammer, D.: Development of timber buckling restrained brace for mass timber-braced frames. *Journal of Structural Engineering*, 147(5):04021050, 2021.

[10] AISC: Seismic Provisions for Structural Steel Buildings. ANSI/AISC 341-16, Chicago, American Institute of Steel Construction, 2016.

[11] Takeuchi T., Terazawa Y., Komuro S., Kurata T. and Sitler B.: Performance and failure modes of mass timber buckling-restrained braces under cyclic loading. *Engineering Structures* 266, 2022.

[12] Dong W., Li M., Lee C., MacRae G., and Abu A.: Experimental testing of full-scale glulam frames with buckling restrained braces. *Engineering Structures* 222, 2020.

[13] Rebouças A.S., Mehdipour Z. Branco J.M. and Lourenço P.B.: Ductile Moment-Resisting Timber Connections: A Review. *Buildings*. 12(240), 2022.

[14] Popovski M., Prion H. G.L., and Karacabeyli E.: Seismic performance of connections in heavy timber construction. *Canadian Journal of Civil Engineering* 29:389-399, 2001.

[15] Ogrizovic J., Wanninger F. and Frangi, A.: Experimental and analytical analysis of moment-resisting connections with glued-in rods. *Engineering Structures.* 145: 322-332, 2017.

[16] Steiger R., Serrano E., Stepinac M., Rajcic V., O'Niell C., McPolin D. and Widmann, R.: Strengthening of timber structures with glued-in rods. *Construction and Building Materials*, 97:90-105, 2015.

[17] Dong, W., Li, M., He, M., Li, Z.: Experimental testing and analytical modeling of glulam moment connections with self-drilling dowels. *Journal of Structural Engineering*, 147(5): 04021047, 2021.

[18] Bouchaïr, A., Racher, P., Bocquet, J.F.: Analysis of dowelled timber to timber moment-resisting joints. *Materials and Structures*, 40:1127-1141, 2007.

[19] APA (The Engineered Wood Association): Freres Mass Ply Panels (MPP), and Mass Ply Lam (MPL) Beams and Columns, Freres Lumber Co.. *Inc. PR-L325*, 2022
[20] Williamson E., Pantelides C. P., Blomgren H.-E. and Rammer D.: Performance of beam-column connections with Mass Ply Lam and steel dowels under cyclic loads. *Journal of Structural Engineering,* 149(6):04023057, 2023.
[21] AWC (American Wood Council): National Design Specification for Wood Construction, 2018.
[22] AWC (American Wood Council): Technical Report 12: General Dowel Equations for Calculating Lateral Connection Values with Appendix A, 2018.
[23] Fan, X., Zhang, S., Qu, W.: Load-carrying behaviour of dowel-type timber connections with slotted-in steel plates. *Applied Mechanics and Materials*, 94-96: 43-47, 2011.
[24] ASTM: Standard Test Methods for Cyclic (Reversed) Load Test for Shear Resistance of Vertical Elements of the Lateral Force Resisting System for Buildings. *ASTM E2126*, 2011
[25] Yasumura M. and Kwai N.: Estimating seismic performance of wood-frame structures." *Proceedings of the 5th World Conference on Timber Engineering*, 1998. Presses Polytechniques et Universitaires Romandes.
[26] Muñoz W., Mohammad M., Salenikovich A. and Quenneville P.: Determination of yield point and ductility of timber assemblies: in search for a harmonized approach. *Engineered Wood Products Association*, 2008.
[27] Xiong H. and Liu Y.: Experimental study of the lateral resistance of bolted glulam timber post and beam structural systems. *Journal of Structural Engineering*, 142(4), 2014.

https://doi.org/10.52202/069179-0265

World Conference on Timber Engineering Oslo 2023

EFFECT OF SMALL DEFORMATION DUE TO MODERATE EARTHQUAKES ON THE SHEAR PERFORMANCE OF SHEAR RESISTING WALL

Ryo Inoue[1] , Takuro Mori[1], Shinya Matsumoto[2]

ABSTRACT: In order to confirm how cyclic deformation due to moderate earthquakes during the use period of a wooden house affects the shear resisting wall, in-plane shear experiments with cyclic deformation on the walls using plywood and gypsum board were conducted. As a result, it was found that the maximum load and the yield load are not significantly affected even if the wall received repeatedly small deformation. The load reduction due to repeated deformation of gypsum board wall was larger than plywood wall. Additionally, the stiffness of repeated specimens was reduced accordingly. The calculated load reduction trend of sheathed walls subjected to repeated small deformations from the experimental results of nailed joints was found to be generally expressible. It was found that the response deformation of wooden houses during the major earthquake may increase as the stiffness of shear resisting walls decreases.

KEYWORDS: Cyclic deformation, Plywood wall, Gypsum board wall, Moderate earthquake, Shear performance

1 INTRODUCTION

Increasing the continuous use of wooden houses after the major earthquake is important not only for maintaining the assets, but also for early city reconstruction. For the purpose, it is necessary to build high seismic performance house and/or to appropriately evaluate the residual seismic performance at the time of seismic diagnosis after moderate earthquakes.

Cyclic deformations due to small and medium-class earthquakes may reduce seismic performance in existing houses. Especially in large deformations, it is known that the deterioration of shear performance due to multiple cyclic deformations. It has been reported that when the amount of repeated deformation is large, such as during a large earthquake, the deterioration of the shear performance is large [1]. In addition, some examples have shown the effect of cyclic loading on the structural performance of shear resisting walls [2].

However, these existing reports are mainly aimed at improving the accuracy of response prediction during large earthquakes and the prediction of seismic behaviour of wooden houses. They are targeted at large deformation for large earthquakes. Therefore, there are very few examples of studies of large numbers of small deformation repetitions, and the effects of such repetitions have not been clarified. In Japan, small and medium earthquakes often occur. For example, in Ibaraki Prefecture, for the past 30 years, there have been about 300 earthquakes of intensity 3 [3]. It is important to understand to what extent the accumulation of small deformation caused by such earthquakes affects the seismic performance of wooden houses and their response deformation during large earthquakes.

Therefore, in the previous report [4], single shear tests in which nailed joints using plywood, OSB, MDF, and gypsum board were repeatedly displaced many times assuming small and medium earthquakes were conducted. As a result, it was clarified that plywood, OSB, and MDF showed almost the same load reduction tendency. And gypsum board had a particularly large load reduction compared to other boards.

In this report, in-plane shear experiments on the walls were conducted to confirm the effect of repeated small deformation on the shear performance of plywood walls and gypsum board walls.

Table 1: *List of specimens*

	SC	NC
Frame only	-	1
Plywood wall	1	2
Gypsum board wall	1	3

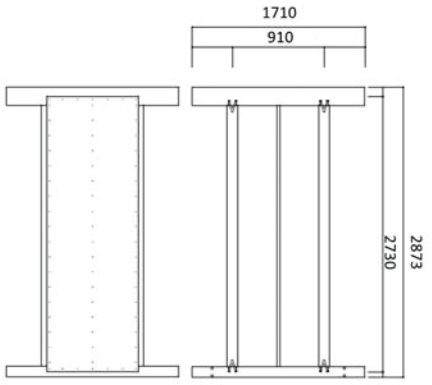

Figure 1: *Configurations of specimens (Unit: mm)*

[1] Ryo Inoue, Hiroshima University, Japan, d204777@hiroshima-u.ac.jp
Takuro Mori, Hiroshima University, Japan, moritaku@hiroshima-u.ac.jp

[2] Shinya Matsumoto, Kindai University, Japan matsumoto@hiro.kindai.ac.jp

https://doi.org/10.52202/069179-0266

2 OUTLINE OF EXPERIMENT

Table 1 shows a list of specimens, and Figure 1 shows the configurations of specimens. The specimen was 1P (b=910, h=2730 mm) wall. Two kinds of panels, plywood (t=9mm) and gypsum board (t=12.5mm) were used. A 105 x 180 mm hybrid beam (E105-F300, Japan Agricultural Standards) was used for the beam. A 105 x 105 mm Sugi glulam lumber (E65-F225, JAS) was used for the columns and base. The base-column and base-beam were joined by two N90 nails and VP plate with a short tenon. Plywood and gypsum board were fastened with N50 nails @ 150mm. There are two types of loading schedules; SC (Standard cyclic schedule) and NC (Numerous cyclic schedule). The SC was set to pull up to 1/15 rad after repeatedly deforming of ± 1/450, ± 1/300, ± 1/200, ± 1/150, ± 1/100, ± 1/75, ± 1/50 and 1/30 rad. For NC specimens, after the loading schedule shown in Table 2, additional loading was performed according to the same schedule as the SC specimen. The target deformation of multiple repetition was set assuming the maximum inter-story deformation of a wooden house during an earthquake with a seismic intensity of 3 to lower 5. The number of repetitions in each step was set by examining the number of observations at each prefectural office location for each seismic intensity from the Seismic Intensity Database [3] and using the maximum number. The loading was performed by displacement control, and the load was applied using a 300 kN jack. Figure 2 shows the test set up and transducer position. Experiments were conducted using a tie-rod system that restrained the column legs from lifting. Loading was displacement-controlled using the true deformation angle (Equation 1). It is obtained by subtracting the slip of the base and vertical displacement of the columns from the top deformation of wall. In equation 1, 2730 mm is the specimen height and 910 mm is the specimen width.

$$\gamma_0 = (\delta_1 - \delta_2)/2730 - (\delta_3 - \delta_4)/910 \quad (1)$$

γ_0: True deformation angle (rad)
δ_1: Top deformation of wall (mm)
δ_2: Slip of the base (mm)
δ_3, δ_4: Vertical displacement of the columns (mm)

Table 2: *Loading schedule of multiple repetitions*

Seismic intensity	Story deformation (rad)	Target deformation (mm)	Number of repetitions
3	1/2000	±1.4	200
	1/1000	±2.7	200
4	1/450	±6.1	50
	1/300	±9.1	50
4~lower 5	1/200	±13.7	10

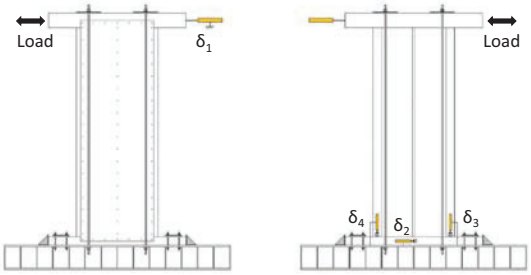

Figure 2: *Test setup and transducer position*

Table 3: *Strength characteristic values*

Plywood	P_{max} (kN)	K (kN/mm)	P_u (kN)	P_y (kN)	$0.2P_u\sqrt{2\mu-1}$ (kN)	$2/3P_{max}$ (kN)	P_{150} (kN)	P_a (kN)	Wall multiplier
SC	7.35	0.92	6.61	4.16	5.34	4.90	5.61	4.16	2.3
NC-1	7.07	1.07	6.42	4.32	4.92	4.71	5.39	4.32	2.4
NC-2	6.42	0.54	5.61	3.91	4.99	4.28	4.61	3.91	2.1
NC-3	7.00	0.66	5.99	3.97	5.42	4.67	4.68	3.97	2.2
NC Mean (CV)	6.83 (0.29)	0.76 (0.22)	6.01 (0.33)	4.06 (0.18)	5.11 (0.22)	4.55 (0.19)	4.89 (0.35)	4.06 (0.18)	2.2 (0.10)
TL	5.91	0.65	4.95	3.49	4.41	3.94	3.78	3.49	1.96
NC / SC	0.93	0.82	0.91	0.98	0.96	0.93	0.87	0.98	0.98

Gypsum board	P_{max} (kN)	K (kN/mm)	P_u (kN)	P_y (kN)	$0.2P_u\sqrt{2\mu-1}$ (kN)	$2/3P_{max}$ (kN)	P_{150} (kN)	P_a (kN)	Wall multiplier
SC	3.93	0.49	3.60	2.55	3.49	2.65	2.82	2.55	1.4
NC-1	4.01	0.91	3.64	2.50	4.62	2.97	3.19	2.50	1.4
NC-2	3.61	0.43	3.13	1.90	3.25	2.41	2.44	1.90	1.0
NC-3	4.59	0.30	4.06	2.91	3.10	3.06	3.29	2.91	1.6
NC Mean (CV)	4.07 (0.40)	0.55 (0.26)	3.61 (0.38)	2.44 (0.41)	3.66 (0.68)	2.71 (0.27)	2.97 (0.38)	2.44 (0.41)	1.3 (0.23)
TL	2.80	0.43	2.41	1.13	1.51	1.87	1.77	1.13	0.63
NC / SC	1.02	1.13	1.00	0.96	1.05	1.02	1.05	0.96	0.96

*Lower tolerance limit value (TL).
P_{max}, P_y, P_u: 95% lower tolerance limit at 75% confidence level.
K: 50% lower tolerance limit at 75% confidence level.

https://doi.org/10.52202/069179-0266

3 RESULT OF EXPERIMENT

Figure 3 shows the load-displacement envelope as the mean of each specimen group. Table 3 shows the strength characteristic values calculated by the perfect elasto-plasticity model [5]. The stiffness calculated using the slope between 0.1 P_{max} and 0.4P_{max}. The ductility factor μ is the ratio of δ_u to δ_y. The short-term allowable shear capacity P_a is the minimum value among P_y, 2/3P_{max}, 0.2$P_u\sqrt{(2\mu-1)}$, and P_{150} (load at 1/150 rad). The wall multiplier is the short-term allowable shear capacity divided by 1.96 kN and the width of the wall (0.91 m in this case), and is an index used in wall amount calculations (a common design method for wooden houses in Japan).

In both cases of plywood and gypsum board, repeated small deformations had no clear effect on the envelope curve of load-deformation relationships and ductility. In addition, comparing the mean values, it was found that there was no significant difference in maximum, yield and ultimate load between the SC and NC specimens regardless of whether the panel was plywood or gypsum board. There was also no difference in wall multiplier, indicating that even when subjected to repeated small deformations, the design performance can be expected to be similar to the shear performance of the sound condition. Furthermore, there was no difference in failure properties (Photo 1) between SC and NC specimen.

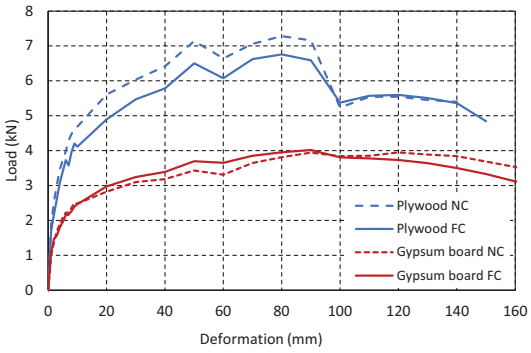

Figure 3: *Load-displacement envelope curve*

Photo 1: *Failure of specimen*
(Right: Gypsum board wall, Left: Plywood wall)

Figure 4 shows the transition of the load residual rate at the target displacement of 1/2000, 1/1000, 1/450, 1/300 and 1/200 rad. Here, the first load for each step is shown as 100%. Similar to the experiment of nailed joint [4], it

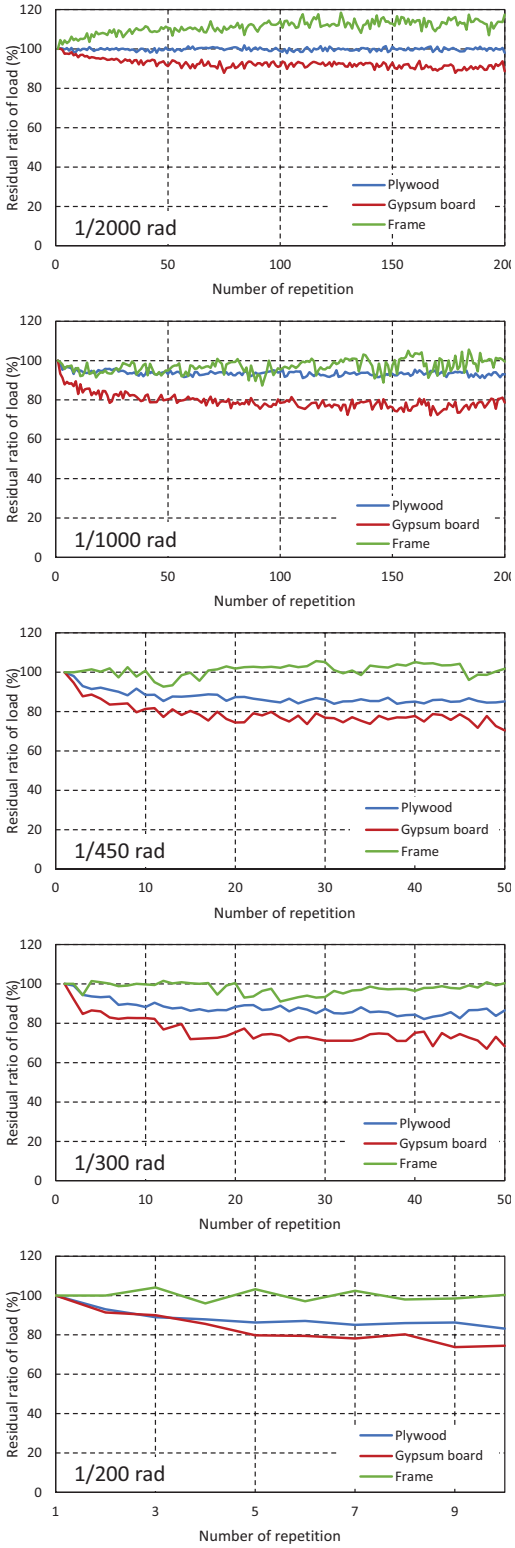

Figure 4: *Transition of the load residual rate*

https://doi.org/10.52202/069179-0266

was found that the load reduction of the gypsum board wall was larger than the plywood wall. In the nailed joint experiment, for example, the load residual ratio at the end of the repetition assuming 1/1000 rad was about 80% for plywood and about 70% for gypsum board. However, in the wall experiment, the load was maintained about 90% on the plywood wall even at the same deformation angle, and the load was maintained about 80% even on the gypsum board. In other words, the load reduction tendency was gradual. It is considered that this is because the target deformation in the nailed joint experiment was set assuming the nail with the largest amount of deformation in the wall, and the amount of deformation of the nail was smaller than expected. No significant tendency for the load to decrease was observed in the range of the number of repetitions of this experiment in the frame only specimen at any deformation angle.

Figure 5 shows the transition of equivalent stiffness and equivalent damping factor obtained by the equivalent linearization method. As with the load reduction, both equivalent stiffness and equivalent damping factor decreased after 5 to 10 repetitions at the beginning of each step, confirming that even small deformations have an effect. However, in subsequent repetitions, a convergence trend was observed, with a gradual decrease or levelling off, and no sudden decrease was observed.

4 PREDICTION AND DISCUSSIONS

The experimental results of the nailed joints [4] are used to examine whether the load residual ratio obtained in the wall experiments can be explained. For the plywood-sugi-N50 nailed joints, the relationship between load residual ratio and number of repetitions at each deformation (step) obtained in the previous report is expressed in both logarithms as shown in Figure 6. The load residual ratio-number of repetition relationship was considered as a proportional relationship, and the slope was calculated for each deformation by linear regression. The intercept of the approximate line was set to 2, since the residual load percentage for the new deformation was 100%. The slopes obtained for each deformation were plotted side by side for each deformation as shown in Figure 7. The larger the deformation, the larger the slope of the approximate straight line, indicating a larger load degradation. Here, it was determined that there is a roughly proportional relationship between the amount of repeated deformation and the slope of the approximate line. Since no load degradation occurs when the deformation is 0, the slope was obtained by linear regression with the intercept set to 0. Using the obtained slope, the equation for residual load at any deformation and any number of repetitions was derived as in Equation 2. The same procedure was performed for gypsum board wall, and the equation for residual load was obtained from Figure 7.

$$\text{Load residual ratio (\%)} = 10^2 \cdot N^a \qquad (2)$$

where a=deceleration index

Plywood: a = -0.047x, gypsum board: a = -0.077x

x: deformation (mm),

N: number of iterations (times)

Several models have been proposed to calculate the load-deformation relationship of sheathed walls using experimental results of nailed joints; Tuomi [6] et al. proposed a relatively simple method to estimate the

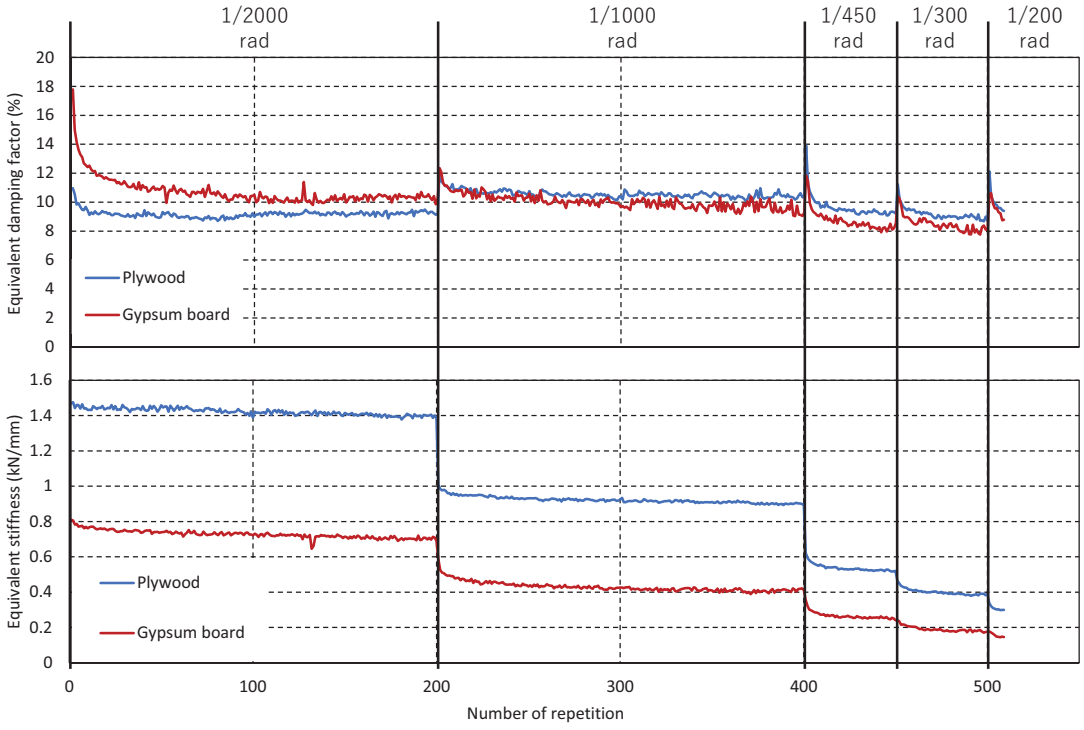

Figure 5: *Transition of equivalent stiffness and damping factor*

https://doi.org/10.52202/069179-0266

deformation behavior based on the assumption that nails driven into the four corners are displaced in the diagonal direction. Kamiya [7] and Murakami [8] proposed a model that determines the direction of rotation of a face material based on the equilibrium of forces.
Furthermore, Toda et al [9] have modified the equation to adapt to the case where part of the nailed joint has deteriorated due to biodeterioration, and where nails with different load-displacement relationships are mixed within the wall. The calculation method is cited from reference [9] as Equation 3 – 14. Since the equations used in the calculations were proposed with the intention of being used in design, the calculated results of load are slightly lower than the experimental results. The distance from the origin of the coordinates to the neutral axis is expressed by Equation 3 and 4, where i is the serial number of each nail and the load by each nail is considered.

$$x_0 = \frac{\sum x_i \times p_i}{\sum p_i} \quad (3)$$

$$y_0 = \frac{\sum y_i \times p_i}{\sum p_i} \quad (4)$$

x_0: Distance from the coordinate origin to the neutral axis in the x direction (mm)
x_i: x-coordinate of nail with number i (mm)
p_i: Load by the nail with number i (mm)
y_0: Distance from the coordinate origin to the neutral axis in the y direction (mm)
y_i: y-coordinate of nail with number i (mm)

The moment-rotation angle relationships in the x- and y-directions are given in Equation 5 – 7, respectively. And the relationship between the deformation angle of the wall and the rotation angle in the x- and y-directions is given in Equation 8.

$$M_x = K_x \times \theta_x \quad (5)$$

$$M_y = K_y \times \theta_y \quad (6)$$

$$M_x = M_y \quad (7)$$

$$R = \theta_x \times \theta_y \quad (8)$$

M_x: Moment in x direction (Nmm)
K_x: Rotational stiffness in x direction (Nmm/rad)
θ_x: Rotation angle in x direction (rad)
M_y: Moment in y direction (Nmm)
K_y: Rotational stiffness in y direction (Nmm/rad)
θ_y: Rotation angle in y direction (rad)
R: Deformation angle of the wall (rad)

Considering the secant stiffness of each nail, the rotational stiffness is shown in Equation 9 and 10. The deformation of each nail is expressed in Equation 13 using Equation 11 and 12.

$$K_x = \sum K_i \times (y_i - y_0)^2 \quad (9)$$

$$K_y = \sum K_i \times (x_i - x_0)^2 \quad (10)$$

$$\delta_{ix} = (y_i - y_0) \times \theta_x \quad (11)$$

$$\delta_{iy} = (x_i - x_0) \times \theta_y \quad (12)$$

$$\delta_i = \sqrt{{\delta_{ix}}^2 + {\delta_{iy}}^2} \quad (13)$$

K_i: Secant stiffness of nail with number i (N/mm)
δ_{ix}: x-direction displacement of nail with number i (mm)
δ_{iy}: y-direction displacement of nail with number i (mm)
δ_i: Displacement of nail with number i (mm)

Equation 3 – 12 can be obtained by convergence calculations, and the relationship between any given deformation angle of the wall and the corresponding shear force can be obtained using Equation 14.

$$P \times H = M_x = M_y = \frac{K_x \times K_y}{K_x + K_y} \times R \quad (14)$$

H: Height of the wall (mm)

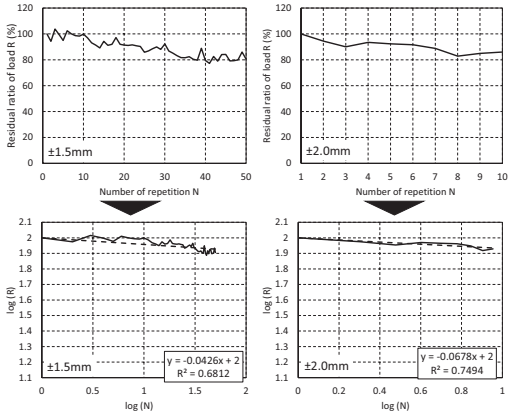

Figure 6: *Relationship between logarithmic load residual ratio and number of repetitions*

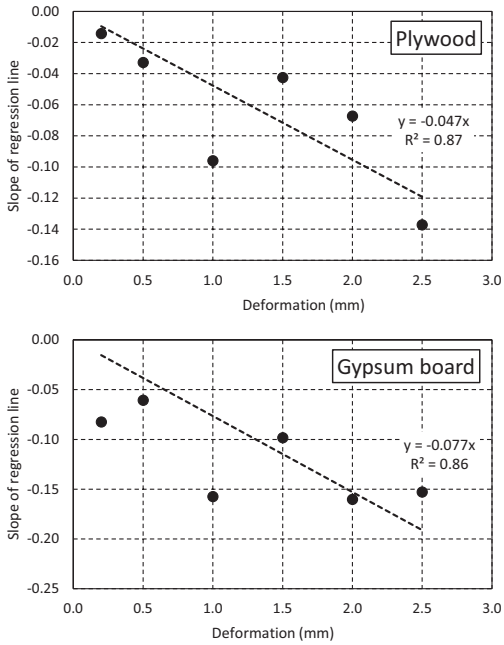

Figure 7: *Relationship between deformation and slope of regression line*

https://doi.org/10.52202/069179-0266

In this study, based on this calculation method, the load residual ratio corresponding to the amount of deformation and repetition for each nail was calculated from Equation 2 and multiplied by the load of each nail to calculate the load on the wall. Then, the load residual ratio of the entire wall was calculated. Comparison of the estimated results with the experimental values is shown in Figure 8. The experimental results are shown up to 1/200 rad, which was the subject of the repeated experiments, and the estimated values are shown up to 1/200 rad with a lower limit of 30% load residual.

For the plywood walls, the load reduction due to the 1/2000 rad repetitions is evaluated somewhat larger, but it can be said that the load reduction trend in the shear experiments of wall can be expressed. For gypsum board, the estimated value at 1/1000 rad repetitions was evaluated to be on the dangerous side compared to the experimental value. The reason for this is unknown. However, for the other deformation repetitions, it can be concluded that the experimental results are well represented. In conclusion, it was confirmed that the load-reducing tendency of shear resisting walls using face materials due to repeated small deformations can be generally estimated by repeated experiments on nailed joints.

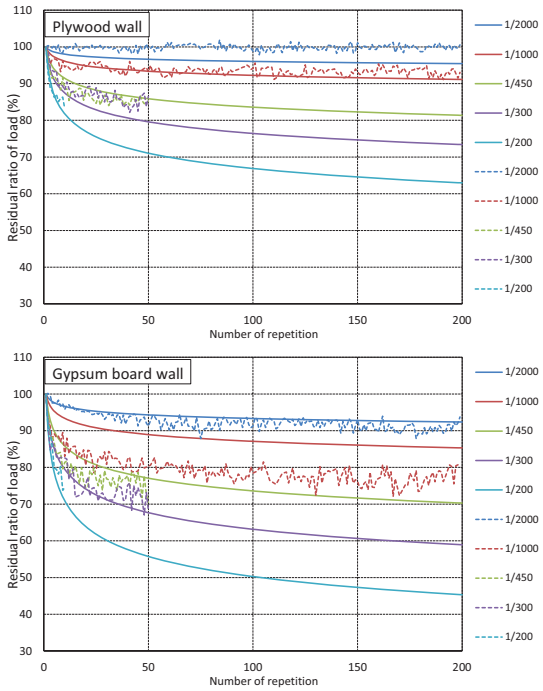

Figure 8: *Comparison between estimated value and test result of load residual ratio*
(*Solid line: test result, dotted line: prediction*)

5 CONCLUSIONS

In-plane shear experiments on the walls were conducted to confirm the effect of repeated small deformation due to moderate earthquakes on the shear performance of plywood walls and gypsum board walls.

As a result, it was found that the load reduction and equivalent stiffness reduction due to repetition of the same deformation were observed even in the case of repeated small deformations for the sheathed wall. Furthermore, the rate of load reduction due to repeated deformation in the gypsum board wall was larger than that in the plywood wall.

On the other hands, it was found that the maximum load and yield load are not significantly affected even if the wall received repeatedly small deformation.

The calculated load reduction trend of sheathed walls subjected to repeated small deformations from the experimental results from nailed joints was found to be generally expressible.

ACKNOWLEDGEMENT

This research was supported by Grant-in-Aid for JSPS Fellows (21J14285). Special thanks to Mr Ryo Shibahashi for assisting the experiments.

REFERENCES

[1] K. Sumida, H. Isoda, T. Mori, K. Tanaka, S. Tesfamariam: Experimental Seismic Response of a Japanese Conventional Wooden House Using 2016 Kumamoto Earthquake Records, J. Perform. Constr. Facil., 2019, 33(2): 04019014

[2] M. He, F. Lam, H.G.L. Prion: Influence of cyclic test protocols on performance of wood-based shear walls, Can. J. Civ. Eng. 25 (1998) 539–550

[3] Japan Meteorological Agency: Seismic intensity database, https://www.data.jma.go.jp/svd/eqdb/data/shindo/index.html, 2020.5, in Japanese.

[4] R. Inoue, T. Mori, A. Ariki, S. Matsumoto: Evaluation of single shear performance of nailed joint damaged by cyclic deformation due to moderate earthquakes, 2021 World conference on timber engineering, 2021.9

[5] Architectural Institute of Japan: Standard for Structural Design of Timber Structures, Maruzen, pp.108-109, 2006. in Japanese

[6] R.L. Tuomi, W.J. McCutcheon, Racking Strength of Light-Frame Nailed Walls, ASCE Journal of Structural Division 144 (ST7) (1978) 1131–1140.

[7] F. Kamiya: Theoretical studies on racking stiffness and strength of wooden sheathed walls, Trans. Of AIJ, 309, pp. 87-94, 1981, in Japanese.

[8] M. Murakami, M. Inayama: Formulae to predict the elastic and plastic behavior of sheathed walls with any nailing arrangement pattern, J. Struct. Constr. Eng., AIJ, 519, 87−93, 1999, in Japanese.

[9] M. Toda: Mokuzai mokushitsumenzairyou no seibutsurekka gamokushitsukouzoubutsu no taishinseinou ni oyobosu eikyou, Doctoral theses, Hokkaido University, 2014, in Japanese.

https://doi.org/10.52202/069179-0266

World Conference on Timber Engineering Oslo 2023

EXPERIMENTAL TESTING OF HIGH-CAPACITY SINGLE AND COUPLED CLT SHEAR WALL SYSTEMS

Ben Moerman[1,2] and Minghao Li[1,3]

ABSTRACT: This paper presents an experimental study on three types of balloon-framed cross-laminated timber (CLT) shear wall configurations: (a) a single wall, (b) a coupled wall with a half-lap joint between wall piers, and (c) a coupled wall with steel link beams between wall piers. Three-storey, 2/3-scale CLT wall specimens were cyclically tested to failure and the results are presented to compare the performance between wall types. All specimens used 5-ply, 205mm-thick CLT wall panels with the same base connections of mixed-angle screw hold-downs and notched shear keys. The beam-coupled wall achieved a peak strength of 592kN and demonstrated the best performance among the wall configurations with the highest strength, stiffness, energy dissipation, and least amount of degradation under repeated load cycles. All the wall specimen exhibited ductile failure modes and demonstrated their feasibility to be designed for lateral load resisting systems in buildings.

KEYWORDS: CLT, Shear Walls, Cyclic Loads, Self-tapping Screws, Coupled Walls, Hold-downs

1 INTRODUCTION

Cross-laminated timber (CLT) buildings are gaining global interest from architects, engineers, and owners. For CLT buildings built in seismic regions, CLT shear walls are critical to providing adequate earthquake resistance. It is well recognised that the lateral performance of typical CLT shear walls is governed by their connections [1], primarily because: (a) CLT panels have inherently high in-plane strength and stiffness and (b) conventional connections used in CLT structures have relatively low strength and stiffness.

Pei et al. [2] presented a review of experimental research on conventional CLT shear walls for seismic resistance which typically follow platform construction methods and use commercially available light gauge metal hold-downs or shear brackets with small diameter nails or screws. Connections with small, slender fasteners can achieve ductile behaviour and dissipate energy by fastener yielding and local timber embedment crushing around the fasteners [3]. They are currently the industry standard for connecting CLT walls as they are readily available and easy to specify. However, these connectors normally have a limited design capacity of less than 100 kN [4] and are often not strong and stiff enough to impose significant in-plane stresses on the CLT wall panels, particularly when relatively thick panels with 5 or 7-ply layups are used. Therefore, conventional connectors are not structurally efficient for applications in multi-storey buildings with CLT shear walls subjected to high seismic or wind demands.

Compared with small diameter nails and screws, larger diameter steel dowels or bolts can be used to create higher capacity hold-downs in CLT shear walls. Large-scale hold-down testing on 5-ply CLT panels with a group of 16-Ø20mm mild steel dowels and 25mm-thick steel knife plates found maximum connection strength exceeded 1000kN [5]. Further experimental research [6] showed the advantages of increased row spacing and end distance to encourage more ductile hold-down responses under cyclic loading.

Self-tapping screws have been widely used in mass timber construction due to their relatively high strength and ease of installation. When installed at 90° to the timber grain, slender screws can provide ductile responses and behave like typical dowel-type fasteners. When installed at an inclined angle to the timber grain, these screws are engaged primarily in withdrawal and can provide high connection strength and stiffness. For mixed angle screw connections, it is possible to achieve a balanced behaviour with high strength, high stiffness, and high ductility. Wright et al. [7,8] tested mixed angle screwed hold-downs and found peak strengths exceeded 600kN.

The previously mentioned experimental programmes on dowelled and screwed hold-downs demonstrate the ability of CLT hold-downs to achieve higher strengths than currently available commercial connectors. Furthermore, shear keys at the base of walls (similar to castellated connections studied by Brown et al. [9]) allow much higher shear capacities when compared to conventional angle brackets with groups of ring shank nails or small diameter screws. The use of these higher capacity

[1]University of Canterbury, New Zealand
[2]Structurecraft, Canada; bmoerman@structurecraft.com
[3]University of British Columbia, Canada; minghao.li@ubc.ca

https://doi.org/10.52202/069179-0267

connections in combination with coupled wall configurations allows CLT shear walls to be a more practical solution in mid-rise buildings.

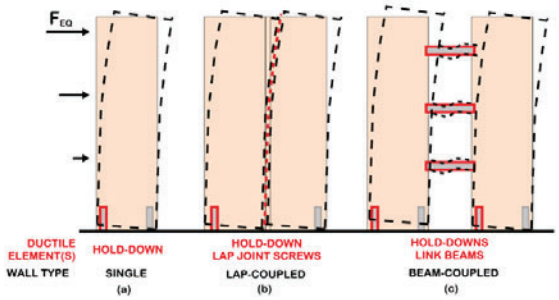

Figure 1: *(a) Single wall, (b) coupled wall with a lap joint, and (c) coupled wall with steel link beams.*

Figure 1 describes three types of multi-storey CLT walls: (a) a single wall, (b) a coupled wall with a screwed vertical half-lap joint (lap-coupled (LC)), and (c) a coupled wall with steel link beams (beam-coupled (BC)). The designated ductile elements where yielding is promoted in each wall type are also highlighted in Figure 1. All other components should be designed to have adequate strength to prevent premature failure in the system that may compromise its integrity during an earthquake. In this study, the hold-downs in each wall type are designed as ductile elements. In the LC and BC wall types, the lap joint screws and link beams, respectively, are additional ductile elements. The BC configuration is a form of hybrid wall system which uses ductile steel elements to enhance the hysteretic energy dissipation of a primarily timber-based structural system, similar in concept to the addition of steel buckling restrained braces in timber frames [10,11].

This study compares the lateral behaviour of the three different wall types with the results of four large-scale cyclic wall tests.

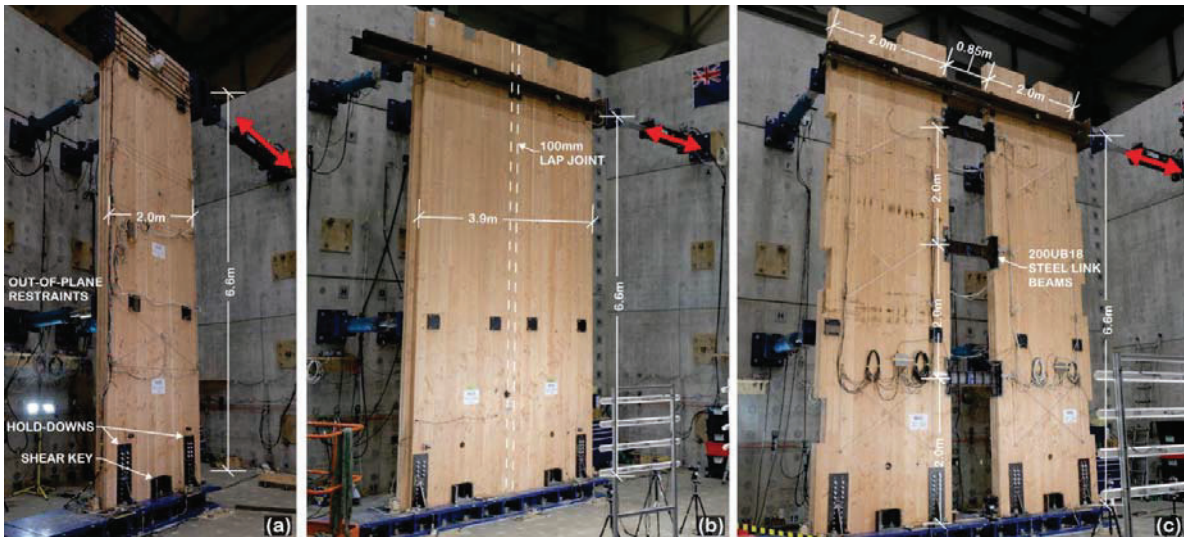

Figure 2: *Test specimen overview and experiment setup: (a) Single wall, (b) Lap-coupled wall, and (c) Beam-coupled wall.*

2 EXPERIMENT DETAILS

The test setup for each CLT wall configuration is shown in Figure 2. The specimens were proportioned and detailed as three-storey walls scaled by a factor of 2/3 and loaded laterally at a height of 6.6m. The CLT panels were created from grade SG8 (per NZS3603 [12]) Douglas-fir boards with a layup of 45/35/45/35/45mm.

Each wall specimen used the same type of mixed-angle screwed hold-downs, based on the previous testing by Wright et al. [7,8]. The ratio between the Ø12x260mm partially threaded inclined screws and the Ø12x180mm partially threaded inclined screws was 1:1.5. One hold-down bracket was installed on each side of the wall specimen. The combination of mixed angle screws creates a hold-down with high stiffness (due to the 45° screws) and reasonably high ductility (due to bending of the 90° screws). The typical hold-down and shear key used in each specimen are shown in Figure 3. The shear keys were installed in a full-depth, 250x350mm notch at the centre of the wall base. The vertical contact faces of the shear key were angled at a slope of 1:25 to prevent binding when the wall base rotated.

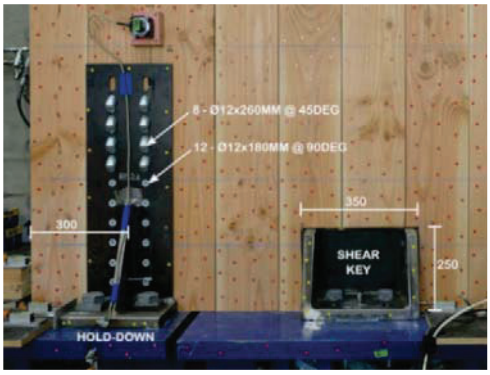

Figure 3: *Mixed-angle screwed hold-downs and shear keys.*

https://doi.org/10.52202/069179-0267

The lap-coupled walls used Ø10x200mm partially threaded screws in the 100mm-wide vertical half-lap joint with spacings of 200mm and 100mm for wall specimens LC1 and LC2, respectively. Therefore, LC2 was designed to achieve a greater degree of coupling.

The beam-coupled wall (Figure 1c) used dissipative, 200UB18 steel link beams with capacity-designed [13] screwed end plate connections to provide coupling action between the CLT panels. Link beams were installed at each level with a vertical spacing of 2m.

Each specimen was subjected to the CUREE cyclic loading protocol [14], shown in Figure 4. The reference wall drifts to define the CUREE protocol were determined based on preliminary pushover analyses and are reported with the results in Table 1.

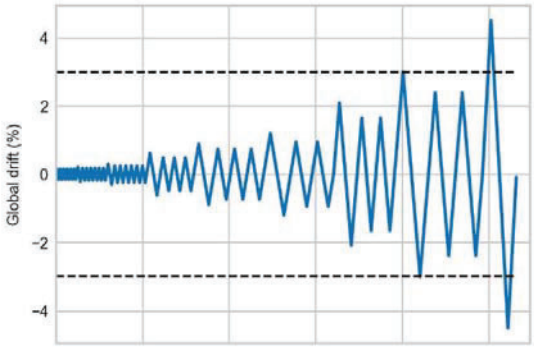

Figure 4: *Example of CUREE loading protocol (D_{ref}=3.0%).*

3 DAMAGE OBSERVATIONS

Each wall specimen primarily experienced damage in its designated ductile elements, which are described in Figure 1. No damage was observed at the shear keys in any test specimen. A moderate degree of toe crushing was experienced by each specimen due to a concentration of compression force but it did not lead to a brittle failure or result in sudden strength loss.

The mixed angle screwed hold-downs in each specimen experienced screw bending and withdrawal, in addition to local embedment crushing around the fasteners, as shown in Figure 5, due to the high uplift force demand. No screws in the hold-downs experienced fracture during the experiments, even though the maximum hold-down uplift displacement exceeded 100mm during the experiments.

The LC walls experienced significant damage to the screws in the vertical lap joint, as shown in Figure 6. Initial damage of screw bending and withdrawal was evident by the screw heads protruding from the timber surface (Figure 6a). Significant local crushing occurred internally around the lap-joint fasteners in the vertical direction (Figure 6b). Following completion of the test, the lap joint screws were uninstalled but many of them fractured due to the applied reverse torque (Figure 6c), indicating significant damage accumulated in the screws. Figure 6d shows the mechanism of a typical screw yielding in the half-lap joint.

Figure 5: *Typical damage observed in mixed-angle screw hold-down connections: (a) screw withdrawal and (b) local wood crushing.*

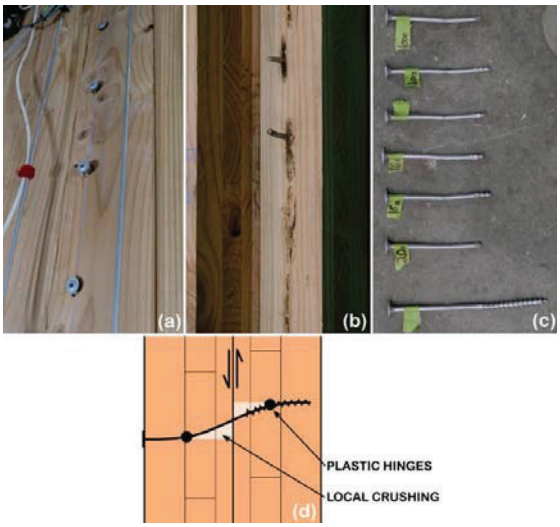

Figure 6: *Observed damage in screwed half-lap joint for LC walls: (a) Screw withdrawal, (b) local crushing inside half-lap. (c) removed screws, and (d) screw yielding mechanism.*

The BC wall experienced severe damage to the steel link beams, as shown in Figure 7. The webs yielded over the full length of the beams. In addition, the flanges adjacent to the end plate stiffeners yielded and eventually buckled inelastically. No damage was observed in the capacity-designed screwed end plate connections; therefore, the capacity design was successful.

https://doi.org/10.52202/069179-0267

Figure 7: *Typical damage to steel link beams in beam-coupled wall specimen.*

4 COMPARISON OF RESULTS

Key experimental results, including wall strength, stiffness, ductility, and energy dissipation are summarized in Table 1. As expected, the single wall had the lowest strength, stiffness, and energy dissipation; however, it may provide the most simple and economic structural form for CLT shear walls. The LC and BC (coupled) walls demonstrated higher strength and stiffness and more energy dissipation. The displacement ductility factors ($\mu=D_u/D_y$), varied between a minimum of 3.5 (LC1) and 7.6 (BC).

The LC walls had the lowest yield drift, which is beneficial because the system's hysteretic damping of the earthquake excitation (i.e., energy dissipation) begins at a lower drift level. As timber lateral systems are often drift-controlled, a low yield drift is advantageous for seismic design [15]. The average peak strength of LC1 normalized by its wall length (F_{max}/L) was 17% less than that of the single wall, despite having the same hold-downs and using twice as much timber volume. This was primarily due to the fastening pattern of its vertical joint in which screws were installed with 90° to the timber surface and with a 200mm spacing. The vertical joint was not sufficiently strong and stiff to promote a significant degree of coupling. LC2 was similar to LC1 except it used a 100mm screw spacing in the vertical joint. In contrast, it obtained 53% greater energy dissipation and peak strengths were 23% and 64% greater than those of LC1 in the positive and negative loading directions, respectively. Furthermore, its stiffnesses were 40% and 26% greater in the positive and negative directions, respectively. Apparently, more fasteners used in the vertical joint provided a more efficient lap-coupled wall type. However, caution must be exercised by the designer because if the half-lap joint is too strong, the energy dissipation of the system may be compromised.

The BC wall exhibited the highest strength, stiffness, drift capacity, and energy dissipation of the three wall types. This configuration involves a greater degree of fabrication and construction complexity. However, given its enhanced structural performance, it is likely that fewer walls would be required in a given building and therefore its application may be more economical than single or lap-coupled walls. Furthermore, it provides a practical wall configuration which can accommodate repetitive window or door openings in the architectural plans.

The force-displacement plots of the four wall specimens are shown in Figure 8. All wall specimens exhibited a ductile failure mode with damage concentrated in the designated regions described previously in Figure 1. The hysteresis loops show typical features of cyclically loaded timber connections: strength and stiffness degradation, and the pinching effect. The pinched behaviour is a result of cumulative local crushing around the yielding screws in the hold-downs and/or half-lap joints. The BC wall test showed the least amount of pinching due to the influence of the ductile link beams which yielded without exhibiting pinched behaviour on a component level.

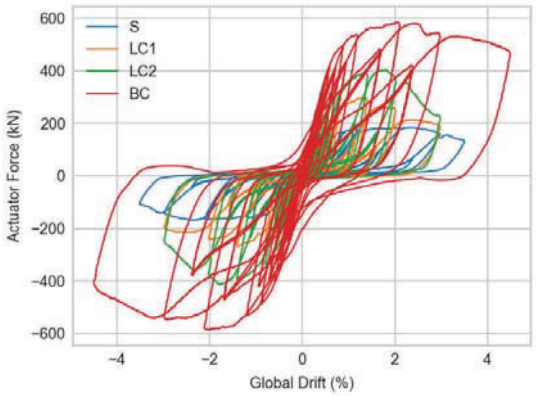

Figure 8: *Comparison of global drift vs. base shear.*

The energy dissipation of the primary and first two trailing cycles (characteristic of the CUREE loading protocol in Figure 4) are shown for each of the four wall tests in Figure 9. The pinched hysteretic behaviour and corresponding loss of energy dissipation is evident when comparing the amount of energy dissipation in the primary and trailing cycles for each wall type. Both the S and LC specimens exhibited minimal energy dissipation on their trailing cycles. However, the BC wall dissipated a reasonable amount of energy on its trailing cycles due to the influence of the steel link beams.

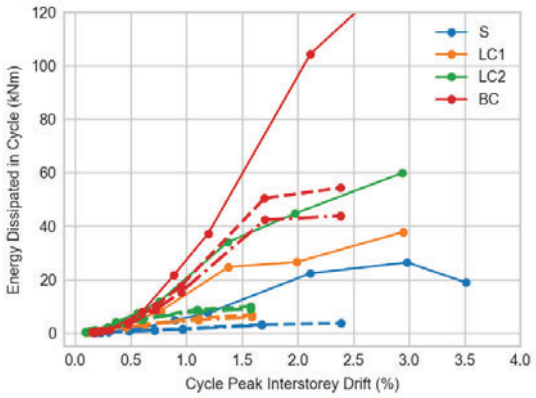

Figure 9: *Comparison of energy dissipation in each wall specimen.*

https://doi.org/10.52202/069179-0267

Table 1: *Summary of wall test results*

	Single Wall (S)	Lap-Coupled Wall 1 (LC1)	Lap-Coupled Wall 2 (LC2)	Beam-Coupled Wall (BC)
D_{ref}[a] (% Drift)	3.0%	2.0%	2.0%	3.0%
F_y (kN)	161 / -138	221 / -182	276 / -299	471 / -465
D_y (% Drift)	0.69% / -0.66%	0.40% / -0.32%	0.35% / -0.43%	0.58% / -0.56%
F_{max} (kN)	185 / -170	300 / -278	409 / -418	590 / -592
F_{max}/L (kN/m)	93 / -85	77 / -71	105 / -107	122 / -122
D_{Fmax} (% Drift)	2.31% / -2.38%	1.28% / -1.39%	1.70% / -1.78%	2.07% / -2.02%
F_u (kN)	140 / -132	236 / -200	317 / -315	470 / -465
D_u (% Drift)	2.99% / -3.17%	1.38% / -1.40%	1.98% / 2.02%	4.37% / -3.91%
K_i[b] (kN/mm)	3.3 / 3.3	8.5 / 7.9	11.9 / 10.0	11.9 / 12.1
Displacement Ductility, μ	4.3 / 4.8	3.5 / 4.4	5.7 / 4.7	7.6 / 6.9
E[c] (kNm)	80	154	236	482

[a]Reference displacement to define the CUREE loading protocol [14]
[b]Initial stiffness
[c]Cumulative energy dissipated up to 3% interstorey drift

5 CONCLUSIONS

This study conducted experimental testing on four balloon-type CLT shear walls with three wall configurations: a single wall, a coupled wall with screwed half lap joints, and a coupled wall with steel link beams. The cyclic performance of each specimen was evaluated and compared. Based on the test results, the following conclusions are drawn:

1. Mixed angle screwed hold-downs can provide a feasible, high-capacity hold-down connection for multi-storey CLT shear walls subjected to earthquake loading.
2. All three wall types in this study exhibited ductile failure modes and experimentally demonstrated their feasibility as lateral load resisting systems.
3. For the coupled walls with screwed half lap joints, the degree of wall coupling was governed by the screw spacing which can be optimized to achieve a balance of wall strength, stiffness, and energy dissipation.
4. Displacement ductility factors varied between the wall types, with the lowest value observed in the lap-coupled wall specimen LC1 and the greatest value observed in the beam-coupled wall specimen BC.
5. The beam-coupled wall BC with steel link beams demonstrated the greatest strength, stiffness, and energy dissipation, while also exhibiting the least amount of pinched hysteresis. However, it is more complex to fabricate and construct than the other wall types.

REFERENCES

[1] FP Innovations. Canadian CLT Handbook. Pointe-Claire, Canada: 2019.

[2] Pei S, van de Lindt JW, Popovski M, Berman JW, Dolan JD, Ricles J, et al. Cross-Laminated Timber for Seismic Regions: Progress and Challenges for Research and Implementation. J Struct Eng 2016;142. https://doi.org/10.1061/(ASCE)ST.1943-541X.0001192.

[3] Dong W, Li M, Ottenhaus L-M, Lim H. Ductility and overstrength of nailed CLT hold-down connections. Engineering Structures 2020;215:110667. https://doi.org/10.1016/j.engstruct.2020.110667.

[4] Rothoblaas. Plates and connectors for timber. 2020.

[5] Ottenhaus L-M, Li M, Smith T. Structural performance of large-scale dowelled CLT connections under monotonic and cyclic loading. Engineering Structures 2018;176:41–8. https://doi.org/10.1016/j.engstruct.2018.09.002.

[6] Brown JR, Li M. Structural performance of dowelled cross-laminated timber hold-down connections with increased row spacing and end distance. Construction and Building Materials 2021;271:121595. https://doi.org/10.1016/j.conbuildmat.2020.121595.

[7] Wright TDW, Li M, Moroder D, Carradine D. Cyclic behaviour of hold-downs using mixed angle self-tapping screws in Douglas-fir CLT. New Zealand Society for Earthquake Engineering 2021 Annual Conference, Christchurch, New Zealand: 2021.

[8] Wright TDW, Li M, Gedyma M, Lim H, Moroder D, Carradine D. Repair and reinstatement of douglas fir CLT hold-down connections using mixed angle self tapping screws. New Zealand Society for Earthquake Engineering 2022 Annual Conference, Christchurch, NZ: 2022.

[9] Brown JR, Li M, Sarti F. Structural performance of CLT shear connections with castellations and angle brackets. Engineering Structures 2021;240:112346. https://doi.org/10.1016/j.engstruct.2021.112346.

[10] Dong W, Li M, Lee C-L, MacRae G, Abu A. Experimental testing of full-scale glulam frames with buckling restrained braces. Engineering Structures 2020;222:111081. https://doi.org/10.1016/j.engstruct.2020.111081.

[11] Dong W, Li M, Lee C-L, MacRae G. Numerical modelling of glulam frames with buckling restrained braces. Engineering Structures 2021;239:112338. https://doi.org/10.1016/j.engstruct.2021.112338.

[12] New Zealand Standard. NZS 3603:1993 Timber Structures Standard 2005.

[13] Paulay T, Priestley MJN. Seismic Design of Reinforced Concrete and Masonry Buildings. John Wiley & Sons Ltd.; 1992.

[14] Krawinkler H, Parisi F, Ibarra L, Ayoub A, Medina R. Development of a Testing Protocol for Woodframe Structures 2001.

[15] Buchanan AH, Smith T. The Displacement Paradox for Seismic Design of Tall Timber Buildings. New Zealand Society for Earthquake Engineering 2015 Annual Conference, Rotorua, New Zealand: 2015.

 https://doi.org/10.52202/069179-0267

World Conference on Timber Engineering Oslo 2023

EXPERIMENTAL TESTING OF MIXED ANGLE SCREWED HOLD-DOWN CONNECTIONS FOR CLT SHEAR WALLS

Thomas Wright[1] and Minghao Li[2]

ABSTRACT: Cross laminated timber (CLT) shear walls are an efficient lateral load resisting system for mass timber buildings. Ductility and energy dissipation of timber buildings is mostly provided by well detailed connections. Therefore, to achieve good seismic performance of CLT shear walls, hold-down connections must be not only strong and stiff but also ductile with sufficient displacement capacity to meet the drift demands. A novel hold-down connection is proposed using a mixture of screws installed at an inclined angle and 90° to the grain. The respective benefits of inclined and 90° screws can be combined to create a strong, stiff, and ductile connection. Two stages of experimental testing were undertaken with target connection capacities of 600 kN and 1200 kN respectively. The experimental results confirmed that mixed angle screws can provide a strong, stiff, and ductile hold-down solution for CLT shear walls. The optimal ratio of φ12mm inclined screws to φ10mm 90° screws was 1:2, and the optimal ratio of φ12 mm inclined screws to φ12 mm 90° screws was 1:1.5. The primary failure modes were screw withdrawal and wood embedment crushing. Only localised damage of timber around the screw holes was observed and this was repaired with epoxy. New screws were then reinstated with a small offset to the original screw locations and the repaired hold-down connections were found to have the same or even slightly better performance.

KEYWORDS: Cross Laminated Timber, CLT, Hold-down Connections, Self-Tapping Screws, Mixed Angle, Cyclic Loading, Shear Walls, Ductility

1 INTRODUCTION

Cross-laminated timber (CLT) shear walls are commonly used as lateral load resisting systems in mass timber buildings. It is well understood that timber exhibits brittle behaviour when it reaches failure loads, particularly under tension. Therefore, when designing a building to resist seismic loading, any ductility or energy dissipation has to be provided by connections between timber elements. Therefore, in seismic countries like New Zealand, CLT shear walls are often designed with capacity design principles so that the CLT wall panels remain elastic while specified connections have ductile behaviour under severe ground shaking. To achieve optimal seismic performance, these ductile connections must be well detailed with sufficient strength, stiffness, and ductility / displacement capacity to allow the building to yield and dissipate earthquake energy.

Self-tapping screws are widely used for mass timber construction including CLT buildings. They are made out high strength steel and are easy to implement on site with hand tools. Previous research on self-tapping screws has highlighted the benefits of installing screws at an inclined angle to the grain in terms of strength and stiffness [1]–[3]. However, it is well recognized that with this increase in strength and stiffness, ductility / displacement capacity is compromised as the inclined screws primarily transfer load in an axial tension action. Screws installed perpendicular to the grain (or 90° screws) have relatively low strength and stiffness compared with inclined screws, but as they are relatively slender and can deform well and have good ductility / displacement capacity when loaded laterally. Previous research on timber to timber connections by Tomasi [4] showed that connections comprised of mixed angle screw installations, i.e. a combination of inclined screws and 90° screws, can lead to optimised connection behaviour with high strength, high stiffness and reasonably good ductility. When both inclined and 90° screws are used in a connection, their contributions are superimposed with the inclined screws providing high strength and stiffness, and the 90° screws providing high ductility and displacement capacity.
Further research has adopted this concept for in-plane joints between CLT shear walls [5] and orthogonal joints for C-shaped post-tensioned CLT shear walls [6]. Given the clear performance benefits of mixed angle screws, over inclined or 90° only installations, it is proposed to extend on previous research and develop mixed angle screwed hold-down connections for CLT shear walls.

Typical timber connections designed with ductility are susceptible to damage during a major seismic event. If these connections can be repaired quickly and economically, seismic resilience of timber buildings can be improved. It is well understood that the timber material

[1] Thomas Wright, University of Canterbury, New Zealand, thomas.wright@pg.canterbury.ac.nz
[2] Minghao Li, University of Canterbury, New Zealand / University of British Columbia, Canada, minghao.li@ubc.ca

https://doi.org/10.52202/069179-0268

is relatively easy to work with on site and likely to be repaired.
Projects such as the SOFIE project have highlighted the feasibility of repairing CLT shear wall buildings [7], [8]. Methods that have been used include removing damaged fasteners and reinstalling new ones at an offset and installing new hold-down brackets. To enact a successful repair, it is important that damage is concentrated to the connections, brittle failure of the timber element itself is avoided, and there is an easy access to conduct the repair.

This paper provides an overview of an experimental research program at the University of Canterbury to develop a robust hold-down connection solution for high capacity CLT shear walls that uses mixed angle self-tapping screws. The key research objectives are listed as follows:

- Assess the performance of mixed angle screws in CLT hold-down connections;
- Determine the optimal ratios of inclined to 90° screws for optimal seismic performance;
- Investigate connection damage under cyclic loading and compare to other connection systems with similar capacity; and
- Determine options for post-earthquake repair and evaluate performance of repaired connections

2 EXPERIMENTAL PROGRAMME

A total of 55 connection tests of mixed angle screwed hold-downs were conducted over two testing stages. Stage 1 consisted of 46 hold-down specimens with approximately 600 kN target capacity. Stage 2 consisted of 9 larger hold-down specimens with approximately 1200 kN target capacity. Of the 55 tests, 36 were conducted on original connections and 19 were conducted on repaired connections.

2.1 TESTING PROGRAMME

Table 1 and Table 2 show the test matrix of Stage 1 (labelled as S1) and Stage 2 (labelled as S2) on the original and repaired connection specimens, respectively. Repairs were not undertaken for all the original specimens due to time constraints. The 36 original connection specimens were grouped into 9 test sets with 5 distinct connection layouts. The 5 connection layouts tested in Stage 1 are shown in Figure 1. Stage 2 only tested one connection layout shown in Figure 2. This layout is a scaled-up version of Configuration 5 from Stage 1. In the test matrices test sets are labelled (stage)-(material species)-(screw configuration). a1 spacings were 60 mm for both Stage 1 and Stage 2. a2 spacings were 65 mm for Stage 1 (32 mm considering fasteners from both sides) and 60 mm (30 mm) for Stage 2. These spacings are shown for a typical connection layout in Figure 3.

2.2 TESTING APPARATUS

The testing apparatus for Stage 1 is shown in Figure 4. A steel reaction frame is used in conjunction with a single 1000 kN hydraulic actuator. Load was transferred to the CLT specimen using an inclined screw connection for Configurations 1-2, 4-5, and a dowelled connection for lower capacity single sided tests of Configuration 3.
Displacement was measured by 4 potentiometers measuring between the steel hold-down and timber surface as shown in Figure 6.
The testing apparatus for Stage 2 is show in Figure 5. The test specimen is laid horizontally compared to the vertical configuration in Stage 1, with two 1000 kN actuators anchored to the strong wall. The reaction force was provided by a steel frame with 1500 kN design capacity. Similar to Stage 1, load is transferred into the CLT specimen using two large inclined screw connections. As the test specimen is laid horizontally, rollers are used to support its gravity load, and also to restrain it from out of plane buckling under compressive loading. Displacement is measured by 6 string potentiometers placed between the timber specimen and the steel hold-down bracket.

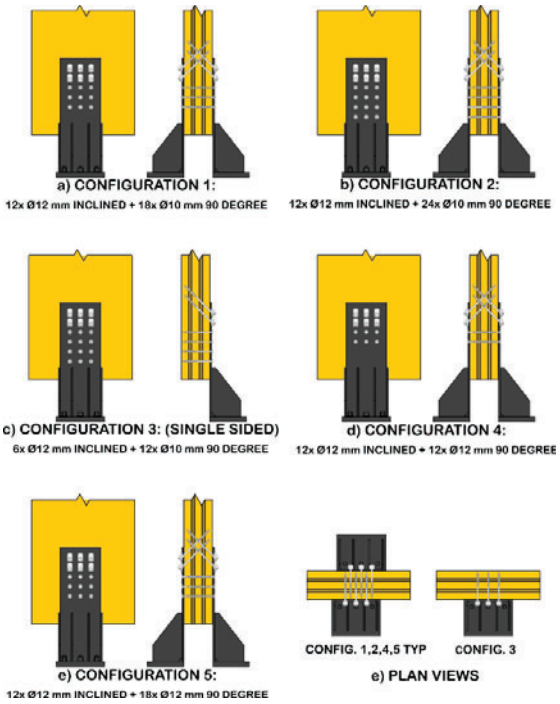

Figure 1: *Stage 1 connection configurations*

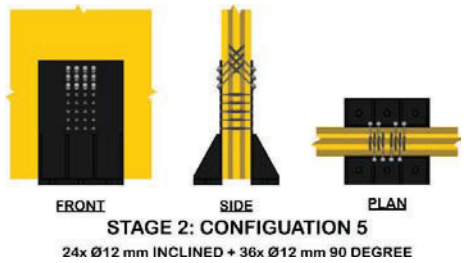

Figure 2: *Stage 2 connection configuration*

https://doi.org/10.52202/069179-0268

Table 1: *Test matrix for original connection tests*

	Test Set	Species	Qty (inclined)	Size (inclined)	Qty (90°)	Size (90°)	Ratio	Mono	Cyclic
S1	S1-DF-1	D. fir	12	12x260 PT	18	10x180 PT	1:1.5	2	3
	S1-DF-2	D. fir	12	12x260 PT	24	10x180 PT	1:2	1	3
	S1-RP-2	Pine	12	12x260 PT	24	10x180 PT	1:2	1	3
	S1-DF-3	D. fir	6	12x260 PT	12	10x180 PT	1:2	2	3
	S1-DF-4	D. fir	12	12x260 PT	12	12x180 PT	1:1	1	3
	S1-RP-4	Pine	12	12x260 PT	12	12x180 PT	1:1	1	3
	S1-RP-5	Pine	12	12x260 PT	18	12x180 PT	1:1.5	1	3
S2	S2-DF-5	D. fir	24	12x260 PT	36	12x180 PT	1:1.5	1	2
	S2-DF-5	Pine	24	12x260 PT	36	12x180 PT	1:1.5	1	2

Table 2: *Test matrix for repaired connection tests*

	Test Set	Species	Qty (inclined)	Size (inclined)	Qty (90°)	Size (90°)	Ratio	Mono	Cyclic
S1	S1-DF-2-R	D. fir	12	12x260 PT	24	10x180 PT	1:2	1	3
	S1-RP-2-R	Pine	12	12x260 PT	24	10x180 PT	1:2	1	3
	S1-DF-4-R	D. fir	12	12x260 PT	12	12x180 PT	1:1	1	3
	S1-RP-4-R	Pine	12	12x260 PT	12	12x180 PT	1:1	1	3
S2	S2-DF-5-R	D. fir	24	12x260 PT	36	12x180 PT	1:1.5	1	2

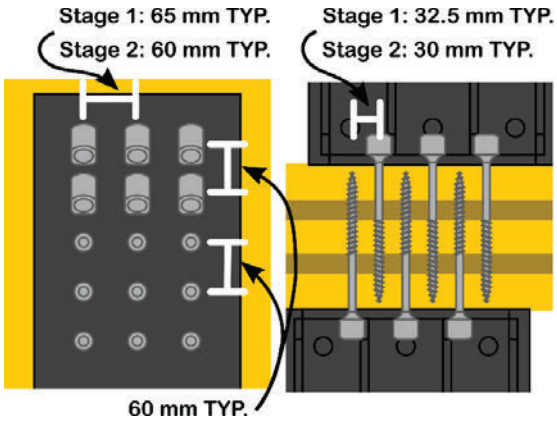

Figure 3: *Typical dimensions for spacings between screws*

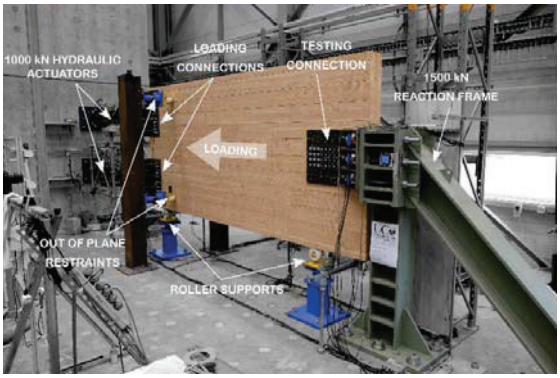

Figure 5: *Annotated photograph of Stage 2 test setup*

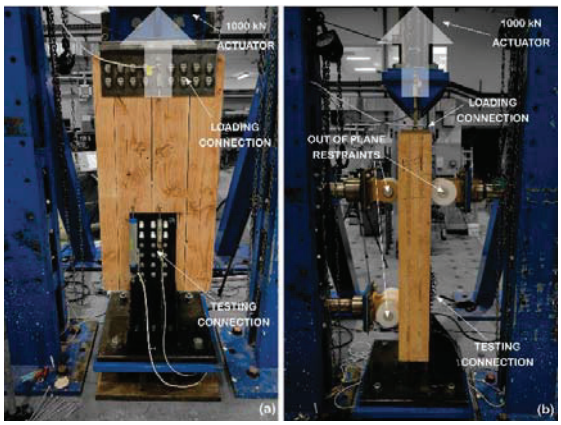

Figure 4: *Annotated photograph of Stage 1 test setup. a) double sided tests b) single sided tests*

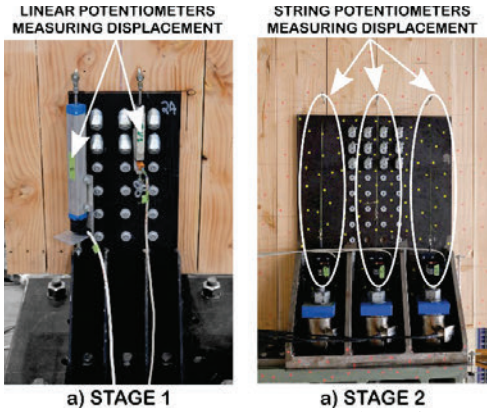

Figure 6: *Instrumentation setup for displacement measurements*

2.3 MATERIALS

All CLT material was manufactured by XLAM New Zealand. Lamella were graded to meet NZS3603:1993 SG8 grade (8 GPa mean elastic modulus), with Douglas fir specimens using New Zealand grown Douglas fir, and radiata pine specimens using New Zealand grown radiata pine [9]. For Stage 1 testing Douglas fir specimens were 5-layer 175 mm thick with a 45/20/45/20/45 layup, and for Stage 2 Douglas fir specimens were 5-layer 205 mm thick with a 45/30/45/30/45 layup. For both stages, radiata pine specimens were 205 mm thick with a 45/30/45/30/45 layup. All moisture contents were found to be approximately 11% following the standard [10]. Density was calculated in accordance with the standard [11], with mean and characteristic densities of both the Douglas fir and radiata pine CLT specimens being presented in Table 3.

Inclined screws were SPAX ϕ12x260 mm partially threaded (PT) screws with countersunk heads. 90° screws were either SPAX ϕ10x180 mm PT screws with washer heads, or SPAX ϕ12x180 mm PT screws with countersunk heads. Inclined angles were achieved using 12 mm Rothoblaas VGU inclined washers.

Table 3 - *Mean and characteristic densities of CLT specimens*

Species	Douglas Fir		Radiata pine
Stage	Stage 1	Stage 2	Stages 1 & 2
Mean Density (kg/m^3)	496	472	460
Characteristic Density (kg/m^3)	440	429	417

2.4 LOADING PROTOCOL

The loading protocol used was from ISO 16670 as shown in Figure 7 [12]. The loading protocol is a half cycle protocol loading only in the tension direction, similar to what would be expected in the hold-down connection of a CLT shear wall. For both stages of testing, the targeted loading rate was 0.2 mm/sec.

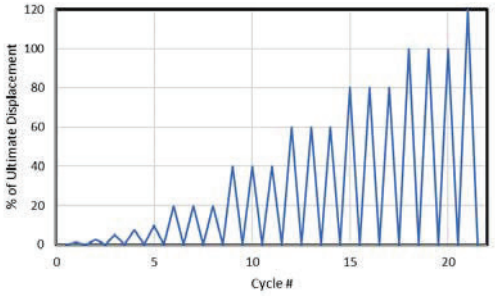

Figure 7: *Cyclic loading protocol based on ISO16670*

2.5 REPAIR METHODOLOGY

The repair process presented in this paper is made up of two steps. The first step is to enact a repair on the timber that has been damaged by screw withdrawal and embedment crushing. The second step is to install new screws at locations with a small horizontal offset to the original locations such that the screws are installed into fresh timber.

2.5.1 Step 1: Repair holes with epoxy

As shown in Figure 10, the failure modes of mixed angle screw connections are primarily withdrawal for inclined fasteners and withdrawal and embedment crushing for 90° fasteners. These embedment failures leave large vertical holes in the timber with loose and torn fibres around the edges. First the holes were cleaned of loose timber. For inclined screws this was done by drilling out the screw hole with a long series drill bit. This drill bit was sized to suit the Hilti Epoxy injection tube such that epoxy could be injected under a small amount of pressure to force out air and fill all the voids. For 90° screws, the holes were first reamed with a drill bit, then the edges where significant embedment failure had occurred were tidied up by removing loose or damaged timber fibres either with pliers and chisel, or with a handheld electric router. Holes were then vacuumed and blown out with compressed air to clear them of dust. Epoxy was then injected into the holes from the inside out, using the pressure of the epoxy to force the nozzle out of the hole. In this study Hilti HIT RE-500 was used with the standard nozzles and extension tubes used for concrete anchors. Excess epoxy was wiped off, and once cured the area sanded to remove any excess epoxy from the timber surface.

2.5.2 Step 2: Reinstate fasteners with an offset

The second step is to reinstate the connection with new fasteners. Small cold-formed hold-downs such as the Rothoblaas WHT with small nails or screws could be reinstalled beside the original hold-down position. However, the mixed angle screw connections tested have fasteners with larger diameter and hence larger row spacing. Due to the much larger dimensions and capacity of these mixed angle screw hold-downs, the change in level arm required to install beside the damaged connection would significantly impact the strength of the wall. A large shift would also require any anchors into the foundations to be moved which may not be practicable if cast in place. Therefore, a small horizontal shift of half row spacing is used. For the connections tested the shift was 16.25 mm for Stage 1, and 15 mm for Stage 2. This shift places the replacement screws half-way in between the repaired holes from the original fasteners.

This horizontal shift may require new brackets to be constructed or can be achieved using well planned details. In Stage 1 testing, the offset was achieved simply using a large tolerance on the hold-down bolt holes. In Stage 2 it was done by creating two sets of brackets with holes offset by 15 mm. These two sets can be used on either end of a shear wall and swapped post-earthquake when repair is required.

3 RESULTS

Experimental results are shown in Table 4 in terms of key performance parameters including strength, stiffness, ductility, and ultimate displacement. For the definition of yield point and ductility, two approaches are presented.

https://doi.org/10.52202/069179-0268

The first approach is described by EN12512, where the yield point is found at the intersection between the initial stiffness and a second line tangent to the curve at 1/6 the slope of the initial stiffness [13]. Due to the high stiffness of these mixed angle screw connections, this approach seems to significantly underestimate the yield force and displacement estimated by visual inspection. The second approach is the equivalent energy elastic plastic (EEEP) approach which derives an equivalent elastic perfectly plastic curve based on equal energy or area under the force displacement curve [14].

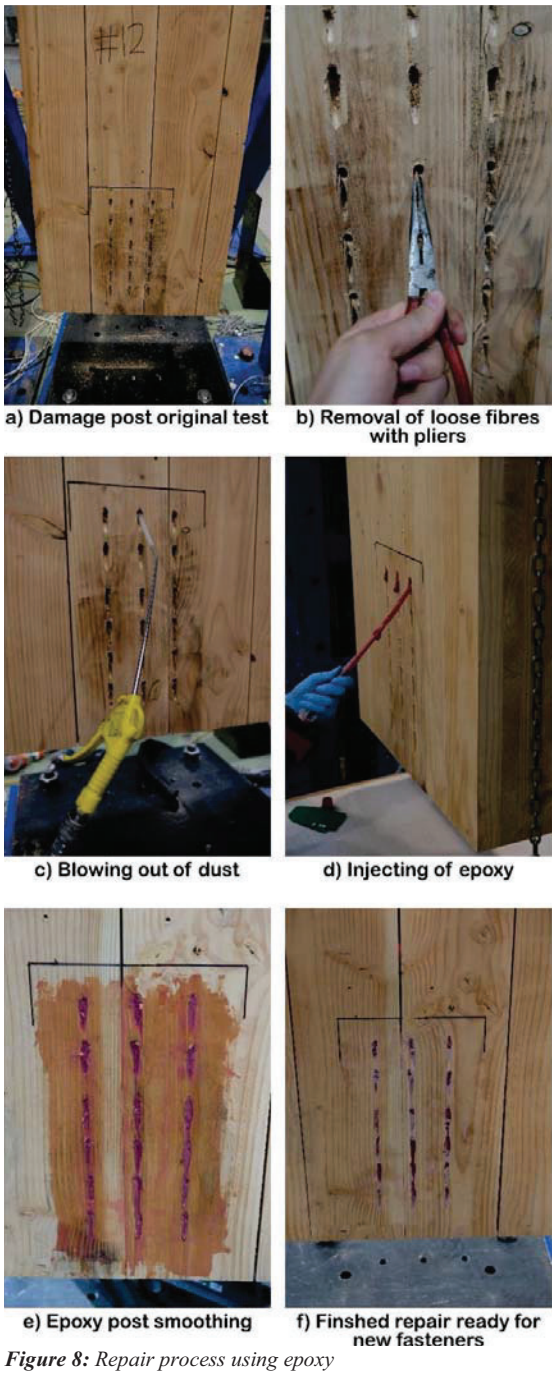

Figure 8: *Repair process using epoxy*

The EEEP method was found to provide a good representation of the yield point compared to what would be visually identified, except in cases where the force increased significantly post-yield. In these cases, the EEEP method was found to slightly overestimate the yield point. Both EN12512 and EEEP results are presented for comparison in Table 4 and Table 5. Due to some initial non-linearity in the elastic portion of the force displacement curve, stiffness values were determined using a similar approach to [15], whereby a regression analysis was undertaken on multiple sections of the initial elastic portion of the force displacement curve.

Representative hysteric force-displacement curves of the mixed angle screw connections are shown in Figure 9. These plots overlay the monotonic and a representative cyclic curve from testing. For the connections where repair was undertaken, the corresponding repaired tests are also shown on the same plot.

4 DISCUSSION

4.1 CONNECTION PERFORMANCE

Overall, satisfactory performance of the mixed angle screw hold-down connections was observed with high strength, stiffness, and ductility. Peak loads F_{max} in Table 4 show the mean value was 500 to 650 kN for Stage 1 double sided connections, 350 kN for Stage 1 single sided connections, and 1081 to 1286 kN for Stage 2 double sided connections. Stiffness values varied between 212 and 269 kN/mm for Stage 1 tests and 361 and 370 kN/mm for Stage 2 tests. Despite using the regression approach described above, the stiffness was found to be quite variable and the expected correlation between the connection tests with more 90° fasteners and higher stiffness was not observed. The variability of stiffness might be due to the initial conditions and friction between the steel side plate and the timber surface. Therefore, more research is required to better understand this. It is also noted that no initial slips were observed or corrected for, with the initial non-linearity in the elastic portion of the force displacement curve being of higher stiffness than that reported.

All of the tested connections exhibited high connection ductility. Ductility is commonly defined as the ratio of ultimate displacement to yield displacement [13]. As discussed, the method of determining yield displacement can have a large impact on the value obtained. Therefore, the ductility and yield displacement values from both the EN12512 approach and the EEEP approach are presented. As the ultimate displacement was relatively large, and the yield displacement was small (between 1 and 3 mm), relatively small changes of the yield displacement can make large changes to the ductility value. For example, if yield displacement changes from 1 to 2 mm, the ductility will be the half. Therefore, for the mixed angle screw connections, it is also recommended to consider the ultimate displacement or displacement capacity of the connection as well. A comparison between S1-RP 4 and S1-RP-2 explains why the ultimate displacement should be considered. The mean ductility of S1-RP-4 is 17.6 with the mean ultimate displacement of 31.4 mm while the mean ductility of S1-RP-2 is 13.2 with the mean ultimate

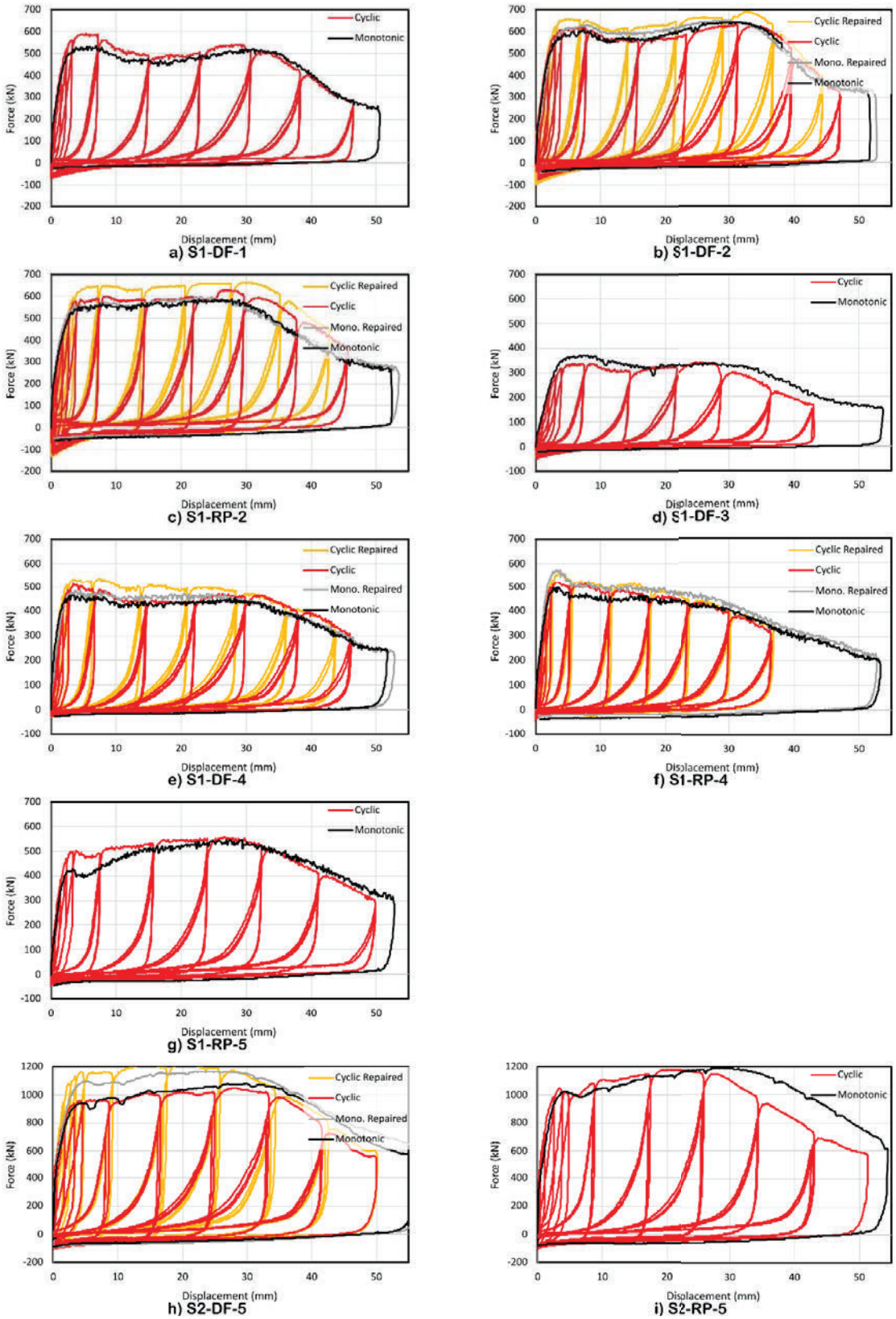

Figure 9: *Representative curves of all tests sets*

https://doi.org/10.52202/069179-0268

Table 4: *Testing results for original tests*

								EN12512			EEEP		
	Test Set	Test #	F_{max} (kN)	F_u (kN)	Δ_{Fmax} (mm)	Δ_u (mm)	K (kN/mm)	F_y (kN)	Δ_y (mm)	μ	F_y (kN)	Δ_y (mm)	μ
Stage 1	S1-DF-1	M1	546	437	6.10	35.8	214	475	1.84	19.5	507	2.37	15.1
		M2	535	428	6.92	38.5	250	448	1.46	26.3	520	2.08	18.5
		C1	614	491	4.38	39.5	284	532	1.55	25.4	601	2.12	18.6
		C2	590	472	5.31	35.4	248	505	1.68	21.1	546	2.20	16.1
		C3	535	428	4.04	36.9	251	459	1.52	24.3	500	1.99	18.6
		Mean	**564**	**451**	**5.35**	**37.2**	**249**	**484**	**1.61**	**23.3**	**535**	**2.15**	**17.4**
	S1-DF-2	M1	643	515	30.0	38.7	233	520	1.91	20.3	615	2.64	14.7
		C1	622	498	35.2	39.8	205	521	2.18	18.3	597	2.91	13.7
		C2	609	487	30.7	39.1	228	507	1.88	20.8	587	2.58	15.1
		C3	633	506	31.2	39.6	236	544	1.93	20.5	621	2.63	15.0
		Mean	**627**	**502**	**31.8**	**39.3**	**226**	**523**	**1.98**	**20.0**	**605**	**2.69**	**14.6**
	S1-RP-2	M1	587	470	25.2	35.3	247	464	1.51	23.3	565	2.29	15.4
		C1	608	487	26.1	36.6	230	484	1.54	23.7	580	2.52	14.5
		C2	628	502	26.8	37.5	204	528	2.17	17.3	594	2.91	12.9
		C3	643	515	26.7	36.8	168	535	2.77	13.3	612	3.64	10.1
		Mean	**617**	**494**	**26.2**	**36.6**	**212**	**503**	**2.00**	**19.4**	**588**	**2.84**	**13.2**
	S1-DF-3	M1	372	297	7.97	35.5	104	333	2.98	11.9	341	3.3	10.8
		M2	314	251	28.0	35.7	97.9	248	2.2	16.2	287	2.93	12.2
		C1	372	298	31.5	39.3	100	319	2.76	14.3	357	3.56	11.1
		C2	342	274	25.5	33.9	85.0	313	3.34	10.2	334	3.93	8.63
		C3	328	262	25.1	34.6	93.9	282	2.63	13.2	315	3.36	10.3
		Mean	**346**	**276**	**23.6**	**35.8**	**96.0**	**299**	**2.78**	**13.2**	**327**	**3.42**	**10.6**
	S1-DF-4	M1	466	373	3.49	38.9	308	390	1.02	38.0	447	1.45	26.8
		C1	515	412	4.72	40.7	208	457	1.92	21.2	492	2.37	17.2
		C2	494	395	4.51	38.1	261	420	1.38	27.6	461	1.77	21.5
		C3	512	410	3.36	36.9	228	455	1.77	20.9	473	2.07	17.8
		Mean	**497**	**398**	**4.02**	**38.7**	**251**	**431**	**1.52**	**26.9**	**468**	**1.92**	**20.8**
	S1-RP-4	M1	500	400	3.41	31.5	240	451	1.59	19.8	456	1.9	16.6
		C1	509	407	3.11	33.4	289	435	1.22	27.4	473	1.64	20.4
		C2	522	418	3.39	27.8	254	468	1.58	17.5	481	1.9	14.6
		C3	540	432	14.9	33.0	291	454	1.37	24.1	510	1.76	18.8
		Mean	**518**	**414**	**6.20**	**31.4**	**269**	**452**	**1.44**	**22.2**	**480**	**1.80**	**17.6**
	S1-RP-5	M1	548	439	27.4	41.8	202	393	1.68	24.9	499	2.46	17.0
		C1	560	448	26.7	38.5	238	444	1.6	24.1	525	2.21	17.4
		C2	599	479	25.8	37.8	238	429	1.46	25.9	548	2.3	16.5
		C3	592	474	26.7	36.9	280	396	1.11	33.3	538	1.92	19.2
		Mean	**575**	**460**	**26.7**	**38.8**	**240**	**416**	**1.46**	**27.1**	**528**	**2.22**	**17.5**
Stage 2	S2-DF-5	M1	1082	865	29.9	42.1	342	828	1.66	25.4	1024	2.99	14.1
		C1	1108	886	28.9	39.6	394	808	1.32	29.9	1039	2.64	15.0
		C2	1052	842	27.7	39.9	385	833	1.28	31.1	1009	2.62	15.2
		Mean	**1081**	**864**	**28.8**	**40.5**	**374**	**823**	**1.42**	**28.8**	**1024**	**2.75**	**14.8**
	S2-RP-5	M1	1194	955	28.7	43.5	309	943	2.16	20.2	1119	3.63	12.0
		C1	1300	1040	24.3	37.8	353	1024	2.18	17.3	1241	3.52	10.7
		C2	1183	946	20.3	34.3	421	922	1.44	23.9	1127	2.68	12.8
		Mean	**1226**	**980**	**24.4**	**38.5**	**361**	**963**	**1.92**	**20.5**	**1162**	**3.27**	**11.9**

Table 5: *Testing results for repaired tests*

								EN12512			EEEP		
	Test Set	Test #	F_{max} (kN)	F_u (kN)	Δ_{Fmax} (mm)	Δ_u (mm)	K (kN/mm)	F_y (kN)	Δ_y (mm)	μ	F_y (kN)	Δ_y (mm)	μ
Stage 1	S1-DF-2-R	M1	653	522	29.4	37.9	207	557	2.41	15.7	625	3.02	12.6
		C1	658	527	6.06	38.4	223	562	2.17	17.7	632	2.83	13.6
		C2	621	497	7.13	36.9	195	561	2.69	13.7	610	3.13	11.8
		C3	692	554	32.6	39.5	233	589	2.1	18.8	660	2.84	13.9
		Mean	**656**	**525**	**18.8**	**38.2**	**215**	**567**	**2.34**	**16.5**	**632**	**2.96**	**13.0**
	S1-RP-2-R	M1	601	481	22.8	34.6	264	470	1.41	24.6	571	2.16	16.0
		C1	630	504	22.1	33.8	250	532	1.78	18.9	611	2.45	13.8
		C2	664	531	29.9	38.8	195	577	2.77	14	643	3.29	11.8
		C3	650	520	24.1	36.8	182	577	2.91	12.7	633	3.47	10.6
		Mean	**636**	**509**	**24.7**	**36.0**	**223**	**539**	**2.22**	**17.6**	**615**	**2.84**	**13.1**
	S1-DF-4-R	M1	484	387	4.46	36.7	226	437	1.72	21.4	464	2.06	17.9
		C1	521	417	8.35	40.3	211	443	1.76	22.8	499	2.37	17.0
		C2	507	405	4.49	36.7	276	428	1.33	27.6	482	1.75	21.0
		C3	542	433	7.64	34.8	263	474	1.54	22.6	504	1.92	18.2
		Mean	**514**	**411**	**6.24**	**37.1**	**244**	**446**	**1.59**	**23.6**	**487**	**2.03**	**18.5**
	S1-RP-4-R	M1	575	460	3.05	27.5	288	514	1.59	17.3	508	1.76	15.6
		C1	526	421	3.09	31.7	291	453	1.31	24.2	498	1.71	18.6
		C2	561	448	3.63	23.7	241	501	1.78	13.4	515	2.14	11.1
		C3	536	429	3.28	33.7	278	476	1.5	22.5	514	1.85	18.2
		Mean	**550**	**440**	**3.26**	**29.2**	**275**	**486**	**1.55**	**19.4**	**509**	**1.87**	**15.9**
Stage 2	S2-DF-5-R	M1	1170	936	24.4	40.6	370	951	1.81	22.4	1126	3.04	13.4
		C1	1199	960	20.5	36.8	470	891	1.21	30.4	1122	2.39	15.4
		C2	1233	987	20.4	36.0	466	1017	1.45	24.9	1172	2.52	14.3
		Mean	**1201**	**961**	**21.8**	**37.8**	**435**	**953**	**1.49**	**25.9**	**1140**	**2.65**	**14.4**

displacement of 36.6 mm. Due to its lower yield displacements, S1-RP-4 turned out to have a higher ductility value even though it had 5 mm less ultimate displacement.

4.2 CONNECTION DAMAGE/FAILURE MODES

As mentioned in Section 2, all the screws used in this study were partially threaded. The inclined screws were designed to fail in the withdrawal mode as the threaded length was controlled to avoid the tensile failure of the screw shank. It is critical to avoid tensile failure of the screws in the mixed angle screw connections as it allows the gradual transfer of load from inclined screws to 90° screws when the deformation increases.

The 90° screws were loaded laterally and caused localised embedment failure. At large displacements they began to withdraw from the timber. In Figure 10a, the elongated holes were caused by embedment crushing, and ***Figure 10***b shows a section cut through the fastener holes, clearly showing the embedment crushing and the fastener plastic hinge location. The hinges formed in the screws are shown in Figure 11. The 90° screws form two hinges, one right under the steel plate, the other at a depth into the timber. The inclined fasteners, as shown in Figure 11 can also form hinges as they undergo bending actions at high displacements as well, but to a lesser extent.

Throughout the testing, no block tear out or other brittle failure modes were observed.

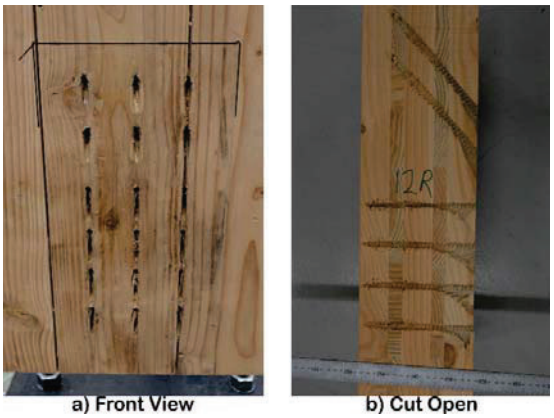

Figure 10: *S1-DF-2 connection with damage*

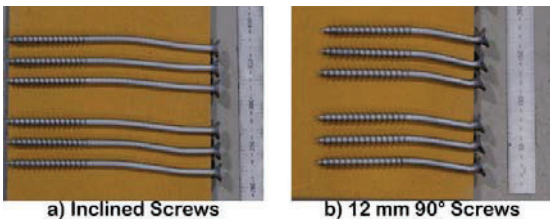

Figure 11: *Pictures of screws after testing the plastic hinges formed*

https://doi.org/10.52202/069179-0268

4.3 OPTIMAL RATIO BETWEEN INCLINED AND 90° SCREWS

For the mixed angle screw connections tested, all the configurations showed high strength, stiffness and ductility. The designer can choose the ratio of inclined to 90° screws based on the performance required. In general, a connection with more 90° screws will have a higher post yield force increase (or post yield stiffness) due to significant rope effect of the 90° screws at high displacements.

To determine a recommended ratio, further criteria would need to be defined. Efficiency, post yield force increase, and energy dissipation are all compared at length in the literature [16]. The conclusions of [16] can be replicated by visual inspection of the force displacement plots in Figure 9. In general, a connection that can sustain the yield force till a large displacement is desired. Literature also suggested that an increase in force post yield is desirable in terms of limiting drift [17]. From Figure 9 it can be determined the connections using Configuration 2 and Configuration 5 meet these criteria better. Therefore, the optimal ratio of ϕ12 mm inclined screws to ϕ10 mm 90° screws was 1:2; and it was 1:1.5 for ϕ12 mm inclined screws and ϕ12 mm 90°.

4.4 FEASIBILITY OF POST-EARTHQUAKE REPAIR

A key observation from this study was the localised and confined damage to the CLT in comparison to extensive damage in the dowelled CLT hold-down connections tested in a previous study [18]. With the localised damage, post-earthquake repair of these connections becomes viable, and tests were undertaken to evaluate the performance of the repair by comparing original and repaired tests of the same experimental specimen.

To evaluate the effectiveness of the repair, strength, stiffness, and ultimate displacement are compared in Figure 12. Figure 12a shows a comparison of maximum force for each original and repaired test. From Figure 12 it can be seen that all repaired tests reached a higher maximum force than the original tests. This increase averaged 5.5% over all tests with a maximum of 15%.

Figure 12b shows a comparison of stiffness, with the original and repaired stiffnesses being similar for most tests.

Figure 12c shows a comparison of ultimate displacement, with repaired tests having lower ultimate displacement for all but two results. This may be in part due to the definition of ultimate displacement being dependent on the maximum force which was higher for the repaired tests. Given the increase in strength, and similar stiffness values, the epoxy repair and shift method is deemed to be effective in repairing this type of connection post-earthquake.

Figure 13 shows the epoxy repair of the connection after the repaired test. Overall the epoxy has filled the damaged holes well, with no large trapped pockets of air. There are some small air bubbles in the epoxy, but given the difference in strength between the epoxy and the surrounding timber material, these are unlikely to cause adverse effects.

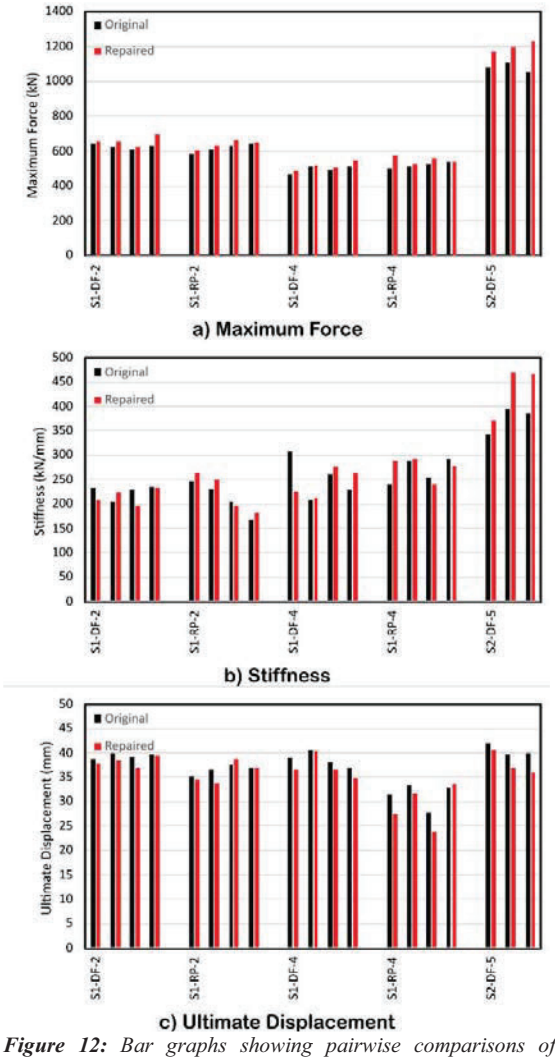

Figure 12: *Bar graphs showing pairwise comparisons of maximum force, initial stiffness, and ultimate displacement between original and repaired tests of the same specimen*

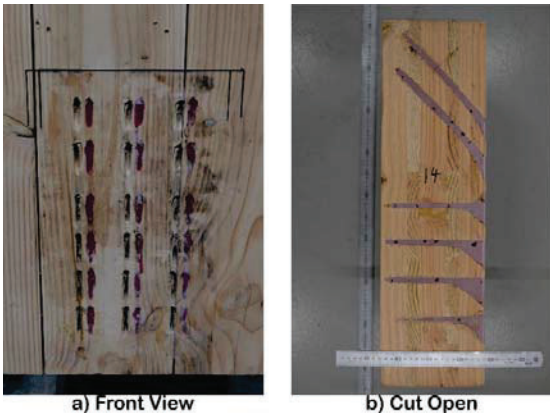

Figure 13: *Picture of repaired S1-DF-2-R connection post testing a) View from front of connection after steel bracket is removed b) Section cut through the epoxy repair*

5 CONCLUSIONS

The paper presents an experimental study on large-capacity CLT hold-downs using mixed angle self-tapping screws. Monotonic and cyclic tests were undertaken to assess the hold-down performance. The key conclusions are:

- Mixed angle screws can provide a strong, stiff, and ductile hold-down connection system for CLT shear walls;
- The optimal ratio of inclined screws to 90° screws was 1:2 for ϕ12 mm inclined and ϕ10 mm 90° screws, and 1:1.5 for ϕ12 mm inclined and ϕ12 mm 90° screws. These ratios led to connections with high strength, high stiffness, and high ductility;
- Under cyclic loading, mixed angle screws can be detailed such that the primary failure modes are screw withdrawal and wood embedment crushing. This leaves only localised damage and results in repairable damage in timber; and
- Localised damage observed in mixed angle screw hold-down connections can be repaired with epoxy and the screws reinstated with a small offset to original fastener holes leading to the same or even slightly better performance.

REFERENCES

[1] H. J. Blaß and I. Bejtka, "Screws with continuous threads in timber connections," in *In: Joints in timber structures. Proceedings of the International RILEM Symposium, Stuttgart, Germany 2001. Ed.: S. Aicher*, 2001, vol. 22, pp. 193–201.

[2] Bejtka and Blaß, "Joints with inclined screws," in *Working Commission W18 - Timber Structures*, Kyoto, Japan, 2002, vol. 35-7–4, p. 141.

[3] Kevarinmaki, "Joints with inclined screws," in *Working Commission W18 - Timber Structures*, Kyoto, Japan, 2002, vol. 35-7–4.

[4] R. Tomasi, M. Piazza, A. Angeli, and M. Mores, "A new ductile approach design of joints assembled with screw connectors," in *WCTE 2006*, Portland, USA, 2006.

[5] A. Hossain, M. Popovski, and T. Tannert, "Cross-laminated timber connections assembled with a combination of screws in withdrawal and screws in shear," *Eng. Struct.*, vol. 168, pp. 1–11, Aug. 2018, doi: 10.1016/j.engstruct.2018.04.052.

[6] J. R. Brown, M. Li, T. Tannert, and D. Moroder, "Experimental study on orthogonal joints in cross-laminated timber with self-tapping screws installed with mixed angles," *Eng. Struct.*, p. 111560, Dec. 2020, doi: 10.1016/j.engstruct.2020.111560.

[7] A. Ceccotti and M. Follesa, "Seismic Behaviour of Multi-Storey XLam Buildings," p. 15, 2006.

[8] A. Ceccotti, C. Sandhaas, M. Okabe, M. Yasumura, C. Minowa, and N. Kawai, "SOFIE project - 3D shaking table test on a seven-storey full-scale cross-laminated timber building: 3D SHAKING TABLE TEST ON A SEVEN-STOREY FULL-SCALE X-LAM BUILDING," *Earthq. Eng. Struct. Dyn.*, vol. 42, no. 13, pp. 2003–2021, Oct. 2013, doi: 10.1002/eqe.2309.

[9] Standards New Zealand, "NZS 3603:1993 Timber Structures Standard," Standards New Zealand, 1993.

[10] Standards New Zealand, *Timber: Moisture content. methods of test*, Second 2012. Sydney, NSW;Wellington; Jointly published by Standards Australia Limited Limited, 2012.

[11] Standards New Zealand, "Timber: methods of test. Method 3, Density." Standards New Zealand, 2000.

[12] International Organization for Standardization, "Timber structures - Joints made with mechanical fasteners - Quasi-static reversed-cyclic test method (ISO 16670:2003)." 2003.

[13] British Standards Institution, "BS EN 12512:2001: Timber structures. Test methods. Cyclic testing of joints made with mechanical fasteners." British Standards Institute, 2001.

[14] ASTM, "E2126 − 11: Test Methods for Cyclic (Reversed) Load Test for Shear Resistance of Vertical Elements of the Lateral Force Resisting Systems for Buildings," ASTM International, 2011. doi: 10.1520/E2126-11.

[15] R. Brandner, "Cross laminated timber (CLT) in compression perpendicular to plane: Testing, properties, design and recommendations for harmonizing design provisions for structural timber products," *Eng. Struct.*, vol. 171, pp. 944–960, Sep. 2018, doi: 10.1016/j.engstruct.2018.02.076.

[16] Wright, M. Li, D. Moroder, and D. Carradine, "DRAFT: Cyclic Behaviour of CLT Shear Wall Hold-Down Connections Using Mixed Angle Self-Tapping Screws," *Eng. Struct.*, vol. (Under Review), 2023.

[17] G. A. MACRAE and K. KAWASHIMA, "POST-EARTHQUAKE RESIDUAL DISPLACEMENTS OF BILINEAR OSCILLATORS," *Earthq. Eng. Struct. Dyn.*, vol. 26, no. 7, pp. 701–716, 1997, doi: https://doi.org/10.1002/(SICI)1096-9845(199707)26:7<701::AID-EQE671>3.0.CO;2-I.

[18] L.-M. Ottenhaus, M. Li, and T. Smith, "Structural performance of large-scale dowelled CLT connections under monotonic and cyclic loading," *Eng. Struct.*, vol. 176, pp. 41–48, Dec. 2018, doi: 10.1016/j.engstruct.2018.09.002.

https://doi.org/10.52202/069179-0268

World Conference on Timber Engineering Oslo 2023

DYNAMIC PERFORMANCE OF A FULL-SCALE WOOD FRAME SUBJECTED TO CYCLIC LOAD TESTING

Félix Bouffard[1], Jean Proulx[2]

ABSTRACT: The strength-to-weight ratio of wood structural elements makes them very attractive on an engineering design point of view. This is one of the reasons why wooden buildings are known to perform well during seismic events of medium and high intensities. However, ductility and over strength factors, making it possible to design structures having the capacity to resist a seismic event by its inelastic properties, are not well characterized and leads to a local over design of assemblies and critical wood sections. The primary objective of this study is to characterize the cyclic behaviour of a diagonally braced full-scale frame. This study focuses on capacity design to have the dowel assemblies as the main dissipator of energy. A full-size frame specimen was subjected to cyclic loading. The frame was built with glulam timber elements joined together with hidden steel plates and fastened with dowels. The cyclic loading results demonstrated a global ductile behaviour, a good redistribution of the internal efforts in the assemblies, a reduction of the secant stiffness after the yielding point, increment of the dissipation of energy, great over-strength, and minor damage in the timber elements. This supports the use of this type of frame with a capacity design focused on a ductile behaviour.

KEYWORDS: Seismic behaviour, Full-scale, Wood frame, Cyclic loading, Glulam, Capacity design, Seismic force resisting system

1 BACKGROUND AND MOTIVATION

Various research studies have been conducted on wood as a material, and there is a greater understanding of its mechanical properties. It is now possible to use wood and to manufacture it in such a way as to obtain structural products with a mechanical resistance increasingly comparable to that of steel, and allowing to build high rise buildings. On a structural engineering point of view, wood is a very light and strong material. Therefore, wooden buildings perform relatively well during seismic events of medium and high intensities. However, wood as a material possesses low ductility properties and brittle failure modes. The National Building Code of Canada (NBCC) [1] is giving more room to allow the design and construction of all-wood Seismic Force Resisting Systems (SFRS) into new buildings. When designing engineered wood structures, ductility and over-strength factors are used. These coefficients, making it possible to design structures entirely in wood having the capacity to resist a seismic event by its inelastic properties, are very low. The problem is that a low global demand stemming from small, underdeveloped force modification factors leads to a local over design of connections and critical wood sections. SFRS built entirely from engineered wood therefore require more material for compliance purposes. In the NBCC, the R_d factor considers the ductility of the system and its ability to absorb energy, and the R_o factor considers the overstrength of the structure.

Due to the increasing use of timber braced frame in practice, multiple configurations of these systems were developed, and this leads to new questions. Previous research [2]–[5] has been conducted to evaluate the behaviour of such systems, investigating the influence of capacity design, connection behaviour, brace configuration as well as the protocols used for cyclic testing. The behaviour of timber braced frames is generally highly influenced by its energy absorption capacity and overall ductility which is governed by a proper design [2]. The main components of interest in capacity design of such structures are generally the connections in the joints, as there is existing knowledge on ductile failure modes. Connectors type and their configuration in wood elements directly influence the behaviour of local wood to steel assemblies and the overall behaviour of a structure [3]. Braced frames with diagonal wood elements have been tested in different configurations to evaluate their performance. Frames with X-brace or K-brace were shown to have desirable lateral stiffness and can be improved with a design focused on ductile failure modes [5]. On a global perspective, other researchers focused their attention on cyclic protocols used to ensure proper characterization of timber frames. Cyclic testing patterns with sequences composed of multiple cycles can be demanding in terms of the effects on the results. It is therefore important to have a representative loading protocol that simulates the behaviour of a real seismic energy demand to correctly establish the properties of interest [4].

The literature review emphasized the need for studies on the dynamic performance of a full-scale braced frame designed according to industry standards, which would give information to professionals in regards of the critical parameters to be used for design. The primary objective of this study is to characterize the cyclic behaviour of a diagonally braced frame of a three-storey wooden building and identify the current design challenges. The full-size specimen is a braced frame with a diagonal glulam wood element connected with two dowel

[1] Félix Bouffard, University of Sherbrooke, Canada, felix.bouffard@usherbrooke.ca

[2] Jean Proulx, University of Sherbrooke, Canada, jean.proulx@usherbrooke.ca

https://doi.org/10.52202/069179-0269

assemblies that are designated to be the fuses in accordance with the principle of capacity design.
A testing methodology was established with suitable properties for a full-scale loading protocol in the structural laboratory of the University of Sherbrooke. This test allowed for the analysis of the energy dissipation capacity, resistance parameters and lateral stiffness of the frame. The results of this research provides information on how to approach such problems and behavioural data for future research.

2 APPROACH

2.1 STANDARD WOOD BUILDING

To incorporate elements that would be observed in an actual timber construction, the fictional "benchmark" building proposed by the Canadian Wood Council (CWC) [6], as shown in Figure 1, was used as a reference. This three-storey building is 12.192 m high, has a ground area of approximately 1440 m^2 and a typical grid spacing of 7.62 m by 7.62 m in each direction. Using SAP2000 [7] and S-Frame [8], the building was modelled and analysed to find the critical load combination, including seismic and snow loads.. The use of different commercial software allowed for a verification of the results to ensure reliable loading targets for laboratory testing. The numerical analysis showed that the critical SFRS was on the long side of the building. The equivalent static load method for a building located in Montréal (City Hall), Canada on a class C soil was used to establish the applied seismic force. The uniformly distributed roof loads are 1.5 kPa and 2.3 kPa for dead load and snow load respectively. For the floors, the uniformly distributed loads are 3 kPa and 2.4 kPa for dead load and live load, respectively. In the context of this research, the R_d and R_o factors for such a structure were chosen to be 2.0 and 1.5 for a moderately ductile system with ductile connections respectively. The total hypothetical weight of the building was assumed to be 11204 kN resulting in a lateral seismic force at ground level of 1481 kN. Accidental torsion was considered during the redistribution of the seismic force in each storey. These forces were then reproduced on the specimen with the experimental setup.

Figure 1: *Standard wood building by the CWC*

2.2 FRAME DESIGN

Due to the fragile properties of wood, there must be pre-assigned ductile elements that will yield firstly to impose a safety measure. All elements that must be oversized compared to an unprotected element are non-energy dissipating elements. The specimen of this research was designed using the capacity design approach. This allowed to pre-determine the components that would fail first. Therefore, all the elements, except for the two dowel assemblies in the brace element were overdesigned to have a linear deformation behaviour. To determine the appropriate geometry of the non-dissipating elements of the specimen, a reduction of the seismic force based only on the overstrength factor was used. As for the ductile assembly, its design was based on the CSA O86-14 adapted the European model [9] for ductile deformation of steel connectors in wood. Both reduction factors accounting for overstrength, and ductility were used to reduce the seismic force for the dowel connections design. The "g" mode was prioritized to be the governing mode of deformation to fully utilize the yield of the dowels and the crushing of the wood.

2.3 CONNECTION STIFFNESS ASSUMPTIONS

During the design phase of the specimen, the challenge was the determination of the connection properties. Since bracing systems, similar to the one in this research, are usually composed of two steel to wood connections and a diagonal element, they have a direct influence on the total drift of the SFRS. The problem is that the stiffness of these connections is not documented by Canadian standards, which means that professionals must rely on values that are not necessarily representative of values that could be observed in the field. This leads to a misrepresentation of the drift ratio of wood SRFS in large-scale buildings.
To solve this issue, the slippage modulus, K_{ser}, established in the SIA 265 standard [10] and by the Eurocode 5 (E5) [11] was used to characterize the stiffness and the drift of the specimen. For Canadian SPF 12c-E class wood, the density of $\rho = 455\ kg/m^3$ was used according to the CSA O86-14 standard. Drift displacement of the whole system was assumed by using the relationship of derivation of connection and system stiffness developed by Chen and Popovski [12].

3 FULL-SCALE WOOD FRAME

3.1 MATERIALS

All the timber elements were joined with grade 350W steel plates and fastened with grade A325 dowels in respect of the ASTM standards. The steel plates connecting the braced assembly were 19.1 mm thick and the column plate were 12.7 mm thick. The 56 dowels (28 at each end) connecting the brace element had a diameter of 9.5 mm and the other 53 dowels had a diameter of 19.1 mm. All the dowels had a length of 342.9 mm. They were hammered in place, as per typical on-site instructions. Yield point of all steel elements was 310 MPa. All the requirements from CSA S16-14 [13] were considered during the design phase of these elements. All the wood members were made of glued laminated Canadian spruce-

https://doi.org/10.52202/069179-0269

pine-fir (SPF) wood produced by Art Massif in accordance with CSA O122-16 [14] and CSA O177-06 [15] for produce and manufacturing requirements respectively. The bracing and column elements had a stress class of 12c-E and the beam element had a stress class of 20f-Ex. The average moisture in the laboratory and of the specimen were respectively 6.6% and 6.2% during the test. The modulus of elasticity considered for 12c-E and 20f-Ex grades were 9700 MPa and 10300 MPa respectively. All the requirements from CSA O86-14 [9] were respected during the design phase of these elements.

3.2 EXPERIMENTAL SPECIMEN

The experimental frame, as shown in Figure 2, represents the braced frame at ground level of the bay perpendicular to the longest length of the standard building. The specimen is 7680 mm long centre to centre of the columns and 4540 mm high from the bottom of the column feet to the centre of the beam. Figure 3 shows the layouts of the specimen as well as the configurations of the connections. The section dimension of the bracing element and columns are 365 mm by 381.7 mm. To ease the manufacturing process and simplify the experimental setup, the beam element was oversized compared to the original plan and were made 365 mm by 555.2 mm. The common design coefficients for all the components of the specimen in respect to the CSA O86-14 standard were load-duration factor (K_D) of 1.15, service-condition factor (K_S) of 1.00, treatment factor (K_T) of 1.00 and system factor (K_H) of 1.00. The resistance of the specimen is governed by the yielding resistance of the brace connections that were assigned to be the ductile elements in the capacity design method used. The resistance of the brace assemblies was calculated to be 552 kN (factored) and 689 kN (nominal). All the other elements were designed to withstand more than the maximum force of the actuators to ensure proper load distribution in the fuses of the whole system.

Figure 2: *Full-scale wood frame*

3.3 SPECIMEN ASSEMBLY CHALLENGES

Assembly of the specimen took place in the structural laboratory of the University of Sherbrooke with the help of the lab technicians, the support of a candidate to the engineering profession and professional engineers.

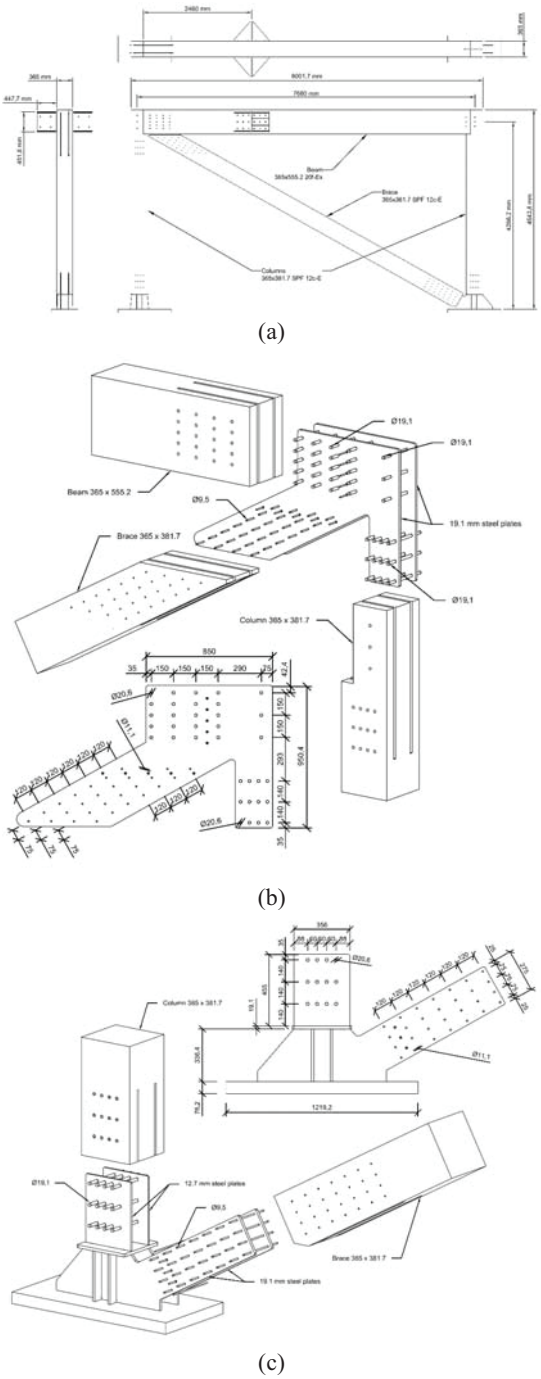

Figure 3: *Specimen layout: full-scale wood frame (a), top brace connection (b) and bottom brace connection (c)*

Some challenges occurred during the assembly due to the scale of the specimen. The wood elements arrived with an unknown degree of humidity which was approximated to be high due to the possible exterior storage of the wood slats prior to assembly. Since the laboratory is well aerated and kept dry, multiple cracks started to appear on the specimen until the day of the test. These cracks, as shown in Figure 4 (a), were carefully monitored to ensure

the integrity of all the components. After testing, the specimen was cut at precise locations to establish the depth of the cracks and none of them were identified as critical. It showed that all the cracks were on the surface only and did not change the integrity of the wood.

Another challenge was the alignment of the holes in the steel plates. Even though all the holes in the wood and in the steel were drilled by a computerized numerical control machine, some holes were not precisely aligned, as shown in Figure 4 (b). In general, the misaligned holes were forced, and the dowels passed through. However, one of the holes in the single column connection was grinded to allow the 19.1 mm dowel to pass through. It was evaluated that only one enlargement of a hole in the single column connection would not affect the results du to the scale of the specimen. It was also established that this would somehow represent errors observed on a construction site and the enlargement technique used was as per typical on-site instructions.

The beam to column connection opposite to the top corner of the diagonal element was composed of a 270 mm by 270 mm by 12.7 mm thick steel plate. A total of six dowels (three in the beam and three in the column) ensured that the pieces would stay together. This assembly was not designed to withstand forces arising from the lifting of the specimen. Therefore, a steel bracing system, as shown in Figure 4 (c), was screwed onto the specimen. Once the specimen was in its testing position and no uplift forces were applied on the beam, the steel brace was removed, and the twelve lag screw holes (six on each side) were filled with the same glue used to manufacture the wood elements. Wooden dowels were used to block the glue filled holes. No cracking was observed du to the installation of the temporary steel bracing prior to the gluing and blocking of the holes.

Since the laboratory setup did not allow for the beam to be dismounted from the simple column throughout the test, a safety block was installed. This 347 mm by 350 mm by 130 mm thick glulam block was installed on the face of the column directly under the beam as shown in Figure 4 (d). Four 8 mm in diameter by 240 mm long screws were installed at a 90-degree angle and 8 mm in diameter by 350 mm long screws were installed at a 45-degree angle. These screws ensured that the beam would be supported in the case of a detachment from the column during the pulling cycles. A clearance of approximately 2 mm was ensured between the beam and the block to allow for movements without interfering the results.

(a)

(b)

(c)

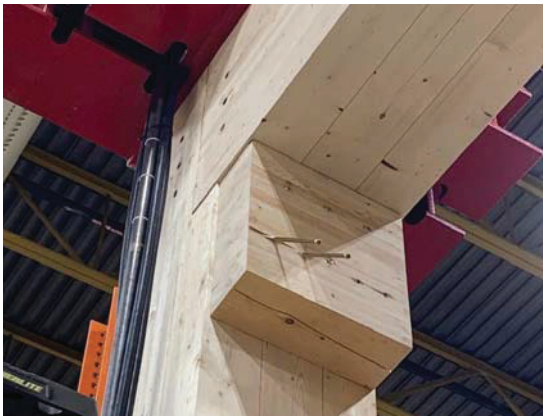

(d)

Figure 4: *Assembly challenges of the specimen: superficial cracks (a), dowel hole misalignment (b), lifting brace (c) and security block (d)*

4 EXPERIMENT PARAMETERS

4.1 TEST SET UP AND INSTRUMENTATION

The experimental setup was composed of three essential systems for the proper functioning of the laboratory tests. The guidance system ensured that the loads are appropriately transmitted to the specimen system. It also ensured that the specimen did not deviate from its lateral trajectory. All of this was documented by the

https://doi.org/10.52202/069179-0269

instrumentation system linking the specimen movements to the data collection tools.

As shown in Figure 5, the specimen was assembled horizontally and temporarily braced with additional timber elements. These braces allowed the specimen to be lifted vertically in its testing position while ensuring minimum efforts in the dowel assemblies. Columns steel bases were made of 15.9 mm and 19.1 mm thick steel plates welded to 1219.2 mm long by 609.6 mm wide and 76.2 mm thick foundation plates. These plates were anchored with high resistance steel rods to the concrete reaction floor.

(a)

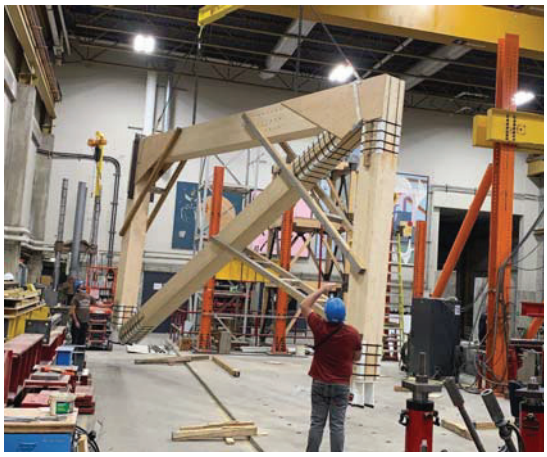

(b)

Figure 5: *Specimen bracing: bracing system (a) and lifting (b)*

A 12 m reinforced concrete reaction wall with a shear strength of 8000 kN, an overturning resistance of 25000 kNm and a punching resistance of 1500 kN was used to anchor two hydraulic actuators. The actuators were from MTS System Corporation and were controlled by the MTS FlexTest-60 system. The maximum capacity of each actuator was 500 kN and they had a displacement range of ±250 mm. The heads of the actuators were anchored to metal braces bolted into the wood beam with 18 one inch in diameter bolts. Hinges at the base and at the head of the actuators allowed to eliminate the bending moment generated by the gravity forces. To simulate the gravity load from above stories, two high-strength rods were anchored in each foundation plates to apply 292 kN of force in the long axis of each of the columns. The rods were connected to a transfer beam at the top of the columns which ensured the correct distribution of the load. The steel beams were connected to a load cell system which ensured that the loading remained constant during the test. The load variation was negligible due to the small angles generated. As shown in Figure 6, the out-of-plane bracing system was made up of four W section steel columns on which two beams were mounted. These beams included a network of rollers and guides ensuring that the specimen did not deviate from its lateral axis when subjected to a cyclic loading.

Potentiometers, linear variable differential transformers (LVDT) and load cells, as shown in Figure 7, were used to capture all the required data for the analysis of the frame's behaviour.

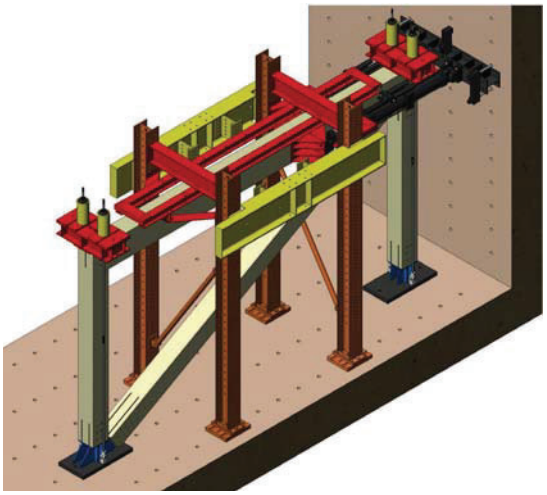

Figure 6: *Guidance system of the laboratory set up*

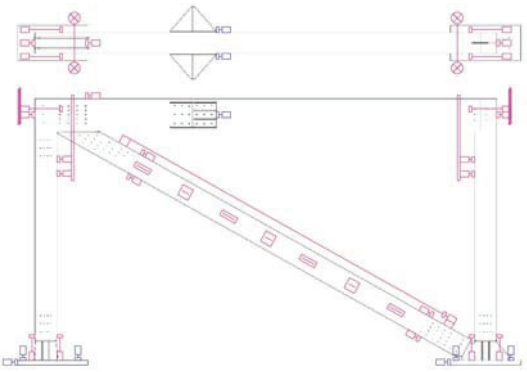

Figure 7: *Instrumentation set up*

4.2 LOADING PROTOCOL

Due to the availability of only one specimen, multiple Due to the availability of only one specimen, multiple parameters were established to ensure proper testing of

the frame. Test method A also known as the Sequential-Phased Displacement Procedure (SPD) in the protocol from the American Society of Testing and Materials E2126-19 [16] was used as a reference. The SPD method shown in Figure 8 involves multiple phases of controlled loading cycles that incrementally increase the displacement of the structure. Two patterns of reversed cyclic loading were applied to the specimens. The first displacement pattern was divided in three phases with the amplitude based on the anticipated first major event (FME). The FME was established to be the first significant limit state to occur. Each phase had a displacement of 25% (step 1), 50% (step 2) and 75% (step 3) of the anticipated FME. The second displacement pattern was composed of an initial phase, a decay phase and a stabilization phase that increased after each cyclic phase of pattern 2 is completed. The initial phase had one cycle at 100% displacement (step 4) of the anticipated FME. The decay phase had three reversed cycles that decreased the initial phase amplitude by steps of 25% of the displacement. The stabilization phase had three cycles that replicated the amplitude of the initial phase. This pattern was repeated until one of the stop criteria was achieved.

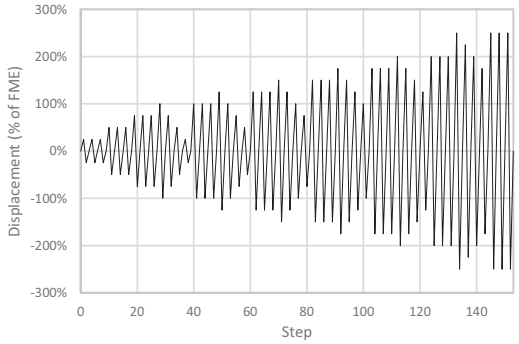

Figure 8: *Loading procedure*

Since only one specimen was available to test, no monotonic test was performed to establish the FME nor the ultimate displacement of the specimen. However, theoretical calculations based on the SIA265 standard [10], Eurocode 5 (E5) [11], E5 platform [17] and Popovski's method [12] were made to evaluate the FME. Due to the capacity design of the frame, the first major event was defined as the yield point of the dowels inside the assemblies of the frame. The lateral force of 482 kN corresponding to an assumption of a 9.21 mm drift was established as the FME for the final test. Through previous testing on large-scale wood structural members at the University of Sherbrooke, it was determined that a loading rate of 0.5 mm/s would be used. This rate was chosen based on the recommendations of the laboratory professionals, as faster loading rate would not have allowed the test to be paused before a possible critical event with potential negative impacts on the specimen. The sampling rate of the instrumentation was set at 50 readings per second.

Two preliminary cyclic load tests followed by a final destructive test were conducted. The first preliminary test (Test 5%) consisted of a triangular wave loading pattern at very low loading rate with a lateral force of 24.1 kN equivalent to 5% of the FME. The goal of the first preliminary test was to ensure proper operation of the instrumentation and loading system. The second loading test (Test 100%) consisted of steps 1 to 4 of method A controlled by force parameters. The goal of the second test was to validate the overall stiffness of the system and to confirm if the theoretical values of the FME were well evaluated. The established limits allowed to stay in the elastic domain and potentially enter the initial phase of the plastic domain. In this case, the force control of the actuators was programmed to perform a lateral thrust of 481.4 kN. Based on the results of the second test, the lateral stiffness of the system and the FME was confirmed. Then the complete loading protocol (Test final) was performed in displacement control until one of two stop criteria was achieved.

The two stop criteria were an observation of a degradation of more than 20% of the specimen's resistance and when the maximum force of 1000 kN of the actuators is achieved. The final test was terminated because the maximum force of the actuators was achieved. However, a maximum lateral force of approximately 1100 kN was applied on the specimen due to a slight increase of the laboratory hydraulic pump capacity.

5 EXPERIMENTAL OBSERVATIONS

5.1 HYSTERETIC BEHAVIOUR OF THE WHOLE FRAME

The hysteretic curves shown in Figure 9 represent the average lateral displacement of the top section of the specimen. It was calculated as the average drift of the two upper assemblies at the vertical centre line of the beam. A correction of the curve in reference to the elongation and compression of the wood was applied to ensure proper representation of the true displacement.

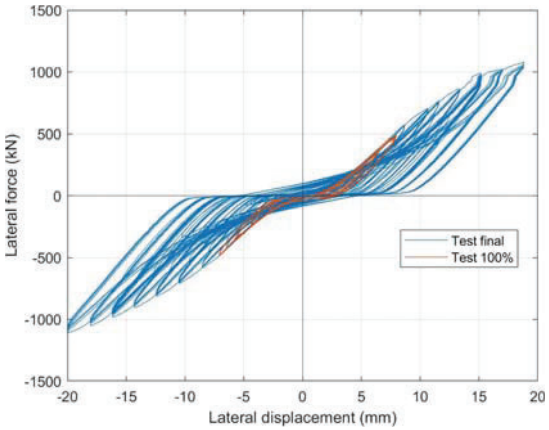

Figure 9: *Hysteresis curve*

It is observed that the curve of the Test 100% shows a very similar elastic behaviour to that of the Test final. In both tests, during return to point zero, the curves don't show any flattening, which means that the specimen remained in the linear deformation domain for both tests. An

https://doi.org/10.52202/069179-0269

average of the difference in displacements at each cycle of about 0.5 mm was recorded. This difference is explained by the fact that the 100% test was performed in force control while the final test was performed in displacement control.

Observation of the hysteresis curve past the yielding point of the brace assemblies shows a broadening of the curves that characterizes an overall ductile behaviour. The stability of each subsequent cycle demonstrates that there is a dissipation of energy increasing at a stable rate. There is also a shift in the curve before the engagement of the elements that resist the lateral force. This phenomenon is common in wood structures and can be explained du to the 1 mm clearance in the connections slots and holes to facilitate assembly. This clearance creates a slight shift in the curves when there is a change in the direction of the force.

5.2 LATERAL STIFFNESS

Lateral stiffness of the system subjected to a cyclic force is determined using the secant stiffness defined by the ratio of force to displacement as shown by the Equation 1 [18]:

$$k_i = \frac{|F_i^+| + |F_i^-|}{|X_i^+| + |X_i^-|} \quad (1)$$

where F_i^+ ; F_i^- are the peak loads of each cycle and X_i^+ ; X_i^- are the relative displacements of the same cycles.

Analysis of the stiffness curve, shown in Figure 10, shows that there is a loss in the overall stiffness of the specimen once the sequence of cycles at the FME amplitude is passed. The FME is achieved when there is a lateral displacement of 9.21 mm. In the test, an average force of approximately 576 kN was required to achieve this displacement. This corresponds to a specimen secant stiffness of 68447 kN/m.

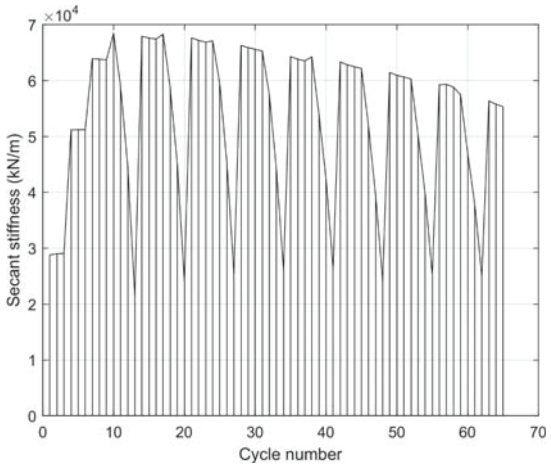

Figure 10: *Secant stiffness curve*

The curve of the following cycles shows that there is a loss of stiffness until the end of the test. Therefore, it can be established that the FME was exceeded, and that the specimen shows a behaviour with plastic failure modes. However, it should be noted that the exceedance of the elastic limit was probably achieved between the FME cycle and the next higher cycle. Hence, the CEN method [19], was used to define the slope of the envelope in the linear domain. Note that the slope (K_α) shown in Figure 11 was evaluated for comparative purposes, as it was not possible to measure the maximum strength of the specimen. As a result, the stiffness in the linear domain is estimated to be 86659 kN/m.

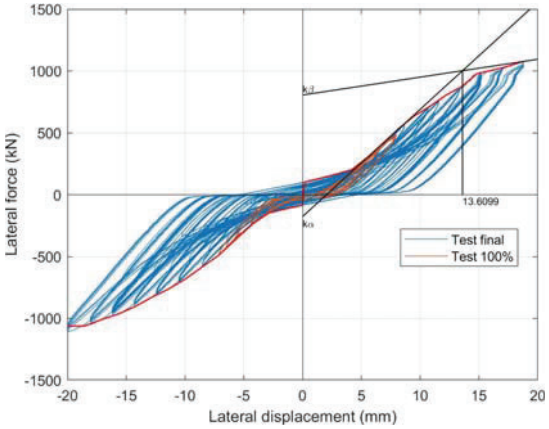

Figure 11: *Approximation of CEN method*

5.3 ENERGY DISSIPATION

The amount of energy dissipated by the specimen is determined by measuring the area of the hysteresis curve in respect of each cycle as shown by Equation 2 [20]:

$$E_{Di} = \int F_i(x)dx \quad (2)$$

where $F_i(x)$ is the hysteresis curve function in accordance with the lateral displacement.

The ratio of dissipated energy is the ability of the overall system to dissipate energy over the strain energy required to deform it. In the case where there are no mechanisms to dissipate energy, the ratio would be zero. However, at each subsequent cycle during the test, there was at least one energy dissipation mode present that ensured a ratio increase. It can be determined using Equation 3 and Equation 4 [20]:

$$E_i = \frac{E_{Di}}{2E_{S0i}} \quad (3)$$

$$E_{S0i} = \frac{k_i u_{0i}^2}{2} \quad (4)$$

where E_{S0i} is the deformation energy per cycle, k_i is the lateral stiffness of the system and u_{0i} is the maximum displacement.

The gradual increase of the energy dissipation ratio shown in Figure 12 is explained as a result of increased friction, cracking, and especially due to the yielding of the brace assemblies.

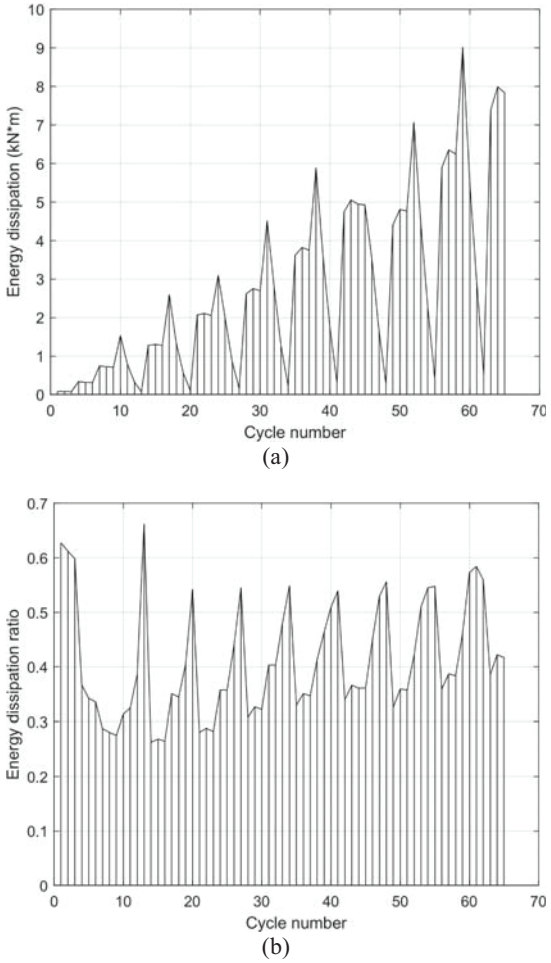

Figure 12: *Energy dissipation: energy dissipation per cycle (a) and energy dissipation ratio (b)*

5.4 STRENGTH DEGRADATION

When a structure is subjected to cyclic forces simulating the forces of earthquake aftershocks, the structure in question may suffer more damage than anticipated. That is why it becomes very important to consider the rate at which SFRS degrade in strength [21]. The degradation under cyclic loads was characterized using the degradation coefficient defined by the equation [18].

$$\lambda_i = \frac{F_i}{F_{max}} \tag{5}$$

where F_i is the force of the observed cycle in a sequence and F_{max} is the peak load of the same sequence.

As expected, the results obtained shows that all the cycles in the elastic domain of the specimen shows negligible strength degradation. Past the elastic limit, the first cycles of each phase corresponds to the maximum load of reference. The subsequent cycle shows a loss of strength due to the crushing of the wood in the connections. Figure 13 illustrates the loss of strength during the test when the lateral load is directed in the east and west directions. The strength degradation trend is relatively stable. Due to the large over-capacity, a degradation of 3.73% was observed when the maximum lateral force was applied.

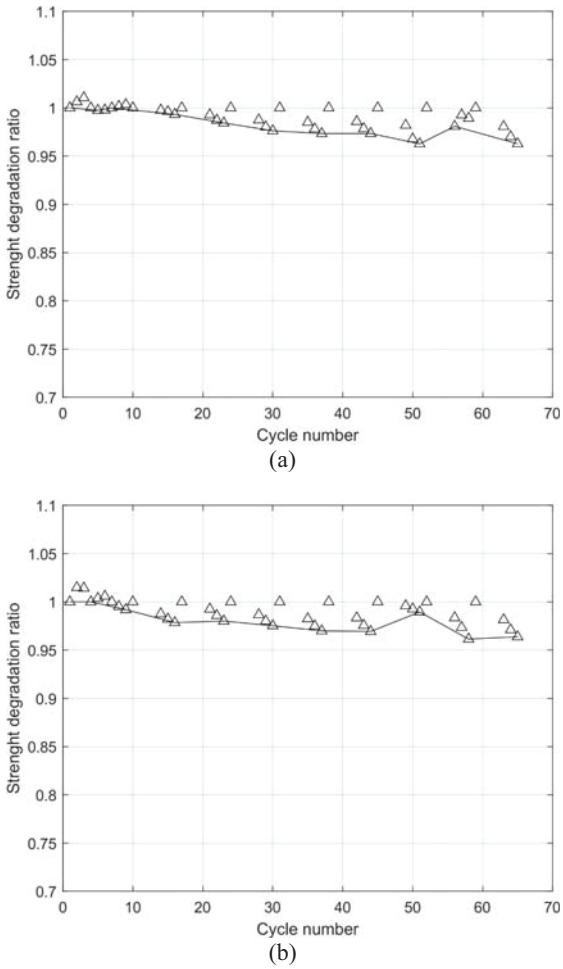

Figure 13: *Strength degradation ratio: load traveling in the east direction (a) and the west direction (b)*

5.5 R_D AND R_O MODIFICATION FACTORS

The R_d factor considers the ductility of the system and its ability to absorb energy, and the R_o factor considers of the excess in resistance of the structure. The force modulation factor R_d ensures that the structural system has the capacity to absorb energy, while having acceptable deformations. When a building is designed with a R_o factor greater than 1, it is considered that the structure can undergo inelastic deformations and that the connections can deform ductile.

According to a study [22], the modification factor R_d is defined by the equation 6.

$$R_d = \sqrt{2\mu - 1} \tag{6}$$

where μ is the ductility expressed as the ratio of displacement at failure to displacement at yield.

The ratio P_{max}/P_y is used to calculate the R_{yield} factor in the evaluation of the coefficient which considers the

https://doi.org/10.52202/069179-0269

excess strength of the structure. Equation 7 is explained in a study [23] to calculate the R_o factor.

$$R_o = R_{size} \cdot R_{\phi} \cdot R_{yield} \cdot R_{sh} \cdot R_{mech} \quad (7)$$

where R_{size} is the overstrength arising from restricted choices for sizes of elements and rounding of sizes and dimensions equal to 1.05; R_{ϕ} is the factor accounting for the difference between nominal and factored resistances equal to 1.43; R_{yield} is the ratio of actual yield strength to minimum specified yield strength; R_{sh} is the overstrength due to the development of strain hardening equal to 1.00 and R_{mech} is the overstrength arising from mobilizing the full capacity of the structure such that a collapse mechanism is formed equal to 1.00.

Since failure of the specimen was not achieved, it is important to note that the value of the displacement and force found with the method used to determine the yielding point can be improved. In addition, it is crucial to obtain the displacement and force at the point of failure in order to properly evaluate the modification factors. Thus, solely to provide an overview of the test results, the following R_d^* and R_o^* values were calculated with the results at the point of maximum force applied to the specimen. The ratio P_{max}/P_y was used to calculate the R_{yield} factor. It is important to consider that the NBCC takes a conservative approach by assuming that the R_{yield} factor is equal to 1.00. However, our tests show that the R_{yield} value is higher and therefore a larger value of the R_o^* factor would be expected. In addition, the calculated values may be considered as underestimated due to the fact that the point of failure is probably higher than the point of maximum force applied on the specimen during testing. R results from our tests lead to calculated value of R_d^* equal to 1.87 and a R_o^* value equal to 2.85.

6 CONCLUSION

Evaluating the seismic behaviour of a full-scale wood frame under cyclic loading to obtain seismic properties for optimization and better understanding of such a system was achieved during this research. The elastic performances of the specimen based on capacity design was evaluated. The following conclusions come from the observations of the specimen and the analysis of the results:

1. The overall behaviour of the system demonstrated that the use of a preliminary test in the elastic domain was an adequate method to validate the elastic stiffness of the specimen in order to establish the limits of a destructive test.
2. The braced frame system, from this research project, demonstrated the same behavior several times during the preliminary tests and during the final test in the elastic domain.
3. In comparison with the study of Xiong and Liu [5], it can be concluded that the overall behaviour of the diagonally braced structure is comparable to a K-braced bolted system.
4. An increase in the ratio of dissipated energy with increasing amplitude of each cycle is observed.
5. There is a loss of stiffness of the overall system passed the elastic limit of the fuse elements.
6. The strength degradation of the system was influenced by the yielding of the fuse elements.
7. The tests in this research project resulted in a value for the R_d^* coefficient that was close to the value established by the 2015 NBCC. The test value is underestimated and therefore a a somewhat higher value would be expected when testing to complete failure. This value would slightly exceed that of the 2015 NBCC.
8. The tests in this research project resulted in a value for the R_o^* coefficient that is much larger than the value established by the 2015 NBCC. This value is also underestimated, as tests were not completed to failure. Thus, there is room for improvement in the proposed CNBC value for system types similar to the one in this research project.
9. Based on the observations of the specimen in this research, a great deal of overstrength is associated with wood frame systems due to the oversizing of the unprotected elements.
10. A lack on information in Canadian standards about stiffness properties of steel connectors in wood was identified. Other national standards can be used to establish preliminary assumptions, but further research should be conducted to provide models with respect to Canadian materials.

In order to better understand the complete behaviour of the frame, it would be appropriate to create a numerical model using different finite element software and use the results for calibration purposes. In this way, a complete model of the SFRS and the structure could be compared to a typical design practice. These results would allow to establish the ductility of the frame and the force modification factors associated with it. To further extend the project, the calibration of such a model could lead to the dynamic finite element analysis of different types of structures with the same SRFS. Thus, these studies could establish a starting point for Canadian standards with respect to the introduction of new requirements related to the seismic behaviour of wood structures.

ACKNOWLEDGEMENT

The authors would like to acknowledge the funding from the National Sciences and Engineering Research Council of Canada and the Québec FRQNT fund. The authors also recognize Art Massif for their collaboration and funding, and for providing the frame for this project. This study was carried out in collaboration with the CIRCERB research Chair at Université Laval, and the CEISCE research centre, Finally, the authors are grateful for the technical support of the staff at Université de Sherbrooke structures laboratory.

REFERENCES

[1] Commission canadienne des codes du bâtiment et de prévention des incendies, « Code national du bâtiment – Canada 2015 », National Research Council of Canada, DOI: 10.4224/40002005, 2015.

[2] M. Popovski et E. Karacabeyli, « Force modification factors and capacity design procedures for braced timber frames », 2008.

[3] C. D. Frenette, « The seismic response of a timber frame with dowel type connections », 1997, doi: 10.14288/1.0050203.

[4] K. Gatto et C.-M. Uang, « Effects of Loading Protocol on the Cyclic Response of Woodframe Shearwalls », *Journal of Structural Engineering*, vol. 129, nº 10, p. 1384-1393, oct. 2003, doi: 10.1061/(ASCE)0733-9445(2003)129:10(1384).

[5] H. Xiong et Y. Liu, « Experimental Study of the Lateral Resistance of Bolted Glulam Timber Post and Beam Structural Systems », *J. Struct. Eng.*, vol. 142, nº 4, p. E4014002, avr. 2016, doi: 10.1061/(ASCE)ST.1943-541X.0001205.

[6] Canadian Wood Council, AKA Architecture + Design, et Art Massif, « Low-Rise Commercial Wood Building Initiative ». Canadian Wood Council, 11 décembre 2019.

[7] CSI, « SAP2000 Integrated Software for Structural Analysis and Design ». Computers and Structures Inc., Berkeley, California, United States.

[8] S-frame, « S-Frame Software Canada ». Altair Engineering Inc., Richmond, BC, Canada.

[9] CSA, « O86-14: Règles de calcul des charpentes en bois », *Canadian Standards Association, Mississauga, Canada*, 2014.

[10] Société suisse des ingénieurs et architectes, « SIA265:2012 Construction en bois ». Société suisse des ingénieurs et architectes, 1 janvier 2012.

[11] NF, « Eurocode 5 : Conception et calcul des structures en bois », *AFNOR*, 1995.

[12] Z. Chen et M. Popovski, « Expanding wood use towards 2025: Seismic perf of braced mass timber frames Yr2 », FPInnovations, févr. 2020. [En ligne]. Disponible à: https://library.fpinnovations.ca/fr/viewer?file=%2fmedia%2fWP%2f36376.pdf#search=Marjan&phrase=false

[13] CSA, « S16–19: Limit States Design of Steel Structures », *Canadian Standards Association, Mississauga, Canada*, 2019.

[14] CSA, « O122-16: Structural Glued-Laminated Timber », *Canadian Standards Association, Mississauga, Canada*, 2016.

[15] CSA, « O177-06 (R2015): Qualification Code for Manufacturers of Structural Glued-Laminated Timber », *Canadian Standards Association, Mississauga, Canada*, 2015.

[16] ASTM International, « E2126-19 Standard Test Methods for Cyclic (Reversed) Load Test for Shear Resistance of Vertical Elements of the Lateral Force Resisting Systems for Buildings », American Society for Testing and Materials, West Conshohocken, PA, 2019. doi: 10.1520/E2126-19.

[17] J.-F. Bocquet, L. Cabaton, D. Calvi, et E. Sauvignet, « Assemblages bois-métal à plans de cisaillement multiples ». Platforme Eurocode 5, 11 janvier 2013.

[18] China Academy of Building Research, « Specification of test methods for earthquake resistant building », Ministry of Construction architectural engineering standards technical focal China Academy of Building Research, JGJ101-96, déc. 1996.

[19] W. Muñoz, M. Mohammad, A. Salenikovich, et P. Quenneville, « Determination of yield point and ductility of timber assemblies: In search for a harmonised approach », Engineered Wood Products Association, Technique, 2008.

[20] P. Paultre, *Dynamics of Structures*. John Wiley & Sons, Ltd, 2013. doi: 10.1002/9781118599792.

[21] M. Popovski, H. G. L. Prion, et E. Karacabeyli, « Shake table tests on single-storey braced timber frames », *Can. J. Civ. Eng.*, vol. 30, nº 6, p. 1089-1100, déc. 2003, doi: 10.1139/l03-060.

[22] F. A. Boudreault, C. Blais, et C. A. Rogers, « Seismic force modification factors for light-gauge steel-frame - wood structural panel shear walls », *Can. J. Civ. Eng.*, vol. 34, nº 1, p. 56-65, janv. 2007, doi: 10.1139/l06-097.

[23] D. Mitchell, R. Tremblay, E. Karacabeyli, P. Paultre, M. Saatcioglu, et D. L. Anderson, « Seismic force modification factors for the proposed 2005 edition of the National Building Code of Canada », *Can. J. Civ. Eng.*, vol. 30, nº 2, p. 308-327, avr. 2003, doi: 10.1139/l02-111.

https://doi.org/10.52202/069179-0269

World Conference on Timber Engineering Oslo 2023

EXPERIMENTAL PARAMETER STUDY ON CLT SHEAR WALLS WITH HIGH-PERFORMANCE SELF-TAPPING SCREW CONNECTIONS

Yuxin Pan[1], Thomas Teflissi[2], Thomas Tannert [3]

ABSTRACT: This paper presents experimental investigations on the performance of Cross-laminated Timber (CLT) shear walls with high-performance self-tapping screw (STS) connections. Hold-down and panel-to-panel connections were tested under monotonic and quasi-static reversed cyclic loading. The derived design values of STS were significantly higher than those calculated using the current Canadian Standard for Engineering Design in Wood. Subsequently, a total of twenty-six CLT shear walls (in single-, double- and triple-panel configurations) were tested under monotonic and quasi-static reversed cyclic loading. The shear walls consisted of 5-ply, 139 mm thick and 3 m high CLT panels with aspect ratio of either 2:1 or 3:1, and different numbers of STS in the connections. The shear wall strength and corresponding displacements increased with the number of screws in hold-downs and spline joints, further it increased with number of connected panels and decreased as a function of aspect ratio.

KEYWORDS: Mass timber; cross laminated timber; self-tapping screws, seismic design

1 INTRODUCTION

High-rise mass timber construction has been successfully re-introduced across North America [1]. The 2020 version of National Building Code of Canada [2] and the 2021 version of the International Building Code [3] have increased the building height limit of mass timber structures up to 12 stories and 18 stories, respectively.

Extensive experimental and analytical research on the seismic performance of Cross-laminated Timber (CLT) shear walls was conducted over the last decade, demonstrating that connections govern their strength, stiffness, ductility, and energy dissipation. A capacity design philosophy is normally employed, where the dissipative components are designed to be ductile and absorb energy while non-dissipative parts are over-designed [4].

However, previous work on self-tapping screws (STS) found connections to be between 2 and 6 times stronger than the design values derived using standard provisions [5]. In consequence, the energy-dissipative connections may be severely over-designed and remain elastic during seismic events. The resulting increased stiffness potentially increases the seismic force demands and put the 'capacity-protected' structural components at risk.

2 OBJECTIVE

In this research, CLT shear walls with high-performance STS connections were investigated to determine the strength, stiffness, yield point, failure point, and ductility of a rocking wall system as a function of the number of STS in the connection, and subsequently develop appropriate and economic design values for the STS.

3 EXPERIMENTAL INVESTIGATIONS

3.1 CONNECTION TESTS

The CLT panels were strength grade 191V2, 5-ply, 139 mm thick. Both HD and SB were made of custom steel plates of grade 44W/300W. The HD was 186 mm wide, 435 mm high, with a 70 mm long base plate, thickness 12.7 mm (vertical part) and 25 mm (base plate). 21 ø13 mm holes were prepared in the vertical part for installing STS; the base plate had 2 ø19 mm holes for installing bolts. The SB was 340 mm wide with a length of the vertical and horizontal plate equal to 127 mm and 89 mm, respectively, and a constant thickness of 6.35 mm. It had 8 ø 11 mm vertical slots, for installing the STS to eliminate any uplift resistance. STS ø12×120 mm were used as fastener for HDs and SBs. The panel-to-panel vertical splines was surface mounted 25×140 mm D-Fir plywood attached with ø8×100 mm STS. Figures 1, 2 and 3 show the drawings for each connection detail.

[1] Yuxin Pan, The Hong Kong University of Science and Technology, Hong Kong, China, ceypan@ust.hk

[2] Thomas Teflissi, Aspect Engineering, Vancouver, Canada, teflissi@aspectengineers.com

[3] Thomas Tannert, University of Northern British Columbia, Canada, Prince George, thomas.tannert@unbc.ca

https://doi.org/10.52202/069179-0270

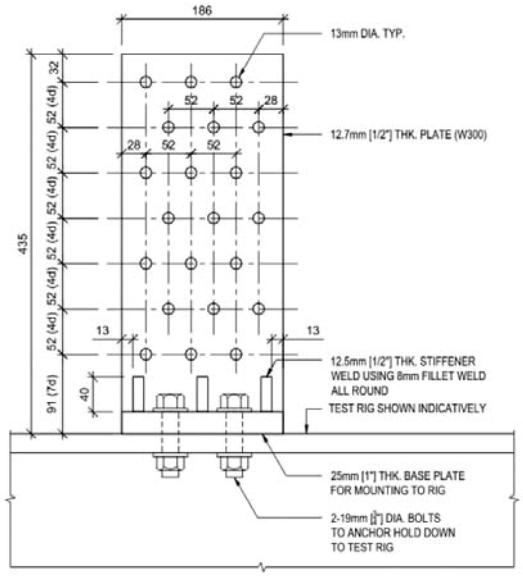

Figure 1: *Hold-down*

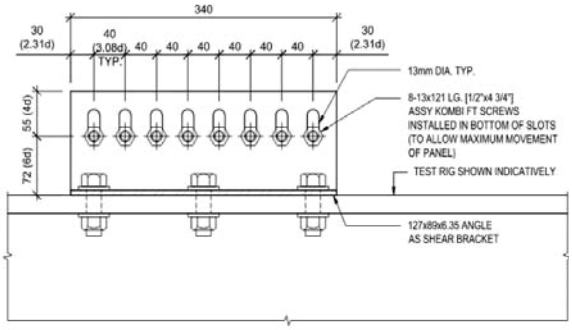

Figure 2: *Shear bracket*

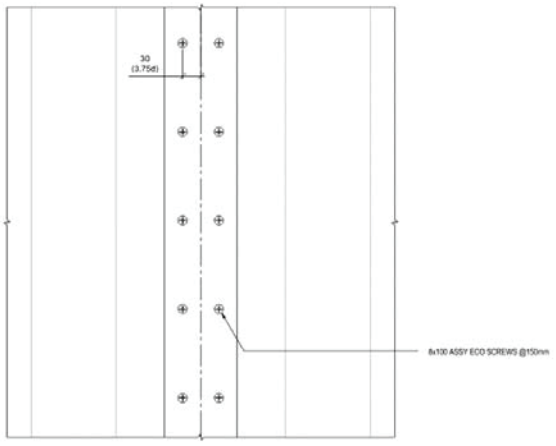

Figure 3: *Spline joint*

3.2 SHEAR WALL TESTS

A total of 26 CLT shear walls were assembled and tested, including 4 single panel (SP), 16 coupled panel (CP), and 6 triple panel (TP) walls. The shear walls consisted of 3 m tall CLT panels, either 1.5 m or 1.0 m wide, resulting in aspect ratios of 2:1 and 3:1, respectively, see Figure 4. All wall configurations were tested with two HDs, CP and TP shear walls with one HD on the outside edge of the outside panels. For all configurations, one SB was mounted at the midpoint of each CLT panel. The CP and TP shear walls were coupled vertically using a screwed plywood spline joint on one side. The splines were attached to the panels with either 13, 16, or 19 screws per panel edge side (total 26, 32, 38 screws per spline). All SBs were fully attached to the walls with 8 STS, while the HDs had 9, 11, 13, or 15 screws each. The screw types matched the connection tests.

The lateral loads were applied by a actuator at the top of the left wall panel through a steel plate connected to steel H-beam. The H-beam was placed on two wooden blocks at the center of each panel. A 10 kN/m superimposed vertical gravity load was applied representing a moderately loaded wall in a two-storey system. This gravity load system simultaneously prevented out-of-plane horizontal movements in addition to allowing for the lateral movement of the shear wall.

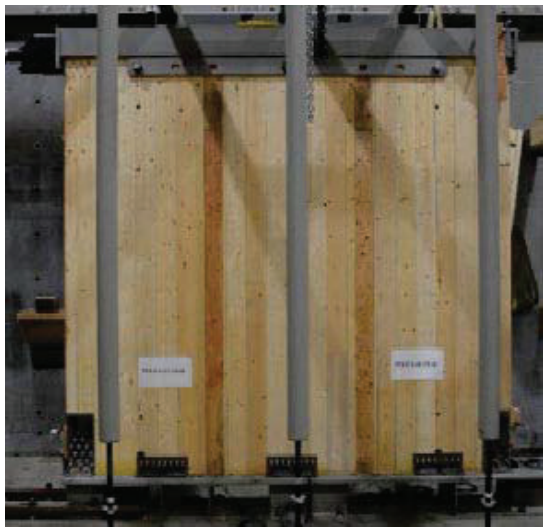

Figure 4: *Full-size triple-panel CLT shear wall tests*

3.3 ANALYSIS

For each connection and shear wall test, the strength, stiffness, displacement, and ductility were determined and analyzed. The maximum forces (load-carrying capacity) from both positive and negative phases (F_{max+} and F_{max-}) were recorded for the reversed cyclic tests. The displacements corresponding to these forces, d_{Fmax+} and d_{Fmax-} were the measurements at the top right corner of the shear walls.

https://doi.org/10.52202/069179-0270

4 RESULTS

4.1 HOLD-DOWN RESULTS

The typical failure mode of the HD was fastener yielding. The corresponding hysteresis behavior of the HD connections combined with a representative monotonic curve are presented in Figure 5. Until reaching capacity, the HD showed little stiffness degradation with increasing displacement. Beyond the capacity, distinct nonlinear degradation and pinching behavior in cyclic re-loading was observed. Throughout the entire loading history, the HDs showed almost the same high unloading stiffness.

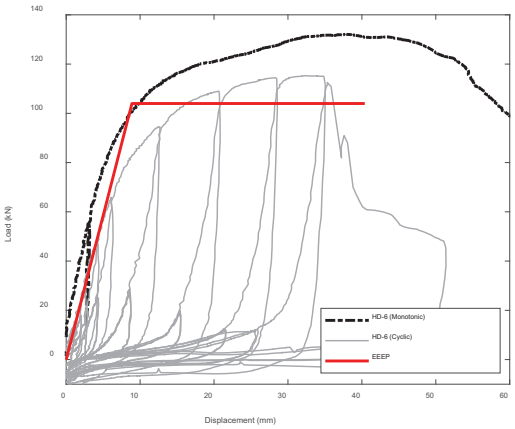

Figure 5: *Typical HD connection hysteresis curve*

4.2 SPLINE RESULTS

The hysteresis behavior of typical spline joints combined with a representative monotonic curve is shown in Figure 6. The curves showed high re-loading stiffness combined with degradation and pinching effects. A small amount of cyclic strength degradation was also observed in the tailing cycles with reduced displacement. Displacement above approximate 30 mm caused brittle failure. Overall, both the strength and displacement capacities under cyclic loading were reduced when compared to monotonic loading. Load-carrying capacity linearly increased with the number of STS. From 2 screws to 8 screws, all strength parameters increased about fourfold regardless of the loading type, e.g. F_{max} increased from 15 kN to 57 kN under monotonic loading and from 11 kN to 46 kN under cyclic loading.

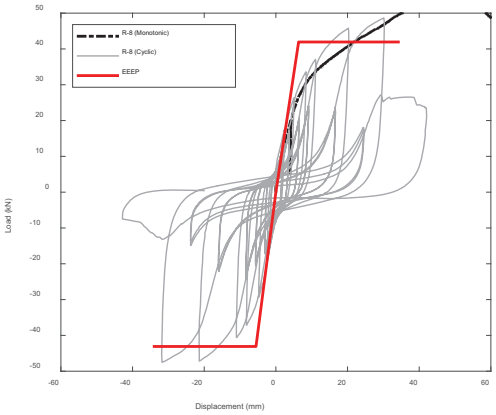

Figure 6: *Typical spline hysteresis curve*

4.3 CONNECTION DESIGN VALUES

Since CSA O86 does not provide any design guidance for STS, the design provisions for lag screws are commonly used by practitioners to calculate the design values. These values are dramatically smaller than the experimental results, see Table 1, confirming that STS in energy-dissipative connections may be severely over-designed and are likely to remain elastic during seismic events. As a consequence, the non-dissipative connections that require capacity protection are also over-designed; however the wood components may no longer be capacity protected.

As an alternative, the test results were used to derive expected performance values: $R_d = k_{mod} \cdot R_k / \gamma_{mod}$, where R_d is the design resistance, R_k is the characteristic value of load-carrying capacity of a single screw, k_{mod} is modification factor taking into account the duration of load and moisture content, and γ_{mod} is the material property factor. Herein, k_{mod} = 0.9 (for short-term action and dry condition) and γ_{mod} = 1.3 were applied. R_k was determined from the test data, assuming that the strength distribution follows a lognormal distribution. The expected performance design values for a single screw in HDs and spline joints were derived using Equation (1) based on $R_{k0.05}$, see Table 5. The design resistance for a single HD screw was 11.8 kN, which was still only 69% of the experimental values, but significantly better than that calculated based on CSA O86 provision (almost 3 times higher). Similarly, the derived resistance for spline joint screw was only 70% of the experimental value but more than 3 times higher than the values based on CSA O86 provisions.

Table 1: *Connection test results*

Connection	Screw Type	Characteristic strength (kN/screw)			Resistance (kN/screw)	
		5th percentile	Mean	95th%	Derived	CSA O86
HD	12Ø×120 ASSY Kombi	17.1	19.4	22.1	11.8	4.1
Spline	8Ø×100 ASSY Eco	4.6	5.0	5.5	3.2	0.9

https://doi.org/10.52202/069179-0270

4.4 SHEAR WALL TEST RESULTS

The effects of four parameters: i) the number of STS in HDs, ii) the number of STS in spline joints, iii) the wall aspect ratio, and iv) the number of panels (SP, CP, TP) on the CLT shear wall performance were investigated. The results are summarized in Table 2; the monotonic load-displacement curves are shown in Figure 7.

Under monotonic loading, the curves were initially linear up to 5 mm displacement when nonlinear behavior started due to plastic deformation in the spline joints connections. After reaching the peak, the curves exhibited a sudden drop because of the HD screws exceeding their capacity.

Figure 7a provides a comparison between SP and CP with different number of STS in HDs (9 vs 15). All shear walls exhibited similar performance at the beginning of loading but reached different load-carrying capacities, F_{max}, as a function of number of STS, following a similar linear relationship observed in HD connection tests. For example, for CP3 and CP1 which had 11 and 15 HD screws, respectively, F_{max} increased from 163 kN to 213 kN (31% increase). The displacement at maximum loads, d_{max}, as well as yield point and failure point were also a function of number of STS.

The impact of the number of STS in the spline joints is illustrated in Figure 7b for CP walls with 13, 16, and 19 STS in the spline and the same HD configuration (9 STS). While the performance of CP4 and CP5 with 19 and 16 screws was similar in terms of strength, displacement, and stiffness, when the number of spline screws was reduced to 13 in CP6, a distinct reduction in performance was observed: when compared with CP4 of 19 screws: F_{max} was reduced by 19%, d_{max} was reduced by 14%,

The significant impact of the panel aspect ratios (2:1 for CP3/5 and 3:1 for CP11/12) on the performance of shear walls with the same connector configuration is shown in Figure 7c. F_{max} for CP3 and CP5 were 23% and 39% higher than those from CP11 and CP 12, respectively.

Finally, the influence of the number of panels for panels with an aspect ratio of 3:1 is illustrated in Figure 7d. Going from CP to TP with the additional SB and spline joint, a higher capacity and stiffness was achieved. F_{max} for TP1 and TP2 were 24% and 42% higher when compared to those from CP11 and CP12

4.5 SHEAR WALL FAILURE MODES

The wall failure modes are presented in Figure 8. All coupled walls exhibited rocking behavior, as seen in Figure 8a. With increasing lateral displacement, some minor plastic deformations occurred in SB, see Figure 8b. Similar to the failure modes observed from connection tests, at the end of each test, the screws in HD were heavily damaged with a failure combination of yielding and withdrawal, and eventually developed plastic hinges, as seen in Figure 8c. Caused by the relative displacement between adjacent panels in the multi-panel tests (CP and TP walls), failure of spline wall-to-wall joints were observed, including screw yielding combined with fracture (TP3), as seen in Figure 8d.

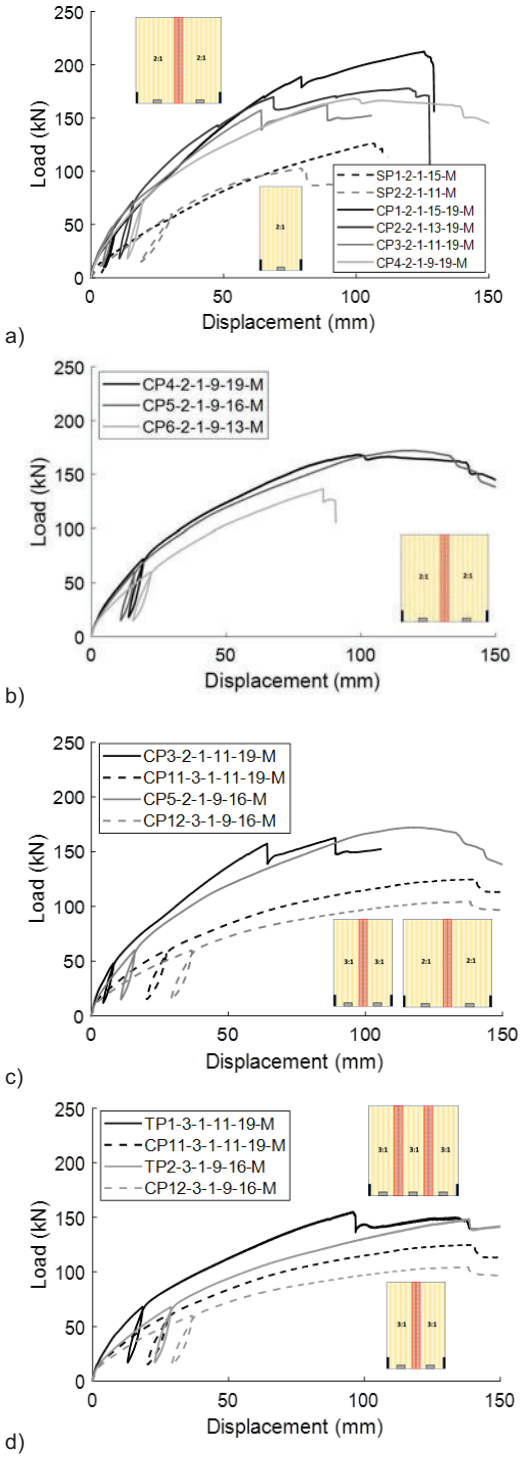

Figure 7: *Monotonic load-displacement curves with effects of: a) HD screws; b) spline screws in CP; c) aspect ratio effect; and d) panel number*

https://doi.org/10.52202/069179-0270

Table 2: *Shear wall test results*

Test ID	F_{max+} [kN]	F_{max-} [kN]	d_{max+} [mm]	d_{max-} [mm]
SP1-2-1-15-M	126.2	-	106.5	-
SP2-2-1-11-M	102.6	-	79.6	-
SP3-2-1-15-C	119.8	-115.7	91.1	-91.1
SP4-2-1-11-C	125.0	-99.9	112.1	-70.1
CP1-2-1-15-19-M	212.6	-	125.6	-
CP2-2-1-13-19-M	177.8	-	119.8	-
CP3-2-1-11-19-M	162.7	-	89.0	-
CP4-2-1-9-19-M	168.4	-	99.3	-
CP5-2-1-9-16-M	172.1	-	116.6	-
CP6-2-1-9-13-M	136.6	-	86.0	-
CP7-2-1-11-19-C	142.4	-153.5	75.0	-75.1
CP8-2-1-11-19-C	174.4	-164.5	70.0	-70.0
CP9-2-1-9-16-C	149.6	-150.8	70.0	-70.1
CP10-2-1-9-16-C	161.1	-146.4	70.0	-70.0
CP11-3-1-11-19-M	124.9	-	140.0	-
CP12-3-1-9-16-M	104.3	-	137.0	-
CP13-3-1-11-19-C	109.7	-106.6	104.1	-104.1
CP14-3-1-11-19-C	102.8	-99.1	80.1	-104.1
CP15-3-1-9-16-C	89.8	-83.6	80.0	-80.1
CP16-3-1-9-16-C	93.6	-96.2	104.1	-104.1
TP1-3-1-11-19-M	155.2	-	95.9	-
TP2-3-1-9-16-M	148.6	-	138.6	-
TP3-3-1-11-19-C	147.5	-132.4	80.1	-80.1
TP4-3-1-11-19-C	150.6	-130.7	104.1	-104.1
TP5-3-1-9-16-C	124.4	-116.2	80.1	-80.1
TP6-3-1-9-16-C	138.0	-122.3	104.1	-104.1

5 CONCLUSIONS

The performance of CLT shear walls with high-performance self-tapping screw connections was investigated under monotonic and cyclic loading. Connection tests and full wall tests were carried out to derive design values of STS. The following conclusions can be drawn:

1) The strength and stiffness of connections were found to linearly increase with the number of screws. The derived design values of STS from the connection tests under short-term cyclic loading were about 3 times higher than those calculated in accordance with the current CSA O86 provisions for lag screws. This shows that STS in energy-dissipating connections are extremely over-designed when designed in accordance with CSA O86 and may not yield as intended.

2) The strength capacity and the corresponding displacement of the shear walls decreased linearly with the reduction of screws in HD. The same trend was also found for the spline joints connections.

3) The aspect ratio had a significant impact on the performance of the coupled shear walls. 2:1 aspect ratios increased load-carrying capacity by 40%, and decreased deformation capacity by 30%.

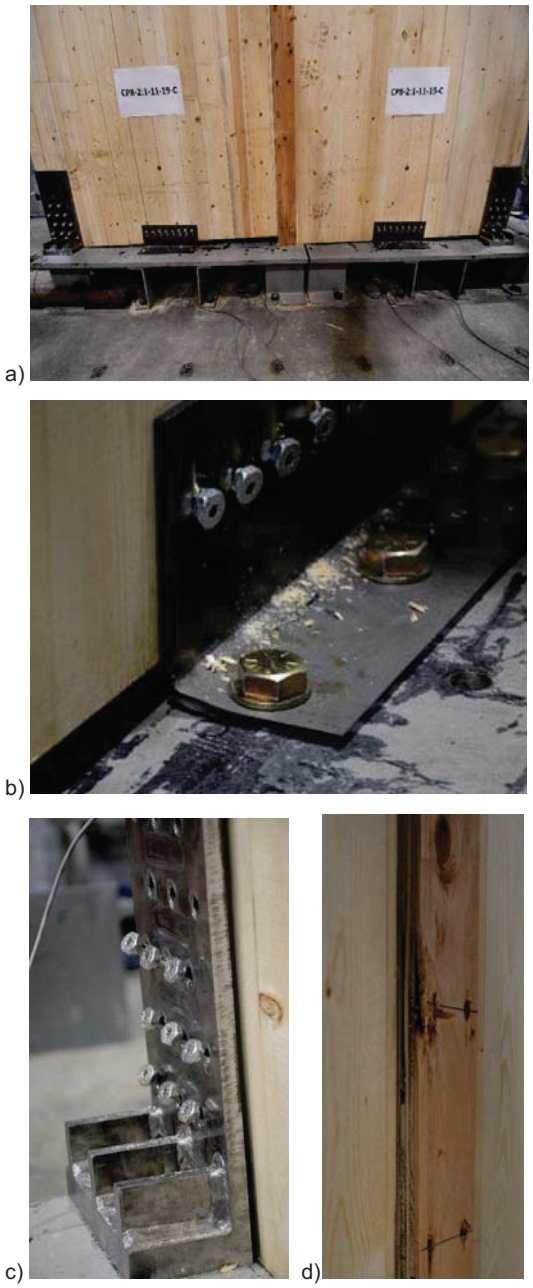

Figure 8: *Observed damages: a) wall rocking, b) deformation of SB, c) screw failure in HD, d) screw failure in spline*

https://doi.org/10.52202/069179-0270

ACKNOWLEDGEMENT

The project was funded by the government of British Columbia through a Forest Innovation Investment grant. The support by the UNBC technicians Michael Billups, James Andal and Ryan Stern, student assistant Anthony Bilodeau, and Adam Gerber from ASPECT Structural Engineers is greatly appreciated. Material was provided by Structurlam Ltd and MTC Solutions.

REFERENCES

[1] Karacabeyli, E., and Gagnon, S.: Canadian CLT Handbook, 2019 Edition. FPInnovations, Pointe-Claire, QC, Canada, 2019.

[2] NBCC, National Building Code of Canada, National Research Council of Canada, Ottawa, Ontario, Canada, 2020.

[3] IBC, International Building Code, International Code Council, Falls Church, VA, USA., 2021.

[4] Masroor M., G. Doudak, D. Casagrande, The effect of bi-axial behaviour of mechanical anchors on the lateral response of multi-panel CLT shearwalls, Engineering Structures 224 (2020) 111202

[5] Sullivan K., T.H. Miller, R. Gupta, Behavior of cross-laminated timber diaphragm connections with self-tapping screws, Engineering Structures 168 (2018) 505-524.

https://doi.org/10.52202/069179-0270

World Conference on Timber Engineering Oslo 2023

HORIZONTAL - LOADING TEST OF STEEL BAR-TIMBER COMPOSITE COLUMNS FOR LOW- RISE BUILDING

Yuuto Shimoirisa[1], Takahiro Iju [2], Takao Ohta [3], Kazuya Mori[4], Shinichi Shioya[5]

ABSTRACT: In light of the current climate crisis, there has been much recent interest in using timber structural members in large buildings, and moreover, in severe earthquake prone, such as Japan, they are more desired on the grounds of light weight of timber members. We are developing a frame system formed by timber members reinforced by deformed steel bars (i.e. rebars) using epoxy resin adhesive. The column could produce, in mechanical properties, better performance than those of reinforced concrete structure (RC). This paper reports horizontal-loading experiment of its column specimens, its results. The specimens were modelled for three-storey buildings, i.e., low-rise buildings. Performance of the specimens indicated to be better than that of RC columns with the same size except difference in material between wood and concrete.

KEYWORDS: Composite timber, Column, Deformed steel bar, Moment-resisting connection, Re-centering

1 INTRODUCTION

In light of the current climate crisis, there has been much recent interest in using timber structural members in large buildings, as timber is as renewable natural resource. Cross-laminated timber (CLT) is a typical timber element, however, CLT structural system very often restricts building planning, owing to CLT being a plate member. The demand for a timber structural system of slender beams and columns is high.

S. Shioya has proposed a structural system for building construction, adopting Hybrid Glulam Timber members using Steel bars (HGTSB, nicknamed as “Samurai” in Japan), has developed the structural design methodology, and has constructed the first prototype building, a two-way frame structure using the structural system [1,2].

We are now developing more refined and more commercial competitive structural system for buildings adopting HGTSB and its structural design methodology. This paper reports an experimental loading test of columns for low-rise buildings with three storeys or less.

2 BACKGROUND

A study on rebar-mixed composite timber to improve bending stiffness and strength of timber beam was initialized by Granholm [3]. Also, after then, studies were and have been being conducted by using other materials beside rebar, however, most of the studies focused on only bending stiffness and strength of the composite beams under short-term or long-term loading. Connection between column and beam has nearly never been studied so as to use performance of the composite members, such as moment-resisting connection for rigid frame.

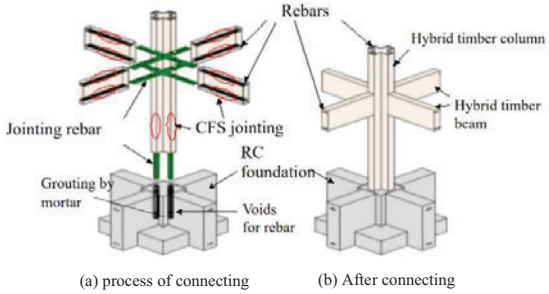

Figure 1: *Beams-column-footing connection*

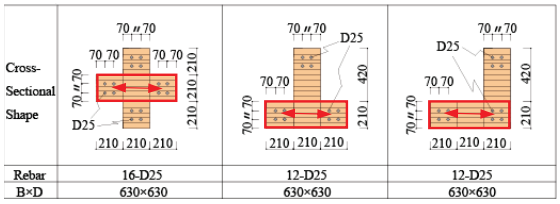

Figure 2: *Representative cross-section of column*

S.Shioya has already developed a technique for rigid connection of rebars inside the composite timber, using carbon fiber plastic sleeve (CFS) and epoxy resin adhesive with works similarly to work process of the glued-in-rod, and reported performance of the column adopted the technique as shown in Figure 1 [2,4].

3 CROSS-SECTIONS OF COLUMN

As Young’s modulus of rebar is approximately 31 times as much as that of timber (Japanese Ceder) by bending, arrangement of rebars nearer the outer on cross-section will produce more increase of bending stiffness and strength. In the panel of connection between column and beam, development length of rebar of beam is required to

[1] Yuuto Shimoirisa, Department of Architecture, Kagoshima University, Japan, k2779317@kadai.jp
[2] Takahiro Iju, Takenaka Corp., Japan, iju.takahiro@takenaka.co.jp
[3] Takao Ohta, Kajima Corp., Japan, ohta-t@kajima.com
[4] Kazuya Mori, Takenaka Corp., Japan, mori.kazuya@takenaka.co.jp
[5] Shinichi Shioya, Department of Architecture, Kagoshima University, Japan, k7347039@kadai.jp

https://doi.org/10.52202/069179-0271

be longer for transmission of axial force of the rebar between the composite beam and column.

On the other hand, in general, magnitude of axial force of columns for low-rise buildings is smaller than that for high-rise buildings. Therefore, the column for low-rise buildings is nearly never required comparative large cross-section area.

As a result of considering them, configurations for cross-section of column for low-rise buildings of two-way-frame may be chosen to be +, T, or L-shaped cross-section as shown in Figure 2, while rectangular portion (enveloped by red line in the figure) in the cross-section mainly resists lateral forces. Also, one-way frame may choose only rectangular cross-section according to planning of buildings. S.Shioya reported a loading experiment of one column specimen with + shaped cross-section for low-rise building [2] and two column specimens with square cross-section for middle rise building [4] . This paper reports an experiment of column specimens with rectangular, T, and a new +-shaped cross-sections.

4 EXPERIMENTAL TEST FOR COLUMN WITH RECTANGULAR CROSS-SECTION

4.1 SPECIMEN

Two columns with rectangular cross-section was selected with scale ratio of 2/3. Figure 3 illustrates the specimen. The specimen was modelled, considering connection between RC foundation and HGTSB column on ground floor of building. Area ratio of rebars (8-D16) to column's gross-area (140mm x 400mm) was 2.8%. The column and RC foundation were connected by using the CFS at joint between rebar and jointing rebar at bottom of its column. The column bottom was connected to a reinforced concrete stub. After shaping the hybrid column, heat-resistant epoxy adhesive shown in Table 1 was filled in insertion hole on column bottom for joint rebar, and then the joint rebar ,8 pieces of D16 for this case, were inserted in the holes each to bond the built-in carbon fiber plastic sleeve (CFS) with the joint rebar. After the adhesive hardened, the column bottom and the RC stub were connected by inserting its joint rebars into voids in the RC stub, for anchorage, and then filling non-shrinkage grout into the column bottom-stub gap and the voids of RC-stub simultaneously. Fresh concrete of nominal strength Fc42 was casted for concrete of the RC-stub. Nominal strength of the no-shrinkage grout is 61.3 N/mm^2 at 4 weeks. Glulam timber was prepared according to E65F255 in Japanese Agriculture Standard, and resorcinol-based resin adhesive was used for glulam timber. Table 1 lists Young's modulus and strengths of laminas of timber of which section size was 25×25mm^2; the number was 10; loading was conducted as four-point bending. Strain was measured by foil strain gauges. Moisture content of lamina test pieces was 14.8%, and those density was 0.45g/cm^3. Table 2 lists mechanical properties of rebar by testing. Table 3 lists mechanical properties in the catalogue of the epoxy adhesives used to bond the rebar.

4.2 CARBON FIBER PLASTIC SLEEVE (CFS)

Figure 4 shows shape and dimensions of a CFS used, which is specified for joint rebar/deformed bar D16. Each rebar is inserted through holes at both ends of the CFS; the CFS is filled with epoxy adhesive shown in Table 3 to join both-side rebars in rigid. This joint was confirmed to produce rigid connection, as shown Figure 5. For more information on CFS, please refer to Reference 2 and 4.

4.3 YIELD SECTION OF REBAR

As shown in Figure 6(a) in the next page, the joint rebar is devised to yield at the section between the RC stubs and the CFS, resulting in plastic elongation and contraction only over the section. The wood around the rebar is devised to be such that even if the rebar yields, the wood portion will not crack.

Table 1: *Lamina properties*

(Unite: N/mm^2)

Grade	Bending test		Compressive test	
	E	F	E	F
L70	8663	68.4	8434	41.4

E: Young's modulus, F: strength

Table 2: *Rebar tensile properties*

(Unite: N/mm^2)

Rebar	E	σ_y	σ_{tk}
D16	1.96x10^5	371	558

E: Young's modulus, σ_y: Yielding strength
σ_{tk}: Braking strength

Table 3: *Epoxy adhesive properties*

(Unite: N/mm^2)

E	Fc	Ft	Fb
2200	76.4	43.4	64.9

E: Young's modulus, Fc: Compresive strer
Ft: Tensile strength, Fb: Bending strenth

Table 4: *CFS tensile properties*

(Unite: N/mm^2)

Specimen	E	σ_y	σ_B
D16	1.94x10^5	363	557
CFS-1	1.76x10^5	363	558
CFS-2	2.11x10^5	352	557

E: Young's modulus, σ_y: Yielding strength
σ_B: Braking strength

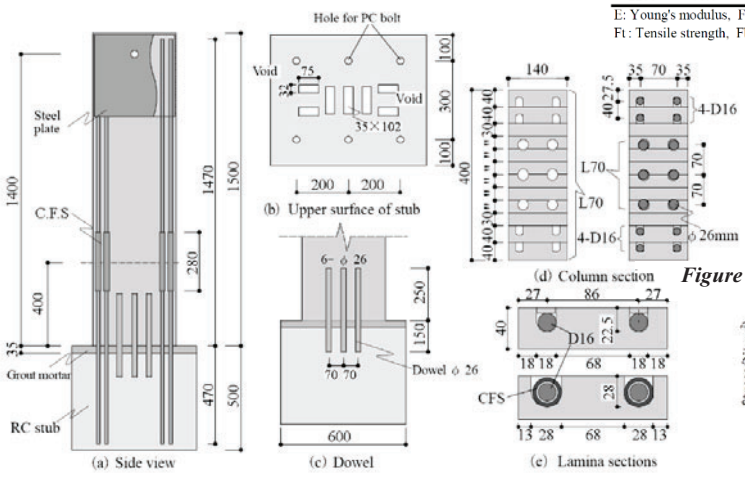

Figure 3: *Specimen configuration and cross-section*

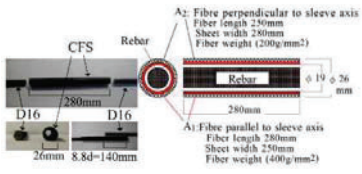

Figure 4: *Carbon-fiber sleeve (CFS) and connection*

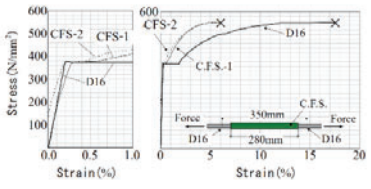

Figure 5: *Tensile stress-strain of CFS*

https://doi.org/10.52202/069179-0271

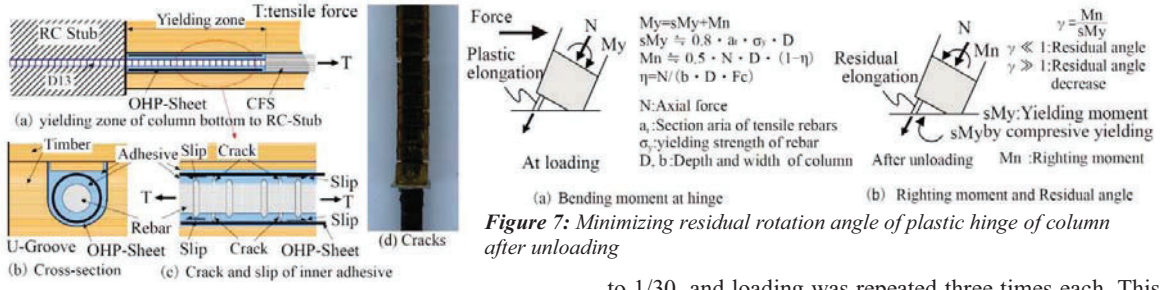

Figure 6: *Yielding length for jointing rebar*

Figure 7: *Minimizing residual rotation angle of plastic hinge of column after unloading*

4.4 MECHANISM OF MINIMIZING RESIDUAL DEFORMATION OF COLUMN

As shown in Figure 7(a), yield bending moment/M_y of a column, which yields in bending by tensile rebar yielding, consists of the moment component/${}_sM_y$ borne by the tensile rebar and the moment component/Mn borne by the axial force. The yielded rebar will generate plastic elongational deformation, resulting in plastic rotation angle in column bottom. After unloading, residual deformation occurs in the column due to its plastic rotation angle. In order to reduce the residual deformation, tensile-yielded rebar needs to yield in compression, and the reduction can be achieved by the moment/Mn by axial force. M_n is defined as restoring moment, and ratio of '$M_n/{}_sM_y$' is named as the restoring moment ratio/γ. When γ is larger than 1.0, the residual deformation of column decreases more. Moreover, when residual vibration after maximum response deformation of building during earthquake is taken into account, the plastic rotation angle can decrease even if 'γ' is smaller than 1.0.

4.5 LOADING

Figure 8 shows set-up for loading. The vertical load/F_v was applied to column head; horizontal deformation at horizontal force height was gradually increased; the horizontal force was applied positively and negatively repeatedly, increasing the horizontal deformation. F_v divided by axial force capacity of column/N_u is defined as 'η' (=F_v/N_u); axial force capacity/N_u is assumed to be product of compressive strength/F_c of glulam timber (F_c=20.6N/mm^2) and cross-sectional area of the column (Fc・b・D). b is column width and D is column depth. Figure 9 shows target displacement protocol for lateral loading. Target deformation angle/R_t was calculated by dividing the horizontal deformation by height h_F (=1400 mm).

i) Specimen No.1(R16)

At first, axial force/F_v was maintained to be constant at an axial force ratio/η of 16%, and target deformation angle was gradually increased up to 1/50 rad. This is the first stage. After this, residual displacement was returned to zero and angel/R_t was returned to 1/200 and again R_t was gradually increased up to 1/50. This is the second stage. Additional residual vibration loading was applied at R_t indicated by symbol '●' in Figure 9 to investigate performance of minimizing residual deformation. The application rule for this residual vibration loading is described in the next section. This is the third stage.

After this stage, in order to investigate the performance under unexpected Mega-earthquake, R_t was increased up to 1/30. and loading was repeated three times each. This stage is the fourth stage. After this, the force was applied until fracture of column. This stage is the fifth stage.

ii) Specimens No.2 (R10) and No.2 (R30)

No.2 was one specimen, but No.2 (R10) was assumed to be characteristic during range where horizontal force was applied at η of 10% and No.2 (R30) was done to be that during range where the horizontal force was applied at η of 30%. With setting η being 10%, reversed repetitive loading was applied gradually increasing Rt from 1/400 to 1/50. This stage is the first stage of No. 2 (R10).

After this, the vertical load/F_v was increased to η of 30%; R_t was returned to 1/400.; lateral force was applied repeatedly with R_t gradually increasing up to 1/50. This is the first stage of No.2 (R30). The same process as the first stage was repeated three times, alternating η between 10% and 30%, as shown in Figure 9(b). These processes are the second, third, and fourth stages of No. 2 (R10) and No. 2 (R30), respectively. At the end of the fourth stage, No. 2 had experienced eight cycles of repetitive loading to 1/50. After this stage, with η setting 30%, repetitive loading was applied by increasing R_t to investigate the

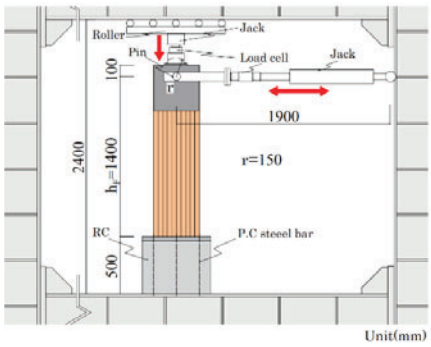

Figure 8: *Set up for loading*

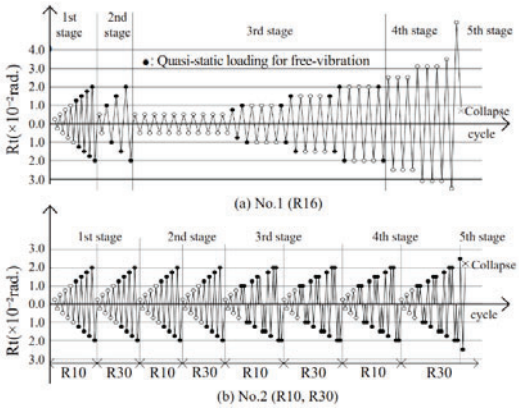

Figure 9: *Target displacement protocol for lateral loading*

performance during unexpected Mega-earthquake until fracture of column. This stage is the fifth stage.

4.6 QUASI-STATIC LOADING FOR FREE-VIBRATION

In order to reveal that residual deformation be minimized after maximum response deformation during an earthquake, quasi-static loading was applied after it reached the target deformation angle/Rt by assuming damped free vibration. For more information of the loading force, please refer to previous reference [4]. Figure 10 schematically shows a hysteresis loop obtained by the loading. Final residual deformation 'δ_F' was taken as the average of 'δ_2' and 'δ_3'.

4.7 MEASUREMENT METHOD

Figure 11 shows set-up for measurement of displacement and strain. Displacement transducer/Disp.1 and Disp.2 were used to measure horizontal deformation between the stub and horizontal force-applied point; Disp.3-Disp.6 were used to measure angle of rotation over hinge region of column bottom; Disp.7and Disp.8 were used to measure shear slip deformation in the loading direction between column bottom and stub surface.

4.8 EXPERIMENTAL RESULTS

4.8.1 Failures and force-deformation relationship

Figure 12 shows final failures. Figure 13 and Figure 14 show horizontal force-deformation angle relationship.

i) No. 1 (R16)

Figure 13(a) shows relationship of the first stage. A tensile rebar yielded at R=+1/137 rad. and bending capacity was almost determined. Figure 13(b) compares loop of the se -cond stage with envelope of the first stage. In the first stage, initial stiffness was maintained up to +75.3 kN at +1/137. In the second stage, the stiffness decreased at 45.1 kN and +1/235. This is due to the Bauschinger effect, as shown in Figure 3(d), where once steel yields, the proportional limit stress decreases in subsequent cyclic loading loops. Figure 13(c) compares envelope over the loops after the third stage with those of the second stage. The envelope of the second stage was almost the same as that of the third stage loops; Figure 13(e) and (f) and (g) show loops at typical target deformation angles. The first loop of the first stage is compared with last loop of the third stage; at R_t=1/100, the proportional limit is reduced as mentioned above; at R_t=1/50, loops of the first and third stages are almost identical. In the third stage, lateral force at Rt=1/400 was applied 10 times, and thereafter, loading was repeated 5 times at each target up to 1/50. When repetitive loading of the first and second stages were added, loading was applied at least seven times from 1/400 to 1/50. Even with such many cyclic loadings, the loops after steel rebar yielded were hardly degraded. Figure 12(a) shows final failures. At the end of the third stage, no damage was observed in timber, and as shown in Figure 12, only thin cracks were observed on the top face of RC stub due to pull-out of joint rebar, and maximum width of cracks was less than 0.3 mm. The damage did not progress at all until the fourth cycle of 1/30. Final fracture occurred at -1/140 to negative direction after the loading was applied up to +1/18.

ii) No.2(R10) and No.2(R30)

Figure 14(a) and (b) show the first stage, in which tensile rebar of No.2(R10) yielded at +1/155. In No.2(R30), force at proportional limit also decreased due to the Bauschinger

effect because the joint rebar of column had already yielded at No.2(R10).

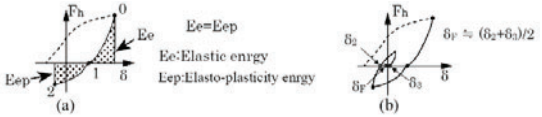

Figure 10: *Quasi-static loading for free -vibration and determination final displacement*

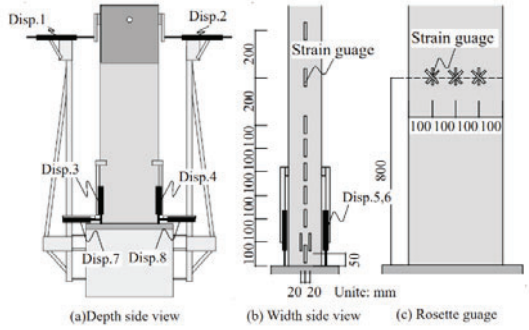

Figure 11: *Set-up for measurement of displacement and strain*

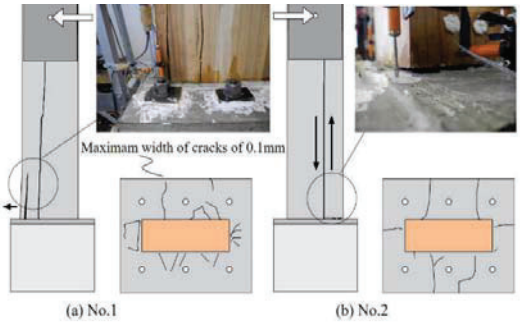

Figure 12: *Observed failures until 5th stage*

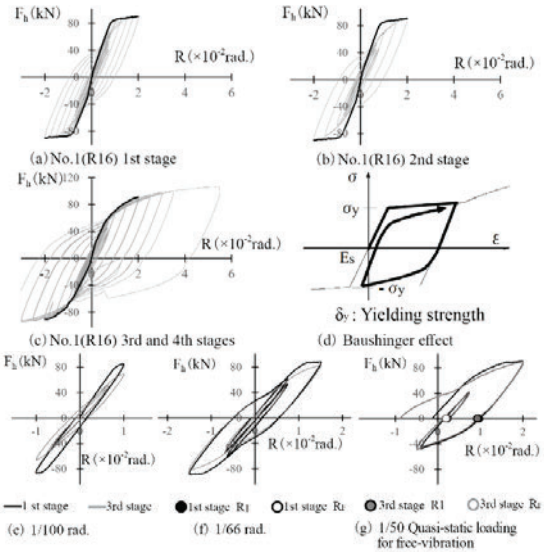

Figure 13: *Lateral force -displacement angle relationship of NO.1*

https://doi.org/10.52202/069179-0271

Figure 14(c) and (d) show the second stage. Envelope of the first stage is shown in comparison with that of the second stage: No.2 (R10) had a lower load at the proportional limit due to the Bauschinger effect; No.2 (R30) had also lower load at the proportional limit in the first stage; envelope of the first and second stages were almost the same in positive loading, and horizontal capacity of the second stage decreased slightly after 1/100 in negative loading.

Figure 14(e)and (f) show a comparison of the third-stage loop and the second-stage envelope; Figure 13(g) and(h) show a comparison of the fourth-stage loop and the third-stage envelope. Envelopes of the third stage almost encircles loops of the fourth stage, and no damage in column occurred after the fourth stage of No. 2 (R30). At the time, the column was subjected to eight cycles of incremental repetitive 1/400-1/50. After this, the fifth stage was applied to confirm final fracture with maintaining axial force ratio η of 30%.

Figure 12(b) shows final failures. The column failed in shear with a vertically crack at the web at +1/45.

From the results of No.1 and No.2 above, it is highly possible to realize a design in which the column connected to RC foundation are subjected to 8 cycles of incremental and repeated loading from 1/400 to 1/50, with axial force ratio η of 10-30%, with little damage and little degradation in loop after joint rebar yielded.

4.8.2 Residual deformation suppression and restoring moment

Figure 13(g) and Figure 14(i) show examples of loops of residual vibration loading at Rt=1/50. Restoring moment ratio γ of each specimen was 0.34 for No.1 (R16), 0.22 for No.2 (R10), and 0.62 for No.2 (R30). Final residual deformation angle/R_F is indicated by symbol '○' according to the method of identifying residual deformation described in Section 4.6. The larger the restoring moment ratio/γ is, the smaller the final residual deformation angle is.

Figure 15 shows variation of residual deformation angle with the target deformation angle/R_t and compares each stage. It can be seen that the angle/R_F decreases from R_1 due to the residual vibration loading, where R_F is deformation/R angle at δ_F in Figure 10(b) and R_1 is the deformation angle at δ_1.

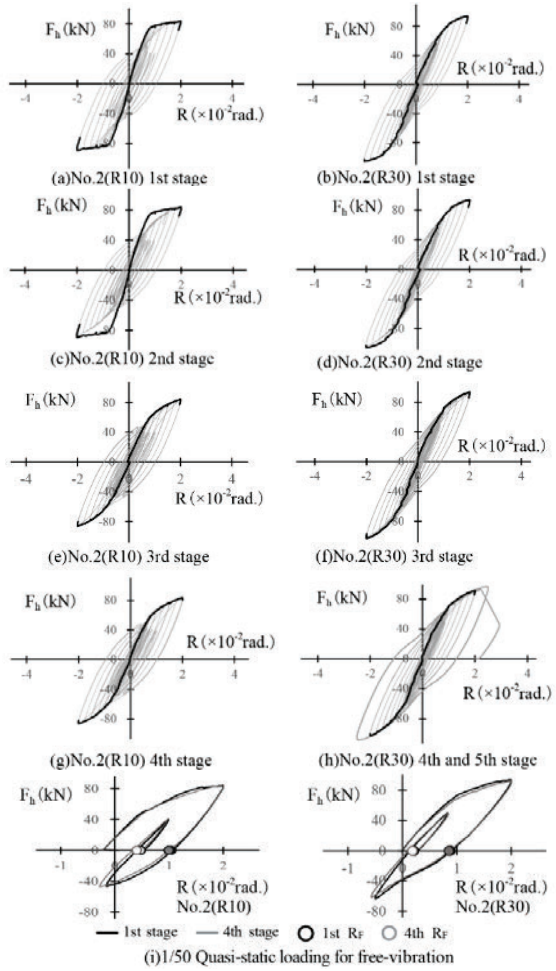

Figure 14: *Lateral force -displacement angle relationship of NO.2*

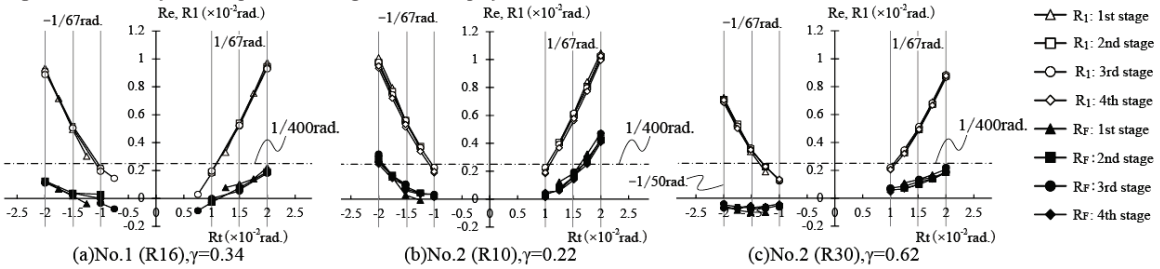

Figure 15: *Relationship of residual displacement angle/R_f -target displacement angle/Rt*

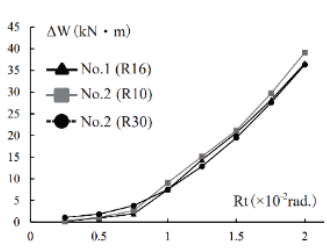

Figure 16: *Dissipation energy*

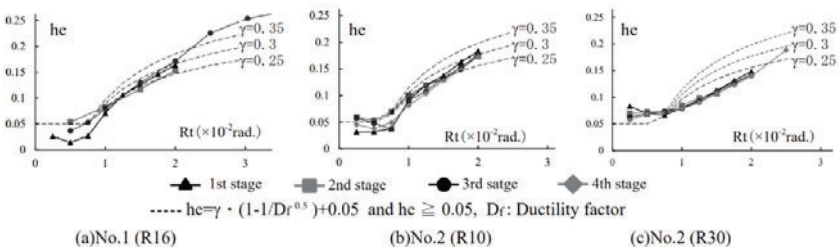

Figure 17: *Equivalent viscous damping factor/ h_e*

https://doi.org/10.52202/069179-0271

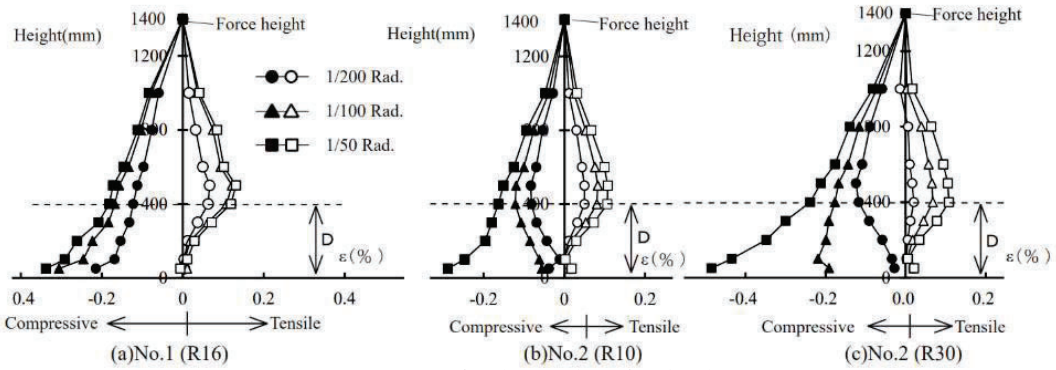

Figure 18: *Strain distribution of wood surface by*

Visually allowable limit angle of 1/400 for the residual deformation angle is shown in the figure as a horizontal, one dot chain line. This value is the upper limit of deformation angle at which column leaning cannot be visually recognized. If γ is greater than 0.34, the residual deformation angle was suppressed to 1/400 or less up to the range where target deformation angle was 1/50 or less.

4.8.3 Dissipated energy and equivalent viscous damping constant

Figure 16 shows variation of the amount of dissipated energy at each target deformation angle loop. Since the dissipated energy is mainly plastic energy by yielding of joint rebar in column, cycles with the same target deformation angle had similar amount in irrespectively of the magnitude of axial force.

Figure 17 shows variation in the equivalent viscous damping constant/h_e of each loop. h_e is smaller for larger values of axial force ratio/η. As h_e is calculated by dividing the amount of dissipation energy of loop by the target deformation and its capacity, larger axial force ratio decreases more the value of h_e. It is necessary to consider the effect of axial force for h_e.

4.8.4 Distribution of strain in column by bending

Figure 18 shows distribution of vertical strain of wood surface by bending. On the compressive surface, the strain distribution increased at the column bottom. On the tensile surface, distribution of strain increases downward from force applied point of column head and decreased to zero from a height of 400 mm to column base. The range is demonstrated not to adhere to the assumption of the plane section used for calculation of bending capacity and stiffness.

4.8.5 Estimation for stiffness and bending capacity

Elastic stiffness was calculated for three cases shown in Figure 19. The column bottom was assumed to be fixed-ended; Cal.1 in Figure 19(a) was calculated using the cross-sectional secondary moment/E_wI_e including the rebar. Cal.2 in Figure 19(b) was calculated using the flexural stiffness E_wI_w of Glulam timber column by ignoring rebar. Cal.3 in Figure 19(c) was calculated by dividing the hinge of column bottom into two half section, with the bending stiffness of the half section on the base side as bending stiffness/E_sI_s resisted by only joint rebar and bending stiffness of the upper half section as average of bending stiffness /E_wI_e of the composite column and E_sI_s. The reduction of tensile strain of wood near the

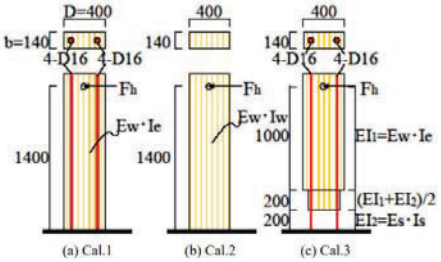

Figure 19: *Assumed bending stiffness for calculations*

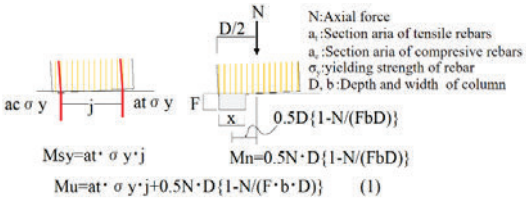

Figure 20: *Stress assumed for ultimate bending moment*

column bottom in Figure 18 was taken into account. Length of the hinge was assumed to be 400 mm of column depth. This is Cal.3. Shear deformation was considered as resisted by the cross-section of timber, with a shape factor of 1.2 and ignoring the rebar. Shear modulus of elasticity of wood was assumed to be 800 N/mm^2 referring to the shear strain in Figure 11(c). Young's modulus for timber and rebar were based on material test. Figure. 21(a) shows loops of horizontal load -deformation angle relationship for No. 1 (R16); the calculated elastic stiffnesses are indicated as straight lines of thick, thin and one dot chain line. The experimental elastic stiffness is between Cal.1 and Cal.2 and close to the elastic stiffness of Cal.3. Figure 21(b) compares those of calculation with the envelope up to joint rebar yielding. On the positive loading, the stiffness by Cal.3 estimates experimental stiffness, while, on the negative loading, the experimental stiffness is somewhat larger. The load-deformation angle relationship calculated by replacing wood of specimen with concrete of compressive strength/Fc(30N/mm^2) is shown in the figure by one dot chain line. The column base was assumed to be fixed ends, taking into account rebar for the bending stiffness of column. The stiffness of RC column is greater until flexural crack occurs, after which The stiffness decreases and approaches that of the specimen. It can be confirmed that the stiffness of the composite columns is close to that of RC column. The capacity was determined by dividing the bending capacity moment/M_u

https://doi.org/10.52202/069179-0271

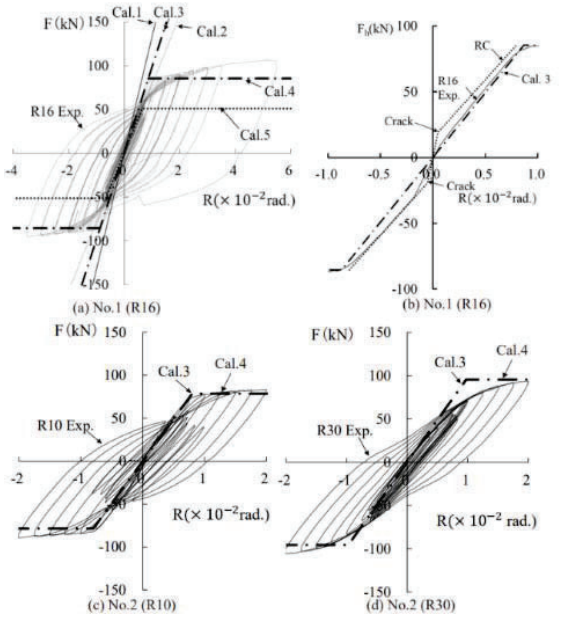

Figure 21: *Skeleton curves of experiment loop and calculation*

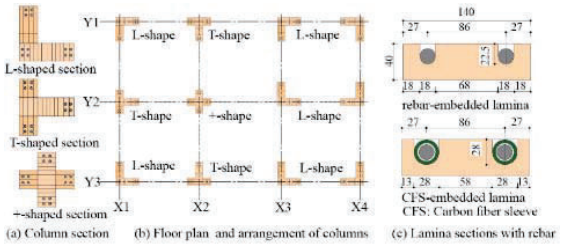

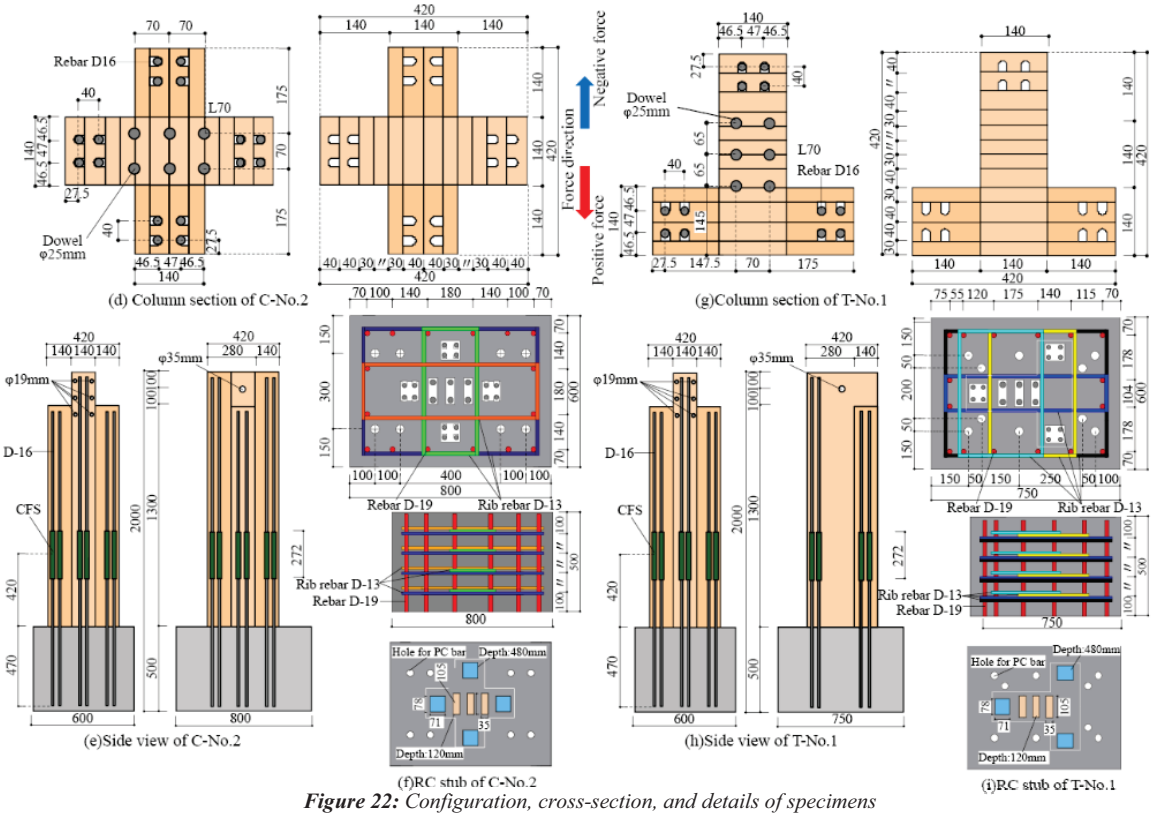

Figure 22: *Configuration, cross-section, and details of specimens*

by the horizontal loading height (h_F=1400 mm) where the joint rebar of column bottom yields, as shown in Figure 20. Sum of bending moment/M_{sy}, which can be resisted by joint rebar in yielding, and bending moment/M_n, which can be resisted by axial force/N and compressive zone of wood. This capacity is Cal.4. Yield strength of rebar was taken as a material test value and compressive strength/F_c of timber was taken as 22.5 N/mm^2, which is a standard value for timber. It can be seen in Figure 21(a) that the calculated capacity almost estimates the capacity at which the rebar yields.

In Figure 21(a), bending capacity of Glulam timber column in Figure 19(b) is shown by horizontal dotted line, where the timber is assumed to reach its bending capacity at column bottom. This is Cal.5. The yield capacity of the specimen is 167% of Cal.5, confirming that connection capacity for the composite column base is extremely high. Figure 21(c) and 21(d) show No. 2; in Figure 21(d), R30 experienced the loading up to 1/50 at No.2(R10) and then started the loading, so that the stiffness of column was reduced before yielding due to the Bauschinger effect and the experimental stiffness was smaller than the calculated relationship. Excluding this, it can be found that skeleton curve by Cal. 3 and Cal. 4 can estimate roughly skeleton curve of experimental force-deformation angle loops.

5 LOADING TEST FOR COLUMN WITH + AND T -SHAPED CROSS-SECTION

As described in Chapter 3, in low-rise buildings, there are three possible shapes of column cross-sections in terms of

https://doi.org/10.52202/069179-0271

architectural plan, as shown in Figure 22(a); L-shaped section column alone, as seen between the X3-X4 axes in Figure 22(b), can constitute a two-way rigid frame.
The L-section column is desirable because of the fitting of column and wall and because of the efficiency of the use of room and corridor.
The L-section column also have the advantage of having only one secondary bonding surface in production.
However, L- section column is difficult to apply in loading test due to eccentricity. If the floor slab is provided for the entire building, effect of the eccentricity in the column is negligible small and therefore, the mechanical performance of the L-shaped column in building will approach that of T-shaped section column.
In this study, it was determined to investigate performance of T-shaped section column specimen.
A horizontal loading test have already been carried out on +-shaped section columns subjected to strong-axis bending of Glulam timber to reveal their elasto-plastic characteristics [2]. This horizontal loading test were carried out on a +-shaped section column subjected to weak-axis bending and a T-shaped section column to investigate the elastic-plastic properties, and the method for estimating the skeleton curve of horizontal load-deformation angle relationship was discussedd.

5.1 SPECIMEN

Figure 22(d)-(i) show cross-sections, shapes, and dimensions of specimens. The number of specimens was two: one with a + shaped cross-section (C-No.2) and the other with a T-shaped cross-section (T-No.1). The height of force point was 1400 mm. Scale of specimen was approximately 2/3 of actual dimensions. The columns were manufactured by first gluing together a rectangular section of 140 x 420 mm (hereafter referred to as the main section) and a square section of 140 x 140 mm (hereafter referred to as the orthogonal 'Part A'), and then gluing these sections together into a +-shaped cross-section and a T-shape section. The +- shaped section column had a total rebar area ratio p_g of 3.24% and a tensile rebar area ratio p_t of 1.62%; the T-section column had a total rebar area ratio p_g of 2.43% and a tensile rebar area ratio p_t of 1.62%. The connection of RC stub and column bottom and the yield length of rebar was the same as in Section 4.3. Glulam timber was JAS cedar laminated timber of the same grade E65F255 (with finger joints) and adhesive for gluing was resorcinol-based resin. Table 5(a) lists mechanical properties of lamina by testpieces. Table 5(b) lists mechanical properties of rebar by testpieces.

Table 5: *Mechanical properties of lamina and rebar*

(a)Lamina (Unit: N/mm²)

Grade	Compression		Bending	
	Ec	Fc	Eb	Fb
L70	8835	34.1	9639	63.6

Fc,Fb: Strength
Ec,Eb: Young's modulus

(b)Rebar (Unit: N/mm²)

Rebar	a_u in mm²	E	σ_y	σ_B
D16	198.6	1.97x10⁵	389	571

a_u: Nominal cross-sectional area of rebar
E : Young's modulus, σ_y: Yielding strength
σ_B: Breaking strength

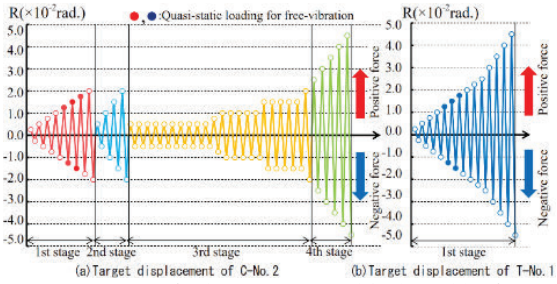

Figure 23: *Target displacement protocol for lateral loading*

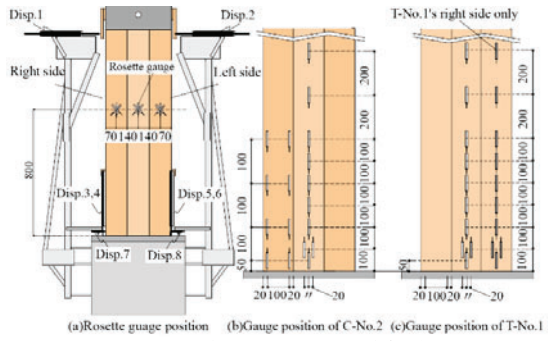

Figure 24: *Set-up for measurement of displacement and strain*

5.2 LOADING AND MEASUREMENT

Method and system for loading were the same as in Figure 8. The axial force on column was chosen to be 194 kN as the axial force ratio η of 10%, while axial force on the T-shaped section column was chosen to be 121 kN as the axial force ratio η of 6%. The axial capacity N_u is the product of the compressive strength F_{wc} (20.6 N/mm²) of standard strength of Glulam timber and the gross cross-sectional area of timber in the column. The deformation angle is the same as Section 4.5.

5.3 EXPERIMENTAL RESULTS

Figure 25 shows final failures and Figure 26 shows the horizontal load-deformation angle relationship of column in the first stage.
i) +-shaped section column (C-No.2)
Under positive loading, rebar in tensile side yielded in tension at +1/118 at +95.0 kN (Y_{t1}), while rebar in compressive side also yielded in compression (Y_{c1}). After this, the second-tier rebar in the tensile side yielded in tension at +1/100 rad., +99.4 kN (Y_{t2}) and the second-tier rebar in the compressive side yielded in compression at +1/78, +105.0 kN (Y_{c2}). These points are shown in Figure 26. After the rebars yield, horizontal stiffness decreased and the load increased at a constant stiffness, i.e., the secondary stiffness. This is seemed to be due to the rebar in Part A still being in elastic and the stiffness of wood in compression. At the peak of the cycle (+121.4 kN, +R=1/57) when the target deformation angle/Rt was +1/57., strain of rebar in the tensile side of Part A was 1743 μ and it had not yielded yet. At R=-1/59 , -125.5 kN on the negative loading, as shown in Figure 25(a), a vertical crack occurred in the Part A near the border with the main section, and then load dropped rapidly. This was the time of maximum load. At this time, strain of the rebar in the main section was 1804μ and it had not yielded yet. From these results, it can be concluded that the specimen failed in shear before the column bottom reached ultimate bending capacity. It is explained that the rebar in the orthogonal sections increased bending capacity and increased shear force of column, and, as a result, shear failure occurred. After this, the column split in two by the

https://doi.org/10.52202/069179-0271

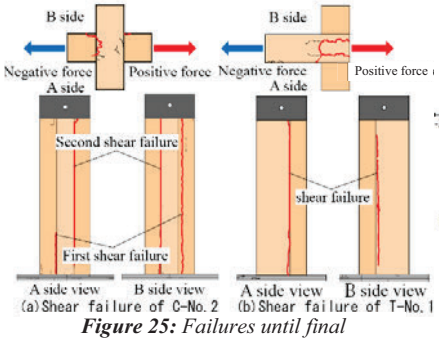

Figure 25: *Failures until final*

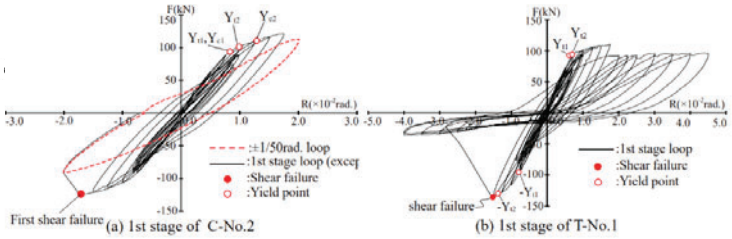

Figure 26: *Lateral force-displacement angle relationship of 1st stage*

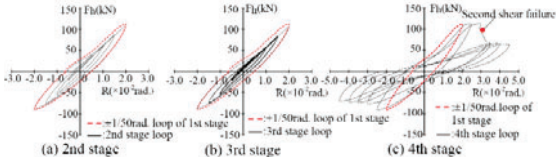

Figure 27: *Lateral force- displacement angle relationship of C-No.2*

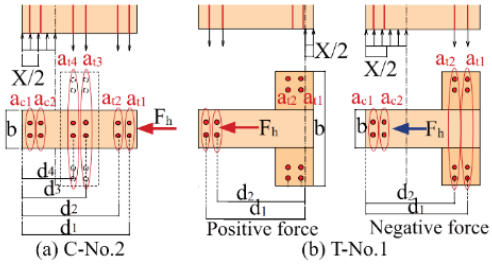

Figure 28: *A model for C-No.2 and T-No.1 at bending capacity*

vertical crack and resisted horizontally and exhibited horizontal capacity and provided a stable loop up to ±1/50 rad. After this, residual deformation was returned to 0.0 mm, and the second stage of loading was applied repeatedly by gradually increasing the target deformation angle from ±1/200 to ±1/50.

Figure 27(a) compares loops of the second stage (solid black line) with the final ±1/50 loop of the first stage (red dotted line). The black loops are enveloped by the red dashed loop, and after the vertical cracking, a stable loop was exhibited by the segmented elements. Figure 27(b) and (c) show loop of the third stage and the loop of the fourth stage at R_t=±1/50. The red dashed loop is the same as those in Figure 27(a).

In Figure 27(b), the loop of R_t=1/50 exhibited almost no deterioration, and in Figure 27(c), it exhibited +114.5 kN up to R_t=+1/33 on positive loading. However, immediately after that, at +100.6 kN during unloading, new vertical cracks occurred as shown in Figure 25(a). After this, the stiffness and capacity decreased in both negative and positive loading, and the capacity was +68.2 kN in the positive loading and -76.3 kN in negative loading. The column resisted as three separated elements and exhibited stable loops up to R=+1/22 such that they could resist the vertical load until the final deformation. Because of the presence of rebars within the divided elements, they could resist to axial forces and a constant horizontal force, even when split by shear failure.

(b) T-shaped section column

On the positive direction, the first outer rebar in tensile side yielded in tension at R=+1/123 at +97.8 kN 'Y_{t1}' and the second rebar in tensile side yielded in tension at R=+1/113 at 98.2 kN 'Y_{t2}'. At this, it can be judged that bending capacity had almost been reached. After this, the load increased with a constant and gradual stiffness, which might be caused by the elastic resistance of the rebar near the tensile side among the two-tier rebar in the flange of the T-section.

On the negative direction, the first rebar in the tensile side yielded in tension at R=-1/117 '-Y_{t1}', and the second-tier rebar yielded in tension at Rt=-1/65, -134.7kN, slightly exceeding yielding strain/ 'Yt_2'. Compressive yielding of rebar in the compression could not be judged from strain gauge values because the rebar had already yielded on the positive direction. Immediately after this, as shown in Figure 25(b), vertical cracks occurred so that the orthogonal section (Part A) and the main section were separated, resulting in a sudden drop in load.

It can be judged that the specimen, on the negative loading, failed in shear just before reaching the bending capacity. After this, the two separated elements resisted as a column, respectively, and capacity on the positive loading was +94.8 kN. The negative load capacity was -34.5 kN.

Even with T-shaped cross-section, care should be taken in design of the column because the bending capacity increases in the direction of loading in which the orthogonal columns are in tension, resulting in shear failure due to the increased shear force.

5.3.1 Elastic stiffness

As well as the calculation in Section 4.8.5, a hinge section in the column bottom was assumed to be column depth of 420 mm.

5.3.2 Yield bending capacity

Equation (1) in Figure 20 can be modified to apply to + and T-shaped cross-sections as follows. Figure 28 shows symbols for assumed cross-sections and dimensions.

$$M_r=\Sigma\alpha_i \cdot a_{t\,i} \cdot \sigma_y \cdot j_i \quad (2)$$

$$M_n=0.5 \cdot N \cdot D \cdot (1-X) \quad (3)$$

$$M_u=M_r + M_n \quad (4)$$

where, $a_{t\,i}$, $a_{c\,i}$: Gross cross-sectional area of rebar in each tier as tensile rebar or compressive rebar, σ_y : yield strength of rebar, α_i : Adjustment factor for stress at bending capacity, j_i : Distance from the centroid of the combined compressive forces to each rebar tier, $j_i=d_i-X/2$, X: Depth of the bending and compressive zone

$$X=(N +\Sigma \alpha_i \cdot a_{t\,i} \cdot \sigma_y - \Sigma a_{ci} \cdot \sigma_y)/(F_{wc} \cdot b) \quad (5)$$

https://doi.org/10.52202/069179-0271

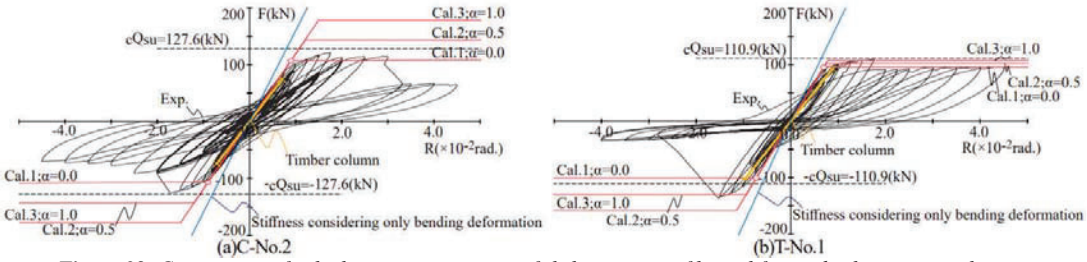

Figure 29: *Comparison of calculation to experiment of skeleton curve of lateral force- displacement angle*

5.3.3 Calculation and Experimental Result

Figure 29 shows a comparison of the calculated result of the skeleton curve and the experimental loops. Initial stiffness was calculated separately for bending and shear deformation. Material test values were used for wood and rebar.

(a) Elastic stiffness

The bending stiffness, assuming the plane cross-section, was calculated for total cross-section area, taking rebar into account. The shear modulus of wood was assumed to be 812 N/mm^2 and the shape factor of shear deformation to be 1.68. The shear resistance area is the horizontal cross -section area of the main cross-section of the wood, the column bottom and in the section from the column head down to column depth. The intermediate section between those were assumed to be the cross-section area of the full cross-section, including the orthotropic sections.

Initial stiffness with only the bending deformation component is shown by blue solid line. The relationship with red solid line shows that added shear deformation. By considering shear deformation, the initial stiffness of both specimens has been accurately estimated by the model shown in Figure 19.

(b) Yielding capacity

+-shaped section columns were assumed to be tension-yielded or compression-yielded, with four two-tier rebar groups on either side of the main section, concentrated at the centroid of each group. The αi in Equation (5) for rebar is assumed to be values at range of 0.0-1.0; the eight rebars in the orthogonal section were also concentrated in the center of the column cross-section. The calculated capacity with αi =0.0 is indicated by symbol '○' as yielding capacity. Shear force was calculated by dividing the yield moment by the height from the loading point to base. Both positive and negative capacities were approximately estimated. After yielding, the column attempted to reach Cal. 3 capacity, i.e. αi=1.0, but it was seemed its shear force had reached the shear capacity and then shear failure has occurred.

The number of rebars resisting in tension in T-shaped section column depends on direction of loading. For positive loading, the two-tier rebar in tensile side were assumed to yield and the α_i of the third rebar in the flange at the orthogonal section was assumed to 0.0, 0.5 and 1.0, where compressive reinforcement bars were neglected. On the negative loading, four rebars in the first-second tiers from the compressive side in the main section were assumed to yield in compression, the first-tier rebar from the tensile side was assumed to yield and α_i was set to 0.0, 0.5 and 1.0 to the second-tier rebar. Yield capacity ○ with α_i being to 0.0 approximately estimates capacity at the positive and negative proportional limits of the experiment. The column width/b was assumed to be 420 mm for the positive loading and 140 mm for the negative loading. In the future, we are going to investigate a method for estimating the shear capacity.

6 CONCLUSION

Horizontal loading tests were conducted on rectangular ,+, and T-shaped cross-sectional columns of which bottoms were planned to yield by bending, assuming the first floor of low-rise building consisting of rigid joined frame using HGTSB, and the elasto-plastic behavior of the column was clarified. The results are summarized below.

1) The horizontal stiffness and the bending capacity of the column was higher than those of ordinary glulam timber column with its same cross-section assuming that the column bottoms were fixed-end.
2) When the column axial force ratio was less than 0.25, they were hardly damaged even after subjected many times, of which one is cyclic loading from 1/400 to 1/50. After joint rebars of the column bottom yielded, its loops were shaped to exhibit abundant energy dissipation. The only degrading property was the reduction in bending moment of the proportional limit, due to the Bauschinger effect that occurs after the rebar yield.

ACKNOWLEDGEMENT

This project was funded as Grants-in-Aid for Scientific Research-B by Japan Society for the Promotion of Science.

REFERENCES

[1] S. Shioya: Hybrid timber-steel bar glulam and its building system. JTCCM JOURNAL,Vol.52, 2016.
[2] S.Shioya, et al.: An innovative hybrid timber structure in Japan: performance of column and beam. World Conference on Timber Engineering, 2016.
[3] Granholm, H.: Armerat Tra (Reinforced timber), Chalmers Tekniska Hogskolas Handlingar. No.154, 68-76, Gothenburg, Sweden, 1954.
[4] M. Mukai, et al.: Horizontal - loading test of steel bar - timber composite column for mid-rise building. World Conference on Timber Engineering, 2021.
[5] N. Fukutomi, S.Shioya, et al.: Design Method to Estimate Stiffness and Strength of Hybrid Timber-Steel Beams. World Conference on Timber Engineering, 2018.

https://doi.org/10.52202/069179-0271

World Conference on Timber Engineering Oslo 2023

EVALUATION OF VIBRATION PROPERTY OF HIGH-DAMPING TWO-STORY TIMBER STRUCTURE BASED ON RESONANCE CURVE

Yuji Miyazu[1]

ABSTRACT: This paper aims to evaluate the vibration property of a two-story timber structure which has energy dissipation devices to enhance the seismic performance. Oil dampers and friction dampers are considered as the energy dissipation devices in this study. Steady-state response of a two-degree-of-freedom system which has the nonlinear springs with the force-deformation relation of timber structure and the dampers is derived by using the equivalent linearization technique and the sequential quadratic programming. Through the comparison of the resonance curves of the models with/without dampers, it is found that the friction damper reduces the story drift mainly around the first mode while the oil damper works to decrease the story drift both around the first and the second modes.

KEYWORDS: Steady-state response, Resonance curve, Two-story timber structure, High-damping structure

1 INTRODUCTION

Recent years in Japan, energy dissipation devices such as oil dampers and friction dampers are widely used to enhance seismic performance of low-rise timber buildings, especially two-story wooden houses. In some previous researches, the effectiveness of installing energy dissipation devices into timber structures is evaluated numerically through time history seismic response analysis; however, it is also important to investigate the effect of dampers theoretically based on dynamics of structures in order to discuss the vibration property of timber structure that have energy dissipation devices.

The author derived steady-state response of a single-degree-of-freedom system which has a nonlinear spring of ENCL model [1] and viscous and friction elements as energy dissipation devices by using Caughey's equivalent linearization technique [2] in the previous work [3]. In this paper, the steady-state response of a two-degree-of-freedom system are derived in a same manner as the previous method [3] and discuss the vibration property based on resonance curves.

At first, a force-deformation relation model and analysis models used in this study are summarized in Chapter 2. Then, the steady-state response of the two-degree-of-freedom system are derived by using Tajimi's [4] and Caughey's methods [2] in Chapter 3. Finally, the vibration property of a two-story timber structure with energy dissipation devices are discussed in Chapter 4.

2 FORCE-DEFORMATION RELATION OF TIMBER STRUCTURE AND ANALYSIS MODEL

The force-deformation relation of a timber structure is simulated by an extended normalized characteristic loop model (ENCL model) [1] expressed by Eq. (1). $L_1(x)$ and $L_2(x)$ are loading and unloading curves, respectively. The variable x is the deformation normalized by the maximum deformation of the hysteresis loop. A, B, n_1, and n_2 are the parameters which control the shape of the hysteresis loop.

$$\left.\begin{aligned} L_1(x) &= \mp Ax^4 + Bx|x|^{n_1} + (1-B)x \pm A \\ L_2(x) &= \pm Ax^4 + Bx|x|^{n_2} + (1-B)x \mp A \end{aligned}\right\} \quad (1)$$

A represents the force at a y-intercept, and an absorbing energy increases with the increase of the value of A. B controls the slip behaviour of the loop, and a tangent stiffness decreases with the increase of the value of B. n_1 and n_2 control the curvature of the loading and unloading curves, and the curvature increases with the increase of the values of n_1 and n_2.

In this paper, these parameters are adjusted to simulate the force-deformation relation obtained through the static cyclic loading test on the timber beam and column frame combined with plywood panel [5]. Figure 1 shows the force-deformation relation simulated by ENCL model, and its parameters are listed in Table 1. The deformation and the force are expressed by μ and r, and these values are normalized by the deformation and the force at 1/360 rad, respectively.

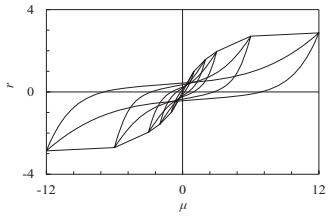

Figure 1: *Force-deformation relation of the timber structure simulated by ENCL model*

[1] Yuji Miyazu, Tokyo University of Science, Japan, miyazu@rs.tus.ac.jp

https://doi.org/10.52202/069179-0272

Table 1: *Parameters of the ENCL model*

Drift angle (rad)	μ	r	A	B	n_1	n_2
0	0	0	0	0	1	1
1/720	0.5	0.5	0	0	1	1
1/360	1	1	0.12	0.3	1	1.6
1/180	2	1.568	0.12	0.54	1	2.4
1/120	3	1.958	0.12	0.66	1.2	2.8
1/60	6	2.704	0.13	0.76	1.9	4.3
1/30	12	2.865	0.15	0.82	2	5.1

Figure 2 illustrates the composition of the analysis models used in this study. The Basic model is the two-degree-of-freedom system which has nonlinear springs with the ENCL model and dashpots representing the inherent structural damping. The VD model has additional dashpots (Dashpot 2) to consider the viscous force added by oil dampers. The FD model has elastic-perfectly plastic springs (EPP springs) which express the stiffness and the friction force added by friction dampers.

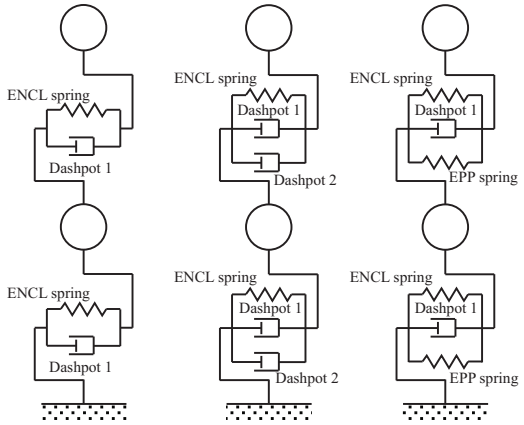

(a) Basic model (b) VD model (c) FD model

Figure 2: *Composition of analysis models*

3 STEADY-STATE RESPONSE

The equation of motion is formulated as Eq. (2) using story deformation represented by u_1 and u_2 for the first and the second stories, respectively.

$$\left.\begin{aligned} &m_2\left(\ddot{u}_2+\ddot{u}_1\right)+\left(c_2+c_{\mathrm{d}2}\right)\dot{u}_2+k_2Q_2=-m_2\alpha\cos pt \\ &m_2\ddot{u}_2+\left(m_1+m_2\right)\ddot{u}_1+\left(c_1+c_{\mathrm{d}1}\right)\dot{u}_1+k_1Q_1=-\left(m_1+m_2\right)\alpha\cos pt \end{aligned}\right\} \tag{2}$$

where m_i is the mass of ith node, c_i is the viscous damping coefficient of the ith story related to inherent damping of timber structure, $c_{\mathrm{d}i}$ is the viscous damping coefficient added by oil dampers in the ith story, k_i is the stiffness of the ith story, Q_i is the function of restoring force of the ith story, α is the magnitude of an excitation, and p is the circular frequency of the excitation. Here, we approximate the solution of Eq. (2) as follows.

$$u_i=\mu_i\cos\left(pt-\varphi_i\right)\qquad\left(i=1,2\right) \tag{3}$$

The restoring force of ith story is approximated as follows by using Caughey's equivalent linearization technique.

$$k_iQ_i=k_i\left(k_{ei}u_i+c_{ei}\dot{u}_i\right) \tag{4}$$

where

$$k_{ei}=C_i,\quad c_{ei}=-\frac{S_i}{p} \tag{5}$$

C_i and S_i in Eq. (5) are the values defined in the Caughey's equivalent linearization technique, and they are calculated as the summation of the values of ENCL and EPP springs as formulated in Eq. (6).

$$\begin{aligned} C_i&=C_{i\_\mathrm{ENCL}}+C_{i\_\mathrm{EPP}} \\ S_i&=S_{i\_\mathrm{ENCL}}+S_{i\_\mathrm{EPP}} \end{aligned} \tag{6}$$

C_{i_ENCL} and S_{i_ENCL} are calculated by Eq. (7) which was derived in the previous study [3].

$$\begin{aligned} C_{i\_\mathrm{ENCL}}&=\frac{2}{\mu_i\pi}\left[\int_{-\frac{\pi}{2}}^{0}r_iL_1\left(\cos\theta\right)\cos\theta d\theta\right. \\ &\qquad\left.+\int_{0}^{\frac{\pi}{2}}r_iL_2\left(\cos\theta\right)\cos\theta d\theta\right] \\ &=\frac{2r_i}{\mu_i\pi}\left\{\frac{\sqrt{\pi}}{2}\left(\frac{\Gamma\left(\frac{n_1+3}{2}\right)}{\Gamma\left(\frac{n_1+4}{2}\right)}+\frac{\Gamma\left(\frac{n_2+3}{2}\right)}{\Gamma\left(\frac{n_2+4}{2}\right)}\right)B+\frac{\pi}{2}\left(1-B\right)\right\} \\ S_{i\_\mathrm{ENCL}}&=\frac{2}{\mu_i\pi}\left[\int_{-\frac{\pi}{2}}^{0}r_iL_1\left(\cos\theta\right)\sin\theta d\theta\right. \\ &\qquad\left.+\int_{0}^{\frac{\pi}{2}}r_iL_2\left(\cos\theta\right)\sin\theta d\theta\right] \\ &=\frac{2r_i}{\mu_i\pi}\left\{-\frac{8}{5}A+\frac{1}{2}\left(\mathrm{B}\left(1,\frac{n_2+2}{2}\right)-\mathrm{B}\left(1,\frac{n_1+2}{2}\right)\right)B\right\} \end{aligned} \tag{7}$$

C_{i_EPP} and S_{i_EPP} are calculated by Eq. (8) based on the method proposed by Caughey [6].

$$C_{i\_\mathrm{EPP}}=\begin{cases}\dfrac{F_i}{\mu_{yi}\pi}\left(\theta^*-\dfrac{\sin2\theta^*}{2}\right) & \mu_i>\mu_{yi} \\ \dfrac{F_i}{\mu_{yi}} & \mu_i\le\mu_{yi}\end{cases} \tag{8}$$

$$S_{i\_\mathrm{EPP}}=\begin{cases}\dfrac{-F_i}{\mu_{yi}\pi}\sin^2\theta^* & \mu_i>\mu_{yi} \\ 0 & \mu_i\le\mu_{yi}\end{cases}$$

where $\theta^*=\cos^{-1}\left(1-2\mu_{yi}/\mu_i\right)$, F_i is the ratio of the yield force of the EPP spring to the force of the ENCL model in the ith story at 1/360 rad. μ_{yi} is the yield deformation of the EPP spring in the ith story. By substituting Eqs. (3) and (5) for Eq. (4), and by replacing $pt-\varphi_i$ with θ_i, the restoring force of the ith story is expressed as follows.

$$k_iQ_i=k_i\mu_i\left(C_i\cos\theta_i+S_i\sin\theta_i\right) \tag{9}$$

First, we replace $pt-\varphi_2$ with θ_2 in Eq. (3) to obtain Eq. (3').

https://doi.org/10.52202/069179-0272

$$u_1 = \mu_1 \cos(\theta_2 + \varphi_2 - \varphi_1), \quad u_2 = \mu_2 \cos\theta_2 \tag{3'}$$

By substituting Eqs. (3') and (9) for the upper equation of Eq. (2), we obtain Eq. (2').

$$\begin{aligned} &-p^2 m_2 \{\mu_2 \cos\theta_2 + \mu_1 \cos\theta_2 \cos(\varphi_2 - \varphi_1) - \mu_1 \sin\theta_2 \sin(\varphi_2 - \varphi_1)\} \\ &-(c_2 + c_{d2}) p \mu_2 \sin\theta_2 + k_2 \mu_2 (C_2 \cos\theta_2 + S_2 \sin\theta_2) \\ &= -m_2 \alpha (\cos\theta_2 \cos\varphi_2 - \sin\theta_2 \sin\varphi_2) \end{aligned} \tag{2'}$$

Since Eq. (2') is an identity, we obtain the following relations.

$$\begin{aligned} &-p^2 m_2 \{\mu_2 + \mu_1 \cos(\varphi_2 - \varphi_1)\} \\ &\qquad + k_2 \mu_2 C_2 = -m_2 \alpha \cos\varphi_2 \end{aligned} \tag{10-1}$$

$$\begin{aligned} &p^2 m_2 \mu_1 \sin(\varphi_2 - \varphi_1) - (c_2 + c_{d2}) p \mu_2 \\ &\qquad + k_2 \mu_2 S_2 = -m_2 \alpha \sin\varphi_2 \end{aligned} \tag{10-2}$$

By multiplying $-i$ to Eq. (10-2) and adding it to Eq. (10-1), we obtain Eq. (11).

$$\begin{aligned} &-p^2 \mu_1 e^{-i\varphi_1} \\ &+\left[-p^2 + \frac{c_2 + c_{d2}}{m_2} pi + \frac{k_2}{m_2}(C_2 - iS_2)\right] \mu_2 e^{-i\varphi_2} = -\alpha \end{aligned} \tag{11}$$

Next, we replace $pt - \varphi_1$ with θ_1 in Eq. (3) to obtain Eq. (3'').

$$u_1 = \mu_1 \cos\theta_1, \quad u_2 = \mu_2 \cos(\theta_1 + \varphi_1 - \varphi_2) \tag{3''}$$

By substituting Eqs. (3'') and (9) for the lower equation of Eq. (2), we obtain Eq. (2'').

$$\begin{aligned} &-p^2 m_2 \mu_2 \{\cos\theta_1 \cos(\varphi_1 - \varphi_2) - \sin\theta_1 \sin(\varphi_1 - \varphi_2)\} \\ &-(m_1 + m_2) p^2 \mu_1 \cos\theta_1 - (c_1 + c_{d1}) p \mu_1 \sin\theta_1 \\ &+ k_1 \mu_1 (C_1 \cos\theta_1 + S_1 \sin\theta_1) \\ &= -(m_1 + m_2) \alpha (\cos\theta_1 \cos\varphi_1 - \sin\theta_1 \sin\varphi_1) \end{aligned} \tag{2''}$$

Since Eq. (2'') is also an identity, we obtain the following relations.

$$\begin{aligned} &-p^2 m_2 \mu_2 \cos(\varphi_1 - \varphi_2) - (m_1 + m_2) p^2 \mu_1 \\ &\qquad + k_1 \mu_1 C_1 = -(m_1 + m_2) \alpha \cos\varphi_1 \end{aligned} \tag{12-1}$$

$$\begin{aligned} &p^2 m_2 \mu_2 \sin(\varphi_1 - \varphi_2) - (c_1 + c_{d1}) p \mu_1 \\ &\qquad + k_1 \mu_1 S_1 = (m_1 + m_2) \alpha \sin\varphi_1 \end{aligned} \tag{12-2}$$

By multiplying $-i$ to Eq. (12-2) and adding it to Eq. (12-1), we obtain Eq. (13).

$$\begin{aligned} &\left[-p^2 + \frac{c_1 + c_{d1}}{m_1 + m_2} pi + \frac{k_1}{m_1 + m_2}(C_1 - iS_1)\right] \mu_1 e^{-i\varphi_1} \\ &\qquad - \frac{m_2}{m_1 + m_2} p^2 \mu_2 e^{-i\varphi_2} = -\alpha \end{aligned} \tag{13}$$

Equations (11) and (13) can be written in matrix form in the same manner as Kikuchi et al [7]:

$$\begin{Bmatrix} \mu_1 e^{-i\varphi_1} \\ \mu_2 e^{-i\varphi_2} \end{Bmatrix} = \begin{bmatrix} A_{11} & A_{12} \\ A_{21} & A_{22} \end{bmatrix}^{-1} \begin{Bmatrix} -\alpha \\ -\alpha \end{Bmatrix} \tag{14}$$

where

$$\begin{aligned} A_{11} &= -p^2 \\ A_{12} &= -p^2 + \frac{c_2 + c_{d2}}{m_2} pi + \frac{k_2}{m_2}(C_2 - iS_2) \\ A_{21} &= -p^2 + \frac{c_1 + c_{d1}}{m_1 + m_2} pi + \frac{k_1}{m_1 + m_2}(C_1 - iS_1) \\ A_{22} &= -\frac{m_2}{m_1 + m_2} p^2 \end{aligned}$$

The story drift μ_i is expressed by Eq. (15).

$$\begin{Bmatrix} \mu_1 \\ \mu_2 \end{Bmatrix} = \frac{\alpha}{|A_{11}A_{22} - A_{12}A_{21}|} \begin{Bmatrix} |A_{22} - A_{12}| \\ |A_{11} - A_{21}| \end{Bmatrix} \tag{15}$$

Equation 15 cannot be solved explicitly since A_{12} and A_{21} are also the function of μ_i; therefore, the sequential quadratic programming (SQP) was used to solve the optimization problem formulated by Eq. (16).

$$\begin{aligned} &\text{Minimize} \quad f = \left|\mu_1 - \frac{|A_{22} - A_{12}|}{|A_{11}A_{22} - A_{12}A_{21}|}\alpha\right| \\ &\qquad + \left|\mu_2 - \frac{|A_{11} - A_{21}|}{|A_{11}A_{22} - A_{12}A_{21}|}\alpha\right| \\ &\text{subject to} \quad 0 \le \mu_i \le 12, \quad i = 1, 2 \end{aligned} \tag{16}$$

4 RESONANCE CURVE

4.1 PARAMETER OF ANALYSIS MODEL

The detail of the analysis models used here is listed on Table 2. The parameters of c_{d1} and c_{d2} are the viscous damping coefficients added by oil dampers in the first and the second story, respectively. In all the models, m_1 and m_2 are unity, and the values of c_1 and c_2 are decided to let the model have the inherent structural damping of 1% to the initial stiffness of the ENCL springs.

The M1 is the basic model in this study. The mode shape of the first mode in the elastic region of the M1 is an inverted triangle, which is expected to have an almost uniform deformation along the height of the model under ground excitation. The k_1 and k_2 of the M1_R_1.25, 1.5 and 2 are 1.25, 1.5 and 2 times larger than those of the M1, respectively. The M1_V_3%, 5% and 10% has dashpots representing oil dampers in all the stories, and the viscous damping coefficients of the dashpots are decided to have the damping ratio of 3%, 5% and 10% to the initial stiffness of the ENCL springs, respectively. The M1_F_0.1, 0.3 and 1 contain EPP springs representing friction dampers in all the stories. The number put after F_ means the value of F_i which is the ratio of the yield force of the EPP spring to the force of the ENCL model in the ith story at 1/360 rad as mentioned in Chapter 3. The yield deformation of the EPP spring is 1/360 rad in all the M1_F models.

The M2 is another basic model in this study. The stiffness k_1 and k_2 of the M2 are unity, so the story drift in the first story is supposed to become larger than that of the second story under ground excitation. This type of two-story wooden houses is very common in Japan because most houses have many rooms, i.e. many walls, in the second story. For the M2 model, strengthening only in the first

Table 2: *Parameters of analysis models*

Name	Model type	m_1	m_2	k_1	k_2	c_{d1}	c_{d2}	F_1	F_2
M1	Basic model	1	1	1	0.667	0	0	0	0
M2	Basic model	1	1	1	1	0	0	0	0
M1_R_1.25	Basic model	1	1	1.25	0.833	0	0	0	0
M1_R_1.5	Basic model	1	1	1.5	1	0	0	0	0
M1_R_2	Basic model	1	1	2	1.333	0	0	0	0
M1_V_3%	VD model	1	1	1	0.667	0.104	0.069	0	0
M1_V_5%	VD model	1	1	1	0.667	0.173	0.115	0	0
M1_V_10%	VD model	1	1	1	0.667	0.346	0.231	0	0
M1_F_0.1	FD model	1	1	1	0.667	0	0	0.1	0.067
M1_F_0.3	FD model	1	1	1	0.667	0	0	0.3	0.2
M1_F_1	FD model	1	1	1	0.667	0	0	1	0.667
M2_R_1.25	Basic model	1	1	1.25	1	0	0	0	0
M2_R_1.5	Basic model	1	1	1.5	1	0	0	0	0
M2_R_2	Basic model	1	1	2	1	0	0	0	0
M2_V_3%	VD model	1	1	1	1	0.085	0	0	0
M2_V_5%	VD model	1	1	1	1	0.141	0	0	0
M2_V_10%	VD model	1	1	1	1	0.283	0	0	0
M2_F_0.1	FD model	1	1	1	1	0	0	0.1	0
M2_F_0.3	FD model	1	1	1	1	0	0	0.3	0
M2_F_1	FD model	1	1	1	1	0	0	1	0

story by increasing stiffness, installing oil dampers, and installing friction dampers are considered in this analysis. In the models of the M2_R_1.25, 1.5 and 2, the stiffness of the first story increases by 1.25, 1.5 and 2 times compared with that of the M2. The M2_V_3%, 5% and 10% have the dashpots the viscous damping coefficients of which are calculated by $c_{d1} = 2h_d\sqrt{(m_1 + m_2)k_1}$ in the first story, where the value of h_d for each model are 0.03, 0.05 and 0.1, respectively. The M2_F_0.1, 0.3 and 1 have the EPP spring in the first story, and the yield forces are 0.1, 0.3 and 1, respectively. The yield deformation of the EPP spring is 1/360 rad in all the M2_F models.

4.2 RESULT AND DISCUSSION

4.2.1 M1 model

Figure 3 shows the resonance curve of each story of the M1 with α = 0.1, 0.2, 0.3 and 0.34. The horizontal axis of the figure is the ratio of circular frequency of excitation p to the first natural circular frequency ω_0 of the M1. As an overall feature, the value of μ_1 and μ_2 in the first mode significantly increase with increase of α, whereas those value around the second mode have little or no increase. It is seen that the value of p/ω_0 at the peak in the first mode moves to the left side, which means the model shows softening behaviour under strong excitation. This result agrees to intuitive understanding because the equivalent stiffness of the model gradually decreases with increase of the story drift as shown in the force-deformation relation in Figure 1. It is also confirmed that the jump phenomenon occurs around the fist-mode peak, which is generally seen in the non-linear system.

When the attention is focused on the result with α = 0.34, the shape of the curve around the first mode dramatically changes, and the model has more than three solutions at the same p/ω_0. It is presumed that this phenomenon is caused by the strong non-linearity in the range of large deformation; however, more investigations including the verification of stability is needed.

4.2.2 M1_R, M1_V and M1_F models

The resonance curves of the M1_R, M1_V and M1_F with α = 0.34 are displayed in Figure 4 (a), (b) and (c), respectively, in comparison with the M1. The purpose here is to clarify the effect of increasing the stiffness, installing oil dampers and installing friction dampers on the reduction in the story drift of structures.

When the stiffness increases by 1.25, 1.5 and 2 times, μ_1 and μ_2 in the first mode gradually decrease and the p/ω_0 at the peak moves to the right side, but in the second mode the maximum values of μ_1 and μ_2 are almost the same as those of the M1. Similar feature is seen in the result of the M1_F models shown in Figure 4 (c), while quite different trend can be seen in the M1_V models shown in Figure 4 (b). First of all, installing oil dampers reduce the story drift not only around the first mode but also around the second mode. Secondly, the change of the value of p/ω_0 at the peak is insignificant compared with the results of M1_R and M1_F. Thirdly, oil dampers does not work to reduce the story drift in the range of $0 \le p/\omega_0 < 0.4$ where external force act as almost static load.

In order to investigate the response characteristics of the three strengthened models, M1_R_2, M1_V_10% and M1_F_1, against large excitation, the resonance curves of these models with α = 0.68 are compared in Figure 5.

https://doi.org/10.52202/069179-0272

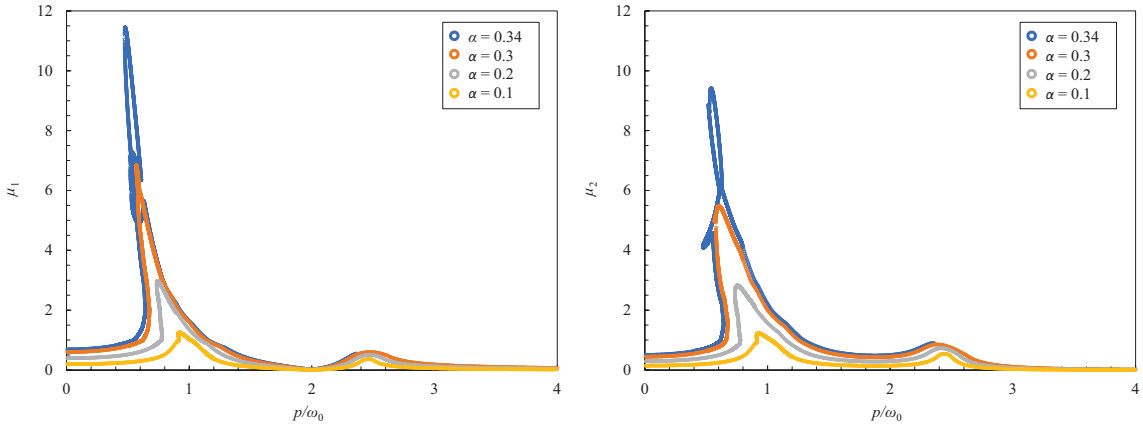

Figure 3: *Resonance curves of the M1 with α = 0.1, 0.2, 0.3 and 0.34 (left: first story, right: second story)*

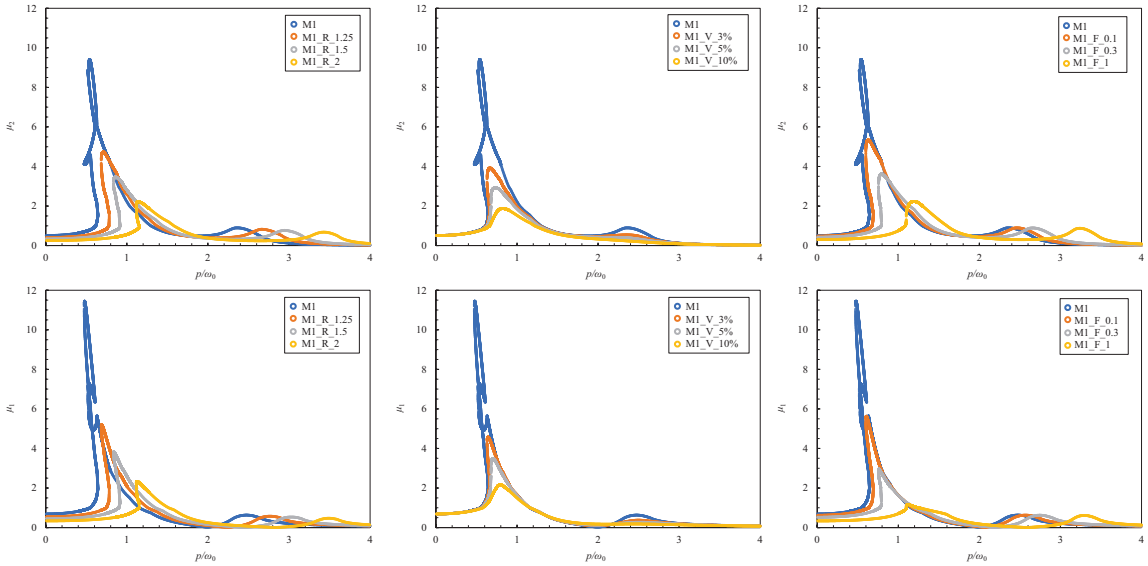

(a) M1 and M1_R_1.25, 1.5, 2 *(b) M1 and M1_V_3%, 5%, 10%* *(c) M1 and M1_F_0.1, 0.3, 1*

Figure 4: *Resonance curves of the M1, M1_R, M1_V and M1_F with α = 0.34 (top: second story, bottom: first story)*

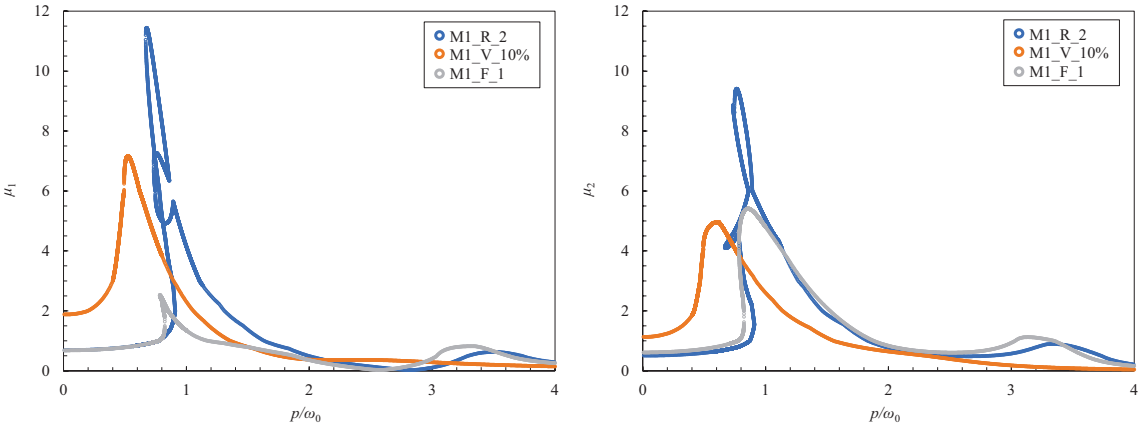

Figure 5: *Resonance curves of the M1_R_2, M1_V_10% and M1_F_1 with α = 0.68 (left: first story, right: second story)*

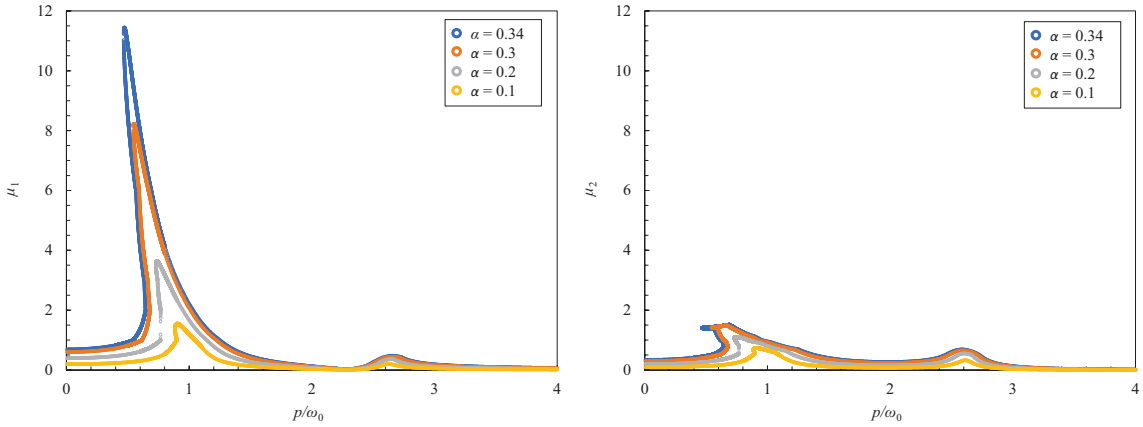

Figure 6: *Resonance curves of the M2 with α = 0.1, 0.2, 0.3 and 0.34 (left: first story, right: second story)*

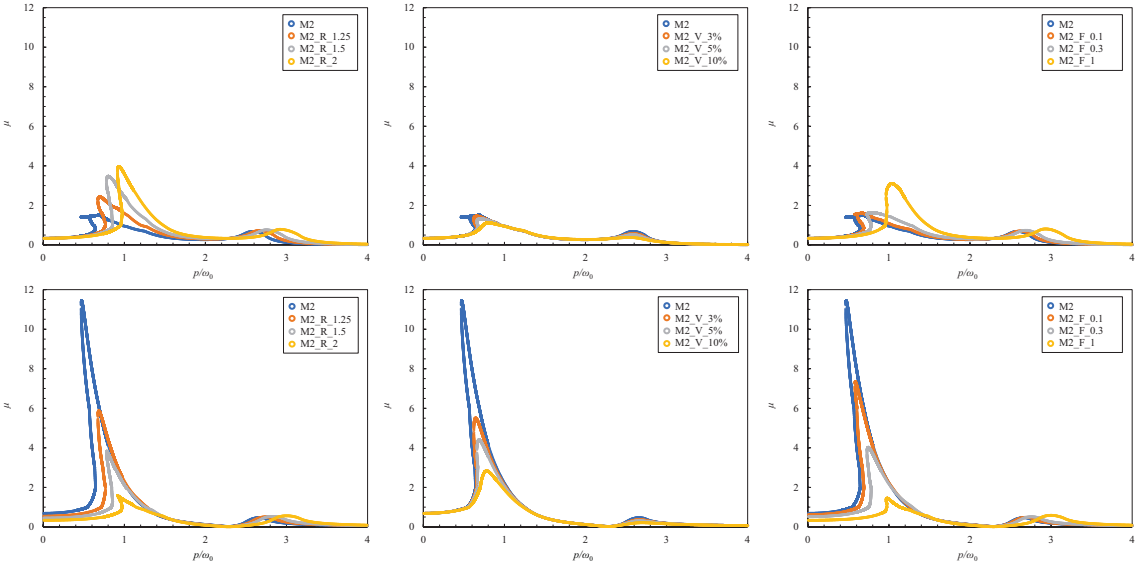

(a) M2 and M2_R_1.25, 1.5, 2 *(b) M2 and M2_V_3%, 5%, 10%* *(c) M2 and M2_F_0.1, 0.3, 1*

Figure 7: *Resonance curves of the M2, M2_R, M2_V and M2_F with α = 0.34 (top: second story, bottom: first story)*

Although these three models have similar peak values of μ_2 under the excitation with $\alpha = 0.34$, the maximum value of μ_2 of the M1_V_10% and M1_F_1 under the excitation with $\alpha = 0.68$ are smaller than that of the M1_R_2. This result indicates that the effect of strengthening by increasing stiffness, installing oil dampers and installing friction dampers highly depends on the magnitude of excitation.

4.2.3 M2 model

Figure 6 indicates the resonance curve of the M2 with α = 0.1, 0.2, 0.3 and 0.34. In this model, the story drift in the first story much larger than that of the second story especially under large excitation. This result explains the soft-story mechanism of two-story wooden houses caused by very strong earthquakes such as 1995 Kobe earthquake and 2016 Kumamoto earthquake occurred in Japan. It is also seen that the jump phenomenon occurs around the first mode and the shape is less complicated than that of the M1.

4.2.4 M2_R, M2_V and M2_F models

In Figure 7, the resonance curves of the M2_R, M2_V and M2_F are compared with that of the M2 in the same manner as Figure 4. It is seen in Figure 7 (a) that the increaseing of the stiffness of the first story decreases the story drift in the first story μ_1 but increases the story drift in the second story μ_2, indicating that when we strengthen only first story, we have to pay attention to the response of the second story even if the original structure has the relatively low stiffness and strength in the first story.

In the case of installing oil dampers or friction dampers only in the first story, the story drift in the first story gradually decreases with increase of the capacity of the dampers without significant increase of the story drift in the second story. It is presumed that the reason of this result is dut to the feature of the damper which works to

https://doi.org/10.52202/069179-0272

increase mainly damping performance not stiffness and strength.

5 CONCLUSIONS

The steady-state response of the two-degree-of-freedom-system with ENCL and EPP springs were derived and the vibration property of two-story timber structure with energy dissipation devices were discussed based on the resonance curve. The following conclusions are obtained from this study:

1. The two-degree-of-freedom-system which has ENCL springs with the parameters of timber structure shows softening behaviour and jump phenomenon around the first mode in the resonance curve.
2. The strengthening by increasing stiffness and installing friction dampers reduce the story drift only around the first mode, whereas installing oil dampers reduces the story drift both around the first and the second modes.
3. In the two-story timber structure which has relatively low stiffness in the first story, installing dampers only in first story reduces the story drift in the first story without significant increase of the story drift in the second story.

REFERENCES

[1] H. Matsunaga, Y. Miyazu, S. Soda: A Universal Modeling Method for Wooden Shear/Nonshear Walls, J. Struct. and Const. Eng., 74-639, pp. 889-896, 2009. (in Japanese)

[2] Caughey T. K.: Equivalent Linearization Techniques, Journal of the Acoustical Society of America , Vol. 35, No. 11, pp. 1706-1711, 1963

[3] Y. Miyazu: Evaluation of vibration characteristics of high-damping structure based on response curve, J. Struct. and Const. Eng., 87-798, pp. 789-798, 2022. (in Japanese)

[4] Hiroshi Tajimi: Introduction to Structural Dynamics, CORONA PUBLISHING, 1965. (in Japanese)

[5] Y. Miyazu, M. Nagano, T. Sato, M. Iguchi, T. Mikoshiba, T. Katada, K. Sugawara: Evaluation of Seismic Performance of Wooden Houses with Friction Dampers by Full-scale Shaking Table Tests, World Conference on Timber Engineering (WCTE2021), 2021.

[6] T. K. Caughey: Sinusoidal Excitation of a System With Bilinear Hysteresis, Journal of Applied Mechanics, Vol. 27, Issue 4, pp. 640-643, 1960.

[7] M. Kikuchi, K. Tamura, M. Ueda: Non-linear Steady-state Vibration of Seismically-isolated Structures with Viscously-damped Isolation System, J. Struct. and Const. Eng., 69-576, pp. 63-70, 2004. (in Japanese)

World Conference on Timber Engineering Oslo 2023

YIELD MECHANISM OF PERFORATED PLATE CONNECTIONS FOR MASS TIMBER SYSTEMS

Hossein Daneshvar [1], Thomas Tannert [2], Ying He Chui [3], Carla Dickof [4]

ABSTRACT: Mechanical connections are often the only source of ductile behaviour in mass-timber systems. This paper presents an experimental study on using perforated steel plates as a dissipating energy device, also called a seismic fuse, to enhance the structural performance of mass timber systems during extreme loading events. A target application of the perforated plate connection is in braced timber frames. Six perforation patterns were developed based on preceding experimental and numerical studies and tested under cyclic loads. These different patterns targeting one or multiple yielding mechanisms: shear, axial (tension and compression), and bending. The hysteresis performance and failure mechanism of the perforated plate systems showed that the selected patterns provided reliable yield mechanisms and that damage to timber elements can be avoided when the fuses are combined with capacity-protected dowel-type fasteners. In addition, the results of cyclic tests demonstrated sufficient ductility and ultimate displacement for specific patterns, e.g., specimens with long oval perforations, to achieve the desired energy dissipation.

KEYWORDS: Braced Timber Frame, Ductile Connections, Structural Fuse, Perforated Steel Plate, Seismic Force Resisting System

1 INTRODUCTION

The design of tall timber buildings in high seismic regions is still a challenge, mainly due to the limited energy dissipating systems and/or connections with high-performance and established practical design procedures for seismic force resisting system (SFRS). Due to the inherent brittleness of wood, other ductile materials, such as steel, are used to provide the ductility required in a seismic event. Conventionally, metal dowel-type fasteners, e.g., nails, drift pins, screws, or bolts, are a common source of ductility in timber structures. However, due to the damage they may cause to the timber components, it is beneficial to localize damage in a certain part of the structure, called seismic fuses, that are replaceable after a seismic event, with little damage to the rest of the structural system. Perforated plates are categorized as a "yielding damper" in which kinetic energy due to seismic motions is dissipated through the yielding of the steel component. In steel frames, the perforated plate fuse concept has been shown to be successful as documented in previous studies [1-8].

Specific to timber structures, Zhang et al. [9] applied glued-in, perforated plates in hold-down connections. Focusing on a specific perforation pattern confirmed their predictive ability and scalability when shear yielding was dominant. Blomgren et al. [10] and Morrell et al. [11] used a specific perforated pattern in panel-to-panel connections in cross-laminated timber shear walls. Dires and Tannert [12] extended the work on such fuses by using the concept of internal panel-to-panel connections and hold-downs. Daneshvar et al. used perforated plate fuses to panel-to-panel connections [13] and base shear connections [14] in shear walls, as well as to end brace connections in braced timber frames (BTF). They developed an analytical model for strength and prediction of ultimate deformation, verified by limited test results on specific perforation patterns. An example of such fuses at the end of a glulam brace member is shown in Figure 1.

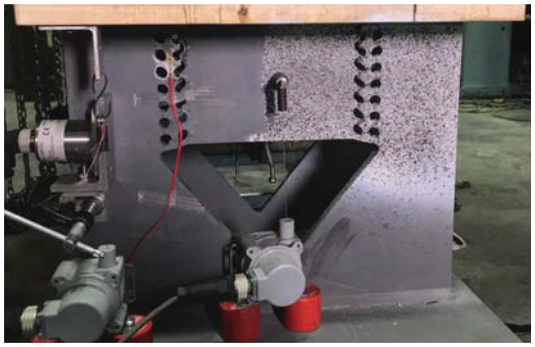

Figure 1: *Shear yielding circular perforations used in end brace connections of BTF as a seismic fuse*

[1] Hossein Daneshvar, University of Alberta, Canada, Hossein.daneshvar@ualberta.ca
[2] Thomas Tannert, University of Northern British Columbia, Canada, thomas.tannert@unbc.ca
[3] Ying-Hei Chui, University of Alberta, Canada, yhc@ualberta.ca
[4] Carla Dickof, Fast + Epp, Canada, cdickof@fastepp.com

https://doi.org/10.52202/069179-0273

Figure 1 showcases an example of shear yielding of a 12 mm thick plate with a 10 mm diameter circular perforation with a centre-to-centre spacing of 25 mm. The "link" element, defined as the minimum clear distance between two adjacent perforations, dictates the behaviour of the connection. Previous studies confirmed that the characteristic behaviour of the link elements could reasonably predict the behaviour of the connection system made of perforated plates [9, 13, 14]. However, despite adequate ductility being achieved under monotonic loading, the corresponding ductility under cyclic loading was substantially decreased, necessitating further investigation.

2 EXPERIMENTAL PROGRAM

2.1 OBJECTIVE

Based on the findings from previous research [9, 13, 14], it was postulated that the reduced ductility under cyclic loading was related to the onset of shear yield failure of the link elements between circular holes. An additional test program was deemed necessary to investigate perforation patterns to achieve flexural and axial yielding of the perforation, as opposed to the shear yielding in the earlier experimental phase. The main goal is to enhance the response of the connections in the cyclic behaviour, increasing the ductility and ultimate displacement the specimens can endure by delaying the fatigue-type failure initiations in the link elements.

2.2 FUSE PATTERNS

Six perforation patterns, as listed in Table 1, were designed and subsequently tested at the UNBC Wood Innovation Research Laboratory in Prince George, Canada. A total of twelve end brace connection specimens were tested using Method C of ASTM E2126 [15]. When the specimens were loaded by an axial force, the stress fields around the perforation zones could be in shear, axial, flexural, or a combination thereof, depending on the perforation shape and pattern. The perforation details for the oval patterns are shown in Figure 2 as a sample.

Table 1: *Fuse types tested*

Type	Fuse Pattern[1]	Specimen code
1	Oval	EBC-O
2	Circular Staggered	EBC-S
3	Circular Staggered – Buckling Restrained	EBC-BR
4	Oval Staggered (Modified)	EBC-OS[2]
5	Long Oval	EBC-LO
6	Smooth Diamond	EBC-SD

[1] Each specimen had two replicas, resulting in twelve total tests labelled, e.g., EBC-O-1 and EBC-O-2.
[2] EBC-OS-1 and EBC-OS-2 had a minor difference, c.f. section 3.4.

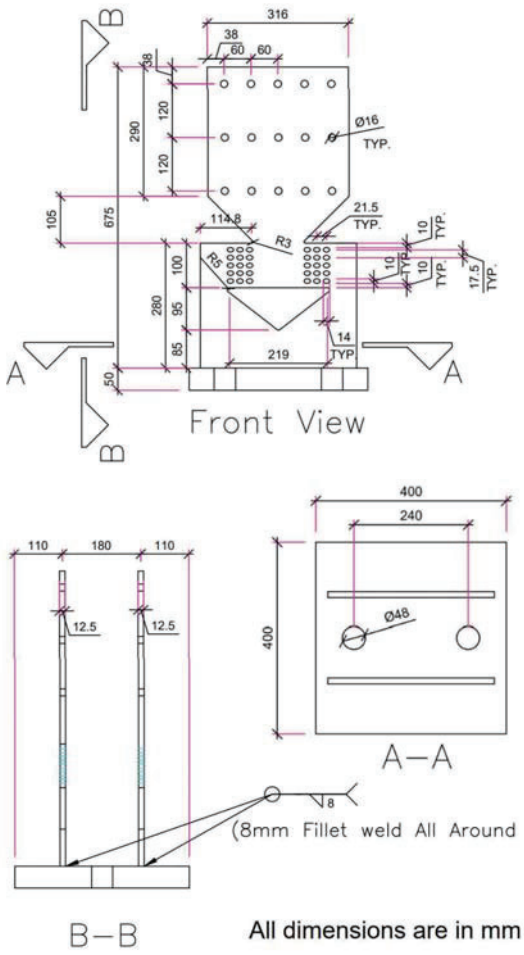

Figure 2: *Sample fuse end for EBC-O*

2.3 MATERIALS, METHOD, AND INSTRUMENTATION

The perforated plate fuses were applied to end brace connections in BTF. However, it can be noted that the perforation patterns can also be utilized in other timber SFRS, such as CLT shear walls. The timber member was 1.1 m long, 365 mm x 380 mm spruce-pine glulam grade 12c-E according to CSA O86 [16].

As shown in Figure 3 (a), the specimens consisted of fuses and capacity-protected dowel-type connections at one end (bottom) and capacity-protected connection at the other end (top). Fifteen and twenty tight-fit steel dowels of diameter 16 mm were used in the capacity-protected and fuse end connections, respectively. The specimens were instrumented using six Linear Variable Differential Transformers (LVDT), as shown in Figure 3 (b), labelled LVDT1 to LVDT6. The average displacement of the perforation zones was recorded by LVDT1 and LVDT2 . LVDT3 to LVDT6 were used to monitor the deformation in the capacity-protected steel dowels.

https://doi.org/10.52202/069179-0273

(a)

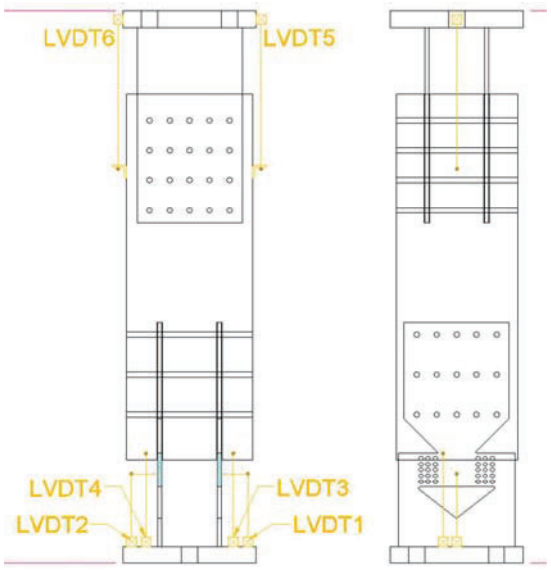

(b)

Figure 3: *Sample specimen: (a) photo, (b) schematic, instrumentation included*

3 RESULTS

The deformed shape and its corresponding load-deformation hysteresis curves for selected specimens are shown in Figures 4 and 5, respectively. Detailed analysis of the test results is currently in progress at the time of writing this paper. Some preliminary findings and test observations are presented below.

3.1 EBC-O

The signs of yielding in all the link elements, both horizontal and vertical, were obvious before failure initiation. It is not easy to distinguish if the yielding of links is flexural or shear; however, considering the link elements' aspect ratio, it seems reasonable to assume shear-flexural yielding. The failure is initiated with a sudden rupture of inner link elements and propagates vertically to other elements in the row. Almost the same failure mode was observed in both replicates; the failure mode of EBC-O-2 is shown in Figure 5 (a). The other rows, while uniformly yielded, did not experience any rupture. Both specimens achieved similar ultimate displacements but different peak loads. The hysteresis curve of EBC-O-2 is shown in Figure 6 (a). As can be seen, the curve is wide, with substantial energy dissipation capability.

3.2 EBC-S

Due to a mistake in load application, EBC-S-1 was subjected to a monotonic load and buckled. EBC-S-2 was loaded cyclically, as anticipated; but similarly failed due to the global buckling of the knife plates, as shown in Figure 5 (b). The weak line was found where the perforation ends, and the triangular cut-out is maximized. While global buckling of the plates could be used as a source of energy dissipation, the difference in tensile and compressive responses, as noted in Figure 6 (b), might make it difficult to predict the onset of yielding. The pinching behaviour due to the buckling of the plate in compression is evident. Pattern EBC-S was initially aimed at achieving axial yielding in the perforation zones. The observed buckling behaviour necessitated modifying the perforation patterns to achieve the target failure mode. This led to the buckling restrained specimens of EBC-BR, as discussed below, in 3.3.

3.3 EBC-BR

EBC-BR contains a larger perforation diameter compared to EBC-S. In addition, four stiff plates were welded to the outer sides of the knife plates. The failure mode of EBC-BR-2 is shown in Figure 5 (c). As can be seen, these two major changes caused the shift in failure mode from global plate buckling to axial yielding of link elements, as intended. The link on the inner rows is mainly ruptured due to excessive yielding, while there were no ruptures observed in other rows, although significant yielding was observed. Figure 6 (c) depicts that this fuse pattern possesses ample wide hysteresis curves, with improved strength and ultimate displacement, compared with EBC-S.

3.4 EBC-OS

EBC-OS-1, similar to EBC-S-1 and EBC-S-2, globally buckled at the weak line of the minimum cross section. Increasing the size of perforations in EBC-OS-2 shifted the failure mode from global buckling to rupture in the perforation zones, as seen in Figure 5 (d). The intended axial yielding mechanism is achieved in the EBC-OS-2. Also, the pinching observed due to buckling in the hysteresis loops of the EBC-OS-1 faded away in the EBC-OS-2 responses, as shown in Figure 6 (d). The larger perforations also allow an increase in ultimate displacement achieved by the specimen.

https://doi.org/10.52202/069179-0273

(a)

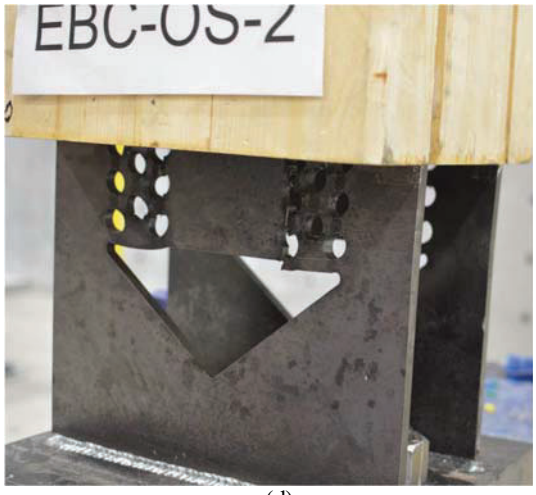

(d)

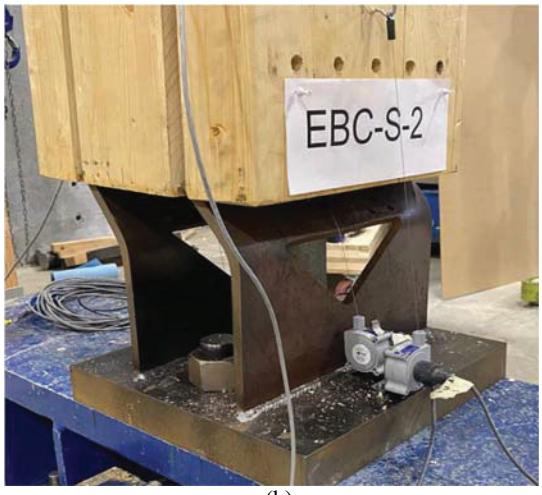

(b)

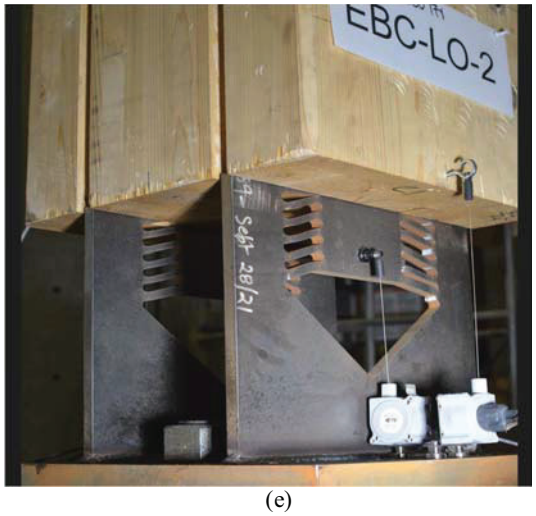

(e)

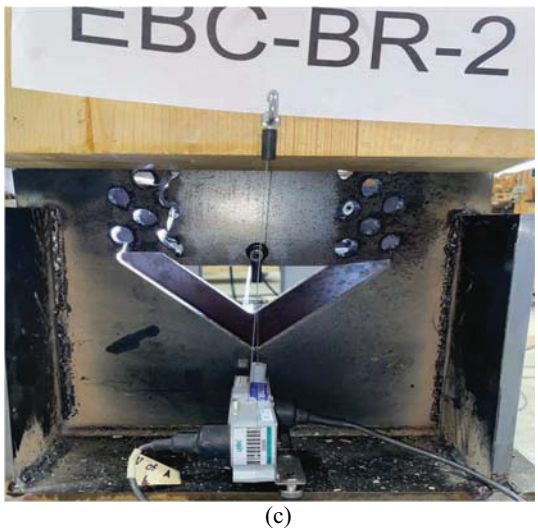

(c)

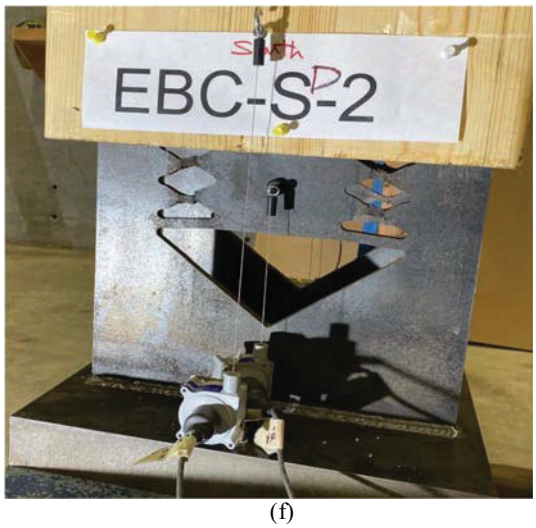

(f)

Figure 4: *Failure modes and deformed shapes*

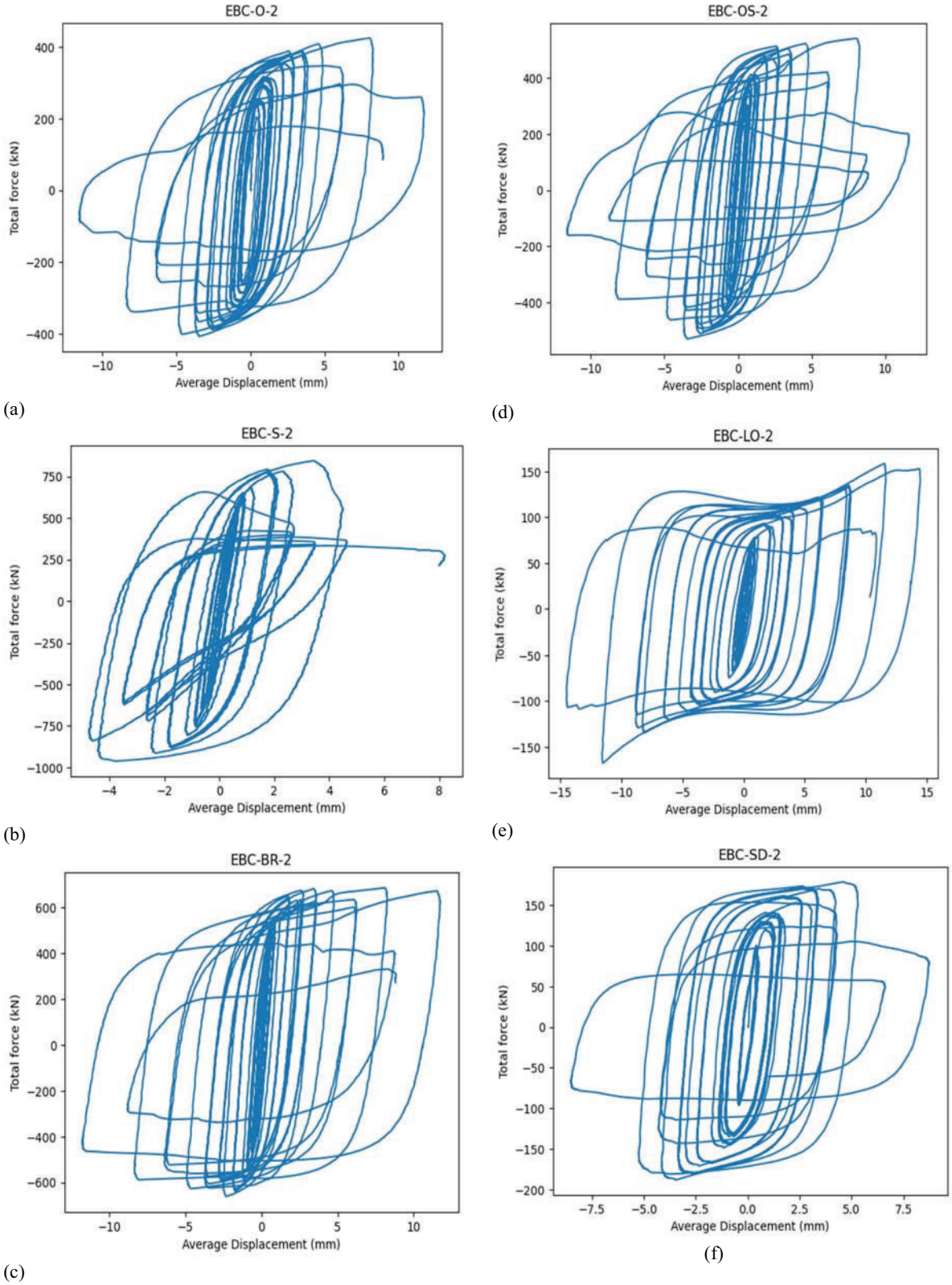

Figure 5: *Hysteresis curves*

https://doi.org/10.52202/069179-0273

3.5 EBC-LO

The target failure mode for this pattern was flexural yielding, achieved by forming two plastic hinges at the ends of link elements. The two specimens behaved almost the same. Figure 5 (e) shows the failure mode of EBC-LO-2); the outer plastic hinges experienced rupture first in the majority of perforation zones, and then the failure propagated to the inner plastic hinges of the link elements. The hysteresis loops of the two specimens were almost the same; see Figure 6 (e) corresponding to EBC-LO-2, for instance. The results show reasonable ductility for the fuses, with large open hysteretic loops reflecting the ability of the fuse to dissipate energy. Significant ultimate displacements were observed with this pattern compared with other patterns, suggesting that the flexural mechanism, achieved with the long oval-shaped perforations, could be the desired pattern to improve the fuse behaviour under cyclic loading.

3.6 EBC-SD

Like EBC-LO specimens, the intended yielding mechanism for EBC-SD specimens was also flexural yielding. However, instead of two plastic hinges at the ends of the link elements, a non-prismatic cross section was used to force the formation of the plastic hinges in the middle of the link elements. The intended failure mode was achieved in both specimens; Figure 5 (f) shows the EBC-LO-1 failure mode. Although the hysteresis loops are wider compared to the EBC-LO pattern, limited ultimate displacement caused the dissipative energy capability of the fuse to be insignificant, see Figure 6 (f). However, the hysteresis behaviour of the fuse, in terms of the area enclosed per cycle, looks promising and may be enhanced with minor revisions in the future.

3.7 FUSE REPLACEABILITY

As illustrated in Figure 7, all damage was concentrated in the perforation zones . The capacity-protected steel dowel connections were undamaged and could be disassembled. The fuse end connection can be easily removed after the cyclic tests, representing the resiliency of the fuse with no damage to the timber component. To reliably design capacity-protected dowel-type connections, research to quantify the over-strength factor is ongoing.

4 CONCLUSIONS

Under cyclic loading, twelve full-scale end brace connection specimens with six different steel plate perforation patterns were tested. These perforated plates, developed based on preceding experimental and numerical studies, were intended to be seismic fuses. The triggered yielding mechanisms were shear, axial, flexural, or a combination. Long oval perforations provided the best performance regarding ductility, energy dissipation, and ultimate displacement. The evaluated perforated plate patterns provided resilient solutions that could be replaced after yielding failure.

Figure 6: *Resiliency in terms of replaceability*

ACKNOWLEDGEMENT

The authors would like to acknowledge the financial support of the Natural Sciences and Engineering Research Council of Canada (NSERC) through the Industrial Research Chair program as well as the Natural Resources Canada (NRCan) through the Green Construction through Wood (GCWood) program—special thanks to Western Archrib for supplying the glulam members. The support by the UNBC technicians Michael Billups, James Andal, and Ryan Stern is greatly appreciated.

REFERENCES

[1] Eatherton, M., Hajjar, J., Deierlein, G., Krawinkler, H., Billington, S. and Ma, X. Controlled Rocking of Steel-framed Buildings with Replaceable Energy-dissipating Fuses. *Proceedings of the 14th World Conference on Earthquake Engineering*, Beijing, China, 2008.

[2] Ma, X. Seismic Design and Behavior of Self-centering Braced Frame with Controlled Rocking and Energy Dissipating Fuses. Ph.D. thesis, Stanford University, Stanford, California, United States, 2011.

[3] Kobori, T. Miura, Y. Fukuzawa, E., Yamada, T., Arita, T., Takenake, Y. and Fukumoto, T. Development and Application of Hysteresis Steel Dampers. *Proceedings of the 10th World Conference on Earthquake Engineering*, Rotterdam, Netherlands, 2341-2346, 1992.

[4] Chan, R.W.K. and F. Albermani. Experimental Study of Steel Slit Damper for Passive Energy Dissipation. Engineering Structures, 30(4): 1058-1066, 2008.

[5] Teruna, D., Majid, T. and Budiono, B. Experimental Study of Hysteretic Steel Damper for Energy Dissipation Capacity. Article ID 631726, *Advances in Civil Engineering,* 2015.

[6] Lee, C.L., Ju, Y.K., Min, J.K., Lho, S.H. and Kim, S.D. Non-uniform Steel Strip Dampers Subjected to Cyclic Loadings. Engineering Structures, 99: 192-204, 2015.

[7] Ahmadie Amiri, H. Najafabadi, E. and Estekanchi, H. Experimental and Analytical Study of Block Slit Damper. Journal of Constructional Steel Research, 141: 167-178, 2018.

[8] Li, T. Experimental Testing and Numerical Modelling of Honeycomb Structural Fuse. MASc thesis, Department of Civil Engineering, University of British Columbia, Vancouver, British Columbia, Canada, 2018.

[9] Zhang, X., Popovski, M., and Tannert, T. High-capacity hold-down for mass-timber buildings. Construction and Building Materials, 164: pp. 688-703, 2018.

[10] Blomgren, H.-E. Pei, S. Powers, J. Dolan, J. Wilson, A. and Jin, Z. Cross-laminated Timber Rocking Wall with Replaceable Fuses: Validation through Full-scale Shake Table Testing. *Proceedings of WCTE 2018: World Conference on Timber Engineering*. Seoul, Republic of Korea, 2018.

[11] Morrell, I., Phillips, A. Dolan, J. and Blomgren, H.-E. Development of an Inter-panel Connector for Cross-laminated Timber Rocking Walls. *Proceedings of WCTE 2018: World Conference on Timber Engineering*, Seoul, South Korea, 2018.

[12] Dires, S. and Tannert, T. Performance of coupled CLT shear walls with internal perforated steel plates as vertical joints and hold-downs. Journal of Construction and Building Materials, 346(3): 128389, 2022.

[13] Daneshvar, H., Niederwestberg, J., Dickof, C., Jackson, R. and Chui, Y.H. Perforated Steel Structural Fuses in Mass Timber Lateral Load Resisting Systems. Engineering Structures, 257: 114097, 2022.

[14] Daneshvar, H., Niederwestberg, J., Letarte, JP., and Chui, Y.H. Yield Mechanism of Base Shear Connections for Cross-Laminated Timber Shear Walls. Journal of Construction and Building Materials, 335: 127498, 2022.

[15] ASTM E2126, Standard Test Methods for Cyclic (Reversed) Load Test for Shear Resistance of Vertical Elements of the Lateral Force Resisting Systems for Buildings. ASTM International, West Conshohocken, PA, 2018.

[16] Canadian Standards Association (CSA): Engineering Design in Wood. CSA Standard 086-19. Toronto, ON, Canada, 2019.

https://doi.org/10.52202/069179-0273

World Conference on Timber Engineering Oslo 2023

EXPERIMENTAL CHARACTERISATION OF GLULAM SHEAR WALLS UNDER LATERAL CYCLIC LOADING

Giuseppe D'Arenzo[1], Werner Seim[2]

ABSTRACT: This paper presents the results of an experimental campaign aimed at investigating the lateral response of glulam (glued laminated) shear walls subjected to horizontal cyclic loads. The objective of the study is to explore the potential of this engineered wood product to be used as an alternative lateral load-resisting element in platform timber constructions. The lateral response of massive wooden shear walls is governed by the wall-base connections; therefore, in addition to shear wall tests, cyclic tests were carried out on hold downs and angle brackets attached to glulam elements. Results of the experimental tests of both connections and shear walls showed failure mechanisms characterised by relatively large plastic deformation of the nails and with significant ductility levels. This results in the potential of glulam shear walls being adopted as the lateral load-resisting element of platform timber constructions in seismic prone areas.

KEYWORDS: Glued Laminated Timber, Shear Walls, Experimental Tests, Cyclic Behaviour

1 INTRODUCTION

Mass Timber constructions are gaining in popularity among designer communities as they respond well to today's need for sustainability, permit design with a large architectural freedom and have overcome many limits of traditional wooden structures. The expression "mass timber" refers to the massive, engineered wood products (EWP) which are used for the construction of these structures; glued laminated (glulam) and cross-laminated timber (CLT) are the most widely spread product types. Glulam is used mostly for structural one-dimensional elements, such as beams and columns, whereas CLT is used mostly for planar elements, such as walls and floors. Today's large availability of different EWPs that respond well to different needs of the construction industry results in the possibility of realising mass timber buildings with different structural systems. Among the latter ones, structural systems with shear walls have been largely adopted in the construction practice, CLT panels being the product adopted most.

CLT buildings with shear walls are realized by connecting the CLT panels by means of mechanical anchors and screws. The mechanical anchors are used at the base of the walls, while the screws are used for panel-to-panel connections. The mechanical anchors typically adopted in CLT shear walls are hold downs and angle brackets; the first ones are used at the wall ends to prevent the wall rocking, while the second ones are spread along the wall base and are used to prevent the shear wall sliding.

The lateral behaviour of structural systems made of CLT shear walls has been largely investigated in the last decade, with particular focus on their seismic performance. Shaking table tests on multi-storey CLT buildings [1], racking tests on CLT shear walls [2,3], and cyclic tests on sub-assemblies and connections [4] were conducted, showing the high dissipation capacity and good seismic performance of CLT structures and sub-components. These experimental programmes were instrumental in understanding the seismic behaviour of these structural typologies and in defining the calculation models and specifications needed for the design.

Structural systems with shear walls can also be realised by using different EWPs, such as glulam or laminated veneer lumber (LVL). However, less studies have been conducted on shear wall systems made of glulam and LVL, having the majority of these experimental investigations been conducted on timber walls with dampers and low-damage connection systems. For instance, Wrzesniak et al. [5] investigated the rocking behaviour of glulam shear walls anchored to the foundation with dampers, while Iqbal et al. [6] investigated the seismic resistance of post-tensioned LVL walls coupled with U-Flexural plate dissipators.

If on one hand the use of low-damage systems and dissipators improves the seismic performance of timber walls, on the other hand traditional connection systems are more adopted in practice due to their simplicity of design. However, to authors' knowledge, no studies investigating the seismic performance of glulam and LVL shear walls anchored with traditional hold downs and angle brackets are available in the literature, with the consequence that the relevant information needed for the design are not available to practitioners. This represents a relevant gap of scientific knowledge, which may negatively impact the spread of innovative timber structural systems.

With the aim of filling this gap, this paper presents an experimental study investigating the lateral response of glulam shear walls subjected to lateral loading, and the cyclic response of traditional hold downs and angle brackets attached to glulam elements. In particular, the cyclic behaviour of such structural components is investigated, to explore the potential of glulam shear wall elements to be used in platform timber buildings in seismic prone areas. The evaluation of quantities relevant

[1] Timber Structures and Building Rehabilitation, University of Kassel, Germany, giuseppe.darenzo@uni-kassel.de
[2] Timber Structures and Building Rehabilitation, University of Kassel, Germany, wseim@uni-kassel.de

https://doi.org/10.52202/069179-0274

for the seismic design, such as the strength, stiffness, ductility of connections, energy dissipation, and impairment of strength, is carried out, providing valuable insights into the seismic design of structures with glulam shear walls.

2 EXPERIMENTAL TESTS

2.1 MATERIALS

Experimental tests were conducted using glulam specimens with strength class GL24h.
Hold downs type HTT22E and angle brackets type AE116 from Simpson Strong Tie were used for the experimental tests. The geometrical and mechanical properties of both hold downs and angle brackets are described in the ETA-07/0285 [7]. The mechanical anchors are shown in Figure 1 (a) and (b).
Annular ringed nails CNA 4×60 mm from Simpson Strong Tie were used for the connection between the mechanical anchors and the timber elements, see Figure 1 (c). The geometrical and mechanical properties of the nails are described in the ETA-04/0013 [8]. The mechanical anchors were connected at the base with bolts M12 and M16, strength class 8.8.

2.2 METHOD

The lateral behaviour of massive wooden shear walls is governed by the wall base connections. Hold down connections are normally used at the extremities of the wall to prevent rocking, while angle bracket connections are used in the centre of the wall to prevent sliding. Accordingly, the methodology used in this study involved experimental investigations of hold downs and angle brackets subjected to tensile and shear loads, respectively, along with full-scale tests at wall level.

2.3 LOAD PROTOCOLS

The connections were tested in monotonic and cyclic regime according to EN26891 [9] and EN12512 [10], respectively.
The monotonic tests were performed in force control, in order to perform the unloading and reloading path prescribed in the EN26891. The load protocol of the monotonic tests is shown in Figure 3 (a). Two different load protocols were used for the cyclic tests of hold downs and angle brackets due to the different test setups. Hold downs, which were tested for tensile loads, were loaded with an only positive displacement path with imposed displacement ranging from zero up to a specific positive value, see Figure 3 (b). Angle brackets, which were tested under shear loads, were loaded with fully reversed displacement path with positive and negative displacements, see Figure 3 (c). Both hold down and angle bracket cyclic tests were performed in displacement control with a rate varying from 0.1 to 0.5 mm/sec.

2.4 EVALUATION OF MECHANICAL PARAMETERS

Mechanical parameters were evaluated according to EN12512 [10]. The stiffness of the connections, K_{el}, was evaluated according to the method B of the EN12512 as the slope of the line that intersects the load displacement curve in the points of ordinate equal to 10% and 40% of the maximum force. The intersection between the stiffness line and the line with slope equal to one-sixth of the stiffness line and tangent to the load displacement curve defines the yielding point, from which the yielding displacement, V_y, and the yielding load, F_y, are evaluated. The point with the highest ordinate of the load displacement curve defines the maximum force, F_{max}, and the relative displacement, V_{max}. The ultimate force, F_{ult}, is evaluated as the ordinate of the load displacement curve when a 20% reduction of the maximum force is reached. The abscissa of the point of ultimate force defines the ultimate displacement, V_{ult}. Finally, the ductility, D, is evaluated as the ratio between the ultimate displacement and the yielding displacement. Figure 2 shows an example of experimental curve with the relative yielding, maximum and ultimate point.
According to EN12512, the cyclic behaviour of the timber connections is expressed using three parameters: the dissipated energy, E_d, the equivalent viscous damping ν_{eq}, and the impairment of strength, ΔF. The dissipated energy is computed as the area enclosed by each hysteretic loop and is useful for evaluating the total energy dissipated

Figure 1: *(a) Hold downs, (b) angle brackets and (c) annular ringed nail used for the experimental tests.*

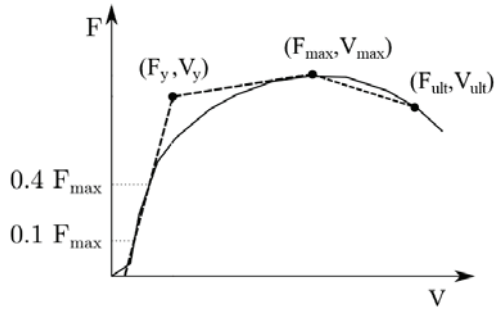

Figure 2: *Representation of the yielding, maximum and ultimate point according to EN12512.*

https://doi.org/10.52202/069179-0274

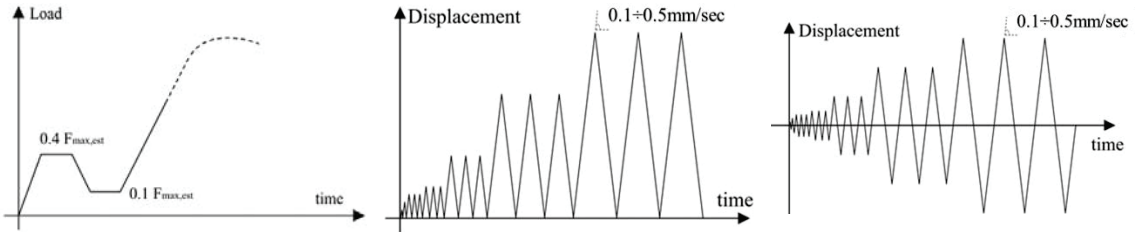

(a) (b) (c)

Figure 3: *Load protocol for (a) monotonic tests, (b) cyclic tests of hold downs, (c) cyclic tests of angle brackets and shear walls.*

during the test when presented cumulatively. The equivalent viscous damping is evaluated at each hysteretic loop and represents the ratio of dissipated energy, E_d, to available potential energy, E_p, multiplied by 2π. The available potential energy E_p is calculated using the maximum force, F_i, in each cycle and the corresponding displacement, V_i, and is expressed as $E_{p,i} = 1/2 \cdot F_i \cdot V_i$. The impairment of strength, ΔF, which quantifies the strength degradation of timber connections, is determined by the difference between the strengths of the first and third envelope curves at the same displacement level. In this study, the normalized form of ΔF, $\Delta F_{1\text{-}3}$, is presented by dividing the impairment of strength by the strength of the first envelope.

2.5 TEST SETUP

2.5.1 Connection Tests

The experimental tests on the mechanical anchors were carried out with the universal machine RBO-2000 with a maximal capacity of 800 kN and a displacement range of ±150 mm. The lamella orientation of the glulam elements was chosen in order to simulate the real condition in which the connections work, when they are anchored to the shear wall. Figure 4 (a) and (b) shows the test setups of the tension and shear tests, for hold downs and angle brackets, respectively. Figure 5 (a) and (b) shows the photos of the hold down and angle bracket test setups. The displacements of the specimens were measured by means of Linear Variable Displacement Transducers (LVDTs) placed on the timber element.

Hold downs were fastened to the glulam elements with 15 annular ringed nails and anchored to the bottom steel plate with one bolt M16. Angle brackets were fastened to the glulam elements with 12 annular ringed nails and anchored to the bottom steel plate with two bolts M12.

One monotonic (n_m) and six cyclic (n_c) tests were performed for each configuration, for a total amount of 14 experimental tests on connections.

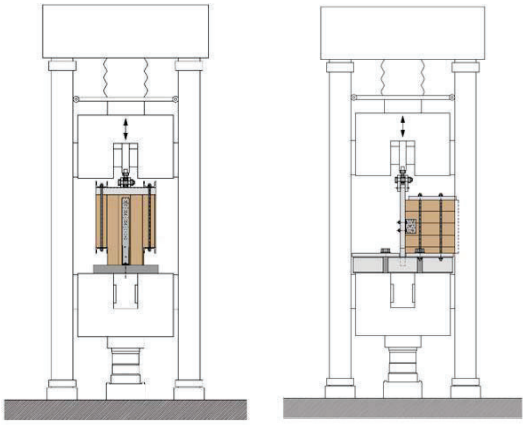

(a) (b)

Figure 4: *Experimental test setup of (a) hold down and (b) angle bracket tests.*

(a) (b)

Figure 5: *Photos of (a) tension test setup of hold downs and (b) shear test setup of angle brackets.*

https://doi.org/10.52202/069179-0274

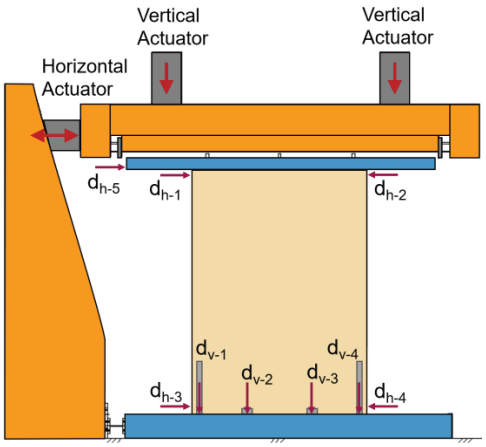

Figure 6: *Shear wall test setup.*

Figure 7: *Photo of the shear wall test setup.*

2.5.2 Shear Wall Tests

Figure 6 and Figure 7 show the test setup used for the shear wall tests. The shear walls had a height of 2500 mm, a length of 1500 mm, and a thickness of 140 mm. All experimental tests were performed with a constant vertical load applied on the top of the shear wall of 30 kN/m. The shear walls were anchored with two hold downs in the shear wall corners, to prevent the shear wall rocking, and with two angle brackets, to prevent the shear wall sliding. Horizontal and vertical loads were applied to the wall specimens through one horizontal and two vertical hydraulic actuators with 400 kN capacity. The vertical actuators were connected to a horizontal steel beam, which was screwed to the shear wall head with self-tapping screws 8×160 mm spaced at 100 mm. The timber walls were anchored through the wall-base connections to a steel beam, which was anchored to a strong floor.

Nine LVDTs were used to measure the wall displacements, see Figure 6. The shear wall lateral displacements were measured with two LVDTs (d_{h-1}, d_{h-2}) placed in the two upper corners of the shear wall. Two horizontal LVDTs (d_{h-3}, d_{h-4}) were used to measure the sliding displacements while four vertical LVDTs (d_{v-1}, d_{v-2}, d_{v-3}, d_{v-4}) were used to measure the rocking of the shear wall as well as the vertical displacements of the two hold downs and the two angle brackets. A horizontal LVDT (d_{h-5}) was used to measure the horizontal displacements of the steel beam connected to the upper side of the shear wall.

The experimental program on shear walls included two cyclic tests in total.

3 RESULTS

3.1 MECHANICAL ANCHORS

The mechanical behaviour of hold down and angle bracket connections was characterised by high ductility and capability to withstand relatively large cyclic displacements. The behaviour of the connection systems was, to a large extent, comparable to that of traditional hold downs and angle brackets attached to CLT elements (see, for instance [4]).

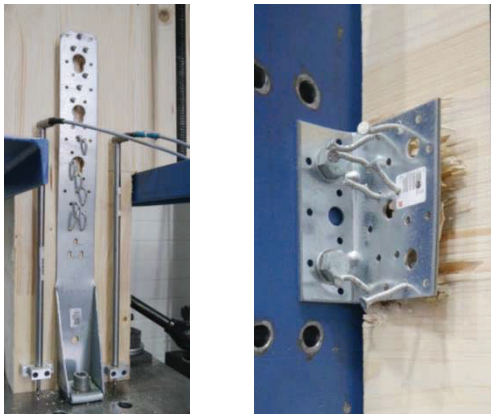

(a) (b)

Figure 8: *Photo of connection specimens at the end of the tests: (a) hold downs, (b) angle brackets.*

Table 1: *Mechanical parameters evaluated from the load displacement curves of monotonic and cyclic connection tests.*

Test type	n_m	n_c	K_{el}	F_y	V_y	F_{max}	V_{max}	F_{ult}	V_{ult}	D
	[-]	[-]	[kN/mm]	[kN]	[mm]	[kN]	[mm]	[kN]	[mm]	[-]
Hold downs	1	6	8.05	43.20	4.96	55.69	15.90	44.55	28.15	5.71
Angle brackets	1	6	3.69	27.90	7.53	32.39	14.70	25.91	21.01	2.99

https://doi.org/10.52202/069179-0274

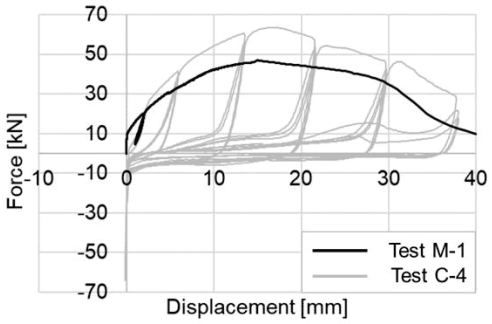

Figure 9: *Typical load displacement curve of a hold down connection.*

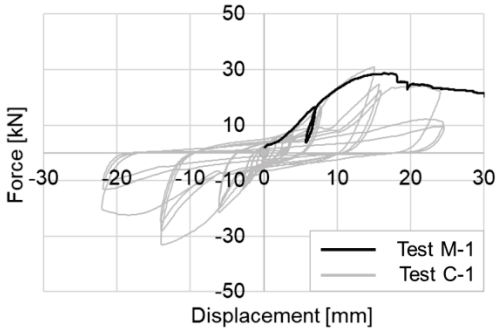

Figure 10*: Typical load displacement curve of an angle bracket connection.*

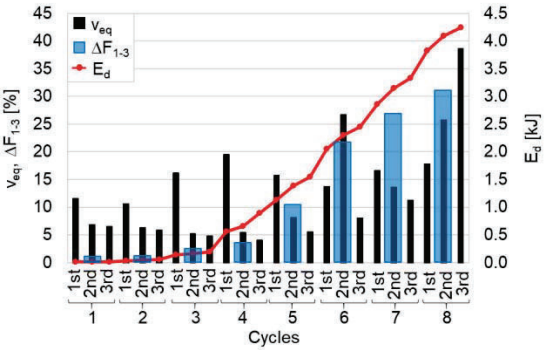

Figure 11: *Average cyclic properties of hold down tests.*

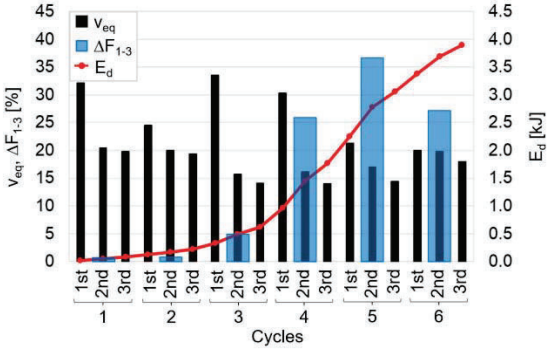

Figure 12: *Average cyclic properties of angle bracket tests.*

In general, hold down connections showed a failure in the nails of the steel-to-timber connection with one or two plastic hinges, see Figure 8 (a). The hold down steel brackets showed small deformation, while the overall displacement of the tests was mainly provided from the nails of the steel-to-timber connection.

Angle brackets connections showed a failure in the nails of the steel-to-timber connection with one or two plastic hinges combined with a failure due to the opening of the wooden lamellas composing the glulam element. In all tests, the metal brackets showed small deformation, while the overall displacement of the tests was mainly provided from the nails of the steel-to-timber connection, see Figure 8 (b).

Typical load displacement curves of hold downs under tension and angle brackets under shear are shown in Figure 9 and Figure 10, respectively. Table 1 summarizes the average mechanical parameters of the connection tests evaluated according to EN12512.

The results show that the hold down connections have a higher stiffness of 8.05 kN/mm as compared to the angle brackets, which have a stiffness of 3.69 kN/mm. The maximum loads the connections can withstand before failure show variation between the two connection types, with the hold down connections having a higher maximum load capacity than the angle bracket connections. For the hold down connections, the maximum load value is 55.69 kN, while for the angle bracket connections, the maximum load value is 32.39 kN. The ductility was higher for the hold down connections with a value of 5.71, compared to the angle bracket connections with a value of 2.99. The higher performances of the hold downs compared with the angle brackets are due to the larger number of nails used in the connection with the timber panel.

Figure 11 and Figure 12 shows the cyclic properties of hold downs and angle brackets, respectively. The graphs report the number of cycles in the horizontal axes, while two vertical axes are used to plot the dissipated energy (E_d), the equivalent viscous damping (ν_{eq}), and the normalised impairment of strength ($\Delta F_{1\text{-}3}$).

Averagely, 4.24 kJ and 3.89 kJ were dissipated at the end of the hold down and angle bracket tests, respectively. The average equivalent viscous damping was 12.7 % and 20.6 % for hold down and angle bracket tests, respectively. The normalised impairment of strength showed an increasing trend up to the failure of the connections with maximum values of 31.5 % and 36.5 % for hold downs and angle brackets, respectively.

3.2 SHEAR WALLS

The mechanical behaviour of the shear walls was governed by the connections and characterised by large ductility and capability to withstand large cyclic displacements. The behaviour of the wall was, to a large extent, comparable to that of traditional CLT shear walls (see, for instance, [2]).

https://doi.org/10.52202/069179-0274

Table 2: *Mechanical parameters evaluated from the load displacement curves of cyclic shear wall tests.*

Test type	n_c	K_{el}	F_y	V_y	F_{max}	V_{max}	F_{ult}	V_{ult}	D
	[-]	[kN/mm]	[kN]	[mm]	[kN]	[mm]	[kN]	[mm]	[-]
Shear walls	2	3.44	33.70	9.90	55.29	55.60	44.23	71.10	7.55

In general, the deformation mechanism was governed by the wall-base connections, while the panel deformation was negligible. The shear walls failed with a prevalent rocking mechanism with failure in the nails of the hold downs, see Figure 13 and Figure 14. The nails of the angle brackets showed also plastic deformations, due to the bidirectional tensile-shear loads they were subjected to. At the end of the tests, the hold down steel brackets showed small deformation whereas larger deformations were reached in the angle brackets' steel.

Figure 15 shows the load displacement curves of the shear wall tests, while Table 2 summarizes the average mechanical parameters of the shear wall tests evaluated according to EN12512.

The results show that the glulam walls have an average stiffness of 3.44 kN/mm, a maximum load of 55.29 kN and an ultimate lateral displacement of 71.10 mm. The average ductility of the shear walls is 7.55, indicating that the shear walls have a significant amount of deformation capacity beyond the yield point.

Figure 16 shows the cyclic properties of wall tests. Averagely, 27.1 kJ were dissipated at the end of the shear wall tests, with an average equivalent viscous damping of 13.6 %. The normalised impairment of strength showed an increasing trend up to the failure of the connections with maximum value of 10.8 %.

Figure 13: *Photo of a shear wall specimen at the end of the test.*

(a) (b)

Figure 14: *Photo of wall-base connections at the end of a shear wall test: (a) hold downs, (b) angle brackets.*

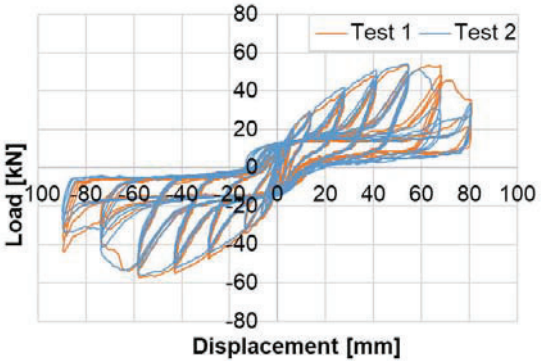

Figure 15: *Load displacement curves of the shear walls.*

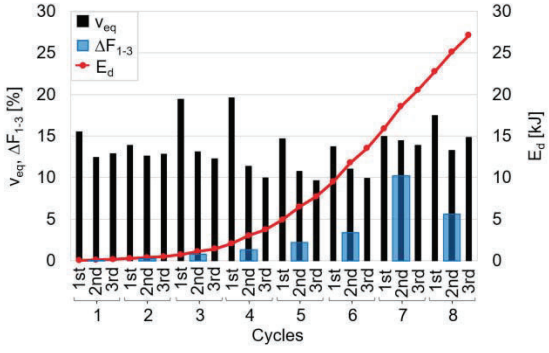

Figure 16: *Average cyclic properties of the shear walls.*

https://doi.org/10.52202/069179-0274

4 CONCLUSIONS

This paper presented an experimental study on the cyclic behaviour of glulam shear walls and typical hold down and angle bracket connection systems fastened to glulam elements with annular ringed nails.

The EN12512 procedure was used to calculate relevant design parameters for connections, including stiffness, strength, ductility, impairment of strength, and equivalent damping ratios. This data is significant when evaluating the seismic performance of timber structures since the majority of seismic forces and energy dissipation occur at the wall-base connections.

The mechanical behaviour of the connections was characterized by local deformation of the nails embedded into the timber and low deformation of the mechanical anchors. Hold down connections showed higher performance in term stiffness, strength, and ductility than angle bracket connections due to the higher number of nails used in the steel-to-timber joint. The mechanical behaviour of the shear walls was governed by the connections and characterised by large ductility and capability to withstand large cyclic displacements.

Results of this experimental study showed that typical hold down and angle bracket connection systems attached to glulam elements and glulam shear walls exhibit a ductile behaviour with mechanical performance similar to that of hold downs and angle brackets attached to CLT elements and CLT shear walls.

REFERENCES

[1] A. Ceccotti, C. Sandhaas, M. Okabe, M. Yasomura CM and NK. SOFIE project-3D shaking table test on a seven-storey full-scale cross-laminated building. Earthq Eng Struct Dyn 2013;42:2003–21. https://doi.org/10.1002/eqe.

[2] Gavric I, Fragiacomo M, Ceccotti A. Cyclic Behavior of CLT Wall Systems : Experimental Tests and Analytical Prediction Models. J Struct Eng 2015;141. https://doi.org/10.1061/(ASCE)ST.1943-541X.0001246.

[3] Hummel J, Flatscher G, Seim W, Schickhofer G. CLT Wall Elements Under Cyclic Loading – Details for Anchorage and Connection. Focus Solid Timber Solut - Eur Conf Cross Laminated Timber 2014:152–65.

[4] Gavric I, Fragiacomo M, Ceccotti A. Cyclic behaviour of typical metal connectors for cross-laminated (CLT) structures. Mater Struct 2015:1841–57. https://doi.org/10.1617/s11527-014-0278-7.

[5] Wrzesniak D, Rodgers GW, Fragiacomo M, Chase JG. Experimental testing of damage-resistant rocking glulam walls with lead extrusion dampers. Constr Build Mater 2016;102:1145–53. https://doi.org/10.1016/j.conbuildmat.2015.09.011.

[6] Iqbal A, Pampanin S, Palermo A, Buchanan AH. Performance and design of LVL walls coupled with UFP dissipaters. J Earthq Eng 2015;19:383–409. https://doi.org/10.1080/13632469.2014.987406.

[7] ETA-07/0285. Simpson Strong-Tie Int. Ltd. Simpson Strong-Tie Hold Downs & Post Bases 2020.

[8] ETA-04/0013. Simpson Strong-Tie Int. Ltd. CAN Connector nails and CSA Connector screws 2019.

[9] EN26891. Timber structures; Joints made with mechanical fasteners; General principles for the determination of strength and deformation characteristics. CEN, Brussel, Belgium. 1991.

[10] EN12512. Timber structures. Test methods. Cyclic testing of joints made with mechanical fasteners. Brussels, Belgium: CEN 2005.

World Conference on Timber Engineering Oslo 2023

CYCLIC LOAD TESTS AND NUMERICAL ANALYSIS OF CLT SHEAR WALLS WITH GIR JOINTS

Shuhei Uesugi[1], Daisuke Kadono[2], Katsuhide Murakami[3], Masahide Murakami[4]

ABSTRACT: Four CLT shear wall specimens with GIR joints were subject to cyclic loading. The tensile anchor pre-yielding type specimens exhibited great performance and non-slip response because the M24 ABR steel anchors connected to the GIR joints contributed to resisting in compression. A numerical model using OpenSees was developed to simulate the global response and confirm the energy absorption. A crack was confirmed in one of the specimens before the GIR exhibited its ultimate strength. It is presumed that edge clearance distance may affect CLT shear walls performance for large deformations. The analysis model results are in good agreement with the experimental testing. Finally, the energy absorbed by the tensile bars on the compression side have been quantified.

KEYWORDS: CLT, CLT shear wall, GIR joints, Cyclic load tests, Numerical analysis

1 INTRODUCTION

Cross-laminated timber (CLT) structures have attracted significant attention during the past decade to realise a low-carbon society and carbon sequestration. CLT shear walls are one of the most effective structural systems because of their high strength and in-plane stiffness. CLT shear walls and hybrid structures, such as combined CLT shear walls and steel moment frames have been proposed in the past [1-5]. CLT shear walls are characterised by their rocking behaviour, and the performance of the joints at the ends has a significant impact on the behaviour of the entire CLT shear wall performance [6]. However, it is difficult to realize high-strength and high ductility CLT walls because the strength and ductility of distributed connectors are limited.

In Japan, where earthquakes occur frequently, there is a need for the development of such high-strength and high ductility CLT walls. Aiming at the development of CLT shear walls which final failure properties can ensure high energy absorption properties with stable and ductile failure at the joint, if sufficient tensile performance can be secured using GIR joints that can ensure relatively high bearing capacity, a design method will be similar to reinforced concrete beam members calculation in terms of bending performance.

The authors designed CLT shear walls using GIR joints with high expected strength and confirmed the structure performance by cyclic loading tests. A numerical model is created using OpenSees to simulate the global response and the characteristics of GIR joints are discussed from the viewpoint of energy absorption.

2 SPECIMENS

Figure 1 shows the configuration of Specimen 1 and the steel base. The 0.95 m width and 1.95 m hight CLT shear wall was made of 5-layer, 7-ply cedar S60A CLT panels (@30 × 7 = 210 mm), which were glued with resorcinol adhesive along the width. The strong axis direction of the CLT panels was set in the vertical direction. The GIR joints were filled with epoxy resin adhesive (AICA Kogyo JB-3) and were used for the tensile and shear resisting joints. The anchorage lengths of the tensile and shear rebars were 750 mm and 210 mm, respectively, with D22 bar diameter and rebar grade SD345 which were manufactured by JFE Steel Corporation / Mizutori Works.

Tensile rebars were connected to M24 ABR anchors (manufactured by Dai-rock Ltd.) via mechanical couplers inside the wall base. The yielding capacities of the tensile rebars and ABR anchors were 133.5 kN and 115.0 kN, respectively, and the ABR anchors were expected to yield first. The lower flange of the steel base was tightened by nuts from the upper and lower side. A horizontal stiffener plate was arranged in the middle of flanges to increase the compressive buckling resistance of the M24 ABR anchors. Due to the nuts and the stiffeners, the M24 steel bars are expected to contribute to high energy absorption. Shear rebars were connected to shear plates (PL-12), and the joints between shear bars and shear plates were reinforced by fillet welding. There were long holes along the loading direction at the upper flange of the steel base so as not to the tensile rebars resist to the horizontal force.

Figure 2 shows the arrangement of the GIR joints of each specimen. Specimen 1 had tensile rebars at the second layer from the outside. Specimen 2 had two tensile rebars

[1] Shuhei Uesugi, Nikken Sekkei Ltd., Japan, uesugi.shuhei@nikken.jp
[2] Daisuke Kadono, Nikken Sekkei Ltd., Japan, kadono.daisuke@nikken.jp
[3] Katsuhide Murakami, Nikken Sekkei Ltd., Japan, murakamik@nikken.jp
[4] Masahide Murakami, KINDAI Univ. Faculty of Architecture, murakami@arch.kindai.ac.jp

https://doi.org/10.52202/069179-0275

at the fourth layer from the outside. Both specimens have eight shear-resistant rebars in the middle, placed in fiber direction layers and in the middle eight shear-resistant rebars were placed in fiber direction layers. Specimen 3 had no shear bars, and specimen 4 had only two shear bars. Specimens 1 and 2 were intended to check the tensile-yielding-procedures while specimens 3 and 4 were for checking the shear-yielding-procedures.

3 TEST SETUP

As shown in Figure 1, the specimens were placed horizontally to the ground and supported vertically by linear slider that do not constrain horizontal deformation, thus out-of-plane stiffening was not provided. A constant axial force of 246 kN was applied.

Loading was applied by gradually increasing the cyclic inter-story drift from 1/450, 1/300, 1/200, 1/150, 1/100, 1/75, 1/50, 1/40, to 1/30. These cycles were repeated three times for each amplitude up to ±1/30. Loading was

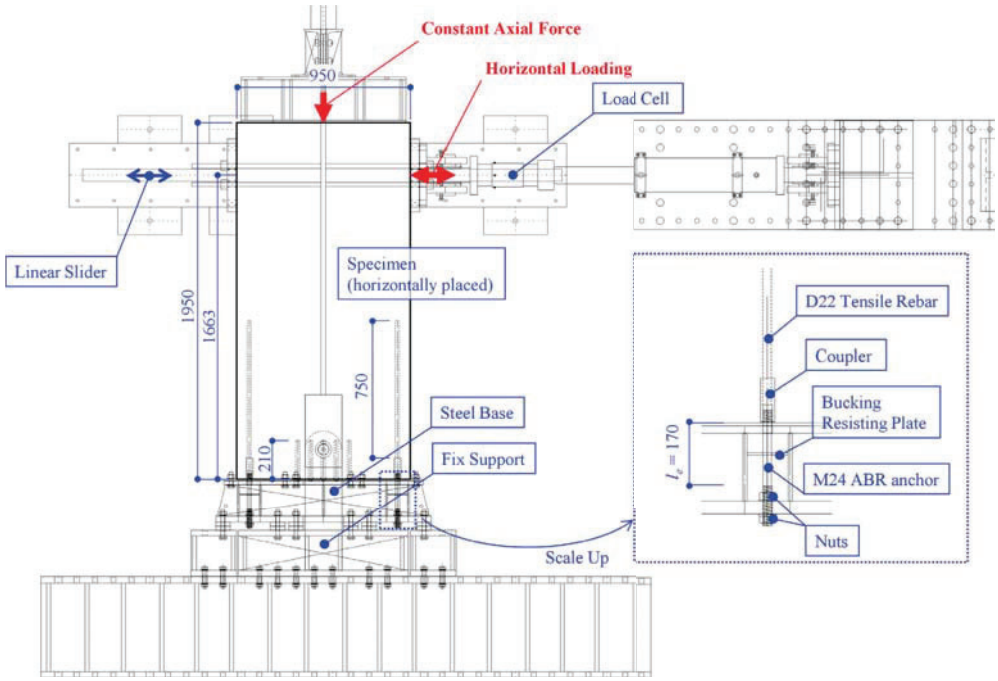

Figure 1: *Configuration of specimen 1 and test setup*

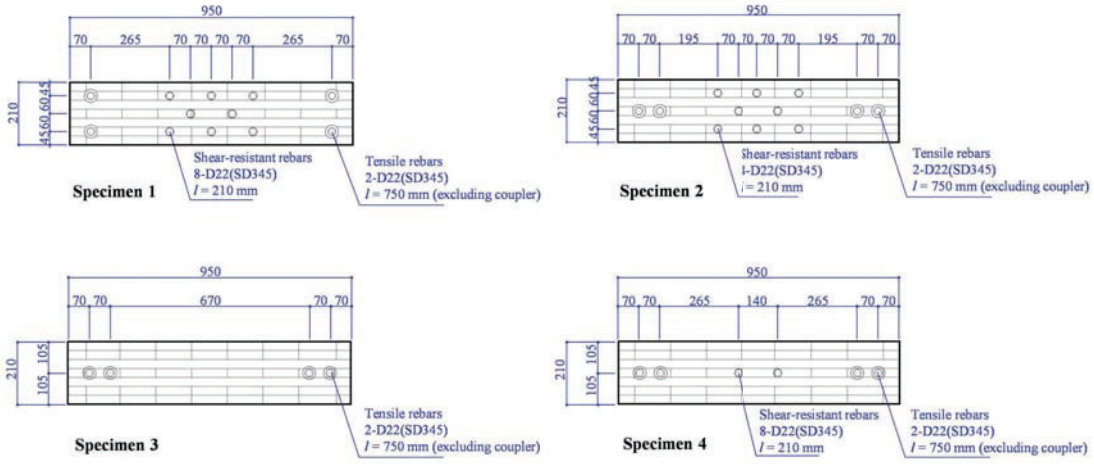

Figure 2: *Arrangement of GIR joints [Unit mm]*

https://doi.org/10.52202/069179-0275

continued until rupture of tensile bars or failure of CLT shear walls was confirmed.

Loading histories for specimen 3 was 1/450 (268kN-3*c*, 402kN-1*c*, 536kN-1*c*), 1/300 (268kN-3*c*, 402kN-1*c*, 536kN-1*c*), 1/100 (268kN-3*c*), 1/75 (402kN-2*c*) and 1/50 (536kN-1*c*). The constant axial force was changed to conform the friction between CLT and steel base and effect of axial force difference. The *c* indicates the number of cycles. In specimen 3, L-shaped steel was installed to restrain horizontal displacement of the CLT shear wall footings at the end of the 1/300 cycle. Figure 3 shows the relationship between shear drift angles and the number of cycles of specimen 3.

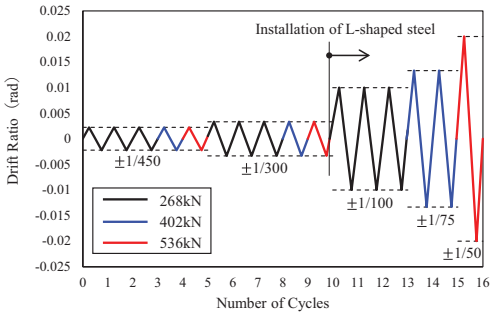

Figure 3: *Loading history at specimen3*

4 TEST RESULTS

4.1 GLOBAL RESPONSE

Figure 4 shows the relationship between horizontal force and horizontal displacement of each specimen (specimen 1 through 4). Specimen 1 exhibited yielding of the tensile rebar during the first excursion up to ±1/100. Subsequently, a stable response was observed up to ±1/75, and CLT cracked at the first excursion up to -1/50. At the second +1/30, the tensile bars were pulled out from CLT, and there was a sudden decrease of the horizontal force. Specimen 2 showed a stable response up to ±1/30, and fracture of the tensile bars was confirmed at a horizontal displacement of about +100 mm. Because tensile bars were arranged inside for specimen 2, the maximum strength of specimen 2 was slightly weaker than specimen 1. In Specimen 3, the adhesive between the CLT and shear plates peeled off after passing 1/450, and the friction between the CLT and shear plates and the shear of the tensile bars resisted against horizontal force up to 1/300. Fracture of the tensile bars was confirmed after the horizontal displacement reached 120 mm. Finally, for specimen 4, the ultimate shear force of 62.0 kN, which is equivalent to the ultimate shear force of two shear bars, was reached at 1/450 of a cycle, but the shear force continued to increase after that because of the tensile rebars acting to resist not only tensile force but also shear force.

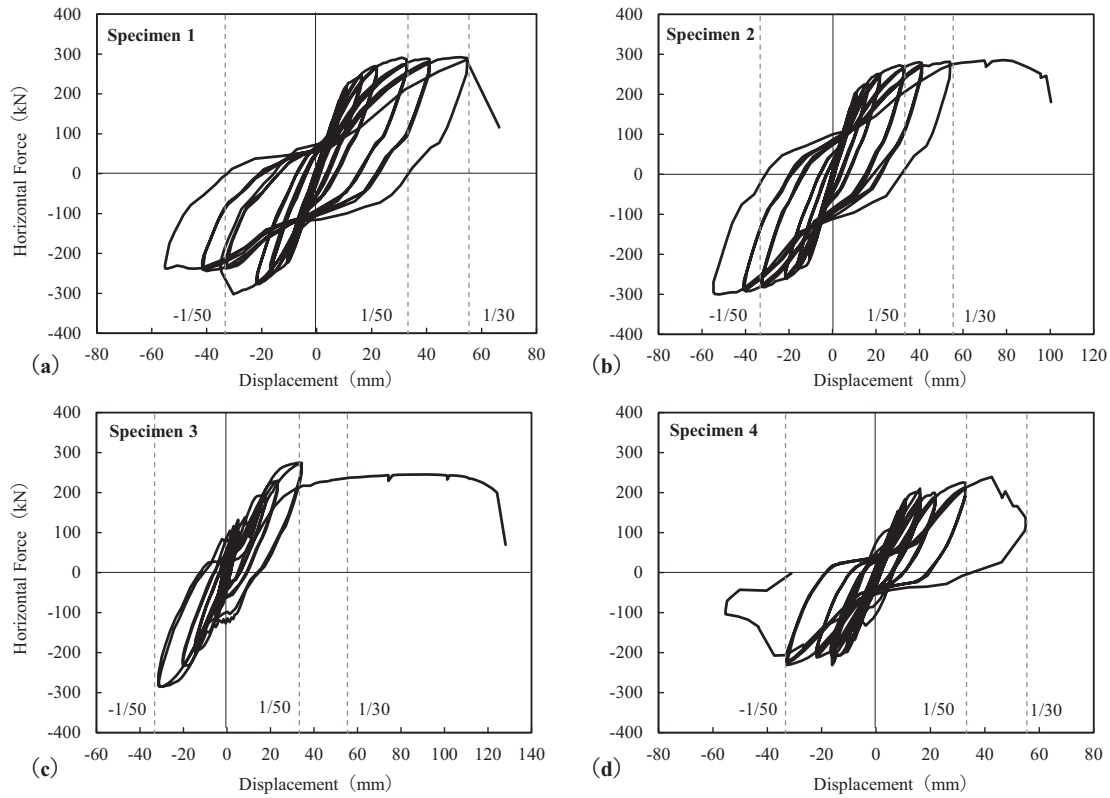

Figure 4: *Global response: (a) Specimen 1; (b) Specimen 2; (c) Specimen 3; (d) Specimen 4*

https://doi.org/10.52202/069179-0275

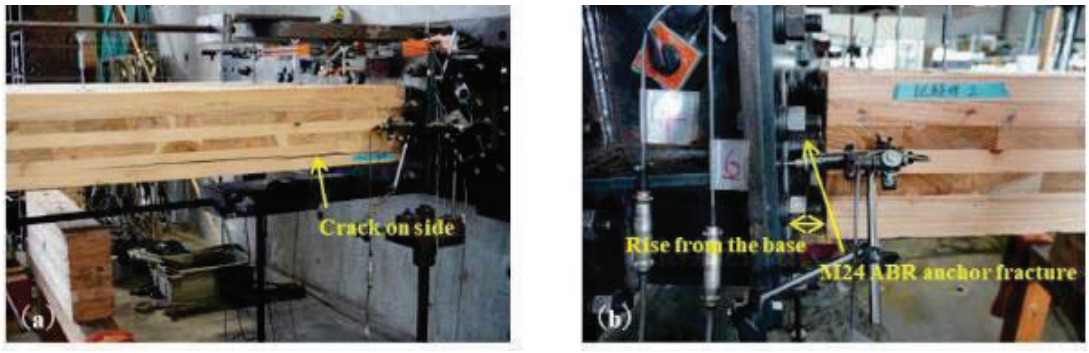

Figure 5: *Damage condition: (a) Specimen 1; (b) Specimen 2*

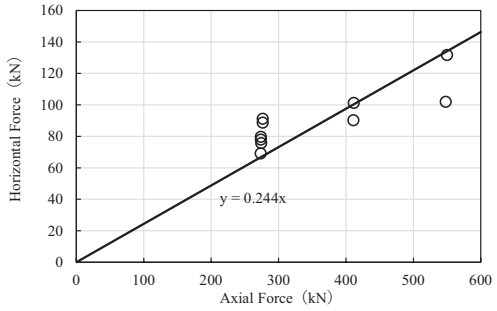

Figure 6: *Friction coefficient measured at specimen3*

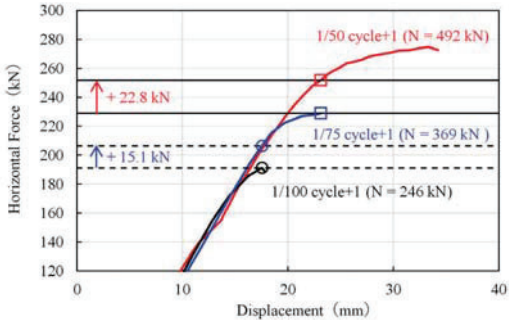

Figure 7: *Effect of axial force measured at specimen3*

The historical response of specimens 1 and 2, which were of the tensile bar pre-yielding type, was spindle-shaped, and energy absorption in the second and fourth quadrants was confirmed.

4.2 DAMAGE CONDITION

Figure 5 shows the damage of specimens 1 and 2. Specimen 1 had a crack on one side whereas specimen 2 had no damage. In the GIR joint with D22 rebar anchored 750 mm into the CLT, it was suggested that the CLT may have cracked and failed before the GIR exhibited its ultimate strength, because of the edge clearance distance. In the large deformation range, the separation between the CLT shear wall footing and the steel base increased, indicating that tensile forces were acting on the shear bars, which were expected to resist only shear forces.

4.3 FRICTION COEFFICIENT

Figure 6 shows the relationship between maximum horizontal and axial forces for each cycle measured on the positive side of the 1/450 and 1/300 cycles of specimen 3. The coefficient of static friction between the CLT and the steel base was calculated by the horizontal force divided by the axial force. The top flange of the steel base had a long hole along loading direction therefore the tensile bars didn't resist the shear force under such a small deformation range. The slope of the regression line (which means the static friction coefficient) was determined to be 0.244 using the least-squares method.

4.4 EFFECT OF AXIAL FORCE

Figure 7 shows the relationship between horizontal force and horizontal displacement for the first positive side up to 1/100, 1/75, and 1/50 for specimen 3. The horizontal forces increased by 15.1 kN by changing the axial force from 1.0 to 1.5 times during the transition from 1/100 to 1/75 cycles, and by 22.8 kN changing the axial force from 1.5 to 2.0 times during the transition from 1/75 to 1/50 cycles. The advantage of the self-centering ability: that the axial force snapped back to the initial position, was observed.

5 NUMERICAL ANALYSIS

5.1 NUMERICAL ANALYSIS MODEL

Hummel proposed a method for analysing the behaviour of CLT walls, which predicts the maximum strength and global response [7].

An attempt was made to reproduce the global response of specimen 2 using OpenSees, a general-purpose structural analysis framework [8]. Figure 7 shows an overview of the numerical analysis model, in which the CLT wall was represented by plastic beam-column elements and multi-springs were placed between the CLT wall footing surface, which was assumed to be rigid body, and the steel foundation. Tensile springs were placed at the same positions of the tensile and shear resisting bars, and a horizontal shear spring was placed in the center of the rigid body to consolidate the stiffness of the eight shear resisting bars.

https://doi.org/10.52202/069179-0275

Table 1 summarizes spring property of each spring. Detailed calculations are showed in the following section.

5.2 TENSILE SPRING PROPERTY OF TENSILE BARS

The elastic stiffness k_e of the tensile spring representing the tensile rebar and anchor was calculated from the following equation.

$$1/k_e = 1/k_{clt} + 1/k_a + 1/k_f \quad (1)$$

where k_{clt} = pull-out stiffness from GIR joint, k_a = tensile stiffness of ABR anchors, k_f = stiffness due to out-of-plane bending of the bottom flange

From previous studies [9,10], the tensile stiffness of the GIR joint with 750 mm anchorage length was 114 kN/mm, and the tensile stiffness of the D22 rebar exposed 300 mm length was 264 kN/mm. Pull-out stiffness from GIR joint was calculated by the series spring relationship.The tensile stiffness of ABR anchor was calculated from the axial stiffness with an effective length of 170 mm.

From the element tensile test of the M24 ABR anchor, the yield strength F_y, the ultimate strength F_u, the displacement of the yield shelf δ_1, and the secondary stiffness K_p were calculated. The stiffness after reaching the ultimate strength was set to zero. The yield strength in compression was set to 121 kN, which is the buckling strength following the Japanese code [11]. The effective buckling length l_b was set to 62.5 mm considering the stiffeners. Factors of safety were not considered when calculating the buckling strength in order to obtain a compression strength close to the actual behaviour. The stiffness after reaching the compressive yield strength was set to zero.

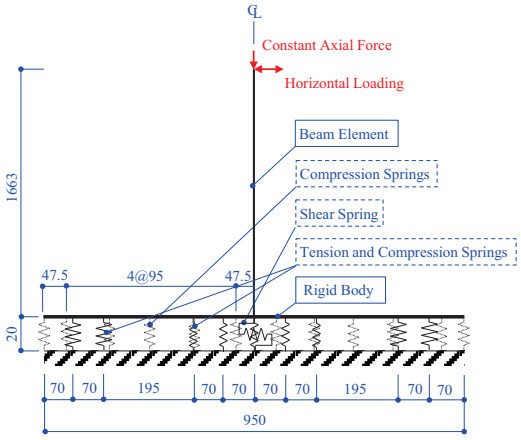

Figure 8: *Numerical analysis model*

5.3 TENSILE SPRING PROPERTY OF SHEAR RESISTING BARS

For the tensile stiffness of the shear resisting bars, a pullout stiffness of 54.5 kN/mm with an anchorage length of 210 mm was substituted for the tensile stiffness of the shear resisting bars from a previous study [12]. The shear resisting bars were assumed to resist only in tension since the effect of the shear resisting bars wasn't ignored in the large deformation range.

5.4 COMPRESSION SPRING PROPERTY OF CLT

The compression spring characteristics of CLT shear wall footing were calculated from the compressive stiffness and stress specified in the CLT-related Notification Manual and the Design and Construction Manual [12]. The effective width of the compression springs was set to 47.5 mm for the springs located at both ends of the rigid body, and 95 mm width for the other compression springs.

5.5 COMPARISION WITH TEST GLOBAL RESPONSE

Figure 9 compares the experimental and analytical global response of specimen 2. The analysis was in good agreement with the experiment results. The initial stiffness of the experimental and analytical results agreed at 19.1 kN/mm, and the maximum positive strength was 286 kN and 316 kN, respectively. The excursion to

Table 1: *Spring properties*

Type of springs	Tensile spring representing tensile resistance bar	Compression spring representing CLT wall	Tensile spring representing shear resistance bar	Shear spring representing shear resistance bar
Relationship between deformation and force	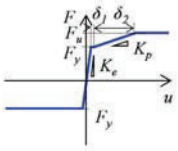	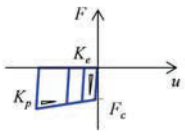	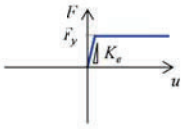	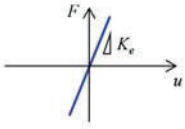
K_e Elastic Stiffness [kN/mm]	128	16.8 (edges) 33.7 (the others)	54.5	14.4
F_y Yielding strength [kN]	141(tension) 121(compression)	115 (edges) 230 (the others)	99.4	–
K_p Plastic Stiffness [kN/mm]	0.581	0.168 (edges) 0.337 (the others)	–	–
F_u Ultimate strength [kN]	201	–	–	–

https://doi.org/10.52202/069179-0275

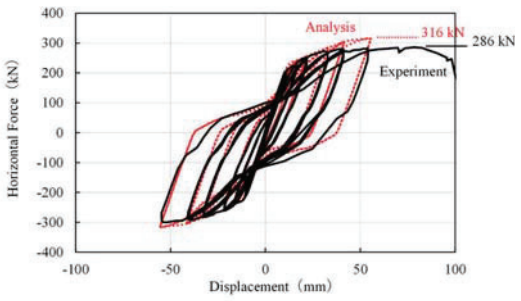

Figure 9: *Comparison experiment vs analysis*

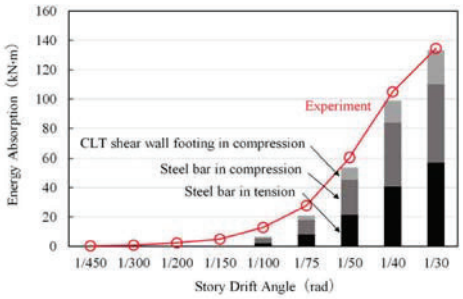

Figure 10: *Energy absorption*

unloading point from the peak strength, the experimental and analytical response showed slightly different behaviour. This difference is presumably due to the unloading stiffness of the tensile spring, that is set to be the same as the initial stiffness on the analysis, and there seems to be room for improvement in the modelling of the tensile spring.

5.6 ENERGY ABSORPTION

Figure 10 shows a comparison between experimental and analytical absorbed energy up to each cycle. The absorbed energy in the experiment is the sum of the horizontal displacement multiplied by the horizontal force at that point, i.e., the area bounded by the curve of the global response. The energy absorbed in the analysis was calculated from the response of tensile springs (simulating tensile resisting rebars) and compression springs (simulating the CLT wall footing). The energy absorption of tensile springs was defined as tension absorption when the axial force of the springs worked in tension and compression absorption was the opposite.

The larger the horizontal displacement, the better the agreement between the experimental and analytical values, with a difference of 3.37% at the 1/30 cycle. For the same cycle, the ratio of steel bars and CLT shear wall footing springs to the total energy absorption was 82.3% and 17.7%, respectively.

The energy absorbed by the steel bars on the compression side was 39.8% of the total energy absorbed, which means that the global response of the CLT shear wall exhibits a non-slip response.

6 CONCLUSION AND SUMMARY

Four CLT shear wall specimens with GIR joints were subjected to cyclic loading to examine the performance. A numerical model using OpenSees was developed to simulate the global response and confirm the energy absorption ability. Key results and observations are summarized below:

Specimens 1 and 2, which focused on using tensile rebars, exhibited great performance up to the 1/75 and exhibited a non-slip response because the M24 ABR steel anchors contributed to resisting in compression. In the GIR joint with D22 rebar anchored to the CLT by 750 mm, it was suggested that the CLT may crack and failed before the GIR exhibited its ultimate strength depending on the distance of edge.

The analysis model following Hummel proposed method reproduced the experimental behaviour of CLT shear wall specimen adequately. However, there was some room for improvement in the modelling of the tensile spring. The energy absorbed by the tensile resisting bars on the compression side was 39.8% of the total energy absorbed.

ACKNOWLEDGEMENTS

The authors are grateful to Yamasa Mokuzai Co.,Ltd., who contributed to making the test specimens and supported the experimental tests. The opinions expressed in this paper are those of the authors and do not necessarily reflect the views of individuals and organizations mentioned herein.

REFERENCES

[1] K. Kanazawa, H. Isoda, A. Kitamori, T. Usami, Y. Araki, Structural Performance OF Composite Structure WITH CLT Wall Infilled IN Steel Frames Using Drift-pin WITH Steel Plate, J. Struct. Constr. Eng., AIJ, Vol. 86, No.788, 1430-1439, Oct., 2021 (in Japanese)

[2] K. Morita, H. Umemori, T. Goshozono, M. Inayama, Development of medium-rise steel frame building with CLT shear wall. Part4 Horizontal load experiment of specimens with improved joint, Architectural Institution of Japan (AIJ) conference, Japan, 2020 (in Japanese)

[3] M. Kimura, S. Tsubata, O. Sadahiro, T. Kawachi, T. Hama, K. Kenji, Development of high strength shear wall using CLT (Part2 Structure experiment of high strength shear wall), Architectural Institution of Japan (AIJ) conference, Japan, 2017 (in Japanese)

[4] A. Mimatsu et al., Various Element Tests for the CLT Shear Wall using GIR Joints, Architectural Institution of Japan (AIJ) conference, Japan, 2018 (in Japanese)

[5] T. Carrero, J. Montañ, S. Berwart, H. S. María1, P. Guindos, Seismic behavior of innovative hybrid CLT-steel shear wall for mid-rise buildings, Bulletin of Earthquake Engineering (2021) 19:5917–5951

[6] I. Gavric, M. Fragiacomo, A. Ceccotti, Cyclic Behavior of CLT Wall Systems: Experimental Tests and Analysis Prediction Models, J. Struct. Eng., 2015, 141(11) 04015034.

[7] J. Hummel, Displacement-based seismic design

for multi-storey cross laminated timber buildings, Ph.D. Dissertation, Faculty of Civil and Environmental Engineering of the University of Kassel, Germany, 2017.
[8] McKenna, F., Object oriented finite element programming frameworks for analysis, algorithms and parallel computing. PhD thesis, University of California, Berkeley, California; 1997.
[9] S. Uesugi, D. Kadono, K. Murakami, Various Element Tests for the CLT Shear Wall using GIR Joints (Part2 GIR Joint Testing for the High Toughness Type CLT), Architectural Institution of Japan (AIJ) conference, Japan, 2021 (in Japanese).
[10] A. Mimatsu et al., Development and Construction of the Design Method of Two-way Flat Slab Using Cross Laminated Timber (Part2 GIR Joint Tensile Test and Shear Key Shear Test), Architectural Institution of Japan (AIJ) conference, Japan, 2019 (in Japanese)
[11] Architectural Institution of Japan (AIJ), Design Standard for Steel Structures -Based on Allowable Stress Concept-, Muruzen, Tokyo, Japan, 2019 (in Japanese)
[12] Japan Housing and Wood Technology Center, Design and Construction Manual for buildings using CLT, Japan, 2016 (in Japanese)

https://doi.org/10.52202/069179-0275

World Conference on Timber Engineering Oslo 2023

FULL-SCALE 3-D SHAKE TABLE TEST OF A TEN-STORY MASS TIMBER BUILDING

Shiling Pei[1], John W van de Lindt[2], Jeffrey Berman[3], Keri Ryan[4], James D. Dolan[5], Steve Pryor[6], Sarah Wichman[7], Aleesha Busch[8], Reid Zimmerman[9]

ABSTRACT: This paper provides a summary of the design, construction, and test planning of a shake table test program of a full-scale ten-story mass timber building. The shake table test program is a component of the experimental research work conducted as part of the NHERI TallWood project funded by the U.S. National Science Foundation. The goal of the NHERI TallWood project is to develop resilience-based seismic design methods for tall wood buildings through the adoption of a mass timber rocking wall lateral system and various detailing strategies for deformation-tolerant structural and non-structural connections and subassemblies. In this paper, the design configuration of the test structure is introduced, the construction process of both the structural and non-structural systems is explained, and the intended testing plan is presented. At the time of this writing, the construction of the building has been completed while the instrumentation process is ongoing. The authors intended to present initial results from the tests at the WCTE 2023 conference.

KEYWORDS: NHERI TallWood project, Shake table test, Tall wood building, Resilience, Seismic Design, Mass timber rocking wall

1 INTRODUCTION

Recently, mass timber construction materials such as cross laminated timber (CLT) have enabled taller wood construction projects including medium-to-high-rise mass timber buildings in the U.S. and around the world. Examples are the 10-story Forte building in Melbourne, Australia; the 18-story Mjøstårnet building in Norway; the 18-story Brock Commons building at the University of British Columbia, and the 27-story Ascent building in the U.S. Many of these tall wood buildings utilized non-wood lateral force-resisting systems such as reinforced concrete core walls or steel braced frames. At the same time, new mass timber-based lateral force-resisting systems have been proposed. Research on such systems continues at an impressive pace worldwide, including on post-tensioned mass timber rocking wall systems [1-3] and platform-framed CLT shear wall systems [4]. It is likely future mass timber buildings will continue to utilize a mixture of conventional and innovative lateral systems. However, amongst new mass timber lateral force-resisting systems, the post-tensioned mass timber rocking wall arguably demonstrates the greatest potential to enable a new type of tall wood building design that can achieve resilience and rapid return to functionality following an earthquake. Thus, the building can remain structurally damage free during design level earthquakes and be quickly repairable after maximum considered earthquakes.

The NHERI TallWood project was initiated in 2016 with the objective of developing a resilience-based seismic design methodology for tall wood buildings. Through funding provided by the U.S. National Science Foundation and U.S. Forest Service, the research team worked collaboratively with industry partners to develop design schematics, modelling tools, and resilience-based assessment methods in the past six years towards the goal of realizing a method to design a mass timber building based on functional recovery time. Based on past experience and assembly test data [2], the project team has completed the design of a 10-story mass timber building specimen with extracted features from realistic archetype buildings and under various physical constraints. One of the major constraints is the NHERI shake table dimensions (7.6x12.2 m) at the University of California San Diego (UCSD).

The shake table at UCSD is the world's largest outdoor shake table, thereby allowing a full-scale 10-story specimen to be constructed totalling approximately 34 meters in height. Building construction was completed in

[1] Associate Professor, Colorado School of Mines, U.S.A. spei@mines.edu
[2] Harold H. Short Endowed Chair, Professor, Colorado State University, U.S.A. jwv@engr.colostate.edu
[3] Professor, University of Washington, U.S.A. jwberman@u.washington.edu
[4] Professor, University of Nevada Reno, U.S.A. klryan@unr.edu
[5] Professor, Washington State University, U.S.A. jddolan@wsu.edu
[6] Advanced Research Manager, Simpson Strong-Tie Co., U.S.A. spryor@strongtie.com
[7] Research Assistant, University of Washington, U.S.A, wichman@uw.edu
[8] Research Assistant, Colorado School of Mines, U.S.A, abusch@mines.edu
[9] Technical Director, KPFF Consulting Engineers, U.S.A. Reid.Zimmerman@kpff.com

https://doi.org/10.52202/069179-0276

December 2022, and instrumentation will continue through February 2023 with over 700 channels of displacement, acceleration, and strain sensors. The tests are scheduled to be conducted between March and May of 2023. The building performance during testing will be compared to the resilience objectives intended during the design process, thus validating resilience-based seismic design approach proposed.

2 BUILDING CONFIGURATIONS

The test building utilizes a mass timber beam-column grid with mass timber floor panels as the gravity force-resisting system. Four post-tensioned rocking walls (two in each direction, constructed using CLT and mass plywood panels (MPP) respectively) serve as the lateral force-resisting system for the building. The gravity system of the building was designed using typical office live load. The beams and columns were sized considering 2 hour fire condition with exposed wood (i.e., considering a sacrificial layer of wood for wood charring). The basic design information about the building is listed in Table 1.

Table 1: *Basic design parameters for the test building*

Building Characteristics	Value
Number of stories	10
Total height	34.1m
Total floor area	840m^2
Design floor load (Dead/Live)	3.1/3.1 kN/m^2
Total building weight	295 MT
Design location	Seattle WA
Estimated period	1.8 sec

There is a large array of different mass timber materials used in the construction of the building, including CLT, Mass Plywood Panel (MPP), Glu-Laminated Timber (GLT), Veneer Laminated Timber (VLT), and Nail/Dowel Laminated Timber (NLT/DLT). The composition of different material types on various building components is shown in Figure 1. Aside from the structural system, selected floors also have non-structural partition walls and exterior envelop installed to evaluate their performance during the tests. A rendered building configuration is shown in Figure 2.

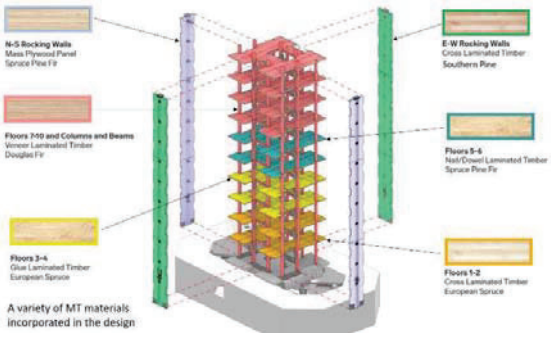

Figure 1: *Variety of mass timber material and components included in the tall wood test building*

Figure 2: *Rendering of the 10-story test building on the NHERI@UCSD outdoor shake table (Rendering courtesy of Lever Architecture)*

3 DESIGN AND CONSTRUCTION PROCESS

The objective of the NHERI TallWood Project is to develop a resilience-based seismic design methodology for tall wood buildings. The test building was designed with the objective of quantifying resilience, essentially time to functionality, as a function of building damage. In order to use resilience as a design metric, one of the first steps is to develop and validate an approach to assess and predict building damage and associated repair time following an earthquake. A fragility-based approach was utilized to link building response (i.e., floor acceleration and inter-story drift) to component and system damage, and then from damage to repair time [5]. This approach will be calibrated and validated using data obtained from the shake table tests.

As for the design of the test building, the project team took an indirect approach to address resilience. First, basic configuration parameters (e.g., rocking wall length, post-tensioning (P/T) force level, etc.) of the building and lateral force-resisting system were estimated using a prescriptive design method developed by collaborators of the project team [6]. This approach is largely force-based using demands generated with the modal response spectrum method from ASCE 7 [7] and a linearized model in ETABS [8]. Then a full nonlinear dynamic model in OpenSees [9] was used to evaluate acceleration and drift limits necessary to achieve the target resilience. Aside from the rocking wall lateral force-resisting system, which is designed to exhibit nonlinear behaviour (i.e., rocking behaviour at the base and yielding of energy dissipaters), all other structural components are designed to remain essentially elastic with negligible damage through providing sufficient overstrength or appropriate connection detailing.

Construction of the test building started in July 2022. Before construction, the outdoor shake table at UC San Diego was expanded by adding 4 cantilevered concrete foundation blocks to the long edge of the shake table. See

https://doi.org/10.52202/069179-0276

Figure 3. This expansion provided a roughly 11 x 11 meter footprint for building construction. Four steel foundation beams were also installed on the shake table serving as the base of the rocking walls. All foundation components were connected to the shake table through post-tensioned steel rods. The post-tension forces were determined based on the calculated shear demands from the numerical models. Before construction started, the ground motions intended to be used during the test were replayed on the shake table to ensure clearance and to determine the tuning parameters for the shake table control.

Figure 3: *Foundation system added on the NHERI@UCSD outdoor shake table before construction started*

Construction of the NHERI TallWood test building structural system lasted for approximately 4.5 months. Swinerton Mass Timber/Timberlab was the structural contractor and planned the erection and construction engineering for the building process. The construction of the test building was especially challenging due to the limited floor plan area on the shake table, which makes temporary bracing congested. Temporary post-tensioning of the rocking walls on the lower floor had to be implemented in order to utilize the partially completed rocking wall panels as the lateral bracing system for construction loads.

The two pairs of mass timber rocking walls are a key component of the test building. Aside from the material and some minor dimensional differences, the CLT and MPP rocking walls utilized the same design. The rocking wall panels are strengthened at the base corners with steel armor plates. The post-tensioning rods were installed on the outside of the wall panels near the centre of the wall. Because of the height of the building, each rocking wall consists of 3 individual mass timber panels that had to be spliced on site. The splice connection was designed as a series of steel tension and shear rods embedded in the wall using special epoxy material. During the fabrication of the wall panels, a number of the predrilled holes at the panel splices were fabricated out of tolerance. This resulted in a change in connection design during construction to use coupler steel plates at the splices in order to bridge the mismatched hole coordinates. Between the rocking wall panel and bounding columns on each side of the wall, steel U-shaped flexural plates (UFP) were installed in order to provide energy dissipation to the lateral force-resisting system. Photos demonstrating the main details along the height of the rocking wall system can be seen in Figure 4.

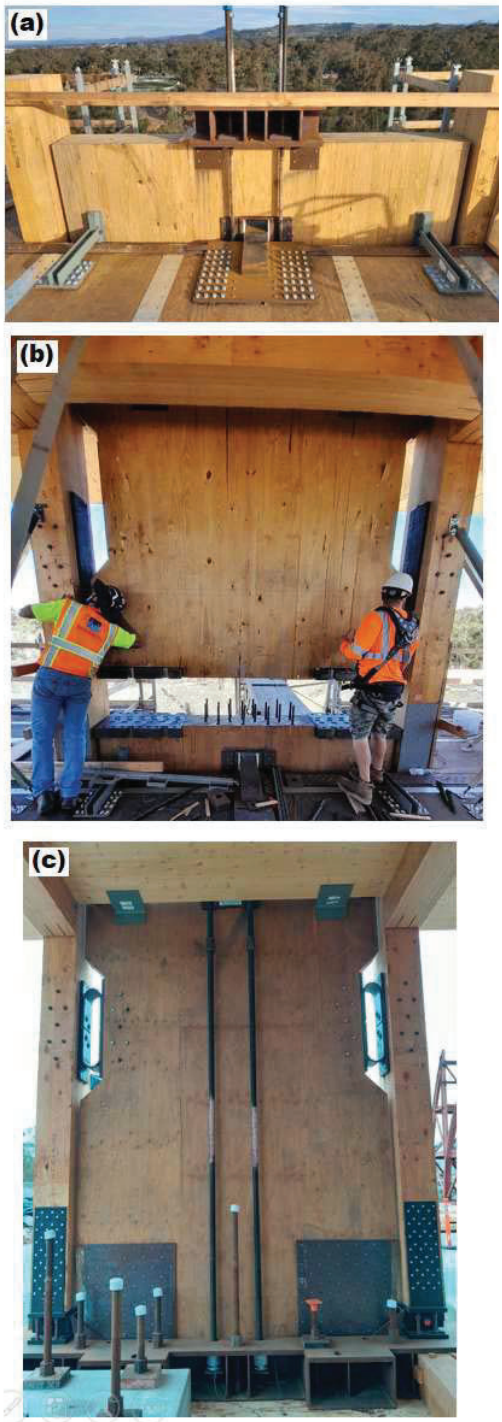

Figure 4: *Post-tensioned rocking wall system (a) PT anchor at wall top (b) Wall splice being installed (c) foundation level detail and UFP devices*

https://doi.org/10.52202/069179-0276

Figure 5: *Construction process of the test building*

The gravity system was erected along with the rocking wall segments. As shown in Figure 5, a modular stair and gravity columns were placed first, followed by the mass timber beam grid and floor panels. Once the gravity system reached the height of the rocking wall segment, the rocking wall panels were installed. This process was repeated 3 times during construction until the building was topped out. After that, the post-tensioning rods were extended to the top of the wall and stressed to complete the lateral force-resisting system. Once the design post-tensioning forces were applied (about 890 kN total post-tension force was applied to each wall), the construction of the structural system was complete.

In order to accurately evaluate repair time from non-structural system damage, the test specimen also included exterior façade subassemblies on the first three floors, interior partition walls, and a 10-story stair tower. Various low-damage deformation compatible details were implemented with the expectation of eliminating damage in small earthquakes and limited damage in design basis earthquakes. The details include horizontal slip joints fr walls, vertical joints at intersecting walls, and specialized joints for connecting stair stringers to mid-landings.

Figure 6: *Selected non-structural systems and components included in the test (a) Curtain wall (b) Exterior wall and windows (c) Interior partition walls.*

Figure 6 shows a few selected non-structural components, including a fire-rated curtain wall system, exterior stud wall with windows, and interior partition wall with low-damage joint details. Non-structural system construction is currently ongoing and is expected to be completed in February 2023.

4 INSTRUMENTATION PLAN

A comprehensive plan for instrumentation of the test building was developed and implemented. There are a total of over 700 instrumentation channels monitoring key aspects of the building response, namely overall building demands, rocking wall behavior, and non-structural system performances.

As shown in Figure 7, a 3D accelerometer was placed near the centre of mass of the floor diaphragm at each floor. String potentiometers will mainly be used to measure inter-story displacement, as well as absolute displacement for lower floors where they can be attached on the safety reference tower. The deformation of the rocking wall and building components are measured using LVDT sensors and tilt meters. Strain gauges were installed on key load-transferring components (e.g., tension straps and floor shear transfer keys) to monitor internal forces. Customized load cells were placed at the post-tensioning rod anchor to record rod forces. Examples of the installed sensors are shown in Figure 7.

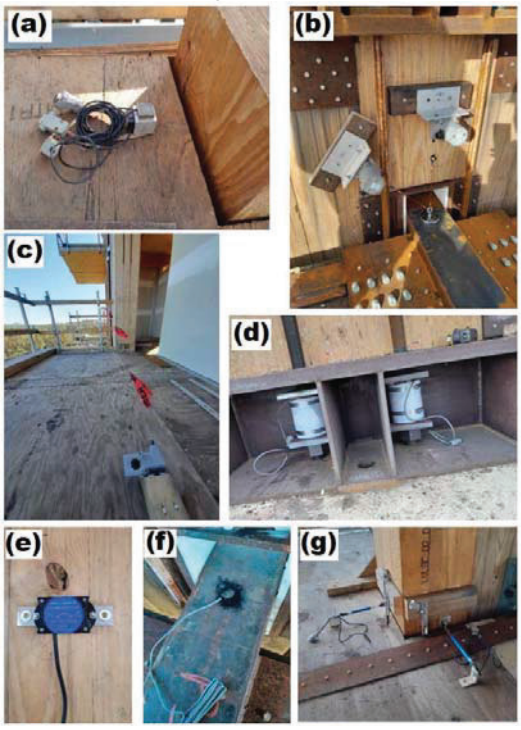

Figure 7: *A variety of sensors installed on the test building (a) Accelerometer on the floor (b) String potentiometer for small deformation (c) String potentiometer for inter-story displacements (d) Custom load cells for PT forces (e) Tilt angle sensor for rocking wall response (f) Strain gauge on key load transferring components (g) LVDT sensor for column rotation*

https://doi.org/10.52202/069179-0276

A summary of all sensors implemented on the test building is listed in Table 2. Data obtained from these sensors during the test will serve multiple purposes, including providing key safety limit information during testing, calibrating and validating numerical models developed by the research team and other engineers after the test, and helping support damage fragility models of structural and non-structural components within the building. The data obtained from the tests will be archived and made public on the DesignSafe-CI database following the end of the NHERI TallWood project.

Table 2: *Summary of instrumentation channels deployed on the tallwood test building*

Building component	Sensor types*	Total number
Global Disp	SP, AC, GPS	139
Gravity system	LD, SP	79
Rocking walls	LC, AC, TL, SG, SP	196
Non-structural	AC, SP, LD	186
Stair	AC, SP, LD	109

* SP-String potentiometer, AC-Accelerometer, LC-Load cell, LD-Liner potentiometer, TL-Tilt meter, SG-Strain gauge, GPS- High precision GPS

5 TEST PROGRAM

The tests of the Tallwood building will be conducted on the newly upgraded 6-DOF high performance outdoor shake table at NHERI@UCSD in San Diego California. The research team plan to subject the building to a suite of ground motions selected and spectrally matched to represent seismic hazard at a site in Seattle WA, the location selected for the design of the building. Earthquake ground motions that will be used during testing have been selected and scaled to represent different hazard levels and sources affecting the site in Seattle, thus providing a realistic evaluation of the performance-based design for the building. The hazard levels include the 225 year, 475 year, 975 year and 2475 year return periods.

In order to achieve the desired range of hazards and sources, a total of 20 3D ground motions were selected, scaled and used to tune the shake table control before construction started. These inputs include recorded ground motions from historical earthquakes with different source types ranging from crustal earthquakes such as the Northridge Earthquake (1994) to interface subduction earthquakes such as the Tohoku, Japan Earthquake (2011). In particular, the interface subduction ground motion records contain significant amounts of excitation energy in long period ranges, which are believed to be especially detrimental to tall buildings. They also have long duration, resulting in many cycles of loading. All the ground motions at the Risk-Targeted Maximum Considered Earthquake (MCE_R) level which approximately corresponds to a 2,475 year return period, were used to tune the shake table. The test program will start at the lower hazard levels (i.e., lower levels of ground motion intensity). It will then continue with ground motions scaled to the larger and larger intensity levels. Numerical simulations will provide insight on the ground motions as the testing continues with decisions made dynamically as information is gathered following each test. The response spectra for the selected ground motions, scaled for different hazard levels, are shown in Figure 8 where the bold lines indicate averages at each hazard level. The ASCE 7 MCE_R spectrum used for design is also shown.

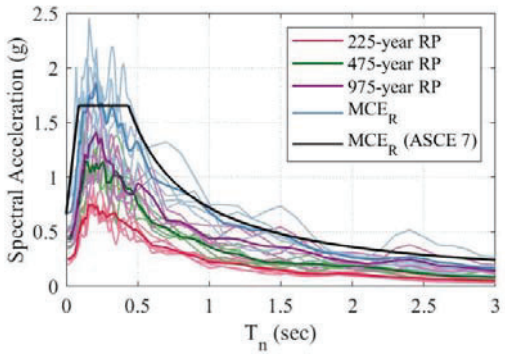

Figure 8: *Response spectra for all candidate ground motions at four representative hazard levels.*

Based on the schedule constraints, the test program will include 30 – 40 seismic tests over a period of about one month. White noise excitation will be implemented before and after each seismic test in order to gather data on the change in building dynamic characteristics. Since most of the practical design calculations currently required by the code do not consider biaxial or tri-axial excitation, the ground motion inputs were planned to first isolate the influence of multi-directional interaction. It is planned that the uniaxial ground motion components will first be applied. This will be followed by applying ground motion in the two horizontal directions and then by a full 3D motion. A typical testing sequence for one 3D seismic input at a given intensity level will include 5 tests and span over two to three days (See Table 3). This test program will help validate the design calculations/checks in a uniaxial configuration. The data from this test sequence will also be able to shed light on building response beyond code requirements in a biaxial and 3D excitation setting.

According to pre-test numerical simulation, the maximum inter-story drift during the planned test program will not exceed 3%, with the maximum drifts occurring in the MCE_R ground motions. Damage to non-structural systems at these drift levels is expected, while the structural system should experience negligible damage (except localized, expected component damage such as UFP energy dissipaters) throughout the test program. Comprehensive inspections of the test building will be conducted on both the structural and non-structural systems following significant testing events. The research team is planning for concluding the first phase of the test by April 2023.

https://doi.org/10.52202/069179-0276

Table 3: *As-planned typical testing sequence for a single seismic hazard level*

Test	GM record	Building direction	Comments
1	GM_H1	X	CLT wall response
2	GM_H1	Y	MPP wall response
3	GM_H2	Y	Biaxial comparison
4	GM_H1H2	XY	Biaxial test
5	GM_H1H2V	XYZ	Tri-axial test

Note: H1, H2 and V represent horizontal 1, horizontal 2 and vertical components of a ground motion.

6 KEY RESULTS

At the time of this writing, the building is still undergoing instrumentation, and no seismic tests have been conducted. The research team is expected to complete instrumentation of the structure by March 2023 and complete all testing by June 2023. It is expected that initial results from these tests will be presented in the conference presentation. It is envisioned that key testing results will include the dynamic response of the building and damage inspection outcome after large tests.

7 CONCLUSIONS

The ten-story Tallwood building test program planned in this study represents one of the most significant research efforts in recent years to experimentally validate tall wood building performance during earthquakes. Through extensive collaboration with the mass timber industry partners, the building archetype and construction details included in the test program are also readily implementable in realistic building projects for high seismic regions. While the test results are not available at the time of this paper, key details and the design methodology utilized in this project were introduced.

It is expected that the test building will have resilient performance, which corresponds to negligible damage under frequent earthquakes, negligible structural damage under design level earthquakes, and be quickly repairable under maximum considered earthquakes. The outcome from this test will help advance knowledge on mass timber structural system design and provide increased confidence to the mass timber market in regions with high seismicity around the world.

ACKNOWLEDGEMENT

The NHERI TallWood Project is a collaborative research project, supported under National Science Foundation (NSF) awards 1636164, 1634204, 1635363, 1635156, 1634628, carried out through collaboration with the U.S. Forest Service (USFS) through the Wood Innovation Fund program, Forest Product Laboratory and a large number of industry partners (see http://nheritallwood.mines.edu/collaboration.html). Any opinion expressed in this material is that of the author and does not necessarily represent the opinion of sponsors.

REFERENCES

[1] Iqbal, Asif, Massimo Fragiacomo, Stefano Pampanin, and Andrew Buchanan. "Seismic resilience of plywood-coupled LVL wall panels." Engineering Structures 167: 750-759, 2018.

[2] Pei S., van de Lindt JW., Barbosa AR., Berman JW., McDonnel E., Dolan JD., Blomgren HE., Zimmerman RB., Huang D., Wichman S., Experimental Seismic Response of a Resilient 2-story Mass-Timber with Post-Tensioned Rocking walls, J. Struct. Eng., 145 (11): 04019120, 2019.

[3] Ceccotti, A., Sandhaas, C., Okabe, M., Yasumura, M., Minowa, C., Kawai, N., SOFIE – 3D shaking table test on a seven-storey full-scale cross-laminated timber building, Earthquake Engineering & Structural Dynamics, 42:2003-2021, 2013.

[4] van de Lindt, J.W., Furley, J., Amini, M.O., Pei, S., Tamagnone, G., Barbosa, A.R., Rammer, D., Line, P., Fragiacomo, M., Popovski, M., Experimental seismic behavior of a two-story CLT platform building, Engineering Structures, 183: 408-422, 2019.

[5] Furley, J., van de Lindt, J.W., Pei, S., Wichman, S., Hasani, H., Berman, J.W., Ryan, K., Daniel Dolan, J., Zimmerman, R.B. and McDonnell, E., Time-to-functionality fragilities for performance assessment of buildings. Journal of Structural Engineering, 147(12), p.04021217, 2021.

[6] Busch, A., R. B. Zimmerman, S. Pei, E. McDonnell, P. Line, and D. Huang. Prescriptive Seismic Design Procedure for Post-Tensioned Mass Timber Rocking Walls. Journal of Structural Engineering 148, no. 3: 04021289, 2022.

[7] ASCE, Minimum Design Loads and Associated Criteria for Buildings and Other Structures (ASCE/SEI 7-22), American Society of Civil Engineers, Reston, VA, 2022.

[8] Computers & Structures Inc. User's manual for ETABS. Walnut Creek, CA, 2022.

[9] Pacific Earthquake Engineering Research Center, User's manual for Opensees. https://opensees.berkeley.edu/ (accessed 1/2023)

https://doi.org/10.52202/069179-0276

World Conference on Timber Engineering Oslo 2023

CONSTRUCTIVE REHABILITATION OF THE FLOOR STRUCTURES OF ZAGREB'S DOWNTOWN BUILT IN THE FIRST HALF OF THE 20TH CENTURY

Dean Čizmar[1], **Krunoslav Pavković**[2], **Marija Babić Tončić**[3], **Ivana Iljkić**[4]

ABSTRACT: The major damage to the buildings in Zagreb's Lower downtown caused by the earthquake is partly the result of the way the timber ceilings were built, which are mostly not connected to the masonry walls on which they rest. In this way, they do not have the properties of rigid diaphragms, which, due to the effect of an earthquake, leads to the loss of the integrity of the construction.

In the paper, we consider the possibility of strengthening timber ceilings with regard to the significant requirements of preserving cultural heritage, and present the results of selected types of reinforcement. The considered types of reinforcement are: reinforcement of the timber beams with a concrete compression slab, reinforcement of the timber beams with wooden elements - OSB boards, and reinforcement with steel elements.

Regarding the possibility of implementation, a conclusion was given on the chosen method that meets the given requirements in terms of horizontal stiffness and the preservation of the cultural and historical heritage of the downtown core.

KEYWORDS: Zagreb earthquake, timber ceilings, horizontal stiffness, seismic analysis

1 INTRODUCTION

Due to the earthquake in Zagreb on March 22, 2020, there was extensive damage to the downtown architecture. Damage is partly due to the way timber ceilings are built. Most of the damaged buildings were built in period 1900 and 1948. In that period, all buildings have deficiencies in terms of meeting the criteria of earthquake resistance, unconnected ceilings with walls, i.e., the inability to transmit horizontal forces, load-bearing walls made of unbounded masonry, and poor connections of basic assemblies and elements without the necessary load-bearing capacity and ductility [1].

Masonry buildings are structural systems of vertical and horizontal parts whose seismic response is the result of the interaction of wall with wall and wall with ceiling or roof. In order for the structure to meet the behaviour during an earthquake, it is necessary to realize the bearing capacity and rigidity of the walls in the plane and to prevent the collapse of the walls outside the plane [2].

In the paper we will analyse the possibility of strengthening the classic timber ceiling structures. These proposals for constructive rehabilitation will enable the strengthening of existing ceiling timber structures but also the preservation of cultural heritage, as damaged. buildings are individually or as an urban entity protected as Immovable Cultural Heritage.

2 CASE STUDY

The subject building is a residential building located in the downtown of the city of Zagreb, at the address Medulićeva street 16/3. The building was built in the first part of the 20th century (before 1920).

[1] Dean Čizmar, Zagreb University of Applied Sciences, Department of Civil Engineering, dean.cizmar@tvz.hr
[2] Krunoslav Pavković, Zagreb University of Applied Sciences, Department of Civil Engineering, krunoslav.pavkovic@tvz.hr
[3] Marija Babić Tončić, Zagreb University of Applied Sciences, Department of Civil Engineering, marija.babic.toncic@tvz.hr
[4] Ivana Iljkić, Zagreb University of Applied Sciences, Department of Civil Engineering, student, ivana.iljkic@tvz.hr

https://doi.org/10.52202/069179-0277

Figure 1: *The western façade (face) of the structure*

The vertical bearing structure consists of brick walls, while the ceiling structure is made of timber beams. The residential building has a basement, ground floor and 3 floors [3].

Figure 2: *The eastern façade (face) of the structure*

In the floor plan, we see a deficiency of walls in the x direction, and we can immediately establish that this is the weaker direction of our building.

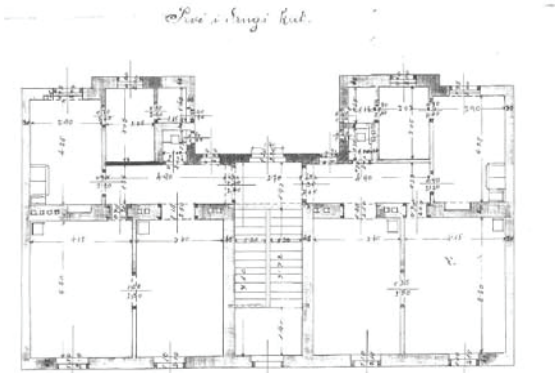

Figure 3: *Archival floor plan of the building (first and second floor)*

In this period [4], buildings are built that have predominantly timber ceiling structures, except for the basement ceilings, which are most often made in the structure of masonry vaults, arches, or Prussian ceilings. The extensive damage due to earthquakes is partly due to the way timber ceilings are built, which do not have the characteristics of rigid diaphragms, they cannot connect all the load-bearing elements into one whole. The consequence of this is the local failure of the walls.
Existing timber beams, meet the criteria of the final ultimate limit state of bearing capacity (ULS) while the limit states of serviceability are generally not met, mostly due to rheological phenomena (creeping). Furthermore, the connections of timber beams and walls are made by direct adhering the beams to the walls, as a rule, without anchoring. This type of design allows only reliable resistance to vertical actions, while resistance to horizontal actions is extremely low [3].

3 REHABILITATION METHODS

The possibility of rehabilitation, i.e., increasing horizontal and vertical stiffness is possible with concrete compression plate, OSB slabs or timber or wood-based elements and steel profiles. To achieve appropriate effect, it is necessary to connect the beams to the walls. In the case of reinforcement with the concrete compression plate [5], a pliable connection between concrete and wood is made.
Considering the weight of the rubble and the weight of the reinforced concrete slab, the own weight of the ceiling structure does not increase significantly. By placing the fasteners in the existing wooden beams, the structure is connected, and in this way, significantly greater load capacity and rigidity is achieved perpendicular to the plane, while inside the plane we get a rigid disc [1]. The pressure plate can be made of classic concrete C25/30 or light concrete EPS.

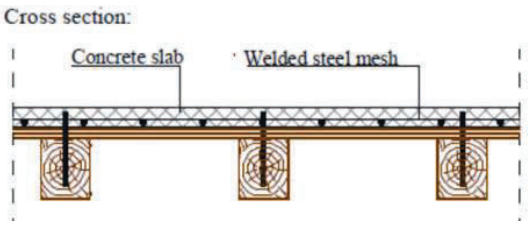

Figure 4. *Reinforcement of the timber beams with a concrete compression slab*

Figure 5. *Reinforcement of the timber beams with a concrete compression slab*

The disadvantages of this method of rehabilitation are changes in the stress state in the T-section and the action of two different materials of different stiffness and rheological characteristics [5].
Rehabilitation and reinforcement with OSB plates (possibly veneer plates or wooden boards) can be done

https://doi.org/10.52202/069179-0277

from the bottom or top side of the timber beam. This way of stiffening is a partially rigid diaphragm.
By placing wooden boards on the existing ceiling structure, i.e., timber beams, a double reinforcement effect is achieved. Reinforcement to vertical load, but also to horizontal action, is achieved if the elements that form the diaphragm are properly connected to each other to take the shear load.
The ceiling structures must be connected to the walls so that they do not separate during the horizontal effects of the earthquake force, but also to enable the proper distribution of the seismic force on the individual walls. Wooden panels made of OSB boards 22 mm thick is placed in two layers, the first layer is placed at an angle of 45° in relation to the beam, and the second layer is placed at an angle of 90° in relation to the first. The connection to the beams is made with self-tapping screws. Each joint is made with a minimum of 2 wood screws [1].
With the diagonal arrangement of the additional layer, we get better pressure resistance and stiffness in both planes [2].
To achieve continuity, it is necessary to adequately secure the joints with the walls.

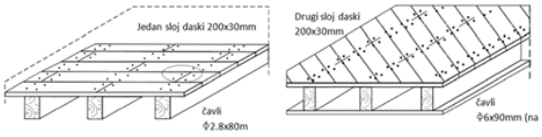

Figure 6. *Reinforcement with OSB boards on the top or bottom*

Rehabilitation and reinforcement with steel elements is usually carried out between the last two ceiling timber beams in such a way as to install steel sheets forming a lattice girder [4]. Horizontal stiffening of wooden ceiling structures with steel elements is carried out when no additional vertical bearing capacity of the structure is required, but only the absorption of horizontal forces [1].

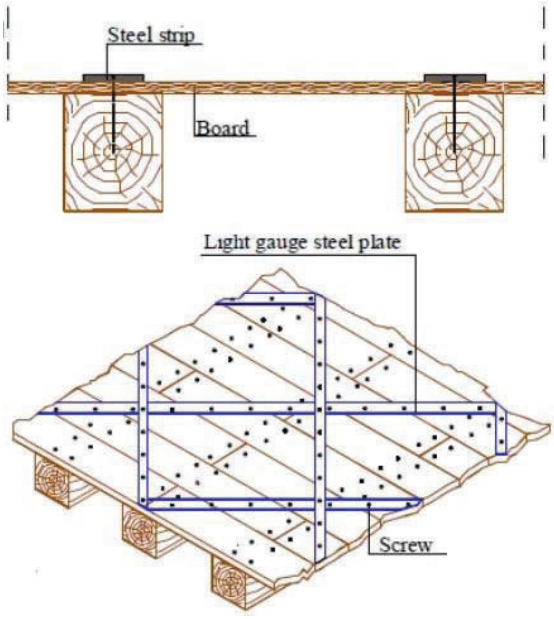

Figure 7: *Reinforcement with steel elements*

Figure 8: *Steel strip*

3.1 NUMERIC MODEL DESCRIPTION

For the purpose of the numerical modelling, an analysis of 3 cases was made – a timber beam without stiffening (existing condition) – model A, a timber beam with an 8 cm concrete plate - model B (composite timber-concrete), a timber beam with an OSB plate 24 mm – model C.
We describe the possibility of strengthening timber ceilings with steel elements, but we did not model it due to the complexity of creating such a model in the program for masonry structures.
Several models of the current state have been made, each of which has its own assumptions in modelling. A linear-elastic model was made. This model is acceptable for engineering practice. The following loads were considered:
LC1 - self-weight
LC2 – additional self-weight
LC3 – live load 2 kN/m2 in residential areas, 0.75 kN/m2 on an impassable roof and 3 kN/m2 on the staircase

https://doi.org/10.52202/069179-0277

LC4 - earthquake in X direction
LC5 - earthquake in the Y direction

A modal spectral analysis was made for the calculation, and the load was taken as if we wanted to strengthen the structure to meet level 2 of the seismic reconstruction. Among other data, soil type C, type 1 spectrum, soil acceleration coefficient 0.13 and behavioural factor 1.5 were assumed, which corresponds to the assumptions in Eurocode Standard for unbounded masonry. For each model, 30 different modes were considered [3].

In the model of the existing state, the beams are modeled so that they carry in the shorter direction, and in this way only the walls in the transverse direction take over the loads on the wall. (Model A). Due to the vertical/longitudinal direction of the earthquake in relation to the timber beam (in the direction of the timber beams), an orthotropic seismic response occurs, i.e., relative displacements of the beams and bending of the floor covering occur, while the load perpendicular to the direction of the timber beams causes bending of the beams and relative movements of the floor covering [2].
The second model is a model with a reinforced concrete pressure plate 8 cm anchored in the walls (model B).
The third model is stiffened using OSB panels on the upper side of the beams (model C). The thickness of the panels is assumed to be 24mm.

3.1.1 Seismic design in 3Muri

A 3D numerical model of the subject building was created using the 3Muri computer program. Seismic analysis of the observed structure was performed using a non-linear static calculation, i.e., a gradual pushover method with a constant gravity load and a monotonically increasing horizontal load.

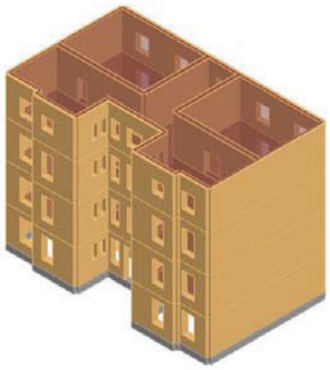

Figure 9: *3D building model - existing condition*

After the response of the structure to seismic excitation, i.e., the so-called capacity of the structure, which is independent of the seismic demand, is obtained, controls are carried out in accordance with the HRN EN 1998-3 standard according to the basic requirements related to the state of damage to the structure, which are defined by limit states.

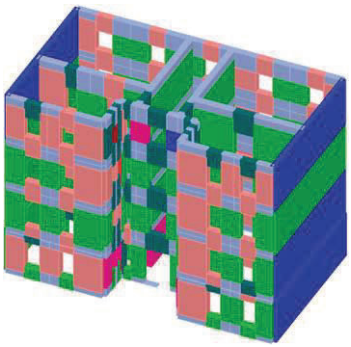

Figure 10: *3D Seismic model - existing condition (Model A)*

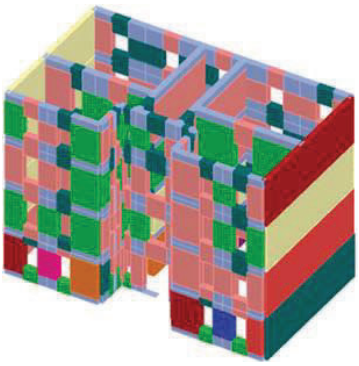

Figure 11: *3D Seismic model - reinforcement with a concrete compression slab (Model B)*

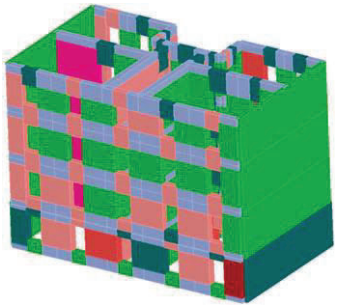

Figure 12: *3D Seismic model - reinforcement with wooden elements - OSB boards (Model C)*

https://doi.org/10.52202/069179-0277

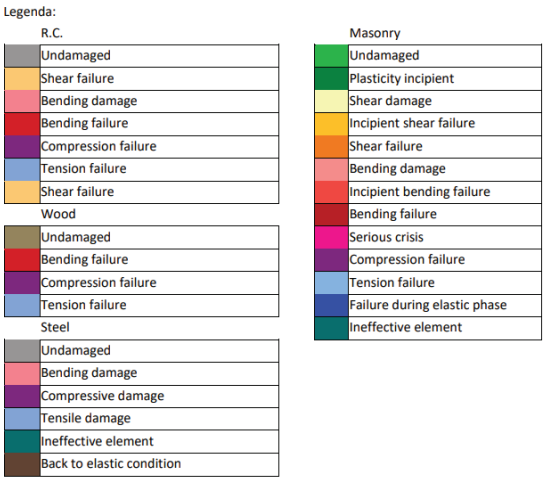

Figure 13: *Legend of structural damage*

The constructed 3D models represent the distribution of stiffness and masses, and thus all significant forms of deformation as well as inertial forces in the observed seismic action are taken into account. The analysis was performed according to Eurocode 8 [5,6].

For the method of gradual pushing, two forms of vertical distribution of lateral forces were used. These are a uniform distribution that is proportional to the mass of the structure on each floor, and a linearly increasing distribution in height that has the shape of an inverted triangle. The mentioned lateral forces act at the locations of the masses in the model. A random eccentricity of 5% was also considered, which takes into account possible uncertainties in the position of the masses. The result of the earthquake analysis is a capacity curve that gives the relationship between the transverse force at the footing and the control displacement.

4 RESULTS

The analysis for the existing condition shows the expected results - local failure of individual elements (walls are not horizontally connected). The largest displacements were achieved on the model of the existing state, where the horizontal stiffness of the timber ceiling is the least, and the smallest displacements are on the model of the reinforced concrete compression slab, which has the highest stiffness of the mentioned models.

Table 1: *Calculated construction shifts for individual models*

Model	Maximum displacement of the structure compared to model A [%]
Model A	100,00%
Model B	73,74%
Model C	65,42%

The tables below show the results of the pushover analysis for displacements under seismic loading for the X and Y directions:

Table 2: *Pushover analysis – displacement (Model A)*

Br.	Seismic load direction	Seismic load	dt SD [cm]	dm SD [cm]	SD Ver.	Sd DL [cm]	d*y DL [cm]	DL Ver.
1	+X	Uniform	10,16	7,46	No	3,74	1,47	No
2	+X	Modal distribution	14,78	0,87	No	5,44	0,85	Ne
3	-X	Uniform	10,38	8,20	No	3,82	1,32	No
4	-X	Modal distribution	15,79	1,01	No	5,82	0,98	No
5	+Y	Uniform	5,53	1,55	No	1,67	1,21	No
6	+Y	Modal distribution	6,23	1,26	No	1,94	1,02	No
7	-Y	Uniform	5,14	2,17	No	1,48	1,01	No
8	-Y	Modal distribution	5,74	1,56	No	1,75	1,15	No

Table 3: *Pushover analysis – displacement (Model B)*

Br.	Seismic load direction	Seismic load	dt SD [cm]	dm SD [cm]	SD Ver.	Sd DL [cm]	d*y DL [cm]	DL Ver.
1	+X	Uniform	10,61	8,03	No	3,96	1,65	No
2	+X	Modal distribution	10,90	3,65	No	4,07	1,49	No
3	-X	Uniform	10,68	8,76	No	3,99	1,46	No
4	-X	Modal distribution	9,80	4,54	No	3,66	1,58	No
5	+Y	Uniform	5,29	3,06	No	1,57	1,27	No
6	+Y	Modal distribution	4,95	2,71	No	1,43	1,21	No
7	-Y	Uniform	5,26	2,27	No	1,52	1,11	No
8	-Y	Modal distribution	4,92	2,15	No	1,38	1,04	No

Table 4: *Pushover analysis – displacement (Model C)*

Br.	Seismic load direction	Seismic load	dt SD [cm]	dm SD [cm]	SD Ver.	Sd DL [cm]	d*y DL [cm]	DL Ver.
1	+X	Uniform	9,67	8,87	No	3,57	1,44	No
2	+X	Modal distribution	9,40	8,87	No	3,47	1,40	No
3	-X	Uniform	9,70	11,03	No	3,58	1,29	No

4	-X	Modal distribution	10,27	10,79	No	3,79	1,58	No
5	+Y	Uniform	4,73	3,16	No	1,33	1,12	No
6	+Y	Modal distribution	5,40	4,01	No	1,57	1,13	No
7	-Y	Uniform	4,77	1,85	No	1,29	0,94	No
8	-Y	Modal distribution	5,41	3,00	No	1,53	0,95	No

The tables below show the results of the pushover analysis for the limit states of significant and limited damage under seismic loading for the X and Y directions:

Table 5: *Pushover analysis – limit states (Model A)*

Br.	Seismic load direction	Seismic load	α SD	α DL
1	+X	Uniform	0,735	0,394
2	+X	Modal distribution	0,059	0,155
3	-X	Uniform	0,790	0,345
4	-X	Modal distribution	0,064	0,169
5	+Y	Uniform	0,354	0,722
6	+Y	Modal distribution	0,249	0,525
7	-Y	Uniform	0,489	0,683
8	-Y	Modal distribution	0,339	0,657

Table 6: *Pushover analysis – limit states (Model B)*

Br.	Seismic load direction	Seismic load	α SD	α DL
1	+X	Uniform	0,758	0,416
2	+X	Modal distribution	0,335	0,367
3	-X	Uniform	0,820	0,366
4	-X	Modal distribution	0,463	0,433
5	+Y	Uniform	0,632	0,811
6	+Y	Modal distribution	0,614	0,847
7	-Y	Uniform	0,500	0,727
8	-Y	Modal distribution	0,514	0,754

Table 7: *Pushover analysis – limit states (Model C)*

Br.	Seismic load direction	Seismic load	α SD	α DL
1	+X	Uniform	0,917	0,403
2	+X	Modal distribution	0,944	0,404
3	-X	Uniform	1,137	0,361
4	-X	Modal distribution	1,050	0,417
5	+Y	Uniform	0,720	0,841
6	+Y	Modal distribution	0,772	0,719
7	-Y	Uniform	0,472	0,726
8	-Y	Modal distribution	0,599	0,624

According to the results of the calculation, the building model without reinforcement (model A) does not satisfy the deformability conditions in all analyses for the limit state of limited damage (DL) and for the limit state of significant damage (SD), with the most unfavourable analysis being 2 in the direction x for which the structure had the ability to withstand 5.9% of the designed peak ground acceleration for a return period of 475 years.
The result of the calculation of model B - the beam reinforced with a concrete compression slab does not satisfy the deformability conditions for any of the limit states, and in the most unfavourable analysis 2 in the x direction, the structure had the ability to withstand 33.5% of the designed peak ground acceleration for a return period of 475 years.

Results for the calculation model C - strengthening with OSB plates, shows that the building does not satisfy the deformability conditions for both limit states of damage, with the most unfavourable analysis being 7 in the y direction, for which the structure had the ability to withstand 47.2% of the designed peak ground acceleration for the return period from 475 years.

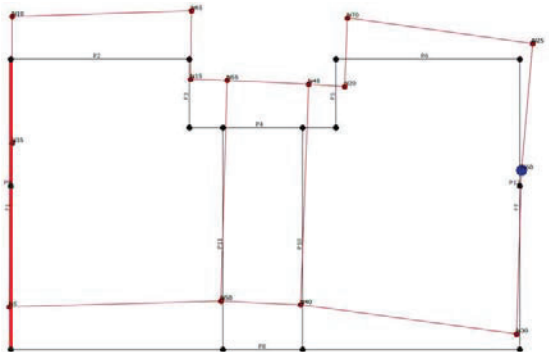

Figure 14: *Seismic analysis no. 2 in the X direction (critical direction), plan view of deformation, (Model A)*

https://doi.org/10.52202/069179-0277

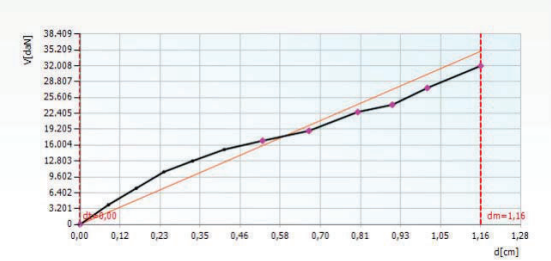

Figure 15: *Pushover curve (analysis n. 2) (Model A)*

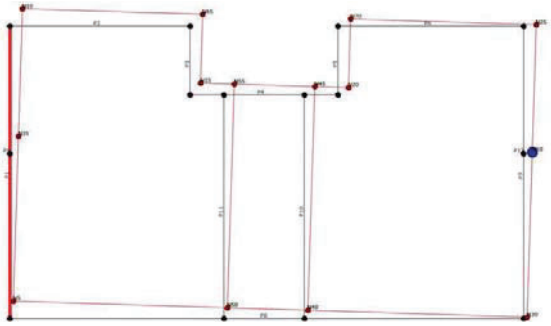

Figure 16: *Seismic analysis no. 2 in the X direction (critical direction), plan view of deformation, (Model B)*

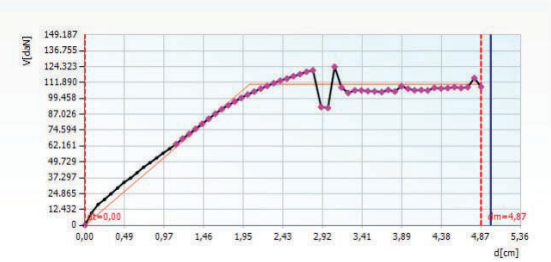

Figure 17: *Pushover curve (analysis n. 2) (Model B)*

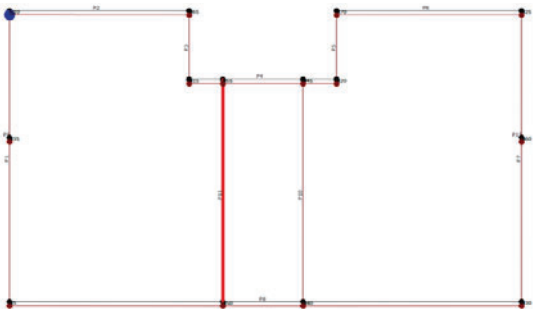

Figure 18: *Seismic analysis no. 7 in the Y direction (critical direction), plan view of deformation, (Model C)*

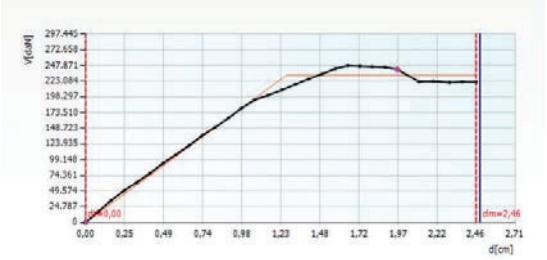

Figure 19: *Pushover curve (analysis n. 7) (Model C)*

5 CONCLUSIONS

After conducting an analysis of various preliminary models of this structure, the best result in terms of increasing the horizontal stiffness of the structure is the use of concrete plate. But there is a problem with the influence of the stiffness of the compression plate on other structural elements, i.e., masonry, and the invasiveness of such a procedure.

However, the analysis showed that despite the high local stiffness of the slab, the calculated displacements of model B are about 11% higher than those of model C. This is explained by the relatively larger mass acting on the walls.

The advantages of strengthening with wooden elements are:

- execution speed,
- low self-weight,
- non-invasiveness
- stiffening in both planes
- can be used for both ceiling and roof systems [2].

Reversible strengthening techniques are preferred when strengthening historical heritage buildings. In this case model B represents an irreversible technique while model C is reversible therefore, option C is presented as the optimal solution.

REFERENCES

[1] Galić J., Vukić H., Andrić D., Stepinac L.: Repair and strengthening techniques of masonry buildings, University of Zagreb, Faculty of Architecture Zagreb, 2020.g.

[2] Bjelanovic, A.: Traditional timber ceiling systems and reinforcements – contribution to the seismic resistance of existing masonry buildings;

[3] Čizmar, D.; Fot, Eduard; Lebo, Ž.; Arbutina, D.; Strengtening of structures of Zagreb's lower city architecture from the aspect of horizontal stiffness. In 8. Assembly of Croatian builders: Construction and climate change, pages. 1-11, 2021.

[4] Uroš, M., Todorić, M., Crnogorac, M., Atalić, J. Šavor M., Lakušić, S., SEISMIC ENGINEERING - *Renovation of masonry buildings*, Faculty of Civil Engineering, University of Zagreb, 2021.

[5] Čizmar, D., Vrančić, M.: Analysis of timber-concrete composite girders, Građevinar journal of the Croatian

Association of Civil Engineers, pages 559-570, 68 (7) 2016.
[6] Rajčić, V.: Tests of coupled wood-lightweight concrete supports. In Građevinar (Builder):, 53 (2001), 1; 1-8
[7] Podnar, H.: Construction project of rehabilitation of residential - office building, Zagreb, 2021
[8] Arbutina D.: Modern methods for making recordings of the existing state, Professional material with seminar, Program of professional training of certified engineers of architecture and construction, Zagreb University of Applied Science, Zagreb, 2011
[9] HRN EN 1996-1-1, Eurocode 6: Design of Masonry Structures—Part 1-1: General Rules for Reinforced and Unreinforced Masonry Structures, 2022.
[10] Eurocode 8: Design of Structures for Earthquake Resistance—Part 3: Assessment and Retrofitting of Buildings—National Annex, 2021.

https://doi.org/10.52202/069179-0277

World Conference on Timber Engineering Oslo 2023

EXPERIMENTAL RESEARCH ON THE SEISMIC PERFORMANCE OF WATTLE AND DAUB INFILLED CHUAN-DOU TYPE TIMBER FRAMES

Rui Xu[1], Yunyang Qi[2], Hao Huang[1,3]

ABSTRACT: In the southwest of China, the Chuan-Dou type timber structure is widely seen in traditional dwellings, temples and halls, among which the wattle and daub (W&D) infilled wall is a relatively common embedded wall. Based on a large-scale field investigation of 30 traditional wooden structures in Chongqing, this paper had conducted experimental research on the quasi-static loading test of one bare Chuan-Dou frame and two W&D infilled Chuan-Dou frames with different wall thickness. The damage characteristic, bearing capacity, stiffness, ductility and energy dissipation of each specimen were analyzed. The results had shown that, compared with bare frame, the W&D infilled frames had obvious better lateral performance; the thicker the infill wall, the higher the bearing capacity, stiffness and dissipated energy of the specimen while also the more intense the damage of the infills.

KEYWORDS: Chuan-Dou type timber frame, Wattle and daub, Seismic performance, Quasi-static

1 INTRODUCTION

Many scholars have carried out some research on the seismic performance of traditional bare timber frames, masonry or wood panel infilled timber frames [1–3]. Finite element simulation is also one of the key research directions, so as to check the failure mode of components in the test and analyse its seismic mechanism [4,5]. However, the W&D infilled timber structure (Figure 1), which is widely distributed in the southwest of China, still lacks adequate research, it is urgent to carry out relevant research to clarify the seismic characteristics of the W&D infilled Chuan-Dou timber frames.

Figure 1: *W&D infilled timber structure*

2 EXPERIMENTAL PROGRAM

2.1 DESIGN OF SPECIMEN

In order to study the effect of the embedded wattle and daub wall and the wall thickness on the properties such as lateral resistance and damage of the wood structure wall of the pierced bucket, a total of three elements were made as follows (Table 1).

Table 1: *Parameters of each specimen (Clay : Straw scraps refers to weight ratio)*

Parameters	CK-1	QH-50	QH-60
Wall Span/mm	1400	1400	1400
Brace spacing/mm	0	350	350
Wall thickness/mm	0	50	60
Clay : Straw scraps	0	130:1	130:1

The wood used in the test was southwest spruce from China, and all walls were full-scale specimens with single layer and single span. In order to fit the structure found during the actual investigation, the footing of the wooden column was floating and the bottom of the frame was in direct contact with the top of the concrete ground beam. The foot of the two wooden columns was actually the structure of the slot directly buckled at the top of the foot. The detailed structural parameters of the standard specimen (QH-50) and the dimensions of the beam and column elements are shown in Figure 2. The size of the pure frame is the same as that of the standard specimen except that there is no embedded wall.

[1] Rui Xu, School of Civil Engineering, Chongqing University, Chongqing 400045, China, 291559092@qq.com
[2] Yunyang Qi, School of Civil Engineering, Chongqing University, Chongqing 400045, China, 2585549565@qq.com
[3] Hao Huang, Key Laboratory of New Technology for Construction of Cities in Mountain Area (Chongqing University), Ministry of Education, Chongqing 400045, China, huanghao@cqu.edu.cn

https://doi.org/10.52202/069179-0278

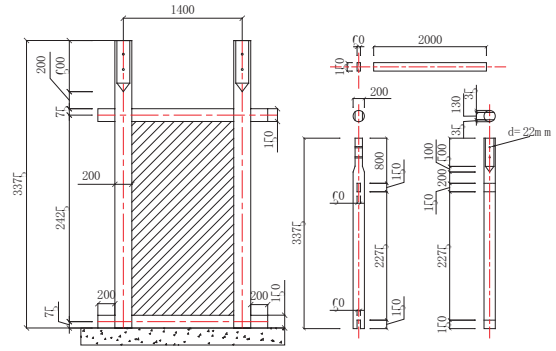

Figure 2: *Dimensions of standard specimen*

2.2 TEST SETUP AND LOADING PROTOCOL

The vertical load of the column is applied by the traditional method of hanging weights which are reinforced concrete columns for about 450kg each. It was decided to hang the weight in front of and behind each wooden column. The weights were lifted after the specimen and sensors were installed, and two weights of a column were lifted simultaneously to avoid a large out-of-plane tilt of the wall. The schematic diagram of the test piece after the overall installation is shown in Figure 3. The loading rate is also controlled at 25mm/min, and the wall cracks were plotted after all the single-cycle loading was finished and each three-cycle loading.

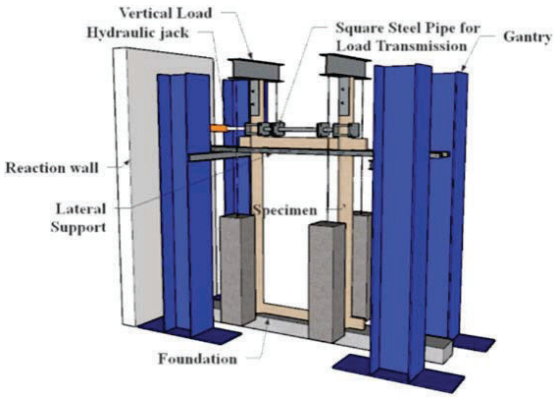

Figure 3: *Test model*

The design of the loading history referred to the international general standard, and the load-displacement curve of the static loading test of the corresponding wall is used to determine the control displacement of the structure under quasi-static loading. Finally, the loading history of pure frame and timber frame with embedded wall is determined as shown in Figure 4.

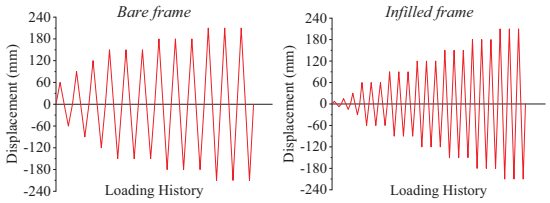

Figure 4: *Loading history*

For the unit wall of the traditional Chuan-Dou timber frame, the main horizontal displacement measurement is concentrated at the bottom of the frame and the load application site, and the vertical displacement is concentrated at the two column bases. In addition, the rotation angle and strain of each joint also need to be measured which is realized in this test with a pair of displacement gauges and strain gauges, respectively (Figure 5).

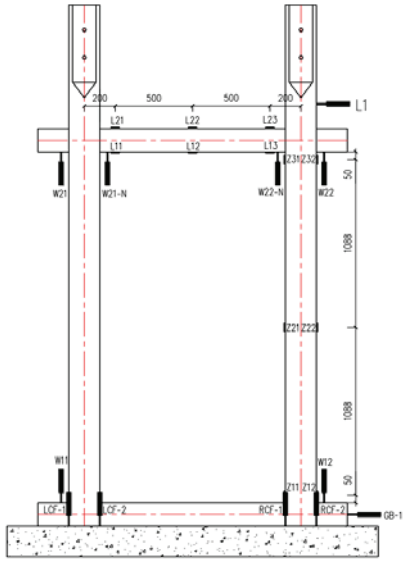

Figure 5: *Gauge arrangement*

3 TEST PHENOMENON

The embedded wall of the specimen is composed of wattle and daub and was finally finished in the form of putty smearing the surface layer. Therefore, there would be initial cracks caused by dry shrinkage cracking of the mud and specimen hoisting before the formal test. The main failure modes of the specimens are concentrated on the peeling off of the surface putty, the large area of the mud falling off, the bareness of the bamboo strips and the embedded wall separated from the frame. However, due to the variation in embedded wall and its thickness, there are differences in the stages of damage formation. The important failure process and the loading stage of each specimen are given in Table 2-4, and the crack development state and the specific failure mode are shown in Figure 6.

https://doi.org/10.52202/069179-0278

Table 2: *Summary of key experimental phenomena of specimen CK-1*

Loading stage	Key phenomena
150mm	The left and right column bases have unequal slip relative to the initial position
Third cycle of 180mm	The force transmission square steel pipe is partially pressed on the top surface of the wooden beam due to the loosening of the screw
First cycle of 210mm	The force transmission square steel pipe is all pressed on the top surface of the wooden beam. The steel parts rub violently against the wood
Second cycle of 210mm	The hysteresis curve does not show the load displacement path correctly and the test is terminated

Table 3: *Summary of key experimental phenomena of specimen QH-50*

Loading stage	Key phenomena
Before the test	Front surface fine cracks are distributed in the upper and lower part of the wall. Reverse surface cracks are spread all over the wall.
7.5-60mm	The new cracks continue to expand. The back putty is partially peeled. Some of the mud at the joints connected to the side of the column is stripped off.
120mm	When one side of the wall is pressed, the embedded wall is separated from the frame on the other side.
150-210mm	The shedding of mud material continues to develop. The embedded bamboo strips are partially exposed.

Table 4: *Summary of key experimental phenomena of specimen QH-60*

Loading stage	Key phenomena
Before the test	The initial cracks are long and thin, and the lifting process causes the putty to peel and fall off
90mm	Putty layer peeling keeps getting worse
120mm	Delamination of local surface mud and internal mud on the wall
150-210mm	Cracks are developing and large pieces of clay material are falling off more and more

Figure 6: *Test phenomenon*

4 ANALYSIS OF TEST RESULTS

4.1 HYSTERETIC LOOPS AND ENVELOPE CURVES

The comparison between hysteresis curves and envelope curves of different components are shown in Figure7.

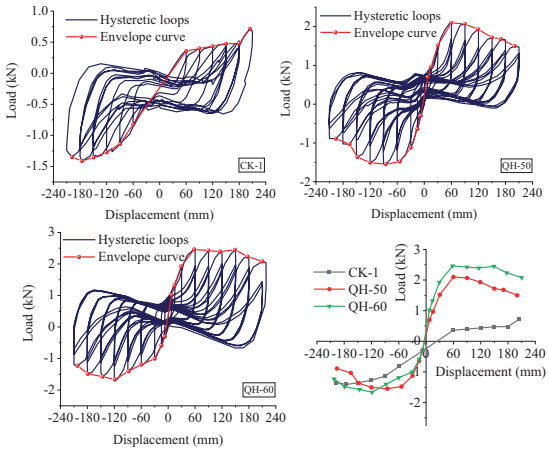

Figure 7: *Hysteretic loops and envelope curves*

Due to the initial existence of gaps in the mortise and tenon joints, the pure frame specimen showed slippage in the first loading level cycle, and the hysteresis curve showed anti-S shape. With the increase of loading level, the mortise and tenon joints exhibited more plastic deformation, and the slippage section of the hysteresis curve became longer and longer. with obvious pinching effect, the hysteresis loops of subsequent loading levels were Z-shaped. As the top force transmission square steel pipe fell on the top surface of the top beam, it was equivalent to become a part of the wall and was stressed together with the wall, so the stiffness and bearing capacity are steeply increased. It is the force transmission square steel pipe that was raised again in the back-tensioning process thus the bearing capacity began to drop at the end of the back-tensioning. It was no longer a part of the wall and the whole specimen exhibited a relatively large plastic deformation at this time which meant that the specimen began to enter yielding stage.

https://doi.org/10.52202/069179-0278

The hysteresis loops of the QH-50 specimen were shuttle-shaped at the loading level of 7.5 mm, and the load displacement was linear overall, indicating that the specimen was still in the elastic stage. With the increase of the loading level, the hysteresis loops gradually transitioned to Z-shaped, and the pinching effect became more and more obvious. The hysteresis loops of the standard specimens were obviously fuller than those of the pure frame specimens, reflecting the improvement of the energy dissipation capacity of the embedded wall with wattle and daub infill.

The development pattern of the hysteresis loop of QH-60 specimen is similar to that of QH-50, which is shuttle-shaped at 7.5 mm and Z-shaped at the subsequent large displacement loading level, and the pinching effect is intensified. The envelope curve of QH-60 specimen shows that the specimen reaches the extreme load of 2.46 kN in the positive direction at 60 mm loading level, but the obvious decrease of the load occurred after 150 mm. The drop of load before this is not significant, combined with the test phenomenon of QH-60 specimen, it can be inferred that the large area of mud shedding occurred at 180mm and afterwards caused a large discount in the bearing capacity of the specimen.

4.2 COMPARISON OF LATERAL RESISTANCE

For all loading specimens, the calculation of the lateral performance parameters is taken from the envelope curve. The calculation method is shown in Equation (1), Equation (2) and Equation (3):

$$K = \frac{0.3F_{\max}}{D_{0.4F_{\max}} - D_{0.1F_{\max}}} \tag{1}$$

$$G = \frac{F_{\max}}{2D_y} \times \frac{H}{L} \tag{2}$$

$$d = \frac{D_{\max}}{D_y} \tag{3}$$

where K = secant stiffness, F =force, D = displacement, G = shear stiffness, H = height, L = width, d = ductility.

The calculation results based on the above formula are shown in Table 5.

Table 5: *Comparison of lateral performance parameters between specimens*

Parameters	CK-1	QH-50	QH-60
K (kN/m)	9.850	55.350	88.618
G (kN/m)	10.063	102.560	171.127
d	3.41	3.47	4.79

It can be found that because there is no embedded wall, the mortise and tenon joints become the main part to resist the lateral force, and the role of the joint alone is relatively limited, so the embedded wall has a significant improvement in the bearing capacity. In terms of ductility, the two specimens (CK-1 and QH-50) also show different characteristics in the positive and negative directions. The ductility of the positive loading is similar, while the ductility of QH-50 is significantly larger than that of the pure frame. The embedded wattle and daub wall also significantly improves the initial stiffness and overall shear stiffness. In general, the bearing capacity, stiffness and ductility of the timber frame are obviously improved by the embedded wall. In terms of bearing capacity, the specimen shows that the thicker the wall, the higher the bearing capacity and the ductility of QH-60 is higher than that of QH-50 at the same time.

4.3 STIFFNESS DEGRADATION

The change in stiffness of a timber frame can reflect the magnitude of the frame's ability to resist deformation. The stiffness degradation reflects the cumulative damage to the joints of the timber frame which can be described by the secant stiffness K_i defined by Equation (4):

$$K_i = \frac{\left|+P_i\right| + \left|-P_i\right|}{\left|+\Delta_i\right| + \left|-\Delta_i\right|} \tag{4}$$

where P = peak load, Δ = displacement.

The comparison of the stiffness degradation between the wall thickness parameter specimens and the standard specimens with each other is shown in Figure 8. From the curve change, it can be found that the initial stiffness of the CK-1 specimen (l=60 mm) is 9.85 kN/m, and its stiffness decreases continuously during the loading process. Finally, it is only 4.91 kN/m which is a decrease of 50.2%.

The other two walls have much greater stiffness than the CK-1 specimen at the same loading level due to the presence of the embedded wall. Figure 8 shows that QH-60 has the largest initial stiffness of 88.13 kN/m, followed by QH-50 with 71.13 kN/m. During the subsequent loading, the stiffness of QH-60 is greater than the other two specimens from beginning to end.

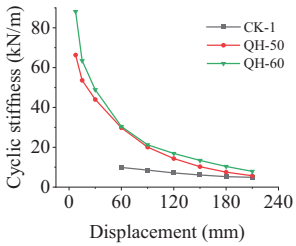

Figure 8: *Stiffness degradation*

The stiffness of all the specimens with embedded walls continuously decreased during the loading process, which was mainly caused by the accumulated plastic deformation of the mortise and tenon joints and the continuous development of the mud shedding in the walls. However, it can be found that the effect of increasing the wall thickness on improving the stiffness of the specimens is relatively obvious.

4.4 STRENGTH DEGRADATION

Strength degradation is caused by cumulative fatigue damage to structural specimens or joints, the magnitude of which determines whether the structure can maintain a good load bearing capacity under multiple cycles of lateral forces. Define R2/R1 as the ratio of the second

https://doi.org/10.52202/069179-0278

cycle peak load to the first cycle peak load at the same displacement control level, and R3/R2 as the ratio of the third cycle peak load to the second cycle peak load at the same displacement control level. These two parameters are used to quantitatively describe the strength degradation of the specimens. The R2/R1 and R3/R2 curves of all specimens are shown in Figure 9.

It can be found that the strength degradation curves of the three walls do not show an obvious rule, but the degradation occurs mainly in the second cycle. The steep increase in R3/R2 at 180 mm for CK-1 is due to the pressure of the force-transmitting square steel tube on the top surface of the top beam, which is mentioned in the test phenomenon before.

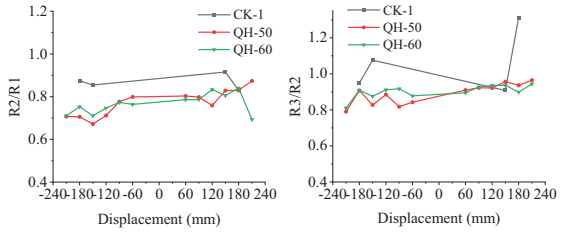

Figure 9: *Strength degradation*

4.5 ENERGY DISSIPATION

The energy dissipation ability of the structure is an important criterion to evaluate the seismic performance. The load-displacement hysteresis curve obtained by the test can calculate the energy dissipated by the structure at different loading levels, which is the area $S_{ABC} + S_{ACD}$ included in the hysteresis loop shown in Fig. 10. The energy dissipation of the structure is mainly manifested as the energy generated by the earthquake or cyclic loading is converted into heat energy or other forms of energy by the deformation and damage of the component or the whole wall.

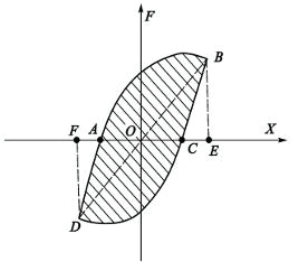

Figure 10: *The schematic diagram of the calculation of the area of hysteretic curve*

In order to better describe the energy dissipation ability of the structure, the equivalent viscous damping ratio (EVDR) is adopted as shown in Equation (5):

$$h_e = \frac{1}{2\pi} \cdot \frac{S_{ABC} + S_{ACD}}{S_{OBE} + S_{ODF}} \quad (5)$$

where h_e = EDVR, S = area.

For the specimens with different wall thickness, the energy dissipation curves and equivalent viscous damping ratio curves at each level are shown in Figure 11 and Figure 12, respectively.

.

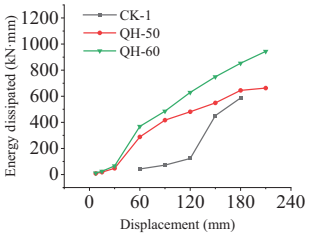

Figure 11: *The energy dissipation curve of all specimens*

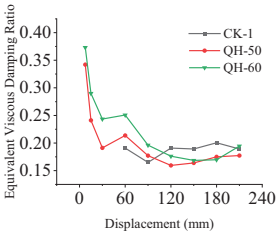

Figure 12: *Energy dissipation and equivalent viscous damping ratio (EVDR)*

It can be found that the pure frame has the lowest energy dissipation among all specimens at each loading level. When the loading displacement was small, the pure frame dissipated energy mainly through the extrusion of the mortise and tenon joints. With the loading displacement increasing, the whole specimen exhibited uncoordinated deformation due to the absence of the restraint of the embedded wall. In addition to the rotation extrusion at the joint of the pure frame specimen, the friction movement deviating from the initial position occurred and the bottom of the wall also rubbed back and forth with the surface of the floor beam during the cyclic loading process, which increased the energy dissipation of the pure frame to a certain extent, so the energy dissipation curve of the pure frame had a relatively obvious increase after 150mm loading displacement.

For both frames with embedded wall, during the whole loading process, the mud gradually dropped in blocks and the bonding between mud and the embedded bamboo strip mesh became worse. Under the large displacement loading section, the structural system cannot be formed between each other, so the energy dissipation ability decreased rapidly with the increase of displacement. In the single-cycle loading section, the energy dissipation of QH-60 was slightly higher than that of the other two specimens, but the overall difference was not significant. In the three-cycle loading section, the energy dissipation of QH-60 specimen was larger than that of QH-50. The comparison of the curves of QH-60 and QH-50 shows that the increase of wall thickness significantly improves the energy dissipation of the specimen.

The trend of the EVDR curve of the two embedded walls is similar, which is reflected in the continuous decline of the single cycle loading section. The curve has a rise when

https://doi.org/10.52202/069179-0278

entering the first three cycles, followed by a slow decline, and finally the curve has risen again. The phenomenon is related to the energy dissipation mechanism of the specimen. The small displacement loading section relied mainly on the nodal energy dissipation of the frame. With the increase of the loading stage, the hysteresis loop transformed from the shuttle shape to the longer anti-S shape of the slip section, and the energy dissipation efficiency was reduced. In the subsequent loading process, the mud wall began to have a relatively large extrusion with the wooden column, and the EVDR value of the specimen began to rise at l = 60mm due to the increase of the energy dissipation part, and the energy dissipation capacity was improved. Subsequently, the wall was damaged to varying degrees, and the EVDR value continued to decline due to the reduction of energy consuming parts. At the end of loading, friction energy dissipation began to occupy the main part, and the energy dissipation efficiency of each specimen was improved. The energy dissipation capacity of QH-60 is only slightly lower than that of QH-50 at 180 mm, while the other loading sections are higher than the standard specimen. It can be seen that the wall thickness improves the energy dissipation capacity.

The resistance of the traditional timber frame with wattle and daub infill mainly comes from the mortise and tenon joints, the mud wall itself and a large amount of frictional slip. The initial gap at the nodes and the wood joints have different effects on the lateral resistance and energy dissipation of the specimens. The main energy dissipation mechanisms of the traditional timber frame with embedded wall are shown in the following aspects. At the beginning of the test, the energy dissipation capacity decreased because the joints mainly provided resistance leading to the development of hysteresis loop pinching and shrinkage. In the middle of the test, the wall started to play more role in energy dissipation, but it decreased again with the increase of wall damage. In the later part of the test, various frictional effects had a greater impact on energy dissipation.

5 CONCLUSIONS

Based on the results of cyclic loading test, the main conclusions can be drawn as follows:

(1) Compared with bare frame, the W&D infilled frames had better bearing capacity and stiffness.
(2) The bearing capacity, stiffness and dissipated energy of W&D infilled frames can be obviously improved by increasing the wall thickness.

ACKNOWLEDGEMENT

This work was financially supported by the National Natural Science Foundation of China (grant no. 51978102).

REFERENCES

[1] Hao H., Yuntian W., Zhao L., et al.: Seismic behavior of Chuan-Dou type timber frames. Engineering Structures, 167:725-739, 2018.
[2] Zhe Q., Xiang F., Shoichi K., et al.: Behavior of masonry infilled Chuandou timber frames subjected to in-plane cyclic loading. Engineering Structures, 211:110449, 2020.
[3] Emile C., Xiaobin S., Yajie W., et al.: Lateral performance of mortise-tenon jointed traditional timber frames with wood panel infill. Engineering Structures, 161: 223-230, 2018.
[4] LI S. Behavior of traditional Chinese mortise-tenon joints: Experimental and numerical insight for coupled vertical and reversed cyclic horizontal loads[J]. Journal of Building Engineering, 2020: 15.
[5] YANG Q. Load resisting mechanism of the mortise-tenon connection with gaps under in-plane forces and moments[J]. Engineering Structures, 2020: 16.

https://doi.org/10.52202/069179-0278

World Conference on Timber Engineering Oslo 2023

EVALUATION OF SEISMIC PERFORMANCE OF WOODEN HOUSES WITH SLIDING BASE BY FULL-SCALE SHAKING TABLE TEST

Ai Tomita[1], Yuji Miyazu[2], Takehiro Wakita[3], Takaki Tojo[4], Takashi Aoki[5], Masayuki Nagano[6]

ABSTRACT: For the purpose of validating the effectiveness of the sliding base for reducing the seismic response, we first conducted a shaking table test of a full-scale two-story wooden frame. In addition, we also propose an evaluation formula for the coefficient of friction and confirm its effectivenes though a time history response analysis that simulates the test results using the calculated friction coefficient. The test results show that the sliding base reduces the maximum story drift angle to 1/100 rad or less even for the input of ground motion that causes severe damage to conventional wooden houses. The analysis results indicated that the test results could be simulated by the time history response analysis using the friction coefficient calculated by the proposed evaluation formula of the friction coefficient.

KEYWORDS: Sliding base, Friction, Contact-pressure, Wooden house, Shaking table test

1 INTRODUCTION

Although research and development of seismic isolation and vibration control technology are being promoted as a method of improving the seismic performance of detached wooden houses, seismic isolation technology is not sufficiently widespread mainly because the installed cost is high. To resolve this situation, a sliding base that can be introduced at low cost has been proposed by Soda [1]. Previous studies have demonstrated the effectiveness of sliding base in reducing seismic response [2] [3]. However, full-scale shaking table test for two-story wooden frame has not yet been conducted. Therefore, in this paper, we conducted full-scale shaking table test of two-story wooden frame assuming a wooden house with standard specifications and examined the behaviour of the sliding base and the seismic response of the superstructure. We also propose an evaluation formula for the coefficient of friction and verify its validity by performing a time history response analysis that simulate the test results using the calculated friction coefficient.

2 OVERVIEW OF SLIDING BASE STRUCTURE

Figure 1 depicts the outline of the sliding base structure. The sliding base is a structure in which a sliding material is inserted between the reinforced concrete (RC) base and the base concrete. Subjected to a severe earthquake ground motion, the superstructure slides on the sliding material to reduce the seismic force acting on the superstructure.

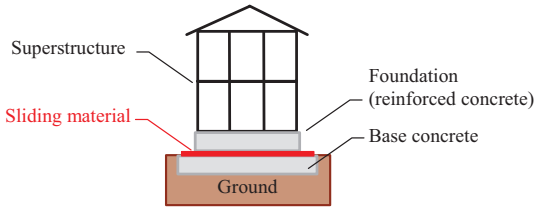

Figure 1: *Overview of sliding base structure.*

3 SHAKING TABLE TEST

3.1 OVERVIEW OF SHAKING TABLE TEST

Figure 2 shows the two-story wooden frame mounted on the shaking table installed in National Research Institute for Earth Science and Disaster Resilience (NIED), in Tsukuba, Japan. Figure 3 shows the elevation of both test frames, and Figure 4 shows the plan of each floor. There were two types of the base: Fixed Base (FB) [4] and Sliding Base (SB). Steel plate weights were installed on the second and the roof so that the mass of the superstructure was 2.61 t on the second floor and 1.73 t on the roof for both. The mass of the RC base of the SB was 6.81 t. There were two types of seismic elements: a 45×90 mm X-shaped brace wall and a structural plywood wall made by connecting 12 mm structural plywood with CN50 nails at a pitch of 150 mm. Figure 5 and Table 1 displays the details of the sliding base and the sliding materials. The base of the sliding base was an RC structure. A fluororesin sheet and a rubber mat as a protective material were laid between the RC base and the base concrete. The base concrete was fixed on the shaking

[1] Ai Tomita, JSPS Research Fellow, (Doctoral Student, Tokyo University of Science), 7121706@ed.tus.ac.jp
[2] Yuji Miyazu, Associate Professor, Tokyo University of Science, Dr. Eng., miyazu@rs.tus.ac.jp
[3] Takehiro Wakita, Guest Associate Professor, Waseda University, Dr. Eng., t.wakita@aoni.waseda.jp
[4] Takaki Tojo, R&D Institute, Takenaka Corporation, toujou.takaki@takenaka.co.jp
[5] Takashi Aoki, National Research Institute for Earth Science and Disaster Resilience (NIED), Dr. Eng., taoki@bosai.go.jp
[6] Masayuki Nagano, Professor, Tokyo University of Science, Dr. Eng., nagano-m@rs.tus.ac.jp

https://doi.org/10.52202/069179-0279

table around four circumferences using steel jigs. In order to constrain the in-plane rotation of the RC base during excitation, a guide rail was installed along the excitation direction on the side of the RC base. In order to reduce the frictional force generated by the contact between the guide rail and the RC base, a polypropylene sheet and a fluororesin sheet were inserted on the contact surface. In the FB, the base was fixed to the H-shaped steel with anchor bolts, and the H-shaped steel was fixed to the shaking table. The first-mode natural period of the superstructure under micro-vibration, which was evaluated by excitation using white noise, was 0.16 seconds for the FB and 0.19 seconds for the SB. Table 2 displays the information of input ground accelerations. An artificially synthesized motion 1 and 2 are the middle- and the large-scale earthquake ground motions defined in the Japanese Building Standards Act, respectively. The time history and pseudo velocity response spectrum of the input ground accelerations are shown in Figures 6 and 7.

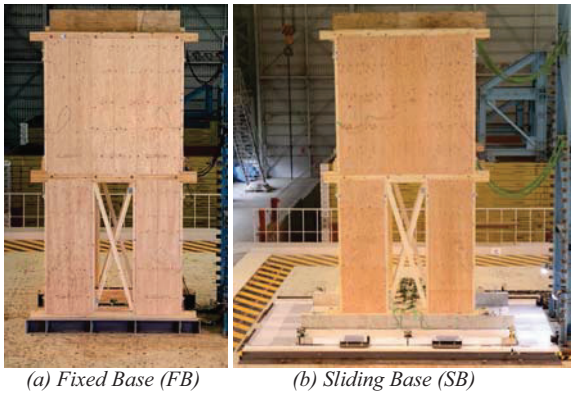

(a) Fixed Base (FB) *(b) Sliding Base (SB)*

Figure 2: *The photograph of the test frames.*

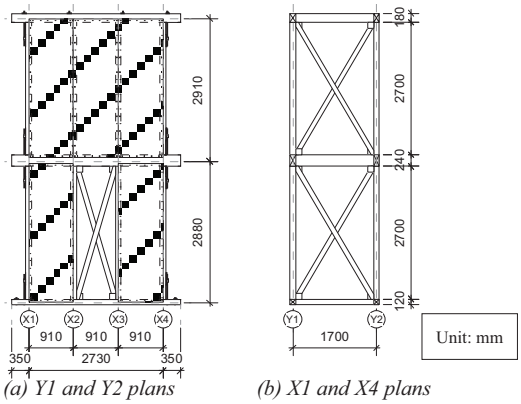

(a) Y1 and Y2 plans *(b) X1 and X4 plans*

Figure 3: *Elevation of the wooden frame.*

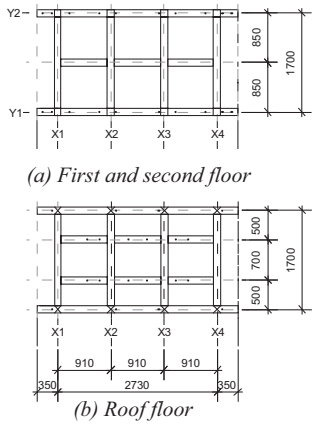

(a) First and second floor

(b) Roof floor

Figure 4: *Plan of the wooden frame.*

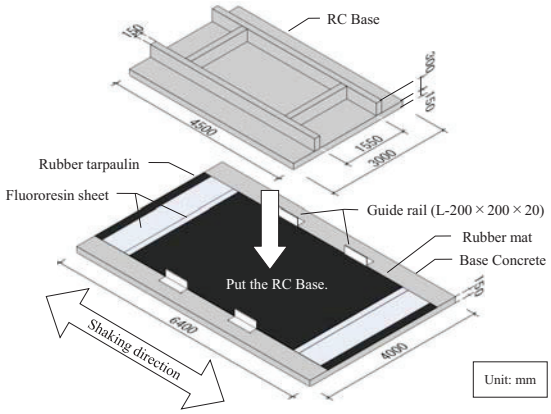

Figure 5: *Detail of the sliding base.*

Table 1: *Materials used for sliding base.*

Sliding material (material thickness)	Use applications
Rubber mat (t = 5 mm)	Installed on the sliding material as a protective material for the upper sliding material
Fluororesin sheet (t = 0.2 mm)	Installed between a rubber tarpaulin and a rubber mat as a lower and upper sliding material
Rubber tarpaulin (t = 2 mm)	Installed on the base concrete as a protective material for the lower sliding material

Table 2: *Input ground accelerations.*

Name	(Abbreviation)	Maximum acceleration (m/s^2)
Artificially Synthesized Motion 1 50%	(BCJ_Lv1*0.5)	1.04
Artificially Synthesized Motion 1 100%	(BCJ_Lv1)	2.07
Artificially Synthesized Motion 2 100%	(BCJ_Lv2)	3.56
2016 Kumamoto earthquake, KiK-net Mashiki Foreshock EW 75%	(MSKf*0.75)	6.94
2016 Kumamoto earthquake, KiK-net Mashiki Mainshock EW 75%	(MSKm*0.75)	8.68
1995 Kobe earthquake, JMA Kobe NS 100%	(KOBE)	8.18

https://doi.org/10.52202/069179-0279

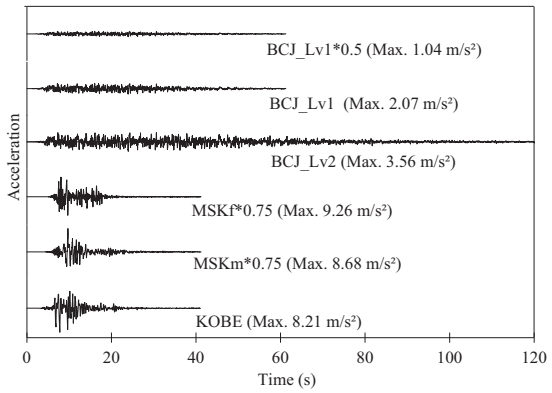

Figure 6: *Time history of the input ground accelerations.*

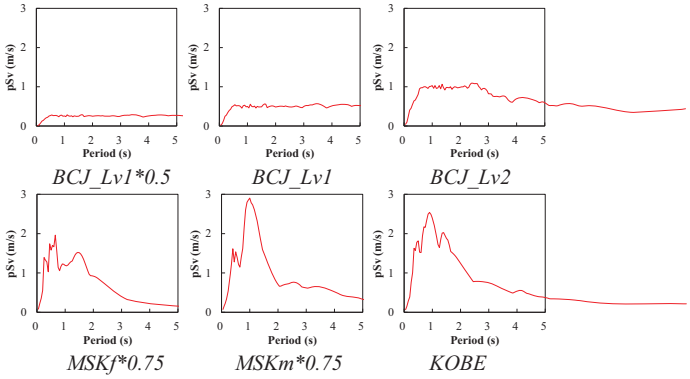

Figure 7: *Pseudo velocity response spectra (h=5%) of the observed wave on the shaking table.*

3.2 CALCULATION METHOD OF THE FRICTION COEFFICIENT

Equation (1) shows the calculation method of the friction coefficient when the cumulative dissipated energy is equivalent, and the vertical ground motion is taken into consideration. The sign of the denominator in Equation (1) is the same as the sign of the slip velocity V defined in Equation (2).

$$\bar{\mu} = \frac{\sum_{t=0}^{T}(N_{t+\Delta t} + N_t)\,(L_{t+\Delta t} - L_t)}{\sum_{t=0}^{T} \pm m(2g + a_{t+\Delta t} + a_t)\,(L_{t+\Delta t} - L_t)} \qquad (1)$$

$$V = \frac{L_{t+\Delta t} - L_t}{\Delta t} = \frac{\Delta L_t}{\Delta t} \qquad (2)$$

where N_t is friction force of the sliding surface at time t, L_t is the sliding displacement at time t, a_t is vertical response acceleration of the sliding base at time t, T is earthquake duration, m is total mass of the structure and g is gravitational acceleration.

In order to eliminate the influence of noise contained in the measurement data, the sliding displacement L_t was subjected to moving average processing with an average interval of 0.02 seconds. In addition, when the value of ΔL_t is less than the threshold shown in Table 3, it was assumed that no sliding occurred during Δt ($\Delta L_t = 0$). The threshold was set for each excitation to be slightly larger than ΔL_t before the start of excitation.

Table 3: *Threshold for calculation of coefficient of friction.*

Name	Threshold (mm)
BCJ_Lv2	0.10
MSKf*0.75, MSKm*0.75, KOBE	0.20

3.3 TEST RESULTS

Figure 8 compares the maximum response for each input ground acceleration. In the FB, first story drift angle of MSKf*0.75-1 increased sharply, and first story drift angle of KOBE-1 further increased. Whereas in the SB, the

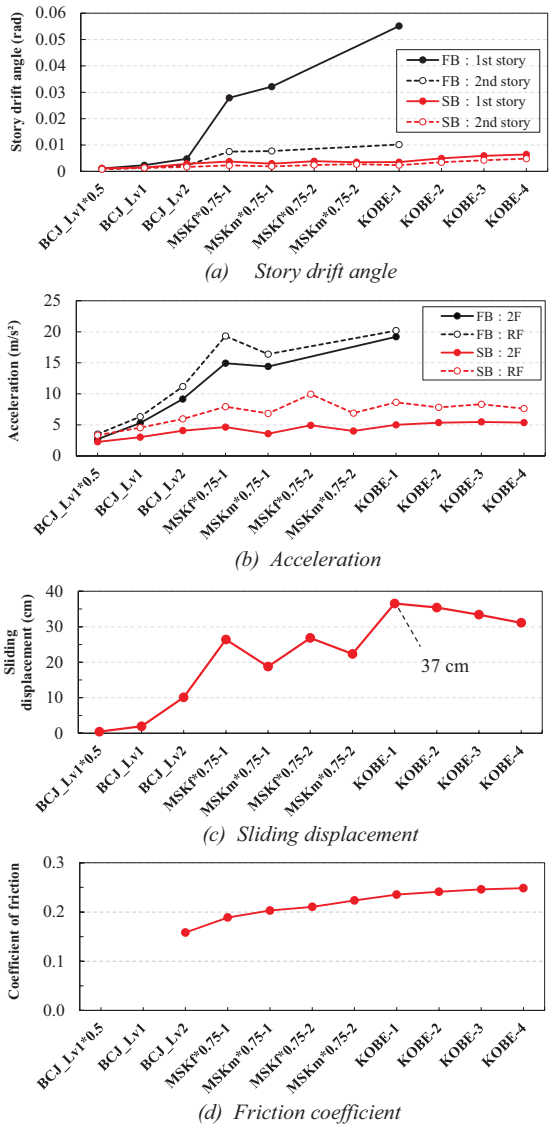

Figure 8: *Maximum response of FB and SB for each input ground acceleration.*

maximum story drift angle is reduced to 1/100 rad or less in all excitations. It is seen that the maximum response acceleration of each floor is also reduced by the sliding base. The maximum sliding displacement was 37 cm at KOBE-1. It can be seen that the coefficient of friction gradually increases with repeated excitation. In addition, it is found that the maximum sliding displacement decreases as the friction coefficient increases due to repeated excitation of KOBE. Figure 9 shows the values obtained by dividing the response values of the SB by those of the FB. By using a sliding base, it is possible to reduce the response, especially against strong ground motions. The maximum story drift angle of the first story was reduced to 13% with excitation of MSKf*0.75-1, 10% with excitation of MSKm*0.75-1, and 8% with excitation of KOBE-1. The maximum response acceleration on the second floor was reduced by 25% with excitation of MSKm*0.75-1, and the maximum response acceleration on the roof floor was reduced to about 40% by excitation of MSKf*0.75-1 to KOBE-1. From the acceleration response spectra on the first and second floors shown in Figures 10 and 11, it can be seen that the frequency characteristics have changed and the response value has been reduced by applying the sliding base. Figure 12 shows the force deformation relations of each story of the FB and the SB. It can be seen that the maximum force of first story can be reduced to about half by applying the sliding base.

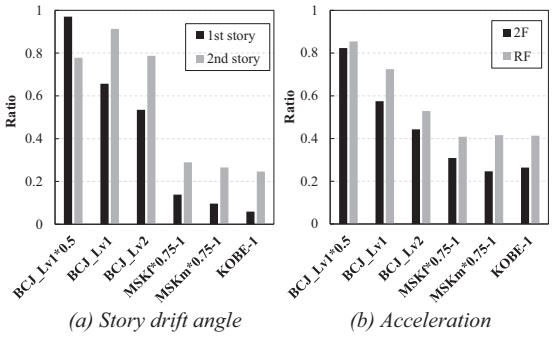

Figure 9: *Ratio of the response of SB to that of FB.*

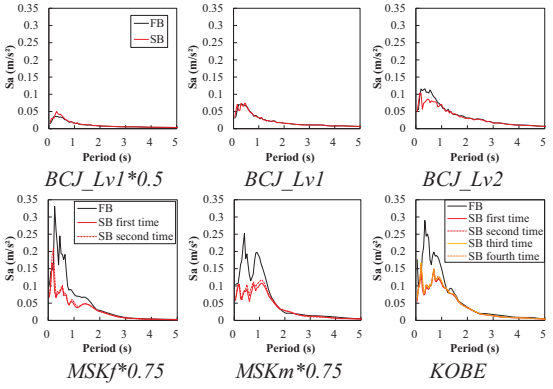

Figure 10: *Acceleration response spectra (h=5%) of the observed wave on the first floor.*

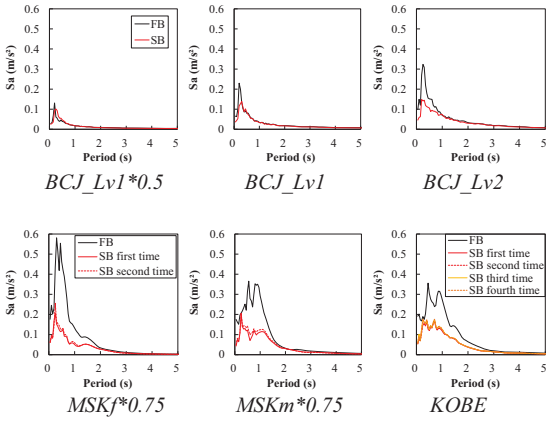

Figure 11: *Acceleration response spectra (h=5%) of the observed wave on the second floor.*

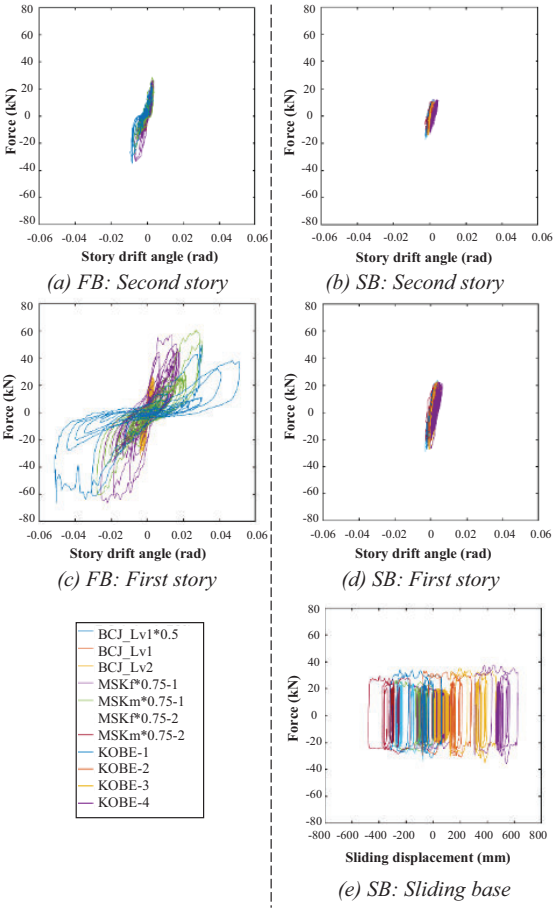

Figure 12: *Force-deformation relations of FB and SB.*

Time history of the sliding displacement, the story drift angle and the acceleration of the FB and the SB are compared in Figures 13 (a), (b) and (c), respectively. It can be seen that the base of the SB moved mainly in one direction and finally stopped with the residual displacement of about 20 cm. The residual displacement highly depends on the characteristic of the input ground motion; however, it is important to take it into

https://doi.org/10.52202/069179-0279

consideration at the design stage of the building with the sliding base. It can be confirmed in Figures 13 (b) and (c) that the story drift of the SB is lower than that of the FB in all the time, whereas the acceleration is reduced mainly during from 12 to 14 s and during from 15 to 16 s when the sliding of the base occurred.

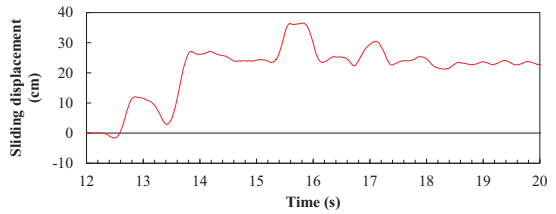

(a) Sliding displacement

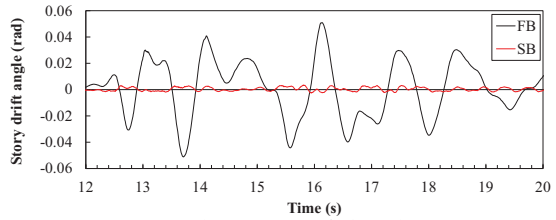

(b) First story drift angle

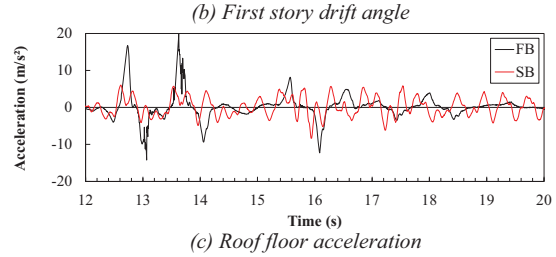

(c) Roof floor acceleration

Figure 13: *Time histories when input KOBE-1.*

The damage condition of the sliding material after all shakings is shown in Figure 14. It was confirmed that the sliding material was torn by about 1.3m after the end of all excitations. Considering this together with the results of maximum response, at least the increase in the friction coefficient and the decrease in the maximum sliding displacement after KOBE-2 can be attributed to damage to the sliding material.

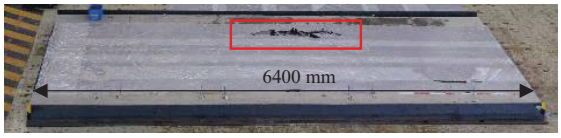

(a) Overall photo of the lower sliding material

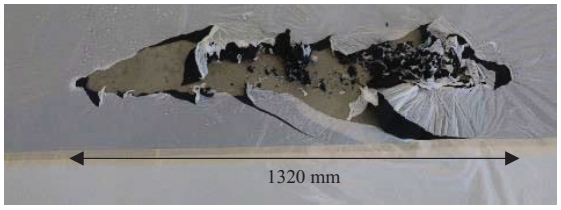

(b) Enlarged photo in red frame

Figure 14: *The photograph of the damage condition of the sliding material after full excitation.*

4 TIME HISTORY SEISMIC RESPONSE ANALYSIS

4.1 OVERVIEW OF ANALYSIS

Each test frame was model in the multi-mass shear system depicted in Figure 15, and the simulation of the experiment was performed by time history response analysis. The mass of each floor was 6.81 t for the sliding base, 2.61 t for the second floor, and 1.73 t for the roof floor. An elastic-perfectly plastic model was used to model the sliding base. The yield force of the elastic-perfectly plastic model was obtained by multiplying the friction coefficient estimated from the test results by the total mass of the SB, 10.84 t. The coefficient of friction was set to 0.197, which is the average value from BCJ_Lv2 to MSKm*0.75-2, taking into account the effect of repetition. The initial stiffness of the elastic-perfectly plastic model was set to reach the yield force at 0.01 mm deformation. For the modelling of the superstructure, we used the ENCL model [5], which simulates the force deformation relations obtained from cyclic loading test on structural plywood walls and X-shaped brace walls. Figure 16 shows the force deformation relations of the ENCL model. The ENCL model for four structural plywood walls and the ENCL model for two X-shaped brace walls were placed in parallel on the first story, and the ENCL model for six structural plywood walls was installed on the second story. The damping of the superstructure was set to 1% of the initial stiffness proportional type, and no viscous damping was applied to the sliding base. The natural periods of the first mode of the FB and the SB are 0.282 s and 0.284, respectively. The input seismic motion was the acceleration measured on the shaking table, and the input acceleration was set to 0 between each excitation for 10 seconds, so that the free vibration after the excitation was sufficiently damped. OpenSees [6] was used to perform the time history analysis, and the Newmark β (β = 0.25) was used for the numerical integration. The step time of the calculation was 1/10000 seconds.

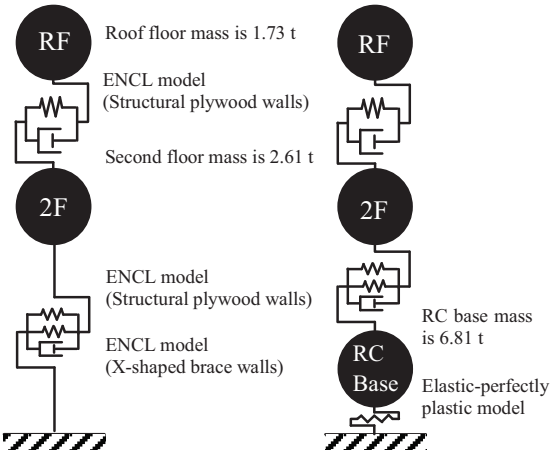

(a) Fixed Base (FB) *(b) Sliding Base (SB)*

Figure 15: *The analysis model of FB and SB.*

https://doi.org/10.52202/069179-0279

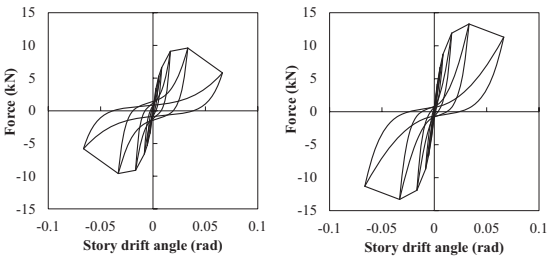

(a) Structural plywood wall *(b) X-shaped brace wall*

Figure 16: *Force-deformation relations of seismic walls.*

4.2 NUMERICAL ANALYSIS RESULTS

Figure 17 shows a comparison of the test results and analysis results for the FB, and Figure 18 shows a comparison of the test results and the analysis results for the SB. In the FB, the maximum story drift angle of the second story agree well with the test results. On the other hand, the analysis results for the first story were larger with excitation up to BCJ_Lv2, and smaller with excitation after the MSKf*0.75-1. Regarding the maximum response acceleration, the test results can be simulated on the second floor and the roof floor with the excitation up to MSKm*0.75-1. The maximum sliding displacement of the SB model generally simulates the test results. The maximum story drift angle is almost the same as the test results for the second story, but for the first story, there is a difference between the test results and the analysis results. As for the maximum response acceleration, the analysis results are excessive for both the second floor and the roof floor.

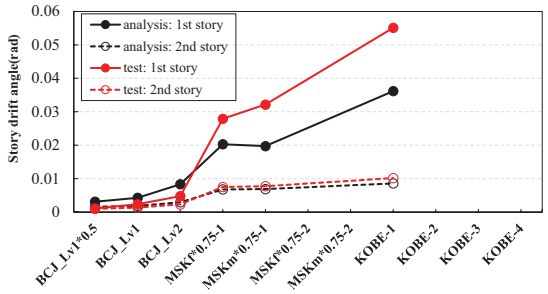

(a) FB: Story drift angle

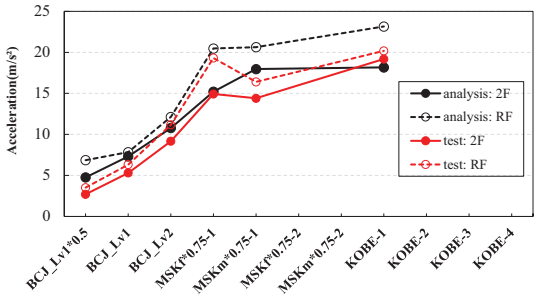

(b) FB: Acceleration

Figure 17: *Maximum response of analysis and test (FB).*

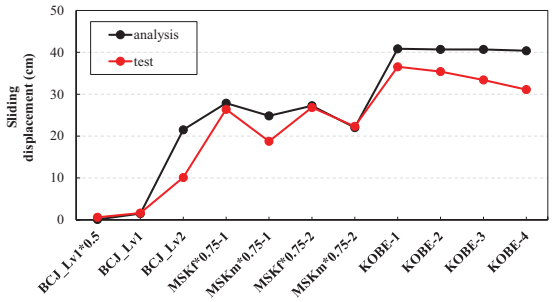

(a) SB: Sliding displacement

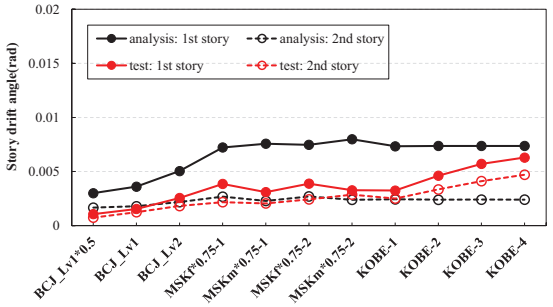

(b) SB: Story drift angle

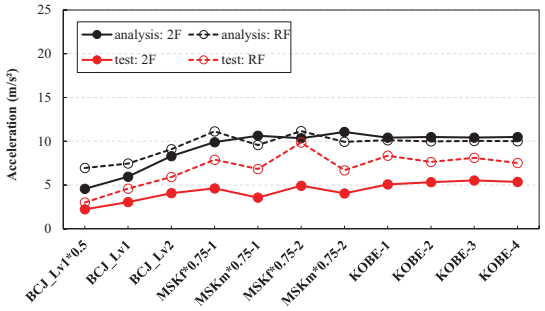

(c) SB: Acceleration

Figure 18: *Maximum response of analysis and test (SB).*

Figure 19 compares the force-deformation relation between test and analysis results. In the test, tthe considerable degradation of the resistance occurred due to the buckling failure of the brace wall, which is not considered in the analysis model. It can be seen that both the maximum deformation and the maximum force of the superstructure of the SB are larger in the analysis results. From the force deformation relations of the sliding base, it can be seen that the difference in cumulative sliding displacement is large. Summarizing the maximum response results, the following two points are considered to be the factors for the difference between the analysis results and the experimental results. (1) Set low stiffness and yield strength of the analytical model in the small deformation region below about 1/100 rad. (2) In the region of large deformation above 1/30 rad, the analytical model does not consider the significant reduction of resistance due to the buckling failure of braces.

https://doi.org/10.52202/069179-0279

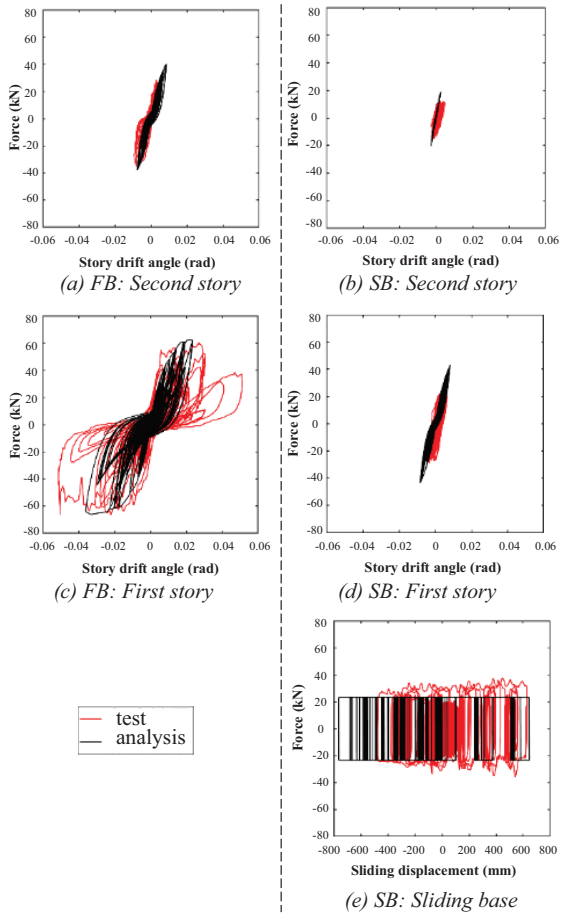

Figure 19: *Force-deformation relations of test and analysis.*

5 CONCLUSIONS

In order to understand the seismic response characteristics of a full-scale two-story wooden frame to which a sliding base is applied, a full-scale shaking table test and time history response analysis were carried out.

1) It is confirmed through the shaking table test that the maximum story drift angle can be reduced to 1/100 rad or less even under extremely strong ground motion by the applying of the sliding base.
The maximum sliding displacement of the sliding base was about 37 cm for the input of KOBE-1.
2) In the analytical study, even with a simple mass-shear system model in which the sliding base is represented by an elastic perfect plastic model, the analysis results shows good agreement with the test result. From this, it can be seen that the friction coefficient calculated by the proposed evaluation formula is appropriate.

ACKNOWLEDGEMENT

This work was supported by the grant from the Japan Society for the Promotion of Science (JSPS KAKENHI Grant Number JP 22J12689) and the Japan Society of Seismic Isolation (JSSI).

REFERENCES

[1] S. Soda, Y. Miyazu: SEISMIC RESPONSE CONTROL OF WOODEN HOUSE PLACED ON SLIDING BASE, Proceedings of the 9th U.S. National and 10th Canadian Conference on Earthquake Engineering, Paper No. 1508, 2010.
[2] Satsuya SODA, Hirosuke FUJITA, Emi MIYAMOTO: Study on seismic response reduction of building on sliding base by full scale shaking table test, Summaries of Technical Papers of Annual Meeting Architectural Institute of Japan, pp. 623-624, 2009. (in Japanese)
[3] Hong-Song Hu, Fan Lin, Yi-chao Gao, Zi-Xiong Guo, Chen Wang: Maximum Superstructure Response of Sliding-Base Structures under Earthquake Excitation, J. Struct Eng., 146(7),2020
[4] T. Katada, Y. Miyazu, S. Kageyama, T. Mori, H. Isoda: Prevention of Soft-Story Mechanism of Wooden Houses Using Continuous Walls., AIJ J. Technol. Des. Vol. 27, No. 67, 1243-1248, 2021. (in Japanese)
[5] H. Matsunaga, Y. Miyazu, S. Soda: A Universal Modelling Method for Wooden Shear/ Nonshear Walls, Journal of Structural and Constraction Engineering, Vol. 74, pp.889-896, 2009. (in Japanese)
[6] PEER: OpenSees, http://opensees.berkeley.edu, reference 2022.

World Conference on Timber Engineering Oslo 2023

CYCLIC TESTS OF INTERLOCKING CROSS LAMINATED TIMBER SHEAR WALLS

Wyatt Payne[1], Alex Winward[2], Johnn Judd[3]

ABSTRACT: Cyclic tests of interlocking cross laminated timber shear walls were conducted to determine hysteretic behavior under lateral load and the effect of anchorage on wall strength. Four 3.05-m tall by 2.44-m long by 288-mm wide shear wall specimens were constructed. Two types of let-in braces (rectangular and dovetailed) and two types of distributed anchor configurations (conventional and a withdrawal type connection) were examined. Shear walls without end anchorage (hold-downs) were compared to shear walls with 14-gauge and 12-gauge strap hold-downs. All specimens successfully resisted cyclic loading up to approximately 2.5% story drift without significant degradation in strength and stiffness. Walls with withdrawal type distributed anchorage increase the lateral strength compared to walls with the conventional configuration of distributed anchorage. The test results showed that hold-down straps increased the wall lateral strength by a factor of two compared to shear walls with only conventionally distributed anchorage.

KEYWORDS: Mass timber, seismic resistance, shear walls

1 INTRODUCTION

Many timber structures typically use high-grade building materials and often involve products that emit volatile organic compounds. The grade of dimensional lumber mainly depends on the slope of grain (fiber alignment relative to the edges of the member) and the size and number of knots (pieces of wood branches that intersect the cross section of the member) [1]. High-grade dimensional lumber has a low slope of grain, and few knots. Light frame construction in the United States often uses Grade No. 2 lumber. This grade of lumber has a low slope of grain and may contain moderate sized knots. In contrast, low-grade lumber has a higher of slope of grain and may contain larger knots. Lumber from trees killed by the Mountain Pine Beetle is an important example of low-grade lumber because it is plentiful in the United States. In Colorado alone, it has been estimated that nearly half of the forest areas have been infested [2]. If left standing, beetle killed trees pose a hazard for wildfires, but if employed as a building material, the wood has the potential to be a low-cost building material. As a result, there has been interest in utilizing beetle kill wood in mass timber systems, such as cross laminated timber, because the cost of the material can be much lower than high-grade materials.

Similar to other engineered wood products, the most common type of cross laminated timber relies on adhesives to bind the layers of wood. Commonly used adhesives include urea-formaldehyde, for interior use wood products, and phenol-formaldehyde, for exterior use wood products. Formaldehyde is a volatile organic compound that is emitted into the surrounding environment. In a building, the concentration of formaldehyde in the environment is increased when the air is refreshed low rates. In the United States, the Department of Housing and Urban Development sets limits on the amount of formaldehyde that may be emitted by building materials. Although formaldehyde emissions from wood products made with urea-formaldehyde or phenol-formaldehyde adhesives are less than the Department's limits, long-term exposure to volatile organic compounds may contribute to building occupants becoming sick proportional to the time spent inside the structure, without any specific illness or cause [3,4], a condition called "sick building syndrome" [5].

Interlocking cross laminated timber is a relatively new type of prefabricated mass timber panel structural system that has the potential to employ low-grade wood without volatile organic compounds [2]. Figure 1 shows an interlocking cross laminated timber structure under construction.

Figure 1: *Interlocking cross laminated timber structure under construction.*

[1] Wyatt Payne, Brigham Young University, USA, Wpayne397@gmail.com
[2] Alex Winward, Brigham Young University, USA, alex.winward@yahoo.com
[3] Johnn Judd, Brigham Young University, USA, johnn@byu.edu

https://doi.org/10.52202/069179-0280

Similar to conventional cross laminated timber, interlocking cross laminated timber is a panel that consists of orthogonal layers (plies) of wood. But unlike conventional cross laminated timber, interlocking cross laminated timber is assembled without adhesives. The plies in a panel can be interlocked using various methods [6]. One of these methods is to create a diagonal "let-in" brace within the panel.

Interlocking cross laminated timber was developed to be fabricated using low-grade wood material [7]. The orthogonal orientation of the plies minimizes the overall effect of the slope of grain on the strength. Thus, interlocking cross laminated timber systems can be sourced from local standing dead timber material, such as beetle-kill trees, and it can decrease the concentrations of pollutants in buildings.

Similar to conventional shear walls, interlocking cross laminated timber shear walls use distributed anchorage to resist sliding, and end anchorage to resist rocking. Figure 2 shows the distributed and end anchorage in a shear wall. The conventional type of distributed anchorage uses small-diameter self-tapping screws to fasten the wall to a wood sole plate that is bolted to the concrete foundation. For wide-segment shear walls with lower lateral demands, strap hold-downs are often used. Strap hold-downs are embedded in the foundation before the concrete hardens, and then later fastened to the face of the shear wall. For narrow segment shear walls, like the one shown in Figure 2, a larger-capacity hold-down is required.

Since interlocking cross laminated timber is relatively new, the structural strength and behavior of interlocking cross laminated shear walls is not yet fully understood. In the first study of the system [7], full-scale specimens of 2.44-m tall by 2.44-m long 340 mm wide five-layer interlocking cross laminated timber shear walls made with beetle killed wood were subjected to a monotonically applied lateral load in the plane of the wall. The lateral monotonic strength of the shear wall was 170 kN, approximately twice the unit shear strength of a comparable conventional shear wall.

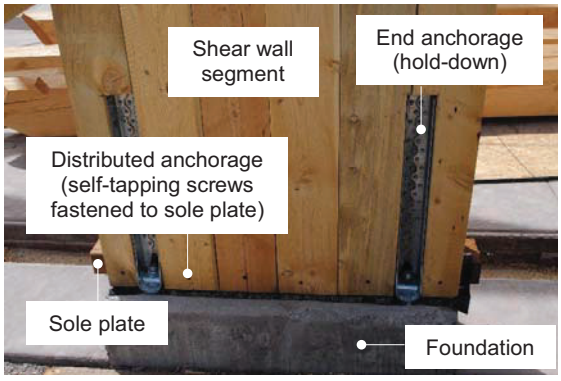

Figure 2: *Distributed and end anchorage in an interlocking cross laminated timber shear wall.*

In a subsequent study [8], 2.44-m tall by 2.44-m long 216 mm wide three-layer interlocking cross laminated timber shear wall specimens made with beetle killed wood were subjected to monotonic in-plane lateral load, and then, in a separate test, the wall was subjected to a monotonic load applied to the face of the wall. The in-plane lateral monotonic strength of the shear wall was 148 kN. Internal crushing of the dovetailed members in the layers of the wall led to ductile in-plane and out-of-plane behavior. In another study [6], 2.44-m tall by 2.44-m long 349 mm wide shear wall specimens using five vertically oriented layers of beetle killed wood were subjected to a monotonically applied in-plane lateral load. The average lateral monotonic strength was 147 kN for shear walls with dovetailed horizontal braces, and 246 kN for shear walls with horizontal and diagonal dovetailed braces.

The focus of the previous studies was on the monotonic lateral strength of the wall. Cyclic strength and behavior of interlocking cross laminated timber shear walls was not investigated. In the authors opinion, this is a significant gap in knowledge because cyclic strength and behavior are important in order to better understand how the shear walls will respond to seismic demands in an earthquake. Furthermore, in the previous studies the shear walls were secured directly to the test frame. No attempt was made to determine the effect on the lateral behavior of distributed and end anchorages that are used in the field. This is also a significant gap in knowledge because lateral behavior of a shear wall is known to be dependent upon anchorage.

In this study, four full-scale interlocking cross laminated timber shear wall specimens were constructed and tested under a cyclic loading sequence to determine hysteretic behavior under lateral load and to determine the effect of anchorage. Two types of let-in brace cross sections (rectangular and dovetailed) were used in this study. Distributed anchorage using medium-diameter self-tapping screws fastened to the wide face of the sole plate was compared to the typical configuration (small-diameter self-tapping screws fastened to the narrow edge of the sole plate). The effect of end anchorage was examined by testing two specimens without hold-downs, and two specimens with strap hold-downs.

2 METHODOLOGY

The shear wall specimens were 3.05-m tall by 2.44-m long by 288-mm wide. The specimens were manufactured by Euclid Timber Frames (https://euclidtf.com/), located in Heber City, Utah, using computer numerical control (CNC) milling machinery. Figure 3 shows a drawing of the shear wall. The wall used 102-mm thick Kiln-dried Douglas fir vertical interior plies, exterior tongue and grove (T&G) plies, and horizontal let-in braces. Specimens 1 and 2 used standard rectangular ("R") cross-section let-in braces (Figure 4a), and Specimens 3 and 4 used dovetailed ("D") braces (Figure 4b). The exterior T&G plies extended below the bottom of the wall to accommodate a rectangular wood sole plate.

https://doi.org/10.52202/069179-0280

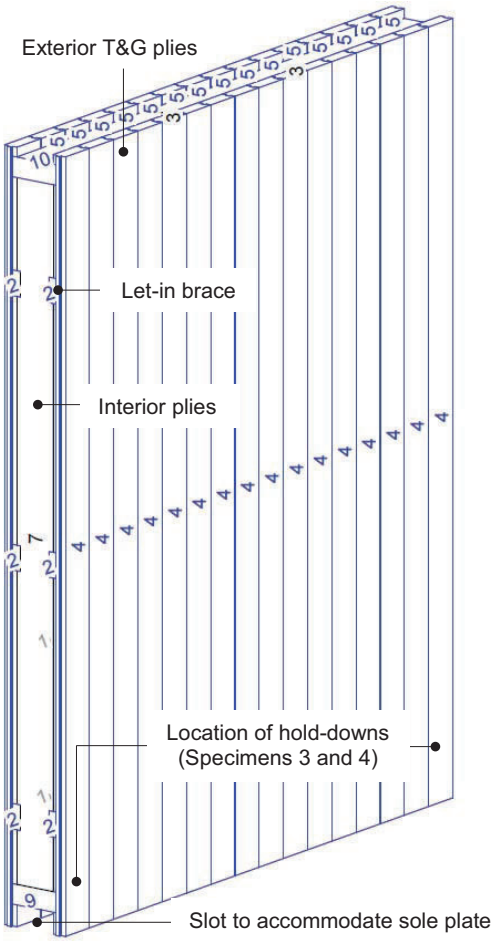

Figure 3: *Drawing of shear wall specimen.*

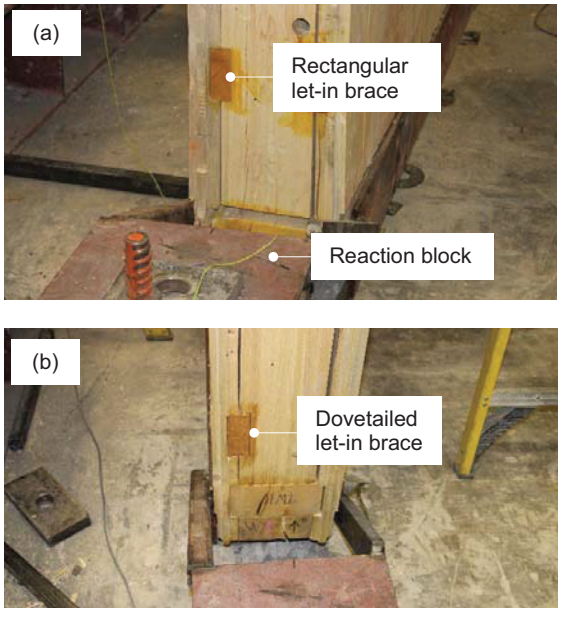

Figure 4: *Let-in braces: (a) rectangular, and (b) dovetail.*

Two types of distributed anchorage were used. For Specimen 1, the distributed anchorage consisted of two rows of 10-mm diameter by 215-mm long TCC self-tapping screws spaced every 76.2 mm. The face of the sole plate was fastened to the web of a steel beam below the wall. The screws passed through the sole plate and into the end grain of the interior plies of the shear wall. In this paper, this anchorage is referred to as type "W". For Specimens 2, 3, and 4, the distributed anchorage consisted of 4.8-mm diameter by 178-mm long OLYLOG self-tapping screws spaced every 203 mm. The screws were fastened through the exterior T&G plies of the shear wall to the narrow edge of the sole plate on both sides of the sole plate. Figure 5 shows the distributed anchorage. This type of distributed anchorage was intended to be representative current construction practices. In this paper, it is termed type "C".

Figure 6 shows the test setup. The top of the shear wall specimen was fastened to the web of a steel beam using 10-mm diameter by 215-mm long TCC self-tapping screws spaced every 76.2 mm. The beam was pin-connected to a spreader beam above. The pin allowed the wall to move vertically (rock). The spreader beam was connected to the end of a hydraulic actuator, and the actuator was mounted to a steel frame. Out-of-plane movement of the shear wall specimen was restrained by a surrounding steel framework. For Specimens 2, 3, and 4, the sole plate was fastened to the web of a steel beam below using 15.9-mm diameter anchor bolts spaced every 914 mm. The steel beam was secured to steel reaction blocks at each end (see Figure 3).

Figure 5: *Distributed anchorage (Specimens 2, 3 and 4).*

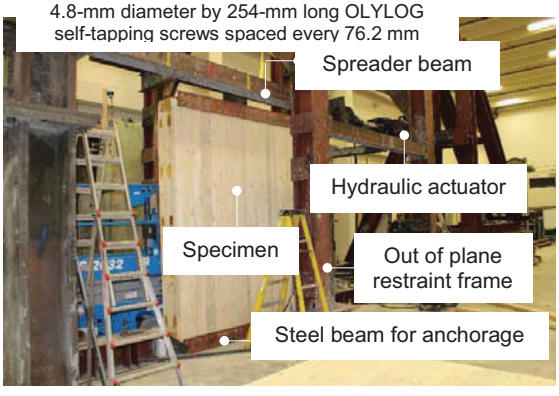

Figure 6: *Test setup.*

https://doi.org/10.52202/069179-0280

Specimens 1 and 2 were installed without hold-downs. Specimen 3 used a 14-gauge LSTHD8 strap hold-down at each end, and Specimen 4 used a 12-gauge STHD14 strap. The upper portion of the strap was fastened to the face of the shear wall according to manufacturer's instructions [9]. The lower portion of the strap is ordinarily embedded in concrete. For testing purposes, this portion was removed and the cut end of the strap was welded directly to the flange of the steel beam, as shown in Figure 7.

The shear wall specimen was subjected to a quasi-static cyclic loading sequence to determine lateral strength, ductility, and cyclic degradation of strength and stiffness. Figure 8 shows the loading sequence. The displacement-controlled loading sequence consisted of an initial two cycles at 1.67% target story drift, followed by two cycles at increments of 1.67% target story drift, continued until failure. The load rate was 50.8 mm/min.

The shear wall specimens were instrumented with string potentiometers (SPs) to measure in-plane and out-of-plane movement of the wall. Figure 9 shows the location of the instrumentation. The actuator internally measured its own displacement and force. The wall displacement was calculated by subtracting the sole plate movement from the displacement at the top of the wall.

Figure 7: *End anchorage placement (Specimens 3 and 4).*

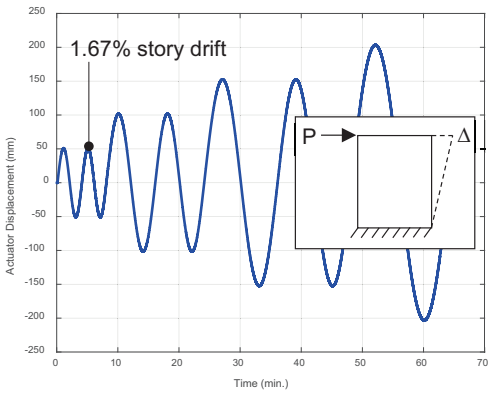

Figure 8: *Cyclic loading sequence.*

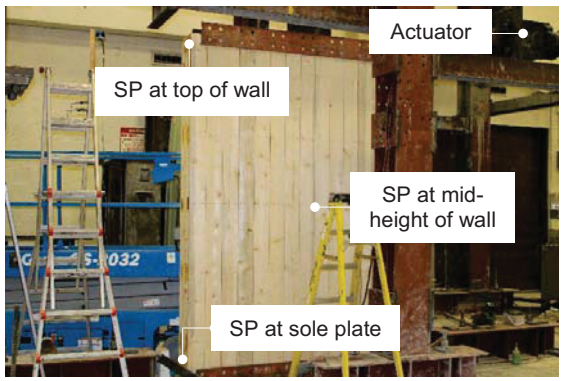

Figure 9: *Instrumentation.*

3 RESULTS

The lateral load versus wall displacement response of Specimen 1 is shown in Figure 10. No substantial damage was observed during the first cycles at 1.21% story drift. During the second cycle at 2.79% drift, vertical cracks initiated at the end of the shear wall. As loading increased, the bottom of the wall withdrew from the TCC self-tapping screws in the sole plate, as shown in Figures 11 and 12. The ultimate load achieved was 97.5 kN. Finally, at 4.39% drift, the sole plate failed in tension perpendicular to grain due to cross-grain bending.

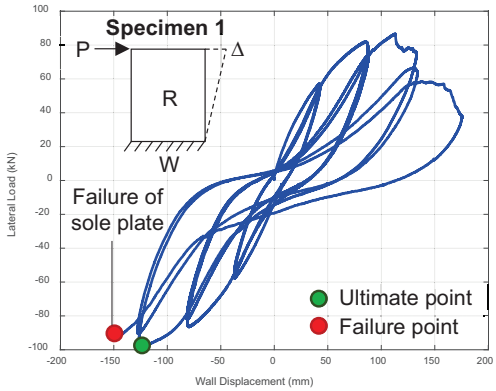

Figure 10: *Specimen 1: load versus displacement response.*

Figure 11: *Specimen 1: wall withdrawal from sole plate.*

https://doi.org/10.52202/069179-0280

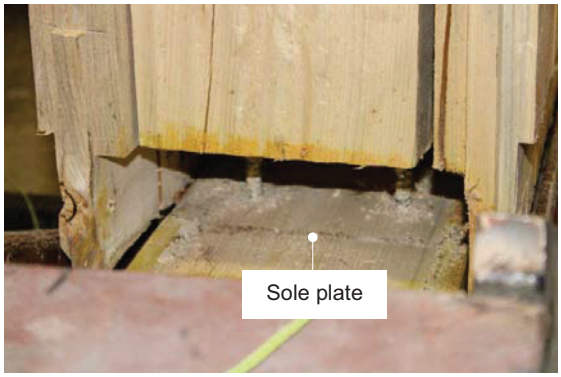

Figure 12: *Specimen 1: wall withdrawal from sole plate.*

Figure 13 shows the response of Specimen 2. As in the previous test, no substantial damage was observed during the first cycles. However, during subsequent cycles, the OLYLOG self-tapping screws tore through the exterior T&G plies, as shown in Figure 14. The ultimate load achieved was 32.8 kN. After completing the third set of cycles, the sole plate failed due to cross-grain bending.

Figure 15 shows the response of Specimen 3. The initial response was similar to the previous tests. As loading progressed, the hold-down straps buckled in compression.

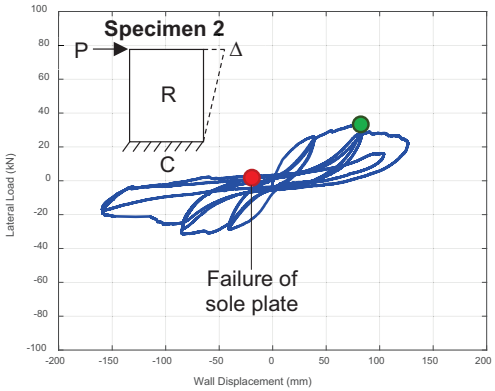

Figure 13: *Specimen 2: load versus displacement response.*

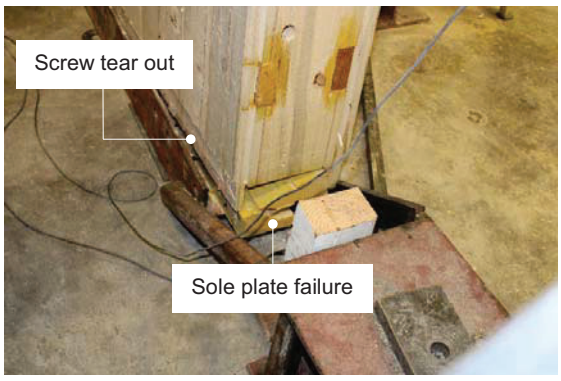

Figure 14: *Specimen 2: screw tear out and sole plate failure.*

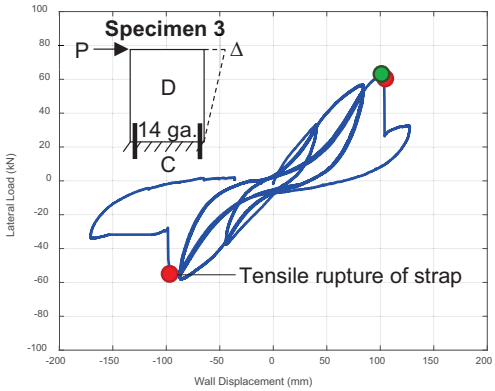

Figure 15: *Specimen 3: load versus displacement response.*

Figure 16a shows the buckled strap. At 3.34% drift, an ultimate load of 62.2 kN was achieved, and one of the straps ruptured in tension (Figure 16b). The loading continued in the reverse direction and the other strap ruptured at 3.23% drift. Finally, the sole plate failed due to cross-grain bending.

Figure 17 shows the response of Specimen 4. The response was similar to the previous test: the straps buckled in compression, then both straps ruptured in tension, and eventually the sole plate failed. The ultimate load achieved was 32.8 kN.at 4.36% drift.

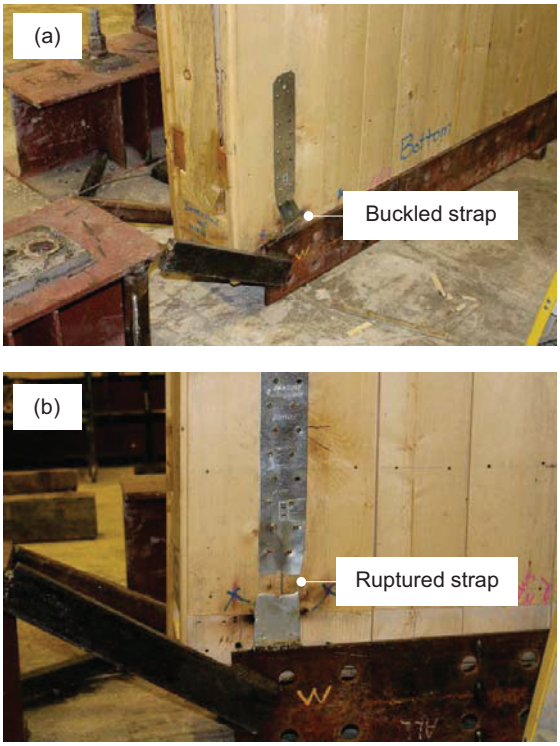

Figure 16: *Specimen 3: (a) buckled strap, and (b) ruptured strap.*

https://doi.org/10.52202/069179-0280

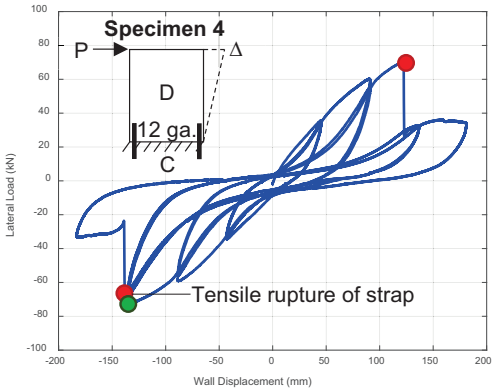

Figure 17: *Specimen 4: load versus displacement response.*

The test results are summarized in Table 1. All specimens successfully resisted cyclic loading up to at least 2.5% story drift without significant degradation in strength and stiffness.

The results indicated that rectangular versus dovetailed let-in bracing did not have a significant effect on the wall response. In contrast, distributed anchorage had a considerable effect. If hold-down straps were not installed, the ultimate strength of the wall with small-diameter self-tapping screws fastened to the narrow edge of the sole plate (Type C distributed anchorage) was a third of the strength compared to medium-diameter self-tapping screws fastened to the wide face of the sole plate (Type W distributed anchorage). The difference in lateral behavior can be attributed to the combined shear and uplift demands that are imposed on the self-tapping screws fastened to the narrow edge of the sole plate when end anchorage is not present to take the uplift loading.

The test results show that hold-down straps successfully resisted the uplift loads until the straps buckled and ruptured after repeated cycles. When the straps failed, the uplift load was transferred to the screws. For both types of distributed anchorage, the drift attained at the ultimate load was approximately 3%. The strength of the wall with Type C distributed anchorage increased by a factor of two if hold-down straps were installed, and the drift attained at ultimate load increased to over 4% drift.

Table 1: *Results of cyclic tests*

Spec.	Anchorage		Strength	
No.	Dist.	End.	P_u (kN)	Δ_u (%)
1	W	--	97.5	3.20
2	C	--	32.8	2.66
3	C	14 ga.	62.2	3.34
4	C	12 ga.	72.1	4.36

Although the results show that distributed anchorage fastened to the face of the sole plate effectively resisted uplift, this type of distributed anchorage configuration would require connecting the sole plate to the shear wall prior to connecting the sole plate to the foundation, which is not the normal construction sequence. Normally, the sole plate is fastened to the foundation wall first and the shear wall is installed later. Therefore, additional research is needed to determine the construction viability of using self-tapping screws fastened to the wide face of the sole plate as a means to anchor the base of the shear wall.

4 CONCLUSIONS

Four 3.05-m tall by 2.44-m long by 288-mm wide interlocking cross laminated timber shear wall specimens were tested under cyclic loads. The test results indicated that the distributed anchorage and the end anchorage have a significant effect on the load deformation response of the shear wall. The type of let-in brace was not significant based on the two cross sections examined. The results show that end anchorage was vital to resist the uplift demands at the base of the shear wall. The conventional configuration for distributed anchorage, using small-diameter self-tapping screws fastened to the narrow edge of the sole plate, led to a shear wall strength that was a third of the strength compared to fastening medium-diameter self-tapping screws to the wide face of the sole plate. However, it is recognized that fastening to the wide face may be challenging to accomplish in the field. In summary, the results suggest that interlocking cross laminated timber shear walls may be a viable lateral system in seismic areas provided sufficient distributed and end anchorages are provided.

ACKNOWLEDGEMENT

The shear wall specimens were generously provided and fabricated by Euclid Timber Frames. The authors also wish to recognize Mr. David Anderson, Lab Manager in the Civil and Construction Engineering Department at Brigham Young University, Rodney Mayo, Structures Laboratory Instrumentation Manager, and Ethan Brown and Micah Harley, Laboratory Assistants, for their help in the experimental tests. The views expressed in this paper are those of the authors and do not necessarily reflect the views of the organizations and people acknowledged.

REFERENCES

[1] Schmidt D., McElroy, Anthony R. Displacement method for measuring knots. Timber Framing, 137(9), 4-8, 2020.

[2] Smith R. Interlocking cross laminated timber: alternative use of waste wood in design and construction. *Building Technology Educators Society Conference*, 2011.

[3] United States Environmental Protection Agency. Indoor air quality: technical overview of volatile organic compounds. https://www.epa.gov/indoor-air-quality-iaq/technical-overview-volatile-organic-compounds.

[4] Wang S., Ang H.M., Tade M.O. Volatile organic compounds in indoor environment and photocatalytic oxidation: state of the art. *Environ. Int.*, 33(5): 694-705, 2007.

[5] Joshi S.M. The sick building syndrome. *Indian J Occup Environ Med*., 12(2):61-4. doi: 10.4103/0019-5278.43262, 2008.
[6] Decker B.T. In-plane lateral load capacities of vertically oriented interlocking timber panels. M.S. thesis, Brigham Young University, Provo, Utah, 2014.
[7] Sanders, S. Behavior of interlocking cross-laminated timber shear walls. M.S. Project, Brigham Young University, Provo, Utah, 2011.
[8] Wilson D.E. Structural properties of ICLT wall panels composed of beetle killed wood. M.S. thesis, Brigham Young University, Provo, Utah, 2012.
[9] Simpson Strong-Tie Company, Inc. *Wood Construction Connectors catalog*. C-C-2021. Pleasanton, California, 2021.

https://doi.org/10.52202/069179-0280

World Conference on Timber Engineering Oslo 2023

FATIGUE RESISTANCE OF ADHESIVE BONDED CONNECTIONS WITH AND WITHOUT INTERNAL STEEL PLATES IN LARGE TIMBER STRUCTURES

Robert Jockwer[1], Pierre Landel[2], Viktor Norbäck[3], Rune Ziethén[4], Erik Dölerud[5], Leo Anderson Naveda[6], Carl-Johan Åkerström[7]

ABSTRACT: A modular wooden wind turbine tower has been developed by the Swedish company Modvion AB, where the prefabricated modular elements are connected by glued timber-timber edge joints and by hybrid timber joints with bonded-in perforated steel plates. The application of wood-based products in such a demanding application and high-performance structure is challenging and a variety of questions had to be solved to ensure a reliable performance. The fatigue performance of the adhesive bonded connections has been evaluated in a research project and is presented in this paper. Test specimens of the fatigue resistance of the adhesive and the bond line has been developed. Different stress ratios with alternating loads and high numbers of load cycles have been tested. The results of the tests are presented in this paper.

KEYWORDS: Bonded-in steel plates, adhesive testing, butt-joints, fatigue strength

1 INTRODUCTION

The transition towards renewable energy supply is more urgent than ever. The need and demand for innovations that enable the construction of tall wind turbines (>150 metres hub height) is very high for Sweden and elsewhere to fully exploit the potential of wind power and reach 100% renewable electricity production.

A modular wooden wind turbine tower has been developed by the Swedish company Modvion AB [1] and a first 30 m tall demonstrator used for research of the Swedish Wind Power Technology Center (SWPTC) at the university of Chalmers has been built near Gothenburg, Sweden (Figure 1).

The tower developed by Modvion has a conical shape and is made of prefabricated modular elements made of LVL, that allow for easy transportation also on remote sites.

Building modular wind turbine towers enables further development towards higher wind turbines and contributes to a lower cost per kWh without logistical barriers. Modular towers made of wood with innovative joining solutions enable tall wind turbines at lower cost, lower weight and provide an efficient installation process. The LCA analysis carried out shows that the wood material contributes to 90% lower CO2 emissions than competing tower structures made of steel and stores Carbon for several years ahead. In addition, there is the possibility of reusing the wooden material in the tower as a construction material.

Nevertheless, the modularity requires strong connections that can be joined on-site. Butt-joints with bonded-in perforated high-strength steel plates are developed for the wooden wind turbine towers by Modvion. These joints are similar to other existing solutions [2].

Figure 1: *Demonstrator of the wooden wind turbine tower used for research on Björkö island near Gothenburg, Sweden*

[1] Robert Jockwer Chalmers University of Technology, Gothenburg, Sweden, robert.jockwer@chalmers.se
[2] Pierre Landel, RISE, Borås, Sweden pierre.landel@ri.se
[3]Viktor Norbäck, RISE, Borås, Sweden viktor.norback@ri.se
[4] Rune Ziethén, RISE, Borås, Sweden rune.ziethen@ri.se
[5] Erik Dölerud, Modvion AB, Sweden erik@modvion.com
[6] Leo Anderson Naveda, Modvion AB, Sweden leo@modvion.com
[7] Carl-Johan Åkerström, Modvion AB, Sweden carljohan@modvion.com

https://doi.org/10.52202/069179-0281

2 DESIGN OF TIMBER TOWERS

2.1 GENERAL

Timber is so far mainly used in buildings and infrastructure applications. Consequently, the design parameters specified in design codes and guidelines, and material properties declared by producers are based on these applications.

Wind turbines made of steel and/or concrete elements can be designed in accordance with the International standard for the design of Wind turbines, IEC 61400 [3]. The design of timber structures follows the basic principles for structural design given in EN 1990, load cases in EN 1991 and specifications for timber materials in EN 1995 (Eurocode 5). These standards are based on similar methods with partial coefficients to achieve sufficient safety margins on both materials and loads. Wooden wind turbine towers can to a large extent be designed by combining these standards. However, there is a gap between innovation and existing design standards as this has not been done before on a large scale.

2.2 FATIGUE OF BONDED JOINTS

2.2.1 General

A good level of knowledge of the fatigue performance of the steel plates exists, however, there is a clear lack of basic and more detailed knowledge of the fatigue performance of the adhesive, its bond to the timber, and the timber itself.

In particular, knowledge and data are missing regarding the fatigue strength of the timber at very large numbers of cycles at low load levels. Current fatigue provisions limit the maximum number of load cycles to approx. $5 \cdot 10^7$. A fatigue threshold (or cut off limit) for wood has been mentioned in some research [4], but not in the design standard for timber bridges EN 1995-2. Existing tests on bonded timber joints [5] are typically below this maximum number of load cycles.

2.3 Fatigue design in Eurocode 5

In the 2004 version of Eurocode 5, the specification on fatigue design is given in the part for bridge structures EN 1995 – 2 (EC5-2) [6]. Kreuzinger and Mohr [7][8] derived the material parameters in the respective chapter based on the literature at the time of drafting.

The specification for the fatigue design of timber structures in the next generation of Eurocode 5 will be incorporated in the main part and can be found in prEN 1995-1-1 [9]. The specifications are based on the same theory and data as in the 2004 version but are slightly more extensive.

The design strength (or analogously the resistance) for the verification of fatigue $f_{fat,d}$ should be calculated from the characteristic strength f_k at static loading according to the following formula:

$$f_{fat,d} = k_{fat} \frac{f_k}{\gamma_{M,fat}} \qquad (1)$$

where k_{fat} is the reduction factor for fatigue and $\gamma_{M,fat}$ is the partial factor for the fatigue resistance, which may be considered as equal to the partial factor under static load unless other information is given in the National Annex.

The reduction factor k_{fat} can be calculated as follows:

$$k_{fat} = 1 - \frac{1 - R_T}{a_{fat}\left(b_{fat} - R_T\right)} \log\left(\beta n_{obs} T_{Life}\right) \qquad (2)$$

where R_T is the stress ratio, n_{obs} is the number of constant amplitude stress cycles per year, T_{Life} is the design service life of the structure expressed in years, and β is the factor based on the damage consequence which can have a value of 1 or 3.

The two coefficients a_{fat} and b_{fat} represent the type of fatigue action and are given in Table 1.

Table 1: *Values of coefficients* $\boldsymbol{a_{fat}}$ *and* $\boldsymbol{b_{fat}}$ *for timber members subjected to arbitrary state of stress*

	a_{fat}	b_{fat}
Timber members with $\sigma_{d,max}$ mainly being		
• compression, perp. or parallel to grain	2,0	9,0
• tension parallel to grain	9,5	1,1
• tension perpendicular to grain	4,7	2,1
Timber members mainly being subjected to		
• shear	6,7	1,3
Connections with		
• dowel-type fasteners with $d \leq 12\ mm$	6,0	2,0
• nails	6,9	1,2

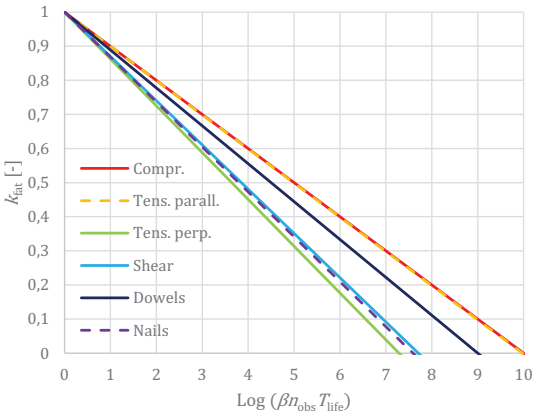

Figure 2: *Example of the reduction factor* $\boldsymbol{k_{fat}}$ *for different stress states and details with* $\boldsymbol{R_T = -1}$.

No specification or values of coefficients are given for the bond line or the glue line failure for different adhesives. The existing test methods for the fatigue testing of bonded joints, such as for glued-in rods when following EN 17334 [10], are not suited to evaluate and potentially classify the fatigue performance of the adhesive itself and the bond line strength. Instead, the steel member is often the element governing the fatigue resistance of the joint [11].

2.4 Impact of testing frequency on fatigue strength

The loading frequency can have an effect on the results of the fatigue tests. Typical frequencies reported in the

https://doi.org/10.52202/069179-0281

literature on connections with mechanical fasteners are in the range of approx. 1-3 Hz.
More detailed studies on the impact of testing frequency on the fatigue strength is reported in the literature for tests on wood-based materials. Bond and Ansell [12] state that at high frequencies adiabatic heating of the specimens may occur due to the hysteresis in the mechanical behaviour of the timber. The good insulation property of the timber limits the heat dissipation and may create heat build-up within the specimen. This can be a particular issue for connections with heat sensitive adhesives. In mechanical connections, also the frictional heating between shear surfaces should be considered. In addition, high frequencies might lead to longer fatigue life (in terms of number of cycles).
A very large range with frequencies from 1-100 Hz has been studied by Thompson et al. [13] on tests on chipboard. For this wide range, a clear impact of the frequency on the fatigue strength was observed: the fatigue strength was higher for the high frequencies of 10 and 100 Hz compared to 1 Hz.
Bonfield and Ansell [14] evaluated the fatigue properties of wood in tension, compression and shear in tests with frequencies of 5 Hz.
Hacker and Ansell [15] performed fatigue tests on wood-epoxy laminates with frequencies between 4 and 7 Hz. It is stated that these frequencies are low enough to avoid sample heating, moisture loss and change in mechanical properties.
Bond and Ansell [12] mention that the rate of stress application (RSA) is the relevant parameter to consider. Different stress levels at constant frequency result in different RSA, which in turn affect the fatigue life of the specimens. They used a constant RSA = 400 MPa/s in their tests resulting in variable frequencies for the different stress levels. Generally, all static and fatigue testing for a particular material should be carried out at the same rate.
Bond and Ansell [12] state that for frequencies exceeding 8 Hz, adiabatic heat generation may cause changes in the properties of the wood.
The frequency of the actual loading in the wooden wind tower is very complex as it is a stochastic phenomenon. For the present case, however, it can be derived that a variable load with $5 \cdot 10^7$ cycles during 20 years' service life has a period of approx. 10 sec (0.1 Hz). It is of course impossible to perform laboratory tests with such low frequency and large number of cycles. Hence, it was decided to perform a first explorative series with different frequencies at high stress ratios and low fatigue life, in order to determine an adequate high frequency.

3 EXPERIMENTS

3.1 OVERVIEW

Different static tension and cyclic fatigue tests of the adhesive bonded joints by Modvion have been carried out at the laboratories of the Swedish institute RISE in Borås, Sweden, between Mars 2022 and January 2023.
The purpose of the experiments was to investigate the fatigue life capacity (curve).
Within the tests, the different stress ratios (-1 < R < 0,1) and loading-ratios have been varied to study the number of cycles to fatigue in the range of approx. $10^4 - 10^7$.
In order to reach the desired high number of cycles in reasonable time, a relatively high loading frequency of up to 10 Hz is desired. In a preliminary test campaign, the static performance of the specimen and the impact of loading frequency were analysed.
It was confirmed that no impact of frequency on the fatigue resistance was observed in the desired range of frequencies between 1-10 Hz.

3.2 MATERIALS

The objective of the test campaign is to study the fatigue performance of the adhesively bonded joints with polyurethane adhesive in the timber tower by Modvion. In particular the bond line fatigue strength between timber and adhesive in the timber-timber edge joints and the glue dowel fatigue strength in the hybrid timber joints shall be evaluated.
The walls of Modvion's timber towers are made of several layers of special Laminated Veneer Lumber (LVL). First, the thick, curved LVL modules are glued together from thinner, special LVL panels. The precise cutting of the LVL modules is done by a CNC-robot. Four of these modules are assembled on-site to build a tubular section of the tower. The sections are then stacked on top of each other to build the tall conical timber tower.
Two different types of joints are present in the tower:

1. the longitudinal (lap) shear joints between LVL modules in the vertical direction of the tower.
2. the transversal, hybrid butt-joints with perforated steel plates between the tower sections in the horizontal direction of the tower.

The test specimens were developed and chosen accordingly, and are denoted as:

1. *Strong Enough Longitudinal* joint or SEL joint
2. *Strong Enough Transversal* joint or SET joint

The dimensions of the joints are carefully calibrated in order to achieve the desired failure in the bond line or in the adhesive dowels going through the perforated steel plates for the SET joint.
In the tests, the mean density of the LVL was 510 kg/m^3. The LVL veneer layup in the specimens was representative of the layup in the final application in the tower.

3.2.1 The edge joint (SEL)

The edge joint technology with a 3 mm thick 2-component polyurethane adhesive is utilized in Modvion's tower to connect two modules along the length.
All specimens were carefully produced in the factory of Modvion AB as solid specimens with an internal thick glue line (Figure 3 top). At the moment of testing at RISE, Borås, two cuts in transversal direction at a distance of 30 mm were cut using a band saw in order to create the bond surface for the shear tests (Figure 3 bottom). The test

was inspired by the lap joint test specimen in EN 302-1 [16].
Steel plates were glued into the specimens in order to clamp the specimens with the same equipment as the SET-specimens. In this case, the glued joint between the steel plate and the LVL was sufficiently overdesigned to prevent failure.

Figure 3: *SEL-specimen without the cutting (top) and with the two cuts for testing (bottom)*

3.2.2 The hybrid timber joint (SET)

The hybrid timber joint is an adhesive connection using a thin perforated steel plate to join two timber members. It is similar to other bonded connections between steel and timber such as glued-in rods for glued structural timber products or the connection system described in [2].
In Modvion's application, a thick steel plate with a large amount of holes are inserted in slots in the LVL members. Then a 2-component polyurethane adhesive is injected between the LVL and the steel plate. When the adhesive cures, bond to the wooden members is established and "glue-dowels" penetrating the steel plate are formed, which lock the steel plates in place and provide strength and stiffness to the connection. These hybrid joints are utilized in Modvion's timber tower to connect two sections on top of each other's to reach the desired height of the tower. The steel plates have a specific hole pattern in order to avoid stress concentrations.

The dimensions of these specimens were carefully designed to achieve the desired failure mode in the adhesive or the bond line. Hence, the steel plates used in the SET samples have small number of holes for the glue dowels to create the connection. An illustration of the specimens is shown in Figure 4. The desired failure mode with bond line failure was confirmed in static tests.

Figure 4: *Illustration of the SET-specimen*

A variety of different configurations of SET-specimens have been tested as shown in Table 2. The configurations include: two different methods for manufacturing the holes of the steel plates, different adhesion inhibitors applied on the steel plates (SET 200 and 400) , a variation of the glue line thickness, and the number of holes in the steel plate have been varied.

Table 2: *The different sets of SET samples*

SET series	# of samples	Hole manufacturing	Slot thickness [mm]
000	13	Laser-cut	6
200	6	Punched	6
400	12	Laser-cut	6
500	8	Laser-cut	9
Double # holes	8	Laser-cut	6
no hole	4	-	6

3.3 METHODS - TESTING EQUIPMENT

3.3.1 Static tensile tests

The static tensile tests aim to evaluate the tensile strength of the samples. The tensile tests have been performed on a universal testing machine (Instron 1253) with a hydraulic cylinder of 50 kN capacity in both compression and tension. The load was recorded using a load cell with a capacity of 50 kN. Before testing, the samples were stored for several weeks in a conditioned climate of 20 °C and 65% relative humidity.
Special grips were designed and manufactured to secure a stiff and strong connection between the steel plates of the specimens and the test machine and to avoid bending stresses in the specimens.

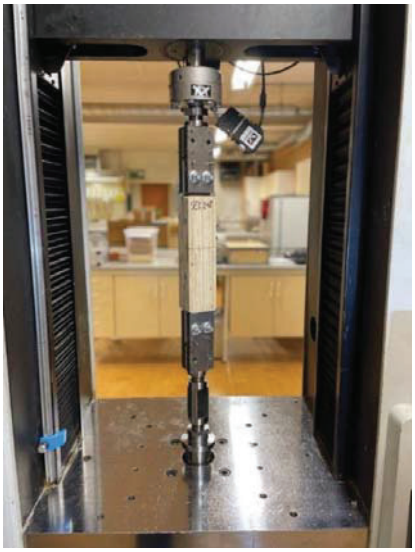

Figure 5: *Test machine Instron 1253 and set-up with SEL sample*

3.3.2 Fatigue tests

In the cyclic fatigue tests the connection's fatigue strength was determined, i.e. the number of loading cycles the connection can withstand for certain loading conditions

https://doi.org/10.52202/069179-0281

before failure. Sinusoidal cyclic loading was applied at frequencies of 5, 6, 8, and 10 Hz.
The loading amplitudes and the mean load values varied, and three different stress ratios $R = \sigma_{d,min}/\sigma_{d,max}$ were tested:

- $R = -1$, the loading is pulsating, e.g. the load varies sinusoidally between -5 kN (compression) and 5 kN (tension), for an example of a load record see Figure 6.
- $R = 0.1$ in tension, e.g. the load varies sinusoidally between 1 kN and 10 kN, an example of a load record see Figure 7.
- $R = 0.5$, e.g. the load varies sinusoidally between 5 kN and 10 kN.

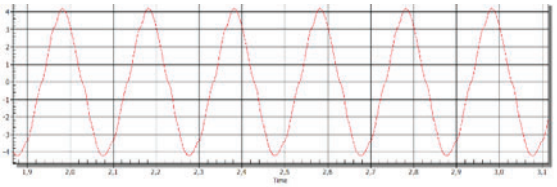

Figure 6: *Example of a load record in machine Instron 1253 during a fatigue test at 5 Hz and R = -1, with pulsating load varying sinusoidally between +4.2 kN and – 4.2 kN. The time in [s] is on the horizontal axis, and the load in [kN] is on the vertical axis.*

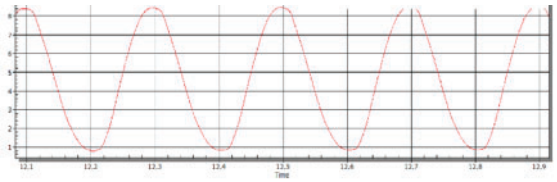

Figure 7: *Example of a load record in machine Instron 1253 during a fatigue test at 5 Hz, and R = 0.1, with load varying sinusoidally between +8.5 kN and +0.85 kN. The time in [s] is on the horizontal axis, and the load in [kN] is on the vertical axis.*

Two machines were used for the fatigue tests at RISE in Borås. The Instron 1253 and a special machine for long-term testing with a hydraulic cylinder (capacity 100 kN) called the Blå-Rigg, (Figure 7). Before testing, the samples were stored for several weeks in a conditioned climate of 20°C and 65% relative humidity. However, the ambient climate during the fatigue testing was not controlled and varied between 19-23ºC and 40-70 % RH.

Figure 8: *Fatigue test machine **Blå-Rigg** and set up with a SET sample*

4 TEST RESULTS

4.1 The edge joint specimens (SEL)

4.1.1 SEL static tests

Ten SEL samples were tested in the Instron 1253 machine. The load was applied at a constant displacement rate of 0.5 mm/min until failure. The mean value of the bonline shear strength is approx. 6 MPa and the CoV is 5.2%.

4.1.2 SEL fatigue tests

For the fatigue tests, 34 samples were tested to failure at different load levels and frequencies. One loading ratio $R = -1$, i.e. pulsating loading from tension to compression, has been studied in this test series.
In Figure 9, the results are presented in a log-linear diagram with the number of cycles to failure with respect to the applied (sinusoidal) stress level in the glue line (SEL Fatigue in blue), and the relative results from the static tests (SEL Static in red).

https://doi.org/10.52202/069179-0281

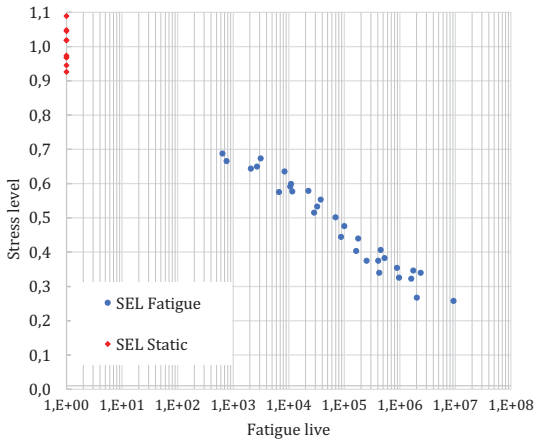

Figure 9: *Results of the SEL fatigue tests*

4.1.3 The SEL failure mode

For both static and fatigue tests the failure mode was similar and happened in both the adhesive, in the wood and/or at the bond line interface between both materials. From visual inspection, the mean value of the surface share with wood failure is approximately 60 %, i.e. about 40 % failure at the adhesive or at the bonding interface. However, a large variation of the surface share ratio can be observed. Some examples of the failure surfaces SEL specimens are shown in Figure 10.

Figure 10: *Examples of failure surfaces of three tested SEL specimens*

4.2 The hybrid timber joint (SET)

4.2.1 SET static test

Results from the static tests on the SET specimens are presented in Table 3 for the different sets of SET configurations summarized in Table 2. The static tests on the specimens with special steel plates show considerable different resistance: the specimens with steel plates of double amount holes (SET double) show an almost double resistance whereas the specimens with steel plates without any holes (SET no hole), i.e. with smooth steel plates show slightly smaller resistance.

Table 3: *Comparison of the relative mean resistance from the test results for the different sets of SET samples*

SET series	Mean max. load [kN]	CoV max. load [%]
SET 000	100%	13.5%
SET 200	101%	6.7%
SET 400	101%	3.1%
SET 500	102%	3.9%
SET double # holes	193%	16.0%
SET no hole	87%	14.6%

4.2.2 The SET fatigue tests

For the fatigue test of series SET 000 at $R = -1$, a preload of 10 kN was applied in tension to all the samples. This simulates the load of a storm with 50-year return period right after erection the tower. No preload was applied to the other series in the fatigue tests.

The results are presented in Figure 11, in a log-linear diagram with the number of cycles to failure with respect to the applied (sinusoidal) stress level for all specimens.

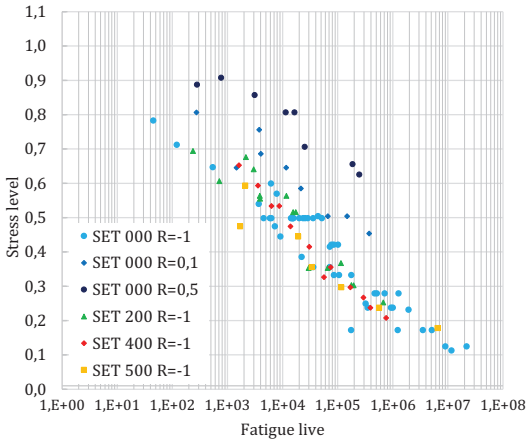

Figure 11*: Results of the SET fatigue tests*

4.2.3 The SET failure mode

For both static and fatigue tests the failure mode is similar and common to most of them: failure always occurred in the glue dowels (100%). But also failures of the bonding at the interface between the steel plate and the adhesive (60-80%), and failures of the bonding at the interface between the wood surface and the adhesive or in the wood material (20-30%) were observed. However, the visual estimation of the ratings is subjective and rough. Figure 12 shows some examples of pictures of tested SET samples and the failure mode.

https://doi.org/10.52202/069179-0281

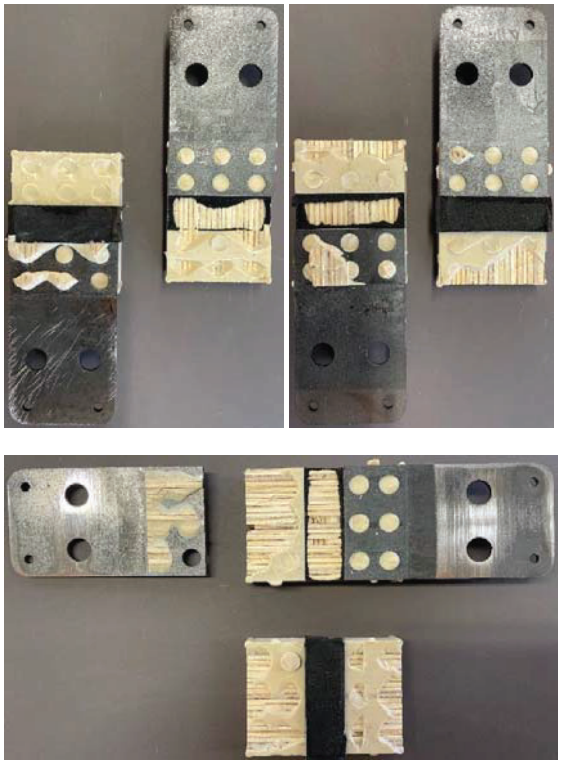

***Figure 12**: Examples of failure surfaces of three tested SET specimens.*

5 CONCLUSIONS

The results of the project described in this paper provide the basis for the design and verification of advanced timber structures for wooden wind turbine towers and allow a better understanding and further development of fatigue-loaded bonded joints in timber construction.

ACKNOWLEDGEMENT

The project "Strong Enough: Testing technology for environmentally friendly and cost-efficient wind turbine towers" with project number 2020-014383 described in this paper was funded by Energimyndigheten, the Swedish Energy Agency.

REFERENCES

[1] Steen, P., P. Landel, E. Dölerud, and O. Lundman. "Structural Design Methods for Tall Timber Towers with Large Wind Turbine." In Proc. of CompWood 2019 Conference, 27–27. Växjö, Sweden, 2019.

[2] Bathon, L., O. Bletz-Mühldorfer, F. Diehl, J. Schmidt, A. Wagner, and M. Weil. "Anwendungen von eingeklebten Lochblechen unter statischen sowie ermüdenden Einwirkungen." In Proc. of 29th IHF, 14. Garmisch-Partenkirchen, Germany, 2014.

[3] IEC 61400-1: Wind turbines – Part 1: Design requirements, International Electrotechnical Commission, 2019.

[4] Clorius, Christian Odin. "Fatigue in Wood: An Investigation in Tension Perpendicular to the Grain." PhD Thesis, BYG-Rapport No. R-038, Technical University of Denmark, 2001.

[5] Zachary, C., and S. Aicher. "Fatigue Behaviour of Timber Composites and Connections for Ultra High Wooden Towers." In Proc. of the World Conference on Timber Engineering WCTE 2016, August, 22–25, 2016, Vienna, Austria.

[6] EN 1995-1-2:2004. Eurocode 5: Design of timber structures – Part 1-1: General – Structural fire design, European Committee for Standardization CEN, Brussels, 2004.

[7] Kreuzinger, H., and B. Mohr. "Holz und Holzverbindungen unter nicht vorwiegend ruhenden Einwirkungen. Abschlußbericht." Bauforschung, Nr.T 2637. Stuttgart, Germany: Fraunhofer IRB, 1994.

[8] Mohr, Bernhard. "Zur Interaktion der Einflüsse aus Dauerstands- und Ermüdungsbeanspruchung im Ingenieurholzbau. " Berichte aus dem konstruktiven Ingenieurbau; 2001,10. Munich, Germany: Technische Universität München, 2001.

[9] prEN 1995-1-1: Eurocode 5 Design of timber structures — Part 1-1: General rules and rules for buildings. CEN/TC 250/SC 5 N 1650, European committee for standardization CEN, Brussels, Belgium, 12-2022.

[10] EN 17334 - Glued-in-Rods in Glued Structural Timber Products — Testing, Requirements and Bond Shear Strength Classification. European Committee for Standardization CEN, Brussels, Belgium, 2021.

[11] Myslicki, S., O. Bletz-Mühldorfer, F. Diehl, C. Lavarec, T. Vallée, R. Scholz, and F. Walther. "Fatigue of Glued-in Rods in Engineered Hardwood Products — Part I: Experimental Results." The Journal of Adhesion 95, no. 5–7 (June 1, 2019): 675–701. DOI: 10.1080/00218464.2018.1555477.

[12] Bond, I., and M. Ansell. "Fatigue Properties of Jointed Wood Composites Part I Statistical Analysis, Fatigue Master Curves and Constant Life Diagrams." Journal of Materials Science 33, no. 11 (1998): 2751–62. https://doi.org/10.1023/A:1017565215274 .

[13] Thompson, R., P. Bonfield, J. Dinwoodie, and M. Ansell. "Fatigue and Creep in Chipboard." Wood Science and Technology 30, no. 5 (1996): 293–305. https://doi.org/10.1007/BF00223550.

[14] Bonfield, P., and M. Ansell. "Fatigue Properties of Wood in Tension, Compression and Shear." Journal of Materials Science 26, no. 17 (1991): 4765–73. https://doi.org/10.1007/BF00612416 .

[15] Hacker, C., and M. Ansell. "Fatigue Damage and Hysteresis in Wood-Epoxy Laminates." Journal of Materials Science 36, no. 3 (2001): 609–21. https://doi.org/10.1023/A:1004812202540 .

[16] EN 302-1 - Adhesives for Load-Bearing Timber Structures - Test Methods - Part 1: Determination of Longitudinal Tensile Shear Strength. European Committee for Standardization CEN, Brussels, Belgium, 2023.

World Conference on Timber Engineering Oslo 2023

TESTING OF STRONG MULTI-LAYERED WOOD FRAME SHEAR WALLS WITH NON-STRUCTURAL LAYERS

Diego Valdivieso[1] , Diego Lopez-Garcia[2], Jairo Montaño[3], Pablo Guindos[4]

ABSTRACT: In areas of high seismic activity it is important to provide Light Frame Timber Buildings (LFTBs) with enhanced levels of lateral stiffness and strength, as well as to prevent excessive levels of non-structural (NSC) damage. Chilean wood-frame shear walls are usually sheathed at both sides with OSB and covered by one/two-ply type X gypsum wallboard (GWB) fastened to the frame with narrow patterns of nails or screws. The result is a multi-layered strong shear wall (MLSSW), which is not considered as such by design codes and mechanical models. The objective of this paper is to report an experimental evaluation of typical Chilean MLSSWs, with emphasis on the influence of NSCs. Connection-level and assembly-level of 1:1 aspect ratio shear walls were evaluated through experimental tests. Results showed increments of 53% and 160% in elastic stiffness and maximum capacity, respectively, while keeping virtually the same deformation capacity and energy dissipation of equivalent bare (non-GWB finished) shear walls. It is postulated that such increases may arise from the high embedment strength of the GWB, and that the deeply screwed GWB may prevent nails from pulling out during hysteresis cycles. It is concluded that GWBs have a significant structural influence on MLSSWs, and such influence should be taken into account in structural design.

KEYWORDS: Wood frame construction, light-frame shear walls, multi-layered, non-structural, gypsum wallboard.

1 INTRODUCTION

Light Frame Timber Building (LFTB) is one of the structural systems currently evaluated by the Chilean construction industry, public authorities, and academia to enhance the sustainability of the Chilean building inventory. Since Chile is subjected to strong earthquakes, it is essential to provide LFTBs with enhanced levels of lateral stiffness and strength. Equally important is the prevention of excessive levels of non-structural damage, as significant costs of damage repairs (i.e.,gypsum wallboard replacement) after earthquake events have been reported [1]. In Chile, wood-frame shear walls usually have a strong structural configuration, consisting of 41 mm × 185 mm (2×8) framing members, sturdy end studs (typically comprising 4 or more members), conventional or continuous holdown devices, wood structural panels (WSPs) -typically OSB on both sides- and closely spaced nails for attachment of sheathing to wood-frame members [2]. On the other hand, the non-structural sheathing customarily consists of one or two layers of Type X gypsum wallboard (GWB) at both sides, fastened to the framing with screws or staples through the OSB. These features cast multi-layered strong shear walls (MLSSWs), as exemplified in Figure 1, whose characteristics have neither been thoroughly investigated nor explicitly considered by design codes or mechanical models. More precisely, although previous investigations have reported a distinct behavior for these types of strong walls (i.e., more prevalence of the rocking effect [2-4]), the influence of the non-structural finishes is rather unknown, and no adequate modeling procedures are currently available. The structural effect of the GWB has been mainly studied in conventional light-frame shear walls (the term conventional was introduced by Estrella et al. [2]), hence a brief summary of the experimental testing of conventional walls with non-structural finishes is presented next.

1.1 EXPERIMENTAL EVALUATION OF THE EFFECT OF NON-STRUCTURAL GWB FINISH LAYERS

GWB is the most common interior wall sheathing material for fire protection used in residential construction [5]. Due to the brittle nature of its core material and its supposedly low stiffness and strength relative to that of wood-based panel materials, the structural contribution of GWB to the lateral response of light-frame buildings is rarely recognized [5]. For this reason, manufacturers have focused on the characterization of GWB for acoustic and fire protection purposes rather than on the mechanical properties that influence the lateral response of a shear wall, such as the shear modulus [6-8]. However, previous research has evaluated the contribution of GWB finish layers to the lateral response of different configurations of

[1] Diego Valdivieso, Pontificia Universidad Católica de Chile, Centro Nacional de Excelencia para la Industria de la Madera (CENAMAD) & Centro de Innovación en Madera (CIM UC-CORMA, Chile, dnvaldivieso@uc.cl
[2] Diego Lopez-Garcia, Pontificia Universidad Catolica de Chile & Research Center for Integrated Disaster Risk Management (CIGIDEN) ANID FONDAP 1522A0005, Chile, dlg@ing.puc.cl
[3] Jairo Montaño, Centro Nacional de Excelencia para la Industria de la Madera (CENAMAD) & Centro de Innovación en Madera (CIM UC-CORMA), Pontificia Universidad Católica de Chile, Chile, jamontano@uc.cl
[4] Pablo Guindos, Pontificia Universidad Católica de Chile, Centro Nacional de Excelencia para la Industria de la Madera (CENAMAD) & Centro de Innovación en Madera (CIM UC-CORMA, Chile, pguindos@ing.puc.cl

https://doi.org/10.52202/069179-0282

conventional shear walls where the OSB and GWB sheathing layers are installed at opposites sides of the frame. For example, the effect of the GWB finish layer on the lateral response of wood-frame shear walls was experimentally evaluated in [9]. A 12% and 60% increase in lateral strength and stiffness, respectively, was found, but also a 31% reduction in deformation capacity due to significant strength degradation. Moreover, GWB impacted the failure mode of the shear walls by limiting the twisting in the stud caused by the eccentricity due to sheathing placed at only one side. In [10] the effect of GWB on a full-scale two-story wood-frame townhouse was evaluated. A reduction of up to 9% of the fundamental period was found because of a 21% increase in the lateral stiffness of shear walls, which was attributed to the incorporation of GWB in the interior side. Also, contrary to other findings [9], when the finish layer was incorporated the lateral stiffness degradation was smaller than that of bare shear walls. The study highlighted the need to develop a seismic design method that takes into account the effect of wall finishes materials.

Even though the aforementioned research results were promising, the experimental evaluation of the MLSSW configuration typically used for mid-rise buildings in highly seismic-prone areas was not considered. In this context, a first approach was given in [11]. Improvements in the performance of GWB in wood-frame shear walls were investigated, motivated by the fact that the configuration typically used in houses (i.e., OSB and GWB panels installed on opposite sides of the frame) tended to trigger substantial damage to the GWB, mainly because of the different lateral stiffness of OSB and GWB. A promising solution was to install the GWB at the top of a shear wall sheathed on both sides with OSB, which resulted in improvement of the GWB performance (i.e., reduction of earthquake damage) due to minimization of the difference in lateral stiffness between both sides of the wall. However, the effect of the finish layer on the lateral behavior of the shear wall (which is of great interest for MLSSWs and mid-rise LFTBs) was not quantified. Recently, in [12] the contribution of Type X GWB to the racking strength of wood-frame shear walls with representative multi-story details (i.e., the racking restraint system was a continuous rod system [13]) was evaluated experimentally. GWB and OSB were installed on opposite sides of the frame, as in previous research [9, 10]. Results showed that Type X GWB increased the peak strength by 3% and the initial stiffness by 11% when shear walls were tested cyclically and monotonically, respectively, compared to bare shear walls. Contrary to previous research, the study reinforced the traditional practice that ignores the contribution of GWB in the seismic design of LFTBs.

In summary, even though several studies have demonstrated the benefits of non-structural finish GWB layers, the experimental evaluations have been limited to wall assemblies that are different from those typically used in mid-rise LFTBs located in highly seismic-prone areas (i.e., MLSSWs). Hence, it becomes important to quantify experimentally and/or numerically the effect of GWB layers in strong shear wall assemblies, particularly in the context of development of tall timber buildings in seismic areas.

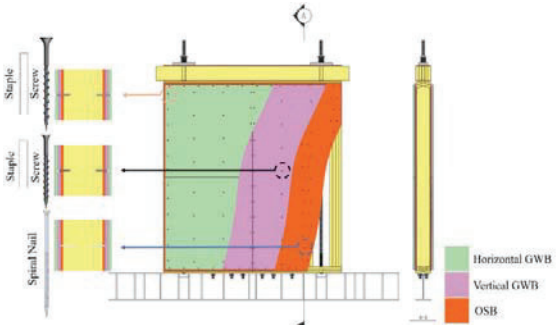

Figure 1: *Typical Chilean MLSSW configuration*

2 SCOPE

In this paper, the contribution of Type X GWB finish layers to the lateral response of multi-layered strong shear walls (MLSSW) is evaluated through reverse cyclic tests on 2.44 m x 2.44 m full-scale MLSSWs and comparisons with previous findings on bare shear walls [3,4].

3 METHODOLOGY

An experimental program was developed to characterize the behavior of multi-layered sheathing-to-frame connections and full-scale shear walls under monotonic and/or cyclic loading.

3.1 CONNECTION-LEVEL TESTS

Three different configurations of multi-layered sheathing-to-frame connections were assembled considering the typical fasteners used for attaching OSB and Type X GWB to wood frames. As shown in Figure 2, the connection-level specimen consisted of a frame of 41 mm x 185 mm (2 x 8) dimensional Chilean radiata pine lumber mechanically graded as C16 according to NCh1198 [14] and attached to different sheathing materials and fastener types (see Table 1). For each configuration, four specimens were considered (i.e., one and three specimens for monotonic and cyclic test, respectively).

Table 1: *Connection-level specimens (all dimensions in millimetres)*

ID	Wood Structural Panel (OSB)		Type X Gypsum Wallboard (GWB)		
	Thick	Nail	Thick.	Type	Fast.
A	11.1	2.9x80	-	-	-
B	11.1	-	15	Screw	4.0x63.5
C	11.1	-	(2) 15	Screw	4.0x76.2

Notes:
a) OSB sheathing layer attached to frame with pneumatically driven wire coil spiral nails (80 x 2.9 x 6.5 mm) according to EN14592:2008+A1:2012 [29].

https://doi.org/10.52202/069179-0282

b) Type X GWB sheathing first layer attached to frame through the OSB with type "W" screws (63.5 x 4.0 x 8.0 mm)
c) Type X GWB sheathing second layer attached to frame through the 1st Type X GWB and OSB with type "W" screws (76.2 x 4.0 x 8.0 mm)

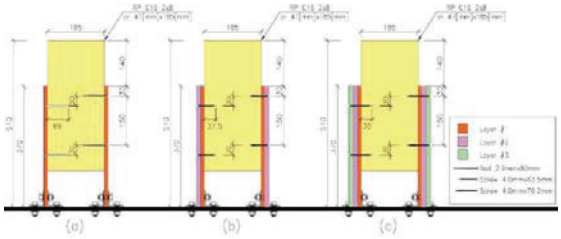

Figure 2: *Multi-layered connection specimen for: (a) Test Group A, (b) Test Group B, and, (c) Test Group C. All dimensions in millimeters*

The test setup is shown in Figure 3. The reaction steel frame is anchored to a concrete floor. A heavy-duty steel beam is installed on the frame at a suitable location to accommodate the specimen, which is attached to the heavy-steel beam through bolted L-shape elements (Figure 3). The load was applied by a double-action cylinder of +/- 86 kN and +/- 75 mm of force and displacement capacity, respectively, which transfers the vertical load to the specimen through a load-transfer system. All specimens were instrumented with two displacement transducers (LVDTs) and one double-effect load cell to capture the slip and shear force between the frame and sheathing multi-layers.

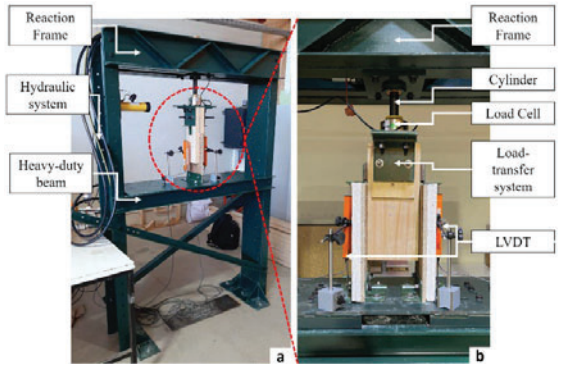

Figure 3: *Connection-level test set-up: (a) general view of the reaction steel frame and (b) detailed view of the specimen set-up*

The loading protocol was established according to ASTM E564-06 [15] and ASTM E2126-19 [16] for the monotonic and cyclic tests, respectively. The ultimate displacement observed in the monotonic test (i.e., the maximum displacement at which the strength has not yet dropped below 80% of the peak strength) was used to compute the reference displacement for the simplified CUREE-Caltech cyclic testing protocol [17] according to method C of ASTM E2126-19 [16]. The loading protocol was displacement-controlled and applied until failure of the specimen.

3.2 ASSEMBLY-LEVEL TESTS

Specimens are representative of typical ground-level walls of a 7-story building designed per the Chilean seismic design code NCh433 [18] (see Figure 4). Four of them are MLSSWs, whereas the remaining one (i.e., the control wall) is a bare strong shear wall. As shown in Figure 4, the walls had a 1:1 aspect ratio (i.e., 2481 mm in height and 2440 mm in length). Wood-frame consisted of eight studs distributed along the length every 400 mm center-to-center distance. Due to the high levels of overturning moments, each sturdy end-stud consisted of four members mechanically joined and located symmetrically with respect to the continuous rod system. Double plates at the top and bottom of the wall were nailed to the studs with ϕ3.0 mm x 80 mm nails. All framing elements were 41 mm x 185 mm (2 x 8) C16 Chilean RP dimensional lumber, with a nominal modulus of elasticity E = 7900 MPa according to NCh1198 [14]. The walls were sheathed on both sides with 11.1 mm thick APA-rated OSB panels [19] with G = 1307.5 MPa (measured in previous studies [3]), and pneumatically driven to the frame with ϕ2.9 mm x 80 mm helical nails. The edge and field nails were installed at 100 mm and 200 mm center-to-center, respectively. According to SDPWS prescriptions [20], edge-nailing at the end studs should be uniformly distributed among the four framing members and spaced at a maximum of 300 mm. The walls were sheathed on both sides with two-ply 15 mm thick Type X GWB panels [6] with a measured G = 1177.9 MPa according to the ASTM D3044-16 [21] prescriptions. The first Type X GWB layer was vertically oriented and attached to the frame through the OSB with ϕ4.0 mm x 63.5 mm (i.e., Nº 8 x 2-½") drywall screws, whereas the second Type X GWB layer was horizontally oriented and attached to the frame through the first GWB layer and OSB with ϕ4.0 mm x 76.2 mm (i.e., Nº 8 x 3") drywall screws. The edge screws and field screws were installed at 200 mm and 300 mm center-to-center, respectively, according to the NCh1198 [14] fire prescription draft. In order to transfer the lateral load to the wall, a built-up collector beam of 205 mm x 207 mm (i.e., five members of 41 mm x 185 mm C16 RP plus an 11.1 mm thick OSB layer on top and bottom) was mechanically attached to the top sole plate through 38 Simpson Strong-Tie's SCDP221100 screws. The MLSSW racking restraint system consisted of a continuous rod system (i.e., Strong-Rod® system [13]) fabricated in Pleasanton, CA, USA. High-Strength ASTM A193 Grade B7 (i.e., ultimate strength equal to 125 ksi) fully threaded steel rods of ϕ38.1 mm were installed on both sides of the specimen. The rods were attached to the walls by a reaction system over the collector beam that consists of (from bottom to top) a 31.75 mm thick bearing plate (i.e., Simpson Strong-Tie PL16-5x12), a take-up device (i.e. Simpson Strong-Tie ATUD14), a 9.5 mm thick bearing plate (i.e. Simpson Strong-Tie BP 1-1/2), and a finger tightened double heavy hexagonal nut ASTM A563 Grade DH. To avoid sliding between the specimen and the reaction beam, 14 ϕ32 mm x 220 mm ASTM A193 Grade B7 anchor bolts were used to attach the bottom double sole plate to the top flange of the reaction steel beam.

https://doi.org/10.52202/069179-0282

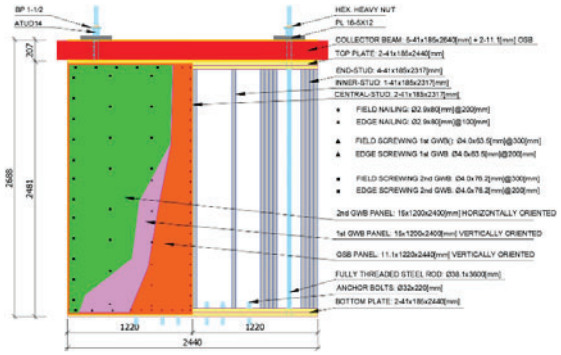

Figure 4: *Monotonic response of connection-level groups*

A cantilever reaction wall, a strong floor, and a reaction steel beam were used to perform the assembly-level tests. As shown in Figure 5, the reaction steel beam was attached to the strong floor by two transversal steel beams attached to the strong floor by four high-strength fully threatened steel rods with a post-tensioned force of 120 kN each, avoiding possible sliding of the reaction beam. The specimens were attached to the reaction beam through a rod-to-steel beam connector (i.e. Simpson Strong-Tie ATS-SBC10H connector) and 14 ϕ32 mm x 220 mm ASTM A193 Grade B7 anchor bolts to prevent overturning and sliding, respectively. The lateral load was applied by a hydraulic bidirectional actuator of +/- 245 kN and +/- 250 mm of force and displacement capacity, respectively, which transfers the lateral load to the specimen through the collector beam. To prevent out-of-plane displacements, the specimens were laterally braced by two steel A-frames which allowed in-plane displacements. To capture the lateral displacement and shear force along the axis of the collector beam, the slip of the wall with respect to the steel reaction beam, the diagonal (shear) deformation, uplift in the exterior edge of the wall, the relative displacement between the multiple layers of the wall, the relative displacement of the steel reaction beam with respect to the strong floor, and the compressive deformation under the bearing plate of the strong-rod system, all specimens were instrumented with thirteen displacement transducers (LVDTs), one laser displacement transducer, and one load cell and displacement transducers (LVDT) incorporated into the actuator. To measure the tension in the rods of the continuous holdown, two unidirectional strain-gauges were attached to the rods.

In order to characterize the in-plane cyclic behavior of specimens, the CUREE-Caltech cyclic testing protocol proposed by Krawinkler et al. [17] was applied. The reference displacement was based either on: a) previous monotonic tests conducted by Guiñez et al. [4] on bare shear walls of comparable specimens features for the case of discrete hold-downs; or b) the shear walls investigated by Estrella et al. [3] for the case of continuous rod systems. The maximum limit for the reference displacement Δ = 61 mm was set for the specimens (i.e. 0.0025 times the wall height) as established in method C (i.e. the simplified CUREE-Caltech protocol) of ASTM E2126-19 [16]. The loading protocol was displacement-controlled and applied until the specimens reached a safe minimum capacity after the peak strength.

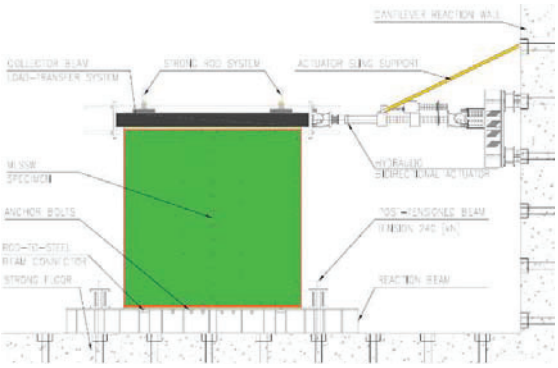

Figure 5: *Front view of the test set-up for assembly-level specimens.*

4 RESULTS

In this section, test results and a discussion of the findings are presented. Failure mode, hysteresis shape, and six engineering parameters were established for connection-level and assembly-level test results: (1) elastic stiffness (K_e); (2) yield displacement (Δ_y); (3) yield force (F_y); (4) ultimate displacement (Δ_u); (5) ultimate force (F_u); and, (6) ductility (μ). Moreover, the lateral behavior of MLSSWs is compared with that of bare SSWs used in this study as reference.

4.1 CONNECTION-LEVEL TESTS

The specimens were inspected after each cyclic test in order to evaluate typical failure modes. On the nailed OSB-to-frame connection (i.e., test group A) two failure modes were identified: (i) excessive bend in the nail leading to shearing-off of the fastener; and (ii) pull out or pull-through of the nail from the OSB-to-frame joint, leading to detachment of the OSB. In both cases, crushing in the wood and OSB panel and fiber tear in the OSB panel were observed. On the screwed 1-ply type X GWB+OSB-to-frame connection (i.e., test group B) two failure modes were identified: (i) excessive bend in the screw leading to shearing-off of the fastener; and (ii) pull-through of the screw from the 1-ply type X GWB+OSB-to-frame joint, leading to detachment of the GWB and OSB sheathing. In both cases, crushing in the wood and panels and tearing in OSB and GWB panels were likewise observed. Finally, on the screwed 2-ply type X GWB+OSB-to-frame connection (i.e., test group C), one failure mode was identified: (i) excessive bend in the screw leading to shearing-off of the fastener. Wood crushing and tearing in OSB and GWB panels were observed.

https://doi.org/10.52202/069179-0282

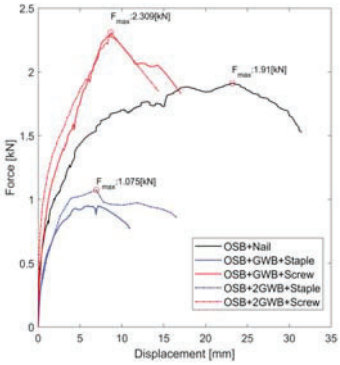

Figure 6: *Monotonic response of connection-level groups*

Table 2: *Engineering parameters from monotonic connection-level test results*

Test Group	K_e kN/mm	Δ_y mm	F_y kN	Δ_u mm	F_u kN	μ
A	0.91	1.87	1.69	31.51	1.53	16.9
B	0.91	2.15	1.94	17.05	1.83	7.9
C	1.89	1.01	1.91	14.39	1.85	14.3

The monotonic force-displacement test response for all the tested groups is presented in Figure 6, in which the reported displacement is the differential slip between the wood frame and the multi-layer sheathing, and the force is that taken by only one fastener along a single shear plane. In specimens with two Type X GWB, two screws are needed (one for each GWB), but results reported in this section refer to either one nail (for bare connections) or one screw, regardless of the number of Type X GWB. This makes possible a direct evaluation of the use of only one fastener in different configurations. Six engineering parameters are summarized in Table 2, where the Equivalent Energy Elastic-Plastic (EEEP) [22] approach was used to estimate the parameters according to ASTM E2126-19 [16]. Monotonic test results indicate that connections A (OSB+nail) and B (OSB+Type X GWB+screw) exhibited almost the same elastic stiffness, even though connection B has multiple layers of sheathing. In contrast, connection C (OSB+(2)Type X GWB+screw) was about twice stiffer than connections A and B. Results for connections A and C were consistent with the analytical stiffness expressions reported in [23]. However, connection B exhibited smaller stiffness than the analytical prediction, attributable to installation defects that tend to leave a gap between the sheathing layer and the wood-frame due to difficulties in screwing throughout the finish layers. Regarding capacity (strength), the screwed connections B and C exhibited stronger capacity than the nailed connection A. The screwed connection takes advantage of the axial capacity of the fastener, whereas the nailed connection is easily pulled out. From a ductility point of view, connection A performs better than all other GWB-sheathed connections. Ductilities of connections B and C were expected because screws are typically less ductile than nails and the reinforcing effect of the Type X GWB produced a more prominent strength degradation and a reduction of the inelastic ultimate displacements. However, the behavior of connection C is similar to the one reported in concrete-to-wood hybrid connections [24] in terms of elastic stiffness (i.e., elastic stiffness is almost twice that of connection B), but the peak strength and the ultimate displacement are similar to the ones of connection B. That is why the ductility of connection C is 80% higher than that of connection B. Likewise, it was found that even when all connections showed comparable yielding displacements of about 1-2 mm, the ultimate displacement of the bare connection A was about twice larger than that of the other connections, indicating that GWB-sheathed connections can clearly undergo lesser inelastic displacements.

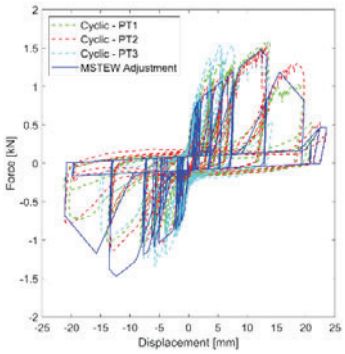

Figure 7: *Force-displacement response of test group A (i.e., nailed OSB-to-frame)*

The cyclic force-displacement test response for all the tested connections is presented in Figures 7 to 9. Again, results are expressed in terms of differential slip per fastener/shear plane. Cyclic test results for all tested connections depict a strong pinching effect due to wood frame and OSB crushing at the shear planes. Moreover, an abrupt strength degradation after repeated cycles at the same target displacement was found in all tests. A markedly asymmetric hysteretic response was found for bare OSB connections (group A), which was not consistent with previous findings [2, 25-27]. This asymmetric response could be attributed to: (1) the threaded portion of the nail is located at its end rather than distributed along the whole length (as in previously reported tests [2]), which would affect the rope effect in the connection [25]; and/or (2) an installation effect (i.e., the use of a pneumatic nail gun). This asymmetric response behavior of full-scale MLSSWs should be analyzed with more detail in the future. Apart from the response asymmetry, cyclic test results were consistent with monotonic test results: larger strength and stiffness of screwed connections, and a significantly larger ultimate displacement capacity of nailed connections.

https://doi.org/10.52202/069179-0282

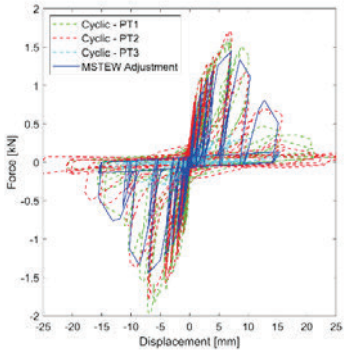

Figure 8: *Force-displacement response of test group B (i.e., screwed one layer Type X GWB+OSB-to-frame).*

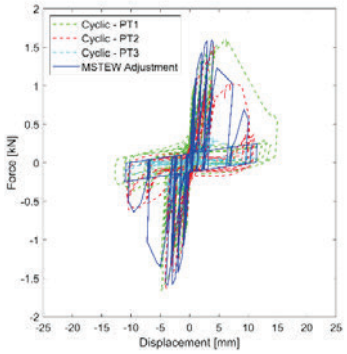

Figure 9: *Force-displacement response of test group C (i.e., screwed two layers Type X GWB+OSB-to-frame).*

4.2 ASSEMBLY-LEVEL TESTS

The wall specimens were inspected after each test in order to evaluate typical failure modes. In all four specimens (all of them had a 2-Type X GWB screwed configuration) five failure modes were identified: (i) pulling out of the nails and screws; (ii) pulling out of the nail and screw heads through the OSB or Type X GWB panels; (iii) shear-off of nails and screws due to excessive fastener bending; (iv) local embedding failure (crushing) in the OSB and Type X GWB panels attributable to an excessive stress concentration around the fastener; and, (v) detachment (out-of-plane unsheathing) of the OSB and GWB panels from the wood-frame because of failure of the fasteners (i.e. nails and screws). In all cases, excessive and moderate crushing in the wood and in the OSB and Type X GWB panels were observed, respectively. The fasteners failure was initiated at the center studs of the walls and propagated to the edge of the walls at the final stages of the loading protocol. This phenomenon is consistent with findings of previous researchers for continuous rod hold-downs [3], and can be explained by the concentration of fasteners in end studs around the continuous rod, which typically initiates failure at interior sheathing edges.

It is remarkable that double shear failure, pull-out, and pull-through of fasteners, along with local embedding of sheathing, were found as failure modes. However, there was no evidence of shear Type X GWB failure, and apparently, there was no reduction of the shear wall racking deformation capacity. Typically, the failure of non-structural finishes has been a cornerstone in restraining the design inter-story drift limit because it is commonly thought that it has much less deformation capacity and is more brittle than OSB. In MLSSWs, however, there was neither evidence of GWB failure nor shortening of the deformation capacity. This behavior is attributed to the fact that OSB sheathing offers protection to GWB [11], preventing brittle failure modes if OSB and GWB are located on both sides of the frame (i.e., the GWB always has a protective OSB layer beneath. Moreover, failure of the nails and detachment of the OSB occurred only at the ultimate stages of the loading protocol because of the minimal reinforcing effect of the GWB after the general failure of the GWB-screwed connections.

Figure 10: *Main failure modes observed in MLSSW specimens: (1) nail and screw failure pattern; (2) and (3) failure of the screwed* Type X GWB+*OSB-to-wood frame connection (in orange) for the 2nd layer and 1st layer, respectively; (4) and (6) pulling out of screws and nails; (5) and (9) local failure of the* Type X GWB *panels and OSB, respectively; (7) pulling through of nails and screws;(8) sheathing layers detachment from the wood-frames; and, (10) double shear failure of the screws.*

The wood frame showed moderate to low damage in all cases. Damage was concentrated mainly on the double central (interior) stud of the specimens and its connection to the top and bottom double plate, and was not as excessive as observed in previous tests on specimens with denser nailing patterns of 50 mm [3]. At the final stages of the loading protocol, detachment between the end studs located at the edge of the specimen and the bottom double plate was observed due to failure of the nailed OSB-to-bottom plate connection.

As expected, the rocking restraint system showed no damage in all the wall tests (it was designed to behave elastically even at the peak strength of the MLSSW specimens). The top-bearing steel plates were not

damaged, as no crushing into the OSB of the collector beam was observed. This was also attributable to the overstrength factor used to design the specimens, which led to predominant nail and screw ductile failures.

The backbone hysteretic curves of the four MLSSW specimens (CT-MLSSW-0i, all comprising 2 screwed Type X GWB) and the control wall (CT-100-38, only with bare OSB without any GWB sheathing) are shown in Figure 10. The reported displacement is the effective displacement of the wall measured at the collector axis where the actuator was located. The effective displacement is the measured lateral displacement at the collector of the wall minus the displacement measured at the specimen-to-reaction beam relative to the reaction beam-to-strong floor. The overall shape of the hysteresis loops was consistent with that reported in previous research [3, 4, 28]. The MLSSW specimens showed elastic response up to a drift of about 1.0%, and then a nonlinear response was observed, attributable to the multilayer sheathing-to-wood frame connection. After the specimens reached the peak strength, progressive and smooth strength and stiffness degradation was found. As expected, high redundancy was evident in the specimens because of the multiple screwed and nailed connections at multiple layers, resulting in high drift levels with no brittle failures. Hence, as the lateral behavior of the MLSSWs was governed by the connection-level response, the MLSSW hysteresis was markedly pinched because of the non-reversible crushing effect of the fasteners (i.e., nails and screws) over the wood-frame components, which leads to a gap between the wood and the fasteners.

The engineering parameters of the backbone curves were estimated according to the Equivalent Energy Elastic-Plastic (EEEP) approach [22] per ASTM E2126-19 [16]. The resulting mean values are summarized in Table 3. All the shear walls tested in this research had a panel edge nail spacing of 100 mm and an anchoring rod of 38 mm in diameter.

Table 3. *Engineering parameters from cyclic MLSSW and control wall test results*

Test Group	K_e [kN/mm]	Δ_y [mm]	F_y [kN]	Δ_u [mm]	F_u [kN]	F_{peak} [kN]	μ
MLSSW	5.9	28.6	157.5	93.6	139.6	174.5	3.5
CT-100-38*	3.8	15.4	58.6	90.2	54.0	67.5	5.9

* CT -NP-AD: CT = cyclic test; NP = nail spacing pattern (i.e., 100 = 100[mm]); AD = anchorage diameter (i.e., 38 = 38[mm]).

The MLSSW specimens showed a mean peak strength of 174.5 kN, which is up to 160% higher (i.e., almost 3 times) than the peak strength (67.5 kN) observed in the equivalent bare strong shear wall specimen (CT-100-38), see Table 3. These surprising results confirm that double sheathing and screwing Type X GWB in timber shear walls can make an enormous structural difference, as it may have an even stronger influence than denser nailing patterns or stronger anchorages (these two parameters are currently among the most important design parameters to increase the capacity of timber shear walls). This enormous increase is thought to be generated not only by the "parallel spring" action of the screws but also because of the axial strength of the screws and their axial sheathing fixing may also reinforce and benefit the nailed OSB-to-wood frame connection, which is believed to control the strength of bare shear walls. This is related to the fact that in MLSSWs the evident pulling-out of OSB-to-wood frame connections took place at the final stage of the testing protocol, whereas in the CT-100-38 specimen the same phenomenon started right after the peak strength was reached.

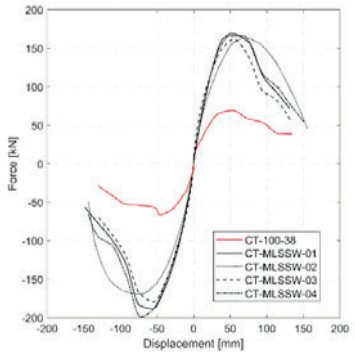

Figure 10: *Comparison between backbone curves of all tested specimens.*

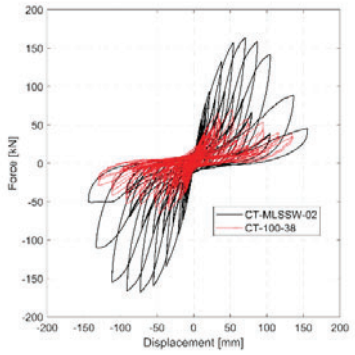

Figure 10: *Comparison between force-displacement hysteretic response of MLSSW sample CT-MLSSW-02 and control wall (i.e., bare strong shear wall) CT-100-38.*

The elastic stiffness of the MLSSWs, CT-100-38 and other research specimens are reported in Table 5. MLSSW specimens show a mean elastic stiffness of 5.854 kN/mm, which is up to 53% higher than the elastic stiffness observed in the control specimen CT-100-38 (3.821 kN/mm). All specimens show a clear stiffness degradation as the lateral drift increases, presenting a residual stiffness between 0.5 kN/mm to 1.5 kN/mm. At 0.1% to 4% lateral drift the MLSSWs exhibit the highest levels of secant stiffness, and the degradation is linear rather than quadratic as observed in bare shear walls. Finally, at lateral drifts smaller than 0.1%, specimen CT-100-38 present a secant stiffness that is 99% smaller than that of the MLSSWs. These results confirm that the actual

https://doi.org/10.52202/069179-0282

elastic and secant stiffness of MLSSWs are greater than those based on the assumption of bare shear wall.

In bare wood-frame strong shear walls the ductility is governed mainly by the nailed sheathing-to-frame connection. MLSSWs, on the other hand, have multiple sheathing-to-frame connections and each of these has a different ductility level, hence the overall ductility of MLSSWs depends on the combined effect of all connections. Values of ductility μ are reported in Table 3. They were computed according to ASTM E2126-19 [16] as the ratio of ultimate to yield displacement: $\mu = \Delta_u/\Delta_y$. MLSSW specimens show a mean ductility of 3.5, which is 42% smaller than the observed ductility in the control specimen CT-100-38 (5.929). This reduction in ductility could be attributed to the screwed 1st/2nd layer GWB+OSB-to-frame connection, which contributes mainly to stiffness and strength rather than to deformation capacity because screws tend to fail first as the lateral drift of the MLSSW increases. In other words, the screwed connections themselves are less ductile than the nailed connections. However, once the screwed connections fail in MLSSWs, a rapid failure of the nails is expected as they are unable to take all the load previously taken by the screws. Therefore, the ductility of the screws (rather than that of the nails) is thought to govern the MLSSW ductility as was reported by previous researchers [3, 4], the nail spacing in OSB-to-frame connection controls the ductility of bare shear wall.

5 CONCLUSIONS

Findings of this investigation reinforce the idea of taking advantage of the effect of the finishes layer on the lateral response of MLSSWs to achieve a cost-effective structural design. Such approach would cast a paramount criterion in the context of targeting earthquake-prone tall timber buildings, and traditional design practices that ignore the contribution of GWB finish layers should be discouraged. Further research is needed to elucidate the potential contributions of the finishes layer on seismic performance factor of light-frame timber buildings.

ACKNOWLEDGEMENTS

Financial support was provided by CONICYT (Doctorado Nacional 2018–21180074), by VRI-UC, by ANID BASAL FB210015 (CENAMAD), and by the Research Center for Integrated Disaster Risk Management (CIGIDEN) ANID FONDAP 1522A0005.

REFERENCES

[1] Kircher, C. A., Reitherman, R. K., Whitman, R. V., & Arnold, C. (1997). Estimation of earthquake losses to buildings. *Earthquake Spectra*, 13(4), 703-720.

[2] Estrella, X., Guindos, P., Almazán, J. L., & Malek, S. (2020). Efficient nonlinear modeling of strong wood frame shear walls for mid-rise buildings. *Engineering Structures*, 215, 110670.

[3] Estrella, X., Malek, S., Almazán, J. L., Guindos, P., & Santa María, H. (2021). Experimental study of the effects of continuous rod hold-down anchorages on the cyclic response of wood frame shear walls. *Engineering Structures*, 230, 111641.

[4] Guíñez, F., Santa María, H., & Almazán, J. L. (2019). Monotonic and cyclic behaviour of wood frame shear walls for mid-height timber buildings. *Engineering Structures*, 189, 100-110.

[5] Wolfe, R. W. (1983). *Contribution of gypsum wall board to racking resistance of light-frame walls* (Vol. 439). US Department of Agriculture, Forest Service, Forest Products Laboratory, Madison, USA.

[6] Etex Group (2022). *Technical Guidelines for Type X Gypsum Wallboard*. Gyplac. Accessed on: May 26, 2022. [Online]. Available: www.gyplac.com/es-cl/productos/gyplac-portafolio/placas-de-yeso/yeso-carton-resistente-fuego/

[7] Rahmanian, I. (2011). Thermal and mechanical properties of gypsum boards and their influences on fire resistance of gypsum board based systems. *Ph.D. Thesis*, The University of Manchester, Manchester, UK.

[8] Cramer, S. M., Friday, O. M., White, R. H., & Sriprutkiat, G. (2003). Mechanical properties of gypsum board at elevated temperatures. *Fire and Materials 2003 Conference*, San Francisco, USA.

[9] Uang, C. M., & Gatto, K. (2003). Effects of finish materials and dynamic loading on the cyclic response of woodframe shearwalls. *Journal of Structural Engineering*, 129(10), 1394-1402.

[10] Filiatrault, A., Christovasilis, I. P., Wanitkorkul, A., & van de Lindt, J. W. (2010). Experimental seismic response of a full-scale light-frame wood building. *Journal of structural engineering*, 136(3), 246-254.

[11] Goodall, S. I., & Gupta, R. (2011). Improving the performance of gypsum wallboard in wood frame shear walls. *Journal of Performance of Constructed Facilities*, 25(4), 287-298.

[12] Line, P., Hohbach, D., & Waltz, N. (2021). Gypsum wallboard finish contribution to the racking strength of wood-frame shear walls with representative multi-story details. *World Conference on Timber Engineering*, Santiago, Chile.

[13] Tyrell, T. (2007). *Full-Scale Three Dimensional Wood Structure Test Project*, Gilb Research Laboratory, Simpson Strong- Tie Company. Detailed information available at: http://www.strongtie.com/news/industry/wall-bracing/3Dtest/index.html. Accessed 15 October 2008.

[14] INN (2014). *Madera - Construcciones en Madera - Cálculo NCh 1198*. Instituto Nacional de Normalización, Santiago, Chile. (in Spanish)

[15] ASTM (2006). *Standard Practice for Static Load Test for Shear Resistance of Framed Walls for Buildings ASTM E564-06*. ASTM International, West Conshohocken, USA.

[16] ASTM (2019). *Standard Test Methods for Cyclic (Reversed) Load Test for Shear Resistance of Vertical Elements of the Lateral Force Resisting Systems for Buildings ASTM E2126-19*. ASTM International, West Conshohocken, USA.

[17] Krawinkler, H., Parisi, F., Ibarra, L., Ayoub, A., & Medina, R. (2001). Development of a testing protocol for woodframe structures. *CUREE Publication No. W-02*, Consortium of Universities for Research in Earthquake Engineering, Richmond, USA.
[18] INN (2009). *Diseño Sísmico de Edificios NCh 433 Of1996 Mod. 2009*. Instituto Nacional de Normalización, Santiago, Chile. (in Spanish)
[19] APA (2012). *Panel Design Specification*. APA - The Engineering Wood Association, Tacoma, USA.
[20] AWC (2021). *Special Design Provisions for Wind and Seismic ANSI/AWC SDPWS-2021*. American Wood Council, Leesburg, USA.
[21] ASTM (2016). *Standard Test Methods for Shear Modulus of Wood-Based Structural Panels ASTM E3044-16*. ASTM International, West Conshohocken, USA.
[22] Foliente, G. C. (1996). Issues in seismic performance testing and evaluation of timber structural systems. *International Wood Engineering Conference*, New Orleans, USA.
[23] CEN (2008). *EN 1995-1-1:2004+AC:2006+A1:2008 Eurocode 5 - Design of Timber Structures - Part 1-1: General - Common Rules and Rules for Buildings*. European Committee for Standardization, Brussels, Belgium.
[24] Carrero, T., Montaño, J., Santa-María, H., & Guindos, P. (2020). Static and dynamic performance of direct hybrid connections of cross-laminated timber with steel, concrete and laminated strand lumber composites. *Latin American Journal of Solids and Structures*, 17(4), e279.
[25] Fonseca, F. S., Rose, S. K., & Campbell, S. H. (2002). Nail, wood screw, and staple fastener connections. *CUREE Publication No. W-16*, Consortium of Universities for Research in Earthquake Engineering, Richmond, USA.
[26] Sartori, T., & Tomasi, R. (2013). Experimental investigation on sheathing-to-framing connections in wood shear walls. *Engineering Structures*, 56, 2197-2205.
[27] Dolan, J. D., & Madsen, B. (1992). Monotonic and cyclic nail connection tests. *Canadian Journal of Civil Engineering*, 19(1), 97-104.
[28] Pei, S., & Van de Lindt, J. W. (2009). Coupled shear-bending formulation for seismic analysis of stacked wood shear wall systems. *Earthquake Engineering & Structural Dynamics*, 38(14), 1631-1647.
[29] BSI (2008). *BS EN 14592:2008+A1:2012 Timber Structures - Dowel-type Fasteners - Requirements*. British Standard Institution, London, UK.

https://doi.org/10.52202/069179-0282

World Conference on Timber Engineering Oslo 2023

TESTING THE INFLUENCE OF 3D COUPLING EFFECTS ON THE LATERAL RESPONSE OF NON-PLANAR T-SHAPE WOOD FRAME SHEAR WALLS

Diego Valdivieso[1], Diego Lopez-Garcia[2], José Luis Almazán[3], Jairo Montaño[4], Pablo Guindos[5]

ABSTRACT: Cumulative shear wall overturning (CSWO) is a common response of structural models of multi-story Light-Frame Timber Buildings (LFTBs) under lateral loads. Governed by holdown uplift and shear wall (SW) bending, large CSWO occurs in LFTBs due to the light self-weight of wood and the dominant rocking flexibility of stiff SWs. Even though CSWO is paramount in seismic design because of its effect on the flexibility of LFTBs (making hard to achieve the inter-story drift limits), this phenomenon is not incorporated into the structural models of LFTBs. For instance, in the design of LFTBs for lateral loads it is assumed that SWs behave as planar isolated elements. However, CSWO may be influenced by 3D coupling effects (3D-SWCE) in non-planar SWs such as T or L assemblies. This paper describes a large full-scale experiment of a 7.32 m x 5.1 m assembly, performed to gather insight into 3D-SWCEs through the cyclic evaluation of a non-planar T-shape SW. Results showed an asymmetric behaviour of the T-shape SW with increments of 20% and 98% in elastic stiffness and maximum capacity, respectively, with respect to those of a planar SW. It is concluded that 3D-SWCEs have a significant structural influence on the response of LFTBs.

KEYWORDS: Wood frame construction, light-frame shear walls, non-planar, T-shape, 3D-SWCE.

1 INTRODUCTION

Light frame timber building (LFTB) is one of the alternatives evaluated by the Chilean construction industry to eventually replace concrete and steel mid-rise buildings, reducing the housing deficit and the contribution of the construction industry to the global greenhouse gas emissions [1].

A LFTB is the result of the assembly of several components with repetitive members such as walls, floors, and roof systems connected by intercomponent connections forming a three-dimensional highly indeterminate structural system. Then, gross simplifying assumptions are made (e.g., walls assumed as in-plane resistant components) for its design and analysis [2]. When LFTBs are subjected to earthquake loads, cumulative rotation effects are presented when the shear walls are assumed to behave as isolated cantilever components due to the hold-down elongation and bending deformation of the wall [3]. However, full-scale test results [4-8] showed that current mechanical models [3,9,10] suffer from several limitations as the system effects are not captured. In this paper system effect refers to the interaction between the components of a building (i.e., shear walls, floor, or roof systems) which modifies the response of isolated components. It is then important to experimentally evaluate the mechanism that controls the system effect considering component-level specimens, as the experimental campaigns in light-frame structures that identified the system effect had been done based on building-level specimens [4-8].

1.1 NON-PLANAR TIMBER SHEAR WALLS

For mid-rise buildings in highly seismic-prone areas, such as Chile, wood-frame shear walls usually adopt a strong structural configuration (i.e., strong shear wall or SSW), consisting of 41 × 185 mm (2×8) framing members, sturdy end studs (typically comprising 4 or more members), strong hold-down, wood structural panel (WSP) - typically OSB on both sides-, and closely spaced

[1] Diego Valdivieso, Pontificia Universidad Catolica de Chile, Centro Nacional de Excelencia para la Industria de la Madera (CENAMAD) & Centro de Innovación en Madera (CIM UC-CORMA, Chile, dnvaldivieso@uc.cl
[2] Diego Lopez-Garcia, Pontificia Universidad Catolica de Chile & Research Center for Integrated Disaster Risk Management (CIGIDEN) ANID FONDAP 1522A0005, Chile, dlg@ing.puc.cl
[3] José Luis Almazán, Pontificia Universidad Catolica de Chile, Centro Nacional de Excelencia para la Industria de la Madera (CENAMAD) & Centro de Innovación en Madera (CIM UC-CORMA, Chile, jlalmaza@ing.puc.cl
[4] Jairo Montaño, Centro Nacional de Excelencia para la Industria de la Madera (CENAMAD) and Centro de Innovación en Madera (CIM UC-CORMA), Chile, jamontano@uc.cl
[5] Pablo Guindos, Pontificia Universidad Católica de Chile, Centro Nacional de Excelencia para la Industria de la Madera (CENAMAD) & Centro de Innovación en Madera (CIM UC-CORMA, Chile, pguindos@ing.puc.cl

https://doi.org/10.52202/069179-0283

edge and field nailing patterns [11-13]. In the layout of a building, SSWs are typically assembled in T-shape, L-shape, and/or U-shape non-planar SSWs based on the architectural project. These non-planar shear walls have been deeply studied in concrete structures [14, 15], identifying coupling effects (i.e., the effect of transverse shear walls on the in-plane response of a wall) that need to be addressed in SSWs. In this paper, the coupling effect presented in non-planar SSWs is denoted 3D shear wall coupling effect (3D-SWCE).

In light-frame timber structures, 3D-SWCE has been identified as one of the key factors to be evaluated for a better understanding of LFTBs [16]. The 3D-SWCE has been evaluated experimentally in conventional shear walls [17, 18] (i.e., the term conventional shear wall was introduced in [11] for referring to wood frame shear wall consisting of a 1.2–2.4 m long wood frame with 38 × 89 mm (2×4) interior studs spaced at 400 mm on center, double end studs, single members for the top and sole plate, and discrete holdowns to prevent overturning of the wall) and partitional walls [19, 20] as an alternative for replacing the installation of hold-downs. Experimental results showed that transverse shear walls have the potential to increase the racking stiffness of a wall to the point where no hold-down is needed. An analytical procedure was introduced in [21] for computing the tying-down effect of transverse walls on the load-carrying capacity of partially anchored conventional shear walls. The procedure demonstrates that transverse shear walls have the potential to increase the lateral in-plane load-carrying capacity of a shear wall. That increment reduces as the aspect ratio of the wall reduces as well (i.e., up to 100% of increment in lateral load for shear walls with a 1:2 aspect ratio, from up to 32% for walls with a 1:0.5 aspect ratio). Even though this procedure is a starting point for the evaluation of 3D-SWCE, it considers only the effect of transverse shear walls by their uplift strength/stiffness, neglecting the out-of-plane strength/stiffness component. Further experimental evaluation is needed in the case where SSWs are used (i.e., as the in-plane/out-of-plane stiffness and strength are higher in SSWs than in conventional shear walls). To the best of the authors' knowledge, no previously published studies have described the cyclic behavior of non-planar SSWs.

The 3D-SWCE has been studied in cross-laminated timber (CLT) shear walls experimentally and numerically [22, 23]. The effect of the out-of-plane walls on the in-plane strength and stiffness of an I-shape CLT non-planar shear wall was reported in [22]. A positive influence on the initial lateral stiffness (i.e., increment of up to 155%) and peak strength (i.e., increment of up to 60%) was found because of the added out-of-plane walls with respect to an isolated wall assembly. Furthermore, the 3D-SWCE seems not to affect the failure mechanism and deformation capacity of the system. The study highlights that a key component for achieving 3D-SWCE is a properly detailed connection between transverse and in-plane walls in order to use them as an uplift restraint system.

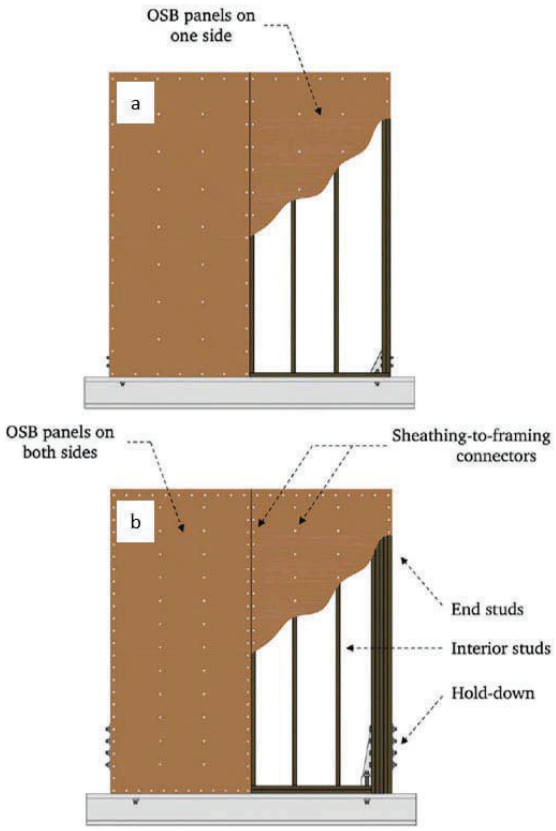

Figure 1: *Schematic configuration of (a) conventional and (b) strong wood frame shear wall. Taken from [11]*

2 SCOPE

This investigation aims at evaluating experimentally the lateral cyclic response of a non-planar T-shape wood frame strong shear wall as a way to represent part of the system effects found in LFTBs. Also, as previous studies identified that the wall-to-wall perpendicular connections are crucial for achieving 3D-SWCEs, two alternatives were evaluated experimentally.

3 METHODOLOGY

Connection-level and assembly-level tests were carried out under monotonic and/or cyclic loading according to ASTM E564-06 [5] and ASTM E2126-19 [6], respectively. The loading protocol was displacement-controlled and applied until failure of the specimen.

3.1 CONNECTION-LEVEL TEST

Two different configurations of wall-to-wall perpendicular connections were assembled. Both connections (i.e., screwed and slotted) were selected to facilitate wall installation considering off-site construction techniques. The connection-level specimens are representative of an end-stud-to-end-stud perpendicular connection (i.e., for a wall-to-wall perpendicular connection, end-studs are connected). Specimens consider two lateral elements and one central element manufactured with 41 mm x 135 mm (2x6)

https://doi.org/10.52202/069179-0283

dimensional Chilean radiata pine (RP) lumber mechanically graded as C16 according to NCh1198 [26]. As SSWs are sheathed with OSB, a layer of OSB is attached at both sides of the central element. Screwed connection considers two pairs per shear plane of four crossed screws in an X-position installed at 45°. Slotted connections consider one slot connector per shear plane. Details of each specimen are summarized in Table 1. Each configuration consists of 3 specimens: 1 for monotonic testing, and 2 for cyclic testing.

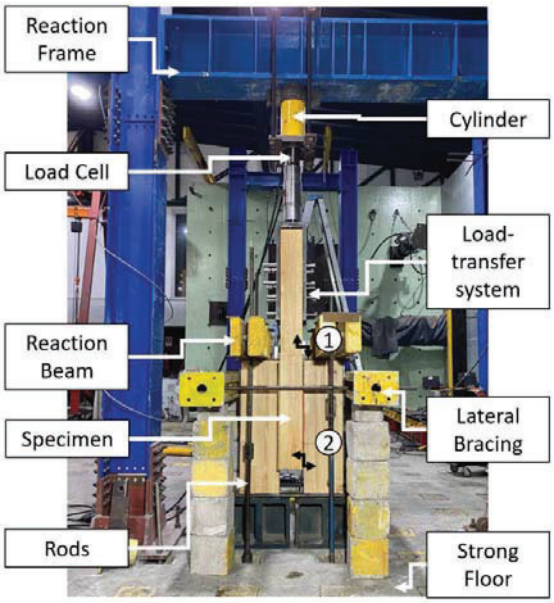

Figure 2: *Connection-level test setup*

A reaction steel frame was used to perform the connection-level tests. As shown in Figure 2, the reaction steel frame is anchored to a strong floor. Two heavy-duty steel beams are installed at each side of the specimen reacting against the strong floor through four high-strength rods (Figure 2). The load was applied by a double-action cylinder of +/- 588 kN and +/- 75 mm of force and displacement capacity, respectively, which transfers the vertical load to the specimen through a load-transfer system that consists of two steel plates attached to the specimen through bolts. As shown in Figure 2, all specimens were instrumented with four (i.e., two per shear plane) displacement transducers (LVDTs) for measuring the slip of the connection (labelled as 1 in Figure 2), two (i.e., one per shear plane) LVDTs for monitoring the rotation of the lateral end-studs (labelled as 2 in Figure 2) and one double-effect load cell to capture the shear force between end-studs.

Table 1: *Connection-level specimen details*

Connection Type	Lateral Element[b]	Central Element[b]	Fast.or Conn. Type
45XSc[a]	(4)41x135	(10)41x135	ESCRFTZ 8.0X300[c]
Slot90	(6)41x135	(12)41x135	SLOT90[d]

Notes:
a) Screw is abbreviated as Sc
b) For assembling each element, wood-frames are glued together following NCh2150 [27] prescriptions.
c) ESCRFTZ 8.0X300 per ETA-13/0796 of 12/15/2017 manufactured by Simpson Strong-Tie.
d) SLOT 90 per ETA-19/0167 of 04/05/2019 manufactured by Rothoblaas.

3.2 ASSEMBLY-LEVEL TEST

Specimens used for the planar and non-planar T-shape walls are representative of typical ground-level walls of a 7-story building designed per the Chilean seismic design code NCh433 [28]. Details of the wall specimens are summarized in Table 2. Double plates at the top and bottom of the wall were nailed to the studs with ϕ3.0 mm x 80 mm smooth shank nails that conform to ASTM F1667 [29]. All framing elements were 41 mm x 185 mm (2x8) C16 Chilean RP dimensional lumber, with a nominal modulus of elasticity E = 7900 MPa according to NCh1198 [26]. The walls were sheathed on both sides with 11.1 mm thick APA-rated OSB panels [30] with G = 1307.5 MPa (measured in previous studies [11]), and pneumatically driven to the frame with ϕ2.9 mm x 80 mm spiral nails. OSB sheathing layers were installed at both sides of the specimens and attached to the lower top plate and to the upper bottom plate as illustrated in Figure 3. According to the SDPWS [31], edge-nailing at the end studs should be uniformly distributed among the four framing members and spaced at a maximum of 300 mm. In order to transfer the lateral load to each specimen, a built-up collector beam of 205 mm x 207 mm (i.e., five members of 41 mm x 185 mm C16 RP plus an 11.1 mm thick OSB layer on top and bottom) was mechanically attached to the top plate through 38 Simpson Strong-Tie's SCDP221100 screws. For assembling the non-planar T-shape SSW, one type A (i.e., for the web) wall and two type B (i.e., for the flange) wall were used. For the wall-to-wall perpendicular connection (i.e., for attaching each flange to the web of the T-shape wall), six SLOT90 connector are used. The connectors are installed into the walls and fixed using two (i.e., one screw for wall) Simpson Strong-Tie's SDCF22614 screws (Figure 3). The planar SSW is a type C wall.

Table 2: *Wall type configuration*

Wall Type	n	Wall size (L by H)	Wood Structural Panel (WSP)		
			Thickness	Sheathing Nails[d]	Spacing edge/field
A[a,c]	1	2440x2481	11.1	ϕ2.9x80	100/200
B[b,c]	2	2440x2481	11.1	ϕ2.9x80	100/200
C[b,c]	1	2440x2481	11.1	ϕ2.9x80	100/200

Notes:
a) Wall framing consisted of 41mm x 185 mm (2x8) C16 Chilean RP [26] studs at 400mm o.c., (2) 41mm x 185 mm used as a central stud, (4) 41mm x 185 mm studs mechanically joined and located symmetrically with respect to the rod and (5) 41mm x 185 mm studs mechanically joined are used as end-studs.
b) Wall framing consisted of 41mm x 185 mm (2x8) C16 Chilean RP [26] studs at 400mm o.c., (2) 41mm x 185 mm used as a central stud, (4) 41mm x 185 mm studs mechanically joined

https://doi.org/10.52202/069179-0283

and located symmetrically with respect to the rod are used as end-studs.
c) Wall shear anchorage consisted of ϕ32 mm x 220 mm ASTM A193 Grade B7 anchor bolts (14 and 15 for wall type A and B, respectively) with ϕ80 mm x 4.0 mm Grade A36 washers. Overturning restraint provided by ϕ38.1 mm ASTM A193 Grade B7 rods with 31.75 mm thick bearing plate (i.e., Simpson Strong-Tie PL16-5x12), a take-up device (i.e., Simpson Strong-Tie ATUD14), a 9.5 mm thick bearing plate (i.e., Simpson Strong-Tie BP 1-1/2), and ASTM A563 Grade DH double hexagonal nut.
d) nails installed considering a minimum of 20/40 mm of end/edge distance, respectively. According to EN14592:2008+A1:2012 [32].

Figure 3: *(a) sliding restrain system for wall type A and B, and, wall-to-wall connection detail; (b) slot disposition; and (c) installation of the SLOT90 connector*

An L-shape cantilever reaction wall, a strong floor, and a T-shape reaction steel beam were used to perform the assembly-level tests following ASTM E2126-19 [25] prescriptions (Figure 4). As shown in Figure 3, the specimens were attached to the reaction beam through 43 ϕ32 mm x 220 mm ASTM A193 Grade B7 anchor bolts to prevent sliding in the T-shape SSW. In order to prevent sliding and to measure the shear force during the cyclic test in the planar SSW, a couple of cylinders reacting against a L-shape connector were installed at each side of the wall (element 9 in Figures 5 and 6). The walls continuous rod system reacts against the top flange of the reaction beam through a system of double hexagonal nuts. Out-of-plane support was provided to the 2D SSW in such a way that in-plane displacements were not affected. In order to capture the 3D response of the T-shape non-planar shear wall, a bidirectional cyclic test was performed according to FEMA 461 [33]. The hexagonal protocol from FEMA 461 [33] consider as a base the test protocol per ASTM E2126-19 [25] method C where a 100% and 50% of the target displacement were applied in the longitudinal and transverse direction. The lateral load was applied by a hydraulic bidirectional actuator of +588 kN/-294kN and +/- 200 mm of force and displacement capacity, respectively, in the longitudinal direction, and by a hydraulic bidirectional actuator of +588 kN/-294kN and +/- 50 mm of force and displacement capacity, respectively, in the transverse direction. Both actuators transfer the lateral load to the specimen through the collector beam. The T-shape non-planar SSW and the planar SSW are connected by a steel pinned-beam, allowing the in-plane loading transferring and decoupling the racking response of the specimens (Figure 4).

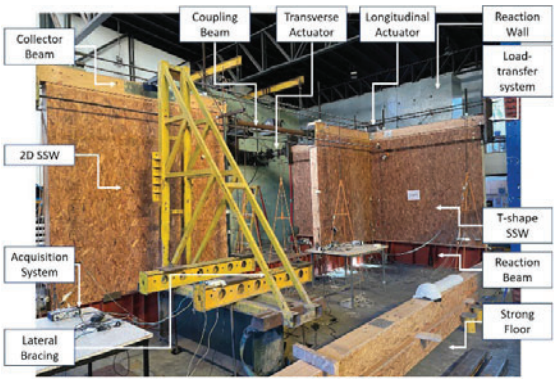

Figure 4: *Assembly-level test setup*

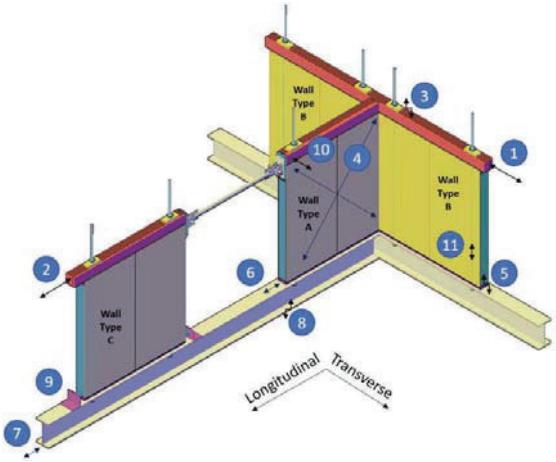

Figure 5: *Assembly-level specimen and instrumentation detail*

The specimen were instrumented with 41 displacement transducers (LVDTs), two cell load at the reaction cylinders (element 9 in Figures 5 and 6), and two load cell and displacement transducers (LVDT) incorporated into the actuator to capture the lateral displacement and shear force along each axis of the specimens (elements 1 and 2 in Figure 5), the slip of the wall with respect to the steel reaction beam (elements 6 and 8 in Figures 5 and 6), the diagonal (shear) deformation (element 4 in Figures 5 and 6), uplift in the exterior edge of the wall (element 5 in Figures 5 and 6), the out-of-plane displacement of the T-shape SSW web (element 10 in Figures 5 and 6), the relative displacement of the steel reaction beam with respect to the strong floor (element 7 in Figure 5), and the compressive deformation under the bearing plate of the strong-rod system (element 3 in Figures 5 and 6). To measure the tension in the rods of the continuous hold-down, seven unidirectional strain-gauges were attached to the rods (element 11 in Figures 5 and 6).

https://doi.org/10.52202/069179-0283

Figure 6: *Test setup: (a) sliding restraint system for the 2D SSW; (b) T-shape SSW instrumentation detail; (c) transverse view of the T-shape SSW; (d) detail of the instrumentation at the wall corners; and (e) strain gauge installation in a rod.*

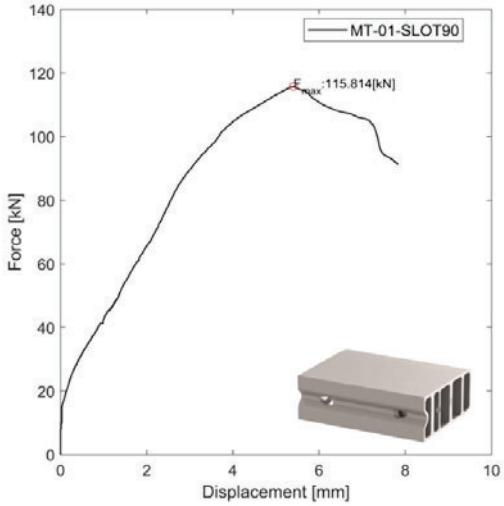

Figure 7: *Monotonic test results of Slot90 wall-to-wall perpendicular connections.*

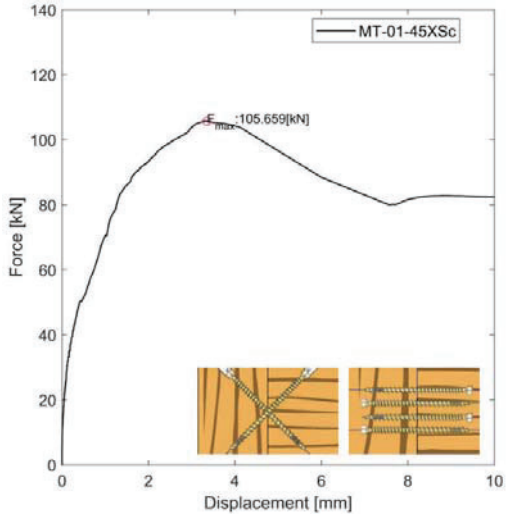

Figure 8: *Monotonic test results of 45XSc wall-to-wall perpendicular connections*

4 RESULTS

Failure mode, hysteresis shape, and six engineering parameters were established for connection-level and assembly-level test results: (1) elastic stiffness (K_e), calculated as the secant stiffness between zero and 40% of maximum load F_{max}; (2) yield displacement (Δ_y); (3) yield force (F_y); (4) ultimate displacement (Δ_u), defined as the displacement after post-peak load where the load dropped to $F_u = 0.8\ F_{max}$; (5) ultimate force (F_u); and, (6) ductility (μ), defined as the ratio of Δ_u to Δ_y. Moreover, the lateral behavior of the T-shape SSW is compared with that of the 2D SSW used in this study as reference.

4.1 CONNECTION-LEVEL TESTS

The slotted connection (i.e., connection type Slot90) shows two failure modes: (i) compression parallel to the grain crushing at the wood studs; and (ii) local yielding in the SLOT90 connector. The screwed connection (i.e., connection type 45XSc) shows two failure modes: (i) excessive bend in the screws, wood crushing and tearing in OSB sheathing layer; (ii) withdrawal failure of at least one screw of the group; (iii) pull-through of the screws head; and (iv) tension failure of at least one screw of the group. Note that in failure modes (ii) to (iv) pulling out of the connected wood members was present.

Monotonic results for each connection-level test are shown in Figures 7 and 8, in which the reported displacement is the differential slip between the wood frames, and the force is that taken by only one SLOT90 or group of four inclined ESCRFTZ 8.0X300 screws along a single shear plane. Based on monotonic test results, engineering parameters are summarized in Table 3. Both connections showed almost the same peak load and higher elastic stiffness which is attributable to the wood parallel to the grain stiffness/strength and axial stiffness of fully threaded screws for the case of connection type Slot90 and 45XSc, respectively. From a ductility point of view, connection type 45XSc showed almost four times higher values than the Slot90 connection. However, this tendency was not evidenced in cyclic test results were the 45XSc and Slot90 connection types show almost the same deformation capacity (Figures 9 and 10). Finally, based on preliminary numerical models, for achieving 3D-SWCE in a T-shape non-planar SSW the wall-to-wall

perpendicular connection needs to have a stiffness equal to 40% of that of the 2D SSW. When 3D-SWCE is achieved, the numerical model predicted a 20% reduction in the lateral displacement of a 1-story SSW. Based on previous evaluation, both connection types are good candidates as wall-to-wall perpendicular connections.

Table 3: *Engineering parameters from monotonic connection-level test results*

Connection Type	K_e kN/mm	Δ_y mm	F_y kN	Δ_u mm	F_u kN	μ
45XSc	156.0	0.59	92.4	6.74	84.5	11.4
Slot	39.2	2.64	103.6	7.72	92.65	2.9

The cyclic force-displacement test response for both connection types is presented in Figures 9 and 10. Again, results are expressed in terms of differential slip per connector or group of fasteners per shear plane. Cyclic test results for all tested connections depict a strong pinching effect due to the wood frame crushing at the shear planes. Moreover, strength and stiffness degradation after repeated cycles were found in all tests. In particular, in the 45XSc connection type, an abrupt reduction of the stiffness and strength was found after reaching the peak load as the withdrawal failure tends to be more brittle than the parallel to the grain crushing evidenced in the Slot90 connection.

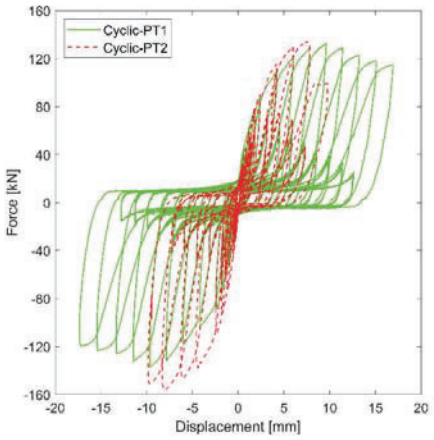

Figure 9: *Cyclic test results of Slot90 wall-to-wall perpendicular connections.*

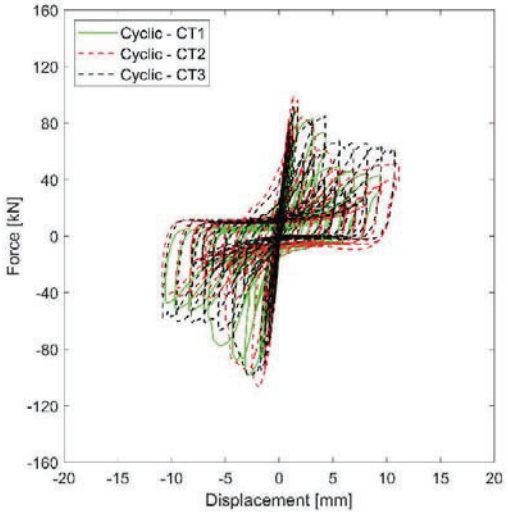

Figure 10: *Cyclic test results of 45XSc wall-to-wall perpendicular connections.*

4.2 ASSEMBLY-LEVEL TESTS

A comparison between the backbone curves obtained from bidirectional cyclic loading on the assemble-level full-scale tests is presented in Figure 11. Based on backbone curves results, engineering parameters are summarized in Table 4. Assembly-level tests showed an asymmetric behaviour of the T-shape SSW with increments of up to 19% and 98% in the elastic stiffness and maximum capacity, respectively, compared to those of a 2D SSW. However, a mean reduction of 44% in ductility was also observed.

The hysteretic curves of the T-shape SSW and the control wall (i.e., 2D SSW) are shown in Figures 12 and 13, respectively. The reported displacement is the effective displacement of the wall measured at the collector axis where the actuator was located (i.e., longitudinal collector). The effective displacement is the measured lateral displacement at the collector of the wall minus the displacement measured at the specimen-to-reaction beam relative to the reaction beam-to-strong floor. The overall shape of the 2D SSW hysteresis loops was consistent with that reported in previous research [12, 13]. However, the T-shape SSW cyclic response was asymmetric (i.e., 44% difference in peak strength) with a faster degradation of strength and stiffness in the flange side of the specimen (i.e., the negative branch of the cyclic response in Figure 13), which is attributable to the premature detachment of the OSB sheathing (i.e., nailed OSB-to-wood frame connection failure) close to the flange of the wall. The 2D SSW and the T-shape SSW specimens showed elastic response up to a drift of about 0.6% and 0.8%, respectively, and then a nonlinear response was observed, attributable to the nailed OSB-to-wood frame connections. After the specimens reached the peak strength, progressive strength and stiffness degradation was found. As expected, high redundancy was evident in the specimens because of the nailed connections, resulting in high drift levels with no brittle failures. Hence, as the

https://doi.org/10.52202/069179-0283

lateral behavior of the specimens was governed by the nailed connection response, the hysteresis was markedly pinched because of the non-reversible crushing effect of the nails.

Table 4: *Engineering parameters from cyclic backbone curves of the assembly-level test results*

Wall Conf.	K_e kN/mm	Δ_y mm	F_y kN	Δ_u mm	F_u kN	μ
T-shape SSW+	4.04	18.9	76.3	68.6	67.3	3.6
T-shape SSW-	4.83	22.7	109.4	64.3	104.2	2.9
T-shape SSW_{mean}	4.44	20.8	92.9	66.5	85.8	3.3
2D-SSW+	3.58	17.1	61.3	88.1	55.3	5.1
2D-SSW-	4.06	13.8	55.9	92.4	52.6	6.7
2D-SSW_{mean}	3.82	15.4	58.6	90.2	54.0	5.9

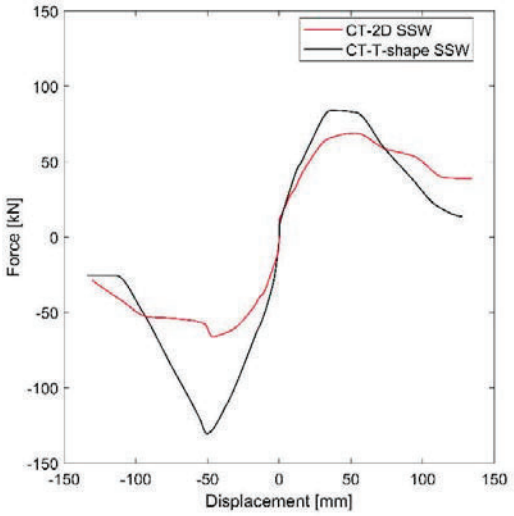

Figure 11: *Comparison between the backbone curves of in-plane response of the T-shape SSW (black) and the 2D SSW (red).*

5 CONCLUSIONS

Findings of this research reinforce the idea of taking advantage of the 3D-SWCE on the lateral response of LFTBs. The ultimate objective is to achieve a cost-effective structural design and to better understand CSWO, so that traditional pseudo-3D design practices be discouraged. The next steps of this research program include the calibration of analytical and numerical models for non-planar timber shear walls. Further research is needed to elucidate potential 3D effects on other non-planar walls such as U- or L-shape assemblies.

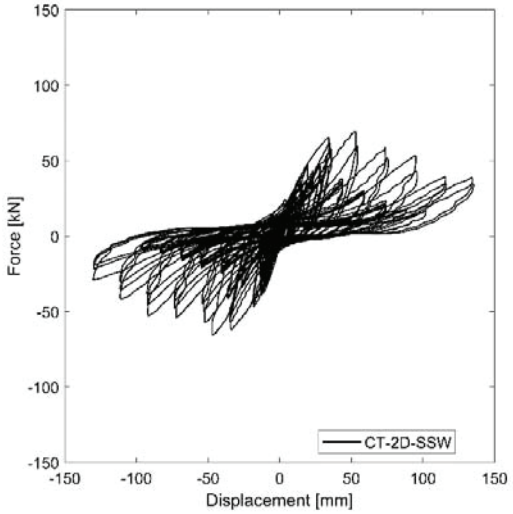

Figure 12: *In-plane cyclic response of the 2D SSW.*

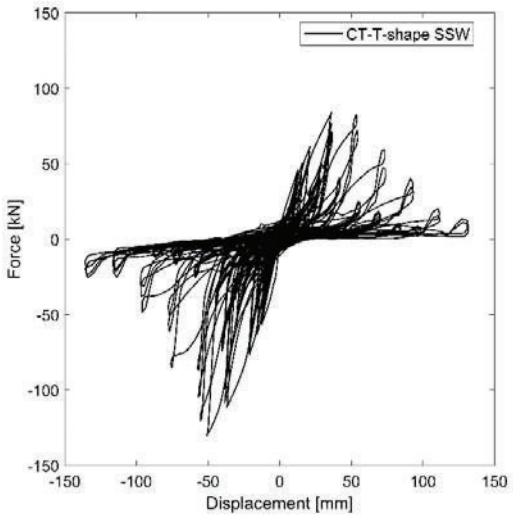

Figure 13: *In-plane cyclic response of the 2D SSW*

ACKNOWLEDGEMENTS

Financial support was provided by CONICYT (Doctorado Nacional 2018–21180074), by VRI-UC, by ANID BASAL FB210015 (CENAMAD), and by the Research Center for Integrated Disaster Risk Management (CIGIDEN) ANID FONDAP 1522A0005.

REFERENCES

[1] Almeida De Araujo, V., Cortez-Barbosa, J., Garcia, J. N., Gava, M., Laroca, C., & César, S. F. (2016). Woodframe: viviendas de entramado ligero para países en desarrollo. *Revista de la Construcción*, 15(2), 78-87.

[2] Hopkins, A. K., Fell, B. V., Deierlein, G. G., & Miranda, E. (2014). Large-scale tests of seismically enhanced planar walls for residential construction.

Report No. 186, John A. Blume Earthquake Engineering Center, Stanford, USA.

[3] Leung, T., Asiz, A., Chui, Y., Hu, L. J., & Mohammad, M. (2010). Predicting lateral deflection and fundamental natural period of multi-storey wood frame buildings. *11th World Conference on Timber Engineering*, Trentino, Italy.

[4] Van de Lindt, J. W., Pei, S., Pryor, S. E., Shimizu, H., & Isoda, H. (2010). Experimental seismic response of a full-scale six-story light-frame wood building. *Journal of Structural Engineering*, 136(10), 1262-1272.

[5] Collins, M., Kasal, B., Paevere, P., & Foliente, G. C. (2005). Three-dimensional model of light frame wood buildings. II: Experimental investigation and validation of analytical model. *Journal of Structural Engineering*, 131(4), 684-692.

[6] Winkel, M., & Smith, I. (2010). Structural behavior of wood light-frame wall segments subjected to in-plane and out-of-plane forces. *Journal of Structural Engineering*, 136(7), 826-836.

[7] Paevere, P. J. (2002). Full-scale testing, modelling and analysis of light-frame structures under lateral loading. *Ph.D. Thesis*, University of Melbourne, Melbourne, Australia.

[8] Tomasi, R., Sartori, T., Casagrande, D., & Piazza, M. (2015). Shaking table testing of a full-scale prefabricated three-story timber-frame building. *Journal of Earthquake Engineering*, 19(3), 505-534.

[9] Pei, S., & Van de Lindt, J. W. (2011). Seismic numerical modeling of a six-story light-frame wood building: comparison with experiments. *Journal of Earthquake Engineering*, 15(6), 924-941.

[10] Pang, W., Ziaei, E., & Filiatrault, A. (2012). A 3D model for collapse analysis of soft-story light-frame wood buildings. *World Conference on Timber Engineering*, Auckland, New Zealand.

[11] Estrella, X., Guindos, P., Almazán, J. L., & Malek, S. (2020). Efficient nonlinear modeling of strong wood frame shear walls for mid-rise buildings. *Engineering Structures*, 215, 110670.

[12] Estrella, X., Malek, S., Almazán, J. L., Guindos, P., & Santa María, H. (2021). Experimental study of the effects of continuous rod hold-down anchorages on the cyclic response of wood frame shear walls. *Engineering Structures*, 230, 111641.

[13] Guíñez, F., Santa María, H., & Almazán, J. L. (2019). Monotonic and cyclic behaviour of wood frame shear walls for mid-height timber buildings. *Engineering Structures*, 189, 100-110.

[14] Kolozvari, K., Kalbasi, K., Orakcal, K., & Wallace, J. (2021). Three-dimensional shear-flexure interaction model for analysis of non-planar reinforced concrete walls. *Journal of Building Engineering*, 44, 102946.

[15] Ramos, L., & Hube, M. (2020). Contribution of coupling elements to the seismic demand of walls in reinforced concrete buildings. *Latin American Journal of Solids and Structures*, 17(2), e256.

[16] Seible, F., Filiatrault, A., & Uang, C. M. (1999). Proceedings of the Invitational Workshop on Seismic Testing, Analysis and Design of Woodframe Construction. *CUREE Publication No. W-01*, Consortium of Universities for Research in Earthquake Engineering, Richmond, USA.

[17] Suzuki, S. (1990). Effect of cross-walls on lateral stiffness of light-frame buildings. *International Timber Engineering Conference*, Tokyo, Japan.

[18] Sugiyama, H., & Isono, R. (1983). The effect of perpendicularly arranged wall on the shear strength of plywood sheathed wall. *1983 Annual Meeting*, Architectural Institute of Japan, Tokyo, Japan.

[19] NAHB Research Center, Inc. (2001). *Wood Shear Walls with Corners*. Partnership for Advanced Technology in Housing, Washington, USA.

[20] Dolan, J. D., & Heine, C. P. (1997). Sequential phased displacement tests of wood-framed shear walls with corners. *Report No. TE-1997-003*, Virginia Polytechnic Institute and State University, Blacksburg, USA.

[21] Girhammar, U. A., & Källsner, B. (2008). Effect of transverse walls on capacity of wood-framed wall diaphragms without tie-downs. *10th World Conference on Timber Engineering*, Miyazaki, Japan.

[22] Stoner, M. W. (2020). Performance of cross-laminated timber as a residential building material subject to tornado events. *Ph.D. Thesis*, Clemson University, Clemson, USA.

[23] Ruggeri, E., D'Arenzo, G., Fossetti, M., & Seim, W. (2022). Investigating the effect of perpendicular walls on the lateral behaviour of cross-laminated timber shear walls. *Structures*, 46, 1679-1695.

[24] ASTM (2006). *Standard Practice for Static Load Test for Shear Resistance of Framed Walls for Buildings ASTM E564-06*. ASTM International, West Conshohocken, USA.

[25] ASTM (2019). *Standard Test Methods for Cyclic (Reversed) Load Test for Shear Resistance of Vertical Elements of the Lateral Force Resisting Systems for Buildings ASTM E2126-19*. ASTM International, West Conshohocken, USA.

[26] INN (2014). *Madera - Construcciones en Madera - Cálculo NCh 1198*. Instituto Nacional de Normalización, Santiago, Chile. (in Spanish)

[27] INN (2022). *Madera Laminada Encolada - Clasificación Mecánica y Visual de Madera Aserrada de Pino Radiata NCh 2150*. Instituto Nacional de Normalización, Santiago, Chile. (in Spanish)

[28] INN (2009). *Diseño Sísmico de Edificios NCh 433 Of1996 Mod. 2009*. Instituto Nacional de Normalización, Santiago, Chile. (in Spanish)

[29] ASTM (2021). *Standard Specification for Driven Fasteners: Nails, Spikes, and Staples ASTM F1667*. ASTM International, West Conshohocken, USA.

[30] APA (2012). *Panel Design Specification*. APA - The Engineering Wood Association, Tacoma, USA.

[31] AWC (2021). *Special Design Provisions for Wind and Seismic ANSI/AWC SDPWS-2021*. American Wood Council, Leesburg, USA.

[32] BSI (2008). *BS EN 14592: 2008+ A1: 2012 Timber Structures - Dowel-type Fasteners - Requirements*. British Standard Institution, London, UK.

https://doi.org/10.52202/069179-0283

[33] ATC (2007). *Interim Testing Protocols for Determining the Seismic Performance Characteristics of Structural and Nonstructural Components FEMA 461*. Federal Emergency Management Agency, Washington, USA.

World Conference on Timber Engineering Oslo 2023

DATA-DRIVEN APPROACH FOR ASSESSMENT OF SEISMIC DAMAGE IN WOOD BUILDINGS

Sifat Muin[1], Asif Iqbal[2], John W. van de Lindt[3]

ABSTRACT: Advances in modern computing techniques and capabilities have been utilized in development of new structural health monitoring techniques that utilize a significant volume of data from instrumentation. These data-driven methods open new possibilities for the damage assessment of wood (or any) buildings. A method known as feature engineering is a key step in developing such tools. This paper presents a feature engineering procedure for wood buildings based on data recorded during seismic events and utilizes a full-scale wood shake table test data set and damage inspection results to illustrate the procedure.

KEYWORDS: Data-driven Damage Assessment, Seismic Performance, Resiliency, Wood Buildings, Feature Engineering, Cumulative absolute velocity

1 INTRODUCTION

Over the past decade, significant progress has been made in structural health monitoring through the application of data-driven damage assessment. Data-driven seismic damage assessment evaluates the potential damage to structures or infrastructure caused by earthquakes using data and analytical techniques. Advances in computing technologies, remote sensing, and data science paved the way for new and improved damage assessment tools, many of which are machine learning algorithm-based [1-3]. These ML-SHM techniques, which utilize structural vibration response as the primary data type, have four stages: *health definition*, *data acquisition*, *feature engineering*, and *machine-learned damage assessment*. Arguments for the damage prediction power of ML have been made in several studies [4-7]. These studies have focused on addressing feature engineering through extracting and selecting features that result in more effective ML model training. This feature engineering step is particularly crucial for ML-based seismic damage assessment as data from the damage class is sparse. Hence, a dataset that provides vibration data from damaged structures is extremely valuable for the development of data-driven damage assessment tools. In this study, feature engineering concepts are applied to a dataset acquired from a series of shake table tests of a four-story full-scale soft-story wood-frame building model. The study's primary goal is to identify the most suitable features for damage assessment of such buildings so that ML-based algorithms would provide the most accurate predictions.

2 FEATURE ENGINEERING

In feature engineering (FE), domain knowledge and data mining techniques are used to identify the most useful features from the data to enhance the performance of ML models. For seismic damage assessment, classifiers or regression models may be used with these features to predict the extent of damage caused to the structure. The data required for the FE are acceleration response histories (RH) and corresponding damage states (DS), or RH-DS pairs. Through *feature extraction*, *exploratory data analysis* ((EDA), and *feature selection*, a vector of damage features is selected that is most suitable for damage classification and localization.

Feature extraction is the process of transforming the measured data into a helpful alternative form. In this step, the RH-DS dataset is transformed into a feature-DS dataset. This transformation reduces the dimension of the dataset keeping the most informative and salient features for damage assessment from the raw data. The extracted damage features include vibration characteristics that have been studied as structural damage indicators by researchers in the past [3]. Past work has shown that these features, referred to as "intensity measures" or "engineering demand parameters" in earthquake engineering, are related to the structural response and are thus likely correlated to damage from a physics-based perspective. Examples of these damage features include peak ground acceleration, peak ground velocity, peak ground displacement, peak responses, cumulative absolute velocity (CAV) [8,9], standardized CAV (CAV_{STD}) [10], Arias Intensity (AI), etc.

[1] Sifat Muin, University of Southern California, USA, muin@usc.edu
[2] Asif Iqbal, University of Northern British Columbia, Canada, asif.iqbal@unbc.ca
[3] John W. van de Lindt, Colorado State University, USA, jwv@colostate.edu

https://doi.org/10.52202/069179-0284

Exploratory data analysis (EDA) is the process of studying the *feature-DS* dataset in detail. EDA aims to gain insights into the underlying structure, patterns, and relationships in the data and to identify any potential problems or outliers. EDA often involves visualizing the data using graphs, plots, histograms, and running summary statistics. By exploring the data this way, researchers can make informed decisions about which features and models to use for further analysis. Figure 1 shows an example of EDA where CAV shows a clear pattern with ductility. This set of data was collected using a finite element model of a building and the displacement ductility was used as a measure of damage. Consequently, it was successfully used as a damage indicator for concrete and steel buildings.

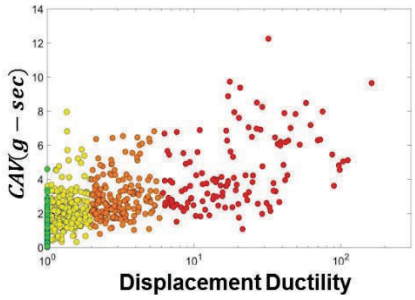

Figure 1. *EDA of CAV showing distinct pattern with increasing ductility (damage) for a reinforced concrete structure. [8]*

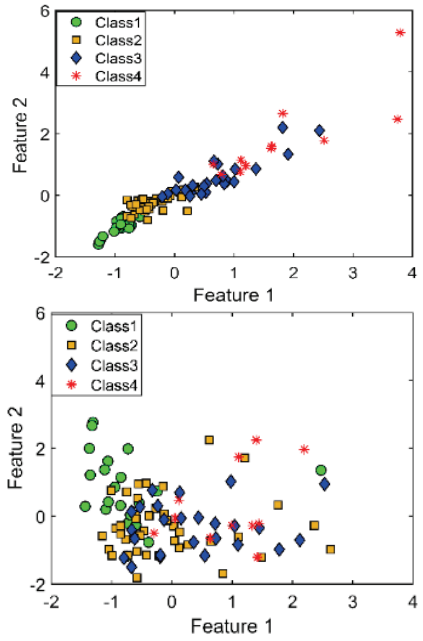

Figure 2. *Discrimination ability of features with high (top) and low (bottom) Fisher scores.*

Feature selection is the process of identifying a subset of the original feature set, which increases the learning efficiency without compromising the classification performance. A filter-based feature selection method is chosen herein called the Fisher Score (FS) because it is computationally inexpensive.). FS determines the relative ability of features to discriminate between categorical classes in a classification model. A larger Fisher score indicates that the feature is more discriminative (Figure 2). Although the Fisher score is known to have limitations as it considers each feature separately and therefore cannot reveal mutual information between features, it is widely used as a heuristic algorithm for feature selection [11].

In this study, the classification model aims to determine which class of DS is indicated by the feature vector. The DSs are ordered in this problem, i.e., if DS0 refers to undamaged and DS1 refers to minor damage, then DS1 is ranked higher than DS0. Due to the ordering of the classes in this model, feature selection that considers *ordinality* is preferred. Thus, an ordinal variant of the Fisher score, the *Ordinal Fisher Score*, is used for feature selection [12]. The ordinal Fisher score (F_{OR}) for the ith feature, x_i is computed following a specific procedure. First, the class discrimination term, $F_O(x_i)$, is defined as follows,

$$F_O(x_i) = \sum_{k=1}^{K}\sum_{j=1}^{K}|k-j|\cdot d^i(C_k,C_j)/\{(K-1)\sum_{k=1}^{K}(\sigma_k^i)^2 \qquad (1)$$

where the class C_k indicates data from one of the K classes, $k,j \in \{1,2,\ldots,K\}, \sigma_k^i$ is the variance of the ith feature in class k, and $d^i(C_k, C_j)$ is the distance between classes C_k and C_j. It is computed using the Hausdorff distance which allows for use of nonlinear, multimodal, or non-normal data, and shown in [12] to perform best for ordinal classification. Second, an ordinality term, $O_R(x_i)$, incorporating the relative distance between classes, is defined as follows,

$$O_R(x_i) = \sum_{k=1}^{K-2}\sum_{j=k+1}^{K-1}\sum_{h=j+1}^{K} I(d^i(C_k,C_h) - d^i(C_k,C_j) > 0)/\sum_{j=2}^{K-1}(K-j) \qquad (2)$$

where $I(\cdot)$ is the indicator function (1 if the inner condition is true & = 0 otherwise). This $O_R(x_i)$ score measures the number of ordinal requirements fulfilled for the ith feature. Finally, the two terms $F_O(x_i)$ and $O_R(x_i)$ are combined in a weighted sum as follows,

$$F_{OR}(x_i) = \alpha \cdot F_O(x^i) + (1-\alpha)\cdot O_R(x_i), \alpha \in (0,1) \qquad (3)$$

The candidate damage features are evaluated using Equation (3) with $\alpha = 0.1$ to identify which features best discriminate between the different classes of DS. Selecting features that can identify ordinality is crucial for accurate damage assessment. Hence, the ordinality term, $O_R(x_i)$, is given a higher weight ($1 - \alpha = 0.9$) compared to the class discrimination term, $F_O(x_i)$. The features with the highest Ordinal Fisher Scores constitute the final damage feature set.

https://doi.org/10.52202/069179-0284

3 FULL WOOD BUILDING APPLICATION

The methodology described above is applied to data acquired from a shake table test program on a four-storied full-scale wood building (Figure 3) tested at the University of California San Diego in 2013 under the project titled "Seismic Risk Reduction for Soft-Story Woodframe buildings (NEES-Soft)" [13, 14]. The model represents many thousands of buildings throughout California, and the United States, generally built before 1970 and many as early as the 1920s, following conventional construction practices of the time which are no longer satisfactory by today's seismic codes and standards. The NEES-Soft project included a major testing program to validate performance-based seismic retrofit methodology developed for these buildings. The penultimate experiment of this program was a collapse test sequence. Data from the collapse test is utilized in this investigation as the structure experienced increasing levels of damage.

Figure 3. *NEES-Soft model building*

3.1 MODEL DESCRIPTION AND TESTING

The building in this study was a 370 m^2 (4,000 sqft) four-story light wood-frame building with a "soft-story" archetype most common in San Francisco Bay Area. It had a plan dimension of 7.3 m x 11.6 m and a total height of 10.9 m. The first story (soft story) mainly serves as a parking area with big wall openings for parking doors. The other three upper stories facilitate two typical two-bedroom apartment units [15]. In order to monitor the behavior of the building during testing, the building was instrumented with two string potentiometers and four accelerometers on the first floor, and three accelerometers on the roof. Moreover, six video cameras monitored the movement of the building. Figure 4 presents the location and details of the instrumentation used in the series of tests leading to the collapse of the test building.

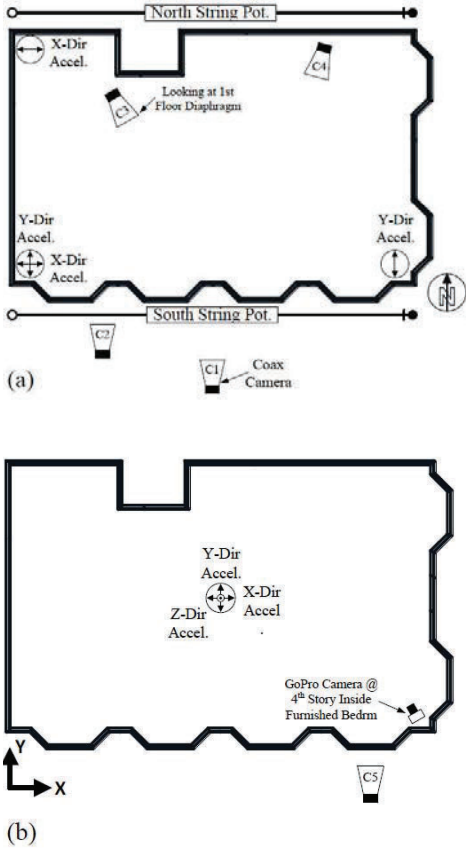

Figure 4. *Instrumentation plan a) first story b) fourth story*

To study the collapse mechanism and behavior of this type of at-risk building, the building was subjected to a range of ground motions with different scaling. Three different ground motions with different intensities were selected. The selections were such that they would provide a range of earthquake records based on differences in ground displacement, even if the seismic intensities as determined through spectral acceleration were similar. The ground motions were then scaled to spectral accelerations ranging from Sa = 0.4g (33% of the design-based earthquake level) to Sa =1.8g (maximum credible earthquake (MCE) level). Table 1 presents the ground motions and test sequences with the corresponding peak ground acceleration (PGA) and peak ground displacement (PGD) for each test.

3.2 DEVELOPMENT OF RH-DS DATABASE

The RH-DS database is created from the acceleration response histories of the eight tests and their corresponding observed damage conditions. The RH data is acquired from the six accelerometers that measured the horizontal responses of the first story and roof. The ground motion RHs were computed from the feedback of the shaketable.

The DS data is based on damages reported during the testing. Due to safety regulations, no damage inspection

https://doi.org/10.52202/069179-0284

and repair was conducted between each consecutive test; therefore, the structural and non-structural damage accumulated during the entire collapse test program. However, building period calculation and residual displacement measurements indicated the level of damage after each test. It was observed that the period of the building increased significantly after Test-4 due to permanent structural damage [16]. But no residual displacements were observed even after Test 5. Test 6 led to extensive permanent damage to the building, bringing it to the verge of collapse with a residual displacement of 350 mm. Then, it was subjected to the same ground motion scaled to Sa=0.9g to evaluate the aftershock performance of the building (Test 7); however, the building did not collapse even with about 406 mm (16 in.) residual drift and 2.3 degrees of residual rotation. The building was then subjected to Test 8, which led to the collapse of the building. Based on these observations, the damage states are classified into four categories, shown in Table 1. These are:

i. DS0 when no damages are reported.
ii. DS1 when the period increase is reported.
iii. DS2 when residual displacement is observed.
iv. DS3 when the building collapsed.

Table 1: *Testing details and damage states*

Seismic Test ID	Eq record	Sa (g)	PGA (g)	PGD (mm)	Damage State
1	Cape Medocino - Rio	0.40	0.21	13.1	DS0
2	Cape Medocino - Rio	0.90	0.44	29.4	DS0
3	Cape Medocino - Rio	1.20	0.56	39.2	DS0
4	Cape Medocino - Rio	1.80	0.90	58.8	DS1
5	Loma Prieta - Gilroy	1.80	0.98	72.1	DS1
6	Superstition Hills	1.80	0.86	277	DS2
7	Superstition Hills	0.90	0.42	138	DS2
8	Superstition Hills	1.80	0.86	277	DS3

4 RESULTS AND DISCUSSION

4.1 FEATURE EXTRACTION:

In the feature extraction phase, the RH-DS database is transformed into a feature-DS database. Six individual features are computed from the RHs. Table 2 shows the feature name and their mathematical definition. For each test, these six features are calculated for the ground response, first story response, and the roof response making the total number of features 18. These 18 features are studied in the EDA phase and utilized in the feature selection phase with corresponding DS shown in Table 1 as their respective class.

Table 2: *Description of candidate damage features*

Feature	Definition
Peak acceleration (PA)	$max(\lvert\ddot{u}(t)\rvert)$
Peak velocity (PV)	$max(\lvert\dot{u}(t)\rvert)$
Peak displacement (PD)	$max(\lvert u(t)\rvert)$
Arias intensity (AI)	$\frac{\pi}{2g}\int_0^T [\ddot{u}(t)]^2 dt$
Cumulative absolute velocity (CAV)	$\int_0^T \lvert\ddot{u}(t)\rvert dt$
Standardized CAV (CAV_{std})	$\sum_{i=1}^{N} H(PA_i - 0.025)\int_{i-1}^{i} \lvert\ddot{u}(t)\rvert dt$ $H(x) = Heaveside\ function = \begin{cases} 0\ , x < 0 \\ 1,\ otherwise \end{cases}$ N: $non-overlapped$ 1 sec $intervals\ with\ PA_i$

4.2 EXPLORATORY DATA ANALYSIS

In this phase, the extracted features are studied to understand their relationship to damage and to point out any outliers. Two different tasks were performed as EDA. Firstly, the relationship between CAV profiles and damage states is investigated. Then all 18 features and their progression with damage are studied.

Figures 5 and 6 show each test's CAV time series and Normalized CAV time series. The normalized CAV is computed by dividing the CAV values by the final CAV, making the ultimate value 1. The responses are calculated from acceleration data of X-direction from the first floor. Figure 5 shows that the damage-inducing tests (4,6,8) have high CAV values (>0.8 g-sec). The normalized CAV plots (Figure 6) show a baseline behavior for tests 1, 2, 3, 4 and a departure from this baseline pattern for tests 5,6,7,8. In previous studies, such deviations coincided with damage [8]. Similar behavior is observed for roof response as well. The figures show that CAV-based

features should be considered as candidate damage features.

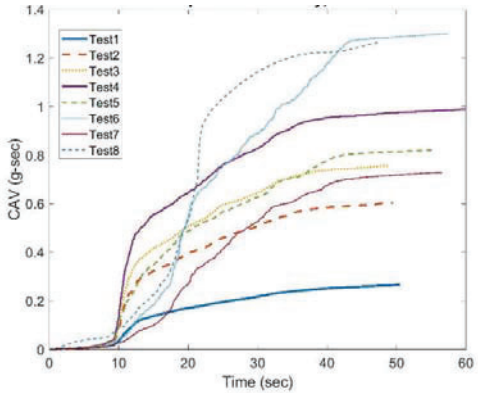

Figure 5. *CAV profile at first floor for X-dir response*

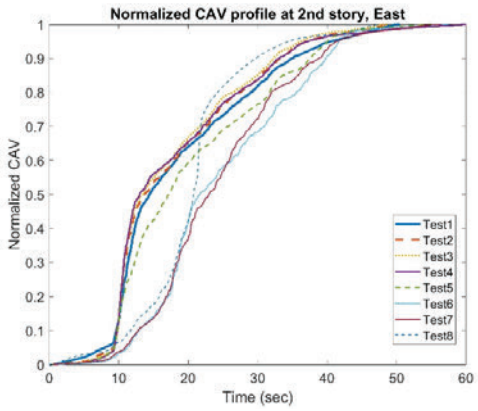

Figure 6. *Normalized CAV profile at first floor for X-dir response*

Figures 7, 8, and 9 show the relationship of the features with the damage states for ground, first floor, and roof response respectively through box plots. The ends of the box plots indicate the quartiles and the line in the middle is the median. The cross inside the box represent the mean. The whiskers (if any) indicate outliers. All ground motion features (Figure 7) depict some trend with increasing damage states. However, for the first floor (Figure 8) and roof responses (Figure 9) the trend is unclear due to the excessively high feature values of DS3. Moreover, the box plots in Figure 8 shows outliers for DS3. Such data, if used in feature selection will produce undesirable outcome. Therefore, DS3 data was not utilized in the feature selection phase following the findings of EDA.

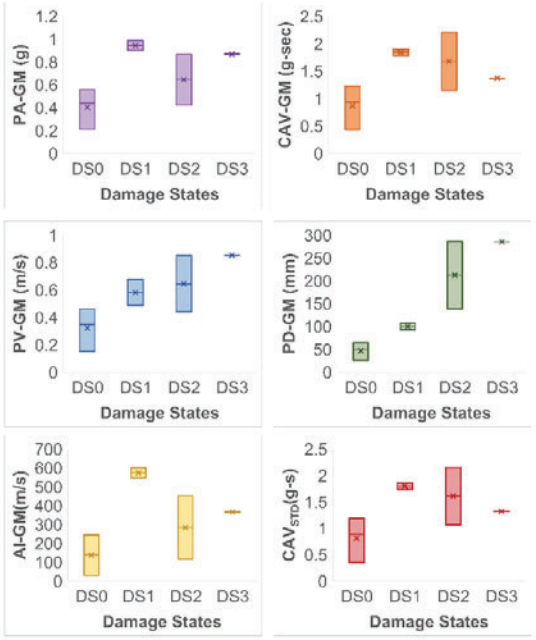

Figure 7. *Features vs damage states computed from the shake table response (ground motion)*

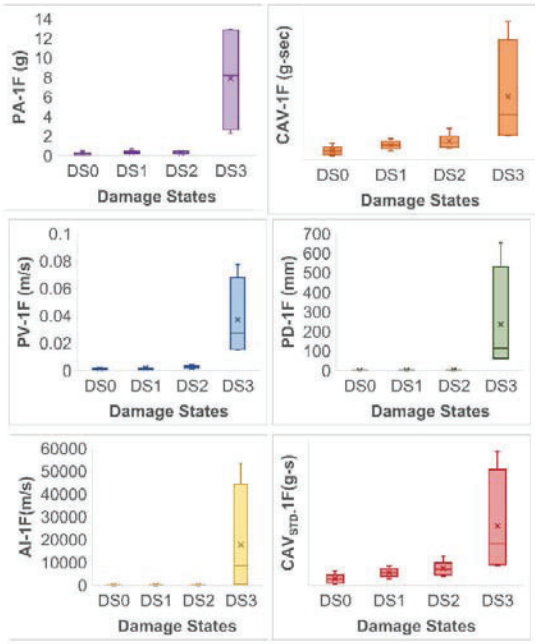

Figure 8. *Features vs damage states computed from the first floor response*

https://doi.org/10.52202/069179-0284

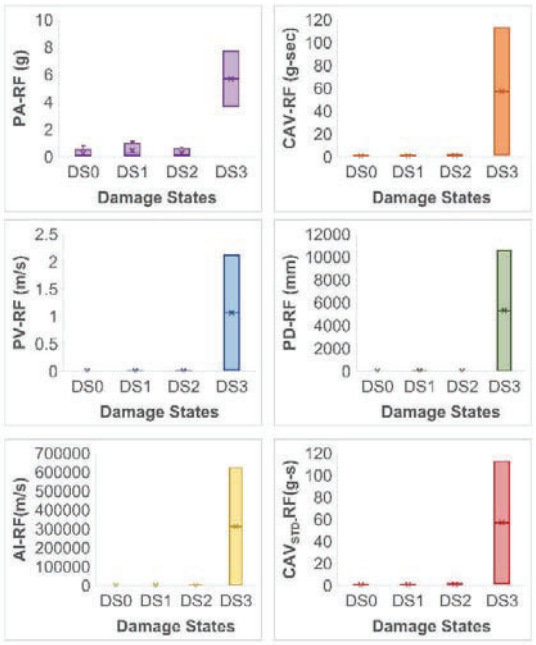

Figure 9. *Features vs damage states computed from the roof response*

4.3 FEATURE SELECTION

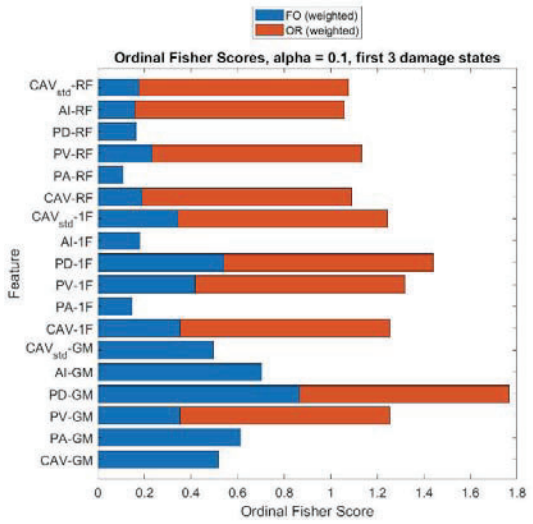

Figure 10. *Ordinal Fisher Scores of the candidate damage features*

In feature selection phase, Fisher score is calculated for all 18 features using Equation 1, 2, and 3. Three damage classes were considered (DS0, DS1, and DS2). Figure 10 shows the ordinal fisher score (F_{OR}). The blue portion is weighted the class discriminatory part and red is the weighted ordinality term. Higher weight is given to the ordinality term so that the features that can identify order of the DS scores higher.

Table 3: *Ordinal Fisher score of the candidate features*

Features	Fisher Score
PD-GM	1.77
PD-1F	1.44
PV-1F	1.32
PV-GM	1.25
CAV-1F	1.25
CAVstd-1F	1.24
PV-RF	1.13
CAV-RF	1.09
CAVstd-RF	1.08
AI-RF	1.06
AI-GM	0.70
PA-GM	0.61
CAV-GM	0.52
CAVstd-GM	0.50
AI-1F	0.18
PD-RF	0.16
PA-1F	0.15
PA-RF	0.11

Table 3 lists the F_{OR} from highest to lowest. Peak displacement of the ground scores the highest among all the features. The high correlation of ground displacement and damage is a well-established observation in the literature. The first floor's peak displacement and peak velocity are the second and third-highest-scoring features. CAV and CAVstd of the first floor, along with the peak velocity of the ground motion, are ranked next with almost the same values. This higher ranking of the CAV features agrees well with Figure 5 and Figure 6 observations. Overall the first-floor features ranked higher than the roof features. This behavior may be due to the "soft-story" mechanism of the structure. One interesting observation is that even though some features (PA-GM, AI-GM) showed a specific trend to damage (Figure 7), their $F_{OR}$was low. Figure 10 shows that these features have high discriminatory terms but very low ordinality terms bringing down the overall score. Therefore, these features would not be suitable for damage classification.

The results imply that for damage assessment of “soft-story” wood-frame buildings, peak displacement and peak velocity of the ground motion are crucial indicators. Moreover, peak displacement, peak velocity, CAV, and CAVstd of the first-floor response will improve the overall performance of an ML model developed toward damage classification. It should be noted that computing displacement values from acceleration by double integrating can sometimes produce erroneous peak values, particularly for low signal-to-noise ratio measurements. CAV values, CAVstd specifically by definition, avoid such noise levels. Therefore, having these features with the peak values will provide a more reliable outcome.

https://doi.org/10.52202/069179-0284

5 CONCLUSIONS

In this study, feature engineering is applied to a dataset acquired from a series of shake table tests of a soft-story wood-frame building. The building was subjected to increasing levels of ground motion until it collapsed, providing a valuable RH-DS dataset. All three phases of feature engineering have been applied to the data set. During the feature extraction phase, peak values of acceleration, velocity, and displacement, and energy representing features such as CAV and AI are extracted. In the exploratory data analysis phase, CAV-based features of the first floor have shown an obvious pattern with increasing damage states. In this phase, all the features are studied for the ground, first floor, and roof in order to identify any outliers. It was discovered that the DS3 values were outliers compared to other DSs. Therefore, in the feature selection phase, DS3 data was left out.

In feature selection, the ordinal Fisher score is used as identifying the order of the DSs is essential to accurate damage assessment. The analysis showed that the peak displacement of the ground and first floor are the most important features. Peak velocities of the ground and the first floor were also critical. Moreover, CAV and CAVstd of the first floor were also identified as important. Therefore, when developing an ML model for damage assessment of a wood-frame soft-story building, these six features should be used.

ACKNOWLEDGEMENT

The work done for the NEES-Soft project was supported by the National Science Foundation under Grant No. CMMI-1314957 (NEES Research) and NEES Operations. Any opinions, findings, and conclusions or recommendations expressed in this material are those of the investigators and do not necessarily reflect the views of the National Science Foundation.

REFERENCES

[1] Sohn, Hoon, et al. "A review of structural health monitoring literature: 1996–2001." Los Alamos National Laboratory, USA 1 (2003): 16.

[2] Fan, Wei, and Pizhong Qiao. "Vibration-based damage identification methods: a review and comparative study." Structural health monitoring 10.1 (2011): 83-111.

[3] Farrar, C. R., & Worden, K. (2012). Structural health monitoring: a machine learning perspective. John Wiley & Sons.

[4] Lam, Heung-Fai, Ka-Veng Yuen, and James L. Beck. "Structural health monitoring via measured Ritz vectors utilizing artificial neural networks." Computer-Aided Civil and Infrastructure Engineering 21.4 (2006): 232-241.

[5] Figueiredo, Eloi, et al. "Machine learning algorithms for damage detection under operational and environmental variability." Structural Health Monitoring 10.6 (2011): 559-572.

[6] Abdul-Aziz, Ali, et al. "Rotor health monitoring combining spin tests and data-driven anomaly detection methods." Structural Health Monitoring 11.1 (2012): 3-12.

[7] Babajanian Bisheh, Hossein, et al. "Damage detection of a cable-stayed bridge using feature extraction and selection methods." Structure and Infrastructure Engineering 15.9 (2019): 1165-1177.

[8] Muin, Sifat, and Khalid M. Mosalam. "Cumulative absolute velocity as a local damage indicator of instrumented structures." Earthquake Spectra 33.2 (2017): 641-664.

[9] Muin S., Mosalam K.: Human-machine collaboration framework for structural health monitoring and resiliency. Engineering Structures, 235: 112084, 2021.

[10] Campbell, Kenneth W., and Yousef Bozorgnia. "A comparison of ground motion prediction equations for Arias intensity and cumulative absolute velocity developed using a consistent database and functional form." Earthquake Spectra 28.3 (2012): 931-941.

[11] Gu, Quanquan, Zhenhui Li, and Jiawei Han. "Generalized fisher score for feature selection." arXiv preprint arXiv:1202.3725 (2012).

[12] Pérez-Ortiz, María, et al. "Fisher score-based feature selection for ordinal classification: a social survey on subjective well-being." Hybrid Artificial Intelligent Systems: 11th International Conference, HAIS 2016, Seville, Spain, April 18-20, 2016, Proceedings 11. Springer International Publishing, 2016.

[13] Bahmani, Pouria, et al. "Experimental seismic behavior of a full-scale four-story soft-story wood-frame building with retrofits. I: Building design, retrofit methodology, and numerical validation." Journal of Structural Engineering 142.4 (2016): E4014003.

[14] van de Lindt, John W., et al. "Experimental seismic behavior of a full-scale four-story soft-story wood-frame building with retrofits. II: Shake table test results." Journal of Structural Engineering 142.4 (2016): E4014004.

[15] Bahmani P., van de Lindt J., Iqbal A., Rammer D.: Mass Timber Rocking Panel Retrofit of a Four-Story Soft-Story Building with Full-Scale Shake Table Validation. *Buildiings.* 7(2): 48, 2017

[16] Bahmani, Pouria; van de Lindt, John; Mochizuki, Gary; Pryor, Steve; Gershfeld, Mikhail; tian, jingjing; Symans, Michael; Rammer, Douglas, (2013), "4-Story Full-Scale Soft-Story Woodframe Building Test at UCSD", DesignSafe-CI [publisher], doi: 10.4231/D3F76678B
https://doi.org/10.4231/D3F76678B

https://doi.org/10.52202/069179-0284

World Conference on Timber Engineering Oslo 2023

EFFECT OF SMALL OPENINGS ON SHEAR CAPACITY OF PLYWOOD SHEATHED SHEAR WALLS

Yuta Sakai [1] , Kenji Aoki[2]

ABSTRACT: In plywood shear walls used for interior walls, small openings are provided for the installation of piping. With the increase in the number of medium and large wooden buildings, it is necessary to accurately calculate the earthquake resistance of each member, as the requirements for the earthquake resistance of elements have increased. The purpose of this study is to verify the effect of small openings on the shear capacity of plywood shear walls. 1820 x 910 mm plywood shear walls with small 350 mm wide square openings were used as a preliminary element test. The results indicate that the location of the opening affects the shear failure behavior of the plywood and its ability to resist loads after maximum load. Based on the results of the element tests, full scale plywood shear walls with small openings were developed with the same performance as those without the opening.

KEYWORDS: small opening, racking test, plywood sheathed shear wall, medium- and large-sized wooden buildings

1 INTRODUCTION

In order to prevent global warming and realize a sustainable society, the use of wood is being promoted worldwide. In recent years, the expansion within medium and large scale wooden buildings has received much attention. However, the change from residential scale to medium and large scale brings challenges in various aspects, such as changes in building design methods and preparation of codes. Small openings in plywood shear walls, which are the subject of this study, are one such example. Small openings are made in interior walls to install ducts, outlet boxes, switch boxes, etc. In the past, for small residential buildings, it was not a problem to consider shear walls with small openings as non-shear walls. This was because the entire building had a surplus of earthquake resistance. In fact, in general wooden houses, openings as small as ventilation ducts were allowed in shear walls at the discretion of the building control officer. Therefore, there was almost no research on shear walls with small openings, and no theory for calculating the shear capacity of walls was established. However, as buildings have become larger, the required earthquake resistance has increased. There is no longer a margin for the earthquake resistance of the entire building, and it is necessary to verify the loss of performance due to small openings. In addition, the current standards for small openings have no experimental or theoretical basis, and their applicability to high-strength shear walls is also unclear. It is dangerous to apply the current standards, which are designed for residential buildings, to medium and large timber buildings. It is urgent to establish a new method to accurately calculate the performance of shear walls with small openings in order to promote medium and large wooden buildings and create a sustainable society. Therefore, the purpose of this study is to verify the effect of small openings on the shear capacity of plywood shear walls and to propose small opening size, location, and reinforcement method for a plywood sheathed shear walls with small openings to have the same performance as those with no openings.

2 PRELIMINARY ELEMENT SPECIMEN

2.1 SPECIMENS

Figure 1 and Table 1 shows the preliminary element test specimen and members, a plywood shear wall. The thickness of the plywood is 24 mm, the density is 0.57g/cm^3, and seven layer. The wall size was 1820 mm in height and

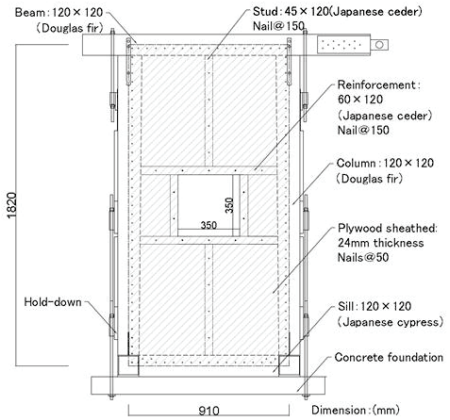

Figure 1: *Preliminary element test specimen*

[1] Yuta Sakai, Yayoi 1-1-1, Bunkyo-ku, Tokyo, Japan. Department of Biomaterials Sciences, Graduate School of Agricultural and Life Sciences, The University of Tokyo, nimajneb1119@g.ecc.u-tokyo.ac.jp

[2]Kenji Aoki, The University of Tokyo, Japan. aoken@g.ecc.u-tokyo.ac.jp

https://doi.org/10.52202/069179-0285

910 mm in width, with a small 350 mm square opening, assuming that the pipes used in medium and large wooden buildings have an outer diameter of about 300 mm. When making small openings, holes are drilled at the four corners and then cut in straight lines. The principle of specimen naming and a simplified diagram of each specification are shown in Figure 2. The first half of the specimen name was named after one of the four types of small opening locations (MM, EE, EM, ME), and the second half was named after the reinforcement method (-N, -S, -HS, -SH). The parameters were the location of small openings and the method of reinforcement, and a total of 12 specimens were made, one for each of the 12 specifications. The nails and screws used are shown in Table 2 and Figure 3.

Table 1: *Members of specimens*

Member	Species	Cross-sectional Area(mm)	Dencity (kg/m^3)	Moisture Content(%)
Beam	Douglass fir	120×120	555	13.3
Column			510	15.6
Sill	Cypress		534	16.8
Stud	Ceder	45×120	390	17.0
Reinforcement		60×120	458	19.4

Common 75 mm long nails were used to join the plywood to the framing at 50 mm pitch and for the studs and opening reinforcement at 150 mm pitch. The studs and opening reinforcement were fastened with two 100 mm long structural screws for each joint. Beam-to-column connections were made with mortise and tenon, foundation-to-column connections were fastened with box-type column leg hardware, and foundation-to-base connections were fastened with hold-down connectors.

2.2 TEST METHODS AND EVALUATION

The static load test was conducted according to the racking test in "Wood Frame House Construction in Japan"[1]. The deformation angle was provided by the horizontal displacement height of the specimen. And the three-time cyclic test was conducted at each deformation angle of 1/450, 1/300, 1/200, 1/150, 1/100, 1/75, 1/50, and 1/30. The envelope curve was determined using the load-displacement test data of cyclic loading. Yield strength (P_y) was obtained from the intersection of the line connecting 0.1 P_{max} point and 0.4 P_{max} point and the tangent line to the envelope curve parallel to the line connecting 0.4 P_{max} point and 0.9 P_{max} point. The stiffness (K) was obtained by dividing the yield strength by the yield displacement (δ_y). Ultimate displacement (δ_u)was obtained from the point where the load dropped to 0.8 P_{max} after P_{max}. Ultimate strength(P_u) was obtained from the point where the area of the trapezoid is equal to the area bounded by the envelope curve and the ultimate displacement. P_y, K, P_u are obtained as shown in Figure 5. Displacements of the test were measured by transducers shown in Figure 4.

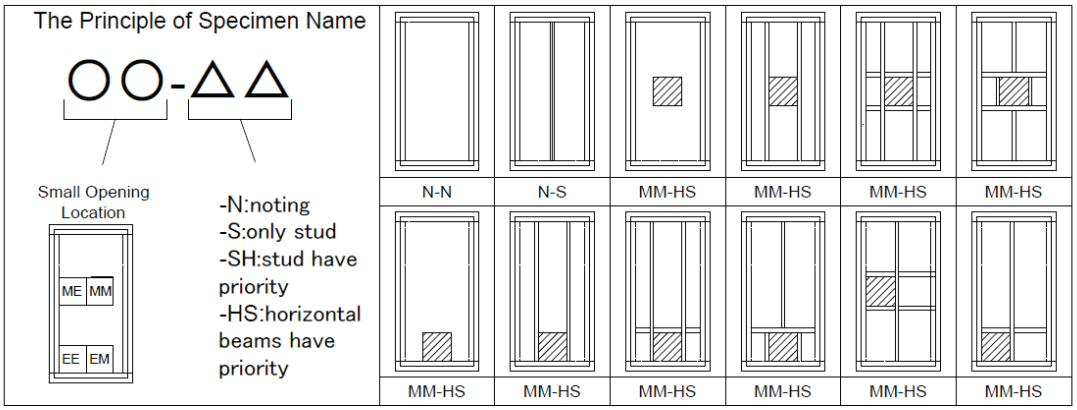

Figure 2: *Preliminary element test specimen*

Table 2: *Detail of Nails and Screws*

	L(mm)	D(mm)	d(mm)	s(mm)
CN75	76.2	7.92	3.76	—
P6-100	100	11.5	6.00	30.0

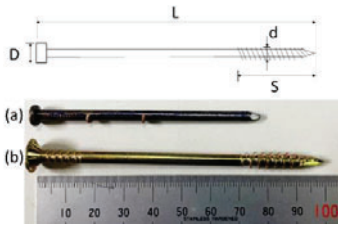

Figure 3: *Nails and Screws*

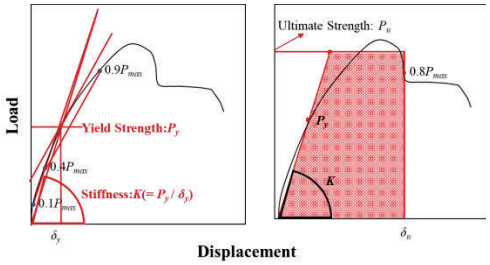

Figure 4: *Evaluation methods on yield strength and ultimate strength*

https://doi.org/10.52202/069179-0285

2.3 TEST RESULTS AND DISCUSSION

Figure 5 shows the load-deformation angle relationship and Table 3 shows the results. Out-of-plane buckling of the plywood did not occur even in the specification with the lowest ability to suppress buckling. The cause of the decrease in strength in the small opening specifications was shear failure of the plywood, as shown in Figure 6. Cracks started at the corners of the small openings at 1/50 rad and expanded with increasing deformation, reaching the edges of the plywood at about 1/30 rad. In the case where the distance from the opening corner to the plywood edge was short as shown in Figure 7, the cracks starting from the opening corner reached the plywood edge relatively early, but the other parts of the plywood were not damaged and the load continued to increase slowly because the shear force was transferred to the column assembly through the opening reinforcement. On the other hand, when the distance was long as shown in Figure 8, it took time for the crack to reach the plywood edge, so the wall deformation proceeded, but after the crack reached the plywood edge, the plywood was damaged more and the load was maintained while the shear failure zone was crushed.

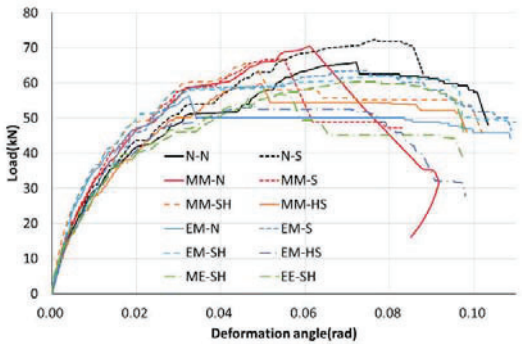

Figure 5: *Load deformation angle relationship of preliminary element test*

Comparing the specification with no openings and those with openings and no reinforcement, it was assumed that the performance of the specification with openings and no reinforcement was lower because of the openings in the plywood. In fact, this trend was confirmed for the EM specification, but the MM-N specification had the highest maximum load of all specifications, an unnatural result that was thought to be due to variation. Therefore, the following discussion is based primarily on the trends in the EM specifications. In comparing the specifications with and without reinforcement, the performance of the specifications with reinforcement was better, confirming the usefulness of the reinforcement. Comparison of the specifications without openings and those with openings and reinforcement indicated that the performance of the specification with openings would be lower, but no significant decrease in stiffness was observed. This is due to the increase in the number of joints because the plywood and the opening reinforcement were fastened with nails, and the opening reinforcement and the frame were fastened with screws. On the other hand, the strength of the plywood was lower because all the openings were

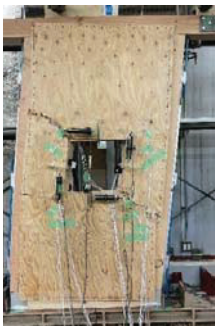

Figure 6: *Failure of entire specimen(MM-HS)*

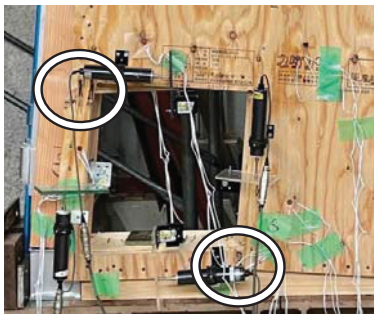

Figure 7: *Short cracks of plywood*

Figure 8: *Long cracks of plywood*

Table 3: *Results of preliminary element test*

	N-N	N-S	MM-N	MM-S	MM-SH	MM-HS	EM-N	EM-S	EM-SH	EM-HS	ME-SH	EE-SH
K(kN/rad)	2462	2775	2541	2918	3887	2391	3989	2763	4114	2558	2642	2447
Py(kN)	35.7	35.8	40.3	38.3	32.1	32.7	29.6	35.5	32.2	31.3	31.3	37.1
Pmax(kN)	65.1	69.9	70.6	66.7	65.5	59.7	56.2	63.3	60.5	54.1	58.2	58.3
Pu(kN)	55.2	58.4	62.8	59.8	57.3	53.2	49.1	57.6	56.1	49.7	50.6	51.0

https://doi.org/10.52202/069179-0285

due to shear failure of the plywood, while those without openings were due to failure at the nail joints. Regarding the method of reinforcement, the -SH specification performed better. It was expected that the short reinforcement would carry the stresses more efficiently. However, contrary to expectations, an extra stud was placed, increasing the number of nails and thus improving the performance of the wall.

3 ANALYSIS

3.1 ANALYSIS MODEL

The analysis was performed to verify the effect of variation in the preliminary test and to confirm the detailed stress state. The analysis was conducted using the SNAP analysis software and the analysis model is shown in Figure 9. The Multi Shear Spring(MSS) model was used for the nails. The restoring force characteristics of the nails were obtained from the results of the nail single shear test, which was carried out as an elementary test through the monotonic loading test of the rocket type shown in Figures 10. As shown in Figure 11, four lines were substituted, including the negative slope after the maximum load. The evaluation of the nail shear test was in accordance with the Wood Frame House Construction in Japan. Each point was set as follows for the average of three specimens based on the element test results.

First point: (P_y, δ_y)
Second point: (P_u, displacement of an arbitrary upper point coinciding with the envelope)
Third point: (P_{max}, δ_{Pmax})
Fourth point: (0.8 P_{max}, δ_u)

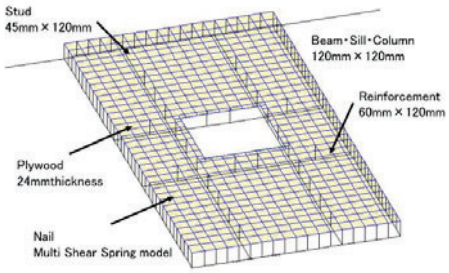

Figure 9: *Analysis model*

Figure 10: *Monotonic loading test of the rocket type*

The boundary conditions were pin supported on one side of the foundation and roller supported on the other. All joints between members were pin joints. The cross sections and nail positions were the same as in the preliminary tests, and only the nails on the four perimeters of the plywood were placed at the edges of the plywood. Physical properties were obtained from the literature. Forced displacement was applied in the positive direction of the x-axis of the beam, with a target displacement of 182 mm and a displacement increment of 0.2 mm per step, for a total of 910 incremental analysis steps.

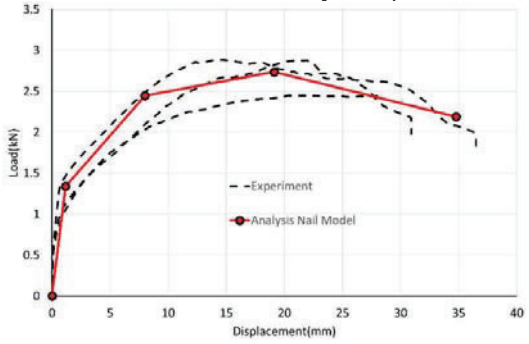

Figure 11: *Load displacement relationship of loading test*

3.2 ANALYSIS RESULT AND DISCUSSION

The load-deformation angle relationships obtained from the analysis are shown in Figure 12, and Table 4 compares each of the analytical values obtained from the analysis with the experimental values. The outline of the curves and the ratio of experimental to analytical values in Table 3 show that, although there are a few large deviations, the overall trend is generally captured.

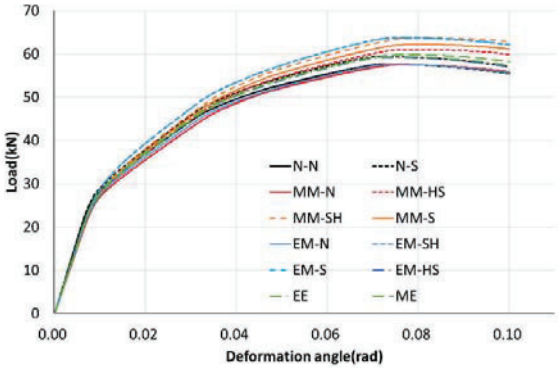

Figure 12: *Load deformation angle relationship of analysis*

The analysis results showed that the specimens with openings and reinforcement had the highest maximum loads, followed by those without openings, and those with openings and no reinforcement had the lowest loads. With no reinforcement, the specimens with openings, which are weak points, had the lowest load capacity. In the case with reinforcement, the load was higher with more nails, supporting that the nails were the main factor in the resistance mechanism.

https://doi.org/10.52202/069179-0285

Table 4: *Results of analysis*

	N-N	Ratio*	N-S	Ratio*	MM-N	Ratio*	MM-S	Ratio*	MM-SH	Ratio*	MM-HS	Ratio*
K(kN/rad)	2846	1.16	2744	0.99	2547	1.00	2494	1.00	2524	0.65	2452	1.23
Py(kN)	28.5	0.80	30.2	0.84	28.0	0.70	29.9	0.70	30.3	0.94	29.4	0.93
Pmax(kN)	56.8	0.87	59.4	0.85	56.1	0.79	60.2	0.79	61.5	0.94	59.2	0.99
Pu(kN)	47.9	0.87	49.9	0.86	47.3	0.75	51.0	0.75	51.9	0.91	50.3	0.94

	EM-N	Ratio*	EM-S	Ratio*	EM-SH	Ratio*	EM-HS	Ratio*	ME-SH	Ratio*	EE-SH	Ratio*
K(kN/rad)	2585	0.65	2481	0.90	2634	0.64	2485	1.20	2661	1.25	2662	1.25
Py(kN)	28.4	0.96	32.3	0.91	31.6	0.98	29.8	0.95	29.3	0.94	29.3	0.87
Pmax(kN)	56.5	1.01	62.7	0.99	62.3	1.03	58.3	1.08	58.5	1.01	58.4	1.02
Pu(kN)	47.8	0.97	52.5	0.91	52.8	0.94	49.7	1.00	49.1	0.99	49.4	0.98

Ratio* means 'Ratio to experimental value' (analsis value/experimental value)

The behavior after yielding was considered to be improved by adding appropriate rotational stiffness to the ends of each member in the analytical model instead of pin joints. The plasticity factor tended to have a large error due to its small value. On the other hand, this analytical model does not consider the shear failure of the plywood, so a new method that can estimate the behavior after the end of the phase is needed to predict the overall behavior.

4 FULL SCALE TEXT

4.1 SPECIMEN

To verify the applicability of the preliminary element test results to the actual building, eight 24 mm plywood sheets, four on the front and four on the back, were attached together for a full-scale test of a 3340 mm height and 1820 mm length shear wall as shown in Figure 13. Beam connectors and hold-downs were used for column head connections. Lag screws (ϕ45, 600 mm) was used for the column legs. 110 mm screws were used to fasten the reinforcement to the frame. As in the preliminary test,

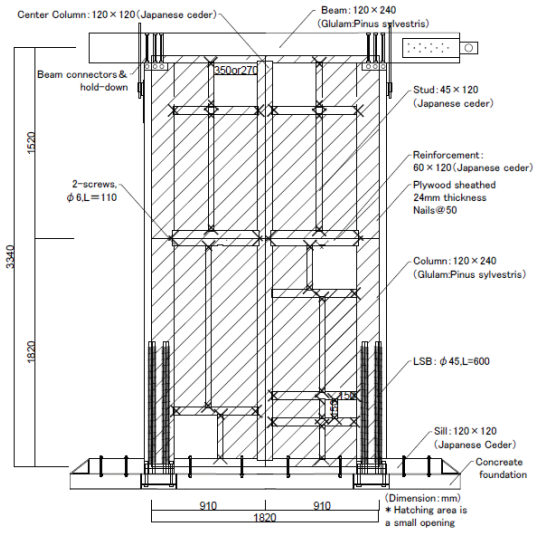

Figure 13: *Full scale test specimen*

a small 350 mm square opening was made in each faceplate. The number of specimens tested was three for the specimen with no opening and four for the specimen with openings including the preliminary test. The small openings were located at the four corners where performance was estimated to be lowest based on the preliminary element test results, assuming actual construction. An additional 150mm opening for a switch box was provided in the bottom plywood to make the specifications similar to actual installation. Based on the preliminary test results, the size of the small openings in the full-scale test was reduced to 270mm square when small openings are provided at the same height, and the nail pitch to the studs and opening reinforcement was modified from 150mm to 100mm.

4.2 TEST RESULTS AND DISCUSSION

Figure 14 shows the load-deformation angle relationship. The experimental values calculated from them are shown in Table 5. The failure of the preliminary test and the main test are shown in Figure 15 for the entire and in Figure 16 for the upper opening(Left:preliminary,Right:main). Preliminary test results showed that the performance similar to that of the no-opening specification could not be achieved because the center columns failed in bending and the load dropped rapidly. The bending failure of the columns was caused by stress concentration on the columns because the plywood could not resist the shear stress after the cracks from the opening corners reached the plywood edges as in the preliminary test. In this test,

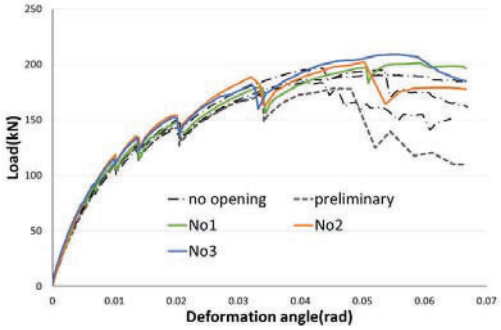

Figure 14: *Load deformation angle relationship of full scale test*

https://doi.org/10.52202/069179-0285

crack propagation from the opening corner was suppressed and brittle failure did not occur up to 1/15 rad, confirming that the performance was equivalent to that of the no opening specification. The failure behavior at the end of the test was that the plywood around the opening on the column leg side failed as shown in Figure 17 and the plywood could no longer bear the load, resulting in collective failure of the LSB on the column leg on the tension side and buckling failure of the columns on the compression side as shown in Figure 18 and 19.

Table 5: *Results of full scale test*

	no opening*	opening			
		Prelininary	No.1	No.2	No.3
K(kN/rad)	11924.3	11292	10230	12392	10774
P_{max}(kN)	190.5	178.4	201.3	202.3	209.0
P_y(kN)	102.9	103.8	113.5	111.0	117.1
P_u(kN)	173.3	157.8	181.1	175.4	186.8

*Average of three specimens

Figure 15: *Failure of entire specimen*

Figure 16: *Failure of upper opening*

Figure 17: *Failure of plywood around the opening on the column leg side*

Figure 18: *Collective failure of the Lag screws*

Figure 19: *Buckling failure of the columns*

5 CONCLUSIONS

Preliminary element tests were conducted on a plywood bearing wall 1820 mm high and 910 mm wide with a small 350 mm square opening for a piping. The results indicate that the location of the opening changes the degree of damage to the plywood and may subsequently affect the shear capacity of the wall. In combination with the results of the analysis, it was estimated that the opening positions with the lowest performance were those closer to the four corners. Based on these results, full-scale tests were conducted on an actual medium- to large-sized wooden shear wall. Preliminary tests revealed that shear walls with small openings did not perform as well as walls without openings. When the small openings were horizontally connected, the nail pitch to the opening reinforcement was narrowed by setting a limit based on the opening size. As a result, it was confirmed that the performance of the wall with small openings was equivalent to that of the wall without openings. In this study, the size, location, and reinforcement method of small openings were proposed to ensure that plywood sheathed shear walls with small openings perform as well as those with no openings.

ACKNOWLEDGEMENT

This research was carried out with the cooperation of Maeda Corporation and supported by Grant-in-Aid for JSPS Research Fellow Grant Number JP 22J12027 I would like to thank all those involved.

REFERENCES

[1]Isao S.: Wood Frame House Construction in Japan, Japan Housing and Wood Technology Center, pages 294–304, 2017.

https://doi.org/10.52202/069179-0285

World Conference on Timber Engineering Oslo 2023

CYCLIC TESTING AND NUMERICAL MODELING OF A THREE-STORY MASS-TIMBER BUILDING WITH A PIVOTING MASS PLY PANEL SPINE AND BUCKLING-RESTRAINED ENERGY DISSIPATORS

Gustavo A. Araujo R.[1], Barbara G. Simpson[2], Tu X. Ho[3], Gustavo F. Orozco O.[4], Andre R. Barbosa[5], and Arijit Sinha[6]

ABSTRACT: Mass timber panels are emerging as an innovative alternative for the design of elastic spines due to their high stiffness- and strength-to-weight ratio, among other factors. Recent research has shown that mass timber panels used in conjunction with steel energy dissipators are promising solutions for enhanced seismic performance. However, the available experimental data at the building scale is still minimal, which limits the understanding, adoption, and development of effective seismic design guidelines for these systems. This research addresses this gap through full-scale quasi-static cyclic testing of a three-story mass timber building. Lateral loads are transferred through Mass Ply Panel (MPP) diaphragms to an MPP spine with vertically-oriented unbonded steel buckling-restrained braces (BRBs) as energy dissipating boundary elements in the first story. The only elements designed to dissipate energy in the inelastic range are the BRBs. The building specimen achieved low-structural damage and enhanced-performance goals, being able to reach a 4% roof drift ratio with little loss of strength and stiffness. The proposed pivoting detail was effective in mitigating compressive damage at the wall toe. To support the experimental campaign and future design procedures, a high-fidelity numerical model of the building was developed using OpenSees.

KEYWORDS: buckling-restrained braces, experimental testing, mass timber, numerical model, pivoting spine

1 INTRODUCTION

The emergence of mass timber as a novel construction material poses new opportunities for the development of innovative seismic force-resisting systems that are designed for enhanced-performance goals beyond the scope of prescriptive codes [1]. For example, mass timber walls can be designed as structural spines. A spine is a stiff and strong vertical element or portion of the structure that is designed to remain essentially elastic in every vibrational mode, thereby imposing a more uniform drift distribution with building height [2], [3], mitigating story mechanisms [4], [5], and enabling the designer to bypass potential geometric or mass irregularities [6]. If detailed properly and combined with supplemental energy dissipators, mass timber spines are capable of deforming well into the inelastic range during strong ground shaking with stable energy dissipation and, in some cases, low-damage seismic performance [7]–[19].

Despite efforts to standardize mass timber wall design in the United States [20]–[23], alternative means and methods, e.g. performance-based design methods [24]–[28], are often needed to design systems employing mass timber spines, since mass timber seismic force-resisting systems frequently fall outside prescriptive clauses [29]–[32]. However, such methods rely on numerical models grounded on extensive experimental data and can be computationally expensive, thereby limiting the design of mass timber spines in practice. Consequently, experimental testing and numerical validation are necessary to support the development of more practical design methods that better reflect the existing seismic design philosophy in the U.S. to facilitate the use of mass timber systems, including those with spines.

This research contributes to existing experimental data through full-scale quasi-static cyclic testing of a three-story mass timber building featuring a seismic force-resisting system employing a Mass Ply Panel (MPP) pivoting spine with vertically-oriented unbonded steel buckling-restrained braces (BRBs). The specimen was tested in October 2022 at the A.A. Red Emmerson Advanced Wood Products Laboratory at Oregon State University as part of ongoing research on low-damage mass timber seismic force-resisting systems. A numerical model was developed to support the experimental campaign and aid in the development and validation of future design procedures.

[1] Gustavo A. Araujo R., Stanford University, Stanford, CA, USA, garaujor@stanford.edu
[2] Barbara G. Simpson, Stanford University, Stanford, CA, USA, bsimpson@stanford.edu
[3] Tu X. Ho, Oregon State University, Corvallis, OR, USA, tu.ho@oregonstate.edu
[4] Gustavo F. Orozco O., Oregon State University, Corvallis, OR, USA, gustavo.orozco@oregonstate.edu
[5] Andre R. Barbosa, Oregon State University, Corvallis, OR, USA, andre.barbosa@oregonstate.edu
[6] Arijit Sinha, Oregon State University, Corvallis, OR, USA, arijit.sinha@oregonstate.edu

https://doi.org/10.52202/069179-0286

2 EXPERIMENTAL PROGRAM

2.1 TEST SPECIMEN

The test specimen consisted of a two-bay by two-bay three-story building segment selected from a case-study building archetype; see Figure 1 through Figure 3. The building segment had a square floor plan with an area of approximately 12.2 m x 12.2 m = 149 m^2 (1,600 ft^2). The first story was slightly taller than the others, with a height of 3.15 m (10.3 ft); the remaining stories had a typical story height of 2.75 m (9 ft).

The gravity system featured four frames made of simply-supported laminated-veneer lumber (LVL) beams and LVL columns. Beams and columns were connected using customized Simpson Strong-Tie column caps with vertically-slotted holes at the column ends to allow for rocking at the beam-to-column interface with minimal moment restraint, effectively accommodating large story drift demands [16]. The gravity connections were braced against lateral-torsional buckling using a L-shaped cross-section steel members. Diaphragm panels were also MPP supported by the LVL beams.

The building specimen was subjected to two separate phases of experimental testing. Phase 1, which is the object of this paper, featured an MPP wall designed as a pivoting spine, supplemented by two-vertically oriented BRBs attached to the wall boundaries in the first-story; see Figure 2(a). The spine is located between two collar beams. In comparison to a rocking wall, the proposed pivoting wall does not impact the foundation during shaking, which alleviates potential crushing at the toe at the base of the wall [33], [34], which might render repairs impractical. Other methods of mitigating crushing at the wall toe have also been proposed [8]. Uplift at the base is restrained by two steel threaded rods connected to a steel plate screwed to the MPP wall at both sides and the external energy dissipators. The base shear is transferred from the spine to the foundation through cross-ply bearing of the MPP on two stiff shear key plates located at the edges of the wall panel. The proposed seismic force-resisting system takes inspiration from previous research on pin-supported reinforced concrete walls [35]–[41] and steel braced frames [42]–[45].

The BRBs are bolted at both ends to gusset plates. The top gusset plate is ultimately connected to the MPP wall through steel side plates and 45-deg inclined, fully threaded screws; see Figure 2(b). The design detail takes advantage of the high strength and stiffness of inclined screws in tension [46], [47], while compressive forces are transferred through bearing of the MPP on top of the timber-to-BRB connection.

To ensure torsional stability of the building specimen during unidirectional cyclic testing, a series of platform-construction MPP walls, termed herein out-of-plane walls, were installed around the perimeter of the building in the perpendicular-to-loading direction. The out-of-plane walls were connected to the MPP floors using standard angle brackets [22] designed to resist 10% of the expected in-plane capacity of the spine.

General dimensions and material properties of the different elements in the specimen are shown in Table 1.

***Table 1**. General dimensions and material properties.*

Element	Material	Dimensions
Floor panels	Freres F16-7 MPP	181 mm thick
Columns	Boise Cascade Douglas-fir LVL	178 mm × 178 mm cross section
Beams	Boise Cascade Douglas-fir LVL	133 mm × 559 mm cross section
Spines	Freres F16-8 MPP	207 mm thick
BRBs	CoreBrace bolted brace	A = 1,290 mm^2 L_{core} = 2.03 m L_{brace} = 3.05 m
Foundation beams (spine and gravity system)	ASTM A992	W12×136 [in×plf]
	Boise Cascade Douglas-fir LVL	178 mm × 356 mm cross section
Beam-to-column connections	Simpson Strong-tie column cap	Customized to project

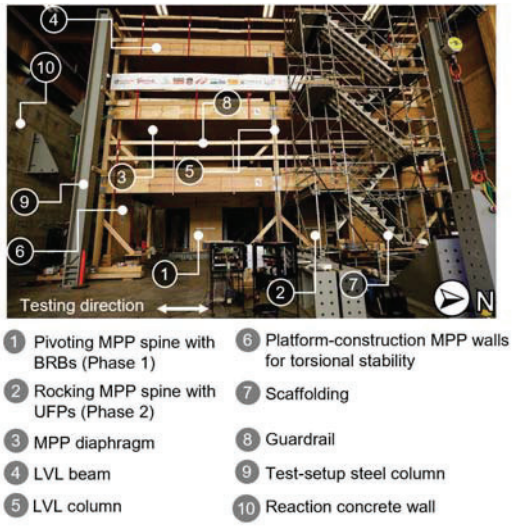

***Figure 1:** Three-story building specimen.*

https://doi.org/10.52202/069179-0286

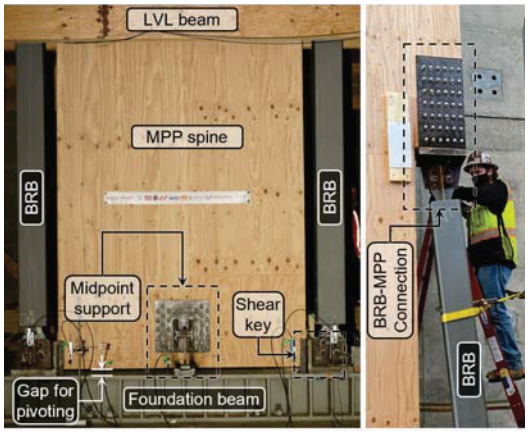

(a) *(b)*

Figure 2: *Pivoting MPP spine specimen: (a) first-story components and (b) BRB-MPP screwed connection.*

2.2 SEISMIC DESIGN

The building was assumed to be representative of an office building archetype located in Seattle, WA, USA (47.58227 N, 122.33111 W). The building specimen was designed following traditional prescriptive seismic design principles from ASCE 7-16 [48], with additional stiffness and strength considerations to include enhanced-performance goals under multiple hazard levels, including seismic demands associated with the Risk-Targeted Maximum Considered Earthquake (MCE_R), in addition to the Design Earthquake (DE). The design method was broken into three major components: (i) design of the BRBs, (ii) design of the spine, and (iii) design of the diaphragm and connection details.

The BRBs were designed to resist the entirety of the overturning moment resulting from the design lateral forces, which were obtained using $R = 8$, consistent with the design of buckling-restrained braced-frames. This value of R will be validated in the future. The yield length of the BRB was selected to keep strain demands in the core at the MCE_R level below 2.5% to mitigate fracture due to low-cycle fatigue and $10\varepsilon_y$ (where ε_y is the yield strain) to target Life Safety per ASCE 41-17 [49].

The spine was proportioned to limit inelastic story drift ratios to 2.0% at the DE level following a displacement-based design approach [49], [50]. In this approach, an equivalent single-degree-of-freedom system is used to estimate the maximum-allowed structural period of the system based on the demands from the DE spectrum. In addition, the MPP spine was designed to remain elastic up to 4.0% roof drift ratio under a first-mode loading pattern to target enhanced performance beyond the MCE_R. Design forces were derived from the expected inelastic forces delivered by the BRBs to the spine at a 4.0% roof drift ratio and the near-elastic demands expected in the higher modes. The seismic design of the spine and the BRBs are covered in detail in ref. [51].

Diaphragms and their components, including splines, coiled straps, collectors, and the shear transfer mechanism, were preliminary designed using the alternative design method from ASCE 7-16 §12.10.3, with timber and fastener strength per NDS 2018 [52] and manufacturer recommendations, respectively. The design was then adjusted for the estimated capacity of the spine at a 4% roof drift ratio. More details on the design and expected performance of the diaphragms can be found in refs. [53], [54].

2.3 TEST SETUP AND INSTRUMENTATION

Lateral cyclic loads were applied to the structure at each floor level using three actuators, one per level, connected through stiff reaction steel beams to an L-shaped, 7.70-m (25.25-ft) tall reaction wall; see Figure 3. The concentrated load from the actuators was distributed across the MPP diaphragm panels using an assembly of load-transfer steel beams at the south side of the building and LVL beams spanning along the north-south direction. The LVL beams are connected to the MPP diaphragm using screwed steel angle plates and brackets.

The instrumentation layout was designed to measure the global load-displacement behaviour of the system and the local deformations in the spine, BRBs, diaphragm panels and connections. Applied loads at each level were recorded using the corresponding actuator load cells. Lateral displacements of the system in the direction of loading were determined using string potentiometers connected to fixed points in the perimeter of the laboratory. LVDTs were used to measure the tilting behaviour of the MPP spine at the base and the axial deformation of the BRBs. Strain gauges were installed in the elastic regions of each BRB and in the pivot-support rods to estimate axial forces in these elements.

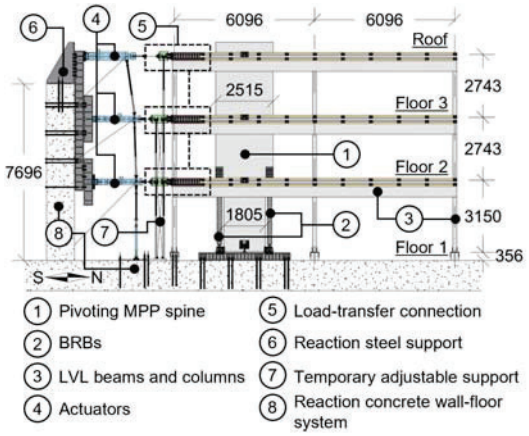

Figure 3: *Test setup. Units: mm.*

2.4 LOADING PROTOCOL

The specimen was subjected to two types of loading protocols:

(i) **First mode:** a quasi-static cyclic loading procedure derived from CUREE [55] to assess the behaviour of the spine subjected to a first-mode loading distribution up to 4% roof drift ratio, which was the displacement demand targeted in the design for enhanced performance; see Figure 4 and Figure 5(a).

(ii) **"Higher mode":** a quasi-static half-cycle procedure following a "higher-mode"-like loading distribution up to a base shear of 178 kN (40 kip) to verify the spine remained elastic in the higher modes; see Figure 5(b). The load distribution was selected to satisfy modal orthogonality assuming uniform mass distribution.

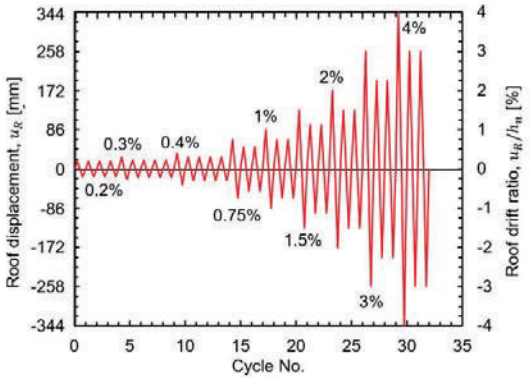

Figure 4: *First-mode displacement protocol with primary-cycle amplitudes labelled.*

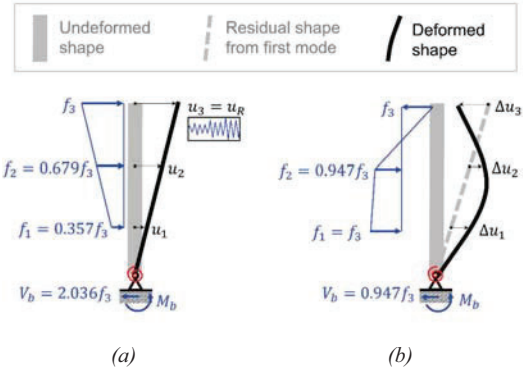

(a) (b)

Figure 5: *Testing load distributions: (a) first mode and (b) "higher mode".*

3 EXPERIMENTAL RESULTS

3.1 GLOBAL FIRST-MODE BEHAVIOUR

Figure 6 shows the global base shear-roof displacement hysteretic behaviour of the building specimen when subjected to a first-mode loading distribution; Figure 7 breaks down the experimental results by primary and trailing cycles of different peak cyclic amplitudes. The specimen performed as intended, maintaining a nearly uniform distribution of lateral drifts across all stories for the entire loading protocol; see Figure 8. The building exhibited a full and stable global hysteretic behaviour, including a complete cycle at the target enhanced-performance drift of $\theta = 4.0\%$ and two subsequent cycles at $\theta = 3.0\%$, without observed loss of lateral strength. In general, the behavior of the system was comparable to the observed in previous tests on steel and concrete pivoting spines supplemented by BRBs [33], [44].

Observed residual drifts significantly increased after yielding of the BRBs due to the absence of a self-centering mechanism in the structure and accumulated residual deformations in the BRBs. After the cycles to $\theta = 2.0\%$ (the target drift at the DE level), the observed residual roof drift ratio was 1.38%. Similarly, the residual drifts after the cycles to $\theta = 3.0\%$ and 4.0% were 2.3% and 3.3%, respectively. Such level of residual drift may result in increased repair costs and downtime after an earthquake event. A plausible solution for this issue would be the use of self-centering BRBs [56]–[58], post-tensioning or other similar devices.

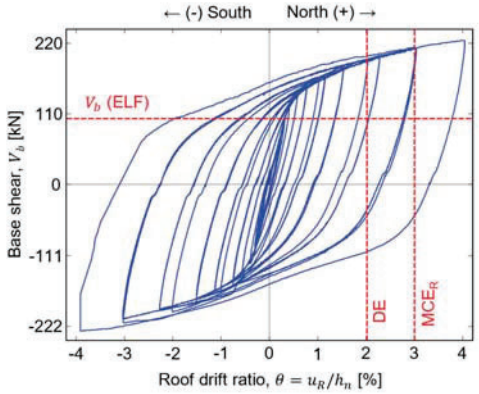

Figure 6: *Global hysteretic behaviour of the specimen subjected a first-mode loading distribution.*

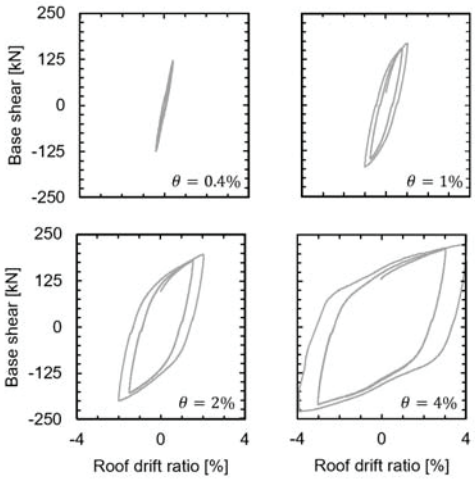

Figure 7: *Global hysteretic loops at 0.4%, 1%, 2%, and 4% primary cycles, and subsequent trailing cycles.*

https://doi.org/10.52202/069179-0286

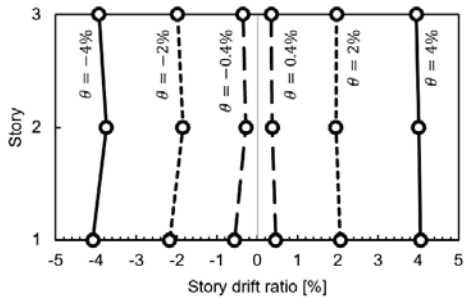

Figure 8: *Story drift profiles at different roof drift levels θ.*

3.2 BRB BEHAVIOUR

Damage investigation after the primary cycles and post-processed instrumentation data were used to assess the behaviour of each of the components of the test specimen, including the BRBs, the MPP spine and connections, MPP diaphragms and the gravity system.

Inelastic behaviour was observed in the BRBs at low drift levels ($\theta > 0.40\%$). After yielding, the BRBs started to exhibit significant residual elongation or shortening of the yielding core when unloaded in tension or compression, respectively. Figure 9(a) shows photographical evidence of the state of the BRBs before testing and after completion of the loading procedure. The BRBs were able to sustain the axial deformation demands imposed by the tilting mode of the spine without fracture or the core or instabilities at the connection regions. Due to inelastic deformations in the BRBs, the BRB-MPP spine system remained tilted towards the south direction at the end of the test, resulting in a residual roof drift ratio of 3.2% after the last cycle; see Figure 9(b).

Both BRBs exhibited similar axial deformations in tension and compression, as shown in Figure 10(a), due to the rod preventing uplift at the pivot support. By vertical equilibrium, without the addition of the rod detail, the wall would have uplifted at the middle and the deformation demands in the BRBs would have been greater in tension than in compression. Deformation demands in the BRBs at the cycles up to $\theta = 4\%$ were in the order of 40 mm (1.57 in), resulting in strains of nearly 2% in the yielding core.

Figure 10(b) presents the estimated hysteretic axial force-deformation behaviour of the BRBs. Axial forces were estimated using the average of the data recorded by four strain gauges installed near the ends of the BRBs, while axial deformations were measured using LVDTs oriented lengthwise on either side of the BRB (assuming deformations occurred primarily in the yielding region of the core). The strain gauges installed in the transition region were expected to remain elastic. In the test, however, flaking at the BRB end connections was observed during damage inspections after the 3.0% cycles, and this strain gage data is suspect. For this reason, the estimated hysteretic behaviour shown in Figure 10(b) is separated into cycles before and after 2.0%. The recorded data suggest that the BRBs exhibited kinematic and isotropic strain hardening after yielding, which is consistent with previous observations on systems employing BRBs [44], [47], [59]–[65]. However, the effects of isotropic hardening were not evident in the observed global behaviour of the system. It is suspected that other sources of softening in the system could have overshadowed the effect of isotropic hardening in the system.

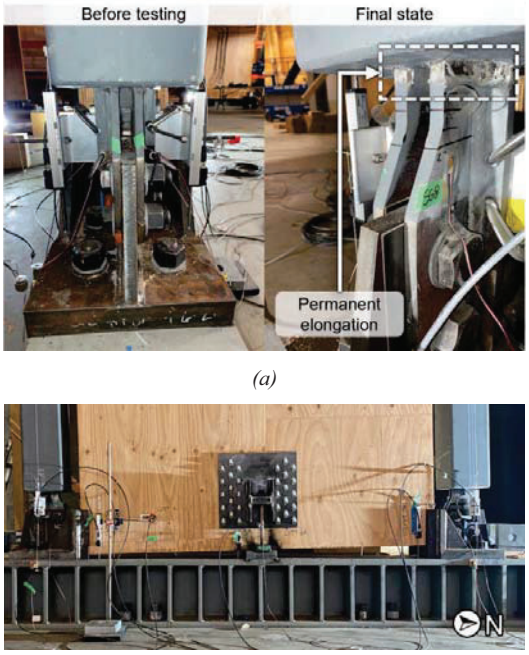

(a)

(b)

Figure 9: *Damage investigation in the BRBs: (a) permanent elongation of the yielding core at the bottom, near the foundation, and (b) permanent tilting mode after the test due to inelastic deformations in the BRBs.*

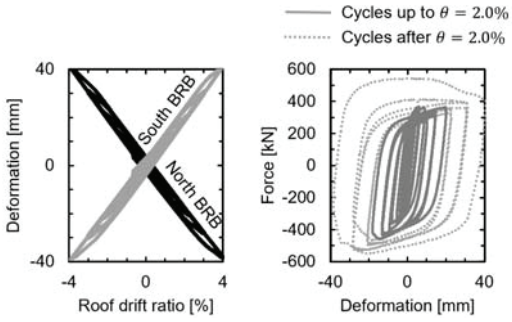

(a) *(b)*

Figure 10: *Experimentally-observed behaviour of BRBs:(a) axial deformation vs roof drift ratio for both BRBs and (b) hysteretic force-displacement behaviour.*

3.3 MPP SPINE AND CONNECTIONS

The MPP spine remained essentially elastic throughout the entire testing protocol. The midpoint pivot support behaved as intended, limiting uplift due to the unbalance force between the two BRBs acting in tension and compression (i.e., by vertical equilibrium). Small southward sliding of the MPP spine with respect to the

foundation was observed from low-amplitude cycles; see Figure 11(a).

Minimal, cosmetic damage was observed in the spine at the location of the base shear keys, as shown in Figure 11(b). The observed damage was attributed to a combination of bearing stresses in the cross-ply direction of the MPP and friction between the steel and the outer MPP plies in the vertical direction.

No visible damage was observed in the MPP spine above the first floor. The BRB-to-MPP connections did not show any signs of slip of the steel plates or splitting/crushing in the MPP boundaries at the screwed connections.

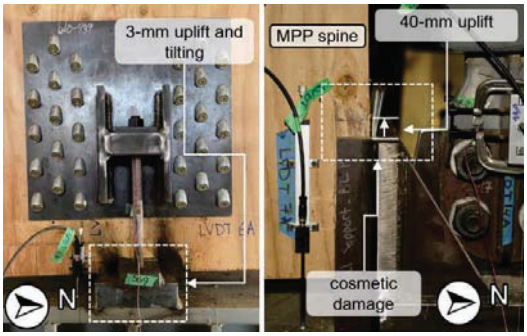

(a) (b)

Figure 11: *Damage observation in the MPP spine after the test: (a) midpoint pivot support, and (b) north base-shear key.*

3.4 DIAPHRAGMS AND GRAVITY SYSTEM

The MPP diaphragms remained essentially elastic throughout the entire test. No visible signs of slip in the plywood splines or openings between the diaphragm panels was observed. Similarly, the beam-to-column connections in the gravity system were able to accommodate story drift demands up to $\theta = 4.0\%$ through rocking, without inducing visible damage to the LVL columns.

3.5 GLOBAL HIGHER-MODE BEHAVIOUR

Figure 12 summarizes the global behaviour of the building when subjected to the "higher-mode"-like loading distribution. The testing procedure started after the full first-mode loading protocol was applied, with the building tilting southwards with a residual drift of $\theta = -2.25\%$. The specimen behaved near-elastic, as is intended for the spine design, under the higher-mode loads. The load-displacement relation reached the maximum targeted base shear in a near-linear way, with high stiffness and little increase in lateral displacements; see Figure 12(a-b). Under this force distribution, the behaviour of the spine resembled that of a simply-supported deep beam under a four-point loading distribution, as shown by the incremental displacement profile in Figure 12(b). No visible damage in the connections or MPP spine was observed at the end of the test. Deformation and force demands in the BRBs did not vary significantly throughout the "higher-mode"-like testing procedure.

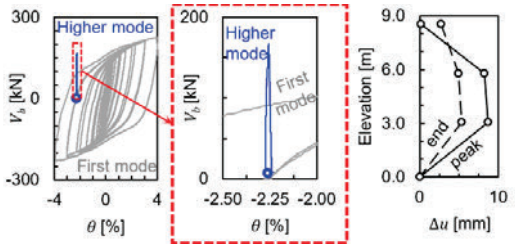

(a) (b)

Figure 12: *"Higher-mode" behaviour of the building: (a) Base shear vs. roof drift ratio; (b) Incremental displacements relative to the first-mode residual deformed shape at peak base shear and at the end of the test.*

4 NUMERICAL VALIDATION

4.1 MODELING SCHEME

The cyclic behaviour of the test specimen was estimated using a two-dimensional nonlinear numerical model in OpenSees [66], as shown in Figure 13. The numerical model included the LVL beams and columns, pivoting MPP spine, BRBs, and foundation beam for the spine. The BRB-to-spine, diaphragm-to-spine, and foundation connections were also modelled. Material properties were based on existing test data at the component level [44], [62], [67]–[69]. More details on the numerical model can be found in ref. [51], [70].

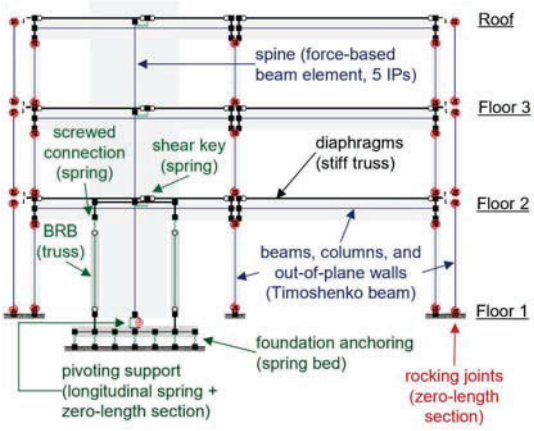

Figure 13: *Two-dimensional numerical model of the building specimen.*

4.2 SIMULATED BEHAVIOUR.

Figure 13 compares the experimentally-measured cyclic behaviour of the building specimen and the BRBs under a first-mode loading distribution against the numerical estimates. At the system level, the simulation results agree well with the observed behaviour of the specimen; see Figure 13(a). At the BRB level, the simulation approximates the experimentally-measured behaviour for cycles up to $\theta = 2.0\%$. For larger values of θ, the simulation significantly diverges from the BRB experimental data, particularly on the tension side. It should be noted that this discrepancy is likely due to the strain gage data used to estimate the axial force in the

https://doi.org/10.52202/069179-0286

BRBs becoming corrupted after $\theta = 2.0\%$. In general terms, the proposed numerical model estimates well the behaviour of the specimen and is suitable for extensive numerical analyses typical in performance and collapse assessment.

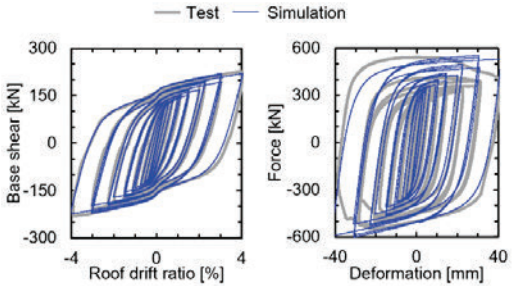

Figure 14: *Experimentally-measured vs simulated behaviour: (a) system level and (b) BRBs.*

5 CONCLUSIONS

This study introduced a seismic force-resisting system employing a mass timber pivoting spine supplemented by BRBs as energy dissipators. The behaviour of the system was studied through experimental quasi-static cyclic testing of a three-story full-scale building specimen and numerical modelling. The study illustrates that mass timber walls can be effectively designed as structural spines with the addition of BRBs as energy dissipators. The specimen achieved low-structural damage and enhanced-performance goals. The proposed pivoting detail was effective in mitigating compressive damage at the wall toe. The behaviour of the system was significantly influenced by the inelastic and strain-hardening behaviour of the BRBs, resulting in high residual drifts due to the absence of self-centering mechanisms.

These findings can be useful for improving the design and evaluation of mass timber structures in future studies. Future work should explore the addition of self-centering devices that help to reduce residual drifts and assess the seismic performance of the system through nonlinear dynamic analysis.

ACKNOWLEDGEMENTS

The authors would like to thank graduate students Steven Kontra, Patricio Uarac, and undergraduate students Kristian Walker, and Tanner Field for their help with instrumentation and testing. In addition, the authors would like to thank the laboratory technicians Byrne Miyamoto, Phil Mann, and Mark Gerig of the Tallwood Design Institute for their support throughout the experimental program.

This project was executed under the USDA Agricultural Research Service Award No. 58-0204-9-165. Part of the work was also supported by the National Science Foundation under awards #2120683, #2120692, and #2120684. Special thanks to our industry partners, KPFF, Holmes, Fortis Construction, Carpenters Union, CoreBrace, Boise Cascade, Simpson Strong-Tie, and Freres Engineered Wood, for supporting this experimental program. The findings, opinions, recommendations, and conclusions in this paper are those of the authors and do not necessarily reflect the views of others, including the sponsors.

REFERENCES

[1] S. Pei, J. D. Dolan, R. B. Zimmerman, E. McDonnell, P. Line, and M. Popovski, "From Testing to Codification: Post-tensioned Cross Laminated Timber Rocking Walls," in *International Network for Timber Engineering Research (INTER)*, 2019.

[2] B. Alavi and H. Krawinkler, "Strengthening of moment-resisting frame structures against near-fault ground motion effects," *Earthq Eng Struct Dyn*, vol. 33, no. 6, pp. 707–722, 2004, doi: https://doi.org/10.1002/eqe.370.

[3] Z. Qu, L. Ye, and A. Wada, "Seismic Damage Mechanism Control of RC Ductile Frames from a Stiffness Point of View," in *8th International Conference on Urban Earthquake Engineering*, 2011. [Online]. Available: http://qu-zhe.net/Resource/Struct/CUEE8-QuZ.pdf

[4] D. Mar, "Design Examples using Mode Shaping Spines for Frame and Wall Buildings," in *9th U.S. National and 10th Canadian Conference on Earthquake Engineering*, 2010.

[5] L. Panian, N. Bucci, and B. Janhunen, "BRBM Frames: An Improved Approach to Seismic-Resistant Design Using Buckling-Restrained Braces," in *Improving the Seismic Performance of Existing Buildings and Other Structures 2015*, 2015, pp. 632–643. doi: doi:10.1061/9780784479728.052.

[6] J. Osteraas, J. Hunt, and G. Luth, "Performance Based Seismic Design of the Gigafactory in Tesla Time," in *2017 SEAOC Convention*, 2017. [Online]. Available: https://cdn.ymaws.com/www.seaoc.org/resource/resmgr/Convention_Proceedings/2017/009_PAPER_Osteraas.pdf

[7] T. Akbas *et al.*, "Analytical and Experimental Lateral-Load Response of Self-Centering Posttensioned CLT Walls," *Journal of Structural Engineering*, vol. 143, no. 6, p. 4017019, 2017, doi: doi:10.1061/(ASCE)ST.1943-541X.0001733.

[8] H.-E. Blomgren *et al.*, "Full-Scale Shake Table Testing of Cross-Laminated Timber Rocking Shear Walls with Replaceable Components," *Journal of Structural Engineering*, vol. 145, no. 10, p. 4019115, 2019, doi: doi:10.1061/(ASCE)ST.1943-541X.0002388.

[9] Z. Chen, M. Popovski, and A. Iqbal, "Structural Performance of Post-Tensioned CLT Shear Walls with Energy Dissipators," *Journal of Structural*

Engineering, vol. 146, no. 4, p. 4020035, 2020, doi: 10.1061/(asce)st.1943-541x.0002569.

[10] D. Fitzgerald, T. H. Miller, A. Sinha, and J. A. Nairn, "Cross-laminated timber rocking walls with slip-friction connections," *Eng Struct*, vol. 220, p. 110973, 2020, doi: https://doi.org/10.1016/j.engstruct.2020.110973.

[11] A. Hashemi and P. Quenneville, "Large-scale testing of low damage rocking Cross Laminated Timber (CLT) wall panels with friction dampers," *Eng Struct*, vol. 206, p. 110166, 2020, doi: https://doi.org/10.1016/j.engstruct.2020.110166.

[12] A. Iqbal, T. Smith, S. Pampanin, M. Fragiacomo, A. Palermo, and A. H. Buchanan, "Experimental Performance and Structural Analysis of Plywood-Coupled LVL Walls," *Journal of Structural Engineering*, vol. 142, no. 2, p. 4015123, 2016, doi: doi:10.1061/(ASCE)ST.1943-541X.0001383.

[13] M. Massari, M. Savoia, and A. R. Barbosa, "Experimental and Numerical Study of Two-Story Post-Tensioned Seismic Resisting CLT Wall with External Hysteretic Energy Dissipaters," in *Atti del XVII Convegno ANIDIS L'ingegneria Sismica in Italia : Pistoia, 17-21 settembre 2017. - (Studi in tema di internet ecosystem)*, Pisa: Pisa University Press, 2017. [Online]. Available: http://digital.casalini.it/4215425

[14] M. P. Newcombe, "Seismic design of post-tensioned timber frame and wall buildings," Christchurch, New Zealand, 2011.

[15] A. Palermo, S. Pampanin, M. Fragiacomo, A. H. Buchanan, and B. L. Deam, "Innovative seismic solutions for multi-storey LVL timber buildings," *9th World Conference on Timber Engineering, WCTE 2006*. Portland, OR, 2006.

[16] S. Pei *et al.*, "Experimental Seismic Response of a Resilient 2-Story Mass-Timber Building with Post-Tensioned Rocking Walls," *Journal of Structural Engineering*, vol. 145, no. 11, p. 4019120, 2019, doi: doi:10.1061/(ASCE)ST.1943-541X.0002382.

[17] F. Sarti, A. Palermo, and S. Pampanin, "Quasi-Static Cyclic Testing of Two-Thirds Scale Unbonded Posttensioned Rocking Dissipative Timber Walls," *Journal of Structural Engineering*, vol. 142, no. 4, p. E4015005, 2016, doi: doi:10.1061/(ASCE)ST.1943-541X.0001291.

[18] F. Sarti, A. Palermo, and S. Pampanin, "Development and Testing of an Alternative Dissipative Posttensioned Rocking Timber Wall with Boundary Columns," *Journal of Structural Engineering*, vol. 142, no. 4, p. E4015011, 2016, doi: doi:10.1061/(ASCE)ST.1943-541X.0001390.

[19] R. Soti, A. Sinha, I. Morrell, and B. T. Miyamoto, "Response of self-centering mass plywood panel shear walls," *Wood and Fiber Science*, vol. 52, no. 1, pp. 102–116, 2020.

[20] ASCE 7, "Minimum Design Loads and Associated Criteria for Buildings and Other Structures (ASCE/SEI 7-22)." American Society of Civil Engineers, Reston, VA, 2022.

[21] AWC, "SDPWS - Special Design Provisions for Wind and Seismic with Commentary," vol. ANSI/AWC SDPWS. American Wood Council, Leesburg, VA, 2021.

[22] FEMA P-2082-1 and Federal Emergency Management Agency, "NEHRP Recommended Seismic Provisions for New Buildings and Other Structures," Federal Emergency Management Agency, Washington, D.C., 2020.

[23] IBC, "2021 International Building Code." International Code Council, Inc., USA, 2020.

[24] G. G. Deierlein, H. Krawinkler, and C. A. Cornell, "A framework for performance-based earthquake engineering," *2003 Pacific Conference on Earthquake Engineering*. New Zealand Society for Earthquake Engineering, Christchurch, New Zealand, 2003. [Online]. Available: https://www.nzsee.org.nz/db/2003/View/Paper140s.pdf

[25] FEMA P-58-6, "Guidelines for Performance-Based Seismic Design of Buildings." Federal Emergency Management Agency, Washington, D.C., 2018.

[26] S. Günay and K. M. Mosalam, "PEER Performance-Based Earthquake Engineering Methodology, Revisited," *Journal of Earthquake Engineering*, vol. 17, no. 6, pp. 829–858, 2013, doi: 10.1080/13632469.2013.787377.

[27] H. Krawinkler and E. Miranda, "Performance-Based Earthquake Engineering," in *Earthquake Engineering: From Engineering Seismology to Performance-Based Engineering*, 1st Edition., Y. Bozorgnia and V. v Bertero, Eds. Boca Raton, FL: CRC Press, 2004. doi: https://doi.org/10.1201/9780203486245.

[28] J. P. Moehle and G. G. Deierlein, "A Framework Methodology for Performance-Based Earthquake Engineering," *13th World Conference on Earthquake Engineering*. Vancouver, Canada, 2004. [Online]. Available: https://www.iitk.ac.in/nicee/wcee/article/13_679.pdf

[29] E. McDonnell and B. Jones, "Performance-Based Engineering Provides Path to More Compelling Mass Timber Projects," *Technology|Architecture + Design*, vol. 4, no. 1, pp. 9–13, 2020, doi: 10.1080/24751448.2020.1705709.

[30] B. T. Teweldebrhan and S. Tesfamariam, "Performance-based design of tall-coupled cross-laminated timber wall building," *Earthq Eng*

https://doi.org/10.52202/069179-0286

Struct Dyn, vol. 51, no. 7, pp. 1677–1696, 2022, doi: https://doi.org/10.1002/eqe.3633.

[31] R. B. Zimmerman, H.-E. Blomgren, J. McCutcheon, and A. Sinha, "Catalyst - A Mass Timber Core Wall Building with High Ductility Hold-Downs in a Seismic Region," *2020 World Conference on Timber Engineering*. Santiago, Chile, 2020.

[32] R. B. Zimmerman and E. McDonnell, "Framework - A tall re-centering mass timber building in the United States," *2017 NZSEE Conference*. Wellington, New Zealand, 2017. [Online]. Available: http://db.nzsee.org.nz/2017/O5C.3_Zimmerman_&_McDonnell.pdf

[33] Q. Jiang *et al.*, "Experimental study and numerical simulation of a reinforced concrete hinged wall with BRBs at the base," *Journal of Building Engineering*, vol. 49, p. 104030, 2022, doi: https://doi.org/10.1016/j.jobe.2022.104030.

[34] Q. Jiang *et al.*, "Analysis and experimental testing of a self-centering controlled rocking wall with buckling-restrained braces at base," *Eng Struct*, vol. 269, p. 114843, 2022, doi: https://doi.org/10.1016/j.engstruct.2022.114843.

[35] B. Janhunen, S. Tipping, and J. Wolfe, "Seismic Retrofit of a 1960s Steel Moment-Frame Highrise Using a Pivoting Spine," in *SEAOC 2013 Convention*, 2013. [Online]. Available: https://www.tippingstructural.com/firm/publications

[36] Q. Jiang *et al.*, "Experimental study and numerical simulation of a reinforced concrete hinged wall with BRBs at the base," *Journal of Building Engineering*, vol. 49, p. 104030, May 2022, doi: 10.1016/J.JOBE.2022.104030.

[37] Z. Qu, A. Wada, S. Motoyui, H. Sakata, and S. Kishiki, "Pin-supported walls for enhancing the seismic performance of building structures," *Earthq Eng Struct Dyn*, vol. 41, no. 14, pp. 2075–2091, 2012, doi: https://doi.org/10.1002/eqe.2175.

[38] T. Sun, Y. C. Kurama, and J. Ou, "Practical displacement-based seismic design approach for PWF structures with supplemental yielding dissipators," *Eng Struct*, vol. 172, pp. 538–553, 2018, doi: https://doi.org/10.1016/j.engstruct.2018.05.120.

[39] A. Wada, Z. Qu, H. Ito, S. Motoyui, H. Sakata, and K. Kasai, "Seismic Retrofit Using Rocking Walls and Steel Dampers," in *Improving the Seismic Performance of Existing Buildings and Other Structures*, 2009, pp. 1010–1021. doi: doi:10.1061/41084(364)92.

[40] A. Wada, Z. Qu, S. Motoyui, and H. Sakata, "Seismic retrofit of existing SRC frames using rocking walls and steel dampers," *Frontiers of Architecture and Civil Engineering in China*, vol. 5, no. 3, p. 259, 2011, doi: 10.1007/s11709-011-0114-x.

[41] X. Wang, T. Wang, and Z. Qu, "An experimental study of a damage-controllable plastic-hinge-supported wall structure," *Earthq Eng Struct Dyn*, vol. 47, no. 3, pp. 594–612, 2018, doi: https://doi.org/10.1002/eqe.2981.

[42] X. Chen, T. Takeuchi, and R. Matsui, "Simplified design procedure for controlled spine frames with energy-dissipating members," *J Constr Steel Res*, vol. 135, pp. 242–252, 2017, doi: https://doi.org/10.1016/j.jcsr.2017.04.017.

[43] L. Gioiella, E. Tubaldi, F. Gara, L. Dezi, and A. Dall'Asta, "Modal properties and seismic behaviour of buildings equipped with external dissipative pinned rocking braced frames," *Eng Struct*, vol. 172, pp. 807–819, 2018, doi: https://doi.org/10.1016/j.engstruct.2018.06.043.

[44] B. G. Simpson and S. A. Mahin, "Experimental and Numerical Investigation of Strongback Braced Frame System to Mitigate Weak Story Behavior," *Journal of Structural Engineering*, vol. 144, no. 2, p. 4017211, 2018, doi: doi:10.1061/(ASCE)ST.1943-541X.0001960.

[45] T. Takeuchi, X. Chen, and R. Matsui, "Seismic performance of controlled spine frames with energy-dissipating members," *J Constr Steel Res*, vol. 114, pp. 51–65, 2015, doi: https://doi.org/10.1016/j.jcsr.2015.07.002.

[46] Z. Chen, M. Popovski, and A. Iqbal, "Structural Performance of Post-Tensioned CLT Shear Walls with Energy Dissipators," *Journal of Structural Engineering*, vol. 146, no. 4, p. 04020035, Jan. 2020, doi: 10.1061/(ASCE)ST.1943-541X.0002569.

[47] W. Dong, M. Li, C. L. Lee, G. MacRae, and A. Abu, "Experimental testing of full-scale glulam frames with buckling restrained braces," *Eng Struct*, vol. 222, p. 111081, Nov. 2020, doi: 10.1016/J.ENGSTRUCT.2020.111081.

[48] ASCE 7, "Minimum Design Loads and Associated Criteria for Buildings and Other Structures (ASCE/SEI 7-16)." American Society of Civil Engineers, Reston, VA, 2016.

[49] ASCE 41, "Seismic Evaluation and Retrofit of Existing Buildings (ASCE/SEI 41-17)." American Society of Civil Engineers, Reston, VA, 2017.

[50] M. Panagiotou and J. I. Restrepo, "Displacement-Based Method of Analysis for Regular Reinforced-Concrete Wall Buildings: Application to a Full-Scale 7-Story Building Slice Tested at UC-San Diego," *Journal of Structural Engineering*, vol. 137, no. 6, pp. 677–690, 2011, doi: doi:10.1061/(ASCE)ST.1943-541X.0000333.

[51] G. A. Araújo R., "Design, Experimental Testing, and Numerical Analysis of a Three-Story Mass

Timber Building with a Pivoting Spine and Buckling-Restrained Energy Dissipators," MS Thesis, Oregon State University, Corvallis, OR, 2022.

[52] AWC, "National Design Specification (NDS) for Wood Construction with Commentary," vol. ANSI/AWC NDS. American Wood Council, Leesburg, VA, 2018.

[53] L. G. Rodrigues, A. R. Barbosa, G. F. Orozco O., J. M. Branco, A. Sinha, and B. G. Simpson, "Analytical model and finite element modeling strategy for the design and assessment of mass timber diaphragms," in *12th National Conference on Earthquake Engineering*, 2022.

[54] G. F. Orozco O., T. X. Ho, G. A. Araújo R., A. R. Barbosa, A. Sinha, and B. G. Simpson, "Innovative Mass Timber Seismic Lateral Force Resisting Systems: Testing of a Full-scale Three-story Building with Mass Ply Panels (MPP) Rocking Walls," in *12th National Conference on Earthquake Engineering*, 2022.

[55] H. Krawinkler, F. Parisi, L. Ibarra, A. Ayoub, and R. Medina, "Development of a Testing Protocol for Woodfram Structures," CUREE - Consortium of Universities for Research in Earthquake Engineering, Richmond, CA, 2001.

[56] H. Dong, X. Du, Q. Han, H. Hao, K. Bi, and X. Wang, "Performance of an innovative self-centering buckling restrained brace for mitigating seismic responses of bridge structures with double-column piers," *Eng Struct*, vol. 148, pp. 47–62, 2017, doi: https://doi.org/10.1016/j.engstruct.2017.06.011.

[57] M. R. Eatherton, L. A. Fahnestock, and D. J. Miller, "Computational study of self-centering buckling-restrained braced frame seismic performance," *Earthq Eng Struct Dyn*, vol. 43, no. 13, pp. 1897–1914, 2014, doi: https://doi.org/10.1002/eqe.2428.

[58] D. J. Miller, L. A. Fahnestock, and M. R. Eatherton, "Development and experimental validation of a nickel–titanium shape memory alloy self-centering buckling-restrained brace," *Eng Struct*, vol. 40, pp. 288–298, 2012, doi: https://doi.org/10.1016/j.engstruct.2012.02.037.

[59] C. J. Black, N. Makris, and I. D. Aiken, "Component Testing, Seismic Evaluation and Characterization of Buckling-Restrained Braces," *Journal of Structural Engineering*, vol. 130, no. 6, pp. 880–894, 2004, doi: doi:10.1061/(ASCE)0733-9445(2004)130:6(880).

[60] V. Budaházy, "Modelling of the Hysteretic Behavior of Buckling Restrained Braces," *Conference of Junior Researchers in Civil Engineering*. Budapest University of Technology and Economics, Budapest, Hungary, pp. 34–41, 2012.

[61] L. A. Fahnestock, J. M. Ricles, and R. Sause, "Experimental Evaluation of a Large-Scale Buckling-Restrained Braced Frame," *Journal of Structural Engineering*, vol. 133, no. 9, pp. 1205–1214, 2007, doi: doi:10.1061/(ASCE)0733-9445(2007)133:9(1205).

[62] S. Merritt, C.-M. Uang, and G. Benzoni, "Subassemblage testing of corebrace buckling-restrained braces," University of California, San Diego, La Jolla, California, 2003.

[63] C. Tong, J. Wu, K. Hua, and L. Xie, "Low-Cycle Fatigue Life Estimation Curve for Buckling-Restrained Braces Based on Cumulative Plastic Deformation," *Journal of Earthquake Engineering*, pp. 1–29, 2020, doi: 10.1080/13632469.2020.1772152.

[64] C.-M. Uang, M. Nakashima, and K.-C. Tsai, "Research and application of buckling-restrained braced frames," *International Journal of Steel Structures*, vol. 4, no. 4, pp. 301–313, 2004.

[65] A. Watanabe, Y. Hitomi, E. Saeki, A. Wada, and M. Fujimoto, "Properties of brace encased in buckling-restraining concrete and steel tube," in *Proceedings of ninth world conference on earthquake engineering*, 1988, vol. 4, pp. 719–724.

[66] F. McKenna, M. H. Scott, and G. L. Fenves, "Nonlinear Finite-Element Analysis Software Architecture Using Object Composition," *Journal of Computing in Civil Engineering*, vol. 24, no. 1, pp. 95–107, 2010, doi: doi:10.1061/(ASCE)CP.1943-5487.0000002.

[67] R. Soti, T. X. Ho, and A. Sinha, "Structural Performance Characterization of Mass Plywood Panels," *Journal of Materials in Civil Engineering*, vol. 33, no. 10, p. 4021275, 2021, doi: doi:10.1061/(ASCE)MT.1943-5533.0003902.

[68] T. X. Ho, A. Arora, and A. Sinha, "In-Plane Shear Properties of Mass Ply Panels in Long-Ply Direction," *Journal of Materials in Civil Engineering*, vol. 34, no. 8, p. 4022170, 2022, doi: doi:10.1061/(ASCE)MT.1943-5533.0004327.

[69] B. G. Simpson and S. Mahin, "Design Development for Steel Strongback Braced Frames to Mitigate Concentrations of Damage," Berkeley, CA, 2018.

[70] G. A. Araújo R, B. Simpson, T. X. Ho, G. F. Orozco O, A. R. Barbosa, and A. Sinha, "Numerical Modelling of a Three-Story Building Using a Hybrid of Mass Timber Walls with Buckling-Restrained Braces," in *Proceedings of the 10th International Conference on Behaviour of Steel Structures in Seismic Areas. STESSA 2022. Lecture Notes in Civil Engineering.*, 2022, vol. 262. doi: 10.1007/978-3-031-03811-2_45.

https://doi.org/10.52202/069179-0286

World Conference on Timber Engineering Oslo 2023

HYSTERESIS - A PYTHON LIBRARY FOR ANALYSING STRUCTURAL DATA

Christian Slotboom[1]

ABSTRACT: Researchers studying the design of timber structures are often required to generate and process a large amount of data from experimental and numerical studies. Hysteretic data coming from seismic tests is particularly challenging to work with, because the x/y curve will change direction through testing. This paper provides an overview of Hysteresis, a software library written in the Python programming language that can be used to quickly process and analyse structural data, including hysteretic curves.
The main structure and algorithms used in the software package are presented, including a summary of how data is represented in the package, and how it can be used. Two case studies are then presented where data is processed using the Hysteresis package. In the first, experimental and numerical data from tests on a shear wall are processed and compared in a variety of ways. The second, Hysteresis is used in an optimization analysis, where a genetic algorithm is used to fit non-linear material data to a structural element.

KEYWORDS: Hysteresis, Connection Testing, Data Analysis, Genetic Algorithm.

1 INTRODUCTION

In seismically active areas, wood structural elements and connections will be exposed to repeated loading. For these elements it's important to understand not just the initial behaviour of the specimen to load, but how the response of the system change over repeated loading in a force deformation hysteresis. Experimentalists testing structural elements and connections will often have to apply load protocols, such as the CUREE method proposed in Krawinkler et al. [1], to their test specimens to understand this behaviour. Common tasks may include finding the area under a curve, finding the back-bone curve of a hysteresis, or fitting a new curve to a back bone, such as in the Equivalent Energy Elastic-Plastic procedure outlined in ASTM E2126 [2]. These data processing tasks are often very time consuming and take away time from high level research.
Structural researchers are also frequently working with hysteretic data coming from a finite element numerical analysis. In addition to processing this data, there are many common tasks that require researchers compare output data a numerical model to those from experiment to see their similarity. Researchers also may want to fit parameters of a non-linear material model, for example Steel02 [3] or pinching4 [4] from the OpenSees [5,6] library, to their experimental data. These tasks are often completed manually, due to the difficulty in matching different hysteresis.
To address these challenges in processing experimental and numerical data, a library in the Python programming language has been developed. This library can be used to work with simple x/y curves, as well as hysteretic data that changes direction in cycles. The following paper describes the Hysteresis library, its main features, and showcases several key use-cases.

2 HYSTERESIS PACKAGE SUMMARY

2.1 BACKGROUND

Data from structural tests is generally represented by a series of (x,y) points, commonly force vs. deformation. In the case of structural data, it can be useful for curves to be divided into regions where the y values are "mostly" increasing or decreasing monotonically. For a CLT wall loaded in shear loaded may have a force deformation curve that increases to a peak value, then decreases after this value. Figure 1 demonstrates this, using the final cycle from a force deformation hysteresis tested by Drexlar et. al. [7], where the cycle has been split into regions of interest.

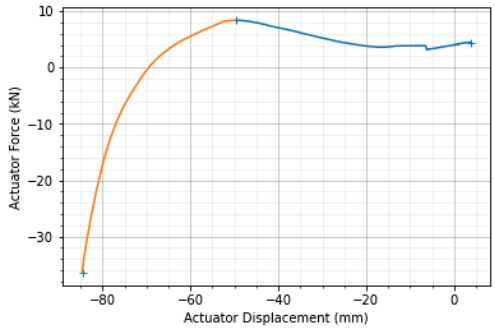

Figure 1: *A data from a shear wall split into regions that are mostly increasing (orange) or decreasing (blue).*

[1] Christian Slotboom, Graduate Engineer, Fast+Epp, cslotboom@fastepp.com

https://doi.org/10.52202/069179-0287

Structural data will also occur in cycles, where the x axis values are either increasing or decreasing monotonically. This commonly occurs in reverse cyclic loading for seismic testing. Figure 2 shows a hysteresis of the same shear wall in Figure 1, highlighting distinct regions where the x values are mostly unchanging. Similar to the monotonic load case, it's often useful to determine where these cycles occur in data.

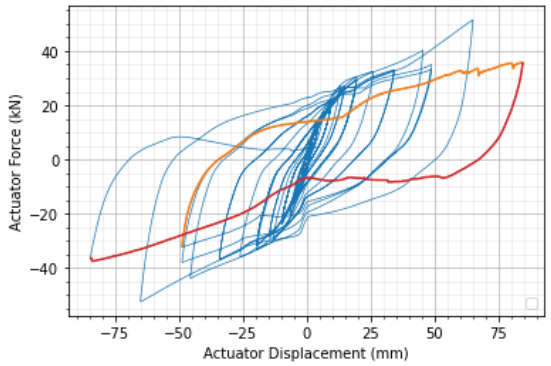

Figure 2: *A positive cycle (orange), and negative cycle (red) noted in a shear wall hysteresis.*

In both Figure 1 and Figure 2, there are small regions where the graph will decrease slightly in a roughly increasing zone. These irregularities are often not important to the data but can complicate finding data.

2.2 ABSTRACTIONS AND CLASS STRUCTURE

To represent x/y curves of structural data, the hysteresis Python package contains three main classes of curve objects:

- The "MonotonicCurve", where the x/y curve does not change in in its vertical axis and its horizontal axis.
- The "SimpleCycle", where data changes only in the y axis only.
- The "Hysteresis", where data in the x/y curve can change in both the both the x and y direction.

The structure of each curve object is nested, so that Hysteresis objects can be broken up into SimpleCycle objects, and SimpleCycle can be broken up into of MonotonicCurve objects.

Hysteresis and SimpleCycle objects divide themselves into sub-curves by finding reversal points in either the x data, or peaks in the y data. Signal filtering functions from the Python library Scipy [8] are used to find these local extreme values in the data. These functions also allow peaks/reversals to be selected based on various criteria, such as number of data points between extremes, or the prominence of the peaks/reversals from other lower points. Providing a method of filtering out smaller peaks in the data allows the main objects to ignore minor irregularities within the input data.

MonotonicCurve, SimpleCycle, and Hysteresis objects all inherit from a common "CurveBase" class that provides functionality to all objects. Included in this base class are a number of methods that can be used to numerically find properties like the curve, such as slope, cumulative change in x, arclength, or area under the curve. Figure 3 showcases some of these properties for a SimpleCycle object. By default, slope and area is calculated with second order finite difference schemes.

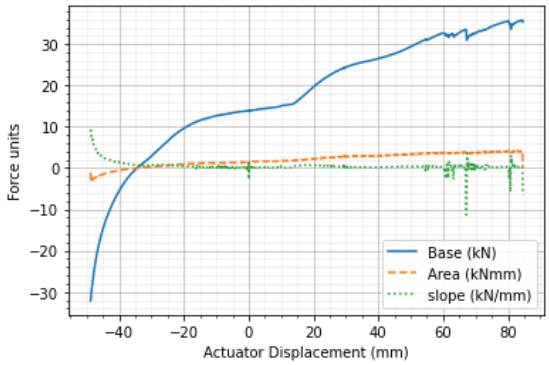

Figure 3: *A SimpleCycle object cycle with its numerically calculated slope, and area under the curve.*

The CurveBase class also includes a number of methods that allow for the curve to be easily plotted. Built in methods include: making a x/y plot of the curve, plotting the cumulative area under the curve, or plotting a curves x value against the index. Plots can also be made to show peak values or reversal points. All plots produced by the hysteresis module make use of the Matplotlib Python library [9] and can be modified with well-known commands. Figure 4 shows two of the plot functions, for the hysteresis in Figure 2 with reversal points highlighted, and the same data with x values plotted against index.

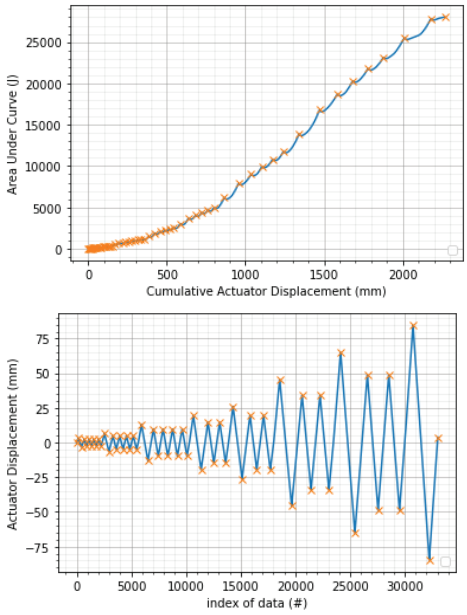

Figure 4: *Top, experiment hysteresis with reversal points highlighted. Bottom, the x displacement plotted against the index used, with reversal points highlighted.*

The Hysteresis package was designed to allow users to customize the behaviour of its key objects. At the time of object creation, functions are assigned to each object. For

https://doi.org/10.52202/069179-0287

example, the "areaFunction" is set, reading from a environment object that contains the default functions used by all objects. The stored areaFunction will then be called later when a request is made to calculate area. Users can implement custom behaviour by either directly overwritten the desired function in individuals object, or by setting a new function in the environment variable. Changing the environment will affect the behaviour of all objects created afterwards.

Figure 5 summarizes the main classes used in the Hysteresis package, and some of their key methods. Arrows represent inheritance relationships, where one class is a subclass of another class, while diamonds represent composition where objects are stored in other objects. Hysteresis classes will contain SimpleCycles in a list of "cycles", and similarly SimpleCycles contain MonotonicCurves in a list of subcycles.

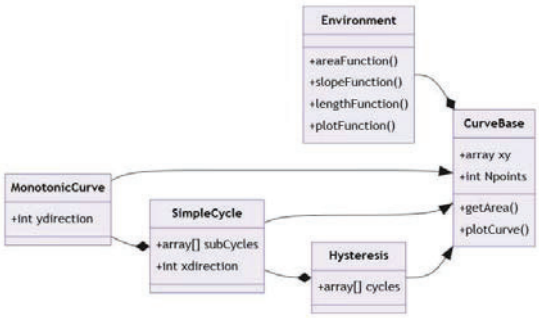

Figure 5: Class diagram for the Hysteresis package's main abstractions, and some key methods for each class.

2.3 BASIC FUNCTIONS

In addition to the basic numerical analysis and plotting functionality provided by the CurveBase class, there are a number of functions in the Hysteresis package that allows users to operate on hysteresis objects. Different object types can be combined can be combined with the "concatenate" function. This allows for more complex objects, such as the SimpleCycle or Hysteresis, to be built up from its component curves, or lists of x/y data.

Another desirable feature is the ability to take an input curve and resample it, which allows for data to be compressed or expanded. The Hysteresis package has a "resample" function, which allows for the number of x axis points to be increased or decreased using linear interpolation. When called on the MonotonicCurve or SimpleCycle Object, resample will change the total number of points in the curve, while when Hysteresis objects are resampled the number of points in each sub-curve is changed. This highlights a major benefit of the class structure used, because complex objects such as the Hysteresis are broken into simpler objects, it's possible to easily resample entire hysteresis by resampling its components. Resampling can be done based on a number of increments between the maximum and minimum x value or based on a sample change in x direction distance. Figure 9 shows the final cycle shown in Figure 1, where the curve has been resampled to only include 5 segments.

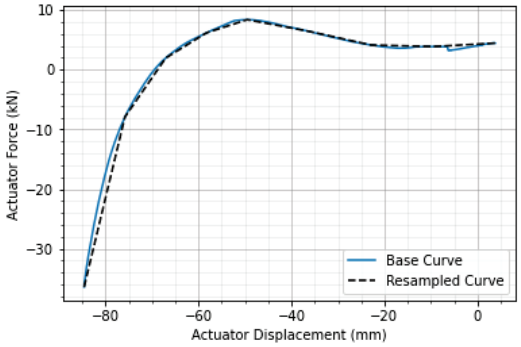

Figure 6: *The x/y curve shown in Figure 1, and a resampled version of that curve.*

A feature enabled by the resample function is the ability to various Curve objects of the same type. Two curves can be compared using the "compare" function by resampling each curve, then summing the Euler distance over all the resulting set of points. Equations (1,2) below overview this calculation for a SimpleCycle and Hysteresis respectively, where: "j" is an index that counts the number of sample point; and "i" is an index that counts the number of SimpleCycles that make up a hysteresis object. While the actual sum of the two curves is not physically significant, it's size will indicate how similar two curves are, and reduce to zero when curves coincide. Like resampling, Hysteresis curves are compared by summing the comparison between the monotonic cycles of each object. Figure 7 showcase the process comparison process, where the final output is the average distance between each point on the curve.

$$\varepsilon_0 = \frac{\sum_j^{N_j} \sqrt{\left(y_j - y_{j-1}\right)^2 + \left(x_j - x_{j-1}\right)^2}}{N_j} \quad (1)$$

$$\varepsilon_{hys} = \sum_i^{N_i} \frac{\sum_j^{N_j} \sqrt{\left(y_j - y_{j-1}\right)^2 + \left(x_j - x_{j-1}\right)^2}}{N_j} \quad (2)$$

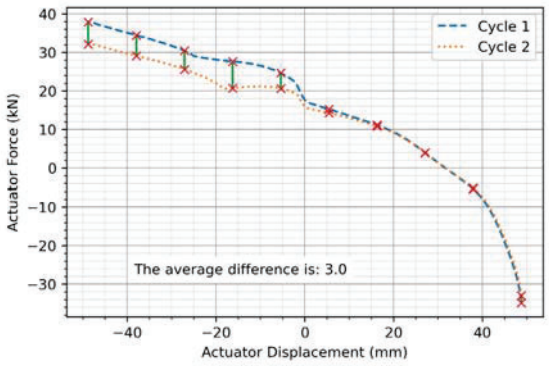

Figure 7: *The average difference in the x/y space between each point for the resampled curves.*

2.4 ENVELOP FUNCTIONS

The Hysteresis library also has functions that can be used to extract data from the envelop of a Hystersis class. A

common task researchers will face is finding the backbone of a hysteresis. Because the reversal points in an input Hysteresis are automatically stored, the Hysteresis library can be used to quickly extract the backbone of data coming from a numerical or experimental hysteresis. A function "getBackbone" can be applied to the curve in question to extract the correct points from an input Hysteresis. Figure 8 shows a backbone curve extracted from a numerical model of a seismic damper [11]. By default the getBackbone function will return all reversal points, but the user can provide the number cycles each step in the load protocol has to the function to skip certain points, for example return only the first cycle.

In addition to the getBackbone function, a second function called "getBackboneAvg" can be used. This function extracts the positive and negative backbones of a Hysteresis objects, takes the absolute value of each x/y points, then an averages to the two curves.

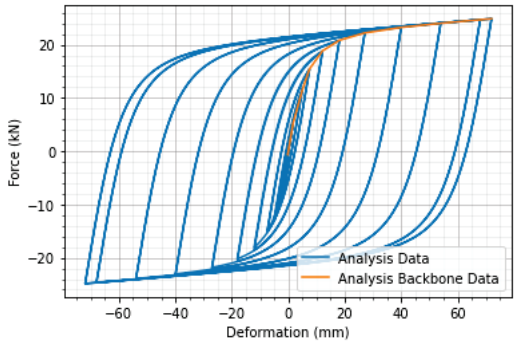

Figure 8: *The extracted backbone curve from a hysteresis.*

A specialized feature of the Hysteresis package is automatically fit an Equivalent Energy Elastic-Plastic (EEEP) Curve to a Hysteresis. In this process, the backbone of the hysteresis is first extracted using the average backbone function and rules outlined in ASTM 2126 [2]. Figure 9 shows a typical use case, where a EEEP curve is fit to the shearwall data from Figure 2.

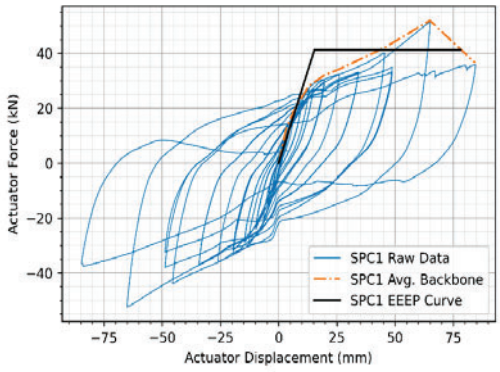

Figure 9*: Raw data from a shearwall test SPC1, overlayed with the calculated back-bone curve and fitted EEEP curve.*

3 CASE STUDIES

3.1 POST PROCESSING OF SHEAR WALL DATA

In the following example, experimental data from a self-centring CLT shear wall is postprocessed, then compared to data coming from numerical models of the shear wall. The CLT wall was approximately 4.5m tall, and a post-tensioned steel tendon was used to apply an initial compression force to the wall. Lateral force was applied to the system in a number of cycles, and the force-deformation of the wall was recorded. A detailed discussion of the experimentation can be found in Ganey [10], where it is labelled as TS1. Data for the numerical model is generated in OpenSees [5] using a models similar to those presented in Slotboom [11]. Figure 10 below shows both models, where both data sets have been "cropped", so they both end at approximately 0.15m of drift.

First the experimental data will be checked to see if reversal have been correctly extracted properly. The "plotLoadProtcol" method is used to clearly see which peaks have been picked up, and can be seen in figure XX. It's noted that that not all of the reversal points alternate between positive and negative, and one of the peaks has a value similar to the prior peak. This incorrectly detected point is removed by recalculating the reversal points using a prominence filter that will removes reversal points which do not change much compared to other points. The updated plot can be seen in Figure XX.

Often data from numerical and experimental studies are compared by plotting directly on top of each other, similar to Figure 12. While this can be used to understand general trends in the data, it is often difficult to tell how each curve compares at different points in the analysis. Using the hysteresis package, it's possible easily extract specific cycles of the curve for comparison. Two other metric can easily be employed to see how similar each curve is at different points:

- Cumulative energy observed by each model.
- A direct comparison of the "error" between each curve.

Figure 13 shows a cycle of the produced by the Hysteresis package, while Figure 14 and Figure 15 overview the cumulative energy and error of each cycle respectively. Looking at the Figure 14 it easily be observed that the experimental model absorbed much more energy per cycle than the numerical model did, something which would have been difficult to observe from Figure 12 alone. Through Figure 13, it can be concluded that the experimental hysteresis was asymmetric, and had an open hysteresis that was absorbing energy, while the numerical model was symmetric and had a purely elastic behaviour. Noting quickly noting these differences could allow the researcher make changes to their experimental setup or numerical model if needed.

https://doi.org/10.52202/069179-0287

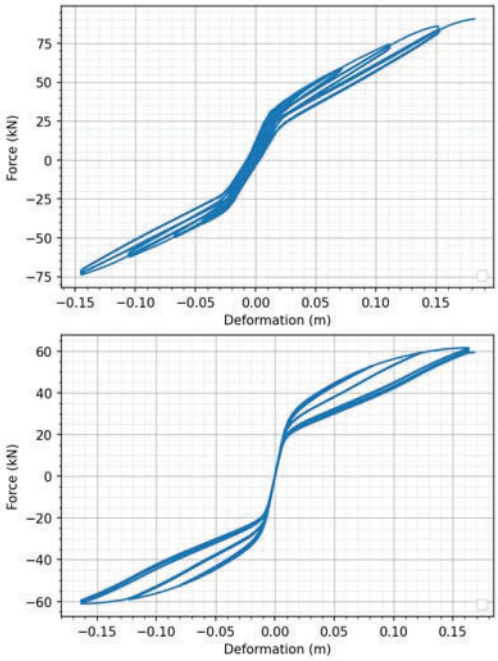

Figure 10: *The raw experimental hysteresis (top), and analysis hysteresis (bottom).*

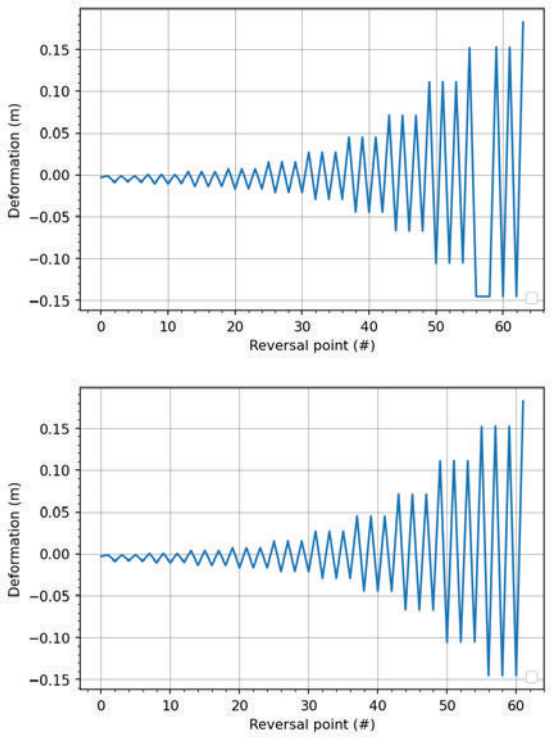

Figure 11: *A plot of detected peaks before (top) and after (bottom) filtering.*

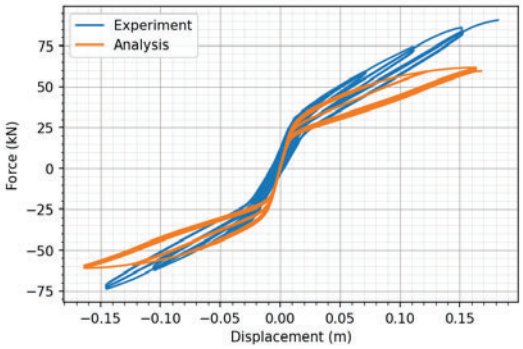

Figure 12: *A typical comparison of experiment/numerical data.*

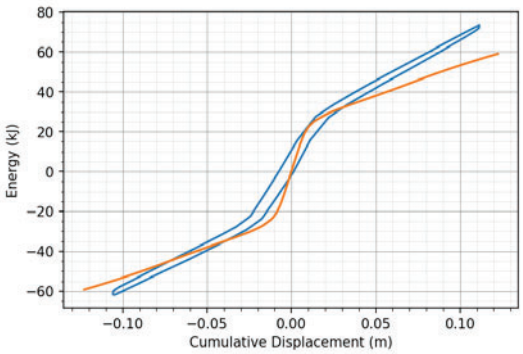

Figure 13: *Experiment and analysis results compared for a single cycle in the hysteresis.*

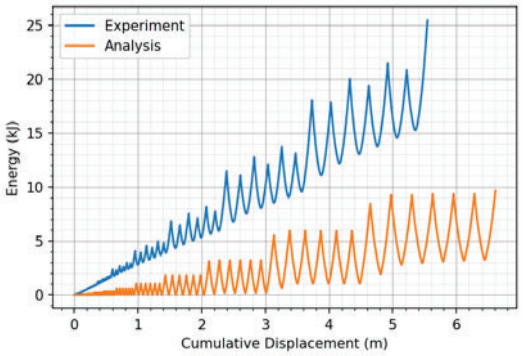

Figure 14: *The energy absorbed by each cycle in the hysteresis.*

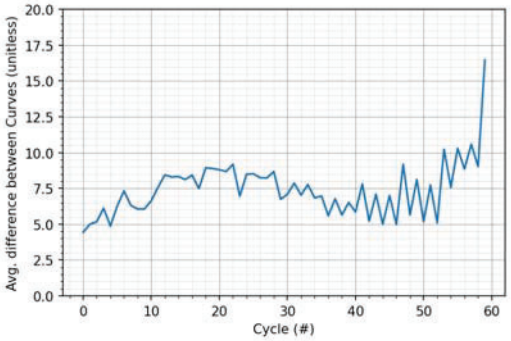

Figure 15: *The average difference between the experiment and numerical analysis.*

3.2 PARAMETER FITTING USING GENETIC ALGORITHMS

A second case study is presented where a nonlinear numerical models are calibrated to match experimental data using a genetic algorithm and the Hysteresis package. As part of a testing program on self-centring shear walls, Ganey tested a number of U-shaped Flexural Plate (UFP) steel dampers. These dampers showed a stable response with a full hysteresis until failure. It's desired to make numerical models of this damper, which can be applied to model of the wall system.

The numerical models of the damper were developed in with the Python implementation of OpenSees, OpenSeesPy [6-7]. A zero-length element was used to model the damper, with a steel02, a Giuffre-Menegotto-Pinto steel material, applied to the element. Force was applied to one of the zero length element's nodes, and the load protocol used matched the testing from Ganey's experiment. To match the damper to experimental results, the OpenSees analysis was first parameterized to take in set of values about the zero-length damper. The significant parameters chosen to be varied were: F_y, the yield strength; E_0, the slope of the elastic tangent; b, the strain hardening ratio between the elastic and plastic tangent lines; and R_0, C_{R1}, and C_{R2}, which are parameters influence how the material transfers from it's elastic to plastic tangent lines.

Once the function was parameterized, the genetic algorithm was set up to iterate through possible values until an optimum was reached. The genetic algorithm used a scheme where a pool of 30 genes was tested over 100 generations. Each gene consisted of the six parameters used to . Initially parameters were randomly generated, with the bounds for the parameters defined in Table 1.

During each generation, all genes in the population were tested by running a OpenSeesPy with those values, then using the Hysteresis Compare function to quantify how similar the experimental and analysis hysteresis was. In each generation, 8 pairs of genes are chosen to pass on their genes to the next round, and results that closely matched experiment were more likely to be chosen. The remaining 14 genes were filled up by randomly generated values within the range of Table 1. Both crossover, where information is swapped between pairs of genes, and mutation, where genes are randomly changed were considered. After 100 generations the analysis was ended, and the optimal value was taken, and is presented in Table 1.

Table 1: *Genetic algorithm parameters and solution.*

Parameter	Minimum	Maximum	Solution
F_y (kN)	0	32	23
E_0 (kN/m)	0	$4x10^6$	$2.9 x10^6$
b	0	0.023	0.002
R_0	0	29	4
C_{R1}	0	1.4	0.57
C_{R2}	0	.23	0.15

Figure 16 compares results from the experimentally tested damper to the solution chosen by the genetic algorithm, showing a close fit between the two hysteresis curves. The Hysteresis package is small part of this process, but it provides a crucial comparison between experiment and numerical data, needed to tell which parameters are good, and which are bad.

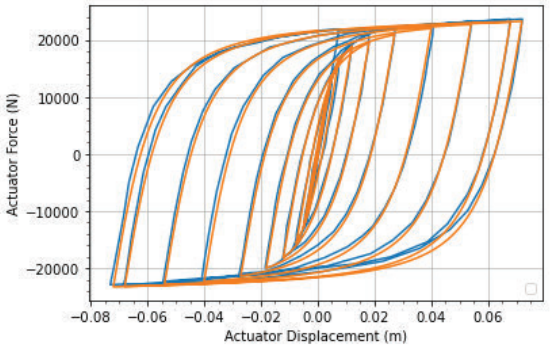

Figure 16: *Experiment (blue) vs. Optimal solution (orange) for the chosen genetic algorithm.*

4 CONCLUSIONS

The Hysteresis Python package can be used to quickly post process structural data, with an emphasis on hysteretic data. The main structure and algorithms used in the package was overviewed, highlighting the three key types of curves (Monotonic, SimpleCycle, and Hysteresis) used to represent structural data. These curve classes all have built in functions for plotting and doing numerical analysis on their data. These classes were designed with customization in mind, and the user can modify these methods by changing the underlying functions in the environment. In addition to the basic functionality, there also exists a number of functions that can be used to extract parameters from an envelop of a Hysteresis object, with some key functions being "getBackbone", and "compare".

Two case studies are then presented, showing how the hysteresis python package can be used to speed up data processing, and enable different types of analyses. The Hystersis package can be used to quickly compare numerical and experimental data in a number of ways. Also, by enabling two hysteresis curves to be compared, the Hysteresis package allows for advanced algorithms or machine learning models to work with Hysteresis dat.

ACKNOWLEDGEMENT

The Author would like to acknowledge data provided by Fast+Epp and Professor Thomas Tannert from the University of Northern British Columbia.

REFERENCES

[1] Krawinkler H, Parisi F., Ibarra L., Ayoub A., Medina R, Development of a Testing Protocol for Woodframe Structures, 2001

[2] ASTM E2126, Standard Test Methods for Cyclic (Reversed) Load Test for Shear Resistance of Vertical Elements of the Lateral Force Resisting

https://doi.org/10.52202/069179-0287

Systems for Buildings, ASTM International, West Conshohocken, PA, 2018
[3] Lowes L, Mitra, N, A Beam-Column Joint Model for Simulating the Earthquake Response of Reinforced Concrete Frames, Pacific Earthquake Engineering Research Center, Report 2003/10, University of Washington, 2003
[4] Filippou, F. C., Popov, E. P., Bertero, V. V., Effects of Bond Deterioration on Hysteretic Behavior of Reinforced Concrete Joints, Report EERC 83-19, Earthquake Engineering Research Center., University of California, Berkeley. 1983
[5] Mckenna F, OpenSees: A Framework for Earthquake Engineering Simulation, Computing in Science and Engineering, 2011
[6] Zhu, Minjie, McKenna, Frank, Scott, Michael H. OpenSeesPy: Python library for the OpenSees finite element framework, 2018
[7] Drexler M, Dires S, Tannert T, Internal perforated-steel-plate connections for CLT shear walls., In proceedings of World Conference for Timber Engineering, Santiago de Chile., 2021
[8] Virtanen P, Gommers R, Oliphant T/, Haberland M., Reddy T., Cournapeau D., Burovski E., Peterson P., Weckesser W., Bright J., van der Walt S., Brett M., Wilson J., Millman K., Mayorov N., Nelson R, Jones E., Kern R., Larson E., Carey C., Polat I, Feng Y., Moore E., VanderPlas J., Laxalde D., Perktold J., Cimrman R., Henriksen I., Quintero E., Harris C., Archibald A., Ribeiro A., Pedregosa F., Mulbregt P., and SciPy 1.0 Contributors. (2020) SciPy 1.0: Fundamental Algorithms for Scientific Computing in Python**.** *Nature Methods*, 17(3), 261-272.
[9] Hunter, J. D., Matplotlib: A 2D graphics environment, computing in Science & Engineering, 9(3) 2007
[10] Ganey, R., Seismic Design and Testing of Rocking Cross Lamiated Timber Walls, MASC. thesis, 2015
[11] Slotboom, C., Numerical Analysis of Self-centering Cross-laminated Timber Walls, MASC thesis, 2020

World Conference on Timber Engineering Oslo 2023

MONOTONIC TESTS ON BEAM-TO-COLUMN JOINT WITH STEEL LINK FOR TIMBER SEISMIC RESISTANT STRUCTURES

Giacomo Iovane[1], Leonardo Rodrigues[2] , Jorge Branco[3], Beatrice Faggiano[1]

ABSTRACT: For the design of dissipative heavy timber frame structures, in the context of modern seismic design approach based on the mechanical triad of strength, stiffness and ductility, brittle timber failure modes can be avoided by integrating modern timber connection technology into hybrid timber-steel system. The overall seismic performance can be improved, entrusting the dissipation function to ad hoc conceived devices, as an alternative to connections. Steel links located at the ends of the beams are very promising solutions, which can develop plastic hinges, thus providing a ductile behaviour, with a significant dissipative capacity. Besides timber members, as well as connections, to be designed with an adequate over-strength, can remain in elastic field. In this perspective, the paper illustrates the mechanical characterisation through monotonic tests of two different configurations of timber beam-to-column joint with steel link for heavy timber frames, consisting of a timber element connected to a steel link by means of a steel end-plate and glued-in steel rods. The experimental results indicate a satisfactory agreement with the theoretical ones, therefore the suitability of the system and of the design criteria.

KEYWORDS: Seismic resistant timber structures, beam-to-column joints with steel link, monotonic test on joint.

1 INTRODUCTION

Timber material has an elastic and fragile behaviour up to failure, so that, the present anti-seismic regulations, like the European Eurocode 8 [1], indicates that for the seismic design of dissipative timber structures, joints should dissipate a part of the seismic energy through plastic deformations of steel connectors. However, joints are primary structural elements, with a crucial role in bearing the design loads, so that their integrity should be preserved [2]. By integrating modern timber connection technology into hybrid timber-steel system, brittle wood failure modes can be avoided and overall seismic performance improved.

With specific reference to the structural type of Moment Resisting Frames (MRF), recently, some authors have proposed different solutions for dissipative timber structures, by coupling a ductile material like steel to timber [3 - 9].

In particular, Montuori and Sagarese [6] and Montuori [7] have applied to timber beams the steel reduced beam sections, commonly proposed for steel MR frames; as well as Gohlich et al. [10] studied hybrid steel-timber structures, such as buckling restrained braced frame (BRBF) and moment resistant frame (DMRF) with steel links; Yang et al. [11] have delegated the dissipative capacity to a steel box connected to the beam and column by glued bars; Tomasi et al. [8] and Andreolli et al. [9] focused on a beam-column timber joint equipped with steel links for dissipative MR frames.

The paper deals with the latter type of device, such as a timber beam-to-column joint with steel link located at the ends of the beam. It is designed so that the plastic hinge forms in the steel link, achieving a ductile behaviour and a significant dissipative capacity, while timber members and steel connections, having an adequate over-strength as respect to the dissipative links, remains in elastic field. Such connection system, further to an advantageous mechanical performance, has some other interesting properties, like versatility and prefabrication [2, 12, 13].

As regard the design criteria of the study joints, the capacity design method was applied to ensure the collapse hierarchy between the connection subcomponents [12, 13]. The joints behaviour was preliminary studied through numerical analyses, by means of the software ABAQUS FEA [14], in terms of key parameters, like ultimate strength, stiffness, rotation capacity and failure mode [13]. Then the ductile joint system and the proposed design criteria were validated through an experimental campaign carried out in 2019 at the Department of Civil

[1] Beatrice Faggiano, faggiano@unina.it, Giacomo Iovane, giacomo.iovane@unina.it, University of Naples Federico II, Department of Structures for Engineering and Architecture, P.le Tecchio 80, 80125, Naples, Italy;
[2] Leonardo Rodrigues, Leonardo.Rodrigues@nottingham.ac.uk, University of Nottingham, Faculty of Engineering, Nottingham, NG7 2RD, United Kingdom;
[3] Jorge Branco, jbranco@civil.uminho.pt, University of Minho, Department of Civil Engineering, Campus de Azurém 4800-058 Guimarães, Portugal.

https://doi.org/10.52202/069179-0288

Engineering (DECivil) of the University of Minho, in Guimaraes (Portugal), in cooperation with the Department of Structures for Engineering and Architecture of the University of Naples Federico II. 2 monotonic and 2 cyclic tests up to collapse were performed for 2 types of specimen.
In particular, in this work the monotonic tests on the two beam-to-column joints with steel link are presented.

2 SPECIMEN FEATURES AND MANUFACTURING PROCESS

The specimens (Figs. 1, 2a; [13]) are made of a laminated timber beam (GL24h) with a 140x320mm rectangular cross section, 850mm long, equipped at one end with a steel link, HE100A or IPE100 profiles 250mm long (steel grade S355) with two welded end-plates (120x230mm, steel grade S275), with 20mm thickness for the HE100A, 15mm thickness for the IPE100 specimens.

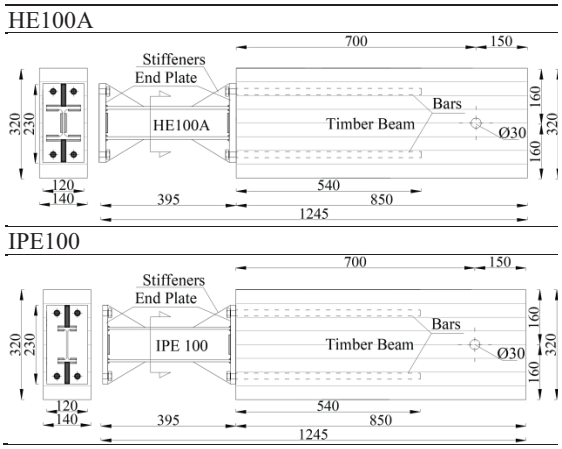

Figure 1: *Specimens geometrical features [mm].*

For both specimens, the link is connected at one side to the timber beam by 4 glued threaded bars (M16, 10.9, 540mm long), at the other side it is rigidly connected to a steel endplate (300x300mm and 40mm thickness) by 4 bolts (M16, 10.9 steel grade, 60mm long). The endplates have four triangular stiffeners (110x67mm for HE100A and 110x65mm for IPE100, with 15mm thickness).
With regards to the insertion of the bars within the timber beam the following manufacturing procedure was applied. On the timber element (Fig. 2b) 4 notches, 49x18mm and 540mm long, were realized guaranteeing an adequate bars anchorage. To ensure the bars centering within the notches, 2mm thick wire was wrapped around each bar, as spacer between bars and internal surface of notches (Fig. 2c). A two-component epoxy resin (Xepox F-liquid, by Rothoblaas) was poured into the notches (Fig. 2d), then the 4 threaded steel bars were inserted. At the end, notches were closed through additional timber elements (31x18mm and 540mm long), previously obtained by the timber rods cut from the timber element for realizing the notches (Fig. 2e, f), ensuring a 18x18mm cavity around the bars. The closing timber elements were sealed using structural timber glue. After gluing, the timber beam was left to dry for 4 days (Fig. 2g).

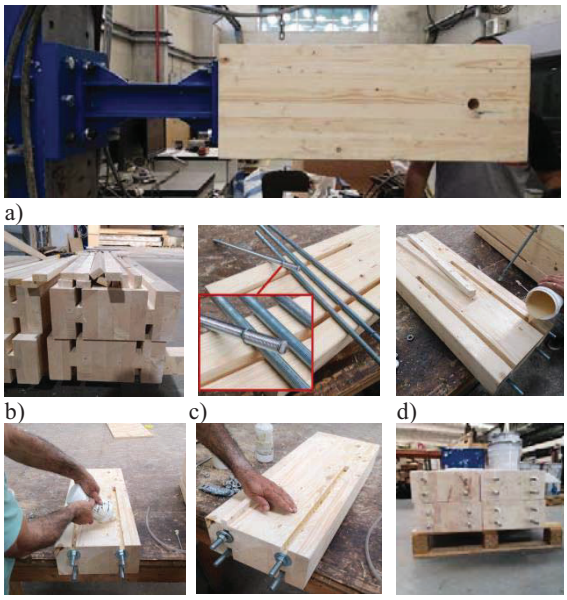

Figure 2: *Manufacturing steps: a) assembled joint; b) notches realization; c) wire spacer around the bars; d) epoxy resin pouring into the notches; e) and f) gluing of additional timber elements; g) timber specimen;.*

3 TEST SET-UP AND EQUIPMENTS

For the tests, a cantilever configuration (Fig. 3a) is realized. At one end, the link is rigidly connected to the reaction steel column of the retaining frame by means of 6 bolts (M12, 10.9 steel grade, 60mm long, Fig. 3b). At the timber beam free-end the load is applied through a pin, inserted in a hole with 30mm diameter drilled at the free-end of the beam. A steel fork connected to the pin ends is used to transfer the load by an hydraulic jack, having a maximum stroke of 200mm (Fig. 3c).

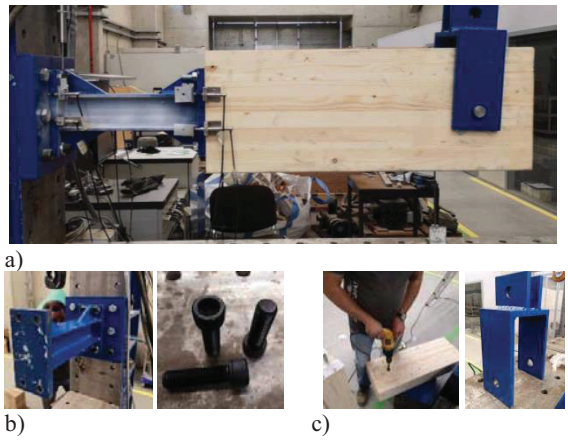

Figure 3: *Test set-up: a) overall set up; details: b) connection of the joint to the retaining frame; c) steel fork.*

The displacements of the specimen during the test are measured by using different types of linear variable displacement transducers (LVDTs). The displacement ranges required to each LVDT were estimated through the preliminary numerical analyses [13]. The LVDTs were installed on the specimen by using aluminium brackets screwed at the timber beam and glued at the steel elements.

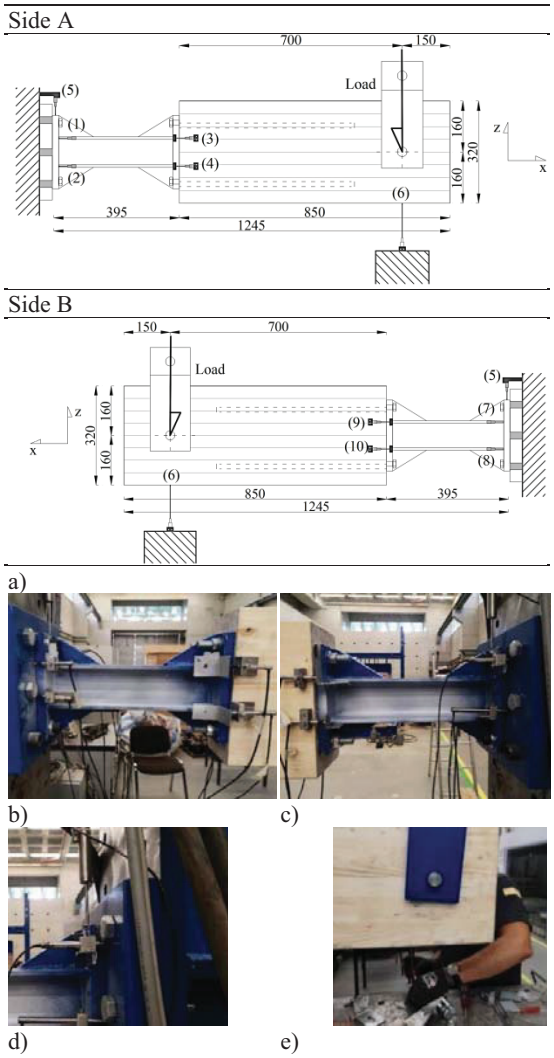

Figure 4: *Displacement transducers position: a) LVDTs on sides A and B [mm]; b) LVDTs nr.1, 2, 3, 4 on side A; c) LVDTs nr.7, 8, 9, 10 on side B; d) LVDT nr.5 at the upper side of the right end-plate; e) LVDT nr.6 at the loading beam section.*

In Figure 4 the position of the LVDTs is shown, they are:

- 4 LVDTs, 2 for each side of the specimens (nr.1 and 2 on side A, Figs. 4a, b; nr. 7 and 8 on side B, Fig. 4a, c) to measure the horizontal displacement between the fixed steel end-plate and the retaining frame;
- 4 LVDTs, 2 for each side of the specimens (nr. 3 and 4 on side A, Fig. 4a, b; nr. 9 and 10 on side B, Fig. 4a, c) to measure the horizontal displacement between the steel link and the timber beam;
- 1 LVDT (nr. 5) placed over the joint end-plate connected to the fixed end-plate to evaluate the possible vertical displacement at the fixed-end of the specimen (Fig. 4a, d);
- 1 LVDT (nr. 6) placed under the hydraulic jack to measure the vertical displacement of the joint at the free-end of the cantilever (Fig. 4a, e).

The LVDTs were calibrated using a large micrometre over a range of ±6 mm. The core of the device is set as close as possible to the zero locations.

The applied force (F) is measured by a load cell (max load: 200kN).

In Figure 5 the overall view of the test set up including the retaining frame is shown.

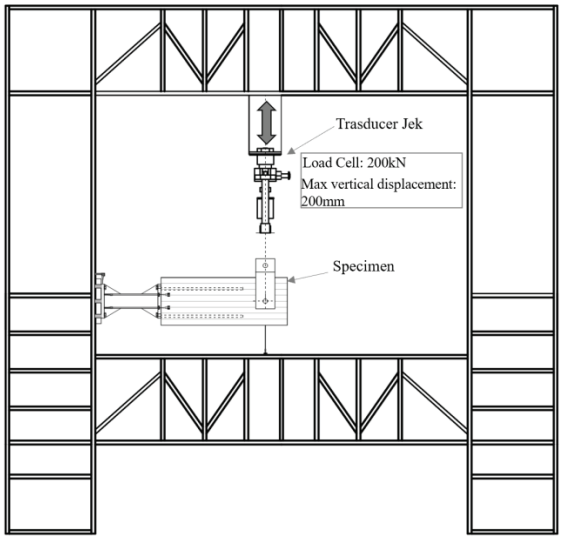

Figure 5: *Overall view of the test set up with the retaining frame.*

4 TEST PROCEDURE AND PERFORMANCE CURVES

The vertical load is applied under displacement control at a constant rate of 0.1mm/s, according to the European standard EN 12512 [15], in order to study the specimen response in elastic-plastic field. Therefore, considering the maximum stroke of the actuator of 200mm, the test end is achieved in about 30 minutes.

The test outputs are provided in terms of force-displacement (F-u) curve. Then, the bending moment-rotation (M-θ) curve is analytically obtained, evaluating the bending moment (M; Eq. 1) and the corresponding rotation (θ; Eq. 2) at the mid-section (M_L point) of the link, according to the following equations (Fig. 6):

$$M = F \cdot L \quad (1)$$

$$\theta = \theta_{Tot} - \theta_A - \theta_B \quad (2)$$

where L is the distance of the mid-section of the link M_L from the load point (L=1020mm); θ_{Tot} is the global rotation of the joint as respect to the retaining frame, θ_A is the rotation of the link left end-plate with respect to the retaining frame, θ_B is the rotation of the link right end-

https://doi.org/10.52202/069179-0288

plate with respect to the timber beam. In particular, the above defined rotations are calculated as it follows with reference to Figure 6:

$$\theta_A = \frac{\delta_{1,7} + \delta_{2,8}}{h_A} \quad (3)$$

$$\theta_B = \frac{\delta_{3,9} + \delta_{4,10}}{h_B} \quad (4)$$

$$\theta_{Tot} = \frac{u_{Tot}}{L_A} \quad (5)$$

where $\delta_{1,7}$ and $\delta_{2,8}$ are the horizontal displacements detected at point A section, evaluated as mean value between the displacements measured with the LVDTs nr. 1, 7 and 2, 8 and h_A is the distance between the LVDTs (Fig. 6b); $\delta_{3,9}$ and $\delta_{4,10}$ are the horizontal x-direction displacements detected at point B section, evaluated as mean value between the displacements measured with the LVDTs nr. 3, 9 and 4, 10 and h_B is the distance between the LVDTs (Fig. 6c); u_{Tot} is the total displacement in vertical z-direction, evaluated at the applied force (F) section by using the LVDT nr. 6 and L_A is the whole length of the joint.

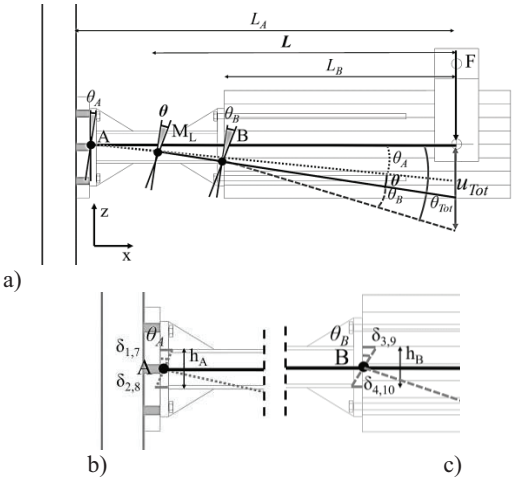

Figure 6: *a) Schematic deformation of the joint and relative rotations between the joint components; b) Rotation between link left end-plate and retaining frame; c) Rotation between link right end-plate and timber beam.*

5 MONOTONIC TEST

In Figure 7, the force-displacement (F-u) curves and the failure modes achieved through the experimental tests are presented. In particular, outputs are noticed at specific selected performance points, defined at the yielding of the steel link (P_Y), the collapse of the specimen (P_C) and a total displacement equal to 200mm (P_{200}), which corresponds to the maximum stroke of the loading actuator.

Both joints show a ductile behaviour with the plastic deformation of the link, achieving the formation of the plastic hinge. HE100A joint reached the maximum stroke of 200mm (coinciding with the end of the test) before the failure (P_C), while IPE100 joint failed (P_C) through the buckling of the link flange, before the achievement of the 200mm total displacement.

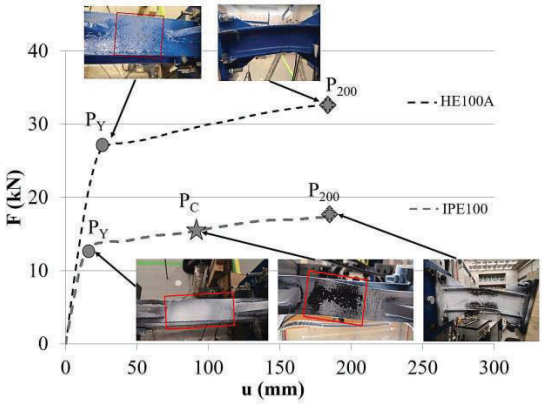

Joint	HE100A		IPE100	
Performance points	**F [kN]**	**u [mm]**	**F [kN]**	**u [mm]**
P_Y	27.11	17.73	12.89	14.96
P_C		-	15.40	97.32
P_{200}	32.71	184.97	17.81	184.97

Figure 7: *Experimental F-u curves of the joints; performance points: Y-yielding, C- collapse, 200-Actuator stroke.*

6 ANALYSIS OF RESULTS

The tests results are discussed in terms of initial stiffness $S_{j,ini}$ (eq. 1), plastic field stiffness $S_{j,pl}$ (eq. 2, 3) and resistance $F_{j,Y}$ at yielding point (P_Y), as well as ductility capacity D_j (eq. 4, 5), evaluated as it follow:

$$S_{j,ini} = \frac{M_{j,el}}{\theta_{j,el}} \quad (1)$$

$$S_{HE100A,pl} = \frac{M_{j,Rd,200}}{\theta_{j,pl,200}} \quad (2)$$

$$S_{IPE100,pl} = \frac{M_{j,Rd,C}}{\theta_{j,pl,C}} \quad (3)$$

$$D_{HE100A} = \frac{u_{200}}{u_Y} \quad (4)$$

$$D_{IPE100} = \frac{u_C}{u_Y} \quad (5)$$

where $M_{j,el}$ and $\theta_{j,el}$ correspond respectively to the elastic bending moment, not exceeding 2/3 $M_{j,Rd}$ ($M_{j,Rd}$ being the design bending strength of the j-joint, [16]), and the rotation at the elastic limit; $M_{j,Rd,C}$ and $\theta_{j,pl,C}$ correspond respectively to the design bending strength and the rotation of the IPE100 at collapse point (P_C); $M_{j,Rd,200}$ and $\theta_{j,pl,200}$ correspond respectively to the design bending strength and the rotation of the HE100A at 200mm vertical displacement (P_{200}); u_{200} is the displacement at P_{200} point, u_C is the displacement at P_C point and u_Y is the displacement at P_Y point.

In particular, HE100A and IPE100 joints performances are compared through the Capacity Ratios (CRs), defined in terms of initial stiffness $S_{j,ini}$ (CR-S_{ini}=$S_{IPE100,ini}$/$S_{HE100A,ini}$), plastic field stiffness $S_{j,pl}$ (CR-S_{pl}=$S_{IPE100,pl}$/$S_{HE100A,pl}$), yielding strength $F_{j,Y}$ (CR-F_Y=$F_{IPE100,Y}$/$F_{HE100A,Y}$) and ductility capacity D_j (CR-

$D_j=D_{IPE100}/D_{HE100A}$). The mechanical parameters are given in Table 1. Observing the experimental results, IPE100 joint shows lower initial and plastic field stiffnesses, strength and ductility, as respect to HE100A, with CR-S_{ini}=75%, CR-S_{pl}=85%, CR-F_Y=48%, CR-D=75%.

***Table 1**: Joints initial stiffness $S_{j,ini}$, plastic field stiffness $S_{j,pl}$, resistance F_j and ductility capacity D_j for study joints: preliminary numerical and experimental values.*

Joint	**HE100A**		**IPE100**	
Performaces	**Test**	**Num.**	**Test**	**Num.**
$S_{j,ini}$ [kN/rad]	1227	1546	936	1054
$S_{j,pl}$ [kN/rad]	38	16	28	17
$F_{j,Y}$ [kN]	27.11	26.50	12.89	11.61
D_j [-]	10.43	11.48	6.51	7.85

With regards to rotations, it has to be noticed that, in both joints, the maximum θ_B and θ_A rotations are negligible compared to the overall rotation θ_{Tot}, being θ_B/θ_{Tot} equal to 2.2% and 2.3% for HE100A and IPE100 respectively, θ_A/θ_{Tot} equal to 0.5% and 0.7% for HE100A and IPE100 respectively (Tab. 2). This also confirms the efficiency as rigid connections of the link end joints.

***Table 2**: Joints rotations θ_B, θ_A and θ_{Tot} in P_{200} and P_C points respectively for HE100A and IPE100.*

Joint	**HE100A**		**IPE100**	
Points	**P_{200}**		**P_C**	
	[rad]	**θ_i/θ_{Tot}** [%]	[rad]	**θ_i/θ_{Tot}** [%]
θ_B	0.004	2.2	0.002	2.3
θ_A	0.0009	0.5	0.0006	0.7
θ_{Tot}	0.18		0.084	

In Figure 8, the experimental force-displacement (F-u) and the analytically moment-rotation (M-θ) curves are given in comparison with the preliminary numerical ones [13]. In particular, further to the previously defined performance points (P_Y, P_C, P_{200}), on the numerical curve also the point, corresponding to the link full plasticization (P_{PN}), is evidenced.

It is apparent that the experimental and numerical curves are very close in the elastic field, while the post-elastic branches differs. This means that the preliminary model perfectly caught the elastic behaviour, while it has to be calibrated after the laboratory tests. This is also quantified through the Capacity Ratios (CRs) evaluated at the selected performance points (P_i, where i is Y, 200, C), in terms of strength $F_{j,i}$ (CR-$F_{j,i}=F_{j,n,i}/F_{j,t,i}$), displacement $u_{j,i}$ (CR-$u_{j,i}=u_{j,n,i}/u_{j,t,i}$), initial stiffness $S_{j,ini}$ (CR-$S_{j,ini}=S_{j,n,ini}/S_{j,t,ini}$), plastic field stiffness $S_{j,pl}$ (CR-$S_{j,pl}=S_{j,n,pl}/S_{j,t,pl}$) and ductility capacity D_j (CR-$D_j=D_{j,n}/D_{j,t}$; Tab. 3).

With regards to the collapse modes it is worth noticing that the preliminary numerical analysis of HE100A joint reached the failure, beyond the test limit of 200mm (P_{200t}), corresponding to the buckling of the link web (F_{Cn}=29.35kN; u_{Cn}=242mm). Besides the same collapse condition is evidenced for IPE100 in both preliminary numerical analysis and test, corresponding to the buckling of the link flange before P_{200}.

It is not possible to evaluate the collapse hierarchy of the joint sub-components through the experimental tests, however by superimposing the images deriving from the numerical analysis with the photos taken at the end of the test (at P_C for IPE100 and P_{200} for HE100A), a very good approximation of the ultimate deformed configuration of the joints is worth noticed (Fig. 9).

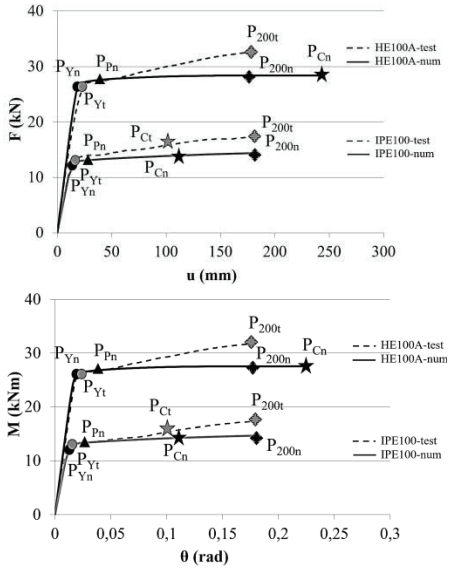

***Figure 8:** Experimental vs preliminary numerical F-u and M-θ curves of the joints; performance points: Y-yielding, C-collapse, 200-Actuator stroke.*

***Table 3**: Joints Capacity Ratios (CRs) in terms $F_{j,i}$, $u_{j,i}$, $S_{j,ini}$, $S_{j,pl}$, and $D_{j,i}$ in P_Y, P_{200} and P_C points for HE100A and IPE100.*

Joint	**HE100A**			**IPE100**		
[%]	**P_Y**	**P_{200}**	**P_C**	**P_Y**	**P_C**	**P_{200}**
Cr-F	98	87	/	90	81	91
Cr-u	98	108	/	89	108	108
CR-S_{ini}	126			114		
Cr-S_{pl}	43			59		
Cr-D	110			121		

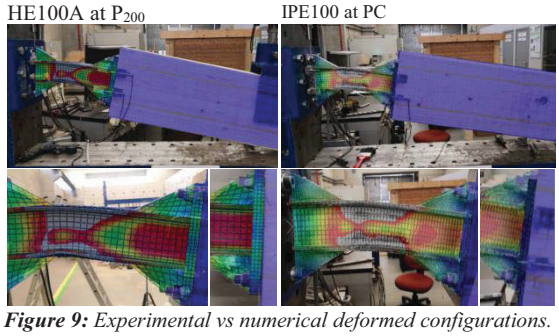

***Figure 9:** Experimental vs numerical deformed configurations.*

7 CONCLUSIVE REMARKS

The paper focuses on beam-to-column joints with dissipative steel link in the timber beam for seismic moment resistant heavy timber framed structures. In

https://doi.org/10.52202/069179-0288

particular, monotonic experimental tests on two joints are presented.

The HE100A and IPE100 joints structural performance was preliminary investigated through monotonic incremental non-linear analyses on refined FE models, examining the key parameters, such as strength, stiffness, rotation capacity and failure modes. Then, the mechanical behaviour of the joints was studied through the capacity curves, F-u and M-θ, obtained through the monotonic tests. The joints performance is evaluated at specific points, corresponding to the link yielding (P_Y), full plasticization of the link (P_P), ultimate strength (P_C) and strength at the actuator stroke equal to 200mm (P_{200}). Results showed that HE100A joint, as respect to IPE100, has higher initial stiffness, plastic field stiffness, strength and ductility. With regards to the collapse conditions, for HE100A joint, the 200mm stroke (P_{200}) occurs before the joint failure, while for IPE100 joint, the failure is achieved before, corresponding to the buckling of the link flange. For HE100A the collapse was attained through the preliminary numerical analysis, corresponding to the buckling of the link web.

Therefore, the experimental results are compared with those of the preliminary numerical analysis. The experimental and numerical curves are coincident in the elastic field, up to the yielding point, while the post-elastic branches are different, evidencing the need to opportunely calibrate the FE models, specially on the basis of the laboratory tests on the materials.

Definitely the tests have validated the theoretical and numerical predictions, confirming the formation of the plastic hinge in the link, which dissipates the energy through plastic deformation, avoiding brittle failures, as well as proving the efficiency of the system and of the proposed design criteria.

The work is in progress toward the development of seismic resistant dissipative timber structures, focusing on the dissipative device design, toward the calibration of the refined numerical model, the extension of both the numerical analyses and test campaigns, to evaluate the cyclic behavior and the dissipation capacity of the beam-to-column joint with steel link. At the same time, the global behavior of seismic resistant timber structure with dissipative links is going to be investigated.

ACKNOWLEDGEMENT

The research project DPC–ReLUIS 2019-2021 and 2022-2024 - WP13 Contribution to standards for timber structures, and the Department of Civil Engineering (DECivil) laboratory of the Minho University, in Guimaraes (Portugal) are acknowledged.

REFERENCES

[1] EN 1998-1: 2004: Eurocode 8: Design of structures for earthquake resistance – Part 1: General rules, seismic actions and rules for buildings (CEN: Comité Européen de Normalisation).

[2] Faggiano B., Iovane G.. First considerations on the design approach and criteria for seismic resistant moment resisting and bracings timber frames. In *World Conf. on Timber Engin.*, 2016. Paper ID1094.

[3] Humbert J., Lee S., Park J., Park M.. Moment resistance of post-and-beam joints with concealed metallic connectors. In *World Conference on Timber Engineering (WCTE)*, 2014.

[4] Komatsu K., Mori T., Kitamori A., Araki Y.. Evaluation on dynamic performance of glulam frame structure composed of slotted bolted connection system. In *World Conference on Timber Engineering*, (WCTE 2014).

[5] Nakatani M., Mori T., Komatsu K.. Performance of semirigid timber frame with Lag screw bolt connections: experimental, analytical, and numerical model results. In *International Journal of Advanced Structural Engineering* 7:387–403, 2015.

[6] Montuori R. and Sagarese V.. The use of steel RBS to increase ductility of wooden beams. In *Engineering Structures.* 169, 154-161. 2018.

[7] Montuori R.. The influence of gravity loads on the seismic design of RBS connections. *The Open Construction and Building Technology Journal*. Betham Open, 8, 248-261, 2014.

[8] Tomasi R., Zandonini R., Piazza M., Andreolli M.. Ductile end connections for glulam beams. In *Structural Engineering International*. 18; 290-296, 2008.

[9] Andreolli M., Piazza M., Tomasi R., Zandonin R.. Ductile moment-resistant steel-timber connections. In Structures and Buildings, 164, SB2, 65-78, 2011.

[10] Gohlich R., Erochko J., Woods J.E.. Experimental testing and numerical modelling of a heavy timber moment-resisting frame with ductile steel links. In *Earthquake Engineering & Structural Dynamics*. 47, 1460-1477, 2018.

[11] Yang H., Wang. C., Hu J., Tao H., Liu J., Tang L., Shi B.. Experimental static and seismic behaviour of glulam beam-to-column connection with screwed-in threaded rod joints. *BioResources* 16(3), 5272-5286, 2021.

[12] Iovane G., Faggiano B., Noviello C., Mazzolani F.M., Landolfo R., Faggiano B.. Beam-to-column joint with steel link for timber structures: system optimization through numerical investigations and design criteria. In *World Conference on Timber Engineering (WCTE),* 2020

[13] Iovane G., Faggiano B.. Timber beam-to-column joint with steel link: design and mechanical characterization through numerical investigation. *8th Int. Conference on Computational Methods in Structural Dynamics and Earthquake Engineering* (COMPDYN), vol. 1, 2359-2365, 2021.

[14] ABAQUS FEA 2022 - Abaqus/CAE, or “Complete Abaqus Environment”.

[15] EN 12512: 2001/A1: 2005: Timber Structures - Test methods - Cyclic testing of joints made with mechanical fasteners (CEN, French: Comité Européen de Normalisation).

[16] EN 1993: 2005: Eurocode 3: Design of steel structures. Part 1-8: Design of joints (CEN: Comité Européen de Normalisation).

World Conference on Timber Engineering Oslo 2023

MODELLING SEISMIC ISOLATION BEARING FOR WOOD BUILDINGS

Asif Iqbal[1], Angelo Aloisio[2] and Massimo Fragiacomo[3]

ABSTRACT: This paper discusses the details of modelling a type of seismic isolator, named RoGlider, suitable for wood buildings. An analytical model of the bearing and estimate the parameters of a classical Bouc-Wen model representative of this device is presented. RoGlider is found to be useful for seismic protection and the proposed model can represent the isolation system with sufficient accuracy.

KEYWORDS: Seismic Isolation, Bouc-Wen Model, Wood Buildings

1. INTRODUCTION

The RoGlider, shown in Figure 1, is a sliding bearing which includes an elastic restoring force [1,2]. The actual configuration is dependent on the details of the structure being isolated and the expected earthquake. It consists of two flat steel plates with a puck between the plates. The puck consists of alternating layers of rubber and sheet steel, similar to the arrangement used in elastomeric bearings and Lead Rubber Bearings. The sliding elements such as PTFE are mounted at the ends of the puck. The two rubber membranes are attached to the puck with each being joined to either the top or the bottom plates thereby making a sealed unit. When the top and bottom plates slide sideways with respect to each other diagonally opposing parts of the membrane undergo tension or compression. The tension components provide the restoring force between the plates.

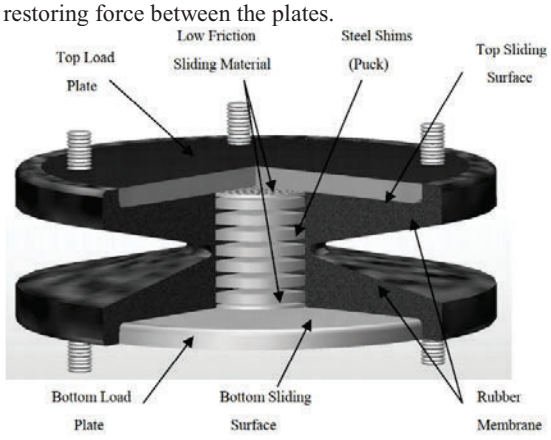

Figure 1: *Sectional view of RoGlider.*

With the special arrangement (Figure 3) and geometry (Figure 4), RoGlider is characterized by a lower lateral stiffness compared to classical elastomeric isolators. This feature enables the RoGlider to be used for isolating lightweight structures. The lower lateral stiffness guarantees the attainment of higher natural periods of vibration. Figure 2 shows a typical hysteresis plot.

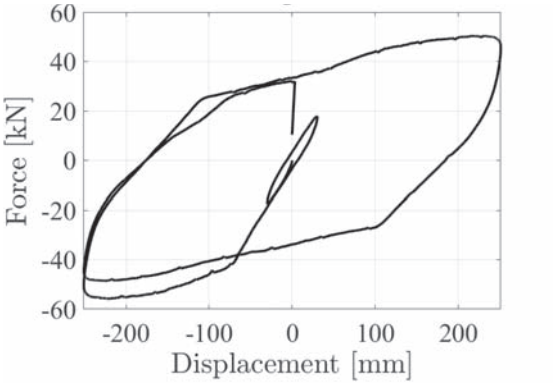

Figure 2*: Hysteresis of RoGlider*

2. ROGLIDER PROPERTIES

RoGlider bearings went through extensive testing by the developers and also during a research project at BRANZ in New Zealand [3]. Robinson et al. tested the bearing at their facility (Figure 4) under a range of vertical loads and displacement range [1]. It is visible that the bearings can carry significant vertical load at design-level (Figure 6) and large displacements (Figure 7). The force displacement plot (Figure 8) shows significant energy dissipation under design-level displacements. The energy dissipation is less under large displacements, but the loading cycles produce very stable loops (Figure 9).

[1] Asif Iqbal, University of Northern British Columbia, Canada, asif.iqbal@unbc.ca
[2] Angelo Aloisio, University of L'Aquila, Italy, angelo.aloisio1@univaq.it
[3] Massimo Fragiacomo, University of L'Aquila, Italy, massimo.fragiacomo@univaq.it

https://doi.org/10.52202/069179-0289

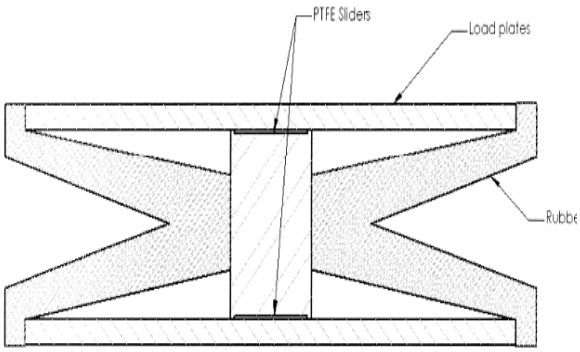

***Figure 3**: Schematic section of RoGlider*

***Figure 4**: Exterior view of RoGlider*

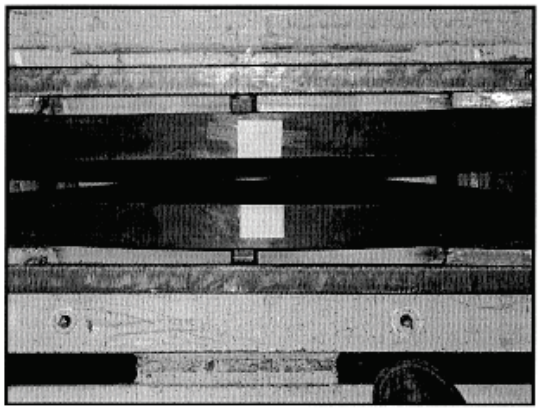

***Figure 5**: View of RoGlider with attachments during testing, under vertical load of 850 kN [1]*

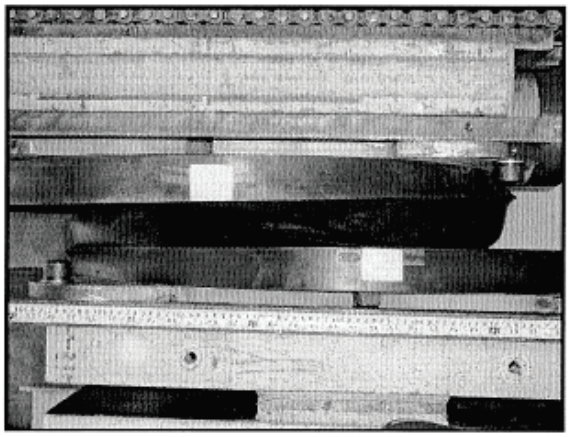

***Figure 6**: Deformed shape of RoGlider during testing, at 150 mm displacement and vertical load of 850 k N [1]*

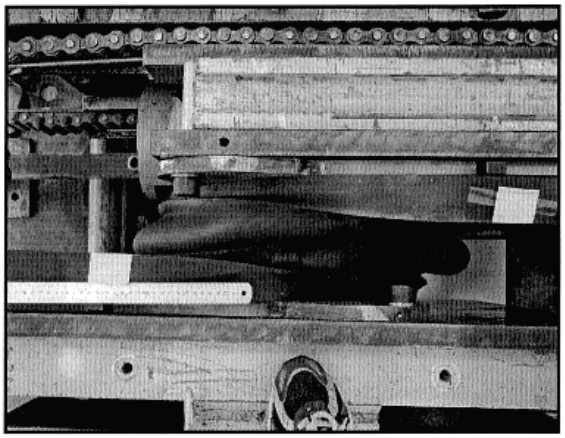

***Figure 7:** Deformed shape of RoGlider during testing, at 575 mm displacement and vertical load of 110 k N [1]*

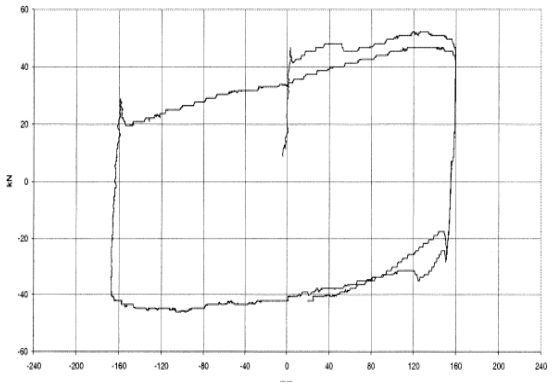

***Figure 8:** Force-displacement plot of RoGlider, under 850 kN vertical load [1]*

https://doi.org/10.52202/069179-0289

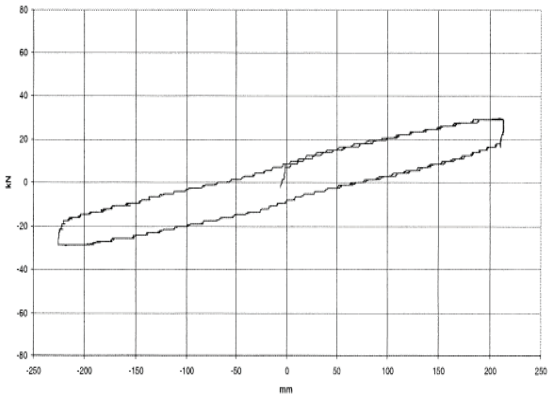

Figure 9: *Force-displacement plot of RoGlider, under 110 kN vertical load [1]*

The bearings also exhibit stable behaviour under sinusoidal loading cycles at slow (Figure 10) and high speeds (Figure 11). The coefficients of friction vary with speed (Figure 12) but the trend is consistent between slow and high speeds.

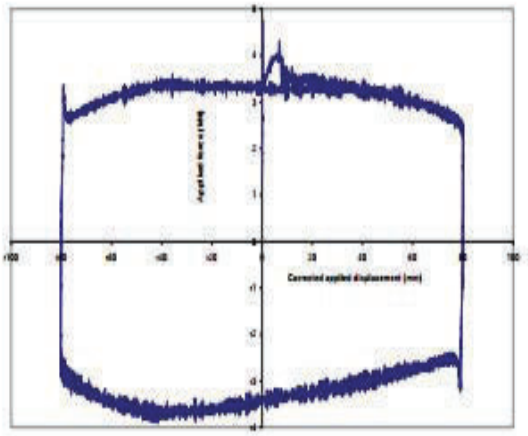

Figure 10: *Hysteresis loops of RoGlider, under sinusoidal displacement to 80 mm at 0.01 Hz [3]*

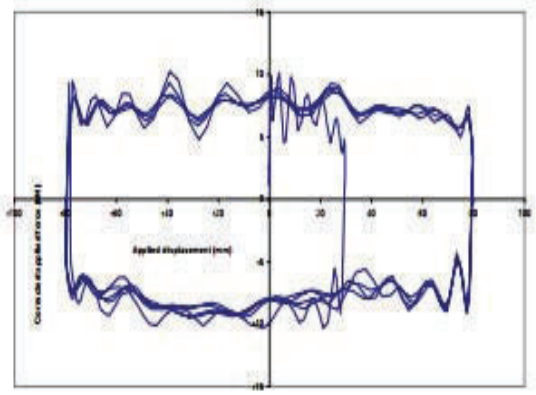

Figure 11: *Hysteresis loops of RoGlider, under sinusoidal displacement to 80 mm at 0.5 Hz [3]*

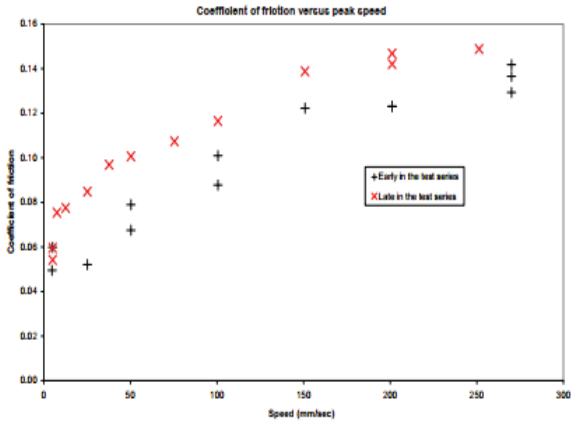

Figure 12: *Effective coefficient of friction of RoGlider [3]*

3. ROGLIDER APPLICATION

Figure 13: *Wanganui Hospital Building in New Zealand [2]*

RoGlider have been used to isolate a hospital building in Wanganui (Figure 13) in the North Island of New Zealand [2]. The bearings have been placed under the steel structure of the building (Figure 13). The load-displacement plots of the bearings used (Figure 14) again show very stable loops with significant energy dissipation capacity.

https://doi.org/10.52202/069179-0289

Figure 13: View of *Wanganui Hospital Building structure with RoGlider bearings [2]*

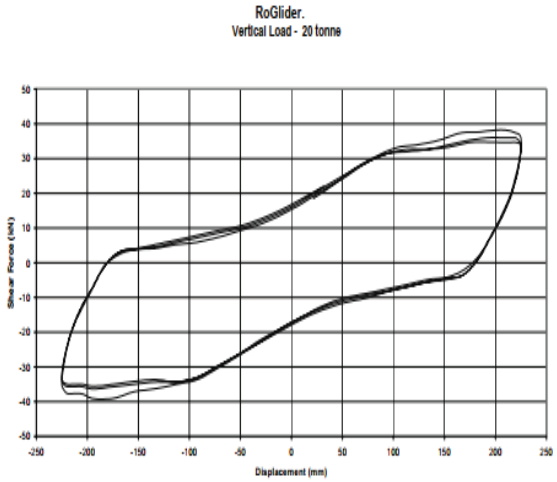

Figure 14: *Hysteresis loops of RoGlider, bearing used in Wanganui Hospital building [2]*

4. HYSTERESIS MODELLING

The authors describe the hysteresis curve of the RoGlider using a classical Bouc-Wen model. For a structural element described by a Bouc–Wen class model, the resisting force is written as

$$f_s(x, \dot{x}, z) = \alpha k_0 x + (1 - \alpha) k_0 z \qquad (1)$$

Where

fs	Resisting force
x	Displacement
x	Derivative of x with respect to time
z	Auxiliary variable representing inelasticity
α	Post- to-pre-yield stiffness ratio
k_0	Initial stiffness

The evolution of z is determined by an auxiliary ordinary differential equation, which can be written in the form

$$\dot{z} = \dot{x}[A - |z|^n \psi(x, \dot{x}, z)] \qquad (2)$$

Where

z	Derivative of z with respect to time;
A	Parameter controlling scale of hysteresis loops;
n	Sharpness parameter of hysteresis loops, n>0;
ψ	Other shape features of the hysteresis loop;

The ψ functions of the original Bouc–Wen model used in this paper is

$$\psi_{Bouc-Wen} = \gamma + \beta sgn(\dot{x}z) \qquad (3)$$

Where

$\psi_{Bouc-Wen}$ Shape parameter, $\gamma > 0$, $-\gamma < \beta < +\gamma$;

5. MODEL VALIDATION AND DETAILS

Comparison between the simulated and experimental data in terms of hysteresis curve, force-time and energy-time functions are shown in Figures 15, 16 and 17, respectively.

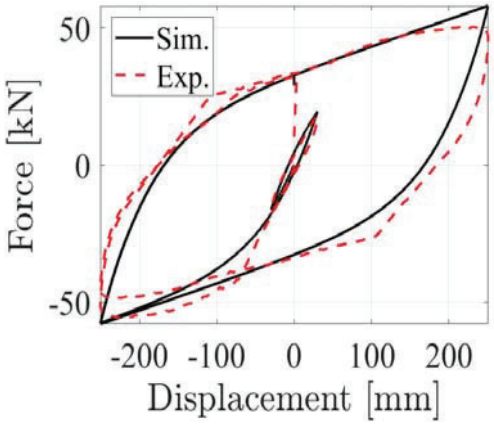

Figure 15: *Hysteresis comparison*

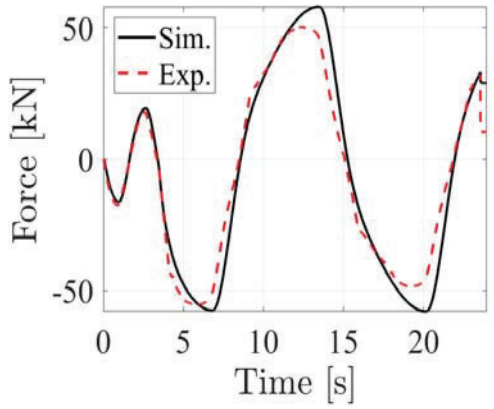

Figure 16: *Comparison of force vs. time*

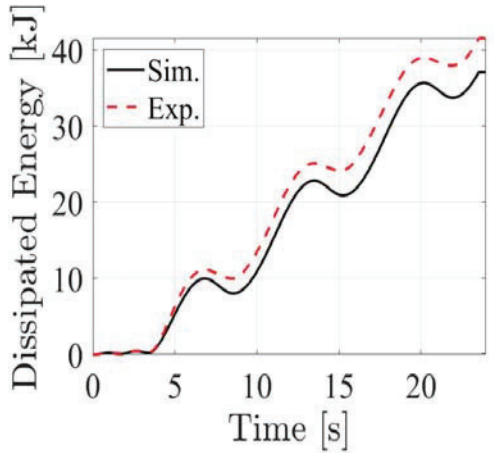

Figure 5: *Energy vs. time functions*

Hysteresis curve parameters in Figures 3, 4 and 5 estimated using Ordinary Least Square Operator [5,6] are:

Table 1: *Estimated classical Bouc-Wen model parameters*

Parameters	RoGlider
α	0.15
k_0	0.65
n	1.08
β	20.5
γ	0.1

6. RESULTS

The paper discusses the effect of variable mass on the gain spectra of a SDOF oscillator, whose restoring force is represented by the Bouc-Wen model in Figure 3. The gain spectra are defined as:

$$\mathcal{G}(T,\xi) = \frac{\max(|x_1(t)|}{\max(|x_2(t)|} \tag{4}$$

where $\mathcal{G}$ is the gain spectrum, ξ is the viscous damping ratio, $x_1(t)$ is the seismic response of a SDOF oscillator with restoring force described by the Bouc-Wen model, $x_1(t)$ seismic response of a viscoelastic SDOF system with damping ξ. If $\mathcal{G} < 1$, the use of the RoGlider is advantageous. The inelastic restoring force contributes to the equilibrium of a single-degree-of-freedom oscillator (SDOF), which is representative of the dynamic response of the RC frame. The analysis focuses on the behavior of a SDOF system neglecting all aspects related to the practical scenario of a full-size building. The equilibrium of a lumped mass above the frame yields the following ordinary differential equation (ODE) under earthquake excitation:

$$m\ddot{x} + f_t = -m\ddot{x}_g \tag{5}$$

where m is the mass equal to 20 t, x is the displacement, $\ddot{x}$ is the double derivative of x with respect to time, f_t is the resisting inelastic force, and $\ddot{x}_g$ is the ground acceleration. Fig.4 shows the comparison between the seismic response of a specific SDOF with mass equal to 20ton, under the El-Centro earthquake.

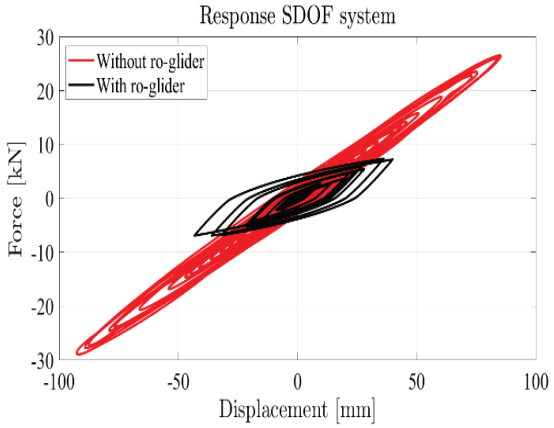

Figure 17: *Response of a SDOF system with mass M=20ton to the El Centro earthquake*

Figure 18 plots the inelastic gain spectra, defined in Eq.(4) estimated using earthquake records listed in Aloisio et al. [6].

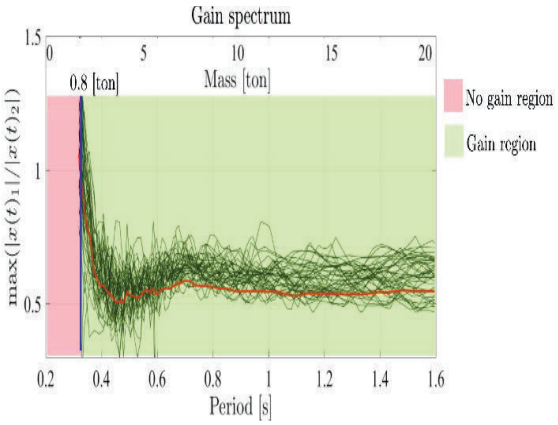

Figure 18: *Gain Spectra*

The averaged gain spectrum, in red, exhibits a peculiar shape. If the lumped mass is lower than 0.8 ton, the maximum displacement attained by the two systems with and without the Ro-glider are equal. This mass value corresponds to a natural period equal to 0.35s. There is a region of minimum between 0.4 and 0.6s, where the gain spectrum attains 0.5. For natural periods higher than 0.6s, the gain spectrum stabilizes at 0.55.

7. CONCLUSIONS

The proposed model promises to represent the isolation system with sufficient accuracy. It also demonstrates usefulness of RoGlider as a practical option for seismic design of lightweight structures. Further work on applicability and seismic performance of the system in multi-story timber buildings is currently underway.

REFERENCES

[1] Robinson, W. H., Gannon, C. R. and Meyer, J. The RoGlider – A sliding bearing with an elastic restoring force, *Bulletin of the New Zealand Society for Earthquake Engineering*, 39(1), 2006, 81-84.

[2] Robinson, W. H. and Gannon, C. R. The A seismic isolation of Wanganui hospital with RoGliders, Bulletin of the New Zealand Society for Earthquake Engineering, 41(4), 2008, 261-263.

[3] Thurston SJ. 2006. 'Base Isolation of Low Rise Light And Medium-Weight Buildings'. BRANZ *Study Report SR 156*. BRANZ Ltd, Judgeford, New Zealand.

[4] Thurston SJ. 'Base Isolation of Timber-Framed Buildings', Bulletin of the New Zealand Society for Earthquake Engineering. Vol. 40, No. 4, December 2007.

[5] Aloisio, A., Alaggio, R., Köhler, J., and Fragiacomo, M. Extension of generalized bouc-wen hysteresis

https://doi.org/10.52202/069179-0289

modeling of wood joints and structural systems. *Journal of Engineering Mechanics*, 2020, 146(3):04020001.

[6] Aloisio, A., Boggian, F., Tomasi, R., and Fragiacomo, M. (2021). Reliability-based assessment of ltf and clt shear walls under in-plane seismic loading using a modified bouc-wen hysteresis model. ASCE-ASME Journal of Risk and Uncertainty in Engineering Systems, Part A: Civil Engineering, 7(4):04021065.

World Conference on Timber Engineering Oslo 2023

EXPERIMENTAL MONOTONIC AND CYCLIC TESTING ON GLULAM BEAM-TO-COLUMN CONNECTIONS

Erica C. Fischer[1], Haley Madland[2], Sujit Bhandari[3], Arijit Sinha[4]

ABSTRACT: During seismic events, mass timber gravity connections must be able to accommodate the induced lateral deformations while still maintaining their load bearing capacity. Large-scale experimental testing can demonstrate and provide data for different connection configurations and numerical simulations can further inform the behaviour of these connections under lateral demands. However, there is a lack of experimental testing on glue laminated (glulam) beam-to-column connections, which presents a lack of data available for benchmarking numerical modelling. This paper will summarize a comprehensive large-scale testing regime performed at Oregon State University on five glulam beam-to-column connections, three custom designed connections and two pre-engineered connections. Each connection was tested under both monotonic and cyclic loading demands and the data from one of the connection tests was used to develop preliminary numerical modelling techniques for glulam beam-to-column connections. The tests demonstrated that all of the connections were able to be tested to 7.2% drift in the monotonic test and 4% drift in the cyclic test without losing load bearing capacity. The experimental testing regime developed data on maximum force demands in the connections, connection rotations, and connection stiffnesses that were used to characterize the connections on a scale of pinned to fixed connections.

KEYWORDS: Mass timber, Beam-to-column connection, Deformation compatibility, Monotonic, Cyclic

1 INTRODUCTION

Gravity beam-to-column connections in a building are designed to transfer shear forces, to be capable of rotation, and to have some small resistance to lateral forces. During a seismic event, where lateral forces are applied to a building, the entire building will also be subjected to deformation demands. Because of this, every member in the structure, including the gravity connections, must be capable of deforming along with the rest of the structure. Loss of load carrying capacity of gravity connections can occur when the connection components do not have sufficient ductility or strength to deform with the remainder of the building under lateral demands. This could potentially have cascading effects leading to a partial or complete collapse of the structure itself. Therefore, it is extremely important that the ductile behaviour of gravity connections under lateral loading is understood and promoted in design. This behaviour is referred to as deformation compatibility.

To better understand the deformation compatibility behaviour of beam-to-column connections, they are tested under monotonic and cyclic lateral loading. The experimental data from these tests informs connection characteristics such as the force-deformation (F-δ) and moment-rotation (M-θ) relationships of the connection. However, there is minimal research on deformation compatibility behaviour glulam beam-to-column connections. Because of this, the deformation compatibility behaviour of glulam beam-to-column connections is not well understood.

Glulam beam-to-column connections typically fall into one of two categories: custom designed connections or pre-engineered connections. For custom design connections, the responsibility of designing the connection is placed on the engineer of record. However, pre-engineered connections are proprietary connections that have been designed, tested, and rated for certain loading by a supplier. This means that once the required capacity of a connection has been determined by the engineer, a pre-engineered connection can be selected using design aids developed by the supplier of the connection. Therefore, while custom connections can be specifically designed to meet the necessary capacity requirements most efficiently, more time spent designing is required of the engineer. Conversely, pre-engineered connections can reduce the design time for the engineer,

[1] Assistant Professor, Oregon State University, School of Civil and Construction Engineering, Corvallis, OR, erica.fischer@oregonstate.edu
[2] Graduate Research Assistant, Oregon State University, School of Civil and Construction Engineering, Corvallis, OR< madlanha@oregonstate.edu
[3] Post-doctoral researcher, Oregon State University, School of Civil and Construction Engineering, Corvallis, OR, sujit.bhandari@oregonstate.edu
[4] Arijit Sinha, Associate Professor, Oregon State University Dept. of Wood Science & Engineering, Corvallis OR, arijit.sinha@oregonstate.edu

https://doi.org/10.52202/069179-0290

but limited options may force the engineer to use an over-designed connection.

The design of custom glulam beam-to-column connections is prescribed by relevant standards, such as ASCE 7-16 [1] and the National Design Specification for Wood [2]. The required lateral capacity of a gravity connection is defined in Section 1.4 of ASCE 7-16 as no less than 5% of the supported members weight, and no less than 5% of the reaction imposed on the supporting member due to the unfactored dead and live loads [1]. Although gravity connections are not intended to resist large lateral forces, these integrity provisions in Section 1.4 ensure that there is some connection between members capable of withstanding a minimum prescribed lateral force. However, although custom connections are designed for this lateral force there is no correlation between this lateral force demand and the deformations or rotations of the connection. Therefore, the behaviour of connections exposed to large deformations is not addressed.

To demonstrate the capacity of pre-engineered connections and provide design aids to the engineer for choosing pre-engineered connections, suppliers must perform experimental testing [3] to establish allowable loads in the connection. This testing prescribes how connection characteristics such as the limiting strength and deflection should be determined but does not address the deformation compatibility behaviour of the connection. Testing such as this creates substantial barriers to the development of pre-engineered connections because of the large time and financial investments that must be spent to perform experimental testing.

The research presented and discussed in this paper serves to develop a fundamental understanding of the behaviour of glulam beam-to-column connections exposed to lateral monotonic and cyclic loading. Monotonic and quasi-static cyclic testing of both custom and pre-engineered glulam beam-to-column connections involving combined lateral and gravity loading were performed, from which quantitative data was collected and qualitative observations were made. From the experimentally collected data, the force-displacement (F-δ) and the moment-rotation (M-θ) relationships were compared between connections. Connection characteristics such as initial and secant stiffness and energy dissipation were calculated and compared across custom and pre-engineered connections. The data developed from the experimental testing regime was used to develop and benchmark a finite element method model and explore numerical modelling methods for glulam beam-to-column connections. Specifically, the objectives of this research are to: (1) quantify the deformation compatibility behaviour of glulam beam-to-column connections under lateral loading demands, (2) compare the deformation compatibility behaviour of custom and pre-engineered beam-to-column connections, and (3) explore numerical modelling methodologies for simulating glulam beam-to-column connections under lateral demands.

2 MATERIALS AND METHODS

2.1 TESTING SETUP

The testing setup (Figure 1) consisted of a 3.66 meter tall 24F-V4 glulam Douglas Fir (DF) column, connected at its base to a pin connection. The beam, a 24F-V4 DF glulam, extended approximately 4.27 meters from the face of the column, at mid-height in all connection types. The beam was 311 mm (W) x 610 mm (D). The column width was 311 mm in all connections, but depth varied on connection type. The end of the beam was supported by a roller support. A 1.2 meter wide, 4.27 meter long, and 175 mm thick SPF CLT (5-ply) deck was connected to the top of the beam. A hydraulic ram applied a constant gravity load throughout the tests.

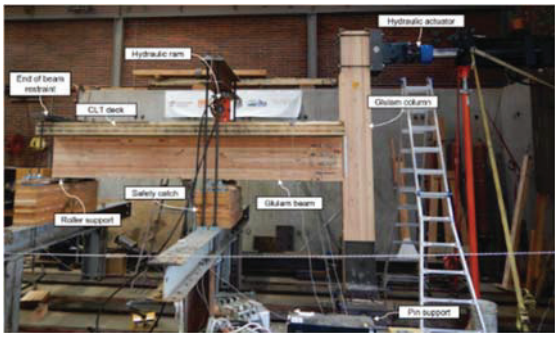

Figure 1: *Testing setup*

2.2 SPECIMEN DESCRIPTIONS

Five connections were investigated. Three connections were designed at Oregon State University per relevant standards [1, 2] and two connections were pre-engineered connections, designed by MTC Solutions. Specimen designations include the connection number, a shortened descriptor of the connection, and loading type (M for monotonic and Cyc for cyclic). For example, C1-KP-Cyc1 refers to connection 1 (C1), the connection uses a knife plate (KP), and the first cyclic test performed (Cyc1) on that connection type. For brevity the connections are referred to only by their designation. Connection C1-KP was a bracketed knife plate connection (Figure 2a). Connections C2-N and C3-N2 were bearing connections where the beam was inserted into a notched column (Figures 2b and 2c). Connection C4-MEG was a MEGANT 450x150x50 concealed beam hanger (Figure 2d), and connection C5-MTCP was a prototype connection designed by MTC (Figure 2e). Both MTC connections involved two interlocking aluminium plates, one screwed to the beam, and one to the column. A more comprehensive description of the connections is provided in [4, 5].

https://doi.org/10.52202/069179-0290

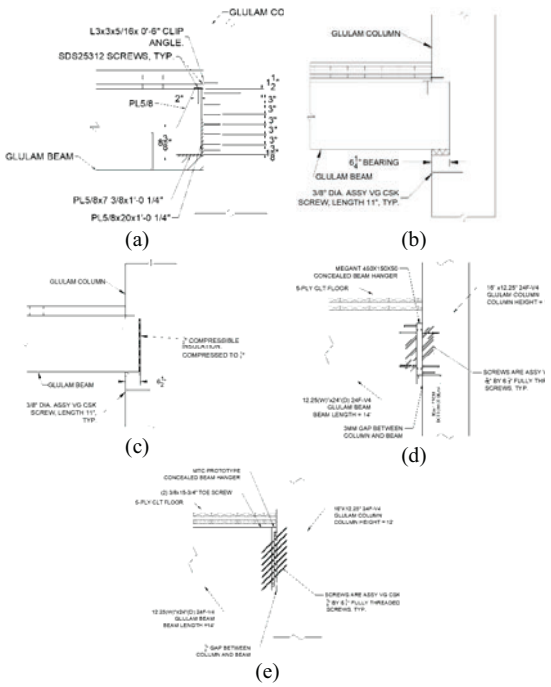

Figure 2: *Glulam beam-to-column connections*

2.3 LOADING PROTOCOL

For monotonic tests, displacement was applied through a hydraulic actuator at a rate of 0.51 mm/second to a target drift of 7.2%. The abbreviated CUREE basic loading history [6] with a target reference deformation of 1.9% drift and maximum displacement of 3.8% drift was used for the cyclic tests (Figure 3). The cyclic test began at a rate of 0.25 mm/second and increased to 0.64 mm/second after the cycle with the reference deformation. The cyclic loading protocol was altered for connections C4-MEG-Cyc2, C5-MTCP-Cyc1, and C5-MTCP-Cyc2, such that the cycle of maximum displacement was increased to 4% drift (from 3.8%), and the following trailing cycle was increased to 75% of the 4% drift cycle.

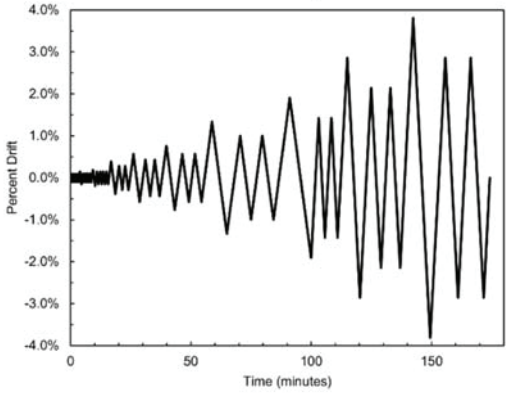

Figure 3: *Cyclic loading protocol per CUREE [6]*

The design shear demands for connections C1-KP, C2-N, and C3-N2 were calculated using an archetype office building with glulam beams spaced at 3.66 m, columns spaced at 8.53 m, and a live load of 2.39 kPa [1]. The design lateral demand were calculated per Section 1.4 of ASCE 7-16 [1]. To resist this lateral demand, and to have a mechanical connection between the glulam beam and column, each of these connections used an L3x3x5/16x152 mm section connected to the beam and column with two SDS25312 screws each. To install this clip angle on the top of the beam, a small portion of the CLT was chipped out to not conflict with the clip angle. The design shear demands for connections C4-MEG-M and C5-MTCP-M were prescribed by the supplier, MTC Solutions. Additional information on these demands can be found in [4, 5]. A summary of these demands and capacities is shown in Table 1.

Table 1: *Summary of gravity and lateral loading demands on connections*

Connection designation	Design shear demand [kN]	Design lateral capacity (demand) [kN]
C1-KP	49.1	6.09 (2.4)
C2-N	49.3	
C3-N2	49.3	
C4-MEG	98	14.5
C5-MTCP	179	17.3

2.4 INSTRUMENTATION LAYOUT

For both the monotonic and cyclic testing, seven linear variable differential transformers (LVDTs) and three load cells were utilized to measure the displacement and calculate the behaviour of the connections (Figure 4). In addition, the hydraulic actuator head displacement and a string potentiometer were utilized to measure the movement of the column. These measurements were used to calculate story drift throughout the test. LVDTs #1 – 4 were utilized to calculate the rotation of the connection assuming rigid body rotation of the column. These connection rotations were then compared with the base connection rotations calculated using LVDTs #5 and #6 to confirm the assumption of rigid body rotation. LVDTs #5 and #6 measured vertical displacements throughout the duration of the test and were centred on the column such that the recorded data could be used in combination with the known distance between the two LVDTs to calculate the column base rotation. Lastly, LVDT #7 was used to measure the differential movement between the top of the CLT and the column itself.

The load cells under the beam end, the ram, and the column base were utilized to calculate the shear in the connection throughout the test (Table 1). Connection moment was calculated throughout the test by multiplying the measured actuator force by the distance between the actuator force and the mid-height of the beam.

https://doi.org/10.52202/069179-0290

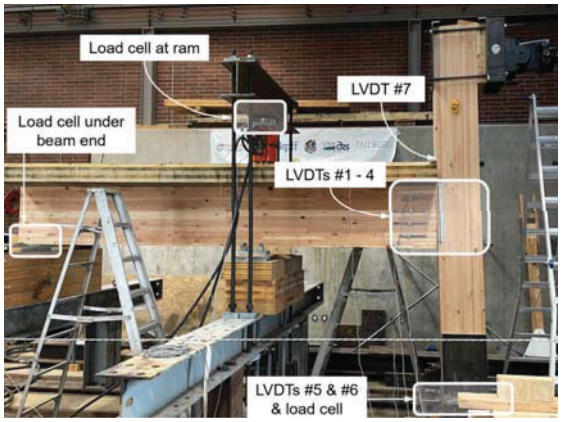

Figure 4: *Instrumentation layout for connection tests*

2.5 NUMERICAL MODELING METHODOLOGY

A three-dimensional finite element method (FEM) model of C2-N-M was developed in the commercially available software, Abaqus CAE, to explore the methodology for simulating glulam beam-to-column connections and to further understand the experimental test. The dimensions of the glulam beam, column, and CLT deck matched those tested in the laboratory at Oregon State University. An additional part was added to the base of the column such that the point of rotation for the column base matched that experimentally tested. Steel material properties were applied to this part to limit deformations. In addition, rather than applying boundary conditions to the beam end directly, an end of beam support was simulated to explore if friction contributed to the stiffness of the connection. Deformations were applied through a displacement-controlled loading protocol at the same rate as described in Section 2.3 at where the centroid of the actuator was located. The FEM model is shown in Figure 5.

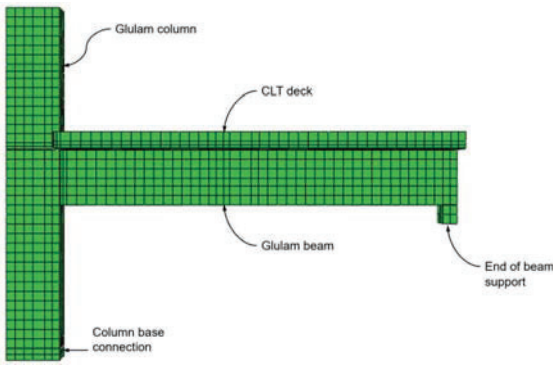

Figure 5: *FEM model of C2-N-M*

The column base was restrained from rotation in the out-of-plane direction and movement in all directions, but allowed to rotate about the base. The beam end was restrained from vertical displacement and rotation but was allowed to move horizontally.

As an anisotropic material, wood's stiffness and strength properties vary in different directions. Usually, the property of wood is defined in three directions: longitudinal (L), radial (R), and tangential (T). The strength and stiffness properties are typically higher in the longitudinal direction compared to radial and tangential directions. The stress-strain relationship for wood is typically linear until brittle failure for tension and shear loading in all directions while the stress-strain relationship is typically nonlinear and ductile in compression. For the FEM model described within this paper, wood has been modelled as orthotropic material with elastic-perfectly plastic behaviour [7, 8]. The stiffness properties for 24F-V4 DF glulam are from NDS and Wood Handbook [2] while the properties for SPF E1 CLT are taken from PRG 320 [9].

The coefficient of friction between the glulam column and beam was assumed to be 0.5 and the coefficient of friction between the glulam beam end and end support was varied to explore the degree of "frictionless" the authors were able to attain.

3 EXPERIMENTAL RESULTS

3.1 MONOTONIC TESTING

The yield load, yield displacement, and initial stiffness were calculated per EN12512 [10] and are summarized in Table 2. Specimen C2-N-M was the only specimen to have post-peak behaviour during monotonic testing. The remainder of the specimens reached maximum load (F_{max}) at maximum displacement.

Specimens C1-KP-M and C2-N-M had the lowest of the F_{max} with F_{max} increasing by 260% between C2-N and C3-N2 connections. The addition of the compressible insulation increased the capacity of the connection. The pre-engineered connections had larger F_{max} than the custom connections, even with the application of larger shear demands throughout the test.

Table 2: *Calculated properties for connections under monotonic loading*

Connection designation	Max. load [kN]	Yield load [kN]	Yield displ. [mm]	Initial stiffness [N/mm]
C1-KP	8.72	4.84	10.9	446
C2-N	11.97	8.87	15	595
C3-N2	21.42	18.46	28.4	649
C4-MEG	29.17	15.82	33.8	467
C5-MTCP	36.48	25.16	27.7	913

A small yield displacement (d_y) can indicate less ductility within the connection whereas a larger d_y, particularly coupled with a larger yield force (F_y) can indicate more ductility within the connection. In addition, higher values of initial stiffness can potentially indicate that the connection has more rotational rigidity. This type of behaviour is more evident in the initial stiffness

https://doi.org/10.52202/069179-0290

calculations where C4-MEG connection has lower initial stiffness than some of the custom connections (C2-N and C3-N2). C5-MTCP-M had the largest initial stiffness, 105% greater than the initial stiffness of specimen C1-KP-M. Connections C3-N2-M, C4-MEG-M, and C5-MTCP-M all had considerably larger d_y values than C1-KP-M and C2-N-M, ranging between 28 – 34 mm.

The design-level drift demand for buildings is 2% drift [1]. The actuator force at a lateral displacement corresponding to 2% drift for each test was compared to the design lateral capacity for each connection. For every connection, the actuator force exceeded the design lateral capacity at a drift of 2%. Table 3 summarizes the ratio of the actuator force at 2% drift ($P_{2\%}$) to the design lateral capacity of connection (P_n). However, failure of the connections (loss of load carrying capacity) was not observed during any of the tests. Therefore, although the lateral capacity of the connection was exceeded, force transfer continued through the connection for the duration of the tests.

Table 3: *Ratio of actuator force at 2% drift to design lateral capacity of tested connections*

Connection designation	$\frac{P_{2\%}}{P_n}$
C1-KP	1.13
C2-N	1.56
C3-N2	3.54
C4-MEG	1.22
C5-MTCP	1.79

During monotonic testing of the connections, screw fracture occurred in the C4-MEG connection, and fracture of the column connection plate occurred in the C5-MTCP connection. In the C2-N and C3-N2 connections, withdrawal of the screws connecting the clip angle to the column was observed.

3.2 CYCLIC TESTING

Backbone curves of all cyclically tested specimens, constructed from the peak actuator force and corresponding story drift in each primary cycle, are plotted in Figure 6. Connections C2-N and C3-N2 had similar forces during pulling cycles, but C3-N2 connections had substantially larger forces during pushing cycles, indicating greater capacity. Overall, custom connections generally had lower actuator forces than pre-engineered connections.

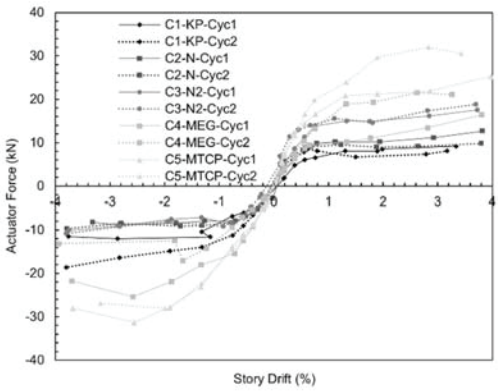

Figure 6: *Backbone curves of cyclic tests*

In Figure 7, the connection moment-rotation relationship is plotted for all cyclically tested specimens, with backbone curves (shown in black) constructed from peak connection moments and corresponding rotations in each primary cycle. The same trends were also observed for actuator forces due to the nature of how connection moments were calculated. As such, pre-engineered connections generally demonstrated larger connection moments than custom connections. The large drop in moment during the pushing cycle of the largest amplitude primary cycle for C5-MTCP-Cyc2 corresponds to the fracture of the column connection plate pocket (Figure 7).

The secant stiffness for each primary cycle was calculated for each connection, similar to previous research [11, 12], and plotted against connection rotation. These plots (Figure 8) show the calculated secant stiffness of the specimens decreases throughout the test. The secant stiffness is the ratio of the summation of the absolute value of the maximum ($+M_i$) and the minimum ($-M_i$) connection moment attained during a primary cycle to the summation of the absolute value of the rotation that corresponds to $+M_i$ ($+\Delta_i$) and the absolute value of the rotation that corresponds to $-M_i$, ($-\Delta_i$). The secant stiffness degraded with increasing connection rotation for each specimen. The secant stiffness decreased 74 – 91% from the first to the last primary cycle. The decrease of secant stiffness can indicate damage accumulating in a connection. While damage is expected, rapid decreases in secant stiffness indicate more brittle behaviour while gently decreasing slopes indicate more ductile behaviour. Although lateral force demands on connections are lower in early primary cycles, it is in these early loading cycles that the greatest stiffness degradation occurred. Greater secant stiffness indicated greater rotational rigidity in the connection as a larger force, or moment, is required to achieve the same connection rotation.

https://doi.org/10.52202/069179-0290

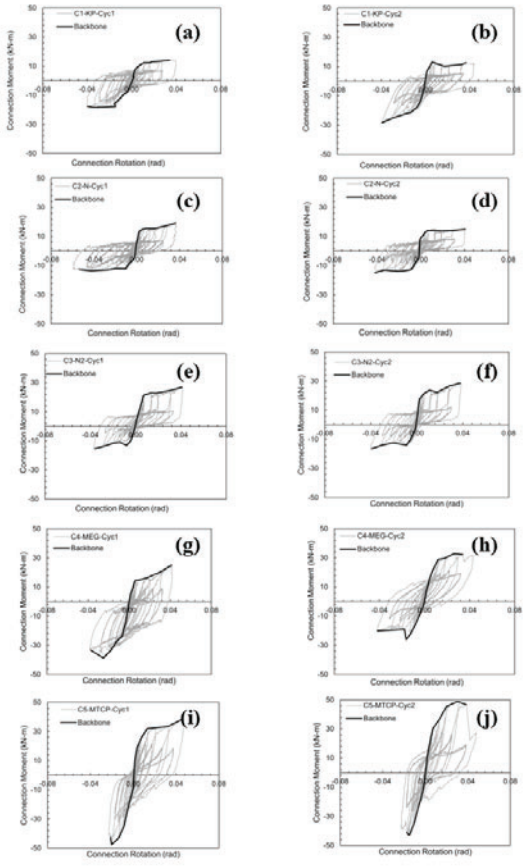

Figure 7: *Connection moment rotation relationship for cyclic tests (a) C1-KP-Cyc1, (b) C1-KP-Cyc2, (c) C2-N-Cyc1, (d) C2-N-Cyc2, (e) C3-N2-Cyc1, (f) C3-N2-Cyc2, (g) C4-MEG-Cyc1, (h) C4-MEG-Cyc2, (i) C5-MTCP-Cyc1, (j) C5-MTCP-Cyc2*

An increase in secant stiffness was observed between the first (0.075△) and second primary cycles (0.1△) except for C1-KP-Cyc2, C3-N2-Cyc1, C4-MEG-Cyc1, and C4-MEG-Cyc2. After the 0.1△ primary cycle, as damage accumulated, specimens demonstrated a non-linear decrease in secant stiffness from one consecutive primary cycle to the next. The largest rate of decreasing secant stiffness occurred between the 0.1△ and 0.2△ primary cycles except for connections C1-KP and C4-MEG. These specimens had the largest rate of decreasing secant stiffness either between primary cycles 0.075△ and 0.1△ (C1-KP-Cyc2, C4-MEG-Cyc1, and C4-MEG-Cyc2), or primary cycles 0.2△ and 0.3△ (C1-KP-Cyc1). Both C2-N specimens exhibited the largest percent degradation of secant stiffness from the first to the last primary cycle (91% in each case). Pre-engineered connections had the largest secant stiffnesses, displaying more rigidity than custom connections. However, C4-MEG specimens had lower rates of decreasing secant stiffness than the C5-MTCP specimens, indicating more ductile behaviour.

To compare the per-cycle energy dissipated, equivalent viscous damping ratio (EVDR) was used. This ratio is the energy enclosed in the moment-rotation hysteretic loop (Figure 7) divided by the corresponding energy that a linear system undergoing the same maximum rotation and corresponding moment would have dissipated. This ratio is then divided by 2π. A higher EVDR indicates that the connection has better energy dissipation. Between the 0.075Δ and 0.1Δ primary cycles, specimens C2-N-Cyc1, C2-N-Cyc2, and C5-MTCP-Cyc1 had large increases (between 54-203%) in EVDR while all other connections tested exhibited either much smaller increases or even decreases in EVDR. These sharp increases indicate damage occurring within the connection due to energy being dissipated. All of the C2-N and C3-N2 connections tested exhibited a small peak in EVDR during the 0.7Δ primary cycle (1.33% drift). During these cycles, the authors observed screw withdrawal of C2-N-Cyc1, and deformation of the clip angle during testing of C2-N-Cyc2. The EVDR of the custom connections either plateaued or decreased between the final primary cycles (1.5Δ to 2.0Δ); however, the EVDR of the pre-engineered connections increased with increasing connection rotation. This behaviour indicates that pre-engineered connections exhibited improved energy dissipation compared to custom connections, with larger total energy dissipation, and increasing EVDR values throughout testing.

4 NUMERICAL MODELING RESULTS

The authors compared the results from the FEM model with the experimental data for only C2-N-M testing to explore modelling methodologies for glulam beam-to-column connections. The authors found that the numerical model and the experimental data had good agreement for drift levels less than 1.4% drift (Figure 8). The comparison of energy differential between the experimental data and the FEM model was less than 20% and reduced substantially throughout testing. The results shown in Figure 8 used a coefficient of friction of 0.1 between the beam end and beam end support. The difference in the experimental data and the numerical modelling resides in the material model. While the behaviour of the FEM model and experimental data at maximum drift look similar (Figure 9), there is crushing of the glulam beam at the top of the connection pocket. The nature of the material model that was utilized within the FEM model described in this paper did not implement simulating crushing of the glulam.

https://doi.org/10.52202/069179-0290

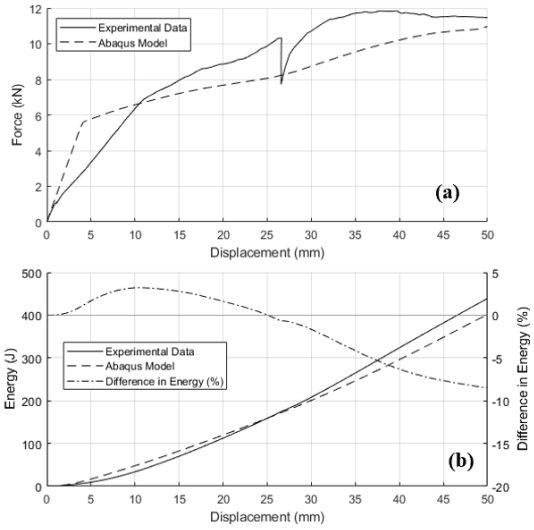

Figure 8: *Comparison of experimental test data to FEM model (a) force-displacement comparison and (b) quantifying energy differences between experimental data and FEM model*

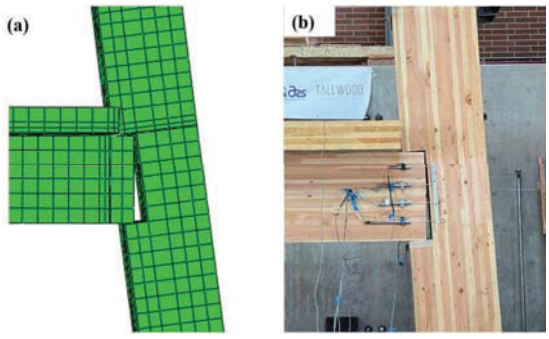

Figure 9: *Comparison of FEM model connection behaviour and experimental test at maximum drift (7.2%)*

Previous researchers have tried to implement damage and crushing material models into FEM simulations to simulate crushing of timber. However, many of these simulation techniques requires the researcher to know where localized crushing will occur prior to the simulation and therefore are limited for predictive modelling of untested connections. Hill yield criterion, sometimes with modifications, has been used to simulate the post-peak behaviour of wood for modelling of timber connections [13 -16]. To simulate the crushing around the steel members in connections, a so-called "foundation" modelling approach based on the theory of a beam on a nonlinear foundation has been used [15, 17, 18]. In these simulations, a material model with lower strength and stiffness was applied where localized crushing was expected. Crushable foam material model has also been used to simulate the crushing of wood in numerical models [19]. While this model simulated crushing at the bearing surfaces and the numerical model provided comparable results to the experiment, this isotropic material model doesn't consider the orthotropic behaviour of wood.

User subroutines incorporating different behaviour of wood have also been used in numerical modelling. Modified Hashin-Hill yield criterion implemented in a user subroutine has been used to model a bolted glulam beam-to-column connection. The model was able to simulate the cracking of wood similar to that seen in the experiment [13]. A more sophisticated constitutive model combining a number of sub-models, including orthotropic elasticity, Yamada-Sun failure criteria, softening, and hardening, was incorporated into a user subroutine for Abaqus [20]. The behaviour of wood in compression was modelled using strain-based damage evolution, plastic-flow, and hardening law. This model was able to reasonably simulate the mechanical as well as thermal behaviour of wood in bending and connections; however, creates a large burden on the researcher to write the subroutine and validate the subroutine against experimental data prior to predictive modelling.

5 CONCLUSIONS

Seismic events can create both force and deformation demands on a building. Beam-to-column connections must be capable of deforming with the rest of the structure during these events while maintaining load-carrying capacity. This behaviour is referred to as deformation compatibility and can be quantified through experimental testing. Because of the novelty of mass timber as a structural material, very limited experimental data has been produced on the deformation compatibility behaviour of glulam beam-to-column connections, therefore this behaviour is not yet well understood. To meet this demand of experimental data, five different connection designs were investigated. Three were custom connections (C1-KP, C2-N, and C3-N2), and two were pre-engineered connections (C4-MEG and C5-MTCP).

Large scale monotonic tests were performed on connections to a target deformation of 7.2% drift. Larger lateral forces were present in connection C3-N2 than C2-N, indicating the addition of compressible insulation increased capacity in the connection. Connection C5-MTCP had the largest initial stiffness and secant stiffness, while C4-MEG had the had the second lowest initial stiffness, and the largest yield displacement, indicating more ductile behaviour.

In cyclic tests, the cycle of maximum displacement corresponded to a target story drift between 3.81 - 4.0%. The hysteretic force-displacement and moment-rotation behaviour of the connections were analysed, and initial stiffness, secant stiffness, and energy dissipation of the connections was compared. Pre-engineered connections had larger total energy dissipation when compared to the custom connections. The EVDR of pre-engineered connections generally increased throughout testing, while custom connections showed a decrease or plateau of

https://doi.org/10.52202/069179-0290

EVDR in the final primary cycles. As damage accumulated, all specimens experienced a degradation of secant stiffness throughout testing. By the final primary cycle of the cyclic testing protocol, all pre-engineered connections had the largest remaining secant stiffness, however, connection C4-MEG demonstrated a much gentler degradation of secant stiffness than the C5-MTCP connection, indicating more ductile behaviour. Similar to the monotonic testing, all connections maintained load carrying capacity throughout the testing protocol.

The data collected within this research is representative only of the five connection designs tested, therefore continued testing and investigation into the behaviour of a wider variety of beam-to-column connections is recommended. Additionally, increasing the cycle of maximum displacement to larger amplitudes would be recommended for future testing, so that the post-peak behaviour of connections could be observed. Examination of the post-peak behaviour of connections would allow for the calculation of connection ductility, as well as comparisons of post-peak degradation of strength and stiffness between different connection designs.

Additional research on numerical modelling methodologies for simulating these connections is necessary to expand the body of knowledge on the behaviour of glulam beam-to-column connections. Specifically, research on the development of material models that simulate crushing of timber in compression is necessary to perform predictive modelling of mass timber connections.

ACKNOWLEDGEMENT

This work was sponsored by the USDA Agricultural Research Service, grant no. 58-0204-6-002. Thank you to Holmes Structures, KPFF, and the Northwest Carpenters Union for donating time and expertise, and to Tyler DeBoodt for assistance during construction and testing.

REFERENCES

[1] American Society of Civil Engineers. *Minimum design loads and associated criteria for buildings and other structures.* ASCE/SEI 7-16. 2017. American Society of Civil Engineers. Reston, VA.

[2] American Wood Council (AWC). 2018. "National Design Specification for Wood Construction (ANSI/AWC NDS 2018)". *AWC.* Leesburg, VA.

[3] American Society for Testing and Materials (ASTM). 2021. "D7147-21:Specification for Testing and Establishing Allowable Loads of Joist Hangers". *ASTM International.* West Conshohocken, PA.

[4] Madland, H., Fischer, E.C., and Sinha. A. (2023). "Monotonic testing of glue laminated beam-to-column connections," *Journal of Structural Engineering*. 149(5).

[5] Madland, H., Fischer, E.C., and Sinha. A. (2023). "Cyclic testing of glue laminated beam-to-column connections," *Journal of Structural Engineering*. 149(4).

[6] Krawinkler H, Parisi F, Ibarra L, Ayoub A, Medina R. Development of a Testing Protocol for Woodframe Structures. 2001. *Consortium of Universities for Research in Earthquake Engineering.* Richmond, CA.

[7] Guo, J., & Shu, Z. (2019). "Theoretical Evaluation of Moment Resistance for Bolted Timber Connections," *MATEC Web of Conferences*, 303(201 9), 03003. https://doi.org/10.1051/matecconf/201930303003

[8] Jalilifar, E., Koliou, M., & Pang, W. (2021). "Experimental and Numerical Characterization of Monotonic and Cyclic Performance of Cross-Laminated Timber Dowel-Type Connections," *Journal of Structural Engineering*, 147(7), 1–20. https://doi.org/10.1061/(asce)st.1943-541x.0003059

[9] ANSI/APA. (2019). Standard for Performance-Rated Cross-Laminated Timber (ANSI/APA PRG 320-2019). *APA – The Engineered Wood Association*, Tacoma, WA.

[10] CEN (European Committee for Standardization). 2005b. *Timber structures – Test methods –Cyclic testing of joints made with mechanical fasteners*. EN12512:2001 including amendment A1:2005. Brussels, Belgium: CEN.

[11] Min-Juan, H., L. Hui-fen. (2015). *"*Comparison of glulam post-to-beam connections reinforced by two different dowel-type fasteners*." Construction and Building Materials.* 99(2015), 99-108. https://doi.org/10.1016/j.conbuildmat.2015.09.005.

[12] Li, Z., He, M., and Wang, K. 2018. "Hysteretic Performance of Self-Centering Glulam Beam-to-Column Connections". *Journal of Structural Engineering*, 144(5): 04018031. https://doi.org/10.1061/(ASCE)ST.1943-541X.0002012

[13] He, M., Luo, J., Tao, D., Li, Z., Sun, Y., & He, G. (2020). "Rotational behavior of bolted glulam beam-to-column connections with knee brace," *Engineering Structures*, 207(September 2019), 110251. https://doi.org/10.1016/j.engstruct.2020.110251

[14] Kharouf, N., McClure, G., & Smith, I. (2003). "Elasto-plastic modeling of wood bolted connections," *Computers and Structures*, 81(8–11), 747–754. https://doi.org/10.1016/S0045-7949(02)00482-0

[15] Leitner, E. (2011). *Three-Dimensional Modeling of Wood Moment Connections* (Issue May) [Pennsylvania State University]. file:///C:/Users/Tanner/Downloads/ejl195_-_MSc_Thesis.pdf

[16] Xu, B. H., Bouchaïr, A., & Racher, P. (2012). "Analytical study and finite element modelling of timber connections with glued-in rods in bending," *Construction and Building Materials,* 34, 337–345. https://doi.org/10.1016/j.conbuildmat.2012.02.087

[17] Hong, J.-P., & Barrett, D. (2010). "Three-Dimensional Finite-Element Modeling of Nailed Connections in Wood," *Journal of Structural*

Engineering, 136(6), 715–722. https://doi.org/10.1061/(asce)st.1943-541x.0000160

[18] Karagiannis, V., Málaga-Chuquitaype, C., & Elghazouli, A. Y. (2016). "Modified foundation modelling of dowel embedment in glulam connections," *Construction and Building Materials*, 102, 1168–1179. https://doi.org/10.1016/j.conbuildmat.2015.09.021

[19] Persson, J. (2011). *Numerical analysis of compression perpendicular to the grain in glulam beams with and without reinforcement* [Lund University]. http://www.byggmek.lth.se

[20] Chen, Z., Ni, C., Dagenais, C., & Kuan, S. (2020). "Wood ST : A Temperature-Dependent Plastic-Damage Constitutive Model Used for Numerical Simulation of Wood-Based Materials and Connections," *Journal of Structural Engineering*, 146(3), 1–14. https://doi.org/10.1061/(asce)st.1943-541x.0002524

https://doi.org/10.52202/069179-0290

World Conference on Timber Engineering Oslo 2023

SEISMIC CONNECTIONS FOR CLT STRUCTURES WITH TUBULAR ELEMENTS AND UNCOUPLED TENSION-SHEAR INTERACTION

Luca Marchi[1], Davide Trutalli[1], Luca Pozza[2], Roberto Scotta[1]

ABSTRACT: Cross Laminated Timber (CLT) panels possess high in-plane stiffness, and traditional earthquake resistant connections, originally designed to counteract separately rocking and sliding phenomena, are subjected to a combined tension-shear interaction. Detailed models involving tension-shear interaction may be considered unpractical to apply by designers with the dilemma of simpler ones not representative of the real behaviour of the panels. This work presents the mechanical response of a novel connection system which limits tension-shear interaction aiming to contribute towards the reliability of capacity design of CLT shear wall assemblies. Such connection system extends the concept of rocking shear-walls with shear keys used for high-rise CLT buildings to the case of low-to medium rise buildings. Latest results from monotonic and cyclic-loading experimental tests of the connection device are presented and the design implication of this solution is analysed via a comparative analysis adopting non-linear numerical simulations of a CLT structure.

KEYWORDS: Earthquake resistant connections, Cross-laminated Timber, Aluminium, Shear test

1 INTRODUCTION

Cross Laminated Timber (CLT) are large factory-manufactured panels commonly used in mass timber construction as both horizontal and vertical structural elements due to their flexibility in interpreting challenging architectural solutions. The high-level of prefabrication ensures a reduced time for the erection of such systems. Their high performance/weight ratio justifies their acceptance in several high-seismicity areas such as Mediterranean European countries, North American territories, Japan and New Zealand.

The seismic response of these structures is strongly dependent on the cyclic behaviour of connections between panels and to foundation because CLT panels behave almost elastically under in-plane forces. In particular when large-sized panels are used where the density of connections is drastically decreased [1]. Although a great effort of the research is toward the developing of novel dissipative connection/damping systems to be used for the realization of tall buildings, CLT is still mostly used to realize low-to medium rise buildings, e.g., residential dwellings and public buildings (schools, community centers). Here, traditional hold-downs and angle brackets, initially designed for intrinsically ductile and dissipative platform-frame structures, are still the most employed fastening systems.

As CLT panels possess high shear stiffness [2], these traditional connections, originally designed to counteract separately rocking (uplift) and sliding (shear) phenomena, are subjected to a combined tension-shear interaction [3, 4]. Furthermore, application of capacity design principles requires the shear connection to be over designed for strength and stiffness [5]; this may inevitably lead to an even higher tension-shear interaction of the connections. This can result in lower-dissipative cyclic response and often unpredictable connection failure; hence conservative behaviour factors are adopted in various International Seismic Codes [6, 7] and revision proposals [8].

Detailed models involving tension-shear interaction may be considered unpractical to apply by designers [9] with the dilemma of simpler ones not representative of the real behaviour of the panels. Therefore, a high number of fasteners are generally required as shear connectors to fulfill capacity design resulting in economically inefficient solutions. From a practical point of view novel connection systems able to simplify and speed up the realization of wall-floor-wall nodes in CLT structures are of paramount relevance.

This paper presents the mechanical response of a novel connection system which limits tension-shear interaction aiming to contribute towards the reliability of capacity design of CLT shear wall assemblies. The idea is to exploit metallic tubular elements inserted edge-wise into predrilled holes operating as shear-keys. They can also operate as tension-resistant connection (such as hold-downs) if the tubular connectors are connected to CLT with screws or dowels. Such connection system extends the concept of rocking shear-walls with shear keys used for high-rise CLT buildings [10] to the case of low-to medium rise buildings. Latest results from monotonic and cyclic-loading experimental tests of the connection device are presented. The obtained mechanical parameters are

[1] Department of Civil, Environmental and Architectural Engineering, University of Padova, via Marzolo 9 - Padova, 35131, Italy. davide.trutalli@dicea.unipd.it; luca.marchi@unipd.it; roberto.scotta@unipd.it.

[2] Department of Civil, Chemical, Environmental and Materials Engineering, University of Bologna, viale Risorgimento 2 - Bologna, 40136, Italy. luca.pozza2@unibo.it

https://doi.org/10.52202/069179-0291

compared in terms of stiffness, strength, and ductility to that of traditional connection systems and to analytical and numerical models.

2 DESIGN AND CONCEIVING

2.1 OVERVIEW OF THE CONNECTION

The investigated connection system exploits tubular elements realized from extruded steel or aluminium inserted into pre-drilled holes at the edge of the timber panels (Figure 1). The location of the tubes along the wall is equivalent to standard hold-down and angle brackets connections, with the elements on the wall edges contrasting the wall rocking and the inner ones opposing to the horizontal slip. While the outer tubes are connected to the wall with dowel-type fasteners to provide a vertical restraint, the inner tubes are meant to work as traditional shear-keys thus restraining the horizontal displacements. The complex tension-shear interaction is almost completely avoided by simply increasing the diameter of the holes on the floor panel where the outer tubes are placed, i.e., forcing the transmission of the shear force by contact of the inner tubes only (Figure 2).

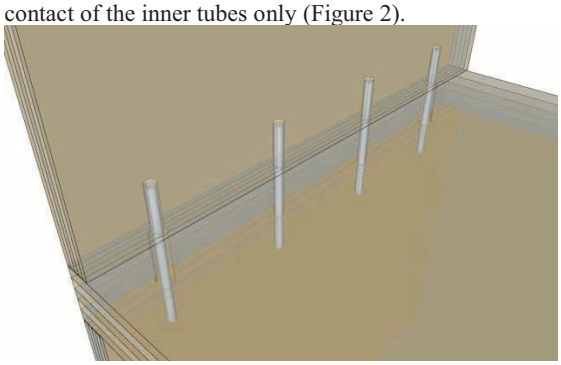

Figure 1: *Conceptualization of the analysed connection system*

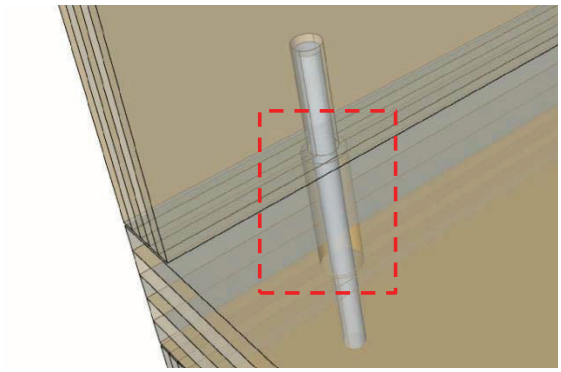

Figure 2: *Gap of the floor panel for the edge connections*

The material properties of the tube are of utmost importance in this application. Aluminium is already being successfully applied as good medium to realize other timber joints thanks to its lightness and good mechanical performance [11, 12]. In this case, its use as tension-resistant connection would benefit for the types of screws or dowels as less drilling force is required to pass through the tube walls. On the contrary, its lower stiffness compared to steel may provide reduced performance as a shear-key connector.

2.2 ANALYTICAL DESIGN

The conceiving phase started with the analytical determination of the load-carrying capacity of a dowel-type fastener drilled into the tube and locking it to the CLT panel. This was mandatory to overdesign the tube cross-section, namely diameter and thickness that guarantee a sufficient overstrength to the element.

The CLT panel thickness and layer arrangement implicitly define the possible failure modes of the dowel-type fasteners used to fasten the tube to the wooden element. Considering that the connection was purposely designed to be used into a low-rise structure (up to two-three storey high), the reference CLT wall panel thickness can be figured in the range of 100-140 mm in a 3-to-5-layer configuration.

Within the 3-layer configuration it is likely possible that the tube will exploit the whole inner layer and therefore the possible failure modes for this condition are already included in the Eurocode 5 [13] for the case of steel plates of any thickness as the central member of a double shear connection:

$$F_{v,Rk} = min \begin{cases} f_{h,k} t d & (f) \\ f_{h,k} t\, d \left[\sqrt{2 + \frac{4 M_{y,Rk}}{f_{h,k} d t^2}} - 1 \right] + \frac{F_{ax,Rk}}{4} & (g) \\ 2{,}3 \sqrt{M_{y,Rk} f_{h,k} d} + \frac{F_{ax,Rk}}{4} & (h) \end{cases}$$

For a 5-layer configuration the failure modes can be reconstructed by following the approach of [14] starting from the Johansen model. In summary, the possibility to obtain one or two plastic hinges is split into two sub-cases as reported in the equations below.

Mode 1 - wood embedment:

$$F_{v,Rk} = f_h \cdot d \cdot t \tag{1}$$

Mode 2.1 - one plastic hinge:

$$F_{v,Rk} = f_h \cdot d \cdot t \left(\sqrt{2} \sqrt{\beta \left[\beta (1-\psi)^2 + \psi (2-\psi) + \frac{M_{y,Rk}}{f_{h1} \cdot d \cdot t^2} \right]} + \beta (\psi - 1) - \psi \right) \tag{2}$$

Mode 2.2 - one plastic hinge:

$$F_{v,Rk} = f_h \cdot d \cdot t \left(\sqrt{2} \sqrt{2 + \psi (\psi - 2) - \beta (1-\psi)^2 + \frac{M_{y,Rk}}{f_{h1} \cdot d \cdot t^2}} + \beta (1-\psi) + \psi - 2 \right) \tag{3}$$

Mode 3.1 - two plastic hinges:

$$F_{v,Rk} = \sqrt{2} \sqrt{2 M_{y,Rk} \cdot f_{h1} \cdot d \cdot \beta} \tag{4}$$

Mode 3.2 - two plastic hinges:

https://doi.org/10.52202/069179-0291

$$F_{v,Rk} = f_h \cdot d \cdot t \left(\sqrt{\left[(1-\psi)^2(1-\beta) + 4\frac{M_{y,Rk}}{f_{h1} \cdot d \cdot t^2} \right]} + \beta(1-\psi) + \psi - 1 \right) \quad (5)$$

The tensile strength of the tube could be easily calculated following provisions from Eurocode 3 [15] or 9 [16], whether steel or aluminium is used.
Main outcomes from the analytical approach suggested that a 4-mm thick extruded profile of aluminium alloy equal to EN AW 6082 [17] with an external diameter equal to 40mm could be used for the purpose. The fastening of the tube shall be entrusted to self-drilling dowels with nominal diameter equal to 7 mm realized with steel grade S275.

3 TENSION-RESISTING JOINT: EXPERIMENTAL TESTS

Monotonic tests were performed to assess the main mechanical parameters of the joint if exploited as tension-resistant element.

3.1 SPECIMEN CHARACTERISTICS

The joint in the tension-resisting configuration was tested according to a simple compression setup using a universal testing machine (Figure 3). The CLT specimens were cut from a 5 layer 100-mm thick CLT panel (20-20-20-20-20) with dimension sufficient to respect actual edge distance provisions valid for the chosen connections. The resistance of the self-drilling was evaluated in two distinct configurations:

- a single dowel with length equal to 93mm placed orthogonally to the CLT panel face;
- a single dowel with length equal to 133mm placed at an angle of 45° to the CLT panel face.

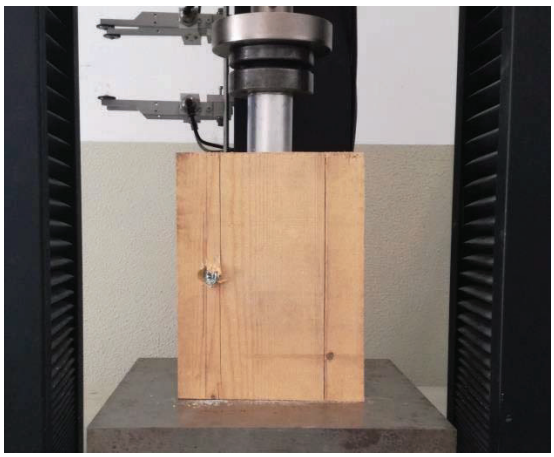

Figure 3: *Tensile test*

3.2 RESULTS

Preliminary tests were conducted to assess the contribution of friction between tube and CLT by pushing the tube into the hole without the insertion of the dowels. Results shows a resistance of about 500N to be reached before the triggering of the slippage phenomena. Force increased up to 1450N at 20mm of insertion.

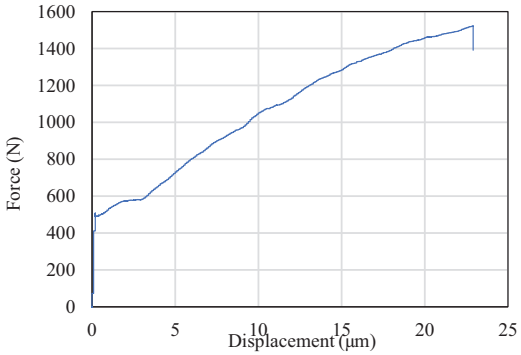

Figure 4: *Frictional contribution between tube and panel*

All monotonic tests returned a combined wood embedment failure coupled with the formation of two plastic hinges, technically the most ductile failure mode achievable for a dowel-type fastener (Figure 5).

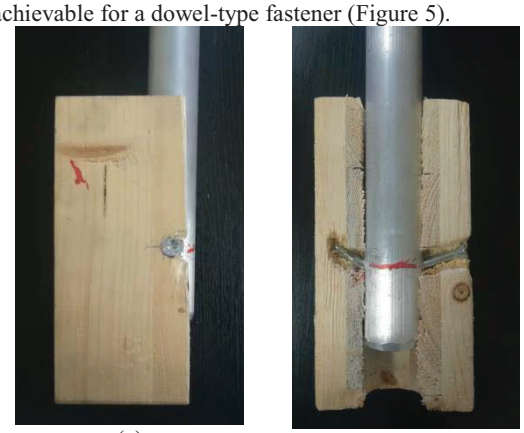

Figure 5: *Specimen inspection at failure*

Table 1 summarize the mechanical parameters calculated from the force displacement curves, for which average trends are reported in Figure 6 and Figure 7.

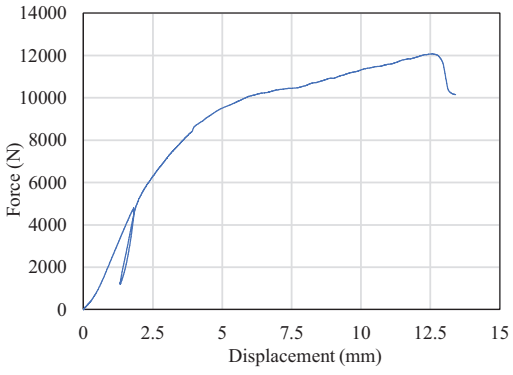

Figure 6: *Average force-displacement curve of a single dowel orthogonal to the panel (90°)*

https://doi.org/10.52202/069179-0291

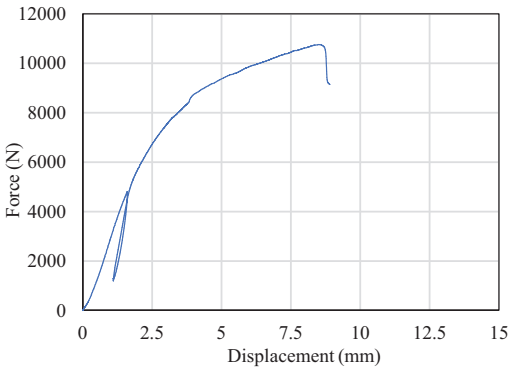

Figure 7: *Average force-displacement curve of a single dowel orthogonal to the panel (45°)*

dowel; iii) elastic-plastic orthotropic response for the timber element.

Large deformations and frictional contact laws were used to simulate the interaction (i.e., force transfer) between the different elements. The CLT panel was discretized according to the different composing layers. A bonded contact was applied between the different layers.

The simulated timber elements were a 200-mm thick CLT panel working as a floor, and a 100-mm thick CLT panel as a wall. A 5-layer configuration was chosen for both elements with 20 mm and 40 mm of thickness for the floor and wall respectively. Symmetry planes were adopted to reduce the computational costs of the models (Figure 8).

Firstly, a parametric analysis was performed to evaluate the changes of the mechanical performance by varying three key parameters defining the aluminium tube: strength class (yielding and ultimate strength in detail),

Table 1: *Summary of tensile tests between the two tested fastening configurations*

	F_{MAX} [kN]	d_{FMAX} [mm]	F_Y [kN]	d_{FY} [mm]	K_{el} [kN/mm]	K_{pl} [kN/mm]	μ [-]	Ductiliy class [-]
Angle 90°								
Mean	12.01	14.80	8.99	2.15	4.60	0.24	7.53	H
Dev.St.	0.62	4.72	1.01	0.13	0.61	0.03		
5% Fractile	10.46		**6.48**					
COV	5.20%	31.88%	11.21%	6.21%	13.33%	10.54%		
Angle 45°								
Mean	11.15	9.95	9.63	2.42	4.93	0.21	5.05	M
Dev.St.	1.09	1.68	1.25	0.31	0.88	0.10		
5% Fractile	8.44		6.53					
COV	9.80%	16.84%	12.98%	12.78%	17.85%	48.84%		

The two configurations show comparable values of the yielding point, expressed by the resistance F_y and displacement d_y (evaluated according to EN 12512 method b [18]). A more pronounced post-elastic response of the dowels placed at 90° allows to reach a greater static ductility value. This returns that only the first configuration can be assigned to the highest ductility class according to [8].

Considering an average load bearing capacity at yielding of about 6.5 kN it results that about 6 to 8 dowels should be fastened to the same tube to obtain an overall capacity comparable to traditional hold-downs fastened with annular ringed-shank nails.

4 SHEAR-RESISTING JOINT: NUMERICAL SIMULATIONS

Given the high complexity and effort of designing a test to investigate in deep the behaviour of the tubular element when used as a shear-resisting connection, a 3D finite element model of the joint was developed with the commercial software Ansys Mechanical Workbench to test the performance of the joint. The analyses included material non-linearities for all the components: i) multilinear Ramberg-Osgood law [19] for the aluminium element; ii) bilinear elastic-plastic constitutive law for the

external diameter and thickness. This becomes important not to overdesign the tube but also to obtain a cost-efficient solution.

A parametric analysis was performed to assess the different response to be obtained when the floor panel is oriented parallel or perpendicular to the wall. Additionally, the contribution of the frictional forces that can develop at the wall-to-panel contact interface and at the CLT-tube interface was also included in the parametric analysis.

4.1 RESULTS

Sections 4.1.1 and 4.1.2 summarize the results obtained by considering the CLT panel representing the floor oriented parallel or perpendicular to the wall respectively. By comparing Figure 8 to Figure 11 it emerges the different location of the plastic hinge that is the consequence of the different stiffness of the external layer of the floor panel (light shaded elements on the left of the figure).

Considering a reference displacement of 15 mm and frictionless boundary conditions, it results in an important difference between the two panel orientations with an applied force equal to 93.5 kN for a parallel layout and 76.6 kN (-18%). Introducing friction at both interfaces raise the force level up to 113.9 kN and 91.1 kN respectively (-20%).

https://doi.org/10.52202/069179-0291

The contribution of the frictional phenomena can also be appreciated from the superposition of the force-displacement curves obtained from the parametric analysis. Such occurrence, to be neglected in the design phase, can produce an increase of the total shear force between 8 to 10% attributed to the panel-to-panel interface and an additional 10% to the tube-to-CLT interface.

By adopting the same bilinearization method of the tensile-resisting configuration the yielding force F_y can be estimated between 50 to 70kN; within this range of shear load bearing capacity, a single tube can easily provide similar or higher performance of the last generation of angle-brackets.

4.1.1 FLOOR PARALLEL TO THE WALL

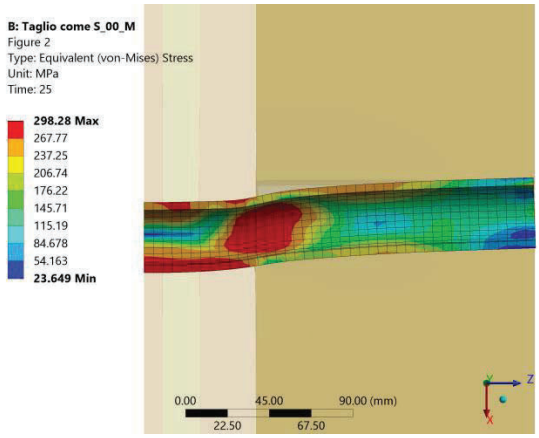

Figure 8: *von-Mises stress in the tube and plastic hinge location*

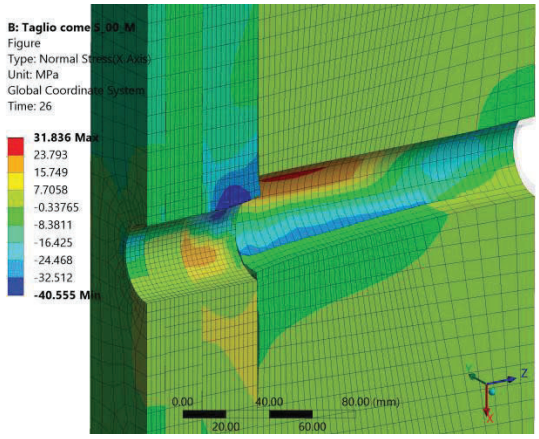

Figure 9: *principal stress in the CLT elements parallel to the loading direction*

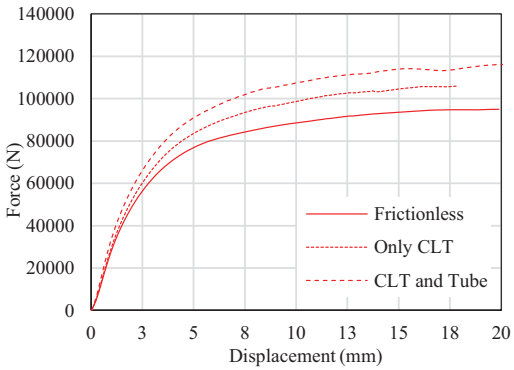

Figure 10: *numerical force-displacement curve with floor direction parallel to the wall*

4.1.2 FLOOR PERPENDICULAR TO THE WALL

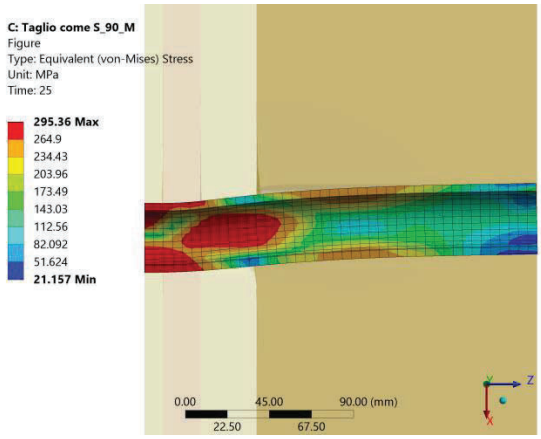

Figure 11: *von-Mises stress in the tube and plastic hinge location*

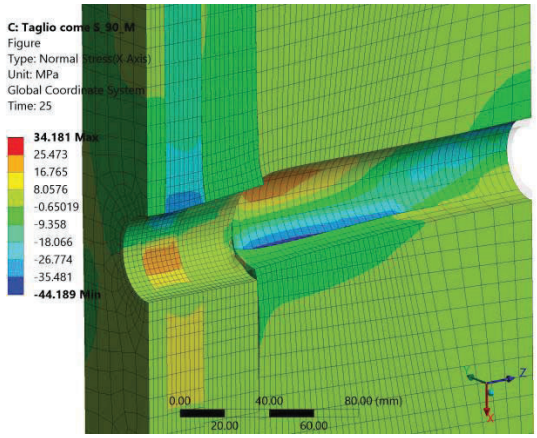

Figure 12: *principal stress in the CLT elements parallel to the loading direction*

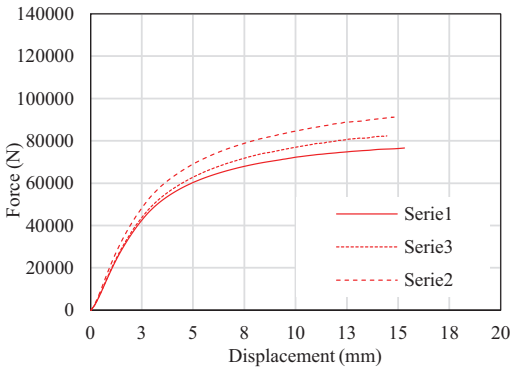

Figure 13: *numerical force-displacement curve with floor direction parallel to the wall*

REFERENCES

1. Scotta R, Pozza L, Trutalli D, Marchi L (2015) Dissipative connections for squat or scarcely jointed CLT buildings . Experimental tests and numerical validation. In: International Network on Timber Engineering Research (INTER). Sibenik, pp 1–14
2. Aloisio A, Boggian F, Tomasi R, Fragiacomo M (2021) The role of the hold-down in the capacity model of LTF and CLT shear walls based on the experimental lateral response. Constr Build Mater 289:123046. https://doi.org/10.1016/J.CONBUILDMAT.2021.123046
3. Pozza L, Saetta A, Savoia M, Talledo D (2018) Angle Bracket connections for CLT structures: experimental characterization and numerical modelling. Constr Build Mater 191:95–113. https://doi.org/10.1016/j.conbuildmat.2018.09.112
4. Liu J, Lam F (2018) Experimental test of coupling effect on CLT angle bracket connections. Eng Struct 171:862–873. https://doi.org/10.1016/j.engstruct.2018.05.013
5. Trutalli D, Marchi L, Scotta R, Pozza L (2019) Capacity design of traditional and innovative ductile connections for earthquake-resistant CLT structures. Bulletin of Earthquake Engineering 17:2115–2136. https://doi.org/10.1007/s10518-018-00536-6
6. CSA Group (2015) CSA 086 Engineering design in wood. Mississauga
7. CEN (2005) EN 1998-3 Eurocode 8 — Design of structures for earthquake resistance —
8. Follesa M, Fragiacomo M, Casagrande D, et al (2016) the New Version of Chapter 8 of Eurocode 8. In: 14th World Conference on Timber Engineering (WCTE)
9. Marchi L, Trutalli D, Scotta R, Pozza L (2020) Macro-element modelling of a dissipative connection for CLT structures. Structures 26:582–600. https://doi.org/10.1016/j.istruc.2020.04.044
10. Brown JR, Li M, Sarti F (2021) Structural performance of CLT shear connections with castellations and angle brackets. Eng Struct 240:112346. https://doi.org/10.1016/J.ENGSTRUCT.2021.112346
11. Scotta R, Marchi L, Trutalli D, Pozza L (2017) Engineered Aluminium Beams for Anchoring Timber Buildings to Foundation. Structural Engineering International 27:158–164. https://doi.org/10.2749/101686617X14881932435736
12. Scotta R, Trutalli D, Marchi L, Pozza L (2018) On the anchoring of timber walls to foundations: Available strategies to prevent wood deterioration and on-site installation problems. In: Procedia Structural Integrity. pp 282–289
13. CEN (2009) EN 1995-1-1 Eurocode 5: Design of timber structures - Part 1-1 : General - Common rules and rules for buildings. CEN, Brussels, Belgium
14. Uibel T, Blaß H (2006) Load carrying capacity of joints with dowel type fasteners in solid wood panels. In: CIB-W18 Meeting 39. Florence, Italy
15. CEN (2015) EN 1993-1-1 Eurocode 3: Design of steel structures - Part 1-1: General rules and rules for buildings. Brussels, Belgium
16. CEN (2007) EN 1999 Eurocode 9: Design of aluminium structures - Part 1-1: General Structural rules. Brussels, Belgium
17. CEN (2016) EN 755-2 Aluminium and aluminium alloys — Extruded rod/bar, tube and profiles Part 2: Mechanical properties. Brussels, Belgium
18. CEN (2011) EN 12512 Timber structures-Test methods: Cyclic testing of joints made with mechanical fasteners. Brussels, Belgium
19. Ramberg W, Osgood WR (1943) Description of stress-strain curves by three parameters. National Advisory Committee For Aeronautics Technical Note No. 902. https://doi.org/10.1016/j.matdes.2009.07.011

https://doi.org/10.52202/069179-0291

World Conference on Timber Engineering Oslo 2023

VARIABILITY OF THE CROSS-LAMINATED TIMBER (CLT) SINGLE-PANEL SHEAR WALLS' RESPONSE UNDER IN-PLANE LATERAL LOADS

Vincenzo Rinaldi[1], Igor Gavrić[2], Massimo Fragiacomo[3]

ABSTRACT: In the past, several studies analysed the seismic response of Cross-Laminated Timber (CLT) shear wall systems using experimental tests and numerical analyses. Usually, these analyses were based on the average mechanical properties of connections, which have the largest effect on the non-linear response of CLT shear walls. This paper investigates the non-linear in-plane response variability of single-panel CLT shear walls accounting for the actual scatter of the connection's mechanical properties. Based on previously obtained experimental results of traditional hold-downs and angle brackets, the response of CLT shear walls subjected to in-plane lateral loads is analysed considering the main engineering parameters variability, such as strength, deformation, and ductility through a simulation approach based on random sampling. The study considers three different shear walls width-to-height aspect ratios (1:3, 1:1, 3:1) analysed by changing the vertical loads. For each scenario, one thousand of numerical analyses are carried out by varying the experimental mechanical properties of every single connection. The outcomes of this study show the variability of the non-linear numerical response of single-panel CLT shear walls, which was found to decrease with an increase in the length of the shear wall, while the engineering parameters varied in a range of 1% to 17%.

KEYWORDS: Cross-Laminated Timber, shear wall, variability, non-linear response, mechanical connections.

1 INTRODUCTION

The numerical modelling of Cross-Laminated Timber (CLT) shear wall behaviour under lateral loads is still a subject of research. Among the proposed modelling strategies [1], several authors implemented the so-called component-level (CL) modelling approach since it allows a detailed analysis of the non-linear behaviour. The CL strategy considers each structural system component (i.e. CLT panels, connections) with linear/non-linear behaviour calibrated through experimental tests or analytical equations. Although significant efforts have been made to investigate the CLT shear walls' behaviour [2,3], no research has been conducted to estimate the variability of the non-linear response due to the variability of the connections' actual behaviour.

The average experimentally obtained properties are commonly used to perform non-linear numerical analyses when adopting a CL approach [4,5,6].

This approach is obviously correct when assessing a CLT shear wall's performance. However, for all structural systems, the seismic response of CLT shear walls is ruled by physical aspects of each structural component, including the deformation mechanisms (CLT shear and bending deformations, sliding and rocking) and the variable behaviour of the structural components.

In the case of CLT shear walls without openings, the total lateral deformation of a shear wall [7] is mostly influenced by the connections' flexibility instead of the panel deformability.

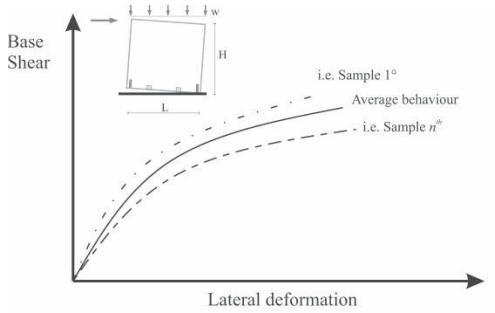

Figure 1: *Different response scenarios due to the connections' variability for the same CLT shear wall configuration*

Due to this phenomenon, the response of a CLT shear wall is predominantly affected by the connection's behaviour [8]. As shown in Figure 1, a CLT shear wall could result in different force-displacement responses due to the variability of the connections' mechanical properties.

In most experimental programmes on timber connections [9-11], a well-defined connection is tested several times to investigate the actual behaviour and the variability of the connection's response. It should be highlighted that mechanical timber connections are prone to a high scatter of results due to the natural variability of the timber as a material [12]. In fact, the fasteners of a connection may be fixed into a quite defective part of the wood (i.e. knot) or layer with less strength which can completely influence the overall behaviour of a connection.

[1] Vincenzo Rinaldi, University of L'Aquila, Italy, vincenzo.rinaldi@univaq.it
[2] Igor Gavrić, InnoRenew CoE & University of Primorska, Slovenia, gavric.igor@gmail.com
[3] Massimo Fragiacomo, University of L'Aquila, Italy, massimo.fragiacomo@univaq.it

https://doi.org/10.52202/069179-0292

In this paper, several CLT single-panel shear wall setups are numerically analysed to investigate the effects of the mechanical variability of traditional CLT connections.
A parametric analysis is carried out by examining three different shear wall aspect ratios (1:3, 1:1, 3:1) varying the levels of applied vertical loads and modifying the experimental backbone curves of each connection of the shear wall through a simulation approach based on random sampling. According to this procedure, each configuration is analysed in terms of aspect ratio and vertical load. The specific objectives of this study are to investigate:

- the variability of CLT shear walls response under different conditions (aspect ratios and vertical loads);
- the variability of the main engineering output parameters, such as strength, deformation and ductility.

2 METHODOLOGY

The randomness and the response variability of single-panel CLT shear wall are investigated through a non-parametric stochastic simulation approach.
The study is based on four main phases: *i)* collection of the experimental data of the mechanical connections and calibration of the numerical parameters, *ii)* definition and validation of a numerical model, *iii)* definition of the shear walls configurations in terms of geometry, vertical loads and number of connections, and *iv)* random sampling generation and analyses of a thousand different CLT shear walls for each configuration.
Non-Linear Static Analyses (NLSA) are used to estimate and compare the variability of strength, deformation, and ductility of each shear wall. The pushover curves are linearised according to EN 12512 [14]. Figure 2 shows the adopted nomenclature.

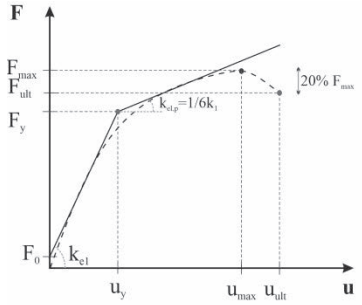

Figure 2: *Linearisation and definition of the parameters according to EN 12512 [14]*

F_0 is the intercept between the elastic branch representing elastic stiffness k_{el} and the y-axis; k_{el} is defined as the secant stiffness between 10% and 40% of the maximum strength F_{max}; $k_{el,pl}$ is the post-elastic branch tangent to the experimental curve and inclined by 1/6 k_{el}. The points (F_y, u_y), (F_{max}, u_{max}) and (F_{ult}, u_{ult}) represent the conventional yielding, maximum strength and ultimate capacity, respectively, where the last one is estimated at the strength drop equal to 20% of F_{max}.

2.1 EXPERIMENTAL DATA AND NUMERICAL CALIBRATION

Traditional timber-to-steel connections such as Hold-Downs (HD) and Angle-Brackets (AB) are considered in this study. The backbone curves of the HD and AB are based on existing experimental data [9]. HD type WHT540 with twelve 4×60 mm annular shanked nails and AB type BMF 90 × 116 × 48 × 3 with 11 annular shanked nails are used (Figure 3).

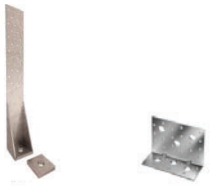

Figure 3: *(a) hold-downs (HD) and (b) angle brackets (AB)*

Several specimens were tested for each configuration of HDs and ABs during the experimental programme (tension and shear tests). Results are available for seven samples of HDs in tension, six samples of AB in tension and six samples of AB in shear and were implemented in this work.
A uni-directional vertical-uplift behaviour is assumed for HD since they do not provide a significant contribution in horizontal-shear direction and assuming a bi-directional behaviour would yield too conservative results [7]. A bi-directional behaviour is considered for AB due to the comparable load-bearing capacity in both directions, shear (horizontal-shear) and tension (vertical-uplift).
The "SAWSMaterial" [13] OpenSees numerical model was implemented in the FE model to reproduce the connections' behaviour. All nineteen experimental curves (seven HDs in tension and six ABs in shear and tension) were calibrated based on a fitting procedure. Figure 4 displays the experimental and numerical curves of the analysed connections. The curves are derived from the first backbone curve of the connections' cyclic tests.

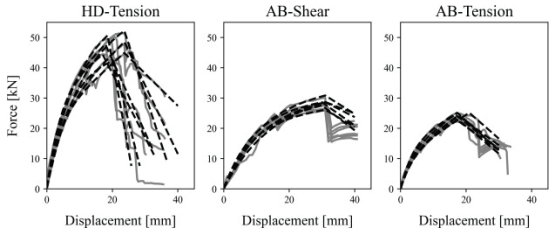

Figure 4: *Experimental data (solid lines) and numerical calibration (dashed lines): HD tension tests (left); AB shear tests (centre); AB tension tests (right)*

https://doi.org/10.52202/069179-0292

Since ABs are considered with a bi-directional behaviour, thirty-six types of different ABs are defined by combining the six experimental tests in the two main directions.
The experimental data highlights the general scatter between the capacity curves. HDs show a higher variation of the backbone curves compared to ABs, as shown in Figure 4. HDs have a higher scatter in terms of strength compared to the ABs. The main reason is the nature of the failure mechanisms: a sudden significant force drop can be recognised in HD tension tests due to several nails failing simultaneously in shear, including cap tear-off. On the other hands, ABs failure mechanism was a combination of progressive nails yielding, deformation of the brackets and embedment of CLT [9].

2.2 NUMERICAL MODEL OF THE CLT SHEAR WALL AND VALIDATION

A simplified two-dimensional FE model is implemented for the non-linear analyses of the shear wall, as reported in [6]. The model consists of an assembly of rigid and flexible frames to reproduce the CLT wall, whereas zero-length springs schematise the connections (Figure 5). The use of a frame-model instead of area-model for the CLT panels allowed the user to reduce the computational effort. As a shear-type model, the frame model includes the CLT panel deformability through analytical equations due to shear and bending deformation. The horizontal frames placed at the top and the bottom of the wall are assumed as rigid, whereas the two vertical frames on the left and the right edge of the wall are modelled as flexible frames. The flexibility of the vertical frames is calibrated by modifying the second moment of area of the element to account for the overall stiffness of the CLT panel.
All CLT panels are 120 mm thick, made of 5-layers (v30-20-v20-20-v30) with timber strength class C24, where "v" represents vertical orientation of laminations.
Axially rigid friction-contact elements with a Coulomb friction coefficient equal to 0.1 were adopted to simulate the steel-to-timber contact. HDs are modelled with a uni-directional behaviour, while ABs are modelled with bi-directional behaviour. A numerical uncoupled behaviour is assumed for the two orthogonal non-linear laws of the ABs.

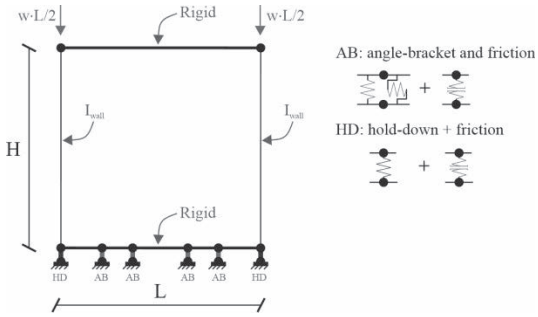

Figure 5: *Finite element model of a CLT shear wall*

The FE model is validated by comparing the experimental response of a CLT shear wall, shown in Figure 6 [7]. The validation was conducted through a NLSA numerical model, where the same connections (HDs and ABs), presented in Section 2.1, were used, in both numerical model and the experimental tests.

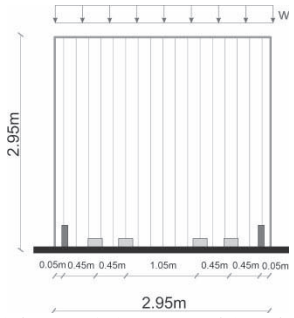

Figure 6: *Validation of the FE model and the parametric procedure of test I.1 [7] with w=18.5kN/m*

The experimental-numerical comparison is made in terms of a mean numerical curve obtained from one thousand different FE shear walls developed with a parametric procedure.
The mean numerical behaviour is reproduced by averaging the parameters of the numerical model respectively for HD in tension and AB in shear and tension. The parametric procedure generated thousand FE shear wall configurations by randomly combining and modifying the properties of every single connection. The parametric shear walls were defined using a random selection among seven different HD responses and thirty-six ABs responses.
As visible in Figure 7, the mean and the parametric curves fit well with the backbone curves of the cyclic experimental test. In addition, for the specific shear wall test, the parametric analysis shows in detail that the maximum strength and the degradation branch have high variability compared to the wall elastic stiffness.

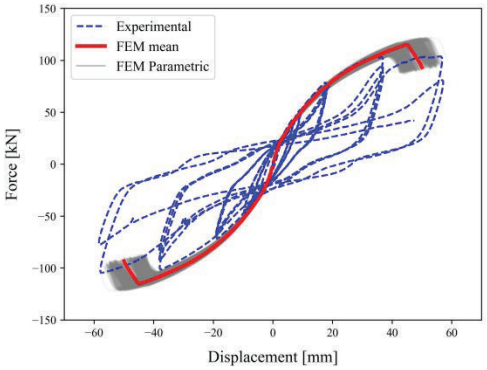

Figure 7: *Numerical validation of test I.1 [7]. Mean numerical curve (red) and a thousand of FE shear walls (gray)*

2.3 CLT SHEAR WALL CONFIGURATIONS

A parametric matrix of CLT shear wall configurations was defined to investigate: *i)* the CLT shear walls response under different conditions and *ii)* the variability of the main engineering parameters (Table 1).

The study considers three different shear wall aspect ratios L:H equal to 1:3 (1 m x 3 m), 1:1 (3 m x 3 m) and 3:1 (9 m x 3 m). The number of ABs is set with 60 cm spacing between the ABs, whereas one HD is placed at each corner of the CLT wall. Three different vertical loads (0 kN/m, 10 kN/m, 20 kN/m) are defined to compare the influence of the gravity loads. A total of nine CLT shear wall configurations are thus defined.

Table 1: *Matrix of the shear walls' configurations for the parametric study*

Vertical load [kN/m]	ID	Aspect ratio L:H		
		1:3 (1m x 3m) 1AB+2HD	1:1 (3m x 3m) 4AB+2HD	3:1 (9m x 3m) 12AB+2HD
0.0	#1	1:3	1:1	3:1
10.0	#2	1:3	1:1	3:1
20.0	#3	1:3	1:1	3:1

2.4 RANDOM SAMPLING AND ANALYSES

Each configuration in Table 1 was analysed with one thousand different shear wall models where each connection has different properties for HDs and ABs randomly generated by combining seven HDs backbone curves and thirty-six types of ABs.

The generation of all shear walls is performed with a Python script using the same random seed to keep the properties and location of each connection constant for the same aspect ratio in all vertical load cases. After applying the vertical loads, each shear wall is analysed through a NLSA with a displacement control approach.

In a post-processing phase, all curves are linearised with EN 12512, and engineering parameters are estimated.

3 RESULTS

Figure 8 shows the pushover curves of all configurations. The outcomes show how the vertical load increases the shear wall's total strength capacity and stiffness. This effect is most evident for 1:3 and 1:1 shear walls where, as expected, the rocking mechanism governed the deformation capacity of the shear wall. The 3:1 aspect ratio is hardly affected by the vertical load variations since the predominant deformation mechanism is sliding. The variability of connection capacity reported in Section 2.1 is evident for 1:3 shear walls, less so for 1:1 shear walls and negligible for 3:1 shear walls. Seven "groups" of pushover curves can be recognised for the 1:3 case. These groups are strictly related to the experimental response of the seven HDs tested since they mostly affect the overall behaviour of the shear wall due to the rocking mechanism. Tables 2-4 list the outcomes in terms of mean value and Coefficient of Variation (CoV) for all configurations, whereas Figures 9-12 represent the CoV of F_y, F_{max}, k_{el} and μ.

As a general trend, the CoV decreases with the length of the shear wall, while they show a limited variation with the vertical loads. The stiffness $k_{el,}$ and $k_{el,p}$ have the same CoV since they depend on each other according to EN 12512.

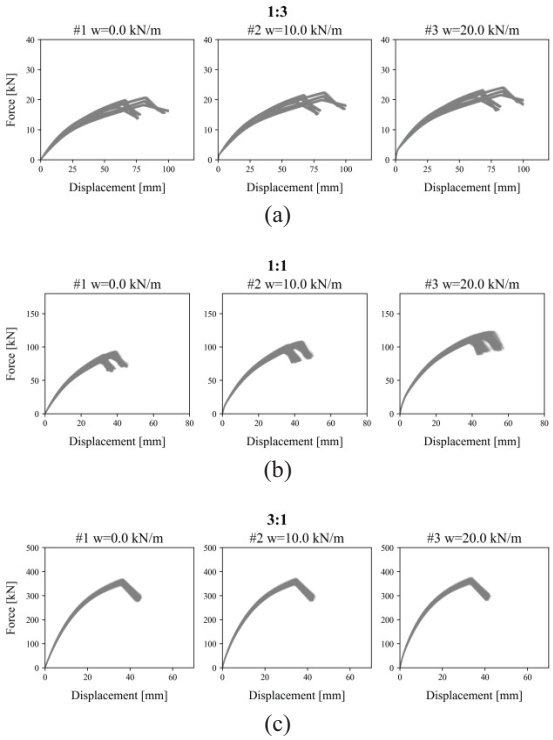

Figure 8: *(a) shear wall 1:3, (b) shear wall 1:1 and (c) shear wall 3:1*

Table 2: *Results of CLT shear wall configuration 1:3*

	1:3			
	w [kN/m]	0.0	10.0	20.0
F_0	mean [kN]	0.39	1.35	1.70
	CoV [%]	16.25	4.01	7.39
F_y	mean [kN]	15.72	17.01	17.64
	CoV [%]	7.96	8.02	8.46
u_y	mean [mm]	33.54	31.90	27.73
	CoV [%]	15.02	15.25	16.78
F_{max}	mean [kN]	18.75	20.41	22.08
	CoV [%]	6.41	5.88	5.44
u_{max}	mean [mm]	71.70	72.68	73.71
	CoV [%]	11.84	11.69	11.53
F_{ult}	mean [kN]	15.20	16.59	18.01
	CoV [%]	6.76	6.58	6.57
u_{ult}	mean [mm]	83.67	85.36	86.94
	CoV [%]	12.84	12.28	11.60
k_{el}	mean [kN/mm]	0.46	0.50	0.58
	CoV [%]	9.67	9.50	9.92
$k_{el,p}$	mean [kN/mm]	0.08	0.08	0.10
	CoV [%]	9.67	9.50	9.92
μ	mean [-]	2.52	2.72	3.20
	CoV [%]	12.67	14.38	15.93

https://doi.org/10.52202/069179-0292

Table 3: *Results of CLT shear wall configuration 1:1*

	1:1			
	w [kN/m]	0.0	10.0	20.0
F_0	mean [kN]	1.74	5.80	6.39
	CoV [%]	13.52	6.68	6.59
F_y	mean [kN]	71.09	83.93	91.21
	CoV [%]	7.61	4.20	3.97
u_y	mean [mm]	17.56	17.63	16.14
	CoV [%]	11.84	7.92	8.24
F_{max}	mean [kN]	85.37	100.33	115.29
	CoV [%]	5.01	4.27	3.72
u_{max}	mean [mm]	33.90	37.90	43.40
	CoV [%]	10.26	9.95	10.10
F_{ult}	mean [kN]	66.69	78.49	89.49
	CoV [%]	8.53	7.53	8.06
u_{ult}	mean [mm]	39.10	43.46	49.19
	CoV [%]	10.08	9.48	9.44
k_{el}	mean [kN/mm]	3.97	4.45	5.27
	CoV [%]	5.16	5.05	4.87
$k_{el,p}$	mean [kN/mm]	0.66	0.74	0.88
	CoV [%]	5.16	5.05	4.87
μ	mean [-]	2.24	2.48	3.06
	CoV [%]	9.12	10.04	8.48

Table 4: *Results of CLT shear wall configuration 3:1*

	3:1			
	w [kN/m]	0.0	10.0	20.0
F_0	mean [kN]	7.47	13.65	13.65
	CoV [%]	7.27	2.43	3.14
F_y	mean [kN]	293.02	283.65	281.45
	CoV [%]	2.26	1.94	1.96
u_y	mean [mm]	15.20	13.05	11.78
	CoV [%]	3.84	3.71	3.94
F_{max}	mean [kN]	355.49	357.64	361.05
	CoV [%]	1.47	1.47	1.44
u_{max}	mean [mm]	35.88	34.10	33.09
	CoV [%]	1.32	1.53	1.23
F_{ult}	mean [kN]	279.47	281.45	279.46
	CoV [%]	3.84	4.25	5.73
u_{ult}	mean [mm]	44.29	42.52	41.63
	CoV [%]	1.29	1.21	1.13
k_{el}	mean [kN/mm]	18.80	20.70	22.75
	CoV [%]	2.31	2.56	2.76
$k_{el,p}$	mean [kN/mm]	3.13	3.45	3.79
	CoV [%]	2.31	2.56	2.76
μ	mean [-]	2.92	3.26	3.54
	CoV [%]	3.07	2.99	3.28

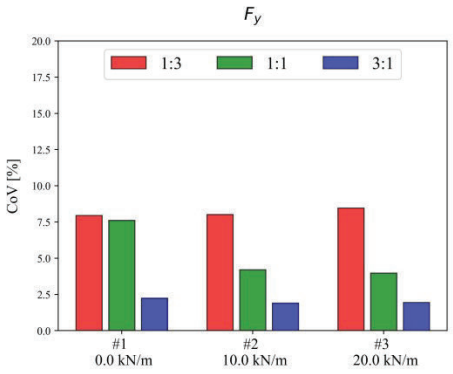

Figure 9: *Coefficient of variation of the yielding strength F_y*

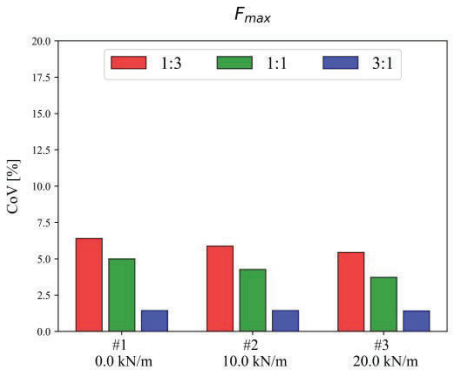

Figure 10: *Coefficient of variation of the maximum strength F_{max}*

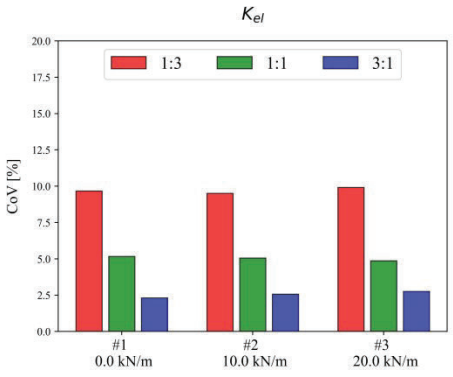

Figure 11: *Coefficient of variation of elastic stiffness k_{el}*

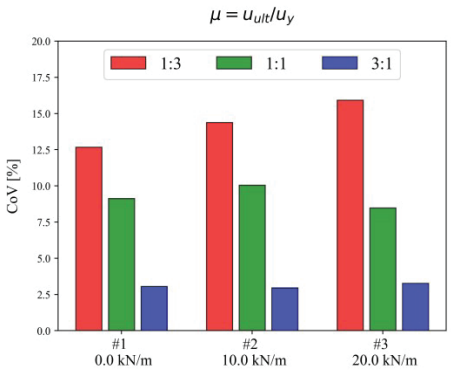

Figure 12: *Covariance of the ductility μ*

Table 5: *Minimum and maximum CoV in percentage*

	1:3 min-max	1:1 min-max	3:1 min-max
F_0	4.0-16.3	6.6-13.5	2.4-7.3
F_y	8.0-8.5	4.0-7.6	1.9-2.3
u_y	15.0-16.8	7.9-11.8	3.7-3.9
F_{max}	5.4-6.4	3.7-5.0	1.4-1.5
u_{max}	11.5-11.8	9.9-10.3	1.2-1.5
F_{ult}	6.6-6.8	7.5-8.5	3.8-5.7
u_{ult}	11.6-12.8	9.4-10.1	1.1-1.3
k_{el}	9.5-9.9	4.9-5.2	2.3-2.8
$k_{el,p}$	9.5-9.9	4.9-5.2	2.3-2.8
μ	12.7-15.9	8.5-10	3.0-3.3

To compare the overall variability, Table 5 summarises the minimum and maximum CoV of all parameters of the three configurations. The following remarks can be done:

- The CoV tends to decrease with the length of the shear wall;
- The strength F_0 shows the most significant variation among all configurations, with the lowest minimum and highest maximum coefficient of variation observed in configuration 1:3 due to the significant role played by the vertical loads;
- The strength F_y is relatively stable across all configurations, with a low coefficient of variation observed in all cases;
- The displacement u_y exhibits significant variations in all configurations, with a higher CoV than the other parameters;
- The parameters F_{max}, u_{max}, F_{ult}, and u_{ult} show variability across the different configurations, but the differences in the CoV among configurations are relatively small;
- The stiffnesses k_{el} and $k_{el,p}$ have the same CoV across all configurations (due to the EN 12512 linearisation);
- The ductility μ significantly varies among the configurations, with the lowest minimum and highest maximum coefficient of variation observed in configuration 1:3.

4 CONCLUSIONS

This paper investigates the variability of Cross-Laminated Timber (CLT) single-panel shear walls' response under in-plane lateral loads. The variability is considered by performing a parametric analysis on three different CLT shear wall configurations consisting of one thousand different finite element shear walls. The mechanical properties of all connections, based on experimental results, are randomly sampled to investigate several possible scenarios of the shear wall.

The results show that all mechanical properties, such as strength (yield, maximum, ultimate), stiffness (elastic, post-elastic), deformations (yield, maximum, ultimate) and ductility are influenced by the geometry of the shear wall and the vertical loads. As a general trend, the Coefficient of Variation (CoV) decreases with the length of the shear wall, whereas it shows limited variation with the vertical loads. All parameters have a different range of minimum and maximum CoV, varying from 1% to 17%.

Future studies are planned to investigate additional shear wall parameters and configurations and extend the analysis to multi-panel CLT shear walls.

ACKNOWLEDGEMENTS

Igor Gavrić gratefully acknowledges receiving funding from Horizon 2020 Framework Programme of the European Union; H2020 WIDESPREAD-2-Teaming: (#739574) and the Republic of Slovenia as well as the ForestValue Research Programme, a transnational research, development and innovation programme jointly funded by national funding organisations within the framework of the ERA-NET Cofund "ForestValue - Innovating Forest-based bioeconomy".

REFERENCES

[1] Rinaldi, V., Casagrande, D., Cimini, C., Follesa, M., & Fragiacomo, M. (2021). An upgrade of existing practice-oriented FE design models for the seismic analysis of CLT buildings. Soil Dynamics and Earthquake Engineering, 149, 106802. doi: 10.1016/j.soildyn.2021.106802

[2] Pozza, L., Savoia, M., Franco, L., Saetta, A., & Talledo, D. (2018). Effect of different modelling approaches on the prediction of the seismic response of multi-storey CLT buildings. Timber Struct Eng, 163. doi: 10.2495/CMEM-V5-N6-953-965

[3] Rinaldin, G., Amadio, C., & Fragiacomo, M. (2013). A component approach for the hysteretic behaviour of connections in cross-laminated wooden structures. Earthquake Engineering & Structural Dynamics, 42(13), 2023-2042. doi: 10.1002/eqe.2310

[4] Sustersic, I., Fragiacomo, M., & Dujic, B. (2016). Seismic analysis of cross-laminated multistory timber buildings using code-prescribed methods: Influence of panel size, connection ductility, and schematisation. Journal of Structural Engineering,

https://doi.org/10.52202/069179-0292

142(4), E4015012. doi: 10.1061/(ASCE)ST.1943-541X.0001344
[5] Seim, W., Hummel, J., & Vogt, T. (2014). Earthquake design of timber structures–Remarks on force-based design procedures for different wall systems. Engineering Structures, 76, 124-137. doi: 10.1016/j.engstruct.2014.06.037
[6] Rinaldi, V., Casagrande, D., & Fragiacomo, M. (2022). Verification of the behaviour factors proposed in the second generation of Eurocode 8 for cross-laminated timber buildings. Earthquake Engineering & Structural Dynamics. doi: 10.1002/eqe.3792
[7] Gavric, I., Fragiacomo, M., & Ceccotti, A. (2015). Cyclic behavior of CLT wall systems: Experimental tests and analytical prediction models. Journal of Structural Engineering, 141(11), 04015034. doi: 10.1061/(ASCE)ST.1943-541X.0001246
[8] Casagrande, D., Rossi, S., Sartori, T., & Tomasi, R. (2016). Proposal of an analytical procedure and a simplified numerical model for elastic response of single-storey timber shear-walls. Construction and Building Materials, 102, 1101-1112. doi: 10.1016/j.conbuildmat.2014.12.114
[9] Gavric, I., Fragiacomo, M., & Ceccotti, A. (2015). Cyclic behaviour of typical metal connectors for cross-laminated (CLT) structures. Materials and structures, 48, 1841-1857. doi: 10.1617/s11527-014-0278-7
[10] Dong, W., Li, M., Ottenhaus, L. M., & Lim, H. (2020). Ductility and overstrength of nailed CLT hold-down connections. Engineering Structures, 215, 110667. doi: 10.1016/j.engstruct.2020.110667
[11] Pozza, L., Saetta, A., Savoia, M., & Talledo, D. (2018). Angle bracket connections for CLT structures: Experimental characterisation and numerical modelling. Construction and Building Materials, 191, 95-113. doi: 10.1016/j.conbuildmat.2018.09.112
[12] Köhler, J., Sørensen, J. D., & Faber, M. H. (2007). Probabilistic modeling of timber structures. Structural safety, 29(4), 255-267. doi: 10.1016/j.strusafe.2006.07.007
[13] Folz, B., & Filiatrault, A. (2002). A computer program for seismic analysis of woodframe structures. Consortium of Universities for Research in Earthquake Engineering. doi:
[14] EN 12512:2001 (2002). Timber structures – Test methods – Cyclic testing of joints made with mechanical fasteners. CEN, Brussels, Belgium.

World Conference on Timber Engineering Oslo 2023

SHEAR PERFORMANCE ESTIMATION OF WOODEN LATHS AND PLASTER WALLS THROUGH EXPERIMENTS AND NUMERICAL ANALYSIS

Naoyuki Matsumoto[1], Katsuhiko Yamawaki[2], Kaori Fujita[3]

ABSTRACT: Structural tests and analytical modelling were conducted to clarify the seismic performance of wooden laths and plaster walls, which are one of the representative types of modern Japanese wooden buildings. Wooden laths and plaster is a construction method where plaster is applied to substrates made with 50 mm wide and 10 mm thick boards. In this study, the plaster wall was fabricated with the four sides of the wall restrained by the frame (columns, a lintel, and a baseboard), and static lateral loading tests were conducted. The results indicated that the wall has two types of resistance mechanisms, one at the point of initial stiffness and the other at the point of reaching the maximum bearing capacity, due to the large influence of the wall restraint by the frame. Secondly, shear element tests of small walls and shear tests of plaster materials were conducted to simulate the two types of resistance mechanisms. Finally, two numerical analysis models were presented to estimate the initial stiffness and maximum bearing capacity in a full-scale test. The numerical analyses showed an initial stiffness of 80% and a maximum bearing capacity of 130%.

KEYWORDS: Wooden lath, Plaster, Lateral loading test, Element test, Shear performance, Analytical model

1 INTRODUCTION

1.1 BACKGROUND

Modern Japanese wooden buildings, from the Meiji Restoration to World War II, are built based on the mixed techniques of traditional and Western buildings, and many do not have reliable standards or data for structural evaluation. With the increase in the preservation and rehabilitation of modern wooden buildings, proper evaluations of their structural mechanisms are imminent. Few studies have focused on the structural systems of modern structural walls, and a variety of walls was found to have surplus capacity [1-3]. This study focuses on a wall with wooden laths as substrates and plaster as the finish. Although this type of wall is one of the most prevalent and existing experiments have reported the reinforcement effect of the plaster finish and its tough behavior, even after plaster failure, its structural mechanism has not yet been clarified. Therefore, establishing a numerical estimation method for evaluating the structural performance of wooden laths and plaster walls will lead to more flexible and appropriate seismic diagnoses and evaluations of modern wooden buildings.

1.2 PURPOSE AND METHODOLOGY

This study aims to experimentally elucidate the horizontal force resistance mechanisms of wooden laths and plaster walls and proposes a mechanical model to estimate the initial stiffness and maximum load as the basic structural performance of the wall. Here, the composition pattern of laths was based on the Japanese style; that is, laths were nailed only between the columns on the small studs next to them **(Figure 1)**.

First, we conducted full-scale lateral loading tests to understand the typical load deformation relationships and failure patterns and then proposed two phases of resistant systems. Subsequently, element tests on the shear performance of the plaster, lath-and-nails, and small laths-and-plaster walls were performed. Finally, in combination with the resulting data, an analytical model is proposed to assume the initial stiffness and maximum load.

2 WOODEN LATHS AND PLASTER

Wooden laths and plaster finishes quickly prevailed in Japan after the Meiji Restoration (1868), referring to the Western techniques and combining them with traditional plastering techniques. Thin wooden lath boards (approximately 50 mm wide and 10 mm thick) were used as substrates, and they were nailed to the columns. Hemp ropes were also nailed for fastening plaster and the laths, and plaster mixed with seaweed glue was applied in layers of approximately 20 mm. This method is commonly used for the walls of Western-style buildings as a substitute for mud walls and is sometimes applied to ceilings. **Figure 1** shows a schematic of wooden laths and plaster walls.

[1] Naoyuki Matsumoto, Department of Civil Engineering and Architecture, Faculty of Eng., Tohoku University, Japan, nmatsu@rcl.archi.tohoku.ac.jp

[2] Katsuhiko Yamawaki, Yamawaki Katsuhiko Architectural Engineering Design, Inc., Japan, yamyam.e.design@gmail.com

[3] Kaori Fujita, Dep. of Arch., Faculty of Eng., The University of Tokyo, Japan, fujita@arch1.t.u-tokyo.ac.jp

https://doi.org/10.52202/069179-0293

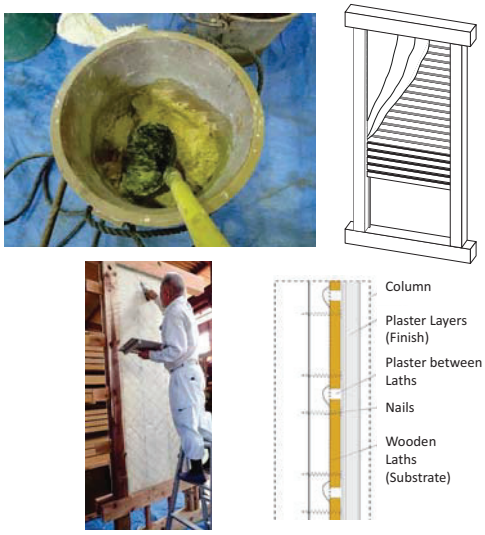

Figure 1: *[clockwise from top left] Plaster material, Composition of the wooden laths and plaster wall, Section details of the wall, and Plastering process*

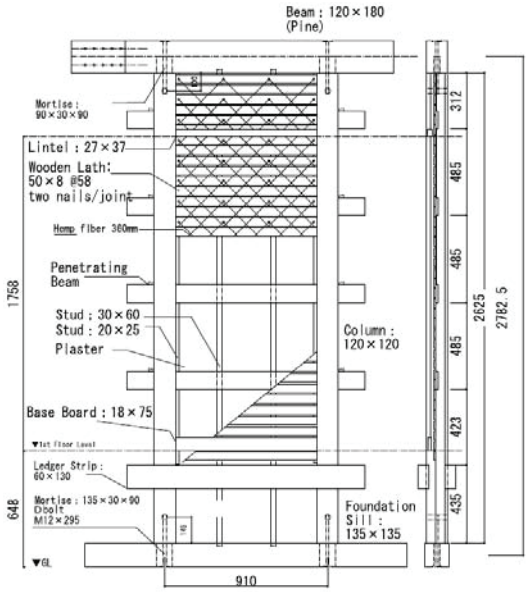

Figure 2: *Dimensions of the specimen [lath and plaster + frame]*

3 FULL-SCALE LATERAL LOADING TESTS

3.1 SUMMARY OF LATERAL LOADING TESTS

Full-scale static loading tests were conducted to clarify the horizontal force resistance mechanisms of the wooden laths and plaster walls. The dimensions of the specimens were based on those of a cultural heritage house built in Tokyo in 1928. To understand clearly the differences in the structural performances and mechanisms, the same tests were conducted on a frame wall (only with penetrating beams) with the same dimensions.

3.2 SPECIMENS

The specifications of the specimens are shown in **Figure 2**. The specimen was made with traditional unit wall dimensions of 910 mm × 2783 mm, referring to the walls of an important cultural property building located in Tokyo (constructed in 1928, modern Japanese-style architecture). The wall has four penetrating beams, two ledger strips at the bottom, and a void below the floor level. The wall was divided into upper and lower sections by a nailed lintel, and at the bottom of the plaster wall, a baseboard was inserted and nailed to the column.

The substrate of the wall was made of 50 mm wide and 8 mm thick wooden lath nailed to the pillar frames, and plaster was applied over the laths. The formulation of the plaster is listed in **Table 2**. Three types of plaster were used: undercoat, middle coat, and finish coat. The formulations conformed to the specifications of the buildings used as the reference. The materials used were slaked lime, sand, hemp fiber, seaweed glue, and water. The plaster material for each layer was prepared by first making a mixture of glue, slaked lime, and hemp fiber, called "*Tsuta-awase*," and then mixing sand into the mixture as needed. The total plaster thickness was approximately 20 mm.

Table 1: *Specifications of specimens [lath and plaster + frame]*

Item	Unit	Dimension/Specification
Column	mm	120×120
Beam	mm	120×180
Foundation	mm	135×135
Stud	mm	30×60, 20×25
Species	—	Sugi (Japanese Cedar)
Wooden Lath	mm	50×8×530 @58
Species	—	Sugi (Japanese Cedar)
Nail	mm	N32 * 2 [30 mm apart] @255; shell diameter: 1.9

Table 2: *Formulation of plaster*

Number of layer	Types of layer	unit	Thickness of each layer	Note on formulation
1st and 2nd layer	Under coat	mm	t = 2+1	*Tsuta-awase* (Plaster with hemp) Slaked lime Water
3rd layer	Flatten layer	mm	t = 1	Same as above
4th, 5th, and 6th layer	Middle layer	mm	t = 4+3+3	Plaster : Sand = 1:2 (or more)
7th layer	Finish coat	mm	t = 2	Plaster (shell ash) and algae glue

A static cyclic load ranging from 1/600 rad to 1/10 rad was applied, one cycle at each step. The test was terminated when the maximum load decreased to 80% or reached 1/10 rad.

https://doi.org/10.52202/069179-0293

3.3 RESULTS OF LATERAL LOADING TESTS

The maximum bearing capacity was 8.7 kN (at 1/60 rad). For the wooden lath and plaster wall, approximately 1.9 times higher than the 4.6 kN (at 1/15 rad) of the frame specimen. Elastic stiffness was 7.5 times greater for the wooden lath and plaster wall than for the frame specimen. The deformation angle at the maximum load capacity was +1/60 rad to −1/75 rad for the wooden lath and plaster wall, whereas the load did not decrease for the frame specimen.

Although the frame wall exhibited some damage to the penetrating beams and ledger strips by embedding, the load increased toward the end of the experiment, at 1/10 rad. In contrast, the wooden lath and plaster wall initially showed a stable high stiffness value; however, after exceeding the maximum load capacity, the load decreased to approximately 60% of the maximum load capacity, indicating a brittle behavior. Subsequently, the load gradually increased and was 1.5 times greater than that of the frame specimen, suggesting that the nails and residual plaster were functional up to large deformations.

Based on the observation of the failure conditions, the resistance mechanism of the wooden plaster and lath wall to horizontal forces can be divided into two phases.

The restraint condition of the plaster layer changes as the deformation progresses and the two lateral members (lintel and baseboard) that support the layers gradually break at their connections with the columns. When the two lateral members and joints are sound, as the initial stiffness is maintained, the shear and compression performances of the plaster are dominant, because the four-round members restrain the plaster layer. However, at approximately the maximum load after the loss of the baseboard restraint, the plaster layer was mainly restrained to only two columns, and the plaster layer began rotating. Then, the lateral resistance is dominated by the rotation-shear force between the plaster layer and the plaster filling the gap between the laths. Based on these two phases of resistance mechanisms, we propose an "initial stiffness estimation model" and a "maximum strength estimation model."

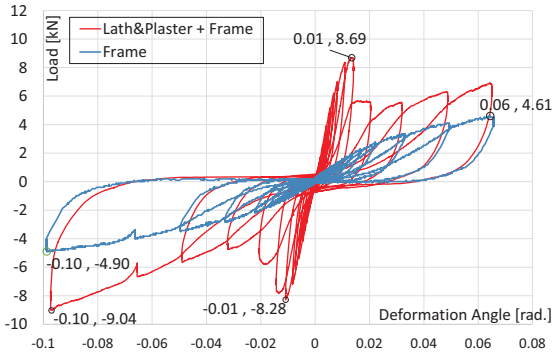

Figure 3: *Comparison of test results for wooden laths and plaster wall and frame wall (columns and beams)*

Table 3: *Characteristic value of full-scale wall test*

Characteristic value		Maximum Strength	Deformation @P_{max}	Yield Strength	Yield Deformation	Ultimate Strength	Ultimate Deformation	Initial Stiffness
		P_{max}	δ_{Pmax}	P_y	δ_y	P_u	δ_u	K
	unit	kN	rad.	kN	rad.	kN	rad.	kN/rad.
Frame	Push	4.61	0.065	2.71	0.024	4.13	0.067	114
	Pull	4.02	0.066	2.37	0.027	3.51	0.067	89
	Ave.	4.31	0.065	2.54	0.025	3.82	0.067	102
Lath and Plaster + Frame	Push	8.69	0.016	5.69	0.007	6.10	0.033	768
	Pull	8.28	0.014	5.27	0.007	5.72	0.034	784
	Ave.	8.49	0.015	5.48	0.007	5.91	0.033	776

Figure 4: (Left) *Ultimate condition of wooden laths and plaster wall (@-1/10 rad).* ***(Right):*** *Major fracture patterns of wooden laths and plaster (shear and compressive failures of the plaster layer, shear failure of the plaster filled within wooden laths' gaps, and fracture at the edge of base board)*

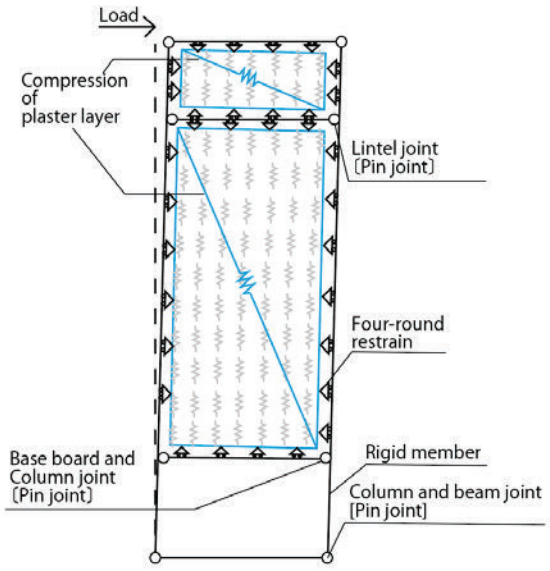

Figure 5: *Lateral resistant mechanism of laths and plaster wall: initial stiffness phase*

https://doi.org/10.52202/069179-0293

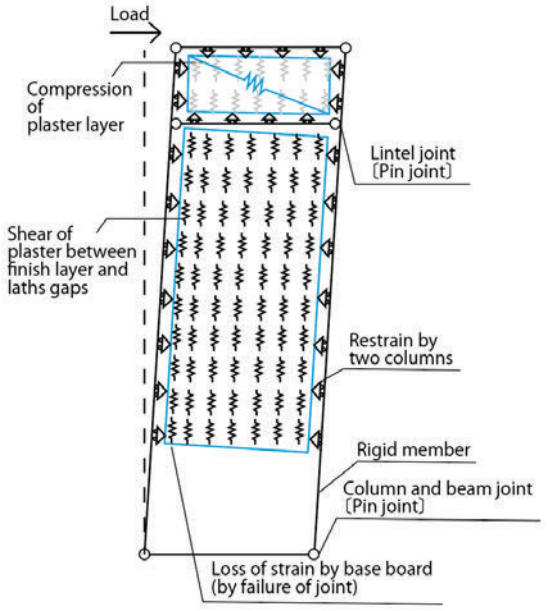

Figure 6: *Lateral resistant mechanism of laths and plaster wall: maximum load phase*

4 ELEMENT TESTS ON WOODEN LATHS AND PLASTER

Two types of element tests were conducted to determine the properties required to fulfil the analytical model: (1) shear tests on 580 mm square small laths and plaster walls, and (2) shear tests on the plaster material

4.1 SHEAR TESTS ON 580 MM SQUARE SMALL LATH AND PLASTER WALL

From the observations of the full-scale tests, it was estimated that the shear resistance of the wooden lath and plaster wall, when fully restrained on all four sides, is mainly due to the shear resistance of the nails, compressive effect of the wooden lath and plaster wall, and shear resistance of the plaster key. To verify these effects, elemental specimens of 580 mm square lath and plaster walls were prepared, and shear element experiments were conducted with and without plaster as parameters. The specimens are shown in **Figure 8**. The specifications of the wooden lath and plaster element wall were identical to those of the full-scale specimen.

WL series: Specimens without plaster finish

As the specimen deformed in shear, shear deformation occurred at the joints of each wooden lath to the supporting wood at the edge by the nails and studs. The distance between the edge of the wooden lath and the wood frame was approximately 1 to 1.5 mm, and the contact between the wood frame and the edge of the wooden lath was observed to be approximately 1/15 rad. Subsequently, the nails of the wood-frame support were pulled out and embedded in the wood frame. Although the load did not decrease, cracks and fractures were observed at the edges of the wooden lath. The maximum loads of three specimens were 1.4 kN (0.11 rad.), 1.4 kN (0.12 rad.), and 0.6 kN (0.1 rad.).

WL+P series: Specimens with plaster finish

In the test of WL+P1, the plaster layer gradually began to swell and went up on the wooden frame before it reached the maximum load. Eventually, the shear failure of the plaster at the gap between the wooden laths and the crushing of the plaster layer at the top and bottom edges occurred. However, shear cracks were not observed. However, in the case of WL+P2, although slip was observed at the beginning, the plaster layer did not protrude, but resisted within the wooden frame surface, and the load decreased after the deformation angle of 0.03 rad. Cracks were observed between the top and bottom at a deformation angle of approximately 1/22 rad.

In both specimens, the behavior was similar; compression between the top and bottom edges became remarkable, as the plaster layer did not follow the shear state in the large deformation. The maximum load was 10.7 kN (0.03 rad) for WL+P1 and 9.7 kN (0.036 rad) for WL+P 2.

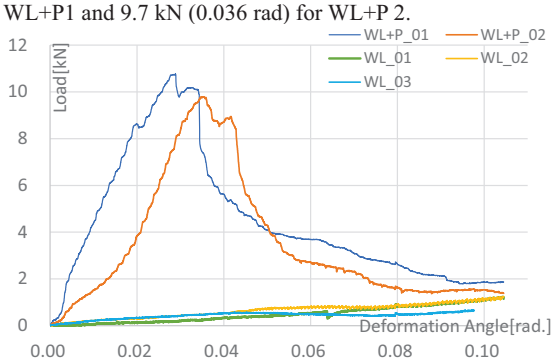

Figure 7: *Results of the Test: WL+P (wooden laths and plaster) and WL (wooden laths)*

Table 4: *Characteristic value of small wall shear tests*

Characteristic Value		Max. Load	Angle at Max. Load	Elastic Shear Stiffness*
		kN	rad.	kN/mm2・rad.
Wooden Lath (WL)	1	1.40	0.1	**0.002
	2	1.40	0.1	**0.002
	3	0.60	0.1	**0.0005
	ave.	1.13	0.1	—
Wooden Lath + Plaster (WL+P)	1	10.7	0.03	0.06
	2	9.7	0.036	0.03－0.04
	ave.	10.2	0.033	—

*2 kN to 8 kN are regarded as the elastic area

**Shear area of WL series are assumed to be same as WL+P

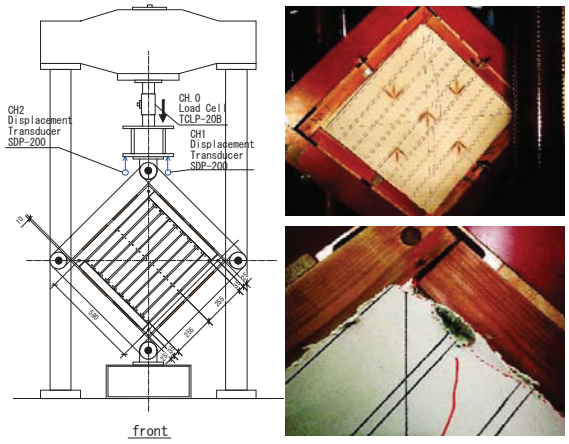

Figure 8: *Setting of shear tests(left), Final condition of shear tests of small wall: (cracks on plaster(up), Crushed plaster edge(down))*

https://doi.org/10.52202/069179-0293

4.2 SHEAR TESTS ON PLASTER MATERIAL

Based on the observation of the full-scale test, it was assumed that the plaster key between the wooden laths would reach the maximum load by shear resistance as a resistance mechanism after the failure of the baseboard. Therefore, material shear tests were conducted on the undercoat plaster to determine its shear stiffness and strength.

Maximum Shear Stress and Failure Process

The experimental results are listed in **Table 5**, and the load-deformation relationships are shown in **Figure 11**. The shear stress, τ, was calculated by dividing the load by the shear area (B * H'), and was generally 0.7–0.8 N/mm^2 for the other specimens, although it was about 1.5 times higher for PS6 and PS7. The overall average is approximately 0.89 N/mm^2. The displacement at the maximum load varied slightly from 0.64 to 1.6 mm, but the failure process was similar. Even after the shear face failed, the load gradually decreased as the plaster fragments became entangled with the fibers of the shear plane **(Figure 10)**. However, edge collapse was observed under the applied force.

Assumption of shear strain angle and elastic stiffness: Comparison with wood plaster

Because it was difficult to measure the shear strain directly, the following assumptions were made: The steel base that holds the specimen down has a 2 mm clearance from the shear plane of the plaster to remove the effect of compression at the corner. Considering the failure situation and assuming that the shear deformation in this area is significant and that the stress distribution is uniform, the shear strain γ is expressed as d/2, where d is the vertical displacement **(Figure 12)**. The shear elastic stiffness calculated with shear strain γ was approximately 3 N/mm^2.

In contrast, shear deformation was estimated to occur close to the surface of the actual plaster wall **(Figure 12)**. In addition, because the undercoat plaster and plaster key are integrated, it is assumed that this area (thickness L) is subjected to shear deformation if the plaster is sufficiently fixed in the gaps of the wooden laths. In this case, it was estimated that the size of the gap between laths affects the maximum shear force and has little effect on the failure displacement.

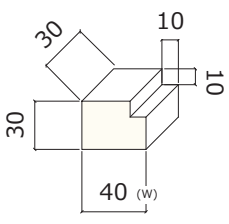

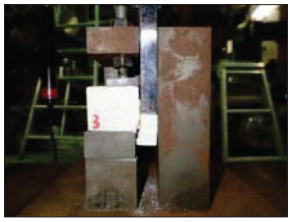

Figure 9: *Dimensions of specimens (left)*
Figure 10 : *Final condition of shear tests (right)*

Table 5*: Result of shear tests*

	P_{max}	τ_{max}	Disp. @P_{max}	Shear Strain @P_{max}	Shear Stiffness*
unit	N	N/mm^2	mm	-	N/mm^2
PS1	421	0.70	0.64	0.32	3.43
PS2	486	0.81	1.00	0.50	2.39
PS3	435	0.83	0.88	0.44	5.19
PS4	460	0.77	1.60	0.80	1.13
PS5	454	0.78	1.54	0.77	2.22
PS6	669	1.17	0.80	0.40	4.98
PS7	698	1.15	1.52	0.76	1.70
Average	518	0.89	1.14	0.57	3.01

*Secant stiffness from 10% to 50% of P_{max}

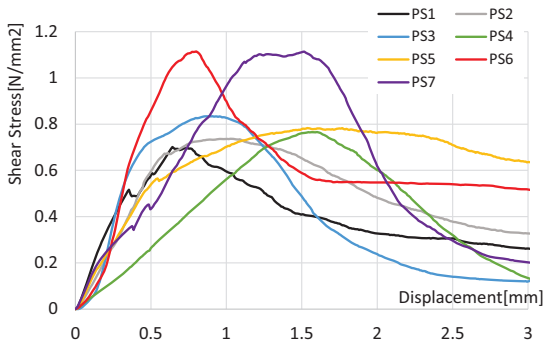

Figure 11: *Shear stress–displacement curves*

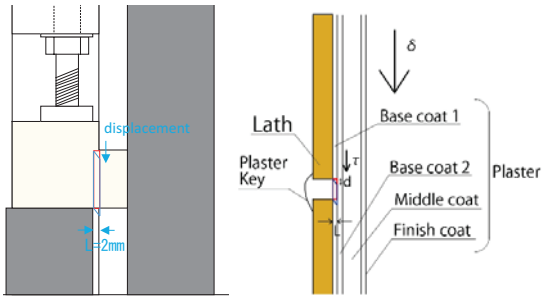

Figure 12: *Settings of shear tests(left) and Hypothesis of Shear Strain in the wall (right)*

5 ANALYSIS OF THE INITIAL STIFFNESS AND MAXIMUM LOAD

Two mechanical models were constructed based on previous tests to analyze the initial stiffness and maximum load. In the initial stiffness estimation model, in which the shear resistance of the wooden lath and plaster (both above and below the lintel) were considered, the shear stiffness was estimated to be approximately 80% accurate. In the model for estimating the maximum load, in which the shear resistance between the finish layer and the gaps of laths was dominant, particularly below the lintel, the maximum load was estimated to be approximately 1.3 times that of the tests. **(Figure 15)**

The horizontal shear stiffness and capacity of the wooden lath and plaster wall were calculated based on the results of the element tests described in Section 4. The calculation was performed on the portion of the wall that did not include the shear resistance of the frame wall (only the effects of the wooden lath and plaster were calculated).

https://doi.org/10.52202/069179-0293

In Section 3, the resistance mechanism of the Japanese-style (rounded by frames) plaster wall is divided into two phases, before and after the baseboard is damaged. The initial stiffness is assumed to be exerted mainly by the shear mechanism of the wall before the baseboard is damaged. The maximum bearing capacity was assumed to be reached through the process of shear failure of the plaster in the gap of the lath after the baseboard was damaged.

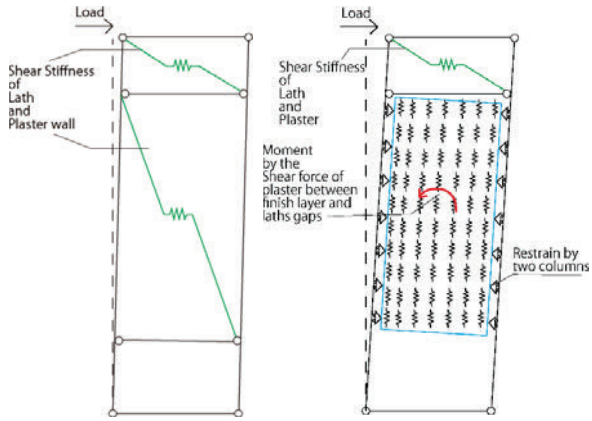

Figure 13: *Analytical model of lath and plaster wall: Initial stiffness phase (left), Maximum strength phase (right)*

1) Sound baseboard condition (initial stiffness model)

In the initial state of resistance, the lath and plaster walls were considered to act as shear-resisting elements. As shown in **Figure 13**, the stiffness and strength of the small-wall experiments were used to evaluate the initial stiffness.

The wall parameters applied to the initial stiffness model are as follows

$\tau_{max} = P_{max}/\sqrt{2}\ /L\ /t = 0.067\ [kN/cm^2]$

The initial stiffness of the hanging wall section is 88 [kN/cm^2] and that of the section from the lintel to the baseboard is 422 [kN/cm^2], totaling about 509 kN/cm^2, which is about 80% of the experimental elastic stiffness **(figure 15)**.

2) After baseboard failure (maximum bearing capacity)

From the observations of the full-scale test, it was estimated that when the base boards were damaged, the vertical restraining effect of the plaster layer was lost. In such a case, as explained in the previous section, it was assumed that the small area between the plaster and wooden lath substrates would resist shear deformation.

In the maximum bearing capacity model, the maximum bearing capacity is calculated based on the shear stiffness of the plaster. It is assumed that the upper and lower restraints are burned out and that only the left and right columns are restrained. The wooden frame was assumed to deform horizontally, whereas the plaster plate on the laths was assumed to deform rotationally while being restrained on the left and right sides. The load-deformation relationship for each angle of deformation was calculated from the balance between the total moment resistance owing to the shear force from the plaster key between the wooden laths and the horizontal force acting on the top.**(Figure 14)** The maximum bearing capacity was 9.1 kN, approximately 1.3 times of the experimental value, as shown in **Figure 15**.

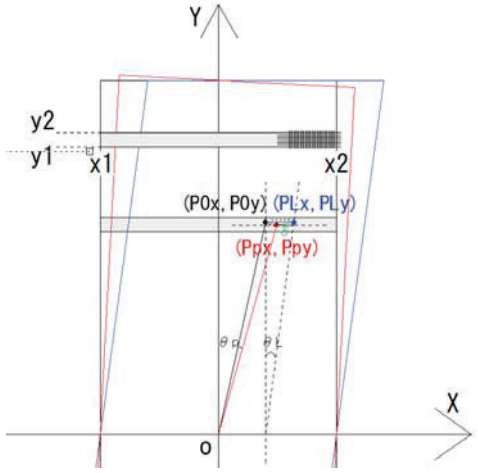

Figure 14: *Diagram of shear displacement of plaster key (plaster between the gaps of laths) from wooden lath*

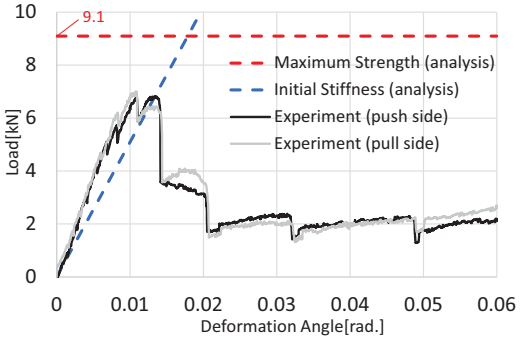

Figure 15: *Shear stress–displacement curves showing the shear test evaluations and shear strain hypothesis*

6 CONCLUSIONS

Lateral loading tests were conducted on laths and plaster walls to clarify their shear performances and failure mechanisms. The results indicate that the restraint conditions of the plaster layer (columns, lintel, and baseboard) significantly affected the resistance mechanism. Through element tests and analysis, we could accurately predict the initial stiffness (80% of the experiment) and maximum load (130% of the experiment). To clarify the proposed system further, the interactive behavior and stress distribution between the plaster and the laths must be investigated in detail.

ACKNOWLEDGEMENT

The authors would like to thank Japan Cultural Heritage Consultancy, Iwase Kenchiku and Osaki Sakan for technical assistance with the production of specimens and conducting the experiments. This work was supported by JSPS KAKENHI 21K14287, Matsui Kakuhei Memorial Foundation and Obayashi Foundation.

REFERENCES

[1] Tanabe H., Goto K., Kikuta M.: Tests on Timber Frames with Wall (European System) under Alternate Horizontal Load (Study on Earthquake Resistant Timber Construction. Part 7)., Journal of Architectural Institute of Japan, 13:210-219, 1939.

[2] Katayama T., Tomitaka R., Sawada K., Hirai T.: Structural Evaluation of Bearing Wall in Kita Ichijo Catholic Church, In: Proceedings of the Annual Conference of Hokkaido branch of the Japan Wood Research Society, 14-17, 2012.

[3] Takino A., Shimokawa C., Ishiyama H., Nakano R.: Experimental Study on Lateral Performance of Shear Wall of Modern Timber Architecture Combined with Brace and Plaster using Wood Lath. Journal of Structural and Construction Engineering, 83(752):1477-1485,2018.

https://doi.org/10.52202/069179-0293

World Conference on Timber Engineering Oslo 2023

A SEISMIC RESPONSE ESTIMATION MODEL FOR CROSS-LAMINATED TIMBER WALLS USING MACHINE LEARNING

Eknara Junda[1], Christian Málaga-Chuquitaype[2]

ABSTRACT: This paper proposes a machine learning-based model for estimating the seismic damage of cross-laminated timber (CLT) walls. Random Forests are used to this end. A database is created using numerical results from nonlinear response history analyses under a large set of ground motions. 69 numerical models of CLT walls with various structural characteristics and design parameters are used. The maximum inter-storey drift ratio (MIDR), which plays an essential role in explaining the seismic damage of buildings, is adopted as the damage predictor target. Two feature selection techniques, sequential forward floating selection and LASSO are applied to evaluate the impact of various input features on the estimation performance. Results show that a high accuracy of the estimation is obtained if six features are employed as inputs. The proposed model performance is assessed and then compared with traditional methods. Finally, the Shapley Additive exPlanation method is employed to interpret the influence of the input features on the MIDR estimates in the machine-learning-based model.

KEYWORDS: Seismic demand estimation, Machine learning, CLT walls, Random Forests, Maximum inter-storey drift ratio

1 INTRODUCTION

Cross-laminated timber (CLT) is an environmentally friendly material that offers several advantages in construction, such as high prefabrication level, good thermal insulation, lightweight, and good fire performance when properly designed. CLT has enhanced mechanical properties springing from its manufacturing process resulting in high in-plane strength and stiffness. Thus, CLT has been widely used for walls as the load-bearing element of CLT buildings, including being considered as the lateral force-resisting system in seismic applications [1].

The advantageous mechanical and environmental characteristics of CLT have made it an attractive option for mid to high-rise buildings in earthquake-prone regions. Typical CLT buildings generally comprise panels linked by metal connectors such as hold-downs, angle brackets, and screws. These connectors play a vital role in dissipating the seismic energy through the nonlinear deformation under seismic actions. On the other hand, the CLT panel is assumed to behave as a rigid body [2]. This causes the lateral deformation of CLT buildings to be fundamentally based on a combination of rocking and sliding responses which are completely different from other structural systems, such as moment frames or braced frames governed by flexural behaviour. Such rocking and sliding deformation of CLT walls are complex and challenging to predict due to the overlying effects of pinching, friction, stiffness and strength degradation phenomena. These complex phenomena could also result in high inelastic deformations under strong earthquakes. All this in the context of the continuous push towards taller CLT buildings driven by current developments in construction technology. Therefore, more complex structural behaviours and high seismic demands are expected. Hence, an accurate tool for estimating and assessing the seismic demands of CLT walls is needed.

Seismic demand estimation using machine learning (ML) have increasingly been applied to various structural systems. As ML algorithms do not need functional forms to predict a target, they can successfully map the complex relations between inputs and the target by learning directly from a given dataset. Such abilities to learn and recognise data patterns make ML beneficial for dealing with high-dimensional spaces [3]. ML models for the estimation of seismically-induced responses have been developed for a variety of systems, from geotechnical structures [4] to extra-terrestrial constructions [5]. Likewise, several ML techniques were used to establish regression-based and classification-based models for reinforced concrete [6] and steel frames [7]. ML techniques were also used for other structural systems in the past few years [8-10]. Even though ML techniques have been used for the seismic response estimation of various structural systems, no previous study has applied such techniques to CLT walls. This despite the fact that, as mentioned earlier regarding the complexity of the seismic response of CLT walls, ML techniques have inherent advantages in handling the highly nonlinear

[1] Eknara Junda, Imperial College London, UK, eknara.junda19@imperial.ac.uk
[2] Christian Málaga-Chuquitaype, Imperial College London, UK, c.malaga@imperial.ac.uk

https://doi.org/10.52202/069179-0294

responses and explore the complex relations among parameters of multi-storey CLT walls.

This paper proposes a ML model for estimating the seismic response of multi-storey CLT walls. The maximum inter-storey drift ratio (MIDR) is chosen as the output target. Thirty input features are used as predictors. These features are composed of intensity measures (IMs) and structural parameters of CLT walls (SPs). Sixty-nine numerical models of CLT wall cases with different structural configurations are created and analysed using nonlinear response history analyses to obtain MIDR. Random Forests, a ML algorithm, is used to develop a regression model for MIDR estimates. Finally, the prediction performance of the ML-based models are evaluated and compared with traditional methods. In addition, the influence of each input features on the MIDR prediction is interpreted using SHAP.

2 CLT STRUCTURAL MODELS AND GROUND MOTIONS

2.1 CLT WALL MODELS

69 CLT structures representing residential multi-storey CLT buildings of different heights and panel fragmentation levels are considered. All buildings share the same plan layout and have a typical storey height of 3.5 m, except for the ground level which height is 4.3 m. Figure 1 shows the configuration of a typical 12-storey CLT building as an example. Dead loads were calculated considering all finishing and insulation, whereas a superimposed load of 2.0 kN/m^2 was assumed. Loads considered for seismic mass are a combination of 100% dead and 30% superimposed load. The response spectrum of Eurocode 8 Type 1 [11,12] at a Peak Ground Acceleration (PGA) of 3.0 m/s^2 with an importance factor of 1.0 was adopted to estimate the seismic load.

In this study, CLT Wall 2-BC was selected as the representative part of the structure. The wall is 8.5 m long (marked with dashed lines in Figure 1). All walls were designed using capacity design principles and current codified guidance. We followed ductile design and failure mode control principles informed by Eurocode 8, Part 1. More details of the design processes of the CLT structure can be found in [12].

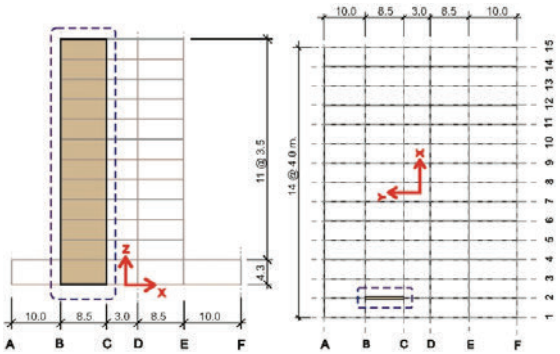

Figure 1: *Typical 12-storey building.*

Several parameters were varied during the design to cover a wide range of CLT buildings and evaluate their effects on the corresponding seismic demands. These parameters comprised the number of storeys, the sub-panel numbers, and the behaviour factors. Table 1 summarises parameters regarding CLT walls adopted in this study.

Table 1: *parameters regarding CLT walls*

Parameters	Variables
Number of stories (N)	6, 8, 12, 16, 20
Number of subpanels per wall (m)	1, 2, 3, 4
Behaviour factor (q)	1.5, 2, 2.5, 3, 4

We developed a series of 2D numerical models of the wall structures in OpenSees [13]. Figure 2 shows a schematic drawing of the model for a wall with m = 2. All CLT panels were discretised into a number of shell elements. In contrast, two-node link elements with zero length represented the three main steel connectors (hold-downs, shear brackets, and vertical screws). The link elements for hold-downs were located at the corners of the panels, represented by blue springs. Angle brackets were distributed along the length of the panels in the X direction (red springs), and self-threaded screws at the vertical joints were lumped into an equivalent single link element, placed at the mid-height of the panels (shown in green).

Since most of the nonlinear deformations in CLT walls under lateral actions occur at their joints and since the CLT panels themselves are expected to remain largely elastic [12,14], an equivalent isotropic material model with linear elastic properties was assumed for the CLT panels. In steel connectors, we used a hysteretic uniaxial material model to capture the global nonlinear responses. Both shear and axial direction capacities were modelled in all types of connectors, considering the uncoupled reaction between the two directions. The strength, deformation values, pinching, strength and stiffness degradation were calibrated against available data from previous experimental studies [15-17]. Moreover, a leaning column, modelled using beam-column elements, was connected to the wall through equal degree-of-freedom constraints to account for P-Delta effects caused by gravity loads. This was done to consider geometric nonlinear effects since the shell element type used in OpenSees only allows for a linear geometric transformation. A Rayleigh damping model with a damping ratio of 0.05 in the first and fifth mode was assumed in all cases.

https://doi.org/10.52202/069179-0294

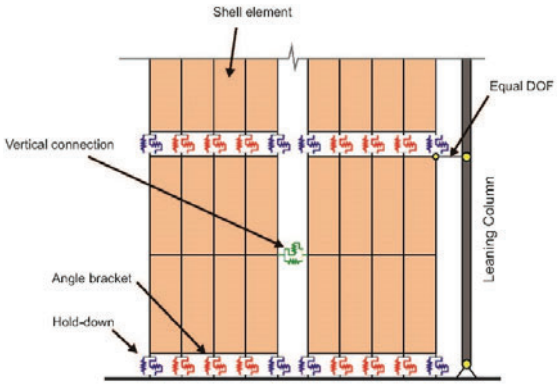

Figure 2: *Numerical model of CLT walls.*

The CLT-walled models mentioned above were validated against experimental results. Two cases of structures, single wall and couple walls are compared and shown In Figures 3 and 4. It is seen from the comparisons that our modelling approach can efficiently reproduce the experimental hysteretic response of CLT assemblages.

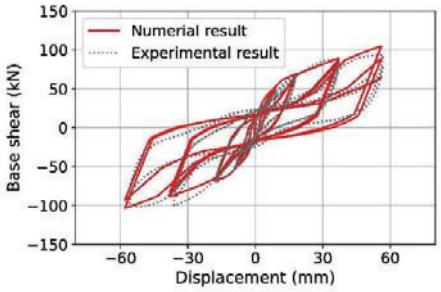

Figure 3: *Validation of the numerical model for a single wall.*

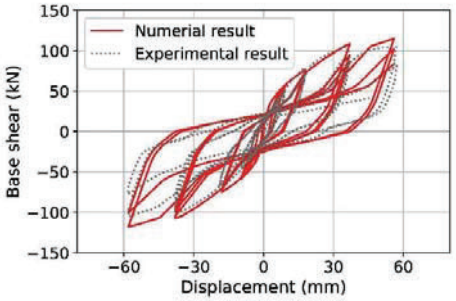

Figure 4: *Validation of the numerical model for coupled walls.*

2.2 GROUND MOTIONS

In this study, we used the 1,656 records selected by Hancock et al. [18] from the NGA-West database [19]. These records come from shallow crust seismic events with moment magnitudes between 5.1 and 7.9 and an average PGA of 1 g. More information regarding the ground motion set can be found in [18]. Moreover, scaling factors of 2 and 1 were used to scale up the original un-scaled records in order to increase the intensity of the ground motions, resulting in more cases of nonlinear responses. Therefore, the total number of ground motion records was 3,312 leading to 228,528 nonlinear response history analyses (NRHA). The massive analysis was performed on the high-performance computing facility (HPC) at Imperial College London.

3 FEATURE SELECTION

To develop an ML model for MIDR estimation, a training dataset was prepared. The dataset consists of the input features (predictors) and the output target (MIDR). Two main parameters were considered for the model development: ground-motion intensity measures (IMs) that describe earthquake characteristics and structural parameters (SPs) that describe structural properties in CLT walls. Nine common IMs were selected based on hazard computability, including Peak Ground Acceleration (PGA), Peak Ground Velocity (PGV), Peak Ground Displacement (PGD), total Arias intensity at the end of the time series (I_a), significant duration ($D_{5–75}$ and $D_{5–95}$), and spectral acceleration values at the building's fundamental period ($S_a(T_1)$) and at n times T_1 ($S_a(nT_1)$) where n was varied from 1.1 to 3.0, the mean period of the ground motion (T_m) and the ratio between the fundamental structural period and the ground-motion mean period (the tuning ratio, T_1/T_m). In addition, six structural parameters (SPs) were also considered as candidate input features. These include the behaviour factor (q), building height (H), slenderness (λ_w), length of fastening lines (FL), joint density (β_w), and wall subdivision ratio (m). These SPs have been reported in the literature to significantly impact the seismic response of CLT wall structures [14, 20, 21]. The total number of input features was 30.

We randomly divided the whole database into training and test sets to avoid overfitting during the model development. The training set contained 70 % of the database and was used for all the activities of the modelling processes, whereas the remaining 30 % of the data was kept as unseen data and was used for performance testing purposes at the final step. We transformed all IMs and MIDR to the log-normal space following the common assumption of lognormality adopted in earthquake engineering [22].

All 30 input features used for the model development were selected using different feature selection techniques, namely sequential forward floating selection (SFFS) and Least Absolute Shrinkage and Selection Operator (LASSO). The feature selection was carried out using the training dataset. Note that the objective of this process is to evaluate the predictive potential of the features and obtain a set of features influencing the prediction. The mean square error (MSE) was used to assess the fit, and a 10-fold cross-validation (CV) was applied to generalise the results, mitigate overfitting, and improve the model's robustness [23]. The features which finally selected were PGV, $S_a(T_s)$, T_1/T_m, q, H, and m. This set was considered

as an optimised combination of predictors, which was used to develop the ML model in this paper.

4 MACHINE LEARNING MODEL DEVELOPMENT

4.1 MODEL TRAINING

As mentioned previously, this paper compares the performance of MIDR estimates between a traditional regression model and an ML-based model. The algorithm used for a traditional method is Multiple Linear Regression, whereas an ML method is Random Forest. We have implemented the algorithms using the Scikit-learn package in the Python-based computational platform. Note that hyper-parameters of Random Forest were tuned to minimise a cost function using GridSearchCV, also available from the Scikit-learn package.

4.2 PERFORMANCE MEASURES

This study employs two performance metrics, the coefficient of determination (R^2) and the root mean square error (RMSE), to assess the applied models' prediction performance. These two indicators, widely adopted in ML performance studies, are provided for training and test sets. The expressions for R^2 and RMSE are given in Equations 1 and 2.

$$R^2 = 1 - \frac{\sum_{i=1}^{n}(y_i - \hat{y}_i)^2}{\sum_{i=1}^{n}(y_i - \bar{y}_i)} \quad (1)$$

$$RMSE = \sqrt{\frac{1}{n}\sum_{i=1}^{n}(y_i - \hat{y}_i)^2} \quad (2)$$

where $\hat{y}_i$ is the estimated target out, y_i is the real target value, and n is the number of data points.

5 RESULTS

5.1 MODEL PERFORMANCES

The prediction performances of the training and test datasets for the regression models are presented in Table 2. The MIDR estimates versus actual values are depicted in Figures 5 and 6 for the linear regression and random forest models, respectively. The result shows a comparable prediction performance between the training and the test set. This indicates that the models developed do not overfit the training data and should perform well on unseen data.

Table 2: *Comparison of the prediction performances*

Algorithm	MIDR			
	Training set		Test set	
	R^2	RMSE	R^2	RMSE
Linear regression	0.778	0.368	0.777	0.369
Random Forest	0.950	0.102	0.946	0.198

The traditional linear regression, which has been broadly applied for estimating seismic demands of structures, shows relatively low prediction power, evidenced by the lower R^2 and higher values of RMSE, compared to the Random Forest. The linear regression model clearly has notable dispersion levels between its predictions and numerical results, especially underestimating MIDRs at higher levels of demand. Lower performances are observed from the linear regression with R^2 of 0.777 and RMSE of 0.369 on the test set for MIDR estimates. This indicates that traditional approaches like Linear Regression might not be able to predict MIDR over the full range of deformation in CLT structures. The low prediction performances can be partially attributed to its inability to describe highly nonlinear processes and complex relationships between the input features and MIDRs. On the other hand, the model developed from Random Forest shows substantial improvements in prediction power over the traditional method, reflected by 21.75% higher values of R^2 and 46.34% lower values of RMSE. The results clearly show that Random Forest can capture better the non-linearity in the drift response of CLT walls.

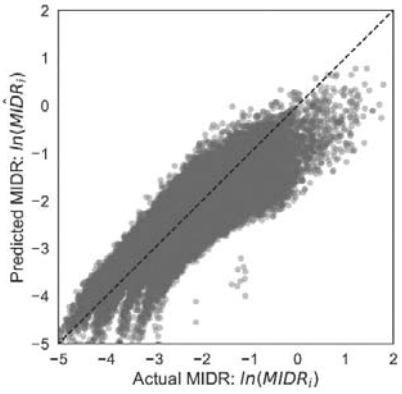

Figure 5: *Comparison between actual and predicted MIDR from the Linear Regression model.*

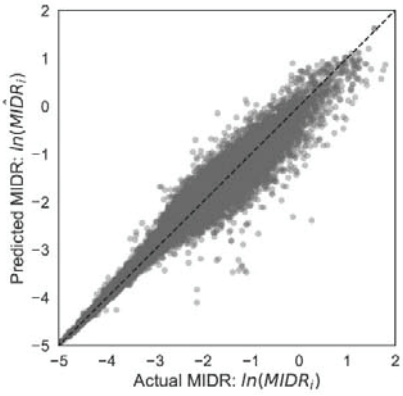

Figure 6: *Comparison between actual and predicted MIDR from the Random Forest model.*

https://doi.org/10.52202/069179-0294

5.2 MODEL INTERPRETATION

Machine learning models can be difficult to understand and are sometimes seen as black boxes due to their complex algorithms. It is essential to know how a model makes predictions and which factors affect the model. To this end, SHAP methodology [24] was used to explain our ML model, Random Forest. Figure 7 shows the SHAP summary plot for MIDR. Each point in this graph shows the relation between the six features and the SHAP value obtained from the Random Forest model. The features are ordered from top to bottom based on their overall importance to the model prediction. It is observed that $\ln(S_a(T_1))$ is the most important feature, followed by H, ln(PGV), m, q, and $\ln(T_1/T_m)$. The variation in colours, from blue to red, represents the variation of the features from low to high, respectively. Moreover, data points that result in the same SHAP value are scattered, leading to different distribution shapes for the features.

The SHAP summary indicates that MIDR positively corresponds to almost input features except for $\ln(T_1/T_m)$. An increase in SHAP value goes along with an increase in $\ln(S_a(T_1))$, H, ln(PGV), m, and q. In the case of $\ln(T_1/T_m)$, lower values have more impact on MIDR than higher values, as the red dots are concentrated approximately in the SHAP value of 0. It is also observed that small SHAP values (SHAP values < 0) are sensitive to the variation of all features, reflected in the long blue tails to the left. This indicates that all features significantly impact the low range of MIDR, especially in the case of $\ln(S_a(T_1))$. The SHAP explanation is consistent with the fact that this range of MIDR is strongly dependent on the elastic stiffness of the structures, as well as their yield strength and structural configuration. On the other hand, ln(PGV) influences the model for large MIDR values significantly. Other features become progressively less influential on the prediction, especially m, q, and $\ln(T_1/T_m)$.

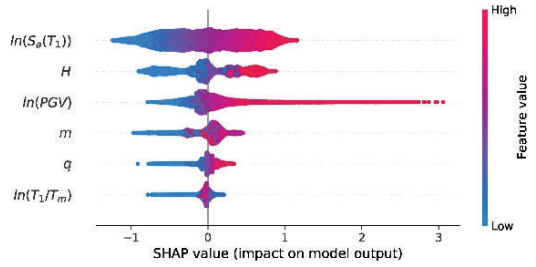

Figure 7: *SHAP summary plots for MIDR.*

Figures 8, 9 and 10 show scatter diagrams displaying local feature importance for the input features and SHAP values. The plots also indicate the interaction between a pair of features considered represented by the transition from blue (low values) to red (high values), as shown on the right of the plots. Overall, it is observed that a highly nonlinear influence of all the IMs examined over the MIDR. $\ln(S_a(T_1))$ and ln(PGV) have a positive relation with MIDR, although they have different trends. This can be explained by the fact that higher values of $\ln(S_a(T_1))$ and ln(PGV) lead to higher SHAP values, which are associated with larger MIDRs. The impact of $\ln(S_a(T_1))$ on the estimation of MIDR decreases moderately, while ln(PGV) tends to increase exponentially.

In the case of $\ln(T_1/T_m)$, a positive impact on the drift estimation is observed until $\ln(T_1/T_m)$ reaches a value of 1. After that, $\ln(T_1/T_m)$ has no impact on the prediction denoted by the almost unchanged SHAP values. This marks an explicit limitation to the predictive power of T_1/T_m that peaks at "resonance" and decays afterwards. This reduction in the predictive ability of T_1/T_m can be partially due to the rise in the importance of structural yielding.

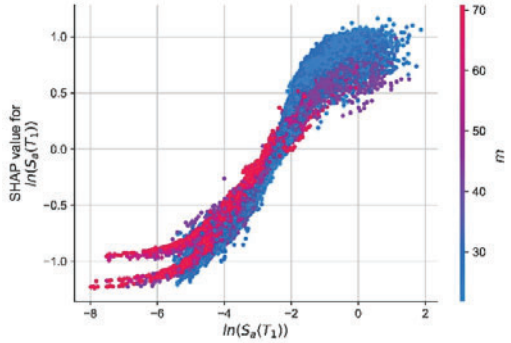

Figure 8: *SHAP dependent plots for MIDR and $\ln(S_a(T_1))$.*

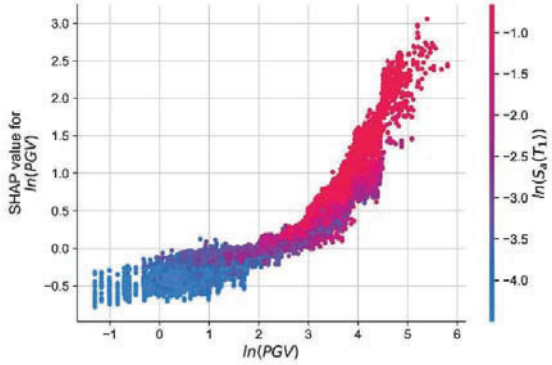

Figure 9: *SHAP-dependent plots for MIDR and ln(PGV).*

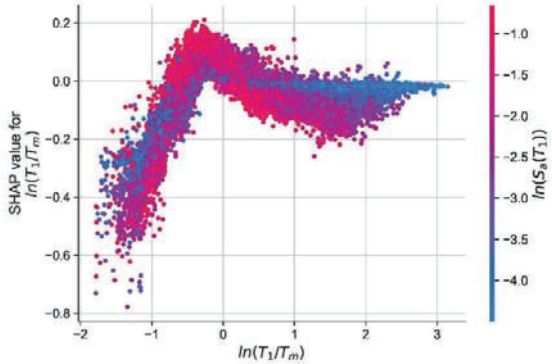

Figure 10: *SHAP-dependent plots for MIDR and $\ln(T_1/T_m)$.*

Figures 11, 12, and 13 depict the SHAP dependency plots for the three structural parameters used to formulate our model. They show that H and q positively impact the MIDR prediction. However, for q values of 3 or larger, MIDR becomes less sensitive to q. On the other hand, the trend of m changes from positive to slightly negative after a value of 3. This suggests that subdividing a CLT wall into more than three sub-panels is unnecessary.

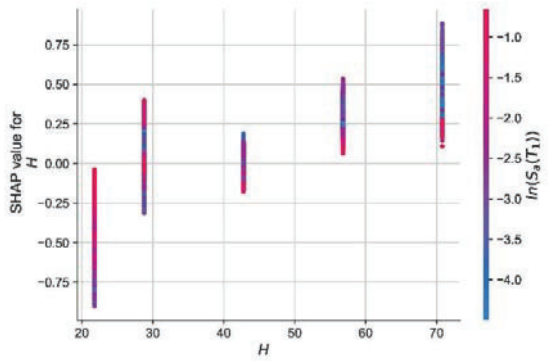

Figure 11: *SHAP-dependent plots for MIDR and H.*

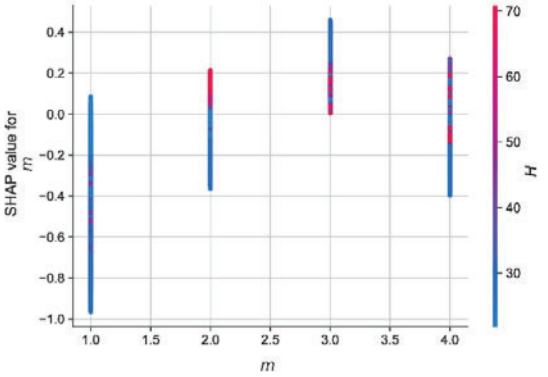

Figure 12: *SHAP-dependent plots for MIDR and m.*

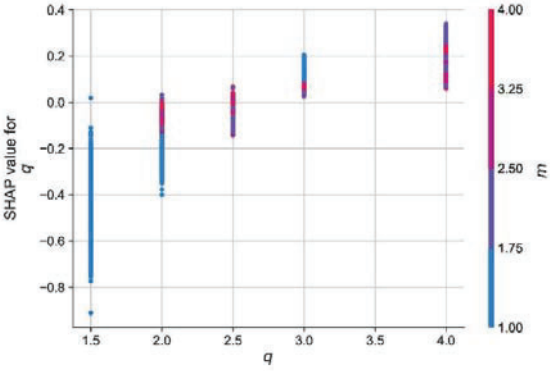

Figure 13: *SHAP-dependent plots for MIDR and q.*

6 CONCLUSION

This paper has investigated the use of machine learning (ML) to estimate the maximum inter-storey drift (MIDR) in multi-story CLT structures and compared it with traditional regression approaches. To do this, we have built numerical models of 69 CLT-walled structures with various structural configurations and design attributes, which reflect a wide variety of CLT building configurations. After calibrating the accuracy of the numerical models against available experimental data, we use them to generate MIDRs of the wall structures using extensive nonlinear response history analyses under a database of 3,312 real ground-motion records scaled with factors of 1.0 and 2.0. The large dataset of seismic drift demands is used as output targets. A total of 30 characteristics, including ground-motion intensity measurements and structural factors, were examined for their influence on the MIDR estimates. Two data-science-based feature selection methods, SFFS and LASSO, are used to inform the suitable set of features to estimate MIDR. A set of six most significant features is obtained, namely the spectral acceleration at T_1 ($S_a(T_1)$), peak ground velocity (PGV), the period ratio (T_1/T_m), behaviour factor (q), structure height (H), and wall ratios (m).

Two regression models are developed and compared with their prediction performances using R^2 and RMSE. The results demonstrate that the traditional linear regression, widely applied for estimating seismic demands of structures, has low prediction power. This indicates that the traditional method oversimplifies the complex nature of the seismic response and cannot provide reliable MIDR estimates over the full range of deformations in CLT structures, but this is especially true at higher deformation levels where the linear model underestimates the drift response. In contrast, the Random Forest model significantly outperforms the traditional method, which is 21.75% higher in R^2 and 46.34% lower in RMSE. The findings show that Random Forest captures better the nonlinearity of MIDR in multi-storey CLT walls.

The SHAP important plots reveal that $S_a(T_1)$ and T_1/T_m strongly influence the drift prediction for tiny drifts where the structure remains elastic while PGV dominates the model at large displacements. The results also imply that a q and an m value of 3 can be optimal for multi-story CLT buildings since an increase in their value beyond those levels will not significantly improve the overall ductility of CLT structures.

REFERENCES

[1] Sullivan K, Miller TH, Gupta R. Behavior of cross-laminated timber diaphragm connections with self-tapping screws. Engineering Structures 2018;168:505–24. https://doi.org/10.1016/j.engstruct.2018.04.094.

[2] Sandoli A, D'Ambra C, Ceraldi C, Calderoni B, Prota A. Sustainable cross-laminated timber structures in a seismic area: Overview and future trends. Applied Sciences (Switzerland) 2021;11:1–24. https://doi.org/10.3390/app11052078.

[3] Málaga-Chuquitaype C. Machine Learning in Structural Design: An Opinionated Review.

https://doi.org/10.52202/069179-0294

Frontiers in Built Environment 2022;8:1–12. https://doi.org/10.3389/fbuil.2022.815717.

[4] Macedo J, Liu C, Soleimani F. Machine-learning-based predictive models for estimating seismically-induced slope displacements. Soil Dynamics and Earthquake Engineering 2021:106795. https://doi.org/10.1016/j.soildyn.2021.106795.

[5] Maqdah J, Memarzadeh M, Kampas G, Málaga-Chuquitaype C. AI-aided exploration of lunar arch forms under in-plane seismic loading. Acta Mechanica 2023. https://doi.org/10.1007/s00707-023-03520-7

[6] Meng X, Shi L, Yao L, Zhang Y, Cui L. Machine learning-based approaches for seismic demand and collapse of ductile reinforced concrete building frames. Colloids and Surfaces A: Physicochemical and Engineering Aspects 2020:124658. https://doi.org/10.1016/j.jobe.2020.101905.

[7] Zahra F, Macedo J, Málaga-Chuquitaype C. Hybrid data-driven hazard-consistent drift models for SMRF. Earthquake Engineering and Structural Dynamics 2023; 52(4):1112-1135. https://doi.org/10.1002/eqe.3807

[8] Wu J, Baker JW. Statistical learning techniques for the estimation of lifeline network performance and retrofit selection. Reliability Engineering and System Safety 2020;200:106921. https://doi.org/10.1016/j.ress.2020.106921.

[9] Ni P, Mangalathu S, Liu K. Enhanced fragility analysis of buried pipelines through Lasso regression. Acta Geotechnica 2020;15:471–87. https://doi.org/10.1007/s11440-018-0719-5.

[10] Mangalathu S, Ph D, Asce AM, Jeon J, Ph D. Machine Learning – Based Failure Mode Recognition of Circular Reinforced Concrete Bridge Columns : Comparative Study. Journal of Structural Engineering 2019;145:1–12. https://doi.org/10.1061/(ASCE)ST.1943-541X.0002402.

[11] (CEN) EC for S. Eurocode 8: Design of structures for earthquake resistance-Part 1: General rules, seismic actions and rules for buildings. 2004. https://doi.org/10.1680/cien.2001.144.6.55.

[12] Málaga-Chuquitaype C. Chapter 8: Design of timber structures in Seismic Design of Buildings to Eurocode 8 (CRC Press, 2016), 213–234.

[13] McKenna F. OpenSees: A framework for earthquake engineering simulation. Computing in Science and Engineering 2011;13:58–66. https://doi.org/10.1109/MCSE.2011.66.

[14] Demirci C, Málaga-Chuquitaype C, Macorini L. Seismic drift demands in multi-storey cross-laminated timber buildings. Earthquake Engineering and Structural Dynamics 2018;47:1014–31. https://doi.org/10.1002/eqe.3003.

[15] Gavric I, Fragiacomo M, Ceccotti A. Cyclic behaviour of typical metal connectors for cross-laminated (CLT) structures. Materials and Structures/Materiaux et Constructions 2015;48:1841–57. https://doi.org/10.1617/s11527-014-0278-7.

[16] Gavric I, Fragiacomo M, Ceccotti A. Cyclic behaviour of typical screwed connections for cross-laminated (CLT) structures 2015:179–91. https://doi.org/10.1007/s00107-014-0877-6.

[17] Gavric I, Fragiacomo M, Ceccotti A. Cyclic behavior of CLT wall systems: Experimental tests and analytical prediction models. Journal of Structural Engineering (United States) 2015;141:1–14. https://doi.org/10.1061/(ASCE)ST.1943-541X.0001246.

[18] Hancock J, Bommer JJ, Stafford PJ. Numbers of scaled and matched accelerograms required for inelastic dynamic analyses. Earthquake Engineering & Structural Dynamics 2008:1585–607. https://doi.org/10.1002/eqe.

[19] Campbell KW, Eeri M, Bozorgnia Y, Eeri M. NGA Ground Motion Model for the Geometric Mean Horizontal Component of NGA Ground Motion Model for the Geometric Mean Horizontal Component of PGA , PGV , PGD and 5 % Damped Linear Elastic Response Spectra for Periods Ranging from 0 . 01 to 10 s. Earthquake Spectra 2008;24:139–71. https://doi.org/10.1193/1.2857546.

[20] Demirci C, Málaga-Chuquitaype C, Macorini L. Seismic shear and acceleration demands in multi-storey cross-laminated timber buildings. Engineering Structures 2019;198:109467. https://doi.org/10.1016/j.engstruct.2019.109467

[21] Pozza L, Trutalli D. An analytical formulation of q-factor for mid-rise CLT buildings based on parametric numerical analyses. Bulletin of Earthquake Engineering 2017;15:2015–33. https://doi.org/10.1007/s10518-016-0047-9.

[22] Shome N, Cornell CA, Bazzurro P, Carballo JE. Earthquakes, records, and nonlinear responses. Earthquake Spectra 1998;14:469–500.

[23] Kohavi R. A study of cross-validation and bootstrap for accuracy estimation and model selection. Ijcai, vol. 14, Montreal, Canada; 1995, p. 1137–45.

[24] Liu GR. Interpretable Machine Learning with Python. 2022. https://doi.org/10.1142/12774.

World Conference on Timber Engineering Oslo 2023

ADAPTIVE COMPOSITE RUBBER BEARINGS FOR TIMBER STRUCTURE: A CASE STUDY FOR EARTHQUAKE-PRONE REGIONS

W.C. Liao[1], Kin Sang Michael Wong[2]

ABSTRACT: Mass timber buildings are becoming more popular in Europe and America for its low carbon footprint compared with traditional construction materials. However, its earthquake resistance should be carefully considered if it is to be used in earthquake-prone areas such as the Asia-Pacific region. The use of traditional base isolators such as lead rubber bearing was already prohibited in Europe due to its toxic gas emission during melting of lead core when large displacement occurs. Therefore, alternative bearing such as adaptive composite rubber bearing (ACRB) made with more environmental-friendly material is being developed. This study applies carbon fabric, layered rubber sheet and novel core materials to fabricate an ACRB base isolator with adjustable damping ratio and lateral shear stiffness. A quasi-isotropic layup of carbon fabric, high temperature resin prepreg system and hot press is adopted in the fabrication of composite laminates. The selection of primer coat between composites and raw rubber is determined by the double lap shear test of a single composite/rubber unit. Through the biaxial test of this novel ACRB base isolator, the equivalent damping ratio, equivalent lateral stiffness and friction coefficient of the isolator can be characterized. Under low shear strain, the damping ratio of the isolator can be as high as 0.58, and the envelopes of their hysteretic loop shows prominent seismic energy absorption capacity. In order to verify the earthquake mitigation performance of these adaptive composite rubber bearings, shaking table tests of several down-scaled multi-story mass timber buildings were carried out.

KEYWORDS: Mass timber building, adaptive rubber bearing, carbon fabric, biaxial test, shaking table seismic test

1 INTRODUCTION

Mass timber buildings includes cross laminated timber (CLT), glued laminated timber (GLT) and dowel laminated timber (DLT) are popular construction materials used for medium to tall buildings in Europe and America. The reason for the trend to use more timber over conventional construction materials is due to its low carbon footprint and urban heat island effect. With the improvement of timber material against fire, corrosion and pest, it is foreseen that timber would become more popular in other urban areas. In order to improve the earthquake resistance of timber buildings, the most cost-effective way would be by the implementation of passive control measures at the base of the timber structure.

During an earthquake, energy was transferred into buildings through forced vibration. As the major frequency of earthquake shown in typical response spectrum coincides with the natural frequency (1-10Hz) of conventional building structures, resonance effect would be resulted during an earthquake. The structural members would exhibit large internal force during resonance vibration and be damaged. Passive isolation makes use of the low stiffness of the isolator to change the natural frequency of the above building to lower than 0.5Hz. Passive control measures include three major principles: base isolation, energy dissipation and vibration mitigation. Energy dissipation method relies on the hysteretic damping through yielding of metal core, friction damping or viscous damping to provide supplementary damping to dissipate the vibration response of the structure.

This study aimed at fabricating an adaptive composite elastomeric base isolator and verify its performance in mass timber structure. In the past, high damping rubber bearing (HDRB) and lead rubber bearing (LRB) were efficient elastomeric base isolators to make use of the low strength of rubber to change the frequency of the structure and dissipate the earthquake energy transferred up to the structure. The addition of lead core could even provide larger energy dissipation through the plastic deformation of the core during extremely large displacement [2][3]. However, in 2009, Kalpakidis and Constantinou [4][5] carried out studies on the effects of heating on the behaviour of lead-core rubber bearings and concluded that the lead core would have zero yield strength when it reached its melting point at 327°C and thus the earthquake energy would be absorbed by the adjacent rubber and resulted in its damage and failure. During the Tohoku earthquake in Japan in 2011, some of the lead core in LRB were found to be having irreversible deformation due to the sudden rise in temperature resulted from extremely large displacement[6][7]. The European Union had banned the use of lead core in LRB in 2011. Therefore, it is urgent to find alternative laminate material that could replace the function of lead core in rubber bearing.

[1] W.C. Liao, Department of Civil Engineering, Feng Chia University, Taiwan, wcliao@fcu.edu.tw

[2] Kin Sang Michael Wong, Department of Civil Engineering, Feng Chia University, Taiwan, m1083495@o365.fcu.edu.tw

https://doi.org/10.52202/069179-0295

In contrary to LRBs, HDRB uses laminated specialized high damping rubber (HDR) and had slightly lower energy dissipation capacity [8].

In this study, carbon fabric, layered rubber sheet and novel core materials were used to fabricate an ACRB base isolator with adjustable damping ratio and lateral shear stiffness. A quasi-isotropic layup of carbon fabric, high temperature prepreg resin system and hot press is adopted in the fabrication of composite laminates. The selection of primer coat between composites and raw rubber is determined by the double lap shear test of a single composite/rubber unit. Through the biaxial test of this novel ACRB base isolator, the equivalent damping ratio, equivalent lateral stiffness and friction coefficient of the isolator can be characterized. Under low shear strain, the damping ratio of the isolator can be as high as 0.58, and the envelopes of their hysteretic loop shows prominent seismic energy absorption capacity. In order to verify the earthquake mitigation performance of these adaptive composite rubber bearings, shaking table tests of several down-scaled multi-story mass timber buildings were carried out.

2 CHARACTERISTICS TEST OF ACRB

2.1 DESIGN AND MANUFACTURING OF AN ADAPTIVE FIBER-REINFORCED RUBBER BEARING BASE ISOLATOR

Carbon roving TC360 from Formosa Plastic Group has a tensile modulus of 250 GPa, and tensile strength of 4890 MPa, respectively, were adopted in this research. The UD carbon laminate has E_1=117.29 GPa, E_2=E_3=7.44 GPa, G_{12}=3.77GPa, and v_{12} = 0.1946. In order to avoid the misalignment in the curing of composite laminate and rubber layers, a quasi-isotropic stacking sequence of [0/90/+45/-45]s is adopted. All carbon plates were made through hot press to about 3mm thick. High temperature resin prepreg of EPO-HTG™ G351N from Epotech Taiwan was applied during the layup. The carbon plates were then cut to Φ130mm discs and stacked with Φ 60mm shim core steel plates and sliding plates to form the core of the ACRB. The outer side of the core layer were filled up by high damping rubber. From 3-D effective moduli theory, we can estimate E_x=E_y = 44.66 GPa, which are close to experimental data. The layup of an adaptive composite rubber bearing is shown in Figure 1.

2.2 BIAXIAL TEST ON ACRB

Biaxial test was used to test the ACRB under different frequency, loading directions and shear strain. The typical experimental setup for ACRB is shown in Figure 2. After setting a vertical force, horizontal displacement would applied through the MTS dynamic system with sine wave movement at different frequencies and amplitudes. Vertical force, horizontal force and displacement were recorded by imc μ-sys to yield hysteresis loops.

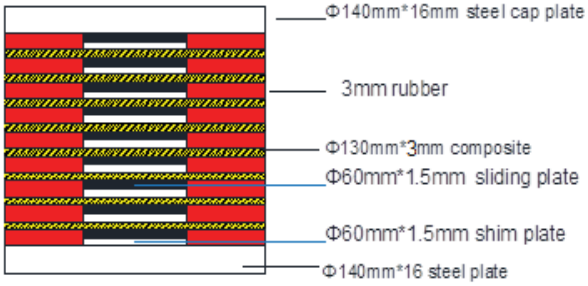

Figure 1: *Scaled down ACRB*

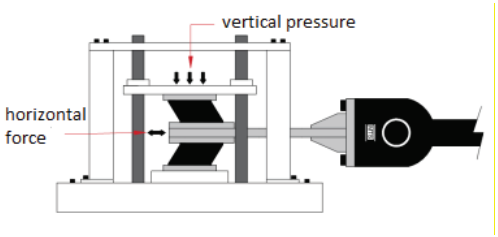

Figure 2: *Setup for biaxial test*

2.3 SHAKING TABLE TEST FOR SCALED TIMBER STRUCTURE WITH ACRB

Four scaled ACRB were then installed under a scaled 3-storey steel structure which was designed to have the weight and natural frequency similar to timber structure to carry out the shaking table test. The earthquake loading used were scaled-down El Centro earthquake (1940) and Chi-Chi earthquake (1999) under x and y directions separately. Control tests with no ACRB were also recorded for comparison with the use of scaled-down earthquakes at 0.05g to prevent extensive damage to the structure. Accelerometers and displacement gauges were installed at every storey to record the acceleration and displacement in x and y directions as shown in Figure 3 and 4. The reason for the use of steel structure instead of real timber structure was due to the consideration on transportation and size limit of the shaking table.

3 RESULTS AND DISCUSSION

3.1 BIAXIAL TEST ON ACRB

Biaxial tests were carried out under 5t(3.7MPa) & 7t(5.2MPa) vertical force with sine wave signals at different frequencies (0.1Hz, 0.2Hz, 0.5Hz, 1.0Hz & 1.5Hz) and different horizontal shear strain (25%, 50%, 100% & 150%) of the total thickness of rubber. Typical hysteresis loops for two repeated cycles under different shear strains are shown in Figure 5 and Figure 6.

The data obtained from the hysteresis loops was used to calculate the effective stiffness (K_{eff}) as demonstrated by Liao, Tsai and Hsieh [9] by the following Equation (1):

https://doi.org/10.52202/069179-0295

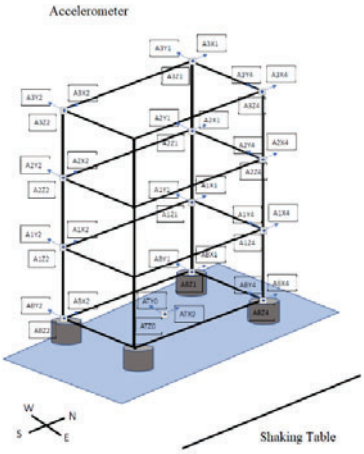

Figure 3: *Setup for accelerometers for shaking table test*

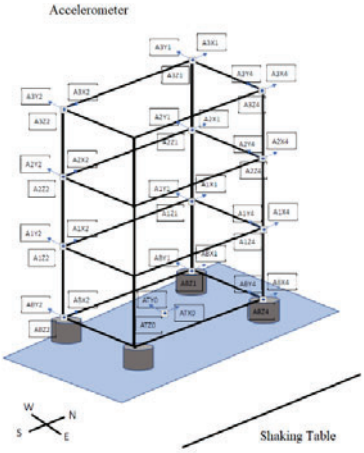

Figure 4: *Setup for displacement gauges for shaking table test*

$$K_{eff} = \frac{F_i^+ - F_i^-}{2\Delta_i} \quad (1)$$

where F_i^+ = maximum horizontal force of ith cycle,
F_i^- = minimum horizontal force of ith cycle,
Δ_i = average horizontal displacement of ith cycle.

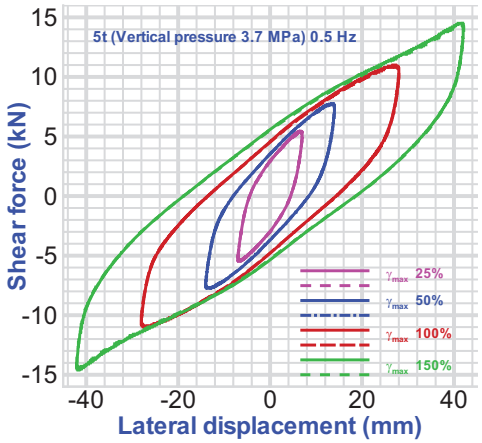

Figure 5: *Hysteresis loop of ACRB at different shear strains under pressure of 3.7MPa at 0.5Hz frequency*

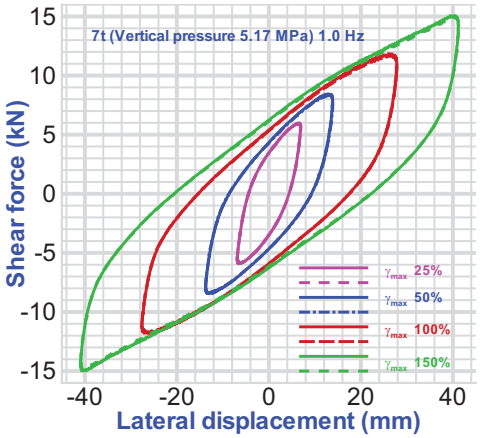

Figure 6: *Hysteresis loop of ACRB at different shear strains under pressure of 5.2MPa at 1.0Hz frequency*

The effective stiffness (K_{eff}) was plotted against the shear strain under different frequencies of loading. As shown in Figure 7 and 8 below, K_{eff} decreased significantly when the shear strain increased. The effect on frequencies was relatively insignificant.

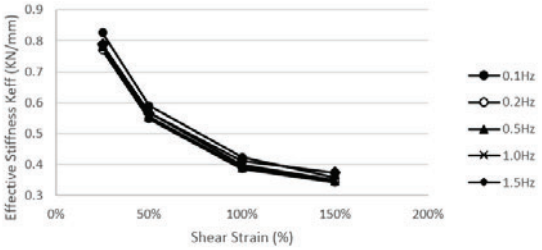

Figure 7: *Effective stiffness against shear strain under pressure of 3.7MPa*

https://doi.org/10.52202/069179-0295

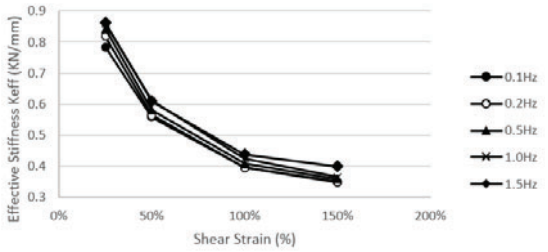

Figure 8: *Effective stiffness against shear strain under pressure of 5.2MPa*

The equivalent damping ratio (ξ_e^i) as demonstrated by Liao, Tsai and Hsieh [9] by the following Equation (2):

$$\xi_e^i = \frac{E_d^i}{2\pi k_{eff}^i \Delta_i^2} \tag{2}$$

where E_d^i= area enclosed by ith cycle in loop.

The test results of equivalent damping ratio under 5t (3.7MPa) and 7t (5.2MPa) are summarized in Table 1 and Table 2 below:

Table 1: *Equivalent damping ratio ξ_e^i of ACRB under 5t(3.7MPa) vertical pressure.*

Shear strain	Frequency				
	0.1Hz	0.2Hz	0.5Hz	1.0Hz	1.5Hz
25%	24.7%	27.5%	27.6%	28.0%	28.3%
50%	22.5%	24.9%	25.2%	25.6%	26.0%
100%	19.8%	22.7%	23.1%	23.4%	23.4%
150%	18.0%	19.1%	19.5%	20.2%	22.2%

Table 2: *Equivalent damping ratio ξ_e^i of ACRB under 7t(5.2MPa) vertical pressure.*

Shear strain	Frequency				
	0.1Hz	0.2Hz	0.5Hz	1.0Hz	1.5Hz
25%	27.9%	28.5%	28.4%	29.4%	29.7%
50%	27.0%	27.6%	27.8%	28.2%	28.7%
100%	24.3%	24.7%	25.5%	26.1%	26.1%
150%	21.4%	21.4%	22.3%	22.4%	25.5%

As shown in the tables above, the equivalent damping ratio is relatively insensitive to frequency of loading. However, it increased when the vertical pressure increased and dropped when the shear strain increased.

3.2 SHAKING TABLE TEST FOR SCALED TIMBER STRUCTURE WITH ACRB

From the shaking table results, the inter-storey displacement and relative acceleration were both significantly reduced after ACRB were installed. The displacement of each storey in x-direction under 0.5g El Centro (NS) earthquake was plotted against time in Figure 9 below:

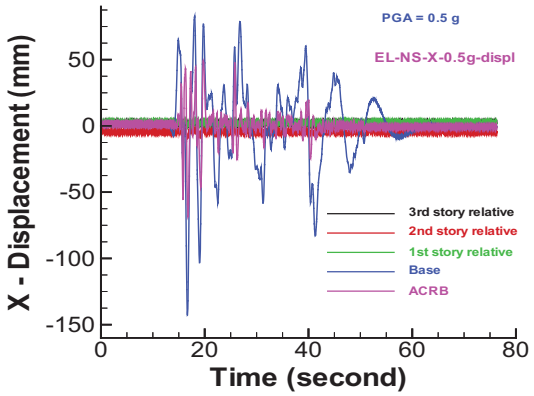

Figure 9: *Displacement of base and relative displacement of different storeys under PGA of 0.5g El Centro (NS) Earthquake.*

The above figure showed that the relative displacement of the structure itself was small and not more than 5mm. When compared with the base displacement (with maximum at about 140mm), the inter-storey movement was almost negligible and the structure was shaking with rigid body motion.

A typical plot about the acceleration at different storeys against time is shown in Figure 10 below.

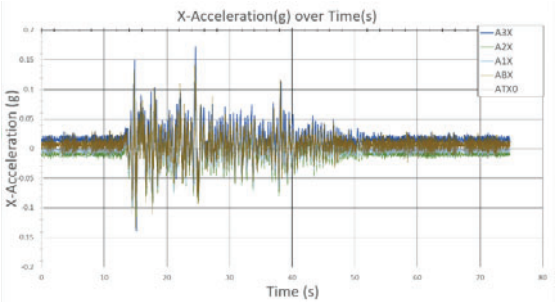

Figure 10: *Acceleration of base, ACRB and each storey under PGA of 0.2g El Centro Earthquake.*

The peak acceleration of each storey within the earthquake was extracted for comparison to calculate the acceleration reduction efficiency of the ACRB. The ratio for comparison would be by comparing the peak ground acceleration (PGA) actually measured by 0.05g loading of the same earthquake. The summary on acceleration reduction efficiency of El Centro-NS loading were compared in Table 3 below.

Table 3: *Acceleration reduction efficiency of ACRB under different levels of El Centro (NS) loading*

	w/o ACRB	w/ ACRB		
Test name	0.05g	0.2g	0.3g	0.4g
PGA (g)	0.060	0.181	0.320	0.424

https://doi.org/10.52202/069179-0295

3F	0.099	0.170	43%	0.371	29%	0.397	43%
2F	0.082	0.154	37%	0.222	49%	0.311	46%
1F	0.068	0.157	23%	0.317	12%	0.358	25%

In order to further check the damping efficiency of the ACRB under earthquake loadings, the base shear was plotted against the average x-displacement of the ACRB to show the relationship between ACRB displacement and base shear under various earthquake acceleration. The base shear was calculated based on the sum of the products of storey mass times average acceleration in x direction for each storey. The result of the hysteresis loops were shown in Figure 11-16 below.

As shown in Figure 11, 14 & 15 where the shear strain was up to 138%, the equivalent damping ratio was up to 23.7%. As shown in Figure 13, 14 & 16 where the shear strain was up to 256%, the equivalent damping ratio would gradually decrease to 15.8%.

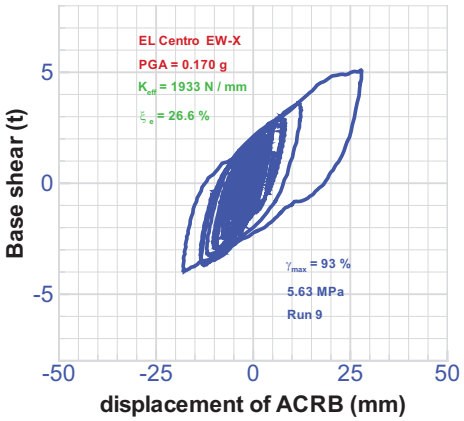

Figure 11: *Hysteresis loop of ACRB under PGA of 0.170g El Centro EW Earthquake.*

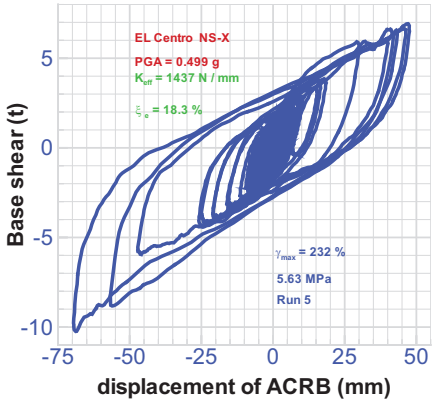

Figure 12: *Hysteresis loop of ACRB under PGA of 0.499g El Centro NS Earthquake.*

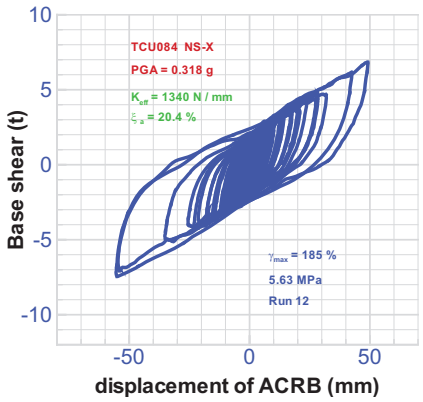

Figure 13: *Hysteresis loop of ACRB under PGA of 0.318g Chi-Chi NS Earthquake...*

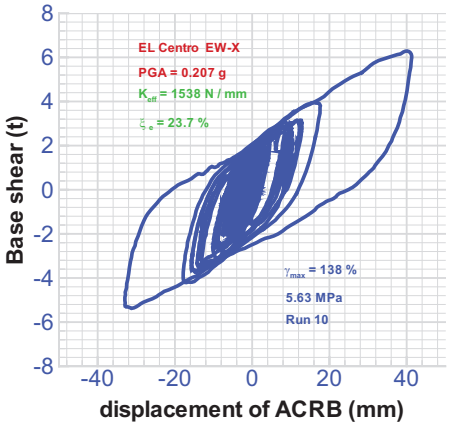

Figure 14: *Hysteresis loop of ACRB under PGA of 0.207g El Centro EW Earthquake.*

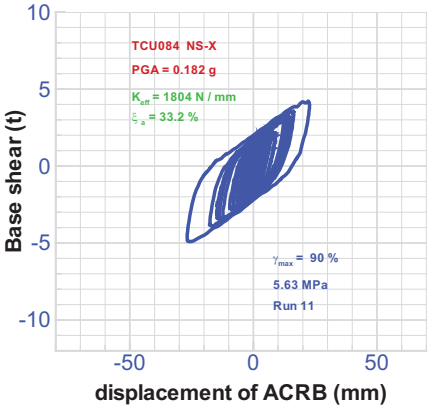

Figure 15: *Hysteresis loop of ACRB under PGA of 0.182g Chi-Chi NS Earthquake.*

https://doi.org/10.52202/069179-0295

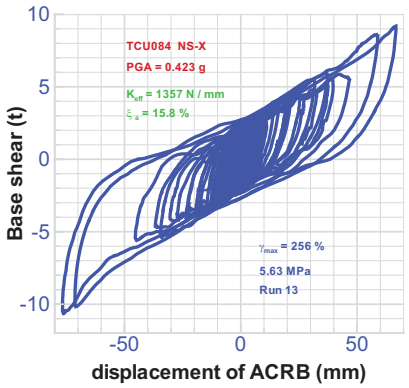

Figure 16: *Hysteresis loop of ACRB under PGA of 0.423g Chi-Chi NS Earthquake.*

4 CONCLUSIONS

Mass timber buildings are becoming more popular in view of the improved characteristics of laminated timber. Existing bearings such as LRB were already banned due to toxic emission. The performance of its alternative (HDRB) relies on the vertical pressure on the bearing. With the decrease in weight of timber structure compared with conventional concrete or steel structure, it is essential to investigate the possibility of improved bearing which could perform. We manufactured ACRB with carbon fabric. The damping efficiency of ACRB on timber structure was demonstrated under the experiments in this paper. The use of this alternative damper could lower the cost and number of dampers and become more environmental-friendly.

ACKNOWLEDGEMENTS

Supports from the Ministry of Science and Technology of Taiwan under grants MOST 110-2221-E-035-024 & MOST 108-2221-E-035-010 are acknowledged.

REFERENCES

[1] Tsai, C. S., Chiang, Tsu-Cheng and Chen, Bo-Jen., 2003, “Component and Shaking Table Tests for Full Scale Multiple Friction Pendulum System”, Earthquake Engineering and Structural Dynamics, Vol. 35, No. 13, pp. 1653-1675.

[2] Asher, J. W., Hoskere, S. N., Ewing, R. D., Van Volkinburg, D. R., Mayes, R. L. and Button, M., 1995, “Seismic Performance of the Base Isolated USC University Hospital in the 1994 Northridge Earthquake.” Proceedings of the 1995 Joint ASME/JSME Pressure Vessels and Piping Conference, HI, USA, Vol. 319, 147-154.

[3] Dowrick D. J., Babor, J., Cousins, W. J. and Skinner, R. I., 1992, “Seismic Isolation of a Printing Press in Wellington, New Zealand.” Bulletin of the New Zealand National Society for Earthquake Engineering, Vol. 25, No. 3, 161-166.

[4] Kalpakidis, I. V. and Constantinou, M. C., 2009a, “Effects of heating on the behaviour of lead–rubber bearings. Ⅰ: theory.” Journal of Structural Engineering, ASCE, 135(12):1440-1449 .

[5] Kalpakidis, I. V. and Constantinou, M. C., 2009b, “Effects of heating on the behavior of lead –rubber bearings. Ⅱ:verification of theory.” Journal of Structural Engineering, ASCE, 135(12):1450-1461.

[6] Takahashi, Yoshikazu (2012) “Damage of rubber bearings and dampers of bridges in 2011 great East Japan earthquake.” Proceedings of the International Symposium on Engineering Lessons Learned from the 2011 Great East Japan Earthquake, March 1-4, 2012, Tokyo, Japan.

[7] Tsai, C. S., 2015 , " Seismic Isolation Devices: History and Recent Developments." In the 2015 ASME Pressure Vessels and Piping Conference, Seismic Engineering, (ed.) by C. S. Tsai, Cleveland, American Society of Mechanical Engineers, Boston, U. S. A.

[8] Mineoh, Takayama, 1997, Road to 4 Seconds Seismic Isolation – Seismic Isolation Structure Design Manual. The Science and Engineering Books.

[9] Tsai, C. S., Chiang, Tsu-Cheng and Chen, Bo-Jen., 2003a, “Component and Shaking Table Tests for Full Scale Multiple Friction Pendulum System”, Earthquake Engineering and Structural Dynamics, Vol. 35, No. 13, pp. 1653-1675.

[10] Tsai, C. S., Lu, P. C., Chen, W. S., Chiang, T. C., Yang, C. T. and Lin, Y. C., 2008,"Finite Element Formulation and Shaking Table Tests of Direction-optimized Friction Pendulum System," Engineering Structures, 30(9), 2321-2329).

[11] Ario Cecotti, Carmen Sandhaas, Minoru Okabe, Motoi Yasumura, Chikahiro Minowa and Naohito Kawai, 2013, “SOFIE Project - 3D Shaking Table on a Seven-Storey Full-Scale Cross-Laminated Timber Building”, Earthquake Engineering and Structural Dynamics, Vol. 42, pp. 2003-2021.

World Conference on Timber Engineering Oslo 2023

SEISMIC DESIGN OF A CLT MULTI-STOREY BUILDING IN DIFFERENT DUCTILITY CLASSES

Giuseppe Cenci[1], Maurizio Follesa[2], Vincenzo Rinaldi[3], Daniele Casagrande[4], Massimo Fragiacomo[5]

ABSTRACT: This study aims to clarify fundamental concepts related to the design of Cross-Laminated Timber (CLT) multi-storey buildings in seismic-prone areas. An in-depth worked example of a CLT multi-storey building design is presented following four different cases of analysis: low and medium ductility according to the current Italian regulations (NTC 2018), and medium and high ductility (DC2 and DC3) according to the new draft of Eurocode 8. Finite Element (FE) models of the building have been implemented to analyse the linear dynamic behaviour of the structure. In high ductility class, a couple-panel behaviour of shear walls is achieved by following the analytical provisions reported in the new draft of the Eurocode 8. As a result, a clear design process is defined for each case analysed. Through the analysis of the individual steps, possible issues in the interpretation and application of the rules are highlighted and resolved. Finally, this study allows an easy and direct comparison between the various cases.

KEYWORDS: CLT buildings, Seismic analysis, Capacity-based design, Practice-oriented.

1 INTRODUCTION

The use of Cross-Laminated Timber (CLT) panels has become widespread for the construction of low-to-mid-rise multi-storey buildings, representing a valuable alternative to other traditional structural types also in seismic-prone areas [1,2]. However, the development of Standard provisions framing the design and calculation of this type of structure is still lacking in Europe, especially for seismic load situations.

1.1 DPC-ReLUIS 2019-2021

Through the DPC-ReLUIS 2019-2021 research project, the Italian Civil Protection Department and the ReLUIS research consortium have promoted the development of pre-normative documents related to structural types not yet considered in the current standards. They have also assisted in the actual drafting of the technical standards. Concerning CLT structures, the aim is to produce effective documentation to support normative review [3]. Therefore, an in-depth worked example of a CLT multi-storey building has been prepared by applying both the Italian Technical Regulations for Construction (NTC 2018) [4] and the new draft of the Eurocode 8 still under revision (prEN 1998-1-2: 2020) [5,6].

2 SCOPE

The primary purpose of the aforementioned document is to clarify fundamental concepts related to the design of CLT buildings in seismic areas, such as: (i) dissipative mechanisms, allowing the use of a specific value of the behaviour factor q; (ii) the minimum ductility values that the dissipative connections should exhibit; (iii) the design conditions for attaining those minimum ductility values; (iv) the over-strength factors used in the design of the non-dissipative components; (v) the partial safety factors to be used in the design while taking into account the strength reduction due to cyclic loading. Therefore, the objective of the present study is to clarify the practical application of the capacity-based design by defining unambiguous procedures.

3 ANALYSIS CASES

A 5-storey CLT residential building (Figures 1, 2 and 3) is designed following four different cases of analysis: low and medium ductility class in accordance with the current Italian regulations (NTC 2018), and medium and high ductility (DC2 and DC3) according to the new draft of Eurocode 8.

[1] Giuseppe Cenci, University of L'Aquila, Italy, cenci.giuseppe@outlook.it
[2] Maurizio Follesa, dedaLEGNO, Italy, follesa@dedalegno.com
[3] Vincenzo Rinaldi, University of L'Aquila, Italy, vincenzo.rinaldi@univaq.it
[4] Daniele Casagrande, National Research Council of Italy CNR-IBE, Italy, daniele.casagrande@ibe.cnr.it
[5] Massimo Fragiacomo, University of L'Aquila, Italy, massimo.fragiacomo@univaq.it

https://doi.org/10.52202/069179-0296

Figure 1: *Rendered view of the case-study building*

The table below summarises the different cases analysed and the corresponding adopted values of the behaviour factor q.

Table 1: *Analysis cases*

Case	Code	Ductility class DC	Behaviour factor q
1	NTC2018	Low	1.5
2.1	NTC2018	Medium	2.5
2.2	prEN 1998-1-2:2020	2	2.0
3	prEN 1998-1-2:2020	3	3.0

The walls with grey hatching in figure 3 are segmented in DC 3.

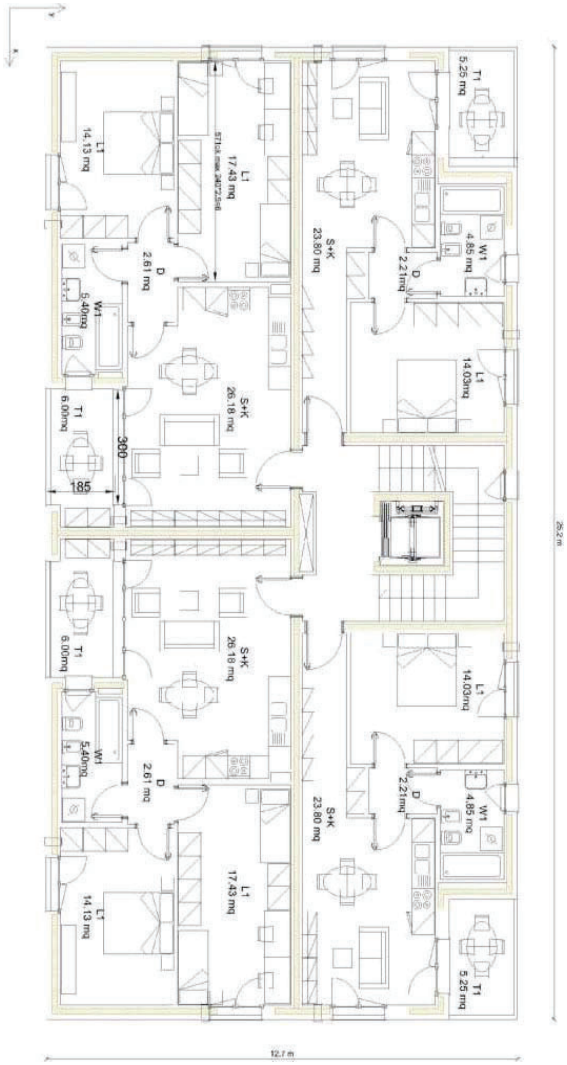

Figure 2: *Architectural plan of a typical floor*

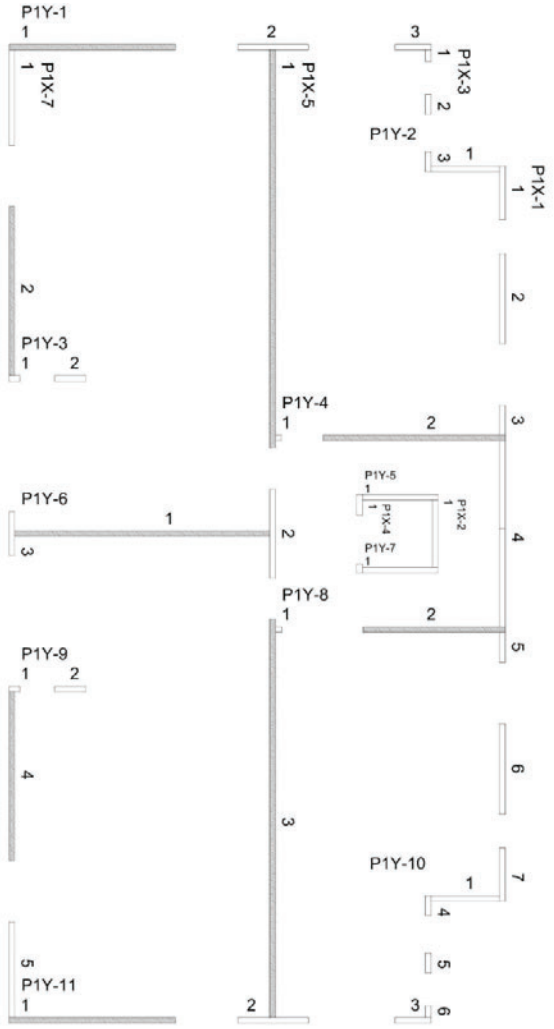

Figure 3: *CLT walls*

4 DESIGN DATA

4.1 THE BUILDING

The building is composed of five storeys, with an inter-storey height of 3.12 m; the total height of the buildings is 17.5 m. The structure is built using CLT panels (walls and slabs); the shear walls are designed to support both gravitational and lateral loads (wind and seismic action). The presence of many openings (windows and balconies) results in a segmentation of the shear walls that was addressed to define the Seismic Force Resisting System. The stairwell and the elevator shaft are also made of CLT panels; the connections with the diaphragm have been designed to ensure an adequate in-plane behaviour of floors. Neither the foundation system nor the soil-structure interaction are taken into account in the analysis. Three different types of panels are used, as shown in the table below.

Table 2: *CLT layup and thickness*

Element	Layup	Thickness
Slab	7 layers	220 mm
Walls level 1 to 3	5 layers	140 mm
Walls level 4 to 5	5 layers	120 mm

4.2 GRAVITY LOADS AND SEISMIC ACTION

Table 3 lists the values of the gravity loads acting on the building while Table 4 reports the parameters of the pseudo-elastic spectrum for the two limit states considered: Significant Damage SD (SLV according to NTC18) and Damage Limitation DL (SLD according to NTC18). Values of the seismic actions are selected with reference to common real cases in Italy. The peak ground accelerations for SD and DL have a probability of exceedance of 10% and 63% in 50 years, respectively. The site is mainly flat (topographic amplification factor S_t = 1) with a soil class C (180 m/s < $v_{s,30}$ < 360 m/s).

Table 3: *Gravitational loads*

Element	G_2	Q_{LIVE}
Slab	2.5 / 3.0 kN/m^2	2.0 / 4.0 kN/m^2
Roof	0.5 kN/m^2	-
Walls	0.5 kN/m^2	-

Table 4: *Seismic action parameters*

Limit state	a_g/g	F_0	T_C*
SD (SLV)	0.266 g	2.312	0.351
DL (SLD)	0.101 g	2.336	0.284

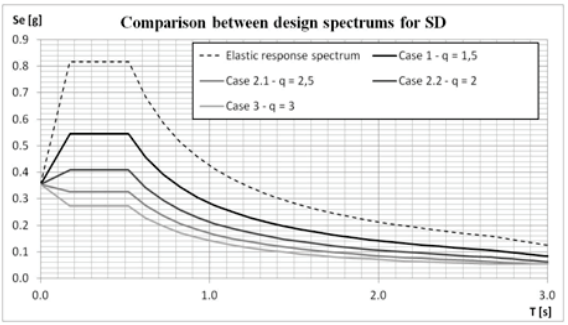

Figure 4: *Comparison between design spectrums for SD*

Given the interest on the seismic behaviour, only the seismic combination is considered, including all the possible variable loads.

$$E + G_1 + G_2 + P + \psi_{21} \cdot Q_{k1} + \psi_{22} \cdot Q_{k2} + \psi_{33} \cdot Q_{k3} \ldots$$

5 DESIGN PRINCIPLES AND FEM MODEL

The seismic design principles used in this example are based on the results of several research projects and of some full-scale tests on earthquake shaking tables (e.g. SOFIE project, IVALSA-CNR institute) [7]. These tests also enabled some modelling methods to be validated, like the one mentioned in the next paragraph.

5.1 FINITE ELEMENT MODEL

A 3D Finite Element (FE) model of the building is defined for each analysis case following the method proposed in [8]. Each model simulates the behaviour of the real structure in the context of linear dynamics.

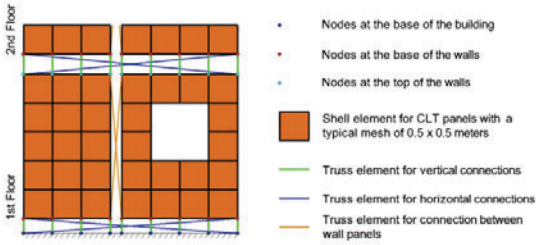

Figure 5: *Typical wall schematisation*

https://doi.org/10.52202/069179-0296

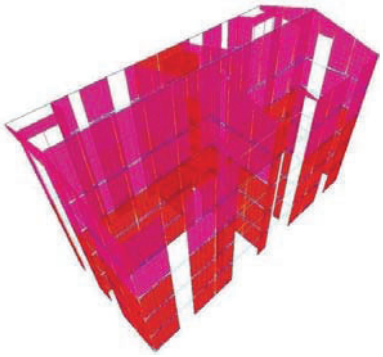

Figure 6: *Finite Element model*

Through an iterative process, it is possible to check the force level of the connections and update the corresponding deformability values which strongly affect the structure's vibration modes.

6 CAPACITY-BASED DESIGN

The design of dissipative seismic-resistant structures requires that a portion of the energy transferred by the earthquake to the structure is dissipated through the plasticisation of some connections. In this case, the seismic actions can be reduced provided that the Lateral Load Resisting System (LLRS) is able to provide an extra post-elastic resistance through well-localised plastic deformations. This means that the plasticisation phenomena must not make the structure unstable and must not compromise its overall behaviour. To achieve this goal, all the elements that must not exceed the elastic phase are designed with an over-strength factor compared to those with ductile behaviour, so that the dissipative phenomena will concentrate on the latter one [9,10].

6.1 OVER-STRENGTH LEVELS

As described below, the over-strength condition affects a structure at different levels:

- Single connector: in connection with Johansen's formulas, the brittle failure modes must have adequate over-strength with respect to ductile failure mode, represented by the plasticisation of the fasteners through one or more plastic hinges.
- Connections: the brittle failure mode of an entire connection must have adequate over-strength with respect to ductile failure mode. Typical brittle failure modes are shear failure in the carpentry nodes, shear or tension failure in wood sections, tensile or shear failure of metal plates and shear or punching shear failure of bolts and screws. Ductile failure modes are typically shear failures of dowel-type fasteners characterised by at least a plastic hinge formation;
- Structural elements and global behaviour: collapse of structural elements with non-dissipative behaviour and the formation of soft storey mechanisms are avoided, enhancing the overall behaviour of the entire structure.

6.1 HIGH DUCTILITY CASES (DC3)

In the new draft of Eurocode 8, a high ductility class (DC3) is proposed for CLT buildings consisting of LLRS made with multi-panel shear walls. In these walls, the panels are connected together with vertical joints that can dissipate energy primarily through the yielding of fasteners, leading to a coupled-panel (CP) behaviour where all the panels remain in contact with the ground or the floor below and a significant slip of vertical joints is attained. In order to ensure that CP behaviour is also attained in the plastic region, vertical joints have to be designed to yield before the hold-downs whereas angle brackets have to be slightly over-designed so that the sliding failure mechanism of the wall is prevented. Non-dissipative elements, typically characterised by a brittle failure mode, are designed to remain elastic when the vertical joints attain the desired level of inelastic displacement according to the capacity-based design approach.
The analytical expressions proposed by Casagrande et al. [9] are used in the draft of the new Eurocode 8 to ensure that CLT shear walls of buildings designed in DC3 attain the desired kinematic mode.

7 DISSIPATIVE CONNECTIONS

Dissipative connections must ensure proper energy dissipation; it is therefore important to analyse the different failure mechanisms in order to provide sufficient over-strength to those that exhibit brittle behaviour.

7.1 ANGLE BRACKETS FOR SHEAR LOAD

Angle brackets for shear load connect the wall panels to the floor panels or to the concrete foundation. To ensure the desired behaviour, the following failure mechanisms have been analysed:

- Shear failure of the steel plates;
- Failure of the plate-to-wall dowel-type connection;
- Failure of the plate-to-slab dowel-type connection.

Four types of angle brackets manufactured by Rothoblaas have been analysed in combination with two different types of fasteners (LBA 4 x 60 mm high bond nails and LBS 5 x 70 mm screws):

- TCN240 for timber-to-concrete connections;
- TTN240 for timber-to-timber connections;
- TTV240 for timber-to-timber connections with reinforcing screws that absorbs the eccentricity in the vertical plate of the bracket;
- TTF200 for timber-to-timber connections for lower loads.

In this case, the energy dissipation is exclusively located in the plate-to-wall screwed connection. The NTC2018 and the draft of the Eurocode 8 used for this work provide different over-strength factors, 1.3 and 1.6, respectively.

https://doi.org/10.52202/069179-0296

These values considerably affect the design resistance of the connection, as shown in the table below.

Table 5: *Angle brackets resistance in each case*

Angle bracket	Non-dissipative joints (from ETA)		Dissipative joints	
	Case 1	Cases 2.1, 2.2, 3	Case 2.1	Cases 2.2, 3
TCN240 + LBA	23.8 kN	33.3 kN	26.8 kN	26.8 kN
TCN240 + LBS	28.5 kN	39.9 kN	33.0 kN	33.0 kN
TTV240 + LBA	46.9 kN	65.7 kN	39.0 kN	31.7 kN
TTV240 + LBS	46.9 kN	65.7 kN	39.1 kN	31.8 kN
TTN240 + LBA	29.8 kN	41.7 kN	26.8 kN	21.8 kN
TTN240 + LBS	36.7 kN	51.4 kN	33.0 kN	26.9 kN
TTF200 + LBA	27.9 kN	39.1 kN	23.4 kN	19.0 kN
TTF200 + LBS	33.4 kN	46.8 kN	29.0 kN	23.6 kN

7.2 HOLD-DOWNS AND TIE-DOWNS

The anchoring connections against uplift (hold-downs, tie-downs) have been similarly analysed. Tie-down anchors through the floor panels have been used in combination with screwed connections between the steel plate and the CLT wall panel. The following failure mechanisms have been analysed:

- Tensile failure of the steel plate;
- Failure in shear of screwed connections between metal plate and CLT panel.

7.3 VERTICAL JOINTS BETWEEN WALL PANELS

In case 3 (high ductility case DC3), the increased demand for energy dissipation is ensured by the panel-to-panel connections; such joints are activated by the coupled-panel (CP) behaviour previously mentioned. The capacity-based design for a segmented wall requires that the vertical joints must yield before the anchoring connections against uplift [11,12]; this condition strongly affects the design of vertical joint between the wall panels. The half-lap joint replaces the step joints made with a cross-layer stripe inserted in grooves on one side of the CLT panels. The step joints are used only for low and medium ductility cases.

The shear force acting on the vertical joints has been calculated by isolating each individual wall (continuous wall from the foundation to the roof) and analysing it as disconnected from the rest of the structure. The actions (lateral load and gravitational loads for seismic combination) are taken from the global model. Once the loads are defined, it is possible to design the joints between adjacent wall panels by using the analytical expressions proposed by Casagrande et al. [9]

8 LINEAR DYNAMIC ANALYSIS

The stiffness of timber structures, particularly the CLT platform-frame type, is markedly affected by the deformability of the connections. However, this deformability can only be determined after the design of the connection itself.

The first step involves the use of a linear static analysis; this analysis allows for the "calibration" of the connections' resistance through a preliminary design.

Both the NTC2018 and the new draft of the Eurocode 8 propose Equation (1) as a method to identify the building's fundamental period of vibration.

$$T_1 = 0.05 \cdot h^{\frac{3}{4}} \quad (1)$$

where h is the height of the building, in [m], measured from the foundation or from the top of a rigid basement.

Once the connections are preliminarily designed, it is possible to calculate the related deformations that will be used to complete the numerical model. The dynamic analysis that, through an iterative process, leads to the convergence of the solution can then be run.

9 ANALYSIS OF RESULTS

The results obtained make it possible to compare the cases analysed, evaluating the differences in relation to various aspects.

9.1 MODAL ANALYSIS

A comparison of the results of the modal analysis demonstrates that the differences between the vibration periods of cases 1, 2.1 and 2.2 are negligible (in the order of a hundredth of a second). On the contrary, for case 3 there is an increase of about one-tenth of a second in the first vibration period; this result reflects the larger deformability of the structure due to the wall segmentation. The following table summarises the values for the first three modes of vibration.

Table 6: *Vibration periods*

Mode	Vibration periods	
	Cases 1, 2.1, 2.2	Case 3
1	0.384 s	0.486 s
2	0.363 s	0.479 s
3	0.294 s	0.398 s

The mode shapes do not present significant variations; the first three mode shapes are translational along the two horizontal directions and rotational along the vertical axis.

https://doi.org/10.52202/069179-0296

9.2 CONNECTIONS

The following subparagraphs compare the loads obtained for the different types of connections. Two shear walls have been chosen for the sake of synthesis: the first P1X-5-1 is a long wall on the first level, with significant gravitational loads; the second P4Y-11-1 is a short external wall on the fourth level, only slightly loaded in terms of vertical loads.

9.2.1 Angle brackets

The following table shows the number of angle brackets for the two walls analysed. It is interesting to compare the values relating to cases 2.1 and 2.2: the number of angle brackets in case 2.2, already increased due to the lower behaviour factor, is further amplified by the lower performance of the angle brackets themselves, caused by the greater over-strength factor.

Table 7: *Number of angle brackets per wall*

Wall (angle bracket)	Number of angle brackets (load) Case 1	Cases 2.1	Case 2.2	Cases 3
P1X-5-1 (TCN240)	14 (535 kN)	9 (324 kN)	13 (380 kN)	4 (118 kN)
P4Y-11-1 (TTN240)	5 (182 kN)	3 (110 kN)	5 (139 kN)	5 (110 kN)

9.2.2 Hold-down/Tie-down

In the case of anchoring connections against uplift, the design loads are shown instead of the connection setup. This is because in case 3, the connection setup was changed to accommodate the needs of the capacity-based design in high ductility.

Table 8: *Uplift forces in hold-down / tie-down*

Wall	Uplift forces Case 1	Cases 2.1	Case 2.2	Cases 3
P1X-5-1	26 kN	0 kN	0 kN	4 kN
P4Y-11-1	69 kN	32 kN	46 kN	42 kN

9.2.3 Non-dissipative connections

For medium and high ductility, the non-dissipative connections must ensure sufficient over-strength in order to remain elastic when the dissipative connections attain the desired level of inelastic displacement. With Equation (2) it is possible to take into account the effective resistance of the dissipative connections before applying the desired over-resistance factor to it.

$$F_{Rd,b} \geq \frac{\gamma_{Rd}}{k_{deg}} \cdot \Omega_d \cdot F_{Ed,E} + F_{Ed,G} \qquad (2)$$

where F_{Rd} = design resistance of the non-dissipative joints, γ_{Rd} = over-resistance factor, k_{deg} = strength reduction factor, $F_{Ed,E}$ = action effect in the non-dissipative joint, or member due to the design seismic action, $F_{Ed,G}$ = action effect in the non-dissipative joint or member due to the non-seismic actions in the design seismic situation, and Ω_d = minimum value of all the over-strength ratios $\Omega_{d,i}$, where i is the storey (see CEN/TC250/SC8 prEN 1998-1-2:2020 for further information).

Table 9 shows the results obtained for the joints between orthogonal walls; due to the heavy loads, these connections are made with angle brackets for shear forces; two connections were chosen in locations where the greatest loads occur.

It is important to point out that these connections are schematised with rigid links in the numerical model.

Table 9: *Number of angle brackets for joints between orthogonal walls*

Wall (angle bracket)	Number of angle brackets (load) Case 1	Cases 2.1	Case 2.2	Cases 3
P1X-5-1 (TTF200)	6 (169 kN)	4 (173 kN)	5 (231 kN)	4 (177 kN)
P4Y-11-1 (TTF200)	2 (66 kN)	2 (68 kN)	3 (96 kN)	2 (85 kN)

9.3 DESIGN COMPLEXITY

Finally, the design complexity of the different cases is analysed. After having calibrated the model through the linear static analysis, few iterations in the dynamic analysis are enough to make the solution converge for low and medium ductility. The angle brackets for shear loads represent the only deformable connections in the numerical model. With the results extracted from the model, it is possible to design all the joints.

In the case of high ductility, one more step must be added: once the global numerical model of the structure is completed, the loads acting on the different connections of the segmented walls are calculated through free body diagrams on each single wall. Horizontal and vertical loads acting on the wall can be extracted from the numerical model. These conditions must be validated through the equations proposed by Casagrande et al. [9] in order to attain the desired kinematic mode.

10 CONCLUSIONS

This study presents the design process of a multi-storey CLT building according to the methods and design provisions included in the new draft of the Eurocode 8. A detailed worked example of design is presented for four different cases of analysis, including also a comparison with the current Italian regulations (NTC 2018). The design process starts from the calibration of the global models through an equivalent static analysis up to the characterization of the main connections that this construction system requires.

Through the detailed analysis of each individual step, possible issues in the interpretation and application of the

rules are highlighted. Some solutions complying with the requirements related to the various cases and ensuring ease of use in the application are then proposed. Such simplified solutions are indispensable for a practical design.

Finally, the results of the various cases analysed are compared. When it comes to capacity-based design, the effects of the over-strength factors strongly characterise the design of each connection as well as the choice of connection types. This over-strength requirement makes the implementation of the connections more difficult in some cases. Furthermore, these coefficients cancel out almost completely the advantage of using higher behaviour factors for all the non-dissipative joints and elements.

Therefore, some serious considerations should be made about the values of the over-strength factors to be used in the seismic design of highly redundant structures like multi-storey CLT buildings. The fairly high values currently proposed in the new Eurocode 8 draft, in fact, may lead to a limited use of these structures in seismic prone areas. On the other hand the full-scale tests conducted so far demonstrated that such structures are capable to withstand severe seismic actions with limited damage and high dissipative behaviour.

Several issues related to the modelling process are also analysed in order to verify the underlying hypotheses and their correspondence with the experimental results.

ACKNOWLEDGEMENT

The authors gratefully acknowledge the financial contribution of the DPC-ReLUIS 2019–21 and 2022-24 Research Projects, WP13 “Timber Structures – Regulatory Contributions”.

REFERENCES

[1] Izzi, M., Casagrande, D., Bezzi, S., Pasca, D., Follesa, M., Tomasi, R.Seismic behaviour of Cross-Laminated Timber structures: A state-of-the-art review (Open Access) (2018) Engineering Structures, 170, pp. 42-52.

[2] Pei, S., Van De Lindt, J.W., Popovski, M., Berman, J.W., Dolan, J.D., Ricles, J., Sause, R., (...), Rammer, D.R. Cross-Laminated Timber for Seismic Regions: Progress and Challenges for Research and Implementation (2016) Journal of Structural Engineering (United States), 142 (4), art. no. E2514001.

[3] Cenci, G., Follesa, M., Rinaldi, V., Casagrande, D., Fragiacomo, M.: Edifici in legno a pannelli massicci: Esempio di calcolo di un edificio a pannelli massicci in zona sismica. Report ReLUIS WP13-Task3, 2022.

[4] C.S.LL.PP. [2018] “Aggiornamento delle norme tecniche per le costruzioni” Supplemento ordinario alla “Gazzetta Ufficiale” n. 8 del 20 febbraio 2018 - Serie generale – n. 42 (In Italian.)

[5] CEN/TC250/SC8. prEN 1998-1-2:2020: Eurocode 8: Design of structures for earthquake resistance. Part 1-2: Rules for new buildings. Draft document. European Committee for Standardization; 2021.

[6] Follesa, M., Fragiacomo, M., Casagrande, D., Tomasi, R., Piazza, M., Vassallo, D., Canetti, D., Rossi, S. The new provisions for the seismic design of timber buildings in Europe (Open Access) (2018) Engineering Structures, 168, pp. 736-747. doi: 10.1016/j.engstruct.2018.04.090

[7] Ceccotti, A., Sandhaas, C., Okabe, M., Yasumura, M., Minowa, C., Kawai, N.SOFIE project - 3D shaking table test on a seven-storey full-scale cross-laminated timber building (2013) Earthquake Engineering and Structural Dynamics, 42 (13), pp. 2003-2021. doi: 10.1002/eqe.2309

[8] Follesa M., Christovasilis I.P., Vassallo D., Fragiacomo M., Ceccotti A.: Seismic design of multi-storey cross laminated timber buildings according to Eurocode 8. Ingegneria Sismica, vol. 30, 2013.

[9] Casagrande, D., Doudak, G., Polastri, A. A proposal for the capacity-design at wall- and building-level in light-frame and cross-laminated timber buildings, (2019) Bulletin of Earthquake Engineering, 17 (6), pp. 3139-3167.

[10] Jorissen, A., Fragiacomo, M. General notes on ductility in timber structures (2011) Engineering Structures, 33 (11), pp. 2987-2997. doi: 10.1016/j.engstruct.2011.07.024

[11] Masroor, M., Doudak, G., Casagrande, D.The effect of bi-axial behaviour of mechanical anchors on the lateral response of multi-panel CLT shearwalls (2020) Engineering Structures, 224, art. no. 111202.

[12] Masroor, M., Doudak, G., Casagrande, D. Design of Multipanel CLT Shear Walls with Bidirectional Mechanical Anchors following Capacity-Based Design Principle, Journal of Performance of Constructed Facilities Volume 36, Issue 11 February 2022 Article number 04021113

https://doi.org/10.52202/069179-0296

World Conference on Timber Engineering Oslo 2023

SEISMIC RESPONSE OF BALLOON TYPE CLT SHEAR WALLS

Zhiyong Chen[1], Marjan Popovski[2]

ABSTRACT: Balloon-type mass timber shear walls are one of the most efficient structural systems to resist lateral loads induced by earthquakes or high winds. This system, however, is not included in the 2020 National Building Code of Canada and has no design guidelines in the 2019 Canadian Standard for Engineering Design in Wood, so it is out of reach of most designers. A multi-year research project has been initiated at FPInnovations to quantify the system performance and develop the necessary technical information to codify balloon-type mass timber shear walls. This paper presents the initial results of a study on the seismic response of balloon-type CLT shear walls. A mechanics-based analytical model was updated to predict the CLT panel resistance, in addition to predicting the deflection and resistance of balloon type CLT shear walls. The influence of specific key parameters such as wall length and thickness, aspect ratio, vertical loads, and vertical joints, on the structural performance of this wall system under lateral loads was investigated using the updated model. The results of this study will give a valuable insight into the seismic performance of balloon type CLT shear walls.

KEYWORDS: Mass timber, CLT, balloon walls, tall wood construction, seismic response, numerical model

1 INTRODUCTION

Balloon-type mass timber shear walls (Figure 1) are one of the most efficient structural systems to resist lateral loads induced by earthquakes or high winds. They allow use of longer mass timber panels, reduction of number of connections, and prevention of the accumulated compression perpendicular to grain in floor panels [1]. This system, however, is not included in the 2020 National Building Code of Canada and has no design guidelines in the 2019 Canadian Standard for Engineering Design in Wood, so it is out of reach of most designers.

***Figure 1: E**xample of a balloon wall in CLT construction*

Most of the research on CLT as a lateral load resisting system so far has been conducted on platform-type construction [2]. A multi-year research project has been initiated at FPInnovations to quantify the system performance and develop the design information to codify balloon-type mass timber shear walls [3]. This paper presents the initial results of the study related to the seismic response of balloon-type CLT shear walls. A mechanics-based analytical model [1] was updated to predict the CLT panel resistance, in addition to predicting the deflection and resistance of these types of CLT shear walls. The influence of wall length and thickness, wall aspect ratio, vertical loads, and vertical joint properties on the structural performance of this wall system under seismic loads was investigated using the developed model.

2 ANALYTICAL MODELS

2.1 DEVELOPED MODELS

Two analytical models (rigid- and elastic-base models) were developed and verified at FPInnovations to predict the resistance and deflection of balloon-type CLT shear walls [4]. Single- and coupled panel balloon-type CLT walls (Figure 2) were considered by the developed models [1]. The seismic actions on these walls create a base shear force and overturning moment(s). As illustrated in Figure 2, the vertical uplift forces are taken by hold-downs at both ends of the wall, while the shear forces are taken by shear connectors, shear keys, or both. The vertical joints between the panels are not only used to connect the panels in the coupled walls, but also add to the energy dissipation properties of the system. Using the capacity design methodology for seismic lateral loads, the capacity of the wall system is governed solely by the capacity of the connections. The CLT panels are designed to exhibit elastic in-plane deformations, while the connections provide all the ductility and energy dissipation [5, 6].

[1] Zhiyong Chen, FPInnovations, Canada, zhiyong.chen@fpinnovations.ca
[2] Marjan Popovski, FPInnovations, Canada, marjan.popovski@fpinnovations.ca

https://doi.org/10.52202/069179-0297

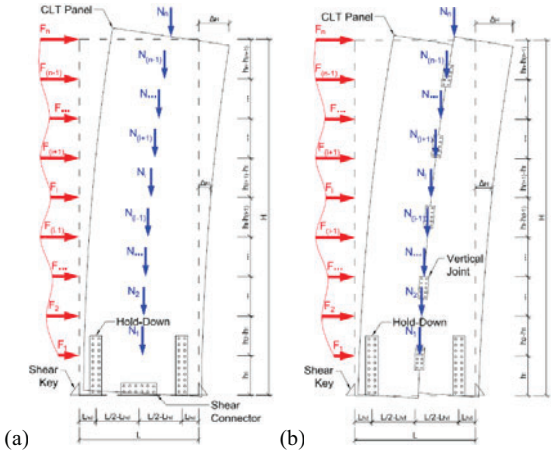

Figure 2: *(a) Single and (b) coupled wall model. Note: F_i and N_i represent the lateral load and the vertical load on the wall at a height level i, respectively [kN]; h_i represents the height level of the lateral and vertical load [m]; the deflection of the wall at the top (level $h_n = H$) and at any level i is designated as Δ_H and Δ_{hi}, respectively [mm]; n indicates the number of load levels.*

The total lateral deflection of a single-panel balloon-type CLT shear wall at any height level *i*, Δ_{hi}, is comprised of four deflection components: wall bending $\Delta_{hi,b}$, wall shear $\Delta_{hi,s}$, rotation (anchorage deformation) $\Delta_{hi,rot}$, and sliding $\Delta_{hi,sld}$, (Figure 3a to 3d). In case of walls with multiple panels an additional component $\Delta_{hi,slp}$ (Figure 3e) that represents the slip between the panels, needs to be added. Thus, the total deflection can be calculated using Eq. (1).

$$\Delta_{hi} = \Delta_{hi,b} + \Delta_{hi,s} + \Delta_{hi,rot} + \Delta_{hi,sld} + \Delta_{hi,slp} \quad (1)$$

The lateral resistance of the system is governed by the strength of the hold-downs, shear connector(s), wood in contact with shear keys, and vertical joints, if present, using three failure scenarios: (a) when shear failure occurs in the bottom connections where the hold-downs and shear connector yield horizontally, and the wood in contact with the shear key at one end crushes successively under base shear; (b) when overturning occurs in single-panel walls where the hold-down at one end yields vertically; and (c) when overturning occurs in coupled walls where the vertical joints yield first followed by yielding of hold-down at one end. The actual resistance can be taken as the minimum resistance derived from the three scenarios.

The balloon-type shear wall is a statically indeterminate system where the connections resist the loads following deformation coordination principle. The deflection and resistance of the wall system can be derived by solving the nonlinear equations of the developed analytical models using the trial-and-error method. Detailed derivation of the deformation components and resistances in different scenarios is provided in Chen and Popovski [1].

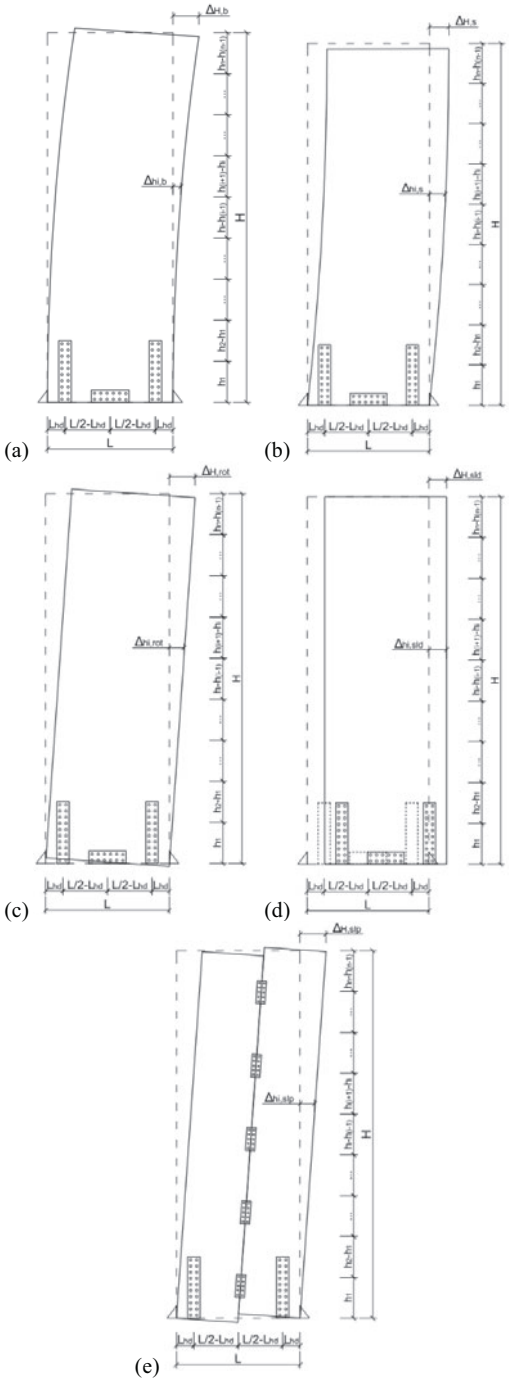

Figure 3: *Lateral deflection components of balloon-type walls: (a) bending; (b) shear; (c) rotation; (d) sliding; and (e) slip*

Generally, the CLT panels in balloon wall system when subjected to in-plane lateral loads present a complex stress state and many failure modes need to be considered in the design [7]. Therefore, the developed elastic-base model was updated in this study to predict the CLT panel resistance to support the capacity design of the balloon-type CLT shear walls.

https://doi.org/10.52202/069179-0297

2.2 PANEL RESISTANCE

CLT panels considered in this study have all longitudinal layer with equal thickness and equal width of the boards in the layers. It is assumed that the resistance of CLT panels is governed by bending and shear failure (gross shear, net shear, rolling shear and torsion). It is also assumed that reinforcing solutions are present in areas where some stress concentration is to be expected, e.g., around openings, bottom of the panels, and others, so that the failure does not occur in the panel.

A balloon-type CLT shear wall acts like a vertical cantilever beam in which the wall panels generally behave elastically. The normal stress distribution due to bending in the cross section of the CLT panel is illustrated in Figure 4. Accordingly, the maximum bending stress, σ_{max}, at the bottom for a balloon-type shear wall under a number of lateral loads at different height levels can be calculated using Eq.(2) that is derived using structural mechanics based on a beam theory.

$$\sigma_{max} = \frac{LE_{mean}}{2(EI)_{eff}} \sum_{j=1}^{n} F_j h_j \qquad (2)$$

where E_{mean} is the mean modulus of elasticity [N/mm^2] of the longitudinal layers (the horizontal layers in Figure 4) of the CLT panel; $(EI)_{eff}$ is the effective bending stiffness [N·mm^2] of the CLT panel which can be calculated using the simplified design method [8], or using the k method (composite theory) provided by Blass and Fellmoser [9].

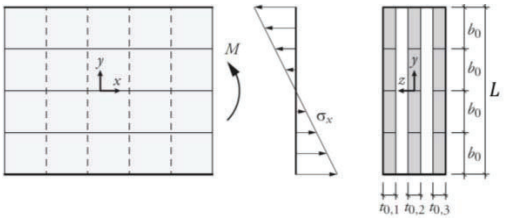

Figure 4. *Illustration of normal stress distribution due to bending [7]*

The calculated maximum stress should not be larger than the bending strength f_b of the CLT panel specified in the material design standards or product manuals. Therefore, the maximum base shear V_b can be calculated using Equation (3).

$$V_b = \frac{2f_b(EI)_{eff}}{LE_{mean}} \Big/ \sum_{j=1}^{n} F_{pattern,j} h_j \qquad (3)$$

where $F_{pattern,j}$ is the normalized lateral load factor for the j_{th} storey according to the lateral load pattern along the height of the wall. Lateral load F_j is the product of V_b and $F_{pattern,j}$.

In CLT cantilever beams where adjacent lamellas (boards) within individual layer are not edge-glued, the thickness is not constant throughout the height of the CLT beam. In cross-sections at unglued joints between neighbouring lamellas, the shear forces can only be transferred by lamellas in the perpendicular direction. Consequently, the shear stresses in these so-called net cross sections are higher than in the gross cross-sections (between unglued joints). The transfer of shear forces between longitudinal and transversal lamellas also causes shear stresses in the crossing areas of orthogonally bonded lamellas. By considering the shear stresses in the lamellas and in the crossing areas, three different failure modes (Figure 5) exist in CLT beams subjected to shear stresses [10].

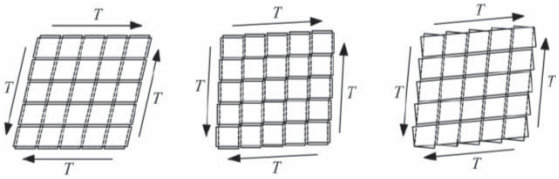

Figure 5. *Failure modes I, II and III in CLT-panel subjected to transversal forces in plane direction (from left to right) [10]*

Failure mode I is characterised by shear failure parallel to the grain in the gross cross-section of the CLT panels. This failure occurs in sections between unglued joints with τ_I equaling to the gross shear strength $f_{v,gross}$ in longitudinal layers and transversal layers. Therefore, the maximum base shear, V_{sI}, can be calculated using Equation (4).

$$V_{sI} = \frac{2Lt_{gross}f_{v,gross}}{3} \qquad (4)$$

where t_{gross} is the gross thickness of the CLT panels.

Failure mode II is characterised by shear failure perpendicular to the grain in the net cross-section of the CLT panels. This failure occurs in sections coinciding with unglued joints with shear stresses only in lamellas perpendicular to the joints. The maximum base shears ($V_{sII,90}$ and $V_{sII,0}$) can be calculated using Eqs. (5) and (6).

$$V_{sII,90} = \frac{2Lt_{net,90}f_v}{3} \qquad (5)$$

$$V_{sII,0} = \frac{2Lt_{net,0}f_v}{3} \qquad (6)$$

where $t_{net,90}$ is the total thickness of all perpendicular layers in the CLT panels; $t_{net,0}$ is the CLT panel net cross-section thickness when considering longitudinal layers only.

Failure mode III is characterised by shear failure within the crossing areas between the orthogonally glued boards (lamellas). This failure mode is caused by torsional and unidirectional shear stresses form the transfer of the shear forces between adjacent layers. The maximum base shear (V_{sIII}) can be calculated using Equation (7).

$$V_{sIII} = \frac{b_0^2 n_{ca}}{\frac{6\left(\frac{1}{m}+\frac{1}{m^3}\right)}{f_{tor}} \frac{b_0 b_{max}}{b_0^2+b_{90}^2} + \frac{6\left(\frac{1}{m^2}+\frac{1}{m^3}\right)1.33}{f_s}} \quad (7)$$

where n_{ca} is the number of crossing areas that longitudinal lamination shares with adjacent transversal laminations; m is the number of horizontal boards in the CLT beam or $m = L/b_0$; q is the local compression [kN/m]; b_{max} is the maximum value for the width of either the longitudinal boards (b_0) or the transversal boards (b_{90}), i.e., $b_{max} = max\{b_0, b_{90}\}$.

3 KEY PARAMETERS AFFECTING STRUCTURAL PERFORMANCE

Using the updated analytical elastic-base model, parametric analyses were conducted to investigate the influence of various key parameters on the structural performance of balloon-type CLT walls. The key parameters that were investigated include (a) CLT panel thickness (number of layers); (b) wall length (panel width); (c) wall aspect ratio; (d) level of vertical loads; and (e) vertical joint properties (coupled walls). The influence of the first four parameters was studied with single-panel shear walls (Figure 2a) under multiple point loads in reversed triangular pattern (Figure 6), while that of the fifth parameter was studied with coupled shear walls (Figure 2b).

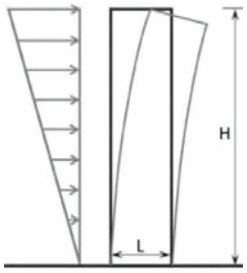

Figure 6: *Reversed triangular lateral load pattern applied to the wall*

The CLT panels and shear connectors were capacity designed; while the hold-downs were designed to yield under lateral loads once the maximum stresses in the panels reach 30% design bending or shear strength, whichever is less, i.e., lateral load level (LLL) = 30%. The distance of hold-downs to the close edge, L_{hd} (Figure 2), was taken as $L/20$.

3.1 WALL LENGTH

The influence of wall length (CLT panel width) was studied on single-panel shear walls with a wall height of 18 m, which is typical for a 6-storey building with a storey height of 3 m. The considered wall lengths, L, were 2.4 m, 3.0 m, 3.6 m, 4.2 m, 4.8 m, 5.4 m, and 6.0 m. The commonly used 5-, 7-, and 9-ply CLT panels were investigated.

Figures 7 and 8 show the relationship of the wall length to the resistance (P_{wall}) and stiffness (K_{wall}) of the analysed balloon-type CLT shear walls. The ratios in Figures 7b and 8b were based on the structural performance properties of the shear walls with 3.0 m wall length and a given wall thickness. With an increase in the wall length, the resistance increased linearly, while the stiffness increased nonlinearly. This is because the resistance of all walls was governed by the shear failure, while the deflection was a combination of bending and shear deformation, rotation, and sliding.

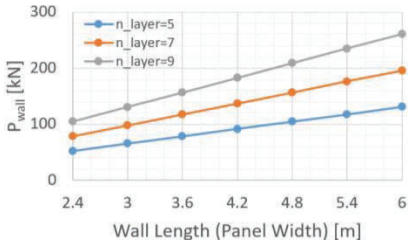

(a)

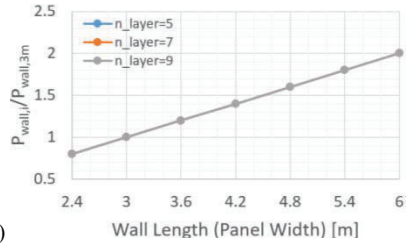

(b)

Figure 7: *Relationship between the wall length and the wall resistance: (a) Absolute values; and (b) Relative values with respect to a 3m long wall*

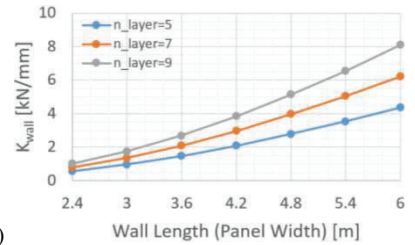

(a)

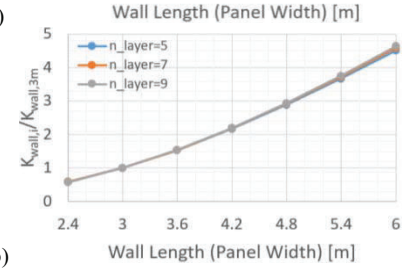

(b)

Figure 8: *Relationship between the wall length and the wall stiffness: (a) Absolute values; and (b) Relative values with respect to 3 m long wall*

The relationship between the wall length and the ratio of the compression zone length to the wall length (L_c/L) for the analysed balloon-type CLT shear walls is shown in Figure 9. The L_c/L ratio was constant for all wall lengths

https://doi.org/10.52202/069179-0297

of the same wall thickness. This is because the lateral loads applied on the walls is governed by shear resistance of the panels, which by itself is in linear relationship with the wall length. Thus, the L_c/L ratio remained constant.

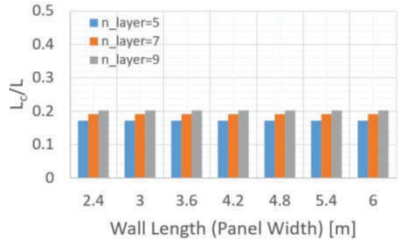

Figure 9: *Relationship between the wall length and the compression zone length*

3.2 WALL THICKNESS

The influence of wall thickness can be analysed by comparing the structural performance of the analysed shear walls with different thickness. The thickness depends on the number of layers in the CLT panel (0.175 m for 5-ply, 0.245 m for 7-ply, and 0.315m for 9-ply panels). The relationship of the wall thickness to the wall resistance and stiffness is shown in Figures 10 and 11. The ratios in Figures. 10b and 11b were based on the structural performance properties of walls with 0.175 m thickness (5-ply) for a given wall length. With an increase in wall thickness, the resistance and the stiffness of the shear walls increased linearly. In both, Figure 10b and 11b, the relationships for all wall lengths are identical. All shear walls were governed by shear (type II in transversal laminations) failure of which the resistance and stiffness increase linearly with the number of transversal laminations (i.e., 2, 3, and 4).

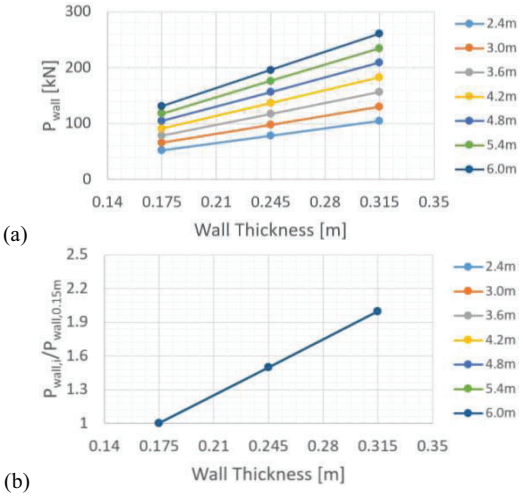

Figure 10: *Relationship between the wall thickness and the wall resistance: (a) Absolute values; and (b) Relative values with respect to 175 mm thick wall*

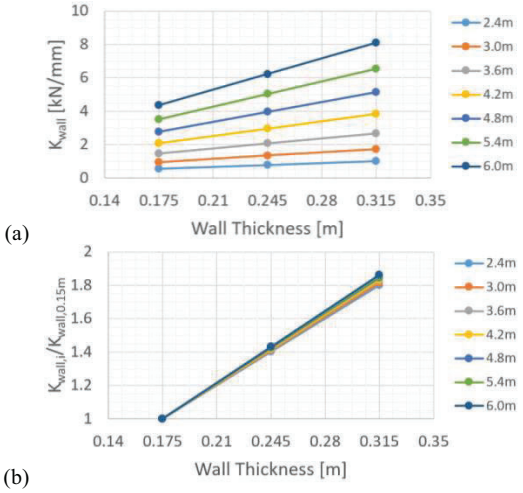

Figure 11: *Relationship between the wall thickness and the wall stiffness: (a) Absolute values; and (b) Relative values with respect to 175 mm thick wall*

The relationship between the wall thickness and the ratio of the compression zone length to the entire wall length (L_c/L) for the analysed balloon walls is shown in Figure 12. The ratio L_c/L increased with an increase in wall thickness.

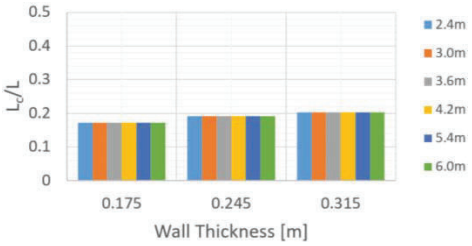

Figure 12: *Relationship between wall thickness and compression length*

3.3 WALL ASPECT RATIO

The influence of the wall aspect ratio was studied on 7-ply single-panel shear walls with a wall length of 1.5 m, 3.0 m, and 6.0 m. The considered aspect ratios were 4, 6, 8, 10, and 12. Correspondingly, the wall heights were 6m, 9 m, 12 m, 15 m, and 18 m for 1.5m long shear walls; 12 m, 18 m, 24 m, 30 m, and 36 m for 3.0 m long walls; and 24 m, 36 m, 48 m, 60 m, and 72 m for 6.0 m long walls.

Figures 13 and 14 show the relationship of the wall aspect ratio to wall resistance and stiffness of the analysed balloon walls. The ratios (Figures 13b and 14b) were based on the structural performance properties of the shear walls with the aspect ratio of 4.0 and a given wall length. The resistance kept constant until the aspect ratio of 8.0. Beyond that it decreased in a nonlinear fashion with an increase in the aspect ratio. This is because the shear failure governed the wider walls while bending failure governed the slender walls. The critical aspect

ratio for the change of governing failure mode was around 8.0. The stiffness decreased in a nonlinear fashion with an increase in the aspect ratio. Slender walls showed to have less resistance and be more flexible, compared to wider walls.

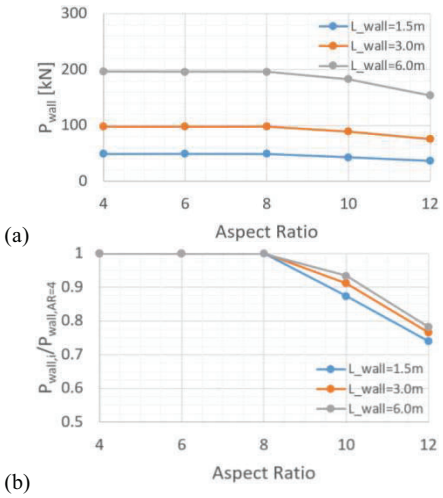

Figure 13: *Relationship between the aspect ratio and the wall resistance: (a) Absolute values; and (b) Relative values with respect to walls with aspect ratio of 4.0*

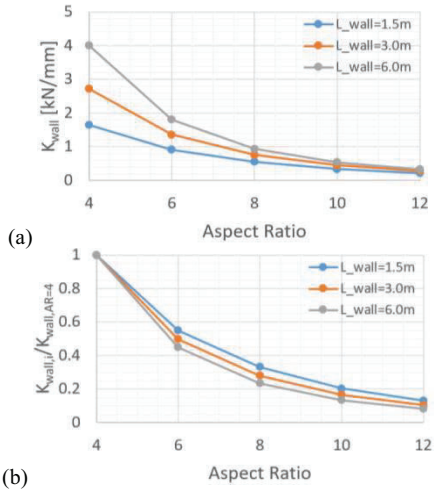

Figure 14: *Relationship between the aspect ratio and wall stiffness: (a) Absolute values; and (b) Relative values with respect to wall with an aspect ratio of 4.0*

The relationship between the wall aspect ratio and the ratio of the compression zone length to the entire wall length (L_c/L) for analysed balloon-type CLT shear walls is shown in Figure 15. As can be seen, an increase in wall aspect ratio resulted in a non-linear increase in the L_c/L ratio until a wall aspect ratio of 8.0, beyond which L_c/L was constant. For the walls governed by shear failure, where the wall aspect ratio is not larger than 8.0, slender walls needed longer L_c to resist larger compression under the same later loads. In walls governed by bending failure, where the wall aspect ratio is over 8.0, a balance was achieved between L_c and the aspect ratio. A larger wall aspect ratio resulted in an increase in the compression stress at the wall base and thus L_c; however, it also reduced the amount lateral load that the wall can carry and thus the compression portion and L_c.

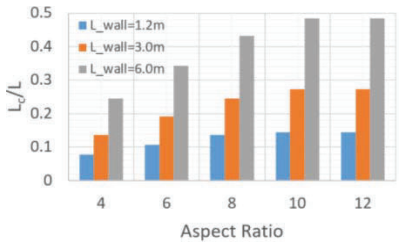

Figure 15: *Relationship between the wall aspect ratio and the compression zone length for walls designed for the same lateral load*

The deflection components of the balloon-type CLT shear walls with different aspect ratios were decoupled and the percentage of each component is shown in Figures 16 to 18. The rotation and bending deflection were the major contributors to the deflection of the walls, while the shear deflection had less contribution. The contribution of sliding was small enough to be ignored. As the wall aspect ratio increased, the walls became slenderer and the contribution of the bending deflection increased and became predominant, while the contribution of rotation and shear deflection decreased. The intersection between the rotation and the bending deformation curves occurred at a lower aspect ratio for longer walls (e.g., 6.0 m) compared to a short wall (e.g., 1.5m). This is due to the fact that the bending deflection is a function of aspect ratio but also of the applied loads. For the same aspect ratio, the higher the loads, the larger the deflection.

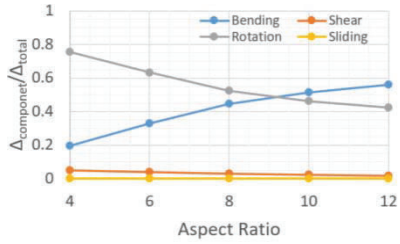

Figure 16: *Influence of wall aspect ratio on the deflection components in 1.5 m long single-panel walls*

https://doi.org/10.52202/069179-0297

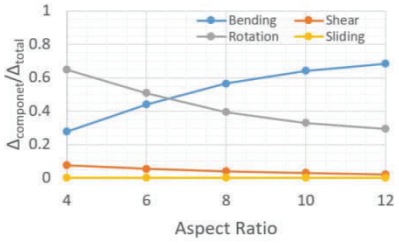

Figure 17: *Influence of wall aspect ratio on the deflection components in 3.0 m long single-panel walls*

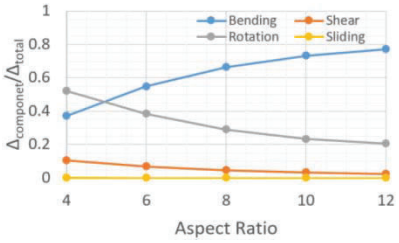

Figure 18: *Influence of wall aspect ratio on the deflection components in 6.0 m long single-panel walls*

3.4 VERTICAL LOADS

Vertical loads applied to the shear walls provide additional overturning resistance to the walls, and as a result, they affect wall's lateral stiffness and resistance. The influence of the vertical loads was studied on 7-ply single-panel shear walls with a wall length of 1.5 m (H = 9 m), 3.0 m (H = 18 m), and 6.0 m (H = 36 m). Six vertical load levels (VLLs), 0%, 20%, 40%, 60%, 80% and 100% of the reference vertical loads, were analysed for each wall length. The reference vertical loads were defined as loads that can counteract the overturning resistance of a wall without vertical loads. Thus, the reference vertical loads were taken as 1200 kN, 2300 kN, and 4300 kN for 1.5 m, 3.0 m, and 6.0 m walls, respectively.

Figures 19 and 20 show the relationship of vertical loads to wall resistance and stiffness of the analysed balloon-type CLT shear walls. The ratios (Figures 19b and 20b) were based on the structural performance properties of the shear walls with the vertical load level of 0% (no vertical loads) and a given wall length. As shown in Figure 19, the resistance of 1.5 m walls increased with an increase in the VLL up to 60% and then started to decrease. The resistance of 3.0 m long walls increased with an increase in the VLL at the beginning, but then very soon after 40% VLL the resistance started to decrease. The resistance of 6.0 m walls decreased with an increase in VLL until VLL reached 60% beyond which the resistance increased with the increases in the VLL. As shown in Figure 20, the stiffness of 1.5 m and 3.0 m long walls increased with an increase in VLL, while the stiffness of 6.0 m walls decreased with an increase in VLL. All these findings indicate that the wall resistance and stiffness were affected by not only the VLL, but also the ratio between compression length and the wall length ($\boldsymbol{L_c/L}$, Figure 21).

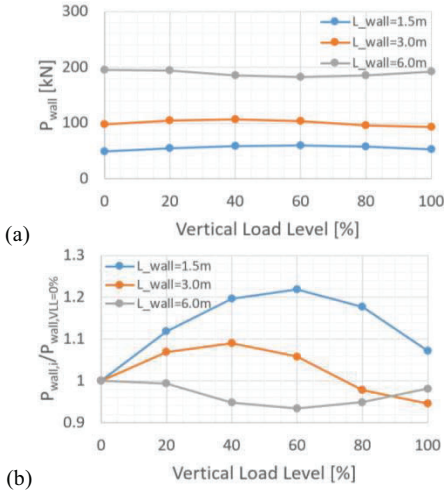

Figure 19: *Relationship between VLL and wall resistance: (a) Absolute values; and (b) Relative values with respect to walls without vertical load*

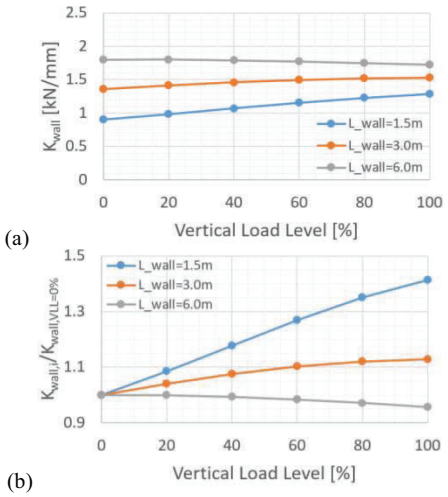

Figure 20: *Relationship between vertical loads level and compression zone length*

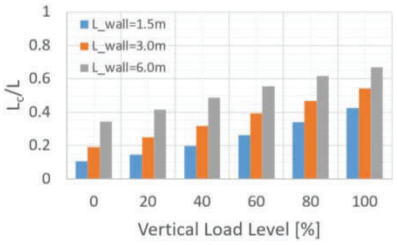

Figure 21: *Relationship between vertical loads level and compression zone length*

The stiffness of the walls increased with an increase in VLL when L_c/L was less than 0.4 and decreased when L_c/L was larger than 0.4. The resistance of walls increased with an increase in VLL when L_c/L was either

less than 0.4 or larger than 0.6, while it decreased with an increase in VLL when L_c/L was between 0.4 and 0.6. This is because the effect of vertical loads changes from been helpful (increasing the resistance) to detrimental (decreasing the resistance) under lateral loads, when L_c/L changes from less than 0.4 to larger than 0.6, with the range of 0.4 to 0.6 L_c/L been the transition zone. For cases with large L_c/L (e.g., over 0.6), the vertical loads provide some kind of prestressing at the wall bottom and thus increase the wall resistance.

3.5 VERTICAL JOINTS

The influence of the vertical joints was studied on a 7-ply coupled balloon-type CLT walls with two configurations. Configuration A was a 9 m high coupled wall with 1.5 m panel width (3.0 m total wall length), while Configuration B was 18 m high coupled wall with 3.0 m panel width and a total wall length of 6.0 m. A shear stiffness ratio (SSR) was defined as the ratio of the stiffness of the vertical joints to the shear stiffness of the wall along the height. Seven (7) shear stiffness ratios (SSR) were considered in the investigation: 0.01, 0.1, 0.2, 0.4, 0.6, 0.8, and 1.0. The ratio between the resistance and the stiffness of the vertical joints was taken as that of the self-tapping screw connections tested at FPInnovations [4], i.e., 5.0.

Figures 22 and 23 show the relationship of the shear stiffness ratio to wall resistance and stiffness of the analysed balloon-type CLT shear walls. The ratios (Figures 22b and 23b) were based on the structural performance properties of the shear walls with the SSR of 0.01 and a given wall length. As shown in Figure 22, the resistance of 3 m and 6 m coupled walls increased with an increase in the SSR until 0.4 and 0.6, respectively, beyond which the resistance of the walls was governed by the hold-downs rather than the vertical joints. The stiffness of both wall configurations (Figure 23), increased dramatically when the SSR was less than 0.4, beyond that the increases became smaller. The relationship between the SSR and the $\boldsymbol{L_c/L}$ for analysed balloon-type walls is shown in Figure 24. The ratio $\boldsymbol{L_c/L}$ stayed constant for different SSRs, indicating that $\boldsymbol{L_c/L}$ of coupled shear walls is not affected by the SSR.

The deflection components of the coupled CLT shear walls with different SSRs were decoupled and the percentage of each component is shown in Figures 25 and 26. Bending, rotation, shear, and sliding deformation increased with an increase in the SSR, while the slip defection decreased. Slip deformation was the major component for coupled walls with a small SSR, while bending deformation became the major component for coupled walls when the SSR was larger than 0.1.

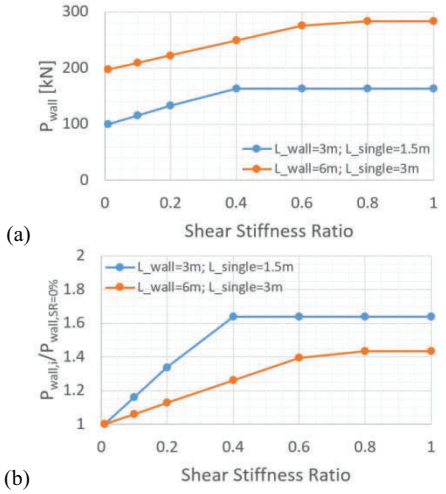

Figure 22: *Relationship between SSR and wall resistance: (a) Absolute values; and (b) Relative values with respect to wall with SSR=0.01*

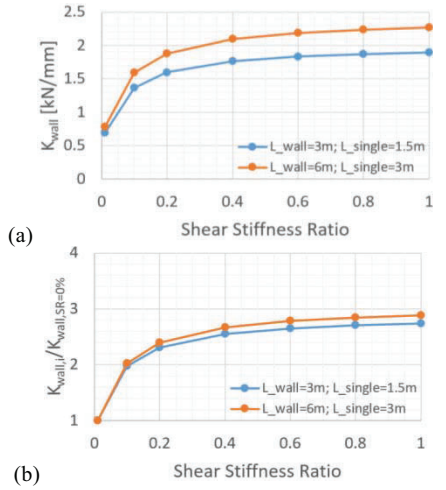

Figure 23: *Relationship between SSR and wall stiffness: (a) Absolute values; and (b) Relative values with respect to wall with SSR=0.01*

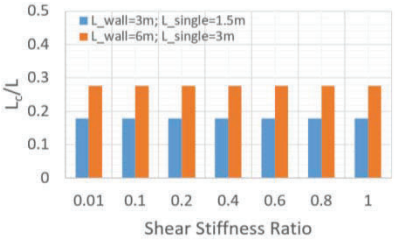

Figure 24: *Relationship between shear stiffness ratio and compression length*

https://doi.org/10.52202/069179-0297

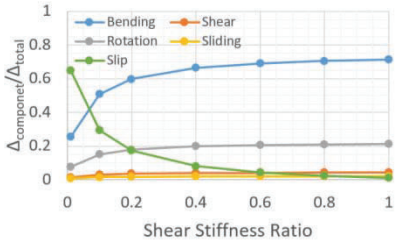

Figure 25: *Influence of wall aspect ratio on the deflection components in 3.0 m coupled walls*

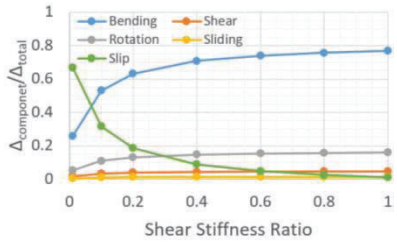

Figure 26: *Influence of wall aspect ratio on the deflection components in 6.0 m coupled walls*

4 CONCLUSIONS

A multi-year research project has been initiated at FPInnovations to quantify the system performance and develop the design information to codify balloon-type mass timber shear walls. A mechanics-based analytical model was updated to predict the CLT panel resistance, in addition to the deflection and resistance of balloon type CLT shear walls. Using this updated model, the influence of wall length and thickness, aspect ratio, vertical loads, and vertical joints on the seismic performance of this wall system was investigated. The findings are listed as follows:

- The lateral resistance and stiffness of balloon-type CLT shear walls increased with an increase in the wall length and thickness and decreased with an increase in the wall aspect ratio.
- The rotation and bending deflection were the two major contributors (e.g., 90% in total) to the total deflection of single panel balloon walls, while the shear deflection was the third one (e.g., 10%). The contribution of sliding was small enough to be ignored. As the wall aspect ratio increased, the walls became slender, and as a result the contribution of bending deflection increased (e.g., from 20% to 80%) and became the largest contributor to the total deflection, while the contribution of the rotation and the shear deflection decreased (e.g., rotational deflection changed from 80% to 20% and shear deflection changed from 10% to 1%).
- The lateral resistance and stiffness were affected by the vertical load level and the ratio of compression zone length to the wall length (L_c/L). The resistance of walls increased with an increase in the vertical load level when L_c/L was either less than 0.4 or larger than 0.6, while it decreased with an increase in vertical load level when L_c/L was between 0.4 and 0.6. The stiffness of walls increased with vertical load level when L_c/L was less than 0.4 and decreased when L_c/L was larger than 0.4.
- The lateral resistance of 3 m and 6 m coupled walls increased with an increase in the shear stiffness ratio until 0.4 and 0.6, respectively, beyond which the resistance of the walls was governed by the hold-downs rather than the vertical joints. The stiffness of both wall configurations increased dramatically when the shear stiffness ratio was less than 0.4, beyond that the increase became smaller.
- In coupled balloon-type CLT shear walls, the bending, rotation, shear, and sliding deflection increased with an increase of the shear stiffness ratio, while the slip deflection decreased with increases in the shear stiffness ratio.

The updated analytical model will assist researchers and structural designers in developing and designing appropriate balloon-type CLT shear walls for timber structures. The analytical model can also be used to quantify the performance of balloon-type CLT structures subjected to seismic loads and thus providing the research background for drafting of the seismic design guidelines for balloon-type CLT construction for CSA O86 and National Building Code of Canada.

ACKNOWLEDGEMENT

This project was financially supported by the Canadian Forest Service and National Resources Canada under the contribution agreement existing between the Government of Canada and FPInnovations.

REFERENCES

[1] Chen, Z., Popovski, M.: Mechanics-based analytical models for balloon-type cross-laminated timber (CLT) shear walls under lateral loads. Engineering Structures, 208:109916, 2020.

[2] Izzi, M., Casagrande, D., Bezzi, S., Pasca, D., Follesa, M., and Tomasi, R.: Seismic behavior of Cross-Laminated Timber structures: A state-of-the-art review. Eng. Struct., 170: 42-52, 2018.

[3] Chen, Z., Popovski, M.: Expanding wood use towards 2025: Seismic performance of balloon mass timber walls – year 2. FPInnovations project report (301014059), Vancouver, 2021.

[4] Chen, Z., Cuerrier-Auclair, S., and Popovski, M.: Advanced Wood-based Solutions for Mid-rise and High-rise Construction: Analytical Prediction Models for Balloon-Type CLT Shear Walls. FPInnovations Project Report (301012205), Vancouver, 2018.

[5] Chen, Z., Tung, D., Karacabeyli, E.: Modelling Guide for Timber Structures. FPInnovations, 2022: web.fpinnovations.ca/modelling

[6] Chen, Z., Popovski, M.: Modelling of mass timber seismic force resisting systems. FPInnovaitons, 2021.

[7] Danielsson, H., & Serrano, E.: Cross laminated timber at in-plane beam loading – Prediction of shear stresses in crossing areas. Eng. Struct., 171, 921-927, 2018.
[8] Gavric, I., Fragiacomo, M., & Ceccotti, A.: Cyclic Behavior of CLT Wall Systems: Experimental Tests and Analytical Prediction Models. Journal of Structural Engineering, 141(11): 04015034, 2015.
[9] Blass, H. J., & Fellmoser, P.: Design of solid wood panels with cross layers. In: 8th World conf. timber eng. 2004.
[10] Flaig, M., & Blass, H. J.: Shear strength and shear stiffness of CLT-beams loaded in plane. In: CIB-W18, 245-258, 2013.
[11] CSA: Engineering design in wood (CSA O86:19). Canadian Standards Association (CSA), Toronto, 2019.
[12] ANSI/APA: PRG 320 Standard for performance-rated cross-laminated timber. APA – The Engineered Wood Association, Tacoma, 2019.

https://doi.org/10.52202/069179-0297

World Conference on Timber Engineering Oslo 2023

EFFECTS OF VARIABLE CLIMATE CONDITIONS ON THE BEHAVIOR OF POST-TENSIONED MASS TIMBER WALL PANELS

Jacob Gesh[1], Esther Baas[2], Ryan Longman[3], Mariapaola Riggio[4], Andre R. Barbosa[5], Lech Muszynski[6], and Gabriele Granello[7]

ABSTRACT: Post-tensioned (PT) mass timber rocking walls are innovative lateral force-resisting systems used in resilient seismic design. The system relies on an initial tensioning of wall panels using high-strength steel rods. However, tension losses are known to occur in PT systems over time, especially when these systems are exposed to variable climate conditions. In mass timber rocking wall designs, existing creep models do not allow for reliable prediction of long-term PT losses. Thus, the purpose of this research is to characterize the long-term behaviour of PT mass-timber wall panels exposed to variable climate conditions and to develop a model for reliable prediction of the effects of such exposures. The mass timber panels consist of ANSI PRG 320 approved cross-laminated timber (CLT) and mass ply panels (MPP). The components of the complex effect of long-term variable climate exposure are isolated by comparing data collected on similar panel specimens exposed to controlled humidity cycles in post-tensioned and unloaded conditions with those collected on loaded specimens exposed to a constant environment. Panel in-plane deformations, loads, and moisture content in the tested systems are continuously monitored. These tests provide data for the development of an in-plane creep model for mass timber panels that will be validated on two monitored full-scale 9.1 m tall post-tensioned rocking walls, exposed to naturally varying indoor conditions in a large-scale structural testing laboratory for 12 months. This paper summarizes the experimental data collected from specimens in the environment with controlled humidity cycles and the constant environment and some lessons learned. The data shows the following trends: (1) it appears that, during the test time frame and under the imposed changing environmental conditions, the PT system's response is dominated by the in-plane shrinkage and swelling of the specimens, (2) the MC profiles of the PT panels have a significant effect on the panel's strain behaviour, and (3) under constant environmental conditions, the CLT panels experienced more viscoelastic creep compared to the MPP panels.

KEY WORDS: Creep, Mass timber panels, Post-tensioning

1 INTRODUCTION

Utilizing timber in large structures is a sustainable option for construction and is made possible with mass timber panels, such as cross-laminated timber (CLT) and mass ply panels (MPP) [1]. Post-tensioned (PT) mass timber rocking walls have been developed as an innovative lateral force-resisting system to allow for resilient, low-damage seismic designs [2-4]. However, substantial tension losses have been recorded in monitored mass timber panel PT systems [4]. Existing models do not allow for reliable prediction of long-term PT losses, due to sparse data and limited understanding of the complex mechanisms of in-plane deformations in loaded mass timber panels experiencing non-uniform moisture variations induced by variable climate conditions. There is a general understanding that such models must be able to account for dynamic moisture transfer through thick composite panels and contributions of resulting hygro-expansion as well as viscoelastic and mechano-sorptive creep and relaxation [4-8]. This paper presents the experimental study conducted to measure the components of strain resulting from these entangled phenomena. However, in the interest of brevity of this conference paper, the isolation of these components is not included

[1] Jacob Gesh, Graduate Student Researcher, School of Civil and Construction Engineering and Department of Wood Science and Engineering, Oregon State University, USA, Jacob.Gesh@oregonstate.edu
[2] Esther Baas, PhD Student, Department of Wood Science and Engineering and School of Civil and Construction Engineering, Oregon State University, USA, esther.baas@oregonstate.edu
[3] Ryan Longman, MS, Department of Wood Science and Engineering and School of Civil and Construction Engineering, Oregon State University, USA, ryan.longman@oregonstate.edu
[4] Mariapaola Riggio, Associate Professor, Department of Wood Science and Engineering, Oregon State University, USA, mariapaola.riggio@oregonstate.edu
[5] Andre R. Barbosa, Professor, School of Civil and Construction Engineering, Oregon State University, USA, andre.barbosa@oregonstate.edu
[6] Lech Muszynski, Professor, Department of Wood Science and Engineering, Oregon State University, USA, lech.muszynski@oregonstate.edu
[7] Gabriele Granello, Adjunct Faculty, Department of Wood Science and Engineering, Oregon State University, USA, gabriele.granello@gmail.com

https://doi.org/10.52202/069179-0298

herein. The presented study is part of a project carried out at Oregon State University, whose overall objective is to provide data and a functional model to allow engineers to confidently incorporate PT mass timber rocking walls in resilient seismic design.

2 METHODOLOGY

The experimental methodology provides for a comprehensive separation of the contribution of the effects of free hygro-expansion, viscoelastic creep, and mechano-sorption [9].

2.1 MEDIUM-SCALE SPECIMENS IN A CONTROLLED VARYING ENVIRONMENT

A total of twelve medium-scale panels have been tested in a climate chamber that has dimensions of 2.48 m x 2.44 m and can maintain temperatures ranging from -30 ℃ to +40 ℃ and relative humidities (RH) from 10% to 90% (Figure 1).

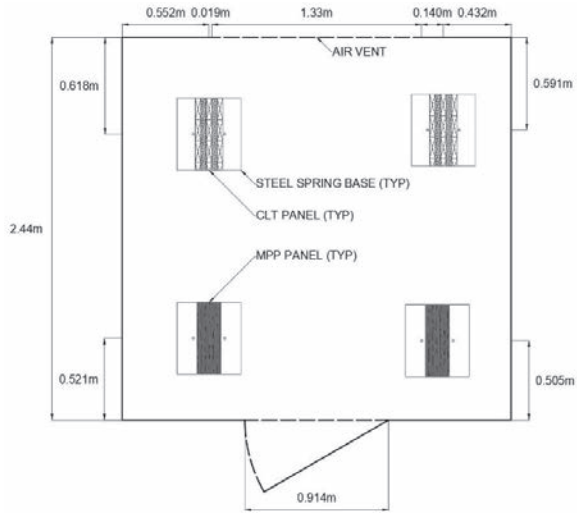

Figure 1: *Plan view of panel layout in climate chamber (approximate actual panel locations).*

Ten specimens are loaded with the tensioning of the PT rods and two are not loaded, designated here as unloaded specimens. One of the unloaded and five of the loaded panels were 5-ply Douglas fir-Larch CLT (1.52 m x 0.457 m x 0.174 m) while the remaining panels were 152.4 mm-thick Douglas fir MPP (1.52 m x 0.457 m x 0.152 m). Since full-scale applications of the mass timber PT wall systems generally have the edges of the walls concealed by other structural components, moisture flow is typically 1-dimensional through the face of the wall [8]. Therefore, in this test, each panel was edge-sealed such that moisture flow was perpendicular to the panel face. Due to the sizes of the panels and the geometry of the chamber, only four panels could be tested at a time thus, there was a total of three batches of specimens. Each test cycle consisted of an initial exposing of the panels to two weeks of uncontrolled environmental conditions to provide more time for the panels to creep under the applied load. Following the two-week period in uncontrolled conditions, three cycles of humidity ranging from 30% RH (two weeks) to 90% RH (two weeks) at constant temperature (20 ℃) were then applied to the panels to determine the complex deformation resulting from the superposition of viscoelastic and mechano-sorptive creep, shrinkage, and swelling [1,5].

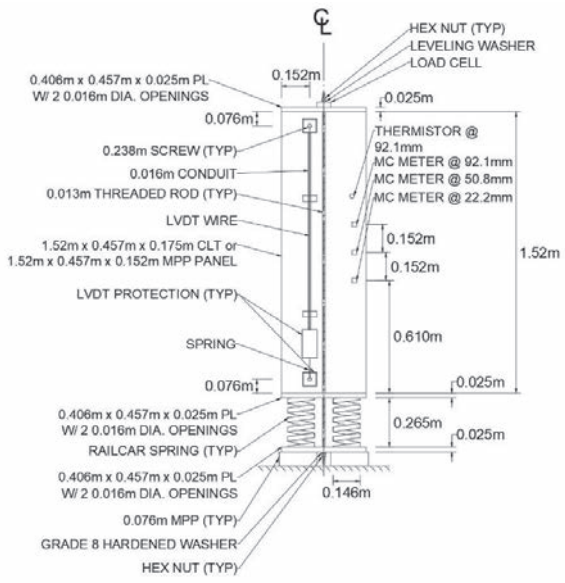

Figure 2: *Test setup for loaded specimens exposed to a controlled varying environment (frontal view).*

Each loaded panel is placed on steel spring bases to minimize the tension losses to less than 2% of the applied force (Figures 2-4). The load is transferred through two post-tensioned threaded steel rods running through holes in the top plate and the bottom of the spring base and monitored by two load cells placed at the end of each rod. The level of applied PT load was chosen to be approximately 7% of the compressive strength of each panel. The loading process was comprised of two phases: during phase 1, the panels were loaded to the chosen level of stress, and during phase 2, the spring bases maintained the applied load within 2% of the initially applied load for the remainder of the test.

The instrumentation setup includes a linear variable differential transformer (LVDT) which measures the vertical deformation of each timber panel. Electric resistance moisture sensors equipped with screws with insulated shafts monitor the moisture content (MC) over an approximate length of 13 mm within the first three plies of the CLT panels and the first, second, and forth plies of the MPP panels as indicated in Figure 5.

Two unloaded reference panels with a similar setup as the loaded panels were tested in the same climate conditions to determine the effect of free shrinkage and swelling [5]. When compared to the loaded panels shown in Figure 2, the unloaded panels did not have a top plate or PT rods installed (Figure 6). The instrumentation on the unloaded panels was similar to the instrumentation installed on the loaded panels except the unloaded panels did not include load cells.

https://doi.org/10.52202/069179-0298

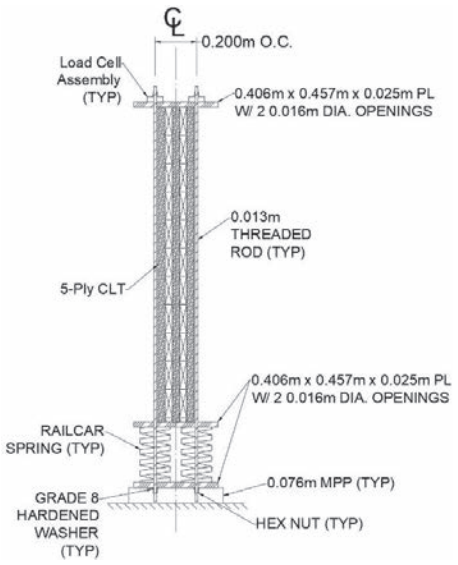

Figure 3: *Test setup for loaded CLT specimens exposed to controlled varying environment (profile cross-section).*

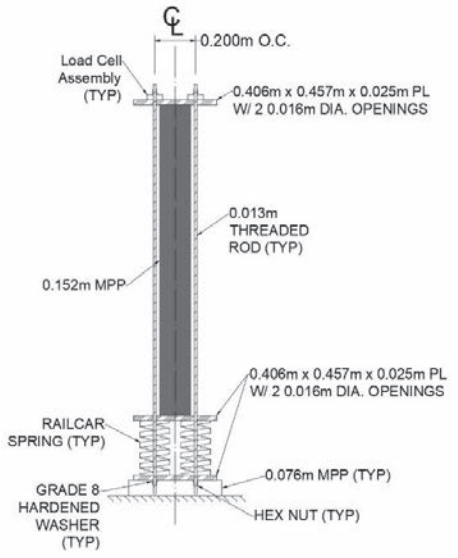

Figure 4: *Test setup for loaded MPP specimens exposed to controlled varying environment (profile cross-section).*

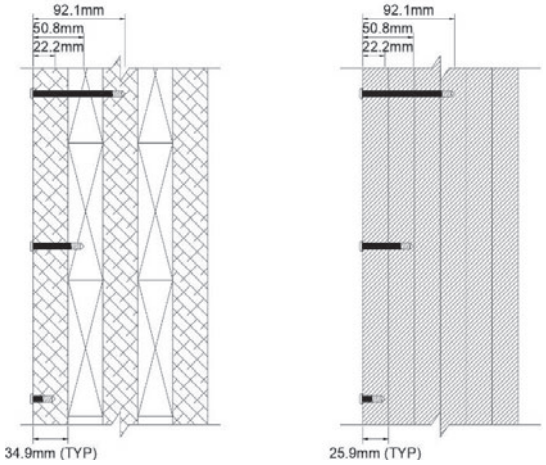

Figure 5: *Electric resistance moisture sensor depths (Left: CLT cross-section along panel height. Right: MPP cross-section along panel height).*

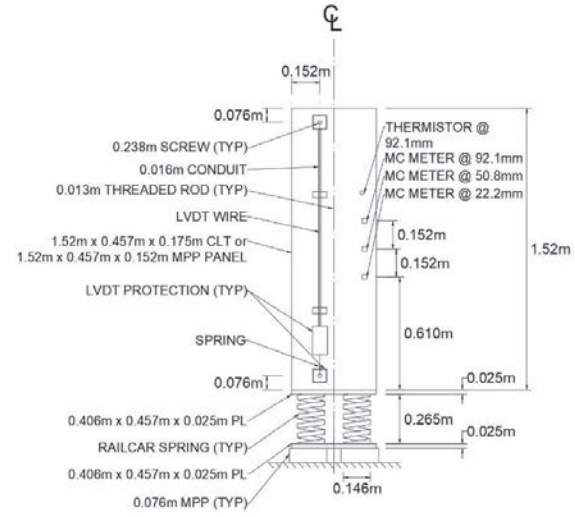

Figure 6: *Test setup for unloaded specimens exposed to controlled varying environment (frontal view).*

For safety reasons, panels were laterally braced with pins at the top of each panel to prevent any tipping motions. The pin connection between the lateral support system and the panels is used to not restrict any vertical deformation of the panels.

https://doi.org/10.52202/069179-0298

Figure 7: *Test setup inside the climate chamber.*

2.2 MEDIUM-SCALE SPECIMENS IN CONSTANT ENVIRONMENT

Three CLT and three MPP panels of the same dimensions as the specimens described in 2.1 are tested in an environment with constant RH and temperature, to isolate the viscoelastic creep component within the panels [5]. The setup is as described in 2.1 except that the specimens are not instrumented with moisture sensors and are not edge sealed. The specimens are PT-loaded at the same level as specimens tested in variable climate conditions.

Figure 8: *Test setup inside constant climate conditions (sensors unattached).*

3 DATA ANALYSIS AND PRELIMINARY RESULTS

The preliminary results presented in this paper include the two unloaded specimens, and six of the ten PT specimens tested in the controlled and varying environment. Additionally, approximately 10.5 months of data from the six specimens in the constant environment are presented. Data processing consisted in three phases: (1) Offsetting, (2) Signal Processing, and (3) Calculations.

3.1 DATA OFFSETS

Prior to loading each specimen, the LVDTs were physically adjusted such that the output reading was approximately zero. However, the readings were not exactly zero, therefore, during post-processing, offsets were applied to the displacement readings of each sample. For consistency, the average of the first three data points prior to the beginning of the loading process was taken as zero displacements and then used as the offset for the respective specimen.

Additionally, the average percent MC (calculated as described in section 3.3.4) of the loaded MPP panel in the first batch of samples had a portion of data with unnatural changes in MC during the third dry cycle. Therefore, for this section of data only, the data line was smoothed to eliminate the obvious signal offsets.

Offsets to zero the load cells were not applied during post processing since at the beginning of the tests, offsets were initially programmed into the data acquisition system. However, for the panels in the constant environment, there were portions of data that had rapid changes in loads throughout the tests. Therefore, the data line was smoothed to eliminate the large erratic changes in measured load.

3.2 SIGNAL PROCESSING

Signal irregularities such as unexplained spikes were removed by means of a median filter with an overall window of 13 data points determined iteratively until all artifacts were removed. It should be noted that the median filter was applied once to the offset LVDT readings, the load cell readings, and the average moisture contents (calculated as described in section 3.3.4).

3.3 CALCULATIONS

The measured data were used to determine the following derived quantities: 1) panel displacement, 2) average strains in the panel, 3) average panel stress, and 4) average moisture content in the panel.

3.3.1 Panel-spring displacement

For the panels in the constant climate only, the LVDT signals were erratic and inconsistent with what would be physically expected. Therefore, the displacements of these panels during loading phase 2 were calculated using the corresponding phase 2 load cell data in combination with the stiffnesses of the spring bases following the general relationship:

https://doi.org/10.52202/069179-0298

$$\delta = \frac{F}{k} \quad (1)$$

in which δ is the displacement of the spring base, F is the force applied to the system, and k is the stiffness of the spring base. At the start of loading phase 2, after the spring bases were compressed under the initially applied load, the displacements of the spring bases would be equal to the displacements of the panels. Therefore, the point at which each panel was fully loaded (beginning of phase 2) was assumed to be zero displacement within the panel.

3.3.2 Panel strain

Following typical convention, positive strains measured indicated panel growth while negative strains indicated panel contraction. Since the LVDTs on the panels in the climate chamber did not have erratic readings, the average longitudinal strains (ε) in the panels were calculated based on the readings from the LVDTs as:

$$\varepsilon = \frac{\delta_{LVDT}}{l_0} \quad (2)$$

where l_0 is the initial length of the specimen between the wood screws used to secure the LVDT wire to the sample (or 1371.6 mm), and δ_{LVDT} is the displacement reading from the LVDT.

For the panels in the constant climate, δ_{LVDT} in Equation 2 was substituted with δ calculated by Equation 1 and l_0 was assumed to be the panel's undeformed height (1524 mm). It should be noted that assuming l_0 to be equal to the panels' undeformed height is not entirely accurate since after loading, the panels would deform elastically and would therefore be shorter overall. However, this assumption gives a reasonable approximation.

3.3.3 Panel stress

The engineering stress (σ) in each panel was calculated using the readings from two load cells as:

$$\sigma = \frac{P_1 + P_2}{A_{panel}} \quad (3)$$

where P_1 and P_2 are the loads measured by the load cells applied at the two post-tensioned rods and A_{panel} is the cross-sectional area of the panels (CLT: 0.080 m^2, MPP: 0.070 m^2).

3.3.4 Average panel moisture content

The average MC in each panel was calculated using data from the resistance sensors embedded into each panel at the various depths shown in Figure 5. More specifically, the first three plies of the CLT panels were monitored while the first, second, and fourth plies of the MPP panels were monitored. Since the panels are symmetric, it was assumed that the moisture profile in the panels would also be symmetric around the centre thickness. Therefore, since the MPP panels have an even number of plies (i.e., six, 25.9 mm-thick plies), the average of the three percent MC readings of each panel can be taken to represent the overall average panel percent MC ($MC_{MPP\ avg}$):

$$MC_{MPP\ avg} = \frac{MC_{ply1} + MC_{ply2} + MC_{ply4}}{3} \quad (4)$$

where MC_{ply1}, MC_{ply2}, and MC_{ply4} are the percent MC readings of the 22 mm, 51 mm, and 92 mm long sensor pins in the MPP panel, respectively.

However, since the CLT has five plies, a weighted average percent MC ($MC_{CLT\ wavg}$) was calculated assuming the sensors capture the percent MC in ply one, ply two, and half of ply three. The equation is as follows:

$$MC_{CLT\ wavg} = \frac{MC_{ply1} + MC_{ply2} + 0.5MC_{ply3}}{2.5} \quad (5)$$

where MC_{ply1}, MC_{ply2}, and MC_{ply3} are the percent MC readings of the 22 mm, 51 mm, and 92 mm long sensor pins in the CLT panel, respectively.

3.3.5 Interpolation of data

Due to differing time steps for the data within both batches of samples tested, it was necessary to interpolate between data points so that displacements and MCs could be compared at specific points in time. Therefore, each data set was linearly interpolated between measured data points to get the displacement and MC readings every 30 seconds throughout the entirety of the tests.

3.3.6 Cumulative moisture content

Although the same humidity cycle program was applied to both batches of samples, the differences in initial MC in the panels, the first two-week period after loading in uncontrolled environments, and mechanical issues with the climate chamber resulted in variability of specimen initial conditions. Because of this, it is difficult to directly compare the deformations recorded on separate batches of panels tested with different humidity programs in the time domain. To facilitate a more meaningful comparison, the cumulative moisture content (CMC) in each panel was calculated (Equation 6) to present strains as a function of CMC rather than time [9], where the CMC is given by:

$$CMC = \sum_{0}^{i} |MC_{i+1} - MC_i| \quad (6)$$

where MC_i and MC_{i+1} is the ith and ith+1 average percent MC sensor readings of an individual panel, respectively. Each CMC value aligns with a corresponding measured strain value thus allowing for convenient comparison.

3.3.7 Summary of data

Figures 9 and 10 summarize the environmental and moisture content data from the first and second batches of CLT and MPP samples tested in the climate chamber in the time domain. Additionally, Figures 11 and 12 summarize the strain and CMC data from the first and second batches of CLT and MPP samples tested in the climate chamber presented in the time domain. The first batch of samples included one loaded CLT and one loaded MPP panel and the two unloaded panels used to capture the free shrinkage and swelling. The second batch of

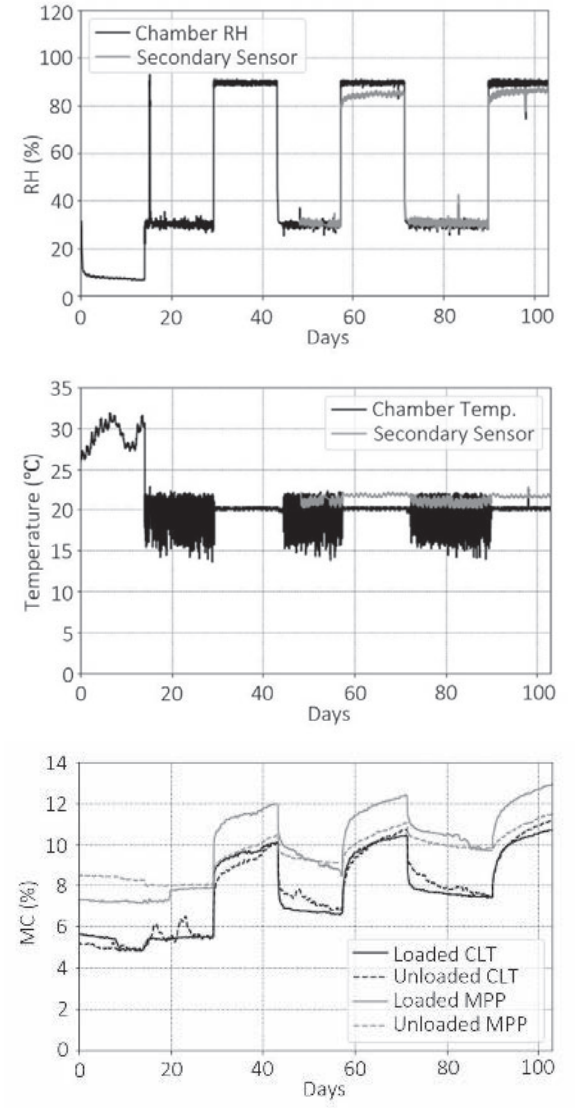

Figure 9: *Batch one environmental and MC data (top: RH over time, middle: temperature over time, bottom: weighted average percent MC over time).*

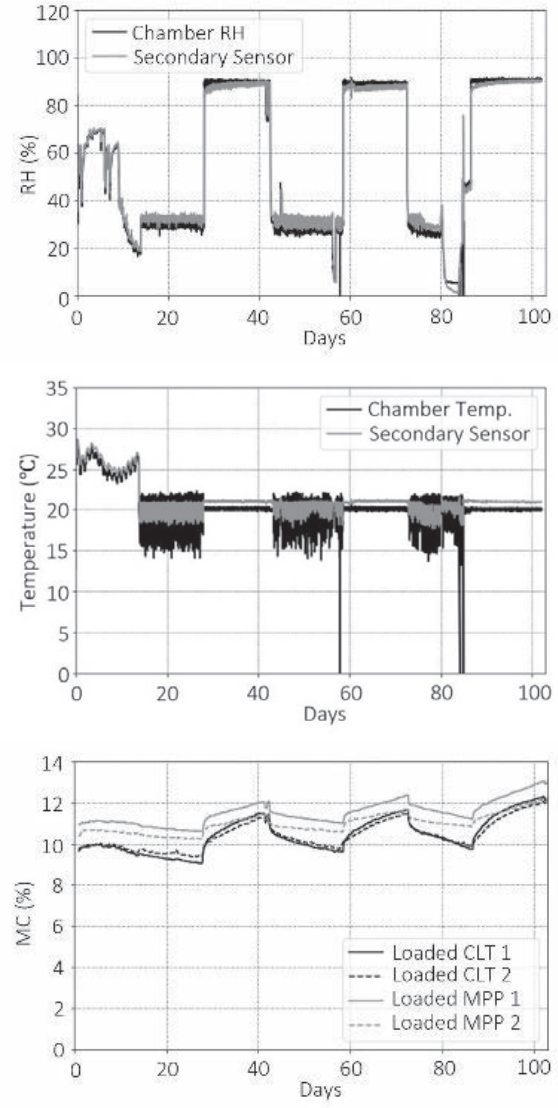

Figure 10: *Batch two environmental and MC data (top: RH over time, middle: temperature over time, bottom: weighted average percent MC over time).*

samples included two loaded CLT panels and two loaded MPP panels. It should be noted that during the second batch of tests, one of the MPP panels was unloaded and re-loaded approximately seven days into the test period in the uncontrolled environment. Therefore, the plots show data for this particular panel starting at the point in time just before the reloading. Throughout the tests, the spring bases were able to maintain the applied stresses within 2% of the initially applied stress. As seen in the strain vs. time plots in Figures 11 and 12, during the first 14 days after initial tensioning, the deformation in the panels was dominated by shrinkage and swelling due to the uncontrolled conditions in the chamber environment (approximately 6-10% RH and 26-32 ℃ for the first batch and 16-70% RH and 23-29 ℃ for the second batch). Following the commencement of the first dry cycle on day 14, a rapid increase in strain indicates a sudden expansion in the panels equilibrating to the 30% RH. As each dry and wet cycle commence, the rate of strain changes. During the dry cycles, the strain rates are negative indicating the effect of shrinkage due to a loss of moisture to the surrounding environment. During the wet cycles, the strain rates are positive indicating the effect of swelling induced by the gain of moisture from the ambient environment.

Unexpectedly, however, the overall trends in the strain of the first batch of samples indicated that the loaded CLT panel (and portions of the loaded MPP panel) experienced more elongation than the unloaded panels.

Based on the strain vs CMC plots, each of these described trends are reiterated; the panels from the second batch experienced less strain and less CMC compared to the first. After plotting the response of both batches of panels together in Figure 13, it can be seen that the free shrinkage

https://doi.org/10.52202/069179-0298

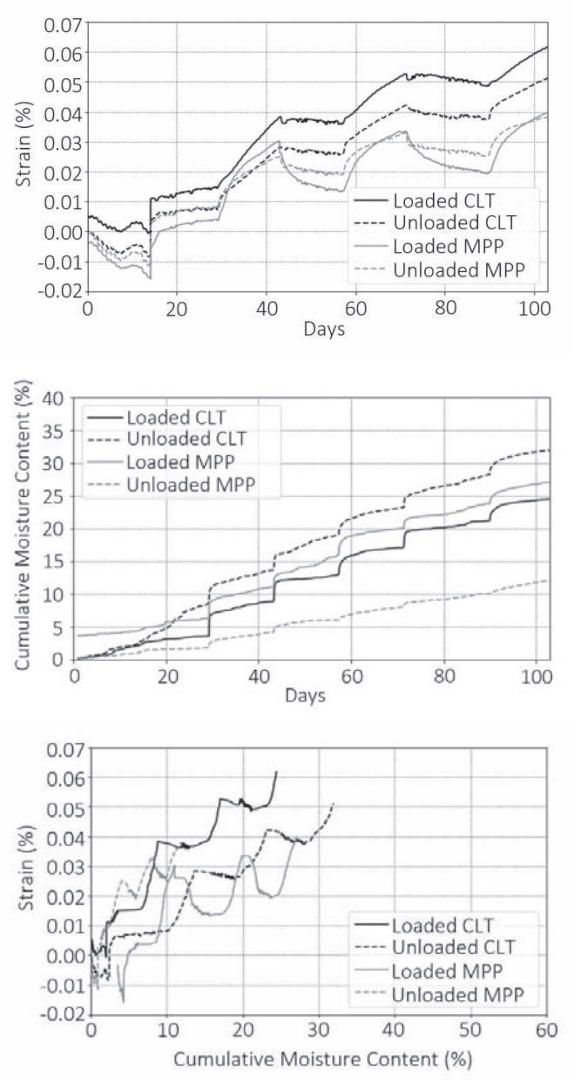

Figure 11: *Batch one specimen data (top: strain over time, middle: CMC over time, bottom: strain versus CMC).*

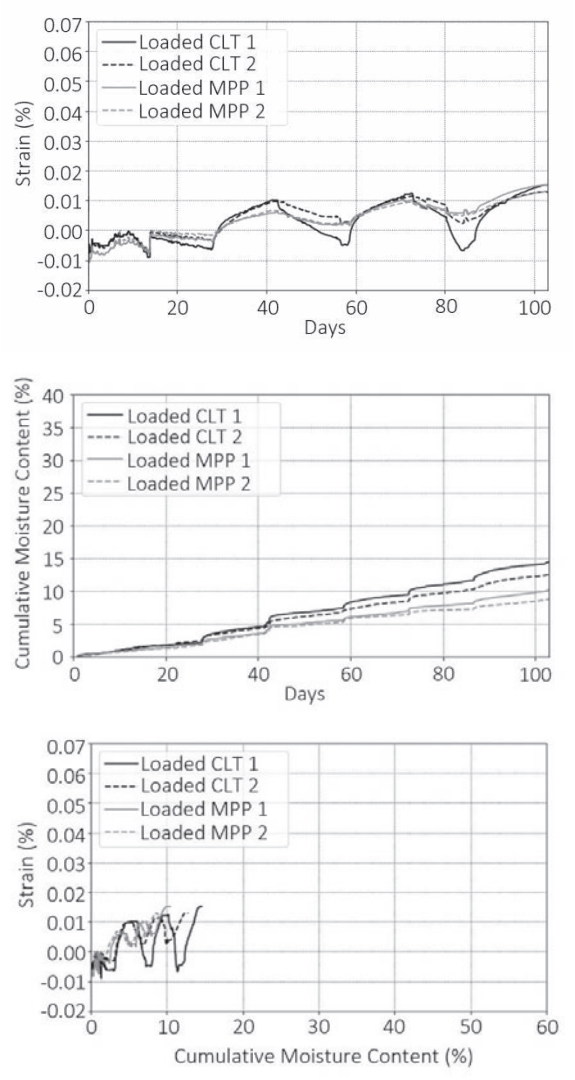

Figure 12: *Batch two specimen data (top: strain over time, middle: CMC over time, bottom: strain versus CMC).*

and swelling strains are in fact generally greater than the total strains of the loaded panels from the second batch (except for the CLT specimens from approximately 4% to 6.4% and from 7.8% to 10.4% CMC).

Figure 14 summarizes the test data from the panels in the constant environment over a period of approximately 10.5 months. It should be noted that the loading of the CLT panels occurred approximately one week after the loading of the MPP panels. Since the panels were close to each other, the loading of the CLT panels disrupted the MPP data around day 7. Additionally, it can be noticed that shortly after the loading of the CLT panels, a portion of data is missing. This data was removed due to an error with the data acquisition system.

As expected, based on the calculated displacements, the panels exhibit an overall shortening over time. In particular, the CLT panels displace more than the MPP panels even though both were loaded to the same percentage of their respective compressive strengths. When compared to the test data from the varying environment (Figure 15) over the same time domain, it can be seen that the panel behaviour between the tests in the different environments nearly mirror each other (excluding the cyclic behaviours from the changing RH). Strains of the panels in the changing environment increase with time to a maximum strain between approximately 0.0004 mm/mm to 0.0006 mm/mm while strains in the constant environment decrease with time to a minimum strain between approximately -0.0003 mm/mm to -0.0007 mm/mm.

4 DISCUSSION

The unusual trend observed in both batches of specimens tested in the climate chamber could be attributed to differences in moisture profiles between the panels as each panel had different initial MCs. It could also be attributed to layup differences between panels which in turn could affect the diffusion coefficients. Another possibility could be caused by inaccurate sensor readings.

https://doi.org/10.52202/069179-0298

For example, as seen at day 0 of the test for the first batch of panels (Figure 11), the loaded CLT panel increases in strain as it is loaded whereas the loaded MPP panel decreases in strain. This would mean that the CLT panel elongates as it is loaded which is not reasonable.

Overall, the second batch of specimens (Figure 12) experienced significantly less amounts of strains which may in part be due to the overall differences in CMC between the panels. It is also important to point out the initial MCs between both batches. The first batch of samples had more dispersed MC levels between approximately 5% and 10% while the second batch of samples had more consistent MC levels of approximately 10% or more. The causes leading to the differences in initial MCs between batches of specimens stems from the storage conditions of the panels. For example, the first batch of panels were left in the chamber powered off for several months prior to testing while the second batch of panels were left outside of the chamber in an uncontrolled indoor environment. Additionally, the first batch of panels began testing in May of 2022 while the second batch of panels began testing at the end of the summer in September of 2022. As might be expected, the higher temperatures and likely higher humidities in the unconditioned indoor environment at the end of the summer likely led to the second batch of samples equilibrating to the larger initial MC levels measured at the beginning of the tests. Since changes in MC inherently affects strains due to shrinkage, swelling and mechano-sorptive creep in timber, it would be expected that more drastic CMC curves would result in more drastic strains. This is evident between the two tests as the first batch of specimens have more CMC and more strain contrary to the second batch of specimens which have less CMC and therefore less strain (Figures 11 and 12). Additionally, beginning at a higher moisture content may mean that the panels have more dimensional stability when exposed to changing MC as they are further along in the moisture sorption isotherm curves.

Another important detail is the relative position of each specimen in the chamber. As seen in Figure 1, for both rounds, the CLT panels were arranged such that they were closest to the chamber vents from which the dry and wet air and temperature were controlled. Therefore, these panels would be the first to experience MC changes which can generally be seen in the data from Figures 11 and 12; most of the MPP panels had less CMC. This observation concerning lower CMC levels in the MPP panels could also be attributed to the larger number of layers of adhesives within the MPP panels which may affect the moisture diffusion properties.

The larger amounts of strain observed in the CLT panels compared to the MPP panels in the constant environment is likely due to differences in the mechanical properties of the panels. Although the wood in both panel types are similar species, the difference in the general layup will affect the overall panel properties.

Another possible contributor to the differences in overall strain between both panel types could stem from differences in the moisture profiles of the panels. While all panels were placed in the constant environment and allowed to react with the environmental conditions, it is possible that the panels did not all reach equilibrium by the start of the test. Based on the observations from the specimens tested in the changing environment, it would be reasonable to suspect that if the initial MC profiles of the specimens are different, then there would likely be large variations in the measured strains.

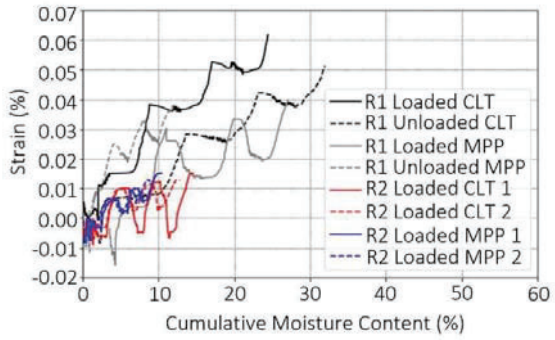

Figure 13: *Batches one (R1) and two (R2) specimen strain verses CMC data comparison.*

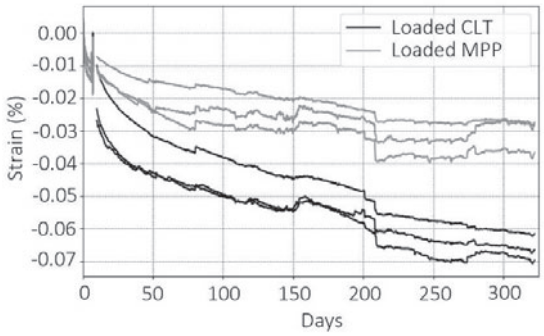

Figure 14: *Specimen strain data in constant environmental conditions.*

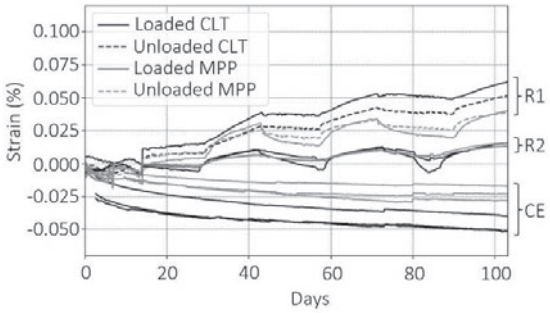

Figure 15: *Batches one (R1), two (R2), and specimens in constant environment (CE) strain data.*

5 PRELIMINARY CONCLUSIONS

This paper presents a preliminary analysis of data of medium-scale PT CLT and MPP systems with the objective of providing data and a functional model to allow engineers to confidently incorporate PT mass

https://doi.org/10.52202/069179-0298

timber rocking walls in resilient seismic design. The data shows the following trends: (1) it appears that, during the test time frame and under the imposed changing environmental conditions, the PT system's response is dominated by the in-plane shrinkage and swelling of the specimens, (2) the MC profiles of the PT panels have a significant effect on the panel's strain behaviour, and (3) under constant environmental conditions, the CLT panels experienced more viscoelastic creep compared to the MPP panels, which is likely due to differences in the material properties of the panels and or differences in panel moisture profiles. The data also allows for the isolation of the viscoelastic and mechano-sorptive creep which will facilitate model development in future works.

The difference in responses of the panels between the two test batches exposed to cyclic climates may be explained by different initial MCs. A practical conclusion for future testing is that prior to testing all panels should be equilibrated to the same MC and that the environment during the two-week period prior to the launching of humidity cycles should be replicated for each batch so that all panels will start the humidity cycles with the same MCs. The MC of panels in the constant environment should be checked prior to testing as well.

In the current study, the CLT panels were located closest to the climate chamber vents in each batch of tests involving cyclic climate conditions and were observed to absorb more moisture. Therefore, in the future work, the effect of panel location in the chamber on the moisture absorbed into the CLT and MPP specimens should be determined.

REFERENCES

[1] J. Cover. Mass timber: The new sustainable choice for tall buildings. International Journal of High-Rise Buildings, 9(1):87-93, 2020.

[2] Granello G., Palermo A., Pampanin S., Pei S., van de Lint J. W.: Pres-Lam buildings: state of the art. Journal of Structural Engineering, 146(6): 04020085, 2020.

[3] Pei S., van de Lindt J. W., Barbosa A. R., Berman J., McDonnell E., Dolan J. D., Blomgren H., Zimmerman E., Huang D., Wichman S.: Experimental seismic response of a resilient 2-story mass-timber building with post-tensioned rocking walls. Journal of Structural Engineering, 145(11): 04019120, 2019.

[4] Baas E. J., Granello G., Barbosa A. R., Riggio M.: Post-tensioned timber wall building: lessons learned from design and construction practice in New Zealand and United States. In: 2021 World Conference on Timber Engineering, 2021.

[5] R. P. Longman. In-plane creep behavior of cross-laminated timber and mass plywood panels: A methodology to evaluate the long-term performance of post-tensioned mass timber walls. Oregon State University, 2021.

[6] Zheng X., He M., Li Z., Luo Q.: Long-term performance of post-tensioned cross-laminated timber (CLT) shear walls: hygro-mechanical model validation and parametric analysis. Archives of Civil and Mechanical Engineering, 22(2):1-18, 2022.

[7] He M., Zheng X., Lam F., Li Z.: Potential loss in prestressing tendon forces under long-term service conditions: cross-laminated timber shear wall applications. Journal of Structural Engineering, 148(3):04021284, 2022.

[8] Nguyen T. T., Dao T. N., Aaleti S., Hossain K., Fridley K. J.: Numerical model for creep behavior of axially loaded CLT panels. Journal of Structural Engineering, 145(1):04018224, 2019.

[9] Muszyński L., Lagaňa R., Davids W., Shaler S. M.: Comments on the experimental methodology for quantitative determination of the hygro-mechanical properties of wood. Holzforschung, 59(2):232-239, 2005.

World Conference on Timber Engineering Oslo 2023

OPTIMIZED CLT-RC FRAME CONNECTION FOR SEISMIC RETROFITTING

Zabih Mehdipour[1], Jorge M. Branco[2], Elisa Poletti[3], Paulo B. Lourenço[4]

ABSTRACT: Cross-laminated timber (CLT) panels have been used as a renovation solution to be adopted in existing masonry-infilled RC buildings, especially those which were designed based on old seismic codes. The connections through which the panels are attached to the RC frames have shown to provide the most contribution to the seismic behaviour of buildings, highly depending on the type of connections used. In this study, to investigate the effect of design procedures of bilinear RC-CLT connections on the dissipated energy and peak displacement of the retrofitted building, their optimum number, location, and mechanical properties, including elastic/inelastic stiffness and yielding displacement, are aimed to be found using genetic a algorithm in a one-bay one-story RC frame. Two structures, (1) a masonry-infilled frame strengthened by CLT panel and (2) a CLT-infilled frame, are used to take the effect of masonry infill into account for two optimization purposes, maximum energy dissipation and minimum structural drift. Results show that under different predefined levels of structural performance, different optimum bilinear curves are achieved. In a parallel study, concerning connectors' arrangement, it was found that their horizontal distribution in beams, starting from the middle and moving to the corners, result in a much better response than a vertical distribution in columns.

KEYWORDS: Cross-laminated timber panel, Infilled RC frame, CLT-RC connection, Optimization, Genetic algorithm

1 INTRODUCTION

Cross-laminated timber (CLT) shear walls have developed recently as an infill added to existing buildings [1][2]. These buildings, mainly made of reinforced concrete frames infilled with masonry walls, have shown to be vulnerable to seismic actions due to in-plane and out-of-plane failures of the infills and shear failure of RC columns [3][4]. CLT panels added to those frames are able to improve elastic response with increasing stiffness and load-carrying capacity and inelastic response with ductile deformations and limited impairment of strength at the same time. Elastic contribution of the walls are made by the panels which are rigid due to their layers arranged crosswise to each other at an angle of 90° [5][6]. On the other hand, inelastic behaviour is improved only by the connections where CLT is attached to the frame [5][7][8]. Many traditional and innovative RC-CLT connections have been suggested to demonstrate their abilities to improve the main frame responses emphasizing on nonlinear analyses [9][10][11][12][13].
A comparison made between those connectors which have various Force/Deformation curves shows how much elastic/inelastic response of the frame strengthened by CLT is associated to the connector curve [2][8]. Stiffer connectors provide more stiffness and strength for the main frame, while energy dissipated by the connectors depends on the yielding displacement. Materials with low-yield displacement produce plastic loops with low load-carrying capacity under cyclic/seismic loadings. Also, the ones with high-yield displacement almost lack plastic loops. In both case, energy dissipated that is represented by the area inside the plastic loops is the lowest. It can be proved that there is a specific yielding point between these two extremities where the energy is the greatest. Moreover, the locations of connectors along the frame are effective in changing the Dissipated Energy (DE), strength or drift of the frame [14]. The problem would have an economically advantage where, among different connectors with the same cyclic performance, the cheapest one can be adopted arranged optimally along the frame.
To find the values resulting in the most favourable response of the frame, an optimization process is carried out using Genetic Algorithm (GA) in binary form, which is a stochastic optimization technique based on the process of natural selection that belongs to the evolutionary algorithm [15]. It is considered as a powerful tool for discrete problems like here where optimum arrangement is sought, and the problems with high degree of nonlinearity where plastic deformations of different materials under dynamic loadings are evaluated.
In this study, a RC-CLT connector is represented by two perpendicular split and uplift springs where Force-Deformation curves are assumed to be bilinear for simplicity. The arrangement and yielding displacement of the connectors are obtained so that the strengthened frame has the highest dissipated energy and strength, and least drift in cyclic and seismic analysis, respectively, for both bare and masonry-infilled RC frames. In the final section, an economical survey is performed between two connectors with different stiffness and prices.

2 Modelling of the infilled RC frame coupled with CLT panel

The first step to proceed with the study's plan is to define and characterize the structure's elements and the renovation solution, and describe how to simulate them. Then, the optimization problem, including the

[1] Zabih Mehdipour, University of Minho, Portugal, zabih.mehdipour@gmail.com.
[2] Jorge M. Branco, University of Minho, Portugal, jbranco@civil.uminho.pt.
[3] Elisa Poletti, University of Minho, Portugal, elisapoletti@gmail.com.
[4] Paulo B. Lourenço, University of Minho, Portugal, pbl@civil.uminho.pt.

https://doi.org/10.52202/069179-0299

optimization algorithm, goal function, variables, constraints, will be defined clearly. The last step is to connect the frame strengthened with the optimization process. All aforementioned will be discussed as follows.

2.1 THE INFILLED RC FRAME COUPLED WITH CLT SHEAR WALL

Due to the nature of the problem, where the hybrid frame is analysed many times to achieve the optimal solution and nonlinear behaviour of materials (RC frame, masonry infill, and RC-CLT connector), the finite element analyses of the frame are carried out in OpenSees [16]. Figure 1 shows the geometry and reinforcement of the RC frame where the beams and columns cross-sections are, respectively, 160×270 mm^2 and 160×160 mm^2 with the rebars made of A400NR and concrete of class C55/67 [17].

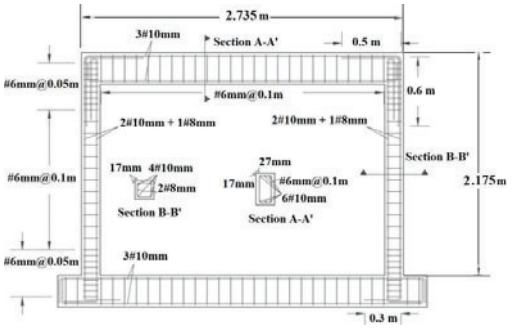

Figure 1: *Reinforcement and geometry of the RC frame*

In simulations, the beams were considered elastic, while the columns were constructed by FiberSection object, available in the software, governed by Concrete02 material assigned to concrete and Steel02 assigned to rebars as shown schematically in Figure 2.

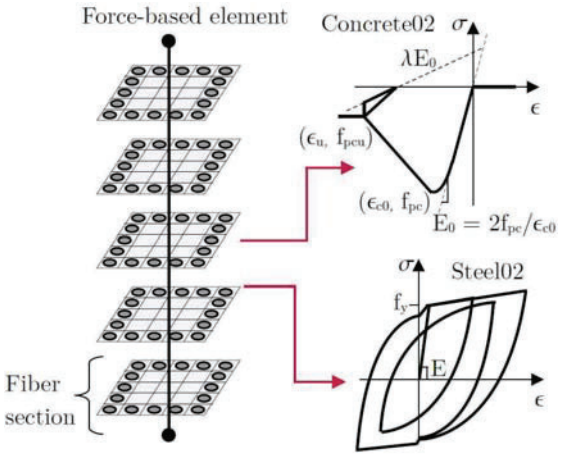

Figure 2: *The materials assigned to the RC elements*

In Table 1 and 2, calibrated parameters of Concrete02 and Steel02 material are presented, respectively. Figure 3 displays the cyclic response of the frame taken from the experimental [17] and numerical analysis, confirming the accuracy of materials used in modelling.

Table 1: *The parameters for Concrete02 material*

f_{pc} (MPa)	ε_{co} (-)	f_{pcu} (MPa)	ε_u (-)	λ (-)	f_t (MPa)	E_{ts} (MPa)
31.20	0.002	6.24	0.05	0.005	4.36	436.5

Table 2: *The parameters for Steel02 material*

f_y (MPa)	E_0 (MPa)	b (-)	R_0 (-)	$cR1$ (-)	$cR2$ (-)
400	205000	0.015	10	0.94	0.20

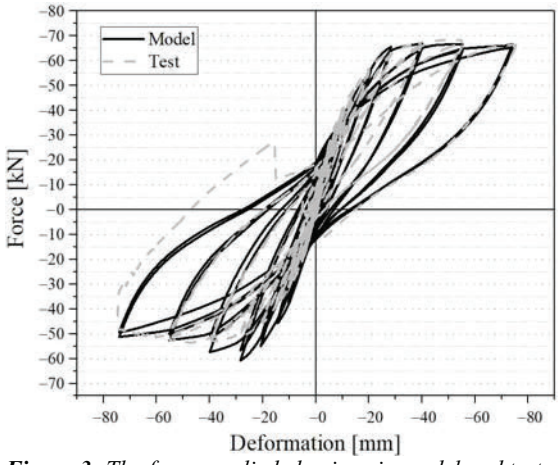

Figure 3: *The frame cyclic behaviour in model and test*

Also, masonry infill is made of vertically perforated masonry units reinforced in bed joints and connected to the RC columns in the interface by metallic connectors [17]. The panels are replaced with the solid parts, made of triangle solid beam elements, that are connected together by Zero-Length element assigned by Pinching4 element, as seen in Figure 4, [18] suitable to consider strength degradation and pinching effect typical of masonry walls due to crack openings. The equivalent scheme for the wall is shown in Figure 5 with the element governing horizontal spring in which the parameters reproduced by Genetic algorithm are listed in Table 3.

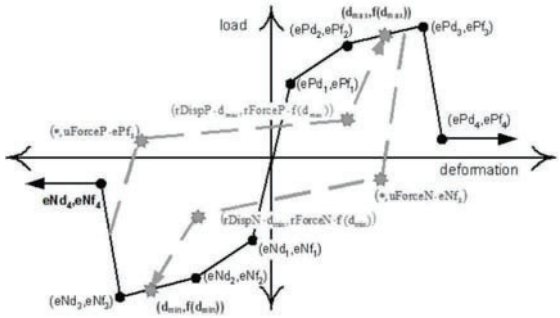

Figure 4: *The behaviour of Pinching4 material*

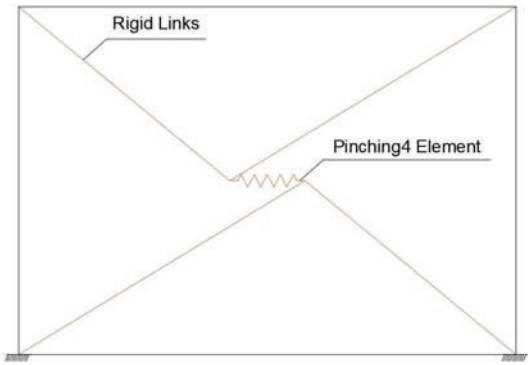

Figure 5: *The masonry infill in modelling*

Table 3: *The parameters for Pinching4 material*

Parameter	Value	Parameter	Value
ePf1 (MPa)	0.0736	*fForceN* (-)	0.2
ePf2 (MPa)	0.157	*uForceN* (-)	0.01
ePf3 (MPa)	0.196	*gK1* (-)	1.3
ePf4 (MPa)	0.177	*gK2* (-)	1.3
ePd1 (-)	0.0024	*gK3* (-)	1.3
ePd2 (-)	0.014	*gK4* (-)	1.3
ePd3 (-)	0.028	*gKLim* (-)	1.3
ePd4 (-)	0.0499	*gD1* (-)	1
eNf1 (MPa)	-0.0736	*gD2* (-)	1
eNf2 (MPa)	-0.1373	*gD3* (-)	4
eNf3 (MPa)	-0.167	*gD4* (-)	4
eNf4 (MPa)	-0.157	*gDLim* (-)	1
eNd1 (-)	0.0024	*gF1* (-)	1
eNd2 (-)	0.014	*gF2* (-)	0
eNd3 (-)	0.028	*gF3* (-)	1
eNd4 (-)	0.0499	*gF4* (-)	1
rDispP (-)	0.5	*gFLim* (-)	1
fForceP (-)	0.2	*gE* (-)	10
uForceP (-)	0.01	*dmgType* (-)	"energy"
rDispN (-)	0.5		

With the above-shown elements representing masonry infill, variation of base shear against peak displacement in the infilled frame resulted from test and simulation are similar (Figure 6).

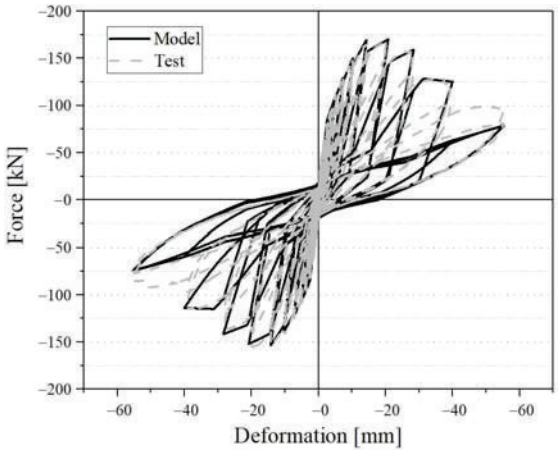

Figure 6*: The infilled frame response in cyclic analyses*

The CLT panel, used here, has 97 mm thickness in three layers, which are 35, 27, and 35 mm, respectively. Because of the panel staying elastic in elastic analyses, only elastic moduli of elasticity, shear modulus, and Poisson's ratio need to be defined (Table 4), and are taken into account in simulations [19][20][21].

Table 4: *The panel characteristics*

Property	Value
E_L	11,000 N/mm²
E_R	370 N/mm²
E_T	370 N/mm²
G_{LR}	688 N/mm²
G_{LT}	688 N/mm²
G_{RT}	68.8 N/mm²
υ_{LR}	0.02
υ_{LT}	0.02
υ_{RT}	0.3

CLT shear wall generally are simulated in the same way as masonry infill did, meaning that, as shown in Figure 7, the wall is replaced by two frames made of solid beam elements at the top and bottom of the frame that attach CLT-frame connectors and a horizontal elastic shear spring at the middle of the wall, representing the CLT lateral stiffness.

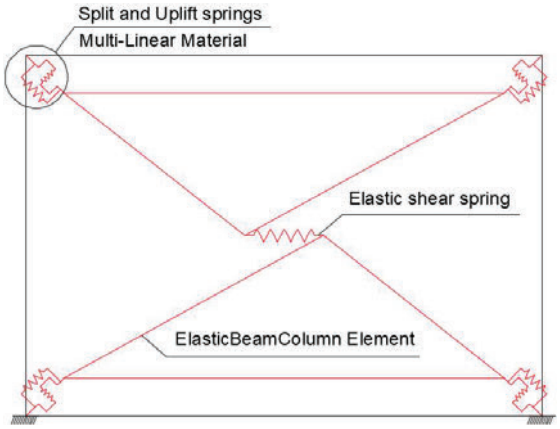

Figure 7: *The panel with the connectors in the model*

The stiffness of the mid-spring in Figure 7 is determined by the following equation [13]:

$$k_{CLT} = \frac{1}{\frac{h^3}{12EI} + \frac{1.2h}{GA}} \quad (1)$$

where h is the panel height, A is the cross-section area, I is the cross-section inertia, and E and G are the moduli of elasticity and shear modulus of the panel, respectively.
Both uplift and split springs that represent the connectors are usually attributed by Pinching4 or SAWS elements [22], but here to satisfy this study's purposes investigating bilinear spring, Multi-Linear material, available in the software library, is assigned to each of them comprising only two lines for simplicity. Stiffness of the second line is assumed as 10% of the first one. It can not be considered

https://doi.org/10.52202/069179-0299

as a separate optimization variable since it has a straight effect on increasing energy dissipated and strength.

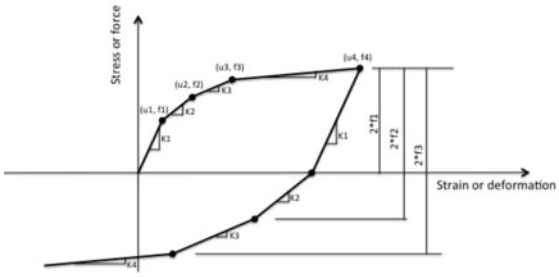

Figure 8: *Multi-Linear material assigned to both split and uplift springs*

2.2 THE OPTIMIZATION PROBLEM

It is supposed that only one kind of CLT-RC connection represented with split and uplift springs being characterized by bilinear Force-Deformation curves is used in the frame. Yielding displacement and elastic stiffness of the split and uplift springs are of four variables of the connector with the inelastic stiffness considered as 10% of the elastic one. Each of RC elements has 6, 8, and 10 potential locations where the connector can connect RC frame to the CLT panel. 6, 8, 10 spots per element (or 24, 32, 40, respectively, spots in total along the frame) are for the problem with 4, 8 and 12, and 16 and 20 connectors, respectively.

Number of possible locations of connectors along the frame, which are 24, 32, and 40, depending on the number of connectors, are of the variables assigned for the possible location of connectors, each of which can be 1, meaning there is the connector, or zero. Optimum locations and connector's properties are sought for specific number of connectors, that is, 4, 8, 12, 16 and 20. Number of population was assumed to be number of variables multiplied by 40. The lower and upper bound for elastic stiffness of springs are respectively 0.1 and 100 *kN/mm* and those of yielding displacement are 0.5 mm and 50 mm, respectively. For the problem where only spring's location is sought, elastic and inelastic stiffness of split springs are taken 3 and 0.5 and those of uplift springs are 2 and 0.6 *kN/mm*, respectively. Also, in the problem where only spring properties are demanded, optimum locations resulted from former analysis are considered for specific number of connectors. In the GA algorithm, for crossover, roulette wheel selection is used, and mutation coefficient is taken 0.2. The algorithm stops when the best answer stays unvaried for 15 iterations. For the sake of simplicity in expressing the variables, especially location of springs, binary genetic algorithm is adopted here meaning that all the variables in the population are expressed as binary numbers in the base-2 numeral system. Two loadings are applied to the bare/infilled frames: cyclic and seismic. The goal function is defined depending on the loading. Table 5 presents in summary all analyse with loading, goal function (GF), frame, and variables.

Table 5: *Optimization problems studied here*

No.	Frame	Loading	GF	Variables
1	Bare	Cyclic	DE	Location/Properties
2	Bare	Cyclic	Strength	Location
3	Infilled	Cyclic	DE	Location/Properties
4	Infilled	Cyclic	Strength	Location
5	Bare	Seismic	DE	Location/Properties
6	Bare	Seismic	Drift	Location
7	Infilled	Seismic	DE	Location/Properties
8	Infilled	Seismic	Drift	Location

2.3 THE LOADINGS PROTOCOL

Two kinds of loadings, cyclic and seismic, are applied to the frame to figure out the dependency of them to the optimum arrangement and properties of the connectors. The loading pattern is obtained according to FEMA 461 [23] and has 16 steps, starting from 0.5 mm, regarding 0.026% drift, and ending in 75, regarding 3.94% drift. Each step is repeated two times with the exception of the first one repeating six times. Also, a set of six earthquake records as the seismic loading, mentioned in Table 6, is exerted on the structure.

Table 6: *The seismic records* [24]

Event Name	Station Name	Year
L'Aquila Italy	V. Aterno - Centro Valle	2009
Kocaeli Turkey	Izmit	1999
Manjil Iran	Abbar	1990
Kalamata Greece-01	Kalamata (bsmt)	1986
Corinth Greece	Corinth	1981
Friuli Italy-01	Barcis	1976

3 RESULTS AND DISCUSSIONS

3.1 OPTIMUM ARRANGMENT

The specific number of connectors (4, 8, 12, 16, and 20) was selected to be a multiple of 4 for regularity as there are four RC joints or four RC elements. In the first section optimum location to attach the panel along the RC frame is shown for those numbers of connectors with the specific properties, as mentioned before.

In the figures schematically shown as follows, the infilled squares show where the connector attach CLT and RC frame resulting in a better response, but cross signs are the potential locations of connectors which are not preferred. In case of using 4 connectors, in all cases, the best arrangement is displayed in Figure 9. As it is usually considered, four connectors in the corners, RC joints, give the most favorable response.

https://doi.org/10.52202/069179-0299

Figure 9: *Optimal locations of 4 connectors*

For 8 connectors, Figure 10 and 11 show the frame with the highest DE, and strength, respectively, under cyclic loading. In the seismic action, the optimal distribution is different from cyclic loading, but in both cases, connectors are located along the beams and columns in terms of DE and strength criteria.

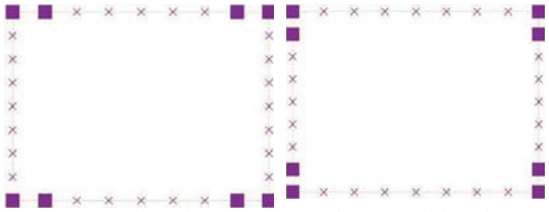

(a) DE-based (b) Strength-based

Figure 10: *Optimal locations of 8 connectors under cyclic loading*

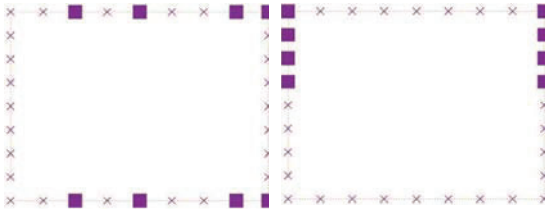

(a) DE-based (b) Drift-based

Figure 11: *Optimal locations of 8 connectors under seismic loading*

With the same order, Figures 12 and 13 demonstrate the connectors optimally arranged under cyclic and seismic loadings, respectively.

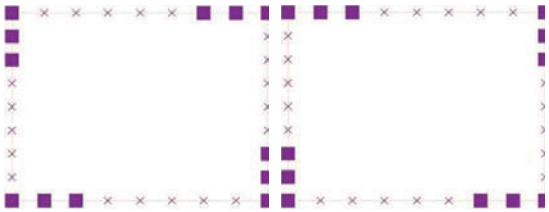

(a) DE-based (b) Strength-based

Figure 12: *Optimal locations of 12 connectors under cyclic loading*

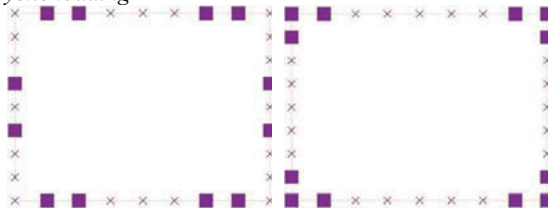

(a) DE-based (b) Drift-based

Figure 13: *Optimal locations of 12 connectors under seismic loading*

The following figures show the distribution of 16 connectors:

Figure 14: *Optimal locations of 16 connectors under cyclic loading*

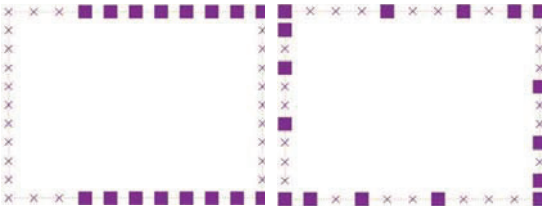

(a) DE-based (b) Drift-based

Figure 15: *Optimal locations of 16 connectors under seismic loading*

And finally, in the presence of 20 connectors, optimal positions of connectors are shown in the following figures:

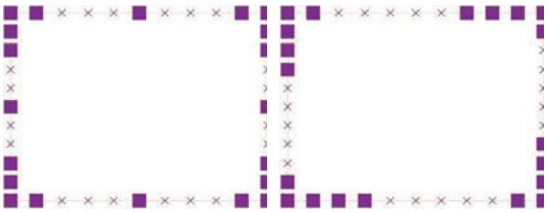

(a) DE-based (b) Strength-based

Figure 16: *Optimal locations of 20 connectors under seismic loading*

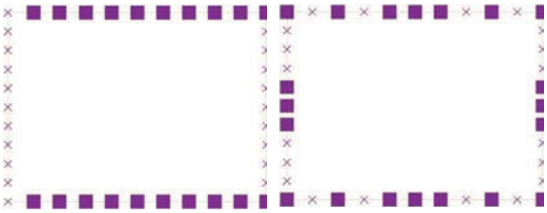

(a) DE-based (b) Drift-based

Figure 17: *Optimal locations of 20 connectors under seismic loading*

The first outcome shown in Figures 9 to 17 is that the optimum arrangement depends on the loading and the criteria used to determine it. That is, the DE of the structure under cyclic loading is completely different from the one under seismic action, or what is obtained as a result of having the highest DE is not the same as the highest strength or lowest drift. By classifying the

https://doi.org/10.52202/069179-0299

problem based on loadings and objective function, some general outlines are extracted: optimal connectors' positions in the frame under seismic loading are equal along the upper and lower beam, leading to the highest DE, while under cyclic loading, the connectors in the corners offer the best response. The connectors, however, often occupy the frame corners while there are few of them in order to achieve the lowest drift, but as their number increases, this ideal location shifts to along the beams. Finally, although usually more strength is associated with less drift, the optimal solution of the frame with the highest strength is not exactly the same as that for the frame with the lowest drift since the locations of the former are concentrated in the frame corners, regardless of their number.

3.2 OPTIMUM BI-LINEAR CURVE

As mentioned before, yielding displacement of connectors is the only feature of the springs on which the dissipated energy of the frame depends. There is a specific point of split and uplift yielding where the dissipated energy is the highest, as demonstrated in Figure 18 for the bare frame attached to the panel by four-in-corners connectors under cyclic loading. Searching all possible variables is time-consuming and adopting an optimization methodology is unavoidable. As mentioned section 3.1, this solution is sought here by GA. Table 7 and 8 present the optimal values of yielding displacements in the bare and infilled frames, respectively, for both horizontal and vertical springs in the presence of different specific even number of connectors, ranging from 4 to 20 optimally arranged along the frame as a result of previous subsection. Here only cyclic analysis was conducted since the seismic loading cannot necessarily push the frame until the yielding point, especially when the frame is equipped with higher number of connectors.

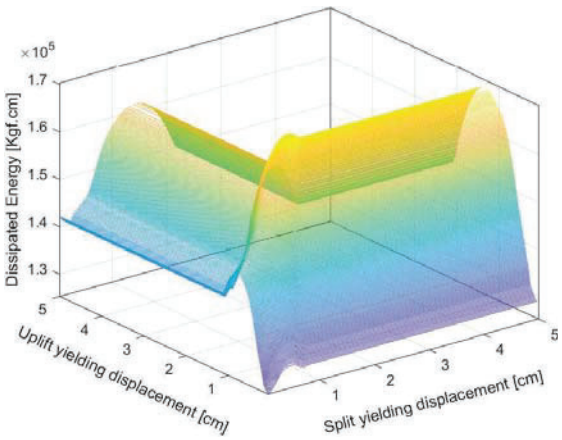

Figure 18: *Energy dissipated versus yielding points of split and uplift springs*

Table 7: *Optimal yielding points of bare RC-CLT connectors*

Connectors number	Split yielding point (cm)	Uplift yielding point (cm)
4	1.32	1.38
6	1.31	1.36
8	1.04	1.19
10	0.92	1.02
12	0.95	0.86
14	1.02	0.92
16	0.86	1.00
18	0.87	1.00
20	0.99	1.17

Table 8: *Optimal yielding points of infilled RC-CLT connectors*

Connectors number	Split yielding point (cm)	Uplift yielding point (cm)
4	1.31	1.47
6	0.95	1.73
8	1.24	1.40
10	1.29	1.58
12	1.42	1.53
14	1.21	1.80
16	1.58	1.49
18	1.13	1.94
20	1.39	1.65

Table 7 and 8 confirm that uplift yielding points are greater than split ones for both bare and infilled frames coupled to the panel by various numbers of connectors. Also, the corresponding split and uplift yielding displacements of the infilled frame strengthened is more than the bare frame for nearly all number of connectors. The average of split and uplift displacements of the reinforced bare frame are 1.03 and 1.10 cm, and those of the reinforced infilled frame are 1.28 and 1.62 cm, respectively.

3.3 ECONOMICAL CONNECTOR

After analysing the optimal yielding displacement and distribution of a specific connector with predefined elastic and inelastic stiffness, the next issue is to find out the connector with optimal stiffness. To achieve it, there needs to be a relationship between the stiffness and price of connectors. The research aims at analysing if a lesser number of stronger connectors (or more expensive ones) is more economical than a greater number of weaker connectors (or cheaper ones), considering an equal structural response with an optimal distributed. Due to lack of the stiffness-price relationship of connectors or a table including different connectors in terms of price and stiffness, the investigation here is summarized as follows comparing two connectors: a traditional angle bracket (AE116) and an innovative connection proposed by Rothoblaas, so-called X-RAD. Tables 9 and 10 compare the price of each connector and their stiffness.

Table 9: *The prices of two connections*

Connector	Unit type	No.	Unit cost (€)	Total (€)
AE116	WBR90110	1	8.5	8.5
	LBA450	21	0.087	1.83
	Total cost (€)			10.33
XRAD	XONE	1	194	194
	XVGS11350	4	8.56	34.24
	MI120	1	105	105
	XBOLT1665	8	2.91	23.28

Total cost (€)		356.52

***Table 10**: The stiffness of two connections*

Connector	Stiffness	Split	Uplift
AE116	Elastic	2857.31	6448.89
	Inelastic	980.85	1008.86
X-RAD	Elastic	8675.80	20751.64
	Inelastic	1392.20	4374.79

A comparison is made between two cases; (1) four strong connectors (X-RAD) in the corners of the frame are installed; and (2) the number and distribution of the weaker one (AE116) is optimally found so that both cases result in an equal energy dissipation. The result shows that 16 AE116 connectors optimally distributed around the frame have approximately the same response, in terms of strength and dissipated energy (Figure 19), to the frame as 4 X-RAD connectors do. However, according to Table 9, the total material price of AE116 used is 165.28 (€), while X-RADs cost 1426.08 (€), confirming the importance of using connectors optimally designed both in number and mechanical properties in reducing expenses. Nonetheless, the former takes more time to be installed and this translates into increasing labour costs, thus resulting in a higher the total cost compared to X-RADs.

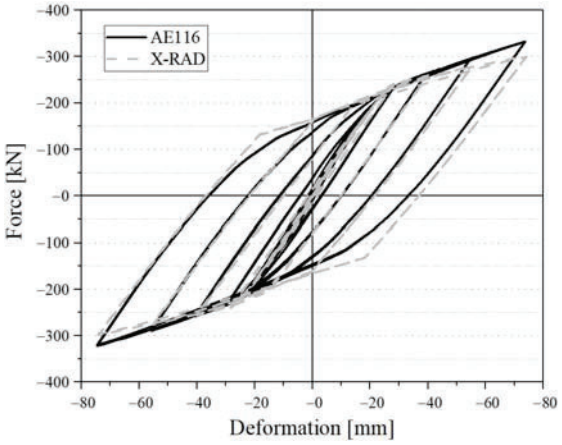

***Figure 19:** Force-Deformation of the reinforced frame for two cases*

4 CONCLUSIONS

In this work, the optimum bilinear CLT-RC connectors on the one hand, and optimum configuration with certain numbers of those connectors on the other hand, were found. The outcome would be beneficial to design a real-case CLT-RC connector with the same properties as the one that was optimally attained here. This connector turned out to have a split and uplift yielding displacement of 1.03 and 1.10 cm for the CLT-infilled RC frame, and 1.28 and 1.62 cm for the masonry-infilled frame coupled with externally added CLT panel, respectively. It was observed that their placements are affected by both loadings and objective functions, though generally, no matter how many of them are utilized, the highest DE and strength are produced by corner-distributed connectors under cyclic loading, whereas the highest DE is produced by along-beam-distributed connectors under seismic loading. In the case of the lowest drift in the frame, both distributions were observed.

ACKNOWLEDGEMENT

This work was financially supported by the Portuguese Science Foundation (Fundação de Ciência e Tecnologia, FCT) under the research project TimQuake - Structural performance of timber joints and structures under earthquakes (015/TT/2021).

REFERENCES

[1] I. Sustersic and B. Dujic, "Seismic shaking table testing of a reinforced concrete frame with masonry infill strengthened with cross laminated timber panels," 2014.

[2] Z. Mehdipour, J. M. Branco, I. Sustersic, L. G. Rodrigues, and P. B. Lourenço, "Masonry-infilled RC frames strengthened with cross-laminated timber panels," in *COMPDYN Proceedings*, 2021, vol. 2021-June.

[3] A. B. Mehrabi and P. B. Shing, "Finite Element Modeling of Masonry-Infilled RC Frames," *J. Struct. Eng.*, vol. 123, no. 5, 1997, doi: 10.1061/(asce)0733-9445(1997)123:5(604).

[4] I. Koutromanos, A. Stavridis, P. B. Shing, and K. Willam, "Numerical modeling of masonry-infilled RC frames subjected to seismic loads," in *Computers and Structures*, 2011, vol. 89, no. 11–12, doi: 10.1016/j.compstruc.2011.01.006.

[5] I. Gavric, M. Fragiacomo, and A. Ceccotti, "Cyclic Behavior of CLT Wall Systems: Experimental Tests and Analytical Prediction Models," *J. Struct. Eng.*, vol. 141, no. 11, 2015, doi: 10.1061/(asce)st.1943-541x.0001246.

[6] V. Hristovski, V. Mircevska, B. Dujic, and M. Garevski, "Comparative dynamic investigation of cross-laminated wooden panel systems: Shaking-table tests and analysis," *Adv. Struct. Eng.*, vol. 21, no. 10, 2018, doi: 10.1177/1369433217749766.

[7] M. Izzi, D. Casagrande, S. Bezzi, D. Pasca, M. Follesa, and R. Tomasi, "Seismic behaviour of Cross-Laminated Timber structures: A state-of-the-art review," *Engineering Structures*, vol. 170. 2018, doi: 10.1016/j.engstruct.2018.05.060.

[8] Z. Mehdipour, E. Poletti, J. M. Branco, and P. B. Lourenço, "Numerical Analysis of Masonry-Infilled RC-CLT Panel Connections," *Buildings*, vol. 12, no. 11, 2022, [Online]. Available: https://doi.org/10.3390/buildings12112009.

[9] J. Schneider, E. Karacabeyli, M. Popovski, S. F. Stiemer, and S. Tesfamariam, "Damage Assessment of Connections Used in Cross-Laminated Timber Subject to Cyclic Loads," *J. Perform. Constr. Facil.*, vol. 28, no. 6, 2014, doi: 10.1061/(asce)cf.1943-5509.0000528.

[10] F. T. Matos, J. M. Branco, P. Rocha, T. Demschner, and P. B. Lourenço, "Quasi-static tests on a two-story CLT building," *Eng. Struct.*, vol. 201, 2019, doi: 10.1016/j.engstruct.2019.109806.

[11] G. D'Arenzo, W. Seim, and M. Fossetti,

https://doi.org/10.52202/069179-0299

"Experimental characterization of a biaxial behaviour connector for CLT wall-to-floor connections under different load directions," *Constr. Build. Mater.*, vol. 295, 2021, doi: 10.1016/j.conbuildmat.2021.123666.

[12] A. Polastri and A. Angeli, "An innovative connection system for CLT structures: Experimental-numerical analysis," 2014.

[13] A. Aloisio, M. Pelliciari, S. Sirotti, F. Boggian, and R. Tomasi, "Optimization of the structural coupling between RC frames, CLT shear walls and asymmetric friction connections," *Bull. Earthq. Eng.*, vol. 20, no. 8, 2022, doi: 10.1007/s10518-022-01337-8.

[14] C. Aranha, J. Branco, P. Lourenço, G. Flatscher, and G. Schickhofer, "Finite element modelling of the cyclic behaviour of CLT connectors and walls," 2016.

[15] R. L. Haupt and S. E. Haupt, *Practical genetic algorithms*. 2004.

[16] S. Mazzoni, F. Mckenna, M. Scott, and G. Fenves, "OpenSees Command Language Manual," *Pacific Earthq. Eng. Res. Cent.*, vol. 264, no. 1, 2006.

[17] L. M. Silva, G. Vasconcelos, P. B. Lourenço, and F. Akhoundi, "Seismic performance of Portuguese masonry infill walls: From traditional systems to new solutions," in *COMPDYN Proceedings*, 2019, vol. 2, doi: 10.7712/120119.7063.19702.

[18] L. N. Lowes, N. Mitra, and A. Altoontash, "A Beam-Column Joint Model for Simulating the Earthquake Response of Reinforced Concrete Frames," *Peer2003/10*, vol. 88, no. 4, 2003.

[19] DIN 1052:2008 Entwurf, *Berechnung und Bemessung von Holzbauwerken – Allgemeine emessungsregeln und Bemessungsregeln für den Hochbau.* .

[20] EN 338:2003, *Structural timber - Strength classes*. 2003.

[21] J. Bodig and B. Jayne, *Mechanics of Wood and Wood Composites*. New York, USA: Van Nostrand Reinhold, 1982.

[22] Y. L. Shen, J. Schneider, S. Tesfamariam, S. F. Stiemer, and Z. G. Mu, "Hysteresis behavior of bracket connection in cross-laminated-timber shear walls," *Constr. Build. Mater.*, vol. 48, 2013, doi: 10.1016/j.conbuildmat.2013.07.050.

[23] F. E. M. A. (FEMA), "Interim Protocols For Determining Seismic Performance Characteristics of Structural and Nonstructural Components Through Laboratory Testing," *FEMA 461*, no. June. 2007.

[24] T. Ancheta, R. Darragh, J. Stewart, and E. Seyhan et al., "PEER 2013/03: PEER NGA-West2 Database," Pacific earthquake engineering research center (PEER), 2013. doi: http://peer.berkeley. edu/publications/.

World Conference on Timber Engineering Oslo 2023

LESSONS LEARNED FROM A DECADE OF RESEARCH ON WOOD ASSEMBLIES UNDER BLAST LOADING

Ghasan Doudak[1], Christian Viau[2], Daniel Lacroix[3]

ABSTRACT: A comprehensive research program, combining experimental and analytical research, has resulted in significant advancements of knowledge pertaining to the behaviour of various structural timber assemblies subjected to blast loads. The full paper will report on key findings obtained from investigating light-frame walls, mass timber elements, and boundary connections. Significant results on the effect of strain rate on the material behaviour, typical failure modes observed, as well as influence on connections will be discussed. The main outcomes from this decade-long research program have paved the way to the development of design methodologies and retrofit options.

KEYWORDS: Design, Blast, Timber, Glulam, CLT, Stud walls, Connections, Retrofits, Mitigation

1 INTRODUCTION AND RESEARCH NEEDS

Targeted attacks or accidental explosions near civilian infrastructures have highlighted the need for developing reliable and robust design methodologies to address the behaviour of structural elements subjected to blast loading. With increasing number of timber structures built around the world, and evidence of their relatively poor performance when subjected to blast loads [1], there is a critical need to establish and enhance the behaviour of timber structural elements under high strain rates. Mid- and high-rise mass-timber structures comprised of engineered wood products (EWPs), such as glued laminated timber (glulam) and cross-laminated timber (CLT), are often accompanied by higher risk of being exposed to potential effects of blast loading.

American and Canadian blast standards (i.e., ASCE/SEI 59-11 and CSA S850) have been developed based on an experimental program on light-frame wood structures [1, 2], which focused on the overall qualitative behaviour of the structures. Since no in-situ properties of the structural members were measured during testing, published data was used to obtain the strength and stiffness of the specimens in order to conduct damage assessment, develop design provisions and propose response limits for wood structures [3]. Investigations into material behaviour under high strain-rate effects necessitates comprehensives experimental research programs, which can be accomplished through live explosion or simulated blast load testing (e.g., shock tube). While the former replicates the complete effects of a blast event (e.g., shock wave, fireball, fragmentation, debris throw, etc.) challenges arise with regard to the collection of reliable data. Conversely, the main benefit of laboratory experimentation simulating the shock wave over live arena testing is the richness of information generated.

A comprehensive research program has been established at the University of Ottawa to investigate the performance of light-frame stud walls, glued laminated timber (glulam) beams and columns, cross-laminated timber (CLT) slabs, and various connections (e.g., bolts, bearing angles, specialized energy-dissipative connections) when subjected to simulated blast loads. This paper presents key research results from the past decade including well over 200 tests conducted at the University of Ottawa Shock Tube Test Facility with the aim of establishing and improving the behaviour of several types of timber systems under blast loading.

2 EXPERIMENTAL PROGRAM

The Shock Tube (Figure 1), used in the experimental campaigns, is a test apparatus capable of simulating shock waves similar to those found in far-field explosions, on small-to-full-scale structural and non-structural components. A wide range of pressure and impulse combinations, representing different charge-weights and stand-off distances can be simulated.

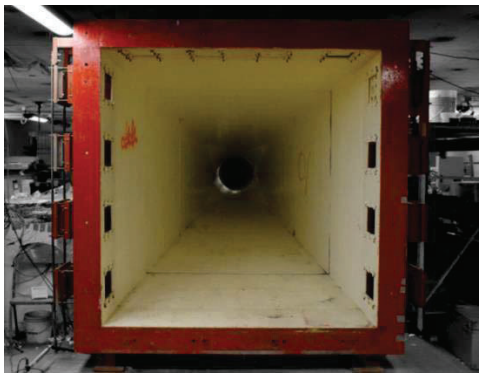

(a) *Expansion section and end-frame (front view)*

[1] Ghasan Doudak, Professor, University of Ottawa, Canada, gdoudak@uottawa.ca
[2] Christian Viau, Assistant Professor, Carleton University, Canada, christian.viau@carleton.ca
[3] Daniel Lacroix, Assistant Professor, University of Waterloo, Canada, daniel.lacroix@uwaterloo.ca

https://doi.org/10.52202/069179-0300

***(b)** Driver section (back view)*

***Figure 1:** University of Ottawa Shock Tube*

The Shock Tube consists of three main components: driver, spool, and expansion sections. The shock wave is created by the release of compressed air stored in the driver section. This forms a shock front that travels along the 6096 mm expansion section and interacts with the specimen mounted at the end-frame (Figure 1b). The reflected pressure can be measured by two dynamic piezoelectric pressure sensors. Strain gauges are typically used to obtain strain data and determine the dynamic failure point for each test. Linear variable displacement transducers (LVDTs) are used to measure the specimen deflection. The data acquisition system is also connected to a full colour high-speed camera, capable of recording videos at a rate of 2000 frames per second.

3 KEY RESEARCH FINDINGS

3.1 MATERIAL PROPERTIES

Structural materials subjected to high strain rates during blast or impact loading tend to experience apparent increases in strength and sometimes stiffness [e.g. 4, 5-7], typically quantified as dynamic increase factors (DIFs). The current version of the Canadian blast design standard (CSA S850) assigns a DIF value of 1.4 to all wood element types [8]. Extensive static and dynamic experimental testing on full-scale studs, stud walls, glulam beams and columns, as well as CLT panels, has provided insight to values of DIFs for various wood products. As shown in Table 1, the current DIF value provided by the Canadian blast design standard [8] is clearly not sufficiently nuanced to capture the behaviour of different timber elements, and it may in several instances lead to a design that is not adequately conservative.

***Table 1:** Observed and code DIF values*

	Experimentally Observed	CSA S850 [8]
Solid Sawn	1.40	
CLT	1.28	1.40
Glulam	1.14	

The values reported in Table 1 were based on testing of fifty-three light frame wood stud walls [6, 9, 10], seventy-one glulam beams [11-14], twenty-five CLT panels [7, 15, 16].

3.2 LIGHT-FRAME WOOD STUD WALLS

Light-frame stud walls of various configurations have been studied experimentally, involving various types and thicknesses of sheathing, stud size, and fasteners. Full-scale flexural tests on lumber elements have shown that the characteristics of the failure often shift from that of splintering failure when loaded under static loading to a brash “cut-through” failure when loaded dynamically (Figure 2).

***(a)** Static* ***(b)** Dynamic*

***Figure 2:** Representative failure modes for studs*

Results also showed indications of premature failure in some sheathing panels prior to achieving full flexural failure in the stud elements (Figure 3a). When sheathing failure occurred, debris was also produced, with some pieces being as large as the gap between the studs. Detachment of failed stud fragments was caused by the weak withdrawal capacity of the nail connections between the sheathing and the stud. While nails behave efficiently in shear when in-plane loads are imparted on the wall (i.e., shearwall), nails involved in out-of-plane motion are eventually loaded in withdrawal, where they are known to be very weak. The use of screws was found to significantly limit debris throw (Figure 3b), which has been shown to be the principal cause of injuries and deaths during blast events [17].

***(a)** Sheathing failure and debris throw*

https://doi.org/10.52202/069179-0300

***(b)** Wall specimen with thicker sheathing and screws*

***Figure 3:** Light-frame wall specimens after testing*

3.3 GLUED-LAMINATED TIMBER

Failure of glulam members have been observed to consistently initiate at a tension-side finger joint or natural defect. In some instances, glulam specimens with localized concentration of finger joints on the tension-side laminate (Figure 4a) lacked the increase observed in specimens containing no finger joints in the middle one-third span (Figure 4b).

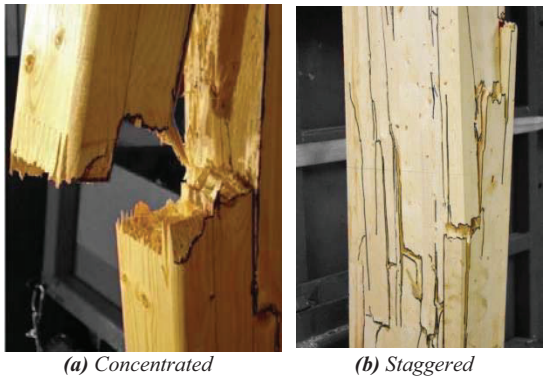

***(a)** Concentrated* ***(b)** Staggered*

***Figure 4:** Glulam finger joints*

The effect of axial load on the dynamic behaviour was also investigated. Three different axial load ratios were considered. The addition of axial load reduced the resistance of the column and contributed to concentrating the damage at midspan when compared to the case without axial load (Figure 5). It should be noted, however, that the contribution of axial loads in actual structures would highly depend on the connection detailing between the columns and the elements they support.

***(a)** Without axial load* ***(b)** With axial load*

***Figure 5:** Effect of axial load on glulam specimens*

3.4 CROSS-LAMINATED TIMBER

Two experimental programs investigating the out-of-plane behaviour of CLT under static and simulated blast loading of twenty-two panels, with different panel thicknesses was undertaken [7, 16]. The dynamic behaviour of CLT panels under bending consisted of a primarily flexural failure mode, accompanied by rolling shear damage in the transverse layers, particularly in specimens with low span-to-depth ratios. The overall behaviour of CLT panels can be generalized as a progression of failure of the longitudinal layers, initiating at the outermost longitudinal laminate, and crack propagation within the transverse laminates due to rolling shear (see Figure 6).

***(a)** 3-ply*

https://doi.org/10.52202/069179-0300

(b) *5-ply* ***(c)*** *7-ply*

Figure 6: *Representative failure modes for CLT panels*

The CLT panels were observed to have significant post-peak resistance [7]. The initial drop in resistance represents the loss of the tension longitudinal and transversal laminates. For example, for a 7-ply specimen, which consist of four longitudinal and three transverse layers, this failure mechanism implies that the specimen would now behave as a 5-ply member, consisting of three longitudinal and two transverse layers.

4 CONNECTIONS

4.1 LIGHT-FRAME CONNECTIONS

Premature failure of the wall connections to the roof and the foundation has been identified as the cause for most collapses [18]. A research study was undertaken to investigate the behaviour of typical nailed boundary connections, designed according to the National Building Code of Canada's prescriptive design guidelines [19]. The results showed that such detailing was not adequate to withstand the blast pressure and resulted in premature connection failure occurring at the top and bottom plates, as shown in Figure 7.

(a) *Arrival of blast wave* ***(b)*** *Top connection failure*

Figure 7: *Failure of nailed stud wall boundary connection*

Off-the-shelf joist hangers, typically used in light-frame wood floor systems, as well as simple angle brackets, were used to connect the studs to the boundary elements, as shown in Figure 8. The results showed that while overdesigned connections allowed the studs to achieve their flexural capacities, walls with connections designed to yield in a controlled manner could withstand greater blast pressures and impulses, and exhibit less damage.

(a) *Failed wall specimen*

(b) *Relatively intact bottom plate connections*

Figure 8: *Wall specimen with joist hanger connections*

4.2 BOLTED GLULAM CONNECTIONS

A study was carried out on single-bolt joints of various slenderness ratios in both principal load direction (i.e., parallel- and perpendicular-to-grain), with the aim to investigated high strain-rate effects on the connections. An average dynamic increase ratio of 1.2 was observed on the yield load of connections designed to fail via wood crushing, while no significant dynamic increase on the yield load or stiffness was found for connections designed to fail in bolt bending and yielding. A loss in connection ductility was also noted when comparing static to dynamic loading, and the use of self-tapping screws (STS) as joint reinforcement was proved effective (see Figure 9).

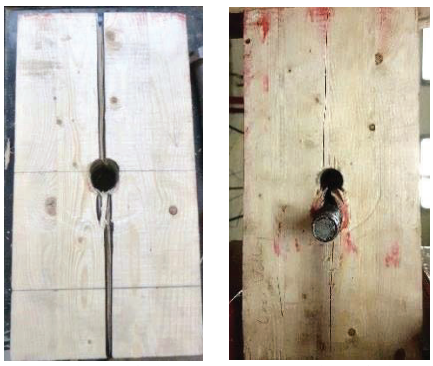

(a) *Splitting failure (unreinforced)* ***(b)*** *Crushing failure (reinforced)*

Figure 9: *Dynamic stocky bolt specimens (parallel-to-grain)*

https://doi.org/10.52202/069179-0300

Glulam beams with bolted end connections with slenderness ratio of 10.8 were tested under shock tube simulated blast loads [12]. It was observed that bolted connections designed to yield and undergo significant inelastic deformations (Figure 10a) had enhanced overall energy dissipation when compared to specimens with overdesigned bolted connections, as required by the CSA S850.

***(a)** Yielding in connection*

***(b)** After blast test*

***Figure 10:** Full-scale bolted glulam specimen*

4.3 SELF-TAPPING SCREWS IN CLT

Self-tapping screws (STS) were used in end-grain with full-scale CLT specimens subjected to simulated blast loads. Significant damage was observed in the STS connections, where tension perpendicular-to-grain failure as well as combination of shear and withdrawal failure were prevalent. To take advantage of timber's relatively high capacity in bearing, the use of angle brackets with STS, which are traditionally used for in-plane loading for wind and seismic, were also investigated. Two angle brackets were tested, representing two distinct design philosophies; a thin and flexible angle bracket, designed to undergo significant yielding and wood crushing, and a robust and stiff angle bracket, designed to remain elastic and not cause significant wood crushing. The flexible angle bracket was found to fail in yielding and wood crushing. The overdesigned and stiff bracket exhibited a brittle failure mode when the capacity of the connection was exceeded, namely by rupturing the fasteners that connect the bracket to the base of the test assembly. As shown in Figure 11, full-scale test specimens with the flexible angle brackets were seen capable of absorbing more blast pressure and impulse prior to failure in the CLT panel.

***(a)** Flexible angle*

***(b)** Overdesigned angle*

***Figure 11:** Full-scale CLT specimens with angled connections*

4.4 ENERGY ABSORBING CONNECTIONS

The use of energy absorbing connections (EAC), which are purposefully designed to dissipate energy through controlled deformations of a steel fuse, were observed to improve the capability of a timber assembly to withstand blast explosions. Various configurations of EACs were investigated, all of which comprised of mild-steel shapes with various thickness and dimensions. The connections that were identified to perform optimally were found to exhibit a bi-linear elastic-perfectly plastic behaviour. The connection deemed the most efficient (Figure 12a) was implemented into full-scale glulam and CLT specimens. In comparison to specimens with simply-supported idealized boundary conditions, or overdesigned connections, the EACs were found to provide around 75%-115% increase in total impulse absorbed by the assembly prior to flexural failure of the wood element. A time lapse of a test is shown in Figure 12b.

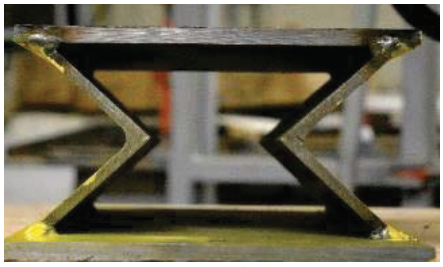

***(a)** Tested EAC*

https://doi.org/10.52202/069179-0300

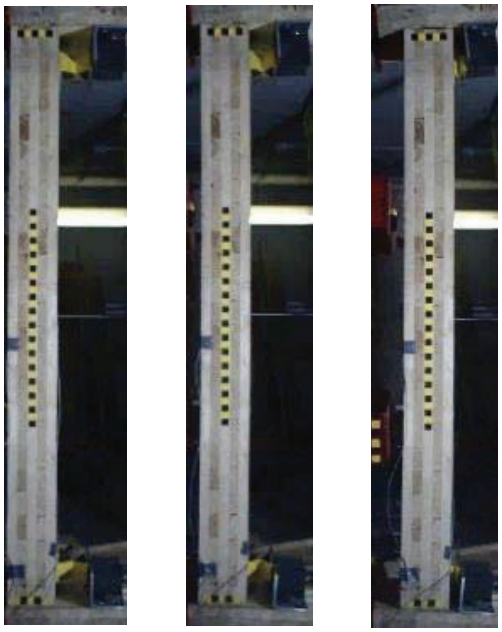

***(b)** Time-lapse*

***Figure 12:** Full-scale CLT specimens with EACs*

5 WOOD ELEMENT RETROFITS

Identified deficiencies found during the research program were used as motivation for investigating possible retrofit options to increase the overall performance of various timber systems. This includes enhancing the performance of sheathing elements, load-bearing elements (i.e., stud, glulam column), boundary connections, as well as minimizing high-velocity flying debris. Stud walls designed according to typical prescriptive requirements often experienced premature failure of sheathing panels [9]. This not only caused flying debris but a loss in structure integrity, where the load-bearing elements cannot achieve their full flexural capacity. The use of thicker wood-based sheathing was found to shift the failures to the studs, while concurrently decrease the amount of sheathing debris. Corrugated steel panels were also tested (Figure 13) and the results showed that they provide significant increase in stiffness and strength.

***Figure 13:** Corrugated steel panels as sheathing retrofit*

Welded-wire-mesh (WWM) was implemented as a sheathing retrofit, as well as a catcher system. In both applications, it was found to perform adequately well. As a sheathing reinforcement, the WWM acted similar to a skin reinforcement, thus reducing the demand on the panel in bending and minimizing overall damage and fragmentation (see Figure 14a), while as a catcher system, it adequately captured all debris of significant sizes (Figure 14b).

***(a)** Sheathing reinforcement* ***(b)** Catcher system*

***Figure 14:** Application of welded wire mesh (WWM) as retrofit*

Different retrofit configurations using fibre-reinforced-polymers (FRP) were investigated for light-frame stud walls, glulam columns, and CLT panels, as shown in Figure 15.

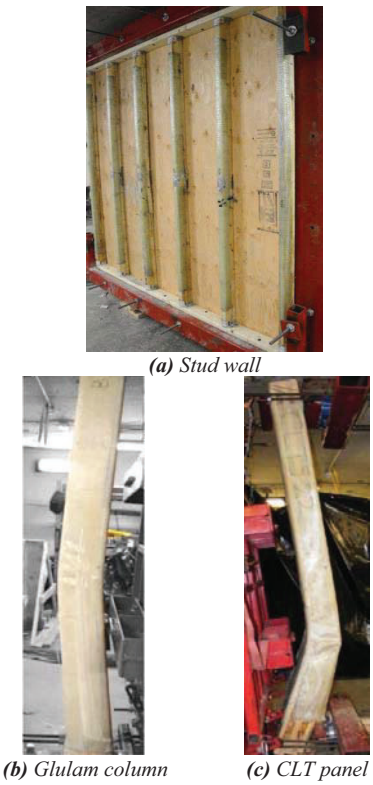

***(a)** Stud wall*

***(b)** Glulam column* ***(c)** CLT panel*

***Figure 15:** Retrofits using fibre-reinforced polymers*

https://doi.org/10.52202/069179-0300

When adequate confinement in tandem with longitudinal tension reinforcement was provided, the application of FRP tended to delay and contain brittle tension parallel-to-grain failure and allowed for the compression-side longitudinal fibres to crush in a ductile manner [20-22]. In general, this allowed for the reinforced specimens to have sustained post-peak capacities, which would otherwise be limited, due to the inherent brittle nature of wood in flexure.

6 CONCLUSIONS

The key findings of a decade-long experimental and analytical research program investigating the behaviour of structural timber systems subjected to blast loads are summarized. High strain rate effects for various structural components and connections have been documented, paving the way for more accurate and resilient structural designs of wood assemblies. Mitigation strategies to improve the blast resistance of wood assemblies have been investigated, including boundary connections, sheathing reinforcements, and the use of fibre-reinforced polymers.

REFERENCES

[1] Marchand, K.A., *BAIT, BASS & RODS Testing Results*. 2002, Applied Research Associates: Prepared for the USAF Force Protection Battlelab.

[2] ASCE, *Blast Protection of Buildings*, in *ASCE/SEI 59-11*. 2011, American Society of Civil Engineers: Reston, VA.

[3] Oswald, C.J., *Component Explosive Damage Assessment Workbook (CEDAW) Methodology Manual V1.0.* 2005, Prepared for the Protective Design Center, US Army Corps of Engineers: San Antonio, TX.

[4] Malvar, L.J., *Review of Static and Dynamic Properties of Steel Reinforcing Bars.* ACI Materials Journal, 1998. 95(5).

[5] Lok, T.S. and P.J. Zhao, *Impact Response of Steel Fiber-Reinforced Concrete Using a Split Hopkinson Pressure Bar.* Journal of Materials in Civil Engineering, 2004. 16(1): p. 54-59.

[6] Lacroix, D.N. and G. Doudak, *Investigation of Dynamic Increase Factors in Light-Frame Wood Stud Walls Subjected to Out-of-Plane Blast Loading.* Journal of Structural Engineering, 2015. 141(6): p. 04014159.

[7] Poulin, M., C. Viau, D.N. Lacroix, and G. Doudak, *Experimental and Analytical Investigation of Cross-Laminated Timber Panels Subjected to Out-of-Plane Blast Loads.* Journal of Structural Engineering, 2018. 144(2): p. 04017197.

[8] CSA, *Design and assessment of buildings subjected to blast loads*, in *CSA S850*. 2012, CSA Group: Mississauga, ON.

[9] Viau, C. and G. Doudak, *Investigating the Behavior of Light-Frame Wood Stud Walls Subjected to Severe Blast Loading.* Journal of Structural Engineering, 2016. 142(12): p. 04016138.

[10] Viau, C., D.N. Lacroix, and G. Doudak, *Damage level assessment of response limits in light-frame wood stud walls subjected to blast loading.* Canadian Journal of Civil Engineering, 2016. 44(2): p. 106-116.

[11] Lacroix, D.N. and G. Doudak, *Determining the Dynamic Increase Factor for Glued-Laminated Timber Beams.* Journal of Structural Engineering, 2018. 144(9): p. 04018160.

[12] Viau, C. and G. Doudak, *Behavior and Modeling of Glulam Beams with Bolted Connections Subjected to Shock Tube-Simulated Blast Loads.* Journal of Structural Engineering, 2021. 147(1): p. 04020305.

[13] Viau, C. and G. Doudak, *Energy-Absorbing Connection for Heavy-Timber Assemblies Subjected to Blast Loads–Concept Development and Application.* Journal of Structural Engineering, 2021. 147(4): p. 04021027.

[14] Wight, N., C. Viau, and P.J. Heffernan, *Behaviour and Resistance of Glued-Laminated Timber Subjected to Impact Loading*, in *CSCE 2022 Annual Conference*. 2022, Canadian Society for Civil Engineering: Whistler, BC.

[15] Viau, C. and G. Doudak, *Behaviour and modelling of cross-laminated timber panels with boundary connections subjected to blast loads.* Engineering Structures, 2019. 197: p. 109404.

[16] Doudak, G., C. Viau, and D.N. Lacroix, *Proposed Design Methods for Timber Members Subjected to Blast Loads.* Journal of Performance of Constructed Facilities, 2022. 36(3): p. 04022020.

[17] Bogosian, D. and H.D. Avanessian, *Blunt trauma from blast-induced building debris*. 2004, DTIC Document.

[18] Sorensen, A. and W.L. McGill, *What to look for in the aftermath of an explosion? A review of blast scene damage observables.* Engineering Failure Analysis, 2011. 18(3): p. 836-845.

[19] NRCC, *National Building Code of Canada*. 2015, Associate Committee on the National Building Code, National Research Council of Canada: Ottawa, ON.

[20] Lacroix, D., C. Viau, E. Battelli, and G. Doudak, *Enhancing the performance of light-frame wood studs using glass fibre-reinforced polymers.* Engineering Structures, 2021. 245: p. 112973.

[21] Lacroix, D. and G. Doudak, *Towards enhancing the post-peak performance of glued-laminated timber beams using multi-directional fibre reinforced polymers.* Engineering Structures, 2020. 215: p. 110680.

[22] Lacroix, D.N. and G. Doudak, *Experimental and Analytical Investigation of FRP Retrofitted Glued-Laminated Beams Subjected to Simulated Blast Loading.* Journal of Structural Engineering, 2018. 144(7): p. 04018089.

https://doi.org/10.52202/069179-0300

World Conference on Timber Engineering Oslo 2023

A NONLINEAR DYNAMIC MODEL FOR COLLAPSE INVESTIGATIONS IN TALL TIMBER BUILDINGS – PRELIMINARY RESULTS

Alex Sixie Cao[1], Lukas Esser[2], Ben Glarner[3] Andrea Frangi[4]

ABSTRACT: Structural robustness of timber buildings is becoming increasingly relevant because of the increasing use of timber in the built environment. An important tool for assessing the robustness of any structure is an efficient numerical model capable of simulating progressive collapse. With such a model, physical tests can be limited to a few carefully selected validation tests and the robustness of a wide range of building typologies and geometries can be investigated efficiently. In this paper, a parametric nonlinear dynamic model for simulating progressive collapse of timber buildings is presented. Because of the parametric capabilities of the model, a vast range of buildings can be modelled. Moreover, the entirety of a collapse can be simulated with the recently developed mixed element method and the implementation of stress- and energy-based failure criteria for normal loading and impact loading. To demonstrate the capabilities of the model, a case study is presented on a symmetrical three-dimensional frame building with varying cross-sectional member dimensions. The model is an indispensable tool for investigating the robustness of timber buildings.

KEYWORDS: Structural robustness, Progressive collapse, Nonlinear dynamic modelling, Impact loading, OpenSees

1 INTRODUCTION

Buildings and other infrastructure are essential in our daily life. They provide us with shelter from the weather, working and leisure spaces, and they serve logistical purposes in our society. When a building is damaged, it may lose its main function of providing shelter and instead become a hazard to its users. To limit such hazards, buildings should be built such that the damage can be confined, and a disproportionate and progressive collapse can be prevented. This property of a structure is its structural robustness, which can be defined as the insensitivity to initial damage [1].

After the progressive collapses of Ronan Point in 1968 and the World Trade Center in 2001 [2,3], substantial efforts have been put into research on the robustness of steel and reinforced concrete structures [3]. At present, most of the building stock in Europe comprises reinforced concrete and masonry buildings [4]. As the use of timber in our built environment is being increasingly recognized as an important carbon sequestration tool [5], more and more timber buildings are also being built [6–8]. However, the knowledge on structural robustness of timber buildings is still scarce [3,9,10].

Dissimilar to steel and reinforced concrete, timber is an intrinsically lightweight material [11,12]. This leads to vastly different behaviour when subjected to lateral loading, such as wind and seismic loading [12–15]. Besides the weight difference, the material and its connections are also dissimilar to its conventional steel and reinforced concrete opponents [16–18]. Therefore, existing knowledge on the robustness of steel and reinforced concrete structures cannot be directly applied to timber buildings [10].

To assess the robustness of any structure, one of the primary tools is an efficient and accurate numerical model [3]. Because of the complexity of the behaviour of timber and its connections, and the highly dynamic nature of a collapse, a nonlinear dynamic model accounting for large deformations is necessary [3,9,19]. [3,9]With such a model, the structural robustness of a vast range of buildings and materials can be investigated, and physical experiments can be reduced to a few validation tests of the model.

In this paper, a fully parametric nonlinear dynamic model for simulating progressive collapse of timber buildings is presented. The model can simulate the entirety of a progressive collapse with large deformations and incremental damping. To facilitate the separation, detachment, and loss of members, the recently developed mixed element method was implemented [20]. Besides commonly used stress-based failure criteria [21], an energy-based failure criterion based on extensive impact tests on full-size timber beams was used [22–25]. The collapse model was written in Python with the open-source finite element framework OpenSees [26].

To demonstrate the model, a three-dimensional frame subjected to a corner, edge, and internal ground-floor column removal was analysed. The frame comprises glued laminated timber beams and columns, and laterally loaded dowel-type connections with slotted-in steel plates. The frames are designed for the vertical gravity loads in the ultimate and serviceability limit states, as well as serviceability-level wind-induced vibrations.

[1] Alex Sixie Cao, Institute of Structural Engineering, ETH Zurich, 8093 Zurich, Switzerland, cao@ibk.baug.ethz.ch
[2] Lukas Esser, Institute of Structural Engineering, ETH Zurich, 8093 Zurich, Switzerland, lukas.esser@ibk.baug.ethz.ch
[3] Ben Glarner, Institute of Structural Engineering, ETH Zurich, 8093 Zurich, Switzerland
[4] Andrea Frangi, Institute of Structural Engineering, ETH Zurich, 8093 Zurich, Switzerland, frangi@ibk.baug.ethz.ch

https://doi.org/10.52202/069179-0301

2 MODEL DESCRIPTION

2.1 CONCEPTUAL FRAMEWORK

The conceptual framework comprises the seven different modules shown in Figure 1. In the framework's development, a basic requirement was the ability to have a fully parametric model with a programmable input interface of the different model parameters. To accommodate this requirement, the building geometry was constrained to an irregular orthogonal grid. This enables an irregular positioning of the orthogonal grid axes, which makes different bay lengths and floor heights possible. Beam elements can be positioned on any of the grid axes, and shell elements can be positioned on any of the three surface planes following the grid. In the future, trusses will be implemented following the same system. For the programmable input interface, a matrix equivalent representation of the building was developed. These features are shown in Figure 1a.

Another requirement was the possibility of adapting the model to commonly used connections in timber buildings, such as laterally loaded dowel-type connections and axially loaded dowel-type connections. It is also possible to implement connection models with hysteresis. The parametric connection model is shown in Figure 1b.

It was decided that the framework would be required to simulate the entirety of a collapse. For this purpose, the mixed element method was developed and verified [20]. The method uses finite elements with physical lengths and properties, interspersed with rigid zero-length elements. For each time-step, a failure detection algorithm detects the exceedance of a failure criterion in the model and removes the rigid zero-length elements at the points of failure. With this, the simulation can continue after the failure of a building member. This is shown in Figure 1c.

To impose initial damage scenarios and to remove elements in the analysis upon failure, an element removal algorithm was developed [27]. The real removal of these elements is advantageous over a stiffness reduction approach, since the stiffness reduction approach may lead to convergence problems. The element removal algorithm is shown in Figure 1d.

If a rigid zero-length element is removed such that a finite element with physical length is entirely disconnected from the rest of the model, a convergence problem would occur. To avoid such convergence problems, any disconnected parts of the model with rigid-body motions were removed. The removal was conducted with the element removal algorithm shown in Figure 1d. In reality, the rigid-body motion of the removed parts would be building debris, which would lead to impact loading at some point. Therefore, a debris tracking algorithm was implemented for any parts with rigid-body motion. The debris tracking algorithm calculates the trajectory of the debris as projectiles. This is shown in Figure 1e.

Besides the debris tracking algorithm, an impact detection and loading algorithm was developed. If the impact detection algorithm detects debris is impacting a member of the remaining structure, the impact loading algorithm is activated. This loads the impacted member over a pre-determined time-step and is shown in Figure 1f.

Based on impact tests of full-size glued laminated timber beams [22–25], an energy-based failure criterion was developed, and the impact time was found. If the kinetic energy of the debris exceeds the energy capacity given by the failure criterion, local failure of the member will occur. This is shown in Figure 1g.

2.2 ANALYSIS DESCRIPTION

The conceptual framework of the collapse model in Section 2.1 was implemented in Python, with the open-source finite element framework OpenSeesPy [26] as the computational engine. To organise the input and output of

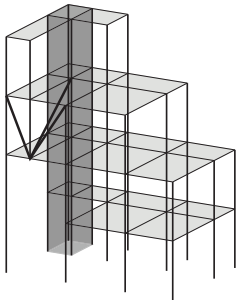

(a) Parametric global model.

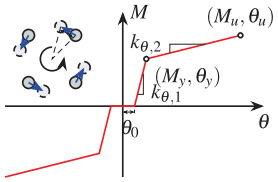

(b) Parametric multi-scale connection model.

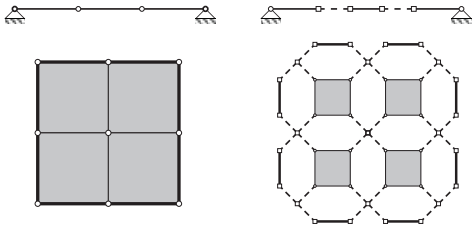

(c) Mixed element method and element separation algorithm.

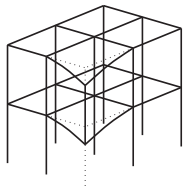

(d) Element removal algorithm

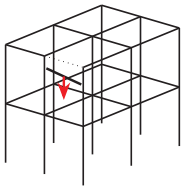

(e) Debris tracking algorithm.

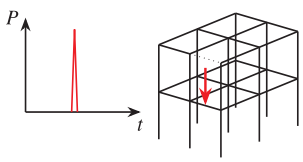

(f) Impact loading.

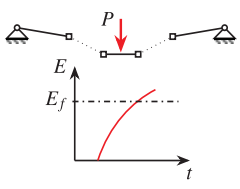

(g) Energy-based failure criterion.

Figure 1: *Conceptual framework of the collapse model and figurative illustrations of the different modules.*

https://doi.org/10.52202/069179-0301

the model, an SQL database was developed with SQLite in Python. In the general framework, one-dimensional *forceBeamColumn* elements were implemented for the beams and the columns, and two-dimensional *ShellMITC4* elements were implemented for wall and slab members. The connections and the rigid links interspersed between the finite elements were modelled with the zero-length element *twoNodeLink*. The beam and column members were modelled with a linear-elastic perfectly brittle material behaviour, which is concurrent with high strain-rate models for glued laminated timber [28]. As a simplification, the connections were also modelled as a linear-elastic perfectly brittle material. A corotational transformation was used for the entire model.

2.2.1 Element-removal algorithm

The element-removal algorithm can be described in the following steps:

1. Solve the system of equations to get the internal forces of the element to be removed.
2. Remove the element from the model and re-apply the internal forces of the removed element.
3. Step down the internal forces of the removed element linearly over a time t_r.

The algorithm can be used for static or dynamic analysis and can also be used for the removal of entire members. In the collapse model, it is used for in situ removal of any failed elements, detached model parts with rigid-body motion, and to impose damage by removing single elements or members. A full description of the element removal algorithm can be found in Cao et al. [27].

For a column-removal scenario, the UFC 4-023-03 [29] states that the removal time t_r must be less than 1/10 of the natural period of the vibration mode associated with the damage, whereas ASCE 7-22 recommends an impact duration between 30 ms for modelling flood-borne debris. In EN 1991-1-7 [30], hard impact for vehicles results an impact time of 70 ms. The results from the impact tests conducted by Cao et al. [22–25] showed that the mean impact time was 12 ms, with an impact velocity of around 9.6 m/s, which corresponds to a free-fall of about 4.7 m. The natural period associated with the initial damage scenario was in the order of 400 ms. On this basis, a removal time t_r of 20 ms was chosen.

2.2.2 Incremental damping

One of the main drawbacks of previous models was the lack of an incremental damping formulation [31], which is also a general weakness for the most common damping implementations [32]. During a collapse, the connections and members may enter the nonlinear range and parts of the building may detach from the surviving structure. Because of the potential nonlinearities of the members, the stiffness of the system may change. Similarly, the detached parts do not contribute to the mass or stiffness of the remaining building. Therefore, a damping scheme which does not account for the changes in the stiffness and mass of the building during a collapse may lead to gross errors. Moreover, modal analysis in the undamaged state will not reflect the vibration modes throughout a collapse.

In the current state of the model, an incremental damping scheme based on Rayleigh damping is implemented. Rayleigh damping considers both stiffness- and mass-proportionate damping in the damping matrix **C**:

$$\mathbf{C} = \alpha\mathbf{M} + \beta\mathbf{K}, \tag{1}$$

where **M** is the mass matrix, **K** is the stiffness matrix, and α and β are calibration parameters. The calibration parameters α and β are selected based on the natural angular frequency ω_i and ω_j, of two vibration modes or frequencies from an eigenvalue analysis, which determine the range of interest for the damping scheme. The two calibration parameters α and β can be computed from:

$$\alpha = \zeta\frac{2\omega_i\omega_j}{\omega_i + \omega_j}, \qquad \beta = \zeta\frac{2}{\omega_i + \omega_j}, \tag{2}$$

where ζ is the damping ratio. Because the vibration modes at the undamaged state of the model will not reflect the vibration modes throughout the collapse, the iterative damping scheme is based on updating the mass **M** and stiffness **K** matrices at each time-step. By doing so, nonlinearities and physical detachments of building parts will be reflected in the damping **C** of the analysis. The calibration parameters α and β are only computed at the start of the analysis because of difficulties with high-frequency modes ω_i and instabilities throughout the simulation. To avoid the calibration parameters α and β coefficients from being computed too close to each other, the frequency j was set as ω_j=5ω_i, and frequency i was set as the first natural frequency ω_i= ω_1.

2.2.3 Convergence check

The dynamic analysis was conducted with an implicit time integration scheme. For the implicit integration, the unconditionally stable average acceleration method in the Newmark family is used. To solve the nonlinear equations of motion, the Newton-Raphson method was used.

Because the failure criteria in the model are checked at each time-step, an optimum maximum time-step had to be determined. If the maximum time-step is too large, the utilization of the members will grossly exceed the capacity. If the maximum time-step is too small, the model will be computationally inefficient. Based on a sensitivity analysis of the maximum time-step, a time-step of 0.5 ms was used for the collapse simulations. Compared to a time-step of 0.1 ms, the difference in the time of the last element failure was about 1.6%. The difference in the vertical deflections of the node above the removed column was about 4.6%, and the maximum utilization in the model was 1.08, compared to 1.04 for a time-step of 0.1 ms.

Like the sensitivity analysis of the maximum time-step, a mesh sensitivity analysis was conducted to determine the best member discretization. A member discretization of five finite elements per member was found as the optimum between computational expenses and accuracy. Compared with a discretization of ten finite elements per member, the difference in the time of the last element failure was about 0.2%, and the difference in the vertical deflections of the node above the removed column was about 0.8%. The computation time of the simulation was approximately 56% shorter for the discretization with five

finite elements per member. The incremental Rayleigh damping scheme in Section 2.2.2 was calibrated for the first and fifth vibration modes.

2.3 FAILURE CRITERIA

For most of the failure checks in the model, stress-based failure criteria according to EN 1995-1-1:2004 [21] were used at each time-step. The design checks were conducted on the mean material strength level, without load factors on the action side. The connections were modelled as linear elastic and perfectly brittle in rotation, with a maximum allowable rotation θ_y of 25.8 mrad, or a moment M_y of 52.4 kNm. For the mean material strengths, parameters from Schilling et al. [33] were used for glued laminated timber of strength class GL24h. For the mean elastic and shear modulus, values from EN 14080:2013 [34] were used for GL24h.

2.3.1 Combined compression and bending action

In the model, a corotational transformation was used. The corotational transformation is suitable for problems with large deformations, which are expected during a collapse. Because of the corotational transformation, a second order failure criterion for combined compression and bending action can be used without buckling coefficients. This is possible because second order P-Δ-effects are automatically considered in the equilibrium computations. Therefore, the failure criterion for combined compression and bending action was:

$$\frac{\sigma_{c,0}}{f_{c,0}} + \frac{\sigma_{m,y} + \sigma_{m,z}}{f_m} \leq 1, \tag{3}$$

where $\sigma_{c,0}$ is the compressive stress parallel to the grain, $f_{t,0}$ is the compressive strength parallel to the grain, $\sigma_{m,y}$ and $\sigma_{m,z}$ are the maximum bending stresses about the strong and weak axis of the cross-section, and f_m is the bending strength.

2.3.2 Energy-based failure criterion

In this paper, the energy-based failure criterion was based on work done on impact loading of timber beams at ETH Zurich [22–25]. Because of the dynamic nature of impact loading, a limit state based on energy was used instead of one based on stresses. From the pendulum impact hammer tests on full-size timber beams, the failure energy E_r was determined directly. The failure energy E_r from the tests is analogous to the strength of a material in terms of stresses. If the strain energy in the member E_s from imposed loads exceeds the failure energy E_r, the member has failed. This can be expressed as:

$$E_s \leq E_r \Leftrightarrow \frac{E_s}{E_r} \leq 1. \tag{4}$$

If the kinetic energy of a projectile from impact loading E_k is considered as well, Equation (4) can be expanded to:

$$\frac{E_s + E_k}{E_r} \leq 1. \tag{5}$$

The kinetic energy of a projectile can be computed from E_k=0.5mv^2, where m is the mass of the projectile, and v is the velocity of the projectile. The velocity v of the projectile can be found directly from classical projectile motion, with the initial velocity vector $\boldsymbol{v}$ from the collapse model. From the impact tests, the failure energy E_r of the beams in this paper is 22.2 kJ.

3 FRAME DESIGN AND SIMULATIONS

3.1 DESIGN OF FRAMES

The design of the frames was conducted for gravity loads according to EN 1990:2002 [35] and EN 1991-1-1:2002 [36], and wind-induced vibrations according to EN 1991-1-4:2005 Annex B [37] and ISO 10137:2007 [38]. The beams and columns were assumed to be spruce glued laminated timber with a strength class of GL24h. For the design of the cross-sections, strength and stiffness parameters were assumed from EN 14080:2013 [34]. The members and connections were designed with EN 1995-1-1:2004 [21].

The load combination for the gravity loads was chosen for office buildings in category B. The beams were designed with the following load combination:

$$p_{Ed} = \xi\gamma_G g_k + \gamma_Q q_k, \tag{6}$$

where ξ is 0.85, γ_G is 1.35, γ_Q is 1.50, g_k is 3.5 kN/m^2, and q_k is 3.0 kN/m^2. For the design of the columns, the design gravity load p_{Ed} in Equation (6) was multiplied with the reduction factor α_n in EN 1991-1-1:2002 [36] for multi-storey buildings.

The connections were designed against the load combination in Equation (6) with laterally loaded steel dowels and a slotted-in steel plate. Based on the joint slip K_{ser}=$\rho_m^{1.5}d$/23 in EN 1995-1-1:2004 [36], the connection stiffness k_θ was computed with:

$$k_\theta = K_{ser} \sum_i^{n_d} r_i^2, \tag{7}$$

where index n_d is the number of dowels in the connection, and r_i is the distance of each dowel from the connection's centre of rotation. To find the connection stiffness per shear plane k_θ in Equation (7), the spacing of the dowels was chosen as the minimum spacing in EN 1995-1-1:2004 [36]. The resulting connection stiffness k_θ was 210 kNm/rad. The connections were assumed to be rigid on the column-side of the beam-column connection.

In the serviceability wind-design, terrain category III and a mean wind velocity of 26 m/s were chosen. Since the frames were symmetrical, only a planar frame was considered in the design against wind-induced vibrations. For the wind-design and the collapse simulations, a damping ratio ζ of 2% was chosen based on ambient vibration tests [39].

In the collapse simulations, the following accidental load combination from EN 1990:2002 [35] was used:

$$p_{Ed} = g_k + \psi_{2,1} q_k, \tag{8}$$

where g_k is 3.5 kN/m^2, q_k is 3.0 kN/m^2, and $\psi_{2,1}$ is 0.3. For all the frames, the initial damage scenario was the rapid loss of a ground-floor corner column.

https://doi.org/10.52202/069179-0301

3.2 FRAME CONFIGURATIONS

The frames were symmetrical in the horizontal plane with four bays and storeys. The beams and columns were placed on an orthogonal grid with a uniform spacing of 3600 mm in each axis direction. Two variations of the beam cross-sections were designed: (1) optimised for maximum utilisation; and (2) 50% utilisation. Both variations were designed for ultimate and serviceability limit states with EN 1995-1-1:2004 [21] with standard glued laminated timber dimensions. Bending stresses in the ultimate limit state was the governing design criterion for the design of the beams.

In the connection design, a dowel diameter of 8 mm and a steel plate thickness of 10 mm were chosen with an S235 steel quality. The dowels were arranged in a 3×2 rectangular pattern. With this layout, the shear capacity of the connection was 30 kN. The rotational stiffness of the connection k_θ was 210 kNm/rad, which resulted in a peak acceleration of the softest frame of 0.053 m/s^2. This satisfies the serviceability criterion of office buildings for wind-induced vibrations in ISO 10137:2013 [38]. For the collapse simulations, a linear-elastic behaviour of the connections and the members was assumed. The incremental damping scheme in Section 2.2.2 was adopted for the collapse simulations, with a damping ratio ζ of 2%. An overview of the different frames is shown in Table 1.

Table 1: *Beam and column cross-sections of the frames.*

No.	Damage	Cross-section $b \times h$ (mm)	
		Beam	Column
120×240C	Corner		
120×240E	Edge	120×240	360×360
120×240I	Inner		
120×320C	Corner		
120×320E	Edge	120×320	360×360
120×320I	Inner		

4 RESULTS AND DISCUSSION

Both the models with the smaller and larger beam cross-sections suffered from near identical collapses when comparing the same column removal scenarios, as shown in Figure 2. This was because of the same failure modes being activated after column removal. In each simulation, after the column removal, the loads were diverted to the beams above the removed column, resulting in increased moments in the connections. The connections of the beams adjacent to and above the removed column were the first to exceed their capacity. For each damage-scenario, the damage propagated progressively from the removed column. The damage-scenario with the least collapsed floor area was the removal of the corner-column with a collapsed floor area of 6.3%, or 51 m^2, including the roof. For the edge-column removal, the collapsed floor area was 12.5% or 104 m^2, and 25% or 207 m^2 for the internal column removal.

The initial maximum static deformations of the frames before the column removals were 10.5 mm for the 120×240 scenarios and 5.6 mm for the 120×320 scenarios. After the progressive collapses, the remaining members almost returned to their initial static deflections because of the complete vertical collapses of the bays adjacent to the removed columns. This is also because of the absence of inelastic material behaviour in the model.

Although the failure criterion of the connections was the maximum rotation θ_y, the maximum deformations of the models at the first failure w_f were different. This can be attributed to the dynamic response of the frames and is shown in Table 2 and is reflected in the maximum moments at the first failure M_f. The progressive collapses of all the damage-scenarios stopped between a failure time t_f between 116 and 136 ms. The first failure in the corner column damage-scenario occurred up to 20 ms later than that of the internal damage-scenario. However, these differences are almost negligible and do not improve the robustness properties of the structure.

Table 2: *Comparison of failure times t_f, durations of the collapse scenarios t_c, maximum deformations at the first failure w_f, and the corresponding moment M_f at the first failure.*

No.	t_f (ms)	t_c (ms)	w_f (mm)	M_f (kNm)
120×240C	136	3	88.3	50.3
120×240E	126	2	85.5	50.4
120×240I	116	4	78.2	48.9
120×320C	136	4	89.4	49.7
120×320E	129	3	88.2	51.4
120×320I	124	4	88.6	49.9

4.1 COLLAPSE MITIGATION

Here, suggestions are made for how the structure could be modified to increase its robustness and also how the model could capture other effects. Because the connections are the primary cause of the progressive collapses in the damage-scenarios, adjustments to their design could improve the robustness. However, changing one property of the connections could directly influence other properties. This can be exemplified in the following scenario. An increase of the moment capacity M_y may be conducted by increasing the distances of the fasteners in a laterally loaded timber connection with dowel-type fasteners. The moment capacity increases proportionally to the distance of the dowels to the centre of rotation of the connection, and the stiffness k_θ increases quadratically, according to Equation (7). Consequently, the elastic rotational capacity $\theta_y = M_y/k_\theta$ will decrease with increased distances. An increased moment capacity M_y of the connection could activate an alternative load path via bending. However, a reduced rotational capacity θ_y would constrain the development of other alternative load paths, which require larger member rotations to be activated. An example is catenary action [40,41]. Moreover, overly strong connections may cause failures of the beams, which in practice is undesirable since timber has a predominantly brittle failure mode in bending [42,43]. Therefore, the modification of connection design without consideration of the impact of this on the larger structure may not necessarily increase the robustness of the structure.

https://doi.org/10.52202/069179-0301

The activation of alternative load paths may cause a progressive collapse [44], similar to the collapse of the Bad Reichenhall ice-arena [45]. Here, transferring loads from a damaged member to the adjacent structure may overload the structure. Considering this, a partial but more confined collapse may be preferable, similar to the collapse of the Siemens Arena [45]. For the considered damage-scenarios, the collapse propagated vertically and is shown in Figure 2. Fuse elements may prevent the horizontal propagation of a collapse, but not a vertical propagation [10]. To prevent the vertical propagation of a collapse, strong floors can be used for compartmentalization [10]. Future work could include scenarios where failure is not concentrated in the connections, and the effect of using members with a surplus capacity reserve could be evaluated. It is uncertain if this will be beneficial for the robustness of such structures, and if the increased material volume will justify such an approach.

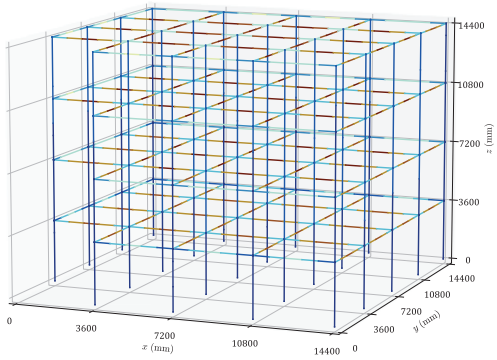

(a) 120x240C: t=139 ms, w=10.53 mm

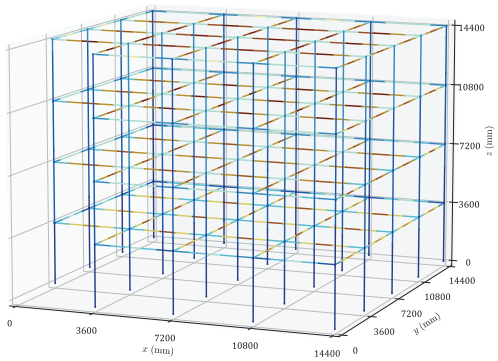

(b) 120x320C: t=140 ms, w=5.58 mm

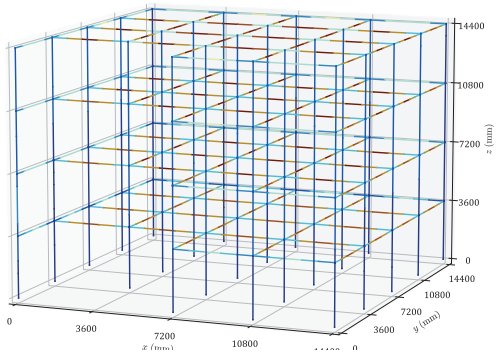

(c) 120x240E: t=128 ms, w=10.53 mm

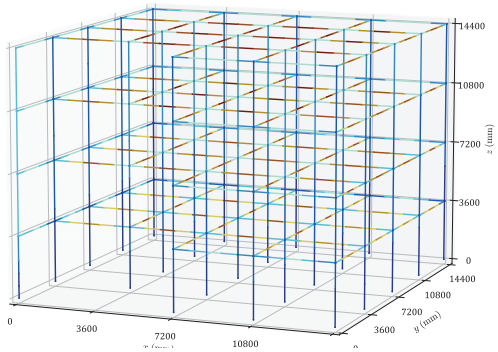

(d) 120x320E: t=132 ms, w=5.62 mm

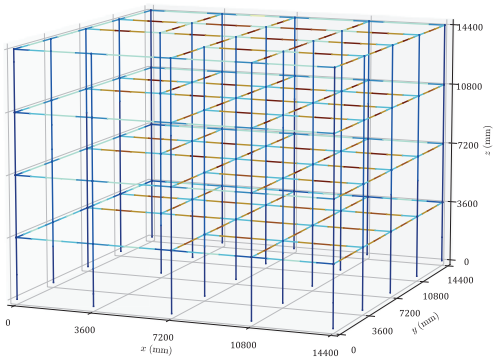

(e) 120x240I: t=120 ms, w=10.54 mm

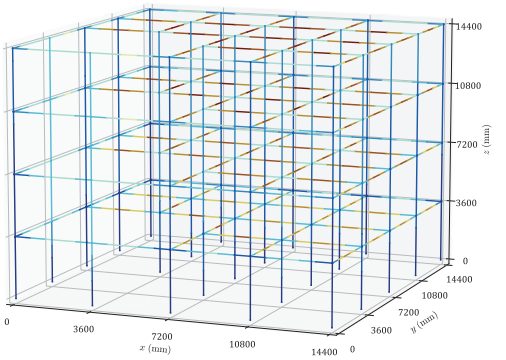

(f) 120x320I: t=128 ms, w=5.68 mm

Figure 2: *Maximum deformations for the frames with different beam cross-sections, immediately after the failure of the last element.*

https://doi.org/10.52202/069179-0301

4.2 PLAUSIBILITY OF DEFORMATIONS

To evaluate the plausibility of the model, the two-dimensional static model depicted in Figure 3 was assessed for a corner-column damage-scenario. The structural system in Figure 3 is similar to the loading conditions in each storey above the removed column. To account for the stiffness of the laterally loaded timber connections with dowel-type fasteners, the beam ends were constrained by rotational springs with a rotational stiffness k_θ, as defined in Section 3.2. The accuracy of the simplified beam model is more dependent on the rotational constraint than the axial constraint. For 120×240C, the maximum static deformation was 224 mm, and 213 mm for 120×320C.

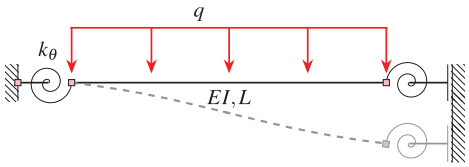

Figure 3: *Simplified beam model of a corner-column damage-scenario.*

To obtain comparable deformations to those of the simplified model, the nonlinear parametric collapse model was modified to neglect the failure of the connection elements. The maximum dynamic deformations from the column removal for 120×240C was 446 mm, and 425 mm for 120×320C. To compare the dynamic deformations from the nonlinear parametric collapse model and the static deformations from the simplified beam model, a dynamic amplification factor was necessary. Here, the dynamic amplification factor was defined as the ratio between the maximum dynamic and the maximum static deformations for the considered damage-scenario. For linear elastic structures without damping, the dynamic amplification factor attains a value of 2.0 [46]. Because of the limited damping for the considered structure, a dynamic amplification factor of 2.0 is reasonable [27]. With this dynamic amplification factor, the deviations between the parametric nonlinear collapse model and the simplified beam model are less than 0.25%. Therefore, the model results are reasonable.

4.3 LIMITATIONS

4.3.1 Connection behaviour

In the presented case study, the connection behaviour is linear elastic and perfectly brittle. This is a large simplification of the real behaviour of laterally loaded dowel-type connections with slotted-in steel plates, which could have hysteresis. The current iteration of the model neglects inelastic material behaviour, shear or tensile failure, as well as any energy dissipation from hysteretic behaviour. For connections which remain in the elastic domain, the modelled behaviour is realistic. For a column-removal scenario with no propagation of the failure, the linear-elastic connection assumption is conservative. This may not hold true if the collapse propagates further. Accounting for inelastic behaviour in the model would have increased the rotational capacity $\underline{\theta}_v$ and may increase the deformations of the members before failure. However, including ductility in the inelastic behaviour of the connections may not increase the robustness of the structure [31]. For edge or internal column damage-scenarios, ductility in the connections could be beneficial. Here, the static system in Figure 3 remains a good approximation of the members above the removed column because of the symmetry. Ductility in the connections or member could cause larger deformations in the system and the activation of catenary action [40,41]. Further research should be conducted on the static and dynamic characterisation of the hysteretic behaviour of laterally loaded dowel-type connections with slotted in steel plates subjected to large deformations, combined loading, and full or partial load reversals.

4.3.2 Slabs and walls

Currently, the model offers a realistic depiction for frame-type buildings with non-load-bearing walls and disconnected floors. However, most buildings include floors and walls, which act as rigid diaphragms to transfer lateral loads. This behaviour is not reflected in the current model and may significantly influence the progressive collapse. Other researchers have shown that walls and slabs are beneficial for the structural robustness [41,47]. Hence, including walls and slabs in future models is important to expand the scope of the model.

4.3.3 Damping formulation

There are notable uncertainties related to the level of damping in the model, which are also difficult to quantify. The implemented amount of damping corresponds to a service-level situation in timber buildings. However, the level of damping in a progressive collapse of a timber building is not known. A collapse situation is also an extreme loading scenario with large deformations and nonlinearities [9], which is dissimilar to the situations in which previous measurements were conducted [39]. The amount of modelled damping may therefore be severely under- or overestimated. Moreover, there is not a clear consensus in the scientific community on how damping should be modelled in such situations [32].

Because glued laminated timber can be considered as a linear-elastic perfectly brittle material, it is safe to assume that any plasticity and energy dissipation will mainly be in the connections. Therefore, implementing hysteretic connection behaviour can reduce the uncertainties related to damping. By introducing damping directly into the connections, the incremental damping can be reduced to a minimum, which will also reduce the modelling uncertainties. Like the connection behaviour, the neglection of damping in a column-removal scenario with no propagation of the failure is conservative.

4.3.4 Model validation

The presented model is not validated with physical column-removal experiments. Because of the intrinsic nature of a collapse, it is difficult to conduct building-scale validation experiments. However, the individual modules of the model which require the input of physical parameters can be validated by component-scale experiments. The validation of the full model can be conducted with full-size dynamic member-removal

experiments on building sub-assemblies. Previously, the implemented mixed element method was verified against the finite element method for both static and dynamic analysis. Moreover, an extensive experimental campaign on impact loading of full-size timber beams was conducted to improve the modelling of the impact loading and the energy-based failure criterion.

5 CONCLUSIONS

In this paper, a nonlinear dynamic model was presented for investigating the progressive collapse of timber buildings. The model is fully parametric and can model the entirety of a progressive collapse, including features such as member failure, element removal, debris tracking, impact loading, and incremental damping. The model was demonstrated on symmetrical three-dimensional frames with four floors and bays. One frame was designed for a maximum utilisation in the ultimate limit state, and another for a 50% utilisation. The frames were subjected to a corner, edge, and internal column-removal scenario.

All simulations resulted in vertically propagating collapses in the bays above the removed column. This was because of the failure of connections in bending. These connections acted as fuse elements and inhibited the horizontal propagation of damage. The capacity reserve in the beams was not activated because of the prior failure of the connections and did not lead to an increased robustness. Increasing the strength of the connections could activate alternative load paths via bending and an increase of the rotational capacity could do so through catenary action. However, a strength increase may not lead to an increase in the rotational capacity and further research is needed to assess the consequences on the failure mode of structures undergoing a column removal scenario.

The presented results are valid for frame-type structures with non-load-bearing walls and disconnected slabs. However, many structures have load slabs and walls acting as diaphragms. The current iteration of the collapse model cannot assess the contribution of these members. Similarly, trusses are also not implemented at the time of writing. These features are planned for the next iteration of the model. Besides the aforementioned limitations, the current incremental damping scheme is based on Rayleigh damping with fixed calibration factors with a damping ratio based on serviceability measurements of the damping ratio. There are several uncertainties related to the damping in this paper. To increase modelling accuracy and to reduce the uncertainties related to damping, more numerical and experimental research is needed.

The results in this paper were for linear elastic and perfectly brittle connections. However, the best practice in timber engineering is to design the connections with ductile behaviour. Future investigations should include inelastic connection behaviour to include connection hysteresis and the possible activation of alternative load paths.

The presented collapse model is an important step in the quantification and prevention of progressive and disproportionate collapse of timber buildings. The plausibility of the deformations in the model was verified with a simplified beam model. However, there are still some hurdles left before the model can be used on a large scale. One of the main challenges is the validation of the model, which is only possible through full-size experiments of an entire building or a representative sub-assembly. Despite the aforementioned limitations, the presented model is an important step for assessing the robustness of timber structures.

ACKNOWLEDGEMENT

This article is part of the project *Robustness of tall timber buildings* at ETH Zurich and is generously funded by the Albert Lück-Stiftung.

REFERENCES

[1] Starossek U, Haberland M. Disproportionate Collapse: Terminology and Procedures. Journal of Performance of Constructed Facilities 2010;24:519–28. https://doi.org/10.1061/(asce)cf.1943-5509.0000138.

[2] Lalkovski N, Starossek U. The Total Collapse of the Twin Towers: What It Would Have Taken to Prevent It Once Collapse Was Initiated. Journal of Structural Engineering 2022;148. https://doi.org/10.1061/(asce)st.1943-541x.0003244.

[3] Adam JM, Parisi F, Sagaseta J, Lu X. Research and practice on progressive collapse and robustness of building structures in the 21st century. Eng Struct 2018;173:122–49. https://doi.org/10.1016/j.engstruct.2018.06.082.

[4] Landolfo R, Formisano A, di Lorenzo G, di Filippo A. Classification of european building stock in technological and typological classes. Journal of Building Engineering 2022;45:103482. https://doi.org/10.1016/j.jobe.2021.103482.

[5] Churkina G, Organschi A, Reyer CPO, Ruff A, Vinke K, Liu Z, et al. Buildings as a global carbon sink. Nat Sustain 2020;3:269–76. https://doi.org/10.1038/s41893-019-0462-4.

[6] Ramage MH, Burridge H, Busse-Wicher M, Fereday G, Reynolds T, Shah DU, et al. The wood from the trees: The use of timber in construction. Renewable and Sustainable Energy Reviews 2017;68:333–59. https://doi.org/10.1016/j.rser.2016.09.107.

[7] Crews KI. Nonconventional timber construction. Nonconventional and Vernacular Construction Materials: Characterisation, Properties and Applications 2020:437–66. https://doi.org/10.1016/B978-0-08-102704-2.00016-0.

[8] Svatoš-Ražnjević H, Orozco L, Menges A. Advanced Timber Construction Industry: A Review of 350 Multi-Storey Timber Projects from 2000–2021. Buildings 2022;12:404. https://doi.org/10.3390/buildings12040404.

[9] Huber JAJ, Ekevad M, Girhammar UA, Berg S. Structural robustness and timber buildings–a review. Wood Mater Sci Eng 2019;14:107–28. https://doi.org/10.1080/17480272.2018.1446052.

[10] Mpidi Bita H, Huber JAJ, Palma P, Tannert T. Prevention of Disproportionate Collapse for Multistory Mass Timber Buildings: Review of

https://doi.org/10.52202/069179-0301

Current Practices and Recent Research. Journal of Structural Engineering 2022;148. https://doi.org/10.1061/(asce)st.1943-541x.0003377.
[11]Abed J, Rayburg S, Rodwell J, Neave M. A Review of the Performance and Benefits of Mass Timber as an Alternative to Concrete and Steel for Improving the Sustainability of Structures. Sustainability (Switzerland) 2022;14. https://doi.org/10.3390/su14095570.
[12]Harte AM. Mass timber – the emergence of a modern construction material. Journal of Structural Integrity and Maintenance 2017;2:121–32. https://doi.org/10.1080/24705314.2017.1354156.
[13]Cao AS, Stamatopoulos H. A theoretical study of the dynamic response of planar timber frames with semi-rigid moment-resisting connections subjected to wind loads. Eng Struct 2021;240. https://doi.org/https://doi.org/10.1016/j.engstruct.2021.112367.
[14]Binck C, Cao AS, Frangi A. Lateral stiffening systems for tall timber buildings–tube-in-tube systems. Wood Mater Sci Eng 2022. https://doi.org/10.1080/17480272.2022.2086066.
[15]Vilguts A, Stamatopoulos H, Malo KA. Parametric analyses and feasibility study of moment-resisting timber frames under service load. Eng Struct 2021;228:111583. https://doi.org/10.1016/j.engstruct.2020.111583.
[16]Malo KA, Siem J, Ellingsbø P. Quantifying ductility in timber structures. Eng Struct 2011;33:2998–3006. https://doi.org/10.1016/j.engstruct.2011.03.002.
[17]Buchanan AH. The challenges for designers of tall timber buildings. WCTE 2016 - World Conference on Timber Engineering 2016;25:24–35.
[18]Franke S, Franke B, Harte AM. Failure modes and reinforcement techniques for timber beams-State of the art. Constr Build Mater 2015;97:2–13. https://doi.org/10.1016/j.conbuildmat.2015.06.021.
[19]Ellingwood BR, Asce F. Mitigating Risk from Abnormal Loads and Progressive Collapse n.d. https://doi.org/10.1061/ASCE0887-3828200620:4315.
[20]Cao AS, Frangi A. Mixed Element Method for Progressive Collapse Analysis: Method Description and Verification. In: di Trapani F, editor. Proceedings of Eurasian OpenSees Days 2022, Torino, Italy: Springer Nature; 2022.
[21]European Committee for Standardization. EN 1995-1-1:2004. Eurocode 5: Design of timber structures - Part 1-1: General - Common rules and rules for buildings. Brussels, Belgium: 2004.
[22]Cao AS, Houen MT, Lolli M, Frangi A. Pendulum Impact Hammer Tests on Glued Laminated Timber Beams. Zurich: 2022. https://doi.org/10.3929/ethz-b-000585619.
[23]Cao AS, Lolli M, Frangi A. Pendulum impact hammer tests on spruce GLT – Preliminary results. In: Topping BHV, Kruis J, editors. Proceedings of the Fourteenth International Conference on Computational Structures Technology, Edinburgh, UK: Civil-Comp Press; 2022, p. 1–8.
[24]Cao AS, Houen M, Lolli M, Frangi A. Pendulum impact hammer tests on glued laminated timber beams. Report 2022-01. Zurich, Switzerland: 2022. https://doi.org/10.3929/ethz-b-000585619.
[25]Cao AS, Frangi A. Pendulum impact hammer tests on timber beams - Experimental setup. WCTE 2023 - World Conference on Timber Engineering 2023.
[26]McKenna F, Scott MH, Fenves GL. Nonlinear Finite-Element Analysis Software Architecture Using Object Composition. Journal of Computing in Civil Engineering 2010;24:95–107. https://doi.org/10.1061/(asce)cp.1943-5487.0000002.
[27]Cao AS, Palma P, Frangi A. Column removal analyses of timber structures - Framework to assess dynamic amplification factors for simplified structural design methods. World Conference on Timber Engineering 2021, WCTE 2021, Santiago, Chile: 2021, p. 1717–24.
[28]Doudak G, Viau C, Lacroix D. Proposed design methodologies for timber assemblies subjected to blast loading. In: Görlacher R, editor. International Network on Timber Engineering Research, INTER: Proceedings, Meeting 55, 21-25 August 2022, Bad Aibling, Germany, Bad Aibling, USA: Timber Scientific Publishing, KIT Holzbau und Baukonstruktionen; 2022, p. 1–15.
[29]U.S. Army Corps of Engineers, Naval Facilities Engineering Command, Air Force Civil Engineer Support Agency. UFC 4-023-03 Design of Buildings to Resist Progressive Collapse. 2009.
[30]European Committee for Standardization. EN 1991-1-7:2006. Eurocode 1: Actions on structures - Part 1-7: General actions - Accidental actions. Brussels, Belgium: 2006.
[31]Voulpiotis K, Schär S, Frangi A. Quantifying robustness in tall timber buildings: A case study. Eng Struct 2022;265:114427. https://doi.org/10.1016/J.ENGSTRUCT.2022.114427.
[32]Chopra AK, McKenna F. Modeling viscous damping in nonlinear response history analysis of buildings for earthquake excitation. Earthq Eng Struct Dyn 2016;45:193–211. https://doi.org/10.1002/eqe.2622.
[33]Schilling S, Palma P, Steiger R, Frangi A. Probabilistic description of the mechanical properties of glued laminated timber made from softwood. In: Görlacher R, editor. International Network on Timber Engineering Research, INTER: Proceedings, Meeting 54, 16-19 August 2021, Online, Timber Scientific Publishing, KIT Holzbau und Baukonstruktionen; 2021, p. 1–16.
[34]European Committee for Standardization. EN 14080:2013 Timber structures - Glued laminated timber and glued solid timber - Requirements. Brussels, Belgium: 2013.
[35]European Committee for Standardization. EN 1990:2002. Eurocode - Basis of structural design. Brussels, Belgium: 2002.
[36]European Committee for Standardization. EN 1991-1-1:2002. Eurocode 1: Actions on structures - Part 1-

1: General actions - Densities, self-weight, imposed loads for buildings. Brussels, Belgium: 2002.
[37]European Committee for Standardization. EN 1991-1-4. Eurocode 1: Actions on structures -Part 1-4: General actions -Wind actions. Brussels, Belgium: 2005.
[38]International Organization for Standardization. ISO 10137:2007. Bases for design of structures - Serviceability of buildings and walkways against vibrations. Geneva, Switzerland: 2007.
[39]Feldmann A, Huang H, Chang W, Harris R, Gräfe M, Hein C. Dynamic properties of tall timber structures under wind-induced vibration. WCTE 2016 - World Conference on Timber Engineering, 2016.
[40]Cao AS, Grönquist P, Frangi A. Manuscript under peer review: Catenary action in strip-reinforced wood and timber beams. Constr Build Mater 2023.
[41]Mpidi Bita H, Tannert T. Disproportionate collapse prevention analysis for post and beam mass timber building. Journal of Building Engineering 2022;56:104744. https://doi.org/10.1016/J.JOBE.2022.104744.
[42]Ottenhaus L, Jockwer R, Drimmelen D Van, Crews K. Designing timber connections for ductility – A review and discussion. Constr Build Mater 2021;304:124621. https://doi.org/10.1016/j.conbuildmat.2021.124621.
[43]Jorissen A, Fragiacomo M. General notes on ductility in timber structures. Eng Struct 2011;33:2987–97. https://doi.org/10.1016/J.ENGSTRUCT.2011.07.024.
[44]Voulpiotis K, Köhler J, Jockwer R, Frangi A. A holistic framework for designing for structural robustness in tall timber buildings. Eng Struct 2021;227:111432. https://doi.org/10.1016/j.engstruct.2020.111432.
[45]Munch-Andersen J, Dietsch P. Robustness of large-span timber roof structures - Two examples. Eng Struct 2011;33:3113–7. https://doi.org/10.1016/j.engstruct.2011.03.015.
[46]Li Y, Lu X, Guan H, Ye L. An energy-based assessment on dynamic amplification factor for linear static analysis in progressive collapse design of ductile rc frame structures. Advances in Structural Engineering 2014;17:1217–25. https://doi.org/10.1260/1369-4332.17.8.1217.
[47]Huber JAJ, Mpidi Bita H, Tannert T, Berg S. Finite element analysis of alternative load paths to prevent disproportionate collapse in platform-type CLT floor systems. Eng Struct 2021;240:112362. https://doi.org/10.1016/j.engstruct.2021.112362.

https://doi.org/10.52202/069179-0301

World Conference on Timber Engineering Oslo 2023

RESEARCH AND DEVELOPMENT OF SMALL-SCALE TIMBER CONSTRUCTION SYSTEM "BI-TREE STRUCTURE" WITH SMALL-DIAMETER TIMBER

Toko Kamata[1], Satoru Ito[2], Yuya Takaiwa[3]

ABSTRACT: We propose a rational small-scale building structure system "Bi-tree structure" that incorporates the idea of biomimetics using red cedar (38 mm square, 900 mm), which is a short piece of wood. A bending loading test was carried out to determine the Young's modulus and the allowable stress, and a finite element analysis was performed using the obtained results to evaluate the allowable stress calculation and structural safety. The validity of the model was confirmed by comparing the analysis results with the tensile loading test results of the shed.

KEYWORDS: Small-Diameter Timber, Biomimetics, Tree structure, Allowable stress degree, Finite element analysis

1 INTRODUCTION

Considering the environment, many methods have been adopted for processing short and small lumber, which is leftover wood when sawing, into woody biomass fuel, wood chips, laminated lumber, and paper raw materials. However, it has been clarified that the above-mentioned method is generally expensive, and it is regarded as a problem. [1] If it can be applied directly to the building structural system without processing the offcuts, it will be an economical and rational way to utilize wood, but there are few such cases. The main reasons for this are that joining details using ready-made hardware cannot be used for short and small materials, and that using fitting details causes large cross-sectional defects and almost no yield strength can be obtained. In addition, although it is possible to propose a building structure with a lattice structure by applying pin joints to short and small materials, the number of members will inevitably increase, so it is rather uneconomical to build a building structure other than a large scale. It becomes a structure. Therefore, in this research, we propose a rational and small-scale building structural system using small-diameter timber.

Here, the dominant load of the structure changes depending on the scale. When constructing a large-scale wooden building, the vertical load (self-weight) becomes dominant compared to the horizontal load, and the vertical load is designed as the dominant load. There are many cases of adopting dendritic pillars and dendritic lattices. For example, "Yamaga City Yamaga Elementary School (Kumamoto Prefecture, Japan)" which designed by Kazumi Kudo + Hiroshi Horiba / Shirakansu K & H [2] shown in Figure 1 and "Roadside Station Aizu Yugawa / Aizu Bange (Fukushima Prefecture, Japan)" which designed by Arsed Building Research Institute shown in Figure 2 [3]. These are considered to be a structural system that regards the leaves of a tree as a load distributed to the entire canopy, supports it with twigs, and transmits it to the trunk by an optimal route. Regarding this tree structure (Figre 3), Gaudi and Frei Otto conducted an upside-down suspension test (Figure 4) to clarify the load propagation path [4] and to set the optimum member arrangement for low-stress members. Research [5] has been conducted to propose a method for removing the stress. However, these are verifications for vertical loads, and in the case of small buildings such as the shed in this study, horizontal loads are the dominant load rather than vertical loads, and the required

Figure 1: *Yamaga City Yamaga Elementary School, Kumamoto Prefecture, Japan [2]*

Figure 2: *Rest stop Aizu Yukawa and Aizu Bange, Fukushima Prefecture, Japan [3]*

[1] Toko Kamata, Toyo University of Science and Technology, Japan, Saitama
[2] Satoru Ito, Associate professor, Toyo University of Science and Technology,Japan, Saitama
[3] Yuya Takaiwa, Associate Professor, Department of Architecture, Faculty of Science and Engineering, Toyo University, Dr. Eng.
takaiwa@toyo.jp 2100 Kujirai, Kawagoe-shi, Saitama, Japan (350-8585)

https://doi.org/10.52202/069179-0302

performance to the dominant load is different from the case of large-scale buildings.

Figure 3: *A model of tree structure [4]*

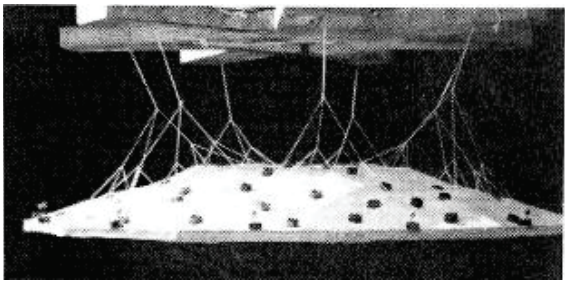

Figure 4: *Upside-down model [4]*

Therefore, in this research, we think that the structural system is different from that when constructing a large-scale building. And in order to construct a small-scale wooden building, we propose a structural system which has a rational dendritic shape not only for vertical load but also for horizontal load. Specifically, a tree system that transmits the load in the shortest path when a vertical load is applied, and a brace structure where the branch part is tensioned and compressed while bending resistance is generated in the trunk part and deformation is released when a horizontal load is applied. In this study, this structure is called "Bi-tree structure". In addition, there are only a few cases in the world where biomimetics are used in architecture, and we believe that this research will contribute to the development of biomimetics by becoming one of these cases.

Based on the above background, the allowable stress of the red cedar used in the proposed structural system was calculated by testing and calculation, and the stress transfer mechanism was clarified by finite element analysis. And a loading test was conducted after the shed construction to make a comparison with analysis model. By doing so, the validity of the analysis is verified.

2 THE OUTLINE OF ARCHITECTURE

2.1 THE OUTLINE OF THE SHED

2.1.1 Materials and dimensions

Figure 5 shows the appearance of the shed. A 38 mm square, 900 mm long red cedar was used as the structural material. Polycarbonate is used for the roofing material and exterior material. The dimensions are 4320 mm in width, 975 mm in depth, and 2000 mm in maximum height. The location is somewhere in Karuizawa Town, Kita-Saku District, Nagano Prefecture, Japan.

Figure 5: *Appearance of the shed*

2.1.2 MATERIALS

Figure 6: *Parts of the shed*

Figure 6 shows a reference to the members of the shed. The shed is made up of three types of members. Here, in this research, a 38 mm square lumber with a material length of 900 mm is a "Single Timber", two Single Timber laminated with an adhesive is a "Piled Beam", and a column which sandwiches three square lumbers between

the two single materials is defined as " Intermitted column ". In the lower photograph of Figure 2, the Piled Beam is shown on the left side, the Intermitted Column is shown on the right side, and the other parts are all made of a Single Timber.

2.2 THE OUTLINE OF RED CEDAR

Figure 7: *Enlargement of a red cedar [6]*

An enlarged photograph of Red Cedar is shown in Figure 7 [6]. Red cedar is a softwood of the Cupressaceae family, and its absolute dry specific density is 0.37, which is close to that of Sugi. In addition to being used as solid wood for

https://doi.org/10.52202/069179-0302

greenhouses and barns, it can also be used for building columns and fences by shaving it into a cylindrical shape.

2.3 ALLOWABLE STRESS OF RED CEDAR

In order to use building materials in buildings, the allowable stress must be defined. However, among the woods designated as building materials in Japan, the allowable stress level of red cedar is not defined as a structural member by the Building Standard Law. Therefore, a test was conducted (see Chapter 4), and the allowable stress level was set by itself based on the obtained results, making it possible to apply it to building structures.

3 STRUCTURAL PLAN

3.1 PROPOSAL OF STRUCTURAL SYSTEM

This time, we propose the following two structural systems. The first is the "Bi-tree structure," in which the axial force fluctuates when vertical or horizontal loads are applied, and also the type of structure changes.

Figure 8 shows the force flow when a vertical load is applied. When a vertical load is applied, a compressive force is transmitted from the upper surface to the tree part, which is decomposed to generate two thrusts, which are offset by acting in opposite directions. This is a structure that imitates the continuous arch in Figure 9.

Figure 8: *The shed when vertical load applies*

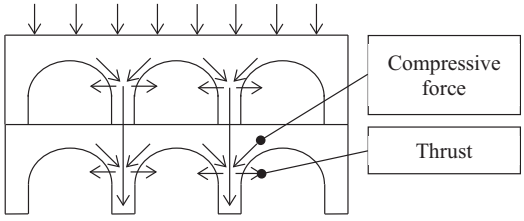

Figure 9: *The continuous arch when vertical load applies*

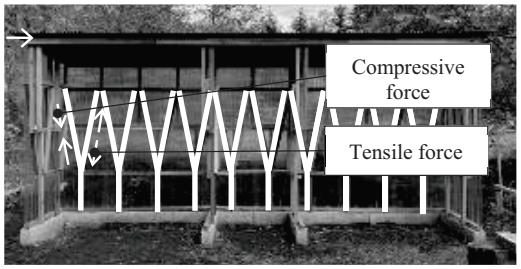

Figure 10: *The shed when a horizontal load applies*

Figure 10 shows the force flow when a horizontal load is applied. When a horizontal load is applied, one diagonal member bears the compressive force and the other diagonal member bears the tensile force in the tree part. This mimics the brace structure shown in Figure 11.

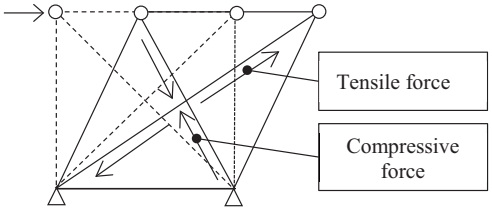

Figure 11: *A brace structure when a horizontal load applies*

The second is a structural system that applies the mechanism of independent columns with hanging walls, which is a traditional Japanese construction method. Independent columns with hanging walls are a construction method that is often used in traditional Japanese wooden houses, and are like the circled parts in Figures 12 and 13.

Figure 12: *An independent column with hanging walls*

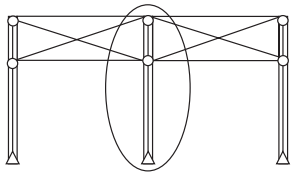

Figure 13: *A diagram of an independent column with hanging walls*

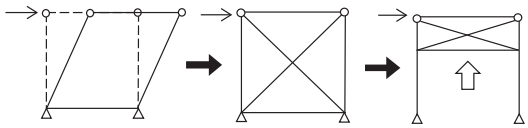

Figure14: *The origin of independent column with hanging walls*

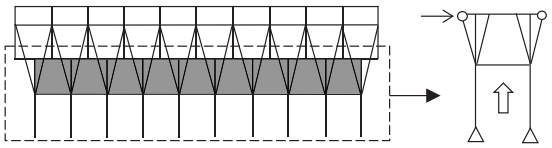

Figure 15: *The relation between trass part of the shed and an independent column with hanging walls*

Figure 14 shows the formation of an independent column with a hanging wall. With only a normal framework, the deformation becomes large when a horizontal load is applied, so a brace is incorporated to suppress the deformation of the entire wall. Furthermore, in order to secure a living space, the wall part is reduced. In this study, we applied this structure to the shed. As shown in Figure 15, the lower part of the truss part "Bi-tree structure" of the shed corresponds to the brace of the independent column with hanging walls. The position of

https://doi.org/10.52202/069179-0302

the truss is raised to keep the truss away from the ground and protect it from moisture and water splashes. In this way, we make proposals to rationally incorporate traditional construction methods.

4 TEST

4.1 BENDING LOAD TEST 1

4.1.1 Purpose

The purpose of this test is to clarify the strength of red cedar and to obtain the value used for the allowable stress calculation.

4.1.2 The outline of specimens

The target materials in this test are the three bodies defined in Chapter 2, Section 2. The Single Timber is the specimen 1, the Piled Beam is the specimen 2, and the Intermitted Column is the specimen 3, as shown in Figures 15 to 17.

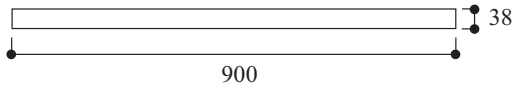

Figure 15: *Single timber; Specimen 1*

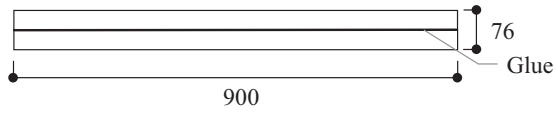

Figure 16: *Piled beam; Specimen 2*

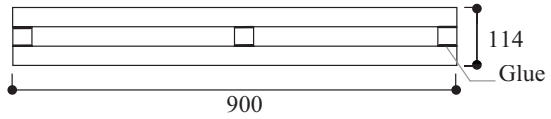

Figure 17: *Intermitted column; Specimen 3*

4.1.3 Test method

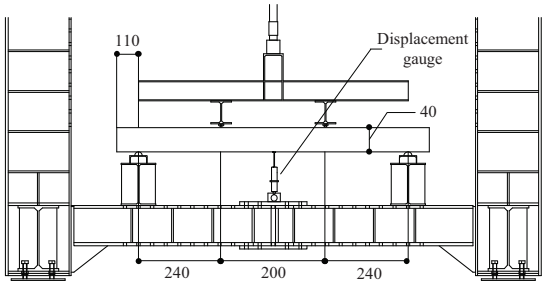

Figure 18: *Distance between fulcrums of a vertical hydraulic jack*

Figure 18 shows the distance between fulcrums and the equipment used. Using a vertical hydraulic jack, a load test was carried out by bending and loading at three equal parts of the push-off point at a load speed of 0.5 mm / sec. For the distance between fulcrums, we referred to the strength test manual [7] for structural timber established by the Japan Housing and Wood Technology Center.

4.1.4 Test result

Table 2: *Test result of Specimen 1*

Specimen	1-1	1-2	1-3	1-4	1-5
F_{max}	10.32	9.92	9.59	7.51	9.00
f_b	68.44	59.25	69.73	47.01	74.20
D	Simple Tension	Cross-grain Tension	Splintering Tension	Simple Tension	Cross-grain Tension

F_{max}: Max load(N)
f_b: Bending Strength(N/mm^2)
D: Destruction Mode [8]

Table 2 shows the test results of Specimen 1. For the strength, the 95% lower allowable limit value at the 75% confidence level was obtained in consideration of the variation of each specimen, and this was treated as the lower limit value of 5%, and the allowable bending stress was evaluated as 39.9N/mm2 from that value. The Young's modulus was 9.268 kN/mm² from the average value of the five bodies.

Table 3: *Test result of Specimen2 and 3*

Specimen	2	3
F_{max}	9250	8500
f_b	25.76	10.23
D	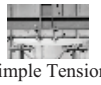 Simple Tension	Cross-grain Tension

F_{max}: Max load(N)
f_b: Bending Strength(N/mm^2)
D: Destruction Mod [8]

Table 3 shows the test results of Specimen 2 and 3, and Specimen 2 showed the highest strength. In addition, the Specimen 3 had cracks not on the adhesive surface but on the base metal part.

4.1.5 CONSIDERATION

Regarding the Specimen 1, the reason why the Specimen 2 had the highest strength is considered to be that the adhesive surface was the widest compared to the other two bodies and it was able to resist bending. In addition, it was confirmed that the adhesive strength was higher than the base metal strength at the location where cracks occurred in the Specimen 3, and there was no problem with the strength of the members.

4.2 BENDING LOAD TEST 2

4.2.1 Purpose

The purpose of this test is to verify that there is no problem in the strength even if the joint part of the Piled Beam (Specimen 2 in Chapter 4.1) is shortened to 450 mm, which is half of 900 mm, and used as a long member. This is because it was necessary to construct a long member in order to provide an opening in a part of the shed.

https://doi.org/10.52202/069179-0302

4.2.2 The outline of specimens

The target materials in this test is shown in Figere 19. This is a specimen whose the adhesive part of the Piled beam (Specimen 2 in Chapter 4.1) is shortened from 900 mm to half of 450 mm. And this is referred to as the Specimen 4.

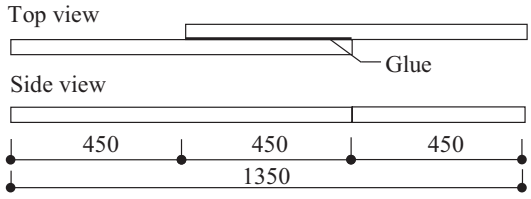

Figure 19: *Piled beams which were shortened their bonded zone in half; Specimen 4*

4.2.3 Test method

The test method is the same as that described in Chapter 4, Section 1, Section 3.

4.2.4 Test result

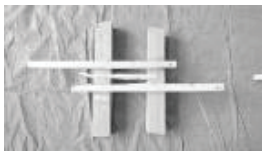

Figure 20: *The condition of specimen No.4 after broken*

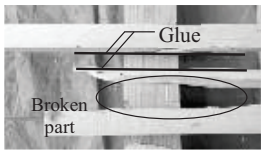

Figure 21: *Enlargement of Figure16*

Figure 20 shows the state after the destruction of the Specimen 4. In addition, as shown in Figure 21, in the loading test, the destruction of the material occurred not in the adhesive part but in the base material part.

4.2.5 CONSIDERATION

Since the destruction of the Specimen 4 occurred not in the adhesive part but in the base material part as in the Specimen 3, it can be confirmed that the adhesive strength is higher than the base material strength and there is no problem in the strength of the member.

5 STRUCTURAL ANALYSIS

5.1 THE OUTLINE OF ALALYSIS

The two types of analysis models created in this analysis are Model 1 and Model 2, respectively. The purpose of this analysis is to calculate the allowable stress using the results obtained from the analysis of Model 1 and to confirm whether the structure is as proposed. In addition, the results obtained from the analysis of Model 2 and the results of the tensile test of the shed in Chapter 6 are used to compare and consider the amount of deformation during load action.

5.2 ANALYSIS METHOD

We created and analyzed models using the finite element analysis software "midas iGen".

5.3 ANALYSIS MODEL SPECIFICATIONS

5.3.1 Model 1

Table 4: *List of elements in analysis Model 1*

	Widen (mm)	Height (mm)	Bending Strength (N/mm^2)	Young's Modulus (kN/mm^2)
Single timber	38	38	39.90	9.268
Piled beams	38	76	25.76	
Intermittent column	38	38	10.23	

Model 1 is model 2 (leftmost column of Figure 18) with the exterior material removed. The specifications are shown in Table 4. For the Young's modulus, the average value of 9.268 kN/mm^2 of the five bodies obtained in Chapter 4, Section 1 is used.

5.3.2 Model 2

Table 5: *List of elements in analysis Model 2*

	W	D	T	E	S
Roof	4300	862	5	2.15	58.8×10^{-9}
Wall	38	76			

References
W: Widen (mm) D: Depth (mm) T: Thickness (mm)
E: Young's Modulus (kN/mm^2) S: Specific Weight (kN/mm^3)

The specifications of Model 2 are shown in Table 5. It is used to compare the amount of displacement with the loading test of the shed.

5.3.3 Joining/supporting

As shown in Figure 19, all the joints are pin joints, and the 15Φ screw is used. The support is also pin-joined.

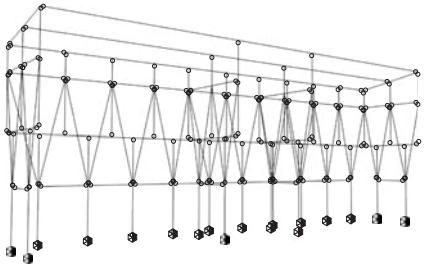

Figure 22*: Structure of joint and support*

5.4 SAFETY EVALUATION USING ANALYSIS RESULTS

To evaluate the structural safety, we carried out the allowable stress calculation. Also, we made sure that the structure of the building was not hindered by deformation or vibration.

https://doi.org/10.52202/069179-0302

5.4.1 The outline of allowable stress calculation

Calculate and confirm whether the design stress is less than the allowable stress.

Table 6: *Testal Result of Specimen from No.1 to No.3*

Specimen	1-1	1-2	1-3	1-4	1-5	2	3
F_{max}	6200	5350	6300	4250	6700	9250	8500
f_b	68.44	59.25	69.73	47.01	74.20	25.76	10.23
f_m			39.90			25.76	10.23

References
F_{max}: Max load(N) f_b: Bending Strength(N/mm^2)
f_m: Adopted Bending Strength(N/mm^2)

Table 7: *Long and short allowable stress degree of Specimen from No.1 to No.3*

Specimen	1	2	3
Long Allowable stress degree(N/mm^2)	14.63	9.45	3.75
Short Allowable stress degree(N/mm^2)	26.60	17.17	6.82

Table 6 shows the outline of the test results in Chapter 4. From this, the long-term and short-term allowable stress of each member is obtained. It is necessary to evaluate long-term allowable stress such as fixed load and snow load using long-term allowable stress, and rarely generated force such as seismic load and wind load using short-term allowable stress. The long-term allowable stress and the short-term allowable stress are calculated by multiplying the reference strength by 1.1 / 3 and 2/3, respectively. Table 7 is the value obtained by the above calculation. We evaluate safety by comparing these with the design stress degree of each member.
The following equation (1) is the equation to obtain the design stress degree of each member.

$$\sigma = \frac{M}{bh^2/6} \quad (1)$$

Here, σ = design stress degree (N / mm²), M = bending moment (N ・ mm), b = wood width (mm), h = wood fault (mm).

5.4.2 Allowable stress degree calculation for Single Timber

We calculate the allowable stress of a single timber. The parts shown in a and b in Figure 23 are composed of a single material, and the maximum bending moments in the vertical and horizontal directions show the same value of 10550 N ・ mm. Therefore, the calculation is as follows from Eq. (1).

$$\sigma = \frac{10550(N \cdot mm)}{38(mm) \times 38(mm) \times 38(mm)/6}$$

From this, the following results can be obtained.

$$\sigma = 1.153594\, N/mm2$$

Comparing this result with the long-term allowable stress of 14.63N / mm2 and the short-term allowable stress of 26.60N / mm2 for a single material in Table 7, the following results are obtained.

$$\sigma = 1.153594\, N/mm2 < 14.63\, N/mm2$$
$$\sigma = 1.153594\, N/mm2 < 26.60\, N/mm2$$

From this, it was confirmed that the values were smaller than the long-term and short-term allowable stress degrees. Here, the long-term allowable stress and the short-term allowable stress divided by the obtained allowable stress are defined as the safety factors in the vertical and horizontal directions, respectively. The calculation is as follows.

【Vertical direction】

$14.63\, N/mm^2 / 1.153594\, N/mm^2 = 8.196 \ldots \fallingdotseq 8.2$

【Horizonal direction】

$26.60\, N/mm^2 / 1.153594\, N/mm^2 = 23.05 \ldots \fallingdotseq 23.1$

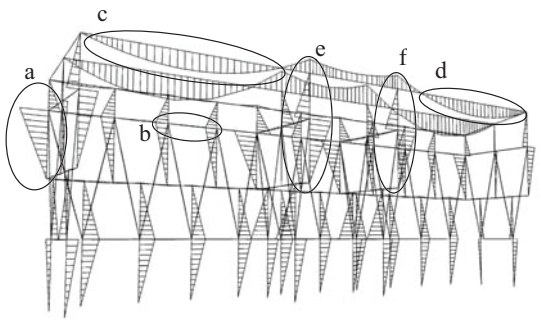

Figure 23: *Bending moment diagram of the shed when dead load and seismic load work*

From this, it can be said that the single timber can withstand up to about 8 times the vertical force and about 23 times the horizontal force.

5.4.3 Allowable stress degree calculation for Piled Beam

Similarly, we calculate the allowable stress of the Piled Beam. C and d in Figure 23 are composed of Piled Beams, which receive bending moments only in the vertical direction. Therefore, the calculation is as follows from Eq. (1).

$$\sigma = \frac{10550(N \cdot mm)}{38(mm) \times 76(mm) \times 76(mm)/6}$$

$$\sigma = 0.288398\, N/mm^2$$

Comparing this with the long-term allowable stress of 9.45 N / mm² for the lap beam in Table 7, the following results are obtained.

https://doi.org/10.52202/069179-0302

$$\sigma = 0.288398\,N/mm2 < 9.45\,N/mm2$$

From this, it was confirmed that the obtained allowable stress is smaller than the long-term allowable stress. If the safety factor is calculated in the same way as for a Single Timber, it will be as follows.

$$9.45\,N/mm2/0.288398N/mm2 = 32.76 \ldots \fallingdotseq 32.8$$

From this, it can be said that the Piled Beam can withstand up to about 33 times the force in the vertical direction.

5.4.4 Allowable stress degree calculation for Intermitted Column

Similarly, we calculate the allowable stress of the Intermitted Column. e and f in Figure 23 composed of Intermitted Column, which receives the bending moment only in the horizontal direction. Therefore, the calculation is as follows from Eq. (1).

$$\sigma = \frac{10550(N \cdot mm)}{38(mm) \times 38(mm) \times 38(mm)/6}$$

$$\sigma = 1.153594\,N/mm2$$

Comparing this with the short-term allowable stress of 6.82 N / mm² for the lap beam in Table 7, the following results are obtained.

$$\sigma = 1.153594\,N/mm2 < 6.82\,N/mm2$$

From this, it was confirmed that the obtained allowable stress is smaller than the short-term allowable stress. When the safety factor is calculated in the same way as for single materials and lap beams, it is as follows.

$$6.82N/mm2/1.153594N/mm2 = 5.91 \ldots \fallingdotseq 5.9$$

From this, it can be said that the Intermitted Column can withstand up to about 6 times the horizontal force.

From the all above calculations, it can be evaluated that the safety of this shed is maintained in small and medium-sized earthquakes and does not collapse in large earthquakes.

5.4.5 Impact on buildings due to deformation and vibration

We check if the building is hindered by vertical and horizontal deformation and vibration.

First, we evaluate the vertical weight and snow load. According to the "Deflection Limit" of the Building Standard Law in Japan, it is necessary to satisfy the condition of the following formula (2) when a fixed load and a live load are applied.

$$\frac{\delta}{\ell} \leq \frac{1}{250} \qquad (2)$$

Here, let δ = deflection amount (mm) and ℓ = member length (mm). From Figure 24, the amount of deflection in the vertical direction σ = 0.21 (mm) and the member length ℓ = 1700 (mm), so the ratio of the amount of deflection to the member length in this shed is as follows.

$$\frac{\delta}{\ell} = \frac{0.21}{1700}$$

Therefore, it can be compared with Eq. (2) as follows.

$$\frac{\delta}{\ell} = \frac{1}{3695.65} \fallingdotseq \frac{1}{3696} < \frac{1}{250}$$

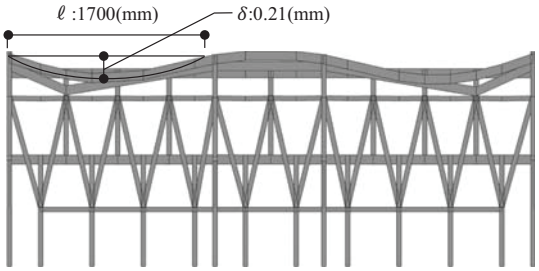

Figure 24: *Displacement diagram of the shed when vertical load works*

From the above, it can be evaluated that the building is not hindered by deformation and vibration caused by its own weight and snow load because it satisfies the deflection limit of the Building Standard Law.

Next, we evaluate the horizontal seismic load and wind load with reference to the guideline of deformation angle and damage rank in wooden buildings. There are four damage ranks: "Minor damage", "Small damage", "Medium damage", and "Great damage". When a horizontal load is applied to the shed, it is desirable that it be suppressed with minor damage, in which case the deformation angle must be less than 1/120, as in Eq. (3).

$$\frac{\delta}{\ell} \leq \frac{1}{120} \qquad (3)$$

Here, δ = deformation amount (mm) and ℓ = member length (mm). From Figure 25, the horizontal deformation amount σ = 15.08 (mm) and the member length ℓ = 1900 (mm), so the ratio of the deformation amount to the member length in this shed is as follows.

$$\frac{\delta}{\ell} = \frac{15.08}{1900}$$

Therefore, it can be compared with Eq. (3) as follows.

$$\frac{\delta}{\ell} = \frac{1}{125.99} \fallingdotseq \frac{1}{126} < \frac{1}{120}$$

https://doi.org/10.52202/069179-0302

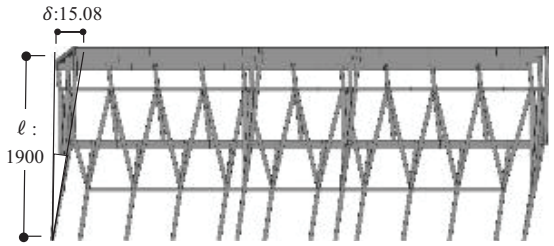

Figure 25: *Displacement diagram of the shed when horizontal load works*

From the above, it can be evaluated that the deformation and vibration caused by the seismic load and the wind load do not cause any trouble to the building because the deformation angle and the damage rank of the wooden building are satisfied.

Here, there was a difference between the comparison result with the deflection limit in the vertical direction and the comparison result with the deformation angle in the horizontal direction and the guideline of the damage rank. We give a reason for this.

Table 8: *Total amount of snowfall (as of May 11,2021)*

Municipalities	Site	Total amount of snowfall (cm)	The ratio this year: Common year(%)	Common value (cm)
Nagano City	Nagano	107	43	250
Karuizawa town, Kita-Saku District	**Karuizawa**	**35**	**30**	**117**

First, we paid attention to the snow load in the vertical direction. When snow accumulates on the upper surface of the shed, the snow load is a load that acts for a long period of time, so the vertical direction was set safely to prevent creep. In addition, as shown in lower column of Table 8, it is hard to say that Karuizawa Town, where the shed is located, is a heavy snowfall area when considering only the amount of snowfall. However, considering the frequency of natural disasters caused by abnormal weather in recent years and the damage situation, it was designed so that it can withstand sufficient strength even in the unlikely event of heavy snowfall.

Next, in the horizontal direction, we focus on earthquakes for evaluation. J-SHIS data show that the probability of earthquake occurrence within 30 and 50 years in the major active fault zone near Karuizawa Town is 0%, and that the ground amplification factor at the same site is low[9]. Therefore, it was judged that the probability of damage to the building due to the earthquake is not high.

The above are reasons for differences between the comparison result with the deflection limit in the vertical direction and the comparison result with the deformation angle in the horizontal direction and the guideline of the damage rank.

5.5 COLLATION OF SUGGESTIONS AND ANALYSIS

Using the axial force diagram obtained from the analysis, we confirm whether the structure of this shed proposed in Chapter 3 is realized. First, we proposed a "Bi-tree structure" in which a force like a continuous arch structure acts on the tree part when a vertical load is applied.

Figure 26 is an axial force diagram when a vertical load is applied to the shed. It can be seen that in the tree structure, the two thrusts generated by the decomposition of the compressive force work in opposite directions and cancel each other out.

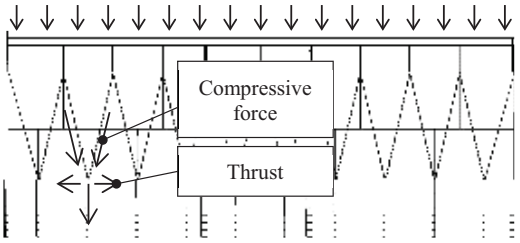

Figure 26: *Axial force diagram of the shed when vertical load works*

We also proposed a frame in which the dendritic part becomes a force flow like a brace structure when a horizontal load is applied.

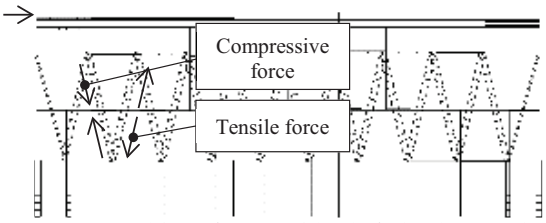

Figure 27: *Axial force diagram of the shed when horizontal load works*

Figure 27 is an axial force diagram when a horizontal load is applied to the shed. The tree part of the shed, which has a brace structure and is a diagonal lumber, bears the compressive and tensile forces, respectively.

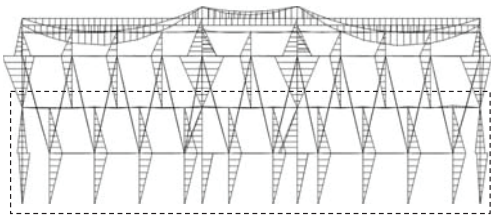

Figure 28: *Bending moment diagram of the shed when dead load and horizontal load work*

Furthermore, we proposed a frame with reference to the structure of an independent column with hanging walls, which is a traditional construction method. Figure 28 is a bending moment diagram of this shed. It can be seen that the bending moment diagram of the lower part (broken line part) of the shed that adopted the structure of the

https://doi.org/10.52202/069179-0302

independent column with hanging walls matches the bending moment diagram of the independent column with hanging walls.
Based on the collations with the above three analysis results, the structural system of this shed is as proposed in Chapter 3.

5.6 COMPARISON OF THE AMOUNT OF DEFORMATION BETWEEN ACTUAL MEASUREMENT AND ANALYSIS

We performed a manual tensile test to show the reproducibility of the analytical model and the validity of the proposal.

Table 9: *Tensile testing and deformation of analysis model*

Z, X, Y	Photo of tensile testing	Deformation (Analysis model No.2)
X-direction		
Y-direction		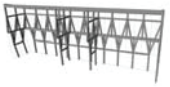
Z-direction		

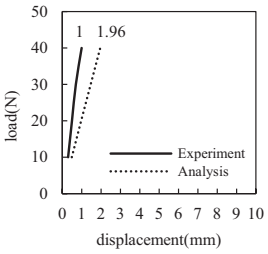

Figure 28: *Load-displacement graph of X-direction*

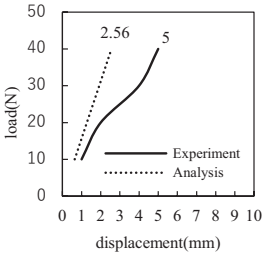

Figure 29: *Load-displacement graph of Y-direction*

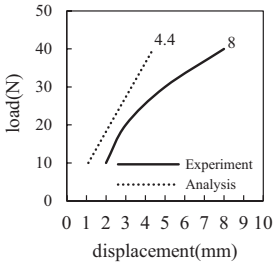

Figure 30: *Load-displacement graph of Z-direction*

As shown in Table 9, we defined three directions in the shed, and compared the amount of deformation when an arbitrary point was manually pulled in each direction with the amount of deformation when a load was applied in the analysis. The model used for the analysis is Model 2 with the exterior material. The displacement charts when a load is applied in each direction are shown in the rightmost column of Table 9, and the graphs comparing the amount of deformation in each direction are shown in Figures 28, 29, and 30.
The maximum value of the displacement error in each direction was 3.6 mm in the Z direction.
From this, it can be said that the analysis model can almost reproduce the real thing, and the proposal is valid.

6 CONCLUSIONS

In this research, we proposed a rational small-scale building structure system "Bio-tree structure" using small-diameter timber. This is a tree system that transmits the load in the shortest path when a vertical load is applied, and a structure in which the branch part becomes a tension / compression brace structure while causing bending resistance in the trunk part and allowing deformation to escape when a horizontal load is applied. In addition, we conducted a bending load test of red cedar, determined the allowable stress level indispensable for building design, calculated the allowable stress degree, evaluated the safety, and it became possible to design a small-scale building. Furthermore, we shown the validity of the proposal by performing numerical analysis and actual loading test on the proposed structural system. These are the results that suggest the possibility that small-diameter timber will be used for building structural systems in the future, and it can be expected to contribute to the development goals of SDGs "11. Creating a town where people can continue to live" and "15. Protecting the abundance of greenery", and the development of biomimetics in architecture.

ACKNOWLEDGEMENT

This work was supported by Toyo University Top Priority Research Program (2021.4～2024.3). Also, Ms. Yagi, Mr. Akimoto, Mr. Ozawa, Mr. Tobari of the Department of Architecture, Faculty of Science and Technology, Toyo University, and Mr. Hosokawa, Ms. Nakata, and Mr. Yoshinuma of the Takaiwa Laboratory of the same department were helped us. We would like to express my gratitude here. Thank you very much.

REFERENCES

[1] Ryuzo Asada and 3 others(2017)：Production Cost Structure and Cost Reduction Scenario of Woody Biomass in Japan. J Jpn For Soc 99: 187―194
[2] SHINKENCHIKU 2012 February issue :123 （SHINKENCHOKU Data）
[3] SHINKENCHIKU 2014 November Issue :136 （SHINKENCHOKU Data）
[4] Frei Otto: Natural Structure (Kajima Institute Publishing)
[5] Architectural Institute of Japan: Theory and Application of Structural Form Creation (Applied Mechanics Series (8)) Book – 2001/3/1

[6] Aidan Walker, Nick Gibbs and 3 others：The Encyclopedia of Wood:180-181
[7] Japan Housing and Wood Technology Center: Structural Wood Strength Test Manual: 8-10
[8] Architectural Institute of Japan: Deformation and Fracture in Timber Structure : 26
[9] National Research Institute for Earth Science and Disaster Prevention : J-SHIS Japan Seismic Hazard Information Station (2011)

https://doi.org/10.52202/069179-0302

World Conference on Timber Engineering Oslo 2023

MODELLING OF TIMBER STRUCTURES

Zhiyong Chen[1], Dorian Tung[2], Erol Karacabeyli[3]

ABSTRACT: Computer modelling is an essential part in the analysis and design of residential and commercial buildings as well as long-span structures. It is also a valuable tool in the development and optimisation of wood-based products, connections, and systems. A survey shows that practicing engineers are typically unfamiliar with timber structure modelling, and researchers generally lack resources for advanced modelling of timber systems. A global collaboration, including research institutes, consulting firms, manufactures, software companies, and government and associations, was initiated by FPInnovations in 2020 to develop a guide for supporting the application of numerical modelling on analysis and design of timber structures, and development and optimisation of wood-based products and systems. The guide – Modelling Guide for Timber Structures – covers a wide range of practical and advanced modelling topics, including a comparison (in terms of modelling) among timber, steel, and concrete structures; key modelling principles, methods, and techniques that are specific to timber structures; modelling approaches and considerations for wood-based components, connections, and assemblies; and analysing approaches and considerations for timber structures during progressive collapse, wind, and earthquake events. This paper provides a high-level overview of this guide, with the goal of assisting practicing engineers in application of computer modelling to timber structures, enriching researchers' resources for advanced computer modelling of timber systems; and assisting software companies to identify the gaps and upgrade programs accordingly to accommodate advanced computer modelling of timber structures.

KEYWORDS: Timber structures, digital twins, performance-based design, modelling, analyses, optimisation

1 INTRODUCTION

Computer modelling is an essential part in the analysis and design of residential and commercial buildings as well as long-span structures. It is also a valuable tool in the development and optimisation of wood-based products, connections, and systems. A survey by FPInnovations [1] shows that practicing engineers are typically unfamiliar with timber structure modelling, and researchers generally lack resources for advanced modelling of timber systems. Furthermore, wood analysis and design modules currently implemented in a few structural analysis software packages are usually not suitable for complex or hybrid timber structures. This will hinder the application and development of timber construction given that timber structures increasingly require demonstration of performance or equivalency through computer modelling, regardless of whether prescriptive or performance-based design procedures are used.

A global collaboration (Figure 1), including research institutes, consulting firms, manufactures, software companies, and government and associations, was initiated by FPInnovations in 2020 to develop a guide for supporting the application of numerical modelling on analysis and design of timber structures, and development and optimisation of wood-based products and systems. The guide – Modelling Guide for Timber Structures [2] (web.fpinnovations.ca/modelling) – has been developed by selecting efficient modelling methodologies and analysis methods, and robust evaluation criteria for timber structures: seismic response, wind-induced response, and progressive collapse robustness; and developing basic principles for the application of computer modelling in timber building design, including modelling assumptions, validation of assumptions and modelling results, and demonstrating compliance with the building code. The guide consists of three parts: Part A – Introduction (in green), Part B – Modelling (in red), and Part C – Analyses (in blue), see Figure 2.

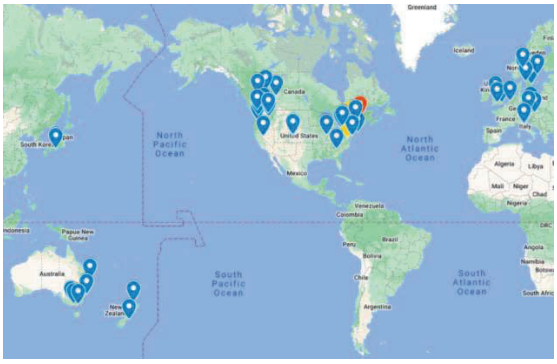

Figure 1: *Locations of more than 100 global collaborators*

[1] Zhiyong Chen, FPInnovations, Canada, zhiyong.chen@fpinnovations.ca
[2] Dorian Tung, FPInnovations, Canada, dorian.tung@fpinnovations.ca
[3] Erol Karacabeyli, FPInnovations, Canada, erol.karacabeyli@fpinnovations.ca

https://doi.org/10.52202/069179-0303

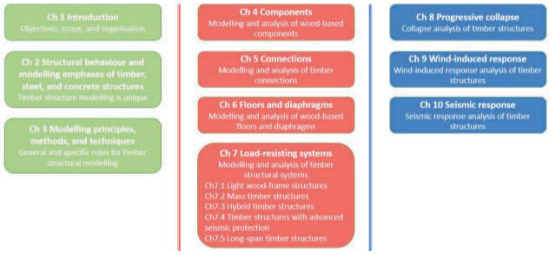

Figure 2: *Organisation of modelling guide*

This paper provides a high-level overview of this guide, including a comparison among timber, steel, and concrete structures, in terms of modelling emphases; key modelling principles, methods, and techniques specific for timber structures; modelling approaches and considerations for timber components, connections, floor diaphragms, and load resisting systems; and analysis approaches and considerations for timber structures during progressive collapse, wind, and earthquake events.

2 DIFFERENCE AMONG TIMBER, STEEL, AND CONCRETE STRUCTURES

Every structural material has unique mechanical characteristics. Consequently, different design strategies have been adopted for structural systems using different materials to optimise the material use. The structural behaviour and modelling emphases of structural systems with different materials vary accordingly.

Steel is a ductile material and is generally considered to be a homogeneous, isotropic, elastoplastic material with equal strength in tension and compression. Reinforced concrete (RC) is a composite material that is concrete into which steel reinforcement bars, plates, or fibres have been incorporated, where the two materials work together, with concrete providing the compressive strength, and steel providing the tensile strength primarily. While wood has characteristic anisotropy due to its fibrous structure, which can be considered as producing three-dimensional orthotropy. Its stiffness and strength properties vary as a function of grain orientation among the longitudinal, radial, and tangential directions. The failure modes and the stress-strain relationships of wood depend on the direction of the load relative to the grain and on the type of load (tension, compression, or shear). For wood in tension and shear, the stress-strain relationship is typically linear, and the failure is brittle, while for wood in compression, the stress-strain relationship is typically nonlinear, and the failure is ductile.

Due to their high strength-to-weight ratio, steel elements are, in general, relatively slender. The design should account for the buckling resistance of slender steel compression and bending elements. Care is needed to ensure that connections do not unduly influence the overall response of a steel structure, especially for seismic design. As a composite material, maintaining composite action requires the transfer of load between the concrete and steel that is achieved by means of bond (anchorage). Thus, detailing of reinforcement, particularly for seismic conditions, is a key design aspect for RC structures. Because of their anisotropic mechanical properties, timber elements possess much higher stiffness and strength in the parallel-to-grain direction than in the perpendicular directions. Due to the presence of growth characteristics (e.g., knots), which significantly impair the tension and shear strength of wood, timber elements are most suitable for use in resisting compression parallel to the grain, followed by bending. Tension strength parallel-to-grain is as good or better than compression strength parallel-to-grain; however, the tension connections are prone to brittle failure. Tension perpendicular to the grain should be avoided or minimised in timber elements whenever possible because the capacity of wood in this direction is limited, and any splits effectively remove this capacity altogether. The main area that requires attention in the design of timber structures is connections. Timber connections typically govern the strength of timber structures, either light wood-frame structures or mass timber structures and can contribute significantly to the stiffness of the structures.

To model steel elements and connections, material models must simulate the homogeneous, isotropic, and elastoplastic behaviour of steel. For simple or equivalent models, RC elements can be simulated using elastic material models with effective stiffness, while an inelastic mechanism can be simulated using plastic hinges. With respect to complex or detailed models, typically, the constitutive response of the concrete and reinforcement comprising the RC are modelled separately. Timber elements generally can be simulated using orthotropic elastic material models. In some cases, such as balloon-type mass timber walls, elastoplastic behaviour of timber elements must be included in the material models at the wall bottom that connects to the foundation. Compared to other connections, timber connections are much more complex due to the highly variable anisotropic mechanical properties of wood, existing growth characteristics such as splits and knots, and other effects, such as moisture content and temperature. Various types of failure modes can occur in timber connections, and they should have ductile failure modes, such as yielding, rather than brittle modes, such as splitting. When properly designed, timber connections can be simulated using models that represent the connection stiffness and strength. For analysing timber systems under cyclic loading, suitable hysteretic models are required to accurately reflect the structural response of timber connections and assemblies, as these may possess highly pinched hysteresis and degradation of strength and stiffness.

General comparisons, in terms of material and structural behaviour, and modelling emphases, among timber, steel, and RC are presented in Chapter 2 of the modelling guide. Selected timber structural systems with analogous ones from steel and concrete are also compared.

https://doi.org/10.52202/069179-0303

3 MODELLING PRINCIPLES, METHODS, AND TECHNIQUES

3.1 PRINCIPLES

To obtain the best possible analysis results, it is important that engineers follow a formal modelling process that is based on sound engineering and finite element (FE) analysis principles. A typical modelling process includes the following key elements: (a) understanding the structure and planning the modelling process; (b) selecting the software; (c) developing the analysis model; (d) verifying the results; (e) performing a sensitivity analysis; and (f) deciding on the accepted model and results. General and specific principles, in terms of the modelling process, model development, model validation, result verification, model interpretation, and competence are introduced in Chapter 3 of the modelling guide.

3.2 METHODS

Various numerical modelling methods are available for simulating the behaviour of structures under different loading conditions. Mechanics-based modelling, FE modelling, hybrid simulation, and material-based modelling are introduced in the modelling guide. Only the former two are briefly summarised in this paper.

3.2.1 Mechanics-based Modelling

Mechanics-based modelling, also called analytical modelling, is used to calculate the forces and deformation in a structure induced by various actions through applying engineering principles and fundamental mechanics. It usually involves establishing and solving equilibrium, compatibility, and constitutive equations. Hand calculation or any engineering calculation program can be adopted depending on the complexity of the equations. Mechanics-based models provide simple methods that help understand and predict the performance of structures. Such models are suitable for conceptual designs and for verifying the results obtained from complex FE models. Once such models are developed, the analysis of corresponding structures with various key parameters (e.g., sensitivity analysis) is straightforward. These types of models are more suitable for analysing relatively simple problems (e.g., static performance) of uncomplicated structures (e.g., elastic material behaviour and/or boundary conditions). With respect to structures for which mechanics-based models do not exist or their development outweighs the benefit, FE modelling is a more efficient approach.

3.2.2 FE Modelling

In this modelling approach, the major structural components and connections are developed using any FE-type software. The software develops and solves equilibrium equations, compatibility equations, and constitutive equations. Problems ranging from simple to complex (e.g., time-history analysis) and models with different levels of complexity (e.g., nonlinear material behaviour and boundary conditions) can be analysed by FE modelling, which is usually limited by software capacity (e.g., material models).

In terms of model scale, two types of models are available: microscale and macroscale. Microscale models form a broad class of computational models that simulate fine-scale details. In contrast, macroscale models amalgamate the details into selected coarse-scale categories. The goals and complexities of the models determine which modelling scale is used for a specific work. In the area of structural engineering, microscale models are commonly used in analyses of structural components and connections, with testing results of materials as model input. These models focus on how the behaviour of the modelled object is influenced by its geometric and material properties. In contrast, macroscale models are widely used in the analyses of structural assemblies and entire buildings. For structures where the storey shear deformation is the major component induced by lateral loads, such as low-rise light wood-frame buildings, mass-spring-damper (Macroscale) models can be used to simulate the entire building or the main lateral load-resisting assemblies at each storey. When bending deformation cannot be ignored under lateral loads (e.g., balloon-type mass timber shear wall structures), mass-spring-damper models are no longer suitable, and the lateral load-resisting assemblies must be modelled in a relatively more detailed approach. The connections in these assemblies, however, can be simulated using suitable nonlinear hysteretic springs.

In the FE modelling approach, the major structural components and connections should be developed using any type of software. Because of the anisotropic material characteristics of wood, orthotropic material properties are required for the 2D or 3D model input for wood-based products. When the capacity design is used, the timber structural components that are capacity-protected can be modelled as orthotropic elastic members.

Connections play a critical role in any timber structural model in terms of stiffness, ductility, and energy dissipation of the entire system. Connections that experience semirigid behaviour can be modelled using spring or connection elements. In cases of conducting nonlinear analyses (pushover or nonlinear dynamic analysis), suitable backbone curve models that can represent the yielding and post-yield behaviour of the connections, as well as hysteretic models that can represent the energy dissipation and the pinching effect of timber connections, must be used. As timber connections have high variability in stiffness and strength, the ranges of these parameters must be established during modelling, and the lower and upper bounds of the connection mechanical properties should be considered. Specific key connections should be considered as semirigid joints when calculating the deformation or stiffness and the natural period of vibration of the building. Upper bound limits should also be used when analysing the natural period of vibration of the buildings because simplified numerical models can easily produce unrealistically high and therefore nonconservative natural vibration periods.

https://doi.org/10.52202/069179-0303

Floor and roof diaphragms as horizontal assemblies distribute the gravity and lateral loads to load-resisting assemblies underneath. Diaphragm flexibility is a key factor affecting the lateral load distribution to the walls and other elements below. It is suggested that diaphragms be modelled in the structural models according to their stiffness and deformability characteristics. Nonstructural components, such as gypsum wallboard, provide considerable additional stiffness to lateral load-resisting systems. Engineers must exercise judgment about whether the contribution of nonstructural components should be considered in the model.

3.3 TECHNIQUES

Due to the highly variable anisotropic mechanical properties of wood, this variability has to be accounted for in the design and analysis of timber structures. The stochastic FE method (SFEM) accounts for the uncertainty of a structure that occurs as a result of variations in geometry, materials, or loading condition, thus being one of the best modelling approaches to quantify or predict the influence and sources of randomness in timber structures. Monte Carlo simulation, perturbation method, and the spectral SFEM are the most commonly used and accepted SFEM. Each method adopts a different approach to represent, solve, and study the randomness of a structure. Computational structural design, including parametric analysis, structural optimisation, and form-finding, can influence or enable the exploration of design space. Its application will dramatically improve the efficiency of identifying the best solutions for the structural design of geometrically complex or free-form timber structures.

BIM is a technology-driven integrated digital process that uses intelligent geometric and data models to provide coordinated, reliable information about a project throughout its entire life cycle. With the BIM revolution, the focus has been on the M—modelling: creating accurate and highly detailed models and drawings which represent the design, effectively creating digital twins (Figure 3). However, the building industry does not merely need increasingly more detailed 3D models; it needs a design for manufacture and assembly (DfMA) process to increase design and on-site efficiency while systematically reducing construction change orders.

Figure 3: *Digital twin model of UBC Brock Common*

4 MODELLING OF WOOD-BASED COMPONENTS

4.1 CONSTITUTIVE MODELS AND KEY INFLUENCING FACTORS

Wood is an anisotropic material. Because of its inherent characteristics, the mechanical behaviour of wood depends on the direction of the grain and the load type, as illustrated in Figure 4. Appropriate material models are the fundamental basis of reliable simulations.

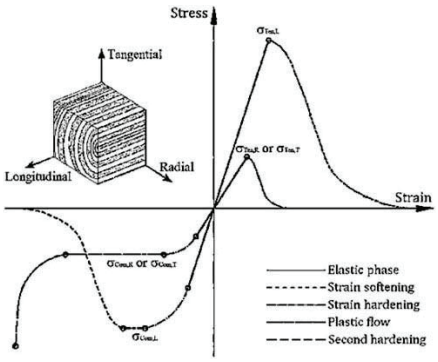

Figure 4: *Typical stress-strain behaviour of wood*

The constitutive models incorporated in existing general design software packages are often limited, making the software unsuitable for accurately predicting the mechanical behaviour and failure modes of wood-based materials. Some researchers have developed specific constitutive models for wood-based members, e.g., Wood^{S} and WoodST. Typically, a material model is composed of sub-models for describing the elastic properties, strength criterion, post-peak softening for quasi-brittle failure modes, plastic flow, and hardening rule for yielding failure modes, and densification perpendicular to grain. Depending on the modelling complexities, scenarios, and demands, however, different constitutive models with various combinations of the sub-models can be adopted.

As tall or large timber structures are becoming a viable option in the construction industry, the structural elements and connections are becoming more complex, and the corresponding design is beyond the compatibility of general design software packages. Designers can still carry out the design using any tools by making more assumptions. The design as well as the assumptions must be verified by testing, numerical simulation, or both. In such a scenario, general purpose FE software with a comprehensive constitutive model of wood-based material is the first choice for the simulation. A comprehensive constitutive model can predict potential failure modes, including those that may be overlooked in design, providing more reliable analysis results to support the design. With the appropriate constitutive model, the strength, stability, and deflection problems of wood-based members can be investigated and evaluated. The outputs still need to be interpreted carefully using engineering judgment.

https://doi.org/10.52202/069179-0303

The mechanical properties of wood change as temperature, moisture, and loading time change. Moreover, growth characteristics such as slope of grain and knots significantly affect the mechanical behaviour of wood-based products. These key influencing factors are discussed in Chapter 4.1 of the guide along with corresponding modelling recommendations.

4.2 STRUCTURAL COMPONENT ANALYSIS

Analyses of timber components under various loads are essential for structural design and product optimisation. Numerous studies have been conducted on traditional wood-based products such as lumber. However, there is limited information on newer wood products such as cross-laminated timber (CLT), nail-laminated timber (NLT), dowel-laminated timber (DLT), and other types of composite components.

Of the two approaches used in the analysis and design of timber components, analytical models are very efficient for the specific cases for which the models have been developed. FE methods are capable of handling complex cases and can provide results that are more comprehensive than those provided by analytical methods. Eigenvalue buckling, linear load-displacement, and nonlinear load-displacement analyses are usually adopted to analyse timber components in FE modelling. Linear analysis is the most common method to determine the deformation, reaction, and stresses when an element is in its elastic stage. With engineering adjustment, the lower bound of resistance and the corresponding failure mode of the components can be predicted manually based on the results of linear elastic analysis, for example, stress distribution and the highest stress, for simple cases. Eigenvalue buckling analysis is commonly used to derive buckling resistances and mode shapes for beams and columns. This analysis is best suited for walls, slender beams, and columns where the members are likely to buckle in the elastic range. Nonlinear analysis is capable of predicting the resistance, failure modes, and post-failure behaviour of analysed components, with or without imperfection (e.g., post-buckling analysis). This analysis requires more refined models, or comprehensive material models and specific input. Key considerations, such as imperfection for the post buckling analysis of columns (Figure 5) and beams, for modelling wood-based components under various loading conditions can be found in Chapter 4.2 of the modelling guide.

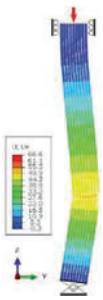

Figure 5: *Deformation (deformation scale factor = 3) of a glulam column under a vertical point load*

4.3 MODELLING PROCESSES AND PROPERTIES OF STRUCTURAL WOOD PRODUCTS

The development of new wood-based products, plus the optimisation of existing products, plays a key role in the expansion of timber construction, especially for taller and larger structures. Manufacture of wood-based products, however, is complex, involving a variety of influencing factors—the properties of the constituents, the structure, and the many parameters of the manufacturing process. Traditional product development and optimisation usually uses trial-and-error laboratory experiments and mill trials, or empirical approaches. While they can offer direct and short-term solutions, experimental studies are generally time consuming and expensive to run; more importantly, they have limitations in providing fundamental understanding. Modelling offers an efficient and cost-effective approach to advancing wood science and industrial composites manufacture. It applies mathematics, physics, and mechanics principles and computer numerical simulation techniques to the field of wood composites. Modelling also helps understand the complex manufacturing process and optimises the product performance by reducing the number and scope of experimental variables.

The production and quality control process are straightforward compared with hot-pressed veneer and strand composites, very few process models are available for lumber-based productions. Many structural models, including empirical models, probabilistic models, and FE models, have been developed for glulam and CLT, to investigate the influence of lumber grades, layup arrangement of graded lumber, species, density, and defects. Several phases of veneer and veneer-based products require careful attention to material and process control as these feed into and affect subsequent steps as well as final product quality and performance. Such processes include log conditioning/heating, peeling, defect and moisture detection, veneer-ribbon clipping, veneer drying, glue application, panel layup, prepressing, and hot-pressing. A series of computer simulation and optimisation models for almost all stages of the process of veneer and veneer-based product manufacture have been developed. FE models are usually used for the mechanical modelling of veneer-based product. Integrative models can be developed on three essential parameter sets for the entire manufacturing process of strand-base products. The first parameter set defines the constituents from which wood composites are made: mainly wood, resin, and wax. The second parameter set defines the structure (the spatial organisation) of the constituents: density, strand orientation, porosity, and contact. The final parameter set concerns major processing steps: strand preparation, drying, blending, forming, and pressing. Various physical models have been developed to simulate strand cutting (from bamboo culms); particulate or strand drying; resin; mat forming and consolidation; and hot-pressing. FE modelling, multiscale modelling, and integrated modelling are used to predict the mechanical properties of strand-based products. Figure 6 illustrates an integrated

https://doi.org/10.52202/069179-0303

model for LSL. More detail information can be found in Chapter 4.3 of the modelling guide.

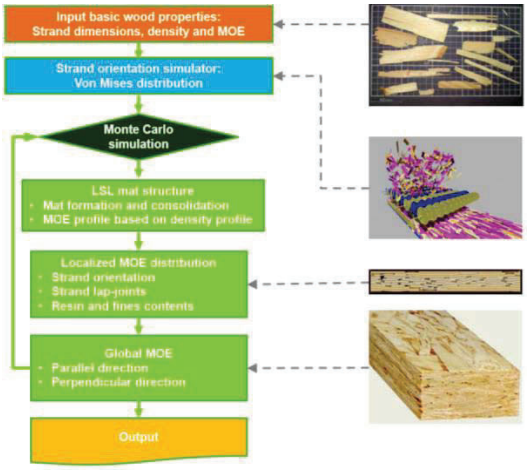

Figure 6: *Schedule diagram of an integrated model for predicting the MOE of LSL*

5 MODELLING OF WOOD-BASED CONNECTIONS

Connections play a crucial role in the integrity and load-resisting mechanism of structures. Well-designed timber connections with mechanical fasteners are usually characterised by highly nonlinear behaviour, strength and stiffness degradation, and pinching effect on their hysteresis loops. All these aspects may pose significant challenges for modelling of timber connections (Figure 7) and how they interact with other elements in the structure.

When modelling timber connections in structures, depending on the purpose of the model, it may be necessary to model the response of the connections, providing upper and lower bounds, particularly for the yielding resistance. These are often built-in to typical backbone curve forms provided in analysis software. When considering modelling stability, it is often useful to implement a post-failure tail to ensure model stability. Where a nonlinear time-history analysis is required, it is also important to properly implement the correct hysteresis form. The main features shown in typical hysteresis loops of timber connections include (a) nonlinear connection behaviour, (b) slightly asymmetric loops, (c) indistinct yield point, (d) stiffness degradation with increasing load cycles, (e) relatively fat initial hysteresis loops that imply large amounts of energy dissipation, (f) narrowed loop areas (pinching effect) in the middle of the hysteretic loops after the first load cycle, (g) strength degradation at the same deformation level for repeating loading cycles, (h) strength degradation for larger deformations, and (i) relatively high values of ductility. Therefore, a hysteretic model capable of predicting stiffness and strength degradation, along with the pinching effect, is desirable for timber connections. During the past several decades, various types of hysteretic models have been developed for dynamic analysis of timber connections and structures. Generally, they can be categorised as three major types: mechanics-based models, piecewise linear functions models, and mathematical models. Chapter 7.1 of the modelling guide discusses the backbone curve and hysteretic models in detail.

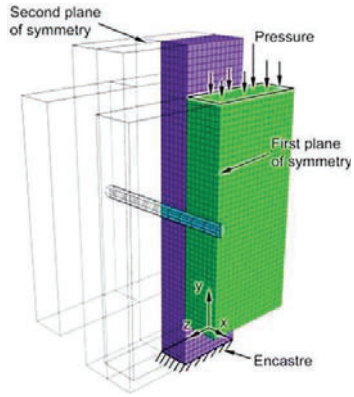

Figure 7: *FE model for bolted connection [3]*

The steel dowel type and glued-in-rod type connections, which involve timber and steel materials, are more complex than the other types of connections composed primarily of steel. Efficient models, e.g., European yield model, have been developed for predicting mechanical properties of ductile failure modes of dowel type connections. However, the brittle failure modes typically can be precited by FE modelling. In such cases, the timber, steel, and contact between them, e.g., gap or glue, must be simulated using proper elements and constitutive models. Figure 8 illustrates modelling examples for dowel type connections.

More information, e.g., the structural behaviour, failure mechanism, design considerations, modelling methods, and key considerations of timber connections can be found in Chapter 5 of the modelling guide.

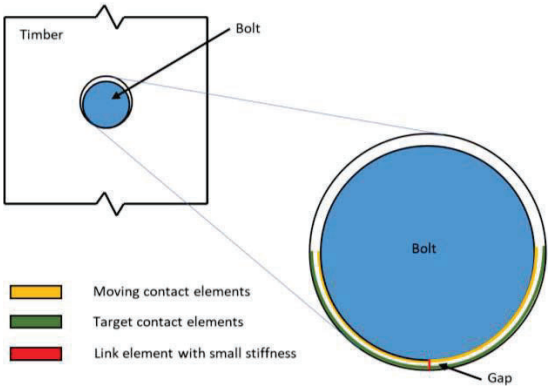

Figure 8: *Example where contact elements are used between fastener and timber*

https://doi.org/10.52202/069179-0303

6 MODELLING OF WOOD-BASED FLOOR DIAPHRAGMS

6.1 FLOOR AND ROOFS

Timber-based roofs and floors, whether light wood-frame, mass timber, or timber-concrete composite (TCC) systems, are complex structures to analyse despite their relatively simple construction. This is because they are constructed with multiple components and multiple materials that are often connected by mechanical fasteners, leading to semi-rigid connections between components, which is called composite action.

In analysing the structural performance of floor systems, composite beam and ribbed-plate models are available. The ribbed-plate models are typically only used for light wood frame floors to account for its two-way action. There are two main categories of beam models in composite systems: continuous bond models and discrete bond models. The continuous bond models, where the connections are modelled as evenly distributed, include the Gamma method and the Shear Analogy method, among others. The discrete bond models, where the connections are modelled as individual members, include beam models with rigid-perfectly plastic connections or elastic-perfectly plastic connections (also called progressive yielding model, release-and-restore method). Continuous bond models are more suited for composite systems with continuous connections or uniformly distributed connections that are closely spaced, while the discrete bond models are more suited for discontinuous connections. Because of their complexity and efficiency, discrete bond models are usually applied to composite systems with nonuniformly and widely spaced distributed connections, for example, TCC floors.

While most floors and roofs can be designed using the analytical approaches, advanced modelling methods such as FE models can be used for cases beyond the scope of the analytical methods and the system development and optimisation. Framework/truss model (Figure 9) and space-exact element model are two typical FE models for floor systems. More details regarding the analytical and FE models, general rules, and specific consideration for developing FE models for different types of floors are provided in Chapter 6.1 of the modelling guide.

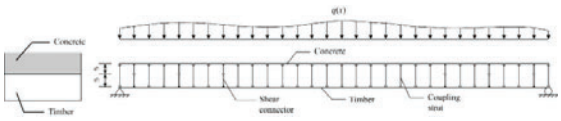

Figure 9: *Framework model*

6.2 DIAPHRAMGS

Diaphragms not only transfer any horizontal load to the vertical lateral load-resisting system (LLRS) but also tie all structural and nonstructural elements together, providing integrity to a building. Several different analysis methods and approaches that can serve to analyse diaphragms include deep beam/girder analogy, shear field analogy, truss analogy, and FE methods. Beam analogy methods provide satisfactory results, as long as the floor is rectangular and does not contain substantial irregularities, such as floor openings, re-entrant corners, and concentrated forces. These influence the load path, leading to stress concentrations, and therefore require more specific designs. The shear field analogy provides a reasonably easy method to analyse wood frame diaphragms with irregularities like openings or re-entrant corners. As the number of irregularities increases, however, this method, based on hand calculations, soon becomes too complex. The assumptions of the shear field analogy are very often violated in real structures. Loads not applied via the framing elements in their axial direction, as well as displacement incompatibilities, cause inconsistencies in the method. The truss analogy can be seen as a compromise between a simple approach like the girder analogy and a sophisticated FE analysis. It allows for irregular geometries and provides a clear force path through all involved members. Complex geometries might need a refined mesh, resulting in a number of different diagonals. Because the forces are introduced as concentrated loads in the nodes, some calculated results (like the axial force in framing members) require post-processing to account for the real force distribution along the member length.

FE analysis of diaphragms provides the most realistic load path and information on the general performance of the diaphragms, but it also requires a high degree of knowledge about the specific software package and a larger number of input parameters. A designer must determine the level of analysis required for the specific diaphragm. For timber diaphragms, this can range from elastic models with homogenous material parameters that have reduced shear stiffness to account for fastener stiffness to orthotropic panels connected with discrete nonlinear links to model the individual fasteners (Figure 10b). Designers need to decide which approach best suits the given problem and what level of accuracy is required. More details on the modelling and design of wood-based diaphragms are presented in Chapter 6.2 of the modelling guide, along with connection options linking diaphragms to lateral load-resisting systems.

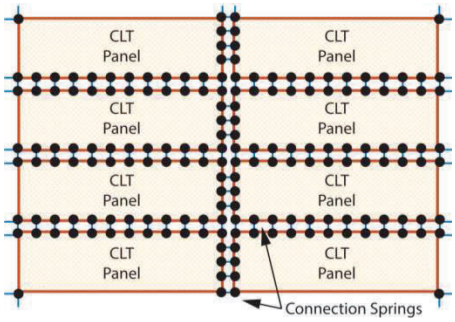

Figure 10: *Discrete panel model with spaced connections [4]*

https://doi.org/10.52202/069179-0303

7 MODELLING OF LOAD-RESISTING SYSTEMS

7.1 LIGHT WOOD-FRAME STRUCTURES

Light wood-frame buildings are constructed using dimensional lumber framing and wood-based sheathing connected to each other with metal fasteners. This type of system has been dominated in timber engineering for a long while and been investigated intensively. Elastic model, plastic models with upper bound method (Kinematic theorem) and lower bound method (static theorem) are the three main analytical models for light wood-frame buildings, the last one has been adopted by many countries' standards to design this system. Regarding advanced FE modelling methods, this system can be simulated using either very detailed models that includes lumber, panels, and nails, or macro-element models where each wall or diaphragm assembly is simulated using an equivalent spring. For both types of models, backbone curve and hysteretic model play a crucial rule in the performance of this system. Generally, mechanics-based models, empirical models, and mathematical models are the three main types of hysteretic models for timber structures. For practical analyses, the shear walls can also be simulated using stick and rotational spring model or equivalent beam model. More information regarding the structural behaviour and modelling considerations can be found in Chapter 7.1 of the modelling guide.

7.2 MASS TIMBER STRUCTURES

Mass timber structures are a viable solution for taller and larger construction. The existing pure mass timber lateral load-resisting systems include platform-type shear walls, balloon-type shear walls, braced frames, and moment frames.

CLT shear walls are the latest lateral load-resisting system of timber structures accepted by codes and standards around the world, while RC shear walls are a system made of other materials that is most similar to CLT shear walls. Unlike RC shear walls, CLT panels are typically capacity-designed, and the connections govern the capacity of the CLT shear walls. CLT panels can be modelled as orthotropic plates, and the connections must be simulated using specific models to represent their stiffness, strength, plastic deformation, and even the hysteretic behaviour, see Figure 11. Braced frames are essentially planar vertically cantilevered trusses. Unlike braced steel frames, braced timber frames yield and dissipate energy primarily through energy-dissipative connections. The diagonal brace assembly or the two end connections must be modelled with equivalent spring elements that can represent their stiffness, strength, plastic deformation, and hysteretic behaviour, while other timber elements can be modelled as elastic truss or beam elements. Moment-resisting frames are rectilinear assemblages of beams and columns, with the beams rigidly connected to the columns. Unlike in moment-resisting frames using steel or concrete, the inelasticity of timber moment-resisting frames is typically concentrated in the beam-to-column connection area due to the nonlinear response of the connections. The beams and columns can be simulated using elastic beam elements, while the connections are modelled using linear or nonlinear spring elements. More information regarding the analytical models and FE modelling considerations for each type of mass timber systems can be found in Chapter 7.2 of the modelling guide.

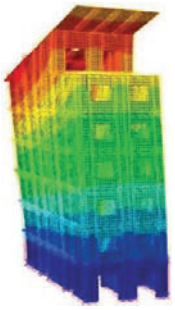

Figure 11: *FE model of a 7-storey CLT building [5]*

7.3 HYBRID TIMBER STRUCTURES

One solution with significant potential for the increased use of wood beyond previous limitations, e.g., building height, involves 'hybrid structures' that integrate wood with different materials. Hybridisation is the process of combining two or more materials to form a system that makes use of the strength of each material and simultaneously overcomes their individual weaknesses.

The gravity load resisting system (GLRS) and LLRS of a hybrid timber structure are typically analysed separately. A main reason for this is to simplify the design by limiting the model contribution of the GLRS to the LLRS, and vice-versa. To conduct a seismic analysis of hybrid timber structures using FE models, it is possible to consider i) the LLRS only; ii) LLRS with connecting GLRS only using appropriate boundary conditions; and iii) both the LLRS and GLRS. For the first approach, one should apply the seismic forces calculated by the ESFP, distributed to the individual LLRS components based on diaphragm flexibility, as a lateral point load at each level. For buildings with core or irregularly shaped LLRSs, the second approach is generally better for determining complex lateral force distribution. The third approach for seismic analysis considers the full building with a complete LLRS, with or without a GLRS, respectively. Special considerations for the design, modelling, and analysis of such structures are provided in Chapter 7.3 of the modelling guide in detail.

7.4 TIMBER STRUCTURES WITH ADVANCED SEISMIC PROTECTION

Timber structures traditionally provided satisfactory seismic performance due to such features as a light weight, high strength-to-weight ratio, structural redundancy, elastic deformation capacity, and the ductility of connections. Nowadays, however, they aim for greater heights and longer spans, resulting in

https://doi.org/10.52202/069179-0303

challenging seismic designs. Rather than increasing the seismic resistance of a structure, more recent work applies advanced seismic protection technologies to reduce the seismic demand from other structures on those made of timber. Such seismic protection technologies can be grouped into supplemental damping, rocking systems, and seismic isolation.

Modelling Press-Lam systems (Post-tensioned shear walls and moment frames) can involve two main categories of model. The first are spring type models, including the rotational spring models and multi-spring models, with either the rocking connections or the gap opening mechanics simulated using spring elements. The second are material- or component-based models, with geometric and material properties as input. The modelling methods for mass timber structures discussed in Section 7.2 are applicable to timber structures with resilient slip friction joints (RSFJs), but RSFJs are different from common timber connections. The models should properly simulate the RSFJ's flag-shaped hysteresis loops. It is advisable to connect the seismic fuse to another link that accounts for the actual stiffness of the connection between the damper and the remaining timber structural element. The modelling of the seismic isolation plays a key role in the analysis of timber structures with seismic isolation. Typical numerical models include plasticity model for coupled shear behaviour, Bouc-Wen model for coupled shear behaviour, advanced model for elastomeric and lead-rubber bearings, extension of bidirectionally coupled models to friction pendulum behaviour, model for tension-capable double pendulum bearing, and model for triple pendulum bearing. More information regarding mechanics-based modelling and advanced modelling methods is provided in Chapter 7.4 of the modelling guide, along with corresponding recommendations.

7.5 LONG-SPAN TIMBER STRUCTURES

Long-span timber structures are usually adopted by stadiums and bridges. Typical structural forms include trusses, portal frames, arches, suspended structures, and domes. Such long-span structures, like roof applications, are typically designed based on static (strength and stability) analyses, however, dynamics often govern the design of some types of long-span structures, e.g., pedestrian bridges and floors. Free-form systems are also an aesthetically attractive and structurally viable options for long-span timber structures. Dynamic relaxation, among others, is an efficient method in form-finding of free-form structures. The modelling approaches discussed in the above sections, i.e., Sections 7.1 to 7.4, can apply to long-span structures, however, some specific modelling methods or tricks have been developed specifically for long-span timber structures, e.g., how to consider the connections at the end of web members in a truss analysis, how to consider the risk of both in-plane and out-of-plane buckling in an arch analysis, whether the first-, second-, or third-order analysis is more suitable for timber-based suspend structures, and the importance of consideration of geometric imperfections in the analysis of domes. The analysis and modelling of the typical structural types of long-span timber structures are described in detail in Chapter 7.5 of the modelling guide, with corresponding recommendations.

8 PROGRESSIVE COLLASPE

Progressive collapse is a phenomenon initiated by local damage to a structure that propagates throughout the structural system in a chain reaction, leading to the partial or entire collapse of the structure, see Figure 12. Typical design and analysis approaches of progressive collapse include tie forces, redundancy, alternative load paths (ALPs) for static analysis and dynamic analysis, compartmentalisation, and the key element method. In the modelling of both platform-type shear wall systems and post-and-beam systems, the model of connections plays a crucial role and needs load-deformation curves as input. The difference between the platform-type buildings and post-and-beam buildings is in the modelling of the beam-to-column connections where it is needed to quantify their residual shear capacity after they undergo large deformation. Model development and analysis of shear wall systems and post-and-beam systems are described in detail in Chapter 8 of the modelling guide. Key modelling considerations for the progressive collapse analysis of hybrid systems, long-span structures, and prefabricated module structures are also provided.

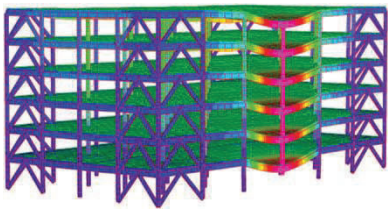

Figure 12: *Progressive collapse analysis of a timber structure*

9 WIND-INDUCED RESPONSE ANALYSIS

Within wind engineering literature and practice, it is generally recognised that wind forces govern the structural design of lightweight and flexible buildings for both safety and serviceability limit states. In general, the action of wind (Figure 13) on tall timber buildings depends on wind hazard, nearby buildings, terrain conditions, building shape, and dynamic structural properties, which is described in the wind loading chain.

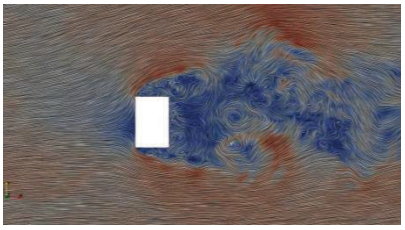

Figure 13: *Wind field around a building*

Wind tunnel techniques are typically used to assess the design wind loads and dynamic wind response of

buildings, while computational fluid dynamics (CFD) simulation is adopted for preliminary design and aerodynamic optimisation applications. As with wind tunnel studies, when modelling wind effects using CFD, care must be taken at each step of the wind loading chain. The structural wind-induced response analysis methods mainly include frequency domain analysis method and time domain analysis method. Among them, the frequency domain method uses Fourier transform to transform the wind load into a series of simple harmonic loads, and finally superimposes the response of the structure under each simple harmonic load to obtain the total response of the structure. The disadvantage of this method is that the non-linearity of the structure cannot be considered, and the calculation results are not accurate enough. The time-domain analysis method is to directly use the wind pressure time history of the wind tunnel test or the wind pressure history of the numerical simulation to be used in the calculation model. The response of the structure can be obtained by directly solving the motion equation in the time domain, and the nonlinear response of the structure can be considered. In addition to the above analyses and modelling with key considerations, a framework for the wind design of timber buildings and performance-based wind engineering approaches are also introduced in Chapter 9 of the modelling guide.

10 SEISMIC RESPONSE ANALYSIS

Seismic response analysis is a crucial evaluation of timber structures in earthquake-prone areas. There are two main types of static analysis: linear and nonlinear. Nonlinear static analysis is used where a structural system is expected to experience changes in its strength and stiffness properties with varying loads over time. There are different approaches for performing nonlinear static pushover analyses and calculating the target displacement. The two most prevalent in North America are the so-called coefficient method and the capacity spectrum method, while in Europe the N2 method is widely used. Response spectrum analysis is a linear dynamic analysis method which determines the contribution from each natural mode of vibration (Figure 14) on structural performance. It provides insight into dynamic behaviour by measuring pseudospectral acceleration, velocity, or displacement as a function of structural period for a given level of damping, thus being accepted as a standard analysis method in many standards. The time-history analysis provides an evaluation of the time evolution of the building response. Generally, two types of time-history analyses can be performed: linear and nonlinear. Both approaches require a numerical model with its characteristics tuned well to represent the lateral resistance mechanism of a real structure, and properly selected and scaled ground motions. Detailed information related to different types and methods of static and dynamic analyses used to quantify the seismic response of timber structures is provided in Chapter 10 of the modelling guide, along with their advantages and drawbacks. It also highlights the specific modelling requirements and considerations for different types of seismic response analyses, along with their suitability for timber structures.

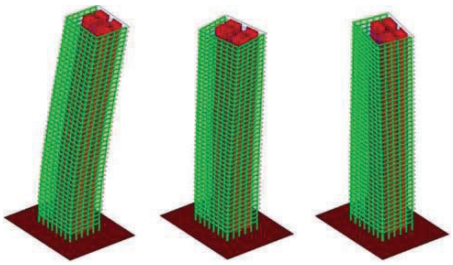

Figure 14: *Mode shapes for the first three modes [6]*

11 SUMMARY

This paper provides a high-level overview of the Modelling Guide for Timber Structures, with the goal of assisting practicing engineers to apply computer modelling to timber structures, enriching researchers' resources for advanced computer modelling of timber systems; and assisting software companies to identify the gaps and upgrade programs accordingly to accommodate advanced computer modelling of timber structures.

ACKNOWLEDGEMENT

This project was financially supported by Natural Resources Canada through the Expanding Wood Use Towards 2025 project and the Green Construction through Wood program. We also acknowledge the financial contribution from Ministère des Forêts de la Faune et des Parcs du Québec. In-kind support provided by NRCan, CWC, AWC, and FII is greatly appreciated. Contributions by more than 100 authors and reviewers of the guide are greatly appreciated.

REFERENCES

[1] Chen, Z., Karacabeyli, E., Lum, C.: A survey on modelling of mass timber. FPInnovations project report (301011232), 2017.

[2] Chen, Z., Tung, D., Karacabeyli, E.: Modelling Guide for Timber Structures. FPInnovations, 2022: web.fpinnovations.ca/modelling

[3] González Fueyo, J. L, Dominguez, M., Cabezas, J. A., Rubio, M. P.: Design of connections with metal dowel-type fasteners in double shear. Materials and Structures, 42:385-397, 2009.

[4] Breneman, S., McDonnell, E., & Zimmerman, R.: An approach to CLT diaphragm modelling for seismic design with application to a US high-rise project. In: the World Conference on Timber Engineering, 2016.

[5] Rinaldin, G., & Fragiacomo, M.: Non-linear simulation of shaking-table tests on 3- and 7-storey X-Lam timber buildings. Engineering Structures, 113: 133-148, 2016.

[6] Nitti, G., Lacidogna, G., Carpinteri, A.: Structural Analysis of High-rise Buildings under Horizontal Loads: A Study on the Piedmont Region Headquarters Tower in Turin. The Open Construction & Building Technology Journal, 13: 81-96, 2019.

https://doi.org/10.52202/069179-0303

World Conference on Timber Engineering Oslo 2023

PREDICTIVE CAPABILITIES OF FINITE ELEMENT MODELLING FOR TIMBER MEMBERS SUBJECTED TO BLAST LOADS

Damian Oliveira[1], Christian Viau[2], Ghasan Doudak[3]

ABSTRACT: High-fidelity modelling used to predict the dynamic behaviour in terms of displacement-time history and failure mechanism of heavy timber elements are presented and validated. A material predictive model was implemented in ABAQUS through a dynamic user subroutine using continuum damage mechanics. Full-scale experimental test results were analysed and used to validate the modelling predictions. Compared with the experimental test results, the finite element models simulated the displacement-time histories and overall failure behaviour reasonably well. The accurate prediction of failure modes and overall responses of timber elements, including those with complex properties such as cross-laminated timber, is important to ensure safer designs, and lead to a better overall understanding of the material behaviour when subjected to very short duration loading.

KEYWORDS: Blast, Glulam, CLT, Dynamic, Finite element, Modelling, Failure, Criteria, Resistance, Damage

1 INTRODUCTION

Investigations into wood behaviour under extreme loadings have historically focussed on small-scale clear wood specimens subjected to impact loading. Recent effort in this field has dealt with full-scale structural elements, such as stud walls, glued-laminated (glulam) members, and cross-laminated timber (CLT) panels under simulated blast loading. The validity of using single-degree-of-freedom (SDOF) analysis to predict and investigate the behaviour of full-scale heavy-timber structural elements subjected to blast loading has been extensively investigated [1-3], while the use and application of FEA has been very limited, in part due the need for material properties that are difficult to isolate and establish experimentally [4].

The continuum damage approach, whereby stress-based criteria are used to initiate the damage process, allows for the detection of both brittle and ductile failure modes, whereas simplified modelling methods, such as SDOF analysis, are typically limited to a single failure mode. The applicability of the SDOF modelling approach has been investigated for wood elements [2, 3, 5-10]. The current study presents and validates a FE modelling approach capable of capturing the behaviour of glulam and CLT elements when subjected to blast loading. Validation of the model is undertaken using published full-scale experimental test results from [11].

2 LITERATURE REVIEW

Analytical and numerical models are often used for the purpose of analysis and design of structural systems due to their low cost and their ability to expand the scope of experimental studies. The most common analysis method for blast is the equivalent single-degree-of-freedom (SDOF) analysis, which consists of lumping continuous structural elements into a system with given resistance function, equivalent mass, and based on assumed deflected shapes [12]. SDOF analysis has been shown to provide adequate numerical predictions with little required computational efforts [2, 3, 5-10]. However, such simplified modelling techniques are limited to their assumed deflected shape and associated failure mode, and may therefore lead to inconsistencies between modelling predictions and actual sequence of damage or failure events in complex structural systems.

Modelling wood components within a finite element analysis (FEA) environment carries challenges related to properly reproducing the anisotropic nature of the wood material and the interactions between various failure mechanisms. Wood may exhibit brittle and ductile failure mechanisms depending on the failure plane and direction, and such failures may need to be considered simultaneously. While brittle failure modes are typically modelled using fracture mechanics or discrete lattice models, which are capable of capturing detailed property variation [13], ductile failure modes are usually captured using plasticity-based models, such as the Hill criterion [14] and the Tsai-Wu criterion [15].

Continuum damage mechanics-based models [16], whereby elements are modelled as being composed of subdivided areas for the purpose of developing formulations that provide average stress and strains, have been widely implemented in a variety of commercial software packages. Sandhaas, et al. [17] developed a static material model for timber in ABAQUS using solid three-dimensional elements within a continuum damage approach, which allowed for the detection of both brittle and ductile failure modes. The model used stress-based

[1] Damian Oliveira, Canadian Wood Council, Canada, doliveira@cwc.ca
[2] Christian Viau, Assistant Professor, Carleton University, Canada, christian.viau@carleton.ca
[3] Ghasan Doudak, Professor, University of Ottawa, Canada, gdoudak@uottawa.ca

https://doi.org/10.52202/069179-0304

criteria, each associated with a specific failure mode, to initiate the damage process.

The current study focuses on developing and validating a FEA model based on the continuum damage approach that can predict the behaviour of full-scale wood elements subjected to far-field blast explosions, and their associated strain rate effects. The numerical investigation will focus on glulam and CLT as these are the dominant engineered wood products (EWPs) currently being used for mid- and high-rise wood and hybrid construction.

3 FINITE ELEMENT MODEL

3.1 MODEL DEFINITION

ABAQUS was chosen for the purpose of this study due to its ability to perform both static and dynamic analyses with a variety of element types and applications. An advancing time-step solution, suitable for high-speed dynamic analyses with nonlinear behaviour, was utilized to determine the kinematic state of the model at every time-step. The non-iterative nature of this specific formulation tends to result in less memory usage and runtime.

The models utilized three-dimensional solid geometries without planes of symmetry. Eight-node continuum linear hexahedral elements (C3D8) were used in all analyses and the overall solution algorithm uses a continuum damage approach [4], based on the approach proposed by Sandhaas, et al. [17]. The model was developed following five assumptions, as follows:

1. the adhesive used for bonding the lamination of the timber elements is at least as strong as the surrounding wood fibres and the modelling of the bonds between individual laminations can be omitted;
2. the ultimate compressive behaviour of wood does not result in complete material failure, leading to element deletion from the model environment;
3. damage accumulation in the tension parallel-to-grain direction does not influence damage in other stress components until complete failure;
4. deletion of elements subjected to only shear stresses require not only the exceedance of the failure criterion associated with shear stress, but also additional stresses which would widen the existing cracks in situ, and;
5. the inclusion of the rolling shear component alongside the longitudinal shear component was found to lead to unrealistic and rapid degradation in tension perpendicular-to-grain, and was therefore omitted from any interaction with the tension perpendicular-to-grain stress component.

A total of eight failure criteria are used to represent the state of damage in a given element. The predicted stresses are evaluated using failure criteria which represent the stress-capacity ratios for the element. The respective damage components are identified using specific subscripts: longitudinal tension (t0), longitudinal compression (c0), radial tension (t90R), radial compression (c90R), tangential tension (t90T), tangential compression (c90T), longitudinal shear with respect to the radial plane (vR), and longitudinal shear with respect to the tangential plane (vT). These are presented as follows:

$$F_{t0}(\sigma) = \frac{\sigma_L}{f_{t0}} \tag{1}$$

$$F_{c0}(\sigma) = \frac{-\sigma_L}{f_{c0}} \tag{2}$$

$$F_{c90R|T}(\sigma) = \frac{-\sigma_{R|T}}{f_{c90}} \tag{3}$$

$$F_{t90T|R}(\sigma) = \frac{\sigma_{R|T}^2}{f_{t90}^2} + \frac{\sigma_{LT|LR}^2}{f_v^2} \tag{4}$$

$$F_{vR|T}(\sigma) = \frac{\sigma_{LT|LR}^2}{f_v^2} + \frac{\sigma_{RT}^2}{f_{roll}^2} \tag{5}$$

Each criterion presented above can be considered as a ratio of applied stress (σ) to the material capacity (f). The damage process is initiated if a failure criterion is evaluated to be greater than unity, at which point it is established that an element stress exceeded the elastic limit.

The criterion result of each stress component is then verified against the respective maximum ratio from the previous time steps to determine if damage within the element has progressed. This is performed through the peak stress-history variable, κ, which is used to calculate damage. Depending on the detected failure mode, the damage progression either weakens the element (i.e., brittle tension failure) or allows for sustained stress to take place while the element deforms (i.e., ductile compression failure). In addition, as shear damage can be initialized by other failure criteria, the method of superposition, or coupling, is utilized to capture the complex interactions occurring within the three shear planes (i.e. RT, LR, and LT), as proposed in [18]. For CLT, it is also proposed in the current study that the rolling shear damage variable (d_{roll}) is comprised of the longitudinal shear (d_{vR} and d_{vT}) and perpendicular-to-grain tension (d_{t90R} and d_{t90T}) damage components. The damage equations are presented below:

$$d_t = 1 - \frac{1}{f_{max}^2 - 2G_f E}\left(f_{max}^2 - \frac{2G_f E}{\kappa}\right) \tag{6}$$

$$d_v = 1 - \frac{1}{f_{max}^2 - 2G_f G}\left(f_{max}^2 - \frac{2G_f G}{\kappa}\right) \tag{7}$$

$$d_c = 1 - \frac{1}{\kappa} \tag{8}$$

$$d_{roll} = 1 - (1 - d_{t90R})(1 - d_{t90T})(1 - d_{vR})(1 - d_{vT}) \tag{9}$$

$$d^{eff}{}_{vR|T} = 1 - \left(1 - d_{t90R|T}\right)\left(1 - d_{vR|T}\right) \tag{10}$$

where d_t is the brittle damage in tension, d_v is the brittle damage in shear, d_c is the ductile damage in compression, and $d^{eff}{}_{vR|T}$ is the effective shear damage variable.

As seen in Equations (9) and (10), the method of superposition was utilized to capture the complex interactions occurring within the three shear planes (i.e. RT, LR, and LT), as proposed in [18], to calculate shear damages.

https://doi.org/10.52202/069179-0304

Viscous stabilization was incorporated into the damage algorithm through a modification of the damage variables using a bulk viscosity parameter to limit the damage development within the element and prevent large sections of the model from being deleted instantaneously, which is an unrealistic behaviour [4].

The cylindrical axes of wood, namely longitudinal, radial, and tangential, were replaced with the default local cartesian system of reference used within ABAQUS (i.e., X, Y, Z). The behaviour assigned to the perpendicular-to-grain axes within the material was smeared into a homogenized plane, whereby the local longitudinal X-axis was assigned parallel-to-grain properties while identical perpendicular-to-grain properties were assigned to the radial and tangential axes. The stress and strains present within a wood element are therefore defined by a total of six components, as shown in Equation (11) and Equation (12), respectively. These are written using unique properties for the three cartesian axes, but the terms are simplified as the implemented version assigns identical perpendicular-to-grain properties to the Y (denoted *R*) and Z (denoted *T*) axes and parallel-to-grain properties to the X (or *L*) axis. The general constitutive relationship equation includes the elastic modulus parallel-to-grain, E_0, and perpendicular-to-grain, E_{90}, for the axial components rather than a unique value for each axis, while a longitudinal shear modulus, G, is implemented for both the LR and LT orientations in combination with a rolling shear modulus, G_{roll}, for the RT orientation. The constitutive relationship is presented in Equation (13), while the stiffness matrix of an element, $[k]$, is provided in the literature [4, 19].

$$\{\sigma\} = \{\sigma_L \quad \sigma_R \quad \sigma_T \quad \sigma_{vR} \quad \sigma_{roll} \quad \sigma_{vT}\}^T \tag{11}$$

$$\{\epsilon\} = \{\epsilon_L \quad \epsilon_R \quad \epsilon_T \quad \epsilon_{vR} \quad \epsilon_{roll} \quad \epsilon_{vT}\}^T \tag{12}$$

$$\{\sigma\} = [k]\{\epsilon\} \tag{13}$$

After receiving new incremental strains from the previous step of the ABAQUS analysis, the material model estimates the new stress based on the assumption of linear elastic behaviour. If a damage parameter is evaluated at a value near to unity, the element is identified for deletion.

3.2 TESTING PROGRAM AND MODELLING INPUT

The test configuration and specimens from an experimental study investigating the behaviour of glulam and CLT structural elements subjected to simulated blast loads were utilized for the purpose of validating the finite element model and modelling approach [11]. The experimental testing was conducted using the Shock Tube Test Facility at the University of Ottawa (see Figure 1).

Figure 1: *University of Ottawa Shock Tube Test Facility*

The specimens, boundary conditions, and loading of ten experimental tests were replicated within the FEA environment and the predicted results (i.e., displacements, reactions, and failure modes) were compared with the experimental test data. The 2,500 mm long specimens consisted of 24f-ES grade glulam beams (86 mm x 178 mm) and E1 grade 5-ply CLT panels (445 mm x 175 mm), subjected to dynamic four-point bending. Strain-rates in the testing varied between 0.10 to 0.32 s^{-1}.

Inputs for the material model pertaining to wood properties were obtained from published manufacturer data and research studies, modified to consider high-strain rate effects. The parallel-to-grain elastic modulus (E_0) was obtained from published design information by the manufacturer. The perpendicular-to-grain modulus of elasticity (E_{90}) and the shear and rolling shear moduli (G and G_{roll}, respectively) were calculated using relationships from the CSA O86 wood design standard [20]. Average strength material properties rather than the design-level properties were obtained from the literature in order to model the in-situ test specimens. The 5th percentile compression and tension parallel-to-grain, as well as perpendicular-to-grain strengths were modified using a load-duration factor (K_D) of 1.25, as well as strength and dynamic increase factors (*SIF* and *DIF*). The *SIF* is used to transform design-level strengths to average static strength values, while the *DIF*, which is the ratio of the dynamic strength over the static strength, takes into consideration high strain-rate effects [21]. The values for the material properties utilized in the FEA models, including elastic moduli (E), shear moduli (G), strengths (f), fracture energies (G_f), and Poisson's ratios (υ), are summarized in Table 1.

Table 1: *Material properties*

Property	Glulam	CLT (Long./Trans.)	Ref.
E_0	13,100 MPa	11,700 / 9,000 MPa	[20]
E_{90}	437 MPa	390 / 300 MPa	[20]
G	819 MPa	731 / 563 MPa	[20]
G_{roll}	81.9 MPa	73.1 / 56.3 MPa	[20]
f_{t0}	33.7 MPa	27.7 / 5.8 MPa	[22, 23]
f_{c0}	54.5 MPa	34.7 / 16.2 MPa	[22, 23]
f_{c90}	11.3 MPa	8.0 / 8.0 MPa	[22, 23]
f_{t90}	1.4 MPa		[24]
f_v	10.9 MPa		[25]
f_{roll}	1.5 MPa		[26]
G_{f0}	6.0 N/mm		[4]
G_{f90}	0.5 N/mm		[4]
G_{fv}	1.2 N/mm		[4]
G_{froll}	0.6 N/mm		[4]
υ_{LR}	0.47		[27]
υ_{LT}	0.37		[27]
υ_{RT}	0.44		[27]

The glulam specimens were modelled as homogenous members, while the plies of the modelled CLT panel were created by portioning sections of the panel geometry. This significantly reduced computational efforts by reducing contact relationships in the analysis. An example of a modelled CLT panel is presented in Figure 2. The boundary supports for the models consisted of four cylindrical rigid bodies, acting as pinned supports, in order to replicate the boundary conditions used during the full-scale experimental tests.

As the validation of the FE model was to be conducted through comparisons with published full-scale test results which utilized a load-transfer device (LTD) to convert the blast pressure into two concentrated point loads, the inertial contribution of the LTD was accounted for by distributing the effective mass of the LTD over the middle third of the member. This was implemented by increasing the material density in the region between the loading areas.

In order to select an appropriate mesh for the finite element material model, an h-refinement based sensitivity analysis was conducted for the glulam and CLT models using a blast load that would induce an elastic response in both specimens. For the purpose of this study, a mesh size of 20 mm was used for the glulam specimens as it provided the highest resolution of results. For the CLT model, considerations were made to include at least two elements for each ply. Overall, the CLT model was found to be more sensitive to mesh size, and a 17.5 mm element size was chosen, since it provided a reasonable balance of result fidelity and runtime.

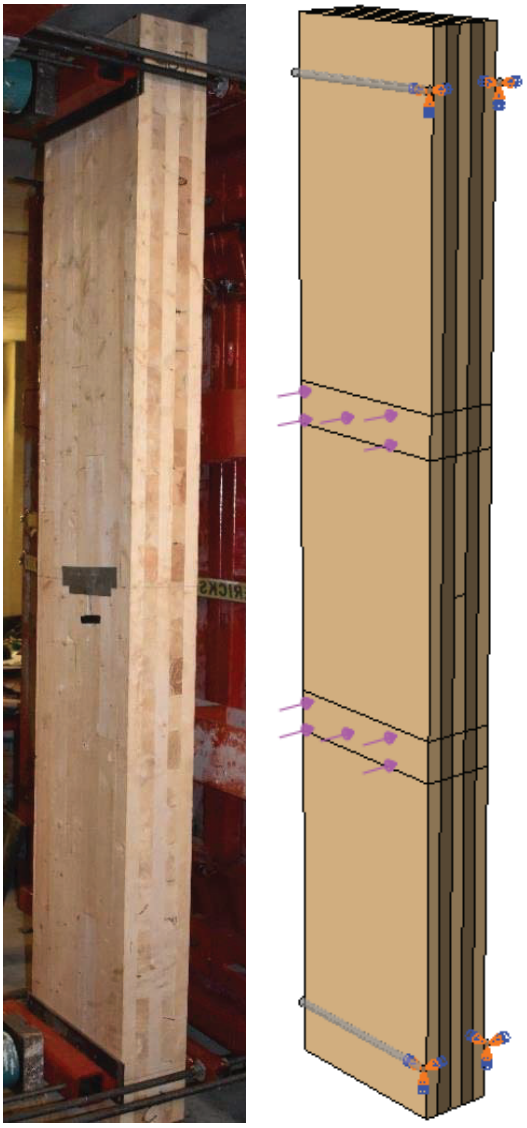

(a) *Experimental* ***(b)*** *FE model*

Figure 2*: Experimental and numerical CLT specimens*

4 RESULTS AND DISCUSSION

The finite element modelling results were evaluated through the displacement-time history and resistance-displacement relationship, as well as the observed overall damage behaviour. The displacement-time history was obtained from a mid-span node, located at mid-depth of the modelled specimen. The numerical results and the corresponding experimental test results are presented in Table 2, which includes the peak resistance and the mid-span displacement occurring at peak resistance.

https://doi.org/10.52202/069179-0304

Table 2: *Summary of numerical and experimental results*

Test Name	Peak Resistance (kN)			Displacement at Peak (mm)		
	Exp.	Num.	Err. (%)	Exp.	Num.	Err. (%)
GL1.1	54	53	-2	26	25	-4
GL2.1	77	61	-21	33	38	+15
GL2.2	79	65	-18	34	42	+24
GL3.1	29	30	+3	13	13	0
GL3.2	66	56	-15	28	28	0
GL3.3	70	63	-10	31	38	+23
CLT1.1	187	188	+1	33	31	-6
CLT2.1	126	150	+19	22	26	+18
CLT2.2	181	170	-6	34	36	+6
CLT3.1	167	176	+5	26	34	+31

The resistance curves and peak resistances were obtained by establishing equilibrium of the dynamic systems, taking into account the dynamic reactions, $V(t)$, imparted blast load, $F(t)$, and mass properties. The closed-form formulation for the resistance at a certain point in time, $R(t)$, is given in Equation (14):

$$R(t) = \frac{6}{L}\left(V(t)x_{eq} + \left(\frac{L}{3} - x_{eq}\right)\frac{F(t)}{2}\right) \qquad (14)$$

where L is the clear span of the specimen, and x_{eq} is the location of the equivalent effective inertial force, which can be determined based on previously derived solutions [28]. The reaction-time histories were obtained from the rigid pins in contact with the tension face of the structural elements at the supports.

On average, the model underpredicted the peak resistance by 4.3 % (COV = 12 %) and overpredicted the displacement-at-peak on average by 10.6 % (COV = 11 %). These ratios are well within the expected margins of variability, considering that the inputs were obtained from the timber design standard (CSA O86) [40], manufacturer's data, and studies on similar specimens. Representative experimental and numerical time histories are shown in Figure 3 for specimen CLT2.1. While the model permitted both the inbound and rebound phases of the response to be investigated, the comparison with the experimental test results only extended to the maximum inbound behaviour and response, due to the underlying assumptions involving the LTD mass. While the model considers that the LTD is constantly in contact with the specimen, experimentally this was often not the case, particularly when specimens experienced failure.

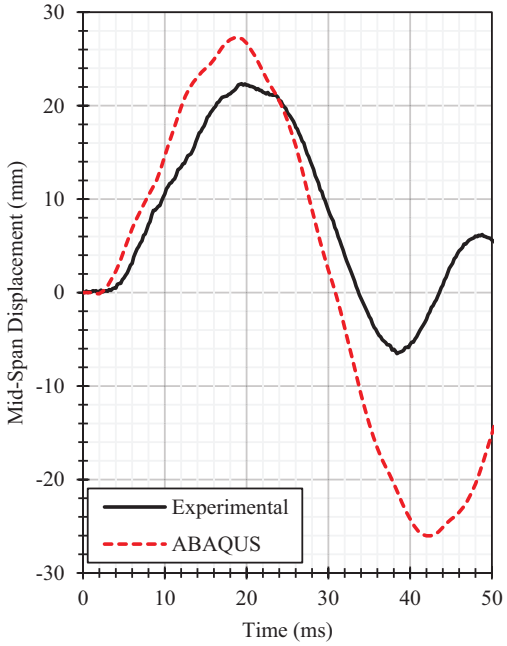

(a) *Displacement-time*

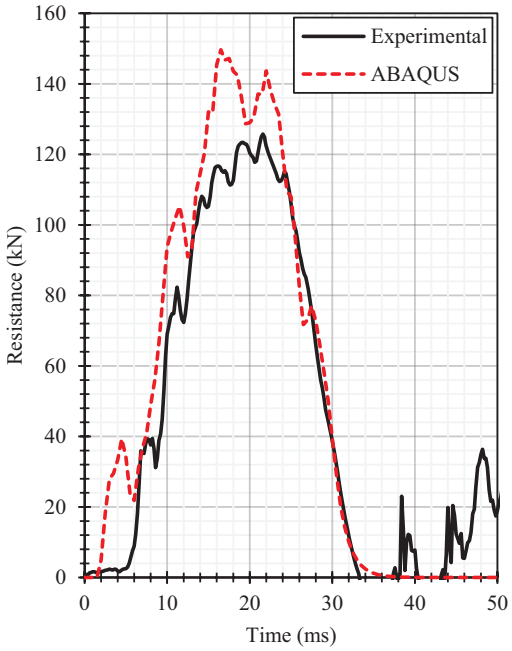

(b) *Resistance-time*

Figure 3*: Representative results (CLT2.1)*

The reaction-time histories included numerical scatter due to the solution method used by ABAQUS, which does not calculate the global stiffness or equilibrium. Another potential cause could be attributed to the mismatch between the frequency at which the results from the model outputs are stored and the stable time increment used within the analysis. The stable time increment is related to stress wave propagation velocity within an element, and

thus the output at a certain integration point can vary depending on whether the stress wave has propagated through that specific point of the model at the given time increment.

The FEM results for the glulam specimens matched well in terms of overall deflected shapes and load-displacement behaviour, and propagation of damage through cracks. Failure in the glulam specimens was always initiated on the tension-side outer laminate near the mid-span, corresponding to initial element deletion, followed by damage propagation towards the rest of the cross-section. As shown in Figure 4, the shape and extent of the damage were consistent among simulations and corresponded generally well to the experimental test results.

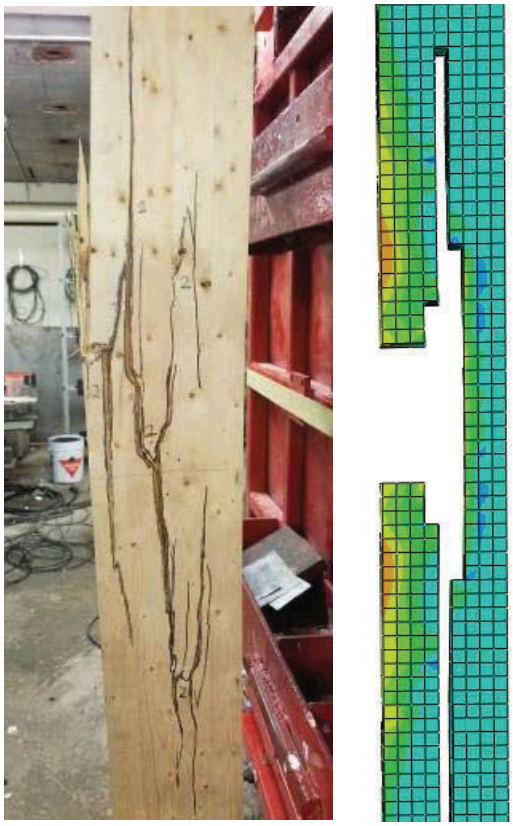

(a) *Experimental* ***(b)*** *FE Model*

Figure 4*: Representative results for glulam*

Similar to glulam, the simulated sequence of failure and overall damage characteristics of CLT elements correlated well with those observed in the experimental test specimens, as shown in Figure 5. Two specific failure mechanisms, namely flexural failure of the longitudinal laminates and rolling shear failure of the transverse laminates, were observed experimentally and within the numerical models. This combination of failure modes caused greater variability in terms of the accuracy of the numerical results. However, the FEM consistently predicted rolling shear damage occurring near or at the instance of flexural failure; an observation that was also documented in the experimental tests.

(a) *Experimental* ***(b)*** *FE Model*

Figure 5*: Representative results for CLT*

Previous studies on CLT panels under blast have underlined the limitations in the use of simplified SDOF modelling due to the inability of the model to consider two concurrent failure modes [3, 29]. Herein lies the significant advantage of the described ABAQUS model, whereby a multitude of damage types and failure mechanisms can be studied simultaneously, and the output of the model can provide the resistance curve; and input that usually required when performing SDOF analysis.

The resistance curves generated by the finite element method generally correlated well with experimental results despite the presence of artificial numerical fluctuation, as shown in (Figure 6).

https://doi.org/10.52202/069179-0304

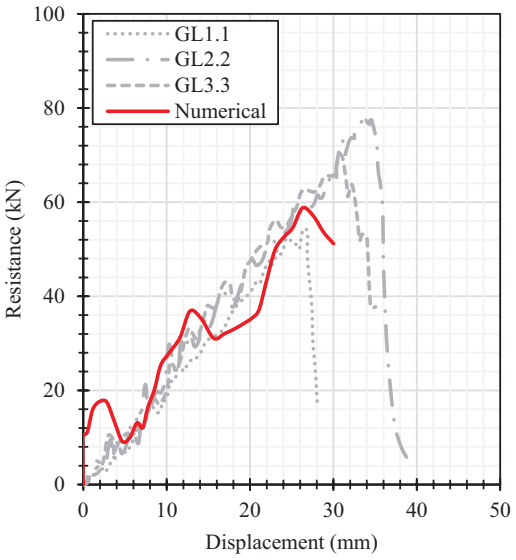

***(a)** Glulam*

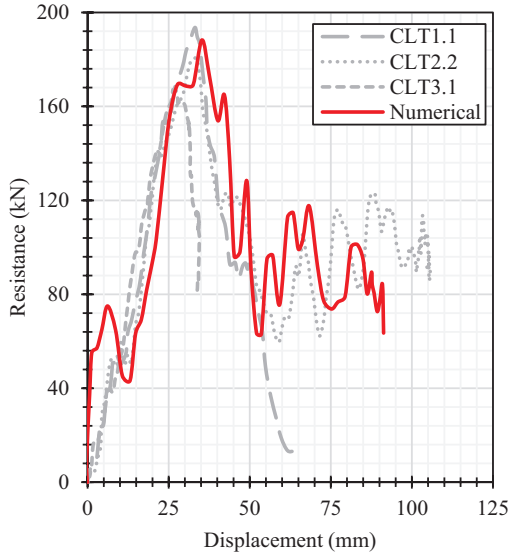

***(b)** CLT*

***Figure 6**: Comparison between experimental and numerical resistance curves*

The overall numerical results in terms of resistance curve within the elastic regime were very consistent with the experimental test results, with the exception that a very high initial stiffness was observed in all models within the first two milliseconds. This phenomenon does not, however, affect the overall accuracy and results from the FEA model. In both the experimental and numerical results, no post-peak behaviour was observed for the glulam specimens, as shown in Figure 6a, while the CLT specimens exhibited significant post-peak capacity, as shown in Figure 6b. The loss of the outermost longitudinal laminates corresponded with the peak resistance of the panel.

5 CONCLUSIONS

A material predictive model for glued-laminated and cross-laminated timber structural elements was implemented into ABAQUS/Explicit through a dynamic user subroutine following a continuum damage approach. The experimental test results of 10 full-scale shock tube tests were used to validate the accuracy of the model, which was determined to be effective in capturing the dynamic response of timber elements. Reasonably accurate numerical predictions were obtained for peak resistance, as well as mid-span displacements at peak resistance. The finite element models were also capable of predicting damage and failure in the specimen, similar to those observed experimentally. The FE model was found to produce resistance-displacement relationships which correlated well to the corresponding experimental results. This finding identifies a key advantage to using sophisticated FEA over simplified modelling methodologies, such as single-degree-of-freedom modelling. While the latter requires that the resistance curve as input, the former produces the resistance curve, given appropriate material properties are implemented by the analyst. The modelling results also show that the lack of actual in-situ material properties does not pose a challenge in obtaining realistic predictions of overall behaviour and resistance curves, as published data from available manufacturer spec sheets, design provisions, and published studies can be used to obtain generally good results.

REFERENCES

[1] Jansson, B., *Impact loading of timber beams*, MSc Thesis, 1992, University of British Columbia: Vancouver, BC.

[2] Lacroix, D.N. and G. Doudak, *Determining the Dynamic Increase Factor for Glued-Laminated Timber Beams.* Journal of Structural Engineering, 2018. 144(9): p. 04018160.

[3] Poulin, M., C. Viau, D.N. Lacroix, and G. Doudak, *Experimental and Analytical Investigation of Cross-Laminated Timber Panels Subjected to Out-of-Plane Blast Loads.* Journal of Structural Engineering, 2018. 144(2): p. 04017197.

[4] Sandhaas, C., *Mechanical behaviour of timber joints with slotted-in steel plates*, Doctoral Dissertation, 2012, TU Delft.

[5] Viau, C. and G. Doudak, *Investigating the Behavior of Light-Frame Wood Stud Walls Subjected to Severe Blast Loading.* Journal of Structural Engineering, 2016. 142(12): p. 04016138.

[6] Viau, C., D.N. Lacroix, and G. Doudak, *Damage level assessment of response limits in light-frame wood stud walls subjected to blast loading.* Canadian Journal of Civil Engineering, 2016. 44(2): p. 106-116.

[7] Lacroix, D. and G. Doudak, *Towards enhancing the post-peak performance of glued-laminated timber beams using multi-directional fibre reinforced polymers.* Engineering Structures, 2020. 215: p. 110680.

[8] Lacroix, D.N. and G. Doudak, *Effects of High Strain Rates on the Response of Glulam Beams and Columns.*

Journal of Structural Engineering, 2018. 144(5): p. 04018029.
[9] Lacroix, D.N. and G. Doudak, *Investigation of Dynamic Increase Factors in Light-Frame Wood Stud Walls Subjected to Out-of-Plane Blast Loading.* Journal of Structural Engineering, 2015. 141(6): p. 04014159.
[10] Lacroix, D.N., G. Doudak, and K. El-Domiaty, *Retrofit Options for Light-Frame Wood Stud Walls Subjected to Blast Loading.* Journal of Structural Engineering, 2014. 140(4): p. 04013104.
[11] Oliveira, D., C. Viau, and G. Doudak, *Behaviour of mass timber members subjected to consecutive blast loads*. International Journal of Impact Engineering, 2023. 173: p. 104454.
[12] Biggs, J.M., *Introduction to Structural Dynamics*. 1964, New York, NY: McGraw-Hill. 341.
[13] Reichert, T., *Development of 3d lattice models for predicting nonlinear timber joint behaviour*, 2009, Edinburgh Napier University: Edinburgh, UK.
[14] Hill, R. and E. Orowan, *A theory of the yielding and plastic flow of anisotropic metals.* Proceedings of the Royal Society of London. Series A. Mathematical and Physical Sciences, 1948. 193(1033): p. 281-297.
[15] Tsai, S.W. and E.M. Wu, *A General Theory of Strength for Anisotropic Materials.* Journal of Composite Materials, 1971. 5(1): p. 58-80.
[16] Matzenmiller, A., J. Lubliner, and R.L. Taylor, *A constitutive model for anisotropic damage in fiber-composites.* Mechanics of Materials, 1995. 20(2): p. 125-152.
[17] Sandhaas, C., J.W.G.V.D. Kuilen, and H.J. Blass, *Constitutive model for wood based on continuum damage mechanics*, in *World Conference on Timber Engineering*. 2012: Auckland, NZ.
[18] Sandhaas, C., A.K. Sarnaghi, and J.-W. van de Kuilen, *Numerical modelling of timber and timber joints: computational aspects.* Wood Science and Technology, 2020. 54(1): p. 31-61.
[19] Chen, Z., D. Tung, and E. Karacabeyli, *Modelling Guide for Timber Structures*, in *Special Publication SP-544*. 2022, FPInnovations: Pointe-Claire, Que.
[20] CSA, *Engineering design in wood*, in *CSA O86*. 2019, CSA Group: Mississauga, ON.
[21] Doudak, G., C. Viau, and D.N. Lacroix, *Proposed Design Methods for Timber Members Subjected to Blast Loads.* Journal of Performance of Constructed Facilities, 2022. 36(3): p. 04022020.
[22] Nordic Structures, *Nordic X-Lam Technical Guide*. 2022, Nordic Structures: Montreal, QC.
[23] Nordic Structures, *Nordic Lam+ Technical Guide*. 2022, Nordic Structures: Montreal, QC.
[24] Jönsson, J. and S. Thelandersson, *The effect of moisture gradients on tensile strength perpendicular to grain in glulam.* Holz als Roh- und Werkstoff, 2003. 61(5): p. 342-348.
[25] Boström, L.A., *Method for determination of the softening behaviour of wood and the applicability of a nonlinear fracture mechanics model.* Report TVBM, 1992.
[26] Wang, Z., J. Zhou, W. Dong, Y. Yao, and M. Gong, *Influence of technical characteristics on the rolling shear properties of cross laminated timber by modified planar shear tests.* Maderas. Ciencia y tecnología, 2018. 20: p. 469-478.
[27] Green, D.W., J.E. Winandy, and D.E. Kretschmann, *Mechanical properties of wood. Wood handbook : wood as an engineering material*, in *General technical report FPL ; GTR-113*. 1999, USDA Forest Service, Forest Products Laboratory: Madison, WI.
[28] Lacroix, D., *Investigating the Behaviour of Glulam Beams and Columns Subjected to Simulated Blast Loading*, PhD Dissertation, 2017, University of Ottawa: Ottawa, ON. p. 294.
[29] Viau, C., D. Lacroix, and G. Doudak, *Design Considerations for Cross-Laminated Timber Panels Subjected to Simulated Blast Loads*, in *CSCE 2018 Annual Conference*. 2018, Canadian Society for Civil Engineering: Fredericton, NB.

https://doi.org/10.52202/069179-0304

World Conference on Timber Engineering Oslo 2023

EXPERIMENTAL INVESTIGATIONS ON CLT PANELS WITH OPENINGS

Xiaoyue Zhang [1], Lu Xuan [2], Weitian Li [3], Thomas Tannert [4]

ABSTRACT: The design of cross-laminated timber (CLT) shear walls demands careful consideration. In order to reduce cost and speed up construction time, large panel sizes are often preferred, yet sometimes openings are required for architectural purposes. However, the Canadian Standard for Engineering Design in Wood (CSA O86-19) prohibits openings in CLT shear walls due to a lack of research quantifying the reduction of stiffness as a function of opening size. To address this research gap, the impact of opening size on the stiffness of CLT panels was investigated. A total of 43 tests were conducted on panels with two different aspect ratios, two different thicknesses, and various opening sizes. The results indicate that the panel stiffness decreases non-linearly with an increase in opening size. However, even opening sizes large in relation to the panel width have only a minimal impact on the panel stiffness. These findings provide valuable insights for future design provisions for openings in CLT shear walls.

KEYWORDS: Cross-laminated timber, Push-over test, In-plane stiffness, Opening size

1 INTRODUCTION

1.1 CLT SHEAR WALLS WITH OPENING

The use of cross-laminated timber (CLT) in construction has significantly increased in the 21st century, with numerous structures built worldwide demonstrating the benefits of this material [1]. One emerging application of CLT is as shear walls, which commonly feature openings for doors and windows. However, such openings create stress concentrations that can reduce the panel's in-plane stiffness and load-carrying capacity.

While previous research has largely focused on the mechanical properties of CLT panels, limited work has been conducted on openings to determine a reduction coefficient. Dujic et al. [2] utilized a combination of experiments and numerical analysis to investigate how the size and shape of openings affect the strength and stiffness of shear walls. Through a parametric study, the authors proposed Equations (1) and (2) to estimate the stiffness and strength of panels with openings:

$$K_{opening} = K_{full} \cdot \frac{r}{2-r} \tag{1}$$

$$F_{opening} = F_{full} \cdot r(2-r) \tag{2}$$

Where $K_{opening}$ and K_{full} denote the stiffness of a CLT wall with and without and openings, respectively. The panel area ratio, r, is calculated using Equation (3):

$$r = \frac{1}{1+\frac{\alpha}{\beta}} \cdot \frac{H\Sigma L_i}{H\Sigma L_i + \Sigma A_i} \tag{3}$$

In this equation, H is the height of wall, ΣL_i is the sum of length of full height wall segments (excluding length of openings from the total length), and ΣA_i is the sum of the openings area. The parameters used in these equations are illustrated in Figure 1.

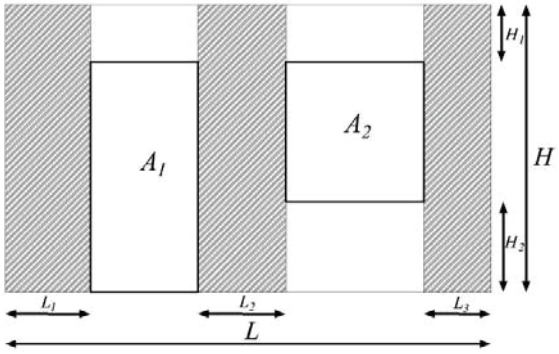

Figure 1: *Opening parameters for Equations (1) and (2)*

[1] Xiaoyue Zhang, School of Civil Engineering, Chongqing University, Chongqing, China, xzhang.ubc@icloud.com

[2] Lu Xuan, School of Civil Engineering, Chongqing University, Chongqing, China, xuanlu@stu.ouc.edu.cn

[3] Weitian Li, School of Engineering, University of Northern British Columbia, Prince George, Canada, Weitian.Li@unbc.ca

[4] Thomas Tannert, School of Engineering, University of Northern British Columbia, Prince George, Canada, Thomas.Tannert@unbc.ca

https://doi.org/10.52202/069179-0305

Ashtari [3] investigated the in-plane stiffness of four configurations of CLT floor diaphragms, with and without openings, utilizing a numerical model. The study determined that several key factors significantly influenced the in-plane stiffness, including the panel-to-panel connections of the CLT, the in-plane shear modulus of the CLT panels, the stiffness of the shear walls, and the configuration of the floor diaphragm. The numerical model was considered to be appropriate for CLT shear walls with openings, but it was noted that the findings require further experimental validation.

Pai et al. [4] studied the force transfer mechanism around openings in CLT shear walls and identified reinforcement requirements for the opening corners. The study revealed high concentrations of shear stress, indicating a likelihood of shear failure. To mitigate this issue, the authors recommended adding reinforcement to the opening.

Yasamura et al. [5] created 3D models and examined the mechanical properties of full-size CLT structures subjected to reverse cyclic horizontal loads. The results highlighted the importance of considering panel failure when designing CLT plates with openings.

Shahnewaz et al. [6] utilized numerical methods to calculate the in-plane stiffness of fenestrated three-ply single CLT walls. Through a parametric study, the authors evaluated the impact of changing the size and shape of openings and proposed Equation (4) to calculate the stiffness reduction as function of opening size and shape.

$$K_{opening} = K_{full} \cdot \left(1 - \frac{r_{o/w}\left({}^{A_0}/_{A_w}\right)}{\sqrt{r_{o/w} + r_o\left({}^{A_0}/_{A_w}\right) - 2\left({}^{r_{off}}/_{r_w}\right)}}\right) \quad (4)$$

Where $K_{opening}$ and K_{full} represent the stiffness of walls with and without opening, respectively. A_0 and A_w represent the areas of walls with and without opening, respectively. The aspect ratio of the opening, r_o, is defined as the ratio of the smaller to larger dimension of the opening. The maximum aspect ratio of opening to wall dimension, $r_{o/w}$ is calculated as the maximum of l_0/L or h_0/H, where L and H are the wall length and height, respectively, and l_0 and h_0 are the opening length and height, respectively. The wall aspect ratio, r_w, is defined as L/H, and the ratio of wall offset to wall dimension, r_{off}, is defined as x_{off}/L or y_{off}/H, respectively). These parameters are illustrated in Figure 2.

Mestar et al. [7] and Casagrande et al. [8] studied CLT shear walls with openings and found that for large lintel slenderness, bending failure occurred. Additionally, a numerical calculation method was proposed for simulating laminated plates using homogeneous shell elements with effective moduli of elasticity and shear.

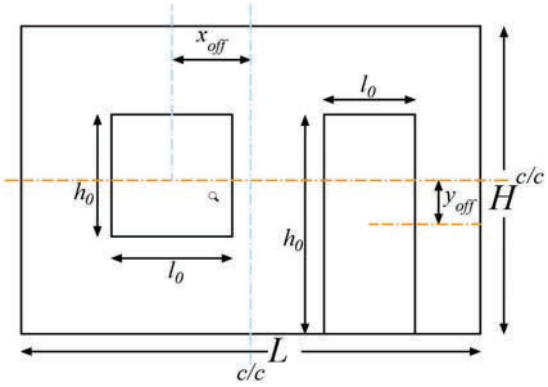

Figure 2: *Opening parameters for Equation (4)*

1.2 OBJECTIVES

Due to a lack of research on the strength and stiffness reduction as a function of the size and location of openings, the current CSA O86 provisions do not allow for any openings in CLT shear walls [9]. To address this knowledge gap, the objective of this study was to investigate experimentally how the size of openings affect the stiffness of CLT panels with different panel thicknesses and aspect ratios.

2 EXPERIMENTAL INVESTIGATIONS

2.1 MATERIALS

CLT panels with two different thicknesses were used in the experiments, namely: 1) 139mm 5-ply grade E1M4; and 2) 175mm 5-ply grade E1M5. The CLT panels were fabricated in accordance with ANSI/APA PRG 320 [10] and were supplied by Structurlam Products Ltd [11]. The wood species used were SPF MSR2100 (major layer)/No. 3 (minor layer). Based on the weight and volume of the CLT panels, the average apparent density of the panels was calculated to be 490 kg/m^3. The moisture content of the wood products was determined to be 12% (±3%) using portable electric resistance meters.

2.2 TESTS ON SINGLE PANELS

Two CLT panels of each layup measuring 1.5 x 3.0m were subjected to testing. Initially, the panels were tested without any opening, and then with gradually increasing opening sizes. The opening sizes were increased in increments of 200mm, up to a maximum size of 1200 x 1200mm, as shown in Figure 3. The panel was fixed at the bottom by three hold-downs, with one placed on each end and one in the panel centre. For ease of preparation, only slots were cut instead of completely removing the material from the opening.

https://doi.org/10.52202/069179-0305

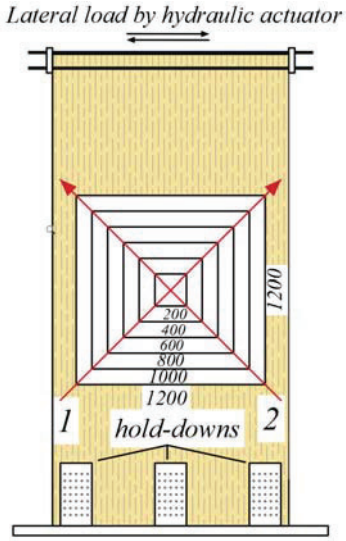

Figure 3: *Size of openings in single panels*

A lateral load was applied at the top end of the panel using a hydraulic actuator. The actuator was attached to steel plates with four pre-stressed rods. For each opening size, the panels were loaded three times to 100kN in both directions. The quasi-static monotonic load was applied at a constant rate of displacement of 10mm/min [12]. To measure the panel distortion, two string pots were used to span diagonally over the opening. In-plane panel movement was prevented by using an HSS profile, which was placed on a Teflon sheet to prevent friction. The experimental setup is illustrated in Figure 4.

Figure 4: *Set-up of single-panel test*

2.3 RESULTS OF SINGLE PANEL TESTS

Figure 5 shows the applied force versus opening distortion for all opening sizes. Figure 6 illustrates the maximum opening distortions as a function of opening size. It can be found that the panel stiffness decreased slightly with increasing opening size, with distortions of around 4mm for opening sizes of up to 800 x 800mm. Only when the opening size reached 1000mm was a significant increase of approximately 10mm observed.

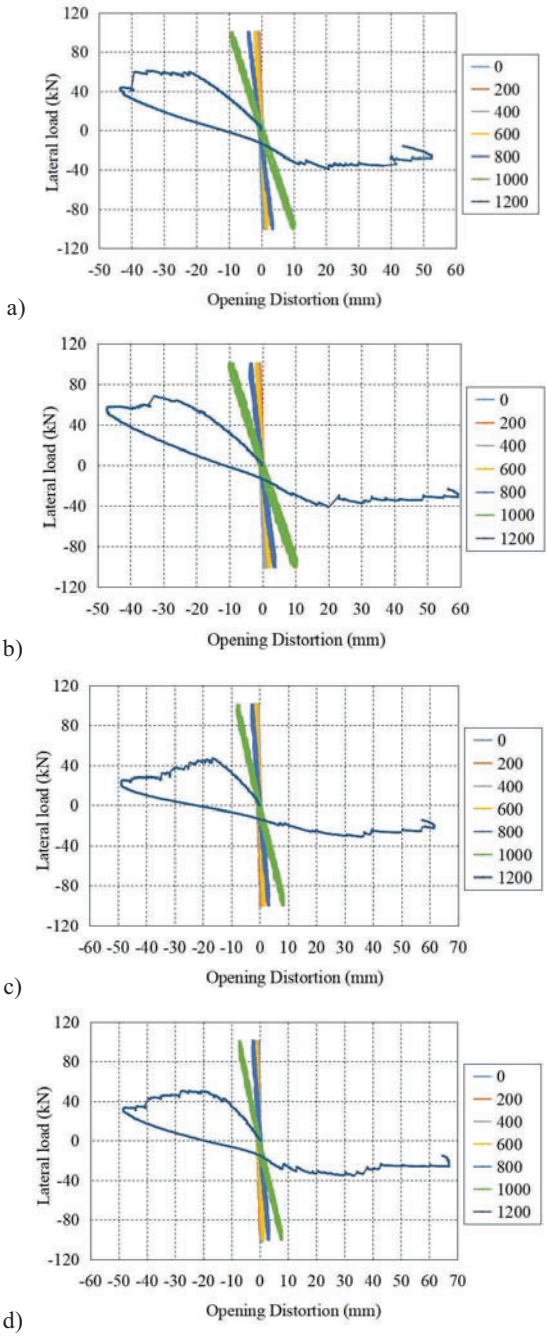

Figure 5: *Lateral load vs Opening distortion curves: (a)139-1; (b)139-2; (c)175-1; (d)175-2*

https://doi.org/10.52202/069179-0305

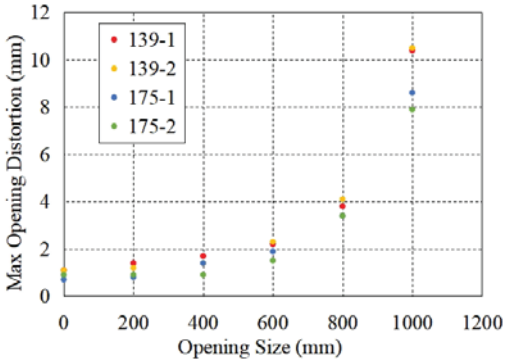

Figure 6: *Maximum opening distortion vs opening size*

The typical failure mode of the panels, when tested with a 1200 x 1200mm opening, is depicted in Figure 7. It be observed that cracks developed in the CLT panels near the corners of the openings, where the stresses peaked.

Figure 7: *Typical failure mode in single-panel test*

2.4 TESTS ON COUPLED PANELS

In the second part of the tests, the impact of different aspect ratios on CLT panels was examined with dimensions of 3 x 1.5 m and 3 x 1 m, corresponding to aspect ratios of 2:1 and 3:1, respectively. Only 139 mm 5-ply CLT panels were utilized for these tests.

Two CLT panels were tested next to each other, initially without any openings and subsequently with openings increasing in size from 150 x 150mm in increments of 150mm. The maximum opening sizes were 750 x 750mm for 1000mm wide panels and 1200 x 1200mm for 1500mm wide panels. To simplify the preparation process, only slots were cut rather than completely removing the material from the openings. The openings were placed eccentrically, with their centers 750mm and 500mm away from the long side of the panels, as depicted in Figure 8.

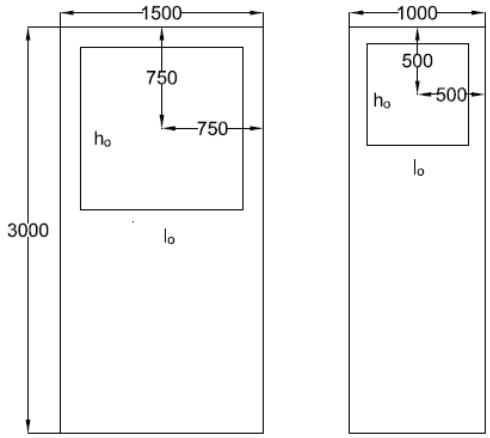

Figure 8: *Size of openings in coupled panels*

A hyperelastic hold-down system, presented by Asgari et al. [13] was used on the outside corners of the panels, and a pin-type shear connector was mounted at the midpoint, as shown in Figure 9. There was no further shear connection between the two panels. A hydraulic actuator was used to apply lateral load to the top of the two CLT panels via pins. A steel frame was used to hold the panels in-plane and to apply a constant dead load to the panels. For each opening size, the panels were subjected to three cycles of lateral loading in both directions, up to 50kN for the 1000mm wide panels and up to 75kN for the 1500mm wide panels. The quasi-static monotonic load was applied at a constant rate of displacement of 10mm/min.

The following parameters were measured during the tests: horizontal panel displacement, individual panel uplifts at both corners, horizontal sliding at the bottom of the panels, and panel distortion. Two string pots were mounted on each panel, spanning diagonally over the openings, to measure the panel distortion.

Figure 9: *Set-up of coupled-panel test*

https://doi.org/10.52202/069179-0305

2.5 RESULTS OF COUPLED PANEL TESTS

Figure 10 illustrates the typical failure mode of the CLT panels when tested with a 1200 x 1200 mm opening. Similar to the single panel test, cracks developed in the panels near the corners of the openings, where the stresses were highest.

Figure 10: *Typical failure mode in single-panel test*

The force versus displacement curves for all opening sizes are depicted in Figure 11, while the panel distortions are illustrated in Figure 12. It is evident that an increase in opening size resulted in a corresponding increase in the maximum displacement, coupled with a decrease in stiffness. Notably, the curves for small to mid-sized openings overlap, indicating that the reduction in stiffness was minimal. The relationship between opening size and maximum distortion is displayed in Figure 13.

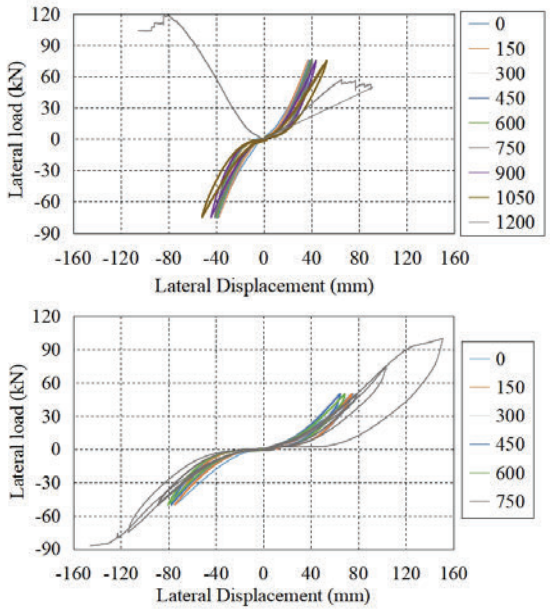

Figure 11:*Load vs displacement curves. Top: 2:1 aspect ratio; bottom: 3:1 aspect ratio*

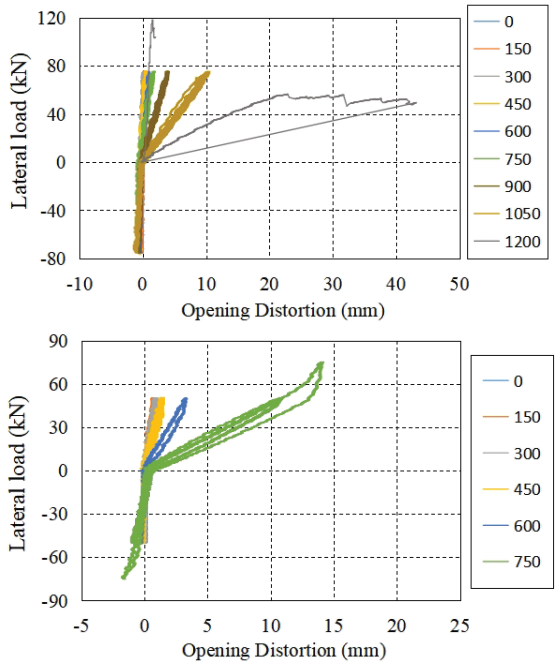

Figure 12: *Opening distortion curves. Top: 2:1 aspect ratio; bottom: 3:1 aspect ratio*

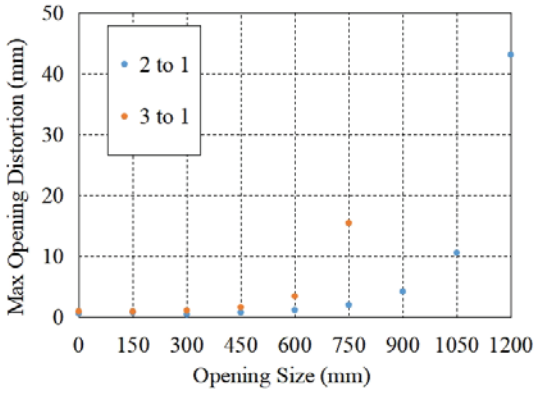

Figure 13: *Maximum opening distortion vs opening size*

3 CONCLUSIONS

The impact of different opening sizes on the in-plane stiffness of CLT panels was investigated experimentally, and the following main conclusions were drawn:

1) Openings do have an impact on the in-plane stiffness of CLT panels, but this impact is minimal for small opening sizes, and only becomes significant for very large opening sizes.

2) From the experimental results of coupled panels, it can be concluded that small openings in CLT shear walls only marginally reduce their stiffness. However, very large openings can reduce the stiffness by up to 35% and significantly reduce the shear resistance, leading to brittle panel failure at small loads.

https://doi.org/10.52202/069179-0305

3) The aspect ratio is a significant factor affecting the stiffness of CLT panels, and panels with different aspect ratios exhibit a considerable difference in stiffness under the same size of CLT panel openings.

4) These findings, once analysed in more depths and used to validate a numerical model for extended parameters studies can guide the development of future design provisions regarding openings in CLT shear walls.

ACKNOWLEDGEMENT

The project was funded by the government of British Columbia through a Forest Innovation Investment grant and a BC Leadership Chair to Dr. Tannert. The support by the UNBC technicians Michael Billups, James Andal, and Ryan Stern is greatly appreciated. The authors also would like to thank the National Natural Science Foundation of China (Grant Nos. 52108192); China Postdoctoral Science Foundation (Grant Nos. 2022M710528); the OEICDI fund (Grant Nos. B13041); the Entrepreneurship and Innovation Support Program for Overseas-educated student in Chongqing China (Grant Nos. CX2021085).

REFERENCES

[1] Karacabeyli, E. and Gagnon S., eds. CLT handbook Canadian edition. 2019. FPInnovations.

[2] Dujic, B, et al. Influence of openings on shear capacity of wooden walls. In proc. of 40th CIB-W18 Meeting, Bled, Slovenia. Paper 40-15-6, 2007.

[3] Ashtari, S. In-plane stiffness of cross-laminated timber floors. MASc dissertation. University of British Columbia, Vancouver, 2012.

[4] Pai, S. et al. Force transfer around openings in cross-laminated timber shear walls." Journal of Structural Engineering 143.4.: 04016215, 2017.

[5] Yasumura, M, et al. Full-scale tests and numerical analysis of low-rise CLT structures under lateral loading. Journal of Structural Engineering 142.4 : E4015007, 2016.

[6] Shahnewaz, Md, et al. In-plane stiffness of cross-laminated timber panels with openings" Structural Engineering International 27.2: 217-223, 2021.

[7] Mestar, M, et al. Investigating the kinematic modes of CLT shear-walls with openings. Engineering Structures 228 : 111475, 2021.

[8] Casagrande, D, et al. Experimental and numerical study on the mechanical behaviour of CLT shearwalls with openings. Construction and Building Materials 298: 123858, 2021.

[9] CSA O86 Engineering Design in Wood.\" CSA Group: Mississauga, Canada, 2019.

[10] ANSI/APA PRG 320-2018 Standard for performance-rated cross-laminated timber. Tacoma, WA: The Engineered Wood Association, 2018.

[11] Mass Timber Technical Guide. Structurlam Mass Timber Corporation Canada, 2021.

[12] ASTM E2126-09. (2009). Standard Test Methods for Cyclic (Reversed) Load Test for Shear Resistance of Walls for Buildings. American Society for Testing and Material.

[13] Asgari, H, et al. Hyperelastic hold-down solution for CLT shear walls. Construction and Building Materials 289: 123173, 2021.

https://doi.org/10.52202/069179-0305

World Conference on Timber Engineering Oslo 2023

SEISMIC PERFORMANCE EVALUATION OF REINFORCED WOODEN TEMPLE BASED ON LONG TERM EARTHQUAKE OBSERVATIONS

Toshiaki Sato[1], Yasuhiro Nambu[2], Yuji Miyazu[3] and Masayuki Nagano[4]

ABSTRACT: The seismic performance of structures is known to change over time, and the causes are affected by the surrounding environment such as temperature and humidity as well as damage caused by disturbances such as earthquakes. In terms of structure, seismic performance has been evaluated based on the construction age, mainly the transition of related laws and regulations, but the seismic performance changes over time, considering the material properties that swell and shrink sensitively due to temperature and humidity. the purpose of this study is to quantitatively evaluate the effects of various influential factors using earthquake observation records which are measured over a long period of time at the main hall of wooden temple. The subspace method was applied to the observation record of target temple, and the transition of the natural frequency due to aging was verified as the environment was changed. As a result of the investigation, the natural frequency changed as the temperature up and down, suggesting the effect of swell and shrink of the joint. Further, in the deformation range about less 3 mm, the variation in the natural frequency may have the same effect as the nonlinearity due to the large and small response.

KEYWORDS: System Identification, Subspace Method, Traditional Wooden buildings

1 INTRODUCTION

The seismic performance of structures is known to change over time, and the causes are affected by the surrounding environment such as temperature and humidity as well as damage caused by disturbances such as earthquakes. In terms of structure, seismic performance has been evaluated based on the construction age, mainly the transition of related laws and regulations, but the seismic performance changes over time, considering the material properties that swell and shrink sensitively due to temperature and humidity in case of timber structure. On the other hand, there is still no way to quantitatively evaluate the seismic performance of the wood structure over time, and it can be said that the accumulation of knowledge is indispensable.

Against this background, the purpose of this study is to quantitatively evaluate the effects of various influential factors using earthquake observation records which are measured over a long period of time at the main hall of wooden temple shown in Fig. 1. In this paper, we first organize the system identification method by the subspace methods used in the subsequent studies, and then describe the results of the analysis focusing on the transition of the natural freq-uency together with the identification results by the earthquake observation records.

***Figure 1**: Photo of the target temple*

2 SYSTEM IDENTIFICATION BASED ON SUBSPACE METHOD

2.1 NUMERICAL CALCULATION BY ORDINARY MOESP METHOD

Since the subspace method has the advantage of being applicable to multi-input multi-output (MIMO) systems, verification work of its identification accuracy has been advanced in previous studies, and considering its significance in this study, the Ordinary MOESP method was adopted. In the subspace method, it is considered that

[1] Toshiaki Sato, Dr. Eng., Assoc. Prof., Kyushu University, Japan, sato@arch.kyushu-u.ac.jp
[2] Yasuhiro Nambu, Dr. Eng., Assist. Prof., Kyushu University, Japan, nambu@arch.kyushu-u.ac.jp
[3] Yuji Miyazu, Dr. Eng., Assoc. Prof., Tokyo University of Science, Japan, miyazu@rs.tus.ac.jp
[4] Masayuki Nagano, Dr. Eng., Prof., Tokyo University of Science, Japan, nagano-m@rs.tus.ac.jp

https://doi.org/10.52202/069179-0306

each expression in Eqs. (1) and (2) are satisfied as the state-space representation of the discrete-time linear time-invariant system of *m* input *l* output [1].

$$\mathbf{x}(k+1) = \mathbf{A}\,\mathbf{x}(k) + \mathbf{B}\,\mathbf{u}(k) + \mathbf{w}(k) \qquad (1)$$

$$\mathbf{y}(k) = \mathbf{C}\,\mathbf{x}(k) + \mathbf{D}\,\mathbf{u}(k) + \mathbf{v}(k) \qquad (2)$$

Where, **x** (*k*) denotes the state vector, **u** (*k*) and **y** (*k*) are the input to the system and the output of the system, respectively. **A**, **B**, **C** and **D** are the constant matrix. These vectors and matrices belong to a set of real numbers. **w** (*k*) and **v** (*k*) are unmeasurable vector signals. They are assumed to be zero mean, stationary, white noise vector sequences. The Eqs. (1) and (2) can be organized as

$$\mathbf{Y} = \mathbf{\Theta}\,\mathbf{X} + \mathbf{\Psi}\mathbf{U} + \mathbf{\Xi}\mathbf{W} + \mathbf{V}\,. \qquad (3)$$

Where, **U** and **Y** denote the Input and output block Hankel matrices, respectively, and **X** is matrix composed by state vectors. These are expressed as follows.

$$\mathbf{U}_p = \begin{bmatrix} \mathbf{u}(k) & \mathbf{u}(k+1) & \cdots & \mathbf{u}(k+N-1) \\ \mathbf{u}(k+1) & \mathbf{u}(k+2) & \cdots & \mathbf{u}(k+N) \\ \vdots & \vdots & \ddots & \vdots \\ \mathbf{u}(k+r-1) & \mathbf{u}(k+r) & \cdots & \mathbf{u}(k+r+N-2) \end{bmatrix}$$

$$\mathbf{U}_f = \begin{bmatrix} \mathbf{u}(k+r) & \mathbf{u}(k+r+1) & \cdots & \mathbf{u}(k+r+N-1) \\ \mathbf{u}(k+r+1) & \mathbf{u}(k+r+2) & \cdots & \mathbf{u}(k+r+N) \\ \vdots & \vdots & \ddots & \vdots \\ \mathbf{u}(k+2r-1) & \mathbf{u}(k+2r) & \cdots & \mathbf{u}(k+2r+N-2) \end{bmatrix}$$

$$\cdots (4\text{-}1,\ 2)$$

$$\mathbf{Y}_p = \begin{bmatrix} \mathbf{y}(k) & \mathbf{y}(k+1) & \cdots & \mathbf{y}(k+N-1) \\ \mathbf{y}(k+1) & \mathbf{y}(k+2) & \cdots & \mathbf{y}(k+N) \\ \vdots & \vdots & \ddots & \vdots \\ \mathbf{y}(k+r-1) & \mathbf{y}(k+r) & \cdots & \mathbf{y}(k+r+N-2) \end{bmatrix}$$

$$\mathbf{Y}_\mathbf{f} = \begin{bmatrix} \mathbf{y}(k+r) & \mathbf{y}(k+r+1) & \cdots & \mathbf{y}(k+r+N-1) \\ \mathbf{y}(k+r+1) & \mathbf{y}(k+r+2) & \cdots & \mathbf{y}(k+r+N) \\ \vdots & \vdots & \ddots & \vdots \\ \mathbf{y}(k+2r-1) & \mathbf{y}(k+2r) & \cdots & \mathbf{y}(k+2r+N-2) \end{bmatrix}$$

$$\cdots (5\text{-}1,\ 2)$$

$$\mathbf{X} = \begin{bmatrix} \mathbf{x}(k) & \mathbf{x}(k+1) & \cdots & \mathbf{x}(k+2r-1) \end{bmatrix} \qquad (6)$$

In respective Eqs. (4) and (5), the scope is divided into two parts, the past and the future based on a certain time for the calculation reasons described later.

The matrix **Θ**, which is designated the expanded observability matrix, and **Ψ** are expressed as follows.

$$\mathbf{\Theta} = \begin{bmatrix} \mathbf{C} \\ \vdots \\ \mathbf{C}\mathbf{A}^{k-1} \\ \mathbf{C}\mathbf{A}^{k} \end{bmatrix},\ \mathbf{\Psi} = \begin{bmatrix} \mathbf{D} & & & \mathbf{0} \\ \vdots & \ddots & & \\ \mathbf{C}\mathbf{A}^{k-2}\mathbf{B} & \cdots & \mathbf{D} & \\ \mathbf{C}\mathbf{A}^{k-1}\mathbf{B} & \cdots & \mathbf{C}\mathbf{B} & \mathbf{D} \end{bmatrix}$$

$$\cdots (7\text{-}1,\ 2)$$

Others shown in Eq. (3) are notes related to noise, but they are not directly used in subsequent calculations, so we will omit them here and proceed with discussions.

In the MOESP method, the expanded observability matrix **Θ** is estimated by using an Eq. (3), and the system matrix **A** and **C** are calculated. First, using the input and output data to execute the LQ decomposition shown in the following equation composed of the block Hankel matrix defined in Eqs. (4) and (5). The Eq. (8) is the LQ decomposition that can be placed in the Ordinary MOESP method is represented.

$$\begin{bmatrix} \mathbf{U}_f \\ \mathbf{Y}_f \end{bmatrix} = \begin{bmatrix} \mathbf{L}_{11} & \mathbf{0} \\ \mathbf{L}_{21} & \mathbf{L}_{22} \end{bmatrix} \begin{bmatrix} \mathbf{Q}_1^T \\ \mathbf{Q}_2^T \end{bmatrix}. \qquad (8)$$

The block matrix $\mathbf{L}_{22}$ obtained by Eq. (8) is applied singular value decomposition as shown in Eq. (9). The block matrix $\mathbf{U}_1\mathbf{\Sigma}_1^{1/2}$ is an estimated value of the expanded observability matrix **Θ**.

$$\mathbf{L}_{22} = \begin{bmatrix} \mathbf{U}_1 & \mathbf{U}_2 \end{bmatrix} \begin{bmatrix} \mathbf{\Sigma}_1 & \mathbf{0} \\ \mathbf{0} & \mathbf{\Sigma}_2 \end{bmatrix} \begin{bmatrix} \mathbf{V}_1^{\mathrm{T}} \\ \mathbf{V}_2^{\mathrm{T}} \end{bmatrix} \approx \mathbf{U}_1\mathbf{\Sigma}_1\mathbf{V}_1^{\mathrm{T}} \qquad (9)$$

The system matrix **A** is calculated from the expanded observability matrix **Θ**. The natural frequency f_j ($j = 1 \sim n$) and damping ratio h_j ($j = 1 \sim n$) are calculated using the eigenvalue λ_j of the system matrix **A**.

$$f_j = \frac{\left|\ln \lambda_j\right|}{2\pi\Delta t}, \quad h_j = -\frac{\ln\left|\lambda_j\right|}{\left|\ln \lambda_j\right|} \qquad (10\text{-}1,\ 2)$$

2.2 SETTING CALCULATION CONDITION

In the Ordinary MOESP method, it is necessary to adjust the system number *N* and the number of lines *r* of the block Hankel matrix. In Previous research [2], we find the two indicators shown in the following equations can accurately determine the system number *N* and the number of lines *r* in each time section.

$${}_1e_i = \frac{\sqrt{\left(\sum_{i=1}^{n} \sigma_i^{\,2}\right)^{\frac{1}{2}}}}{\left(\sum_{i=1}^{rl} \sigma_i^{\,2}\right)^{\frac{1}{2}}} \times 100 \qquad (11)$$

$${}_2e_i = \sqrt{\frac{\sum_{i=1}^{N_k} \left({}_rZ_i - {}_{ave}Z_i\right)^2}{N_k}} \qquad (12)$$

Where N_k means the total number of time intervals when the input and output data are divided into multiple intervals on the time axis, and ${}_rZ_i$ is the frequency and damping ratio which identified in time interval *i*. ${}_{ave}Z_i$ represents the average value of all block rows of frequencies and/or damping ratio identified in time interval *i*.

As a result of the preliminary examination, it was determined that appropriate calculation results could be obtained for values exceeding 98% of the index ${}_1e_i$ in each time interval. In addition, since it is necessary to secure a

https://doi.org/10.52202/069179-0306

sufficient number of Hankel rows in order to ensure the accuracy of identification, the upper limit was set to the number of Hankel rows.

In accordance with the above-mentioned identification method, dynamic characteristics can be calculated by using earthquake observation. To investigate the time dependent changes in these characteristics, the observed time history is split into 4 s, and a half of this dividing time is processed for each computation.

3 SEISMIC PERFORMANCE OF WOODEN TEMPLE EVALUATED BY EARTHQUAKE OBSERVATION

3.1 SEISMIC OBSERBATION FOR REINFORCED WOODEN TEMPLE

The target building is a wooden one-story temple the roof is copper tiled, the height of the building is about 9.5 m, the plane is about 14 m × 19 m. The timber, that constructs the main frame, is almost entirely Japanese pine, and parts of the columns are composed of zelkova serrate. The primary structural frame is made with post and beam construction. The main aseismic elements of the vertical plane include traditional mud walls and hanging walls finished with ordinary plaster, and the building was seismically retrofitted in 2013 through 2014 by adding to Plywood. the outline is shown in the Fig. 2. As shown in the Fig. 2, accelerometers are installed at 7 locations in the temple for seismic observation. These are the same as the seismometer arrangement before reinforcement reported in the previous study [3].

Acceleration data from 2012 to 2019 can be obtained. All sensors were able to measure to a limit 1500 cm/s (resolution: 0.01 cm/s) at intervals of 0.01 s, and to record acceleration in three directions. Sensors 1 and 2 observed input motions; the other sensors, located on girders on the roof frame, observed the seismic responses of this target building.

As system identification, the assumed characteristics include that the orthogonal directions, which means the X- and Y-directions shown in Fig. 2, affect each other, therefore cannot be operated independently in each direction. In this paper, the following results are computed for a two input (the records of X- and Y- directions by Sensor-2) and ten output (the records of X- and Y-directions by Sensors 3~7) system. Sensor 1 is not used in this study because Sensor 2 can represent the feature of input motion by previous research [3].

3.2 THE EARTHQUSKE OBSERVATION

Many observational results were obtained during the period from 2012 to 2019, including the issue of trigger settings. In this study, observation records were selected on the condition that PGA in at least one of the two horizontal directions exceeded 10 gal. 44 seismic observation records satisfy these conditions, and the system identification results for these are shown below.

For reference, the observed waveforms in the X and Y directions on July 17, 2016, when the maximum PGA was recorded, are shown in Fig. 3, and the response spectrum obtained from them is shown in Fig. 4.

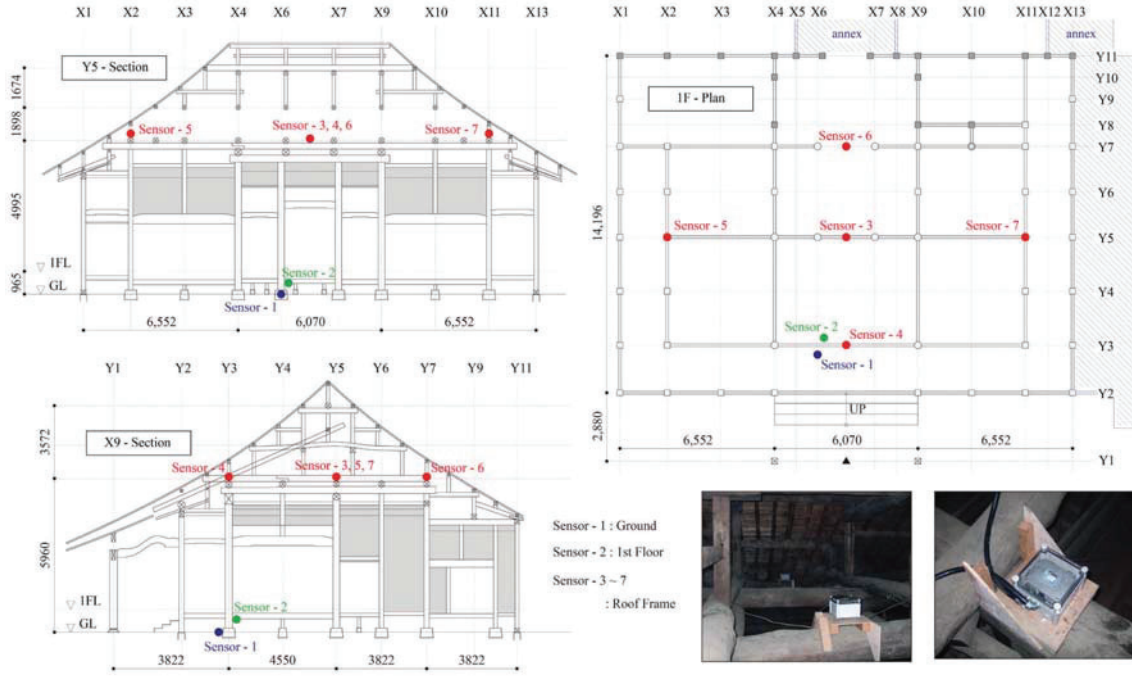

***Figure 2**: Outline of the measuring points on the earthquake observation* [3]

https://doi.org/10.52202/069179-0306

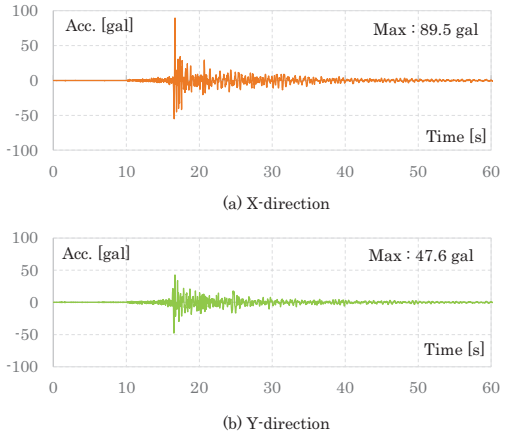

***Figure 3**: Acceleration time history (17th, July, 2016)*

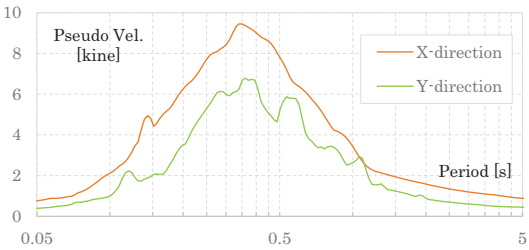

***Figure 4**: Pseudo velocity response spectrum (17th, July, 2016)*

As can be seen in Fig. 3, there is no standard definition of earthquake duration. In this paper, using the effective duration evaluated by the following equation [4] as a measure, we cut off the calculation target interval from each observation record. In addition, in order to remove high-frequency noise that can also be seen in the waveform of Fig. 3, processing was performed using 0.5 through10 Hz bandpass filter.

$$a(t) = \frac{\int_0^{t_0} \ddot{z}^2(t)\,dt}{\int_0^{t} \ddot{z}^2(t)\,dt}$$

Where $a(t)$ means the time history with no dimension of acceleration power, $\ddot{z}$ (t) denotes the acceleration of ground motion, t_0 denotes target time. When $a(t)$ is in the range of

$$0.01 \le a(t) \le 0.95\,,$$

the duration of earthquake is verified the efficiency in this research.

The Fourier spectrum shown in Fig. 4 indicates that the dominant frequency recorded in this earthquake is approximately 3 Hz. Most of the observation records investigated in this study are intraplate earthquakes, which, like this record, are dominated by relatively short periods of 1Hz or more. We add that the target temple also responds clearly to these seismic motions, since it also has a relatively short period.

3.3 UNDERSTANDING THE EFFECT OF NONLINEARLITY

As a result of system identification, Fig. 5 shows the change over time of the natural frequency and story drift for the earthquake that recorded the maximum ground acceleration in the observation record, which discusses Fig. 3 and 4. The story drift is calculated by integration of the acceleration data recorder by Sensor-2 and 3 on each direction.

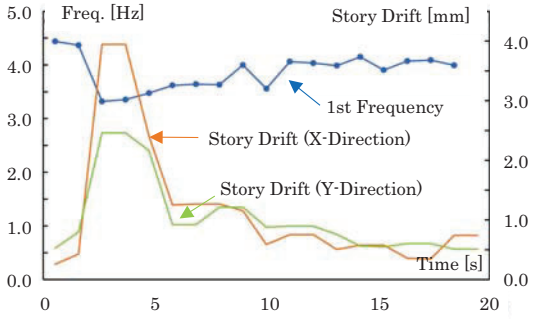

***Figure 5**: Changes in natural frequency and story drift over time estimated by the records on 17th, July, 2016*

Fig. 5 shows that the natural frequency is about 1 Hz as the story drift increases. This is considered to be the result of the nonlinearity of the strain-dependent of a timber structure. In addition, comparing the natural frequency before and after the earthquake, it is also suggested that a decrease of about 0.5 Hz has been observed, causing damage.

In order to confirm the change in vibration properties due to nonlinearity, comparing the vibration mode for each range of story drift corresponding to the identification results shown in Fig. 5. Fig. 6. shows a result comparing the vibration mode of each deformation range. The figure is created by standardizing the maximum value to 1.0 among the eigenvalue mode in each measurement position, and also taking into account the phase difference of each channels.

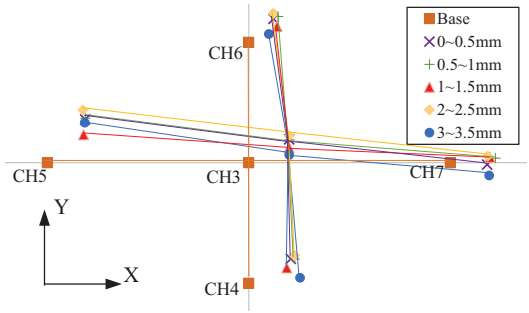

***Figure 6**: Comparison of vibration mode due to difference of story drift estimated by the records on 17th, July, 2016*

All vibration mode is not the same, but no significant difference is observed as shown in Fig. 6. From the above-mentioned results, it is presumed that the vibration properties itself do not change significantly even if the natural frequency due to nonlinearity is reduced.

https://doi.org/10.52202/069179-0306

3.4 INVESTIGATING THE TREND FOR LONG OBSERVSTION PERIOD

Following the discussion of short-term natural frequency changes in the same earthquake described above, only long-term changes are investigated. Fig. 7 shows the average values obtained from the identification results of each observation record, arranged in order by observation period. In this figure, the seasons are color-coded.

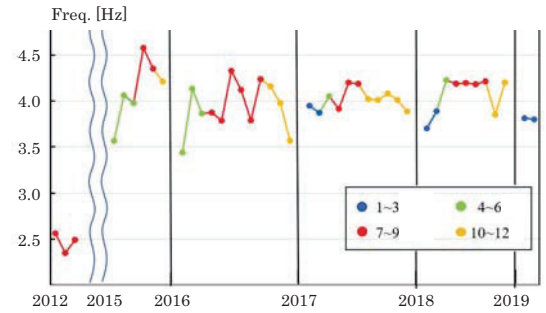

(a) Long-term change of the natural frequency

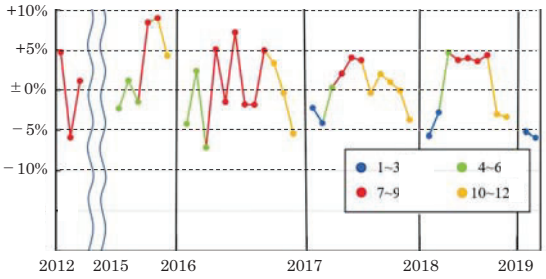

(b) the range of changing caused by seasons

***Figure 7**: Changes in natural frequency for Long-period*

From Fig. 7 (a), it can be confirmed that the natural frequency is greatly improved by the seismic reinforcement, and also can be seen that there is a certain amount of periodic variation in each season. In order to clarify the range of seasonal fluctuations, the Fig. 7 (b) shows the results standardized by the average value for before and after seismic retrofit respectively. From this result, it can be seen that the seasonal variation is about 10 % for the natural frequency, and about 20 % for the stiffness assuming that the mass is the same.

4 ANALYSIS OF LONG-TERM STRUCTURAL PERFORMANCE

4.1 CHANGES IN VIBRATION CHARACTERISTICS DUE TO THE SURROUNDING ENVIRONMENT

We investigate the factors that affect the change in the natural frequency of traditional wooden buildings. Fig. 8 shows a comparison between the outside temperature at the location of the target temple, where is Kasukabe-city, Saitama prefecture (near Tokyo), and the natural frequency for each seismic response of story drift. The temperature is the average of the day published by the Japan Meteorological Agency [5]. In the same figure, symbols are displayed separately for each story drift, and the reasons that the multiple results are plotted on the same horizontal axis, is given multiple identification results as the same event as shown in Fig. 5. In addition, the horizontal axis does not show the real time, but the events that occurred in the year are arranged in order of occurrence.

From Fig. 8, it can be seen that the natural frequency decreases as story drift increases, as in the previous result. First, in order to understand the overall trend, focusing on the results of deformation of 0.5 mm or less, which is the most identified result as the equivalent deformation range,

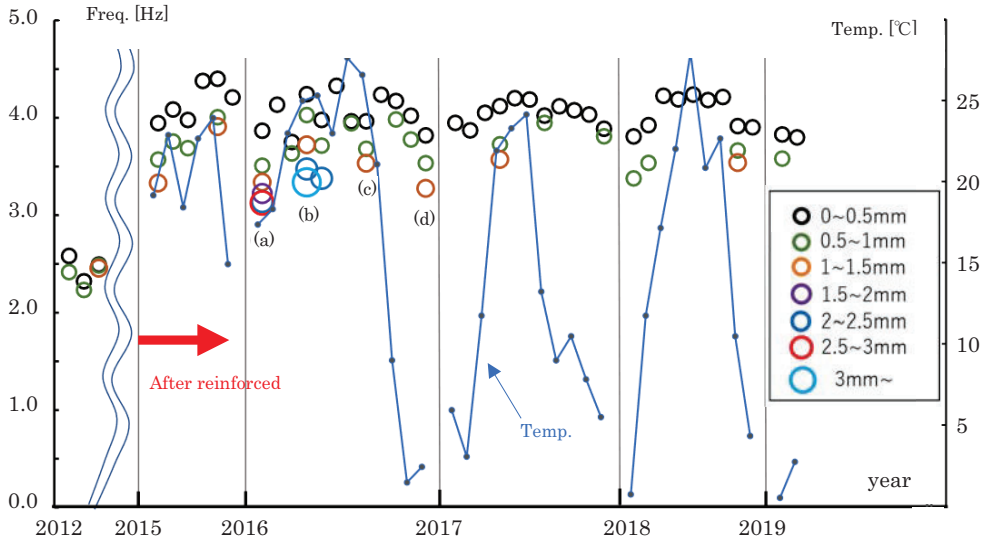

***Figure 8**: Changes in natural frequency for each story drift due to seasonal changes*

https://doi.org/10.52202/069179-0306

it can be seen that the natural frequency has been gradually decreasing since 2015 after the seismic reinforcement. There are two possible reasons. One is the accumulation of damage caused by earthquakes, and the other is the viscoelastic property of wood. The former was also confirmed in the results of Fig. 5, suggesting that there are factors that accumulate in addition to changes in the natural frequency due to nonlinearity. The latter does not even have method to assess its impact. Although there is a possibility that the result was obtained because it was a traditional wooden building where the properties of wood are likely to appear, it is considered to be a problem that can occur in all timber structures.

Next, focusing on the correspondence between the temperature and the natural frequency of the surrounding environment, it can be seen that the natural frequency clearly increases as the temperature increases, and conversely, the natural frequency decreases as the temperature decreases. It is understood the reason that the wood swelled due to the increase in the amount of moisture in the air accompanying the temperature rise, and conversely, the wood contracted due to drying accompanying the temperature drop. The effect is relatively large, because it can be evaluated that the change corresponding to the decrease in the natural frequency for about five years, which discussed above, is repeated in one year.

Finally, in order to confirm the changes in the vibration properties accompanying these changes in the natural frequency, Fig. 9 shows the comparison results of the eigenmodes for the same seasons during three years from 2016, and Fig. 10 shows the comparison results of the eigenmodes identified for the events (a) to (d) appended to Fig. 8, which means the changes occurring over the course of one year. From the results shown in both figures, it is verified that even if some factors change the natural frequency, there is no significant effect on the vibration characteristics. This view is based on various pre-conditions such as the appropriateness of the arrangement of seismic elements, but it is an important property confirmed in this study.

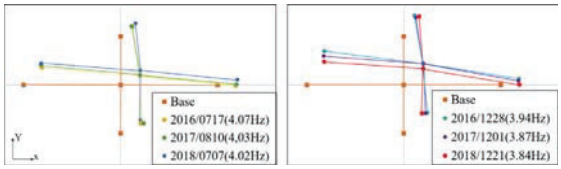

(a) Hot seasons *(b) Cold seasons*

***Figure 9**: Comparison of vibration mode in hot and cold seasons*

5 CONCLUSIONS

In this paper, the subspace method is applied to the observation records of traditional wooden buildings, and the transition of natural frequency over time is verified along with the changes in the environment. The findings are summarized as follows.

- The natural frequency changed as the temperature up and down, suggesting the effect of swell and shrink of the wood composed the target temple.
- It was confirmed that even if the natural frequency changes depending on the surrounding environment, there is no significant difference in the vibration characteristics.
- In the small deformation range about less 3 mm, the variation in the natural frequency may have the same effect as the nonlinearity due to the large and small response.

ACKNOWLEDGEMENT

We would like to our sincere gratitude toward the chief priest of Jyou - syun - in, Seihou Ishida and sub-chief, Ri-gyou Ishida for their help during this earthquake observation; and former assist. prof. Takenori Hida, Tokyo Univ. of science, for advice about system identification. A part of this study was carried out under support by Junichiro Hara and Naoki Tomiyama, former graduate students, to compute identification results and to organize the data.

REFERENCES

[1] Verhaegen, M. and Verdult, V. : Filtering and System Identification A Least Square Approach, Cambridge University Press, 2012. 7

[2] Hara, J. and Sato, T. : Applicability of subspace method to MIMO systems based on identification error - Accuracy verification of three calculation methods for timber structures -, Journal of Structural and Construction Engineering (Transaction of AIJ), 2023 (in preparation).

[3] Sato, T., Nagano, M. and Mochizuki, E : Seismic Performance of A Wooden Temple Inferred from Earthquake Observation and Seismic Diagnosis, WCTE 2014, Quebec, 2014. 8

[4] Akiyama, H. and Kitamura, H. : Relationship between energy spectra and velocity response spectra, Journal of Structural and Construction Engineering (Transaction of AIJ), No. 608, pp.37-43, 2006. 10 (in Japanese).

[5] Japan Meteorological Agency (/www.jma.go.jp)

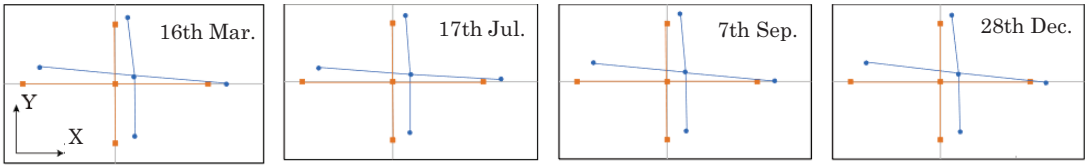

(a) Record – a *(b) Record – b* *(c) Record – c* *(d) Record – d*

***Figure 10**: Comparison of vibration mode changing by seasons*

https://doi.org/10.52202/069179-0306

World Conference on Timber Engineering Oslo 2023

GLUED-LAMINATED TIMBER BEAMS WITH LARGE ROUND HOLES: AN EXPERIMENTAL AND NUMERICAL INVESTIGATION

Francesco Mirko Massaro[1], Kjell Arne Malo[2]

ABSTRACT: Timber beams are oftentimes used as joists in timber floors. Especially for small timber buildings like two-story housing for single or few families, it may be necessary to let service pipes pass through the joists to avoid a reduction of the story height. Therefore, there is a need to have large holes in the timber joists, which under the current local guidelines and the future European regulations, leads to the use of timber beams of significant height. In this study, the capacity of glued-laminated timber beams with large round holes is evaluated. The paper presents results from novel experiments performed on beams with round holes positioned in two different configurations. The holes are considered as large, i.e. the diameter of the holes is 50% of the timber beam height or larger. The objectives are, in addition to the experimental investigations, to establish a numerical simulation approach of these experiments which can be used to future studies of possible solutions to the challenge of large holes in timber joists. For comparison, an analytical evaluation of the beams capacity in accordance with the future European regulations is added.

KEYWORDS: timber beams, large holes, glulam, numerical modelling, cohesive zone

1 INTRODUCTION

Timber is one of the most used structural materials because of its excellent mechanical properties. Moreover, due to its advantage of being environmental friendly, there has been a renewed interest in its usage. In the recent years, examples of buildings such as Treet and Mjøstårnet, both in Norway, have shown that timber can be a good material choice also for high-rise structures [1, 2]. However, for the Nordic timber industry the use of timber in houses for single and few families is still more important. The flooring in these smaller building consists usually of traditional joisted floors with simple solutions for ceiling and decking of the floors, as acoustic properties are of little relevance within single apartments. In these buildings, it is preferable to let pipes, used by e.g. water, heating, or ventilation systems, pass through beams in the floors to reduce the height of the building. The design criteria for these types of floors are usually deformations and vibrations, and one or two large holes in the beams, larger than half of the height, do not increase the deformation significantly, as the portion of the beams having reduced bending stiffness will be very small. Nevertheless, it is a very cheap improvement to reduce the spacing of the beams, in areas where the beams have large holes, to compensate for the reduction in stiffness and strength. Therefore, the presence of large holes for pipes in timber beams is very beneficial and leads to effective building systems without unnecessary use of material and space. The presence of holes generates concentrations of shear and tensile stresses orthogonal to grain in proximity of the hole. The exact location of the stress concentrations depends on the acting forces on the member, i.e. on the ratio between the bending moment M and the shear force V in the hole section (see Figure 1).

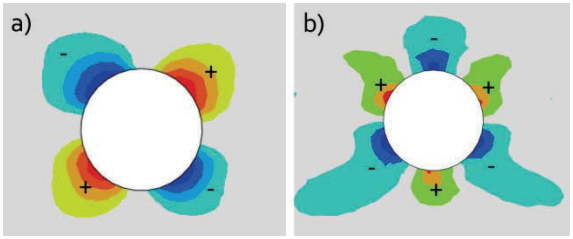

Figure 1: *Stress concentration around circular holes: a) dominant shear (M/V=1h where h is the beam height), b) pure bending (M/V=∞). The symbols + and – indicate tension and compression, respectively.*

Aicher and Höfflin [3] have studied the location of the stress concentrations around a circular hole in a beam subjected to various loading modes, concluding that at approximately 45° from the center of the hole, stress concentrations occur at the edge of the hole.
The strength of timber in tension perpendicular to grain is relatively small and therefore the stress concentrations lead to a reduction of the capacity of the timber element. Consequently, the design of timber members with holes is challenging. Indeed, Eurocode 5 [4] still does not include any normative rule about the presence of holes in timber beams. Nonetheless, there exist national regulations, such as the German National Annex to Eurocode 5 [5], or local guidelines [6] that provide an indication on the maximum hole size. An overview on recent developments on design guidelines can be found in Tapia and Aicher [7].

[1] Francesco Mirko Massaro, NTNU Norwegian University of Science and Technology, Norway, francemm@ntnu.no
[2] Kjell Arne Malo, NTNU Norwegian University of Science and Technology, Norway

https://doi.org/10.52202/069179-0307

Moreover, the future generation of Eurocode 5 will include normative rules, based on Danzer et al. [8], about the design of timber members with holes, although the diameter of the hole, *d*, will be limited to 30% of the timber beam height, *h*, if unreinforced [9]. For joisted floors in small wooden houses, the height of the joists is in the range of 220 mm to 300 mm. Typical water pipes in buildings can have diameter of about 160 mm and thus the limitation on the ratio *d*/*h* increases the necessary beam height significantly with the presence of a hole.

Numerous experiments have been performed on glued-laminated timber beams with round holes over the time, i.a. Johannesson [10], Höfflin [11], Aicher and Höfflin [12], Danzer et al. [13]. However, in these studies the diameter of the holes was always smaller than 50% of the beam height.

Several methods were proposed to analyze the failure load of timber beams with holes, such as i.a. models based on linear elastic fracture mechanics (LEFM) [14], Weibull based models [15, 16], cohesive zone models (CZM) [17]. The use of numerical models with cohesive elements has provided good accuracy in the evaluation of the failure load of timber structural elements, such as for laminate veneer lumber (LVL) beams with round holes [18] and glulam beams with rectangular holes [19].

The main objectives of the present study are to evaluate the experimental capacity and a numerical model of glued-laminated timber beams with large round holes. In this study, a hole is defined as large by having a diameter larger than 50% of the beam height. Thus, novel experiments on timber beams with large round holes were performed. The experimental results were then used to validate the numerical model using cohesive elements with definition of a traction-separation law. Finally, an analytical evaluation of the failure load of timber beams with large round holes, based on the latest draft of the new generation of Eurocode 5, is provided.

2 MATERIAL AND METHODS

2.1 EXPERIMENTS

The experimental investigation was carried out on glued-laminated beams with large holes at the Norwegian University of Science and Technology, Trondheim. The experiments were conducted on K-beams made of Norway Spruce (Picea abies). The K-beams, manufactured by Inntre Kjeldstad AS, are not covered by the EN 14080:2013 standard [20], and therefore they have their own technical approval [21]. Their inner lamellae, classified as LT20 according to the INSTA 142:2009 standard [22], are 17 or 19 mm thick, while the two outermost lamellae are 47 mm thick and are classified as C24 according to the EN 338:2016 standard [23].

Sixty-nine tests were conducted on beams with dimension 36×300×4200 mm^3. Sixty of the tested beams have a hole of 150 to 170 mm diameter, which corresponds to 50 to 56.7% of the beam height. The series name reflects the position and the diameter of the hole: M indicates that the hole is located in a moment-dominated zone, while V indicates that the hole is located in a shear-dominated zone. Moreover, an additional series of nine experiments on K-beams without holes was performed and it is denominated with the letter K. An overview of the performed experiments is given in Table 1 and the geometrical properties are explained in Figure 2.

***Table 1**: Summary of the performed experiments*

Series name	n. of tests	*d* [mm]	l_V [mm]	l_A [mm]	l_L [mm]
M170	9	170	1630	1530	300
V170	10	170	700	600	1230
M160	11	160	1640	1540	300
V160	10	160	700	600	1240
M150	10	150	1650	1550	300
V150	10	150	700	600	1250
K	9	-	-	-	-

The beams were tested with a 3-point bending configuration (see Figure 2), with the supports centered at 100 mm from the beam ends. Prior to testing, the glulam beams were located in a room with the constant climate of 20 °C of temperature and 65% relative humidity (RH) of the air for the time necessary to reach a moisture content (MC) of approximately 12% in the beams.

The load was applied by means of a hydraulic actuator and it was distributed over an aluminum U-profile 140 mm long and 4 mm thick, to avoid local compression deformation (see Figure 2). Moreover, the load was continuously recorded by the test machine together with the displacement of the actuator.

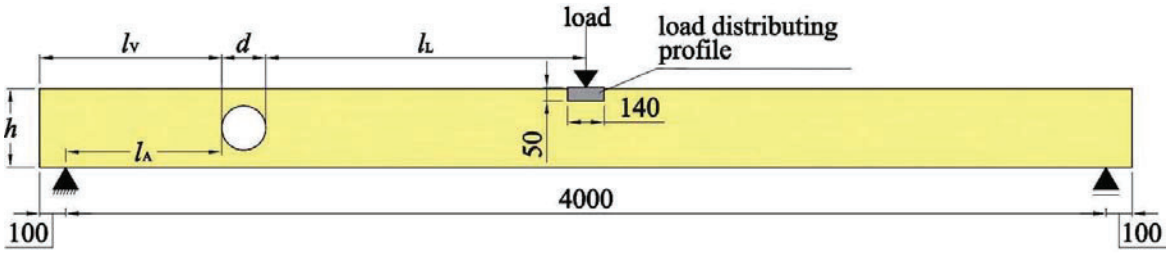

***Figure 2:** Test setup with location of the hole and the load.*

https://doi.org/10.52202/069179-0307

The tests were conducted in displacement control and performed in agreement with the standard EN 380:1993 [24] for the determination of the load at failure. After an initial loading/unloading cycle with the force cycling between ca. 1 and 2 kN, the displacement is increased and then kept constant in order to reach and maintain a loading force of ca. 3 kN. Finally, the displacement is further increased until the failure of the beam is obtained.

2.2 NUMERICAL SIMULATIONS

A numerical model to simulate the behavior of the glulam beams was developed in the FEM software program Abaqus [25].

Timber can be considered as an orthotropic material. However, in the two transversal directions the same material properties were used. Nevertheless, it should be noted that the shear moduli are independent from the normal moduli and thus the material was modeled differently from transversally isotropic. The normal moduli E_x, E_y, E_z and the shear moduli G_{xy}, G_{xz} are chosen according to the K-beams technical approval [21], while G_{yz} as 1/10 of the other shear moduli, and the Poisson's ratios are selected based on Dahl [26] and Massaro et al. [27]. The elastic material properties used in the numerical model are given in Table 2, where the subscript "x" indicates the grain direction. The coordinate system is depicted in Figure 3.

The geometry of the model resembles the geometry of the tested beams, i.e. the model consists of a beam, 4200 mm long and cross-section of 36×300 mm^2. The beam has a hole located according to the geometry given in Table 1 and illustrated in Figure 2.

The beam movements in the y-direction are on the supports on the bottom beam surface, centered at 100 mm from the ends of the beam as displayed in Figure 3b, resembling the experimental supports. The beam is loaded by applying a displacement on a 36×140 mm^2 surface on the middle of the beam top surface, i.e. in the xz-plane (Figure 3a). The loading surface resembles the load distributing area of the experimental configurations.

The behavior in compression parallel to grain is considered to be elastic-perfectly plastic, with elastic limit $f_{c,0}$ (see Table 2). Moreover, the location of the highest transversal tensile stresses around the hole, as determined with an elastic analysis for each configuration, is at the hole edge in a plane at approximatively 40° - 60° from the center of the hole. In correspondence of the highest transversal stress, cohesive layers (layers A and B in Figure 3a), crossing the entire length of the beam, were then introduced in the model. An additional cohesive layer (layer C) is located vertically under the hole, as this area may be subjected to high tensile stress parallel to grain due to bending (see Figure 3a).

A cohesive layer requires the definition of a traction-separation law, i.e. stiffness properties, a damage initiation criterion and a damage evolution phase. The traction-separation law used in this model is a bilinear law, with an initial elastic phase succeeded by a linear softening which starts when the chosen damage initiation criterion is fulfilled (see Figure 4).

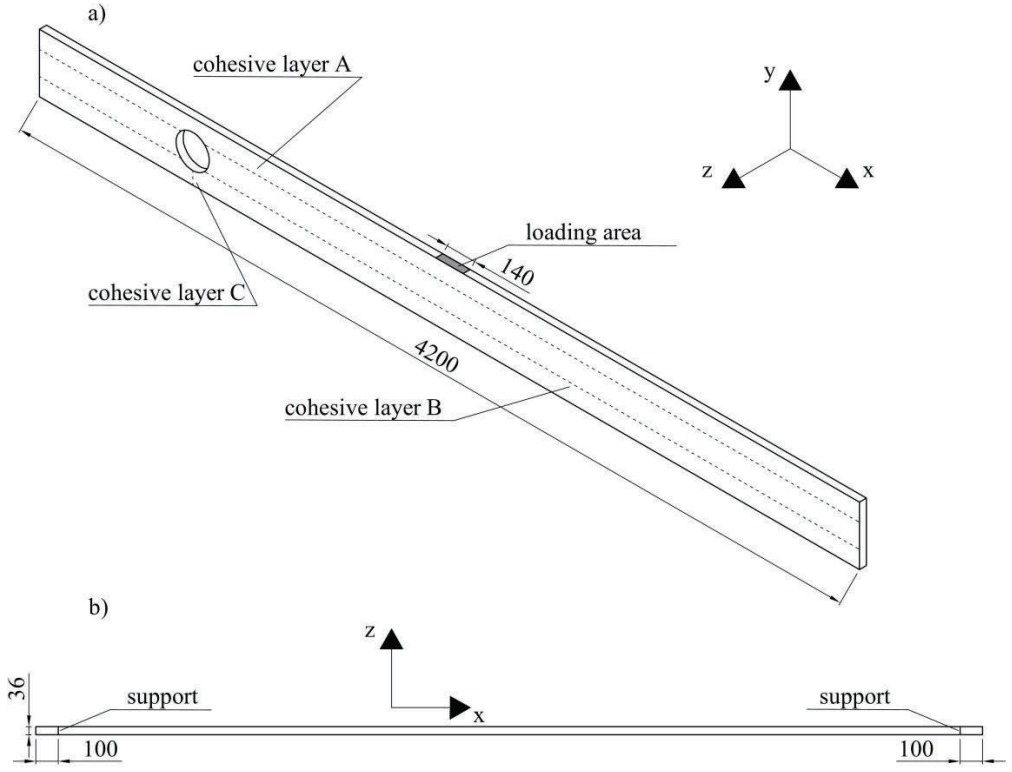

Figure 3: *Geometry of numerical model: a) isometric view and location of the cohesive layers, b) bottom plan view*

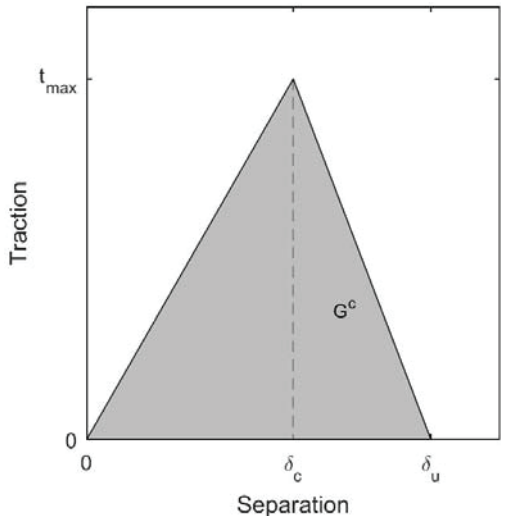

Figure 4: *Traction-separation law*

The elastic stiffness values of the cohesive layers are equal to the stiffness values used for the timber parts. As damage initiation criterion, the maximum stress criterion has been used, i.e. the damage starts when either the tensile stress orthogonal to the cohesive layer or the shear stress in the layer reaches the maximum allowed value. The criterion is expressed as in Equation (1), where t_n, t_s, t_t represent the normal and the two shear tractions, respectively. Note that the angular brackets specify that t_n is a tension stress and can thus only be positive. The subscript max indicates the elastic limit stress in the specific direction. These limit values are chosen as the mean values of the respective strengths.

$$\max\left\{\frac{\langle t_n\rangle}{t_{n\max}};\frac{t_s}{t_{s\max}};\frac{t_t}{t_{t\max}}\right\}=1 \qquad (1)$$

The mean values for shear and tension parallel to grain strength have been obtained from the results of the experiments performed by Treteknisk [28-30] on the K-beams. On the other hand, the tension orthogonal to grain mean strength has been assumed based on Dahl [26] and Massaro et al. [27], while the compression parallel to grain mean strength was based on the K-beams Technical Approval [21, 31].

The damage evolution phase in the layers A and B is controlled by the energy method with linear softening [18, 32]. The critical values of the fracture energy for the opening mode (mode I) and shearing mode (mode II) are chosen as the average of the values reported by Ostapska [33] and Ostapska and Malo [34]. Furthermore, the mixed mode, usually relevant in beams with holes, is here described by Wu's criterion [35, 36] presented in Equation (2).

$$\left(\frac{G_I}{G_{Ic}}\right)^{0.5}+\frac{G_{II}}{G_{IIc}}=1 \qquad (2)$$

In Equation (2), G_I and G_{II} represent the fracture energies for mode I and mode II, respectively, while G_{Ic} and G_{IIc} denote the respective critical values.

The material properties of wood and of the cohesive layers are summarized and given in Table 2.

Table 2: *Material properties of wood and of the cohesive layers used in numerical simulations*

Elastic properties of wood	Normal moduli	E_x	11000 MPa	[21]
		$E_y \equiv E_z$	370 MPa	
	Shear moduli	$G_{xy} \equiv G_{xz}$	690 MPa	
		G_{yz}	69 MPa	[20]
	Poisson's ratios	ν_{xy}	0.5	[26, 27]
		ν_{xz}	0.6	
		ν_{yz}	0.6	
Mean strengths	Tension orthogonal to grain	$f_{t,90}$	2 MPa	[26, 27]
	Tension parallel to grain	$f_{t,0}$	40 MPa	[29, 30]
	Shear	f_v	4 MPa	[28]
	Compression parallel to grain	$f_{c,0}$	26 MPa	[21, 31]
Fracture energies (layers A and B)	Mode I	G_{Ic}	0.24 N/mm	[33, 34]
	Mode II	G_{IIc}	0.79 N/mm	[33]

The elements in the cohesive layer C followed a different damage evolution since they have to represent tensile failure parallel to grain. These elements, if the damage initiation criterion is satisfied, immediately lose their stiffness. This is obtained by imposing $\delta_u \cong \delta_c$ as their damage evolution law (see Figure 4).

Eight-node three-dimensional elements were used in the model: C3D8 (i.e. full integration) for the wooden material and COH3D8 for the cohesive layers with viscous parameter chosen equal to 10^{-3} [18]. Note that the viscous parameter is only necessary to ensure convergence of the analysis and does not have physical meaning. After a sensitivity mesh study, the mesh size has been chosen equal to 20 mm for the timber parts, and equal to 5 mm for the cohesive layers, thus in agreement with Abaqus guidelines [25].

https://doi.org/10.52202/069179-0307

3 RESULTS AND DISCUSSION

3.1 EXPERIMENTAL RESULTS

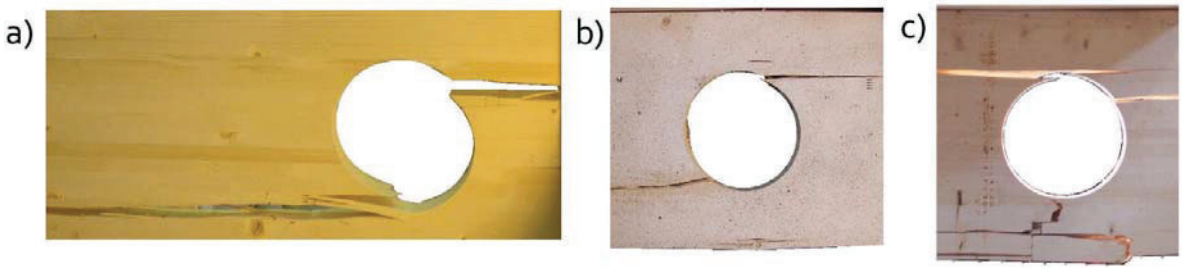

***Figure 5**: Examples of beams at failure: a) Test V170-5; b) Test M150-1; c) Test M150-4*

Figure 5 shows typical examples of beam failure. The cracks were usually initiating either at the top right or at the bottom left of the hole circumference, and then they propagated from there, usually until the beam ends. It should be noted that some beams of the M-series presented additional cracks on the bottom chord of the beam (see e.g. Figure 5c), likely due to bending stresses and thus tension parallel to grain. The failure load F_f, i.e. the maximum load reached in an experimental test, for each tested beam is given in Figure 6, together with the mean value of the series.

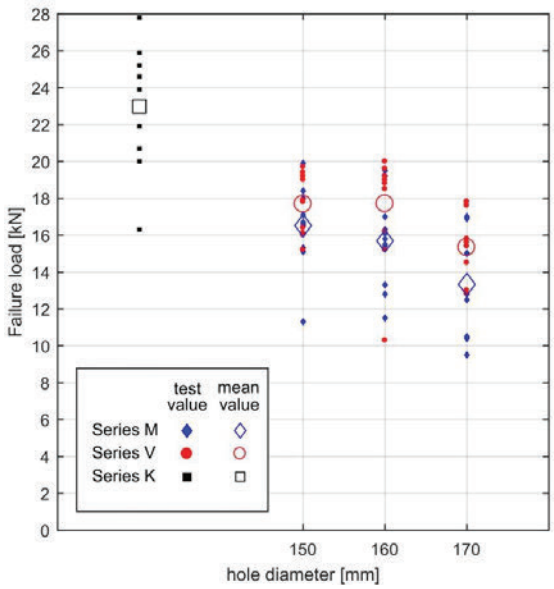

***Figure 6:** Experimental failure loads.*

In Figures 7 and 8, the red dashed lines depict a typical representative outcome of the results of the conducted investigation, described in Chapter 2.1, for the series with the largest holes, i.e. M170 and V170, respectively. The response is given by loading force vs. displacement.

The results show, after the initial loading/unloading phase, a linear increase of the loading force with respect to the deformation applied in agreement with loading procedure described in Chapter 2.1. By increasing the load, the first crack appeared and it gradually spread over the whole beam thickness. Thus, the corresponding load is defined as cracking load (F_{cr}). Afterwards, the crack propagated and new cracks were formed, until a sudden drop in the force occurs corresponding to failure. In some cases, especially in the M-series, the loading force increased again after the first drop, probably because of the presence of knots and finger joints or fiber bridging, but it was followed again by further sudden drops in the force, thus reaching failure.

The distribution of the failure load may be considered lognormal [37]. Thus, the mean and characteristic values of the measured cracking loads, $F_{cr,mean}$ and $F_{cr,k}$ respectively, and failure loads, $F_{f,mean}$ and $F_{f,k}$ respectively, were then determined according to EN14358. The values are reported in Table 3.

***Table 3:** Experimental results: mean and characteristic values. (Values in kN. Coefficient of variation in parentheses.)*

Series	$F_{cr,mean}$	$F_{cr,k}$	$F_{f,mean}$	$F_{f,k}$
M170	11.03 (0.323)	5.37	13.33 (0.220)	8.20
V170	12.70 (0.094)	10.41	15.33 (0.134)	11.50
M160	13.02 (0.169)	9.05	15.69 (0.162)	11.12
V160	15.56 (0.559)	4.35	17.70 (0.206)	11.34
M150	12.70 (0.286)	6.62	16.52 (0.154)	11.85
V150	13.44 (0.221)	8.14	17.68 (0.094)	14.46
K	-	-	22.97 (0.165)	16.00

The results in Table 3 and Figure 6 show that the failure load of the M-series is lower than in the V-series, arguably due to high tensile stress parallel to grain under the hole, in addition to the stress concentrations around the hole. Indeed, the reduction of the mean failure load, from the

reference value for beams without holes (i.e. K-series), ranges between 23% and 33% for the V-series, while for the M-series it ranges between 28% and 42%. The difference between the failure load of the M-series and the V-series is in the order of 2 kN. Moreover, the V-series seems to be less affected than the M-series by the presence of larger holes. Indeed, increasing the diameter of the hole from 150 mm to 170 mm, i.e. from $d/h = 0.5$ to $d/h = 0.57$, the beams of the M-series observe a reduction of the failure load of about 19%, while the reduction is lower for the V-series beams, i.e. approximately 13%.

3.2 NUMERICAL RESULTS

The numerical simulations of the timber beams were performed with the parameters given in Chapter 2.2, and their results are given in Table 4. Additionally, in Table 4, the mean experimental capacity of each configuration, $F_{f,mean}$, and the relative difference with the numerical results are given, showing that the model is in good agreement with the test results and can evaluate the failure load with good accuracy.

Furthermore, the results of the simulations for the M170 and V170 configurations are given in Figures 7 and 8, respectively, in terms of force vs. displacement curves and compared with the experimental results. The force is the load applied in the model, and the deflection is the displacement measured at mid-span. In Figures 7 and 8, the dash-dotted lines represent the experimental results while the continuous lines represent the results obtained from the simulations. Additionally, in the plots the mean failure load obtained from the experiments is depicted with a horizontal dash-dotted line.
The curves in Figures 7 and 8 show good agreement between the experimental and the numerical results. Nevertheless, the stiffness of the simulated beams is slightly higher than in the experiments. The deflection in the experimental investigation is the measured movement of the loading actuator. Thus, the deflection is affected from the flexibility of the test rig, leading to a measured value slightly larger than in the idealized numerical model.

Table 4: *Comparison between numerical and experimental results*

Series	$F_{f,num}$ [kN]	$F_{f,mean}$ [kN]	Relative difference
M170	14.08	13.33	5.6%
V170	15.53	15.33	1.3%
M160	14.81	15.69	5.6%
V160	16.63	17.70	6.0%
M150	15.59	16.52	5.6%
V150	17.69	17.68	0.1%

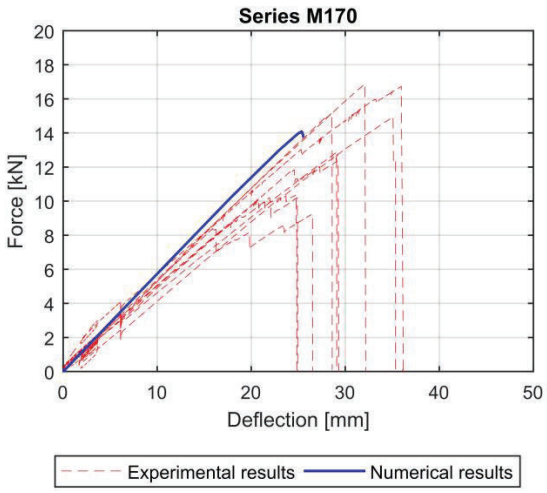

Figure 7: *Comparison between experimental results and numerical simulations: series M170.*

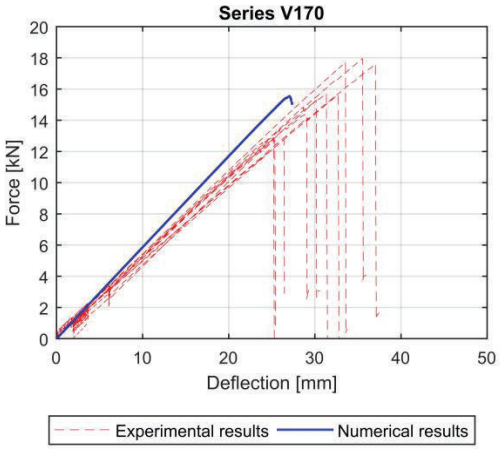

Figure 8: *Comparison between experimental results and numerical simulations: series V170.*

3.3 COMPARISON WITH REGULATIONS

The new generation of Eurocode 5 [9] includes normative regulations for the evaluation of timber member with holes. However, the diameter of the hole is limited to 30% of the beam height in case of unreinforced holes [9]. Herein, the Eurocode equations are however applied for holes with diameter larger than the limit. According to the new draft of Eurocode 5, the characteristic capacity F_k of a timber beam resembling load conditions and geometry of the tested beams is evaluated by taking into account the three conditions expressed in Equations (3), (4) and (5).

https://doi.org/10.52202/069179-0307

$$F_k = \frac{b \cdot \left(\frac{4 \cdot V_{\text{ref}}}{b \cdot d^2}\right)^{0.2}}{\frac{7}{52 \cdot h} \cdot \left[3 - \left(0.7 \cdot \frac{d}{h}\right)^2\right] \cdot \left[1.1 + 1.3 \cdot \frac{d}{h} - 1.3 \cdot \left(\frac{d}{h}\right)^2\right] + \frac{0.9 \cdot (l_A + d)}{8 \cdot d \cdot h} \cdot \left(\frac{d}{h}\right)^2} \cdot f_{\text{t,90,k}} \; ; \; V_{\text{ref}} = 0.01 \text{ m}^3 \quad (3)$$

$$F_k = \frac{2 \cdot b \cdot (h^3 - d^3)}{6 \cdot (l_A + d) \cdot h} \cdot f_{\text{m,k}} \quad (4)$$

$$F_k = \frac{2 \cdot b \cdot (h - 0.7 \cdot d)}{1.5 \cdot 1.8 \cdot \left(1 + 0.7 \cdot \frac{d}{h}\right) \cdot \left(\frac{0.7 \cdot d}{h}\right)^{0.2}} \cdot f_{\text{v,k}} \quad (5)$$

Equation (3) limits the capacity due to the tensile stresses perpendicular to grain generated by the transfer of bending and shear stresses around the hole, while Equations (4) and (5) limit the capacity because of the bending stresses and shear stresses generated in the residual cross-section, respectively.

The characteristic values of the strength are chosen according to the Technical Approval for K-beams [21], i.e. the tensile strength perpendicular to grain $f_{\text{t,90,k}}$ is chosen as 0.4 MPa, the bending strength $f_{\text{m,k}}$ as 24 MPa and the shear strength $f_{\text{v,k}}$ as 3.5 MPa. By inserting these strength values and the geometric parameters given in Table 1 into Equations (3), (4) and (5), the characteristic capacity F_k is obtained for all tested configurations.

The results are summarized in Table 5, together with a comparison with the experimental results. Furthermore, it is given the relative difference δ between the experimental results and Eq. (3).

Table 5: *Comparison experimental results vs regulations*

Series	F_k [kN] Eq. (3)	F_k [kN] Eq. (4)	F_k [kN] Eq. (5)	$F_{f,k}$ [kN] (exp.)	δ [%]
M170	9.9	12.5	14.6	8.2	+17.3
V170	12.7	27.5	14.6	11.5	+9.3
M160	10.4	13.0	15.6	11.1	-6.8
V160	13.1	28.9	15.6	11.3	+13.6
M150	10.9	13.5	16.6	11.9	-8.2
V150	13.6	30.2	16.6	14.5	-5.8

It can be noted that also for the Eurocode regulations the critical failure mechanism in the beams is splitting perpendicular to grain starting from the edge of the holes, in accordance with the experiments.

The perpendicular to grain splitting failure mechanism, represented by Equation (3), gives a safe estimation for holes of 150 mm, i.e. $d/h = 0.5$. However, for larger holes, it overestimates the characteristic capacity of the beams up to 17%. Indeed, Equation (3) is only valid up to $d/h = 0.3$ for unreinforced holes, and it may need adjusting in order to consider round holes with large diameters.

4 CONCLUSIONS

The objectives of this study were to experimentally evaluate the capacity of glued-laminated timber beams with large round holes and to validate a numerical model for the description of such beams.

Six series of experiments were performed on glued-laminated beams having a hole of diameter varying between 50% and 56.7% of the beam height, for a total of sixty tests. The series differed in the location of the hole: the M-series exhibited a hole in a moment-dominated cross-section, while the V-series presented it in a shear-dominated cross-section. The experiments showcased that the beams have a mean capacity ranging between 13.3 and 16.5 kN for the M-series, and between 15.3 and 17.7 kN for the V-series, respectively. This resulted in a decrease of the capacity of the beam, with respect to a beam without holes, up to 43% when the hole is positioned in a moment-dominated area. On the other hand, the presence of holes in a shear-dominated area has a lower influence, with a drop of the capacity up to 33%.

A numerical model, which resembled the beams geometry, was utilized to study their capacity and fracture process. The model presents horizontal cohesive layers in the location of the predicted fracture planes. An additional vertical cohesive layer was introduced underneath the hole in order to take into account the possibility of longitudinal tensile failure of the beams. The mechanical parameters of the cohesive layers were either chosen according to experimental investigations performed on the beams (Technical Approval) or relevant literature. The model exhibited an overall good agreement. Indeed, the relative difference of the numerical model does not exceed 6%, thus allowing for a proper evaluation of the failure load. Therefore, the numerical model may be used for further studies on the topic of large round holes in timber joists.

Finally, an analytical evaluation of the characteristic capacity of the beams according to the future European regulations was provided. As expected, the splitting verification was the most restrictive and it provided a fair evaluation of the failure load, especially for 150 mm hole diameter. However, the limitations on the size of holes in beams in joisted floors appear to be restrictive, as the beams having circular holes of about 57% of the height

show a residual strength exceeding 57% relative to a beam without any hole.
Furthermore, for a joisted floor having beams with large hole in an area, the spacing between the beams can be halved and the strength of that area becomes unaltered. However, some precautions should be made to avoid drying cracks starting at the hole. Possible actions are painting the hole surface and screw reinforcement.

ACKNOWLEDGMENTS

The authors would also like to acknowledge Atis Degro, Pål Østen Solberg and Noh Weldeab, for their contribution in performing experimental tests and numerical simulations. Furthermore, the supply of the test beams from Inntre Kjeldstad AS is gratefully acknowledged.

REFERENCES

[1] Abrahamsen, R. and Malo, K.A., *Structural design and assembly of "treet" - A 14-storey timber residential building in Norway*, in *WCTE 2014 - World Conference on Timber Engineering*. 2014: Quebec City, Canada.

[2] Abrahamsen, R., *Mjøstårnet - 18 storey timber building completed*, in *24. Internationales Holzbau-Forum IHF*. 2018: Garmisch-Partenkirchen, Germany.

[3] Aicher, S. and Höfflin, L., *Runde Durchbrüche in Biegeträgern aus Brettschichtholz - Teil 1: Berechnung.* Bautechnik, 2001. 78(10): p. 706-715.

[4] CEN, *Eurocode 5: Design of timber structures – Part 1-1: General rules and rules for buildings*, in *EN 1995-1-1:2004*. 2004, Comité Européen de Normalisation

[5] DIN, *Nationaler Anhang - National festgelegte Parameter - Eurocode 5: Bemessung und Konstruktion von Holzbauten - Teil 1-1: Allgemeines - Allgemeine Regeln und Regeln für den Hochbau*, in *DIN EN 1995-1-1:2004/NA:2013*. 2013, Deutsche Institut für Normung e.V.

[6] SINTEF, *Trebjelkelag. Dimensjonering og utførelse.* 2011.

[7] Tapia, C. and Aicher, S., *Evaluation of design concepts for holes in glulam beams - comparison with test results.* Otto-Graf-Journal, 2019. 18: p. 329-344.

[8] Danzer, M., Dietsch, P., and Winter, S., *Round holes in glulam beams arranged eccentrically or in groups*, in *INTER International Network on Timber Engineering Research - Meeting 50*. 2017: Kyoto, Japan.

[9] CEN, *Eurocode 5: Design of timber structures – Part 1-1: General rules and rules for buildings*, in *prEN 1995-1-1:20XX*. 2021, Comité Européen de Normalisation

[10] Johannesson, B., *Design problems for glulam beams with holes: stresses and stress concentrations, fracture criteria, design considerations*, in *Department of Structural Engineering, Division of Steel and Timber Structures*. 1983, Chalmers University of Technology: Göteborg.

[11] Höfflin, L., *Runde Durchbrüche in Brettschichtholzträger – Experimentelle und theoretische Untersuchungen*, in *MPA Otto-Graf-Institute*. 2005, University of Stuttgart: Stuttgart.

[12] Aicher, S. and Höfflin, L., *Tragfähigkeit und Bemessung von Brettschichtholzträgern mit runden Durchbrüchen – Sicherheitsrelevante Modifikationen der Bemessungsverfahren nach Eurocode 5 und DIN 1052.*, in *MPA Otto-Graf-Institute*. 2006, University of Stuttgart: Stuttgart.

[13] Danzer, M., Dietsch, P., and Winter, S., *Reinforcement of round holes in glulam beams arranged eccentrically or in groups*, in *WCTE 2016 - World Conference on Timber Engineering*. 2016: Wien, Austria.

[14] Aicher, S., Schmidt, J., and Brunold, S., *Design of timber beams with holes by means of fracture mechanics*, in *CIB-W18/28*. 1995: Copenhagen, Denmark.

[15] Aicher, S. and Höfflin, L., *Fracture behavior and design of glulam beams with round holes*, in *WCTE 2008 - 10th World Conference on Timber Engineering*. 2008: Miyazaki, Japan. p. 132-140.

[16] Danielsson, H. and Gustafsson, P.J., *A probabilistic fracture mechanics method and strength analysis of glulam beams with holes.* European Journal of Wood and Wood Products, 2011. 69(3): p. 407-419.

[17] Schmidt, J. and Kaliske, M., *Models for numerical failure analysis of wooden structures.* Engineering Structures, 2009. 31(2): p. 571-579.

[18] Ardalany, M., Fragiacomo, M., and Moss, P., *Modeling of Laminated Veneer Lumber Beams with Holes Using Cohesive Elements.* Journal of Structural Engineering, 2016. 142(1): p. 04015102.

[19] Danielsson, H. and Gustafsson, P.J., *Fracture analysis of glued laminated timber beams with a hole using a 3D cohesive zone model.* Engineering Fracture Mechanics, 2014. 124-125: p. 182-195.

[20] CEN, *Timber structures - Glued laminated timber and glued solid timber*, in *EN 14080:2013*. 2013, Comité Européen de Normalisation

[21] SINTEF, *Teknisk Godkjenning K-bjelken*. 2014, SINTEF Byggforsk: Oslo.

[22] INSTA, *Nordic visual strength grading rules for timber*, in *INSTA 142:2009*. 2009, Internordic Standardization.

[23] CEN, *Structural timber - Strength classes*, in *EN 338:2016*. 2016, Comité Européen de Normalisation

[24] CEN, *Timber structures - Test methods - General principles for static load testing*, in *EN 380:1993*. 1993, Comité Européen de Normalisation

[25] Dassault Systemes, *Abaqus/CAE*, in *Abaqus*. 2014.

[26] Dahl, K.B., *Mechanical properties of clear wood from Norway spruce*, in *Faculty of Engineering Science and Technology, Department of Structural*

https://doi.org/10.52202/069179-0307

Engineering. 2009, Norwegian University of Science and Technology: Trondheim.
[27] Massaro, F.M., Stamatopoulos, H., Andersen, J., and Brekke-Rasmussen, E., *Finite element modelling and experimental verification of timber halved and tabled scarf joints.* International Wood Products Journal, 2022: p. 1-10.
[28] Norsk Treteknisk Institutt, *Skjærtest av K-bjelken*. 2003, Norsk Treteknisk Institutt: Oslo.
[29] Norsk Treteknisk Institutt, *Bøyetest av K-bjelken*. 2003, Norsk Treteknisk Institutt: Oslo.
[30] Norsk Treteknisk Institutt, *Test av K-bjelken*. 2009, Norsk Treteknisk Institutt: Oslo.
[31] JCSS, *Jcss Probabilistic Model Code*, in *Part 3: Resistance Models*. 2006, Joint Committee on Structural Safety. p. 16.
[32] Schoenmakers, J.C.M., *Fracture and failure mechanisms in timber loaded perpendicular to the grain by mechanical connections*. 2010, Eindhoven University of Technology: Eindhoven.
[33] Ostapska, K., *Fracture in wood of Norway spruce*, in *Faculty of Engineering Science and Technology, Department of Structural Engineering*. 2020, Norwegian University of Science and Technology: Trondheim.
[34] Ostapska, K. and Malo, K.A., *Wedge splitting test of wood for fracture parameters estimation of Norway Spruce.* Engineering Fracture Mechanics, 2020. 232: p. 107024.
[35] Wu, E.M., *Application of Fracture Mechanics to Anisotropic Plates.* Journal of Applied Mechanics, 1967. 34(4): p. 967-974.
[36] Jernkvist, L.O., *Fracture of wood under mixed mode loading: I. Derivation of fracture criteria.* Engineering Fracture Mechanics, 2001. 68(5): p. 549-563.
[37] CEN, *Timber structures - Calculation and verification of characteristic values*, in *EN 14358:2016*. 2016, Comité Européen de Normalisation

World Conference on Timber Engineering Oslo 2023

ASSESSMENT OF THE FUNDAMENTAL PERIOD OF MULTI-STOREY CROSS LAMINATED TIMBER BUILDINGS

Ebenezer Ussher[1], Angelo Aloisio[2], Roberto Tomasi[1]

ABSTRACT: Cross laminated timber has entered the building industry as an alternative to reinforced concrete with interest for employing them in buildings in high seismic regions because they are lightweight. It is envisaged simplified methods have limitations in predicting design level demands on CLT systems due to the complexities and challenges associated with the material. The objective of this work is assessing the efficiency of proposed analytical methods in predicting the fundamental period (T_1) of building superstructures made of CLT. This is because T_1 is the basis for the equivalent lateral force method in seismic analysis of buildings. The assessment is conducted by comparing predictions from verified numerical modal models with estimates from available empirical formulas. Suggestions are made for the minimum requirements for assessing CLT buildings under dynamic loads.

KEYWORDS: Analytical formulas, buildings, cross-laminated timber, fundamental period, seismic design

1 INTRODUCTION

Timber has been identified as a renewable and sustainable construction material capable of being part of the solution to the global warming menace [1-3]. This is because carbon dioxide ((CO_2) the primary anthropogenic greenhouse gas, accounting for 78% of the human contribution to the greenhouse effect) can be absorbed and stored by timber and timber-related products in their lifetime [1]. This reflects that engineered wood products (EWP) such as cross laminated timber (CLT) has better green credentials than mineral resourced-based construction products including concrete and steel. Development of Fire Engineering tools in recent times have also been at the forefront in erasing the concerns associated with timber as a combustible construction material in the building industry [4]. This has enabled the adaptation of massive EWP and other timber materials as new structural forms to meet sustainable housing demands and challenges.

CLT construction systems are manufactured with three or more layers of lumber arranged and bonded in an orthogonal manner enhancing its split resistance to in-plane loading. Commercially they are available in thicknesses ranging between < 100mm and about 500mm [5,6]. Developed and used in Europe for nearly two decades CLT construction systems have become popular across the globe for putting up low- to medium-rise buildings. CLT products have high stiffness to mass ratios and have similar load carrying characteristics to reinforced concrete (RC) [6]. These make them suitable for building in high seismic-prone regions and in areas with soft soil conditions. Consequently, they have become popular as an alternative to RC for the construction of floors and walls including shear walls [4]. However, among the challenges in respect of using new building systems especially those prefabricated from timber like CLT, is employment of empirical design formulas that are applicable to simple design cases, and which may not work well for those new products. Most design codes and guidelines [7-9] recommend that seismic analysis of buildings whose responses are not significantly influenced by contributions from higher-order modes be conducted using the Equivalent Static Force Procedure (ESFP). Such buildings are required to satisfy some criteria for regularity both in footprint and in elevation. The prediction of the fundamental period (T_1) is therefore the most important parameter in determining the base shear to be proportioned along the height of the building [7,8]. Various formulas have been proposed for predicting the fundamental period (T_1) of buildings as a precursor in determining the horizontal seismic forces under the ESFP. For buildings with heights up to 40 *m* the Eurocode [7] recommends estimating T_1 from Equation (1):

$$T_1 = C_t H^{0.75} \quad (1)$$

where C_t is 0.085 for moment resisting space steel frames, 0.075 for moment resistant space concrete frames and eccentrically braced steel frames and 0.05 for all other structures; and H is the height of the building, in *m*, from the foundation or from the top of a rigid basement. Similar expressions such as given on Equation (1) are outlined in the National Building code of Canada (NBC) [8] and the

[1] Ebenezer Ussher, Norwegian University of Life Sciences, (NMBU), Norway, ebenezer.ussher@nmbu.no
[2] Angelo Aloisio, Università degli Studi dell'Aquila, Via Giovanni Gronchi n. (UNIVAQ), Italy, angelo.aloisio@univaq.it
[3] Roberto Tomasi, Norwegian University of Life Sciences, (NMBU), Norway, roberto.tomasi@nmbu.no

https://doi.org/10.52202/069179-0308

Indian standard (IS) – criteria for Earthquake Resistant Design of Structures [9]. However, the NBC [8] suggests estimating the fundamental period for other moment resisting frames as $T_1 = 0.1N$, where N is the total number of storeys above exterior grade to level n. The fundamental period for all other buildings may be obtained from Equation (2), according to the Indian Standard [9], where H is the height of the building in m and d is the base dimension of the building at the plinth level along the considered direction of earthquake shaking in m.

$$T_1 = \frac{0.09}{\sqrt{d}} \tag{2}$$

The objective of this study is to assess the capabilities of existing empirical formulas in various design guidelines in accurately estimating T_1 of CLT buildings. In particular, the study focuses on the so-called platform buildings in which CLT floor framings are supported on load bearing CLT walls; with an erected floor serving as the platform for building the next storey. The assessment is based on using verified numerical models capable of fully representing construction features that exist in actual buildings. Attention is placed on predicting mode shapes and associated modal frequencies. This includes demonstrating whether the discrepancies that can arise out of using simplified assumptions and approaches outlined in various design guidelines for seismic analysis may be acceptable for emerging construction systems.

2 NUMERICAL MODELS

This section describes the scope, assumptions, and calibration of the numerical model techniques employed in this study.

2.1 SCOPE AND ASSUMPTIONS

The numerical models presented in this study represent CLT buildings that are rectangular on plan and satisfy Platform Construction methodology. Building models ranging between 4- and 12-storey heights with footprint and wall locations shown in Figure 1, were considered to match current trend of multi-storey mass timber buildings. Axes of material symmetry (1, 2, 3) of CLT plates are considered to lie parallel to orthogonal axis directions x, y, z that define the length, width and thickness of elements. Linear-elastic small deflection theory is assumed valid since amplitudes of system displacements are several orders of magnitude less than overall building superstructure dimensions.

The limitation of the scope to buildings with rectangular floors was adopted because it illustrates choices of design variables that ensures geometrical regularities for the ESFP in the event of seismic analysis and design without limiting the generality of the adopted concepts. Buildings which are regular in both footprint and elevation are typical for many practical occupancy applications.

2.2 MODELLING TECHNIQUES

The Numerical models were developed using the commercial software package TimberTech [10] whose choice was made because it has the capabilities for simulating direct CLT walls and floors with various connectors to make accurate representation of platform construction arrangements. Furthermore, the program is associated with ease of creating elements and structural systems that facilitates openings for windows, doors, stairs and lift wells.

Successful numerical models depend on accurately simulating the system's geometry and applying the appropriate material properties, boundary conditions and the expected external forces. In developing the geometries of the buildings, the floor plans were laid out with nodes at the locations of both internal and external walls. Thin plates of required thickness and heights representing CLT walls were inserted in between nodes to create loading bearing (including shear walls) and partition walls. Lintels were introduced for window and door openings. CLT floor elements were modelled, supported on both exterior and interior walls along the shorter plan dimension of the buildings. This created a platform upon which upper storeys were added on until the roof. CLT floor elements (180 mm thick) and roof (200 mm thick) were assigned residential and roof live loads respectively. Table 1 and Table 2 respectively summarize CLT type and material properties employed for modelling and analyses with the adoption of a Poisson's ratio of 0.3 for all CLT materials [11]. Figure 2 illustrates an 8-storey FE model with footprint as illustrated in Figure 1.

Table 1: *CLT type and layup configuration used in FE models*

CLT-panel layup	Thickness (mm)
CLT 90 3S (30-30-30)	90
CLT 100 5S (20-20-20-20-20)	100
CLT 120 5S (30-20-20-20-30)	120
CLT 140 5S (40-20-20-20-40)	140
CLT 160 5S (40-20-40-20-40)	160
CLT 180 5S (40-30-40-30-40)	180
CLT 200 5S (40-40-40-40-40)	200

As has been mentioned, TimberTech provides the flexibility of link elements between wall and floor elements. The stiffness applied to the different types of link elements, were estimated from the results of experimental analysis from Gavric et al. [12]. For the angle brackets and hold-downs, a linear relationship between the number of screws and stiffness value is

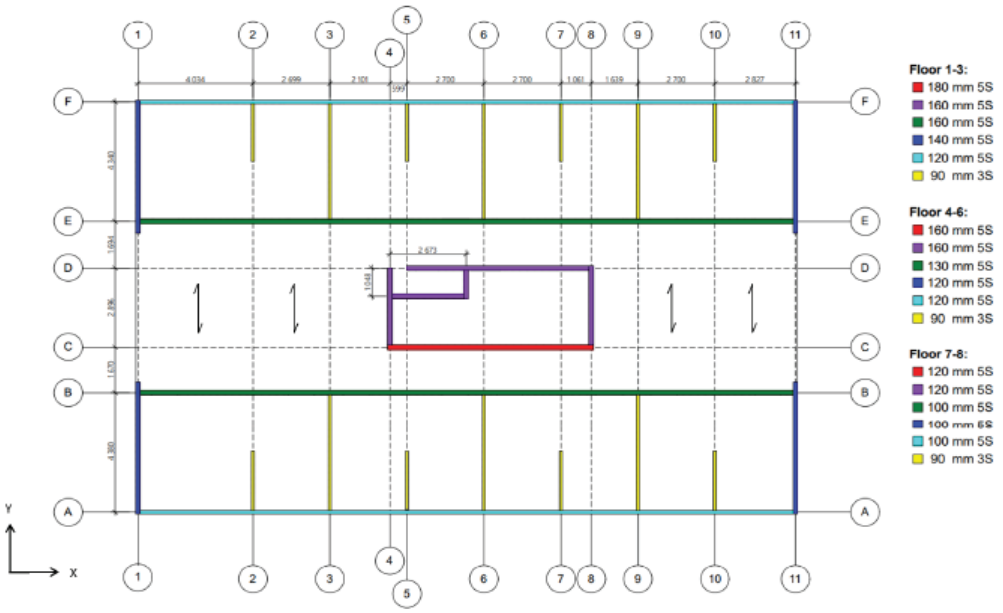

(a) Floor plan of the case study building

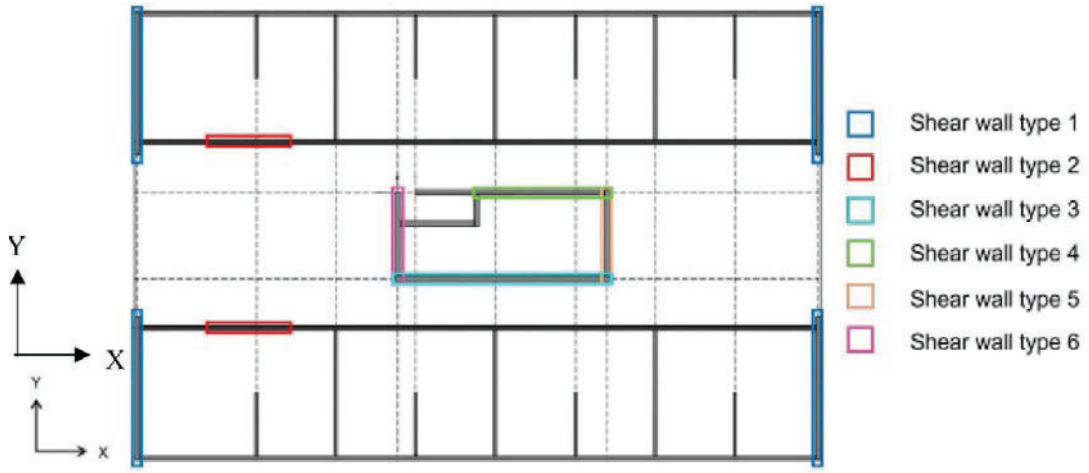

(b) Shear wall location in the case study building

Figure 1: *Floor plan and shear wall locations of the case study building*

https://doi.org/10.52202/069179-0308

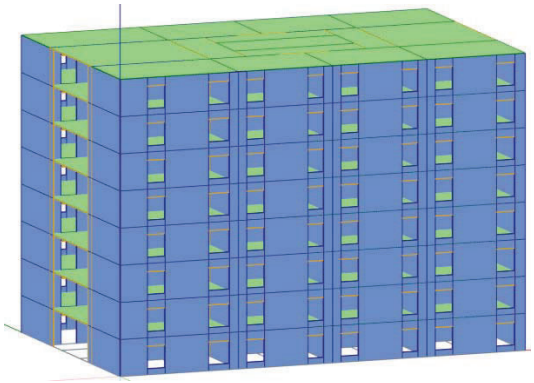

Figure 2: *FE model of 8-storey CLT building*

Table 2: *Apparent properties of CLT used in FE models**

CLT-panel layup	Units	Value
Density, ρ	Kg/m^3	460
Elastic moduli:		
E_1	GPa	11.0
E_2	GPa	4.00
E_3	GPa	0.40
Shear moduli:		
G_1	GPa	0.69
G_2	GPa	0.04
G_3	GPa	0.04

**Parallel to face laminations (direction-1); perpendicular to face laminations (direction-2); direction-3 is perpendicular to plate.*

assumed, and the values for tensile and shear stiffness are estimated by Equation (3): where k_a is the analytical stiffness value from (Gavric et al. 2015), n_a is the number of nails used in the analytical connector, and n_{exp} is the number of nails used in the experiment. Table 3 illustrates estimated hold-down stiffnesses employed along the storey heights of FE models.

Table 3: *Stiffnesses of hold-down anchors in FE analyses*

Storey level	Type of hold-down	# of brackets	Tensile stiffness [KN/mm])
1	HD-1	5	13.3
2	HD-2	4	10.6
3	HD-2	4	10.6
4	HD-3	3	7.95
5	HD-3	3	7.95
6	HD-3	3	7.95
7	HD-4	2	5.30
8	HD-4	2	5.30
>9	HD-5	1	2.65

$$K_a = \frac{K_{exp}}{n_{exp}} \tag{3}$$

2.3 NUMERICAL MODEL VERIFICATION

Results from field campaign of ambient vibration measurements of one of the two identical Palisaden student residence buildings on the campus of the Norwegian University of Life Sciences (NMBU) in Ås, Norway, were used to verify the numerical models. The case study building shown in Figure 3 is 8-storey high and matches the configurations of the numerical model described in Figures 1 and 2. Shallow CLT spine elements form structural walls, and horizontal floor and roof slabs which act as structural diaphragms. Except for stair and lift wells on plan, the horizontal floor elements have widths up to 2.5 m and span continuously over 15 m in line with the shorter plan axis dimension. Horizontal floor and roof elements are supported on both exterior and interior CLT walls, reflecting that building configuration conforms to the Platform Construction type.

Figure 3: *Photograph of case study building*

From the lower to the upper storeys the thicknesses of the wall elements decrease, thus the storey masses decrease along the building height, (Figure 1a). CLT floor slab elements have a constant thickness of 180 mm whilst the roof slab elements composed of 200 mm thick CLT plates. The thickness of roof elements indicates that design snow loads are of much significance in Ås, Norway than corresponding design live loads for the floors. Walls designated to act as shear walls are those indicated in Figure 1b. The structure has a central core as shown in Figure 1, which houses a staircase, an elevator and services ducts. The core is surrounded by CLT walls connected to the floor and roof elements thus constituting part of the lateral load transfer system.

Figure 4 compare modal natural frequencies and mode shapes of the numerical model with the results from the field campaign of modes 1–3. As can be seen from Figure 4, modal model results are in good agreement with results from the ambient vibration measurements. Discrepancies between modal model and test results especially between

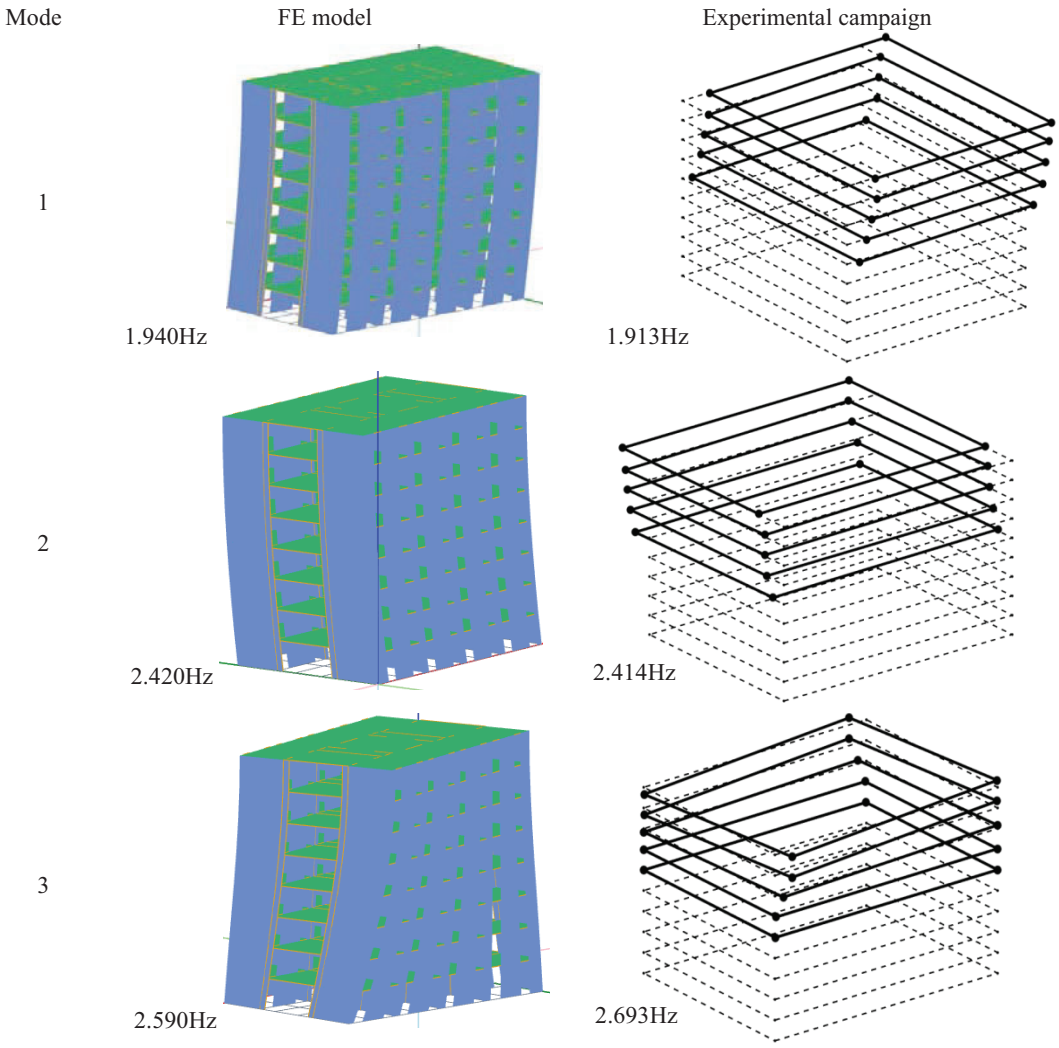

Figure 4: *Comparison of modal frequencies and modal shapes of FE model modal analysis and field campaign of results of the case study building*

mode 3 natural frequencies may be attributed to simplification of the numerical model not accounting for the stiffness due to the end-wall non-CLT materials adjacent to the communal corridor space present in each storey. Presence of non-CLT wall construction elements potentially added to the overall system stiffness consequently influencing low-amplitude ambient vibration measurements. Furthermore, variations between the model and field campaign results may be due to numerical model not accounting for minor differences in material properties and construction imperfections. Also, construction features including door and window openings were simplified and differences between real and model superstructure and wall anchoring conditions were ignored. Overall, the authors consider the obtained balance between the model accuracy and computational efficiency reasonable for extending the presented modelling techniques to assess the reliability and robustness of simplified formulas in estimating T_1.

3 ESTIMATING THE FUNDAMENTAL PERIOD OF CLT PLATFORM-TYPE BUILDINGS

Analytical formulas provided in various design codes [7-9] are employed in estimating T_1 of CLT platform-type buildings. Evaluations are compared with predictions obtained from verified numerical models which offer the needed basis for commenting on the accuracy and

https://doi.org/10.52202/069179-0308

reliability of extrapolating empirical design formulas to systems outside their calibration range.

From Eurocode 8 [7], Equation (1) is applied on the case study building in which C_t is defined by Equation (4)

$$C_t = \frac{0.075}{\sqrt{A_c}} \quad (4)$$

where, A_c is the total effective area of shear walls in the first storey of the building, in m^2 defined by Equation (5):

$$A_c = \sum \left[A_i \left(0.2 + (l_{wi}/H) \right)^2 \right] \quad (5)$$

A_i is the effective cross-sectional area of shear wall i in the direction considered in the first storey of the building, in m^2; H is the building height in m, from the foundation; and l_{wi} is the length of the shear wall i in the first storey in the direction parallel to the applied forces, in m, with $l_{wi} \leq 0.9$. The choice of Equation (4) for calculating C_t is made to reflect the application of CLT shear walls in the case study building and corresponding numerical model. Further comparisons are made with Equation (2) which is part of the Indian Standards [9] provisions for seismic analysis of buildings. From Equation 2, C_t is defined as $C_t = 1/\sqrt{d}$

Table 4 compares model predictions of T_1 of the case building with alternative analytical estimations. As may be observed from Table 4, there are huge discrepancies between the predictions from the Eurocode 8 (Equation (1)) [7] approach and the verified numerical model. However, there appears reasonable variations between the provision from the Indian Standard (Equation (2)) [9] and the numerical model estimates.

Table 4: *Comparison of FE model prediction versus analytical approaches of T_1*

Weak stiffness direction			
Analysis Type	C_t	T_1[s]	%Var
FE	--	0.515	0.000
Eq.-1 [7]	0.068	0.736	42.91
Eq.-2 [9]	0.258	0.548	6.488
Strong stiffness direction			
Analysis Type	C_t	T_1	%Var
FE	--	0.413	0.000
Eq.-1 [7]	0.055	0.587	42.10
Eq.-2 [9]	0.209	0.443	7.236

This suggests that not accounting for both floor plan dimension in addition to the building height in the desired seismic direction affect the accuracy of the formula as may be seen from the Eurocode method versus the Indian design guide formula. For both directions of the building on plan the simplified approach in estimating the fundamental period of the case study building by Equation 2 (from the Indian design guidelines) predicts less than 10% variation from the numerical method. Construction features such as CLT plates edge-to-edge jointing, wall to floor connections, location of shear walls as well as the presence of openings for staircase, lifts, doors and windows all affect the modal stiffness to mass ratios in low amplitude vibration of CLT platform-like buildings. This is demonstrated in the numerical model and providing factors that account for such features in analytical expressions may improve their accuracy for seismic analyses for regular CLT buildings.

4 EFFECT OF BUILDING HEIGHT

Analytical formulas provided in the various design codes [7-9] for the prediction of T_1 for buildings classified as regular in both footprint and elevation, mostly depend on the building height, H in m. As demonstrated in Equations (1) and (2), it is expected that the distribution of stiffness and mass along the height of the building will facilitate over 90% of the energy released in the fundamental mode during seismic action. Therefore, the calibrated numerical model is applied in evaluating effect of building height on T_1 and comparing them with the analytical formulas. Analyses are carried out for four to twelve storeys reflecting a height of between11.8 m and 35.4 m.

Table 5 Compares the FE models prediction of T_1 with analytical provisions based on varying the building height. A couple of inferences may be made from Table 5. First, increasing the number of storeys resulting in increasing the building height results in increasing the fundamental period. This may be attributed to the fact that

Table 5: *Effect building height on T_1 based FE model versus analytical approaches*

Weak stiffness direction			
# of storeys		T_1[s]	
	FE	Eq.-1 [7]	Eq.-2 [9]
4	0.259	0.438	0.274
6	0.385	0.593	0.411
8	0.515	0.736	0.548
10	0.625	0.870	0.686
12	0.735	0.998	0.823
Strong stiffness direction			
# of storeys		T_1[s]	
	FE	Eq.-1 [7]	Eq.-2 [9]
4	0.205	0.349	0.221
6	0.310	0.473	0.332
8	0.413	0.589	0.443
10	0.508	0.694	0.554
12	0.613	0.795	0.664

increasing the storey height results in increases in the systems overall mass without corresponding increases in the overall stiffness. This may be because of changes in wall thickness and uneven distribution of connection details along the building height. Second, numerical predictions compare relatively well with the analytical formula that takes into consideration the building footprint dimension in the direction of ground motion under consideration. Relatively high discrepancies are noted between FE model predictions and the analytical method that considers only the building height.

As the above comparisons between verified numerical models and analytical predictions of T_1 of CLT platform-type buildings demonstrate, it is impossible to judge the suitability of simplified formulas provided in design codes in a generalised manner. The ability of some current simplified representations to estimate T_1 is associated with significant errors whilst others perform relatively better. Implication of this is use of explicit formulas or numerical models not accounting for basic building geometric properties such as floor plan dimension may not be a reliable way of estimating T_1. Additionally, CLT plates have orthotropic representation and slabs, and walls often contain features like intra-plate construction joints. Therefore, design level models should be based on explicit formulas that predict the fundamental frequencies of CLT structures accounting for orthotropic nature of the material and other architectural variables.

5 CONCLUSIONS

Numerical model representations have the capabilities of incorporating construction features that include building plan geometry, material characteristics and other architectural features. This enables the development of viable cost-effective simulations as alternative to expensive field campaigns for determining vibration characteristics of multi-storey CLT buildings. Model techniques also have the advantage of being employed to evaluate the effect of various parameters on a system.

Analyses from the modelling approach presented in this study and compared with analytical methods provided in various design codes point out the limitations in applying simplified analytical formulas for assessing the seismic demands on CLT buildings. Verified numerical analyses prove that in addition to the building height, floor plan dimension in the desired seismic direction should be accounted for in estimating the fundamental period as basis for determining the seismic forces on the structure. This is because the distribution of system mass to stiffness ratios depends on both footprint and the storey height of the building. Furthermore, presented analysis show that construction features influencing modal stiffnesses such as metal shear connectors and tiedown anchors in connections should be accounted for predicting low amplitude vibrations characteristic and forces due to extreme seismic events on CLT buildings.

REFERENCES

[1] IPCC, Climate Change 2014: Synthesis Report. Contribution of Working Groups I, II and III to the Fifth Assessment Report of the Intergovernmental Panel on Climate Change [Core Writing Team, R.K. Pachauri and L.A. Meyer (eds.)]. IPCC, Geneva, Switzerland, 151, 2014.

[2] Buchanan A. H.: How will timber buildings help New Zealand meet the Kyoto protocol commitments? New Zealand Timber Design Journal, (13):9-13, 2005.

[3] International Energy Agency (IEA) for the Global Alliance for Buildings and Construction (GlobalABC). Global Status Report for Buildings and Construction Towards a zero-emissions, efficient and resilient buildings and construction sector, ISBN No: 978-92 807-3768-4, 2019.

[4] I. Smith, and A. Frangi. Structural use of timber in tall multi-storey buildings, structural engineering document 13: International Association for Bridge and Structural Engineering, Zurich, Switzerland, 2014.

[5] American National Standards Institute (ANSI). Standard for performance-rated cross-laminated timber, Standard ANSI/APA PRG 320-2012. Page 29. New York, NY, USA: ANSI; 2012.

[6] A. Ceccotti. New technologies for construction of medium-rise buildings in seismic regions: the XLAM case. Structural Engineering International, 18(2),156–65, 2008.

[7] European Committee for Standardization (2004c). EN 1998-1 (English): Design of structures for earthquake resistance - Part 1: General rules, seismic actions and rules for buildings. The European Union, 2004.

[8] National Research Council (NRC). National building code. Ottawa, Canada: NRC; 2010, 2015.

[9] IS:1893:2016. “Criteria for Earthquake Resistant Design of Structures,” Bureau of Indian Standards, New Delhi, [Online]. 2016. Available at: https://archive.org/details/1893Part1.

[10] Design software for timber structures TimberTech Buildings Version 95 - 2022 user's manual; 95-12/2022, 2022.

[11] Wallner-Novak M., Koppelhuber J. and Pock K. Cross-Laminated Timber Structural Design. proHolz Austria, p. 191. 2014. www.proholz.at.

[12] Gavric I., Fragiacomo M. and Ceccotti, A. Cyclic behavior of CLT wall systems: Experimental tests and analytical prediction models. Journal of Structural Engineering, 141(11), 04015034, 2015.

ACKNOWLEDGEMENT

The authors are very grateful to Dr. Mauro Andreolli of TimberTech Buildings for facilitating the use of the software.

https://doi.org/10.52202/069179-0308

APPENDIX A1: SELECTED NUMERICAL ANALYSIS MODELS OF CLT BUILDINGS

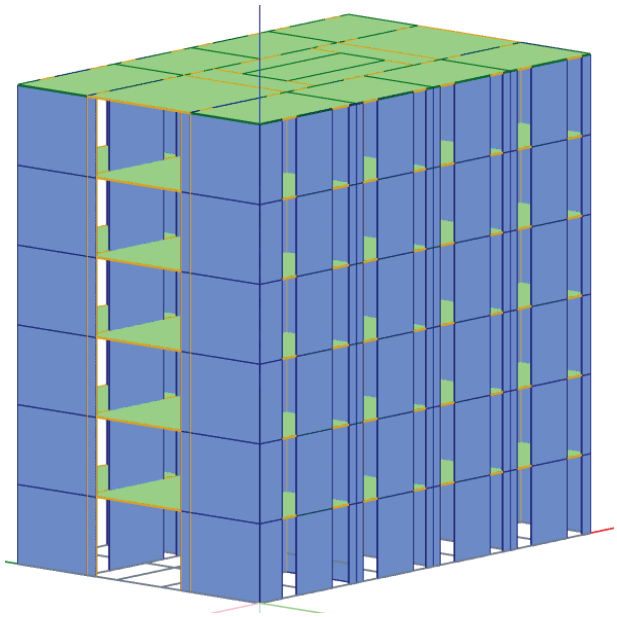

(a) FE Analysis model of 6-storey CLT building

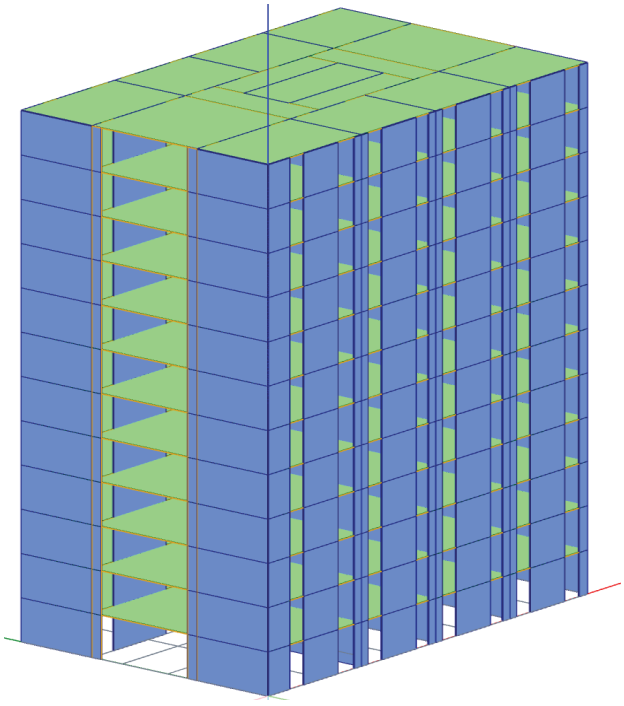

(b) FE Analysis model of 12-storey CLT building

Figure A1: *FE analysis models of 6- and 12-storey CLT buildings*

https://doi.org/10.52202/069179-0308

World Conference on Timber Engineering Oslo 2023

NUMERICAL MODELLING OF LIGHT TIMBER FRAME WALLS – COMPARATIVE STUDY OF THREE FASTENER REPRESENTATIONS

Lukas Rauber[1], Benno Hoffmeister[2]

ABSTRACT: The lateral load-bearing capacity and stiffness of light timber frame walls (LTFW) depend on the mechanical properties and interaction of their components (frame, sheathing, fasteners and anchorage). The fasteners are decisive for the structural performance (resistance, stiffness) of LTFW. Therefore, numerical modelling focuses on the representation of the fasteners. In this paper, different modelling approaches for fasteners of LTFW are presented and compared with regard to applicability in research and practice – (i) an engineering model with line releases; (ii) a model with oriented springs and (iii) a model with beam elements. The models were validated and compared to experimental results from tests conducted at RWTH Aachen. All models represent the load-bearing capacity closer than the analytical approach of Eurocode 5. The model with line releases is recommended for engineering while the model with oriented springs is recommended for research. The modelling of GFB sheathing needs further investigation.

KEYWORDS: timber frame walls, shear walls, numerical modelling, push-over tests, load-bearing capacity, stiffness

1 INTRODUCTION

Light Timber Frame construction is a resource-efficient construction method with a high degree of prefabrication and short construction times. Light Timber Frame Walls (LTFW) consist of several components (frame, sheathing, fasteners). Frame and sheathing provide a load-bearing element when fastened in shear. The load-bearing behaviour is usually governed by the shear-connection between sheathing and frame as well as by the anchoring or the connection to adjacent building components.

In Europe, the horizontal load-bearing capacity and the displacement of LTFW are calculated according to the "pure shear" model ("Method A") of *Eurocode 5* [1]. This model is based on the lower bound theorem of plasticity theory and assumes that all fasteners are loaded with the same force and parallel to the sheathing edges. In addition, detailing provisions are given to ensure that yielding of the fasteners governs the failure mode of the diaphragm.
In *Eurocode 5* areas containing large openings, like windows or doors, are neglected in the determination of the load-bearing behaviour. It is assumed that wall sections with large openings do not contribute to the load-bearing capacity of the wall [1].

Eurocode 5 does not contain explicit provisions for the calculation of the horizontal stiffness of LTFW [1]. Engineers may calculate the deformation according to the "pure shear" model, by determining the contributions of the individual components – fastener deformation, shear deformation of the sheathing, axial displacement of the frame parts, deformation perpendicular to the grain of the bottom rail and deformation of the anchorage [2].

Test results [3–5] show that prediction of the load-bearing behaviour of LTFW using the "pure shear" model of *Eurocode 5* leads to very conservative results .
For seismic actions LTFW need to be verified according to seismic codes, e.g. *Eurocode 8* [6]. The seismic resistance may be determined assuming ductile and dissipative behaviour represented by a behaviour factor. The application of a behaviour factor of $q > 1.5$ assumes ductile fastener behaviour and requires prevention of brittle failure of other structural wall components. The condition for the achievement of ductile behaviour is the application of so-called capacity design rules. An accurate estimation of the load-bearing behaviour of all structural components is therefore essential for safe seismic design. Due to the lack of adequate provisions for calculating the realistic load-bearing behaviour of LTFW in *Eurocode 5*, non-linear numerical simulations are good alternatives for the calculation of load-bearing capacity and stiffness.

The objective of this contribution is to assess three promising numerical models regarding their applicability in research and engineering. The requirements according to which the models were preselected are the following:

- The model should be able to calculate the load-bearing capacity and the stiffness of LTFW and give more accurate results than the analytical model of *Eurocode 5*.
- The model output can be used as basis for the non-linear analyses of timber frame buildings.
- The model should have reasonable computing time for the application in engineering.

[1] Lukas Rauber, RWTH Aachen University, Germany, Institute of Steel Construction, l.rauber@stb.rwth-aachen.de
[2] Benno Hoffmeister, RWTH Aachen University, Germany, Institute of Steel Construction, hoff@stb.rwth-aachen.de

https://doi.org/10.52202/069179-0309

2 NUMERICAL MODELS

The reference structure used with the three presented numerical models is shown in Figure 1. For the frame all models use beam elements with linear-elastic material properties. The studs were hinged to the rails – this is common practice for numerical models of LTFW; whereas in the "pure shear" model of *Eurocode 5* studs and rails are considered contactless. The sheathing was modelled by means of linear-elastic shell elements. The anchorage was represented as a linear-elastic spring.

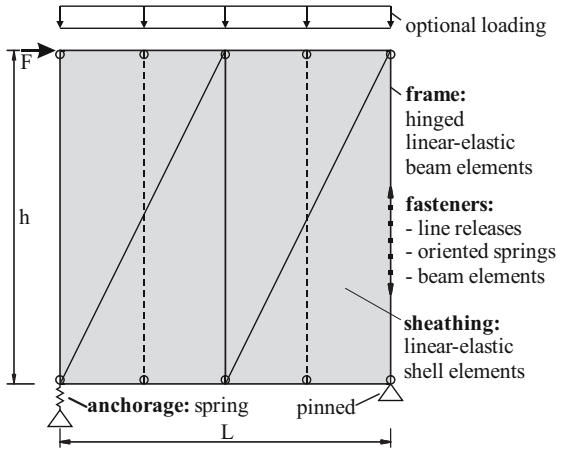

Figure 1: *Basic structure of the numerical models*

The three models differ in the representation of the non-linear fastener behaviour as seen in Figure 2. In model 1 (M1) the connection was modelled using "line releases". Model 2 (M2) used oriented springs to represent the connection between frame and sheathing. In model 3 (M3) flexible beam elements in bending were used according to *Vogt* [3].
M2 (oriented springs) and M3 (Vogt) were implemented in ABAQUS 2019 with "B31" beam elements for the frame and "S4R" shell elements for the sheathing. M1 (line releases) was realized in Dlubal RFEM 5.26 which uses automatic mesh generation.

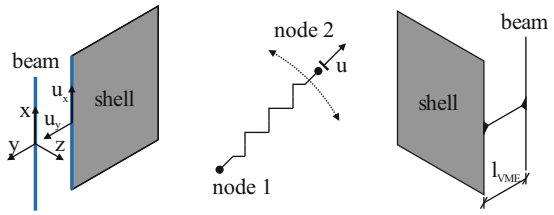

Figure 2: *Different fastener representations of the models*

2.1 LINE RELEASES (M1)

M1 used continuous cartesian spring elements for the representation of the connection between sheathing and frame. RFEM was chosen for the implementation of the model because of the availability and the simple applicability of continuous springs – called "line releases".

The input for line releases is defined as load-displacement per unit length. As shown in Figure 2 a, load-displacement behaviour is represented by continuous springs with degrees of freedom parallel and perpendicular to the sheathing edge. Since cartesian springs only act on their predefined axes, the resulting load-bearing capacity and stiffness are overestimated for oblique load directions [3]. Herein, both spring directions used non-linear curves from tests on connection units as input values as described in chapter 2.4 (0° for u_x and 90° for u_y).
The wall models were solved according to the theory of the third order with large displacements.

2.2 ORIENTED SPRINGS (M2)

M2 used non-linear oriented springs (Figure 2 b) for the representation of the individual fasteners. The model was implemented in ABAQUS.
For modelling the oriented springs "connectors" between sheathing and frame nodes were used with the translational type "axial". With this definition the springs acted in direction of their individual deformation. For modelling the non-linear fastener behaviour, input curves from tests on connection units were used (chapter 2.4).
"Static general" with large displacements (*NLgeom on*) was used as solving method.

2.3 BEAM ELEMENTS (M3)

M3 was also implemented in ABAQUS and used the same elements for frame and sheathing as M2. To model the fastener behaviour, beam elements as described by *Vogt* [3] were used (Figure 2 c).
The fastener elements (*B33*) were connected as "fixed" to frame and sheathing. They used elastic-plastic material behaviour and circular cross-sections to exhibit the same load-bearing behaviour in each load direction.
The fasteners remained elastic until plastic hinges occurred on both ends after the yield point of the material was reached.
To represent the load-bearing capacity of the connection F_f the length of the beam elements was calculated with:

$$l_{VME} = \frac{2 \cdot M_{pl}}{F_f} \tag{1}$$

To represent the stiffness of the connection *K*, a factor s_l was used for reducing *EI* in the numerical definition [3].
The input values for the model presented by *Vogt* [3] used the shear strength $F_{f,Rk}$ and stiffness K_{ser} calculated according to *Eurocode 5*.
For this paper mean values derived from connection tests were used for F_f while *K* was calculated as K_{ser} according to *Eurocode 5* [1].

2.4 INPUT DATA

The input data for the modelling of the fasteners' plastic behaviour was derived from connection tests conducted at RWTH Aachen [4] and the Optimberquake project [7].
At RWTH a test program with a total of 78 connection units was conducted in accordance with *ISO 6891* [8] for the monotonic tests used in this contribution.

https://doi.org/10.52202/069179-0309

The test setup is shown in Figure 3. Structural timber grade C24 was used for the frame part.
Sheathing materials, staple diameters and force grain angles (0° and 90°) were varied. For the validation in this paper only monotonic tests with OSB/3 sheathing (t =15 mm) and staples of diameter 1.8 mm and a length of 65 mm were used.

Figure 3: *Test setup of connection units at RWTH with load acting 0° (left) and 90° (right) to the timber grain*

For the validation with walls tested in the Optimberquake [9] project, tests on connection units [7] performed in this project were used. Relevant for the validation were monotonic tests on OSB/3 sheathing with nails of diameter 2.8 mm and a length of 65 mm. Also relevant were monotonic tests on gypsum fibre board (GFB) with a thickness of 18 mm and staples (⌀ 1.53 mm and length 55 mm).

The non-linear input curves per fastener were derived directly from the test results and used in tabular form for defining fastener load-deformation properties of M1 (line releases) and M2 (oriented springs).
The input values used for the models and the calculation according to *Eurocode 5* are shown in Table 1. M1 and M2 used nonlinear input curves generated from tests on connection units (Figure 4). M3 used mean values of F_f derived from the connection tests. The analytical calculations according to *Eurocode 5* were performed with both mean (m) and characteristic (k) values of F_f.
The E-moduli were set to 11000 N/mm² for the frame components and 380 N/mm² for the sheathing.
In order to simulate the tests at RWTH Aachen the anchorage was simplified by pinned supports. For the Optimberquake walls the spring stiffness of the anchorage was set to 11150 N/mm (from *Vogt* [3]).
The process of the generation of input curves is described in Figure 4. First the mean curves of the monotonic tests were generated per connection variant. Afterwards the curve was scaled down to one fastener for the input of M2 (oriented springs). For M1 (line releases) the input curves still had to be divided by the fastener spacing of the modelled wall to obtain to the load-displacement curves per unit length.

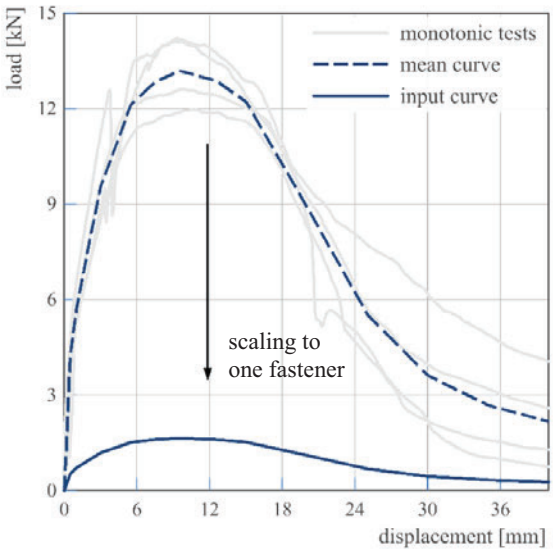

Figure 4: *Generating the fastener input curves from test results*

3 VALIDATION

3.1 TESTS ON WALL ELEMENTS

To validate the models, results of wall tests conducted at RWTH Aachen [4] and the Optimberquake project [9] were used. The tests for the validation are listed in Table 2. All tests were conducted with the monotonic loading protocol according to *ISO 21581* [10].

The experimental investigations conducted at RWTH include tests on standard reference walls as well as newly developed triple-sheathing walls. A total of 12 full scale wall tests were performed at RWTH. Four tests were conducted with and eight without additional vertical loading. In Figure 5 the test setup for a LTFW with vertical loading is shown. A vertical load of 37 kN was applied on each stud (111 kN in total) – representing loads of a four-story building.
All test specimens consisted of C24 frames and OSB/3 sheathing with a thickness of 15 mm which was fastened using resin coated staples (⌀ 1.80 mm and length 65 mm) with a spacing of 75 mm. Specimens with aspect ratios of 1.25 × 2.50 m and 2.50 × 2.50 m were tested.

Table 1: *Input values of the parameters used for the validation of the numerical models for the different tests (see Table 2)*

Test	Fastener parameter		M1 (LR) M2 (OS)	M3 (Vogt)	EC 5 (m)	EC 5 (k)
h-m-xx	K	[N/mm]	non-linear curve from	450	450	450
	F_f	[N]	test series OSB15-st1.80	1609.5	1609.5	908.5
WL-1.1	K	[N/mm]	non-linear curve from	859.5	859.5	859.5
	F_f	[N]	test series na2.8-o18-m	1071	1071	819
WL-2.1	K	[N/mm]	non-linear curve from	643.7	643.7	643.7
	F_f	[N]	test st1.53-g18-m-1	1225	1225	682.7

https://doi.org/10.52202/069179-0309

Table 2: *Test data of timber frame walls used for the validation of the numerical models*

Test	L × h [m]	Sheathing t [mm]	Fasteners ⌀ - length - spacing [mm]	Loading	Project
h-m-02/03	1.25 × 2.50	2 × OSB 15	Staples 1.80 - 65 - 75	horizontal	
h-m-04	1.25 ×2.50	2 × OSB 15	Staples 1.80 - 65 - 75	horizontal + vertical	
h-m-11	1.25 × 2.50	3 × OSB 15	Staples 1.80 - 65 - 75	horizontal	RWTH [4]
h-m-12	2.50 × 2.50	3 × OSB 15	Staples 1.80 - 65 - 75	horizontal	
h-m-13	1.25 × 2.50	3 × OSB 15	Staples 1.80 - 65 - 75	horizontal + vertical	
WL-1.1	2.50 × 2.50	2 × OSB 18	Nails 2.80 - 65 - 75	horizontal + vertical	Optimber-
WL-2.1	2.50 × 2.50	2 × GFB 18	Staples 1.53 - 55 - 75	horizontal + vertical	quake [9]

The anchorage was designed as non-dissipative including sufficient overstrength. The "shear response" according to *Dujic* [11] was ensured for all tests. For this purpose, two anchorages of the type HTT31 of Simpson Strong-Tie as well as horizontal cleats were used at each support.

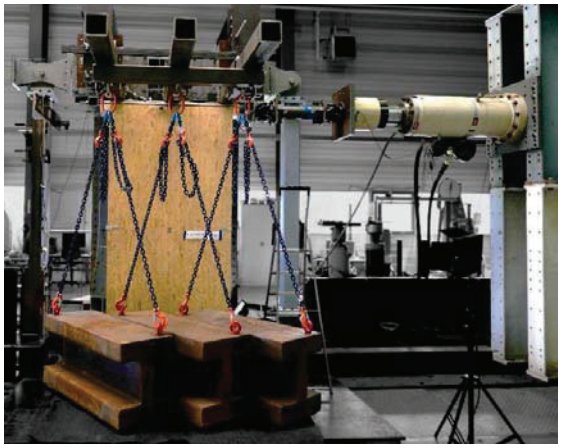

Figure 5: *Test setup for LTFW with vertical loading*

Further test results on LTFW elements from the Optimberquake program [9] were used for validation. Two test setups were selected: (i) specimens with 18 mm OSB sheathing and nails (⌀ 2.80 mm and length 65 mm) and (ii) specimens with 18 mm GFB sheathing and staples (⌀ 1.53 mm and length 55 mm).

3.2 NUMERICAL RESULTS

Figure 6 shows the comparison of the load-bearing capacities (F_{max}) from tests, by numerical models and according to *Eurocode 5* calculated with characteristic (k) and mean test (m) input values.
For M1 and M2 maximum values were used to determine the load-bearing capacity while M3 (Vogt) was evaluated at 60 mm displacement in this paper, since this model does not include decreasing of resistance (Figure 7).

The load-bearing capacity was underestimated for all OSB sheathed test specimens (*h-m-xx* and *WL-1.1*), by the models and by *Eurocode 5* design rules.
F_{max} of the GFB sheathed specimen (*WL-2.1*) was overestimated by all models and *Eurocode 5* when using test data from connection units (*m*).
Comparable tests without (*h-m-02* and *h-m-11*) and tests with vertical loads (*h-m-04* and *h-m-13*) showed no significant difference for F_{max}. The same was the case for the numerical models and the analytical calculations.

The load-displacement curves of the models are compared to the test results of *h-m-02* and *h-m-03* and shown in Figure 7 (left).

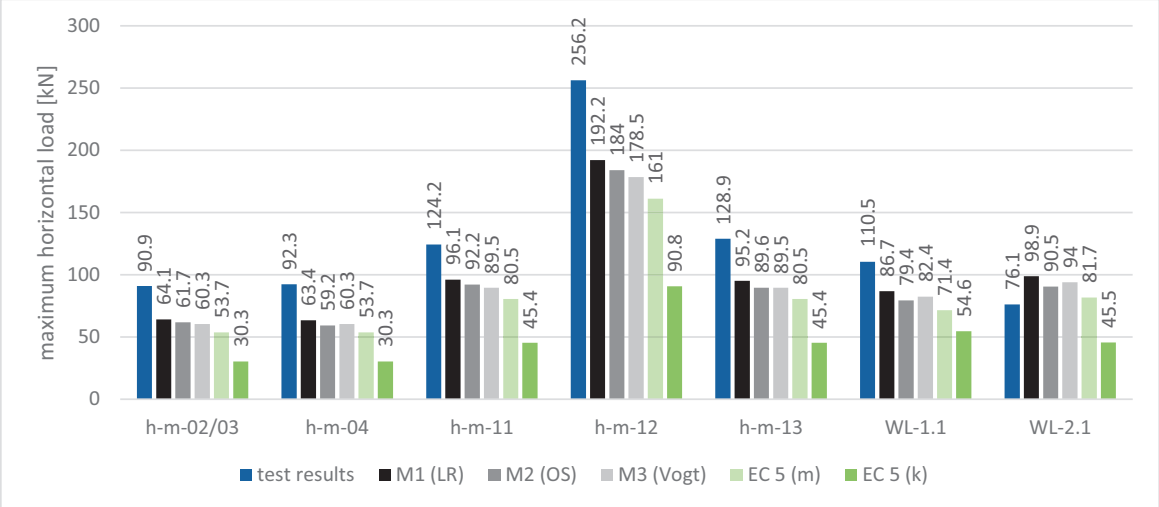

Figure 6: *Bar chart comparison of the load-bearing capacity between mean test results, numerical models and analytical calculation*

https://doi.org/10.52202/069179-0309

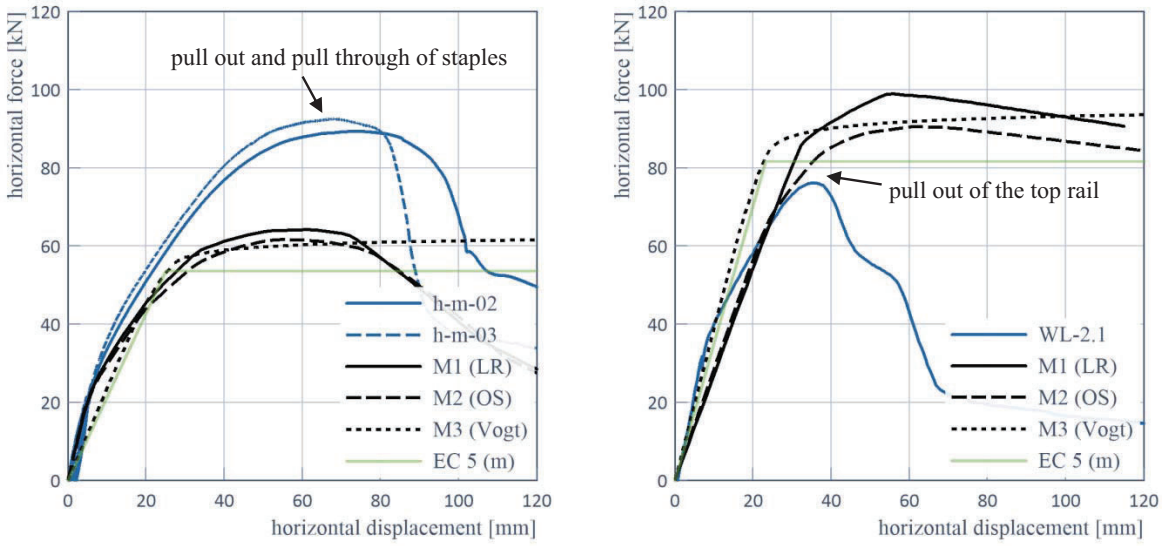

Figure 7: *Load displacement comparison of tests vs models for walls made of OSB with staples (left) and of GFB with staples (right)*

M1 (line releases) and M2 (oriented springs) resembled the scaled non-linear input curves for fasteners (Figure 4) while M3 (beam elements) showed almost ideal elastic-plastic behaviour.

As seen before, all models underestimated the load-bearing capacity of the tests. This model behaviour looked similar for all comparisons to tests *h-m-xx* (OSB and staples) and *WL-1.1* (OSB and nails).

In Figure 7 (right) the load-displacement diagram of specimen *WL-2.1* is shown – the only test with GFB sheathing. F_{max} was overestimated by all models compared to the test result. The initial stiffness was underestimated with M1 and M2 while M3 was closer to the initial stiffness of the test curve.

For the evaluation of the initial stiffness of the tests as well as the model results the calculation of K according to *ISO 21581* [10] was carried out with:

$$K = \frac{0.3\ F_{max}}{u_{40\%F_{max}} - u_{10\%F_{max}}} \qquad (2)$$

The comparison of the evaluated initial stiffnesses of wall tests, models and analytical calculations (according to [2] but also named EC 5) is shown in Figure 8.

For the test series *h-m-xx* (OSB and staples) the following order applies to the stiffness: M1 is the stiffest, followed by M2, M3 and *Eurocode 5*.

Tests on nominally equal walls without (*h-m-02* and *h-m-11*) and tests with vertical loads (*h-m-04* and *h-m-13*) showed no significant difference regarding the initial stiffness. This was also observed for the numerical models and the analytical calculations.

The mean average percentage error (*MAPE*) was used for the comparison between models and test results and was calculated for F_{max} and the initial stiffness by:

$$MAPE = \frac{100\%}{n} \sum_{i=1}^{n} \left| \frac{A_i - F_i}{A_i} \right| \qquad (3)$$

with A_i as the test value and F_i as the model value.

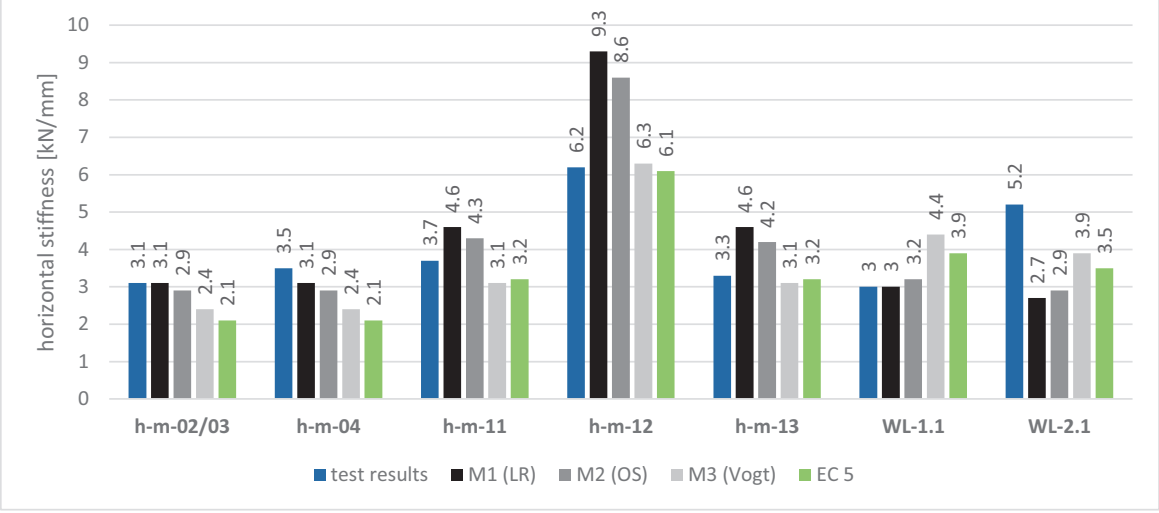

Figure 8: *Bar chart comparison of the stiffness between mean test results, numerical models and analytical calculation*

https://doi.org/10.52202/069179-0309

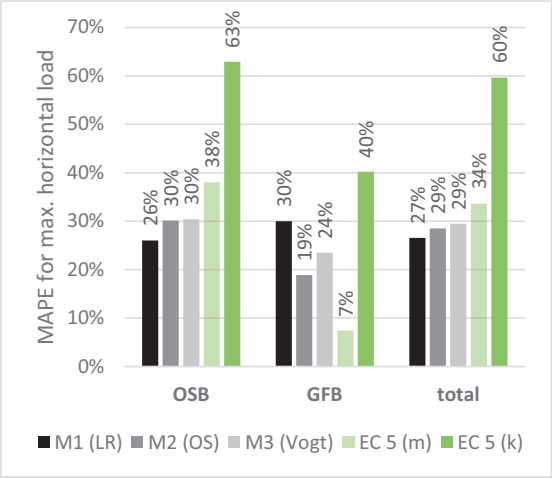

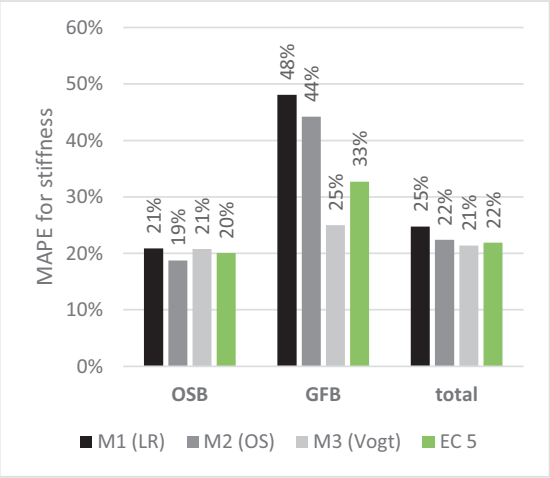

Figure 9: *Comparison of the MAPE of models and Eurocode 5 to test results for F_{max} (left) and for stiffness (right)*

The comparison of *MAPE* between the different models and *Eurocode 5* was evaluated for OSB sheathing, GFB sheathing and the total of all tests. The results are shown in Figure 9 for F_{max} (left) and stiffness (right).
M1 showed the least total error with regard to F_{max}, followed by M2, M3 and EC 5 (mean). For the test with GFB sheathing M1 had the biggest model error, followed by M3, M2 and EC 5 (mean).
With regard to stiffness M1 showed the greatest total error, followed by M2, EC 5 and M3. For OSB sheathing the error is approximately 20% for all models.

3.3 DISCUSSION

The presented numerical models showed a better representation of the load-bearing capacity than the analytical "pure shear" model of *Eurocode 5*.
However, all models show large deviations from the load-bearing capacity as obtained by tests. The differences were significantly higher than expected.

For OSB sheathing the load-bearing capacity was strongly underestimated by all models. This might be due to friction effects between sheathing and frame and/or scale effects of the fastener behaviour – in particular the behaviour of large groups compared to few fasteners in the connection tests – which both might not be represented by the conducted tests on connection units (Figure 3).
For GFB sheathing the load-bearing capacity was overestimated by all numerical models. This might be due to the limited test data from GFB tests – only one connection test and one wall test were used here. Nevertheless, the models' overestimation of load-bearing capacity for GFB is a safety risk for the calculation with these methods. More tests with GFB are needed to calibrate and validate the models.
With regard to stiffness estimation all model results are only as good as the calculation with the model in *Eurocode 5* (calculated with [2]) for OSB test specimens.

In the following the known abilities and limitations of the models are listed and related to the models (named in parentheses).

Abilities

- Calculate the load-bearing capacity and stiffness more accurately than *Eurocode 5* for OSB (all).
- Failure of other wall components (studs, anchorage, sheathing) may also be assessed (all).
- Resulting load-displacement curves may be used as basis for simplified full scale building models (all).
- Wall parts with large openings due to windows and doors can be included in the calculation (all).

Limitations

- Model relies on test results – ideally non-linear test curves – of connection units for best results (all).
- Not applicable for huge and complex engineering models of buildings due to time consuming modelling and long computation time (M2, M3).
- Overestimation of oblique fastener loads and stiffness by using cartesian spring pairs (M1).
- Sheathing failure (e.g. shear and tension) cannot be represented by the models if using linear-elastic material representation. This can lead to overestimation of the load-bearing capacity when sheathing failure occurs for the LTFW (all).
- Seismic behaviour cannot be derived directly because the models' lack the representation of damage (strength reduction) due to cyclic loading (all).

The limitations might be overcome by the following modifications:

- Instead of test data, characteristic values could also be used as model input for safe-sided estimates leading to less model error than *Eurocode 5*.
- M1 could be used in engineering applications, as it requires low computing times and gives reasonable results. The overestimation due to the cartesian spring pair could be overcome by using just the main load direction of the fasteners (u_x) or reducing the second input values (u_y).
- Sheathing stress could be assessed continuously in the models to determine premature sheathing failure.

https://doi.org/10.52202/069179-0309

4 CONCLUSIONS

Three different numerical approaches of fastener representation for LTFW were presented – (i) an engineering model with line releases; (ii) a model with oriented springs and (iii) a model with beam elements.
The comparison of the test results with numerical models demonstrates the difficult venture of modelling load-bearing behaviour of LTFW. The transfer of experimental data from connections to full-scale walls does not lead to the expected (realistic) results.
The results indicate that a scale effect between connection tests to LTFW tests exists. Further research is needed in this regard.

Nevertheless, all models represent the load-bearing capacity of OSB sheathing better than the "pure shear" model given in *Eurocode 5*.
The following conclusions can be drawn with regard to load-bearing capacity:

- All models underestimated the maximum load for the OSB sheathed specimens.
- All models overestimate the maximum load for the GFB specimen. As long as the models cannot represent the load-bearing capacity of GFB sheathed walls, wall tests are recommended.
- Tests and models with and without vertical loading show no significant difference regarding lateral performance.

The following conclusions can be drawn with regard to stiffness:

- The numerical models represent the stiffness of OSB specimens as good as the "pure shear" model.
- No influence from vertical loading is observed for both tests and numerical models.

Model 1 (line releases) shall be particularly interesting for engineers, as it is simple, quick to apply and contains all wall components required for capacity design. However, the effects due to usage of the cartesian spring pair need to be considered.
Model 2 (oriented springs) is suggested for the application in research as it gives valuable output about the individual fastener forces and displacements. Model 3 leads to better estimations than the analytical model of *Eurocode 5* but showed high computational demand and modelling times.

Model 1 (line releases) and model 2 (oriented springs) might be especially interesting for nonlinear pushover analyses of timber frame buildings. Although results are not as good as individual wall tests the models are a less expensive alternative to testing. Both models might also be used to estimate the ductility of LTFW with data from tests on connection units only, but this still needs to be investigated. If the shown model limitations could be overcome, the number of wall tests required to validate the performance would become significantly less in the future.

ACKNOWLEDGEMENT

The authors gratefully acknowledge the financial support of the ZIM research project *HOLZBEBEN* by the BMWI and the FNR research project *HELEPOLIS* funded by BMEL. We are also grateful for the cooperation with the project partners Walter • Reif Ingenieurgesellschaft mbH and Adams Holzbau-Fertigbau GmbH.

REFERENCES

[1] EN 1995-1-1: Eurocode 5: Design of timber structures - Part 1-1: General – Common rules and rules for buildings, 2004.
[2] Blaß H. J., Ehlbeck J., Kreuzinger H., Steck G.: Erläuterungen zu DIN 1052: 2004-08: Entwurf, Berechnung und Bemessung von Holzbauwerken. 1st ed. München, 2004.
[3] Vogt T., Seim W.: Advanced modelling of timber-framed wall elements for application in engineering practice. INTER, Bath, 2014.
[4] Wilden V., Hoffmeister B.: Experimental analyses of innovative wood-shear walls under seismic loads. IABSE Congress, 2021.
[5] Schick M., Vogt T., Seim W.: Connections and anchoring for wall and slab elements in seismic design. CIB-W18/46-15-4, 2013.
[6] EN 1998-1: Eurocode 8: Design of structures for earthquake resistance - Part 1: General rules, seismic actions and rules for buildings, 2009.
[7] Seim W., Vogt T.: OptimberQuake - Deliverable 2A: Connection units – monotonic and cyclic testing. Kassel, 2013.
[8] ISO 6891: Timber structures - Joints made with mechanical fasteners -· General principles for the determination of strength and deformation characteristics, 1983.
[9] Seim W., Vogt T.: OptimberQuake - Deliverable 2B: Timber framed wall elements – monotonic and cyclic testing. Kassel, 2013.
[10] ISO 21581: Timber structures - Static and cyclic lateral load test methods for shear walls, 2010.
[11] Dujic B., Aicher S., Zarnič R.: Investigations on in-plane loaded wooden elements: influence of loading and boundary conditions. Otto-Graf-Journal 200516:259–72.

https://doi.org/10.52202/069179-0309

World Conference on Timber Engineering Oslo 2023

INCREMENTAL DYNAMIC ANALYSIS OF A FIVE STOREYS CLT BUILDING DESIGNED THROUGH FORCE-BASED METHODS

Franco Benedetti[1], Tomás Valenzuela[2], Alan Jara-Cisterna[3], Alexander Opazo-Vega[4], Víctor Rosales[5]

ABSTRACT: Since the large seismic demands in Chile, there is a high level of uncertainty regarding the seismic safety behavior of timber structures. Besides, in the last decade, there has been a worldwide rise in the construction of cross-laminated timber (CLT) buildings, explained by the ease of industrialization of CLT panels and for being a sustainable material. However, its massification in high earthquake-prone zones is still under development. This research analyzes the seismic fragility of a 5-story CLT building. The aim of this research is to determine the seismic safety level of a CLT midrise building designed by Chilean force-based code regulations by means of Static Nonlinear Analysis and Incremental Dynamic Analysis. For IDA curves, a set of 540 nonlinear time-history analyses were performed using parallel computing tools. The main results show that for the collapse of the building to occur, large pseudo-acceleration values need to be reached. Besides, the collapse margin ratio (CMR) is calculated for the two principal directions, achieving values larger than 3 for 50% collapse probability. These results suggest a large margin of seismic safety of the CLT building designed in this research.

KEYWORDS: Seismic fragility of CLT mid-rise buildings, Timber construction, Incremental Dynamic Analysis.

1 INTRODUCTION

In the last decade, there has been a growing interest in promoting sustainable and industrialized construction materials, in which timber structures have advantages against other materials. In terms of construction systems, CLT is one of the most attractive systems that satisfy all these purposes. It is also a resistant system with good structural performance that has been extensively tested at element [1] and full scale [2] levels.

In general, there is sufficient evidence that shows that CLT can withstand high gravitational load and have an optimal behavior against seismic loads [3]. This last aspect is crucial in a highly seismic country such as Chile. However, in Chile there are no explicit seismic design regulations for CLT. This means, for example, that CLT buildings must meet the same deformation requirements of a reinforced concrete structure. This fact can generate over stiffened and oversized structures that do not take advantage of the deformation capacity that CLT can provide. Additionally, the application of traditional force-based design methods based on the seismic behavior of other structural systems creates uncertainty about the earthquake response and safety of CLT structures. This research aims to quantify through incremental dynamic analyses (IDA) the seismic safety of a panelized CLT mid-rise building designed under the force-based methods approach.

2 PYMELAB BUILDING

The Pymelab building was developed through a collaborative effort between public and private organizations [4]. It was funded by the Production Development Corporation of the Chilean Ministry of Economy (CORFO) and executed by the University of Bío-Bío (Concepción, Chile). It is a project that gathers a large number of SMEs in the timber sector to innovate and create associative support networks. As a result of this collaborative project, a non-habitable 5-story cross-laminated timber building was built (Pymelab Building), providing the timber companies with a living laboratory to test and validate their products and manufacturing capacities.

2.1 BUILDING DESCRIPTION

The 5-story CLT building has a plan dimension of 6.6 m length by 4.2 m width, with 2.5 m of inter-story height. Three representative views of the studied building are shown in Figure 1. On the first three floors, the platform system is employed considering 150 mm thick walls (5 layers CLT panels); while on the upper 2 storeys, the balloon frame system with 100 mm thick walls (3 layers

[1] Franco Benedetti, University of Bio Bio, Chile, fbenedet@ubiobio.cl
Centro Nacional de Excelencia para la Industria de la Madera (CENAMAD), Pontificia Universidad Católica de Chile.
[2] Tomas Valenzuela, University of Bio Bio, Chile, tomas.valenzuela1601@alumnos.ubiobio.cl
[3] Alan Jara-Cisterna, University of Bio Bio, Chile, afjara@ubiobio.cl
[4]Alexander Opazo-Vega, University of Bio Bio, Chile, aopazove@ubiobio.cl
Centro Nacional de Excelencia para la Industria de la Madera (CENAMAD), Pontificia Universidad Católica de Chile.
[6]Victor Rosales, University of Bio Bio, Chile, vrosaleg@ubiobio.cl
Centro Nacional de Excelencia para la Industria de la Madera (CENAMAD), Pontificia Universidad Católica de Chile.

https://doi.org/10.52202/069179-0310

panels) is used. Besides, following the local industry manufacturing capacity, walls and slabs consider a panelized configuration with panels of a maximum width of 1.2 m (walls) and 1.8 m (slabs). Spline joints are used for the parallel in-plane panel-to-panel connection, and self-tapping screws are employed for the perpendicular wall-to-wall and slab-to-wall connections. The geometry and structural information of the Pymelab structures are presented in Table 1. The structural system is based on the concept of a simple regular prism with stiff and strong corners and concentrated openings in the middle zone of each elevation, providing vertical continuous load paths.

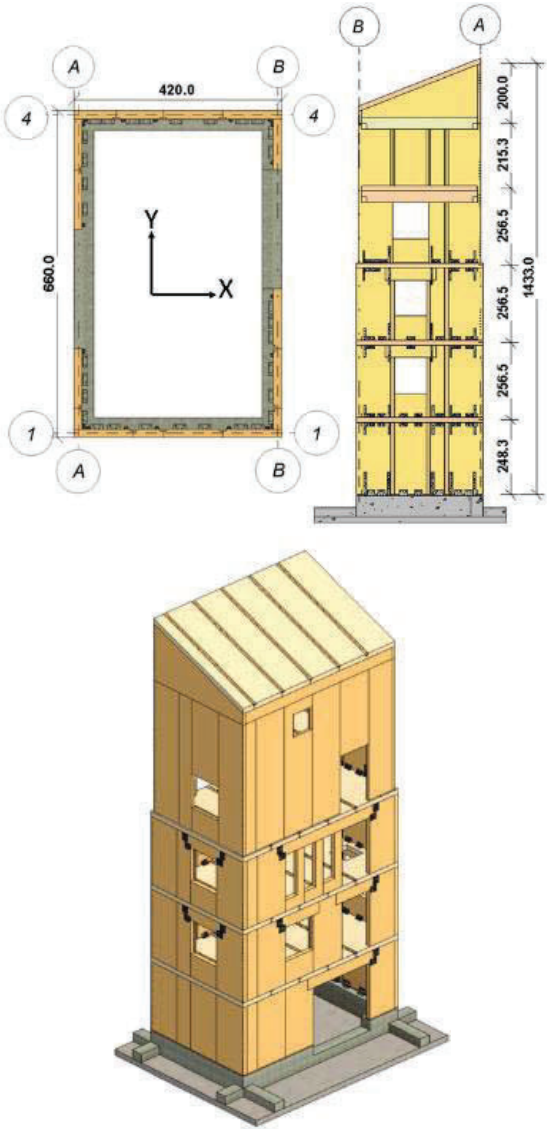

Figure 1: *Floor plan, elevation (top), and 3D view of the general structural configuration (bottom)*

Table 1: *Summary of main properties of the PymeLab building [5]*

Property	Value
N° Stories (Height)	5 (12.5 m)
Story area	27.7 m^2
Wall thickness	165 mm – 100 mm
Slabs thickness	165 mm
N° Metal connectors	2.0 /m^2
Total Wall Ratio (1st story)	10%
CLT Volume	0.34 m^3/m^2

2.2 SEISMIC DESIGN PROCEDURE

For the structural design, the allowable stress design approach was used, following the Chilean seismic code [6], the Chilean structural wood design standard [7], and international recommendations [8]. The mechanical properties of radiata pine CLT panels used in the walls and slabs are listed in Table 2.

Table 2: *Mechanical properties of CLT walls and slabs*

Mechanical properties	Value
Elastic Modulus Ex (3 layers)	2750 MPa
Elastic Modulus Ey (3 layers)	5250 MPa
Elastic Modulus Ex (5 layers)	1755 MPa
Elastic Modulus Ey (5 layers)	6250 MPa
Shear Modulus	324 MPa
Poisson Coefficient	0.3
Density	450 kg/m^3

SAP2000 [9] finite element software was utilized to develop the structural analysis for the design. All connections were considered flexible and modeled using link elements. Non-dissipative elements were modeled as elastic springs, while dissipative elements were modeled as multi-linear springs. Additionally, GAP contact elements were included to simulate the contact between wall-to-wall, wall-to-slab, slab-to-wall, and wall-to-foundation interfaces. Figure 2 displays an elevation of a case study, the graphical representation of the model created in SAP2000, and an example of the deformation of one elevation subjected to lateral seismic loads.

Regarding the seismic design, according to the Chilean code (NCh 433 [6]), the lateral load demand is defined using the maximum seismic coefficient C=0.46, which is established for non-traditional structures and calculated using a load reduction factor R=2. Additionally, the lateral load design must comply with a maximum center of mass inter-story drift of 0.2% under reduced seismic loads. This deformation limit applies to all structural systems regardless of the material used. The seismic demand is applied as lateral forces in the mass center of each floor slab. Additionally, to take into account the accidental torsion at each story level, the mass center where displaced 10% of the plan whith. Lateral forces and weight per story are summarized in Table 3. The seismic weight is determined as the Dead Load plus 25% of the

https://doi.org/10.52202/069179-0310

Live Load, resulting in 2.5 kN/m^2/story and a base shear of 142 kN.

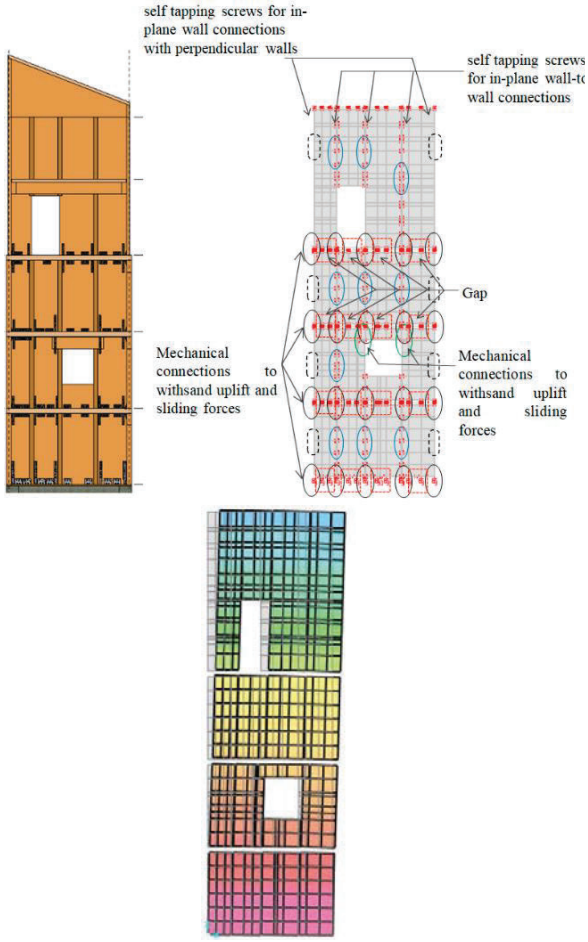

Figure 2: *1-Axis elevation, numerical design model (top), and deformed shape under seismic loads (bottom)*

Concerning the dynamic response, the design periods calculated using the Ritz vector method for the X and Y directions are 0.318 s and 0.274 s, respectively.

Table 3: *Summary of the seismic weight and lateral load demand used in the design stage*

Story	Lateral Force (kN)	Seismic weight (kN)
1	17.9	70.1
2	20.7	68.2
3	22.0	70.2
4	26.3	61.0
5	55.3	44.2

The foundation is a 20 cm thick reinforced concrete mat of 8 m x 6.4 m, stiffened with 0.7 m x 0.4 m beams. The foundation system design was challenging due to the site soil conditions, as well as the slenderness of the building. The soil beneath the mat is a medium-compacted and low-bearing capacity sandy silt. One of the main problems of the foundation is that the structure, being so light and slender, has overturning stability issues. To address this situation, additional weight was added over the foundation to improve the overturning safety, achieving stability safety factors of 1.3 and 1.7 for Y and X directions, respectively.

In terms of connections design, Izzi et al. (2018) [10] recommendations and authors' experience were followed to define the dissipative and non-dissipative connections. The joints that resist the rocking and the wall-in-plane splines are designed to be dissipative to improve the deformation capacity of the system. On the other hand, shear brackets, perpendicular joints, slab-to-wall, and slab-to-slab spline connections were considered non-dissipative.

2.3 STRUCTURAL DETAILING

Due to the panelized configuration of the building, a large number of metal plates and screw connectors are required. Examples of the connectors and metal plates used in this case study include:

Self-tapping screws: used for joints between panels at perpendicular joints. Among the screws used are ESCRC 8x240 screws for perpendicular joints between wall panels, and ESCRC 10x240 screws for joints between walls and slabs.

Angle Brackets: angular-type metal connectors are typically used to resist shear and uplift forces resulting from seismic demands. The angular type brackets used are ABR255 and ABR255SO models fastened with CNA 4x60 annular shank nails.

Hold-Down: HTT31, HTT22e, and HTT5 devices fastened with CNA 4x60 annular shank nails are employed to resist uplift loads and to create vertical load transfer paths.

Spline joints: employed for the in-plane panel-to-panel connection. In this case, radiata pine boards fastened with ESCRC 8x80, ESCRC 8x120, and DSVR312R5LB screws were considered.

Table 4 shows the per-story amount of shear brackets and hold-down connectors used in the Pymelab building.

Table 4: *List of shear and hold-down connectors per story (C: ceiling, F: floor)*

		Shear Brackets		Hold-down		
Story		ABR255SO	ABR255	HTT31	HTT22e	HTT5
5	C	0	0	0	0	0
	F	0	0	0	0	0
4	C	0	0	0	0	0
	F	0	28	0	6	12
3	C	0	26	0	6	12
	F	0	30	0	7	10
2	C	0	18	0	7	10
	F	0	32	0	3	14
1	C	0	32	0	3	14
	F	31	0	19	0	0

https://doi.org/10.52202/069179-0310

Due to the strict requirements of the Chilean seismic design code (NCh433 [6]), a crowded connector layout is obtained. Figure 3 provides an elevation view and a plan of the metal connector distribution.

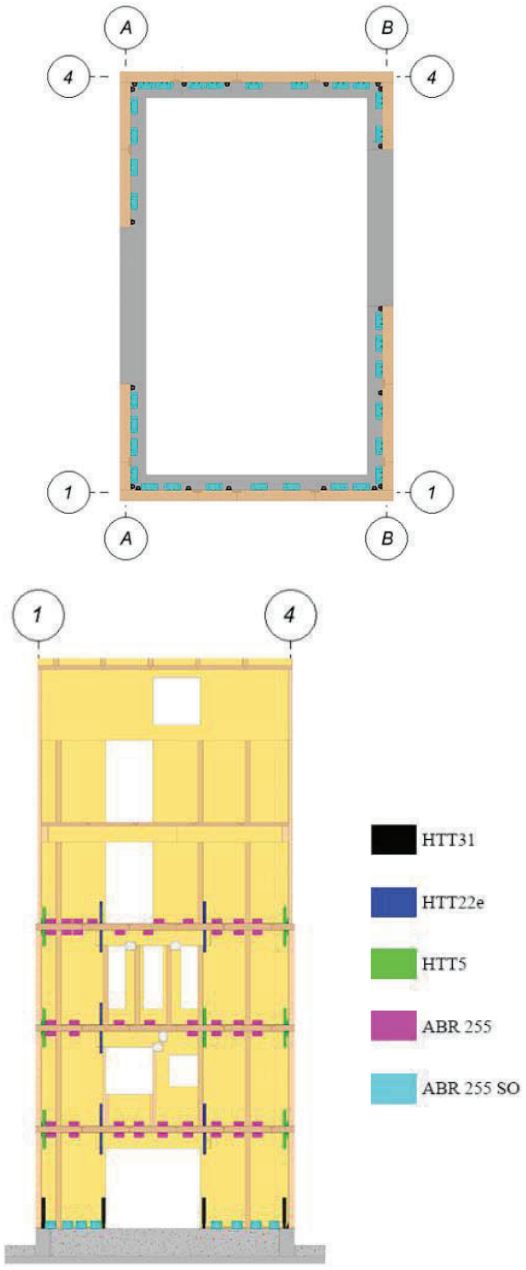

Figure 3: *Mechanical connectors distribution at foundation level (top) and A-axis elevation (bottom)*

3 INCREMENTAL DYNAMIC ANALYSIS APPROACH

Aiming the assessment of the safety level of the seismic design of the Pymelab Building, an incremental dynamic analysis (IDA) has been carried out. To perform this analysis, a robust and detailed model is required in which every deformation mechanism can be properly modeled. Given the model complexities and the large amount of nonlinear time history analyses involved in the IDA, OpenSees [11] models were developed using parallel computing techniques.

3.1 NUMERICAL MODEL DEVELOPMENT

The models consider linear and nonlinear components. Elastic orthotropic shell elements were employed for the CLT boards, and hysteretic nonlinear springs were assigned to the connection elements to simulate their nonlinear mechanical behavior. Moreover, a friction interface was used to represent the contact between walls, slabs, and the foundation. The proposed modeling approach is illustrated in Figure 4, while the mechanical properties of mechanical devices are presented in Table 5. Further details of the modeling process are available in Benedetti et al. (2023) [5].

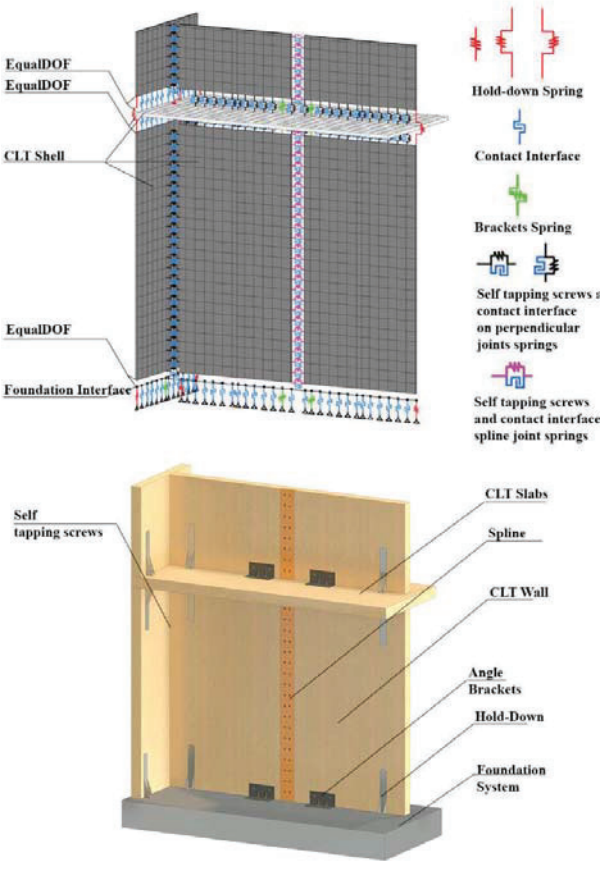

Figure 4: *Cross Laminated Timber (CLT) shear wall components (below) and model implementation (top) [5]*

https://doi.org/10.52202/069179-0310

Table 5: *General mechanical properties of connections in the models*

Connection	Yield displacement Δ_y (mm)	Load capacity F_{max} (kN)	Elastic Stiffness K_e (kN/mm)
Hold Downs (tension)	8.9	72.3	5.88
Shear Brackets (shear)	6.1	110.1	15.15
Shear Brackets (tension)	7.2	88.19	9.83
Metal Plate(shear and tension)	2.4	174.8	42.73

In terms of the parallel modeling approach, several strategies have been developed to segment nonlinear computational domains [12]. However, this study focuses on a static decomposition approach due to its simplicity and straightforwardness. Moreover, the decomposition is conducted with the intent of preventing load imbalances between the processing cores.

Additionally, an iterative approach was employed to address the numerical integration and convergence issues caused by the high nonlinearity of the complex numerical model. An algorithm was used to dynamically and adaptively modify the nonlinear solver, time step (or displacement step), and convergence tolerance, if necessary in order to ease the solving of the analyses [5].

3.2 SEISMIC DEMANDS FOR THE IDA

A combination of Chilean earthquakes and other well-known seismic recordings from around the world were used in the IDA. The seismic response of the structural model was evaluated using 18 acceleration time series, including the horizontal components of the Mw 8.0 Algarrobo 1985, Mw 8.1 México 1985, Mw 6.9 Loma Prieta 1989, and Mw 8.8 Maule 2010 earthquakes. Figure 5 shows the response spectrum of the seismic demands considered, and Table 6 shows their main parameters. To perform the IDA, each seismic record is normalized and scaled according to FEMA recommendations [13].

Table 6: *Main pareameters of the seismic demands employed in the IDA*

Year	M_w	Station	Component	PGA (g)	PGV (m/s)
2010	8.8	CCP	L	0.40	0.67
			T	0.28	0.51
		CSP	EO	0.60	0.43
			NS	0.65	0.37
		Angol	EO	0.69	0.37
			NS	0.93	0.33
		Peñalolén	EO	0.29	0.22
			NS	0.29	0.29
		Valdivia	EO	0.13	0.18
			NS	0.09	0.13
1985	8.0	Llolleo	10	0.71	0.40
			100	0.44	0.23
1985	8.1	SCT	EO	0.16	0.58
			NS	0.09	0.35
1989	6.9	Treasure Island	0	0.09	0.15
			90	0.15	0.33
		Yerba buena	0	0.02	0.04
			90	0.06	0.14

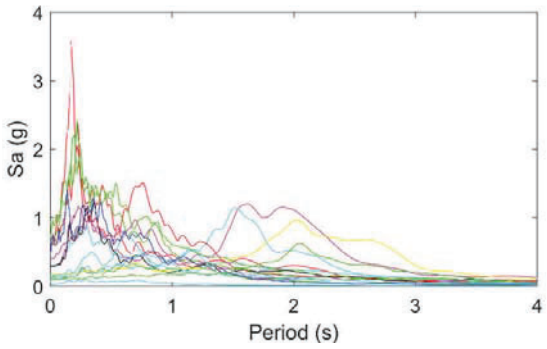

Figure 5: *Acceleration spectra of the seismic demands used in the Incremental Dynamic Analyses*

4 RESULTS AND DISCUSSION

4.1 MODEL VALIDATION

A comparison of the first mode period calculated with OpenSees detailed model with respect to the design model and ambient vibration measurements was performed to validate the model used for the IDA.

To determine the period of the first mode in the IDA numerical model, free vibration tests were conducted under initial conditions that excite the first mode, but are small enough to prevent the response from exceeding the system's yield. The results of the free vibration analysis are presented in Figure 6, showing periods of 0.32 s and 0.28 s for the X and Y directions, respectively.

Moreover, given that the Pymelab building is already built, vibration measurements and modal analysis were carried out with ARTEeMIS software [14]. With this software tool, fundamental vibration modes and

frequencies were identified. Table 7 shows the periods obtained from the measurements, as well as the calculated with both implemented models.

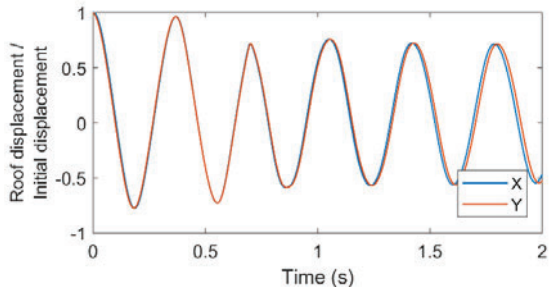

Figure 6: *Free vibration analysis of the IDA model for X and Y directions*

Table 7 periods suggest that the model used for the IDA is able to properly replicate the dominant dynamic response, with differences not larger than 7% with respect to the actual periods. Besides, the design model's and IDA model's fundamental mode periods match closely.

Table 7: *Period comparison among different models and experimental data.*

Model	Tx (s)	Ty (s)
Design model (SAP2000)	0.318	0.274
IDA Model (OpenSeeS)	0.32	0.28
Experimental Data	0.31	0.26

4.2 STATIC NONLINEAR ANALYSIS

Using the IDA OpenSees model, a nonlinear static analysis is performed to analyze the deformation capacity and the overall response of the structure in both directions. The result of the pushover analysis is shown in Figure 7.

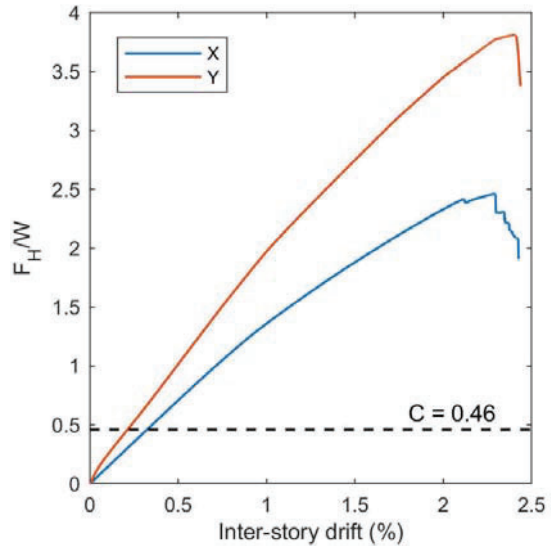

Figure 7: *Static nonlinear curves for X and Y directions*

The capacity curves obtained suggest that the global behavior of the structure for both principal directions is nearly linear during the whole drift range until de maximum capacity is achieved. However, around an inter-story drift of 1%, a break in the curve is observed, which is related to the system's yielding. The elastic stiffness calculated with the first slope of the curves are 155.9 kN/m and 252.1 kN/m for the X and Y directions, respectively.

Notwithstanding that the X-direction is more flexible and weaker than the Y-direction, both reached the maximum capacity and ultimate state at similar inter-story drifts (between 2.3% to 2.4%). Besides, the response of the structure seems to be brittle because of the abrupt drop in the lateral load capacity at the ultimate state.

Additionally, comparing the maximum lateral load capacity with the design seismic coefficient (C=0.46) and base shear, it is observed that the structure's overstrength factors (**Ω**) are 5.4 in the X-direction and 8.3 in the Y-direction (Table 8). Moreover, the system remains in the elastic range for this level of demand.

Table 8: *Maximum capacity (Fmax) and overstrength factor (Ω) in X and Y directions*

Design Base	X-Direction		Y-Direction	
Shear (kN)	Fmax(kN)	Ω	Fmax(kN)	Ω
142.6	763.2	5.4	1181.1	8.3

4.3 INCREMENTAL DYNAMIC ANALYSIS

For the IDA curves construction, a set of 540 nonlinear time-history analyses were performed. The structural damage index considered is the maximum inter-story drift demand, while the first mode elastic pseudo-acceleration spectral coordinate is used as the intensity index.

Using the results of the IDA, fragility curves are calculated for each direction considering four levels of structural damage, which are defined in terms of the inter-story drifts and set at 0.5% for Immediate Occupancy (IO), 1.0% for Operational (O),1.5% for Life Safety (LS), and 2.5% for Near Collapse (NC) (Figure 8). These inter-story drift limits are defined arbitrarily but consistent with the pushover results (Figure 7).

Fragility curves results show that the elastic pseudo-acceleration necessary to reach a 100% probability of achieving the NC state is larger than 7.5 g in and 9.0 g for the X and Y directions, respectively. On the other hand, in the range of elastic pseudo-accelerations between 1.5 g to 2.0 g it is achieved a 100% probability of reaching the IO level.

Moreover, the Collapse Margin Ratio (CMR) is evaluated for different collapse probabilities to determine the level of seismic safety. The CMR values are defined as the ratio between the elastic pseudo-acceleration required to achieve a certain NC state probability (S_{CT}) divided by the maximum expected earthquake demand (S_{MT}). According to Chilean codes (NCh 2745 [15]), S_{MT} demand level can be defined as the elastic design spectrum (S_E) amplified by 1.2 (S_{MT}=1.2S_D). Figure 9 presents the S_E and S_{MT}

https://doi.org/10.52202/069179-0310

demand spectra, as well as the SMT acceleration coordinates obtained for each analysis direction.

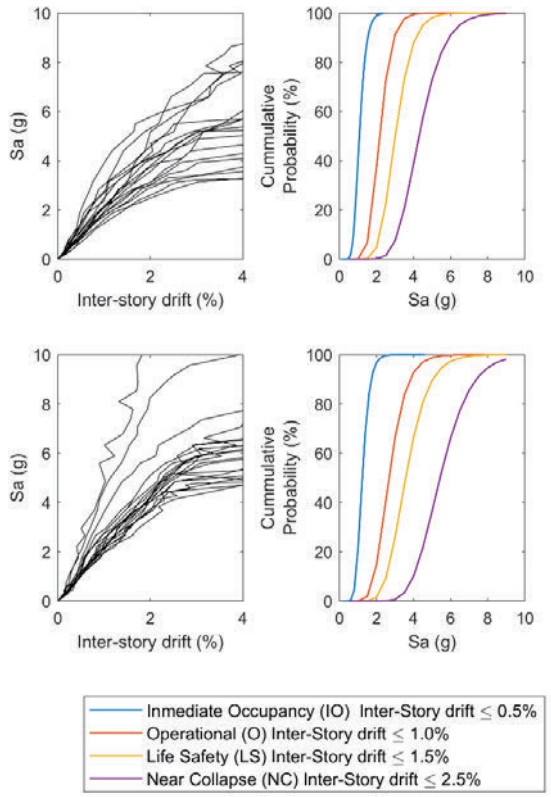

Figure 8: *IDA curves and fragility curves for X-direction (top) and Y-direction (bottom)*

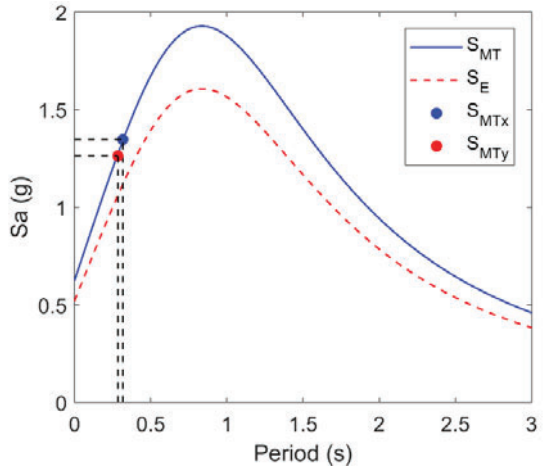

Figure 9: *Maximum considered earthquake spectrum (S_{MT}) and the elastic spectrum (S_a).*

Table 9 presents the obtained CMR values. It is observed that the Y-direction has higher collapse margin ratios due to lower S_{MT} demands and larger S_{CT} at all probability levels considered. However, for both directions, the CMR tends to be high, suggesting that the building's design is able to provide a significant safety margin against earthquake loads (CMR>3 for a 50% NC probability).

Table 9: *Collapse Margin Ratio (CMR) for different NC probabilities*

NC probability	X-Direction			Y-Direction		
	S_{CT}	S_{MT}	CMR	S_{CT}	S_{MT}	CMR
25%	3.63	1.34	2.71	4.62	1.26	3.67
50%	4.30	1.34	3.20	5.45	1.26	4.32
75%	5.05	1.34	3.76	6.46	1.26	5.13

4.4 INTER STORY DRIFT VS ROOF DRIFT RELATIONSHIP

Using the IDA analysis results, it is possible to establish the relationship between the maximum roof drift and maximum inter-story drift. Figure 9 shows the relation obtained and the linear fits for each direction.

The results of Figure 9 show a strong correlation between the maximum roof drift and inter-story drift for the Pymelab building. The linear fits point out that the slope angle is 42° and 36° for the X and Y directions, respectively. These angles suggest that the inter-story drift distribution among the building stories tends to be more uniform X-direction, hinting that the Y-direction could be more prone to concentrated story deformations and eventual soft story mechanisms. Furthermore, linear fit slope angles are close to Gohbarah (2014) [16] findings for reinforced concrete buildings.

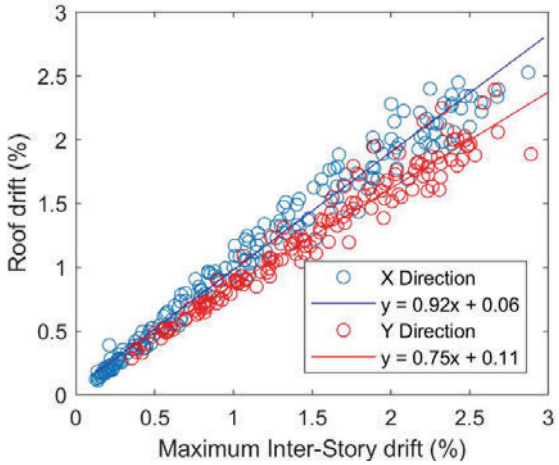

Figure 9: *Relationship between maximum inter-story drift and maximum roof drift of the Pymelab building*

5 CONCLUSIONS

This research analyzes the seismic response and safety of a CLT building designed through traditional force-based methods under seismic codes that do not recognize the intrinsic wooden building characteristics. Complementary, aiming to achieve better earthquake

performance, capacity-based design principles were also considered.

Results appear to show that the building is able to provide significant lateral load strength, but its deformation capacity can be limited. This fact is based on the large overstrength values (Ω >5) and the low displacement ductility ratios (μ<2.5) obtained. The latter might be a consequence of the large seismic force demand considered in the design due to the small load reduction factor (R=2) established by the Chilean code for CLT structures.

Regarding the seismic safety, fragility curves show that the probability of achieving a Near Collapse state is close to 0% for the maximum expected Chilean seismic demand (elastic pseudo-acceleration of 1.36 g). In addition, collapse margin ratio values suggest that the safety margin of the Pymelab Building against earthquake demands is appropriate.

Finally, results suggest that current Chilean force-based design regulations promote safe CLT structures, but it appears that there is still a wide room for the optimization of the designs. Nevertheless, capacity-based design principles should complement the design process in order to promote a suitable failure mode.

ACKNOWLEDGEMENT

Collaborations of SIMPSON Strong-Tie, CMPC Maderas, Alto Horizonte, Promaest, Forestal Tricahue, JMS Ingenieros, Premad, Cortelima, Constructora IMB, Oxiquim S.A., Láminas Chile, Lemu Products, EBCO, as well as the funding and support provided by MacroFacultad, CIPYCS, and CORFO are deeply acknowledged. Finally, we also thank ANID BASAL FB210015 for their ongoing scientific collaboration with our academic departments.

REFERENCES

[1] Baño, V., Godoy, D., Figueredo, D., & Vega, A. (2018). Characterization and structural performance in bending of CLT panels made from small-diameter logs of loblolly/slash pine. Materials

[2] Matos, F. T., Branco, J. M., Rocha, P., Demschner, T., & Lourenço, P. B. (2019). Quasi-static tests on a two-story CLT building. Engineering Structures

[3] Shahnewaz, M., Pan, Y., Shahria Alam, M., & Tannert, T. (2020). Seismic fragility estimates for cross-laminated timber platform building. Journal of Structural Engineering

[4] Rosales V., Benedetti F., Suazo M., Vargas M., Rojas I., Jara A., Rebolledo A. (2021). Associativity between SMEs towards mid-rise building timber construction: Pymelab project. World Conference on Timber Engineering 2021, WCTE 2021

[5] Benedetti, F., Jara-Cisterna, A., Meza, S., Castillo, J., Casanova, E. (2023). Nonlinear modeling of midrise cross-laminated timber through parallel and sequential computing techniques. Proceedings of the OpenSees Days 2022 Eurasia in Lecture Notes on Civil Engineering. Accepted.

[6] INN. Norma Chilena Oficial NCh433 of. 1996, "Diseño Sísmico de Edifcios"

[7] INN. NCh1198, "Madera-Construcciones en madera-Cálculo"

[8] E. Karacebeyli, B. Douglas, CLT Handbook - US Edition, FPInnovations and Binational Softwood Lumber Council, Point-Claire, Quebec, 2013.

[9] Computers and Structures, Inc. (2017). SAP2000 integrated software for structural analysis and design.

[10] Izzi, M., Casagrande, D., Bezzi, S., Pasca, D., Follesa, M., & Tomasi, R. (2018). Seismic behaviour of Cross-Laminated Timber structures: A state-of-the-art review. Engineering structures, 170, 42-52.

[11] McKenna, F.; Scott, M.H.; Fenves, G.L. Nonlinear Finite—Element analysis architecture using object composition. J. Comput. Civ. Eng. 2010, 24, 95–107

[12] Al-Sayegh, A.T.; Sotelino, E.D. A new row-wise parallel finite element analysis algorithm with dynamic load balancing. Int. J. Earthq. Impact Eng. 2020, 3, 120–142

[13] Applied Technology Council. Quantification of building seismic performance factors. Redwood City, USA: FEMA; 2009: P695.

[14] ARTeMIS Modal Pro, Version 5.3, Structural Vibration Solutions A/S, Aalborg Denmark, Copyright 1999–2013.

[15] INN. Norma Chilena Oficial. NCh 2745. Análisis y diseño sísmico de edificios con aislación sísmica.

[16] Ghobarah, A. On drift limits associated with different damage levels. In Proceedings of the International Workshop on Performance-Based Seismic Design Concepts and Implementation, Bled, Slovenia, 28 June–1 July 2004; Fajfar, P., Krawinkler, H., Eds.; Pacific Earthquake Engineering Research Center: Berkeley, CA, USA, 2004; pp. 321–332

https://doi.org/10.52202/069179-0310

World Conference on Timber Engineering Oslo 2023

ESTIMATION METHOD OF DEGRADATION STATE FOR TIMBER BRIDGES USING VIBRATION ANALYSIS

Daisuke Oikawa[1], Shuya Nemoto[2], Humihiko Gotou[3], Yukari Aoki[4]

ABSTRACT: In this study, a new degradation diagnosis method is developed by vibration analysis. The natural frequency of aging timber bridge is normally decreased due to decay and degradation partially and entirely. In Japan, one of the timber bridges has been in service more than 35 years and its natural frequency is about 8.7Hz. In this study, a numerical bridge model is designed by FEM software considering the decay parts which are end supports and connections between spandrel column and arch rib. When the bridge members are healthy, the Young's modulus is 9.6GPa and the natural frequency is about 12.7Hz. In order to adjust calculated value to the measured value 8.7Hz, the Young's modulus of the bridge model has to be decreased to 4.49 GPa, which is significantly low. Furthermore, we calculated frequencies for each mode parametrically varying the decay parts to find the most affected parts to decrease the natural frequency of the bridge. According to this analysis, the connection between spandrel column and arch rib is the most affected.

KEYWORDS: Glulam timber bridges, Natural frequency, Elastic modulus, Decay, Degradation diagnosis method

1 INTRODUCTION

While degradation diagnosis for timber bridges is important, it is not possible to measure the strength and stiffness by extracting partial members from an existing bridge. In that sense vibration analysis, which makes it possible to measure the natural frequency of an entire bridge by non-destructive test method, is useful. In the real bridges, especially aging ones, decay and degradation would be found at every part especially end support and connection. Thus, when the vibration analysis is adopted as degradation diagnosis, the local decay and degradation should be considered. Unfortunately, a current used vibration method in the literatures[1], [1], [1] can not take into account the local decay.

In this study, we at first evaluate typical modal analysis model using beam/shell element and more exact model using tetrahedral element. Then we adopt the better model to find the effect of the local decay and degradation for the bridges.

3D numerical bridge model (Kajika Bridge in Japan) is created for includes the localized decay and degradation by decreasing Young's modulus. To validate this numerical model, we used for which the natural frequencies obtained by the numerical analysis and by the vibration test are compared.

By this method, we can determine whether natural frequency of the bridge model would decrease or not, that is, how the local decay would affect to the stiffness and strength of the entire bridge. By this method, we can determine whether natural frequency of the bridge model would decrease or not, that is, how the local decay would affect to the stiffness and strength of the entire bridge.

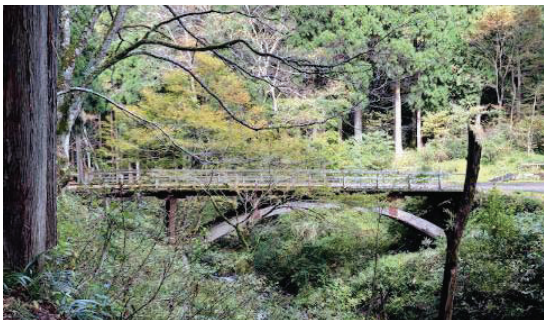

Figure 1: *Kajika Bridge in Ishikawa prefecture1*

Figure 2: *Kajika Bridge in Ishikawa prefecture2*

[1] Daisuke Oikawa, Akita University, Graduate School of Engineering Science, Japan, d.oikawa1987@gmail.com
[2] Shuya Nemoto, Akita University, Faculty of Engineering Science, Japan,
[3] Humihiko Gotou, Akita University, Graduate School of Engineering Science, Japan, gotou@gipc.akita-u.ac.jp
[4] Yukari Aoki, Akita University, Graduate School of Engineering Science, Japan, yaoki@gipc.akita-u.ac.jp

https://doi.org/10.52202/069179-0311

2 MODEL SETTING

In this study, measured data for the existing bridge 'Kajika Bridge' in Ishikawa prefecture in Japan, is used. This bridge shown in Figure.1, 2 is a two-hinged deck arch bridge built in 1987. This bridge has been used as roadway bridge for 35 years till now. In 2019, measurements such as investigations of natural frequencies and of degradation area for the bridge were carried out [1]. Here we numerically simulate the measured condition of the bridge by vibration analysis using FEM tool Salome-Meca[1].

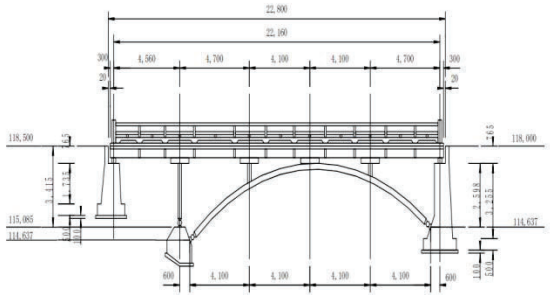

Figure 3: General drawing of Kajika Bridg

Table 1: *Properties of Kajika Bridge*

Location	Ishikawa pref, Japan
Type	Deck arch bridge
Total length	22.8m
Span	16.4m
Traveled way width	3.0m
Design load	Roadway 6tf
Completion	1987-12
Material	Glulam of Hiba (Thujopsis)

3 COMPARISON OF TWO MODELS

In modal analysis for bridges such as truss, arch and so on, which consist of slender members, beam element is generally used, while solid element such as tetrahedral element is not often used because of large calculation load. In this section we compare typical modal analysis model using beam/shell element and more exact model using tetrahedral element for Kajika Bridge.

3.1 CONVERGENCY OF TETRAHEDRAL ELEMENT

Here we investigate convergency of tetrahedral element. In the case of linear element, it needs 6,640,476 elements for natural frequency to be converged to two significant digit, while in the case of quadratic element, it needs 1,596,360 to be converged to two significant digit. Figure. 5 shows convergency for the vibration mode of vertically antisymmetric two sin half-waves, which is the most dominant mode for Kajika Bridge.

According to this result, quadratic element, which can obtain high accuracy with less number of elements, is adopted for the analysis hereafter.

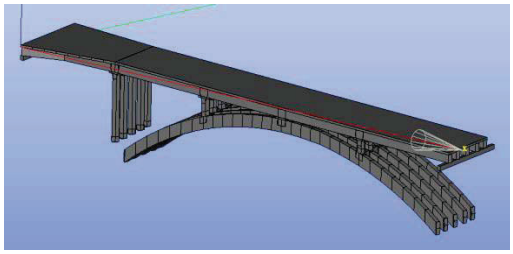

Figure 4: *Numerical Model for Kajika Bridg*e

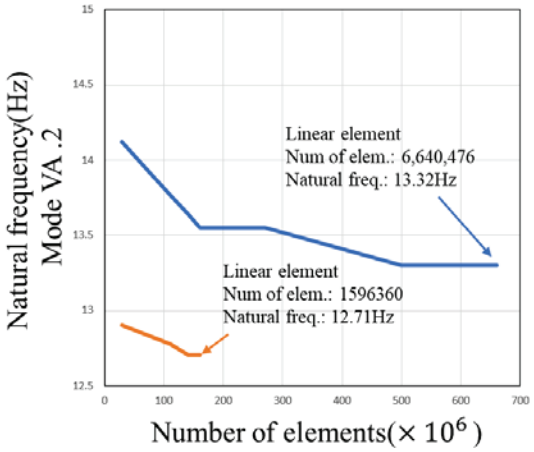

Figure 5: Convergency of tetrahedral element

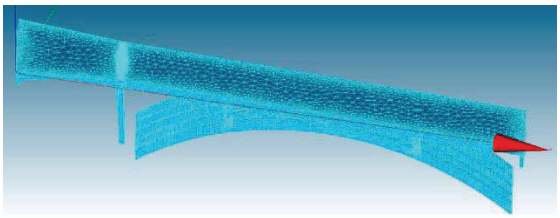

Figure 6: *Mesh of tetrahedral element*

3.2 COMPARISON TO MEASURED VALUE UNDER FITED YOUNG'S MODULUS

Natural frequencies measured in 2004, which is the first year of measurement since the beginning of service in 1987 for Kajika Bridge are shown in Table 2 for the following four dominant modes: H.S.1 is horizontally symmetric one sin half-wave shown in Figure. 6; V.A.2 is vertically antisymmetric two sin half-waves shown in Figure7; V.S.1 is vertically symmetric one sin half-wave shown in Figure.8 and V.S.4 is vertically symmetric four sin half-waves shown in Figure.9

We try to compare accuracy of the tetrahedral element model with beam/shell element model. Beam/shell element mode means the model in which the deck part is modeled by shell element, while the other parts such as arch, longitudinal beam and spandrel column are modeled by beam element shown in Figure 10. Each Young's

https://doi.org/10.52202/069179-0311

modulus of the tetrahedral element model and of the beam/shell element model is fitted to each appropriate value so that the natural frequency for the dominant vibration mode V.A.2 can coincide with the measured value 11.62Hz. Natural frequencies for the other three modes are calculated for the two models as shown in Table. 2. The relative errors for H.S.1 and V.S.1 of the tetrahedral element mode are smaller than those of the beam/shell element model. Although relative error for V.S.4 of the tetrahedral element mode are larger than that of the beam/shell element model. we think that this

Table 2: *Comparison of analysis accuracy*

Vibration mode	Natural frequency Measurement value (2004)	tetrahedral element	beam/shell element
H.S.1	11.62 Hz	4.95 Hz (-4.3%)	4.57 Hz (-13.2%)
V.A.2	5.17 Hz	11.62 Hz (0%)	11.62 Hz (0%)
V.S.1	15.82Hz	15.20 Hz (-3.9%)	14.00 Hz (-11.5%)
V.S.4	19.14Hz	20.77 Hz (8.5%)	18.00 Hz (-5.5%)

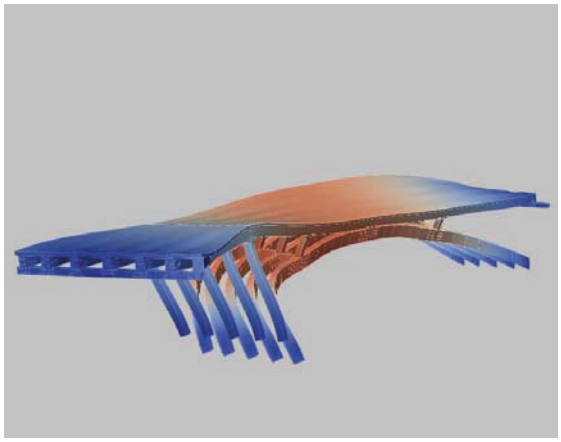

Figure 6: *Horizontally symmetric 1 sin half-wave (H.S.)*

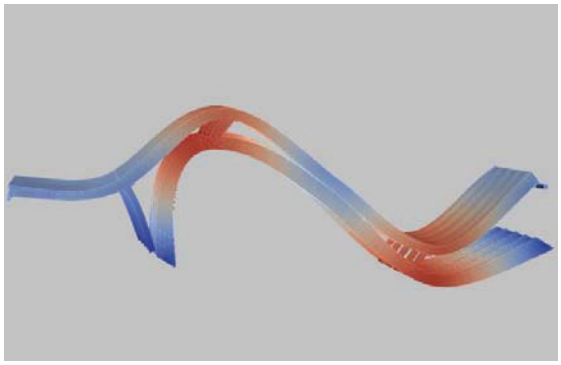

Figure 7: Vertically antisymmetric 2 sin half-waves (V.A.)

because of loss of measurement accuracy in higher mode vibration. According to the above, the tetrahedral element model is more suitable for modal analysis and this model will be used for all analyses hereafter. Incidentally materials for deck parts are orthotropic, while material for arch parts and so other parts is isotropic, since it is difficult to set appropriate othotropic condition corresponding to each local coordinate along the arch rib. Handrails with less influence to structure is not modeled.

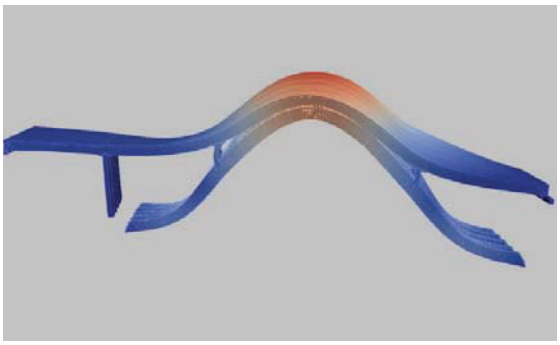

Figure 8: *Vertically symmetric 1 sin half-wave (V.S.)*

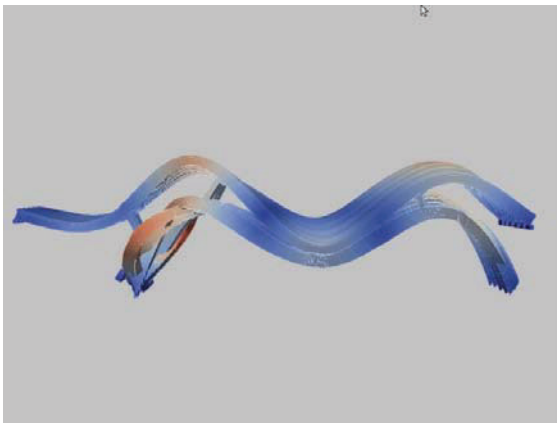

Figure 9: *Vertically symmetric four sin half-waves (V.S.4)*

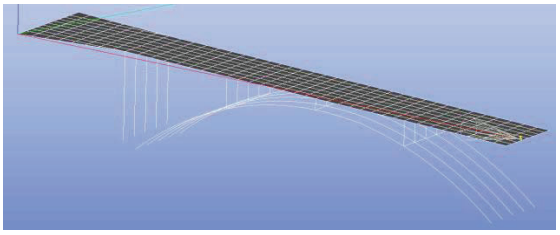

Figure 10: *Beam/shell element model*

https://doi.org/10.52202/069179-0311

Table 3 Natural frequencies for measured value and calculated value, also estimated Young's modulus

	1987 years	2004 year		2012 year		2015 year		2017 year		2019 year	
	Analysis value	Measured value	Analysis value	Measured value	Analysis value	Measured value	Analysis value	Measured value	Analysis value	Measured value	Analysis value
V.A.2	12.71	11.62	11.62	9.47	9.47	9.46	9.46	8.79	8.79	8.69	8.69
H.S.1	9.34	5.17	8.56	3.12	6.98	2.92	6.98	2.81	6.46	2.73	6.39
V.S.1	20.02	15.82	19.25	15.82	15.68	15.51	15.67	15.43	13.85	15.38	13.69
V.S.4	29.79	19.14	27.67	18.95	22.54	18.04	22.52	17.68	20.63	17.18	20.39
Estimated Young's modulus											
Deck parts (GPa)		8.60		5.71		5.70		4.92		4.81	
Other parts (GPa)		8.03		5.33		5.32		4.59		4.49	
Decreasing rate (%)		16.44		44.52		44.63		52.17		53.23	

4 YOUNG'S MODULUS FITTING TO MEASURED VALUE

The natural frequencies of the four modes for Kajika Bridge measured five times during fifteen years are shown in Table.4. The natural frequency for V.A.2, which is 11.62Hz in 2004, decreases to 8.69Hz in 2019. When we adjust Young's modulus in the tetrahedral element model so that the natural frequency for V.A.2 can be fitted to the value 8.69Hz, the Young's modulus for members of deck part becomes 4.81GPa and that for members of the other parts becomes 4.49GPa. If we assume that Young's modulus for all members decreases uniformly, it follows that Young's modulus for members of Kajika Bridge decreases by 53.23%, drastically. Young's moduluses adjusted in the same fitting manner for the measured values are also shown in Table 3. Figure 11 shows decreasing of the adjusted Young's moduluses for the measurement years. Young's moduluses decrease sharply from 2004 to 2012 and from 2015 to 2017, while Young's modulus decrease gradually in the other periods.

However from the realistic view point, the situation that the Young's moduluses for all members decrease uniformly by 53.23% is unlikely to happen, whether they sharply decrease or gradually decrease depending on periods during fifteen years. We guess that the decrease of the natural frequency is significantly influenced by partial decay of members. In fact the typical examples of partial decay are recognized at easily decayable parts such as ends of arch rib, connection between members and so on, which are shown in Figures 11, 12, 13 and 14. On the other hand, it seems that most of parts except for the decayable parts are not decayed so much by visual inspection.

Therefor we try a new approach fitting natural frequency by adjusting Young's modulus of partially set decay parts instead of adjusting Young's modulus of all members in the following section.

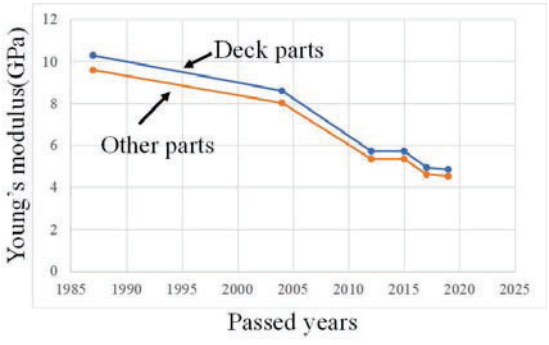

Figure 11: *Reduction in Young's modulus by passing age*

Figure 12: *Decay at the end of arch rib*

https://doi.org/10.52202/069179-0311

Figure 13: *Decay of connection between longitudinal beam and sleeper berm*

Figure 14: *Decay of connection between spandrel column and arch rib*

5 EVALUATION OF DECAY EFFECT

Here we numerically simulate the measured condition of the bridge by vibration analysis using FEM tool Salome-Meca considering decayed areas such as connection between longitudinal beam and sleeper beam, connection between spandrel column and arch rib, and end supports corresponding to the measurement. The numerical model with decayed areas is shown in Fig.15, 16.

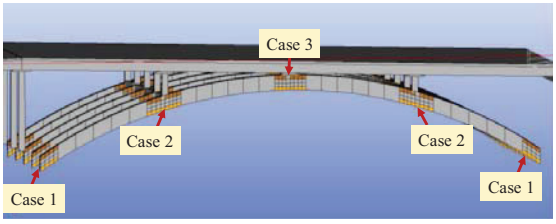

Figure 15: *Bridge model with decayed areas*

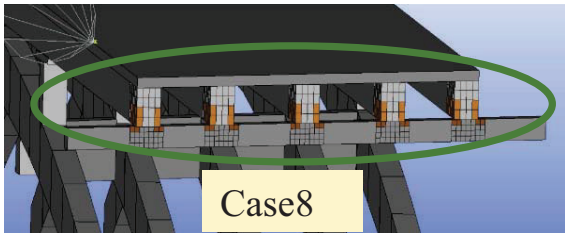

Figure 16: *Bridge model with decayed areas(sleeper beam)*

6 NUMERICAL ANALYSIS METHOD

In this study, the FEM model for the bridge is meshed by tetrahedral solid elements and the ends of each arch rib are hinged at the middle line of the section. The following two types of analyses are carried out.

6.1 COMPARISON BETWEEN MEASURED DATA AND NUMERICALLY DERIVED DATA

According to the measurement in 2019, the dominant natural frequency of Kajika bridge is 8.69Hz. In the numerical estimation, we firstly assume the model with only healthy areas whose Young's modulus is 9.6GPa (without decay), secondly we set the decayed areas whose Yong's modulus is 96MPa (Reduction 0%) and thirdly we gradually reduce the Young's modulus for the healthy areas (from 10% to 50%) with the same Young's modulus 96MPa for the decayed areas, until the natural frequency of the model would be enough close to the measured value.

6.2 EFFECT ESTIMATION FOR LOCAL DECAY PARTS

The case study has been conducted to identify the most significant part affecting the natural frequencies. The following cases shown in Table 4 are considered. It should be noted that the decay part for analysis 6.1 includes all cases, that is, the combination of Case 7 and Case 8.

Table 4: *Cases considering decay parts*

	Decay parts
Case 1	End supports
Case 2	Connection between spandrel column and arch rib
Case 3	Connection between deck and arch rib at center
Case 4	Combination of Case 1 and Case 2
Case 5	Combination of Case 1 and Case 3
Case 6	Combination of Case 2 and Case 3
Case 7	Combination of Case 1, Case 2 and Case 3
Case 8	Connection between longitudinal and sleeper beams

7 RESULTS AND DISCUSSION

The results of the analysis 6.1 are shown in Table 5. The dominant vibration mode of the arch bridge has vertically in-plane two sine half-waves as shown in Figure 3. While the measured natural frequency for Kajika bridge is 8.69Hz, that of numerical model with the decay parts and the healthy parts whose Young's modulus remains 9.6GPa (Reduction 0%) is 11.79Hz, which is about twice as large as the measured value. When Young's modulus of healthy parts is reduced by 40%, the calculated natural frequency is close to the measured value. And when the Young's modulus is reduced by 45.59%, the calculated natural frequency almost coincides with the measured value. At this time, the Young's modulus of this bridge is 5.22GPa which is less than half of the model without

https://doi.org/10.52202/069179-0311

decay. This estimation is smaller than expected and not realistic.

The results of the analysis 6.2 are shown in Table 6. According to the results, Case 2, 4, 6, and 7 shows the lower frequencies. The decay parts in these cases includes connection between spandrel column and arch rib. Therefore, the connection has significant influence on natural frequencies.

Table 5: *Young's modulus estimation*

	Mode V.A. (Hz)	Young's modulus estimation (GPa)
Measured value	8.69	
Without decay	12.71	9.60
Reduction 0%	11.79	9.60
Reduction10%	11.19	8.64
Reduction20%	10.55	7.68
Reduction30%	9.87	6.72
Reduction40%	9.13	5.76
Reduction50%	8.34	4.80
Reduction45.59%	8.69	5.22

Table 6: *Effect of decay parts*

	Frequency (Hz)	Relative error
Without decay	12.71	0.00%
Case1	12.68	0.20%
Case2	11.97	5.79%
Case3	12.53	1.41%
Case4	11.95	5.95%
Case5	12.50	1.64%
Case6	11.87	6.57%
Case7	11.85	6.73%
Case8	12.67	0.31%

8 CONCLUDING REMARKS

In this study, we carried out vibration analysis to estimate the proper Young's modulus and the most significant decay part affected to decreasing of the natural frequency for the bridge model with the considered local decay, comparing calculated values to the measured value. Basing on the results of the study, the following conclusions are made:

1) According to numerical comparison between tetrahedral element model and beam/shell element model, it is found that tetrahedral element mode gives more fitted natural frequencies for each dominant vibration mode than beam/shell element model.
2) As a result of simplified analysis, in which Young's moduluses for all members decrease uniformly, the adjusted value of Young's modulus becomes 53.23% to the original, while it is unlikely to happen.
3) In order to adjust the calculated natural frequency to the measured value, the Young's modulus of the healthy parts of the bridge has to be 5.22GPa, which is significantly low and still not realistic.
4) The decay at connection between spandrel column and arch rib has significant influence on natural frequencies of the bridge.

It is difficult to estimate which is more significant, reduction of Young's modulus for healthy parts or influence of decay parts. In the further study, the decay parts should be more parametrically studied considering conditions such as size, position, level of decay and so on.

REFERENCES

[1] Nakada, Y. Honda, H. and Ueno, Y.: Structural characteristics of half through arch timber highway bridge with stringer, Journal of Structural Engineering, Vol. 55, pp.915-924, 2009.

[2] Nukayama, N. and Honda, H.: Actual Evaluation on Structural Performance of Modern Glulam Timber Bridges, Paper Reports on Use of Wood for Civil Engineering9, pp.146-157, 2010.

[3] Toyoda, A. Honda, H. Shinohara, M. and Kato, S.: Structural Rigidity Based On Dynamic Performance Of Timber Bridge By Passing Age, Paper Reports on Use of Wood for Civil Engineering 17, pp.24-30, 2018/12.

[4] Oikawa, D. The Late Suganuma, G. Honda, H. and Gotou, H.: Structural Performance And Soundness Evaluation Of Aging Timber Arch Highway Bridge, Paper Reports on Wood Engineering 19, pp.72-79, 2021/2.

[5] https://code-aster.org/(browsed in 2022/06/15)

https://doi.org/10.52202/069179-0311

World Conference on Timber Engineering Oslo 2023

TECHNICAL DESGIN GUIDE FOR TIMBER-CONCRETE COMPOSITE FLOORS – A CANADIAN APPROACH

Samuel Cuerrier Auclair[1], Christian Dagenais[2], Sylvain Gagnon[3]

ABSTRACT: FPInnovations, a not-for-profit research organisation for the Canadian forest sector and affiliated industries, developed a technical design guide for timber-concrete composite (TCC) floors meeting multi-design requirements. It provides the design criteria along with the calculation methods to control the elastic and long-term deflection, the vibration induced by human walking and the structural resistance, as well as guidance for the fire-resistance design and the behaviour of the shear connection. The technical guide has been used to develop design provisions that are expected to be implemented in the next 2024 edition of CSA O86. This paper presents a summary of this Canadian design method.

KEYWORDS: Timber-concrete composite (TCC), multi-criteria design, floor vibration, fire resistance, shear connector

1 INTRODUCTION

A timber-concrete composite (TCC) system consists of two distinct layers, a timber layer and a concrete layer, joined together by shear connectors; typically, the concrete slab is the top layer. The properties of both materials are better exploited as a composite element, since tension forces from bending are mainly resisted by the timber while compression forces from bending are resisted by the concrete. This construction technique is used to strengthen and stiffen timber floors of existing and new constructions, especially in multi-storey buildings and long-span applications. When the two materials are well connected together, the load-carrying capacity and the bending stiffness are significantly increased compared to a traditional timber floor system [1]. The concrete layer is usually a reinforced concrete slab. The timber part can be solid wood lumber, glued laminated timber (Glulam), structural composite lumber (SCL), cross-laminated timber (CLT), nail-laminated timber (NLT) or made of other engineered wood products. The shear connectors can be discrete fasteners (e.g., nails, screws, or notches cut in the wooden part) or shear connectors transferring the load to a larger surface (e.g., embedded plates, glue). A combination of different shear connectors is also possible.

The development of the TCC system was initiated after the First World War to find an alternative for reinforced concrete and steel, because of a lack of availability of steel. Several connection systems were patented [2, 3]. In the 1930's, this construction technique was applied to bridges mainly located in the U.S.A. [4]. In the 1950's, TCC building structures appeared in Australia and New Zealand [5]. It was ignored in most parts of the world until the 1990's, when TCC structures started to be used when refurbishing old historical buildings in European cities, in order to meet the new requirements regarding sound insulation and fire-resistance [6].

TCC systems can be a cost-competitive solution in the construction of buildings with floors having longer spans, since the mechanical properties of the two materials would be used efficiently. Furthermore, the additional mass from the concrete can improve the acoustic performance, compared to that of a timber floor system alone. Nevertheless, TCC floors are not commonly used in buildings in Canada, due to the absence of technical guidelines in the Canadian wood engineering design standard CSA O86-19 [7].

2 OBJECTIVES

The objectives of this paper are to present the multi-criteria design guide for TCC floors in Canada written by FPInnovations [8]. The criteria considered in the design are:

1) the elastic and the long-term deflections,
2) the vibration performance due to human normal walking,
3) the ultimate limit state design (bending and shear resistance) and,
4) the structural fire resistance.

The methodology used to verify those criteria are based on the gamma-method (γ-method) which was developed by Möhler [9] in 1956 by applying a sinusoidal load on a composite beam.

[1] Samuel Cuerrier Auclair, FPInnovations, Canada, samuel.cuerrier-auclair@fpinnovations.ca
[2] Christian Dagenais, FPInnovations, Canada, christian.dagenais@fpinnovations.ca
[3] Sylvain Gagnon, FPInnovations, Canada, sylvain.gagnon@fpinnovations.ca

https://doi.org/10.52202/069179-0312

3 EVALUATION OF THE EFFECTIVE BENDING STIFFNESS

Using the γ-method, available in Annex B of the Eurocode 5 [10], the effective bending stiffness of the composite system can be evaluated. The γ-method assumes a uniformly distributed shear stiffness, K, between the two connected components, being timber and concrete. If the spacing of the shear connector is not constant along the span, an effective spacing needs to be estimated as follows:

$$s_{eff} = 0.75s_{min} + 0.25s_{max} \quad (1)$$

where s_{min} is the spacing of the shear connector near the supports in mm and s_{max} is the connector spacing in the mid-span section in mm. The uniformly distributed shear stiffness is then calculated as follows:

$$K = \frac{nk}{s_{eff}} \quad (2)$$

where n is the number of rows of the shear connectors and k is stiffness of a single shear connector in N/mm.

The tension contribution of the concrete must be neglected to be in-line with the concrete design standard in Canada (CSA A23.3) [11]. Figure 1 shows the nomenclature used and the cross-section with the associated axial deformation used for the calculation.

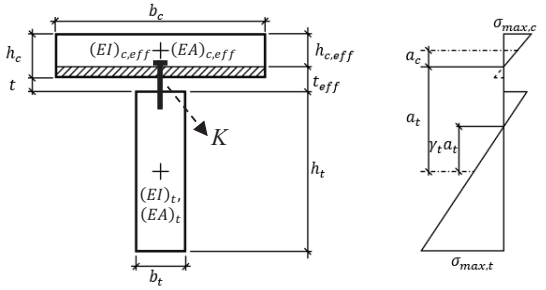

Figure 1: *Cross-section and axial deformation of a TCC beam neglecting the concrete solicited in tension*

$$(EI)_{eff} = (EI)_{c,eff} + (EI)_{t,eff} + \gamma_c(EA)_c a_c^2 + \gamma_t(EA)_t a_t^2 \quad (3)$$

Where,

$$\gamma_c = 1 \text{ and } \gamma_t = \frac{1}{1 + \frac{\pi^2(EA)_t}{KL^2}} \quad (4)$$

$$h_{c,eff} = \min\left(\sqrt{\alpha^2 + \alpha(h_t + 2h_c + 2t)} - \alpha; h_c\right) \quad (5)$$

$$\alpha = \frac{\gamma_t(EA)_t}{E_c b_c} \quad (6)$$

$$(EA)_{c,eff} = E_c b_c h_{c,eff} \text{ and } (EI)_{c,eff} = \frac{E_c b_c h_{c,eff}^3}{12} \quad (7)$$

$$a_c = \frac{\gamma_t(EA)_t r}{(EA)_{c,eff} + \gamma_t(EA)_t} \text{ and } a_t = r - a_c \quad (8)$$

$$r = \frac{h_t}{2} + t + h_c - \frac{h_{c,eff}}{2} \quad (9)$$

Where $(EI)_{eff}$ is the effective bending stiffness in N-mm^2. $(EI)_{c,eff}$ and $(EA)_{c,eff}$ are the effective bending stiffness and the axial stiffness of the concrete slab by neglecting the portion in concrete in N-mm^2 and in N, respectively. $(EI)_t$ and $(EA)_t$ are the bending stiffness and the axial stiffness of the timber component in N-mm^2 and in N, respectively.γ_c and γ_t are the composite factor of the concrete and wood component, respectively. E_c, b_c and h_c are the modulus of elasticity, the effective width and the thickness of the concrete slab in MPa, mm and mm, respectively. h_t is the height of the wood component in mm. a_c and a_t are the distance between the centroid of the concrete slab and the timber to the neutral axis of the concrete slab in mm, respectively. L is the span of the TCC floor in mm. t is the gap between the concrete slab and the timber component in mm. r is the distance between the centroids of the concrete slab and the wood component in mm.

4 SHEAR CONNECTION PROPERTIES

The type of shear connection between the timber and concrete components greatly influences the structural properties of TCC floors. A wide range of connection systems are available, ranging from mechanical connectors such as bolts [12], lag screws [13], or self-tapping screws (STS) [14], glued-in perforated steel plates [15], composite connectors [16], adhesive bonds [17], notched connections [18], or steel kerf plates [19].

When possible, the shear resistance of the shear connector should be estimated with the appropriate Clause 12 in CSA O86-19 [7]. When not possible, the shear resistance needs to be estimated through laboratory testing.

CSA O86-19 [7] does not give equation to estimate the slip modulus of connectors. Thus, this property needs to be evaluated in a laboratory. The testing need to be performed in accordance with the standard ISO 6891 [20].

5 ELASTIC AND LONG-TERM DEFLECTIONS

5.1 ELASTIC DEFLECTIONS

In Canada, the deflection limit for timber structure under serviceability loads are prescribed by CSA O86-19 [7]. Estimating the elastic deflection is relatively straightforward, the effective bending stiffness is estimated using the standard-term properties of each

https://doi.org/10.52202/069179-0312

material and using the serviceability limit state slips modulus of the shear connector. Once this, effective bending stiffness is estimated, the instantaneous deflection can be estimated with the serviceability load combination considered.

5.2 LONG-TERM DEFLECTION

The long-term deflection is estimated by the superimposition principles. Two portions of the total deflection can be defined:

1) the elastic deflection due to transient load evaluated with the previous subsection and
2) the long-term deflection, which includes the elastic and creep portion, due to quasi-permanent and permanent loads.

The second portion is evaluated by dividing the stiffness properties of each material (e.g., timber, concrete and shear connector) by their respective creep modification factors. Creep modification factors are numerically equivalent to the creep coefficient by adding 1 to the value. Once the stiffness of each material is modified, the long-term effective bending stiffness can be estimated to calculate the long-term deflection due to quasi-permanent and permanent loads.

6 VIBRATION PERFORMANCE DUE TO WALKING

Human normal walking excites the floor through its footstep. Significant efforts were made towards understanding the nature of footsteps [21-24]. Based on their findings, it can be concluded that the footstep force generated by walking comprises two components [22]. One component is a short duration impact force induced by the heel of each footstep on the floor surface where the duration of the heel impact varies from about 30 ms to 100 ms depending on the conditions and the materials of the two contact surfaces (that of the floor and the footwear of the walking person), and on the weight and gait of the person. The other component is the walking rate, a series of footsteps consisting of a wave train of harmonics, at multiples of about 2 Hz.

To understand how TCC floors behave under walking vibration, FPInnovations tested three different laboratory floors:

1- NLT-concrete composite slab floor with a nail plate as shear connectors;
2- CLT-concrete composite slab floor with self-tapping screws as shear connectors;
3- Concrete slab - glulam beams composite floor with self-tapping screws as shear connectors.

The three floors have been tested according to the ISO 18324 [25] and ISO 21136 [26] in order to evaluate their natural frequency, damping ratio, static deflection under a concentrated load and their vibration performance under a subjective evaluation. From these tests, design criteria to limit the span due to vibration induce by walking has been developed. More information on the tested laboratory TCC floors can be found in [27].

Using the subjective evaluation results of the three tested TCC floor along with their calculated natural frequencies and deflections, the following design criterion was derived using the method described in ISO 21136 [26].

$$\frac{f_1}{d_{1kN}^{0.14}} \geq 5.75 \tag{10}$$

where f_1 is the fundamental natural frequency in Hz and d_{1kN} is the static deflection under a 1 kN point load in mm. Assuming a simple span floor with a centre point load, Equation (10) can be rewritten as follows to limit the span.

$$L \leq 0.329 \frac{\left((EI)_{eff}^{1m}\right)^{0.264}}{m_L^{0.207}} \tag{11}$$

where L is the maximum allowable clear span in meter for the vibration criterion. $(EI)_{eff}^{1m}$ is the effective bending stiffness of the floor calculated with Equations (3) considering the standard-term material properties for 1-meter-wide floor in N-m^2 and m_L is the structural mass only of the 1-meter-wide floor in kg/m.

Figure 2 illustrates the verification of the proposed design criterion for TCC floors using the limited laboratory data and the field floor data. Each symbol represented a subjectively rated TCC floor.

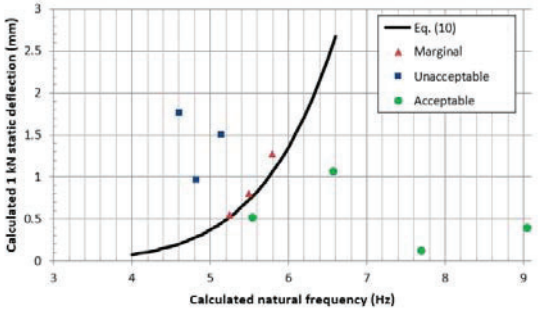

Figure 2: *Verification of the proposed design criterion for controlling vibration of TCC floors*

7 ULTIMATE LIMIT STATE DESIGN

TCC floors are made of three components: timber, concrete and shear connectors, where each of them can limit the strength of the floor. In the following section, equations are developed to evaluate the bending moment and the shear resistance of the whole TCC floors by considering the component that would fail first.

The shear connector can be 1) brittle or is not allowed to yield or 2) ductile and is allowed to yield. In these two different scenarios, the resisting equations are not the same. In the first scenario, the γ-method is used to estimate the force in each component. The TCC floor

design resistance is achieved when the first component achieved its ultimate resistance. The second scenario assumes that each connector has yielded which changes the equilibrium cinematic compared to the γ-method. Consequently, an elasto-plastic model (EPM) [28] is used to estimate the force on each component and the TCC floor ultimate resistance is achieved when the timber or the concrete achieved its ultimate resistance. It should be noted that the shear connector under serviceability load must remain in its elastic behaviour which is verified with the γ-method.

If the connector is ductile and the resistance of the TCC floor is limited by the γ-method, the floor will likely be brittle. Comparatively, if the resistance is limited by the EPM, the floor will have inelastic deformation before collapse. Figure 3 shows typical load-deflection curve of TCC floor. The γ-method will limit the resistance of the floor if the floor fails in the first circled portion and the EPM will limit the resistance of the floor if the floor fail in the second circled portion.

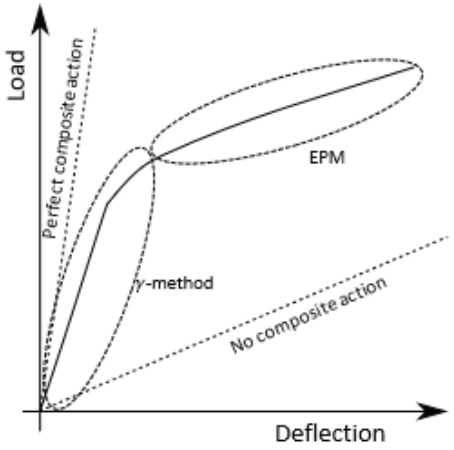

Figure 3: *Failure mechanism of TCC floors*

If not all the connectors have yielded when the floor fails, that situation is not directly accounted either in the γ-method and the EPM. However, in the γ-method the shear stiffness of the connectors is usually reduced when calculating the ultimate resistance of the floor which partially accounts this situation. Moreover, in the EPM the total shear load given by all the yielded connectors is estimated with their design resistance. Due to repeatability effect, the total shear load given by the connectors in the EPM gives a smaller probability of failure compared to a single shear connector. Consequently, in the design calculation, the EPM gives a conservative design value if all the connectors have yielded.

7.1 BENDING RESISTANCE

7.1.1 Gamma method

A bending moment applied on a composite floor (M) induced a bending moment (M_i) and an axial force (N_i) on each layer where i is used to either represent the timber component, t, or the concrete component, c. According to the γ-method, the axial force and the bending moment on each layer is calculated with the following formulae:

$$N_i = \frac{\gamma_i (EA)_i a_i}{(EI)_{eff}} M \tag{12}$$

$$M_i = \frac{(EI)_i}{(EI)_{eff}} M \tag{13}$$

The maximum axial stress on a given component is equal to the following equation:

$$\sigma_{max,i} = \frac{M}{b_i h_i (EI)_{eff}} \left(\frac{6(EI)_i}{h_i} + \gamma_i (EA)_i a_i \right) \tag{14}$$

However, for the timber element, only looking the maximum stress is not sufficient. The interaction between the axial force and the bending moment need verification with the following combined efforts interaction in accordance with CSA O86-19 [7]:

$$\frac{T_{f,t}}{T_{r,t}} + \frac{M_{f,t}}{M_{r,t}} \leq 1.0 \tag{15}$$

Where $T_{r,t}$ and $M_{r,t}$ are the tension and bending moment resistance, respectively, for the timber element evaluated with the CSA O86-19 [7] and $T_{f,t}$ and $M_{f,t}$ are the tension and bending moment force resisted by the timber component. The bending moment resistance of a TCC floor limited by the timber can be determined by substituting Equations (12) and (13) into Equation(14):

$$M_{r,\gamma,t} = \frac{(EI)_{eff} T_{r,t} M_{r,t}}{\gamma_t (EA)_t a_t M_{r,t} + (EI)_t T_{r,t}} \tag{16}$$

The bending moment resistance of a TCC floor limited by the concrete component is determined by ensuring that the maximum axial stress of the concrete does not exceed $0.9\phi_c f_c'$ which is in consistent with CSA A23.3-19 [11]. However, ensuring that the concrete never exceeds $0.9\phi_c f_c'$ with a triangular stress distribution is very conservative since concrete is able to have some inelastic deformation.

$$M_{r,\gamma,c} = 0.9\phi_c f_c' S_c \tag{17}$$

$$S_c = \frac{(EI)_{eff}}{E_c (0.5h_c + \gamma_c a_c)} \tag{18}$$

As a result, the bending moment resistance of a TCC floor when the shear connectors are brittle or not allowed to yield is:

$$M_{r,\gamma} = \min\left(M_{r,\gamma,t}; M_{r,\gamma,c}\right) \tag{19}$$

7.1.2 Elasto-plastic model

The bending moment resistance evaluated with the γ-method assumes that each component has a linear elastic behaviour. However, if the connector yields before failure

https://doi.org/10.52202/069179-0312

of the timber or the concrete element, bending moment resistance given by the γ-method may overestimate the resistance which is why bending moment resistance needs to be limited as a function of the connection's strength determined from the EPM ($M_{r,EP}$). When calculating the resistance with the EPM, the connectors must exhibit a ductile behaviour.

To consider the ductility of the connectors, Frangi & Fontana [28] proposed a method which accounts the strength of the connectors. The principles of this method are similar to the method in CSA S16-19 [29] for calculating the bending moment resistance of a steel-concrete beam, with some minor differences. When the connectors are allowed to yield, the following equation needs to be respected:

$$M_r = \min\left(M_{r,\gamma,t}; M_{r,\gamma,c}; M_{r.EP}\right) \tag{20}$$

where $M_{r,EP}$ is the bending moment resistance evaluated with the EPM developed by Frangi & Fontana [28] describes in this section. They developed the equations to evaluate the bending moment resistance considering that the timber fails first, while a part of the concrete is in tension, which is usually the case. However, to consider all possible scenarios, the equations for the bending resistance in the event that the concrete fails first or when the entire thickness of the concrete is in compression were also developed.

Based on the assumption that all connectors have yielded at the collapse mechanism, the maximum shear force that can be transferred to each layer is calculated from the design connector strength ($V_{r,conn}$) and the number of connectors (m) located between the critical cross-section and one point of zero moment:

$$N_c = N_t = N = mV_{r,conn} \leq \min\left(T_{r,t}; 0.9\phi_c f_c' A_c\right) \tag{21}$$

If $mV_{r,conn} \geq \min\left(T_{r,t}; 0.9\phi_c f_c' A_c\right)$, it means that the concrete or the timber will reach its resistance before that all the connectors have yielded. In that case, $N = \min\left(T_{r,t}; 0.9\phi_c f_c' A_c\right)$, $h_{c,eff} = h_c$, $\sigma_{b,t} = \sigma_{b,c} = 0$, when evaluating $M_{r,EP}$ with Equation (31).

If the bending moment resistance of the composite floor is governed by the timber design strength, the bending stress applied on the timber $\sigma_{b,t}$ is calculated as follows:

$$\sigma_{b,t} = \left(1.0 - \frac{N}{T_{r,t}}\right)\frac{6M_{r,t}}{b_t h_t^2} \tag{22}$$

If a part of the concrete is in tension, $h_{c,eff}$ and $\sigma_{b,c}$ are calculated as:

$$h_{c,eff} = \sqrt{\frac{NE_t h_t}{E_c \sigma_{b,t} b_c}} \leq h_c \tag{23}$$

$$\sigma_{b,c} = \frac{N}{b_c h_{c,eff}} \leq 0.45\phi_c f_c' \tag{24}$$

Note that E_t in the EPM is equal to $12(EI)_t/(b_t h_t^3)$. If the limitation of Equation (23) is not respected, then the entire thickness of the concrete is in compression and $h_{c,eff} = h_c$ and $\sigma_{b,c}$ is calculated as:

$$\sigma_{b,c} = \frac{E_c h_{c,eff}}{E_t h_t}\sigma_{b,t} \leq \left(0.9\phi_c f_c' - \frac{N}{b_c h_{c,eff}}\right) \tag{25}$$

If the limitation of Equation (24) or (25) is not respected then the bending moment resistance of the composite floor is governed by the concrete strength. If a part of the concrete is in tension, $h_{c,eff}$, $\sigma_{b,c}$ and $\sigma_{b,t}$ are calculated as follows:

$$h_{c,eff} = \frac{2N}{0.9\phi_c f_c' b_c} \leq h_c \tag{26}$$

$$\sigma_{b,c} = 0.45\phi_c f_c' \tag{27}$$

$$\sigma_{b,t} = \frac{E_t h_t b_c (0.9\phi_c f_c')^2}{4E_c N} \leq \left(1.0 - \frac{N}{T_{r,t}}\right)\frac{6M_{r,t}}{b_t h_t^2} \tag{28}$$

If the limitation of Equation (26) is not respected then the entire thickness of the concrete is in compression and $h_{c,eff} = h_c$ and $\sigma_{b,c}$ and $\sigma_{b,t}$ are calculated as follows:

$$\sigma_{b,c} = 0.9\phi_c f_c' - \frac{N}{b_c h_{c,eff}} \leq \frac{N}{b_c h_{c,eff}} \tag{29}$$

$$\sigma_{b,t} = \frac{E_t h_t}{E_c h_c}\left(0.9\phi_c f_c' - \frac{N}{b_c h_{c,eff}}\right) \leq \left(1.0 - \frac{N}{T_{r,t}}\right)\frac{6M_{r,t}}{b_t h_t^2} \tag{30}$$

Once N, $h_{c,eff}$, $\sigma_{b,c}$ and $\sigma_{b,t}$ are known, the bending moment resistance of the composite floor is calculated as follows:

$$M_{r,EP} = N\left(\frac{h_t}{2} + t + h_c - \frac{h_{c,eff}}{2}\right) + \sigma_{b,c}\frac{b_c h_{c,eff}^2}{6} + \sigma_{b,t}\frac{b_t h_t^2}{6} \tag{31}$$

7.2 SHEAR RESISTANCE

7.2.1 Gamma method

The shear resistance of a TCC floor can be dictated by the strength of the connectors, the timber or the concrete. From the Eurocode 5 [10], the shear flow at the connection interface (τ_{conn}) is evaluated with the following formulae:

$$\tau_{conn} = \frac{\gamma_t (EA)_t a_t}{(EI)_{eff}} V \quad (32)$$

V is the applied shear force on the whole TCC section. The applied shear force at one connector (V_{conn}) is afterwards evaluated with the following equation:

$$V_{conn} = \frac{\tau_{conn} s}{n} = \frac{\gamma_t (EA)_t a_t s}{n(EI)_{eff}} V \quad (33)$$

Where s is the tributary spacing of the considered shear connector and n is the number of rows of shear connectors. Equation (33) can be rewritten to estimate the shear resistance of the whole composite floor dictated by the connection shear resistance with the γ-method ($V_{r,\gamma,conn}$) as follows:

$$V_{r,\gamma,conn} = \frac{n(EI)_{eff}}{\gamma_t (EA)_t a_t s} V_{r,conn} \quad (34)$$

where $V_{r,conn}$ is the design connection shear resistance.

The vertical shear stress in the timber and concrete elements according to the classical beam theory (and the theory of mechanically jointed beams [10]) is calculated as follows:

$$\tau_{max,i} = \frac{V(EQ)_i}{(EI)_{eff} b_i} \quad (35)$$

where,

$$(EQ)_i = \frac{y_i}{h_i}\left(\frac{6(EI)_i}{h_i}\left(1 - \frac{y_i}{h_i}\right) + \gamma_i (EA)_i a_i\right) \quad (36)$$

y_i is the position at which the shear stress is evaluated. Knowing that the shear stress is critical at the neutral axis evaluated as $y_{NA,i} = h_i/2 + \gamma_i a_i$ the maximum stress within a layer is then:

$$\tau_{max,i} = \begin{cases} \dfrac{0.5E_i\left(\frac{h_i}{2} + \gamma_i a_i\right)^2}{(EI)_{eff}} V, & y_{NA,i} < h_i \\ \dfrac{E_i h_i \gamma_i a_i}{(EI)_{eff}} V, & y_{NA,i} \geq h_i \end{cases} \quad (37)$$

If there is no neutral axis in the layer, the shear stress is maximal at the interface, as dictated from the second expression in Equation (37).

In Canada, the verification according to design standard is based on the force instead of the stress. According to the theory of mechanically jointed beams, the shear force in each component is calculated with the following equation:

$$V_i = \frac{(EI)_i + 0.5\gamma_i (EA)_i h_i a_i}{(EI)_{eff}} V \quad (38)$$

Equation (38) can be rewritten to estimate the shear resistance of the whole composite floor dictated by the timber shear resistance or the concrete shear resistance with the γ-method as follows:

$$V_{r,\gamma,t} = \frac{(EI)_{eff}}{(EI)_t + 0.5\gamma_t (EA)_t (h_t + t) a_t} V_{r,t} \quad (39)$$

$$V_{r,\gamma,c} = \frac{(EI)_{eff}}{(EI)_c + 0.5\gamma_c (EA)_c (2h_c - h_{c,eff} + t) a_c} V_{r,c} \quad (40)$$

where $V_{r,t}$ is the design shear resistance of the timber component and $V_{r,c}$ is the design shear resistance of the concrete slab. It must be noted that in Equations (39) and (40) the gap, t, have been added in the equation to ensure that the total vertical shear force can be resisted by the concrete and the timber component.

The shear resistance of the whole TCC floors is reached when the first component reaches its strength. Thus, the following equation gives the shear resistance of the whole TCC floors ($V_{r,\gamma}$).

$$V_r = \min\left(V_{r,\gamma,conn}; V_{r,\gamma,t}; V_{r,\gamma,c}\right) \quad (41)$$

If the connector resistance is reached before the shear resistance of the timber or the concrete, that doesn't necessarily mean failure of the TCC floor if the connectors exhibit a ductile behaviour [28,30,31]. When the capacity of the ductile shear connector is reached, it will transfer its forces to the concrete and timber elements until one of them fail. As a conservative design, Equation (41) may be used to evaluate the shear resistance of the TCC floor when the connector is ductile. However, if the designer wants to benefit on the ductility of the connector, the following equation can be used:

$$V_r = \min\left(V_{r,\gamma,t}; V_{r,\gamma,c}; V_{r,EP,t}; V_{r,EP,c}\right) \quad (42)$$

where $V_{r,EP}$ is the shear resistance following the EPM. Although the shear connectors are ductile, the shear resistance limited by the shear connector, $V_{r,\gamma,conn}$, must be higher than the serviceability shear load in order to limit the fatigue phenomena and ensuring accuracy in the deflection calculation.

7.2.2 Elasto-plastic model

More details for the shear resistance calculated with the EPM is given in the design guide for TCC floors in Canada written by FPInnovations [8].

8 STRUCTURAL FIRE-RESISTANCE

This section addresses the structural fire-resistance of a TCC floors subjected to a standard fire from underneath and does not address all the other subjects related to the

https://doi.org/10.52202/069179-0312

fire safety, such as the separating function of floor assemblies. In order to develop and validate a calculation method to predict the time of structural fire-resistance for a TCC floor, FPInnovations [32, 33] tested three different TCC floors exposed to a standard fire such as that specified in CAN/ULC-S101 and ASTM E119. The span of these three floors was 4815 mm with an applied live load of 2.4 kPa. One of the floors consisted of a series of nine screw-laminated 2x8 "beams" (38 x 184 mm, on the edge), where each build-up beams consisted of five pieces of lumber boards. Conventional truss plates were used as shear connectors into 89 mm reinforced concrete as shown in Figure 4a. A second floor consisted of a 5-ply (175 mm) E1 stress grade CLT and 89 mm concrete, connected using self-tapping screws driven at 45° into the CLT, as shown in Figure 4b. The third floor consisted of 5¼" x 16" (133 x 406 mm, on flat) laminated veneer lumber (LVL). Lag screws were used as shear connectors, as shown in Figure 4c, to 89 mm concrete topping. All of these floors were fully exposed to the standard fire from underneath (i.e. timber components were exposed to fire).

a) 2x8 screw laminated wood with a truss plate

b) CLT with self-tapping screws

c) LVL with lag screw

Figure 4: *TCC floors under construction for fire-resistance testing*

Based on the data gathered from the tested TCC floors exposed to the CAN/ULC S101 standard fire, it was found that the shear connectors have little to no impact on the heat transfer into the assembly. Even the lag screws' larger diameter did not create a significant increase in heat transfer through the assembly as the shear connector becomes exposed to fire from underneath. Consequently, as long as the connector is not exposed to fire (i.e., remains in the reduced timber cross-section), it can be assumed that the shear resistance and the shear stiffness of the connector are not affected. However, when the timber element is exposed to fire on its side and underneath (e.g. timber beam), the wood that covers the shear connector on the side must be at least 35 mm to remain thermally thick (i.e. to limit heat transfer up to the connector). When the wood cover is less than 35 mm, the temperature into the connection can increase significantly and then greatly affect its mechanical properties.

When the connector becomes exposed to fire from underneath, its shear resistance should be estimated using the appropriate design provisions as a function of its residual penetration depth into the timber. If it is not possible to estimate the shear resistance with those design provisions, its strength may be reduced proportionally to its remaining depth. This design assumption may not be applicable for all shear connectors. Consequently, applying this assumption is at the judgment of the structural engineer of record.

When no test data are available, the reduced shear stiffness of the shear connector could be proportional to the loss of strength. This assumption may not be applicable for all shear connectors, but has been validated with self-tapping screws inserted with an angle of 45°, lag screws and truss plates in the following references [32, 33]. It is at the judgment of the structural engineer of record to apply or not this hypothesis in function of the shear connector.

Table 1 gives the structural failure times obtained from these three tested floors and those predicted using the methodology proposed herein.

Table 1: *Fire-resistance of TCC floors – Test data vs. calculation method*

	NLT-Concrete	CLT-Concrete	LVL-Concrete
Shear connector	Truss plate	Self-tapping screws	Lag screws
Test failure time (min)	>214*	214	191
Predicted failure time	247	198**	165

*Test was stopped when the CLT-concrete floor failed. No failure was reached for the NLT-concrete floor.
**Using the effective charring model from Annex B of CSA O86-19 [7]

The predicted structural fire-resistance failure times are calculated using laboratory shear connector test results (stiffness and resistance). The shear connector properties were proportionally reduced linearly as a function of its remaining penetration depth once it was exposed to fire. The predicted times are conservative for the CLT-concrete and LVL-concrete composite floors. For the NLT-concrete floor, the predicted failure time seems realistic, but it is uncertain whether the estimation is conservative, or not, since the test was stopped after 214 min; time at which the CLT-concrete floor failed first (CLT and NLT were tested simultaneously in the same furnace).

Figure 5 shows the predicted deflection as a function of time for the LVL-concrete composite floor with two different assumptions. One predicted curve assumes that the stiffness of the connectors is reduced proportionally to its remaining penetration depth and the other curve uses the stiffness of the connectors based on shear test results conducted at different remaining penetration depths into

the LVL. The deflection was estimated by reducing the thickness of the wood through time and the shear connector stiffness which impacted the calculated $(EI)_{eff}$. For the LVL-concrete composite floor with lag screws as shear connectors, the estimated deflection and residual resistance are conservative when assuming that the properties of the shear connector are reduced proportionally to its remaining penetration depth. The predicted deflection is also quite accurate when compared to the experimental results using shear connector properties being modified based on experimental shear test results.

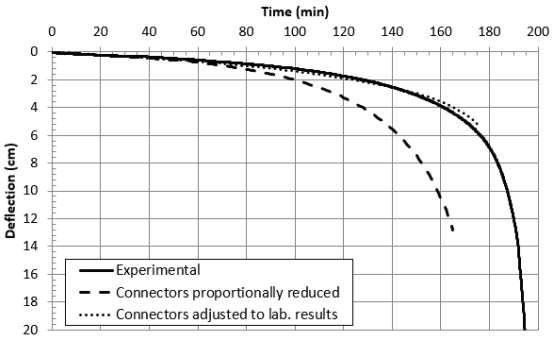

Figure 5: *Comparison between the experimental and the predicted deflections in function of time curves*

From these tests, it is concluded that when the composite floor is made with a timber slab (bottom), the timber effectively protects the concrete (top) from the thermal effects from fire underneath. Consequently, the strength of the TCC slab floor can be calculated by simply reducing the timber cross-section due to charring and the connector properties as a function of its remaining penetration depth. However, when the floor is made with timber beams instead of a timber slab, the concrete located between beams becomes fully exposed to fire and its fire resistance shall be calculated in accordance with the applicable design provisions found in the NBC [34].

9 CONCLUSIONS

With the information currently available in the literature and laboratory test results, FPInnovations developed a design guide for timber-concrete composite floors with a focus on the Canadian design code. This paper presents a summary of this design method.

At the time of writing this paper, design provisions were developed for implementations in the next 2024 edition of CSA O86. The methodology presented in the technical guide was used to develop the provisions, which have been slightly modified based on CSA O86 Task Group members. Limitations are also proposed, such as simple span TCC floors and TCC floors consisted of slab elements only.

ACKNOWLEDGEMENT

FPInnovations would like to thank its industry members and Natural Resources Canada (Canadian Forest Service) for their financial supports of this work.

REFERENCES

[1] A. Ceccotti, "Composite concrete-timber structures," *Progress in Structural Engineering and Materials,* vol. 4, no. 3, pp. 264-275, 2002.

[2] P. Mueller, "Decke aus hochkantig stehenden Holzbohlen oder Holzbrettern und Betondeckschicht". 1921.

[3] O. Schaub, "Wood reinforced concrete structural member". 1931.

[4] F. E. Richart and C. B. Williams, "Tests of composite timber and concrete beams," *University of Illinois bulletin,* vol. 40, no. 38, 1943.

[5] J. N. Rodrigues, A. M. P. G. Dias and P. Providência, "Timber-concrete composite bridges: state-of-the-art review," *BioResources,* vol. 8, no. 4, pp. 6630-6649, 2013.

[6] D. Yeoh, M. Fragiacomo, M. De Franceschi and K. Heng Boon, "State of the art on timber-concrete composite structures: Literature review," *Journal of structural engineering,* vol. 137, no. 10, pp. 1085-1095, 2010.

[7] CSA O86-19, Engineering design in wood, Mississauga, Ontario, Canada: Canadian standard associsation, 2019.

[8] S. Cuerrier-Auclair, "Design Guide for Timber-Concrete Composite Floors in Canada : Special Publication SP-540E," FPInnovations, Pointe-Claire, Qc, Canada, 2020.

[9] K. Möhler, Über das Tragverhalten von Biegeträgern und Druckstäben mit zusammengesetzten Querschnitten und nachgiebigen Verbindungsmitteln, Karlsruhe, 1956.

[10] European Committee for Standadization (CEN), Eurocode 5 - Design of timber structures - Part 1-1: General rules and rules for buildings (EN 1995-1-1:2004+A1:2008), 2008.

[11] CSA A23.3-19, Design of concrete structures, Mississauga, Ontario, Canada: Canadian standard associsation, 2019.

[12] A. Dias, S. Lopes, J. Van de Kuilen and H. Cruz, "Load-carrying capacity of timber concrete joints with dowel-type fasteners," *Journal of Structural Engineering,* vol. 133, no. 5, pp. 720-727, 2007.

[13] A. Dias, U. Kuhlmann, K. Kudla and S. Mönch, "Performance of dowel-type fasteners and notches for hybrid timber structures," *Engineering Structures,* vol. 171, pp. 40-46, 2018.

[14] M. Derikvand and G. Fink, "Deconstructable connector for TCC floors using self-tapping screws," *Journal of Building Engineering,* vol. 42, 2021.

[15] P. Clouston and A. Schreyer, "Design and use of wood-concrete composites," *Practice Periodical on Structural Design and Construction,* vol. 4, no. 13, pp. 167-174, 2008.

https://doi.org/10.52202/069179-0312

[16] S. Cuerrier-Auclair, L. Sorelli and A. Salenikovich, "A new composite connector for timber concrete composite structures," *Construction and Building Materials,* vol. 112, pp. 84-92, 2016.

[17] M. Brunner, M. Romer and M. Schnüriger, "Timber-concrete-composite with an adhesive connector (wet on wet process)," *Materials and Structures,* vol. 40, pp. 119-126, 2007.

[18] D. Yeoh, M. Fragiacomo, M. De Franceschi and A. Buchanan, "Experimental Tests of Notched and Plate Connectors for LVL-Concrete Composite Beams," *Journal of Structural Engineering,* vol. 137, no. 2, 2011.

[19] M. Shahnewaz, R. Jackson and T. Tannert, "CLT concrete composite floors with steel kerf plate connectors," *Construction and Building Materials,* vol. 319, 2022.

[20] International Organisation for Standardization, ISO 6891:1983, Timber structures — Joints made with mechanical fasteners — General principles for the determination of strength and deformation characteristics, Geneva, 1983.

[21] J. H. Rainer and G. Pernica, Vertical dynamic forces from footsteps, Ottawa: National Research Council Canada, 1986.

[22] S. V. Ohlsson, "Serviceability criteria - especially floor vibration criteria," *Proceedings of 1991 International Timber Engineering Conference,* pp. 58-65, September 1991.

[23] A. Ebrahimpour, R. L. Sack, W. N. Patten and A. Hamam, "Experimental measurements of dynamic loads imposed by moving crowds," *Structures Congress XII,* pp. 1385-1390, 1994.

[24] S. C. Kerr and N. W. M. Bishop, "Human induced loading on flexible staircases," *Engineering Structures,* vol. 23, no. 1, pp. 37-45, 2001.

[25] International Organisation for Standardization, ISO 18324:2016, Timber structures -- Test methods -- Floor vibration performance, Geneva, 2016.

[26] International Organisation for Standardization, ISO 21136:2017, Timber structures -- Vibration performance criteria for timber floors, Geneva, 2017.

[27] S. Cuerrier-Auclair, L. Hu and R. Ramzi, "Design method for vibration control of timber-concrete composite floor," FPInnovations, 2018.

[28] A. Frangi and M. Fontana, "Elasto-plastic model for timber-concrete composite beams with ductile connection," *Structural Engineering International,* vol. 13, no. 1, pp. 47-57, 2003.

[29] CSA S16-19, Design of steel structures, Mississauga, Ontario, Canada: Canadian Standars Association, 2019.

[30] S. Cuerrier-Auclair, L. Sorelli and A. Salenikovich, "Simplified nonlinear model for timber-concrete composite beams," *International Journal of Mechanical Sciences,* vol. 117, pp. 30-42, 2016.

[31] A. M. Dias and L. F. Jorge, "The effect of ductile connectors on the behaviour of timber–concrete composite beams," *Engineering Structures,* vol. 33, no. 11, pp. 3033-3042, 2011.

[32] L. Osborne, «Fire Resistance of Long Span Composite Wood-Concrete Floor Systems (Project No. 301009649),» FPInnovations, 2015.

[33] L. Ranger, C. Dagenais and S. C.-Auclair, Fire-resistance of timber-concrete composite floor using laminated veneer lumber, Project Report No. 301010618, FPInnovations, 2016.

[34] Canadian Commission on Building and Fire Codes, "National Building Code of Canada: 2020," National Research Council of Canada, 2022.

World Conference on Timber Engineering Oslo 2023

AN ENGINEERING MODEL FOR THE DESIGN OF CUT-BACKS IN RIBBED PANELS

Medhanye Biedebrhan Tekleab[1], Manfred Augustin[2], Gerhard Schickhofer[3]

ABSTRACT: This paper deals with the modelling and analysis of ribbed panels with 'cut-back' ribs. A critical point in the design of these members is on the determination of the occurring forces and stresses - in particular in tension perpendicular to grain - at the end of the ribs, potentially inducing a splitting failure. Thus, ribbed panels with cut-back ribs in practice always have to be reinforced by appropriate methods (e. g. self-tapping screws or glued-in rods). The open question for the designer is on the determination and the intensity of the design force for the reinforcement.

In this contribution a pure analytical solution procedure based on a simple engineering model has been used. A detailed discussion on modes of load resistance and corresponding deformations has been made, taking into account effects of geometrical & mechanical properties of the components, cut-back length, component-interface properties and load intensity. As a result, simple expressions for the prediction of forces in the reinforcement under transverse loading situations were obtained. All results and discussions may also be applied to systems of beam-beam as well as plate-plate composites with cut-backs and notches of the lower component respectively.

KEYWORDS: CLT, GLT, Stiffening, ribbed-panels, cut-back ribs, shear connection, relative slip, splitting, linear elastic analysis, reinforcement, stresses perpendicular to grain

1 INTRODUCTION

With the increased demand and use of CLT and LVL plates as slabs in structural timber systems, panels with longer spans are desired. One possibility to fulfil the requirements regarding strength, serviceability and economical aspects of long span plates is through the application of wooden ribbed panels. Such structural components consist usually of equally spaced ribs (e.g. glulam) and a plate (e.g. CLT or LVL). These ribs are in general eccentrically glued to the plate along their upper edge (interface line or contact surface).
Ribbed panels/plates with ribs having depths commonly used in practice are regarded as stiffened panels/plates. With relatively deeper ribs, the case of 'folded plates/structures', consisting of a system of rectangular cover plate and a sequence of parallel equidistant ribs may come into picture.

2 LOAD-CARRYING BEHAVIOUR

Ribs oriented in the longitudinal direction to increase the flexural stiffness of the plates are due to constructional and economical reasons shorter in length than the longitudinal dimension of the cover plate, i.e. there is a 'cut-back' at the end of the ribs. Such ribs are not supported at the transverse edges of the structural system. The ribs therefore are taking part in the load-carrying process of the complete structural system via distributed 'interaction' forces along the interface lines, i.e. interaction shear forces parallel to the interface line & interaction transverse normal forces in the direction orthogonal to the mid-plane of the ribbed panel.
Apart from the usual design of ribbed panels in ULS and SLS this detail requires a special consideration.
To get an overview about the phenomenon as well as to calibrate the developed model tests were driven. In Figure 1 the used test configuration is shown, while in Figure 2 the potential failure mode is depicted.

[1] Medhanye Biedebrhan Tekleab, holz.bau forschungs GmbH, Graz, Austria, medhanye.tekleab@tugraz.at
[2] Manfred Augustin, holz.bau forschungs GmbH, Graz, Austria, manfred.augustin@tugraz.at
[3] Gerhard Schickhofer, holz.bau forschungs GmbH, Graz, Austria, and Institute of Timber Engineering and Wood Technology, Graz University of Technology, Austria, gerhard.schickhofer@tugraz.at

https://doi.org/10.52202/069179-0313

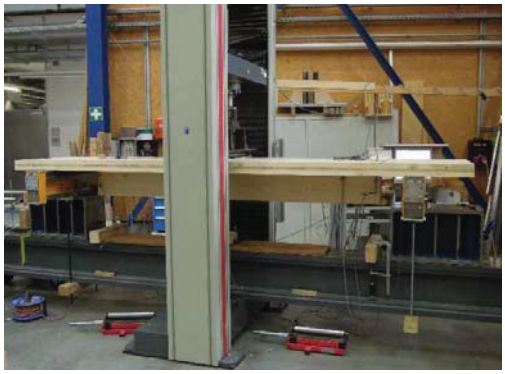

Figure 1: *Test configuration*

Figure 2: *Potential failure mode: 'splitting at the cut-back of the rib'*

3 PRACTICAL CONSIDERATIONS

When designing ribbed panels, the usual loadings have to be taken into consideration. In addition, effects from changing moisture contents may occur but are usually neglected in the verification as well as in this paper. While shear forces at the interface are covered (up to a certain limit) by the glue-line, the tension stresses perpendicular tend to induce a splitting-failure at the end of the cut-back. In practise, the resulting tension force has to be taken by appropriate reinforcements (e. g. self-tapping screws or glued-in rods) because of the magnitude and sensitivity of this strength. Currently no specific model for the design of cut-back reinforcements is known.

There have been many studies that directly or indirectly dealt with reinforcements of notches in beam members (see section 5.4) which are to some extent comparable with cut-backs in ribbed panels. Results of such studies have been included in guidelines and standards and are used by practicing engineers. Most studies, if not all, however mix 'transverse tensile stress resultant' as given, for example, in the DIN 1052:1988 [5] formula $F_{t,90} = 1.3\,[3(1-\alpha)^2 - 2(1-\alpha)^3]\,V$, which is only valid for unreinforced cases or equivalent, 'force in a given reinforcing screw' referring to any reinforced system irrespective of crack extent or system strength and 'required screwing/reinforcing force' for cases with pre-specified crack extent or intended system strength.

From the viewpoint of practice, one may not definitely speak about avoiding splitting at the end of the cut-back; one may even say cracking at its vicinity is inevitable. Once splitting happens there, the (local) shear resistance will be lost. This effect keeps increasing as crack line grows as a result of load increase.

To cover the requirements in practice, a model for the determination of design forces for the reinforcement of cut-backs in this paper is developed based on a beam model enabling a transparent and understandable design.

4 STRUCTURAL MODELLING

The structural system will be modelled as a plate system with rib stiffeners. The rectangular plate is assumed simply supported along both (parallel) transverse edges and extends to 'infinity' in the other direction (Figure 3).

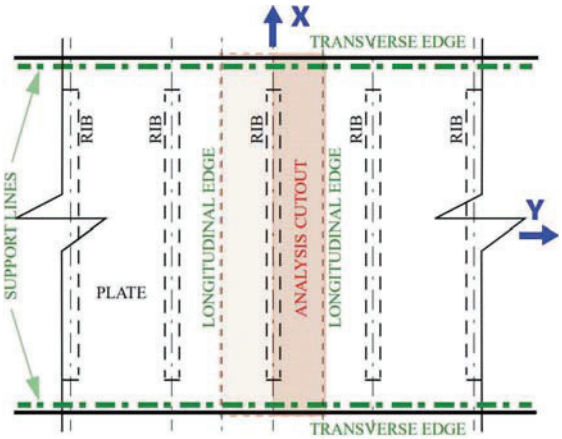

Figure 3: *Plan view of the structural system*

Due to an assumed independence of the load distribution on the transverse Y-coordinate it becomes possible to reduce the investigation to a suitable analysis 'cut out', applying symmetry conditions along the longitudinal edges of the structural model. The representative analysis 'cut out' will consist of one full rib and a strip of the covering plate composed as T-shaped model (Figure 4). Due to symmetry this model may further be reduced to half of the rib and plate flange. Figure 5 shows sectional views of uncracked and partly cracked interfaces, respectively.

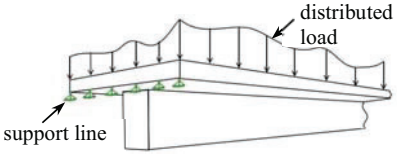

Figure 4: *Symmetric T-shaped model*

https://doi.org/10.52202/069179-0313

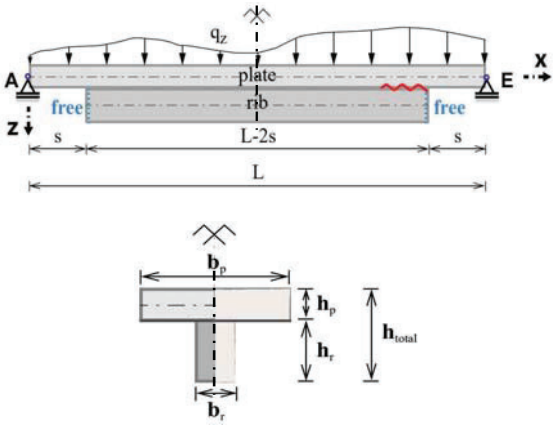

Figure 5: *Sectional views: uncracked interface (rib left side) and cracked interface (rib right side) at the cut-back*

The first question of interest is how the (linear elastic) structural behavior changes if the support conditions switch from the 'standard situation' where ribs are supported alongside the cover plate to the 'non-standard situation' where ribs are of the same length as the cover plate but are not supported, i.e. cut-back length s = 0. The second question of interest is how this change of behavior will further be affected if the cut-back length 's' becomes greater than zero, i.e. s > 0 as shown in Figure 10.

5 SOLUTION APPROACH

There will be an interaction of interface shear stress with interface normal stress in resisting applied system loading. For the sake of simplicity, special cases of no relative slip (rigid shear connection) and unrestricted relative slip (without shear connection) have been considered in the current study. Moreover, for simplicity, only bending deformations are considered. Figure 6 shows a substitute system of a general two-element system (cut-back length s = 0) that will help to understand the solution approach implemented. In the 'substitute system' both elements are first considered supported with a follower step that counterbalances the forces at the free edge of the lower structural element.

In the intermediate step of the 'substitute system' where both elements are supported, the load share between the elements depends on their flexural stiffnesses for the case of a system with unrestricted relative slip (without shear connection) as given by Equations (1) and (2).

$$q_{z,1} = \frac{E_1 I_1}{E_1 I_1 + E_2 I_2}\, q_z \tag{1}$$

$$q_{z,2} = \frac{E_2 I_2}{E_1 I_1 + E_2 I_2}\, q_z \tag{2}$$

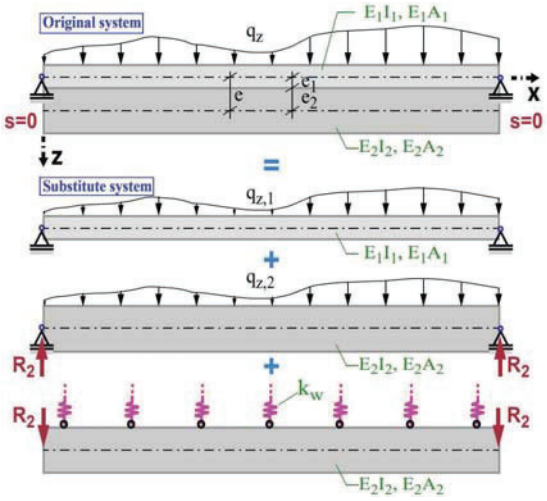

Figure 6: *Substitute system and load sharing*

For the case of the system with no relative slip (rigid shear connection), the load share between the elements will depend on the axial stiffnesses of the elements in addition to their flexural stiffnesses. The load share in such a case is given by Equations (3) and (4) and the axial force at a section resulting from the stiffness of the interface in shear by Equation (5).

$$q_{z,1} = \frac{E_1 I_1 + \rho\, e_1\, e}{E_1 I_1 + E_2 I_2 + \rho\, e^2}\, q_z \tag{3}$$

$$q_{z,2} = \frac{E_2 I_2 + \rho\, e_2\, e}{E_1 I_1 + E_2 I_2 + \rho\, e^2}\, q_z \tag{4}$$

$$N_x = -\rho\, e\, \frac{\partial^2 w}{\partial x^2} \tag{5}$$

where

$$\rho = \frac{E_1 A_1 \cdot E_2 A_2}{E_1 A_1 + E_2 A_2} \tag{6}$$

It should be noted that for structural components commonly used in practice, the rib contribution towards the system resistance remains almost unaffected when the interface is taken as shear rigid. This is true because the axial stiffness in general has a very small effect when compared with the flexural stiffness.

As far as design of cut-back reinforcement against splitting is concerned, the relative transverse displacement between the plate and rib becomes relevant. For the development of a solution method, a step-by-step procedure based on the superposition of different intermediate steps is proposed.

5.1 ZERO CUT-BACK LENGTH, s = 0

As part of the solution, the plate will be analysed and the rib stiffening effects will be introduced as boundary conditions for the plate structure as shown in Figure 7. The basic case where ribs are of the same length as the

https://doi.org/10.52202/069179-0313

cover plate but unsupported (cut-back length s = 0) will be considered first.

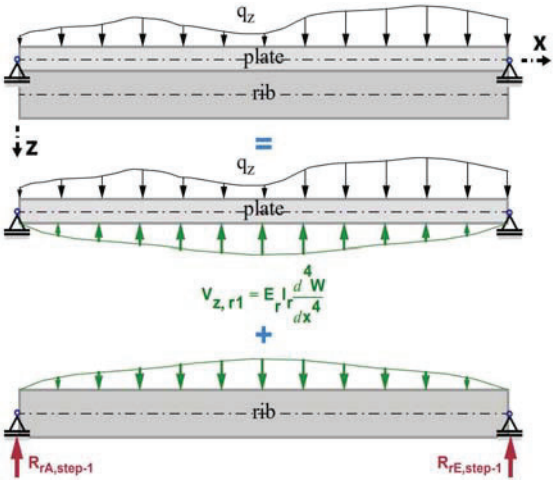

Figure 7: *Intermediate structural system: rib-effect as boundary condition*

The orthotropic plate differential equation with 'w' representing the transversal plate bending deformation (downward positive) is given as follows:

$$K_x \frac{\partial^4 w}{\partial x^4} + 2\left(K_\nu + 2K_{xy}\right)\frac{\partial^4 w}{\partial x^2 \partial y^2} + K_y \frac{\partial^4 w}{\partial y^4} = q_z(x,y) \quad (7)$$

where w is the transverse deformation, $q_z(x,y)$ is the transverse distributed loading, K_x and K_y are bending stiffnesses, K_ν is coupled bending stiffness, and K_{xy} is torsional stiffness (for CLT, $K_\nu = 0$ due to cracks & gaps).

5.1.1 First step

As a first step in the solution procedure, Equation (7) can easily be solved taking the following plate boundary conditions into account. In this particular step the ribs, together with the plate, will be considered as simply supported representing a standard simply supported system.

at x = 0 and x = L_r:

$$\begin{aligned} w &= 0 \\ \partial^2 w/\partial x^2 &= 0 \end{aligned} \quad (8)$$

at y = 0:

$$\begin{aligned} \partial w/\partial y &= 0 \\ V_z = -\left[K_y \frac{\partial^3 w}{\partial y^3} + \left(K_\nu + 4K_{xy}\right)\frac{\partial^3 w}{\partial x^2 \partial y}\right] &= \frac{1}{2} E_r I_r \frac{\partial^4 w}{\partial x^4} \end{aligned} \quad (9)$$

at y = b/2:

$$\begin{aligned} \partial w/\partial y &= 0 \\ V_z = \left[K_y \frac{\partial^3 w}{\partial y^3} + \left(K_\nu + 4K_{xy}\right)\frac{\partial^3 w}{\partial x^2 \partial y}\right] &= 0 \end{aligned} \quad (10)$$

where V_z = transverse shear force along the edge parallel to X-axis, E_r = rib elastic modulus, I_r = rib moment of inertia and L_r = length of the rib.

In order to fully solve Equation (7), a particular solution w_{part} and a homogeneous solution w_{hom} will be introduced and superposed.

$$w_{p1} = w_{r1} = w_{part} + w_{hom} \quad (11)$$

in which w_{p1} = plate transversal deformation and w_{r1} = rib transversal deformation, both from step-1.

In the following equation, the particular solution w_{part} is shown for a strip acting just like a beam under a constant loading $q_z(x)$ and fulfilling the aforementioned boundary conditions.

$$w_{part} = \frac{q_z}{24\,K_x}\left(x^4 - 2L_r x^3 + {L_r}^3 x\right) \quad (12)$$

When Equation (12) is expressed in Fourier series form, it is given by:

$$w_{part} = \frac{4\,q_z {L_r}^4}{\pi^5\,K_x} \sum_{1,3,5\ldots}^{\infty} \frac{1}{m^5} \sin\frac{m\pi x}{L_r} \quad (13)$$

and w_{hom} should fulfil the following homogeneous equation:

$$K_x \frac{\partial^4 w}{\partial x^4} + 2\left(K_\nu + 2K_{xy}\right)\frac{\partial^4 w}{\partial x^2 \partial y^2} + K_y \frac{\partial^4 w}{\partial y^4} = 0 \quad (14)$$

For a single span system with hinged end-supports, one can choose a solution for w_{hom} of the type

$$w_{hom} = \sum_{1,3,5\ldots}^{\infty} Y_m \sin\frac{m\pi x}{L_r} \quad (15)$$

where Y_m is a function of y only.

For cases where $\left(K_\nu + 2K_{xy}\right)^2 < K_x K_y$, just like in the case of CLT plates, substituting w_{hom} into Equation (14) and solving for Y_m gives:

$$\begin{aligned} Y_m = \frac{q_z {L_r}^4}{K_x}\big(&e^{\varphi y}(A_{m1}\cos\psi y + B_{m1}\sin\psi y) \\ &+ e^{-\varphi y}(C_{m1}\cos\psi y + D_{m1}\sin\psi y)\big) \end{aligned} \quad (16)$$

where

$$\begin{aligned} \varphi &= \frac{m\pi}{L_r}\sqrt{\frac{1}{2}\left(\sqrt{\frac{K_x}{K_y}} + \frac{K_\nu + 2K_{xy}}{K_y}\right)} \\ \psi &= \frac{m\pi}{L_r}\sqrt{\frac{1}{2}\left(\sqrt{\frac{K_x}{K_y}} - \frac{K_\nu + 2K_{xy}}{K_y}\right)} \end{aligned}, \quad (17)$$

The constants A_{m1}, B_{m1}, C_{m1}, and D_{m1} can be found from fulfilling the aforementioned boundary conditions of the plate at y = 0 and y = b/2. For plates with $K_\nu = 0$, the expressions for the constants A_{m1}, B_{m1}, C_{m1}, and D_{m1} are given in ANNEX-A.

https://doi.org/10.52202/069179-0313

5.1.2 Second step

The second step will involve balancing/zeroing the end shear of the rib, i.e. re-applying the rib-end reaction forces of the intermediate structural system in the opposite direction. Since this force will result in a fast decaying interface tensile stress (Figure 11) and later be mostly carried by reinforcements very close to the supported edges, it results in very small deformation of the plate. It is thus possible to consider the effects of the tip-loaded rib alone on a beam-on-elastic foundation model.

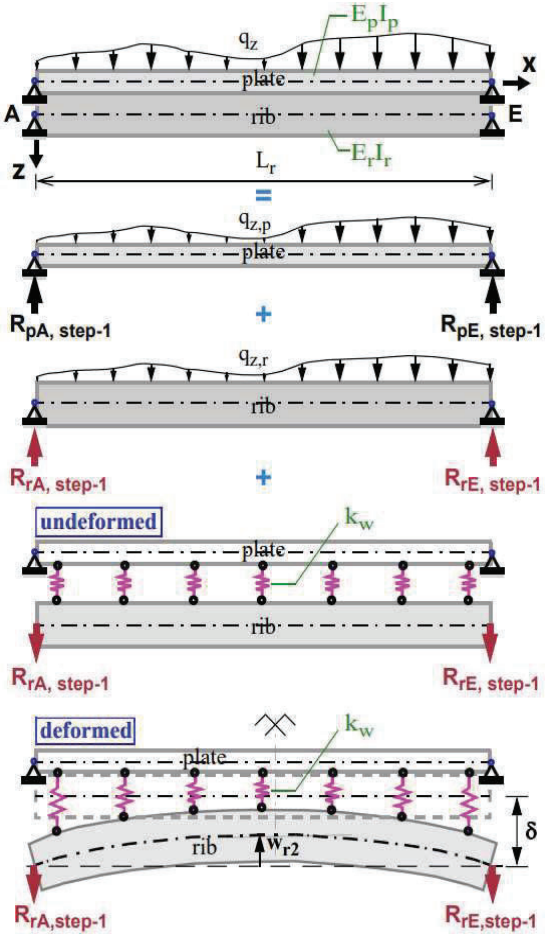

Figure 8: *Rib-end shear balancing*

The following equation results from equilibrium considerations of the rib:

$$E_r I_r \frac{\partial^4 w_{r2}}{\partial x^4} = k_w(\delta - w_{r2}) \tag{18}$$

where k_w = interface transversal stiffness, δ represents rib-tip transverse deformation of step-2, obtained from force equilibrium equation as given by Equation (19), $R_{r1} = R_{rA,step\text{-}1} = R_{rE,step\text{-}1}$ is the rib-tip reaction force from step-1 and w_{r2} is rib deformation under rib-tip action R_{r1} (see deformed system, Figure 8).

$$\delta = \frac{1}{L_r}\left(\frac{R_{r1}}{k_w} + \int_0^{L_r/2} w_{r2}\ dx\right) \tag{19}$$

As part of the second step in the solution procedure, the above differential equation can be solved considering the following rib boundary conditions:
at x = 0 and x = L_r:

$$\begin{aligned} w_{r2} &= 0 \\ \partial^2 w_{r2}/\partial x^2 &= 0 \end{aligned} \tag{20}$$

The resulting rib transverse deformation will then be given by:

$$\begin{aligned} w_{r2} = \delta &+ e^{\lambda x}(C_1 \cos\lambda x + C_2 \sin\lambda x) \\ &+ e^{-\lambda x}(C_3 \cos\lambda x + C_4 \sin\lambda x) \end{aligned} \tag{21}$$

where

$$\begin{aligned} C_1 &= -\frac{1 + e^{\lambda L_r}\cos\lambda L_r}{1 + e^{2\lambda L_r} + 2e^{\lambda L_r}\cos\lambda L_r}\delta, \\ C_2 = C_4 &= -\frac{\sin\lambda L_r}{2(\cos\lambda L_r + \cosh\lambda L_r)}\delta, \\ C_3 &= -\frac{1}{2}\left(1 + \frac{\sin\lambda L_r}{\cos\lambda L_r + \cosh\lambda L_r}\right)\delta, \end{aligned} \tag{22}$$

$$\lambda = \sqrt[4]{\frac{k_w}{4\,E_r I_r}} \tag{23}$$

The fast-decaying elastic foundation reaction given by $V_{z,r2} = k_w(\delta - w_{r2})$ can also be represented by a Fourier series as follows:

$$V_{z,r2} = \sum_{1,3,5\ldots}^{\infty} E_m \sin\frac{m\pi x}{L_r} \tag{24}$$

where

$$E_m = \frac{32m^3\pi^3 e^{\lambda L_r}\lambda^4 E_r I_r(\cos\lambda L_r + \cosh\lambda L_r)}{(m^4\pi^4 + 4\lambda^4 {L_r}^4)(1 + e^{2\lambda L_r} + 2e^{\lambda L_r}\cos\lambda L_r)}\delta \tag{25}$$

The resultant tensile force of the decaying elastic foundation reaction can then be determined. One is able to compute the total rib boundary effect on the plate and repeat the calculations to determine the plate total deformation.
In the shown form, the mutual deformations of both structural components affect the distribution of forces in the elastic foundation. Since the deformations in the plate at the end of the rib are small, as a simplification, the plate can be assumed rigid. This leads to the structural system of a beam/rib-on-elastic foundation from which the resultant tensile force and the reinforcement force in the region of the cut-back can be determined analytically (Figure 9). The computation of the resultant tensile force of the decaying elastic foundation reaction of such a beam is shown in ANNEX-B.

https://doi.org/10.52202/069179-0313

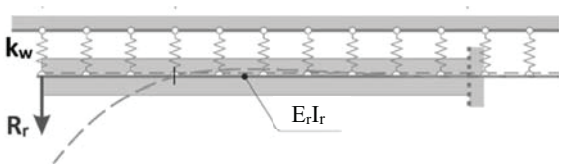

Figure 9: *Model for the cut-back based on a beam on an elastic foundation*

5.2 NON-ZERO CUT-BACK LENGTH, s > 0

The presented structural model can also be used to compute the transverse tensile stress resultants for 'cut-back' lengths larger than zero. Similar to the s = 0 case two intermediate steps are involved in the solution procedure.

5.2.1 First step

The first step in the modelling considers a simply supported system (system span length equal to rib span length) with symmetrical end moments obtained by simple mechanics (Figure 10). The rib restraining force/reaction and the corresponding bending contribution of the rib will then be computed.

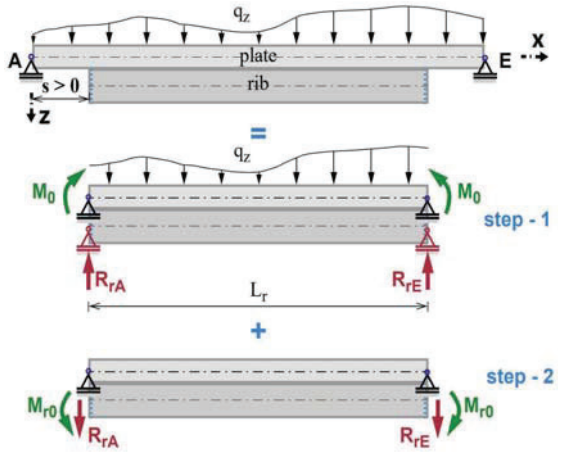

Figure 10: *step-by-step solution procedure*

5.2.2 Second step

The second step will deal with a rib-tip loaded system that counterbalances the restraining force/reaction and corresponding bending contribution. These are believed to be the main causes for the possible relative displacement between the structural components. It can also be treated as a beam on an elastic foundation.

The resulting interface tensile stress distributions which depend on the interface stiffness against splitting are shown in Figure 11 and Figure 12 for cases with no interface crack and partly cracked, respectively. As can be seen from both figures, the larger the interface tension stiffness is the faster the decay would be. This fact can be related to the need for relatively stiff reinforcement at the cut-back disturbance zone edge.

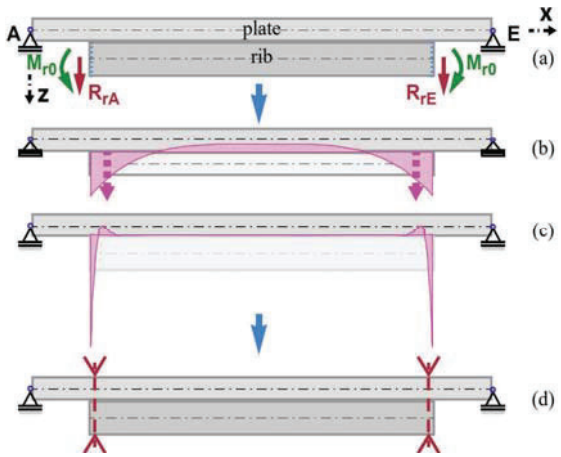

Figure 11: *No interface crack: (a) rib-tip actions, (b) transverse stress distribution for smaller interface stiffness, (c) transverse stress distribution for larger interface stiffness and (d) reinforcement*

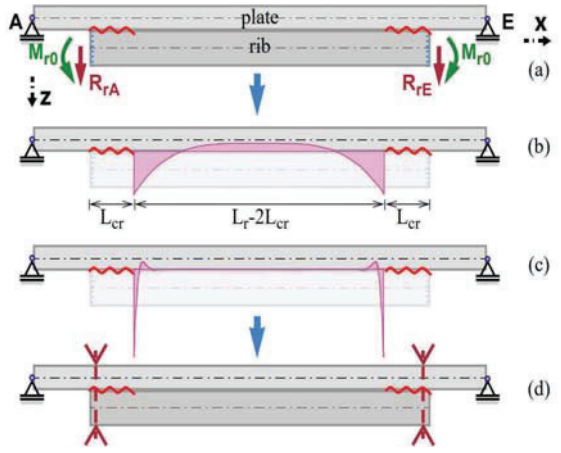

Figure 12: *Partly cracked interface (with L_{cr} = crack length): (a) rib-tip actions, (b) transverse stress distribution for smaller interface stiffness, (c) transverse stress distribution for larger interface stiffness and (d) reinforcement*

5.3 CALCULATION OF THE FORCE IN THE REINFORCEMENT

The tensile stress resultants (up to the first root) and its distance from the end of the rib can be computed as functions of the applied rib-tip force $R_r = R_{rA} = R_{rE}$ and the moment $M_r = M_{r0} = \left(E_r I_r / \left(E_r I_r + E_p I_p\right)\right) M_0$ as given by Equations (27) & (28) (see ANNEX-B.1 and ANNEX-B.2). The rib-tip moment M_r is expressed as:

$$M_r = \frac{E_r I_r}{E_r I_r + E_p I_p} \cdot M_0 = \frac{M_0}{1 + \frac{1}{\gamma_r}} \qquad (26)$$

It should also be noted that in the following analysis the rib is assumed to be long enough to have enough decay

length for any edge effect, i.e. to avoid effects of one edge on the other.

$$F_{t,90;R_r} = \left(1 + e^{-\frac{\pi}{2}}\right) R_r \approx 1.21\, R_r \; (for\; x_1 = \frac{\pi}{2\,\lambda}) \quad (27)$$

$$F_{t,90;M_r} = \sqrt{2}\, e^{-\frac{\pi}{4}}\, M_r \lambda \approx 0.645\, M_r \lambda \; (for\; x_1 = \frac{\pi}{4\,\lambda}) \quad (28)$$

In a simultaneous presence of both actions R_r and M_r at the rib-tip, one can compute the combined tensile stress resultant as a rough estimation leading to satisfactory results from the resulting combined stress distribution of the decaying interface tensile stress using Equation (30). In particular this procedure gives results numerically close to the exact solution if the interface stiffness is large. The resultant transverse tensile force for this case is given approximately by Equation (29).

$$\begin{aligned} F_{t,90;R_r+M_r,\text{large }\lambda} &\approx \frac{V}{1+\frac{1}{\gamma_r}} \left(1 + e^{-\pi/2} + \sqrt{2}\, e^{-\pi/4}\, \lambda\, s\right) \\ &\approx \frac{V}{1+\frac{1}{\gamma_r}} \left(1.21 + 0.645\, \lambda\, s\right) \end{aligned} \quad (29)$$

For general cases, however, the actual transverse tensile stress resultant caused by a simultaneous loading by the rib-tip actions R_r and M_r can be obtained from Equation (30) (see ANNEX-B.3). It represents the tensile stress resultant of the total decaying function up to the first root (zero-point) under the assumption that $M_r \approx R_r \cdot s$.

$$F_{t,90;R_r+M_r} = \frac{V}{1+\frac{1}{\gamma_r}} \left(1 + a \cdot e^{-b}\right) \quad (30)$$

where

$$a = \sqrt{1 + 2\,\lambda\, s\,(1+\lambda\, s)};\; b = \tan^{-1}\left(1 + \tfrac{1}{\lambda\, s}\right) \ldots \text{ [rad]}$$

5.4 COMPARISON WITH KNOWN APPROACHES (VALID FOR BEAMS)

A comparison of results from different approaches (beam theory, DIN 1052-1:1988 [5], Henrici ([6],[7]), draft prEN 1995-1-1:2021 [4]) that dealt with 'transverse tensile stress resultant' and the results from the current study have been made. In this context it has to be mentioned, that these studies are valid, from a strict point of view, only for notched beams with rectangular cross-sections, but since no alternatives are known they were used for the comparison.

The expressions used in the following comparison are given by Equations (31) to (35). In the comparison, since no proven methods for the determination of the interface normal stiffness k_w are known yet, the assumption of a constant transverse stress distribution along the rib-depth: $k_w = b_r \cdot E_{90,mean}/h_r$ has been used for the current study.

$$F_{BT} = [3(1-\alpha)^2 - 2(1-\alpha)^3]\, V \quad (31)$$

$$F_{DIN} = 1.3\; [3(1-\alpha)^2 - 2(1-\alpha)^3]\, V \quad (32)$$

$$F_{Hen} = \kappa_\beta\, \kappa_s\, \kappa_\alpha\; V \quad (33)$$

$$F_{Tek} = \frac{V}{1+\frac{1}{\gamma_2}} \left(1 + a \cdot e^{-b}\right) \quad (34)$$

$$\begin{aligned} F_{prEN} = (0.9 + 0.5(2\alpha-1)^2) \cdot (1+2\beta) \\ \cdot (3(1-\alpha)^2 - 2(1-\alpha)^3)\, V \end{aligned} \quad (35)$$

where
$\alpha = h_1/h_{total}$ (valid for beams only),
$\kappa_\beta = 1 + 2\beta$,
$\kappa_s = 1 + (s_0 - 1)[1.44(1-\alpha)(1-2\alpha) - 0.1]$,
$\kappa_\alpha = 1.5\big(1 - 0.7(1-\alpha)(3(1-\alpha)^2 - 2(1-\alpha)^3)\big)$,
$s_0 = \sqrt[4]{E_0/E_{90}}$ (in the comparison, $s_0 = 1.81$ is used [6]),
$\gamma_2 = E_2 I_2 / E_1 I_1$,
$\beta = s/h_{total}$
V … vertical force
F_{BT} … force using beam theory
F_{DIN} … force using DIN 1052-1:1988 [5]
F_{Hen} … force using Henrici ([6],[7])
F_{Tek} … force from this study (see Equation (30))
F_{prEN} … force using prEN 1995-1-1:2021 [4]

Figure 13 shows the comparison for the case of $s/h_{total} = 0.2$ and Figure 14 for the case of $s/h_{total} = 0.4$, where s = cut-back length, h_1 = depth of upper element, h_{total} = total depth of the system and V = beam reaction force. For CLT-GLT ribbed panels, the practical range for the h_1/h_{total}-ratio lies between 1/3 and 1/4 [11]. This range is represented by the gray shaded regions in Figure 13 and Figure 14. It can be observed from Figure 13 and Figure 14 that the 'transverse tensile stress resultant' decreases with an increase in the h_1/h-ratio, i.e. the stiffening effect from the lower-beam and its contribution to the system strength decreases.

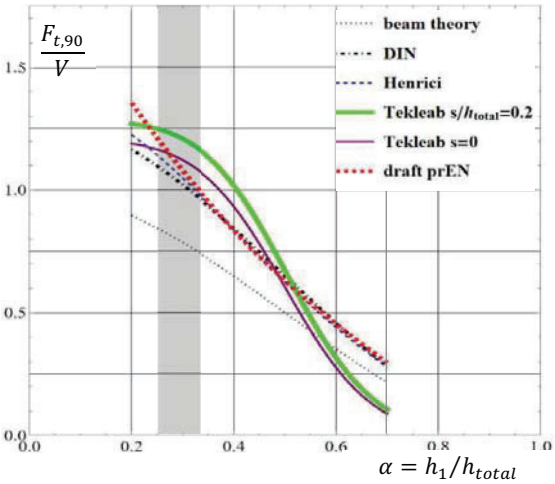

Figure 13: *Transverse tensile stress resultants for $s/h_{total} = 0.2$*

https://doi.org/10.52202/069179-0313

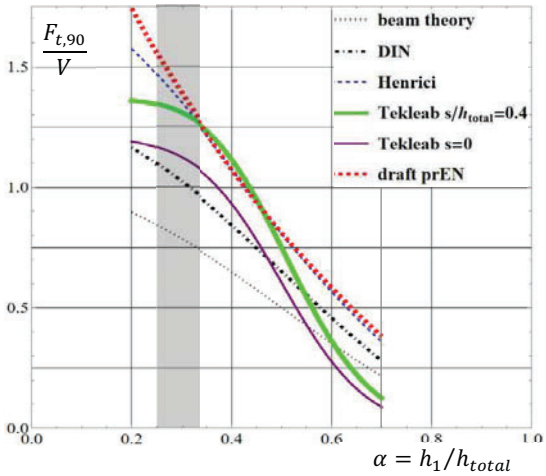

Figure 14: *Transverse tensile stress resultants for s/h_{total} = 0.4*

One can easily recognise from the graphical comparisons that the beam theory and DIN results do not directly include cut-back length effects in addition to the perpendicular to grain stiffness effects.

Figure 15 shows the effect of the cut-back length *s* on the transverse tensile stress resultant ratio, $F_{t,90}/R_r$, of a system example. It can be seen that with an increasing distance from the supporting line, the transverse stress resultant increases. Due to restrictions of the model this tendency will be valid only for small β-values. Further studies regarding the scope of application are necessary.

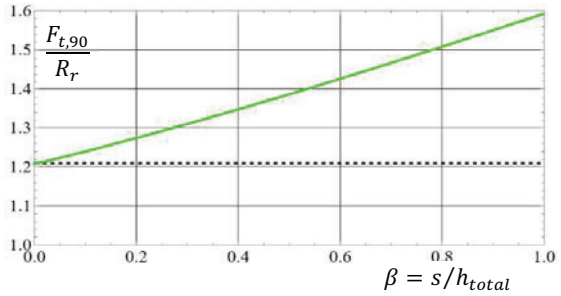

Figure 15: *cut-back length effect on tensile stress resultant*

The discussions so far dealt with 'transverse tensile stress resultants' of unreinforced cases. It is evident that the 'force in a reinforcement' is influenced by the tensile load-carrying of the timber and its stiffness as well as the stiffness of the reinforcement. Further efforts on the area will deal with this topic.

6 APPLICATION EXAMPLE

As an example (see Figure 16), a ribbed plate consisting of a glulam rib b_r/h_r = 160/280 mm and a 5-layer CLT panel with layer thicknesses of 40-20-20-20-40 mm (h_p = 140 mm) and width b_p = 800 mm has been considered. The system is a single span simply supported beam with length L = 10.0 m and cut-back length s = 200 mm. The materials used for the 7-layer combined glulam rib are T21 for the two lower layers & T14 for the upper five layers and GL24h* for the CLT panel. The system is loaded by its own weight $g_{1,k}$ = 1.0 kN/m², a permanent load $g_{2,k}$ = 2.0 kN/m² and a live load q_k = 3.0 kN/m². It is reinforced with self-tapping screws of ϕ10/400 mm at 'cut-backs' with an end distance of 50 mm.

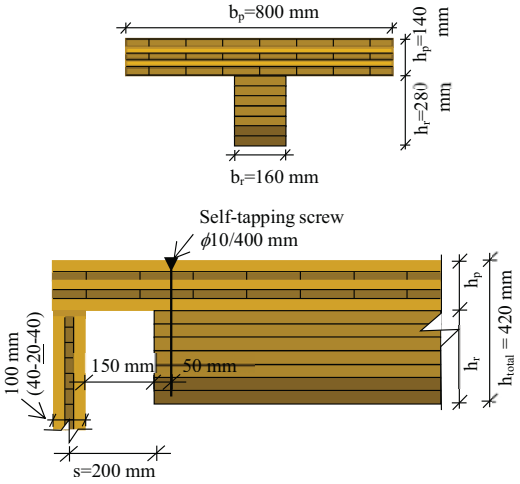

Figure 16: *cross-section (upper) and cut-back details (lower)*

In order to determine the force in the given screw, one will first obtain the following quantities:

$$q_d = [1.35 \cdot (1.0 + 2.0) + 1.50 \cdot 3.0] \cdot 0.800 = 6.84\ kN/m$$

$$A_d = \frac{q_d\, L}{2} = \frac{6.84 \cdot 10.0}{2} = 34.2\ kN$$

$$V_d = A_d - q_d \cdot s = 34.2 - 6.84 \cdot 0.200 = 32.8\ kN$$

$$E_p I_p = 1.96 \text{ x } 10^{12}\ N\ mm^2$$

$$E_r I_r = 3.48 \text{ x } 10^{12}\ \text{N mm}^2$$

$$\rightarrow \gamma_r = \frac{E_r I_r}{E_p I_p} = \frac{3.48\ x\ 10^{12}}{1.96\ x\ 10^{12}} = 1.78$$

$$R_{r,d} = \frac{V_d}{1 + \frac{1}{\gamma_r}} = \frac{32.8}{1 + \frac{1}{1.78}} = 21.0\ kN$$

$$M_{r,d} = R_{r,d} \cdot s = 21.0 \cdot 0.200 = 4.20\ kNm$$

$$k_w = \frac{b_r \cdot E_{90,mean}}{h_r} = \frac{160 \cdot 300}{280} = 171 N/mm^2$$

$$\lambda = \sqrt[4]{\frac{k_w}{4 \cdot E_r I_r}} = \sqrt[4]{\frac{171}{4 \cdot 3.48x10^{12}}} = 0.00187\ [1/mm]$$

- $R_{r,d}$ and $M_{r,d}$ considered solely and added up

$$F_{t,90,d;R_r+M_r,\lambda} \approx 1.21 \cdot 21.0 + 0.645 \cdot 1.87 \cdot 4.20 \approx 30.5\ kN$$

- $R_{r,d}$ and $M_{r,d}$ considered simultaneously

$$a = \sqrt{1 + 2 \cdot 1.87 \cdot 0.2 \cdot (1 + 1.87 \cdot 0.2)} = 1.42$$

$$b = tan^{-1}\left(1 + \frac{1}{1.87 \cdot 0.2}\right) = 1.31$$

$$F_{t,90,d;R_r+M_r} = 21.0\ (1 + 1.42 \cdot e^{-1.31}) = 29.0\ kN$$

For comparison:

- DIN 1052-1:1988 [5]

$$\alpha = h_{ef}/h_{total} = 140/420 = 1/3$$

$$F_{t,90,d} = 1.3 \cdot V_d \cdot [3(1-\alpha)^2 - 2(1-\alpha)^3]$$

$$F_{t,90,d} = 1.3 \cdot 32.8 \cdot \left[3\left(1 - \frac{1}{3}\right)^2 - 2\left(1 - \frac{1}{3}\right)^3\right] = 31.6\ kN$$

- with DIN 1052 adapted for ribbed panels:

for the composite cross-section: $e_{z,s}$ = 273 mm (from the lower edge), $(EI)_{ef} = 2.08 \cdot 10^{13} Nmm^2$,

$$F_{t,90,d} = 1.3 \cdot V_d \cdot \frac{b_r}{6} \cdot \frac{\mathrm{E_r}}{(EI)_{ef}} \cdot (3 \cdot z_s \cdot h_r^2 - h_r^3)$$

$$F_{t,90,d} = 1.3 \cdot 32.8 \cdot \frac{160}{6} \cdot \frac{12500}{2.08x10^{13}} \cdot (3 \cdot 273 \cdot 280^2 - 280^3) = 28.9\ kN$$

Verification of the reinforcement:

The design resistance per screw is computed applying the following values (screw data from an approval):

- for the verification of the withdrawal resistance: with the withdrawal strength $f_{ax,90,k}$ = 10.0 N/mm², the modification factor k_{mod} = 0.80 and the partial safety factor γ_M = 1.30 for the reinforcement (joint); since the smaller penetration depth is in the CLT plate it becomes crucial for the design.

$$F_{ax,Rd} = k_{mod} \cdot \frac{f_{ax,90,k} \cdot d \cdot l}{\gamma_M} = 0.80 \cdot \frac{10.0 \cdot 10.0 \cdot 140}{1.30} = 8{,}615\ N = 8.62\ kN$$

- for the verification of the screw tensile strength: tensile strength of the screw $F_{tens,k}$ =32.0 kN and the related partial safety factor γ_{M2} = 1.25.

$$F_{tens,d} = \frac{F_{tens,k}}{\gamma_{M2}} = \frac{32{,}000}{1.25} = 25{,}600\ N = 25.6\ kN$$

- design resistance per screw:

$$\mathrm{R}_{ax,d} = \min\{F_{ax,Rd}; F_{tens,d}\} = \min\{8.62\ kN; 25.6\ kN\} = 8.62\ kN$$

with n_{ef} = n, the required screws to cover the force:

$$n_{req} = \frac{\mathrm{F}_{t,90,d;R_r+M_r}}{R_{ax,d}} = \frac{29.0}{8.62} = 3.36$$

Applied at each cut-back: 4 x Ø 10/400 mm screws.

The rules regarding spacings and end distances etc. have to be met. Special conditions for the detailing of the reinforcement at the 'cut-back' can be found in ([1], [2]).

7 CONCLUSIONS AND OUTLOOK

Ribbed timber panels are interesting possibility to expand the range of application in timber engineering due to the possibility of realizing floors with larger spans. Because of technical and economic reasons, the ribs of such floor systems are often 'cut-back', i. e. end at a distance from the supports.

The ends of ribs in this case have to be reinforced by appropriate methods (e. g. self-tapping screws). As known to the authors no explicit rules for this mentioned design situation are known or given in relevant standards. Since no alternatives are given, one may use the equations given in the National Annexes to EN 1995-1-1 in Germany and Austria, mentioned for the first time in DIN 1052:1988 [5] for reinforced notches of rectangular cross-sections. It is, however, evident that this approach doesn't cover the given situation of ribbed panels with 'cut-backs' and is thus not valid for this case.

In the current study, simplified expressions for the 'transverse tensile stress resultants' (of unreinforced cases) based on a simple engineering approach applying a beam on elastic foundation were derived. With the developed equations one can easily calculate the force to be covered by the reinforcement. Since a general approach was used, the presented modelling, analysis and results can also be applied to plate-plate and beam-beam composites. The usual verifications like verifications of bending and shear stresses in ULS as well as deflection and vibration in SLS have to be done. This is important because due to the limited load-carrying capacity of the CLT, too high β-values will not be possible.

In addition to the presented results the interface tensile stiffness, the consideration of shear-deformation effects, interaction of interface shear stress with interface normal stress, non-linear interface behaviour, crack length etc. will be part of the ongoing analysis and experimental research. Moreover, the range of application (regarding α- and β-values) is under investigation. In particular, tests with different lay-ups (γ_r-values and h_p/h_{total}-values) and different β-values are in preparation.

ACKNOWLEDGEMENT

This research work was financed by the Austrian Research Promotion Agency (FFG) and is part of an ongoing study and experimental research on ribbed timber panels being carried out at the competence centre holz.bau forschungs gmbh, Graz, Austria.

REFERENCES

[1] Augustin, M., et al.: A contribution to the design of ribbed plates, World Conference on Timber Engineering, Vienna, Austria, 2016.

[2] Augustin, M.: Recommendations regarding the design of CLT ribbed panels. *Research report*, holz.bau forschungs gmbh, Graz, Austria, 2020.

[3] Bogensperger, T., & Silly, G.: Zweiachsige Lastabtragung von Brettsperrholzplatten. Bautechnik, 91(10), 742-752, 2014.

[4] CEN/TC 250/SC 5 "Eurocode 5: Design of timber structures" consolidated draft prEN 1995-1-1, 2021.

[5] DIN 1052-1:1988: Holzbauwerke; Berechnung und Ausfuhrung. DIN Deutsches Institut fur Normung e.V., Berlin, Germany, 1988.

[6] Henrici, D.: Beitrag zur Bemessung ausgeklinkter Brettschichtholzträger ein Vergleich mit der DIN 1052. Bauen mit Holz 11/90, München, Germany, 1990.

[7] Henrici, D.: Beitrag zur Spannungsermittlung in ausgeklinkten Biegeträgern aus Holz. Dissertation, Technische Universität München, München, Germany, 1984.

[8] Hetenyi, M.: Beams on elastic foundation, theory with applications in the fields of civil and mechanical engineering, University of Michigan, 1946.

[9] Papastavrou, P., et al.: The design of cross-Laminated timber slabs with cut-back glulam rib downstands – from research to live project, World Conference on Timber Engineering, 2016.

[10] Timoshenko S., Woinowsky-Krieger S.: Theory of plates and shells. Second edition. McGraw-Hill book company, 1959.

[11] Wallner-Novak, M., et al.: Cross-Laminated Timber Structural Design - Volume 2, proHolz Austria, 2018.

https://doi.org/10.52202/069179-0313

ANNEX-A: *Coefficients in Equation* (16) *for single-span orthotropic plate with constant distributed loading*

$$Am1 = -\frac{b^5 e^{-\varphi b}\zeta\,(\varphi^2+\psi^2)\left(3\varphi^2\psi^2-\psi^4+e^{\varphi b}\left((\varphi^2+\psi^2)^2+\varphi(\varphi^2-3\psi^2)(-\varphi\cos[b\,\psi]+\psi\sin[b\,\psi])\right)\right)}{16{L_r}^4\,{\alpha_m}^5\left(L_r\zeta((\varphi^2+\psi^2)^3-\varphi^2(\varphi^2-3\psi^2)(\varphi^2+\psi^2)\cos[b\,\psi])+\psi\left(4\varphi^2(\varphi^2-3\psi^2)\sin[b\,\psi]-\psi(-3\varphi^2+\psi^2)(L_r\zeta(\varphi^2+\psi^2)\cosh[b\,\varphi]-4\varphi\sinh[b\,\varphi])\right)\right)}$$

$$Bm1 = -\frac{b^5 e^{-\varphi b}\zeta\,\varphi(\varphi^2+\psi^2)\left(-3\varphi^2\psi+\psi^3-e^{\varphi b}(\varphi^2-3\psi^2)(\psi\cos[b\,\psi]+\varphi\sin[b\,\psi])\right)}{16{L_r}^4\,{\alpha_m}^5\left(L_r\zeta((\varphi^2+\psi^2)^3-\varphi^2(\varphi^2-3\psi^2)(\varphi^2+\psi^2)\cos[b\,\psi])+\psi\left(4\varphi^2(\varphi^2-3\psi^2)\sin[b\,\psi]-\psi(-3\varphi^2+\psi^2)(L_r\zeta(\varphi^2+\psi^2)\cosh[b\,\varphi]-4\varphi\sinh[b\,\varphi])\right)\right)}$$

$$Cm1 = -\frac{b^5\zeta\,(\varphi^2+\psi^2)\left(e^{\varphi b}\psi^2(-3\varphi^2+\psi^2)-(\varphi^2+\psi^2)^2+\varphi(\varphi^2-3\psi^2)(\varphi\cos[b\,\psi]+\psi\sin[b\,\psi])\right)}{16{L_r}^4\,{\alpha_m}^5\left(L_r\zeta(\varphi^2+\psi^2)(-(\varphi^2+\psi^2)^2+\varphi^2(\varphi^2-3\psi^2)\cos[b\,\psi])+\psi\left(-4\varphi^2(\varphi^2-3\psi^2)\sin[b\,\psi]+\psi(-3\varphi^2+\psi^2)(L_r\zeta(\varphi^2+\psi^2)\cosh[b\,\varphi]-4\varphi\sinh[b\,\varphi])\right)\right)}$$

$$Dm1 = \frac{b^5\zeta\,\varphi\,(\varphi^2+\psi^2)\left(-e^{\varphi b}\psi(-3\varphi^2+\psi^2)-(\varphi^2-3\psi^2)(-\psi\cos[b\,\psi]+\varphi\sin[b\,\psi])\right)}{16{L_r}^4\,{\alpha_m}^5\left(L_r\zeta(\varphi^2+\psi^2)(-(\varphi^2+\psi^2)^2+\varphi^2(\varphi^2-3\psi^2)\cos[b\,\psi])+\psi\left(-4\varphi^2(\varphi^2-3\psi^2)\sin[b\,\psi]+\psi(-3\varphi^2+\psi^2)(L_r\zeta(\varphi^2+\psi^2)\cosh[b\,\varphi]-4\varphi\sinh[b\,\varphi])\right)\right)}$$

where $\alpha_m = \frac{b\,m\,\pi}{2\,L_r}$ and $\zeta = \frac{E_r I_r}{K_X\,L_r}$

ANNEX-B:

B.1: *Semi-infinite Euler-Bernoulli beam with beam-end concentrated force*

Deflection: $w(x) = \frac{2\cdot\lambda\cdot R_r}{k_w}\cdot e^{-\lambda\cdot x}\cdot cos(\lambda\cdot x)$ with $\lambda = \sqrt[4]{\frac{k_w}{4\cdot E_r I_r}}$

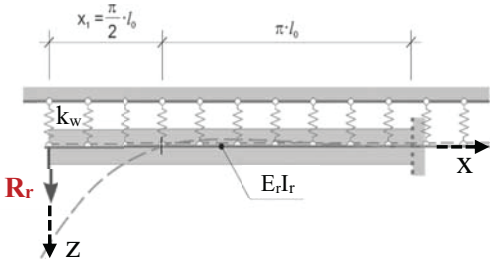

Position of the first root (zero-point):

$$w(x) = \frac{2\cdot\lambda\cdot R_r}{k_w}\cdot e^{-\lambda\cdot x}\cdot cos(\lambda\cdot x) = 0 \Rightarrow e^{-\lambda\cdot x}\cdot cos(\lambda\cdot x) = 0 \Rightarrow cos(\lambda\cdot x) = 0$$

$$\Rightarrow x_1 = \frac{\pi}{2\cdot\lambda} = \frac{\pi}{2}\cdot\sqrt[4]{\frac{4\cdot E_r I_r}{k_w}}$$

Integral up to the distance of the first root (= tensile stress resultant):

$$F_{t,90} = \int_0^{x_1}\bar{p}(x)\,dx = 2\cdot\lambda\cdot R_r\cdot\int_0^{x_1} e^{-\lambda\cdot x}\cdot\cos(\lambda\cdot x)\,dx = 2\cdot\lambda\cdot R_r\cdot\left[\frac{e^{-\lambda\cdot x}}{2\cdot\lambda}\cdot(\sin(\lambda\cdot x)-\cos(\lambda\cdot x))\right]\Bigg|_0^{x_1} =$$

$$= R_r\cdot\left[\left(e^{-\lambda\cdot x_1}\cdot\left(\underbrace{\sin(\lambda\cdot x_1)}_{1}-\underbrace{\cos(\lambda\cdot x_1)}_{0}\right)-\underbrace{e^{-\lambda\cdot 0}}_{1}\cdot\left(\underbrace{\sin(\lambda\cdot 0)}_{0}-\underbrace{\cos(\lambda\cdot 0)}_{1}\right)\right)\right] = R_r\cdot\left[1+e^{-\lambda\frac{\pi}{2\cdot\lambda}}\right] = \mathbf{1.21\ R_r}$$

where $R_r = q_z\cdot\frac{b\cdot l}{2}\cdot\frac{1}{1+\frac{1}{\gamma_r}}$ and $F_{t,90} = 1.21\cdot q_z\cdot\frac{b\cdot l}{2}\cdot\frac{1}{1+\frac{1}{\gamma_r}}$ with $\gamma_r = \frac{E_r I_r}{E_p I_p}$

B.2: *Semi-infinite Euler-Bernoulli beam with beam-end concentrated moment*

Deflection: $w(x) = \frac{2\cdot\lambda^2\cdot M_r}{k_w}\cdot e^{-\lambda\cdot x}\cdot[cos(\lambda\cdot x)-\sin(\lambda\cdot x)]$ with $\lambda = \sqrt[4]{\frac{k_w}{4\cdot E_r I_r}}$

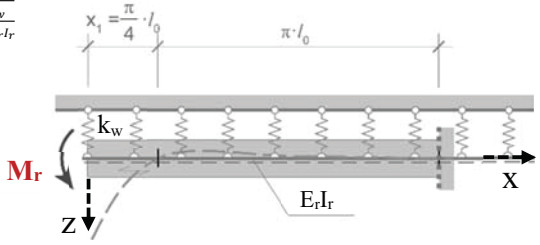

Position of the first root (zero-point):

$$w(x) = \frac{2\cdot\lambda^2\cdot M_r}{k_w}\cdot e^{-\lambda\cdot x}\cdot[cos(\lambda\cdot x)-\sin(\lambda\cdot x)] = 0$$

$$\Longrightarrow e^{-\lambda\cdot x}\cdot[cos(\lambda\cdot x)-\sin(\lambda\cdot x)] = 0 \Longrightarrow cos(\lambda\cdot x)-\sin(\lambda\cdot x) = 0$$

$$\Rightarrow x_1 = \frac{\pi}{4\cdot\lambda} = \frac{\pi}{2}\cdot\sqrt[4]{\frac{4\cdot E_r I_r}{k_w}}$$

https://doi.org/10.52202/069179-0313

Integral up to the distance of the first root (= tensile stress resultant):

$$F_{t,90} = \int_0^{x_1} \bar{p}(x)\,dx = 2\cdot\lambda^2\cdot M_r\cdot\int_0^{x_1} e^{-\lambda\cdot x}\cdot[cos(\lambda\cdot x)-\sin(\lambda\cdot x)]\,dx = 2\cdot\lambda^2\cdot M_r\cdot\left[\frac{e^{-\lambda\cdot x}}{\lambda}\cdot\sin(\lambda\cdot x)\right]\Big|_0^{x_1} =$$

$$= 2\cdot\lambda\cdot M_r\cdot\left[\left(e^{-\lambda\cdot x_1}\cdot\left(\underbrace{\sin(\lambda\cdot x_1)}_{1/\sqrt{2}}\right)-\underbrace{e^{-\lambda\cdot 0}}_{1}\cdot\left(\underbrace{\sin(\lambda\cdot 0)}_{0}\right)\right)\right] = M_r\cdot\lambda\cdot\left[\sqrt{2}\,e^{-\lambda\cdot\frac{\pi}{4\cdot\lambda}}\right] = \mathbf{0.645}\,\boldsymbol{M_r\cdot\lambda}$$

B.3: *Semi-infinite Euler-Bernoulli beam with beam-end concentrated force and moment*

Deflection: $w(x) = \frac{2\cdot\lambda\cdot R_r}{k_w}\cdot e^{-\lambda\cdot x}\cdot cos(\lambda\cdot x) + \frac{2\cdot\lambda^2\cdot M_r}{k_w}\cdot e^{-\lambda\cdot x}\cdot[cos(\lambda\cdot x)-\sin(\lambda\cdot x)]$ with $\lambda = \sqrt[4]{\frac{k_w}{4\cdot E_r I_r}}$

Position of the first root (zero-point): $w(x) = \frac{2\cdot\lambda}{k_w}(R_r+\lambda\cdot M_r)\cdot e^{-\lambda\cdot x}\cdot cos(\lambda\cdot x) - \frac{2\cdot\lambda^2\cdot M_r}{k_w}\cdot e^{-\lambda\cdot x}\cdot\sin(\lambda\cdot x) = 0$

$\Longrightarrow (R_r+\lambda\cdot M_r)\cdot cos(\lambda\cdot x)-\lambda\cdot M_r\cdot\sin(\lambda\cdot x) = 0 \;\Longrightarrow \frac{R_r+\lambda\cdot M_r}{\lambda\cdot M_r} = \tan(\lambda\cdot x) \;\Rightarrow x_1 = \frac{\tan^{-1}\left(1+\frac{R_r}{\lambda\cdot M_r}\right)}{\lambda}$

Integral up to the distance of the first root (= tensile stress resultant):

$$F_{t,90} = \int_0^{x_1} \bar{p}(x)\,dx = 2\cdot\lambda\cdot R_r\cdot\left[\frac{e^{-\lambda\cdot x}}{2\cdot\lambda}\cdot(\sin(\lambda\cdot x)-\cos(\lambda\cdot x))\right]\Big|_0^{x_1} + 2\cdot\lambda^2\cdot M_r\cdot\left[\frac{e^{-\lambda\cdot x}}{\lambda}\cdot\sin(\lambda\cdot x)\right]\Big|_0^{x_1} =$$

$$= R_r\cdot\left[\left(e^{-\lambda\cdot x_1}\cdot(\sin(\lambda\cdot x_1)-\cos(\lambda\cdot x_1))-\underbrace{e^{-\lambda\cdot 0}}_{1}\cdot\left(\underbrace{\sin(\lambda\cdot 0)}_{0}-\underbrace{\cos(\lambda\cdot 0)}_{1}\right)\right)\right] + 2\cdot\lambda\cdot M_r\cdot\left[\left(e^{-\lambda\cdot x_1}\cdot(\sin(\lambda\cdot x_1))-\underbrace{e^{-\lambda\cdot 0}}_{1}\cdot\left(\underbrace{\sin(\lambda\cdot 0)}_{0}\right)\right)\right] = 0$$

$$= R_r + \underbrace{e^{-\tan^{-1}\left(1+\frac{R_r}{\lambda\cdot M_r}\right)}\cdot\sqrt{2\cdot\lambda^2\cdot {M_r}^2 + 2\cdot\lambda\cdot M_r\cdot R_r + {R_r}^2}}_{\Delta R_{r,s}}$$

Where $\Delta R_{r,s}$ represents an additional term resulting from both rib-tip force R_r and the cut-back length s

https://doi.org/10.52202/069179-0313

World Conference on Timber Engineering Oslo 2023

LATERAL DEFORMATION AND KINEMATIC MODES OF MULTI-PANEL BALLOON-TYPE CLT SHEARWALL SYSTEM

Dalu Xing[1], Ghasan Doudak[2], Daniele Casagrande[3]

ABSTRACT: Balloon-type Cross-Laminated Timber (CLT) shearwall systems have been widely used as lateral load resisting systems (LLRS) in several mid- and high-rise timber buildings. Contrary to platform-type shearwalls, balloon framing contains continuous panels along multiple storeys in the vertical direction, which helps avoid perpendicular-to-grain compression failure in the floors. Despite some of the advantages associated with this type of construction, design provisions have not yet been introduced to various timber codes and standards, mainly due to the scarcity in research on their behaviours. This paper presents a numerical analysis model with the aim of investigating the lateral deformation and kinematic modes of balloon-type CLT shearwall systems. A finite element (FE) model is proposed, and a discussion on various key parameters affecting the behaviour of the shearwall, including aspect ratios (*h/b*), stiffness of the connectors, vertical loads and the number of panels, is presented.

KEYWORDS: Balloon-type, Cross-laminated timber, Aspect ratio, Multi-panel, Kinematic behaviour

1 INTRODUCTION

Numerous research projects and case studies have highlighted the ability of cross-laminated timber (CLT) shearwalls to resist lateral wind and seismic loads in timber buildings, mainly due to their high in-plane strength and stiffness. When the wall aspect ratio (i.e., height-to-length) is limited between 2:1 to 4:1, it has been demonstrated that CLT shearwalls are capable of dissipating energy through rocking behaviour and engagement of panel-to-panel connections as well as mechanical boundary anchors (hold-downs and angle brackets). This aspect ratio range is usually suitable for platform-type construction, where the wall extends between two consecutive floors. The development of analytical and experimental models for platform-type CLT shearwalls, including establishing the lateral behaviour and kinematic modes of multi-panel shearwall systems, has been undertaken by several researchers [1,2,3,4]. In terms of manufacturing, transportation and installation, it is sometimes desirable to produce longer panels that can extend multiple storeys along the height of the building. Another benefit of this so-called balloon-type construction is the avoidance of having accumulated axial load in the wall that could cause perpendicular-to-grain compression failure in the floors [5].

Balloon-type CLT shearwall systems have already been adopted in several construction projects, such as the Arboratum Project [6], which employs a CLT shearwall core with aspect ratios of the panels ranging from 5:1 to 20:1. Another example is the Arbora Condos in Montreal [7], which contain shearwall panels spanning 7 storeys with aspect ratios between 3:1 and 11:1. Despite the presence of these type of buildings in practice, research activities investigating the performance of balloon-frame CLT shearwalls have been scarce. Some studies have focused on predicting the lateral deformation of a two-panel balloon-type CLT shearwall system [8,9], while others have investigated the impact of ledger beams on the wall performance [10,11].

It is important to note that there are currently no design provisions for balloon-frame CLT shearwalls in various codes and standards (e.g., CSA O86 [12] and Eurocode 5 [13]), mainly due to a lack of fundamental research output involving this system. The review of available research clearly indicates that more research towards developing an understanding of the behaviour of multi-panel balloon-type CLT shearwall systems is necessary.

The current research aims at contributing to the gaps in knowledge in this field by investigating the lateral deflection and kinematic modes of balloon-type multi-panel CLT shearwall systems through a numerical FE approach.

2 SENSITIVITY ANALYSIS

2.1 MODEL DESCRIPTION

A finite numerical element (FE) model has been adopted to conduct sensitivity analyses with the aim of understanding the impact of key parameters governing the

[1] Dalu Xing, University of Ottawa, Canada
dxing010@uottawa.ca
[2] Ghasan Doudak, University of Ottawa, Canada
gdoudak@uottawa.ca
[3] Daniele Casagrande, Institute for Bioeconomy-National Research Council of Italy (CNR-IBE), Italy
daniele.casagrande@ibe.cnr.it

https://doi.org/10.52202/069179-0314

mechanical behaviour of multi-panel balloon-type shearwall systems subjected to lateral loads. The proposed FE model consists of shearwalls with a total height, a total width and a panel width of h, B and b, respectively, subjected to lateral point force F stemming from wind or seismic loads applied at the diaphragm level of each storey. The panels are assumed to be connected to the foundation by hold-downs with axial stiffness, k_{hd}, along the vertical direction, while the panel sliding along the horizontal direction is restricted. Adjacent panels are connected to each other by means of uniformly placed vertical joints with total shear stiffness k_{vj}. Vertical uniformly distributed gravity loads, q, are assumed to be applied at each floor level. Figure 1 shows a two-panel model with a height representing three storeys.

The numerical analysis is carried out using the commercially available FE software package SAP2000 [14]. A total of 548 different models were developed based on a series of varying parameters, including panel aspect ratio h/b, stiffness of hold-down and vertical joints, vertical loads and the number of panels.

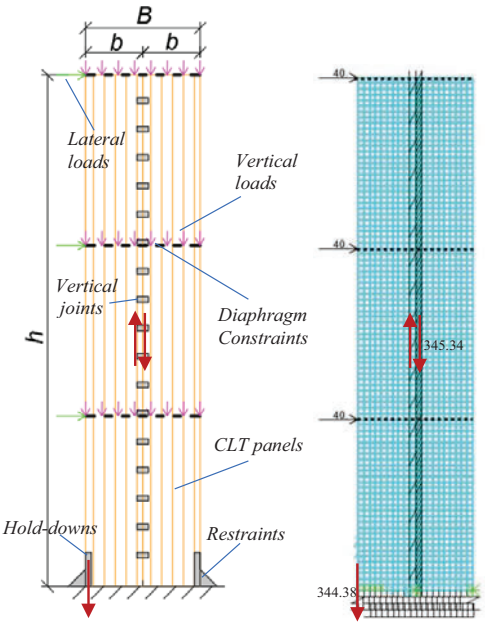

Figure 1: *Two-panel three-storey CLT shearwall model*

2.2 MODEL CONFIGURATION AND PARAMETERS

The FE model adopts thick-shell type elements to simulate the behaviour of the shearwall panels. The mesh size was selected to be 100 mm × 100 mm, based on a mesh sensitivity analysis. It should be noted that when the meshing size was reduced from 100 mm × 100 mm to 10 mm × 10 mm, the difference in the total lateral deformation was within 3%.

Equivalent material properties of the CLT panels were determined using the method proposed by Brandner et al. [15], as presented in Equations (1) and (2) for the effective modulus of elasticity along the vertical, $E_{0,eff}$, and lateral, $E_{90,eff}$, directions, respectively.

$$E_{0,eff} = \frac{E_0 t_0 + E_{90} t_{90}}{t} \quad (1)$$

$$E_{90,eff} = \frac{E_0 t_{90} + E_{90} t_0}{t} \quad (2)$$

where

E_0 is the modulus of elasticity parallel to grain,
E_{90} is the modulus of elasticity perpendicular to grain,
t_0 is the total thickness of vertical layers,
t_{90} is the total thickness of lateral layers,
t is the total thickness of the panel.

For the purpose of the sensitivity analysis, E_{90} is assumed equal to $E_0/30$ [12,16], and E_0 is assumed to be the same in both the longitudinal and transverse layers. The effective in-plane shear modulus, G^*, was estimated according to the method proposed by Bogensperger et al. [17].

Link elements were assumed to simulate the behaviours of hold-downs, vertical joints and foundation supports. Additionally, restraints are applied at the bottom of each panel to restrict their lateral sliding. In order to ensure the same lateral displacements at the top of the panels, a diaphragm constraint at the floor level was imposed.

Table 1 summarises the input parameters used in the sensitivity analysis, while Table 2 indicates the range of aspect ratios investigated.

Table 1: *Values of the basic parameters of models*

Parameter	Symbol	Values
Storey number	n (-)	1; 2; 3; 4
Number of panels	m (-)	1; 2; 3; 4
Lateral load per storey	F (kN/m)	20
Vertical load per storey	q (kN/m)	0; 20
Stiffness of foundation	k_f (1) (kN/m)	1.0×10^6
Panel thickness	t (mm)	175 (5 layers)
Young's modulus and shear modulus	E_0(2), G_0(3) (MPa)	12000; 690
Stiffness of hold-down	k_{hd} (kN/mm)	10; 25; 50; 100
Stiffness of unit vertical-joint	k_{vj}/h (kN/mm/m)	3; 7.5; 15

Note: (1), (2), and (3) refer to the values adopted by [1], [12] and [18], respectively.

Table 2: *Aspect ratio (h/b) matrix in the sensitivity analysis*

	h = 3m	h = 6m	h = 9m	h = 12m
b = 0.25m	12			
b = 0.5m	6	12		
b = 0.75m	4	8	12	
b = 1m	3	6	9	12
b = 2m	1.5	3	4.5	6
b = 3m	1	2	3	4
b = 6m		1	1.5	2
b = 9m			1	1.3
b = 12m				1

The naming convention of the models follows a format where, for example, for "*M12/1 - P3 - VL20 - H10V3*", "*M12/1*" indicates a model (*M*) with a panel aspect ratio of 12 to 1, "*P3*" refers to the number of panels being three, "*VL20*" highlights a value of vertical load (*VL*) equal to 20 kN/m/storey, and "*H10V3"* indicates that the values of

https://doi.org/10.52202/069179-0314

the stiffness of hold-downs (H) and the unit stiffness of vertical-joint (V) are 10 kN/mm and 3 kN/mm/m, respectively.

2.3 VALIDATION OF THE MODEL

The methodology proposed in this paper is verified against the shearwall test conducted by Chen and Popovski [8], which consists of a two-panel balloon frame CLT shearwall, as shown in Figure 2. The panels consist of 5-ply CLT (Grade E1) with dimensions of each panel equal to 4125 mm (height) × 420 mm (width). Two sets of hold-downs are placed at both outer corners, and five pairs of panel-to-panel joints (half in the front and half in the back) are used to attach the two panels with an equal spacing distance of 825 mm. Lateral restraints are used to prevent sliding. A uniformly distributed gravity load with a magnitude of 2.1 kN/m is applied on the top of two panels. A concentrated horizontal load is applied at the top of the wall.

Model input parameters were consistent with those used in the study and included modulus of elasticity in the longitudinal layers are E_0 = 11700 MPa and E_{90} = 390 MPa, while the transverse layers were assigned values of E_0 = 9000 MPa and E_{90} = 300 MPa [12]. As a result, the effective moduli of elasticity obtained using Equation (1) and (2) are calculated to be $E_{0,eff}$ = 7140 MPa, and $E_{90,eff}$ = 3834 MPa, respectively. The shear modulus G is assumed equal to 731 MPa, and hence the effective shear modulus G^* is calculated equal to be 380.47 MPa [17].

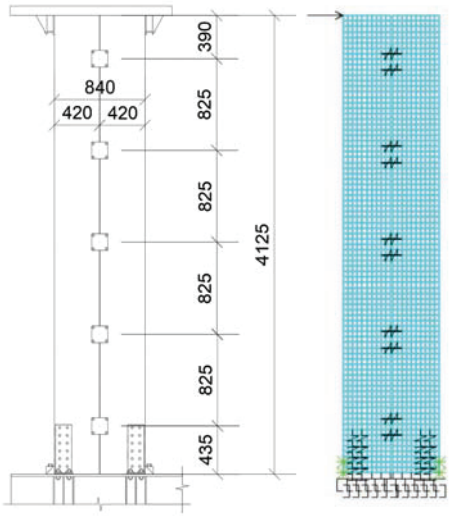

Figure 2: *Shearwall configuration (left) [8] and FE model (right)*

The results of the comparison (Figure 3) clearly show the ability of the proposed model to mimic the behaviour of the shearwall. Discrepancies are likely related to the values of the assumptions associated with the mechanical properties of the connectors, which have been simplified to bi-linear curves in the FE modelling analysis.

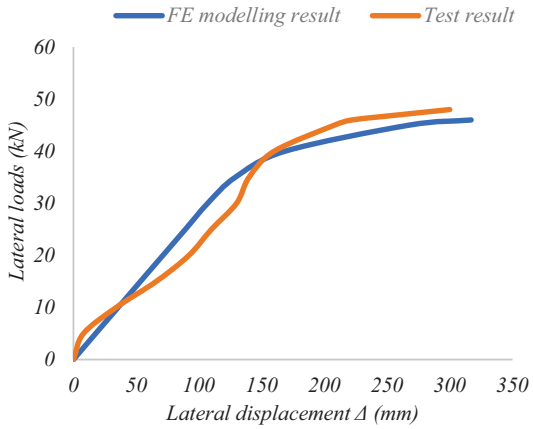

Figure 3: *Result comparison between FE modelling and test [8]*

3 RESULTS AND DISCUSSION

The results from sensitivity analysis are discussed in the context of the total lateral stiffness, K, defined as the ratio between total lateral loads, ΣF, and the total lateral displacement at the top of the shearwall, Δ_{total}. The relative rocking deformation, r, is defined as a percent ratio that the rocking deformation, $\Delta_{rocking}$, constitutes relative to the total deformation, Δ_{total}, ($r = \Delta_{rocking}/\Delta_{total} \times 100\%$). The discussion also includes the kinematic behaviours that are expressed in terms of coupled-panel (CP) behaviour, which involves rotation of the individual panels about their respective centres of rotation, single-wall (SW) behaviour, where the entire shearwall rotates about one centre of rotation at its end, and intermediate (IN) behaviour that falls between the CP and SW behaviours [1].

3.1 IMPACT OF PANEL ASPECT RATIO

The conducted sensitivity analysis of multi-panel balloon-type CLT shearwall systems shows that aspect ratio h/b significantly impacts the lateral deformation and kinematic modes of the walls. As expected, the results from all cases show that $1/K$ increases with increasing aspect ratio h/b, as shown in Figure 4 for the models *M h/b-P2-VL20-H10V3*.

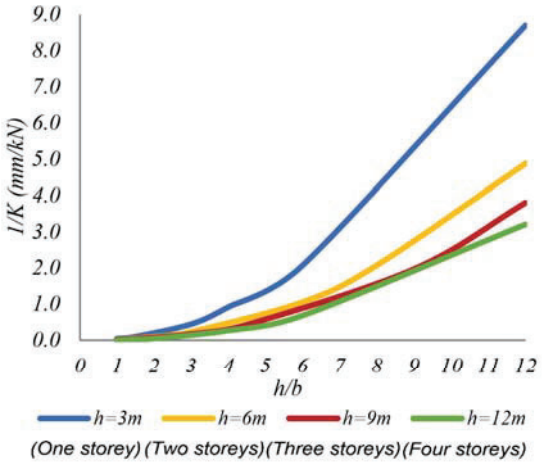

Figure 4: *Relationship between 1/k and h/b for the models M h/b-P2-VL20-H10V3*

Figure 5 shows the relationship between the relative rocking deformation *r* and panel aspect ratio *h/b,* for wall height equal to 6 m. Similar results were also obtained for wall heights equal to 9 m and 12 m. The results reveal consistent tendencies for walls with higher stiffness of hold-downs and vertical-joint to exhibit less rocking. This can be attributed to the restraining effect of the hold-down with higher stiffness, as well as the contribution of the vertical joints with higher stiffness to cause the panels to behave more in SW mode.

It can also be noted that the rocking behaviour is dominant in the range of aspect ratios between 3 and 6, which could be attributed to a largely shear-driven behaviour when the aspect ratio is low (≤ 2), and flexural-driven behaviour for high aspect ratios.

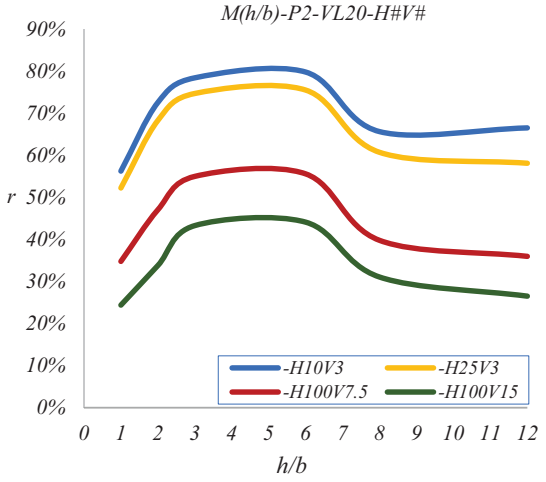

Figure 5: *Relationship between h/b and r when h equals 6 m and vertical load equals 20 kN/m for two-panel models*

3.2 IMPACT OF CONNECTION STIFFNESS

Due to the large range of stiffness values found in the results for connection stiffness, an approach involving normalised lateral stiffness, K_{hd}^* and K_{vj}^*, defined as the ratio between the total lateral stiffness of the wall, *K*, and the value of stiffness related to specific hold-down stiffness, k_{hd}, equals 10 kN/mm in Equation (3), or the specific unit vertical-joint stiffness of k_{vj}/h, equal to 3 kN/mm/m in Equation (4), respectively, is used in this study. The normalised vertical joint stiffness k_{vj} * is defined as a ratio between the value of unit vertical-joint stiffness and the specific value equal to 3 kN/mm/m in Equation (5).

$$K_{hd}^* = \frac{K}{K_{(k_{hd}=10kN/mm)}} \quad (3)$$

$$K_{vj}^* = \frac{K}{K_{(k_{vj}/h=3kN/mm/m)}} \quad (4)$$

$$k_{vj}{}^* = \frac{k_{vj}/h}{3} \quad (5)$$

Figure 6 presents the relationship between the normalised total lateral stiffness K_{hd}^* and hold-down stiffness k_{hd} for $b = 1\ m$, $b = 2\ m$, and $b = 3\ m$, without the application of vertical loads. Generally, it is found that the relationship between K_{hd}^* and k_{hd} is non-linear, and the rate of increase becomes less significant following an increasing hold-down stiffness.

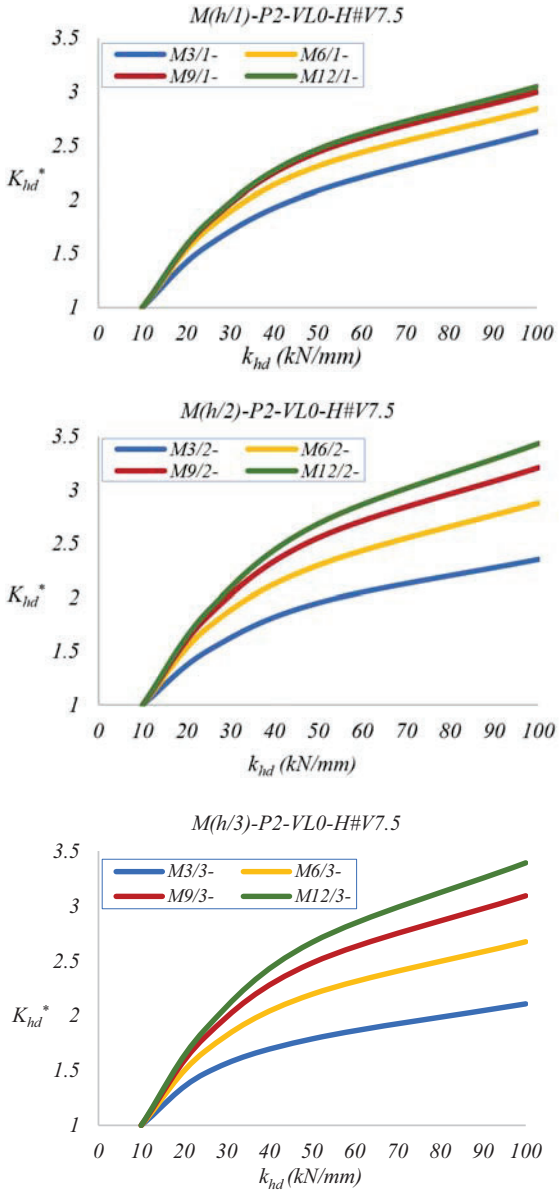

Figure 6*: Relationship between* k_{hd} *and normalised total lateral stiffness* K_{hd}^* *when* k_{vj}/h *equals 7.5 kN/mm/m, and there is no vertical load for two-panel models*

Figure 7 presents the relationship between K_{vj}^* and the normalised vertical-joint stiffness k_{vj}^* for $h = 3\ m$, $h = 6\ m$, $h = 9\ m$ and $h = 12\ m$, including the application of vertical loads. Generally, the trends are consistent with those observed for the hold-down stiffness. When the aspect ratios of panels are low (e.g., 1:1, as in models

https://doi.org/10.52202/069179-0314

M3/3-, M6/6-, M9/9- and *M12/12-*), K_{vj}^* increases less significantly than those with higher aspect ratios following the growth of the stiffness of vertical joints.

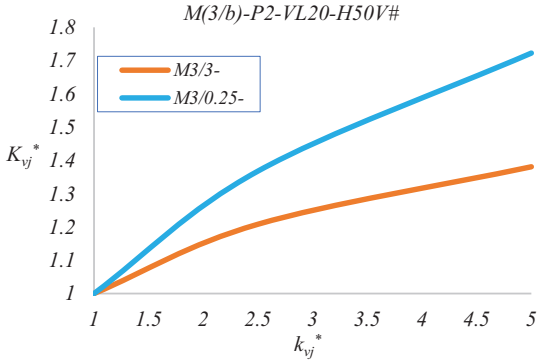

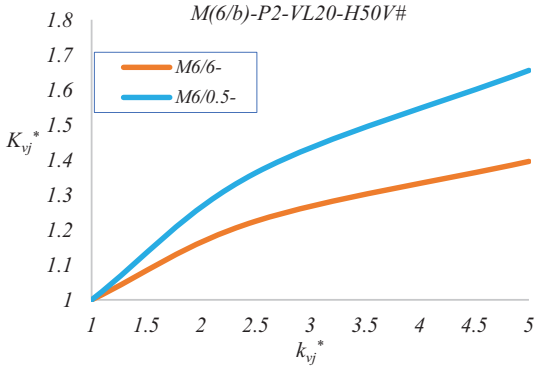

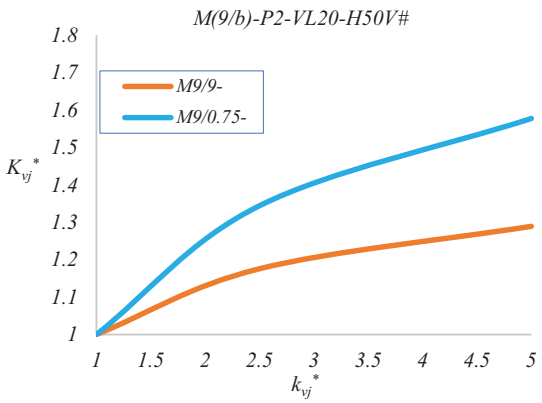

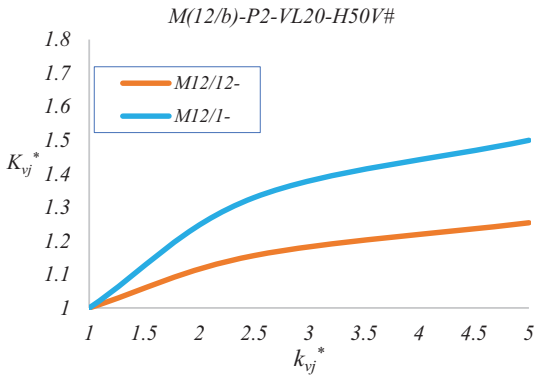

***Figure** 7: Relationship between normalised vertical-joint stiffness k_{vj}^* and normalised total lateral stiffness K_{vj}^* when k_{hd} equals 50 kN/mm, and vertical loads equal 20 kN/m for two-panel models*

Table 3 illustrates the percentage of two-panel models with CP mode as a function of an increase in hold-down stiffness (includes 72 models), while Table 4 presents the percentage of two-panel models with SW mode when the unit stiffness of vertical joints is varied (includes 96 models). It can be observed that similar to what was found from research on platform-type shearwalls, balloon-type construction tends to be more dominated by CP mode when the stiffness of hold-downs increases, while SW mode is more prevalent when the stiffness of unit vertical-joint increases.

***Table 3:** Percentage of the CP mode using different values of the hold-down stiffness*

k_{hd} (kN/mm)	Percentages of the CP mode#
10	16.7%
25	41.7%
50	68.1%
100	88.9%

#: The percentage of CP mode is calculated by

$$\frac{No.\,of\ the\ models\ shown\ as\ CP\ mode}{No.\,of\ the\ total\ models\ (=72)} \times 100\%.$$

***Table 4:** Percentage of the SW mode using different values of the vertical-joint stiffness*

k_{vj}/h (kN/mm/m)	Percentages of the SW mode#
3	21.9%
7.5	46.9%
15	69.8%

#: The percentage of SW mode is calculated by

$$\frac{No.\,of\ the\ models\ shown\ as\ SW\ mode}{No.\,of\ the\ total\ models\ (=96)} \times 100\%.$$

The relationships between the hold-down or unit vertical-joint stiffness and the percentage of rocking deformation are depicted in Figure 8 and Figure 9, respectively. It can be noted that the shearwalls with higher aspect ratios are more sensitive to hold-down stiffness, while the ones with lower aspect ratios are more sensitive to the unit vertical-joint stiffness. This may be attributed to the fact that when the panel aspect ratio is higher, hold-down stiffness has a more significant influence on the distribution between rocking deformation and flexural deformation, while when the aspect ratio is lower with panels performing more rigidly, vertical-joint stiffness has more impact on the distribution between rocking deformation and shear deformation.

https://doi.org/10.52202/069179-0314

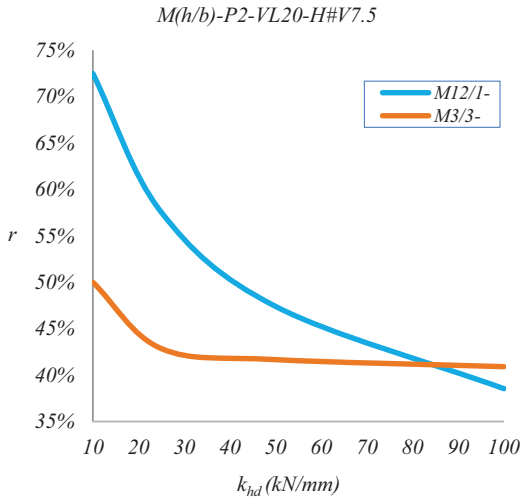

***Figure 8**: Relationship between k_{hd} and r when k_{vj}/h equals 7.5 kN/mm/m, and vertical loads equal 20 kN/m for two-panel models*

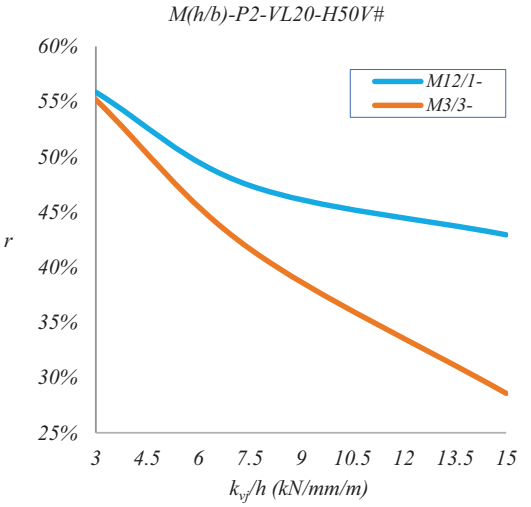

***Figure 9**: Relationship between k_{vj}/h and r when k_{hd} equals 50 kN/mm, and vertical loads equal 20 kN/m for two-panel models*

3.3 THE IMPACT OF VERTICAL LOADS

Models with vertical loads show higher total lateral stiffness K compared with those with no vertical loads applied. Figure 10 compares the average total lateral stiffness between the cases that include or exclude the vertical loads when aspect ratios vary from 3 to 12 for two-panel models. It is noted that although the averaged total lateral stiffness is positively affected by the increase in vertical loads, the effect is much less pronounced when the panel aspect ratio increases. It is also found that the presence of vertical loads yields more cases with CP mode. For example, when a vertical load of 20 kN/m/storey is applied, the number of cases with CP mode increases from 130 out of 288 (45.1%) to 180 out of 288 (62.5%).

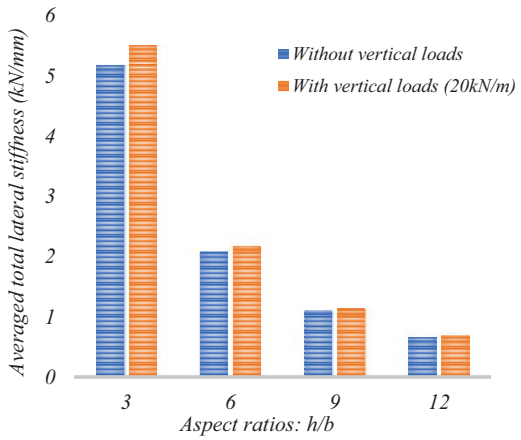

***Figure 10**: Impact of vertical loads on the averaged total lateral stiffness with varying aspect ratios when b equals 1 m for two-panel models*

3.4 THE IMPACT OF THE NUMBER OF PANELS

This part of the analysis considers two conditions, namely a fixed ratio of h to B, and a fixed ratio of h to b, as shown in Figure 11.

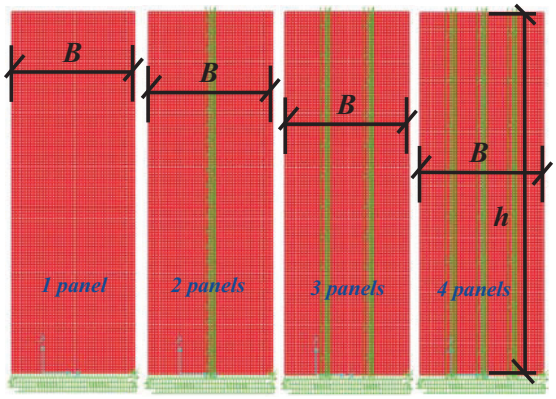

(a) Varying panel number with fixed h/B (12:4)

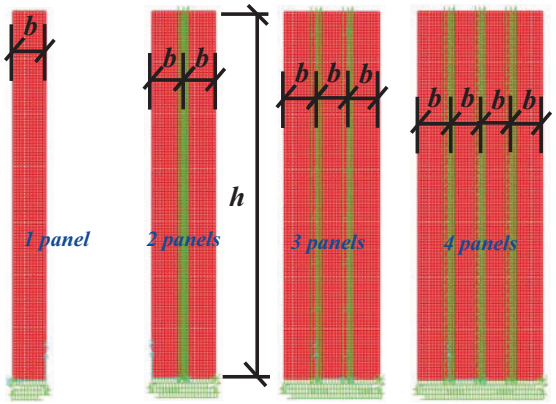

(b) Varying panel number with fixed h/b (12:1)

***Figure 11:** Analysis of multi-panel behaviours*

https://doi.org/10.52202/069179-0314

The analysis for the fixed h/B ratio found that increasing the number of panels resulted in a decrease in the total lateral stiffness of the wall (Figure 12). In comparison, the models with higher relative stiffness $\tilde{k}$ defined as a ratio between k_{hd} and k_{vj} ($\tilde{k} = k_{hd}/k_{vj}$) showed a much larger reduction in stiffness than those with lower relative stiffness values.

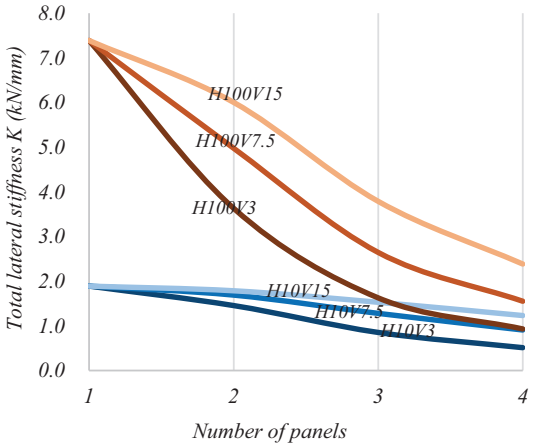

Figure 12: *Relationship between the number of panels and K when h/B is fixed to be 12:4 and vertical loads equal to 20 kN/m*

It can be observed from the results that the number of panels affects the percentage of rocking deformation, with the general tendency for a higher percentage of rocking behaviour when more panels are used, as illustrated in Figure 13.

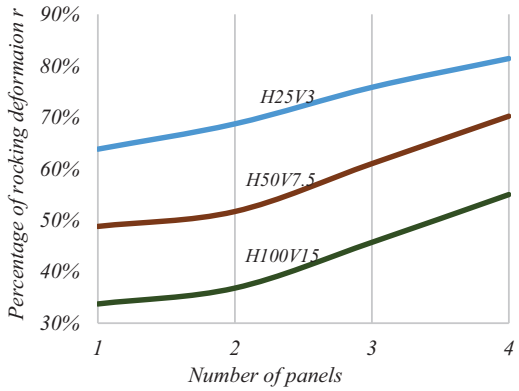

Figure 13: *Relationship between the number of panels and r for the models with CP mode when h/B is fixed to be 12:4 and vertical loads equal to 20 kN/m*

With respect to the kinematic modes, the models with CP mode tend to maintain that behaviour following an increase in the number of panels. However, models with SW mode could shift to IN behaviour when more panels are added. Figure 14 shows an example from model *M h/b -P# - VL20 - H25V15*, where when the number of panels increases from 2 to 4, the kinematic mode changes from SW to IN.

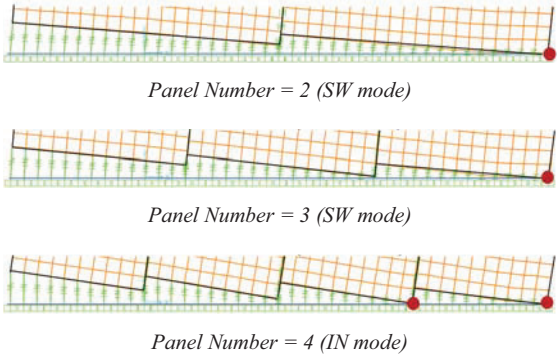

Figure 14: *Kinematic modes of the models with varying panel numbers.*

The analysis found that the total lateral stiffness tends to increase when the number of panels is increased while maintaining a constant ratio of *h/b*.

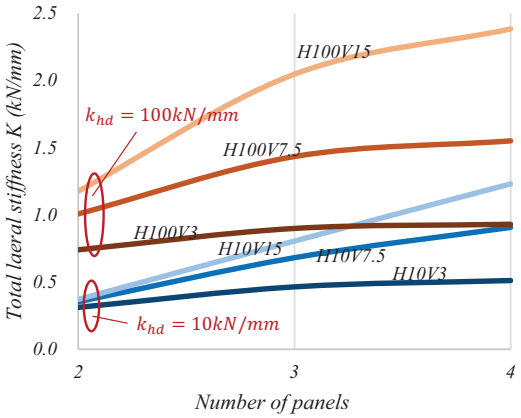

Figure 15: *Relationship between the number of panels and K when h/b is fixed to be 12:1 and vertical loads equal to 20 kN/m*

Similar to the result from the condition with a fixed *h/B* ratio, a higher percentage of rocking deformation is observed for systems using more panels with a fixed *h/b* ratio.

4 CONCLUSIONS

Analysis of the lateral deformation and kinematic modes of multi-panel balloon-type CLT shearwall systems is presented in this paper. A multi-panel shearwall model is proposed, and the effect of key parameters on the behaviour of the shearwall is presented and discussed.

The results highlight the importance of the panel aspect ratio (*h/b*) and the stiffness of connectors. It is found that the total lateral stiffness of the wall is higher when panels with lower aspect ratio, hold-down and vertical joints with higher stiffness and larger vertical loads are adopted. Increasing the number of panels for a shearwall system with a fixed total height-to-width ratio (*h/B*) results in lower total lateral stiffness, while increasing the number of panels with a fixed panel aspect ratio (*h/b*) results in higher total lateral stiffness.

The results also indicate that the lateral flexural deformation for balloon-type shearwalls should not be

https://doi.org/10.52202/069179-0314

ignored. In general, a higher aspect ratio, higher stiffness of hold-downs and vertical joints, and fewer number of panels all lead to a higher percentage of flexural deformation.

Finally, it is found that balloon-type CLT system with higher relative stiffness in the connections and higher vertical loads tends to be dominated by CP mode.

5 REFERENCES

[1] D. Casagrande, G. Doudak, L. Mauro, and A. Polastri, "Analytical approach to establishing the elastic behavior of multi-panel CLT shear walls subjected to lateral loads," *Journal of Structural Engineering*, vol. 144, no. 2, p. 04017193, 2018.

[2] G. Tamagnone, and M. Fragiacomo, "On the rocking behavior of CLT wall assemblies", *In Proceedings of the World Conference on Timber Engineering (WCTE2018)*, Seoul, 2018.

[3] I. Gavric, M. Fragiacomo and A. Ceccotti, "Capacity seismic design of X-LAM wall systems based on connection mechanical properties", *In Proceedings of the Meeting*, Vol. 46, 2013.

[4] A. Polastri, and D. Casagrande, "Mechanical behaviour of multi-panel cross laminated timber shear-walls with stiff connectors", *Construction and Building Materials*, 332, 127275, 2022.

[5] E. Karacabeyli, and S. Gagnon. "Canadian CLT handbook: 2019 edition", *FPInnovations*: Pointe-Claire, QC, Canada, 2019.

[6] AMC, "Project Arboretum: Erection isometric view and list of plans", 90 Arboretum Drive, Newington, N.H., United States, 03801, 2019.

[7] MB, "Project Arbora: Montage vue d'ensemble et liste des dessins", Condos Griffintown, 2018.

[8] Z. Chen and M. Popovski, "Mechanics-based analytical models for balloon-type cross-laminated timber (CLT) shear walls under lateral loads," *Engineering Structures*, vol. 208, p. 109916, 2020.

[9] Z. Li, X. Wang, and M. He, "Experimental and analytical investigations into lateral performance of cross-laminated timber (CLT) shear walls with different construction methods," *Journal of Earthquake Engineering*, pp. 1–23, 2020.

[10] C. Dickof, M. Shahnewaz, N. Bevilacqu and T. Tannert, "Experimental investigations on balloon frame CLT shearwalls", *In Proceedings of World Conference on Timber Engineering (WCTE 2020)*, Chile, 2020.

[11] M. Shahnewaz, C. Dickof, and T. Tannert, "Seismic behavior of Balloon Frame CLT shear walls with different ledgers," *Journal of Structural Engineering*, vol. 147, no. 9, p. 04021137, 2021.

[12] CSA O86-19. "Engineering design in wood", *CSA Group*, Mississauga, Ontario, Canada; 2019.

[13] EN 1995-1-1:2004/A2. "Eurocode 5: Design of timber structures. Part 1–1: General. Common rules and rules for buildings", CEN, Brussels, Belgium; 2014.

[14] CSI. "SAP2000 Integrated Software for Structural Analysis and Design", Berkeley, California: Computers and Structures Inc. 2021.

[15] R. Brandner, P. Dietsch, J. Dröscher, M. Schulte-Wrede, H. Kreuzinger, and M. Sieder, "Cross laminated timber (CLT) diaphragms under shear: Test configuration, properties and Design", *Construction and Building Materials*, vol. 147, pp. 312–327, 2017.

[16] H.J. Blass and P. Fellmoser, "Design of solid wood panels with cross layers", *In 8th World Conference on Timber Engineering*, Vol. 14, No. 17.6, p., 2004.

[17] T. Bogensperger, T. Moosbrugger and G. Silly, "Verification of CLT-Plates Under Loads in Plane", *WCTE*, Riva del Garda, Italy, 2010.

[18] "European technical assessment ETA 12/0362-essepi.it." [Online]. Available: https://www.essepi.it/wp-content/uploads/2020/04/ETA-12_0362.pdf

https://doi.org/10.52202/069179-0314

World Conference on Timber Engineering Oslo 2023

SEISMIC ASSESSMENT OF BALLOON-FRAMED CLT BUILDING WITH SELF-CENTERING HOLD-DOWN

Yuxin Pan[1], Md Shahnewaz[2], Carla Dickof[3], Thomas Tannert[4]

ABSTRACT: Balloon-framed cross-laminated timber (CLT) construction has a number of advantages when compared to platform-type construction. To date, however, only limited studies are reported on the performance of the former during earthquake shaking, and the seismic design provisions of many buildings codes only apply to the latter. Applications of innovative self-centering, energy-dissipation devices in balloon-framed CLT building are not yet well understood either. This study assesses the seismic performance of a balloon-framed CLT building with friction-based self-centering hold-downs (HD). A three-dimensional nonlinear finite element model was developed with the connections calibrated with test data. A tri-hazard ground motion selection approach was adopted to select and scale proper earthquake motions for the building site in Vancouver, Canada. The impact of the choice of hold-down on the seismic performance and damage potential of the building was assessed through nonlinear time history and incremental dynamic analyses. At design level, the building had an maximum drift of 0.67%, which met the 2.5% design limit. For comparison, a second building model with traditional HD was established and analysed, where larger drift was observed. The results confirmed the good seismic performance of the self-centering HD for balloon-framed CLT building.

KEYWORDS: Cross-laminated timber, seismic fragility, nonlinear modelling, resilience

1 INTRODUCTION

Most recent cross-laminated timber (CLT) projects applied a platform-type approach where each floor serves as a platform for erecting the walls of the next floor [1]. The platform construction has several disadvantages, mainly, it requires high compression resistance of the base floor in perpendicular-to-grain direction, and it requires more time for on-site assembly [2]. Balloon-framed construction, in which the walls are continuous from the base to the roof with floors can solve these problems. However, limited studies on balloon-framed construction are available and the design guideline for balloon-frame construction is not specified in Canadian Standard for Engineering Design in Wood CSA O86 [3].

A shake table tests on a 2-storey balloon-framed building with post-tensioned CLT rocking walls was conducted at UCSD laboratory [4]. It was observed that the building performed well at the maximum considered earthquake level. Li et al. [5] conducted a series of reversed cyclic tests on the balloon-framed shear walls and developed analytical equations for estimating the wall resistance. FPInnovations [6] in Canada proposed a mechanics-based model to predict the deflection and resistance of the balloon-type CLT building with an aspect ratio up to 12:1. Shahnewaz et al. [7] conducted static monotonic and cyclic tests on 2-storey balloon-framed CLT shear walls and identified that the rocking behavior of the CLT was not affected by the ledgers. Zhang et al. [8] developed 3D ETABS model for tall balloon-framed CLT building (12-story and 18-story) to investigate the influence of different connections on the overall characteristics of the building. Recently, Pan et al. [9] studied the collapse risk of a 2-storey school building retrofitted with balloon-framed CLT shear walls and found the building designed with the seismic reduction factors of that from the platform system can meet the requirement.

Another challenge for balloon-framed construction is the design of the tall walls' base connections, which require larger shear and overturning resistances. Common CLT buildings experience damage due to yielding and nail withdrawal of steel connectors (e.g., spline joint, hold-down, shear connections) during earthquake excitations, while the wall panels exhibit almost rigid behaviour [10]. With the increase of the wall height, larger demands will be posed to the base connectors, therefore, high-performance connectors are needed to accommodate this demand. Amongst the several high-performance connectors that have been developed in recent years [11],

[1] Yuxin Pan, The Hong Kong University of Science and Technology, Hong Kong, China, ceypan@ust.hk

[2] Md Shahnewaz, Fast + Epp, Canada, md.shahnewaz@alumni.ubc.ca

[3] Carla Dickof, Fast + Epp, Canada, cdickof@fastepp.com

[4] Thomas Tannert, University of Northern British Columbia, Canada, thomas.tannert@unbc.ca

https://doi.org/10.52202/069179-0315

a friction-based self-centering device used as hold-down (HD), commercially available under the trademark 'Tectonus', has shown great energy dissipation while causing low damage. Hashemi et al. [12] conducted large-scale experimental test conducted on a rocking CLT wall with this self-centering HD device and demonstrated that this novel device showed excellent behaviour and can achieve a damage-avoidant and seismic-resilient design.

This paper aims to assess the seismic performance of a balloon-framed CLT building with such self-centering device through nonlinear time history analysis (NLTHA).

2 BUILDING DESCRIPTION

The 4-storey, 16 m tall CLT building, located in Vancouver, Canada, has a dimension of 36.8 m×11.4 m and story height of 3.6 m, as shown in Figure 1. The building is the new office centre for Fast + Epp. It was designed with a live load of 2.4 kPa and a superimposed dead load of 2.5 kPa. The 2015 version of National Building Code of Canada (NBCC) [13] was used for the seismic design for a Class B Vancouver site (rock conditions). The CLT walls were designed with different thickness - 139 mm and 190 mm for the long direction, and 245 mm for the short direction. The walls are balloon-framed with ledgers at the middle. Seismic design reduction factors R_d and R_o of 2.0 and 1.5, respectively were used for the lateral system design which corresponds to the requirement for rocking platform CLT wall [3]. CLT is also utilized throughout the building for the floors, stairwells, elevator cores, as well as the demising firewall.

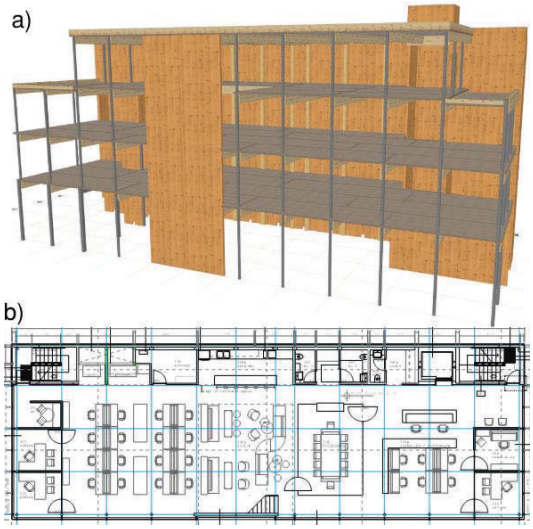

Figure 1: *3D isotropic a) and plan b) view of the building*

The walls are balloon-framed for every two storeys connected with ϕ 8 × 130 mm fully threaded screws installed in horizontal half-lap joints. The vertical panel-to-panel connections are provided with 19 mm ×200 mm D. Fir plywood surface spline joints using both partially threaded screws and smooth shank nails at a spacing of 500 mm and 64 mm, respectively. Base connections include concrete shear keys (SK) for each panel and two Tectonus HD at both ends of the coupled walls. For SK, a concrete upstand of 250 mm height and 300 mm width was designed with 4-15M U-bars embedded.

The Tectonus HD act as shock absorbers for the building during an earthquake, providing energy dissipation and damping through the earthquake cycles, with the ability to snap back to its original position once shaking ends. The Tectonus connectors remain damage-free, a feature that might allow immediate return to occupancy after a significant earthquake, without facing uncertain delays expected with conventional systems. Figure 2 shows a photo of the installed Tectonus device and a typical "flagshaped" hysteresis curve with self-centering characteristics. The design parameters are as follows: F_{slip}=350 kN, F_{ult}=700 kN, $F_{restoring}$=350 kN, $F_{residual}$=165 kN, and Δ_{ult}=15 mm.

In the original design, a steel braced frame was placed in the short direction of the building. As this study focused on the impact of the self-centering HD device, the building was modified by replacing the brace system with a coupled balloon-framed CLT shear wall. A total of 12 Tectonus HDs were used in the updated building model for assessment.

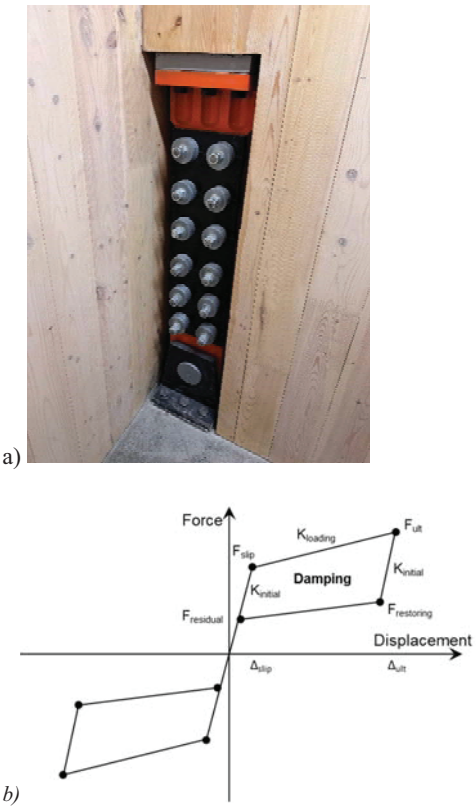

Figure 2: *Tectonus HD device: a) photo, b) hysteresis curve*

https://doi.org/10.52202/069179-0315

3 MODELING

A nonlinear three-dimensional (3D) model of the building was developed in OpenSees [14]. Isotropic elastic shell elements were used to model the CLT wall panels and nonlinear spring elements (either zeroLength or twoNodeLink) were used to simulate the connections, as seen in Figure 3. Pinching4 model and SelfCentering models were used and calibrated to model the nonlinear behaviour of the connections, including cyclic degradation and pinching at large deformation.

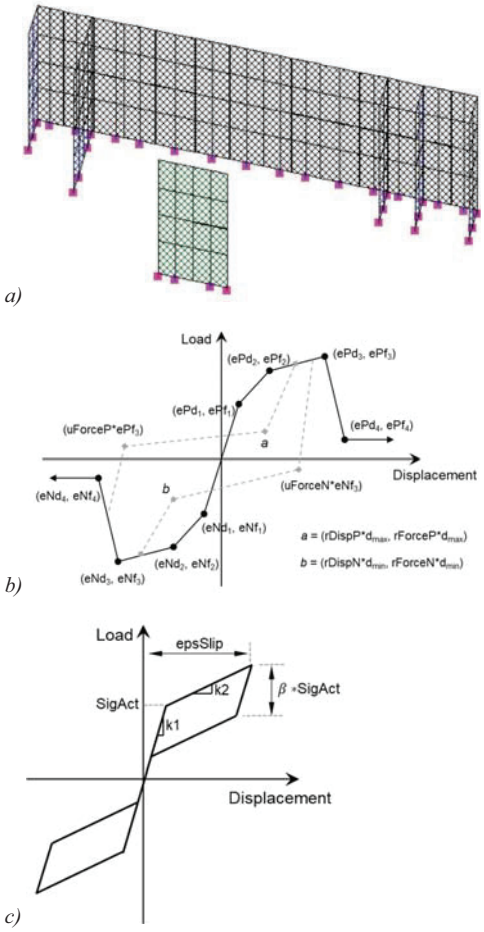

Figure 3: *Numerical model in OpenSees: a) 3D model of the building, b) Pinching4 material model, c) SelfCentering material model for connections*

For comparison purpose, a second building model with conventional dowel-type HD was established and modelled. The HD was manufactured with customized stell plate (975 mm high, 370 mm wide, 102 mm long at base, and 28 mm thick) and attached with 32 fully threaded ϕ12×120 self-tapping screws. It was tested at the UNBC lab with the same peak capacity of 700 kN.

All the connections were calibrated with experimental data available in the literature or conducted at UNBC lab. Considering the limitation of the SelfCentering model where the unloading stiffness has to be the same with the loading stiffness (different in actual behavior of the Tectous HD), an energy equivalent assumption was made: by controlling the *Frestoring* in Figure 2 (i.e., β in Figure 3b), the total energy enclosed by the numerical backbone curves was almost the same as the area enclosed by the design parameter.

Figure 4 shows the first two preliminary mode shapes of the developed model. The building had a fundamental period T of 0.8 sec in the short direction (East-West) and 0.5 sec in the long direction (North-South). The sliding and rocking behaviour of the CLT panels can be identified. The obtained information will be used to select proper ground motion input records that represent the seismicity for the nonlinear dynamic analysis.

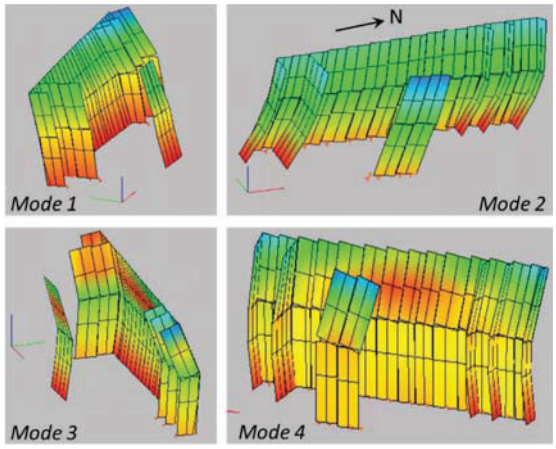

Figure 4: *Mode shapes of the building model*

4 ANALYSIS

To assess the seismic performance of the two buildings, NLTHA was performed on their models. This procedure requires proper selection and scaling of representative ground motions. For the building site of Vancouver, which is located in the complex Cascadia Subduction Zone, there are three types of earthquake hazards: 1) shallow crustal earthquakes, 2) subduction inslab earthquakes, and 3) subduction interface earthquakes. By conducting a probabilistic seismic hazard analysis for the site using Canada's 5th Generation Seismic Hazard Model, the contributions from each hazard are 8%, 72%, and 20%, respectively. As per the NBCC, a total of 21 pairs (two horizontal components) of ground motion records, 7 from each earthquake type, were selected from global databases and matched to the design spectrum of the building over a period range of 0.2T to 2.0T. Figure 5 shows the response spectra of selected motions matched to the design spectrum.

https://doi.org/10.52202/069179-0315

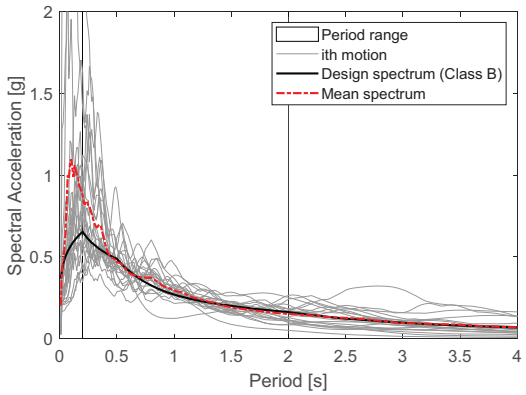

Figure 5: *Ground motion selection and scaling*

With the established models and the selected motios, NLTHA were conducted at the design intensity level for two building models. Figure 6a compares the maximum drifts at both directions of the buildings. For the Tectonus one, the maximum drift on average were 0.22% at the second story for the long direction and 0.67% at the roof floor for the short direction, which were far below the 2.5% drift limit specified in NBCC for normal importance category buildings. It was observed that the Tectonus HD had negligible impact on drift in the strong long direction, but decreased 30% drift for the short direction when compared to the conventional HD. It is worth mentioning that although the two HD devices had the same peak capacity, the initial stiffness were different, therefore, different seismic performance at design intensity levels were expected. This can be seen in Figure 6b. Due to lower initial stiffness, traditional HD showed twice the displacement at 32% lower force than the Tectonus HD.

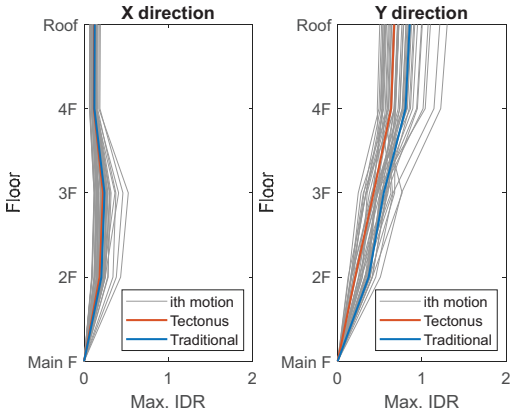

a)

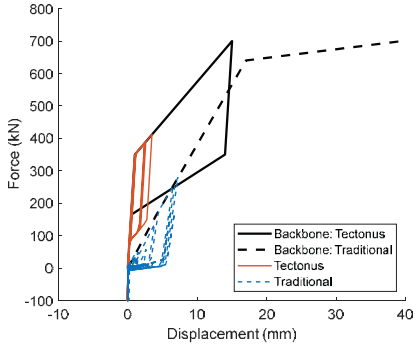

b)

Figure 6: *Comparison of two building models at design intensity level: a) drift, b) HD hysteresis*

For illustration, roof displacement time histories in the short direction of the building with Tectonus HD are presented in Figure 7, are categorized for each earthquake type. The average of the maximum roof displacements for the long and short directions were 24 mm and 64 mm, respectively, where the maximum displacement of 89 mm was observed from one subduction inslab motion – the Michoacan motion in the short direction.

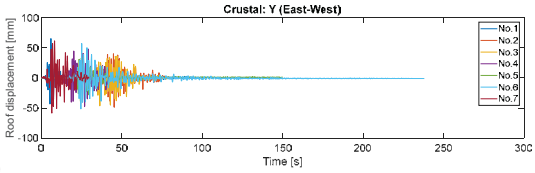

a)

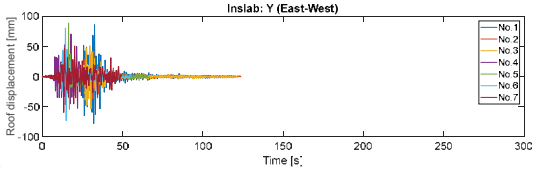

b)

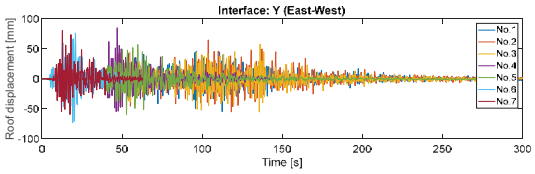

c)

Figure 7: *Roof displacement time histories in the short direction of the building model with Tectonus HD: a) crustal, b) subduction inslab, c) subduction interface*

Hysteresis curves of the Tectonus building model and representative connections subjected to the Michoacan subduction inslab motion (No. 4 at station Caleta De Campos) at design level are presented in Figure 8. Highly nonlinear behaviour including stiffness and strength degradation, as well as pinching can be observed. It can be seen that the horizontal panel-to-panel spline connection was the primary source for energy dissipation.

https://doi.org/10.52202/069179-0315

The spline connections in both directions of the building showed large relative displacements and dissipated large amount of the energy. This was followed by the Tectonus HD. The rocking behaviour for this design level shaking resulted in 2 mm uplift and almost 400 kN tension force. The vertical floor-to-floor half-lap connections were capacity protected, and therefor showed almost linear behaviour.

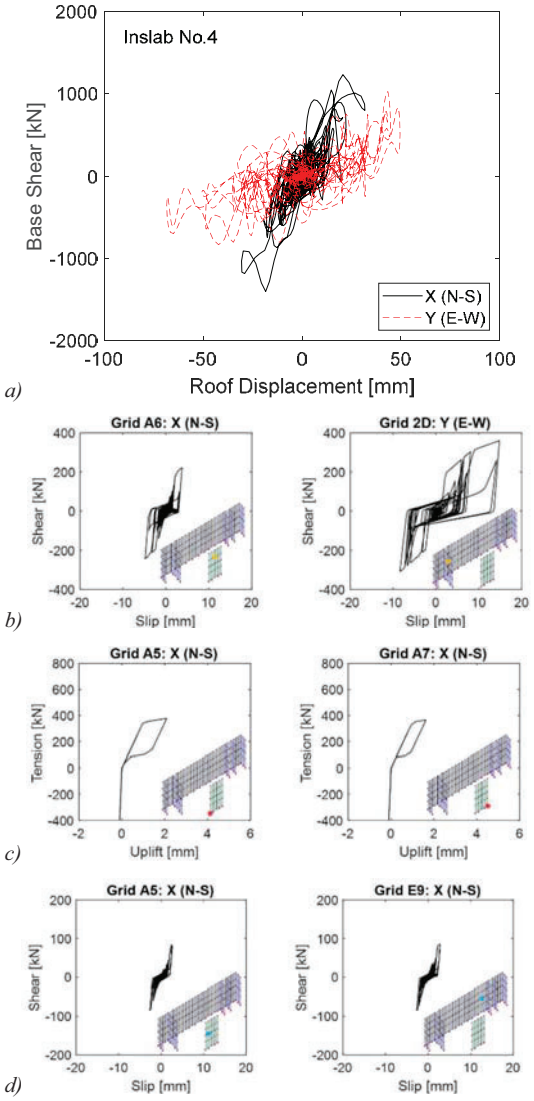

Figure 8: *Nonlinear hysteresis curves during subduction inslab motion: a) global curve, b) horizontal panel-to-panel spline joint, c) Tectonus HD, and d) vertical floor-to-floor half-lap joint*

5 CONCLUSIONS

In this study, a 3D finite element model for a balloon-framed CLT building was developed and calibrated with test data. The building was equipped with a resilient friction-based self-centering device as HD – the first in Canada. For comparison, a second building model designed with conventional dowel-type HD was also developed. The SelfCentering and Pinching4 material models in OpenSees were used for modelling the connections. Twenty-one pairs of ground motion records were selected based on the seismic hazard of the building site for the nonlinear time history analysis. Based on the analysis results, both building models met the drift limit of 2.5% specified in NBCC at the design level. The model with the Tectonus HD showed lower drift compared to the traditional one. Further studies on the collapse capacity and damage fragility of the building model will be conducted to have a comprehensive understanding of the effectiveness of the Tectonus HD for seismic resilience design.

ACKNOWLEDGEMENT

The project was supported by Government of Canada through a Canada Research Chair and by Natural Resources Canada (NRCan) through the Green Construction Wood (GCWood) program.

REFERENCES

[1] Karacabeyli, E., and Gagnon, S.: Canadian CLT Handbook, 2019 Edition. FPInnovations, Pointe-Claire, QC, Canada, 2019.

[2] Shahnewaz, M., Dickof, C., and Tannert, T.: Seismic Behavior of Balloon Frame CLT Shear Walls with Different Ledgers. *Journal of Structural Engineering*, 147(9), 04021137, 2021.

[3] CSA: CSA O86-19 Engineering Design in Wood, Canadian Standard Association. Mississauga, Canada, 2019.

[4] Pei, S., van de Lindt, J. W., Barbosa, A. R., Berman, J. W., McDonnell, E., Daniel Dolan, J., Blomgren, H.-E., Zimmerman, R. B., Huang, D., and Wichman, S.: Experimental seismic response of a resilient 2-story mass-timber building with post-tensioned rocking walls. *Journal of Structural Engineering*, 145(11), 04019120, 2019

[5] Li, Z., Wang, X., and He, M.: Experimental and analytical investigations into lateral performance of cross-laminated timber (CLT) shear walls with different construction methods. *Journal of Earthquake Engineering*, 1-23, 2020.

[6] Chen, Z., and Popovski, M.: Mechanics-based analytical models for balloon-type cross-laminated timber (CLT) shear walls under lateral loads. *Engineering Structures*, 208, 109916, 2020.

[7] Shahnewaz, M., Dickof, C., and Tannert, T.: Seismic Behavior of Balloon Frame CLT Shear Walls with Different Ledgers. *Journal of Structural Engineering*, 147(9), 04021137, 2021.

[8] Zhang, X., Pan, Y., and Tannert, T.: The influence of connection stiffness on the dynamic properties and seismic performance of tall cross-laminated timber buildings. *Engineering Structures,* 238, 112261, 2021.

[9] Pan, Y., Shahnewaz, M. and Tannert, T.: Seismic Performance and Collapse Fragility of Balloon-Framed CLT School Building. *Journal of Earthquake Engineering*, pp.1-21, 2022.

[10] Hashemi, A., Quenneville, P.: Large-scale testing of low damage rocking Cross Laminated Timber (CLT) wall panels with friction dampers. *Engineering Structures*, 206, 110166, 2020.

[11] Tannert, T., Loss, C.: Contemporary and Novel Hold-Down Solutions for Mass Timber Shear Walls. *Buildings*, 12(2), 202, 2022.

[12] Hashemi A, Zarnani P, Masoudnia R, Quenneville P.: Experimental testing of rocking cross-laminated timber walls with resilient slip friction joints. *Journal of Structural Engineering*. 144:04017180, 2018.

[13] NRCC: National Building Code of Canada (NBCC). Associate Committee on the National Building Code, National Research Council of Canada (NRCC). Ottawa, Canada, 2015.

[14] Mazzoni, S., McKenna, F., Scott, M. H., and Fenves, G. L.: OpenSees command language manual, Pacific Earthquake Engineering Research (PEER) Center. Berkeley, CA, 137-158, 2006.

https://doi.org/10.52202/069179-0315

World Conference on Timber Engineering Oslo 2023

STUDY OF THE EFECT OF SEISMIC REINFORCEMENT USING CFRTP STRANDS ON WOODEN BUILDINGS

Koji Kubo[1], Nobuji Sakurai[1], Yuya Takaiwa[2]

ABSTRACT: In this study, we conduct seismic reinforcement work using CFRTP (Carbon Fiber Reinforced Thermo-Plastics) strands on an actual wooden building, conduct microtremor measurement before and after the work, and grasp the change in natural vibration characteristics. Additionally, the numerical analysis before and after the work confirm that to what extent yield strength is raised by the seismic reinforcement. These results reveal that the effectiveness of the seismic reinforcement using CFRTP strands on wooden buildings is not a bad influence on the period of the actual building.

KEYWORDS: Wooden architecture, Microtremor measurement, Seismic performance

1. INTRODUCTION

We can raise yield strength by seismic reinforcement members as a result of conducting seismic reinforcement on wooden buildings. Moreover, we can raise stiffness. The rising of stiffness changes the natural period. In consequence, there is a possibility that the building resonates with seismic motion of the periodic band which used to not resonate before seismic reinforcement. Accordingly, in seismic reinforcement design, we need to grasp the possible spectral shape in the area as a result of surveys of the fault around the site and historical earthquake. On the other hand, if there are seismic reinforcement members raise yield strength and not change stiffness, we can keep resonance with the periodic band unchanged before and after the seismic reinforcement. However, conventional seismic reinforcement members of wooden buildings, for example, plywood, reinforcing bar brace, and diagonal brace, raise not only yield strength but also stiffness. Therefore, we developed a seismic reinforcement method for wooden buildings using CFRTP strands that having high yield strength, and moreover, low stiffness at large deformation. Carbon fiber composite materials are advanced materials used in a wide range of fields of engineering, and are also gathering attention in the field of construction [1]. In the previous study, the authors developed an end fixing structure for CFRTP strands having toughness [2][3][4]. We showed that CFRTP stands have high yield strength at large deformation, moreover, have low stiffness as a result of conducting an in-plane shear test on wooden frame reinforcement walls using CFRTP strands [5]. In this study, we conduct seismic reinforcement work using CFRTP strands on an actual wooden building, conduct microtremor measurement before and after the work, and grasp the change in the natural vibration characteristic. Additionally, the numerical analysis before and after the work confirm that to what extent yield strength is raised by the seismic reinforcement. The purpose of this study is that these results reveal the effectiveness of the seismic reinforcement using CFRTP strands on wooden buildings.

2. TARGET BUILDING

2.1 OUTLINE OF THE BUILDINGS

The “shumaku” displayed in Natural Museum of Ethnology since 1999 is a reproduction of a facility that was built around 1920 for Korean Peninsula travelers to eat and sleep. In order to exhibit, the original roof was changed from thatching to copper plate. The planar shape is L-shaped, and the floor plan is composed of accommodation rooms such as Japanese “Hatagoya” and “Uchiniwa” (cooking area).

Photo 1: *Appearance of the target building (Before reinforcement)*

[1] Koji Kubo, Nobuji Sakurai, Nose Structural Corporation Co., Ltd. , k_kubo@nosekenchiku.co.jp

[2] Yuya Takaiwa, Associate Professer, Dept. of Architecture, Faculty of Science and Engineering, Toyo University, Dr. Eng. takaiwa@toyo.jp

https://doi.org/10.52202/069179-0316

2.2 OUTLINE OF STRUCTURE

The frame by the wooden framework construction method is constructed with 150mm × 150mm columns, 150mm × 200mm beams, 90mm × 150mm rails, and walls are plywood Shinkabe:japanese traditional column-exposed wall. The wooden frame members are all made of pine, and the column bases are Ishibadate:Japanese traditional construction method, columns set up on stones instead of anchoring to the ground. The roof truss is copper roofing using Japanese roof truss. Table 1 shows the building weight. Figure 1 shows roof truss frame and framing elevation.

Table 1: *Building weight.*

Floor		height H (m)	weight W(kN)	area A(m^2)	W/A (kN/m^2)
1		3.270	114.61	61.76	1.85

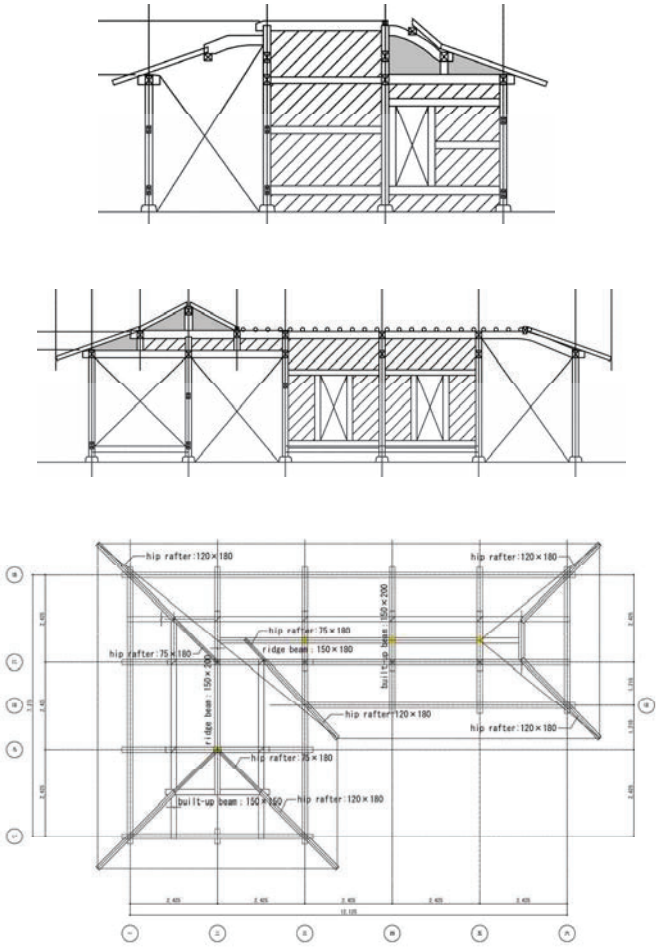

Figure 1: *roof truss flame plan, framing elevation*

2.3 OUTLINE OF REINFORCEMENT

We needed to conduct a reinforcement to maintain the exterior and the interior of the building. Therefore, we selected reinforcement members installed on the current wall. We adopted CFRTP strands made of carbon fiber composites as seismic reinforcement members and conduct seismic reinforcement. CfRTP strands were arranged in well balanced manner on the structure of each frame (top and bottom of girts), and the entire building was considered so that there was no behavior of twisting. The seismic reinforcement work was completed at the end of March 2022.

Photo 2: *Appearance of the target building (After reinforcement)*

Photo 3: *Appearance of the target building (After reinforcement)*

Photo 4: *Control of tightening torque*

https://doi.org/10.52202/069179-0316

Photo 5: *Control of tightening torque*

3. MICROTREMOR MEASUREMENT

3.1 OUTLINE OF THE MEASUREMENT

The eigenfrequency and vibration mode shape are estimated by measurement. Figure 2 shows the measurement position. The measurement was performed at the capital and ground level using a 3-axis accelerometer:RS-ONE.
Data for 180 seconds was sampled at a sampling frequency of 100 Hz.

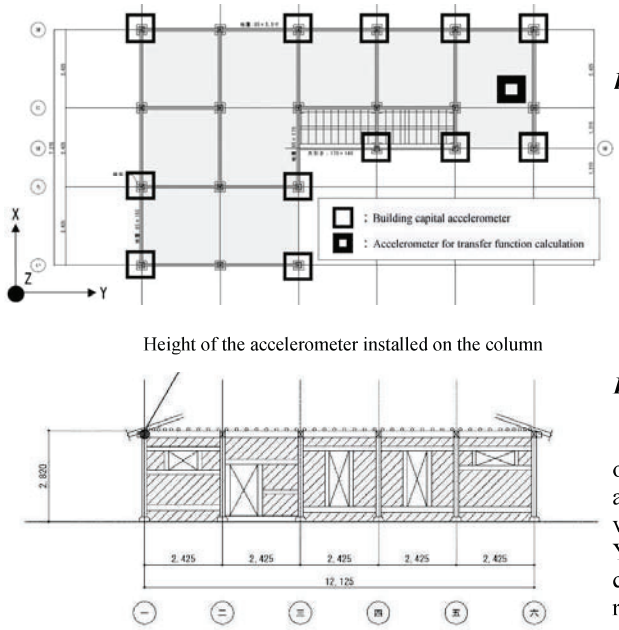

Height of the accelerometer installed on the column

Figure 2: *measurement position*

3.2 MEASUREMENT RESULT

Figure 3, 4 (Before reinforcement) and Figure 5, 6 (After reinforcement) show analysis results.

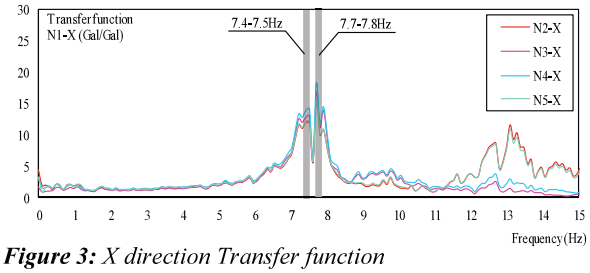

Figure 3: *X direction Transfer function*

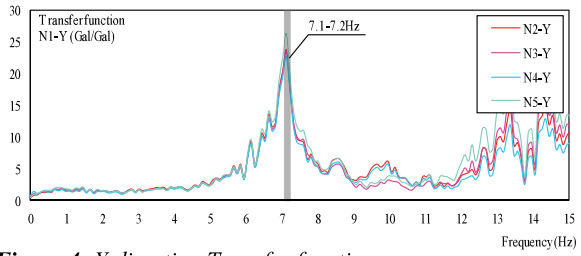

Figure 4: *Y direction Transfer function*

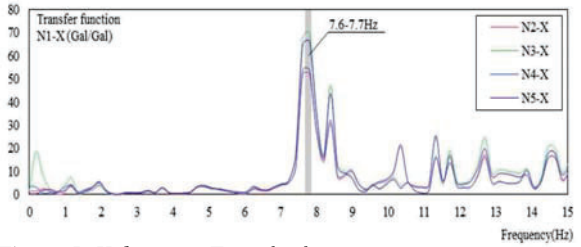

Figure 5: *X direction Transfer function*

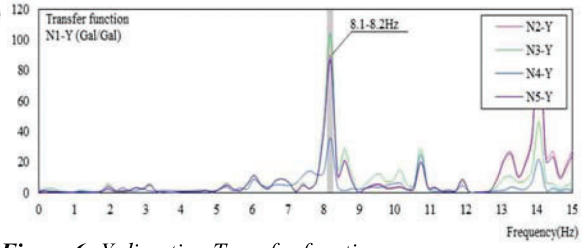

Figure 6: *Y direction Transfer function*

Before reinforcement, it had a natural vibration mode of X component around 7.4 - 7.5 Hz and Y component around 7.1 – 7.3 Hz. After reinforcement, it had a natural vibration mode of X component around 7.6 - 7.7 Hz and Y component around 8.1 – 8.2 Hz. There is almost no change in the periodic band before and after reinforcement.

4. ESTIMATION OF STIFFNESS AND YIELD STRENGTH

We calculated stiffness and ultimate horizontal yield strength before and after seismic reinforcement by numerical analysis, and compared the change of stiffness before and after seismic reinforcement.

https://doi.org/10.52202/069179-0316

4.1 OUTLINE OF THE ANALYSIS MODEL

This analysis model express horizontal diaphragm stiffness in pole plate level contributed by roof truss. We replaced seismic reinforcement members arranged on the wall with wire braces. Figure 7 shows analysis model.

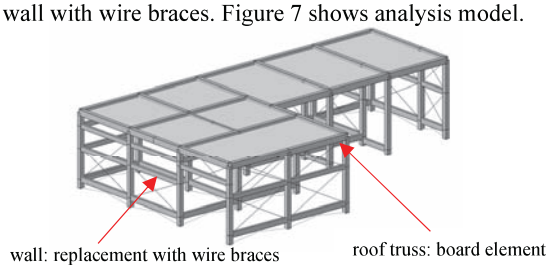

Figure 7: *analysis model*

4.2 EIGENVALUE ANALYSIS

We conducted eigenvalue analysis before and after seismic reinforcement. Table 2 is comparative table of analysis result and microtremor measurement result. Figure 8 and 9 show primary mode.

Table 2: *Eigenfrequency (Hz)*

	Microtremor measurement		Analysis result	
	X direction	Y direction	X direction	Y direction
Before reinforce -ment	7.40	7.10	0.001	0.005
After reinforce -ment	7.60	8.10	2.535	2.805

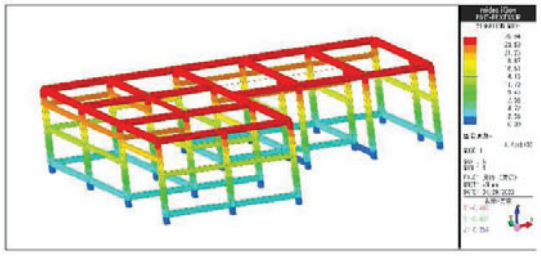

Figure 8: *Primary mode chart (Y direction before reinforcement)*

Figure 9: *Primary mode chart (Y direction after reinforcement)*

4.3 STATIC ELASTIC ANALYSIS

We conducted static elastic analysis before and after seismic reinforcement, and compared horizontal stiffness and ultimate horizontal yield strength. We adopted ultimate horizontal yield strength in 1/15 rad. Figure 10 and 11 show load-deformation relationship. Table 3 shows ultimate horizontal yield strength.

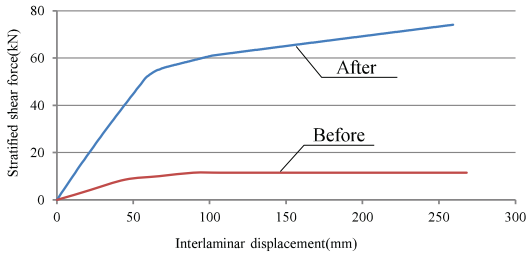

Figure 10: *X direction Load-deformation relationship*

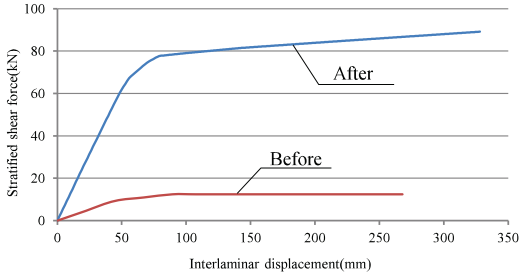

Figure 11: *Y direction Load-deformation relationship*

Table 3: *ultimate horizontal yield strength*

	Horizontal Stiffness (kN/mm)		Ultimate horizontal yield strength (kN)	
	X direction	Y direction	X direction	Y direction
Before reinforce -ment	0.083	0.090	11.5	12.50
After reinforce -ment	1.010	1.236	70.42	78.87

According to analysis results, we can see that stiffness and ultimate horizontal yield strength increased greatly from before reinforcement. By contrast, according to results of microtremor measurement, we can see that eigenfrequency is about the same. Therefore, we suggest that initial stiffness is almost unchanged.

https://doi.org/10.52202/069179-0316

5. EFFECT ON THE BUILDING BY CHANGE OF STIFFNESS

There's a wide variety of seismic reinforcement from high-stiffness members to low-stiffness members. We need to grasp the period of the building, to attenuate the effect on the building by the change of stiffness.

5.1 SEISMIC REINFORCEMENT WITH DIFFERENT STIFFNESS REINFORCEMENT MEMBERS

In the case of seismic reinforcement using high-stiffness members, the natural period fluctuates due to increasing stiffness. In consequence, there is a possibility that the building resonates with seismic motion of the periodic band which used to not resonate before seismic reinforcement.

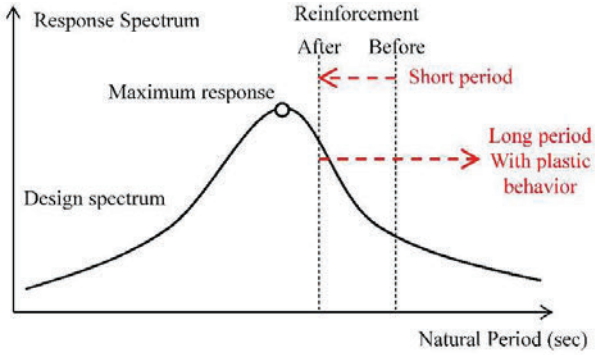

Figure 12: *Seismic reinforcement using high-stiffness members (Steel material brace, plywood, diagonal brace etc.)*

By contrast, seismic reinforcement using low-stiffness members raise yield strength without change of stiffness. In consequence, we can keep the same periodic band which the building resonates before and after seismic reinforcement.

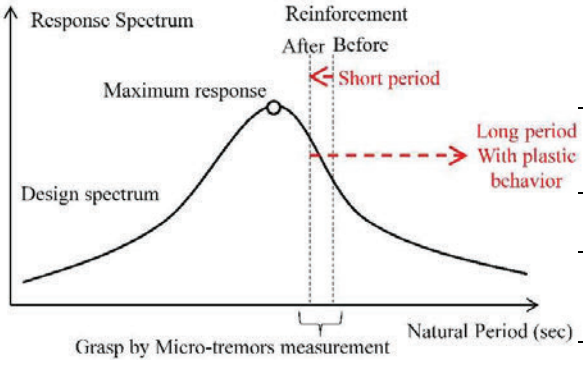

Figure 13: *Seismic reinforcement using low-stiffness members (CFRTP strand proposed by this study)*

5.2 COMPARATION WITH HIGH STIFFNESS MEMBERS

We compared by analysis seismic reinforcement with high-stiffness against low-stiffness members, and considered the change of eigenfrequency after reinforcement. We employed high-stiffness wire braces as high-stiffness members, and CFRTP strands as low-stiffness members. We calculated eigenfrequency and horizontal stiffness in 1/120 rad. Figure 14 and 15 show load-deformation relationship. Table 4 is comparative table of eigenfrequency and stiffness.

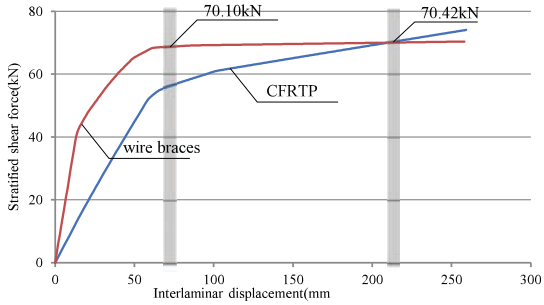

Figure 14: *X direction Load-deformation relationship*

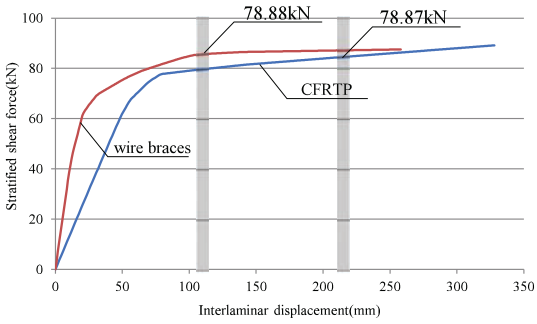

Figure 15: *X direction Load – deformation relationship*

Table 4: *Comparative table of eigenfrequency*

Reinforceme -nt members	CFRTP strand		Wire brace	
Direction	X direction	Y direction	X direction	Y direction
Horizontal stiffness	0.945	1.236	1.963	2.403
Eigenfreque-ncy	2.535	2.805	2.776	3.112

https://doi.org/10.52202/069179-0316

Figure 16 shows mode chart after seismic reinforcement with high-stiffness members.

Figure 16: *Primary mode chart (Y direction after reinforcement)*

Analysis results demonstrated that eigenfrequency of high-stiffness members is up 1.10 times in X direction, and 1.11 times in Y direction than low-stiffness members. We confirmed that horizontal stiffness of high-stiffness members is up around 2 times in both direction than low-stiffness members.

6. CONCLUSIONS

We confirmed that horizontal stiffness calculated by actual measurement value of microtremor measurement is almost unchanged before and after reinforcement. Numerical analysis demonstrated that yield strength after reinforcement is up than before reinforcement. We employed high-stiffness wire braces and low-stiffness CFRTP strands as seismic reinforcement members, and confirmed differences in stiffness between the two by numerical analysis. According to the result, we confirmed that eigenfrequency of using wire braces is higher than using CFRTP strands in the case that each ultimate horizontal yield strength is almost the same. We presume that CFRTP strands employed as seismic reinforcement members in this study are high-yield strength and low-stiffness members. The building reinforced with these seismic reinforcement members function as fail safe in large deformation. Moreover, we confirmed that seismic reinforcement with CFRTP strands have no negative effect on periodic characteristic of the existing building.

ACKNOWLEDGEMENT

The owner of the target wooden building, National Museum of Ethnology gave us huge help.
We would like to express our gratitude to them.

REFERENCES

[1] Kiyoshi Uzawa, Yoshihiro Saito, Atsushi Hokura : APPLICATION OF COMPOSITE MATERIALS TO CIVIL ENGINEERING AND CONSTRUCTION FIELDS – NEW INITIATIVES THROUGH ADVANCED MATERIALS AND INNOVATIVE MANUFACTURING TECHNOLOGY - , Journal of Japan Society of Civil Engineers, Ser. AI (Structural Engineering & Earthquake Engineering (SE/EE)) 73(5), II_1- II_9,2017.5

[2] Yuya Takaiwa, Katsuhiko Nunotani, Kiyoshi Uzawa : DEVELOPMENT AND RESERCH OF END FIXING STRUCTURE FOR EXPANDING THE USE OF CFRP STRANDS, AIJ Journal of Technology and Design 28(68), pp.36-41, 2022.2

[3] Yuya Takaiwa, Katsuhiko Nunotani, Kiyoshi Uzawa : Development of tough CFRP strand end fixation, AIJ Journal of Technology and Design 27(65), pp.108-113, 2021.2

[4] Yuya Takaiwa, Katsuhiko Nunotani, Atsushi Hokura, Shiro Noguchi, Nobuaki Inui, Tadashi Sakuma, Kiyoshi Uzawa : INFLUENCE OF WELDING TEMPERATURE ON ADHESION PERFORMANCE OF CFRTP STRAND ROD-SOCKET, 16th Japan International SAMPE Symposium & Exhibition 3A-06 2019.9

[5] Hina Takizawa, Hiroki Matsumoto, Nobuji Sakurai, Kiyoshi Uzawa, Yuya Takaiwa: Structural Performance Evaluation of Timber Frame with CFRTP Reinforcement, 17th Japan International SAMPE Symposium & Exhibition S01 2021.12

https://doi.org/10.52202/069179-0316

World Conference on Timber Engineering Oslo 2023

SHEAR FAILURE MECHANISM III IN CROSS LAMINATED TIMBER – NUMERICAL INVESTIGATIONS OF FRACTURE BEHAVIOUR

Henrik Danielsson[1], Erik Serrano[2]

ABSTRACT: The paper deals with numerical investigations of load-bearing capacity and fracture behaviour of Cross Laminated Timber at in-plane shear loading. Focus is on shear failure mechanism III, *i.e.* failure in the crossing areas between flatwise bonded laminations, and on evaluating test methods for that failure mode. In current design provisions, this failure mode is characterised by the rolling shear strength, $f_{v,R}$, and the torsional shear strength, $f_{v,tor}$, and therefore testing including both transverse (rolling) shear and torsional shear is needed. Two such test set-ups are investigated, one aiming at evaluating torsional shear strength and one aiming at evaluating rolling shear strength. Full 3D finite element analyses applying a cohesive zone model approach were used to study the strength and fracture behaviour. Failure criteria for structural design, material strength parameters, and the suitability of the two test configurations to determine strength parameters are discussed in relation to findings from the numerical investigations. One main conclusion from the investigation is that expected test results using the torsional test set-up are less size dependent as compared to test results using the transverse set-up. The numerical analyses suggest a very small influence from tensile loading perpendicular to the crossing area, for both test set-ups.

KEYWORDS: CLT, in-plane shear, failure mechanism III, fracture mechanics, finite element modelling

1 INTRODUCTION

Prediction of load-bearing capacity of Cross Laminated Timber (CLT) at in-plane shear loading (see Figure 1) is relatively complex and involves three potential shear failure mechanisms (FM): Gross shear failure (I), net shear failure and (II) and shear failure at the crossing areas between bonded laminations of adjacent layers (III).

This paper deals with investigations regarding load-bearing capacity and fracture behaviour for shear FM III, based on 3D finite element (FE) models including a cohesive zone modelling approach to describe the fracture behaviour at the crossing area between flatwise bonded laminations. The numerical studies include test configurations for determination of strength parameters to be used for structural design: one test set-up for torsional shear loading and one for uniaxial shear force loading.

The influence of test specimen geometry, test specimen size and lamination growth ring pattern on the fracture over the crossing area and on the load-bearing capacity is studied.

The purpose of the work presented is to gain knowledge of the fracture behaviour of CLT at in-plane shear loading, specifically for combined rolling and longitudinal shear over the crossing areas.

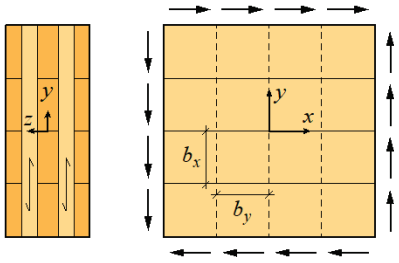

Figure 1: *CLT at in-plane shear loading*

For the applied cohesive zone modelling approach, the behaviour is governed by the material strength, the stiffness, the fracture energy, and the shape of the curve

[1] Henrik Danielsson, Division of Structural Mechanics, Lund University, P.O. Box 118, SE-221 00 Lund, Sweden. Email: henrik.danielsson@construction.lth.se
[2] Erik Serrano, Division of Structural Mechanics, Lund University, P.O. Box 118, SE-221 00 Lund, Sweden.

https://doi.org/10.52202/069179-0317

describing the stress versus deformation relationship within the fracture process region. For rolling shear, very little information is found in the research literature regarding fracture properties at the local scale. For the present application, with combined longitudinal and rolling shear loading, the lack of available information is even further emphasized.

2 FAILURE CRITERIA FOR DESIGN

FM III is in general relevant for CLT elements without edge-bonding, involving shear stresses acting in the *xy*-plane (see Figure 1) and over the crossing areas between adjacent laminations of different layers. These shear stresses represent both longitudinal shear and rolling shear in the two bonded laminations.

For structural design of CLT, both *pure in-plane shear* loading and in-plane shear loading at *beam loading conditions* is relevant. The following failure criteria have been proposed in [1, 2] to be used for structural design:

$$\frac{\tau_{tor}}{f_{v,tor}}+\frac{\tau_{zx}}{f_{v,R}} \le 1.0 \quad \text{and} \quad \frac{\tau_{tor}}{f_{v,tor}}+\frac{\tau_{zy}}{f_{v,R}} \le 1.0 \qquad (1a, 1b)$$

Here τ_{tor} is a shear stress due to torsion by relative rotation between the laminations and τ_{zx} and τ_{zy} are the shear stresses due to relative translation between the laminations (see Figure 2). The corresponding strength parameters are the rolling shear strength, $f_{v,R}$, and a torsional shear strength parameter, $f_{v,tor}$.

In structural design, the two shear stress components τ_{zx} and τ_{zy} are commonly assumed to have uniform distributions over the crossing areas. The torsional stress τ_{tor} is calculated from the polar moment of inertia, $I_{P,CA}$, of the bonded area according to

$$\tau_{tor}=\frac{M_{tor}}{I_{P,CA}}\frac{b_{max}}{2} \qquad \text{with} \qquad I_{P,CA}=\frac{b_x b_y}{12}\left(b_x^2+b_y^2\right) \qquad (2)$$

where M_{tor} is the torsional moment, b_x and b_y are the widths of the laminations, and where $b_{max} = \max\{b_x, b_y\}$. The stress τ_{tor} according to Equation (2) refers to the maximum value at the four mid-points of the sides of the crossing area, see Figure 2, and can also be expressed as

$$\tau_{tor}=\frac{M_{tor}}{W_{P,CA}} \qquad \text{with} \qquad W_{P,CA}=\frac{b_x b_y}{6 b_{max}}\left(b_x^2+b_y^2\right) \qquad (3)$$

where $W_{P,CA}$ represents a corresponding torsional section modulus.

As pointed out in [3], it is from the view of continuum mechanics confusing that the shear stress components in Equations (1a) and (1b) are evaluated against two different strength values: $f_{v,R}$ for stress components τ_{zx} and τ_{zy}, and $f_{v,tor}$ for the torsional shear stress τ_{tor}. The torsional shear strength should in this this sense be seen as representing a structural property, rather than a material property.

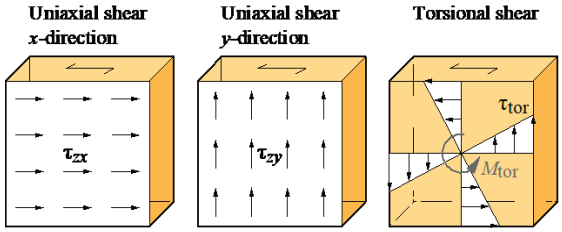

Figure 2: *Illustrations of assumed shear stress distributions*

Alternative approaches for verification of the load-bearing capacity for shear FM III are outlined in [3] and further discussed in [4]. This approach is based on consideration of only the rolling shear strength of the laminations, which would make it possible to abandon the torsional shear strength parameter, $f_{v,tor}$. This is motivated by the relatively large difference in material strength between rolling shear and longitudinal shear. For orthogonally bonded laminations, a material point on one side of the bonding area loaded in longitudinal shear will have a neighbouring material point on the other side of the bonding area which is loaded in rolling shear. By this reasoning, a *maximum stress* criterion based on the rolling shear strength of the lamination was suggested in [3], according to the illustration in Figure 3 (which is based on an assumed strength ratio as $f_v/f_{v,R} = 2.0$).

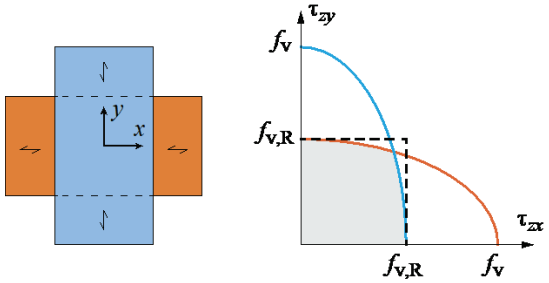

Figure 3: *Suggested maximum stress criterion from [3], based on only rolling shear strength $f_{v,R}$ (dashed lines)*

3 ANALYTICAL MODELS

Simple analytical models can be formulated for approximate estimation of the load-bearing capacity of a crossing area loaded in either pure uniaxial shear or in torsion. A system of two rigid surfaces, connected by a shear-flexible medium, is considered. Two different failure/yield surfaces are considered here. These are denoted A and B and are based on a quadratic stress interaction and on a maximum stress criterion, according to Equations (4) and (5), respectively. The yield surfaces are illustrated in Figure 4, with f_s representing the shear strength.

Surface A: $$\sqrt{\tau_{zx}^2+\tau_{zy}^2} \le f_s \qquad (4)$$

Surface B: $$\max\left\{\tau_{zx}, \tau_{zy}\right\} \le f_s \qquad (5)$$

https://doi.org/10.52202/069179-0317

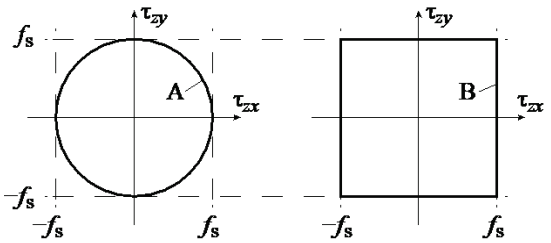

Figure 4: *Failure/yield surfaces A and B*

Expressions for the elastic and ideally plastic load-bearing capacities for a square area loaded in uniaxial shear or in torsion are given in [4] for the respective failure/yield surfaces. These elastic/plastic limits are used below, for comparison to results obtained by numerical analyses.

4 NUMERICAL MODELLING

Test configurations for determination of the rolling shear strength, $f_{v,R}$, and the torsional shear strength parameter, $f_{v,tor}$, were studied by numerical methods. The numerical models are based on non-linear FE-modelling and a cohesive zone approach, including strain softening after reaching the local material strength, for modelling of the fracture initiation and propagation over the crossing area.

The studied test configurations include situations of torsional loading and uniaxial shear force loading. For these test configurations, numerical parameter studies were carried out in order to investigate the influence of specimen geometry (lamination sizes) and the influence of the growth ring pattern of the laminations on the load-bearing capacity and fracture behaviour.

The software Abaqus [5, 6] was used for the numerical analyses. The timber laminations were modelled as linear elastic parts with orthotropic stiffness properties according to Table 1 and considering a cylindrical coordinate system, LRT. Linear 3D brick elements (C3D8 in Abaqus) were used for the timber laminations. The bonding between the laminations was modelled as a surface-to-surface contact. The contact formulation was assigned as hard contact in compression normal to the contact surface. For the two in-plane shear directions and for the normal direction in tension, a cohesive behaviour was implemented. This behaviour is defined by local material strengths for the two in-plane shear directions (f_{s1} and f_{s2}), the tensile strength for loading perpendicular to the contact surface (f_n), the fracture energy (G_f) and a softening law defining the descending part of the local stress versus deformation response. The initial stiffness for the contact formulation in the two shear directions and in the normal direction is further defined by the stiffness values k_{s1}, k_{s2} and k_n, respectively.

For the parameters defining the contact formulation and the softening behaviour, reference values were chosen in accordance with the reference values used in [4]: $f_{s,1} = f_{s,2} = 3.0$ MPa, $f_n = 5.0$ MPa, $G_f = 1.2$ Nmm/mm^2 and $k_{s1} = k_{s2} = k_n = 100$ N/mm^3. For the softening, a linear relation between deformation and decreasing stress was assumed.

Table 1: *Material stiffness parameters used for the timber laminations*

Modulus of Elasticity	E_L	12 000	MPa
	E_T	400	MPa
	E_R	600	MPa
Shear modulus	G_{LT}	750	MPa
	G_{LR}	600	MPa
	G_{TR}	75	MPa
Poisson's ratio	ν_{LT}	0.50	-
	ν_{LR}	0.50	-
	ν_{TR}	0.33	-

In order to study the influence of the choice of damage initiation criterion, two different criteria were used. A maximum stress criterion according to

$$\max\left\{\frac{\langle\sigma_n\rangle}{f_n}, \frac{\tau_{s1}}{f_{s1}}, \frac{\tau_{s2}}{f_{s2}}\right\} = 1.0 \tag{6}$$

and a criterion considering quadratic stress interaction according to

$$\left(\frac{\langle\sigma_n\rangle}{f_n}\right)^2 + \left(\frac{\tau_{s1}}{f_{s1}}\right)^2 + \left(\frac{\tau_{s2}}{f_{s2}}\right)^2 = 1.0 \tag{7}$$

were considered. For these criteria, σ_n represents the normal (tensile) stress over the crossing area while τ_{s1} and τ_{s2} represent the two in-plane shear stresses. For all analyses presented below, equal values for the two in-plane shear strengths are assumed and a notation as $f_{s1} = f_{s2} = f_s$ is hence used below.

For comparison of results, a non-dimensional brittleness ratio is defined according to b/l_{ch}, where b is a characteristic length of the considered body and where the material characteristic length is defined according to

$$l_{ch} = \frac{G_{TR} G_f}{f_s^2} \tag{8}$$

where G_{TR} is the rolling shear stiffness, G_f the fracture energy and f_s the local material shear strength. With reference values for these parameters as given above, the characteristic material length is $l_{ch} = 10$ mm.

4.1 TORSIONAL SHEAR LOADING

For pure torsional loading, the test set-up suggested in EN 16351:2021 [7] (as an alternative method) for determination of the torsional shear strength parameter $f_{v,tor}$ is considered.

The specimen geometry is shown in Figure 5, while the applied boundary conditions and considered lamination growth ring patterns are illustrated in Figures 6 and 7, respectively. For the back surface of the lamination with grain direction parallel to the x-direction, displacements were prescribed as $u_x = u_y = u_z = 0$. The front surface of the lamination with grain direction parallel to the y-direction, was constrained by a kinematic coupling to the surface midpoint which was used as a reference point. For this reference point, boundary conditions were implemented such that the displacements $u_x = u_y = u_z = 0$ and the loading was applied by a prescribed rotation θ_z.

https://doi.org/10.52202/069179-0317

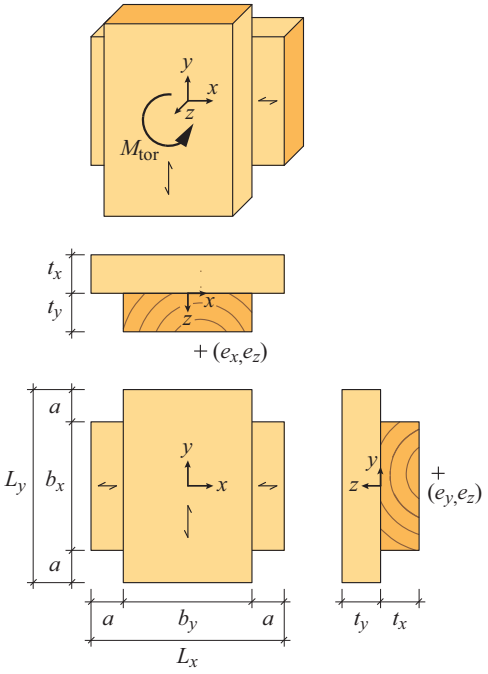

Figure 5: *Definition of geometry for pure torsional loading*

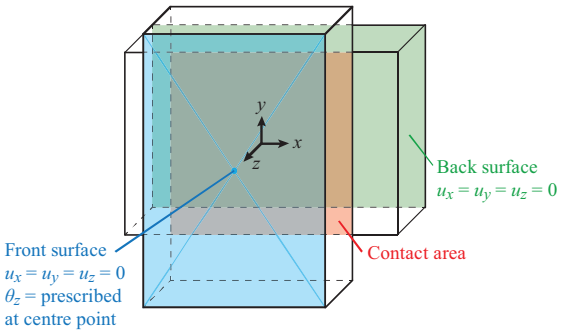

Figure 6: *Boundary conditions for pure torsional loading*

According to EN 16351:2021, no restraints from compression or tension in the direction of the rotation axis should be introduced. The influence of boundary conditions was studied by releasing the constraint of the displacement in the *z*-direction for the front surface, *cf.* Figure 6.

The lamination lengths (here denoted L_x and L_y) should according to EN 16351:2021 furthermore be such that the laminations extend a minimum of 30 mm on each side of the tested crossing area. No further instructions are given regarding the absolute or relative size of the laminations.

Torsional tests of single crossing areas are reported in [8, 9], for six test series with different lamination growth ring patterns and crossing area sizes: 145×100 mm², 145×150 mm² and 145×200 mm². Those tests gave an overall mean torsional strength of 3.46 MPa, with test series mean values varying between 3.00 MPa and 4.13 MPa, without a clear trend regarding the size influence on the load-bearing capacity.

Numerical results for models loaded in pure torsional shear are expressed by the *apparent* torsional shear stress as defined according to Equations (2) and (3), using the resulting torsional moment over the crossing area M_{tor} as found from the FE-analyses.

An initial parameter study was carried out, aimed at investigating the influence of model parameters on the numerical results. Based on the reference values of material strengths, fracture energy and lamination stiffness properties as defined above, a parameter study on the influence of the initial stiffness of the contact area was performed. Stiffness values $k_{s1} = k_{s2} = k_n$ in the range from 10 N/mm³ to 4 000 N/mm³ were used. The lamination geometry was defined by setting $b = b_x = b_y = 120$ mm, $t_x = t_y = 30$ mm and $a = 30$ mm, and the growth ring pattern RB was considered. The element mesh was chosen to obtain roughly cubically shaped elements with a side length of approximately $t_x/6 = 5$ mm.

The calculated maximum load increases slightly with increased crossing area stiffness. The reference stiffness (100 N/mm³) gives however only a 0.7% difference in maximum value compared to a stiffness of 4 000 N/mm³. Since the numerical stability is enhanced using moderate crossing area stiffness values, the reference stiffness of 100 N/mm³ was considered as a reasonable trade-off between numerical stability and accuracy.

The influence of the element size on the results was also studied. Decreasing the element side length by a factor 2.0 (from 5 mm to 2.5 mm) gave only a 0.2% difference in maximum load. The difference in overall torsional stiffness of the specimen was influenced to a greater extent by that element refinement: a reduction of the stiffness by 1.5% was found. An approximate element side length of 1/6 of the lamination width was used for results presented below and relating to torsional loading, since it was considered as a reasonable trade-off between numerical efficiency and accuracy.

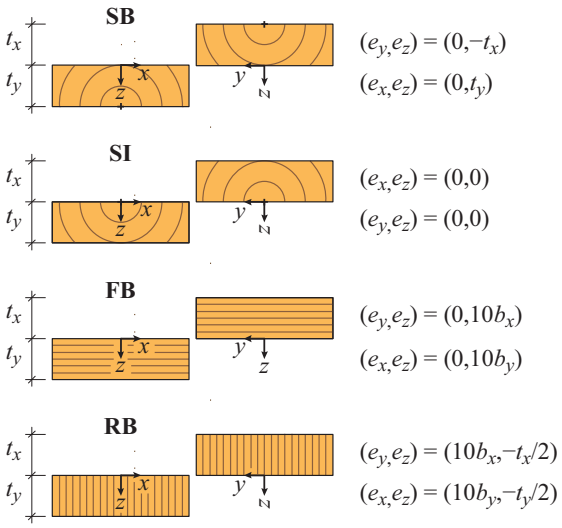

Figure 7: *Considered growth ring patterns for pure torsional loading*

https://doi.org/10.52202/069179-0317

Results for analyses considering the two different criteria for damage initiation according to Equations (6) and (7) are shown in Figure 8. For both criteria, results are presented for assumptions of material tensile strength as either $f_n = 5.0$ MPa (reference value) or $f_n = 2.5$ MPa and for boundary conditions as prescribed by EN 16351:2021, *i.e.* with $u_x = u_y = 0$ but disregarding $u_z = 0$ for the surface with prescribed rotation (denoted EN in Figure 8). The results relate to a specimen with geometry $b_x = b_y = 120$ mm, $t_x = t_y = 30$ mm, $a = 30$ mm and with growth ring pattern RB according to Figure 7.

Using the maximum stress criterion (MS) according to Equation (6) compared to the quadratic interaction criterion (QT) according to Equation (7) gives an increase of the maximum apparent torsional stress of about 6%. Within the two groups of curves (three curves in each group), representing the two criteria, very similar or identical results were found. Identical results for the torsional shear stress were found for material tensile strengths $f_n = 2.5$ MPa, 5.0 MPa and 50 MPa (not shown in Figure 8) for the maximum stress criterion. A very small influence of the material tensile strength was also found for the damage initiation criterion based on quadratic traction (QT), with differences being below 0.2% for load-bearing capacity. The change of boundary conditions regarding free/restricted movement in the z-direction has also a very small influence on the load-bearing capacity, for both damage initiation criteria.

The response in terms of the apparent torsional stress versus prescribed rotation is shown in Figure 9 for $b_x = b_y = 120$ mm, $t_x = t_y = 30$ mm, $a = 30$ mm, growth ring pattern RB, reference values for materials strengths and using the damage initiation criterion based on maximum stress. For these results, a slightly refined mesh was used with approximate elements side lengths as $t_x/8$. In subfigures a), b) and c), the stress distributions over the crossing area are illustrated by the maximum value of the two shear stress components τ_{zx} and τ_{zy} acting in the plane of the crossing area, at three instants during loading: a) at initiation of softening, b) about midway between initiation of softening and maximum load and c) at maximum load.

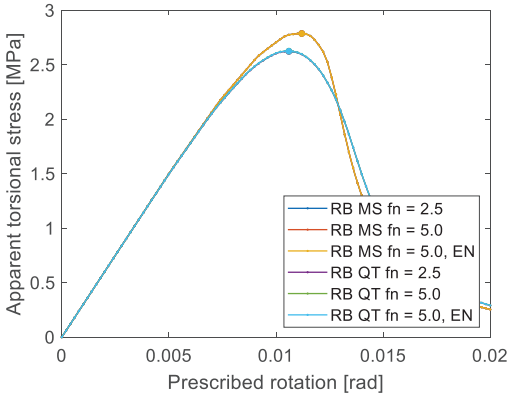

Figure 8: *Apparent torsional stress versus prescribed rotation for different choices of criteria for initiation of softening (MS and QT), for different material tensile strengths f_n, and for different boundary conditions*

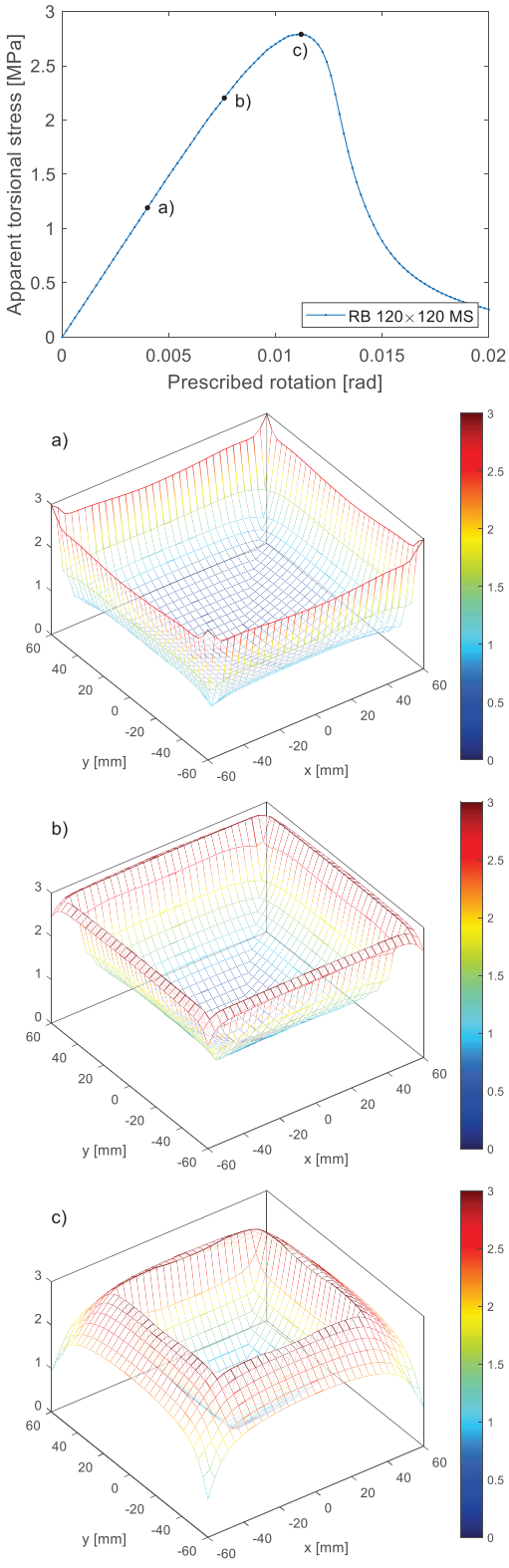

Figure 9: *Apparent torsional stress versus rotation for geometry RB 120×120 with damage initiation criterion from Equation (6) and stress distributions for $\tau = \max(\tau_{zx},\tau_{zy})$ at instants a), b) and c) during loading*

Results in terms of apparent torsional strength are given in Figure 10, based on a specimen geometry with $b = b_x = b_y$, $L_x = L_y = 1.5b_x$, and $t_x = t_y = b_x/4$ and for lamination widths b within the range of 5 mm to 200 mm. Results for all geometries, and all growth ring patterns as illustrated in Figure 7 and considering the damage initiation criteria according to Equation (6) are given. In addition, results for growth ring pattern RB, and initiation criterion according to Equation (7) are also shown. For the specimen geometries considered here, the demand $a \geq 30$ mm given in EN 16351:2021 is not fulfilled for laminations widths $b < 120$ mm.

The same results are shown in Figure 11, but now expressed as the relationship between the brittleness ratio b/l_{ch} and the normalised torsional strength, $\tau_{tor,max}/f_s$. The considered lamination widths b give brittleness ratios b/l_{ch} in the range of 0.5 to 20.

The differences in load-bearing capacity between the different growth ring patterns is fairly small and there is no strong influence of the specimen size for practically relevant dimensions of the laminations.

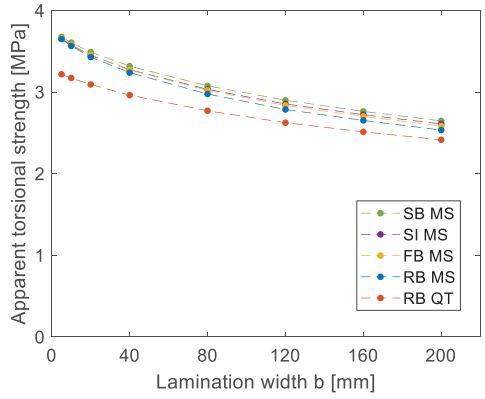

Figure 10: *Apparent torsional shear strength, $M_{tor,max}/W_{P,CA}$ according to Equation (3), for different growth ring patterns and lamination widths $b = b_x = b_y$*

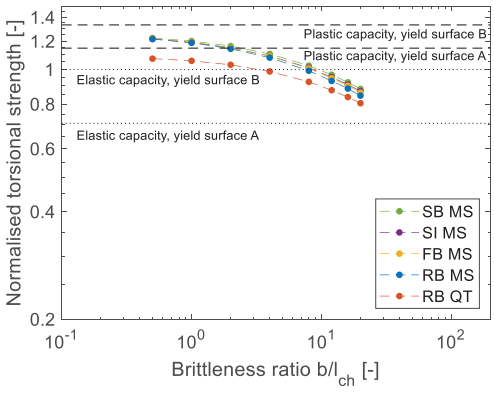

Figure 11: *Normalised torsional strength, $\tau_{tor,max}/f_s$, as influenced by brittleness ratio for different growth ring patterns and considering damage initiation criteria according to Equations (6) and (7)*

The influence of the individual lamination widths, and hence the size and shape of the crossing area, was studied. Results for different widths b_y (20 mm to 220 mm) of the lamination oriented in the y-direction, for a fixed width $b_x = 120$ mm of the lamination oriented in the x-direction, are shown in Figure 12. These results are based on lamination thicknesses $t_x = t_y = 30$ mm, $a = 30$ mm, growth ring pattern RB according to Figure 7 and damage initiation according to Equation (6).

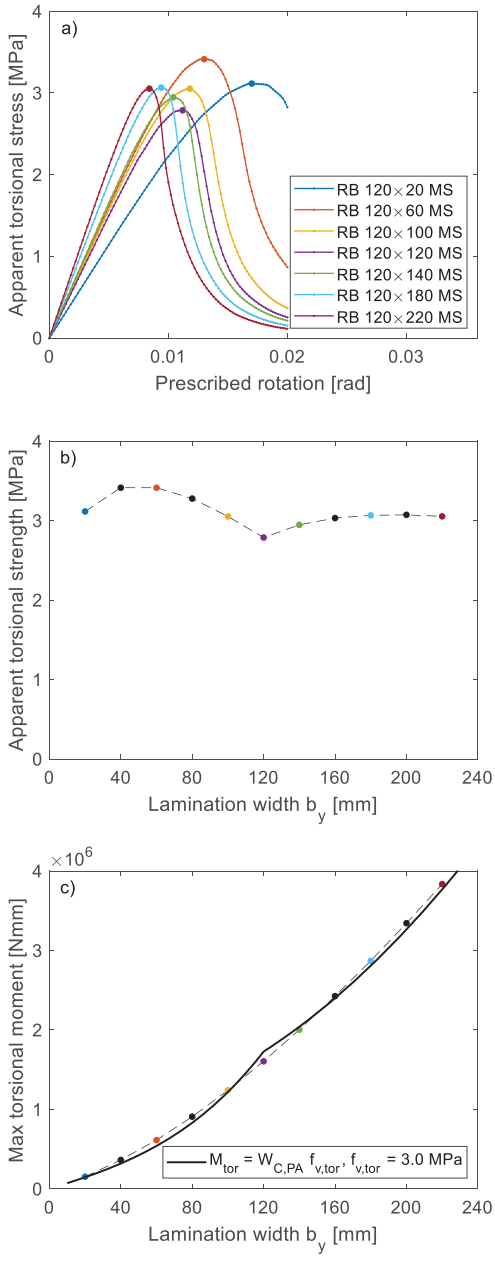

Figure 12: *Results for $b_x = 120$ mm and different lamination widths b_y in terms of a) torsional stress versus rotation, b) apparent torsional strength and c) maximum torsional moment*

https://doi.org/10.52202/069179-0317

Results presented in Figure 12 relate to specimens with 11 different geometries. Results in terms of apparent torsional stress versus rotation are shown in Figure 12a) for seven of these analyses, while results in Figures 12b) and c) are given for all 11 geometries.

The differences in the apparent torsional strength according to Figure 12b) can be explained by essentially two effects; a size effect and an effect of the change of the specimen shape. The two geometries with laminations $b_x \times b_y$ = 120×80 mm^2 and $b_x \times b_y$ = 120×180 mm^2 are equal in shape with a ratio of 1:1.5 between the side lengths of the crossing area. The difference in apparent torsional strength, 3.28 MPa for 120×80 mm^2 and 3.07 MPa for 120×180 mm^2, is hence related to a size effect and, possibly to the effect of changed stiffness ratio between the crossing area torsional stiffness and the rolling shear stiffness of the laminations.

The maximum torsional moments are shown in Figure 12c), where also the torsional moment capacity according to the design criteria from Equations (1) – (3) is given for an assumed torsional strength parameter $f_{v,tor}$ = 3.0 MPa. The ratio between the numerically found values of the maximum torsional moment and the capacity according to the design criteria varies between 0.93 and 1.14 for this assumption.

In order to further study the influence of the shape of the crossing area, a number of analyses were carried out for geometries with a fixed value of the torsional section modulus defined in Equation (3), $W_{P,CA}$ = 576 000 mm^3 (as for b_x = b_y = 120 mm), by varying both lamination widths, b_x and b_y. Also for these analyses, geometries with lamination thicknesses $t_x = t_y = 30$ mm and $a = 30$ mm were considered and results are presented in Figure 13.

Results in terms of stress versus rotation response are given in Figure 13a) for six out of the 11 geometries considered. The apparent torsional strength is shown in Figure 13b) and the maximum torsional moment in Figure 13c).

From the present results, a maximum load-bearing capacity appears to be found for a side length ratio of the crossing area of about 1.8. Equal lamination widths (here $b_x = b_y = 120$ mm) and hence a square shape of the crossing area gives the lowest load-bearing capacity among the geometries considered here. The difference between the highest and lowest capacities (found for geometries 174×90 mm^2 and 120×120 mm^2, respectively) is 15%.

The maximum torsional moments are shown in Figure 13c), where also the torsional moment capacity according to the design criteria from Equation (1) – (3) is given for an assumed value $f_{v,tor}$ = 3.0 MPa. The ratio between the numerically found values of maximum torsional moment and the design criteria varies between 0.93 and 1.07.

The results presented in Figures 12 and 13 concern specimen geometries with a large span of the aspect ratio of the crossing area side lengths: ratios up to 1:6 for results presented in Figure 12 and ratios up to 1:3 for results presented in Figure 13. The numerical results in terms of the maximum torsional moment are yet in fairly good agreement with the load-bearing capacities given by the design criteria from Equations (1) – (3), with the torsional moment capacity being proportional to the value of $W_{P,CA}$, defined in Equation (3).

The shear stress distribution over the crossing area (as found from the FE-analyses) varies during loading, as illustrated in Figure 9, due to initiation of local softening and development of fracture process zones. Although the stress distribution at maximum load does not agree very well with the assumed stress distribution according to the design approach (see Figure 2), similar load-bearing capacities are predicted.

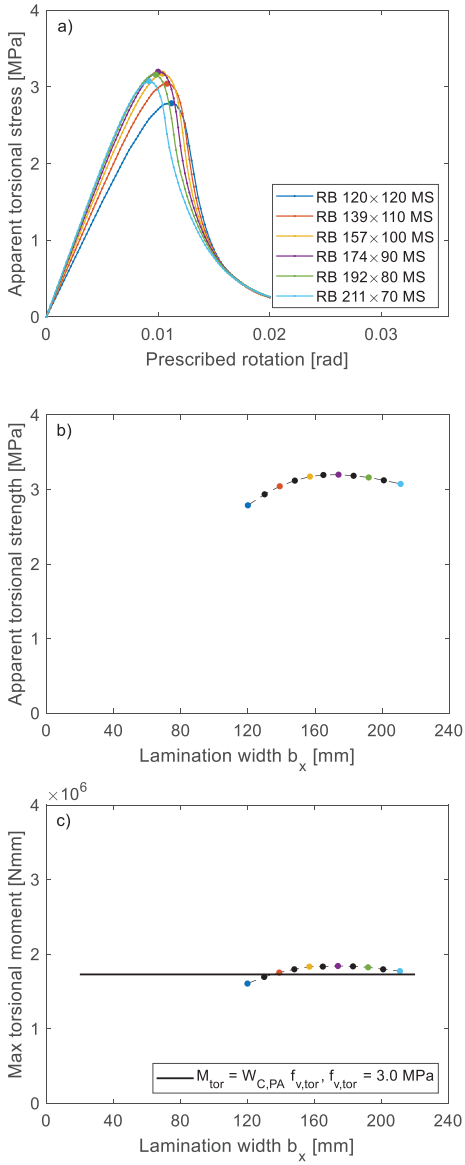

Figure 13: *Results for different laminations widths $b_x \times b_y$ with constant value of $W_{P,CA}$ = 576 000 mm^3 in terms of a) torsional stress versus rotation, b) apparent torsional strength and c) maximum torsional moment*

4.2 UNIAXIAL SHEAR LOADING

For the load case of *pure uniaxial* shear, a test set-up introducing shear over two crossing areas (by compression loading) of a symmetrical test specimen is considered, as illustrated in Figure 14.

Such tests are for example reported in [10], with specimens cut from CLT with lay-up 40-20-40 and testing a crossing area of 150×150 mm^2. Tests of six nominally equal samples gave a mean rolling shear strength $f_{v,R}$ = 1.39 MPa with CoV = 13%.

The numerical results presented here relate to the influence of specimen size and the influence of the growth ring pattern of the laminations, considering material stiffness properties according to Table 1 and boundary conditions according to Figure 15. For the FE-model, the symmetry with respect to the z-direction was considered and only half of the specimen was modelled. The parameters describing the contact formulation and the softening behaviour were according to the reference values stated in Section 4. A study of the influence of the choice for the tensile material strength f_n was carried out and results showed a very small influence on the load bearing capacity for strength values of 2.5 MPa and 50 MPa, compared to the reference value of 5.0 MPa.

For the study of the influence of the specimen size, geometry parameters were chosen according to: $b_x = b_y$, $t_x = t_y = b_x/4$, $L_x = b_x$ and $a = b_x/6$. For this basic geometry, the lamination widths $b = b_x = b_y$ were varied from 5 mm to 200 mm. Three different growth ring orientations were considered for this loading situation, see Figure 16.

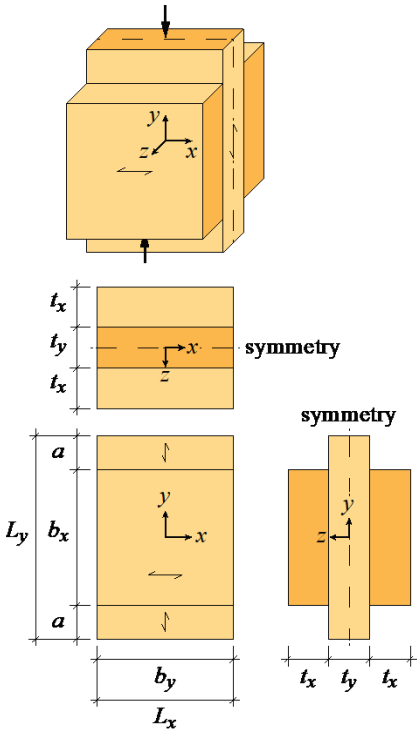

Figure 14: *Definition of geometry for pure shear loading*

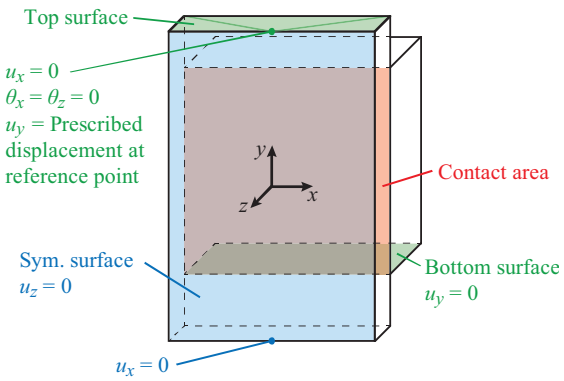

Figure 15: *Boundary conditions for pure shear loading*

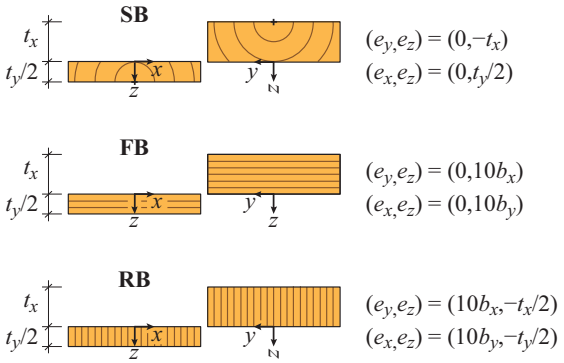

Figure 16: *Considered growth ring patterns for pure shear loading*

Results in terms of *apparent* shear strength, defined as the mean shear stress over the crossing area at maximum loading, are given in Figure 17. The same results are shown in Figure 18, as the relationship between the brittleness ratio b/l_{ch} and the normalised shear strength.

For growth ring pattern RB, results are presented for damage initiation criteria according to Equations (6) and (7). The differences are overall very small, indicating a uniaxial shear stress distribution over the crossing area with little influence from τ_{zx} on the results.

As the specimen size is decreased, the mean shear stress at maximum load approaches the material strength f_s. For a small size of the crossing area, the fracture process zone is relatively large and the behaviour approaches the case of an ideally plastic behaviour over the crossing area. For a uniform stress distribution, the elastic/plastic capacities for yield/failure surfaces A and B are all equal (f_s).

The numerical results show a strong influence of the specimen size for lamination widths $b = b_x = b_y$ above approximately 100 mm. For these specimen sizes, the trend of the numerical results resembles the size influence predicted by LEFM (the dashed line in Figure 18), with load-bearing capacity inversely proportional to the square root of the size. The size influence found from the numerical analyses presented in Figure 18, considering pure uniaxial shear, is stronger than found for the case of torsional loading with results presented in Figure 11.

https://doi.org/10.52202/069179-0317

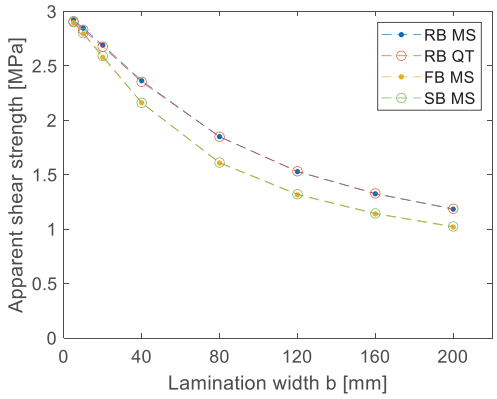

Figure 17: *Apparent shear strengths for different growth ring patterns and lamination widths $b = b_x = b_y$ and considering damage initiation criteria according to Equations (6) and (7)*

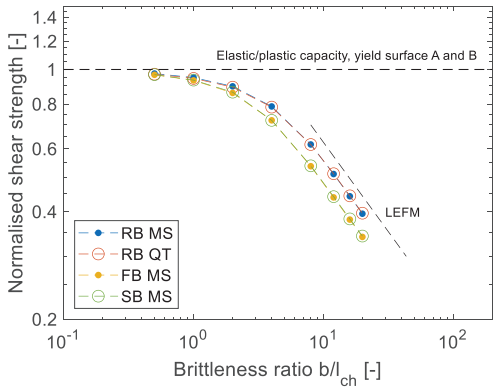

Figure 18: *Normalised shear strength as influenced by brittleness ratio for different growth ring patterns and considering damage initiation criteria according to Equations (6) and (7)*

The response in terms of mean shear stress versus prescribed displacement is shown in Figure 19, for a specimen with geometry according to $b_x = b_y = 120$ mm, $t_x = t_y = 30$ mm, $a = 20$ mm and with growth ring pattern SB according to Figure 16. The stress distribution for the shear stress component τ_{zy} over the crossing area is illustrated for three instants during loading: a) at initiation of softening, b) about midway between initiation of softening and maximum load and c) at maximum load.

The stress distribution before initiation of softening is very uneven, with a high stress concentration along the edge of the crossing area close to the support. At increased loading, a fracture process zone develops and its front moves in the y-direction at increasing load. At maximum load, a small traction-free crack has formed and the stress at the opposite side of the crossing area is approaching the material strength.

During the complete course of loading, the distribution of the shear stress τ_{zy} is very uniform with respect to the x-direction.

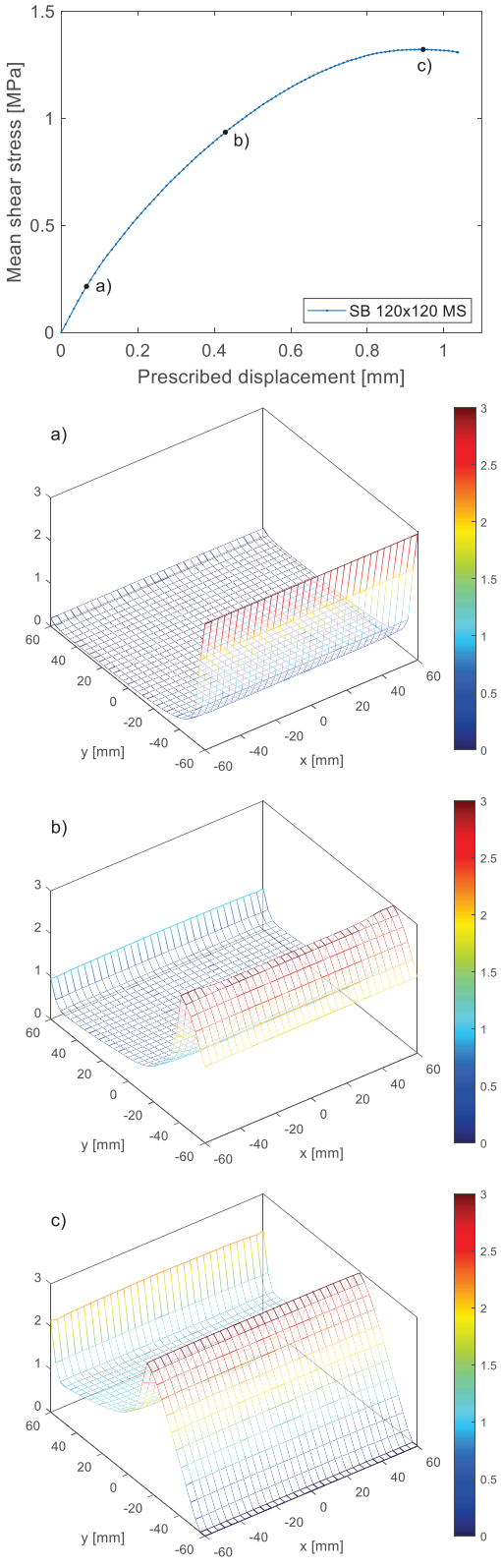

Figure 19: *Load versus displacement for geometry SB 120×120 with damage initiation criterion from Equation (6) and stress distributions for τ_{zy} at instants a), b) and c) during loading*

https://doi.org/10.52202/069179-0317

5 DISCUSSION AND CONCLUSIONS

The general failure criteria for shear failure mechanism III according to Equations (1a) and (1b) are appealing in the sense that they represent criteria which are easy to use for structural engineers. The concept of using two different strength parameters, the rolling shear strength $f_{v,R}$ and the torsional shear strength $f_{v,tor}$, is however somewhat confusing from the view point of continuum mechanics.

Numerical results for pure torsional loading, based on a cohesive zone modelling approach and use of a damage initiation criterion based on maximum stress values and a single shear strength parameter, f_s, are presented in Figures 12 and 13 for different crossing area sizes and shapes. The numerical analyses gave maximum torsional moments which agree reasonably well with predictions of the design approach according to Equations (1) – (3). This agreement regarding load-bearing capacity is not obvious, since the basic concepts of the numerical modelling approach and of the mechanical model underlying the design approach are very different.

Selecting appropriate values for material parameters (especially material strengths and fracture energy) for the present type of numerical analyses is furthermore not obvious, this issue is discussed in *e.g.* [4]. For the reference values of material parameters used in this work, load-bearing capacities as found for the numerical analyses for both torsional and uniaxial shear loading do however roughly agree with test results as presented in *e.g.* [8–10].

The investigations presented here are limited to consideration of one single crossing area which is loaded in *either* pure torsion *or* uniaxial shear. For practical design situations involving in-plane shear of CLT, such as in-plane beam loading, there is typically a large number of crossing areas within the member with combined torsion and uniaxial shear loading. Proposed design approaches for CLT beams, as presented in [1–2, 11], are based on models considering linear elastic behaviour and do not account for gradual damage and strain-softening over the crossing areas during increased loading. To gain better understanding of the mechanical behaviour, further numerical analyses considering full-sized CLT beams modelled with softening contact are suggested.

Considering the specific test set-ups studied here, one important conclusion is that the set-up for uniaxial shear loading according to Figure 14 should be expected to give results for the rolling shear strength which are highly dependent on the specimen size (see Figure 18), especially for practically relevant lamination dimensions with $b > 100$ mm. The numerical results for the test set-up for torsional loading according to Figure 5 do not show the same strong size influence on the load-bearing capacity (see Figure 11). A drawback of torsional testing may however be that the tests are rather complicated to carry out and that torsional testing machines might not be considered as standard test equipment. From the numerical investigation presented, neither of the test set-ups appear to be influenced by tensile loading perpendicular to the crossing area.

ACKNOWLEDGEMENTS

The financial support from FORMAS for the project *Strength and fracture analysis of cross laminated timber* (grant 2019-01354) is gratefully acknowledged.

The financial support for the project *InnoCrossLam* is also gratefully acknowledged. The project *InnoCrossLam* is supported under the umbrella of ERA-NET Cofund ForestValue with Swedish support from Vinnova, FORMAS and the Swedish Energy Agency. ForestValue has received funding from the European Union's Horizon 2020 research and innovation programme under grant agreement N° 773324.

The computations were enabled by resources provided by *Lunarc* – the center for scientific and technical computing at Lund University.

REFERENCES

[1] M. Flaig: Biegeträger aus Brettsperrholz bei Beanspruch in Plattebene. Doctoral thesis. Karlsruhe Institute of Technology, Karlsruhe, Germany, 2013.

[2] M. Flaig, H.J. Blass: Shear strength and shear stiffness of CLT-beams loaded in plane. In: Proc. CIB-W18, CIB-W18/46-12-3, Vancouver, Canada, 2013.

[3] E. Serrano: Test methods for in-plane shear tests of cross laminated timber. In: Properties, testing and design of cross laminated timber: A state-of-the-art report by COST Action FP1402/WG2, Shaker Verlag, Aachen, Germany, 2018.

[4] H. Danielsson, E. Serrano: Cross laminated timber at in-plane shear loading – Strength and fracture analysis of shear mode III. In: Proc. WCTE 2020/21.

[5] Dassault Systemes Simulia Corp. ABAQUS/CAE, Version 2019, 2018.

[6] Dassault Systemes Simulia Corp. ABAQUS/CAE, Version 2021, 2020.

[7] CEN European Committee for Standardization. EN 16351:2021. Timber structures – Cross laminated timber – Requirements.

[8] G. Jeitler: Versuchstechnische Ermittlung der Verdrehungskenngrössen von orthogonal verklebten Brettlamellen. Diploma thesis, TU Graz, 2004.

[9] R. Joebstl, T. Bogensperger et al: Mechanical behaviour of two orthogonally glued boards. In: Proc WCTE, Lahti, Finland, 2004.

[10] M. Jeleč et al: Advancement in prediction of shear strength and stiffness of cross laminated timber beams. *Eng Struct* 238 (2021) 112247.

[11] H. Danielsson, M. Jelec: A unified design proposal for shear stress prediction in crossing areas for cross laminated timber at in-plane shear and beam loading conditions. *Constr Build Mater* 355 (2022) 129167.

https://doi.org/10.52202/069179-0317

World Conference on Timber Engineering Oslo 2023

ANALYTICAL STUDY ON P-Δ EFFECT ON MEDIUM-RISE WOODEN BUILDINGS

Shogo Aoki[1], Naohito Kawai[2], Takafumi Nakagawa[3]

ABSTRACT: In recent years, medium to high rise buildings up to about 10 stories of wooden structure have become a reality in Japan. However, analytical research is still insufficient. In this report, we aim to clarify the influence of the P-Δ effect by pushover analysis, capacity spectrum method, and time history response analysis for wooden buildings of 3 to 5 stories, and to obtain basic data for seismic design method. The result was that the influence of the P-Δ effect on the seismic performance of the medium-rise wooden buildings was small according to the capacity spectrum method, but the increase rate may reach 22 % in time history response analysis, so future examination is required.

KEYWORDS: Wood frame construction, Capacity spectrum method, Time history response analysis

1 INTRODUCTION

1.1 BACKGROUND

In recent years medium to high rise buildings up to about 10 stories of wooden structure have become a reality in Japan. In addition, by using wood as a structural material for sustainable forest management, we can expect to reduce climate change. In other words, wooden structures are good for the environment. Demand for medium to high rise wooden buildings that use a large amount of wood is increasing. However, analytical research is still insufficient.

For conventional low-rise wooden buildings up to about three stories, the safety limit deformation angle against large earthquake motion is considered to be about 1/30. On the other hand, the problem is pointed out whether large deformation is allowed even in medium to high rise wooden buildings such as 5-10 stories.

Among the discussion on whether or not the safety limit deformation angle should be reduced for medium to high rise wooden buildings, there is an opinion that the influence of the P-Δ effect cannot be ignored in medium to high rise wooden buildings because the vertical load is large. However, in theory, there should be no big difference between low-rise wooden buildings and high-rise wooden buildings as far as the ratio to the seismic force is concerned.

1.2 PURPOSE

In this study, we examine the P-Δ effect of medium-rise wooden buildings, for which analytical research is insufficient. The P-Δ effect is the effect of additional bending moment due to the axial force of vertical members and horizontal displacement of the story. In this report, we aim to clarify the influence of the P-Δ effect for wooden buildings, and to obtain basic data for seismic design method. Specifically, 3- to 5-story building models by wood frame construction are created and are analysed using an analysis software, wallstat [1]. And the influence of the P-Δ effect is discussed from the difference of earthquake response between the models with and without P-Δ effect.

2 ANALYSIS MODEL

The analysis models are 3- to 5-story building models by wood frame construction. The floor plan is shown in Fig. 1, and the appearance of 3- to 5- story models are shown in Figs. 2 to 4.

Any construction method can be used for the purpose of this study as the P-Δ effect only depends on the vertical load and the deformation angle. The reason for using wood frame construction method is to make the models simple as the main structural elements against seismic force is shear walls in wood frame construction, and deformation state of one floor does not affect the performance of other floors. The height of each floor was set to 3 maters. We prepared two types of analysis models, the standard model and the soft first story model. For the standard models, the sufficiency rate, the ratio of the allowable strength of a story to the requirement by allowable stress design, is 2 for all the story. For the soft first story models, the sufficiency rate of 1st story is 3, and that of 2nd story or higher is 6.

[1] Shogo Aoki, Graduate Student, Grad. School of Arch. Kogakuin University, Japan, dm22001@ns.kogakuin.ac.jp
[2] Naohito Kawai, Professor, Kogakuin University, Japan, kawai-nk@cc.kogakuin.ac.jp
[3] Takafumi Nakagawa, Associate Professor, Kyoto University, Japan, tkfm0820@gmail.com

https://doi.org/10.52202/069179-0318

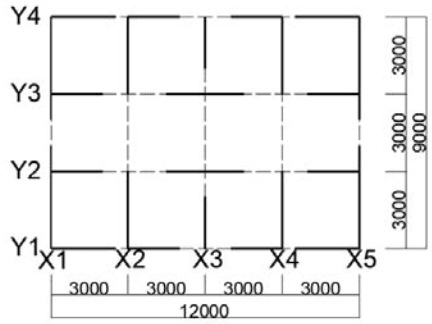

Figure 1: *Floor plan of the model*

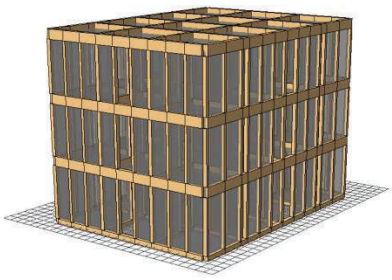

Figure 2: *3 story model*

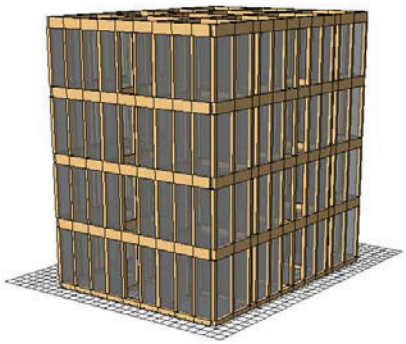

Figure 3: *4 story model*

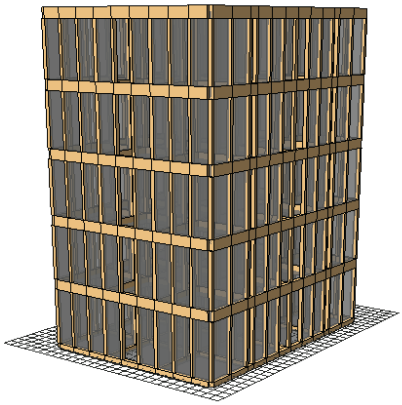

Figure 4: *5 story model*

3 ANALYSIS METHOD

3.1 ANALYSIS SOFTWARE

The analysis model is created using wallstat ver.4.3.13. Originally, it was an analysis software for the conventional wooden framework construction method, but we created a model by replacing it with the wood frame construction. At that time, not all studs and joists were modelled. The studs were modelled at the position of columns of the conventional wooden framework construction method. We use the presence or absence of gravity to determine whether the P-Δ effect should be considered in the design.

3.2 INPUT EXTERNAL FORCE

There are three types of external forces to be input. The first is a pushover analysis so that the deformation angles between the layers are equal in each layer. This is done to confirm the validity of the analysis using wallstat by comparing with the load-displacement relationships of input shear wall data. The second is a pushover analysis using distribution coefficient Ai which is provided in the Building Standard Law (BSL) of Japan as seismic shear force distribution. Using the result of second push over, the maximum response displacement against strong ground motion is calculated using equivalent linearization method or the method known as capacity spectrum method [2, 3] and the response spectrum of type 2 ground stipulated in the BSL. The third is time history response analysis. Five artificial seismic waves conforming to the response spectrum of type 2 ground stipulated in the BSL are input, and the response displacement is calculated.

4 DATA OF ANALYSIS MODEL

4.1 BUILDING MATERIALS

The Young's modulus and flexural strength of wood were set to 1.24×10^4 N/mm^2 and 40.0 N/mm^2, respectively, referring to the material for design [4].

Table 1: *Young's modulus and flexural strength of wood*

Young's modulus	1.24×10^4 [N/mm^2]
Flexural strength	40.0 [N/mm^2]

4.2 BUILDING WEIGHT

Weights were set as shown below with reference to the material of trial design [5].

Table 2: *Weight of 3story model*

	weight[kN]
W_R	275
W_3	481
W_2	481
W_1	240

Table 3: *Weight of 4 story model*

	weight[kN]
W_R	275
W_4	481
W_3	481
W_2	481
W_1	273

https://doi.org/10.52202/069179-0318

Table 4: *Weight of 5 story model*

	weight[kN]
W_R	275
W_5	481
W_4	481
W_3	481
W_2	546
W_1	306

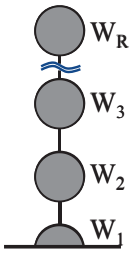

4.3 JOINTS OF BUILDING MATERIALS

Tension & compression springs and rotational springs are set between stud and beam and between beams. The load-displacement relationships of these joints are set as shown in Tables 5 and 6. The tension spring is assumed to be a joint with an allowable strength of 100 kN. The joint at the top or the bottom of each stud is assumed to have no moment resistance, so the stiffness of the rotational spring is close to 0 Nmm.

Table 5: *Tension & compression springs*

	K_{s1}[kN/mm]	K_{s2}[kN/mm]	K_{s3}[kN/mm]	D_1[mm]	D_2[mm]
Tension springs	50.0	13.6	-10.0	4.00	15.0

Table 6: *Rotational springs*

	K_{s1}[kNm/rad]	K_{s2}[kNm/rad]	K_{s3}[kNm/rad]	D_1[rad]	D_2[rad]
Rotaional splings	61.5	30.0	-0.100	8.30×10^{-3}	1.67×10^{-2}
Rotaional splings of all studs	6.15×10^{-2}	3.00×10^{-2}	-1.00×10^{-4}	8.30×10^{-3}	1.67×10^{-2}

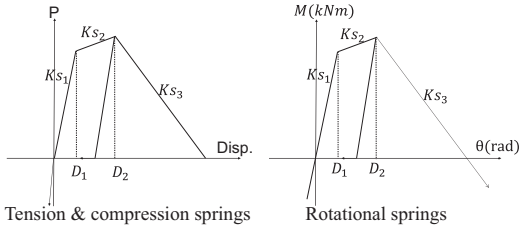

Tension & compression springs Rotational springs

K_{s1}: Primary stiffness of slip spring
K_{s2}: Secondary stiffness of slip spring
K_{s3}: Tertiary stiffness of slip spring
D_1, D_2: Inflection point of curve of slip spring

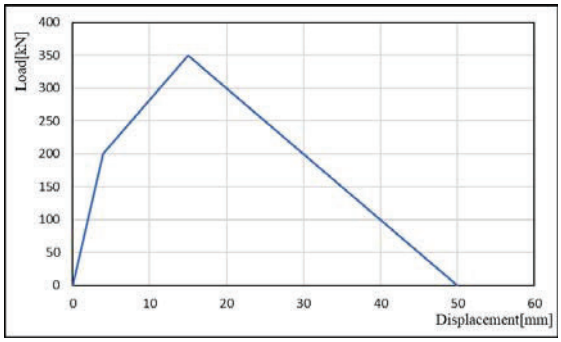

Figure 5: *Restoring force characteristics of tension springs*

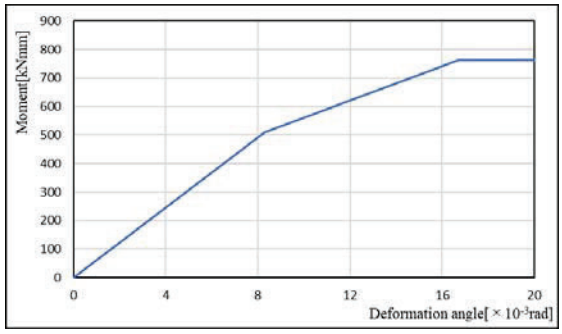

Figure 6: *Restoring force characteristics of rotational springs*

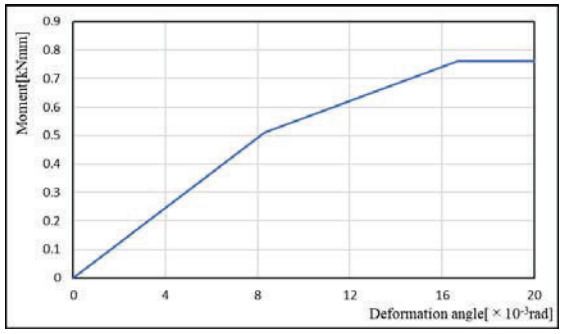

Figure 7: *Restoring force characteristics of stud's rotational springs*

4.4 SHEAR WALLS AND FLOOR STRUCTURES

The structure was set to be shown in Table 7 and 8 based on References [6] and [7]. The values of viscous dumping ratio of all the shear walls and floor structures are set to be 2%. The stiffness values in the table are those for the wall length of 0.91 meters and are converted to the stiffness of the wall length in the model automatically in the software. Floor structures are assumed rigid enough. In the models, the stiffness and the strength are the same as those of the shear walls at the first story. Fig. 8 shows the hysteresis characteristics of the shear wall.

Table 7: *Shear walls and floor structures of standard model settings*

		K_{s1} [N/mm]	K_{s2} [N/mm]	K_{s3} [N/mm]	K_{b1} [N/mm]	K_{b2} [N/mm]	D_1 [mm]	D_2 [mm]	D_3 [mm]	D_4 [mm]
3 stories	3rd story	230	21.9	-32.9	318	11.0	4.00	20.0	70.0	420
	2nd story	484	46.1	-69.2	668	23.1	4.00	20.0	70.0	420
	1st story	660	62.9	-94.3	912	31.4	4.00	20.0	70.0	420
	Floor structure	660	62.9	-94.3	912	31.4	4.00	20.0	70.0	420
4 stories	4th story	266	25.3	-38.0	367	12.7	4.00	20.0	70.0	420
	3rd story	553	52.6	-79.0	763	26.3	4.00	20.0	70.0	420
	2nd story	765	72.9	-109	1057	36.4	4.00	20.0	70.0	420
	1st story	917	87.3	-131	1266	43.7	4.00	20.0	70.0	420
	Floor structure	917	87.3	-131	1266	43.7	4.00	20.0	70.0	420
5 stories	5th story	301	28.7	-43.0	416	14.3	4.00	20.0	70.0	420
	4th story	619	59.0	-88.5	855	29.5	4.00	20.0	70.0	420
	3rd story	864	82.3	-123	1193	41.2	4.00	20.0	70.0	420
	2nd story	1054	100	-151	1455	50.2	4.00	20.0	70.0	420
	1st story	1208	115	-173	1669	57.5	4.00	20.0	70.0	420
	Floor structure	1208	115	-173	1699	57.5	4.00	20.0	70.0	420

https://doi.org/10.52202/069179-0318

Table 8: *Shear walls and floor structures of soft first story model settings*

		K_{s1} [N/mm]	K_{s2} [N/mm]	K_{s3} [N/mm]	K_{b1} [N/mm]	K_{b2} [N/mm]	D_1 [mm]	D_2 [mm]	D_3 [mm]	D_4 [mm]
3 stories	3rd story	690	65.7	-98.6	953	32.9	4.00	20.0	70.0	420
	2nd story	1452	138	-207	2005	69.2	4.00	20.0	70.0	420
	1st story	990	94.3	-141	1368	47.2	4.00	20.0	70.0	420
	Floor structure	990	94.3	-141	1368	47.2	4.00	20.0	70.0	420
4 stories	4th story	797	75.9	-114	1101	38.0	4.00	20.0	70.0	420
	3rd story	1658	158	-237	2290	79.0	4.00	20.0	70.0	420
	2nd story	2295	219	-328	3170	109	4.00	20.0	70.0	420
	1st story	1375	131	-196	1899	65.5	4.00	20.0	70.0	420
	Floor structure	1375	131	-196	1899	65.5	4.00	20.0	70.0	420
5 stories	5th story	904	86.1	-129	1248	43.0	4.00	20.0	70.0	420
	4th story	1858	177	-265	2566	88.5	4.00	20.0	70.0	420
	3rd story	2593	247	-370	3580	123	4.00	20.0	70.0	420
	2nd story	3161	301	-452	4365	151	4.00	20.0	70.0	420
	1st story	1813	173	-259	2503	86.3	4.00	20.0	70.0	420
	Floor structure	1813	173	-259	2503	86.3	4.00	20.0	70.0	420

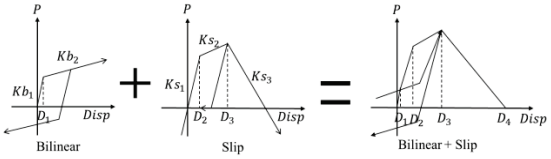

K_{s1}~K_{s3}: Slip stiffness[N/mm]
K_{b1}~K_{b2}: Bilinear stiffness[N/mm]
D_1~D_4: Displacement of break point[mm]

Figure 8: *Hysteresis characteristics of the shear wall*

5 PUSHOVER ANALYSIS RESULTS

5.1 SUMMARY

Pushover analysis is performed so that the story deformation angle is equal in each layer. This is to confirm the validity of the analysis using wallstat.

5.2 STANDARD MODEL ANALYSIS RESULTS

Figs. 9 and 10 shows the result of pushover analysis on 5-story models as the samples. The "assumed wall" with gravity is theoretical solution considering the P-Δ effect. The results of the pushover analysis were generally in agreement with that, and it was confirmed that the P-Δ effect was included in the same degree as the theory.

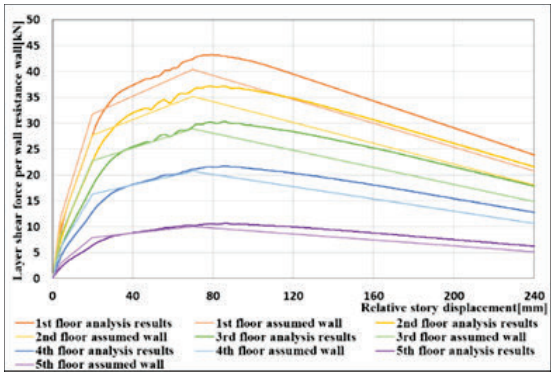

Figure 9: *The results of pushover analysis in case of 5-story without gravity model*

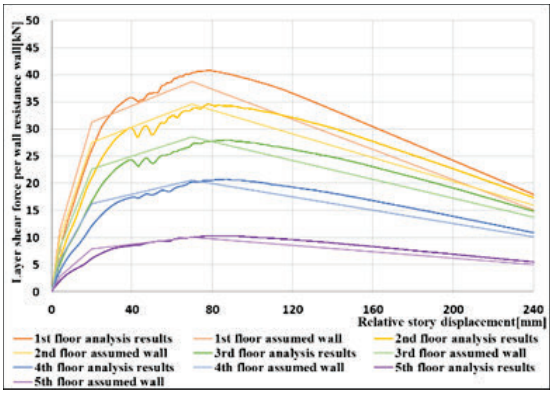

Figure 10: *The results of pushover analysis in case of 5-story with gravity model*

5.3 SOFT FIRST STORY MODEL ANALYSIS RESULTS

Figs. 11 and 12 shows the result of the pushover analysis on 5-story models as the samples.

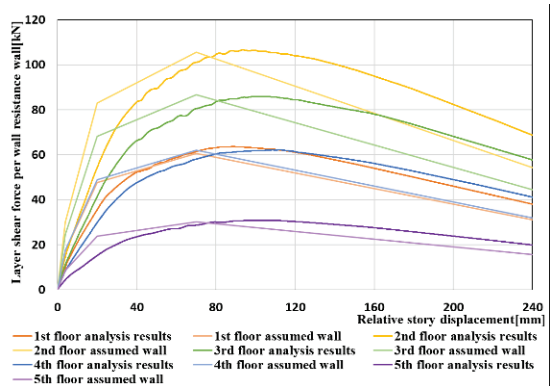

Figure 11: *The results of pushover analysis in case of 5-story without gravity model*

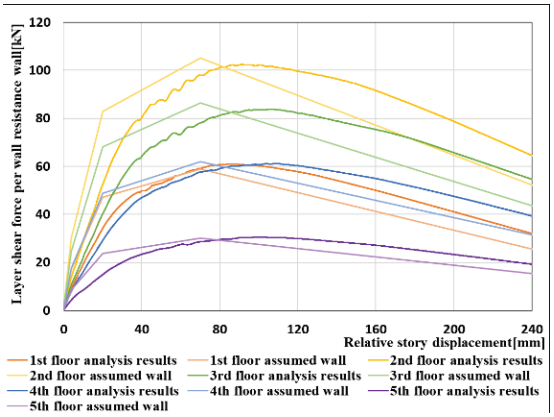

Figure 12: *The results of pushover analysis in case of 5-story with gravity model*

https://doi.org/10.52202/069179-0318

6 RESPONSE PREDICTION BY CAPACITY SPECTRUM METHOD

6.1 OVERVIEW

Capacity spectrum method is a simple prediction method for elasto-plastic response proposed in a 1976 paper by Akenori Sibata et al. The idea of capacity spectrum method is to consider a steady vibration at a certain displacement, replace it with an equivalent linear response, and predict the response using the response spectrum. In the case of a multi-story building, it is necessary to replace it with an equivalent one-degree-of-freedom system. We calculated acceleration response spectrum and displacement response spectrum according to the Building Standard Law of Japan [8]. We used Equations (1) and (2).

$$S_a = \frac{\sum_{i=1}^{N} m_i \cdot {\delta_i}^2}{(\sum_{i=1}^{N} m_i \cdot \delta_i)^2} \cdot Q_B \tag{1}$$

$$S_d = \frac{\sum_{i=1}^{N} m_i \cdot {\delta_i}^2}{\sum_{i=1}^{N} P_i \cdot \delta_i} \cdot S_a \tag{2}$$

m_i: Mass of i-th story (kg)
δ_i: Displacement relative to the ground on i-th story (m)
Q_B: Base shear (N)
P_i: Load on i-th story (N)

6.2 STANDARD MODEL ANALYSIS RESULTS

Table 9 shows the values of maximum relative story displacement and story deformation angle by capacity spectrum method. The rate of increase in interlayer displacement due to the P-Δ effect of the standard model was -4.64 % to 8.68 %. Figs. 21 to 26 show the analysis results of the standard models.

Table 9: *Comparison of response values by capacity spectrum method in a standard model*

		Without Gravity		With Gravity		Increase rate due to P-Δ effect
		Relative story displacement	story deformation angle	Relative story displacement	story deformation angle	Relative story displacement
		$_1\delta$[mm]	θ[$\times10^{-3}$rad]	$_2\delta$[mm]	θ[$\times10^{-3}$rad]	$(_2\delta-{}_1\delta)/{}_1\delta\times100$[%]
3 stories	3rd story	73.6	24.5	72.2	24.1	-1.88
	2nd story	73.5	24.5	78.3	26.1	6.55
	1st story	71.4	23.8	73.5	24.5	2.95
4 stories	4th story	66.8	22.3	63.7	21.2	-4.64
	3rd story	66.4	22.1	70.1	23.4	5.57
	2nd story	65.2	21.7	68.9	23.0	5.73
	1st story	62.9	21.0	61.8	20.6	-1.77
5 stories	5th story	59.2	19.7	56.5	18.8	-4.53
	4th story	62.5	20.8	62.8	20.9	0.493
	3rd story	63.0	21.0	67.1	22.4	6.54
	2nd story	58.9	19.6	64.0	21.3	8.68
	1st story	54.2	18.1	53.5	17.8	-1.26

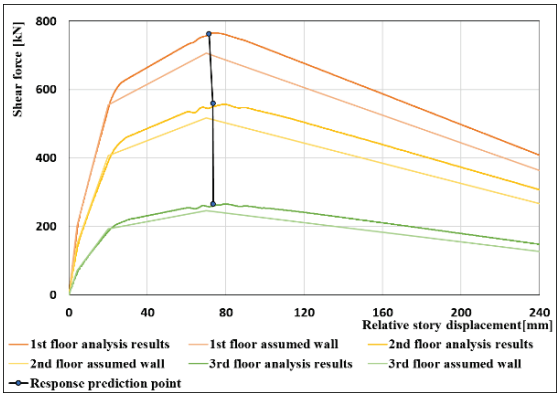

Figure 21: *The results of capacity spectrum method in case of 3-story without gravity model*

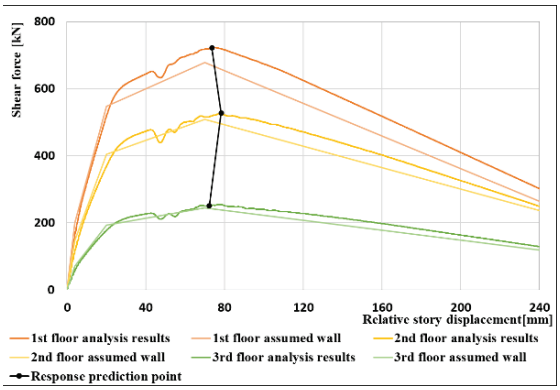

Figure 22: *The results of capacity spectrum method in case of 3-story with gravity model*

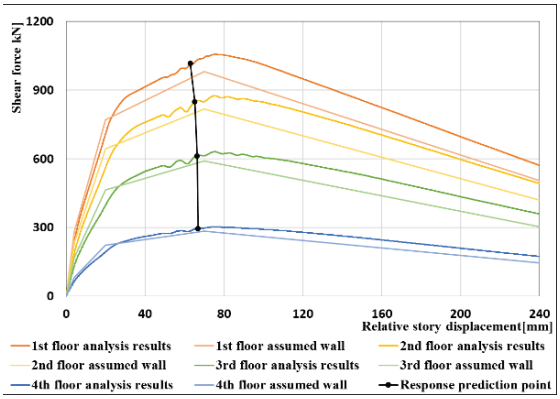

Figure 23: *The results of capacity spectrum method in case of 4-story without gravity model*

https://doi.org/10.52202/069179-0318

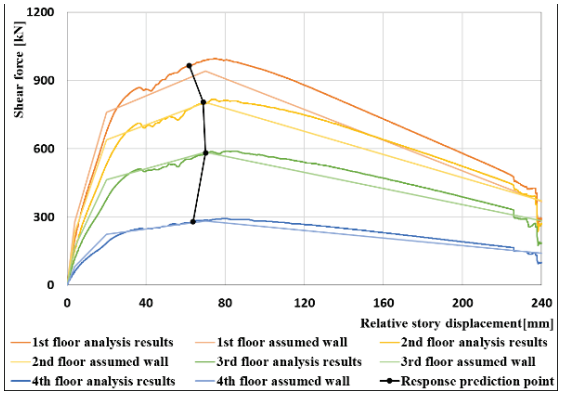

Figure 24: *The results of capacity spectrum method in case of 4-story with gravity model*

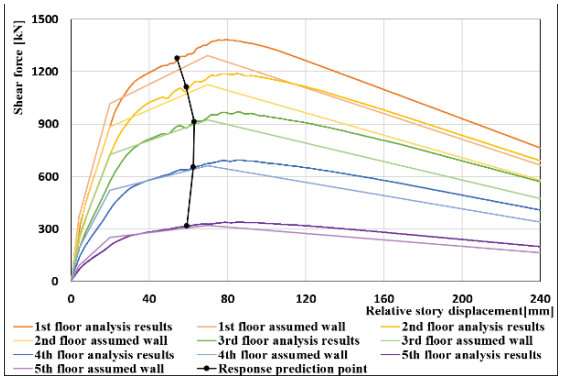

Figure 25: *The results of capacity spectrum method in case of 5-story without gravity model*

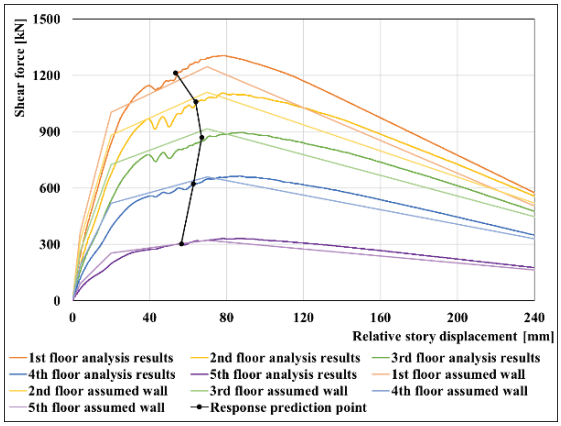

Figure 26: *The results of capacity spectrum method in case of 5-story with gravity model*

6.3 SOFT FIRST STORY MODEL ANALYSIS RESULTS

Table 10 shows the values of maximum relative story displacement and story deformation angle by capacity spectrum method. The rate of increase in interlayer displacement due to the P-Δ effect of the soft first story model was 2.22 % to 8.97 %. Figs. 27 to 32 show the analysis results of the soft first story models.

Table 10: *Comparison of response values by capacity spectrum method in a soft first story model*

		Without Gravity		With Gravity		Increase rate due to P-Δ effect
		Relative story displacement	story deformation angle	Relative story displacement	story deformation angle	Relative story displacement
		$_1\delta$[mm]	θ[$\times10^{-3}$rad]	$_2\delta$[mm]	θ[$\times10^{-3}$rad]	$(_2\delta-{}_1\delta)/{}_1\delta\times100$[%]
3 stories	3rd story	16.2	5.40	16.9	5.63	4.25
	2nd story	15.4	5.13	16.2	5.40	4.75
	1st story	56.7	18.9	61.5	20.5	8.58
4 stories	4th story	19.0	6.33	19.4	6.47	2.31
	3rd story	19.3	6.43	19.9	6.63	3.41
	2nd story	18.4	6.13	19.1	6.37	3.54
	1st story	62.5	20.8	66.7	22.2	6.69
5 stories	5th story	21.6	7.20	22.1	7.37	2.22
	4th story	22.3	7.43	23.0	7.67	3.07
	3rd story	22.5	7.50	23.4	7.80	3.92
	2nd story	21.3	7.10	22.2	7.40	4.27
	1st story	64.9	21.6	70.8	23.6	8.97

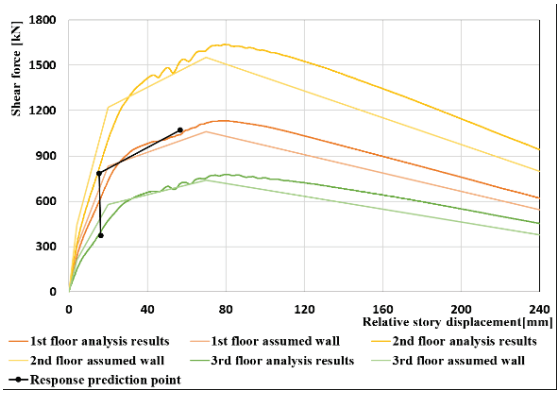

Figure 27: *The results of capacity spectrum method in case of 3-story without gravity model*

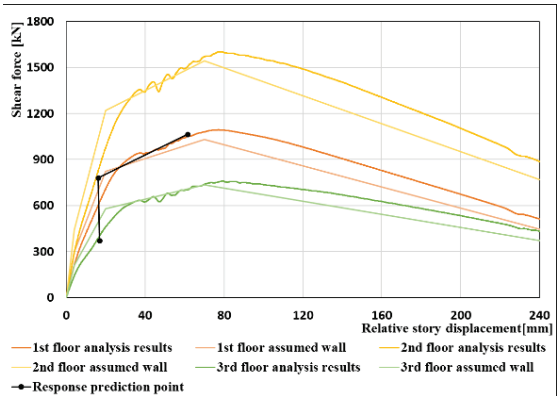

Figure 28: *The results of capacity spectrum method in case of 3-story with gravity model*

https://doi.org/10.52202/069179-0318

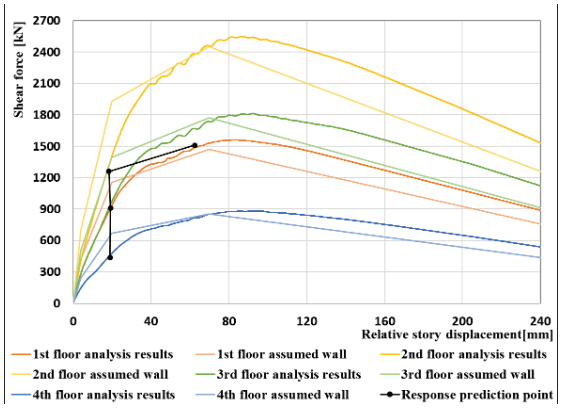

Figure 29: *The results of capacity spectrum method in case of 4-story without gravity model*

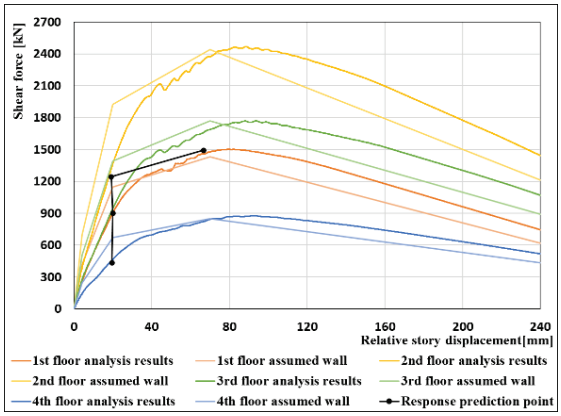

Figure 30: *The results of capacity spectrum method in case of 4-story with gravity model*

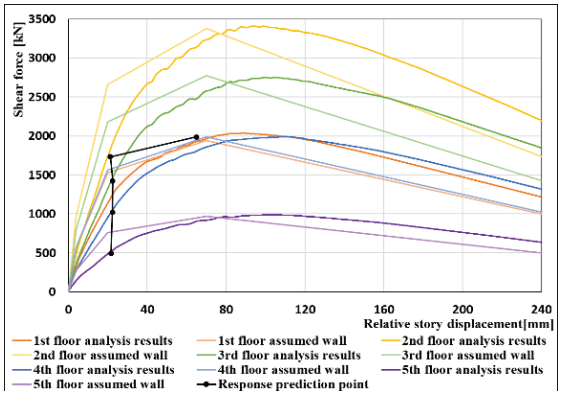

Figure 31: *The results of capacity spectrum method in case of 5-story without gravity model*

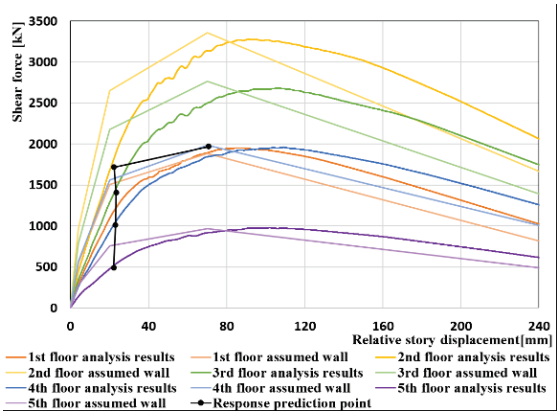

Figure 32: *The results of capacity spectrum method in case of 5-story with gravity model*

7 TIME HISTORY RESPONSE ANALYSIS

7.1 STANDARD MODEL ANALYSIS RESULTS

Table 11 shows the average values of maximum story displacement and story deformation angle by time history analysis using five artificial seismic waves. The rate of increase in interlayer displacement due to the P-Δ effect of the standard model was -34.4 % to 22.2 %. Figs. 33 to 38 show the analysis results of the standard models.

Table 11: *Comparison time history response analysis in standard models*

		Without Gravity		With Gravity		Increase rate due to P-Δ effect
		Relative story displacement	story deformation angle	Relative story displacement	story deformation angle	Relative story displacement
		${}_1\delta$[mm]	$\theta[\times 10^{-3}$rad]	${}_2\delta$[mm]	$\theta[\times 10^{-3}$rad]	$({}_2\delta - {}_1\delta)/{}_1\delta \times 100$[%]
3 stories	3rd story	88.8	29.6	58.2	19.4	-34.4
	2nd story	77.3	25.8	94.1	31.4	21.7
	1st story	41.5	13.8	45.7	15.2	10.0
4 stories	4th story	66.8	22.3	49.4	16.5	-26.1
	3rd story	75.0	25.0	78.9	26.3	5.24
	2nd story	47.3	15.8	52.8	17.6	11.8
	1st story	42.3	14.1	40.7	13.6	-3.66
5 stories	5th story	69.3	23.1	55.9	18.6	-19.4
	4th story	58.1	19.4	66.8	22.3	15.1
	3rd story	41.1	13.7	50.2	16.7	22.2
	2nd story	41.8	13.9	43.5	14.5	4.09
	1st story	39.2	13.1	40.2	13.4	2.64

https://doi.org/10.52202/069179-0318

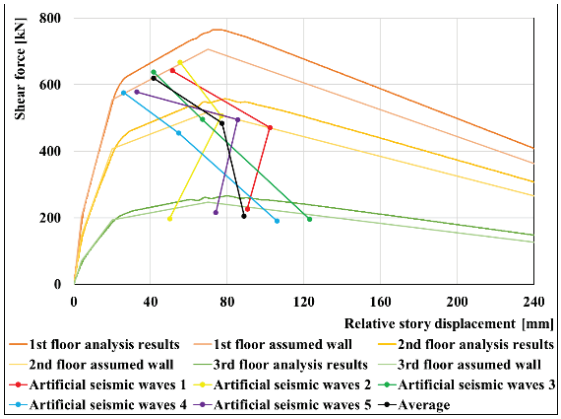

Figure 33: *The results of time history response analysis in case of 3-story without gravity model*

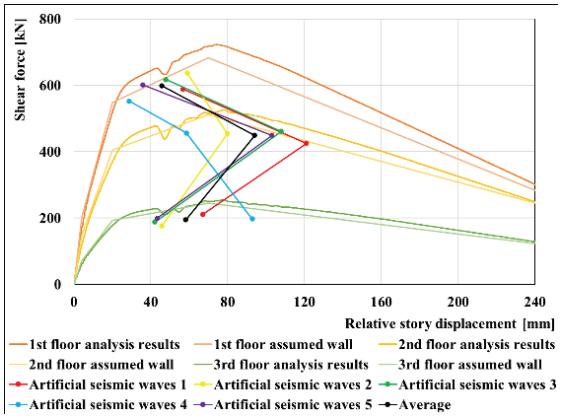

Figure 34: *The results of time history response analysis in case of 3-story with gravity model*

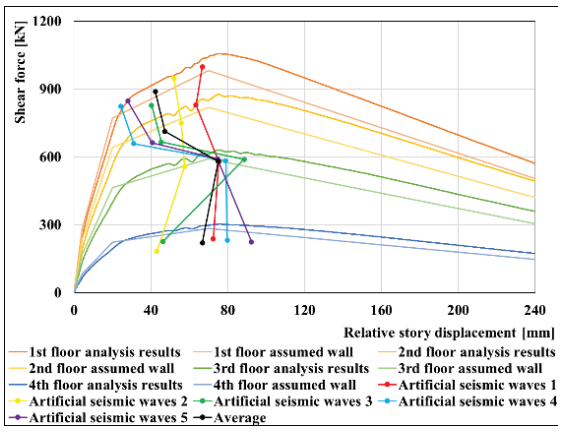

Figure 35: *The results of time history response analysis in case of 4-story without gravity model*

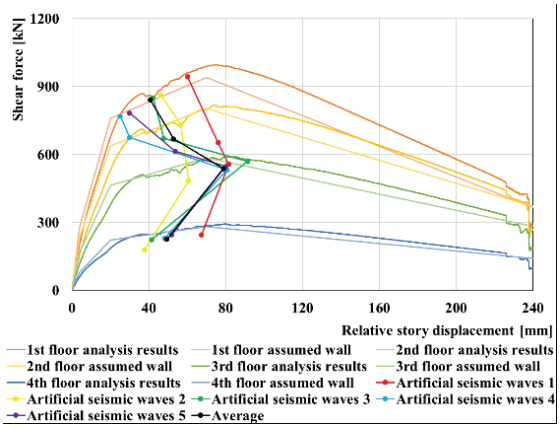

Figure 36: *The results of time history response analysis in case of 4-story with gravity model*

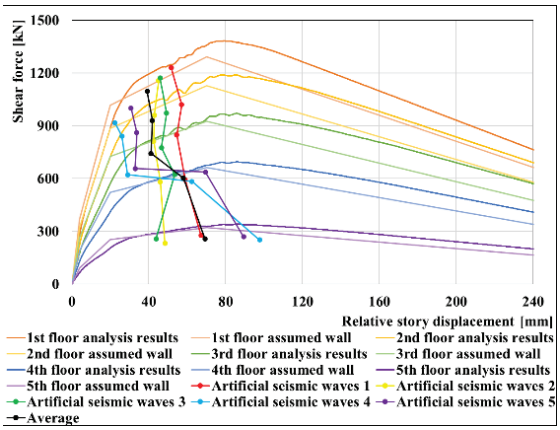

Figure 37: *The results of time history response analysis in case of 5-story without gravity model*

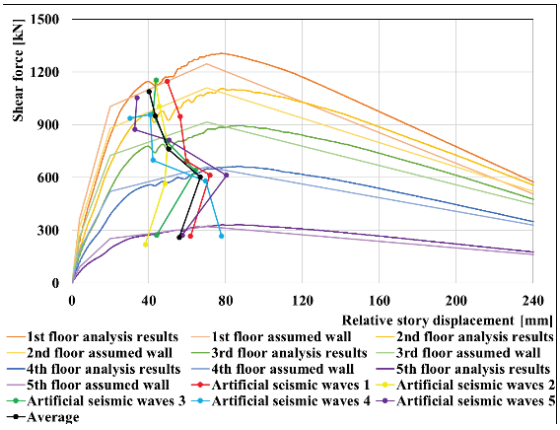

Figure 38: *The results of time history response analysis in case of 5-story with gravity model*

https://doi.org/10.52202/069179-0318

7.2 SOFT FIRST STORY MODEL ANALYSIS RESULTS

Table 12 shows the average values of maximum story displacement and story deformation angle by time history analysis using five artificial seismic waves. The rate of increase in interlayer displacement due to the P-Δ effect of the soft first story model was 0.494 % to 11.9 %. Figs. 39 to 44 show the analysis results of the soft first story models.

Table 12: *Comparison time history response analysis in soft first story models*

		Without Gravity		With Gravity		Increase rate due to P-Δ effect
		Relative story displacement	story deformation angle	Relative story displacement	story deformation angle	Relative story displacement
		$_1\delta$[mm]	θ[$\times10^{-3}$rad]	$_2\delta$[mm]	θ[$\times10^{-3}$rad]	$(_2\delta-{}_1\delta)/{}_1\delta\times100$[%]
3 stories	3rd story	10.9	3.64	11.4	3.79	4.30
	2nd story	10.7	3.58	10.9	3.65	1.73
	1st story	29.3	9.76	29.7	9.90	1.46
4 stories	4th story	12.2	4.05	12.9	4.31	6.41
	3rd story	12.6	4.20	12.8	4.26	1.61
	2nd story	12.6	4.19	12.6	4.21	0.494
	1st story	29.8	9.92	33.3	11.1	11.9
5 stories	5th story	14.1	4.70	15.1	5.05	7.43
	4th story	15.3	5.11	15.6	5.21	1.88
	3rd story	15.1	5.02	15.8	5.27	5.01
	2nd story	14.5	4.83	15.4	5.14	6.35
	1st story	36.0	12.0	40.1	13.4	11.5

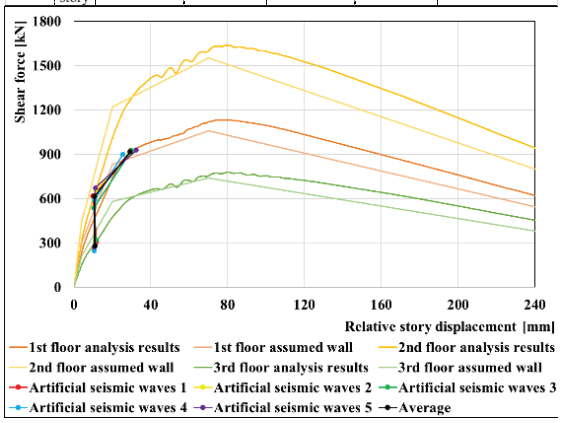

Figure 39: *The results of time history response analysis in case of 3-story without gravity model*

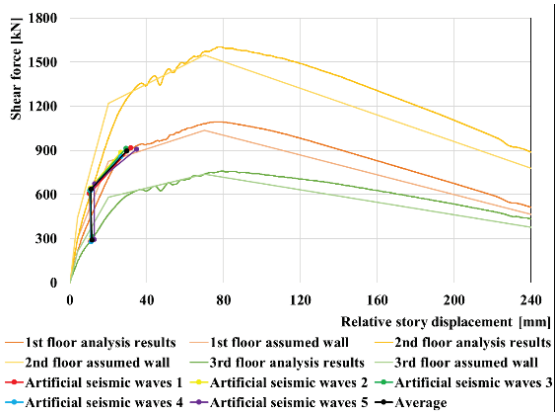

Figure 40: *The results of time history response analysis in case of 3-story with gravity model*

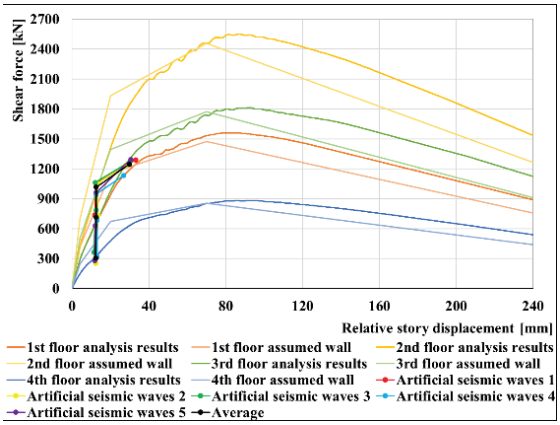

Figure 41: *The results of time history response analysis in case of 4-story without gravity model*

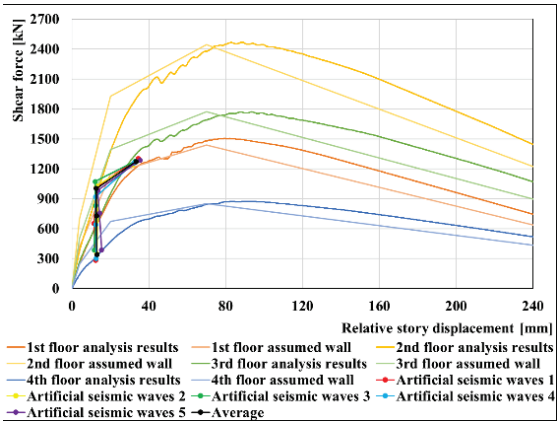

Figure 42: *The results of time history response analysis in case of 4-story with gravity model*

https://doi.org/10.52202/069179-0318

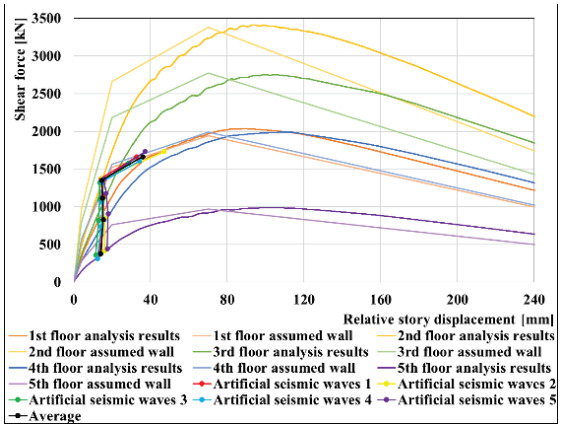

Figure 43: *The results of time history response analysis in case of 5-story without gravity model*

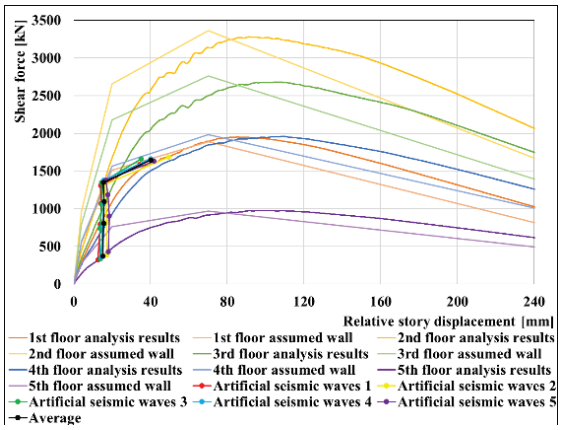

Figure 44: *The results of time history response analysis in case of 5-story with gravity model*

8 CONCLUSION

We aim to clarify the influence of the P-Δ effect by pushover analysis, capacity spectrum method, and time history response analysis for wooden buildings of 3 to 5 stories, and to obtain basic data for seismic design method. In the pushover analysis, it was confirmed that the analysis using wallstat was appropriate by comparing the load deformation relationship of the wall assumed with the analysis result. The increase rate of relative story displacement due to the P-Δ effect was up to 8.97% for the capacity spectrum method and up to 22.2% on average for 5 artificial seismic waves in the time history response analysis. Looking at the results of the capacity spectrum method, it can be said that the effect of the P-Δ effect on the seismic performance of medium-rise wooden buildings is small. However, the rate of increase may reach 22.2% in the time history response analysis, so future examination is required.

ACKNOWLEDGEMENT

This research was carried out as a part of the joint usage and collaborative research of Research Institute for Sustainable Humanosphere, Kyoto University. Authors would like to thank to all the persons concerned.

REFERENCES

[1] T. Nakagawa, M. Ohta, et. al. Collapsing process simulations of timber structures under dynamic loading III: Numerical simulations of the real size wooden houses , Jounal of Wood Science, Vol.56, No.4, pp. 284-292 (2010)

[2] Shibata, A. and Sozen, M. A., Substitute-structure method for seismic design in R/C, Proceedings of the ASCE, Journal of the Structural Division, Vol. 102, ST 1-3, 1976

[3] Freeman, S.A., Nicoletti, S.P., Matsumura, Jeorge, Seismic Design Guidelines for Essential Buildings, the 8th World Conference on Earthquake Engineering. San Francisco, 1984

[4] Japan 2×4 home builders association, 2018 Design guide for wood frame construction buildings (in Japanese), p. 315, 2018

[5] Wooden home builders association of Japan, 2015 Research on wooden framework construction methods, Structural design of medium-rise buildings (in Japanese), p. 120, 2016

[6] N. Kawai, Seismic performance testing on wood framed shear walls, CIB-W18 Proceeding Meeting 31, 31-15-1:1-8, 1998

[7] Mitsui Home Co. Ltd. and Japan 2×4 home builders association, Examination of rationalization of structural design method for medium-rise buildings by wood frame construction (in Japanese), 2019

[8] Building research Institute, Technical background of the structural regulations of the revised Building Standards Law (in Japanese), Gyosei Co., Ltd., pp. 20-21, 2001

https://doi.org/10.52202/069179-0318

World Conference on Timber Engineering Oslo 2023

DETERMINATION OF THE EFFECTIVE WIDTH OF CROSS-LAMINATED TIMBER RIB PANELS USING DIGITAL IMAGE CORRELATION

Miriam Kleinhenz[1], Martin Viertel[2], Thomas Demschner[3], Andrea Frangi[4]

ABSTRACT: The effective width of cross-laminated timber rib panels is analysed. The floor system consists of cross-laminated timber plates rigidly bonded to glued-laminated timber ribs by means of screw-press gluing. Ultimate-load tests were performed on four different cross-sections. Digital image correlation was used to visualize and monitor the strain distribution on top of the cross-laminated timber plates at midspan. The longitudinal strain distributions along the cross-laminated timber width were obtained for the determination of the effective width. The experimental results are compared to numerical results of a finite element model and to Eurocode 5 estimations. The longitudinal strain distributions show good agreement and confirm digital image correlation as a suitable measurement technique.

KEYWORDS: Massive timber rib panel, cross-laminated timber, effective width, optical measurement technique, finite-element modelling, strain distribution

1 INTRODUCTION

Long-span floor systems are required for building types such as commercial office buildings, residential buildings, schools, and industrial buildings. As a long-span floor system with spans up to 16 m, cross-laminated timber rib panels consist of cross-laminated timber (CLT) plates connected to glued-laminated timber (glulam) ribs. Full composite action is provided by a rigid connection between the composite components by means of screw-press gluing [1] (Figure 1).

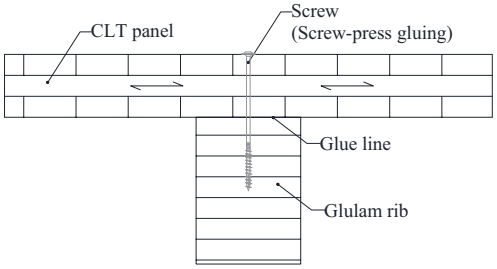

Figure 1: *Cross-section of cross-laminated timber rib panels.*

For such ribbed cross-sections, the assumption that the cross-section remains plane is incorrect. The simple beam theory according to Euler-Bernoulli is not applicable because the strains in the flange vary with the distance from the rib due to the in-plane shear flexibility of the flange. This leads to a non-uniform distribution of the longitudinal strains along the CLT width.
In a research project, ultimate-load tests were performed for the analysis of the structural behaviour. The system's stiffness and the resulting effective width were analysed [2]. This paper focuses on the strain distributions on top of the CLT plate being monitored during the ultimate-load tests using digital image correlation (DIC). The longitudinal strains obtained from the DIC measurements are compared to the numerical results of a finite element (FE) model. Both methods were validated by the measurements at midspan of a linear variable differential transformer (LVDT). Of both methods, the resulting effective widths are compared to the estimated effective width of Eurocode 5 [3].

2 SIMPLIFIED DESIGN METHOD

For simplified structural analysis, the effective width defines an equivalent cross-section that provides the same maximum bending stress and effective bending stiffness as the actual cross-section [4]. Figure 2 illustrates how the non-uniform stress distribution over the entire CLT width is replaced by a uniform stress distribution in the region of the effective width b_{ef}. Equation (1) shall apply:

$$\sigma_{x,max}(z) \cdot b_{ef} = \int \sigma_x(y,z)dy \qquad (1)$$

where $\sigma_{x,max}(z)$ is the maximum longitudinal bending stress distribution along the thickness of the CLT plate at rib centre, b_{ef} is the effective width, and $\int\sigma_x(y,z)dy$ is the integral of the longitudinal bending stresses along the thickness and along the width of the CLT plate.
The chapter on CLT design in the final draft [5] for a revised version of the European design standard for timber structures EN 1995-1-1 (Eurocode 5) [3] proposes simplified equations to estimate the effective width for

[1] Miriam Kleinhenz, Chair of Structural Engineering - Timber Structures, Institute of Structural Engineering, ETH Zurich, Switzerland, kleinhenz@ibk.baug.ethz.ch
[2] Martin Viertel, Bauhallenteam, Institute of Structural Engineering, ETH Zurich, Switzerland, viertel@ibk.baug.ethz.ch
[3] Thomas Demschner, Stora Enso Wood Products GmbH, Austria, thomas.demschner@storaenso.com
[4] Andrea Frangi, Chair of Structural Engineering - Timber Structures, Institute of Structural Engineering, ETH Zurich, Switzerland, frangi@ibk.baug.ethz.ch

https://doi.org/10.52202/069179-0319

ribbed plates build up from CLT plates. In the case of uniformly distributed loads, Equation (2) determines the effective width of Eurocode 5 $b_{ef,EC5}$:

$$b_{ef,EC5} = b_{rib} + \sum b_{ef,i} \tag{2}$$

$$= b_{rib} + b_{f,i} \cdot (0.5 - 0.35 \cdot \left(\frac{b_{f,i}}{l}\right)^{0.9} \cdot \left(\frac{(EA)_x}{(GA)_{xy}}\right)^{0.45})$$

where $b_{ef,i}$ is the effective width at each side of the rib width b_{rib}, $b_{f,i} = (b - b_{rib})$ is the clear rib distance, l is the span, and $(EA)_x/(GA)_{xy}$ is the ratio per meter width between the in-plane stiffness of the longitudinal CLT layers and the shear stiffness in plane of the gross CLT cross-section. The geometry is explained in Figure 3.

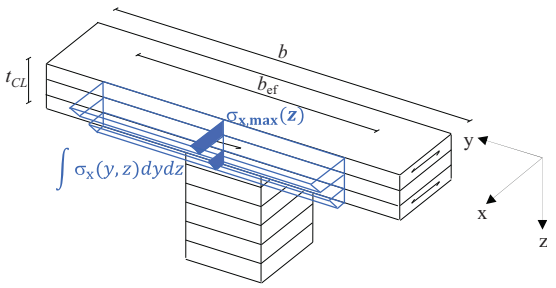

Figure 2: *Determination of the effective width.*

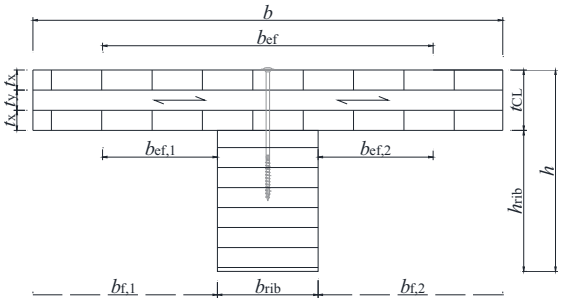

Figure 3: *Geometry of the cross-section.*

For the verification of stresses, the calculation method of rigidly bonded components (Bernoulli-beam) is applied. The calculation method is based on the assumption of full composite action between the CLT plate and glulam rib. The neutral axis is located in the centre of gravity of the composite cross-section z_s, determined by Equation (3):

$$z_s = \frac{\sum_{i=1}^{n+1}(E_i \cdot A_i \cdot a_i)}{\sum_{i=1}^{n+1}(E_i \cdot A_i)} \tag{3}$$

where E_i is the mean value of the modulus of elasticity of component i, A_i is its cross-section area, and a_i is the distance to its centroid from a selected origin.
The effective bending stiffness of the composite cross-section about the y-axis $(EI)_{ef}$ is defined by Equation (4):

$$(EI)_{ef} = \sum_{i=1}^{n+1}(EI)_i = \sum_{i=1}^{n+1}\left(\frac{E_i \cdot b_i \cdot h_i^3}{12} + E_i \cdot b_i \cdot h_i \cdot z_i^2\right) \tag{4}$$

where $(EI)_i$ is the bending stiffness of component i, E_i is the mean value of its modulus of elasticity, b_i is its width, h_i is its height, and z_i is the distance of its centroid to the global centre of gravity z_s.
The effective width b_{ef} defines the width b_i of n-longitudinal CLT layers (n = 1 for top CLT layer, n = 2 for second CLT layer etc.). Therefore, it is involved in both the determination of the global centre of gravity z_s, and the effective bending stiffness of the composite cross-section $(EI)_{ef}$. The rib is considered as (n+1)-component.

3 EXPERIMENTAL INVESTIGATIONS

3.1 CROSS-SECTIONS

Four cross-sections were tested, as presented in Figure 4 (A, B, C, and D), including T-sections (one CLT plate as top flange) and box-sections (CLT plates as top and bottom flanges). Twelve test specimens were tested using three replicates per cross-section (A1-A3, B1-B3, C1-C3, and D1-D3).

3.2 TEST SETUP AND PROCEDURE

The ultimate-load tests were performed as four point bending tests in accordance with EN 408 [6]. The test setup had a span l of 5.20 m (Figure 5). The span complies with the length of the horizontal furnace of later performed full-scale fire tests [2]. The test specimens were simply supported with a CLT width b of 0.933 m. Cross-sections B and D were tested without gypsum plasterboards. For bending at two points, two hydraulic cylinders applied the load uniformly with steel profiles of 200 mm depths along the test specimen's width.

3.3 MEASUREMENTS

Table 1 lists the measurements per test specimen. Load cells measured the applied cylinder forces F_{cyl}. At failure time, the maximum load per cylinder $F_{cyl,max}$ was on average 107 kN. The deflection w at midspan, as described in Figure 5, was recorded by the LVDT as w_{LVDT}. The maximum deflection $w_{LVDT,max}$ was on average 41 mm. The failure led in the linear-elastic load-deflection behaviour to a significant load drop.
An Optotrak Certus position sensor (NDI) was installed to record the local deflection on the front of the test specimen. NDI markers were fixed on the surface of the test specimen, which allowed for a 3D tracking of these markers throughout the testing. Their locations are shown in Figure 5. One NDI marker was located at the bottom edge at midspan. The LVDT at midspan confirmed the accuracy of this NDI measurement. To determine the local effective bending stiffness in the shear-free zone, further markers were placed on the front side of the test specimen below the force application points at a distance l_1 of 1.26 m according to EN 408 [6].

https://doi.org/10.52202/069179-0319

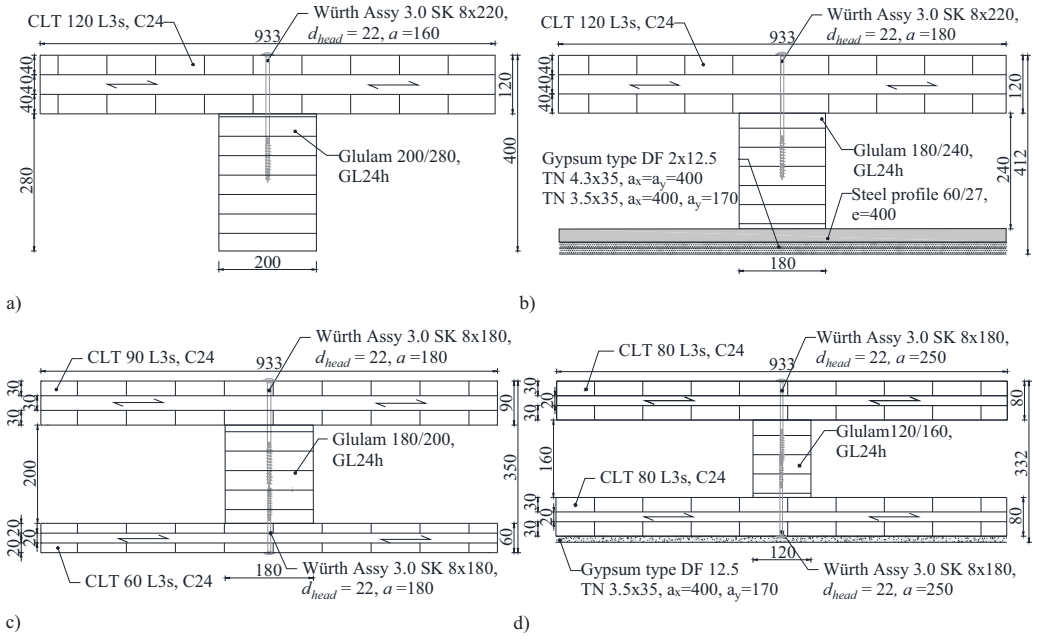

Figure 4: *Cross-section types of the experimental program, in [mm]: a) T-section (A); b) T-section initially protected (B); c) Box-section (C); d) Box-section initially protected (D).*

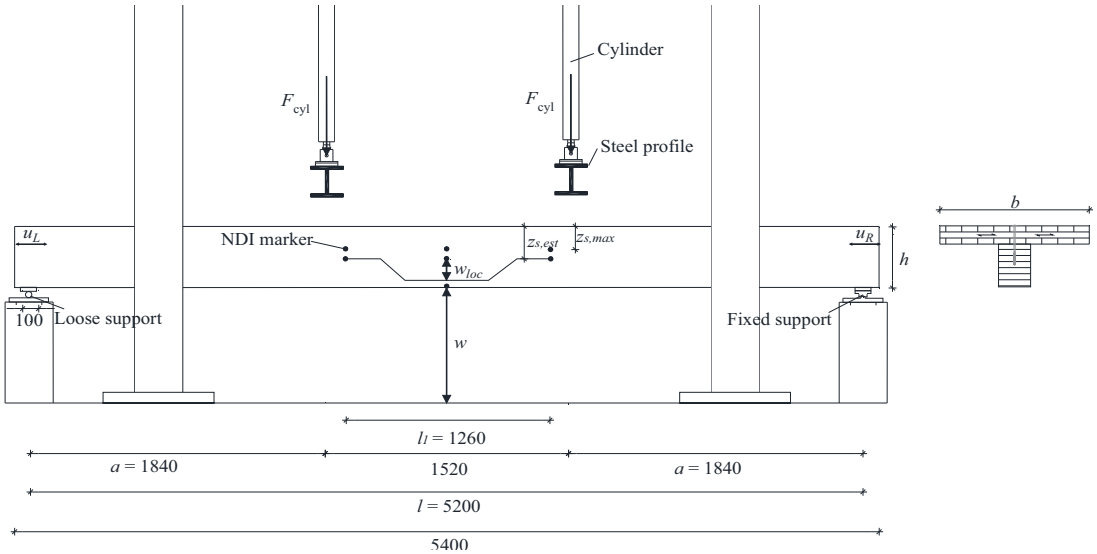

Figure 5: *Test setup in accordance with EN 408* ***[6]****.*

Over the height of the test specimen, these markers were located at two estimated positions of the neutral axis (= global centre of gravity): at $z_{s,max}$ for the maximum system (width b), and at $z_{s,est}$ for the estimated system according to Equation (2) (width $b_{ef,EC5}$). As the actual position can be assumed to be within these limits, the mean on both cases was calculated as local deflection w_{loc}. At failure, the maximum local deflection $w_{loc,max}$ was on average 2.2 mm.

3.4 EXPERIMENTAL RESULTS

3.4.1 Experimental effective bending stiffness

A linear regression was used to determine the slope of the load-deflection curve $\Delta F/\Delta w_{loc}$ [7]. In accordance with EN 408 [6], the experimental effective bending stiffness was calculated as local effective bending stiffness $(EI)_{ef,l}$ according to Equation (5):

$$(EI)_{ef,l} = \frac{a \cdot l_1^2}{16} \frac{\Delta F}{\Delta w_{loc}} = \frac{a \cdot l_1^2}{16} \frac{(2\Delta F_{cyl})}{\Delta w_{loc}} \quad (5)$$

https://doi.org/10.52202/069179-0319

Table 1: *Experimental measurements and results per test specimen – Maximum load per cylinder, ultimate load including self-weight, corresponding maximum deflection measured by the LVDT and maximum local deflection, local effective bending stiffness, experimental effective width, and maximum experimental bending stress on top of the top CLT plate.*

Test specimen	Cross-section type	$F_{cyl,max}$	F_{max}	$w_{LVDT,max}$	$w_{loc,max}$	$(EI)_{ef,l}$	$b_{ef,test}$	$b_{ef,test}/b$	$\sigma_{max,test}(z_{top})$
		[kN]	[kN]	[mm]	[mm]	[MNm^2]	[m]	[-]	[N/mm^2]
A1	T	180	363	53	2.7	24.2	0.92	0.98	-26.4
A2*		88	181	31	1.5	20.9	0.90	0.96	-14.3
A3		106	216	38	2.1	19.1	0.74	0.79	-19.9
B1*		93	190	46	2.9	12.8	0.73	0.78	-23.3
B2		78	160	42	2.5	12.2	0.63	0.68	-20.7
B3		76	156	38	2.3	12.0	0.65	0.70	-19.5
C1*	Box	102	208	34	1.8	20.9	0.80	0.86	-19.3
C2		147	298	52	2.7	20.7	0.74	0.80	-29.4
C3		110	224	38	2.1	19.9	0.74	0.79	-22.1
D1		112	228	43	2.2	18.7	0.71	0.76	-24.7
D2		99	202	38	2.0	18.1	0.68	0.73	-22.6
D3*		98	200	37	2.0	18.0	0.72	0.77	-21.5
mean		107	219	41	2.2	18.1	0.75	0.80	-22.0
SD		28	56	6.4	0.4	3.7	0.08	0.09	3.7
CoV		0.26	0.26	0.16	0.17	0.20	0.11	0.11	0.17

* Selected test specimens for the DIC technique.

where l_1 is the gauge length for the determination of modulus of elasticity, and a is the distance between support and force application, as shown in Figure 5.
Table 1 lists the local effective bending stiffness $(EI)_{ef,l}$ per test specimen; on average 18.1 MNm^2.

3.4.2 Experimental effective width

Due to the correlation between the effective bending stiffness $(EI)_{ef}$ and the effective width b_{ef}, the experimental effective widths $b_{ef,test}$ per test specimen were calculated by equating Equation (4) to the local effective bending stiffness $(EI)_{ef,l}$ of Table 1. A solve-function of nonlinear equations was used. Table 1 lists the experimental effective widths $b_{ef,test}$ per test specimen. Here, the experimental effective width $b_{ef,test}$ defines the width b_i of the longitudinal CLT layers of the top and bottom CLT plate.
Figure 6 presents the results in relation to the CLT width b. In addition, estimated effective widths of Eurocode 5 $b_{ef,EC5}$ were calculated according to Equation (2). Since no formula is given for loading in bending at two points, the formula for uniformly distributed loads was used. For box-sections, an average value of the top and bottom CLT plate is given. While the experimental effective width $b_{ef,test}$ was on average 80% of the CLT width, it would have been estimated at 60% by Eurocode 5 ($b_{ef,EC5}$).

3.4.3 Maximum experimental bending stress

Based on the calculation method of rigidly bonded components, the maximum experimental bending stress on top of the top CLT plate $\sigma_{max,test}(z_{bot})$ is calculated according to Formula (6):

$$\sigma_{max,test}(z_{top}) = \frac{M_{max} E_{CLT}}{(EI)_{ef,l}} \cdot (z_1 + \tfrac{h_1}{2}) \qquad (6)$$

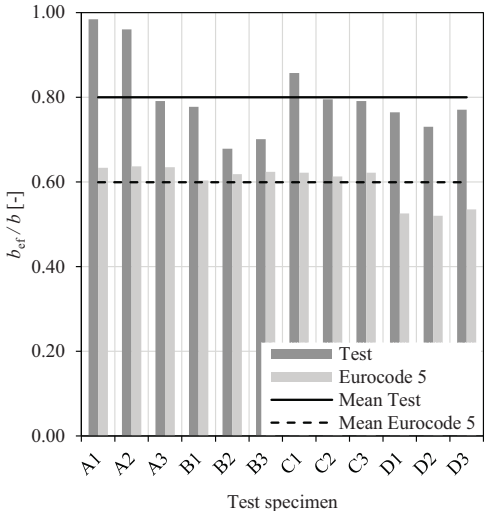

Figure 6: *Experimental and by Eurocode 5 estimated effective width of the tests specimens in relation to the CLT width.*

With

$$M_{max} = F_{max}/2 \cdot a \qquad (7)$$

where E_{CLT} is the modulus of elasticity of the top CLT plate, $(EI)_{ef,l}$ is the local effective bending stiffness (Table 1), and h_1 and z_1 are the height and the distance to the global centre of gravity z_s according to Equation (3) of the top CLT layer, and a is the distance between support and force application, as shown in Figure 5. The ultimate load F_{max} includes the self-weight of the test specimen (see Table 1). The modulus of elasticity of the top CLT plate E_{CLT} and the dimensions of the single CLT plates and glulam ribs have been measured in advance and were

https://doi.org/10.52202/069179-0319

taken from [7]. Table 1 lists the maximum experimental bending stress on top of the top CLT plate $\sigma_{max,test}(z_{bot})$ per test specimen. At failure, the compressive stress value was on average 22 N/mm^2. The top side of the top CLT plate was under compression.

4 DIGITAL IMAGE CORRELATION

4.1 TEST SETUP AND PROCEDURE

In [8], LVDTs were installed at midspan side by side along the CLT width to measure the deformations on the CLT surface. Digital image correlation (DIC) is an optical measurement technique to capture relative 3D changes in sequential images. In this research project, the DIC technique was used at midspan to obtain the strain field distributions on top of the CLT plate of four selected test specimens (A2, B1, C1, and D3). Therefore, a rectangular area of interest of around 1.17 m^2 (0.90 m x 1.30 m) was observed between the two cylinders of the test setup (Figure 7). In the area of interest, a regular, black speckle pattern was applied with a paint roller on top of a white undercoat (speckle size: 1.8 mm). The contrast between speckle and undercoat improves the analysis' accuracy [9,10]. To improve the analysis' quality, LED floodlight illuminated the area of interest.

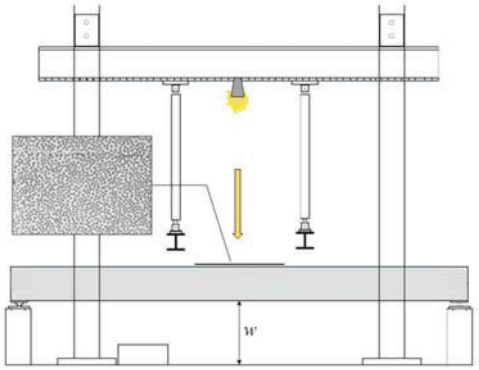

Figure 7: *Test setup in accordance with EN 408* ***[6]*** *including the measurements of the digital image correlation at midspan (area of interest).*

Digital images were simultaneously taken using a set of two cameras, type FLIR, Grasshopper 3, 12.3 MP. The resolution obtained was 4096x3000. The cameras were attached to the universal testing machine by an additional support frame with a distance to the area of interest of approximately 2.20 m. The baseline between the cameras and the distance between the cameras and the test specimen were checked after calibration of the DIC system. Digital images were taken during the ultimate-load tests (frame rate: 30 fps). In a zero-displacement test, the correlation error was checked in dependency of the speckle size, and the subset size. A subset size of 45 pixels on average was used for the image correlation. Displacements were calculated from the digital images by the comparison of virtual subsets containing a certain amount of pixels in original and deformed states at different instants of time. Therefore, a reference image was chosen that was taken in the unloaded phase. Since the projection error did not exceed the value of 0.1, the test specimen's movement or its distance to the cameras remained small. For the calculation, the origin of a coordinate system was set in the centre of the test specimen, thus in the middle of the area of interest. The software VIC-3D Digital Image Correlation Version 9.1.6 [11] was used for calibration, collection of digital images, running the correlation, and calculation of the displacements.

4.2 VALIDATION

The DIC measurements of the four selected test specimens were validated by comparing the maximum vertical displacements $w_{DIC,max}$ at the centre of the area of interest with the maximum deflections measured by the LVDT $w_{LVDT,max}$ (Figure 8). The results show perfect correlation.

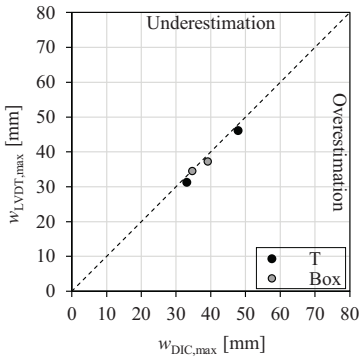

Figure 8: *Maximum deflections - Experimental results measured by the digital image correlation (DIC) and by the linear voltage displacement transducer (LVDT).*

5 NUMERICAL INVESTIGATIONS

5.1 FINITE ELEMENT MODEL

The modelling framework is developed using the Python programming language [12] and Abaqus Unified FEA software suite for finite element analysis [13]. The cross-section of a T-section was sketched and extruded to one deformable part. A geometric symmetry simplification was considered in the form of a vertical symmetry plane in the middle of the cross-section in longitudinal direction and a vertical symmetry plane at midspan (Figure 9). The support was defined as roller support. The generated part was partitioned into flange and rib. The flange was partitioned into the CLT layers, the material orientations of which were defined by local coordinate systems. The contact interactions between flange and rib, and the CLT layers were considered as rigid. The flexible-in-shear multi-layered FE model was loaded as four point bending test. As in the test setup, the mechanical load was applied uniformly at the position of the cylinder along the CLT width over a depth of 200 mm. A gravity load could be activated using a gravity acceleration of 9806.65 mm/s^2. Based on a sensitivity study [14], a mesh of 20x20 mm^2 was chosen. The incompatible mode eight-node brick element (C3D8I) was used for the analyses. Material properties were discussed as linear-elastic and orthotropic using the material properties of Table 2 for the nine engi-

https://doi.org/10.52202/069179-0319

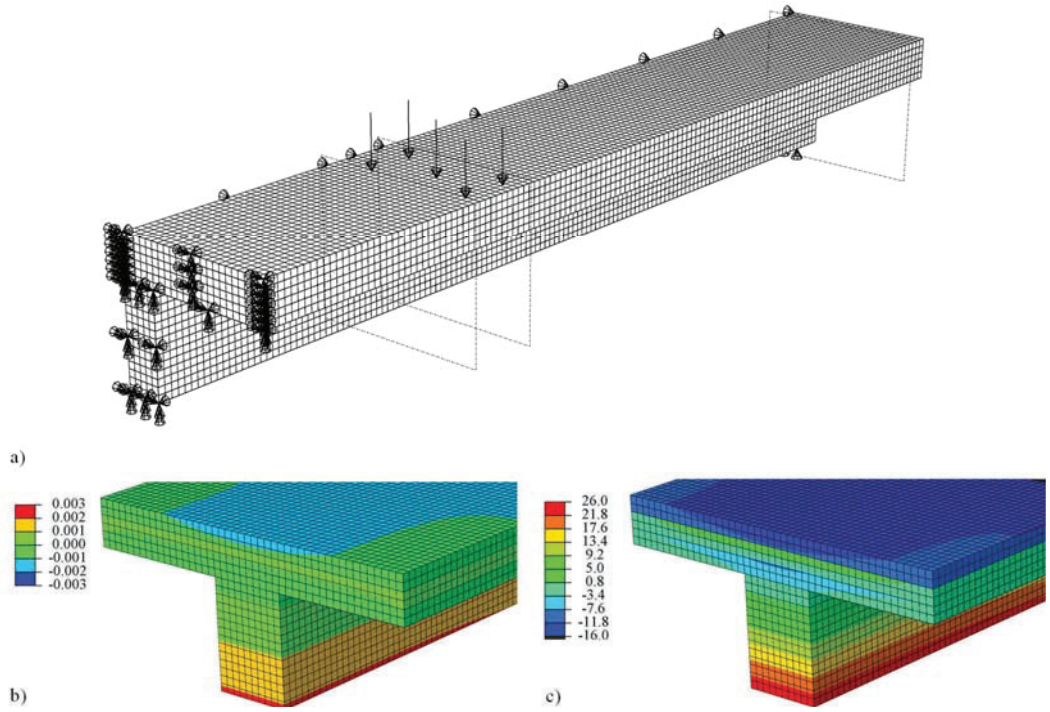

Figure 9: *Finite element model and numerical results mirrored by the vertical symmetry plane (b) and c)): a) 3D FE model; b) Longitudinal strains at midspan, in [-]; c) Longitudinal stresses at midspan, in [N/mm²].*

Table 2: *Material properties for CLT [6] and glulam [17].*

Material	Class	E_x	E_y	E_z	G_{xy}	G_{xz}	G_r	ν_{xy} [2)]	ν_{xz} [2)]	ν_{yz} [2)]
		[N/mm²]	[N/mm²]	[N/mm²]	[N/mm²]	[N/mm²]	[N/mm²]	[-]	[-]	[-]
CLT	CLT24	12500 [1)]	450	450	Eq. (8)	650	Eq. (9)	0.395	0.395	0.410
Gluam	GL24h	11500	300	300	650	650	65	0.395	0.395	0.410

[1)] Value given by Stora Enso.
[2)] Values based on Bodig and Jayne [15].

neering constants. The materials were assigned to the CLT layers as CLT and to the rib as glulam. The shear modulus in-plane of the gross CLT cross-section G_{xy} and the rolling shear modulus of CLT G_r were determined according to Equation (8) and Equation (9):

$$G_{xy} = min\left(\frac{650}{1 + 2.6 \cdot \left(\frac{t_l}{b_l}\right)^{1.2}}; 450\right) \quad (8)$$

$$G_r = min\left(30 + 17.5 \cdot \left(\frac{b_l}{t_l}\right); 100\right) \quad (9)$$

where t_l is the thickness of the lamination, and b_l is either the width of the lamination, the distance between the edge and a groove or the spacing between grooves within the lamination [16,17]. The latter was taken as average distance between grooves of the edge-bonded laminations, declared as 150 mm by Stora Enso.
The FE model was generated for each test specimen of the ultimate-load tests based on the specified dimensions, density, and the determined local modulus of elasticity as modulus of elasticity in x-direction E_x of the single components (CLT plates and glulam ribs), taken from [7]. The maximum load per cylinder $F_{cyl,max}$ was applied per test specimen (Table 1).

5.2 VALIDATION

The gravity load was deactivated in the FE model and the deflection at midspan was requested in the middle of the bottom edge in the post-processing. The FE model was validated by comparing the maximum numerical deflections $w_{sim,max}$ to the maximum deflections measured by the LVDT $w_{LVDT,max}$ (Figure 10). The results show good correlation with a coefficient value of 0.96.
Then, the gravity load was activated in the FE model. The flexible-in-shear multi-layered FE model resulted in a non-uniform stress distribution along the CLT width. On top of the CLT plate at midspan, the stress value in longitudinal direction at rib centre was requested from the created output database. Figure 11 presents per test specimen the maximum longitudinal stress values

https://doi.org/10.52202/069179-0319

$\sigma_{x,max,sim}(z_{top})$ of the FE model in comparison to the maximum experimental bending stresses $\sigma_{max,test}(z_{top})$ (Table 1). The results show good correlation with a coefficient value of 0.91.

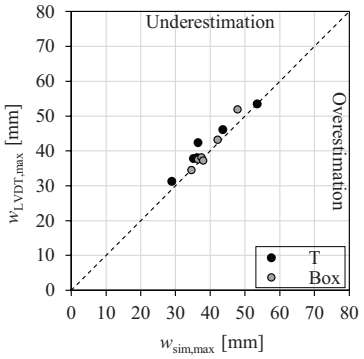

Figure 10: *Maximum deflections – Numerical results (sim) in comparison to experimental results measured by the linear voltage displacement transducer (LVDT).*

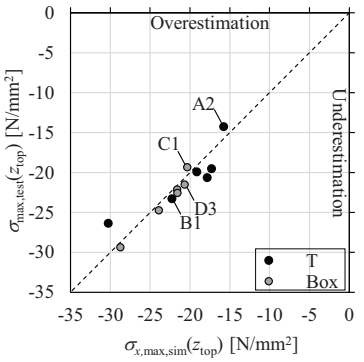

Figure 11: *Maximum stress values on top of the top CLT plate - Numerical results (sim) taken as longitudinal stress values at rib centre in comparison to experimental results (test) calculated as bending stresses according to Formula (6).*

6 RESULTS

6.1 STRAIN DISTRIBUTION

6.1.1 Digital image correlation

The DIC technique measured displacements on top of the top CLT plate. The software VIC-3D Digital Image Correlation Version 9.1.6 [11] was used for the determination of strains. The in-plane strains, i.e. longitudinal strains $\varepsilon_{xx,DIC}$, were calculated from the displacements as engineering strains. The accuracy was influenced by cracks and damages on the surface. Therefore, the longitudinal strains were averaged over the best illuminated region of the area of interest. Figure 12 presents the strain fields at failure of the selected test specimens. It should be noted that the region could only cover around 0.90 m of the CLT width b of 0.933 m.

Then, the averaged longitudinal strains $\varepsilon_{xx,DIC}$ were smoothed over the CLT width by taking the mean over a window length of 100 mm. Figure 13 presents the smoothed longitudinal strain distribution $\varepsilon_{xx,DIC}$ along the CLT width of the four selected test specimens (A2, B1, C1, and D3) at failure time. The strains result in compressive strains between 0.0006 and 0.0014. The results indicate a non-uniform stress distribution along the CLT width of the ribbed cross-sections.

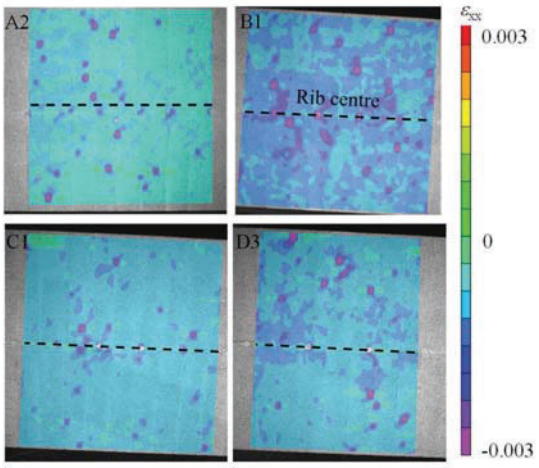

Figure 12: *Strain field on top of the top CLT plate at midspan - Longitudinal strains measured by the digital image correlation (DIC) of the four selected test specimens (Digital image at failure, contour range: -0.003 – 0.003 [-]).*

6.1.2 Finite element model

The gravity load was deactivated in the FE model. For comparison with the DIC results, the strains in longitudinal direction $\varepsilon_{xx,sim}$ along the CLT width were requested on top of the top CLT plate at midspan from the created output database (Figure 13). The strains result in compressive strains between 0.0008 and 0.0016. The flexible-in-shear multi-layered FE model resulted in a non-uniform stress distribution along the CLT width.

6.2 MAXIMUM STRAIN AND STRESS

The strains on top of the top CLT plate vary with the distance from the rib due to the in-plane shear flexibility of the flange. At rib centre, both the maximum longitudinal strain as well as the maximum stress value occur. Table 3 lists the results at midspan based on the DIC measurements and the FE model. The maximum longitudinal strain value at rib centre $\varepsilon_{xx,max}$ resulted on average in -0.00116 for the DIC measurements and in -0.00147 for the FE model. Figure 14 compares the maximum stress values on top of the top CLT plate at rib centre $\sigma_{x,max}(z_{top})$ between the FE model and the DIC measurements. The maximum stress value in longitudinal direction $\sigma_{x,max,sim}(z_{top})$ was requested from the created output database, as in Figure 11. The maximum stress value of the DIC measurements $\sigma_{x,max,DIC}(z_{top})$ was calculated by multiplying the maximum longitudinal strain value at rib centre $\varepsilon_{xx,max,DIC}$ with the modulus of elasticity of the top CLT plate $E_{CLT,}$ taken from [7]. The maximum stress value on top of the top CLT plate at rib centre $\sigma_{x,max}(z_{top})$ resulted in a compressive stress of on average 15.7 N/mm² for the DIC measurements and 19.8 N/mm² for the FE model.

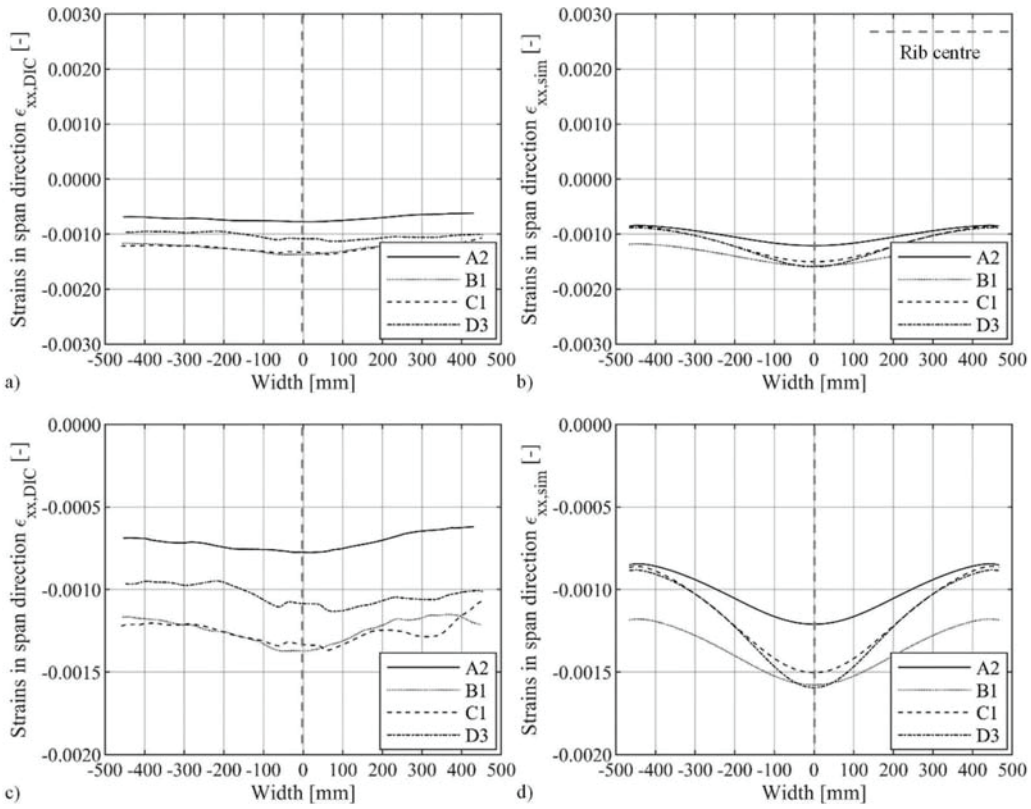

Figure 13: *Strain field distributions on top of the CLT plate - Longitudinal strains along the CLT width of the four selected test specimens a)+c) measured by the digital image correlation (DIC); b)+d) taken from the created output database of the FE model.*

Table 3: *Results based on the DIC measurements and the FE model (sim) per test specimen – Maximum longitudinal strain at rib centre, modulus of elasticity of the top CLT plate, and maximum bending stress and effective width on top of the top CLT plate.*

Test specimen	$\varepsilon_{xx,max,DIC}$	$\varepsilon_{xx,max,sim}$	E_{CLT}[1)]	$\sigma_{x,max,DIC}(z_{top})$	$\sigma_{x,max,sim}(z_{top})$	$b_{ef,top,DIC}/b$	$b_{ef,top,sim}/b$
	[-]	[-]	[N/mm²]	[N/mm²]	[N/mm²]	[-]	[-]
A2	-0.00078	-0.00121	12936	-10.0	-15.7	0.87	0.85
B1	-0.00137	-0.00158	14008	-19.2	-22.3	0.88	0.87
C1	-0.00137	-0.00150	13563	-18.6	-20.3	0.89	0.80
D3	-0.00113	-0.00160	13329	-15.1	-20.7	0.88	0.80
mean	-0.00116	-0.00147	13459	-15.7	-19.8	0.88	0.83
SD	0.00024	0.00016	388	3.7	2.5	0.01	0.03
CoV	-0.21	-0.11	0.03	-0.23	-0.12	0.01	0.04

[1)] Values taken from [7].

6.3 EFFECTIVE WIDTH

In this paper, longitudinal strains ε_{xx} were obtained at midspan only on the top side of the top CLT plate; for both the DIC technique and the FE model. Equation (10) shall apply in accordance with Equation (1) and Figure 2:

$$\varepsilon_{xx,max}(z_{top}) \cdot b_{ef,top} = \int \varepsilon_{xx}(y, z_{top})dy \qquad (10)$$

where $\varepsilon_{xx,max}(z_{top})$ is the maximum longitudinal strain value on top of the top CLT plate at rib centre, and $\int\varepsilon_{xx}(y,z_{top})dy$ is the integral of all longitudinal strains along the width of the CLT plate on top of the top CLT plate.

The effective width on top of the top CLT plate $b_{ef,top}$, is determined according to Equation (11):

$$b_{ef,top} = \frac{\int \varepsilon_{xx}(y, z_{top})dy}{\varepsilon_{xx,max}(z_{top})} \qquad (11)$$

The effective widths on top of the top CLT plate $b_{ef,top}$ were calculated for the four selected test specimens (A2, B1, C1, and D3) based on the longitudinal strains of the FE model and based on the DIC measurements. Table 3 lists the results in relation to the CLT width b. Figure 15 shows the comparison between the two models. Both the results of the DIC measurements and the FE model show

https://doi.org/10.52202/069179-0319

a low deviation between the results of maximum 4%. For the DIC results, the effective widths on top of the top CLT plate $b_{ef,top}$ resulted on average in 88% of the CLT width for all test specimens (CoV = 1%). For the numerical results, a distinction can be made between T-sections (86% of the CLT width) and box-sections (80% of the CLT width).

7 DISCUSSION

7.1 STRAIN DISTRIBUTION

The strain distributions along the CLT width on top of the top CLT plate are compared between DIC measurements and the FE model. The strain distributions show complete compression along the CLT width, as expected for the system of a simply supported beam under positive moment. The DIC results are in a range close to the expected range of the numerical results of the FE model. The DIC results of the T-sections (A2, B1) show good agreement in the shape of the strain distribution in comparison to the FE results. The DIC results of the box-sections (C1, D3) show a less pronounced decrease in strains with the distance from the rib centre. The composite system exhibited a lower shear lag effect as estimated by the FE model. Especially, the thinner top CLT plates of the box-sections proved to be less flexible in plane. The strain distributions at midspan might have been effected through a clinching effect of the steel profiles of the experimental test setup.

7.2 MAXIMUM STRAIN AND STRESS VALUE

The best fit can be seen for test specimen B1. Here, not only the shape of the strain distribution but also the maximum longitudinal strain value at rib centre $\varepsilon_{xx,max}$ comply between the DIC technique and the FE model. The FE model overestimates the maximum longitudinal strain value at rib centre $\varepsilon_{xx,max}$ by only 15%. For specimen A2, however, the FE model overestimates the value by 55%.

The maximum stress values on top of the top CLT plate at rib centre $\sigma_{x,max}(z_{top})$ are calculated from the maximum longitudinal strain value at rib centre $\varepsilon_{xx,max}$. Figure 14 outlines the overestimation by the FE model by up to 55%. The average error is 4.4 N/mm^2 (RMSE).

7.3 EFFECTIVE WIDTH

The effective widths on top of the top CLT plate $b_{ef,top}$ are in good agreement between the DIC technique and the FE model for the T-sections. The FE model underestimates the effective widths of the box-sections by 10%. This is based on the more pronounced non-uniform strain distribution along the CLT width. The small deviation between the results of the individual models (CoV ≤ 4%) illustrates the small influence of the material properties on the strain distribution. As outlined in [7], the effective width b_{ef} mainly depends on the stiffness of the floor system, e.g. the ratio of clear rib distance to span $b_{f,i}/l$, which was about 0.15 of the tested system.

Figure 15 puts the results in relation to the mean value of the estimated effective width of Eurocode 5 $b_{ef,EC5}$, taken from Figure 6. The effective width by Eurocode 5 $b_{ef,EC5}$ shows the approach on the safe side with an estimate of 60% of the CLT width on average.

Figure 15 puts the results in relation to the mean value of the experimental effective width $b_{ef,test}$, taken from Figure 6. The experimental effective width $b_{ef,test}$ was on average 80% of the CLT width. The higher deviation between the experimental results (CoV = 11%) illustrates the sensitivity of the experimental results based on the local deflections of less than 3 mm (see Table 1). The mean value of 80% of the CLT width complies well with the numerical investigations presented in [18]. There, the effective width would have been determined around 75% of the CLT width (Abb. 20, MM_Bsp3s_q).

The effective widths on top of the top CLT plate $b_{ef,top}$ of the DIC measurements and the FE model lay slightly above the mean value of the experimental effective width $b_{ef,test}$. It should be noted that the effective width b_{ef} of the entire flange or system is expected to be smaller than the effective width on top of the top CLT plate $b_{ef,top}$.

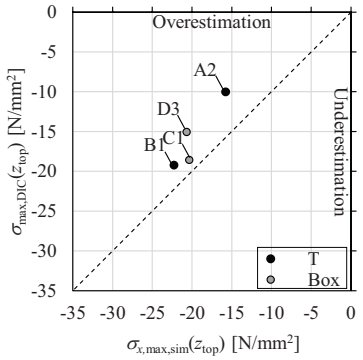

Figure 14: *Maximum stress values on top of the top CLT plate - Numerical results (sim) in comparison to results based on the DIC measurements (DIC).*

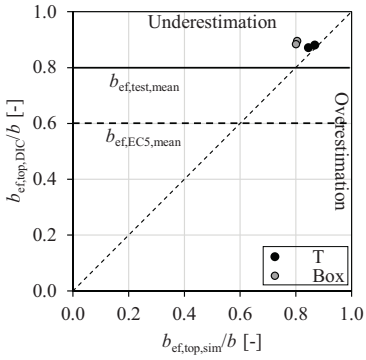

Figure 15: *Effective width - Results on top of the top CLT plate based on the FE model (sim) in comparison to the ones based on the DIC measurements (DIC); incl. mean values of the experimental and by Eurocode 5 estimated effective width.*

8 CONCLUSIONS

The DIC analysis allows visualizing the strain field on top of the CLT plate. In comparison to strain gauges and LVDTs, entire field measurements are possible. The proposed paper investigates DIC as a suitable measurement technique for the determination of the

effective width b_{ef}. The investigations apply to a floor system with a ratio of clear rib distance to span $b_{f,i}/l$ of about 0.15. The strain and stress distributions along the CLT width on top of the top CLT plate are compared between DIC measurements and the FE model. The DIC measurements and the numerical results of the FE model were validated against the experimental results of four tested cross-sections. Based on the DIC results, the composite system exhibited a lower shear lag effect as estimated by the FE model.

Although the in-plane stiffness was underestimated by the FE model, the results of the effective width on top of the top CLT plate $b_{ef,top}$ show good agreement between the DIC measurements and the FE model. Furthermore, the results comply with the effective width b_{ef} of the experimental results, which is on average 80% of the CLT width. Eurocode 5 gives an estimate on the safe side of 60% of the CLT width on average.

The numerical investigations formed the basis for thermo-mechanical investigations [7]. The aim was the determination of the effective width in fire over the entire height of the CLT plate. The 3D FE model resulted in a non-uniform, temperature-dependent strain distribution along the CLT width [19]. The temperature-dependent longitudinal bending stresses were taken along the CLT width and along the thickness of the longitudinal CLT layers per specified time step. A parametric study analysed the effective width in fire $b_{ef,fi}$ for a parameter range expected in practice.

ACKNOWLEDGEMENT

The authors gratefully acknowledge the financial and technical support by Stora Enso Wood Products GmbH in Ybbs, Austria. The numerical work has been supported by the students' work of Julian Brogli and Marco Lamberti.

REFERENCES

[1] K. Bratulic, M. Augustin, G. Schickhofer, Investigations concerning screw-press gluing of assemblies with CLT, in: International Network on Timber Engineering Research (INTER) – Proceedings of the 6th Meeting, Tacoma, USA, 2019.

[2] M. Kleinhenz, A. Just, A. Frangi, Experimental analysis of cross-laminated timber rib panels at normal temperature and in fire, Engineering Structures. 246 (2021) 113091. https://doi.org/10.1016/j.engstruct.2021.113091.

[3] EN 1995-1-1, Eurocode 5: Design of timber structures - Part 1-1: General - Common rules and rules for buildings, European Committee for Standardization (CEN), Brussels, 2004.

[4] S.P. Timoshenko, Strength of materials - Part II Advanced Theory and Problems, 2nd ed., D. Van Nostrand Company, inc., New York - Toronto - London, 1940.

[5] CEN/TC 250/SC 5 N 892: M515 SC5.T1 Phase 1 Final deliverables - SC5.T1 Final Document of prEN 1995-1-1 on CLT, CEN - CENELEC, Brussels, 2018.

[6] EN 408, Timber structures - Structural timber and glued laminated timber - Determination of some physical and mechanical properties, European Committee for Standardization (CEN), Brussels, 2012.

[7] M. Kleinhenz, Cross-laminated timber rib panels in fire, ETH Zurich, 2022. https://doi.org/10.3929/ETHZ-B-000577457.

[8] R. Masoudnia, A. Hashemi, P. Quenneville, Predicting the Effective Flange Width of a CLT Slab in Timber Composite Beams, J. Struct. Eng. 144 (2018) 04018084. https://doi.org/10.1061/(ASCE)ST.1943-541X.0001979.

[9] R.A. Freire, H. Di Benedetto, C. Sauzéat, S. Pouget, D. Lesueur, Crack propagation analysis in bituminous mixtures reinforced by different types of geogrids using digital image correlation, Construction and Building Materials. 303 (2021) 124522. https://doi.org/10.1016/j.conbuildmat.2021.124522.

[10] S.A. Hadigheh, R. McDougall, C. Wiseman, L. Reid, Evaluation of composite action in cross laminated timber-concrete composite beams with CFRP reinforcing bar and plate connectors using Digital Image Correlation (DIC), Engineering Structures. 232 (2021) 111791. https://doi.org/10.1016/j.engstruct.2020.111791.

[11] Correlated Solutions, Inc., VIC-3D Digital Image Correlation (Version 9.1.6), (2020).

[12] Python Software Foundation, Python (version 3.7), (2018). https://www.python.org/.

[13] Dassault Systemes, Abaqus FEA, (2019). https://www.3ds.com/products-services/simulia/products/abaqus/.

[14] P. Hodel, CLT Rib Panels - Simulation der Tragfähigkeit im Brandfall, Master thesis, ETH, 2021.

[15] J. Bodig, B.A. Jayne, Mechanics of wood and wood composites, Reprint ed., Krieger Pub, Malabar, Fla., 1993.

[16] R. Brandner, G. Flatscher, A. Ringhofer, G. Schickhofer, A. Thiel, Cross laminated timber (CLT): overview and development, Eur. J. Wood Prod. 74 (2016) 331–351. https://doi.org/10.1007/s00107-015-0999-5.

[17] T. Ehrhart, R. Brandner, G. Schickhofer, A. Frangi, Rolling Shear Properties of some European Timber Species with Focus on Cross Laminated Timber (CLT): Test Configuration and Parameter Study, in: International Network on Timber Engineering Research (INTER) – Proceedings of the 2nd Meeting, ETH Zurich, Šibenik, Croatia, 2015. https://doi.org/10.3929/ETHZ-A-010548168.

[18] T. Bogensperger, Darstellung und praxistaugliche Aufbereitung für die Ermittlung mitwirkender Plattenbreiten von BSP-Elementen, Research Report focus_sts 2.2.3_1, Graz, Austria, 2013.

[19] M. Kleinhenz, A. Frangi, A. Just, The effective width of cross-laminated timber rib panels in fire, in: International Network on Timber Engineering Research (INTER) – Proceedings of the 9th Meeting, Bad Aibling, Germany, 2022.

https://doi.org/10.52202/069179-0319

World Conference on Timber Engineering Oslo 2023

MODELLING OF OSB SANDWICH PANELS WITH ORIGAMI-INSPIRED CORE

Jan Pełczyński[1], Kamila Martyniuk-Sienkiewicz[2], Anna Al Sabouni-Zawadzka[3]

ABSTRACT: This research is focused on the development, and experimental and numerical testing of wood-based sandwich panels with both covers and a core made of oriented strand boards (OSBs). The core shapes are inspired with an origami pattern. Wood-based sandwich panels are structural elements that maintain essential features of wood, such as lightness, while having an increased load-bearing capacity and stiffness. Thanks to these properties, they find application in high-rise and residential construction. Laboratory tests presented in this study are aimed at determining selected material properties of the boards, namely the Young's moduli in the longitudinal and transverse direction. The experimentally identified parameters are afterwards used as orthotropic coefficients in the numerical analysis of six sandwich panels, differing in the core type and the thickness of the core boards. The numerical models are prepared in the Abaqus environment and analysed using the finite element method (FEM). Two types of models are built for each panel: a 3D shell model of the whole panel and a 3D solid submodel of a section of the panel. The submodels are aimed at the detailed analysis of stress distributions in the areas of the connections between the covers and the core.

KEYWORDS: Sandwich panel, OSB, FEM, Submodelling

1 INTRODUCTION

Modern civil engineering faces many problems that force engineers to seek for new, creative solutions, both within materials and structures. Due to the rapidly progressing urbanisation and the increasingly frequent requirement to strive for sustainable solutions, scientists have started to pay more attention to wood, which has been used in the construction for centuries. One of the first steps toward the improvement of this natural material was the development of wood-based products such as oriented strand board (OSB), laminated veneer lumber (LVL), glued or cross-laminated timber (GLT or CLT). These materials can be used in multi-storey buildings thanks to their improved load-bearing capacity and good elastic properties while maintaining a low weight.

OSBs consist of slender strands of wood which are bonded together using water-resistant resins [1]. The boards have usually three layers of strands, which are oriented perpendicularly to one another, and the strands of outer layers are mostly oriented along the main axis of the board. OSBs are widely used as engineering products in the construction industry due to their favourable mechanical properties [2].

The research on OSB has focused mainly on the determination of its physical and mechanical properties, using both the numerical and experimental studies. Zhu et al. [3] investigated material properties of OSB by performing experimental tests covering in-plane behaviour of the boards as well as their properties in the perpendicular direction. They proved that OSB is an orthotropic material with better mechanical properties along the main strands orientation direction. Moreover, they proposed an elastic-plastic constitutive model of OSB, which they implemented in the finite element (FE) analysis. Islam et al. [2] conducted laboratory tests on OSB samples in order to determine various technical parameters of the boards, e.g. ultimate strengths, Young's modulus, shear modulus, and Poisson's ratio. They tested samples which were cut from the board along three directions: transverse, diagonal and longitudinal. Hrázský and Král [4] studied the effect of density and glue amount changes on the mechanical behaviour of OSB. They determined bending strength, modulus of elasticity and tensile strength of OSBs of different thicknesses, varying in density and the amount of glue. Plenzler et al. [1] performed experiments aimed at determining elastic and strength properties of the layers of commercial OSB panels. They confirmed that the physical and mechanical properties of the face and core layers of OSB differ significantly. Feraboli [5] studied the notched response of OSB wood composites. He collected a large experimental database proving that OSB may be considered a notch-insensitive material thanks to its heterogeneous inner structure.

Although the OSB is a well-known material that has been used since a very long time in various civil engineering applications, and many studies on its mechanical properties can be found in the literature, it is still problematic to find full information on the mechanical behaviour of specific types of OSBs. Therefore, the authors of this paper have decided to perform

[1] Jan Pełczyński, Warsaw University of Technology, Faculty of Civil Engineering, Poland, jan.pelczynski@pw.edu.pl
[2] Kamila Martyniuk-Sienkiewicz, Warsaw University of Technology, Faculty of Civil Engineering, Poland, kamila.martyniuk-sienkiewicz.dokt@pw.edu.pl
[3] Anna Al Sabouni-Zawadzka, Warsaw University of Technology, Faculty of Civil Engineering, Poland, anna.zawadzka@pw.edu.pl

https://doi.org/10.52202/069179-0320

experimental tests aimed at identifying certain orthotropic coefficients of the boards used for the construction of the investigated OSB-based sandwich panels.

Wood-based sandwich panels are understood here as composite slabs consisting of two thin covers and a thick but lightweight core. Such structural elements maintain the essential features of wood, such as lightness, while having the increased load-bearing capacity and stiffness [6]. Thanks to these properties, sandwich structures would find application in high-rise and residential construction. Covers can be made of wood-based materials like OSB, CLT or composite elements. For the core, there is a wide range of structural systems used, including basic trapezoidal or trapezoidal-like shapes [7], or light openwork structures such as lattice-shaped cores [6], especially XX-type lattice [8] and 2D lattice truss [9]. Each shape responds differently under the load, allowing for the design of structures that meet even very high demands. Sandwich structures could be assembled using traditional wood and wood-based materials or, more surprising, bamboo [10] or jute fabrics/epoxy composite [11].

The subject of the research presented in this paper is the development and experimental and numerical testing of a wood-based sandwich structure with both covers and a core made of OSBs. The core shape is inspired with an origami pattern [12, 13]. An example of a physical model of a section of the analysed structure is presented in Figure 1. This is an illustrative example aimed at showing the authors' idea, not the model that has been tested in the laboratory.

Figure 1: *Physical model of the OSB sandwich plate section*

This study focuses on two aspects of the broader research, which is a part of the research project realized by the authors at the Warsaw University of Technology, funded by the National Science Centre in Poland. In Section 2, results of laboratory tests conducted on OSB samples of various thicknesses are presented. The tests were aimed at determining selected orthotropic coefficients of the boards, that is Young's moduli in two directions: longitudinal and transverse. Section 3 contains results of numerical analyses of sandwich panels carried out in Abaqus software using the finite element method (FEM) [14], with the material properties determined in the experimental study.

2 EXPERIMENTAL TESTS

In order to determine selected material parameters of OSB, experimental tests on OSB samples of three different thicknesses were conducted. Altogether, 60 OSB samples were tested: three different board thicknesses (10 mm, 15 mm, and 22 mm), and for each board ten samples cut in each of the two directions (along the longitudinal axis and transverse to it). The tested samples were rectangular with the following dimensions: 25 mm x 200 mm for the 10 mm thick OSB, 25 mm x 300 mm for the 15 mm thick OSB, and 25 mm x 400 mm for the 22 mm thick OSB. The specified lengths of the samples are not their actual lengths, but their spans (distances between the supports in the testing machine). Figure 2 shows 20 samples cut from the 22 mm thick OSB: ten in the longitudinal direction (T00) and ten in the transverse direction (T90).

The tests were aimed at determining the Young's moduli in two directions: longitudinal (E_1) and transverse (E_2).

Figure 2: *Samples of the 22 mm thick OSB in two directions: T00 – longitudinal, T90 – transverse*

https://doi.org/10.52202/069179-0320

Three-point bending tests were performed using a universal testing machine Instron 3382, with one concentrated force applied in the middle of the span. The loading was applied using a displacement-controlled method with the speed of 10 mm/min, and the displacements of the samples were measured with a laser sensor, which observed the bottom surface of the sample. The test setup is showed in Figure 3, which depicts one of the 22 mm thick OSB samples under bending.

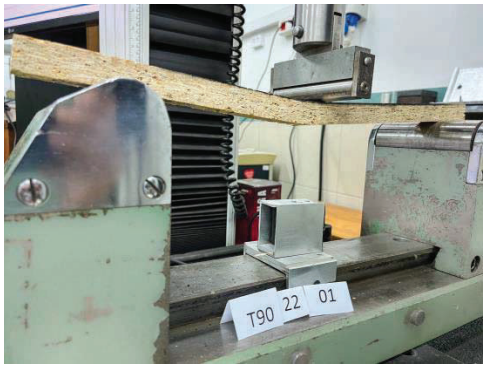

Figure 3: *Bending test on the 22 mm thick OSB sample in the transverse direction*

Figures 4 and 5 present results obtained from the bending tests (force-displacement curves) for the 22 mm thick OSB samples. Similar tests were performed on the 10 mm and 15 mm thick boards. However, as the main aim of this study was to determine the Young's moduli, the curves obtained for other samples are not presented here. Instead, all results (calculated values of the Young's moduli) are gathered in Table 1.

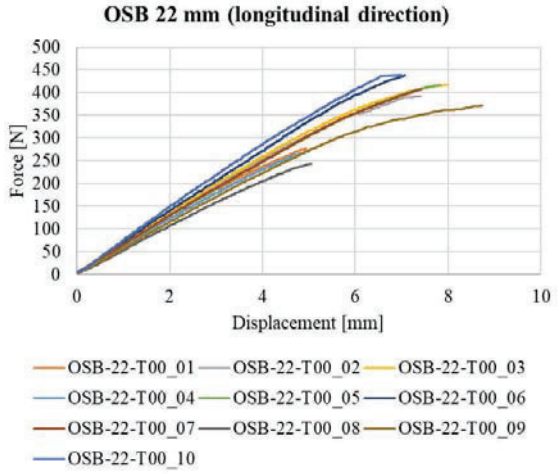

Figure 4: *Results of bending tests performed on the 22 mm thick OSB samples in the longitudinal direction*

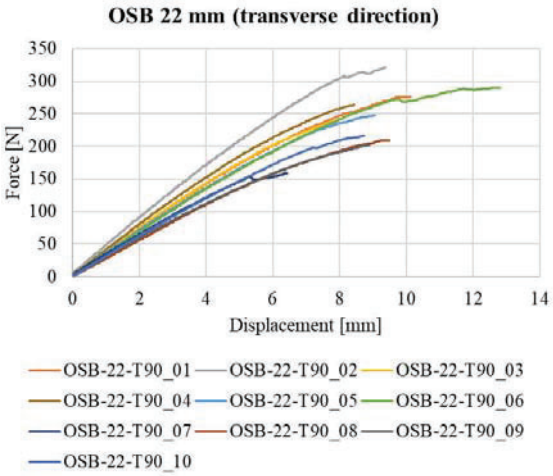

Figure 5: *Results of bending tests performed on the 22 mm thick OSB samples in the transverse direction*

Table 1: *Young's moduli of OSB determined in the experimental tests*

OSB thickness [mm]	Direction	Young's modulus [N/mm^2]: E_1 (T00) and E_2 (T90)		
		Average	Median	Standard deviation
10	T00	5191.22	5079.47	379.38
	T90	3471.12	3481.40	378.91
15	T00	4317.95	4202.95	615.03
	T90	2321.04	2316.10	270.40
22	T00	4072.05	4052.48	357.34
	T90	2271.99	2332.63	312.54

The Young's moduli were calculated using the formula

$$E = \frac{(F_{40} - F_{10})L^3}{48\, I(u_{40} - u_{10})}, \tag{1}$$

where:
E – Young's modulus,
F_{40} – force corresponding to 40% of the breaking load,
F_{10} – force corresponding to 10% of the breaking load,
u_{40} – vertical displacement at 40% of the breaking load,
u_{10} – vertical displacement at 10% of the breaking load,
L – span,
I – moment of inertia.

Calculated values of the Young's moduli were afterwards used in the numerical models of the considered sandwich panels.

3 NUMERICAL MODELLING

Finite element models of the OSB-based sandwich panels were developed in two stages using the Abaqus environment:

- stage 1 – 3D shell model of the panel;
- stage 2 – 3D solid submodel of a section of the panel.

https://doi.org/10.52202/069179-0320

The shell model was built using 4-node general-purpose shell elements with reduced integration (S4R) within the linear elasticity with an orthotropic material model, and the adopted finite element size was 0.01 m. The connection between the core and cover boards was modelled using the tie contact in Abaqus with automatic discretization. The uniformly distributed load of 2 kN/m^2 was applied to the upper cover of the panel in the vertical direction (direction 3 – perpendicular to the panel surface). The panel was supported at shorter edges of the lower cover: at one edge displacement constraints in two directions (U1 and U3) were applied, along the other edge the constraints were applied in the vertical direction (U3) and, additionally, constraints in the horizontal direction (U2) were applied in two corner nodes.

The submodel was generated using the Abaqus built-in procedure, which allows for the automatic reading of the boundary conditions and introducing them into the defined submodel. A shell-to-solid submodelling was used, where shell corresponds to the full model, and solid to the submodel. It is important to locate the submodel in the same coordinate system, so that it is consistent with the location of the corresponding elements of the shell model.

The submodel was built using 8-node linear brick elements with reduced integration (C3D8R) within the linear elasticity with an orthotropic material model, and the adopted finite element size was 0.0025 m. The connection between the core and cover boards was modelled using the tie contact in Abaqus with automatic discretization. The same uniformly distributed load of 2 kN/m^2 was applied to the upper cover of the panel, and the boundary conditions were applied automatically, based on the displacements of the shell model.

Using the procedure described above, six different sandwich panels were analysed. All panels had the same 22 mm thick OSB covers and different core structures:

- panel 1 – continuous core (full), 15 mm thick OSBs (Figure 6a);
- panel 2 – continuous core (full), 10 mm thick OSBs;
- panel 3 – discontinuous core (50% of the full core material), 15 mm thick OSBs (Figure 6b);
- panel 4 – discontinuous core (50% of the full core material), 10 mm thick OSBs;
- panel 5 – discontinuous core (25% of the full core material), 15 mm thick OSBs (Figure 6c);
- panel 6 – discontinuous core (25% of the full core material), 10 mm thick OSBs.

For each sandwich panel two FEM models were created: a shell model and a solid submodel (see Figure 6). Shell models had dimensions of 2.50 m x 1.25 m x 0.25 m, and the dimensions of the submodels differed depending on the panel: 0.25 m x 0.30 m x 0.12 m (panel 1 and 2), 0.25 m x 0.50 m x 0.20 m (panel 3 and 4), 0.25 m x 0.565 m x 0.20 m (panel 5 and 6). All submodels were cut from the same location of the shell models.

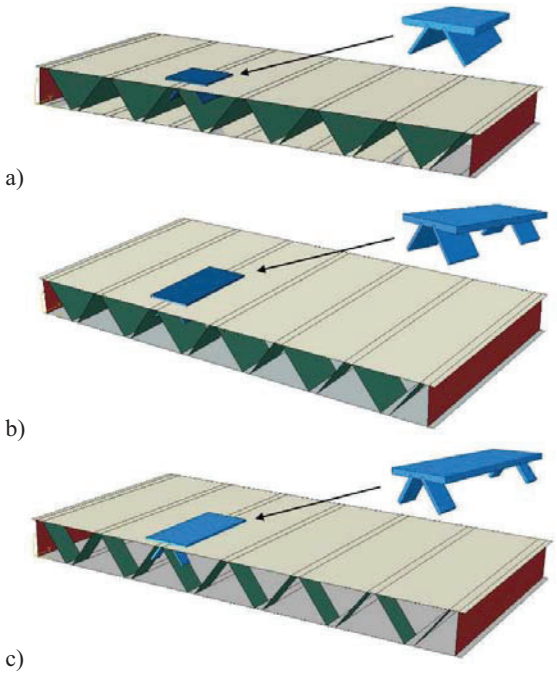

Figure 6: *3D shell models with 3D solid submodels: a) panel 1; b) panel 3; c) panel 5*

The material properties used in the numerical analysis are presented in Table 2. Values of the Young's moduli in two horizontal directions (longitudinal and transverse) were taken from the experimental tests described in Section 2, and all other parameters were adopted based on the literature study – due to the fact that those parameters have much smaller effect on the mechanical behaviour of the structure that the tested Young's moduli, equal values in all directions and for all OSB thicknesses were applied. However, in the future study the authors plan to identify all orthotropic coefficients experimentally.

Table 2: *Material parameters used in the FE analysis*

OSB thickness [mm]	10	15	22
E_1* [N/mm^2]	5191.22	4317.95	4072.05
E_2* [N/mm^2]	3471.12	2321.04	2271.99
E_3** [N/mm^2]	1800	1800	1800
ν**	0.2	0.2	0.2
G** [N/mm^2]	1100	1100	1100

* values identified experimentally
** values based on the literature

Selected results of the numerical analysis are presented in Figures 7-10. Figure 7 depicts magnitudes of displacements obtained in three shell models of selected sandwich panels: 1, 3, and 5.

https://doi.org/10.52202/069179-0320

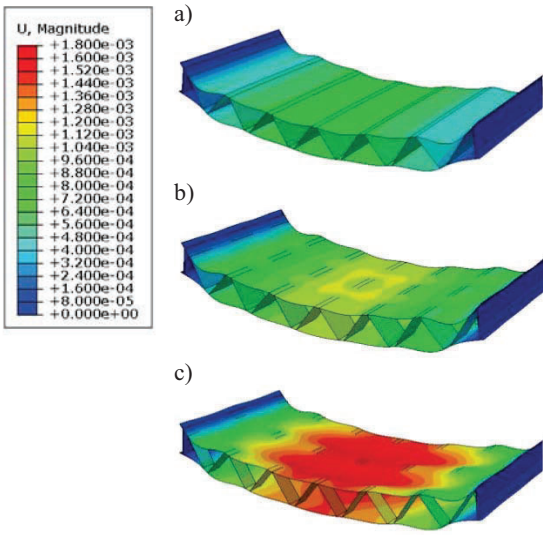

Figure 7: *Magnitude of displacements: a) panel 1; b) panel 3; c) panel 5*

It can be noticed that the reduction of the core material results in increased displacements of the panel. The following maximum displacements were obtained in sandwich panels with the 15 mm thick core boards: 0.79 mm for the full core, 1.14 mm for the 50% reduced core, and 1.72 mm for the 25% reduced core. Similarly, in sandwich panels with the 10 mm thick core boards, the maximum displacements were: 1.00 mm for the full core (26.6% increase in relation to the 15 mm thick core boards), 1.18 mm for the 50% reduced core (3.5% increase), and 1.80 mm for the 25% reduced core (4.7% increase).

Figures 8-10 show distributions of normal stress in the longitudinal direction in the submodels of six panels.

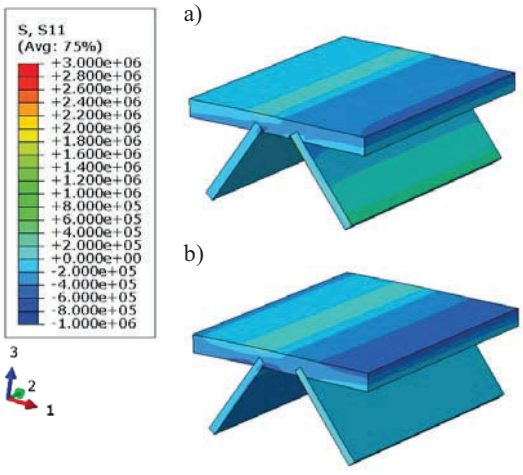

Figure 8: *Distribution of normal stress in the longitudinal direction: a) panel 1; b) panel 2*

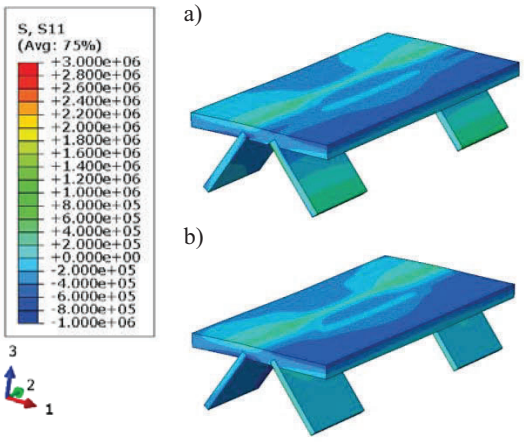

Figure 9: *Distribution of normal stress in the longitudinal direction: a) panel 3; b) panel 4*

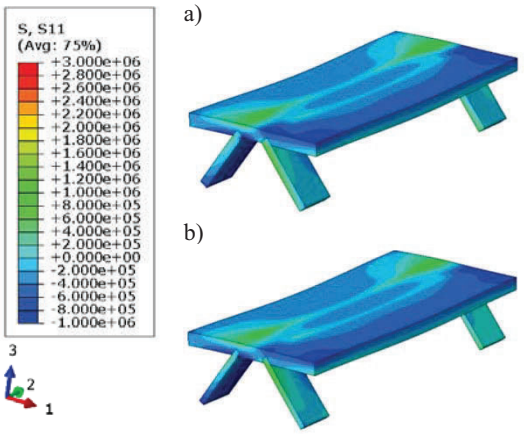

Figure 10: *Distribution of normal stress in the longitudinal direction: a) panel 5; b) panel 6*

The stress distribution is regular in the panels with full cores, and visible concentrations of stresses are observed in the panels with reduced cores, in OSB covers in the areas above the connections with the core boards. Changing the thickness of the core boards from 15 mm to 10 mm, does not affect much the distribution or values of normal stress in the longitudinal direction.

4 SUMMARY

This research focused on the development, and experimental and numerical testing of wood-based sandwich panels with two covers and an origami-inspired core made of OSB. First, laboratory tests on OSB samples of three various thicknesses (10 mm, 15 mm, and 22 mm) were conducted, in order to determine selected material properties of the boards – the Young's moduli in the longitudinal and transverse direction. The experimentally identified parameters were afterwards used in the finite element analysis of six sandwich panels, differing in the core type and the thickness of the core boards.

Three types of cores were considered: full, reduced by 50%, and reduced by 25%. For each developed panel, two numerical models were built: a 3D shell model of the whole panel and a 3D solid submodel of a section of the panel. While the shell models showed the general behaviour of the panels under the assumed uniformly distributed load, the submodels allowed the authors to analyse stress distributions in the areas of the connections between the OSB covers and the core.

The future research will focus on the experimental identification of other orthotropic coefficients of OSB, and other core types will be studied, e.g. tensegrity-inspired cores.

FUNDING

This research was funded in whole by the National Science Centre, Poland, grant number 2021/43/D/ST8/02238. For the purpose of Open Access, the author has applied a CC-BY public copyright licence to any Author Accepted Manuscript (AAM) version arising from this submission.

REFERENCES

[1] Plenzler R., Ludwiczak-Niewiadomska L., Strzelecki P.: Elastic and Strength Properties of OSB Layers. Drvna industrija, 68(1):3-9, 2017.

[2] Islam M.S., Islam M., Alam M.S. Properties of Oriented Strand Board (OSB), and Timber to Evaluate the Stiffness of Timber I-Joist. In: Canadian Society for Civil Engineering, Annual Conference and General Meeting, Leadership In Sustainable Infrastructure, Vancouver, Canada, 2017.

[3] Zhu E. C., Guan Z. W., Rodd P. D., Pope D. J: A constitutive model for OSB and its application in finite element analysis. Holz Roh-Werkst, 63(2):87-93, 2005.

[4] Hrázský J., Král P.: Determination of relationships between density, amount of glue and mechanical properties of OSB. Drvna industrija, 60(1), 2009.

[5] Feraboli P.: Notched response of OSB wood composites. Composites Part A: Applied Science and Manufacturing, 39(9):1355-1361, 2008.

[6] Smardzewski J., Maslej M., Wojciechowski K. W.: Compression and low velocity impact response of wood-based sandwich panels with auxetic lattice core. European Journal of Wood and Wood Products, 79(4):797-810, 2021.

[7] Mohammadabadi M., Jarvis J., Yadama V., Cofer, W.: Predictive models for elastic bending behavior of a wood composite sandwich panel. Forests, 11(6):624, 2020.

[8] Zheng T., Li S., Xu Q., Hu, Y.: Core and panel types affect the mechanical properties and failure modes of the wood-based XX-type lattice sandwich structure. European Journal of Wood and Wood Products, 79(5):1253-1268, 2021.

[9] Jin M., Hu Y., Wang B.: Compressive and bending behaviours of wood-based two-dimensional lattice truss core sandwich structures. Composite Structures, 124:337-344, 2015.

[10] Darzi S., Karampour H., Gilbert B. P., Bailleres H.: Numerical study on the flexural capacity of ultra-light composite timber sandwich panels. Composites Part B: Engineering, 155:212-224, 2018.

[11] Wang X., Shi X. L., Meng Q. K., Hu Y. C., Wang L. H.: Bending behaviors of three grid sandwich structures with wood facing and jute fabrics/epoxy composites cores. Composite Structures, 252:112666, 2020.

[12] Buri H., Weinand Y.: ORIGAMI – Folded Plate Structures. In: Infoscience, EPFL scientific publications, Proc. of the 10th World Conference on Timber Engineering, Miyazaki, Japan, 2018.

[13] Gilewski W., Pełczyński J., Stawarz P.: A comparative study of Origami inspired folded plates. Procedia Engineering, 91:220-225, 2014.

[14] Hughes T.: The Finite Element Method: Linear Static and Dynamic Finite Element Analysis. Dover Publications, 78, 2000.

[15] Hao H., Chen W., Chen S., Meng Q.: Finite element analysis of structural insulated panel with OSB skins against windborne debris impacts. In: Proceedings of 1st Pan-American congress on computational mechanics (PANACM), Buenos Aires, Argentina 27-29, 2015.

https://doi.org/10.52202/069179-0320

World Conference on Timber Engineering Oslo 2023

INNOCROSSLAM – ADDING KNOWLEDGE TOWARDS INCREASED USE OF CROSS LAMINATED TIMBER (CLT)

Boris Azinović[1], Erik Serrano[2], Henrik Danielsson[2], Josef Füssl[3] Markus Lukacevic[3], Philipp Dietsch[4], Matthias Arnold[5], Martin Schenk[5], Stefan Winter[5], Jose Manuel Cabrero[6], Pablo Gonzalez Serna[6], Tomaž Pazlar[1]

ABSTRACT: The research project *Innovative Solutions for Cross Laminated Timber Structures* (InnoCrossLam) was recently finished. The project aimed at increasing the competitiveness of CLT as a versatile engineered product, by increasing its predictability in demanding design situations not covered by the guidelines of today, or standards and codes foreseeable in the near future (*e.g.,* second generation of European design standards). This paper summarises the main project findings in the context of innovative CLT structures, such as: *i*. contemporary design approaches *ii.* the use of (non)linear FE modelling *iii.* experimental investigation of complex details for CLT structures, *iv*. investigation of multifunctional CLT. In this paper, the motivation behind the research topics within the project InnoCrossLam is explained and backed-up by exemplary results and discussion on future work.

KEYWORDS: mass timber, cross laminated timber, CLT properties, structural design, FE modelling, experimental investigation, multifunctional CLT, diagonal laminated timber, DLT

1 INTRODUCTION

1.1 BACKGROUND AND AIMS

Multi-storey timber construction has seen an important development over the last two decades, especially due to the introduction of cross laminated timber (CLT). Although the introduction of CLT to the market must be described as a success story, from a European perspective, the increased use of CLT is still slowed down by the lack of supporting provisions for design. Thus, there is still a lack of harmonised standard and unified design approaches in structural design codes. In addition, other complementing engineering tools such as handbooks are fragmented, national and, as a result, there is a risk of such documents leading to diverging recommendations. Finally, several common design situations are not covered [1].

1.2 OVERVIEW OF PRESENT WORK

Within InnoCrossLam, both basic research efforts and applied studies of innovative concepts have been performed. The work has covered studies to gain in-depth and basic knowledge of the mechanical behaviour of CLT, including joints and moisture related behaviour. Furthermore, the work has addressed more applied research by including investigations on prototypes of innovative concepts related to CLT with embedded functionality in terms of heating and ventilation (known as thermal activation). Finally, the project InnoCrossLam has aimed at proposing practical design approaches and formulae, for inclusion in future structural codes and standards.

2 PROJECT TOPICS AND RESULTS

2.1 SURVEY OF CURRENT CLT PRACTICE

Due to the crosswise arrangement of layers, CLT requires special approaches in the calculation of its mechanical properties and the evaluation of its structural performance compared to typical timber products such as solid structural timber or glulam (GLT). Therefore, as part of the project, it was deemed necessary to conduct a global survey of current practices. The results of the survey can be found in [2]. The questionnaire was distributed digitally worldwide to those who can produce, process, design or install CLT (i.e., CLT manufacturers, suppliers, engineers in construction companies, structural engineers, and researchers in institutions). A large part of the participants came from the main area of the CLT industry, i.e., Germany and Austria.

[1] Boris Azinović & Tomaž Pazlar, Slovenian National Building and Civil Engineering Institute (ZAG Ljubljana), Slovenia, boris.azinovic@zag.si & tomaz.pazlar@zag.si
[2] Erik Serrano & Henrik Danielsson, Lund University, Sweden, erik.serrano@construction.lth.se & henrik.danielsson@construction.lth.se
[3] Josef Füssl & Markus Lukacevic, Technical University of Vienna (TUW), Austria, josef.fuessl@tuwien.ac.at & markus.lukacevic@tuwien.ac.at
[4] Philipp Dietsch, Karlsruhe Institute of Technology (KIT), Germany, dietsch@kit.edu
[5] Matthias Arnold & Martin Schenk, Stefan Winter, Technical University of Munich (TUM), Germany, matthias.arnold@tum.de & martin.schenk@tum.de
[6] José Manuel Cabrero & Pablo González Serna, University of Navarra (UNAV), Spain, jcabrero@unav.es & pgonzalezse@unav.es

https://doi.org/10.52202/069179-0321

More than 70% of the respondents are involved in practice, either in a design office or in a construction company. About 20% of the participants was from research and the remaining from construction companies.

Respondents proved to be quite experienced, most of them having worked in the field for more than 11 years (52.5%). Considering the recent introduction of CLT in practice and the experience of the respondents, it is possible that most of the respondents are self-taught on CLT design. Although most of them, 85%, consider that they have a reasonable knowledge of cross laminated timber structures, the obtained results show a very diverse level of knowledge. The design practice is also very different. While material parameters are uniformly applied to some extent, the approach to design is documented in a very heterogeneous manner, as shown by the wide range of literature used for design practice. No uniformly used background document could be identified.

Regarding the type of software or tools used for CLT verification, practice-oriented finite element (FE) modeling software is most commonly used, especially by designers and constructors in practice (about 70%). CLT-oriented software is used comparatively often, especially in the construction sector. In most cases, however, designers must additionally develop their own tools for certain analyses and verifications.

The most challenging design aspects in practice were openings in walls/floors (cca. 18% and 15%), point supports, and concentrated loads (23%). The majority pointed out the lack of design provisions as the main reason. In addition, connections, vibration, and fire measurements were also reported, again due to the lack of existing design regulations. The results of the survey mainly point to the lack of standardization and incomplete regulations as the main problems for practitioners. This unclear situation leads to the fact that the design of a structure in solid timber construction requires experience and further qualification and can therefore be performed only by some well-trained engineers. There is a need for the development of appropriate tools and models for the product, as well as simple design rules.

2.2 CLT AND MOISTURE

CLT is commonly used as a base for Timber Concrete Composites (TCC), and in this application the issues of moisture transport, drying and moisture-induced deformation are of interest. These were investigated with the help of accurate 3D FE models.

In general, wood moisture plays a major role in the design of timber structures, as wood is a highly hygroscopic material in which changes in moisture lead to changes in almost all physical properties. Due to its directionally dependent material properties, this can lead to cracking. However, the determination of the moisture condition in a timber member is relatively complex and the condition is variable both spatially and temporally, which is why only a very simplified consideration is used in the current version of the standard for the design and construction of timber structures. Water can occur in wood as bound water in the cell walls and as water vapor or free water in the cell lumen. Transport in the respective phases can be described by diffusion (bound water and water vapor) or capillary transport (free water). The phases are also connected by sorption (between water vapor or free water and bound water) and evaporation/condensation (between water vapor and free water). These mechanisms can be described with a so-called multi-Fickian transport model, which was previously implemented and validated with the finite element method and the commercial software Abaqus within a user element subroutine [3].

Next, this simulation tool was used to study the moisture loads that can occur in buildings. The first winter (heating phase) after the installation of the wood component is particularly critical when using timber elements indoors. To simulate such changes in humidity, moisture loads were applied to different wood elements in [4]. Starting from different initial wood moisture contents, fictitious reductions in relative humidity were applied to all exterior surfaces of the cross-sections and held for 720 h. The results were then used to simulate the moisture content of the cross-sections. Depending on the applied difference in relative humidity, the moisture content (MC) differed between 1% and 15% between the outside and inside of the cross-section. Based on the moisture simulations, the stresses can be calculated using expansion coefficients and the stiffness tensor. In unfavourable cases, these stresses can exceed the strength of the wood, causing plastic deformations and cracks [5]. Based on simulation results at the level of individual wood cells, a multisurface failure criterion was developed [6-8] that can reveal ductile (plastic) and brittle (cracking) failure mechanisms that can be used in commercial finite element software to predict the nonlinear behaviour of timber elements under moisture loading. The resulting crack patterns were analysed, and the maximum crack depths at specific time points are shown in Figure 1 for an initial wood moisture content of 15.3%.

From this figure, it can be seen, that the cracking is completed at different times depending on the cross-section width. In the case of the smallest cross-section with a width of 6 cm, this is already the case after 72 h, while in the case of the largest cross-section (GLT 20/40) an increase is already evident after 720 h. This is due to the difference in the cross-section widths: the difference in wood MC (and thus the wood moisture gradient) between the surface and the centre decreases as soon as the moisture flow from the surface reaches the centre of the cross-section. This is also roughly the time when cracking is complete. It is also easy to see that short-term changes of less than 8 hours cause only very small cracks, as a significant wood moisture gradient develops only near the edge. It can also be seen that small moisture differences in small cross-sections still lead to no or only small crack depths, while cracks or significantly deeper cracks can already occur in larger cross-sections. According to [9], cracks up to a depth of 15 mm per side are considered harmless.

https://doi.org/10.52202/069179-0321

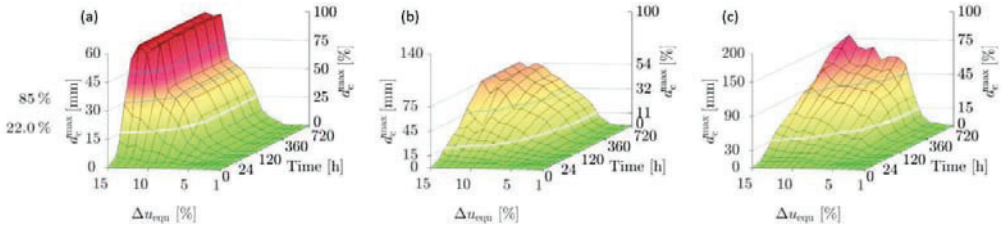

Figure 1: *Development of the maximum crack depth (sum of maximum crack depths of both cross-section sides), given in absolute and relative crack depth, for the cross-sections (a) solid timber 6/8, (b) solid timber 14/28 and (c) GLT 20/40 with an initial wood MC = 15.3% at different moisture content (MC) differences during 30 days (720 h) [9,10].*

The ultimate and serviceability limit states must be respected in the design of a timber structure according to EC 5. Changing climatic conditions and associated moisture-induced stresses are not taken into account directly in the current version of this standard, but via adjusted material parameters [10]. Compared to other environmental effects on the structure, such as wind and snow, no similar site-specific data are available for wood.

The following application of the models to a timber concrete composite demonstrates the capability of such an approach in studying critical conditions. Nowadays, the common method of manufacturing TCC elements with notches as shear connections is to apply fresh concrete directly to the CLT element. However, the fresh concrete releases moisture after application, which is absorbed by the highly hygroscopic wood and may lead to critical reduction of mechanical properties or problematic situations due to different expansion behaviour. Therefore, we used the moisture simulation tool to investigate the influence of the fictitious application of fresh concrete and then a realistic indoor climate applied to the bottom of the CLT element on the moisture behaviour of the timber parts [11]. Figure 3 shows the model of the CLT element and the path along which the wood MC is evaluated over the simulation period.

The resulting wood MC along the path over the simulated period are first shown in Figure 2 (below) for the original model without sealing. Moisture peaks above 70% occur in the uppermost lamella, corresponding to a value above the fibre saturation point and thus free water in the wood cells. Approximately the top half of the slab is affected in wood MC by the application of the fresh concrete. Depending on the indoor climate, the additional moisture introduced is removed over the course of nine to ten months before the entire slab dries out and an equilibrium MC of between 8% and 9% is reached. After that, only the lowest two lamellas are affected by the indoor climate. In addition, local sealing in the area of the end faces of the notches effectively reduces the moisture peak that occurs (see Figure 2). This means that such a sealing could possibly replace commonly used separating foils, which cause a high labour input or can reduce the load transfer.

In the next step, the implementation of more advanced crack modelling techniques [11,13] will also allow to represent in more detail the variability of, e.g., the strength properties of such timber products, leading to even better performance predictions, which have already successfully been shown for studying the so-called size effect of glulam [14,15].

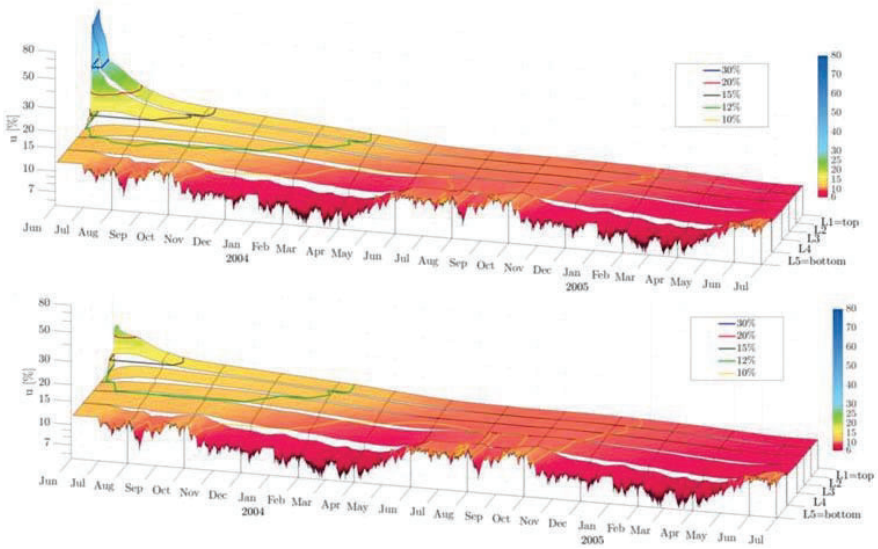

Figure 2: *Course of wood moisture content (MC) along the CLT plate thickness (from L1=top lamella to L5=bottom lamella), plotted over two years for the unsealed model (top) and the model with sealed end faces in the area of the notches (bottom) [11].*

https://doi.org/10.52202/069179-0321

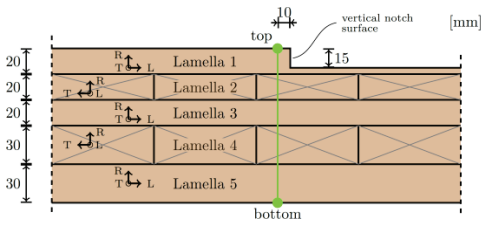

Figure 3: *Sketch showing the structure of the CLT element with local coordinate systems and path (green) for the evaluation of the MC curves over the simulation time [12].*

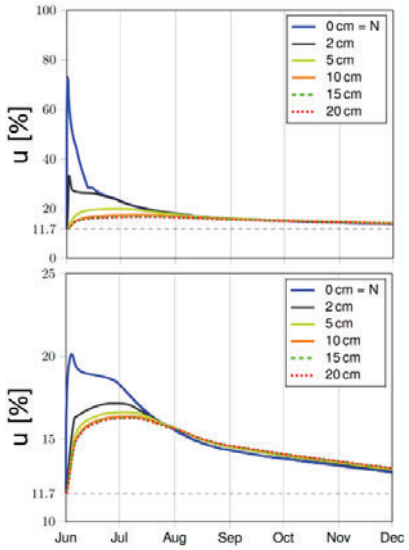

Figure 4: *Course of moisture content (MC) in the shear plane for the unsealed model (top) and the model with sealed end-grain surfaces (bottom) [12].*

2.3 CLT IN-PLANE SHEAR

For in-plane shear loading of CLT, two types of loading situations may be considered: pure in-plane shear loading and in-plane beam loading. The pure in-plane shear loading case is relevant for the loading situation in a shear wall or in a floor diaphragm, while the in-plane beam loading case would represent the loading situation for a lintel, or a pointsupported wall element.

For shear, three possible failure modes - gross shear failure (I), net shear failure (FM II), and shear failure in the crossing areas (FM III) - must generally be considered in the design. The methods proposed for verifying the ultimate capacity with respect to these three shear failure modes vary considerably among the design codes, design manuals, and ETAs of CLT manufacturers. The differences mainly relate to the determination of the design relevant stress components for FM II and FM III and the underlying mechanical models for stress analysis.

Within InnoCrossLam, investigations of the in-plane shear behaviour of CLT focused on the development of rational and unified design approaches for the cases of pure in-plane shear and in-plane beam loading conditions, considering design with respect to FM III.

An analytical model for prediction of internal forces and stresses acting in crossing areas between laminations of adjacent layers has been developed. The model is derived by considering the static equilibrium of individual laminations in CLT without narrow face bonding and loaded in pure in-plane shear. Stress predictions from the developed analytical model, predictions of design-relevant stresses from methods found in codes and handbooks and results from full 3D finite element simulations are compared for 3- and 5-layer CLT in [16] and for 7-layer CLT in [17]. The modelling approaches are limited to consideration of linear elastic behaviour, and the studies focused on the influence of CLT layup (i.e., individual layer thicknesses) on the magnitude and distribution of shear stresses acting on the crossing areas between adjacent layers. The results reported in [16] and [17] show large discrepancies between the considered models in terms of the magnitude of the stresses relevant for shear FM III.

An analytical model for stress analysis of CLT at in-plane beam loading was previously developed by Flaig & Blass, see e.g. [18]. This approach formed the basis for the design equations which were included in previous draft-versions of the new Eurocode 5 and the design equations suggested in the Canadian CLT Handbook. Modifications of the original model by Flaig & Blass have been suggested in [19], aimed at improving predictions of the stress state at loading (compared to the results of finite element simulations). A unified design approach, covering both the case of pure in-plane shear loading and in-plane beam loading, has been developed and is presented in [20]. This approach is based on the analytical model for pure shear loading and the modified model for the beam loading case, with some simplifications and approximations to arrive at rather simple and compact design equations.

In addition, experimental tests of CLT beams have been carried out at ZAG, Slovenia, using a 4-point bending test setup as shown in Figure 5. Six test series with a total of 36 individual tests were performed on beams with a gross cross section b×h = 140×600 mm^2. The study included investigations of three parameters: the individual lamination width, the cross-section lay-up in terms of thickness of each longitudinal layer, and the beam overhang at the supports. The general load versus displacement response was similar in all tests: after an initial linear response, a gradual decrease in stiffness was observed before reaching the maximum load and final failure. At the ultimate limit state, the beam failed due to bending (combined bending and tension) of the individual longitudinal laminations. Digital Image Correlation (DIC) measurements of surface strains and measurements of relative displacement between adjacent longitudinal laminations in the external layers showed significant sliding between the laminations. Sliding between laminations could also be observed at the end faces of the beams, as shown in Figure 6. The gradual decrease in stiffness - before reaching the maximum load - indicates damage and loss of stiffness of the bonding over the crossing areas.

https://doi.org/10.52202/069179-0321

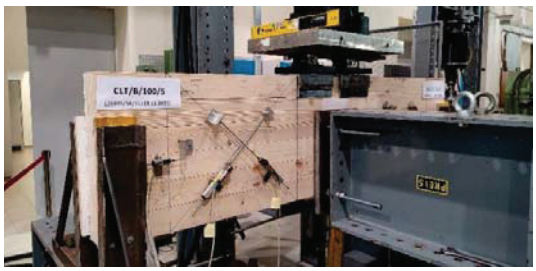

Figure 5: *Test setup for CLT at in-plane beam loading.*

Figure 6: *Shear failure in crossing areas at beam ends.*

The test results are yet to be fully analysed and published. However, the results indicate very little or no effect of the lamination width or of the element layup on load-bearing capacity. These two findings are not consistent with the predictions of the proposed design equations. There are several plausible reasons that could explain the differences between the model predictions and the experimental results for the load-bearing capacity. The models and the failure criterion are based on the assumption of linear elastic behaviour. There appears to be gradual damage of the bonding over the crossing areas between the laminations of adjacent layers appear to take place, before the maximum load is reached. This damage and the corresponding local stiffness reduction could lead to stress redistribution effects and a stress state that deviates significantly from the model assumptions.

Moreover, the failure criterion itself, which is based on consideration of rolling shear stress and a torsional shear stress acting in the crossing areas, may not be suitable for accurate prediction of the load-bearing capacity. Failure criteria for FM III and test setups for determining the relevant strength parameters are further investigated and discussed in [21].

2.4 CLT WITH OPENINGS

An often-faced challenge relates to the design of CLT floors with openings. Within the project this situation has been studied both numerically and experimentally at Technical University of Munich (Figure 7) to find practical design recommendations. Two sets of specimens were designed to understand the different contribution of bending and shear to the overall deformation. Different types of holes were used for each set: a central hole for the bending specimens and holes on the supported edges for the shear specimens. For comparison purposes, three different hole sizes were tested: no holes, a 300x300 mm^2 hole for bending specimens, and 200x300 mm^2 holes for the shear specimens, both of which were eventually enlarged to 600 mm. The different holes were applied sequentially to each specimen, which were therefore tested only in the elastic region. As expected, in both cases the deformation increases with increasing hole size (and thus the stiffness decreases).

As can be seen from the survey [2], FE modelling based on shell elements is the most widely used approach. In the case of holes, the Beam Grillage Model (BGM) was proposed in [22], which simplifies the slab to a beam grid with effective stiffness. These two modelling approaches were compared with the obtained experimental results. Both show poor accuracy compared to the test results, especially in the case of shear dominated configurations. The FE model appears to be more accurate than the BGM for both bending and shear configurations. Although the BGM model is less accurate, it is shown to be conservative for the bending cases (which could be the main case in realistic applications). Both models need to be improved to be considered adequate approaches for this design challenge. For more information, see the companion paper [23,24].

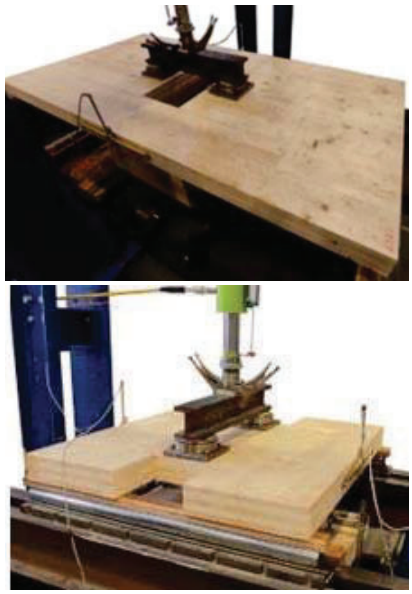

Figure 7: *Experiments on CLT floors with centred openings (bending series, top) and in the supports (shear series, bottom).*

2.5 CLT JOINTS

As with all structural timber elements, understanding the behaviour of joints is crucial also in CLT. As part of InnoCrossLam, particular emphasis was placed on quantifying brittle fracture through an experimental investigation (Figure 8) and reviewing previously available design approaches for their applicability to CLT. Currently existing brittle failure models have been developed mainly for timber products such as glulam and LVL [25-27]. Due to the load distribution between adjacent layers within a CLT element, i.e., due to cross-layer reinforcements, these models cannot be directly applied to CLT. Zarnani and Quenneville [28] made some modifications to their original model [29] to adapt it for CLT and verified the new approach for riveted CLT

https://doi.org/10.52202/069179-0321

connections. Within the project, an experimental campaign was conducted at ZAG (the Laboratory for Structures) on connections with self-tapping screws subjected to tensile loads parallel to the outer layer of the CLT. The experimental campaign, the obtained results and the observed failure modes are described in [30], while the explanation of the existing model, its application to the performed experiments and the obtained results can be found in [31].

The experimental results described in [30] indicate that the load-bearing capacity of the connection increases with the width of the CLT specimen; for example, a 45% increase was observed between the width w = 250 mm and w = 750 mm. However, the increase in specimen width does not seem to affect the resulting elastic stiffness. The length of the screws was found to have a large effect on the elastic stiffness; for example, an increase of more than 70% was observed between 40 mm and 100 mm fastener lengths. The CLT layup does not seem to have a significant influence on the elastic stiffness, while it has an effect on the resulting load-bearing capacity, especially in relation to the penetration of the fastener into the different layers.

Figure 8: *Example of brittle CLT connection failure.*

It was also found that brittle failure typically occurs after the yielding of the fastener has already begun. Quite low ductility values are typically observed, in the range of 1.5-2.5, making these types of connections unsuitable for use in earthquake-prone areas where higher local ductility would be desirable. The existing model developed by Zarnani and Quenneville [28] has given rather inconsistent results compared to the experimental values of the connections performed in [30]. A major reason for this is the significant difference between the reported material properties. It must be emphasised that the need for reliable material properties is (as always) an important task. Moreover, they should be obtained from tests under conditions comparable to those assumed in the model. In addition, the trends presented for moisture may be affected by the reliability of the characteristic level due to the small number of replicates.

2.6 INNOVATIVE CLT

2.6.1 Multifunctional CLT in terms of thermal activation

Introduction and definitions

As part of the work on specific CLT panels, the InnoCrossLam project addressed the properties of application-optimised, multifunctional CLT wall elements. The objective of the presented research was to further develop a previously proposed CLT element (proof-of-concept [32,33]), which is multifunctional in terms of its thermal activation, to application maturity.

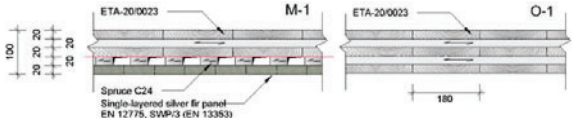

Figure 9: *Exemplary layup of a multifunctional CLT series (left) and a reference series (right) [mm].*

CLT wall elements with channels in which conditioned air circulates (Figure 9), enable the conditioning of massive timber buildings that meet the energy standards currently required in Central Europe [29]. The Construction Product Regulation (CPR) defines the essential requirements and key deliverables for the development and introduction of new construction products on the European market. By determining several essential properties of the multifunctional CLT, the relevant requirements covered in the CPR were answered.

Experimental investigations on the mechanical resistance and moisture changes in the cross section

The experimental investigations have proven that the reduction of the cross-sectional area by the channels does not necessarily have a significant effect on the compressive strength and stiffness of the elements [34]. On the other hand, the climatic tests clearly show that the quality of the front layer is of crucial importance for the deformation behaviour and the cracking pattern under thermal loading. It is therefore advisable to use high-quality 1-layered or better 3-layered solid wood panels for the outer layer [35].

Experimental and analytical investigations on the fire resistance

Safety in case of fire is a key issue in mass timber construction; such as the determination of mass burning rates and the fire protection closure. In large-scale fire tests, the time-temperature curves, the mass burning rate, and fire protection closure were investigated with and without cladding (Figure 10). Additional studies were conducted to analyse the effects of the fire within the channels. For the cavity fire studies, test specimens were moved inside the furnace (Figure 11, right). The specimens had the dimension w/l = 0.5 m / 0.5 m.

Figure 10: *Test specimen in the climate chamber.*

https://doi.org/10.52202/069179-0321

The charts in Figure 11 show examples of the time-temperature curves behind each layer of test specimens (i.e., at a depth of 20, 40, 60, and 80 mm) for a fire event following the ISO 834 [33] curve. Compared to a standard CLT (O-1 series), the discrepancy between the curves measured at 40 mm depth with and without channels differs significantly. For the M-1 series, the flash point of 300 degrees is reached about 15 minutes earlier than for the O-1 series within the middle layer. Smoke and heat passage for M-1 is reached after 60 minutes. A burn-through after 90 minutes. Comparing the M-1 series without additional cavity fire to the M-1 series with additional cavity fire it is clear that the additional cavity fire leads to a reduction in fire resistance of an additional 10 minutes. The question of how to limit or extinguish cavity fires is a question of causality of a fire event that can only be answered analytically: Either a burning-in must be prevented by fire bulkheads or intumescent stripes must be introduced into the cavities during production [35].

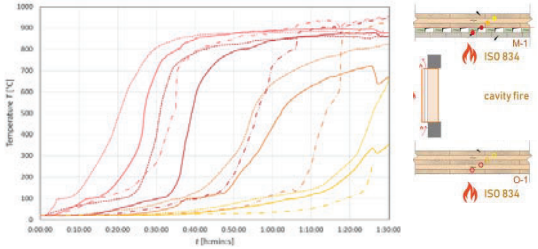

Figure 11: *Time-temperature curves of O-1 and M-1 series with and without cavity fire.*

2.6.2 CLT with diagonal layer arrangements

Introduction and definitions

In addition to research on multifunctional CLT, the mechanical properties of innovative Diagonal Laminated Timber (DLT) were investigated. DLT is a massive timber element, which is innovative in terms of its out-of-plane load-bearing capacity under biaxial bending and homogenization effects of stress distribution. DLT represents an application-optimised evolution of CLT. Conventional CLT consists of individual layers made from softwood laminations which are glued together in crosswise arrangement; this is done at angles of 90°. In DLT, on the other hand, 5 to 9 layers are glued together at specific angles Θ. For each –Θ layer, there is a +Θ layer within the laminate (Figure 12). In this context, DLT can be considered as a standard counterpart to CLT, offering improved mechanical properties when using the same material properties and layer thicknesses.

The diagonal arrangement of the individual layers promises increased in-plane and out-of-plane stiffness properties. Thus, for DLT, smaller deformations compared to conventional CLT are to be expected. In addition, the diagonal arrangement of the layers promises further homogenization of the orthotropic stiffness and strength properties. This can have a positive effect on the stress distribution due to the introduction of concentrated loads.

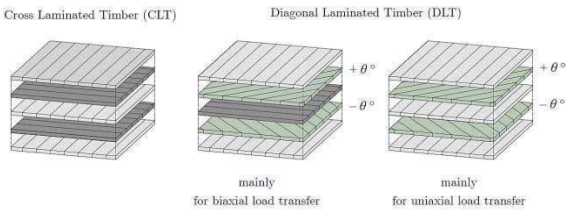

Figure 12: *Exemplary layup of a CLT series and DLT series*

Analytical, experimental and numerical investigations

The aim of this research was to determine the stiffness properties of DLT in terms of number and orientation of the layers. Therefore, the stiffness properties (out-of-plane shear stiffness, torsional stiffness, bending stiffness) have been determined by means of analytical, numerical, and unique experimental investigations (Figure 13). Parts of the results of this research have already been published in [36] and form the basis of further publications [36] and a future dissertation [38].

Following the studies on out-of-plane stiffness properties, a quantitative statement was made on the increase of the in-plane stiffness properties of DLT compared to CLT. This is particularly relevant to the use of DLT for stiffening wall and slab elements and for deep beams with large openings and notches. In addition, the objective was to implement the stiffness parameters in 2D FE models used for deformation analysis related to different static systems of mass timber slabs. The stress distribution in the load application region of point-supported CLT and DLT panels was investigated using large-scale 3D FE models.

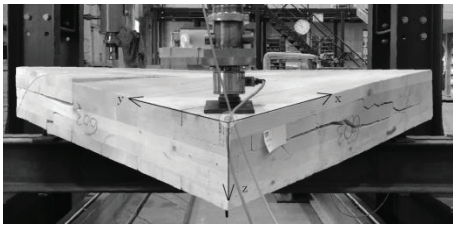

Figure 13: *Experimental investigations on the torsional stiffness of DLT.*

Ratio of homogenization

The terminology "ratio of homogenization" in terms of the number of diagonally or transversely oriented layers relative to the total number of layers oriented in the global x-direction was introduced. By the ratio of the sum of the thicknesses of diagonally and orthogonally oriented layers $t_{d,i}$ to the total thickness t_i, this terminology is quantified. Here, diagonally or transversely arranged layers are accounted for by the square of the cosine function of the respective angle Θi ($cos^2\Theta i$). For a 5-layered DLT element with two layers arranged at 45° - as shown in Figure 12, centre - the ratio is ξ=0.600 (equation (1)).

$$\xi = \frac{\sum t_{d,i}}{t} = \frac{(cos\,45°)^2 \cdot 30 \cdot 2 + (cos\,45°)^2 \cdot 30 \cdot 2 + (cos\,90°)^2 \cdot 30}{150} \quad (1)$$

Therefore, an isotropic plate element could be given as an extreme value that gives the ratio ξ=1.000. A 5-layered CLT of series O-1 has a homogenization ratio of ξ=0.429. The homogenization ratio serves as an indicator of the applicability of the chosen layup, regarding structures governed by uniaxial or biaxial bending in the serviceability limit state (SLS).

2.7 SEISMIC DESIGN OF CLT STRUCTURES

Extending the use of CLT structures to earthquake-prone areas and/or the architecturally driven development of asymmetrical and tall CLT structures requires more accurate numerical models and engineering design tools. The use of (non)linear FE models was investigated and evaluated from an engineering perspective.

The seismic force-resisting system (SFRS) in CLT structures consists of shear walls connected to the foundation or floors through various types of connectors to resist uplift and shear forces [39]. In general, CLT panels exhibit in-plane elastic deformation, while the desired seismic behaviour is achieved with sufficient overstrength design for possible brittle failures, such as splitting, and dissipative zone yielding of predefined ductile connections [40]. The decision on the type of FE analysis, linear and/or nonlinear, is mainly determined by the height and complexity of the structure and by the design approach chosen - Force-Based Design (FBD) or Displacement-Based Design (DBD).

Force-Based Design (FBD) approach

The two most common linear methods of analysis, regardless of structure type, the lateral force method (LFM) and the response spectrum method (RSA), both adopted in EN 1998-1:2004 [41], are based on the design spectrum and used for the force-based design (FBD) approach. In this case, although CLT structures provide a good ability to withstand earthquakes without serious damage, behaviour factors higher than 3.0 can hardly be achieved for taller buildings [42], so they should be selected with caution. Depending on the complexity of the structure and the ability to dissipate energy, values between 1.5 and 3.0 are recommended as suitable values in previous studies [43].

Since the CLT panels have a significant effect on the vibration frequency of the structure, the anisotropic material properties of the wood and the cross-laminated layers of the panels must be considered to accurately determine the stiffness of the building. When modelled as shell elements, design-oriented FE software packages include additional modules based on laminate theory [44] that could be easily adapted to CLT panels. However, orthotropic material model methods such as the equivalent orthotropic shell model-composite theory [45] or the shear analogy method [46] provide a satisfactory estimate of stiffness compared to experimental results at the global scale [47]. In addition, dissipative vertical connections between adjacent wall panels, shear connections, and hold-downs or anchors should be simulated in the wall models by introducing linear springs or other equivalent elements with appropriate stiffness values. Connections between adjacent panels should always be hinged. The supports to RC foundation are usually also hinged and with implemented shear and uplift stiffness parameters of the corresponding connection.

In addition, underestimation of building vibration frequencies and consequently non-conservative calculation of seismic forces with longer vibration periods and/or over-design under serviceability criteria for wind loads may be caused by secondary non-structural elements, as they have a greater influence on the overall stiffness of a lightweight CLT structure, as shown in [47,48]. As shown in Figure 14, a multi-phase approach using diagonal members at location of the openings can be used to represent the influence of the non-structural elements in the exterior façade. Since the total mass has the greatest influence on the natural frequencies, the most important global mode shapes, with the highest effective modal masses can be easily excluded from the local mode shapes in the modal analysis (e.g., by implementing nodal constraints as in-plane rigid floor diaphragms and manually calculated joint masses at each floor). Following these linear FE modelling principles can save engineers time, reduce errors, and improve the final design of the CLT building.

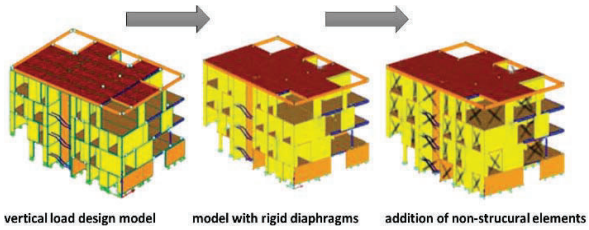

Figure 14: *FE model of a CLT building illustrating a multi-phase modelling approach and introduction of secondary elements stiffness by introducing diagonal spring members.*

Displacement-Based Design (DBD) approach

Since drift limits and target displacements are a common seismic performance objective for innovative performance-based design (PBD), the traditional FBD approach is not best suited for such a design concept. Such predefined objectives are better suited for the DBD approach, which is usually associated with the nonlinear static or pushover analysis - N2 method as described in Annex B of EN 1998-1:2004 [41]. The basis of the method uses the nonlinear response of the predefined components of the ductile structure beyond the elastic resistance and replaces the reduced response spectrum with the transformed bilinear capacity spectrum type curve of the structure under consideration. Although a minimal modification of the N2 method has been proposed in some studies on the design of multistorey CLT buildings [49], the present Eurocode 8 yields higher values for the displacement demands, so that the results are on the conservative side and thus can be safely used in the design process of CLT structures. Since the method requires a nonlinear FE model of the structure to analyse the seismic behaviour, the modelling process is consequently more complex and time-consuming.

https://doi.org/10.52202/069179-0321

In addition, the nonlinear behaviour of the selected ductile connection elements should be defined with a bilinear or multilinear relationship in such a way as to reduce the problems associated with the convergence criteria. To overcome these difficulties, all the modelling principles and simplifications of the global structure as previously discussed for the FBD approach should be implemented in the nonlinear model. In order to simplify the model and reduce the number of FE elements and consequently shorten the computation time, the vertical load can be applied directly to the wall panels and the floors can be modelled as in-plane connected diaphragms only. Since different lateral loading patterns and/or positive and negative directions of load application can be crucial for undesirable structural behaviour of CLT structures at both global and local scales, all loading scenarios should be analysed, and the most undesirable result should be selected for the final design phase (Figure 15). Moreover, the effects of irregularities and their influence on the behaviour of the structure can be analysed using the extended N2 method, which provides a simple estimation of their possible unfavourable effects using the calculated correction factors [50].

An implementation of the N2 method and DBD of a case-study multi-storey CLT platform type building with a simplified nonlinear FE modelling approach, based on a validated single wall model, is presented in [51] where the adequacy of the designed building is assessed to various seismic loading. In a next step, more complex nonlinear seismic analysis methods will allow to validate and develop clear guidelines for the application of the DBD and N2 method to CLT structures.

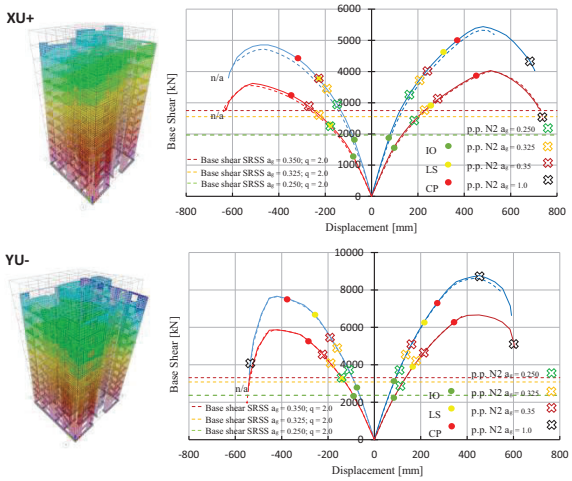

Figure 15: *Pushover analysis and capacity curves with indicated global limit states, N2 performance points and total base shear obtained based on different design spectra for a multi-storey case-study CLT building.*

3 CONCLUSIONS

The project InnoCrossLam has resulted in:

- new in-depth understanding of the mechanical behaviour of CLT components and joints,
- advanced modelling techniques,
- further development of design provisions for CLT by proposing rationally based formulae,
- recommendations for the design of CLT connections in terms of avoiding brittle CLT failure and designing connections with flexible insulation,
- properties of multifunctional CLT in terms of its mechanical and climatic performance and other.

ACKNOWLEDGEMENTS

InnoCrossLam has received support within ERA-NET Cofund ForestValue by MIZŠ, VINNOVA, FORMAS, STEM, BMLFUW, FNR and MINECO-AEI and has received funding from the European Union's Horizon 2020 research and innovation programme under grant agreement N° 773324.

REFERENCES

[1] M. Schenk, P. González-Serna, and J. M. Cabrero. Future research on cross laminated timber (CLT) for multi-storey buildings – a questionnaire among engineers active in practice. In *WCTE 2020/21*, 2021.

[2] M. Schenk, C. Hübner, and J. M. Cabrero. Cross-Laminated Timber: A Survey on Design Methods and Concepts in Practice. *CivilEng.*, vol. 3, no. 3, 2022.

[3] M. Autengruber, M. Lukacevic, and J. Füssl. Finite-element-based moisture transport model for wood including free water above the fiber saturation point. *Int. J. Heat Mass Transf.*, vol. 161, p. 120228, 2020.

[4] M. Autengruber, M. Lukacevic, G. Wenighofer, R. Mauritz, and J. Füssl. Finite-element-based concept to predict stiffness, strength, and failure of wood composite I-joist beams under various loads and climatic conditions. *Eng. Struct.*, vol. 245, p. 112908, 2021.

[5] M. Autengruber, M. Lukacevic, C. Gröstlinger, and J. Füssl. Finite-element-based prediction of moisture-induced crack patterns for cross sections of solid wood and glued laminated timber exposed to a realistic climate condition. *Constr. Build. Mater.*, vol. 271, 2021.

[6] M. Lukacevic, J. Füssl, and R. Lampert. Failure mechanisms of clear wood identified at wood cell level by an approach based on the extended finite element method. *Eng. Fract. Mech.*, vol. 144, pp. 158–175, 2015.

[7] M. Lukacevic and J. Füssl. Application of a multisurface discrete crack model for clear wood taking into account the inherent microstructural characteristics of wood cells. *Holzforschung*, vol. 70, no. 9, pp. 845–853, 2016.

[8] M. Lukacevic, W. Lederer, and J. Füssl. A microstructure-based multisurface failure criterion for the description of brittle and ductile failure mechanisms of clear-wood. *Eng. Fract. Mech.*, vol. 176, pp. 83–99, 2017.

[9] P. Frech. Beurteilungskriterien für Rissbildungen im konstruktiven Holzbau*: Forschungsvorhaben E-85/20, durchgeführt im Auftrag der Entwicklungsgemeinschaft Holzbau (EGH) in der Deutschen Gesellschaft für Holzforschung eV (DGFH)*. IRB Verlag, 1986.

[10] S. Svensson, G. Turk, and T. Hozjan. Predicting moisture state of timber members in a continuously varying climate. *Eng. Struct.*, vol. 33, no. 11, 2011.

[11] S. Pech, M. Lukacevic, and J. Füssl. Validation of a hybrid multi-phase field model for fracture of wood. *Eng. Fract. Mech.*, vol. 275, p. 108819, 2022.

[12] M. Lukacevic, M. Autengruber, T. Raimer, J. Eberhardsteiner, and J. Füssl. Effect of cast-in-place concrete application on moisture distribution in timber-concrete composite floors with notched connections, investigated via finite element simulations. *J. Build. Eng.*, vol. 42, p. 103005, 2021.

[13] S. Pech, M. Lukacevic, and J. Füssl. A hybrid multi-phase field model to describe cohesive failure in orthotropic materials, assessed by modeling failure mechanisms in wood. *Eng. Fract. Mech.*, vol. 271, 2022.
[14] C. Vida, M. Lukacevic, G. Hochreiner, and J. Füssl. Size effect on bending strength of glued laminated timber predicted by a numerical simulation concept including discrete cracking. *Mater. Des.*, vol. 225, p. 111550, 2023.
[15] C. Vida, M. Lukacevic, J. Eberhardsteiner, and J. Füssl. Modeling approach to estimate the bending strength and failure mechanisms of glued laminated timber beams. *Eng. Struct.*, vol. 255, p. 113862, 2022.
[16] H. Danielsson and E. Serrano. Cross laminated timber at in-plane shear loading–Comparison of model predictions. In *INTER/52-12-2*, 2019.
[17] H. Danielsson, M. Jeleč, and E. Serrano. Prediction of Torsional Stress at In-plane Shear Loading of Cross Laminated Timber. In *INTER/53-12-3*, 2020.
[18] M. Flaig and H. J. Blaß. Shear strength and shear stiffness of CLT-beams loaded in plane. In *Proceedings of 46th CIB-W18 Meeting*, Vancouver, 2013.
[19] M. Jeleč, H. Danielsson, V. Rajčić, and E. Serrano. Experimental and numerical investigations of cross-laminated timber elements at in-plane beam loading conditions. *Constr. Build. Mater.*, vol. 206, 2019.
[20] H. Danielsson and M. Jeleč. A unified design proposal for shear stress prediction in crossing areas for cross laminated timber at in-plane shear and beam loading conditions. *Constr. Build. Mater.*, vol. 355, 2022.
[21] H. Danielsson and E. Serrano. Cross laminated timber at in-plane shear loading: Strength and Fracture analysis of shear mode III. In *WCTE 2020/21*, pages 904–913, 2021.
[22] M. Wallner-Novak, M. Augustin, J. Koppelhuber, and K. Pock.: Brettsperrholz Bemessung Band II– Anwendungsfälle, *ProHolz Austria*, 2018.
[23] P. González-Serna, M. Yurrita, and J. M. Cabrero. Experimental analysis of the influence of openings in cross-laminated timber plates loaded out of plane. In *WCTE 2023*, Oslo, 2023.
[24] M. Schenk, A. Husel, P. Dietsch and S. Winter. Cross laminated timber floors with openings – serviceability limit state verifications. In *WCTE 2023*, Oslo, 2023
[25] J. M. Cabrero and M. Yurrita. A review of the existing models for brittle failure in connections loaded parallel to the grain. In C. Sandhaas, J. Munch-Andersen and P. Dietsch Eds., *Design of Connections in Timber Structures: A State-of-the-art Report by COST Action FP1402/WG3*, pp. 127–141, Germany: Shaker Verlag, 2018.
[26] J. M. Cabrero and M. Yurrita. Performance assessment of existing models to predict brittle failure modes of steel-to-timber connections loaded parallel-to-grain with dowel-type fasteners. *Eng. Struct.*, vol. 171, 895–910, 2018.
[27] M. Yurrita and J. M. Cabrero. New design model for brittle failure in the parallel-to-grain direction of timber connections with large diameter fasteners. *Eng. Struct.*, vol. 217, p. 110557, 2020.
[28] P. Zarnani and P. Quenneville. New design approach for controlling brittle failure modes of small-dowel-type connections in Cross-laminated Timber (CLT). *Constr. Build. Mater.*, vol. 100, pages 172–182, 2015.
[29] P. Zarnani and P. Quenneville. Wood block tear-out resistance and failure modes of timber rivet connections: A stiffness-based approach. *J. Struct. Eng.*, vol. 140, no. 2, p. 04013055, 2014.
[30] B. Azinović, J. M. Cabrero, H. Danielsson, and T. Pazlar. Brittle failure of laterally loaded self-tapping screw connections for cross-laminated timber structures. *Eng. Struct.*, vol. 266, p. 114556, 2022.
[31] J. M. Cabrero *et al.* Brittle failures of connections with self-tapping screws on CLT plates. In *INTER/55-7-2*, 2022.
[32] K. Mindrup. Raumklimatisierung durch thermisch aktivierte Massivholzelemente. Dissertation, TUM, Munich, 2020.
[33] K. Mindrup and S. Winter. Thermal activation of solid timber elements for indoor climate control. In *WCTE 2018*, Seoul, South Korea, 2018.
[34] M. Arnold, P. Dietsch, and S. Winter. Mechanical properties of innovative multifunctional cross laminated timber. In *WCTE 2020/21*, 2021.
[35] M. Arnold et al. Schlussbericht zum Europäischen Forschungsvorhaben InnoCrossLam – Innovative Solutions for Cross Laminated Timber Structures; Arbeitspakete 5 und 6 (Deutschland). FNR, 2023.
[36] M. Arnold, P. Dietsch, R. Maderebner, and S. Winter. Diagonal laminated timber - Experimental, analytical, and numerical studies on the torsional stiffness. *Constr. Build. Mater.*, vol. 322, p. 126455, 2022.
[37] M. Arnold, R. Maderebner, P. Dietsch, and S. Winter. Diagonal Laminated Timber (DLT) - Teil 1: Bestimmung der Steifigkeitsparameter und Verformungsanalysen. *Bautechnik,* expected 2023.
[38] M. Arnold. Mechanical Properties of Diagonal Laminated Timber (DLT) with Respect to Point-Supported Mass Timber Slabs. Dissertation in progress, TUM, Munich, expected 2023.
[39] A. Sandoli, C. D'Ambra, C. Ceraldi, B. Calderoni, and A. Prota. Sustainable cross-laminated timber structures in a seismic area: Overview and future trends. *Appl. Sci. (Switz.)*, vol. 11, no. 5, pp. 1–24, 2021.
[40] M. Izzi, D. Casagrande, S. Bezzi, D. Pasca, M. Follesa, and R. Tomasi.: Seismic behaviour of Cross-Laminated Timber structures: A state-of-the-art review. *Eng. Struct.*, vol. 170, pp. 42–52, 2018.
[41] EN 1998-1: Eurocode 8: Design of structures for earthquake resistance – Part 1: General rules, seismic actions and rules for buildings, 2004.
[42] J. Hummel and W. Seim. Displacement-based design approach to evaluate the behaviour factor for multi-storey CLT buildings. *Eng. Struct.*, vol. 201, 2019.
[43] S. Bezzi. Assessment of the q-factor for timber buildings with CLT panels: state of the art. In R. Brandner et al., *Properties, Testing and Design of Cross Laminated Timber*, Germany: Shaker Verlag, 2018.
[44] Staab G. H.: Laminar Composites (Second Edition), Butterworth-Heinemann, 2015.
[45] H. J. Blass and P. Fellmoser. Design of solid wood panels with cross layers. In *8th WCTE,* Lahti, Finland, 2004.
[46] H. Kreuzinger. Platten, Scheiben und Schalen: Ein Berechnungsmodell für gängige Statikprogramme. *Bau. mit Holz*, vol. 1, pages. 33–39, 1999.
[47] I. Gavrić, L. Naumovski, B. Azinović, and I. Šušteršič. Influence of non-structural elements on dynamic response of a multi-storey CLT building: in-situ measurements in different construction stages and numerical modelling. Journal paper in progress, expected 2023.
[48] I. Mugabo, A. R. Barbosa, and M. Riggio. Dynamic characterization and vibration analysis of a four-story mass timber building. *Front. Built Environ.*, vol. 5, 2019.
[49] J. Hummel, W. Seim, and S. Schwendner. N2 method-adaption to CLT structures. Conference Paper, In *WCTE 2018*, Seoul, South Korea, 2018.
[50] M. Kreslin and P. Fajfar. The extended N2 method considering higher mode effects in both plan and elevation. *Bull. Earthq. Eng.*, vol. 10, no. 2, 2012.
[51] L. Naumovski. Nonlinear static analysis of a multi-storey cross laminated timber building. MSc Thesis, FGG, University of Ljubljana, 2022.

https://doi.org/10.52202/069179-0321

World Conference on Timber Engineering Oslo 2023

REINFORCED NOTCHED CROSS-LAMINATED TIMBER PLATES: LOAD-BEARING CAPACITY AND METHODOLOGY FOR PREDICTING THE FORCE IN REINFORCEMENT

Alen Malagic[1], Erik Serrano[3], Manfred Augustin[1], Gerhard Schickhofer[1, 2]

ABSTRACT: This paper deals with the estimation of the design force in self-tapping screws used as a reinforcement of notched cross laminated timber plates (CLT). With the reinforcement, apart from an increased load-carrying capacity, a more ductile behaviour of this detail can be achieved. An analytical model based on the Timoshenko Beam Theory was developed, enabling the estimation of the axial force in the reinforcement. A parametric numerical analysis was conducted to verify the model and to provide possible ways for the calibration. The results show a good matching of the model with the numerical results. The load-bearing capacity is analysed using a simple fracture mechanics model taking into consideration the effect of the reinforcement to correctly depict the increase in performance. Theoretical and numerical results are compared with experimental findings and show acceptable correlations encouraging a further development and a subsequent implementation in EN 1995-1-1.

KEYWORDS: reinforcement, self-tapping screw, notches, fracture mechanics, screw stiffness, CLT

1 INTRODUCTION

Unreinforced "notches" in cross laminated timber (CLT) plates (Figure 1), severely reduce the load-bearing capacity of this member and fail in general by delamination in a brittle manner. Hence, they should be generally avoided, and if unavoidable, notches should be reinforced. Since the efforts required for their application are small compared to the increase in the load-bearing capacity, ductility and robustness, an effective way for the reinforcement is the application of fully threaded, self-tapping screws. With this method, beside increased load-bearing capacity even up to the level of the unnotched configuration, also a stabilisation of crack growth and prevention of complete delamination of the plate along the crack plane can be achieved, if the screws are designed accordingly.

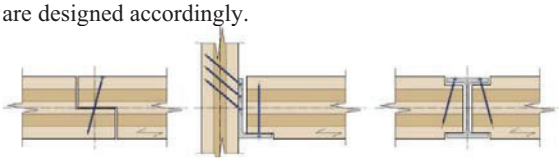

Figure 1: *Various types of notches in CLT plates*

In addition to mechanical loading the crack initiation and growth can also be caused by climate changes [1]. The geometry of the notch makes the timber in the area of the notch significantly more susceptible to moisture content (MC) variations and hence induced residual stresses. These constant MC variations lead to a crack initiation and with each subsequent MC variation to an increase in crack length. The crack lengths are relatively small but they tend to increase over time potentially, reaching critical crack lengths and leading to the failure. The reinforcement increases the critical crack length by a factor 2 and improves the overall behaviour [1], thus mitigating the influence of the moisture variations.

At present, as known to the authors, no explicit rules and expressions are given in standards, guidelines, approvals or in the literature for the calculation of the load-bearing capacity of unreinforced as well as reinforced notches in layered timber products like CLT. Nevertheless, it is evident that the layered structure has an influence on the mechanical behaviour of such members. Thus, known approaches developed and valid for unlayered products and beams out of structural timber and glulam are not mechanically consistent as they disregard the influence of the timber fracture properties and the layup. For these reasons a mechanically consistent approach is desired and should be developed.

The development of such approach for the calculation of the load-bearing capacity suitable for the hand calculation is complex. The main difficulty is the constantly changing mode mixity at the crack tip G_{II} / G_I (τ_{zx} / σ_z) as a function of the crack length, therefore complicating the decomposition of the mixed energy release rate (ERR). An attempt to develop such mechanically consistent approach, still applicable for the implementation in standards or guidelines is presented in this paper.

[1] holz.bau forschungs GmbH, Graz, Austria, alen.malagic@tugraz.at, manfred.augustin@tugraz.at,
[2] Institute of Timber Engineering and Wood Technology, Faculty of Civil Engineering, Graz University of Technology, Graz, Austria, gerhard.schickhofer@tugraz.at

[3] Division of Structural Mechanics, Lund University, Lund, Sweden, erik.serrano@construction.lth.se

https://doi.org/10.52202/069179-0322

2 STATE OF THE ART

2.1 RULES FOR REINFORCED NOTCHED BEAMS IN STANDARDS

Due to the lack of specific rules for CLT, the following review is related to the comparable situation for unlayered timber products (beams) only. Although no related rules are mentioned in EN 1995-1-1:2004/A2:2014 [2], specific sections are given in the German and Austrian National Annex DIN EN 1995-1-1:2010 [3] and ÖNORM B 1995-1-1:2019 [4].

The design force $F_{t,90,d}$, to be carried by the reinforcement, is defined there as a function of the shear force V_d and the notch parameter α. This design approach was developed by Henrici [5] simplifying his findings into the condensed form of Eq. (1).

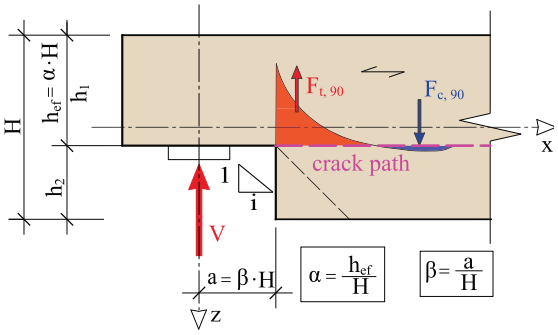

Figure 2: *Geometrical parameters of a notched beam [4]*

$$F_{t,90,d} = 1.3 \cdot V_d \cdot \left[3 \cdot (1-\alpha)^2 - 2 \cdot (1-\alpha)^3\right] \qquad (1)$$

with V_d … design value of the shear force, α …ratio of heights h_{ef} / H

Remark:
To avoid misunderstandings, in the following the denotation for the height ratio α (valid for unlayered timber products) is substituted by ω (valid for layered products like CLT).

In Eq. (1) the force in the reinforcement is calculated by integrating the parabolic shear stresses up to the crack line. The pre-factor 1.3, being a product of the elastic analysis in [5], considers the orthotropy of the timber and the geometry of the notch, leading to conservative values for $\alpha < 0.65$ and $\beta < 0.3$.

Recently, a modified format of Eq. (1) with additional parameters k_α and k_β was proposed in the draft code prEN 1995-1-1:20XX [6] as

$$F_{t,90,d} = k_\alpha \cdot k_\beta \cdot V_d \cdot \left[3 \cdot (1-\alpha)^2 - 2 \cdot (1-\alpha)^3\right] \qquad (2)$$

where

$$k_\alpha = 0.9 + 0.5 \cdot (2\alpha - 1)^2, \; k_\beta = 1 + 2 \cdot \beta$$

for $\alpha \leq 0.6$ and $\beta \leq 0.2$ the product $k_\alpha \cdot k_\beta$ may be taken as $k_\alpha \cdot k_\beta = 1.3$

As an intermediate summary it can be stated that current methodologies for predicting the force in reinforced notches (of unlayered timber members) disregard several important aspects such as: properties and position of the reinforcement as well as length of the crack. Thus, a mechanically more accurate and robust approach considering the mentioned parameters is desired and should be developed.

2.2 LOAD-BEARING CAPACITY

Relatively big notches with $\alpha < 0.7$, drastically decrease the load-bearing capacity of notched timber members. By reinforcing them, an increase of the load-bearing capacity by a factor of 1.5 up to 2.5 can be achieved. The failure of the reinforced notch is governed by the axial and the shear capacity of the reinforcement and the splitting strength of the timber respectively. Since the strength of the timber is disregarded in the current design procedures, the load-bearing capacity is proportional to the axial load-bearing capacity of the reinforcement and the number of reinforcing elements. By substituting the axial capacity of the reinforcement in Eq. (1) the failure load at the notch $V_{f,d}$ can be calculated (for unlayered products) as follows:

$$V_{f,d} = \frac{n_{ef} \cdot R_{ax,d}}{1.3 \cdot \left[3 \cdot (1-\alpha)^2 - 2 \cdot (1-\alpha)^3\right]} \qquad (3)$$

with $n_{ef} = n$ and $R_{ax,d}$ … design value of the axial load-carrying capacity per screw

The strength of the timber is indirectly considered in a proposal authored by Dietsch [7] and also mentioned in prEN 1995-1-1:20XX [6]. The load-bearing capacity there is limited to twice the value of the unreinforced notch. This simple and practical proposal for standards is based on insights made in [1] on a basis of extensive experimental test results and the theoretical insights regarding the fracture energy in pure mode II failure. However, an implementation in this form is questionable for highly orthotropic products such as CLT due to the increased influence of the rolling shear behaviour. Significant discrepancies between the load-bearing capacity calculated by Eq. (3) and experimental results were observed in [1] and [10]. The Eq. (3) provided unsafe results in some configurations. Placing a large amount of reinforcements at the notch can cause this disagreement due to the shift of the failure mode from the reinforcement to the failure at the notch by excessive cracking and subsequent delamination. In CLT notches this fact transforms to: failure in the screw (underreinforced), failure due to the splitting of the timber at the crack tip (overreinforced) and failure due to the splitting and simultaneous failure of the screw (balanced). Naturally, the balanced case is hardly achievable.

The predictions by Eq. (3) have been also compared with the experimental results conducted on reinforced notched CLT plates, see chapter 5.

The load-bearing capacity of reinforced notches in beams was investigated by Jockwer ([1], [8]), proposing an analytical model based on energy balance method of *Linear Elastic Fracture Mechanics* (LEFM). The total energy release rate (ERR) in the mixed fracture mode was evaluated and then a mode partitioning according to the approach from Riipola [9] was applied. A pronounced influence of the crack shearing (mode II) with increasing

https://doi.org/10.52202/069179-0322

crack length and α-value was noted, leading to the reported increase of the load-bearing capacity. The increase of the load-bearing capacity by a factor of about 2 reported in [1] corresponds well with around 4 times larger fracture energy in pure mode II leading to increase in the load-bearing capacity $\sqrt{G_{II} / G_I} \approx 2$ according to LEFM.

A more detailed approach is given by Sorin et. al. [10]. The load-bearing capacity of the notch is calculated according to the *Equivalent Linear Elastic Fracture Mechanics* (Equiv. LEFM) taking into account the quasi-brittleness of the timber and employing crack growth curves (R curves). The linear elastic calculations are made iteratively on different crack lengths. Each crack length has a unique crack growth resistance in separate fracture modes. This model can accurately predict the force evolution and failure load as a function of the crack length, however on the cost of simplicity when compared to [8].

The increase of the load-bearing capacity of reinforced notches can be vividly illustrated by an analogy regarding the timber anatomy: It is a well-known occurrence during the testing of fracture properties on timber specimens that the presence of knots along the fracture plane cause an increase in fracture energy and failure load of the tested specimen. Such specimens are not desired in the analysis and will be commonly disregarded but show a positive influence of knots on the fracture parameters. The knots in such cases are carrying forces between the cross sections divided by the crack and therefore lead to an increase in system stiffness and fracture energy. A similar effect can be achieved by placing self-tapped screws at the notch.

2.3 FORCE IN THE REINFORCEMENT

Literature references regarding the calculation of the design forces in the reinforcement at the notch – in particular for layered timber products – are rather scarce, if not missing. An analytical model for unlayered notched beams based on the Timoshenko Beam Theory was presented in Jockwer [1]. As known to the authors, no other paper of such matter is present, consequently there is a need for further investigations on this topic.

3 METHODOLOGY FOR PREDICTING THE FORCE IN REINFORCEMENT

In the chapters 3 and 4 diagrams regarding the force in reinforcement and the load-bearing capacity of notched CLT plates will be shown. All presented diagrams are related to a reference case in order to clearly present results and parameter relations. The reference case is a 5-layered CLT-plate with the layup: 30-30-30-30-30 mm (underlined numbers indicate the thickness of cross-layers). For a consistent comparison a constant parameter $\beta = 0.5$ was chosen. In all presented diagrams dashed lines refer to the analytical beam model (section 3.1 and 4.1), while solid lines refer to the numerical model (section 3.2).

3.1 ANALYTICAL MODEL

The analytical model is based on the Timoshenko Beam Theory. The used system is graphically depicted in Figure 3. For the application of the model a crack-length L_{crack} has to be pre-assumed. The screw (group) is substituted by spring element of equivalent stiffness. However, to enable a closed form solution, the lateral screw stiffness is ignored. The impact of this simplification is further investigated in the scope of the numerical parametric analysis.

The axial stiffness for part of the single screw under/above the crack is calculated according to Eq. (4) from Ringhofer [11]. The axial stiffness of the whole screw K_{ser} is calculated taking into account the series effect acting on the screw because of the crack.

$$K_{ser,i} = k_{ax} \cdot 160 \cdot \left(\frac{\rho_{12}}{420} \right)^{0.85} \cdot d^{0.9} \cdot l_{ef,i}^{0.6} \qquad (4)$$

with k_{ax} = 1.0 for α = 90°, ρ_{12} … density at moisture content u = 12% [kg/m³], d … diameter of the screw [mm], $l_{ef,i}$ …penetration length of the screw in timber under the crack and above the crack [mm], $K_{ser,i}$ … axial stiffness for part of the screw under/above the crack interface resp. [N/mm]

Remark: The stiffness of the screw group is given as: $K_{ser} \cdot n_{screw}$, where n_{screw} … number of screws, $K_{ser\ ...}$ stiffness of the whole screw

The forces in the reinforcement are calculated by applying the principle of virtual forces on the first order statically indeterminate system shown in Figure 3.

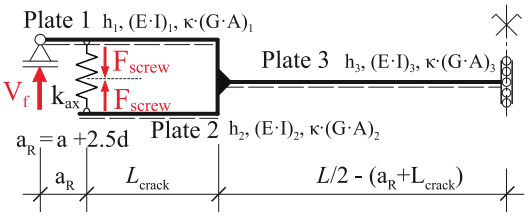

Figure 3: *Analytical beam model*

After simplification the axial force in the reinforcement $F_{t,90,d}$ in the notched CLT plate of width w is as follows:

$$F_{t,90,d} = \frac{\frac{L_{crack}^{\ 2}}{6 \cdot EI_1} \cdot \left(3 \cdot a_R + 2 \cdot L_{crack}\right) + \frac{L_{crack}}{GA_1}}{\frac{L_{crack}^{\ 3}}{3} \cdot \left(\frac{1}{EI_1} + \frac{1}{EI_2}\right) + \frac{1}{k_{ax}} + \left(\frac{1}{GA_1} + \frac{1}{GA_2}\right) \cdot L_{crack}} \qquad (5)$$

3.2 (PARAMETRIC) NUMERICAL MODEL

In order to verify the analytical model from section 3.1 a parametric numerical analysis was conducted. In its frame 3-, 5- and 7-layered CLT plates were investigated. The calculation was elaborated using the finite element software package ANSYS APDL 2021 R1. For ease of work, sets with a range of parameters were submitted as batch file to the solver. Detailed information regarding the considered layups are given in Table 1. The geometry, loading and boundary conditions of the analysed model are illustrated in Figure 4.

https://doi.org/10.52202/069179-0322

A plane stress model was applied on the plate width w = 600 mm to match the width of CLT plates from experimental tests. The plate is loaded by a point load in the symmetric mid span 3-point bending configuration. The support is modelled by means of a steel plate to avoid singularity and unrealistic deformations. It is restrained in the Z-direction and free in X-direction, with free rotation about the Y-axis (Figure 4). A global mesh size of 5 mm was used, while the local mesh refinement at the crack tip and along the crack interface was applied in sizes of 1.5 to 2.0 mm. The material model is linear elastic orthotropic represented by the properties given in Table 2.

Table 1: *Parameters used in the numerical analysis*

Input and analysis parameters for the analytical and numerical models			
Num. of layers	3	5	7
Layup[a)] [mm]	40-<u>40</u>-40	30-<u>30</u>-30-<u>30</u>-30 40-<u>20</u>-40-<u>20</u>-40 40-<u>20</u>-20-<u>20</u>-40 40-<u>40</u>-40-<u>40</u>-40	30-<u>30</u>-30-<u>30</u>-30-<u>30</u>-30 30-30-<u>30</u>-30-<u>30</u>-30
ω [-]	$0.5 \leq \omega < 1.0$		
β [-]	0.25, 0.5, 1.0		
L_{crack} [mm]	$2.5 \cdot d_{screw} \leq L_{crack} \leq 2 \cdot H_{plate}$		

[a)] Underlined numbers indicate the thickness of cross layers

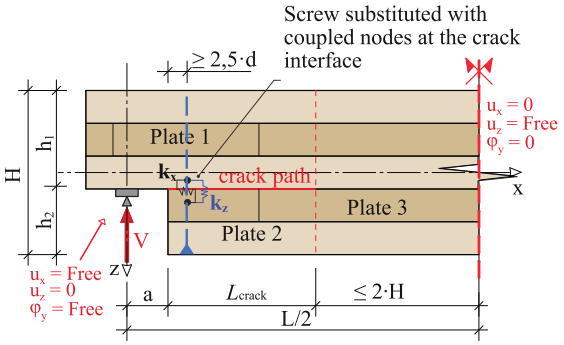

Figure 4: *Illustration of the (parametric) numerical model*

Due to the application of a plane stress model the screw could not be considered as a beam element. Instead, a coupling of the nodes with spring elements at the crack interface was applied. The number of parameters to be considered for the definition of the numerical model in a notched layered member is significantly higher compared to the notched beams made of structural timber or glulam. For example, the parameters defining the number of layers and the layup of the CLT plate need to be defined in addition. Subsequently, the complexity of the parametric analysis, as well as the needed computational time increase exponentially.

Table 2: *Material properties used in the numerical analysis*

Parameter	Value	Description
E_0 E_{90}	11000; 390	MOE longitudinal; transversal [MPa]
$G_{0,\,90}$ $G_{90,\,90}$	690; 69.0	Shear modulus, longitudinal; transversal [MPa]
$G_{c,\,I}$ $G_{c,\,II}$	0.30; 0.90	Critical energy release rate, Mode I; Mode II [mJ/mm²]
$\nu_{,\,LR}$ $\nu_{,\,RT}$	0.56; 0.03	Poisson ratios [-]

In the present analysis the number of considered parameters was reduced by introducing several assumptions in line with the features of CLT-plates and construction practice: The most relevant adoption was made involving the type of reinforcement used in notched CLT-plates as well as the configuration of the reinforcement. Due to the relatively small thickness of the CLT-plate and a width of up to 3 m, the only feasible way of reinforcing such elements in practice is the application of self-tapping screws. In line with the proposals in [7] the reinforcement should be placed in one row and at a distance of about $2.5 \cdot d_{screw}$ from the notch face to the screw. Moreover, the width of the CLT-plates requires a maximum screw distance in a row to be defined. Otherwise, a crack propagation between the screws may occur, severely reducing the load-bearing capacity. In this work a maximum screw distance of 150 mm is proposed and considered. This distance is in line with the situation in practice, however, a maximal distance should be determined on the basis of experimental tests. Screws of the nominal diameter d = 8 mm and a length equal to the plate thickness with an inclination angle of $\alpha = 90°$ were assumed for the reinforcement in this work. With the mentioned assumptions the stiffness of a group of screws can be defined. The axial screw stiffness was considered as given by Eq. (4).

In the numerical model the fracture parameters at the crack tip were obtained as a function of the crack length. The total (mixed) energy release rates and respective modal contributions in the modes I and II were evaluated with the built-in software module "Virtual-crack-closing-technique" (VCCT). To verify the mixed ERR from VCCT the J-integral was applied in the numerical analysis. The modal contributions were verified with the ratio of shear and normal stresses (τ_{zx} / σ_z) giving the mode mixity ratio G_{II} / G_I. The verification calculations for the total ERR showed no difference to the VCCT method and mode partitioning showed minor differences but the same tendency in results.

3.3 FORCES IN THE REINFORCMENT

Predictions for the forces in the reinforcement were computed at specific positions for different notch heights as illustrated in Figure 5.

https://doi.org/10.52202/069179-0322

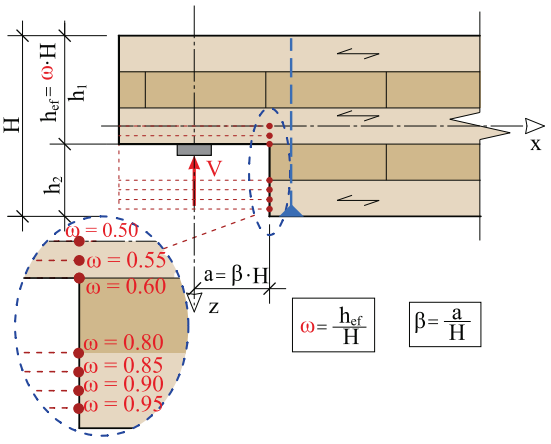

Figure 5: *Positions of notches used in comparison*

The notches in the CLT have a special failure mode when the notch is situated in a transversal layer: The crack there propagates under an angle of approximately 45° up to the layer interface and then continues along the interface [12]. As a consequence, the transversal layer should be excluded from the calculations of the load-bearing capacity in the notched CLT-plates and also excluded from the predictions of the force in the screw, Eq. (5).

The reinforcement leads to an exchange of forces between the upper and lower part of the plate. This exchange depends on the geometry parameters of the notch (ω, β), but also on the crack length L_{crack} and the stiffness of the screw.

In Figure 6 the results from the numerical and analytical analysis regarding the influence of the crack length on the force in the screw are depicted.

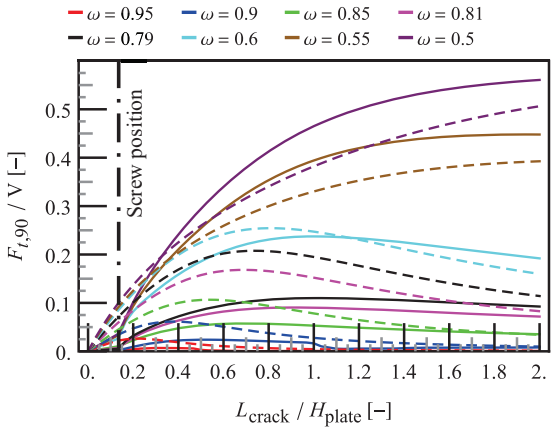

Figure 6: *Axial force in the screw depending on the crack length (dashed lines … analytical model, solid lines … numerical model)*

The analytical and the numerical model show a comparable tendency of an increasing force in the reinforcement with an increasing crack length. This was verified for all investigated ω-values. Additionally, it can be recognised that for bigger crack lengths a decreasing trend in the force of the screw may occur. This can be explained by the fact that the stiffness of the system decreases with an increasing L_{crack}. In the analytical model the point of the local maximum could be obtained by applying the condition $dF / dL_{crack} = 0$. However, this point is not of practical relevance for the design of the reinforcement.

The crack propagation is initiated at the notch tip "behind" the position of the screw. However, until the crack passed the screw position no force, or even compression forces, in the screw were observed. Thus, forces at $L_{crack} = 0$ are assumed to be zero in the numerical analysis.

Jockwer [1] mentions the possibility of an interaction between the member parts under and above the crack in reinforced notches during the crack growth. This occurrence renders the analytical model inappropriate due to the assumption, that the crack interface is not in contact. This assumption was investigated in the numerical model by defining contact elements along the opening crack interface. Within the inspected layups from Table 1 a consistent behaviour could be recognised. The interaction at the crack interface occurs for larger crack lengths and small notches of up to $h_2 = 15$ mm. The analytical model in this range of ω shows conservative results in comparison to the numerical one. This is noted on all inspected CLT layups, therefore the applicability of the taken assumption in the analytical model is acceptable.

As mentioned, the failure of reinforced notches can occur due to the pull-out of the reinforcement. In order to determine the occurring failure mode in the analysed notches the predicted force in the reinforcement for the screw group was compared with their load-bearing capacity determined as

$$\left(\frac{F_{ax,Ed}}{F_{ax,Rd}}\right)^2 + \left(\frac{F_{v,Ed}}{F_{v,Rd}}\right)^2 = 1\,. \qquad (6)$$

with $F_{ax,Rd}$,, $F_{v,Rd}$ … axial and lateral load-bearing capacity of the screw group

The load-bearing capacity was determined according to the expressions given in EN 1995-1-1 [2], sections 8.3 and 8.5. The detailed calculation is excluded here for simplicity. The acting shear force is taken from the numerical analysis and was included in Eq. (6). In order to simplify the results, the maximal shear force obtained for each ω was used.

The resulting load-bearing capacity for the screw group is illustrated in Figure 7. Their failure load capacities are significantly higher than the maximal forces in the reinforcement for the relevant crack lengths, i.e. pointing out a low risk of screw pull-out during the crack propagation. This leads to the "over-reinforced" case of the notch; hence the failure in the timber occurs due to crack propagation. This hypothesis is questioned on the basis of the experimental results in chapter 5.

https://doi.org/10.52202/069179-0322

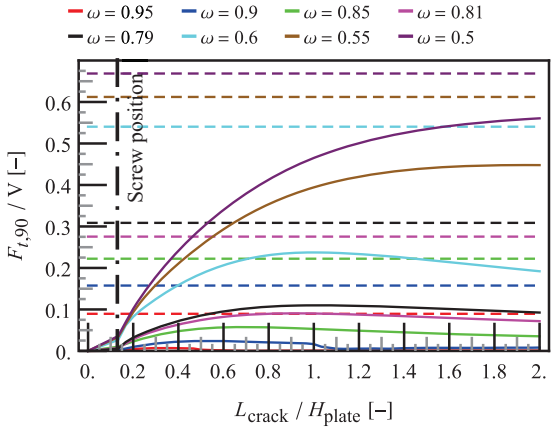

Figure 7: *Comparison of the axial force in the screw to the load-bearing capacity of the applied screws group depending on the crack length (solid lines ... numerical model, dashed lines ... load-bearing capacity of the screw group, Eq. (6.))*

In contrast to the axial force $F_{t,90}$, the shear force F_v shows a constant increase of the force in the screw with increasing crack length (Figure 8). Thus, the load-bearing capacity of the reinforcement in shear is relevant for the determination of the load-bearing capacity of the notched CLT plate for larger notch parameter β and larger crack lengths. The main goal of a reinforcement is to reduce and limit the crack opening at small crack lengths. However, that increases the shear loading at the crack and induces a mode II failure at the crack tip. In order to further increase the load-bearing capacity, the shear loading at the crack should be reduced by increasing the lateral stiffness of the screw. This is accomplished, e.g. by inclining the screws at an angle to grain below 60° ([1],[8]).

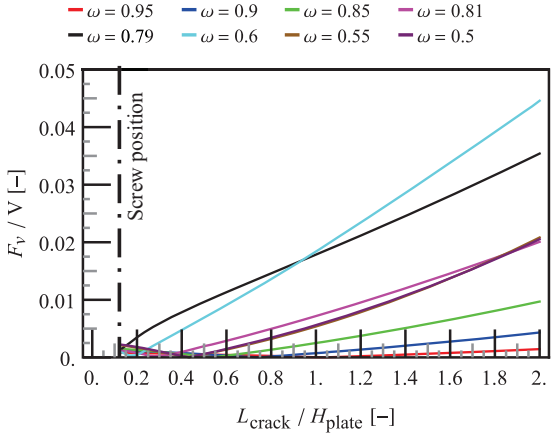

Figure 8: *Shear force in the screws depending on the crack length (numerical model)*

An interesting occurrence can be recognised in the distribution of the shear force: The maximum shear force in the reference case is obtained for ω = 0.6 and ω = 0.79 instead of ω = 0.5 as expected from the distribution of the axial forces. This occurs at the interface of the transversal and longitudinal layer due to the increased compliance caused by rolling shear in the transversal layer. This implies a bigger influence of the mode II failure at the interface of the layers, cf. section 4.2.

The influence of the parameter β on the axial force in the screw is illustrated in Figure 9. The crack length in the analysis was assumed as L_{crack} = 150 mm. This assumption is based on observations from experimental tests conducted by the author ([12]) and found in literature [1] respectively, as the approximate, where a failure of the reinforced notch occurred. The chosen length refers to failures in cases, where inclined screws were used. The lengths for non-inclined screws are smaller and can be expected in the region of 80 to 100 mm. However, a bigger crack length was chosen for the analysis in order to obtain more conservative results.

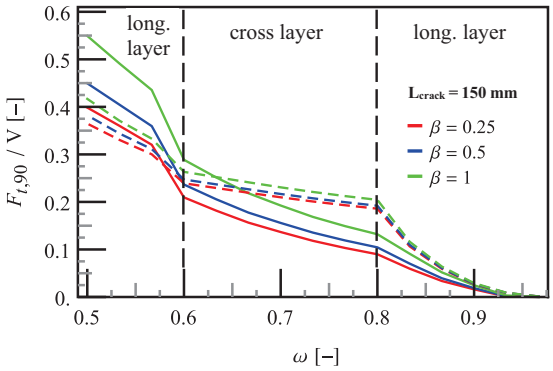

Figure 9: *Axial force in the screw for L_{crack} = 150 mm depending on the parameter ω and β (dashed line ... analytical model, solid line ... numerical model)*

It can be seen that the analytical model is conservative in the area of the first longitudinal and transversal layer ($\omega \geq$ 0.6), but with an increasing notch height the results diverge to the unsafe region compared to the numerical results. This was observed for all considered layups. The differences in the reference case are equal to 15% of the force at the support; for other lay-ups the differences grow up to 25%. As a consequence this implies that the analytical approach should be applied only in the region $\beta \leq$ 0.5. Alternatively, a correction factor increasing the effective notch length as a function of β could be applied.

3.4 COMPARISON OF DIFFERENT METHODS AND VERIFICATION

In this section a comparison of methods for the prediction of the force in the reinforcement related to the reference configuration is given. Beside the analytical and numerical method explained in the sections 3.1 and 3.2, also present methods for unlayered notched beams (see section 2.1; Eq. (1) and (2)) were included, although they are not mechanically consistent with the layered timber product CLT.

A comparison of the results for the axial force in the screw between the analytical and numerical approach is shown in Figure 10. With an increasing crack length, the analytical model converges to the numerical one. This behaviour can be explained due to the assumptions made

https://doi.org/10.52202/069179-0322

in the Timoshenko Beam Theory characterised by a dominant shear deformation of the cracked plate parts under and above the crack interface for small crack lengths and small notch heights. Improved results can be obtained by increasing the effective crack length to overcome the restrictions of the beam theory. In general, the predictions of the analytical model significantly overestimate the forces in the reinforcement predicted by numerical model. On the other side for $\omega < 0.6$ the analytical model underestimates forces in numerical model in range of 20%. These differences are significant and can't be neglected, therefore further investigation and refinement of the model is needed!

In Figure 10 for $\omega = 0.95$ and 0.9 the roughness of the curves is noted. The roughness is caused by the predictions in the numerical model. In mentioned range, the crack interface is in contact and it is causing constant change in force in the screw in contrary to assumption of analytical model.

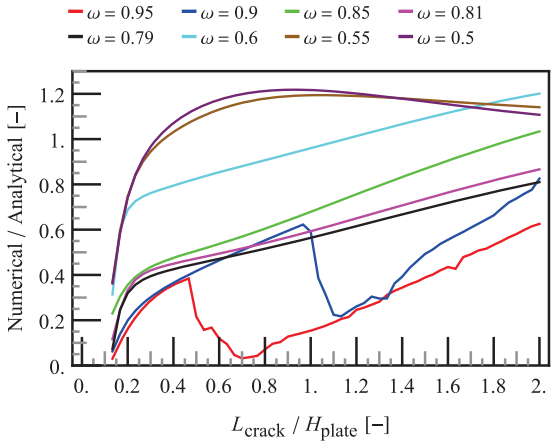

Figure 10: *Comparison of the axial force in the screw between the numerical and analytical model for the reference configuration*

A comparison of different methods for the prediction of the force in the screw of the reference CLT plate is shown in Figure 11. The analytical and numerical solutions were computed for the crack lengths L_{crack} = 100 mm and 150 mm, i.e. in the domain relevant for failure of the notch (cf. section 3.3). In order to check their applicability, although the methods are not consistent with the layered timber products like CLT, in addition results for the regulations valid for unlayered notched timber products specified in the National Annexes [3] and [4] to EN 1995-1-1 and the current draft prEN 1995-1-1:20XX [6] are included.

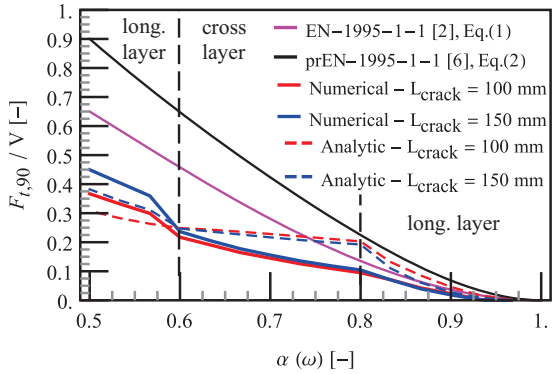

Figure 11: *Force in the screw according to different methods for different parameter ω and $\beta = 0.5$*

In the draft prEN1995-1-1:20XX [6] (Eq. 2) a new approach for the calculation of the force in the reinforcement is specified as described in section 2.1. This method is compared with the regulations in the National Annexes in [3] and [4] (Eq. 1) (Figure 12). It can be recognised that the new approach in the draft standard leads to substantially higher forces in the reinforcement for the full range of the investigated parameter α and β.

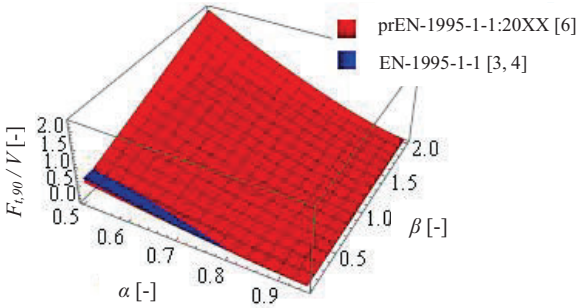

Figure 12: *Illustration of the force in the reinforcement (screw) depending on the parameter α and β for the methods in [3], [4] and [6] resp.*

In Table 3 a comparison of results for different layups applying the mentioned methods is listed. The analytical model and the numerical model for CLT show a good match. The approaches in [3], [4] and [6] resp. are leading to very conservative results, which was expected as these methods are not considering the layered structure of CLT and the influences of cracks, as well as the reinforcements are not taken into account.

If the stiffness of the screw is ignored, the results of the analytical method for the prediction of the force in the reinforcement of CLT plates, Eq. (5), is approaching the results in the National Annexes to the standard EN-1995-1-1, [3] and [4]. This can be achieved by assuming an infinite stiffness for the screw. Further the crack length is assumed again as L_{crack} = 150 mm. The results over the complete range of the important parameters ω and β are presented in Figure 13. If an infinite stiffness of the screw is assumed, the results of the analytical model lead to increased forces in the screw in an expected range of 20% to 30% for all analysed configurations.

https://doi.org/10.52202/069179-0322

Table 3: *Comparison of results for the prediction of the force in the screw according to the different methods and different layups; parameter β = 0.5 and crack length L_{crack} = 150 mm (results are normalised to $F_{t,90}$ / V; the comparison is given in % and normalised to the numerical solution)*

Method	Layup			
	40-20-20-20-40 mm		30-30-30-30-30-30 mm	
	α (ω) = 0.57	α (ω) = 0.50	α (ω) = 0.57	α (ω)= 0.43*
	$F_{t,90}$ / V [-]		$F_{t,90}$ / V [-]	
Analytical model - CLT	0.29 (+26%)	0.37 (-16%)	0.36 (-5%)	0.38 (-15%)
Numerical model - CLT	0.23	0.44	0.38	0.45
prEN 1995-1-1:20XX	0.72 (+213%)	0.90 (+104%)	0.72 (+90%)	1.09 (+142%)
EN 1995-1-1	0.51 (+121%)	0.65 (+47%)	0.51 (+34%)	0.78 (+73%)

* α (ω) = 0.43 is used as α (ω) = 0.5 is situated in a transversal layer

With the increased forces considering an infinite stiffness of the screw the results match better with the approach in the National Annexes (Eq. 1). However, these results underestimate the level of the force in the first layer of the CLT and overestimate the force at the top of the transversal layer. The matching of the methods depends heavily on the layups, but in general the differences are small for $\beta < 1.0$. It can be concluded that the mentioned procedure can be used for standardisation, but in addition the influence of the CLT layup should be taken into account by a fitting factor.

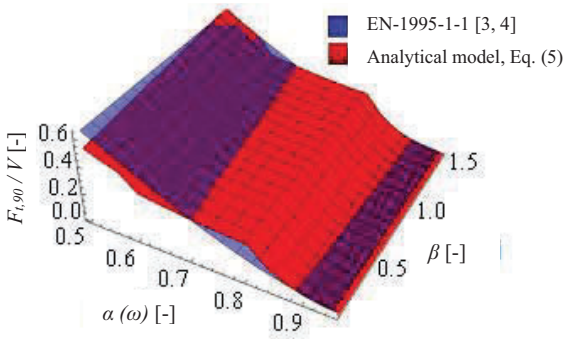

Figure 13: *Comparison of the force in the screw according to [3], [4] and the analytical model (assuming a crack length L_{crack} = 150 mm) for different parameter β, α and ω respectively*

4 LOAD-BEARING CAPACITY

In comparison to the unreinforced notches in CLT the development of mechanically consistent model but also appropriate for hand calculation for reinforced case is more difficult. Due to the pronounced mixed mode failure in reinforced notches a failure criterion needs to be considered.

In this chapter the basics for the computation of the load-bearing capacity of the reinforced notched CLT-plate will be briefly described. The proposed model is based on the energy balance method of LEFM considering all important parameters influencing the load-bearing capacity. Furthermore, assumptions of the critical crack length need to be made for hand calculations with the analytical model.

4.1 ANALYTICAL MODEL FOR THE PREDICTION OF THE MODE MIXITY AND LOAD-BEARING CAPACITY IN REINFORCED CLT-PLATES

The total energy release rate (ERR) of the system in Figure 3 in the frame of the LEFM (expecting a brittle failure in the interface) is given as:

$$G_m = \left[\left(\frac{M_1^2}{EI_1}\right)+\left(\frac{M_2^2}{EI_2}\right)-\left(\frac{M_3^2}{EI_3}\right)\right]+\left[\left(\frac{V_1^2}{\kappa GA_1}\right)+\left(\frac{V_2^2}{\kappa GA_2}\right)-\left(\frac{V_3^2}{\kappa GA_3}\right)\right] \quad (7)$$

where

κGA_i, shear stiffnesses for the plate parts 1, 2, 3

EI_i, bending stiffnesses for the plate parts 1, 2, 3

M_i, V_i moment and shear forces at the crack tip of the plate parts 1, 2, 3

The main challenge regarding Eq. (7) is to decompose it in modal ERR constituents, i.e. mode I and mode II respectively. In the literature the mode decomposition of unlayered cross sections as well as for laminates is well researched. In the pioneering work of Williams [15] a so called "global method" of decomposition was developed. Williams proposed a partitioning method based on the assumptions that: (i) a pure mode I exist when opposite moments act on the plates above and below the crack; and (ii) a pure mode II is obtained when the curvature in the two plates separated by the crack is the same. Such assumptions, however, lead to incorrect results when they are applied to laminates with unsymmetric layups and layers not of the same thickness. For that reason, the accuracy of Williams theory is often questioned when applying it to laminate cross sections such as CLT. The applicability of Williams method was briefly investigated in the scope of this paper. A mode decomposition showed a good matching for the symmetric case with ω = 0.5, but greater deviations for ω ≠ 0.5 compared to the numerical model were observed.

The mode mixity is evaluated as a function of the crack length with the numerical method based on VCCT. The numerical approach is considered as a reliable method for the analysis of fracture properties and mode mixity. Nonetheless, an analytical approach was also developed for easier handling of the parameters and to verify the possibility of using an analytical model for the mode decomposition.

"An Elastic Interface Model for Coupled Laminates" developed by Bennati [16] was used to derive the mode mixity in notched CLT plates. The model is based on the Timoshenko Laminate Theory. The solution is derived based on the crack tip element (CTE) illustrated in Figure 14. The CTE includes the crack tip and a part of the beam behind the crack tip. The CLT laminate is divided by a crack interface into two sublaminates, which are coupled with continuously distributed linear elastic springs

https://doi.org/10.52202/069179-0322

enabling a better description of the deformation at the crack tip. This step requires a fitting with experimental or numerical results. The sensitivity of the spring stiffness on mode mixity was analysed and it has been shown that for $k_z > 1000$ N/mm the mode mixity is constant, therefore $k_z = 1000$ N/mm was taken. To include the influence of transversal layers, the stiffness k_x was defined as $k_z / k_x = 10$. The strain, displacement and stress distributions in the CTE are derived by simultaneously solving a set of two differential equations which define the interface stresses. Then, the mixed energy release rate and its mode I and mode II contributions are evaluated based on Rice's J -integral. The solution of this integral for the total ERR in mode I and II is given in Eq. (8)

$$G_I = \frac{\sigma_z^2}{2 \cdot k_z} \qquad G_{II} = \frac{\tau_{zx}^2}{2 \cdot k_x} \tag{8}$$

with

G_I, G_{II}	ERR in mode I and II [mJ/ m^2]
k_x, k_z	spring stiffness in the horizontal (x) and the vertical (z) direction
σ_z	maximum normal stress at x = 0 (crack tip) in direction perpendicular to grain
τ_{zx}	maximum shear stress at x = 0 (crack tip)

The mode mixity is represented as the phase angle $\psi = \arctan\left(\sqrt{G_{II} / G_I}\right)$ where $\psi = 90°$ refers to the pure mode II and $\psi = 0°$ to the pure mode I fracture.

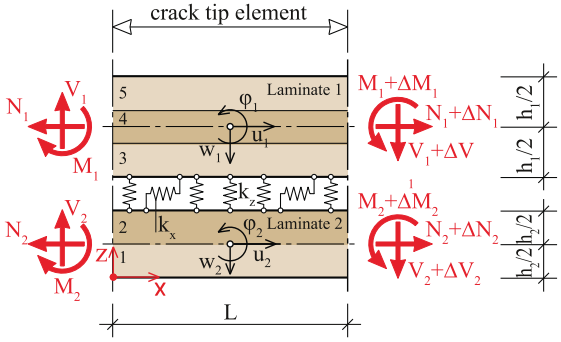

Figure 14: *Crack tip element (CTE) - Elastic Interface model*

4.2 FRACTURE BEHAVIOUR OF REINFORCED CLT NOTCHES

The distribution of the mode I ERR (G_I) as a function of the crack length normalized to the height of the plate is shown for the reference case in Figure 15. The diagram clearly shows the decreasing tendency of the G_I with an increasing crack length. For comparison the G_I in unreinforced notches is causing the failure of the notch as G_I increases with a crack length leading to the failure at relatively small crack lengths of around 50 mm.

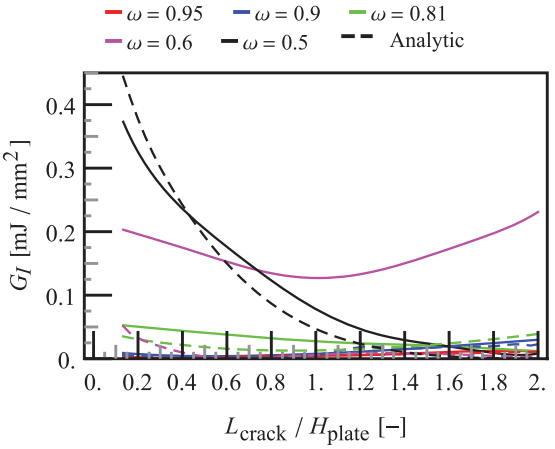

Figure 15: *ERR in mode I for the reference layup*

The effect of the reinforcement is clearly recognisable as the reinforcement reduces the cracking tendency of the plate, as it reduces the crack opening and hence the mode I influence. This effect is increasing with stiffer reinforcements. The agreement of the analytical and numerical model for G_I is relatively poor, especially at the interface between the longitudinal and transversal layer mainly due to the influence of significantly different shear and elastic modulus between them. However, G_I shows the same tendency for all notch heights in the numerical model, excluding the solution at the interface.

The distribution of the mode II ERR (G_{II}) is shown in Figure 16. In this case the G_{II} increases with the crack length. Again, for the same reason the agreement with the numerical model is poor at the interface. Otherwise, a good agreement between the models was observed.

The increasing mode II is also present in the unreinforced notches [1], but the ratio G_{II} / G_I is significantly lower compared to the reinforced case. Moreover, the value of G_{II} doesn't influence the load-bearing capacity of the unreinforced notches significantly as the fracture energy in mode I is up to three times lower compared to that of mode II.

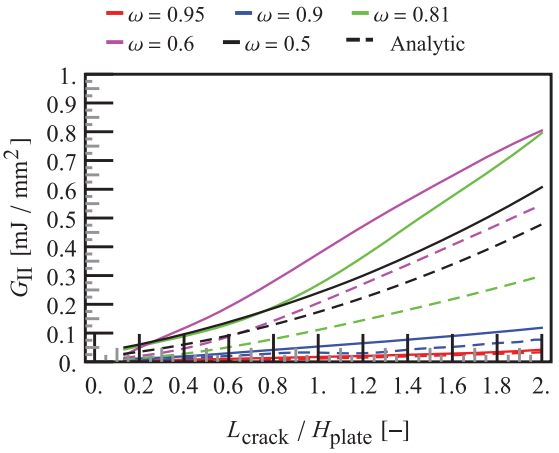

Figure 16: *ERR in mode II for the reference layup*

https://doi.org/10.52202/069179-0322

The load-bearing capacity of reinforced CLT notches is heavily dependent upon the dominant mode of fracture. Therefore, the plots of the mixed mode ratio and mode mixity were investigated. The mixed mode ratio for mode I is shown in Figure 17. It can be seen that the share of the mode I in total mixed mode ERR (G_{mixed}) shows a descending tendency when a reinforcement is applied. This decreasing tendency is especially pronounced in the range $\omega = 0.5$ to 0.6, where for smaller crack lengths the mode I failure is dominant. The decrease of G_I is mainly responsible for the significant increase of the load-bearing capacity in reinforced notches (see Table 4).

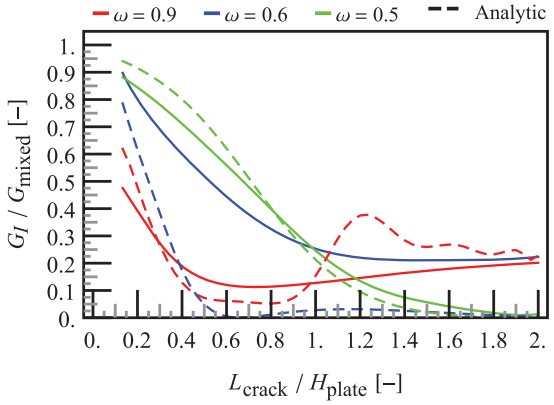

Figure 17: *Mixed mode ratio of mode I for reference layup*

For big ω-values the mode II is dominant, already at small crack lengths. For larger crack lengths they converge to constant value (Figure 18). It is noted that for $\omega = 0.9$ and large crack lengths the delaminated parts of the plate are in contact, therefore producing a significant portion of mode II.

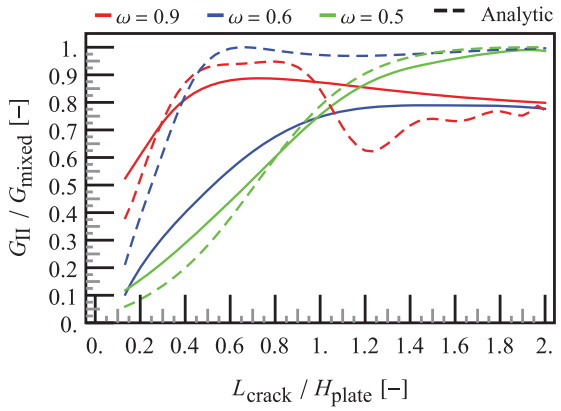

Figure 18: *Mixed mode ratio of mode II for reference layup*

Two plots of the mode mixity are shown with the intention to investigate the influence of the force in the screw on the mode mixity and subsequently on the load-bearing capacity. The Figure 19 and Figure 20 refer to the solution with forces from the numerical and analytical analysis respectively.

It can be seen that the force in the screw plays a big role on the accuracy of the mode mixity. To increase accuracy, a correction factor for Eq. (5) can be developed.

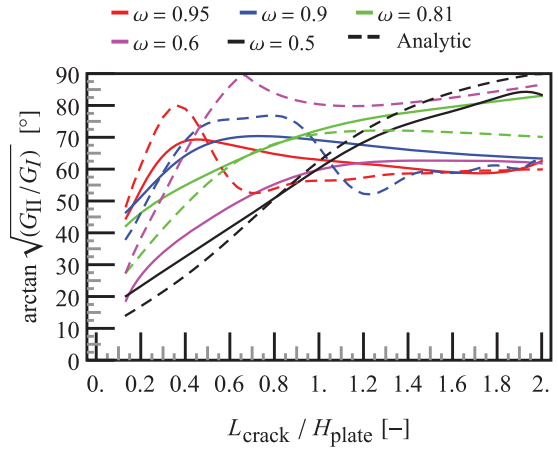

Figure 19: *Mode mixity of the reference layup with forces in the reinforcement from the numerical analysis*

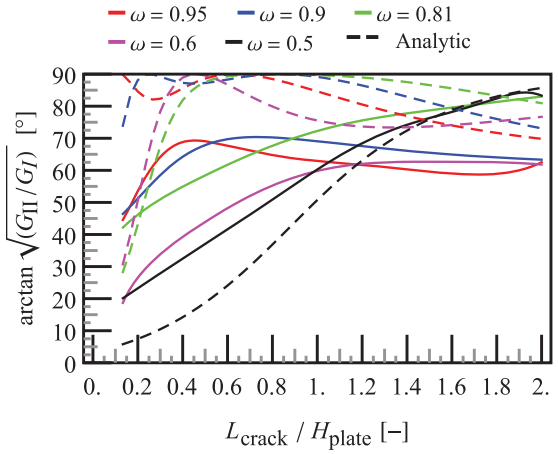

Figure 20: *Mode mixity of the reference layup with forces in the reinforcement from the analytical solution*

4.3 LOAD-BEARING CAPACITY

The load-bearing capacity of a reinforced CLT notch can be explicitly calculated applying Eq. (7) if the mode mixity is known. For that reason, an effort is made in the following to determine the mode mixity. The closed form solution of the mode mixity can't be defined with an expression which would be suitable for the application in standards. Therefore, a regression curve can be developed based on important geometric parameters (ω, β) and the CLT layup. The significant mode mixity of the reinforced beam in failure endorses the implementation of a failure criterion. In Eq. (9) a semi-quadratic criterion was used. However, other failure criteria could also be appropriate.

$$\left(\frac{G_I}{G_{I,C}}\right)+\left(\frac{G_{II}}{G_{II,C}}\right)^2 = 1 \qquad (9)$$

with

$G_{I,C}$ and $G_{II,C}$ critical ERR in mode I and II, respectively

https://doi.org/10.52202/069179-0322

The solution of Eq. (9) is illustrated in Figure 21.

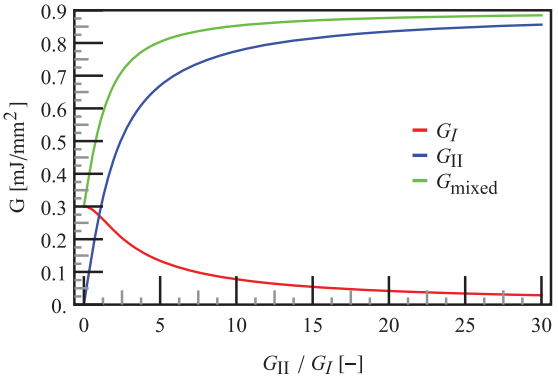

Figure 21: *Progression of the critical ERR in mode I, II and mixed mode G_{mixed} as a function of G_{II} / G_I*

Next, a brief methodology for the determination of the load-bearing capacity for the proposed analytical model is given.

(i) Determine the force in the screw applying Eq. (5), assuming L_{crack} = 150 mm – a conservative approximation compared to L_{crack} = 100 mm.

(ii) Obtain the phase angle of the mode mixity from a regression curve obtained from the analytical or numerical model. In the regression curve a critical crack length should be assumed – proposal from experimental results in this work and from literature for not inclined screws is L_{crack} = 100 mm

(iii) Determine from Eq. (9) or with a regression curve the critical mixed mode ERR G_{mixed} and calculate the load-bearing capacity with Eq. (10)

$$V_{f,d} = \sqrt{\frac{2 \cdot w \cdot G_{mixed}}{\left(\frac{(1-\eta)^2}{(\kappa GA)_1} + \frac{\eta^2}{(\kappa GA)_2} - \frac{1}{(\kappa GA)_3}\right) + H \cdot \left(\frac{(1+\beta-\eta)^2}{(EI)_1} + \frac{\eta^2}{(EI)_2} - \frac{(1+\beta)^2}{(EI)_3}\right)}} \quad (10)$$

where
$\eta = F_{t,90} / V_d$

5 EXPERIMENTAL RESULTS AND VERIFICATION

For the analytical method described in the previous section a comparison of the predicted load-bearing capacity with experimental results presented in [12] was prepared. The summary of the conducted experimental tests on reinforced notched CLT plates is illustrated in Table 4. For determining the mode mixity the results from Figure 19 were taken, as a better matching was obtained. The comparison showed conservative predictions of the model in a range of 10% to 17% (Figure 22). The results show that this method can be used to explicitly predict the failure load of reinforced notched CLT plates. It should be noted that the analytical method for the prediction of the force in the screw and also Elastic Interface model can be utilised for solid timber or glulam beams.

Table 4: *Detailed overview of experimental tests on reinforced notched CLT elements*

Layup [mm]	Series	n_{screws}	Screw angle [°]	α / β	$V_{f,mean,unreinforced}$ [kN]	$V_{f,mean,reinforced}$ [kN]	$V_{f,reinf}/V_{f,unreinf}$
30-30-30-30-30	5A-R1	4	45	0.50/0.40	48.1	84.0	**1.75**
	5A-R2	4	90			78.0	**1.62**
	5A-R3	4*				79.8	1.66
	5C-R1	4	90	0.60/0.40	70.7	92.6	1.31
		4*				88.5	1.25
	5C-R2	**2**				80.2	**1.13**
		2*				80.3	**1.14**
30-30-30-30-30-30	7A-R	3	90	0.62/0.40	75.1	105	1.40
30-30-30-30-30-30	7C-R	3		0.57/0.40	72.9	100	1.37

* Reinforcement applied from top of the plate

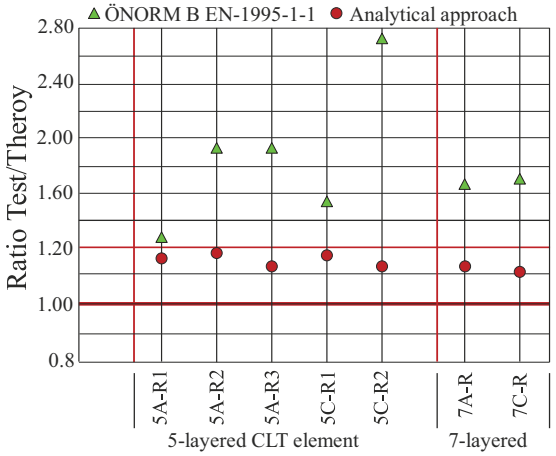

Figure 22: *Comparison of the load-bearing capacity from the experimental tests and the analytical models*

6 CONCLUSIONS

In this paper a contribution for prediction of the force in the reinforcement and the load-bearing capacity in reinforced notched CLT plates is given. In general, notches should be avoided due to the severe impact on the load-bearing capacity, robustness and ductility of load-bearing timber members, but if used they should be reinforced in any case.

The proposed way of reinforcing notched CLT plates is with self-tapping screws placed in one row at a maximum distance a_1 = 150 mm and distance $a_{3c} = 2.5 \cdot d_{screw}$ from the notch tip. A force in the screw can be calculated with Eq. (5), assuming a conservative crack length L_{crack} = H, for simplification. The current method for unlayered reinforced notches in the National Annexes [3] and [4] to EC-1995-1-1 also potentially show a possibility to predict the force in the reinforcement of notched CLT plates. However, more investigations should be conducted. Nonetheless, it is questionable, if such mechanical inconsistent approaches should be utilized in standards and guidelines for CLT after all.

An explicit and mechanically consistent analytical model for the prediction of the load-bearing capacity in reinforced notches of CLT plates was presented. The analytical model showed a good accuracy with the numerical model in scope of mode mixity, being important for the determination of the load-bearing capacity. The analytical model also showed a good correspondence with conducted experimental results. Nonetheless the analytical approach should be further refined and simplified as much as possible in order to be applicable in standards and guidelines.

For a further refinement of the analytical model, it would be of interest to apply fracture mechanics based methods of higher order, e.g. Zig-Zag theory, as the shear in the transversal layers has a big influence on the deformations at the crack tip and therefore on the load-bearing capacity. For the future work it is essential to conduct additional experimental tests on reinforced notched CLT plates including a wide range of different layups and parameters ω and β in order to further verify the given proposals.

ACKNOWLEDGEMENT

This research work was prepared within the frame of the project "Notches in CLT and CLT ribbed panels" which was funded in the program line FFG Collective Research by the Austrian Research Promotion Agency FFG.
The work of Erik Serrano was part of the project InnoCrossLam, supported under the umbrella of ERA-NET Cofund ForestValue.

REFERENCES

[1] Jockwer, R.: Structural Behaviour of Glued Laminated Timber Beams with Unreinforced and Reinforced Notches, Dissertation, ETH Zurich, 2014
[2] EN 1995-1-1:2004: Design of timber structures - Part 1-1: General and rules for buildings. CEN.
[3] DIN EN 1995-1-1/NA:2013: Nationaler Anhang - National festgelegte Parameter - Eurocode 5: Bemessung und Konstruktion von Holzbauten - Teil 1-1: Allgemeines - Allgemeine Regeln und Regeln für den Hochbau
[4] ÖNORM B 1995-1-1:2019: Bemessung und Konstruktion von Holzbauten, Teil 1-1: Allgemeines - Allgemeine Regeln und Regeln für den Hochbau, Ausgabe: 2019-06-01.
[5] Henrici, D.: Beitrag zur Spannungsermittlung in ausgeklinkten Biegeträgern aus Holz, PhD thesis, Technische Universität München, Germany, 1984.
[6] prEN 1995-1-1:20XX: Comment on consolidated draft prEN 1995-1-1, informal enquiry, CEN/TC 250/SC 5 "Eurocode 5: Design of timber structures"
[7] Dietsch, P.: Reinforcement of Timber Structures-a New Section for Eurocode 5, in World conference on Timber Engineering, Vienna, Austria, 2016.
[8] Jockwer, R., et.al.: Enchanced design approach for reinforced notched beams, 46th CIB-W18 Meeting, 26 to 29 August 2013, Vancouver, Canada, 2013.
[9] Riipola, K.: Dimensioning of beams with cracks, notches and holes. An application of fracture mechanics, In: Proc. Of the CIB-W18 Meeting 23, Paper No. CIB-W18/a 23-19-1, Lisbon, Portugal, 1990
[10] Sorin. E., Coureau J.L., Chaplain M.: Prediction of the ultimate load-carrying capacity of wooden notched beams with and without reinforcements using a splitting model. Construction and Building Materials 271 (2021) 121518, 2021
[11] Ringhofer, A.;Screw_Stiffness: highlights, Vortrag im Rahmen der Beiratssitzung des IHBV, 7.10.2021., Wien
[12] Malagic A., Augustin M., Silly G., Thiel A., Schickhofer G.: Load-bearing Capacity and Fracture Behaviour of Notched Cross Laminated Timber Plates, in: International Network on Timber Engineering Research – Proceedings Meeting 54, Paper INTER/54-12-5, Online, 2021.
[13] Blaß, H.J., Bejtka, I.: Querzugverstärkungen in gefährdeten Bereichen mit selbstbohrenden Holzschrauben. Deutsche Gesellschaft für Holzforschung, Universität Fridericiana Karlsruhe, Stuttgart, Germany, 2003
[14] Serrano, E., Danielsson, H. (2020): Fracture Mechanics Based Design of CLT plates– Notches at Supports and Half and-Half Joints. In: International Network on Timber Engineering Research – Proceedings Meeting 53, Paper INTER/53-12-2, Online
[15] Wiliams, J. G.: On the Calculation of Energy Release Rates for Cracked Laminates. International Journal of Fracture 36, 101-119, 1988.
[16] Bennati, S., Fisicaro, P., Taglialegne, L., Valvo, P.S.: An Elastic Interface Model for the Delamination of Bending-Extension Coupled Laminates, Article in Applied Sciences, August, 2019

https://doi.org/10.52202/069179-0322

World Conference on Timber Engineering Oslo 2023

ANALYSIS OF DIFFERENT NUMERICAL MODELLING STRATEGIES OF MULTI-STOREY CLT SHEAR WALLS

Elisabetta Maria Ruggeri[1], Giuseppe D'Arenzo[2], Marinella Fossetti[3], Werner Seim[4]

ABSTRACT: CLT platform-type buildings are characterized by a high level of redundancy due to the high number of connections used in the perimeter of the CLT panels. In this regard, in addition to the connections placed at the base of the walls, other structural components including the floor diaphragms and the lintels above the openings, along with their connections, influence the lateral performances of CLT shear walls. In this paper, an extensive analysis on the lateral behaviour of multi-storey CLT shear walls with openings realized with two different construction techniques is conducted. The study compares the results obtained from a simplified modelling strategy commonly used in practical design with more advanced modelling strategies that consider in detail the effects of structural interactions between floors and wall segments and between lintels and wall segments. The results of the elastic analyses conducted in this study showed significant differences in the lateral behaviour of systems analysed with the two modelling strategies, emphasizing that the simplified modelling strategies cannot always be reliable methodologies to describe the lateral behaviour of multi-storey CLT shear walls due to the significant effect of structural interactions provided by floors and lintels.

KEYWORDS: CLT structures, Multi-storey shear walls, Structural interactions, Numerical modelling, Elastic analyses

1 INTRODUCTION

CLT "box-type" buildings, and in particular those erected using the platform construction method, present a high level of structural redundancy due to the numerous connections between external walls, internal partitions and floor diaphragms, see Figure 1. Connections of this type, which are typically neglected in practical design, generate structural interactions that have a significant impact on the lateral performance of CLT shear walls and, as a result, the entire structure subjected to lateral loads.
Typically, in the practical design, the lateral stiffness of a CLT building is calculated based on the shear walls and their individual stiffness in the direction of the horizontal load. However, the high number of connections used in the perimeter of the CLT panels, provide an additional stiffening contribution due to the interaction between floor diaphragms and wall segments and between lintels and wall segments, which modifies the deformation mechanisms of a generic shear wall, see for instance [1–5].
The effects of the interactions between lintels and wall segments also depend on the method used for the construction of the openings, which include opening cut

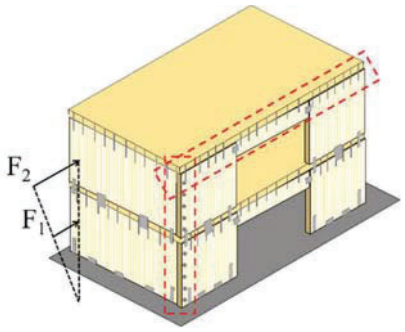

Figure 1: *CLT "box-type" building erected using the platform construction method under lateral loads.*

out of the panel or opening realized by assembling different CLT panel elements. In case where the openings are directly cut out of the CLT panel, the structural continuity between lintels and wall segments is ensured and the shear wall behaves as a unique structural element, see Figure 2 (a). On the other hand, in case where the openings are realized by assembling wall segments and lintels through mechanical connections, such as screws or

[1] Elisabetta Maria Ruggeri, Faculty of Engineering and Architecture, Kore University of Enna, Italy, elisabettamaria.ruggeri@unikorestudent.it
[2] Giuseppe D'Arenzo, Timber Structures and Building Rehabilitation, University of Kassel, Germany, giuseppe.darenzo@uni-kassel.de
[3] Marinella Fossetti, Faculty of Engineering and Architecture, Kore University of Enna, Italy, marinella.fossetti@unikore.it
[4] Werner Seim, Timber Structures and Building Rehabilitation, University of Kassel, Germany, wseim@uni-kassel.de

https://doi.org/10.52202/069179-0323

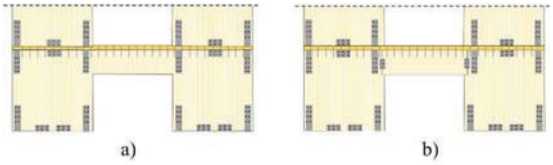

Figure 2: *a)shear wall as monolithic element, b) shear wall with assembled wall segments and lintels.*

metal brackets, a full structural continuity is difficult to achieve and, in this case, the wall segments can be assumed as independent cantilever elements [6], see Figure 2 (b). The lateral performance of CLT buildings realized with these two construction techniques has been the focus of different experimental studies, see for instance [7–9], which showed a different lateral behaviour for multi-storey CLT systems realized with the two construction techniques.

The results of various studies conducted in the literature, [7,10,11], reveal that the lateral behaviour of multi-storey CLT shear walls is influenced by the structural interactions between the wall segments and the surrounding structural elements and the different construction techniques used to realize the openings. Despite these structural interactions have an impact on the lateral behaviour of multi-storey CLT systems, they are often not considered in practical design and in simplified models.

This study investigates in detail the effects of the structural interactions provided by floors and lintels on the lateral behaviour of multi-storey CLT shear walls. The approach used in this study consisted of comparing the results obtained from the elastic analyses of simplified modelling strategies, in which the effects of the structural interactions are not taken into account, with those obtained from more advanced modelling strategies, which consider the structural interactions due to floors and lintels. Results of this numerical study show how the different modelling strategies lead to different lateral performance of the systems, highlighting the need to more carefully consider the different structural elements of CLT systems in the analysis of their lateral behaviour.

2 NUMERICAL STUDY

2.1 MODELLING STRATEGIES

Typically, multi-storey CLT shear walls are modelled by means of a simplified modelling strategy, identified as SM in this study, see Figure 3. In this case, stability for horizontal loads of multi-storey CLT shear walls is provided by wall segments, schematized as cantilever elements. Whereas, lintels are modelled as pinned elements, which connect the wall segments and have the only function of transferring horizontal and vertical loads to the wall segments, and have no ability to transfer moment at their extremities. The lateral stability of the system is ensured by the wall base connections, namely, hold-downs, which are placed at the two extremities of each wall segment, and angle brackets, which are placed along the length of the wall panels.

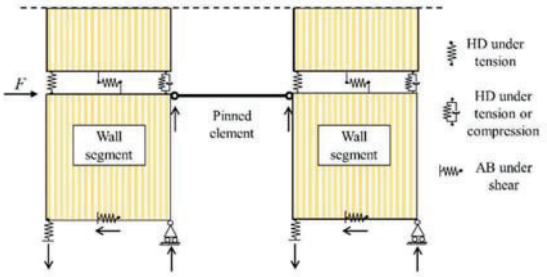

Figure 3: *Simplified modelling strategy of multi-storey CLT shear walls (SM).*

With this modelling strategy, the bending contribution of the floor diaphragms and lintels is neglected, and as a result, no bending moment is transmitted between the wall segments and the lintels, and the system failure occurs in the mechanical anchors placed at the base of the wall segments.

In order to realistically simulate the lateral behaviour of multi-storey CLT shear walls, a more advanced modelling strategy that takes into account the interactions between floor diaphragms and wall segments and between lintels and wall segments is required. In this regard, an advanced modelling strategy that considers these structural interactions (IM) is proposed and applied to the two construction techniques shown in Figure 2, for the case of monolithic (IM-MSW) and assembled (IM-ASW) multi-storey shear walls, see Figure 4 and Figure 5, respectively.

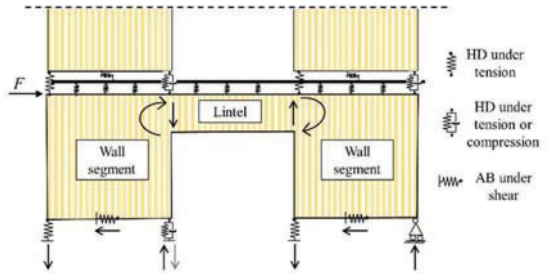

Figure 4: *Advanced modelling strategy with interactions in case of monolithic multi-storey CLT shear walls (IM-MSW).*

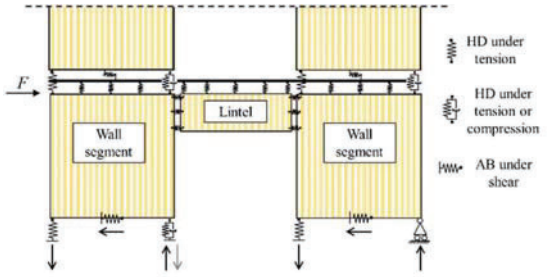

Figure 5: *Advanced modelling strategy with interactions in case of assembled multi-storey CLT shear walls (IM-ASW).*

https://doi.org/10.52202/069179-0323

When structural interactions are taken into account, higher lateral performance and different lateral deformation mechanisms are expected than the SM strategy, due to the bending contribution of the floor diaphragms and, in case of monolithic walls, also due to the capability of the lintel to transfer bending actions. In case of monolithic shear walls (IM-MSW) the system failure can occur either in the connections at the base of the wall segments or in the corner of the openings in correspondence of the lintel element, depending on the stresses level in this critical zone [7,8,12]. On the other hand, in case of assembled shear walls (IM-ASW), the system failure may occur in the floor panel or in the base connections. In the following, the configurations and the mechanical parameters used for the numerical analysis are presented.

2.2 STRUCTURAL CONFIGURATIONS CONSIDERED IN THE STUDY

In order to investigate the effects of the structural interactions, a numerical analysis was performed considering different multi-storey CLT shear wall systems. An investigation was conducted to analyse the impact of different modelling strategies on two construction techniques involving shear walls. These construction techniques include the creation of shear walls as monolithic elements with openings or as assemblies of different CLT elements with openings. The numerical analysis was developed considering nine different multi-storey CLT shear walls structures consisting of one-, three- and five-storey systems and three different geometries, see Figure 6.

The first geometry, Geometry 1, has one opening of 3 m in length; the second geometry, Geometry 2, has two openings of 1 m in length; while the third geometry, Geometry 3, has three openings of 1 m in length. The height of the wall segments is equal to 3 m for all configurations analysed, while the lintels and the floors are 400 and 200 mm high, respectively. Geometrical dimensions of the three geometries are shown in Figure 7.

The numerical study was conducted considering three different thicknesses of CLT wall panels along the height of the structures. The distribution of the different wall panels along the height of the structures is reported in Table 1. Wall panel 1 (WP1) consists of a three-layered

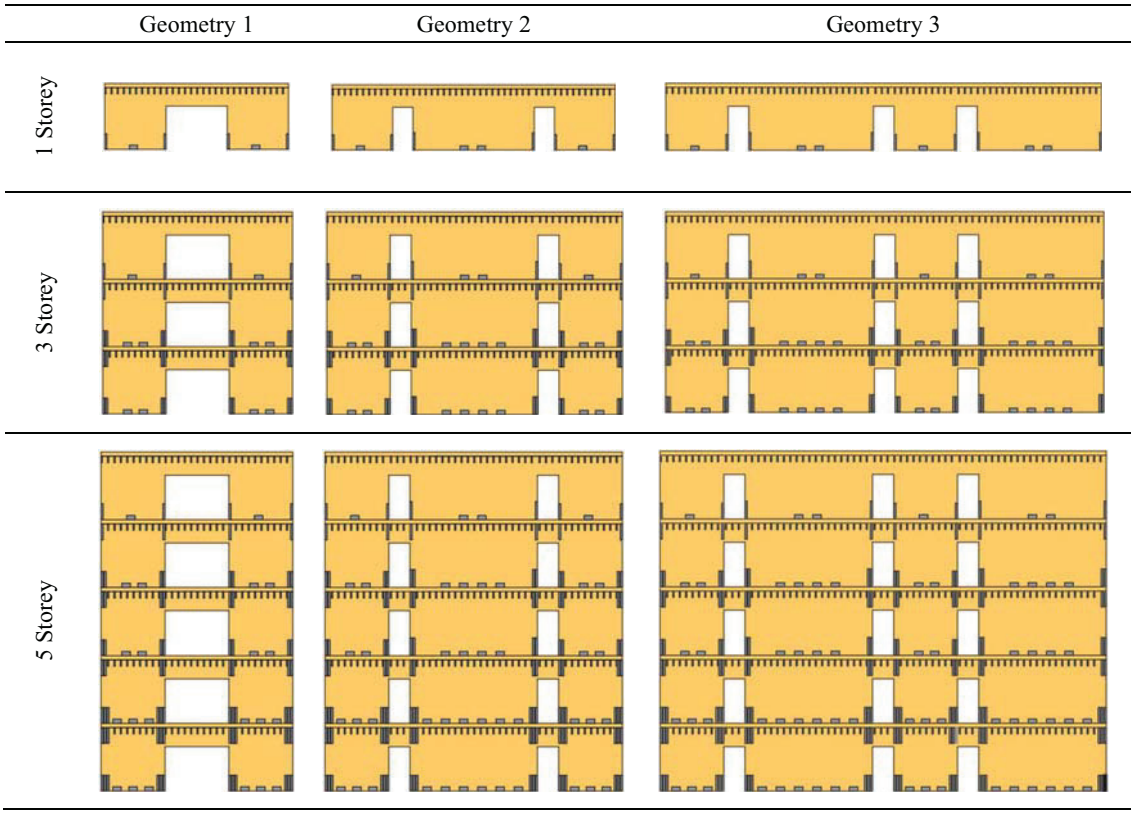

Figure 6: *Multi-storey CLT shear walls configurations and mechanical anchors distribution.*

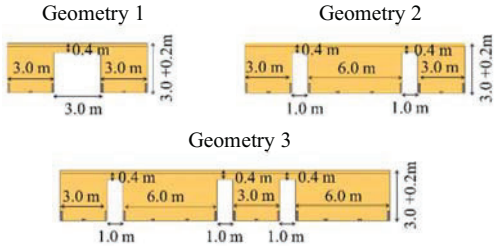

Figure 7: *CLT shear walls geometries and dimensions.*

panel with a thickness of 80 mm and layer thicknesses of **30**-20-**30** mm (in bold the layers of wooden laminated arranged in the vertical direction). Wall panel 2 (WP2) consists of a five-layered panel with a thickness of 120 mm and layer thicknesses of **30**-20-**20**-20-**30** mm. Wall panel 3 (WP3) consists of a five-layered panel with a thickness of 160 mm and layer thicknesses of **40**-20-**40**-20-**40** mm.

Table 1: *Distribution of the CLT panels thicknesses.*

	1 storey	3 storey	5 storey
Fifth storey			WP1
Fourth storey			WP2
Third storey		WP1	WP2
Second storey		WP2	WP3
First storey	WP1	WP2	WP3

A different direction of the external wooden laminates was adopted for the wall segments and the lintels: in case of monolithic shear walls, the orientation of the external wooden laminates of the CLT panels was assumed in the vertical direction for both wall segments and lintels, while in case of assembled shear wall, a vertical orientation was assumed for wall segments and a horizontal orientation for lintels (Figure 2). For all configurations, a floor panel (FP) with a total thickness of 200 mm and five layers with thicknesses of **40**-40-**40**-40-**40** mm, was adopted.

Regarding the elastic properties of CLT panels, the modulus of elasticity parallel to the grain (E_0), the modulus of elasticity perpendicular to the grain (E_{90}), and the shear modulus in the plane (G_0) of the wooden laminates were assumed equal to 11700 MPa, 390 MPa and 730 MPa, respectively.

The values of the elastic stiffness of the base connections, hold-downs and angle brackets, were defined according to the experimental results of Casagrande et al [13]. On the basis of this study, hold-downs (HDs) type WHT440 with thirty 4×60 mm annular ring nails were used and the value of vertical elastic stiffness was set equal to 6.61 kN/mm. Whereas, angle brackets (ABs) type TTF200 with thirty 4×60 mm annular ring nails were used and the value of horizontal elastic stiffness was set equal to 8.94 kN/mm. The distribution of the base connections, hold-downs and angle brackets, of the multi-storey CLT shear walls was determined based on the increase of the shear force from the upper storeys to the foundation, see Figure 6. Mechanical properties of the floor-to-wall connections (f-w) were assigned according to the experimental results of Gavric et al. [14]. Based on this study, the vertical stiffness (withdrawal, w-w_v) and the horizontal stiffness (shear, w-w_h) of one screw was set equal to 4.00 and 1.45 kN/mm, respectively. A spacing of 300 mm was chosen for these connections in all the analyses.

Table 2 summarizes the elastic stiffnesses used in the numerical analyses for one hold-down in the vertical direction, one angle bracket in the horizontal direction, and one floor-to-wall connection in both vertical (v) and horizontal (h) directions.

Table 2: *Stiffness of the connections used for the numerical analyses.*

	K_{el} [kN/mm]
HD	6.61
AB	8.94
w-w_v	4.00
w-w_h	1.45

The values of the elastic stiffness of the base connections, hold-downs and angle brackets, reported in Table 2, were modified to account for the significative influence of the connection properties on the lateral deformation of a CLT shear wall. In this context, the stiffness of each hold-down and angle bracket was multiplied by three different coefficients α equal to 0.5, 1.0, and 1.5, which lead to 3 different arrangements of connection stiffnesses in multi-storey shear walls. Table 3 provides a summary of these arrangements.

Table 3: *Stiffness of connections as function of α.*

	α=0.5	α=1.0	α=1.5
K_{HD} [kN/mm]	3.30	6.61	9.91
K_{AB} [kN/mm]	4.47	8.94	13.41

A vertical load *q* equal to 10 kN/m was applied on each storey of the system, while a triangular distribution of horizontal loads *F* was adopted. The values of the horizontal loads used in each geometry are reported in Table 4.

https://doi.org/10.52202/069179-0323

Table 4: *Horizontal loads F adopted in the numerical analyses.*

Storey configuration			N° storeys	Geometry 1	Geometry 2	Geometry 3
		5	Fifth storey	107.14	166.67	250.00
			Fourth storey	85.71	133.33	200.00
	3		Third storey	64.29	100.00	150.00
			Second storey	42.86	66.67	100.00
1			First storey	21.43	33.33	50.00

2.3 NUMERICAL MODELS

The elastic behaviour of multi-storey CLT shear walls with openings was investigated using finite element models (FEM) developed in the software package SAP2000 [15].

To accurately capture the elastic behaviour of wall segments and lintels with varying thicknesses, orthotropic shell elements were adopted in the numerical models. Specifically, the CLT panels were simulated using four-node quadrilateral shell elements with a mesh size of 100×100 mm. The mechanical properties of CLT panels were assigned considering the layered structure of the three different sections, WP1, WP2 and WP3, according to the composite theory of Blaß and Fellmoser [17]. The effective moduli of elasticity in the vertical direction, $E_{eff,v}$, and horizontal direction, $E_{eff,h}$, of the panel were defined according to Equation (1) and Equation (2), where t_v and t_h represent the total thickness of the vertical and horizontal wooden laminates, while t_{CLT} denotes the total thickness of the CLT panel.

$$E_{eff,v} = \frac{E_0 t_v + E_{90} t_h}{t_{CLT}} \quad (1)$$

$$E_{eff,h} = \frac{E_0 t_h + E_{90} t_v}{t_{CLT}} \quad (2)$$

The effective in-plane shear modulus of the wooden laminates, G_{eff}, was defined according to Bogensperger et al. [18], see Equation (3), in which w denotes the width of the wooden boards, t_{mean} represents the mean thickness of the wooden laminates and can be calculated with Equation (4), while α_T can be calculated by using Equation (5).

$$G_{eff} = \frac{G_0}{1 + 6\alpha_T \left(\frac{t_{mean}}{w}\right)^2} \quad (3)$$

$$t_{mean} = \frac{t_{CLT}}{N} \quad (4)$$

$$\alpha_T = p \left(\frac{t_{mean}}{w}\right)^{-0.79} \quad (5)$$

In Equation (4) and Equation (5), N is the number of the section's layers, while p is a parameter equal to 0.535 and 0.425 for three- and five-layered CLT panels, respectively. The elastic properties of the CLT panels adopted for wall segments and lintels are summarized in Table 5.

Table 5: *Elastic properties of CLT wall panels.*

	$E_{eff,z}$ [MPa]	$E_{eff,x}$ [MPa]	G_{eff} [MPa]
WP1	8872	3217	573
WP2	7930	4160	598
WP3	8872	3217	570

In the following, Figure 8, Figure 9 and Figure 10 illustrate the different modelling strategies employed in this study for the case of Geometry 1 and three-storey. A representation of the simplified modelling strategy of multi-storey CLT shear walls (SM) is shown in Figure 8. The lintels were modelled as pinned beam elements with infinite axial stiffness. In case of the SM strategy, analyses were conducted by applying the horizontal forces F at the top of the wall segments to each storey, while a vertical load q was applied to the first row of shell elements as equivalent load per unit area and as uniformly distributed load on the pinned elements.

A representation of the advanced modelling strategies of multi-storey CLT shear walls in case of monolithic (IM-MSW) and assembled (IM-ASW) systems is shown in Figure 9 (a) and (b), respectively. According to Figure 9 (a), in case of monolithic shear walls analysed with the advanced modelling strategy (IM-MSW), the wall segments and the lintels were modelled as unique shell element with the same orientation of the external wooden laminates (z-direction). Whereas, in case of assembled shear walls (IM-ASW), the wall segments and lintels were modelled as separate shell elements with different orientation of the external wooden laminates (z- and x-direction, respectively). According to Figure 9 (b), wall

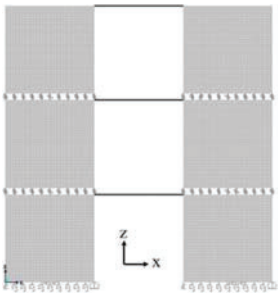

Figure 8: *Simplified modelling strategy of multi-storey CLT shear walls (SM).*

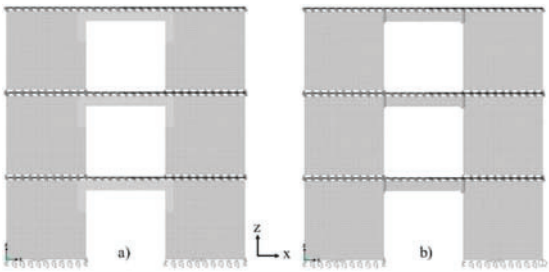

Figure 9: *Advanced modelling strategy with interactions of multi-storey CLT shear walls: a) IM-MSW, b) IM-ASW.*

segments and lintels were connected through the wall-to-lintel connections (w-l). In the modelling strategies with interactions, the floor panels were modelled as beam elements. The assigned bending stiffness, E_0I_{eff}, was determined based on the FP's layered structure outlined in section 2.2, considering only the layers arranged parallelly to the bending stresses. The effective moment of inertia, I_{eff}, was calculated by using Equation (6), where t_i is the thickness of each layer considered in the calculation, a_i is the distance of each layer from the centroid of the section, while b_f represents the floor width. The floor width b_f depends on the effective collaborative section that works in case of internal bending actions, which was calculated using the methodology proposed by Masoudnia et al [19].

$$I_{eff} = \frac{\sum_{i=1}^{n} t_i^3 \, b_f}{12} + \sum_{i=1}^{n} t_i b_f a_i^2 \qquad (6)$$

In these modelling strategies, the horizontal loads F were applied on the top of the wall segments at each storey and a vertical load q was applied to the first row of shell elements as equivalent load per unit area.

Modelling strategies that consider structural interactions (IM-MSW and IM-ASW) were compared with the SM strategy and another additional numerical model that represents a comparison system, called CS, see Figure 10. The CS strategy takes into account the structural interactions due to floors and walls and considers the same configurations of the multi-storey CLT shear walls without openings. As the SM and CS strategies represent the cases of maximum and minimum lateral flexibility,

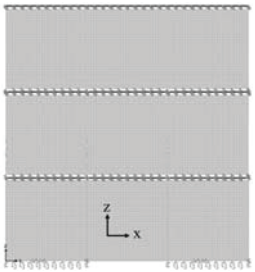

Figure 10: *Advanced modelling strategy with interactions in case of multi-storey CLT shear walls without openings (CS).*

respectively, the CS can offer valuable information on the lateral behaviour of multi-storey CLT shear walls.

For both modelling strategies SM and IM, multi-linear elastic links were employed to model the connections. In particular, mechanical anchors were modelled by means of one- and two-joint multi-linear elastic links from SAP2000 library. Figure 11 provides the force–displacement curves of the connections adopted in the numerical models for the elastic analyses. According to Polastri et al. [20], the hold-downs (HDs) were modelled with different behaviour for tensile and compressive forces (z-direction): for tensile forces the tensile stiffness of the hold-downs was considered, while for compressive forces the link simulated the contact between panel and foundation through high stiffness, see Figure 11 (a). Angle brackets (ABs) were modelled with symmetric elastic behaviour in the horizontal direction (x-direction), according to Yasumura et al. [8], in order to reproduce the behaviour of the angle brackets for shear loads, see Figure 11 (b). In order to reproduce the contact between the wall segments and the foundation, both the SM and IM modelling strategies utilized gap elements with rigid compression-only behaviour, see Figure 11 (c). Additionally, these gap elements were employed between the wall segments of two consecutive storeys in the SM strategy.

In case of IM strategies, the floor-to-wall connections (f-w) were modelled as a series of two-joint multilinear elastic links from SAP2000 [15] library. These connections were characterized by a symmetric elastic behaviour in the horizontal shear direction (x-direction), Figure 11 (b), while they were modelled with elastic behaviour, for tensile loads, in order to simulate the withdrawal behaviour of the connection, and with a stiff behaviour, for compressive loads, to simulate the contact between floor and wall, see Figure 11 (a). In case of assembled shear wall (IM-ASW) the wall-to-lintel connections (w-l) were modelled as a series of two-joint multi-linear elastic links with rigid compression-only behaviour in the horizontal direction (x-direction), in order to reproduce the contact between wall segments and lintels, neglecting the relative low stiffness contribution of these connections, see Figure 11 (c).

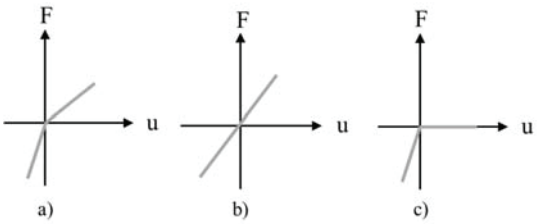

Figure 11: *Force-displacement curves of the connections used in the numerical models: a) HD and f-w in z-direction, b) AB and f-w in x direction, c) GAP in z-direction and w-l in x-direction.*

https://doi.org/10.52202/069179-0323

3 RESULTS AND DISCUSSION

The results of the elastic analyses in terms of lateral storey displacements, lateral stiffness and deformation mechanisms are presented in this section. Results obtained from the advanced modelling strategy (IM) were compared with those obtained from the simplified modelling strategy (SM) and the comparison system (CS). Figure 12 shows the results in terms of lateral storey displacements of multi-storey CLT shear walls. Each graph reports four curves representing the lateral storey displacement of each structure obtained from the four modelling strategies SM, IM-ASW, IM-MSW and CS. In particular, the lateral storey displacement values are normalized with respect to the lateral storey displacement of the upper storey obtained through the SM strategy.

From Figure 12 it can be observed that the deformed shape of the monolithic (IM-MSW) and assembled shear walls (IM-ASW) modelled with interactions is very close, meaning that the floor alone strongly influences the lateral behaviour of the systems. The largest difference between the deformed shape of the IM-MSW and IM-ASW strategies is reached in case of Geometry 1 and five-storey systems, which is the case of the minimum bending stiffness of lintels and floors and the maximum lateral flexibility of the multi-storey system. In general, it can be observed that the lateral storey displacements decrease when moving from Geometry 1 to Geometry 3. This trend can be attributed to the increase in stiffness of the systems.

The graphs illustrated in Figure 12 indicate that when employing the IM-MSW and IM-ASW modelling strategies, which incorporate structural interactions, the lateral storey displacements are lower compared to those obtained using the SM strategy. In particular, the lateral storey displacements are much closer to those obtained from the CS strategy. According to Figure 12, in case of three-storey systems, the lateral storey displacements obtained from the modelling strategies with interactions of monolithic and assembled shear wall (IM-MSW and IM-ASW, respectively) reach both a maximum of 42% of those obtained from the SM strategy. Whereas, in case of five-storey systems, the lateral storey displacements obtained from the IM-MSW and IM-ASW strategies reach a maximum of 36% and 42% of those obtained from the SM strategy, respectively.

Figure 13 shows the results in terms of normalized lateral stiffness of multi-storey CLT shear walls against the coefficient α used to modify the stiffness of the wall base connections, see Table 3. Each graph shows four curves, representing the lateral stiffness of a multi-storey CLT shear wall modelled with the four modelling strategies (SM, IM-ASW, IM-MSW and CS) and normalized respect to the lateral stiffness obtained from the CS strategy. The lateral stiffness of each system was calculated as the ratio between the base shear and the lateral displacement at the top of the shear wall obtained from the numerical analyses.

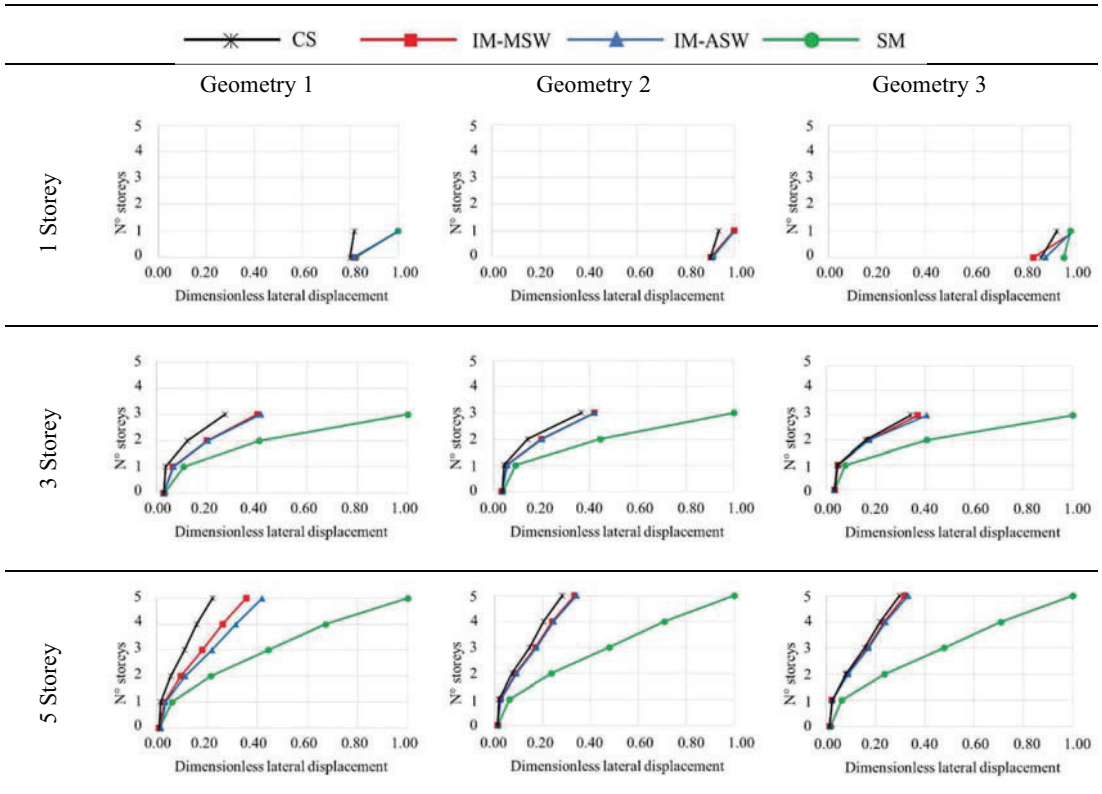

Figure 12: *Results in terms of lateral storey displacement.*

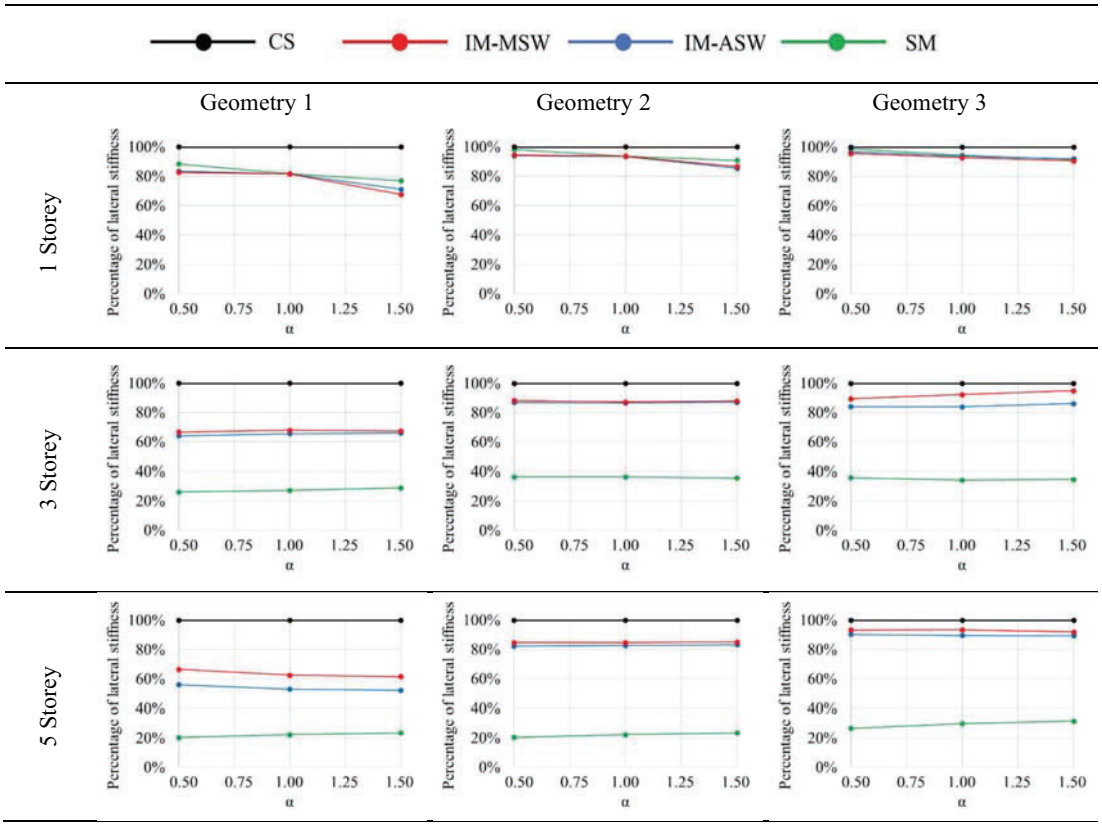

Figure 13: *Results in terms of lateral stiffness.*

The results about the lateral stiffness, depicted in Figure 13, align with those obtained for lateral storey displacements. The findings of Figure 13 demonstrate that IM-MSW and IM-ASW, which incorporate the structural interactions, have lateral stiffness between that of the SM and CS strategies. Specifically, the curves obtained from the monolithic and assembled shear walls (IM-MSW and IM-ASW, respectively) are much closer to those obtained from the comparison system (CS).

According to Figure 13, in case of one-storey systems, the curves representing the lateral stiffnesses lie approximately on the same level of the CS strategy. This is due to the fact that the systems deform with a predominant sliding mechanism and low rocking, generating negligible structural interactions.

Figure 13 shows that the overall lateral stiffness of multi-storey CLT shear walls is similar for both construction techniques depicted in Figure 2 (IM-MSW and IM-ASW). In this regard, the maximum differences between the IM-MSW and IM-ASW strategies are equal to 9%, for Geometry 3 and three-storey, and 11%, for Geometry 1 and five-storey.

Moreover, Figure 13 shows that, in case of Geometry 1, the monolithic and assembled shear walls modelled with interactions (IM-MSW and IM-ASW, respectively) have normalized lateral stiffness values all greater than 60% and 50% for three- and five-storey systems, respectively. However, in case of Geometry 2, these values are greater than 80% for both three- and five-storey systems. Whereas, in case of Geometry 3, the normalized lateral stiffness values are greater than 80% and 90% for three- and five-storey systems, respectively.

Figure 14 shows the structures in the deformed configuration obtained from the four modelling strategies, SM, IM-ASW, IM-MSW and CS, in case of Geometry 1. It can be observed that moving from SM to CS (from left to right of Figure 14), the rocking contribution decreases and the sliding contribution increases, due to the effects of the structural interactions. From Figure 14 it can be observed the significant effect of the interactions due to floors and lintels; in fact, the multi-storey systems with interactions deform similarly to multi-storey systems without openings (CS).

In particular, in case of SM strategy and CS strategy, the predominant deformation mechanisms were rocking and sliding, respectively, while in case of IM-MSW and IM-ASW a combination of sliding and rocking mechanism, with predominant sliding, were performed.

Results obtained from the elastic analyses, show that the interactions between lintels and wall segments and between floors and wall segments strongly influence the deformation mechanism of multi-storey CLT shear wall systems, which is closer to that of multi-storey shear wall systems without openings (CS) rather than that of multi-storey shear wall systems modelled with the SM strategy, in which these interactions are not taken into account.

https://doi.org/10.52202/069179-0323

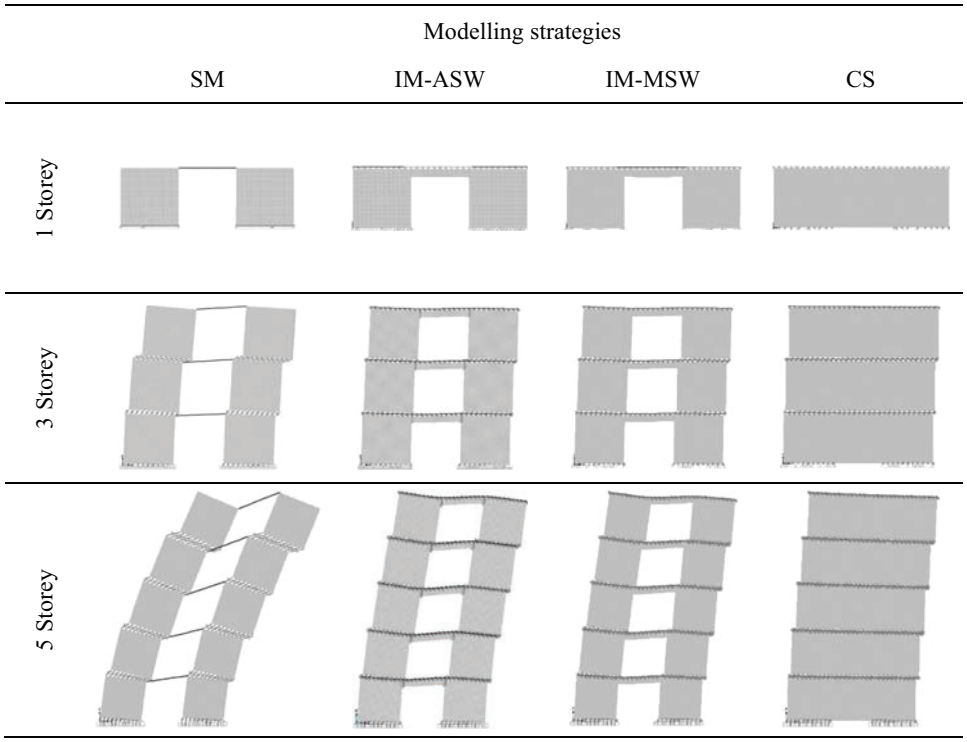

Figure 14: *Deformation mechanisms of the systems in case of Geometry 1.*

4 CONCLUSIONS

This paper presented a numerical study that aims to examine how the lateral behaviour of multi-storey CLT shear wall systems, constructed using monolithic and assembled shear walls, is affected by structural interactions provided by floor diaphragms and lintels. In particular, the effects of the structural interactions were studied by considering both simplified modelling strategy (SM) and more advanced modelling strategies (IM), which consider these structural interactions. The numerical study was conducted considering nine structural configurations, consisting of one-, three- and five-storey systems, and including three multi-storey shear wall geometries and different mechanical properties of the connections placed at the base of the wall segments. The study was conducted by comparing the results, in terms of lateral storey displacements, lateral stiffness and deformation mechanisms, obtained from the advanced modelling strategies with interactions, in case of monolithic and assembled shear walls (IM-MSW and IM-ASW), with those obtained from the SM strategy. Moreover, an additional numerical model representing a comparison system (CS), which considers the same configurations of multi-storey CLT shear walls without openings, was developed only for purpose of comparisons.

Results of the elastic analyses show that the structural interactions due to floors and lintels modify the deformation mechanism of multi-storey CLT systems compared to the cases in which these structural interactions are neglected. In particular, these structural interactions reduce the rocking component of the lateral displacement and increase the overall lateral stiffness of the multi-storey systems, which becomes closer to that that of an equivalent system without openings.

Results of this study show that the simplified modelling strategies, often adopted in the design practice, may not always properly describe the behaviour of the multi-storey CLT shear walls subjected to lateral loads.

As result, this study suggests to take into account the contribution given by lintels and floors in the numerical modelling of multi-storey CLT shear walls, since they significantly modify the lateral performance of the system, which is typically modelled by means of simplified modelling strategy.

ACKNOWLEDGEMENT

The presented research was carried out during a research stay of the first author at the University of Kassel (Germany). The support of the scientific staff of the University of Kassel are gratefully acknowledged.

REFERENCES

[1] Tamagnone G, Rinaldin G, Fragiacomo M. Influence of the Floor Diaphragm on the Rocking Behavior of CLT Walls. J Struct Eng 2020;146:1–11. https://doi.org/10.1061/(ASCE)ST.1943-541X.0002546.

[2] D'Arenzo G, Schwendner S, Seim W. The effect of the floor-to-wall interaction on the rocking stiffness of segmented CLT shear-walls. Eng Struct 2021;249:113219. https://doi.org/10.1016/j.engstruct.2021.113219.

[3] Ruggeri EM, D'Arenzo G, Fossetti M, Seim W. Investigating the effect of perpendicular walls on the lateral behaviour of Cross-Laminated Timber shear walls. Structures 2022;46:1679–95. https://doi.org/10.1016/j.istruc.2022.10.141.

[4] Khajehpour M, Casagrande D, Doudak G. The role of lintels and parapets on the mechanical performance of multi-storey cross laminated timber shearwalls with openings. Eng Struct 2022;255:113912. https://doi.org/10.1016/j.engstruct.2022.113912.

[5] D'Arenzo G. An elastic model for the prediction of the lateral response of Cross-Laminated Timber shear walls with openings. Eng Struct 2023;274:115055. https://doi.org/10.1016/j.engstruct.2022.115055.

[6] Casagrande D, Fanti R, Doudak G, Polastri A. Experimental and numerical study on the mechanical behaviour of CLT shearwalls with openings. Constr Build Mater 2021;298:123858. https://doi.org/10.1016/j.conbuildmat.2021.123858.

[7] Popovski M, Gavric I. Performance of a 2-Story CLT House Subjected to Lateral Loads. J Struct Eng 2015;142:1–12. https://doi.org/10.1061/(asce)st.1943-541x.0001315.

[8] Yasumura M, Kobayashi K, Okabe M, Miyake T, Matsumoto K. Full-Scale Tests and Numerical Analysis of Low-Rise CLT Structures under Lateral Loading. J Struct Eng (United States) 2016;142:1–12. https://doi.org/10.1061/(ASCE)ST.1943-541X.0001348.

[9] Sato M, Isoda H, Araki Y, Nakagawa T, Kawai N, Miyake T. A seismic behavior and numerical model of narrow paneled cross-laminated timber building. Eng Struct 2019;179:9–22. https://doi.org/10.1016/j.engstruct.2018.09.054.

[10] Yasumura M, Kobayashi K, Okabe M, Miyake T, Matsumoto K. Full-Scale Tests and Numerical Analysis of Low-Rise CLT Structures under Lateral Loading. J Struct Eng 2016;142:1–12. https://doi.org/10.1061/(asce)st.1943-541x.0001348.

[11] Kawai N, Tsuchimoto T, Tsuda C, Murakami S, Miura S, Isoda H, et al. Lateral loading tests on CLT shear walls by assembly of narrow panels and by a large panel with an opening. WCTE 2014 - World Conf Timber Eng Proc 2014.

[12] Yue K, Liang B, Shao Y, Xie C, Hu W, Zhao M, et al. Lateral behavior of wood frame shear walls sheathed with densified plywood under monotonic loading. Thin-Walled Struct 2021;166:108082. https://doi.org/10.1016/j.tws.2021.108082.

[13] Casagrande D, Polastri A, Sartori T, Loss C, Chiodega M. Experimental campaign for the mechanical characterization of connection systems in the seismic design of timber buildings. WCTE 2016 - World Conf Timber Eng 2016.

[14] Gavric I, Fragiacomo M, Ceccotti A. Cyclic behavior of typical screwed connections for cross-laminated (CLT) structures. Eur J Wood Wood Prod Vol 2015;73:179–91. https://doi.org/10.1007/s00107-014-0877-6.

[15] CSI. Integrated software for structural analysis and design. CSI-SAP2000. Berkeley, CA: CSI. I Berkeley (CA, USA) Comput Struct INC 2013.

[16] Izzi M, Casagrande D, Bezzi S, Pasca D, Follesa M, Tomasi R. Seismic behaviour of Cross-Laminated Timber structures : A state-of-the-art review. Eng Struct 2018;170:42–52. https://doi.org/10.1016/j.engstruct.2018.05.060.

[17] Blaß HJ, Fellmoser P. Design of solid wood panels with cross layers. Proc, World Conf Timber Eng Helsinki, Finl Finnish Assoc Civ Eng © 2004:604.

[18] Bogensperger T, Moosbrugger T, Silly G. Verification of CLT-plates under loads in plane. 11th World Conf Timber Eng 2010, WCTE 2010 2010;1:231–40.

[19] Masoudnia R, Hashemi A, Quenneville P. Predicting the Effective Flange Width of a CLT Slab in Timber Composite Beams. J Struct Eng 2018;144:04018084. https://doi.org/10.1061/(asce)st.1943-541x.0001979.

[20] Polastri A, Izzi M, Pozza L, Loss C, Smith I. Seismic analysis of multi - storey timber buildings braced with a CLT core and perimeter shear - walls. Bull Earthq Eng 2018. https://doi.org/10.1007/s10518-018-0467-9.

https://doi.org/10.52202/069179-0323

World Conference on Timber Engineering Oslo 2023

IN-PLANE DEFLECTION OF CROSS-LAMINATED TIMBER DIAPHRAGMS

Mahboobeh Fakhrzarei[1], Hossein Daneshvar[2], Ying Hei Chui[3]

ABSTRACT: Cross-Laminated Timber (CLT) is a reliable alternative to heavy structural components due to its dimensional stability and environmental benefits. However, there is currently no universally accepted design method for calculating the load-bearing capacity and deformation of a CLT diaphragm. The main objective of this study is to develop an analytical model for diaphragm deflection calculation when the major direction of panels is perpendicular to the load and confirm the results with the Finite Element (FE) analysis. In the absence of an experimental study aligned with the derived formula, an FE model was developed based on a full-scale diaphragm test subjected to loading parallel and perpendicular to the panel length. A parametric study was performed on the influence of the diaphragm length and the panel-to-panel connection stiffness. The contribution of bending, shear, and connection's slip to the total diaphragm deflection was quantified. The study reveals that the flexibility of the floor is primarily influenced by two factors: the shear deformation of the CLT panels when the load is perpendicular to the panel length and the stiffness of the panel-to-panel connection when the load is parallel to the panel length.

KEYWORDS: Cross Laminated Timber (CLT) diaphragms, Lateral load, Connections, In-plane deflection

1 INTRODUCTION

Floor diaphragms play an essential role in distributing the applied lateral load to the vertical elements of the lateral load-resisting systems of buildings. Cross Laminated Timber (CLT) panels have become more prevalent in recent years, such as diaphragm components in mid- to high-rise structures, primarily for sustainability reasons [1]. Several studies have investigated the impact of the rigidity or flexibility of CLT diaphragms on the distribution of lateral forces. A rigid diaphragm transmits loads to supports in proportion to the stiffness of the supports, whereas flexible diaphragms deformed in-plane through bending [2]. The lateral load distribution is influenced by the material properties and the load-slip behaviour of the connections between the adjacent panels (called panel-to-panel connections) and panel-to-beam connections [3]. Beairsto, in 2020 [4], evaluated the ductility of two large CLT diaphragms under monotonic and cyclic loads. The test indicated that the ductile design of the CLT diaphragm depended heavily on the panel-to-panel connections.

Pei et al. [5] conducted a series of experiments on a CLT building that was two-story high and 6.7 meters tall, using a shaking table to simulate seismic motions. The floors in this building were made up of 3-ply CLT panels, which were connected using a plywood surface spline and screws. The study found that the CLT diaphragms were significantly stiffer than wood frame floor diaphragms with wood-based sheathing panels, with satisfactory seismic performance. The researchers concluded that the design of a diaphragm needs to consider various sources of overstrength in the diaphragm components, e.g., the strength of the panel-to-panel connections, the stiffness of the boundary elements, and the strength of the fasteners used. Furthermore, Mohammadi [6] conducted experiments to evaluate the seismic performance of CLT diaphragms with multiple configurations. They found that the panel-to-panel connection stiffness significantly affected the in-plane stiffness of CLT diaphragms and recommended that the connections should be designed carefully.

Ashtari [7] investigated selected configurations of CLT floor diaphragm using a two-dimensional (2-D) FE analysis. The comparison between the FE and test results showed that the in-plane stiffness of CLT floors mainly depends on the panel-to-panel connection stiffness and shear modulus of the panels. It is important to note that CLT diaphragms can be loaded either parallel or perpendicular to the major panel axis, as shown in Figure 1. Spickler et al. [8] have provided a procedure for designing CLT diaphragms based on U.S. standards, assuming that the load is applied perpendicular to the panel length. The procedure covers diaphragm design for wind or seismic loads. However, their design approach has certain drawbacks that require attention, such as the failure to consider the impact of panel-to-panel connections on the overall behaviour of the diaphragm. Additionally, utilizing the chord width to determine the bending deflection of the diaphragm may not be a valid assumption.

[1] Mahboobeh Fakhrzarei, University of Alberta, Edmonton, AB, Canada, Fakhrzar@ualberta.ca
[2] Hossein Daneshvar, University of Alberta, Edmonton, AB, Canada, Daneshva@ualberta.ca
[3] Ying Hei Chui, University of Alberta, Edmonton, AB, Canada, yhc@ualberta.ca

https://doi.org/10.52202/069179-0324

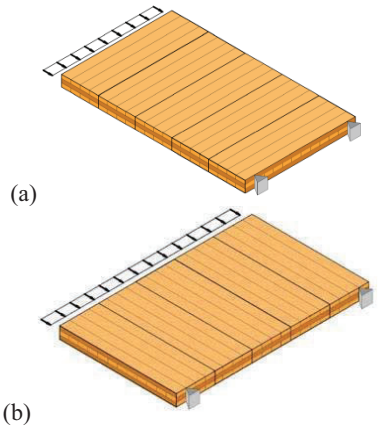

Figure 1: *CLT panels subjected to load (a) perpendicular and (b) parallel to the panel direction.*

Wallner-Novak et al. [9] conducted a technical investigation on the design of CLT floor diaphragms according to the Eurocode 5 specifications [10]. The report focused on diaphragms loaded parallel to the panel length and identified panel-to-panel connections that played a significant role in the diaphragm's performance. The study found that the diaphragm's deflection under shear force was primarily caused by the slip in the connections between the CLT panels, while the deflection due to bending resulted from the rotation of the panels. However, the study did not address scenarios where the applied load is perpendicular to the panel length.

Recently, Line et al. [11] conducted an experimental study to evaluate the current design provisions for CLT diaphragms in ANSI/AWC 2021 [12]. The study involved testing two CLT diaphragms that were loaded parallel and perpendicular to the panel length. The CLT panels were connected using plywood surface splines and fastened to glulam beams using self-tapping screws. Following the CLT diaphragm test [11], Line et al. [13] conducted a series of diaphragm connection tests to provide input data for models predicting the load-displacement response of the CLT diaphragms. The objective of the research was to analyse the behaviour of CLT diaphragms when loaded parallel or perpendicular to the panel length. The findings of the study provide helpful information regarding the different sizes and configurations of diaphragms which can contribute to the next edition of the Timber Design Standards in the USA.

This paper studies the effect of connections between CLT panels, assuming a simply supported diaphragm subjected to a uniformly distributed load perpendicular to the panel length. An analytical model is developed and validated using a finite element model. The effect of different connection stiffness values on the diaphragm's behaviour is evaluated.

The researchers also used a similar modelling technique to develop the FE model for CLT diaphragm loading in parallel and perpendicular directions and compared it with the experimental results. The findings show that the FE models agree well with the experimental results, confirming the effectiveness of the models in predicting the behaviour of CLT diaphragms.

This study has practical implications for the design of CLT diaphragms, as it provides a better understanding of the effect of connections on the diaphragm's performance. Additionally, it emphasizes the importance of incorporating different connection stiffness values and the size of the diaphragm length into the design process. Overall, this research contributes to the advancement of CLT diaphragm design and can potentially improve the performance of CLT structures.

2 ANALYTICAL MODEL DEVELOPMENT

When floor diaphragms are considered deep beams, their in-plane deformation can be separated into two components: deformation in the X and Y directions, as shown in Figure 2. The deflection in the X direction is primarily due to the slip between the panels. In the Y direction, deflection is caused by shear and bending in the CLT panels, as well as interlayer slip between the panels. Simple supports are assumed to be located at both ends of the diaphragm. The diaphragm centreline experiences an external in-plane load, q, which is then conveyed to the shear walls below by the CLT panels.

2.1 SLIPPING AMONG THE PANELS

Figure 2 shows an infinitesimal floor segment of finite length dx, the internal forces and moment, and the strain distribution in a typical floor diaphragm system cross-section.

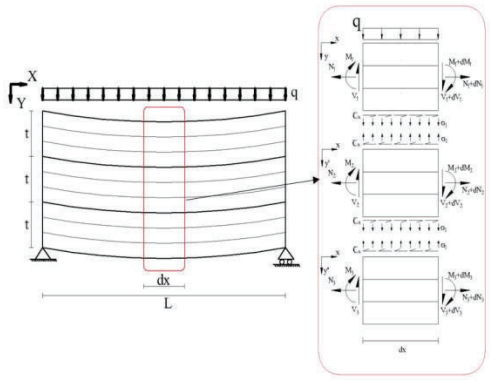

Figure 2: *CLT diaphragm internal force and strain*

The strain in the CLT panel cross-section near the interfaces is caused by the action of the bending moment and displacement in the X direction. First, a longitudinal displacement function (U^N) is assumed for each panel as Equation (1).

https://doi.org/10.52202/069179-0324

$$U_n^N(x,y) = A_n(x).{y_n}^2 + B_n(x).y_n + C_n(x) \quad (1)$$

The variable n = the panel number and y_n" = the reference point for the local coordinate system upper surface of each panel denoted as. Coefficients named "A_n", "B_n", and "Cn" are determined based on the boundary conditions. With the substitution of a derivative of Equation (1) into the distribution of shear stress throughout the depth of the panels, the shear stress for each panel can be written as:

$$\sigma_{xy(1)} = G_{xy}(2A_1y + B_1) \quad (2)$$

$$\sigma_{xy'(2)} = G_{xy}(2A_2y' + B_2) \quad (3)$$

$$\sigma_{xy''(3)} = G_{xy}(2A_3y'' + B_3) \quad (4)$$

where G_{xy} = the shear modulus, and $\sigma_{xy}(n)$ = shear stress throughout the depth of each panel. It is worth mentioning that, in this study, the analytical model was initially developed for a diaphragm system consisting of three panels. The local coordinates are centred on the upper surface of each panel and are represented as y for the top panel, y' for the middle panel, and y" for the bottom panel. By applying the boundary condition, the shear stresses in the panels can be calculated, and in turn, the shear strain in the panels is obtained as:

$$\gamma_{xy(1)} = \gamma_1 = \frac{\tau(x)}{G_{xy}t}y \quad (5)$$

$$\gamma_{xy(2)} = \gamma_2 = \frac{\tau(x)}{G_{xy}} \quad (6)$$

$$\gamma_{xy(3)} = \gamma_3 = \frac{\tau(x)}{G_{xy}}\left(1 - \frac{y''}{t}\right) \quad (7)$$

γ_{xy} = the shear strain of each panel. The longitudinal displacement function, U_n^N, due to longitudinal forces, is given by:

$$U_n^N = U_n^N(0) + \int_0^y \gamma_n(y)\,dy + U_n^N(t_n) \quad (8)$$

$U_n^N(0)$ and $U_n^N(t_n)$ indicate panel displacement at a panel's top and bottom edges, respectively, and can be calculated by subtracting the panel displacement at each interface from the connection displacement. The longitudinal force acting on each panel is equal to:

$$N_n = Eb\int_0^t \frac{dU_n^N}{dx}dy \quad (9)$$

where t = width (depth) of the panel, b = thickness of the panel, and E = Young's modulus. by substituting a derivative of Equation (8) into Equation (8), the strain at each panel edge is obtained. The shear stress between two adjacent panels can be expressed as Equation (10).

$$\tau(x) = \frac{K_s.n^*}{S}\left(u_{n+1}(x) - u_n(x)\right) \quad (10)$$

K_s = the shear stiffness of a fastener in units of (kN/mm). S = the distance between two fasteners and n* = the number of fasteners per row. The longitudinal displacements are described as $u_{n+1}(x)$ and $u_n(x)$, corresponding to the top of panel n+1 and the bottom of panel n, respectively.

The equations can be supplemented by the equilibrium equations assuming the same deflection for all panels. After some algebraic calculations, Equation (11) can be obtained for panel shear stress, where τ(x) is the shear stress at the interface.

$$\tau(x) = -m\frac{q}{\lambda}\left(\tanh\left(\frac{\lambda L}{2}\right)\cosh(\lambda x) - \sinh(\lambda x)\right) + mq\left(\frac{L}{2} - x\right) \quad (11)$$

Variables m and λ are determined in Equations (12) and (13), respectively. q = uniformly distributed load, and L = length of the CLT diaphragm.

$$m = \frac{1}{\left(\frac{1}{K_s} + \left(\frac{5t}{6G}\right)\right)\lambda^2}\left(\frac{t}{3EI}\right) \quad (12)$$

$$\lambda^2 = \frac{b}{\frac{1}{K_s} + \left(\frac{5t}{6G}\right)}\left(\frac{2t^2}{3EI} + \frac{1}{EA}\right) \quad (13)$$

where A = cross-sectional area of the panel, I = moment of inertia, and G = in-plane shear modulus. After substituting the value of τ(x) into horizontal equilibrium, the maximum amount of axial force can be calculated at the edge of the panels (x= 0 or L):

$$N(x) = \left(-m\frac{q}{\lambda^2}\left(tanh\left(\frac{\lambda l}{2}\right)Sinh(\lambda x) - Cosh(\lambda x) + 1\right) + mq\left(\frac{L}{2}x - \frac{x^2}{2}\right)\right) \quad (14)$$

2.2 DIAPHRAGM DEFORMATION

Diaphragm deformation corresponds to the conventional equation for a deep beam. However, it has an additional term to account for interlayer movement, including the panels' shear deformation. Using Timoshenko's theory [14] to establish the following relationship between the

bending moment, shear force, deflection, and rotation of the cross-section:

$$\frac{dw}{dx} = \theta - \frac{EI}{kAG}\left(\frac{d\theta^2}{dx^2}\right) \quad (15)$$

$$\frac{d\theta}{dx} = -\frac{M_T(x) - b\int \tau(x).2t}{3EI} \quad (16)$$

Where w = the deflection of the panels in the *y*-direction and θ = the cross-section angle of rotation and $M_T(x)$ = the applied moment. By substituting Equation (11) into Equation (16) to include the effect of shear stress on the deformation and adding the interlayered movement, we obtain Equation (17), which gives the mid-span deformation of the diaphragm.

$$w(x) = \frac{5qL^4}{384EI_s} + \frac{qL^2}{8kAG} + \frac{mqL^2}{4t}\left(\frac{1}{K_s} + \left(\frac{5t}{6G}\right)\right) \quad (17)$$

3 FE MODEL DEVELOPMENT

A three-dimensional (3D) model was created in Abaqus [15] to calculate the mid-span in-plane deformation of the diaphragm and replicate the layout illustrated in Figure 2. The model comprised a rectangular CLT floor consisting of three 10-meter-long and 2.4-meter-wide panels. Line springs were evenly distributed along the length of the panels to connect them. In addition, butt joint connections were strengthened by using screws oriented at a 45° angle relative to the edge face of the CLT panels to enhance the structure's load-carrying capacity. The comparison of the mid-span deflection of the floor between the FE and analytical models revealed a difference of less than 2%, with the deflection values of 3.3 mm and 3.36 mm, respectively. This indicates that the two models are in agreement with each other and can be relied upon to predict the behaviour of the floor accurately.

3.1 COMPARATIVE ANALYSIS OF CONNECTION STIFFNESS

The stiffness of connectors in the joints of CLT panels was determined through experimental tests from multiple sources, including studies [16-18], where 8mm screws were used. The stiffness values obtained were compared to the analytical model predictions, as shown in Figure 3. The comparison showed that the difference between the experimentally determined stiffness values and the predictions of the analytical model was less than 5%. The finding suggests that the developed formula is accurate for the assumed range of stiffness values. Hence, the analytical model can confidently predict the behaviour of CLT panel joints.

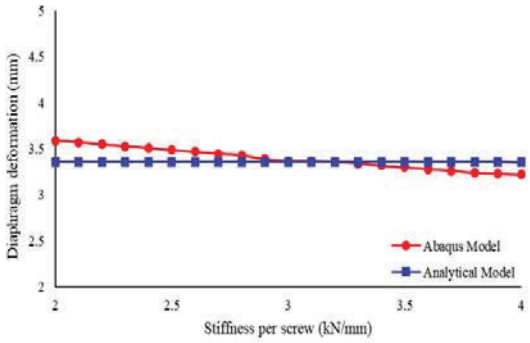

Figure 3: *The diaphragm deformation versus stiffness of the connection*

3.2 FE MODEL VALIDATION THROUGH EXPERIMENTAL STUDY

To the best of the authors' knowledge, no empirical investigations have been conducted to date on the behaviour of a CLT diaphragm subjected to a perpendicular load with the specific boundary conditions assumed in the developed analytical model. Therefore, to validate the modelling approach, the results of full-scale CLT diaphragm tests reported in [11] were compared with the FE model developed to ensure the accuracy of the proposed numerical models.

3.3 FE MODEL SETUP

The experimental study examined the behaviour of two diaphragms, one loaded parallel to the panel length and the other loaded perpendicular to the panel length, as shown in Figure 4.

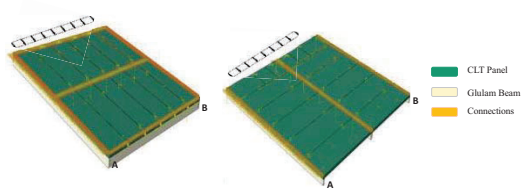

(a) (b)

Figure 4: *Diaphragm assemblies when the load direction is (a) parallel to the panel length, (b) perpendicular to the panel length.*

For each diaphragm, twelve 1.22 × 3.66 m CLT panels were modelled with a proposed thickness of 105 mm using a three-ply layup. The panel-to-panel spline connection was made using 18.3 mm plywood and 8d common power-driven nails. To establish connections between panels and beams in the FE model, two-point spring elements were utilized. These spring elements were linked to the CLT panel at each fastener point by connector elements that tied the displacement and rotation

https://doi.org/10.52202/069179-0324

of each fastener point to the average displacement and rotation of the neighbouring nodes. As for the experimental study, the diaphragms were pinned at their far corners in the plane of loading (points A and B in Figure 4). The perimeter beams' edges were pinned, allowing the assembly to bend inward while restraining its movement in the direction of loading.

3.4 COMPARING THE RESULTS

The load-displacement curves at the mid-span of the diaphragms subjected to parallel and perpendicular loading to the panel length, obtained from both experimental and numerical analyses, are presented in Figure 5. The results demonstrate a close agreement up to the maximum force, suggesting that the numerical model was successfully validated and can be trusted to predict the behaviour of comparable CLT diaphragms under various loading conditions.

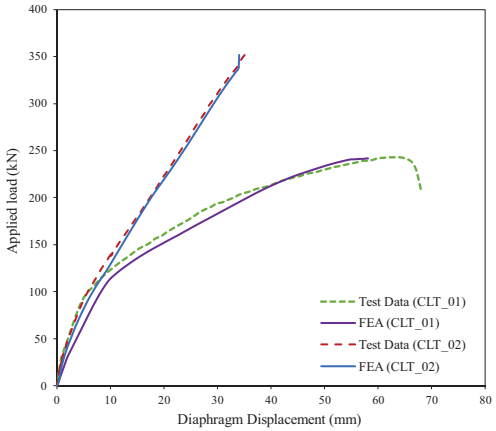

Figure 5: *The mid-span load-displacement curve for diaphragm under in-plane loading; numerical versus experimental.*

The numerical model was based on the assumption of linear-elastic behaviour of the wood components, with the connections exhibiting nonlinear behaviour. Plastic deformation was observed at a load of approximately 100 kN, leading to failure. However, due to numerical instabilities, the simulation was stopped once the load reached its maximum point, and the connections failed. Comparing the experimental and numerical load-displacement curves indicated that the developed numerical model effectively predicted the diaphragms' overall behaviour. These findings suggest that the numerical model can accurately simulate and predict the behaviour of similar CLT diaphragms under varying loading conditions.

4 THE PARAMETRIC STUDY

A comprehensive parametric study was conducted to augment the database on CLT diaphragms by varying parameters such as panel thicknesses and the Aspect Ratio (AR) of the CLT diaphragms, which is the ratio of the diaphragm length to its depth.

4.1 DIAPHRAGM LOADED PERPENDICULAR TO THE PANEL LENGTH

Table 1 presents six archetypes categorized based on the thickness of the CLT panels, with each group comprising three different panel sizes. Each configuration comprises six panels and three glulam beams placed underneath the panel joints.

Table 1: *Summary of characteristics feature of diaphragm loaded perpendicular to the panel length in FE models.*

Archetype No.	Diaphragm Size			Number of layers	Associated Sketch
	Length (m)	Depth (m)	Thickness (mm)		
1	9	7.2	175	5	
2	11	7.2	175	5	
3	13	7.2	175	5	
4	9	7.2	245	7	
5	11	7.2	245	7	
6	13	7.2	245	7	

The deformation of the CLT diaphragm under perpendicular loading to the panel length is illustrated in Figure 6. The results indicate an increase in the diaphragm deformation as the length increases. Interestingly, the study found that the thickness of the CLT panels did not significantly impact the deformation of the diaphragm in this configuration.

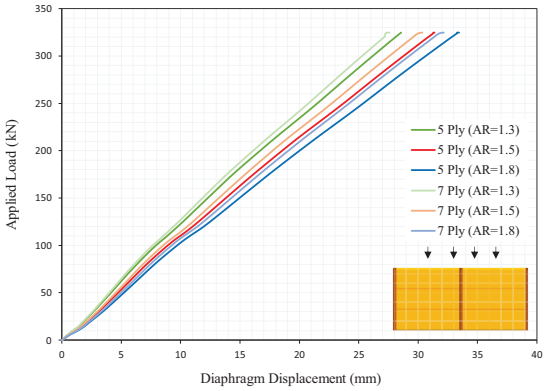

Figure 6: *Load-displacement curves for diaphragm with different diaphragm aspect ratios and thicknesses for loading perpendicular to panel length.*

4.2 DIAPHRAGM LOADED PARALLEL TO THE PANEL LENGTH

Table 2 summarizes the analysis results of six archetypes subjected to in-plane loads parallel to the panel length.

https://doi.org/10.52202/069179-0324

Similar to the analysis of perpendicular loading, the archetypes were divided into two groups based on the thickness of the panels.

Table 2: *Summary of characteristics of a diaphragm loaded parallel to the panel length in FE models.*

Archetype No.	Diaphragm Size			Number of layers	Associated sketch
	Length (m)	Depth (m)	Thickness (mm)		
1	9	7.2	175	5	
2	11	7.2	175	5	
3	13	7.2	175	5	
4	9	7.2	245	7	
5	11	7.2	245	7	
6	13	7.2	245	7	

The results presented in Figure 7 indicate that, for archetypes 1- 6, the diaphragm deflection decreased as the diaphragm length increased under loading parallel to the panel length. The panel thickness did not significantly affect the diaphragm deflection in this configuration. However, it was observed that, for loading parallel to the panel length, the chosen panel depth used in the parametric study, which was twice that of the experimental analysis, resulted in significantly less deformation than the experimental results. These findings highlight the importance of considering the appropriate panel depth to accurately predict the behaviour of CLT diaphragms under in-plane loads parallel to the panel length.

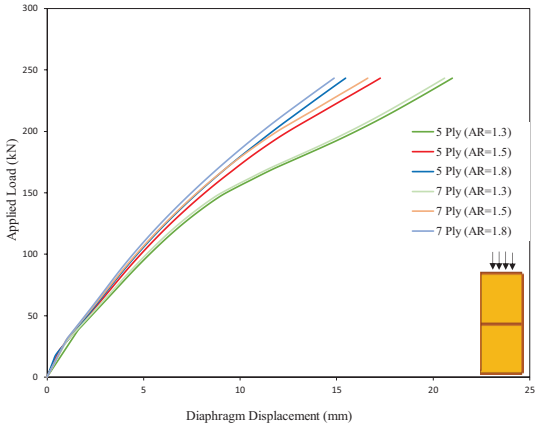

Figure 7: *Load-displacement curves for diaphragm with different diaphragm aspect ratios and thickness for loading parallel to panel length.*

5 DISCUSSION

Figure 8 summarizes the effect of diaphragm length and panel thickness on the behaviour of archetypes 1 to 6 under in-plane loading, both parallel and perpendicular to the panel length. The diaphragms loaded parallel to the panel length are denoted as "parallel," while those loaded perpendicular to the panel length are labelled as "perpendicular." The results reveal that the aspect ratio has the most significant effect on diaphragm deformation, particularly for aspect ratios below 1.5, while panel thickness is not an important parameter. For the diaphragm loaded parallel to the panel length, the stiffness was found to be unaffected by the panel thickness.

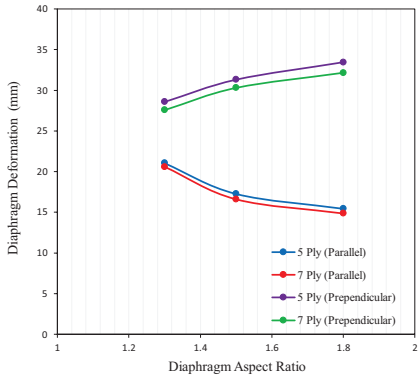

Figure 8: *The effect of the aspect ratio and panel thickness in diaphragm displacement for the archetype 1 to 6.*

6 CONCLUSIONS

This study presents an analytical model to calculate the mid-span deflection of a simply supported diaphragm and predict the force in the connection between adjacent CLT panels when the load is perpendicular to the panel length. The model accounts for the effect of bending and shear deflections of each panel and slip between the panels. To validate the analytical model, a FE model was developed and compared to the behaviour of CLT diaphragms under in-plane loading. The comparison showed good agreement between the predictions of the analytical and FE models, confirming the accuracy of the analytical model.

In addition, proposed FE models were compared to the results of full-scale CLT diaphragm tests to evaluate the modelling approach. A comprehensive parametric study was conducted to identify the most influential parameters contributing to in-plane deformation in CLT floor diaphragms. The behaviour of the employed diaphragm was investigated by varying the aspect ratio and thickness of the CLT diaphragm. It was found that when the load was perpendicular to the panel length, shear deflection in the CLT panels provided the most significant contribution to total diaphragm deflection, while the slip in the connections was the most influential parameter when the load was parallel to the panel length. The study also revealed that the thickness of the panels is not a key parameter in the deformation of the diaphragm under lateral loading.

https://doi.org/10.52202/069179-0324

The results of this study provide valuable insights into the behaviour of CLT diaphragms under in-plane loading that can be used by practitioners in the design of CLT diaphragms in both loading orientations. The developed analytical model can be applied to predict the mid-span deflection and force in the connections between adjacent CLT panels, enabling the more efficient and accurate design of CLT diaphragms.

ACKNOWLEDGEMENTS

The authors would like to thank the Natural Sciences and Engineering Research Council of Canada (NSERC) for the financial support of this study under the Industrial Research Chair Program. Financial support was also provided by the Landmark Group of Companies, FPInnovations, Canadian Wood Council, MTC Solutions, Rotho Blaas, Western Archrib, and Alberta Innovates. Their support is gratefully acknowledged.

REFERENCES

[1] Lenon, C. 2015., "Design and behavior of a mid-rise cross-laminated timber building" *Masters of Science Thesis. Colorado School of Mines.*

[2] NBCC. 2015. "National Building Code of Canada 2015." Institute for Research in Construction, Ottawa: National Research Council of Canada.

[3] G. D'Arenzo, D. Casagrande, T. Reynolds, and M. Fossetti, "In-plane elastic flexibility of cross laminated timber floor diaphragms," *Construction and Building Materials*, vol. 209, pp. 709–724, 2019.

[4] Beairsto, C. J. 2020. Monotonic and cyclic testing of cross-laminated timber diaphragms. https://ascelibrary.org/doi/abs/10.1061/%28ASCE%29SC.1943-5576.0000658

[5] Pei, S., J. Van de Lindt, A.R. Barbosa, J. Berman, H-E. Blomgren, J. Dolan, E. McDonnell, R. Zimmerman, M. Fragiacomo, D. Rammer. 2018. Full-scale shake table test of a two-story mass-timber building with resilient rocking walls. In: Proceedings, 16th European Conference on Earthquake Engineering. Thessaloniki, Greece, June 18–21. 1–10.

[6] Mohammadi, J., & Khalili, M. (2016). Seismic performance of cross-laminated timber floor diaphragms with different configurations. Engineering Structures, 111, 296-307.

[7] Ashtari, "In-plane stiffness of cross-laminated timber floors." University of British Columbia, 2012.

[8] K. Spickler, M. Closen, P. Line, and M. Pohll, "Cross laminated timber: Horizontal diaphragm design example," *White paper reference*, 2015.

[9] M. Wallner-Novak, M. Augustin, J. Koppelhuber, and K. Pock, "Cross-Laminated Timber Structural Design Volume 2: Applications." ProHolz Austria, 2018.

[10] CEN, E.N. 2004. EN 1995-1-1: Eurocode 5: Design of timber structures. Part 1–1: General–Common rules and rules for buildings. The European Union per regulation 305/2011, Directive 98/34/EC, Directive 2004/18/EC. Committee for Standardization CEN. Bruxelles, Belgium. https://www.phd.eng.br/wp-content/uploads/2015/12/en.1995.1.1.2004.pdf.

[11] Line, P., S. Nyseth, N. Waltz. 2022a. Full-scale Cross-laminated timber diaphragm evaluation. I: Design and full-scale diaphragm testing. Journal of Structural Engineering, 148 (5) 4022037. American Society of Civil Engineers.

[12] ANSI/AWC 2021. 2021. Special design provisions for wind and seismic. ANSI/AWC SDPWS-2021. Leesburg, VA: American Wood Council.

[13] Line, P., S. Nyseth, N. Waltz. 2022b. Full-scale cross-laminated timber diaphragm evaluation. II: CLT diaphragm connection tests. J. of Structural Eng., 148 (5) 4022038. American Society of Civil Engineers.

[14] Timoshenko, S. 1983. *History of strength of materials: With a brief account of the history of theory of elasticity and theory of structures*. Dover Publications.

[15] G. Abaqus, "Abaqus 6.11," *Dassault Systemes Simulia Corporation, Providence, RI, USA*, 2011.

[16] Loss, C., M. Piazza, and R. Zandonini. 2016. "Connections for steel–timber hybrid prefabricated buildings. Part I: Experimental tests." Constr. Build. Mat., 122 (S1): 781–795. DOI:10.1016/j.conbuildmat.2015.12.002

[17] Hossain, A., M. Popovski, and T. Tannert. 2019. "Group effects for shear connections with self-tapping screws in CLT." J. Struct. Eng., 145 (8): 4019068. https://ascelibrary.org/doi/10.1061/%28ASCE%29ST.1943-541X.0002357

[18] Joyce, T. P. R. D. 2014. "Connections for CLT diaphragms in steel-frame buildings." Masters Thesis. University of New Brunswick. https://www.researchgate.net/publication/337063778_Connections_for_CLT_diaphragms_in_steel-framed_buildings

World Conference on Timber Engineering Oslo 2023

EVALUATION OF THE BEHAVIOUR FACTOR BY INCREMENTAL DYNAMIC ANALYSES FOR THE SEISMIC DESIGN OF LIGHT-FRAME TIMBER BUILDINGS

Alessandra Gubana[1], Alessandro Mazelli[1]

ABSTRACT: Light Frame Wood structures are today a valid alternative to Cross Laminated Timber structures for low and medium height buildings, both in terms of performance and environmental impact, given the lower volume of wood used. Light wood frames demonstrate a ductile behavior under seismic actions, linked to the plastic deformation of the connections, but uncertainties still regard the value of the behaviour factor associated to these types of structures.
This paper presents the evaluation of the behaviour factor 'q', used for the seismic design, based on Incremental Dynamic Analyses for Light-Frame Timber Buildings. Papers in literature regarding its evaluation are mostly based on static non-linear pushover analyses. Example buildings with 2, 3 and 4 storeys, were designed according to capacity design and then analysed by varying the displacement-ductility of the sheathing-to-frame connection. The results are then compared with the requirements provided by codes.

KEYWORDS: Light-frame timber buildings, Incremental Dynamic Analyses, Behaviour factor.

1 INTRODUCTION

Timber structures have a long tradition in several areas of the world, where residential balloon-frame and platform-frame houses constitute a large amount of the building stock. In the past, the carpenters' expertise drew the building construction process.
In the last years the use of timber in construction significantly developed, due to the growing attention to sustainability and environmental impact [1]. The appearance on the traditional market of new wood engineered products as Cross Laminated Timber (CLT) opened new technical possibilities and consequently also high multi-storey buildings can be built [2]. Thanks to prefabricated technologies, construction time can be strongly reduced with economic benefits on the real estate investment.
Light-frame wood (LFW) structures still represent a valid alternative to CLT structures for low and medium rise buildings, both in terms of performance and environmental impact, as the involved necessary timber mass is lower than in case of CLT. The advantages of the precast processes are also extended to LFW buildings, especially in Europe, where Light Frame Walls are built in prefabrication plants, often completed with the electrical and hydraulic systems and insulating materials and then connected in the building yards.
The good performance of timber buildings under earthquake excitations is well known and largely acquired, due to the limited mass and the high ductility ensured by, for instance, mechanical connections between sheathing to framing, wall to wall, wall to foundation. Besides, hysteretic behaviour of LFW structures were investigated by means of tests on shake tables in past years. [3-5]
It also well known that a reduction of seismic forces is possible due to the beneficial effects of energy dissipation in ductile structures and to inherent over-strength. This theoretical acquisition is considered in seismic design standards and codes, where force reduction factors (e.g. the 'behaviour factor' q in Eurocode 8 [6], or the 'response modification factor' R in US codes) are indicated to quantify the seismic design loads. The entity of these factors was initially based on empirical observations of the behaviour of common structural systems, but uncertainties still regard the value of q [7].
More recently, several numerical studies have been performed to determinate appropriate values, and most of them refer to non-linear static analyses results. A recent work by Rossi et al. [8] proposes the evaluation of q by static non-linear analysis, providing an important contribution to the calibration of the behaviour factor. However, static analysis does not consider the frequency of seismic input motion and the influence of higher vibration modes of the structure [9].
In the present work, a study for the evaluation of the behaviour factor q for LFW structures by means of Incremental Dynamic Analysis (IDA) is described.
Example buildings with 2, 3 and 4 storeys were designed according to capacity design and then analysed by varying the displacement-ductility of the panel. The results are then compared with the requirements provided by codes.

[1] DPIA Polytechnic Department of Engineering and Architecture, University of Udine (Italy).
alessandro.mazelli@uniud.it

https://doi.org/10.52202/069179-0325

2 LIGHT FRAME WOOD WALLS MODELLING AND VALIDATION

Light Frame Wood (LFW) shear walls are made up of timber-based panels (typically Oriented Strength Board OSB or plywood) and a timber frame connected together by small diameter nails. Angle brackets are used for shear forces at the base and the top of the panel, while hold-downs are placed at the corners to absorb tension and compression induced by bending moment.

Recent codes provide analytical methods to evaluate the stiffness or the top displacement of a LFW wall subjected to a horizontal force. The New Zealand standard [10], the American International Building Code IBC [11] and the Canadian Standard Association CSA O86 [12] consider the top displacement of a LFW wall as the sum of four terms: the base rotation δ_c, the shear deformation of the wood panel δ_s, the shear deformation of the sheathing-to-frame connection δ_{ps} and the bending deformation δ_b. The total displacement of the wall δ_w is evaluated by means of equation 1.

$$\delta_w = \delta_c + \delta_s + \delta_{ps} + \delta_b \quad (1)$$

It is worth noticing that the contribution due to the deformation of the angle brackets is not considered in equation 1. The slip is negligible only if the connectors are extremely stiff, consequence of a Capacity Design approach. Otherwise, it is always possible to add the base slip contribution to equation 1.

In order to assemble the example buildings with parameterized sheathing-to-frame connections, two wall FEM models were built: a detailed model (Figure 1a) and a simplified model (Figure 1b). Both were then calibrated thanks to the results of a cyclic test on a real scale LFW (3 m × 3 m) Technical Report [13].

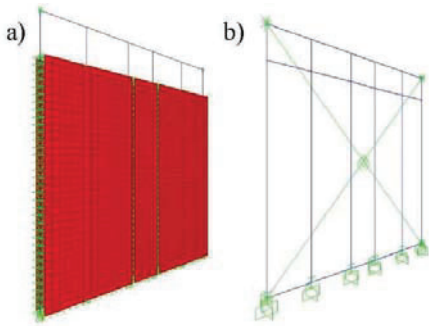

Figure 1: *Analysis models of the wall: complete (a) and with equivalent non-linear springs (b).*

The model of Figure 1a was built in SAP2000. OSB panel were modelled as *flat-shell* elements and timber studs as pinned *frames*. Non-linear links were used for hold-downs, angle brackets and for the nailed connection along the perimeter of the panels. It is worth noticing that the independent behaviour of the nail link in x and y directions leads to overestimate the strength of the connection in intermediate directions, and a squared rather than circular force domain is considered [14]. The detailed model was validated through a pushover analysis (Figure 2). This model was then used to create the set of parameterized walls, varying the displacement ductility of the sheathing-to-frame connection.

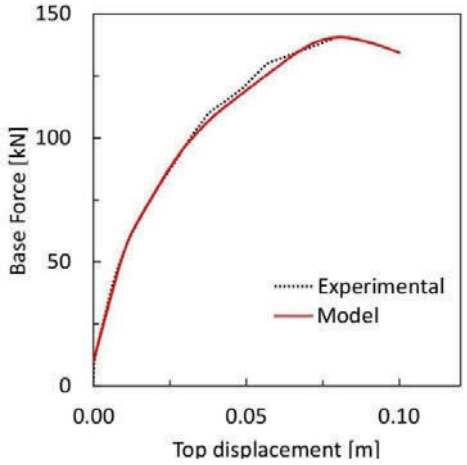

Figure 2*: Comparison between experimental and analytical monotonic behaviour of the wall.*

The model of Figure 1b was used to calibrate the pivot hysteresis parameters for non-linear uniaxial springs which represent the sheathing-to-frame connection, the hold-downs and the angle brackets separately. The walls were modelled by means of 5 non-linear springs each: two vertical springs for the hold-downs, one horizontal spring for the angle brackets and two inclined springs for the sheathing-to-frame connection. Their cyclic behaviour was validated by minimizing the difference with the experimental test in terms of dissipated energy (Figure 3). The simplified wall was then used in the modelling of the example buildings.

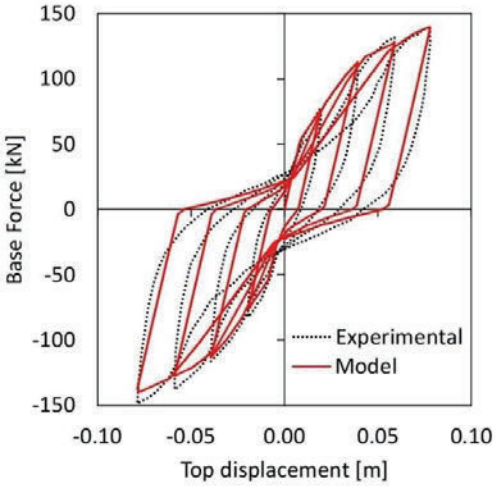

Figure 3*: Comparison between experimental and analytical cyclic behaviour of the wall.*

https://doi.org/10.52202/069179-0325

3 MULTI-STOREY TIMBER BUILDINGS

Example buildings with dimensions in plan of 6.50 m ×10.70 m with two up to four storeys, were built assembling 3 m × 3 m walls, in order to refer directly to the experimental test, and were calculated according to EN 1995-1-1:2005 [15] and EN 1998-1:2013 [6], following the Capacity Design (Figure 4). Each block can stand alone or be connected to other ones to have more surface area of the apartments.

The Life Safety ultimate state was verified by means of the Eurocode response spectrum with a PGA of 0.35 g, soil type A and q-factor equal to 3. The choice of q in the design procedure was necessary only to obtain realistic LFW wall structural dimensions, as the typical ones used in engineering design practice. The q equal to 3, in fact, affects the results only in term of resistance of the wall. The ductility of the nailed connection, in fact, will be parameterized. Furthermore, Rossi et al. [8] shows that the soil type has a negligible influence on the ductility evaluation.

An overstrength factor equal to 1 was chosen for the sheathing-to-frame connection, so that the nominal strength is equal to the design strength. On the other hand, hold-down and angle brackets were designed according to the Capacity Design approach [16], with an overstrength factor of 1.6. Because of this choice, the contribute to dissipation of hold-down and angle brackets was not considered, as they were over strengthened, and all the plastic deformation were concentrated in the sheathing-to-frame connection. Each wall of the example buildings was modelled with the simplified method (Figure 1b).

4 PARAMETRIZATION OF LFW WALLS

Starting from the validate detailed model of Figure 1a, a set of LFW walls was created, varying the ductility of the sheathing-to-frame connection. Three classes were selected: 4, 6 and 8. The yield limit and the ductility of the nailed connection was evaluated according to an Equivalent Energy Elastic Plastic EEEP approach.

Moreover, it was necessary to build set of walls that corresponds to the strength capacity required by the design procedure of the three example buildings. Thus, the connectors spacing and resistance was varied, and the OSB panels were placed on one or both sides. Table 1 reports the characteristics of the walls used to assemble the example buildings, obtained by means of pushover analyses.

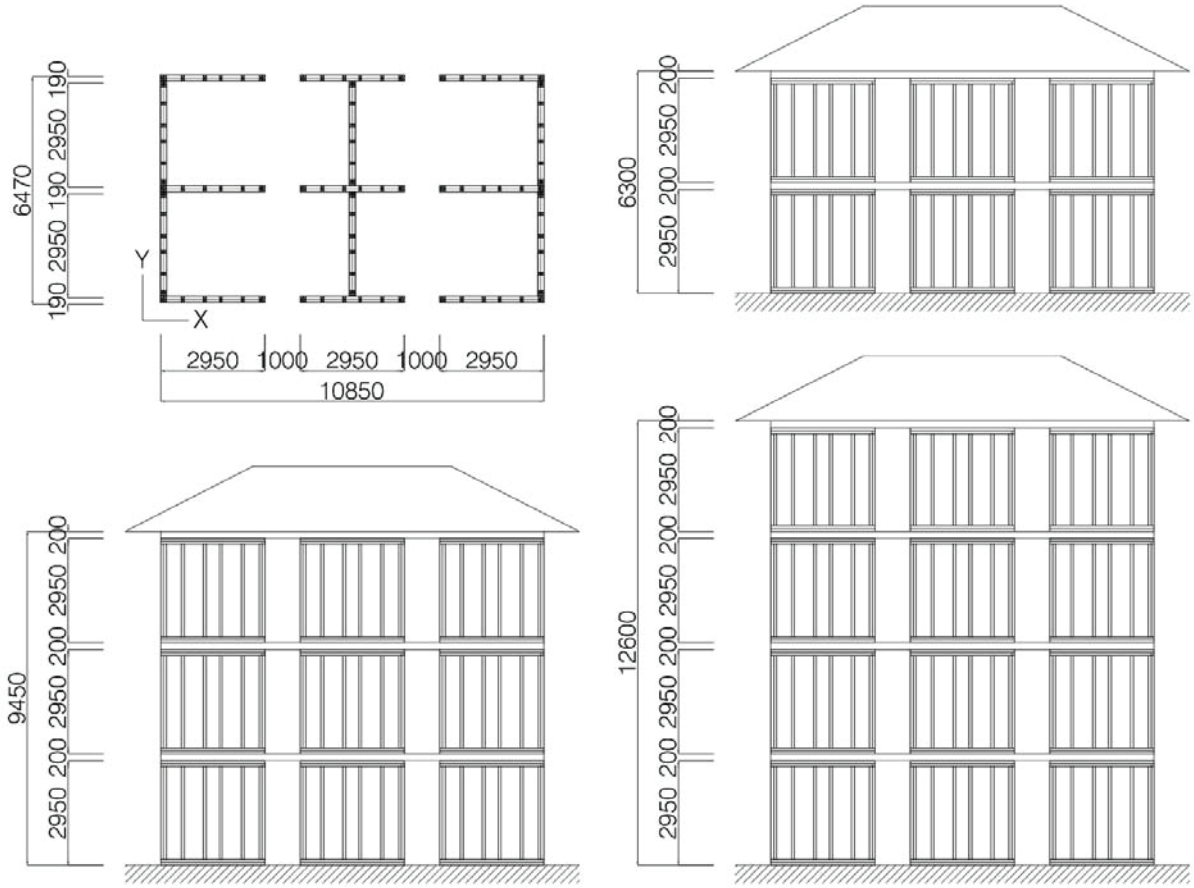

Figure 4: *Example buildings (dimensions in mm).*

https://doi.org/10.52202/069179-0325

F_{max} is the maximum resistant shear force of the wall, while d_y and d_u are the top horizontal displacement of the wall at yield and ultimate condition respectively. Each wall has a label that refers to the nail spacing (75 mm or 150 mm), the sides covered by OSB (1 or 2) and the resistance of the sheathing-to-frame connection, referred to only one nail (720 N or 1000 N).

Table 1: *Parameterized walls used in the assembling of example buildings.*

	LFW connection ductility 4		
Wall type	**F_{max} [kN]**	**d_y [m]**	**d_u [m]**
75(1)720	23.1	0.015	0.037
150(1)720	11.2	0.012	0.036
75(1)1000	29.9	0.017	0.039
150(1)1000	18.6	0.014	0.042
150(2)1000	36.5	0.012	0.030
	LFW connection ductility 6		
Wall type	**F_{max} [kN]**	**d_y [mm]**	**d_u [mm]**
75(1)720	25.6	0.017	0.058
150(1)720	12.3	0.013	0.048
75(1)1000	32.9	0.019	0.058
150(1)1000	20.6	0.015	0.055
150(2)1000	36.9	0.011	0.043
	LFW connection ductility 8		
Wall type	**F_{max} [kN]**	**d_y [mm]**	**d_u [mm]**
75(1)720	27.0	0.019	0.077
150(1)720	12.7	0.014	0.062
75(1)1000	35.5	0.021	0.078
150(1)1000	21.7	0.016	0.072
150(2)1000	37.1	0.012	0.056

The increasing of the ductility of the sheathing-to-frame connection affects slightly F_{max} and d_y, while it influences widely d_u.

The pushover curves of each wall of each set were transformed into multilinear relationship. Then, the behaviour was adapted to the non-linear diagonal springs of the simplified models. The procedure is shown in Figure 5, where F and d are the shear force and the top displacement respectively. The subscript 45 refers to the 45° inclined spring.

Hysteretic pivot parameters of the sheathing-to-frame connection were already calibrated in section 2.

An elastic behaviour was associated with hold-downs and angle brackets, since they were calculated according to the Capacity Design approach.

5 IDA PROCEDURE

The example buildings were analysed by means of IDA procedure [17].

The IDA consists in the execution of several non-linear dynamic analyses under a multiply scaled set of ground motion records. Every IDA curve represents the relationship between the Energy Demand Parameter (EDP) and the Intensity Measure IM. In the present study, the Peak Ground Acceleration (PGA) was chosen as IM and the ratio between the maximum roof displacement and the height of the building was selected as EDP (Mean Interstorey Drift Ratio MIDR). The choice of this couple (PGA, MIDR) allows to compare IDA curves at the same scale for each ductility class and for each number of storeys.

A set of 10 couples of records was chosen by means software REXEL [18] (Table 2).

Generally, the estimation of the q factor is obtained by means of non-linear static analysis via procedure present in the literature (e.g. Fajfar [19], Newmark and Hall [20]).

Table 2: *Record selected for IDA procedure.*

Earthquake name	**Waveform ID**	**PGAX (m/s^2)**	**PGAY (m/s^2)**
Friuli Earthq 1st shock	IT0014	3.39	3.09
L'Aquila Mainshock	IT0792	5.35	6.44
Campano Lucano	000291	1.53	1.73
Friuli (Aftershock)	000146	3.40	3.30
Kalamata	000414	2.35	2.67
Erzican	000535	3.81	5.03
Umbria Marche	000594	5.14	4.54
Montenegro	000196	4.45	3.00
South Iceland	004673	2.04	4.68
Bam (Iran)	000230	7.85	6.28

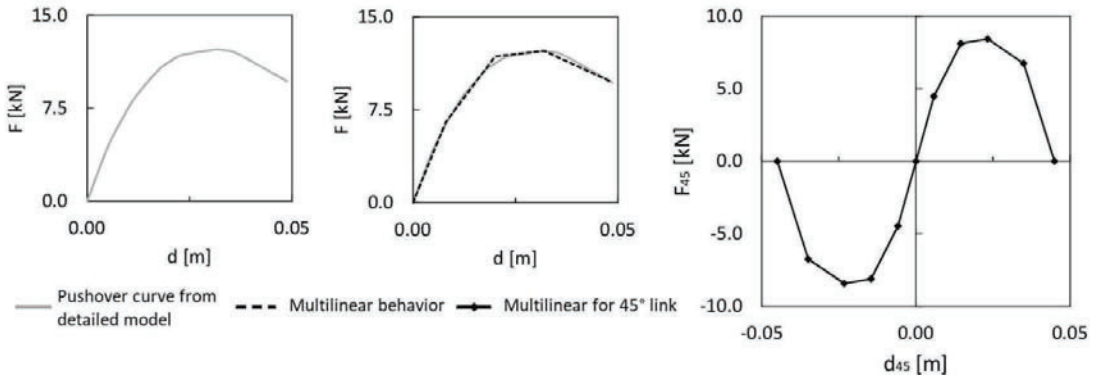

Figure 5: *Procedure to obtain multilinear behaviour for uniaxial non-linear springs of the simplified LFW wall model.*

https://doi.org/10.52202/069179-0325

Several methods to evaluate q by means on non-linear dynamic analysis are available, considering experimental, numerical or hybrid procedures [21]. Some were already used for CLT buildings [22,23] In this work, a numerical method to evaluate q was chosen.
In fact, the behaviour factor q was obtained as the product of a ductility factor q_μ, connected to the non-linear behaviour of the structure, and an overstrength factor q_D, which takes into account the post-elastic hardening and the structural redundancy [24]:

$$q = q_\mu \cdot q_D \tag{2}$$

The obtained q is intrinsic and code independent, because the design overstrength factor for the sheathing-to-frame connection was set to 1.
The two factors of equation 2 follow the expression (3) and (4) respectively.

$$q_\mu = \frac{V_{b(Dyn,e)}}{V_{b(Dyn,y)}} \tag{3}$$

$$q_D = \frac{V_{b(Dyn,y)}}{V_{b(St,s)}} \tag{4}$$

where $V_{b(Dyn,y)}$ is the base shear which corresponds to the collapse of the structure, and $V_{b(Dyn,e)}$ is the base shear obtained by an elastic analysis of the structure under the same records. $V_{b(St,s)}$ is the base shear corresponding to the first yield in the structure and it is evaluated by means of a static non-linear analysis.
The use of non-linear static analysis avoids the problem of yield point detection. In fact, in an IDA, there could be more IM intensities with only one wall that has reached the yield displacement. This solution was used in other literature works [25,26].
It is worth noticing that the choice of IM and EDP did not affect the final results, since the q-factors were evaluated by base shear force ratios.

6 RESULTS

In this section, the result of the 90 IDA are reported.
Figure 6 illustrates two examples of wall reaching the ultimate displacement for a ductility class equal to 6, one in X direction and one in Y, according to Figure 4.
The diagrams show the relationship between the shear force on the wall F and its top horizontal displacement d. The sheathing-to-frame connection reaches the ultimate displacement under the scaled Kalamata earthquake for a PGA = 0.13 g. (Figure 6a). In Y direction, the wall attains to its ultimate displacement under the South Iceland accelerograms for a PGA = 0.35 g (Figure 6b).
In Figure 7 the complete IDA study is reported. The curves for each example building and for each ductility class are illustrated at the same scale, in order to perform comparison. Each graph shows the Mean Interstorey Drift Ratio versus the PGA.

On the basis of these first results, for a fixed ductility class, the MIDR shows a decreasing tendency when the number of storeys increases. On the other hand, the MIDR increases for higher ductility classes.
Finally, to a higher ductility class corresponds a higher average PGA at collapse.

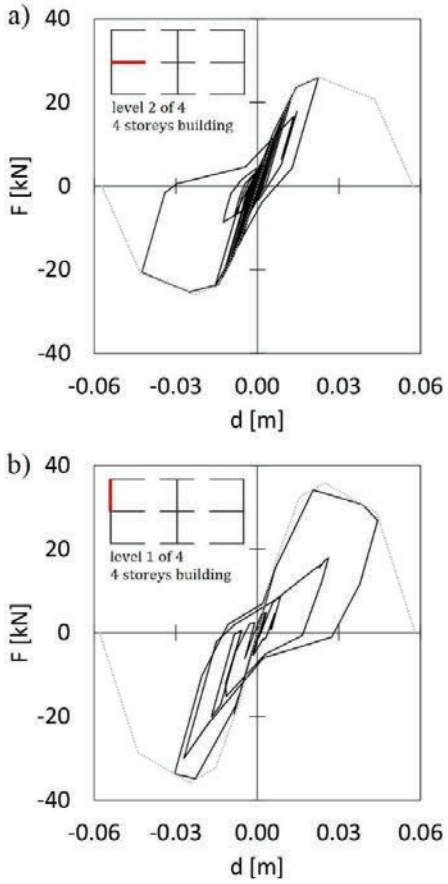

Figure 6: *Hysteresis cycles for two walls attaining the ultimate displacement for a sheathing-to-frame connection ductility equal to 6 under Kalamata (a) and South Iceland (b) earthquakes.*

Results of the IDA studies were used to evaluate the q factor, following equations 2, 3 and 4. Table 3 reports the minimum, mean and maximum values of the ductility factor q_μ, the overstrength factor q_D and the intrinsic factor q. Furthermore, the CoV is also reported for all the classes.
As expected, the ductility factor q_μ increases when increasing the ductility class of the sheathing-to-frame connection. Furthermore, the data are more scattered for higher values of ductility.
The overstrength factor q_D is higher as the ductility increases. Besides, the dispersion is lower with respect to the ductility factor.
The values of q reported in Table 3 are intrinsic and code independent. It can be noted that the value of 2.3 obtained for ductility class 6 correspond to the results reported in [8].

https://doi.org/10.52202/069179-0325

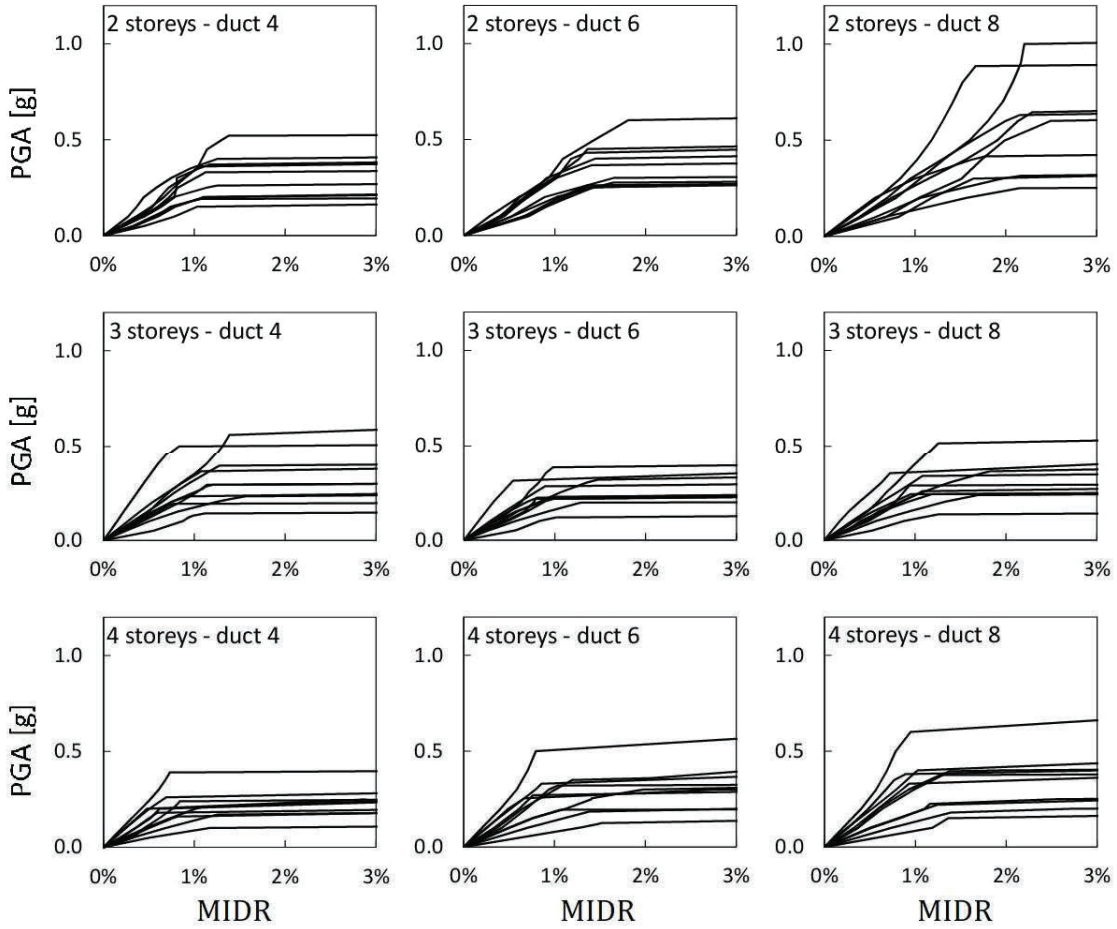

Figure 7: *IDA study for each ductility class and for each building, representing the Mean Interstorey Drift Ratio (MIDR) vs the PGA.*

Table 3: *Ductility factor q_μ, overstrength factor q_D and intrinsic behaviour factor q for each ductility class and for each building.*

LFW connection ductility 4												
	q_μ				**q_D**				**q**			
Storeys	2	3	4	global	2	3	4	global	2	3	4	global
Min	1.1	1.3	1.2	1.1	1.0	1.0	1.0	1.0	1.2	1.3	1.3	1.2
Mean	1.7	1.5	1.5	1.6	1.4	1.2	1.1	1.2	2.4	1.8	1.6	1.9
Max	2.3	2.3	2.9	2.3	1.6	1.3	1.3	1.6	3.6	2.2	2.3	3.6
CoV	0.22	0.18	0.22	0.19	0.19	0.11	0.12	0.16	0.30	0.15	0.21	0.30
LFW connection ductility 6												
	q_μ				**q_D**				**q**			
Storeys	2	3	4	global	2	3	4	global	2	3	4	global
Min	1.2	1.3	1.2	1.2	1.2	1.0	1.0	1.0	1.6	1.6	1.4	1.4
Mean	2.1	1.6	1.7	1.8	1.4	1.1	1.2	1.2	2.8	1.8	2.2	2.3
Max	2.7	2.3	2.3	2.7	1.4	1.4	1.5	1.5	3.6	2.2	3.4	3.6
CoV	0.23	0.18	0.20	0.23	0.05	0.12	0.17	0.14	0.22	0.11	0.30	0.29
LFW connection ductility 8												
	q_μ				**q_D**				**q**			
Storeys	2	3	4	global	2	3	4	global	2	3	4	global
Min	1.5	1.5	1.4	1.4	1.3	1.1	1.1	1.1	2.4	2.1	1.7	1.7
Mean	2.3	1.8	2.0	2.0	1.6	1.3	1.3	1.4	3.8	2.4	2.6	2.9
Max	3.7	2.7	2.6	3.7	2.1	1.5	1.5	2.1	6.3	2.9	3.6	6.3
CoV	0.29	0.20	0.19	0.25	0.21	0.12	0.11	0.20	0.36	0.13	0.24	0.36

https://doi.org/10.52202/069179-0325

However, it is not possible to perform a direct comparison between these values and those provided by codes. In this study, the overstrength factor for the sheathing-to-frame connection was set to 1. Though, it is possible to multiply the intrinsic q by 1.5, which is the q-factor suggested by Eurocode 8 for a global non-dissipative behaviour, in order to calculate the q_{code} (code dependent q-factor)(Table 4).

Table 4: *Mean value of the q_{code} factor for each ductility class.*

Ductility Class	Storeys			global
	2	3	4	
4	3.6	2.6	2.4	**2.9**
6	4.3	2.8	3.3	**3.4**
8	5.6	3.6	4.0	**4.4**

For a ductility class equal to 4, a value of 2.9 was obtained, which confirms the q=3 provided by the Italian building code [27] for Low Ductility Class timber structures. On the other hand, a value of 3.4 was obtained for a ductility class 6, which is widely lower than 5, value suggested for Ductility Class High (DCH) by Eurocode 8 [6] and Italian Building Code [27]. Even a ductility class 8 is not sufficient to comply with Eurocode provision (a mean intrinsic q equal to 2.9, and a q-factor equal to 4.4). It is worth noticing that, in this work, all the dissipation is concentrated in the sheathing-to-frame connection, and the contribution of hold-downs and shear brackets are not taken in to account.

7 CONCLUSIONS

In this work, an Incremental Dynamic Analysis approach was used, in order to evaluate the behaviour factor for Light Frame Wood structures. Compared to the non-linear static approach, the dynamic analysis considers the cyclic behaviour of the walls and the frequency of the ground motion.

Three example buildings were calculated according to Eurocode and Capacity Design. Starting from an experimental test on a full-scale LFW wall, a set of walls was obtained, varying the ductility of the sheathing-to-frame connection, and an IDAs procedure was applied to the building assembled with parameterized walls.

The obtained results confirm the behaviour factor for Low Ductility Class according to the Italian building code. However, the q-factor for High Ductility Class is lower than that provided by Eurocode 8.

The results presented belong to a larger study. In the next phases, the influence of the non-regularity of buildings will be investigated and a greater number of accelerograms and ductility classes will be considered, in order to expand the dataset.

ACKNOWLEDGEMENT

This research work was partly financed by the ReLUIS Consortium (Italian University Network of Seismic Engineering Laboratories), within the frame of the ReLUIS-DPC 2022-2024 project WP13 "Timber Structures – Code contributions".

REFERENCES

[1] Mishra A., Humpenöder F., Churkina G. et al.: Land use change and carbon emissions of a transformation to timber cities. Nat Commun13, 4889, 2022. https://doi.org/10.1038/s41467-022-32244-w www.nature.com/articles/s41467-022-32244-w

[2] Safarik D., Elbrecht J., Miranda W.: State of Tall timber 2022, CTBUH (Council on Tall Buildings and Urban Habitat) Journal , 2022 Issue.

[3] Filiatrault A., Christovasilis I.P., Wanitkorkul A., van de Lindt J.W.: Experimental seismic response of a full-scale light-frame wood building. J Struct Eng, 136(3):246–254, 2009.

[4] Van de Lindt J.W., Pei S., Pryor S.E., Shimizu H., Isoda H.: Experimental seismic response of a full-scale six-story light-frame wood building. J Struct Eng,136(10):1262–1272, 2010.

[5] Tomasi R., Casagrande D., Grossi P., Sartori T.: Shaking table tests on a three-storey timber building. Proc Inst Civil Eng Struct Build, 168(11):853–867, 2015. https://doi.org/10.1680/jstbu .14.00026

[6] EN 1998-1:2013. Eurocode 8: design of structures for earthquake resistance part 1: general rules, seismic actions and rules for buildings. Brussels, Belgium: CEN, European Committee for Standardization, 2013.

[7] Faggiano B., Sandoli A., Iovane G., Fragiacomo M., Bedon C., Gubana A., Ceraldi C., Follesa M., Gattesco N., Giubileo C., Pio Lauriola M., Podestà S., Calderoni B.: The Italian instructions for the design, execution and control of timber constructions (CNR-DT 206 R1/2018). Engineering Structures, 253, art. no. 113753, 2022. DOI: 10.1016/j.engstruct.2021.113753

[8] Rossi S., Giongo I., Casagrande D., Tomasi R., Piazza M.: Evaluation of the displacement ductility for the seismic design of light-frame wood buildings. Bulletin of Earthquake Engineering, 17 (9), pp. 5313 – 5338, 2019. DOI: 10.1007/s10518-019-00659-4

[9] Demirci C., Malaga-Chuquitaype C., Macorini L.: Seismic shear and acceleration demands in multi-storey cross-laminated timber buildings. Engineering Structures, 198, 2019. doi/10.1016/j.engstruct.2019.109467

[10] NZS 3603, New Zealand Timber Structures Standards, 1993

[11] IBC, International Building code, 2021.

[12] Canadian Standards Association CSA O86, 2014.

[13] Gubana A., Tomasi G.: Results analysis of an experimental shear test on a light frame timber wall. Technical Report UNIUD 01, Reluis project 2010-2013 (in Italian), 2013.

[14] Melotto M.: Wood-based in-plane strengthening solutions for the seismic retrofit of traditional timber floors in masonry buildings. Doctoral Thesis, University of Brescia, Italy, 2017, tutor Alessandra Gubana.

[15] EN 1995-1-1:2005. Eurocode 5: design of timber structures—part 1-1: general—common rules and rules for building, 2013.

[16] Casagrande D., Sartori T., Tomasi R.: Capacity design approach for multi-storey timber-frame buildings. In: INTER conference, Bath 2014

[17] Vamvatsikos D., Cornell C.A.: Incremental dynamic analysis, Earthquake Engineering and Structural Dynamics 31(3): 491–514, 2002.

[18] Iervolino I., Galasso C., Cosenza E.: REXEL: computer

https://doi.org/10.52202/069179-0325

aided record selection for code-based seismic structural analysis. Bulletin of Earthquake Engineering, 8:339-362, 2009. DOI 10.1007/s10518-009-9146-1
[19] Fajfar P.: Capacity Spectrum Method Based On Inelastic demand Spectra. Earthquake Engineering And Structural Dynamics, Vol. 28, 979-993, 1999.
[20] Newmark N.M., Hall W.J.: Earthquake Spectra and Design. Earthquake Engineering Research Institute Monograph Series, 1982
[21] Ceccotti A., Massari M., Pozza L.: Procedures for seismic characterization of traditional and modern wooden building types. Int J Quality Res, 10(1):47–70, 2016. doi:10.18421/IJQR10.01-02
[22] Ceccotti A., Sandhaas C.: A proposal for a standard procedure to establish the seismic behaviour factor q of timber buildings. In: Proceedings of the 11th world conference on timber engineering WCTE, Riva del Garda, Italy, 2010.
[23] Aloisio A., Alaggio R., Fragiacomo M.: Fragility functions and behavior factors estimation of multi-story cross-laminated timber structures characterized by an energy-dependent hysteretic model. *Earthquake Spectra*, 37(1):134-159, 2021. doi:10.1177/8755293020936696
[24] Mwafy A.M., Elnashai A.S.: Calibration of force reduction factors of RC buildings. J Earthq Eng, 6:239–73, 2002.
[25] Fanaie N., Ezzatshoar S.: Studying the seismic behavior of gate braced frames by incremental dynamic analysis (IDA), Journal of Constructional Steel Research, 99:111-120, 2014. https://doi.org/10.1016/j.jcsr.2014.04.008.
[26] Oggu P., Gopikrishna K., Nagariya A.: Seismic behavior and response reduction factors for concrete moment-resisting frames. Bull Earthquake Eng 19:5643–5663, 2021. https://doi.org/10.1007/s10518-021-01184-z
[27] Italian Building Code NTC 2018, Ministerial Decree of 17th January 2018, M.I.T., Rome, 2018 (in Italian).

World Conference on Timber Engineering Oslo 2023

MODULE FOR ANALYSIS AND CAPACITY-BASED DESIGN OF BRACED TIMBER FRAMES

Hossein Daneshvar [1], Brian Qi [2], Tahiat Goni [3] , Md. Abdul Hamid Mirdad [4], Marjan Popovski [5], Zhiyong Chen [6] Ying Hei Chui [7]

ABSTRACT: The National Building Code of Canada (NBCC) specifies values for the ductility-related force modification factor (R_d) for different seismic force resisting systems (SFRSs), which reflects their ability to dissipate energy during a seismic event. For braced timber frames (BTF), NBCC 2020 recognizes two ductility categories: braced frames with moderate and limited ductility, which are assigned an R_d value of 2.0 and 1.5, respectively. However, these values were primarily based on engineering judgment, qualitative comparisons, and experience rather than rigorous analysis using a recognized procedure. Additionally, the Canadian Standard for Engineering Design in Wood, CSA O86, needs to provide specific guidance on how to achieve these two ductility levels. To address this gap, the University of Alberta and FPInnovations are conducting an extensive study to develop specific design provisions for BTFs, including detailed procedures to achieve performance requirements for each level of ductility. This paper represents the first research stage, which involves developing software to analyse and design a range of archetype BTFs using capacity-based design principles.

KEYWORDS: Braced Timber Frame (BTF), Ductile End Brace Connections, Seismic Force Resisting System (SFRS), ductility-related force modification factors (R_d), ductile and moderately ductile connections.

1 INTRODUCTION

The National Building Code of Canada (NBCC) [1] specifies ductility-related force modification factors (R_d) and over-strength-related force modification factors (R_o) for different seismic force-resisting systems (SFRS) to account for a structure's ability to dissipate energy through inelastic behaviour and its dependable reserve strength, respectively. The NBCC 2020 considers Braced Timber Frames (BTFs) with two levels of ductility performance: moderate and limited ductility. The NBCC specifies values of 2.0 and 1.5 for R_d and R_o, respectively, for moderately ductile BTFs. The corresponding values for BTFs with limited ductility are 1.5 and 1.5 [1]. These recommended values were primarily based on engineering judgment, qualitative comparisons, and experience rather than rigorous analysis using a recognized procedure. In addition, no specific guidance is provided in CSA O86 [2] on achieving these ductility levels in terms of end brace connection details as the primary source of ductile behaviour in BTFs. Also, there is no specific design methodology and corresponding tool to design such frames to achieve the desired ductility levels. This project aims to contribute to developing seismic design provisions for BTFs that can be incorporated into the next edition of CSA O86, specifically provisions to achieve the stated R_d factors in NBCC.

2 METHODOLOGY

To achieve the project goals, the technical guide NRC-CONST-56478E published by Construction Canadian Construction Materials Centre (CCMC), National Research Council of Canada (NRCC), herein referred to as CCMC guideline, is used as the primary reference [3]. This guideline is a simplified version of the FEMA P695 guideline [4]. The procedure requires the study of various archetypes with different attributes that may affect the seismic performance of a building, such as storey heights, number of floors, number of bays, types of dowel-type connections, and earthquake intensities. The nonlinear time history analysis (NLTHA) approach at 100% and 200% of the Uniform Hazard Spectrum (UHS) is suggested to investigate whether the performance criteria are met for the designed archetypes [3]. To facilitate the required tasks, a computer platform is developed with the two modules shown in Figure 1. The first module is a BTF

[1] Hossein Daneshvar, University of Alberta, Canada, Hossein.daneshvar@ualberta.ca
[2] Brian Qi, University of Alberta, Canada, bqi1@ualberta.ca
[3] Tahiat Goni, University of Alberta, Canada, tahiat@ualberta.ca
[4] MD Abdul Mirdad, University of Illinois, mirdad@illinois.edu
[5] Marjan Popovski, FPInnovations, Canada, Marjan.Popovski@fpinnovations.ca
[6] Zhiyong Chen, FPInnovations, Canada, zhiyong.chen@fpinnovations.ca
[7] Ying-Hei Chui, University of Alberta, Canada, yhc@ualberta.ca

https://doi.org/10.52202/069179-0326

linear analysis and capacity-based design module with an in-house developed analysis engine that can mass produce archetype models and the hysteresis loops of selected dowel-type connections necessary for performing NLTHA. These archetypes will be analysed using the OpenSeesPy program [5] and post-processed within module 2 to evaluate their responses to selected seismic motions, scaled according to NBCC [1]. As highlighted in Figure 2, this paper focuses on developing module 1 as a stand-alone software to create the necessary archetype buildings and hysteresis loops of selected dowel-type connections for performing NLTHA.

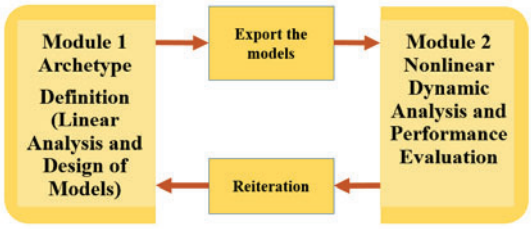

***Figure 1**: Modules 1 and 2 of the developed software to evaluate seismic force modification factors for BTFs*

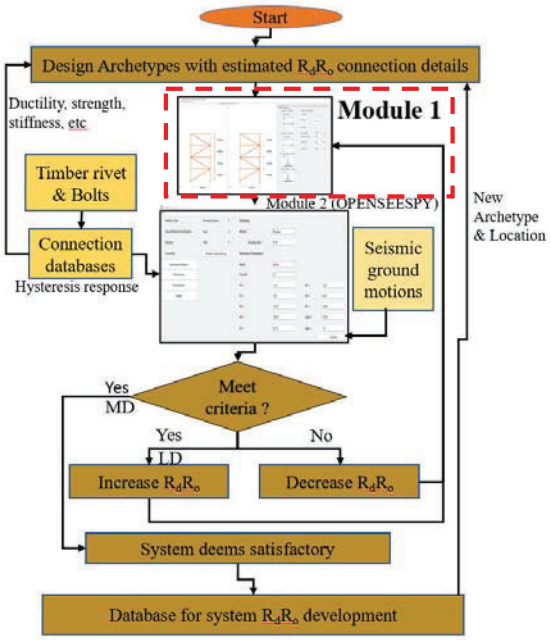

***Figure 2**: Process to evaluate seismic force modification factors for BTF (LD: Limited ductility; MD: Moderately ductile frames)*

3 FRAME ANALYSIS SOFTWARE

Module 1 was developed using Python [6] to calculate loading, analysis and design BTFs. The development of module 2 is in progress to perform NLTHA with the OpenSeesPy library using the exported file from module 1. Module 1 software interface includes a set of general and specialized tabs menus that enables users to create an archetype and, subsequently, analyze and design it in a step-by-step procedure. The steps followed are based on principles of the capacity-based design approach, as explained and demonstrated below in sections 3.1 to 3.9

3.1 PROJECT INFORMATION

In this section, the user is asked to input the model's name, description, revision number, the engineer's name, and the checker's name, as shown in Figure 3. The software automatically assigns the name to the file based on the input provided. It is noted that properly labelling the created archetypes is essential to help manage the large number of archetypes.

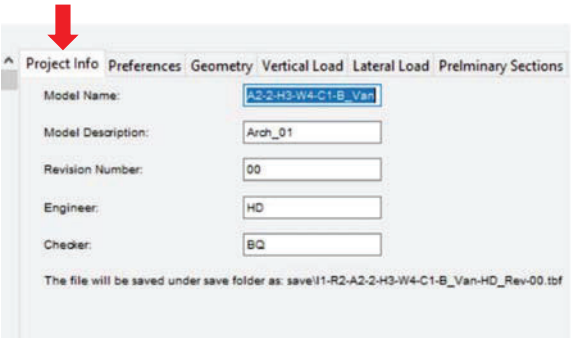

***Figure 3**: Software interface: project information*

3.2 PREFERENCES

In this section, the user selects the unit system (metric or imperial), design code (currently just CSA O86-19 [2]), the loading code (NBCC 2015 [7] or NBCC 2020 [1]), and the location of archetypes. The software currently incorporates four Canadian cities, as shown in Figure 4. Their associated design load values, such as 1-in-50-year ground snow loads, 1-in-50-year associated rain load, 1-in-10-year and 1-in-50-year wind reference velocity pressures, as well as 5% damped spectral response acceleration (S_a), are embedded and taken from NBCC 2015 [7] and NBCC 2020 [1]. More cities will be added later as the use of the module expands.

***Figure 4**: Software interface: preferences*

3.3 GEOMETRY AND BOUNDARY DEFINITIONS

This menu possesses two tabs. In the first one, the user inputs the required values to define the geometry of the archetype building, such as the number of storeys, the number of bays, their width in x- and y- directions, and the height of the first and subsequent stories, as shown in Figure 5. The user is also asked to input the type of braced frame in each direction (single diagonal versus cross bracing) and the kind of support condition at the bottom, either pinned or fixed (the pinned support is recommended for BTF). In the second tab, the user can select the locations of the braced bays within the interactive plan view (see Figure 6). The graphic interface will show a view of brace frames in each direction, as shown in Figure 7. By the end of this step, the archetype model's geometry is developed.

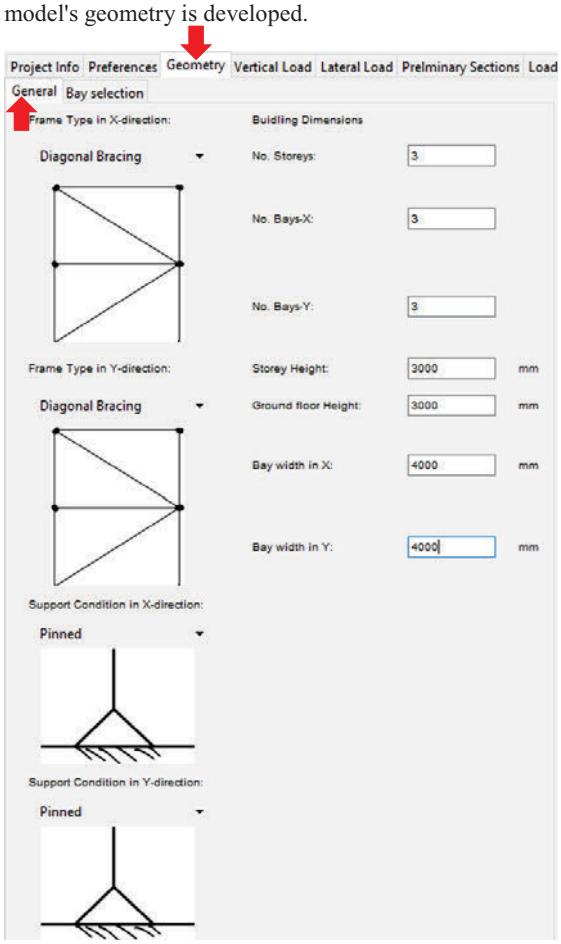

***Figure 5**: Software interface: geometry definition - braced frame specifications*

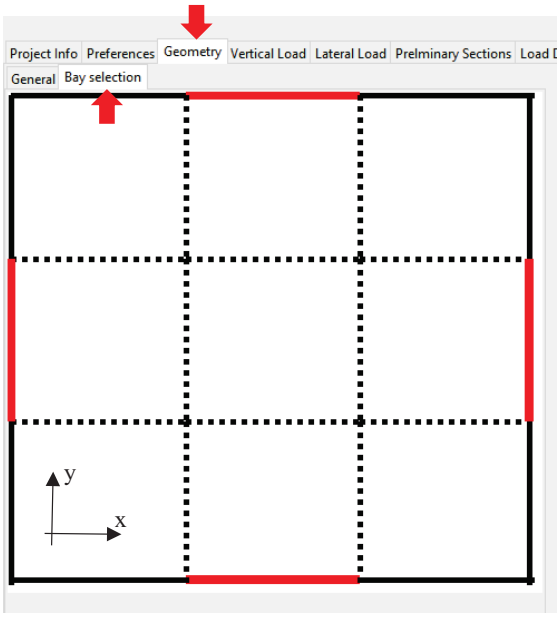

***Figure 6**: Software interface: geometry definition - braced frame locations*

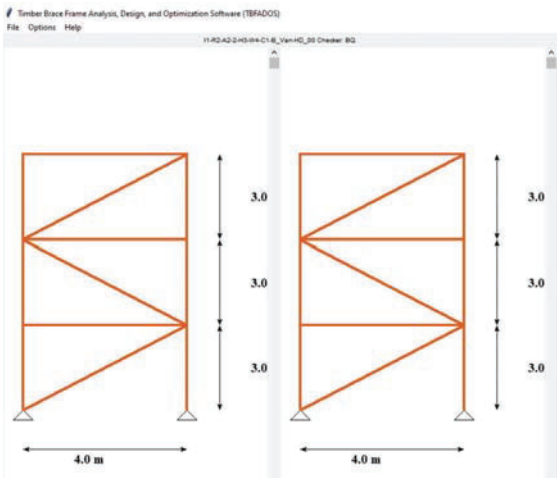

***Figure 7**: Software interface: geometry creation*

3.4 VERTICAL LOAD DEFINITION

In this section, the user inputs the distributed dead and live load with associated factors for calculating the snow load, i.e., wind exposure factor (C_b), slope factor (C_s), and accumulation factor (C_a), as shown in Figure 8. The software will calculate the share of each frame from the vertical loads considering the tributary area of each frame. The seismic weight of the archetype building is calculated based on the input provided in the section, according to the selected loading code. It is noted that the BTFs, as a part of SFRS, do not support any vertical load. The ability to support the vertical load in addition to the lateral load will be added in future revisions of the module.

https://doi.org/10.52202/069179-0326

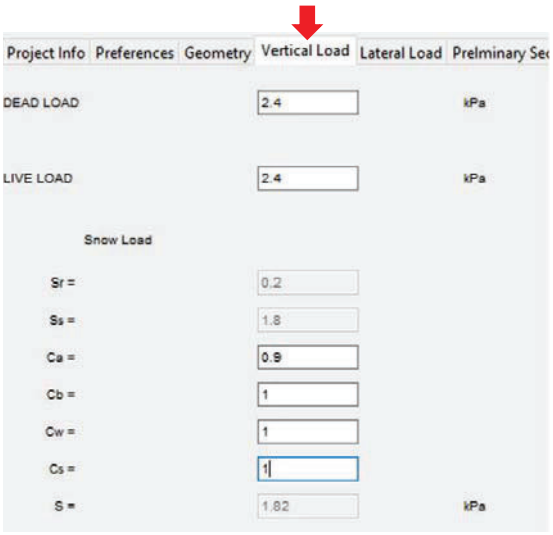

***Figure 8**: Software interface: vertical load*

3.5 LATERAL LOAD DEFINITIONS

This software section contains two tabs: one dedicated to wind load calculation and the other to seismic load, as shown in Figure 9 and Figure 10, respectively. To calculate the wind pressure, the user needs to select the importance category of the building, i.e., low, normal, high, or post-disaster, as well as the option to calculate the wind load; for either the ultimate limit state (ULS) or serviceability limit state (SLS). After that, the software will automatically select the appropriate values for the exposure, topographic, and external and internal pressure factors. The user can choose a factor of 2 or 2.5 for the gust factor. It is noted that the wind load calculation is used solely in period calculations based on the Rayleigh method in module 1 of the developed software.

In the seismic tab (See Figure 10 (a) to (c)), the user is asked to input the necessary values to calculate the induced lateral seismic loads based on the equivalent static load method according to NBCC 2015 or NBCC 2020, e.g., the soil type (Class A to E), importance category, and accidental eccentricities. The spectral acceleration values (S) are automatically calculated based on the archetype location, with reference values anticipated in the preference menu (S_a). One significant difference between NBCC 2015 [7] and NBCC 2020 [1] is the introduction of seismic design categories (SC) in the 2020 version of NBCC [1], which will be determined as shown in Figure 10 (c). Another difference is the substantially higher seismic design load adopted in NBCC 2020 for several major cities in Canada. In addition, the user can select ductility-related force modification, overstrength-related force modification factors, and the R_d and R_o factors, respectively, for each direction. The R_d and R_o factors are also used to calculate the estimated inelastic drifts of each floor. Additionally, the period of the structure is calculated using four different methods shown in Figure 10 (c); or can be overruled by the user. The period calculation method selected by the user will be used for base shear calculation (the default value is the NBCC's recommended relationship, depending on the height of the archetype solely). Finally, the software will calculate the base shear total force in each direction based on the information provided in this sheet.

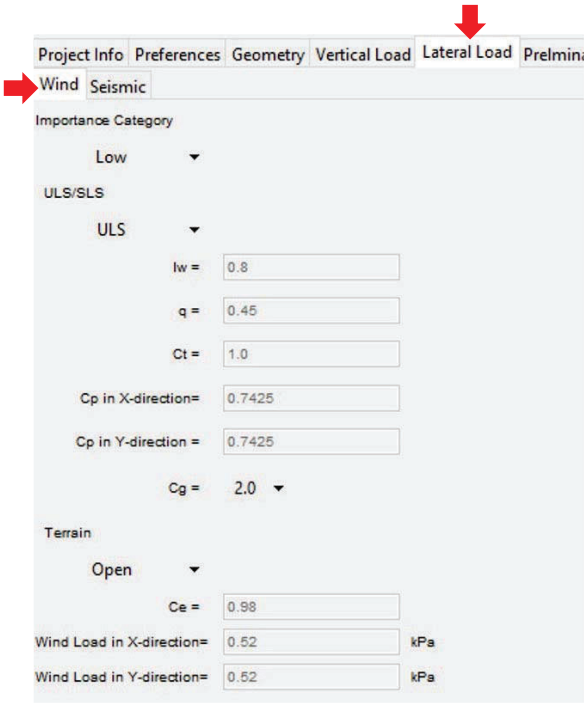

***Figure 9**: Software interface: lateral load – wind*

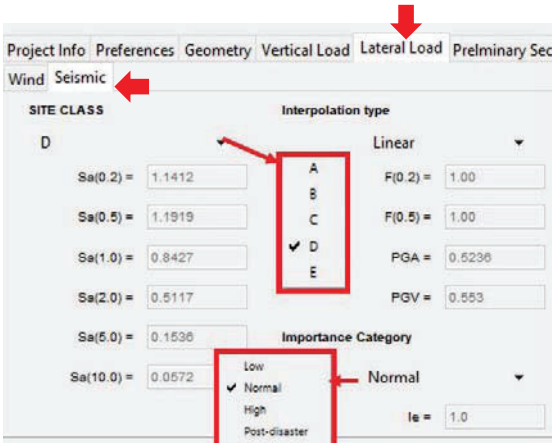

(a)

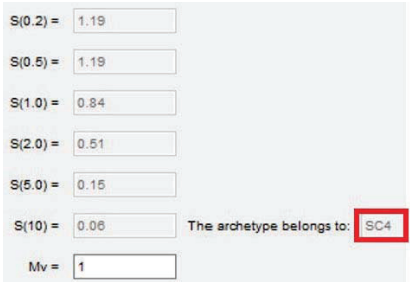

(b)

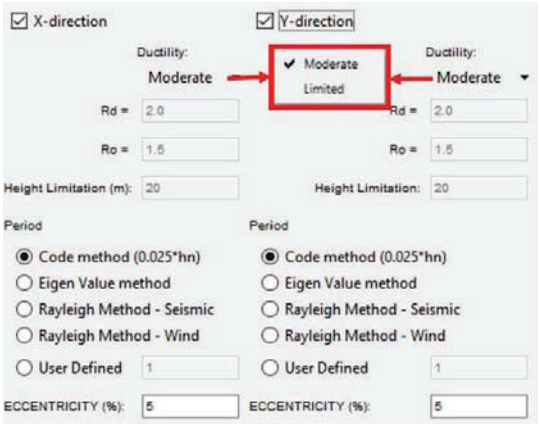

(c)

***Figure 10**: Software interface: lateral load – earthquake*

3.6 SECTION DEFINITIONS

In this software interface section (See Figure 11), the preliminary sections and associated dimensions and materials are assigned to the braces, beams, and columns. The available products are sawn lumber and glulam, with different species and grades. In addition, the connection types for the end brace connections (dissipative connections) can be either timber rivet or bolted connection. The need to limit the choices to these two dowel-type connections is because background load-slip data on these connections have been obtained by experiments [8]. Other types of connections or fuses can be incorporated in the future.

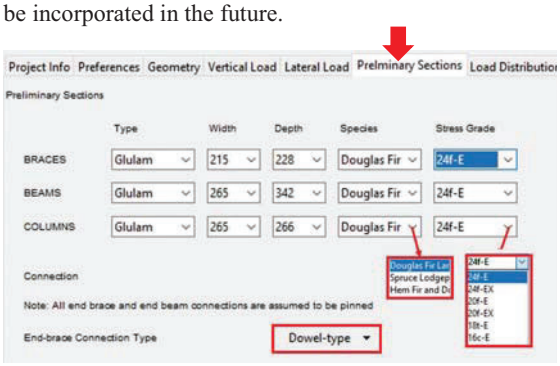

***Figure 11**: Software interface: preliminary sections*

3.7 DIAPHRAGM DEFINITION AND TWO-DIMENSIONAL (2-D) FRAME SELECTION

In this menu, as shown in Figure 12, the diaphragm type (flexible versus rigid) can be selected to distribute the seismic-induced forces among the frame within -z floors. The three-dimensional archetype produced at the beginning is loaded, while the analysis and design will be performed on the chosen 2-D frames, as suggested by CCMC [3] and FEMA P695 [4] guidelines. The BTFs are then analysed and designed based on the selected design loads. The load distribution and results are shown in Figure 12. Figure 13 shows the load distribution at different floor levels of the selected frame in the graphical interface. The period of the structure is calculated and reported using different methods, as shown in Figure 14. The variability of results for different period calculation methods indicates the need for investigating this issue more profoundly, as the current equation for the braced frames ($0.025h_n$; in which h_n is the building height) [1] is empirically obtained for the steel braced frames.

3.8 ANALYSIS

In this menu, as shown in Figure 15, running the analysis performs the linear static analysis with the option to include p-delta effects. The axial force for the braces is displayed in the graphical interface, along with the absolute elastic displacement. The elastic and plastic drift can be calculated (See Table 1) and compared with allowable values based on the importance category of the building specified in section 3.5. The analysis engine is created based on the matrix structural analysis method (displacement method), fully verified against third-party commercial software, SAP2000 [9].

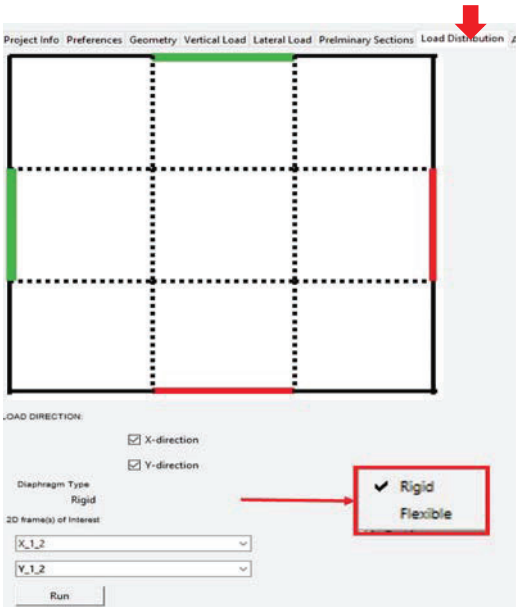

***Figure 12**: Software interface: load distribution among the frames*

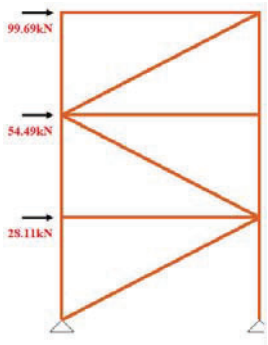

(a)

https://doi.org/10.52202/069179-0326

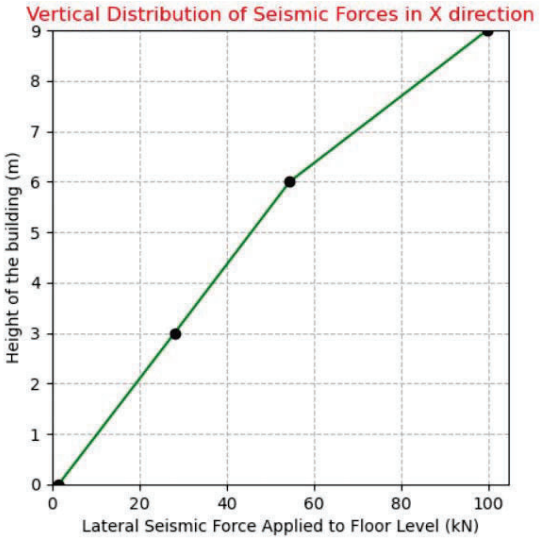

(b)

***Figure 13**: Software interface: sample results for load distribution among the frames*

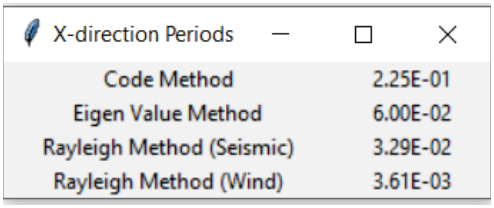

***Figure 14**: Software interface: period calculation*

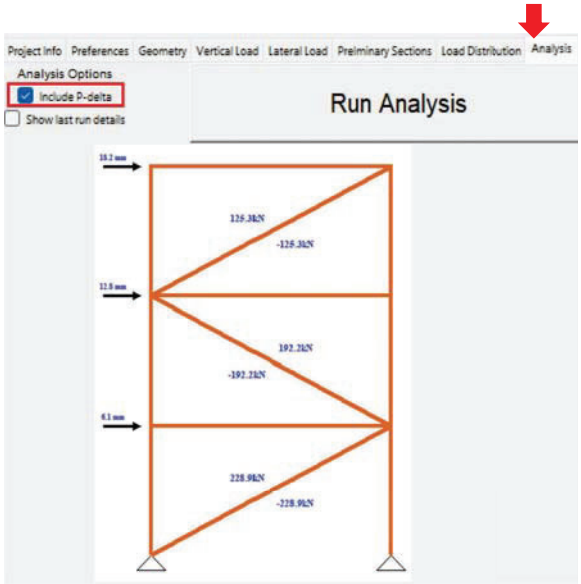

***Figure 15**: Software interface: analysis results – brace force and displacements*

***Table 1:** Software interface: analysis results – drift calculations for three floors in X-direction*

No. Floor	Absolute Displacement (mm)	Elastic Drift	Allowable Drift	Plastic Drift	Status
1	6.106	0.0020	0.025	0.0061	OK
2	12.733	0.0023	0.025	0.0066	OK
3	18.238	0.0018	0.025	0.0055	OK

3.9 DESIGN

This module segment has two tabs: one dedicated to designing dowel-type end brace connections; and the other for the design of members. The latter consists of three subsequent tabs devoted to braces, beams, and columns. Only the brace design interface is discussed in this paper.

3.9.1 End brace connections

For the end brace connection design, two types of fasteners are considered: bolts and timber rivets, due to the availability of the test results for these specific applications [8]. To keep the scope of the designed connection configurations manageable, four patterns for the bolted connections (C1-B, C1-B-R, C2-B, and C2-B-R) and two patterns for the riveted connections (G5-40-12 and G5-65-10) are selected as standard connection types, as shown in Figure 16 (a). The connection patterns for the C1-B and C2-B connection types are shown in Figure 17. C1-B-R and C2-B-R possess the same pattern as C1-B and C2-B, respectively, but were reinforced with self-tapping screws. G5-40-12 and G5-65-10 consist of twenty 5x40 and 5x65 timber rivets, respectively, with 25 mm spacing in both directions. The user can either revise the default design parameters for each type of standard connection, such as modification factors (Figure 16***Figure 16*** (b)), fastener specifications (Figure 16(c)), main and side member properties (Figure (d) and (e), respectively), or assign a scale factor (Figure (a)) to satisfy the strength requirement for the end brace connections, i.e., the strength of the end brace connection exceeds the force calculated in Section 3.8 (Figure 16 (f)).

An additional feature within this section is intended to perform a parametrization task in which the hysteresis loops of the connections are quantified by selecting a model. While this step is not vital for the archetype analysis and design within module 1, it is necessary to produce the required input to perform nonlinear dynamic analysis in module 2. The SAWS model, illustrated in Figure 18 ***Figure 18*** (a), available in OpenSeesPy [5], was selected to model both bolted and timber rivet connections, and is appropriate for modelling timber dowel-type connections in general. While this part of the module has been fully developed, it has not yet been discussed herein, as a thorough discussion of the subject is deemed outside the scope of this paper. However, the results of the parametrization exercise for the six types of standard connections mentioned above are summarized in Table 2. The test results compared to the SAWS model

with the obtained parameters are shown in Figure 18***Figure 18*** (b) and Figure 18 (c) as examples for C1-B and C2-B.

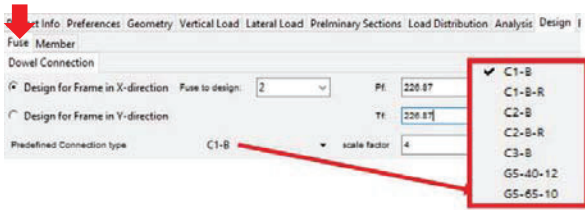

(a)

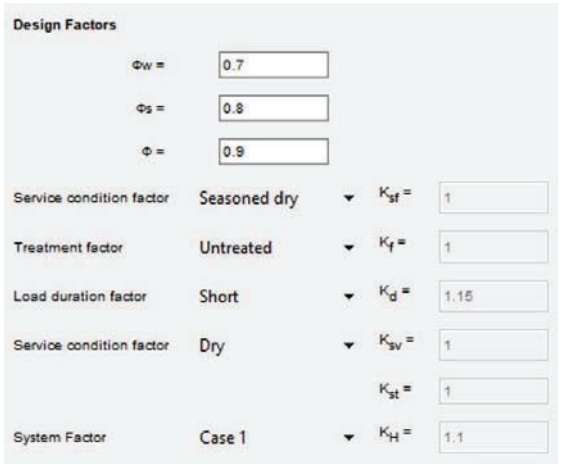

(b)

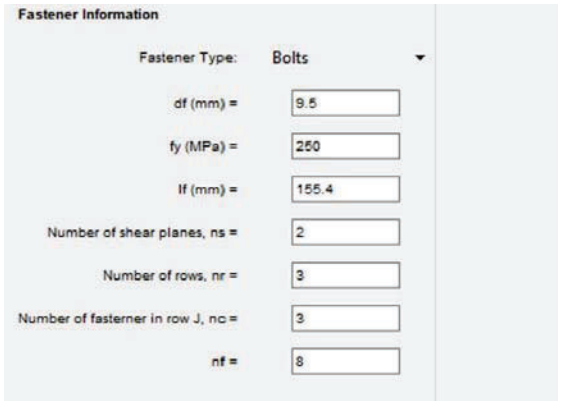

(c)

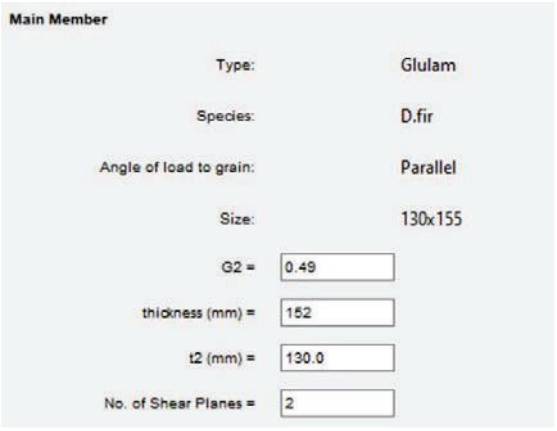

(d)

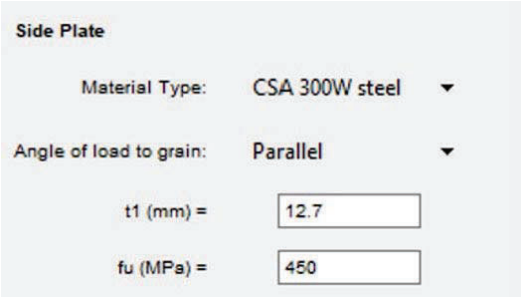

(e)

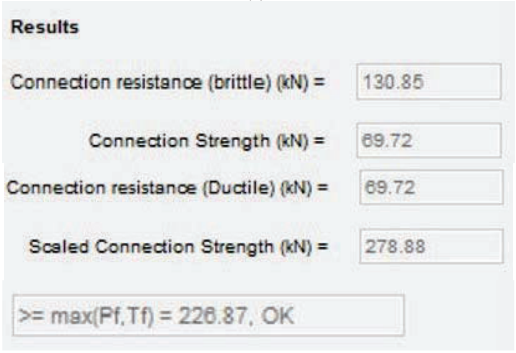

(f)

Figure 16*: Software interface: design – end brace connections (a) design force, standard connection type and scale factor (b) design factors (c) fastener information (d) main member (e) side member (f) results satisfying strength requirement*

https://doi.org/10.52202/069179-0326

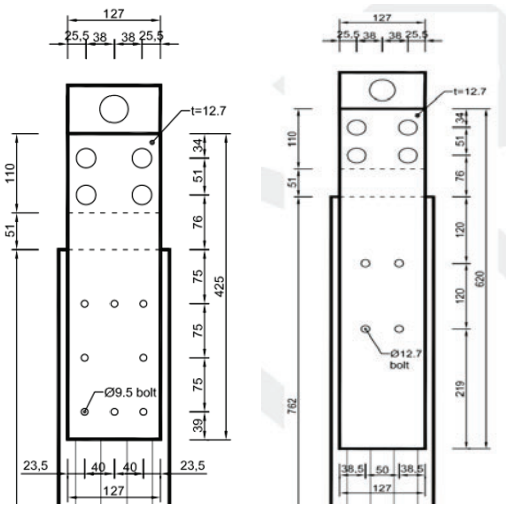

(a) (b)

***Figure 17**: Sample standard end brace connections (a) C1-B (b) C2-B*

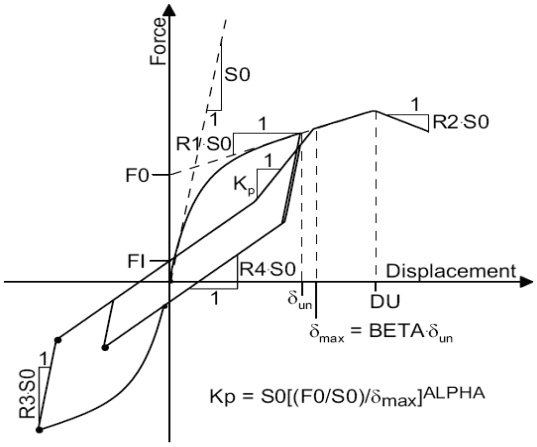

(a)

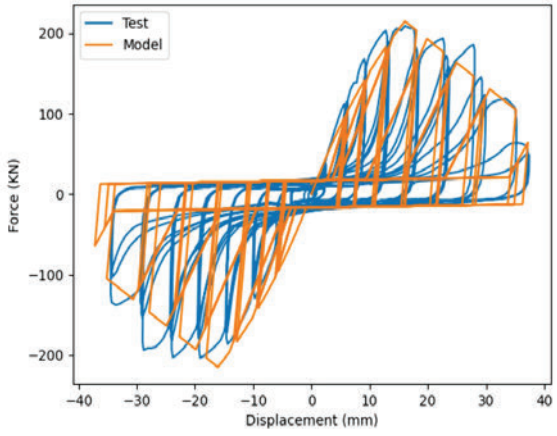

(b)

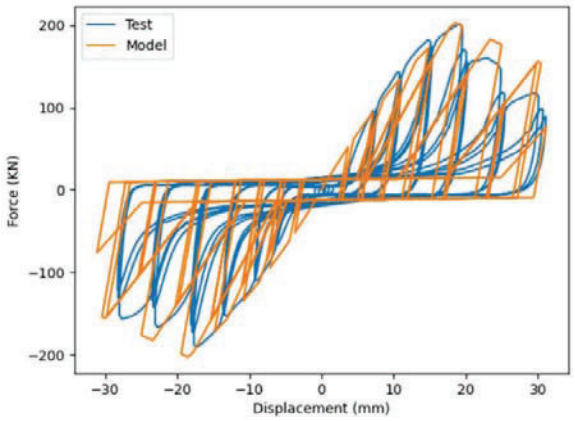

(c)

***Figure 18**: (a) SAWS model [5] (b) C1-B: test versus SAWS model (c) C2-B: test versus SAWS model*

***Table 2:** SAWS model parameters for standard connection types*

Specimen Label	C1-B	C1-B-R	C2-B	C2-B-R	G5-40-12	G5-65-10
F0	245.7	242.7	290.6	218.33	109.4	137.1
FI	16.87	15.31	12.56	15.96	7.51	5.13
DU	16.07	27.38	18.49	38.04	7.51	6.4
S0	19.35	26.61	15.07	17.34	69.20	86.36
R1	0.17	0.035	0.14	0.03	0.002	0.004
R2	-0.29	-0.07	-0.27	-0.12	-0.08	-0.04
R3	4.29	4.2	3.33	4.55	0.82	1.16
R4	0.006	0.01	0.007	0.0092	0.001	0.001
Alpha	0.33	0.32	0.68	0.03	0.03	0.78
Beta	1.1	1.1	1.2	1.08	1.05	1.1

3.9.2 Members

After designing the end brace connections, where energy can be dissipated through yielding, it is necessary to design other components, namely braces, beams, and columns. The members are intended to remain elastic and undamaged, based on the capacity-based design principle. Figures (a) to (c) illustrate the details of designing a brace as an axial member for tension and compression, following CSA O86-19 [2]. Capacity protection is ensured by applying an over-strength factor, Figure 19 (b) and (c), for compression and tension, respectively. Although a factor of 1.1 is used in Figure 19 for demonstration purposes, this value could be increased based on the available test results and the design engineer's judgement. Work is currently underway to develop appropriate values for this factor based on a review of the typical coefficient of variation of connection test data that would meet the philosophy in CSA O86-19 [2] of designing capacity-protected elements based on the 95th percentile of ultimate strength of the energy dissipative connection.

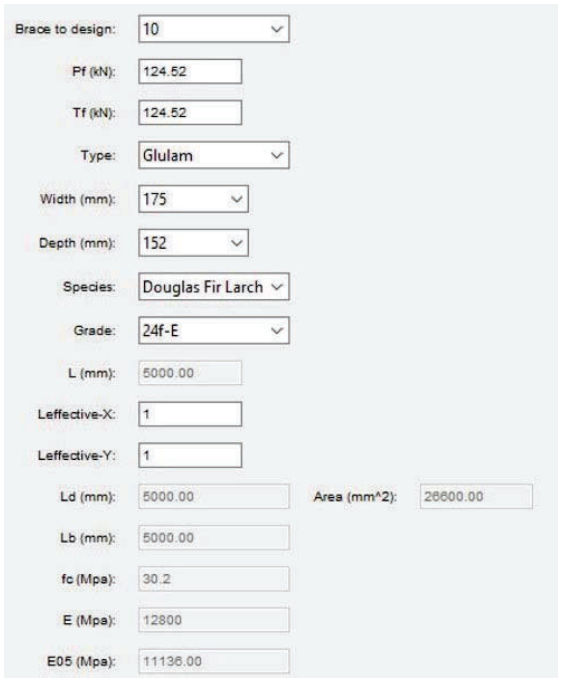

(a)

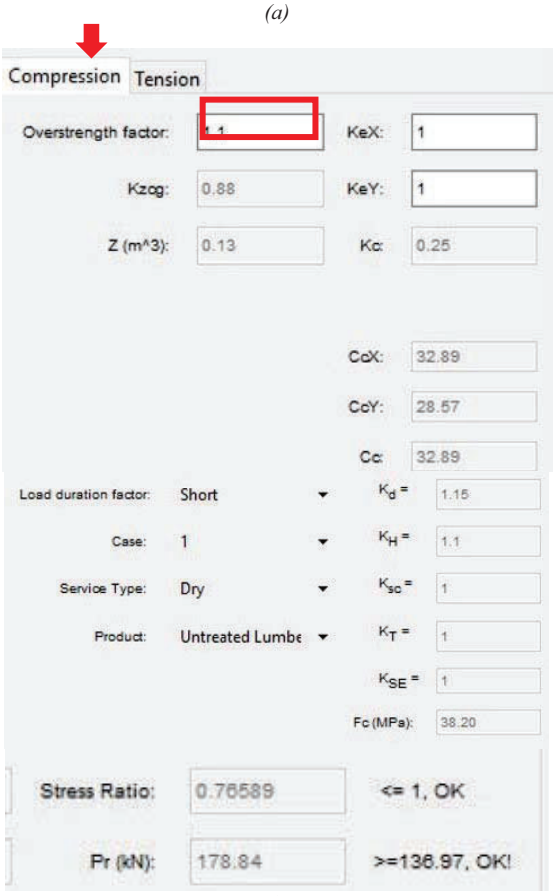

(b)

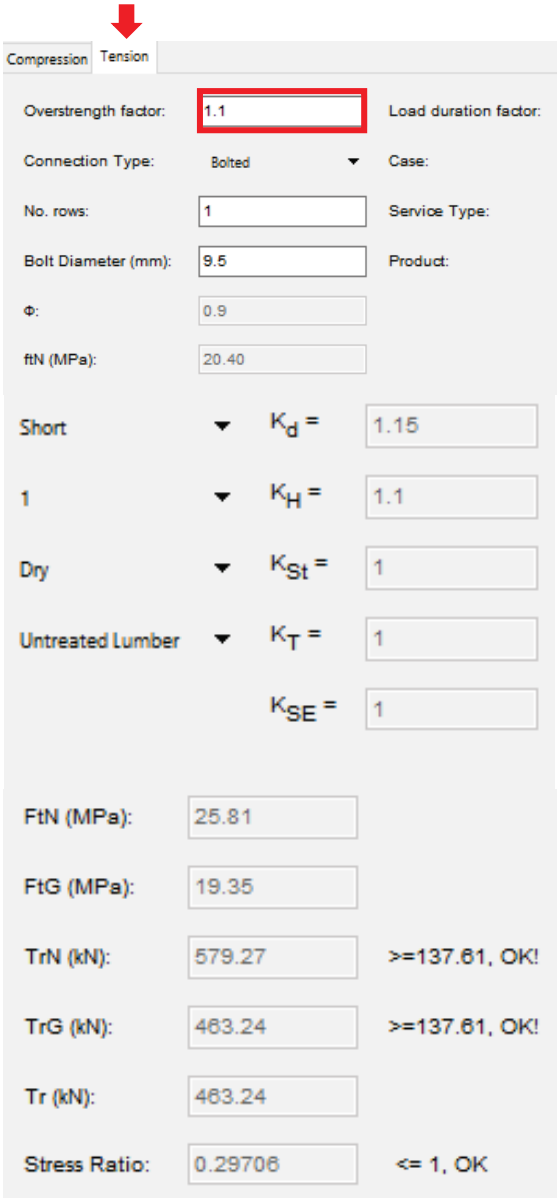

(c)

***Figure 19**: Software interface: design – braces (a) selected brace force and section and general design parameters (b) design parameters for compression (c) design parameters for tension*

4 RESULTS

After the results of the load distribution calculation, analysis, and design of connections and members are obtained; the last two tabs of the module should be accessed. They include the summary of the results and the export process of the model details and results to use in module 2 for performing NLTHA.

https://doi.org/10.52202/069179-0326

4.1 RESULTS

Figure 20 demonstrates a sample result summary of this module of the software. The geometry of the model includes the node coordinates (Figure 20 (a)), member types with their associated material types, section size, species, and grade, which the user can verify (Figure 20 (b)). The maximum governing stress ratio and status are also presented (Figure 20 (b)). Finally, the user can verify the number and type of end-brace connections with the scale factor used for design and the associated SAWS model parameters (Figure 20 (c)).

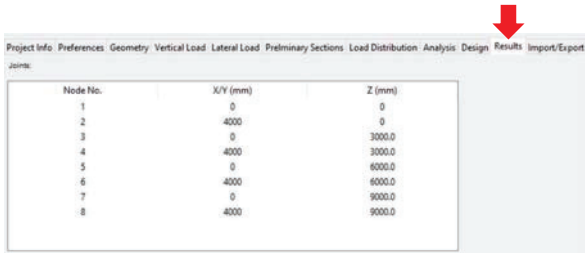

(a)

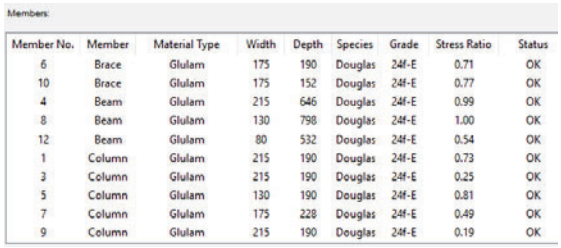

(b)

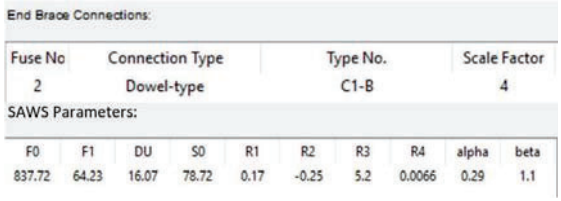

(c)

***Figure 20**: Software interface: results (a) node coordinates (b) members and their associated types, material, sections, stress ratios (c) end brace connection types and associated SAWS model parameters*

4.2 EXPORT TO MODULE 2

In the last section of the first module of the software, the results are exported as a file with the .py extension, which can be imported to module 2 to perform nonlinear dynamic analysis using the OpenSeesPy analysis engine [5].

5 SUMMARY AND CONCLUSIONS

This research project aims to contribute to developing design provisions on BTFs that could be implemented in the next edition of CSA O86-19 [2]. As the initial part of the research, a software module responsible for analysing statically (with the option to include p-delta) and designing a variety of archetype braced timber frames based on the principle of capacity-based design. The methodology established in the developed module provides specific connection details and system specifications permitted to use with the stated ductility-related seismic force modification factors specified in NBCC [1 & 7], namely limited and moderate ductility.

ACKNOWLEDGEMENTS

The authors gratefully acknowledge the financial support of the Natural Sciences and Engineering Research Council of Canada (NSERC) through the Industrial Research Chair program as well as contributions of the Natural Resources Canada (NRCan) and the Canadian Wood Council (CWC). We also thank Dr. Dorian Tung of FPInnovations and Dr. Ali Mikael of CWC for their thoughtful insights.

REFERENCES

[1] National Research Council of Canada (NRC): National Building Code of Canada (NBCC). Ottawa, ON, Canada, 2020.

[2] Canadian Standards Association (CSA): Engineering Design in Wood. CSA Standard 086-19. Toronto, ON, Canada, 2019.

[3] Canadian Construction Materials Centre (CCMC). Technical Guide for Evaluation of Seismic Force Resisting Systems and Their Force Modification Factors for Use in the National Building Code of Canada with Concepts Illustrated Using a Cantilevered Wood CLT Shear Wall Example. Ottawa, ON, Canada, 2021.

[4] Applied Technology Council (ATC): Quantification of Building Seismic Performance Factors. Redwood City, California, 2009.

[5] Zhu, M. OpenSeesPy Documentation Release 3.4.0.2, Corvallis, Oregon, 2023. (https://openseespydoc.readthedocs.io/en/latest/)

[6] Python Software Foundation, Python Language Reference, version 3.8.10, 2022.

[7] National Research Council of Canada (NRC): National Building Code of Canada (NBCC). Ottawa, ON, Canada, 2015.

[8] Chen, Z. and Popovski, M. Expanding Wood Use Towards 2025: Seismic Performance Of Braced Mass Timber Frames – Year 2 (Project Number: 301013618: Task: Braced Frames, 2020.

[9] Computers & Structures. Sap2000: Integrated Solution for Structural Analysis and Design; Computers & Structures: Berkeley, CA, USA, 2021.

World Conference on Timber Engineering Oslo 2023

INVESTIGATING THE EFFECTS OF THE INTERACTIONS BETWEEN FLOOR DIAPHRAGMS AND SEGMENTED CROSS-LAMINATED TIMBER SHEAR WALLS

Giuseppe D'Arenzo[1], Werner Seim[2]

ABSTRACT: This paper presents a study on the effects of the interactions between floor diaphragms and segmented cross-laminated timber shear walls. An analytical model of a beam on a bed of elastic springs is used to describe such an interaction for the case of two- and three-panel segmented shear walls. The analytical model is, firstly, validated by comparing its results with those of a numerical model developed in SAP2000 and, secondly, used for the definition of an equivalent spring which simulates the effects of the floor-wall interaction in a simpler yet reliable way. In the study, it is shown that the equivalent spring can be used to take into account the effects of the floor-wall interactions for the cases of two- and three-panel segmented shear walls. The internal actions of the floor element as well as the increase of rocking stiffness due to such interaction are discussed in the final part of the study.

KEYWORDS: Cross-Laminated Timber, Multi-Panel Shear Walls, Floor-Wall Interaction.

1 INTRODUCTION

Cross-laminated timber (CLT) is a structural typology which offers many advantages in terms of sustainability, speed of construction and structural performance. Given their excellent in- and out-of-plane structural properties, CLT panels are used in these structures as both vertical and horizontal load-bearing elements. The assemblage of the CLT panels is realized by means of mechanical joints, which permit the creation of structures with excellent lateral performance.

This assemblage represents a key aspect of the structural behaviour of CLT buildings, which, *inter alia*, entails structural interactions, such as those between perpendicular walls or vertical walls and horizontal floors. These structural interactions are usually not directly considered when the lateral performances of CLT buildings are assessed, as most of the attention is paid to the wall-base connections, namely, hold-downs and angle brackets. However, several experimental campaigns aimed at investigating the lateral behaviour of platform CLT buildings have revealed that these structural interactions modify the lateral response of the structure, leading to higher mechanical performance [1] or, ultimately, unexpected failure mechanisms [2].

This paper deals specifically with the problem of the interaction between floor diaphragms and segmented shear walls (see Figure 1). Among the several effects, the interaction between these structural components contributes to stiffening the lateral response of segmented shear walls and, under some conditions, can even lead to local failures of the floor panels.

In particular, the current paper provides a generalization of the methodology proposed by D'Arenzo et al. [3], in which an analytical model describing the interaction mechanism of two-panel segmented CLT shear walls and

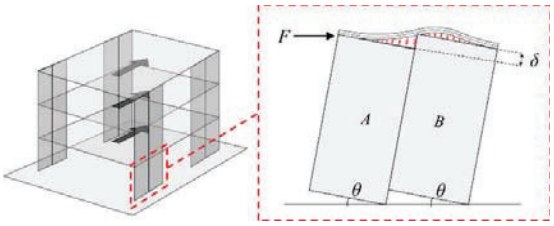

Figure 1: *Representation of the interaction between floor diaphragms and segmented CLT shear walls.*

CLT floors was presented. The analytical model, which is based on the theory of a beam on a bed of elastic springs, will be used in this study to describe the floor-to-wall interaction in the case of three-panel segmented walls. The reliability of the analytical model will be proved by means of numerical simulations and a parametric analysis, in which several wall geoemtries and connection stiffnesses are considered.

2 ANALYTICAL MODEL

The majority of the mechanical models available in the literature used for the prediction of the lateral response of CLT shear walls take into account the properties of the CLT wall segments and the wall base connections, yet do not consider the connections which are on the perimeter of the CLT panels, such as the connections between perpendicular walls or between floor and wall panels (see, for instance, Lukacs et al. [4]). In the model proposed by D'Arenzo et al. [3], the mechanical system is enlarged by considering the additional contribution of the floor elements and the floor-to-wall connections to account for

[1] Timber Structures and Building Rehabilitation, University of Kassel, Germany, giuseppe.darenzo@uni-kassel.de
[2] Timber Structures and Building Rehabilitation, University of Kassel, Germany, wseim@uni-kassel.de

https://doi.org/10.52202/069179-0327

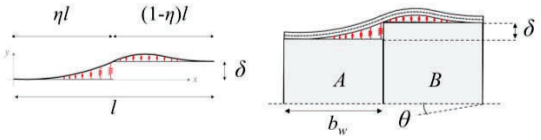

(a) (b)

***Figure 2**: Analytical model of floor-wall interaction.*

the effects of the interaction between segmented CLT shear walls and horizontal floor diaphragms. The effect of this interaction mainly contributes to reducing the slip between the vertical joints of the wall panels and, consequently, results in an increase of the rocking stiffness of the shear wall.

This interaction can be described by means of a mechanical model of a beam on a bed of springs, in which the beam represents the floor element and the springs represent the floor-to-wall connections. Figure 2 depicts the mechanical problem of this interaction, while Eq. (1) represents the differential equation governing the problem.

$$w^{IV}(x) + 4\lambda^4 w(x) = 0 \tag{1}$$

In Eq. (1), $w(x)$ represents the transversal displacement of the beam and λ is an elastic parameter, which takes into account the elastic properties of the system, i.e., the bending stiffness of the beam EI and the stiffness per unit length of the springs k, see Eq. (2).

$$\lambda = \sqrt[4]{\frac{k}{4EI}} \tag{2}$$

The solution to the differential Eq. (1) can be written as piecewise function defined over the two segments of length ηl and $(1-\eta)l$, see Figure 2 and Eq. (3).

$$w(x) = \begin{cases} w_A(x) = w_{g,A}(x); & 0 \le x \le \eta l \\ w_B(x) = w_{g,B}(x) + \delta; & \eta l \le x \le l \end{cases} \tag{3}$$

In Eq. (3), the functions $w_{g,A}(x)$ and $w_{g,B}(x)$ represent exponential functions solution of Eq. (1), which depend on constants to be defined in accordance to the boundary conditions of the system. δ represents the slip between the two wall panels, which triggers the resisting mechanism of the floor-wall interaction.

The boundary conditions of the system depicted in Figure 2 are reported in Table 1 and take into account the rotation, the bending moment, and the shear of the floor-beam, expressed as derivative of the transversal displacement.

It should be noted that the mechanical behaviour of the floor-to-wall connections is different for tensile and compressive forces. While the stiffness of the floor-to-wall connection is engaged in case of tensile forces, a contact mechanism takes place in case of compressive forces. This implies a nonlinearity of the mechanical behaviour of the floor-to-wall connections, which, however, cannot be described with the linear elastic model presented in this study. The solution adopted by D'Arenzo et al. [3] was to consider a linear behaviour of the floor-to-wall connections and to check downstream that the solution found is consistent with the real mechanical behaviour of the system.

***Table 1:** Boundary conditions of the analytical model of floor-wall interaction.*

$x = 0$	$x = \eta l$	$x = l$
$w''_A(0) = 0$	$w'_A(\eta l) = w'_B(\eta l)$	$w''_B(0) = 0$
$w'''_B(0) = 0$	$w''_A(\eta l) = w''_B(\eta l)$	$w'''_B(0) = 0$
	$w'_A(\eta l) = \delta$	
	$w'_B(\eta l) = \delta$	

3 EQUIVALENT SPRING

In D'Arenzo et al. [3], the expression of an equivalent spring to be placed between the vertical joints of two-panel segmented shear walls was presented, to provide a simple strategy to consider the effects of the floor-to-wall interaction (Figure 3). In this study, the equivalent spring will be validated for the case of three-panel segmented shear walls.

The mechanical system consisting of the floor and floor-to-wall connections provides stiffness that reduces the slip between the wall panels. This stiffness can be represented by a vertical equivalent spring in the joint of two wall panels, and can be calculated as the ratio between the shear force in the floor beam, $V(b_w)$, and the slip of the vertical joint of the wall, δ. This equivalent spring reproduces the effect of the floor-wall interaction for the rocking behavior of the segmented shear wall, based on the elastic properties of the floor beam and floor-to-wall connections, and independent of the kinematic behaviour of the segmented shear wall.

The stiffness of the equivalent spring, $k_{f-w,eq}$, can be determined using the polynomial function in Eq. (4), which depends on the bending stiffness of the floor beam, EI, the elastic parameter, λ, and the length of structural system, l (see Figure 2 and Figure 3).

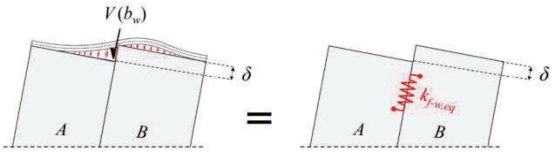

***Figure 3:** Representation of the equivalent spring.*

$$k_{f-w,eq} = \frac{V(b_w)}{\delta} = EI \cdot (p_{00} + p_{10} l + p_{01} \lambda + p_{11}\, l\, \lambda + p_{20} l^2 + p_{02} \lambda^2) \quad (4)$$

Table 2: *Polynomial coefficients for the calculation of the equivalent spring stiffness (Eq. (4)).*

$\lambda\ [m^{-1}]$	p_{00}	p_{10}	p_{01}	p_{11}	p_{20}	p_{02}
$0.5 \leq \lambda \leq 0.7$	0.73100	0.05060	-4.28300	0.21595	-0.01507	5.19500
$0.7 \leq \lambda \leq 1.2$	2.84650	0.12635	-10.2850	0.32880	-0.03467	8.91500
$1.2 \leq \lambda \leq 2.0$	8.02500	1.41600	-22.6350	0.06530	-0.14895	14.3100

The polynomial coefficients, p_{ij}, are listed in Table 2 for three different ranges of the elastic parameter, λ. Eq. (4) and the coefficients in Table 2 can be used to calculate the stiffness of the equivalent spring, $k_{f-w,eq}$, in $[kN/m]$ by using the bending stiffness, EI, in $[kNm^2]$, the system length, l, in $[m]$ and the elastic parameter, λ, in $[m^{-1}]$.

4 METHODOLOGY

To predict the floor-wall interaction for three-panel shear wall sytems, the analytical model is used to describe the shear force of the floor element by considering the three-panel system as the superimposition of two two-panel systems which share the central panel, see Figure 4. In particular, the analytical model is used to predict the shear force of the floor-beam in the region above the two vertical joints of the shear wall, as this represents the shear force value relevant for the definition of the equivalent spring. If the analytical model predict with sufficient accuracy the shear force in the region above the vertical joints of the shear wall, the equivalent spring can then be used for the case of three-panel shear wall systems.
The methodology used in this study involved comparison between the results obtained from the analytical model presented in the previous section and the numerical models presented in the next section. The numerical models were distinguished in deatailed models and simplified models. In the deatailed models, the floor-wall interactions was considered by modelling the floor and the floor-to-wall connections, while in the simplified models, the floor-wall interactions was considered through the equivalent spring.

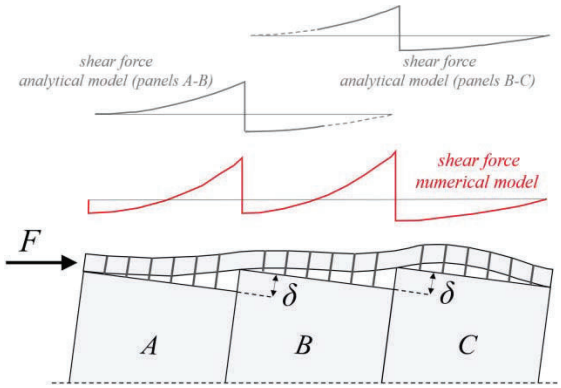

Figure 4: *Representation of the methodology adopted to use the analytical model for three-panel shear walls.*

Two types of analysis were considered: (i) local analysis, at floor level, to evaluate the capability of the analytical model to describe the internal actions of the floor, and (ii) global analysis, at wall level, to evaluate the capability of the equivalent spring to simulate the effect of the floor-wall interaction in three-panel shear wall systems. In the first analysis, the comparison is conducted by directly comparing the shear force functions of the floor, as shown in Figure 4. In the second analysis, the comparison is conducted by comparing the rocking stiffnesses of the shear walls, calculated as the ratio between the lateral force applied on the top of the wall, F, and the rocking displacement, Δ_{rock}, namely the lateral displacmenet on the top of the wall.

5 NUMERICAL MODELS

In this section the numerical models are presented. Three different numerical models were considered: (i) shear walls with floor-wall interactions considered through a detailed modelling of the floor and the floor-to-wall connections (Det-Model), (ii) shear walls with floor-wall interactions considered through the equivalent spring (EqSp-Model), and (iii) shear walls without floor-wall interactions (NoFl-Model). The last numerical model is considered for purpose of comparison, to evaluate the effects of the floor-to-wall interaction on the rocking stiffness of the shear wall. An illustration of the Det-Model for a three-panel shear wall system can be seen in Figure 5.
The same modelling strategy was used to model the wall segments and the base connections of the numerical three models considered. The wall panels were modeled as shell elements with orthotropic elastic material. To simulate the rocking behaviour of the shear walls, the external corner of the shell element under compression was hinged while the internal corner was restrained with a gap element. This allowed for free uplift of the internal corner while preventing displacement in the opposite direction to simulate the wall-to-foundation contact. The sliding mechanism of the shear-wall was disregarded as it has no influence on the rocking behaviour of the shear-wall. The external corner under tension was restrained with a vertical spring that represents the vertical stiffness of the hold down or the weighted vertical stiffness of all wall base connections. 2-joint links with high compression stiffness, no tension stiffness, and linear elastic stiffness in the transversal direction were placed between the two shell elements to prevent wall panel interpenetration and simulate the wall-to-wall connection flexibility in the transversal direction.

https://doi.org/10.52202/069179-0327

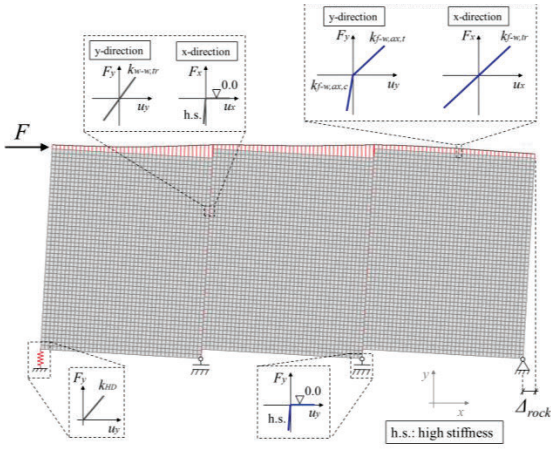

Figure 5: *Numerical model of floor-wall interaction (Det-Model).*

In the Det-Model, the floor was modeled as a linear elastic beam with an orthotropic material. The connections between the floor and the walls were modeled to account for their different behavior under tensile and compressive forces. While for tensile forces the behaviour of the floor-to-wall connection depends on the withdrawal stiffness of the connections, for compressive loads, the floor-to-wall contact takes place. This different behaviour for tensile and compressive forces was modelled with a 2-joint link with multilinear behaviour. For tensile forces the behaviour was assumed with stiffness of the floor-to-wall connection, while for compressive forces an equivalent stiffness that simulates the floor-to-wall contact was considered. Additionally, the horizontal stiffness of the floor-to-wall connection was considered in these links.

In the EqSp-Model, one equivalent spring was placed in the vertical joints between the shell elements representing the wall panels, in addition to the wall-to-wall connections.

A horizontal force was applied to the top of the wall panel, in all numerical models. Nonlinear static analyses were conducted to account for the multilinear behavior of the links simulating hold down, wall-to-wall, and wall-to-floor connections.

6 PARAMETRIC ANALYSIS

The analytical model is validated through a parametric analysis using common geometrical and mechanical parameters used in construction. The analysis considers two symmetric systems, each consisting of two or three wall panels of equal width anchored at both ends with two hold downs and an overlying horizontal floor with evenly spaced floor-to-wall connections, as depicted in Figure 6. For the validation, three wall panel aspect ratios were utilized, each with a height equal to $h = 2.5\ m$ and widths of $b_w = \{1.5 - 2.0 - 2.5\}\ m$. A 5-layer panel with a total thickness of $t_w = 120\ mm$ and individual layer thicknesses of **30**-20-**20**-20-**30** mm (with the thickness of the vertically arranged layers in bold) was considered in the analysis. Three different floor panels typologies with

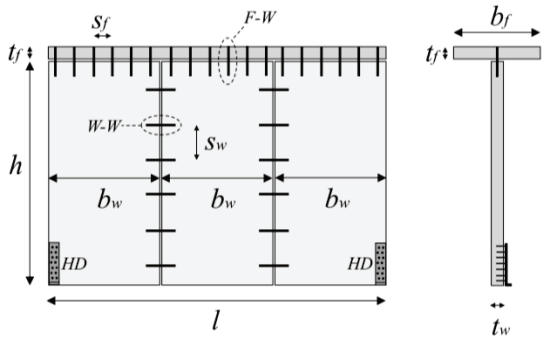

Figure 6: *Reference system used for the parametric analysis.*

total thickness equal to $t_f = \{140 - 180 - 220\}\ mm$ and layer thicknesses as shown in Table 3 were analysed. The floor width was not chosen a priori as it depends on the effective section that contributes to internal bending actions, as per composite section beam theory. The effective width was calculated using the methodology developed by Masoudnia et al. [21], which demonstrates that the effective width is dependent on the wooden layer structure of the CLT panel. The values obtained for the three floor-panels were $b_f = \{1006 - 479 - 636\}\ mm$.

Table 3: *Thickness (in mm) of the floor panels used in the parametric analysis.*

ID	t_f	t_1	t_2	t_3	t_4	t_5	t_6	t_7
1	140	**30**	25	**30**	25	**30**	-	-
2	180	**30**	**30**	20	**20**	20	**30**	**30**
3	220	**30**	**30**	35	**30**	35	**30**	**30**

The floor-to-wall connection spacing and withdrawal stiffness were selected to provide a broad range of stiffness per unit length k in the analytical model. The withdrawal stiffness of the screws was set at $k_{with} = 4kN/mm$, as reported in the experimental study of Gavric et al. [5]. This value is representative of floor-to-wall connections with partially threaded screws 10×260 mm. The screw spacing in the floor-to-wall connection was set at $s_f = \{900 - 300 - 100\}\ mm$. The shear stiffness of the floor-to-wall connections was set at $k_{sh} = 4kN/mm$, based on the experimental results from Gavric et al. [5]. The hold down stiffness was chosen as $k_{HD} = 10\ kN/mm$, as reported by Hummel et al. [6]. The CLT panels of both floor and walls were assumed to be made of wooden boards with an elastic modulus in the longitudinal direction of $E_0 = 11.6\ GPa$.

6.1 MECHANICAL PROPERTIES OF THE ANALYTICAL MODEL

The stiffness per unit length k of the analytical model was determined using Eq. (5), based on the withdrawal stiffness and the spacing of the floor-to-wall connections. The values presented in the previous section were utilized to calculate the stiffnesses per unit length as $k = \{4.4 - 13.3 - 40.0\}\ N/mm^2$.

https://doi.org/10.52202/069179-0327

$$k = \frac{k_{with}}{s_f} \tag{5}$$

The bending stiffness of the floor-beam was calculated based on the layered structure of the floor panel, as described by Blaß and Fellmoser [7], excluding the effect of the wooden boards in the transverse direction. Using the geometrical and elastic properties of the floor outlined in the previous section, the following bending stiffnesses were adopted for the floor beam in the analytical model: $EI = \{2197.7 - 2606.5 - 5947.6\}\, kNm^2$.

6.2 MECHANICAL PROPERTIES OF THE NUMERICAL MODEL

The wall panels were modeled as shell elements and their elastic properties were assigned based on the layered structure of CLT panels. Equivalent longitudinal and transversal elastic moduli of $E_{eq,l} = 7.7\ GPa$ and $E_{eq,t} = 3.9\ GPa$ were assigned to the orthotropic shell elements, based on the methodology proposed by Blaß and Fellmoser [7]. Equivalent shear modulus of $G_{eq} = 0.5\ GPa$ was assigned using the methodology proposed by Brandner et al. [8]. The floor-to-wall connections were modeled as links with spacing $a_f = 50mm$. The tensile stiffness of these links was calculated using Eq. (6), based on the stiffness per unit length of the analytical model and the spacing of the links in the numerical model.

$$k_{f-w,ax,t} = k \cdot a_f \tag{6}$$

The axial stiffnesses of the links simulating the floor-to-wall connections were determined using the values in the previous section, resulting in $k_{f-w,ax,t} = \{0.22 - 0.67 - 2.00\}\, kN/mm$.

The compressive stiffness of the links simulating the floor-to-wall connections, $k_{f-w,ax,c}$, was calculated using Eq. (7) as described by Schickhofer and Ringhofer [9] and Blaß and Görlacher [10].

$$k_{f-w,ax,c} = \frac{E_{90} \cdot A_{ef}}{t_f} = \frac{E_{90} \cdot l_{ef} \cdot a_f}{t_f} \tag{7}$$

The equation considers the effective area under compression in the floor element, A_{ef}, and the elastic modulus perpendicular to the grain of the floor, E_{90}. The effective area was determined by multiplying an effective length, l_{ef}, by the spacing of the link elements, a_f. The effective length was calculated based on a stress distribution line with an inclination of 1:3, according to Eurocode 5 [11] specifications. The resulting compression stiffnesses for the links simulating the floor-to-wall contact were $k_{f-w,ax,c} = \{45.7 - 40.0 - 36.4\}\, kN/mm$.

The transversal stiffness of the floor-to-wall connections was computed using Eq. (8), which considers the different spacings of the numerical model, a_f, and the reference system, s_f.

$$k_{f-w,tr} = \frac{a_f}{s_f} \cdot k_{sh} \tag{8}$$

Based on the values presented in previous sections, the following transversal stiffnesses were utilized for the floor-to-wall connections: $k_{f-w,tr} = \{0.22 - 0.67 - 2.00\}\, kN/mm$. The high stiffness of the wall-to-wall connections and gap element was set to $10^6 kN/mm$.

7 RESULTS AND DISCUSSION

7.1 ANALYSIS AT FLOOR LEVEL

The validation of the analytical model is carried out by comparing the displacement, the bending moment, and the shear force of the floor-beam obtained from analytical and numerical models. Figure 7 shows this comparison for the case of systems with two-panel shear walls with width $b_w = 2.0\ m$, floor bending stiffness $EI = 2606.6\ kNm^2$, and floor-to-wall connection stiffness per unit length $k = 13.3\ N/mm^2$. It can be observed that the analytical and numerical model results converge starting from a point of conjunction, located in the first half of the floor length.

For the case of three-panel shear walls, the analytical model is used to describe the shear force of the floor element. This is done by considering the three-panel system as the composition of two two-panel systems, as discussed in section 4. Figure 8 shows the comparison between the shear force obtained from the analytical and numerical model for the case of three-panel shear walls with width $b_w = \{1.5 - 2.0 - 2.5\}\, m$, floor bending

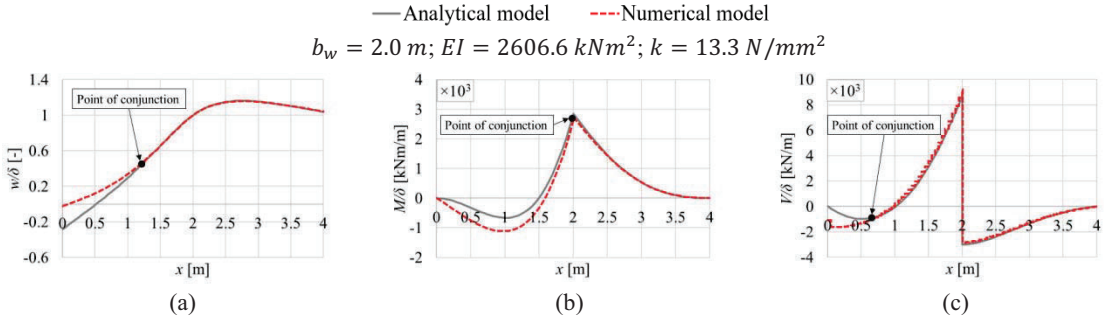

Figure 7: *Displacement, bending moment, and shear force function of the floor element for the two-panel shear walls.*

https://doi.org/10.52202/069179-0327

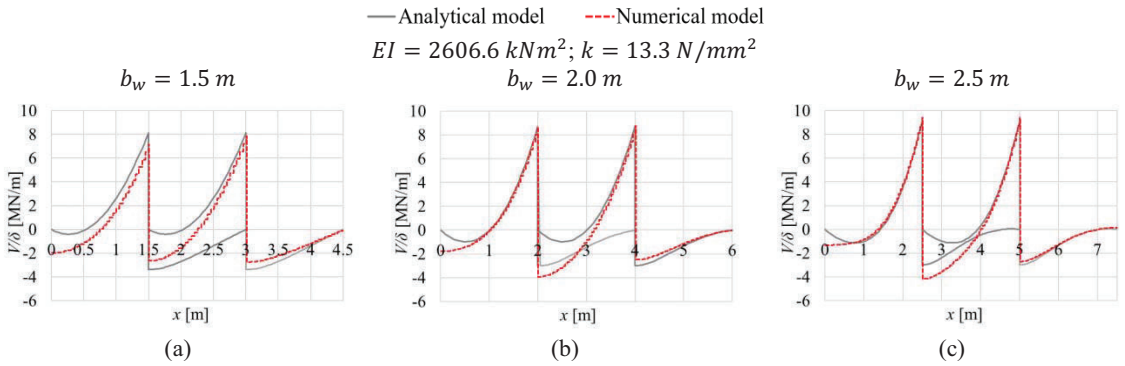

Figure 8: *Shear force function of the floor element for the three-panel shear walls.*

stiffness $EI = 2606.6\ kNm^2$, and floor-to-wall connection stiffenss per unit of length $k = 13.3\ N/mm^2$. It can be observed that the trend of the shear force for the three-panel system is similar to that of the two-panel system. In particular, the analytical and numerical models show a good agreement in the region above the vertical joints of the shear walls, with identical values for the cases with $b_w = 2.0\ m$ and $b_w = 2.5\ m$, and reasonably close values for the cases with $b_w = 1.5\ m$. This allows the equivalent spring defined for two-panel shear walls to be used for three-panel shear walls as well.

7.2 ANALYSIS AT WALL LEVEL

In this section the effect of the floor-wall interaction is evaluated at wall level. The results of the three numerical models described in section 5 are compared, (i) to evaluate the impact of the the floor-wall interaction on the lateral behavior of the shear wall, and (ii) to validate the equivalent spring in case of three-panel shear wall systems. In particular, the rocking stiffness of the models that consideres the floor-wall interaction (Det-Model and EqSp-Model) are compared with the rocking stiffness of the models without floor-wall interaction (NoFl-Model). Figure 9 shows the comparison of the dimensioneless rocking stiffness of the systems with width $b_w = \{1.5 - 2.0 - 2.5\}\ m$, floor-to-wall connection stiffenss per unit length $k = \{4.4 - 13.3 - 40.0\}\ N/mm^2$, and floor bending stiffness $EI = 2606.6\ kNm^2$. The dimensionless rocking stiffness, $\tilde{K}_{rock}$, was calculated as the ratio between the rocking stiffness of the models that consideres the floor-wall interaction and the rocking stiffness of the model without floor-wall interaction.

In general, the graphs show that the floor-wall interaction increases the rocking stiffness of the shear walls. The increase of rocking stiffness is primarily governed by the withdrawal stiffness of the floor-to-wall connections. For instance, for the systems with panel width $b_w = 2.0\ m$, the increase of rocking stiffness associated to the stiffness per unit length $k = \{4.4 - 13.3 - 40.0\}\ N/mm^2$ are equal to 24.8 %, 48.5 %, and 84.9 %, respectively. The panel width also affects the increase of rocking stiffness; for a floor-to-wall connection stiffness of $k = 13.3\ N/mm^2$, the increase of rocking stiffness associated to the panel widths $b_w = \{1.5 - 2.0 - 2.5\}\ m$ is equal to 43.8 %, 48.5 %, and 50.8 %, respectively.

The graph also reports the kinematic behaviour associated to each system. It is possible to see that if the effect of the floor-wall connection is neglected, the shear walls deform with a couple panel (CP) kinamtic behaviour, namely with

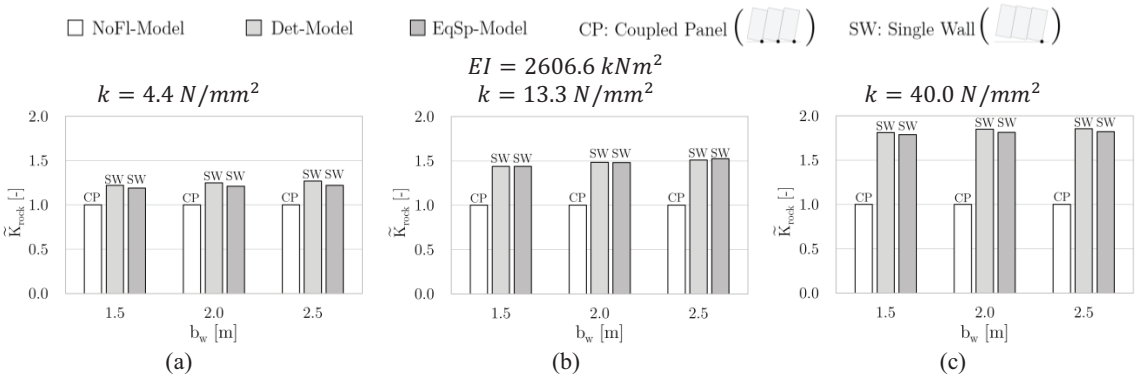

Figure 9: *Dimensionless rocking stiffness of the three-panel shear walls with and without floor-wall interaction.*

each wall panel being in contact with the foundation and the shear wall having multiple centre of rotations. On the other hand, when the floor-wall interaction is considered the kinamtic behaviour switchs to Single Wall (SW), meaning with only one panel in contact with the foundation and with the whole shear wall pivoting about one point. This is due to the fact that the floor-interaction fictitiously increases the overall stiffness of the wall panel vertical joints.

From Figure 9, it is also possible to observe the accuracy of the models with the equivalent springs (EqSp-Model). In fact, the values of rocking stiffness of these models are very close to those obtained from the models with detailed modelling of the floor-wall interaction. The largest discrepancy between these models is 3.8 % and is found in the case of system with $b_w = 2.5\ m$ and $k = 4.4\ N/mm^2$.

The results showed in Figure 9 reveal that the floor-wall interaction increases the rocking stiffness of segmented shear walls and may lead in some cases to modification of the kinematic behaviour, from coupled panel to single wall. This is particualry important to be considered in contexts of seismic design, when highly dissipative behaviours are expected from the vertical joints of segmented shear walls.

8 CONCLUSIONS

This paper presents a study on the effect of the floor-wall interaction on the rocking behaviour of multi-panel CLT shear walls. Previous research on two-panel wall systems conducted by D'Arenzo et al. [3] showed that the floor-wall interaction generates internal actions in the floor element and reduces the slip in the vertical joints of the wall panels. The internal actions can be described with an analytical model of beam on elastic springs, while the reduction of slip in the vertical joints of the wall panels can be simulated by means of an equivalent spring. In this study, the analytical model and the equivalent spring presented by D'Arenzo et al. [3] were used to describe the effects of the floor-wall interaction in the case of three-panel wall systems.

The results of this study showed that the analytical model can be used to describe the shear force of floor elements connected to three-panel shear wall systems. The comparison of the shear force obtained from the analytical and numerical models for three-panel systems showed a good agreement in the region above the vertical joints of the shear walls, with identical values for the cases with 2.0 m and 2.5 m panel width and reasonably close values for the case with 1.5 m panel width. This allowed the equivalent spring defined for two-panel systems to be used for three-panel systems.

At wall level, the results showed that the floor-wall interaction increases the rocking stiffness of the wall. It was found that the increases of rocking stiffness is primarily governed by the stiffness of the floor-to-wall connections and affected by the wall panel width. The increase of rocking stiffness was observed for all the systems, with the highest increase observed for the systems with the highest floor-to-wall connection stiffness and largest wall panels width.

These results demonstrate the significance of considering the interaction between floor diaphragms and segmented shear walls when evaluating the lateral response of multi-panel CLT shear walls. Nonetheless, further research is required to extend the findings of this study to the case of multi-panel systems with more than three panels both for linear elastic and nonlinear analyses.

The study provides valuable insights into the interaction between floor diaphragms and segmented shear walls in CLT buildings, demonstrating that these interactions can significantly modify the lateral response of CLT structures. The analytical model developed in this study provides a useful tool to account for the floor-to-wall interaction in the analysis of CLT buildings.

ACKNOWLEDGMENTS

Authors would like to thank Matthias Schwind from Univervisty of Kassel, for the support given in the numerical simulations.

REFERENCES

[1] Popovski M, Gavric I. Performance of a 2-Story CLT House Subjected to Lateral Loads. J Struct Eng 2016;142:1–12. https://doi.org/10.1061/(ASCE)ST.1943-541X.0001315.

[2] Yasumura M, Kobayashi K, Okabe M, Miyake T, Matsumoto K. Full-Scale Tests and Numerical Analysis of Low-Rise CLT Structures under Lateral Loading. J Struct Eng (United States) 2016;142:1–12. https://doi.org/10.1061/(ASCE)ST.1943-541X.0001348.

[3] D'Arenzo G, Schwendner S, Seim W. The effect of the floor-to-wall interaction on the rocking stiffness of segmented CLT shear-walls. Eng Struct 2021;249:113219. https://doi.org/10.1016/j.engstruct.2021.113219.

[4] Lukacs I, Björnfot A, Tomasi R. Strength and stiffness of cross-laminated timber (CLT) shear walls: State-of-the-art of analytical approaches. Eng Struct 2019;178:136–47. https://doi.org/10.1016/j.engstruct.2018.05.126.

[5] Gavric I, Fragiacomo M, Ceccotti A. Cyclic behavior of typical screwed connections for cross-laminated (CLT) structures. Eur J Wood Wood Prod 2015:179–91. https://doi.org/10.1007/s00107-014-0877-6.

[6] Hummel J, Seim W. Displacement-based design approach to evaluate the behaviour factor for multi-storey CLT buildings. Eng Struct 2019;201:109711. https://doi.org/10.1016/j.engstruct.2019.109711.

[7] Blaß HJ, Fellmoser P. Design of solid wood panels with cross layers. World Conf. Timber Eng., Lathi, Finland: 2004.

[8] Brandner R, Dietsch P, Dröscher J, Schulte-Wrede M, Kreuzinger H, Sieder M. Cross laminated timber (CLT) diaphragms under shear:

https://doi.org/10.52202/069179-0327

Test configuration, properties and design. Constr Build Mater 2017;147:312–27. https://doi.org/10.1016/j.conbuildmat.2017.04.153.
[9] Schickhofer G, Ringhofer A. The seismic behaviour of buildings erected in Solid Timber Construction. Graz: 2012.
[10] Blaß HJ, Görlacher R. Compression perpendicular to the grain. World Conf. Timber Eng., Lathi, Finland: 2004, p. 435–40.
[11] EN1995-1-1. Eurocode 5: Design of timber structures – Part 1–1: General – Common rules and rules for buildings. European Standard, European Committee for Standardization 2008.

World Conference on Timber Engineering Oslo 2023

EXPERIMENTAL CHARACTERIZATION OF STIFF ALUMINIUM CONNECTORS FOR MULTI-PANEL CLT SHEAR-WALLS

Pietro Rigo[1], Andrea Polastri[2], Daniele Casagrande[3], Ernesto Callegari[4], Alvise Ramazzini[5], Luca Sestigiani[6]

ABSTRACT: Cross-Laminated Timber (CLT) shear-walls composed of multiple panels are nowadays a viable alternative to single-panel CLT walls in mid-rise construction sector. Prefabrication process, transport and erection limits are some of the reasons why short panels, vertically-jointed by means of mechanical fasteners, are preferred to CLT single-panel walls. When a significant amount of energy dissipation in the vertical joint is not required (i.e. low seismic prone areas), stiff vertical joints are preferred: the wall behaves mostly like a single-panel wall and vertical joints are designed to minimize the relative displacement between the panels. This paper presents an experimental campaign on aluminium stiff shear-key connector, as an alternative to traditional screwed connections for stiff vertical joints in multi-panels CLT walls. Monotonic tests were performed on shear-key connectors and full-scale tests on multi-panel CLT shear-walls were carried out. A numerical model was developed in order to extend the experimental results on full-scale tests by means of a sensitivity analysis.

KEYWORDS: Cross-laminated timber, Multi-panel, shear walls, Shear-key connectors, Hold-down, Vertical joints.

1 INTRODUCTION

Cross-Laminated Timber (CLT) shear-walls composed of multiple panels are nowadays a viable option for mid-rise buildings. Prefabrication process, transport and erection limits are some of the reasons for which short panels, vertically-jointed by means of mechanical fasteners, are preferred to CLT single-panel walls. The lateral load resistance of multi-panel walls is mainly provided by mechanical connections while CLT panels behave mostly like rigid elements. Either nailed or screwed connections are commonly adopted for connecting the panels.

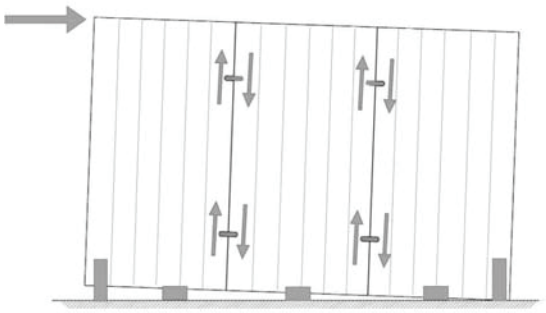

Figure 1: *Multi-panel shear wall with stiff connectors*

As derived by Casagrande et al. and Masroor et al. [1,20], the relative stiffness and strength capacity of vertical joints and hold-downs have a significant influence on the behaviour of multi-panel CLT shear-walls. When a significant amount of energy dissipation is not required (i.e. low seismic prone areas), relatively stiff vertical joints are preferred: the wall behaves mostly as single-panel wall, see Figure 1, and vertical joints are designed to minimize the relative displacement between the panels so that the stiffness and strength capacity of the wall is approximately equal to that of a single panel wall.

1.1 LITERATURE REVIEW

Several studies have been conducted in order to characterize the mechanical behaviour of CLT panel-to-panel joints. Monotonic and cyclic tests were carried out by Gavric et al. [2] on screwed half-lap and spline joints, showing high ductility and energy dissipation. Hossain et al. [3] performed monotonic tests on spline, half-lap and butt joints where fully- and partially-threated screws with different inclinations were adopted.

Loss et al. [4] presented an experimental campaign on butt joints with crossed self-tapping screws inserted in CLT panels with different inclinations. Half-lap and spline joints connected with partially- and fully-threated self-tapping screws were tested by Sullivan et al. [5], comparing the experimental results with the analytical preditcion in terms of strength and stiffness.

More recently, innovative steel devices have been presented as an alternative to traditional screwed connec-

1 P.Rigo, Institute for Bioeconomy-National Research Council of Italy (CNR-IBE), Italy, pietro.rigo@ibe.cnr.it
2 A. Polastri, Institute for Bioeconomy-National Research Council of Italy (CNR-IBE), Italy, andrea.polastri@ibe.cnr.it
3 D. Casagrande, Institute for Bioeconomy-National Research Council of Italy (CNR-IBE), Italy, daniele.casagrande@ibe.cnr.it
4 E. Callegari, Rotho Blaas, Italy, ernesto.callegari@rothoblaas.com
5 A. Ramazzini, Rotho Blaas, Italy, alvise.ramazzini@rothoblaas.com
6 L. Sestigiani, Rotho Blaas, Italy, luca.sestigiani@rothoblaas.com

https://doi.org/10.52202/069179-0328

tions. Schmidt and Blaas [6] developed a highly dissipative connection made with thin steel plate inserted perpendicularly to the vertical joint. Marchi et al. [7] performed cyclic tests on an innovative X steel bracket, showing high ductility, negligible strength degradation and a limited pinching behaviour.

A significant number of full-scale testes on multi-panel CLT shear-walls with vertical joints assembled with dowel-type fasteners has been conducted. Two-panel CLT shear-walls with half-lap and spline screwed vertical joints were tested by Gravic et al [8], showing an almost rigid behaviour of the CLT panels and a significant energy dissipation in the vertical joints. The cyclic behaviour of single- and multi-panel CLT shear-wall was also investigated by Popovski and Karacabeyli [9].

Conversely, a limited number of tests has been performed with the aim to characterise the behaviour of multi-panel shear walls with stiff vertical joints. This type of shear-walls, regardless the smaller energy dissipation capacity than shear-walls with flexible vertical joints, may be a viable alternative in low seismic prone areas.

1.2 OBJECTIVE

This paper presents an experimental campaign on a innovative stiff aluminium shear-key connector developed with the aim of providing an alternative to nailed or screwed connections for stiff vertical joints in multi-panel CLT walls. The connector is named "SLOT" and is produced by Rotho Blaas company [10]. SLOT connector is made with aluminium EN AW-6005A T6 (yield tensile strength equal to R_y = 225 N/mm^2 and ultimate tensile strength equal to R_u=270 N/mm^2). The length, the width and the thickness of the SLOT connector are equal to l_{SL} = 120 mm, b_{SL} = 89 mm and t_{SL} = 40 mm, respectively, see Figure 2.

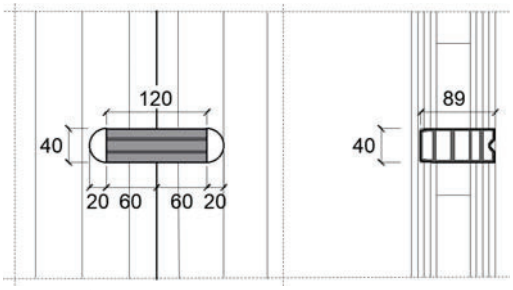

Figure 2: *Aluminium SLOT connector*

Monotonic shear tests were performed both at connector and shear wall level. Numerical finite element models were implemented to predict the mechanical behaviour of tested shear-walls.

2 MONOTONIC TESTS ON STIFF SHEAR-KEY CONNECTORS

2.1 MATERIALS AND METHODS

Monotonic shear tests were performed on CLT panel-to panel joints assembled with SLOT connectors.

Two grooves of dimensions equal to 90x60x40 mm were cut in the panels in order to insert each SLOT perpendicular to the vertical joint line and aligned to the outer face of CLT panels.

Different specimen configurations using different types of CLT panels were assembled for a total of 10 tests. The total thickness and the layout the of CLT panels are reported in Table 1. Tests on spline joints were also performed and the results were compared with those obtained in tests with SLOT connectors. The spline joints were made by connecting the CLT panels to a 27x150 mm LVL beech board by means of 6x70 mm screws, see Figure 3. For spline joints two different values of spacing (50, 100 mm) were tested, yielding a total of 4 tests (Table 1).

The mean value of the moisture content of the CLT panels was equal to 10.1% while the 5th percentile and the mean value of density of the CLT panels were equal to 402 kg/m^3 and 454 kg/m^3, respectively.

Table 1: *Test layout on SLOT connectors and screwed vertical joint*

Test on joints with SLOT connectors			
ID	Test	CLT thickness	CLT layout
SL01	I II III	90 mm	3s (24-42-24)
SL02	I II	100 mm	3s (33-34-33)
SL03	I	100 mm	3s (29-42-29)
SL04	I II III	100 mm	5s (20-20-20-20-20)
SL05	I	145 mm	5s (20+20-20-20-20-45)*
*Slot connector aligned to the outer layer with thickness equal to 20 mm			
Test on joints with screwed connections			
ID	Test	Screw spacing	CLT thickness	CLT layout
SP01	I II	50 mm	100 mm	3s (30-40-40)
SP02	I II	100 mm	100 mm	3s (30-40-40)

The inner panel of each specimen was vertically loaded, while the two outer panels were laterally restrained. The load was applied with a constant load rate equal to 0.1 mm/s and according to EN 26891 [11] the failure occurred within 300 seconds. The relative slip between the inner and the outer panels was measured by means of four LVDTs and the load applied was measured by a 250 kN load cell.

The results in terms of maximum shear load F_{max} and stiffness K_s are reported in Table 2 and 3.

For each specimen the slip value was determined as the average from four LVDTs. The shear load F acting on each single connector was obtained from the ratio between the total shear load measured by the load cell and

the number of connectors. The value of stiffness and shear load for spline joints is reported per couple of screws.

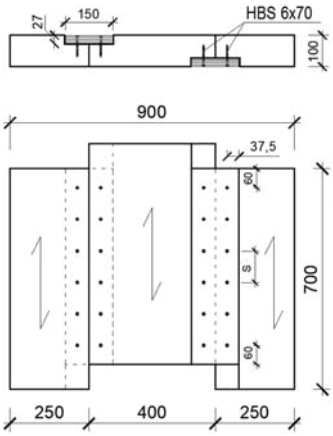

Figure 3: *Monotonic shear tests on spline joint*

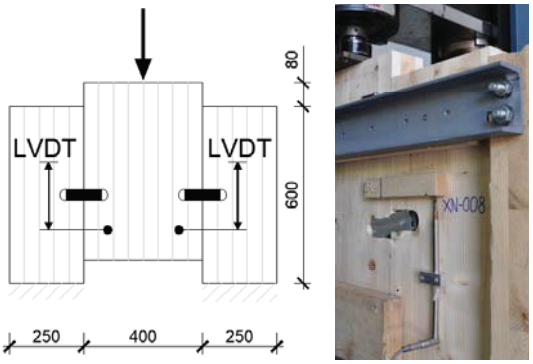

Figure 4: *Monotonic shear tests on aluminium CLT-to-CLT shear-key connector*

2.2 RESULTS AND DISCUSSION

Tests conducted on specimens with SLOTs showed a rigid body rotation of the connectors with no residual plastic deformation. A failure mode characterised by the localized crushing of the wood was observed. In spline joint tests, a plastic deformation of the screws and a local embedment crushing of the wood around the fasteners were detected.

The load-slip curves for test SL01-II and SP01-II are reported in Figure 5. The gap between the SLOT connector and the CLT panels caused an initial slip (0.3 and 0.5 mm) after which an elastic-almost perfectly plastic behaviour is observed. The initial slip was not observed in the tests on screwed joints where, conversely, a significant rope effect after the yielding of the fasters was detected.

The effective number of screws equal to a single SLOT connector in terms of strength and stiffness $n_{eff,Fmax}$ and $n_{eff,Ks}$ have been defined with the aim to compare the performance of joints with SLOT connectors to those with screwed joints. Using the average values of strength and stiffness determined from Table 3 and assuming an effective width $b_{eff,SL}$ of the SLOT connectors equal to 53 mm (see Figure 2, section), the effective number of screws $n_{eff,Fmax}$ and $n_{eff,Ks}$ are equal to 12.6 and 13.0 respectively.

Table 2: *Test results on SLOT connectors*

ID	Test	F_{max} [kN]	K_s [kN/mm]
SL01	I	60.35	13.99
	II	62.30	12.69
	III	58.74	14.75
SL02	I	53.83	14.91
	II	63.24	17.89
SL03	I	60.92	15.43
SL04	I	62.56	13.09
	II	74.88	15.56
	II	71.11	15.34
SL05	I	68.12	13.30

Table 3: *Test results on spline joints*

ID	Test	F_{max} [kN]	K_s [kN/mm]
SP01	I	5.37	0.88
	II	4.75	1.57
SP02	I	5.10	0.92
	II	4.90	1.17

The load and stiffness values are reported per couple of screws

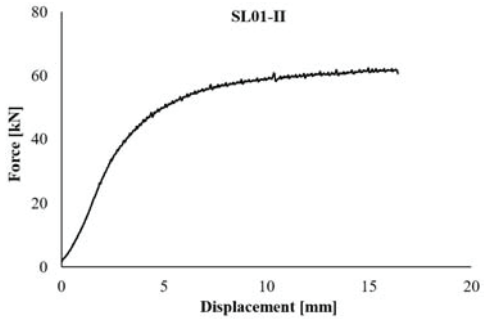

(a)

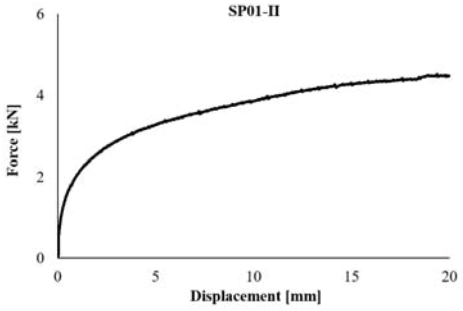

(b)

Figure 5: *Load-vs-displacement curves for test on (a) SLOT connectors (b) spline joints*

https://doi.org/10.52202/069179-0328

3 FULL-SCALE TESTS ON MULTI-PANEL CLT SHEAR-WALLS

3.1 TEST-LAYOUT AND SET-UP

Two monotonic full-scale tests were carried out to investigate the mechanical behaviour of 3-panel 100 mm thick CLT [13] shear-walls with SLOT connectors, see Figure 6a and 6b. Either two or four connectors along each vertical joint were used. An additional multi-panel shear-wall with spline vertical joints was tested, see Figure 6c. As in shear tests on panel-to-panel joints, 6x70mm screws were used with a spacing of 50 mm.

Two typologies of hold-down (WHT 340 and WHT620) were used to limit the rocking of shear-walls, whereas the sliding of each panel was prevented by the contact of the panels bottom edges with properly designed steel devices. The same displacement was applied on the top of each panel according to the analytical model developed by Casagrande et al. (2018) [1]; no vertical load was applied. In accordance with EN 594 [14], displacement-controlled monotonic tests with load rate equal to 0.2 mm/s were adopted.

3.2 ANALYSIS METHOD

Two transducers (LVDTs) were used in order to measure the top lateral displacement of shear-walls, while another LVDT was used to measure the panel sliding.

The difference between the total lateral displacement and the sliding represents the lateral displacement Δ due to the rocking behaviour and the panel deformation.

Trilinear curves were drawn in order to approximate the experimental load-displacement curves. These curves were obtained by connecting the yield point Y, the maximum point M and the ultimate point U determined according to the procedure reported in EN 12512 [15]. The ratio between the yielding load F_Y and the yielding displacement Δ_Y represent the elastic stiffness K, while the ratio between the yielding displacement Δ_Y and the ultimate displacement Δ_U represent the ductility of the shear-wall μ.

Table 4: *Shear-wall test layout*

Test	N. of panels	Type of connector in vertical joint	N. of connector	Hold-down
Wall-I	3	SLOT connector	2	WHT 340
Wall-II	3	SLOT connector	4	WHT 620
Wall-III	3	Spline joint – 6x70 mm screws	44 / spacing 50 mm	WHT 340

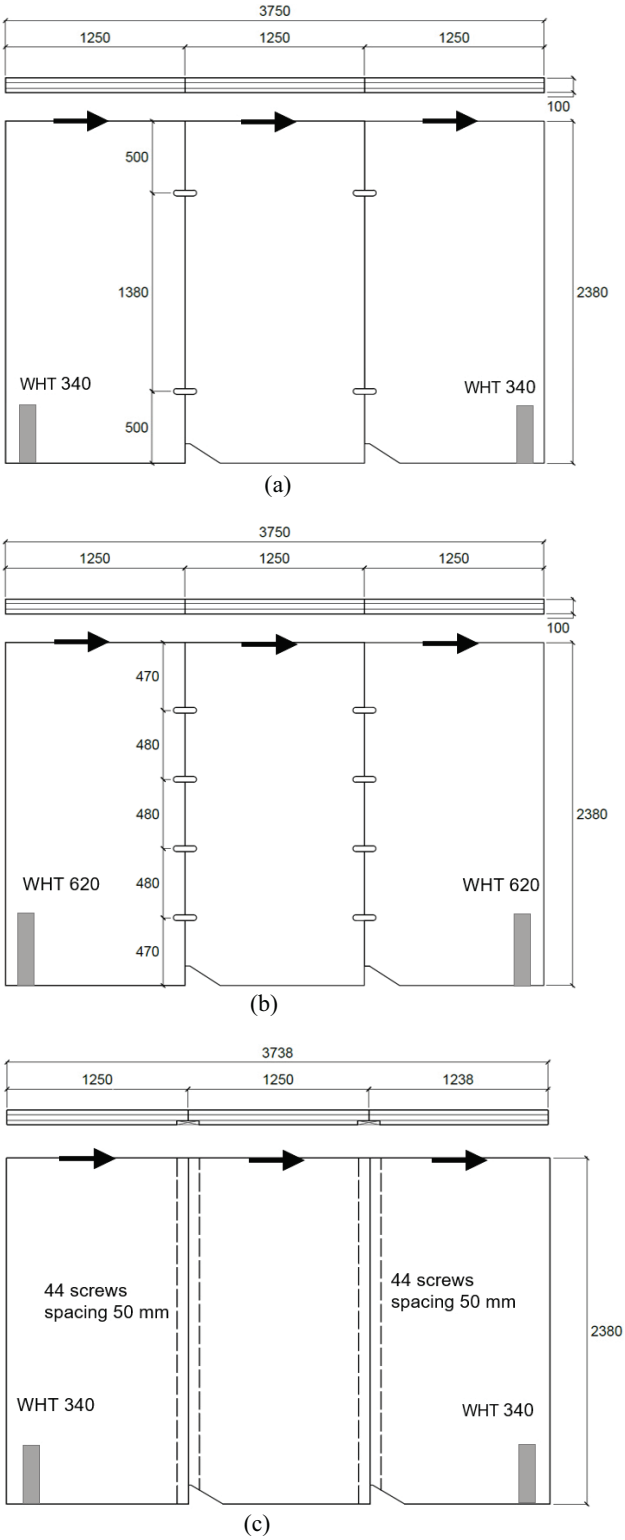

Figure 6: *Shear-wall test specimens (a) Wall-I, (b) Wall-II, (c) Wall-III*

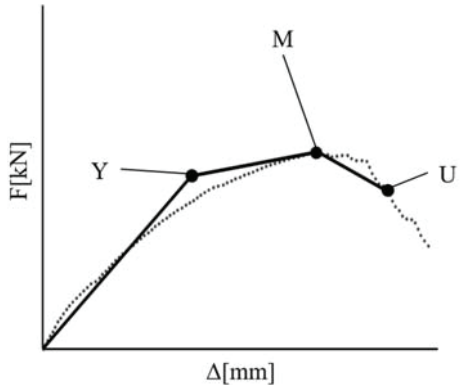

Figure 7: *Load F vs displacement Δ curves, trilinear approximation.*

3.3 RESULTS AND DISCUSSION

All the tested walls showed a kinematic mode characterised by a single global centre of rotation (see Figure 8), as also confirmed by a value of uplift of the hold-down greater than the panel-to-panel slip, see Table 5.

Table 5: *Uplift of hold-down and relative panel-to-panel slip corresponding to the maximum lateral load*

Test	Maximum load	Uplift hold-down	Slip panel 1-panel 2	Slip panel 2-panel 3
	F_M [kN]	v_{H-D} [mm]	$\delta_{1.2}$ [mm]	$\delta_{2.3}$ [mm]
Wall-I	115	19.5	2.0	2.0
Wall-II	167	16.0	1.1	1.2
Wall-III	120	20.8	2.4	3.5

The failure of the hold-down was achieved in all three tests: ductile failure with plastic deformation of nails was observed for WHT340 in Wall-I, while in Wall-III a brittle failure of the steel plate was observed. A brittle failure of the steel plate occurred also in the test on Wall-II, where WHT620 was used. Either SLOT connectors and screwed joints exhibited an almost elastic behaviour with no residual deformations. The force and displacement values related to the yield point Y, the maximum point M and the ultimate point U are reported in Table 6, whereas the experimental load-vs-displacement curve and the corresponding trilinear curve are reported in Figure 7.

Table 6: *Mechanical parameters obtained from tri-linear curves of shear-wall tests*

Test	F_Y	Δ_Y	F_M	Δ_M	F_U	Δ_U	K	μ
	[kN]	[mm]	[kN]	[mm]	[kN]	[mm]	[kN/mm]	[-]
Wall-I	101	9.4	115	17.4	92	21.8	10.7	2.3
Wall-II	141	5.9	167	13.5	167	13.5	23.8	2.3
Wall-III	86	5.0	120	19.5	116	20.2	17.3	4.1

As shown in Figure 9, the load-vs-displacement curves of the test on Wall-I and that on Wall-III are comparable. The maximum shear load reached in both tests is very similar, but due to the physical gap between the SLOT connector and the CLT panels, the stiffness of Wall-I is lower than that of Wall-III.

Figure 8: *Centre of rotation in a monotonic full-scale test on 3-panel CLT shear-wall with SLOT connector*

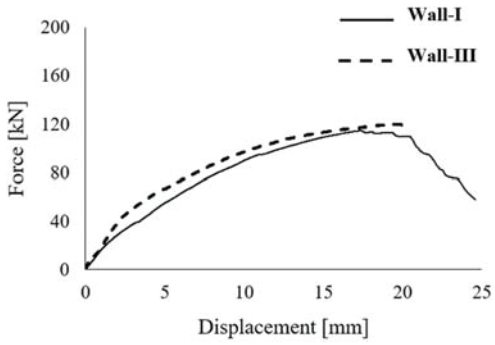

Figure 9: *Load-vs-displacement curves obtained from Wall-I and Wall-II*

4 FINITE ELEMENT NUMERICAL ANALYSES ON SHEAR-WALLS

Finite Element (FE) numerical models were implemented with the commercial software SAP2000 [16] to predict the mechanical behaviour of the three tested shear-walls, see Figure 10. Orthotropic homogenous elastic 100 mm thick shell elements were adopted for the modelling of CLT panels. Effective modulus of elasticity $E_{eff.v}$ and $E_{eff.h}$ were defined along the vertical and horizontal direction. Respectively, according to the composite theory presented by Blass and Fellmoser [17] and adapted to CLT panels as expressed by Equations 2 and 3:

$$E_{eff.v} = \frac{E_0 \cdot \sum t_{v.i}}{t} = 7200MPa \quad (2)$$

$$E_{eff.h} = \frac{E_0 \cdot \sum t_{h.j}}{t} = 4800MPa \quad (3)$$

where E_0 is the modulus of elasticity of wooden boards equal to 12000 MPa, t is the total thickness of the panel equal to 100 mm, $\sum t_{v.i}$ and $\sum t_{h.j}$ are the total thickness of the vertical and horizontal layers equal to 60 mm and 40 mm, respectively.

An effective in-plane shear modulus G_{eff} equal to 479 MPa was assigned to shell elements according to the expressions proposed by Brandner et al. [18] to take into account the effective shear and torsional deformation of wooden boards. Rigid gap elements were adopted to model the contact of CLT panels with the ground. The shear-key connectors or the screwed connections along the vertical joints were modelled by 2-joint uni-axial multi-linear link elements.

https://doi.org/10.52202/069179-0328

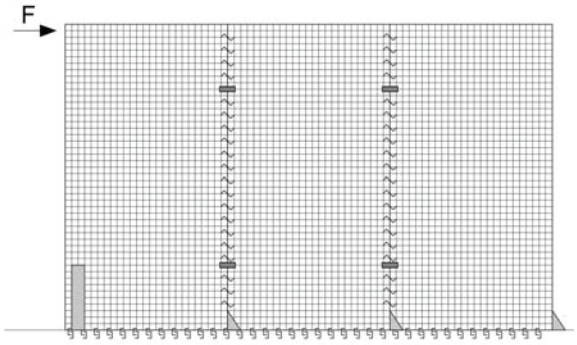

Figure 10: *FE numerical model for Wall-I*

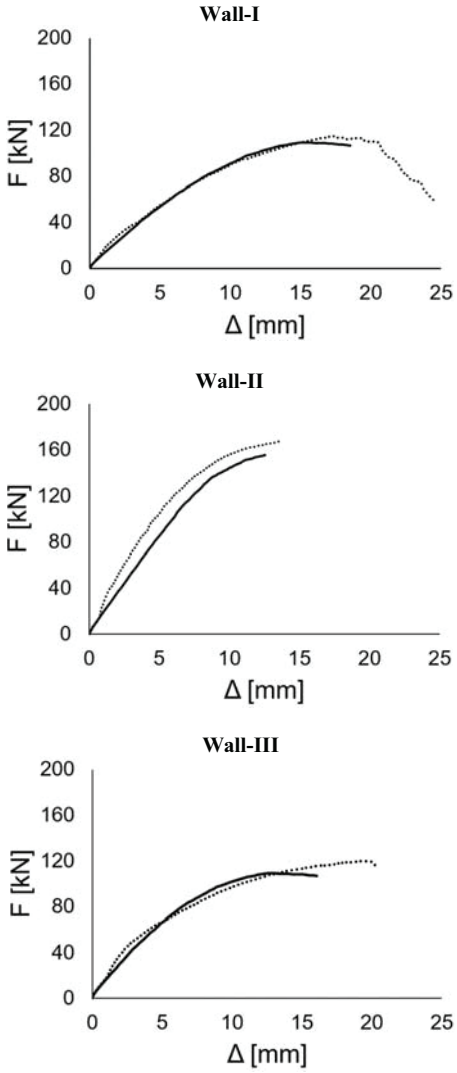

Figure 11: *Load-vs-displacement curves obtained from FE model (continuous line) and shear-wall tests (dot line)*

The multi-linear behaviour assigned to the link along the direction parallel to vertical joint was defined elaborating the experimental curves obtained from the tests on connectors presented in Section 3. In order to simulate the panel-to-paper contact, rigid gap elements acting along the direction perpendicular to the joint were used.

A multi-linear 1-joint uni-axial link element was adopted to model the hold-down when subjected to a vertical tensile load. In order to characterize the non-linear behaviour of hold-down link element, four monotonic tests were carried out on WHT 340 hold-down. The experimental curve for WHT620 is conversely available in Casagrande et. al 2021 [19].

A diaphragm constraint was applied at joints of the FE model on the top of each panel. Non-linear static analyses were performed by increasing the lateral displacement at the top of the wall from zero up to the value corresponding to the global failure condition.

The validation of the FE models with the experimental results was carried out in terms of load F vs displacement Δ curves as shown in Figure 11. It is noteworthy to mention that the values of the lateral displacement Δ were measured in the model at the same location of the LVDTs used during the tests to monitor the lateral displacement of the shear-wall. A reasonable fit is obtained for all analysed tests.

5 CONCLUSIONS

This paper presents an experimental campaign on aluminium rigid shear-key SLOT connectors. The tests were carried out both at connector and wall level. The curves related to connector tests, after an initial slip due to the gap between the connector and the CLT panels, showed an almost elasto-perfectly plastic behaviour.

At wall level, a single-wall kinematic mode with a single global centre of rotation was observed; all tested wall specimens showed a failure mode related to the hold-down.

The shear-wall with two SLOT connectors in each vertical joint (Wall-I) and the shear-wall with screwed vertical joints (Wall-III) showed similar behaviors: the maximum shear load was almost the same, but, due to the physical gap between the SLOT connector and the CLT panels, the stiffness calculated analytically was smaller in Wall-I than that in Wall-III.

The load-vs-displacement curves obtained from the FE numerical model reasonably fit the experimental curves obtained from the shear-wall tests. The numerical models can hence be adopted to predict the mechanical behaviour of multi-panel with rigid shear-key connectors for different geometrical dimensions and mechanical properties.

The results of the experimental and numerical investigations showed how these connectors can be considered to be a viable alternative to traditional connections for stiff vertical joints in multi-panels CLT walls.

6 ACKNOWLEDGEMENTS

Eng. Matteo Magelli is acknowledged for his great help in the processing of data of all tests.

7 REFERENCES

[1] Casagrande D. Doudak G. Mauro L. Polastri A. (2018) Analytical approach to establish the elastic behaviour of multipanel CLT shear-walls subjected to lateral loads. J. Struct. Eng. 144(2).

[2] Gavric I. Fragiacomo M. Ceccotti A. (2015) Cyclic behavior of typical screwed connections for cross-laminated (CLT) structures. Eur J Wood Wood Prod 2015;73(2):179–91. http://dx.doi.org/10.1007/s00107-014-0877-6.

[3] Hossain A. Danzig I. Tannert T. (2016) Cross-laminated timber shear connections with double-angled self-tapping screw assemblies. J Struct Eng 2016;142(11):04016099.

[4] Loss. C. Hossain. A. Tannert. T. (2018) Simple cross-laminated timber shear connections with spatially arranged screws (Open Access) (2018) Engineering Structures. 173. pp. 340-356. doi: 0.1016/j.engstruct.2018.07.004

[5] Sullivan K. Miller T.H. Gupta R. (2018) Behavior of cross-laminated timber diaphragm connections with self-tapping screws Engineering Structures. 168. pp. 505-524. doi: 10.1016/j.engstruct.2018.04.094

[6] Schmidt T. Blass H.J. (2016) Contact joints in engineered wood products. In Proc. 2016 World Conference on Timber Engineering (WCTE). August 22-25. World Conference on Timber Engineering. Vienna. Austria.

[7] Marchi. L. Trutalli. D. Scotta. R. Pozza. L. (2020) Macro-element modelling of a dissipative connection for CLT structures. Structures 26. pp. 582-600. DOI: 10.1016/j.istruc.2020.04.044

[8] Gavric I. Fragiacomo M. Ceccotti A. (2015) Cyclic Behaviour of CLT wall systems: Experimental tests and analytical prediction models. J Struct Eng 2015;vol. 141. no. 11. 2015. https://doi.org/10.1061/(ASCE)ST.1943-541X.0001246.

[9] Popovski M. Karacabeyli E. (2011) Seismic performance of Cross-Laminated Wood panels. 44th CIB-W18 meeting. Alghero. Italy. Paper 44-15-7.

[10] ETA-19/0167 (2019) Rotho Blaas Slot Connectors - ETA-Denmark; https://www.eota.eu/etassessments/9190

[11] EN 26891:1991 (1991) Timber structures – Joints made with mechanical fasteners – General principles for the determination of strength and deformation characteristics. Brussels. Belgium: CEN. European Committee for Standardization.

[12] ETA-19/0167 (2019) Rotho Blaas Slot Connectors - ETA-Denmark; https://www.eota.eu/etassessments/9190

[13] ETA 12/0362 (2020) Essepi XXL - Solid wood slab elements to be used as structural elements in buildings - Eurofins Expert Services

[14] EN 594 (2011) Timber Structures – Test Methods – Racking Strength and Stiffness of Timber Frame Wall Panels, EN 594. . European Committee for Standardization: Brussels, Belgium.

[15] EN 12512:2001 (2005) Timber structures – Test methods –cyclic testing of joints made with mechanical fasteners. Brussels, Belgium: CEN.

[16] CSI. “SAP2000 Integrated Software for Structural Analysis and Design.” Computersand Structures Inc.. Berkeley. California.

[17] Blass H.J. Fellmoser P. (2004) Design of solid wood panels with cross layers. In Proceedings of World Conference on Timber Engineering (WCTE), Lahti, Finland, vol. 2, pp. 543–548.

[18] Brandner R. Dietsch P. Dröscher J. et al. (2017) Cross laminated timber (CLT) diaphragms under shear: test configuration, properties and design. Construction and Building Materials 147: 312–327.

[19] Casagrande D. Fanti R. Doudak. G. Polastri A. (2021) Experimental and numerical study on the mechanical behaviour of CLT shearwalls with openings. Construction and Building Materials. Vol 298. Art n.123858 DOI 10.1016/j.conbuildmat.2021.123858

[20] Masroor, M., Doudak, G., Casagrande, D. (2020= The effect of bi-axial behaviour of mechanical anchors on the lateral response of multi-panel CLT shearwalls (2020) Engineering Structures, 224, art. no. 111202.

https://doi.org/10.52202/069179-0328

World Conference on Timber Engineering Oslo 2023

REPRODUCTIVE ANALYSIS OF FULL-SCALE SHAKING TABLE TESTS OF WOODEN HOUSES USING QUALITY ENGINEERING

Tokikatsu Namba[1], Takafumi Nakagawa[2], Yuji Kado[3], Atsuo Takino[4], Hiroshi Isoda[5]

ABSTRACT: Since the Great Hanshin-Awaji Earthquake in Japan, many full-scale shaking table tests have been conducted for the purpose of analysing the seismic performance of wooden houses. Therefore, the knowledge obtained in the experiment needs to be fed back to the simulation such as structural analysis. However, as a premise that makes them possible, it is indispensable to be able to perform reproductive analysis. In this study, as reproductive analysis, we tried the data assimilation using quality for seismic response analysis of wooden houses engineering.

KEYWORDS: Data assimilation, Reproductive analysis, Full-scale shaking table test, Quality engineering

1 INTRODUCTION

Since the Great Hanshin-Awaji Earthquake in Japan, many full-scale shaking table tests have been conducted for the purpose of analysing the seismic performance of wooden houses [1]. The purpose of these experiments was to determine the seismic performance of the houses and to establish analysis methods. If there is an analytical method that can reproduce the behaviour, it will be possible to determine the seismic performance of the building without conducting experiments. However, if a time history response analysis is conducted in advance by simple addition of load-deformation relationships of individual walls, the response deformation tends to be larger, i.e., the performance of the building at the time of the experiment often exceeds the prediction. As a result, the parameters of walls and joints are reviewed to obtain parameters that match the experimental results, and the parameters will be compared before and after the review to consider the reason for the increase in the capacity. The review is performed manually while considering the reason for the increase, but it is a time-consuming process, and even if the failure process of the obtained solution is different, the inter-story displacement may happen to be similar to the experimental results.

This study discusses a data assimilation method, rather than trial and error, for the review process. Data assimilation is a method of finding parameters that are consistent with observations [2]. This method has been developed primarily in the field of weather forecasting, and it has also been applied to the development and validation of mathematical models in meteorology, climatology, geophysics, geology, and hydrology. In recent years, data assimilation has also been applied to numerical simulations in the fields of geophysics and biology to improve the reliability of numerical simulations [3,4]. In the fields of architecture and civil engineering, it is also known as "system identification," a theory for identifying the modal properties and analytical parameters of structures by observing their response to earthquakes and using microtremor measurements [5]. For example, Nakamura et al. (2000) proposed and validated method for identifying layer stiffness and damping of shear mass system structures using actual earthquake records [6]. In wooden houses, studies have been conducted to estimate layer stiffness by microtremor observation [7]. But there have been few research cases of system identification of nonlinear behaviour of wooden houses, which is the target in this study. As mentioned above, there are several studies on estimating seismic performance by analysis and reproducing experimental results that are closely related to the parameters. For example, Sugiyama et al. (1987), in a static load test of a two-story wood-frame frame house, compared the seismic capacity during a full-scale experiment with the estimated bearing capacity calculated from an experiment on a single wall, and reported that the capacity during the experiment was about 30% greater than the estimated capacity [8]. Miyoshi et al. (2001) reported that static loading force and shaking table experiments on a two-story wood-frame frame house estimated the load-deformation relationship in shaking table experiments by adding up wall experiment and found that it was possible to estimate about 90% of the stiffness up to 1/75 rad, but not the maximum capacity and toughness in the large-deformation region [9]. Comparing the results of shake table tests of several full-scale wooden houses with the calculation results of adding up the load-deformation relationships of all the walls of those structures, Isoda et al. (2021) reported that the capacity during full-scale

[1] Tokikatsu Namba, RISH, Research Institute for Sustainable Humanosphere, Kyoto university, Japan, tokikatsu_namba@rish.kyoto-u.ac.jp
[2] Takafumi Nakagawa, RISH, Kyoto university, Japan, nakagawa@rish.kyoto-u.ac.jp
[3] Yuji Kado, JAXA, Japan Aerospace Exploration Agency, Japan, kado.yuji@jaxa.jp
[4] Atsuo Takino, Osaka Institute of Technology, Japan, atsuo.takino@oit.ac.jp
[5] Hiroshi Isoda, RISH, Kyoto university, Japan, hisoda@rish.kyoto-u.ac.jp

https://doi.org/10.52202/069179-0329

shake table tests was larger than the addition results, about 1.2 times larger at small deformations and about 1.5 times larger at large deformations [10]. It is not easy to accurately estimate the performance of a full-scale shaking table test from experiments for individual walls. In most of these previous studies, shear deformation of each floor is the target. In this study, on the other hand, a three-dimensional analytical model that includes the behaviour of joints, rather than a shear system model that only covers the response of the layers, was constructed to present the damage of each part in detail. In other words, the number of parameters to be considered is enormous.

Here, we focused on quality engineering to reduce the computational complexity in data assimilation and to more efficiently assimilate analytical parameters from shaking table tests. Quality engineering is a statistical method based on the design of experiment method and is sometimes called the robust design method [11]. Developed to improve product quality, orthogonal tables are employed to analyse a large number of variables with a relatively small number of experiments, for example [12]. And inferences obtained using orthogonal tables are said to yield results similar to those obtained by exhaustive examination, and have recently been applied in various fields, such as biotechnology. In the data assimilation method using quality engineering, parameters are defined by multiplying a correction factor with the nominal value set to 1 by the actual physical property value, and the parameters are reproduced by manipulating the correction factor [13].

Based on the quality engineering, this study attempted to establish a method for searching parameters in an analytical model that can accurately reproduce the response of a shake table test. By analysing the results obtained from the actual performance during the full-scale shaking table test and the results of elemental experiments for each seismic element, the main objective of this study is to discuss points and problems that have not been considered in previous studies and to help improve the accuracy of future seismic simulations.

2 EXPERIMENT

The full-scale shaking table experiment targeted in this study was conducted as part of the Ministry of Land, Infrastructure, Transport and Tourism-subsidized project "Design Method Verification Project for 3-Story Wooden Frame Construction" [14]. There were four specimens, each with different wall amounts, joints, and their arrangement, etc. The target specimens to be analysed in this study are specimens 1 and 2 (Figure 1), which have the same plan and elevation plan, but the design of the joints is different (Figure 2). Both are three-story wood-frame frame construction buildings with a plan dimension of 4.55 m x 10.01 m and an eave height of 8.905 m.

3 NUMERICAL ANALYSIS

3.1 Analysis model

In this study, we used “wallstat” [15], an analysis software based on the discrete element method, was used for the time history response analysis. The individual element method is an analysis method for discontinuous bodies such as collapsed bedrock, but the authors have proposed an analysis method using a three-dimensional framework model that can trace the collapse of a wooden house16). Figure 3 shows the analytical model. The number of nodes is 1716 and the number of springs is 3050. The shaft members were assumed to be beam elements, and the bending strength was set to 60 N/mm^2, considering the actual values of the glued laminated wood used in the test specimens. Young's modulus was set to the value based on JAS for each member, respectively.

***Figure 1**: The specimen of the test*

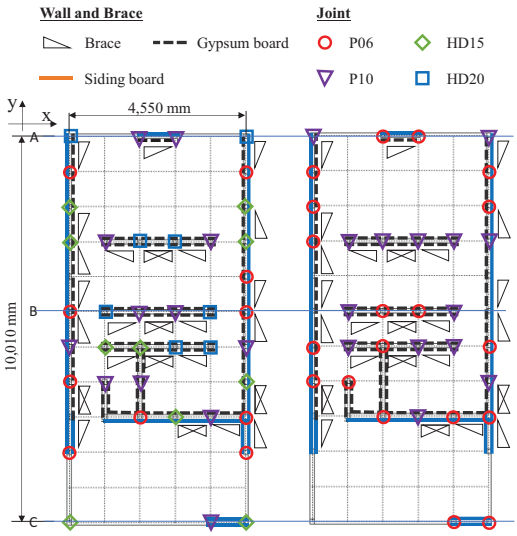

(a) Specimen No.1 *(b) Specimen No.2*

***Figure 2**: Plan views at the 1st floor of the specimen*

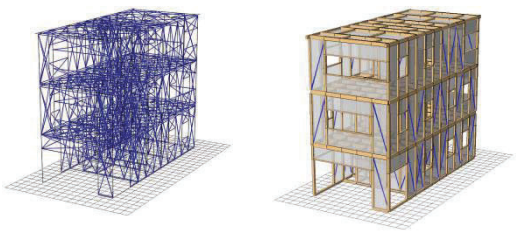

(a) Beam and truss elements *(b) Overview*

***Figure 3**: Analysis model (1716 Nodes, 3050 elements)*

https://doi.org/10.52202/069179-0329

The shear resistance of the wall and brace were modelled as shown in Figures 4(a) and (b), with bracing substituted by truss elements for the walls and two truss elements for the fascia walls with separate load-deformation relationships on the tensile and compressive sides. Each spring acts only in the compression and tension directions. The joints were modelled with rotational springs, compressional and tensile springs (rigid against shear), as shown in Figure 4(c). The skeletal curves were defined based on the results of flexural and tensile tests of the joints. The tensile spring was assumed to be a spring with slip-type characteristics, and the compressional spring was assumed to be an elastic spring. The rotational spring acts independently in the strong and weak axial directions. Figure 5 shows the skeleton curve of the walls and braces, and the skeleton curves of the tensile and rotational springs. The resilience characteristics of the walls and braces are the bilinear + slip skeleton curve [15] (Figure 6), which is used as a simple modelling method for walls of wooden houses, while the tensile and rotational springs are defined as slip-type history characteristics.

The input seismic motion was the acceleration measured at the center of the shaking table; the time history of acceleration at 100% BSL and the acceleration response spectrum are shown in Figure 7. As in the experiment, the seismic motion was input in the order of 90% BSL to 160% BSL.

Numerical integration was performed using the average integration method with a step of every 10^{-5} seconds. Viscous damping was set to 2% with instantaneous stiffness proportional to the instantaneous stiffness, and zero damping was set when the instantaneous stiffness was negative. The weight of each layer was set to be equal to the weight measured in the full-scale shake table test by distributing half of the wall load to the upper and lower layers at the center of each floor height. (1F: 50.1 kN, 2F: 103.1 kN, 3F: 104.3 kN, RF: 61.2 kN)

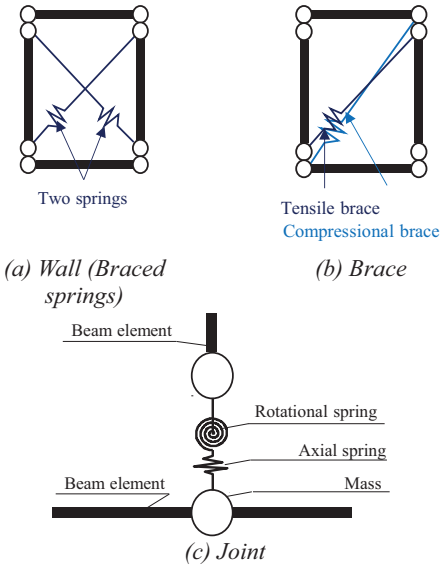

(a) Wall (Braced springs) *(b) Brace*

(c) Joint

***Figure 4**: The details of the elements*

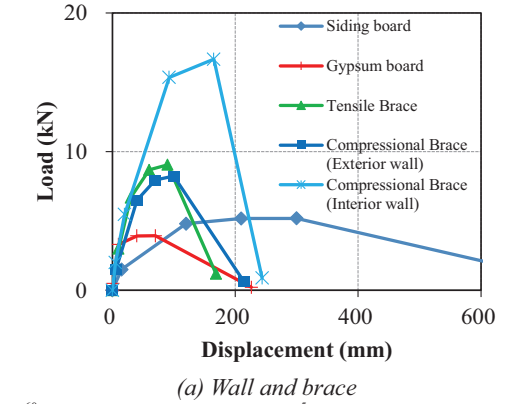

(a) Wall and brace

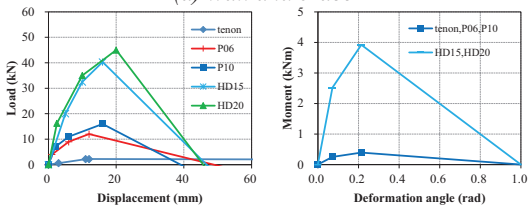

(b) Tensile spring *(c) Rotational spring*

***Figure 5**: The backbone curves of the springs*

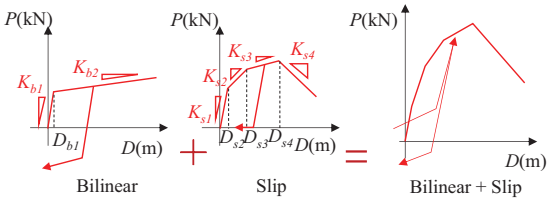

***Figure 6**: Hysteresis rule of the wall and brace*

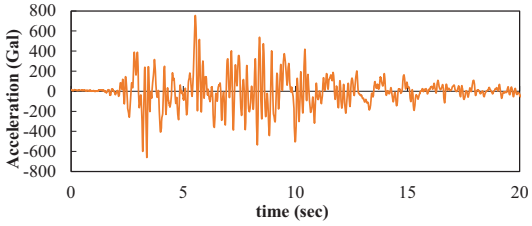

(a) Time history curve

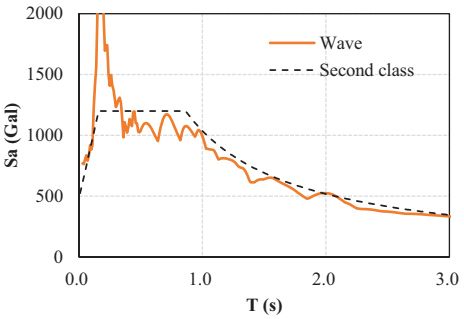

(b) Spectrum acceleration

***Figure 7**: Outline of the BSL wave*

3.2 Analysis and experimental results

The time history response analysis was performed with analytical parameters based on the elemental tests. Figure 10 shows the test image of the BSL160% BSL and a simulation image of the same time in the time history response analysis. In the full-scale shaking table test, almost all of the column leg joints pulled out in specimen 2, and the entire building slid sideways. In specimen 1, the column legs did not pull out, but instead the damage was concentrated in the walls, resulting in the collapse of the building due to a 1F collapse. On the other hand, in the simulation, both specimens 1 and 2 collapsed and did not reproduce the experiment.

4 REPRODUCTIVE ANALYSIS

4.1 Outline of data assimilation

To analyse responses of the test, a 3-D simulation program "wallstat" was used. Figure 3 provides an overview of the data assimilation using orthogonal arrays. First, various skeletal curves are created by multiplying the parameters that simulate elemental experiments by correction factors (1. Definition of the parameters). These parameters are set as the skeletal curves for the springs in the analytical model, and multiple analyses are conducted (2. Numerical analysis). The results of the multiple analyses are compared with the experiments, and the correction factor range are analysed (3. Comparison). Then, the factor ranges are narrowed down by reviewing the initial range (4. Narrowing down the range of factor). Data assimilation was attempted by repeating this flow multiple times. In this study, we were able to obtain accurate results by repeating this process three times.

4.1.1 Definition of the parameters

In this study, mainly focusing on the input parameters for the walls, braces and joints, correction factors were multiplied to set the skeleton curve of the spring. The correction factor multiplied to the parameters are indicated in Figure 10.

Taguchi methods are statistical and based on the design of experiments (DOE), also called quality engineering to improve the quality of manufactured goods [16]. In the theory, the orthogonal array (OA) is a factorial-based approach combining statistical and engineering techniques [17]. The Taguchi technique employs OAs to analyze numerous variables with fewer experiments [18]. Moreover, inferences from the reduced number of experiments apply to the entire experimental region spanned by control factors and levels [19]. Therefore, this method allows data assimilation of many parameters without too much numerical analysis. Therefore, OAs in the Taguchi method was applied to conduct the time history response analysis. The OA is a type of general fractional factorial design. It is a highly fractional orthogonal design based on a design matrix proposed by Taguchi and allows one to consider a selected subset of combinations of multiple factors at multiple levels. OAs are balanced to ensure that all levels of all factors are considered equally. Therefore, the factors can be evaluated independently, despite the fractionality of the

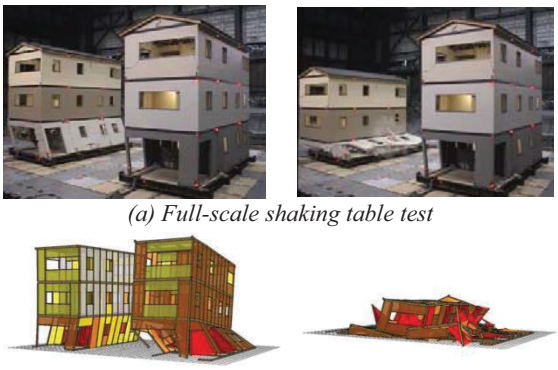

(a) Full-scale shaking table test

Step 1 *Step 2*

(b) Pre-analysis

***Figure 8**: Movie snapshots in BSL160%.*

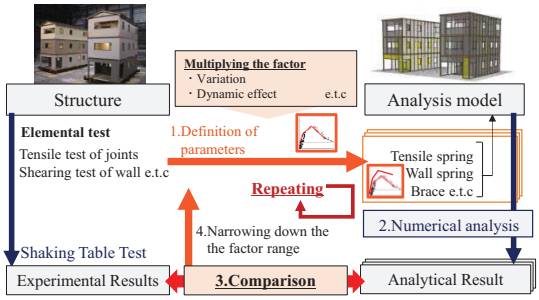

***Figure 9**: Flow diagram of data assimilation.*

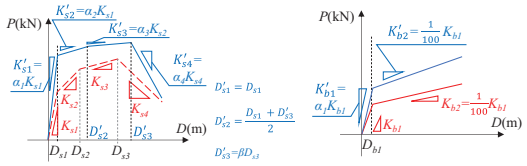

(a) Slip *(b) Bilinear*

***Figure 10**: Definition of backbone curves.*

design. In this study, 12 eleven-level factors and the orthogonal array, which is to examine the effects of those factors and called L121, were adopted. In L121, to clarify all effects of 12 eleven-level factors, 121 combinations are planned. Table 5 shows two orthogonal arrays (L121) that targets the 11 significant analytical parameters of rotational springs and young's modulus, along with the factor levels of the coefficient. The correction factors were set as 11 levels, equally spaced from minimum to maximum. In the numerical analysis, we multiplied the coefficient and the property. If we try to conduct all combinations, 9.85×10^{24} (= (1112)2) cases are simulated. Using combination of two OAs, 14641 (=1212) cases are needed.

4.1.2 Numerical analysis

The analyses planed in phase 1 were conducted using JAXA's HPC "JSS3" [20]. Using a common computer will take 600 days but using the supercomputer JSS3, it took 15 hours to complete 14,641 analysis cases.

https://doi.org/10.52202/069179-0329

4.1.3 Comparison

Focusing on the inter-story displacement, shear force, and uplifts deformation of walls measured in the full-scale shaking table tests, four model validation criteria related to the difference between the analytical and experimental results, shown below, were calculated for each case of analysis (14641 cases).

(i) Total distance of points on the graph in the load-deformation relationship for each layer

Draw the load-deformation relationship and sum the distances between the plots in the analysis and the plots in the experiment at all times. The interlaminar deformation was measured in 7 streets for each layer, but three streets, one at both ends and the center street, were targeted for the inter-story drift, and all the summed values were calculated. (Equation-(1))

$$nSm = \sum_{k=1}^{3}\sum_{i=0}^{20}\sqrt{({}_{anmk}D_i - {}_{exmk}D_i)^2 + ({}_{anmk}Q_i - {}_{exmk}Q_i)^2} \quad (1)$$

where *exmkDi*: inter-story drift in the *m*-story *k*-street in experiment at *i* second, *anmkDi*: inter-story drift in the *m*-story *k*-street in analysis at *i* second, *exmkQi*: shear force at in the *m*-story *k*-street in experiment, *anmkQi*: shear force in the *m*-story *k*-street in analysis.

(ii) Inter-story drift in each layer

The difference in Inter-story drift between the analytical and experimental results for all layers at all times when the earthquake motion was input was summed for each sampling period of 0.01 (s). The inter-story displacement was measured at seven streets in each layer, and calculations were made for three streets: the streets at both ends and the center street. (Equation-(2))

$$nDm = \sum_{k=1}^{3}\sum_{i=0}^{20}|{}_{anmk}D_i - {}_{exmk}D_i| \quad (2)$$

(iii) Shear force in each layer

The difference between the analytical and experimental results for the layer shear force was calculated at all times when the earthquake motion was input. (Equation-(3))

$$nQm = \sum_{k=1}^{3}\sum_{i=0}^{20}|{}_{anmk}Q_i - {}_{exmk}Q_i| \quad (3)$$

(iv) Uplift deformation of walls in 1F (14 locations)

The difference of uplift deformation of 1-story walls between the analysis and the experiment was summed up at all times. The difference of load-deformation curves between layers was evaluated in (1). However, if the results of the lifting of the legs were different, it could not be said that the three-dimensional behaviour during the experiment was reproduced, so the uplift deformation was also included in the evaluation. (Equation-(4))

$$nUD = \sum_{l=1}^{14}\sum_{i=0}^{20}|{}_{anl}UD_i - {}_{exl}UD_i| \quad (4)$$

Where, *anlUDi* : the uplift deformation of wall leg at point l in the analysis at i second, and *exlUDi* : the uplift deformation of wall leg at point l in the experiment.

These values are calculated separately for BSL90% and 160%, and the difference between the analytical and experimental results is evaluated to create a factorial effect diagram. For all criteria, the closer the values are to zero, the smaller the difference between the analytical and experimental results.

A comparison of the calculated results of each model validation for 14,641 analysis cases is shown in Figure 11.

The horizontal axis of each figure is 1S1, which is the distance between the points on the graph for the load-deformation curve in 1F at BSL90%, and the values on the vertical axis are changed. In (a), the vertical axis is 1UD targeting the uplift deformation at BSL90%, with values of 1UD greater than 40 x 10^6 shown in black and others in grey plot. The same trend can be seen in graphs (b) and (c), where the vertical axes are 1D1 and 1Q1 for inter-story drift and shear force in 1F, and the graphs are generally polarized with black values of 1UD greater than 40 x 10^6 and grey values for the other points. The positive correlation can be confirmed from (d) and (e). On the other hand, (f) shows that there is no significant correlation between 1S1 and 2S1.

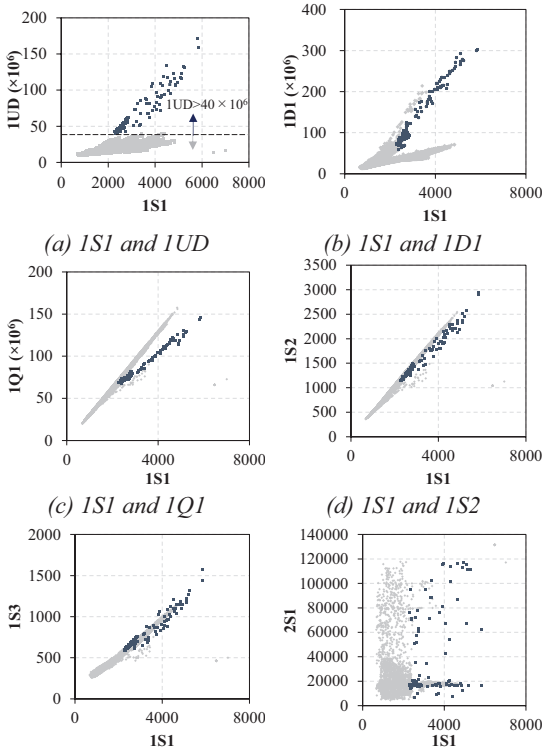

***Figure 11**: Comparison of evaluation (Wall_K_s1 of the Specimen No.1)*

4.1.4 Narrowing down the range of factor

The results of the analysis were evaluated using a factorial effect diagram in quality engineering. This figure is used to identify input parameters that are sensitive to output parameters and to analyse the range of correction factors that reduce the difference between experimental and analytical results. To minimize the difference between the analytical and experimental results, the next step is narrowing the factor range of each parameter. From the results in this phase 3, we can make the graph of factorial effect for each parameter, and we can narrow the ranges of other parameters to move to the second cycle. For the next, the same procedure was conducted, and the ranges were narrowed down using the figures. In the presentation, detailed results and the process will be discussed.

5 RESULT AND DISCUSSION

Figure 12 indicates comparison of the images from the full-scale shake table test, and reproductive analysis, respectively. In the test, almost all of the column legs were uplifted in specimen 2 and the entire building slid, while in specimen 1, the column legs did not pull out, but instead the damage was concentrated in the walls and the building collapsed. In reproductive analysis, the same behaviour of the test was confirmed and the proposed method in this study was verified. As for the load-deformation curves, similar results were got.

(a) Full-scale shaking table test

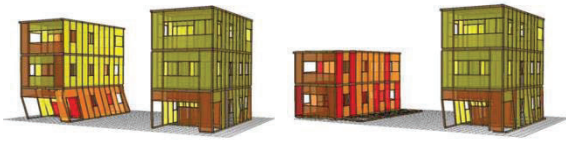

Step 1 *Step 2*

(c) Reproductive analysis

Figure 12: *Movie snapshots in BSL160%.*

6 CONCLUSIONS

In this study, we tried the reproductive analysis of the full-scale shaking table test on two 3-story wooden houses to verify the validity of the proposed data assimilation method using quality engineering. The reproducibility of the analysis confirmed the validity of the data assimilation method, as it was able to track the experiment behaviour well.

ACKNOWLEDGEMENT

This research was conducted as part of a collaborative research by Kyoto University, Osaka Institute of Technology, and JAXA, "Examination of data assimilation method for simulation of collapse analysis of wooden houses using quality engineering". In the time-response analysis, we used the Japan Aerospace Exploration Agency supercomputer system "JSS3". The full-scale shaking table test targeted in this study was conducted as part of the Ministry of Land, Infrastructure, Transport and Tourism-subsidized project “Design Method Verification Project for Three-Story Wooden Frame Construction Methods”.

REFERENCES

[1] Isao Sakamoto. 2005. “Overview of Shaking Table Tests after Osaka-Kobe Earthquake” Journal of the Japan Wood Research Society 61(3):151-161 (in Japanese)

[2] Kalnay, E., 2003. “Atmospheric Modeling, Data assimilation and Predictability” Cambridge University Press, Cambridge, MA, USA

[3] Blum, J.; Le Dimet, F.X.; Navon, I.M., 2009. “Data assimilation for geophysical fluids” In Handbook of Numerical Analysis; Elsevier: Amsterdam, The Netherlands, Volume 14, pp. 385–441.

[4] D’Elia, M.; Perego, M.; Veneziani, A. 2012 “A variational data assimilation procedure for the incompressible Navier-Stokes equations in hemodynamics” J. Sci. Comput. 52, 340–359.

[5] Housncr, G., et al., 1997. “Special issue; Structural control: past, present, and future” J. Eng. Mech., ASCE, Vol.123, No.9, pp.897-971

[6] Mitsuru Nakamura, Izuru Takewaki, Yuzuru Yasui, Koji Uetani : Simultaneous Identification of Stiffness and Damping of Building Structures using Limited Earthquake Records, Journal of Structural and Construction Engineering (Transaction of AIJ), No.528, pp.75-82, 2000.2 (in Japanese)

[7] Takuro Habara, Takahiro Sada, Kazuki Kishimoto, Shinta Yoshitomi : Initial Stiffness Estimation Model for Wooden House Considering Non-Structural Elements Using Information and Micro-Tremor Measurement, Journal of Structural and Construction Engineering (Transaction of AIJ), Vol.87, No.791, pp.42-48, 2022.1 (in Japanese)

[8] Hideo Sugiyama et al.: Experimental Study on The Behavior of Full-size Japanese Traditional Wooden House Subjected to Horizontal Force Part1~2, Summaries of Technical Papers of Annual Meeting, Architectural Institute of Japan, pp.1335-1338, 1987.8 (in Japanese)

[9] Hideyuki Nasu et al.: Full-scale static loading test of the wooden house which consists of board bearing walls Part1~3, Summaries of Technical Papers of Annual Meeting, Architectural Institute of Japan, pp.109-114, 2002.8 (in Japanese)

[10] Kokoro Yoshida: Estimation of strength and stiffness of wooden house based on addition of load deformation relation of wall, master thesis in Shinshu University, 2020.3 (in Japanese)

[11] Genichi Taguchi, 1994. “Quality Engineering for Technology Development” Japanese Standards Association Group

[12] Byrne, D.M. & Taguchi, S. (1987). The Taguchi approach to parameter design. Quality Progress, 19–26.

[13] wallstat ver.4.3.11 [Computer Software]. Research Institute for Sustainable Humanosphere, Kyoto University, Kyoto, Japan

[14] Naohito Kawai, Masahiro Tsuchimoto et al.: Design Methods and Shaking Table Tests on 3-story Wood Houses by Post and Beam Construction Part1~14, Summaries of Technical Papers of Annual Meeting, Architectural Institute of Japan, pp.229-254, 2010.7 (in Japanese)

[15] Hiroshi Isoda, Naohito Kawai: Hysteresis Model of Walls on Japanese Conventional Construction : Study on seismic behavior of wooden construction, Journal of Structural and Construction Engineering (Transaction of AIJ), No.616, pp.157-163, 2007.6 (in Japanese)

[16] Taguchi, G.. 1994. “Quality Engineering for Technology Development” Japanese Standards Association Group, Japan

[17] Mitra, A. 1998. Fundamentals of Quality Control and Improvement. Delhi: Pearson Educational Asia

[18] Pignatiello, J. J. Jr. 1988. “An overview of the strategy and tactics of Taguchi.” IIE Trans., 20 (3), 247–254

[19] Phadke, M. S. 1989. Quality Engineering Using Robust Design. Englewood Cliffs, New Jersey: Prentice-Hall

[20] JSS3 [Supercomputer]. Japan Aerospace eXploration Agency, Ibaragi, Japan

https://doi.org/10.52202/069179-0329

World Conference on Timber Engineering Oslo 2023

TIMBER-BASED SEISMIC RETROFIT TECHNIQUES FOR EXISTING MASONRY STRUCTURES IN NORTH EUROPE

Joakim P. Munden[1], Francesco Graziotti[2], Guido Magenes[3], Roberto Tomasi[4]

ABSTRACT: This paper presents the results of an application of seismic retrofitting techniques to an existing masonry structure in Oslo. Due to low seismicity, the Norwegian National annex of 1998-1 (EC8-1, Standard Norge, 2021) allows omission from seismic design of several structures. Furthermore, the EC8-3 Norwegian National annex (Standard Norge, 2013) states that, unless the probability of collapse in the case of an earthquake changes significantly as result of a general refurbishment of the structure, it is not necessary to perform seismic retrofitting of the building. However there are cases where, depending on the geographical site, intended use or changes to the lateral force resisting structure, it is necessary to perform seismic analysis and possibly strengthen the building's resistance to seismic forces. In this paper, a real case study is used to investigate how the effect of changes to shear walls due to a refurbishment intervention can reduce the capacity of a masonry building, and how two combined timber based retrofit systems can reduce the probability of collapse after the interventions: timber posts working as "strong-backs" with nailed OSB connected to the internal surface of the masonry walls; OSB panels applied to the timber floor.

KEYWORDS: Strengthening masonry structures; timber engineering; masonry shear walls; earthquake strengthening.

1 INTRODUCTION

The background of this study is the need to understand how seismic loads should be evaluated for changes such as renovation or change of use for existing masonry buildings, with a focus on a masonry type construction which is typical in Oslo. Oslo is located in an ancient deep rift zone corresponding to Oslofjorden, which is relatively active but with fairly low seismic loads [1]. The biggest recorded seismic event occurred in 1904, with the Ms 5.4 Oslofjorden earthquake. Masonry buildings constructed during the period 1850-1920 make up a significant part of the building stock in Oslo (Oslo Byleksikon [2], see Figure 1). The constructions are typically unreinforced masonry consisting of clay bricks and lime mortar. The floors are wooden beams.

Building standards for designing resistance to seismic forces were introduced with the Eurocodes in Norway in 2004. For certain buildings the codes require demonstration of capacity against earthquakes for both new buildings and changes in existing buildings. In cases where seismic design cannot be omitted according to EC8-1[3] , the construction must be demonstrated to be resistant to seismic forces.

EC8-1 has a set of criteria for when seismic evaluation is not necessary. The latest revision as of June 2021 has a new set of rules regarding omission of seismic evaluation of structures. According to the National annex of EC8-1, most structures in Oslo in seismic class II or lower, will no longer need to be evaluated for seismic loads. However, if ground conditions are unfavourable and the building project involves a change in use, masses and/or altering of stabilizing constructions, a seismic evaluation should be performed. EC8-3 guidelines are given for the design of existing structures. The National Annex, paragraph NA.2.1[4], states the following:

"*The reinforcement of existing structures that have not been exposed to earthquake damage can be limited to changes or additions that change the load effect and/or the carrying capacity in such a way that the probability of collapse during an earthquake increases significantly if the structure is not reinforced. In the assessment, NS-EN 1998-1 is used for calculation of load effect both before and after the change/addition (Standard Norge, 2013, page 2 in the National Supplement, authors' translation)*."

The standard does not provide provisions for what is considered a significant increase in the probability of collapse. However, RIF - The Norwegian Association of Consulting Engineering Firms has a published the paper "Dimensjonering for jordskjelv av eksisterende konstruksjoner" [5]). In this paper, a significant increase is defined as a 20% increase in the risk of collapse during an earthquake. The RIF guide reviews EC8-3 and EC8-1 for use in the design of existing buildings, and provides recommendations for calculation methods for demonstration of significant increase. However, the paper does not go into detail on the practical application for masonry buildings.

[1] Joakim P. Munden is a structural engineer based in Oslo, Norway, joakim@iogm.net
[2] Francesco Graziotti, Università di Pavia, Italy, francesco.graziotti@unipv.it
[3] Guido Magenes, Università di Pavia, Italy, guido.magenes@unipv.it
[4] Roberto Tomasi, Norwegian University of Life Science, NMBU, Norway, roberto.tomasi@nmbu.no

https://doi.org/10.52202/069179-0330

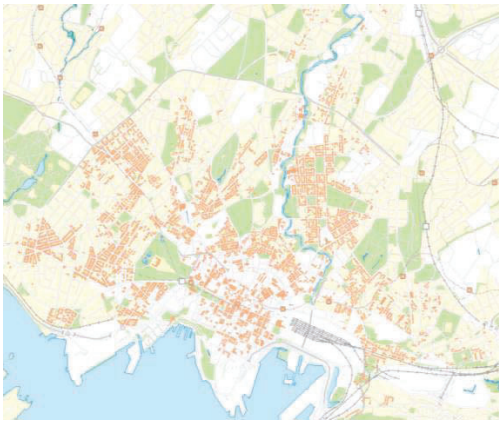

Figure 1: *Murbyen Kristiania, construction before 1915 (reproduced from Kart: Byantikvaren, 2011* [6]*)*

In Oslo (and probably Norway in general), seismic retrofitting of masonry structures is uncommon, and the perception amongst most building owners and people in general is probably that earthquakes don't impose a real threat in Norway. The aim of the study is therefore to look at simple seismic retrofitting strategies that are cost efficient and can improve the seismic resistance of the building structure so that the structure can withstand the design seismic load. For an existing construction where the lateral resistance is below seismic design loads, and the probability of collapse increases significantly after the changes have been made to the construction, the aforementioned guidelines are relevant to decide the need for retrofitting.

A large part of the building stock in inner Oslo consists of older masonry buildings that require repurposing or renovation.

The purpose of this study is to propose a retrofit technique when changes in masses, stiffness and/or strength constitute a significant increase for risk of collapse under seismic influence.

2 DESCRIPTION OF THE CASE STUDY

The project is a case study where a sample building is modelled with different situations where the walls' geometry is altered, introducing openings in lateral force resisting elements of the building.

The building in the case study is a typical masonry structure built around 1890 in the Grünerløkka quarter in Oslo, located in a densely populated residential area with buildings from the same era and with approximately equivalent geometry and construction methods.

The structures have a fairly consistent building design, with a load-bearing structure with piers and spandrels of unreinforced masonry of solid bricks and with timber floors and roofs. The floor slabs consist of floor joists that are supported by the façade wall, the central wall, and the back wall.

Normally, the timber floors have a dimension of approximately 170mm x 220mm, spaced 700mm–900mm. Dried clay, often from the construction site was used between the floor beams to increase the capacities for insulation, fire-resistance and sound insulation (see for example Figure 2).

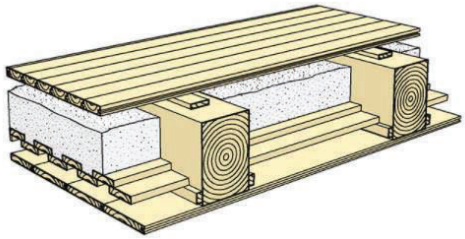

Figure 2: *Typical floor construction (Sintef Byggforsk 2017, reproduced from* [7]*)*

The building is relatively symmetrically designed, even if not completely regular on the ground floor. In the sample building, the structural design was changed in the 1960s by partially demolishing the load-bearing walls at the ground floor, to create more open spaces better suited for serving or retailing. All changes were in the main load-bearing walls in the X direction (façade wall, central wall, and back wall, see Figure 3). For the calculations, the existing/original situation is as it was before the renovation, while the new situation largely coincides with the actual changes in the load-bearing walls that were carried out in the 1960s.

The original (existing) and new situations for load-bearing walls in the X direction are shown in Figure 4. In the existing situation, the beams are dimensioned for the facade openings and the openings in the central wall. For changes in the new situation, both beams and columns are dimensioned.

The case study will be analysed both in the original situation and after the opening of the structure, in order to evaluate the effect of changes in terms of capacity of the building. The type of retrofitting techniques considered in this analysis will be the stiffening of timber floors and the application of timber strong backs with nailed OSB in the masonry walls in X direction.

A numerical model of the capacity of the structure is presented and the results are expressed in term of push-over curve, with respect to five design situations: original building; building after the opening; building with timber floors stiffened at the first storey; building with one wall retrofitted with timber strong-backs and OSB; building with timber floors stiffened at the first storey and one wall retrofitted with timber strong-backs and OSB.

The push-over capacity curve has been derived considering the mean mechanical parameters reported in Table 1 based on common practice in Norway for week mortar brick type of masonry with an assumption for cohesion value (i.e. 0.4).

https://doi.org/10.52202/069179-0330

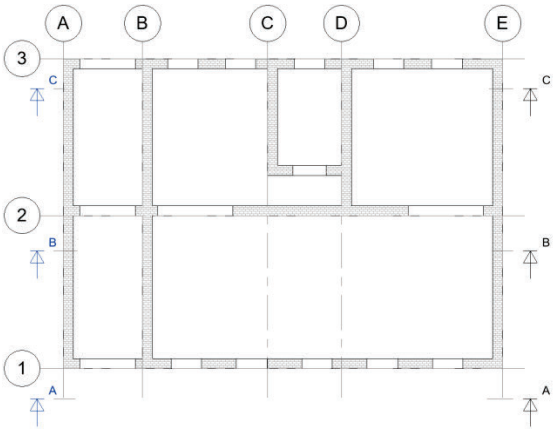

Figure 3: *Plan of structure, existing situation*

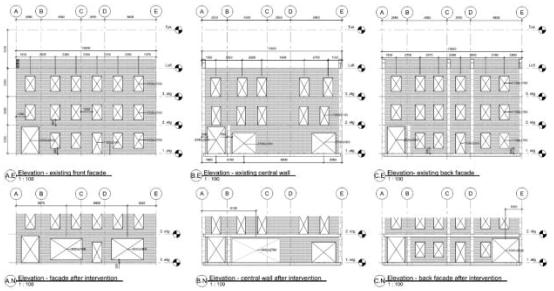

Figure 4: *Three load bearing walls before and after changes*

Table 1: *Mechanical parameters adopted in the model*

Parameter	Mean Value
Cohesion	0.1 MPa
Friction coefficient	0.4
Compression strength *fc*	2.1 MPa
Elastic modulus	1050 MPa

3 PROPOSED RETROFIT TECNIQUES

3.1 ENHANCEMENT OF THE MASONRY

The proposed retrofit system is based on the strengthening solutions proposed and tested by Dizhur et al. [8], which involves the use of vertical timber posts connected to masonry walls to improve their out-of-plane capacity. The solution herein reported has been further developed by Guerrini et al. [9] and Miglietta et al. [10] to also improve the in-plane strength and deformation capacity of piers and the connection between masonry and floor systems. In fact, the lack of connections between masonry and flooring is a significant weakness in existing URM buildings and is addressed by the proposed retrofit system.

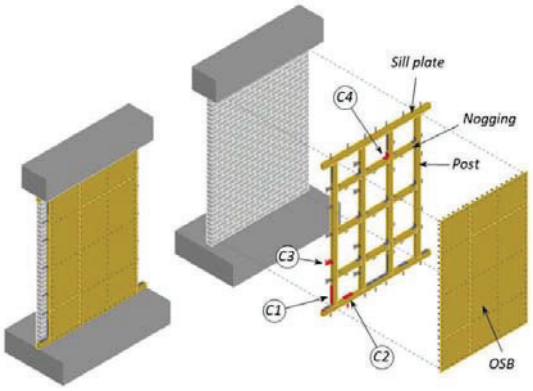

Figure 5: *Retrofit components and layout* [9]

The proposed retrofit system aims at improving the in-plane capacity of piers by adding horizontal timber members (nogging or blocking) between vertical posts to create a timber frame connected to the masonry. As shown in Figure 5, the frame is completed with top and bottom sill plates that connect to the floor and foundation. There are four different connection types: C1 (connections between posts and sill plates), C2 (anchorages between sill plates and floor/foundation), C3 (connections between timber frame and masonry wall), and C4 (connections between timber frame components).

The vertical posts improve the masonry wall's out-of-plane response by acting as strong-backs in flexure. The timber frame and OSB panels increase the pier's in-plane capacity by interacting with the masonry through connections C3. The posts and tie-down connections (C1) contribute to in-plane flexural strength, while the OSB layer and nailing contribute to in-plane shear strength.

The connection enhancement between masonry and floor offered by the retrofit system is critical in improving seismic performance as it promotes a global box-type response, preventing the onset of undesirable local mechanisms that can greatly reduce the building's seismic capacity. The system could be applied in one or both sides of the masonry, considering architectural limitations and required level of improvement.

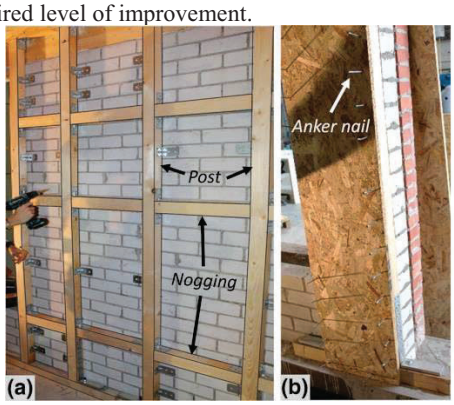

Figure 6*: Pictures of the retrofit system during the application on a building specimen tested on shake table: a) wall timber frame, b) nailing of a OSB for in-plane strengthening of longitudinal walls* [10]

This retrofit technique has been validated through components [9] and shake table tests on an entire URM building [10], as reported in **Error! Reference source not found.**. Analytical formulations to design this retrofit intervention are reported in Damiani et al. [11].

3.2 ENHANCEMENT OF THE FLOOR DIAPHRAGMS

Another structural element that may require to be stiffened and strengthened to transfer the shear between walls on different vertical planes and to assure a box-type response are the flexible timber diaphragms. Different strengthening techniques have been proposed in the past (see [12, 13]), but a typical in-plane floor reinforcement might use 18-mm thick OSB panels attached to the existing planks using anker nails and timber blocking beams inserted between joists. The blocking elements and joists have to be connected using steel angles and screws.

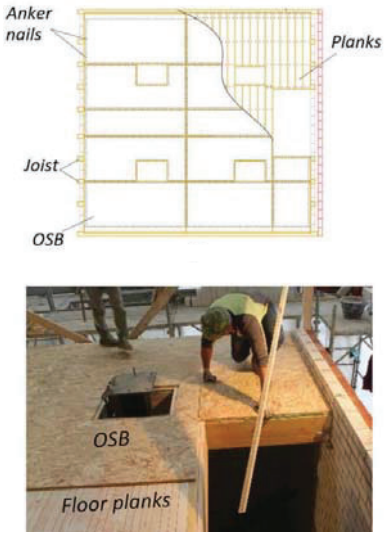

Figure 7: *OSB panels layout and picture of the diaphragm retrofit system during the application on a building specimen tested on shake table* [10].

The system could in principle be applied from underneath the diaphragm or on top of the diaphragm adapting the adequate detailing. Analytical formulations to design this retrofit intervention are reported in Damiani et al. [11]

4 MODELING OF THE RETROFIT INTERVENTIONS

4.1 STRUCTURAL ANALYSIS SOFTWARE

The commercial software selected for the analyses is 3Muri. It is based on the macro-element approach (with elastoplastic pier and spandrel behaviour) and allows execution of nonlinear static (i.e. pushover) and analyses of entire masonry buildings, by means of an equivalent-frame idealisation of the structure (Lagomarsino et al. [12]. This analyses allow to estimate the global capacity and behaviour of the structure.

The nonlinear static analyses were carried out with two different force distributions (e.g. mass proportional and first mode distributions), indicated by several codes (e.g. EN 1998-1, 2004, Eurocode [3]), to account for the dynamic response in the different phases of damage evolution.

The force distribution is applied along two orthogonal directions (both positive and negative), also taking into account accidental eccentricities introduced by the codes to account for uncertainties in the location of masses. Since the building originally has flexible timber floors, the position of the control node is critical. For this reason, one of the nodes belonging to the central wall at the top level was selected, as it was considered representative for the portion of the building with a higher displacement.

The proposed analyses are valid for evaluating the overall behaviour of the structure. Local analyses, such as the evaluation of out-of-plane mechanisms of masonry or the actual effectiveness of the steel beam inserted in place of the removed portion of masonry, should be evaluated with specific methods or software (these calculations are beyond the scope of this paper).

4.2 DEFINITION OF THE INTERVENTIONS

The building work carried out on the ground floor, such as the widening of openings, and in particular the central wall, worsens the seismic capacity both in terms of maximum shear at the base and displacement. Structural retrofit solutions must therefore be aimed at restoring the original structure's resistance and deformation capacity. In order to minimize the cost of the intervention, especially in terms of invasiveness for residents on the upper floors, it may be possible to intervene locally only on the ground floor.

The best solution from a seismic performance point of view would be to retrofit all the diaphragms and all the masonry piers and spandrels. Considering that this solution may be too expensive and also takes up valuable space, three more cost-effective solutions are investigated in this paper: (i) the first is to retrofit only underneath the first diaphragm above ground floor to redistribute the shear between walls and give the structure a more box-like behaviour; (ii) the second is to retrofit the main pier in the central wall on both faces, as the length of this structural element has been heavily reduced, and (iii) the third solution is to retrofit both the floor and the wall pier. A scheme of the retrofit solutions can be seen in Figure 8.

Regarding retrofit of the masonry (ii, iii), increasing the shear and deformation capacity on the shortened pier appears to be the only solution that maximizes the cost/benefit ratio. As shown in Figure 9 in section number 5 in the original structure (at the top), the pier remained undamaged (green) until the structure's ultimate capacity was reached, while after enlargement of the openings, (central figure), the remaining pier was the first to reach ultimate deformation (orange). Retrofitting it by increasing both its strength and deformation capacities

https://doi.org/10.52202/069179-0330

allows the entire structure to have beneficial effect both in terms of base shear and displacement capacity.

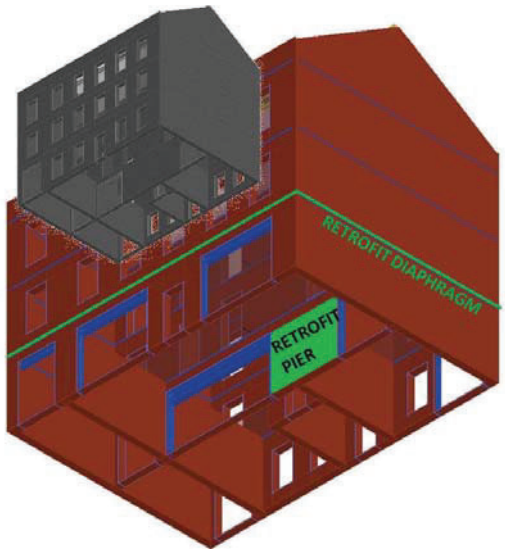

Figure 8: *Original and enlarged openings structures with scheme of the proposed structural interventions* [9]

4.3 MODELLING OF THE RETROFIT INTERVENTIONS

Detailed analytical formulations to design retrofit intervention are reported in Damiani et al. [13]. A detailed modelling of the same type of retrofit is also possible as reported in Damiani et al. [11]. For the preliminary study proposed in this paper, the retrofit was not designed in detail. The increase in shear strength and diaphragm stiffness was based on test results, and can therefore be considered plausible, but valid only for the specific details reported in Miglietta et al. [10]. The strength of the retrofitted masonry and the stiffness of the diaphragm may be increased or decreased depending on the nail spacing and/or on the thickness of the OSB or other detailing.

In particular, to model the presence of the retrofit for the masonry, the shear strength of masonry was increased by approximately 10 kN/m for the pier as experimentally assessed when retrofitting one side of the wall. As the pier is 3.6 meters in length, a retrofitting on both faces adds up to a shear strength increase of approximately 72 kN (about 1.5 times the strength of the non-retrofitted pier).

The ultimate shear deformation capacity of the retrofitted pier was increased from 0.5% to 0.8%. The latter value is conservative, as demonstrated by the physical testing described in [9]. For comparison 0.8% is the deformation capacity prescribed by Eurocode for reinforced masonry.

Concerning the diaphragm, the shear stiffness (expressed in terms of shear modulus times the thickness of the floor $G \cdot t$) was increased from 400 N/mm, a value assumed realistic for a flexible timber diaphragm with nailed planks, to 6300 N/mm for the diaphragm retrofitted with OSB, a value that can be considered plausible and valid for the specific detailing reported in Miglietta et al. [10]

5 RESULTS OF THE ANALYSES

As previously reported, the analyses were performed in all directions and for both force distributions (i.e. proportional to the first mode of vibration and proportional to the masses). For the sake of simplicity, only the results of the most critical analyses are reported here: parallel to the enlarged openings, with forces proportional to the masses and applying forces from left to right with no eccentricity.

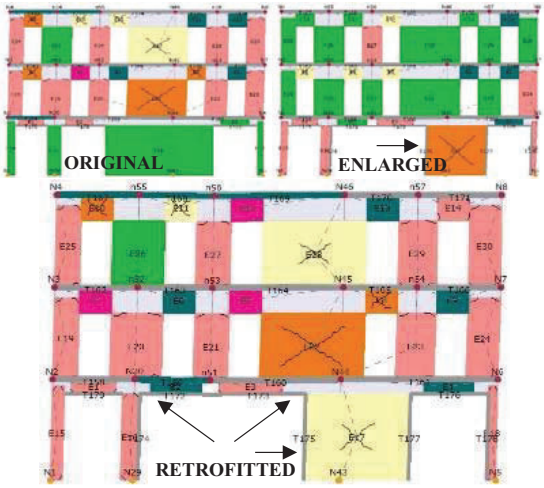

Figure 9: *Visualization of deformed shape and damage at ULS of the central wall for original (top left), enlarged openings w/o retrofit (top right) and retrofitted masonry and diaphragm (iii) (bottom) buildings.*

Figure 9 shows the deformed shape and damage at the ultimate limit state of the central wall (wall number 2 as per Figure 3) for the original (top left), enlarged openings without retrofit (top right), and retrofitted masonry and diaphragm (iii) (bottom). Analysing the top part of the figure, it is evident that the enlargement of the opening significantly affects the structure's behaviour. In the original building (top), the near-collapse condition is reached due to failures at the second storey, while the construction with enlarged openings collapses due to premature failure of the shortened pier at the ground floor, with walls in the upper floors almost undamaged. These results clearly suggest that a retrofit intervention should be focused on an enhancement of that particular portion of the building, both in terms of strength and deformation capacity.

The lower part of Figure 9 shows how the application of the retrofit to the masonry and diaphragm allows for more diffused damage through the storeys. In particular, the diffusion of damage throughout the storeys of the retrofitted structure is similar to the one obtained with the original one. This allows to avoid the soft-storey

mechanism of the building with enlarged openings increasing the displacement capacity of the building.
Figure 10 shows the deformed shape at ULS of the first diaphragm for enlarged openings without retrofit (left) and retrofitted masonry and diaphragm (iii) (right).

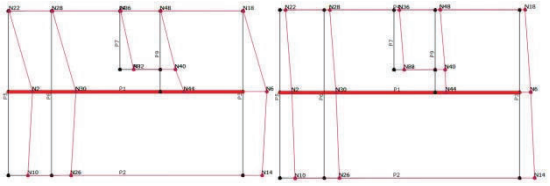

Figure 10: *Visualization of deformed shape at ULS of first diaphragm for enlarged openings w/o retrofit (left) and retrofitted masonry and diaphragm (iii) (right) buildings.*

The result of the analysis is shown in Figure 11. Firstly, comparing the original situation (black line) with the enlarged openings (red line) it is possible to observe a significant reduction both in terms of strength and displacement capacity (-16% both in terms of a_y* and d_u* according the bilinearization proposed by EC8).
Figure 11 reports the capacity (i.e. pushover) curves associated with the different models in terms of equivalent SDOF acceleration and displacement.

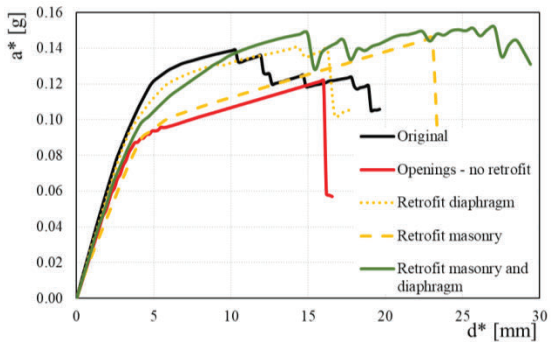

Figure 11: *Capacity curves associated with the different models in terms of equivalent SDOF acceleration and displacement.*

From the figure it is also evident that applying a retrofit intervention on the diaphragm alone (i) is beneficial for the overall strength, nearly restoring the capacity of the original situation. This is due to the inertia force primarily acting on the central wall with flexible diaphragm, while with the strengthened diaphragm loads are transferred also to the other walls, making use of their flexural/shear capacity. On the other hand, it is evident that this intervention does not restore the full displacement capacity of the original building. A representation of the difference between the behaviour of the original and the retrofitted diaphragm can be seen in Figure 10. Retrofitting only the central pier (ii) gives a different behaviour: this limited intervention is not able to restore the full strength of the building, but the displacement capacity is higher than the original situation (+21%); as visible in Figure 9, this is due to the combined effect of increase of displacement capacity of the ground floor pier and the increase of its strength, allowing for a better spread of damage throughout the storeys (i.e. avoiding the soft-story mechanism happening in the structure with enlarged opening but without retrofit interventions). Considering the positive effects of (i) and (ii), the best solution appears to be a combined retrofit of masonry and diaphragm. In this case (green line), both the strength and the displacement capacities were enhanced (+7% and +50% respectively from the original configuration).
Table 2 reports the SDOF parameters according EC8 [3]which summarize the results graphically represented in terms of capacity curves in Figure 11.

Table 2: *SDOF parameters associated with the different models according to the bilinearization proposed by EC8.*

	a_y* [g]	d_u* [mm]	Γ [-]
Original	0.13	19	1.31
Opening-no retrofit	0.11	16	1.28
(i) Retrofit diaphragm	0.13	16	1.26
(ii) Retrofit masonry	0.13	23	1.28
(iii) Retrofit masonry and diaphragm	0.14	29	1.29

6 CONCLUSIONS

Norway can be seen as a low to intermediate seismicity area, with a low seismic hazard and a low exposure level except the area around Oslo and on the west coast. The original motivation of this study is the need to understand how seismic capacity should be evaluated for changes such as renovation or change of use for existing masonry buildings, with a focus on a masonry type construction which is typical in Oslo. For that purpose, a case study of an existing brick masonry building has been analysed before and after a typical refurbishment intervention which introduces some opening in the lateral resisting masonry walls. The different design situations were investigated by means of a global analysis of the building through an equivalent frame macro-element model, using the commercial software 3Muri specific for masonry structures. The results of the analysis for the different cases were reported in terms of capacity curves.
The results showed that the intervention produced a significant weakening of the lateral capacity of the case study (around 16% both in terms of acceleration and displacement), even if, due to the low seismic input of Oslo area (PGA of 0.03g), the verification for seismic resistance could be still considered satisfied after the structural intervention. However, since these types of constructions are typical also of other area in Norway (and more generally in Northern Europe) where the conditions could be more unfavourable (higher seismic hazard, ground amplification), two retrofitting techniques, based on timber elements reinforcing the building structural elements, were investigated to reduce the probability of collapse after the weakening intervention: timber strong-backs with nailed OSB applied to both surface of a central masonry pier; OSB panels applied to the first floor level.

https://doi.org/10.52202/069179-0330

The results of the analysis showed both retrofitting solutions effectively improve the global performance of the building, and that a combined retrofit of floors and diaphragms produces the best performance both in terms of capacity and displacement.

ACKNOWLEDGEMENT

The execution of the analyses was partially funded by the DPC-ReLUIS within the framework of WP5 2022–2024 'Interventi di rapida esecuzione a basso impatto ed integrati'. The authors acknowledge Abdelghani Meslem for his suggestion and guidance during the preliminary analysis of the case study.

REFERENCES

[1] Rønnquist A, Remseth S, Lindholm C. *Earthquake engineering design practice in Norway: Implementation of Eurocode 8*.

[2] Oslo Byleksikon. Murbyen. *https://oslobyleksikon.no/side/Murbyen Accessed 26 Feb 2021*.

[3] NS-EN 1998-1:2004+A1:2013+NA:2021. Eurocode 8 — Design of structures for earthquake resistance — Part 1: General rules, seismic actions and rules for buildings. *2021*.

[4] NS-EN 1998-3:2005+NA:2013. Eurocode 8: Design of structures for earthquake resistance - Part 3: Assessment and retrofitting of buildings.

[5] RIF - Rådgivende ingeniørers forening. *Dimensjonering for jordskjelv av eksisterende konstruksjoner*. 2013.

[6] Wikipedia. Murbyen . *Accessed 02.2023 https://no.wikipedia.org/wiki/Murbyen_(Oslo)*.

[7] Sintef Byggforsk. Trebjelkelag i eldre boligbygninger. Metoder og materialer. *accessed 29.04.2022 https://byggforsk.no/dokument/667/trebjelkelag_i_eldre_boligbygninger_metoder_og_materialer*.

[8] Dizhur D, Giaretton M, Giongo I, et al. Seismic retrofit of masonry walls using timber strong-backs. *SESOC Journal* 2017; 30: 30–44.

[9] Guerrini G, Damiani N, Miglietta M, et al. Cyclic response of masonry piers retrofitted with timber frames and boards. *Proceedings of the Institution of Civil Engineers: Structures and Buildings* 2021; 174: 372–388.

[10] Miglietta M, Damiani N, Guerrini G, et al. Full-scale shake-table tests on two unreinforced masonry cavity-wall buildings: effect of an innovative timber retrofit. *Bulletin of Earthquake Engineering* 2021; 19: 2561–2596.

[11] Damiani N, Guerrini G, Miglietta M, et al. An innovative timber system for the seismic retrofit of URM buildings. Part 2: validation of analytical formulations. *Eng Struct*; Submitted.

[12] Lagomarsino S, Penna A, Galasco A, et al. TREMURI program: An equivalent frame model for the nonlinear seismic analysis of masonry buildings. *Eng Struct* 2013; 56: 1787–1799.

[13] Damiani N, Guerrini G, Miglietta M, et al. An innovative timber system for the seismic retrofit of URM buildings. Part 1: concept, design, and analytical formulations. *Eng Struct*; Submitted.

World Conference on Timber Engineering Oslo 2023

MODAL IDENTIFICATION AND MODEL UPDATING OF AN INNOVATIVE AUTOMATIC SELF-SUPPORTING TIMBER WAREHOUSE: THE CASE STUDY OF ROTHOBLAAS HEADQUARTERS EXPANSION

Ernesto Callegari[1], Roberto Girardi[2], Luca Gottardi[3], Andrea Incerti[4], Claudio Mazzotti[5], Luca Pozza[6], Sebastian Rodemeier[7], Luca Sestigiani[8], Mirko Tommasini[9]

ABSTRACT: Automatic Self-Supporting Timber Warehouse (ASSTW) is an innovative and sustainable structural system with a modal response strongly influenced by both the actual mechanical behaviour of structural elements and the load conditions. The structural analysis of ASSTW is typically carried out using numerical models calibrated referring to codified materials and connection properties. The reliability of the numerical simulations, used in the design phase, can be verified through modal identification on-site tests that also allow for a subsequent model update. This paper reports the main results of the modal identification on-site campaign, conducted by CIRI-EC laboratory of University of Bologna, of the new Rotho Blaas S.r.l. ASSTW in two different load conditions: unloaded warehouse with only the mass of the structural elements and partially loaded warehouse with eccentric mass. The subsequent model update phase is presented carrying out the most significant mechanical parameters to grasp the actual modal response of the structure.

KEYWORDS: Modal identification, Model updating, Self-Supporting Wooden warehouse, Timber structures.

1 INTRODUCTION

In recent years the use of wooden structural systems is increasingly widespread also for special building types typically made only of steel. Automatic self-supporting warehouse is a structural typology that can be profitably built using engineered wood-based products (EWP) allowing to optimize at the meantime: costs, sustainability aspects, aesthetic value and structural efficiency. This is due to the improved performances of the EWP and connection systems and to the use of advanced structural analysis and design methods [1].
Design of an Automatic Self-Supporting Timber Warehouse (ASSTW) can be developed in accordance with the current standard for the static and seismic actions [2,3] and for the fire safety [4].
The structural analysis of a ASSTW can be profitably carried out using numerical models calibrated referring to codified materials and connection properties [5]. Numerical models must be able to faithfully reproduce the static and dynamic response of structural systems characterized by significant plan dimensions and height. Modal identification on-site test represents a robust strategy for defining the actual building response and for the verification of the reliability of numerical simulations and for the subsequent model updating [6].
In this work, the case study of Rotho Blaas headquarters expansion, depicted in Figure 1, is used to describe both the innovative construction solution for ASSTW and the modal identification on-site tests adopted for the definition of modal response and for the model updating. Rotho Blaas ASSTW is one of the tallest wood warehouses in Europe, but also among the first to be fully automated, using conveyers, lifts and sliding shelving to speed and simplify the process (Figure 1-b).

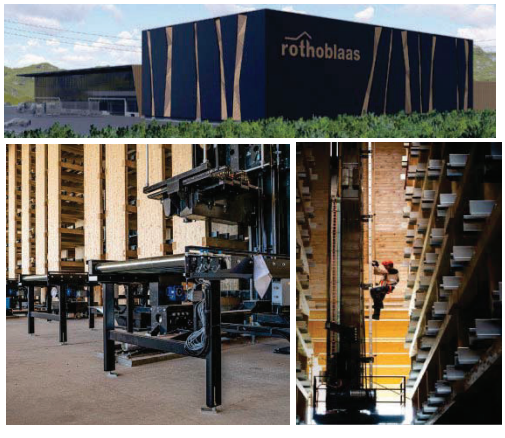

Figure 1: *View of Rotho Blaas ASSTW: a) external view, b) internal view with automatic lifting system.*

[1] Ernesto Callegari - Rotho Blaas srl - Via Dell'Adige 2/1 Cortaccia (BZ), Italy. ernesto.callegari@rothoblaas.com

[2] Roberto Girardi - Armalam Srl - Loc. Fratte 51 Pergine Valsugana (TN), Italy. roberto.girardi@armalam.it

3 Luca Gottardi - Armalam Srl - Loc. Fratte 51 Pergine Valsugana (TN), Italy. luca.gottardi@armalam.it

[4] Andrea Incerti - CIRI Buildings and Construction (CIRI-EC), University of Bologna, Via del Lazzaretto 15/5, Bologna, Italy. andrea.incerti@unibo.it

[5] Claudio Mazzotti - Department of Civil, Chemical, Environmental and Materials Engineering (DICAM), University of Bologna, Viale Risorgimento 2, Bologna, Italy. claudio.mazzotti@unibo.it

[6] Luca Pozza - Department of Civil, Chemical, Environmental and Materials Engineering (DICAM), University of Bologna, Viale Risorgimento 2, Bologna, Italy. luca.pozza2@unibo.it

[7] Sebastian Rodemeier - Merz kley partner GmbH – Sägerstraße 6 A-6850 Dornbirn. s.rodemeier@mkp-ing.com

[8] Luca Sestigiani - Rotho Blaas srl - Via Dell'Adige 2/1 Cortaccia (BZ), Italy. luca.sestigiani@rothoblaas.com

9 Mirko Tommasini - Armalam Srl - Loc. Fratte 51 Pergine Valsugana (TN), Italy. mirko.tommasini@armalam.it

https://doi.org/10.52202/069179-0331

2 DESCRIPTION OF ASSTW CASE STUDY

The ASSTW consists of a multifunctional timber skeleton: the shelving is part of the constructive system of the building together with the roofing and plugging elements. The shelves, which transfer the weights of the stored goods to the ground, also act as a load-bearing structure for the warehouse itself.

The Rotho Blaas ASSTW case study is schematically represented in Figure 2 and consists of three distinct volumes as follows:

- a main volume (1), to be used as an automatic warehouse, measuring 75 x 40 meters and 21 meters high;
- secondary volume (2), which will contain the goods entrance;
- an accessory volume (3), which will connect the new warehouse with the current one (4).

In the following the focus will be only on the main body of ASSTW (1).

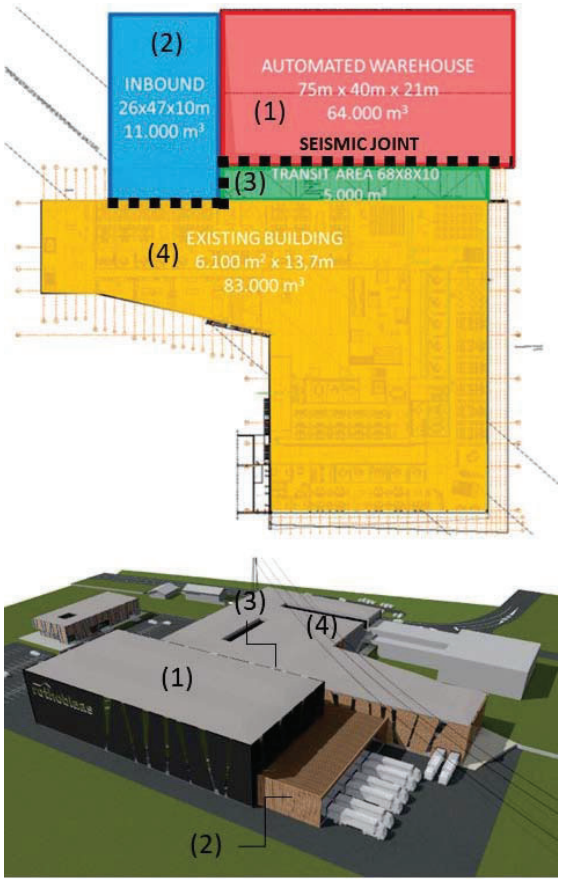

Figure 2: *3D scheme of the Rotho Blaas ASSTW*

3 MULTI-CRITERIA DESIGN

The architectural and compositional design recall the choices made for the existing buildings, which are characterized by large windows and a significant presence of timber, used both for structures and for flooring and coverings. Fire safety requirements, however, have imposed different solutions for the automatic warehouse which is almost entirely covered in aluminium, while the current sloping windows will be replaced by high-quality three-dimensional coatings made of larch strips, recalling the internal timber structures (Figure 3).

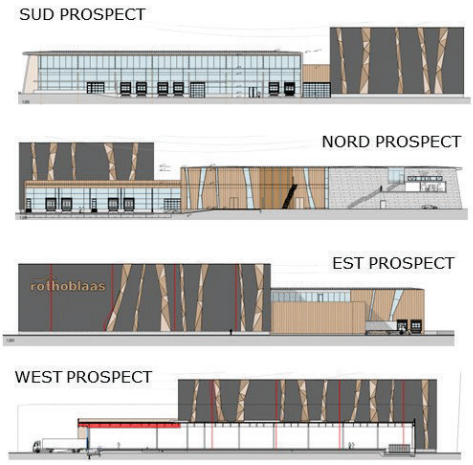

Figure 3: *External prospect of Rotho Blaas ASSTW*

As regard the structural layout, the Rotho Blaas ASSTW has a wooden skeleton (Glulam shelves and beams) enclosed by a CLT skin (roof and perimetral walls). More in details, the ASSTW is braced with two independent systems in the two directions (Figure 4).

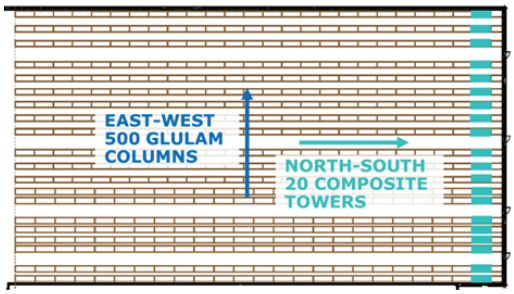

Figure 4: *Scheme of the bracing system for the north-south and East-West directions*

In the north-south direction (long side) twenty bracing towers consisting of a composite box section in LVL and glulam have been used (Figure 5). All the shelving is connected to the bracing towers in order to transfer the seismic forces onto them.

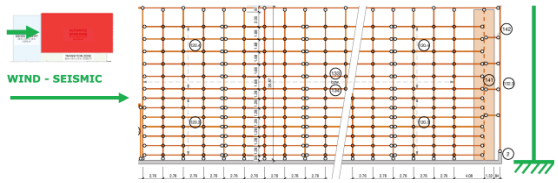

Figure 5: *Scheme of north-south bracing system.*

https://doi.org/10.52202/069179-0331

The composite box towers are embedded in the foundation by means of plates pre-inserted in the poured concrete (Figure 6).

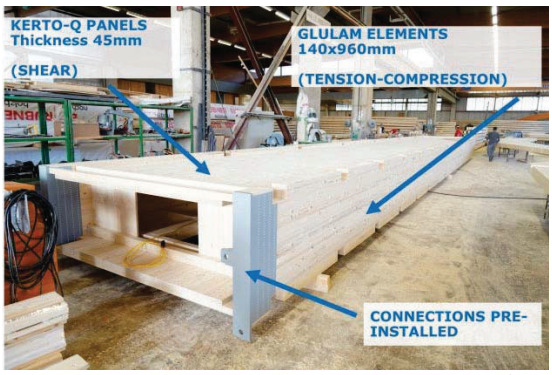

Figure 6: *View of the precast composite bracing tower during the manufacturing phase.*

In the east-west direction, the bracing system is constituted by the shelving itself (Figure 7), with the five hundred cantilevers interlocked at the base and connected to each other only at the roof (Figure 8). The roof is constituted by a framework of glulam beams and CLT panels, which create a limitedly deformable diaphragm.

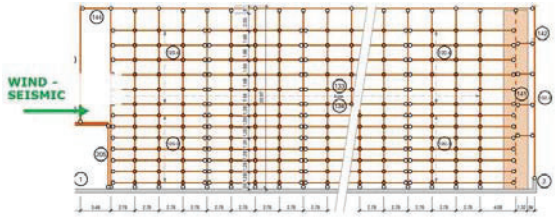

Figure 7: *Scheme of east-west bracing system.*

Figure 8: *Detail of the Glulam cantilever during the manufacturing phase.*

The main critical point of these structures is the deformability towards wind actions, which must be limited in order to allow the machines functionality. In fact, due to operational requirements, the project includes a displacement at the top (at a height of 20 meters) of only 19 millimetres in the east-west direction and 12 in the north-south direction (Figure 9).

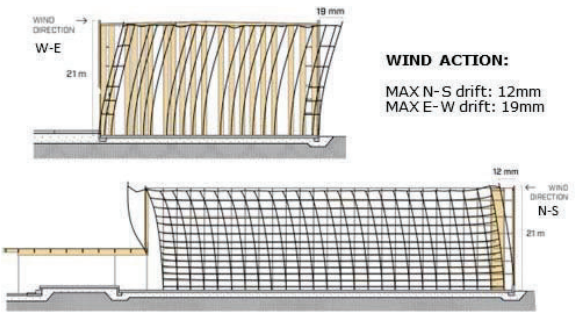

Figure 9: *Deformed shape and max drift of the ASSTW under the horizontal wind action in W-E and N-S directions.*

The ASSTW, is located in northern Italy, in an area classified as low seismic hazard. However, given the height of the building and the isostatic construction system, the seismic design was particularly challenging.
Therefore, a non-dissipative design was chosen, with a structure factor of 1.5 according to EN 1998-1 [3]. Since the building adheres to the existing building, it was necessary to create a seismic joint to decouple the dynamic behaviour between old and new structures (Figure 2).
Regarding to the fire safety, a R30 resistance for all the structures of the warehouse was adopted. It is worth nothing that, it is relatively easy to achieve the R30 requirement with properly designed timber structures. The R30 requirement also shifted the design of connections to solutions without exposed plates, using innovative timber-based materials instead of steel plates. Solutions with intumescent coatings to protect the steel were adopted where this was deemed unfeasible.
A further relevant aspect of warehouse design concerns the in-situ construction phases. In particular, the installation must ensure the stability of the structural system by exploiting the bracing elements of the system itself. Figure 10 shows some explanatory photos of the assembly sequence.

Figure 10: *In situ assembly phases – photo gallery.*

4 ON-SITE MODAL IDENTIFICATION

Goals of the on-site modal identification are:

- Characterization of the modal response of the warehouse in the initial post-construction configuration in order to verify over time, by means of periodic repetition of the dynamic tests, any

https://doi.org/10.52202/069179-0331

changes in the modal response and any system performance decay.

- Validation of the FE numerical model used for the seismic design and subsequent model updating for refined analyses to predict the warehouse response under different mass distribution.
- Identification of the interaction between the contiguous buildings and the stiffening effect of the external facade system.

On site modal identification tests were conducted by CIRI-EC laboratory of University of Bologna.

The modal identification on-site tests were performed installing 12 accelerometers (acc.1-12 in Figure 11) to measure the absolute accelerations of the structure along the longitudinal and transversal direction. Signal acquisitions were carried out when the ASSTW was subject to natural vibrations induced by wind or external vibrations [6].

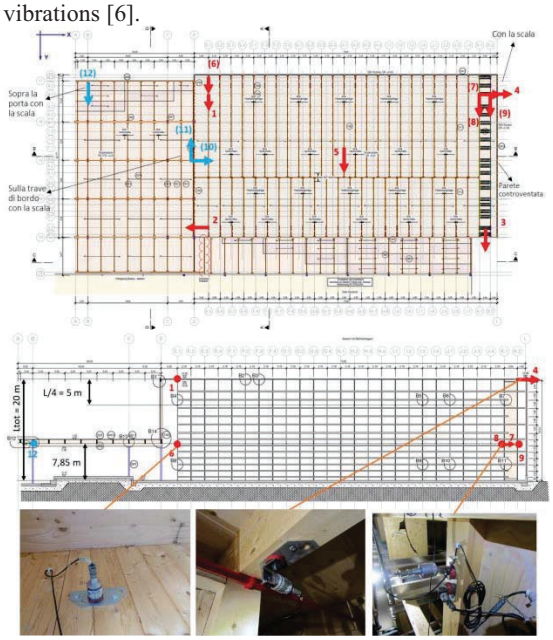

Figure 11: *Plan view and longitudianl section of the structural timber skeleton with indicated the localization of accelerometers employed for the modal identification.*

Two different load conditions were investigated: unloaded warehouse with only the mass of the structural elements and partially loaded warehouse with eccentric mass.

The Enhanced Frequency Domain Decomposition (EFDD) method [7,8] was used to process the on-site acceleration acquisitions obtaining an estimation of eigen frequencies and modal deformations of the Rotho Blaas ASSTW. The method derived from the on-site acceleration acquisition the power spectral density and subsequently the vibration eigenfrequency and modal deformed shape.

Results of modal identification are depicted, in terms of deformed shapes associated to the two principal eigen frequencies, in Figure 12 for the unloaded configuration and in Figure 13 for the partially loaded warehouse with eccentric mass.

Results demonstrate that the additional eccentric mass induces a variation in the principal eigen frequency and correspondent modal shapes. In detail it was observed a reduction of 1st eigen frequency value and modification of the modal response from translational to torsional. Moreover, a reduction of 2nd eigen frequency value was observed without significant modification of the modal response (translational in longitudinal direction).

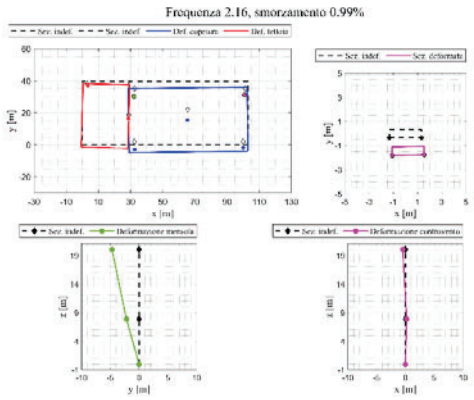

a)

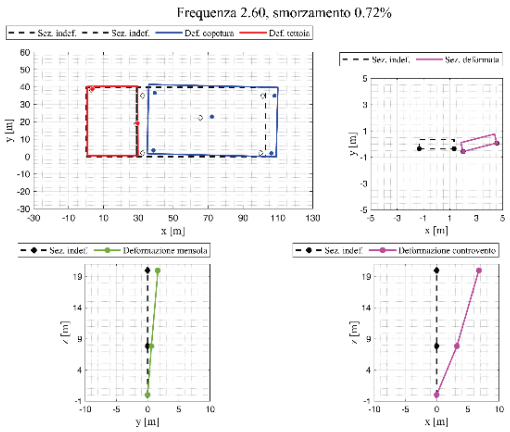

b)

Figure 12: *Unloaded configuration - deformed shape associated to the: a) 1st mode; b) 2nd mode.*

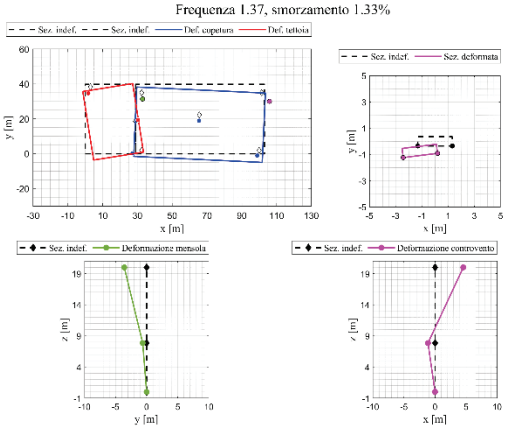

a)

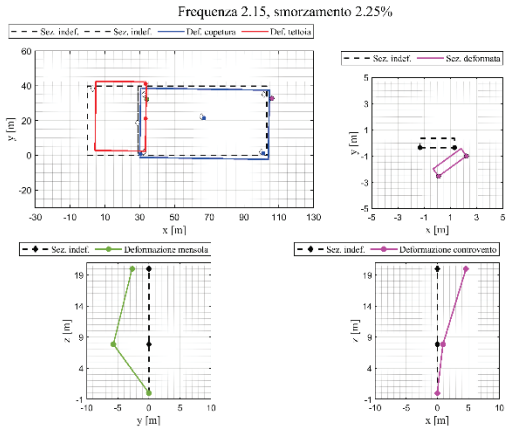

b)

Figure 13: *Partially loaded configuration - deformed shape associated to the: a) 1st mode; b) 2nd mode.*

5 MODEL UPDATING

The modal analyses of the ASSTW, in the different loading configuration, was carried out implementing a detailed Finite Element Model (FEM) considering both the main bracing elements and the stiffening contribution provided by the external massive walls made of CLT panels. The shelves were modelled as cantilever beam elements as well as the bracing towers while plate elements were used for the CLT outer skin panel and for the roof diaphragm. (Figure 14).

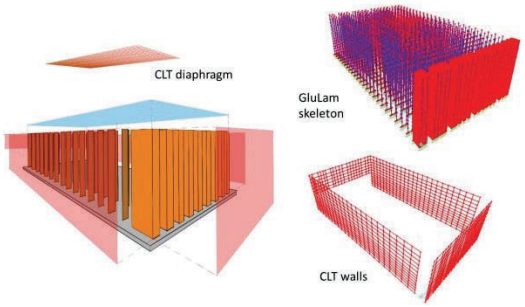

Figure 14: *Scheme of FE model components used for the model updating.*

Different modelling approaches [9] were used to predict the actual response of the warehouse: considering rigid or semi-rigid connections of the shelves and bracing tower; rigid or deformable diaphragm; considering all CLT walls, north and east wall, and no walls [10].
Results form analyses performed considering different modelling hypothesis demonstrate that, for the unloaded configuration, the most accurate model is the one with: fixed shelves and bracing towers; all external CLT walls and deformable diaphragm. This model ensures a good correspondence between FE analyses and identification results for both eigen frequency and modal shape. A comparison between updated FEM results and on-site identification test outputs is reported in Figure 15 for the 1st and 2nd vibration modes.

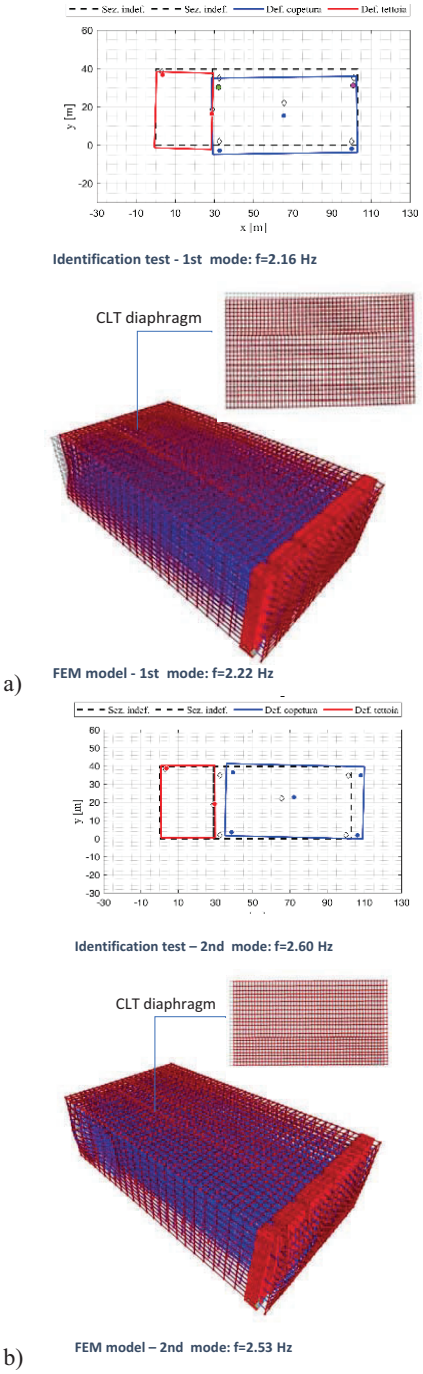

Figure 15: *Partially loaded configuration – comparison between FEM and on-site identification results: a) 1st mode; b) 2nd mode.*

Results substantially demonstrate that for small amplitude vibration (i.e. white noise) all the structural component are activated with a very stiff behavior. ***The*** FEM was also used to investigate the effect of the external CLT walls on the global response of the systems. It was observed that considering only the transversal walls the 1st eigen frequency is reduced from 2.22Hz to 1.46Hz. Otherwise, the system without CLT walls shows a 1st eigen frequency equal to 1.41Hz.

https://doi.org/10.52202/069179-0331

Comparative analyses demonstrate that external walls stiffen the system but do not modify the 1st deformed shape of the warehouse that is governed by the bracing tower. The in-plane stiffness of the roof diaphragm was also investigated. Results highlight that whit a rigid diaphragm the 1st eigen frequency is equal to 2.58 Hz and therefore greater than the reference one (deformable diaphragm - 2.22 Hz). It means that, despite the rigid panel to panel joint, the significant in plant dimension of the floor diaphragm requires a deformable modelling approach.Finally, the updated FEM was used to predict the response of the structure in different load cases: empty; 30% eccentrically loaded; 100% loaded. Figure 16 reports the results from the FE analyses.

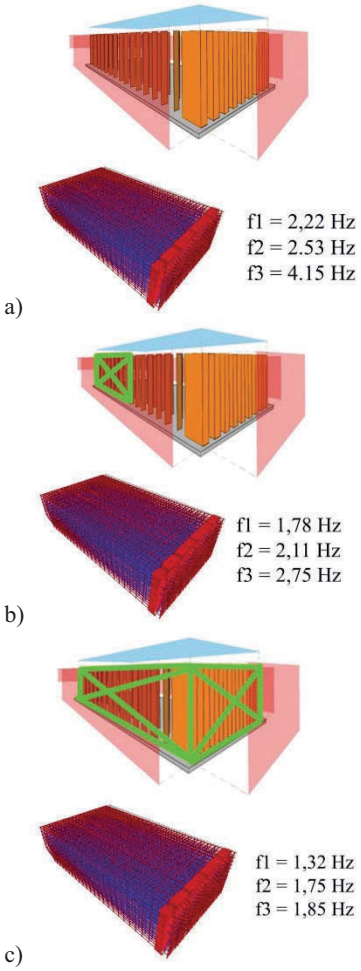

Figure 16: *principal eigen frequencies carried out with FEM analyses for different loading condition of the warehouse: a) empty; b) 30% eccentrically loaded and c) 100% loaded.*

It can be noted that for the 30% eccentrically loaded configuration, results demonstrate a good agreement with outcomes from on-site identification tests. Moreover, a significant reduction of the 1st eigenfrequency is observed for the 100% loaded configuration.

CONCLUSIONS

This work demonstrates the possibility to realize efficient and safe automatic self-supporting warehouse using EWP and high-performance connection elements.
Modal response of such special timber structure can be profitably verified using on-site model identification tests. The FEM can be therefore updated using results of on-site modal identification thus providing a more reliable simulation of actual structural response at global and local level.

REFERENCES

[1] Pozza, L., Savoia, M., Franco, L., Saetta, A., Talledo, D., (2017). Effect of different modelling approaches on the prediction of the seismic response of multi-storey CLT buildings. Int. J. Comp. Meth. and Exp. Meas., Vol. 5, No. 6 (2017) 953–965. DOI: 10.2495/CMEM-V5-N6-953-965.

[2] CEN European Committee for Standardization. (2009) Design of timber structures—Part 1-1: General—Common rules and rules for buildings. Eurocode 5, CEN, Brussels, Belgium, 2009.

[3] CEN European Committee for Standardization. (2013). "Design of structures for earthquake resistance—Part 1: General rules, seismic actions and rules for buildings." Eurocode 8, CEN, Brussels, Belgium.

[4] CEN European Committee for Standardization. (2009) Design of timber structures—Part 1-2: General rules – structural fire design. Eurocode 5, CEN, Brussels, Belgium, 1996.

[5] Loss, C., Pacchioli, S., Polastri, A., Casagrande, D., Pozza, L. & Smith, I., (2018) Numerical study of alternative seismic-resisting system for CLT buildings. Buildings 2018, 8, 162.

[6] Mugabo, I., Barbosa, A. R., Riggio, M. (2019) Dynamic Characterization and Vibration Analysis of a Four-Story Mass Timber Building. Frontiers in Built Environment, 5(86). doi:10.3389/fbuil.2019.00086

[7] Allemang, R.J. & Brown, D-L. 1998. A unified matrix polynomial approach to modal identification. Journal of sound and Vibration, 211(3), 301-322.

[8] Brincker, R., Zhang, L., Andersen, P., 2000. Modal identification from ambient responses using frequency domain decomposition, Atti del 18° SEM - International Modal Analysis Conference - USA.

[9] Mordini, A., Savov, K., Wenzel, H. (2017) The finite element model updating: A powerful tool for structural health monitoring. Structural Engineering International: Journal of the International Association for Bridge and Structural Engineering (IABSE) 17(4), 352– 358. doi: 10.2749/101686607782359010.

[10] Polastri, A., Izzi, M., Pozza, L., Loss, C., Smith, I. Seismic analysis of multi-storey timber buildings braced with a CLT core and perimeter shear-walls. Bull Earthq Eng 2019;17:1009–28. doi:10.1007/s10518-018-0467-9.

World Conference on Timber Engineering Oslo 2023

EVALUATION OF THE STRUCTURAL PERFORMANCE OF SHEAR WALLS BUILT WITH MULTI-LAYER COMPOSITE LAMINATED PANELS

Lin Zheng[1], Sigong Zhang[2], Meng Gong[3],Ying Hei Chui[1]

ABSTRACT: An innovative multi-layer composite laminated panel (CLP), comparable to CLT, has been developed by combining Laminated Strand Lumber (LSL) and dimension lumber to overcome the rolling shear failure while maintaining high mechanical performance and the aesthetic appearance of natural wood. Experimental investigations have been conducted to assess the lateral resistance of CLP connections using self-tapping screws, as well as full-scale CLP shearwalls with varying connection layouts to achieve the target kinematic wall behaviour under both monotonic and cyclic loading. The findings indicate that incorporating Laminated Strand Lumber (LSL) in the laminations has a substantial impact on the mechanical properties of the connections. Replacing lumber with Laminated Strand Lumber (LSL) in the core layer exhibited a remarkable increase in stiffness and strength, and tended to fail in a ductile manner, while the utilisation of LSL in face layers enhanced stiffness and strength, but reduced ductility. Furthermore, the shear wall layout and the number of self-tapping screws in each connection were found to dramatically affect the overall structural performance of the shear wall.

KEYWORDS: Composite Laminated Panel (CLP), Shear walls, Connection properties, Mechanical properties.

1 INTRODUCTION

Over the past decade, mass timber panels (MTPs) have been increasingly implemented in construction as a sustainable and cost-effective building material. The best-known MTP product is cross-laminated timber (CLT), made from sawn lumber planks orthogonally glued together. As a viable product in the mid- and high-rise construction market, CLT offers a promising solution for a diverse range of structural applications in both all-wood and wood-hybrid buildings, including roof, floor, and wall assemblies, and is increasingly replacing other traditional materials such as steel and concrete. The panels can be easily connected to other structural members or materials using fasteners and connectors. The invention of CLT has significantly advanced panelised building technologies.

Although CLT possesses both good dimensional stability and the ability to transfer forces in two-way directions due to its crosswise lamination, its transverse layers are prone to rolling shear failure under out-of-plane loading. This is why new generations of MTPs are being driven forward. The prototype of the next generation of MTP is a combination of lumber and Structural Composite lumber. An innovative multi-layer composite laminated panel has recently been developed by combining laminated strand lumber (LSL) and dimensional lumber to overcome the rolling shear failure while maintaining the high mechanical performance and aesthetic appearance of natural wood, which is referred to here as composite laminated panel (CLP). Test results [14] show that the shear strength, bending stiffness, and moment resistance of CLP were up to 143%, 43%, and 87% higher than their counterparts of regular CLT, respectively, and the use of LSL in transverse layers could eliminate the potential rolling shear failure in CLT. The above promising performance of CLP has prompted researchers to further explore the potential for using CLP as a means of providing lateral load resistance in building systems.

Currently, the most commonly used approach for MTP walls is to consider the MTP as a rigid body and the lateral resistance of the whole wall is mainly governed by connection systems. This theory is based on a set of experimental investigations on full-scale CLT shear walls subjected to lateral loads. [3-4, 7-8] As there are presently no standardized provisions for determining the lateral resistance of CLP shear walls, it is necessary to further investigate this innovative engineered wood product, CLP, used as a lateral load resisting system (LLRS). Additionally, two types of LLRS are typically considered in CLT buildings: monolithic shear walls and multi-panel shear wall configurations. However, in North America, the multi-panel wall configurations are favoured over monolithic shear walls, primarily due to its transportation convenience and potential to enhance energy dissipation in the panel joint connections. (Masroor et al. [13]). Hence, the structural performance of full-scale CLP coupled-panel shear walls were fully evaluated through both monotonic and cyclic loading tests. Accurate quantification of the CLP screw connections was also presented, as it is essential for understanding the shear wall behaviours.

[1] Lin Zheng, University of Alberta, Canada, lzheng1@ualberta.ca
Ying Hei Chui, University of Alberta, Canada, yhc@ualberta.ca
[2] Sigong Zhang, School of Engineering, Newcastle University, Newcastle upon Tyne, UK, Sigong.zhang@newcastle.ac.uk
[3] Meng Gong, University of New Brunswick, Canada, mgong@unb.ca

https://doi.org/10.52202/069179-0332

2 MATERIALS

2.1 SPECIMENS

In total, 21 three-ply MTPs were manufactured by InnoTech Alberta (Edmonton, AB), consisting of 19 three-ply CLP panels with 4 different layer arrangements, and 2 three-ply CLT panels. Figure 1 gives an illustration of the four CLP layups. All shear wall specimens were assembled by placing two panels of the same type side-by-side and connecting them to each other using splice connections. Four shear wall specimen types were fabricated with these four layups respectively. Two specimens were produced for each type with one subjected to a monotonic test and the other to a cyclic test. In addition, one CLT shear wall was also tested as a reference under cyclic loading. Afterwards, specimens for connection tests were obtained by cutting the CLP panels from the undamaged parts of the panels after the shear wall tests.

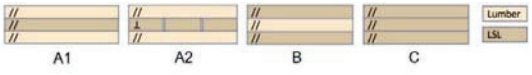

Figure 1: Illustration of CLP layups

2.2 FASTENERS

The study utilized SDS25300 self-tapping screws (STS) with a diameter of 6.35 mm and a length of 63.5 mm, as illustrated in Figure 2. They were made of SAE J403 low-carbon steel wire, possessing a bending yield strength of 1130 MPa (164000 psi), as stated by the manufacturer (SAE 2014). This type of screw has high strength in structural application with no-predrilling installation requirements, which is recommended for wood-to-wood and wood-to-steel connections.

Figure 2: SDS25300 wood screws (courtesy of Simpson Strong-Tie®)

2.3 STEEL PLATES

The steel side plate (HRS416Z) depicted in Figure 3 was manufactured from galvanized steel complying with ASTM A653, SS Grade 33, with a minimum yield strength of 227 MPa (33,000 psi) and a minimum ultimate tensile strength of 310 MPa (45,000 psi) based on the data provided by the supplier.

Figure 3: Steel side plate-HRS416Z (courtesy of Simpson Strong-Tie®)

3 EXPERIMENTAL PROGRAM

This section presents the experimental campaign conducted to investigate the mechanical properties of CLP screw connections as well as full-scale CLP shear walls. All tests were carried out at the Wood Science and Technology Centre, University of New Brunswick, in Fredericton, Canada.

3.1 CONNECTION TESTS

3.1.1 Test setup and procedure

The screw connection tests included 60 specimens with half being subjected to monotonic loading and the other half to reversed cyclic loading. CLP specimens with 4 different layups were tested, as well as a CLT specimen group used as a reference. Table 1 shows the connection specimen configurations. Three replicates were tested for each configuration.

The specimen dimensions were 200 mm × 120 mm × 107 mm for those with the load applied parallel to the face layer grain and 200 mm × 200 mm × 107 mm for those with the load applied perpendicular to the face layer grain. Each side of the CLP member had a 3mm thick steel plate attached using two STSs (SDS HEAVY-DUTY SDS25300), leading to a total of 4 STSs in 2 single-shear connections per specimen. The test setup is shown in Figure 4.

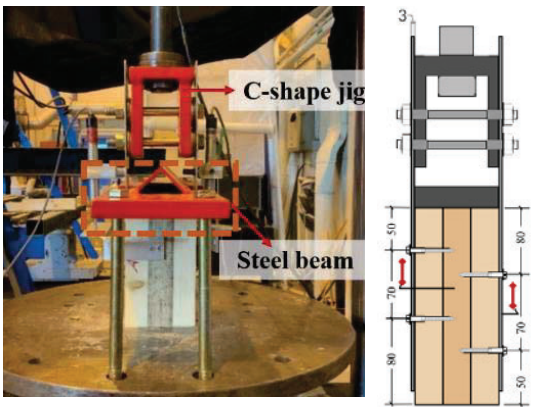

Figure 4: Connection test setup

The monotonic test was conducted at a loading rate of 5 mm/min prior to the cyclic test to obtain a reference displacement value for the cyclic test. The cyclic test was conducted using the reversed loading protocol based on the displacement-controlled loading procedure outlined in ASTM E2126 (Method B) [1].

https://doi.org/10.52202/069179-0332

Table 1: Test matrix for connection tests

Test series	CLP layup	Loading direction	Loading type
A1	L-LSL (par)-L	Par/Perp	m/c
A2	L-LSL (perp)-L	Par/Perp	m/c
B	LSL-L-LSL	Par/Perp	m/c
C	LSL-LSL-LSL	Par/Perp	m/c
CLT	L-L-L	Par/Perp	m/c

Note: "L" is lumber; "LSL" is laminated strand lumber. "Par" indicates the load applied parallel to grain, "Perp" indicates the load applied perpendicular to grain. "m" and "c" means monotonic and cyclic, respectively.

3.2 SHEAR WALL TESTS

3.2.1 Test setup

The CLP walls were anchored to a steel foundation using hold-downs and base shear connectors. As the rollers had horizontal translational and rotational degrees of freedom, four rollers (Ø 7 mm) were placed at the bottom of the panel in order to ensure that the movement of the panel was not restricted and also to prevent friction. A C-shaped channel was attached to the load cell and the actuator, transferring the lateral load through the pin joints to the CLP shear walls. The C-shaped channel was attached to the top of the CLP panel using two 25.4-mm bolts, evenly spaced. It should be noted that lateral supports were used in all the tests to prevent the out-of-plane movement of the wall by using parallel rigid bars and wooden blocks between the guides and specimen. Figure 5 illustrates the shear wall test setup. The shear wall test used Simpson Strong-Tie® steel brackets (Bracket AE116: 90 × 48 × 116 mm), hold-downs (HDU8: 422.5 × 90 × 35 mm). The steel plates used in the panel joint connections were identical to those used in the connection tests. Additionally, the same type of screw was used for all connections, as those tested in the connection tests. Table 2 describes all of the wall configurations tested.

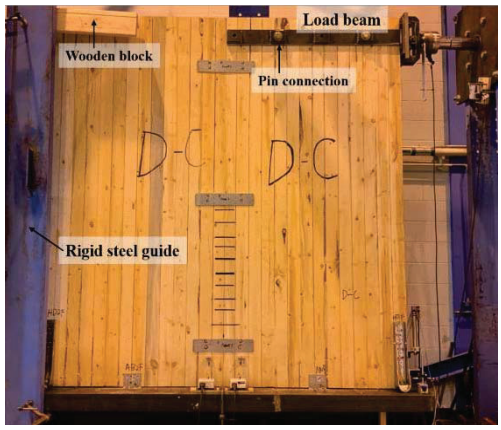

Figure 5: Shearwall test setup

Six linear variable differential transformers (LVDTs) were installed on the specimen as shown in Figure 6.

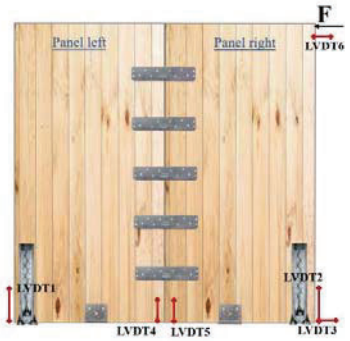

LVDT1: Bottom left corner uplift (negative)
LVDT2: Bottom right corner uplift (positive)
LVDT3: Sliding
LVDT4: Central panel uplift (positive)
LVDT5: Central panel uplift (negative)
LVDT6: Top horizontal displacement

Figure 6: The shear wall sketch with measurement instrumentation

3.2.2 Test Configurations

In this study, three main connections in the shearwalls were panel-to-panel, hold-down, and base shear connections. All these connections share a common characteristic that they can be represented by a steel-to-wood screw connection.

To investigate the kinematic wall behaviour and aspect ratios of the wall panels, different connection layouts were designed by varying number of STS in these connections. Specifically, two target kinematic wall behaviours were considered according to [3]: (a) **Coupled wall** - the wall segments of the coupled wall are connected with a relatively weak panel joint (yielding of the panel joint occurs before yielding of the hold-down/base shear connections) and the wall segment can slide relative to each other under lateral loading; (b) **Single wall** - two panels are connected with a stiff and strong panel joint (yielding of the panel joint occurs after yielding of the hold-downs/base shear connections) and the wall would rotate as a single panel under lateral loading, as illustrated in Figure 7. Identical heights of 2400 mm and widths of 1200 mm were adopted for all CLP panel segments, resulting in an aspect ratio of 2:1 for coupled panel kinematic behaviour and 1:1 for single wall behaviour.

Table 2: Shearwall test matrix

Test Wall ID	No. of screws in brackets	No. of screws in Hold-down	No. of vertical joints	Kinematic behaviour
A1-m	6	9	10	Single
A1-c	6	9	10	Single
A2-m	6	8	6	Coupled
A2-c	6	8	6	Coupled
B-m	6	7	6	Coupled
B-c	6	7	6	Coupled
C-m	6	7	6	Coupled
C-c	6	6	6	Single
D-c	6	8	6	Coupled

A total of 9 shear wall tests were conducted, four of which were monotonic tests and the remaining five being cyclic tests. Table 2 provides a detailed overview of the wall

https://doi.org/10.52202/069179-0332

configurations tested. All the tests were performed with no vertical load applied.

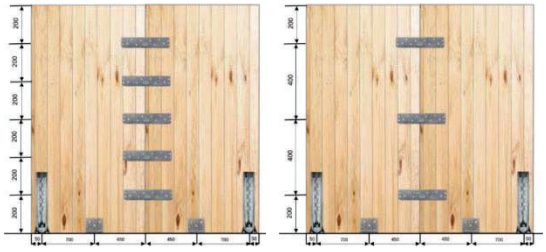

Figure 7: Kinematic wall behaviours: (a) Single wall behaviour (SW); (b) Coupled-panel behaviour (CP) (dimensions in mm)

4 RESULTS AND DISCUSSION

4.1 CONNECTION TESTS

4.1.1 Monotonic tests

Figure 8 and Figure 9 present the load-displacement curves (dashed lines) and their mean value curves (solid lines) of specimens subjected to monotonic loading parallel and perpendicular to the grain, respectively. The measured load values were divided by the total number of screws used to assess the capacity of an individual screw.

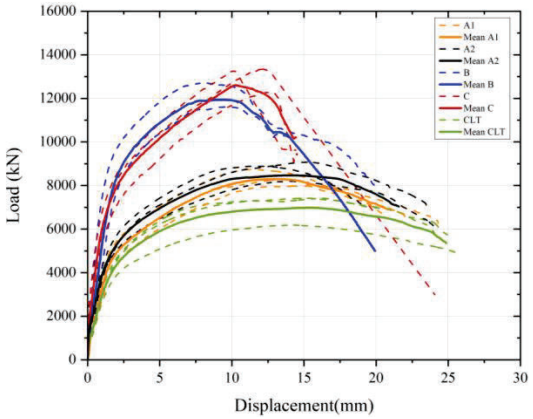

Figure 8: Load-displacement and mean value curves under monotonic load applied parallel to grain (per screw)

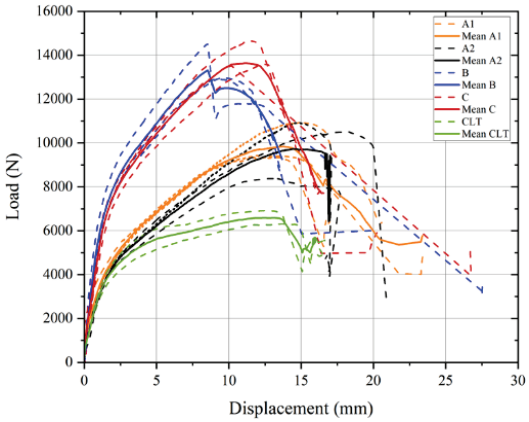

Figure 9: Load-displacement and mean value curves under monotonic load applied perpendicular to grain (per screw)

The presented figures highlight the distinctive behaviours of two test groups, categorized as layup A and traditional CLT in the first group, and layups B and C in the second. It can be observed that specimens A1, A2, and traditional CLT exhibited similar ductile behaviour, with comparable stiffness, yield strength, and ductility. Their load-displacement responses demonstrated that they could be loaded continuously beyond their yield point without significant loss of strength.

In contrast, the screws in specimens B and C demonstrated notably higher strength and stiffness but relatively low ductility. This phenomenon can be attributed to the use of LSL as the face layer of CLP. In other words, CLP with LSL on the face tends to have higher strength and stiffness than lumber on the face. This is because LSL had a higher density than sawn lumber. However, despite the higher strength of specimens B and C, the displacements at failure were extremely small. This observation becomes more apparent when the connection was loaded parallel to grain.

4.1.2 Cyclic tests

The cyclic test results are evaluated in terms of the peak load P_{peak}, yield strength P_{yield}, displacement at capacity Δ_u, displacement at yield load Δ_{yield}, stiffness K_e, ductility ratio μ and dissipated energy E_d according to the standard procedure ASTM E2126 [1]. The mechanical properties were analysed by considering both sides of the hysteresis loops. The mean values of the mechanical properties for each test group, together with the corresponding range of minimum and maximum values (values in brackets are the range of measured values), are presented in

Table 3. The cyclic mechanical properties of the testing group exhibit a trend similar to monotonic cases.

Table 3: Mechanical properties of CLP screw connections under cyclic loads

Specimen ID	K_e (kN/mm)	P_{yield} (kN)	Δ_{yield} (mm)	P_{peak} (kN)	Δ_u (mm)	E_d (kJ)	$\mu = \frac{\Delta_u}{\Delta_{yield}}$
A1-//-c	3.81	6.80	3.45	8.00	6.35	707.88	2.31
	(3.6 - 4.0)	(6.6 - 7.0)	(2.7 - 4.6)	(6.7 - 8.2)	(5.9 - 7.1)	(670.8 - 744.9)	(2.2 - 2.4)
A2-//-c	4.20	7.98	4.30	9.39	8.74	1048.66	2.08
	(3.8 - 4.4)	(7.6 - 8.5)	(3.4 - 5.0)	(9.0 - 10.3)	(8.3 - 9.0)	(852.2 - 1348.8)	(1.8 - 2.5)
B-//-c	4.11	8.63	3.98	10.22	7.44	1013.25	1.87
	(4.1 - 4.8)	(8.6 - 8.9)	(3.9 - 4.1)	(9.7 - 10.6)	(7.2 - 7.7)	(982.2 - 1030.6)	(1.8 - 1.9)
C-//-c	4.98	8.65	3.74	10.19	6.04	754.52	1.62
	(4.9 - 5.0)	(8.5 - 8.8)	(3.6 - 4.0)	(10.0 - 10.5)	(5.8 - 6.3)	(650.4 - 878.6)	(1.5 - 1.8)
CLT-//-c	3.57	6.25	3.54	7.36	10.44	910.00	2.42
	(2.7 - 4.6)	(5.4 - 6.9)	(3.0 - 4.0)	(6.3 - 8.1)	(9.2 - 11.5)	(724.6 - 1100.8)	(2.2 - 2.6)
A1-⊥-c	3.92	7.05	3.0	8.50	8.00	658.97	2.59
	(3.3 - 4.5)	(6.9 - 7.5)	(2.9 - 3.1)	(8.2 - 8.8)	(6.4 - 9.1)	(618.8 - 735.1)	(2.2 - 3.1)
A2-⊥-c	3.22	6.65	4.73	7.89	8.80	713.28	1.78
	(2.8 - 3.4)	(6.6 - 6.8)	(4.4 - 5.1)	(7.8 - 8.0)	(7.5 - 10.1)	(702.8 - 722.1)	(1.7 - 2.0)
B-⊥-c	4.56	8.99	3.83	10.58	6.88	762.28	1.67
	(3.9 - 6.1)	(7.8 - 9.6)	(3.3 - 4.3)	(9.1 - 11.4)	(6.2 - 7.9)	(714.3 - 822.2)	(1.6 - 1.8)
C-⊥-c	6.61	10.34	4.50	11.62	6.20	939.49	1.76
	(6.2 - 7.0)	(9.4 - 11.3)	(3.9 - 5.1)	(10.5 - 13.2)	(5.5 - 6.9)	(800.7 - 1120.9)	(1.7 - 1.8)
CLT-⊥-c	3.70	5.91	4.02	6.95	9.62	735.82	2.42
	(3.3 - 4.1)	(5.5 - 6.3)	(3.7 - 4.4)	(6.5 - 7.4)	(9.6 - 9.7)	(708.1 - 763.6)	(2.2 - 2.7)

4.2 SHEAR WALL TESTS

4.2.1 Failure modes

The CLP shear walls behaved almost as rigid bodies during the test. The failure modes occurred mainly at the connections under both monotonic loading and cyclic loading, as displayed in Figure 10.

For monotonic loading cases, CLPA1-m failed due to both excessive uplift and shear of screws in the hold-down, resulting in slight plastic deformation of the hold-down (right corner), along with wood crushing and wood splitting around the hold-down and angle bracket were observed, while panel joint connection behaved elastically with no visible deformation or failure.

CLPA2-m failed mainly due to brittle failures occurring at the base shear connections (wood splitting and panel edge tear-out) (see Figure 10(d)). In addition, CLPB-m showed an obvious deformation in the hold-down (right corner) with screws pull-out (see Figure 10(a)). No failure was observed on CLPC-m due to the capacity of the test frame. The test was stopped before CLPC-m could fail.

In light of these observations, although CLPA2 and CLPB were designed to have flexible panel connections, the failures were predominantly localized at the hold-downs and base shear connections under monotonic loading. Nevertheless, it is noteworthy that the panel joint connection behaved in an almost elastic manner for all cases tested.

On the other hand, the dominant failure mode observed in the cyclic loading test was the screw yielding followed by screw withdrawal at the panel joint connections. The steel plate also exhibited some degree of plastic deformation, as shown in Figure 10(e) and (f).

(a)

(b)

https://doi.org/10.52202/069179-0332

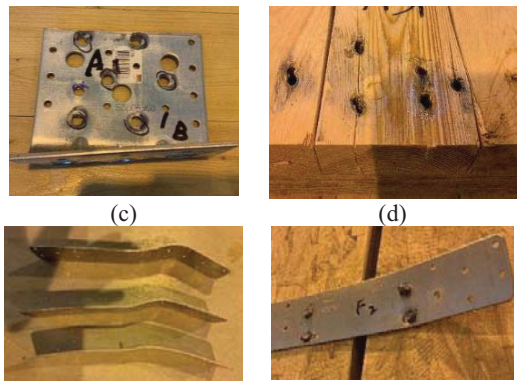

Figure 10: Typical failure modes of shear walls

4.2.2 Load-deformation response

The load-displacement response of each shear wall specimen under monotonic and cyclic tests was obtained. In addition, the envelope curve was generated from the cyclic load response by connecting the peak point of each load cycle. Figure 11 shows the monotonic and cyclic responses of the different wall layouts and the associated envelope curves. The EEEP curve analysis was performed in the same manner as the connection test data and the corresponding mechanical properties are given in

Table 4 and
Table 5.

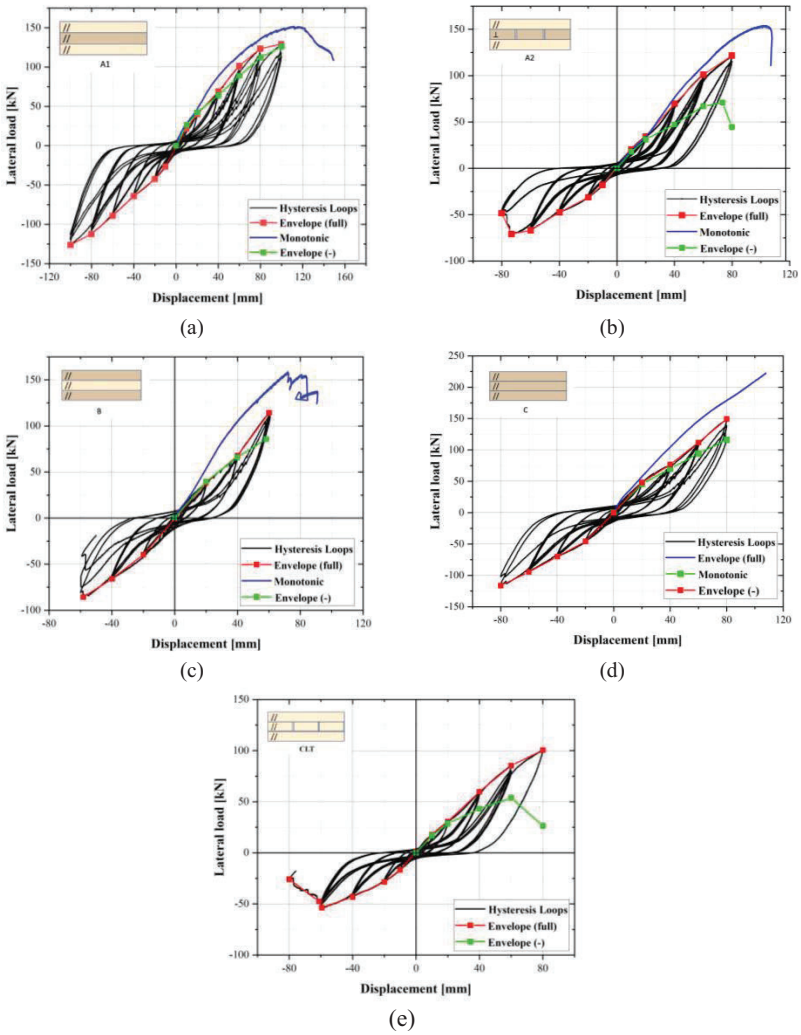

Figure 11: Comparisons of A1-c and A1-m(a), A2-c and A2-m (b), B-c and B-m (c), C-c and C-m (d) and CLT-c

Table 4: Test results of CLP shear wall tests under monotonic loading

Wall ID	K_e (kN/mm)	P_{yield} (kN)	Δ_{yield} (mm)	P_{peak} (kN)	Δ_{peak} (mm)	Δ_u (mm)	E_d (kJ)	$\mu = \Delta_u/\Delta_{yield}$
CLPA1-m	2.32	98.62	52.32	151.73	111.51	142.53	11.96	2.72
CLPA2-m	1.78	104.71	69.21	154.00	118.06	122.19	10.97	1.76
CLPB-m	2.39	80.28	57.25	158.89	91.1	157.77	12.12	2.75
CLPC-m	2.89	-	-	222.48*	95.59*	-	-	-

Note: * testing of wall CLPC was stopped before failure occurred.

Table 5: Test results of CLP shear wall tests under cyclic loading

Wall ID	K_e(+) (kN/mm)	K_e(-) (kN/mm)	P_{peak}(+) (kN)	P_{peak}(-) (kN)	Δ_{ult}(+) (mm)	Δ_{ult}(-) (mm)
CLPA1-c	1.81	1.90	129.18	126.17	99.59	100.1
CLPA2-c	1.78	1.73	121.77	70.92	79.85	79.53
CLPB-c	1.92	1.98	114.31	85.65	60.14	58.19
CLPC-c	2.38	2.26	149.33	116.32	80.03	80.01
CLT-c	1.49	1.65	100.66	53.77	79.97	77.53

The load-displacement response figures above clearly show the differences between the monotonic and reversed cyclic results. The peak loads from the monotonic tests were greater than the corresponding values for the cyclic tests, which was also observed by Popovski [8]. The peak loads from cyclic tests were reduced by 17.4%, 26.5%, 38.9%, and 48.9%, respectively, compared to the corresponding monotonic values. Furthermore, the ultimate displacements obtained from monotonic tests were also greater than the corresponding values obtained from cyclic tests.

In terms of initial stiffness, there is a reduction (20%) when compared to the monotonic test results. The largest difference was for the CLPC wall, with a 35% loss in stiffness under cyclic loading, which can be explained by the different connection details between the monotonic and cyclic tests. It should be noted that to reach the failure limit state of the CLPC wall under cyclic loading, the total number of screws in connection systems of the wall was reduced in the cyclic tests. Furthermore, it can be observed that CLPA1, CLPA2, and CLT walls showed progressively decreasing stiffness values before reaching the ultimate load, whereas a slight increase can be observed for wall CLPB and CLPC walls at displacements between 40 mm and 60 mm. This phenomenon further proves that the use of LSL in the face layer instead of lumber has made a difference.

In addition, the load-displacement responses of all the specimens appeared to exhibit relatively symmetrical load-deflection behaviour. The CLPA2 and CLT walls appeared to have some asymmetric response characteristics. A closer examination of the load-deflection responses would suggest that these walls exhibit apparent asymmetric load-deflection loops, as they failed in one direction before being able to reach the same level of displacement in the opposite direction. It should be noted that several previous studies (Popovski [8]; Dires et al. [5]) also observed the unsymmetrical lateral force-deformation curves for cyclic tests, and low-cycle fatigue may be one of the reasons.

5 CONCLUSIONS

Connection tests and full-scale shearwall tests were carried out for an innovative mass timber panel, CLP, to better understand their performance under lateral loads. From the connection test results, the core layer of the CLP had a non-negligible effect on the lateral strength of the STS connections but the overall performance of connections is less affected by the orientation of the core layer made of the same type of material. However, the face layer of LSL in the CLP significantly increases the stiffness and strength as the density of the face layer increased. Overall, it can be concluded that CLP had higher strength and stiffness than CLT regardless of whether LSL was placed in the face or core layer. However, specimens with lumber as the face layer and LSL as the core, i.e., A1 and A2, exhibited higher strength, stiffness and comparable ductility compared with CLT. This made them more suitable for seismic applications than traditional CLT and CLP with LSL as face layers (B and C).

Furthermore, the shear wall tests revealed that the resistance of coupled shear walls is mainly determined

https://doi.org/10.52202/069179-0332

by the panel-to-panel joints, as well as the hold-down and base shear connections reaching their respective yield strengths. The results indicated that the use of stiffer panel-to-panel connections may be difficult to realise the single wall behaviour in practice, but did make some difference to the entire wall behaviour. The panel-to-panel joint between adjacent panels is critical in determining the kinematic behaviour of the wall system. However, some unexpected brittle failures were observed in the connections during the shear wall tests. Therefore, it is necessary to implement a capacity-based design approach for CLP shear walls. The non-dissipative elements should be over-designed to remain elastic and prevent brittle failures.

REFERENCES

[1] ASTM Standard E2126 (2019). ASTM E2126-11 - Standard Test Methods for Cyclic (Reversed) Load Test for Shear Resistance of Vertical Elements of the Lateral Force Resisting Systems for Buildings. ASTM Int., West Conshohocken, PA, 2019:1–15. https://doi.org/10.1520/E2126—19.

[2] CSA O86 (2019). Engineering design in wood. CSA Group, Mississauga, CA.

[3] Ceccotti, A. (2008). New technologies for construction of medium-rise buildings in seismic regions: the XLAM case. Structural Engineering International, 18(2), 156-165.

[4] D'Arenzo, G., Casagrande, D., Polastri, A., Fossetti, M., Fragiacomo, M., and Seim, W. (2021). CLT shear walls anchored with shear-tension angle brackets: Experimental tests and finite-element modeling. Journal of Structural Engineering, 147(7). https://doi.org/10.1061/(asce)st.1943-541x.0003008

[5] Dires, S., and Tannert, T. (2022). Performance of coupled CLT shear walls with internal perforated steel plates as vertical joints and hold-downs. Construction and Building Materials, 346, 128389.

[6] Gavric, I., & Popovski, M. (2014). Design models for CLT shearwalls and assemblies based on connection properties. International Network on Timber Engineering Research, 18.

[7] Gavric, I., Fragiacomo, M., and Ceccotti, A. (2015). Cyclic Behavior of CLT Wall Systems: Experimental Tests and Analytical Prediction Models. Journal of Structural Engineering, 141(11), 04015034. https://doi.org/10.1061/(asce)st.1943-541x.0001246

[8] Popovski, M., Schneider, J., and Schweinsteiger, M. (2010). Lateral load resistance of cross-laminated wood panels. In World Conference on Timber Engineering (Vol. 20, p. 24), Riva del Garda, Italy.

[9] Pozza, L., Ferracuti, B., Massari, M., and Savoia, M. (2018). Axial – Shear interaction on CLT hold-down connections – Experimental investigation. Engineering Structures, 160, 95–110. https://doi.org/10.1016/j.engstruct.2018.01.021

[10] Shahnewaz, M., Popovski, M., and Tannert, T. (2019). Resistance of cross-laminated timber shear walls for platform-type construction. Journal of Structural Engineering, 145(12), 04019149.

[11] Shahnewaz, M., Popovski, M., and Tannert, T. (2020). Deflection of cross-laminated timber shear walls for platform-type construction. Engineering Structures, 221. https://doi.org/10.1016/j.engstruct.2020.111091

[12] Tomasi, R., and Smith, I. (2015). Experimental characterization of monotonic and cyclic loading responses of CLT panel-to-foundation angle bracket Connections. Journal of Materials in Civil Engineering, 27(6). https://doi.org/10.1061/(asce)mt.1943-5533.0001144

[13] Masroor, M., Doudak, G., and Casagrande, D. (2022). Design of multi-panel CLT shear walls with bidirectional mechanical anchors following capacity-based design principle. Journal of Performance of Constructed Facilities, 36(1), 04021113

[14] Niederwestberg, J.; Zhou, J.; Chui, Y.-H. (2018) Mechanical Properties of Innovative, Multi-Layer Composite Laminated Panels. Buildings, 8, 142.

World Conference on Timber Engineering Oslo 2023

TIMBER INTERACTIVE MODELLING AND POST-PROCESSING SOFTWARE (TIMPS)

Manuel Sánchez-Solís[1], Màxim Lliso[2], Fernando Ibáñez[3]

ABSTRACT: Timber Interactive Modelling and Post-Processing Software (TIMPS) is an internal programming routine implemented by Degree of Freedom for the scope of the analysis and design of timber structures acting as a plug-in for the most common commercial FEM software. Design timber codes and technical approvals from manufacturers are continuously being updated, therefore, design methods should also be adjusted to the latest equations. TIMPS is able to be customized for each project according to the current regulations and previous experiences in order to optimize the design of glulam members, CLT panels and connections specially for constructions with large amount of timber structural elements. The mechanical properties of the timber and its connections are calculated and transformed into typical inputs of commercial software, where the analysis is performed. Once the analysis is finished, TIMPS reads the software output and performs all verifications included in the codes. When the structure is optimized, final reports and graphics are printed.

KEYWORDS: Post-processing, Finite Element Method, analysis, timber, glued-laminated, CLT, cross-laminated, connections

1 INTRODUCTION

In the last two decades, the use of wood as a structural material in construction has experienced exponential growth all around the world. In some countries, structural timber is usually used in roofs, walkways, and single-family homes, limiting its use in big buildings which tend to have additional complexity, with a large floor volume or even a considerable height (up to 20-25 floors).

In this last application, the structural typology based on surface elements (walls and slabs) predominates globally, using panels of cross-laminated wood or CLT.

Regarding the structural design of this type of buildings, two great challenges appear compared to the calculation of conventional buildings: the modelling/verification of the linear elements and panels as structural elements and the modelling/design of the joints between panels.

One of the main characteristics of CLT panels is their orthotropy (both sectional and at the material level), which adds complexity to structural modelling in non-specific commercial calculation software, since a pre-process is required to transform the characteristics of the panel. to the characteristics of the finite element (different for each software).

Regarding its verification, again a specific formulation is required, not included in the usual software, which requires an external post-processing by the user to transform the forces of the finite element into stresses and demand/capacity ratios.

In relation to the joints between panels, the situation is analogous. It is possible to model them in conventional software with additional effort, while external post-processing is required to allow the joints to be dimensioned.

Regarding the first point, there are several programs aimed at sectional calculation and design of isolated elements of timber. The use of these programs is very useful in the design of small-scale buildings and in the pre-dimensioning of elements.

Among the commercial calculation software, there is a range of alternatives for the design of both linear and planar timber elements, however, not always the demands from the project are satisfied because of the available manufacturers of each region or the latest technical approvals or codes.

Furthermore, this software does not resolve all aspects of the design, since the results in joints between panels are limited to the mere obtaining of forces, also requiring external post-processing. Lastly, they do not have the versatility and power of other more advanced commercial software that allow for more complex applications to be carried out.

2 MODELLING SPECIFICITIES USING FEM FOR WOODEN STRUCTURES

FEM is a powerful extended tool in the structural professional practice regarding common structural elements (beams, shells) and materials (steel, concrete) thanks to its calculation capacity which translates to both precision and speed. However, important mechanical concepts need to be taken into account for the modelling of CLT panels and the adaptation of some aspects must be

[1] Manuel Sánchez-Solís, Degree of Freedom SLU, Valencia, Spain, m.sanchez@dofengineers.com
[2] Màxim Lliso, Degree of Freedom SLU, Valencia, Spain, m.lliso@dofengineers.com
[3] Fernando Ibáñez, Degree of Freedom SLU, Valencia, Spain, f.ibanez@dofengineers.com

https://doi.org/10.52202/069179-0333

implemented in order to correctly represent and control the behaviour of this shell elements.

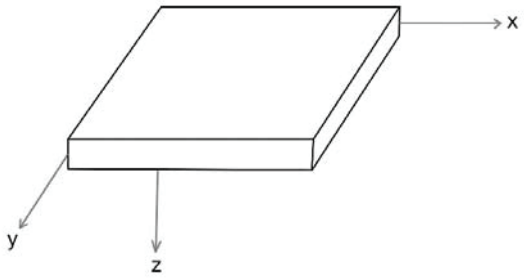

Figure 1: *Axes of orthotropic shells*

2.1 MATERIAL AND SECTIONAL ORTHOTROPIC PROPERTIES

CLT panels are shell elements constituted by different wooden layers which are orthogonally orientated with respect to the direction of their fibres. This fact consequently introduces two types of orthotropy: a material orthotropy in each layer and a sectional orthotropy in a given cross-section. In structural terms this has a particular impact on the shell stiffness since the double orthogonal symmetry of an orthotropic material originates a specific stiffness matrix shape.

In the case of isotropic shells in an elastic regime respecting the Infinitesimal Strain Theory, the stiffness matrix regarding stresses and strains is:

$$C = \begin{bmatrix} C_{11} & C_{12} & C_{13} & 0 & 0 & 0 \\ C_{21} & C_{22} & C_{23} & 0 & 0 & 0 \\ C_{31} & C_{32} & C_{33} & 0 & 0 & 0 \\ 0 & 0 & 0 & D_{11} & 0 & 0 \\ 0 & 0 & 0 & 0 & D_{22} & 0 \\ 0 & 0 & 0 & 0 & 0 & D_{33} \end{bmatrix} \quad (1)$$

In which the terms are:

$$C_{ii} = \frac{(1-\nu)E}{(1+\nu)(1-2\nu)} \quad (2)$$

$$C_{ij} = \frac{\nu\, E}{(1+\nu)(1-2\nu)} \quad (3)$$

$$D_{ii} = \frac{E}{2\,(1+\nu)} \quad (4)$$

Note the fact that only two parameters, the Young Modulus and the Poisson Coefficient, are required to define the stiffness matrix of an isotropic material.

As the study case is based on an orthotropic material, more parameters are needed to define the elastic properties of a cross-section. Those parameters are:

- Three Young Modulus:
  - E_{11}, E_{22} and E_{33}
- Three Poisson Coefficients:
  - ν_{12}, ν_{13} and ν_{23}
- Three Shear Modulus:
  - G_{12}, G_{13} and G_{23}

The stiffness matrix coefficients become then:

- Axial part:

$$C_{ii} = \frac{E_i(1-\nu_{jk}\nu_{kj})}{\Delta} \quad (5)$$

$$C_{ij} = \frac{E_j(\nu_{ij}+\nu_{kj}\nu_{ik})}{\Delta} \quad (6)$$

- Transverse part:

$$D_{ii} = \Delta G_{jk} \quad (7)$$

Where indices *i*, *j* and *k* are always different and vary from 1 to 3 and:

$$\Delta = 1 - \nu_{23}\nu_{32} - \nu_{31}\nu_{13} - \nu_{12}\nu_{21} - \nu_{12}\nu_{23}\nu_{31} - \nu_{32}\nu_{21}\nu_{13} \quad (8)$$

In the context of plate mechanics, no stress or strain is considered in the Z axe and a planar stress state occurs. Furthermore, it is possible to work with only one stiffness matrix with the shape of the one regarding the isotropic case if the cross-sectional orthotropy is physically represented in an equivalent single-layer shell. A method that fulfils this purpose is defined in section 3.1. By contrast, several coupled stiffness matrixes (one per layer) should be used to represent the global behaviour of the shell, which makes the analysis more complex.

These parameters are defined by the user in a later stage.

2.2 FINITE ELEMENT METHOD IMPLEMENTATION

As the FEM for static cases operates with force, stiffness, and displacement matrixes, these must be defined. The stiffness matrix of one layer is then computed in terms of force and displacement assuming the inexistence of work deformation in the Z axis (perpendicular to the plane of the shell). This matrix is introduced by the user into the calculation tool and will be called the elementary stiffness matrix hereafter.

Thus, external forces are:

$$F = \begin{pmatrix} M_x \\ M_y \\ M_{x,y} \\ V_x \\ V_y \\ N_x \\ N_y \\ N_{x,y} \end{pmatrix} \quad (9)$$

Where m_x and m_y are bending moments, $m_{x,y}$ is the torsional torque, V_x and V_y are the shear efforts due to bending, n_x and n_y are the membrane efforts and finally $n_{x,y}$ is the shear effort due to membrane loading. The associated stiffness matrix is:

https://doi.org/10.52202/069179-0333

$$K = \begin{bmatrix} k_x & k_v & 0 & 0 & 0 & 0 & 0 & 0 \\ k_v & k_y & 0 & 0 & 0 & 0 & 0 & 0 \\ 0 & 0 & k_{x,y} & 0 & 0 & 0 & 0 & 0 \\ 0 & 0 & 0 & S_x & 0 & 0 & 0 & 0 \\ 0 & 0 & 0 & 0 & S_y & 0 & 0 & 0 \\ 0 & 0 & 0 & 0 & 0 & D_x & D_{x,y} & 0 \\ 0 & 0 & 0 & 0 & 0 & D_{x,y} & D_y & 0 \\ 0 & 0 & 0 & 0 & 0 & 0 & 0 & D_S \end{bmatrix} \quad (10)$$

These terms are calculated according to the Eurocode 5: Design of Timber Structures and Reissner-Mindlin plate theory, where K_z bending is not considered.
Finally, the displacement vector is given as:

$$U = \begin{pmatrix} \frac{\partial \Phi y}{\partial x} \\ -\frac{\partial \Phi x}{\partial y} \\ \frac{\partial \Phi y}{\partial y} - \frac{\partial \Phi x}{\partial x} \\ \frac{\partial uz}{\partial x} + \Phi y \\ \frac{\partial uz}{\partial y} - \Phi x \\ \frac{\partial ux}{\partial x} \\ \frac{\partial uy}{\partial y} \\ \frac{\partial ux}{\partial y} - \frac{\partial uy}{\partial x} \end{pmatrix} \quad (11)$$

Obviously, this formulation applies in the Continuous Medium Mechanics framework. The conversion into finite element exploitable objects is automatically done by the industrial calculation software by meshing the shells. Consequently, the size of the finite element stiffness matrix will depend on the level of discretisation reached.
All equations above are further simplified for frame finite elements (beams and columns).

2.3 STRUCTURAL JOINTS

The connection between different elements is modelled by the use of the finite element type "link" from industrial software, which connects two nodes with different properties. The stiffness for each degree of freedom is defined according to the slip modulus calculated for each connection.
For direct contact connections, a high stiffness value is defined to ensure that the loads are transferred as expected. For released degrees of freedom, a low stiffness value is used (instead of 0) to prevent from numerical errors during analysis.
The slip modulus to define the correct stiffness value of the connection is calculated according to Eurocode 5, chapter 7.1. The table below show the equations to obtain the shear stiffness of the connections based on the connector type, timber density and diameter of the screws. The axial slip modulus is not included in the Eurocode as these values are normally defined by the producers.

Table 1: *Values of k_{ser} for fasteners and connectors in N/mm in timber-to-timber and wook-based panel-to-timber connections. EC 5.*

Fastener type	K_{ser}
Dowels Bolts with or without clearance[a] Screws Nails (with pre-drilling)	$\rho_m^{1,5} \cdot d/23$
Nails (without pre-drilling)	$\rho_m^{1,5} \cdot d^{0,8}/30$
Staples	$\rho_m^{1,5} \cdot d^{0,8}/80$
Split-ring connectors A (EN 912) Shear-plate connectors B (EN 912)	$\rho_m \cdot d_c/2$
Toothed-plate connectors: - C1 to C9 (EN 912) - C10 and C11 (EN 912)	 $1{,}5 \cdot \rho_m \cdot d_c/4$ $\rho_m \cdot d_c/2$
[a]The clearance should be added separately to the deformation	

Th Eurocode states that for steel-to-timber connections, shear stiffness can be multiplied by 2.
The way in which screws are oriented along a CLT joint has an impact on both strength and stiffness of the connection. It is commonly assumed in the timber design references that only screws inserted perpendicular to the external force will work with a shear mechanism while any inclination of the fastener will make it work axially. Therefore, crossed-screws connections are very typical in timber industry. This concept is described in the following figure.

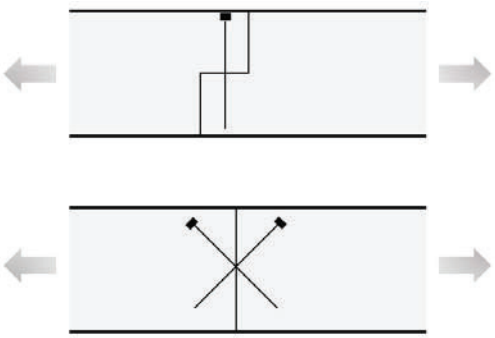

Figure 2: *Different screws resistance mechanisms*

3 TIMPS WORKFLOW

The improvement achieved in the logistical aspect of data processing is obvious. All the design process is now confined in two interfaces (the industrial FEM software and our self-elaborated routine) and the need of manually importing data sets is removed. The calculation stages are explained hereafter.

3.1 COMPUTATION OF THE ELEMENTARY STIFFNESS MATRIX

The elementary stiffness matrix is computed by using the Gamma Method for wooden structures developed in the Eurocode 5 or the Extended Gamma Method if the cross-section contains more than three longitudinal layers. By using this method, the shear stiffness of each layer is considered in the calculus by diminishing the second moment of inertia of the whole cross-section. This

https://doi.org/10.52202/069179-0333

approximation allows for the transition from a multi-layered material to a single-layered one, making it possible to build a single stiffness matrix for the complete orthotropic cross-section. Moreover, the coefficients of wood's transverse expansion ν_{ij} are often considered to be zero. This results in a diagonal matrix since $k_\nu = D_{x,y} = 0$ and therefore in a classical beam stiffness matrix for a generalised 3D situation.

3.2 STRUCTURAL MODELLING AND COMPUTATION

Structural modelling and computation are the only parts of the process elaborated by means of industrial FEM software. Therefore, the user defines the geometry, its boundary conditions, the loads and the load combinations of a given structure using wooden beams and CLT shells, which will be identified by groups. These shells are meshed and the model is computed. Various files containing the computation results are finally automatically created. Among data results, those of interest are the ones associated to nodal forces since they are needed in order to perform the stress analysis and verifications at the multi-layered element scale.

3.3 MODEL DATA ACCES THROUGH PROGRAMMING TOOLS

Once the FEM model is computed, several data packages are extracted using self-elaborated Python routines. Then, results can be selected, exported and manipulated. A significant improvement regarding post-processing computations is achieved by filtering datasets because the amount of data to be treated is well classified and defined. This improvement is appreciated when working with wooden buildings of more than ten floors since more structural effects and parameters, particularly linked to wind loading, need to be precisely considered. This translates into a relatively large amount of data to manage, so it is essential to only work with the necessary inputs with the aim of making post-processing approachable.
The extracted data is then:

- Connectivity chart: this chart identifies each finite element with the nodes that form it.
- Node properties: each node is identified with a number according to their group. Their degrees of freedom as well as their global coordinates are obtained.
- Nodal forces: forces at each node.

This data is stocked in text files.

3.4 MODEL DATA SELECTION BY STRUCTURAL GROUPS AND LOAD CASES/COMBINATIONS

As all data coming from the finite element model belongs to a certain node, it is possible to filter it by the group to which it belongs. As stated before, these groups are created by the user when modelling the structure by means of the industrial software. The advantage of working with group data is that it allows for the possibility to only analyse the selected CLT shells or glulam frames.
On the other hand, a load combination analysis is also feasible. Results of a certain load case or combination can be extracted as well as the results of all ULS or SLS combinations. It is also possible to determine the most unfavourable load combination for each structural element in ULS and SLS so the design calculus can be directly done.
Thus, not all the finite element model's generated data is used to further develop the post-processing analysis.

3.5 IMPLEMENTATION OF VERIFICATION EQUATIONS ACCORDING TO EUROPEAN STRUCTURAL REGULATION

Stress limits are stablished by the Eurocode 5: Design of Timber Structures for ULS. Deformation limits are stablished the same way for SLS.
These equations are implemented in the calculation tool. The ULS verifications carried out are listed below.
Axial and bending verification for timber elements:

- Tension:

$$\frac{\sigma_{t,0,d}}{f_{t,0,d}} + \frac{\sigma_{m,y,d}}{f_{m,y,d}} \leq 1 \tag{12}$$

- Compression:

$$\left(\frac{\sigma_{c,0,d}}{f_{c,0,d}}\right)^2 + \frac{\sigma_{m,y,d}}{f_{m,y,d}} \leq 1 \tag{13}$$

Axial and bending verification for walls and columns. Buckling:

$$\frac{\sigma_{c,0,d}}{k_{c,y}\, f_{c,0,d}} + \frac{\sigma_{m,d}}{f_{m,d}} \tag{14}$$

Shear:

$$\tau_{v,R,d} \leq f_{v,R,d} \tag{15}$$

In-plane shear for CLT panels:

- Shearing-off failure of the boards along a joint:

$$\tau_{v,s,d} \leq f_{v,CLT,d} \tag{16}$$

- Shearing failure of the glued surfaces in the intersection points:

$$\tau_{v,T,d} \leq f_{T,CLT,d} \tag{17}$$

- Shear failure of the entire plate:

$$\tau_{v,d} \leq f_{vgross,CLT,d} \tag{18}$$

With regards to SLS verifications, quasi-permanent and characteristic design situations are taken into account. The verifications are the following:

Deflection:

- Characteristic design situation:

$$w_{inst} \leq \frac{L}{300} \tag{19}$$

- Quasi-permanent design situation:

$$w_{fin} = w_{inst} + w_{creep} \leq \frac{L}{250} \tag{20}$$

Shear wall deformation:

$$w_{hor} = w_M + w_V + w_z + 2w_F \leq \frac{H}{300} \tag{21}$$

Where w_M is the bending deformation, w_V is the shear deformation, w_Z is the expansion of the tie rods and w_F is the displacement of the joints between wall and ceiling.

3.6 RESULT PLOTTING

Designing structures is an iterative process in which many parameters need to be considered. The variation of one of those parameters can significantly impact the results and it may not be easy to detect them, so a graphical representation is needed. Nodal displacements and stresses of the CLT shells or timber frames are plotted so that structural design judgement can be properly done.

As the TIMPS can work with several industrial software by interacting with their API, an interpolation module is provided for the cases in which data extracted is not interpolated so accurate plots can be done.

3.6.1 Examples

This section includes some of the outputs provided by this tool in different projects.

Results for planar elements, linear elements and joints between CLT panels are shown below.

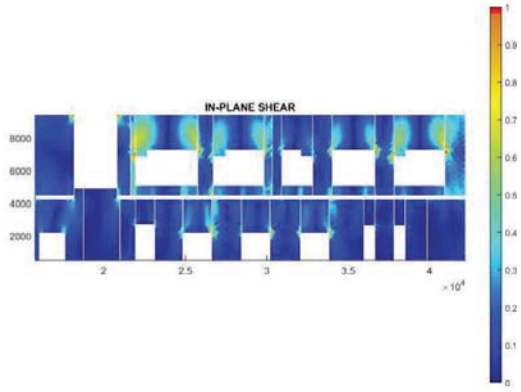

Figure 3: *In-plane shear verification of façade CLT walls*

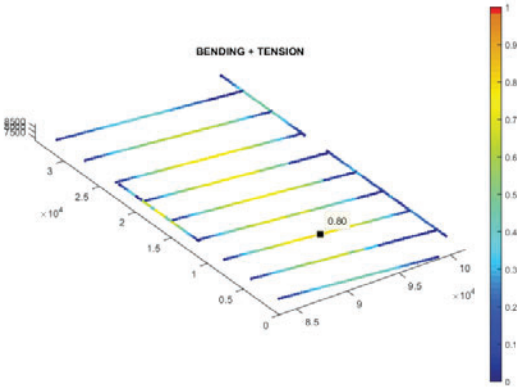

Figure 4: *Bending verification of roof timber beams*

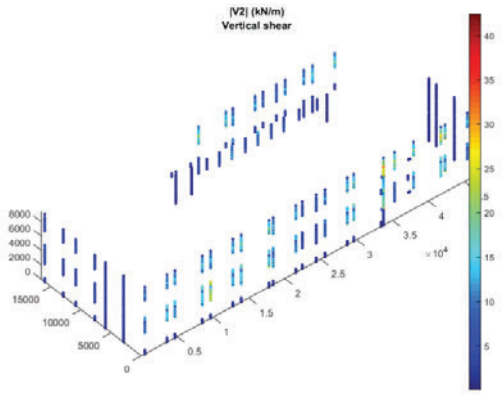

Figure 5: *Vertical shear forces in CLT joints*

3.6.2 Documentation generation

Once the iterative design process is finished, design reports and CAD files with required spacing of screws are exported.

The complete process performed by TIMPS is described in the following figure.

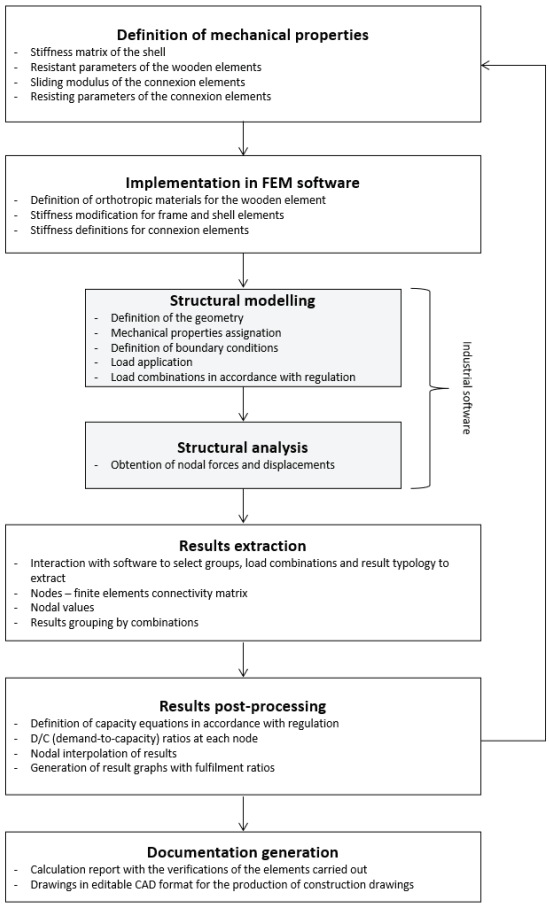

Figure 6: *TIMPS design workflow*

https://doi.org/10.52202/069179-0333

4 POTENTIAL IMPROVEMENTS

Several improvements are planned for the future of this tool. Some of them are listed below.

1) Predefinition of connection type catalogue with already calculated stiffness and strength to allow the user to check the most common joint solutions.
2) Connection to different software in the scope of the parametric design.
3) Improvement of CAD export function to minimize time consumed during detailed drawings production.
4) Evaluation of the transverse Poisson's Coefficients of the material in CLT shell computations. By considering them the results would be more accurate since the stiffness would be increased and best represented.

5 CONCLUSION

Timber Interactive Modelling and Post-Processing Software (TIMPS) is a design tool compatible with many of the commercial software for the purpose of the analysis, design and optimization of big timber structures based on the latest codes and technical approvals. The main goal of the application is to allow for quick updates of equations based on latest regulations and approaches from suppliers and producers in order to optimize future constructions by reducing the engineering time consumed for the verifications as a result of the iterative process inherent in the timber design sequence and the amount of data which needs to be evaluated by the structural engineer.

REFERENCES

[1] Eurocode 5: Design of Timber Structures EN 1995.
[2] M. Wallner-Novak, J. Koppelhuber, K. Pock. Cross-Laminated Timber Structural Design. Basic design and engineering principles according to Eurocode, proHolz. Graz, Austria, 2014.
[3] M. Wallner-Novak, M. Augustin, J. Koppelhuber, K. Pock. Cross-Laminated Timber Structural Design. Volume 2, proHolz. Graz, Austria, 2018.
[4] Lebée, A. Modélisation des Structures Multicouches. Paris, France, 2022.

https://doi.org/10.52202/069179-0333

World Conference on
Timber Engineering
Oslo 2023

NUMERICAL AND EXPERIMENTAL INVESTIGATIONS ON THE STRESS STATE OF CLT-PLATES NEAR CONCENTRATED LOADS

Heinz Wimmer[1], Christoph Huber[2], Robert Eder[3]

ABSTRACT: Cross laminated timber (CLT), as a structural plate-like timber product has been successfully established in civil engineering practice as a load bearing product for walls, floor and roof elements. In a bending situation with transverse shear the cross section does not remain in a plane form due to the strong flexibility of crossing layers. The deformed cross section shows a significant warping which follows a zigzag pattern that influences the stress state. Comparative studies are worked out to investigate the efficiency of two different structural theories. It turned out, that the traditionally used First Order Shear Deformation Theory (FSDT) does not reflect satisfactorily the local stress state near concentrated loads. It is demonstrated that the relatively new Refined Zigzag Theory (RZT) is much better able to represent the stresses in different layers of CLT-plates in such a case. In particular, the rolling shear stress and the maximum bending stress will be strongly underestimated by FSDT, while RZT will provide accurate results. This finding was confirmed by alternative analysis with high-resolution FE continuum elements and by experimental tests using linear strain gauges and a digital image correlation system (DIC) to record the deformations in the area of interest.

KEYWORDS: Cross Laminated Timber, First Order Shear Deformation Theory, Refined Zigzag Theory, Stress state, Rolling shear stress, Concentrated load, Digital image correlation (DIC)

[1] Heinz Wimmer, MPT Engineering GmbH A-4221 Steyregg, Austria, Carinthia University of Applied Sciences, 9800 Spittal /Drau and Upper Austria University of Applied Sciences, 4600 Wels, h.wimmer@fh-kaernten.at
[2] Christoph Huber, KASTNER ZT-GmbH (Civil Engineering), A-9020 Klagenfurt, Austria, c.huber@fh-kaernten.at
[3] Robert Eder, Poltnigg & Klammer ZT-GmbH (Civil Engineering), A-9800 Spittal/Drau, Austria, r.eder@pundk.at

https://doi.org/10.52202/069179-0334

1 INTRODUCTION

Cross laminated timber (CLT), applied as structural plate-like products has revolutionized timber construction for many years. The worldwide production volume is still increasing [1]. For floor systems, single-span strips are predominantly used, characterized by bending with uniaxial load transfer. For the analysis of these types of structural elements many methods exist. A well-known procedure is the Gamma-method [2], originally developed for composite beams with interlayer slip by Möhler [3], which can be modified for applications of CLT. The Shear Analogy (SA) method introduced by Kreuzinger [4] and worked out by Scholz [5,6] provides more capability concerning the local stress state. For beams and plates, the First Order Shear Deformation Theory (FSDT) [7,8] can be used when an appropriate shear correction factor is installed. For multi-span systems as well as for systems with concentrated loads most of the above-mentioned analysis tools are not sufficient to accurately predict the structural behavior, especially the local stress state. In these cases, a higher order plate theory which considers the specific warping phenomenon should be applied. While elaborate 3D analysis is indicated in cases of ultimate load determinations and predictions of damage histories [9], it is useful to resort to structural theories for everyday design tasks. The latter are less complex and easier to handle. In the wide field of theories of composite laminated structures, the following groups are distinguished: Equivalent single layer theories (ESL) [10], Layer-wise theories (LW) [11] and Zigzag Theories [12]. ESL models provide poor results of local variables when employed to highly heterogeneous laminates. The abrupt change of the mechanical properties between layers leads to a change in slope of the in-plane displacements. LW-theories, wherein kinematic assumptions are made for each layer, can reproduce these kinks very well, but the numerical effort increases with the number of plies involved. A good compromise between computational cost and accuracy is offered by the Zigzag models.

The Refined Zigzag Theory (RZT) [13] is an efficient structural theory based on the well-known First Order Shear Deformation Theory, enhanced by local kinematic terms, which allow for the particular attention of warping that arises in the cross section due to shear-elastic layers. The great accuracy of this approach was assessed by comparison with 2D and 3D analytical solutions and 2D-FE solutions as well [13,14]. In a recently published paper, the application of RZT to uniaxial spanned CLT-plates and other shear elastic timber structures like timber-concrete composite beams and timber beams with discrete shear dowels is demonstrated [15]. For single span beams with uniformly distributed loads, there is no significant difference in stress state between FSDT and RZT. In continuous beams and/or when concentrated loads are applied, there are considerable deviations that can no longer be ignored. The Refined Zigzag Theory can work out the qualitative differences that arise from the constrained warping deformations, while FSDT shows an unvarying stress pattern along the whole beam.

2 REFINED ZIGZAG THEORY

The Refined Zigzag Theory was founded in 2010 by Alexander Tessler (NASA) and co-workers from Politecnico di Torino [13]. Since that time many papers have been published, see e.g. references [16–19], showing the tremendous capability of this approach.

2.1 PLATE KINEMATICS

The plate is referred to a Cartesian coordinate system $(\boldsymbol{x}_\beta, z,\ \beta = 1,2)$ (Figure 1). Its thickness h consists of N completely bonded orthotropic layers. The normal surface load $q_z\ (\boldsymbol{x}_\beta)$ is acting on the mid-plane in the positive z-direction. The kinematic field in classical RZT-plate theory is written as

$$\boldsymbol{u}_\alpha^{(k)}(\boldsymbol{x}_\beta, z) = \boldsymbol{u}_\alpha(\boldsymbol{x}_\beta) + z.\theta_\alpha(\boldsymbol{x}_\beta) + \phi_{\alpha\rho}^{(k)}(z).\psi_\alpha(\boldsymbol{x}_\beta)$$
$$u_z^{(k)}(\boldsymbol{x}_\beta, z) = w(\boldsymbol{x}_\beta) \qquad (1)$$

$\boldsymbol{u}_\alpha^{(k)}(\alpha, \rho = 1,2)$ denote the in-plane displacements, $u_z^{(k)}$ the transversal deflection of the k-th layer. $\boldsymbol{u}_\alpha,\ w,\ \theta_\alpha$ represent the displacements of the mid-plane and the rotations of cross sections respectively. $\phi_{\alpha\rho}^{(k)}$ are the layer-wise linear zigzag functions (Figure 2), which are only dependent of the layer setup and the transversal shear moduli. Finally, ψ_α mean the zigzag rotations which are the two additional degrees of kinematic freedom, by which the warping of the cross section will be controlled. Transverse normal deformation (thickness stretching) is neglected. For angle-ply layers, additional coupling terms $\phi_{12}^{(k)}$ and $\phi_{21}^{(k)}$ should be used in the kinematic equations [20]. With these enhanced kinematic terms also diagonal laminated timber plates (DLT) [21] can be treated.

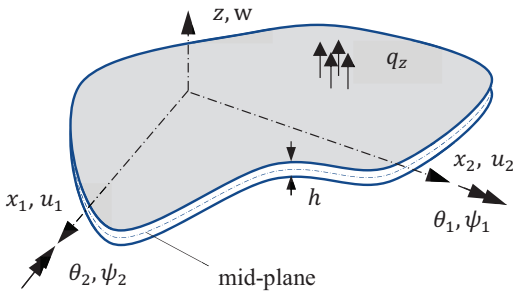

Figure 1: *General plate notation*

Using Green-Lagrange strain-displacement relations with limitation to moderate rotations (von Karman terms) we obtain for the in-plane strains (index p) of a laminated composite plate

https://doi.org/10.52202/069179-0334

$$\boldsymbol{E}_p^{(k)} = \boldsymbol{E}^{(m)} + z.\boldsymbol{E}^{(b)} + \boldsymbol{\Phi}_p^{(k)}(z)\boldsymbol{E}^{(\phi)} \qquad (2)$$

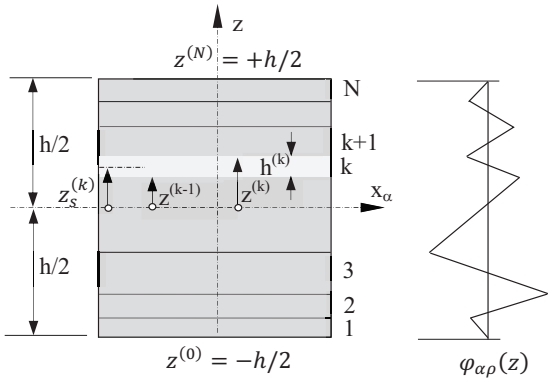

Figure 2: *General layer notation and zigzag function*

Split into the membrane part, the bending part and the zigzag part and with the abbreviation $(.)_{,\alpha} = \frac{\partial}{\partial x_\alpha}$ it follows

$$\boldsymbol{E}^{(m)} = \begin{Bmatrix} u_{,1} + \frac{1}{2}w_{,1}.w_{,1} \\ v_{,2} + \frac{1}{2}w_{,2}.w_{,2} \\ u_{,2} + v_{,1} + w_{,1}.w_{,2} \end{Bmatrix} \qquad (3a)$$

$$\boldsymbol{E}^{(b)} = \begin{Bmatrix} \theta_{1,1} \\ \theta_{2,2} \\ \theta_{1,2} + \theta_{2,1} \end{Bmatrix} \qquad \boldsymbol{E}^{(\phi)} = \begin{Bmatrix} \psi_{1,1} \\ \psi_{2,2} \\ \psi_{1,2} \\ \psi_{2,1} \end{Bmatrix} \qquad (3b, c)$$

$$\boldsymbol{\Phi}_p^{(k)}(z) = \begin{bmatrix} \phi_{11}^{(k)} & 0 & 0 & \phi_{12}^{(k)} \\ 0 & \phi_{22}^{(k)} & \phi_{21}^{(k)} & 0 \\ \phi_{21}^{(k)} & \phi_{12}^{(k)} & \phi_{11}^{(k)} & \phi_{22}^{(k)} \end{bmatrix} \qquad (4)$$

The transverse shear strains (index t) is given by

$$\boldsymbol{E}_t^{(k)} = \boldsymbol{E}_t^{(0)} + \boldsymbol{\Phi}_{t,z}^{(k)}(z)\boldsymbol{\psi} = \boldsymbol{E}_t^{(0)} + \boldsymbol{\beta}^{(k)}\boldsymbol{\psi} \qquad (5)$$

It can be split up into a constant averaged shear part and layer-dependent part

$$\boldsymbol{E}_t^{(0)} = \boldsymbol{\gamma}_t^{(0)} = \begin{Bmatrix} \gamma_1^{(0)} \\ \gamma_2^{(0)} \end{Bmatrix} = \begin{Bmatrix} w_{,1} + \theta_1 \\ w_{,2} + \theta_2 \end{Bmatrix} \quad \boldsymbol{\psi} = \begin{Bmatrix} \psi_1 \\ \psi_2 \end{Bmatrix} \qquad (6a, b)$$

$$\boldsymbol{\Phi}_t^{(k)} = \begin{bmatrix} \phi_{11}^{(k)} & \phi_{12}^{(k)} \\ \phi_{21}^{(k)} & \phi_{22}^{(k)} \end{bmatrix} \qquad \boldsymbol{\beta}^{(k)} = \frac{\partial}{\partial z}\boldsymbol{\Phi}_t^{(k)} = \begin{bmatrix} \beta_{11}^{(k)} & \beta_{12}^{(k)} \\ \beta_{21}^{(k)} & \beta_{22}^{(k)} \end{bmatrix} \qquad (7a, b)$$

Since the zigzag functions $\phi_{\alpha\rho}^{(k)}$ are chosen as layer-wise linear functions, the $\beta_{\alpha\rho}^{(k)}$ functions which influence the shear stresses (see Equation (7) and (8)) are constant for each layer, leading to mean values of shear stress. This means that in the classical RZT the local equilibrium condition of shear stresses at the interlayer and on top and bottom is violated, just like in FSDT. It has been shown by Tessler and co-workers [22,23], that by the application of Reissner´s mixed variational principle (RZT^m) this deficiency can be eliminated.

According to the assumption of plane stress state ($S_{33} = 0$) these strains are connected by the elastic Hookean law with the corresponding second Piola-Kirchhoff stress quantities

$$\boldsymbol{S}_p^{(k)} = \begin{Bmatrix} S_{11} \\ S_{22} \\ S_{12} \end{Bmatrix}^{(k)} = \bar{\boldsymbol{Q}}_p\boldsymbol{E}_p^{(k)} \qquad \boldsymbol{S}_t^{(k)} = \begin{Bmatrix} S_{13} \\ S_{23} \end{Bmatrix}^{(k)} = \bar{\boldsymbol{Q}}_t\boldsymbol{\gamma}_t^{(k)} \qquad (8a, b)$$

The matrices $\bar{\boldsymbol{Q}}$ contain the transformed plane stress reduced stiffness coefficients [7,8].

$$\bar{\boldsymbol{Q}}_p^{(k)} = \begin{bmatrix} \bar{Q}_{11} & \bar{Q}_{12} & \bar{Q}_{16} \\ \bar{Q}_{12} & \bar{Q}_{22} & \bar{Q}_{26} \\ \bar{Q}_{16} & \bar{Q}_{26} & \bar{Q}_{66} \end{bmatrix}^{(k)} \qquad \bar{\boldsymbol{Q}}_t^{(k)} = \begin{bmatrix} \bar{Q}_{44} & \bar{Q}_{45} \\ \bar{Q}_{45} & \bar{Q}_{55} \end{bmatrix}^{(k)} \qquad (9a, b)$$

To establish the discretized problem the principle of virtual work says

$$\delta W_{int} - \delta W_{ext} = 0 \qquad (10)$$

In detail the virtual work done by the inner forces reads

$$\delta W_{int} = \int \delta\boldsymbol{E}_p^T\boldsymbol{S}_p\, dV + \int \delta\boldsymbol{E}_t^T\boldsymbol{S}_t\, dV \qquad (11)$$

Integration over the thickness of the first part leads to

$$\delta W_{int} = \int \delta\boldsymbol{E}_p^T\boldsymbol{R}_p\, dA + \int \delta\boldsymbol{E}_t^T\boldsymbol{R}_t\, dA \qquad (12)$$

with the second Piola-Kirchoff-stress resultants

$$\boldsymbol{R}_p = \begin{Bmatrix} \boldsymbol{N} \\ \boldsymbol{M} \\ \boldsymbol{M}_\phi \end{Bmatrix} \qquad \boldsymbol{R}_t = \begin{Bmatrix} \boldsymbol{T} \\ \boldsymbol{T}_\phi \end{Bmatrix} \qquad (13)$$

2.2 CONSTITUTIVE RELATIONS OF THE WHOLE LAMINATE

From the above equations we get in summary the special plate constitutive equation. In full we have 14 strain components and stress resultants

$$\boldsymbol{R} = \begin{Bmatrix} \boldsymbol{R}_p \\ \boldsymbol{R}_t \end{Bmatrix} = \boldsymbol{C}\boldsymbol{E} = \boldsymbol{C}\begin{Bmatrix} \boldsymbol{E}^{(m)} \\ \boldsymbol{E}^{(b)} \\ \boldsymbol{E}^{(\phi)} \\ \boldsymbol{\gamma}^{(0)} \\ \boldsymbol{\psi} \end{Bmatrix} \qquad (14)$$

In detail we have

$$\begin{Bmatrix} \boldsymbol{N} \\ \boldsymbol{M} \\ \boldsymbol{M}^{(\boldsymbol{\phi})} \\ \boldsymbol{T} \\ \boldsymbol{T}^{(\boldsymbol{\phi})} \end{Bmatrix} = \begin{bmatrix} \boldsymbol{A} & \boldsymbol{B} & \boldsymbol{A}^{\boldsymbol{\phi}} & 0 & \boldsymbol{0} \\ \boldsymbol{B}^{\boldsymbol{T}} & \boldsymbol{D} & \boldsymbol{B}^{\boldsymbol{\phi}} & 0 & 0 \\ \boldsymbol{A}^{\boldsymbol{\phi}T} & \boldsymbol{B}^{\boldsymbol{\phi}T} & \boldsymbol{D}^{\boldsymbol{\phi}} & 0 & 0 \\ 0 & 0 & 0 & \boldsymbol{A}_t & \boldsymbol{B}_t^{(\phi)} \\ 0 & 0 & 0 & \boldsymbol{B}_t^{(\phi)T} & \boldsymbol{D}_t^{(\phi)} \end{bmatrix} \begin{Bmatrix} \boldsymbol{E}^{(m)} \\ \boldsymbol{E}^{(b)} \\ \boldsymbol{E}^{(\phi)} \\ \boldsymbol{\gamma}^{(0)} \\ \boldsymbol{\psi} \end{Bmatrix} \qquad (15)$$

https://doi.org/10.52202/069179-0334

The constitutive matrix **C** is built up by the following sub matrices, emerging from the integration of the weighted, reduced elastic stiffness coefficients over the thickness.

$$(\boldsymbol{A},\boldsymbol{B},\boldsymbol{D}) \equiv \int_{-\frac{h}{2}}^{+\frac{h}{2}} (1,z,z^2)\,\overline{\boldsymbol{Q}}_p^{(k)}\,dz \tag{16a}$$

$$\left(\boldsymbol{A}^{\boldsymbol{\phi}},\boldsymbol{B}^{\boldsymbol{\phi}},\boldsymbol{D}^{\boldsymbol{\phi}}\right) \equiv \int_{-\frac{h}{2}}^{+\frac{h}{2}} \left(1,z,\boldsymbol{\Phi}_p^{(k)T}\right)\overline{\boldsymbol{Q}}_p^{(k)}\boldsymbol{\Phi}_p^{(k)}\,dz \tag{16b}$$

$$\left(\boldsymbol{A}_t,\boldsymbol{B}_t^{(\phi)}\right) \equiv \int_{-\frac{h}{2}}^{+\frac{h}{2}} \left(1,\boldsymbol{\beta}^{(k)}\right)\overline{\boldsymbol{Q}}_t^{(k)}\,dz \tag{16c}$$

$$\boldsymbol{D}_t^{(\phi)} \equiv \int_{-\frac{h}{2}}^{+\frac{h}{2}} \boldsymbol{\beta}^{(k)T}\overline{\boldsymbol{Q}}_t^{(k)}\boldsymbol{\beta}^{(k)}\,dz \tag{16d}$$

The enhanced zigzag functions are established by layer-wise integration of the $\boldsymbol{\beta}^{(k)}$ functions. The latter are derived from a relaxed continuity condition of shear stresses at the interlayer and the assumption that the zigzag functions vanish at the top and bottom surfaces of the plate, see Sorrenti et al. [20]. The model allows for a piecewise constant distribution of transverse shear stresses that is accurate in an average sense.

The corresponding relations for the laminated beam in the x-z-plane can be found in [24]:

$$\begin{Bmatrix} N_x \\ M_x \\ M_\phi \end{Bmatrix} \equiv \begin{bmatrix} A_{11} & B_{12} & B_{13} \\ B_{12} & D_{11} & D_{12} \\ B_{13} & D_{12} & D_{22} \end{bmatrix} \begin{Bmatrix} u_{,x} \\ \theta_{,x} \\ \psi_{,x} \end{Bmatrix} \tag{17}$$

The stiffness coefficients are defined as

$$[A_{11},B_{12},D_{11}] \equiv \int_A C_{11}^{(k)}[1,z,z^2]b^{(k)}(z)\,dz \tag{18a}$$

$$[B_{13},D_{12},D_{22}] \equiv \int_A C_{11}^{(k)}\phi^{(k)}\left[1,z,\phi^{(k)}\right]b^{(k)}(z)\,dz \tag{18b}$$

which can be calculated analytically. For a beam in plane strain in width direction b, $C_{11}^{(k)} = E_x^{(k)}/\left(1-\nu_{xy}^{(k)}\nu_{yx}^{(k)}\right)$ and for beam in plane stress $C_{11}^{(k)} = E_x^{(k)}$, where $E_x^{(k)}$ is the Young´s modulus of the *k*-th layer in axial direction *x* and $\nu_{xy}^{(k)}$, $\nu_{yx}^{(k)}$ are the Poisson´s ratios. Beams with unequal ply width can also be analyzed when a modification of the shear modulus $G_{xz}^{(k)}$ is performed [15].

3 FINITE ELEMENTS

This section summarizes the main finite element developments of the last ten years based on refined zigzag kinematics.

3.1 BEAM ELEMENT

The first numerical implementation was presented by Gherlone et al. [25] using a C^0-element based on an anisoparametric interpolation scheme originally proposed by Tessler and Dong [26]. Di Sciuva et al. [27] has given an extension to a class of higher-order elements. Wimmer et al. [24] provided explicit representations for the stiffness, the geometric stiffness and the mass matrix and an exact version of the stiffness matrix has been worked out in [28]. Flores et al. [29] reflected some limitations of RZT when modelling delamination. Kefal and coworkers [30] presented an iso-geometric beam element based on RZT^m.

There are only a few papers that explicitly report on the experimental verification of RZT. Experimental evaluations of the static and dynamic response of sandwich beams are presented by Iurlaro et al. [31,32]. Buckling test are performed and reported by Ascione et al. [33].

It should be pointed out, that in FSDT beam analysis the shear stress pattern in the cross section does not vary along the beam axis, while in RZT it happens due to the additional kinematic degree of freedom ψ, as can be seen from Equation (5). The mean shear stress obtained by the corresponding constitutive equation of FSDT therefore underestimates the real value dramatically (see Figure 5). For this reason, the shear stress distribution is usually calculated by integrating the local equilibrium equation (Cauchy´s equation) [34]. An analogous procedure derived by Tessler [22] leads to

$$\begin{aligned}\tau_{xz}^{(k)}(x,z) = {} & \theta_{,xx}(x)\left[\frac{B_{12}}{A_{11}}\tau_u^{(k)}(z) - \tau_\theta^{(k)}(z)\right] + \\ & + \psi_{,xx}(x)\left[\frac{B_{13}}{A_{11}}\tau_u^{(k)}(z) - \tau_\psi^{(k)}(z)\right]\end{aligned} \tag{19}$$

with the integrals

$$\tau_u^{(k)}(z) \equiv \int_{-h/2}^{z} C_{11}^{(k)}\,d\bar{z} \tag{20a}$$

$$\tau_\theta^{(k)}(z) \equiv \int_{-h/2}^{z} \bar{z}\,C_{11}^{(k)}\,d\bar{z} \tag{20b}$$

$$\tau_\psi^{(k)}(z) \equiv \int_{-h/2}^{z} \phi^{(k)}(\bar{z})\,C_{11}^{(k)}\,d\bar{z} \tag{20c}$$

In case of shear stresses on the top and bottom side an additional term must be considered. When referring to FSDT all terms associated with ψ are omitted.

3.2 PLATE ELEMENT

A first application for bi-axial plate bending is given by Versino [16], who extended Tessler´s anisoparametric shape functions originally presented in the well-known homogeneous plate element MIN3 to RZT-kinematics. Recently Sorrenti et al. [18] reported a robust quadrilateral version which achieves reliable results even in the ultra-thin range. Wimmer et al. [17] has demonstrated the advantages that can be reaped when the so-called smoothed finite element technique is employed. Hasim et al. [35] has presented an iso-geometric variant that allows for plates with curvilinear fibers. Wimmer and co-workers [36] has recently shown the extension to buckling and geometrical-nonlinear bending.

4 NUMERICAL RESULTS

Two representative examples are given in this section. As a first example a continuous beam is investigated. In

another example, the biaxial bending state of a CLT strip intermediately supported by a column is treated.

4.1 UNIAXIAL BENDING

A two-span CLT-beam is investigated as a beam model (with RZT and FSDT) and as a 2D-continuum. The cross-section consists of five layers of equal thickness with $h^{(k)} = 0.04$ m.

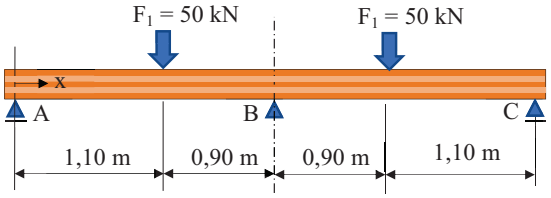

Figure 3: *System of a two-span continuous test beam under concentrated loads (uniaxial bending)*

The single boards are edge-glued. The beam has a width of b = 0.50 m and an overhang of 0.20 m at both ends. Two concentrated loads $F_1 = 50$ kN act approximately in the middle of the span (Figure 3 and 10). An additional force of $\Delta F_1 = 1.84$ kN was taken into account for the load transmission beam. As the structure is first analyzed as a beam model [24], the forces as well as the support reactions are applied via distributed loads with respect to the axis of the beam. At the force application point, a parabolic line load with amplitude $q_F = 243$ kN/m is modeled, acting over a length of 0.32 m, while the line load at the intermediate support has an amplitude of $q_B = -475.6$ kN/m, distributed over a width of 0.24 m, resulting in a reaction force B = 76.1 kN. In the 2D-continuum model the actions are located as uniform pressures on the top and the bottom side of the beam.

The material data for the numerical model were chosen as mean values from component tests of the single boards. To achieve the experimentally determined maximum deflection of $w_{max} = 2.85$ mm, the rolling shear modulus had to be adjusted concerning the experimental measure-ments (see section 5.3):

$E_x = E_0 = 11600$ MPa, $E_y = E_z = E_{90} = 370$ MPa, $G_{xz} = G_{090} = 560$ MPa, $G_{xz} = G_{yz} = G_{9090} = 120$ MPa.

4.1.1 Longitudinal Stress

The maximum bending stress distribution along the beam is given in Figure 4. It shows the significant influence of the cross sectional warping close to the load transfer zone.

In addition, the structure is modeled with 2D-continuum elements of high resolution (3 rows of solid elements for each layer). The maximum deflection must be corrected for thickness deformation when comparing with the beam solution. The peak values of RZT-beam solution are quite well confirmed by 2D-FE analysis. It should be noted that when using 2D continuum elements, no rotational degree of freedom at the nodes of the interlayer boundaries should be present (or it should be released). Otherwise, the typical kink is numerically cancelled, and the stress state could be locally distorted as a result. The measured values of the linear strain gauges (mean values of three specimens), which are attached to the tensile side of the load application points (Figure 10), impressively confirm the numerical values of the RZT.

4.1.2 Shear Stress

The standard method of RZT and FSDT as well provides only mean values of the shear stresses in each layer. It

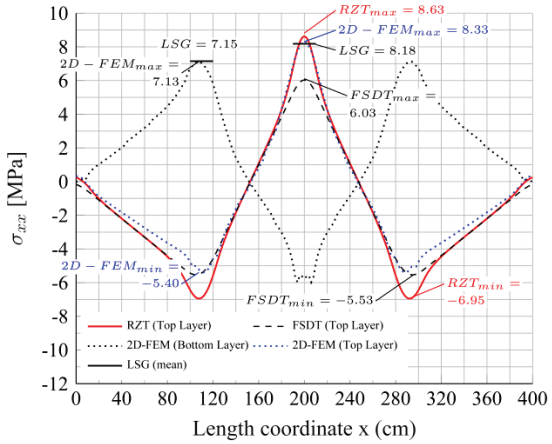

Figure 4: *Maximum bending stress along the axis of a two-span continuous beam for different composite beam theories, from 2D continuum analysis and experimental results.*

turned out that the standard FSDT is not able to reflect the stress state accurately. In particular, the rolling shear stress in the second layer is completely miscalculated qualitatively and quantitatively. It became apparent, that FSDT significantly underestimates the mean values of rolling shear stress (Figure 5) when using the constitutive equation. Figure 6 presents the shear stress distributions $\tau_{xz}(z)$ along several sections (see Figure 10) coming from

different calculation approaches. Figure 6 (upper graph) shows the mean values (FSDTm) recovered from the constitutive equations and the values which result from

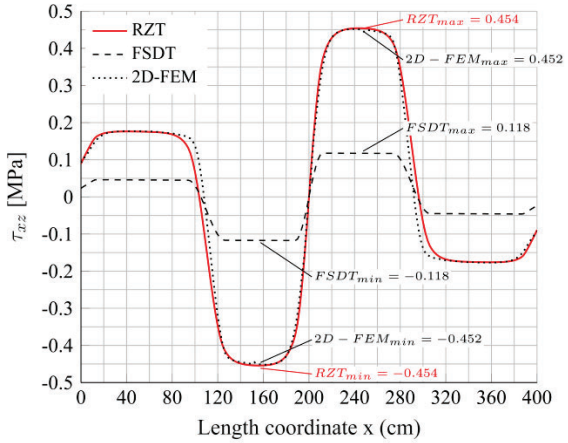

Figure 5: *Rolling shear stress in the second layer along the axis of a two-span continuous beam under concentrated loads for different composite beam theories and 2D continuum analysis.*

https://doi.org/10.52202/069179-0334

integration of Cauchy´s equation (FSDTc, Eq.19, 20). Figure 6 (lower graph) gives the corresponding results for RZT. It is noticeable, that RZT provides accurate values of the rolling shear stress in the second layer even if the constitutive equation is applied. Outside the warping zone, both theories give the same result when the integration technique is applied. In the load transfer zone, the symmetry is lost under the influence of the transverse normal stress σ_{zz}, as can be seen in section 0 - 0, but the maximum shear stress given by the RZT and the integration method reproduces the 2D solution quite well.

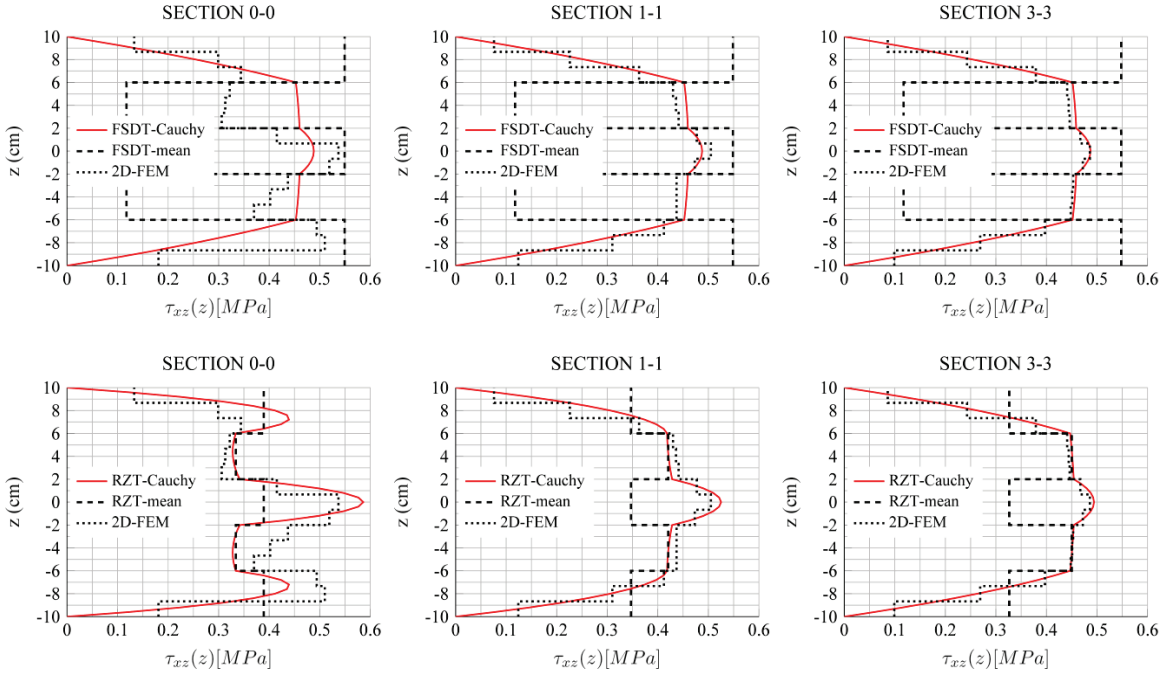

Figure 6: *Shear stress distributions $\tau_{xz}(z)$ (mean values, Cauchy-integrated and unsmoothed 2D-solution) for FSDT (upper graph) and for RZT (bottom graph) along different cross sections*

4.2 BIAXIAL BENDING

A double-symmetric, two-span rectangular CLT-plate (Figure 7) with dimensions 7.80 / 2.40 / 0.20 m, resting on a line support at both ends and a point intermediate bearing (30 x 30 cm) is studied with a plate model [17] considering the above two theories and a 3D continuum model. A quarter of the plate (3.90 / 1.20 m) is modeled and subjected by a constant surface load on the upper side of q_z = -10 kN/m^2. The contact area at the corner (0.15 / 0.15 m) has a subgrade reaction modulus of 3.3 10^6 kN/m^3. The cross section consists of 5 layers, each with equal thickness of 4 cm. The following material parameter were applied:

E_1 = 11500 MPa, $E_2 = E_3$ = 370 MPa, $G_{12} = G_{13}$ = 690 MPa, G_{23} = 50 MPa. ν_{12} = 0.38, ν_{13} = 0.22, ν_{23} = 0.203.

The material axis 1 coincide with the x_1-axis. The layer setup is 0/90/0/90/0°.

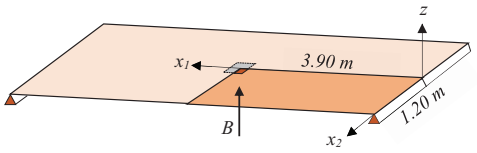

Figure 7: *Biaxial bending of CLT-plate with point intermediate support*

Table 1: *Maximum deflection and bending stresses in the upper two layers of a CLT-plate (symmetry point) under biaxial bending, 3D deflection corrected from thickness compression*

	FSDT	RZT	3D
max w [mm]	5.91	5.18	5.39
max σ_{11} [MPa]	5.68	9.23	9.71
max σ_{22} [MPa]	6.92	10.64	10.98

For comparison the plate is analyzed with the FE-program ABAQUS using more than 40 000 quadratic solids elements of type C3D20. Figure 8 shows the transverse deformation u3 = w and clearly the typical zigzag pattern arising from the heterogeneous cross section under high transverse shear stresses. In Table 1

https://doi.org/10.52202/069179-0334

essential results are presented. Figure 9 gives the through- thickness distribution of stresses at the center point of the whole plate in both directions. It demonstrates the superior accuracy of RZT against FSDT. As with the uniaxial example, it can be seen that FSDT significantly underestimates the maximum bending stresses.

5 EXPERIMENTAL RESULTS

In the following, the experimental configurations as well as the measurement systems for the test beam (see Figure 3) are described. Furthermore, the measured data are analyzed and compared with the results from the numerical analysis.

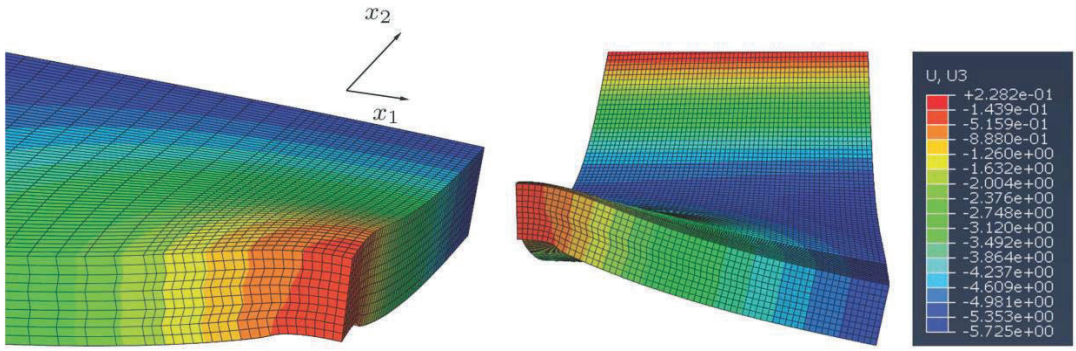

Figure 8: *Warping deformation near the point support along the planes of symmetry with typical zigzag pattern*

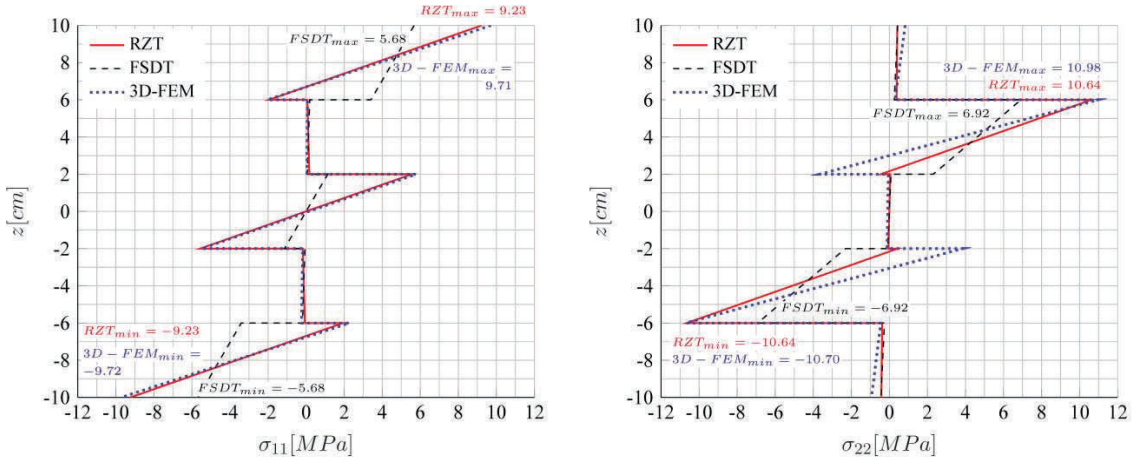

Figure 9: *Bending stresses distribution at the symmetry point by different structural theories*

5.1 EXPERIMENTAL SETUP

Figure 10 shows the experimental setup for the bending test. The hydraulic jack is fixed on a rigid loading frame. The latter is clamped to the rigid floor with anchor bolts. The load is applied via a crossbeam (HEM 280). The two-span beam has three roller supports. For dimensions and loads see section 4.1. The cross section of the test beam has a width of 50 cm.

The shear slenderness at the supports in both bays is a/d = 110/20 = 5.5 and concerning the inner support a/d = 90/20 = 4.5. The test program includes three test specimens. Figure 10 shows the four measurement methods used. A measuring box in the hydraulic jack reported the test load. In the range of the load application as well as above the intermediate support, linear strain gauges (LSG) were responsible for measuring the strains of the top and bottom fiber. To measure the vertical deflection, a displacement sensor was placed under the load application point. A DIC-System is used to detect strains in the area of interest (AOI). The load rate is determined at 0.5 mm/min. for all tests.

https://doi.org/10.52202/069179-0334

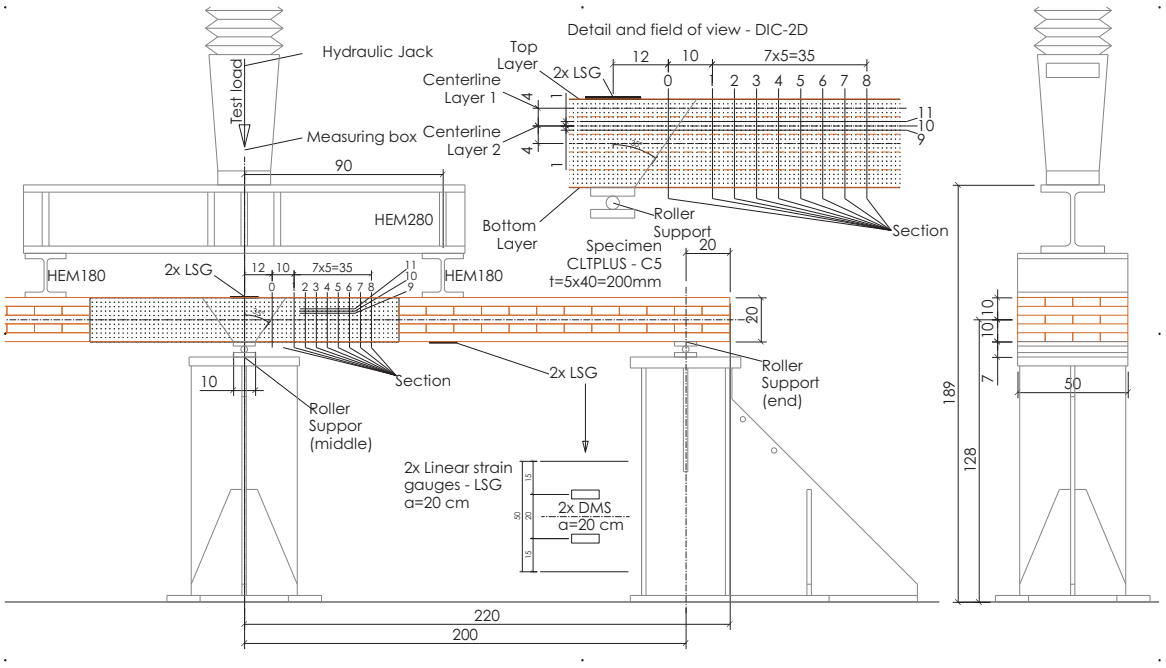

Figure 10: *Experimental setup of a CLT-beam*

5.2 Digital image correlation (DIC)

The DIC-System as an optical, contactless deformation measurement method combines image registration and tracking system for precise 2D measurements to reconstruct the strain state in a structural component. In this study, the DIC-System was used to monitor the strains and deformations near the intermediate support. Just left and right of this support the lateral surface of the beam was speckled randomly and 2D measurement method is employed. The strains and deformations are measured in the area of interest and compared with the numerical results.

5.3 Evaluation of strains

The DIC system provides Green-Lagrange strains. The evaluation of shear angles $\gamma_{xz} = 2\varepsilon_{xz}$ was carried out along vertical sections 0 – 8 (see Figure 10) and showed an unsteady distribution related to the strong inhomogeneity caused by the individual fibers. (Figure 11). Based on these distributions, mean values $\gamma_{xz,m}$ are calculated for each layer. Subsequently they were multiplied layer-wise by those shear moduli G_{xz} that lead to match with the results from 2D-FE analysis which in turn fulfil the equilibrium conditions.

The calibration procedure is performed for all vertical sections marked in Figure 10, separated according to layers, resulting in the following mean values: G_{9090} = 120 MPa, G_{090} = 560 MPa.

A comparison with extensive tests reported in [37] as well as numerical investigations [38] showed good congruence of these values.

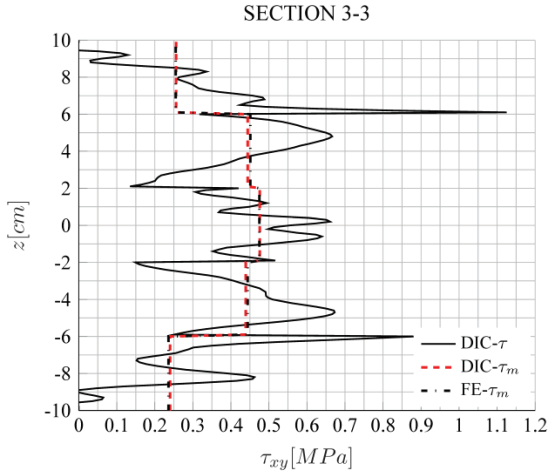

Figure 11: *Shear stress distribution measured by DIC and mean values per layer*

6 ULS-DESIGN

The clearly recognizable stress peaks in the examples shown have a non-negligible influence on the design process. The utilization factor with respect to the axial stresses in the grain direction, which is given in Tables 2, 3 and 4, was evaluated by the formula of Equation (21), where $\sigma_{t/c,0,CLT,d}$ and $f_{t/c,0,CLT,d}$ denote the design values of max/min. stress and strength parallel to the grain for

$$U_{t/c} = \frac{|\sigma_{t/c,0,mean,d}|}{f_{t/c,0,CLT,d}} + \frac{|\sigma_{m,CLT,d}|}{f_{m,CLT,d}} \qquad (21)$$

pure tension (t) or compression (c), respectively. $\sigma_{t/c,mean,d}$ represents the mean value of the linearly varying stress distribution in the uppermost or lowermost layer. The second part $\sigma_{m,CLT,d}$ is given by the nonuniform part of bending stress deviating from the above-mentioned mean value and the bending strength $f_{m,CLT,d}$. For the comparison we refer to the design format of Eurocode 5 and the following material parameters, proposed in [1]: $f_{m,CLT,k}$ = 24 N/mm^2, $f_{c,0,CLT,k}$ = 24 N/mm^2, $f_{t,0,CLT,k}$ = 16 N/mm^2. For the corresponding design values, $k_{mod} = 0.80, \gamma_M = 1.25$ was chosen.

Table 2: *Comparison of utilization factor $U_{c/t}$ concerning axial stresses of example 1 (uniaxial bending) at the intermediate support.*

Layer	z-Pos. [mm]		FSDT [MPa]	RZT [MPa]	Δ %
5/1	±100	$\pm\sigma_{t,0,CLT,d}$	6.03	8.63	43
	±80	$\pm\sigma_{t,0,mean,d}$	4.835	4.525	
		$\pm\sigma_{m,CLT,d}$	1.195	4.105	
5	+100	U_t	0.550	0.709	29
1	-100	U_c	0,393	0,562	43

Table 3: *Comparison of utilization factor $U_{c/t}$ concerning axial stresses of example 2 (symmetry point) in x-direction*

Layer	z-Pos. [mm]		FSDT [MPa]	RZT [MPa]	Δ %
5/1	±100	$\pm\sigma_{t,0,CLT,d}$	5.68	9.23	63
	±80	$\pm\sigma_{t,0,mean,d}$	4.545	3.645	
		$\pm\sigma_{m,CLT,d}$	1.135	5.585	
5	+100	U_t	0.518	0.720	39
1	-100	U_c	0.37	0.601	63

Table 4: *Comparison of utilization factor $U_{c/t}$ concerning axial stresses of example 2 (symmetry point) in y-direction*

Layer	z-Pos. [mm]		FSDT [MPa]	RZT [MPa]	Δ %
4/2	±60	$\pm\sigma_{t,0,CLT,d}$	6.92	10.64	54
	±40	$\pm\sigma_{t,0,mean,d}$	4.62	5.10	
		$\pm\sigma_{m,CLT,d}$	2.31	5.54	
4	+60	U_t	0.601	0.859	43
2	-60	U_c	0.451	0.693	54

7 CONCLUSIONS

Comparative studies on uniaxial and biaxial loaded CLT-plates under concentrated loads have shown the superiority of Refined Zigzag Theory over the traditionally used First Order Shear Deformation Theory. The bending and shear stresses predicted by the RZT are impressively confirmed by numerical comparative calculations with continuum elements and experimental measurements. It could be proven that using the FSDT-based axial stress values leads to an underestimation of the corresponding utilization factor of CLT-plates up to 50 % and more. When applying the FSDT the rolling shear stress must be determined by integration of Cauchy´s equilibrium equation otherwise it is dramatically underestimated. In case of uniaxial bending the RZT already reliably predicts the rolling shear stress in the standard procedure using the constitutive equation. The propagated RZT forms a good compromise in terms of computational effort and achieved accuracy. It does not require a shear correction factor. It represents a consistent extension of the FSDT showing a great similarity to that between Saint Venant's torsion and warping torsion. Since it is the simplest variant among the numerous higher-order shear deformation theories, it should be used as the new standard tool for the analysis of CLT plates and other shear-elastic structures in the everday design process.

ACKNOWLEDGEMENT

This work would not have been possible without the financial and technical support of the following involved parties, the Innovation Voucher - Program of the Austria FFG Funding Service, consultancy firm Poltnigg & Klammer ZT-GmbH & KASTNER ZT-GmbH, Carinthia, Theurl - Timber Structures GmbH and the Baulabor of the Carinthia University of Applied Sciences. Special thanks to Tamas Meszöly and Lukas Kepplinger for their contributions.

REFERENCES

[1] Brandner R., Flatscher G., Ringhofer A., Schickhofer G., Thiel A.: Cross laminated timber (CLT): overview and development. European Journal of Wood and Wood Products 74:331-351, 2016.

[2] EN 1995-1-1, Eurocode 5: Design of timber structures – Part 1-1: Genera–common rules and rules for buildings, 2019.

[3] Möhler K.: Über das Tragverhalten von Biegeträgern und Druckstäben mit zusammengesetzten Quer-schnitten und nachgiebigen Verbindungsmittels, Habilitation TH Karlsruhe (in German), 1956.

[4] Kreuzinger H.: Flächentragwerke, Platten, Scheiben und Schalen, Berechnungsmethoden und Beispiele. In: Brücken aus Holz. Informationsdienst Holz, Arbeitsgemeinschaft Holz e.V. Düsseldorf (in German), 1999.

[5] Scholz A.: Structural analysis of wooden plate structures. 4th International PhD Symposium in Civil Engineering, Munich, 2002.

[6] Scholz A.: Ein Beitrag zur Berechnung von Flächentragwerken aus Holz. PhD thesis Technische Universität München (in German), 2004.

[7] Altenbach H., Altenbach J., Kissing W.: Mechanics of Composite Structural Elements. Springer Berlin 2004.

[8] Reddy J.N.: Mechanics of laminated composite plates and shells. CRC Press, London, 2004.

https://doi.org/10.52202/069179-0334

[9] Hochreiner G., Füssl J., Eberhardsteiner J.: Cross-laminated timber plates subjected to concentrated loading - Experimental identification of failure mechanisms. Strain, 50:68-81, 2013.
[10] Abrate S., Di Sciuva M.: Equivalent single layer theories for composite and sandwich structures: A review. Compos. Struct., 179:482-494, 2017.
[11] Liew K.M., Pan Z.Z., Zhang L.W.: An overview of layerwise theories for composite laminates and structures: Development, numerical implementation and application. Comp. Struct., 216:240-259, 2019.
[12] Icardi U., Sola F.: Assessment of recent zig-zag theories for laminated and sandwich structures. Composites Part B, 97:26-52, 2016.
[13] Tessler A., Di Sciuva M., Gherlone M.: A consistent refinement of first-order shear deformation theory for laminated composite and sandwich plates using improved zigzag kinematics. J. Mech. Mat. Struct., 5:341–367, 2010.
[14] Iurlaro L., Gherlone M., Di Sciuva M., Tessler A.: Assessment of the refined zigzag theory for bending, vibration, and buckling of sandwich plates: a comparative study of different theories. Compos. Struct., 106:777–792, 2013.
[15] Wimmer H., Hochhauser W., Nachbagauer K.: Refined Zigzag Theory: an appropriate tool for the analysis of CLT-plates and other shear-elastic timber structures. European Journal of Wood and Wood Products. https://doi.org/10.1007/s00107-020-01586-x, 2020.
[16] Versino D., Gherlone M., Mattone M., Di Sciuva M., Tessler A.: C0 triangular elements based on the Refined Zigzag Theory for multilayer composite and sandwich plates. Composites Part B, 44:218-230, 2013.
[17] Wimmer H., Celigoj Ch.: An edge-based smoothed three-node composite plate element with refined zigzag kinematics. Compos. Struct., 274, 114204, 2021.
[18] Sorrenti M., Di Sciuva M., Tessler A.: A robust four-node quadrilateral element for laminated composite and sandwich plates based on refined zigzag theory. Computers & Structures, 242, 106369, 2021.
[19] Gherlone M., Versino D., Zarra V.: Multilayered triangular and quadrilateral flat shell elements based on the Refined Zigzag Theory. Composite Structures, 233, 111629, 2020.
[20] Sorrenti M., Di Sciuva M.: An Enhancement of Warping Shear Functions of Refined Zigzag Theory. J. Appl. Mech., 88, 084501-1, 2021.
[21] Arnold M., Dietsch Ph., Maderebner R., Winter S.: Diagonal laminated timber — Experimental, analytical, and numerical studies on the torsional stiffness. Construction and Building Materials, 322, doi.org/10.1016/j.conbuildmat.2022.126455, 2022.
[22] Tessler A.: Refined zigzag theory for homogeneous, laminated composite, and sandwich beams derived from Reissner´s mixed variational principle. Meccanica, 50:2621-2648, 2015.
[23] Groh R.M.J., Tessler A.: Computationally efficient beam elements for accurate stresses in sandwich laminates and laminated composites with delaminations. Comp. Methods Appl. Mech. Engrg., 320:369-395, 2017.
[24] Wimmer H., Gherlone M., Explicit matrices for a composite beam-column with refined zigzag kinematics. Acta Mech., 228:2107–2117, 2017.
[25] Gherlone M., Tessler A., Di Sciuva M.: C0 beam elements based on Refined Zigzag Theory for multilayered composite and sandwich laminates. Composite Structures, 93:2882-2894, 2011.
[26] Tessler A., Dong S.B.: On a hierarchy of conforming Timoshenko beam elements. Computers & Structures, 14:335-344, 1981.
[27] Di Sciuva M., Gherlone M. Iurlaro L., Tessler A.: A class of higher order C0 composite and sandwich bean elements based on the Refined Zigzag Theory. Composite Structures, 132:784-803, 2015.
[28] Wimmer H., Nachbagauer K.: Exact transfer- and stiffness matrix for the composite beam-column with Refined Zigzag Kinematics. Composite Structures, 189:700-706, 2018.
[29] Flores G.F., Oller S., Nallim L.G.: On the analysis of non-homogeneuos laminates using the refined zigzag theory. Composite Structures, 204:791-802, 2018.
[30] Kefal A., Hasim K.A., Yildiz M.: A novel isogeometric beam element based on mixed form of refined zigzag theory for thick sandwich and multilayered composite beams. Composites Part B, 167:100-121, 2019.
[31] Iurlaro L., Gherlone M., Mattone M., Di Sciuva M.: Experimental assessment of the Refined Zigzag Theory for the static bending analysis of sandwich beams. J. Sandwich Structures and Materials, 20:86-105, 2018.
[32] Iurlaro L., Ascione A., Gherlone M., Mattone M., Di Sciuva M.: Free vibration analysis of sandwich beams using the refined zigzag theory: an experimental assessment. Mecchanica, 50:2525-2535, 2015.
[33] Ascione A., Orifici A.C., Gherlone M.: Experimental and Numerical Investigations of the Refined Zigzag Theory for the Accurate Buckling Analysis of Highly Heterogeneous Sandwich Beams. Int. J. Struct. Stab. Dyn., 20 (7): 2050078, 2020.
[34] Rolfes R., Rohwer K.: Improved transverse shear stresses in composite finite element based on first order shear deformation theory. Int. J. Num. Meth. Eng., 40:51-60, 1997.
[35] Hasim K.A., Kefal A.: Isogeometric static analysis of laminated plates with curvilinear fibers based on Refined Zigzag Theory. Composite Structures, 256: 113097, 2021.
[36] Wimmer H., Celigoj Chr., Timmers R.: Bending and Buckling of Shear-elastic Angle-ply Laminated Plates using Enhanced Refined Zigzag Theory. 14th International Conference on Computational Structures Technology, Montpellier, 2022.
[37] Erhart T., Brandner R., Schickhofer G., Frangi A.: Rolling Shear of some European Timber Species with Focus on Cross Laminated Timber (CLT): Test

Configuration and Parameter Study. INTER Proceedings, Meeting 48, Paper 48-6-1, 2015.
[38] Aicher S., Dill-Langer G.: Basic Considerations to Rolling Shear Modulus in Wooden Boards. Otto - Graf-Journal 11:157-165, 2000.

https://doi.org/10.52202/069179-0334

World Conference on Timber Engineering Oslo 2023

ANALYTICAL STUDY ON SEISMIC BEHAVIOR OF NEWLY BUILT FIVE STORY PAGODA IN TENDO-CITY JAPAN

Naohito Kawai[1], Mikio Koshihara[2], Iuko Tsuwa[3], Kohei Nakamichi[4]

ABSTRACT: A five story pagoda was built in Tendo-city Japan in 2019 using traditional construction method and structural calculation based on recent technology. First in this paper, the result of micro tremor measurement of the five story pagoda is summarized, next the result of lateral loading test on a shear wall with the same specification of the pagoda is summarized, and finally, the seismic performance of the pagoda is discussed based on the result of time history response analysis using a ten mass system model which is made with considering shear resistance of board walls, rotational resistance of joints between column and penetrating member, *nuki*, and column rocking resistance. As input earthquake waves, we used three artificial waves created with using the response spectrum of extremely rare ground motion stipulated in Building Standard Law of Japan. As the result of the analysis, the pagoda does not collapse even against the strong ground motion though the deformation angle of first story reaches 1/15 radian in some cases.

KEYWORDS: Micro tremor measurement, Time history response analysis, Ten mass system model

1 INTRODUCTION

It is said that there is no historical record that five story pagoda collapsed by earthquake. In the last 100 or so years, many discussions have been made on the seismic performance of five story pagoda in Japan. And even recently, five story pagodas are built using traditional construction method. As one of them, the five story pagoda of *Joan-ji* Temple was built in Tendo-city Japan in 2019 using traditional construction method and structural calculation based on recent technology.

First in this paper, the result of micro tremor measurement of *Joan-ji* five story pagoda is summarized, next the result of lateral loading test on a shear wall with the same specification of the pagoda is summarized, and finally, the seismic performance of the pagoda is discussed based on the result of time history response analysis using the ten mass system model which is made considering the results of the shear wall test.

2 *JOAN-JI* FIVE STORY PAGODA

Figure 1 shows the exterior photograph of the pagoda. Construction of the *Joan-ji* five story pagoda began in 2016 and was completed in August 2019. Height of the pagoda is 32.7 m and the side length of the first floor is 4.62 m.

Species of the structural members is cypress grown in Aomori prefecture. Although traditional construction method is used, engineered structural calculation was made to confirm structural safety according to the current Building Standard Law of Japan.

***Figure 1**: Exterior photograph of the pagoda*

3 MICRO TREMOR MEASUREMENT

3.1 MEASURING METHOD

Figure 2 shows the arrangement of measuring points in the pagoda. Total 14 velocity sensors are placed in sequence on the ground, beams and the center post of the pagoda to cover these 45 measuring points. Time length of one measurement is 500 sec with the sampling frequency 100 Hz. After measuring velocity twice at the same sensor placement we measured displacement also using integrator circuit built into the measuring system.

[1] Naohito Kawai, Kogakuin University, Japan, kawai-nk@cc.kogakuin.ac.jp
[2] Mikio Koshihara, Institute of Industrial Science, The University of Tokyo, Japan, kos@iis.u-tokyo.ac.jp
[3] Iuko Tsuwa, The Japanese Association for Conservation of Architectural Monuments, Japan, tsuwaiuko@gmail.com
[4] Kohei Nakamichi, Tomoe Corporation, Japan, k_nakamichi@tomoe-corporation.co.jp

https://doi.org/10.52202/069179-0335

And after obtaining the values of natural frequencies, we conducted human power excitation at first and second natural frequencies by two persons pushing columns in fifth story for first natural frequency and in third story for second natural frequency, adjusting the pressing time interval to each natural frequency.

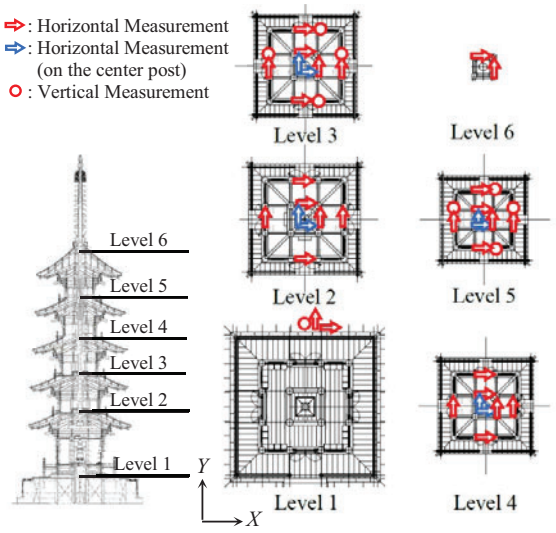

Figure 2: *Arrangement of measuring points*

3.2 RESULT OF MICRO TREMOR MEASUREMENT

By FFT analysis on the measured time history waves, we obtained some values of spectrum peaks. Figure 3 shows the result of FFT analysis. Values of frequency of main spectrum peaks are 1.12 Hz, 3.15 Hz and 5.88 Hz, which are regarded as first to third natural frequencies of the main structure of the pagoda. These observed values are the same in both the X and Y directions.

Figure 4 shows vibration modes in Y direction created by using the ratio of amplitude and the phase difference between measurement points. From Figure 4, we can see that the center column also vibrates with the main structure at first and second natural frequencies. At the third natural frequency, amplitude of the center column is far larger than that of main structure and it is omitted from Figure 4.

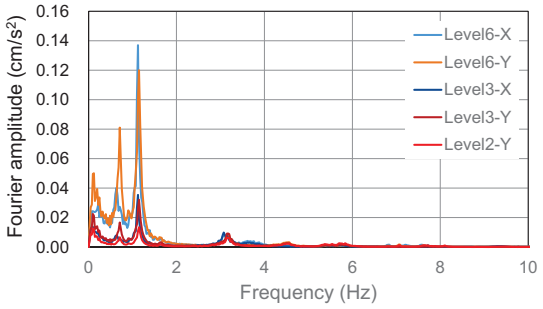

Figure 3: *Result of FFT analysis*

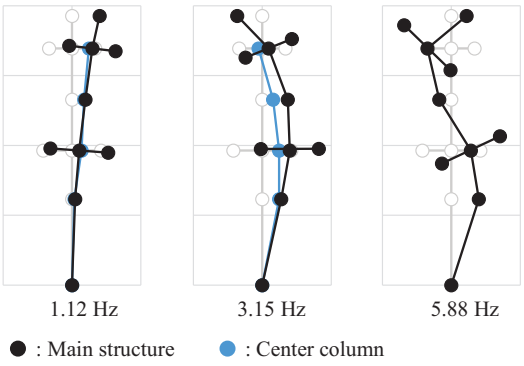

Figure 4: *Vibration mode*

Figure 5 shows the samples of time history waveforms obtained by human power excitation. And Table 1 shows the values of damping ratio at the first and second natural frequencies calculated as the values of logarithmic decrement from the time history waveforms.

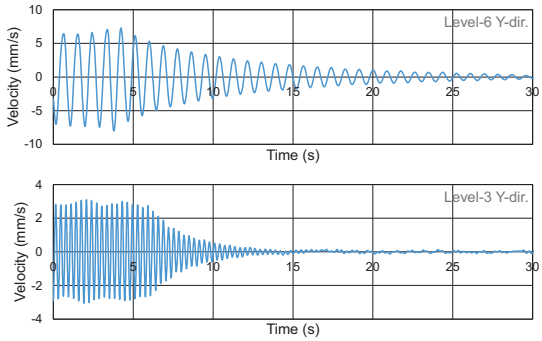

Figure 5: *Samples of time history wave forms obtained by human power excitation*

Table 1: *Values of damping ratio*

Natural frequency (Hz)		Damping ratio (%)
1st	1.12	1.73
2nd	3.15	2.02

4 SHEAR WALL TEST

4.1 TEST SPECIMEN AND TEST METHOD

Figure 6 shows the whole view of the shear wall test, and Figure 7 shows the elevation of the test specimen. The specification of the specimen is same as the wall used in third story of the pagoda.

The species of the members, two column, a sill, a beam and wall boards is cypress. Boards with 50 mm thickness are dropped along the groove of the column and the boards are held together with 9 dowels in each layer. The dowels are made using zelkova. The section of dowels is square of 15 mm by 15 mm, and the length is 120 mm.

https://doi.org/10.52202/069179-0335

The sill of the specimen is fixed by bolts to the base structure and lateral load is applied to the beam using hydraulic actuator.

Lateral cyclic load is applied with 3 cycles at ten target deformation angles, 1/450, 1/300, 1/200, 1/100, 1/75, 1/50, 1/30, 1/20 and 1/15 radians, and finally the displacement reached 123 mm, which is about 1/10 radian in deformation angle.

Figure 6: *Whole view of the shear wall test*

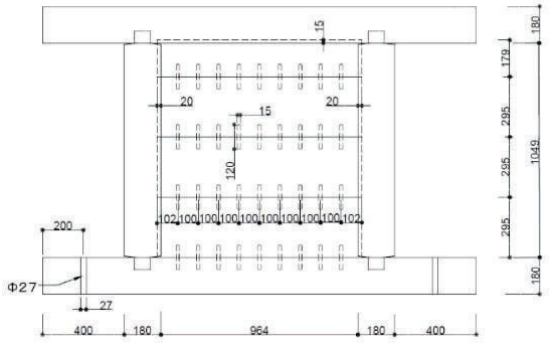

Figure 7: *Elevation of the shear wall specimen (unit: mm)*

4.2 TEST RESULT

Figure 8 shows the load-displacement relationship obtained by the loading test. The load keeps increasing even in a large deformation of 1/10 radian.

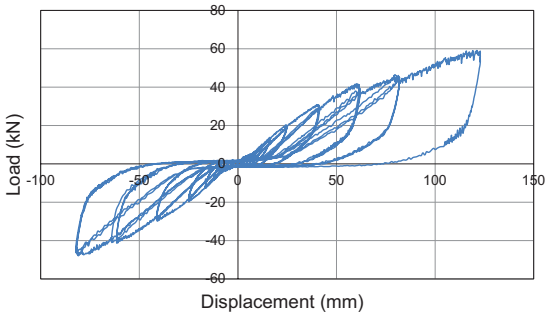

Figure 8: *Load-displacement relationship obtained by the test*

5 TIME HISTORY ANALYSIS

5.1 ANALYSIS METHOD

5.1.1 Overview of the vibration model

Figure 9 shows the concept of ten mass system model and the model for the software "wallstat" [1]. In the model for wallstat, each story consists of two layers. The lower part is is corresponding to the frames and walls and this area deforms by story shear force. The upper part is corresponding to the roof structure and is assumed to be a rigid body. Horizontal resistance of each story is calculated considering shear walls, rotation resistance of joints between column and penetrating member named *nuki* and column rocking resistance. P-Δ effect is also considered as it is built in by default in wallstat. The values of viscous damping is assumed to be 0.02 as instantaneous stiffness proportional type.

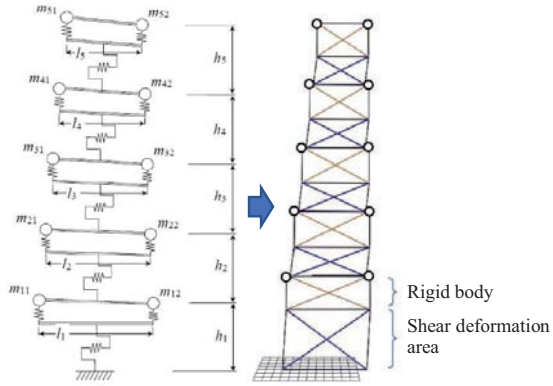

(a) Ten mass system model (b) Model for "wallstat"

Figure 9: *Vibration model*

5.1.2 Values of some parameters

Table 2 shows the values of masses which are obtained by accumulating masses of all the members and roof materials, and values of the length and the height used in the model.

In the roof structure of pagodas, there are some horizontally used timber members and it behaves like vertical springs. The vertical springs are located just below the masses and are assumed to be elastic in this analysis. The value of the spring constant is determined to be 1.81×10^4 kN/m with consulting the result of push over analysis on the three dimensional model which was used in structural calculation in the process of structural design.

Table 2: *Values of masses, length and height in the model*

Story	m_{i1} (ton)	m_{i2} (ton)	L_i (m)	H_i (m)
1st	15.08	15.08	4.62	5.12
2nd	15.21	15.21	4.20	3.65
3rd	13.17	13.17	3.78	3.65
4th	12.19	12.19	3.36	3.65
5th	13.02	13.02	2.94	3.57

https://doi.org/10.52202/069179-0335

5.1.3 Load displacement relationship of shear wall

In order to create the load-deformation relationship of the shear walls in the model, we planned to use theoretical equations for drop board walls given in a guidebook [3], and firstly confirmed the validity between the equations and the experimental results. According to the guidebook, initial stiffness and yield strength of the board wall can be calculated using Equations (1) and (2).

$$K = \frac{1}{\frac{1}{K_a}+\frac{1}{K_b}+\frac{1}{K_c}+\frac{1}{K_d}+\frac{1}{K_s}} \quad (1)$$

where,

K_a = stiffness of the boards as a compression brace,

$$K_a = \frac{E_\theta L t}{2\log\left(L\cos\theta\right)+\frac{1}{\cos^2\theta}-2}$$

K_b = embedment stiffness of the board to the beam,

$$K_b = \frac{L^3 t C_{yb} E_{\perp b}}{15 H d_b}$$

K_c = embedment stiffness of the board to the column,

$$K_c = \frac{aHtC_{yc}E_{\perp c}}{4d_c}$$

K_d = shear stiffness due to dowels,

$$K_d = an_d k_d$$

K_s = shear stiffness of the boards,

$$K_s = GLt$$

$$P_y = \min\left(P_{yd}, P_{ya}\right) \quad (2)$$

where,

P_{yd} = shear strength due to dowels,

$$P_{yd} = n_d \cdot \Delta P_y \left(1+\mu\frac{H}{L}\right)$$

P_{ya} = compression strength when the area of 5% of the diagonal length reaches yield strength,

$$P_{ya} = 0.05Ht\frac{F_\theta}{\sin^2\theta}$$

Parameters L, H, a, t, d_b, d_c, $E_{\perp b}$, $E_{\perp c}$, G, C_{yb}, C_{yc}, n_d, k_d, ΔP_y, μ, θ, E_θ and F_θ for the shear wall test specimen mentioned above are as shown in Table 3.

Figure 10 shows the comparison of load displacement relationship between the calculation result and the test result. The initial stiffness and the yield strength agreed well. As relatively large secondary stiffness was observed in the test result, we assumed secondary stiffness as 35% of the initial stiffness. Moreover, we added first broken point on the relationship of small displacement area to create the proper ratio of bilinear and slip in the hysteresis loop which is built in in the software wallstat as shown in Figure 11.

Table 3: *Values of parameters in Equations (1) and (2) for shear walls in 3rd story*

Symbol	Meaning	Value
L	Inner length of board wall (mm)	964
H	Height of board wall (mm)	1049
a	Board width (mm)	295
t	Board thickness (mm)	50
d_b	Beam height (mm)	180
d_c	Column width (mm)	180
$E_{\perp b}$	Young's modulus perpendicular to the grain of beam (kN/mm^2)	0.3
$E_{\perp c}$	Young's modulus perpendicular to the grain of column (kN/mm^2)	0.3
G	Shear modulus (kN/mm^2)	0.6
C_{yb}	Coefficient of end distance effect of beam	1.8
C_{yc}	Coefficient of end distance effect of column	1.8
n_d	Number of dowels	9
k_d	Shear stiffness of one dowel joint (kN/mm)	1.5
ΔP_y	Shear strength of one dowel joint (kN)	3.8
μ	Coefficient of friction	0.4
θ	Angle of diagonal (rad)	0.828
E_θ	Young's modulus in the direction of diagonal (kN/mm^2)	0.538
F_θ	Compression strength in the direction of diagonal (N/mm^2)	4.78

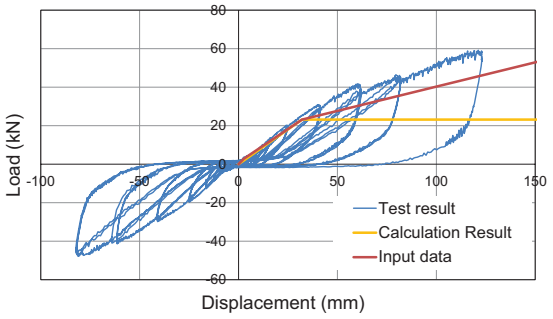

Figure 10: *Comparison of load displacement relationship between calculation result and test result*

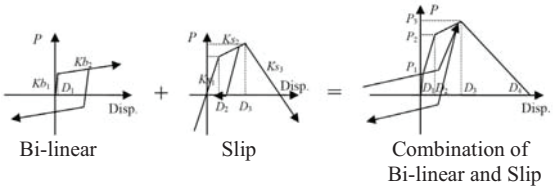

Figure 11: *Hysteresis characteristics of load displacement relationship in the software wallstat* [1]

Thus, we derived load displacement relationship of the shear wall in each story. Table 4 shows the values of parameters in each story. The obtained load value is multiplied by 4 as there located four shear walls in one direction in each story. Table 5 and Figure 12 show the load displacement relationships of the shear deformation

https://doi.org/10.52202/069179-0335

area in each story of the vibration model. The last downward slope after the deformation angle 1/5 radian is a dummy for running the analysis.

Table 4: *Values of parameters in equations (1) and (2) for shear walls in each story*

Story	L (mm)	H (mm)	n_d	θ (rad)	E_θ (kN/mm^2)	F_θ (N/mm^2)
1st	1134	2585	11	1.157	0.355	3.37
2nd	1049	1049	10	0.785	0.581	5.09
3rd	964	1049	9	0.828	0.538	4.78
4th	844	1049	8	0.893	0.484	4.38
5th	724	1049	7	0.967	0.436	4.01

Table 5: *Parameters of load displacement relationship due to shear walls for the shear deformation area*

Story	P1 (kN)	P2 (kN)	P3 (kN)	D1 (mm)	D2 (mm)	D3 (mm)
1st	12.5	103.8	304.6	8.01	100.2	654
2nd	12.8	106.7	446.9	2.58	32.3	326
3rd	11.1	92.5	389.6	2.56	32.1	326
4th	9.1	75.7	317.3	2.58	32.2	326
5th	7.5	62.2	250.2	2.70	33.8	326

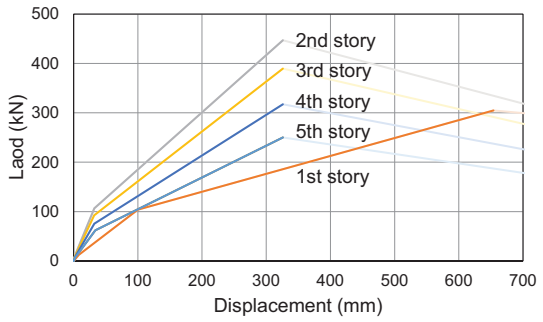

Figure 12: *Load displacement relationship of the shear deformation area in the vibration model due to shear walls*

5.1.4 Load displacement relationship due to rotational resistance of column-*nuki* joint

In order to create the load displacement relationship due to the rotational resistance of column-*nuki* joints, we used theoretical equations given in a design manual [4]. Initial rotational stiffness and yield moment of column-*nuki* joints can be calculated using Equations (3) and (4).

$$K_{\theta b} = {x_p}^2 y_p E_\perp \left\{ \frac{x_p}{Z_0}\left(C_{xm} - \frac{1}{3} \right) + 0.5\mu C_{xm} \right\} \quad (3)$$

$$M_{yb} = \frac{K_{\theta b} Z_0 F_m}{x_p E_\perp C_{xm} \sqrt{C_{ym}}} \quad (4)$$

where,

F_m = Embedment yield stress when end and edge distances are infinite

$$F_m \simeq \frac{2.4}{3} F_{cv}$$

F_{cv}: Embedment strength, F_{cv} = 7.8 (N/mm^2)

C_{xm}: Coefficient of end distance effect in length direction of *nuki*

$$C_{xm} = 1 + \frac{4Z_0}{3x_p}$$

C_{ym}: Coefficient of edge distance effect in width direction of *nuki*

$$C_{ym} = 1 + \frac{4Z_0}{3ny_p}$$

Table 6 shows the meaning of symbols, x_p, y_p, Z_0, $E_\perp$, n *and* μ, and Table 7 shows the values in each story. And Table 8 shows the calculated values of initial rotational stiffness $K_{\theta b}$ and yield moment M_{yb} in each story and of each column diameter.

Table 6: *Meaning of symbols in Equations (3) and (4)*

Symbol	Meaning
x_p	Half of column width or diameter (mm)
y_p	Width of *nuki* (mm)
Z_0	Height of *nuki* (mm)
$E_\perp$	Young's modulus perpendicular to grain of *nuki* (kN/mm^2)
n	Replacement factor of X and Y directions
μ	Coefficient of friction

Table 7: *Values of parameters in each story*

Symbol	Story	Value
x_p (mm)	5th story*1	150, 130
	4th story*1	160, 140
	3rd story*1	170, 150
	2nd story*1	180, 160
	1st story*1	190, 170
y_p (mm)	2nd to 5th story	115
	1st story	100
Z_0 (mm)	2nd to 5th story	175
	1st story	210
$E_\perp$ (kN/mm^2)		0.18
n		6
μ		0.8

*1: First is x_p of inner column and second is of outer column.

Table 8: *Values of initial rotational stiffness and yield moment in each story*

Story	x_p (mm)	Number of joints	$K_{\theta b}$ (kNm/rad)	M_{yb} (kNm)
1st	190	4	3026	25.19
	170	8	2251	10.94
2nd	180	4	2672	25.70
	160	8	1948	21.08
3rd	170	4	2291	23.34
	150	8	1640	18.94
4th	160	4	1948	21.08
	140	8	1367	16.90
5th	150	4	1640	18.94
	130	8	1124	14.98

https://doi.org/10.52202/069179-0335

To create the load displacement relationships due to the rotational resistance of column-*nuki* joints in each story, the load is calculated as the summation of moment of joints divided by the height of shear deformation area of the vibration model, and the displacement is calculated as the product of height of shear deformation area and rotation angle of joint. Though the diameter of column differs between the inner column and outer column in the same story, the difference of the rotation angle of yield point is small. Therefore, we used the summation of the initial stiffness and the summation of the yield moment in each story to derive the load displacement relationship of shear deformation area of each story.

Moreover, it is known that the relationship of moment and rotation angle of these joints has a relatively large secondary stiffness, so we assumed secondary stiffness of 1/12 of initial stiffness with reference to the result of the preceding study [5]. And we added first broken point on the relationship of small displacement area to create the proper ratio of bilinear and slip in the hysteresis loop.

Table 9 and Figure 13 show the load displacement relationships due to the rotational resistance of column-*nuki* joints in each story used in the shear deformation area of the vibration model. The last downward slope after the deformation angle 1/5 radian is a dummy for running the analysis.

Table 9: *Parameters of load displacement relationship for the shear deformation area in each story of the vibration model*

Story	P1 (kN)	P2 (kN)	P3 (kN)	D1 (mm)	D2 (mm)	D3 (mm)
1st	8.2	82.1	228.7	1.46	29.1	654
2nd	16.7	166.5	421.3	0.84	16.8	326
3rd	15.0	150.2	365.6	0.90	17.9	326
4th	13.5	134.7	314.9	0.96	19.1	326
5th	12.0	120.0	269.0	1.02	20.5	326

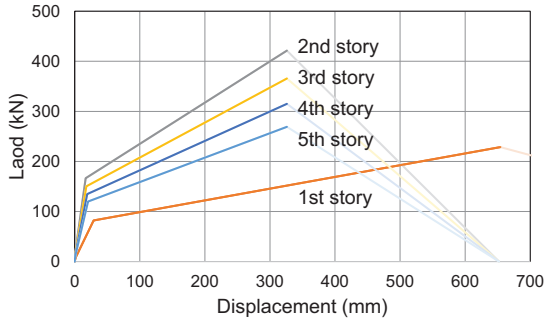

Figure 13: *Load displacement relationship of the shear deformation area due to rotational resistance of column-nuki joints*

5.1.5 Column rocking resistance

When a thick column tilts by lateral load, vertical load on the column works to reduce the tilting angle. This effect is called column rocking resistance and is one of the important seismic element of traditional timber buildings [6]. The function is built into the software wallstat to add column rocking resistance as the moment at the bottom of column.

Table 10 shows the parameters input to the vibration model. There are two columns in each story in the model, the values of vertical load in Table 10 are that of one column. And the values of vertical load from 2nd to 5th stories are decreased to 5/8 of the original values as these columns are surrounded by wood on top and bottom and the effect is smaller than the column on foundation stone. Figure 14 shows the load displacement relationship due to column rocking resistance calculated by Equation (5), which is based on the equation originally derived from the experiment result on circular section column by Ban [7], but does not contain the P-Δ effect as the P-Δ effect is considered for the whole model in the software wallstat.

$$P_c = \frac{b}{h} W \left(1 + 0.99625 e^{-0.03027\delta} - \frac{19.9625}{\delta + 10} \right) \qquad (5)$$

where, P_c = lateral load due to column rocking resistance (kN), b = column diameter (mm), h = column height (mm), W = vertical load (kN) and δ = displacement (mm).

Table 10: *Parameters of column rocking resistance of one column in the vibration model*

Story	Column diameter b (mm)	Column height h (mm)	Vertical load W (kN)
1st	340	3270	673.4
2nd	320	1630	328.5
3rd	300	1630	235.3
4th	280	1630	154.5
5th	260	1630	79.8

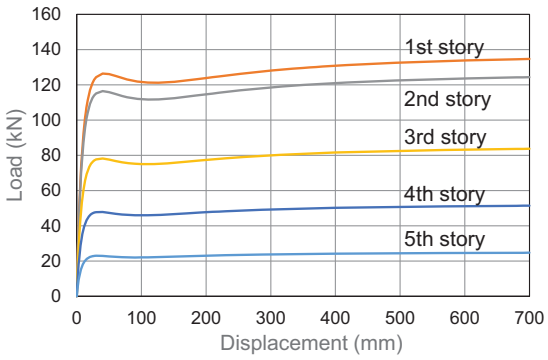

Figure 14: *Load displacement relationship of the shear deformation area due to column rocking resistance*

5.2 INPUT EARTHQUAKE WAVE

As the input earthquake waves, we used three artificial waves created with using the response spectrum of extremely rare ground motion stipulated in Building Standard Law of Japan. Figure 15 shows the acceleration response spectrum and Figure 16 shows the time history of acceleration of these waves.

https://doi.org/10.52202/069179-0335

Hachinohe-NS is created using an amplification factor of acceleration by surface ground G_s calculated by the boring data near the site and the phase spectrum of the observed wave at Hachinohe during the Tokachi-oki earthquake in 1968. Tendo-EW is also created using the boring data and the phase spectrum of the observed wave at Tendo during the 2011 off the Pacific coast of Tohoku earthquake. BSL1 is using G_s of type 1 ground stipulated in Building Standard Law of Japan and a random phase spectrum.

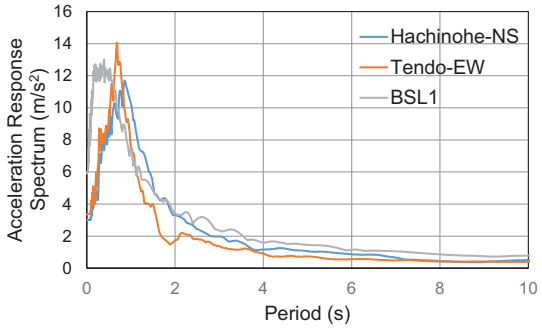

Figure 15: *Acceleration response spectrum of input waves*

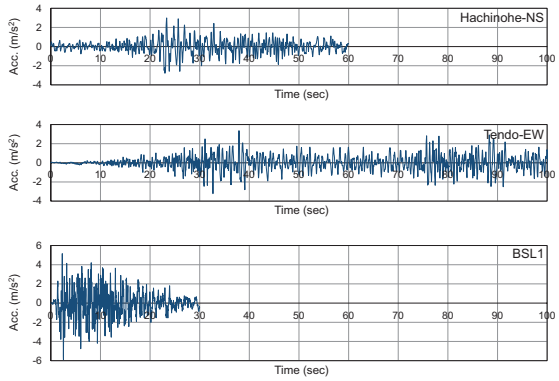

Figure 16: *Time history of acceleration of input waves*

5.3 ANALYSIS RESULT

As an example of the result of time history analysis, Figures 17 and 18 show the time history waveform of story drift and the relationships between story shear force and story drift, against the input wave using Hachinohe-NS phase. Table 11 and Table 12 show the maximum values of story drift δ_{max} and shear deformation angle γ_{max} against each input wave.

From Table 11 and Table 12 we can see that the maximum story drift of first story is far larger than other stories and it reaches 342.7 mm against BSL1, which is about 1/15 radian by story shear deformation angle. However, the pagoda does not collapse against the strong ground motion according to the requirement of Building Standard Law of Japan.

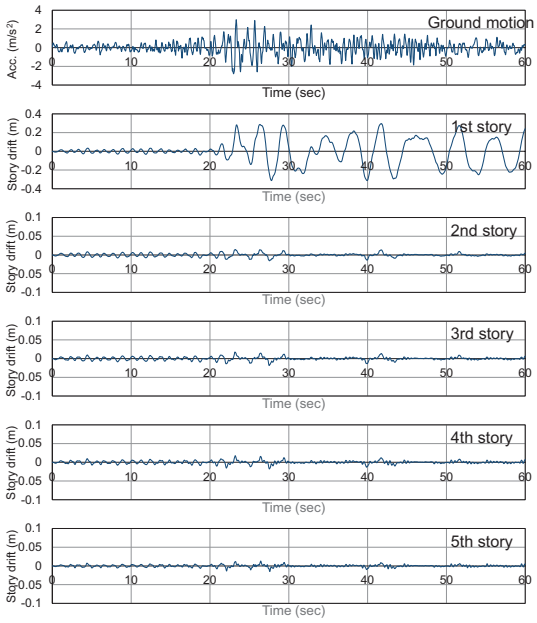

Figure 17: *Time history of story drift against Hachinohe-NS as an example of the analysis result*

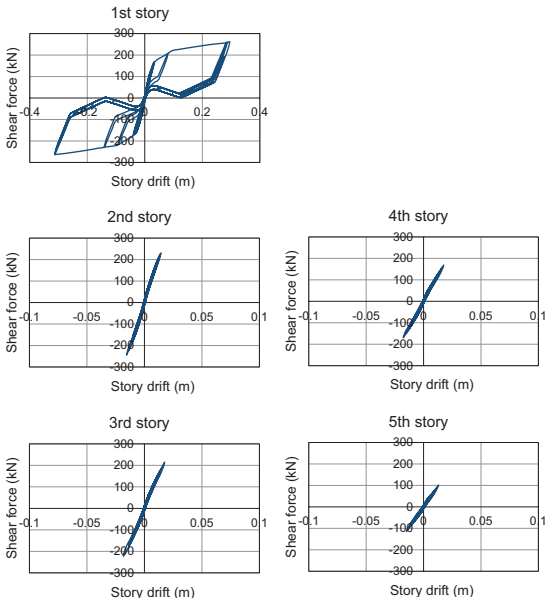

Figure 18: *Relationship between story shear force and story drift against Hachinohe-NS as an example of the analysis result*

Table 11: *Maximum values of story drift δ_{max} (mm)*

Story	Story drift δ_{max} (mm)		
	Input waves		
	Hachinohe-NS	Tendo-EW	BSL1
1st	312.9	295.0	336.5
2nd	15.6	16.3	15.8
3rd	18.4	18.9	16.3
4th	17.8	19.1	15.8
5th	15.0	15.0	15.1

https://doi.org/10.52202/069179-0335

Table 12: *Maximum values of shear deformation angle γ_{max}*

Story	Shear deformation angle γ_{max} (10^{-3} rad)		
	Input waves		
	Hachinohe-NS	Tendo-EW	BSL1
1st	61.1	57.6	65.7
2nd	4.3	4.5	4.3
3rd	5.0	5.2	4.5
4th	4.9	5.2	4.3
5th	4.1	4.1	4.1

In this analysis, only the main seismic elements are considered but there are other structural element that can be considered such as rotational resistance of many other joints. Especially, the ratio of shear stiffness of first story to other stories seems smaller considering the result of microtremor measurement. Therefore, actual maximum displacement may smaller than this analysis result and further study for more appropriate modeling seems necessary.

6 CONCLUSIONS

We conducted micro tremor measurement and performed time history response analysis on the newly built five story pagoda of *Joan-ji* temple in Tendo-city Japan. As the result of micro tremor measurement, we obtained natural frequencies and vibration modes. And the result of the time history analysis considering shear resistance of board walls, rotational resistance of the joints between column and *nuki*, and column rocking resistance, clarified that the pagoda does not collapse against the strong ground motion at the level of the requirement of standard though the deformation angle of first story reaches 1/15 radian in some cases.

ACKNOWLEDGMENT

Authors would like to thank Mr. Yasuo Matsuoka, the chief priest of *Joan-ji* Temple, for his full cooperation in this research, Dr. Takafumi Nakagawa, Associate Professor of Kyoto University, for his advice to use the analysis software wallstat, Mr. Takahiro Sato, who designed the structure of the pagoda, for his provision of technical data and all the members of Kawai laboratory in Kogakuin University who assisted with experiments, measurements and so on.

REFERENCES

[1] T. Nakagawa, M. Ohta, et. al.: Collapsing process simulations of timber structures under dynamic loading III Numerical simulations of the real size wooden houses, Journal of Wood Science, Vol.56, No.4, 284-292, 2010.

[2] A. Kuramoto, N. Kawai, et. al.: Analytical study on seismic performances of a newly built five-storied pagoda, Proceedings of WCTE 2018, 2018.

[3] Technical guidebook on wall multiplying factors for clay walls, lattice walls, and drop board walls (in Japanese), HOWTEC, 2004.

[4] Design manual for engineered timber joints (in Japanese), Architectural Institute of Japan, 2009.

[5] S. Murai and M. Miyamoto: Experimental study on structural performance evaluation of column-to-*nuki* connection in traditional timber shrines and temples, AIJ Journal of Technology and Design, Vol. 27, No.66, 714-719, 2021.

[6] N. Kawai: Static loading test and shake table test on column rocking resistance using scale models, Proceedings of WCTE 2018, 2018.

[7] S. Ban: Study of statics on structure of temples and shrines Part 1 (in Japanese). Technical papers of annual meeting, Architectural Institute of Japan, 1941.

https://doi.org/10.52202/069179-0335

World Conference on Timber Engineering Oslo 2023

INNOVATIVE HIGH PERFORMANCE SEISMIC RESILIENT TIMBER WALL STRUCTURES WITH LOW DAMAGE FLOOR CONNECTIONS

Soheil Assadi[1], Ashkan Hashemi[2], Pierre Quenneville[3]

ABSTRACT: Rocking timber walls provide superior seismic performance in comparison with conventional light timber structures. Nevertheless, there is an uplift movement at the base of the wall that is translated as vertical displacement and rotation demands at the floor levels. With current conventional approach, not only floors and connections are prone to damage, but also the rocking movement is compromised. Presented in this paper is a new wall-to-floor and beam-to-floor solution for mass timber wall structures that not only transfer the lateral loads but also provide full self-centering while dissipating seismic energy without damage. A new shear key like system including friction dampers is proposed, to both safely allow wall uplift relative to floor and at the same time dissipate energy. Among the advantages of the new system are increased damping capacity of the system, elimination of bulky and expensive fastener connections, mitigation of displacement demands on the structure, reduction in the size and capacity of the hold-downs, and the possibility of reducing the size and number of walls. As a result, the design is more economical and cost-effective, while delivering a high-performance, competitive solution compared to conventional timber structures.

KEYWORDS: Low damage, Rocking wall, Cross Laminated Timber, Damage avoidance, Self-centring, Energy dissipation.

1 INTRODUCTION

There has been an increase in the use of engineered (mass) timber products in structures in the past decade due to the advantages they present over conventional light timber and concrete, such as construction speed, efficiency, sustainability, and reduced seismic loads due to their light weight. Shear walls (including rocking walls) are one of the most economical and efficient Lateral Load Resisting Systems (LLRS) to construct. They have been around for decades and have earned an excellent reputation. It has become increasingly popular among engineers and researchers to employ Cross Laminated Timber (CLT) rocking walls due to their reliability and efficiency in terms of seismic performance. In rocking walls, there is an uplift movement at the base of the wall that is translated as vertical displacement and rotation demands at the floor levels. So far, two general approaches have been taken to deal with these demands. Firstly, the coupled approach where the timber floors (or beams) are rigidly or semi-rigidly connected to the timber walls which are typically plywood shear walls. With this approach, not only floors and connections are prone to damage, but also the rocking movement is compromised. Secondly, the decoupled approach, where the floors are isolated from the walls. The extent of damage is relatively less with the decoupled approach; however, the gravity system is separated, and the wall capacity is not fully utilized. Conventionally, rigid or semi-rigid bracket plates and fasteners are utilized for either of these approaches, where not only the floors and connections are susceptible to damage, but also the overall seismic performance of the system is compromised. To date, there has been no solution to address the current shortcomings. This paper introduces an innovative system that addresses current shortcomings while taking advantage of the wall uplift at the floors to dissipate energy and increase the seismic resistance efficiency of the structure.

1.1 INADEQUACIES OF THE CURRENT WALL-TO-FLOOR DESIGN

To understand the performance of CLT walls in a variety of configurations, numerous numerical and experimental studies have been conducted [1-6]. Furthermore, extensive research and experimental tests have been conducted to assess the performance and failure modes of the conventional wall-to-floor connections [7-9]. Based on all of these studies, it can be concluded that CLT walls exhibit a reliable behavior, remaining intact with minimal damage, while plasticization and non-linearity occurring locally at the point of connections and fasteners (see Figure 1). Additionally, boundary conditions have been found to have a significant impact on the lateral resistance capacity of CLT walls. This includes bottom wall connections, i.e., hold-downs and shear keys, as well as the connections between walls and floors (diaphragms). In experimental tests, there were repeated instances of damage to CLT floor panels as a result of displacement incompatibility between the rocking motion and the

[1] Soheil Assadi, University of Auckland, New Zealand, skha858@aucklanduni.ac.nz
[2] Ashkan Hashemi, University of Auckland, New Zealand, a.hashemi@auckland.ac.nz
[3] Pierre Quenneville, University of Auckland, New Zealand, p.quenneville@auckland.ac.nz

https://doi.org/10.52202/069179-0336

floor's swaying motion. Experimental and numerical studies using conventional rigid and semi-rigid connections with conventional hold-downs demonstrate pinching hysteresis and stiffness degradation after each cycle. The pinching hysteresis indicates yield and permanent damage to the rigid or semi-rigid connections and hold-downs, resulting in considerable residual drift and leaving the structure vulnerable to aftershocks. Thus, it is not desirable, nor is it consistent with mass timber structure's objective of seismic resilience and stainability. Presented in Figure 2 are the common failure modes associated with these conventional connections.

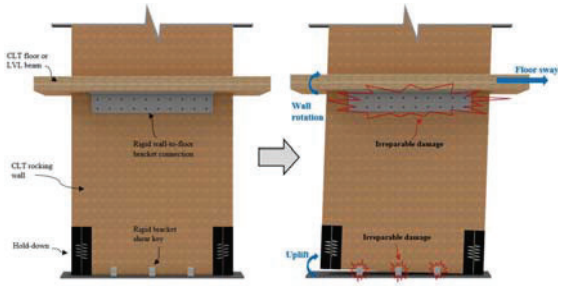

Figure 1. *Rocking wall motion and its interaction with the floor and the rigid connection, leading to irreversible and irreparable damage.*

Figure 2. *Connection failure modes: (a) fasteners withdrawal, (b) fasteners head pull-through, (c) metal bracket buckling, (d & e) timber panel brittle failure (tearing).*

2 CONCEPT OF THE PROPOSED SYSTEM

The new concept utilizes the established Resilient Slip Friction Joint (RSFJ) [10] as hold-downs to provide energy dissipation, self-centering, and allow safe rocking movement of the wall. It not only provides the necessary energy dissipation and complete self-centring behaviour, but also additional mechanism such as secondary fuse activation (collapse prevention) to ensure life safety during a major earthquake event. RSFJ consists of grooved cap plates, grooved middle plates, disk springs and pre-stressed bolts or rods. RSFJ is activated when force demand exceeds the slip force (resisting friction force between clamped plates). It is the friction between the grooved plates that dissipates energy as the cap plates slide onto the middle plates, while the pre-stressed bolts and disk springs are compressed together increasing the friction force required to slide the plates, and thus forcing the grooved cap plates to return to their original position, which leads to self-centering behavior. A more detailed description of the RSFJ mechanism can be found in [3, 11].

Experimental testing of a rocking CLT wall with RSFJ hold-downs demonstrated that these joints provide outstanding seismic performance while allowing damage-free deformation and ductility [3]. The RSFJ assembly and parameters of its flag-shaped load-deformation behavior are displayed in Figure 3.

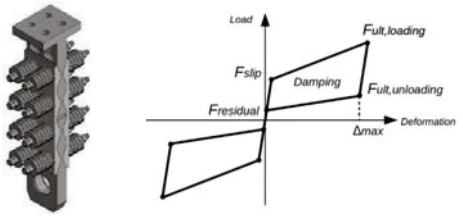

Figure 3: *Resilient Slip Friction Joint (RSFJ): (a) hold-down assembly (b) flagged shaped hysteresis.*

Additionally, slip friction dampers are employed at floor levels to take advantage of the uplift and enhance the damping capacity of the structure. Slip friction dampers are derivatives of symmetric slip-friction dampers introduced by Loo et al. [12]. The symmetric slip friction joint is composed of sliding steel plates clamped together with bolts, Belleville disks, and nuts (no shims are used). Friction dampers dissipate energy through friction between clamped plates, with the inner steel plate incorporating a slot to facilitate free movement of the outer plates without damage while providing Isotropic loop hysteresis behaviour (see Figure 4). The joint was successfully tested in an individual configuration as well as a hold-down for a LVL rocking wall, providing repeatable hysteresis while retaining strength and stiffness [12, 13].

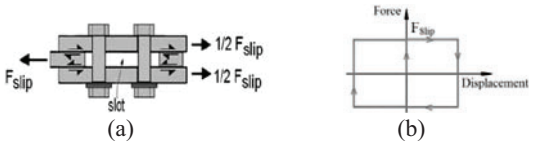

Figure 4: *Symmetric slip friction joint: (a) joint assembly (b) idealized joint isotropic hysteresis*

As an important component of this concept, the innovative shear key developed by Hashemi [3] is incorporated to ensure adequate shear transfer while accommodating the rocking of the CLT wall (Figure 5). It is further proposed to provide a similar shear key at the locations of wall-to-floor to subsequently transfer lateral demands from floor panel (essentially diaphragm) to wall and allow safe and damage free rocking motion. An illustration of the proposed concept assembly is shown in Figure 6. The proposed concept, in summary, utilizes RSFJs as hold-downs of the rocking CLT wall, while friction dampers are utilized at the locations of wall-to-floor, and the innovative shear key is employed at the base of the rocking wall as well as the locations of wall-to-floor.

https://doi.org/10.52202/069179-0336

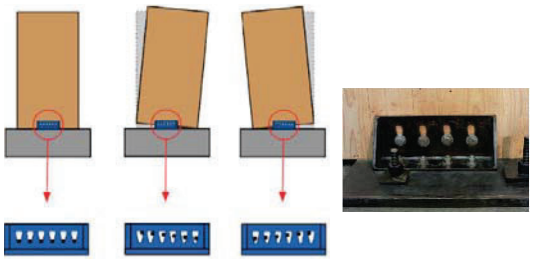

Figure 5: *Innovative shear key*

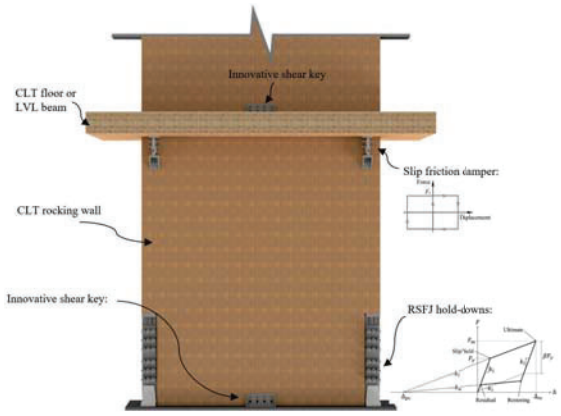

Figure 6: *Proposed concept configuration with RSFJ hold-downs and friction dampers at floor connection.*

3 METHODOLOGY

Through numerical analyses of case study structures with various number of storeys and configurations, this study provides a comprehensive assessment of the proposed CLT rocking wall system. Table 1 presents a summary of the case study structures and Figure 7 illustrates the assembly of the largest case study structure (seven storey K7-FD) as an example. As a means of highlighting the benefits of friction dampers, numerical analysis of each case study structure was conducted in two configurations, one with friction dampers at floor levels, the other without. It should be noted that the loading considerations are assumed to be for a commercial structure. While the first-floor measures 4.8 meters in height, all subsequent floors measure an equal 3.8 meters in height. Gravity is completely taken by the LVL gravity frame, hence the rocking CLT wall is decoupled from the gravity load resisting frame for the purposes of this study. CLT rocking walls are composed of Machine Stress Graded sawn timber with a modulus of elasticity of 8 GPa (MSG8) in the longitudinal direction and MSG6 in the transverse direction. ETABS software [14] is used for the numerical analysis. Non-linear pushover analyses are carried out to highlight the key performance characteristics of the proposed systems, followed by dynamic time history analyses that provide a wide range of variables suitable for comprehensive analytical study. Dynamic time history analyses are conducted by scaling seven ground motion records in accordance with NZS1170.5 guidelines [15].

Table 1: *Summary of the case study structures.*

Case study wall structure:	Configuration, Ki	Number of storeys	Structure height (m)
K2	K2 - FD K2 – R	2	8.6
K3	K3 - FD K3 – R	3	12.4
K4	K4 - FD K4 – R	4	16.2
K5	K5 - FD K5 – R	5	20.0
K6	K6 - FD K6 – R	6	23.8
K7	K7 - FD K7 – R	7	27.6

Configuration, Ki	Number of hold-downs	Number of shear keys	Number of friction dampers
K2 - FD K2 – R	2	2	4 -
K3 - FD K3 – R	2	3	6 -
K4 - FD K4 – R	2	4	8 -
K5 - FD K5 – R	2	5	10 -
K6 - FD K6 – R	2	6	12 -
K7 - FD K7 – R	2	7	14 -

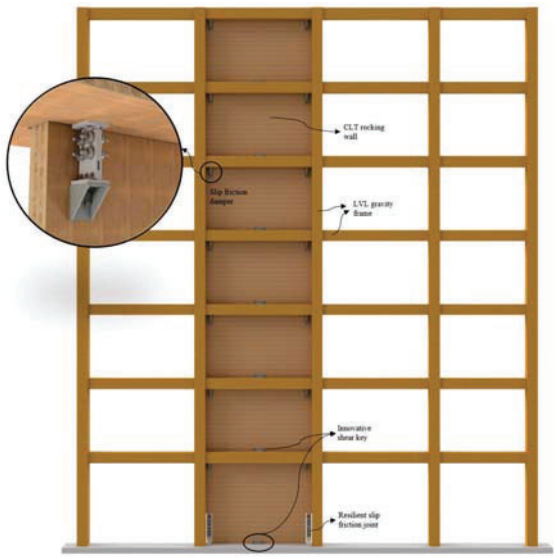

Figure 7: *Assembly of the case study structure (seven story K7-FD)*

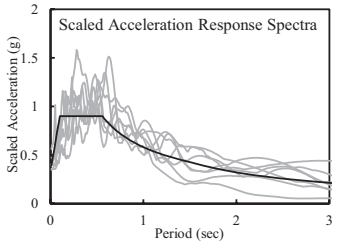

Figure 8: *Scaled ground motion accelerations*

The design envisages that there to be notches at both the bottom corners of the walls to fit the RSFJ hold downs, therefore, the rocking wall lever arm is from the rocking toe to the opposite RSFJ hold down. In practice, the RSFJ hold downs will be equipped with spherical swivel bearings at their base to allow rotation in line with the rocking wall. Thus, a pinned boundary condition is assigned to the bottom of the link elements representing the RSFJs in the numerical model. RFSJ hold downs are modelled using "Damper-friction spring" and slip friction dampers are modelled using "multilinear plastic" link elements in ETABS. The validity of the modelling techniques has already been confirmed by several studies [6, 16, 17].

4 PROPOSED SYSTEM PERFORMANCE

It is appropriate to use non-linear pushover analysis for this study since the case study structures are regular low- to mid-rise structures and the first mode of vibration is the governing mode (fundamental mode). In order to determine the optimal friction damper slip force for each case study structure, nonlinear pushover analysis iterations (tuning) were conducted. Each system was optimized by minimizing the residual force-displacement at the end of every quadrant cycle while maximising energy dissipation (damping). When the friction damper slip force is low, even though complete self-centering is achieved without any residual force, the flag-shaped hysteresis is narrow, and it is possible to increase the damping capacity of the system by increasing the slip force (capacity) of the friction damper in order to enlarge the hysteresis area. When the slip force of the friction damper is high, considerable residual displacement and force are experienced, which most likely result in significant residual deformation after an earthquake.

Hysteretic damping ($\xi_{hysteresis}$) is calculated via Jacobsen's simplified method (hysteresis area) [18] with the provided backbone curves from cyclic pushover analyses. In Figure 9, the load-deformation curve (hysteresis) of the system is shown for cases with friction dampers (Ki-FD series) versus cases without friction dampers (Ki-R series). Non-linear pushover results show that hysteretic damping capacity ($\xi_{hysteresis}$) has increased by 7% on average with the implementation of tuned friction dampers. Increases in damping capacity is correlated with an increase in stories, or in other words, an increase in friction dampers.

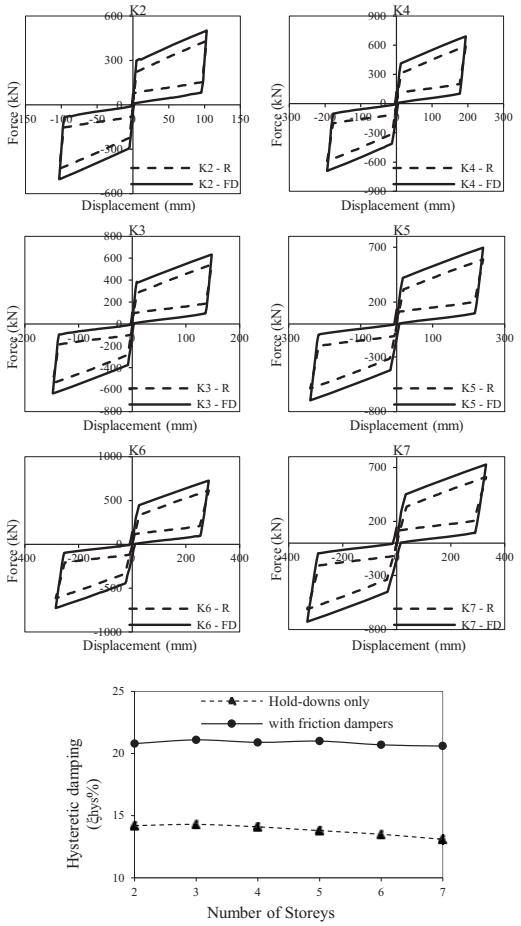

Figure 9: *Comparison of system load-deformation curves of cases with and without friction dampers.*

Dynamic time history offers not only a wide array of variables for this study, but also incorporates all modes of vibration, thereby capturing any dynamic effects that may have been overlooked in nonlinear pushover analysis. Furthermore, dynamic time history appropriately accommodates the non-linearity of members, links (dampers), and boundary conditions such as gaps with their respective inherent and hysteretic damping. For each case study "mean of seven" approach [19] is used as a means of interpreting the results. One of the most noticeable advantages of the proposed system is the reduction in displacement demands on the structure (as an important index); where roof drifts have been significantly reduced by an average of 35% (see Figure 10). It is observed that the greatest reduction in roof drift is about 65%, while the least reduction is about 10%. Based on these results, it is evident that the proposed system is effective in curtailing lateral displacement demands under a variety of cases.

https://doi.org/10.52202/069179-0336

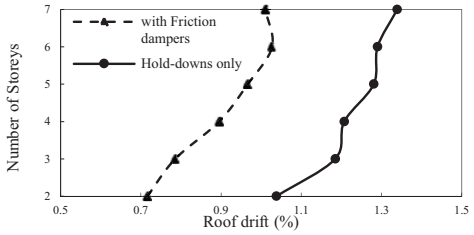

Figure 10: *Performance of the case study structures via dynamic time history analyses, roof drift comparison.*

Seismic force demands (base shear) have been reduced by about 15% on average. This decrease becomes more significant with taller structures, demonstrating an indication of the potential benefit of the proposed system on mitigating higher mode effects which have been of concern with tall wall structures [20, 21]. While complete self-centering behavior is observed in all cases, the proposed system appeared to be more effective in controlling residual drifts, especially for taller walls (see Figure 11). This provides further confidence in its likely performance during a major event in which ground motions exceeding the design level are experienced, developing force and displacement demands exceeding the design levels due to dynamic amplification caused by higher mode effects. All residual drifts fall well under the permissible residual drifts levels suggested by McCormick et al. [22] where 0.5% residual drift is a suitable threshold, after which the structure requires repairs to ensure structural soundness. Combined with RSFJ hold-downs, the concerns regarding self-centring of friction dampers, discussed in the previous section, are rendered irrelevant.

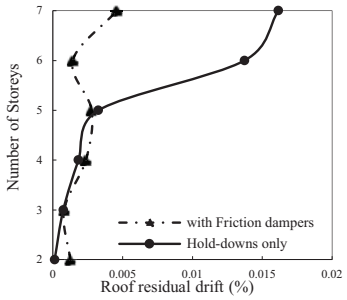

Figure 11: *Performance of the case study structures via dynamic time history analyses, roof residual drift comparison.*

Consequently, there is a reduction in both the force and displacement demands of the hold-downs, resulting in smaller hold-downs required. The reduction in force and displacement demands of the hold-downs is substantial, where force demand have been significantly reduced by an average of 40%, and displacement demand have been reduced by an average of 25%. Similar to the system, the hold-down force demand reduction becomes more evident with taller structures, validating that the presence of friction dampers helps control lateral demand, enhances lateral force distribution, and mitigates higher mode effects. These reductions entail a considerable decrease in capacity, size, and cost of the hold-downs. Figure 12 presents comparison of the hold-down load-deformation (hysteresis) obtained for El Centro (1940) ground motion. Furthermore, it is perceived that by utilizing smaller hold-downs, the stresses induced to critical points of CLT rocking walls can be reduced by approximately 20%. It is therefore possible to reduce the number of layers in the CLT wall or reduce the manufacturing grade of the CLT.

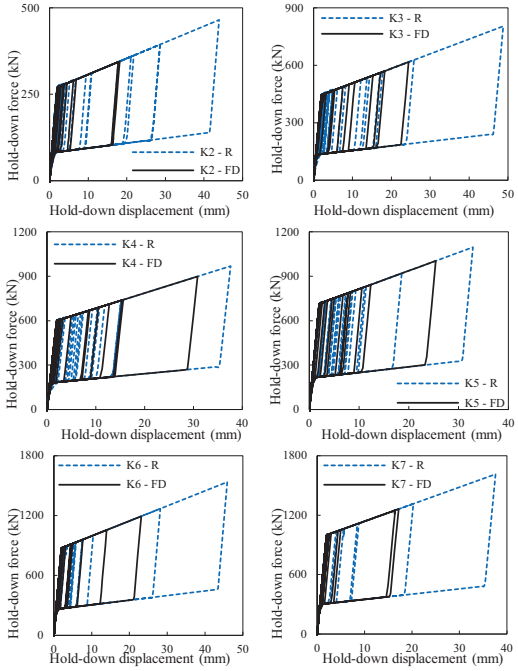

Figure 12: *Comparison of critical hold-down load-deformation (hysteresis) of the case study structures for El Centro (1940) ground motion.*

5 CONCLUSIONS

A new wall-to-floor and wall-to-beam system is presented in this paper that eliminates bulky rigid connections and addresses the shortcomings of existing conventional methods. A new shear key-like system, incorporating friction dampers, has been proposed to allow safe wall uplift, while dissipating energy at the same time. A numerical investigation of the proposed concept was conducted by selecting seven case study structures. By implementing friction dampers, the hysteretic damping capacity ($\xi_{hysteresis}$) has increased by 7% on average. According to the results of dynamic time history analyses, the most notable advantage of the proposed system is the reduction in displacement and force demand by about 35% and 15%, respectively. Furthermore, the force and displacement demand of the hold-downs has reduced noticeably by 40% and 25% respectively, leading to smaller capacity, reduced size, and more affordable hold-downs. The result is a more economical and cost-effective design as a whole, while delivering a high-performance, competitive solution compared to conventional timber structures. The cost of friction dampers can be offset by

eliminating the conventional bracket connections and reducing the number of fasteners.

ACKNOWLEDGEMENT

The authors would like to acknowledge WIDE Trust New Zealand for providing the opportunity and funding for this research.

REFERENCES

[1] Ceccotti, A., C. Sandhaas, M. Okabe, et al., *SOFIE project - 3D shaking table test on a seven-storey full-scale cross-laminated timber building: 3d shaking table test on a seven-storey full-scale x-lam building.* Earthquake engineering & structural dynamics, 2013. **42**(13): p. 2003-2021.

[2] Gavric, I., M. Fragiacomo, and A. Ceccotti, *Cyclic Behavior of CLT Wall Systems: Experimental Tests and Analytical Prediction Models.* Journal of structural engineering (New York, N.Y.), 2015. **141**(11).

[3] Hashemi, A., P. Zarnani, R. Masoudnia, et al., *Experimental Testing of Rocking Cross-Laminated Timber Walls with Resilient Slip Friction Joints.* Journal of structural engineering (New York, N.Y.), 2018. **144**(1).

[4] Popovski, M. and I. Gavric, *Performance of a 2-Story CLT House Subjected to Lateral Loads.* Journal of structural engineering (New York, N.Y.), 2016. **142**(4).

[5] Yasumura, M., K. Kobayashi, M. Okabe, et al., *Full-Scale Tests and Numerical Analysis of Low-Rise CLT Structures under Lateral Loading.* Journal of structural engineering (New York, N.Y.), 2016. **142**(4).

[6] Hashemi, A., P. Zarnani, and P. Quenneville, *Seismic assessment of rocking timber walls with energy dissipation devices.* Engineering structures, 2020. **221**: p. 111053.

[7] D'Arenzo, G., W. Seim, and M. Fossetti, *Experimental characterization of a biaxial behaviour connector for CLT wall-to-floor connections under different load directions.* Construction & building materials, 2021. **295**: p. 123666.

[8] Gavric, I., M. Fragiacomo, and A. Ceccotti, *Cyclic behaviour of typical metal connectors for cross-laminated (CLT) structures.* Materials and structures, 2015. **48**(6): p. 1841-1857.

[9] Tomasi, R. and I. Smith, *Experimental Characterization of Monotonic and Cyclic Loading Responses of CLT Panel-To-Foundation Angle Bracket Connections.* Journal of materials in civil engineering, 2015. **27**(6).

[10] Zarnani, P. and P. Quenneville, *Resilient Slip Friction Joint*, N.I.O.P.N. WO2016185432A1, Editor. 2015: New Zealand.

[11] Hashemi, A., S.M.M. Yousef-Beik, F. Mohammadi Darani, et al., *Seismic performance of a damage avoidance self-centring brace with collapse prevention mechanism.* Journal of constructional steel research, 2019. **155**: p. 273-285.

[12] Loo, W.Y., P. Quenneville, and N. Chouw, *A new type of symmetric slip-friction connector.* Journal of constructional steel research, 2014. **94**: p. 11-22.

[13] Loo, W.Y., C. Kun, P. Quenneville, et al., *Experimental testing of a rocking timber shear wall with slip-friction connectors.* Earthquake engineering & structural dynamics, 2014. **43**(11): p. 1621-1639.

[14] Computers and Structures Inc, *ETABS*. Computers and Structures, Inc ;: Berkeley, California.

[15] Standards New Zealand *NZS 1170.5 Structural Design Actions - Part 5: Earthquake actions - Incorporating Amendment 1 (2016)*. 2004: Wellington, New Zealand.

[16] Loo, W.Y., P. Quenneville, and N. Chouw, *A numerical study of the seismic behaviour of timber shear walls with slip-friction connectors.* Engineering structures, 2012. **34**: p. 233-243.

[17] Hashemi, A., P. Zarnani, R. Masoudnia, et al., *Seismic resilient lateral load resisting system for timber structures.* Construction & building materials, 2017. **149**: p. 432-443.

[18] Chan, N., A. Hashemi, P. Zarnani, et al., *Damping-Ductility Relationships for Flag-Shaped Hysteresis.* Journal of structural engineering (New York, N.Y.), 2021. **147**(7).

[19] Bradley, B.A., *Seismic performance criteria based on response history analysis: Alternative metrics for practical application in NZ.* Bulletin of the New Zealand Society for Earthquake Engineering, 2014. **47**(3): p. 224-228.

[20] Priestley, M.J.N., *Does capacity design do the job? : An examination of higher mode effects in cantilever walls.* Bulletin of the New Zealand Society for Earthquake Engineering, 2003. **36**(4): p. 276-292.

[21] Priestley, M.J.N. and A. Amaris. *Dynamic Amplification of Seismic Moments and Shear Forces in Cantilever Walls*. 2003.

[22] McCormick, J., H. Aburano, M. Ikenaga, et al. *Permissible residual deformation levels for building structures considering both safety and human elements*. 2008.

https://doi.org/10.52202/069179-0336

World Conference on Timber Engineering Oslo 2023

EVALUATION OF SEISMIC PERFORMANCE FACTORS AND FRAGILITY FUNCTIONS FOR POST-TENSIONED MASS PLY PANEL ROCKING WALLS

Tu X. Ho[1], Patricio Uarac P.[2], Andre R. Barbosa [3], Arijit Sinha[4], Barbara Simpson[5], Gustavo A. Araújo R.[6], Gustavo F. Orozco[7]

ABSTRACT: This paper presents the statistical and numerical investigation of the seismic performance of a three-story post-tensioned mass ply panel (MPP) rocking wall lateral force-resisting system prototype whose main components are MPP, U-shaped flexural steel plates (UFPs), and high-strength steel post-tensioned rods. Uncertainties in material properties and geometry of the components are considered in the assessment of the performance of this lateral force-resisting system based on recent experimental data on MPP, experimental data available in the literature for the UFPs and post-tensioning rods, as well as some additional structural design considerations. In the assessment of the seismic performance factors, first, random realizations of the structural design are generated using Monte Carlo simulation. Second, for each realization, a nonlinear finite element model is developed. For each realization, two types of analysis are performed, nonlinear static analyses, and incremental dynamic analyses. Results of the nonlinear static and dynamic analyses are then used to estimate the seismic design factors (e.g., R-factor) and limit state-based fragility functions, the latter being based on exceeding limit states defined for each component based on existing experimental data.

KEYWORDS: Fragility function, incremental dynamic analysis, mass ply panel, post-tensioned rocking wall, pushover analysis, R-factor.

1 INTRODUCTION

Mass timber materials have gained public attention and are finding expanded uses in the building sector. The International Building Code [1] introduced new building types in the last code revision cycle, which now allows for the design and construction of mass timber buildings up to 18 stories tall. Innovative lateral force-resisting systems (LFRS), such as post-tensioned rocking walls coupled with different energy dissipation solutions, have been designed for use in buildings per (i) the equivalent lateral force procedure in ASCE 7 [2] assuming a conservative seismic response modification coefficient (R-factor) [3], or (ii) state-of-the-art performance-based design methods requiring the use of alternative means and methods of design and analysis, which were mentioned by FEMA P-58 [4]. However, even though a few buildings have been built using these LFRS [5], few studies have focused on the seismic performance of mass timber post-tensioned rocking walls, and therefore, the seismic design factors (e.g., R-factor) of the system, which is used in ASCE 7 and other seismic design standards, and fragility functions needed to fully adopt the FEMA P-58 methodology have been based on expert judgement [6] that have been largely conservative. Based on existing knowledge and recent experimental test data, this paper summarizes the nonlinear modelling of post-tensioned mass ply panel (MPP) rocking walls coupled with U-shaped flexural plates (UFPs) and presents the seismic performance assessment of a three-story building adopting this LFRS [7]. Effects of epistemic and aleatory uncertainties were explicitly accounted for in the seismic performance assessment of the rocking wall system, following a validated method available in the literature [8]. Results of the nonlinear analyses are presented in terms of collapse fragility functions and seismic performance factors, which may be used as a first step in the determination of low- and mid-rise building archetypes consisting of post-tensioned mass timber walls.

[1] Tu X. Ho, Department of Wood Science and Engineering, Oregon State University, tu.ho@oregonstate.edu
[2] Patricio Uarac P., School of Civil and Construction Engineering, Oregon State University, uaracpip@oregonstate.edu
[3] Andre R. Barbosa, School of Civil and Construction Engineering, Oregon State University, andre.barbosa@oregonstate.edu
[4] Arijit Sinha, Department of Wood Science and Engineering, Oregon State University, arijit.sinha@oregonstate.edu
[5] Barbara Simpson, Department of Civil and Environmental Engineering, Stanford University, bsimpson@stanford.edu
[6] Gustavo A. Araújo R., Department of Civil and Environmental Engineering, Stanford University, garaujor@stanford.edu
[7] Gustavo F. Orozco, School of Civil and Construction Engineering, Oregon State University, gustavo.orozco@oregonstate.edu

https://doi.org/10.52202/069179-0337

2 METHODOLOGY

2.1 DESCRIPTION OF STRUCTURE

The LFRS was designed for an occupancy consistent with that of an office building archetype located at a site in Seattle, Washington, USA with soil class D and seismic response spectral values, S_{DS} = 0.97 g, S_{D1} = 0.61 g. The direct displacement-based design (DDBD) method [9]–[11] was used for the design of the LFRS. The design base shear was determined by using the capacity spectrum approach [9] and was utilized to design shear wall dimensions, UFPs, and high-strength post-tensioned rods. In the design, a flag shape hysteretic model [11] was utilized to estimate the effective damping of the post-tensioned rocking wall, assuming a damping ratio of 10%. The LFRS was designed to meet requirements of three performance levels [Immediate Occupancy (IO), Life Safety (LS), and Collapse Prevention (CP)], each corresponding to an earthquake hazard intensity level [Service Level Earthquake (SLE), Design Earthquake (DE), and risk-targeted Maximum Considered Earthquake (MCE_R), respectively]. Table 1 lists the performance targets for each performance level. The targets are defined in terms of peak inter-story drift (D_{max}), strains in the post-tensioning rods (ε_{PTmax}), and MPP compression strains at the rocking interface (ε_{MPPmax}). The thresholds strains for the post-tensioning rods and MPP wall are defined such that they remain in the elastic range at IO and LS levels, while both tension rods and MPP are allowed to yield at CP level, but without exceeding their ultimate strains in tension and compression, respectively.

Table 1: *Performance levels and targets*

Performance Level	EQ Levels	Performance thresholds		
		D_{max}	ε_{PTmax}	ε_{MPPmax}
IO	SLE	1.0%	0.0044	0.0032
LS	DE	2.0%	0.0044	0.0032
CP	MCE_R	4.0%	0.0066	0.0075

The investigated post-tensioned rocking wall LFRS shown in Figure 1 (UFP wall) consists of an MPP shear wall (9144 mm × 2134 mm × 181 mm, F16 wall panel [12]), two pairs of post-tensioning rods (diameter 31.8 mm; ASTM A354 Grade BD [13]) connecting the top of the MPP shear wall to the foundation, and 20 UFP devices (152 mm wide, 12.7 mm thick and 102 mm bending diameter, ASTM A572 Grade 42 [14]). The UFPs are attached to the MPP and steel bounding columns that connect to the foundation. The steel bounding column is designed to remain elastic at MCE_R. The MPP walls are connected to the MPP floor slabs through one shear key at each floor level and two shear keys at its base. The MPP floor slabs are supported by laminated veneer lumber (LVL) beams and columns.

2.2 FINITE ELEMENT MODEL OF STRUCTURE

Two-dimensional (2D) finite element models were developed in OpenSees [15] to characterize the building geometry shown in Figure 1. For the gravity system, elastic beam-column elements (elasticBeamColumn) were used. The elastic beam-column elements were connected to the beam-column joint using zero-length, elastic elements to account for the rotational stiffness of the connection. For the LFRS, the MPP panel itself was modelled using elastic beam-column elements along the height of the building, with nonlinear springs placed between the base of the wall and the foundation to represent the rocking behaviour and any potential inelasticity due to panel crushing and gap opening at the base of the wall. The nonlinear base springs consisted of 19 zero-length, elastic-perfectly plastic (ElasticPPGap) elements that work only in compression, assuming the compression strength in the major direction of the MPP (f_{c_0}) as the elastic limit and considering a plastic hinge length of two times the thickness of the MPP [16]. The springs were located based on the Gauss-Legendre quadrature points along the width of the panel. The UFPs were also modelled with zero-length elements with a force-displacement relation based on the uniaxial material Giuffre-Menegotto-Pinto [17] model. Properties of the UFPs were calibrated to match available numerical models developed using a Ramberg-Osgood material model [18]. Finally, the post-tensioning rods were modelled as trusses with an initial strain based on the design post-tensioning force and a tension-only nonlinear material model. The model of the LFRS is shown graphically in Figure 2.

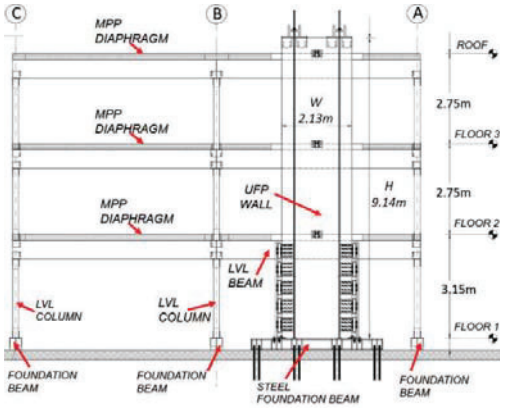

Figure 1: *Elevation of the LFRS archetype*

The finite element models were subjected to nonlinear static pushover analyses and nonlinear time history analyses (NLTHA). For each realization, the fundamental period (T_1) and the associated first-mode shape are computed and used as input parameters for the nonlinear static analysis, where at each floor level, a force is applied following this first-mode distribution with displacement control at the roof level. Each pushover realization is pushed until an 8% roof drift ratio or until is numerically unstable. For the NLTHA, the fundamental period is used to define the target damping ratios for the Rayleigh damping matrix, using committed stiffness and 2% damping associated with the elongated period $1.5T_1$ and short period $0.2T_1$.

https://doi.org/10.52202/069179-0337

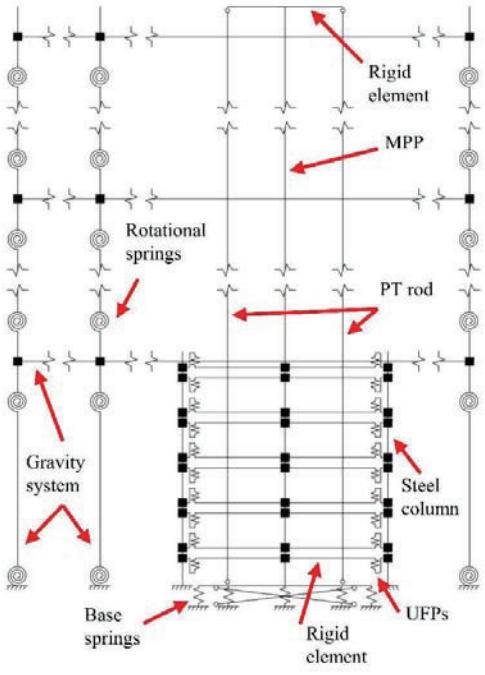

Figure 2: *Finite element model*

2.3 RANDOM VARIABLES AND THEIR STATISTICAL CORRELATIONS

The variability of component properties and dimensions affects the stiffness, strength, and dynamic properties of the structure, and, therefore, its response to loading. Based on the material properties described in this section, a set of 100 structural models were randomly generated. Each model represents a realization of the random variables defining the wall design. Considerations in the model development performed are described in the next subsections.

2.3.1 Material properties

Uncertainties in material properties were based on information available in the literature [19]–[25]. For MPP, Table 2 lists four random variables and their parameters, including mean and coefficients of variation (CoV) for density (ρ_w), modulus of elasticity (E_w), compressive strength in the major direction (f_{c_0}), and shear modulus (G). Expected values were based on the material testing results [24], [25]. Coefficients of variation (CoVs) were determined based on values and formula for glue-laminated timber [22], [23], because currently there is no reliable study on the CoVs of material parameters for MPP, which vary based on base materials, quality control, and material selection schemes implemented in the production of the panels. The density followed a normal distribution while the other properties are lognormally distributed. The four random variables were assumed to be correlated, based on data available for timber materials [22], as shown in Table 3.

Table 2: *Random variables for MPP material properties*

Variable	Dist.	Mean	CoV
ρ_w (kg/m^3)	Normal	34.0	0.10
E_w (MPa)	Lognormal	13626.0	0.13
f_{c_0} (MPa)	Lognormal	44.9	0.12
G (MPa)	Lognormal	509.7	0.13

Table 3: *Correlation coefficient matrix for MPP material properties*

Variable	ρ_w	E_w	$f_{c\ 0}$	G
ρ_w	1.0	0.6	0.8	0.6
E_w	0.6	1.0	0.6	0.6
f_{c0}	0.6	0.6	1.0	0.4
G	0.6	0.6	0.4	1.0

The probabilistic model parameters associated with the mechanical properties of the high-strength rod and other structural steel components are presented in Table 4 and Table 5, respectively. The random variables for the high-strength rods follow a normal distribution, while the structural steel follow lognormal distributions, including the elastic modulus (E_s) and yield strength (f_{sy}) for the UFP components, and on elastic modulus (E_s) and Poisson's ratio (v_s) for the steel bounding columns. The expected values and CoVs were derived from the literature [19], [20].

Table 4: *Random variables for high-strength steel rod properties*

Property	Dist.	Mean	CoV
E_p (GPa)	Normal	200	0.020
f_{pt} (MPa)	Normal	1075.6	0.025
e_u (mm/mm)	Normal	0.05	0.060

Table 5: *Random variables for structural steel properties*

Property	Dist.	Mean	CoV
f_{sy} (MPa)	Lognormal	423	0.105
E_s (GPa)	Lognormal	200	0.045
v_s	Lognormal	0.3	0.045

2.3.2 Component dimensions

Geometric deviations from specified dimensions that also contribute to model uncertainties were accounted for in the probabilistic modelling. For each considered variable, the distribution, mean value, standard deviation, and tolerance are presented in Table 6, where the mean values correspond to the dimensions used for the initial design. Tolerances were considered as the amount by which a measurement might change and still be acceptable [26]; this implies that no realization had geometric values outside the mean plus/minus the tolerance. Values from previous studies were used for the standard deviation and tolerances of each component. For the MPP, standard deviations and tolerances from [27] and [28] were used, respectively. For the UFP thickness, the standard deviation is assumed to be a third of the tolerance from [29]. For the other dimensions, the standard deviation is assumed as half of the tolerance from [30]. For the C-section steel column, the standard deviations are based on [31] and [32], along with tolerances from [30].

https://doi.org/10.52202/069179-0337

Table 6: *Random variables of component dimensions*

Variable	Dist.	Mean [mm]	Std Dev [mm]	Tol. [mm]
Timber panel				
Thickness	Normal	181.0	0.80	1.59
Width	Normal	2133.6	1.59	3.18
Length	Normal	9483.7	3.18	6.35
UFP (Steel Plate)				
Thickness	Lognormal	12.7	0.25	0.76
Width	Normal	152.4	5.56	11.11
Length	Normal	482.6	7.94	15.88
Bending diameter	Normal	88.9	0.89	+0.0 -1.78
C-section steel column				
Depth	Normal	254.0	1.02	+3.18 -2.38
Flange width	Normal	73.4	0.66	+3.18 -3.97
Web thickness	Normal	13.4	0.49	N/A*
Flange thickness	Normal	11.1	0.51	N/A*
High-strength rod				
Diameter	Normal	31.8	0.32	0.25

*N/A: Tolerances not applicable or not available [30].

2.4 PERFORMANCE ASSESSMENT

2.4.1 Damage State Definition

Damage state thresholds were defined using the peak inter-story drift ratio limit as a proxy for damage based on drift limits estimated from component-based (UFP, wall, PT rod, etc.) strain limits developed from experimental data available in the literature. The damage states are associated with the building capacity curve. Three different damage state levels, including Immediate Occupancy (IO), Life Safety (LS), and Collapse Prevention (CP), are defined in this study. The IO damage state is associated with the effective yielding of any components in the building occurs. In the MPP wall LFRS, yielding of UFP devices usually happens at relatively small drift ratios; therefore, yielding of the UFPs is chosen as the indicator of IO damage state in this study. The LS damage state is associated with crushing of the MPP panel or yielding of the PT bar, whichever occurs first. Lastly, the CP damage states are associated with the first occurrence of the following cases: (1) the PT bar strain is greater than the ultimate capacity strain, (2) the peak inter-story drift ratio exceeds 0.1, or (3) the inter-story residual drift is greater than 0.015 [33].

2.4.2 Assessment of the seismic performance factors

The assessment of the seismic performance factors (R-factor, deflection amplification factor, and the over-strength factor) was implemented based on the nonlinear static analyses applied to the set of 100 generated structures. The pushover analysis was used to determine the damage state levels and impact of uncertainties on the R-factor and building capacity. The base shear versus roof drift ratio results were used to obtain the distribution of the building capacity. The mean (μ), mean minus standard deviation (μ-σ), and mean plus standard deviation (μ+σ) of each variable in Figure 3 are determined using the capacity curves. Overall, procedures followed in this study are described in [8] and [34]. The seismic performance factors include: (1) normalized reference yield force, F_y/W, where W is the weight of the structure, (2) reference yield roof drift ratio, d_y/H, where H is the height of the building, (3) displacement ductility factor $\mu = d_u/d_y$ (4) system overstrength factor $\Omega_s = F_y/F_d$, where F_d is the design base shear, and (5) both the seismic modification factor, R, and displacement amplification factor C_d , set equal to the product of the $R_\mu \cdot \Omega_s$., where R_μ is the seismic modification factor associated with the ductility of the system and, thus, set equal to the displacement ductility for this bilinear fitted model.

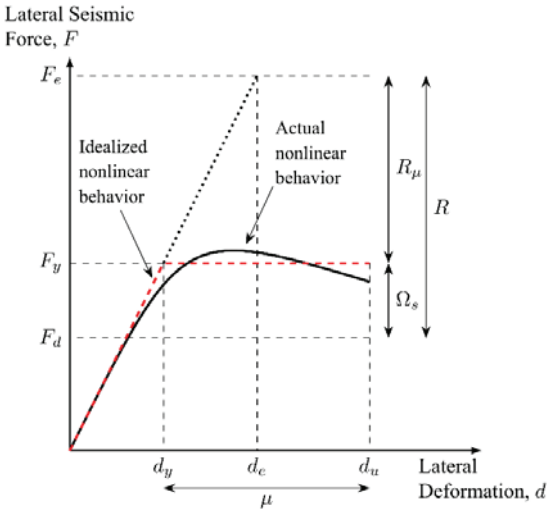

Figure 3: *Equivalent bilinear inelastic model*

2.4.3 Fragility functions

The uncertainties in seismic response were investigated using an incremental dynamic analysis (IDA) for the set of 100 structures. In the IDA, each structure is subjected to the suite of 44 far-field ground motions defined in FEMA P-695 [35]. To reduce computational cost, the 5%-damped response spectral acceleration at the first mode was scaled up to an upper limit of 5g, resulting in a truncated IDA [36]. For each ground motion (GM), increments of 0.2 g were used in the IDA, such that a total of 4,400 IDA was performed. At the IO level, the UFP yielding is chosen as indicator; however, since UFPs reach yielding at relatively small drift ratios, the nonlinear static analysis is used to identify the mean drift ratio where the first-yield of the system occurs, point associated with a 10% drop of the initial stiffness. Using the first-yield drift ratio as threshold on the IDA, a distribution of the amount of UFPs at yielding is obtained and its mean value is used to develop the component fragility function. At CP level, four collapse criteria were used: (1) maximum inter-story drift ratio greater or equal to 0.1, (2) maximum inter-story residual drift ratio greater than 0.015, as recommended by [33], (3) strain in the post-tensioned rods exceeding the maximum strain limit, and (4) numerical non-convergence. As part of the numerical model, the limit states of the UFPs and the MPP panels

https://doi.org/10.52202/069179-0337

were using the uniaxial material 'MinMax' in OpenSees but were not considered a collapse criterion. The use of this 'MinMax' material model means that for strains below or above the ultimate strain of the component, the component fails and returns zero stress.

Based on the IDA results, the fragility functions were fit to a lognormal cumulative distribution function (CDF) with an empirical section and a fitted-extrapolated section, as considered in [37].

3 RESULTS

3.1 SEISMIC PERFORMANCE FACTORS

Figure 4 shows the results of the nonlinear pushover analyses. The results for all 100 structures are shown in grey, while the black curve corresponds to the mean of all the pushover curves. The red line corresponds to a bilinear model calibrated using the Energy Equivalent Elasto-Plastic method [38] fit to the mean pushover curve. A similar calibration process was conducted to obtain the mean plus and minus standard deviation curves (not shown in the figure). Table 7 lists the normalized calibrated factors, reference yield force, and reference yield drift ratio (F_y/W, and d_y/H) for all three calibrated curves. In addition, Table 7 also lists the seismic performance factors. The base shear at the ultimate roof drift ratio of 0.07 represents the lowest force obtained in the mean pushover results.

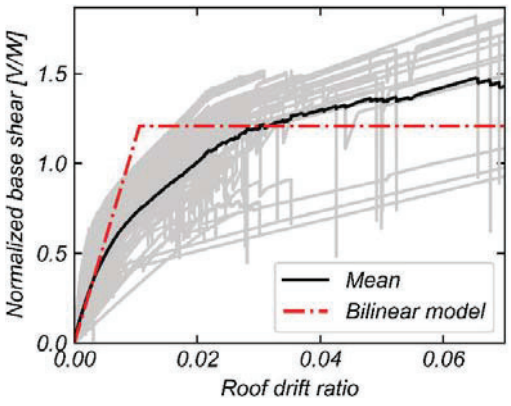

Figure 4: *Pushover results and fitted elastoplastic bilinear model.*

3.2 INCREMENTAL DYNAMIC ANALYSIS (IDA)

Figure 5 shows the results of the IDA, where each grey dot represents the maximum of the absolute peak inter-story drift ratios obtained for each NLTHA for a given realization and ground motion record scaled to the linear elastic, 5%-damped spectral acceleration at the fundamental period of the structure, $S_a(T_1)$. The blue curve represents a typical IDA curve for an individual ground motion and IM_{max} corresponds to the truncated value of the spectral acceleration considered. The mean curve indicates that the LFRS remains essentially elastic up to 0.02 maximum inter-story drift ratio, a soft transition occurs from this point before reaching the plateau of the system around 0.05 maximum inter-story drift ratio associated with IM of 3.3g, which is 3.6 times the S_{DS} value. Note, not all IDA reached the peak inter-story drift ratio of 10%, e.g. at 2%, 4% and 8% of peak inter-story drift ratio, 98%, 79% and 50% of the IDA reached or passed the values respectively.

Table 7: *Seismic performance factor statistics*

Variable	Mean – Std Dev	Mean	Mean + Std Dev
F_y/W	0.95	1.22	1.49
d_y/H	0.0083	0.0122	0.0161
$\mu = R_\mu = d_u/d_y$	4.35	5.74	8.45
$\Omega_s = F_y/F_d$	1.49	1.91	2.34
$R = C_d = R_\mu \cdot \Omega_s$	6.48	11.0	19.8

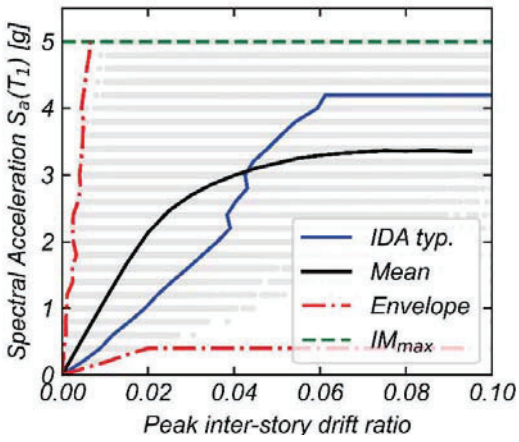

Figure 5: *IDA results for 100 realizations of the structure subjected to 44 FEMA P-695 far-field ground motions.*

As stated on the methodology, at the IO level, the UFPs yield at relatively small drift ratios. From the nonlinear static analysis, it was found that this occurs for an inter-story drift ratio of 0.001 (Figure 4) and the mean first-yield of the system is associated with the yield of one UFP.

Based on the IDA results, for each component, fragility functions were developed in terms of the spectral acceleration versus the normalized peak displacement over the yielding displacement of the UFP (d_u/d_y), normalized maximum stress over the crushing stress of the MPP wall (σ_u/σ_y), and normalized peak strain over the yielding strain on the PT rods ($\varepsilon_u/\varepsilon_y$), which are shown in Figure 6.

https://doi.org/10.52202/069179-0337

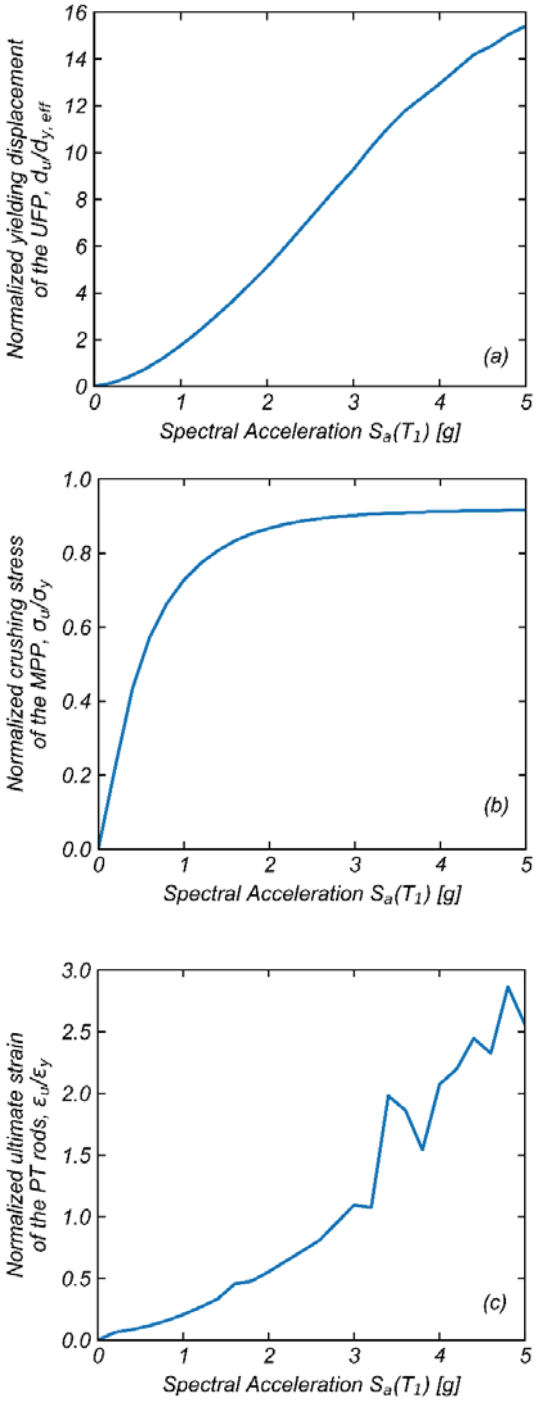

***Figure 6: Mean** empirical component fragility functions for: (a) UFP, (b) MPP panel, (c) PT rod.*

As stated previously, the UFPs reach yielding at small drift ratios compared with peak inter-story drift ratio limit on Table 1 for IO, and similar conclusions can be obtained from the fragility functions, where the IM at yielding is 0.708 g, which is 0.73 times S_{DS}. Between 1 g and 3.5 g, the fragility function is mostly linear and shows a large component displacement ductility of 15.4 at 5 g. The MPP fragility function shows that the MPP wall behaves in the elastic range for all considered IMs, although a plateau forms above 2 g (2.06 times S_{DS}) when the component can no longer resist additional stresses for all limit states. In the case of the PT rod fragility function, the function increases monotonically until yielding at 3 g (3.09 times SDS). After yielding, the function shows abrupt changes that could be related with the snap-back presented in typical IDA.

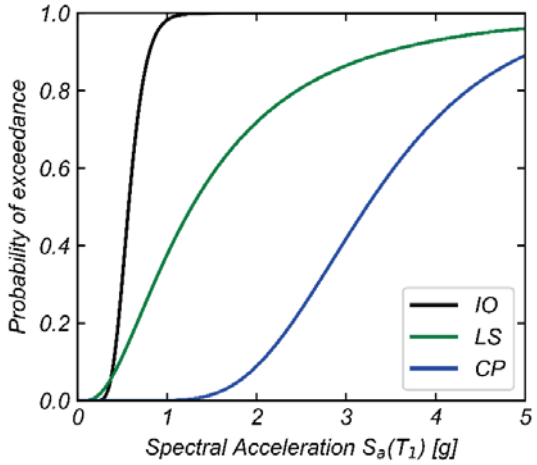

***Figure 7:** Empirical system fragility function for each damage state.*

***Table 8:** IM capacities for different damage states*

	IM		
Damage State	16th percentile	Mean	84th percentile
IO [g]	0.437	0.571	0.744
LS [g]	0.591	1.28	2.76
CP [g]	2.69	3.23	4.60

Table 8 lists the IM for the three damage states considered in this study fitted to a lognormal distribution, the values presented along with the Figure 7 show an overlap of the IO an LS damage for spectral accelerations below 0.5 g which is related to limit states used at each damage state. For IO, the only limit state considered was yield displacement of the UFPs, while for LS either crushing on the MPP or yield of the PT rods were used as limit states. The overlap implies that there is a probability below 5% that the system will sustain damage associated with either IO or LS damage state. Similarly, analysing the components that controls each of these states, UFPs for IO and MPP and PT rods for LS, the larger standard deviation at LS can be attributed to the MPP due its contribution to the nonlinear response at the base spring for each realization, which is a function of the elastic modulus (E_w) and its CoV, which is one order of magnitude greater than the other components. Similarly, at CP, the uncertainties on the MPP play a significant role on the standard deviation of the fragility function.

https://doi.org/10.52202/069179-0337

4 CONCLUSIONS

A statistical and numerical investigation of the seismic performance of post-tensioned MPP rocking walls on a 3-story building is conducted. The uncertainties in material properties of components are considered by generation of the basic random variables to model a set of 100 structures. Nonlinear static analyses and IDA are conducted for each structural realization. From the nonlinear static analysis, the seismic performance factors were estimated. The lower bounds and mean (listed in parentheses) are 6.48 (11.0) for the R-factor, 1.49 (1.91) for the system overstrength, and 4.35 (5.74) for the displacement ductility. From the IDA, empirical component fragility functions were developed as well as system fragility functions for different damage states. The component fragility function shows that the UFPs are the main ductility contributors to the system. The overlap on the system fragility functions for IO and LS damage state shows that there are gaps that must be addressed in the characterization of the uncertainties for mass timber products.

ACKNOWLEDGEMENT

This study is supported by the United States Department of Agriculture (USDA), Agricultural Research Service, Award number: 58-2024-9-165 and by the National Science Foundation (NSF) under award #2120683. We would also like to acknowledge the USDA Agricultural Research Service, the TallWood Design Institute, and our industry partners for supporting this experimental program. Any opinions, findings, and conclusions are those of the authors and do not necessarily reflect views of the supporting agencies.

REFERENCES

[1] International Code Council (IBC), 2021 International Building Code, International Code Council, Inc., 2021.

[2] American Society of Civil Engineers (ASCE), Minimum Design Loads and Associated Criteria for Buildings and Other Structures (ASCE/SEI 7-16). 2017.

[3] A. Busch, R. B. Zimmerman, S. Pei, E. McDonnell, P. Line, D. Huang, Prescriptive Seismic Design Procedure for Post-Tensioned Mass Timber Rocking Walls, *J. Struct. Eng.*, 148(3), 2022.

[4] Applied Technology Council (ATC), Seismic Performance Assessment of Buildings (FEMA P-58), 2018.

[5] E. G. Baas, A. R. Barbosa, M. Riggio, Post-tensioned timber wall buildings: Design & construction practice in New Zealand & United States, *World Conference on Timber Engineering*, 2021.

[6] A. N. Papadopoulos, D. Vamvatsikos, A. K. Kazantzi, Development and Application of FEMA P-58 Compatible Story Loss Functions, *Earthq. Spectra*, 35(1), 95–112, 2019.

[7] G. F. Orozco O., T. X. Ho, G. A. Araújo R., A. R. Barbosa, A. Sinha, B. G. Simpson, Innovative mass timber seismic lateral force resisting systems: Testing of a full-scale three-story building with mass ply panels (MPP) rocking walls, *Proceedings of the 12th National Conference on Earthquake Engineering*, 2022.

[8] L. G. Rodrigues, J. M. Branco, L. A. C. Neves, A. R. Barbosa, Seismic assessment of a heavy-timber frame structure with ring-doweled moment-resisting connections, *Bull. Earthq. Eng.*, 16(3), 1341–1371, 2018.

[9] W. Pang, D. V. Rosowsky, S. Pei, J. W. van de Lindt, Simplified Direct Displacement Design of Six-Story Woodframe Building and Pretest Seismic Performance Assessment, *J. Struct. Eng.*, 136(7), 813–825, 2010.

[10] C. Loss, T. Tannert, S. Tesfamariam, State-of-the-art review of displacement-based seismic design of timber buildings, *Constr. Build. Mater.*, 191, 481–497, 2018.

[11] A. D. Cesare, F. C. Ponzo, S. Pampanin, T. Smith, D. Nigro, N. Lamarucciola, Displacement based design of post-tensioned timber framed buildings with dissipative rocking mechanism, *Soil Dyn. Earthq. Eng.*, 116, 317–330, 2019.

[12] A.-T. E. W. Association, Freres Mass Ply Panels (MPP) and Mass Ply Lam (MPL) Beams and Columns (PR-L325), APA - The Engineered Wood Association, 2022.

[13] ASTM, A354 Standard Specification for Quenched and Tempered Alloy Steel Bolts, Studs, and Other Externally Threaded Fasteners, American Society for Testing and Materials (ASTM) International, 2017.

[14] ASTM, A572/A572M Standard Specification for High-Strength Low-Alloy Columbium-Vanadium Structural Steel, American Society for Testing and Materials (ASTM) International, 2018.

[15] F. McKenna, M. H. Scott, G. L. Fenves, Nonlinear Finite-Element Analysis Software Architecture Using Object Composition, *J. Comput. Civ. Eng.*, 24(1), 95–107, 2010.

[16] T. Akbas *et al.*, Analytical and Experimental Lateral-Load Response of Self-Centering Posttensioned CLT Walls, *J. Struct. Eng.*, 143(6), 2017.

[17] F. C. Filippou, E. P. Popov, V. V. Bertero, Effects of bond deterioration on hysteretic behavior of reinforced concrete joints, 1983.

[18] A. Baird, T. J. Smith, A. Palermo, S. Pampanin, Experimental and numerical Study of U-shape Flexural Plate (UFP) dissipators, *New Zealand Society of Earthquake Engineering*, Mar. 2014. [Online].

[19] J. C. on S. Safety (JCSS), Probabilistic Model Code, Part III - Resistance Models. Section 3.02: Static Properties of Structural Steel (Rolled Sections), 2001.

[20] BS, Hot rolled round steel bars for general purposes - Dimensions and tolerances on shape and dimensions (EN 10060), 2003.

[21] J. C. on S. Safety (JCSS), Probabilistic Model Code, Part III - Resistance Models. Section 3.04: Static Properties of Prestressing Steel (Prestressed Concrete), 2005.

[22] J. C. on S. Safety (JCSS), Probabilistic Model Code, Part III - Resistance Models. Section 3.05: Properties of Timber, 2006,
[23] J. Köhler, J. D. Sørensen, M. H. Faber, Probabilistic modeling of timber structures, *Struct. Saf.*, 29(4), 255–267, 2007.
[24] R. Soti, T. X. Ho, A. Sinha, Structural Performance Characterization of Mass Plywood Panels, *J. Mater. Civ. Eng.*, 33(10), 2021.
[25] T. X. Ho, A. Arora, A. Sinha, In-Plane Shear Properties of Mass Ply Panels in Long-Ply Direction, *J. Mater. Civ. Eng.*, 34(8), 2022.
[26] Cambridge University Press, Cambridge Dictionary: Find Definitions, Meanings & Translations. Accessed: Feb. 24, 2023. [Online].
[27] H. Mpidi Bita, T. Tannert, Disproportionate collapse prevention analysis for a mid-rise flat-plate cross-laminated timber building, *Eng. Struct.*, 178, 460–471, 2019.
[28] APA, ANSI/APA PRG 320: Standard for Performance-Rated Cross-Laminated Timber, 2018. [Online].
[29] P. E. Hess, D. Bruchman, I. A. Assakkaf, B. M. Ayyub, Uncertainties in Material and Geometric Strength and Load Variables, *Nav. Eng. J.*, 114(2), 139–166, 2002.
[30] ASTM, Standard Specification for General Requirements for Rolled Structural Steel Bars, Plates, Shapes, and Sheet Piling (A6-19), 2021.
[31] Z. Kala, J. Melcher, L. Puklický, Material and Geometrical Characteristics Of Structural Steels Based On Statistical Analysis Of Metallurgical Products, *J. Civ. Eng. Manag.*, 15(3), 299–307, 2009.
[32] W. M. Bulleit, Uncertainty in Structural Engineering, *Pract. Period. Struct. Des. Constr.*, 13(1), 24–30, 2008.
[33] Los Angeles Tall Building Structural Design Council, An Alternative Procedure for Seismic Analysis and Design of Tall Buildings Located in the Los Angeles Region, 2020.
[34] J. Varela, J. Tanner, R. Klingner, Development Of Response Modification Coefficient And Deflection Amplification Factor For Design Of Aac Structural Systems, *13th World Conference on Earthquake Engineering*, 2004.
[35] Applied Technology Council (ATC), Quantification of Building Seismic Performance Factors (FEMA P-695), 2009.
[36] J. W. Baker, C. A. Cornell, A vector-valued ground motion intensity measure consisting of spectral acceleration and epsilon, *Earthq. Eng. Struct. Dyn.*, 34(10), 1193–1217, 2005.
[37] J. W. Baker, Efficient analytical fragility function fitting using dynamic structural analysis, *Earthq. Spectra*, 31(1), 579–599, 2015,
[38] W. Muñoz, M. Mohammad, A. Salenikovich, P. Quenneville, Determination of Yield Point and Ductility of Timber Assemblies: in Search for a Harmonised Approach, *Meeting 41 of CIB-W18*, 2008.

https://doi.org/10.52202/069179-0337

World Conference on
Timber Engineering
Oslo 2023

THE USE OF PARAMETRIC WORKFLOW ON TIMBER CONSTRUCTION AT SERVICE STATION TORGHATTEN

Paul Hufnagel[1], **Philipp Vehrenberg**[2], **Matthias Stracke**[3]

ABSTRACT: This paper deals with the planning and design process of the service station Torghatten which should provide better tourism infrastructure for one of the Norwegian scenic routes. It describes parametric and automated workflows used across the various project planning phases and their benefits. Based on the project presented, it will also be shown how using these workflows makes it possible to combine modern design and complex geometries even with traditional construction methods.

KEYWORDS: Timber log structure, solid timber structure, complex geometry, parametric modelling

1 INTRODUCTION

The project 'service station Torghatten' is a collaboration between the architecture studio Atelier Oslo AS and Bollinger+Grohmann on behalf of the road authority 'Statens vegvesen' of Norway.

As part of the 'Nasjonale turistveger', the Norwegian scenic routes, the project has a prestige character within the tourism industry in Norway. The Norwegian scenic routes deliver a scenic alternative to the main roads and is suited for tourists who want to explore unique natural qualities such as fjords, mountains or waterfalls by car. To make these natural sights more accessible, each stop provides parking spaces, sanitary facilities, or information boards. The service areas aim to combine beautiful Norwegian nature with Nordic architecture and art.

Today, the Norwegian authorities established 18 scenic routes totaling more than two thousand kilometres. The new service station is part of the section 'Helgelandskysten' and situated on an island in Brønnøy commune. The connected natural sight is Torghatten, a geological formation of a mountain with a hole going through from one side to the other, shown in Figure 1.

Figure 1: *Photography of Torghatten by Atelier Oslo*

The project will be located at the foot of this mountain. It contains parking lots, benches, and rooms for sanitary, technical and exhibition usage. The rooms share one cantilevered roof structure made of timber. In addition, there is a steel stair structure planned, which leads up to the hole. This structure is not part of this paper.

[1] Paul Hufnagel, Bollinger + Grohmann Ingeniører AS, phufnagel@bollinger-grohmann.no

[2] Philipp Vehrenberg, Bollinger + Grohmann Ingeniører AS, pvehrenberg@bollinger-grohmann.no

[3] Matthias Stracke, Bollinger + Grohmann Ingeniører AS, mstracke@bollinger-grohmann.no

https://doi.org/10.52202/069179-0338

2 CONCEPT

The location of the service station forms a transition between the organised forecourt and the wild nature of Torghatten in the background (see Figure 2).

Three volumes where the cantilevered roof structure rests offer shelter and space for toilets and exhibition areas. The covered outdoor area below the canopy roof creates open spaces equipped with bicycle parking spaces and seating.

Figure 2: *Visualization of the service station by Atelier Oslo*

Except for the foundation, the whole building consists of solid timber beams arranged in layers on top of each other. The alternating overlapping of the layers of timber creates a log structure, which has a long tradition in Norway and is known as 'lafteverk'. This concept continues in the roof structure which is made of overlapping beams in several layers and irregular placement (see Figure 3). The construction method with its traditional roots represents a low-tech solution common in rural areas and differs from many high-tech solutions in urban construction. Due to this irregular placement of the timber beams and the glass roof around the structure, varied shadow plays can be observed throughout the day.

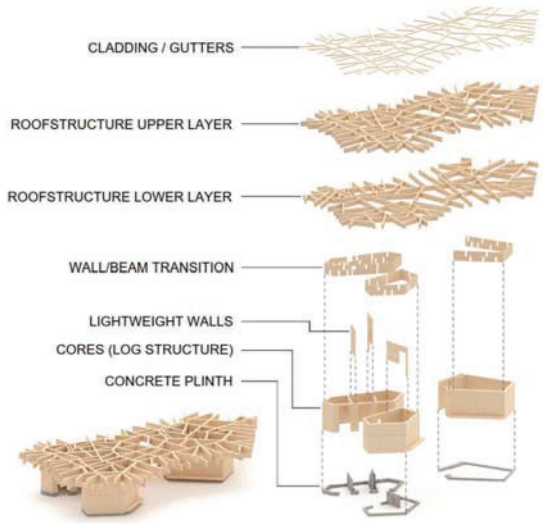

Figure 3: *Illustration of the service building components by Atelier Oslo (translated)*

The simple screw connections and the renunciation of glued timber connections allow the building to be easily dismantled at the end of its lifetime. Just in 2022 these regulations for the reuse of building materials were relaxed in Norway, making it easier to reuse the screws afterwards. A sustainable solution for the project could be found through the predominant use of renewable materials and consideration of the entire life cycle of the building.

3 STRUCTURE – WALLS

3.1 STRUCTURAL CONCEPT

The walls follow the traditionally used 'lafteverk'-concept, where each timber member is placed on top of the other. Each member interlocks on the top and bottom sides to create a horizontal shear connection between the layers.

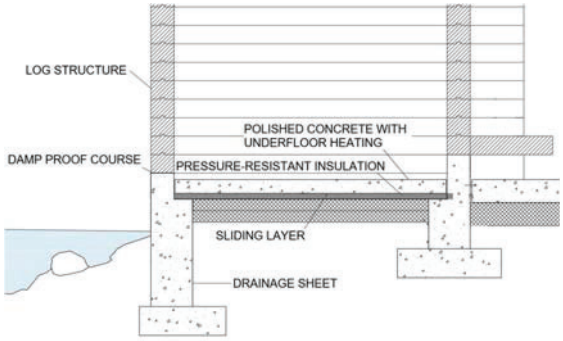

Figure 4: *Section through the service station by Atelier Oslo (translated version of an early presentation)*

In the intersections of two walls, the members alternately overlap in layers. This concept results in a structure of rigid wooden boxes that do not require any additional fasteners except for the door openings. Since the openings interrupt the interlocking principle, other timber dowels and vertical members were planned to ensure the stability of the walls.

3.2 ANCHORAGE/FOUNDATION

The cantilevers of the roof structure, the wind pressure from the passing wind underneath and the wind suction from above lead to uplifting forces that need to be anchored in the foundation. A detailed wind simulation was performed to estimate realistic values for the resulting wind forces that also take the blockage of the canopy roof into account (see Figure 5).

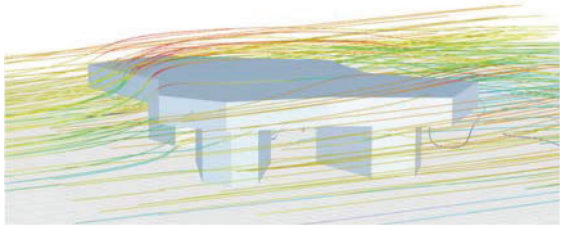

Figure 5: *Extract from the FE-wind calculation*

https://doi.org/10.52202/069179-0338

The resulting uplift forces are transferred by screws from the roof structure into the walls. As shown in Figure 6, the three upper beam layers are screwed to the three lower beam layers screwed to the upper members of the walls. A threaded rod that goes through all wall members is anchored in the foundation and receives a steel plate inside an opening in the top member of the walls. Through this threaded rod, the anchorage of the building can be adjusted according to the long-term deformations of the walls.

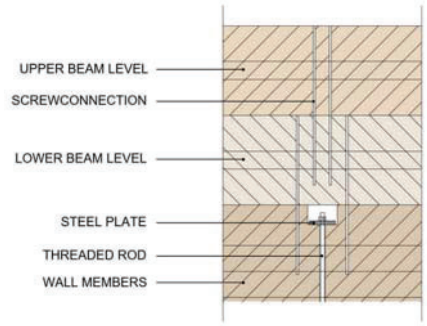

Figure 6: *Anchorage detail*

4 STRUCTURE – ROOF

4.1 STRUCTURAL CONCEPT

4.1.1 Lafteverk-concept within the roof structure

Like the walls, the roof structure also follows the 'lafteverk' principle. Each beam consists of three solid timber members, that are screwed together to create one stiffer member. In the intersections of two beams of the same level, the upper and lower layer of the primary beam (see Figure 7 in orange) continue. In contrast, the inner beam layer stops to give room for the inner layer of the secondary beam (see Figure 7 in green).

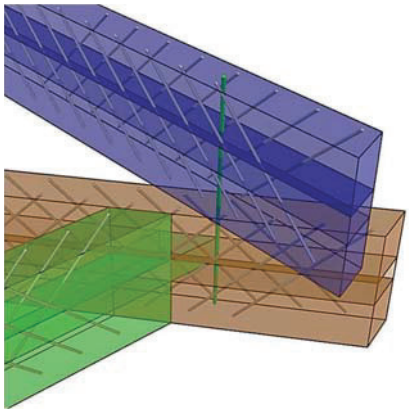

Figure 7: *Illustration of a connection of three beams*

This overlapping of the beam layers creates a vertical support for the secondary beam. This support is unsuitable for transferring moments, so it can be assumed to be hinged. To enable the cantilevers of the canopy roof, another level of beams has to be introduced (see Figure 7 in blue) to support the cantilevered beams that would be structurally unstable, with their only support being hinged. The beams must be placed so that every unstable secondary beam of one level can be supported by a structurally stable beam of the other level. This concept and the resulting structural systems are shown in Figure 8. As shown, it does not matter if a beam from the upper layer supports a beam from the lower layer or the other way around.

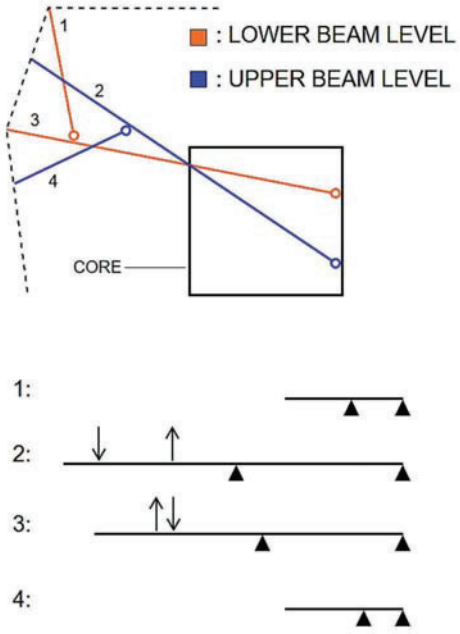

Figure 8: *Illustration of the structural concept of the roof*

Each level on its own would therefore be unstable. Only the combination of the two levels create a stable system where the acting forces travel up and down in the levels and end at the cores.

4.1.2 Form-finding

The architectural design showed the roof geometry as a disordered interaction of beams (see Figure 9).

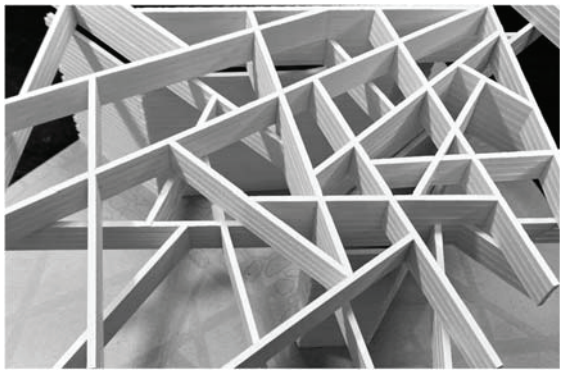

Figure 9: *Photography of an early model by Atelier Oslo*

The task was, therefore, to optimise the beam layout in a way that combines the architectural concept and an efficient structural design.

https://doi.org/10.52202/069179-0338

First, a variation of beam geometries was created using Rhino 3D and its plug-in Grasshopper. For this purpose, short lines were generated along the wall supports defined as fixed positions. Each of these were given a ranking. The short lines were then successively extended in the order of their ranking. If the lines meet the defined building boundary or hit another line, they are not extended any further. In the next step, the lines' ranking varied, which led to endless new patterns. The principle is shown in Figure 10. This approach made it possible to obtain various beam layouts that always sit on the supporting walls.

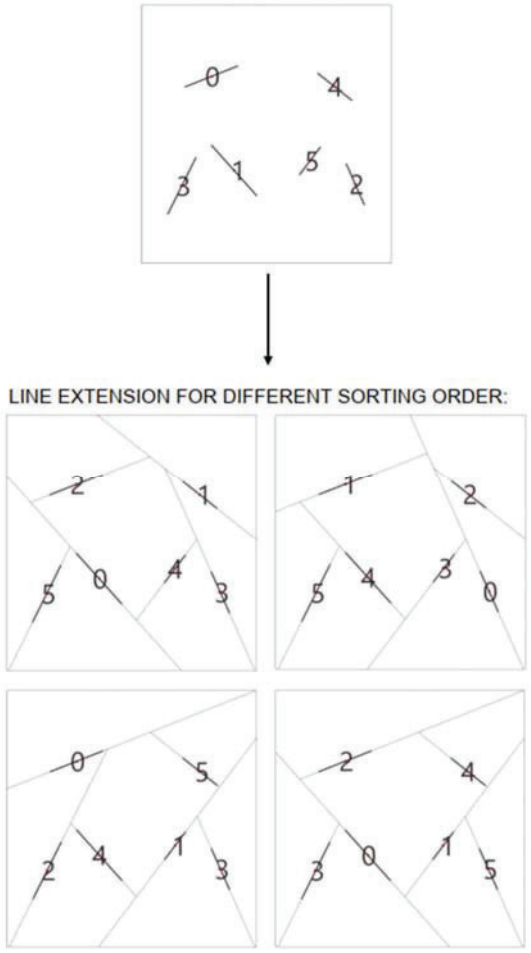

Figure 10: *Illustration of the form finding concept*

To get a tighter beam grid and to optimise the wall positions, additional lines and boundary conditions for the wall geometry were implemented.

In a further step, a structural analysis including FE-calculations was performed using the Grasshopper application Karamba in combination with a multi-objective optimization using the application Octopus. The results of the optimization were rated according to the three variation criteria "deformation", "deviation of the wall geometry" and "beam diversity". The architects used the optimisation variants (examples shown in Figure 11) as the basis for discussion and further development of the roof geometry.

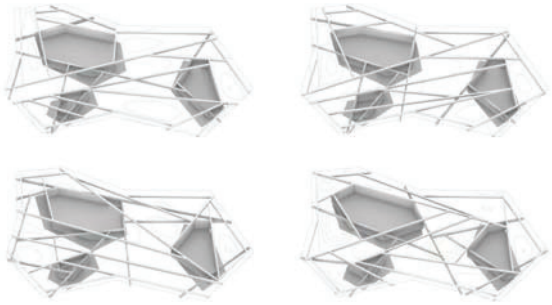

Figure 11: *Selection of results of the form-finding process*

The last adjustments, which led to the final geometry, were made in collaboration between Bollinger+Grohmann and Atelier Oslo based on more detailed FE calculation models using RFEM.

4.1.3 **Modelling**

The structural calculation model was created by using the FE-Software RFEM by Dlubal. The Eurocode refers to the gamma method in EN 1995-1-1 Annex B to model mechanically jointed beams. The gamma method is a simplified calculation in which the reduction factor gamma considers the resilience of the mechanical connection. This factor makes calculating an effective bending stiffness and the resulting deformation and inner forces possible. However, the calculation of the gamma values requires certain boundary conditions. For a mechanically jointed beam consisting of three members, the gamma values can be calculated as shown below:

$$\gamma_2 = 1 \qquad (1)$$

For i = 1 and i = 3:

$$\gamma_i = [1 + \pi^2 \, E_i \, A_i \, s_i / (K_i \, l^2)]^{-1} \qquad (2)$$

Ei Ai: axial stiffness

Ki: slip modulus

si: spacing between the fasteners

l: span

The shown equation (2) sets limits such as a uniform compound of the connection, constant cross-sections and simplified structural support conditions. Especially the last-mentioned limitation is hard to combine with the shown project. The span l can be defined as follows:

Single span beams with a span l: $l = l$

Continuous beams with a span l_i: $l = 0{,}8 \, l_i$

Cantilever with a cantilever length l_c = $2 \, l_c$

Even though RFEM offers the opportunity to define mechanically jointed beams according to their gamma values, each beam would have a different gamma value because of the varying support conditions. Furthermore,

https://doi.org/10.52202/069179-0338

the simplified structural systems used in the code to define the value for l are not feasible for more complex geometries like the roof structure. This premise meant that the gamma method was only used for preliminary calculations and as a plausibility check for individual beams.

A more precise approach was considered to model the stiffness reduction within the mechanically jointed beams, including the screws in the FE-model. The slip modulus of a mechanical connection influences the deformation behaviour of load-bearing systems. In addition, it directly affects the distribution of internal forces in the case of flexibly connected bending beams [1]. For this reason, each screw member had to be modelled according to its slip modulus.

Each combined beam's upper and lower beam layer was modelled for the calculation model according to their cross sections and material properties. Between these layers, the screws were added as spring members at a 45° angle and with a hinged connection to the beams. Each spring member was modelled with a capacity limit and a spring constant according to its slip modulus for the different limit states ULS and SLS and the time $t = 0$ and $t = \infty$. The resulting model acts as a truss system with realistic stiffness values. Additional vertical compression members, which fail if tension occurs, were added to simulate the beams laying on each other. As a simplification, the middle beam layer was only modelled as a load. To gain better control of the internal forces, every truss received a result beam that can show the combined inner forces of the upper and lower beam (see Figure 12).

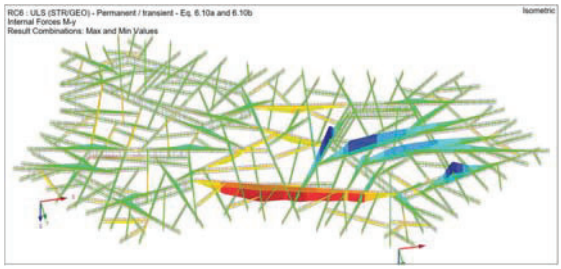

Figure 12: *Moment diagram of the result beams*

Figure 13 shows the FE model equivalent of a combined beam consisting of three individual beams screwed together.

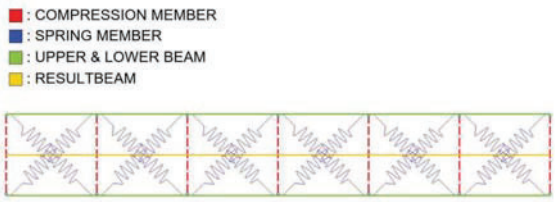

Figure 13: *Illustration of a beam in the structural model*

4.1.4 Interaction between FE-calculation model and parametric model

By having a representative member for each screw of the roof structure, the FE-model gained much complexity. To still react quickly and efficiently to changes in geometry or screwing, interfaces were created between the parametric 3D model and the calculation model.

The Rhino 3D plug-in Grasshopper made it possible to determine the centre lines of each beam for the calculation model from the architects' 3D model. Cross-sections and material properties could already be assigned to these centre lines. In a further step, the centerlines of the screws were generated, and for the screws fixed boundary conditions and variables were defined. One example for a variable parameter was the screw spacing. This made it possible to change the distances between screws in Grasshopper easily, and all the screw centre lines were automatically updated. Figure 14 shows an extract from the parametrically generated centre lines of the screws.

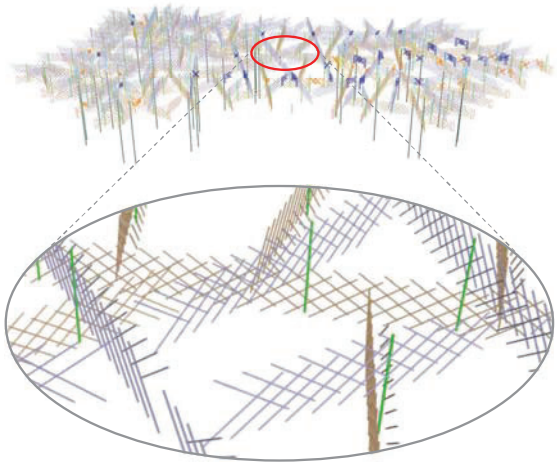

Figure 14: *Generated centre lines of the screws*

After the import into RFEM, only a few adjustments had to be made to get the results from the FE calculation.

5 PARAMETRIC COLLISION CHECK

The two super-positioned structural levels must be connected and also to the cores at particular points, thus creating constraints for the insertion of fasteners. Additionally, intertwining the beam layers within each level of the roof structure induces many potential clashing situations between fasteners and timber beam edges. Since the three beam layers of every level must create a stiff member, the density of necessary screws must be relatively high, increasing the complexity even further.

Over six thousand fasteners of at least eight different types varying in position, length, diameter, and angle had to be placed within this complex structure.

https://doi.org/10.52202/069179-0338

Some screws penetrate not only the three intertwining beams of one roof level but also those of the roof level beneath or the top layers of the walls. This posed a challenge for their modelling, but even more so for ensuring that all fasteners keep a minimum distance to each other and any other element, edge or opening.

By informing each element with a set of key and value properties, such as for the screws their type and beam affiliation, and for the beams their dimensions and beam group affiliation, they could easily be filtered and integrated into custom checks. For example, one review was to model a pipe around a set of screws, with the pipe's radius representing the minimum distance to other objects as defined in the code. Then, the pipe was used for clash detection towards another set of screws or towards beam or opening edges.

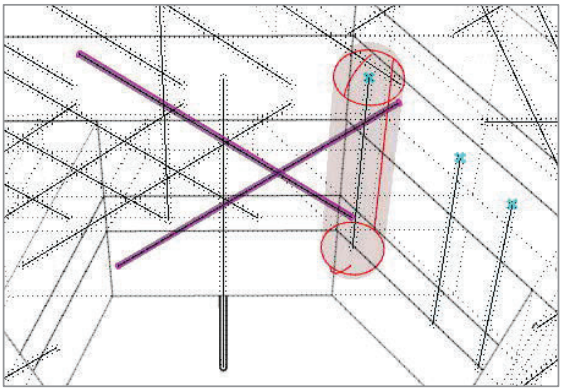

Figure 15: *Showcasing a collision check example*

Even with the 3-dimensional model at hand, it sometimes proved difficult to orient within the structure and avoid confusion. But without using both a 3-dimensional model and a parametric tool, this task for sure could not have been achieved within a reasonable timeframe.

6 PARAMETRIC SHOP DRAWINGS

By choosing a parametric workflow for this project, it was possible to automate almost the entire shop drawing process. This required setting up and maintaining a highly detailed, consistent, and data-informed 3D representation of the whole structure. Therefore, all structural parts, like beams, screws etc., were developed parametrically by Grasshopper scripts. Especially the complex intertwining beam layout proved to be an exciting challenge.

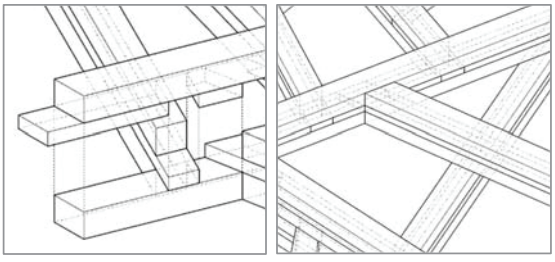

Figure 16: *Intertwined beam layers*

On the one hand, the beams were modelled as simple beams with rectangular plans, with each beam aware of its raw dimensions. On this basis, an excel sheet was exported containing all the necessary information to purchase the raw timber beams, since they had to be dried early on for the later construction process. On the other hand, the beams were also modelled in detail, with their heads cut according to their intersections to produce plans for their manufacture (see Figure 17).

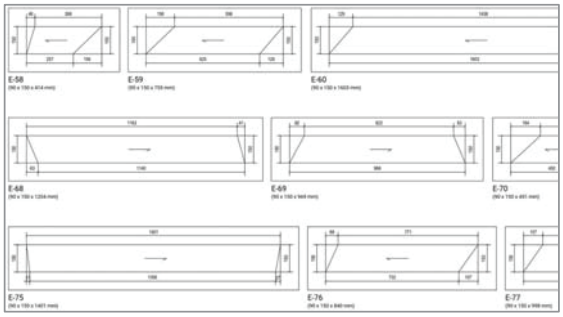

Figure 17: *Extract from the cutting drawing*

Since most elements for the drawings were extracted from or created based on the model, but also to enable an easy check of consistency between the 3D model and the 2D plans, they were made in 3D space at their actual location in the roof structure (see Figure 18). The geometrical elements of the drawing, dimensions, drawing titles, leaders and texts were generated in the parametric process. Once a set of elements was not supposed to change at a certain point in the design process, its final version was stored in the 3D model to reduce the number of elements in the scripting pipeline. To integrate them in the later stage plan production, they inherited the keys and values of their 3D parents and received new information on their purpose.

To conceive meaningful screw position plans, the almost one thousand beams making up the roof structure had to be sorted into roughly two hundred beam groups according to which beams were parallel and connected. Each resulting beam group received geometry and information from neighbouring groups, such as connecting beams and relevant screws that should be displayed along with themselves for orientation. Per beam group, one top view and one section plan were generated. For example, the model's 3D screw lines were transformed into 2D circles at their tips for the top views and to 2D offsets along their length for the sections. The diameter was retrieved from a table according to the screw type information each line contained.

https://doi.org/10.52202/069179-0338

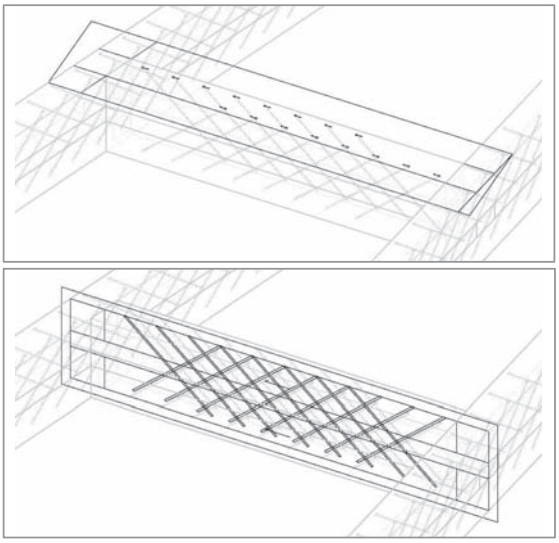

Figure 18: *'Raw' drawings at their origin within the 3D model*

In total, 16 A0 plans were produced for the beam cutting plans and 19 A0 plans for the screw position plans, plus a few more for overviews etc. Considering this number of plans and because every A0 sheet can contain up to one hundred beam cut drawings or up to twenty screw position drawings, it was a challenge to figure out a smart layout for each plan. Therefore, also this task was delegated to a computational tool: A nesting algorithm automatically distributed differently sized rectangles representing each drawing on A0 sheet boundaries, resulting in a spatially optimized layout (see Figure 19). The distributed rectangles contained information as to which drawing, they belonged, so the drawings could be placed on the A0 sheets accordingly.

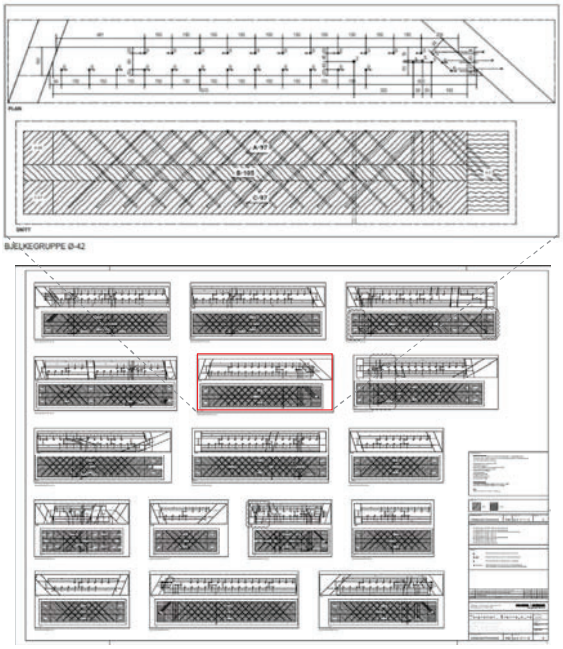

Figure 19: *Extract from the screw position drawings*

Since the entire workflow from modeling to plan production is parametric, changes to the structure or the drawings can be made relatively fast, and automated checks can be performed to enhance quality and oversight. Nevertheless, it was of course necessary to also double-check every plan manually in case of overlapping drawing elements or potential errors. These manual corrections alone proved to be so time-consuming due the number of drawings, that a manual production of all drawings in projects of this complexity can hardly be imagined.

7 CONCLUSION

The project 'service station Torghatten' presented several challenges for the planning architects and engineers due to its disorderly roof geometry and the chosen construction method resulting in an enormous number of fasteners. However, the successful course of the project showed how a parametrised workflow of the complex geometry in all project phases could help to overcome these challenges. The parametric form-finding process also made it possible to achieve an optimised solution in terms of costs, material consumption and sustainability. The interface between the parametric model and the FE software ensured that changes in the design could easily be imported into the analytical model. Custom scripts facilitated the handling of the geometry, for example, to automate edge distance control and collision checks of the screws. This led to more precise results and time savings. Thanks to the automated plan production process, hundreds of individual beams and thousands of screws could be transcribed with their exact position from a 3D model into 2D plans within a short time.

This project has shown that modern planning methods, such as the described parametric workflow, can give new input to traditional construction methods, such as the Norwegian 'lafteverk'.

REFERENCES

[1] Blass, H. J., & Steige, Y.: Steifigkeit axial beanspruchter Vollgewindeschrauben. KIT Scientific Publishing, Karlsruhe, 2019.

https://doi.org/10.52202/069179-0338

World Conference on Timber Engineering Oslo 2023

TIMBER PAVILION CONSTRUCTED IN COMBINATION WITH PARAMETRIC DESIGN AND THE ZOLLINGER CONNECTION SYSTEM

Franziska Häuptle [1], **Camilla By Kampenes**[2], **Matthias Stracke**[3]

ABSTRACT: The engineering workflow in the pavilion project in Belgium has combined a particular connection / joint strategy to fulfil the architect's organic design intentions in a timber pavilion. The client and the architect set high artistic, cost, and environmental ambitions. The goal was to develop a grid-shell mesh consisting mainly of straight beams and continuous for both flat and double-curved surfaces. The structure was created by a combination of parametric engineering design and a grid-shell system called the Zollinger system, invented by Friedrich Zollinger in the 1920s. The paper describes the requirements and limitations set for the timber shell and gives specific features of the timber roof that influenced the design process. To consider all factors in the parametric workflow, a Grasshopper algorithm was set up and used in combination with the design software RFEM to analyse and optimise the grid shell structure efficiently. The paper shows that timber construction with high design ambitions by organic look can be achieved if the parametric design is combined with the Zollinger system. An outlook is provided on how using a parametric design tool can simplify the detailed design and generation of drawings.

KEYWORDS Zollinger system, timber structure, pavilion, parametric design

1 INTRODUCTION

A wooden pavilion for a private client should be designed mainly for the art exhibition. A gallery where the roof should be part of the exhibition, a work of art itself. Therefore, it will be exposed internally and some parts also externally. The Oslo-based architectural firm Snøhetta designed an organic shaped roof with flat, double-curved surfaces. Thus, a structural system needs to be created which sets not only high ambitions on aesthetics but also on the structural efficiency, costs, and environmental impacts. Consequently, the Zollinger system was chosen as a basis for designing a structural grid shell made of mostly straight beams with the help of parametrical design tools.

Figure 1: *Exterior views ©Snøhetta*

[1] Franziska Häuptle, Bollinger + Grohmann Ingeniører AS, fhaeuptle@bollinger-grohmann.no

[2] Camilla By Kampenes, Bollinger + Grohmann Ingeniører AS, ckampenes@bollinger-grohmann.no

[3] Matthias Stracke, Bollinger + Grohmann Ingeniører AS, mstracke@bollinger-grohmann.no

https://doi.org/10.52202/069179-0339

2 THE PAVILION

2.1 THE ZOLLINGER SYSTEM

The Zollinger system is named after the German architect Friedrich Zollinger who patented the structure during the recession in the 1920s. Rhombical arranged lamellas form a grid shell that can span large spans, using timber beams with a limited length and simple connection details. Both factors make prefabrication possible and an easy installation process on site. Mostly single-curved arched vaults were built for which the benefits of using the Zollinger structures show in general additional material savings.

Figure 2: *Interior view ©Snøhetta*

The main pattern of a Zollinger lamella roof is shown in figure 3. Beams are arranged at angles to each other so that two lamellas meet in the middle of one continuous lamella, forming a rhombus. The pattern enables the lamellas to be connected without moment transfer and still provides a stiff system. While the forces are transferred in several directions, the Zollinger system allows for large openings.

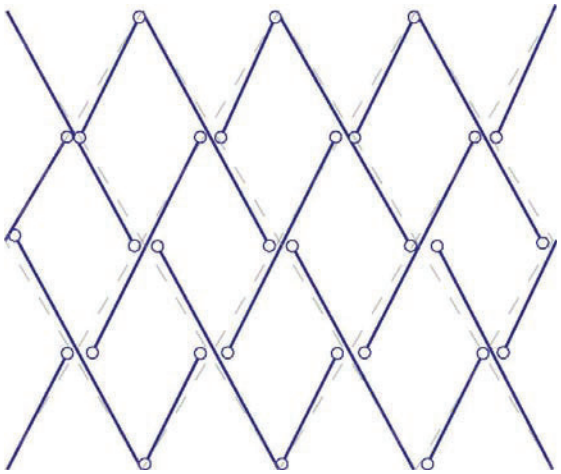

Figure 3: Principal pattern of the Zollinger lamella structure

The Zollinger system is not limited to the structures mentioned above, but it also allows to form double-curved structures out of straight beams while keeping the connection details simple. The system's disadvantages are that the installation process takes longer due to the many details. Therefore, it will be necessary to prefabricate larger elements in the workshop and assemble them on the construction site.

2.2 THE PAVILION'S GEOMETRY

The roof of the pavilion is a composition of double and single-curved surfaces; therefore, a definition for the grid must have been found, which allows a smooth transition between the different types of surfaces, see figure 4.

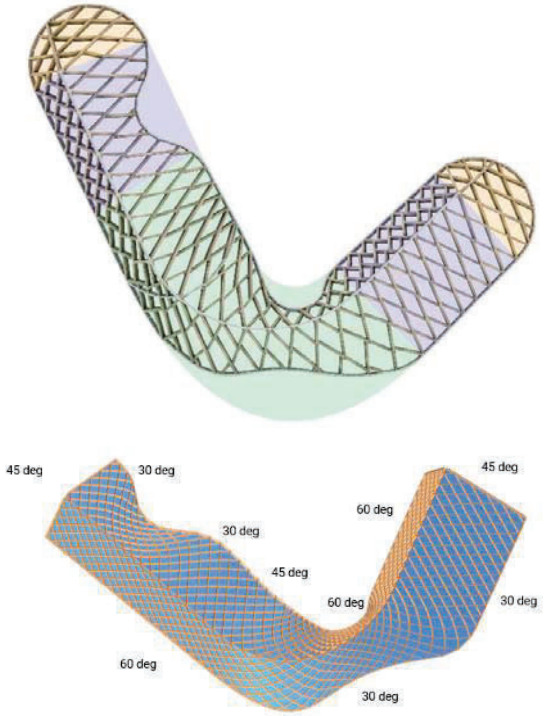

Figure 4: *Different types of surfaces (top) and roof angles (bottom). Top figure: blue: flat surface; green: double-curved surface; orange: double-curved, ellipsoid*

The roof can geometrically be split up into 3 different types. The first type, marked in blue, is a flat surface above the glass-roofed greenhouse and partially above the exhibition/living area. The second type is a double-curved structure marked in green. It represents the entrance area and parts of the residential/ exhibition area. Both pieces will be covered with timber plates and finished with the traditional Japanese shou sugi ban method to make it weather resistant. The areas at each end are part of an ellipsoid with a strong curvature. In addition to the double curvature, the geometry is not symmetrical to the top beam, and the vertical angles differ. This challenge could only be solved with the help of the parametric design described in chapter 3. Several geometries were studied to find an alternative meeting all requirements and limitations.

https://doi.org/10.52202/069179-0339

The requirements and limitations to design an efficient roof structure were:

- Straight beams for the whole roof structure.

- The grid should be as regular as possible to avoid many different node details and different types of beams

- The number of nodes should be kept to a minimum while still being able to establish the Zollinger system and the curved surfaces. With a denser mesh, the surface better approximates the curved architectural geometry, but requires more nodes and, in some areas, more complicated details.

- Simple design detail

- The maximum edge length of the rhombus is given by the glass elements and the plates of the roof membrane

- For each rhombus, a mostly flat surface must be established to mount the timber plates

- Double curved edge beams should be avoided due to the costs and complexity of the production

- The structure must be supported on rigid foundation walls

- The Zollinger system should be applied to all parts of the roof

2.3 SPECIFIC FEATURES FOR THE DESIGN PROCESS OF THE MESH

Specific features of the pavilion's geometry influenced the solution for the mesh.

2.3.1 Double curvature

The nodes in the areas of double curvature will have several different angles, which will influence the detail design. In addition, the mesh must be chosen, such as the timber plates for the roof membrane can be primarily flat or split up into triangulars.

2.3.2 Transition between cold (entrance and glass house) and warm (residential/ exhibition) area.

The roof above the exhibition area will be heated and therefore insulated, while the entrance area and the greenhouse will be uninsulated. Therefore, the thickness of the roof built-up differs. The offset should not be seen, and the top roof surface should be kept at one level. Therefore, the offset in the roof between the cold and warm areas must be handled in the structural system. The beams will be split and moved horizontally apart. Due to the vertical eccentricity, a moment-rigid connection is required, which is made using slotted steel sheets. To avoid complex details, the mesh was chosen so that the façade line (break line) generally does not go through a mesh node but through a continuous system beam.

2.3.3 Foundation

The timber roof will be based on cantilevering concrete walls. The influence of the horizontal deformations of the walls during the lifetime of the pavilion (creep) is considered in the support conditions in the calculation model. Those deformations will lead to vertical deformations of the roof and affect the force transfer.

2.3.4 Edge beams

The edge beams must gap the unsupported areas over the entrances. A double curvature of the beams should be avoided while, at the same time, their geometry should align with the architectural geometry. In addition, the edge beams must be contributed enough stiffness to the roof structure to avoid big deformations. This concerns mostly the long-spanning beam with big curvatures at the entrance area.

Therefore, an alternative geometry was developed that is close to the architectural geometry but only with single curved edge beams.

2.3.5 Half cones

Figure 5: *Alternative for ellipsoids with single curved beams*

The half-cone-shaped surfaces have a small radius of curvature which is challenging for the Zollinger system. Several alternatives were analysed in terms of the complexity of the details, the transition to the other roof areas, the curvature of the beams, the installation process, and the deviations to the architectural geometry.

The Zollinger system is applied but with single-curved beams. The advantages are that the same details can be used, and the visual impression of the main roof is retained. Using single-curved beams can keep the deviation from the architectural geometry to a minimum. Other alternatives were, e.g., a reciprocal frame with pinned connections or solutions with double-curved beams or straight beams spanning between the top and the edge beam.

https://doi.org/10.52202/069179-0339

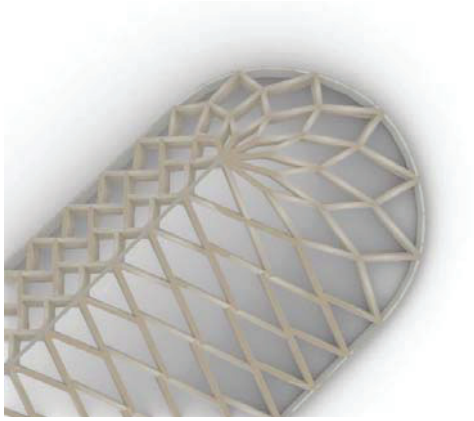

Figure 6: *Alternative for ellipsoids – reciprocal approach*

2.3.6 **Unsymmetrical roof geometry.**

Both parts of the roof must be split up in the same number of pieces to guarantee that the beams meet at the same position at the top beam. Since the outer edge line is longer than the inner one, the size of the mesh, especially over the double-curved entrance area, differs a lot. It needed to be ensured that the mesh of the inner part gets manageable since this will lead to many complex details and an enclosed look of the surface. At the same time, the mesh must be dense enough to establish rhombuses on the outer part. Several alternatives were studied. Two alternatives are shown in figure 7.

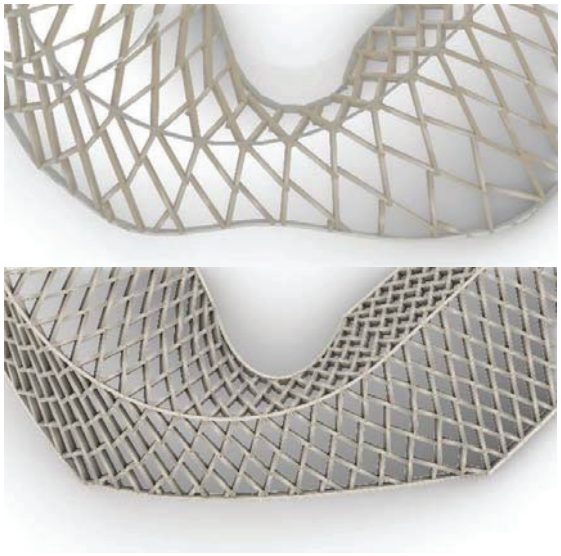

Figure 7: *Mesh above the entrance area – Top: wide mesh – Bottom: dense mesh with a single curved edge beam*

2.4 NODE DETAILS

Joints and connections are crucial points in timber structures and are generally critical to the structure's design. The strength of the connectors in the joint will dictate the strength of the timber structure [1].

Several types of details can be considered for the connection of the timber beams. Several factors influence the choice of relationship. Such as

-Types and sizes of internal forces which need to be transferred

-Geometry of the node. There are different angles in different directions, plus a possible eccentricity between the two ending beams

-The installation process. The number of nodes to be mounted on site must be considered, as what kind of angles are present and how much space is available.

- Collision between the connection elements of the two connecting lamellas.

2.4.1 **Zollinger pin**

The pin can transfer mainly axial forces. Its advantage is that it is easy and fast to install and has only one pin per node. The eccentricity required to install the pins can be large to use the pin for double curved surfaces. Especially at the inner area over the entrance where the mesh is denser, this will be problematic. Due to the shrinking of the timber elements, tightening the pin at regular intervals can be necessary.

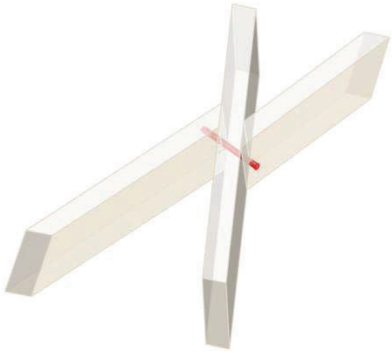

Figure 8: *Zollinger pin*

2.4.2 **Connection with slotted-in plates and dowels / screws**

A connection with steel plates will contribute more stiffness to the structure and allow the transfer of axial and vertical forces. Due to the different angles of the surfaces, this type of detail would lead to many different shaped steel plates, leading to a complicated planning and installation process.

https://doi.org/10.52202/069179-0339

Figure 9: *Detail with slotted-in steel plates of Frans Masereel Centrum in Kasterlee, Belgium*

2.4.3 Connection with screws

In this kind of connection vertical and axial forces can be transferred. To avoid a possible collision between the screws of the two end beams an eccentricity between the two ending lamellas is necessary. For the double-curved surfaces, the angles for the screws can be adjusted. Several screws will be required per node, leading to more connection elements than with the Zollinger pin.

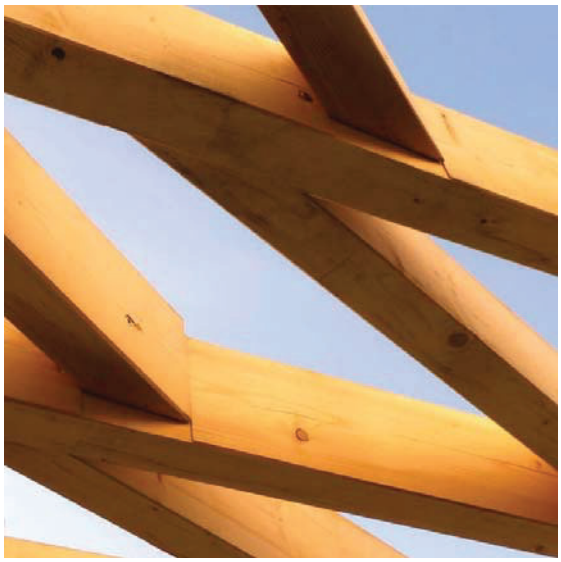

Figure 10: *General detail of Frans Masereel Centrum in Kasterlee, Belgium.*

2.4.4 Connection to the pavilion

For all the above connection requirements it has been determined to use a screwed connection for the general detail and where required by geometry or force a slotted plate as shown in figure 9.

3 PARAMETRIC DESIGN PROCESS

Parametric design tools are used to establish the mesh's geometry with the specifications and requirements mentioned in chapter 2. Unlike being designed directly, the parametric design method is shaped according to algorithmic processes. The aim is to be flexible with few basic parameters, to allow for fast analysis of different alternatives.

3.1 PARAMETRIC TOOLS

To define the geometry GRASSHOPPER was used. Once the boundary conditions were defined, an algorithm was set up that easily allows to adjust of the mesh size. It efficiently and quickly contributes to the study and identification of geometrical problems, such as collisions between the Zollinger roof and the facade line or the evenness of the roof membrane.

The definition was based on architectural geometry. The algorithm's input is the roof's outer lines, which represent the edge beams, and the top line, representing the ridge. In addition, the architectural surfaces of the roof were required, to define a mesh which is as close as possible to the architectural geometry. The input geometry was slightly adjusted to optimise the transition between the flat and double-curved surfaces.

In chapters 2.2 and 2.3 the geometrical specifics of the pavilion roof are given.

In the first step, the outer line without the end parts and the top line were split into the same number of segments. The reasons are given in 2.3.6. Also, the surfaces along the top line are split up normally to the plane in a specified number of segments. It applies the same design approach as for the outer and top lines. The designer chooses the number of segments but it must be a number that can be divided by 2 into a natural number. Only then a Zollinger grid can be established.

In the second step, a diagrid is set up. The nodes from the bottom lines are connected with the ridge nodes. In figure 11 the diagrid is shown as dashed lines.

To apply the Zollinger system the lines in the defined main direction of the diagrid are split at every second node. The received segments represent the continuous lamellas. The same way the second direction is handled but starting the segmentation at the first node, then every other. Now the principle of the Zollinger system is established.

Dependent on the design of the node detail, the eccentricity of the two ending lamellas is required. To study all consequences of the eccentricities on the mesh geometry and other design aspects, the definition of the eccentricities was included in the GRASSHOPPER definition. Therefore, the vectors of the lines of the diagrid are identified. Depending on the vector's direction, the line's end is moved upwards or downwards from the node on the continuous lamella. The principal can be seen in figure 11.

https://doi.org/10.52202/069179-0339

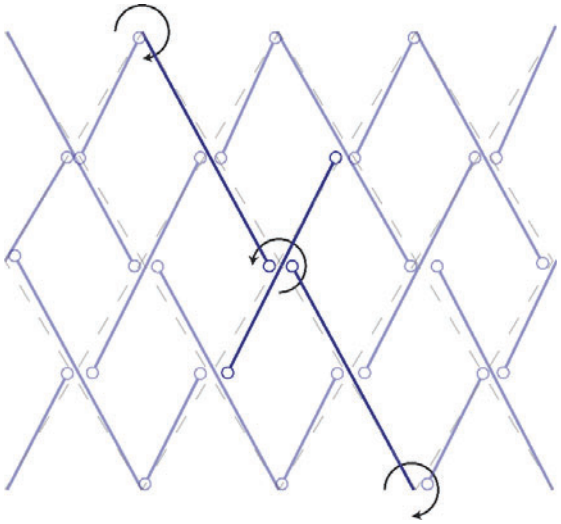

Figure 11: *Diagrid and set up of the eccentricities*

For the ellipsoids, the definition must be due to the strong curvature of the surface and the fact that the meshes of each side of the top line meet adjusted. Dependent on the chosen design approach.

Once the geometry is final, the model can be used to set up a calculation model. For the analysis, the software RFEM from Dlubal was used. Among others are the cross-section, beam hinges, support condition and loads defined in GRASSHOPPER and exported to RFEM.

3.2 CALCULATION MODEL

3.2.1 Geometry, node and support conditions

The geometry defined in GRASSHOPPER was used to set up a calculation model in RFEM. This way, it is possible to make changes to the geometry, such as optimising the curvature of the edge beams or changing the mesh size, without spending much time setting up a new model each time.

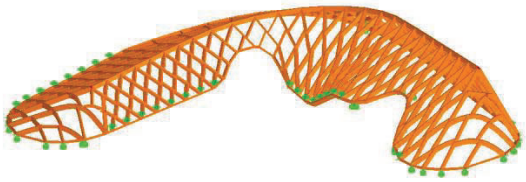

Figure 12: *RFEM Modell*

The connections between the lamellas are assumed as whole hinges. This represents the properties of the Zollinger pin. For other types of details, the stiffness of the connection is determined to check the influences on the roof system and the connection forces.

The vertical support is fixed, while the supports in the direction perpendicular to the concrete wall / outer beam are modelled as springs to account for the horizontal stiffness and long-term effects of the concrete wall.

3.2.2 Wind loads

The Eurocode only gives Cp-values for simple geometries of buildings; thus, the pavilion's plan geometry and the Eurocode assumptions do not cover the double-curved surface. Therefore, the add-on module RF-WIND was used to define the C_p-values for the wind loads for different wind directions. RF WIND is an add-on module to RFEM.

With the C_p-values and areas given from RF WIND the wind loads on each node of the structure were calculated within GRASSHOPPER and applied to the structure. The add-on module can also apply the wind loads directly to the structural model. Still, additional surfaces must be defined, which could adulterate the stiffness behaviour of the structure. In addition, the wind loads would need to be newly defined by RF WIND each time something was changed in the model. Using only the C_p- values can better control and check the load size.

To verify the C_p-values of RF WIND, they were compared to values from the EC 1-4 for a simpler roof geometry. It turned out that the values corresponded well and that the values from RF WIND could be used for the calculations.

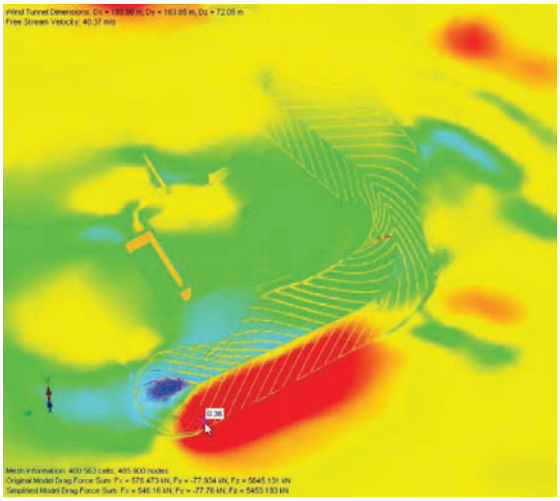

Figure 13: *RF WIND Simulation*

3.2.3 Analysis

With the calculation model, weak points of the structure were identified and optimised in cooperation with GRASSHOPPER according to the limitation and requirements given in chapter 2.2. For this purpose, among other things, the eigenforms of the roof were studied, and the force flow was analysed.

https://doi.org/10.52202/069179-0339

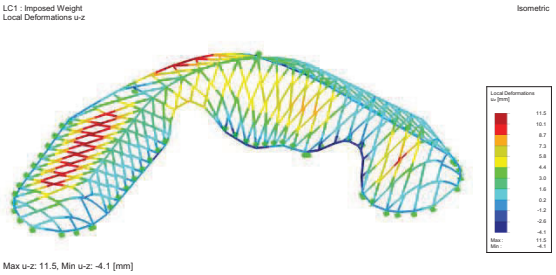

Figure 14: *Deformation print-out RFEM*

4 OUTLOOK

A parametric workflow could be developed to create drawings in a later design phase of the project. This will be especially helpful since, due to the complexity of the double-curved geometry, the length of the different beams and the angles of the connection details will differ. In addition, with the help of parametric tools, clashes of connection elements are quickly identified, and controls to guarantee the feasibility of each node are established.

The forces to transfer at each node can be retrieved from RFEM and checked in GRASSHOPPER for the governing combination. Especially with many different angles, it will take much work to identify manually relevant nodes for the calculation design.

5 CONCLUSION

The studies and analysis for this project show that a combination of a double-curved roof structure and flat surfaces made of straight timber beams using the Zollinger-System in combination with parametric design is possible.

Several factors must be included in the design process for the definition and the setup of the final mesh, such as the design of the nodes, evenness of the roof membrane, types of surfaces, base geometry (symmetrical, unsymmetrical, size of curvature, …), number of nodes, size and regularity of the mesh and the function of the building. All these factors can be included in the parametric design workflow.

The integration of a parametric workflow makes an efficient planning process possible. It helps to identify structural and geometrical problems early and allows quick adjustments in the structure's design.

GRASSHOPPER in combination with the calculation software RFEM from Dlubal allows changes in the geometry easily and therefore an optimised geometry which covers all requirements can be achieved.

REFERENCES

[1] Livingstone, Andrew: *Timber Connection.* Centre for Offsite Construction + Innovative Structure, 2015 A.Livingstone@napier.ac.uk

https://doi.org/10.52202/069179-0339

World Conference on Timber Engineering Oslo 2023

DEVELOPMENT OF THE ANALYTICAL METHOD TO REPRODUCE SEISMIC BEHAVIOR OF CLT BUILDINGS AT LARGE DEFORMATION

So Momose[1], Tatsuya Miyake[2], Hiroshi Isoda[3], Takafumi Nakagawa[4]

ABSTRACT: Understanding the seismic resistance mechanisms and safety limits of cross-laminated timber (CLT) buildings is critical. However, the knowledge of shaking table tests of CLT buildings is limited. As a first step toward collapse analysis, in this study, it was attempted to reproduce full-scale two-story shaking table test results with maximum interstory drift of 8.77%. For that, the results which matched the experimental results were searched by performing data assimilation. Consequently, the analysis results after assimilation agreed well with the experimental results, indicating the validity of this study's analytical method, but the trend of the analytical results have to be addressed in the future.

KEYWORDS: CLT building, Large deformation, Reproductive analysis, Shaking table test

1. INTRODUCTION

The seismic performance of CLT buildings has been investigated using monotonic and quasistatic cycle tests on full-scale CLT buildings [1,2]. In 2007, full-scale shaking table tests of three-, and seven-story CLT buildings were performed as part of the Construction System Fiemme (SOFIE) project [3,4]. During the tests, no residual damage was observed after the destructive earthquakes. The maximum interstory drift of the seven-story building was 67 mm, which was 2.2% against the story height of 3.1 m between the second and third floors of the building during the Japan Meteorological Agency (JMA) Kobe 100%. Further, a five-story CLT building with narrowed panel CLT was tested on a shaking table [5]. During the JMA Kobe 100% test, the compressive rupture of CLT and yielding of all tensile bolts were observed, and a maximum interstory drift of 3.7% was measured on the Y0 plane on the second story. In the USA, a full-scale shaking table test of a two-story CLT building with replaceable components has been performed in a series of research projects on CLT buildings [6]. Interstory drift 4.29% during the Northridge of MCE+ hazard level was measured. In this study, we attempted to reproduce a shaking table test with a maximum interstory drift of 8.77% via numerical analysis, which was 263 mm for a floor height of 3 m at JMA Kobe 140% intensity, exceeding the abovementioned values.

In earthquake-prone areas, such as Japan, USA, and Italy, it is critical to clarify the safety limits and collapse mechanism of CLT buildings through collapse experiments and reproductive analysis as well as to achieve accurate seismic performance evaluation of CLT buildings to protect human lives in the event of a massive earthquake. Consequently, the authors developed the analysis software "wallstat" [7], which is based on the extended distinct element method (EDEM). In this study, the authors modified and developed "wallstat" for CLT buildings. Using the developed software, we attempted to reproduce the experiment results when CLT buildings encountered large deformation. Elemental experiments were used to define the mechanical properties of CLTs and joints. According to a previous study [8], the simple combinations of elemental experiments cannot accurately reproduce full-scale experimental results. An analysis called data assimilation [9] was performed. The process of data assimilation is shown in Fig. 1. First, spring and element parameters were multiplied by the correction factors to create various skeleton curves for the spring. Then, the analytical and experimental results were compared in terms of only the shear force–interstory drift of the first story; finally, the analytical results with the smallest error from the experimental results was extracted. Consequently, the experimental results were reproduced, and the validity of the analytical method was confirmed. Afterward, the analysis results before and after the data assimilation were compared, and the causes of the differences were discussed. This paper is part of the project funded by the Japanese forest agency and includes content that has been in press [10].

2. OUTLINE OF ANALYSIS METHOD

Previous research [11-14]. has widely used numerical calculations based on FEM, as represented using the matrix method, for the time history response analysis of buildings. However, FEM is a tool developed for the stress analysis of continuum, and geometric and material nonlinearities must be considered to trace a specimen to failure analytically. In particular, the problem of handling disproportionate forces in the calculation arises for extreme failures such as member rupture (wood fracture)

[1] So Momose, RISH, Kyoto university, Japan, momose.so.72w@st.kyoto-u.ac.jp
[2] Tatsuya Miyake, Nihon System Sekkei Architects & Engineers Inc., Japan, miyake@nittem.co.jp
[3] Hiroshi Isoda, RISH, Kyoto university, Japan, hisoda@rish.kyoto-u.ac.jp
[4] Takafumi Nakagawa, RISH, Kyoto university, Japan, nakagawa@rish.kyoto-u.ac.jp

https://doi.org/10.52202/069179-0340

and crack propagation. The individual element method [15] is an analytical method that solves these problems and can trace the collapse process. The distinct element method, also known as the "discontinuity analytical method" (a method for calculating the behavior of discrete objects), was originally developed to calculate the collapse of soil and bedrock; hence, it can naturally analyse large deformations and collapse. EDEM [16] is an extended method in which the distinct element method's discontinuum elements are connected by springs, allowing the behavior of the continuum before failure to be tracked. To reproduce the behavior as continuum before failure as in FEM, "wallstat" uses beam elements. Shear, rotational, tensile–compressional, truss springs, and beam elements, which are commonly used in structural analysis in architecture, are incorporated between the elements as springs in EDEM. This has successfully reproduced the rocking and collapse behaviors of low-rise conventional-axle construction buildings [17-21]. "Wallstat" was used to analyse CLT buildings in this study by incorporating multiple-spring (described in Fig. 11) and shear spring models to account for the rocking behavior of CLT panels.

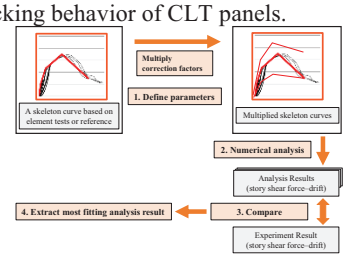

Fig. 1: *Overview of data assimilation*

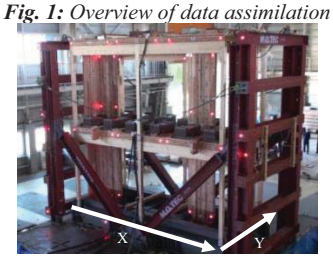

Fig. 2: *Specimen of shaking table test*

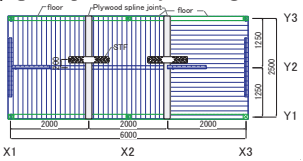

(a) Floor plan of second story

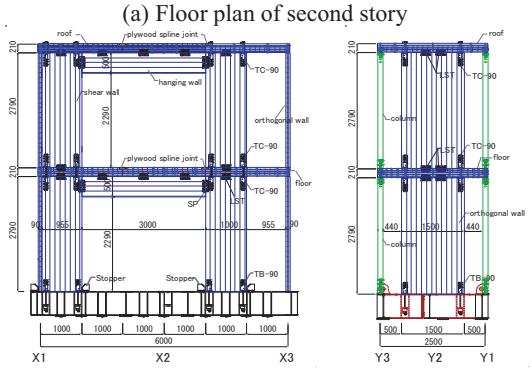

(b)Y2 plane (c)X1 plane

Fig. 3: *Floor plan and elevation of the specimen*

3. SHAKE TABLE TESTS

Fig. 2 shows the specimen of the shaking table test. The test specimen is a full-scale two-story CLT building with a narrow panel frame, consisting of a gravity frame and CLT wall, floor and roof. the floor plan of the second story (Fig. 3(a)), and its elevation in the Y2 and X1 planes where the CLT shear walls were located (Fig. 3(b, c)) are shown. The specimen size is 6.0 m long in the X direction, 2.5 m wide in the Y direction, and 6.0 m high. Two arrangements were made for the floor, one with the outermost lamina parallel to the X direction and the other with a perpendicular one, to verify various conditions. As the main seismic structure, two CLT shear walls were at the center along the X direction on the first and second stories. The strength grading of glulam, which is E95-F315, is specified in the Japan Agricultural Standard.

The meaning of E95 is the laminas in all layers have an average Young's modulus of 9.5 kN/mm^2 and above, whereas F315 means the bending strength of the glulam is 31.5MPa. The material of columns and beams was Glued Laminated Timber (Glulam) made of Scotch pine (*Pinus sylvestris*), which have 2 different strength grading of E95–F315 and E105–F300. The cross-section area was 120 (width) × 120 (height) mm, 120 (width) × 300 (height) mm, respectively. The horizontal diaphragm was made up of seven-layered 210-mm thick CLT panels of Japanese cedar (*Cryptomeria japonica*) grade Mx60 in JAS. The average Young's modulus of the lamina in the outer layers was equal to or more than 6.0 kN/mm^2, whereas it was 3.0 kN/mm^2 in the inner layers. The vertical diaphragm, e.g., shear wall, hanging wall, and orthogonal wall, comprised three-layered 90-mm thick CLT panels of Japanese cedar grade S60, meaning that the average Young's modulus of the lamina in every lamina was equal to or more than 6.0 kN/mm^2.

Fig. 4 shows details of the connectors and which spring corresponds to, and Fig. 5 shows images of the joints. Tensile bolts (ABR490, M16) and U-shaped connectors (TB-90) with holes for screws were used in the wall–foundation joints. Further, it is not common in Japan to install a stopper to resist shear force, but the purpose of this experiment was to excite up to a large deformation domain. Thus, stoppers were introduced to prevent the experiment from stopping early due to the shear failure of the CLT shear wall foot of the first story [Fig. 5(a)]. The metal protectors were attached between the wall panel and stoppers to prevent the shear wall from being embedded in the stoppers due to drifting during excitation. At the wall–wall and wall–roof joints, bolts (ABR490, M20) and U-shaped metal connectors (TC-90) with holes for screws were used as tensile connectors [Fig. 5(b)], and angle brackets (LST) with holes for screws were used as shear connectors [Fig. 5(c)]. Wall–hanging wall and floor–floor connections were made with steel plates secured with screws [Fig. 5(d)]. The screw STS6.5F was used for plywood and long steel plates in the floor–floor shear joint, and STSC65 was used for other joints. The specimen was designed according to "Route 1" provided in CLT manual [Japan Housing and Wood Technology Center Design and construction manual for CLT buildings, 2016]. "Route 1" was the simple method of allowable stress design against

https://doi.org/10.52202/069179-0340

0.2 base shear capacity for moderate earthquake and ultimate strength design against 1.0 base shear capacity for maximum considerable earthquake. The total seismic weight of the specimen was set to 175.95 kN based on the specimen specifications according to the Japanese building standard law (Notification 611 of the Ministry of Land, Infrastructure, Transport and Tourism (2016)).

As shown in Table 1, the specimen was subjected to sine wave of which the frequency was constant in Sequence 0, and the north–south (N–S) component of JMA Kobe waves, which was recorded during the Osaka–Kobe Earthquake in 1995, at 100% and 140% intensity in Sequence 1 and 2, respectively. The exciting direction was the X direction. The acceleration response spectrum of the three seismic waves is presented in Fig. 6.

The displacement where the stickers and LED lights as showed in **Fig. 5**((a)~(c)) were attached was measured with cameras, which is called "image measurement".

Fourier transformation was performed on the acceleration response time history on the shaking table and on the roof of the specimen in Sequence 0, Sequence 1, and Sequence 2; then, the Fourier spectrum was calculated. The Fourier spectrum of the roof was divided by that of the shaking table to obtain a spectral ratio (transfer function), and the lowest frequency among the peaks of the spectral ratio was defined as the natural frequency. In addition, the base shear capacity was derived from dividing the maximum shear force by the total seismic weight, in which the maximum shear force was determined from the acceleration observed during excitation. **Table 2** shows the natural frequency and base shear capacity. The specimen's maximum overall drift and interstory drift in Sequences 1 and 2 are listed in Table 3. During Sequence 1, the maximum roof displacement was 200 mm, corresponding to 3.33% overall drift. A split was seen at the edge of the CLT shear wall due to pulling by the hanging wall, but there was no significant damage other than the split [Fig. 7(a)]. During Sequence 2, the maximum roof displacement was 397 mm, corresponding to 6.62% overall drift, and the interstory drift of the first story was 8.77%. In addition, wall head embedment into the floor panel was observed [Fig. 7(b)]. No repair work was performed after Sequence 1. Some damage and deterioration in the specimen from Sequence 1 was considered in the analysis because the numerical models were subjected to Sequence 1 and 2 in a row.

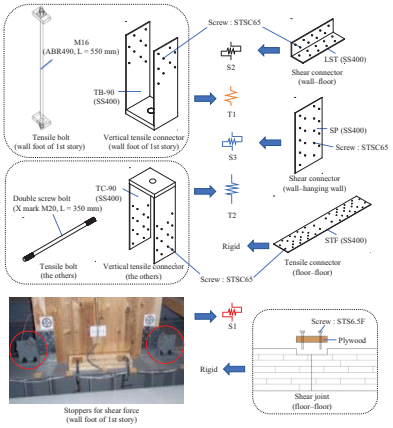

Fig. 4: *Details of connectors and the corresponding springs*

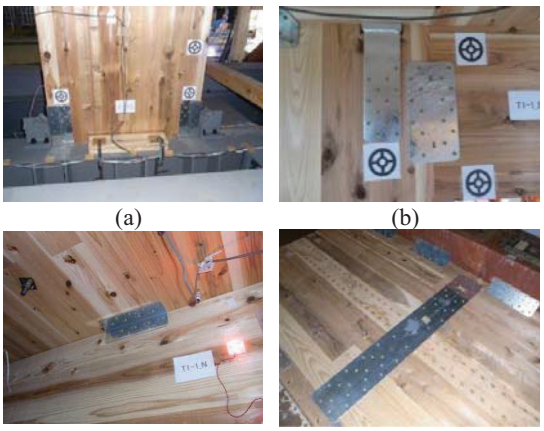

(a) (b) (c) (d)

Fig. 5: *Pictures of the joints*

Table 1: *Input seismic waves*

Sequence	Input seismic waves
0	Sine wave
1	JMA Kobe 100%
2	JMA Kobe 140%

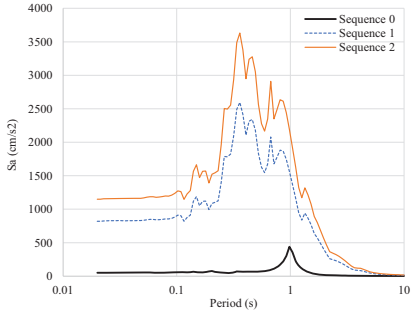

Fig. 6: *Acceleration response spectrum of input waves*

Table 2: *The natural frequency and base shear capacity in Sequence 0, 1, and 2*

Sequence	Natural frequency (Hz)	Max shear force (kN)	Total seismic weight (kN)	Base shear capacity
0	3.198	–		–
1	1.379	244.8	175.95	1.391
2	0.9155	281.0		1.597

Table 3: *Maximum overall and interstory drifts of the first story in the shaking table test*

Sequence	Max overall drift		Max interstory drift of the first story	
	(mm)	(%)	(mm)	(%)
1	200	3.33	115	3.83
2	397	6.62	263	8.77

(a) (b)

Fig. 7: *The fracture properties*

https://doi.org/10.52202/069179-0340

4. MODELING METHOD

Fig. 8 provides the analysis model created according to the joint specifications of the specimen. The number of nodes is 382 and that of springs is 668. his model was fixed in the Y direction of translation because the twisting of the specimen was not observed in the shaking table test. Fig. 9 shows the spring arrangement on the Y2 plane. The analysis model included tensile, shear, and compression springs. Two tensile springs were used for the two types of tensile joints in "wall–foundation" (T1) and "wall–wall" or "wall–roof" (T2). Three types of shear springs were inserted corresponding to the stoppers in "wall–foundation" (S1) and shear joints with steel-plated screws in "wall–floor" or "wall–roof" (S2) and "wall–hanging wall" (S3). Three differently defined compression springs were inserted to express the embedment ability of CLT under loads applied to "wall–foundation" (C1), "wall–floor, wall–roof" (C2), and "wall–hanging wall" and "orthogonal wall–floor" (C3). Other planes, such as Y1 and X1, were modeled similarly.

The modeling method for the CLT shear wall is shown in Fig. 10: the CLT shear wall was replaced by a beam element with rigid beams at its top and bottom ends corresponding to the wall width. The joints at the wall head and foot were modeled with tensile springs, shear springs, and 11 compression springs. The 11 compression springs at equal intervals was called "multiple-spring"; this modeling method has been used in some numerical analyses of specimens with CLT to reproduce the rocking behavior of the CLT shear wall [22,23]. The orthogonal walls, hanging walls, and floor panels were all modeled with beam elements and rigid beams, similar to the CLT shear walls. The beam elements were given only one Young's modulus, which was applicable for both bending and compression. The Young's modulus was set to 4.0 kN/mm^2 for CLT shear walls and hanging walls because the major direction layer was seen as 0 kN/mm^2 according to CLT manual. In addition, it was set to 2.571 kN/mm^2 for the floor panels along the major direction, and 1.285 kN/mm^2 along the minor direction. When establishing the floor panel parameters, the cooperation width was considered. The gravity frame was modeled as a beam element with elastoplastic rotational springs at the element ends. The columns and beams' Young's modulus were set to 9.5 and 10.5 kN/mm^2, respectively, and the bending strength were set to 31.5 and 30.0 Mpa, respectively. This Young's modulus was applied for both bending and compression. Nonlinear tensile shear springs were used to simulate each joint, and nonlinear compression springs were used to model the CLT's embedment properties. Fig. 11 shows hysteretic rules of tensile–compressional and shear springs. The tensile–compressional spring was modeled as a slip type in tension and elastoplastic in compression. Shear springs were set to bilinear for blind prediction, and later wall–foundation shear springs were reset to slip type considering the load–displacement relationship of the experimental results.

The ultimate capacity for tensile springs at the wall–foundation joint (T1) were determined to be 59.3 and 93 kN, and the Young's modulus and effective area of tensile bolts (ABR490, M16) were 205 kN/mm^2 and 157 mm^2 according to JIS B 1220. In addition, the length between the nuts was 400 mm, therefore, the first stiffness and the ultimate displacement for the T1 spring were set to 26.0 kN/mm and 41 mm based on CLT manual. Similarly, for the wall–wall joint (T2), the Young's modulus and effective area of tensile bolts (ABR490, M20) were 205 kN/mm^2 and 245 mm^2 according to JIS B 1220, and the length between the nuts was 200 mm. Therefore, the first stiffness and the ultimate displacement for the T2 spring were set to 30.0 kN/mm and 20 mm according to CLT manual. For shear spring at wall–floor (S2), the yielding and ultimate capacity of the two angle brackets were determined to 54 and 90 kN, respectively, based on CLT manual. In addition, considering friction, the first stiffness was assumed to be like rigid, and the value obtained by multiplying the allowable (79.6 kN) and ultimate capacity (93.0 kN) of the tensile joint from JIS B 1220 by a friction coefficient of 0.3 were added to 54 and 90 kN, which is equivalent to 77.9 and 118 kN. As the four shear springs were distributed at the wall–floor joint as Fig. 10, the calculated yielding and ultimate capacity were divided by 2. Finally, yielding and ultimate capacity for the shear spring were set to 38.9 and 59.0 kN. The ultimate displacement was set to 23.86mm based on CLT manual. Skeleton curves of the wall–hanging wall shear spring (S3) and wall–foundation compression spring (C1) were determined from the element test results (Fig. 12(c, d)). The critical tensile–compressional and shear spring properties in this analysis model are presented in Table 4 and Table 5. All analytical results were generated using a time-integration step of 10^{-6} s. The numerical analysis used the measured acceleration at the center of the shaking table as ground motions. The model weights were equal to the seismic weights of the full-scale specimen, including members and loaded weights, and the weights of the first and second stories were set to 100.54 and 75.41 kN, respectively.

Fig. 8: *Analysis model*

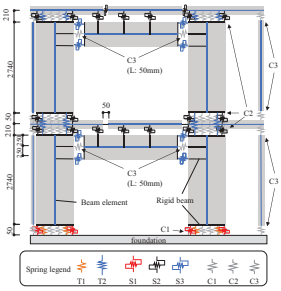

Fig. 9: *The spring arrangement on the Y2 plane*

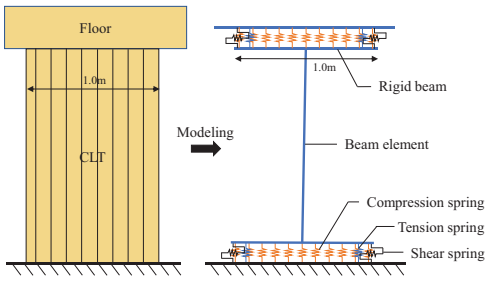

Fig. 10: *Modeling for CLT shear wall*

https://doi.org/10.52202/069179-0340

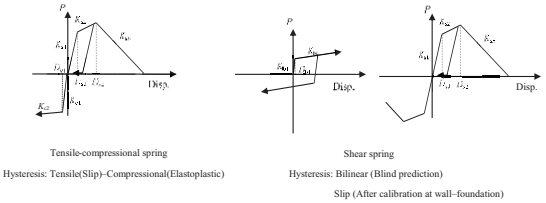

Fig. 11: *Hysteresis rules of tensile–compressional and shear springs*

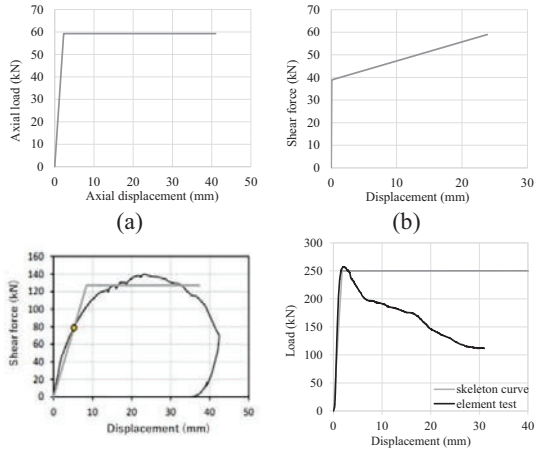

Fig. 12: *Skeleton curve of springs used in blind prediction*

Table 4(a): *Tensile–compressional spring properties based on the element tests and reference values (tensile side)*

Spring	K_{s1} (kN/mm)	K_{s2} (kN/mm)	K_{s3} (kN/mm)	D_{s1} (mm)	D_{s2} (mm)	D_{s3} (mm)
Wall–foundation (T1)	26	0.001	-0.001	2.3	40	41
Wall–wall (T2)	30	0.001	-0.001	3.1	10	20
Wall–foundation (C1)	0.001	0.0001	-0.001	13.5	21.6	1000

Table 4(b): *Tensile–compressional spring properties based on the element tests and reference values (compressional side)*

Spring	K_{c1} (kN/mm)	K_{c2} (kN/mm)	D_{c1} (mm)
Wall–foundation (T1)	0.001	–	–
Wall–wall (T2)	0.001	–	–
Wall–foundation (C1)	140.4	0.001	1.78

Table 5: *Shear spring properties based on the element tests and reference values*

Spring	K_{b1} (kN/mm)	K_{b2} (kN/mm)	D_{b1} (mm)	D_{b2} (mm)
Wall–foundation (S1)	Rigid			
Wall–floor (S2)	486.75	0.8445	0.08	23.86
Wall–hanging wall (S3)	15	0.001	8.5	37

5. BLIND PREDICTION

In the push-over analysis (blind prediction), the skeleton curves of the springs were determined based on the elemental tests results of seismic elements. The analysis results and experimental results are shown in Fig. 13. The first stiffness agreed with the experiments for both the first and second stories, but the maximum capacity of the second story and the ductility of the first and second stories were insufficient, indicating that the analysis cannot reproduce the full-scale shaking table test results when the parameters of the springs were determined by element test results as described in previous papers [8]. Thus, reproductive analysis was performed to better match the experimental results.

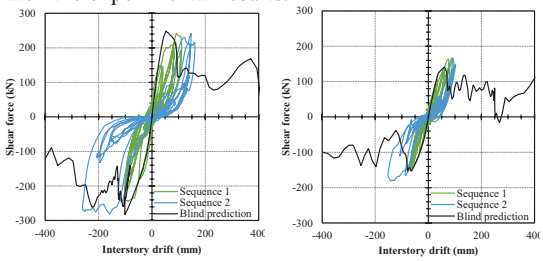

Fig. 13: *Push-over analysis (blind prediction)*

6. REPRODUCTIVE ANALYSIS METHOD

As previously stated, pushover analysis based on elemental tests and references could not reproduce the behavior of full-scale shaking table test at large deformation. The shaking table test results were used to calibrate the spring parameters for the wall–foundation tensile and shear joints (Fig. 14). For the tensile spring, the axial force–displacement relationship of the tensile bolts at the wall–foundation was traced and the skeleton curve was redefined by the slip-type hysteresis rules. In addition, a pretension load of 20 kN was added according to the experimental condition. Half of the shear force for the first story against wall–foundation relative displacement was traced for the shear spring skeleton curve. Half of that was used because there were two CLT shear walls on the first story. The skeleton curve was redefined by the slip-type hysteresis characteristics. Table 6 shows the two spring properties after calibration. Comparing the skeleton curve in blind prediction and after calibration, the tensile spring parameters after calibration matched well with those in blind prediction. For the shear spring, the difference in the first stiffness was large, indicating that the shear resistance ability of the stoppers was not rigid due to the embedment of the CLT shear wall even if the metal protectors were installed.

Further, to enhance reproducibility, the analytical method of this study [9], data assimilation, was performed for the reproductive analysis. Fig. 1 shows an overview of data assimilation executed as the reproductive analysis. The critical 24 parameters of springs and elements in **Table 7** were the target of data assimilation and multiplied by the correction factors to create various skeleton curves, and the parameter combinations when fit to the

experiment result were explored. The correction factors had the range to account for variations in materials and resistance factors which were not considered in the analytical model. Assuming the variation due to these uncertainties was expressed as the correction factors' coefficient of variation CV = 0.2 and the mean value of the correction factors μ was 1, the standard deviation σ = 0.2 was derived from Eq. (1). Assuming that the correction factor x was normally distributed, standardization was performed using the random variable z according to Eq. (2). In this case, $0.5 < x < 2.0$ accounts for 99.38% of the total, which can cover almost all patterns. Therefore, the correction factors were varied in the range of 0.5 to 2.0 with the interval of 0.15 for the Young's modulus, first stiffness, and first yield point. For the second stiffness, the correction factors were varied in the range of 0.0001 to 0.8 with the interval of 0.08, considering that the most possible values of the stiffness after yielding were covered.

$$CV = \frac{\sigma}{\mu} \quad (1)$$

$$\boldsymbol{z = \frac{x - \mu}{\sigma}} \quad (2)$$

With this method, various skeleton curves for the springs were created. Then, the experimental results and many analytical results were compared in terms of only the shear force–interstory drift of the first story through Sequence 1 and 2, not in terms of the time history of interstory drift and uplift displacement. Then, the analytical results with the smallest error from the experimental results was extracted. Later, when comparing the skeleton curves between before assimilation and after assimilation, five analysis results with the smallest five errors from the experimental results were extracted. Thus, assimilation was performed to match both Sequence 1 and 2. Therefore, the damage from Sequence 1 was also considered in the analytical results after data assimilation. In addition, because all springs and elements were free in all directions except the Y direction of translation, if multiple factors are included in the springs and elements, data assimilation of the parameters will result in an accurate analysis model.

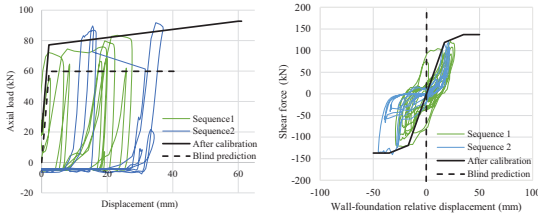

(a) (b)

Fig. 14: *The hysteresis of shaking table test and the spring skeleton curves in blind prediction and after calibration*

Table 6: *Calibrated spring properties based on the shaking table test results*

Spring	K_{s1} kN/mm	K_{s2} kN/mm	K_{s3} kN/mm	D_{s1} mm	D_{s2} mm	D_{s3} mm	K_c kN/mm
Wall–foundation (T1)	26	0.2685	-0.001	2.2	60	61	0.001
Wall–foundation (S1)	7	1	-0.001	17	35	50	–

Table 7: *The list of parameters multiplied by correction factors*

Spring position	Joint type	Spring type	Multiplied parameters
CLT shear wall	–	Beam element	Bending Young's modulus
Hanging wall	–	Beam element	Bending Young's modulus
Floor panel, beam	–	Beam element	Bending Young's modulus
Wall–wall	Tensile	Tensile–compressional	K_{s1}, K_{s2}, D_{s1}
Wall–hanging wall	Tensile	Tensile–compressional	K_{s1}, K_{s2}, D_{s1}
Column foot	Tensile	Tensile–compressional	K_{s1}, K_{s2}, D_{s1}
Wall–wall	Shear	Shear	K_{b1}, K_{b2}, D_{b1}
Wall–hanging wall	Shear	Shear	K_{b1}, K_{b2}, D_{b1}
Wall–foundation	Compression	Tensile–compressional	K_{c1}, K_{c2}, D_{c1}
Wall–hanging wall	Compression	Tensile–compressional	K_{c1}, K_{c2}, D_{c1}

7. REPRODUCTIVE ANALYSIS RESULT

The interstory drift time history for the first and second stories in Sequence 1 and 2 from data assimilation is illustrated in Fig. 15, together with the blind prediction and experimental results. The blind prediction did not agree with the experiment results except for the initial drift response to the excitation. Meanwhile, after assimilation, both the interstory drift and phase agreed well with the experimental results through Sequence 1. Even in Sequence 2, there was a slight error in interstory drift with the experiment results after the maximum drift, but the trends of the interstory drift and phase agreed well, implying a good reproduction result. Fig. 16 illustrates the shear force–interstory drift relationships for the first story in Sequence 1 and 2 in the experiment, in blind prediction, and after assimilation. For the blind prediction, the maximum load was nearly reproduced in Sequence 1, but not in Sequence 2. Nevertheless, the interstory drift and stiffness were not consistent with the experiment results. However, the analytical results after assimilation were almost identical to the experimental result, indicating that the overall behavior of the specimen could be tracked by reproductive analysis. Fig. 17 shows the uplift displacement time history at the CLT shear wall foot of the first story in Sequence 2 in the experiment and the analysis results after assimilation. The analytical result after assimilation agreed with the experimental results in drift and phase, demonstrating that the detailed behavior of the two-story CLT building was reproduced. Fig. 18 and Fig. 19 show the comparison of specimen's behavior in Sequence 1 and 2 between the experiment (red line and spheres depicted by image measurement data) and reproductive analysis (shown as Fig. 8) and the interstory drift time history (Fig. 15(a, c)) with the moment which the image exhibits. It could be seen that the analysis results agreed with the experiment results in appearance in Sequence 1 and 2. Therefore, it was verified that the analysis results were identical to the experiment results.

https://doi.org/10.52202/069179-0340

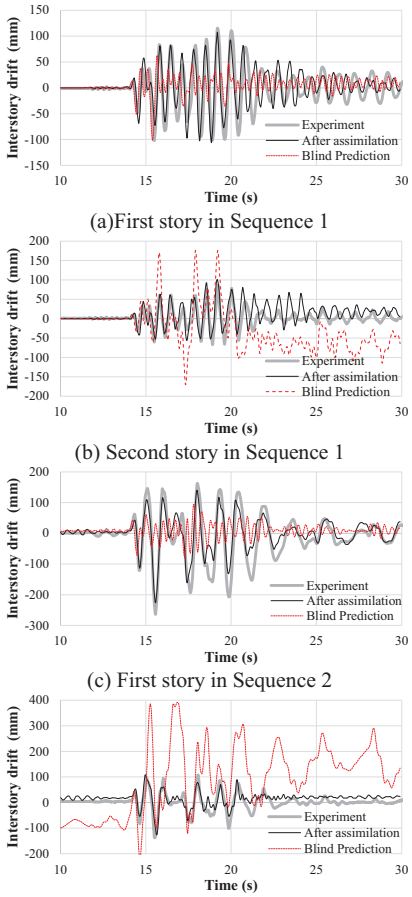

(a)First story in Sequence 1

(b) Second story in Sequence 1

(c) First story in Sequence 2

(d) Second story in Sequence 2

Fig. 15: *The interstory drift time history of the shaking table tests, blind prediction, and after data assimilation*

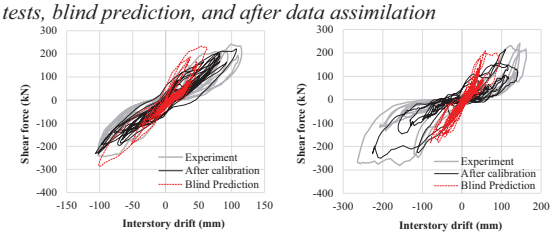

(a) Sequence 1 (b)Sequence 2

Fig. 16: *The story shear force–interstory drift relationship of the experiment, blind prediction, and after data assimilation for 1st story*

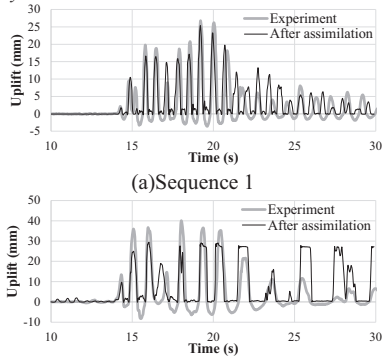

(a)Sequence 1

(b)Sequence 2

Fig. 17: *The time history of uplift displacement at the CLT shear wall foot for the first story in the experiment and after data assimilation*

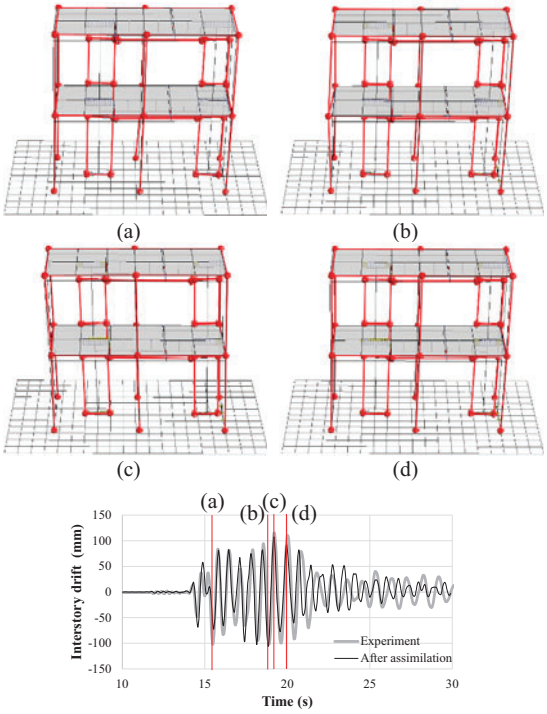

Fig. 18: *The comparison of specimen's behavior between the experiment and analysis in Sequence 1*

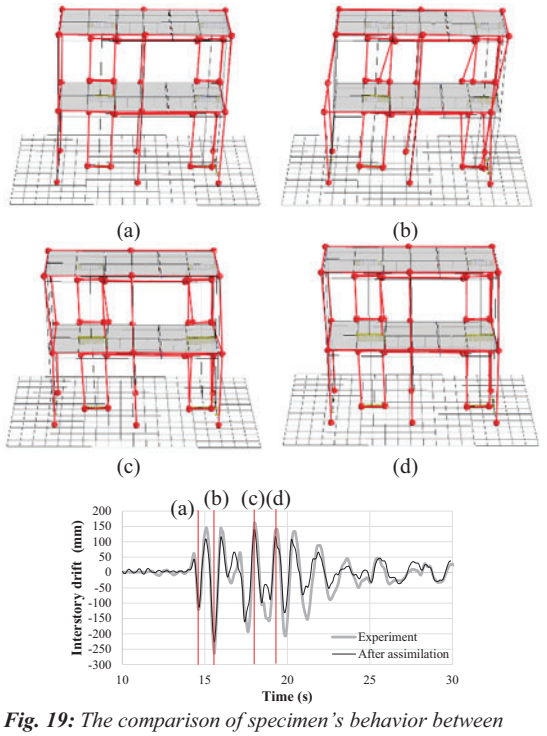

Fig. 19: *The comparison of specimen's behavior between the experiment and analysis in Sequence 2*

Fig. 20 shows the skeleton curves for the four springs before and after assimilation. The blue solid lines in each of **Fig. 20** (a)–(d) are skeleton curves in the analysis results with the five smallest errors from the experimental results. The five analytical results (smallest one was labelled (1), second smallest (2), third smallest (3), fourth smallest (4), and fifth smallest (5)) are shown to grasp the trend of how the skeleton curves changed.

For the wall–wall tensile springs (**Fig. 20**(a)), a clear trend of the first stiffness and yielding capacity was not seen. For the wall–floor shear spring (**Fig. 20**(b)) considering friction when determining the parameters, the skeleton curves tend to be the same before and after assimilation. For the wall–hanging wall shear spring (**Fig. 20**(c)) without considering friction, both stiffness and yield capacity tended to increase after assimilation. This implies that the friction between the shear connectors under suppressed force contributed to an increase in both stiffness and yielding capacity. However, it is recommended to reconsider the friction coefficient which is assumed as 0.3 in the paper. In addition, the difference in the loading speed between the dynamic loading during the full-scale shaking table test and the static loading in the element tests can be another reason because steel strength increases as the strain velocity increases. Also, for the (5), the yielding capacity of wall–floor shear spring was highest although the first stiffness and yielding capacity of wall–hanging wall shear spring were smallest, inferring that the wall–floor and wall–hanging wall shear springs were in a inverse relationship. An increasing trend of the first stiffness and yielding capacity was also seen in the case of compression springs (**Fig. 20**(d)). Similar to shear springs, the dynamic effects of loading can be a contributing factor to the increase in stiffness and yielding capacity. Another possible factor is that the dead weights were fixed to the floor with screws in the experiment, which increased the floor rigidity significantly and suppressed the vertical deformation caused by the rocking of the CLT shear walls." These inverse interaction and factors for increase of stiffness and capacity such as friction, dynamic effects, and increase of floor rigidity will be verified by comparing the detailed behavior and performing static loading tests in the future.

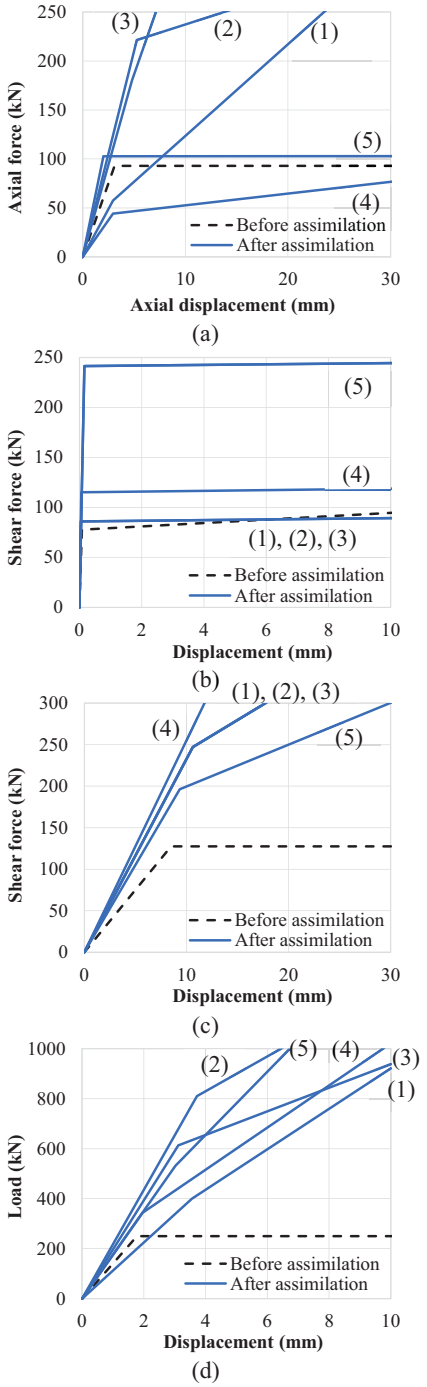

Fig. 20: *Skeleton curves of springs before and after data assimilation*

https://doi.org/10.52202/069179-0340

8. CONCLUSION

In this study, a model that can replicate the seismic behavior of CLT buildings up to a large deformation region is proposed using "wallstat," which was modified to consider the restoring force and P–δ effects due to the rocking behavior of CLT panels. The shaking table test on a two-story full-scale CLT building validated the analytical method.

- A split was observed at a wall–hanging wall joint. Despite the 8.77% interstory drift of the first story in Sequence 2, further damage, such as wall head embedment into the floor panel, was negligible.
- In pushover analysis, blind prediction agreed well with the experimental result in terms of the first stiffness but not the maximum capacity of the second story and the ductility of the first and second stories.
- The shaking table test results of the two-story full-scale CLT building were analyzed using "wallstat," which was modified to include multiple-spring and shear spring models, to account for restoring force and P–δ effects due to the rocking behavior of the CLT panels. Using wallstat, we attempted to replicate the seismic behavior of the two-story full-scale CLT building up to a large deformation domain. Blind prediction could not reproduce the experimental results in the time history interstory drift and hysteresis curves of the shear force–interstory drift of the first story. However, the analytical results after assimilation were consistent with the experimental results in interstory drift and phase in both the first and second stories although the discrepancy between the analysis and experiment after the maximum drift will be the subject of future research, demonstrating that the overall behavior of the CLT building specimen was reproduced with this analytical method even in the large deformation domain.
- The uplift displacement and phase trends of the CLT shear wall of the first story were analyzed for the uplift displacement time history. The outcomes suggest that our analysis model can even replicate the detailed behavior of a full-scale specimen at large deformation as well as the overall behavior.
- The overall behavior of analysis model could be seen identical to that of the specimen in appearance as well as on the graph.
- The skeleton curves of shear and compression springs after data assimilation tended to increase in both stiffness and yielding load compared with those before assimilation. For this, the suppression of deformation due to friction resistance, the difference in the loading speed between the element tests and the shaking table test, and the increment in floor rigidity due to fixed dead weights were considered to be the cause.

Hence, the analysis results after assimilation agreed well with the experimental results, indicating the validity of this study's analytical method. However, it is not possible to predict the responses of CLT buildings without experimental results from this study alone. In this study, as a result of varying the characteristic values for joints and members over the statistically determined range, analytical results that agree with the experimental results were obtained, and the trend of the analytical results was shown. Friction, dynamic effects, and an increase in floor rigidity due to fixed dead weights were thought to be the causes of the increase trend of stiffness and yielding capacity of shear and compression spring. In addition, as the inverse relationship between the properties of the shear springs was confirmed, the interaction among the tensile, shear, compression springs, and beam elements can also exist. These interactions in analysis models of this study have to be verified in the future through behavior comparisons of detailed part and static loading tests, and it is believed that the verification will lead to predict the seismic behavior of CLT buildings at large deformation without experimental results.

ACKNOWLEDGEMENT

This research was conducted as part of a Forestry Agency–subsidized project to study the relaxation of earthquake resistance standards by simplifying joints and reducing the number of walls, etc., based on an understanding of the seismic boundary performance of CLT panel construction method buildings. We would like to express our gratitude to all the parties involved. We used the Japan Aerospace Exploration Agency supercomputer system "JSS3" in the reproductive analysis. [24].

REFERENCES

[1] Zhang X., Isoda H., Sumida K., Araki Y., Nakashima S., Nakagawa T., Akaiyama N. 2021. "Seismic Performance of Three-Story Cross-Laminated Timber Structures in Japan" *J. Struct. Eng.*, 147 (2): 04020319. DOI: 10.1061/(ASCE)ST.1943-541X.0002897.

[2] Popovski, M., and I. Garvic. 2016. "Performance of two－storey CLT house subjected to lateral loads." *J. Struct. Eng.*, 142 (4), 2016.

[3] Ceccotti, A. 2008. "Few technologies for construction of medium－rise buildings in seismic regions." *Struct. Eng. Int.,* 18 (2), 156–165: https://doi.org/10.2749/101686608784218680.

[4] Ceccotti, A., C. Sandhaas, M. Okabe, M. Yasumura, C. Minowa, N. Kawai. 2013. "SOFIE 3D shaking table test on a seven－storey full－scale cross－laminated timber building." *Earthquake Eng. Struct. Dynam*., 42 (13), 2003–2021.

[5] Sato, M., H. Isoda, Y. Araki, T. Nakagawa, N. Kawai, and T. Miyake. 2019. "A seismic behavior and numerical model of narrow paneled cross－laminated timber building." *Eng. Struct.*, 179 (15), 9–22.

[6] Blomgren, H. E., S. Pei, Z. Jin, J. Powers, J. Dolam, J. W. van de Lindt, A. R. Barbosa, and D. Huang. 2019. "Full－scale shake table testing of cross－laminated timber rocking shear walls with replaceable components" *J. Struct. Eng.*, 145 (10): 04019115. https://doi.org/10.1061/(ASCE)ST.1943

－541X.0002388.
[7] wallstat ver.4.3.11 [Computer Software]. Research Institute for Sustainable Humanosphere, Kyoto University, Kyoto, Japan.
[8] Yasumura, M., K. Kobayashi, M. Okabe, T. Miyake, and K. Matsumoto. 2016. “Full－scale tests and numerical analysis of low－rise CLT structures under lateral loading.” *J. Struct. Eng.*, 142 (4), E4015007(12). https://doi.org/10.1061/(ASCE)ST.1943－541X.0001348.
[9] Namba, T., T. Nakagawa, Y. Kado, H. Isoda, Y. Kado, R. Odani, A. Takino. 2023. “Seismic Response Comparison of Full-Scale Moment Resisting Timber Frame and Joint Test Result” *J. Struct. Eng.* [10.1061/JSENDH/STENG-12165]. (in press)
[10] Momose S., T. Nakagawa, T. Namba, H. Isoda, and T. Miyake. 2023. “An Analytical Method to Reproduce Seismic Behavior of Two-Story Cross-Laminated Timber Building at Large Deformation” *J. Struct. Eng*. [10.1061/JSENDH/STENG-11711] (in press)
[11] Ceccotti, A., and M. Follesa. 2006. “Seismic behavior of multi－story Xlam buildings.” In *Proc., of international workshop on earthquake engineering on timber structures*., 11 University of Coimbra, Coimbra: Portugal.
[12] Dujic B., K. Strus, R. Zarnic, and A. Ceccotti. 2010. “Prediction of dynamic response of a 7－ storey massive Xlam building tested on a shaking table” In: Proceedings of WCTE 2010, world conference on timber engineering. DVD.
[13] Rinaldin, G., and M. Fragiacomo. 2016. “Non－linear simulation of shaking–table tests on 3 – and 7 – storey X－Lam timber buildings.” *Eng. Struct.*, 113 (15), 133–148.
[14] Pei, S., M. Popovski, and J. W. van de Lindt. 2013. “Analytical study on seismic force modification factors for cross－laminated timber buildings.” *Can J. Civ. Eng.*, 40 (9), 887–896.
[15] Cundall, P. A1971. “A computer model for simulating progressive, large－scale, movements, in blocky rock system.” Symposium ISRM, Nancy, 129–136.
[16] Meguro, K., and M. Hakuno. 1991. “Simulation of Structural Collapse due to Earthquakes Using Extended Distinct Element Method.” Summaries of Technical Papers of Annual Meeting. Architectural Press Institute of Japan, 763–764.
[17] Nakagawa, T., and M. Ohta. 2003. “Collapsing process simulations of timber structures under dynamic loading I: simulations of two－story frame models.” *J. Wood Sci.,* 49 (5), 392–397.
[18] Nakagawa, T., and M. Ohta. 2003. “Collapsing process simulations of timber structures under dynamic loading II: simplification and qualification of the calculating method.” *J. Wood Sci.*, 49 (6), 499–504.
[19] Nakagawa, T., T. Hidaka, and M. Inayama. 2013. “Damage investigation and collapsing process analysis of Myokenji Hondo damaged from the Great East Japan EARTHQUAKE: Part 2 Collapsing process analysis using 3D space frame model.” [In Japanese.] *J. Struct. Eng. B AIJ*, 59B, 573–578.
[20] Hidaka, T., T. Nakagawa, and M. Inayama. 2013. “Damage investigation and collapsing process analysis of Myokenji Hondo damaged from the Great East Japan EARTHQUAKE: Part 1 Damage investigation and measurement survey.” [In Japanese.] *J. Struct. Eng. B AIJ*, 59B, 567–572.
[21] Sumida, K., T. Nakagawa, and H. Isoda. 2020. “Seismic testing and analysis of rocking motions of Japanese after and－beam construction.” *J. Struct. Eng.*, 147 (2), 04020323.
[22] Sato, M., H. Isoda, Y. Araki, T. Nakagawa, T. Miyake. 2017. “Proposal of analysis model of CLT structure for small width panel and accuracy verification intended.” [in Japanese.] *J. Struct. Constr. Eng*., 82 (741), 1719–1726.
[23] Azumi Y., T. Miyake, K. Matsumoto, I. Sakurai, and N. Kawai. 2019. “A study on expansion and improvement of the structural design method for CLT panel construction, Part 2 Simplification of numerical analysis model by Multiple Spring element.” *Summaries of Technical Papers of Annual Meeting,* Architectural Institute of Japan, [In Japanese.] 461–462.
[24] JSS3 [Supercomputer]. Japan Aerospace Exploration Agency, Ibaraki, Japan

https://doi.org/10.52202/069179-0340

World Conference on Timber Engineering Oslo 2023

RACKING RESISTANCE OF CLT PANELS MANUFACTURED FROM C16 GRADE TIMBER

Conan O'Ceallaigh[1], Rimjhim Kashyap[2], Annette M. Harte[3], Patrick J. McGetrick[4]

ABSTRACT: This study examines the typical lateral/racking resistance of cross-laminated timber (CLT). The use of CLT in construction has grown in many regions of the world, not only due to its impressive structural properties but also the improved environmental performance achieved for this mass-timber system compared to more traditional construction materials. In Europe, CLT is primarily manufactured with C24 grade timber or a combination of C24 with small proportions of C16 grade material in internal layers. In many parts of the world, the supply of C24 timber is limited and it is important to establish the structural properties of CLT manufactured with lower-grade material. This study presents a numerical model developed to predict the load-displacement behaviour and structural racking resistance of CLT panels and will inform the experimental testing of CLT panels manufactured from C16 grade material in combination with typical connections utilised in structural mass timber systems.

KEYWORDS: Connections; Cross Laminated Timber (CLT); Engineered Wood Products (EWPs); Racking resistance; Sitka spruce

1 INTRODUCTION

In recent years, there has been a significant rise in the number of advanced engineered wood products (EWPs) coming to market. Cross-laminated timber (CLT) presented in Figure 1 is one of the most significant advances in EWP technology and has been responsible for the rise in timber structures and has the potential to significantly reduce the environmental footprint of the built environment in the fight against climate change [1].

Figure 1: *Typical cross laminated timber (CLT) panel.*

In Europe, this product is primarily manufactured using C24 grade [2] material with limited quantities of lower-grade material being used [3]. As the market interest in mass-timber increases, the demand for natural timber resources will benefit from increased knowledge of the structural properties of CLT manufactured from lower-grade materials. To date, there has been a significant amount of work carried out to establish the manufacturing properties of CLT from lower-grade materials [4–6] however, there is limited information on the racking resistance of C16-grade CLT panels [7]. In this study, a numerical model is developed to examine the racking resistance of CLT panels subjected to in-plane racking loads. The numerical model is validated against experimental tests on C24 grade CLT carried out by Hughes [8]. In the study by Hughes [8], a 5-layer CLT panel manufactured from C24 grade material was subjected to a racking test.

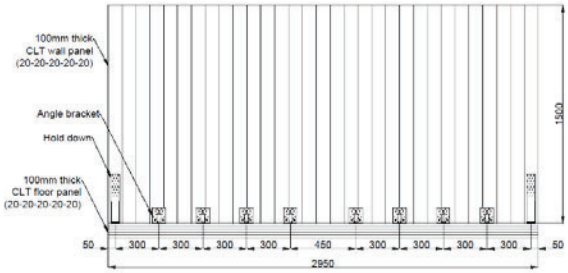

Figure 2: *CLT test set-up* [8] *(Dims. in mm).*

The CLT wall panel measured 1.5 m in height and 2.95 m in length as shown in Figure 2. The panel was connected to a CLT floor with a series of typical brackets (hold downs and angle brackets) and the floor panel itself was anchored to the ground at four fixing points. The vertical load was varied to understand its influence on the load-displacement behaviour of the CLT panel. The developed numerical model is validated based on the results presented by Hughes [8] and utilised to examine the

[1] Conan O'Ceallaigh, Timber Engineering Research Group, University of Galway, conan.oceallaigh@universityofgalway.ie
[2] Rimjhim Kashyap, Timber Engineering Research Group, University of Galway, r.kashyap1@universityofgalway.ie
[3] Annette M. Harte, Timber Engineering Research Group, University of Galway, annette.harte@universityofgalway.ie
[4] Patrick J. McGetrick, Timber Engineering Research Group, University of Galway, patrick.mcgetrick@universityofgalway.ie

https://doi.org/10.52202/069179-0341

corresponding load-displacement behaviour of CLT panels manufactured from C16-grade timber. This numerical study will then inform the experimental testing programme of CLT subjected to racking tests in accordance with EN 594 [9].

2 RACKING RESISTANCE OF CLT

CLT wall panels are typically connected to floor panels through a combination of angle brackets and hold-downs. Angle brackets are used to resist shear and hold-downs are used to resist overturning. Dujic et al. [10] tested 2.44 m x 2.44 m glued lamellate panels subjected to monotonous and cyclic horizontal loads in combination with a constant vertical load. The tested wooden panels have relatively high stiffness and load-bearing capacity, therefore the influence of the anchoring system on the shear stiffness and strength of the wall was studied. It was observed that the racking behaviour of cantilever massive wood walls is very sensitive to the magnitude of vertical load and the type of anchorage system. Ceccotti et al. [11] performed a series of full-scale wall tests as part of the SOFIE project. 2.95 m x 2.95 m wall panels anchored using commercially available hold-downs and angle brackets were subjected to monotonic and cyclic tests to assess their racking behaviour. The panels were designed to behave rigidly and the connections were designed to exhibit ductile behaviour. Due to this, all forces and displacements were locally concentrated around the connections leading to local failure, confirming that the dissipated energy results from the connections. Subsequently, full-scale 3-storey and 7-storey buildings were designed as per Eurocode 8 [12] and tested for seismic loads using a 1D and a 3D shaking table respectively. Ductile failure modes with fastener bending and embedment were observed in these buildings. The buildings were observed to resist a whole series of earthquakes in 1D and 3D, keep their shapes and remain fully operational. Gavric et al. [13] investigated the behaviour of several configurations of single and coupled CLT wall panels subjected to cyclic loads according to EN 12512 [14]. Angle brackets and hold-downs were used to anchor the CLT walls to a steel foundation. The experimental results were then compared to advanced analytical models which were developed for nonlinear pushover analysis of the CLT wall system, which showed that angle brackets have sufficient tension capacity in addition to the shear capacity. However, hold-downs did not exhibit significant shear strength. Izzi et al. [15] proposed a numerical model to predict the mechanical behaviour and failure mechanisms of CLT wall systems. The CLT wall and the element to which it is anchored are modelled as 3D solid bodies using ABAQUS, while the connections are modelled as nonlinear hysteretic springs. Racking tests by Gavric et al. [13] were reproduced on the numerical models. The results of these analyses highlighted that in order to obtain a realistic prediction of the load-carrying capacity of the angle brackets, it is necessary to consider the axial load resistance of the angle brackets. Hughes et al. [7] studied the behaviour of tall CLT buildings under monotonic lateral loading. This was achieved by subjecting the CLT wall system to a constant vertical load replicating gravity loads at storeys within a 10-storey CLT building. Non-linear relationships between vertical load and total lateral displacement, and between vertical load and uplift were observed, which implied that vertical load has a significant influence on the behaviour of CLT wall systems.

3 FINITE ELEMENT MODEL

This section discusses the development of a 3-Dimensional finite element model (FEM) of CLT panels subjected to vertical loads and horizontal racking loads using ABAQUS FEM software.

3.1 MODEL GEOMETRY

The model was developed in line with the study presented by Hughes [7,8]. This comprised a 5-layer CLT wall and floor panel with dimensions of 1.5 m in height, 2.95 m in length and 0.1 m thick. The CLT panels were modelled as an orthotropic elastic material with each layer and corresponding grain direction (longitudinal, radial and tangential) being specified within the model. The CLT panels were meshed with 8-noded linear brick elements with reduced integration (C3D8R). The connections were not discretely modelled, however, connector elements with specified elastic and plastic stiffness were specified to mimic the hold-down and angle bracket behaviour.
A steel plate was utilised to apply the structural racking load and hard contact was defined between the surface of the timber and the steel plate with a tangential friction coefficient of 0.3. The vertical pressure was applied to the top surface of the CLT wall, and the base of the floor was fixed to mimic the experimental conditions.

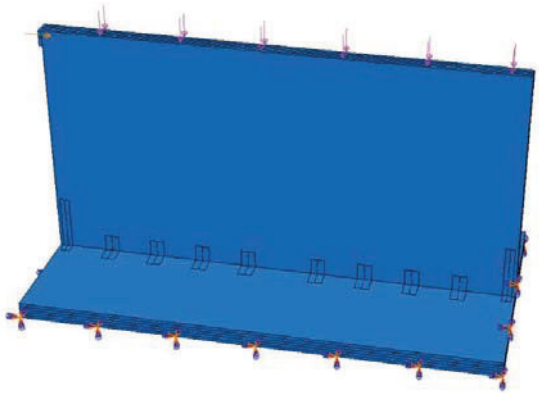

Figure 3: *FEM model geometry*

3.2 MATERIAL PROPERTIES

The material properties of the C24-grade CLT timber presented in Table 1 were sourced from a study by Uí Chúláin [16]. The subscripts *L*, *R* and *T* refer, respectively, to the directions of assumed elastic symmetry, longitudinal, radial and tangential directions. *E* and *G* represent the elastic modulus and shear modulus, respectively. The steel plate was modelled as a linear elastic isotropic material with an elastic modulus of 210 GPa and a Poisson's ratio of 0.3.

https://doi.org/10.52202/069179-0341

Table 1: *FEM material properties for C24 grade timber*

Property	Timber (C24)	Unit
E_L	12000	MPa
E_R	370	MPa
E_T	370	MPa
G_{LR}	690	MPa
G_{LT}	690	MPa
G_{RT}	50	MPa
ν_{LR}	0.511	-
ν_{LT}	0.511	-
ν_{RT}	0.203	-

4 FEM RESULTS

This section presents the result of the finite element model which is validated based on the study performed by Hughes [8]. The validated model is then used to examine the corresponding behaviour for C16-grade CLT.

4.1 MODEL VALIDATION

The simulated load-displacement behaviour of the finite element model results is presented in Figure 4. The results compare the lateral/racking displacement (U_{LAT}) and the lateral stiffness (k_{LAT}) of the panel. The lateral displacement is defined as the horizontal displacement of the top of the wall, measured on the top right corner, minus the horizontal displacement of the floor panel measured at the top of the floor panel directly under the wall panel at the right-hand end of the wall panel. This allows the relative movement of the wall panel to be examined. The numerically simulated horizontal movement of the CLT wall is graphically presented in Figure 5a. The simulated uplift of the wall was examined at the bottom left corner of the wall panel which can be graphically seen in Figure 5b. In Figure 4, the lateral displacement versus the applied lateral load is compared to the simulated results for a series of different vertical loads. The different vertical loads of 10.5 kN/m, 31.5 kN/m and 84.0 kN/m correspond to the associated structural loads of a 2-storey (T1 [8]), 4-storey (T6 [8]) and 9-storey (T8 [8]) CLT building, respectively. It can be seen that the behaviour for different vertical loads can be relatively well predicted. The behaviour of the T8 specimen [8] with a vertical load of 10.5 kN/m was found to have the largest lateral deflection when subjected to a lateral load of 50 kN. This was found to be 4.00 mm and the numerical model demonstrated good agreement and predicted a lateral displacement of 4.24 mm for a common vertical load. The connection properties of the hold-down and angle brackets utilised in this study were based on results presented by Hughes [8]. It was stated in this study that the vertical load had a significant effect on the stiffness behaviour of the individual connections and the associated load-displacement behaviour. This was also noted upon increasing the vertical load within the numerical model and utilising common properties for the connections. It was observed that the load-displacement behaviour deviated from that observed experimentally. It can be seen in Figure 4 that the load-displacement behaviour of Specimen T6, which is subjected to a vertical load of 31.5 kN/m, does not match that of the experimental curve initially as a much stiffer response was simulated than that observed for T8 which was only subjected to a vertical load of 10.5 kN/m. The yielding of the connections was also observed in the numerical model. Similarly, a stiffer response was simulated for Specimen T1 which had a vertical loading of 84 kN/m (equivalent to a 9-storey building).

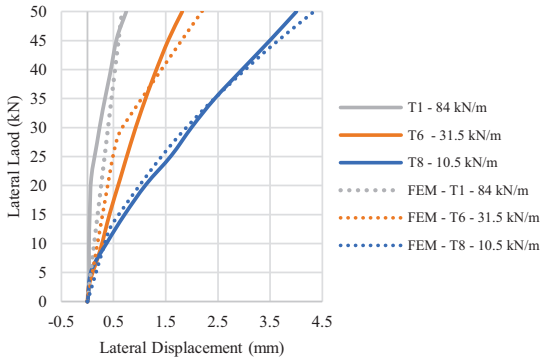

Figure 4: *Load-displacement behaviour of CLT tests [8] compared to the FEM model results.*

The model was also utilised to compare the experimentally determined lateral stiffness of the panel under different vertical loads. The results are presented in Table 2 and graphically presented in Figure 6. It can be seen that with increasing vertical load, the lateral stiffness of the panel increases as expected and the numerical model predicts the trend observed experimentally.

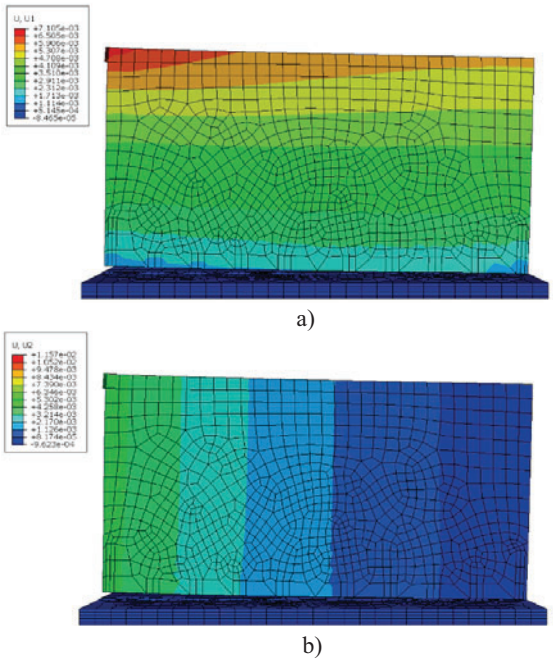

a)

b)

Figure 5: *CLT Racking FEM displacement results at a horizontal load of 100 kN: a) horizontal slip/movement (U1) and b) Vertical uplift (U2). Dimensions are presented in meters and a deformation scale factor of 10 was applied.*

In all cases examined in this study, the predicted lateral stiffness is greater than that observed experimentally. The experimental values of T1, T6 and T8 were found to be 13.5 kN/mm, 26.8 kN/mm and 45.0 kN/mm, respectively.

https://doi.org/10.52202/069179-0341

The results of the model which were taken between 10% and 40% of the maximum load were found to provide values of 15.8 kN/mm, 31.3 kN/mm and 51.7 kN/mm, for T1, T6 and T8, respectively.

Table 2: *Experimental results [8] vs numerical model (FEM)*

FEM Model	Vertical Load (kN/m)	Experimental		FEM	
		U_{LAT} (mm)	k_{LAT} (kN/mm)	U_{LAT} (mm)	k_{LAT} (kN/mm)
FEM-10.5	10.5	4.00	13.5	4.24	15.8
FEM-31.5	31.5	1.82	26.8	2.17	31.3
FEM-84.0	84.0	0.74	45.0	0.62	51.7

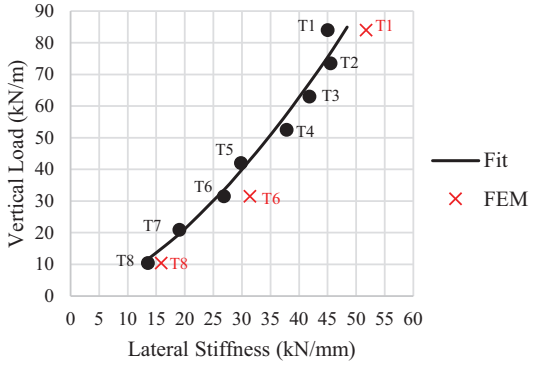

Figure 6: *Vertical load versus the mean lateral stiffness presented by Hughes [8] and the FEM results.*

4.2 RACKING OF C16 GRADE CLT

The developed model was subjected to similar structural loads, however, the structural properties of the CLT were changed from C24-grade material properties to C16-grade properties in accordance with O'Ceallaigh [17] to examine the influence of the grade of timber used to manufacture the CLT. The material properties are presented in Table 3.

Table 3: *FEM material properties for C16 grade timber*

Property	Timber (C16)	Unit
E_L	9222	MPa
E_R	663	MPa
E_T	415	MPa
G_{LR}	659	MPa
G_{LT}	619	MPa
G_{RT}	66	MPa
ν_{LR}	0.529	-
ν_{LT}	0.333	-
ν_{RT}	0.558	-

The results of both models are presented in Figure 7. It can be seen that the stiffness of the CLT has an insignificant effect on the overall lateral displacement and the connections govern a significant proportion of the behaviour. The connection properties are not varied in this study but will form a significant component of future testing on typical bracket connections under tension and shear loading. The developed model will inform the experimental test programme for C16-grade CLT connections.

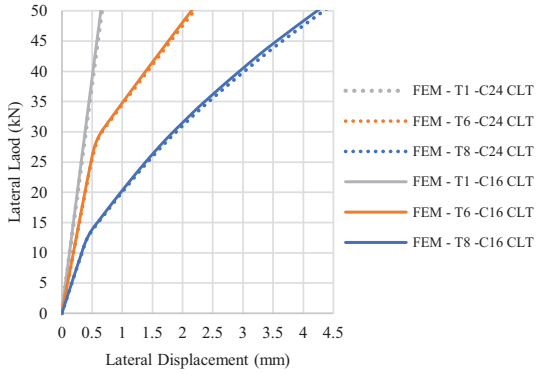

Figure 7: *Comparison of the load-displacement behaviour of CLT manufactured from C24-grade timber and C16-grade timber under different vertical loading situations.*

5 FUTURE EXPERIMENTAL TESTING

This section discusses the planned manufacture and experimental testing of C16-grade CLT under racking loads in accordance with EN 594 [9]. The further development of a suitable numerical model for the prediction of the behaviour of C16-grade CLT connections requires a series of experimental tests to be carried out. While a significant amount of research has been carried out for CLT connections, most of the testing has been carried out for C24-grade CLT. Only a limited number of studies focused on C16-grade timber. O'Ceallaigh & Harte [5] used C16 grade CLT panels to study the behaviour of commonly available steel-to-timber angle bracket connections. The connections were subjected to monotonic and cyclic loadings and were tested for different fastener lengths. The experimental results were compared to analytical models developed using the provisions of Eurocode 5 [18] and the analytical model developed by Blaß & Uibel [19,20]. The results were shown to perform well for C16-grade material. Therefore, it is proposed to test C16-grade CLT connections comprising individual brackets which will allow for an improved numerical model to be developed for C16-grade CLT. It is proposed to extend upon this testing to examine a series of brackets/connections in racking wall systems.

5.1 C16 CLT MANUFACTURE

For the proposed testing, the CLT will be manufactured in accordance with EN 16351 [1]. Two different sizes and test configurations of CLT panels will be manufactured, namely a 3-layer (40-40-40) and a 5-layer (40-20-20-20-40) panel. Boards of C16 Irish Sitka spruce (*Picea sitchensis*) with nominal cross-sectional dimensions of 100 mm × 35 mm (for panels comprising 20 mm thick layers), and 175 mm × 47 mm (for panels comprising 40 mm thick layers), will be used to manufacture the CLT panels. The boards will be initially stored in a conditioning chamber at a relative humidity of 65 ± 5% and at a temperature of 20 ± 2°C, before specimen preparation. Prior to fabrication, all of the sides of the boards will be planed to the desired board thickness (20

https://doi.org/10.52202/069179-0341

mm and 40 mm) and width (80 mm and 160 mm). All of the panels will be bonded using a one-component PUR adhesive (PURBOND HB S309), with a spreading rate of 160 g/m^2, and a pressure (face bonding only, no edge bonding) of 0.6 N/mm^2.

5.2 CONNECTION TESTING

It is proposed that typical CLT bracket connections are to be subjected to compression and shear testing. The influence of three different fastener lengths is to be studied to establish the elastic and ductile behaviour of these connectors for C16 grade CLT. Five sets of tests for each fastener length are proposed for both compression and shear loads. In addition to angle brackets, timber plates or stud rails connected using self-tapping screws is an alternate method for floor-to-wall connections and will be investigated.

5.3 RACKING TEST SET-UP

The connection testing will inform the racking tests. Racking panels, measuring 2.4 m x 2.4 m, will be manufactured in accordance with EN 16351 [1] and tested in accordance with EN 594 [9], which governs the test procedure for determining the racking strength and stiffness of timber frame wall panels. The test protocol allows for comparative performance values for the materials used in the manufacture of the panels to be determined and provides evidence in the form of experimental data for use in structural design. The racking frame in the University of Galway can be seen in Figure 8.

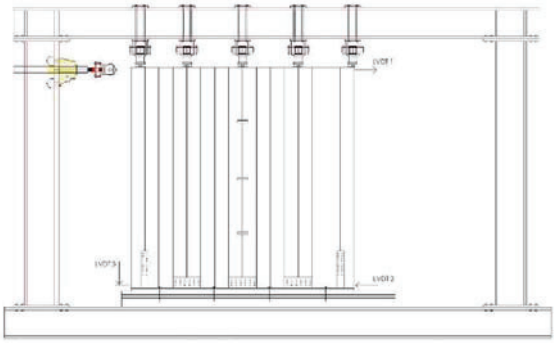

Figure 8: *Racking frame test set-up*

The self-restraining racking frame has the capability to apply a horizontal racking load of up to 200 kN and a series of vertical loads ranging from 1-5 kN. The lateral or racking load (F) is applied via a contact roller to the top left of the panel. The panels will be tested with no vertical load and with the vertical loads (F_v) set to apply a maximum vertical load of 5 kN at five different points along with the top of the wall panel. The five vertical loads are equally spaced along the top of the panel allowing for 100 mm from the leading edge of the wall in accordance with EN 594 [9]. For the purpose of this testing, the leading edge of the panel is the left edge (Figure 8) and the lateral/racking load is applied to the top of the leading edge of the wall panel. The right edge of the panel (see Figure 8) is referred to as the trailing edge.

The displacements of the panel will be monitored using linear variable differential transducers (LVDTs) at locations indicated LVDT 1, LVDT 2 and LVDT 3 (see Figure 8). The deformation (v) for the calculation of the lateral/racking displacement is taken as displacement at LVDT 1 minus the displacement at LVDT 2. The displacement at LVDT 3, which represents the vertical displacement or uplift of the panel is reported separately.
The horizontal racking load will be applied at an appropriate rate to ensure the rate of loading achieves 90 % of the maximum racking load (F_{max}) within 300 ± 120 s in accordance with EN 594 [9].
The lateral/racking displacement of the panel is calculated as shown in Eq. (1).

$$v = v_{LVDT1} - v_{LVDT2} \tag{1}$$

Where v_{LVDT1} is the lateral displacement at LVDT 1 and v_{LVDT2} is the lateral displacement at LVDT 2 (see Figure 8). The racking strength of the panel is the maximum load attained during the test as shown in Eq. (2).

$$F = F_{max} \tag{2}$$

where F_{max} = the maximum load attained.
The lateral/racking stiffness (R) is calculated as shown in Eq. (3).

$$R = \frac{F_{40} - F_{10}}{v_{40} - v_{10}} \tag{3}$$

where F_{10} and F_{40} = are the loads corresponding to 10% and 40% of F_{max} and v_{10} and v_{40} = are the displacements corresponding to 10% and 40% of F_{max}. Essentially, the Racking Stiffness (R) is the slope of the line between 10% and 40% of F_{max}.

6 CONCLUSIONS

A finite element model capable of replicating the load-displacement behaviour of wall-floor CLT connections has been presented. The model has been shown to perform well when examining the load-displacement behaviour and lateral stiffness of C24-grade CLT. The model was also utilised to examine the influence of the timber grade used in the manufacture of the CLT. The numerical results have demonstrated the potential for significant lateral/racking resistance to be achieved from CLT panels manufactured from C16 grade material but it was shown that the stiffness of the CLT itself may not be as important as the defined connection behaviour. This finding must be examined experimentally and is a key focus of future work which will further calibrate the connections utilised in the developed model to better predict the behaviour not only under monotonic loading but also under cyclic loading situations. The development of a refined model will allow a series of different configurations of connections to be examined utilising different grades of CLT. The model and its findings will provide designers with confidence in this product and may encourage producers to incorporate C16-grade material into the production of CLT.

https://doi.org/10.52202/069179-0341

ACKNOWLEDGEMENT

The authors would like to express their gratitude for the support and funding of the Department of Agriculture, Food and the Marine's Competitive Research Funding Programmes, Project Ref: 2019R471 (MODCONS).

REFERENCES

[1] A.M. Harte, Mass timber – the emergence of a modern construction material, J. Struct. Integr. Maint. 2 (2017) 121–132. doi:10.1080/24705314.2017.1354156.

[2] CEN, EN 338. Structural timber - Strength classes, Comité Européen de Normalisation, Brussels, Belgium, 2016.

[3] R. Brandner, G. Flatscher, A. Ringhofer, G. Schickhofer, A. Thiel, Cross laminated timber (CLT): overview and development, Eur. J. Wood Wood Prod. 74 (2016) 331–351. doi:10.1007/s00107-015-0999-5.

[4] C. O'Ceallaigh, K. Sikora, A.M. Harte, The Influence of Panel Lay-Up on the Characteristic Bending and Rolling Shear Strength of CLT, Buildings. 8 (2018) 15. doi:10.3390/buildings8090114.

[5] C. O'Ceallaigh, A.M. Harte, The elastic and ductile behaviour of CLT wall-floor connections and the influence of fastener length, Eng. Struct. 189 (2019) 319–331. doi:10.1016/j.engstruct.2019.03.100.

[6] C. Sigrist, M. Lehmann, Potential of CLT produced from non-structural grade australian pinus radiata, Proc. World Conf. Timber Eng. 2014. (2014).

[7] C. Hughes, D. McPolin, P. McGetrick, D. McCrum, Behaviour of cross-laminated timber wall systems under monotonic lateral loading, J. Struct. Integr. Maint. 4 (2019) 153–161. doi:10.1080/24705314.2019.1622187.

[8] C. Hughes, Behaviour of multi-storey cross-laminated timber buildings under lateral loading, Queens University Belfast, 2020.

[9] CEN, EN 594. Timber Structures - Test methods - Racking strength and stiffness of timber frame wall panels, Comité Européen de Normalisation, Brussels, Belgium, 2011.

[10] B. Dujic, J. Pucelj, R. Zarnic, Testing of racking behavior of massive wooden wall panels, in: 37th CIB-W18 Meet. Edinburgh, Scotl., Edinburgh, Scotland, 2004.

[11] A. Ceccotti, C. Sandhaas, M. Okabe, M. Yasumura, C. Minowa, N. Kawai, SOFIE project - 3D shaking table test on a seven-storey full-scale cross-laminated timber building, Earthq. Eng. Struct. Dyn. 42 (2013) 2003–2021. doi:10.1002/eqe.2309.

[12] CEN, EN 1998-1. Eurocode 8: Design od structures for Earthquake resistance - Part 1: General rules, seismic actions and rules for buildings, Comité Européen de Normalisation, Brussels, Belgium, 2005.

[13] I. Gavric, M. Fragiacomo, A. Ceccotti, Cyclic Behavior of CLT Wall Systems : Experimental Tests and Analytical Prediction Models, J. Struct. Eng. 141 (2015) 1–14. doi:10.1061/(ASCE)ST.1943-541X.0001246.

[14] CEN, EN 12512. Timber Structures - Test methods - Cyclic testing of joints made with mechanical fasteners, Comité Européen de Normalisation, Brussels, Belgium, 2005.

[15] M. Izzi, A. Polastri, M. Fragiacomo, Investigating the Hysteretic Behavior of Cross-Laminated Timber Wall Systems due to Connections, J. Struct. Eng. 144 (2018) 1–10. doi:10.1061/(asce)st.1943-541x.0002022.

[16] C. Uí Chúláin, Experimental and Finite Element Investigations of the Serviceability Behaviour of CLT Floors, National University of Ireland Galway, 2019. doi:10.13140/RG.2.2.21044.12165.

[17] C. O'Ceallaigh, K. Sikora, D. McPolin, A.M. Harte, Modelling the hygro-mechanical creep behaviour of FRP reinforced timber elements, Constr. Build. Mater. 259 (2020). doi:10.1016/j.conbuildmat.2020.119899.

[18] CEN, EN 1995-1-1. Eurocode 5: Design of timber structures - Part 1-1: General - Common rules and rules for buildings, Comité Européen de Normalisation, Brussels, Belgium, 2005.

[19] H.J. Blaß, T. Uibel, Tragfähigkeit von stiftförmigen Verbindungsmitteln in Brettsperrholz, Universitätsverlang Karlsruhe, 2007.

[20] T. Uibel, H.J. Blaß, Joints with Dowel Type Fasteners in CLT Structures, in: R. Harris, A. Ringhofer, G. Schickhofer (Eds.), Focus Solid Timber Solut. - Eur. Conf. Cross Laminated Timber, The University of Bath, 2014: pp. 119–134.

https://doi.org/10.52202/069179-0341

World Conference on Timber Engineering Oslo 2023

NUMERICAL ANALYSIS OF BIAXIAL HOLLOW TIMBER SLAB ELEMENTS

Dominik Bissig[1], Marcel Muster[2], Andrea Frangi[3]

ABSTRACT: The inventions of the company Timber Structures 3.0 (TS3) facilitate the construction of point supported flat slabs made of cross laminated timber (CLT) elements. The CLT of the entire slab area is designed to bridge the largest span and to resist the largest forces at the point supports. Thus, major portions of the flat slab are overdesigned and much of the built-in structural timber is wasted. To tackle this problem, a biaxial hollow timber slab element is developed, to replace the CLT elements wherever their high performance is not needed. The hollow elements consist of a grid of notched, linear timber beams, covered on both sides with thin CLT plates. The notches in the timber grid cause stress concentrations perpendicular to the grain that can lead to an early brittle failure in regions with large shear forces. Therefore, possibilities to optimise the hollow elements' shear resistance are analysed with the help of finite element (FE) models. The models are compared to experimental results and the chosen methods are validated. The geometry of the FE model is parametrised, and the results of 1024 geometry combinations are analysed to study the influence of the geometry parameters on the structural properties of the hollow elements. The results show that geometries with multiple smaller notches have a significantly higher shear resistance than those with only one notch. Furthermore, the shear resistance can be increased by using a wider web with a smaller spacing. Contrary to the initial assumption, the use of CLT instead of glued laminated timber (GLT) in the web grid does not lead to a significant increase of the shear resistance.

KEYWORDS: TS3, point supported flat slab, biaxial hollow slab elements, FEM, Abaqus, parameter study

1 INTRODUCTION

Point supported flat slabs are often used to build modern office buildings and apartments, allowing for versatile floor plans. Most of these slabs are built with reinforced concrete, a low-cost building material that is well known and widely available. The goal of the company Timber Structures 3.0 (TS3) is to provide a cost efficient and sustainable timber alternative to concrete flat slabs. Thus, TS3 has initiated several research projects to develop a point supported timber flat slab. It consists of cross laminated timber (CLT) elements, which are connected on site with the TS3 resin [1]. The timber flat slab has been realised in several projects in Switzerland [2], but the high strength and stiffness of CLT is not needed in all areas of the point supported slab. Thus, the idea of a biaxial hollow timber slab was presented in [3]. An additional research project was launched in 2021 to investigate the biaxial hollow slab. The goal of the project is to replace the CLT elements in those parts of the slab, where the mass timber solution is not needed from a structural point of view. The conceptual idea of the new hollow slab system is illustrated in Figure 1. The new hollow elements aim to optimise the material usage and to be even more economically competitive than the current TS3 slab system by reducing the amount of valuable structural timber needed. The aim is for the hollow elements to contain at least 30% less timber than CLT elements of an equivalent thickness.

The biaxial hollow slab elements are composed of a bottom and a top CLT plate that are glued to a grid of

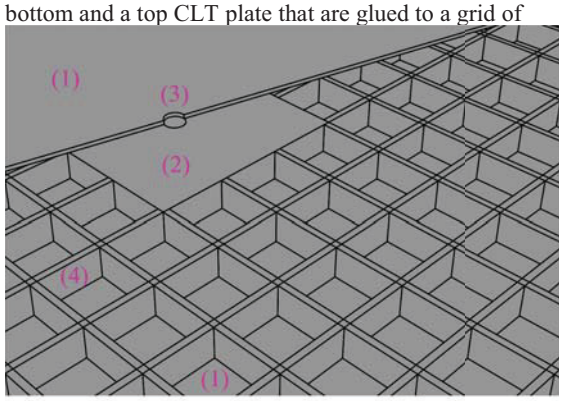

Figure 1: *Sketch of the conceptual idea for a biaxial hollow timber flat slab. (1) upper and lower CLT plate, (2) column head made of CLT, (3) connection and load transfer support, (4) hollow slab grid for biaxial load carrying action.*

linear glued laminated timber (GLT) beams, as illustrated in Figure 1. Figure 2 shows three possibilities how the intersection points of the grid can be accomplished with notches. As presented in many publications of the past decades (summarised e.g. in [4]), the notches cause stress concentrations in the timber beams. The stress concentrations can lead to an early, brittle failure of the timber beams, especially in regions of high shear forces. Therefore, the high shear forces occurring around the load

[1] Dominik Bissig, Institute of Structural Engineering, ETH Zurich, Switzerland, bissig@ibk.baug.ethz.ch
[2] Marcel Muster, Institute of Structural Engineering, ETH Zurich, Switzerland, muster@ibk.baug.ethz.ch
[3] Andrea Frangi, Institute of Structural Engineering, ETH Zurich, Switzerland, frangi@ibk.baug.ethz.ch

https://doi.org/10.52202/069179-0342

introduction of the point supported flat slabs can become the governing design parameter of the new hollow slab. A lower shear resistance of the hollow elements requires larger CLT elements introducing the loads into the point supports. The goal is to reduce the size of the CLT areas, to cut back on the usage of timber as much as possible. Therefore, a high shear resistance of the new hollow element is needed, and the optimisation of the grid intersection points is a crucial task in the current research project.

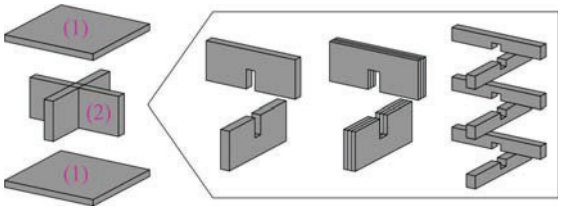

Figure 2: *Layout of the different compounds of the biaxial hollow slab elements and the different web intersection designs tested in* [5]. *(1) CLT plates, (2) GLT / CLT beams with the different notched intersection options.*

A first experimental investigation on biaxial hollow timber elements with different intersection types (as illustrated in Figure 2) was performed in 2021 at ETH Zurich [5]. The uniaxial 4-point bending tests were performed to find the bending stiffness, the shear stiffness and the shear resistance of the different element types. The experiments showed, that multiple smaller notches or the use of a wider CLT instead of a slimmer GLT beam grid increases the shear load bearing capacity of the element by 35% on average [5]. After the experiments, the three intersection types illustrated in Figure 2 were chosen to further investigate with finite element (FE) models.

To investigate the influence of the different geometrical properties on the different structural properties of the elements, the FE-models are parametrised, and a parameter study is performed. The main goal of the parameter study is to find an option with large shear resistance due to the reasons mentioned before. The bending resistance, bending stiffness and shear stiffness are also investigated, but are assumed to be less important. It is assumed that the bending resistance and the bending stiffness can easily be controlled with the hight of the element and the thickness of the CLT plates. According to previous experiences with the TS3 slab system, the shear stiffness has only a minor influence on the global deformations and vibrations in comparison to the bending stiffness. However, the influence of the notch geometry, the web width and web material on the shear resistance is of special interest for this investigation. It is assumed, that these are the most efficient parameters to be manipulated to enlarge the shear resistance. A literature review and the experimental campaign suggest that multiple smaller notches enlarge the shear resistance of all element geometries. Since the production of multiple small notches is more expensive than the production of one larger notch, the parameter study has to proof the structural benefits of the smaller notches over a variety of geometry combinations. Also, the influence of the web width on the shear resistance has to be investigated. A wider web (the same width is used in both directions) enlarges not only the webs cross sectional area, but also the width of the notch. The parameter study should also show, whether the use of CLT in the web is generally beneficial for the shear resistance. Finally, the findings from this parameter study are needed to further optimise and finalise the cross section geometry of the new slab elements.

2 MATERIAL AND METHODS

2.1 FRAMEWORK AND MODELLING

The parameter study was performed in the FE program Abaqus [6]. A Python script was used to generate and execute a volumetric, linear elastic model in Abaqus Standard. The script reads deformations and stresses from the output database generated by Abaqus and stores the information in text files. The text files were read and visualised with the help of a Matlab [7] script.

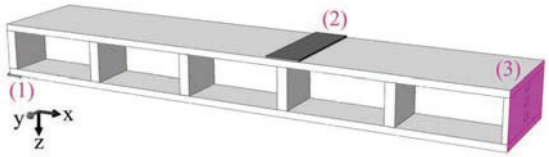

Figure 3: *Illustration of the FE model in Abaqus. (1) steel plate support, (2) steel plate load introduction, (3) symmetry plane.*

The 4-point bending test was modelled in Abaqus with volumetric timber elements. The timber plates were modelled as single parts and the timber webs were modelled as single parts with openings. To model CLT, the parts were partitioned, and each layer was assigned the correct material orientation. Side face gluing of all layers was assumed. The plate and web parts were connected rigidly with each other to form the assembly shown in Figure 3. A hard contact with a tangential friction coefficient of 0.3 was applied between timber and steel plates (support and load introduction), as well as between all timber parts that are not glued together. No glued connection was modelled at the notched intersection of the longitudinal and the cross web parts. The notches were modelled with 1 mm air around all three edges to account for the production. Each steel plate was constrained in all degrees of freedom to a reference point lying centrically below/above the plate (see Figure 4). The reference point at the support was fixed in the directions u_y, u_z (deflections), r_x and r_z (rotations), to model a rolling support. The reference point at the load introduction was fixed in u_x and u_y direction. A point load of $F_{cyl} = 10$ kN was introduced to the reference point above the load introduction steel plate. The symmetry plane in the middle of the specimen was fixed in the directions u_x, r_y, r_z.

The Abaqus mesh element type C3D8 (brick element with 8 integration points) was chosen. A preliminary investigation showed, that this element type has the best result quality to computation time ratio for the on hand study. The mesh size was chosen according to the CLT plate layer thickness h_h. For $h_h \leq 20$ mm, a mesh size of 20 mm was chosen, for $h_h > 20$ mm a mesh size of 30 mm was chosen. A mesh refinement region was

https://doi.org/10.52202/069179-0342

implemented around the notch nearest to the support and at the symmetry plane. In the refinement region, a mesh size of 10 mm was chosen. The refinement region stretched 60 mm from the cross web, followed by a mesh transition zone of 40 mm, as illustrated in Figure 4.

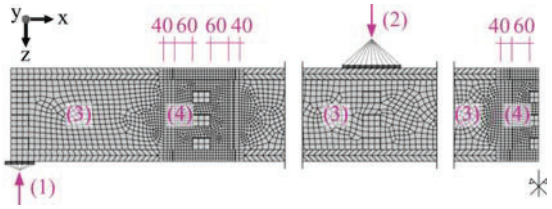

Figure 4: *Longitudinal section of a specimen in Abaqus with the mesh of C3D8 elements, generated according to the defined restrictions. (1) support on reference point, (2) load introduction to reference point, (3) general mesh 20..30 mm, (4) fine mesh 10 mm.*

The elastic material parameters for the longitudinal (L, 1), tangential (T, 2) and radial (R, 3) direction shown in Table 1 were used to model the timber parts. The material model does not distinguish between radial and tangential properties (transversely isotropic material model). Average values of the Poisson's ratio after [8] were used.

Table 1: *Elastic properties of the modelled timber parts for a moisture content of 12%.*

E_1 $E_2 = E_3$	11'500 MPa 300 MPa	Elastic modulus [9]
$G_{12} = G_{13}$ G_{23}	650 MPa 65 MPa	Shear modulus [9]
$\nu_{12} = \nu_{13}$ ν_{23}	0.395 0.41	Poisson's ratio [8]

To verify the FE-model with the experimental results, the actual average timber moisture content of 9% was taken into account. The moisture dependent stiffness parameters after Neuhaus [10] were used to scale the stiffness parameters listed in Table 1 according to Equation (1).

$$E_{FE} = E_{EN} \cdot \frac{E_{NH}(9\%)}{E_{NH}(12\%)} \quad (1)$$

with: E_{FE} Elastic modulus used in the FE-model
E_{EN} Elastic modulus defined in Table 1
E_{NH} Elastic modulus after [10] in dependence of the timber moisture content

2.2 GEOMETRY

The geometric properties of the modelled elements were parametrised to study their influence on the structural properties of the slab elements. The parameters illustrated in Figure 5 were varied with the values listed in Table 2.

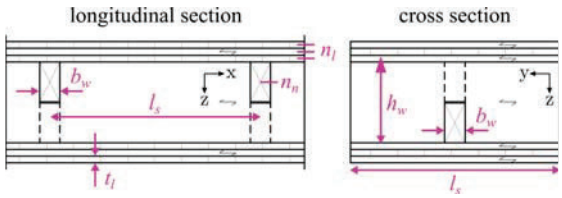

Figure 5: *Illustration of the geometric parameters that are varied within the scope of the parameter study (see Table 2). Longitudinal and cross section of one element configuration modelled with the setup of a uniaxial 4-point bending test.*

Table 2: *Parameters of the hollow elements that are varied within the scope of the parameter study (see Figure 5 for an illustration of the geometric parameters).*

Name	Range	Description
b_w	60, 120, 180 mm	web width
h_w	80, 180, 280 mm	web height
l_s	375, 500, 625 mm	web spacing
n_n	1, 3	number of notches
t_l	20, 40 mm	thickness of CLT layers
n_l	2, 3	number of CLT layers
PN	top, bottom	position of notch
GD	0°, 90°	grain dir. CLT top layer
MW	GLT, CLT	material web

The width of the element was chosen equal to the web spacing l_s to model a representative section of the slab. The number of openings between the cross web parts was kept at a constant number of $n_o = 5$. Thus, the total length of the specimen varied with the chosen web spacing l_s.
A total of 1728 combinations result from the parameters listed in Table 2. The following combinations were excluded from the analysis, since they are not viable either from a productional or from a structural point of view:

- $b_w = 180$ mm and $l_s = 375$ mm
- $h_w = 80$ mm and $n_n = 3$
- MW = CLT and $n_n = 3$

Thus, a total of 1024 geometry combinations result, which leads to the same number of models to be created.
Furthermore, six models with the geometric parameters given by the experimental analysis (see [5]) were created. These models were used to verify the FE results of the failure load and the stiffness by comparing them to the corresponding experimental results. The geometry and the naming of the verification models is summarised in Table 3 and described in detail in [5].

Table 3: *Names and geometry of the verification models. All verification models had a web hight* $\boldsymbol{h_w = 240}$ *mm, a web spacing* $\boldsymbol{l_s = 625}$ *mm, a CLT layer thickness* $\boldsymbol{t_l = 20}$ *mm and a number of CLT layers* $\boldsymbol{n_l = 2}$.

	NL-LX	NL-XL	NX-LX	NX-XL	CL-LX	LL-LX
	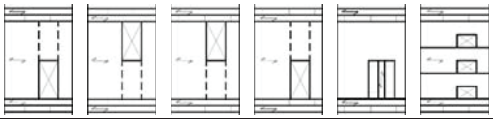					
b_w	60 mm	60 mm	60 mm	60 mm	80 mm	60 mm
n_n	1	1	1	1	1	3
PN	B	T	T	B	B	B

GD	0°	90°	0°	90°	0°	0°
MW	GLT	GLT	GLT	GLT	CLT	GLT

2.3 DATA OUTPUT AND CALCULATIONS

The deflections were evaluated in the pure bending region at the symmetry plane and at a distance of 250 mm from the load introduction point, as illustrated in Figure 6. The bending and shear stiffness can be calculated from the two deflections after Equation (2) and (6).

$$EI_{eff} = \frac{F_{cyl}\, a\, l_w^2}{8\,(w_2 - w_1)} \tag{2}$$

With the assumption that only bending deformations occur in the whole specimen, the apparent bending stiffness can be calculated from Equation (3).

$$EI_{app} = \frac{F_{cyl}}{24\, w_2}\,(3\, a\, l^2 - 4\, a^3) \tag{3}$$

Since the total deformation in the middle of the specimen compounds of bending and shear deformations, the shear stiffness GA_v can be calculated as follows.

$$w_2 = w_2(M) + w_2(V) \tag{4}$$

$$w_2 = \frac{F_{cyl}}{24\, EI_{eff}}(3\, a\, l^2 - 4\, a^3) + \frac{F_{cyl}\, a}{GA_v} \tag{5}$$

$$GA_v = \frac{F_{cyl}\, a}{w_2 - \frac{F_{cyl}}{24\, EI_{eff}}(3\, a\, l^2 - 4\, a^3)} \tag{6}$$

with:
- EI_{eff} Bending stiffness
- GA_v Shear stiffness
- EI_{app} Apparent bending stiffness, assuming $GA_v \to \infty$
- F_{cyl} Force applied per cylinder (10 kN)
- a Distance between support and load introduction (see Figure 6)
- l_w Distance between third point deformation measurements (see Figure 6)
- l Distance between supports (see Figure 6)
- w_i Deformation (see Figure 6)

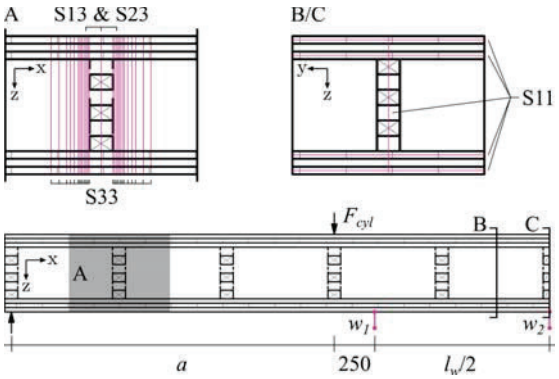

Figure 6: *Evaluation positions of the shear stress (S13, S23), stress perpendicular to grain (S33) and stress parallel to grain (S11) as well as the deformations w_i.*

The bending tension and compression stresses (S11) parallel to grain were evaluated in the pure bending region in the cross sections B and C illustrated in Figure 6. They were evaluated in the centre of each longitudinal layer of the plates and along a vertical section in the middle of the model. The shear (S13) and rolling shear (S23) stresses were evaluated along three vertical lines in the middle and 10 mm to the left and right of the notch next to the support as illustrated in Figure 6. The stresses perpendicular to grain (S33) were evaluated at the same notch, but along 12 vertical lines left and right of the notch. Since the self weight is neglected in the parameter study, the shear force between support and load introduction is constant. Hence, the shear stresses and the stresses perpendicular to grain were not measured at the support to avoid the local influence of the supporting steel plate. For the specimens with a GLT web, the vertical evaluation lines were placed in the centre of the web. To capture the stress perpendicular to grain in the specimens with a CLT web, the vertical evaluation lines in these models were placed in the layer with horizontal grain direction 1 mm from the edge of the web.

The evaluated maximum stresses were compared to the corresponding strength to estimate the load bearing capacity. Preliminary investigations showed that the peak stress positions of the different stress directions do not coincide. Thus, the load bearing capacity of each linear elastic model was estimated after Equation (7) and no stress interactions were considered.

$$F_R = \min\left\{F_{cyl} \cdot \frac{f_i}{\sigma_i}\right\} \tag{7}$$

with:
- F_R Load bearing capacity
- F_{cyl} Applied cylinder force
- f_i Strength in direction *i*
- σ_i Maximum stress occurring in direction *i*

To estimate the load bearing capacity, the average strength values for GL24h listed in Table 4 were used. The compression strength perpendicular to grain was neglected since the tension strength perpendicular to grain is decisive in every case due to symmetry. The tensile strength perpendicular to grain was chosen after the glulam specimens tested by [11] for a small reference volume of 0.75 to 1.5 dm^3.

Table 4: *Mean strength values for GL24h used to estimate the load bearing capacity.*

Name		Value (MPa)	Source
S11	$f_{t,0,m}$	27	[12]
	$f_{c,0,m}$	40	[12]
S13	$f_{v,m}$	4.1	[13]
S23	$f_{r,m}$	1.88	[14]
S33	$f_{t,90,m}$	1.5	after [11]

2.4 EVALUATION METHODS

The stress and strain output database of the verification FE-models was analysed manually in Abaqus' 3D viewer and compared to the automatically produced result data vectors to ensure the quality of the automated data output.

https://doi.org/10.52202/069179-0342

Due to the number of models used in the parameter study, only the automated data output was used for its analysis. The Kendall rank correlation coefficient [15] was used to get an overview of the relations between the different geometry parameters and the structural properties. Furthermore, box- and scatter plots were used to validate the correlation numbers visually and to get a quantitative overview of the results. The boxplots show a box between the 25th and the 75th percentile. All values lying outside the boundaries of 1.5 times the interquartile range are marked as outliers. The median is marked by the centre line and the notches indicate the 5% significance range of the median after [16].

3 RESULTS AND DISCUSSION

3.1 VERIFICATION

Figure 7 shows the force displacement diagrams from the experiments and from the corresponding linear elastic FE models. A longitudinal section and the short name in each diagram indicate the corresponding specimen type. The first two failures estimated by the FE model are indicated in the diagrams with circles.

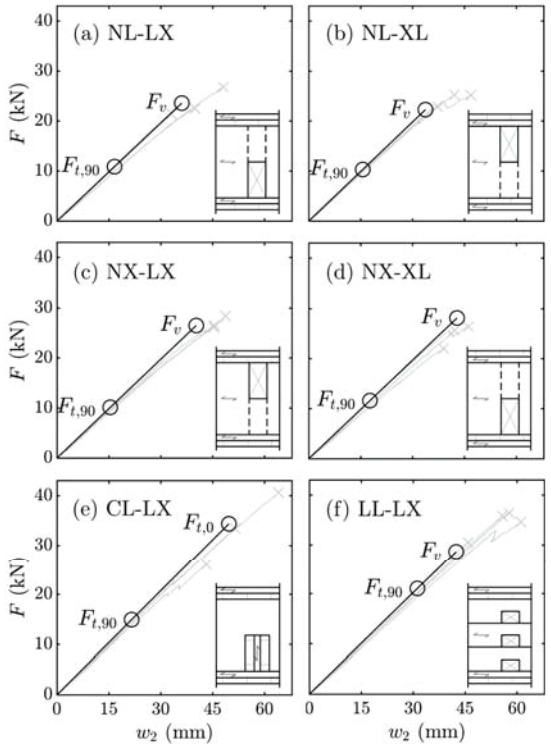

Figure 7: *Force displacement diagrams of the verification models. Results from the FE analysis (black) and the experimental analysis (grey). The circles indicate the first two failures estimated by the FE model.*

Only a negligibly small difference between the grey lines and the black line can be seen between 10% and 40% of the estimated failure load. This indicates that the model predicts the stiffness well in the region of interest. Towards the end of the curve, the grey lines show larger deflections than the black line. This softening is probably caused by the cracks propagating from the notch's corners along the web, which is not reproduced by the linear elastic FE-models. Since the softening occurs in a late state of the experiment, it is not relevant for the derivation of the stiffness parameters and the chosen method is assumed to be suitable. The estimation of the failure load is less straight forward. As observed in the experimental campaign, the first failure occurs in tension perpendicular to grain ($F_{t,90}$) for all specimen types. The magnitude of the first failure load also corresponds well with the observations made during the experiments. It was observed that the cracks formed at the notches corners and expanded until a shear failure occurred. The shear failure (F_v) is also predicted as a second failure by the FE model for the types NL, NX and LL. Although the cross section reduction by crack propagation is not taken into account by the FE model, the magnitude of the shear failure load for these types fits the observed failure load well. The second failure load of the CL type is predicted to be in tension parallel to grain ($F_{t,0}$) in the bending region. No bending failure was observed in the experimental campaign, however, a shear and rolling shear failure in the glue line was observed after the crack propagation. Nevertheless, the first failure type is predicted well for all specimen types. Thus, the first failure type is chosen for further comparisons of the shear resistance. Although this failure does not necessarily correspond to a global failure of the specimen, it still allows for a relative comparison of the models analysed in the parameter study.

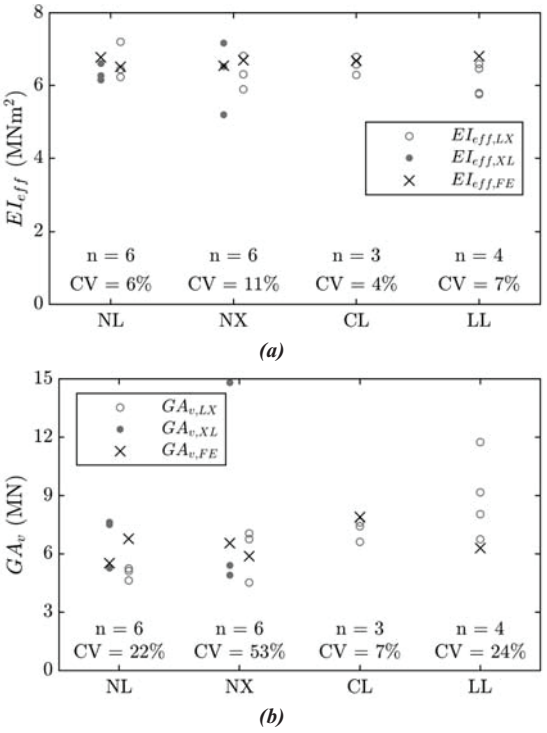

Figure 8: *Bending stiffness* ***(a)*** *and shear stiffness* ***(b)*** *of the different element types, derived from the experimental campaign and the FE-models.*

Figure 8 compares the experimentally determined and numerically predicted bending (EI_{eff}) and shear stiffness

(GA_v). The experimentally determined shear stiffness shows a large scattering for the element type LL. This can partly be explained by the fact, that for two of the LL specimens, only one of two LVDTs measuring w_1 was used due to a malfunction of the other one. The outlier shear stiffness measurement of the specimen type NL showed a large longitudinal crack in the web in the pure bending region already before the test. It is assumed that the specimen cracked due to swelling and shrinking and that the larger deformations in the pure bending region lead to an underestimation of the bending stiffness and an overestimation of the shear stiffness. Given the small number of experiments and the scattering of the results, it still can be stated that the FE-model predicts both stiffnesses accurately for all specimen types. Thus, the chosen material parameters, the element type and the mesh size are assumed to be suitable.

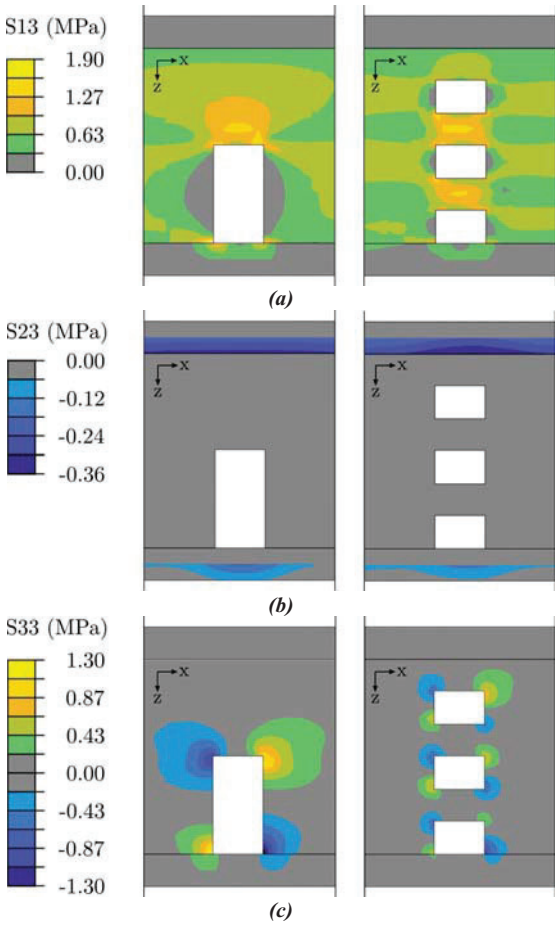

Figure 9: *Stresses acting near the first notch after the support of the specimens NL-LX (left) and LL-LX (right). Acting on the sections: shear load V = 10 kN, bending moment M = 6.3 kNm.* ***(a)*** *shear stress (S13 =* $\boldsymbol{\sigma_v}$*),* ***(b)*** *rolling shear stress (S23 =* $\boldsymbol{\sigma_r}$*),* ***(c)*** *stress perpendicular to the grain (S33 =* $\boldsymbol{\sigma_{t/c,90}}$*).*

Figure 9 illustrates the shear and rolling shear stress as well as the stress perpendicular to grain in the NL-LX and the LL-LX models at the notch next to the support (section A as illustrated in Figure 6). Figure 9 (a) and (b) show, that the largest shear and rolling shear stresses occur in the centre line of the notches. The magnitude and the volume subjected to large shear stresses is similar for both the NL and the LL model. Figure 9 (c) shows, that the NL specimen experiences a higher peak in stresses perpendicular to grain than the LL specimen. Additionally, the timber volume subjected to stresses perpendicular to grain is larger for the NL specimen. Figure 10 illustrates the bending stress of the NL-LX and the LL-LX models at the symmetry plane. It shows, that the tension stress parallel to grain is largest near the web and a stress peak forms under the notch. This peak is higher for the NL model than for the LL model. Nevertheless, the full width of the flange is activated in tension and compression in both models.

It can be concluded that the chosen positions for the evaluation of the stresses as illustrated in Figure 6 cover the maximum stress peaks for all stress directions. This can also be shown for the other reference specimens NX and CL.

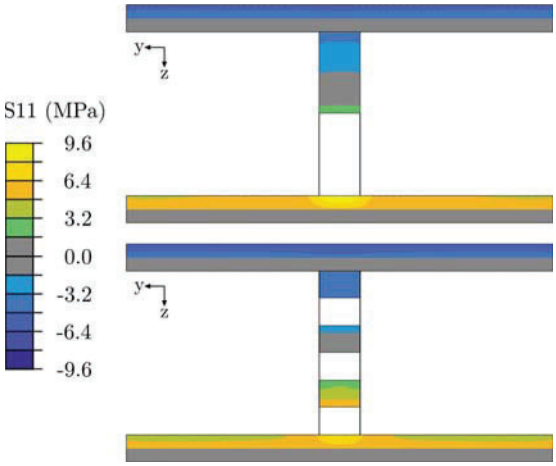

Figure 10: *Bending stress (S11 =* $\boldsymbol{\sigma_{t/c,0}}$*, resp.* $\boldsymbol{\sigma_m}$*) at the symmetry plane of the specimens NL-LX (top) and LL-LX (bottom). Acting on the sections: bending moment M = 18.75 kNm.*

3.2 PARAMETER STUDY

The Kendall rank correlation coefficient for the different geometry parameters and the different structural properties of the elements is shown in Figure 11. This coefficient can only be used to get a first overview of the results, since the coefficient was calculated over the whole dataset and some geometry combinations were excluded from the analysis from the beginning (see Section 2.2). The presented results were normalised for one meter width.

The absolute value of all correlations over the whole dataset is smaller than 0.6, which can be explained by the fact, that all structural parameters are influenced by multiple geometry parameters. Nevertheless, the figure shows, which geometrical parameters can be tackled to manipulate the different structural parameters efficiently. As expected, the bending resistance and the bending stiffness show the largest positive correlation with the height of the web and the thickness of the CLT plates

https://doi.org/10.52202/069179-0342

defined by the number (n_l) and thickness (t_l) of the single CLT layers. They also show a small negative correlation with the grain direction, which can be explained by the modelling of three-layered plates, which are stronger in one direction. Both parameters show little to no correlation with the web width and the web spacing. Since the bending resistance and the bending stiffness can easily be manipulated with the geometry parameters mentioned and since they are not decisive for the success of the hollow slab system, they are not discussed further.

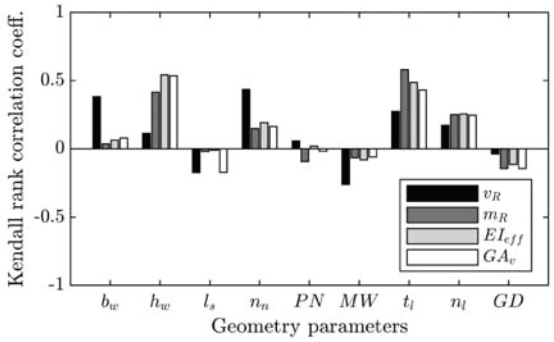

Figure 11: *Kendall rank correlation coefficient for the geometry parameters explained in Table 2 (positive correlation with respect to the values listed in Table 2 from left to right) and the structural parameters* $\boldsymbol{v_R}$ *(shear resistance),* $\boldsymbol{m_R}$ *(bending resistance),* $\boldsymbol{EI_{eff}}$ *(bending stiffness) and* $\boldsymbol{GA_v}$ *(shear stiffness). All structural parameters are evaluated per meter width.*

The shear stiffness also shows the largest positive correlation with the hight of the web and the thickness of the CLT plates, which have a direct influence on the cross-sectional area. It is assumed that the web width shows only a small positive correlation with the shear stiffness due to the exclusion of the mentioned parameter combination of a web width of 180 mm and a web spacing of 375 mm. The web spacing and the shear stiffness show a small negative correlation, which implies that a smaller web spacing is beneficial for the shear stiffness. Since the shear stiffness has only a minor impact on the global deformations of the hollow timber slab, it is not discussed further.

The position of the notch shows little to no correlation with any of the structural parameters. The negligible influence of the position of the notch can also be shown with more detailed scatter- and box plots and the findings coincide with the experimental investigations. The grain direction shows no correlation with the shear resistance and it shows only a small negative correlation with the other structural parameters. Therefore, these parameters are not discussed further.

The shear resistance is mainly influenced by the web width and the number of notches. The width of the web shows a positive correlation with the shear resistance. Thus, the positive effect of a wider web seems to dominate the assumed negative influence of a wider notch (see also Figure 12). The hight of the web does not correlate with the shear resistance, which is an indicator that the shear resistance is dominated by a failure in tension perpendicular to grain. A closer examination shows, that all 1024 models first fail in tension perpendicular to grain. The web spacing and the shear resistance show a small negative correlation, which implies that a smaller web spacing is beneficial for the shear resistance. It is assumed that this correlation would even be larger, if the combination with a web width of 180 mm and a web spacing of 375 mm would not have been excluded from the analysis. As assumed, the number of notches correlates positively with the shear resistance (see Figure 12). The thickness and number of the CLT plate layers also show a positive, but smaller correlation with the shear resistance. Since the plate thickness should stay as small as possible to save as much timber as possible, these parameters are not predestined to enlarge the elements shear resistance. The influence of web width, web spacing, number of notches and thickness of CLT plate layers on the shear resistance is illustrated in Figure 12. The figure confirms the previously stated assumptions and findings.

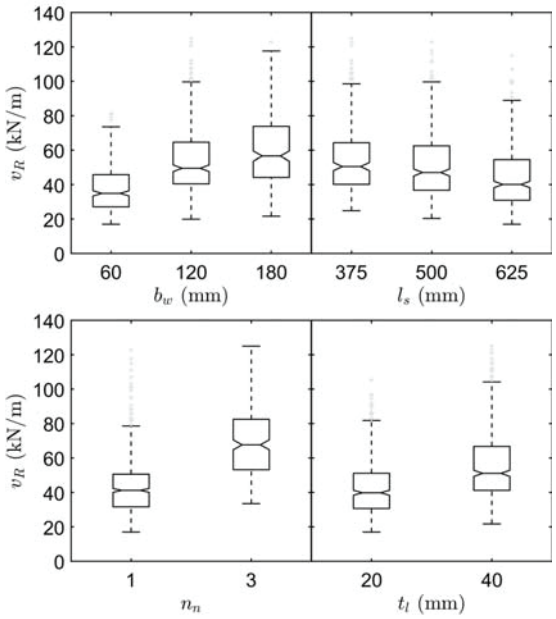

Figure 12: *Boxplots that show the relationship between the shear resistance and the web width (*$\boldsymbol{b_w}$*), the web spacing (*$\boldsymbol{l_s}$*), the number of notches (*$\boldsymbol{n_n}$*) and the thickness of the CLT plate layers (*$\boldsymbol{t_l}$*) for all models analysed within the parameter study.*

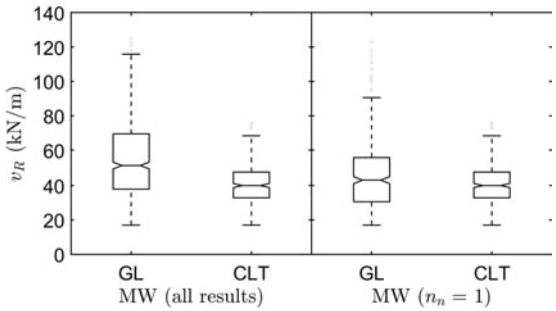

Figure 13: *Boxplots that illustrate the influence of the different web materials (MW) on the shear resistance. Two datasets are illustrated: all results (left) and only specimens with one notch (right).*

https://doi.org/10.52202/069179-0342

The material of the web shows a negative correlation with the shear resistance, which implies that using CLT to build the web does not bring benefits. As illustrated in Figure 13, the effect of a CLT web disappears in the statistical evaluation due to other, more important geometry parameters. The height of the notch dominates the influence on the shear resistance and the negative correlation partially originates from the fact, that the combinations with CLT web and three notches were excluded from the analysis. Figure 13 illustrates the relationship between the shear resistance and the material of the web for two different sets of results. If all results are considered, a negative correlation and a significantly smaller median follows for the CLT web specimens. If only the results for specimens with one notch ($n_n = 1$) are plotted, no significant difference between the medians can be found. Additionally, a smaller scattering of the CLT web specimens can be observed. This may arise from the measuring method of the stresses perpendicular to grain. It is possible that the stress measured only 1 mm from the edge of the CLT web captured a numerical stress peak and thus leads to more conservative shear resistance estimations. But even if the CLT web specimens showed a slightly higher shear resistance, they should not be preferred over the glulam option with one notch, since the stress concentration between web and plate will be the same for both options. The reinforcing vertical middle CLT layer can only be activated in the centre of the web, not at the boundary between plate and web.

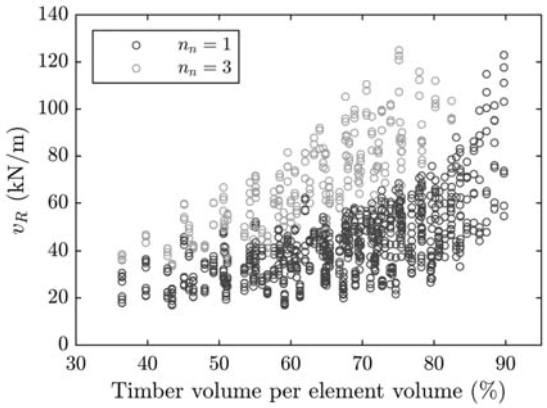

Figure 14: *Shear resistance of all geometry combinations plotted over their average timber volume per element volume. The number of notches ($\boldsymbol{n_n}$) of the individual specimens is illustrated by the marker's brightness.*

The correlations indicate that the shear resistance of the biaxial hollow slab elements is most efficiently maximised by using multiple notches, a wider web and a smaller web spacing. Figure 14 shows a plot of the shear resistance of each geometry combination over its average timber volume per element volume. The two groups of elements with only one notch and elements with three notches represented in black and grey can easily be distinguished. It can be seen, that the elements with three notches have a larger shear resistance overall. The plot clearly illustrates that multiple notches outrival the single notched web specimens in terms of shear resistance over the whole range of geometry combinations. It also shows that the largest shear resistances are achieved by using 70% of timber per element volume or more. As described in Section 1, the timber volume of the hollow elements should be as small as possible, and it should not exceed 70% of the total volume of the element. Thus, a geometry with multiple notches should be chosen in favour of an option with only one notch to build a biaxial hollow slab system.

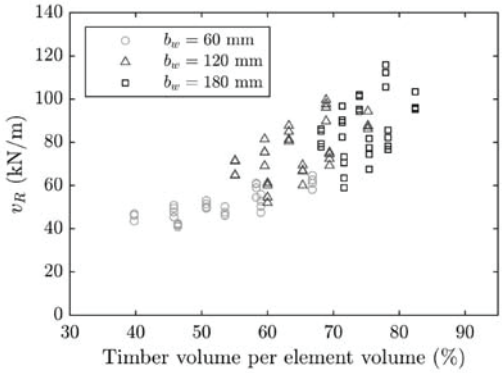

Figure 15: *Shear resistance of the specimens with three notches ($\boldsymbol{n_n = 3}$) and a web spacing ($\boldsymbol{l_s}$) of 500 mm. The web width ($\boldsymbol{b_w}$) of the individual specimens is illustrated by the markers shape and brightness.*

Enlarging the web width also leads to higher shear resistances, as illustrated in Figure 15 for specimens with three notches ($n_n = 3$) and a web spacing (l_s) of 500 mm. The overall smallest shear resistance is achieved with a web width of 60 mm, whereas the overall largest shear resistance is achieved with a web width of 180 mm. The figure also illustrates that less timber can be saved with wider webs. Since the timber volume of the hollow elements should be as small as possible, the results suggest, that web widths larger than 120 mm are not efficient.

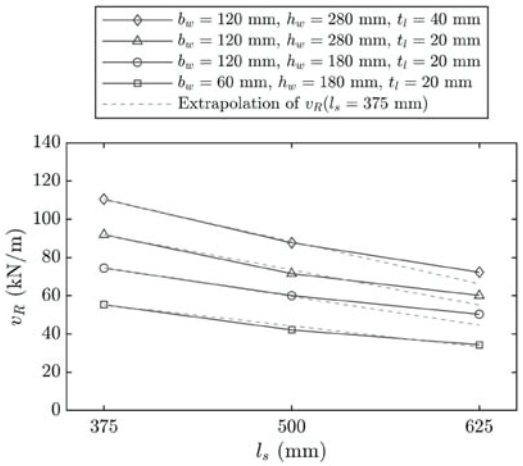

Figure 16: *Shear resistance over web spacing for four example geometry combinations with the common parameters $\boldsymbol{n_n = 3}$, $\boldsymbol{n_l = 2}$, $\boldsymbol{PN = bottom}$, $\boldsymbol{GD = 0°}$, $\boldsymbol{MW = GLT}$ and the varied parameters listed in the legend. The dashed line shows the shear resistance estimated by linear extrapolation of the shear resistance per web with $\boldsymbol{l_s = 375}$ mm.*

https://doi.org/10.52202/069179-0342

Figure 16 illustrates, how the web spacing influences the shear resistance on four different geometry combinations on which only the web spacing was varied. The shear resistance varies linearly with the web spacing. The dashed line in the graph was calculated with the shear resistance per web of the specimens with $l_s = 375$ mm. This shear resistance was linearly extrapolated to get the shear resistance per meter width for web spacings of 375 mm, 500 mm, and 625 mm. The results only marginally deviate from the dashed lines. Thus, it is assumed that the shear resistance varies directly proportional with the web spacing for values within the analysed boundaries and no mentionable stress interactions resulting from smaller web spacings occur.

4 CONCLUSIONS AND OUTLOOK

As expected, the bending resistance and the bending stiffness of the hollow elements can easily be enlarged by enlarging the thickness of the CLT plates and the total thickness of the elements. The same parameters have a positive influence on the shear stiffness too, which is however, less important than the bending stiffness for the serviceability limit state design. Multiple notches, a wider web and a closer web spacing have a positive influence on the shear resistance of the elements. The shear resistance of elements with multiple notches is significantly larger than the one of elements with one single notch over the whole set of geometry combinations. The number of notches proves to be the parameter with the largest influence on the shear resistance of the elements. Web widths larger than 120 mm lead to larger shear resistances, but also consume more timber and are consequently not to be used. The shear resistance per meter width of the element is directly proportional to the web spacing. In opposition to the initial assumption, no positive influence of a CLT web was found.

The different geometry combinations have been compared to each other and the relative best solutions and methods to optimise the mechanical properties were found. To find the absolute best solution for different point supported slab layouts, further studies are needed. Only by comparing different slab layouts, the total timber saving and the impact of the production cost on the total slab cost can be estimated. Hence, different examples of point supported slab arrangements should be analysed. Furthermore, a suitable analytical calculation method is of great importance to allow for an easy and efficient design process. Different analytical models for the calculation of bending and shear resistance and stiffness will be analysed and compared to the data achieved with the FE parameter study.

ACKNOWLEDGEMENT

The presented research project is funded by Innosuisse and supported by the project partners Timber Structures 3.0 AG, Schilliger Holz AG and Henkel & Cie AG. The research project is a collaboration between the ETH Zurich and the Bern University of Applied Sciences.

REFERENCES

[1] S. Zöllig, M. Muster, and A. Themessl, “Butt-Joint Bonding of Timber as a Key Technology for Point-Supported, Biaxial Load Bearing Flat Slabs Made of Cross-Laminated Timber,” *IOP Conf. Ser. Earth Environ. Sci.*, vol. 323, p. 012144, 2019.

[2] Timber Structures 3.0 AG, “References,” 2022. [Online]. https://www.ts3.biz/en/referenzprojekte/. [Accessed: 21-Feb-2023].

[3] S. Franke, B. Franke, and F. J. Niederwolfsgruber, “Bi-Axial Load Transfering Timber Grid-Box Elements for Floor Systems,” in *Proceedings of the 2021 World Conference on Timber Engineering (WCTE)*, 2021.

[4] R. Jockwer, R. Steiger, and A. Frangi, “State-of-the-Art Review of Approaches for the Design of Timber Beams with Notches,” *J. Struct. Eng.*, vol. 140, no. 3, p. 04013068, 2014.

[5] D. Bissig and A. Frangi, “Variantenstudium zur Entwicklung einer zweiachsig tragenden Hohlkastendecke aus Holz,” in *9. Doktorandenkolloquium „Holzbau Forschung + Praxis“ (DoKo 2022), Stuttgart*, 2022, pp. 89–96.

[6] Dassault Systèmes, “Abaqus 2019.” 78946 Vélizy-Villacoublay Cedex (FR), 2019.

[7] MathWorks, “Matlab R2021b.” Natick, Massachusetts 01760-2098 (US), 2021.

[8] J. Bodig and B. Jayne, *Mechanics of wood and wood composites*. Florida: Krieger Publishing Company, 1993.

[9] CEN, “SN EN 14080:2013 Holzbauwerke – Brettschichtholz und Balkenschichtholz – Anforderungen,” vol. 2. Schweizer Ingenieur- und Architektenverein, 2013.

[10] H. Neuhaus, “Elastizitätszahlen von Fichtenholz in Abhängigkeit von der Holzfeuchtigkeit,” Bochum, 1981.

[11] H. J. Blaß and M. Schmid, “Ermittlung der Querzugfestigkeit von Voll- und Brettschichtholz,” Karlsruhe, 1998.

[12] M. Frese, “Computergestützte Verfahren zur pragmatischen Beurteilung der Tragwiderstände von Brettschichtholz: Zusammenfassung exemplarischer Simulationsstudien,” Karlsruher Institut für Technologie, 2016.

[13] G. Schickhofer, “Determination of shear strength values for GLT using visual and machine graded spruce laminations,” in *CIB-W18 Meeting 34*, 2001, no. 34-12–6.

[14] T. Ehrhart, R. Brandner, G. Schickhofer, and A. Frangi, “Rolling Shear Properties of some European Timber Species with Focus on Cross Laminated Timber (CLT): Test Configuration and Parameter Study,” in *INTER Meeting 48*, 2015, no. 48-6–1.

[15] M. G. Kendall, *Rank correlation methods*, 4th ed. London: Griffin, 1970.

[16] R. McGill, J. W. Tukey, and W. A. Larsen, “Variations of box plots,” *Am. Stat.*, vol. 32, no. 1, pp. 12–16, 1978.

World Conference on Timber Engineering Oslo 2023

EFFICIENT FINITE ELEMENT MODELS FOR ADHESIVE-FREE MULTI-LAYERED TIMBER STRUCTURES

J. Paroissien[1,2], T.A. Bui[3], M. Oudjene[1], P. Lardeur[2]

ABSTRACT: This paper presents finite element models to assess the vibration performance of multi-layered timber structures assembled through compressed wood dowels. Starting from a solid model which is considered as a reference, a new methodology using a solid-beam approach for the dowels and a solid-shell approach for the layers is described. Kinematic assumptions are applied throughout the cross-section of the dowels and the thickness of layers, leading to a significant reduction of the number of variables. The models are assessed for the calculation of frequencies and mode shapes of multi-layered timber beams and timber panels. The efficiency of this approach, in terms of quality of results and model size, is highlighted.

KEYWORDS: timber construction, wood dowels, finite element, solid-shell, solid-beam.

1 INTRODUCTION

The construction sector faces an increasing need for more sustainable materials. This is brought together by institutions that impose increasingly stringent standards and consumers who transform the market through their more ecological demands.

Adhesive-free multi-layered timber structures aim to replace glue-laminated timber structures as an eco-friendly alternative by improving their durability and recyclability. Indeed, at high temperatures, glue emits toxic gases, especially formaldehyde which is carcinogenic to humans [1].

A concern for timber construction is the vibration serviceability of timber floors, glued or not. Human activity and children jumping in a residential or commercial building induce annoying vibrations in timber floors since they are lightweight structural elements.

Bui et al. [2,3] performed an experimental and numerical investigation on the vibration performance of Adhesive-Free Laminated Beams (AFLB) (Figure 1) and Adhesive-Free Cross-Laminated Timber (AFCLT) panels (Figure 2) assembled through compressed wood dowels.

Namely, this study highlighted a high variability level of frequencies. A finite element model made of solid elements was proposed for the layers and the dowels. Bui et al. [4] developed the Modal Stability Procedure (MSP) for the evaluation of the variability of frequencies, using this solid finite element model. This model is satisfactory in terms of quality of results but is time-consuming, particularly in the context of variability assessment or optimization where a large number of analyses may be necessary.

Figure 1: *Manufactured Adhesive-Free Laminated Beam (AFLB) [5]*

Figure 2: *Manufactured Adhesive-Free Cross-Laminated Timber (AFCLT) panels [5]*

[1] Université Laval, Département de Génie Civil et de Génie des Eaux, Faculté des Sciences et de Génie, Québec, Canada, marc.oudjene@gci.ulaval.ca

[2] Université de Technologie de Compiègne, Laboratoire Roberval, Compiègne, France, pascal.lardeur@utc.fr

[3] Kumoh National Institute of Technology, Gyeongbuk, South Korea, tuan-anh.bui@kumoh.ac.kr

https://doi.org/10.52202/069179-0343

Models using classical beam elements for the dowels and classical shell elements for the layers were tested by Bui [5]. These models lead to several difficulties, namely due to the complex deformation of dowels and the specific geometry representation, and are finally unsatisfactory.
Solid-shell and solid-beam approaches were developed by Wei et al. [6,7]. These approaches have the advantages to use solid elements and to reduce the number of degrees of freedom in a model by applying beam or shell theories.
These approaches are applicable to AFLB and AFCLT panels to reduce the model while keeping the solid geometry of the structure. However, adapting the solid-shell and solid-beam approaches to industrial structures is a novelty.
In this paper, we first recall the main experimental results obtained for AFLB and AFCLT panels. Then we present the reference finite element model of multi-layered timber beams and timber panels for modal analysis in free-free conditions. To reduce computational time using these reference models, reduced models using solid-beam and solid-shell approaches are also presented. Finally, a method to calculate variability is described.

2 SUMMARY OF EXPERIMENTAL DATA

In Bui et al. study [2], two wood species were considered for the layers: spruce and oak. The experimental campaign and the results were obtained in free-free conditions to minimize boundary conditions effects, with the hammer impact technique. The experimental set-up for the assessment of vibration behavior of AFLB and AFCLT panels is shown in Figure 3.

(a)

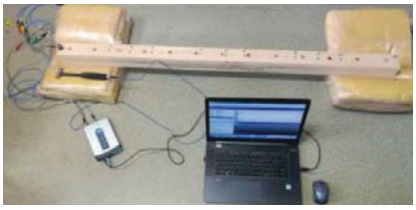

(b)

Figure 3: *Experimental set-up for (a) AFLB, (b) AFCLT panels [5]*

For the beams, 11 measurement points are chosen along the longitudinal axis, and for the panels 15 measurement points are distributed over the whole surface.
In this paper, we consider AFLB and AFCLT panels composed of oak for the layers and compressed spruce for the dowels. The moisture content during the experiments was 9 %.
The first three bending modes for both types of structures are presented.
The AFLB pictured in Figures 1 and 3a is composed of three oak layers and 27 compressed spruce dowels. The beam has a length of 1450 mm for a width of 70 mm and a height of 67.5 mm.
The results for the experimental mean natural frequencies, damping ratios and their respective coefficients of variation are summarized in Table 1 for five AFLBs and Table 2 for five AFCLT panels.

Table 1: *Experimental natural frequencies and damping ratios [2] for five AFLBs*

		Mean value	CoV (%)
f1	frequency (Hz)	118.2	6.0
	damping (%)	4.3	9.0
f2	frequency (Hz)	281.0	5.3
	damping (%)	2.1	4.6
f3	frequency (Hz)	471.1	4.2
	damping (%)	1.9	13.7

The vibrational serviceability performance of AFLB was demonstrated by comparison to their glued counterparts by Bui et al. [5]. It was proved that while the difference between frequencies increase slightly with higher modes, the damping ratio is much higher for AFLB.
The AFCLT panels pictured in Figures 2 and 3b are composed of three oak layers, 28 boards and 196 compressed spruce dowels in total. Each external layer contains 7 boards, while the interior one contains 14 boards in the perpendicular direction. These panels have a length of 2100 mm for a width of 1050 mm and a height of 75 mm.

Table 2: *Experimental natural frequencies and damping ratios [2] for five AFCLT panels*

		Mean	CoV (%)
f_2	frequency (Hz)	54.5	2.5
	damping (%)	0.72	10.8
f_3	frequency (Hz)	56.3	8.5
	damping (%)	0.87	13.7
f_7	frequency (Hz)	110.3	3.0
	damping (%)	0.97	6.9

The vibrational characteristics for the assembled beams and panels show high variability levels as stated before. This highlights the need for a complete variability assessment of the structures.

3 REFERENCE FINITE ELEMENT MODEL

3.1 FINITE ELEMENT MODEL

The models for both AFLB and AFCLT panel using the Verification and Validation methods [8] are presented.
Finite element models are created using the software Abaqus/Standard©, and the twenty-node hexahedral solid element with reduced integration (C3D20R of Abaqus [9]) is exploited. After testing several solid elements, this choice has been made as it is the most efficient for convergence of frequencies and leads to a minimization of model size for these timber structures.
As finite element models must be as close as possible to the physical reality, assumptions based on experimental observations [2] related to the connection between the different parts, are made. On the one hand, in the following models, there are no interactions between the boards or the layers with each other. On the other hand, as the dowels are densified and tend to expand to keep their shape memory, contact without sliding is considered. Because meshes of layers and dowels are not coincident at their interfaces, the interaction between dowels and layers must be modelled. To stick the surfaces of the dowels and holes of the boards, the *Tie* option in Abaqus is chosen.
Finally, the mechanical properties of the oak boards, are a mix of experimental results from [2] for the density and the longitudinal modulus. For all the other elastic properties, empirical relations from Jodin's book [10] are used. For the compressed wood that constitutes the dowels, the properties were identified using a quasi-inverse problem by Bouhala et al. [11].

3.2 VERIFICATION STEP

The Verification process is completed when the convergence of frequencies to the accurate solution is achieved. For the Verification stage, a highly accurate solution is obtained with a very fine model as no analytical solution exists.
For the AFLB the results of the convergence study given in Figure 4 lead to an optimal mesh with about 13 000 elements and 220 000 degrees of freedom.
This model is described in Figure 5. It is important to note that in the dowels the mesh is refined near the interfaces between layers as shear stress gradients are high in these areas.
The same method is applied to the AFCLT panel. In particular, the same refinement technique is applied to the dowels. The convergence study illustrated in Figure 6 leads to an optimal mesh with about 86 000 elements and 1 500 000 degrees of freedom. This mesh is shown in Figure 7.

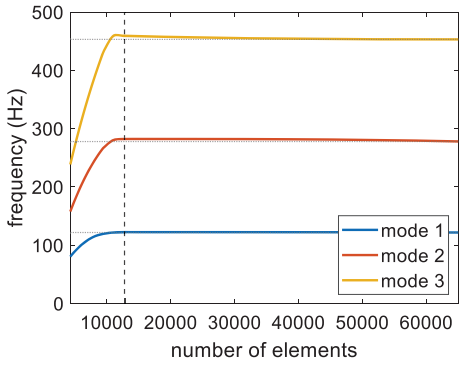

Figure 4: *Convergence study for AFLB*

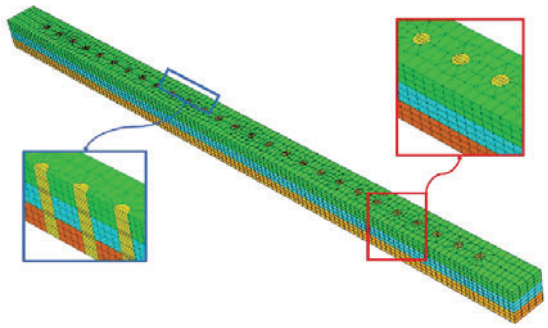

Figure 5: *AFLB finite element model*

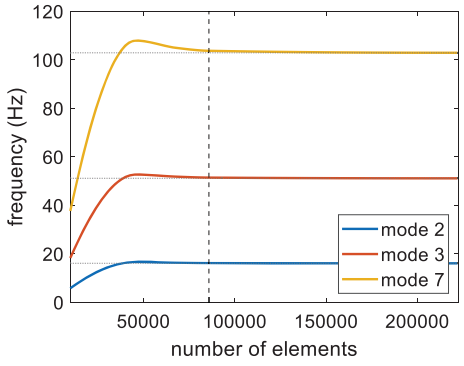

Figure 6: *Convergence study for AFCLT panel*

Table 3: *Elastic mechanical properties for dowels and layers*

	E_1 (MPa)	E_2 (MPa)	E_3 (MPa)	G_{12} (MPa)	G_{13} (MPa)	G_{23} (MPa)	ν_{12}	ν_{13}	ν_{23}
Oak [2,10]	11 380	1 045	1 871	977	1 275	361	0.4	0.32	0.43
Compressed spruce [11]	26 000	1 033	1 082	800	800	100	0.41	0.41	0.37

https://doi.org/10.52202/069179-0343

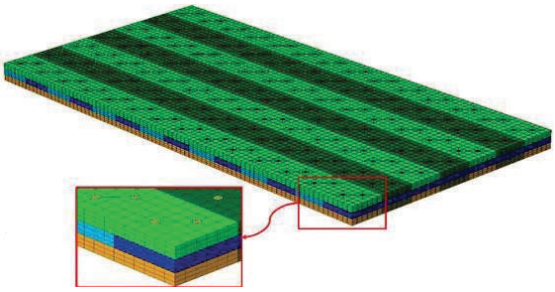

Figure 7: *AFCLT panel finite element model*

3.3 VALIDATION STEP

The Validation stage deals with the comparison between the numerical results obtained with the verified finite element model (from the previous Verification step) and the experimental results. As stated in section 2, we consider three frequencies that correspond to the first three bending modes illustrated in Figure 8 for the beam and Figure 9 for the panel.

Here, the Validation concerns only the mean behaviour of the structures, so numerical frequencies are compared to the mean experimental frequencies. Results are shown in Table 4 for AFLB and Table 5 for AFCLT panel.

Table 4: *Frequencies comparison between mean experimental data [2] and finite element model for AFLB*

	Mean experimental frequencies	Numerical frequencies	Diff.
f_1	118.2 Hz	119.1 Hz	0.7 %
f_2	281.0 Hz	278.2 Hz	-1.0 %
f_3	471.1 Hz	459.6 Hz	-2.4 %

Table 5: *Frequencies comparison between mean experimental data [2] and finite element model for AFCLT panel*

	Mean experimental frequencies	Numerical frequencies	Diff.
f_2	54.5 Hz	54.3 Hz	-0.3 %
f_3	56.3 Hz	55.9 Hz	-0.7 %
f_7	110.3 Hz	108.6 Hz	-1.6 %

Numerical and mean experimental results are in good agreement both for AFLB and AFCLT panel.

The small errors between numerical and experimental frequencies demonstrate that the adopted interaction assumptions are relevant despite that they may be questionable with regard to the complex physics involved in the connections.

This finite element modelling may lead to large-size models. In order to reduce the model size, a new methodology based on specific solid-beam and solid-shell approaches was developed.

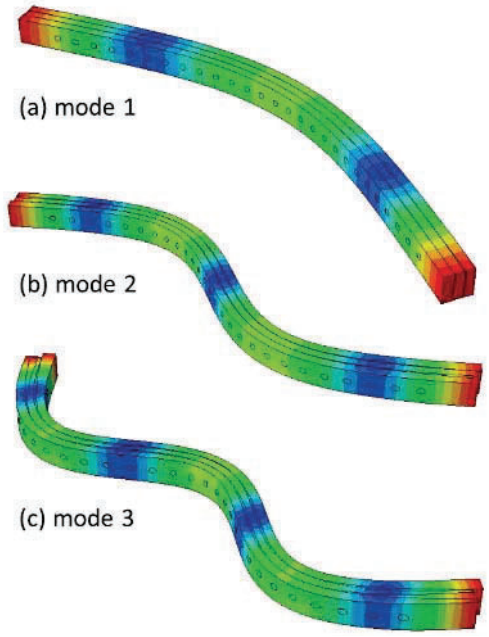

Figure 8: *Mode shapes for AFLB finite element model*

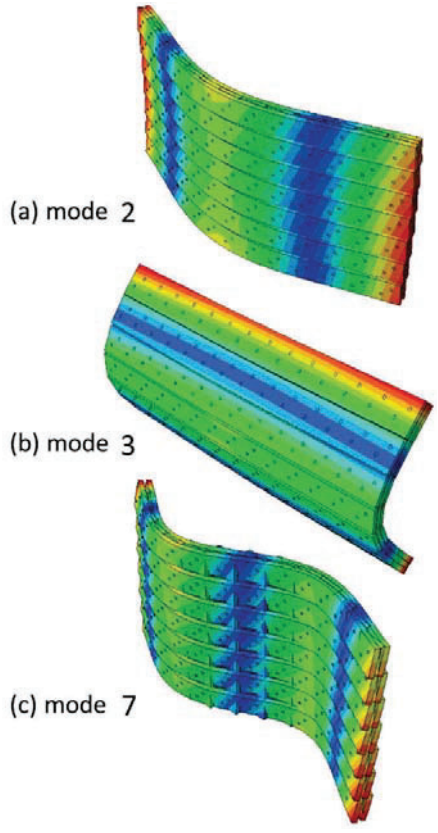

Figure 9: *Mode shapes for AFCLT panel finite element model*

4 SOLID-BEAM AND SOLID-SHELL BASED MODELS

4.1 PRINCIPLE OF SOLID-SHELL AND SOLID-BEAM APPROACHES

The solid-beam and solid-shell approaches used to build a reduced model exploit a methodology that was initially developed by Wei et al. [6,7].

The structure is first modelled with solid finite elements, for layers as well as dowels. Shell theory is considered for the layers and beam theory for the dowels. Then for layers, through-the-thickness shell equations are applied directly to the solid model. In the same way, through-the-section beam equations are applied for dowels. The concept of master and slave nodes is used, only master nodes are kept in the final model and slave nodes are eliminated. This process modifies the system of algebraic equations and leads to a reduction of the model size compared to the initial solid model.

First-order, as well as higher-order theories, can be considered. In this paper, we only use modified first-order theories.

A MATLAB© code produces the set of linear equations. In the Abaqus input file, these equations are introduced using the keyword 'EQUATION' [9].

4.2 DISTRIBUTIONS AND NODE LOCATIONS FOR SOLID-SHELL APPROACH

For the layers, the displacement field in Equation (1) was exploited by Wei et al. [7], using the Reissner-Mindlin theory [12,13], modified to correctly consider the Poisson effect through the thickness. The displacement field is linear through the thickness for *u* and *v* and quadratic for *w*.

$$\begin{cases} u(z) = za_1 + a_2 \\ v(z) = zb_1 + b_2 \\ w(z) = z^2c_1 + zc_2 + c_3 \end{cases} \quad (1)$$

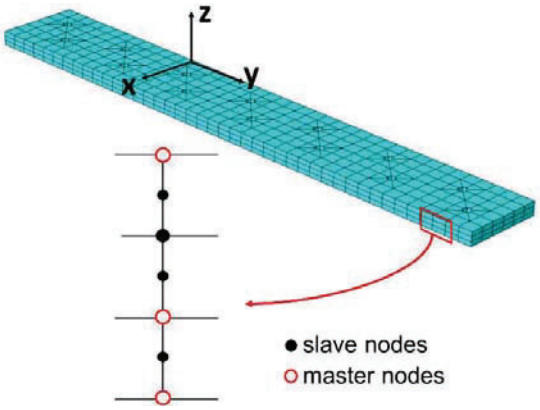

Figure 10: *Master and slave nodes locations for the modified first-order solid-shell approach*

The displacement field is applied through the thickness of a layer as represented in Figure 10. The coefficients in Equation (1) are identified using the coordinates of nodes and displacements at degrees of freedom of master nodes. Then this displacement field is applied to the degrees of freedom of slave nodes which are eliminated. The location of master and slave nodes is described in Figure 10.

4.3 DISTRIBUTIONS AND NODE LOCATIONS FOR SOLID-BEAM APPROACH

For the dowels, the displacement field in Equation (2) was exploited by Wei et al. [6], using the modified Timoshenko theory [14,15]. The reader can find complementary information in the paper by Wei et al. [6].

$$\begin{cases} u(y,z) = ya_1 + za_2 + a_3 \\ v(y,z) = y^2b_1 + z^2b_2 + yzb_3 + yb_4 + zb_5 + b_6 \\ w(y,z) = y^2c_1 + z^2c_2 + yzc_3 + yc_4 + zc_5 + c_6 \end{cases} \quad (2)$$

The displacement field in Equation (2) is applied through the cross-section of each dowel. The distribution is linear for *u* (longitudinal displacement) and quadratic for *v* and *w* (transverse displacement).

The same principle using slave and master nodes is applied again. Figure 11 describes the location of master and slave nodes.

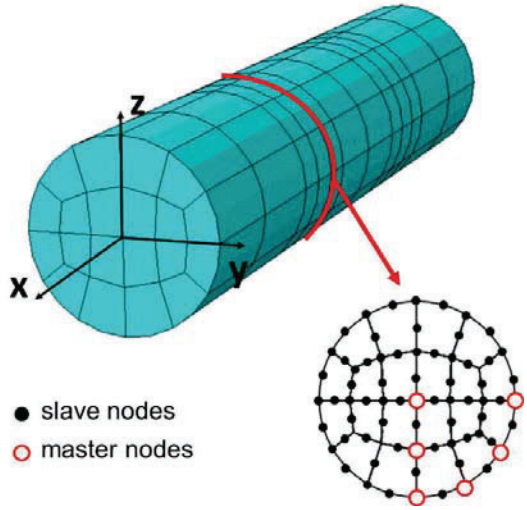

Figure 11: *Master and slave nodes locations for the modified first-order solid-beam approach*

4.4 RESULTS WITH REDUCED MODELS

The reference models respectively for AFLB and AFCLT panel are the ones described in section 3.2 and obtained with the Verification and Validation process. Reduced models for both AFLB and AFCLT panel are created using the methodology presented in sections 4.2 and 4.3. In this section, the reduced models are compared to the reference models. The quality of results and cost reduction are also highlighted.

4.4.1 AFLB reduced model

Table 6 compares, for AFLB, the numerical frequencies obtained with the reference and the reduced finite element

https://doi.org/10.52202/069179-0343

models. The difference between the two models in terms of quality is acceptable with a maximum difference of 5.8 % for the highest frequency.
The comparison of model size and computational cost is summarized in Table 7. The reduction in number of floating-point operations is 97 %. The number of degrees of freedom (d.o.f.) is reduced by 76 %.

Table 6: *Comparison of frequencies between the reference and the reduced models for the AFLB*

	Reference model	Reduced model	Diff.
f_1	119.1 Hz	121.1 Hz	1.7 %
f_2	278.2 Hz	290.0 Hz	4.2 %
f_3	459.6 Hz	486.4 Hz	5.8 %

Table 7: *Comparison of size and computational cost between the reference and the reduced models for the AFLB*

	Reference model	Reduced model	Reduction
Number of d.o.f.	221 220	53 553	76 %
Number of floating point operations	1.34×10^{11}	4.13×10^{9}	97 %

4.4.2 AFCLT panel reduced model

Table 8 compares, for AFCLT panel, the numerical frequencies obtained with the reference and the reduced finite element models. The frequencies obtained with the reduced and solid models are very close to each other. The maximum difference is 3.5 % for the highest frequency.
The comparison of model size and computational cost is summarized in Table 9. The number of d.o.f. and number of floating-point operations are reduced by 77 % and 96 % respectively.

Table 8: *Comparison of frequencies between the reference and the reduced models for AFCLT panel*

	Reference model	Reduced model	Diff.
f_2	54.3 Hz	55.6 Hz	2.4 %
f_3	55.9 Hz	56.2 Hz	0.5 %
f_7	108.6 Hz	112.4 Hz	3.5 %

Table 9: *Comparison of size and computational cost between the reference and the reduced models for the AFCLT panel*

	Reference model	Reduced model	Reduction
Number of d.o.f.	1 460 256	335 356	77.0 %
Number of floating point operations	1.49×10^{12}	6.03×10^{10}	96.0 %

The reduction level is comparable for beams and panels models. However, for cross-laminated timber panels, the size of the numerical models is much larger than for beams. Consequently, reducing the size of the model is even more interesting in this case, especially for a variability or optimization assessment.

4.5 DISCUSSION ON REDUCED MODELS BASED ON HIGHER-ORDER THEORIES

The difference between the reference models and the reduced models for both the AFLB and the AFCLT panel is acceptable in terms of quality. However, some might find it too high for a comparison between two finite element models. The reason for this slight discrepancy is due to the fact that only first-order theories are used here and applied to the totality of the layers and dowels.
Higher-order beam and shell, as well as a mix between beam, shell and solid theories, have also been considered. These other approaches allow us to obtain a better quality of results between the reference and reduced models but in that case, the reduction level is lower. In this paper, only modified first-order theories, which lead to the largest reduction level, are presented.

5 CONSIDERING VARIABILITY WITH A PROBABILISTIC APPROACH

Bui et al. [4] assessed the variability of the vibration frequencies of AFLB and AFCLT panel using the Modal Stability Procedure (MSP). Here, and based on this previous study, we recall the principle of the MSP. Then we apply it to calculate the variability of two frequencies of the AFCLT panel and compare it to the direct Monte Carlo Simulation (MCS).
One way to assess the variability is to use a probabilistic approach which assumes that statistical laws (distribution type, mean value, standard deviation) define the input parameters. Then, statistical characteristics of the output quantities are obtained.
The direct MCS is a robust probabilistic method. In this method, a large number of trials is required with random input values to estimate the statistical characteristics of the output quantities. The computational time of one analysis is multiplied by the number of trials. Consequently, this approach is very computationally time-consuming.
The MSP, a less time-consuming variability assessment methodology, is investigated here.

5.1 THE MODAL STABILITY PROCEDURE

The MSP methodology was developed by Arnoult et al. [16]. Its efficiency in terms of quality of results and computational cost has been proven in multiple studies.
MSP assumes that the mode shape does not change between the original structure (subscript 0) and a perturbated one (subscript p), so $\phi_p = \phi_0$. Consequently, this methodology requires only one finite element analysis in the nominal configuration to extract the mode shapes ϕ_0 and modal strains ε_0.
Thanks to the previous assumption, we obtain the perturbed natural angular frequency for a given mode

using the perturbed stiffness matrix K_p and the perturbed mass matrix M_p:

$$\omega_p^2 = \frac{\phi_0^T K_p \phi_0}{\phi_0^T M_p \phi_0} \quad (3)$$

Equation (3) can be transformed as a summation over all n elements of the finite element model. The elementary internal strain energy of an element j can be expressed as the integration over the elementary volume V_j of the product of the stresses by the strains. Using the generalized Hooke's law to developpe the stress, we then obtain our metamodel as follows:

$$\omega_p^2 = \frac{\sum_{j=1}^{n} \int_{V_j} \varepsilon_{0j}^T C_{pj} \varepsilon_{0j} dV}{\sum_{j=1}^{n} \phi_{0j}^T m_{pj} \phi_{0j}} \quad (4)$$

with C_{pj} the constitutive law matrix and m_{pj} the perturbed mass matrix of the jth element.
The metamodel in Equation (4) is used in a fast MCS, allowing the evaluation of perturbed natural frequencies for each trial. The variability (mean value, standard deviation, coefficient of variation and distribution) of natural frequencies can subsequently be obtained.
Figure 12 presents a flowchart explaining the whole methodology.

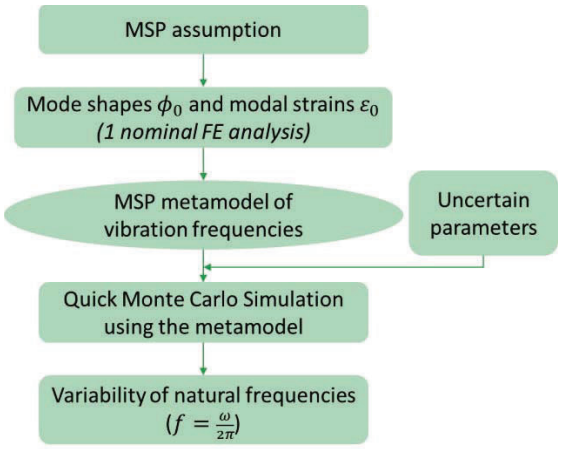

Figure 12: *MSP flowchart*

5.2 VARIABILITY OF AFCLT PANEL FREQUENCIES

The MSP results are presented for two frequencies of the AFCLT panel f_2 and f_3. The reference model is exploited here.

5.2.1 Inputs variability

Uncertain parameters are the material properties of dowels and boards. The parameters distribution is assumed to be Gaussian, however, the distribution law is truncated (±3σ) in order to avoid non-physical values.

Table 10 gives the mean value and coefficient of variation of the uncertain parameters. Four uncertain parameters are defined for each of the 28 boards and 3 uncertain parameters for each of the 196 dowels, leading to 700 independent uncertain parameters.

Table 10: *Variability levels of uncertain parameters*

		Mean value	CoV
board	ρ (kg/m^3)	624	6.5 %
	E_1 (MPa)	11400	13.6 %
	G_{12} (MPa)	1200	14 %
	G_{13} (MPa)	920	14 %
dowel	ρ (kg/m^3)	1133	4.2 %
	E_3 (MPa)	1100	9.5 %
	G_{13} (MPa)	800	10 %

5.2.2 Results

Simulations with 2000 trials using the MSP metamodel and the direct MCS are performed. Figure 13 illustrates the distribution of two frequencies.

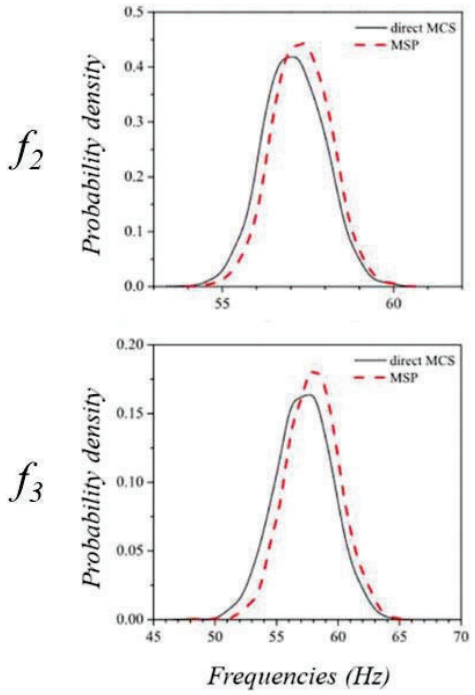

Figure 13: *Distribution of frequencies of AFCLT panel obtained with 2000 trials*

There is a good correlation between results obtained with MSP and direct MCS, even if limited shifts are observed. The maximal difference, observed for mode 3, is about 1 % for the mean value and 8 % for the standard deviation. MSP computational time is divided by about 1000 compared with direct MCS. We can thus conclude that MSP is satisfactory for the assessment of variability of frequencies of a AFCLT panel.

https://doi.org/10.52202/069179-0343

6 CONCLUSION AND PERSPECTIVES

Finite element models to assess the vibration behaviour of AFLB and AFCLT panel have been presented. The Verification and Validation approach shows that the reference model, composed of solid elements, is able to correctly reproduce the experimental frequencies.

A reduction technique, based on the application of solid-beam and solid-shell approaches for dowels and boards respectively, has been introduced. First-order beam and shell theories have been exploited, but higher-order theories can also be considered. The reduced finite element models show good results in terms of quality and significant model size and computational cost reduction compared to the reference models.

The MSP has been presented and applied to evaluate the variability of frequencies of a AFCLT panel using the reference models. The MSP is satisfactory in terms of quality and is much less time-consuming than the classical direct MCS approach.

A next step of this study will be to couple the MSP with reduced models.

Investigating the confrontation between experimental and numerical variability more deeply is also a perspective.

ACKNOWLEDGEMENT

The authors would like to thank the Hauts-de-France Region (France) and the Natural Sciences and Engineering Research Council of Canada (NSERC) for funding this work.

REFERENCES

[1] List of Classifications – IARC Monographs on the Identification of Carcinogenic Hazards to Humans. https://monographs.iarc.who.int/list-of-classifications.

[2] Bui T.A., Lardeur P., Oudjene M., Khelifa M., and Rogaume Y.: Towards experimental and numerical assessment of the vibrational serviceability comfort of adhesive free laminated timber beams and CLT panels assembled using compressed wood dowels. Eng. Struct., 216:110586, 2020.

[3] Bui T.A., Lardeur P., Oudjene M., Khelifa M., and Rogaume Y.: Vibration performance of adhesive free multi-layered timber beams assembled through compressed wood dowels. In: World Conference on Timber Engineering, 2018.

[4] Bui T.A., Lardeur P., Oudjene M., and Park J.: Numerical modelling of the variability of the vibration frequencies of multi-layered timber structures using the modal stability procedure. Compos. Struct., 285:115226, 2022.

[5] Bui T.A.: Experimental and numerical uncertain vibration analysis of multilayered timber structures assembled using compressed wood dowels. *PhD thesis*, University of Lorraine, 2020.

[6] Wei G., Lardeur P., and Druesne F.: A new solid-beam approach based on first or higher-order beam theories for finite element analysis of thin to thick structures. Finite Elem. Anal. Des., 200:103655, 2022.

[7] Wei G., Lardeur P., and Druesne F.: Solid-shell approach based on a first-order or higher-order plate and shell theories for the finite element analysis of thin to very thick structures. Eur. J. Mech. - ASolids, 94:104591, 2022.

[8] Lardeur P., Scigliano R., and Scionti M.: Verification and validation for the vibration study of automotive structures modelled by finite elements. J. Strain Anal. Eng. Des., 48:59-72, 2013.

[9] Simulia: ABAQUS Analysis User's Manual (version 6.14).

[10] Jodin P.: Le bois, matériau d'ingénierie. Association pour la recherche sur le bois en Lorraine Nancy, 1994.

[11] Bouhala L., Fiorelli D., Makradi A., Belouettar S., Sotayo A., Bradeley D.F., Guan Z..: Advanced numerical investigation on adhesive free timber structures. Compos. Struct., 246:112389, 2020.

[12] Reissner E.: The Effect of Transverse Shear Deformation on the Bending of Elastic Plates. J. Appl. Mech., 12(2):A69-A77, 1945.

[13] Mindlin R. D.: Influence of Rotatory Inertia and Shear on Flexural Motions of Isotropic, Elastic Plates. J. Appl. Mech., 18(1):31-38, 1951.

[14] Timoshenko S. P.: On the correction for shear of the differential equation for transverse vibrations of prismatic bars. Lond. Edinb. Dublin Philos. Mag. J. Sci., 41(245):744-746, 1921.

[15] Timoshenko S. P.: On the transverse vibrations of bars of uniform cross-section. Lond. Edinb. Dublin Philos. Mag. J. Sci., 43(253):125-131, 1922.

[16] Arnoult E., Lardeur P., and Martini L.: The modal stability procedure for dynamic and linear finite element analysis with variability. Finite Elem. Anal. Des., 47(1):30–45, 2011.

World Conference on Timber Engineering Oslo 2023

STUDY ON THE STRUCTURAL PERFORMANCE OF PLYWOOD BEARING WALL WITH THE RUSTED NAIL AND DECAYED WOOD

Yuki Ota[1], Hiroki Ishiyama[2], Shigefumi Okamoto[3]

ABSTRACT: In this study, based on the study of the past, deterioration degree of nail and wood is classified because there is a correlation between the maximum load and not only the deterioration degree of the nail by visual inspection but also the penetration depth by pilodyn measurement in the decayed part of wood[1)2)].
And the formula which predicts characteristic of a deformation-load relation when the nail rust and wood decay is developed. Also, using the result and analysing, the structural characteristic of the plywood bearing wall with the nails rusted wood decayed according to the degree of deterioration of the nail and wood can be predicted. As a result,

1. It is revealed that the maximum strength doesn't decrease remarkably when only the sill of plywood bearing wall deteriorates.
2. When the column deteriorates, the rigidity after yield is remarkably reduced.
3. even if the wood decay a little, the strength increases due to the influence of rusting of the nail, and it decreases when further deterioration progresses.

KEYWORDS: Wooden structure, Nail joint, Biological deterioration, Shear strength, Durability, Pull-out force

1 INTRODUCTION

Wooden houses may be required to ensure their safe and long-term use as living spaces. In the deterioration diagnosis currently used, bearing capacity of wall magnification is reduced based on the results of the determination of some deteriorated conditions, such as balconies. And wooden houses may not be adequately repaired according to the degree of deterioration.
So, the shear resistance of the nail joint with rusted nail and decayed wood is formulated based on the study of the past, and the structural characteristic of the plywood bearing wall according to the degree of deterioration of the nail and wood is estimated using the results.

2 ESTIMATION OF THE SHEAR CAPACITY OF JOINT

2.1 CLASSIFICATION OF DETERIORATION DEGREE

The deterioration degree is divided to concisely calculate the shear capacity of nail joint according to the deterioration degree. There is a correlation between the maximum load and the deterioration degree of the nail by visual inspection (Table 1[1)], Fig.1[2)]). And according to Fig.2, it is found that the same behaviour is shown in the case of the same deterioration degree of the nail. Also, there is a correlation between the maximum load and the penetration depth by pilodyn measurement in the decayed part of wood (Fig.3)[3)]. The degree of decay of wood is divided into four stages: pilodyn driving depth of less than 23.5 mm, 23.5 mm or more and less than 27.5 mm, 27.5 mm or more and less than 35 mm, and 35 mm or more. Separated in this way, from Fig.4, the test specimen at the same stage exhibits generally similar behavior. Therefore, the deterioration degree division is Table 2. However, in this study, it is dealt with the degree of deterioration shown in the shaded part of Table2, because moisture is the main cause of both rusting of nails and decay of wood and it is unlikely that only either of them is deteriorate significantly.

Table 1: *Standard of the deterioration grade*

Rating	Standard	Example
1	Scarcely rusted	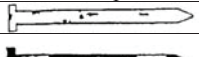
2	Partially rusted, no visible defect	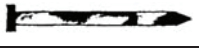
3	Totally rusted, no defect inside	
4	Partially defect, with original length	
5	failure	

[1] Yuki Ota, Osaka Metropolitan University, Japan, uo49yfwhq9o75yuq98y@gmail.com
[2] Hiroki, Ishiyama, Osaka Metropolitan University, Japan, ishiyama@omu.ac.jp
[3] Shigefumi Okamoto, Osaka Metropolitan University, Japan, okmt@omu.ac.jp

https://doi.org/10.52202/069179-0344

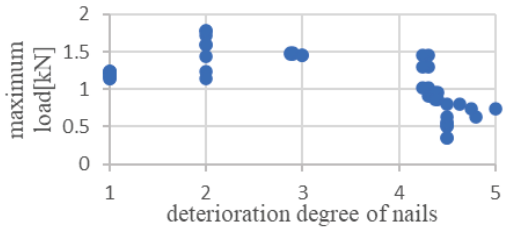

Figure 1: *A correlation between the maximum load and the deterioration degree of the nail*

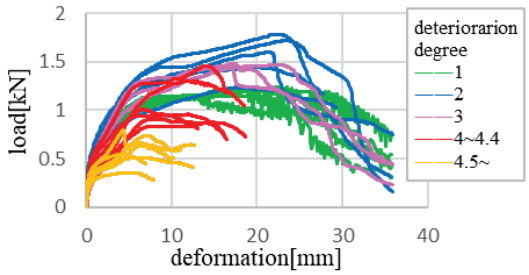

Figure 2: *Experimental results of unit joints with rusted nail*

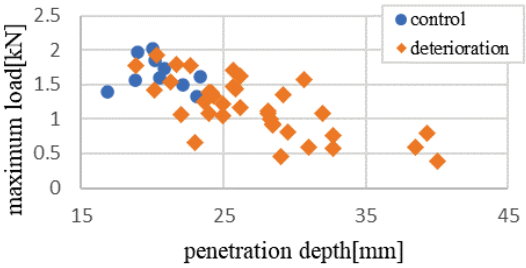

Figure 3: *A correlation between the maximum load and the penetration depth by pilodyn*

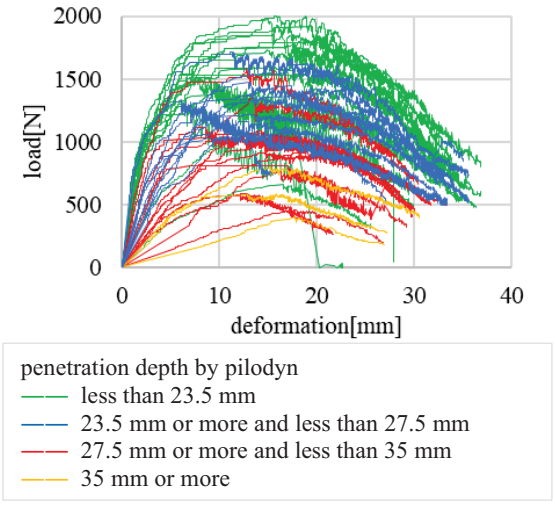

Figure 4: *Experimental results of unit joints with decayed wood*

Table 2: *Division of deterioration degree*

		Deterioration degree of nail					
		1	2	2.5 ~3.5	4 ~4.5	4.5~	
Penetration depth[mm]	~23.5	Aa	Ba	Ca	Da	Ea	Fa
	23.5~27.5	Ab	Bb	Cb	Db	Eb	Fb
	27.5~35	Ac	Bc	Cc	Dc	Ec	Fc
	35~	Ad	Bd	Cd	Dd	Ed	Fd

2.2 ESTIMATION OF TENSILE STRENGTH WITH DETERIORATED NAIL AND WOOD

It is believed that when a shear load is added to the nail joint and the displacement increases, the deflection angle of the nail increases, and resulting in nail pull-out, punching out, or braking. Therefore, it is a breaking point where the axial force of the nail is reached either the pull-out stress intensity of the nail, the nail head penetration bearing capacity of plywood, or the tensile strength of the nail. And the nail head penetration strength of plywood and the tensile strength of nails are determined in the same manner as in previous studies [2]. So, the penetration strength is determined as a stress intensity of 1404 N/mm^2 based on the experimental results of previous study[2] and the tensile strength is calculated by multiplying the lower limit of the tensile strength ($690N/mm^2$) of the iron wire for nail (JISG3562 SWM-N) by the cross-sectional area of the nail body diameter. On the other hand, the pull-out stress intensity of the nail is determined by equation (1).

$$P_d = 4r \int_{\theta_1}^{\theta_2} F(\theta)\mu_{sta}(\theta)d\theta \quad (1)$$

Where, $F(\theta)$ =uniaxial compressive strength of wood [kN], $\mu sta(\theta)$ = static friction coefficient, θ = angle [°] and r = nail radius [mm].
Therefore, the uniaxial compressive strength of wood, the coefficient of statin friction between the rusted nail and the wood, and the range which involved in pull-out resistance of nail (Fig.5) is determined from the study of the past[2)4)5)]. The method is shown below.

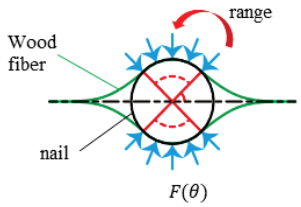

Figure 5: *Range which involved in pull-out resistance of nail*

2.2.1 Uniaxial compressive strength of wood

As for the uniaxial compressive strength, based on the research results[4)], the supporting strength of the wood in the parallel direction of the fiber and the direction in the direction of the fiber perpendicular is adopted. So, the uniaxial compressive strength of wood in fiber

https://doi.org/10.52202/069179-0344

equilibrium direction and the fiber orthogonal direction is represented by the formula (2) and (3), respectively.

fiber equilibrium direction:

$$F_l = -0.7867(x - 20.5) + 35.655 \quad (2)$$

fiber orthogonal direction:

$$F_r = -1.0316(x - 20.5) + 41.271 \quad (3)$$

Where, x =penetration depth by pilodyn.

2.2.2 The coefficient of statin friction between no damage nail and wood

The coefficient of statin friction between no damage nail and wood is adopted by the study[5]. So, coefficient of statin friction between no damage nail and wood in fiber equilibrium direction and the fiber orthogonal direction is represented by the formula (4) and (5), respectively.

fiber equilibrium direction:

$$\mu_{sta_l} = -0.325r_u + 0.409 \quad (4)$$

fiber orthogonal direction:

$$\mu_{sta_r} = -0.386r_u + 0.318 \quad (5)$$

Where, r_u =specific gravity of wood.

2.2.3 The range which involved in pull-out resistance of nail

Using the Hankinson's equation, $F(\theta)$ and $\mu_{sta}(\theta)$ are presented by equation (6) and (7), respectively.

$$F(\theta) = \frac{F_l \times F_r}{F_l sin^2(\theta) + F_r cos^2(\theta)} \quad (6)$$

$$\mu_{sta}(\theta) = \frac{\mu_{sta_l} \times \mu_{sta_r}}{\mu_{sta_l} sin^2(\theta) + \mu_{sta_r} cos^2(\theta)} \quad (7)$$

Further, by substituting into equation (1), the following equation (8) is obtained.

$$P_d = 4r \int_{\theta_1}^{\theta_2} \frac{F_l \times F_r}{F_l sin^2(\theta) + F_r cos^2(\theta)} \times \frac{\mu_{sta_l} \times \mu_{sta_r}}{\mu_{sta_l} sin^2(\theta) + \mu_{sta_r} cos^2(\theta)} d\theta \quad (8)$$

From previous research[2], since the pull-out resistance of the CN65 nail (P_d) is 627.2[N], the required range is θ_{65}~90[°] satisfying equation (9).

$$627.2 = 4r_{65} \int_{\theta_{65}}^{90°} \frac{F_l \times F_r}{F_l sin^2(\theta) + F_r cos^2(\theta)} \times \frac{\mu_{sta_l} \times \mu_{sta_r}}{\mu_{sta_l} sin^2(\theta) + \mu_{sta_r} cos^2(\theta)} d\theta \quad (9)$$

Where, r_{65}=CN65 nail radius [mm]=1.665.
Here, when $\theta_{65} = 89.65°$ and when $\theta_{65} = 89.7°$, the value of equation (9) is 629.9 and 539.9, respectively. So, θ_{65} is found to be about 89.65°.

Then, a range of 89.95 ~ 90 [°] related to the extraction resistance in the case of CN65 nail is applied to the N50 nail. Assuming that the state of the wood when the wood fibers are pushed apart by driving a nail is the same as in the case of CN65 nail and N50 nail, the nail joint at that time is considered to be as shown in Fig.6.

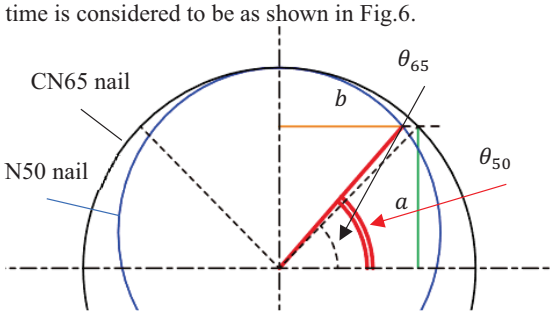

Figure 6: *Schematic of the nail joint when CN65 and N50 nails are driven into wood*

At the time, the range of θ_{50} ~90[°] that affects the extraction resistance in the case of the N 50 nail is represented by the formula (10).

$$\theta_{50} = \tan^{-1}\left(\frac{a}{b}\right) = \tan^{-1}\left(\frac{r_{65} \sin\theta_{65}}{\sqrt{{r_{50}}^2 - (r_{65}\sin\theta_{65} - r_{65} + r_{50})^2}}\right) \quad (10)$$

Where, r_{50}=N50 nail radius [mm]=1.375.
Therefore, when $\theta_{65} = 89.65°$ is substituted into equation (10), $\theta_{50} = 89.7°$, so the range which involved in pull-out resistance of N50 nail is revealed that 89.7~90[°].

2.2.4 The coefficient of statin friction between rusted nail and no damage wood

The coefficient of statin friction between rusted nail and no damage wood is determined based on the results of the pull-out experiment about CN65 nail in previous study[2]. The method is shown below. First, it is calculated how many times the static friction coefficient between rusted nail and no damage wood is that between no damage nail and wood in the case of CN65 nail. Assuming that the rate of increasing static friction is expressed by equation (11), the weight remaining rate of the nail and the rate are shown in Table 3 from the experimental study[2].

$$R = M_R / M_N \quad (11)$$

Where, R =rate of increasing static friction, M_R = maximum pull-out strength with rusted nail and M_N = maximum pull-out strength with no damage nail.
And, assuming that the corrosion depth of the nails when the degree of deterioration of the nails is the same, the weight residual rate of N50 nails having a corrosion depth equivalent to that of CN65 nails with a certain weight residual rate is calculated. The schematic diagram of the rusted nail looks like Fig. 7, so if the nail rust occurs uniformly throughout the nail, the corrosion depth is expressed by formula (12).

https://doi.org/10.52202/069179-0344

Table 3: *static friction (CN65 nail)*

Weight Residual rate	Maximum pull-out strength	Rate of Increasing static friction
100.00[%]	627.2[N]	1.00
97.3[%]	1821.8[N]	2.90
93.4[%]	3011.5[N]	4.80
83.5[%]	3405.1[N]	5.43

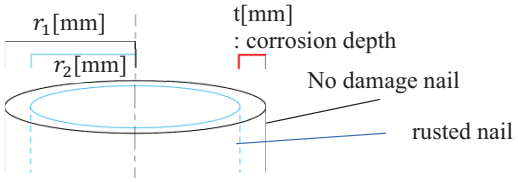

Figure 7: *Schematic of rusted nails*

$$t = r_1\left(1 - \sqrt{q}\right) \tag{12}$$

Where, r_1=body diameter of no damage nail, r_2=body diameter of rusted nail and q=weight residual ratio = $\frac{{r_2}^2}{{r_1}^2}$.
Therefore, when the corrosion depths of the CN65 nail and the N50 nail are equal, the weight residual ratio of the N50 nail is expressed by Equation (13).

$$q_{50} = \left\{1 + \frac{r_{65}}{r_{50}}\left(\sqrt{q_{65}} - 1\right)\right\}^2 \tag{13}$$

Where, q_{65} =weight residual ratio of CN65 nail, q_{50}=weight residual ratio of N50 nail, r_{65}= body diameter of CN65 nail and r_{50}= body diameter of N50 nail.
And the rate of increasing static friction of N50 nail at the time of nail rusting is shown in Table 4.

Table 4: *static friction (N50 nail)*

Weight Residual rate	Rate of Increasing static friction
100.00[%]	1.00
96.74[%]	2.90
92.03[%]	4.80
80.21[%]	5.43

2.3 THE FORMULA OF DEFORMATION-LOAD RELATION

2.3.1 Creating formula on two-later ground

The formula which predicts change of a deformation-load relation when the nail rust and wood decay is developed by expanding the study of the past[2]. In other words, assuming that wood is a two-layer configuration of the decay part and the no damage part, using the horizontal resistance calculation formula of piles[6], the wood is regarded as the ground and the nail is regarded as the piles, and formulas are created for each protruding and fixing conditions of the nail head on two-layer ground. Therefore, equations (14), (15) and (16) are solved for the boundary conditions in the assumed nail head state, and constants A_n, B_n, C_n, and D_n satisfying these conditions are calculated.

$$\begin{aligned} y_1(x) = {} & A_n e^{\beta_1 x}\cos(\beta_1 x) + B_n e^{\beta_1 x}\sin(\beta_1 x) \\ & + C_n e^{-\beta_1 x}\cos(\beta_1 x) \\ & + D_n e^{-\beta_1 x}\sin(\beta_1 x) \end{aligned} \tag{14}$$

$$\begin{aligned} y_2(x) = {} & A_{n+1} e^{\beta_2 x}\cos(\beta_2 x) + B_{n+1} e^{\beta_2 x}\sin(\beta_2 x) \\ & + C_{n+1} e^{-\beta_2 x}\cos(\beta_2 x) \\ & + D_{n*1} e^{-\beta_2 x}\sin(\beta_2 x) \end{aligned} \tag{15}$$

$$y_3(x) = A_{n+2} + B_{n+2}x + C_{n+2}x^2 + D_{n+2}x^3 \tag{16}$$

Where, fixed numbers are shown in Table 5~8.

Table 5: *Fixed number (1)*

H	N	Load
H_0	N	Load at the nail head
y_n	mm	Horizontal displacement of the nail in nth layer
x	mm	Depth
θ	rad	Nail angle
θ_0	rad	Nail head angle
M	$N \cdot mm$	Moment
M_0	$N \cdot mm$	Moment at the nail head
Kh_1	N/mm^2	Horizontal ground reaction coefficient of no damage wood at depth of $x[mm]$
Kh_2	N/mm^2	Horizontal ground reaction coefficient of decayed wood at depth of $x[mm]$
B	mm	Body diameter of nail
E	N/mm^2	Young's modulus of nail = 160000
I	mm^4	Moment of inertia of area of nail
ℓ	mm	Depth to boundary between no damage part and decayed part of wood
ℓ_m	mm	Depth of maximum moment occurrence
h	mm	Nail protrusion depth
$\beta_1 = \sqrt[4]{\frac{Kh_1}{EI}}$, $\beta_2 = \sqrt[4]{\frac{Kh_2}{EI}}$		
$\mathrm{F} = \frac{H}{4EI{\beta_1}^3}$, $\mathrm{F}' = \frac{H}{4EI{\beta_2}^3}$		
$a_1 = e^{\beta_1 \ell}$, $a_2 = e^{\beta_1 \ell}$		
$b_1 = a_1 a_2 + 4sin(\beta_1\ell)cos(\beta_1\ell)$ $b_2 = a_1 a_2 - 4sin(\beta_1\ell)cos(\beta_1\ell)$ $b_3 = {a_1}^2 - 4sin^2(\beta_1\ell)$, $b_4 = {a_2}^2 + 4sin^2(\beta_1\ell)$ $b_5 = {a_1}^2 + 4cos^2(\beta_1\ell)$, $b_6 = {a_2}^2 - 4sin^2(\beta_1\ell)$		
$c_1 = \beta_1\beta_2 b_3 + {\beta_2}^2 b_1$, $c_2 = {\beta_1}^2 b_2 + \beta_1\beta_2 b_3$ $c_3 = \beta_1\beta_2 b_2 + {\beta_2}^2 b_6$, $c_4 = {\beta_1}^2 b_4 + \beta_1\beta_2 b_2$ $c_5 = \beta_1\beta_2 b_1 + {\beta_2}^2 b_4$, $c_6 = {\beta_1}^2 b_6 + \beta_1\beta_2 b_1$ $c_7 = \beta_1\beta_2 b_2 + {\beta_2}^2 b_5$, $c_8 = \beta_1\beta_2 b_2 - {\beta_2}^2 b_5$ $c_9 = {\beta_1}^2 b_4 - \beta_1\beta_2 b_2$, $c_{10} = {\beta_1}^2 b_2 + \beta_1\beta_2 b_5$ $c_{11} = \beta_1\beta_2 b_4 + {\beta_2}^2 b_2$, $c_{12} = {\beta_1}^2 b_3 + \beta_1\beta_2 b_1$ $c_{13} = \beta_1\beta_2 b_2 + {\beta_2}^2 b_3$, $c_{14} = {\beta_1}^2 b_1 + \beta_1\beta_2 b_4$ $c_{15} = \beta_1\beta_2 b_6 + {\beta_2}^2 b_1$		

Table 6: *Fixed number (2)*

$d_1 = \beta_1{\beta_2}^2 b_2 + {\beta_2}^3 b_3,\ d_2 = {\beta_1}^3 b_1 + {\beta_2}^3 b_3$ $d_3 = \beta_1{\beta_2}^2 b_4 + {\beta_2}^3 b_2,\ d_4 = {\beta_1}^3 b_6 + {\beta_2}^3 b_2$ $d_5 = \beta_1{\beta_2}^2 b_4 - {\beta_2}^3 b_2,\ d_6 = {\beta_1}^3 b_6 - {\beta_2}^3 b_2$
$f_1 = a_2 d_1 sin(\beta_1\ell) + \beta_1 a_1 c_1 cos(\beta_1\ell)$ $f_2 = a_2 d_2 sin(\beta_1\ell) - \beta_1 a_1 c_2 cos(\beta_1\ell)$ $f_3 = d_3 i_1 - \beta_1 c_7 i_2,\ f_4 = d_4 i_1 + \beta_1 c_4 i_2$ $f_5 = f_3 + f_4,\ f_6 = f_3 - f_4$ $f_7 = d_5 i_1 + \beta_1 c_8 i_2,\ f_8 = d_6 i_1 + \beta_1 c_9 i_2$
$g_1 = {\beta_2}^2 a_2 c_2 sin(\beta_1\ell) + {\beta_1}^2 a_1 c_1 cos(\beta_1\ell)$ $g_2 = {\beta_1}^2 a_2 c_1 sin(\beta_1\ell) + {\beta_2}^2 a_1 c_2 cos(\beta_1\ell)$
$h_1 = c_1 d_2 + c_2 d_1$ $h_2 = {\beta_1}^2 a_2 f_1 sin(\beta_1\ell) + {\beta_2}^2 a_1 f_2 cos(\beta_1\ell)$ $h_3 = -{\beta_2}^2 a_2 f_3 sin(\beta_1\ell) + {\beta_1}^2 a_1 f_1 cos(\beta_1\ell)$ $h_4 = c_4 d_3 + c_7 d_4$ $h_5 = {\beta_1}^2 a_2 f_3 sin(\beta_1\ell) + {\beta_2}^2 a_1 f_4 cos(\beta_1\ell)$ $h_6 = {\beta_1}^2\{(a_1 + a_2) sin(\beta_1\ell) - a_2 cos(\beta_1\ell)\} f_3$ $+ {\beta_2}^2\{a_1 sin(\beta_1\ell) + (a_1$ $+ a_2) cos(\beta_1\ell)\} f_4$ $h_7 = c_7 d_5 + c_8 d_3,\ h_8 = c_4 d_6 - c_9 d_4$ $h_9 = c_7 d_6 + c_9 d_3,\ h_{10} = c_4 d_5 - c_8 d_4$ $h_{11} = c_8 d_6 - c_9 d_5$
$i_1 = a_1 sin(\beta_1\ell) + a_2 cos(\beta_1\ell)$ $i_2 = a_1 sin(\beta_1\ell) - a_2 cos(\beta_1\ell)$
$j_1 = f_5 h_{10} - f_6 h_7,\ j_2 = f_5 h_8 - f_6 h_9$ $j_3 = f_3 h_{10} + f_4 h_7,\ j_4 = f_3 h_8 + f_4 h_9$ $j_5 = f_5 h_9 - f_6 h_7,\ j_6 = f_5 h_8 - f_6 h_{10}$ $j_7 = f_3 h_7 - f_4 h_9,\ j_8 = f_3 h_{10} - f_4 h_8$
$G_1 = j_1 sin(\beta_2\ell) + j_2 cos(\beta_2\ell)$ $G_2 = j_2 sin(\beta_2\ell) - j_1 cos(\beta_2\ell)$ $G_3 = \{f_5 sin(\beta_2\ell) + f_6 cos(\beta_2\ell)\} h_4$ $G_4 = \{f_6 sin(\beta_2\ell) - f_5 cos(\beta_2\ell)\} h_4$ $G_5 = j_3 sin(\beta_2\ell) + j_4 cos(\beta_2\ell)$ $G_6 = j_4 sin(\beta_2\ell) - j_3 cos(\beta_2\ell)$ $G_7 = \{f_4 sin(\beta_2\ell) + f_3 cos(\beta_2\ell)\} h_4$ $G_8 = \{f_3 sin(\beta_2\ell) - f_4 cos(\beta_2\ell)\} h_4$ $G_9 = j_5 sin(\beta_2\ell) + j_6 cos(\beta_2\ell)$ $G_{10} = j_6 sin(\beta_2\ell) - j_5 cos(\beta_2\ell)$ $G_{11} = \{f_5 sin(\beta_2\ell) + f_6 cos(\beta_2\ell)\} h_{11}$ $G_{12} = \{f_6 sin(\beta_2\ell) - f_5 cos(\beta_2\ell)\} h_{11}$ $G_{13} = j_7 sin(\beta_2\ell) + j_8 cos(\beta_2\ell)$ $G_{14} = j_8 sin(\beta_2\ell) - j_7 cos(\beta_2\ell)$ $G_{15} = \{f_3 sin(\beta_2\ell) - f_4 cos(\beta_2\ell)\} h_{11}$ $G_{16} = \{f_4 sin(\beta_2\ell) + f_3 cos(\beta_2\ell)\} h_{11}$
$J_1 = G_5 e^{\beta_2(2\ell - \ell_m)} + G_7 e^{\beta_2\ell_m}$ $J_2 = G_1 e^{\beta_2(2\ell - \ell_m)} - G_3 e^{\beta_2\ell_m}$ $J_3 = G_6 e^{\beta_2(2\ell - \ell_m)} + G_8 e^{\beta_2\ell_m}$ $J_4 = G_2 e^{\beta_2(2\ell - \ell_m)} - G_4 e^{\beta_2\ell_m}$ $J_5 = G_{13} e^{\beta_2(\ell_m - 2\ell)} + G_{15} e^{-\beta_2\ell_m}$ $J_6 = G_9 e^{\beta_2(\ell_m - 2\ell)} + G_{11} e^{-\beta_2\ell_m}$ $J_7 = G_{14} e^{\beta_2(\ell_m - 2\ell)} - G_{16} e^{-\beta_2\ell_m}$ $J_8 = G_{10} e^{\beta_2(\ell_m - 2\ell)} + G_{12} e^{-\beta_2\ell_m}$
$\mathcal{P}_1 = f_5 f_8 - f_6 f_7,\ \mathcal{P}_2 = f_3 f_7 - f_4 f_8$

Table 7: *Fixed number (3)*

$q_1 = {\beta_1}^2 i_2 \mathcal{J}_3 + {\beta_2}^2 i_1 \mathcal{J}_4$ $q_2 = ({\beta_1}^2 f_4 i_2 + {\beta_2}^2 f_3 i_1) h_4$ $q_3 = {\beta_1}^2 i_2 \mathcal{J}_1 + {\beta_2}^2 i_1 \mathcal{J}_2$ $q_4 = ({\beta_1}^2 f_5 i_2 + {\beta_2}^2 f_6 i_1) h_4$ $q_5' = \mathcal{P}_1(-{\beta_1}^2 i_2 \mathcal{J}_7 + {\beta_2}^2 i_1 \mathcal{J}_8) + \mathcal{P}_2({\beta_1}^2 i_2 \mathcal{J}_5$ $- {\beta_2}^2 i_1 \mathcal{J}_6)$ $q_6' = \mathcal{P}_1({\beta_1}^2 f_3 i_2 + {\beta_2}^2 f_4 i_1) h_{11} - \mathcal{P}_2({\beta_1}^2 f_5 i_2$ $- {\beta_2}^2 f_6 i_1) h_{11}$ $q_7 = {\beta_1}^2 i_2 \mathcal{J}_5 - {\beta_2}^2 i_1 \mathcal{J}_6$ $q_8 = ({\beta_1}^2 f_5 i_2 - {\beta_2}^2 f_6 i_1) h_{11}$ $q_9 = {\beta_1}^2 a_2 \mathcal{J}_3 sin(\beta_1\ell) + {\beta_2}^2 a_1 \mathcal{J}_4 cos(\beta_1\ell)$ $q_{10} = \{{\beta_1}^2 a_2 f_4 sin(\beta_1\ell) + {\beta_2}^2 a_1 f_3 cos(\beta_1\ell)\} h_4$ $q_{11} = {\beta_1}^2 a_2 \mathcal{J}_1 sin(\beta_1\ell) + {\beta_2}^2 a_1 \mathcal{J}_2 cos(\beta_1\ell)$ $q_{12} = \{{\beta_1}^2 a_2 f_5 sin(\beta_1\ell) + {\beta_2}^2 a_1 f_6 cos(\beta_1\ell)\} h_4$ $q_{13}' = \mathcal{P}_1\{{\beta_1}^2 a_2 \mathcal{J}_7 sin(\beta_1\ell) - {\beta_2}^2 a_1 \mathcal{J}_8 cos(\beta_1\ell)\}$ $- \mathcal{P}_2\{{\beta_1}^2 a_2 \mathcal{J}_5 sin(\beta_1\ell)$ $- {\beta_2}^2 a_1 \mathcal{J}_6 cos(\beta_1\ell)\}$ $q_{14}' = \mathcal{P}_1\{{\beta_1}^2 a_2 f_3 sin(\beta_1\ell) + {\beta_2}^2 a_1 f_4 cos(\beta_1\ell)\} h_{11}$ $- \mathcal{P}_2\{{\beta_1}^2 a_2 f_5 sin(\beta_1\ell)$ $- {\beta_2}^2 a_1 f_6 cos(\beta_1\ell)\} h_{11}$ $q_{15} = {\beta_1}^2 a_2 \mathcal{J}_5 sin(\beta_1\ell) - {\beta_2}^2 a_1 \mathcal{J}_6 cos(\beta_1\ell)$ $q_{16} = \{{\beta_1}^2 a_2 f_5 sin(\beta_1\ell) - {\beta_2}^2 a_1 f_6 cos(\beta_1\ell)\} h_{11}$
$Q_1 = 4{\beta_1}^2 e^{\beta_2(\ell - \ell_m)} \times \frac{({f_3}^2 + {f_4}^2)}{J_1 J_4 - J_2 J_3}$ $Q_2 = \frac{1}{sin(\beta_2 \ell_m)} \times \frac{G_3}{J_1 J_4 - J_2 J_3}$ $Q_3' = 4{\beta_1}^2 e^{\beta_2(\ell_m - \ell)} \times \frac{1}{J_5 J_8 - J_6 J_7}$ $Q_4 = \frac{1}{sin(\beta_2 \ell_m)} \times \frac{G_{11}}{J_5 J_8 - J_6 J_7}$
$\mathcal{R}_1 = Q_1 e^{\beta_2\ell}\{q_1 e^{\beta_2(2\ell - \ell_m)} + q_2 e^{\beta_2\ell_m)}\}$ $\mathcal{R}_2 = Q_2 e^{\beta_2\ell}\{q_3 e^{\beta_2(2\ell - \ell_m)} - q_4 e^{\beta_2\ell_m)}\}$ $\mathcal{R}_3 = Q_3' e^{-\beta_2\ell}\{q_5' e^{\beta_2(\ell_m - 2\ell)} - q_6' e^{-\beta_2\ell_m)}\}$ $\mathcal{R}_4 = Q_4 e^{-\beta_2\ell}\{q_7 e^{\beta_2(\ell_m - 2\ell)} + q_8 e^{-\beta_2\ell_m)}\}$ $\mathcal{R}_5 = Q_1 e^{\beta_2\ell}\{q_9 e^{\beta_2(2\ell - \ell_m)} + q_{10} e^{\beta_2\ell_m)}\}$ $\mathcal{R}_6 = Q_2 e^{\beta_2\ell}\{q_{11} e^{\beta_2(2\ell - \ell_m)} - q_{12} e^{\beta_2\ell_m)}\}$ $\mathcal{R}_7 = Q_3' e^{-\beta_2\ell}\{q_{13}' e^{\beta_2(\ell_m - 2\ell)} + q_{14}' e^{-\beta_2\ell_m)}\}$ $\mathcal{R}_8 = Q_4 e^{-\beta_2\ell}\{q_{15} e^{\beta_2(\ell_m - 2\ell)} + q_{16} e^{-\beta_2\ell_m)}\}$
$S_1 = f_5 sin(\beta_2\ell) + f_6 cos(\beta_1\ell)$ $S_2 = f_6 sin(\beta_2\ell) - f_5 cos(\beta_1\ell)$ $S_3 = (-f_3 + 3f_4) sin(\beta_2\ell) + f_6 cos(\beta_1\ell)$ $S_4 = f_6 sin(\beta_2\ell) + (f_3 - 3f_4) cos(\beta_1\ell)$
$t_1 = {\beta_1}^2 a_2 sin(\beta_1\ell) + \beta_1\beta_2 i_2 - {\beta_2}^2 a_1 cos(\beta_1\ell)$ $t_2 = {\beta_1}^2 i_2 - 2\beta_1\beta_2 a_1 cos(\beta_1\ell) - {\beta_2}^2 i_1$ $t_3 = {\beta_1}^2 a_1 cos(\beta_1\ell) + \beta_1\beta_2 i_1 + {\beta_2}^2 a_2 sin(\beta_1\ell)$ $t_4 = {\beta_1}^2 i_1 + 2\beta_1\beta_2 a_2 sin(\beta_1\ell) + {\beta_2}^2 i_2$
$u_1 = {\beta_1}^3 i_1 + {\beta_1}^2\beta_2 a_2 sin(\beta_1\ell) + {\beta_2}^3 a_1 cos(\beta_1\ell)$ $u_2 = 2{\beta_1}^3 a_2 sin(\beta_1\ell) + {\beta_1}^2\beta_2 i_2 + {\beta_2}^3 i_1$ $u_3 = {\beta_1}^3 i_2 - {\beta_1}^2\beta_2 a_1 cos(\beta_1\ell) + {\beta_2}^3 a_2 sin(\beta_1\ell)$ $u_4 = 2{\beta_1}^3 a_1 cos(\beta_1\ell) + {\beta_1}^2\beta_2 i_1 - {\beta_2}^3 i_2$

https://doi.org/10.52202/069179-0344

Table 8: *Fixed number (4)*

$v_1 = {\beta_1}^3\beta_2 b_4 + 2{\beta_1}^2{\beta_2}^2 b_2 + \beta_1{\beta_2}^3 b_5$ $v_2 = {\beta_1}^3\beta_2 b_4 - \beta_1{\beta_2}^3 b_5$ $v_3 = {\beta_1}^3\beta_2 b_2 + 2{\beta_1}^2{\beta_2}^2 b_3 + \beta_1{\beta_2}^3 b_1$ $v_4 = {\beta_1}^3\beta_2 b_2 - \beta_1{\beta_2}^3 b_1$ $v_5 = {\beta_1}^3\beta_2 b_6 + 2{\beta_1}^2{\beta_2}^2 b_1 + \beta_1{\beta_2}^3 b_4$ $v_6 = {\beta_1}^3\beta_2 b_6 - \beta_1{\beta_2}^3 b_4$
$T_1 = t_1u_2 - t_2u_1,\ T_2 = t_1u_3 + t_3u_1$ $T_3 = -t_1u_4 + t_4u_1$
$U_1 = c_{12}T_1 - c_{10}T_2,\ U_2 = c_{13}T_1 - c_{11}T_2$ $U_3 = c_{14}T_1 - c_{10}T_3,\ U_4 = c_{15}T_1 - c_{11}T_3$ $U_5 = c_{14}T_2 - c_{12}T_3,\ U_6 = c_{15}T_2 - c_{13}T_3$
$V_1 = sin(\beta_2\ell) + cos(\beta_2\ell)$ $V_2 = sin(\beta_2\ell) - cos(\beta_2\ell)$
$W_1 = {\beta_1}^2\hbar^2(-{\beta_1}^2U_2V_2 + {\beta_2}^2U_1V_1)$ $+ \beta_1\hbar(-{\beta_1}^2U_4V_2 + {\beta_2}^2U_3V_1)$ $+ (-{\beta_1}^2U_6V_2 + {\beta_2}^2U_5V_1)$ $W_2 = {\beta_1}^2\hbar^2(-{\beta_1}^2U_2V_1 + {\beta_2}^2U_1V_2)$ $+ \beta_1\hbar(-{\beta_1}^2U_4V_1 + {\beta_2}^2U_3V_2)$ $+ (-{\beta_1}^2U_6V_1 + {\beta_2}^2U_5V_2)$
$X_1 = W_1sin(\beta_2\ell) + W_2\ cos(\beta_2\ell)$ $X_2 = W_2sin(\beta_2\ell) - W_1\ cos(\beta_2\ell)$
$Y_1 = {\beta_1}^2\hbar^2(-{\beta_1}^2U_2X_1 - {\beta_2}^2U_1X_2)$ $+ \beta_1\hbar(-{\beta_1}^2U_4X_1 - {\beta_2}^2U_3X_2)$ $+ (-{\beta_1}^2U_6X_1 - {\beta_2}^2U_5X_2)$

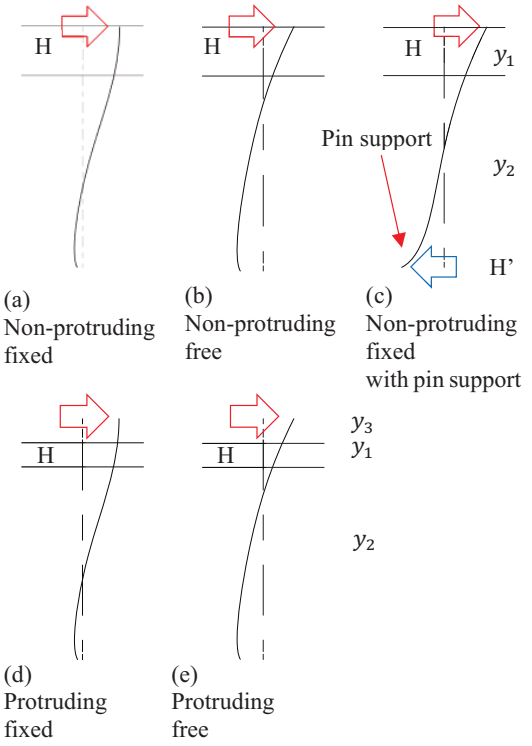

Figure 8: *Schematic diagram of the nail joint under all nail head conditions*

2.3.1.1. Non-protruding and fixed

Fig. 8 (a) shows a nail joint when the nail head condition is non-protruding and fixed. The boundary conditions at this time are that θ_0=0 $[rad]$ and the horizontal load at the nail head is $H[N]$. And the calculations are equation (17) and (18).

$$y_1(0) = \frac{b_2h_1 + 8h_3}{4EI{\beta_1}^3b_3h_1}H \tag{17}$$

$$H_0 = -\frac{2\beta_1b_3h_1}{b_1h_1 - 8h_2}M_0 \tag{18}$$

2.3.1.2. Non-protruding and free

Fig. 8 (b) shows a nail joint when the nail head condition is non-protruding and free. The boundary conditions at this time are that M_0=0 $[N \cdot mm]$ and the horizontal load at the nail head is $H[N]$. And the calculations are equation (19) ~ (22).

$$y_1(0) = \frac{b_4h_4 + 4h_5 - 4h_6}{2EI{\beta_1}^3b_2h_4}H \tag{19}$$

$$\ell_m = \frac{1}{\beta_2}tan^{-1}\left(-\frac{f_5sin(\beta_2\ell) + f_6cos(\beta_2\ell)}{f_6sin(\beta_2\ell) - f_5cos(\beta_2\ell)}\right) \tag{20}$$

$$H(\ell_m) = \frac{\beta_1M(\ell_m)(f_5sin(\beta_2\ell) + f_6cos(\beta_2\ell))h_4}{2{\beta_2}^2({f_3}^2 + {f_4}^2)sin(\beta_2\ell_m)}e^{\beta_2\ell_m - \beta_2\ell} \tag{21}$$

$$H(0) = \frac{\beta_1M(0)h_4}{2{\beta_2}^2f_4} \tag{22}$$

2.3.1.3. Non-protruding and free with pin support

Fig. 8 (c) shows a nail joint when the nail head condition is non-protruding and free with pin support in no damage part of wood. The boundary conditions at this time are that M_0=0 $[N \cdot mm]$, $M(\ell_m) = 0$, the horizontal load at the nail head is $H[N]$ and the horizontal load at $\ell_m$is $H'[N]$. And the calculations are equation (23) ~ (25).

$$y_1(0) = \frac{{\beta_1}^2b_4 + R_1 + R_3}{2EI{\beta_1}^5b_2}H + \frac{R_2 + R_4}{2EI{\beta_1}^2{\beta_2}^3b_2}H' \tag{23}$$

$$\theta(0) = \frac{{\beta_1}^2b_1 + 2R_5 - 2R_7}{2EI{\beta_1}^4b_2}H + \frac{R_6 + R_8}{2EI\beta_1{\beta_2}^3b_2}H' \tag{24}$$

$$\theta(\ell_m) = \frac{S_1 - S_3}{2EI{\beta_1}^3} \times \frac{\beta_2\sin(\beta_2\ell_m)}{f_5\sin(\beta_2\ell) + f_6\cos(\beta_2\ell)}H + \frac{S_2 + S_4}{2EI{\beta_2}^2} \times \frac{sin(\beta_2\ell_m)}{f_5sin(\beta_2\ell) + f_6cos(\beta_2\ell)}H' \tag{25}$$

2.3.1.4. Protruding and fixed

Fig. 8 (d) shows a nail joint when the nail head condition is protruding and fixed. The boundary conditions at this time are that $M(-h)$=0 $[rad]$ and the horizontal load at

the nail head is $H[N]$. And the calculations are equation (26) ~ (29).

$$\ell_m = \frac{1}{\beta_2} tan^{-1}\left(\frac{W_1}{W_2}\right) \tag{26}$$

$$H_{\ell_m} = \frac{4{\beta_1}^3 M(\ell_m) t_1 (\beta_1 h T_1 + T_2) W_1 e^{\beta_2(\ell_m - \ell)}}{Y_1 sin(\beta_2 \ell_m)} \tag{27}$$

$$y_3(-h) = \frac{H}{12EI{\beta_1}^3 t_1(\beta_1 h T_1 + T_2)} \times \begin{Bmatrix} {\beta_1}^4 h^4 t_1 T_1 + 4{\beta_1}^3 h^3 t_1 T_2 \\ +3{\beta_1}^2 h^2 (t_1 T_3 + t_2 T_2 + t_3 T_1) \\ +3\beta_1 h(t_2 T_3 + t_4 T_1) + 3(-t_3 T_3 + t_4 T_2) \end{Bmatrix} \tag{28}$$

$$H_\ell = -\frac{4\beta_1 M(\ell) t_1 (\beta_1 h T_1 + T_2)}{{\beta_1}^2 h^2 U_2 + \beta_1 h U_4 + U_6} \tag{29}$$

2.3.1.5. Protruding and free

Fig. 8 (e) shows a nail joint when the nail head condition is protruding and free. The boundary conditions at this time are that $\theta(-h)$=0 $[rad]$ and the horizontal load at the nail head is $H[N]$. And the calculations are equation (30) and (31).

$$y_3(-h) = \frac{1}{12EI{\beta_1}^3 t_1 T_1}\{4{\beta_1}^3 h^3 t_1 T_1 + 12{\beta_1}^2 h^2 t_1 T_2 + 6\beta_1 h(t_1 T_3 + t_2 T_2 + t_3 T_1) + 3(t_2 T_3 + t_4 T_1)\} H \tag{30}$$

$$y_3'(-h) = -\frac{{\beta_1}^2 h^2 T_1 + 2\beta_1 h T_2 + T_3}{2EI{\beta_1}^2 T_1} H \tag{31}$$

2.3.2 The formula deformation-load relation

Fixed numbers are shown in Table 9.

Table 9: *Fixed number (5)*

H_n	Horizontal load of the nail head at the nth change point of the load-deformation relationship
y_n	Horizontal displacement of the nail head at the nth change point of the load-deformation relationship
σ_{yp}	Yield stress of plywood to the nail side =4105
A_p	Cross-sectional area of plywood to the nail side
Z_n	Section modulus of nail
σ_n	Yield stress of nail =734.6
P_d	Pull-out stress intensity of the nail
P_h	The nail head penetration bearing capacity of plywood
P_n	The tensile strength of the nail

2.3.2.1. No damage wood and rusted nail

Fig.9 is a schematic of no damage wood and rusted nail using plywood as the side material. In this case, first, the wood yield in the state where the nail head is non-protruding and fixed, then the nail yield in the state of nail head protruding and fixed. And the finally, the nail is pulled out, the nail is broken, or the nail head is punching out in the state of nail head protruding and free. The horizontal load and horizontal displacement of the nail head at these times are expressed by equation (32) ~ (37), respectively.

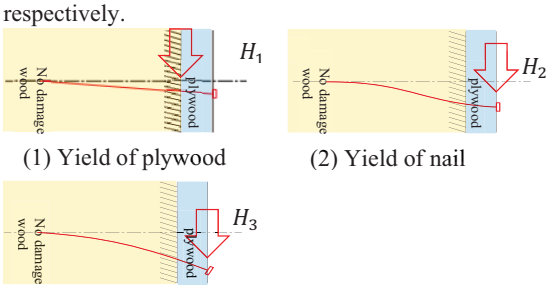

(1) Yield of plywood (2) Yield of nail

(3) Pull-out, punching out or break of nail

Figure 9: *No damage wood and rusted nail*

$$H_1 = \frac{\sigma_{yp} \times A_p}{2} \tag{32}$$

$$y_1 = \frac{H_1}{4EI{\beta_1}^3} \tag{33}$$

$$H_2 = \frac{2\beta_1 Z_n \sigma_n}{\sqrt{1 + (\beta_1 h)^2} exp[-tan^{-1}(1/\beta_1 h)]} \tag{34}$$

$$y_2 = \frac{(1 + \beta_1 h)^3 + 2}{12EI{\beta_1}^3} H_2 \tag{35}$$

$$H_3 = \sqrt{\frac{6/\alpha^2 - \sqrt{36/\alpha^4 - 24N/\alpha^3}}{2}} \tag{36}$$

$$y_3 = \frac{(1 + \beta_1 h)^3 + 1/2}{3EI{\beta_1}^3} H_3 \tag{37}$$

Where, $\alpha = \frac{(1+\beta h)^2}{2EI\beta^2}$.

2.3.2.2. Decayed wood and no damage nail

Fig.10 is a schematic of decayed wood and no damage nail using steel plate as the side material. In this case, first, the nail head yields in the state where the nail head is non-protruding and fixed. Then the nail body yields in the no damage part of wood or at the boundary between the no damage part and the decay part of wood in the state where the nail head is non-protruding and free, and finally the nail pulls out. The nail head conditions for pulling out are protruding and free when the yield of nail body occurs in the no damage part of wood, and non-protruding and free when it occurs at the boundary between the no damage part and the decay part of wood. The horizontal load and horizontal displacement of the nail head at these times are expressed by equation (38) ~ (50), respectively.

https://doi.org/10.52202/069179-0344

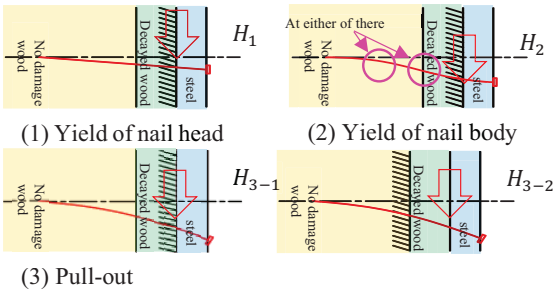

Figure 10: *Decayed wood and no damage nail*

$$H_1 = -\frac{2\beta_1 b_3 h_1}{b_1 h_1 - 8h_2} Z_n \sigma_n \tag{38}$$

$$y_1 = \frac{b_2 h_1 + 8h_3}{4EI{\beta_1}^3 b_3 h_1} H_1 \tag{39}$$

$$H_{2-1} = \frac{\beta_1 Z_n \sigma_n (f_5 sin(\beta_2 \ell) + f_6 cos(\beta_2 \ell)) h_4}{2{\beta_2}^2 ({f_3}^2 + {f_4}^2) sin(\beta_2 \ell_m)} e^{\beta_2 \ell_m - \beta_2 \ell} \tag{40}$$

$$\ell_{m-1} = \frac{1}{\beta_2} tan^{-1}\left(-\frac{f_5 sin(\beta_2 \ell) + f_6 cos(\beta_2 \ell)}{f_6 sin(\beta_2 \ell) - f_5 cos(\beta_2 \ell)}\right) \tag{41}$$

$$y_{2-1} = \frac{b_4 h_4 + 4h_5 - 4h_6}{2EI{\beta_1}^3 b_2 h_4} H_{2-1} \tag{42}$$

$$H_{2-2} = \frac{\beta_1 Z_n \sigma_n h_4}{2{\beta_2}^2 f_4} \tag{43}$$

$$y_{2-2} = \frac{b_4 h_4 + 4h_5 - 4h_6}{2EI{\beta_1}^3 b_2 h_4} H_{2-2} \tag{44}$$

$$H_{3-1}{}' = \sqrt{\frac{6/\alpha'^2 - \sqrt{36/\alpha'^4 - 24{P_d}'/\alpha'^3}}{2}} \tag{45}$$

$${y_{3-1}}' = \frac{1}{2EI{\beta_2}^3} {H_{3-1}}' \tag{46}$$

$$H_{3-1} = \frac{P_d + {H_{3-1}}' sin(\gamma_2 {H_{3-1}}')}{sin(\gamma_1 {H_{3-1}}') - {H_{3-1}}' \alpha_2 cos(\gamma_2 {H_{3-1}}')} \tag{47}$$

$$y_{3-1} = \frac{{\beta_1}^2 b_4 + R_1 + R_3}{2EI{\beta_1}^5 b_2} H_{3-1} + \frac{R_2 + R_4}{2EI{\beta_1}^2 {\beta_2}^3 b_2} {H_{3-1}}' + {y_{3-1}}' \tag{48}$$

$$H_{3-2} = \sqrt{\frac{6/\alpha^2 - \sqrt{36/\alpha^4 - 24N/\alpha^3}}{2}} \tag{49}$$

$$y_{3-2} = \frac{(1 + \beta_1 \hbar)^3 + 1/2}{3EI{\beta_1}^3} H_{3-2} \tag{50}$$

Where, $\alpha' = \frac{1}{2EI\beta^2}$, $\alpha_1 = \frac{{\beta_1}^2 b_1 + 2R_5 - 2R_7}{2EI{\beta_1}^4 b_2}$, $\alpha_2 = \frac{S_1 - S_3}{2EI{\beta_1}^3} \times \frac{\beta_2 sin(\beta_2 \ell_m)}{f_5 sin(\beta_2 \ell) + f_6 cos(\beta_2 \ell)}$, $\gamma_1 = \frac{R_6 + R_8}{2EI\beta_1 {\beta_2}^3 b_2}$, $\gamma_2 = \frac{S_2 + S_4}{2EI{\beta_2}^2} \times \frac{sin(\beta_2 \ell_m)}{f_5 sin(\beta_2 \ell) + f_6 cos(\beta_2 \ell)}$, $\alpha = \frac{(1 + \beta\hbar)^2}{2EI{\beta_1}^2}$

2.3.2.3. Decayed wood and rusted nail

Table 10 shows the nail head conditions and joint behavior at the situation of no damage wood and rusted nail and decayed wood and no damage nail. And Fig. 11 shows experimental results and estimates at the situation. From Fig.11, the formulas are correct because the experimental result and the estimated value match. Therefore, considering these results, nail head conditions and nail joint behavior are expected when wood decay and nail rust occur in combination. The first change point of the load-deformation relationship is the point where the plywood yields when the nail head condition is non-protruding and fixed. This is because, in wooden houses, plywood is used as the side material, so the nail head will not yield. Next, the second change point is the point where the nail yields in the no damage part of the wood or at the boundary between the no damage part and the decayed part of the wood when the nail head condition is protruding and fixed. The reason why the nail head condition is protruding is that the deflection angle of the nail head increase due to the yield of the plywood, and it is thought that it protrudes. Finally, the third change point is the point at which the nail pulls out, breaks, or punching out when the nail head condition is protruding and free. The horizontal load and horizontal displacement of the nail head at these times are expressed by equation (51) ~ (58), respectively. There are summarized as shown in Fig.12. Fig. 13 shows the behavior of the nail joint for each degree of deterioration calculated using these results.

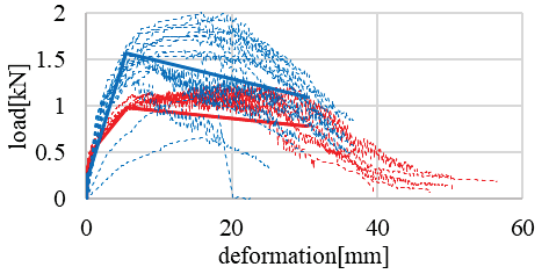

Figure 11: *Experimental results and estimates with rusted nail or wood decayed*

$$H_1 = \frac{\sigma_{yp} \times A_p}{2} \tag{51}$$

$$y_1 = \frac{b_2 h_1 + 8h_3}{4EI{\beta_1}^3 h_1 b_3} H_1 \tag{52}$$

Table 10: *Expected nail head conditions and nail joint behaviour with rusted nail or decayed wood*

	No damage wood and rusted nail		Decayed wood and no damage wood			
	Nail head condition	Behavior	Nail head condition		Behavior	
1	Non-protruding/ fixed	Yield of plywood	Nail pulls out		Yield of nail head	
2	Protruding/ fixed	Yield of nail body	Non-protruding/ free		Yield of nail body	
					At the no damage part	At the boundary between the no damage part and the decay part
3	Protruding/ free	Nail pulls out, breaks, or punching out	Non-protruding/ free with pin support	Protruding/ free	Nail pulls out	

$$H_{2-1} = \frac{4\beta_1 Z_n \sigma_n t_1 (\beta_1 \hbar T_1 + T_2) W_1 e^{\beta_2(\ell_m - \ell)}}{Y_1 \sin(\beta_2 \ell_m)} \quad (53)$$

$$H_{2-2} = -\frac{4\beta_1 Z_n \sigma_n t_1 (\beta_1 \hbar T_1 + T_2)}{{\beta_1}^2 \hbar^2 U_2 + \beta_1 \hbar U_4 + U_6} \quad (54)$$

$$y_2 = \frac{H_2}{12EI{\beta_1}^3 t_1 (\beta_1 \hbar T_1 + T_2)} \times \begin{Bmatrix} {\beta_1}^4 \hbar^4 t_1 T_1 + 4{\beta_1}^3 \hbar^3 t_1 T_2 \\ +3{\beta_1}^2 \hbar^2 (t_1 T_3 + t_2 T_2 + t_3 T_1) \\ +3\beta_1 \hbar (t_2 T_3 + t_4 T_1) + 3(-t_3 T_3 + t_4 T_2) \end{Bmatrix} \quad (55)$$

$$H_3 = \sqrt{\frac{6/\alpha^2 - \sqrt{36/\alpha^4 - 24N/\alpha^3}}{2}} \quad (56)$$

$$y_{3-1} = \frac{H_3}{12EI{\beta_1}^3 t_1 T_1} \{4{\beta_1}^3 \hbar^3 t_1 T_1 + 12{\beta_1}^2 \hbar^2 t_1 T_2 + 6\beta_1 \hbar (t_1 T_3 + t_2 T_2 + t_3 T_1) + 3(t_2 T_3 + t_4 T_1)\} \quad (57)$$

$$y_{3-2} = \frac{H_3}{3EI{\beta_2}^3} \{(1 + \beta_2 \hbar)^3 + 1/2\} \quad (58)$$

Where, $\alpha_1 = \frac{{\beta_1}^2 \hbar^2 T_1 + 2\beta_1 \hbar T_2 + T_3}{2EI{\beta_1}^2 T_1}$, $\alpha_2 = \frac{(\beta_2 \hbar + 1)^2}{2EI{\beta_2}^2}$.

3 MODELING AND ANALYSIS

3.1 OUTLINE

Based on the estimated value by the formula in 2.3.2, the elastoplastic analysis of the plywood bearing wall model is carried out using the analysis software SNAP. The model is shown in Fig.14. To analyze the strength of the plywood bearing wall based on the estimated shear resistance of the nail joint, two frame models are connected with a spring 1, and the estimated value calculated in 2.3.2 is input to spring 1. Further, one of the frame models a wooden frame in the plywood bearing wall and the other models a frame when the structural plywood is expanded using brace expansion.

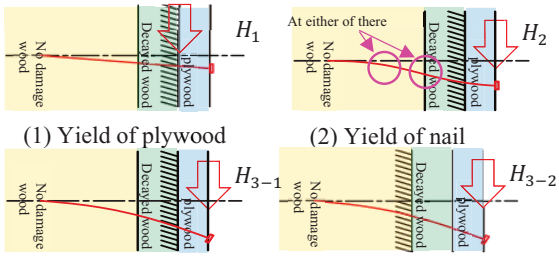

Figure 12: *Decayed wood and rusted nail*

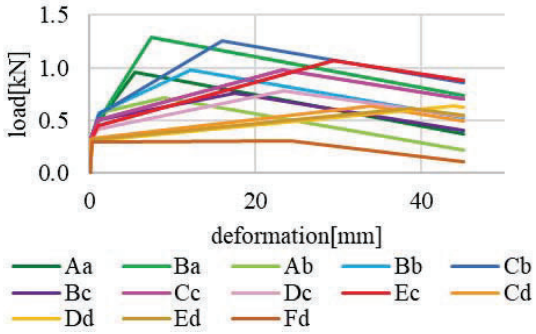

Figure 13: *The performance of nails in each deterioration degree*

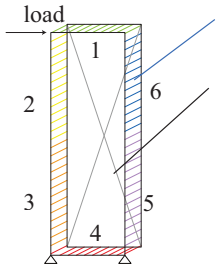

Figure 14: *Model of wall and location of deterioration*

Spring1:
Shear performance of nail

Spring2: plywood
Rigidity:16.5[kN/mm]
Elastoplastic property: elasticity

Table 11: *Pattern of deterioration position*

Pattern	Deterioration position
(α)	No damage
(β)	4
(γ)	5,6
(ω)	1,2,6

https://doi.org/10.52202/069179-0344

3.2 LOCATION OF DETERIORATION

The plywood bearing wall is divided into areas as shown in Fig14, and the deterioration position that is likely to occur is divided into patterns assuming deterioration in the house. This is shown in Table 11. The analysis is carried out when the nail joint at these 4 pattern positions become about 13 levels of deterioration shown in the shaded portion of Table 2.

3.3 ANALYSIS RESULT

Fig.15(α) shows the analysis result and the experimental result of the past[7] with the no damaged nail and wood. The analysis result agrees well with the experimental result. Next, the analysis results of patterns (β), (γ) and (ω) are also shown in Fig.15. In the case of (β), the load-deformation relationship is almost the same regardless of the degree of deterioration of the foundation. In the case of (γ), the deformation increases as the deterioration progresses, but there is no significant effect on the maximum strength. In the case of (ω), the maximum strength and rigidity after yield decreases remarkably as the deterioration progresses.

4 CONCLUSIONS

The structural performance of plywood bearing wall with the nails rusted and columns decayed can be predicted by deterioration degree of nails and columns. The maximum strength doesn't decrease remarkably when only the foundation of plywood bearing wall deteriorates. On the other hand, when the pillar deteriorates, the rigidity after yield is greatly reduced. In addition, even if the wood decay a little, the strength increases due to the influence of rusting of the nail, and it decreases when further deterioration progresses.

ACKNOWLEDGEMENT

This study was carried out with support from the Asahi Glass Foundation.

REFERENCES

[1] Hiroto Imamura, Makoto Kiguchi, Akio Okuro: The Deteriorating Circumstances of Wood Viewed from the Deterioration of Nails in the Exterior Wall of Wooden Houses, Bull. For. & For. Prod. Res. Inst, No.345, pp.101-149, 1987

[2] Hiroki Ishiyama, Mikio Koshihara: Experimental study on the performance of the nailed joint with rust -Study on the structural performance of wooden houses when deteriorated(Part 1)-, Journal of Structural and Construction Engineering, Vol.74, No.646, pp.2281-2289, 2009.12.

[3] Nakaba Wada, Hiroki Ishiyama: The Structural Performance of the Nail Driven into the Decayed Wood. Summaries of technical papers of annual meeting, Architectural Institute of Japan (Hokuriku), September 2019.

[4] Kotaro Kawano, Takumi Nakahata, Yuhei Mouri, Takuro Mori, Yoshiyuki Yanase, Kei Tanaka, Masafumi Inoue: The study on the evaluation of the remaining seismic performance of wooden buildings subjected to biodegradation, AIJ Kyushu chapter architectural research meeting, 2016.3

[5] Qingjun Meng, Takuro Hirai, Akio Koizumi: Frictional coefficients between timber and some structural sheet materials, Journal of the Japan Wood Research Society, Vol.54, No.5, pp.281-288, 2008

[6] Architectural Institute of Japan: Recommendations for design of building foundation(2003 Edition), pp.262-297

[7] Hiroki Ishiyama, Mikio Koshihara: Experimental study on the performance of the shear wall with the nails rusting, Journal of Structural and Construction Engineering, Vol.77, No.676, pp.911-918,

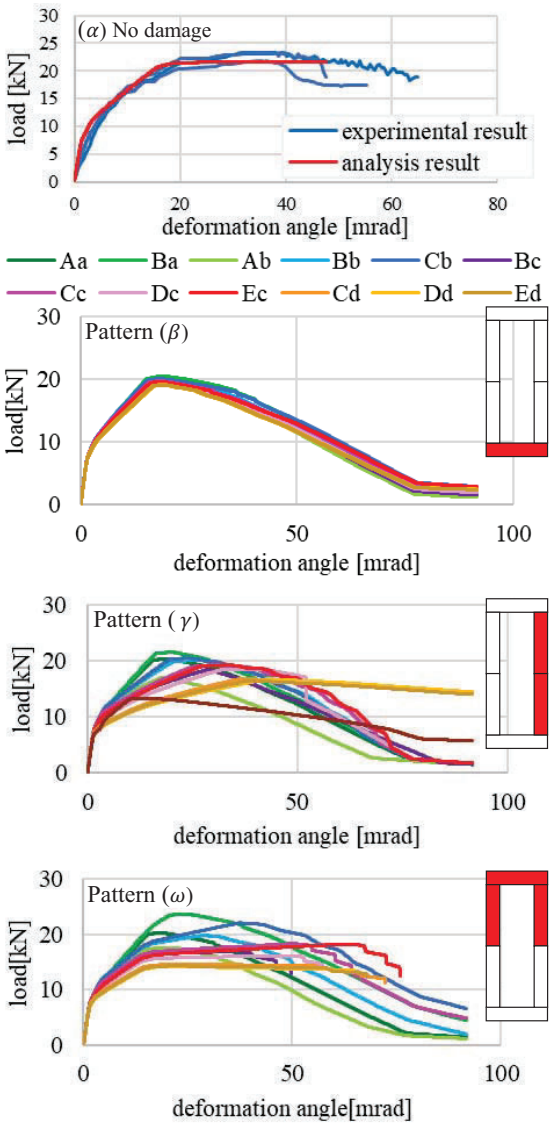

Figure 15: *The analysis result and the experimental result*

World Conference on Timber Engineering Oslo 2023

DEVELOPMENT OF A NUMERICAL MODEL TO CONSIDER THE FOUNDATION FLEXIBILITY EFFECTS IN CLT ROCKING WALLS

Irshad Qureshi[1], Gustavo Acuña[2], Daniel Dolan[3],

ABSTRACT: This work developed a numerical model to consider the effects of foundation flexibility in cross laminated timber rocking wall structures. The model was validated against the test results of a quasi-static cyclic and dynamic tests. In both tests, the foundation behaved as a flexible member with significant yielding. A multi-spring model was used in the study and two different approaches for solid and steel section beam foundations were employed to calculate the axial stiffness of contact springs. The proposed techniques were found to be not only able to consider the foundation flexibility but to also omit the need to use empirical relationships or calibration with experiments to calculate plastic hinge length to be used for calculation of axial stiffness for the base springs. Following the validation of the numerical model, a parametric study was performed to study the effects of foundation flexibility on the shear-drift response of rocking wall structures.

KEYWORDS: Cross laminated timber, Rocking wall, Wall-foundation interaction, Numerical modeling

1 INTRODUCTION

Recently, there has been an increasing focus on the use of sustainable materials in construction. A global effort to reduce carbon emissions has instigated renewed interest in the use of engineered timber like cross laminated timber (CLT) and mass plywood for building structures, which promise a green construction material with higher strength-to-weight ratio, comparable stiffness and ductility, faster installation, and improved thermal performance. CLT rocking wall structures have been in a development phase as a resilient and sustainable alternative to conventional concrete and steel structures. Rocking structures promise damage avoidance design with minimal residual drift and decent energy dissipation.

The U.S. National Science Foundation funded NHERI Tall wood project is a major research initiative [1]. As an initial step, a series of CLT rocking walls with varying design parameters like area and initial force of post-tensioning, single and coupled walls, and varying flexibility of foundation were used [2]. A uniaxial shake table test of a 2-story CLT rocking wall structure followed [3], and a 10-story rocking wall structure is being tested on the NHERI shake table at the University of California-San Diego [4]. During the testing of the 2-story structure, it was observed that the base beam, used as a foundation for the rocking wall, yielded with significant permanent deformation. This unintended inelastic behavior of foundation increased the fundamental period of the building [5], resulting in lower-than-expected damage in the structural members especially at the wall toes; however, the displacement demand on members increased. Based on these results, it is important to explore the effect of foundation flexibility on the overall lateral behavior of rocking wall structures and develop guidelines to achieve optimum solutions with minimal damage and manageable drift demands. To achieve this, numerical models capable of incorporating the effects of foundation flexibility are required, which can then be used to further investigate different aspects of this rocking wall-foundation interaction.

This study is focused on the development of a numerical model to account for the foundation flexibility effects in rocking wall structures. Two different modeling approaches are proposed in this study to model two different tests from literature where the foundation of rocking wall behaved nonlinearly with significant yielding/crushing, one was a static [2] while the other was a dynamic test [3]. A multi-spring model was used in this study to model the rocking behavior along with two different approaches to model contact stiffness at the interface of rocking wall and flexible foundation. A parametric study was then performed to understand the effects of foundation flexibility on the seismic force and displacement demands against two levels of initial post-tensioning.

2 CASE STUDY STRUCTURES

Ganey [2] tested single and coupled CLT rocking walls using quasi-static cyclic lateral loading and the response of these rocking walls were numerically modelled in several studies [2,6,7]. However, to the best of the authors' knowledge, Specimen 4 from the testing has been

[1] Visiting Fulbright Scholar, Washington State University, m.qureshi2@wsu.edu
[2] PhD Scholar, Washington State University, Pullman WA, USA g.acunaalegria@wsu.edu
[3] Professor, Washington State University, Pullman WA, USA jddolan@wsu.edu

https://doi.org/10.52202/069179-0345

modeled in the past studies. Specimen 4 consisted of a single CLT rocking wall resting on a CLT foundation. Since the rocking wall rested on the weaker axis of the CLT foundation, the nonlinear behavior was confined to crushing of the foundation only, resulting in a flexible foundation condition. The CLT rocking wall consisted of two Hem-Fir 5-ply CLT panels joined by steel plates using SDS screws. Cross-sectional dimensions were approximately 1.22 m by 0.17 m while the wall height was 4.43 m. Lateral loading was applied at a height of 4.1m. A 31.5 mm rod with an initial post-tensioning force of $0.4f_{pt,u}$ was used, where $f_{pt,u}$ was the ultimate stress of PT rod. The material properties of CLT and PT are shown in Table 1 while the testing setup for Specimen 4 is shown in Figure 1.

Table 1: *Properties of CLT and PT used for Specimen 4*

CLT Property (Units)	Value	PT Property (Units)	Value
E_1 (MPa)	3042	E_{pt} (GPa)	220
E_2 (MPa)	900	$f_{pt,y}$ (MPa)	929
E_3 (MPa)	2080	$f_{pt,u}$ (MPa)	1091
G_1, G_2, G_3 (MPa)	345	$F_{pt,i}$ (kN)	338
ν_1, ν_2, ν_3	0.3		
f_y (Direction 1*) (MPa) (For rocking wall)	24.8		
f_y (Direction 2*) (MPa) (For CLT foundation)	5.93		

*Directions 1, 2 and 3 coincide with the height, length, and thickness of the CLT wall panel

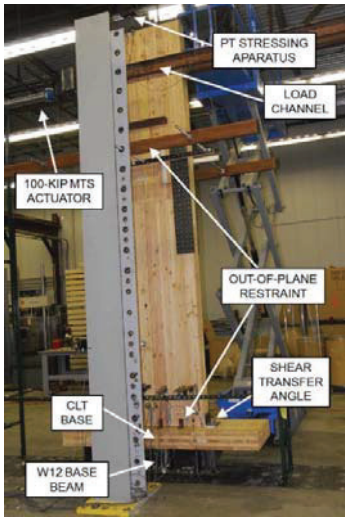

Figure 1: *Testing setup for Specimen 4 (CLT wall) resting on CLT foundation* [2]

The dynamic test considered was the full-scale 2-story CLT rocking wall structure with two rocking shear walls in the direction of shaking [3]. The rocking wall panels were 5-ply having grade E2-M1 CLT. The modulus of elasticity, shear modulus and yielding stress for CLT were 8536 MPa, 552 MPa and 25 MPa, respectively. For each wall, two balloon framed CLT panels were used. The CLT panels in each wall were joined by five equally spaced U-shaped flexural plates along the height of the wall to provide a minimum energy dissipation ratio of 0.3. Modulus of elasticity and yielding stress of each U-shaped plate were $2x10^5$ MPa and 414 MPa. Post-tensioning was provided by using four 19 mm bars in each wall with an average initial post-tensioning force equal to 40% of yield strength (53 KN for each bar). Each wall had a height, length, and thickness of 7.32 m, 1.52 m, and 0.17 m, respectively. Shear transfer angles were used at the wall ends to transfer shear and avoid lateral slip. Wall-to-diaphragm shear transfer connections were used to transfer lateral demands while out-of-plane movement was constrained using bracing. As explained earlier, the steel foundation of the 2-story building, which was expected to behave as rigid, exhibited nonlinear behavior with permanent deformations right below the wall ends (i.e., at the center of rotation during the rocking motion.) A total of 14 excitations were used for the dynamic testing of the structure, with effective PGA for the excitations varying from 0.13g to 0.85g representing service level earthquake (SLE), design basis earthquake (DBE) and maximum considered earthquake (MCE). Details of the test structure, rocking wall and foundation are shown in Figures 2 and 3. Further information about the structure, testing setup and dynamic testing can be found in [8].

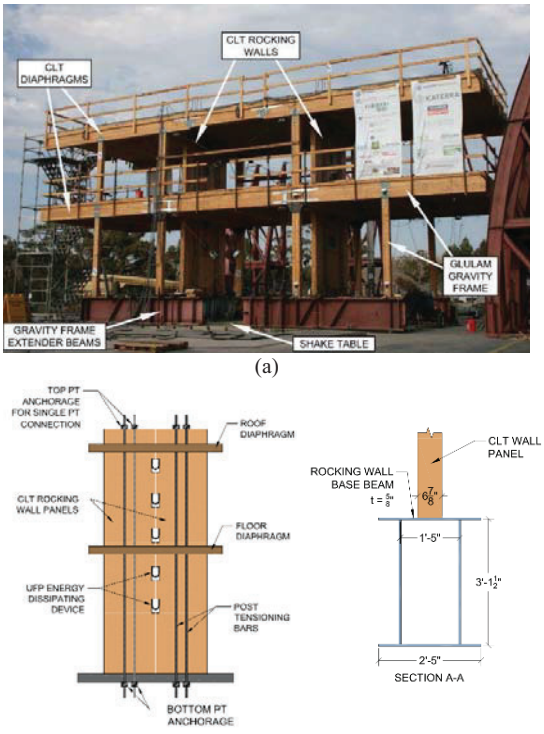

Figure 2: *(a) Full-scale 2-story structure (b) CLT rocking wall (c) Steel base beam [8]*

https://doi.org/10.52202/069179-0345

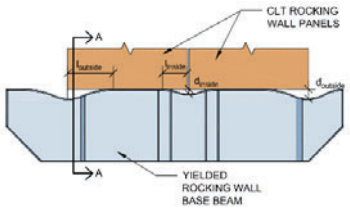

Figure 3: *Full-scale 2-story structure Steel base beam after yielding* [8]

3 PROPOSED NUMERICAL MODELS

Several techniques have been used to model the behavior of rocking walls including monolithic beam analogy, lumped plasticity model, multi-spring model, fiber model, and finite element model. Except for finite element models, all the above-mentioned models need iterative procedures or calibration using experimental results to determine the compression zone/plastic hinge length, and do not consider foundation flexibility. In the current study, a multi-spring (MS) model has been used, as shown in Figure 4, for the 2-story coupled rocking wall with energy dissipation mechanisms, that was tested on the shake table. The MS model for the quasi-static test on single rocking wall without any external energy dissipation mechanism was also based on the same principles for the modeling of the wall, PT steel, contact modeling, placement of rigid links, etc., but it is not shown here for brevity. The rocking wall was modeled using a beam-column element, the post-tensioning was modeled using axial springs with prestress force, and the contact was modeled using 50 compression-only springs at the base. Adjusting the stiffness of the contact springs is an active area of research. Several empirical formulas have been proposed in the past to determine the length of the plastic hinge (L_e), which is used to find the contact stiffness by equating it to EA/L_e where, E and A are modulus of elasticity of wall and contact area. [9,10] proposed empirical relationships to find out the plastic hinge length for rocking timber walls. A plastic hinge length of two times the wall thickness has also been proposed and used in the past [5,11] while for concrete rocking connections, a plastic hinge length equal to the half the length of the walls has been proposed [12,13]. All these empirical relationships try to a provide a measure for the axial stiffness of the rocking wall assuming the foundation to act as rigid, however, both the case study structures selected in the current work showed a permanent deformation due to yielding in the foundation, rendering the available empirical formulas unsuitable. Therefore, different techniques were proposed in this study.

The stiffness of the contact springs was calculated using principles of contact mechanics. [14] argued that the volume with dimension of the contact length in all three spatial dimensions represents the maximum stress concentration region and should be used to find different parameters of contact. It has been shown that although it's an assumption, it gives results within a 10% margin of error [14]. If the indentation at contact interface of a length $2a$ against a force F is d, then axial stress and axial strain are $\frac{F}{(2a)^2}$ and $\frac{d}{2a}$, respectively. Solving for the equation $\sigma = E\varepsilon$ results in

$$F = 2aEd \tag{1}$$

where, $2aE$ represents contact stiffness and E is the modulus of elasticity of elastic half space. However, this formulation is valid for solid foundations only and a different technique is used to model the 2-story rocking wall test on shake table.

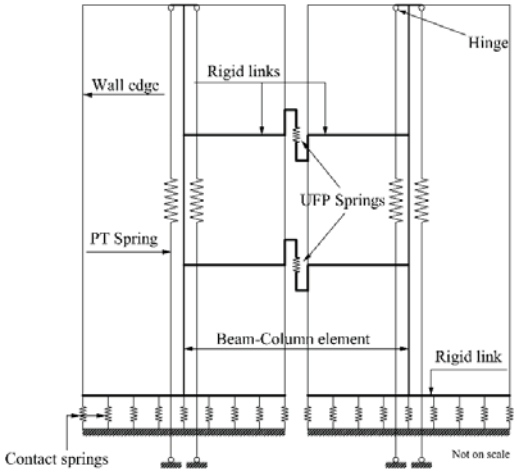

Figure 4: *Multi-spring model*

A steel beam was used as foundation in the dynamic test which showed yielding and permanent deformation. To quantify the contact stiffness at wall-foundation interface, a finite element model for the steel base beam resting on the ground was developed in ABAQUS [15]. Solid 8-noded linear brick elements (C3D8R) with reduced integration were used to model the base beam. A mesh sensitivity study was conducted before choosing the mesh size. Self-weight of the base beam was ignored. Yielding stress for the steel beam was assumed to be 414 MPa. To simulate contact behavior during rocking motion, a triangular force pattern was applied at the expected contact area on the steel beam. The problem was considered as a two-dimensional and the axial stiffness for the contact springs was determined by dividing the force in the tributary area of each spring divided by the average deformation in that region. The finite element model, and the stress distribution in the steel base beam after applying the loading is shown in Figure 5. It is important to mention that the finite element model showed yielding in the base beam even for the loading corresponding to the service level earthquakes. Using the MS model described earlier with contact stiffness from the results of finite element analysis, all 14 ground motions were applied to the 2-story rocking wall in the sequence used during the experiments and the yielding observed in any test in the contact springs was used as initial condition for those springs in the next

https://doi.org/10.52202/069179-0345

tests. However, it was observed that assuming an undamaged base beam for each test did not alter the analysis results significantly as the beam started yielding at the corners at the start of the test, and the condition of the beam against the maximum response time span was almost same.

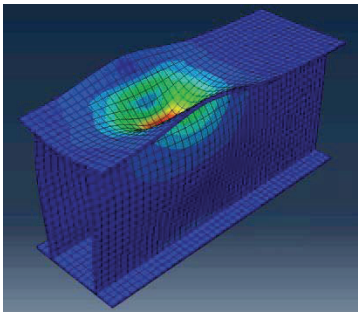

Figure 5: *3D Finite element model of base beam after applying loading*

4 NUMERICAL MODEL VALIDATION

Loss in PT force against increasing drift demand was observed in the test for Specimen 4; however, the model used here cannot account for it. Therefore, a maximum drift of 4% is considered for the comparison purpose as the losses in PT steel during the test were within reasonable range up to this drift. Equation 1 was used to model the stiffness of the foundation which is considered to dominate the contact behavior at the wall-foundation interface because of a much lower modulus of elasticity of CLT in transverse direction of the foundation when compared to the in-plane direction in wall. This stiffness is, therefore, used as axial stiffness for contact springs. The experimental results for only one 5-ply CLT panel was available in the out of plane direction; therefore, an average value of yield stress for four 3-ply and one 5-ply CLT panels in the direction of interest were used to adjust the yielding stress of the CLT foundation.

Wall Specimen 4 was modeled using the MS model explained in earlier sections. Initially, a single layer of axial springs representing a flexible foundation was used. However, two layers of springs can also be used representing the axial stiffness of wall and transverse stiffness of foundation. An important point in this regard is the use of a plastic hinge length for the springs representing the rocking wall. Equating Equation (1) with the expression EA/L_e gives an effective length of the wall equal to the thickness of wall. It's important to mention here that several past studies have proposed an effective length of two times the wall thickness for CLT walls [7, 11, 16]. Results with one and two layers exhibited almost identical results in this study and are not shown here for brevity.

Comparison of force-drift behavior from the experimental results and numerical model is shown in Figure 6. The CLT rocking wall showed slightly different behavior in positive and negative direction of motion. As the first cycle of lateral deformation was provided in positive direction, the comparison in the positive direction of response is considered and discussed here. The numerical model was found to model the initial stiffness accurately. Since the yielding stress for the 5-ply CLT in the transverse direction was taken as average of different samples, a monotonic response considering the CLT wall to be linear elastic is shown. The nonlinear behavior in monotonic response is purely due to geometric nonlinearity. Comparing these two responses shows that the CLT wall showed yielding before gap opening behavior which also caused a softening of post gap-opening stiffness. The numerical model was able to predict this response accurately and the assumed average yield stress value was found to be reasonable. The hysteretic behavior, on the other hand, showed some mismatch with the numerical model showing lower energy dissipation than the experimental results. It's important to mention here that this is due to unavailability of a reliable hysteretic model for the transverse direction response of CLT and future works need to focus on this. Single and coupled rocking walls tested by Ganey were also modeled using this approach and results showed a similar or better accuracy compared to some of the earlier works that calculated plastic hinge length by using trial-and-error approach; however, these walls had rigid-like footing condition and their results are not presented here for brevity and for the reason that this work is focused on the response of rocking structures on flexible foundations.

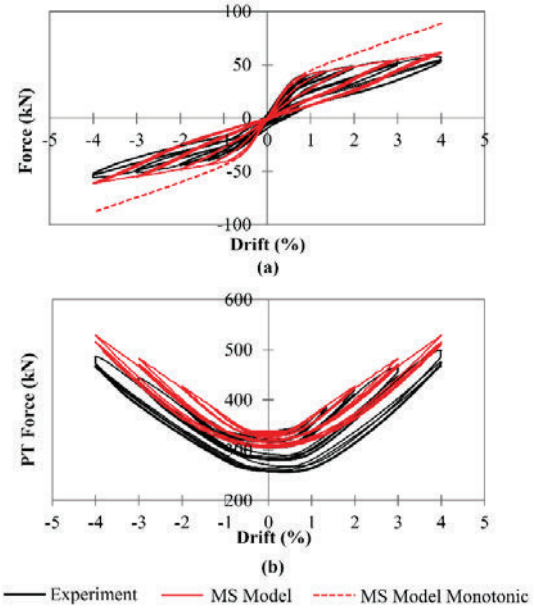

Figure 6: *Comparison of (a) force-drift and (b) PT force-drift response from experiment and MS model for Specimen 4*

As explained earlier, the stiffness of the base springs for the dynamic test was calibrated using a finite element model. All the other aspects of the MS model were same except for the calculation of contact stiffness as described

earlier. Results from two SLE (Tests 2 and 4), one DBE (Test 6) and one MCE (Test 12) level ground motions are shown in Figure 7. The MS model was able to predict the displacement demands in terms of pattern and maximum values with significant accuracy. Barring some under-prediction in a few cycles, the numerical model was found to be efficient in simulating the displacement results of rocking wall resting on flexible foundation. Although not shown here, the results of roof acceleration and base shear, however, showed underprediction for most tests. Two different techniques were used in the current study to model the foundation flexibility effects in solid and steel section beam foundations, and the proposed techniques have shown promising results. Further verification of the proposed techniques is needed in the future to develop a more generalized approach for modeling contact behavior in rocking walls with or without rigid foundations, omitting the need to calibrate the numerical models with experimental results.

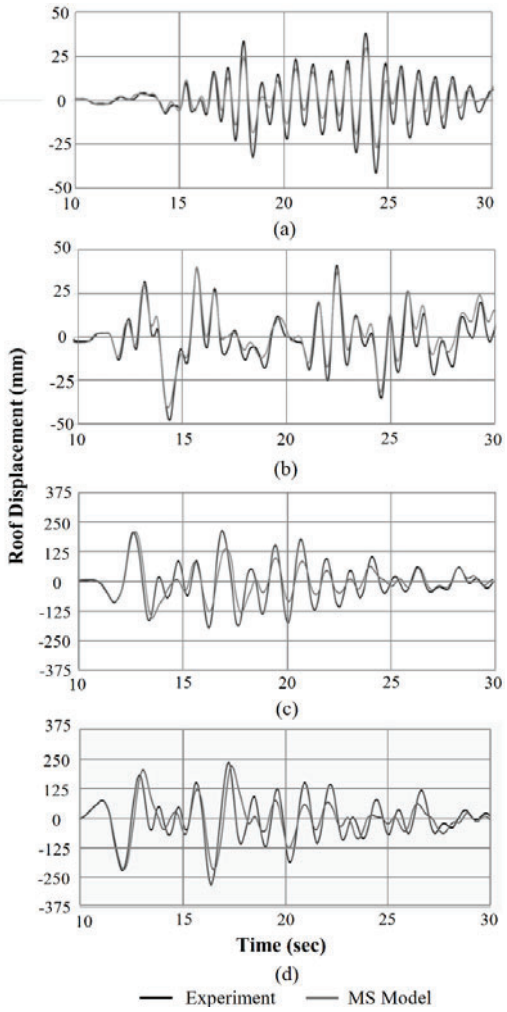

Fig 7: *Comparison of roof displacements from experiment and MS model for (a) Test 2, (b) Test 4, (c) Test 6 and (d) Test 12*

As the proposed MS model can include the effects related to foundation flexibility, a parametric study was conducted to further explore these effects on the base shear demands of rocking walls against different levels of foundation flexibility.

5 PARAMETRIC STUDY

To further explore the effects of foundation flexibility on the lateral behavior of rocking walls, the validated numerical model was used to simulate different combinations of wall and foundation stiffness. Ganey used two levels of initial post-tensioning for different specimens (i.e., 10% and 40% of ultimate strength of PT steel.) In this part, the Ganey wall was used with different foundation stiffness values, ranging from rigid to a stiffness value equal to 10% of the axial stiffness of the wall against two levels of initial post-tensioning, as shown in Table 2. Axial springs representing stiffness of wall and foundation were considered to be acting in series to calculate equivalent interacting stiffness. All the other parameters were kept constant for all the iterations. In this part, both the wall and the foundation were assumed to be linear elastic with geometric nonlinearity acting as sole contributor for inelastic behavior. As the foundation flexibility increased,
the decompression rotation increased while the forces against any particular drift decreased, as shown in Figure 8. When the foundation stiffness was one tenth of the axial stiffness of the wall, the maximum force demands against 3% drift reduced by 30% and 27% for the cases with initial PT force equal to 10% and 40% of the ultimate PT force, respectively. There was also a visible decrement in initial stiffness of the rocking system which will change the modal properties of the system with a lengthened fundamental period, modified mass participation and changes in modal force patterns along the height.

Table 2: *Variables used in parametric investigation*

Initial PT	Parameter studied	Parameter variations				
$f_{pt,i} = 0.1f_{pt,}$	Ratio of foundation to wall stiffness	Rigid	1	0.5	0.25	0.1
$f_{pt,i} = 0.4f_{pt,}$	Ratio of foundation to wall stiffness	Rigid	1	0.5	0.25	0.1

Although the modeling techniques proposed in the current work were focused on the timber rocking walls, future works need to ascertain their general applicability by using them for the modeling of concrete and steel rocking structures. Furthermore, the proposed contact mechanics technique for solid foundations suggests that a concrete rocking wall resting on a concrete foundation with a similar value of modulus of elasticity, as is usually the case, should not be considered rigid as the real contact stiffness value would be lower than the axial stiffness of the wall in the contact region.

https://doi.org/10.52202/069179-0345

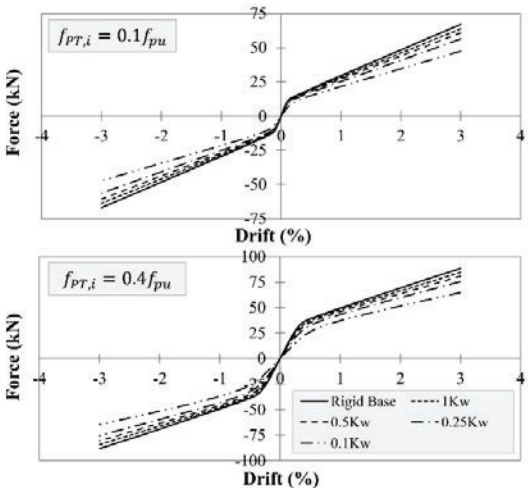

Figure 8: *Effect of foundation stiffness on the force-drift response.*

6 CONCLUSIONS

This study was focused on the development of a simple numerical model to account for the foundation flexibility effects in rocking wall structures. Results from a static and a dynamic test of rocking walls with flexible foundations were used in the current study. Two different approaches for the modeling of contact behavior at wall-flexible foundation interface were proposed. For the solid flexible foundation, a technique based on the principles of contact mechanics was used. Albeit some mismatch in the hysteretic response, the proposed technique was found to predict the force and displacement responses of the case study rocking wall resting on a yielding foundation with significant accuracy. On the other hand, using the results of foundation stiffness from a finite element model to adjust the contact stiffness in the multi-spring model proved to be an effective technique, and accurately predicted the displacement responses of the structure against varying levels of seismic intensity. A decrease in foundation stiffness is found to reduce the initial stiffness and the force demand in rocking structures. Future works are needed to check the general applicability of proposed techniques by modeling the concrete and steel rocking walls.

ACKNOWLEDGEMENT

Authors would like to acknowledge the Fulbright Commission, USA for provide the Visiting Scholar Fellowship to the first author.

REFERENCES

[1] S. Pei *et al.* Development and full-scale validation of resilience-based seismic design of tall wood buildings: the NEHRI Tallwood Project. In *Proc. 2017 NZSEE Conf. Proc. Wellingt. NZ N.Z. Soc. Earthq. Eng.,* pages 1-8, 2017.

[2] Ganey R.S.: Seismic design and testing of rocking cross laminated timber walls. Master's Thesis, University of Washington, Seattle, WA, 2015.

[3] Pei. S. *et al.:* Experimental seismic response of a resilient 2-Story mass-timber building with post-tensioned rocking walls. Journal of Structural Engineering, 145(11), 2019

[4] Pei S.. NHERI TallWood Project. http://nheritallwood.mines.edu

[5] Wichman S., Berman J.W., Pei. S.: Experimental investigation and numerical modeling of rocking cross laminated timber walls on a flexible foundation. Earthquake Engineering and Structural Dynamics, 51(7):1697-1717, 2022.

[6] Wilson A., Motter C., Phillips A., Dolan. J.D.: Modeling techniques for post-tensioned cross-laminated timber rocking walls. Engineering Structures, 195:299-308, 2019.

[7] Slotboom. C.: Numerical analysis of self-centring cross-laminated timber walls. Master's Thesis, University of British Columbia, 2020.

[8] Wichman. S.: Large-Scale dynamic testing of rocking cross laminated timber walls. Master's Thesis, University of Washington, 2018.

[9] Newcombe M.P.: Seismic design of post-tensioned timber frame and wall buildings. Doctoral Dissertation, University of Canterbury, 2011.

[10] Newcombe. M.P.: The connection response of rocking timber walls. New Zealand. Timber Design Journal, 23(1):21-28, p. 8, 2015.

[11] Akbas. T. *et al.*: Analytical and experimental lateral-load response of self-centering posttensioned CLT walls. Journal of Structural Engineering 143(6), 2017.

[12] Spieth. H.A., Carr. A.J., Murahidy. A.G., Arnolds. D., Davies. M., and Mander. J.B.: Modelling of post-tensioned precast reinforced concrete frame structures with rocking beam-column connections. In *2004 NZSEE conference*, 2004.

[13] Qureshi I.M., Warnitchai. P.: Computer modeling of dynamic behavior of rocking wall structures including the impact-related effects. Journal of Advances in Structural Engineering, 19(8):1245-1261, 2016.

[14] Popov V.L.: Contact Mechanics and Friction: Physical Principles and Applications. Springer-Heidelberg Dordrecht London New York Berlin, 2010.

[15] ABAQUS. Dassault Systèmes, S.J.T. and Manuals, U.S., 2018.

[16] Wichman. S., Berman. J.W., Pei. S.: Experimental investigation and numerical modeling of rocking cross laminated timber walls on a flexible foundation. Earthquake Engineering and Structural Dynamics, 51(7):1697-1717, 2022.

World Conference on Timber Engineering Oslo 2023

PRESCRIPTIVE SEISMIC DESIGN PROCEDURE FOR POST-TENSIONED MASS TIMBER ROCKING WALLS IN THE UNITED STATES

Aleesha Busch[1], Reid B. Zimmerman[2], Shiling Pei[3], Eric McDonnell[4], Philip Line[5], Da Huang[6]

ABSTRACT: This paper describes a prescriptive seismic design procedure for a lateral force-resisting system composed of post-tensioned mass timber rocking walls. This procedure utilizes techniques and analysis methods routinely adopted by industry and adheres to force-based approaches found in the current U.S. seismic loading standard. Unlike performance-based design approaches that are more complex and require peer review, this design procedure targets future adoption into model codes by providing a basis for the prescriptive design of mass timber rocking wall lateral force-resisting systems. To illustrate this procedure, a series of example buildings were designed using the methods described in this paper.

KEYWORDS: Tall wood building, Seismic design, Mass timber rocking wall, Cross-laminated timber

1 INTRODUCTION

With the recent growth and popularity of mass timber in the United States, the number of mass timber building projects is expected to multiply. Although there has been increased traction for mass timber lateral force-resisting systems (LFRSs)—which utilize mass timber panels such as cross-laminated timber (CLT), laminated veneer lumber (LVL), and mass plywood panels—in research and development, the U.S. building code and its reference design standards provide limited options for mass timber seismic force-resisting systems as of the end of 2022. The one currently permitted system comprises platform-framed, conventionally connected CLT walls.

Out of the many potential mass timber LFRSs, post-tensioned mass timber rocking walls are thought to be the competitive choice for mass timber building projects in regions with high seismicity, particularly because they are considered a low-damage lateral system. The mechanism of this system is very similar to that of a precast concrete rocking wall system, which was heavily researched and tested in the 1990s and then codified via ACI ITG-5.1-07 and ITG-5.2-09 [1,2]. Researchers in New Zealand conceptualized the first timber version of this system, using LVL walls, and continued the development with several real building project applications [3]. The U.S. also adopted this system and has had real projects that were either permitted [4] or built [5,6]. However, all of these existing designs and analyses were conducted using advanced tools and procedures (performance-based design and nonlinear response history analysis), which are not typically used in average design offices. This situation calls for a prescriptive design method for post-tensioned mass timber rocking wall systems.

2 MASS TIMBER ROCKING WALL SYSTEM

The design procedure described in this paper is suitable for post-tensioned mass timber rocking wall LFRSs like those shown in Figure 1.

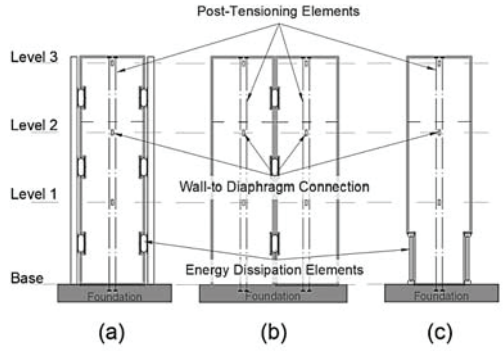

Figure 1: *(a) Conceptual configuration of a post-tensioned mass timber rocking wall with bounding columns; (b) conceptual configuration of coupled post-tensioned mass timber*

[1] Graduate Student, Colorado School of Mines, U.S.A. abusch@mines.edu
[2] Technical Director, KPFF Consulting Engineers, U.S.A. reid.zimmerman@kpff.com
[3] Associate Professor, Colorado School of Mines, U.S.A. spei@mines.edu
[4] Principal, Holmes Structures, U.S.A. eric.mcdonnell@holmesstructures.com
[5] Director of Structural Engineering, American Wood Council, U.S.A. pline@awc.org
[6] Graduate Student, Colorado School of Mines, U.S.A. huang@mines.edu

https://doi.org/10.52202/069179-0346

rocking walls; and (c) conceptual configuration of an uncoupled post-tensioned mass timber rocking wall.

The walls consist of mass timber panels attached to the floor diaphragms in a balloon-framing configuration, and the panels can either be coupled or uncoupled. The material of the wall panels can be of the engineer's choice, given they meet the requirements of the National Design Specification (NDS) for Wood Construction's Chapter 8 for structural composite lumber or Chapter 10 for cross-laminated timber [7]. The wall panels are post-tensioned (P/T) at the center of the wall with high-strength steel strands or threaded rods. Energy dissipation (ED) elements, which can be yielding or frictional devices or specialized friction dampers, must also be part of the system to help absorb the earthquake input energy during the rocking motion. These damping elements can include, but are not limited to, U-shaped flexural plates (UFPs) or buckling restrained devices (BRBs). Connections between the walls and the diaphragms, and between the wall and the foundation must also be detailed to complete the lateral load path.

3 SEISMIC DESIGN APPROACH

This design methodology was created to be used by practicing engineers in the United States to design post-tensioned mass timber rocking walls as a lateral force-resisting system [8]. To accomplish this, a prescriptive design method using either the Equivalent Lateral Force (ELF) method or Modal Response Spectrum Analysis (MRSA) from ASCE 7 Chapter 12 [9] was created. The overall design is completed at the design basis earthquake (DBE) with some additional checks at the maximum considered earthquake (MCE_R). The approach can be broken into the five major steps described below:

3.1 PRELIMINARY DESIGN

This section contains the architectural design and the creation of a linear analysis model of the building.

3.2 DRIFT ANALYSIS

This section calls for the calculation of the building drifts and checking them against the allowable story drifts in ASCE 7 Chapter 12 [9].

3.3 ROTATIONAL DEMAND AT THE ROCKING INTERFACE

This section addresses the calculation of the gap opening at both DBE and MCE_R levels. This is done for each of the hazard levels by following Equations 1 and 2, respectively:

$$\theta_{design} = \frac{C_1 * \delta_x - \delta_{xe,y}}{h_w} \quad (1)$$

$$\theta_{maximum} = \frac{1.5 * C_1 * \delta_x - \delta_{xe,y}}{h_w} \quad (2)$$

Where δ_x is the elastic roof displacement from a fixed-base, elastic model, C_1 is a factor that relates displacements from a linear model to expected inelastic displacements, $\delta_{xe,y}$ is displacement due to the elastic flexibility of the wall panel itself, and h_w is the height of the wall.

3.4 SYSTEM LEVEL DESIGN AND CHECKS

This section contains the determination of the system moment and shear demands from the fixed-based model and their scaling, when appropriate. In addition, the calculation of the system capacity using sectional analysis is also determined. Following the determination of the demands and capacities, a check is performed to ensure the strength of the system is sufficient. The moment capacity of the system shall be determined at the center of the wall for a single wall panel, and at the center of the system for a coupled rocking wall. The moment check can be determined using Equation 3.

$$M_{u,rm} \leq \phi_{rm} * M_{n,rm} \quad (3)$$

Where $M_{u,\ rm}$ is the moment demand of the rocking mechanism from ASCE 7 LRFD factored load combinations, excluding overstrength load combinations, φ_{rm} is the strength reduction factor for the rocking mechanism, and $M_{n,rm}$ is the nominal moment capacity of the rocking mechanism and can be calculated following Equation 4a for single wall panels and Equation 4b for coupled wall panels.

$$M_n = M_{ed,comp} + M_{wood,comp1} + M_{wood,comp2} + M_{ed,tens} \quad (4a)$$

$$M_n = M_{ed,comp} + M_{wood,comp1} + M_{wood,comp2} + M_{ed,tens} + M_{PT\Delta} \quad (4b)$$

Where $M_{ed.comp}$ is the moment due to the ED elements at the wall toe (i.e., compression end of the wall), $M_{wood,comp1}$ is the moment due to the compression of the wood in the linearly varying stress portion, $M_{wood,comp2}$ is the moment due to the compression of the wood in the constant stress portion, $M_{ed,tens}$ is the moment due to the ED elements at the wall heel (i.e., tension end of the wall), and $M_{PT\Delta}$ is the moment due to the incremental force from elongation of the P/T elements during rocking (i.e., total force in P/T elements minus initial P/T force). Each of these moments is defined further in Equations 5 through 9. It should be noted here that the following equations are derived for when the moment is being taken about the center of the wall. When the moment is being taken about a different point (e.g., in a coupled wall system), adjustment to the equations is required. In addition, Equation 9 is only needed for the coupled wall as indicated in Equation 4b.

$$M_{ed,comp} = \frac{F_{ed,comp} * - L_w}{2} \quad (5)$$

$$M_{wood,comp1} = F_{wood,comp1}\left(-\frac{L_w}{2} + c_2 + \frac{c_1}{3}\right) \quad (6)$$

$$M_{wood,comp2} = F_{wood,comp2}\left(-\frac{L_w}{2} + \frac{c_2}{2}\right) \quad (7)$$

$$M_{ed,tens} \ \frac{F_{ed,tens} * L_w}{2} \quad (8)$$

$$M_{PT\Delta} = F_{PT\Delta} * \frac{L_w}{2} \quad (9)$$

Where $F_{ed,\ comp}$ is the force due to the ED elements at the wall toe (i.e., compression end of the wall), $F_{wood,comp1}$ is the force in the wood in the region of linearly varying stress, $F_{wood,comp2}$ is the force in the wood in the region of constant compressive stress, $F_{ed,tems}$ is the force due to the ED elements at the wall heel (i.e., tension end of the wall), $F_{PT\Delta}$ is the force due to the elongation of the P/T elements during rocking (i.e., total force in P/T elements minus initial P/T force), L_w is the length of the wall, c_1 is the length of the linearly varying stress portion in the wall toe, and c_2 is the length of the constant compressive stress in the wall toe. It should be noted that c_1 and c_2 summed together will give c, the neutral axis depth of the wall. These forces are illustrated in the free body diagram in Figure 2 and can be calculated using sectional analysis. The probable moment of the system will be calculated using the same process but using the gap opening rotation at the MCE_R and expected/ultimate material properties.

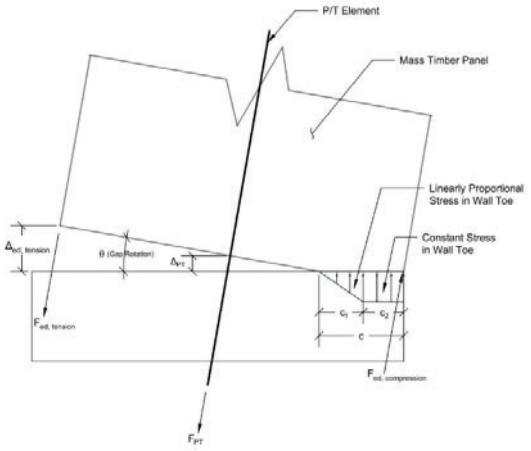

Figure 2: **Free body diagram of mass timber panel at the rocking interface.**

The shear check can be determined using Equation 10 which is also found in the NDS [7].

$$F_v' \geq f_v \tag{10}$$

Where F'_v is the adjusted shear design capacity determined per the NDS and f_v is the in-plane shear capacity of the mass timber panel. It should be noted that dynamic shear amplification may need to be accounted for due to the reduction of yielding in modes other than the fundamental mode for the wall.

3.5 LOCAL COMPONENT DESIGN AND CHECKS

The steps in this section are responsible for the determination of the wall hardware including the P/T and ED elements. Following the determination of these elements, several local checks—detailed below—are completed.

3.5.1 Restoring Ratio

This ensures the rocking wall will re-center after shaking up to and including the design basis earthquake. This is done by comparing the resisting force provided by the initial P/T force plus the additional dead load to the force provided by the ED components on the tension end of the wall at their ultimate capacity. This can be done following Equation 11 below.

$$F_{PTi} + 0.9 * P_u > 2 * F_u * A_{ed,tens} \tag{11}$$

Where F_{PTi} is the initial post-tensioning force in the P/T components, P_u is the vertical dead load in the wall at its base including the wall self-weight, F_u is the ultimate strength of the energy dissipation elements, and $A_{ed,tens}$ is the area of the energy dissipation elements on the tension end of the wall.

3.5.2 Energy Dissipation Ratio

This ratio enforces that there will be some energy dissipation from the system. To calculate this, a ratio of the moment capacity resulting from the energy dissipation devices to the total moment capacity is compared to a minimum limit. This ratio can be calculated using Equation 12 detailed below.

$$\frac{(M_n - M_{noed})}{M_n} \geq 0.25 \tag{12}$$

Where M_n is the nominal moment capacity of the wall and M_{noed} is the nominal moment capacity of the wall if there were no energy dissipation elements in the system.

3.5.3 Limited Wall-Toe Crushing at DBE

This ensures minimal damage occurs at the toe of the rocking wall for shaking up to and including the design basis earthquake and is completed by checking the strains in the wood. This can be calculated using Equation 13 detailed below.

$$\varepsilon_{wood,compr} \leq 0.9 * \varepsilon_{mtmax} \tag{13}$$

Where $\varepsilon_{wood,compr}$ is the strain in the extreme compression fiber and ε_{mtmax} is the maximum useable strain of the mass timber panel. The maximum useable strain shall not be taken greater than the strain at which the post-peak stress reaches 80 percent of the peak compression stress determined from an edgewise compression stress-strain curve.

3.5.4 No P/T Yielding at DBE

This is another check to ensure that re-centering will occur after shaking up to and including the design basis earthquake since P/T yielding compromises re-centering capability. This check is done by comparing the demand to yield stress of the P/T and can be calculated using Equation 14 detailed below.

$$f_{PT} \leq 0.9 * f_{yPT} \tag{14}$$

Where f_{PT} is the stress demand in the P/T elements at DBE and f_{yPT} is the yield stress.

3.5.5 No P/T Failure at MCE_R

This check is to ensure the P/T system will not fail at MCE_R. This is determined by calculating the strain in the P/T elements using Equation 15 detailed below.

$$\varepsilon_{PTf} \leq 0.85 * \varepsilon_{PT,u} \tag{15}$$

https://doi.org/10.52202/069179-0346

Where ε_{PTf} is the strain demand in the P/T elements at the MCE_R and $\varepsilon_{PT,u}$ is the ultimate strain capacity of the P/T element.

3.5.6 No ED Failure at MCE_R

This check is to ensure the ED elements will not fail at MCE_R. This is determined by calculating the strain or deformation in the ED elements using Equations 16a or 16b detailed below.

$$\varepsilon_{ed,tens} \leq 0.85 * \varepsilon_{ed,u} \quad (16a)$$

$$\Delta_{ed,tens} \leq 0.85 * \Delta_{ed,u} \quad (16b)$$

Where $\varepsilon_{ed,tens}$ or $\Delta_{ed,tens}$ is the strain or deformation of the ED elements in tension due to elongation, and $\varepsilon_{ed,u}$ or $\Delta_{ed,u}$ is the ultimate strain or deformation capacity of the ED elements.

4 DESIGN EXAMPLES

To illustrate the use of the proposed design approach, two design examples will be presented. The first example is a six-story mixed-use building featuring post-tensioned mass timber rocking walls with bounding columns. The second example features a three-story academic building with coupled post-tensioned mass timber rocking walls.

4.1 SIX-STORY EXAMPLE

4.1.1 Preliminary Design

This example features an office building located in Seattle, WA on Site Class C and a Seismic Design Category of D. The building features a 6.1m first story with the remaining stories being 3.7m in height. The floor plan of the building is shown below in Figure 3.

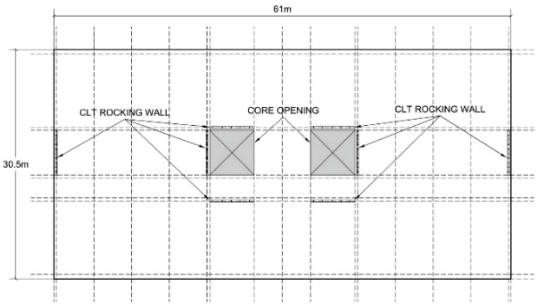

Figure 3: *Floor plan of the 6-story example building.*

The lateral system is composed of eight, 5.9m post-tensioned mass timber rocking walls consisting of 7-ply E1M1 CLT in a bounding column configuration. The wall components for this example are shown in Figure 4. Since this system's response modification factor was not yet available, it was assumed to be equivalent to that of a special reinforced concrete shear wall, giving an R = 6. Additionally, C_d was taken equal to R based on the recommendations made by Uang et. al [10]. Furthermore, the CLT panel material is isotropic and therefore needs to be modeled with appropriate stiffness parameters.

The linear elastic model for this example was built in ETABS with the seismic ground motion parameters listed in Table 1, which were determined using the ATC Hazards by Location Tool [11,12].

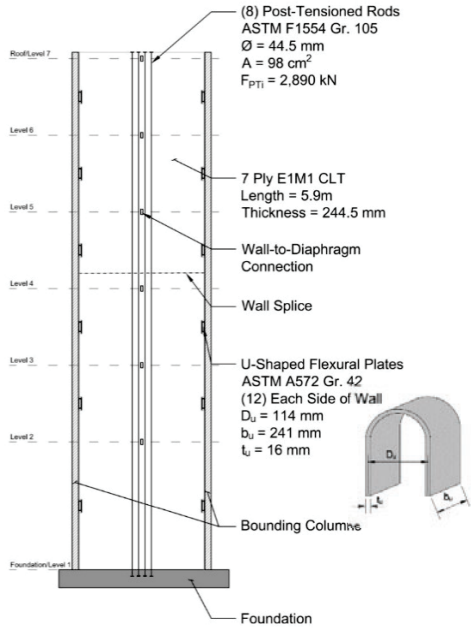

Figure 4: **Description of wall components, including UFP dimensions, for the 6-story example.**

Table 1: *List of seismic ground parameters for the 6-story example.*

Seismic Ground Motion Parameters	
The mapped MCE_R spectral response acceleration parameter at short periods, S_s	1.38
The mapped MCE_R spectral response acceleration parameter at a period of 1s, S_1	0.48
Short-Period Site Coefficient, F_a	1.2
Long-Period Site Coefficient, F_v	1.5
The MCE_R spectral response acceleration parameters for short periods, S_{MS}	1.65
The MCE_R spectral response acceleration parameters at a period of 1s, S_{M1}	0.72
The design spectral response acceleration parameter at short periods, S_{DS}	1.10
The design spectral response acceleration parameter at a period of 1s, S_{D1}	0.48

4.1.2 Drift Analysis

The drift of the building was determined using the linear elastic ETABS model and is shown in Figure 5. ASCE 7-16 Table 12.12-1 gives the Allowable Story Drift [9]. With the classification of "All other structures" and a Risk Category of II, the allowable story drift is 2%. Based on the data presented in Figure 5, it is evident that the drift in both directions does not exceed the 2% limit, therefore validating the current building layout and allowing for the design of the wall to continue.

https://doi.org/10.52202/069179-0346

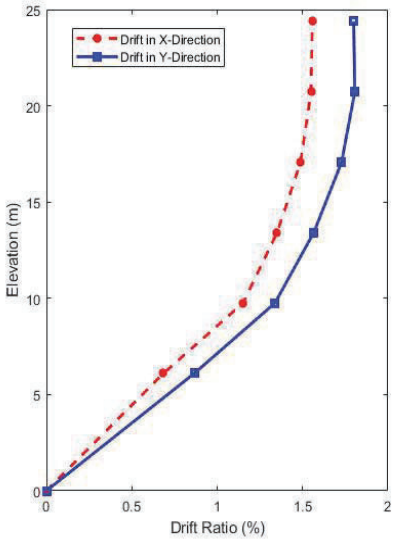

Figure 5: *Drift responses at each story for the 6-story example.*

4.1.3 Rotational Demand at the Rocking Interface

Using the analysis from the linear structural model created in the previous step, the deflections needed to calculate the rotations at the rocking interface can be determined. The design rotation at the rocking interface was given by Equation 1 and can be calculated as follows:

$$\theta_{design} = \frac{1.0*0.273m-0.093m}{24.4m} = 0.007\ rad$$

The maximum rotation at the rocking interface was given by Equation 2 and can be calculated as follows:

$$\theta_{max} = \frac{1.5*1.0*0.273m-0.093m}{24.4m} = 0.013\ rad$$

4.1.4 System Level Design and Checks

The nominal moment capacity of the wall system is calculated using Equation 4a, and subsequently Equations 5 through 8. The forces needed to calculate the moment capacity of the wall were determined using sectional analysis and are listed in Table 2.

Table 2: *Parameters needed to calculate moment capacity for the 6-story example.*

Parameter	Value
$F_{ed,\ comp}$	924 kN
$F_{wood,comp1}$	-472 kN
$F_{wood,comp2}$	-3513 kN
$F_{ed,tems}$	924 kN
c_1	0.22m
c_2	0.81m

Using the values populated in the table above, the individual moment capacities can be computed following Equations 5 through 8.

$$M_{ed,comp} = \frac{-924\ kN*-5.9m}{2} = 2{,}747\ kN*m$$

$$M_{wood,comp1} = -472\ kN\left(-\frac{5.9m}{2} + 0.81m + \frac{0.22m}{3}\right) = 986\ kN*m$$

$$M_{wood,comp2} = -3513\ kN\left(-\frac{5.9m}{2} + \frac{0.81m}{2}\right) = 9017\ kN*m$$

$$M_{ed,tens} = \frac{924\ kN*5.9m}{2} = 2{,}747\ kN*m$$

Following the individual moment capacity calculations, the nominal moment for the wall system can be calculated following Equation 4 as the following:

$$M_n = 2{,}747\ kN*m + 986\ kN*m + 9{,}017\ kN*m + 2{,}747\ kN*m = 15{,}497\ kN*m$$

The probable moment for this system would also be computed using the same equations, but with the maximum gap opening rotation and expected/ultimate material properties. For this example, the probable moment was calculated to be 19,421 kN*m.

Following the nominal moment capacity calculation, Equation 3 can be used to determine if the capacity is sufficient for the demand taken from the ETABS model.

$$13{,}367\ kN*m \leq\ 0.9*15{,}497\ kN*m = 13{,}947\ kN*m$$

Based on the calculation above, the strength of the rocking mechanism is satisfied.

The shear check for this example can be computed following Equation 10 and is detailed below.

$$4.0\ MPa \geq 2.9\ MPa$$

Based on the calculation above, the in-plane shear capacity of the wall is sufficient. It should be noted that the in-plane shear at any section of the mass timber panel shall be calculated using the wall shear demand from ASCE 7-16 factored load combinations (excluding overstrength load combinations) [9]. For this example, the shear demand was determined considering amplification due to flexural overstrength and higher mode effects as reported elsewhere [8].

4.1.5 Local Component Design and Checks

4.1.5.1 Restoring Ratio

Based on Equation 11 and the wall components, the restoring ratio can be determined as the following:

$$2891\ kN + 0.9*0 > 2*\frac{110\ kN}{UFP}*12\ UFPs$$

This then gives the following:

$$2891\ kN > 2640\ kN$$

It should be noted that since this wall is in a bounding column configuration there is no additional dead load from the floors. Furthermore, the self-weight of the wall is conservatively neglected. Based on the calculation above, the system will be able to re-center.

https://doi.org/10.52202/069179-0346

4.1.5.2 Energy Dissipation Ratio

Based on Equation 12 and the wall components and the previous calculations, the energy dissipation ratio can be determined as the following:

$$\frac{(15{,}497 kN*m - 10{,}002\ kN*m)}{15{,}497\ kN*m} = 0.35 \geq 0.25$$

Based on the calculation above, the energy dissipation of the system is sufficient.

4.1.5.3 Limited Wall-Toe Crushing at DBE

Based on Equation 13 and the wall components, the following can be computed:

$$0.0118 \leq 0.9 * 0.015 = 0.0135$$

Based on the calculation above, the strain of the extreme compression fiber of the mass timber panel is satisfied.

4.1.5.4 No P/T Yielding at DBE

Based on Equation 14 and the wall components, the following can be computed:

$$407\ MPa \leq 0.9 * 724 MPa = 652\ MPa$$

Based on the calculation above, there is no yielding of the P/T bars during DBE.

4.1.5.5 No P/T Fracture at MCE_R

Based on Equation 15 and the wall components, the following can be computed:

$$0.0024 \leq 0.85 * 0.05 = 0.043$$

Based on the calculation above, there is no fracturing of the P/T bars at the MCE_R.

4.1.5.6 No ED Fracture at MCE_R

For UFPs, the critical design property is the distance from the start of the 180-degree bend to the nearest attachment point (e.g., weld or bolt) on the straight portion. Based on Equation 16b and the wall components the following can be computed:

$$71.8\ mm \leq 0.85 * 127\ mm = 108\ mm$$

Based on the calculation above, there is no ED fracture at the MCE_R.

Since all the system and local level component checks are satisfied, the overall design of the wall is complete.

4.2 THREE-STORY EXAMPLE

4.2.1 Preliminary Design

This example features an academic building located in Seattle, WA on Site Class C and a Seismic Design Category of D. The building features story heights of 3.7m. The floor plan of the building is shown below in Figure 6.

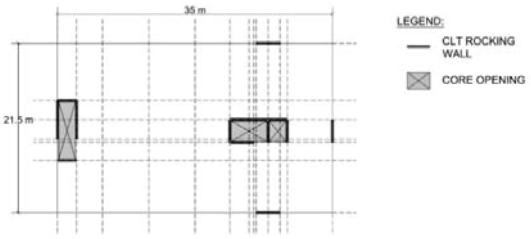

Figure 6: *Floor plan of the 3-story example building.*

The lateral system is composed of eight, 2.44m post-tensioned mass timber rocking walls consisting of 9-ply E1M1 CLT in a coupled wall configuration (not all walls in the floorplan are coupled). The wall components for this example are shown in Figure 7. The response modification factor for this system, since not yet available, was assumed to be equivalent to that of a special reinforced concrete shear wall, giving an R = 6. Additionally, C_d was taken equal to R based on the recommendations made by Uang et. al [10]. Furthermore, the CLT panel material is isotropic and therefore needs to be modeled with appropriate stiffness parameters.

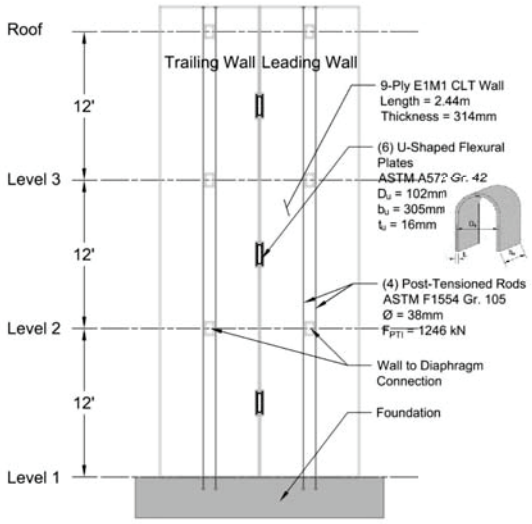

Figure 7: *Description of wall components, including UFP dimensions, for the 3-story example.*

The linear elastic model for this example was built in ETABS with the seismic ground parameters listed in Table 1.

4.2.2 Drift Analysis

The drift of the building was determined using the linear elastic model and is shown in Figure 8. ASCE 7-16 Table 12.12-1 gives the Allowable Story Drift [9]. With the classification of "All other structures" and a Risk Category of III, the allowable story drift is 1.5%. Based on the data presented in Figure 8, it is evident that the drift in both directions does not exceed the 1.5% limit, therefore validating the current building layout and allowing for the design of the wall to continue.

https://doi.org/10.52202/069179-0346

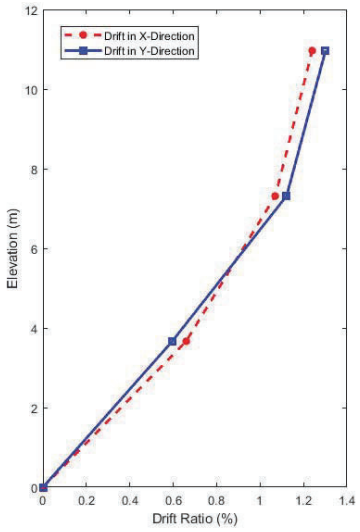

Figure 8: *Drift responses at each story for the 3-story example.*

4.2.3 Rotational Demand at the Rocking Interface

Using the analysis from the linear structural model created in the previous step, the deflections needed to calculate the rotations at the rocking interface can be determined. Since the coupled wall is symmetric in the linear analysis model, the design rotations at the rocking interface will be the same for both walls. The design rotation at the rocking interface was given by Equation 1 and can be calculated as follows:

$$\theta_{design} = \frac{1.1*0.094m-0.028m}{11.0m} = 0.007\ rad$$

The maximum rotation at the rocking interface of each wall was given by Equation 2 and can be calculated as follows:

$$\theta_{max} = \frac{1.5*1.1*0.094m-0.028m}{11.0m} = 0.013\ rad$$

Note that it is a coincidence that the design and maximum rotations at the rocking interface for this example match those of the 6-story example presented in Section 4.1.3.

4.2.4 System Level Design and Checks

For a coupled wall system, the subsequent calculations are broken down into the values for the trailing wall (subscript Tw) and leading wall (subscript Lw). The orientation of these walls is illustrated in Figure 7. The nominal moment capacity of each wall is calculated using Equation 4b, and subsequently Equations 5 through 9, with some modifications to the moment arm as mentioned previously and detailed below. Following the calculation of each wall's nominal moment capacity, the moment for the wall system will be determined following the summation from each wall. The forces needed to calculate the moment capacity of each wall were determined using sectional analysis and are listed in Table 3.

Table 3: *Parameters needed to calculate moment capacity for the 3-story example.*

Parameter	Value
Trailing Wall	
$F_{ed,\ comp}$	-657 kN
$F_{wood,comp1}$	-590 kN
$F_{wood,comp2}$	-368 kN
$F_{ed,tens}$	N/A
$F_{PT\Delta}$	411 kN
c_1	0.22 m
c_2	0.069 m
Leading Wall	
$F_{ed,\ comp}$	N/A
$F_{wood,comp1}$	-590 kN
$F_{wood,comp2}$	-1583 kN
$F_{ed,tens}$	657 kN
$F_{PT\Delta}$	312 kN
c_1	0.22 m
c_2	0.29 m

Using the values populated in the table above, the individual moment capacities can be computed following Equations 5 through 9. As previously mentioned, these equations need modifications to reflect the moment arm for summing moments about the center of the coupled wall system (rather than the center of each respective wall) and are reflected below:

$$M_{ed,comp\_TW} = F_{ed,comp\_TW} * 0 = -657\ kN * 0\ m = 0\ kN * m$$

$$M_{wood,comp1\_TW} = F_{wood,comp1\_TW} * \left(c_{2_{TW}} + \frac{c_{1_{TW}}}{3}\right) = -590\ kN\left(0.069\ m + \frac{0.218\ m}{3}\right) = -83.4\ kN * m$$

$$M_{wood,comp2\_TW} = F_{wood,comp2\_TW} * \left(\frac{c_{2_{TW}}}{2}\right) = -368\ kN\left(\frac{0.069\ m}{2}\right) = -12.6\ kN * m$$

$$M_{PT\Delta\_TW} = F_{PT\Delta} * \frac{L_w}{2} = 411\ kN * \frac{2.44\ m}{2} = 501.1\ kN * m$$

$$M_{ed,tens\_TW} = N/A$$

$$M_{ed,comp\_LW} = N/A$$

$$M_{wood,comp1\_LW} = -F_{wood,comp1\_LW} * \left(L_w - (c_{2_{LW}} + \frac{c_{1_{LW}}}{3})\right) = 590\ kN\left(2.44\ m - \left(0.29\ m + \frac{0.218\ m}{3}\right)\right) = 1{,}223\ kN * m$$

$$M_{wood,comp2\_LW} = -F_{wood,comp2\_LW} * \left(L_w - \frac{c_{2_{LW}}}{2}\right) = 1583\ kN\left(2.44m - \frac{0.29\ m}{2}\right) = 3{,}628.1\ kN * m$$

$$M_{PT\Delta\_TW} = -F_{PT\Delta} * \frac{L_w}{2} = 312.3\ kN * \frac{2.44\ m}{2} = -380.7\ kN * m$$

https://doi.org/10.52202/069179-0346

$$M_{ed,tens\_LW} = F_{ed,tens\_LW} * 0 = 657\ kN * 0\ m = 0\ kN * m$$

Based on the calculations above, the moment capacity for each wall can be computed following Equation 4b as the following:

$$M_{n\_TW} = 0\ kN * m - 83.4\ kN * m - 12.6\ kN * m + 501.1\ kN * m = 405.1\ kN * m$$

$$M_{n_{LW}} = 1{,}223\ kN * m + 3{,}628.1\ kN * m - 380.7\ kN * m + 0\ kN * m = 4{,}470.4\ kN * m$$

$$M_{n\_tot} = 405.1\ kN * m + 4{,}470.4\ kN * m = 4{,}875.5\ kN * m$$

The probable moment for this system would also be computed using the same equations, but with the maximum design values. For this example, the probable moment was calculated to be 6,070 kN*m.

Following the determination of the moment capacity of the wall system, Equation 3 can be used to determine if the capacity is sufficient compared to the demand determined by the linear analysis model.

$$3{,}510.4\ kN * m \leq 0.9 * 4{,}875.5\ kN * m = 4{,}388\ kN * m$$

Based on the calculation above the strength of the rocking mechanism is satisfied.

The shear check for this example can be computed following Equation 10 and is detailed below.

$$4.0\ MPa \geq 1.2\ MPa$$

Based on the calculation above the in-plane shear capacity of the wall is sufficient. It should be noted that the in-plane shear at any section of the mass timber panel shall be calculated using the wall shear demand from ASCE 7-16 factored load combinations (excluding overstrength load combinations).

4.2.5 Local Component Design and Checks

The restoring and energy dissipation ratios will be checked at the system level for the coupled walls. However, all other local component checks will be broken down by the individual wall panel.

4.2.5.1 Restoring Ratio

Equation 11 will be used to determine the restoring ratio for the wall system. Since there are two walls in the system, the restoring force provided by each wall will need to be considered in the calculation. This can be done by summing the two forces as follows:

$$(1245.5\ kN + 0.9 * 42.3\ kN) + (1245.5\ kN + 0.9 * 42.3\ kN) > 2 * \frac{156.4\ kN}{UFP} * 6\ UFPs$$

This then gives the following:

$$2567.1\ kN > 1876.8\ kN$$

Based on the calculation above, the system will be able to re-center.

4.2.5.2 Energy Dissipation Ratio

Equation 12 will be used to determine the energy dissipation ratio for the wall system. Since there are two walls in the system, the moment contribution from both walls will need to be considered in the calculation. This can be done by summing the moments as follows:

$$\frac{(405.1\ kN*m - 204.4\ kN*m) + (4470.4\ kN*m - 3138.4\ kN*m)}{405.1\ kN*m + 4470.4\ kN*m} = 0.314 \geq 0.25$$

Based on the calculation above, the energy dissipation of the system is sufficient.

4.2.5.3 Limited Wall-Toe Crushing at DBE

The strain in the extreme compression fiber of the trailing wall can be calculated following Equation 13. This check is calculated below:

$$0.0032 \leq 0.9 * 0.015 = 0.0135$$

The strain in the extreme compression fiber of the leading wall can be calculated following Equation 13. This check is calculated below:

$$0.0058 \leq 0.9 * 0.015 = 0.0135$$

Based on the calculations above, the strain in the extreme compression fiber of both mass timber panels is satisfied.

4.2.5.4 No P/T Yielding at DBE

The stress in the P/T components of the trailing wall can be computed following Equation 14 and is shown below:

$$481\ MPa \leq 0.9 * 724MPa = 652\ MPa$$

The stress in the P/T components of the leading wall can be computed following Equation 14 and is shown below:

$$451\ MPa \leq 0.9 * 724MPa = 652\ MPa$$

Based on the calculations above, there is no yielding of the P/T bars during DBE in either wall panel.

4.2.5.5 No P/T Fracture at MCE_R

The strain in the P/T elements for the trailing wall can be calculated following Equation 15 and is shown below:

$$0.00295 \leq 0.85 * 0.05 = 0.043$$

The strain in the P/T elements for the leading wall can be calculated following Equation 15 and is shown below:

$$0.00259 \leq 0.85 * 0.05 = 0.043$$

Based on the calculations above there is no fracturing of the P/T elements during MCE_R in either wall panel.

4.2.5.6 No ED Fracture at MCE_R

The strain in ED elements between the trailing and leading wall can be calculated following Equation 16 and is shown below:

$$33.5mm \leq 0.85 * 127mm = 108mm$$

Based on the calculations above, there is no fracturing of the ED elements during MCE_R.

Since all the system and local-level component checks are satisfied, the overall design of the wall system is complete.

5 CONCLUSIONS

This paper describes a prescriptive design procedure for post-tensioned mass timber rocking walls. Based on the existing design procedure for precast concrete walls, this design procedure was developed with a prescriptive format so that it can be integrated into the provisions of ASCE 7 [8] and the National Design Specification (NDS) for Wood Construction [9]. The design procedure includes an assessment of drift limits and an estimation of gap openings. It also checks the wall's ability to re-center, the minimum energy dissipation, and several local element checks. In addition to the ideology of the checks and calculations, two full building examples highlighting different wall configurations are also presented.

ACKNOWLEDGEMENT

The authors would like to acknowledge funding support for the development of the design procedure by the US Forest Services through the Wood Innovation Grant. The use of ETABs software was provided by Computers and Structures Inc. (CSI). The numerical model used for validation in this study was supported by research funding from the National Science Foundation through grant CMMI 1636164. The opinions and conclusions presented in this article are of the authors themselves but not the sponsors. The authors would also like to acknowledge Jonathan Heppner and Thomas Robinson at LEVER Architecture for coordinating an architectural floor plan, which worked with the 6-story example building used in this study.

REFERENCES

[1] ACI (American Concrete Institute). 2007. Acceptance criteria for special unbonded post-tensioned precast structural walls based on validation testing. ACI ITG-5.1-07. Farmington Hills, MI: ACI.

[2] ACI (American Concrete Institute). 2009. Requirements for design of a special unbounded post-tensioned precast shear wall. ACI ITG-5.1 and Commentary. Farmington Hills, MI: ACI.

[3] Palermo, A., Sarti, F., Baird, A., Bonardi, D., Dekker, D., & Chung, S. (2012, September). From theory to practice: Design, analysis and construction of dissipative timber rocking post-tensioning wall system for Carterton Events Centre, New Zealand. In *Proceedings of the 15th World Conference on earthquake engineering, Lisbon, Portugal* (pp. 24-28).

[4] Zimmerman, R. B., & McDonnell, E. (2018). Framework—Innovation in re-centering mass timber wall buildings. In *Proceedings, 11th US National Conf. on Earthquake Engineering*.

[5] Sarti, F., Smith, T., Danzig, I., & Karsh, E. (2017, April). Pres-Lam in the US: The seismic design of the peavy building at Oregon State University. In *Proceedings of the New Zealand society of structural engineering conference*.

[6] Baas, E. J., Riggio, M., Schmidt, E., Mugabo, I., & Barbosa, A. R. (2019, September). Living lab at Peavy Hall: Structural health monitoring of mass timber buildings. In *Proceedings of the 5th International Conference on Structural Health Assessment of Timber Structures, Guimarães, Portugal* (pp. 25-27).

[7] American Wood Council (ANSI/AWC). (2018). "National Design Specification (NDS) for Wood Construction." *Leesburg, VA*.

[8] Busch, A., Zimmerman, R. B., Pei, S., McDonnell, E., Line, P., & Huang, D. (2022). Prescriptive Seismic Design Procedure for Post-Tensioned Mass Timber Rocking Walls. *Journal of Structural Engineering*, *148*(3), 04021289.

[9] ASCE, American Society of Civil Engineers (2016). "Minimum Design Loads for Building and Other Structures." *ASCE Standard ASC/SEI 7-16*, Reston, Virginia.

[10] Uang, C. M., & Maarouf, A. (1994). Deflection amplification factor for seismic design provisions. *Journal of structural engineering*, *120*(8), 2423-2436.

[11] ATC (Applied Technology Council). 2016. "Hazards by Location." Accessed February 17, 2021. https://hazards.atcouncil.org/.

[12] CSI (Computers and Structures, Inc.). 2013. *CSI Analysis Reference Manual*. Walnut Creek, CA: CSI.

https://doi.org/10.52202/069179-0346

World Conference on Timber Engineering Oslo 2023

EFFECT OF THE ASPECT RATIO ON THE SEISMIC PERFORMACE OF POST-TENSIONED CROSS-LAMINATED TIMBER ROCKING WALL SYSTEMS

Gustavo Acuña[1], J. Daniel Dolan[2], Irshad Qureshi[3].

ABSTRACT: With the increased interest on the use of Cross-Laminated Timber (CLT) rocking walls as primarily lateral resistance system, some challenges arise, and special considerations might be considered in the design and structural analysis of this type of system. The influence in the dynamic response of the CLT panel aspect ratio is a parameter that has not been thoroughly studied, nor regulated by current codes and standards. The use of narrower panels leads to an amplification of higher-mode effects, due to the lower flexural stiffness of these elements, negatively affecting both the seismic performance and serviceability of this structural system. The objective of this investigation was to determine the variation in the dynamic behavior of a set of mid-rise Post-Tensioned Cross-Laminated Timber rocking wall structures, considering CLT panels with various aspect ratios. Nonlinear time-history analyses, including P-Δ effects, were performed to predict the seismic behavior. The results clearly showed that the use of wider panels improved the dynamic performance of these type of systems, highlighting reductions in the acceleration and seismic demands, as a consequence of a decrease in the higher-mode amplitudes. Lower aspect ratios also were associated with better displacement, drift ratio, and damage performances.

KEYWORDS: Cross-Laminated Timber, Rocking Walls, Aspect Ratio, Higher-Mode Effects, Nonlinear Analysis.

1 INTRODUCTION

The use of Post-Tensioned Cross-Laminated Timber (PT CLT) walls as primarily lateral resistant system brings both benefits and challenges. It has been demonstrated that CLT rocking wall systems can potentially withstand major earthquake events, and at the same time represents a viable sustainable construction alternative, which makes it very attractive to the designers. However, one of the major concerns with rocking systems and CLT construction is the important presence of higher modes in their dynamic response, including in low- and mid-rise structures.

Past research (Wiebe and Christopoulos [1], Ceccotti [2], Wiebe et al. [3-4], Qureshi [5], Li [6]) have found and shown the significant contribution of higher modes through testing and numerical simulations. The higher-mode contribution increases the acceleration demand in the entire structure, with a more noticeable effect at the upper stories, producing a whip-action. This increase in the acceleration response also increases the internal forces during seismic excitations, as well as the observable damage at the CLT wall toes. This structural drawback, combined with a drop in the serviceability due to excessive floor accelerations, can potentially reduce the overall feasibility of these type of systems in the mid-rise range. Hence, it is crucial to determine the main factors that affect the higher-mode amplification in PT CLT rocking wall structures.

One of the factors that can affect the dynamic performance of these rocking systems is the wall aspect ratio. Even the ever-increasing research in rocking systems, the current state-of-the-art has not evaluated its influence on balloon CLT rocking structures as far as the authors can determine. Moreover, the current codes and standards in the United States only provide guidelines for the wall aspect ratio for platform construction in light-frame wood construction. This aspect ratio limitation is provided by the National Design Specification for Wood Construction [7], and naturally, it is tied to the inter-story wall dimensions, rather than its global dimensions.

Therefore, the objective of this investigation was to quantify the difference in the seismic performance of a set of 6-story PT CLT walls with various global aspect ratios. The mean maximum responses of floor accelerations, floor displacements, inter-story drift ratios, shear and moment in the CLT walls, and damaged volume on the CLT wall toes were used as metrics to evaluate the effect of wall aspect ratio. In addition, the higher-mode influence was investigated by analyzing the roof acceleration time-history results.

[1] Gustavo A. Acuña Alegría, Former Doctoral Student, Washington State University, United States, g.acunaalegria@wsu.edu
[2] James Daniel Dolan, Professor Emeritus, Washington State University, United States, jddolan@wsu.edu
[3] Muhammad Irshad Qureshi, Fulbright Scholar, Washington State University, United States, m.qureshi2@wsu.edu

https://doi.org/10.52202/069179-0347

The results presented, herein, are part of the investigation developed by Acuña [8] and are valid only for the structural configurations defined in later sections of this manuscript. These results must be complemented with further research and experimental testing to determine the maximum practical height-to-length ratio for this type of system.

2 METHODOLOGY

2.1 GENERAL PROCEDURE

The main steps used in this investigation are briefly described in this section. First, the general rocking wall properties were defined, including the number of stories, wall dimensions, seismic weight, and position of the post-tensioned rods. Next, the initial estimates of the seismic demands were computed, following the Equivalent Lateral Force Method (ELF) described by the ASCE 7-16 [9] guidelines.

To determine the number, size, and initial force on the post-tensioned rods, the Cross-Sectional Analysis, developed by Ganey [10] for PT CLT walls, was followed. This method solves the equilibrium equations and stress distributions iteratively to estimate the moment capacity of the post-tensioned rocking wall, given a fixed displacement.

The structures were then evaluated through nonlinear time-history analysis using SAP2000 [11], considering P-Δ effects. Each individual structure was subjected to forty-four far field traces, scaled to Design Basis Earthquake level, according to ASCE 7-16 [9] procedures.

To determine the frequency content of the roof acceleration time-history responses, Fourier analysis was used with the time trace of the roof response from the program. This approach allowed the amplitude, and therefore the influence, of each mode detected on the acceleration response to be calculated. The Discrete Fourier Transform (DFT) and the Amplitude Spectrum were computed using the MATLAB [12] Function "fft", corresponding to the "Fast Fourier Transform" algorithm.

2.2 MODEL CHARACTERIZATION

The CLT rocking walls were modeled with a simplified 2D model, consisting of a linear elastic frame element to represent the wall panel, and two nonlinear rotational springs at the base of each rocking wall to characterize the rocking behavior. This is a computationally efficient and accurate method of modeling CLT rocking systems, developed by Wilson [13], and it is shown in Figure 1. The modeling technique was further validated against the shake table test results carried out by Pei et al. [14] in a full-scale 2-story post-tensioned CLT rocking wall building. Additional details about the model validation can be found on Acuña [8] and Wilson [13].

U-Shaped Flexural plates (UFPs) were utilized to couple adjacent CLT wall panels and to connect the outer CLT panels to the bounding columns. A rigid foundation was assumed for all the cases. A representation of a 3-panel wall model is illustrated in Figure 2.

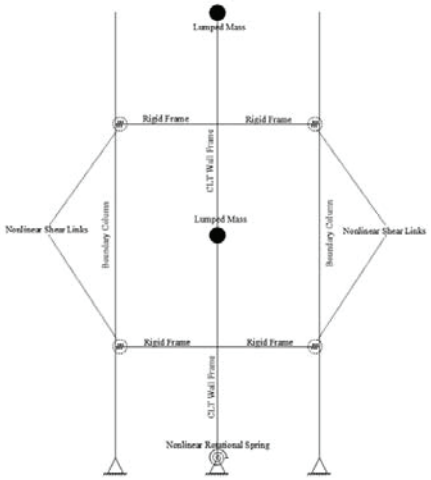

Figure 1: *Simplified CLT rocking wall model*

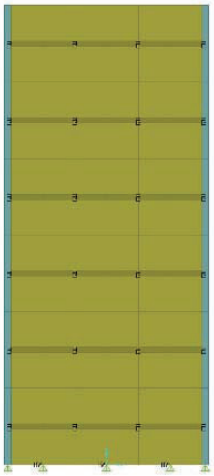

Figure 2: *Coupled wall model*

2.3 SELECTION AND SCALING OF GROUND MOTIONS

Twenty-two far-field acceleration record pairs from the PEER database [15], typically used for FEMA P-695 [16] analyses, were selected for numerical evaluation. Scaling of the traces was carried out following the Amplitude Scaling process, according to ASCE 7-16 [9]; where one single scale factor is used for all the acceleration traces to match the average maximum direction spectrum (RotD100) with the target spectrum at the target period.

https://doi.org/10.52202/069179-0347

The target spectrum was defined assuming the buildings to be in Downtown Seattle, WA (47.622, -122.337). Site Class C and Importance Factor II were assumed for the building, according to ASCE 7-16 [9]. The Modified Response Factor (R-factor) was selected as 6, based on the observations presented by Pei et al. [17], Ganey [10], and Wilson [13]. The design moment demand for all of the structures was 3,192 kN-m. The target spectrum, the mean RotD100 spectrum, and the individual RotD100 spectra for the 22 ground motions are shown in Figure 3.

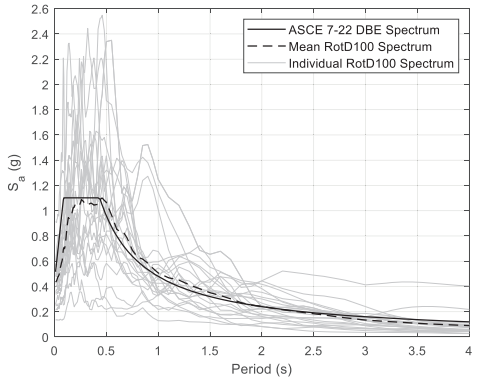

Figure 3: *ASCE 7-22, mean RotD100, and individual RotD100 acceleration spectra*

3 CASE STUDY

3.1 MATERIAL PROPERTIES

3.1.1 Cross-laminated timber

E1M5 rated panels, according to the Structurlam [18] specification, were selected for the CLT rocking walls. The properties of a 9-ply CLT panel were derived from crushing and shear tests performed in a 5-ply CLT panel by OSU and PSU [19]. The adjusted properties for a 9-ply panel were: 7,037 MPa for the modulus of elasticity in the longitudinal direction, 4,520 MPa for the modulus of elasticity in the transverse direction, 552 MPa for the shear modulus, 18.2 MPa for the yield stress, 0.0026 mm/mm for the yield strain, and 0.0082 mm/mm for the crushing strain. The Poisson's ratio was assumed as 0.3 in all directions. The post-yield behavior of the wood crushing was assumed as elastic-perfectly plastic.

3.1.2 Post-tensioned rods

Fully threaded, high-strength steel rods were selected for the PT rods, with denomination ATS-HSRX, according to Simpson Strong-Tie [20]. ATS-HSRX rods use ASTM F1554 Gr.105 steel for diameters equal or greater than 28.58 mm; with modulus of elasticity of 200,000 MPa, yield strength of 724 MPa, and tensile strength of 862 MPa.

3.1.3 U-shaped flexural plates

ASTM A572 Gr.42 steel plates were selected for the UFPs. The elastic modulus was 200,000 MPa, and the yield stress was 290 MPa.

3.2 SPECIMEN DESIGN

Four CLT panel lengths were selected for the numerical evaluation. These panel lengths were chosen to contain the practical range of the CLT panel manufacturing (up to 3.05 m), while an additional length (4.57 m) was included in the analyses for numerical purposes (it is understood that field connecting multiple CLT panels to construct the walls longer than can be manufactured is currently problematic, but for this analysis the connectivity to construct a continuous 4.57 m panel was assumed to be perfect).

For comparison reasons, a target wall length of 9.14 m was defined, and the required number of panels to cover the target length was calculated. These wall segments were connected by using UFPs. The panel length, aspect ratio, and the required number of segments are shown in Table 1.

The number of stories, inter-story height, wall thickness, story weight, roof weight, and position of the post-tensioned rods were held constant throughout all the cases, assuming 6 stories, 3.66 m, 31.43 cm, 333.6 kN, 166.8 kN, and wall centerline respectively. The UFP's size was also held constant; the bend diameter, width, and thickness were set to 15.24 cm, 6.35 cm, and 0.953 cm, respectively.

Table 1: *Wall Length and Aspect Ratio*

#ID	Wall Panel Length (m)	Aspect Ratio (H:L)	# Segments
1	1.52	14.4 : 1	6
2	2.29	9.6 : 1	4
3	3.05	7.2 : 1	3
4	4.57	4.8 : 1	2

To conduct the performance comparison, the rocking wall structures were designed to provide a similar moment capacity at 2.0% drift ratio. The required PT size, number, and initial force were determined using the Cross-Sectional Analysis. The PT properties are summarized in Table 2, and the moment-drift ratio relationship for the wall specimens are shown in Figure 3.

Table 2: *Post-tensioning properties*

#ID	ϕ_{PT} (mm)	#PT Rods	Segment Initial PT Force (kN)	Specimen Capacity (kN-m)
6-5	28.58	4	667	3,452
6-7.5	28.58	4	489	3,553
6-10	28.58	4	311	3,557
6-15	34.93	2	111	3,510

https://doi.org/10.52202/069179-0347

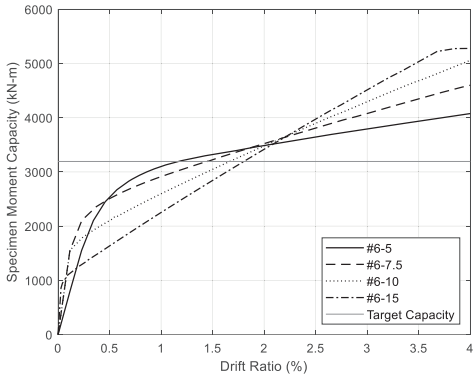

Figure 4: *Specimen capacities and target capacity*

4 RESULTS

The main results from the nonlinear time-history analyses are presented in this section. These results include acceleration, displacement, inter-story drift, shear force, and moment envelopes, modal amplitudes, and damage on CLT walls. The relative differences presented in this section were computed considering the results for Specimen #6-5 as baseline.

4.1 ACCELERATION RESPONSE

The time-history analysis results showed that the magnitude of the peak floor acceleration is directly related to the wall aspect ratio. The mean maximum profiles, presented in Figure 4, indicate a reduced acceleration response for specimens with lower global panel aspect ratio, essentially in the entire structure. A decrease in the whip-action at the upper stories is also noticeable, indicating less influence of the higher vibration modes.

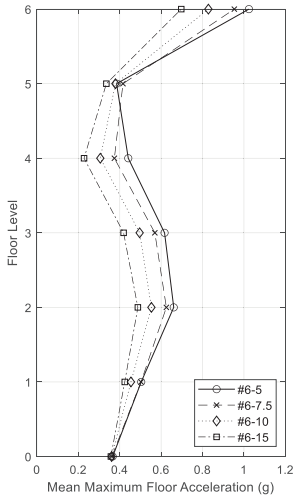

Figure 5: *Average peak floor acceleration*

It was observed that the largest average peak roof acceleration in Specimen #6-5, had a mean value of 1.02 g, while the smallest peak roof acceleration response was obtained in Specimen #6-15, with a value of 0.70 g. This is a respective difference reduction of 31.4%. The remaining average peak roof accelerations and differences are summarized in Table 3.

Table 3: *Average peak roof acceleration*

#ID	Average Peak Roof Acceleration (g)	Difference (%)
6-5	1.02	-
6-7.5	0.95	-6.9
6-10	0.83	-18.6
6-15	0.70	-31.4

4.2 FREQUENCY ANALYSIS

The 90th percentile Fourier amplitude spectra are presented in Figure 5. It is observed that both the first and second mode amplitude increase as the aspect ratio of the wall segment increases, showing the largest amplitudes in Specimen #6-5 and the smallest in Specimen #6-15. A significant shift in the second mode frequency is also exhibited, moving from the 3.5-4.0 Hz range for Specimen #6-5 to the 7.0-7.5 Hz range for Specimen #6-15; this change in the second-mode frequency can potentially reduce the seismic demands by moving the dynamic response out of the plateau region of the design spectrum.

The first and second mode amplitudes for Specimen #6-5 were 0.108 g and 0.145 g, respectively. For comparison, the first and second mode amplitude for Specimen #6-15 were 0.061 g and 0.067 g, respectively. The relative comparison between these two structures yielded an amplitude reduction of 43.5% and 53.8% for first and second mode, respectively. The Fourier amplitudes for the structures considered in this study are shown in Table 6.

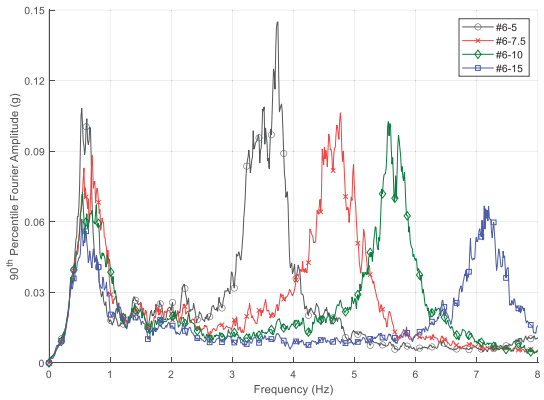

Figure 6: *90th percentile Fourier amplitude spectra*

https://doi.org/10.52202/069179-0347

Table 4: *90th percentile Fourier amplitude spectra*

#ID\ Mode	Frequency (Hz)		90th Percentile Amplitude (g)		Amplitude Difference (%)	
	1	2	1	2	1	2
6-5	0.54	3.75	0.108	0.145	-	-
6-7.5	0.70	4.77	0.088	0.106	-18.5	-26.9
6-10	0.55	5.55	0.072	0.103	-33.3	-29.0
6-15	0.54	7.12	0.061	0.067	-43.5	-53.8

4.3 DISPLACEMENT RESPONSE

The average peak floor displacement profiles, shown in Figure 6, increases with the aspect ratio. It can also be observed that the wall aspect ratio impacts the shape of the displacement envelope, indicating a relative change between the different displacement mechanisms.

The largest peak roof displacement was obtained in Specimen #6-5, with an average of 28.7 cm. While, the minimum average peak roof displacement in Specimen #6-15 was averaged 23.1 cm. The displacement difference between these two structures showed a reduction of 19.5%. The remaining peak roof displacements are presented in Table 5.

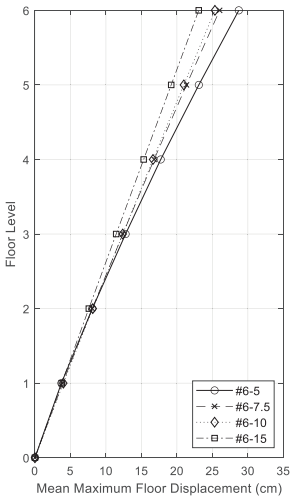

Figure 7: *Average peak floor displacement*

Table 5: *Average peak roof displacement*

#ID	Average Peak Roof Displacement (cm)	Difference (%)
6-5	28.7	-
6-7.5	25.9	-9.7
6-10	25.4	-11.5
6-15	23.1	-19.5

4.4 INTER-STORY DRIFT RESPONSE

Similar to the displacement results, the average peak inter-story drift ratio increased as the wall aspect ratio increased. Additionally, it was verified that the rocking behavior governed the displacement response of the structure with the lowest aspect ratio panels, given by its relatively uniform deformation pattern. In contrast, the structure with the highest aspect ratio panels presented a non-uniform drift ratio distribution, with higher drifts in its upper section, indicating an important presence of bending relative to the rocking motion. The average peak inter-story drift profiles are shown in Figure 7.

The analysis results showed that the maximum inter-story drift ratio was produced in Specimen #6-5, with an average of 1.59%. The lowest drift ratio was observed in Specimen #6-15, with an average of 1.07%. Their relative difference resulted in a drift reduction of 32.7%. The rest of the average peak inter-story drift values and differences are presented in Table 6. Note that these peak values are the maximum observations, regardless of where it was produced (i.e., they are not bound to a specific story.)

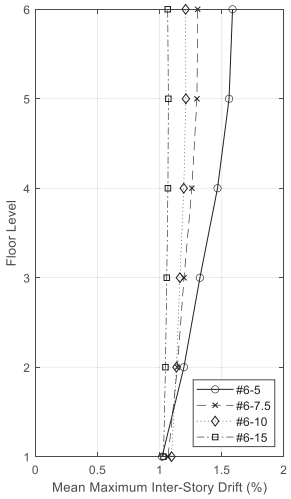

Figure 8: *Average peak inter-story drift ratio*

Table 6: *Average peak roof displacement*

#ID	Average Peak Inter-Story Drift Ratio (%)	Difference (%)
6-5	1.59	-
6-7.5	1.31	-17.6
6-10	1.21	-23.9
6-15	1.07	-32.7

4.5 SHEAR RESPONSE

The shear force results, shown in Figure 8, indicate that the use of longer CLT wall segments reduced the seismic forces into the structure. This patter is observed essentially in the entire structure, and it follows a similar trend as the acceleration envelopes, presented in previous sections. The seismic shear reduction is also a

https://doi.org/10.52202/069179-0347

consequence of the difference on the higher-mode amplitudes.

The largest base shear was observed in Specimen #6-5, with a peak average of 490 kN, while the smallest seismic base shear was on Specimen #6-15 with a maximum average of 358 kN. Their relative difference was a reduction of 26.9%. The rest of the mean maximum base shears are summarized in Table 7.

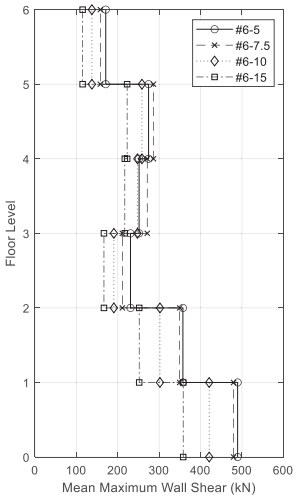

Figure 9: *Average peak wall shear*

Table 7: *Average peak base shear*

#ID	Average Peak Base Shear (kN)	Difference (%)
6-5	490	-
6-7.5	480	-2.0
6-10	421	-14.1
6-15	358	-26.9

4.6 MOMENT RESPONSE

The moment results followed a similar pattern compared to the shear force distribution, as shown in Figure 9, presenting the lowest seismic demand in Specimen #6-15. This performance difference was expected, based on the acceleration and modal amplitude results.

The largest average peak base moment was obtained in Specimen #6-5, with a moment of 3,111 kN-m, while the smallest peak moment was observed in Structure #6-15, with a mean maximum base moment of 2,306 kN-m. The improvement in the response was a reduction of 25.9%. The remaining average maximum base moments are summarized in Table 8.

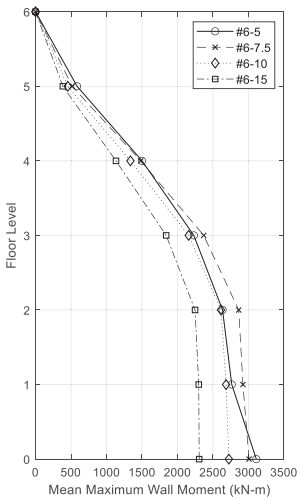

Figure 10: *Average peak wall moment*

Table 8: *Average peak base moment*

#ID	Average Peak Base Moment (kN-m)	Difference (%)
6-5	3,111	-
6-7.5	3,008	-3.3
6-10	2,724	-12.4
6-15	2,306	-25.9

4.7 DAMAGED CLT

The damage analysis also continued with the trend observed for the other performance indicators, showing larger damage in the CLT wall toes in structures with higher aspect ratios. This is a direct consequence of the increase of displacements and moment demands for structures with higher wall aspect ratios, as well as for the reduction in their internal lever arm (to achieve a similar moment, there are required higher strains and stresses at the toes, hence more damage is expected).

The maximum average damage was observed on Specimen #6-5, while the minimum damage was obtained on Specimen #6-15. The average damaged volumes for these two configurations were 18,108 cm^3 and 4,097 cm^3, respectively. The damage difference was a reduction of 77.4%. The remaining CLT damage and their respective percentage differences are summarized in Table 9.

Table 9: *Average damaged volume on CLT wall toes*

#ID	Average Damaged Volume (cm^3)	Difference (%)
6-5	18,108	-
6-7.5	11,930	-34.1
6-10	7,833	-56.7
6-15	4,097	-77.4

https://doi.org/10.52202/069179-0347

5 CONCLUSIONS

The effect of wall segment aspect ratio on the seismic behavior of CLT rocking walls was determined. The results showed that structures with lower aspect ratios (i.e., wider wall segments) have a better seismic performance than structures with narrower segments, due to a reduction of the higher-mode influence on its dynamic behavior, as demonstrated through the Fourier amplitude spectrum. The mean maximum acceleration, displacement, and drift ratio envelopes reduced as the aspect ratio decreased. The internal forces (story shear and moments) presented identical trends as mentioned before. The aspect ratio of the segments also affected the local performance of the rocking walls, exhibiting less damage on the CLT wall specimens with lower aspect ratios.

Based on the findings of this investigation, it is highly recommended to use longer wall panels rather than a series of slender panels coupled with UFPs. However, further investigations are needed to determine the overall upper bound of the wall aspect ratio for this type of systems, also considering the effect of the total building height. This would be crucial to develop new code regulations for CLT rocking wall systems and potentially fully develop its use in mid-rise construction.

The acceleration results showed the highest response in Specimen #6-5, with an average peak roof acceleration of 1.02 g. The structure with the lowest acceleration response was Specimen #6-15, with an average maximum of 0.70 g. Their relative difference was 31.4%. The shape of the acceleration distributions showed a reduction in the whip-action at the upper stories in structures with lower wall aspect ratio.; this also suggested a reduction on the higher-mode contribution, which was confirmed through the frequency analysis.

The Fourier amplitude spectra showed the difference in the frequency content on the roof acceleration response. It was verified a reduction in both the first- and second-mode amplitude in structures with lower aspect ratios. The relative differences between Specimens #6-5 and #6-15 were reductions of 43.5% and 53.8% for the first and second mode, respectively.

Both the displacement and inter-story drift ratio distributions showed that the increase on the wall aspect ratio increased the influence of bending deformation, relative to the rocking motion. It was also verified that structures with higher aspect ratio presented higher displacements and inter-story drifts. The maximum roof displacement and inter-story drift were found for Structure #6-5, with an average displacement of 28.7 cm and 1.59%, respectively. Structure #6-15 presented the lowest average peak displacement and drift ratios, with mean maximum values of 23.1 cm and 1.07, respectively. Their respective relative differences were 19.5% for displacements, and 32.7% for drift ratios. It was also verified that the structures presented in this study did not exceed the drift limit of 2.0% specified in ASCE 7-22 for design level earthquakes.

The internal forces presented similar trends, showing a general decrease as the aspect ratio decreases. The maximum base shear and base moment were observed in Specimen #6-5, with values of 490 kN and 3,111 kN-m. The minimum base shear and moment were found on Structure #6-15, with values of 358 kN and 2,306 kN-m. Their relative differences were reductions of 26.9% and 25.9% for shear and moment, respectively.

The damage on the CLT walls increased as the aspect ratio increased. Specimen #6-5 exhibited the largest average damage, with a volume of 18,108 cm^3, while Specimen #6-15 presented the lowest damage, with an average of 4,097 cm^3. Their relative difference was 77.4%.

ACKNOWLEDGEMENT

This work was supported by the scholarship provided by the Chilean Agencia Nacional de Investigación y Desarrollo, ANID (formerly known as Comisión Nacional de Investigación Científica y Tecnológica, CONICYT) PFCHA/Doctorado Becas Chile/2017 - 72180372.

REFERENCES

[1] Wiebe, L., and C. Christopoulos: Mitigation of Higher Mode Effects in Base-Rocking Systems by Using Multiple Rocking Sections. Journal of Earthquake Engineering, 13 (S1): 83–108, 2009.

[2] Ceccotti, A., C. Sandhaas, M. Okabe, M. Yasumura, C. Minowa, and N. Kawai.: SOFIE project - 3D shaking table test on a seven-storey full-scale cross-laminated timber building. Earthquake Engineering and Structural Dynamics, 42 (13): 2003–2021, 2013.

[3] Wiebe, L., C. Christopoulos, R. Tremblay, and M. Leclerc: Mechanisms to limit higher mode effects in a controlled rocking steel frame. 1: Concept, modelling, and low-amplitude shake table testing. Earthquake Engineering and Structural Dynamics, 42 (7): 1053–1068, 2013.

[4] Wiebe, L., C. Christopoulos, R. Tremblay, and M. Leclerc: Mechanisms to limit higher mode effects in a controlled rocking steel frame. 2: Large-amplitude shake table testing. Earthquake Engineering and Structural Dynamics, 42 (7): 1069–1086, 2013.

[5] Qureshi, I. M., P. Warnitchai, and T. Mehmood: Investigation of Dynamic Response of Rocking Wall Structures Using Inelastic Modal Decomposition Technique. In *5th ECCOMAS Thematic Conference on Computational Methods in Structural Dynamics and Earthquake Engineering*, 3139–3150. Crete Island, Greece, 2015.

[6] Li, T., J. W. Berman, and R. Wiebe: Parametric study of seismic performance of structures with multiple rocking joints. Engineering Structures, 146: 75–92, 2017.

[7] American Wood Council. National Design Specification for Wood Construction, Special Design Provisions for Wind & Seismic. ANSI/AWC SDPWS-2018. American Wood Council, Leesburg, VA. 2018.
[8] Acuña, G.: Effects of Geometric, Damping, and Boundary Parameters on the Dynamic Response of Cross-Laminated Timber Rocking Wall Systems. Doctoral Dissertation. Washington State University, Pullman, WA. 2022.
[9] American Society for Civil Engineers. Minimum Design Loads and Associated Criteria for Buildings and Other Structures. ASCE/SEI 7-16. American Society for Civil Engineers, Reston, VA. 2017.
[10] Ganey R.: Seismic Design and Testing of Rocking Cross Laminated Timber Walls. M.S. Thesis, University of Washington, Seattle, WA. 2015.
[11] Computers and Structures, Inc. CSI Analysis Reference Manual: For SAP2000, ETABS, SAFE, and CSI Bridge. Computers and Structures, Inc., Berkeley, CA. 2010.
[12] The MathWorks, Inc. MATLAB, version 9.12.0.1884302 (R2022a). The MathWorks, Inc., Natick, MA. 2022.
[13] Wilson A.: Numerical Modeling and Seismic Performance of Post-Tensioned Cross-Laminated Timber Rocking Walls. M.S. Thesis, Washington State University, Pullman, WA. 2018.
[14] Pei, S., J. W. van de Lindt, A. R. Barbosa, J. W. Berman, E. McDonnell, J. D. Dolan, H.-E. Blomgren, R. B. Zimmerman, D. Huang, and S. Wichman: Experimental Seismic Response of a Resilient 2-Story Mass-Timber Building with Post-Tensioned Rocking Walls. Journal of Structural Engineering, 145 (11): 04019120, 2019.
[15] Pacific Earthquake Engineering Research Center. PEER Ground Motion Database. 2013. https://ngawest2.berkeley.edu/. Accessed December 2019.
[16] Applied Technology Council. Quantification of Building Seismic Performance Factors. Report No. P-695, FEMA. 2009.
[17] Pei, S., J. W. van de Lindt, and M. Popovski: Approximate R-Factor for Cross-Laminated Timber Walls in Multistory Buildings. Journal of Architectural Engineering, 19 (4): 245–255, 2013.
[18] Structurlam. CrossLam® CLT - Technical Design Guide - v4.0-USA. Structurlam, Penticton, BC. 2018.
[19] Oregon State University and Portland State University. Framework Project. Deliverable 18: Structural Testing. Corvallis, OR, and Portland, OR. 2017.
[20] Simpson Strong-Tie. F-L-SRS18 - Design Guide: Strong-RodTM Systems. Simpson Strong-Tie Company Inc. 2018.

https://doi.org/10.52202/069179-0347

World Conference on Timber Engineering Oslo 2023

THE ROLE OF INTERMODULAR CONNECTIONS IN THE GLOBAL BEHAVIOR OF HIGH-RISE MASS TIMBER BUILDINGS

Juan S. Zambrano Jaramillo[1] and Erica C. Fischer[2]

ABSTRACT: The use of mass timber as a pre-engineered product combined with prefabrication processes to assemble volumetric modular units contributes to optimizing the construction by reducing time, waste, and the weight of the structures for high-rise buildings located in high seismic regions. The performance of modular buildings subjected to lateral loads demonstrated that the connections between the modules play an important role in the diaphragm behavior and the structural response of the buildings. To study the building response, a parametric analysis was performed on 9-, 12-, and 18-story mass timber modular buildings simulated in OpenSees, to identify the influence of the stiffness of the intermodule connections and their location between the modular units. The analysis identified key parameters that govern the diaphragm behavior and how it affects the building's performance. The results demonstrated that the horizontal translational stiffness of the intermodular connections controls the diaphragm behavior thereby controlling the classification of the diaphragm as rigid, semi-rigid, and flexible diaphragm ranges for modular buildings. Additionally, the location of the intermodular connection modifies the diaphragm deflections and the envelope of the column force demands for the gravity system.

KEYWORDS: Mass timber, modular construction, intermodular connections, stiffness, high-rise buildings.

1 INTRODUCTION

1.1 INTRODUCTION TO MODULAR CONSTRUCTION AND MASS TIMBER

The architecture, engineering, and construction industry has acknowledged a shared commitment to increasing the speed of construction [1]. With the emergence of fabrication technology, including robotics, pre-fabrication of structural members and systems is possible. This results in the ability of structural frames or modules to be fabricated prior to arrival on site. Modular building construction takes advantage of this pre-fabrication ability and has been increasing in popularity to reduce the housing demands [2]. In most cases, these modular buildings use light steel frames to assemble modular units for residential buildings, and their dimensions are mainly limited by transportation requirements [3].

The benefits of modular buildings are reduction in construction waste, noise, and cost. Research has shown that 43% of the manufacturing waste can be recycled in a factory environment, resulting in waste of 5% of the total weight of the building compared to traditional construction with an average of 10 - 13% [4]. The use of modular units results in a 70% reduction in the number of trucks used to deliver construction materials to the site, which reduces the construction noise. Lastly, there is a 25 - 50% reduction in construction time of a mass timber building as compared to conventional building construction materials [4,5]. For all these reasons, mass timber modular buildings have the capability of increasing the speed of construction, reduction of waste, and reduction of noise during construction.

Modular building construction requires additional planning during the schematic design and design development phases to coordinate the floor plan such that it meets the functionality requirements of the building based on different arrangements of the modular units. Because of this additional planning, researchers have investigated optimal designs of the modular units for different occupancies [6,7]. Previous research shows that buildings with both office and residential occupancies can be developed using steel modular construction.

Connections are key elements that define the performance of modular buildings and modular units have three main types of connections [8]: intramodule, intermodule, and module to foundation connections. Intramodule connections connect the structural components within the module and are used to assemble the volumetric unit. These connections are designed to provide module stability during transportation and construction and to resist the gravity load demands. Intermodule connections constitute the module to module connection and transfer horizontal and vertical forces. These connections are designed for ease of construction and maintenance. Previous researchers have investigated the behavior of

[1] Juan Sebastian Zambrano Jaramillo, Oregon State University, United States, zambraju@oregonstate.edu
[2] Dr. Erica Claire Fischer, Oregon State University, United States, erica.fischer@oregonstate.edu

https://doi.org/10.52202/069179-0348

these types of connection in steel modular buildings and concluded that they can greatly influence the global behavior of the building [9,10]. The last type of connection is the module to foundation connection which transfers the vertical and lateral loads of the gravity system to the foundation. These connections are designed to restrain displacements and give support at the base of the building so each column can have the required conditions to develop its full strength. Concrete is mainly used for the foundation, and based on previous studies in steel modular buildings, these connections require additional on-site work due to welding and precautions to avoid corrosion [8].

Mass timber as a construction material is becoming more popular as a building construction material. From an analysis by Svatoš-Ražnjević et al. [11], the number of mass timber buildings and the number of stories in those buildings has increased between 2000 - 2021. Of the mass timber buildings constructed during this time, 7.3% of the buildings were classified as using volumetric units [11]. Fernandes Carvalho et al. [12] performed a case study analysis of nine modular mass timber buildings. These structures are used as schools, apartments, and hotels. All of them use either linear, planar, or volumetric modular units to assemble the mass timber structures. A hybrid high-rise hotel building was assembled using CLT panels, glulam beams and columns, and reinforced concrete walls up to 24 stories [13]. One of the major barriers to constructing more modular buildings using volumetric units is data on the behavior of inter and intramodular connections, how to simulate the building under lateral load demands, and proof-of-concept connection types, particularly for high-rise modular buildings.

1.2 PREVIOUS RESEARCH ON MODELING DIAPHRAGMS MASS TIMBER BUILDINGS

To simulate high-rise mass timber buildings under varying lateral force demands, researchers have used finite element (FE) modeling methodologies. However, previous researchers have utilized different methods of modeling mass timber diaphragm behavior.

Ávila et al. [14] simulated CLT diaphragm seismic behavior in a high-rise building with reinforced concrete shear walls. They concluded that using a rigid versus flexible diaphragm impacted the demands in the shear walls and the diaphragms themselves such that a rigid diaphragm produced larger demands in the walls than a flexible diaphragm; however, a rigid diaphragm produced smaller diaphragm demands than a flexible diaphragm [14]. Blomgren et al. [15] also studied CLT diaphragm behavior under seismic loads using the data from a two-story mass timber building tested at the University of California San Diego shake table. The conclusions of this research were that the ratio of the lateral stiffness of the CLT panels to the rigidity of the lateral system can influence whether the diaphragm behaves like a rigid, flexible, or semi-rigid diaphragm.
In general, diaphragms are designed as elastic elements so they can resist gravity loads and transfer the lateral loads without any substantial damage [16]. For code-based design, the diaphragm flexibility must be defined to simulate force distribution and to account for differential displacements of the diaphragm that may occur depending on its flexibility. For modular systems, diaphragms play an important role in the building behavior. During the construction stage, they provide stability to the module while as part of the building they transfer the force to the lateral system [17]. However, there is limited research on how to simulate modular building diaphragms, particularly considering the stiffness of the intermodular connections.

Diaphragms are classified based on their deformation capacity. Specifically, diaphragms are classified by the ratio between the maximum computed in-plane deflection of the diaphragm when subjected to lateral loads and the average drift of the elements of the seismic force-resisting system of the story below the diaphragm under consideration [18]. This ratio can be used to classify the diaphragm as rigid, semirigid, or flexible. The code-prescribed limit for rigid diaphragms is the ratio less than or equal to 0.5, flexible diaphragms greater than 2.0, and semirigid or stiff diaphragms between 0.5 and 2.0. While this diaphragm classification was developed for conventional construction, it has been applied to modular steel buildings in previous research of steel modular buildings [19] and therefore used by the authors.

Previous researchers have explored how intermodular connections can have an impact on the global behavior of a building. Chen et al. [20] developed and tested a steel intermodular connection that was later simulated by Peng et al. [21] to identify the behavior of steel modular buildings under seismic demands. They concluded that the fundamental period of the structure is 14% smaller when the intermodular connections are assumed to be rigid compared to the stiffness obtained from the tested steel connection that add more flexibility to the frame model.

Lacey et al. [22] and Fathieh [23] explored how the stiffness of the intermodule connections affected the structural response of modular buildings. Both researchers used individual spring elements to simulate the horizontal and vertical components of the connections and concluded that the translational stiffness of the intermodule connection had the biggest influence on the global structural behavior of the building. A connection with high translational stiffness resulted in a building with a smaller period and larger base shear forces, while a connection with smaller translational stiffness resulted in larger inter-story drifts. In addition, the translational stiffness of the intermodule connections has shown to increase the modal periods of the structure and cause higher mode participation [19]. The rotational stiffness of the intermodule connection showed to have little effect on the global building behavior [22,23].

This paper aims to explore how to simulate and design mass timber high-rise modular buildings by examining how the structural behavior was influenced by the stiffness of the intermodular connections, the

https://doi.org/10.52202/069179-0348

intermodular connection location, the geometric transformation type, and the diaphragm property definition. Specifically, the objectives of this research are to: (1) develop a numerical modeling methodology to simulate mass timber high-rise modular buildings; (2) explore the influence of the stiffness of the intermodular connections on the diaphragm behavior of mass timber modular buildings; and (3) investigate the influence of intermodular connection and its location on the global structural response of mass timber modular buildings.

2 DESIGN DETAILS AND MODEL DESCRIPTION

2.1 BUILDING DESIGN

To achieve the research objectives, the authors used 9-, 12-, and 18-story modular buildings designed per to ASCE 7 [18] and IBC [24]. The buildings were assumed to be located in Seattle, Washington with site class D. Residential occupancy was considered to calculate the seismic design loads and a risk category II was assumed for the analysis. The gravity system of the structure used mass timber modular elements designed as volumetric units (Figure 1), and for the lateral force-resisting system double core reinforced concrete shear walls were located at the quarter points of the structure length (Figure 2). The building was designed with nine load combinations (Table 1), including seismic load cases. The loads considered are dead load (D), live load (L) due to residential occupancy and at the roof level (Lr), snow load (S), and earthquake load (Eh). The earthquake loads were calculated based on the equivalent lateral force method (ELF).

Table 1: *Load combinations for Allowable Stress Design (ASD)*

Comb	Load Combinations
1	D
2	D + L
3	D + Lr
4	D + S
5	D + 0.75L + 0.75Lr
6	D + 0.75L + 0.75S
7	$1.0D + 0.7E_h$
8	$1.0D + 0.525E_h + 0.75L + 0.75S$
9	$0.6D + 0.7E_h$

The gravity system was designed considering a corner-supported modular system, similar to previous research [4,7]. Each module consisted of four glue-laminated (glulam) columns, four perimeter glulam beams at the floor level, and four at the ceiling level. The floor was a cross-laminated timber (CLT) panel which spanned between the glulam beams and which was assumed to behave as a discrete diaphragm for each module. At the ceiling level, ponderosa pine CLT panels were used to ensure the stability of the module during the transportation and building construction. Since this panel did not resist gravity or lateral load demands, the authors chose a low grade CLT panel. Ponderosa pine is a biproduct of forest restoration for wildfire mitigation in the western states and exploring its usage within building construction would improve the sustainability of the building itself [25].

The superimposed dead load was 0.48 kN/m2 considering finishes at the floor levels. Live load was 2.40 kN/m2, which corresponds to a residential live load per IBC [24], 0.48 kN/m2 was applied at the ceiling level, and 0.96 kN/m2 for a non-occupied roof. The snow load for Seattle was 1.20 kN/m2 [26]. All the mass timber elements were Douglas-Fir and the dimensions were selected from commercially available material [27].

The frame elements used to assemble the modular units of the gravity system were designed per the National Design Specification (NDS) [28]. The centerline dimensions of the volumetric modules (Figure 1) were 3048 mm wide and 6096 mm long, with a total height of 4572 mm. For the 9- and 12-story buildings, the columns were 216 mm by 222 mm. The 18-story building used 260 mm square columns. The floor beams were 130 mm by 337 mm, while the ceiling beams were 130 mm by 298 mm. The floor beams and the ceiling beams were located such that there was a clear distance of 305 mm between the top of the ceiling and the bottom of the floor beam of the module above. This interstitial space was for plumbing and HVAC ductwork throughout the building and a common design for modular buildings. The CLT panel for the floor level was a 5-ply V2M1.1 grade 175 mm thick, and the ceiling panel was a 3-ply 105 mm thick CLT panel.

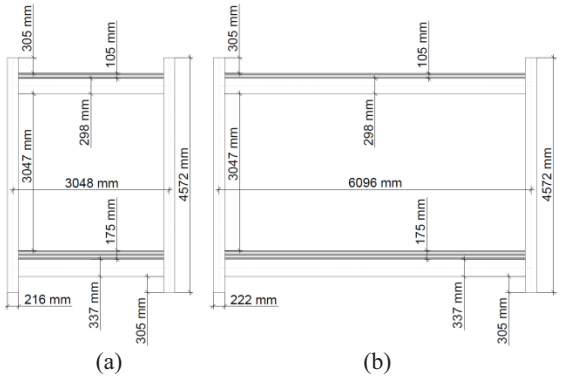

Figure 1: *Module elevation a) in the short direction, b) in the long direction*

Using the designed mass timber modules, a floor plan was proposed based on a double-core shear wall system, similar to the Brock Commons Student Residence project [29]. The proposed floor plan and layout consisted of 41 modules per story, arranged in three rows in the E – W direction (Figure 2). The first and third rows contain 15 modules each while the second row contains 11 modules. At the quarter point along the length of the building, the concrete cores were located in a space equal to that of two modules (Figure 2). All the building cases have 457 mm thick concrete shear walls arranged in a C shape with an opening toward the center of the building. The wall thickness was selected to satisfy the drift limit

requirements in both directions [18]. The modules are oriented with the longest side in the N – S direction, creating a space for the cores with a width-to-length ratio close to unity. The goal of the modular arrangement was to distribute the modules in a way to avoid structure irregularities or inherent torsion while still maintaining functionality of the building.

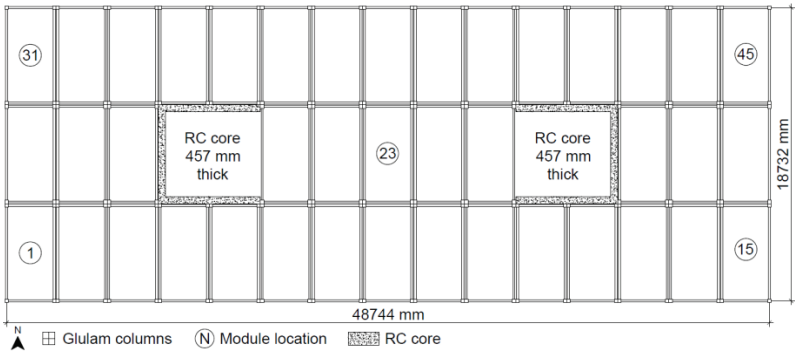

Figure 2: *General plan configuration for modular buildings*

2.2 NUMERICAL MODELING

2.2.1 Modeling geometry

Three-dimensional (3D) finite element models were developed for the 9-, 12- and 18-story mass timber modular buildings using the open-sourced finite element program, OpenSees [30]. All of the mass timber elements were simulated using elastic beam-column elements for the beams and the columns. Zero-length elements were used at the base of the columns to simulate different boundary conditions and three elastic beam-column elements were used to simulate the interstitial space (Figure 3). The beams of the module used zero-length elements at the ends to provide a pinned boundary condition representing the intramodule connection. Finally, a rigid diaphragm property was assigned to the floor level of each module.

To connect the modules together throughout each floor, the intermodule connections were simulated using two-node link elements. This modeling methodology was similar to the modeling methodology implemented by previous research on steel modular buildings [7,22,31]. The two-node link spanned between the column nodes of each module on the same floor. To connect modules together between floors, a rigid zero-length element was used thereby assuming that load was always transferred vertically between the floors and continuity of the module columns was achieved through the connection. In addition, all intermodule connections remained elastic throughout the analysis. The benefit of considering link-type elements in the modeling process was the capacity to explore the impact of each DOF on the global behavior of the building. In addition, each DOF can be defined by assigning elastic materials that can be updated to include material nonlinearity.

Two locations for the intermodule connection were considered (Figure 3). The first location (Figure 3a) considers the intermodule connection (and two-node link) coinciding with the location of the floor beams. The second location (Figure 3b) considers the intermodule connection (and two-node link) located at the column joint. Both locations were considered to compare how the location of the intermodule connection influences the building behavior. For the remainder of the paper, the location shown in Figure 3a will be referred to as *the case with the link at the diaphragm level* and Figure 3b will be referred to as *the case with the link at the column joint location*.

The concrete shear wall elements were simulated using elastic beam-column elements with a fixed base. The dimensions of the walls depended on the location, for the E-W walls two elements were used for each side of the core, while in the N-S direction only one element was used. Connections between the modular elements and the concrete walls were modeled with two node link elements. Because the main objective of this study is to examine how the stiffness of the intermodular connections influences the global behavior of the building, the concrete walls were assumed to be undamaged and uncracked throughout the analysis. Therefore, only the elastic concrete material properties were utilized with an inertia reduction ratio of 0.70. For the purposes of this research, the intramodule connections were considered rigid enough to remain elastic and satisfy the gravity demands for the applied loads in each module

Second-order effects were included through corotational geometric transformation for all elements to take into account the influence of the tolerance limits of the modular elements during the construction process [32].

All the buildings were modeled using elastic uniaxial materials and manually adjusting the stiffness of the two-node link elements used to simulate the intermodule connections to perform the parametric analysis and evaluate the influence of each DOF of the connection on the modular building behavior. Glulam properties for elastic beam-column elements were used from commercial providers [27].

https://doi.org/10.52202/069179-0348

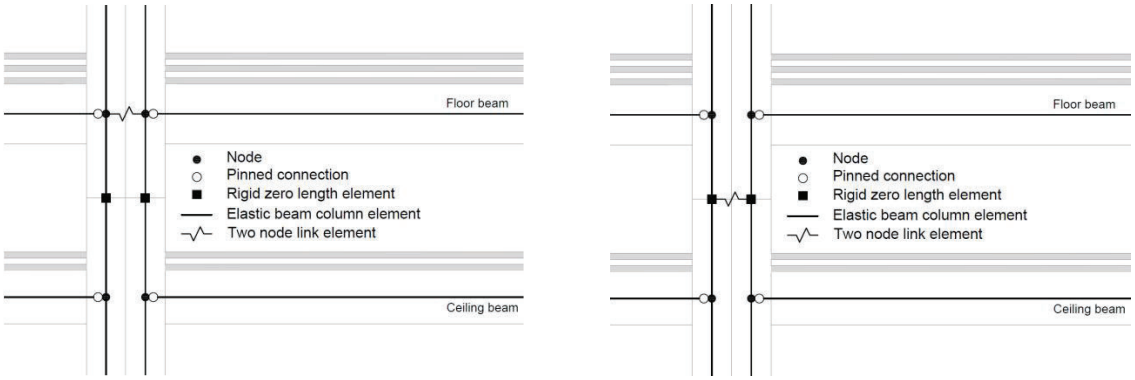

Figure 3: *Horizontal link located a) at the diaphragm level, and b) at the column join level*

2.2.2 Diaphragm modeling

The diaphragm of the case study buildings was assumed to be located at the floor level of the modules. The ceiling level had lower stiffness than the floor because ponderosa pine CLT was utilized for the ceiling panels. CLT diaphragms were considered to behave as rigid elements under design-level earthquake loads [33]. Therefore, the floor panels for each module were considered discrete elements with a rigid diaphragm property to avoid in-plane deformation. This modeling methodology also contributed to the analysis of the structural behavior of the entire floor diaphragm based on the stiffness of the intermodule connections.

The authors assumed a symmetric connection in the X and Y direction. With a parametric analysis the stiffness of the connections was modified in the translational and the rotational DOF to measure the diaphragm deflections. ASCE 7 [18] methodology was used to classify the building diaphragms according to their in-plane deflection compared to the lateral system deflection when both are subjected to lateral loading. The authors used the maximum deflection ratio to classify the diaphragm of each one of the simulations.

2.2.3 Gravity and lateral loads

The gravity loads were included in the model as distributed loads along the module beams based on an equivalent tributary area at the floor and the ceiling beams. Self-weight was assigned as concentrated loads directly to the nodes for columns and the reinforced concrete shear walls. The structure effective mass was considered to be the total structure self-weight plus the superimposed dead load. The mass was assigned to the nodes at the floor and the ceiling level as concentrated mass. Lateral loads were assigned to the model based on the approaches used to simulate the diaphragm. When discrete diaphragms are assigned to each module, the lateral loads were uniformly distributed between the nodes of the columns located at the floor level. This approach allows to simulate the loading distribution required for semi-rigid or flexible diaphragms. In the case of a rigid diaphragm, the same uniform load distribution was applied.

2.3 SENSITIVITY ANALYSIS

A sensitivity analysis was performed to examine the influence of the intermodular connection location (Figure 3) and the influence of the stiffness of each DOF of the intermodular connection. This sensitivity analysis was also performed to increase computational efficiency. The results of the sensitivity analysis were carried through in the remainder of the investigation described in this paper. To perform this sensitivity analysis, a base model was defined. The base model consists of a building with rigid intermodular connections and a rigid diaphragm property assigned to each module in the building. The ranges of considered stiffnesses of the column links are summarized in Table 2.

Table 2: *Parameters analyzed in the sensitivity analysis*

Properties	Direction	Condition/Range
Link location	--	Diaphragm or Column joint
Horizontal links	X, Y	Range: 1.75×10^{-1} – $1.75 \times 10^{+8}$ kN/mm
Rotational links	θX, θY, θZ	Pinned or Fixed

The ranges of stiffnesses provided in Table 2 were used to evaluate the influence of intermodule connection stiffness on diaphragm behavior, specifically the influence of the translational DOF stiffness. The horizontal translational stiffness (X and Y) was adjusted manually to fixed values while the remaining DOF of the connections were assumed to be rigid. The deformation ratio of the diaphragm, the modal periods, and the inter-story drifts of the buildings were calculated for each stiffness value.

3 RESULTS AND DISCUSSION

3.1 INTER-STORY DRIFTS

For all case study buildings and both locations of the intermodular connections (Figure 3), the maximum inter-story drift was below 1.5% (Figure 4). The inter-story drift increased when the intermodular connections were located at the column joint location. Analyzing each location independently, the buildings with connections at the diaphragm level, had higher inter-story drifts in the X direction than in the Y direction, while the buildings with

connections at the column joint locations had larger drifts in the Y direction than in the X direction. The intermodule connection location also influenced the location of the maximum inter-story drift (Figure 4). For the buildings where the intermodular connections are located at the column joints, the maximum inter-story drift ratio was located at about 60% of the height of the building (Figure 4); whereas when the intermodular connection was located at the diaphragm, the maximum inter-story drift ratio was located at about 80% of the height of the building (Figure 4).

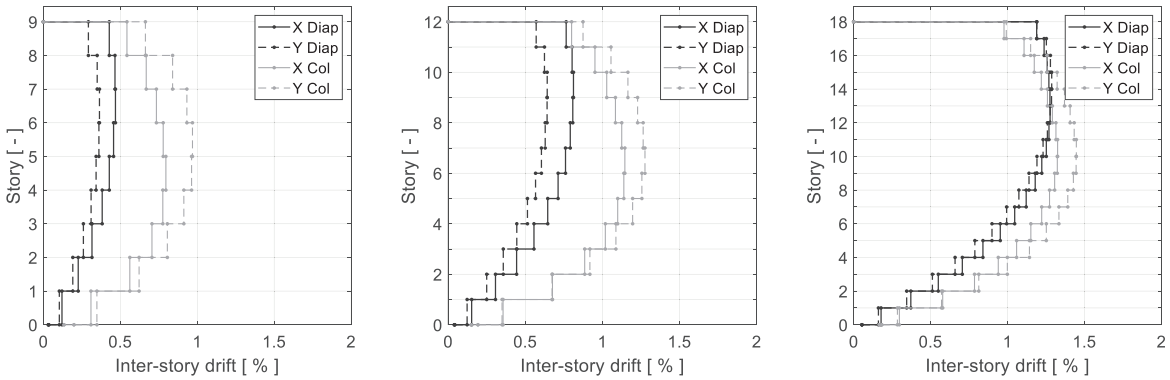

Figure 4: *Design inter-story drifts for the diaphragm and column joint link cases: a) 9-story, b) 12-story, and c) 18-story*

3.2 DIAPHRAGM BEHAVIOR

Regardless of the location of the intermodule connection, as the translational DOF stiffness of the connection decreased, the diaphragm deflection increased exponentially (Figure 5). Based on static analysis results (Figure 5), the 9- and 12-story building required high translational stiffness for the intermodule connection to obtain the same diaphragm deflection ratio as the 18-story building with a less stiff connection. This horizontal stiffness of the intermodular connections influence the deflection of the diaphragms and requires a connection with larger translational stiffness to reach a certain deflection with shorter buildings. This response is opposite to the common behavior of the stiffness of traditional lateral force resisting systems (LFRS) that requires higher stiffness for taller buildings to satisfy the building drift demands.

The difference in diaphragm deflection based on the location of the intermodular connection is more pronounced for the 9-story building (Figure 5a), than for the 18-story building (Figure 5c) and for stiffer connections, than for more flexible connections. In general, buildings with intermodular connections at the column joint location require higher connection stiffness to obtain a rigid diaphragm property definition. On the contrary, regardless of the intermodular connection location, similar connection stiffnesses were required to obtain a semi-rigid or flexible diaphragm definition. Based on the diaphragm behavior shown in Figure 5, the authors assumed a rigid diaphragm could be obtained with an intermodular connection stiffness of 100 kN/mm, regardless of the building height as this connection stiffness results in diaphragm deflection less than 0.5.

The building in-plane configuration, particularly of the LFRS, was observed to have some influence over the diaphragm stiffness. All the cases were analyzed with the same building geometry, however, in the Y direction, when the lateral loads are applied on the long side of the building, the diaphragm deflection is greater than the deflection in the X direction for the same translational stiffness. This is because for the case study building, in the X direction, the lateral displacements are controlled by four shear walls, while in the Y direction, two shear walls control the displacements.

In addition to diaphragm deflection, the authors explored the impact that intermodular connection translational stiffness and location has on the model translational periods in each direction (Figure 6). The results (Figure 6) show that the translational periods are constant for connection stiffnesses greater than 100 kN/mm, which correspond to a rigid diaphragm (deflection ratio less or equal to 0.5). At connection stiffnesses less than 100 kN/mm, the building periods increase with small reductions in the translational stiffness of the intermodule connections. The location of the intermodule connection also has an impact on the translational period of the building. When the intermodule connection is located at the column joint, the buildings have a larger period than when the intermodule connection is located at the diaphragm. This result was observed regardless of building height.

Further analysis considered the modal shapes of the buildings to determine the direction of the translational modes and define if they are affected by the translational stiffness of the connections. Comparing the translational period in the X and Y direction, the same behavior occurred in all the story cases such that the buildings with the connections at the diaphragm change the direction of the fundamental period to the orthogonal direction in the semirigid range. For instance, in Figure 6 the influence of the location of the connection and its stiffness was important over the structure period. For the values at the

https://doi.org/10.52202/069179-0348

bottom of the curve the differences in the periods of the buildings were in some cases more than 1s while for the stiffer cases at the top, the differences remain in less than 0.5 s for all the buildings. For the column joint connection cases, the direction of the fundamental period remained the same for the entire range.

While Figure 5 and Figure 6 show the results of modifying the translational stiffness of the intermodule connections, Figure 7 shows the results of modifying the translational stiffness and the rotational DOF of the intermodule connections. The translational stiffness of the intermodule connections were varied in addition to the rotational DOF varying between pinned and fixed. This variation was performed in in both directions and with both locations of the intermodule connection. In the case of the fixed rotational DOF, the results shown in Figure 7 are the same as those shown in Figure 5 for comparison.

In the X and Y directions (Figure 7), there were small differences between the models with fixed and pinned rotational DOF when the connections were located at the diaphragm level (17.6% for the X direction and 13.2% for the Y direction, on average). However, when the intermodule connection is located at the column joint, the models with pinned rotational DOF had larger diaphragm deflections, on average 25.3% larger in the X direction and 29.8% larger in the Y-direction than models with fixed rotational DOF. In some cases, the location of the intermodular connection changed the diaphragm classification from rigid to semi-rigid. This effect was less pronounced for the 18-story building than for the 9-story building.

The simulation results in Figures 5 – 7 demonstrate that the translational stiffness of the intermodular connections had more of an influence on the diaphragm behavior than the rotational stiffness. This conclusion was consistent with previous research on modular buildings [22]

3.3 ELEMENT FORCES

The modular building design was implemented using an envelope of forces within the structural elements for the two intermodular connection locations (Figure 3). The envelopes of the design forces are shown in Figure 8 for the 12-story building. The forces in the other two buildings were proportional to their height.

The location of the intermodular connection did not substantially influence the axial force demands in the gravity columns (Figure 8a). Rather, there was an 8.7% difference between the axial force demands when the intermodular connections were located at the diaphragm as opposed to the column joint. However, the intermodular connection location did influence the shear demands within the gravity columns (Figure 8b and c). The shear force envelopes in the connection region for when the intermodular connection was located at the diaphragm was on average 33.6% lower in the strong axis (Figure 8b) and 66.8% lower in the weak axis (Figure 8c) than when the intermodular connection is located at the column joint. Similarly, the moment demands in the gravity columns were on average 13.2% lower in the weak axis (Figure 8d) and 26.4% lower in the strong axis (Figure 8e) when the intermodular connection was located at the diaphragm than at the column joint. Columns strong axis is located parallel to E-W direction (Figure 2).

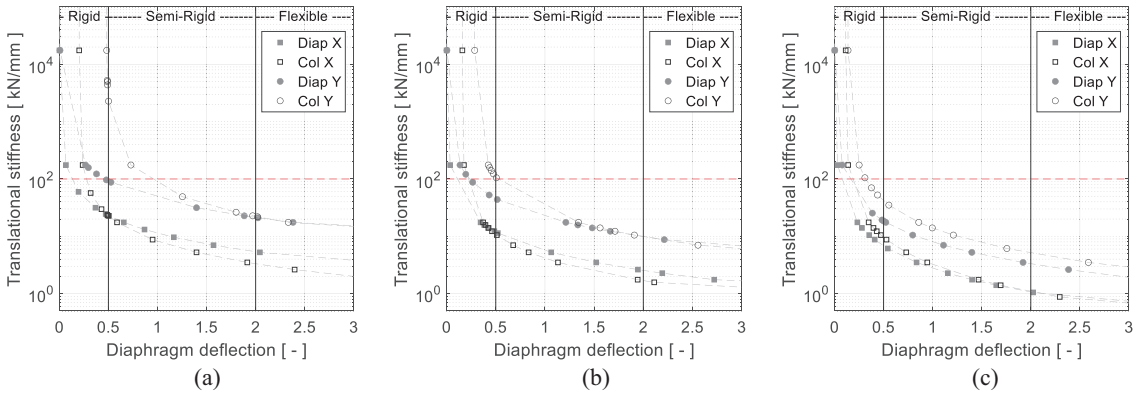

Figure 5: *Diaphragm flexibility for the diaphragm and column joint link cases: a) 9-story, b) 12-story, and c) 18-story*

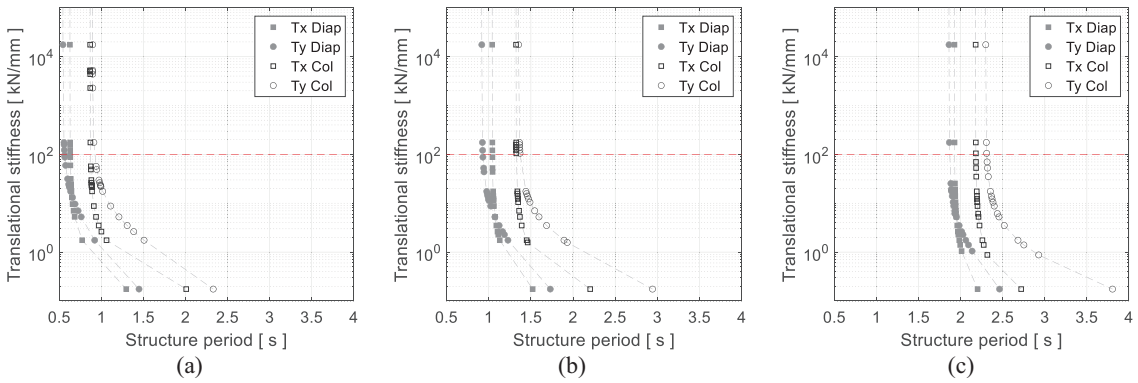

Figure 6: *Structure period for the diaphragm and column joint link cases: a) 9-story, b) 12-story, and c) 18-story*

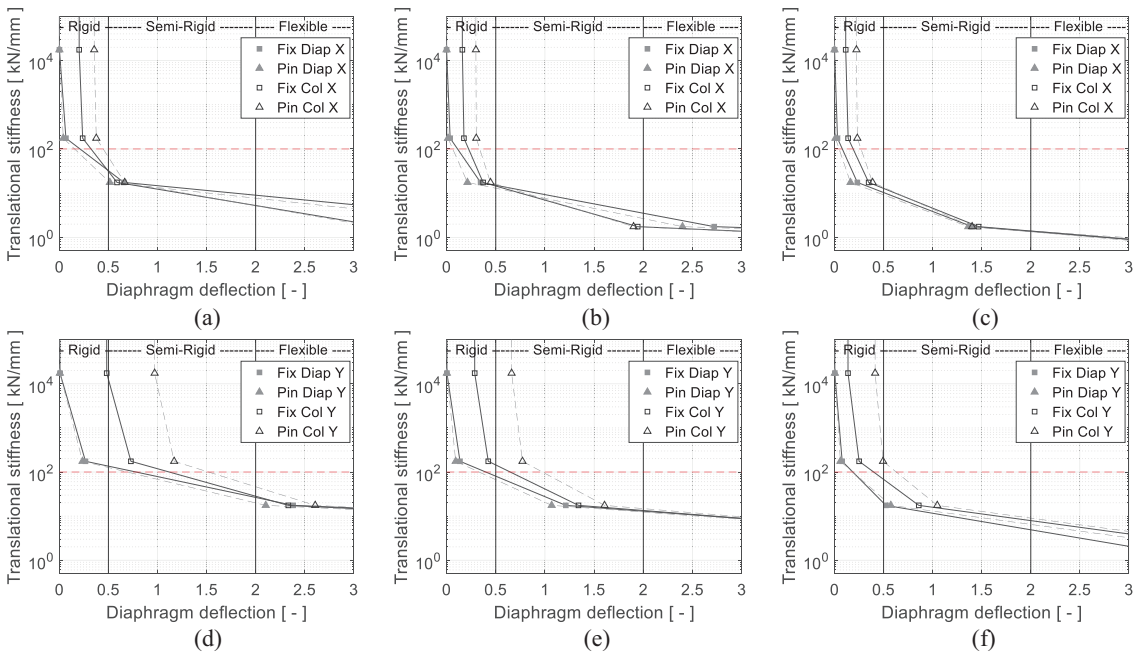

Figure 7: *Diaphragm deflections for varying locations of intermodular connections with pinned and fixed rotational stiffness: a) 9-story X direction, b) 12-story X direction, c) 18-story X direction, d) 9-story Y direction, e) 12-story Y direction, and f) 18-story Y direction*

4 CONCLUSIONS AND FUTURE WORK

This paper presented the results of the analysis of a 9–, 12-, and 18-story mass timber modular building with two reinforced concrete cores. 3D elastic models were developed in OpenSees and used to evaluate the influence of the stiffness and location of intermodule connections on the global response of modular buildings under combined gravity and lateral loads. The modeling methodology developed in this research and summarized within this paper can be utilized to simulate high rise mass timber modular buildings. The numerical simulation approach with beam and column elements to assemble the volumetric units, generated similar response for mass timber modular buildings compared to steel modular buildings reported in previous studies. Therefore, the authors can conclude that the structural behavior described in this paper and the conclusions made herein can be generalized for modular construction independent to the material used to simulate the modular units.

The stiffness of the translational DOF of the intermodular connections showed an inverse exponential relation with the diaphragm deflections for all the building heights. However, taller buildings required a less stiff connection than shorter buildings to have a rigid diaphragm behavior. Figure 5 can be utilized by designers to determine the required connection stiffness to obtain specific diaphragm flexibility given a building height. Simulations demonstrated that the period of mass timber modular buildings remains constant if the diaphragm can be classified as rigid (Figure 6) regardless of the building height, however the building period increases with small reductions of the translational stiffness of the intermodule connections when the diaphragm is classified as either semi-rigid or flexible.

https://doi.org/10.52202/069179-0348

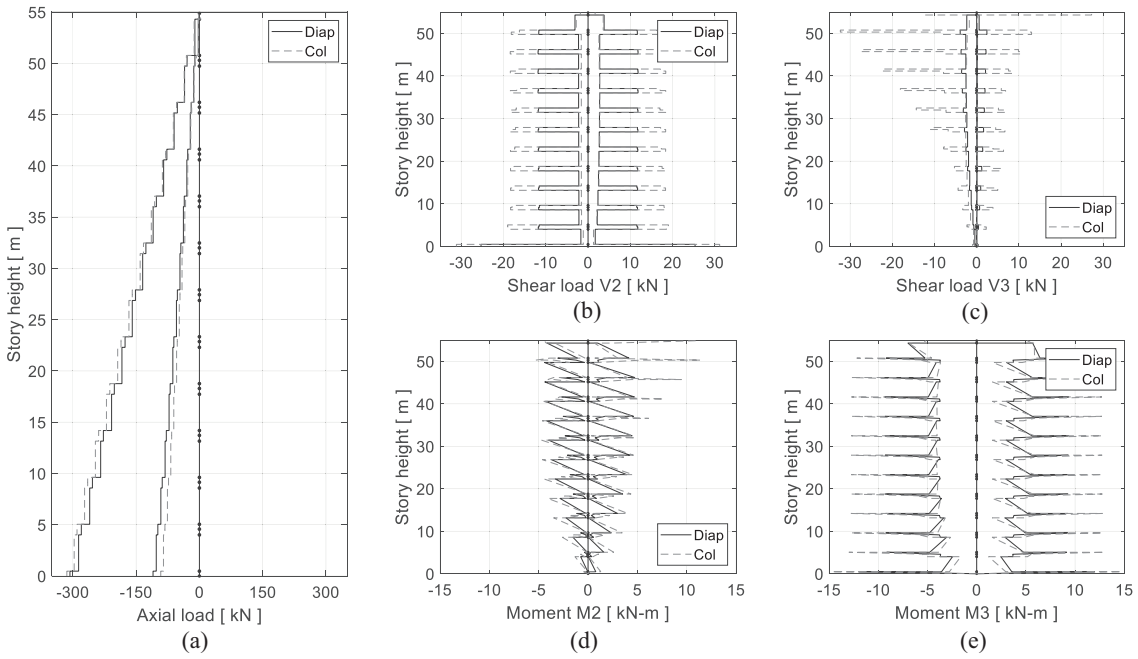

Figure 8: *Design element forces for 12-story buildings: a) axial load, b) shear load in the strong axis, c) shear load in the weak axis, d) moment around the weak axis, e) moment around the strong axis*

The rotational DOF of the intermodule connections has little effect on the diaphragm deflections compared to the influence of the translational stiffness. When the location of the connections was considered, the rotational DOF of the intermodule connections showed a slight increase of the diaphragm deflections for the buildings with the connections at the column joint.

Two different locations of the intermodule connections for the modular buildings were explored in the analyses. The building performed better when the connection was located at the diaphragm level. Specifically, the periods and drifts distribution were influenced by the location of the connection. When the intermodule connection was located at the column joint, the connection required larger translational stiffness to obtain lower diaphragm deflections in all the buildings. In addition, when the intermodule connection was located at the column joint, the shear and moment demands in the column elements were higher.

To identify a better relation between the diaphragm flexibility and the in-plane configuration of the building, additional analyses should be performed to compare different model geometries, however, it is considered out of the scope of the current research. Future research on this topic should also explore the dynamic response of the structures to verify the building behavior under earthquake hazards and define the required strength to design and test the inter-modular connections.

ACKNOWLEDGEMENT

This research is funded by the National Science Foundation (CMMI 2046001).

REFERENCES

[1] American Institute of Steel Construction, Need for Speed. 2022, [Online]. Available: https://www.aisc.org/why-steel/innovative-systems/need-for-speed/

[2] E. M. Generalova, V. P. Generalov, and A. A. Kuznetsova. Modular Buildings in Modern Construction, *Procedia Engineering*, vol. 153, pp. 167–172, 2016, doi: 10.1016/j.proeng.2016.08.098.

[3] M. T. . Gorgolewski, P. J. Grubb, and M. Lawson. Modular Construction using Light Steel Framing Design of Residential Buildings, pp. 1–112, 2001.

[4] R. M. Lawson, R. G. Ogden, and R. Bergin. Application of Modular Construction in High-Rise Buildings. *J. Archit. Eng.*, vol. 18, no. 2, pp. 148–154, Jun. 2012, doi: 10.1061/(ASCE)AE.1943-5568.0000057.

[5] J. Cover. Mass Timber: The New Sustainable Choice for Tall Buildings. *International Journal of High-Rise Buildings*, vol. 9, no. 1, pp. 87–93, Mar. 2020, doi: 10.21022/IJHRB.2020.9.1.87.

[6] M. Almashaqbeh and K. El-Rayes. Optimizing the modularization of floor plans in modular construction projects. *Journal of Building Engineering*, vol. 39, Jul. 2021, doi: 10.1016/j.jobe.2021.102316.

[7] J. Y. R. Liew, Y. S. Chua, and Z. Dai. Steel concrete composite systems for modular construction of high-rise buildings. *Structures*, vol. 21, pp. 135–149, Oct. 2019, doi: 10.1016/j.istruc.2019.02.010.

[8] A. W. Lacey, W. Chen, H. Hao, and K. Bi. Structural response of modular buildings – An overview. *Journal of Building Engineering*, vol. 16, pp. 45–56, Mar. 2018, doi: 10.1016/j.jobe.2017.12.008.

[9] S. Srisangeerthanan, M. J. Hashemi, P. Rajeev, E. Gad, and S. Fernando. Review of performance requirements for inter-module connections in multi-story modular buildings. *Journal of Building Engineering*, vol. 28, Mar. 2020, doi: 10.1016/j.jobe.2019.101087.

[10] H. Rajanayagam, K. Poologanathan, P. Gatheeshgar, G. E. Varelis, P. Sherlock, B. Nagaratnam, P. Hackney. A-State-Of-The-Art review on modular building connections. *Structures*, vol. 34, pp. 1903–1922, Dec. 2021, doi: 10.1016/j.istruc.2021.08.114.

[11] H. Svatoš-Ražnjević, L. Orozco, and A. Menges. Advanced Timber Construction Industry: A Review of 350 Multi-Storey Timber Projects from 2000–2021. *Buildings*, vol. 12, no. 4, p. 404, Mar. 2022, doi: 10.3390/buildings12040404.

[12] L. Fernandes Carvalho, L. Filipe Carvalho Jorge, and R. Jerónimo. Plug-and-Play Multistory Mass Timber Buildings: Achievements and Potentials. 2020, doi: 10.1061/(ASCE)AE.1943.

[13] Lightwood. World's tallest Timber Building 'HoHo Tower' in Vienna. Aug. 2018.

[14] F. Ávila, P. Dechent, and A. Opazo. Seismic behaviour evaluation of CLT horizontal diaphragms on hybrid buildings with reinforced concrete shear walls. *Engineering Structures*, vol. 244, p. 112698, Oct. 2021, doi: 10.1016/j.engstruct.2021.112698.

[15] H.-E. Blomgren, S. Pei, Z. Jin, J. Powers, J. D. Dolan, J. W. van de Lindt, A. R. Barbosa, D. Huang. Full-Scale Shake Table Testing of Cross-Laminated Timber Rocking Shear Walls with Replaceable Components. *J. Struct. Eng.*, vol. 145, no. 10, p. 04019115, Oct. 2019, doi: 10.1061/(ASCE)ST.1943-541X.0002388.

[16] A. R. Barbosa, L. Rodrigues, A. Sinha, C. Higgins, R. B. Zimmerman, S. Breneman, S. Pei, J. van de Lindt, J. Berman, Eric McDonnell, J. M. Branco, L. C. Neves. Numerical modeling of CLT diaphragms tested on a shake-table experiment. 2018.

[17] I. J. Ramaji and A. M. Memari. Identification of structural issues in design and construction of multi-story modular buildings. Presented at the 1st Residential Building Design & Construction Conference, 2013.

[18] American Society of Civil Engineers. Minimum Design Loads and Associated Criteria for Buildings and Other Structures. American Society of Civil Engineers (ASCE), 9780784479964, 2016. doi: 10.1061/9780784414248.

[19] S. Srisangeerthanan, M. J. Hashemi, P. Rajeev, E. Gad, and S. Fernando. Numerical study on the effects of diaphragm stiffness and strength on the seismic response of multi-story modular buildings. *Engineering Structures*, vol. 163, pp. 25–37, May 2018, doi: 10.1016/j.engstruct.2018.02.048.

[20] Z. Chen, J. Liu, and Y. Yu. Experimental study on interior connections in modular steel buildings. *Engineering Structures*, vol. 147, pp. 625–638, Sep. 2017, doi: 10.1016/j.engstruct.2017.06.002.

[21] J. Peng, C. Hou, and L. Shen. Lateral resistance of multi-story modular buildings using tenon-connected inter-module connections. *Journal of Constructional Steel Research*, vol. 177, p. 106453, Feb. 2021, doi: 10.1016/j.jcsr.2020.106453.

[22] A. W. Lacey, W. Chen, H. Hao, and K. Bi. Effect of inter-module connection stiffness on structural response of a modular steel building subjected to wind and earthquake load. *Engineering Structures*, vol. 213, p. 110628, Jun. 2020, doi: 10.1016/j.engstruct.2020.110628.

[23] A. Fathieh. Nonlinear Dynamic Analysis of Modular Steel Buildings in Two and Three Dimensions. 2013.

[24] International Code Council. 2021 International building code (IBC). Falls Church, Va. : International Code Council, 2000-, 978-1-60983-955–0, 2021. [Online]. Available: https://codes.iccsafe.org/content/IBC2021P2

[25] S. Bhandari, M. Riggio, L. Muszynski, E. Fischer, and S. Jahedi's. Behavior of In-plane Butt-joints with 45° Screws in Ponderosa Pine CLT. *Proceedings of the 2021 Society of Wood Science and Technology International Convention*, Flagstaff, Arizona, Aug. 2021.

[26] Building Code (SBC). 2018, [Online]. Available: https://www.seattle.gov/sdci/codes/codes-we-enforce-(a-z)/building-code

[27] Structurlam. Mass Timber Technical Guide for CrossLam ® CLT and GlulamPLUS ®. 2021.

[28] American Wood Council. NDS ® 2018 NATIONAL DESIGN SPECIFICATION® for Wood Construction 2018. 2018. [Online]. Available: www.awc.org.

[29] P. Fast, B. Gafner, R. Jackson, and J. Li. Case study: An 18 storey tall mass timber hybrid student residence at The University of British Columbia, Vancouver. 2016.

[30] F. Mckenna, M. H. Scott, and G. L. Fenves. Nonlinear Finite-Element Analysis Software Architecture Using Object Composition. *Journal of Computing in Civil Engineering ASCE*, 2010, doi: 10.1061/ASCECP.1943-5487.0000002.

[31] T. Gunawardena, T. Ngo, and P. Mendis. Behaviour of Multi-Storey Prefabricated Modular Buildings under seismic loads. *Earthquakes and Structures*, vol. 11, no. 6, pp. 1061–1076, Dec. 2016, doi: 10.12989/EAS.2016.11.6.1061.

[32] R. M. Lawson and J. Richards. Modular design for high-rise buildings. *Proceedings of the Institution of Civil Engineers - Structures and Buildings*, vol. 163, no. 3, pp. 151–164, Jun. 2010, doi: 10.1680/stbu.2010.163.3.151.

[33] S. Breneman, E. McDonnel, B. Tremayne, D. Llanes, J. Houston, E. Mengzhe, R. Zimmerman, G. Montgomery. CLT Diaphragm Design for Wind and Seismic Resistance Using SDPWS 2021 and ASCE 7-16. 2022.

https://doi.org/10.52202/069179-0348

World Conference on Timber Engineering Oslo 2023

A Comparison of Punching Shear Design Approaches for Point Supported CLT Panels

Christian Slotboom[1], Carla Dickof[2], Robert Jackson[3]

ABSTRACT: The following study examines different methods of punching shear design for point supported Cross Laminated timber (CLT) panels. A literature review was completed, summarizing CLT rolling shear capacity, as determined in both European and North America research as well as code and material standard documents. Analysis methods for calculating internal stresses in CLT slabs were then reviewed, with an emphasis on simplified design equations. Several design checks were then completed by comparing predicted capacity to tested strength for CLT panels from existing experimental programs. Predictions from each method were compared to actual panel capacities from testing, and it was found the methods used predicted failure at approximately 3x the input load or higher for the specific panel examined. A parametric study was completed where a number of panels were analysed using the different analysis methods outlined. The parameters studied include panel number of spans, length, width, grade, thickness, and support size. It was shown that simplified analysis methods make predictions that were comparable to FEM predictions, but FEM results varied more with respect to these parameters. It was also shown that the support stiffness was a significant parameter on the distribution of shear forces and the peak model forces observed.

KEYWORDS: Tall wood buildings, CLT Floors, Point-supported floors, two-way floor action, Punching Shear, Rolling Shear.

1 INTRODUCTION

Recent changes to the National Building Code of Canada [1] and International Building [2] have increased height limitations on tall timber buildings up to 12 and 18 storeys respectively. These tall timber provisions accommodate a quickly growing segment of the market, one with many benefits such as decreased embodied carbon in buildings and shorter construction times. One structural system gaining popularity is point supported Cross Laminated Timber (CLT) a gravity system where panels are supported directly on columns without intermediate beams. Buildings using the point supported CLT structural system minimize floor assembly depth. They also reduce material volumes and construction timelines due to the limited components.

The force distribution of point supported CLT differs from typical CLT on beams, and shear forces near the supports are much higher. As such, this type of system is more frequently governed by shear design instead of bending or deflection. While CLT has been studied significantly over the past 20 years, there is minimal code guidance for the design of CLT in this condition. One prominent building in North America using point supported CLT panels is TallWood House at the University of British Columbia [3], where physical testing of full scale CLT panels [4] was used to validate the design of the point supported structural system.

Since the UBC TallWood House was completed, a number of research programs have studied point supported CLT, evaluating both the rolling shear strength of CLT and analysis methods to assess internal stresses. However, few studies to date have compared the predictions made by different design methods. To help address this knowledge gap, the following paper reviews various methods to determine the capacity and demands for CLT punching shear, and compares their predicted results. The analysis and capacity methods examined were applied to a design example where a number of design cases are considered on an experimentally tested panel. Finally, a parametric study was used to examine the effect a wide range of variables on panel response.

2 CLT PUNCHING SHEAR CAPACITY

There are two significant parameters for point supported CLT: the rolling shear strength (f_s), which describes the strength of the base CLT fibre; and the punching shear amplification factor (k_s), which increases the base strength of CLT near columns to it's punching shear strength (f_p). A summary of the rolling and punching shear amplification of CLT is outlined in the following section.

2.1 ROLLING SHEAR STRENGTH

In North American material standards and CLT fabrication standards "specified strength in rolling shear, fs, is taken as approximately 1/3 of the specified strength in shear, f_v, for the corresponding species combination" [5,6]. The rolling shear strengths specified in the fabrication standards are consistent with this rule instead

[1] Christian Slotboom, Graduate Engineer, Fast+Epp, cslotboom@fastepp.com

[2] Carla Dickof, Associate Principle. Fast+Epp, cdickof@fastepp.com

[3] Robert Jackson, Partner, Fast+Epp, rjackson@fastepp.com

https://doi.org/10.52202/069179-0349

of being developed based on test results in material studies.

The rolling shear strength of CLT can be determined experimentally using either inclined direct shear test or four point bending test. Inclined shear tests load a small specimen of CLT in shear directly through a single layer oriented for rolling shear. Many tests on different European species of wood were completed by Erhert et al. [7,8]. It was noted that the strength of CLT was influenced by the aspect ratio of the boards used. Other studies using inclined shear tests include Wang et al. [9], Mestek [10], and Muster [11]. Four-point bend tests load a CLT specimen in bending to failure. The internal stress is indirectly determined using an analytic or numerical assessment of the CLT beam based on the known shear failure load and the CLT layup. Several studies used this method on European [12], Asian [13], Oceanic [14] CLT. While the experimentally measured rolling shear strength varies, impacted by parameters such as species, width-to-depth ratio of the lamella, etc., strengths reported for softwood have been shown within the range of 0.8MPa to 2.0MPa. Table 3 summarizes the 5th percentile strengths observed in different studies and compares them to the characteristic rolling shear strength specified by the material standard CSA O86. To be compared with the short-term test results with the CSA O86 [5] values have a short term load duration factor of 1.15 applied to the standards specified value.

Table 1: *Comparison of 5th percentile strength with CSA 086 code values.*

Reference	f_s (MPa)
CSA O86 SPF [6]	0.50
Wang et al. [9]	0.76
Ehrhart (2015) [7]	1.51
Mestek (2011) [10]	1.47

2.2 PUNCHING SHEAR STRENGTH

Point supported CLT is loaded with a more complex load path than those used in rolling shear tests. The punching shear strength of CLT can be predicted using direct punching tests where a point load is applied to a CLT panel supported or 3 or 4 sides. Based on the ultimate strength observed in testing, the internal shear stresses are determined using analytical methods or numerical methods such as FEM models. Recent studies [10,11,15] have shown that the stress predicted at failure corresponds to a higher shear capacity than the observed base rolling shear strength. Mestek [10] noted that point supported CLT specimens failed at internal stress 1.6 times the predicted capacity associated with base rolling shear strength. Similar increases in strength were noted by Bogensberger et al. [15] and Muster [11].

Possible factors contributing to the observed strength increase include additional confinement from compression, the restraining effect of top and bottom layers, and nonlinear redistribution of forces at failure. Bogensberger proposed a nonlinear strength model of CLT model that could account for the observed higher shear stress [15]. The effect of compression on rolling shear strength was observed by Mestek [10], where the shear strength observed where compression was applied to inclined shear specimens was consistently higher.

Based on the observed data, a draft Eurocode document [16] proposed a factor, k_p=1.6, to increase the base rolling shear strength for punching shear in CLT. In a later study, Muster [11] proposed decreasing k_p to 1.3 at supports at panel edges.

3 POINT SUPPORTED CLT ANALYSIS

Internal stresses can be estimated using ether finite element models, or simplified design equations. The following sections highlight existing methods used to predict demands in CLT panels.

3.1 FINITE ELEMENT MODELS

Three types of Finite element models (FEM) have primarily been used for analysis and design of CLT in punching shear:

- Solid 3D element models.
- Shell 2D element models.
- Beam models using the shear analogy.

Solid 3D models are the most detailed analysis approach of the above three. Each layer of wood is modelled with interaction properties between layers defined. These models can show complex behaviour such as the effect of edge glue, the contact stresses between layers or supports, and the interaction between bending and shear forces. Internal stresses are generally read directly from FEM models. Solid models have been used in a number of studies [10,11,15] to predict internal panel stress, or compare to other design methods in research.

Shell element 2D models represented the CLT with either an orthotropic shell element with equivalent section properties, or a layered shell element. In layered shell elements, stresses can be extracted from layers directly, and some software products, such as Dulbal's RFEM, have layered shell representations of CLT [17]. Stresses through the depth of the panel are then calculated based on established analytical models such as beam shear models. If orthotropic shell elements are used, then stresses are calculated using a section analysis.

Muster [11] presents a modelling approach where 2D shell provided similar stresses to 3D finite element models. In this approach, the supports are modelled as springs with a spring stiffness tuned so that bending stresses were similar between the two models. The simplicity of 2D shell element modelling makes this method attractive to practicing designers.

A grid of beam elements in conjunction with the shear analogy method can also be used to model point supported CLT. This method was used by Mestek [10] to determine the distribution of shear forces on column supports, in lieu of the solid 3D model or a calibrated 2D shell element model. Girder-girder models avoid the extreme stress concentrations that can occur in solid or shell element models.

https://doi.org/10.52202/069179-0349

3.2 SIMPLIFIED MODELS

In addition to FEM, a number of simplified analysis methods have been proposed. Simplified analysis methods typically first determine shear forces on each face of a column, then find internal stress using those forces. The accuracy of these methods is generally determined by comparing to FEM analysis. Three simplified analysis methods were considered in this study:

- Tributary Area simplified method [3].
- Mestek's simplified method [10].
- Muster's simplified method [8].

The Tributary Area simplified analysis method was proposed in a study for the UBC TallWood House [3]. This method determines column face forces (V_i) using associated tributary area. Internal stresses, (τ_i) are then evaluated based by evenly distributing force across the width of the effective support, then using beam bending equation as described in equation 1. The effective depth (d_i) is taken as the height of CLT between layers longitudinal to CLT face being evaluated. The effective width of the support ($b_{i,eff}$) is as half the effective depth (d_i) from the respective face of the column.

$$\tau_i = \frac{1.5V_i}{b_{i,eff}d_i} \quad (1)$$

Mestek's simplified analysis method was developed and calibrated from a parametric study using FEM grid-beam CLT models used to determine forces at the face of column supports. From the support forces, the internal stress across the effective support width and through the depth of the panel are based on equations from DIN 1052 [18]. Conditions for supports at corners of panels, and another for supports in the centre of a panel were considered.

To determine the distribution of forces, a FEM based parametric study was implemented considering:

- Three ratios of strong-to-weak axis lamella thickness, 1, 1.5, and 2
- depths of CLT from 100mm to 220mm with 5 to 11 symmetrical layers depending on thickness and layup
- A single span with a span length-to-width ratio between 1-3

Support size and bay size were not considered in the parametric study. The study also assumes no narrow side edge gluing. Based on outputs from these parametric studies, equations for calculating the force on the strong axis face (V_x) and the force on the weak axis face (V_y) were determined using regression equations. The study found that the distribution of force on each support face had a strong correlation with both number of CLT layers, and the ratio between CLT layer thicknesses. Two equations are developed for both columns at edges and columns away from any panel edge.

Given the support shear force(s), an equation simplified from the German design code [18] is used to calculate peak stress (τ_i) as described in equation 1. This equation is based on the lamella thicknesses in each direction (t_x, t_y), effective support width ($b_{i,eff}$) and two modifications factors: a stress concentration factor (k_A) and a pre-calculated modification factor (k_R). The effective support widths ($b_{i,eff}$) was taken as 35° from the face of column support.

$$\tau_i = \frac{K_{A,i}1.5V_i}{k_{R,i}b_{i,eff}(t_x + t_y)} \quad (2)$$

The stress concentration factor (k_A) accounts for the ratio between the peak stress and average stress across the effective support width in the FEM model for panels supported at their edge. The factor ranges from 1.35 to 1.6 depending on effective support width and panel thickness, but is taken as 1.0 for panels supported away from their edge. The factor k_R is a coefficient precalculated from the section analysis method presented in DIN. Table 2 summarizes values of k_R for a corner support.

Table 2: *Values for K_R in the x and y direction for a corner support.*

Factor	Number of Lamella			
Orientation	5	7	9	11
$k_{R,x}$	2	2.5	3.3	3.89
$k_{R,y}$	1	2	2.5	3.3

Mestek also compared the proposed simplified equation to the FEM results of the parametric study. The predictions from the simplified equations were typically higher than the FEM results, with most in the range of 20% higher. One exception was the weak axis CLT shear stress for 5ply CLT, which was 40-70% higher than the FEM results.

Muster also developed a simplified analysis method, where column face forces (V_i) were calculated using a strip method modified from Hillerborg [19]. Once column face forces were determined, beam bending equations on an effective section were used to determine internal stresses, as shown in equation 3. Two k factors were included in this equation. The stress concentration (k_A) was taken from Mestek and accounts for the ratio between the peak and stress. The stress concentration factor (k_{edge}) was derived from comparisons with FEM data, and represent additional stress concentrations resulting from openings through the panel at supports at panel edges. The effective width is calculated by taking a combination of 45° and 15° angles from the column support for through parallel and perpendicular to grain shear loading respectively.

$$\tau_i = \frac{k_A K_{edge}1.5V_i}{b_{i,eff}d} \quad (3)$$

Muster compared the simplified equation to 3D FEM models, and it was found that both models had similar trends, but a large scatter between the Muster's simplified analysis method and 3D solid FEM stresses.

4 POINT SUPPORTED DESIGN METHODS

The following section compares several design cases for point supported CLT in a design case study using test data

from the UBC TallWood House building. Each design case was completed by choosing an approach for calculating panel capacity as presented in Section 2, to internal stresses predicted by an analysis method from Section 3.

4.1 OVERVIEW OF CONSIDERED DESIGN METHODS

The analysis methods chosen for use in each design case were a mix of FEM and simplified methods. For the simplified analysis methods, both the Tributary Area and Muster simplified analysis method from Section 3.2 were chosen because of their simplicity and flexibility. While the tributary method does not account for centre span hogging, it has no limitations on panel configuration and column locations. Muster's method accounts for hogging of centre columns and panel stiffness, and can analyse any number of panel spans. Mestek's simplified analysis method was excluded because it is limited to single span panels with columns at corner, or columns located at the middle of panel.

For the FEM analysis methods, only the 2D shell analysis were examined due to the complexity associated with making 3D solid modelling and grid-beam models. Several hybrid analysis methods are also examined, where the FEM models are used to calculate V_i on each column face, then simplified analysis equations are used to calculate internal stresses.

Three types of capacity methods were used in the design cases considered: the base code strength, the code strength amplified by k_p, and 5th percentile characteristic strength from test data presented in Table 1. The code strength represents the most conservative assumption, while using test data with k_p is the least. The design cases considered are summarized in Table 3, which describes the methods used to both analyse and determine the capacity of each panel.

Table 3: *Design methods considered.*

Design Case	Analysis Method	Capacity Method
D1	Tributary Area	PRG
D2	Muster's simplified method	PRG & k_p
D3	Hybrid approach, FEM with Muster simplified	PRG & k_p
D4	FEM RF-Laminate	PRG & k_p
D5	Hybrid approach, FEM with Muster simplified (support stiffness x10)	PRG & k_p
D6	FEM RF-Laminate (support stiffness x10)	PRG & k_p
D7	Hybrid approach, FEM with Muster simplified	Test data & k_p

Design case D1 uses the Tributary Area simplified method compared against O86/PRG rolling shear values without punching amplification factors. Case D2 uses the Muster simplified analysis method and compares peak stresses against O86/PRG rolling shear values amplified by the Muster punching shear amplification factors. Case D3 is a proposed hybridized method, which used a FEM 2D shell model of the system with spring supports as presented by Muster to predict column face forces (Vi) [11]. The equations from Muster's simplified method were used to predict peak stress in the system, and compared with the amplified O86/PRG capacities. Case D4 is a full FEM approach using a similar model to the one used in D3. Peak stresses in individual lamella from the RF-Laminate module were extracted from the model and compared with amplified O86/PRG capacities. Cases D5 and D6 used similar models and capacities to D3 and D4 respectively, but with support spring stiffness increased by a factor of 10 to evaluate the sensitivity of the model to stiffness. Finally, design case D7 used a similar model to that in D3, with unchanged spring stiffness, but compares the peak stresses against a 5th percentile base rolling shear strength of 0.75Mpa, along with Muster amplification factors. The base strength value for this case more closely aligning with results from testing [9],

4.2 COMPARISON WITH PREVIOUS TESTING FOR UBC TALLWOOD

The design cases presented in Table 3 were evaluated by comparing their design strength to internal stress for point supported panels in the UBC TallWood House testing [3]. For this evaluation, the panel from Manufacturer III was used, which was a two-span continuous 5ply panel, 169mm thick. Failure occurred in punching shear at the middle support in the strong axis. An average ultimate load of 402kN (201kN per bay) was applied to the system. Figure 1 shows the geometry of the panel tested.

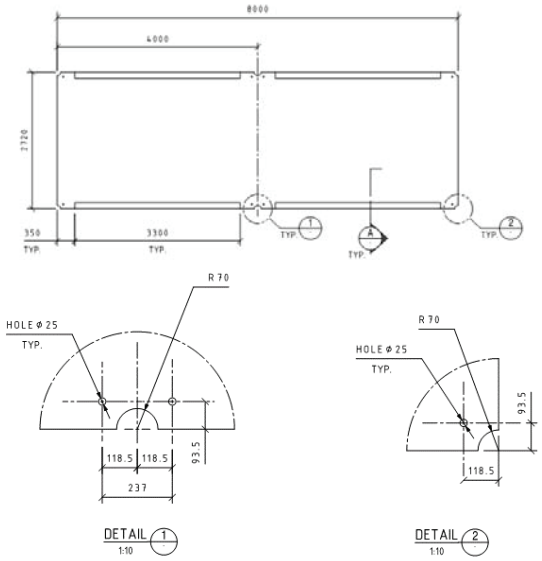

Figure 1: *Geometry of panel considered for Testing.*

For each design case from Table 3, the CLT panel from experimental was analysed using it's failure load to determine the stress demands at failure. For the case D1 and D2, the load was simplified as an equivalent uniform load. For the remaining series the loads were applied as discrete area loads to match the true test setup as shown

https://doi.org/10.52202/069179-0349

in [3]. Table 4 summarizes predicted column face shear for the middle the column, where V_x is the maximum force on the left and right face (i.e. face perpendicular to primary span), and V_y is the shear on the top or bottom face (i.e. face parallel to primary span).

The column face forces predicted by each design case was similar with a few exceptions. In D1 the force in the weak axis was smaller than all other design cases. There was also a notable difference between FEM models with 10x support stiffness used, where stiffer models (D5/D6) attracted more force in the weak axis.

A significant spread is observed in the stress predicted by each design case. Case D1 predicted lower shear stresses than other methods, likely because of not including any stress concentration factors. Comparing design cases that used hybrid analysis (D3, D5) with design cases that used pure FEM (D4, D6), the hybrid methods predicted higher stresses for the baseline model, but lower stresses when the support stiffness was increased. When similar design cases that used different support stiffnesses (D4 vs. D6, D5 vs. D7) were compared, it was found that the spring stiffness significantly impacts the load distribution between column faces, with stiffer supports leading to more force in the y axis and higher stress peaks.

Table 4: *Design Demands*

Design Case	V_x (kN)	V_y (kN)	τ_x (Mpa)	τ_y (Mpa)
D1	32	33	1.55	1.3
D2	33	55	2.81	1.5
D3	34	60	2.94	1.65
D4	34	60	2.28	1.8
D5	26	71	2.25	1.98
D6	26	71	3.05	2.24
D7	34	60	2.94	1.65

Table 5 summarizes the shear strength(s) considered in each design method (D1-D7) for the strong and weak axis faces. The characteristic strength used was multiplied by a phi factor of 0.9 from CSA O86 to determine the design rolling shear strength (f_s'). The punching shear strengths in each direction (f_{px}, f_{py}) were determined based on amplifying the design rolling shear strength by punching factors where applicable. An Overstrength Factor (OF), defined as the ratio between the punching shear stress at failure and the capacity, is also shown. Lastly the predicted failure axis, where the predicted shear stress and the punching capacity the closest, is presented.

Table 5: *Capacity and Overstrength Factor (OF) for design cases considered.*

Design Case	f_s' (Mpa)	f_{px} (Mpa)	f_{py} (Mpa)	OF	Governing Axis
D1	0.45	0.45	0.45	3.44	strong
D2	0.45	0.585	0.72	4.79	strong
D3	0.45	0.585	0.72	4.96	strong
D4	0.45	0.585	0.72	3.90	strong
D5	0.45	0.585	0.72	3.85	strong
D6	0.45	0.585	0.72	5.21	strong
D7	0.68	0.884	1.088	3.33	strong

In all design cases, the strong axis governed the shear capacity, which matched observations from testing [3]. In addition, all design cases using PRG based rolling shear strength had an OF above 3.4, with the series D1 showing the lowest predicted value. For series D7, where a larger rolling shear strength was used, there was still a significant margin of safety in the system, with an overstrength of 3.33.

5 PARAMETRIC STUDIES

To further understand how the analysis methods presented in Section 3 compare, a parametric study was completed. The output column face shear forces from simplified analysis methods were compared with outputs from FEM. The impact of different parameters on outputs of the shell FEM approach presented in Muster were also examined.

5.1 STUDY OVERVIEW

For simplified methods, the parametric study uses 175mm thick CLT panels 5 layers of 35mm thick laminates, 1950f-1.7E SPF in the strong axis and No.1/No.2 SPF in the weak axis. The parameters considered include:

- number of spans (1,2,3)
- span length (3.6m – 4.4m, increments of .2m)
- span width (2.7m – 3.5m, increments of .2m)

For FEM models, the panel was modelled using the 2D shell elements and support conditions as specified by Muster. Near supports a mesh refinement was used. The following parameters were varied in addition to those above in each trial analysis:

- Effective width of support along the weak axis face (0.3m-0.5m, increments of 0.05m, strong axis face is half this value.)
- Spring stiffness (0.1x, 1x, 10x the stiffness equation proposed by Muster)
- CLT panel type (139, 175, 191, 245)
- Grade (E and V)

The 175mm and 245mm thick panels had 5 and 7 layers of 35mm. These panels used 2100f -1.7E SPF in the strong axis and No.1/No.2 SPF in the weak axis for E rated panels, while V rated panels used No.1/No.2 SPF in both directions. The 139mm and 191mm had layers 35mm thick in the strong axis and 18mm thick in the weak axis. These panels used 2100f-1.7E SPF in the strong axis and No.3 and better SPF in the weak axis for E rated panels, while V rated panels used No.1/No.2 SPF in the strong axis, and No.3 and better SPF in the weak axis.

https://doi.org/10.52202/069179-0349

All panels have an edge cantilever of 0.3m on either side of the first and last column. In FEM, the effective dimension of the strong axis face is taken to be half the width of the weak axis face. All panels were loaded with a unit 1kPa load, and results were presented in kN/kPa. A total of 150 trials were run for each simplified method panel, and 2250 trials for each FEM model.

5.2 SIMPLIFIED METHODS COMPARISON

The column face shear forces were compared for the Tributary Area analysis method, Muster simplified analysis method, and FEM models. Because there were multiple columns, each plot shows the shear force for the worst-case column. Figure 2 shows the strong axis column face forces (V_x), and Figure 3 shows the weak axis column face forces (V_y). Width had a small effect on V_x and similarly, changes in length had a small effect on V_y. For this method number of spans had a moderate effect on V_x, but a large effect on V_y.

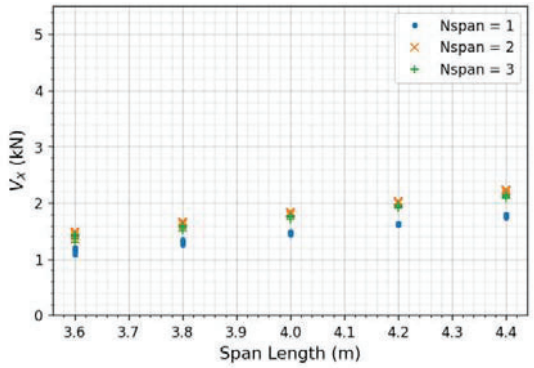

Figure 2: *Shear on X column face for Muster Simplified method.*

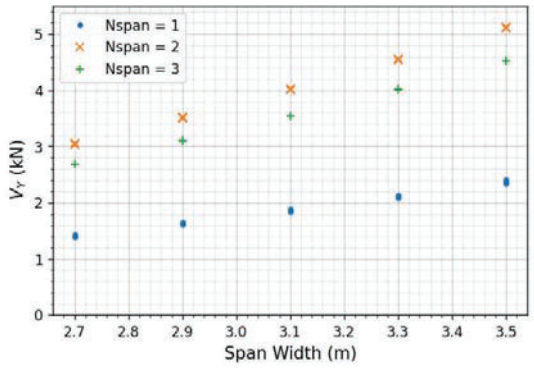

Figure 3: *Shear on Y column face for Muster Simplified method.*

Figure 4 and Figure 5 show the column face forces for the Tributary Area analysis method. Like the Muster analysis method, changes in width had a small effect on V_x and changes to length had no effect on V_y. Similarly, the number of spans had no effect on V_x, and only effects V_y, going from one to two spans. As such, results are only presented for two span panels.

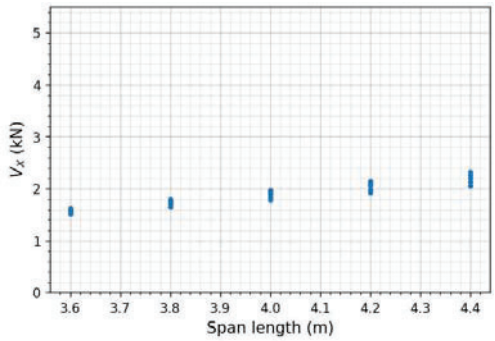

Figure 4*: Shear on X column faces for Trib. Area Method.*

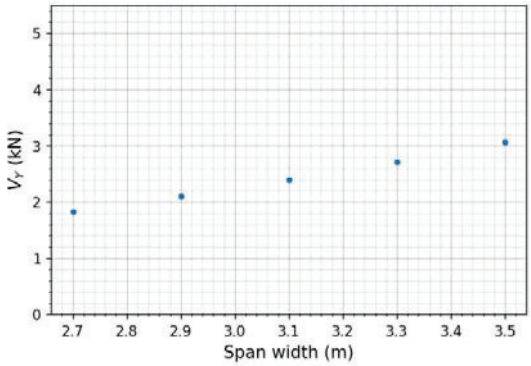

Figure 5: *Shear on Y column faces for Trib. Area Method.*

Results for the Tributary Area and Muster simplified analysis methods were also compared to results from FEM models. The shear force at each column face was extracted from the model for each combination of input variables, and the largest value from all columns was reported. For the FEM models, there was a much larger spread in results, indicating that factors like the out of plane grid dimension (width in this case) or support size had a larger impact on the distribution of forces. Table 6 summarizes the spread in V_x observed, where length is fixed at 3.6m and 4.4m, the number of spans is fixed at two, three or four, and all other parameters were allowed to vary. For the spread of values at each length/span combination, the smallest (min) and largest (max) values from all other combination of parameter were reported, as well as the average value observed. For the Tributary Area simplified analysis method, values were the same for every number of spans, and so not separated out.

Table 6: *Comparison of V_x from simplified methods and FEM*

L (m)	Analysis Method	N_{span}	V_x (kN)		
			Min.	Avg.	Max.
3.6	Muster	2	1.09	1.16	1.20
		3	1.35	1.44	1.49
		4	1.35	1.38	1.43
	Trib. Area	-	1.52	1.58	1.62
	FEM	2	1.10	1.29	1.45
		3	1.39	1.65	1.97
		4	1.39	1.58	1.87

https://doi.org/10.52202/069179-0349

		2	1.74	1.78	1.80
	Muster	3	2.17	2.21	2.23
		4	2.17	2.13	2.15
4.4	Trib. Area	-	2.06	2.20	2.32
		2	1.37	1.64	1.86
	FEM	3	1.75	2.07	2.46
		4	1.75	1.98	2.31

5.3 EFFECT OF PARAMETERS ON SHEAR FORCE

Data from the parametric study was also used to understand how the studied variables change the shear force predicted by FE models. As with the data from section 5.2, it was found that there was a large spread in predicted shear force when comparing applied shear with the span length in that direction (V_x vs. span length, V_y vs. span width). Correlations on the dataset were calculated to highlight which variables are most significant when predicting shear force. Table 7 summarizes the correlations coefficient determined for span length (L), span width (w), number of spans (N_{span}), effective support dimensions (d_{sup}), lamination grades (V or E Grade), and support stiffness (k_s) on the output shear (V_x, V_y).

In Table 7 the shear force generally correlated strongly with the span direction perpendicular to the support face, but there was also a strong correlation with the opposite span length as well. Grade and support size had less of an effect on the distribution of shear force. Strong correlations were also noted for support stiffness and number of spans.

Table 7: *Correlations of various parameters on Shear forces.*

Panel	Correlation Coefficient with V_{xh}					
	L	w	N_{span}	d_{sup}	Grade	k_s
139	0.23	0.08	0.11	-0.11	-0.05	-0.51
175	0.25	0.21	0.22	-0.06	-0.06	-0.35
191	0.27	0.24	0.28	-0.07	-0.06	-0.31
245	0.25	0.27	0.32	0.02	-0.07	0.00
Panel	Correlation Coefficient with V_y					
	L	w	N_{span}	d_{sup}	Grade	k_s
139	0.15	0.35	0.49	0.02	0.01	0.41
175	0.19	0.32	0.53	0.00	0.02	0.34
191	0.18	0.31	0.50	0.03	0.02	0.35
245	0.23	0.30	0.57	-0.01	0.02	0.18

The strong correlation of V_x with support stiffness, but not support width was highlighted below in Figure 6, where a 175 V rated panel with two spans and a 4.2mx2.9m grid has been examined. In this small subset of the data, a large difference between the shear force for different support stiffnesses values (x0.1, x1, x10) was shown. However, shear force was relatively constant for different values of effective support width.

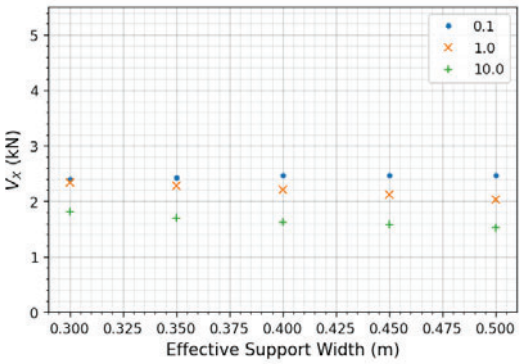

Figure 6: *V_x vs. support width for a trace of data on a 175 V rated panel, and different factors applied ot the support stiffness.*

5.4 FEM MODEL MEASURED K_A

Another quantity measured in the parametric study was the ratio between the peak and average shear force observed in FEM models across a wide variety of panels. In Figure 7-Figure 10, these values were compared to the baseline K_A value proposed by Mestek. The parameters of the parametric study were as presented in Section 5.2.

For each of the panels considered, two series were presented: the baseline formula for spring stiffness from Muster, and x10 the spring stiffness proposed from Muster. For all FEM models the peak value in V_x/m was extracted from the model, and compared to the average value of V_x/m. A large spread in peak/average can be observed that for some series, with thinner panels having a larger distribution in stresses. This may be because Muster's formula for the spring stiffness changes at a negative third power of the panel thickness, so the base stiffness for each panel can be significantly different. The difference in stress ratio suggests significantly different behaviour at supports between the 139mm panels and 245mm panels. Despite the large differences observed between different panels, K_A was lower than the values proposed by Mestek for many panels.

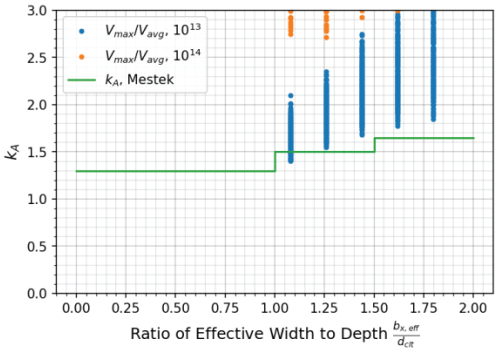

Figure 7: *Calculated K_A for 139 panels.*

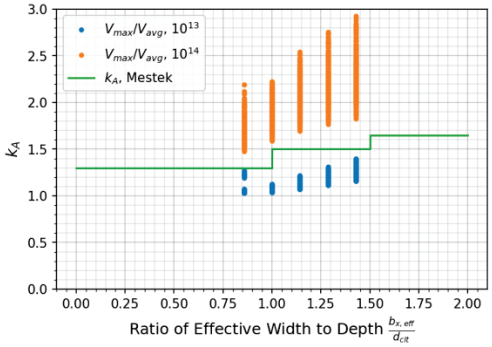

Figure 8: *Calculated K_A for 175 panels.*

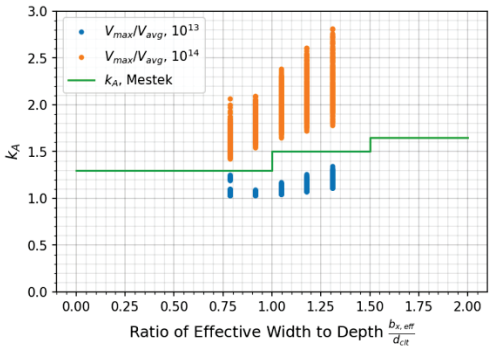

Figure 9: *Calculated K_A for 191 panels.*

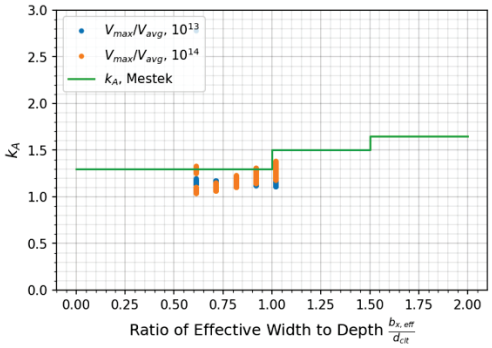

Figure 10: *Calculated K_A for 245 panels.*

The effect of support stiffness as predicted by Muster [11] can also be qualitatively observed in Figure 11 for a single data point. Here a set of four panels is shown where the top pair was 139E rated, the bottom pair was 245E rated, and all other variables are the same between panels. For each pair, the bottom panel uses the baseline formula's constant of 10^{13} (1x stiffness), and the top panel uses 10^{14} (10x stiffness). For these panels, there is a significantly different deformation profile over column supports for the baseline model of 245E vs. 139E, with the 245 behaving much more flexibly.

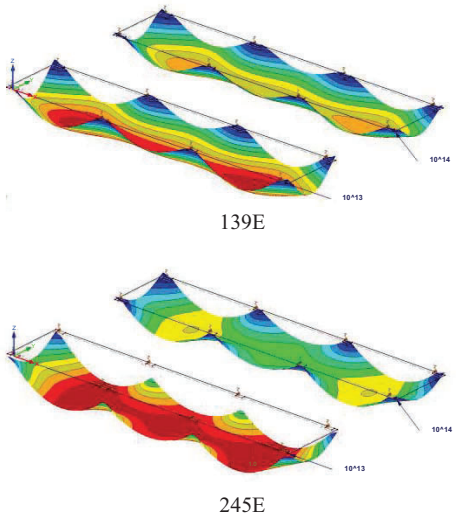

Figure 11: *Deformation over supports for 139E and 245E panels, colour indicates vertical deflection with red being the highest and blue the lowest.*

6 CONCLUSIONS

Reviewing the code and North American material standards for determining capacity of point supported CLT, it was observed that PRG specified shear strength values were generally lower than characteristic strengths determined in experimental test. Several simplified analysis methods were reviewed, with the method presented by Muster [11] being the most flexible.

The capacity and analysis methods were applied to CLT panel tests in a number of design cases. In addition to the simplified analysis methods examined, a Hybrid analysis method was also examined, that takes forces from column faces in the FEM model, and the stress formula from the Muster simplified analysis method. When compared to test data from the UBC TallWood House testing program, the design cases assessed had a significant margin of safety when using current strength specified values in the PRG 320, with ratios of strength to capacity in the range of 3.4-5.2. Even using strength values from experiment, the ratio between failure load and predicted capacity was 3.3 for the Muster Simplified method.

In both the sample design and parametric study, it was noted that the stiffness of column supports had a significant impact on the FEM predicted forces and stresses. In the parametric study it was noted simplified methods predicted column face shears that were comparable to FEM predictions, however, it was observed that FEM predictions had a larger spread in data. This indicates that parameters like the out of span width affect results more than simplified methods. In general FEM results were more sensitive to the span perpendicular to load, e.g. width on V_x, than the simplified models.

The parametric study also showed that the support stiffness was the parameter that had the most influence on support shear forces. The length, width, and number of spans also had a significant effect on shear force, while the type of panel used and support size did not. The parametric study showed that the support stiffness also

https://doi.org/10.52202/069179-0349

had a significant effect on the peak model shear forces of all studied parameters. The ratio of peak to average stress varied significantly for different panel layups and support stiffnesses. A large difference in behaviour at the supports was observed between different panels in the parametric study. Because support stiffness was observed to have a significant influence on shear stress distribution in FEM models, further study is recommended to refine this stiffness for a wider set of parameters and ensure its interaction with factors such as k_A is appropriate.

ACKNOWLEDGEMENT

We gratefully acknowledge the financial support of the Province of British Columbia through the Ministry of Energy, Mines and Low Carbon Innovation.

REFERENCES

[1] National Research Council of Canada (NRC), National Building Code of Canada (NBCC 2020), Ottawa, ON, Canada: NRC, 2020.

[2] International Code Council (ICC), 2021 International Building Code (IBC 2021), Country Club Hills, IL USA, 2021

[3] Fast, P, Gafner B., Jackson R., Li J, Case Study: An 18 Storey Tall Mass Timber Hybrid Student Residence At The University Of British Columbia, Vancouver in *14th World Conference on Timber Engineering,* 2016

[4] Popovski M., Chen Z., Gafner B., Structural behaviour of Point-supported CLT floor Systems, in *14th World Conference on Timber Engineering,* 2016

[5] Canadian Standards Association (CSA), Engineering Design in Wood, CSA Standard O86-19, Toronto, ON, Canada: CSA, 2019.

[6] APA – The Engineered Wood Association, PRG 320-2019 ANSI/APA - Standard for Performance-Rated Cross-Laminated Timber. Tacoma, WA, USA, 2019

[7] Ehrhart T., Brandner R, Frangi A., Rolling Shear Properties of some European Timber Species with Focus on Cross Laminated Timber (CLT): Test Configuration and Parameter Study. *2nd Meeting International Network on Timber Engineering Research (INTER),* 2015

[8] Ehrhart T., Brandner R, Rolling shear: Test configurations and properties of some European soft- and hardwood species. *Engineering Structures.* 172:554-572, 2018.

[9] Wang Z., Zhou J., Dong W., Yao, Y., Gong M., Influence of technical characteristics on the rolling shear properties of cross laminated timber by modified planar shear tests. *Maderas: Ciencia y Tecnologia,* 20(3):469-478, 2018.

[10] Mestek P., "Punktgestützte Flächentragwerke aus Brettsperrholz (BSP) – Schubbemessung unter Berücksichtigung von Schubverstärkungen", Ph.D. dissertation, Technische Universität München , 2011

[11] Muster M., "Column-Slab Connection In Timber Flat Slabs", Ph.D. dissertation, ETH Zurich, 2020

[12] Sandoli A, Calderoni B., The rolling shear influence on the out-of-plane behavior of CLT panels: A comparative analysis, *Buildings* 10(3), 2020

[13] Ukyo S., Miyatake A., Shindo, K., Hiramatsu Y., Shear strength properties of hybrid (hinoki cypress and Japanese cedar) cross-laminated timber, *Journal of Wood Science* 67:1, 2021.

[14] Nero R, Christopher P., Ngo, T., Investigation of rolling shear properties of cross-laminated timber (CLT) and comparison of experimental approaches, *Construction and Building Materials*, 316, 2022

[15] Bogensperger T., Joebstl R., Augustin M., Concentrated load introduction in CLT elements perpendicular to plane - Experimental and numerical investigations, *WCTE 2016 - World Conference on Timber Engineering*, 2016

[16] Dietsch P., Schickhofer G., Brunauer A., Tomasi R, Hübner U., Krenn H., Mestek P., Thomas Moosbrugger T. Wiegand T. Eurocode 5:2022 – Einführung in die neuen Abschnitte Brettsperrholz und Verstärkungen, Holzbau – Forschung für die Praxis, 2018

[17] Dubal Software GmbH, RF-LAMINATE: Design of Laminate Surfaces, 2016

[18] DIN 1052:2008-12: Entwurf, Berechnung und Bemessung von Holzbauwerken. Allgemeine Bemessungsregeln und Bemessungsregeln für den Hochbau.

[19] A. Hillerborg. Strip Method of Design. 2nd Edition. Cement and Concrete Association, 1975

World Conference on Timber Engineering Oslo 2023

SEISMIC AND ENERGY RETROFIT OF MULTIFAMILY LIGHT-FRAME TIMBER RESIDENTIAL BUILDINGS USING MASS PLY PANEL (MPP) WALL FAÇADE SYSTEM

Gustavo F. Orozco O.[1], Andre R. Barbosa[2], Mark Fretz[3], Judith Sheine[4], Jason Stenson[5], Kevin Van Den Wymelenberg[6], Payton Narancic[7], Flynn Casey[8]

ABSTRACT: The most common type of construction in the US for single and multifamily housing is known as Light-Wood-Frame (LWF). This system has been widely used for decades, following prescriptive design rules and usually without an engineered-based analysis. Due to the evolution of knowledge on the seismic hazard in the Pacific Northwest, retrofitting these structures built before the 1990s has become a necessity. In addition, these buildings also lack the energy efficiency required to reduce our global carbon footprint. This paper presents a novel façade retrofit solution consisting of prefabricated mass ply panels (MPP) that can be rapidly applied on-site over existing building cladding to upgrade older LWF one- to three-story buildings. The structural design of an existing prototype two-story LWF building in Portland, OR is presented. Custom steel connections resist design forces following the Equivalent Lateral Force (ELF) method from ASCE 7-16. Nonlinear displacement validation is performed using analytical models (AM) and finite element models (FEM), obtaining lateral drifts of 0.50% for the design earthquake (DE) reducing the expected damage in the building. Over-strength factors are calculated, considering the contribution of existing LWF walls and steel connections. A follow-up experimental setup is described for future validation of the initial assumptions.

KEYWORDS: Façade, Light-Wood-Frame, Mass Timber, Retrofitting, Seismic Vulnerability.

1 INTRODUCTION

In the US, the majority of low-rise residential buildings consist of Light-Wood-Frame (LWF) lateral force-resisting system (LFRS). The LWF structural system makes use of dimensional lumber elements equally spaced forming walls, floor diaphragms, and roofs. These elements are generally joined together using nails and panelised sheeting, such as plywood, oriented-strand board (OSB), or gypsum wallboard (GWB). Even though this solution has been prevalent and overall well-designed buildings tend to perform well under seismic loading, the 1994 Northridge Earthquake resulted in many residential buildings sustaining damage due to excessive lateral drifts [1,2]. In addition, in the Pacific Northwest, the Cascadia Subduction Zone, which drives the high seismic risk of existing structures in the region [3] was only recognized in the early 1990s, and buildings in the region constructed prior to this date were designed to sustain relatively low levels of seismic loading.

Besides the inadequate seismic resistance of many existing buildings constructed before the 1990s, many US buildings were constructed before the advent of building energy codes. In 1975, the American Society of Heating, Refrigerating, and Air-Conditioning Engineers (ASHRAE) promulgated Standard 90-75, which is widely recognized as the first US residential energy code. Since that time, housing energy efficiency has significantly improved in many states. However, pre-code housing remains a significant fraction of the nation's housing stock. According to the Northwest Energy Efficiency Alliance (NEEA) Residential Building Stock Assessment, 88% of this housing stock in the Pacific Northwest is one- to three-story light-wood-frame structures and were constructed between 1960-1994 with very low wall insulation levels (64% had R8-R12 wall insulation) [4]. In addition, the majority of the 88% of the housing stock was constructed with 2x4 studs (38 mm x 76 mm) at 406 mm (16") on-centre [4].

[1] Gustavo F. Orozco O., Oregon State University, USA, gustavo.orozco@oregonstate.edu
[2] Andre Barbosa, Oregon State University, USA, andre.barbosa@oregonstate.edu
[3] Mark Fretz, University of Oregon (UO), USA, mfretz@ uoregon.edu
[4] Judith Sheine, University of Oregon, USA jesheine@uoregon.edu
[5] Jason Stenson, University of Oregon, USA jstenson@uoregon.edu
[6] Kevin Van Den Wymelenberg, University of Oregon, USA kevinvdw@uoregon.edu
[7] Payton Narancic, University of Oregon, USA pcn@uoregon.edu
[8] Flynn Casey, University of Oregon, USA

https://doi.org/10.52202/069179-0350

Such outdated buildings can benefit from a retrofit solution that minimizes impact on the interior of the units, thus minimizing downtime, combining increase energy and seismic performance. The solution proposed in this study involves performing most, if not all, interventions on the exterior of the building through the development of a façade retrofit solution. While other successful energy façade retrofit programs exist in Europe, such as the *Energiesprong* [5] method that provides many lessons for the US, energy façade retrofits on the Pacific Northwest must also contend with seismic upgrades, which are often automatically triggered with the mass of an existing building increases by 10% relative to the mass of the existing building.

In the development of a novel façade retrofit solution, this study adopts a recent product known as mass ply panel (MPP) [6] in the development of structural and non-structural retrofit façade panels that enable seismic and energy retrofit of LWF buildings. Specifically, this paper proposes a structural design methodology for the structural façade panels, considering custom-designed connectors that attach the façade retrofit solution to the existing concrete foundation and existing LWF structure. In addition, considerations needed for the design of the non-structural façade panels are also presented.

1.1 EXAMPLE CASE STUDY

An existing two-story LWF structure built in 1971 in the city of Portland, Oregon (45.51179, -122.67563) is selected as an application example to demonstrate the seismic design retrofit procedures and dimensioning of structural elements of the retrofit façade system and considerations for non-structural elements.

Figure 1: *Visualization of case study multifamily building used for façade retrofit study, pre-retrofit [7].*

The two-story building shown in Figure 1 consists of multiple two-unit modules illustrated in Figure 2a and b. For the existing building, based on the NEEA study [4], it is assumed that there are two types of walls, including (1) exterior walls consisting of 8x8 plywood sheathed wood structural panels (WSP) with 6d nails spaced a 150 mm and (2) interior walls consisting of gypsum sheathed walls.

1.2 FAÇADE RETROFIT SOLUTION

A façade system is proposed, formed by two different types of MT panels. First, the non-structural MPP with slotted-hole connections resisting out-of-plane loads only (highlighted in yellow in Figure 2 and Figure 3), and second the structural walls that resist lateral forces (highlighted in red in Figure 2 and Figure 3).

The MPP structural walls have increased over-turning capacity due to the steel plate hold-downs that transfer overturning tension and compression forces caused by lateral loads to the foundation. A shear steel plate is installed at the base of the MPP transferring the base shear reaction to an upgraded foundation. Fasteners distribute the tension forces from the steel plates to the MPP, and expansion bolts connect the steel plates to the concrete foundation. The MPP walls are connected to MPP transfer joists that transfer the load from the existing LWF to the retrofit system (see Figure 4a).

Insulation layers are attached to both structural and non-structural MPP panels, including wood fibre insulation infill and siding. Windows, doors, field-installed foundation insulation with vertical siding elements used to conceal the hold-downs and other panel-to-panel joints on the completed façade.

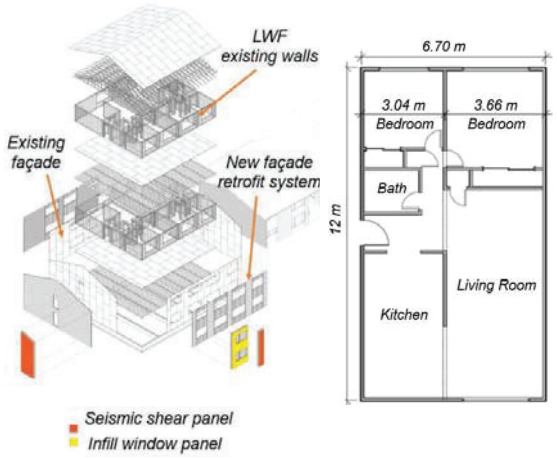

(a) (b)

Figure 2: *(a) 3D exploded view of a two-unit module of the case study multifamily building and example retrofit panels, with structural panels shown in orange and non-structural in-fill panels shown in yellow, (b) Individual unit in case study building.*

This paper focuses on structural design aspects of the study. For more on architectural design considerations, energy retrofit design, construction details, and a mock-up of the proposed solutions, we direct the interested reader to a separate paper [7].

https://doi.org/10.52202/069179-0350

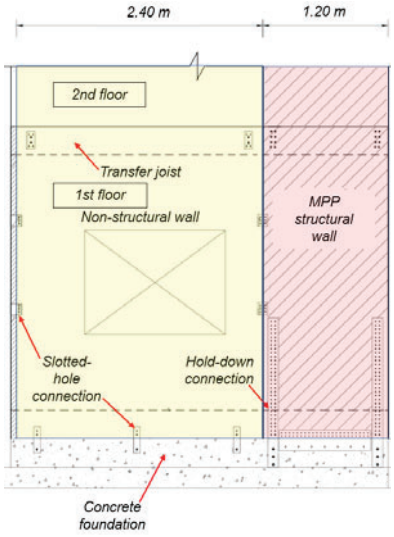

Figure 3: *MPP non-structural and structural wall panels with their various connections. The non-structural panel is highlighted in yellow, and the structural panel is shown in red.*

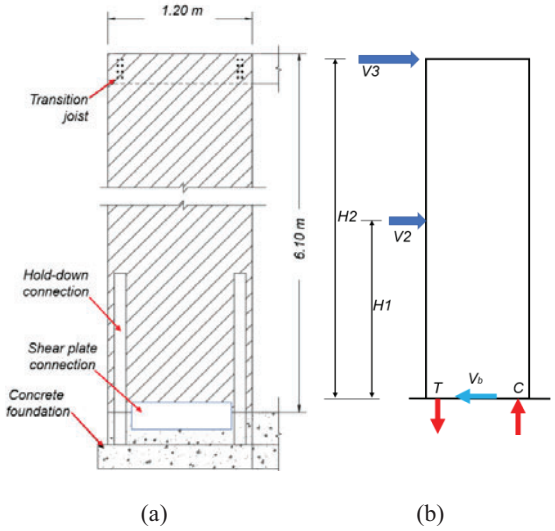

Figure 4. *(a) Single wall components, (b) Reaction forces generated at the base of the MPP.*

2 STRUCTURAL DESIGN PROCEDURES

The design of the new lateral force resisting system (LFRS) follows a capacity-based design approach, where hold-downs are designed as structural fuse elements, while shear transferring elements are designed to remain essentially elastic by considering an over-strength factor (Ω), precluding brittle failures and allowing the wall to develop large deformations without loss of structural capacity.

The design of the structural wall panel followed existing standards, including ASCE 41-17 [8] and ASCE 7-16 [9], and consisted of determining: (1) the tributary seismic weight to be resisted by the structural wall panel, (2) the design seismic base shear, (3) design of the components of the structural wall and connections, (4) a drift analysis, and (5) capacity-based design of elements that are designed to remain essentially elastic. For the non-structural walls, the design consisted of displacement compatibility checks, namely through the design of slotted connections in panel-to-panel, panel-to-transfer joist, and panel-to-foundation connections. The existing and upgraded concrete foundation requires the design of epoxied dowels, shear transfer between the upgraded foundation and the existing foundation, and geotechnical foundation stability checks.

2.1 SINGLE WALL ANALYSIS

In a single structural wall, lateral design forces are calculated and distributed assuming a triangular distribution of forces (see Figure 4b).

Tension and compression reaction forces generated at the base of the wall, T and C, respectively, are determined using the following expression:

$$T = C = \frac{(V_3 \times H_2) + (V_2 \times H_1)}{L_1 + \frac{2}{3}a} \quad (1)$$

where V_3 is the lateral load at floor level 3, H_2 the height at floor level 3, V_2 is the lateral load at floor level 2, H_1 is the height at floor level 2, L_1 is the length between the center of the hold-down connection and the initial point where the wall starts lifting, and a is the length of the compression zone. Additional details on these dimensions are shown in Figure 6a.

The foundation will most probably need to be retrofitted since typical stem walls in existing buildings will not have the bearing area needed to support the new façade panels. Also, due to the addition of extra walls on the façade, the existing diaphragm needs to be evaluated to verify if additional retrofit elements are needed to resist added capacity provided by the façade panels. Upon determination of the diaphragm forces, it may be necessary to provide additional floor sheathing and/or steel coiled straps that may work as collectors or diaphragm tension chords. The need for these elements will vary from project to project, and are therefore not detailed in this paper. Example cross-sections on how the MPP is attached to the existing façade and additional non-structural insulation materials are shown in Figure 5a and b for foundation and roof heave connections, respectively. Additional details on other necessary considerations are provided elsewhere [7].

https://doi.org/10.52202/069179-0350

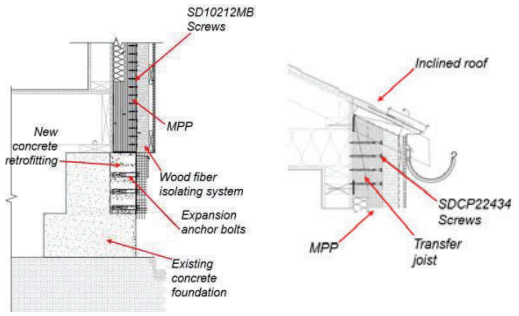

(a) (b)

Figure 5. *Section cut of (a) MPP to the concrete foundation, (b) MPP to transfer joist connection.*

2.2 LATERAL DEFORMATION ANALYSIS=

Lateral deformations of the new LFRS can be verified using a nonlinear analytical model, that considers three types of deformation types in the wall: (1) lateral deformation due to the rocking of the panel, (2) lateral deformation due to the flexural deformation of the panel, (3) lateral deformation due to the shear deformations of the panel (see Figure 6b).

Figure 6a illustrated a simplified model to capture the effects induced by the rocking of the wall. As the wall rocks about one end, the opposite end tends to uplift resulting in compression and tension of either hold-down. For the hold-down that goes into tension an equivalent stiffness K_e for the hold-down connection is given by:

$$\frac{1}{K_e} = \frac{1}{K_{sc}} + \frac{1}{K_{sp}} + \frac{1}{K_{ab}} \qquad (2)$$

where $\boldsymbol{K_{sc}}$ is the stiffness provided by the screws, $\boldsymbol{K_{sp}}$ is the stiffness of the steel plate, and $\boldsymbol{K_{ab}}$ is the stiffness provided by the anchor bolts.

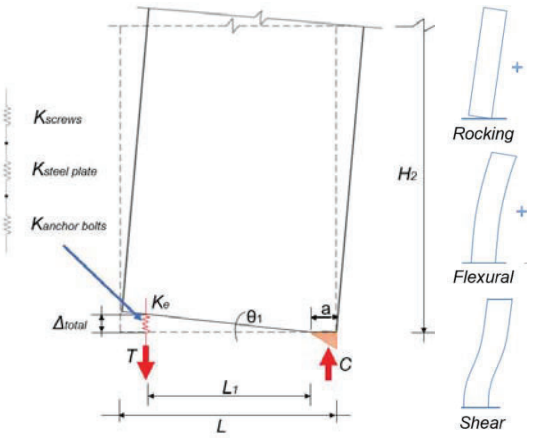

(a) (b)

Figure 6. *(a) Simplified model for rocking deformation analysis, (b) Types of lateral deformations in the wall.*

The lateral displacement at the top of an MPP wall D_{total} is given by:

$$D_{total} = D_{hold-down} + D_{flexure} + D_{shear} \qquad (3)$$

$$D_{hold-down} = H \times \theta_1 \qquad (4)$$

$$\theta_1 = 90^o - \cos^{-1}\left(\frac{\Delta_{total}}{L_1}\right) \qquad (5)$$

$$D_{flexure} = \frac{V_2 {H_1}^3}{3E_{app}I} + \frac{V_3 {H_2}^3}{3E_{app}I} \qquad (6)$$

$$D_{shear} = \frac{V_2 H_1}{G_{app}A} + \frac{V_3 H_2}{G_{app}A} \qquad (7)$$

where $D_{hold-down}$ is the lateral displacement due to hold-down deformation, $D_{flexure}$ is the displacement due to wall flexure, and D_{shear} is the displacement due to wall shear; θ_1 is the rotation at the base of the wall; Δ_{total} is the opening at the base of the wall; H is the height of the wall, $E_{app}I$ is the apparent wall's flexural stiffness (I = 1/12 $t_w L^3$), and $G_{app}A$ is the wall's apparent shear stiffness (A = $t_w L$).

2.3 NONLINEAR CAPACITY OF LWF WALLS

The capacity-based design methodology requires the calculation of any source of over-strength that can affect the new LFRS. In the present application, the main contributor to over-strength in the system is the existing LWF structure. To obtain the lateral stiffness of these walls, simplified backbone curves can be calculated from experimental tests, considering different types of sheathing and length of walls [10]. Structural walls are considered the ones with proper sheathing, with WSP. Infill walls are initially not considered in the lateral resistance of the exiting LWF, and are only considered for over-strength factor calculation. Nevertheless, depending on the contribution of the nonstructural walls, they may be considered structural for structural assessment.

3 EXAMPLE BUILDING APPLICATION

The loads considered to act on the structure are: (1) Dead loads, including self-weight and over-imposed loads of 1.05 kN/m^2 and 0.72 kN/m^2 for intermediate floors and roof, respectively, and (2) live loads of 1.91 kN/m^2 and 0.96 kN/m^2 for intermediate floors and roof, respectively. The performance level for existing structures defined in ASCE 41-17 (BSE-1E) requires an earthquake with a 20% of probability of return in 50 years. For existing structures, ASCE 41-17 and local design codes [11] allow for the use of a design limit of 75% of the seismic demand used for new buildings (BSE-1N), or 10% in 50 years, also known as Design Earthquake (DE).

The design approach included the following steps. First, the two-unit structure shown in Figure 2a was assumed to

https://doi.org/10.52202/069179-0350

be retrofitted by six MPP structural wall segments for the LFRS, for the direction of the building with more openings. The other direction of the building is not presented in this paper, since the more critical direction is analysed. Each MPP structural wall segment has dimensions: 1.20 m wide, 6.10 m height, and 76.2 mm thick. Second, a seismic modification factor (R-factor) of 3 is assumed for the MPP walls [12]. The building is a risk category II structure, therefore a base shear (V_b) of 22% of the seismic weight is determined for the BSE-1N design level earthquake (DE). Applying the limit of 75% the BSE-1E design base shear of 16.8% is obtained. Note that this level is higher than what would be needed for the existing structure with light-frame-wood walls, which would be allowed to be designed for a corresponding R-factor value of 6.5. This would result in a BSE-1N force value of 10.1% of the buildings seismic weight and a corresponding BSE-1E force value of 7.6% of the seismic weight.

Note that this increased level of design force for the façade retrofit solution compared to a retrofit solution of existing LWF walls using additional and stronger sheathing, the façade retrofit solution enhances building performance by reducing drifts and mitigates soft-story failure modes, thus allowing for an enhanced resilient design. Nonetheless, the solution may raise questions from structural engineers and some building owners since it does require that the existing structure be retrofitted to a higher seismic force level.

For the example building, a seismic weight of 400 kN was determined, considering the dead load and 25% of live load. Following allowable stress design (ASD) [9] combinations (with 0.70 factor for seismic forces), a horizontal force of 7.87 kN is obtained for each of the MPP walls, and tension and compression forces of 36.61 kN are obtained for the hold-downs and MPP structural wall panel, respectively.

3.1 HOLD-DOWN CONNECTION DESIGN

The number of screws needed to resist the tension forces is determined following the NDS yielding modes [13], considering a modifying factor $C_d = 1.6$, a group factor $C_g = 0.86$, and additional factors equal to 1.0. The steel plate is sized following the requirements in AISC 360-16 [14], including tension and shear checks. The design checks for the expansion bolts follow the design manual provided by the manufacturer [15]. Shear and compression stresses on the MPP structural wall are checked to verify the thickness of the panel. The ASTM A572-50 [16] steel plate hold-downs obtained are 3.2 mm thick, 101 mm wide, and 1460 mm high, and require a total of 60 screws type SD10212MB [17], and three carbon steel expansion bolts with a diameter of 16 mm (see Figure 7).

To determine the hold-down equivalent stiffness (K_e in Figure 6), the stiffness used for an individual fastener is obtained from shear tests of angle bracket connections using nails with similar diameters [18]. For the steel plate, an axial stiffness relationship, E_sA/L, is used, where E_s is the steel Young's modulus, A is the cross-section area, and L is the effective length of the steel plate. Elastic and plastic shear stiffness and yield forces for an anchor bolt are assumed following engineering first principles. Backbone values per component are shown in Table 1.

Table 1: *Backbone parameters for the hold-down connection.*

Element	Yield force (kN)	Yield disp. (mm)	$K_{elastic}$, (kN/mm)	$K_{plastic}$, (kN/mm)
Bolts	345	38	9	12
Steel plate	122	2	52	3
Screws	96	9	11	4

3.2 SHEAR TRANSFER CONNECTIONS

For this example, an overstrength factor, Ω, of 4 is initially considered. Based on this assumption, the ASTM 572 shear plate connection is 3.2 mm thick, 171 mm wide, 889 mm long, and requiring a total of 46 SD10212MB screws, and seven carbon steel expansion bolts with a diameter of 9.5 mm.

For the transfer joists, 16 screws type SDCP22434 [17] are needed. Note that these are designed with slotted hole connections that allow the wall to rock relative to the transfer joist without inducing uplift forces on the joist. Details are shown in Figure 7.

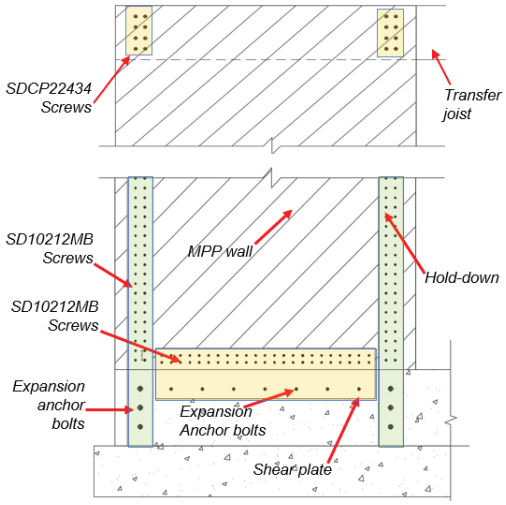

Figure 7. *Hold-down, shear plate connections, and transfer joist details.*

3.3 LWF CONTRIBUTION TO STRENGTH AND STIFFNESS

The exterior and interior walls of the existing structure contribute to the performance of the building by increasing its apparent strength and stiffness. For each MPP structural wall, a tributary length of existing exterior and interior walls and type of sheathing are considered. For the interior gypsum board walls, a tributary length of 3 m is assumed. For the exterior walls, which are assumed to be wood structural panels with 6d nails spaced at 150 mm on-center (8x8 WSP 6d @ 150 mm), a length of 1.20

https://doi.org/10.52202/069179-0350

m is assumed. The contribution of the existing exterior walls with window or door openings was neglected. The resulting backbone curves based on the considerations described in this paragraph are shown in Figure 8 based on experimental data available in [10].

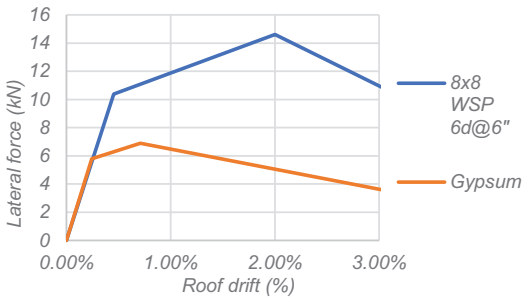

Figure 8. *Nonlinear backbone capacity of existing LWF walls based on their tributary length assigned to an MPP structural wall panel for this façade retrofit example.*

4 FINITE ELEMENT MODEL

Figure 9 illustrates a detailed Finite Element Model (FEM) that was developed to predict the response of the retrofitted building and validate the analytical methodology described in the previous sections. The FEM software used is ETABS [19]. The MPP structural walls are modelled using elastic shell elements for the panel and nonlinear fiber shell elements for the steel plate, both with a mesh size of 50 mm x 50 mm. Orthotropic material properties for the MPP are assumed, based on experimental data [20], using 12362 MPa for Ex, 2979 MPa for E_y, 206 MPa for Ez, 861 MPa for Gxy, 820 MPa for Gyz, and 145 MPa for Gzx. Multilinear elastic links are used to model the nonlinear behavior of screws and bolts. Compression-only nonlinear elastoplastic contact springs are assigned to the FEM to simulate the uplift/contact behavior of the panel with the foundation, considering a yield stress for MPP of 42.95 MPa, a corresponding yield strain of 0.0032, and ultimate strain of 0.007, with the tributary area for each spring and a plastic hinge length of twice the panel width (152.4 mm) [21].

The existing LWF structure is modelled using X-braced frames that can deform axially only and capture the horizontal story force-displacement response shown in Figure 8. Compression and tension plastic hinges are assigned for two braced frames acting in parallel to capture the shear response of the exterior and interior walls. The vertical and horizontal elements are assumed to be nearly rigid elements with moment releases at the ends.

A nonlinear static analysis is performed, using a displacement-controlled analysis, until reaching a target displacement at the top of the MPP wall of 244 mm, which corresponds to 4% roof drift ratio. The nonlinear parameters used in the software are: Newton-Raphson for positive iterations, Constant-Stiffness for negative iterations, solution scheme is Event-to-Event Only, event lumping tolerance (relative) of 0.001, maximum events per step of 200, minimum event step size of 0.001, and the maximum number of null events per step of 5.

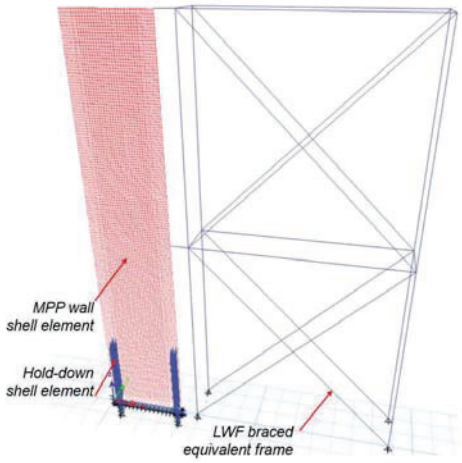

Figure 9. *Two-dimensional FEM developed in ETABS. The MPP structural wall is modelled as shell elements. Steel connections are discretized with shell elements with nonlinear materials. Screws, bolts, and contact elements are modelled as nonlinear multilinear springs. The existing LWF exterior and interior walls are modelled using equivalent braced frames.*

5 RESULTS AND DISCUSSION

5.1 CAPACITY CURVES AND OVER-STRENGTH FACTORS

Figure 10 shows the response for different models. The black line shows the FEM pushover analysis response of a model consisting of only the existing LWF structural walls (WSP walls). The yield force of this system is reached at approximately 11.9% of the seismic weight. After the system yields, damage concentrates on the first floor of the existing building, creating a soft-story mechanism. For reference, the ASCE 41-17 BSE-1E required design force (7.79%) of the LWF walls, shown as a green dash-dot line, is slightly smaller than the yield force of the existing structural wall. Using a typical NDS safety factor of 3.0, the yield point of the capacity curve should be equal to 23.4%. It can be seen in the figure that the LWF structural capacity curve is below this value, therefore the existing LWF structure requires retrofit.

Note that the nonstructural components such as the interior walls should be classified as structural elements if stiffness or strength exceeds 10% of the exterior structural walls [8]. In this case study, including the contribution of the interior walls, the yield force increases 82% from just considering exterior walls to 21.7%. Therefore, even accounting for the nonstructural elements, this LWF structure requires retrofit.

Additionally, Figure 10 shows three different FEM results. The FEM-1 curve is the capacity curve for the MPP structural wall where only the contact springs and

hold-down steel plate and screw connections are modelled explicitly, or in other words, where the horizontal shear steel plate is not modelled. FEM-1 shows a higher ductility than the WSP walls, reaching the first yield point at 1.50% drift. The FEM-2 results show the capacity curve of the model with the shear steel plate and thus illustrate the effect of adding the shear plate at the base of the MPP relative to FEM-1. The addition of the shear steel plate at the base of the wall increases the lateral stiffness and strength of the system. Finally, FEM-3 corresponds to the model shown in Figure 9. The results indicate the increase in capacity required in terms of base shear (over-strength) when the contribution of the existing exterior and interior LWF, WSP, and gypsum walls, respectively, are also added to the model.

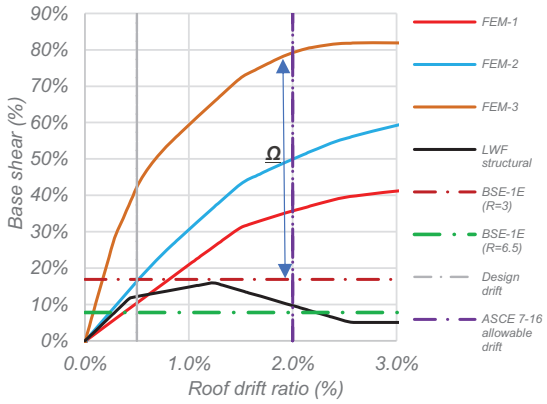

Figure 10: *Capacity curves for the following systems: WSP structural capacity (black), MPP structural wall (red), MPP structural wall with shear plate connection (blue), MPP structural wall with shear plate connection, and existing LWF (orange). The horizontal dashed-dot lines correspond to the BSE-1E force levels.*

The analysis results presented in Figure 10, illustrate that the over-strength in the system originates from two main sources. First, through the engagement of the shear plate connection at the base of the MPP, and second through the lateral stiffness provided by the existing LWF exterior and interior walls. At 2% drift, the over-strength from the shear plate contribution is approximately 143%, while the over-strength originating from the existing LWF walls is 476%.

5.2 STRESS ANALYSIS OF MPP AND STEEL PLATES

MPP walls need to resist the stresses induced by the lateral loads at higher drifts, allowing the connections to develop their nonlinear capacity. Using MPP allowable stresses: tension F_{t0} = 8.96 MPa, bending F_{b0} =13.1 MPa, compression F_{c0} =16.55 MPa, and shear F_{v0} =1.76 MPa [6]. The stress distribution in the MPP and steel plates, at the design force level (7.87 kN), is shown in Figure 11. At this level, the steel plates and the MPP show elastic properties, satisfying one of the initial assumptions in the design process. Nevertheless, the FEM shows shear stress concentration at the base of the wall at higher deformations, shown in Figure 12 for 2% drift. A follow-up experimental test will provide further validation of these results.

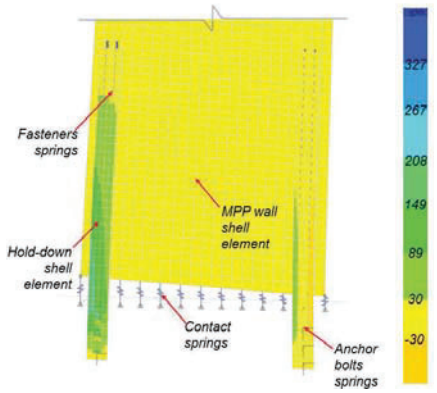

Figure 11: *Axial stresses (F22) for design level (MPa), for hold-down and MPP shell elements. Non-linear springs representing the fasteners and rocking effect at the base of the wall.*

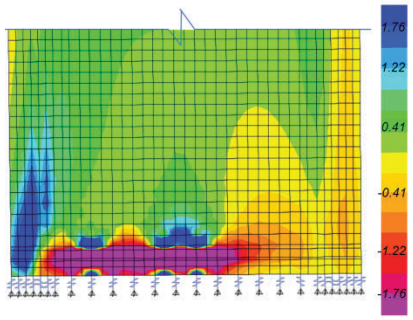

Figure 12: *Shear stress (F12) concentration in MPP at 2% drift ratio.*

5.3 ANALYTICAL MODEL AND FEM COMPARED.

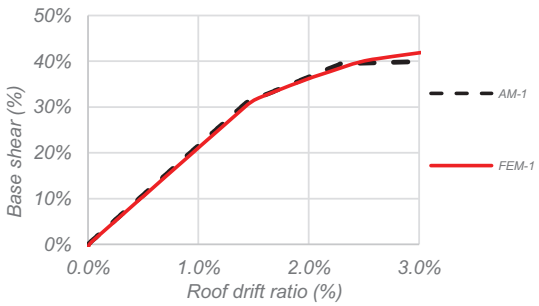

Figure 13. *Capacity curves for AM and FEM for MPP wall with hold-down connections only.*

After applying Equations 3 to 9, the analytical model describes the capacity curve of the LFRS and the yielding points of the components. Compared with the detailed FEM, the results were practically identical, obtaining the yielding points for fasteners and steel plates (see Figure 13).

https://doi.org/10.52202/069179-0350

6 CONCLUSIONS

The implementation of a combined energy and seismic façade retrofit system using MPP provides a practical solution for existing LWF buildings.

A force-based lateral load calculation (ELF) from ASCE 7-16 can be used to size steel connections in a retrofit system. In addition, the lateral stiffness of the existing LWF is an important factor to consider when developing over-strength factors. The lateral transfer system from the existing structure to the new LFRS needs to be designed following capacity-based design demands, increasing the ductility of the system.

A simplified analytical model can be used to obtain the nonlinear capacity curve of the LFRS, following the geometric and mechanical properties of the wall, which was later validated by a detailed finite element model.
An experimental test is needed to validate the assumptions made in the design and the modelling of the LRFS.

7 FUTURE WORK AND EXPERIMENTAL TEST

The analytical model presented in this document presents the equations for the MPP wall only, a future implementation of the existing LWF structure is planned, with the development of the stiffness matrix describing the behavior of 2- and 3-story buildings.

This project has been accompanied initially by the construction of a mock-up, real-scale specimen, built to verify the connections matched with the panels and the foundation. A follow-up experimental test is being developed in parallel, where a real-scale MPP with steel connections attached to a concrete beam will be subjected to a quasistatic lateral protocol load. From the experiment, a validation of the stiffness of the connection is expected, also showing the probable damage at the base of the MPP.

Based on ASCE 41-17, further performance assessment of the system is planned, determining performance points and implementing the methodology from this standard. Response history analysis will be also implemented to determine ductility factors and dynamic effects in the behaviour of the LFRS.

ACKNOWLEDGEMENT

This work was supported by a U.S. Forest Service Wood Innovation Grant #2020-DG-11062765-737 and by the TallWood Design Institute. Any opinions, findings, and conclusions are those of the authors and do not necessarily reflect the views of the supporting agencies.

REFERENCES

[1] Ellingwood B.R., Rosowsky D.V., Li Y., Kim J.H.: Fragility assessment of light-frame wood construction subjected to wind and earthquake hazards. Journal Structural Engineering 130 (12): 1921–1930, 2004.

[2] NAHB Research Center Inc.: Assessment of damage to residential buildings caused by the Northridge Earthquake. NAHB Research Center Report, Upper Marlboro, MD, 1994.

[3] Liel A., Raghunandan M.: Investigation of structural collapse risk in the Cascadia subduction zone, part 2: collapse risk of buildings in the Pacific Northwest region due to subduction earthquakes. Boulder, CO, U.S. Geological Survey, 2013.

[4] Northwest Energy Efficiency Alliance. Residential Building Stock Assessment II: Multifamily Buildings Report 2016-2017, Revised 2019.

[5] Energiesprong. (2023, February 11). [Website]. Retrieved from https://energiesprong.org.

[6] ICC-ES.: Joint Evaluation Report ESR-4760. www.frereslumber.com, 2022.

[7] Fretz, M., Stenson, J., Orozco, G., Narancic, P., Casey, F., Northcutt, Dale., Van Den Wymelenberg, K., Sheine, J., Barbosa, A. R.: Developing an Application for Mass Plywood Panels in Seismic and Energy Wall Retrofits. In: 2023 World Conference in Timber Engineering (WCTE 2023), 2023.

[8] ASCE standard, ASCE/SEI, 41-17: seismic evaluation and retrofit of existing buildings, American Society of Civil Engineers, Reston, VA, 2017.

[9] ASCE/SEI 7-16: Minimum Design Loads and Associated Criteria for Buildings and Other Structures, American Society of Civil Engineers, Reston, VA, 2016.

[10] NIST GCR 17-917-45: Recommended Modeling Parameters and Acceptance Criteria for Nonlinear Analysis in Support of Seismic Evaluation, Retrofit, and Design. National Institute of Standards and Technology, US Department of Commerce, Applied Technology Council, 597, 2017.

[11] Department of Building and Safety: Procedures for the Application of ASCE 41-17 to Existing Buildings, Informative Bulletin. P/BC 2020-148, City of Los Angeles, 2020.

[12] Federal Emergency Management Agency (FEMA): Seismic Evaluation and Retrofit of Multi-Unit Wood-Frame Buildings with Weak First Stories, Technical Report FEMA P-807, Washington, D.C., 2012.

[13] ANSI/AWC: National Design Specification (NDS) for Wood Construction, American Wood Council, Leesburg, VA, 2018.

[14] ANSI/AISC 360-16: American Institute of Steel Construction, Chicago, IL, 2016.

[15] Simpson Strong-Tie: Strong-bolt 2 Design Information. Pleasanton, CA. Simpson Strong-Tie Company Inc, 2021.

[16] ASTM International: Standard Specification for High-Strength Low-Alloy Columbium-Vanadium Structural Steel. ASTM A572 / A572M - 18, ASTM International, West Conshohocken, PA, doi: 10.1520/A0572_A0572M-18, 2018.

[17] ICC-ES.: Evaluation Report ESR-3046, 2022.

[18] Miyamoto B. T., Sinha A., & Morrell I.: Connection performance of mass plywood panels. Forest Products Journal, 70(1), 88-99, 2020.

[19] Computer and Structure, Inc.: ETABS 2016, 2020.

[20] Soti R., Ho T. X., & Sinha A.: Structural performance characterization of mass plywood panels. Journal of Materials in Civil Engineering, 33(10), 04021275, 2021.
[21] T. Akbas *et al.*, Analytical and Experimental Lateral-Load Response of Self-Centering Posttensioned CLT Walls, *J. Struct. Eng.*, 143(6), 2017.

https://doi.org/10.52202/069179-0350

World Conference on Timber Engineering Oslo 2023

CROSS-LAMINATED TIMBER FLOORS WITH OPENINGS – SERVICEABILITY LIMIT STATE VERIFICATIONS

Martin Schenk[1], Anja Husel[2], Philipp Dietsch[3], Pablo González-Serna[4], José Manuel Cabrero[5], Stefan Winter[6]

ABSTRACT: This paper contributes information about the influence of openings in cross laminated timber (CLT) floors in serviceability limit state (SLS) design. SLS verifications according to the European structural design standard for timber structures - Eurocode 5 - comprise functionality, appearance and the user's comfort. The verifications are based on deformation and vibration criteria. The investigation presented describes the influence of openings on the basis of experimental and theoretical investigations. Rectangular centralized openings in CLT elements were tested. The experimental results were used for the calibration of the numerical models used for theoretical investigations. The numerical models were geometrically parameterized. Towards application for practice, modification factors were derived to enable determination of the respective deformation and first natural frequency.

KEYWORDS: mass timber, cross laminated timber, serviceability, openings in floors, deformation, vibration

1 INTRODUCTION

Structural design of openings in walls and floors is of crucial interest to enhance the competitiveness of cross-laminated timber (CLT) with other building materials [1]. Already for spans larger than 4 m – 5 m, serviceability limit state design (SLS) is decisive for the height of floor constructions in timber buildings [2]. Openings, e.g. for staircases or passages of technical building equipment (pipes, ventilation, etc.) locally reduce the mass and stiffness of floors and have therefor an influence on this important design situation. The verifications of serviceability limit states according to the European structural design standards [3], the Eurocodes, ensure (a) the functionality under typical conditions of use, (b) the appearance of the structure and (c) the comfort of intended users. According to the European design rules for timber structures [4] those verifications comprise criteria on deformations for (a-b) and on vibrations for (c). Research results on the performance of CLT floors with openings are available in e.g. [5, 6]. As presented in [7], simplified rules for the assessment and design of openings in CLT floors seem to vary significantly worldwide.

Striving towards a harmonization of rules, the aim of the present investigations is to contribute to existing studies on the influence of openings in CLT floors on SLS design. To achieve this, static load and vibration tests of 6 CLT elements by one single manufacturer without and with openings were carried out at the laboratories of the Technical University of Munich, Germany (MPA BAU), see Figure 1. Four-point bending tests were conducted to obtain the (i) stiffness, (ii) strength, (iii) deformations, and (iv) failure modes of the single span CLT elements. Vibration tests were conducted to derive the (v) natural frequencies of the system. The influence of openings was investigated for two sizes of openings, see Figure 2 and Figure 3. The test results, presented in Chapter 2 and in the companion paper [8], not only gave an insight into the structural behaviour of the system, but also provided data that has been used for the calibration of a numerical model, see Chapter 3, followed by a parametrized

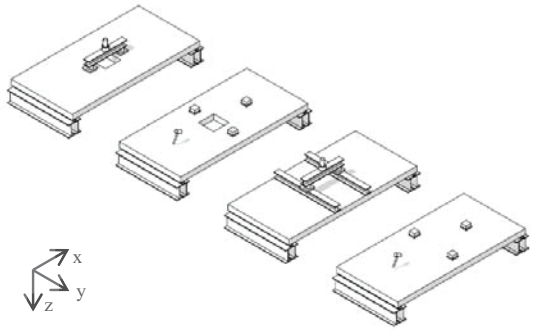

Figure 1: *Deformation and vibration test set-up for a single span CLT floor with and without opening*

[1] Martin Schenk, TUM Technical University of Munich, Germany, martin.schenk@tum.de
[2] Anja Husel, KIT Karlsruhe Institute of Technology, Germany, anja.husel@web.de
[3] Philipp Dietsch, KIT Karlsruhe Institute of Technology, Germany, dietsch@kit.edu
[4] Pablo González-Serna, UNAV University of Navarra, Spain, glezsernapablo@gmail.com
[5] José Manuel Cabrero, UNAV University of Navarra, Spain, jcabrero@unav.es
[6] Stefan Winter, TUM Technical University of Munich, Germany, winter@tum.de

https://doi.org/10.52202/069179-0351

numerical study on the influence of openings on deformations and frequencies in the system, see Chapter 4.

2 EXPERIMENTAL INVESTIGATIONS

A total of six non-edge-glued CLT specimens according to ETA-06/0138 [9] with an element height of 100 mm were tested in bending to determine the element stiffness and natural frequencies. The test set-up for bending corresponded to the test provisions of EN 16351 [10] in conjunction with EN 408 [11]. The lamination height of the five layers of the elements was 20 mm each with the outer layers oriented in span direction, see Table 1 and Figure 4. The strength class of the sorted laminations corresponded to C24 according to EN 338 [12]. The elements had a length of 2,50 m and width of 1,20 m. The span of the simple supported test set-up was 2,40 m. The ratio of plate thickness t to span L was 1/24.

Table 1: *Layer thickness and orientation relative to the x-axis of the element and total element thickness*

layer	1	2	3	4	5	Σ	unit
thickness	20	20	20	20	20	100	[mm]
orientation	0	90	0	90	0	–	[°]

The panels where tested in three series: (i) without opening, (ii) with an opening size of 300 mm x 300 mm and (iii) with an opening size of 600 mm x 300 mm, each in the centre of the elements, see Figure 2. Thus, the opening size corresponded to 12,5 % of the span and to 25 % of the panel width in case (ii) and to 50 % of the panel width in case (iii). In the test series with small opening (ii), the edge distance of the opening was 450 mm. In the test series with bigger opening (iii), the edge distance was 300 mm. Four panels (A2, A3, A4, A6) were tested in all opening stages while two panels (A1, A5) served as reference panels without openings. In this evaluation, the series with openings are presented. All CLT specimens were stored in standard climate until moisture balance with a temperature of around 20 °C and a relative humidity of about 65 % in the test laboratory. The mass of all panels and the moisture content of the CLT panels was determined according to EN 13183-2 [13], see Table 2. The elements had a mean density of 437,5 kg/m^3 (COV: 10,2) and an average moisture content of 11,3 m-% (COV: 0,083). Three different load configurations were tested: (a) two uniformly distributed linear loads over the full element width, (b) two concentrated point loads, both for deformation investigations and (c) an unloaded state for vibration investigations (self-weight only), see Figure 2. The loads F were applied with a displacement-controlled hydraulic actuator in the distance of 900 mm to the supports. The hydraulic cylinder was jointed to a self-contained steel frame, fixed to the ground. The point loads were applied via steel plates of 200 mm x 200 mm width, the linearly distributed loads via two respective spreader beams (HEB), which were linked with a steel coupler. To avoid compressive deformations perpendicular to the grain in the outermost layers, a hardwood lamella was placed as load distributing element onto the roller supports, see Figure 4. Via nine displacement transducers (w1-w9 in Figure 2), global and local deformations were recorded.

Table 2: *Average moisture content according to EN 13183-2 [13] and total element mass without opening*

specimen	A2	A3	A4	A6	unit
moisture	11,3	11,2	11,6	10,9	m-%
mass	132	132	130	131	[kg]

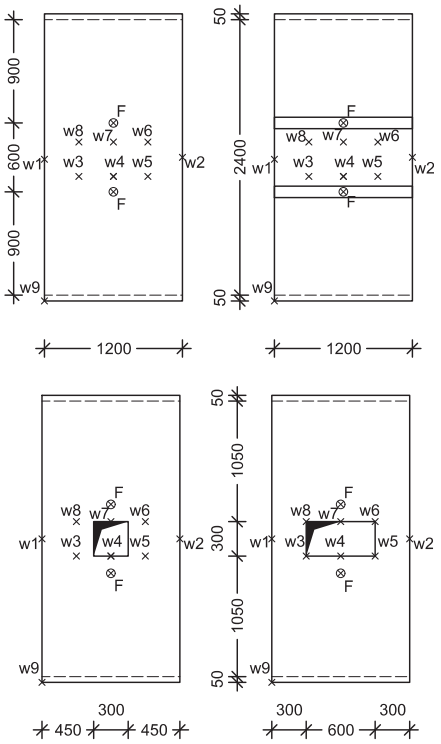

Figure 2: *CLT deformation tests: plan view with locations of the displacement transducers (w1-w9) and distributed load / concentrated load*

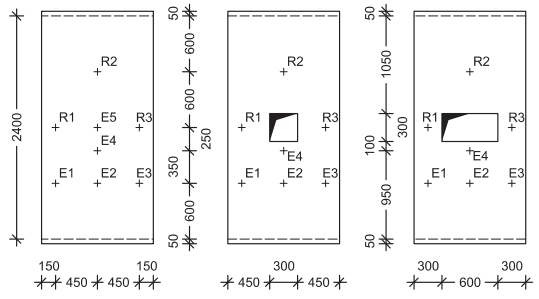

Figure 3: *CLT vibration tests: plan view of excitation points (E1-E5) and locations of the reception (R1-R3)*

https://doi.org/10.52202/069179-0351

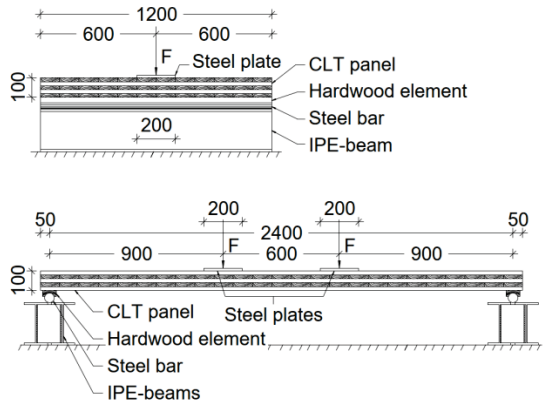

Figure 4: *CLT tests: side view in width (above) and length (below) direction*

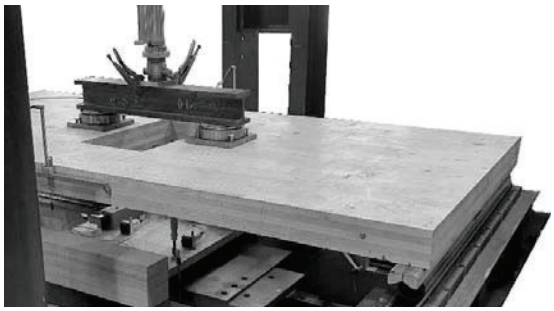

Figure 5*: View on the bending test set-up*

Figure 6: *View on displacement transducer arrangement*

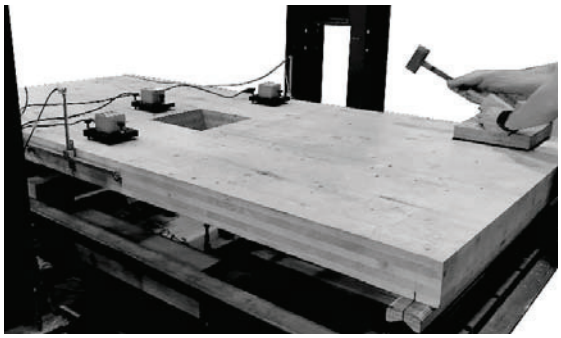

Figure 7: *View on the vibration test set-up*

Spherical bearings at the cylinder and at the concentrated loads ensured uniformly orthogonal load application, see Figure 5. Each concentrated load corresponded to the load $F/2$. An estimated failure load $F_{max,est}$ was determined by numerical calculations according to [14]. In order to achieve deformations in the elastic range and also to reduce the risk of damage such as cracks or plastic deformations to the specimen, a conservative load limitation $F_{lim,est}$ to 40 % of the estimated maximum load $F_{max,est}$ was made for the non-destructive deformation tests. The non-destructive tests were stopped manually when the estimated limit load was reached. For, e.g. panel A2, the estimated limit load $F_{lim,est}$ reached approximately 34 % of the destructively tested limit load $F_{max,test}$, see Figure 8 and Figure 9. Figure 10 shows the evaluated moduli of elasticity in span direction x as average between the left panel edge (transducer w1) and the right panel edge (transducer w2) for all test series in load configuration (a) and (b). The specimens in this series were tested without opening. The in total smallest evaluated value of the modulus of elasticity was $E_{net,x,min} = 12.468$ N/mm^2. The in total largest evaluated value of the modulus of elasticity was $E_{net,x,max} = 14.558$ N/mm^2. The mean values were evaluated as $E_{net,x,mean} = 13.596$ N/mm^2 in case (a) and $E_{net,x,mean} = 13.243$ N/mm^2 in case (b), see Figure 10. The corresponding value according to the manufacturer was 12.000 N/mm^2. One reason for the relatively high tested values could be the inclusion of higher quality boards in

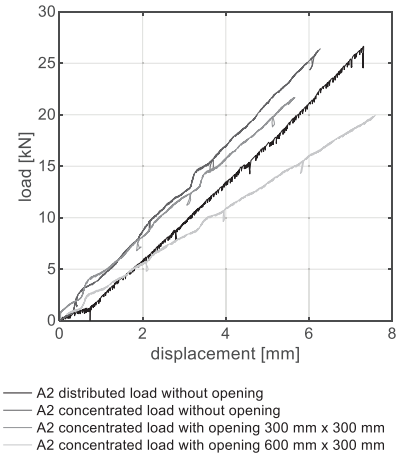

Figure 8: *Example of a load-displacement curve of specimen A2 at global w2 (non-destructive test until $F_{lim,est} = 0{,}4 \cdot F_{max,est}$)*

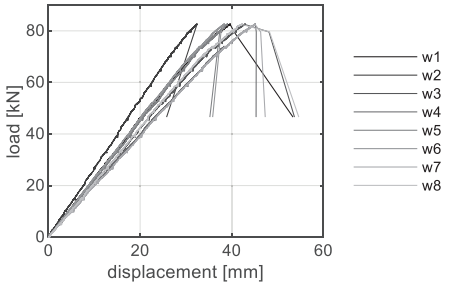

Figure 9: *Overview of load-displacement curves at all transducers of specimen A2 with concentrated load and opening 600 mm x 300 mm (destructive test) according to [15]*

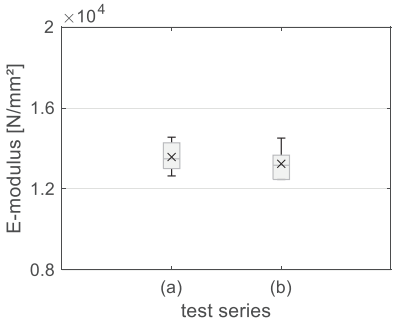

Figure 10: *(a) E-modulus tested according to [9] with uniformly distributed linear load without opening and (b) equivalent E-modulus tested with concentrated load without opening*

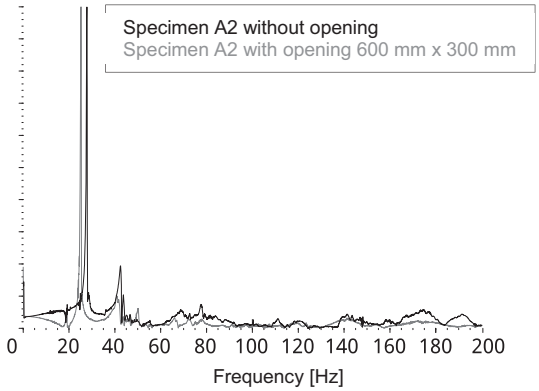

Figure 11: *Example of a vibration test of specimen A2 at locations E3 and R3*

Table 3: *Fundamental natural frequency of the CLT elements at locations E3 and R3: tested (A2 – A6) and simulated (FEA)**

	frequencies [Hz]		
specimen	without opening	with opening 300 mm x 300 mm	with opening 600 mm x 300 mm
A2	27,6	26,6	25,2
A3	27,7	27,4	26,0
A4	26,5	26,1	24,7
A6	27,8	27,2	24,5
mean	27,4	26,8	25,1
FEA*	29,8	28,0	24,5

* see Chapter 3

the grading process. While the laminations have a stiffness more than 10 % higher than stated in declaration of performance, the resulting values for series (a) and (b) are at similar level. The averaged modulus of elasticity $E_{net,x,mean}$ in the case of testing according to [10] (a) is 2,6 % higher than the respective value in the case of concentrated loading (b). To obtain the dynamic characteristics of the elements, the CLT panels were excited at midspan, in the quarter points and at the opening edge by a falling impact hammer in all test stages, see Figure 7 and E1 – E5 in Figure 3. The response was read via accelerometers fixed to the panels in midspan and in the quarter of the span, see Figure 7 and R1 – R3 in Figure 3. The time history acceleration responses from the hammer impacts were converted into frequency domain using the Fast Fourier Transform algorithm, see Figure 11. Table 3 shows the first natural frequency of the elements with and without openings. In general, the first natural frequency of the CLT panels without openings was relatively similar in all elements. The mean fundamental frequency of the CLT panels without opening was 27,4 Hz. With opening, the scatter of the measured fundamental frequencies was a little wider, see Table 3. Due to an opening of 300 mm x 300 mm in the elements, the mean value for the natural frequency of the panels dropped by 2,2 % to 26,8 Hz. An extended opening width of 600 mm x 300 mm lead to a further decrease of the mean value of the fundamental frequency to 25,1 Hz and thus by 8,4 % compared to the condition without opening. For an in-depth view into the determination of values according to EN 384 [16], destructive test-results and further test- set ups, their execution and evaluation see the companion paper [8].

3 NUMERICAL INVESTIGATIONS

There are numerical or analytical methods for solving the plate differential equations, see e.g. [17 – 19], the latter usually being valid for very special cases only. In the present study, a linear elastic finite element (FE) analysis with the software SOFiSTiK 2020 (version 2020.13-1) [20] was used for numerical evaluations.

There are various ways of representing the material and load-bearing behaviour of cross laminated timber elements in finite element models. Figure 12 shows the considered models: (A) modelling of each individual lamination as 2D Timoshenko-beam element, (B) modelling as a multi-layered structure with shell elements and (C) modelling as an equivalent single layered shell element with adjusted material values. For the discussion of further structural models of CLT elements with openings, see [8]. For an overview of the advantages and disadvantages of the investigated model types (A) – (C), see [15].

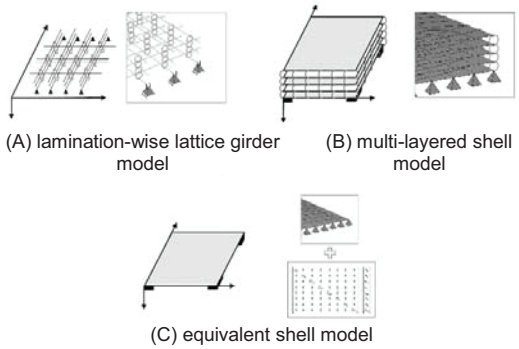

Figure 12: *Overview of considered FE models [13]*

https://doi.org/10.52202/069179-0351

The investigation on hand was carried out using 4-noded Bathe-Dvorkin shell elements, to avoid locking effects [20], with adapted stiffness properties (type C in Figure 12). Further information on locking effects can be found in [21] and [22]. A regular mesh size of the finite elements with a maximum width of 50 mm was chosen. For a convergence study on the mesh size, see [15]. In the applied models, the support conditions were fixed against translation in the *y*- and *z*-directions on one side of the span and against translations in *x*-, *y*- and *z*-directions on the other side. Both support conditions did not fix torsional deformations. A uniformly distributed load of 5 kN/m² was applied to the model for the evaluation of parametrized deformations.

Due to ratio of the investigated total panel thickness t to the span L, it might be assumed that deformations due to shear would not contribute considerably to the calculation results and might be neglected according to Kirchhoff's plate theory. According to Mestek [23], shear deformations of the cross-laminated timber panels may be neglected in the mechanical modelling for threshold ratios $t/L = 1/20 \ldots 1/30$. Additionally, Mestek [23] recommends to always consider shear deformation in serviceability limit state verifications. For the investigation on hand, shear deformations were considered throughout the models. The examined cross-laminated timber panels did not have edge bonding on the narrow edges of the laminations. Therefore, the Poisson's ratios were generally set to zero. For the same reason, the modulus of elasticity perpendicular to the grain in plane was set to zero as well. The adjustment of the torsional stiffness B_{xy} was made according to the declarations specified by the manufacturer [9]. For an in-deep view into the material properties of cross laminated timber, see e.g. Brandner et al. [24]. The applied stiffness values based on the test results are shown in Table 4. For a deeper insight into the evaluation of these stiffness values by calibration on the test results according to Chapter 2, see [15]. For the evaluation of the natural frequencies under dead load, the method according to Lanczos [25] was used. For an in-depth view into modelling of natural frequencies of CLT and respective model uncertainties, see e.g. Labonnote and Malo [26]. The numerical model was parameterized in the geometries span of the element $L_x = 3.000 \ldots 7.000$ mm, width of the opening $l_y = 0{,}10 \ldots 0{,}80 \cdot L_y$ and length of the opening $l_x = 1.000 \ldots 1.500$ mm according to Figure 13.

Table 4: *Material parameters for the model evaluated in [15]*

B_x [kNm/m]	B_y [kNm/m]	B_{xy} [kNm/m]	S_{xz} [kN/m]	S_{yz} [kN/m]
792	208	33,8	7.980	4.420

B_x; B_y = bending stiffness
B_{xy} = torsional stiffness
S_{xz}; S_{yz} = shear stiffness

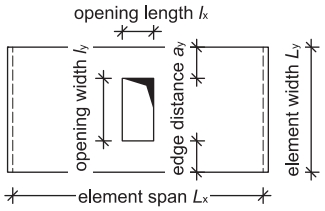

Figure 13: *Definition of geometries according to [15]*

4 RESULTS

The results of the calibrated and parameterized FE analysis were internal forces and deformations, each in the respective element nodes, as well as natural frequencies. The post-processing of the data was carried out with SOFiSTiK, Microsoft Excel and a Python script. Under the two concentrated loads, the CLT elements deformed in both the longitudinal and transversal direction, see Figure 14. The deformed shape of the CLT panels with and without openings was similar under the uniformly distributed load of 5 kN/m². The maximum deflection occurred usually in the area of transducer w4 respectively w7, see Figure 2. The first eigenmode, each with and without opening, reflected an expected semi-sinusoidal shape, see Figure 15.

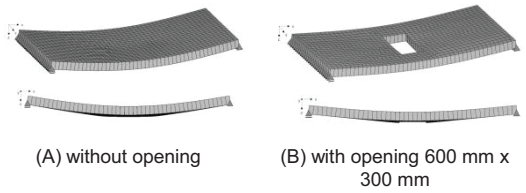

Figure 14: *Deformed shape of the CLT element with visualized element height [15]*

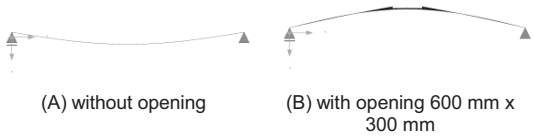

Figure 15: *Semi-sinusoidal eigenmode of the CLT element*

Figure 16 shows the non-normally distributed scatter of the maximum deformation expressed as increase factor k_w, normalized on the deformation without opening for centralized rectangular openings with a fixed opening length of $l_x = 1.000$ mm, see Figure 16 (A), and length of $l_x = 1.500$ mm, see Figure 16 (B), respectively, and a span parametrized between $L_x = 3.000 \ldots 7.000$ mm according to equation (1). Table 5 lists the respective mean values.

https://doi.org/10.52202/069179-0351

$$k_X = \frac{X_2}{X_1} \quad (1)$$

with
$X = w$ for the deformation (2)
$X = f_1$ for the first natural frequency (3)

where
k_X = influence factor of the opening on an effect of action named X;
X_1 = value of the effect of action without opening;
X_2 = value of the effect of action with opening.

It was noted that the relative influence of the opening width l_y on the deformation increases exponentially with the increase of the same in the investigated set-up. As expected with a uniaxial load-bearing system, increasing the opening length l_x in span direction has positive effect on the deformations in case of large opening widths, see Figure 16. From the data obtained, it also appears that the influence of the opening width l_y increases as the span increases. The observations on the deformation can be transferred to the eigenvalues, see Figure 17. Here, too, the influence increases more with increasing opening width compared to increasing opening length. In addition to the stiffness, the influence of the reduced self-weight due to the opening on the natural frequency should not be neglected.

Table 5: *Mean values of influence factor k_w according to [15] and k_{f1} for a span in the range of L_x = 3.000…7.000 mm and for an opening length l_x = 1.000 mm*

l_y/L_y	0,10	0,25	0,50	0,67	0,80
k_w	1,02	1,15	1,54	2,12	3,04
k_{f1}	0,99	0,94	0,83	0,72	0,60

l_y = opening width
L_y = element width

5 CONCLUSIONS AND OUTLOOK

Eurocode 5 provides SLS design verifications for functionality, appearance and the user's comfort in form of deformation and vibration criteria [4]. According to the current draft of the second generation of Eurocode 5 [27], deformations have to be verified using the characteristic, frequent, or quasi-permanent combination of actions given in Eurocode 0 [28]. Based on the investigations of e.g. [29 – 31], vibration verification according to prEN 1995-1-1 [27] comprises frequency criteria, stiffness criteria, velocity and acceleration criteria which are adapted to human perception. The investigations presented showed that openings in CLT floors have a decisive influence on the deformations and the natural frequencies and hence influence the respective verifications in SLS design. Simplified design rules for the verification of deformations of CLT floors with openings do not yet exist in the European design standard.

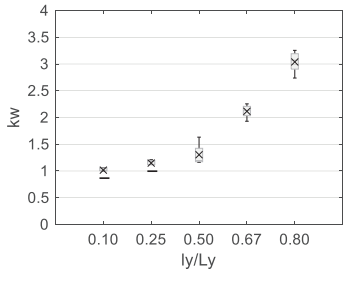

(A) l_x = 1.000 mm

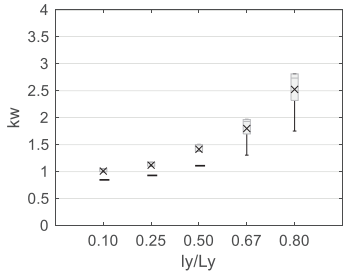

(B) l_x = 1.500 mm

Figure 16: *Non-normally distributed scatter of the increase factor k_w for a span in the range of L_x = 3.000…7.000 mm under uniformly distributed load of 5 kN/m² according to [15]*

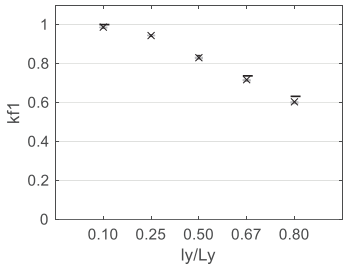

(A) l_x = 1.000 mm

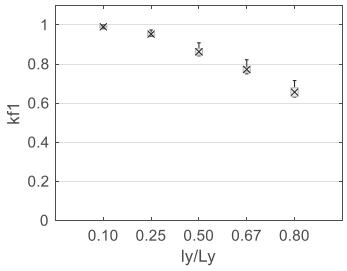

(B) l_x = 1.500 mm

Figure 17: *Non-normally distributed scatter of the increase factor k_{f1} for a span in the range of L_x = 3.000…7.000 mm under self-weight*

https://doi.org/10.52202/069179-0351

According to prEN 1995-1-1 [27], under certain boundaries, openings in floors may be generally neglected in the vibration verification provided that the plan area of the opening area and that no individual opening dimension is greater than 40 % of the respective floor dimension.

Further introduction of simplified rules for SLS design of CLT floors with openings would not only strengthen the competitiveness of timber structures but could also support the resource-efficient use of the material in general. Subsequently, with further harmonisation of its structural design, application of CLT will become more and more user-friendly and attractive globally [32].

ACKNOWLEDGEMENT

Project InnoCrossLam was supported under the umbrella of ERA-NET Cofund ForestValue by MIZŠ, INNOVA, FORMAS, STEM, BMLFUW, FNR and MINECO-AEI and has received funding from the European Union's Horizon 2020 research and innovation programme under grant agreement N° 773324.

The financial support provided by Fachagentur Nachwachsende Rohstoffe e. V. (FNR) of the German Federal Ministry of Food and Agriculture (BMEL) and the Spanish Ministerio de Ciencia, Innovación y Universidades – Agencia Estatal de Investigación under contract PCI2019-103591 AEI is gratefully acknowledged.

Special thanks go to KLH Massivholz GmbH and the colleagues from UNAV, KIT and TUM for excellence collaboration.

REFERENCES

[1] Schenk M., González-Serna P., J. M. Cabrero: Future research on cross laminated timber (CLT) for multi-storey buildings – a questionnaire among engineers active in practice. In: Proceedings WCTE 2020, Chile, 2020/21.

[2] Moosbrugger Th., Bogensperger Th., Krenn H.; Bemessungsdiagramme für den biegebeanspruchten Stab im Holzbau – Teil 2: Deckentragwerke mit inhomogenen Stabquerschnitt. Bautechnik 92, 2015.

[3] EN 1990:2010 Basis of structural design; EN 1990:2002 + A1:2005 + AC:2010. Comité Européen de Normalisation (CEN), Belgium, 2010.

[4] EN 1995-1-1:2014 Eurocode 5: Design of timber structures – Part 1-1: General – Common rules and rules for buildings; EN 1995-1-1:2004 + AC:2006 + A1:2008 + A2:2014. Comité Européen de Normalisation (CEN), Belgium, 2014.

[5] Popovski M., Chen Z.; Structural behaviour of point-supported CLT floor systems. In: Proceedings WCTE 2016, Austria, 2016.

[6] Kozaric L., Bursac S., Vojnic Purcar M., Besevic M., Tekic Z.: Finite Element Analysis of Dynamic Characteristics and Bending Stiffness for Cross Lamianted Timber Floor Panels with and without Openings. Drvna Industrija, 2021.

[7] Arnold M., Schenk M., Kainz N., Dietsch P., Cabrero J. M.; Maderebner R.; Winter S.: Schlussbericht zum Europäischen Forschungsvorhaben InnoCrossLam – Innovative Lösungen für das zukünftige Bauen mit Brettsperrholz - Arbeitspakete 5 und 6 (Deutschland). Research report, Germany 2022.

[8] González-Serna P., Yurrita M., J. M. Cabrero: Experimental analysis of the influence of openings in cross-laminated timber plates loaded out of plane. In: Proceedings WCTE 2023, Norway, 2023.

[9] ETA-06/0138 based on EAD 130005-00-0304 – Solid wood slab element to be used as a structural element in buildings. Österreichisches Institut für Bautechnik (OIB), Austria, 2021.

[10] EN 16351:2021 Timber structures – Cross laminated timber – Requirements. Comité Européen de Normalisation (CEN), Belgium, 2021.

[11] EN 408:2012 Timber structures – Structural timber and glued laminated timber – Determination of some physical and mechanical properties; EN 408:2010+A1:2012. Comité Européen de Normalisation (CEN), Belgium, 2012.

[12] EN 338:2016 Structural timber – Strength classes. Comité Européen de Normalisation (CEN), Belgium, 2016.

[13] EN 13183-2:2002 Moisture content of a piece of sawn timber – Part 2: Estimation by electrical resistance method. Comité Européen de Normalisation (CEN), Belgium, 2002.

[14] González-Serna P. (unpublished): Proposal for testing CLT floor plates with openings. Internal paper, Spain, 2021.

[15] Husel A.: Preliminary studies on openings in cross laminated timber plates. Master thesis, Karlsruhe Institute of Technology, Germany, 2022.

[16] EN 384:2018 Structural timber – Determination of characteristic values of mechanical properties and density; EN 338:2016+A1:2018. Comité Européen de Normalisation (CEN), Belgium, 2018.

[17] Timoshenko T., Woinowsky-Krieger S.: Theory of plates and shells. American Society of Civil Engineers, United States of Amerika, 1959.

[18] Reddy J. N.: Mechanics of Laminated Composite Plates and Shells - Theory and Analysis, CRC Press, United States of Amerika, 1997.

[19] Bogensperger T., Silly G., Schickhofer G.: Comparison of Methods of Approximate Verification Procedures for Cross Laminated Timber. Research Report, Graz University of Technology, Austria, 2012.

[20] SOFiSTiK AG (ed): SOFiSTiK - Manual. Germany, 2020.

[21] Bathe K.-J., Dvorkin, E. N.: A continuum mechanics based four-node shell element for general non-linear analysis. Massachusetts Institute of Technology Cambridge, United States of Amerika, 1983.

[22] Koschnick F.: Geometrische Locking-Effekte bei Finiten Elementen und ein allgemeines Konzept zu ihrer Vermeidung. Dissertation, Technical University of Munich, Germany, 2004.

[23] Mestek P: Punktgestützte Flächentragwerke aus Brettsperrholz (BSP) – Schubbemessung unter

Berücksichtigung von Schubverstärkungen. Dissertation, Technical University of Munich, Germany, 2011.
[24] Brandner R., Flatscher G., Ringhofer A., Schickhofer G., Thiel A.: Cross laminated timber (CLT): overview and development. European Journal of Wood and Wood Products, Germany, 2016.
[25] Lanczos C.: An Iteration Method for the Solution of the Eigenvalue Problem of Linear Differential and Integral Operators. Journal of Research of the National Bureau of Standards, United States of Amerika, 1950.
[26] Labonnote N., Malo K. A.: Vibration properties of cross laminated timber floors. Proceedings ICSA 2010, Portugal, 2010.
[27] prEN 1995-1-1:2023 Eurocode 5: Design of timber structures – Part 1-1: General rules and rules for buildings. Comité Européen de Normalisation (CEN), Belgium, 2023.
[28] EN 1990:2023 Basis of structural design. Comité Européen de Normalisation (CEN), Belgium, 2023.
[29] Ohlsson S.: Floor Vibrations and Human Discomfort. Dissertation, Chalmers University of Technology, Sweden, 1982.
[30] Willford M. R., Young P.: A Design Guide for Footfall induced Vibration of Structures – A tool for designers to engineer the footfall vibration characteristics of buildings or bridges. The Concrete Society, United Kingdom, 2006.
[31] Hamm P., Marcroft J., Toratti T.: Vibrations of floors – Comparison of measured data and suggested design. INTER 53 - 20 – 1, International Network on Timber Engineering Research, Germany, 2020.
[32] Azinović A., et al.: InnoCrossLam – adding knowledge towards increased use of cross laminated timber (CLT). In: Proceedings WCTE 2023, Norway, 2023.

https://doi.org/10.52202/069179-0351

World Conference on Timber Engineering Oslo 2023

TIMBER-FRAMED SHEAR WALLS WITH LARGE OPENINGS AS PART OF THE LATERAL FORCE-RESISTING SYSTEM - OPTIMIZATION OF THE SHEATHING-TO-FRAMING CONNECTION LAYOUT

Nadja Manser[1], René Steiger[2], Martin Geiser[3], Lukas Kramer[4], Andrea Frangi[5]

ABSTRACT: For lateral force-resisting systems of multi-storey timber-framed buildings, the usual policy of current standards is to only consider timber-framed shear wall segments ranging continuously from the ground floor to the top edge of the building and to neglect wall elements with openings. Developing a design method that allows taking wall elements with openings into account, would make the lateral force-resisting system more efficient and respective buildings more economic. This paper presents investigations of the combination of sheathing thickness and arrangement of the fasteners connecting the sheathing to the framing to maximize the load-carrying capacity of the wall while guaranteeing a ductile failure of the connection. The results of the study provide the basis for further experimental investigations on one- and two-story wall elements with large openings with the final goal of developing a design method for timber-framed shear walls with openings.

KEYWORDS: Timber-framed walls, shear walls, sheathing, OSB/3, openings, lateral stiffness, design

1 INTRODUCTION

Timber-framed shear walls are commonly used for the construction of buildings of low to medium heights. It is the usual policy in several current design standards, e.g. SIA 265, 2021 [1], DIN 1052, 2008-12 [2], EN 1995-1-1, 2008 [3], to adopt the so-called segmentation approach for the design of timber-framed shear walls contributing to the lateral force-resisting system (Figure 1, left). Thus, only wall segments, which continuously range from the ground floor to the top of the building can be considered to contribute to the lateral force-resisting system.

Figure 1: *Segmentation approach in the design of timber-framed shear walls with openings (left) versus considering all parts of wall elements with openings (right).*

However, modern architectural designs often demand flexible interior room arrangements, making exterior wall stiffening more important. Since modern architectural designs are characterized by numerous and in particular large openings (Figure 2), designing the lateral force-resisting system of a building using timber-framed shear walls gets very challenging, and sometimes even becomes impossible, since not enough continuous wall segments may be available to resist the lateral forces. The efficiency of the lateral force-resisting system could be enhanced by mobilizing wall segments with openings in the design (Figure 1, right). A beneficial side effect of this design approach is that the number of expensive anchorages is reduced.

Figure 2*: Buildings showing the recent trend in modern architectural design towards façade walls with large openings. [4]*

The objective of an ongoing research project in Switzerland, which forms the basis for the subsequent investigations and findings presented in this paper, is to develop a design method for timber-framed shear walls with openings. This will be accomplished by executing full-scale experiments on such walls and by an analysis of their behaviour under lateral loading. In order to come to an efficient design of wall specimens with openings, it is necessary to first of all define an appropriate and optimized sheathing-to-framing connection layout. This particular

[1] Nadja Manser, Empa – Swiss Federal Laboratories for Materials Science and Technology, Switzerland, nadja.manser@empa.ch
[2] René Steiger, Empa – Swiss Federal Laboratories for Materials Science and Technology, Switzerland, rene.steiger@empa.ch
[3] Martin Geiser, BFH – Bern University of Applied Sciences, Switzerland, martin.geiser@bfh.ch
[4] Lukas Kramer, BFH – Bern University of Applied Sciences, Switzerland, lukas.kramer@bfh.ch
[5] Andrea Frangi, ETH Zürich – Swiss Federal Institute of Technology, Zurich, Switzerland, frangi@ibk.baug.ethz.ch

https://doi.org/10.52202/069179-0352

first-step investigations were performed on wall elements *without* openings.

In seismic active areas, timber-framed shear walls are typically designed to exhibit ductile failure of the sheathing-to-framing connection. This requires that buckling and shear failure of the sheathing and a failure of the framing elements is prevented in order to ensure that ductile failure of the sheathing-to-framing connection remains the governing failure mode. An optimal sheathing-to-framing connection layout allows for the maximization of the load-carrying capacity of the wall, while ensuring that the fasteners undergo ductile failure when the load-carrying capacity is reached and avoiding brittle failure of the sheathing.

2 STATE OF THE ART

2.1 TIMBER-FRAMED WALL CONSTRUCTION

The regional differences in the construction of timber-framed shear walls can be observed comparing the dimensions of the framing elements, the thickness and the materialization of the sheathing, and the type of fasteners utilized. In Europe, the dimensions of the framing elements are generally larger compared to e.g. North-America and the thickness of the OSB/3 sheathing is commonly 15 mm. The typical construction of timber-framed shear walls in Switzerland and in other European countries involves the application of staples for the sheathing-to-framing connection. In Switzerland, more than one row of fasteners is not an uncommon practice. Since the study presented in this paper is a part of a research project in Switzerland, the focus is on the type of timber-framed shear walls prevalent in Switzerland and Europe.

2.2 RULES FOR THE DESIGN OF WALLS WITHOUT OPENINGS

2.2.1 Swiss standard SIA 265, 2021

In the Swiss standard, SIA 265, 2021, some general specifications for the design of timber-framed shear walls without openings are provided but no specific design rules are available. Hence, design rules taken from either EN 1995-1-1, 2008 or from DIN 1052, 2008-12 are applied.

2.2.2 European standard EN 1995-1-1, 2008

According to EN 1995-1-1, 2008, the design shear capacity of a timber-framed shear wall $F_{\mathrm{i,v,Rd}}$ can be determined from Formula (1).

$$F_{\mathrm{i,v,Rd}} = \frac{F_{\mathrm{f,Rd}} \cdot b_{\mathrm{i}} \cdot c_{\mathrm{i}}}{s} \tag{1}$$

where $F_{\mathrm{f,Rd}}$ = design load-carrying capacity of a single fastener, b_{i} = width of a single shear wall element, s = distance between fasteners, $c_{\mathrm{i}} = 1.0$ if $b_{\mathrm{i}} \geq b_0$ and $c_{\mathrm{i}} = b_{\mathrm{i}}/b_0$ if $b_{\mathrm{i}} < b_0$, where $b_0 = h/2$ with h = height of the shear wall element.

In EN 1995-1-1, 2008 it is assumed that the load-carrying capacity of the sheathing-to-framing connection is the governing factor for any wall geometry. This corresponds to the assumption that the resistance of the fasteners is always lower than the resistance of the sheathing. However, this assumption may not be valid when multiple rows of fasteners are used.

2.2.3 German standard DIN 1052, 2008-12

According to DIN 1052, 2008-12 the design shear strength of a timber-framed shear wall without opening can be calculated using Formula (2).

$$f_{\mathrm{v,0,d}} = \min \begin{cases} k_{\mathrm{v,1}} \cdot R_{\mathrm{d}}/a_{\mathrm{v}} \\ k_{\mathrm{v,1}} \cdot k_{\mathrm{v,2}} \cdot f_{\mathrm{v,d}} \cdot t \\ k_{\mathrm{v,1}} \cdot k_{\mathrm{v,2}} \cdot f_{\mathrm{v,d}} \cdot 35 \cdot t^2/a_{\mathrm{r}} \end{cases} \tag{2}$$

where $k_{\mathrm{v,1}}$ = factor to account for the arrangement and the way of connecting the panels ($k_{\mathrm{v,1}} = 1.0$ if the sheathing is connected to the framing on all edges in a sufficiently stiff manner in terms of transferring of shear stresses), $k_{\mathrm{v,2}}$ = factor to account for additional stresses (influences described in the next paragraph), R_{d} = design load-carrying capacity of a single fastener, a_{v} = distance between the fasteners, $f_{\mathrm{v,d}}$ = design shear strength of the panel, t = thickness of the sheathing, a_{r} = distance between the studs.

The first line in Formula (2) considers the limit given by the resistance of the sheathing-to-framing connection. The second line describes the limit given by the resistance of the panel and the third line the limit given by the buckling resistance of the panel. The $k_{\mathrm{v,2}}$ factor serves in accounting for additional stresses, which lead to a reduction of the shear strength of the sheathing. These stresses may originate from:

- the distance between the axis of the framing elements and the sheathing (Figure 3, a)),
- a discontinuous shear flow (Figure 3, b)),
- forces acting perpendicular to the axes of the framing elements (Figure 3, c)).

In DIN 1052, 2008-12 the $k_{\mathrm{v,2}}$ factor is set to 0.33 for the design of sheathing placed on only one side of the wall and to 0.50 for sheathing placed on both sides of the wall.

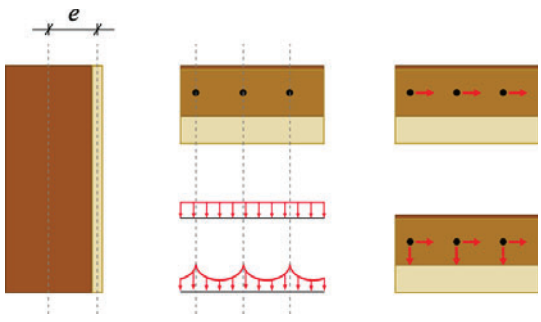

a) *b)* *c)*

***Figure 3**: Influences reducing the shear strength of the sheathing in timber-framed shear walls described in DIN 1052, 2008-12. a) Eccentricity between framing axis and sheathing axis, b) deviation from the model assumption of a continuous shear flow (top: model assumption, bottom reality), c) deviation from the model assumption of forces acting only parallel to the framing element axis (top: model assumption, bottom: reality).*

https://doi.org/10.52202/069179-0352

2.2.4 Current working draft of Eurocode 5, prEN 1995-1-1, 2022

The rules for the design of wall diaphragms in the current working draft of Eurocode 5, prEN 1995-1-1, 2022 [5] are based on the design procedure specified in DIN 1052, 2008-12. The $k_{v,2}$ factor was renamed to $k_{p,model}$ and increased to 0.5 for sheathing placed on one, and to 0.67 for sheathing placed on both sides of the wall. In addition to the three influences listed in DIN 1052, 2008-12, along with the design rules in prEN1995-1-1, 2022 two additional influences which need to be accounted in shear wall design (via the $k_{p,model}$ factor) are mentioned:

- Model assumption of pinned connections between ribs while the actual connections are often weaker (Figure 4, a)),
- Eccentricity of the axes of the framing if the framing elements are of different depth in cross-section (Figure 4, b)).

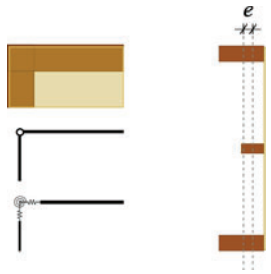

***Figure 4**: Influences reducing the shear strength of the sheathing in timber-framed shear walls compared to DIN 1052, 2008-12 additionally described in prEN 1995-1-1, 2022. a) Deviation from the model assumption of pinned connected framing elements (top: model assumption, bottom: reality), b) eccentricities within the framing elements.*

3 GOAL OF THE STUDY

The $k_{v,2}$ factor specified in DIN 1052, 2008-12 seems to have been introduced to overcome the problem of unaccounted additional stressed in the shear wall designs, which can reduce the shear strength of the sheathing. When looking at literature, it is unclear, to what extent these values are based on experimental research. Up to now, no results from experiments on timber-framed shear walls using OSB panels as sheathing material are available. This leads to the conclusion that the basis in terms of experimental data for the determination of the $k_{v,2}$ factor (or $k_{p,model}$ factor, respectively) is still poor.

In Switzerland, it is common practice to design the fasteners (i.e. the staples) of the sheathing-to-framing connection in multiple rows. In consequence, the need for a more accurate quantification of the $k_{v,2}$ factor needed for an accurate calculation of the shear strength of the sheathing of timber-framed shear walls arises. The results of this study will help in defining the optimal combination of sheathing thickness and fastener layout in order to maximize the load-carrying capacity of the wall element, while avoiding brittle failure of the sheathing.

An experimental campaign was conducted to investigate the shear resistance of OSB/3 panels in timber-framed shear walls without openings. The resulting shear resistance of the OSB/3 panels was compared to analytic estimations based on the design rules available in the standards mentioned above. The ratios calculated from a comparison of experimental data and estimate from design code formulae correspond to the reduction of the shear strength of the OSB/3 sheathing for applications in timber-framed shear walls.

4 MATERIALS

4.1 SHEATHING PANELS

The panels investigated were of type OSB/3 with thicknesses of 12 mm, 15 mm, 18 mm and 25 mm, and dimensions (i.e. width and height) of 1250 mm and 2500 mm. The panels for all test specimens originated from one single production batch for each panel thickness. The moisture content was determined by using the oven-dry method in accordance with the test procedure specified in EN 322, 1993 [6] and was $7.2 \pm 0.4\%$, which fulfils the requirements of EN 300, 2006 [7].

4.2 FRAMING ELEMENTS

The framing elements were composed of Swiss-grown Norway spruce (*picea abies*) glulam GL24h (EN 14080, 2013 [8]). The moisture content was determined by measuring the electic resistance and was $10.3 \pm 0.7\%$.

4.3 SHEATHING-TO-FRAMING CONNECTION

For the sheathing-to-framing connection, two different types of fastener were used:

- resined staples with a diameter of 1.53 mm and a length of 50 mm (Haubold, KG 700),
- threaded nails with a diameter of 3.10 mm and a length of 90 mm. (Haubold 3.10 x 90 Ring Wire Weld).

5 METHODS

Experiments on wall elements, as well as on OSB/3 panels were carried out. The latter aimed at determining the mechanical properties of the OSB/3 panels.

5.1 TESTS ON OSB/3 PANELS

The shear strength of the OSB/3 panels was determined in accordance with the test procedure specified in the European standard EN 789, 2005 [9]. Five specimens were tested for each sheathing thickness for both parallel and perpendicular strand orientation of the top layer.

5.2 SHEAR WALL TESTS

In order to evaluate the shear resistance of OSB/3 panels when applied as sheathing in timber-framed shear walls, full-scale wall elements were tested. The study focused on wall configurations where the OSB/3 sheathing was placed on one side only. The test setup, including the terminology used for the framing elements and the definitions of fastener distances, is depicted in Figure 7.

https://doi.org/10.52202/069179-0352

5.2.1 Design of the specimens

The specimens were designed to ensure that failure would occur in the sheathing, rather than in the sheathing-to-framing connection. To provoke this particular failure mode, sheathing-to-framing connection, anchoring, and framing elements were over-designed in comparison to the shear resistance of the sheathing. The shear resistance and the resistance against buckling of the panels (as described in the second and third line of Formula (2)) were evaluated on design level, using:

- $k_{v,1} = 1.0$,
- $k_{v,2} = 1.0$, assumption as starting point for the factor to be investigated,
- $f_{v,d} = k_{mod} \cdot f_{v,k}/\gamma_M = 6.23\ N/mm^2$, where k_{mod}, γ_M, and $f_{v,k}$ are 1.1, 1.2, and 6.8 N/mm^2, respectively, according to EN 1995-1-1, 2008,
- t: Thickness of the sheathing (nominal values).

Due to lack of information the over-strength factor to design the sheathing-to-framing connection and the anchoring was conservatively selected 1.5. This resulted in a high number of fastener rows. The space needed to arrange the fasteners influenced the width of the edge studs and the top and the bottom rail. In consequence, the framing elements compared to the sheathing, have an over-strength higher than 1.5.

The panels with thicknesses 12 mm, 15 mm, and 18 mm, were connected to the framing elements by means of resined staples. For the 25 mm thick panels, threaded nails were used, since the resined staples used in practice are technically difficult to insert in the 25 mm thick OSB/3 panel and the penetration depth in the framing members would be critically low.

The size of the specimen was governed by the dimensions of the panels (2.50 m and 1.25 m) and an offset of 20 mm (Figure 7 d_1) on all edges to prevent local crushing of the sheathing due to increasing deformations during the tests. The width and the height of the specimen were 1.29 m and 2.54 m respectively. To ensure comparability, the geometric configuration of the three stapled wall types was kept identical. The layout of the sheathing-to-framing connection and the dimensions of the framing elements as well as of the anchoring were taken based on the test specimens with the 18 mm thick sheathing, while the number of inner rails was taken based on the test specimens with the 12 mm thick panel since the resistance against buckling failure is minimal for the thinnest panel. Three specimens were tested for each wall type. In Table 1 the materials used and the geometrical properties are listed for all the four wall types investigated.

In order to prevent compression failure parallel to the grain of the edge studs and the top and the bottom rail, the corners of the walls were designed in such way that the rails and the edge studs both ranged continuously to the edges of the wall elements (mortise and tenon joints). The top and the bottom rails were constructed overlapping in order to simplify the installation of the test specimens in the test rig as well as the force transfer from the hydraulic jack to the specimen. (Figure 5)

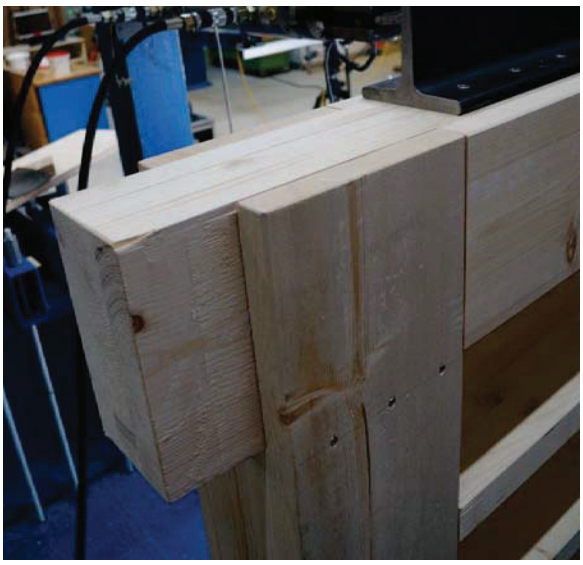

***Figure 5**: Construction detail of mortise and tenon joints at the corners of the tested timber-framed shear wall elements.*

5.2.2 Loading protocol

The walls were tested according to the testing standard ISO 21581, 2010 [10], using the force controlled testing protocol shown in Figure 6. $F_{max,est}$ was determined by estimating the shear capacity of the wall element resulting from the shear resistance of the panel (as described in the second line of Formula (2)) taking the parameters as follows:

- $k_{v,1} = 1.0$,
- $k_{v,2} = 1.0$, assumption as starting point for the factor to be investigated,
- $f_{v,mean,est} = 9.4\ N/mm^2$ [1],
- t: Thickness of the sheathing (nominal values)

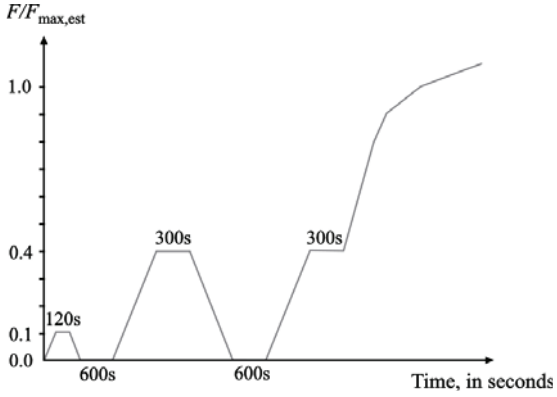

***Figure 6**: ISO 21581 loading protocol applied in the timber-framed shear wall tests.*

https://doi.org/10.52202/069179-0352

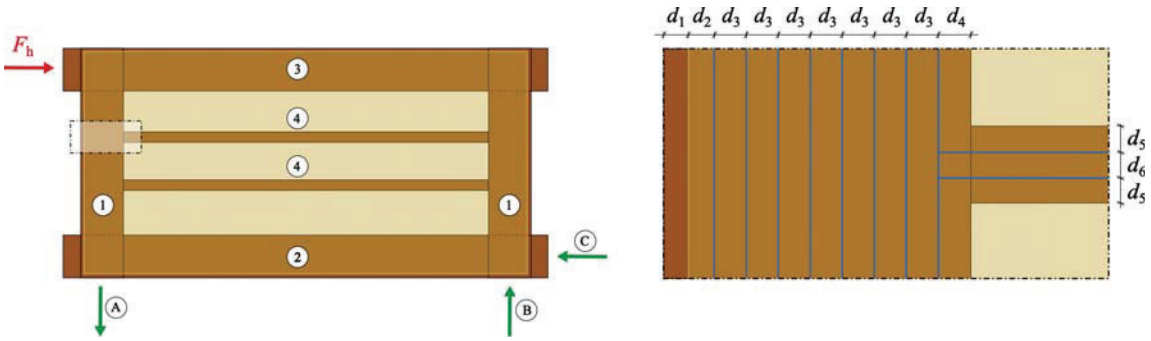

a) *b)*

***Figure 7**: a) Overview of the tested specimen with framing elements labelled with numbers (1: edge studs, 2: bottom rail, 3: top rail, 4: inner rails) and with reaction forces A, B, C induced by the applied force F_h. The dashed-dotted marked area is shown in Figure b). The blue lines indicate the rows, where the fasteners connecting the sheathing to the framing elements are placed.*

***Table 1**: Geometry of the four tested wall configurations. The distances d_1 to d_6 are illustrated in Figure 7, a_v describes the distance between two fasteners in the same row.*

			Wall configuration			
			12-S	**15-S**	**18-S**	**25-N**
Sheathing	Thickness	[mm]	12	15	18	25
Framing	Bottom and top rail (width x height)	[mm]	240 x 200	240 x 200	240 x 200	280 x 200
	Edge studs (width x height)	[mm]	240 x 200	240 x 200	240 x 200	280 x 200
	Inner rails (width x height)	[mm]	60 x 200	60 x 200	60 x 200	100 x 200
	Number of inner rails	[-]	2	2	2	1
Fasteners	Type	[-]	Staples	Staples	Staples	Nails
	Rows at the edges of the sheathing panels	[-]	8	8	8	10
	Rows on inner rails	[-]	2	2	2	2
Distances	d_1	[mm]	20	20	20	20
	d_2	[mm]	20	20	20	30
	d_3	[mm]	25	25	25	20
	d_4	[mm]	25	25	25	50
	d_5	[mm]	20	20	20	35
	d_6	[mm]	20	20	20	30
	a_v	[mm]	23	23	23	40

5.2.3 Realization in the lab

The force was applied centrically on the top rail of the specimen using a 1000 kN hydraulic jack (Figure 8 and Figure 9). Due to the non-perfect stiffness of the test rig, small test rig deformations in direction of the applied force could not be prevented. Since the effective deformation ($d_{\mathrm{max,rel}}$) of the timber-framed shear wall was determined in accordance with the procedure given in the standard ISO 21581 as the difference between the deformation in direction of the applied force on the top rail and the bottom rail, these small test rig deformations were neglected. The horizontal displacement in the centre of the bottom edge of the wall was measured using a mechanical displacement sensor with a measuring range of 10 mm and a precision of 0.04 mm, the horizontal displacement in the centre of the top edge of the wall was measured using a laser distance sensor with precision of 0.11 mm.

The anchoring of the vertical tensile and compressive forces and the resulting horizontal force is shown in Figure 9 and in Figure 10. Due to the asymmetry of the wall elements with sheathing on one side, out-of-plane forces developed during loading. To prevent tilting of the wall, a steel support was attached to the top rail of the wall and a 50 kN hydraulic jack was used to stabilize the wall (Figure 11). By forcing the stroke of this hydraulic jack to a displacement of 0 mm, tilting of the wall was avoided.

***Figure 8**: Timber-framed shear wall specimen mounted in the test rig and ready for investigation of the shear resistance of the OSB/3 panels applied as sheathing material.*

***Figure 10**: The horizontal reaction force was transferred to the test rig via a massive steel angle bracket. The vertical compressive force was transmitted through contact.*

***Figure 9**: The force was applied by the red hydraulic jack. The rail construction on top of the specimen is freely movable in horizontal direction. The tensile reaction forces were transmitted through the edge studs to the top edge of the specimen, where they were then transferred to a steel plate and brought back to the specimen via four steel rods.*

***Figure 11**: Tilting of the specimen was prevented by means of a 50 kN hydraulic jack maintaining the out-of-plane displacement on the top rail at a value of 0 mm.*

https://doi.org/10.52202/069179-0352

6 RESULTS AND DISCUSSION

6.1 TESTS ON OSB/3 PANELS

The results of the shear tests performed on the OSB/3 panels are presented in Table 2. The coefficients of variation (CoV) of the shear strength were in the range of 3.6% to 10.8%. The mean value of the shear strength of OSB/3 panels reported in the literature (9.4 N/mm^2, [11]) was not confirmed by the results obtained from the tests conducted in this study. The 5% fractile values calculated from the test data according to the procedure in the European Standard EN 14358, 2016 [12] were lower than the value specified in EN 1995-1-1, 2008 and in the declaration of performance (6.8 N/mm^2) for all test series except for the 12 mm and 15 mm thick panels tested perpendicular to the strand orientation of the top layer. Investigations are planned to identify the causes of the insufficient shear strengths of the panels.

***Table 2**: Mean values, standard deviations and coefficients of variation (CoV) of the shear strength obtained from the tests on the OSB/3 panels. The 5% fractile values were calculated in accordance with the procedure given in EN 14358, 2016.*

	n [-]	Mean [N/mm^2]	Stdev [N/mm^2]	CoV [%]	5% fractile [N/mm^2]
12, ⊥	5	7.69	0.28	3.6	6.79
15, ⊥	5	7.84	0.36	4.6	6.92
18, ⊥	5	7.61	0.41	5.4	6.63
25, ⊥	5	6.36	0.69	10.8	4.86
12, ∥	5	6.97	0.38	5.5	6.08
15, ∥	5	7.40	0.42	5.6	6.41
18, ∥	5	7.28	0.46	6.3	6.21
25, ∥	5	6.37	0.27	4.3	5.62

6.2 SHEAR WALL TESTS

In all the 12 tests performed on timber-framed shear wall elements, the sheathing failed in a brittle manner, in direction of the force flow, connecting the point of the applied force and the point where the horizontal force is transferred to the test rig. The initial failure occurred either along one of the fastener rows (Figure 12), or in diagonal direction in the field of the sheathing (Figure 13).

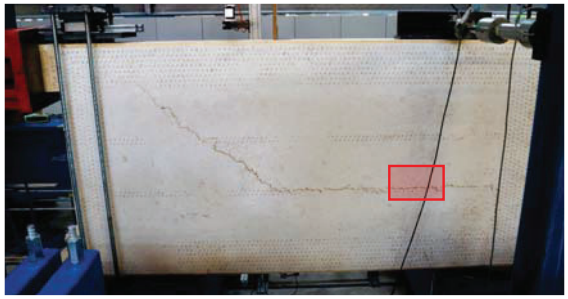

***Figure 12**: The initial failure in the 12-S-2 shear wall test occurred along the fastener row on the lower inner rail (marked in red).*

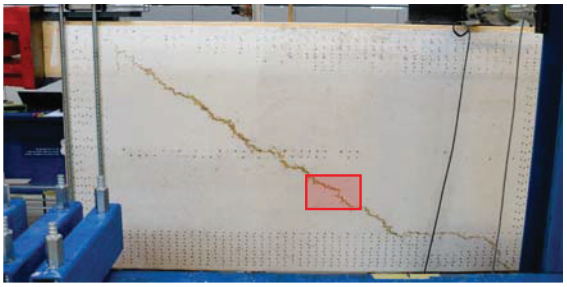

***Figure 13**: The initial failure of the 25-N-3 shear wall test occurred in diagonal direction in the field of the sheathing (marked in red).*

The applied maximum force and the respective maximum of the relative horizontal displacement ($d_{max,rel}$, see 5.2.3) are listed in Table 3 for each of the specimens tested. Since the displacement and the resulting stiffness of the tested wall elements are important for the comparison of numerical calculations with test results, the displacements are given for the sake of completeness, without being further discussed in this paper.

***Table 3**: Applied maximal horizontal force F_{max} and respective maximal relative displacement $d_{max,rel}$ at failure for each of the timber-framed shear wall specimens tested.*

	Specimen	F_{max} [kN]	$d_{max,rel}$ [mm]
12-S	12-S-1	181	9.5
	12-S-2	186	10.1
	12-S-3	178	9.5
15-S	15-S-1	241	12.5
	15-S-2	221	10.6
	15-S-3	229	10.6
18-S	18-S-1	299	11.9
	18-S-2	290	11.7
	18-S-3	305	12.9
25-N	25-S-1	394	16.6
	25-S-2	405	16.3
	25-S-3	379	14.5

The $k_{v,2}$ factor can be determined by equating the shear resistance of the OSB/3 panel in timber-framed shear walls estimated using the second line in Formula (2) multiplied by the length of the wall, and the maximum force F_{max} at failure determined in the experiments. Solving for $k_{v,2}$ leads to Formula (3).

$$k_{v,2} = \frac{F_{max}}{F_{max,est}} = \frac{F_{max}}{k_{v,1} \cdot f_{v,est,mean} \cdot t \cdot l} \qquad (3)$$

where F_{max} = applied force at failure, $k_{v,1} = 1.0$, $f_{v,est,mean}$ = estimated shear strength of the panel on mean level, t = nominal thickness of the sheathing, l = length of the wall.

The mean value of the shear strength of OSB/3 panels $f_{v,est,mean}$ was estimated starting from the characteristic shear strength specified in EN 1995-1-1, 2008 (i.e. $f_{v,k} = 6.8\ N/mm^2$). Based on the assumption of a

log-normal distribution, the mean value was calculated using the definition of the moments and the cumulative distribution function of the log-normal distribution (Formulae (4) - (6)).

$$\mu_X = e^{\lambda+\zeta^2/2} \tag{4}$$

$$\mathrm{CoV}_X = \sqrt{e^{\zeta^2} - 1} \tag{5}$$

$$F_X(x) = \Phi\left(\frac{\ln(x)-\lambda}{\zeta}\right) \tag{6}$$

where ζ and λ = distribution parameters, μ_X = mean value of the population, CoV_X = coefficient of variation of the population.

In the JCSS Probabilistic Model Code [13], there is no information about the CoV of the shear strength of OSB/3 panels. In the present study, it was decided to use a CoV of 15% as the upper bound for the investigations, a value equal to the one specified in the JCSS Probabilistic Model Code for the shear strength of glued laminated timber (GLT). The mean CoV determined from the tests carried out to assess the shear strength of the OSB/3 panels was 6%. This low value can be explained by the fact that all panels tested were part of one single production batch. Hence, in the investigations, the 6% CoV was chosen as the lower bound. Additionally, calculations were also performed using a CoV of 11%. The $k_{v,2}$ factors resulting from these calculations (i.e. from the comparison between estimates and experimental data) are listed in Table 4. In the presented study, the $k_{v,2}$ factors for timber-framed shear walls sheathed with OSB/3 panels on one side were found to range between 0.69 and 0.88, depending on the thickness of the panels and the CoV outlined above accounted for in the calculation. The results show that the $k_{v,2}$ factor of 0.33 given in DIN 1995-1-1, 2004-08 for sheathing placed on one side is very conservative. However, the specified value of 0.5 specified in the working draft of prEN 1995-1-1, 2022 matches the experimental results of this study better.

***Table 4**: $k_{v,2}$ factors determined by applying Formula (3) and using the estimated shear strength $f_{v,est,mean}$ evaluated by assuming different* CoV*'s for the distribution of the shear strength of the OSB/3 panels.*

CoV*	$f_{v,est,mean}$	$k_{v,2}$			
		12-S	15-S	18-S	25-N
6%	7.52 N/mm²	0.81	0.82	**0.88**	0.84
11%	8.19 N/mm²	0.74	0.75	0.81	0.77
15%	8.78 N/mm²	**0.69**	0.70	0.75	0.72

* CoV 6%: Lower bound value based on the mean value of the shear strength measured in the experiments on OSB/3 panels, CoV 15%: Upper bound value based on the CoV given for GLT in JCSS.

In addition to the influencing factors, which induce additional stresses as listed in DIN 1052, 2008-12 (see 2.2.3) and in prEN 1995-1-1, 2022 (see 2.2.4), there are additional influences, which may reduce the shear resistance of OSB/3 panels when applied as sheathing material in timber-framed shear walls. These factors include:

- Additional stresses resulting from eccentricities in the connection of the ceiling to the wall.
- Weakened sheathing due to the attachment of steel bracket angles as anchoring.

These influences were not considered in the experiments, and hence, also not considered in the calculated $k_{v,2}$ factors in Table 4.

When investigating the maximum number of fasteners that can be applied while still ensuring a ductile failure of the connection, an over-strength factor of 1.6 was assumed [14]. By comparing the resistance of the sheathing-to-framing connection and the shear resistance of the panel (first and second line in Formula (2)) and using the over-strength factor 1.6, the minimum distance $a_{v,min}$ between the fasteners can be calculated with different assumptions in terms of $k_{v,2}$ factor with Formula (7):

$$a_{v.min} = \frac{1.6 \cdot R_d}{k_{v,2} \cdot f_{v,d} \cdot t} \tag{7}$$

where $k_{v,2}$ = factor to account for additional stresses, $f_{v,d}$ = design shear strength of the panel, t = thickness of the sheathing, R_d = design load-carrying capacity of one single fastener.

The characteristic load-carrying capacity $F_{v,Rk}$ of a single nail and a single staple was calculated according to the standard EN 1995-1-1, 2008 (Clause 8.2.2, Equation 8.6). The design load-carrying capacity R_d according to EN 1995-1-1, 2008 is $R_d = k_{mod} \cdot F_{v,Rk}/\gamma_M$, where k_{mod} and γ_M are 1.1 and 1.2, respectively, according to EN 1995-1-1, 2008. For a single nail, the design load-carrying capacity R_d is equal to 0.66 kN and for a single staple the respective value is 0.52 kN.

Taking the data and $k_{v,2}$ factors listed in Table 4 and applying Formula (7), the minimum fastener distances were calculated for $k_{v,2}$ values between 0.55 and 0.75. The resulting minimum distances $a_{v,min}$ are listed in Table 5.

***Table 5**: Resulting minimal fastener distances $a_{v,min}$ for the four investigated sheathing thicknesses (12 mm, 15 mm, 18 mm and 25 mm) assuming different $k_{v,2}$ factors.*

$k_{v,2}$	$a_{v,min}$			
	12 mm	**15 mm**	18 mm	25 mm
0.60	18.6	**14.8**	12.4	11.2
0.65	17.1	13.7	11.4	10.4
0.70	15.9	12.7	10.6	9.6
0.75	14.8	11.9	9.9	9.0
0.80	13.9	11.1	9.3	8.4

For example, for a 15 mm thick sheathing and assuming a conservative value of 0.6 for the $k_{v,2}$ factor, based on the results listed in Table 4, the minimum $a_{v,min}$ distance between the staples was calculated to be 14.8 mm (→ 15 mm). When arranging two rows of staples, the minimum distance between the staples would be 29.6 mm (→ 30 mm). According to the Swiss standard SIA 265/1,

https://doi.org/10.52202/069179-0352

2018 [15] the minimum distances of the connection need to be increased by a factor of 1.5 to ensure a ductile behavior. The minimum distance between the staples in Switzerland would be 34.4 mm (→ 35 mm)

7 CONCLUSIONS AND OUTLOOK

The factor $k_{v,2}$ specified in DIN 1052, 2008-12 (0.33 for sheathings placed on one side), which accounts for additional stresses that are reducing the shear resistance of the sheathing in timber-framed shear walls seems to be quite conservative, compared to the results from the experiments conducted in the presented study. The values for $k_{v,2}$ resulting from the experiments range between 0.69 and 0.88 depending on the estimated mean value $f_{v,est,mean}$ of the shear strength of the panels. The value for $k_{v,2}$ (renamed to $k_{p,model}$ in prEN 1995-1-1, 2022) matches the experimental results of this study better.

The test results indicate that by specifying reasonable minimum distances a_v between the fasteners (i.e. for instance 30 mm for two rows of staples in a 15 mm thick OSB/3 sheathing and choosing a $k_{v,2}$ factor of 0.60), multiple rows of fasteners can be planned while ensuring a ductile failure of the fasteners and avoiding a brittle failure of the sheathing.

Further investigations (i.e. additional experiments accompanied by numerical analyses) are required to determine the accurate value of the $k_{v,2}$ factor used in the calculation of the shear resistance of OSB/3 sheathings in timber-framed shear walls. The study presented here only investigated wall elements with OSB/3 sheathing placed on one side of the wall. Additional experiments recently performed on OSB/3 sheathed timber-framed shear walls can be taken into consideration to determine the values of the $k_{v,2}$ factor more reliably. An increase of this factor compared to the values currently specified in prEN 1995-1-1, 2022 (i.e. 0.50 for sheathings on one side and 0.67 for sheathings on both sides) would lead to an increased load-carrying capacity of timber-framed shear walls.

This study represents the first step of a series of investigations in a research project where further experiments will be performed on one- and two-storey wall elements with large openings, with the ultimate goal of developing a design method for timber-framed shear walls with openings as part of the lateral force-resisting system in timber buildings. The use of timber-framed shear walls with openings in the lateral force-resisting system has the potential to provide more economical design solutions in timber construction.

ACKNOWLEDGEMENT

The presented study was supported by the *Swiss Federal Office for the Environment FOEN* within the framework of the initiative *Aktionsplan Holz 2021 – 2026*.

REFERENCES

[1] SIA 265: Holzbau, Swiss Society of Engineers and Architects SIA, Zurich, Switzerland, 2021.*
[2] DIN 1052: Design of timber structures. General rules and rules for buildings, Germany, 2008-12.
[3] EN 1995-1-1: Eurocode 5 – Design of timber structures - Part 1-1: General - Common rules and rules for buildings, CEN, Brussels, Belgium, 2008.
[4] https://www.schaerholzbau.ch/
[5] prEN 1995-1-1: CEN/TC 250/SC 5 N 1650, Eurocode 5 – Design of timber structures, CEN, Brussels, Belgium, 2022.
[6] EN 322: Wood-based panels - Determination of moisture content, CEN, Brussels, Belgium, 1993.
[7] EN 300: Oriented Strand Boards (OSB) - Definitions, classification and specifications, CEN, Brussels, Belgium, 2006.
[8] EN 14080: Timber structures - Glued laminated timber and glued laminated solid timber - Requirements, CEN, Brussels, Belgium, 2013.
[9] EN 789: Timber structures - Test methods - Determination of mechanical properties of wood based panels, CEN, Brussels, Belgium, 2005.
[10] ISO 21581: Timber structures - Static and cyclic lateral load test methods for shear walls, ISO, Geneva, Switzerland, 2010.
[11] Schick M., Probabilistic investigations on overstrengths of nailed timber-framed wall elements, Kassel, Germany, 2017. *
[12] EN 14358: Timber structures - Calculation and verification of characteristic values, CEN, Brussels, Belgium, 2016.
[13] JCSS 3.05: Probabilistic Model Code - Part 3.05: Resistance Models: Timber, 2006.
[14] Ratsch G., Geiser M., Erdbebenbemessung von Holztragwerken nach dem duktilen Tragwerksverhalten – Die schwierige Frage der Überfestigkeit, In: 16th *D-A-CH Tagung Erdbebeningenieurwesen & Baudynamik*, 2019. *
[15] SIA 265/1: Holzbau – Ergänzende Festlegungen, Swiss Society of Engineers and Architects SIA, Zurich, Switzerland, 2018.*

* Only available in German

World Conference on Timber Engineering Oslo 2023

EXPERIMENTAL AND NUMERICAL INVESTIGATION ON THE EFFECT OF CIRCULAR HOLES ON GLULAM COMPOSITE BEAMS

Dag Pasquale Pasca[1], Yuri De Santis[2], Angelo Aloisio[3], Andreas Stenstad[4], Karl-Christian Mahnert[5],

ABSTRACT: This paper presents an extensive experimental investigation on the effect of circular holes with and without reinforcement on glulam joists' behaviour. The tests consider the variability of hole position, number and strength class of the beam. Furthermore, a finite element model based on fracture mechanics was developed and validated against the experimental force-displacement curves of thirteen configurations. The model reproduces crack initiation and propagation through the adoption of cohesive contact layers. The satisfactory agreement with the experimental data has been the base of extensive parametric analyses considering multiple beam and hole geometry selections and two load arrangements at the upper and lower side of the beam. Finally, the results of the parametric analyses, initially used for a qualitative understanding of the structural behaviour, are used for calibrating probabilistic capacity models of the capacity of simply-supported beams with circular holes. The mechanics-based probabilistic model calculates the capacity as the product between the analytical capacity associated with the reduced cross-section and an adimensional correction factor. The factor is expressed as a linear combination of a set of explanatory variables selected after a step-wise deletion process.

KEYWORDS: Holes; Glulam; Reinforcement; NLFM; Experimental tests; FEM.

1 INTRODUCTION

The use of holes in timber beams is a widespread structural solution, especially in the case of interference with pipeline services. The occurrence of tensile stresses perpendicular to grain due to holes, shrinkage, external loads, or a combination of these factors in timber beams can significantly impair the bearing capacity, given the low tensile strength perpendicular to grain [1-3].
Most existing research on beams with holes focuses on experimental tests rather than numerical modelling [4-6]. Experimental tests [7], finite element analysis [8, 9], analytical modelling and design provisions [10] demonstrated the detrimental impact of the holes and notches on the load carrying capacity of the bare timber beams (without slabs) as well as timber composite I-joist with oriented strand board (OSB) webs [11].

The failure of timber beams with openings is typically associated with cracks initiated from the top quarter of the holes (towards mid-span) and/or from the bottom quarter of the holes (towards the support). Similar failure modes and delamination and shear failure of the flanges have been observed in the timber I-joists with web openings [11-13]. The results of laboratory testing and FE modelling have been used to develop empirical equations for estimating the load-carrying capacity of the timber I-joists with web openings [14, 15]. Moreover, for the practical design of OSB webbed timber I-joists with openings, critical (minimum) spacing between the web openings was determined based on the results of FE analyses [15]. To minimize the impact of openings and notches on the peak load of the timber beams, different methods such as externally bonded plywood/OSB and steel plates [12, 13], and fully threaded screws or glued-in rods have been proposed. Their performance has been experimentally and analytically examined by [16, 17].

Karimi and Valipour [18] tested eleven different types of Laminated Veneer Lumber- Cross Laminated Timber (LVL-CLT) and Glued Laminated Timber (GLT)-CLT beams and four types of bare LVL-GLT beams without and with circular and square openings in the LVL-GLT webs under three-point bending to produce benchmark experimental data required for assessing the effect of the web openings on the failure mode and load carrying capacity of the Timber-Timber-Composite (TTC) beams. In addition, digital image correlation (DIC) was used to capture the strain profile around the holes up to the initiation of cracks (onset of fracture) and shed light on failure mechanisms generated by the combination of bending, shear, and tension perpendicular to the grain.

[1] Dag Pasquale Pasca, Norsk Treteknisk Institutt (Norwegian Institute of Wood Technology), Norway, dpa@treteknisk.no
[2] Yuri De Santis, Department of Civil Engineering, University of L'Aquila, Italy
[3] Angelo Aloisio, Department of Civil Engineering, University of L'Aquila, Italy
[4] Andreas Stenstad, Norsk Treteknisk Institutt (Norwegian Institute of Wood Technology), Norway
[5] Karl-Christian Mahnert, Norsk Treteknisk Institutt (Norwegian Institute of Wood Technology), Norway

https://doi.org/10.52202/069179-0353

Several capacity models underestimate the peak loading capacity of timber beams or maybe only applicable to the beams with specific details or cross-section dimensions. For instance, Danielsson [3] showed that the empirical method adopted in the Swedish glulam handbook [10] tends to underestimate the experimental load-bearing capacities of the GLT beams with rectangular openings.
Karimi and Valipour [19] numerically investigate the structural behaviour of the LVL and GLT beams with openings and highlight the importance and need for applying robust localization limiters (regularisation technique).
Recently, Gilbert et al [20] carried out tests on timber Circular Hollow Section (CHS) beams showing failure modes not usually encountered in timber structures.

Fracture mechanics approaches are needed for accurate predictions of the post-elastic behaviour of beams with holes [21]. Therefore, complex mechanical formulations are required, like those based on linear elastic fracture mechanics (LEFM) [22-24] and Weibull theory-based damage model [25].
Nonetheless, the predictions with LEFM might lead to conservative results, as highlighted by Adalany et al. [26], who considered LVL beams with holes.

Guan and Zhu [27] developed a nonlinear finite element model capable of simulating crack propagation based on stress monitoring. The model eliminates the structural contribution by setting the stiffness to zero when the yield strength is reached. However, despite the mentioned improvement, the model does not allow sudden crack propagation, typical of the shear failure of beams with holes.

More recently, methods based on nonlinear fracture mechanics (NLFM) proved to be more effective and capable of simulating the post-failure behaviour with crack propagation [21, 28].
Ardalany et al. [21] developed an NLFM-based tridimensional FE model to investigate the effect of shape, size and position of the openings of a glulam beam and to derive an optimal reinforcement strategy. Continuum damage models (CDM) were developed by Sandhaas [29] and modified by Gharib et al. [30] who enriched it with an anisotropic non-local integral-type model. The non-local CDM is implemented in FE software and then is employed to predict the nonlinear behaviour and capture failure of timber under complex multiaxial stress states generated by the presence of holes/openings.

This paper presents an experimental and numerical study on composite glulam joists with one or two circular holes in different positions. The experimental campaign aims at identifying the influence of hole position, hole number and distance on the reduction of the joist capacity. Furthermore, a finite element model, which accounts for crack initiation and propagation, is developed and validated against the experimental results. Differently from what has been done by [21], cohesive contacts have been used to reproduce the crack formation. The efficient tridimensional FE model has been parameterized and used to extend the results of the experimental campaign.

In synthesis, the main aspects of novelty and originality of this research are:

- Extensive experimental campaign on glulam joist with different hole geometry, position and reinforcement.
- Validation of a nonlinear finite element model based on fracture mechanics.
- Parametrization of the model and extensive analyses to assess the dependence of the capacity of beams with circular holes by varying the following parameters: hole diameter and position, beam geometry, the position of the load (upper side and lower side).

The main limitations of this research are twofold. The first relates to the experimental tests, where only one value for the hole-depth ratio was considered. Therefore, the FE model has only been validated for a specific hole/depth ratio. The second aspect relates to the computational burden of the analyses. The authors only varied the geometric parameters of the beam, assuming deterministic mechanical parameters, which were validated against the experimental tests. Future research efforts will assess the effect of the fracture mechanics properties by considering suitable probability distributions, thus providing a probabilistic estimate of the capacity for given geometric configurations.

2 EXPERIMENTAL TESTS

2.1 MATERIALS AND CONFIGURATIONS

The experimental campaign involved glue-laminated timber joist of length l=5700 mm, with a cross-section width b of 36 mm or 48 mm and with a cross-section height h of 300 mm (Figure 1).
In addition to the reference configurations without holes, joists with one or two holes of diameter d=170 mm in different positions along the joist axis were tested. The tests include configurations with a hole at mid-span and configurations with one or two holes near the supports or under the loading point. The position of the holes of each configuration is shown in Table 1.

Two different series have been considered to assess the glulam class influence on the mechanical properties reduction due to holes. The joists of both series are combined glulam with 19 mm thick ungraded internal lamellae and 47 mm thick external lamellae. The external lamellae of the first and second series are made of C30 and C40 lamellae, respectively. The mean density of the specimens is 460 kg/m^3
The tests covered both unreinforced beams and beam reinforced by glulam or plywood plates glued to the outer faces of the beams. Figure 2 shows the geometry and dimensions of the specimens with exterior reinforcements of the holes.

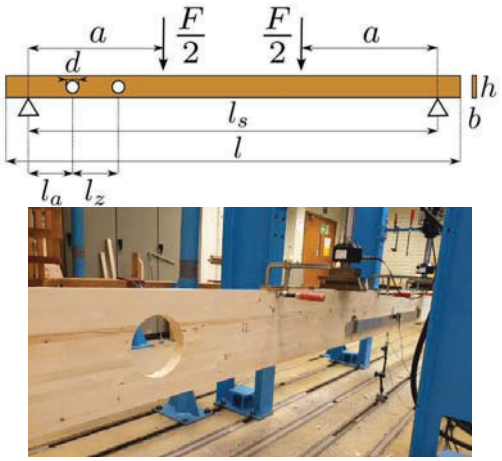

Figure 1 - *(up) Geometric configuration of the beam; (down) Experimental setup*

The plywood plate reinforcement has a length b_r of 1200 mm, a height h_r of 290 mm and a thickness t_r of 12 mm. The employed plywood has 5 layers and belongs to strength class F20/15 and MOE class E 45/25 according to EN 13986 and EN 636. The glulam reinforcement is made of the same material as the reinforced joist with the timber grain parallel to the joist axis. In both cases, the reinforcement has been glued to the joist with a phenol-resorcinol adhesive together with self-tapping screws d=5 mm and l=50 mm. Also, a specimen with non-structural glue was tested. Different quantities of glue and number of screws were tested (Table 1).

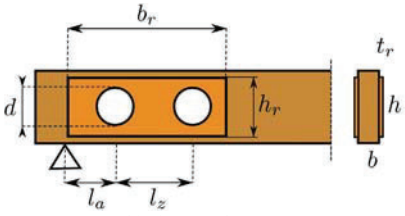

Figure 2 - *Geometry of holes reinforcement*

Table 1*: Mechanical and geometrical properties of the configurations.*

Configuration name	holes (n°)	l_a (m)	l_z (m)	Reinforcement	External lamellae	Specimen (n°)
REF-C30	0	-	-	-	C30	15
UNR-C30-2.7	1	2.7	-	-	C30	10
UNR-C30-0.6-0.6	2	0.6	0.6	-	C30	10
REIN-C30-0.6-0.6-PLY1	2	0.6	0.6	Plywood, PRF 500g/m^2, 8 screws	C30	3
REIN-C30-0.6-0.6-PLY2	2	0.6	0.6	Plywood, PRF 300g/m^2, 8 screws	C30	1
REIN-C30-0.6-0.6-PLY3	2	0.6	0.6	Plywood, Non-struct. glue, 8 screws	C30	1
REIN-C30-0.6-0.6-GL	2	0.6	0.6	Glulam, PRF 300g/m^2, 6 screws	C30	3
DIC-UNR-C30-0.6-0.6	2	0.6	0.6	-	C30	2
DIC-REIN-C30-0.6-0.6	2	0.6	0.6		C30	2
REF-C40	0	-	-	-	C40	20
UNR-C40-2.7	1	2.7	-	-	C40	10
UNR-C40-0.6	1	0.6	-	-	C40	10
UNR-C40-1.7	1	1.7	-	-	C40	10
UNR-C40-0.6-0.6	2	0.6	0.6	-	C40	10
UNR-C40-2.4-0.6	2	2.4	0.6	-	C40	10

2.2 TEST METHODS

The glulam joists were tested according to the four-point bending test procedure outlined in the EN-408 standard [31]. The distance between the base supports was set to l_s=18h=5400 mm, and the distance between a loading points position and the nearest support has been set to a=6h=1800 mm (Figure 1).

The bending strength f_m has been determined with the following equation:

$$f_m = \frac{F_{max} a}{2W} \quad (1)$$

Where F_{max} is the overall maximum load applied by the two jacks, a is the loading points distance from the nearest support and $W=bh^2/6$ is the section modulus.

The global modulus of elasticity in bending $E_{m,g}$ has been calculated from the load-deflection linear regression between F_1 and F_2 and the corresponding deflections w_1 and w_2. The global displacement was measured using LVDT placed under the beams at mid-span, as outlined by the standard. According to EN 408 $F_1=0.1F_{max}$ and $F_2=0.4F_{max}$ or at least $F_2=0.3F_{max}$ with $R2>0.99$, and $w_1=w(F_1)$ and $w_2=w(F_2)$.

The following equation gives the global modulus of elasticity in bending:

https://doi.org/10.52202/069179-0353

$$E_{m,g} = \frac{l^3(F_2 - F_1)}{bh^2(w_2 - w_1)}\left[\left(\frac{3a}{4l}\right) - \left(\frac{a}{l}\right)^3\right] \quad (2)$$

where l is the beam span and $a=6h=l/3$ is the distance from support to the nearest load application point.
The shear strength of the glue line parallel to the direction of the grain of glulam-glulam and glulam-plywood specimens has been tested according to EN-392. The shear test was carried out on specimens with rectangular parallelepiped shapes with two sides of length b=50 mm and the third of t=36 mm or t=48 mm. The offset between each half of the specimen was b_o=5 mm (Figure 3).

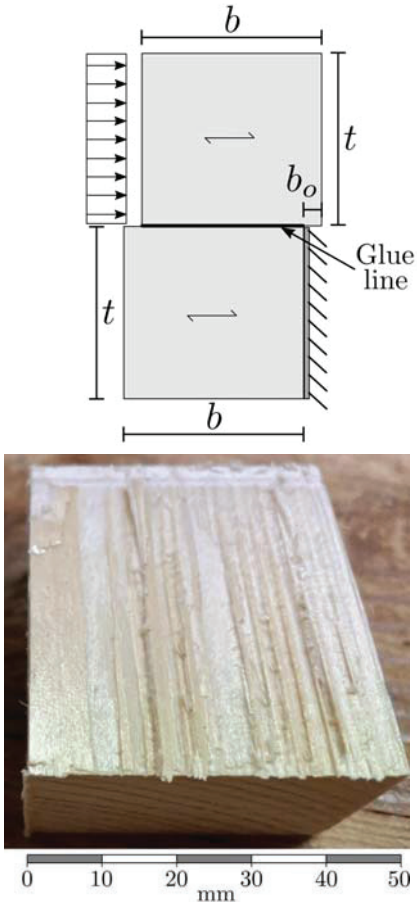

Figure 3 - *Shear tests: (up) dimension and setup; (down) failure surface*

2.3 TEST RESULTS

The overall applied force-midspan deflection results are reported in Figure 4 and Figure 5. The maximum load, the ultimate displacement, the global modulus of elasticity in bending and the bending strength are reported in Table 2. In the reference configurations without holes and configurations with holes in the constant moment area, the joists fail in bending. In contrast, in the joists with one or two holes in the constant shear area, the failure happens due to the longitudinal cracks around the holes (Figure 6).

No appreciable maximum load reduction was observed in configurations with a single hole at midspan (l_a=*2.7 m*). An appreciable decay of the strength of the joist was observed for single hole configurations with l_a=*0.6 m* or l_a=*1.7 m*. The double hole configurations with $l_a=l_z$=*0.6 m* led to the greater reduction in strength of -27% and -33% for C30 and C40 test series, respectively.
The reinforcement of the joists with $l_a=l_z$=*0.6 m* led to a total recovery of the resistance. No significant differences were found in the percentage of strength recovery for varying reinforcement configurations.

Regarding the shear tests, the shear strength and the percentage of timber and glue failures are reported in Table 3. It is worth noting that since the percentage of the timber failure is predominant, the τ_{max} is intended as the shear strength of timber in the direction parallel to the grain.

2.4 PREDICTED LOAD VIA STANDARD FORMULATION

The experimental results have been compared with the predicted load of the formulation prescribed in the DIN-1052. According to the formulation given by this standard, the failure load can be predicted by superposing the effects in terms of traction perpendicular to the grain of the shear and moment component as in the following equation:

$$F_{t,90} = F_{t,V} + F_{t,M} \quad (3)$$

where the shear component $F_{t,V}$ is calculated by integrating the shear tension according to the Euler-Bernoulli theory over the section area delimited by the crack. This area is conventionally defined by the intersection of a 45° line from the hole centre with the hole circumference itself:

$$F_{t,V} = \frac{Vh_d}{4h}\left[3 - \left(\frac{h_d}{h}\right)^2\right] \quad (4)$$

where V is the shear force in the beam, h_d is equal to $d{\cdot}cos(\pi/4)$ for circular openings, d is the diameter of the hole, h the height of the section of the beam.
The moment component $F_{t,M}$ is calculated by an empirical equation by Kolb and Epple [32]:

$$F_{t,M} = 0.008\frac{M}{h_r} \quad (5)$$

where M is the bending moment in the beam and h_r depends on the remaining height above (h_{ro}) or underneath (h_{ru}) the hole crack and can be assumed equal to $h_r=min(h_{ro}+0.15h_d;\ h_{ru}+0.15h_d)$.

Table 2: *Mean experimental results and coefficients of variation of four-point bending tests. B = failure due to bending, H = failure due to longitudinal cracking around the hole.*

Configuration name	F_{max} (kN)	CoV (%)	F_{max} /$F_{max,REF}$	Failure mode	u_u (mm)	CoV (%)	$E_{m,g}$ (N/mm^2)	CoV (%)	f_m (N/mm^2)	CoV (%)
REF-C30	20.3	12.0	-	B	59.5	14.3	11.0	3.3	33.9	12.0
UNR-C30-2.7	21.4	8.3	1.05	B	61.9	8.3	11.2	5.6	35.6	8.3
UNR-C30-0.6-0.6	14.9	5.8	0.73	H	48.8	10.6	10.5	3.5	24.8	5.8
REIN-C30-0.6-0.6-PLY1	21.9	8.6	1.08	B	64.9	17.3	11.9	7.6	36.5	8.6
REIN-C30-0.6-0.6-PLY2	23.0	0.0	1.13	B	70.4	0.0	11.3	0.0	38.4	0.0
REIN-C30-0.6-0.6-PLY3	22.6	0.0	1.11	B	63.6	0.0	12.2	0.0	37.6	0.0
REIN-C30-0.6-0.6-GL	22.7	5.7	1.12	B	66.3	11.5	12.0	5.5	37.8	5.7
DIC-UNR-C30-0.6-0.6	11.2	8.4	-	H	42.5	15.8	10.2	3.1	18.7	8.4
DIC-REIN-C30-0.6-0.6	12.7	2.4	-	H	47.1	1.1	10.7	0.7	21.2	2.4
REF-C40	31.9	12.2	-	B	58.9	16.3	13.4	3.3	39.9	12.2
UNR-C40-2.7	29.0	10.6	0.91	B	63.6	11.3	11.5	4.7	36.2	10.6
UNR-C40-0.6	26.0	14.4	0.81	H	51.9	17.1	12.3	3.5	32.5	14.4
UNR-C40-1.7	26.0	11.3	0.81	H	55.0	14.4	11.7	3.0	32.5	11.3
UNR-C40-0.6-0.6	21.5	11.5	0.67	H	43.9	13.2	11.7	3.1	26.8	11.5
UNR-C40-2.4-0.6	26.9	10.2	0.84	H	59.9	12.7	11.2	7.3	33.7	10.2

Table 3*: Mean experimental results and coefficients of variation of glue shear tests.*

Configuration name	Specimens (n)	Timber failure (%)	Glue Failure (%)	tau max (MPa)	CoV (%)
PRF Plywood	14	97	3	5.8	23.6
PRF Glulam	10	74	26	7.8	12.3

The load of Eq.3 is then compared to the tensile strength of the area subjected to stresses perpendicular to the grain. It is worth noting that according to this model when the crack is located nearest to the mid-height of the section of the beam, the shear contribution defined in Eq.4 increases while the bending contribution defined in Eq.5 decreases. The results in terms of predicted load and percentage deviations from the experimental load are shown in Table 4. The formulation provides accurate predictions in almost all cases that experimentally exhibit failure due to crack propagation around the holes.

3 FINITE ELEMENT MODELLING

A three-dimensional finite-element model capable of reproducing the joist failure mode due to tensile crack formation was implemented in ABAQUS. The model assembly, analysis and post-processing were performed through a Python script to automatise the process and allow for extended validation and parametric analyses.

3.1 MODEL DESCRIPTION

Due to the symmetry of the joist and holes (see Table 1) in the vertical-longitudinal *yz* plane, it was possible to reproduce only half of the actual geometry. On the symmetry plane, the displacement in the out-of-plane direction was restrained $u_x=0$. The hinge support restraint has been reproduced by imposing $u_y=u_z=0$ on the contact line nodes, whilst the roller restraint has been reproduced by imposing $u_z=0$ on the contact line nodes (Figure 7).
An imposed linearly increasing displacement was applied to the nodes of the contact areas between the beam and the distribution plate under the hydraulic jacks ($u_{imp}=100$ *mm*).
The joist has been discretized through C3D8R general-purpose linear brick element, with reduced integration (ABAQUS/Standard library). The mesh dimensions are approximate $m_s \approx b/4$.

https://doi.org/10.52202/069179-0353

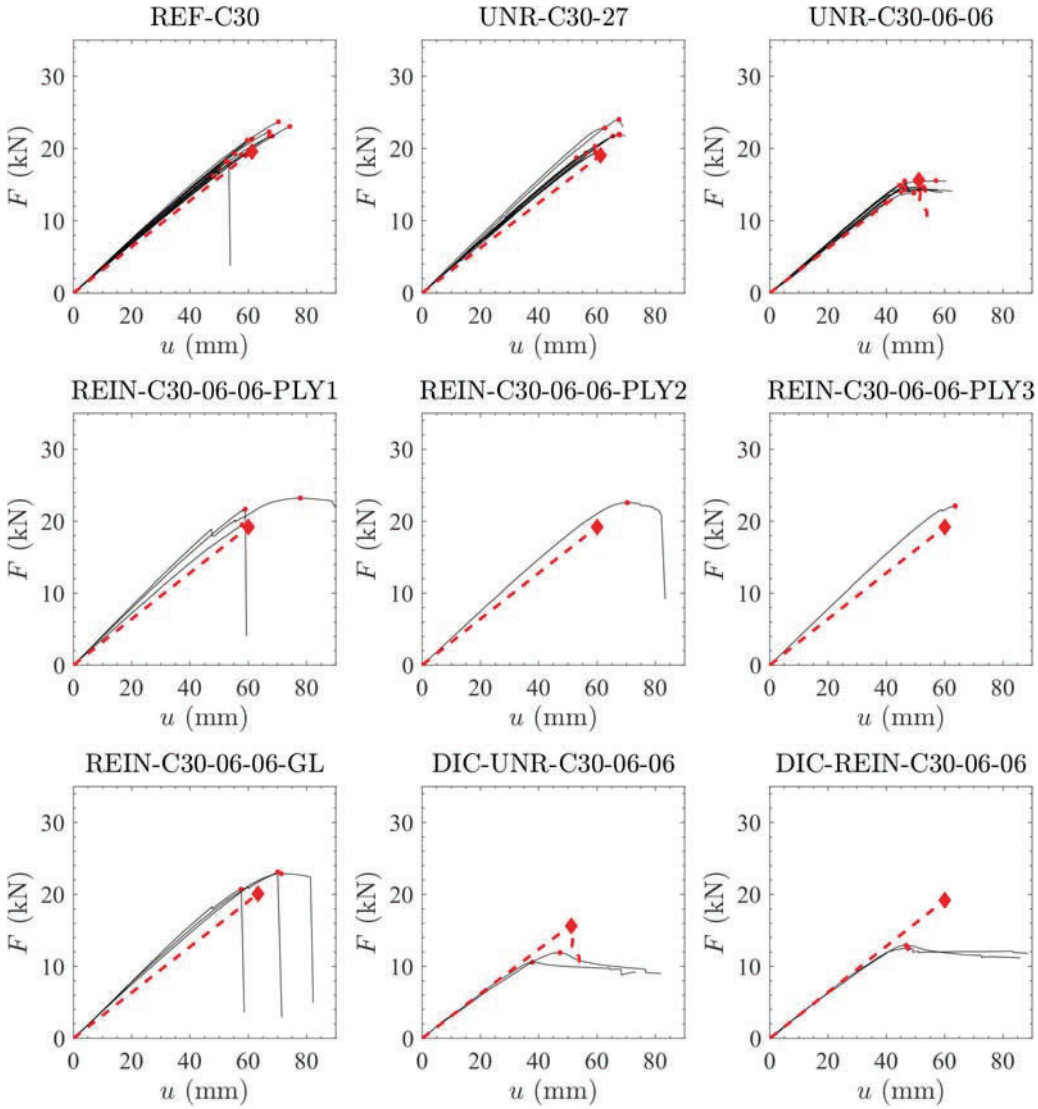

Figure 4: *Force-displacement curves for C30 test series (black line: experimental, red line: finite element model).*

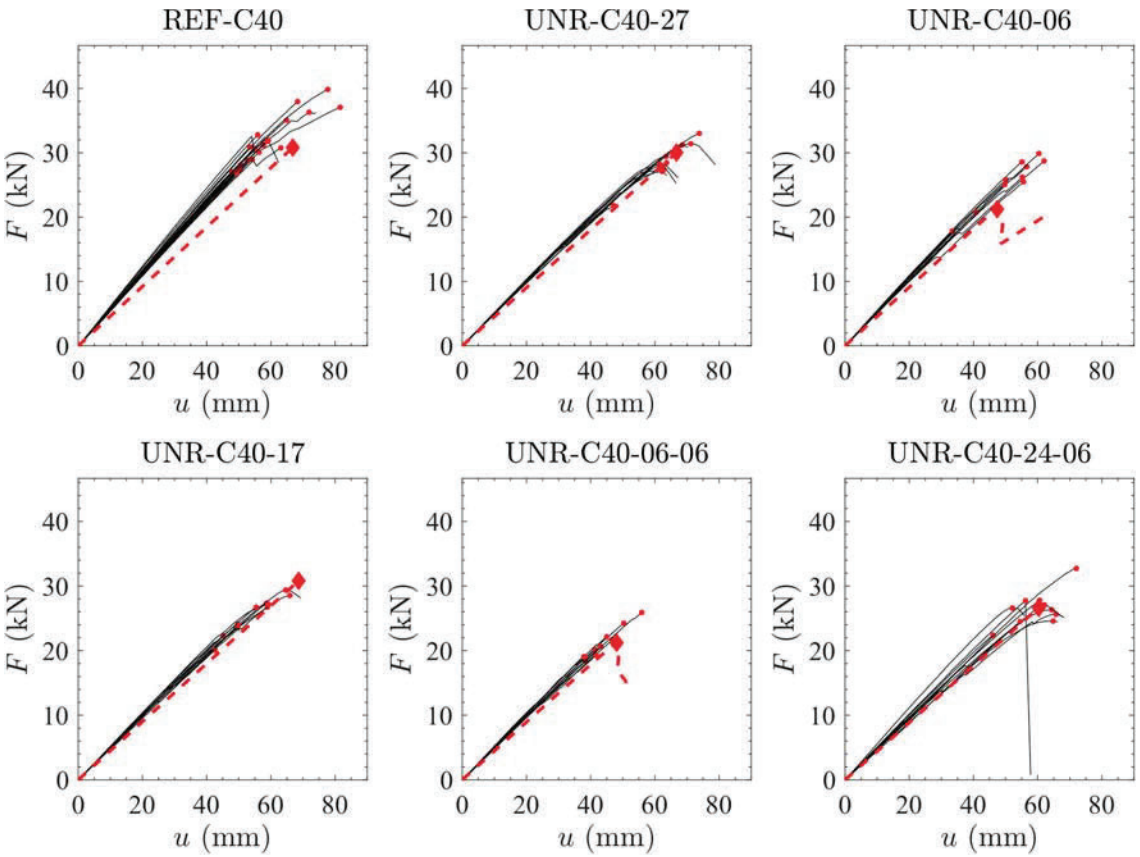

Figure 5: *Force-displacement curves for C40 test series (black line: experimental, red line: finite element model).*

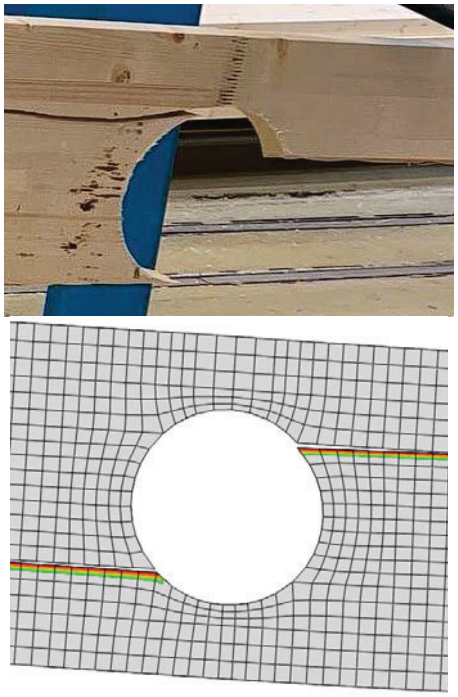

Figure 6: *Hole failure mode: (up) Experimental (down) Finite element model.*

A linear elastic constitutive law has been assigned to outer and inner lamellae domain portions. The material has been modelled as orthotropic and the elasticity moduli and the shear moduli were related to the elastic module in the direction parallel to the grain according to EN-338 [33]. The elastic moduli in the direction perpendicular to the grain have been assumed as $E_x=E_y=E_z/30$, and the shear modules have been assumed as $G_{zy}=G_{zx}=E_z/16$ and the rolling shear moduli has been assumed as $G_{xy}=G_{zy}/10$. Similarly, the plywood reinforcement mechanical properties have been chosen according to EN 13986 and EN 636 and are reported in Table 5.

Cohesive contacts are assigned to surfaces explicitly introduced into the model to reproduce the crack formation and propagation around the hole. No stress interaction was considered for the cohesive layer; the damage is initiated where and when the stresses in the main local direction reach their relative strength values. Conventionally, the crack around the hole is assumed to be at an angle of 45° to the longitudinal axis of the beam. In the finite element models herein developed, the position of the cohesive contacts has been assumed coincident with the point of attainment of the maximum tensile stress perpendicular to the grain on the hole circumference. This position has been determined using preliminary elastic analyses conducted on a single-hole beam} for varying hole positions and both the case of

https://doi.org/10.52202/069179-0353

four-point bending and uniformly distributed load (Figure 8).

***Table 4**: Finite element model results and experimental scatters (*the experimental failure load is due to bending while the DIN predicted failure load is due to hole failure).*

Configuration name	F_{max} (kN)	$S_{FEM-EXP}$ (%)	$E_{m,g,FEM}$ (N/mm^2)	$S_{FEM-EXP}$ (%)	$F_{max,DIN}$ (kN)	$S_{DIN-EXP}$ (%)
REF-C30	19.6	-3.7	11.0	0.2	-	-
UNR-C30-2.7	19.1	-10.9	10.8	-3.8	31.8	48.8
UNR-C30-0.6-0.6	15.6	5.0	10.7	2.0	13.9	-6.6
REIN-C30-0.6-0.6-PLY1	19.2	-12.3	11.1	-7.3		
REIN-C30-0.6-0.6-PLY2	19.2	-16.6	11.1	-2.3		
REIN-C30-0.6-0.6-PLY3	19.2	-14.9	11.1	-8.9		
REIN-C30-0.6-0.6-GL	20.1	-11.4	11.0	-8.2		
DIC-UNR-C30-0.6-0.6	15.6	39.1	10.7	4.5	13.9	23.7
DIC-REIN-C30-0.6-0.6	19.2	51.0	11.1	3.0		
REF-C40	30.8	-3.5	11.9	-10.7	-	-
UNR-C40-2.7	30.0	3.5	11.7	1.5	42.4	46.2
UNR-C40-0.6	21.2	-18.4	11.8	-4.3	21.7	-16.6
UNR-C40-1.7	30.8	18.3	11.7	-0.3	16.5	-36.6
UNR-C40-0.6-0.6	21.2	-1.2	11.6	-1.1	18.5	-13.8
UNR-C40-2.4-0.6	26.6	-1.2	11.5	2.6	42.4	57.3

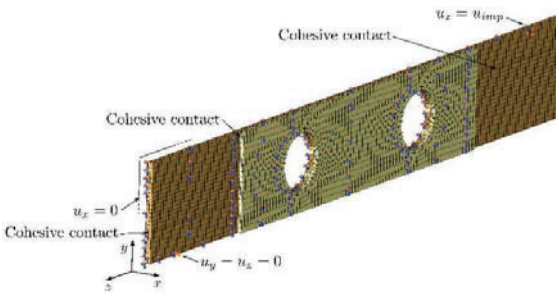

***Figure 7**: Finite element model*

In the case of uniformly distributed load, the maximum stress around the hole is reached between 30° and 40° to the longitudinal axis of the beam with a descending trend if the hole moves towards the mid-span (increasing l_a). Beams with a hole close to the mid-span exhibited lower stresses than those with hole close to the end support. In the four-point bending configuration, tension perpendicular to the grain increases in the part of the beam subjected to linearly increasing bending moment, while a stress drop and a sudden change of the maximum stress location is observed immediately after the loading point location which is at $l_a=6h=1800$ *mm*. Due to the local effect of the loading point, when the hole is under the external load, the maximum stress is reached near the bottom part of the hole.

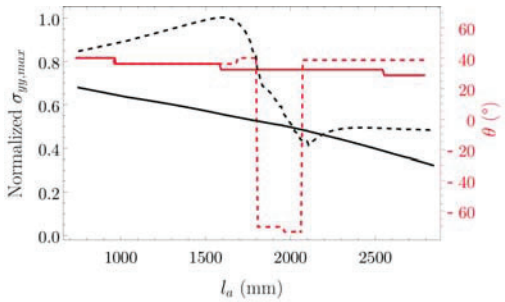

***Figure 8:** Normalized maximum stress and attainment position on the hole circumference for varying hole-support distance l_a (**Figure 1**) (Continuous lines: uniformly distributed load; Dashed lines: four-point bending).*

The interaction between the beam lateral surface and the reinforcement has also been modelled with cohesive contacts to make the model able to predict the failure on the reinforcement-joists contact surface. The screws used to restrain the reinforcement to the beam during the glue curing are neglected in the model. This assumption is made since the stiffness of screws perpendicular to the sliding plane is much lower than the stiffness of the glued connection and therefore, when the reinforced system fails, the contribution of the screws in terms of forces is negligible [34, 35].

The cohesive contacts are specialized constitutive laws used to simulate crack initiation and propagation [21]. Despite timber exhibiting exponential softening behaviour in experimental fracture tests, a bilinear curve is commonly used for this traction-separation curve [36].

The cohesive contacts behaviour is governed by a damage initiation criterion and a traction-separation curve, which relates element traction (stress) to *mode I* (opening) and *mode II* (shearing) displacement.
The bilinear traction-separation relationship consists of an initial elastic region showing the interfacial strength; and a subsequent softening region where zero stress is reached (see Figure 9). *D* is the damage parameter, which changes from *D=0* in the undamaged state to *D=1* in the fully damaged state:

$$D = \frac{\delta_e(\delta - \delta_c)}{\delta(\delta_e - \delta_c)} \quad (6)$$

δ_c indicates the separation corresponding to damage initiation, and δ_e is the final separation corresponding to the full fracture of the element. The total area under the curve is the fracture energy of the material. The stress-strain relationship is assumed for material outside the fracture process zone, and the stress versus separation curve is used for the material in the fracture process zone. However, the traction-separation laws become active only after a damage initiation criterion is met, e.g., when the stress exceeds the material's strength. When it comes to damage evolution, Wu's mixed mode fracture criterion was used [37, 38]:

$$\left(\frac{G_I}{G_{IC}}\right)^m + \left(\frac{G_{II}}{G_{IIC}}\right)^n = 1 \quad (6)$$

G_I and G_{II} indicate the fracture energies for mode I and II, respectively, and G_{IC}, G_{IIC} instead their critical energy release rate values, m and n denote the power of the equation.
The damage initiation parameters σ_n and τ_l have been chosen equal to the inner lamellae tensile strength in the direction perpendicular to the grain and inner lamellae shear strength in the direction parallel to the grain, as explained in the following paragraphs. The shear strength is assumed from experimental tests. In contrast, the tensile strength perpendicular to the grain derives from the model calibration using the experimental test results of the beams in terms of ultimate load. The propagation parameters of the cohesive contact have been chosen according to the results of [21] and are reported in Table 6.
According to [39], the critical fracture energy G_{IC} for mode I varies between 150-600J/m^2 for softwood species. In contrast, the critical fracture energy for mode II can be assumed as $G_{IIC}=3G_{IC}$.

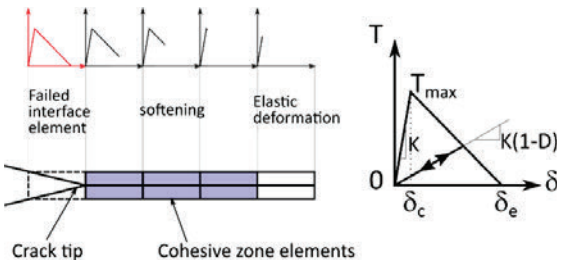

***Figure 9**: Cohesive elements and traction separation curve.*

3.2 MODEL CALIBRATION AND VALIDATION

Firstly, the elastic properties (i.e. the MoE perpendicular to grain, and the shear modulus) of the external and internal lamellae were calibrated according to the reference test series without holes. A sensitivity analysis was conducted on the numerical model to investigate which combination of parameters would minimise the difference with the experimental results. The investigated parameters were the elastic moduli perpendicular to grain and the shear modulus of both the external and internal lamellae. The bounds of the sampling domain were set to $E_{z,ol}$=*13 GPa ±25%*, $G_{zy,ol}=G_{zx,ol}$=*0.75 GPa ±25%*, $E_{z,il}$=*9 GPa ±25%*, $G_{zy,il}=G_{zx,il}$=*0.56 GPa ±25%*. The domain was sampled adopting Saltelli's sampling scheme [40, 41]. The error between the experimental and numerical results was assessed by the squared difference of the ratio of the applied force to the displacement at mid-span (SS).
A graphical representation of the results is shown in Figure 10. Here each point is a triplet of values $E_{z,il}$, $E_{z,ol}$ and the squared differences in terms of stiffness between the experimental and finite element model results) with the two MoE shown on the two horizontal axis. The figure clearly shows that a combination of values that minimises the error exists. By imposing a low threshold value for the error and fitting with linear regression, a relation between $E_{z,il}$ and $E_{z,ol}$ were found. The analysis confirmed also that the shear moduli $G_{zy,il}$ did not have any effect on the results.

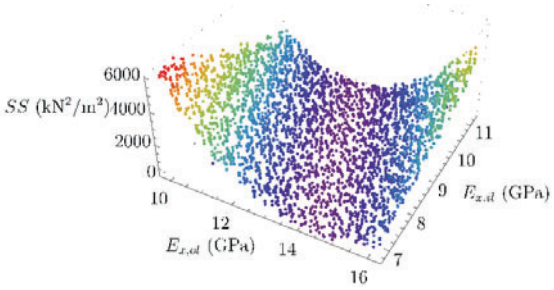

***Figure 10**: Squared differences in terms of stiffness between the experimental and finite element model results for various combinations of $E_{z,ol}$, $E_{z,il}$ and $G_{zy,il}$.*

Experimental tests carried out on the outer lamellae provided a mean value for $E_{z,ol}$ equal to 14.5 and 12.5 for the C40 and C30 timber. Therefore, assuming the above values for the MoE of the outer lamellae, the estimated value of the MoE of the inner lamellae is $E_{z,il}$ ≈10.5 GPa. The resume of all mechanical parameters is shown in Table 5.

In the second stage, the parameters governing the cohesive contact of the beam and the reinforcement were studied. Since the results of the shear test of glued specimens had demonstrated that the failure happens mainly on the timber side, the shear damage initiation parameter τ_l was assumed equal to the experimentally determined value, which corresponds to the actual shear strength of glulam (Table 3 and Table 6).

https://doi.org/10.52202/069179-0353

***Table 5**: Mechanical properties.*

Material name	E_z (Gpa)	$E_x = E_y$ (Gpa)	$G_{zy} = G_{zx}$ (Gpa)	G_{xy} (Gpa)	ν
C40	14.5	0.48	0.91	0.091	0.4
C30	12.5	0.42	0.78	0.078	0.4
Inner lamellae	10.5	0.35	0.66	0.066	0.4
Plywood	8	6	0.35	0.05	0

The tensile strength perpendicular to the grain σ_n and the fracture energy G_{IC} was estimated by minimizing the error between the numerical and experimental result of the unreinforced beams in terms of ultimate load.
The parameter G_{IIC} was derived from the previously mentioned relation according to [39].

A comparison between the results of the calibrated models and the test results is shown in Figure 4 and Figure 5 and Table 4.

***Table 6:** Mechanical properties of the choesive contacts.*

	σ_n (MPa)	τ_I (MPa)	G_{IC} (J/m^2)	G_{IIC} (J/m^2)	m	n
Inner lamellae	1.2	7.9	400	1200	0.5	0.5
Reinforcement Joist	5.4	5.8	400	1200	0.5	0.5

Overall a good agreement between experiments and numerical simulations is achieved. The elastic analyses confirmed that the crack starts at about 28-40° with respect to the longitudinal axis of the beam (Figure 8), which is a well-known result in literature [1, 39] and also confirmed by the experimental outcomes Figure 6.
In some cases (e.g. hole at mid-span, reinforced holes) the cohesive layer failed when the stress perpendicular to the grain on the outermost fibre had already passed values that would have led to a bending failure of the beam. For this reason, an additional failure criterion based on the tensile stresses reached in the outermost elements was introduced. The ultimate tensile stress was assumed to be equal to the one found by the tests on the reference beam, and namely f_m=33.9 MPa and f_m=39.9 for C30 and C40 test series respectively.

3.3 PARAMETRIC ANALYSES

In this section, the results of some parametric studies performed to identify the parameters that have the greatest impact on the ultimate load of the joists are reported.
It is assumed in the finite element models of all studied cases that the external lamellae are strong enough to avoid the bending failure of the joist. In this way, the finite element model can only account for the combined shear-tension perpendicular to the grain failure, so the hole is always the weak point from which the cracks that lead to the failure of the joist propagate.\\
The following plots show the failure load associated with the hole crack propagation determined through the parametric finite element model (contour of Figure 11, Figure 12 and). On the same plots, the analytically determined flexural limit loads of the joist mid-span section (grey surface) and of the hole section (magenta surface) are reported. The flexural limit loads have been determined as the loads which cause the tensile failure of the outermost lamella accounting for the heterogeneous section and the hole in the section modulus calculation (W_{ef} and $W_{ef,hole}$ respectively). The associated maximum forces have been determined from Navier's equation. For the mid-span failure load:

$$f_m = \frac{M_{max}\left(\frac{l}{2}\right)}{W_{ef}\left(\frac{E_{ol}}{E_{il}}, h_{ol}, h_{il}\right)} \tag{8}$$

and for the hole-section failure load:

$$f_m = \frac{M_{max}(l_a + l_s)}{W_{ef,hole}\left(d, \frac{E_{ol}}{E_{il}}, h_{ol}, h_{il}\right)} \tag{9}$$

By substituting in Eqs. 8 and 9 the expression of bending moment M_{max} as function of F_{max} for uniformly distributed load or four-bending configuration and solving for F_{max} the corresponding expressions for the analytically determined bending capacity F_a were found:

$$F_{max} = \begin{cases} \frac{2f_m W_{ef}}{l} \; mid\ span, unif.dist. \\ \frac{2f_m W_{ef,hole} l}{(l_a+l_z)(l-l_z-l_z)} \; hole, unif.dist \\ \frac{2f_m W_{ef}}{a} \; mid\ span, 4\ p.b. \\ \frac{2f_m W_{ef,hole}}{l_a+l_z} \; hole\ and\ l_a + l_z \le a, 4\ p.b. \\ \frac{2f_m W_{ef,hole}}{a} \; hole\ and\ l_a + l_z > a, 4\ p.b. \end{cases}$$

The first parametric study identifies the influence of hole diameter and hole position for a four-point bending configuration. As can be seen from Figure 11 (up) which shows the results for joists similar to that of configuration UNR-C30-0.6-0.6, moving the two holes closer to the load application point causes a slight increase in strength of the hole-failure mechanism. As shown in Figure 8, when the hole is about at 1_d from the load application point l_a=*1.5 m*, the external load-induced compression perpendicular to the grain causes a significant reduction of the tensile stresses (Figure 8).

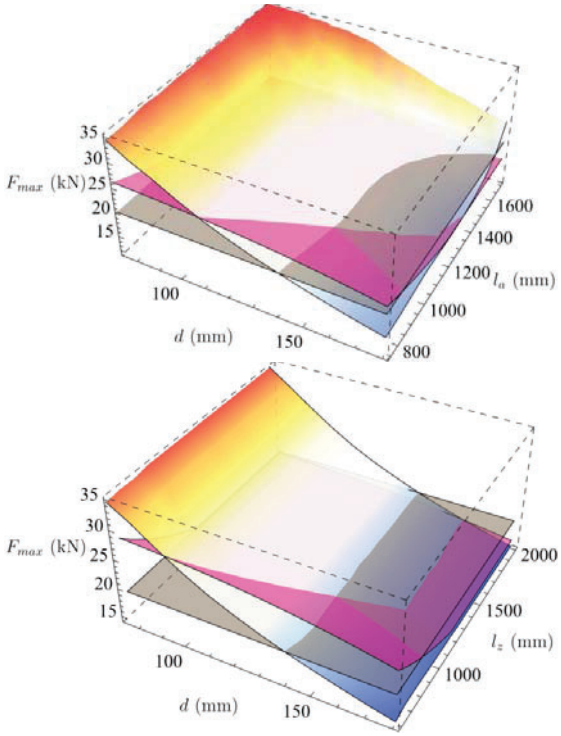

***Figure 11**: Failure load for varying hole diameter and hole position in four-point bending configuration: (up) varying the position of both holes simultaneously (l_a), (down) varying second hole position (l_z) (Contour: FEM hole crack failure load, gray: failure load of mid-span section without hole, magenta: failure load of hole-section).*

Keeping fixed the position of the hole nearest to the support l_a=*0.6 m*) and moving the position of the second hole does not affect the capacity associated with the hole failure because the limit load is related to the failure of the first hole (Figure 11 (down)). In both cases, the hole diameter has a strong influence on the strength reduction.

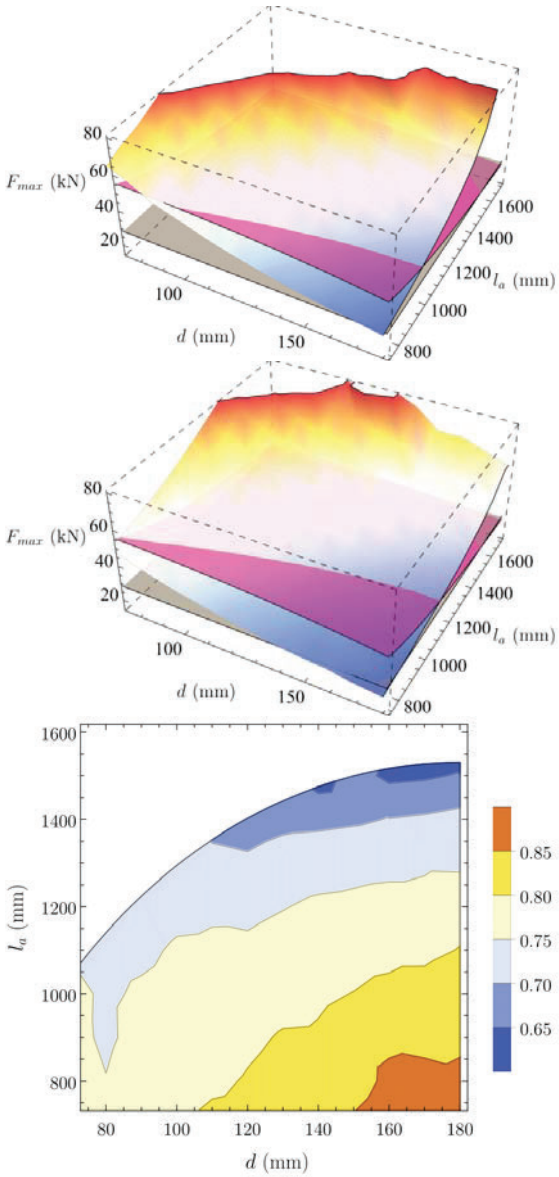

***Figure 12**: Failure load for varying hole diameter and hole position in the uniformly distributed configuration: (up) load at the upper side, (mid) load at the lower side, (down) ratio between the failure load of the lower side and upper side. (Contour: FEM hole crack failure load, grey: failure load of mid-span section without hole, magenta: failure of hole-section*

The second set of parametric studies deals with the case of uniformly distributed load. In both the cases of load applied at the lower side of the beam and load applied at the upper side of the beam, the hole position has proven to be a more significant parameter than in four-point bending configuration in determining the ultimate load for hole area-cracking failure mode (Figure 12). This behaviour is justified by the different arrangements of the internal forces. In the four-point bending configuration, the hole position was varied along the part of the beam in constant shear and linearly increasing bending moment, whilst in uniformly distributed load configuration the beam is subjected to linearly decreasing shear towards the mid-span and parabolic bending moment. As a

https://doi.org/10.52202/069179-0353

consequence when increasing l_a in a four-point bending configuration the tensile stresses perpendicular to the grain due to the combined shear and bending effect increases and reduce only when the local effect of the external load is significant, whilst in uniformly distributed load configuration an almost linear reduction of tensile stresses perpendicular to the grain for increasing l_a can be observed (Figure 8).

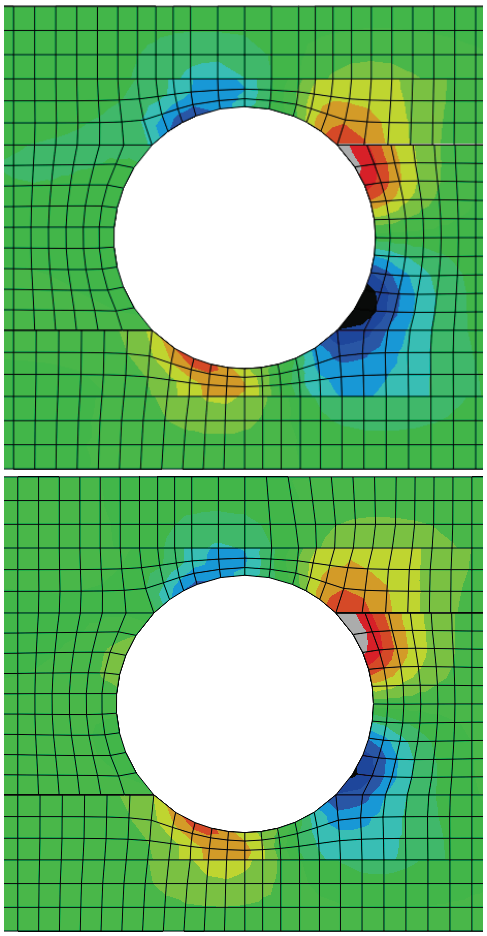

***Figure 13**: Tensile stresses perpendicular to the grain: (up) upper side load, (down) lower side load.*

Applying the load at the lower side causes a reduction in the ultimate load comprised between 40% and 15%. For fixed hole position the reduction is higher for lower diameters. The closer the hole is near the midspan, the higher the reduction. It was observed that applying the same load at the lower side causes an increase in the tensile stresses perpendicular to the grain around the hole (Figure 13).

In the last parametric study, the height of the beam h=300 mm and the relative position of the hole $l_a/l = 0.1$ were maintained constant while varying the length of the beam l and the hole diameter d. This study revealed how for shorter-span beams, the influence of the hole diameter is higher with respect to longer-span beams (Figure 14).

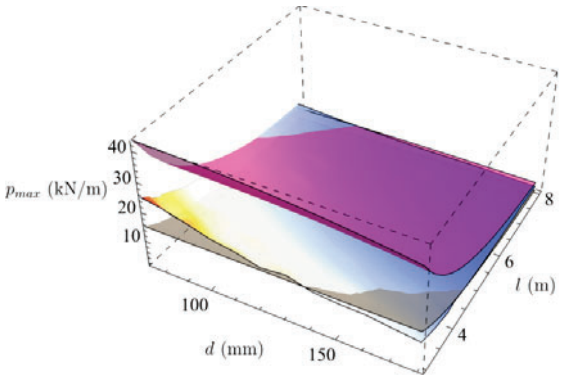

***Figure 14**: Failure load for varying hole diameter and beam length. (Contour: FEM hole crack failure load, grey: failure load of mid-span section without hole, magenta: failure load of hole-section).*

4 CONCLUSIONS

An extended experimental investigation has been conducted on composite glulam joists. The tests highlighted strength reductions up to 33% when in a four-point bending configuration the hole is located in the constant shear zone. No significant differences were found between plywood and glulam reinforcements or between PRF and non-structural glue types. In all cited cases a complete restoration of the joist bending strength was observed.

The developed finite element model provided accurate results in terms of strength and stiffness. The results of the parametric study can be itemized as follow:

- the hole position is a more relevant parameter in beams loaded by a uniformly distributed load than in beams under four-point bending;
- in four-point bending configuration the applied load prevents crack formation; so when the hole is under the load application point the failure load increase;
- applying the load at the lower side causes a reduction in the ultimate load comprised between 40% and 15% with respect to applying the load at the upper side;
- the strength reduction caused by the hole is more pronounced for shorter span beams

Although a satisfying correspondence was found between the formulation provided by the DIN-1052 and the experimental results, the authors proposed a mechanics-based probabilistic formulation for the determination of the strength reduction of beams with holes. Both the case of uniformly distributed load applied at the upper side and lower side have been considered. The proposed formulas are elementary and therefore could be implemented in codes or easily used by practitioners as a possible improvement of the current experimentally derived formulation.

https://doi.org/10.52202/069179-0353

ACKNOWLEDGEMENT

Enter acknowledgements directly before the references. Use the format of primary section headers, but do not number the acknowledgement and references sections.

REFERENCES

1. Aicher, S., L. Höfflin, and H.W. Reinhardt, *Runde durchbrüche in biegeträgern aus brettschichtholz–teil 2: tragfähigkeit und bemessung.* Bautechnik, 2007. **84**(12): p. 867-880.
2. Ardalany, M., B.L. Deam, and M. Fragiacomo, *Numerical investigation of the load carrying capacity of Laminated Veneer Lumber (LVL) joists with holes*, in *11th World Conference on Timber Engineering 2010, WCTE 2010*. 2010. p. 690-699 ,.
3. Danielsson, H., The Strength of Glulam Beams with Holes: A Survey of Tests and Calculation Methods, 2007: p. 1-91 ,.
4. Foliente, G.C. and T.E. McLain, *Strength of end-notched wood beams: A critical fillet hoop stress approach.* Wood Fiber Sci., 1992. **24**(2): p. 168-180 ,.
5. Lee, Y.C., A Study of the Elastic Stresses Around Holes in A Wide-flange Beam with A Concentrated Load, 1969.
6. Smith, C.B., *Mimeo 1510: Effect ofElliptic or Circular Holes on the Stress Distribution in Plates of Wood or Plywood Considered as Orthotropic Materials.* Effect of Elliptic or Circular Holes on the Stress Distribution in Plates of Wood or Plywood Considered As Orthotropic Materials, 1944.
7. Danielsson, H. and P.J. Gustafsson, *Strength of glulam beams with holes-Tests of quadratic holes and literature test result compilation, International Council for Research and Innovation in Building and Construction, Working Commission W18-Timber Structures.* Cib-W18, 2008.
8. Danielsson, H. and P.J. Gustafsson, *A probabilistic fracture mechanics method and strength analysis of glulam beams with holes.* European Journal of Wood and Wood Products, 2011. **69**(3): p. 407-419.
9. Schmidt, J. and M. Kaliske, *Simulation of cracks in wood using a coupled material model for interface elements.* Holzforschung, 2007. **61**(4): p. 382-389.
10. Carling, O., Swedish Glulam Handbook, 2001.
11. Zhu, E.C., et al., *Effect of openings on oriented strand board webbed wood I-joists.* Journal of Structural Engineering, 2007. **133**(1): p. 145-149.
12. Morrissey, G.C., D.W. Dinehart, and W.G. Dunn, *Wood I-joists with excessive web openings: An experimental and analytical investigation.* Journal of Structural Engineering, 2009. **135**(6): p. 655-665.
13. Shahnewaz, M., et al., *Reinforced Wood I-Joists with Web Openings.* Journal of Structural Engineering (United States), 2017. **143**(6).
14. Guan, Z.W. and E.C. Zhu, *Finite element modelling of anisotropic elasto-plastic timber composite beams with openings.* Engineering Structures, 2009. **31**(2): p. 394-403.
15. Zhu, E.C., et al., *Finite element modelling of OSB webbed timber I-beams with interactions between openings.* Advances in Engineering Software, 2005. **36**(11-12): p. 797-805.
16. Danzer, M., P. Dietsch, and S. Winter. *Reinforcement of round holes in glulam beams arranged eccentrically or in groups*. in *World Conf. on Timber Eng*. 2016.
17. Aicher, S. and L. Höfflin, *Glulam beams with holes reinforced by steel bars.* Intl. Council for Research and Innovation in Building and Construction, Working Commission 18-Timber Structures, 2009.
18. Karimi-Nobandegani, A. and H. Valipour, *Effect of web openings on timber composite beams: Testing and analytical modelling.* Engineering Structures, 2022. **256**(January): p. 114064.
19. Karimi-Nobandegani, A. and H. Valipour, *Timber beams with openings: Laboratory testing and nonlocal finite element modelling.* Engineering Structures, 2021. **245**.
20. Gilbert, B.P., et al., *Veneer-based timber circular hollow section beams: behaviour, modelling and design.* Construction and Building Materials, 2020. **258**: p. 120380.
21. Ardalany, M., M. Fragiacomo, and P. Moss, *Modeling of Laminated Veneer Lumber Beams with Holes Using Cohesive Elements.* Journal of Structural Engineering (United States), 2016. **142**(1).
22. Aicher, S., Fracture Mechanics Models for Strength Analysis of Timber Beams with A Hole or A Notch: A Report of RILEM TC-133, 1993.
23. Aicher, S., J. Schmidt, and S. Brunold, *Design of timber beams with holes by means of fracture mechanics.* Proc. CIB Working Commission 18: Timber Structures Meeting 28, 1995.
24. Gustafsson, P.J., *Mean stress approach and initial crack approach.* Fracture Mechanics Models for Analysis of Timber Beams with A Hole or A Notch-a Report of RILEM TC-133. Report TVSM-7134, 2002.
25. Aicher, S. and L. Hofflin, Fracture Behavior and Design of Glulam Beams with Round Holes, 2008.
26. Ardalany, M., *Analysis and Design of Laminated Veneer Lumber Beams with Holes.* Thesis, 2012(September): p. 315.
27. Guan, Z.W. and E.C. Zhu, *Nonlinear finite element modeling of crack behavior in oriented strand board webbed wood I-beams with openings.* Journal of Structural Engineering, 2004. **130**(10): p. 1562-1569.
28. Serrano, E. and P.J. Gustafsson, *Fracture mechanics in timber engineering - Strength*

https://doi.org/10.52202/069179-0353

analyses of components and joints. Materials and Structures/Materiaux et Constructions, 2007. **40**(1): p. 87--96.
29. Sandhaas, C., J. Van de Kuilen, and H.J. Blass. *A 3D constitutive wood model using the concepts of continuum damage mechanics*. in *CDROM Proceedings of the 6th European Congress on Computational Methods in Applied Sciences and Engineering (ECCOMAS 2012), Vienna University of Technology, Austria, iSBN*. 2012.
30. Gharib, M., et al., *Three-dimensional constitutive modelling of arbitrarily orientated timber based on continuum damage mechanics.* Finite Elements in Analysis and Design, 2017. **135**: p. 79-90.
31. *BS EN 408, Timber structures - Structural timber and glued laminated timber - Determination of some physical and mechanical properties.* BSI Standards Limited, 2012.
32. Kolb, H., *Verstärkung von durchbrochenen Brettschichtbindern*. 1985: Forschungs-und Materialprüfungsanst. Baden-Württemberg.
33. *BS EN 338, Structural timber—Strength classes.* BSI Standards Limited., 2009.
34. Yuri De, S. and F. Massimo, *Timber-to-timber and steel-to-timber screw connections: Derivation of the slip modulus via beam on elastic foundation model.* Engineering Structures, 2021. **244**: p. 112798 , publisher = Elsevier Ltd.
35. Tannert, T., A. Gerber, and T. Vallee, *Hybrid adhesively bonded timber-concrete-composite floors.* International Journal of Adhesion and Adhesives, 2020. **97**.
36. Harper, P.W. and S.R. Hallett, *Cohesive zone length in numerical simulations of composite delamination.* Engineering Fracture Mechanics, 2008. **75**(16): p. 4774-4792.
37. Jernkvist, L.O., *Fracture of wood under mixed model loading I. Derivation of fracture criteria.* Engineering Fracture Mechanics, 2001. **68**(5): p. 549-563.
38. Jernkvist, L.O., *Fracture of wood under mixed model loading II. Experimental investigation of Picea abies.* Engineering Fracture Mechanics, 2001. **68**(5): p. 565-576.
39. Blaß, H.J. and C. Sandhaas, *Timber engineering-principles for design*. 2017: KIT Scientific Publishing.
40. Francesca, C., S. Andrea, and C. Jessica, *From screening to quantitative sensitivity analysis. A unified approach.* Computer Physics Communications, 2011. **182**(4): p. 978-988.
41. Sobol, I.M., *Global sensitivity indices for nonlinear mathematical models and their Monte Carlo estimates.* Mathematics and Computers in Simulation, 2001. **55**(1): p. 271-280.

World Conference on Timber Engineering Oslo 2023

EVALUATION OF HARDENING MODELS TO SIMULATE JOINTS IN TIMBER SHEAR WALLS

Rajan Maharjan[1], Johan Vessby[2], Le Kuai[3]

ABSTRACT: The properties of sheathing-to-framing joints considerably affect the load carrying capacity of a light-frame timber shear wall. A fastener with isotropic or kinematic hardening properties is modelled for the sheathing-to-framing joints with a zero-length element, with coupled properties in two perpendicular (orthogonal translational) directions to avoid the overestimation achieved with an uncoupled alternative. A single fastener experiment is performed to determine the elastic and plastic properties. For both fastener level and wall level modelling, monotonic as well as cyclic loading scheme is analysed. A concept of modelling the elasto-plastic coupled behaviour with hardening of the connector model for the fasteners is suggested. A damage response of the fastener is also studied to estimate the failure in load capacity of the connector model and decrease in the wall capacity after the maximum loading.

KEYWORDS: Light-frame timber shear wall, Sheathing-to-framing joints, Single fastener test, Connector model

1 INTRODUCTION

A timber shear wall is built by timber frame members, studs and rails, and sheathing panels attached together by means of mechanical fasteners. The walls are common in multi-story timber buildings since they act as structural diaphragms and transfer lateral loads like wind and seismic loads to the foundation by in-plane action. Furthermore, they are lightweight and can be pre-fabricated at highly automated indoor facilities at high speed in an efficient manner.

From previous studies e.g. [1, 2], it is observed that the mechanical fasteners used as sheathing-to-framing connections are the most important elements affecting the in-plane stiffness and load carrying capacity of the light-frame timber shear wall. To fully comprehend the response of the wall subjected to the in-plane loading, it is essential to study the behaviour of the fasteners used in such connections, a topic that has been addressed by several researchers during the last decades. These include studies with assumed linear elastic response [3] and plastic response [4] of the fastener as well as simulations based on characteristics from Eurocode expressions [5].

The laterally loaded sheathing-to-framing connections are generally timber-steel-timber connections that undergo elasto-plastic deformation when subjected to the loading. A typical mechanical fastener initially behaves elastic up to the yield force and a plastic displacement develops beyond that force. Further displacement beyond the yield initiation is referred to as 'hardening' if the force is increased and 'softening' if the force decreases.

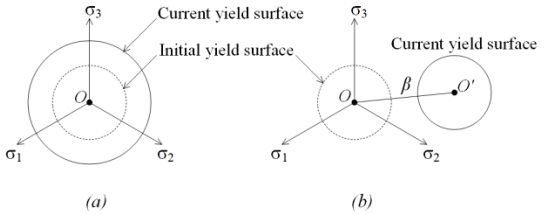

Figure 1: *Initial and current yield surfaces for (a) isotropic and (b) kinematic hardening in the deviatoric plane.*

Hardening can be classified as isotropic hardening or kinematic hardening [6] and they may both be used to simulate the plastic behaviour of the fasteners. The initial yield surface and current yield surfaces for isotropic and kinematic hardening are shown in Figure 1 in the deviatoric plane, perpendicular to the hydrostatic axis.

With an increase in loading, if the subsequent yield surface expands uniformly in all direction in the stress space, the hardening is isotropic. When the yield surface shifts in the stress space, without change in the shape while loading and unloading, the hardening is kinematic. In Figure 1(b), the shift perpendicular to the hydrostatic axis of the current yield field space β is termed as back-stress. For a typical fastener of the type studied, plastic deformation proceeds the failure of the joint. The failure in turn may occur pre or post the average peak load of the fastener type. The peak load is the maximum load registered in the fastener during an experimental test.

Several studies were performed previously on various fasteners to study the performance of mechanical fasteners under monotonic or cyclic loading. Models for

[1] Rajan Maharjan, Karlstad University, Sweden, rajan.maharjan@kau.se
[2] Johan Vessby, Karlstad University, Sweden, johan.vessby@kau.se
[3] Le Kuai, Linnaeus University, Sweden, le.kuai@lnu.se

https://doi.org/10.52202/069179-0354

both monotonic and cyclic lateral behaviours of the nail connection was established in the 1990s e.g. [7]. A hysteresis model, based on modification of the Bouc, Wen, Baber and Noori model, was used [8] in non-linear dynamic analysis of a single-degree-of-freedom wood systems. It was modified to a non-linear and history dependent hysteretic behaviour of a nailed joint [2] which was performed using an user defined element in the finite element (FE) based software ABAQUS.

A recent study on modelling the fastener with a coupled zero-length element was applied on seismic analysis of wood-frame structures [9]. The coupled properties of the zero-length element were implemented to avoid an overestimation of the forces when the load is applied in two orthogonal directions simultaneously. Such coupling may be performed in various ways and some of those are scrutinized by [10]. As previously stated, an accurate model of the fastener is crucial for a correct simulation of a whole shear wall. Many of the previous studies on fasteners also include simulations of different types of shear walls and conclude that the fastener model works well for the wall level e.g. [11].

The aim with the current paper is to evaluate any possible effect in the load-displacement response of choosing an isotropic or kinematic hardening model for the fasteners. To do so, they are modelled in a FE-software using a zero-length coupled element under monotonic and cyclic loading in a 2-D space. The study is performed for a single fastener and for a three panelled shear wall unit. The pinching effect in the cyclic loading is not considered in the simulations performed. An analysis of the damage response of the fasteners is also performed both for the single fastener level and the shear wall level.

2 MATERIAL AND METHODS

2.1 EXPERIMENTAL STUDY

For the experimental study, a timber frame, 45·120 mm in cross-section and of strength class C24 are used. Furthermore, a 12 mm plywood sheathing panel of quality K20/70 and a 3.9·55 mm screw were used for the single fastener test. Monotonic and cyclic tests were performed according to EN 12512 [12] for a single fastener to obtain the load displacement curves and to study a typical loading cycle of the fastener which is loaded parallel to the fibre direction of the timber member.

2.1.1 Monotonic test of a single fastener

A screw was fastened to the sheathing panel (plywood 250·100·12 mm) and the frame (C24 and cross section dimensions 120·45 mm) at the distance of 50 mm from the closest edge in the loading direction, see Figure 2 . The timber frame was fixed to the steel frame by using four Ø 8 mm and 250 mm long steel threaded rods and bolts. The sheathing panel was connected with four bolts, Ø = 4 mm, to the 45·3 mm steel plate that was clamped to the hydraulic wedge grip of the MTS machine having a capacity of ± 100 kN and ± 0.1% linear tolerance interval. The relative displacements between the frame and the panel were acquired by means of two linear variable

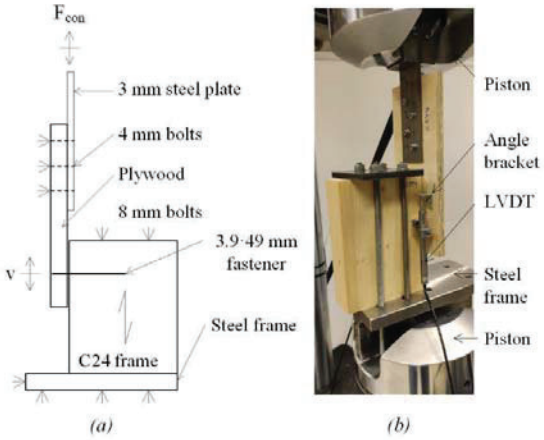

Figure 2: *(a) Setup of the single fastener test and (b) on-going test of the single fastener.*

differential transformers (LVDTs) that were placed at each side of the frame member. The LVDTs were mounted, to the closest possible location of the fastener, on the frame and measured relative to a 15 mm aluminium angle bracket in turn secured to the panel. The monotonic tests were performed under displacement control at a rate of 0.2 mm/sec and from the load-displacement plot of the test the yield displacement v_y was calculated. For the load displacement curve having two clearly linear components, the yield values are determined from the intersection of the two lines according to the procedure suggested in EN 12512 [12].

2.1.2 Cyclic test of a single fastener

The cyclic tests were also performed in the same setup with the load protocol illustrated in Figure 3 where v_y is the yield displacement determined from the monotonic test. The first cycle consists of compression load (towards the steel frame) until the LVDT displacement of $0.25 \cdot v_y$, followed by unloading to zero displacement,

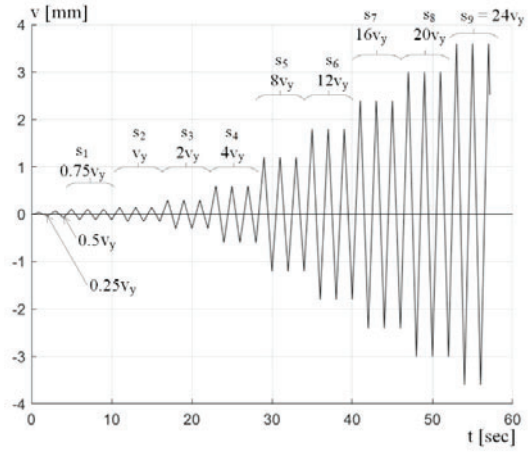

Figure 3: *Loading protocol for the cyclic test where v_y is estimated yield displacement calculated from monotonic test.*

reloading to tensile load (away from the steel frame) up to the LVDT displacement of $0.25 \cdot v_y$ and followed again by unloading to the zero displacement. The second cycle consists of similar loading scheme but this time to the maximum displacement of $0.5 \cdot v_y$. A series (s_1) of three cycles are introduced thereafter with the maximum displacement of $0.75 \cdot v_y$ and so forth with increasing factors for the maximum displacement until failure or until a maximum displacement of v = 30 mm is reached. For both monotonic and cyclic tests, the test frame and the sheathing panel were placed inside a climate chamber with controlled temperature of 20°C and relative humidity of 65% prior to the test, to secure a moisture content around 12% in the timber. The screw was driven by an electric screwdriver after the test setup was prepared.

2.2 NUMERICAL STUDY

2.2.1 FEM model of the single fastener

A two-dimensional connector model of the zero-length element consisting of two orthogonal coupled springs was developed for simulation of the fastener in the commercial FE software ABAQUS. The linear elastic and the non-linear plastic hardening properties of the connector model were assigned based on the results from the cyclic experimental tests. A comparative study on isotropic hardening and kinematic hardening during cyclic loading was performed.

For the isotropic hardening, the yield surface F^0 is a function of equivalent plastic relative displacement $\bar{u}^{pl}$ that can be expressed as:

$$F^0 = \bar{F}_0 + Q_{inf}(1 - e^{-b \cdot \bar{u}^{pl}}) \qquad (1)$$

where, $\bar{F}_0$ is the yield force value at zero plastic relative displacement, and Q_{inf} and b are material parameters affecting the shape of the hardening curve.

Similarly, for the kinematic hardening, the change in the backforce over a half cycle of a unidirectional tension or compression experiment is expressed as:

$$F_j = (F_j{}^0 + \beta_j), \qquad \beta = \frac{C}{\gamma}\left(1 - e^{-\gamma \cdot u^{pl}}\right) \qquad (2)$$

where, $F_j{}^0$ is the initial yield force value, β is the backforce, u^{pl} is the plastic relative displacement, and C and γ are material parameters that are calibrated from the test [13]. The backforce for the connector model is interpreted similar to the back stress in Figure 1(b). The values of Q_{inf} and b for isotropic hardening and C and γ for kinematic hardening were determined by plotting the best fit curve to the envelope curve of the cyclic experimental load-displacement relation.

Since the fasteners in the shear walls experience forces in both orthogonal directions, a coupled behaviour of the fastener is desirable. Therefore the plastic properties of the connector model were modelled as coupled for both hardening models studied. The linear elastic stiffness of the connector was defined as $k = 2 \cdot 10^6$ N/m in both orthogonal directions. The yield force for the cyclic test denotes the boundary between linear elastic and non-linear plastic hardening behaviours studied.

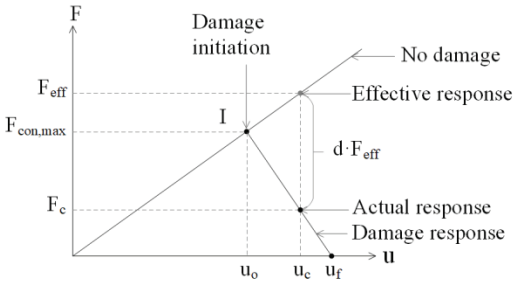

Figure 4: *Damage initiation and damage response.*

When the force in the connector model that is under plastic hardening exceeds its critical value, an irreversible damage is initiated and additional loading leads to further evolution of damage, eventually leading to failure of the fastener. The force response of the connector component i when damage take place is determined as

$$F_i = F_{effi}(1 - d_i), \qquad 0 \le d_i \le 1 \qquad (3)$$

where, d_i is a scalar damage variable and F_{effi} is the effective response in the available connector component under assumption of no damage.

Figure 4 illustrates a simple linear elastic response of a fictive connector with and without damage response. If damage is not defined, the effective response is when the force in the connector is F_{eff} at a displacement u_c. When a damage initiation is introduced at point I by using a damage criteria, the corresponding displacement is u_o. After the connecter is loaded more so that the displacement increase to u_c, the connector force reduces to the current force as determined in Equation (3) depending upon the value of d. Further loading of the connector gradually reduces the response, leading subsequently to the ultimate failure displacement u_f. At the failure displacement, d = 1, which is its maximum value, and at this point the connector loses the ability to carry any load [13].

A force-based damage initiation criterion was specified by defining the lower or compression limit $F_{con,min}$ and the upper or tension limit $F_{con,max}$ for the damage initiation force values. The limits were determined from the maximum load carrying capacity of the fastener from the cyclic tests. Since coupled connector are used, when the resultant of the forces in the connector between two orthogonal directions is outside the range of the two limit values for the first time, the damage initiation occurs. In addition, a linear evolution law is defined by specifying a relative displacement u_{dam} which is the difference between the relative displacement at ultimate failure and the relative displacement at damage initiation $u_{dam} = u_f - u_o$. It describes the additional linear deformation after the damage initiation for the connector to reach the zero force level. A small value of u_{dam} indicates that the connector has brittle property and on the contrary if u_{dam} is large the failure behaviour in the connector is more ductile.

https://doi.org/10.52202/069179-0354

2.2.2 FEM model of simple light-frame shear wall

A shear wall 3.6·3.0 m^2 with three wall panels of width 1.2 m was modelled in a 2-D space with C24 timber frames (cross section 45·120 mm) as beam elements and 12 mm plywood panels as shell elements. The sheathing-to-framing joints for 3.9·55 mm mechanical fasteners were modelled by using one of the two aforementioned connector models. The centre-to-centre spacing between the fasteners at the outer edges of the sheathing panels was assigned as s = 100 mm and that for the intermediate stud at the middle of the panel was assigned as s_{mid} = 200 mm, see Figure 5. The connections between the rails and the studs, which generally consist of 2-3 nails of dimensions 3.1·90 mm, were modelled as a hinge joint so that only the effect of sheathing-to-framing fasteners could be assessed for the global behaviour of the wall. The bottom rail of the wall was fixed to the ground and a displacement controlled horizontal load F_w was applied at the left end of the top rail. A monotonic loading up to a prescribed displacement u_{pres} and a cyclic loading with different displacement amplitude were applied to analyse the global behaviour and the local fastener behaviour. Results from the models were used to compare load-displacement curves for the two hardening models, and to illustrate forces from all fasteners acting on the wall panel at a current load stage and force history during the whole load event for some selected fasteners.

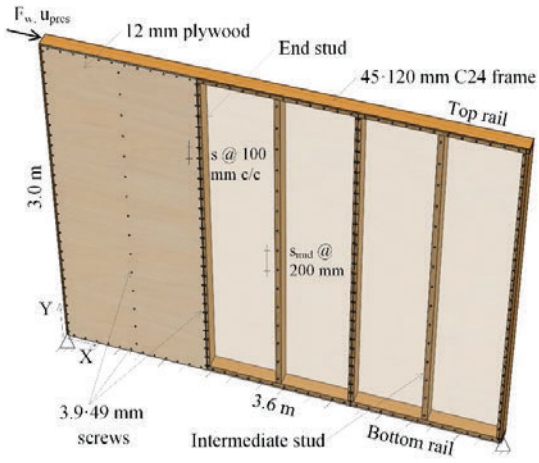

Figure 5: *A simple shear wall model with geometry and spacing of fasteners.*

3 RESULT AND DISCUSSION

3.1 EXPERIMENTS OF A SINGLE FASTENER

The result of single fastener experimental test is illustrated in terms of load-displacement diagram. The force value is taken from the MTS load cell and the displacement value is taken as an average of the two LVDTs that were placed on each side of the fastener.

Among many monotonic tests performed, a typical test result is illustrated to show the calculation method of the yield displacement. From the single fastener monotonic test, the yield load F_y = 588 N and yield displacement v_y = 0.15 mm were determined from the intersection of the two clearly visible linear components (indicated with dotted lines), see Figure 6. The maximum force experienced by the screw in the load-displacement curve is 2340 N at the displacement 10.4 mm.

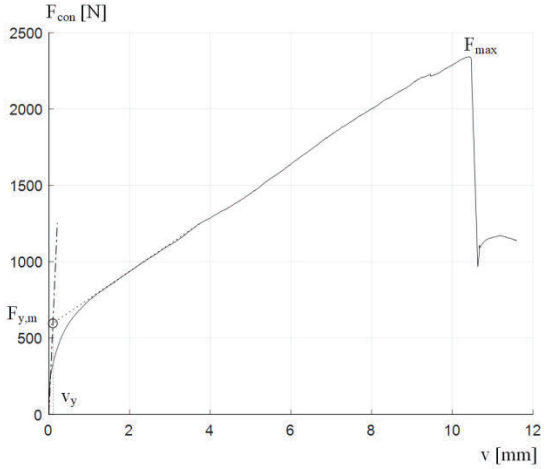

Figure 6: *Load displacement curve from a monotonic test of single fastener showing the yield force F_y from the intersection of two linear components (dotted lines) of the curve.*

Similarly a typical test result from the cyclic loading experiment is shown in Figure 7, which illustrates the load-displacement response for the loading protocol with the yield displacement v_y = 0.15 mm. The experimental data is shifted by + 50 N to the tension zone to adjust the centre of the hysteresis curve about the force axis. The black curve illustrated in the figure is the envelope curve for the test, which is obtained by connecting the force values from the first cycle of each series of the cyclic test, see Figure 3. The envelope response from the cyclic test is observed to yield at F_y = 490 N at a displacement of 0.135 mm, and thus, the elastic modulus is calculated as k_E = 3630000 N/m.

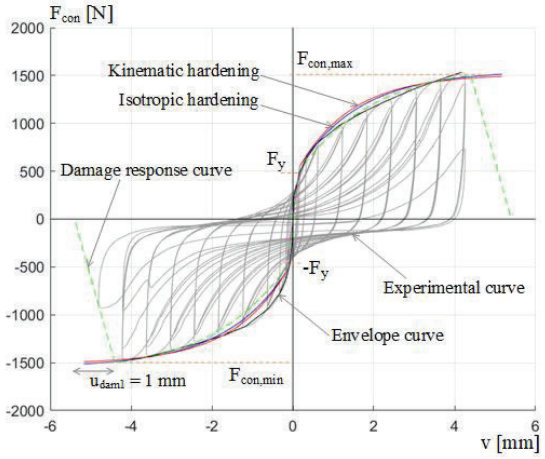

Figure 7: *Load displacement curve for a cyclic loading of the single fastener test with an envelope curve, hardening curves and curves with damage response for v_y = 0.15 mm.*

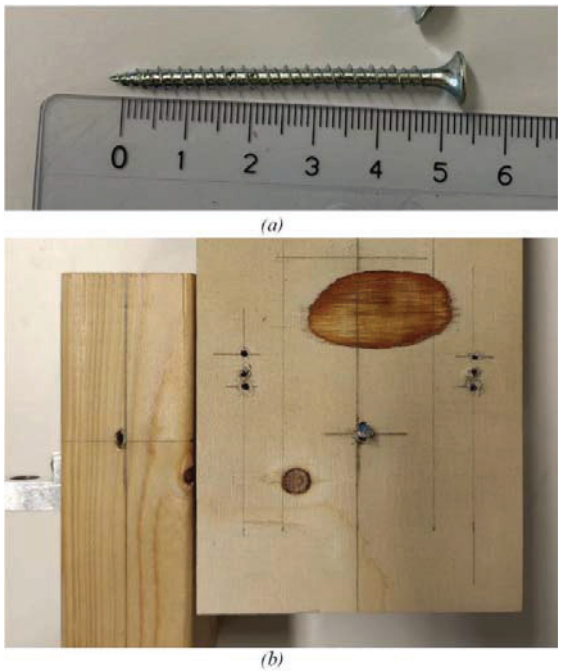

Figure 8: *The screw (a) before the test and (b) after the ultimate failure in the cyclic test.*

The isotropic hardening parameters are obtained by adjusting the parameters in Equation (1) so that the response fits the envelope curve from the experimental results which occurs for Q_{inf} = 1100 and b = 630.
Similarly the kinematic hardening parameters C = 660000 and γ = 590 in Equation (2) are used to fit the experimental results. The lower half-cycle curve for the both hardening properties are obtained by using F_y = - 490 N so that a symmetry in the force-displacement curve is obtained.
From Figure 7, it is observed that during the cyclic test, the screw reached the maximum load carrying capacity $F_{con,max}$ = 1500 N at the cyclic displacement v = 4.2 mm, which is the 10th series of the loading protocol. Therefore, the damage initiation limits, $F_{con,max}$ = 1500 N and $F_{con,min}$ = -1500 N are used for both hardening models. Moreover, two alternate relative displacements u_{dam1} = 1 mm and u_{dam3} = 3 mm are assumed for the connector model which is an estimation of the further deformation of the fastener after the peak load up to the ultimate failure displacement u_f of the fastener. The test screw before and after the ultimate failure from the cyclic test is shown in Figure 8.

3.2 MODELLING OF A SINGLE FASTENER

The input parameters for both hardening models are obtained from the cyclic experimental data to model the response of the single fastener. The simulation results for a typical load cycle with the displacement amplitude v_A = 1.2 mm are illustrated in Figure 9 along with the hysteresis curve from the experiment at that amplitude. The amplitude $v_A = 8 \cdot v_y$ is selected from the 5th series of the loading protocol, see Figure 3. The time displacement graph for the model is illustrated in the subfigure where the solid lines represent the load cycle that are extracted for the hysteresis curve. The isotropic hardening model simulated higher force values whereas the kinematic hardening simulated the force values closer to the experimental values at the selected cycle. The shape of the experimental hysteresis curve is similar to the load cycle of the kinematic hardening, provided the simplifications that the pinching effect achieved in the test is not included and only the linear elastic stiffness k_E is considered during the modelling.

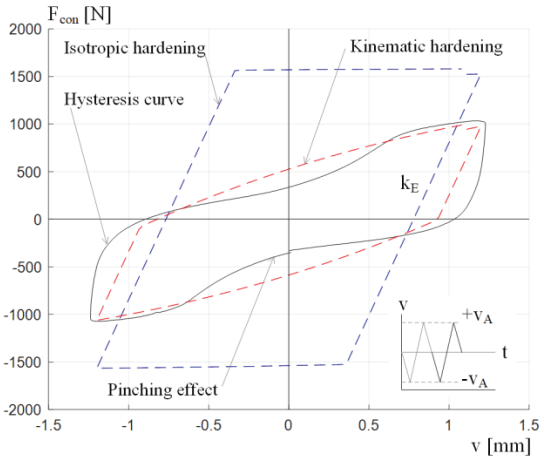

Figure 9: *A typical load cycle at a displacement amplitude of v_A = 1.2 mm from the single fastener cyclic test and models simulating isotropic and kinematic hardening.*

3.3 MODELLING OF A SHEAR WALL

The FEM model of the shear wall is used for both the monotonic and the cyclic loading. The monotonic loading for a prescribed displacement, u_{pres}, is illustrated in Figure 10 that shows the global behaviour of the wall for both hardening models of the fasteners. The blue curves illustrate the response while isotropic hardening is used in the fasteners and the red curves show the results if kinematic hardening is used for the monotonic loading of the wall. Two curves show the global response of the wall without defining the damage response in the connector model. The load in the wall increases asymptotically for both the hardening models, which is unrealistic from an experiment point of view. The two other loading curves show the global response with the damage initiation limit equal to the maximum load carrying capacity of the fastener from the test, $F_{con,max}$ = 1500 N and the relative displacement u_{dam1} = 1 mm. The damage response on the fasteners resulted in numerical instability in the model at the wall displacement around u_w = 24 mm. The reason for the instability is the significant drop in load carrying capacity of the fasteners (because of the steep gradient) after reaching the peak load, which is also an indication of the brittleness in the fasteners.

https://doi.org/10.52202/069179-0354

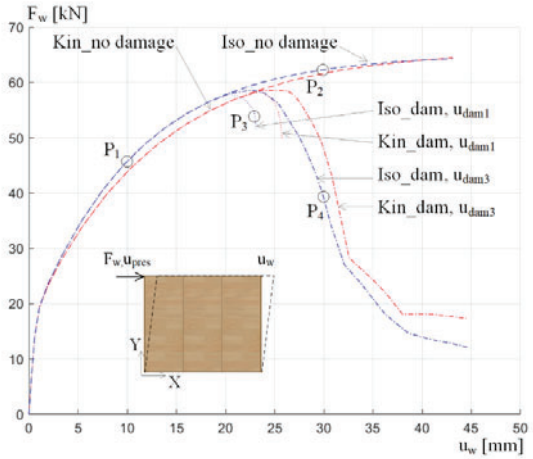

Figure 10: *Load displacement diagram of a shear wall model with damage response u_{dam1}, u_{dam3} and without damage response for both hardening models.*

To model the connector with an increased ductility, the damage response of the fasteners is redefined with u_{dam3} = 3 mm, and a third loading is performed. With the increase in the relative displacement, u_{dam3}, after the peak load in the connectors, the gradient is not so steep and the response of the wall is added in the load-displacement diagram, see Figure 10.

To comprehend the local phenomenon experienced by the fasteners, vector plots of the connector forces in the wall are plotted at different stages and for different assumptions regarding damage response, as positions marked by circles and denoted as P_1-P_4 in Figure 10. Since both hardening models showed similar global behaviour in monotonic loading, the force vector plots are presented only for the kinematic hardening model.

Figure 11 (a) and (b) show the vector plots at the position P_1 (u_w = 10 mm) and P_2 (u_w = 30 mm) respectively for the connector response with no damage defined. The green arrows show scaled vector plot of the forces in the connector at loads lower than the yield load F_y = 490 N and the pink arrows illustrate the vector plot of the forces between F_y and the maximum load carrying capacity of the connector, $F_{con,max}$ = 1500 N. Similarly the red arrows show the vector plot of the connector forces that are greater than $F_{con,max}$. It is observed that the fasteners at the corners of the wall panels reach their peak load first, followed by other fasteners placed close to them. As the displacement in the wall increases, the forces in the connectors also increase and at position P_2, most of the connectors have surpassed the defined peak load of the connectors.

Since the experimental results reveal that fasteners fail at $F_{con,max}$ = 1500 N, the wall model is analysed with the damage response on the connector model. Figure 11(c) illustrates the vector plot of the forces on the connectors at the position P_3 (u_w = 24 mm), which has the damage response definition by the force limit $F_{con,max}$ and the relative displacement u_{dam1} = 1 mm. The connectors at the

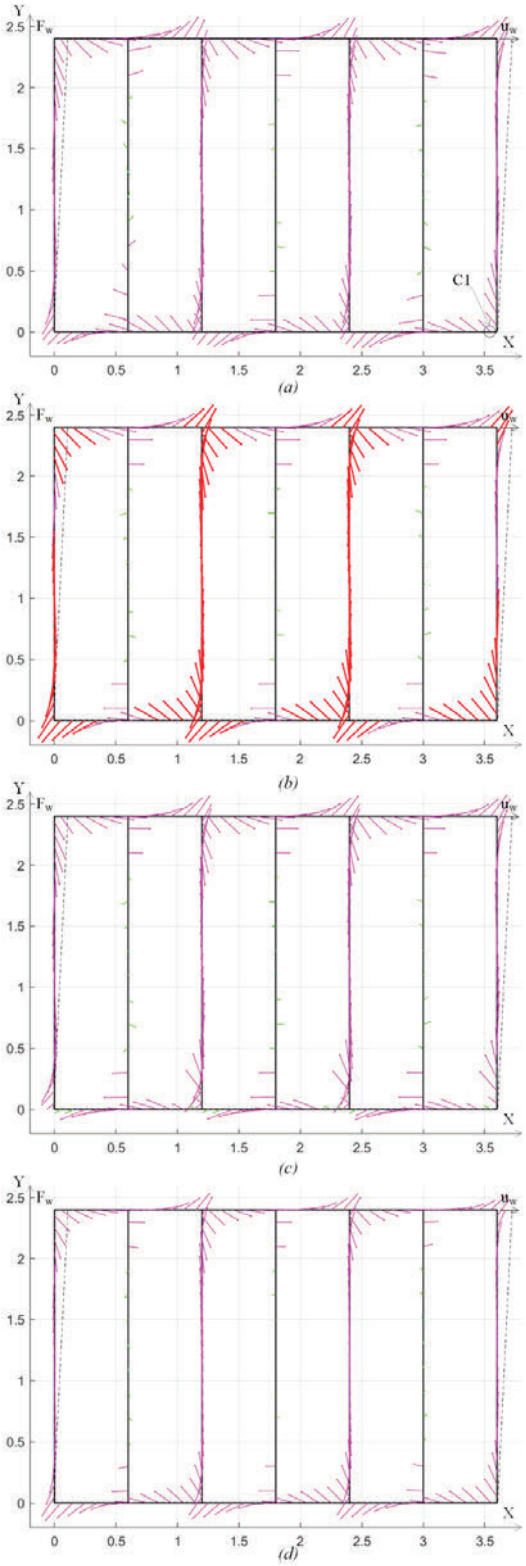

Figure 11: *Force distribution on fasteners of the shear wall model for monotonic displacements at positions (a) P_1, (b) P_2, (c) P_3 and (d) P_4 indicated in the Figure 10.*

https://doi.org/10.52202/069179-0354

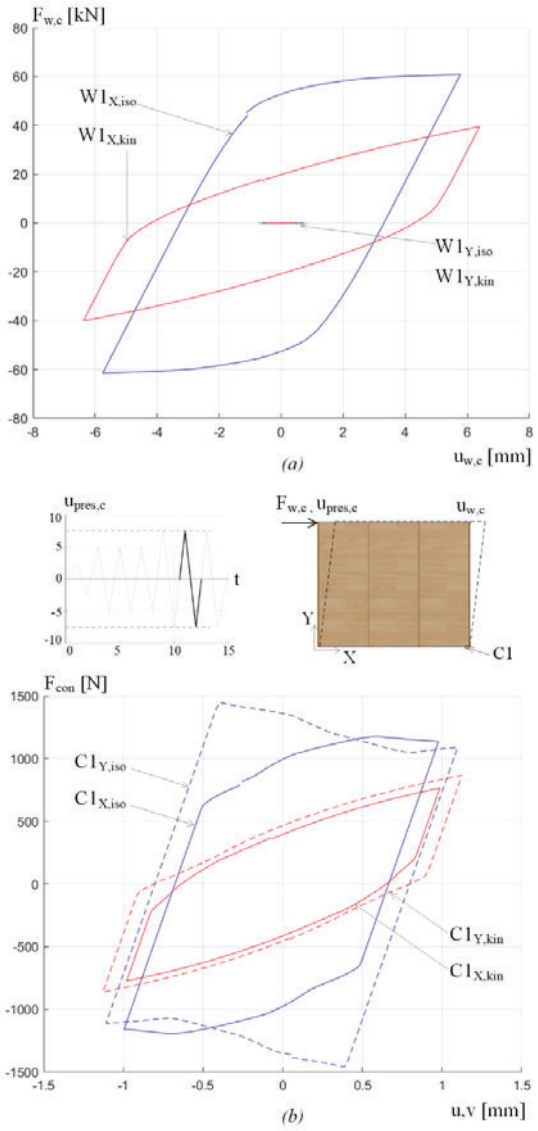

Figure 12: *Load displacement diagram for both hardening models in two orthogonal directions for the displacement amplitude $u_{pres,c}$ = 7.5 mm for (a) shear wall model and (b) for the most loaded fastener denoted C1.*

bottom corners of the three sheathing panels have drastically lower force values, which indicate that they have suffered the damage response the most, thus resulting to the numerical instability.

A comparison of the local connector behaviour is performed for the wall without damage response and with the damage response defined by the force limit $F_{con,max}$ and the relative displacement u_{dam3} = 3 mm. The vector plots for the former is discussed earlier in Figure 11(b) and the latter, at the position *P4* (u_w = 30 mm), is illustrated Figure 11(d). With the damage response u_{dam3}, the forces in the connectors don't exceed the maximum load carrying capacity, $F_{con,max}$. Moreover, the most loaded fasteners at the bottom corners of the sheathing panels have surpassed the $F_{con,max}$ and are in the state of decreasing load bearing capacity at that displacement.

The cyclic loading of the wall model is also simulated and the hysteresis curve for the prescribed displacement amplitude $u_{pres,c}$ = ± 7.5 mm is illustrated Figure 12(a) for the isotropic and the kinematic hardening models of the connector in both horizontal and vertical direction. The damage response for the connector models are not defined for the cyclic loading of the wall model. The displacement amplitude is increased from 2.5 mm with scale factors similar to those used for the single connector model, see subfigure. Since the load was applied along the horizontal (*X*) direction, the sum of the reaction force for the wall along the vertical (*Y*) direction is null. The load-displacement response of the wall exhibits similar shape as the connector model for both hardening models. Moreover, the maximum load applied for the wall with isotropic hardening model is higher compared to the maximum load with the kinematic hardening model, which correlates well with the results for the single connector model.

In order to compare the global wall behaviour with the local fastener behaviour, the force-displacement diagram for the most loaded connector *C1*, indicated in Figure 11(a) at the right end of the bottom rail without the damage response, is illustrated in Figure 12(b). Both the connector forces, defined as F_{con} in the *X*- direction and the *Y*- direction, are illustrated in the figure for both hardening models with respect to the connector displacement u and v in the *X* and *Y*- directions respectively. The connector properties are expressed in orthogonal directions, therefore the resultant of the connector force components in orthogonal directions is the total connector force in action. The kinematic hardening of the fastener for the load amplitude used has similar shape in the force-displacement diagram as the wall. The exception is that for the connector with isotropic hardening model, the vertical component $C1_{Y,iso}$ has higher force than at the horizontal component $C1_{X,iso}$.

4 CONCLUSIONS

The single fastener experimental tests were used to fit two types of elasto-plastic, zero-length coupled elements to the test results, one using isotropic hardening and the other using kinematic hardening. Both models used for the single fastener simulation and the wall simulation are appealing due to their wide availability, their degree of establishment and their simplicity. The comparison between results from simulation using the two models for plasticity and the experimental results indicate the considerable advantage of using a kinematic hardening model compared to the isotropic one for the current application. A benefit with both models is that different properties may be assigned in the two orthogonal directions so that orthotropy in the timber and in some of the sheathing panels may be included in the simulations. These properties influence results from analysis of shear

https://doi.org/10.52202/069179-0354

walls, in particular when the load directions in the fasteners vary during the loading of the wall.
Furthermore, the shear wall models were simulated with the connector models for monotonic and cyclic loading and it was observed that the shape of the load-displacement curve for the global behaviour of the wall was similar to that of the local behaviour of the connector for the most loaded fastener in the wall.
Moreover, the damage response for the connector model was defined to simulate the decreasing load carrying capacity of the fastener after the peak load and until the failure of the fastener. The suggested method for simulating the damage is efficient and the distinct effect of failure in fasteners on the load carrying capacity in the shear wall is shown.

5 FURTHER STUDY

In the current paper, the properties parallel and perpendicular to the fibers are assumed similar. To increase the accuracy of the model, orthotropic properties should be used for the fastener. A series of single fastener experiment for the loading perpendicular to the fibre direction can be performed in order to verify the orthotropic behaviour of the fastener. An experiment on cyclic loading for a simple wall can also be performed to validate the wall model with the zero-length element connector model. Moreover, the effects of large deformation in the connector and the pinching effect of the fasteners can also be included in the further studies.

ACKNOWLEDGEMENT

The research is financially supported by several wood construction companies in Sweden and by the strategic innovation programme Smart Built Environment and Formas. The authors acknowledge that support with great gratitude.

REFERENCES

[1] Sartori, T. and R. Tomasi, Experimental investigation on sheathing-to-framing connections in wood shear walls. *Engineering Structures*, 56: p. 2197-2205, 2013.
[2] Xu, J. and J. Dolan, Development of nailed wood joint element in ABAQUS. *Journal of Structural Engineering-ASCE*, 135, 2009.
[3] Källsner, B. and U.A. Girhammar, Analysis of fully anchored light-frame timber shear walls—elastic model. *Materials and Structures*, 42: p. 301-320, 2009.
[4] Källsner, B. and U.A. Girhammar, Plastic models for analysis of fully anchored light-frame timber shear walls. *Engineering Structures*, 31(9): p. 2171-2181, 2009.
[5] Kuai, L., S. Ormarsson, J. Vessby, and R. Maharjan, A numerical and experimental investigation of non-linear deformation behaviours in light-frame timber walls. *Engineering Structures*, 252: p. 113599, 2022.
[6] Ottosen, N.S. and M. Ristinmaa, The Mechanics of Constitutive Modeling. Elsevier Science Ltd: Oxford. p. 247-264, 2005.
[7] Dolan, J.D. and B. Madsen, Monotonic and cyclic nail connection tests. *Canadian Journal of Civil Engineering*, 19(1): p. 97-104, 1992.
[8] Foliente Greg, C., Hysteresis Modeling of Wood Joints and Structural Systems. *Journal of Structural Engineering*, 121(6): p. 1013-1022, 1995.
[9] Di Gangi, G., C. Demartino, G. Quaranta, and G. Monti, Dissipation in sheathing-to-framing connections of light-frame timber shear walls under seismic loads. *Engineering Structures*, 208, 2020.
[10] Vessby, J., E. Serrano, and A. Olsson, Coupled and uncoupled nonlinear elastic finite element models formonotonically loaded sheathing-to-framing joints in timber based shear walls. *Engineering structures*, 32(11): p. 3433-3442, 2010.
[11] Xu, J. and J. Dolan, Development of a wood-frame shear wall model in ABAQUS. *Journal of Structural Engineering-ASCE*, 135, 2009.
[12] EN12512:2001, Timber structures - Test methods - Cyclic testing of joints made with mechanical fasteners: Brussels, Belgium, 2001.
[13] Dassault-Systèmes, Simulia user assistance 2020: Abaqus/cae user's guide: Vèlizy-Villacoublay, France., 2020.

World Conference on Timber Engineering Oslo 2023

COLLAPSE FRAGILITY OF A 5-STORY CLT STRUCTURE UNDER CHILEAN SUBDUCTION EARTHQUAKE RECORDS

Alberto Aravena[1], Alan Hellman[2], Joaquín Miranda[3], Franco Silva[4], Diego Valdivieso[5]

ABSTRACT: Mass timber structures have been utilized in North America, Europe, and Oceania, and are being evaluated in Latin America to decrease the housing shortage and the construction industry's contribution to greenhouse gas emissions. In Chile, where seismic activity is common, it is crucial to provide resilient timber structures that safeguard life safety and reduce earthquake-induced damage and repair costs. The Performance-Based Earthquake Engineering (PBEE) framework offers a practical alternative for designing more efficient timber buildings and assessing the risks related to seismic hazards, potential damage, and economic losses. In this paper, the PBEE framework is employed to assess the likelihood of a government-subsidized 5-story cross-laminated timber building collapsing under seismic stress in Chile. The probabilistic seismic hazard analysis (PSHA) was used for hazard site characterization, and the collapse probability analysis indicated a probability of less than 0.1% for a building with the mentioned characteristic, making it suitable for construction in Chile. Further research is required to achieve loss estimation under the PBEE framework, such as quantifying damage fragility curves of representative engineering details for Chilean construction.

KEYWORDS: PBEE, CLT, PSHA, Conditional Mean Spectrum, Record Selection, Collapse

1 INTRODUCTION

Cross-laminated timber (CLT) is a mass timber product increasingly used in the construction of mid-rise and high-rise buildings, as an alternative to the traditional materials like concrete, steel, and masonry [2]. The usual constructive system in CLT buildings is the platform type, it consists of walls and slabs composed of solid timber panels with high stiffness and strength in their plane, attached through metal brackets and fasteners [3]. In these constructions, the floor panels are supported by the walls of the lower story, therefore the walls are interrupted at each level [4] and the main source of energy dissipation comes from the wall-to-wall parallel connections and overturning restraint system (i.e. hold-downs) as it is illustrated in Figure 1 [5].

In Chile, cross-laminated timber is a scarcely used product, unlike Europe and North America, where midrise and high-rise buildings have been built using CLT panels as the main material for walls and floor diaphragms [6-8]. However, recent studies [9-12] seek to promote the use of the CLT platform system using radiata pine grown in Chile as raw material by proposing design recommendations such as seismic performance factors (i.e., seismic response modification factor R = 2.0 and inter-story drift limit of 0.2%) and design procedures that are waiting for its incorporation in national design codes. Considering the high seismicity of the country and the lack of formal code-based recommendations, it is essential to provide resilient timber structures where structural and non-structural components adequately protect life safety and reduce earthquake-induced damage and repair costs. In this context, Performance-Based Earthquake Engineering (PBEE) becomes a convenient alternative when the structure's critical elements (CLT-to-CLT connections) exhibit non-linear behaviour, allowing for the design of more efficient buildings and assessing the risk associated with the seismic hazards, potential damage, and economical losses according to the location where they are built. In this paper, the PBEE framework will be employed to assess the probability of collapse of a government-subsidized 5-story cross-laminated timber building designed under the Chilean seismic design code considering the proposed seismic performance factors developed in [11].

[1] Alberto Aravena, Universidad de Santiago de Chile, Chile, alberto.aravena.c@usach.cl
[2] Alan Hellman, Universidad de Santiago de Chile, Chile, alan.hellman@usach.cl
[3] Joaquín Miranda, Universidad de Santiago de Chile, Chile, joaquin.miranda@usach.cl
[4] Franco Silva, Universidad de Santiago de Chile, Chile, franco.silva.c@usach.cl
[5] Diego Valdivieso, Pontificia Universidad Católica de Chile, Centro Nacional de Excelencia para la Industria de la Madera (CENAMAD) & Centro de Innovación en Madera (CIM UC-CORMA, Chile, dnvaldivieso@uc.cl. University of Colorado at Boulder, USA, diego.valdivieso@colorado.edu

https://doi.org/10.52202/069179-0355

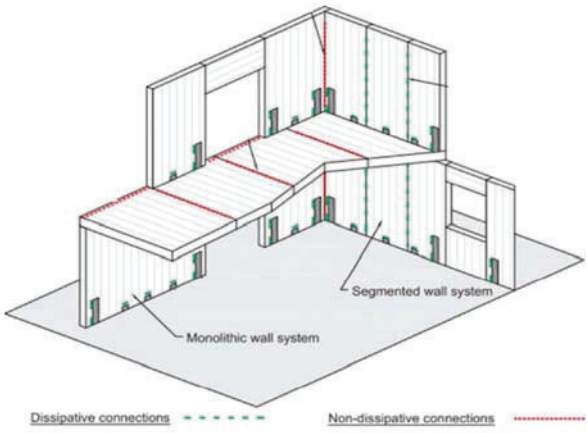

***Figure 1**: Schematics of a CLT structure (platform system) with the indication of the dissipative and non-dissipative connections (taken from [5]).*

2 BUILDING DESCRIPTION

It is important to clarify that the building being studied is still in the project stage. It was defined based on the criteria for government-subsidized housing in Chile, taking into consideration the specific needs and requirements of the target population. The projected building has five floors with a height of 2.6 m each. The length, width, and height of the building are 20.55 m, 7.05 m, and 10.4 m, respectively, with floors and walls made of 3-ply CLT (i.e., 120mm of thickness), using Chilean radiata pine as raw material, with two apartments in each level (55 m^2 per apartment). The building structure has been designed with monolithic wall as a lateral system with hold-downs and shear keys as overturning and sliding restraint systems, respectively. The staircase that provides access to the apartments is located in the middle. It was assumed that the building will be built on a typical soil type in the city of Santiago (i.e., Vs30 > 350 m/sec). The archetype of the building is illustrated in Figure 2. Figure 3 shows corresponding panels in a red box on the floor plan (a) to indicate the panel distribution on the elevations (b).

3 NUMERICAL MODELING

In order to evaluate the response of the building, two modeling variants were considered to illustrate the impact of considering a simplified 2D approach and the possible system effect on the response of the 3D structure. These are (i) a representative 2D planar elevation of the structure (i.e., A-A axis), and (ii) a full 3D representation of the building structure. Both numerical models were developed on OpenSeesPy [13]. Shell elements (i.e. shellMITC4 element) with isotropic material were used for the CLT walls panels and nonlinear springs (i.e. zeroLength element) were used for the hold-downs and shear keys (see Figure 4) as according to [5] both connection are responsible for the energy dissipation in the monolithic wall system. The wall-to-wall perpendicular connection was considered non-dissipative and perfectly rigid. The test data reported in [10] on full-scale CLT shear walls and in [14] on hold-downs and shear keys were considered for the calibration of the numerical model. The modeling and calibration procedure described in [12] was used as a base for the development of the input parameters (i.e., elastic parameters for shell elements and SAWS constitutive parameters for the zeroLength elements) models. Based on previous numerical studies [15], the floor and the roof were modelled as rigid diaphragms with mass lumped at each story.

***Figure 2:** Building considered: (a) typical floor plan, (b) exterior longitudinal elevation, (c) inside longitudinal elevation, and (d) transverse elevation. All dimensions in millimeter.*

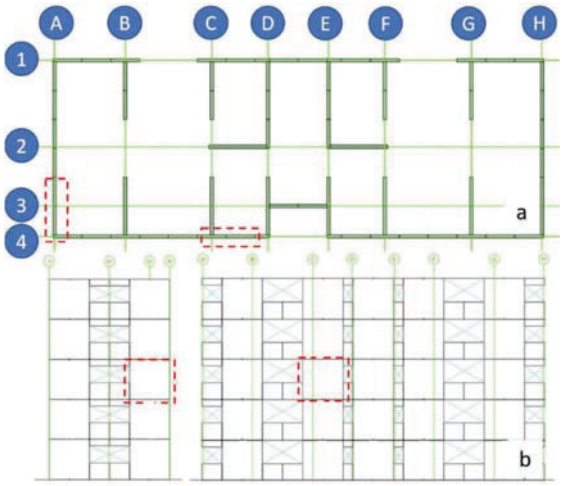

***Figure 3:** CLT shear wall distribution in (a) plan and (b) elevation (along A-A and 1-1).*

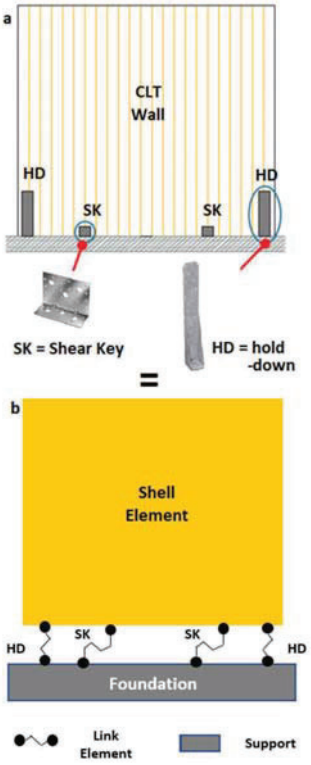

Figure 4: *(a) Typical CLT shear wall configuration used in the building, (b) schematic of FE model for CLT shear walls.*

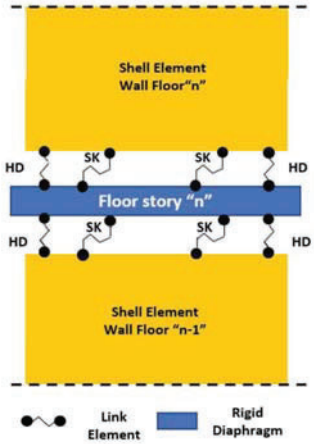

Figure 5: *Schematic of FE model for CLT shear walls at the story "n"*

For the 2D structure, the first fundamental period of the nonlinear structural model was determined as 0.515 sec. For the 3D building model, the first fundamental periods of the nonlinear building model at both translational directions were determined as 0.292 sec and 0.257 sec. The first mode is predominately in the X direction and the second mode is in the Y direction.

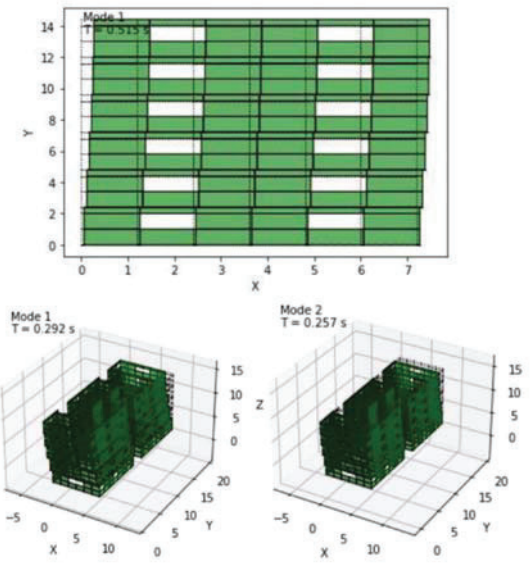

Figure 6: *Mode shape of the structure for (top) 2D simplified model and (bottom) 3D model.*

4 SEISMIC HAZARD

Chile is located in a highly seismic-prone area. Megathrust earthquakes are mainly attributable to the subduction of the Nazca plate beneath the continental South American plate. This subductive interaction is considered the only source of earthquake hazard to perform nonlinear time history analysis (NLTHA) and Multiple Stripe Analysis (MSA).

A probabilistic seismic hazard analysis (PSHA) was conducted to compute the seismic hazard associated with the site location of the building. For the development of the PSHA, the recurrence model developed in [16] and the Ground-motion prediction equation (GMPE) for the Chilean subduction zone developed in [17] were used. An example of the seismic deaggregation for the site of the building is presented in Figure 4 considering a return period of 4975 years (a 1% probability of exceedance in 50 years) at the spectral acceleration of the building period.

Table 1: *Deaggregation results.*

Mean Scenario	*Period (sec)*		
	0.515	*0.292*	*0.257*
Magnitude	*7.80*	*7.83*	*7.83*
Distance (km)	*135.2*	*147.3*	*145.8*

Ground motion (GM) records from the SIBER-RISK database were selected to match the target Conditional Mean Spectrum (CMS) on the period of interest considering the procedure developed in [18] and a maximum scale factor (SF) of 2.0. Figure 5 shows the response spectra of all selected motions adjusted to the CMS. Some of the selected records are summarized in Table 2.

https://doi.org/10.52202/069179-0355

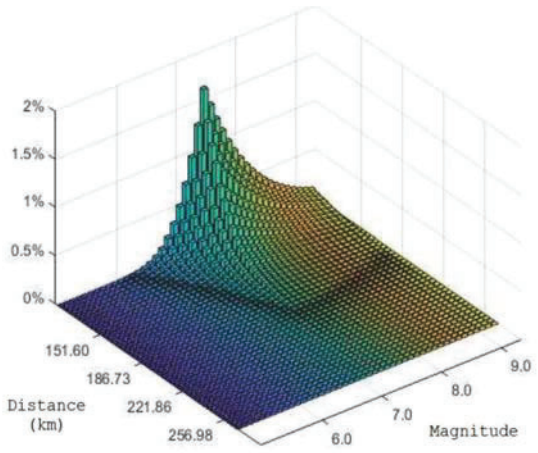

Figure 4: *Deaggregation for the considered site associated with the first mode of the 3D structure.*

In Figure 5, the conditioned spectra for both the 2D and 3D models are shown. Although these are different due to obvious reasons, such as the bidirectional quality for the 3D model, the records that fit these spectra turn out to be virtually the same. This is mainly due to the unique characteristics of the building, such as its stiffness and the parameters established, such as the selected return period.

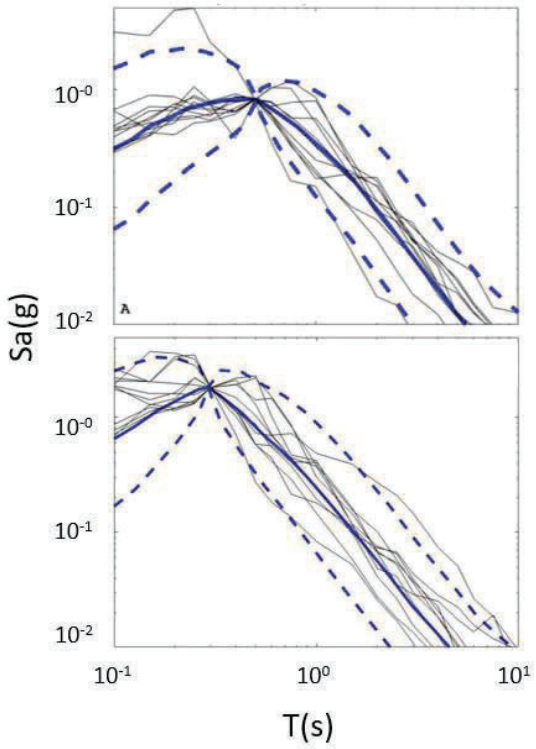

Figure 5 *Response spectra of selected motions matched to the target spectrum for (top) 2D simplified model and (bottom) 3D building model.*

Table 2: *Information on the selected ground motions.*

Location	*Year*	*Mw*	*Distance (km)*	*Station*
Quillota	*2014*	*6.4*	*54.92*	*V18A*
Algarrobo	*1985*	*7.9*	*46.92*	*MAUL06S*
Coquimbo	*2015*	*6.3*	*99.82*	*C11O*
Algarrobo	*1985*	*7.9*	*36.70*	*VALP11S*
Coquimbo	*2015*	*8.2*	*46.31*	*C11O*
Iquique	*2014*	*8.2*	*65.97*	*T10A*
Tarapacá	*2005*	*7.9*	*110.72*	*PICA*
Alto Hospicio	*2014*	*7.6*	*56.58*	*T10A*
Algarrobo	*1985*	*7.9*	*98.77*	*RANC02S*
Coquimbo	*2015*	*8.4*	*49.87*	*C23O*
Maule	*2010*	*7.9*	*50.13*	*ANGOL*

5 RESULTS AND DISCUSSION

The Multiple Stripe Analysis (MSA) method was used for evaluate the structure fragility as is illustrated in Figure 6 and 7. As expected from any structure that is subjected to earthquake loads, major forces are found at the base of the structure. In this model case, base shear keys are the ones that present the biggest internal forces and displacements due to assuming spring-like supports instead of fixed or pinned supports, making these elements the ones that dissipate more energy during a seismic event. For the model developed in this study, an improvement proposal could be to consider different connections at the base than on higher floors or tension rods to prevent the exceeding of the collapse drift limit.

In Figure 8 and 9, the collapse fragility curves for the 2D simplified model and the 3D model shows that the 2D model collapses for lower IM levels in comparison to the 3D full scale model. The collapse fragility function is computed assuming that collapse observations are independent and fit into a binomial distribution, given that a record can either cause collapse of the structure or not.

The collapse margin ratio (CMR) is an important output from the MSA, defined as the ratio between median collapse capacity and the maximum considered earthquake intensity in the Chilean code (i.e., 2% in 50 years) SMT:

$$CMR = \frac{S_{CT}}{S_{MT}} \quad (1)$$

For the 2D simplified case SMT = 0.92g whereas for the 3D building model SMT = 1.35g. Then, the computed CMR is 3.8 and 2.45 for the 2D simplified case and 3D building model case, respectively. Shahnewaz et al. (2020) estimated the CMR for a 4-story CLT building as 2.78-3.55 at collapse drift ranging from 5% to 10% considering a 2% in 50 years scenario for Vancouver. Based on the results, the simplified 2D numerical model tends to underestimate the CMR making it a not good

representation of the response of the building. Having said that, this approximation could be a good estimation for buildings with a symmetric distribution of the structural components.

For the analysed structure and hazard scenario, the collapse probability is 0.5% and less than 0.1% for the 2D and 3D numerical models of the structure, respectively. This is mainly attributable to the strict design requirements of the Chilean seismic design code (i.e., mainly the inter-story drift limit of 0.2% for reduced seismic forces in an elastic design approach.

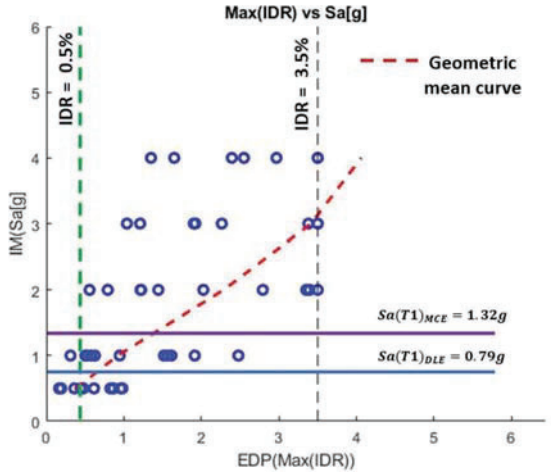

Figure 6: *MSA curves of all ground motions for the 2D simplified structure.*

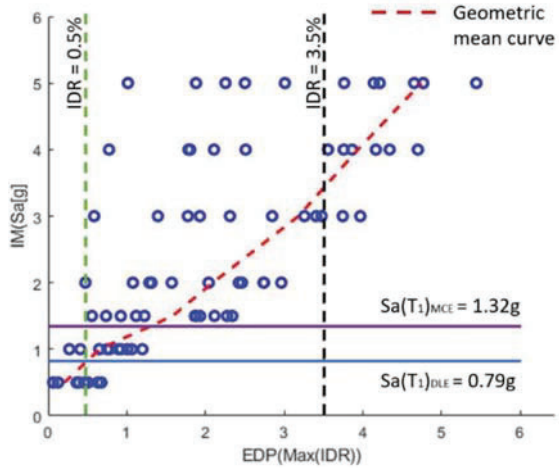

Figure 7: *MSA curves of all ground motions for the 3D building model.*

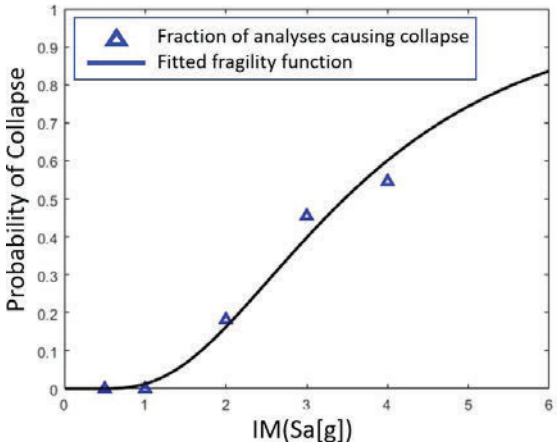

Figure 8*: Fragility curve for collapse for the 2D simplified case.*

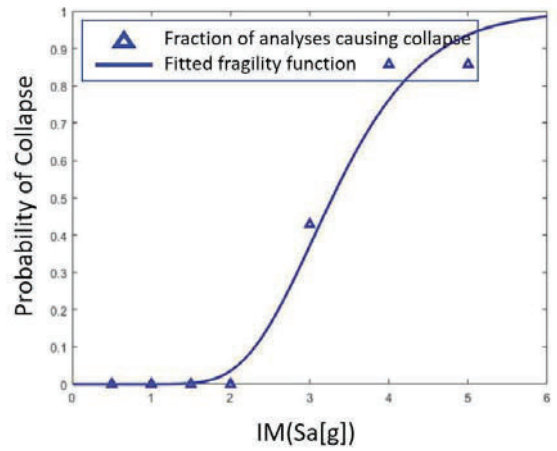

Figure 9: *Fragility curve for collapse for the 3D building mode.*

6 CONCLUSIONS

In summary, the Performance-Based Earthquake Engineering (PBEE) framework can offer a practical approach to designing resilient mass timber structures capable of withstanding seismic activity in highly prone areas such as Chile. The analysis of the collapse probability of a 5-story cross-laminated timber (CLT) building designed under Chilean seismic design code indicated a low probability of less than 0.1%, which suggests that CLT structures could be safely constructed in Chile. The simplified 2D axis has a different structural behaviour in relation to the same axis from the 3D model. From this, it can be concluded that the 2D model may not be a good representation of the behaviour of a full CLT structure given that it collapses to lower IM levels in comparison to the 3D full scale model.

Further research is necessary to improve the PBEE analysis and to obtain damage fragility curves associated with demand parameters such as inter-story drift (IDR) for structural and non-structural elements associated with CLT building design. To add depth and achieve a full

https://doi.org/10.52202/069179-0355

representation of the energy dissipated by the model, it can also be considered the perpendicular wall-to-wall connection in possible iterations of the analysis. To better estimate the effects from damage and the economic loss produced, it is necessary to develop fragility curves for typical structural connections used in timber buildings.

Non-structural components, such as MEP and fire protection installations should also be considered in a more complete risk assessment analysis, which adds more variables to the damage and economic loss estimation for a type of building that requires to manage the uncertainty of using technologies that have not been mass used before in the region, in the scale that it is proposed for future development of the timber industry in Chile. Thus, opening more opportunities for research through public-private partnership in design stages and building specifications for tall timber structures, making it possible to define the pros and cons of building in CLT and other timber engineered products and innovative construction materials.

It is also important to remember that in this present study, only the maximum values of IDR independent of its direction and location have been presented. Therefore, it would eventually be of interest to establish a more detailed description of these variables to better understand the behaviour of mid-rise buildings constructed using CLT. This is necessary for estimating economic losses and providing a full probabilistic risk assessment, which would enhance decision-making support for designers, investors, and stakeholders. Regardless, the use of mass timber structures in construction presents a promising method to reduce the housing deficit and greenhouse gas emissions while ensuring building safety and resilience in earthquake-prone regions.

ACKNOWLEDGEMENT

The research presented in this paper was made possible using SIBER-RISK, a ground-motion database for earthquakes in Chile. We express our gratitude to the creators and contributors of this research project for providing us the necessary information to get the results shown.

We would also like to extend our appreciation to the professor Jack Baker, who generously made all his knowledge available through his webpage, documents and code. The resources provided by Professor Baker played a crucial role in our research and we are grateful for his support and contributions.

REFERENCES

[1] Der Kiureghian, A., and Ditlevsen, O. (2009). “Aleatory or epistemic? Does it matter?” Structural Safety, 31(2), 105–112.

[2] Breneman S. (2016). “Cross-Laminated Timber Structural Floor and Roof Design”. Structure Magazine June 2016:12-15.

[3] González-Rodrigo, B., Fraile-de-Lerma, A., & Mosquera-Feijoo, J. C. (2018). Análisis del comportamiento sísmico de estructuras con paneles prefabricados de madera contralaminada. DYNA-Ingeniería e Industria, 94(2).

[4] Tamagnone, G., Rinaldin, G., & Fragiacomo, M. (2018). A novel method for non-linear design of CLT wall systems. Engineering Structures, 167, 760-771.

[5] Izzi, M., Casagrande, D., Bezzi, S., Pasca, D., Follesa, M., & Tomasi, R. (2018). Seismic behavior of Cross-Laminated Timber structures: A state-of-the-art review. Engineering Structures, 170, 42-52.

[6] Wells, M. (2011). Stadthaus, London: raising the bar for timber buildings. In Proceedings of the Institution of Civil Engineers-Civil Engineering (Vol. 164, No. 3, pp. 122-128). Thomas Telford Ltd.

[7] Abrahamsen, R. (2017). Mjøstårnet-Construction of an 81 m tall timber building. In Internationales Holzbau-Forum IHF (Vol. 2017).

[8] Poirier, E., Moudgil, M., Fallahi, A., Staub-French, S., & Tannert, T. (2016). Design and construction of a 53-meter-tall timber building at the University of British Columbia. In Proceedings of the world conference on timber engineering, Vienna, Austria.

[9] Benedetti, F., Rosales, V., & Opazo, A. (2017). Cyclic behavior of foundation-wall connection in cross laminated timber shear walls. In 16th World Conference on Earthquake, 16WCEE.

[10] Pérez, E., González, P., Saavedra, E., Tapia, S., Torelli, J., & Orellana, S. (2017). Mechanical characterization and hysteretic behavior of CLT panels made of Chilean radiata pine. In 16th World Conference on Earthquake Engineering, 16th WCEE.

[11] Valdivieso, D., Ulloa, C., González, P., Pérez, E. & Burgos, C. (2019). Determinación del factor de modificación de la respuesta estructural para edificio estructurado con muros y losas de madera contralaminada. In XII Congreso Chileno de Sismologia e Ingenieria Sismica, Valdivia, Chile.

[12] Villegas, J., & Valdivieso, D. (2021). Numerical analysis of the cyclic behavior of CLT walls made with radiata pine grown in Chile. In Proceedings of the world conference on timber engineering, Santiago, Chile.

[13] Zhu, M., McKenna, F., & Scott, M. H. (2018). OpenSeesPy: Python library for the OpenSees finite element framework. SoftwareX, 7, 6-11.

[14] Matus, E., & Salgado, S. (2016). Estudio del comportamiento de uniones en madera contralaminada mediantes conectores metálicos bajo carga cíclica. Memoria de título de Ingeniero Civil en Obras Civiles. Universidad de Santiago de Chile.

[15] Shahnewaz, M., Pan, Y., Shahria Alam, M., & Tannert, T. (2020). Seismic fragility estimates for cross-laminated timber platform building. Journal of Structural Engineering, 146(12), 04020256.

[16] Poulos, A., Monsalve, M., Zamora, N., & de la Llera, J. C. (2019). An Updated Recurrence Model for Chilean Subduction Seismicity and Statistical Validation of Its Poisson Nature. An Updated Recurrence Model for Chilean Subduction Seismicity and Statistical Validation of Its Poisson Nature.

Bulletin of the Seismological Society of America, 109(1), 66-74.
[17] Montalva, G. A., Bastías, N., & Rodriguez-Marek, A. (2017). Ground-motion prediction equation for the Chilean subduction zone. Bulletin of the Seismological Society of America, 107(2), 901-911.
[18] Jayaram, N., Lin, T., & Baker, J. W. (2011). A computationally efficient ground-motion selection algorithm for matching a target response spectrum mean and variance. Earthquake spectra, 27(3), 797-815.
[19] Baker, J. W. (2015). Efficient analytical fragility function fitting using dynamic structural analysis. Earthquake Spectra, 31(1), 579-599.
[20] Pan, Y., Shahnewaz, M., & Tannert, T. (2022). Seismic Performance and Collapse Fragility of Balloon-Framed CLT School Building. Journal of Earthquake Engineering, 1-21.

https://doi.org/10.52202/069179-0355

World Conference on Timber Engineering Oslo 2023

FINITE ELEMENT ANALYSIS OF GLULAM BEAMS WITH TRANSVERSE AND LONGITUDINAL NOTCHES

Sardar Malek [1], Azadeh Goodarzi[2], Roger Parra[3], Parham Khoshkbari[4]

ABSTRACT: Laminated wood composites, such as glued-laminated timber (Glulam) and cross-laminated Timber (CLT), are increasingly being used in the design of mass timber buildings. In solid timber (sawn lumber) and engineered wood products (EWPs), transverse notches are generally used at connections or at supports to reduce the height of beams. Small longitudinal notches may also be cut along beams and columns for aesthetic purposes. It is known that abrupt cross-section changes create stress concentrations, which can cause the structural member to fail at lower loads compared to an unnotched member. European (Eurocode 5), Canadian (CSA O86-19), and American (NDS 2018) codes provide guidance on designing solid timber and Glulam beams with transverse notches. However, no recommendation has been provided for longitudinal notches along Glulam beams. To address this gap, a 3D Finite Element (FE) model is developed in ANSYS© software to assess the stress field of Glulam beams with the transverse end notches. The developed model is validated with experiments from the literature. The predicted load-bearing capacities are compared with those of notched beams based on the design equations provided in the codes and existing test data. The validated model is then used to comprehensively assess the effect of rounded notched corners and longitudinal notches on the stress fields of Glulam beams.

KEYWORDS: Glulam, Notch, CSA O86, Eurocode 5, NDS, Finite Element Analysis (FEA)

1 INTRODUCTION

Transverse notches are commonly used in solid timber and engineered wood products (EWPs) for various purposes. These notches are typically placed at connections like mortise and tenon or dovetail joints or at supports. In order to achieve a desired visual effect, it is also possible to create small longitudinal notches on structural members. It is well known that tension side transverse notches significantly reduce the load-bearing capacity of Glulam beams. This capacity reduction is mainly due to stress concentration near notched corners and the low tensile strength of timber perpendicular to the grain direction. The structural behavior of Glulam beams with transverse end notches has been studied experimentally and numerically in the literature [1-4].

European (Eurocode 5 [5]), Canadian (CSA O86-19 [6]), and U.S. codes (NDS 2018 [7]) provide design provisions for Glulam beams with the tension side transverse notches. However, currently, there are no guidelines or recommendations regarding longitudinal notches in Glulam beams.

In this paper, first, the design provisions for Glulam beams with transverse notches in their tension sides are reviewed and compared. A detailed review of the design equations, the considered notch geometry parameters, and limitations on maximum notch depth is provided. Then, the stress fields in a Glulam beam with the tension side transverse end notches are analyzed based on a 3D FE model developed in ANSYS software. The material and geometric parameters are selected based on the four-point bending test reported in [2]. The shear resistance of the end-notched Glulam beam based on provisions in various standards is compared with available test data [2] and the predictions of the developed FE model. The validated model is then used to numerically assess the effect of a rounded notch corner on the stress components. Finally, two longitudinal notches are added in the model, and the effects of these notches on the stress fields are investigated.

2 DESIGN APPROACHES FOR NOTCHED GLULAM BEAMS

A typical notched Glulam beam with a rectangular cross-section with a width of b and a depth of d, has been shown in Figure 1. In this figure, the d_n and i are the notch depth and notch inclination, respectively. The notch length, e, is defined as the horizontal distance from the support to the notched corner. The effective depth of the notched beam, d_{ef}, is obtained by:

$$d_{ef} = d - d_n \quad (1)$$

[1] Sardar Malek, University of Victoria, Canada, smalek@uvic.ca
[2] Azadeh Goodarzi, University of Victoria, Canada, azadehgoodarzi@uvic.ca
[3] Roger Parra, Degenkolb Engineers, USA
[4] Parham Khoshkbari, Google LLC, California, USA

https://doi.org/10.52202/069179-0356

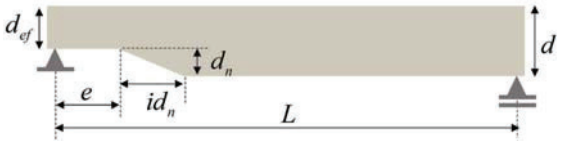

Figure 1: *Schematic of a typical notched beam.*

Based on the design provision provided in Eurocode 5 [5], the shear force at the notched support of the beam should be verified using:

$$V \leq \frac{2}{3} bd_{ef} k_v f_{v,d} \tag{2}$$

where $f_{v,d}$ is the design shear strength and k_v is a reduction factor calculated by the following equation for the Glulam beam:

$$k_v = \min\left\{ \frac{6.5\left(1 + \frac{1.1\, i^{1.5}}{\sqrt{d}}\right)}{\sqrt{d}\left(\sqrt{\alpha(1-\alpha)} + 0.8\, \frac{e}{d}\sqrt{\frac{1}{\alpha} - \alpha^2}\right)}, 1 \right\} \tag{3}$$

here, α is the notch ratio defined by $\alpha = d_{ef}/d$.
According to the design provisions in CSA O86-19 [6], the shear force at the notched support of a Glulam beam with less than 2.0 m^3 in volume should be verified by:

$$V \leq F_r \tag{4}$$

and

$$V \leq V_r \tag{5}$$

where F_r is the factored fracture shear resistance at a notch on the tension side at support obtained by:

$$F_r = 0.9 F_f d b K_N \tag{6}$$

In Equation (6), $F_f = f_f(K_D K_H K_{Sf} K_T)$. It should be noted that f_f is the specified fracture shear strength at a notch and obtained by $2.5(b)^{-0.2}$ or 0.9 MPa (whichever is greater). Other factors, K_D, K_H, K_{Sf}, and K_T are the load-duration factor, system factor, service-condition factor for fracture shear, and treatment factor, respectively. K_N is the notch factor calculated as follows:

$$K_N = \left[0.006d\left(1.6\left(\frac{1}{\alpha} - 1\right) + \left(\frac{e}{d}\right)^2\left(\frac{1}{\alpha^3} - 1\right)\right)\right]^{\frac{-1}{2}} \tag{7}$$

In Equation (5), V_r is the factored shear resistance obtained by:

$$V_r = 0.9 F_v \frac{2bd}{3} \tag{8}$$

for $e < d$, and

$$V_r = 0.9 F_v \frac{2bd_{ef}}{3} \tag{9}$$

for $e > d$. In the above equations $F_v = f_v(K_D K_H K_{SV} K_T)$. f_v is the specified strength in shear and K_{SV} is the service-condition factor for shear.
According to the design approach provided in NDS 2018 [7], the shear force at support should satisfy the following equation:

$$V \leq 0.48 F_v' b d_{ef} \left(\frac{d_{ef}}{d}\right)^2 \tag{10}$$

in which, F_v' is the adjusted shear design value parallel to the grain. A general comparison of the limitations stated for notched Glulam members in Canadian, European, and U.S. codes has been provided in Table 1.

Table 1: *Comparison of design approaches for notched Glulam beams in Eurocode 5, CSA O86-19, and NDS 2018 Standards, considering taper notches, notch length, and allowable notch depth.*

Standards	Taper Notch	Notch Length	Limitation on Maximum Notch Depth
CSA O86-19	-	✓	0.25 d
Eurocode 5	✓	✓	-
NDS 2018	-	-	0.1 d or 3"

Table 1 shows that CSA O86-19 and Eurocode 5 account for notch length, while taper notches are only considered in Eurocode 5. On the other hand, NDS 2018 and CSA O86-19 impose strict limitations on notch depth, while Eurocode 5 is comparatively more flexible.

3 FE MODELLING

3.1 TRANSVERSE NOTCH

A 3D finite element (FE) model corresponding to a notched Glulam beam with reported performance in the literature [2] is developed in ANSYS software. The Glulam beam has seven layers with uniform thickness (see Figure 2). The beam has a rectangular cross-section with a width of 100 mm, a total height of 220 mm, and an overall length of 4000 mm. The beam is notched at both ends, the depth of each notch is 110 mm (half of the depth of the beam), and the notch length is 250 mm. The beam is simply supported at two ends. Two-point loads of 5 kN (F=10 kN) are applied to the beam at a 1200 mm distance from the supports. Four steel plates with a width of 100 mm, length of 140 mm, and thickness of 10 mm are placed at the load application and support positions to reduce the effect of local indentations. All the above-mentioned geometric parameters of the beam are illustrated in Figure 2.
All of the geometric parameters, loads, and boundary conditions are symmetric in this problem. Therefore, the symmetric constraint is considered in the middle of the span of the beam, and just half of the beam (Figure 3) has been modelled.

https://doi.org/10.52202/069179-0356

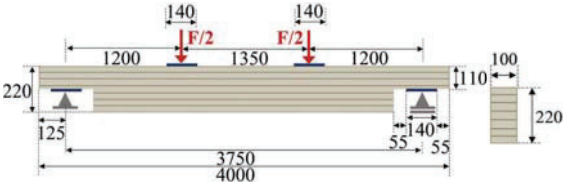

Figure 2: *Schematic of the notched glulam beam considered in [2] and the selected geometric parameters for model validation. All dimensions are in mm.*

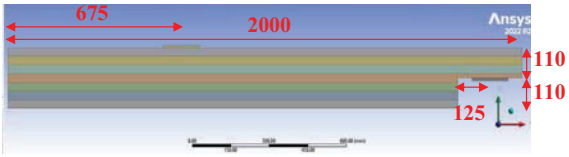

Figure 3: *Developed FE model corresponding to the beam in Figure 2. All dimensions are in mm. Half of the beam has been considered due to symmetry.*

3.2 ROUNDED NOTCH EFFECT

To investigate the effect of a rounded notch, two Glulam beams with rounded notched corners with a radius of 10 mm and 16 mm (see Figure 4) are analyzed in ANSYS Workbench. The stress fields in these models are compared with those of the Glulam beam with sharp notches in Section 4.3.

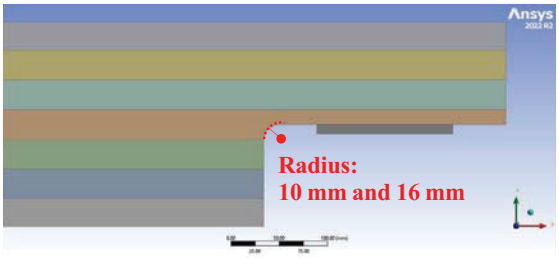

Figure 4: *Rounded notched corner.*

3.3 LONGITUDINAL AND TRANSVERSE NOTCH

In addition to the transverse end notches, two longitudinal notches are also included along the beam to investigate the effect of longitudinal notches on the stress fields (see Figure 5). The longitudinal notches have a square cross-section (20 mm × 20 mm) and are located under the sixth layer on both face sides of the Glulam beam.

4 RESULTS

4.1 VALIDATION OF THE MODEL

To validate the developed model, the predicted load-deflection curve of the selected Glulam beam with transverse notches is compared with experimental data as well as other reported models in the literature [2,3].
In experiments reported in [2], a linear elastic behaviour has been observed for the notched Glulam beam up to failure. In the FE model developed in [3], a linear elastic behaviour has also been predicted for the notched Glulam beam. Therefore, the comparisons are made based on the slope of the linear region of the load-deflection curves. The values of loads, deflections, and slopes of load-deflection lines are listed in Table 2. Preliminary results show a very good agreement between the models and experimental data (see Figure 6). The differences between the predicted slope of the load-deflection line in the current FE model and those obtained experimentally in [2] and those predicted in [3] are approximately 10% and 2%, respectively.

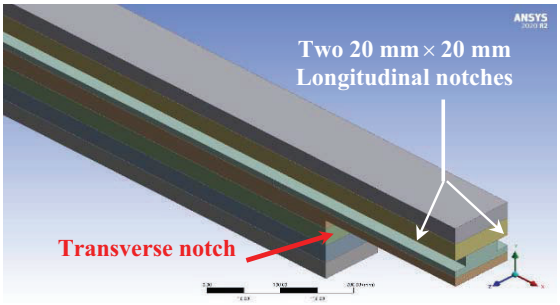

Figure 5: *3D FEM of the Glulam beam with the transverse and longitudinal notches.*

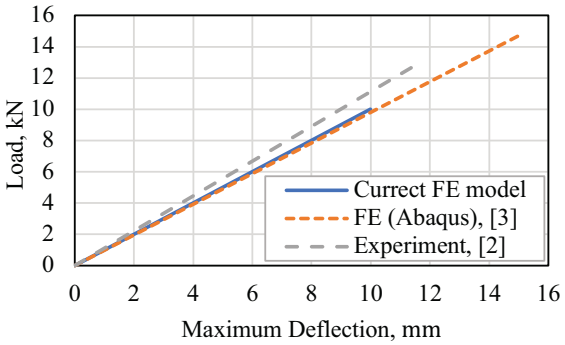

Figure 6: *Comparison between the elastic region of the load-deflection curves of the notched Glulam beam of the current FEM in ANSYS©, experiment [2], and FEM in ABAQUS© [3].*

Table 2: *Loads, deflections, and initial slopes of load-deflection curves of the notched Glulam beam of the current FE model in ANSYS©, experiment [2], and FEM in ABAQUS© [3].*

	Load (kN)	Deflection (mm)	Slope $10^6 \frac{N}{m}$
Experiment, [2]	12.8	11.5	1.113
FE Model in ABAQUS, [3]	14.8	15.1	0.980
Current FE Model (ANSYS)	10.0	9.98	1.001

4.2 EFFECT OF THE TRANSVERSE NOTCH ON INDUCED STRESSES

The distribution of perpendicular to the grain stress is shown in Figure 7. It is noted that the maximum value of this normal stress, σ_y, is 3.7 MPa and occurs at the notched corner.

The stress stress distribution is shown in Figure 8. The maximum value of the shear stress, σ_{xy}, (3.0 MPa) is highlighted at the notched corner.

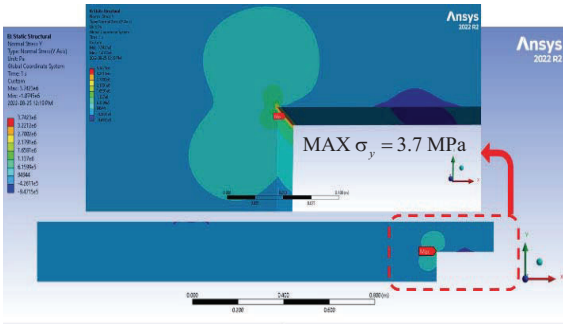

Figure 7: *Distribution of normal stress σ_y (Pa) under the applied load of 10 kN.*

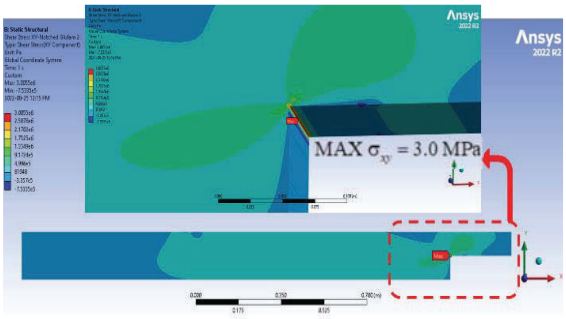

Figure 8: *Distribution of shear stress σ_{xy} (Pa) under the applied load of 10 kN.*

To study the state of stress at the notch vicinity, a path is defined in the model from the notched corner to the other end of the beam parallel to the beam direction. The yy and xy components of the stress components along this path are shown in Figures 9 and 10, respectively. An abrupt increase of the tensile stress perpendicular to the grain and shear stress at the notched corner has been noted.

It is noted that the values of shear stress and tensile stress perpendicular to the grain are increased significantly near the notch. These stress concentrations are the main cause for Mode I and II crack initiation at the notched corner and the reported brittle failure of notched Glulam beams in the literature [2].

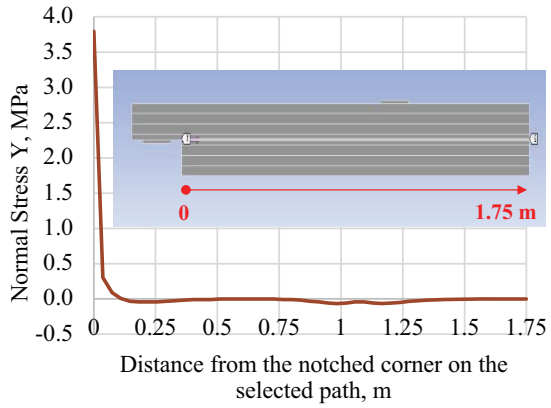

Figure 9: *Normal stress σ_y (MPa) along the selected path.*

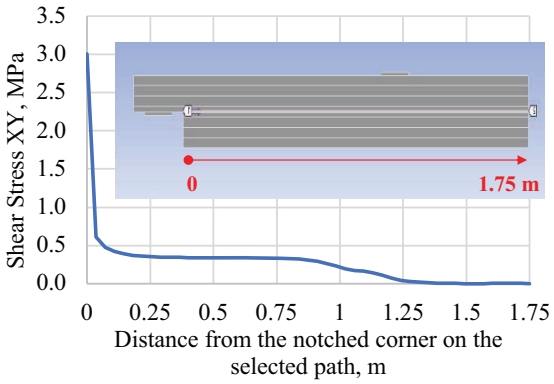

Figure 10: *Shear stress σ_{xy} (MPa) along the selected path.*

To define the input material properties in ANSYS, similar to [2], we have used the mechanical properties of spruce timber that is classified under strength class C22 in accordance with EN 338 [8]. The shear strength of the material is 3.8 MPa as highlighted in [2] and [8].

For verification purposes, a comparison was made between the measured capacity of the Glulam beam with deep, transverse notches reported in the literature [2] and the expected capacity of the end-notched Glulam beam using design equations provided in Eurocode 5, CSA O86-19, and NDS 2018 (see Figure 11). It should be noted similar strength values have been considered in Equations (2), (6) and (10) for this comparison (dry condition). Considering various adjustment factors and clauses highlighted in different standards (see Section 2), slight differences are expected for the beam capacity.

Figure 11 shows that Eurocode 5 and CSA O86-19 overestimate the capacity of the notched Glulam beam, while NDS 2018 underestimates it. Considering the differences between the definitions of adjustment factors in various standards, such discrepancies may be justifiable. Also, it is noted that the predicted load-bearing capacity using the current FE model (12.66 kN) is in good agreement with the measured capacity (12.80 kN). The beam capacity (12.66 kN) has been estimated numerically assuming the material behaviour is linear followed by a brittle failure when the shear stress at the notch corner

https://doi.org/10.52202/069179-0356

reaches the the shear strength of the selected spruce grade (3.8 MPa).

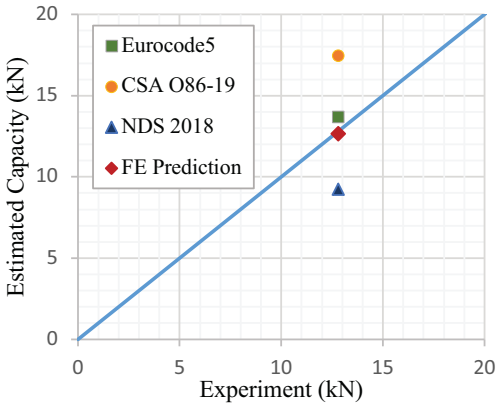

Figure 11: *Comparison between the estimated capacity based on Eurocode 5 [5], CSA O86-19 [6], NDS 2018 [7], FE model prediction and the measured capacity [2].*

4.3 EFFECT OF THE ROUNDED NOTCHED CORNER ON THE STRESS FIELD

4.3.1 Rounded notched corner with a radius of 10 mm

The validated model is used to conduct a range of parametric studies on the notch geometry. The yy component of the stress (perpendicular to the grain stress) in Glulam beam with a rounded notched corner with a radius of 10 mm is shown in Figure 12. The xy component of the stress tensor is also shown in Figure 13.

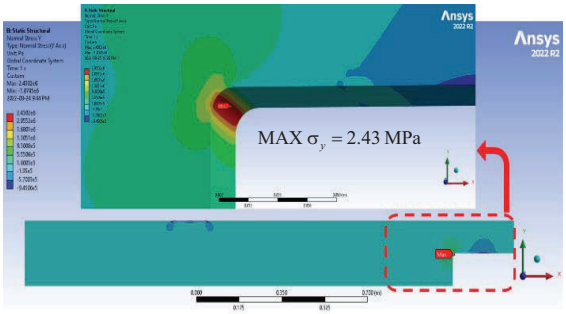

Figure 12: *Distribution of normal stress σ_{yy} (Pa) for the case of the rounded notched corner with a radius of 10 mm, under the applied load of 10 kN.*

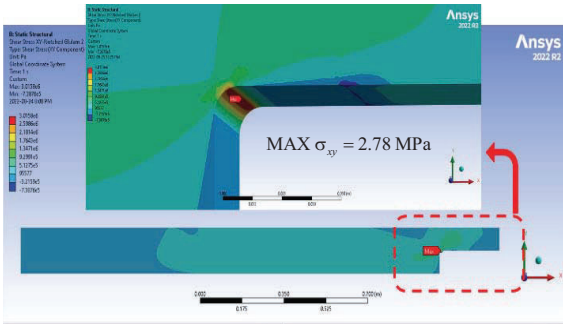

Figure 13: *Distribution of shear stress σ_{xy} (Pa) for the case of the rounded notched corner with a radius of 10 mm, under the applied load of 10 kN.*

4.3.2 Rounded notched corner with a radius of 16 mm

The yy component of the stress tensor of the Glulam beam with a rounded notched corner with a radius of 16 mm is shown in Figure 14. It can be seen that the maximum normal stress, σ_y, occurs at the rounded notched corner, reaching a value of 1.89 MPa under the applied load of 10 kN. The xy component of the stress tensor is also shown in Figure 15. Under the same applied load, the maximum shear stress, σ_{xy}, is 2.39 MPa which occurs at the notched corner.

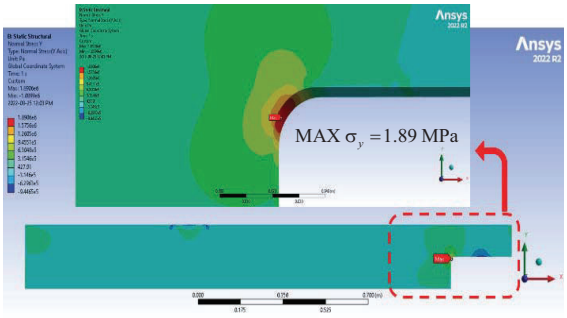

Figure 14: *Distribution of normal stress σ_{yy} (Pa) for the case of the rounded notched corner with a radius of 16 mm, under the applied load of 10 kN.*

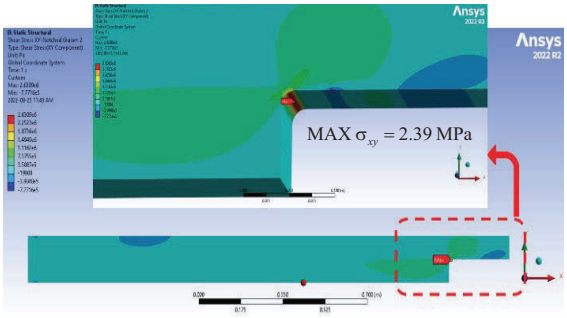

Figure 15: *Distribution of normal stress σ_{xy} (Pa) for the case of the rounded notched corner with a radius of 16 mm, under the applied load of 10 kN.*

4.3.3 Stress Field Comparison between Glulam Beams with Sharp Notch and Rounded Corners

A path is defined parallel to the beam axis starting from the location of the maximum stress component at the notched corner. The normal stress, σ_y, and shear stress, σ_{xy}, along the beam with the sharp notch, the beam with the rounded notched corner with a radius of 10 mm, and the beam with the rounded notched corner with a radius of 16 mm are shown in Figures 16 and 17, respectively.
According to Figure 16, it can be seen that the rounded notched corners with a radius of 10 mm and 16 mm reduce the maximum value of the normal stress, σ_y, by 34% and 49%, respectively. Based on Figure 17, using rounded notched corners with a radius of 10 mm or 16 mm can decrease the maximum shear stress, σ_{xy}, by 7% and 20%, respectively.

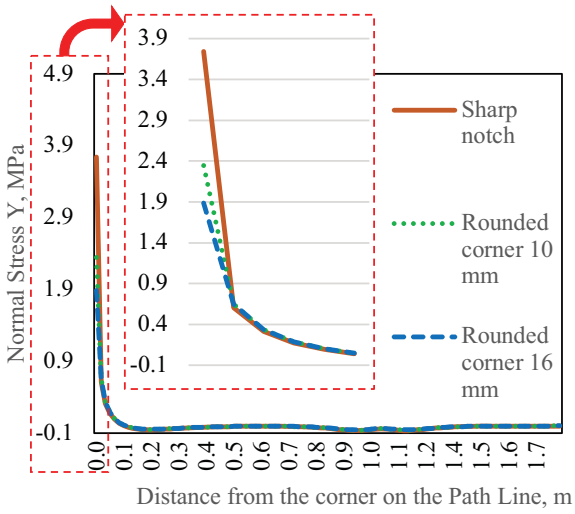

Figure 16: *Normal stress, σ_y, along the selected path.*

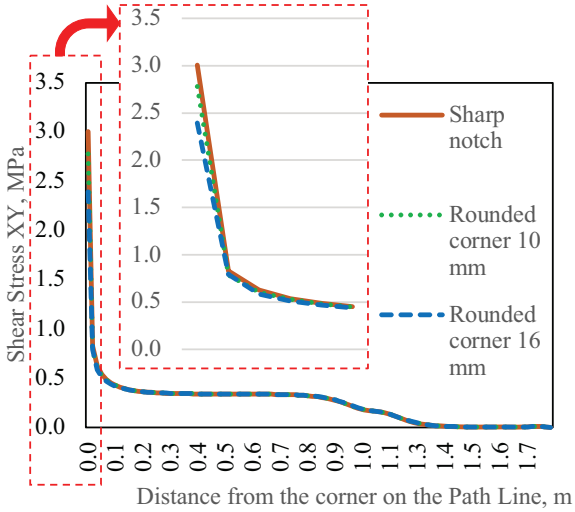

Figure 17: *Shear stress, σ_{xy}, along the selected path.*

4.4 EFFECT OF THE LONGITUDINAL NOTCH

For the case when the Glulam beam has two longitudinal notches in addition to the transverse end notches, the distribution of normal stress, σ_y, and shear stress, σ_{xy}, are shown in Figures 18 and 19, respectively.
The maximum values of normal stress, σ_y, and shear stress, σ_{xy}, for the Glulam beam with the longitudinal notches are 4.17 MPa and 3.33 MPa, respectively, occurring at the notched corner. It can be seen that the maximum values of normal stress, σ_y, and shear stress, σ_{xy}, for this beam are increased by 13% and 11%, respectively, compared to those values in the beam without the longitudinal notch.

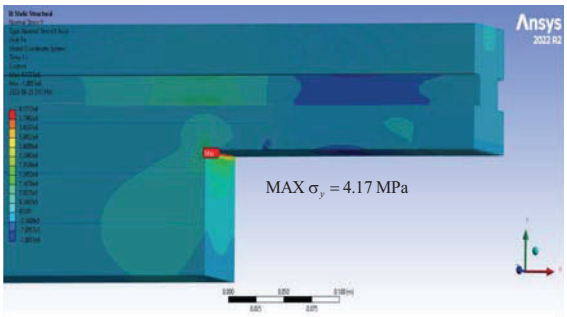

Figure 18: *Normal stress σ_y (Pa) distribution in the Glulam beam with the longitudinal and transverse notches, under the applied load of 10 kN.*

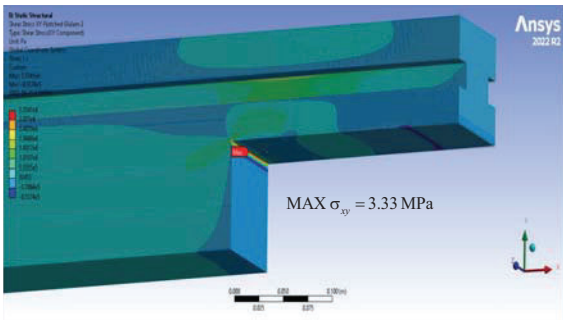

Figure 19: *Shear stress σ_{xy} distribution in the Glulam beam with the longitudinal and transverse notches, under the applied load of 10 kN.*

The stress distributions of σ_y and σ_{xy} for the layer of the Glulam beam in which the longitudinal notches are located are shown in Figures 20 and 21.
It is noted that at the longitudinal notch above the notched corner, the normal stress perpendicular to the grain, σ_y, has a maximum value of 1 MPa (see Figure 20). The maximum shear stress, σ_{xy}, also reaches 1.78 MPa (occurring at a location between the support and the notched corner) which is significant for the longitudinal notch (see Figure 21).

https://doi.org/10.52202/069179-0356

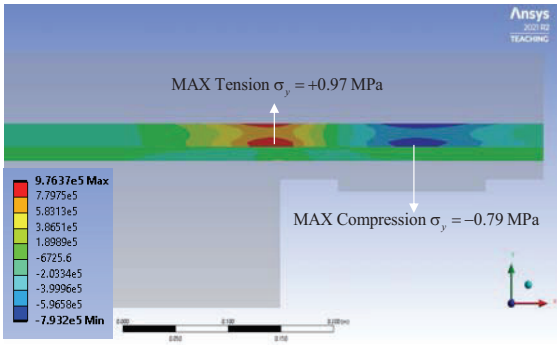

Figure 20: *Normal stress $\sigma_y(Pa)$ distribution in the layer of the Glulam beam in which the longitudinal notches are cut.*

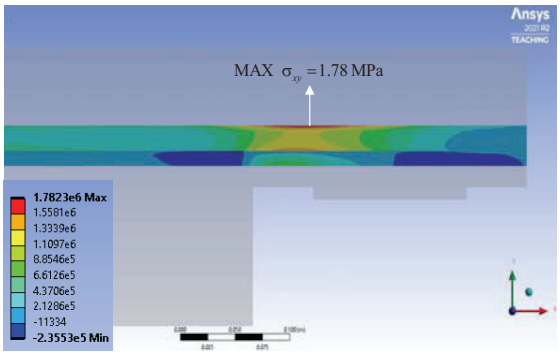

Figure 21: *Shear stress σ_{xy} (Pa) distribution in the layer of the Glulam beam in which the longitudinal notches are cut.*

5 CONCLUSIONS

A comprehensive review of design equations given in different standards for calculating the capacity of Glulam beams with transverse notches was conducted. Slight discrepancies were noted, which was expected due to various adjustment and safety factors. It was found that the Canadian standard (CSA O86-19) and Eurocode 5 consider the length of notches, while only Eurocode 5 accounts for taper notches. The maximum allowable notch depth is restricted by NDS 2018 and CSA O86-19, whereas Eurocode 5 is comparatively more flexible. There is currently a lack of provisions for notched columns subjected to combined axial and bending loads, which necessitates further investigation in the future.

To understand the effect of notch geometry and the interaction of notches cut in different directions, a FE model was developed and validated using experimental data. It was shown that the model predictions and experimental data in the literature are in agreement in terms of stiffness and strength. The difference between the predicted slope of the load-deflection line in the current FE model and the experimental value in the literature was approximately 10%. The current FE model also predicted a load-bearing capacity that is approximately 1.1% less from the test data reported in the literature [2].

The developed model in this paper was used to assess the notch effect on the stress distribution (normal and shear) in the tested Glulam beam for various notches and notched corners. It was shown that the longitudinal notches could interact with transverse notches and increase the stress levels. In the beam with both longitudinal and transverse notches, the maximum normal stress, σ_{yy}, and shear stress, σ_{xy}, at the notched corner were increased by 13% and 11%, respectively, compared to the values in the notched beam without a longitudinal notch. An increase in shear stress and normal stress perpendicular to the grain was also noted at the longitudinal notch near the transverse notch. It was shown that rounded notched corners with a radius of 10 mm or 16 mm could reduce the maximum normal stress, σ_{yy}, by 34% and 49%, respectively, and decrease the maximum shear stress, σ_{xy}, by 7% and 20%, respectively.

ACKNOWLEDGMENTS

Financial support from the National Sciences and Engineering Research Council (NSERC) through a Discovery grant is gratefully acknowledged. The authors would like to thank Professor Thomas Tannert (UNBC) for scientific discussions on notched timber products.

REFERENCES

[1] Jockwer, R.: Structural Behaviour of Glued Laminated Timber Beams with Unreinforced and Reinforced Notches. PhD Thesis. ETH, Zurich, Switzerland, 2014.

[2] Todorović M., Glišović I., Stevanović B.: Experimental Investigation of Cracked Notched Glulam Beams Repaired with Screws. In: *Proceedings of World Conference on Timber Engineering*. Seoul, South Korea, 2018.

[3] Todorović M., Glišović I., Stevanović B.: Numerical modelling of end-notched glulam beams reinforced with GFRP bars: *Proceedings of World Conference on Timber Engineering*. Santiago, Chile, 2020.

[4] Todorović M., Glišović I., Stevanović B.: Experimental investigation of end-notched glulam beams reinforced with GFRP bars: European Journal of Wood and Wood Products, 80:1071–1085, 2022.

[5] European Committee for Standardization: Eurocode 5: design of timber structure. Brussels, Belgium, 2008.

[6] National Standard of Canada, CSA O86:19, Engineering design in wood, 2019.

[7] National Design Specification for wood construction, NDS: American Wood Council, 2018.

[8] European Committee For Standardization: EN 338: Structural timber - Strength classes. Brussels, Belgium, 2016.

World Conference on Timber Engineering Oslo 2023

A STUDY ON THE SEISMIC PERFORMANCE OF SHEAR WALLS UNDER A DYNAMIC LOAD

Tomoki Furuta[1] and Masato Nakao[2]

KEYWORDS: Post-and-beam construction system, Plywood shear wall, Braced shear wall, Shake table test

1 INTRODUCTION

In recent years, the number of Japanese buildings that have suffered damage due to multiple large earthquakes has increased. As timber buildings do not have an obvious yield point, the shear stiffness of these buildings decreases gradually during the occurrence of multiple earthquakes. Consequently, there is concern about a decrease in seismic performance, which may result in the collapse of timber houses even during relatively small earthquakes.

Regarding timber shear walls, to investigate the dynamic performance and to build an analysis model in order to predict earthquake response, several experimental and numerical studies have been conducted, e.g. [1-5]. Nowadays, It has become possible to predict the earthquake response of timber houses.

Nevertheless, it remains difficult to predict the earthquake response of timber houses when there are multiple earthquake motions. For this reason, a shake table test of the shear walls of the Japanese post-and-beam construction system was conducted to understand the dynamic characteristics of shear walls during multiple earthquakes. Hysteresis models of the shear walls for earthquake response analysis are proposed using the shake table test results. Moreover, an equivalent linearization method as a simple prediction method for a maximum response displacement was tried.

2 SHAKE TABLE TEST

2.1 OUTLINE

Specimens for the shake table test were constructed using the Japanese post-and-beam construction system. The wall length of each specimen was 2730 mm, and the specimens contained four columns as shown in Figure 1. Two kinds of shear walls were tested. The first, a plywood shear wall, was 910 mm × 2730 mm in size. A sheet of plywood was nailed to the frame using N50 nails spaced at 150 mm. The second was a braced shear wall, two 45 mm × 90 mm timber braces were attached crosswise to the frame. Conventional brace connectors (C-brace) were used to connect the ends of the braces and the columns. Newly-developed ductile brace connectors (D-brace) were also used as a variation of the braced shear wall.

The new brace connector, as shown in Figure 2, includes a damping mechanism. The thickness of the steel for the connector is 3.2mm. As the lateral displacement of the braced shear wall increases, the bridges deform to absorb a displacement between a column and a brace. Damping force is produced by the plastic deformation of the bridges. The steel core is covered with high-damping rubber to use as a brace connector.

A 15.8 kN weight was applied to the beam (Figure 1). Rollers were arranged along the longitudinal direction of the weight. 25 kN hold-down connectors were installed to reinforce the joint between the ends of the columns and the horizontal members.

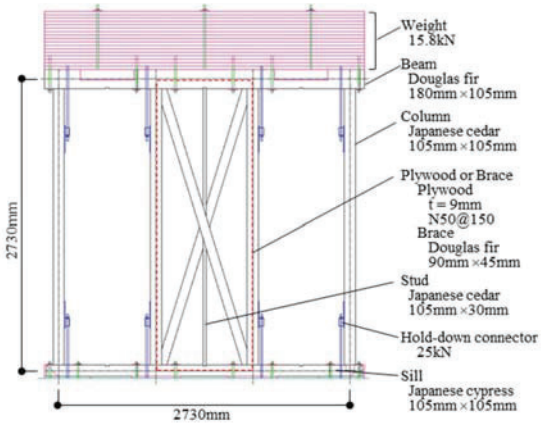

Figure 1: *Specimen for the shake table test*

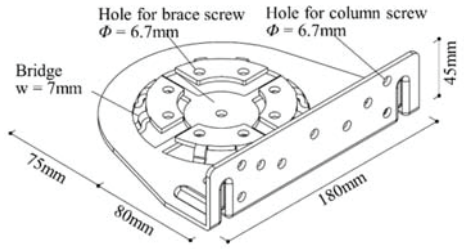

Figure 2: *Core of newly-developed ductile brace connector (To use as a brace connector, this steel core is covered with high damping rubber.)*

[1] Tomoki Furuta, Nishinippon Institute of Technology, Japan, furuta@nishitech.ac.jp
[2] Masato Nakao, Yokohama National University, Japan, mnakao@ynu.ac.jp

https://doi.org/10.52202/069179-0357

The seismic waves of the 1995 JMA Kobe NS earthquake (as observed at the Kobe branch of the Japan Meteorological Agency on January 17th, 1995) were applied to the specimen. The time history of acceleration and the response acceleration are shown in Figures 3 and 4, respectively.

The input level was stepped up to 80% for the plywood shear wall and up to 100% for the braced shear wall. Before each input step level, 50% of the previous level was applied in order to evaluate the earthquake response characteristics after the stiffness degradation of the shear walls, as shown in Figure 5. In this paper, the step-up input is referred to as "1st", whereas 50% of the previous level input is referred to as "2nd."

Accelerometers were attached to the shake table, the sill, and the beam of the specimens. The story displacement was measured between the beam and the sill.

2.2 SHEAR FORCE-DISPLACEMENT RELATIONSHIP AND FAILURE MODE

The shear force-displacement relationship of the plywood shear walls is shown in Figure 6. The shear force Q was calculated using Equation (1).

$$Q = m \cdot a \tag{1}$$

where m is mass(16kN/9800mm/sec^2), a is acceleration(mm/sec^2).

A remarkable degradation of shear stiffness was seen under the 40% input load. During the 80% input load, the shear stiffness significantly decreased. Pull-out, punch-out, and fracture of nails were observed as shown in Figure 7.

For the conventional brace connector, a remarkable decrease in the shear stiffness was observed during the 80% input load as shown in Figure 8. After the application of the 100% input load, as shown in Figure 9, the pull-out of the screws on the column and buckling of the stud were observed.

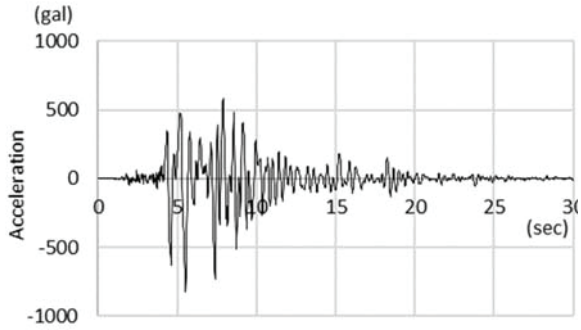

Figure 3: *Time history of JMA Kobe NS wave*

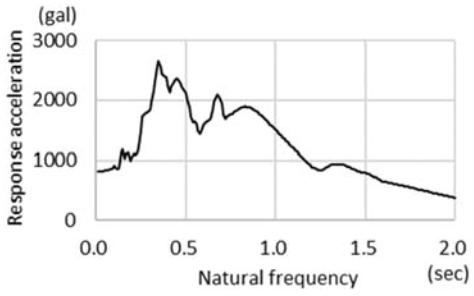

Figure 4: *Acceleration response spectrum of JMA Kobe wave (h=5%)*

Figure 5: *Input level of the JMA Kobe wave*

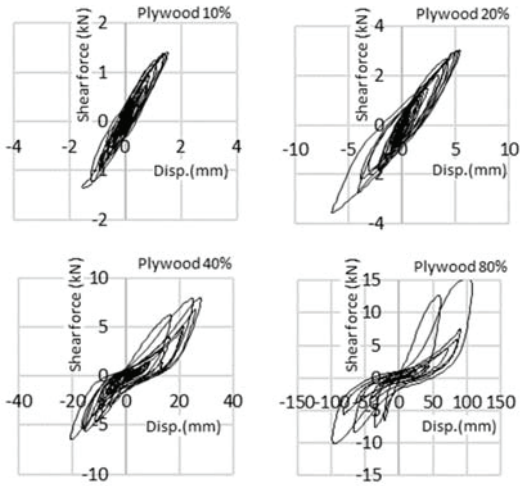

Figure 6: *Shear force-displacement relationships of plywood shear wall specimen on each input*

Figure 7: *Plywood shear wall specimen and nails after the test*

No shear stiffness reduction was seen in the shear force-displacement relationship of the braced shear wall with ductile brace connectors during the series of inputs as shown in Figure 10. There was no visible damage to the connectors even after the 100% input load, as shown in Figure 11.

The degradation of the shear stiffness can be found easily from the combined shear force-displacement relationships as shown in Figures 12 to 14. Skeleton curves of the shear force-displacement relationships are shown in Figure 15. The ratio of the shear forces at 1/120 rad for plywood shear wall: braced shear wall with conventional brace connectors: braced shear wall with ductile brace

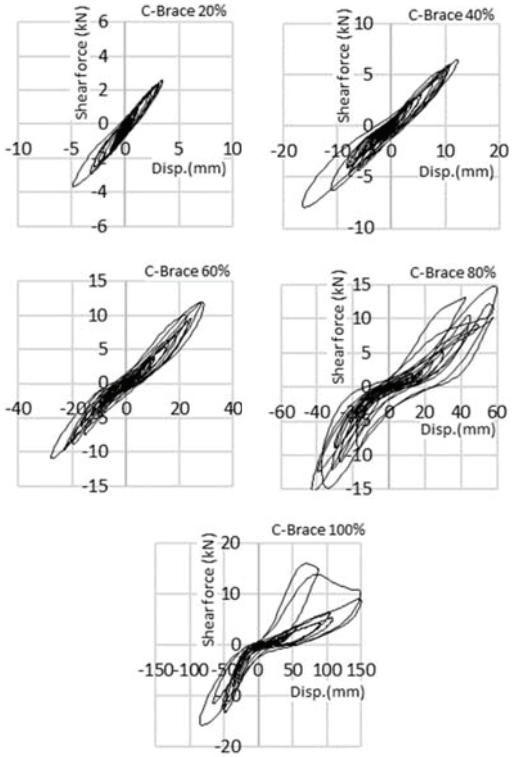

Figure 8: *Shear force-displacement relationships of braced shear wall specimen with conventional brace connectors on each input*

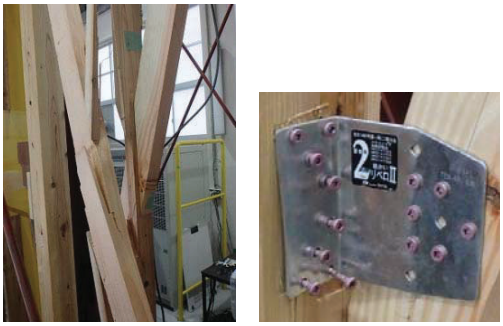

Figure 9: *Braced shear wall specimen with conventional brace connectors after the test*

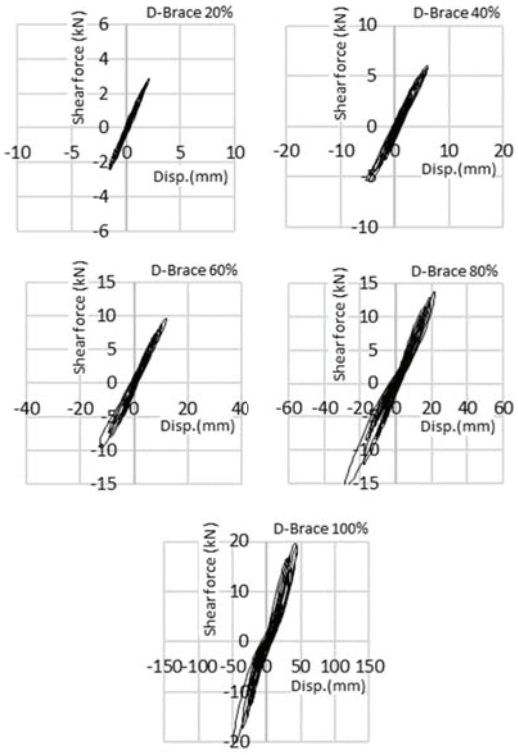

Figure 10: *Shear force-displacement relationships of braced shear wall specimen with ductile brace connectors on each input*

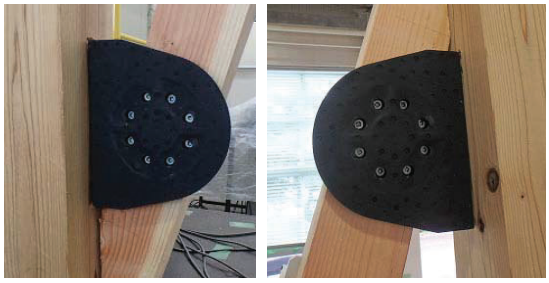

Figure 11: *Ductile brace connectors after the test*

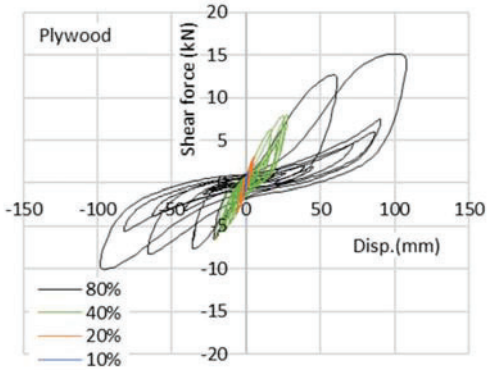

Figure 12: *Shear force-displacement relationships of plywood shear wall specimen*

https://doi.org/10.52202/069179-0357

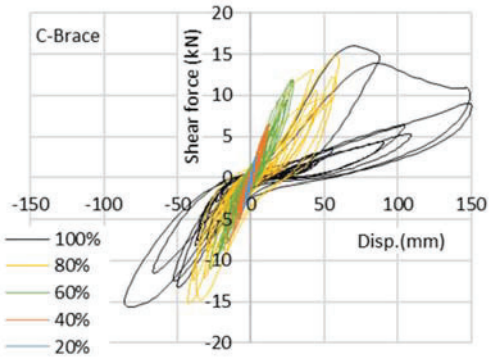

Figure 13: *Shear force-displacement relationships of braced shear wall specimen with conventional brace connectors*

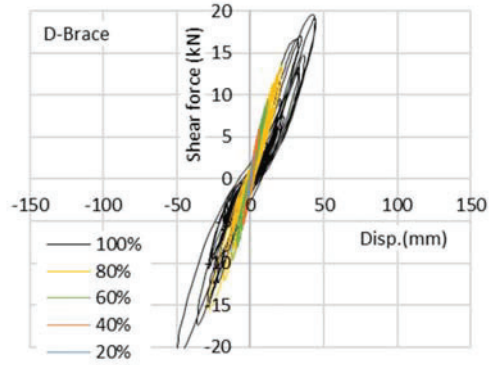

Figure 14: *Shear force-displacement relationships of braced shear wall specimen with ductile brace connectors*

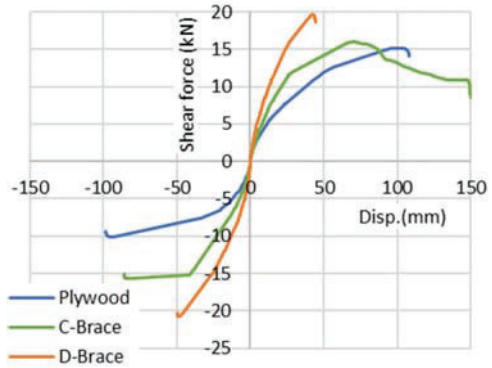

Figure 15: *Skeleton curves of shear force-displacement relationships of shear wall specimens*

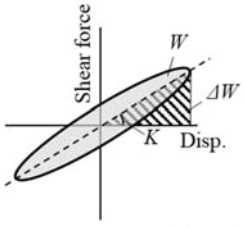

Figure 16: *Notations in Equation (2) for calculation of H_{eq}*

connectors was 1.0:1.4:2.0. It is obvious that the shear stiffness of the ductile brace connector is superior to the plywood shear wall and the braced shear wall with conventional brace connectors.

2.3 TRANSITION OF STRUCTURAL PERFORMANCE OF SPECIMEN

To grasp the structural performance transition of the specimens during a series of loading, the equivalent damping factor(H_{eq}) was calculated using Equation (2) on each input load. The notations refer to Figure 16.

$$H_{eq} = \frac{W}{4\pi\Delta W} \tag{2}$$

In addition to that, the shear stiffness of one shear force-displacement loop (K) that involves a maximum displacement was calculated. For a comparison, initial stiffness (K_0) was also calculated on each input load. The amplitude of one loop picked out for the calculation was approximately 0.5mm to 1.0mm.

Figure 17 shows the structural performance transition of the plywood shear wall. It is found that the H_{eq} is about 15% regardless of input level. It is also found that the

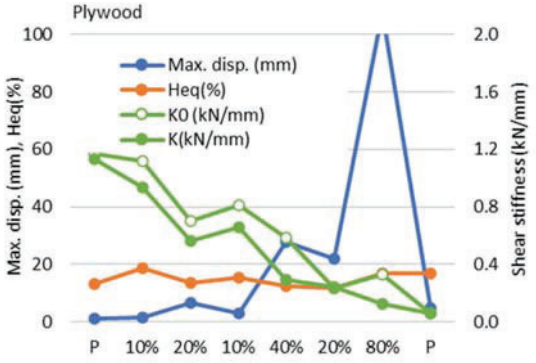

Figure 17: *Maximum displacement, equivalent damping factor(H_{eq}), shear stiffness K_0 and shear stiffness K of plywood shear wall specimen*

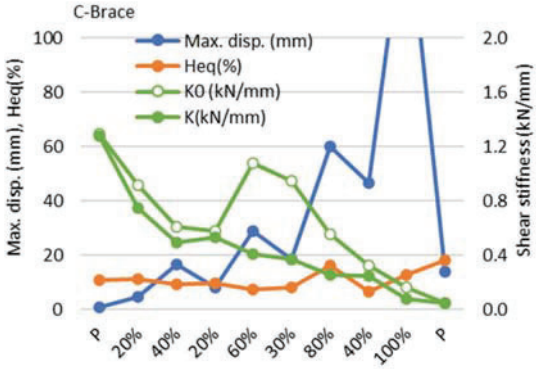

Figure 18: *Maximum displacement, equivalent damping factor(H_{eq}), shear stiffness K_0 and shear stiffness K of braced shear wall specimen with conventional brace connectors*

https://doi.org/10.52202/069179-0357

shear stiffness decreases as the maximum displacement increases. In terms of K_0, it is larger than K during a series of input loads.

Figure 18 shows the ones of the braced shear wall with convention brace connectors. H_{eq} is about 10 to 15% through the series of input loads. It is also found that the shear stiffness decreases as the maximum displacement increases same as the plywood shear wall. Unlike the plywood shear wall, the difference between K and K_0 is relatively large. It implies that the degradation of shear stiffness of the braced shear wall with convention brace fasteners is remarkable.

Figure 19 shows the ones of the braced shear wall with ductile brace connectors. H_{eq} is about 10%, it is lower than the plywood shear wall and the braced shear wall with conventional brace connectors. As in the previous Figure 14, the braced shear wall with the ductile brace connectors was almost elastic during the series of input loads, it is considered that damping due to plasticity is not contained in H_{eq}. Moreover, K_0 is close to K, and degradation of shear stiffness is considered to be little.

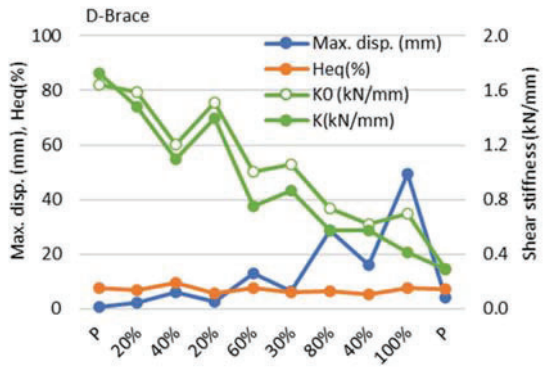

Figure 19: *Maximum displacement, equivalent damping factor(H_{eq}), shear stiffness K_0 and shear stiffness K of braced shear wall specimen with ductile brace connectors*

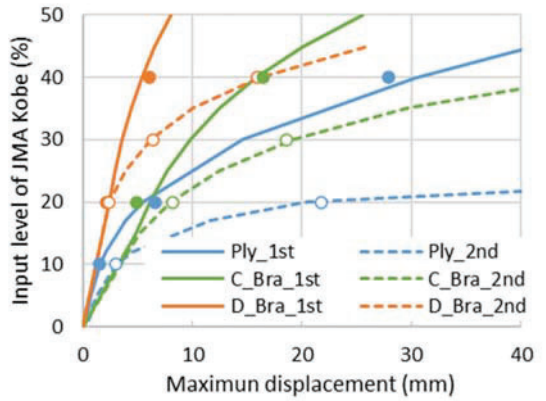

Figure 20: *Maximum displacement for different input levels*

2.4 EFFECT OF MULTIPLE INPUTS

Figure 20 shows the relationship between the input level of the JMA Kobe NS wave and the maximum response displacement of the shear walls. The regression curves for the 1st and 2nd inputs are also indicated in the figure. For the plywood shear wall, the 2nd displacement at 10% input was twice that of the 1st displacement. The 2nd displacement of the braced shear wall with ductile brace connectors exceeded that of the 1st displacement at an input over 20%, whereas the 2nd displacement of the braced shear wall with conventional brace connectors exceeded that of the 1st displacement at an input over 15%. From the regression curves, it can be seen that the response displacement of the 2nd input increases rapidly with the input level.

Figure 21 shows the relationship between the maximum displacement and the natural period of the three shear walls, where the maximum displacements were divided by the input level to convert to the one under 100% wave. The displacement response spectrums of the JMA Kobe NS 100% wave with 10%, 15%, and 20% damping ratio is also displayed in the figure. The natural period T was calculated using the mass, m=16kN/g (g=9800mm/sec^2), and shear stiffness, K(kN/mm).

$$T = 2\pi\sqrt{\frac{m}{K}} \tag{3}$$

Most of the maximum displacements are located between the displacement response spectrums of damping ratios of 15% and 20%. There is no remarkable difference between 1st and 2nd inputs. From the figure, it is found that a maximum response displacement can be estimated using the natural period based on K and the displacement response spectrum. Suppose the displacement response spectrum of a 15% damping ratio is used, predicted

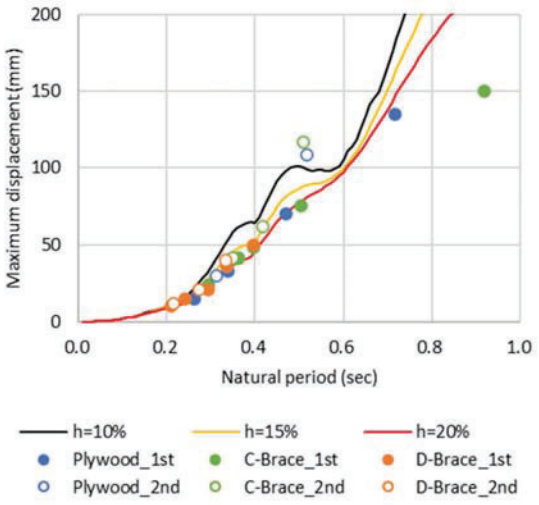

Figure 21: *Relationship between maximum displacement and natural period based on shear stiffness K*

https://doi.org/10.52202/069179-0357

response displacement would be the safe side for the three shear walls.
However, there is an issue that for predicting a maximum response displacement using a displacement response spectrum, it is impossible to grasp K beforehand because K is let from a maximum response displacement.

3 RESPONSE DISPLACEMENT PREDICTION

3.1 EARTHQUAKE RESPONSE ANALYSIS

On the basis of the shake table test results, hysteresis models of the plywood shear wall and the braced shear wall were set as shown in Figures 22 to 24. Earthquake response analysis was conducted using input waves on the shake table test. 16kN of weight and 10% of viscous damping were applied to single degree of freedom analysis model.
Figures 25 to 27 show maximum response displacements. A comparison of the earthquake response analysis using the hysteresis models and the shake table test results shows that the maximum response displacements of the analysis and the shake table test showed a good degree of correspondence in a small displacement range. In a large displacement range, there is a relatively large difference, which implies that more parameters of the hysteresis model are needed to predict maximum response displacements accurately in a wide displacement range.

3.2 EQUIVALENT LINEARIZATION METHOD

There was an issue that K derived from the maximum response displacement is needed to calculate the natural period for the prediction of maximum response displacement using a displacement response spectrum. As one solution for the above-expressed issue, in place of K, there is a possibility that K_0 is rather useful for the prediction of a maximum response displacement because K_0 can be calculated based on approximately 0.5mm to 1mm of amplitude. If time history data of displacement and acceleration could be recorded even under relatively small input, K_0 can be calculated.
Figure 28 shows the relationship between the natural period calculated using K_0 and the maximum displacement of the shear walls, where the maximum displacements were converted to the one under 100% wave. The displacement response spectrum of the JMA Kobe NS 100% wave with a 5% damping ratio is added to the figure as well as 10%, 15%, and 20%. Most of the maximum displacements of the shear walls are located near the displacement response spectrum of a 5% damping ratio, which implies that the response displacement can be predicted using the natural period based on K_0 regardless of the 1st or 2nd input.
Comparing the experimental maximum displacements and the displacement response spectrum, most of the maximum displacement was lower than the displacement response spectrum. Therefore, safe side prediction regarding maximum displacements is expected.
In case displacement and acceleration data can't be obtained, to grasp K_0 for the prediction of a maximum response displacement, it is valid to make use of the largest displacement in experienced displacements so far because there is a close relationship between the largest displacement in the past and K_0.
Figure 29 shows the relationship between the shear stiffness degradation ratio and the maximum displacement. The x value of each point is the largest

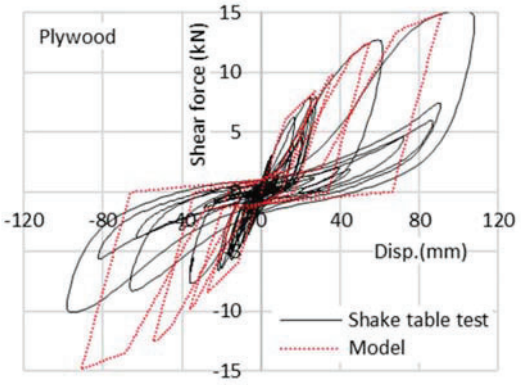

Figure 22: *Shear force-displacement relationship model of plywood shear wall*

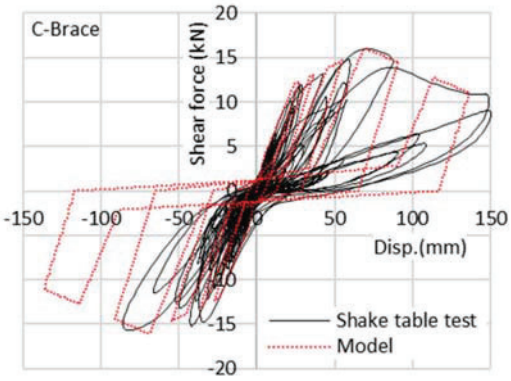

Figure 23: *Shear force-displacement relationship model of braced shear wall with conventional brace connectors*

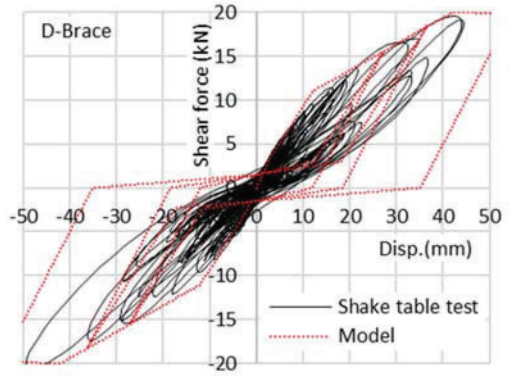

Figure 24: *Shear force-displacement relationship model of braced shear wall with ductile brace connectors*

https://doi.org/10.52202/069179-0357

displacement up to the time, and the y value, shear stiffness degradation ratio, is a ratio of the shear stiffness(K_0) after the input load where the largest displacement is recorded to the initial shear stiffness.
Ignoring the difference of 1st and 2nd inputs, regression lines according to the points belonging to each shear wall are also indicated in the figure. Equations (4), (5), and (6) represent regression lines of the plywood shear wall, the braced shear wall with conventional brace connectors, and the braced shear wall with ductile brace connectors, respectively.

$$y = x^{-0.4} - x/1000 \quad (4)$$
$$y = x^{-0.25} - x/500 \quad (5)$$
$$y = x^{-0.22} - x/500 \quad (6)$$

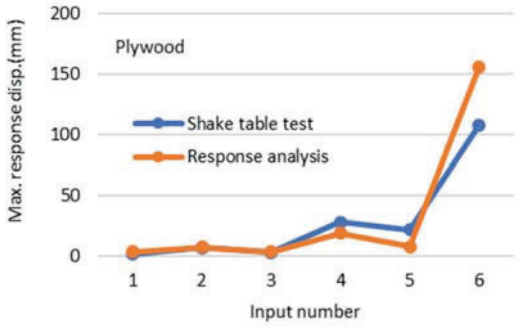

Figure 25: *Maximum response displacement of plywood shear wall*

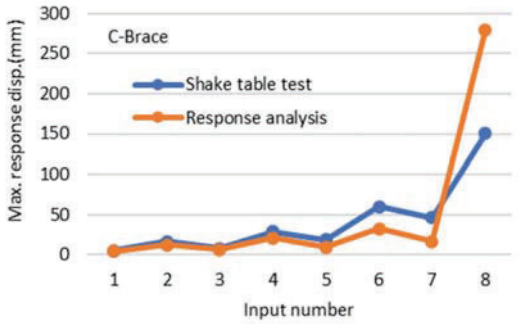

Figure 26: *Maximum response displacement of braced shear wall with conventional brace connectors*

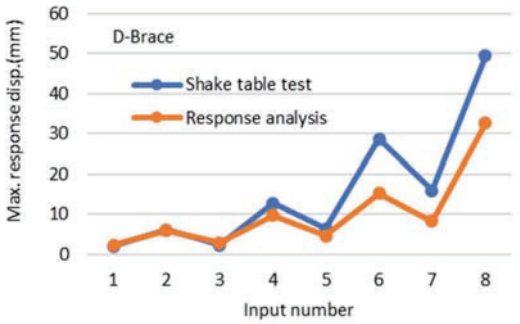

Figure 27: *Maximum response displacement of braced shear wall with ductile brace connectors*

In the case that the experienced largest displacement is known, the ratio of stiffness can be found using the equations, and K_0 can be calculated by multiplying the initial stiffness of the shear wall and the ratio of stiffness. Furthermore, using the displacement response spectrum of a 5% damping ratio, a maximum response displacement under the next input wave can be predicted. Figures 30 to 32 show maximum response displacements. Though the equivalent linearization method is simple, predicted response displacements are close to the maximum displacements obtained by the shake table test. With the derived regression curves from the shake table test results, the equivalent linearization method is

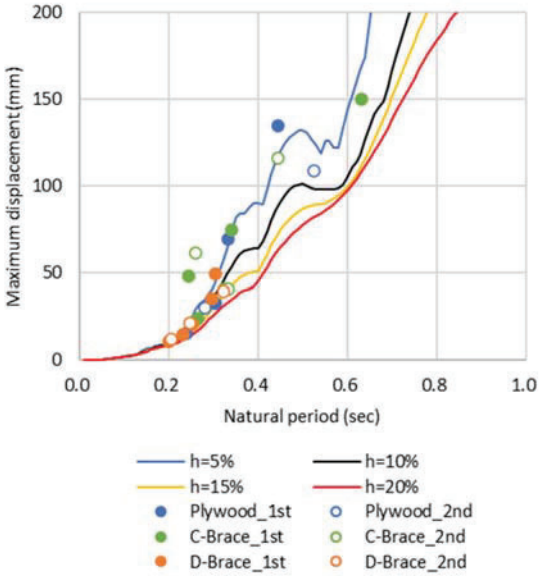

Figure 28: *Relationship between maximum displacement and natural period based on shear stiffness K_0*

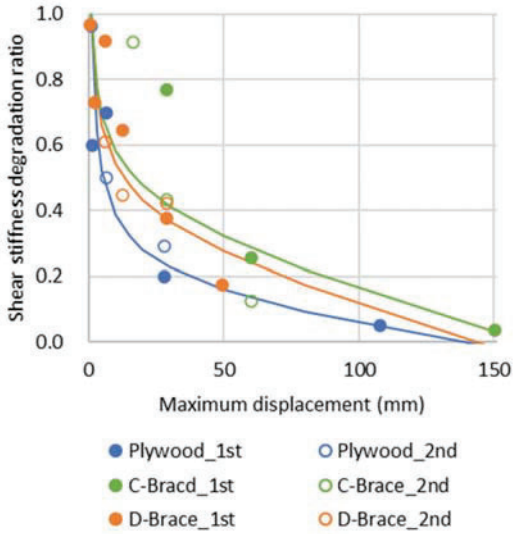

Figure 29: *Relationship between shear stiffness degradation ratio to initial shear stiffness and maximum displacement*

https://doi.org/10.52202/069179-0357

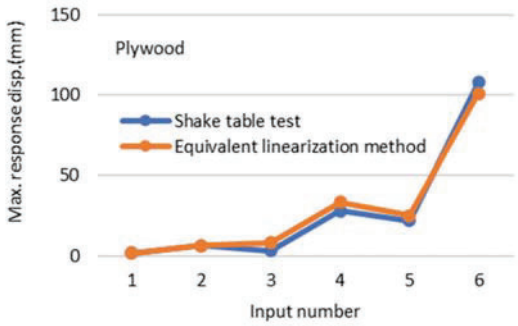

Figure 30: *Maximum response displacement of plywood shear wall*

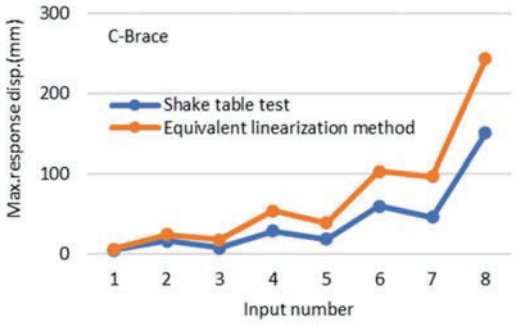

Figure 31: *Maximum response displacement of braced shear wall with conventional brace connectors*

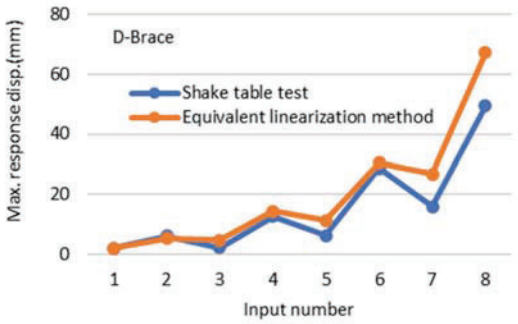

Figure 32: *Maximum response displacement of braced shear wall with ductile brace connectors*

considered to be a useful method to predict maximum response displacements even under multiple input waves.

4 CONCLUSIONS

Shake table tests of a plywood shear wall and braced shear walls were conducted to understand their dynamic characteristics under multiple earthquake inputs. Moreover, hysteresis models of the shear walls were proposed based on the shake table test results, and earthquake response analysis was conducted. The maximum response displacements from the analysis results were relatively close to the shake table test results in a small displacement range. Additionally, an equivalent linearization method as a simple prediction method for a maximum response displacement was tried. Using the initial shear stiffness and the shear stiffness degradation ratio derived from the shake table test results, the prediction results showed good correspondence with the shake table test results.

ACKNOWLEDGEMENT

Authors express our gratitude for the great support on the shake table test by Dr. Hideo Fujitani and Dr. Yoichi Mukai of Kobe university.

REFERENCES

[1] Nobuyoshi Yamaguchi, Chikahiro Minowa, and Masashi Miyamura: Seismic Performance of Wooden Shear Walls on Dynamic Condition. Proceedings of 12th World Conference on Earthquake Engineering, 2000

[2] Jennifer Durham, Frank Lam, and Helmut G. L. Prion: Seismic Resistance of Wood Shear Walls with Large OSB Panels. Journal of Structural Engineering, 127(12), 1460-1466, 2001

[3] John W. van de Lindt, Hongyan Liu, and Shiling Pei: Performance of a Woodframe Structure during Full-Scale Shake-Table Tests: Drift, Damage, and Effect of Partition Wall. Journal of Performance of Constructed Facilities, 21(1), 35-43, 2007

[4] Erol Varoglu, Erol Karacabeyli, Siegfried Stiemer, Chun Ni, Marlen Buitelaar, and Dan Lungu: Midply Wood Shear Wall System: Performance in Dynamic Testing. Journal of Structural Engineering, 133(7), 1035-1042, 2007

[5] C. Boudaud, J. Humbert, J. Baroth, S. Hameury, and L. Daudeville: Joints and wood shear walls modelling II: Experimental tests and FE models under seismic loading. Engineering Structures, 101, 743-749, 2015

World Conference on Timber Engineering Oslo 2023

STRUCTURAL PERFORMANCE EVALUATION OF A TIMBER HOUSE USING NEW CONSTRUCTION SYSTEM WITH CLT HORIZONTAL DIAPHRAGM

Masato Nakao[1] and Tomoki Furuta[2]

KEYWORDS: Post-and-beam construction system, CLT, Horizontal diaphragm, Braced shear wall

1 INTRODUCTION

Japanese forest resources have been abandoned and accumulated for a long time. Making much use of CLT(Cross Laminated Timber) leads to consuming the forest resources effectively, it is necessary to develop various ways to use CLT.

As one of the ways to use CLT, authors have developed a new post-and-beam construction system with a CLT horizontal diaphragm. In the developed construction system, CLTs are used as a horizontal diaphragm, whereas beams are omitted. It may realize a short construction period, high structural performance, and high sound insulation.

This paper presents the structural performance evaluation of the newly developed construction system through the static incremental analysis of a prototype timber house.

2 OUTLINE OF PROTOTYPE HOUSE

Figure 1 shows the conventional post-and-beam construction system and the new construction system with a CLT horizontal diaphragm. In the new construction system, the floor system of the conventional post-and-beam construction system is replaced by CLTs. Because CLT has mortises, tenons of the end of columns can be joined to CLTs directly.

Figures 2 to 4 show a prototype house with the new construction system. Thanks to the rigidity of CLT, a large balcony can be placed on the southern part of the house, and it is tolerated that the external wall of the second story is not arranged just above the one on the first story. The CLT grade of the horizontal diaphragm at the floor level on the second story is Mx60-5-5[1]. The species of the CLTs is Japanese cedar.

Braces are used as the shear wall in the prototype house while the plywood shear wall is not used. The ends of the braces are connected by newly developed ductile brace connectors. 15kN hold-down connectors are installed on the ends of columns. CLTs as the second story floor are arranged as shown in Figure 5.

A half-lapped joint was adopted as the joint between CLTs of the horizontal diaphragm. Screws, 7 mm in diameter and 200 mm long, are driven at an angle of 45 degrees on the joint for reinforcement.

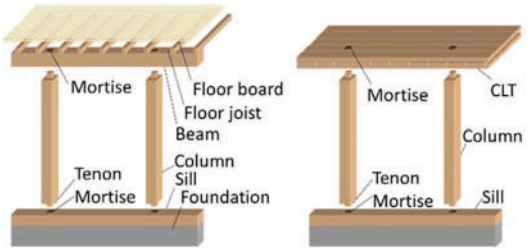

Figure 1: *Conventional post-and-beam construction system(left) and new construction system with CLT horizontal diaphragm(right)*

Figure 2: *South elevation of the prototype house*

Figure 3: *East elevation of the prototype house*

[1] Masato Nakao, Yokohama National University, Japan, mnakao@ynu.ac.jp
[1] Tomoki Furuta, Nishinippon Institute of Technology, Japan, furuta@nishitech.ac.jp

https://doi.org/10.52202/069179-0358

The weight of the first story of the prototype house is estimated as 191.1 kN, while the one of the second story is 120.7 kN, where the live load was assumed as 600 N/m^2[2].

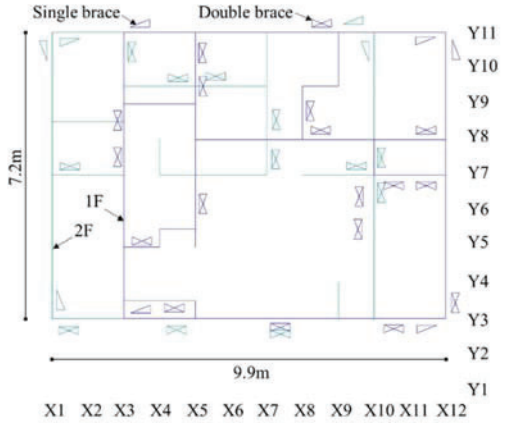

Figure 4: *Plan of the prototype house*

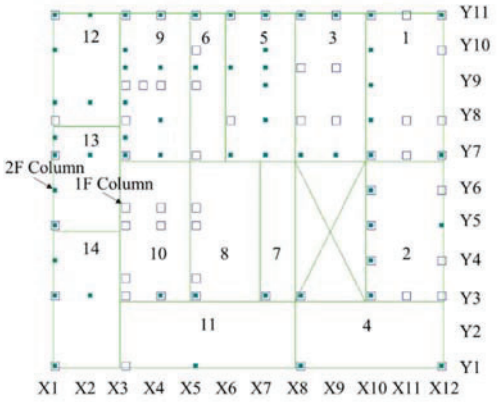

Figure 5: *Arrangement of CLTs at the floor level on the second story*

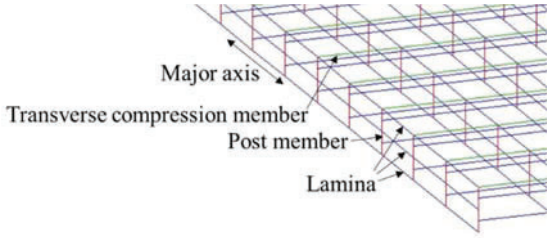

Figure 6: *Analysis Model of CLT*

Table 1: *Young's modulus and shear modulus of CLT analysis model*

	Young's modulus (N/mm^2)	Shear modulus (N/mm^2)
Lamina	7350	637
Post member	590	326
Trans. comp. mem.	590	637

3 PROTOTYPE HOUSE MODELING AND INCREMENTAL ANALYSIS

To evaluate the structural performance of the prototype house, a 3D structural model for static incremental analysis was built.

3.1 CLT AS HORIZONTAL DIAPHRAGM

Because an evaluation method of the out-plane two-way bending stiffness of CLT is not established, the CLT model that consists of laminas as shown in Figure 6 was adopted. The section of the lamina was 227.5mm x 30mm, and the laminas were connected by the post members. On the top layer, the side of the lamina is expected to touch the next lamina under a bending moment of minor direction. Therefore, transverse compression members were arranged between laminas on the top layer. Young's modulus and shear modulus of the members that compose the CLT are listed in Table 1, where every member is assumed as elastic.

3.2 CLT-CLT JOINT

3.2.1 Tensile direction

To evaluate the tensile force-displacement relationship of a CLT-CLT joint of the second-story floor diaphragm, a tensile loading test was conducted. The joint type is a half-lapped joint with long screws that is 7mm in diameter and 200mm long. Figure 7 shows the specimen. There were major axis specimens and minor axis specimens regarding the lamina direction as shown in Figure 8, and three specimens were prepared for each axis. Two screws were driven to the specimen. Figure 9 shows a specimen set in the test apparatus. One directional tensile load was applied to the specimen.

Figure 10 shows the tensile force-displacement relationships of all specimens. The variation of minor axis specimens is relatively large, while the average curve of major axis specimens and of minor axis specimens are about the same level. The average maximum tensile force per screw was approximately 12.5kN. For major axis specimens, failure around the screw occurred, while split along the edge occurred in minor axis specimens as shown in Figure 11. Large plastic deformation of the screws was not found in both major axis or minor axis specimens.

The spring which represents the screw on the joint between CLTs was set to 4 kN/mm of stiffness for tensile direction considering the experimental data. Because a large axial force is not expected to be produced through the incremental analysis, the spring was elastic. Regarding the compression side, the stiffness was set to 4kN/mm same as the tensile direction.

https://doi.org/10.52202/069179-0358

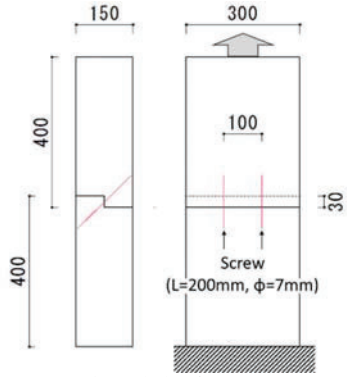

Figure 7: *Specimen of tensile loading test*

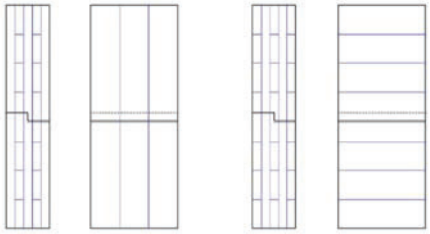

(a) Major axis specimen *(b) Minor axis specimen*

Figure 8: *Direction of lamina*

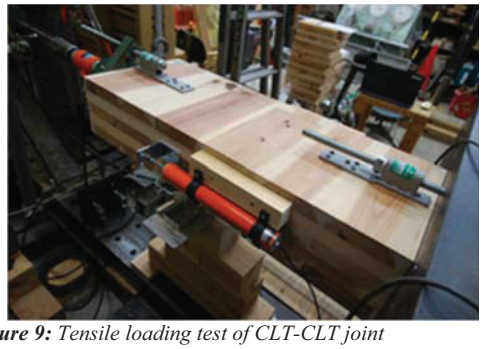

Figure 9: *Tensile loading test of CLT-CLT joint*

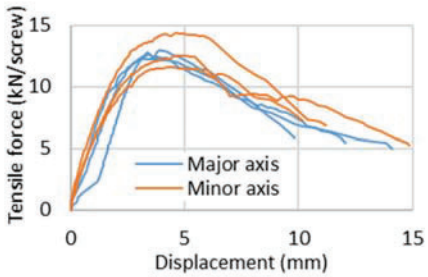

Figure 10: *Tensile force-disp. relationship of CLT-CLT joint*

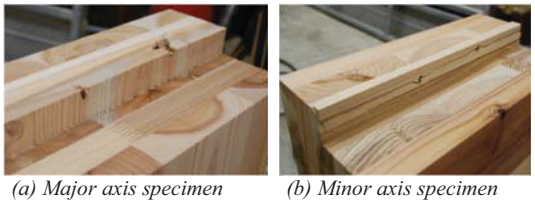

(a) Major axis specimen *(b) Minor axis specimen*

Figure 11: *Specimen after tensile loading test*

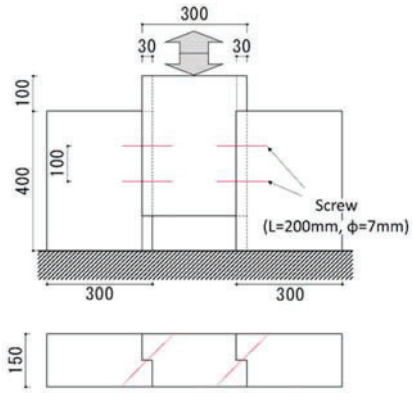

Figure 12: *Specimen of shear loading test*

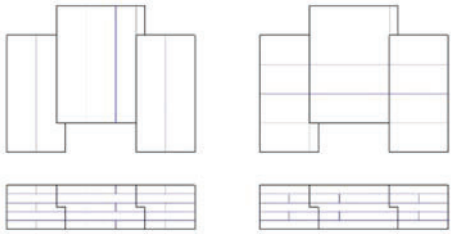

(a) Major axis specimen *(b) Minor axis specimen*

Figure 13: *Direction of lamina*

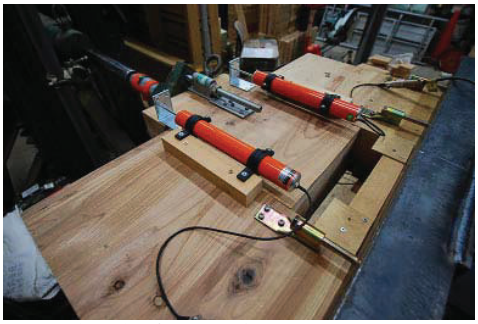

Figure 14: *Shear loading test of CLT-CLT joint*

3.2.2 Shear direction

To evaluate the shear force-displace relationship of a CLT-CLT joint of the second story floor diaphragm, a shear loading test was conducted. The joint type is also a half-lapped joint with long screws.

Figure 12 shows the specimen. There were major axis specimens and minor axis specimens regarding the lamina direction as shown in Figure. 13, and three specimens were prepared for each axis. Four screws were driven to Major axis 1 and Minor axis 1 specimens, while two screws were driven in the other specimens. Figure 14 shows a specimen set in the test apparatus. The repeated load was applied to the center peace of the specimen.

The results of the tests are shown in Figure 15. The maximum shear force per screw was approximately 10kN, and the screw was bent largely or fractured as shown in Figure 16. Figure 17 shows the skeleton curves of all specimens. The variation of major axis specimens is relatively large, while the average curve of the major axis specimens and the one of the minor axis specimens are about the same level.

https://doi.org/10.52202/069179-0358

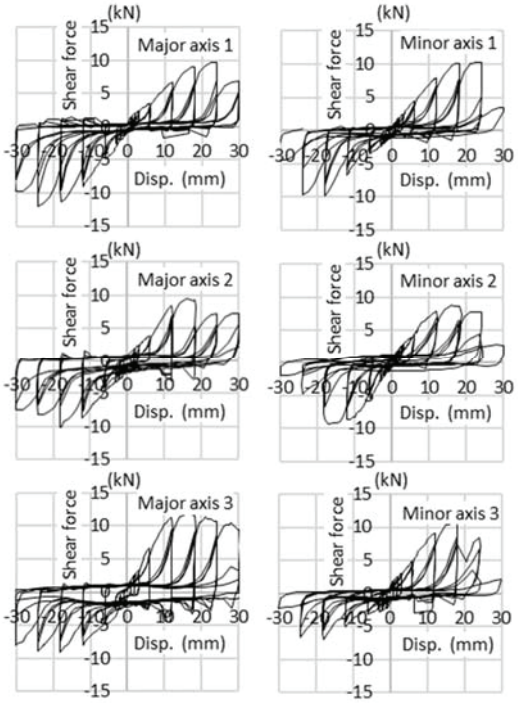

Figure 15: *Shear force-disp. relationship of CLT-CLT joint*

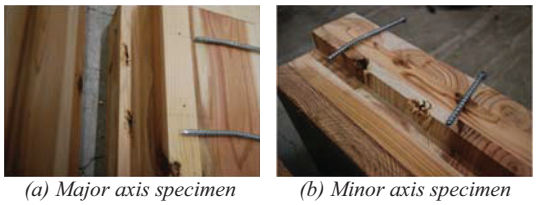

(a) Major axis specimen *(b) Minor axis specimen*

Figure 16: *Specimen after shear loading test*

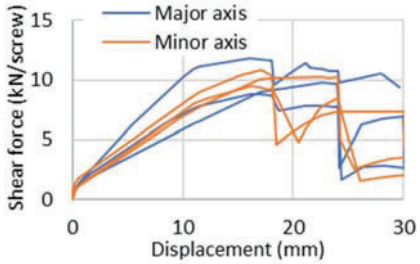

Figure 17: *Skeleton curves of shear force-disp. relationship*

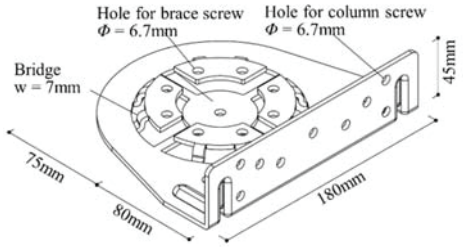

Figure 18: *Steel core of ductile brace connector*
(To use as a brace connector, this steel core is covered with high damping rubber.)

The spring which represents the screw on the joint between CLTs had 0.8 kN/mm of stiffness for in-plane shear direction. The spring was elastic, and the stiffness was derived from the experimental data.

3.3 BRACE

Regarding shear walls, braced shear walls are arranged in the prototype house. For reinforcing the joint between the end of a brace and a column, the ductile brace connector was used.

The ductile brace connector, as shown in Figure 18, includes a damping mechanism. The thickness of the steel for the connector is 3.2mm. As the lateral displacement of the braced shear wall increases, the bridges deform to absorb a displacement between a brace and a column. Damping force is produced by the plastic deformation of the bridges. To use as a brace connector, the steel core is covered with high-damping rubber.

Figure 19 shows a shear force-drift angle relationship of a single braced shear wall specimen as shown in Figure 20. Repeated lateral shear load was applied to the beam up to 0.02rad. After that, a one-directional shear force that causes tensile failure at the joint between the end of a brace and a column was applied.

The axial force-displacement relationship model of the brace with the ductile brace connectors is shown in Figure 21, where the compressive yield force of the model is the buckling strength of the brace.

3.4 COLUMN-CLT JOINT

To evaluate the tensile force-displace relationship of a joint between the end of the column and the CLT of the floor diaphragm on the second story, a tensile loading test was conducted.

Figure 22 shows the specimen, which has a tenon on the end of the column and a mortise on the CLT. A connector to prevent pull-out of the column was installed at the joint. Three specimens were prepared for the test, and a repeated load was applied to the column.

Figure 23 shows the axial force-displacement relationship of the joint between the end of the column and the CLT. Screws driven to the CLT were pulled out as shown in Figure 24, and the applied load decreased.

After the tensile loading test, a compressive loading test was conducted with the same specimen as the tensile loading test. The compressive load was applied to the specimen up to 50kN due to a limitation of the test apparatus, and relationships between compressive force and relative displacement between the end of the column and the CLT were derived as shown in Figure 25.

From the test results, an axial force-displacement relationship model at the end of the column, as shown in Figure 26, was set, and applied to the 3D prototype house model.

3.5 BUILDING UP OF 3D PROTOTYPE HOUSE MODEL

The 3D structural model of the prototype house is shown in Figure 27, which contains 8944 nodes and 16747 members, where the out-plane shear stiffness of the CLT-CLT joint was set as 10 kN/mm.

https://doi.org/10.52202/069179-0358

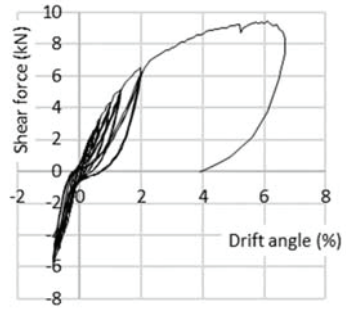

Figure 19: *Shear force-drift angle relationship*

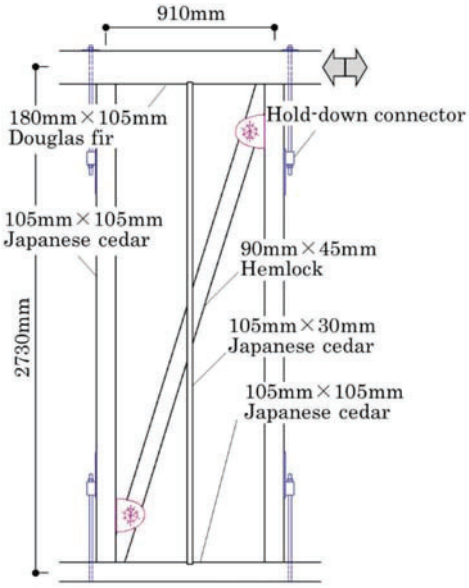

Figure 20: *Single brace shear wall specimen*

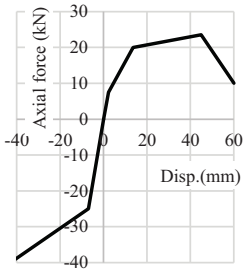

Figure 21: *Axial force-disp. relationship of brace*

Figure 22: *Tensile loading test of column-CLT joint*

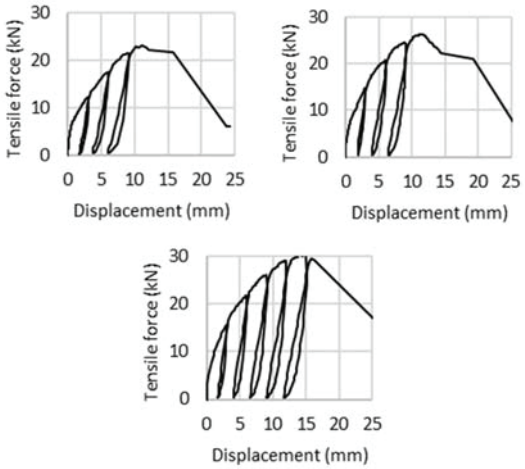

Figure 23: *Tensile force-disp. relationship of column-CLT joint*

Figure 24: *Joint of specimen after tensile loading test*

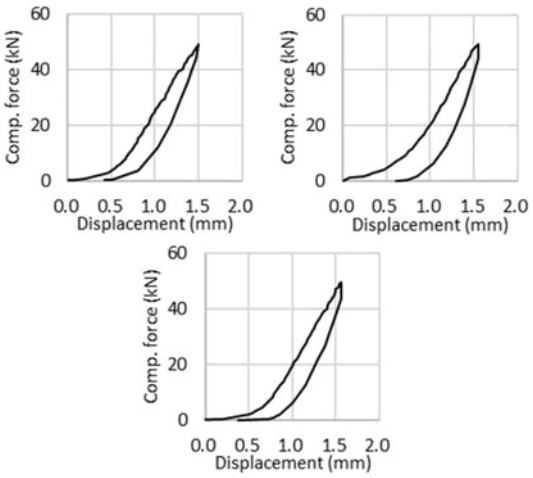

Figure 25: *Compressive force-disp. relationship of column-CLT joint*

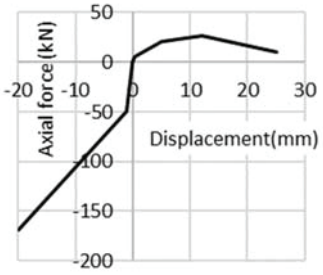

Figure 26: *Axial force-disp. relationship of column-CLT joint*

https://doi.org/10.52202/069179-0358

4 RESULT OF INCREMENTAL ANALYSIS

Figure 28 shows the story shear force-story displacement relationship from the static incremental analysis. Though the shear force along the Y-direction is slightly low compared to the one along the X-direction.

Regarding C_0=0.2 and C_0=0.3, where C_0 is the value of the story shear force divided by the weight the story carries, the maximum stress of the laminas and the maximum force of the screws on the CLT-CLT joint are listed in Table 2. The maximum bending stress of all laminas is 77% of the lower limit strength under C_0=0.3 shear force. For the maximum tensile stress, it is 21% of the lower limit strength, therefore CLTs are not considered to have damage even under relatively large earthquakes.

Regarding the tensile and shear forces carried by the spring at the CLT-CLT joint, they are considered to be in the elastic range compared to the test results such as Figures 10 and 17. As for the out-plane shear force, because no experimental data exist, an out-plane shear loading test will be planned to be conducted.

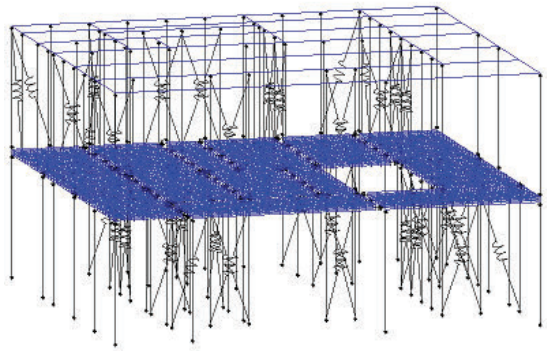

Figure 27: *3D structural model of the prototype house*

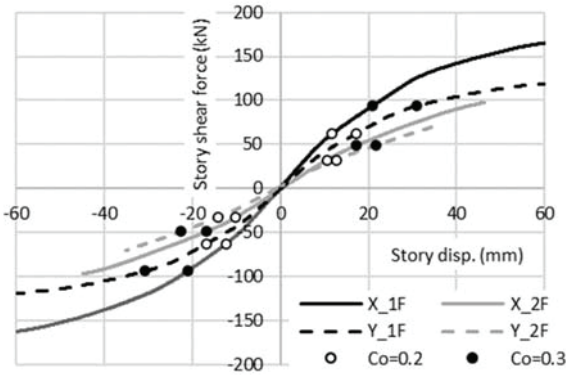

Figure 28: *Story shear force-story displacement relationship*

Table 2: *Maximum stress and force*

	Lamina (N/mm^2)		Spring between CLTs (kN)		
	Bending	Tension	Tension	In-plane shear	Out-plane shear
C_0=0.2	10.89	1.57	5.19	2.16	5.30
C_0=0.3	15.49	2.56	7.80	3.33	7.24

5 CONCLUSIONS

Static incremental analysis of the prototype timber house which is designed with the new post-and-beam construction system with a CLT horizontal diaphragm was conducted. From the experimental and numerical test results, it was confirmed that no damage to the CLT horizontal diaphragm was expected even under relatively large earthquakes.

REFERENCES

[1] Japanese Agricultural Standard of Closs Laminated Timber. Notification No.683 of the Ministry of Agriculture, Forestry and Fisheries, 2018. (in Japanese)

[2] Structural Design and Construction Manual using CLT. Japan Housing and Wood Technology Center, 2018. (in Japanese)

https://doi.org/10.52202/069179-0358

World Conference on Timber Engineering Oslo 2023

NUMERICAL ANALYSIS ON SEISMIC BEHAVIOUR OF TIMBER FRAME STRUCTURE WITH HYBRID SCREWED-IN ROD CONNECTIONS

Jiwei Liu[1], Benkai Shi[2], Huifeng Yang[3]

ABSTRACT: A hybrid connection with steel bracket and screwed-in rods was developed for timber structures or hybrid steel-timber structures. Cyclic tests have been conducted upon the proposed connection and then compared it with the traditional bolted connections. Test results showed that the hybrid connection had better stiffness, energy dissipating capacity, and moment resisting capacity, compared with the bolted connection. The numerical models for the two types of connections were established. Bayesian parameter identification method was used to calibrate the parameters of the model. These two connection models were applied to a three-story frame numerical model in Open System for Earthquake Engineering Simulation (Opensees), and the seismic performances of the three-story frame with hybrid connection or bolted connections were evaluated, which can provide guidance for the application of the innovative connection hybrid connection. The results show that the hybrid connection can reduce the displacement response of the structure and improve the seismic performance of the structure, especially under rare earthquakes.

KEYWORDS: Steel bracket, Screwed rods, Bolted connection with steel plate, Three layers frame

1 INTRODUCTION

The bolted connections with steel plate are widely used in modern timber structures for convenient fabrication. However, bolted suffered lots of problems. Low initial stiffness may be caused by the space reserved for installation. Insufficient tensile and shear strength of timber results in low moment resisting capacity. Brittle failure mode of wood in tension and shear direction leads to brittle failure of joints [1-4]. In order to solve the above problems, screwed rods has been proposed to connect the beam and column. The joints connected by screwed rods have satisfactory initial stiffness and moment resisting capacity.

But the limitation in energy dissipating capacity restricts the ability of structures to reduce seismic response [5-7]. In this paper, screwed rods and steel bracket are used in beam-column connections. Cyclic loading test are implemented on bolted connection and hybrid connection to evaluate the initial stiffness, moment resisting capacity, and energy dissipating capacity. The connection numerical models are established in the OpenSees environment. Model parameters are identified by Bayesian method. The numerical models for bolted connection and hybrid connections are applied to a three-story structure model for nonlinear time history analysis. The interlayer displacement angles of the two structures are compared.

[1] Jiwei Liu, Southeast University, China, liujiwei2f@163.com
[2] Benkai Shi, Nanjing Tech University, China, benkaishi@njtech.edu.cn
[3] Huifeng Yang, Nanjing Tech University, China, hfyang@njtech.edu.cn

2 NUMERICAL ANLYSIS OF BEAM-TO-COLUMN CONNECTION

2.1 NUMERICAL MODEL

Figure 1 show the specimen design of the hybrid connection. The specimen had a timber beam member (135 mm × 420 mm in cross section, 1500 mm in length), a steel column member (350mm × 160mm × 20mm in cross section, 1500 mm in length). The steel bracket was a replaceable ductile energy dissipation element. Steel bracket was connected by bolts to the steel column. Steel bracket was connected to the screwed rods at the end of the timber beam. The test data of bolted connection with steel plate were compared with the hybrid connection.

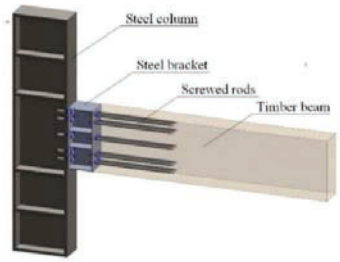

Figure 1: *Details of Hybrid connection*

https://doi.org/10.52202/069179-0359

In order to meet the need of nonlinear time history analysis of the structure, fiber model is used for finite calculation of the structure. Figure 2 shows the model of the connection. The steel column was modelled by dispBeamColumn element with steel02 material. The model has high precision and high numerical stability, and can effectively simulate the Bauschinger effect of rebar. The glulam beam was modelled by dispBeamColumn element with Concrete02 material. The model parameters were determined according to results of the mechanical tests of glulam. The steel bracket was simplified to a rotational spring. Compared with the experimental data of the connection, the multi-parameter Pinching4 material model could better simulate the degradation and damage of the steel bracket, as shown in Figure 3. The model parameters are calibrated by Bayesian method. The method of parameter identification is referred to the literature [8]. Parameter identification results are shown in Table 1.

Table 1 *Identified parameter*

Tag	Bolted connection	Hybrid connection
ePf1/kN·m	26.76	34.96
ePf2/kN·m	42.04	53.61
ePf3/kN·m	55.12	72.60
ePf4/kN·m	39.43	50.65
ePd1/rad	8.89E-03	6.25E03
ePd2/rad	2.02E-02	1.56E02
ePd3/rad	2.74E-02	3.86E02
ePd4/rad	6.00E-02	8.00E02
eNf1/kN·m	-35.51	-44.99
eNf2/kN·m	-45.45	-67.92
eNf3/kN·m	-70.29	-91.22
eNf4/kN·m	-51.70	-69.44
eNd1/rad	-8.86E-03	-6.25E03
eNd2/rad	-1.76E-02	-1.61E02
eNd3/rad	-3.52E-02	-3.80E02
eNd4/rad	-6.00E-02	-8.00E02
rDisP	3.50E-01	6.80E-01
rForceP	8.57E-02	2.73E-01
uForceP	2.01E-03	-3.01E-01
rDisN	1.67E-01	6.46E-01
rForceN	4.10E-02	5.50E-01
uForceN	3.03E-02	1.20E-01
gK1	9.50E-01	-5.15E-02
gK2	5.77E-01	1.29E-01
gK3	7.23E-01	1.62E-01
gK4	8.38E-01	8.67E-01
gKLim	4.01E-02	2.32E-02
gF1	9.31E-01	2.78E-01
gF2	8.40E-01	4.25E-01
gF3	6.09E-01	7.83E-01
gF4	5.13E-01	4.81E-01
gFLim	8.74E-03	1.19E-01
gD1	9.93E-01	-1.52E-03
gD2	4.01E-02	-1.58E-03
gD3	8.10E-01	4.71E-06
gD4	9.08E-01	4.78E-05
gDLim	8.46E-04	-1.64E-03

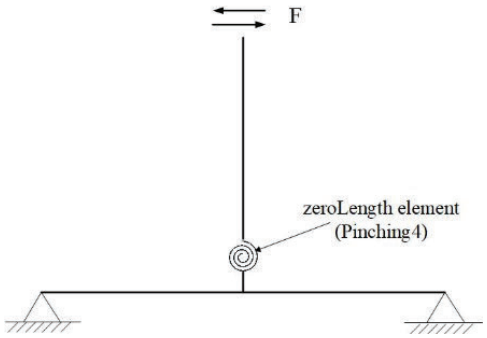

Figure 2: *Numerical mode of the connection.*

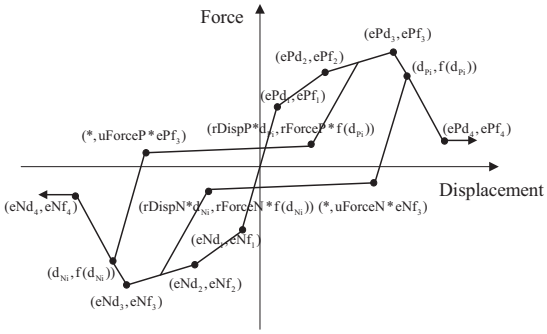

Figure 3: *Pinching4 constitutive model.*

2.2 CALIBRATION

In order to verify the accuracy of the numerical model, the simulation hysteresis curve of the connection model is compared with the experimental hysteresis curve. The hybrid connection test results are provided by the literatures [9]. Figure 4 and Figure 5 show the simulated result. The loading stiffness, bearing capacity and unloading stiffness obtained by numerical model are consistent with the experimental results, which proves that the model is effective and the parameter selection is reasonable.

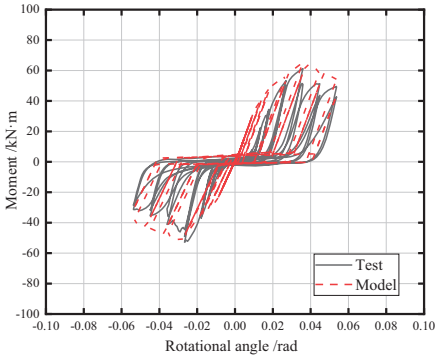

Figure 4: *Comparison of hysteretic curves (bolted connection)*

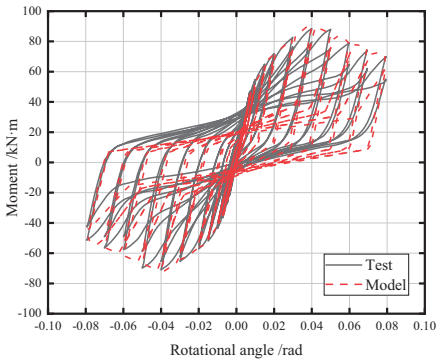

Figure 5: *Comparison of hysteretic curves (hybrid connection)*

3 NUMERICAL ANLYSIS OF FRAME STRUCTURE

3.1 NUMERICAL MODEL

According to Chinese code for seismic design of buildings (GB50011-2010) [10], a three-storey frame structure is designed. The structure is located in the 8 degree fortified area, the second group, the second site classification. As the structure is regular, the torsion effect can be ignored. Therefore, a longitudinal frame is proposed to reflect the longitudinal seismic performance of the whole structure. The frame consists of 3 spans of 5 meters each. Each layer of the frame is 4 meters in height, and the whole frame is 12 meters in height. Figure 6 shows the model of a three-story structure. A two dimensional three-storey frame was simulated. The model of beam, column and connection is established by the modelling method of Section 2. Spring elements using elastic materials with high stiffness were arranged at column base.

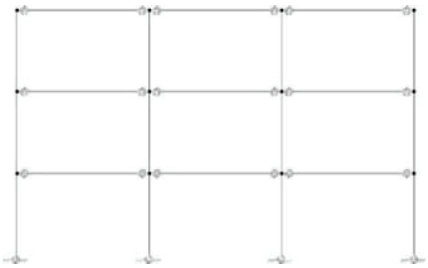

Figure 6: 3.1 *Numerical model for a three-story structure*

The modal analysis of the two frames is carried out respectively. The periods of the first two modes of the two frames are shown in the Table 2.

Table 2 Structural natural period of vibration

Specimen ID	First mode period /s	Second mode period /s
BC[a]	1.170	0.226
HC[b]	1.026	0.216

[a]BC (Bolted connection)
[b]HC (Hybrid connection)

Four natural ground motions were selected according to the site category of the structure, the design seismic grouping, the spectral characteristics of the standardized response spectrum and the first two natural vibration periods of the structure. The characteristics of each ground motion are shown in Table 3. The acceleration spectrum of each ground motion, the mean acceleration spectrum diagram and the target response spectrum are compared under the action of 8-degree frequent and 8-degree rare earthquakes as shown in Figure 7 and Figure 8.

Table 3 Main characteristics of selected earthquakes.

GM ID	Earthquake Name	Magnitude	PGA/g
GM1[a]	Imperial Valley-06	6.53	0.17
GM2	Coalinga-01	6.36	0.60
GM3	Chi-Chi_ Taiwan	7.62	0.21
GM4	San Simeon_ CA	6.52	0.44

[a]GM (Ground motion)

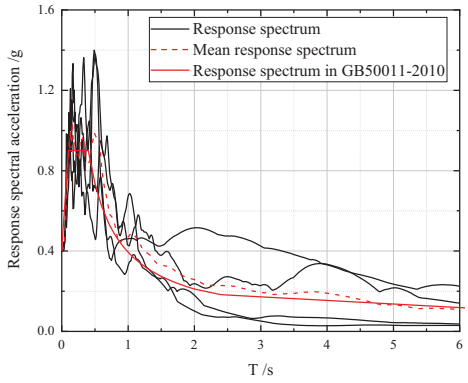

Figure 7: *Rare earthquake response spectrum.*

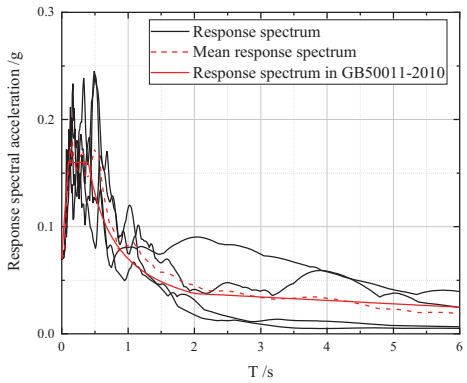

Figure 8: *Frequent earthquake response spectrum.*

3.2 RESULT AND DISCUSSION

According to different fortification standards, the time history analysis after amplitude modulation is carried out on the four ground motions before time history analysis. The top-level displacement-time history curves of the two frames under different seismic waves are shown in the Figure 9-Figure 12 (Rare earthquake) and Figure 13-Figure 16 (Frequent earthquake). The maximum displacement response and maximum interlayer displacement Angle are shown in the Under rare

https://doi.org/10.52202/069179-0359

earthquakes, hybrid connections can reduce the maximum displacement response by 19.62%, while under frequent earthquakes, hybrid connections can reduce the maximum displacement response by 9.38%. According to the simulation results, the hybrid connection can reduce the seismic response of the structure and improve the seismic performance of the structure. In rare earthquakes, the effect of lifting is more obvious.

Table ***4*** and Table 5.

By comparing the simulation results, it can be found that under rare earthquakes, the maximum displacement of the frame with hybrid connection is smaller than that with bolted connection. Under frequent earthquakes, the average maximum displacement of the frame with hybrid connection is smaller than that of the frame with bolted connection. However, the maximum displacement response of the frame with bolted connection is larger than that of the frame with hybrid connection under GM2.

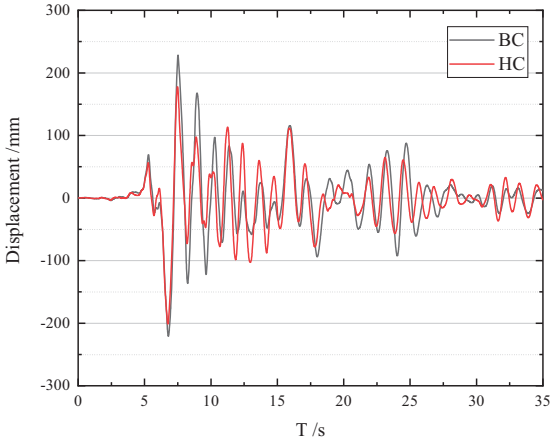

Figure 9: *Comparison of displacement time histories of the top layer of two frames under GM1 (Rare earthquake).*

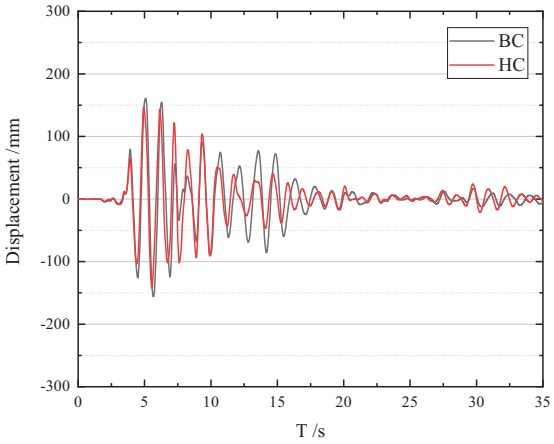

Figure 10: *Comparison of displacement time histories of the top layer of two frames under GM2 (Rare earthquake).*

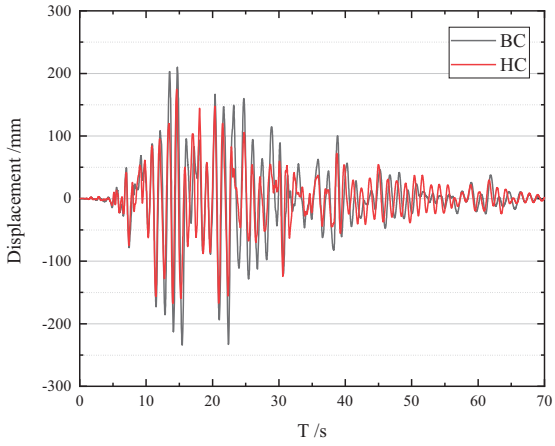

Figure 11: *Comparison of displacement time histories of the top layer of two frames under GM3 (Rare earthquake).*

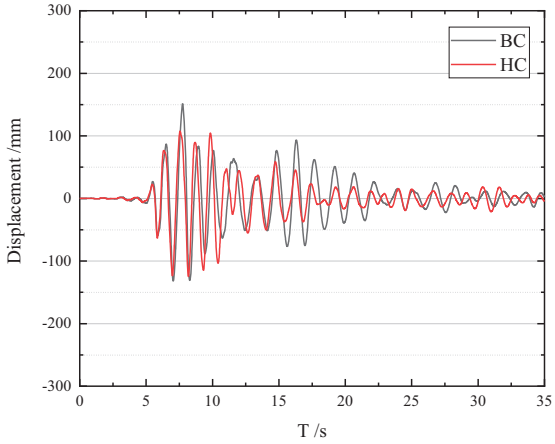

Figure 12: *Comparison of displacement time histories of the top layer of two frames under GM4 (Rare earthquake).*

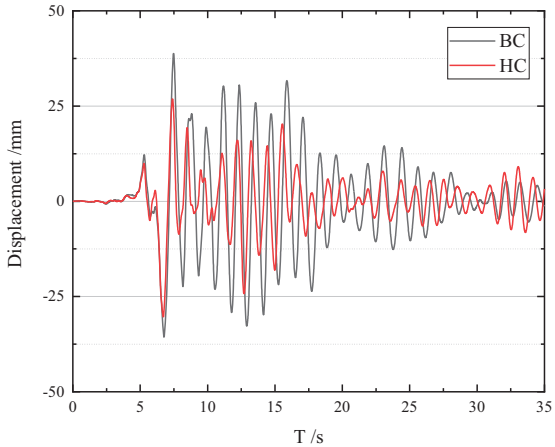

Figure 13: *Comparison of displacement time histories of the top layer of two frames under GM1 (Frequent earthquake).*

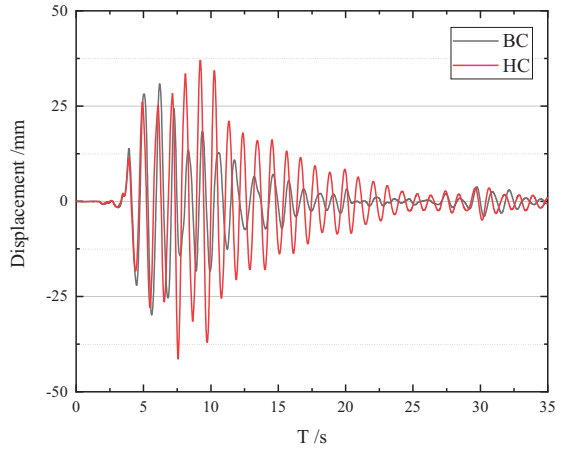

Figure 14: *Comparison of displacement time histories of the top layer of two frames under GM2 (Frequent earthquake).*

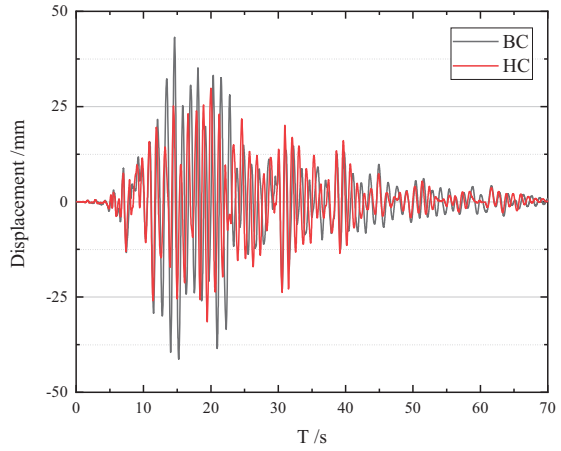

Figure 15: *Comparison of displacement time histories of the top layer of two frames under GM3 (Frequent earthquake).*

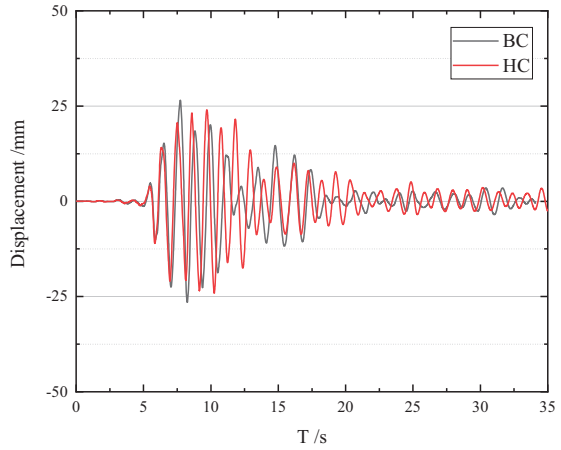

Figure 16: *Comparison of displacement time histories of the top layer of two frames under GM4 (Frequent earthquake).*

Under rare earthquakes, hybrid connections can reduce the maximum displacement response by 19.62%, while under frequent earthquakes, hybrid connections can reduce the maximum displacement response by 9.38%. According to the simulation results, the hybrid connection can reduce the seismic response of the structure and improve the seismic performance of the structure. In rare earthquakes, the effect of lifting is more obvious.

Table 4 Comparison of maximum deformation under rare earthquakes

GM ID	Maximum displacement /mm		Maximum displacement Angle /%		Difference ratio /%
	BC	HC	BC	HC	
GM1	228.37	201.34	1.90	1.68	13.42
GM2	160.83	147.06	1.34	1.23	9.36
GM3	234.05	174.59	1.95	1.45	34.06
GM4	151.40	124.60	1.26	1.04	21.51
Total	193.66	161.90	1.61	1.35	19.62

Table 5 Comparison of maximum deformation under frequent earthquakes

GM ID	Maximum displacement /mm		Maximum displacement Angle /%		Difference ratio /%
	BC	HC	BC	HC	
GM1	38.78	30.31	0.32	0.25	27.96
GM2	30.83	41.40	0.26	0.35	25.54
GM3	43.14	31.50	0.36	0.26	36.96
GM4	26.54	24.13	0.22	0.20	9.97
Total	34.82	31.84	0.29	0.27	9.38

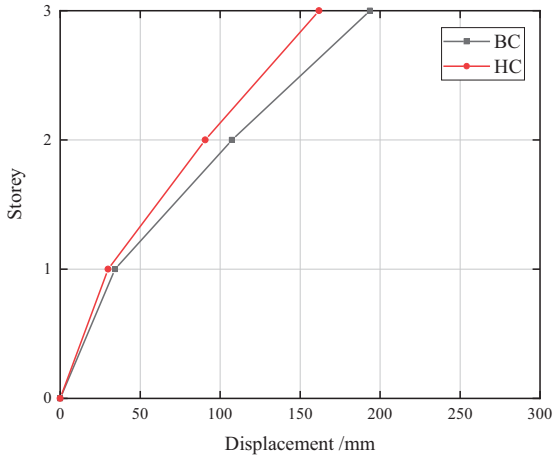

Figure 17: *Comparison of displacement between layers of the two frames (Rare earthquake).*

https://doi.org/10.52202/069179-0359

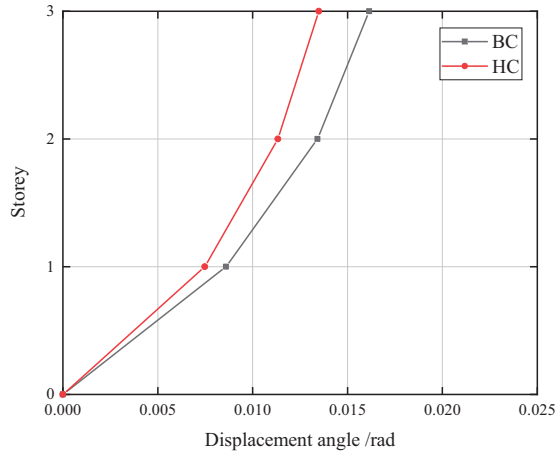

Figure 18: *Comparison of displacement angle between layers of the two frames (Rare earthquake).*

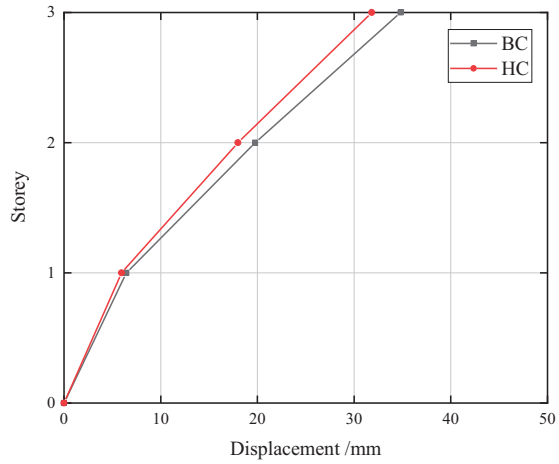

Figure 19: *Comparison of displacement between layers of the two frames (Frequent earthquake).*

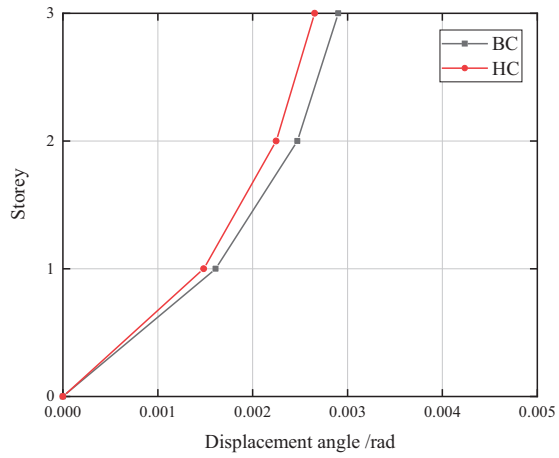

Figure 20: *Comparison of displacement angle between layers of the two frames (Frequent earthquake).*

Figure 17- Figure 20 shows the mean displacement and the mean displacement angle of each layer under different ground motions according to different fortification standards. The displacement response of each floor of the mixed connected frame is smaller than that of the traditional connected frame

4 CONCLUSIONS

In this paper, a ductile beam-column connection, named as hybrid connection, was proposed and investigated. Compared with the traditional bolted connection, hybrid connection has higher stiffness, moment resisting capacity, and energy dissipating capacity. The joint models are established and compared with the experimental results to verify the accuracy of the model. Also, these two kinds of connections are applied to a three-story structure model. The interlayer displacement angles and interlayer displacement are compared. The following conclusions can be drawn:

1. The connection modelling method has been verified by experimental data with accuracy and can be used for connection modelling.
2. The frame with hybrid connection can reduce the displacement response of each layer of the structure and improve the seismic performance of the structure under the ground motions according to different fortification standards.
3. It is more obvious that the frame with hybrid connection can improve the seismic performance of the structure under rare earthquakes.

ACKNOWLEDGEMENT

This work was supported by National Natural Science Foundation of China (Grant No. 51878344, 51578284), which are highly appreciated.

REFERENCES

[1] Lam F., Gehloff M., Closen M.: Moment-resisting bolted timber connections. *Proc. Inst. Civil Eng. Struct. Build.* 163(4):267-274, 2010.

[2] Wang M., Song X., Gu X., Zhang Y., Luo L.: Rotational Behavior of Bolted Beam-to-Column Connections with Locally Cross-Laminated Glulam, *J. Struct. Eng.* 141(4), 2015.

[3] He M., Liu H.: Comparison of glulam post-to-beam connections reinforced by two different dowel-type fasteners. *Constr. Build. Mater.* 99:99-108, 2015.

[4] Sun X., Qu Y., Liu W., Lu W., Yuan S.: Rotational behavior and modeling of bolted glulam beam-to-column connections with slotted-in steel plate. *Adv. Struct. Eng.* 23(9):1989-2000, 2020.

[5] Mori T., Nakatani M., Tesfamariam S.: Performance of semirigid timber frame with Lagscrewbolt connections: experimental, analytical, and numerical model results. *Int. J. Adv. Struct. Eng.* 7(4):387-403, 2015.

[6] Buchanan A., Fairweather R.: Seismic design of glulam structures. *Bull New Zeal Natl Soc Earthquake Eng.* 26(4):415–36, 1993.

[7] Gohlich R., Erochko J., Woods J.: Experimental testing and numerical modelling of a heavy timber

moment-resisting frame with ductile steel links. *Earthq. Eng. Struct. Dyn.* 47(6):1460-1477, 2018.
[8] Liu J., Yang H.: Parameter identification of ductile timber beam-to-steel column connections: Procedure and assessment. *Engineering Structures*. 259, 114179, 2022.
[9] Yang H., Wang C., Hu J., Tao H., Liu J., Tang L., Shi B.: Experimental static and seismic behaviour of glulam beam-to-column connection with screwed-in threaded rod joints. *Bioresources.* 16(3):5272-5286, 2021.
[10] GB/T 50011. Code for seismic design of buildings. Standardlization administration of China, Beijing, China, 2010

https://doi.org/10.52202/069179-0359

EXPERIMENTAL AND NUMERICAL ANALYSIS OF HIGH-CAPACITY SHEAR WALLS WITH MULTIPLE ROWS OF NAILS

Ruite Qiang[1], Lina Zhou[2], Chun Ni[3]

ABSTRACT: With the increase of building height in light wood-frame construction and seismic design spectra in the 2015 edition of National Building Code of Canada, stronger shear wall systems have been facing higher demands, especially for mid-rise wood-frame buildings located in high seismic zones. In collaboration with FPInnovations, a new high-capacity shear wall system with two and three rows of nails was developed. A total of 30 shear walls had been tested under reversed cyclic loading. Results showed that the lateral resistance of shear walls with multiple rows of nails is roughly proportional to the number of rows compared to a standard shear wall with the same sheathing thickness, nail diameter and nail spacing. However, new failure modes, such as splitting of bottom plates, out-of-plane separation of end studs from bottom plates, rupture of sheathing panels, etc. have limited the post-peak deformation of the high-capacity shear wall and its ductility. A better understanding on the stress-strain development of wood material and connections is needed to develop design details to prevent these failure modes and increase the ductility and design resistance of wood shear walls with multiple rows of nails. A preliminary 3D numerical model of high-capacity shear walls with multiple rows of nails were developed using ABAQUS to simulate the lateral performance and failure modes of high-capacity shear walls. Testing data from previous research by the authors was used to verify the modeling techniques developed in this study. Results show that the detailed 3D shear wall model can reasonably simulate the lateral resistance of high-capacity shear walls and the failure modes that are not common in regular shear walls.

KEYWORDS: high-capacity shear wall, multiple rows of nails, lateral load, numerical modelling

1 INTRODUCTION

Light wood frame shear wall systems have been widely used in the construction of multi-story residential and commercial wood buildings in North America. Consisting of wood framing members, wood-based sheathing panels and fasteners, wood frame shear walls are the main vertical component in resisting lateral loads caused by wind or seismic actions.

The height limit of wood frame buildings has been firstly increased from 4 to 6 stories since 2009 in BC, and the seismic design spectra have also been increased substantially for all site classes in the provincial and national building codes of Canada (NBCC) [1,2]. Therefore, the demand for higher lateral load resisting systems for mid-rise wood frame buildings has increased, especially in high seismic zones. To respond to this demand, a high-capacity shear wall system with multiple rows of nails along sheathing edges has been jointly developed by FPInnovations and University of Victoria. There were 30 high-capacity shear walls with two and three rows of nails along sheathing edges tested over a three-year period [3,4]. Results showed that the lateral resistance of shear wall with multiple rows of nails is almost proportional to the number of rows. However, new failure modes that are not common in standard shear walls were observed in high-capacity shear walls, such as splitting of bottom plates, out-of-plane separation of end studs from bottom plates, rupture of sheathing panels, etc. Present of these new failure modes limited the post-peak deformation of the high-capacity shear wall system and its ductility. Additional design details had been tried in the past few years to prevent these new failure modes. For example, double bottom plates were used to avoid splitting of bottom plates. However, reinforcing one element of the wall system may shift the weakest point to another location. A better understanding on the stress-stain development of sheathing panels, framing members and connections is needed to develop design details to prevent these undesirable brittle failures and increase the ductility and design resistance of wood shear walls with multiple rows of nails.

Numerical models of light wood frame shear walls have been developed with different methods in the past [4].

[1] Ruite Qiang, Department of Civil Engineering,
University of Victoria, Victoria BC, Canada, ruiteqiang@uvic.ca
[2] Lina Zhou, Department of Civil Engineering,
University of Victoria, Victoria BC, Canada, linazhou@uvic.ca
[3] Chun Ni, Advanced Building Systems, FPInnovations,
Vancouver BC, Canada, Chun.Ni@fpinnovations.ca

https://doi.org/10.52202/069179-0360

Different approaches were used to describe the monotonic and reversed-cyclic behavior of nail joints and shear walls in light wood frame buildings [5–8]. For shear wall models, framing members and sheathing panels are usually defined as elastic beam-type and shell-type element, respectively, while the sheathing-to-framing nail joints are represented by nonlinear link elements [9–12]. In a standard shear wall, the wall performance is mainly governed by sheathing-to-framing nail joints. The assumption of elastic behavior of framing members and sheathing panels, and pin connections between studs and plates, is usually acceptable. However, for high-capacity shear walls, in order to simulate the framing septation, wood splitting, sheathing rupture, etc. more realistic framing member connection performance and wood material damage should be considered in the model.

The objective of this study is to develop a detailed 3D shear wall model to predict the structural performance of high-capacity shear walls and simulate the failure modes including those that are not common in regular shear walls. The numerical models of high-capacity shear walls with three rows of nails were verified with the test results obtained in previous research by the authors [4]. Detailed wall components and boundary conditions were included in the model to regenerate the lateral behavior and failure modes of high-capacity shear walls tested in the lab. The modelling will provide insights for design and future testing of high-capacity shear walls.

2 EXPERIMENTAL STUDY

2.1 SHEAR WALL SPECIMEN AND TEST SETUP

There have been 30 high-capacity shear walls with two or three rows of nails along sheathing edges and reference walls tested in the past three years. Table 1 summarizes the details of the 22 shear walls tested in the first two years [3,4]. The wall details cover a combination of different sheathing panel thicknesses, nail sizes and nail spacings. For each configuration except the 9.5 mm panel thickness walls, a standard shear wall with one row of nails was also tested as reference. The shear wall specimens are 2.4 m × 2.4 m in dimension, constructed with 2 × 4 or 2 × 6 Douglas Fir dimension lumber, and vertically sheathed with 1.2 m × 2.4 m OSB panels on one side. Figure 1 shows the configuration of a shear wall specimen with three rows of nails.

Construction details and test set up of shear walls with three rows of nails are presented in this section as the numerical modelling described in this paper was based on shear walls with three rows of nails which are more prone to fail in the new failure modes.

The framing members were connected using F1667 NLCMMS69 (76.2 mm × 3.05 mm) power driven common nails. There were two rows of nails spaced at 200 mm on center for built-up end studs, built-up interior end studs, and top and bottom plates. For built-up center studs, three rows of nails (76.2 mm × 3.05 mm) spaced at 100 mm were used to prevent separation of center studs [4].

The shear wall specimens were fabricated and installed according to ASTM E2126 [13]. Figure 2 shows the schematic test set up. For all shear wall specimens, continuous 28.6 mm (1-1/8 in.) diameter tie-rods were used to resist overturning moment. 6 Hex A325 anchor bolts (22.2 mm in diameter) with steel bearing plates (127 mm in length × 127 mm in width × 6 mm in thickness) were used to connect both top and bottom plates to load spreader beam (C180 × 18) and foundation steel beam, respectively. Steel bearing plates (165 mm in length × 114 mm in width × 25 mm in thickness) were used to hold the tie-rod against the top plates (Fig. 2 B-B). The lateral load was applied through the steel load spreader beam to the top of the shear wall, as shown in Figure 2a. There was no vertical load applied on the wall specimens. Reversed cyclic loading was applied on tested specimens, following the CUREE protocol (method C) in ASTM E2126 [13].

Table 1: *Shear wall test configurations*

Wall #	OSB thickness (mm)	Nail size (mm)	Row of nails	Nail spacing along panel edges (mm)
1	9.5	63.5 × 3.33	2	100
2	9.5	63.5 × 3.33	2	75
3	11	63.5 × 3.33	3	100
4	11	63.5 × 3.33	3	75
4r	11	63.5 × 3.33	1	75
5	15	76 × 3.76	2	100
6	15	76 × 3.76	2	75
6r	15	76 × 3.76	1	75
7	15	76 × 3.76	3	100
8	15	76 × 3.76	3	75
8r	15	76 × 3.76	1	75

Note: "r" refers to regular shear walls with one row of nails along sheathing edges.

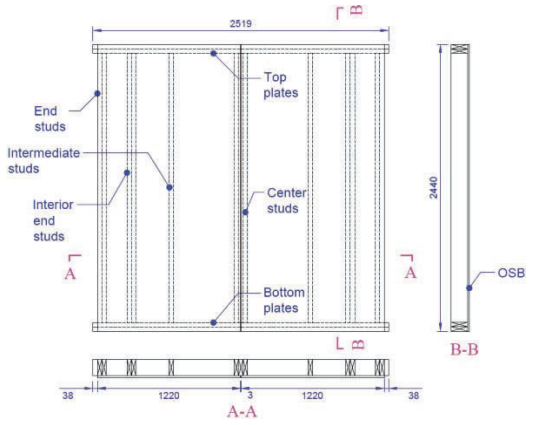

Figure 1*: Shear wall with three rows of nails [4] (Unit: mm)*

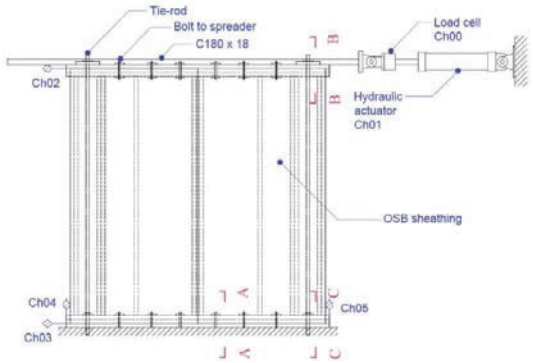

https://doi.org/10.52202/069179-0360

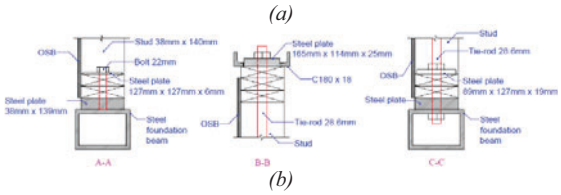

Figure 2: *Schematic of shear wall test set up: (a) front view, (b) cross section view [4]*

2.2 TEST RESULTS

Test results showed that shear walls with two rows of nails have approximately 2 times the lateral load resistance and energy dissipation capacity of a standard shear wall with the same sheathing thickness, nail diameter and nail spacing. According to seismic equivalency requirement in ASTMD7989 [14], a design value of 1.8 times standard shear walls can be assigned to shear walls with two rows of nails [3].

In general, shear walls with three rows of nails achieved approximately 3 times the lateral load resistance and energy dissipation capacity of a standard shear wall with the same sheathing thickness, nail diameter and nail spacing. However, a design value much less than three times of standard shear walls must be used to meet the ductility requirements. This is due to the undesirable failure modes which caused shear walls to lose resistance rapidly after the peak point [4].

Figure 3 shows the load-displacement response of walls with three rows of nails compared to a standard shear wall with one row of nails.

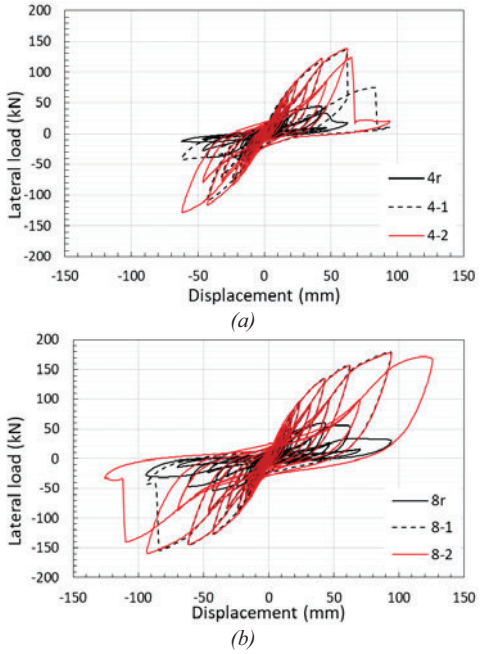

Figure 3: *Comparison of hysteresis loops of (a) Wall 4r, Wall 4-1, Wall 4-2, (b) Wall 8r, Wall 8-1, Wall 8-2*

2.3 FAILURE MODES

Besides common failure modes such as nail head pull through sheathing, nail chip-out from sheathing edge, nail withdrawal and fracture, other failure modes were also observed in the testing of high-capacity shear walls, including bottom plate splitting, end stud pull-out from bottom plates, center stud separation, and sheathing rupture.

In Wall 3 and Wall 4 (Table 1), bottom plates split due to a combination of factors (Figure 4 a), such as increased uplift force from three rows of nails, while the end of bottom plates was not restrained from uplifting. The splitting of bottom plates is brittle and undesired. This failure mode was prevented after installing bearing plates on bottom plates where tie-rods were located.

For most of the shear wall specimens with three rows of nails, end studs were separated from bottom plates (Figure 4 b), which led to the rupture of the sheathing panels in some cases (Figure 4 c). This is because the shear walls were only sheathed on one side which caused an out-of-plane moment on the end studs. This moment was amplified with increase of the number of rows of nails and using of 2 × 6 lumber compared to a 2 × 4 standard wall. The nails that connect bottom plates to end studs were not able to hold end studs and bottom plates together. The failure mode of end stud separation is brittle and need to be prevented.

Sheathing rupture was also observed in one of the shear walls (Figure 4 d). To prevent such failure, sheathing panels with higher thickness should be used.

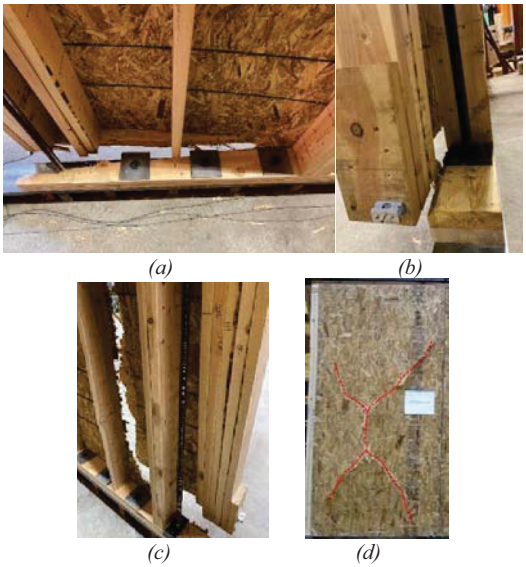

Figure 4: *Failure modes: (a) Splitting of bottom plates, (b) Separation of end studs, (c) Sheathing rupture due to end stud separation, (d) Sheathing rupture due to buckling and tension [4]*

2.4 NAIL JOINT TESTS

Nail joints made from the same materials (dimension lumber, OSB panels, and nails) as shear walls with two rows of nails were tested [3]. The test results were used in

https://doi.org/10.52202/069179-0360

the modelling of shear walls. Nail size of 63.5 mm × 3.33 mm and 76 mm × 3.76 mm were combined with sheathing thickness of 15 mm (Table 2). Figure 5 shows the test setup and configurations of the nail joint. The reversed cyclic loading protocol (CUREE) used for shear wall testing were adopted for nail joint testing, with half the displacement amplitude.

Table 2 shows the details of nail joint configurations and the average peak resistance of all replicates. It was found that the tested peak resistance of nail joints for both nail sizes is approximately 1.7 times the design value based on CSA O86 [15].

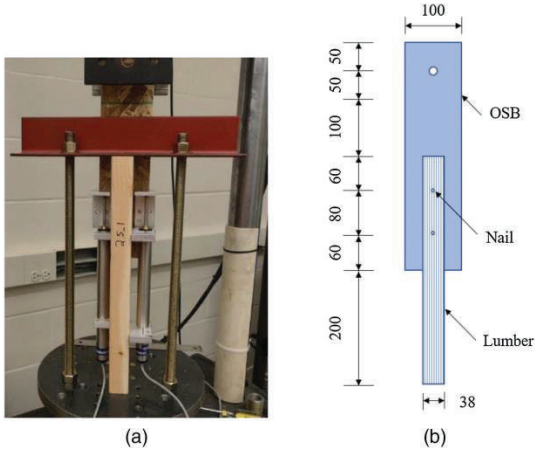

Figure 5: *Nail joint test: (a) Test set up, (b) Specimen dimension (mm) [3]*

Table 2: *Configuration and test results of the nail joints[3]*

Nail joint #	OSB thickness (mm)	Nail size (mm)	Peak resistance[1] (N)	Design resistance (N)
N2.5	15	63.5 × 3.33	1619	954
N3	15	76 × 3.76	1835	1105

1. The peak resistance is based on nail joint with one nail.

3 NUMERICAL MODELLING

Numerical models of the shear walls with three rows of nails were developed in ABAQUS. The sheathing-to-framing and framing-to-framing nail joints were simulated by a nonlinear fastener (link) element. The nail joint test data was used to derive the properties of fastener elements through fitting the load-displacement curve to the test curve. These properties of fasteners were then implemented in the shear wall models.

3.1 NAIL JOINT ELEMENT PROPERTIES

The tested nail joints with 15 mm sheathing thickness and 63.5 mm × 3.33 mm and 76.2 mm × 3.76 mm nails were modeled. The two nails connecting OSB panel and lumber were modelled using mesh independent fasteners. The fastener properties were derived from the average backbone curves and its corresponding EEEP parameters [13].

The fastener elements in ABAQUS were used to define a point-to-point connection between surfaces of OSB panel and lumber. An influence radius equal to the diameter of nail shank was used for each type of nails. A connector section was assigned to the fastener element, which allows behavior in three local directions. Elastic, plastic and damage behavior were assigned in the connector section. For elastic behavior, spring stiffness was assigned for each local direction. The average secant stiffness, *D*, derived from the tested nail joints was used, as shown in Table 3. Coupled plastic behavior with nonlinear isotropic hardening was defined using exponential law as shown in the following Equation (1):

$$F_0 = F|_0 + Q_{inf}\left(1 - e^{-b\bar{u}^{pl}}\right) \quad (1)$$

where F_0 is the yield surface size defined as the equivalent force in the connector, $F|_0$ is the yield force at zero plastic motion, Q_{inf} is the maximum change of yield surface, $\bar{u}^{pl}$ is the relative plastic motion, b is the rate of the change of the yield surface. The relative motion components are coupled in a quadratic form by defining the potential function [16]. Coupled damage behavior was also defined based on relative plastic motion, where linear softening was assumed.

The parameters for plastic and damage behavior were derived from the average backbone curve of the tests, as shown in Figure 6. Table 4 summarizes the properties of the fasteners, in which b is modified after back calculated from test data using Equation (1), plastic motion at failure was modified based on actual failure displacement to fit the test curve.

Monotonic push-over displacement was applied in the modeled nail joint. Load-displacement relationship of the models is compared with the average backbone curve of the tested nail joints, as shown in Figure 7. Overall, the parameters listed in Table 4 give a good fitting of the performance of the nail joints to the test data and can capture the post peak load-displacement behavior.

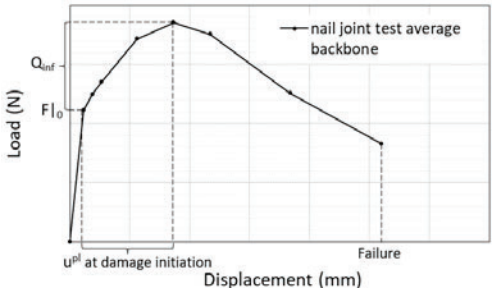

Figure 6: *Plastic and damage parameters from tested backbone curve*

Table 3: *Properties of fastener element for nail joints*

Connector property	Nail size (mm)	
	63.5 × 3.33	76 × 3.76
D (N/mm)	827.5	980.6
$F\|_0$ (N)	964.8	1100.1
Q_{inf} (N)	607.9	743.1
b	0.4	0.4
Plastic motion at damage initiation (mm)	7.6	7.5
Plastic motion at failure (mm)	30	30

https://doi.org/10.52202/069179-0360

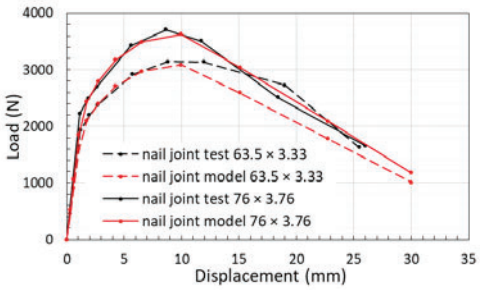

***Figure 7:**. Comparison of load displacement curves between nail joint tests and models*

3.2 SHEAR WALL MODEL

In the shear wall model, more details of the shear wall are included to simulate both the overall load displacement behavior and the possible new failure modes.

The framing members were represented with solid elements (C3D8R), and sheathings panels were modelled with continuum shell elements (CS8R). The framing members and sheathing were both assumed to be elastic. Table 3 summarizes the elastic properties of Douglas fir lumber and OSB panel. Sheathing-to-framing nails, nails for built-up studs and plates, nails connecting studs to plates were all represented by the fastener elements, in which both shear and withdrawal components were included. For sheathing-to-framing nails, properties are derived from nail joint fitting process (Table 3). Since properties in Table 3 refers to 15 mm sheathing thickness, a factor of 0.89 was used to adjust the resistance for 11 mm sheathing panel with combination of 63.5 mm × 3.33 mm nails based on the ratio of design resistance of these two different nail joints in O86-19 [15]. For nail joints in built-up studs and plates (76.2 mm × 3.05 mm), a factor of 0.98 was applied to the properties of 63.5 mm × 3.33 mm nail joint in Table 3. For nails connecting studs to top and bottom plates, an end grain factor of 0.67 was applied to the nail joints for built-up members to further reduce the resistance [15]. Table 5 and Table 6 shows the modified connector properties used for sheathing panels and framing nails.

***Table 4:** Material properties of nail joint model*

Material property	Douglas-Fir[1] (Mpa)	OSB[2] (Mpa)
E_1	11000	5323
E_2	748	3231
E_3	550	-
G_{12}	704	1574
G_{13}	758	1574
G_{23}	77	1574
μ_{12}	0.29	0.31
μ_{13}	0.45	-
μ_{23}	0.39	-

1. Properties of Douglas-Fir are obtained from O86 and Wood Handbook [15,17].
2. Properties of OSB are obtained from studies of Islam et al. [18].

***Table 5:** Properties of fastener elements used for sheathing-to-framing nails*

Connector property	Nail size (mm)	
	63.5 × 3.33	76 × 3.76
D_{11} (N/mm)	734.3	980.6
D_{22} (N/mm)	734.3	980.6
D_{33}[1] (N/mm)	9.6	10.6
$F\|_0$ (N)	856.1	1100.1
Q_{inf} (N)	539.4	743.1
b	0.4	0.4
Plastic motion at damage initiation (mm)	7.6	7.5
Plastic motion at failure (mm)	30	30

1. D_{33} is the nail withdrawal stiffness of sheathing-to-framing nails based on the local coordinate, which was assumed to be a small percentage of the lateral stiffness in this preliminary modeling with the assumption that the withdrawal resistance is limited after yielding of nails in shear and losing of friction from the surrounding wood when the nail is pulling out from studs.

***Table 6:** Properties of fastener element used in framing members*

Connector property	Nail type	
	Built-up member	Stud to plate
D_{11} (N/mm)	811.5	543.7
D_{22}[1] (N/mm)	811.5	543.7
D_{33} (N/mm)	811.5	543.7
$F\|_0$ (N)	946.0	633.8
Q_{inf} (N)	596.1	399.4
b	0.4	0.4
Plastic motion at damage initiation (mm)	7.6	7.6
Plastic motion at failure (mm)	30	30

1. D_{22} is the nail withdrawal stiffness of built-up members and stud-to-plate connections based on the local coordinates. No reduction of the lateral stiffness was used in this preliminary model.

Figure 8 shows a shear wall model. The assembly includes the shear wall panel, steel loading beam and foundation beam. The fastener elements were assigned for all built-up studs, top and bottom plates, stud-to-plates connections, and sheathing-to-framing connections. The top and bottom plates have pre-dill holes representing locations of anchor bolts and hold-downs (tie-rods). The hold-downs were represented by axial connector elements with a stiffness of 42.34 kN/mm [19], where the top of the hold-down element was coupled with the top plates over a surface area of the same size of the bearing plates. The bottom of the hold-down element was fixed at the foundation. The bottom plates were anchored to the foundation beam at the surfaces of the same size of bearing plates. The top plates and loading beam are simplified as tie constrained to eliminate slip between top plates and loading beam. A monotonic lateral displacement is applied through the loading beam. There's no out-of-plane degree of freedom allowed on the loading beam.

https://doi.org/10.52202/069179-0360

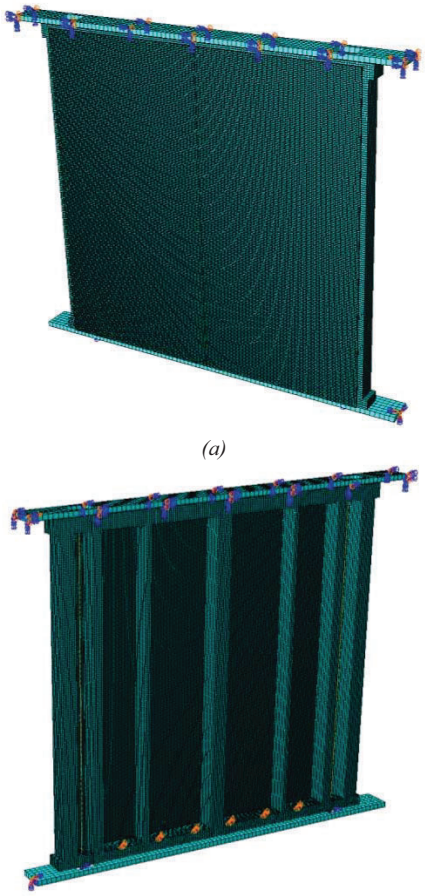

(a)

(b)

Figure 8: *Shear wall model: (a) Front view, (b) Back view*

The load-displacement curves of the models are compared with the hysteresis loops of the tests. There are in total 6 wall configurations (Wall 3, 4, 4r, 7, 8, 8r in Table 2) modelled, including two reference wall models. The results are shown in Figure 9.

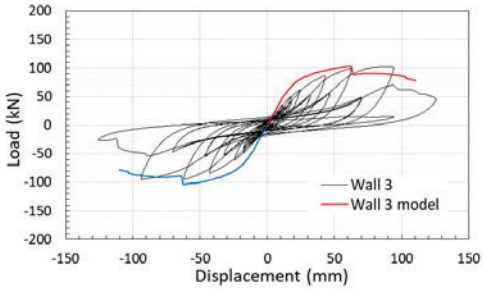

(a)

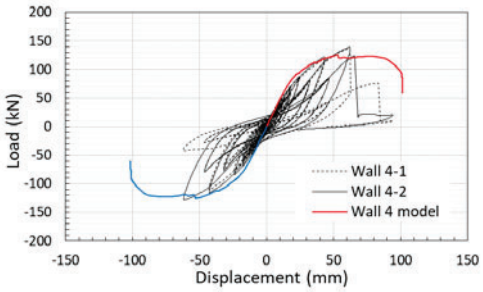

(b)

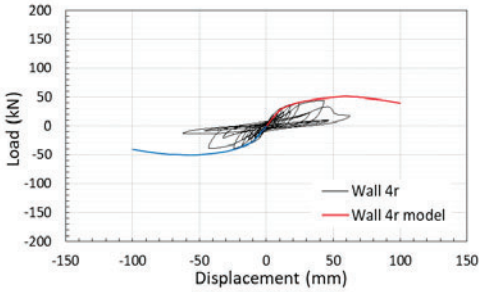

(c)

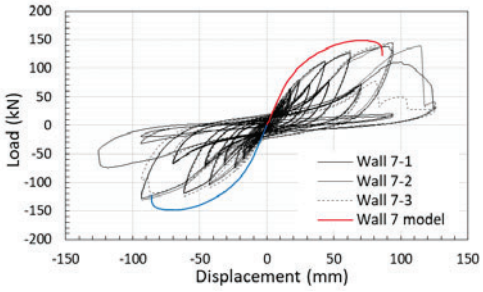

(d)

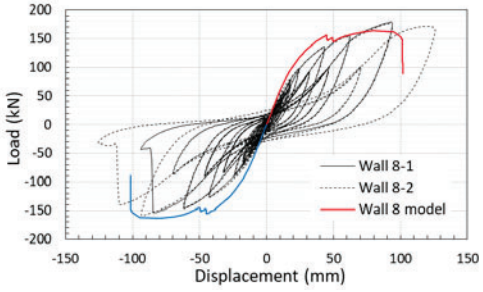

(e)

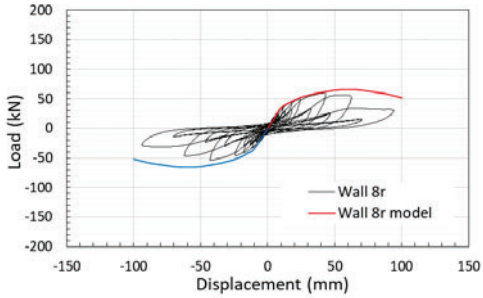

(f)

Figure 9: *Comparison between model and test results: a) Wall 3, (b) Wall 4, (c) Wall 4r, (d) Wall 7, (e)Wall 8, (f) Wall 8r*

Overall, the model can predict the nonlinear behavior of

https://doi.org/10.52202/069179-0360

the shear wall including the post-peak load drop. The peak resistance of models and test results are compared in Table 7. It can be seen that the discrepancy of peak load is with 10% for most cases. In all shear walls with three rows of nails, namely Wall 3, Wall 4, Wall 7 and Wall 8, the stiffness of the models appears to be higher than the tested shear walls (Figure 9 a, b, d, e). In the reference shear walls, namely Wall 4r and Wall 8r, the models reach their peak load at a larger displacement than the tested walls, and the models do not have a significant load drop after peak load (Figure 9 c, f).

Table 7: *Comparison of the tested peak resistance and model peak resistance*

Wall #	Test P_{peak} (kN)	Model P_{peak} (kN)	Model peak/Test peak
3	91.5	103.5	1.1
4-1	114.1	125.5	1.1
4-2	133.7	125.5	0.9
4r	41.7	50.7	1.2
7-1	132.1	148.6	1.1
7-2	137.6	148.6	1.1
7-3	131.2	148.6	1.1
8-1	166.7	155.7	0.9
8-2	168.4	155.7	0.9
8r	57.2	65.7	1.1

In the shear wall models with three rows of nails, end stud separation from bottom plates was observed, as shown in Figure 10 a, which caused the load drop at the end of the load-displacement curves in Wall 4, Wall 7 and Wall 8. The end studs on the opposite side of the wall have also separated slightly from the top plates (Figure 10 b). The separation of end studs is due to the eccentric moment on end studs caused by sheathing only on one side of the wall and the relatively low resistance of fasteners connecting the end studs to the bottom and top plates, which are not strong enough to counteract the out-of-plane moment. The failure modes were also observed in shear wall tests. Separation of end stud from bottom and top plate can be prevented through reinforcing the stud-to-plate connections.

As framing members and sheathing panels were assumed to be linear elastic in this preliminary model to reduce convergence difficulty, the failure modes such as bottom plate splitting and sheathing rupture was not captured. Figure 11 shows the axil stress on framing elements. It can be seen that the compression stress was concentrated on end studs which indicates that the compression force due to over-turning moment is mainly resisted by the end studs. The contribution from the interior end studs (Figure 1) is limited. Therefore, when tie-rods are used in shear walls as hold-downs, the interior studs should neither be counted for resisting the compression force due to over-turning, nor the bearing area of the bottom plates. Figure 12 shows the principal stress distributed on the sheathing panels before end stud separation. It can be seen that the principal tensile and compressive stress developed on the sheathing panels are diagonal, which explains the failure in one of the Wall 4 replicates tested, in which 'X' shape fracture occurred in one of the sheathing panels (Figure 4 d).

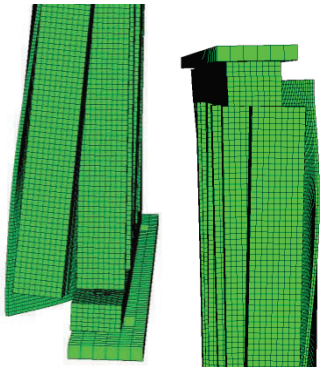

(a) (b)

Figure 10: *Failure of the shear wall model (Wall 4): (a) End stud separation from bottom plates, (b) End stud separation from top plates*

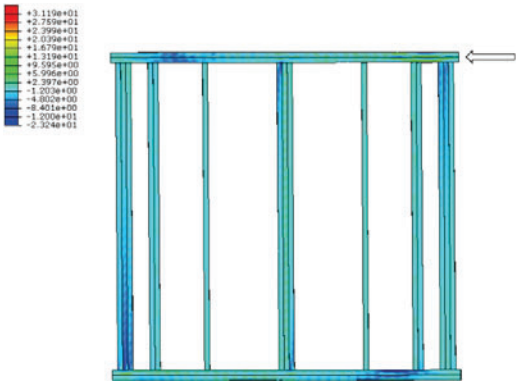

Figure 11: *Stress S11 along grain direction of framing members in Wall 4 model(MPa)*

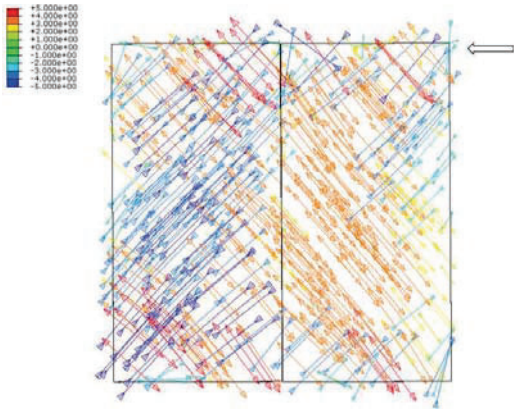

Figure 12: *Principal Tensile and compressive stress in sheathing panels of shear wall model (Wall 4) before end stud separation (MPa)*

Overall, the models can generally predict the load-displacement behavior and the end stud separation in walls with three rows of nails. With only fastener behavior assumed to be non-linear, the models are not able to predict material failure in sheathing panels and framing members. Although the stress distribution in sheathings showed potential cause for sheathing rupture, additional

wood damage definition is needed to simulate those failure modes.

3.3 ON-GOING WORKS

To better understand the split of bottom plate of shear walls with multiple rows of nails, a more detailed 3D sub-model of the shear wall is being developed only including the bottom plates and foundation beam. Steel anchor bolts and bearing plates are installed in the bottom plates. Nails and initial imperfections (cracks, checking) on wood will be added (Figure 13). The objective of this modeling is to capture the crack propagation parallel to grain under the one-sided shear force on the bottom plate. Moreover, more detailed material definition will be included in the shear wall model to capture the fracture of sheathing panel due to buckling or tension.

Figure 13: *Detailed sub-model of bottom plates*

4 CONCLUSIONS

In this study, high-capacity shear walls with multiple rows of nails were introduced and numerically simulated using ABAQUS. Test results of shear walls with two and three rows of nails were presented. The lateral load resistance is proportional to number of rows of nails. Failure modes that are not commonly observed in regular shear walls were found in shear walls with multiple rows of nails. To study the behavior of high-capacity shear walls, a preliminary 3D shear wall model with three rows of nails was developed. Fastener elements were used to simulate the non-linear behavior of nails, firstly, the properties for fastener elements were derived from the nail joint tests and through a fitting process. The fastener properties were then implemented in the shear wall models. In the shear wall model, all the framing-to-framing and framing-to-sheathing nails were represented by the non-linear fastener elements, while framing members and sheathing panels were assumed to be linear elastic. Components such as anchors, hold-downs, foundation beam and loading beam were also included. The main findings of the numerical modeling analysis are summarized as follows:

- The preliminary 3D model developed in this study can well capture the load-displacement performance of the high-capacity shear walls with multiple rows of nails, and predict the end-stud separation from the bottom plate.
- Failure on sheathing and framing members cannot be captured by the current preliminary model due to linear elastic material assumption.
- The principal stress developed on sheathing panels is diagonal, which explains the “X” shape fracture observed in one of the wall panels in the test.
- Compression force due to over-turning moment is mainly resisted by the end studs. The interior end studs should neither be counted for resisting this compression force in design, nor the bearing area of the bottom plates in a shear wall when tie-rods are used as hold-downs.

More detailed modelling and material damage definition need to be added to the current model to study the splitting of bottom plates, sheathing panel fracture, and other failure modes of high-capacity shear walls.

ACKNOWLEDGEMENT

This project is funded by Canadian Forest Service of Natural Resources Canada and Forestry Innovation Investment Ltd. in BC – Wood First Program. Donation of continuous threaded steel rods, coupler nuts and nuts by Simpson-Strong Tie, which have been used for tie-downs of the shear wall specimens, is greatly appreciated.

REFERENCE

[1] Canadian Commission on Building and Fire Codes. National Building Code of Canada: 2020 2020.

[2] Canadian Commission on Building and Fire Codes. National Building Code of Canada 2015. https://doi.org/10.4224/40002005.

[3] Derakhshan SS, Ni C, Zhou L, Qiang R, Huang D. Cyclic test and seismic equivalency evaluation of high-capacity light wood-frame shear walls for midrise buildings. J Struct Eng, 148: 4022168, 2022.

[4] Qiang R, Zhou L, Ni C, Huang D. Seismic performance of high-capacity light wood frame shear walls with three rows of nails. Eng Struct, 268:114767,2022. https://doi.org/10.1016/j.engstruct.2022.114767.

[5] Ayoub A. Seismic analysis of wood building structures. Eng Struct, 29:213–23, 2007. https://doi.org/10.1016/j.engstruct.2006.04.011.

[6] Boudaud C, Humbert J, Baroth J, Hameury S, Daudeville L. Joints and wood shear walls modelling II: Experimental tests and FE models under seismic loading. Eng Struct,101:743–9, 2015. https://doi.org/10.1016/j.engstruct.2014.10.053.

[7] Humbert J, Boudaud C, Baroth J, Hameury S, Daudeville L. Joints and wood shear walls modelling I: Constitutive law, experimental tests and FE model under quasi-static loading. Eng Struct;65:52–61,2014. https://doi.org/10.1016/j.engstruct.2014.01.047.

[8] Pang WC, Rosowsky D V., Pei S, Van De Lindt JW. Evolutionary parameter hysteretic model for wood shearwalls. J Struct Eng,133(8):1118–29, 2007. https://doi.org/10.1061/(asce)0733-9445(2007)133:8(1118).

[9] Xu J, Dolan JD. Development of nailed wood joint element in ABAQUS. J Struct Eng, 135:968–76,2009. https://doi.org/10.1061/(asce)st.1943-

https://doi.org/10.52202/069179-0360

541x.0000030.
[10] Peng C, El Damatty AA, Musa A, Hamada A. Simplified numerical approach for the lateral load analysis of light-frame wood shear wall structures. Eng Struct, 219:110921, 2020. https://doi.org/10.1016/j.engstruct.2020.110921.
[11] Collins M, Kasal B, Paevere P, Foliente GC. Three-dimensional model of light frame wood buildings. II: Experimental investigation and validation of analytical model. J Struct Eng, 131:684–92,2005. https://doi.org/10.1061/(asce)0733-9445(2005)131:4(684).
[12] Gattesco N, Boem I. Stress distribution among sheathing-to-frame nails of timber shear walls related to different base connections: Experimental tests and numerical modelling. Constr Build Mater, 122:149–62, 2016. https://doi.org/10.1016/j.conbuildmat.2016.06.079.
[13] ASTM - American Society for Testing and Materials. E2126 - Standard Test Methods for Cyclic (Reversed) Load Test for Shear Resistance of Vertical Elements of the Lateral Force Resisting Systems for Buildings, i:1–14, 2019. https://doi.org/10.1520/E2126.
[14] ASTM - American Society for Testing and Materials. D7989 - Standard Practice for Demonstrating Equivalent In-Plane Lateral Seismic Performance to Wood-Frame Shear Walls Sheathed with Wood Structural Panels, i:1–9, 2018. https://doi.org/10.1520/D7989-18.
[15] Canadian Standards Association. CAN/CSA-086:19. Engineering design in wood, 1, 2019.
[16] Abaqus 6.14 Analysis User's Guide. Dassault Systèmes 2014.
[17] Forest Products Laboratory. Wood handbook : wood as an engineering material. 1999. https://doi.org/10.2737/FPL-GTR-113.
[18] Shahidul Islam M, Islam MN, Shahria Alam M. Properties of oriented strand board (OSB), and timber to evaluate the stiffness of timber L-joist. 6th Int Conf Eng Mech Mater 2017, 2:790–801, 2017.
[19] Simpson Strong-Tie Company Inc. Strong-Rod™ Systems Seismic and Wind Anchor Tiedown System Guide 2022.

World Conference on Timber Engineering Oslo 2023

BUCKLING ANALYSES OF CROSS LAMINATED TIMBER PANELS

Martina Sciomenta[1], Yuri De Santis[2], Chiara Bedon[3], Massimo Fragiacomo[4]

ABSTRACT: This paper investigates the column buckling behaviour of three-layer Cross Laminated Timber (CLT) panels under compression, from both the experimental and numerical point of view. The main aim of present study is hence to define the expected load-bearing capacity for these composite CLT solutions, and to assess the typical fracture mechanism for two different series of specimens of possible technical interest for construction applications. To this aim, a total of 14 column buckling experiments is carried out. First, a set of 7 homogeneous specimens ("HO" series), which are entirely made of beech, are investigated. Their load-bearing capacity is compared with the column buckling performance of 7 hybrid specimens ("HB" series), whose inner layers are made of Corsican pine. Overall, the experimental analysis gives evidence of a rather stable column buckling capacity for CLT panels, with evidence of major failure mode due to out-of-plane bending phenomena, but also rolling shear and delamination. Finally, further assessment of experimental evidence is provided by extended analytical calculations (based on existing formulations, including the Eurocode 5 approach). Comparative results are discussed in terms of structural performance, capacity, weakness of analytical models for CLT solutions.

KEYWORDS: Cross-Laminated Timber (CLT), beech wood (Fagus sylvatica L.), Buckling, Experimental tests, Load-bearing capacity, Standards

1 INTRODUCTION

In the last years the Cross Laminated Timber (CLT) has become a widespread construction material in the framework of panel mid- and high-rise buildings [1]. The high prefabrication and the well-known advantages [2], such as the high dimensional stability, the elevated in-plane isotropic strength and stiffness with respect to sawn timber and the high speed of installation [3] contributed to spread their applicability, in addition with the great environmental benefits, in terms ot carbon absprtion and sustainability.

Several researches have been carried on to assess how and which parameters mainly influence the load-bearing capacity of this engineered wood product.

The results confirmed that the response of CLT is influenced by the lamellas' material and geometry, and in particular by: *i)* the layer thickness [4,5] ; *ii)* the wood species [6,7], and *iii)* the type of adhesive [8,9].

The choice of wood species is so relevant that different studies focused on this point even to emphasize the potential use of wood species other than fir and spruce [10,11,12] which are the most widespread used for commercial applications.

In this framework, native hardwoods species such as beech which is extensively available in European forests [13] proved to have relevant mechanical features for CLT structural applications [14]. Many researches have been also conducted to better understand the CLT behavior under different load conditions as bending [15], compression [16,17], and shear [18,19], nevertheless the CLT in-plane behavior under compressive loads, leading to column buckling is currently poorly investigated as for softwood [20,21] as for hardwood species.

For timber structural components and systems, stability issues have a critical role in design procedures, due to the challenging trend of modern applications towards the construction of high-rise timber buildings as well for the intrinsic material's nature.

In particular, due to the low modulus of elasticity parallel to the grain of timber in general and of the even lower shear modulus which affects the ortogonal layers, CLT is more prone to undergo instability phenomena.

CLT members, depending on the boundary conditions, can be addressed as: *i)* one-way elements if they are restrained on two opposite sides; or as *ii)* two-way elements if them are constrained on three or all sides.

Few studies that have addressed the buckling behavior of CLT members considered them as one-way elements [22]. Some researchers have been carried by performing experimental tests; [23] investigated the axial compression behavior of both cross-laminated timber columns (CLTCs) and control glued-laminated timber columns (GLTCs). It was discovered that CLT column specimens had better ductility and energy absorption. [24] carried on tests on Chilean radiata pine CLT panel, focalizing on the variation of the number of layers while keeping the panel thickness constant. At last, the test

[1] Martina Sciomenta, University of L'Aquila, Italy, martina.sciomenta@univaq.it
[2] Yuri De Santis, University of L'Aquila, Italy, yuri.desantis@.univaq.it
[3] Chiara Bedon, University of Trieste, Italy, chiara.bedon@dia.units.it
[4] Massimo Fragiacomo, University of L'Aquila, Italy, Massimo.fragiacomo@univaq.it

https://doi.org/10.52202/069179-0361

evidences were compared with the numerical predictions and successfully validated.

Kudo *et al*. [25] conducted a series of buckling tests on full-size Japanese Cedar or Japanese Cypress CLT members. The buckling loads were compared with those calculated following the formulas of the Japanese Building Code; it was found that the formulas given in the national standard provided conservative results.

The worldwide standards (i.e. Eurocode 5 [26]) and national codes available for the calculation methods of the buckling capacity (or the stability coefficient) of axially loaded CLT members are only applicable to one-way CLT members.

The currend handbook/standards provide two methods for the calculation of the load-bearing capacity of axially compressed columns with and without eccentricity; the most simple one is based on the Effective Length Method (ELM), while, the other accounts for a 2nd order analysis of the structure. This latter, by the way, considers timber as an elastic material so, is not able to take into account its material non-linearity. The ELM assumes a simple equivalent column hinged at both ends. The simplicity of the approach is that the P-delta effect is taken implicitly into account through a buckling factor, k_c. The buckling factor has the role to reduce the compressive strength of the timber column, in the direction parallel to the grain, and strictly depends on the effective length of the structural element, which is conventionally expressed in terms of slenderness ratio λ.

2 EXPERIMENTAL TESTS

The herein reported buckling tests are part of a wider experimental campaign [27,28] performed at the Laboratory of Structures, Tests and Materials of the University of L'Aquila (Italy), aiming to investigate the possible structural applications of two of the most interesting Italian broad-leaved and conifer timber species, namely beech and Corsican pine [14].

The raw material for both species came from Calabrian forests – South Italy. A list of different preliminary steps was carried out to obtaining the final composition of investigated CLT specimens. Boards were at first strength graded according to EN 14081-2:2018 rules [29] by the grading machine ViSCAN-Portable (Mi-CROTEC). The machine settings used for the strength grading of the boards of both beech and pine were developed in previous studies [30,31,32]. The strength class combinations used to qualify the raw material were D40 and rejects for beech and C20 and rejects for pine (EN 338:2016 [33]). The outcomes are summarized in Table 1. Boards were planed to a thickness of 18 mm to guarantee the adequate planar surface necessary for the face gluing. Two different series of three-layer CLT panels, made respectively of beech and Corsican pine and only beech, were realized by bonding the boards and gluing them with a Melamine Urea Formaldehyde (MUF) adhesive (GripProTM Design – AkzoNobel). The narrow board edges were not bonded. The average of glue grammage was 190 g/m^2. The adhesive was applied in a factory condition of 17° C, with an environmental moisture of 50%. Formed panels were then cold-pressed for two hours, with a pressure of 1.4 N/mm^2.

Table 1: *Mean properties of timber species, as derived from the non-destructive measurements [14].*

Timber species	ρ (kg/m^3)	MOE_{dyn} (N/mm^2)	MoR (N/mm^2)	MOE_{global} (N/mm^2)
Beech	756	16077	80.1	16154
Corsican Pine	512	9650	38.2	9748

Seven specimens for each series were tested under central axial compression loading conditions.

The specimens' geometrical features are characterized by nominal dimensions equal to b=144 mm, t=54 mm and l=800 mm. The three constituent layers had identical nominal thickness t_i = 18 mm.

The buckling tests were carried out by applying a central axial compression on the top surface of the CLT specimens for an average duration of 30 minutes. This condition was pledged by a setup able to provide the desired loading and boundary conditions to the tested CLT beams (Fig. 1).

Each specimen was positioned between a couple of one-way knife hinges whose shape has been designed to ensure the right positioning in the underlying and overlying wedges. The distance between the axes of end hinges was set equal to L=1064 mm.

The horizontal displacements in the loading stage were measured by using four laser displacement transducers, which were placed perpendicularly to the lateral surfaces of each specimen (Fig. 1). In particular, two transducers were located at the midpoint and two near the corners, to account for possible torsional phenomena (Fig.1). Displacement-control tests with a limit of 15 mm to the vertical lowering of the machine crossbeam were carried out by means of an Instron-Schenck machine system. Load vs. mid-span deflections of each beam specimen was monitored and plotted with a sampling rate of 0.5 Hz. Two different speed rates were taken into account during each experiment. At first, until the critical load was reached for each sample, was set equal to 0.44 mm/s. Once the critical load was reached, the speed rate was then reduced to 0.33 mm/s.

https://doi.org/10.52202/069179-0361

Figure 1: *Experimental tests setup*

The experimental evidences related to buckling test are summarized in Table 2 and Table 3. For most of tested HO and HB samples, the typical failure mode was characterized by out-of-plane bending deflection due to buckling (all the HO specimens except for the HO-6 and HB-1). Nevertheless, rolling shear (HB-2, HB-3 and HB-5) and delamination phenomena (HB-6 and HB-7) occurred in a certain stage of the tests, especially for HB specimens. Typical failure mode outcomes are summarized in Fig. 2.

Figure 2: *Failure modes: left) compressed fibres; right) rolling shear*

Table 2: *Buckling tests experimental evidences for HO= homogeneous series. Failure mode key: b= bending / buckling; r= rolling shear; d= delamination; s_y= the standard deviation, m_k =5th percentile*

ID	F_b (kN)	v_{max} (mm)	Failure Modes
HO -1	211	9.3	b
HO -2	183	4.9	b
HO -3	165	11.6	b
HO -4	203	5.0	b
HO -5	205	4.0	b
HO -6	218	2.4	d
HO -7	217	7.2	b
Average	200	6.3	
s_y	200	6.3	
m_k	19	3.2	

Table 3: *Buckling tests experimental evidences for HB= hybrid series. Failure mode key: b= bending / buckling; r= rolling shear; d= delamination, s_y= the standard deviation, m_k =5th percentile*

ID	F_b (kN)	v_{max} (mm)	Failure Modes
HB -1	234	3.6	b
HB -2	187	6.3	r
HB -3	134	14.0	r
HB -4	241	2.7	r+d
HB -5	204	2.5	r+d
HB -6	204	2.1	d
HB -7	141	11.4	d+b
Average	192	6.1	
s_y	41	4.8	
m_k	99	-4.6	

3 BUCKLING FORMULATIONS

In a typical column buckling analysis, two key aspects should be considered, namely: *i)* a geometric effect called P-delta, which describes the non-linear increasing of deformations due to the increasing eccentricity of the axial load, and *ii)* the non-linear behaviour of timber material under compression actions parallel to the grain. A large investigation on the P-Delta effect on axial compressed timber elements was carried on by Tetmajer *et al* [34] and confirmed by test campaign by Larsen and Pedersen [35], the influence of non-linearity of timber on the interaction between moment and axial force was numerically defined by Buchanan [36].

In this section, a comparison of commonly used analytical formulas for the critical buckling load evaluation was provided. At first, the Euler formulation for column buckling is defined; at a second stage, it is extended in order to account for a possible initial geometric curvature. Thereafter, the existing Eurocode 5 formulation for timber columns subjected to combined bending and axial compression parallel to the grain is discussed.

The buckling strength of CLT specimens under in-plane vertical compression could be provided by classical analytical formulations of axially compressed, monolithic columns [37]. The corresponding Eulerian critical load could be reasonably estimated as:

$$P_e = \frac{\pi^2 E I_{\text{ef}}}{l_0^2} \tag{1}$$

with:

https://doi.org/10.52202/069179-0361

$$I_{\text{ef}} = \frac{bt_i^2}{12} + (bt_i) \cdot \left(\frac{t_i}{2}\right)^2 \quad (2)$$

The flexural moment of inertia, for outer layers and for the inner layer; and

$$l_0 = \beta L \quad (3)$$

with l_0 the effective buckling length.
In Eq.(3), L is the maximum distance between the hinges center, while β is the buckling coefficient accounting for the actual restraint conditions, in this study it was set equal to 1 for pinned-pinned specimens.
The latter Eq. (1) describes the behaviour of an ideal compressed beam (Eulerian instability), without taking into account the material non-linearity as well the possible geometrical clearances caused by production tolerances that lead to an inevitable rectilinear imperfection, which must be taken into account when calculating the buckling load. To take into account this phenomenon, the initial specimen deflection must be considered. A stability analysis of the beam in its deformed configuration was carried out.
The initial deformation is schematized as in Fig. 4, by imposing a sinusoidal deformation where represents its maximum amplitude:

$$\tilde{v}(x) = e_0 \, sin\left(\frac{\pi \cdot x}{L}\right) \quad (4)$$

The elastic displacement behaviour can be hence modelled as:

$$Pv(x) = -EI_{\text{ef}}\left(v''(x) - \tilde{v}''(x)\right) \quad (5)$$

which can be rewritten as:

$$v''(x) + \alpha^2 v(x) - \tilde{v}''(x) = 0 \quad (6)$$

Where
Replacing Eq. (4) and (1) in Eq. (6) and solving, the solution of differential equilibrium equation is:

$$v(x) = e_0 \frac{1}{1 - \frac{PL^2}{\pi^2 EI_{\text{ef}}}} sin\left(\frac{\pi x}{L}\right) = e_0 \frac{1}{1 - \frac{P}{P_e}} sin\left(\frac{\pi x}{L}\right) \quad (7)$$

Its maximum displacement is reached in the middle point of the beam:

$$v\left(\frac{L}{2}\right) = e_0 \frac{1}{1 - \frac{P}{P_e}} \quad (8)$$

The limit load can be written as

$$P = \left(\frac{\alpha L}{\pi}\right)^2 P_e \quad (9)$$

3.1 EUROCODE 5

Based on the Eurocode 5 [26] approach, the buckling verification of timber columns subjected to combined bending and axial compression parallel to the grain is performed by taking into account its minimum relative slenderness ratio:

$$\lambda_{\text{rel}} = \frac{\lambda}{\pi} \sqrt{\frac{f_{c,0,k}}{E_{0,05}}} \quad (10)$$

with

$$\lambda = \frac{l_0}{\rho_{min} \sqrt{\frac{A}{I_{\text{min}}}}} \quad (11)$$

with A the cross-sectional area, $f_{c,0,k}$ is the characteristic compressive strength parallel to the grain, $E_{0.05}$ represents the fifth percentile value of the MOE parallel to the grain, β=1 is the factor for buckling depending on the support conditions and the load, L is the element length. The stability check of the member in pure compression requires that the design compressive stress $\sigma_{c,0,d}$ along the member would satisfy the condition:

$$\sigma_{\text{c,0,d}} \leq k_c \cdot f_{\text{c,0,d}} \quad (12)$$

where $f_{c,0,d}$ represents the design compressive strength in the direction parallel to the grain and k_c is a buckling reduction factor given by:

$$k_c = \frac{1}{k + \sqrt{k^2 - \lambda_{\text{rel}}}} \quad (13)$$

With:

$$k = 0.5(1 + \beta_c(\lambda_{\text{rel}} - 0.3) + \lambda_{\text{rel}}^2) \quad (14)$$

βc an imperfection factor equals to 0.2 or 0.1 for solid timber or glued laminated timber and LVL, respectively, while the coefficient $\beta_0 = 0.3$ in Eq. (14) finally, represents the minimum relative slenderness ratio λ_{rel} beyond which flexural buckling phenomena may occur in the column.

3.2 CANADIAN CLT HANDBOOK

According to the Canadian standard [38], when CLT panels are loaded under in-plane axial loads, only the layers with laminations oriented parallel to the applied axial load should be assumed to carry that load.
The compressive resistance is calculated as:

$$F_{\text{b}} = 0.8K_C K_{Zc} f_{c,0,d} A_{eff} \quad (15)$$

Where A_{eff} is the effective cross-sectional area of the panel accounting only for the layers with laminations oriented parallel to the axial load, K_C is the slenderness factor for compression members:

$$K_C = \left(1 + \frac{f_{c,0,d} K_{Zc} C_c^3}{35E}\right)^{-1} \quad (16)$$

Where E is the modulus of elasticity of the laminations oriented parallel to the axial load, K_{Zc} is the size factor for compression:

$$K_{Z,c} = \min(6.3\left(2\sqrt{3} r_{eff} l\right)^{-0.13}; 1.3) \quad (17)$$

Where r_{eff} is the radius of gyration accounting only for the layers with laminations oriented parallel to the axial load. C_c is the slenderness ratio:

$$C_c = \min(\frac{l}{\sqrt{12} r_{eff}}; 43) \quad (18)$$

3.3 CLT HANDBOOK U.S. EDITION

According to the U.S Edition of CLT handbook [39], for wall design, the failure load is given by the product of the adjusted compression strength for buckling times the area of the laminations where the grain is running parallel to the load.

$$F_{\text{b}} = C_p f_{c,0,d} A_{eff} \quad (19)$$

Where the column stability reduction factor is:

$$C_p = \frac{1 + \text{P}_{\text{cE}}/\text{P}_{\text{c}}^*}{1.8} - \sqrt{\left(\frac{1 + \text{P}_{\text{cE}}/\text{P}_{\text{c}}^*}{1.8}\right)^2 - \frac{\text{P}_{\text{cE}}/\text{P}_{\text{c}}^*}{1.8}} \quad (20)$$

Where P_{c}^* is the composite compression capacity and:

$$\text{P}_{\text{cE}} = \frac{\pi^2 E I_{app-min}}{l^2} \quad (21)$$

The minimum value of the apparent stiffness is to be determined as:

$$EI_{app-min} = 0.5184 EI_{app} \quad (22)$$

EI_{app} is a reduced effective bending stiffness to account for shear deformation.

4 COMPARISON WITH EXPERIMENTAL RESULTS

Table 2 summarize the average experimental loads and the predicted loads by means of standards formulations. The closest prediction is given by the Eurocode 5 formulation. It is worth noting that Canadian standard predict the same failure load for both homogenous and hybrid configurations. The Canadian standard completely neglect the mechanical properties of the layers perpendicular to the load. In the American standard the influence of the mid-layer is accounted only in the apparent stiffness calculation, while the effective area refers only to layers parallel to the load. The American standard predictions for the two cases are close together.

Table 2: *Comparison between experimental failure loads and predicted loads via standards formulations (HO= homogeneous; HB= hybrid).*

		F_b (kN)	F_b/N_c	Scatter (%)
HO	Experimental	200		
	Eurocode 5	210	0.92	4.9
	Canad.Handb	176	0.88	-12.3
	U.S. Handb.	156	0.78	-21.9
HB	Experimental	192		
	Eurocode 5	194	0.93	1.0
	Canad.Handb	176	0.88	-8.5
	U.S. Handb.	157	0.78	-18.5

5 CONCLUSIONS

Among others, stability issues are particularly critical in timber load-bearing components, due to their intrinsic anisotropy and to the increasing trend towards challenging high-rise timber buildings. As such, this possible vulnerability is even more pronounced for Cross Laminated Timber (CLT) components, due to their intrinsic composition and layout.
In this paper, a major attention was given to the column buckling behaviour of three-layer CLT panels. Technical advantage for the assessment of load-bearing capacity, failure mode and potentials was based on a set of experimental tests and also analytical models. Two different configurations were considered, the first (HO) composed of three layers made with the same timber specie, whereas the second was assembled with the inner layer made of a different timber specie (HB). Overall, the tested panels (14 in total) showed different failure mechanisms but little scattered results in terms of load-bearing capacity. Specifically, the hybrid (HB) specimens resulted in standard deviation.
In terms of analytical estimation of actual CLT capacities in column buckling setup, the attention was given to existing analytical models of literature, including the existing Eurocode and Handbook formulations.

https://doi.org/10.52202/069179-0361

Most importantly, the results provided by the analytical formulation, even though very close to the experimental ones, resulted always in favour of safety, since the analytical limit loads were found smaller than those obtained experimentally.

REFERENCES

[1] Brandner, R., Flatscher, G., Ringhofer, A., Schickhofer, G., & Thiel, A. (2016). Cross laminated timber (CLT): overview and development. European *Journal of Wood and Wood Products*, 74(3). https://doi.org/10.1007/s00107-015-0999-5

[2] Jeleč, M., Varevac, D., Rajčić, V.: Cross-laminated timber (CLT) – a state of the art report, *GRAĐEVINAR*, 70 (2018) 2, pp. 75-95, doi: https://doi.org/10.14256/JCE.2071.2017

[3] Van De Kuilen J.W.G., Ceccotti A., Xia Z., He M.,Very Tall Wooden Buildings with Cross Laminated Timber, *Procedia Engineering*, Volume 14, 2011, Pages 1621-1628, ISSN 1877-7058, https://doi.org/10.1016/j.proeng.2011.07.204

[4] Sikora K. S., McPolin D. O., and Harte A. M., "Effects of thickness of cross-laminated timber (CLT) panels made from Sitka spruce on mechanical performance in bending and shear," *Constr. Build. Mater.*, vol. 116, pp. 141–150, 2016.

[5] Wang, Z.; Fu, H.; Gong, M.; Luo, J.; Dong, W.; Wang, T.; Chui, Y.H. Planar shear and bending properties of hybrid CLT fabricatedwith lumber and LVL.*Constr. Build. Mater*. ,151, 172–177. 2017

[6] Yusoh, P. M. Tahir, M. K. A. Uyup, S. H. Lee, H. Husain, &M. Khaidzir. "Effect of wood species, clamping pressure and glue spread rate on the bonding properties of cross-laminated timber (CLT) manufactured from tropical hardwoods." *Construction and Building Materials*. 2020. doi: 121721. 10.1016/j.conbuildmat.2020.121721.

[7] Azambuja R.R, DeVallance D., McNeel. J. "Evaluation of Low-Grade Yellow-Poplar (Liriodendron tulipifera) as Raw Material for Cross-Laminated Timber Panel Production." *Forest Products Journal*. 72. 2022. Doi: 1-10. 10.13073/FPJ-D-21-00050.

[8] Adnan N. A., Tahir P. Md., Husain H., Lee S.H. , Khairun Anwar Uyup M., Arip M. N. M. & Ashaari Z.. "Effect of ACQ treatment on surface quality and bonding performance of four Malaysian hardwoods and cross laminated timber (CLT)". European *Journal of Wood and Wood Products*. 2021.

[9] Musah M., Wang X., Dickinson Y., Robert R., Rudnicki M. & Xie X.. "Durability of the adhesive bond in cross-laminated northern hardwoods and softwoods." *Construction and Building Materials*. 2021. doi: 307. 124267. 10.1016/j.conbuildmat.2021.124267.

[10] Aicher S., Christian Z., and Dill-Langer G., "Hardwood glulams – emerging timber products of superior mechanical properties," Sep. 2014, doi: 10.13140/2.1.5170.1120.

[11] Franke S., "Mechanical properties of beech CLT," in *WCTE 2016* - World Conference on Timber Engineering, 2016.

[12] Crovella P., & Kurzinski S.. "Predicting the Strength and Serviceability Performance of Cross-laminated Timber (CLT) Panels Fabricated with High-Density Hardwood." in *WCTE 2020* - World Conference on Timber Engineering, 2021.

[13] Kovryga, S. Peter, and Jan Willem G van de Kuilen, "Mechanical properties and their interrelationships for medium-density European hardwoods, focusing on ash and beech," *Wood Mater. Sci. Eng*., pp. 289–302, 2019, doi: https://doi.org/10.1080/17480272.2019.1596158.

[14] Sciomenta M., Spera L., Bedon C., Rinaldi V., Nocetti M., Brunetti M., Fragiacomo M., Romagnoli M. "Mechanical characterization of novel Homogeneous Beech and hybrid Beech-Corsican Pine thin Cross-Laminated timber panels". *Constr. Build. Mater*., vol. 271, 2021, doi: 10.1016/j.conbuildmat.2020.121589

[15] Pang, S.-J.; Jeong, G.Y. Effects of combinations of lamina grade and thickness, and span-to-depth ratios on bending properties ofcross-laminated timber (CLT) floor. *Constr. Build. Mater*.,222, 142–151. 2019

[16] Gong, Y.; Ye, Q.; Wu, G.; Ren, H.; Guan, C. Effect of size on compressive strength parallel to the grain of cross-laminated timbermade with domestic larch.Chin. *J. Wood Sci. Technol*. ,35, 42–46. 2020a.

[17] Gong, Y.; Ye, Q.; Wu, G.; Ren, H.; Guan, C. Prediction of the compressive strength of cross-laminated timber (CLT) made bydomestic Larix Kaempferi. *J. Northwest For. Univ*.,35, 234–237. 2020b

[18] Li, Q.; Wang, Z.; Liang, Z.; Li, L.; Gong, M.; Zhou, J. Shear properties of hybrid CLT fabricated with lumber and OSB. *Constr.Build. Mater*.,261, 120504. 2020

[19] Wang, F.; Wang, X.; Yang, S.; Jiang, G.; Que, Z.; Zhou, H. Effect of different laminate thickness on mechanical properties of cross-laminated timber made from Chinese fir. *Sci. Silvae Sin*.,56, 168–175.13. 2020

[20] Perret O., Douthe C., Lebée A., Sab K., 'A shear strength criterion for the buckling analysis of CLT walls', *Engineering Strucutres*, Vol. 211, 2020. https://doi.org/10.1016/j.engstruct.2020.110344

[21] Ye Q, Gong Y, Ren H, Guan C, Wu G, Chen X. Analysis and Calculation of Stability Coefficients of Cross-Laminated Timber Axial Compression Member. *Polymers* (Basel). 2021 Dec 6;13(23):4267. doi: 10.3390/polym13234267.

[22] Ye Q, Gong Y, Ren H, Guan C, Wu G, Chen X. Analysis and Calculation of Stability Coefficients of Cross-Laminated Timber Axial Compression Member. *Polymers* (Basel). 2021 Dec 6;13(23):4267. doi: 10.3390/polym13234267.

[23] Wei, Peixing & Wang, Brad & Li, Hao & Wang, Libin & Peng, Si & Zhang, Long. (2019). A comparative study of compression behaviors of cross-laminated timber and glued-laminated timber columns. *Construction and Building Materials*. 222. 86-95. 10.1016/j.conbuildmat.2019.06.139.

[24] Pina J.C, Saavedra Flores E. I. a, Saavedra K.,b Numerical study on the elastic buckling of cross-laminated timber walls subject to compression, *Construction and Building Materials,* Volume 199, 2019, Pages 82-91, ISSN 0950-0618
[25] Kudo, Y.; Nakajima, S.; Miyatake, A.; Araki, Y.; Shibusawa, T.; Haramiishi, T. Evaluation of buckling strength of cross laminated timber. In Proceedings of the World Conference on Timber Engineering (*WCTE2016*), Vienna, Austria, 22–25 August 2016
[26] EN 1995 Eurocode 5 2003. Design of timber structures, part 1-1: General-Common rules and rules for buildings. CEN/TC 250, European Committee for Standardisation, Brussels.
[27] Sciomenta M., Spera L., Peditto A., Ciuffetelli E., Savini F., Bedon C., Romagnoli M., Nocetti M., Brunetti M., Fragiacomo M., Mechanical characterization of homogeneous and hybrid beech-Corsican pine glue-laminated timber beams, *Engineering Structures*, Volume 264, 2022, 114450, ISSN 0141-0296
[28] Scarascia Mugnozza G, Romagnoli M, Fragiacomo M, Piazza M, Lasserre B, Brunetti M, Zanuttini R, Fioravanti M, Marchetti M, Todaro L, Togni M, Ferrante T, Maesano M, Nocetti M, De Dato GB, Sciomenta M, Villani T (2021). La filiera corta del legno: un'opportunità per la bio-economia forestale in Italia. *Forest@* 18: 64-71. – doi: 10.3832/efor0052-018 [online 2021-08-26]
[29] CEN (European Committee for Standardization), ''Timber Structures – Strength graded structural timber with rectangular cross section – Part 2: Machine grading; additional requirements for type testing," EN 14081-2, 2018.
[30] Nocetti M., Bacher M., Brunetti M., Crivellaro A., van de Kuilen J. W. G., "Machine grading of Italian structural timber: preliminary results on different wood species", in *WCTE 2010* - World conference on timber engineering, 2010
[31] Brunetti M., Nocetti M., Pizzo B., Negro F., Aminti G., Burato P., Cremonini C., Zanuttini R., Comparison of different bonding parameters in the production of beech and combined beech-spruce CLT by standard and optimized tests methods, *Construction and Building Materials*, Volume 265, 2020a, 120168, ISSN 0950-0618, https://doi.org/10.1016/j.conbuildmat.2020.120168.
[32] Brunetti, M., Nocetti, M., Pizzo, B. et al. Structural products made of beech wood: quality assessment of the raw material. *Eur. J. Wood Prod*. 78, 961–970, 2020b. https://doi.org/10.1007/s00107-020-01542-9
[33] CEN (European Committee for Standardization), "Structural timber - Strength classes," EN 338, 2016.
[34] Tetmajer L. (1896). Die Gesetze der Knickungs- und der zusammengesetzten Druckfestigkeit der technisch wichtigsten Baustoffe. *Materialprüfungs-Anstalt am Schweiz*. Polytechnikum Zurich. Zurich.
[35] Larsen HJ., Pedersen SS. (1975). Tests with centrally loaded timber columns. In: Proceedings of *CIB-W18 meeting 4*: Paper No. 4-2-1. Paris.
[36] Buchanan AH. (1984). Strength model and design methods for bending and axial load interaction in timber members.
[37] Timoshenko S.P., Gere J.M.(1961). Theory of Elastic Stability, McGraw-Hill, International Book Company
[38] Karacabeyli E., Gagnon S. FPInnovations, Canadian CLT Handbook, 2019 Edition. Volume I
[39] Karacabeyli E., Gagnon S. FPInnovations, U.S Edition CLT Handbook, v2013

https://doi.org/10.52202/069179-0361

World Conference on Timber Engineering Oslo 2023

CONNECTIONS TESTING AND RELIABILITY ASSESSMENT OF TIMBER CONNECTIONS WITH DOWEL-TYPE FASTENERS.

E. Moreno-Zapata[1], B. Iraola[2], R. Quinteros-Mayne[3], I. de Arteaga[4], P. Tanner[5], C. Lara[6], J.M. Cabrero[7]

ABSTRACT: The accurate description of the structural behaviour of structural timber connections is still an open issue, which poses many unresolved challenges. The REACT research project engages in developing a reliable framework for the design of structural timber connections. Based on an extensive experimental campaign and novel multi-scale models, it will provide a sound reliability assessment of timber connections. This knowledge will stem from a multilevel analysis, ranging from the material up to the connection level, with a special focus on the interaction of timber with dowel-type fasteners.

As a major contribution, the project will deliver information for design practice, allowing to make use of the obtained knowledge in a simple yet efficient way.

KEYWORDS: Timber structures, Structural connections, Experimental tests, FEM, Multi-scale modelling, Computational mechanics, MonteCarlo Analysis

1 INTRODUCTION

Although timber is one of the oldest construction materials known to man, the scientific knowledge about its material behaviour is often surprisingly poor. Due to its orthotropic material structure, growth irregularities, and hundreds of different species, wood, as a natural material, is one of the most complex building materials.

The required development of appropriate design rules for current tall buildings poses a challenge to satisfy the required design criteria (e.g., vibrations, creep, avoidance of brittle failure modes, robustness) [1]. Furthermore, many unresolved challenges hinder the designer from obtaining a realistic prediction of the actual performance and reliability of structural timber connections.

Though Finite Element Models are the main technique to simulate timber structural behaviour, the required material models for comprehensive modelling of timber response are not yet fully developed, and moreover, offer high accuracy at the expense of high computational costs. Many different approaches have been developed by several researchers [8,12-14,19,20,33,34]. Among others, the main challenging points in timber structures simulation are high variability in material properties, presence of random singularities such as knots, complex microscopical structure with fibres and layers, surface finish and influence on contact behaviour, different behaviour in tension and compression; different failure mechanisms (brittle and ductile) for different orientations and loadings.

There are strong economic and safety reasons for developing a reliability assessment of the design framework of structural timber connections, which explicitly takes into account the interaction between components, and predicts the associated failure mechanism [2].

The REACT project, *Towards a Reliable and Efficient Analysis of Connections in Timber: material and interaction testing, and numerical modelling*, financed by the Spanish Ministry of Science and Innovation, and conducted in collaboration between the Onesta Wood Chair at the University of Navarra and researchers from the Institute for Construction Science Eduardo Torroja, aims at providing a new insight into the response and modelling of structural timber connection with dowel type fasteners. The following sections describe the proposed multiscale approach, which is explained in Figure 1 as well.

2 PROJECT TOPICS

The research project has the following objectives:

- Provide a multi-scale understanding of timber connections, from the material (micro-level) to the connection level (macro-level), with a

[1,2,4,7] Department of Building Construction, Services and Structures, ONESTA Wood Chair, University of Navarra, Spain; [1] emorenoz@unav.es; [2] bisaenz@unav.es; [4] iarteaga@unav.es; [7] jcabrero@unav.es
[3] Facultad de Ingeniería, Pontificia Universidad Católica de Valparaíso, Chile; roberto.quinteros@pucv.cl
[5,6] Institute for Construction Science Eduardo Torroja (IETcc-CSIC), Spain; [5] tannerp@ietcc.csic.es; [6] carloslara@ietcc.csic.es

https://doi.org/10.52202/069179-0362

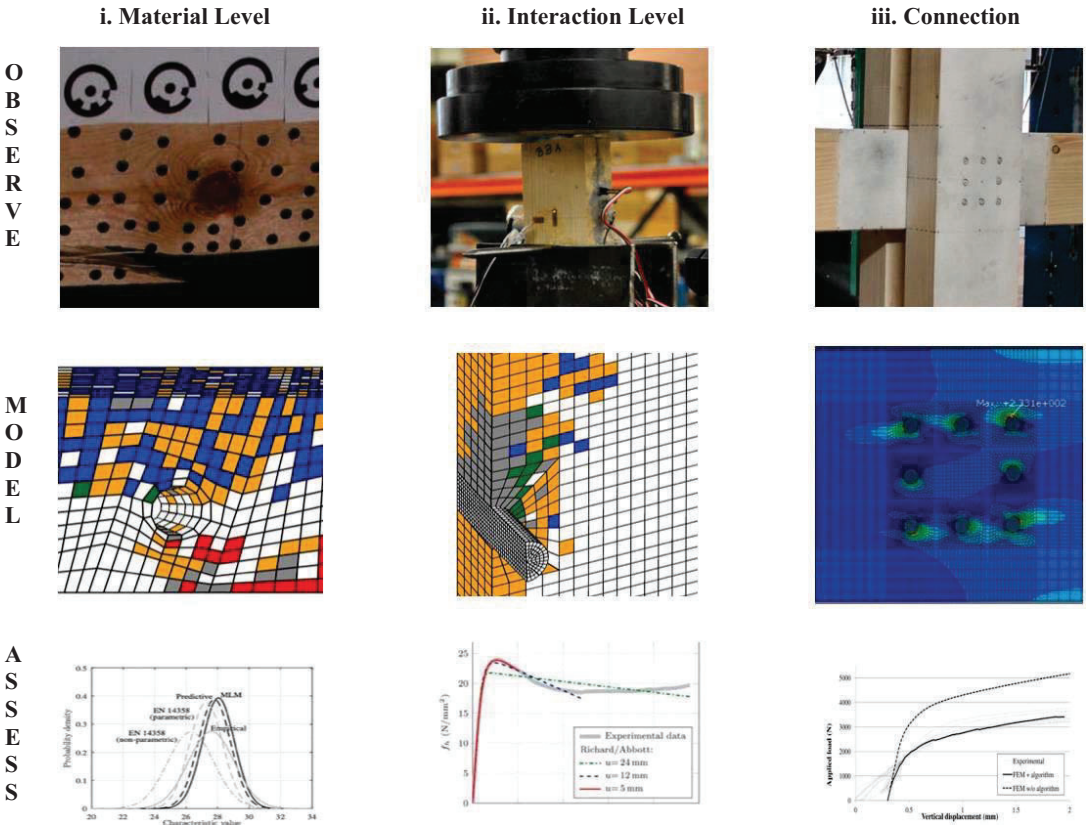

Figure 1: *Levels of analysis and related activities and results for each aim: tests, models and obtained results from the assessment. [10,17-20,31]*

particular focus on the interaction with the fasteners.

- Characterize more comprehensively the structural response of timber connections (stiffness, capacity and ductility) when submitted to realistic loads (i.e., different levels of interaction of forces, bending moment and shear and axial interaction…), with an emphasis of the capacity and type of failure.
- Develop three-dimensional models of structural timber connections based on a multi-scale modelling approach based on FEM, incorporating timber fracture.
- Assess the reliability of design models for timber connections.
- Deliver practical developments for the structural analysis and design of timber connections: verify and propose design models and criteria (i.e., overstrength) to ensure the ductile failure of the connection, an interaction criteria for the different types of loads and directions, an adequate design concept of the connection.

To accomplish these objectives, the project focuses on three different levels: material, interaction, and connection as a whole, and makes use of experimental tests, numerical finite elements modelling, and analytical models. The following sections describe the different topics.

2.1 OBSERVE THE BEHAVIOUR

A solid experimental foundation on which further theoretical and numerical developments can be built and validated is of course a preliminary and strong requirement. The experimental work plan is structured in the different levels to progressively apprehend the involved parameters and the complexity of the system. It is focus on products (solid wood and glulam) made of a representative species for softwood (spruce, Picea Abies), and two types of fasteners (dowels and self-taping screws). For each configuration, several replicates are testing to get statistically relevant distributions and properties. Such detailed results will be later used for different aims within the project, i.e., to validate the models for each level in detail, to provide material properties and their statistical distribution.

Additionally, to the traditional parallel and perpendicular loading testing, testing in intermediate angles (off-axis tests) are performed. Since parallel and perpendicular failure modes are different (i.e., plug-shear failure for the parallel tension loading and splitting for the perpendicular tension), the interaction at different angles and different connectors configurations needs to be studied. Figure 2 shows a depiction of the type connections to be tested. The

https://doi.org/10.52202/069179-0362

project challenges the current test setups by developing a new test philosophy, based on the available DIC techniques [21, 22] and off-axis tests to get new knowledge into timber response.

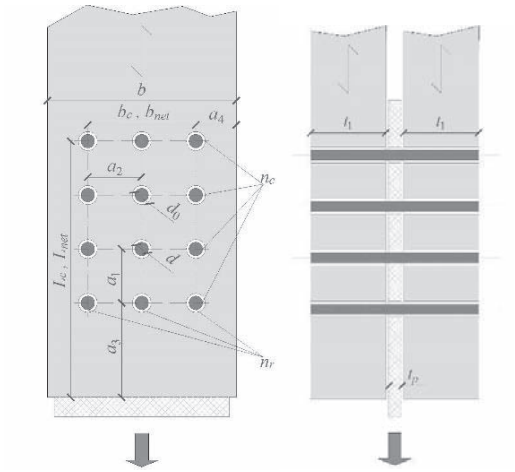

Figure 2: *Representative depiction of the types of connections to be tested with slotted-in-plates and dowel-type fasteners [9]: front (left) and side (right) views.*

2.1.1 Material tests

The experimental campaign at this comprehension level focuses on the mechanical response of timber. Samples with different anatomical features (with defects, i.e., knots, finger-joints) are tested instead of the classical approach of testing clear wood specimens (with no defects).

Material properties will be obtained using the current standard procedures [23], and by a novel experimental procedure, based on off-axis tests (as those depicted in Figure 3) and the use of DIC techniques [21,22]. The tests will provide the characterization of the different required material parameters (classical tests provide strength parameters and not actual material properties [3]), their variance, and correlation, as required for the reliability analysis. Non-destructive techniques (i.e., ultrasound) will be additionally used at each piece, to have an additional source of information, and a way to assess how to indirectly obtain material properties.

This level will give us a comprehensive description of the behaviour of the material, its fracture behaviour, the coupling among the different material orientations, their statistical properties, as well as the influence of the different anatomical defects.

2.1.2 Interaction test

This level will deal with the interaction of timber with a single dowel-type fastener, conceived as a system property [24]. Existing test standards will be again challenged. Two main configuration types, at different load and fastener angles to the grain, related to the distinct roles of the fasteners are developed: load transfer through contact between fasteners and timber by the standard [25] and novel off-axis [26] embedment tests; and the application of reinforcement by performing off-axis tests of reinforced timber. The versatility of the novel approach and the detailed description obtained employing the DIC will provide an improved understanding of the occurring phenomena.

The following phenomena are expected to be understood in more detail: rope effect, friction, clamping, residual stress around the fastener, the influence of load-to-grain angle, predrilling, and possible execution tolerances. The different required properties of the fasteners (i.e., withdrawal strength, head pull-through capacity) will be tested employing standard procedures [25,27-32].

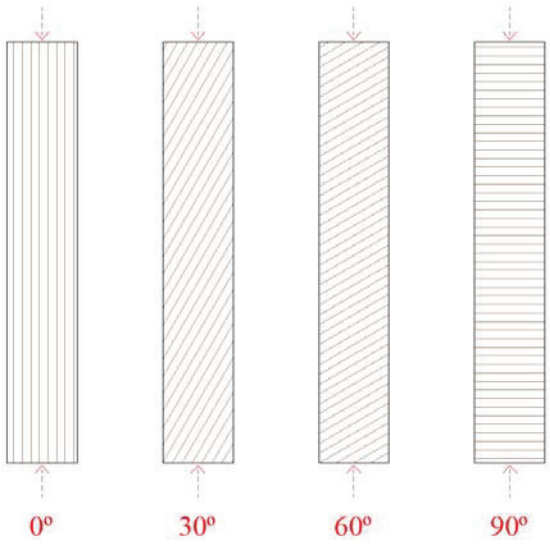

Figure 3: *Off-axis tests for the material level. Depicted, the concept for compression tests.*

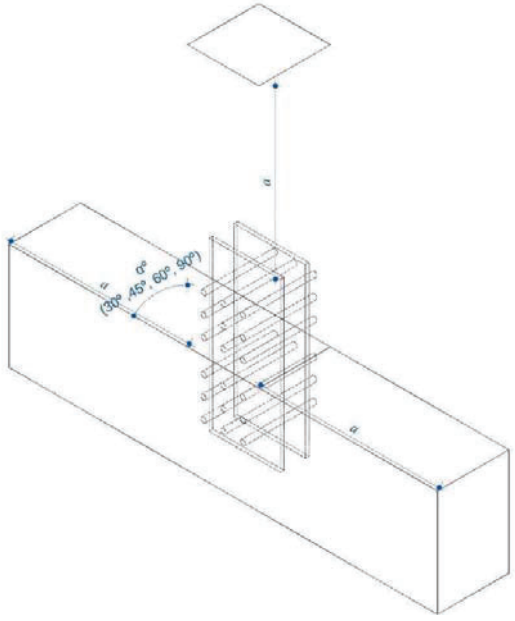

Figure 4: *Main concept and scheme for the tests of the structural connections, with a varying angle between members.*

This study will give us a new comprehension of the complexity of the stress field around dowel-type fasteners, the resulting stress field, and the related failure process.

2.1.3 Connection tests

Reinforced and unreinforced connections with different geometrical parameters and load orientation will be tested. While most available experimental studies focus on parallel tension loading [31,32], we will pursue load application setups to achieve complex and realistic load patterns, in which bending, shear, and axial interaction are present, to provide an understanding of the existing interaction, related to those observed in the previous levels. Figure 4 shows a depiction of the proposed test specimens.

A detailed description of the actual geometry after assembling the specimen will be obtained, which will provide a reliable source to quantify the execution defects before testing (i.e., misalignment, straightness of fasteners, actual positioning). These measurements will provide a database for its additional use for the uncertainty of execution in the reliability analysis.

The actual material properties of both timber and fasteners employed in the connections tests will be obtained after the tests, to reduce the uncertainties in the performed tests. To that purpose, pieces of the undamaged material will be extracted after testing and will be performed the corresponding material tests.

This study will give us a new perspective on the behaviour of connections. Based on the previous levels, which provide the influence of anatomical features and the interaction with the fasteners, here an understanding of the interaction of these different mechanisms altogether and their influence on the global response will be reached.

2.2 MODEL THE RESPONSE

This topic will develop an efficient FEM modelling framework of the connection, aiming at two different types of Finite Element Models. Within this work package, first, a usual (in research practice) three-dimensional FEM models for comprehensive modelling of the full response of the connections will be developed. ABAQUS will be used as the main platform [11,16,18,19], which will serve as the basis of the developments within this aim.

Subroutines for the material and the interaction levels within the FEM platform will be developed in two iterative steps: the first-generation models will serve as a validation of the techniques applied at each level and will be based on usual 3D models with solid (hexahedral) elements, in which the material and interaction levels will be implemented within user-defined routines into the commercial FEM code Abaqus via the different available interfaces, i.e. UMAT, UINT.

However, these 3D models are cost-intensive, not appropriate for practice. Carrying out reliability analysis based on them would be unfeasible. Therefore, to reduce the computational time, second-generation multi-scale models will be developed. These models, though simple, will be able to incorporate the material fracture, so they provide comprehensive modelling of the behaviour of timber connections at a reduced computational cost. These models will be used for the development of the required dataset for the subsequent reliability analysis. To that extent, realistic properties, mostly based on the obtained dataset from the experimental set and analysed in the following Aim, will be fed into the model. Moreover, these models, may provide a simple and reliable way to model connections in future practice.

To obtain the interaction and linking between the different models and ABAQUS, and the required parameterization for the stochastic models, a framework with the additional use of MatLab, Python, and C++ will be developed.

2.2.1 Material model

The main focus of this level is the modelling of the timber failure response, defined by the onset of failure, based on appropriate failure criteria for timber [33,34], and the following behaviour, either ductile or brittle, for the different stress combinations, and the different anatomical features.

Three-dimensional models reproducing the tests at this level consisting of simple geometries will be used to validate the developed material model. It will allow to develop appropriate modelling techniques for the material, and to incorporate in a realistic way timber defects, such as knots and grain deviation.

An appropriate homogenization technique will be developed, i.e., by adequate mixture rules to assign anatomical features and their corresponding properties to each element or representative volume element [15] to derive a product model for its use at higher levels. The developed script will provide realistic modelling of the material behaviour of timber products.

2.2.2 Interaction model

This level aims at developing an efficient technique for the modelling of load transfer through direct contact and reinforcement by embedment of fasteners into the timber. This model's developments will already take advantage of the previous material model since it is needed to reproduce the timber response. These models will be validated against the experimental tests.

2.2.3 Connection model

In the FEM it is crucial to appropriately define the coupling conditions for the different components. A full and detailed description of the connections' response (i.e., full non-linear load-slip behaviour, ultimate displacement, failure type…), and the resulting stress fields and interactions among the constitutive components will be obtained. These models will be validated against the existing tests.

https://doi.org/10.52202/069179-0362

2.2.4 Multiscale model

A multiscale model will be developed based on previous achievements. The proposal will be based on previous developments. Mainly based on the Beam on Elastic Foundation [8,37-39]. Such models, which make use of connector, beam and shell elements, reduce the computational cost to a fraction (results in the order of minutes), in comparison to the 3D models used in the previous parts. The multiscale model will incorporate fracture behaviour of timber, allowing for the first time for a full multiscale model of timber connections incorporating all the required parameters.

2.3 ASSESS THE RELIABILITY

This topic will develop a framework for the reliability assessment of timber connections, based on the dataset derived from the previously developed multiscale FEM models and the connection tests. The performed analyses will include material, execution, and geometric parameters as stochastic variables, based on the probabilistic properties derived in Section 2.1 and databases from the literature [40]. The developed framework in Section 2.2 will serve to calibrate existing and newly proposed design models to achieve the required level of calibration required for the relevant design situations. For this purpose, the uncertainties associated with such models must be quantified, which constitutes a crucial step to provide safe and efficient use of timber structures.

Load carrying capacity models should be calibrated to achieve the level of reliability required for the relevant design situations. For this purpose, the uncertainties associated with such models must be quantified, which is typically done by adjusting the model based on a best-fit criterion and by comparing the model outcome to the results of measurements and experimental tests. The degree of uncertainty of the model may be described in terms of the bias and the coefficient of variation that result from such comparisons. Additional conditions, such as measurement errors and statistical uncertainties due to a limited data set, real structure-specific conditions and scale effects should also be taken into account if required. Moreover, uncertainties describing random effects that are neglected in a resistance model and simplifications in the mathematical relationships on which it is based should be additionally incorporated.

For the calculation of the design value of the resistance, the Eurocode [41] makes a distinction between a partial factor associated with the uncertainty of the resistance model, γ_{Rd}, and a partial factor for material properties, γ_m. Depending on the type of structure considered, the partial factor γ_{Rd} may cover uncertainties in the resistance model; the bias in the resistance model, when relevant; and geometric deviations, if these are not modelled explicitly.

For certain types of structure, γ_{Rd} and γ_m may be combined into a single partial material factor, γ_M, and applied to material properties. Similarly, when applying partial factors to resistance for certain types of structure, γ_{Rd} and γ_m may be combined into a single partial resistance factor, γ_R.

The statistical determination and calibration of resistance models based on tests must consider the statistical uncertainty due to a limited number of results. To overcome such problems, the research project will involve the use of numerical models to complement the available test results. The model uncertainty should be treated as a random variable, and this research proposal will do so. In this context, it should be noted that if advanced models are used to calibrate simplified engineering models, then model and statistical uncertainties are present on both levels and should be taken into account simultaneously.

2.3.1 Dataset description

A detailed analysis of the test results from the experimental tests (see Section 2.1) will be performed, adequate for the assessment procedure to obtain the adequate statistical description, and analysis of the obtained results, assuming the appropriate distribution function for its uncertainty and variability. Probabilistic models for uncertain resistance characteristics may in principle be formulated at any level of approximation within the range of a purely scientific mathematical description of the physical phenomena governing the problem at hand (micro-level) and a purely empirical description based on observations and tests (macro-level).

In engineering analysis, the physical modelling is, however, normally performed at an intermediate level sometimes referred to as the meso-level. Reliability analysis will, therefore, in general, be based on a physical understanding of the problem but due to various simplifications and approximations, it will always to some extent be empirical. This essentially means that if experimental results are compared to predictions obtained through physical modelling, omitting some effect, then there will be a lack of fit. The lack of fit introduces a so-called model of uncertainty, which is associated with the level of approximation applied in the physical formulation of the problem.

It is important that the model uncertainty is fully appreciated and taken into account in the uncertainty modelling. This will be done in the project, following the principles established in the JCSS Probabilistic Model Code [40].

2.3.2 Montecarlo analysis

A Montecarlo analysis will be developed at the connections' level, including stochastic variables with values derived from the measurements within the experimental campaign. It is envisaged to also include the execution tolerances, taken from existing execution standards. The developed framework will provide a detailed insight into the response and reliability of timber connections, which is needed in current practice. It will provide an answer into problems such as overstrength, ductility, and type of failure, by giving special attention to estimating the proportion of different connection failure types within the considered design.

https://doi.org/10.52202/069179-0362

2.3.3 Model's uncertainty

This aim focuses on assessing the model uncertainty. The assessment of this variable is based on a comparison of model and test results and the determination of the associated partial factors include the following steps:

- Compilation of available test results.
- Calculation of the resistance for each of the tested specimens by using resistance models for relevant failure modes and measured values for dimensions and material properties.
- Determination of the theoretical load-bearing capacity and the associated failure mode.
- Comparison with experimental failure mode and capacity.
- Statistical evaluation of the results, in which the theoretical and the observed failure mode match.
- Suitable probabilistic description of the model uncertainty (lognormal distribution is commonly an appropriate distribution function).
- Determination of resistance model uncertainty partial factors depending on the partial factor format, parameters of the model uncertainty variable, target reliability and sensitivity factor.

When generalizing the model uncertainty beyond the scope of the database, trends with regard to mean and scatter should be carefully considered.

2.4 APPLY IN PRACTICE

Scientific knowledge, such as the herein proposed, must be made available for practice. Therefore, as a final step, all the developed scientific knowledge and strategies will be incorporated into tools for practice: design models for their consideration in design codes, such as the Eurocode.

Reports will be circulated and presented at the relevant Working Groups and Committees within the European standardization framework.

Such resistance design models are usually based on a combination of mechanical principles and empirical relationships. Newly developed models for inclusion in structural design codes should preferably be based on mechanical principles and meet the required level of reliability.

The expected outcome of the research plan will moreover allow developing improved design models for the capacity of the connections. It is expected to develop design models for the brittle failure of connections in the parallel and perpendicular direction and provide an interaction rule among these two capacities. The calibration procedure within Section 2.3 will allow providing a sound and consistent reliability background to the used fitting and safety coefficients in those models.

2.4.1 Design model

Based on the deep gained understanding of the behaviour of timber connections and their components, a design model will be developed to improve those existing (or still non-existing) within design codes. These models will be based on the existing design models from the literature (i.e., EYM) for the capacity of timber connections, for both failure types, ductile (EYM) and brittle, and will be calibrated, as described in Section 2.3. Additionally, it is expected to deliver a sound model for the brittle failure of timber connections for different load types and interactions. The developed design models will provide design principles and application rules for the design of timber connections in the future generations of timber design standards.

2.4.2 Reliability parameters

The statistical description of the uncertainty and the proposal of the developed reliability framework, which may be derived based on the JCSS Probabilistic Model Code [40], will be developed and presented at the appropriate standardization committees. The developed reliability assessment will allow proposing adequate safety concepts and calibration parameters for the design of timber structures and connections.

3 CONCLUSIONS

Tall timber buildings are becoming increasingly popular while challenging our surprisingly poor scientific knowledge of timber structures. However, current design approaches are still based on experience and tradition, and they are neither efficient nor reliable: while most members in timber structures are around 40-60% over-designed due to connection requirements [4,5], almost 25% of recent collapses of timber structures were related to connections. [2,6,7]

REACT engages in developing a reliable framework for the design of structural timber connections and structures. Based on the described extensive experimental campaign and the developed finite element models, both 3D-based and the novel multi-scale models, it will provide a sound reliability assessment of timber connections. This knowledge will stem from the described multilevel analysis, ranging from the material up to the connection level, with a special focus on the interaction of timber with dowel-type fasteners.

The experimental campaign focuses on three observation levels: material, timber-fastener interaction, based on standard and novel techniques; and connections. In this latter, the focus will be on realistic load patterns, in which bending, shear, and axial are present, to provide an understanding of the existing interaction among them. This challenges the current knowledge, mostly based on simple loading schemes.

This level-based experimental knowledge will inform the development of a multi-scale numerical model for timber connections which will be used to carry out the required stochastic models for the MonteCarlo Simulation and the subsequent reliability analysis of structural timber connections.

https://doi.org/10.52202/069179-0362

As a major contribution, the project will deliver information for design practice, allowing to make use of the obtained knowledge in a simple yet efficient way.

To exploit its extraordinary ecological potential and to enable its structural use, improved comprehension of the structural response of timber connections is required. REACT can make a significant difference towards more efficient, reliable, and safe timber constructions.

ACKNOWLEDGEMENTS

The financial support provided by the Spanish Ministerio de Ciencia e Innovación and Fondo Europeo de Desarrollo Regional under contract PID2020-118569GB-C21 MINECO/FEDER UE is gratefully acknowledged. The first author is supported by a PhD fellowship from the Programa de Becas FPU del Ministerio de Educación y Formación Profesional (Spain) under the Grant No. FPU20/03012.

REFERENCES

[1] K. Voulpiotis, J. Köhler, R. Jockwer, A. Frangi, Quantifying Robustness in Tall Timber Buildings, in: International Network on Timber Engineering (INTER), 2020: p. Paper 53-22-1.

[2] J.M. Cabrero, B. Iraola, M. Yurrita. Failure of timber constructions. In Handbook of Materials Failure Analysis 2018 Jan 1 (pp. 123-152). Butterworth-Heinemann. https://doi.org/10.1016/B978-0-08-101928-3.00007-0

[3] R. Jockwer, G. Fink, J. Köhler, Review of the reliability of timber structures in the 2020s, in: International Network on Timber Engineering (INTER), 2020: p. Paper 53-01-01.

[4] H.J. Blaß, C. Sandhaas, Timber Engineering Principles For Design, KIT Scientific Publishing, Karlsruhe, 2017. https://doi.org/10.5445/KSP/1000069616.

[5] M.U. Pedersen, Dowel Type Timber Connections, 2002.

[6] E. Frühwald Hansson, Analysis of structural failures in timber structures: Typical causes for failure and failure modes, Engineering Structures. 33 (2011) 2978–2982. https://doi.org/10.1016/j.engstruct.2011.02.045.

[7] E. Frühwald, E. Serrano, T. Toratti, A. Emilsson, S. Thelandersson, Design of safe timber structures – How can we learn from structural failures in concrete, steel and timber ? Design of safe timber structures – Report TVBK-3053, 2007.

[8] R. Lemaitre, J.-F. Bocquet, M. Schweigler, T.K. Bader, Beam-on-Foundation Modelling as an Alternative Design Method for Timber Joints with Dowel-Type Fasteners – Part 4: Joints Subjected to In-Plane Loading, in: International Network on Timber Engineering (INTER), 2020: p. Paper 53-7-4.

[9] M. Yurrita, J.M. Cabrero, New design model for brittle failure in the parallel-to-grain direction of timber connections with large diameter fasteners, Engineering Structures. 217 (2020) 110557. https://doi.org/10.1016/j.engstruct.2020.110557.

[10] T.A.C.M. van der Put, The tensorpolynomial failure criterion for wood, Delft Wood Science Foundation, Delft, the Netherlands, 2005

[11] J.M. Cabrero, B. Iraola, Wood or timber? Considerations on the numerical modelling of wood and its fracture, in: EUROMECH Colloquium 556. Theoretical, Numerical and Experimental Analyses in Wood Mechanics, Dresden, Germany, 2015.

[12] M. Lukacevic, J. Füssl, R. Lampert, Failure mechanisms of clear wood identified at wood cell level by an approach based on the extended finite element method, Engineering Fracture Mechanics. 144 (2015) 158–175.

[13] M. Lukacevic, J. Füssl, Application of a multisurface discrete crack model for clear wood taking into account the inherent microstructural characteristics of wood cells, Holzforschung. 70 (2016) 845–853.

[14] M. Lukacevic, W. Lederer, J. Füssl, A microstructure-based multisurface failure criterion for the description of brittle and ductile failure mechanisms of clear-wood, Engineering Fracture Mechanics. 176 (2017) 83–99.

[15] G. Fink, A. Frangi, J. Kohler, Probabilistic approach for modelling the load-bearing capacity of glued laminated timber, Engineering Structures. 100 (2015) 751–762. https://doi.org/10.1016/j.engstruct.2015.06.015.

[16] B. Iraola, J.M. Cabrero, B. Gil, Pressure-overclosure law for the simulation of contact in spruce joints, in: WCTE 2016 - World Conference on Timber Engineering, 2016.

[17] B. Iraola, J.M. Cabrero, An algorithm to model wood accounting for different tension and compression elastic and failure behaviors, Engineering Structures. 117 (2016) 332–343. https://doi.org/10.1016/j.engstruct.2016.03.021.

[18] Basterrechea-Arevalo M, Cabrero JM, Iraola B, Goñi R. Modelling of moment transmitting beam-to-column timber connections accounting for frictional transmission. Engineering Structures. 2021 Nov 15;247:113122. https://doi.org/10.1016/j.engstruct.2021.113122

[19] B. Iraola. Simulación del comportamiento mecánico de la madera en uniones estructurales y su aplicación mediante modelos tridimensionales de elementos finitos. PhD Thesis. Universidad de Navarra, 2016. URI: https://hdl.handle.net/10171/42120

[20] M. Schweigler, T.K. Bader, J.-F. Bocquet, R. Lemaitre, C. Sandhaas, Embedment test analysis and data in the context of phenomenological modeling for dowelled timber joint design, (2019). http://urn.kb.se/resolve?urn=urn:nbn:se:lnu:diva-89339 (accessed August 18, 2020).

[21] J. Xavier, A. Majano-Majano, J. Fernandez-Cabo, On the identifiability of stiffness components of clear wood from a 3D off-axes prismatic specimen: angle orientation and friction effects, European Journal of Wood and Wood Products. 74 (2016) 285–290. https://doi.org/10.1007/s00107-016-1032-3.

[22] A. Majano-Majano, J.L. Fernandez-Cabo, S. Hoheisel, M. Klein, A Test Method for Characterizing Clear Wood Using a Single

Specimen, Experimental Mechanics. 52 (2012) 1079–1096. https://doi.org/10.1007/s11340-011-9560-6.
[23] CEN, EN 408:2010+A1:2012. Timber structures - Structural timber and glued laminated timber - Determination of some physical and mechanical properties, 2012.
[24] M. Yurrita, J.M. Cabrero, New criteria for the determination of the parallel-to-grain embedment strength of wood, Construction and Building Materials. 173 (2018) 238–250. https://doi.org/10.1016/j.conbuildmat.2018.03.127.
[25] CEN, EN 383:2007. Timber Structures - Test methods - Determination of embedment strength and foundation values for dowel type fasteners, 2007.
[26] M. Schweigler, T.K. Bader, G. Hochreiner, G. Unger, J. Eberhardsteiner, Load-to-grain angle dependence of the embedment behavior of dowel-type fasteners in laminated veneer lumber, Construction and Building Materials. 126 (2016) 1020–1033. https://doi.org/10.1016/j.conbuildmat.2016.09.051.
[27] CEN, EN 1380:2009. Timber structures - Test methods - Load bearing nails, screws, dowels and bolts, 2009.
[28] CEN, EN 1383:2016. Timber structures - Test methods - Pull through resistance of timber fasteners, (2016).
[29] CEN, EN 409:2009. Timber structures - Test methods - Determination of the yield moment of dowel type fasteners, 2009.
[30] CEN, EN 1382:2016. Timber Structures - Test methods - Withdrawal capacity of timber fasteners, 2016.
[31] CEN, EN 26891:1991. Timber structures - Joints made with mechanical fasteners - General principles for the determination of strength and deformation characteristics, 1991.
[32] CEN, EN ISO 8970:2020. Timber structures - Testing of joints made with mechanical fasteners - Requirements for timber density, 2020.
[33] C. Blanco, J.M. Cabrero, A. Martin-meizoso, K.G. Gebremedhin, Design oriented failure model for wood accounting for different tensile and compressive behavior, International Journal Of Mechanics And Materials. 83 (2015) 103–109. https://doi.org/10.1016/j.mechmat.2015.01.001.
[34] J.M. Cabrero, C. Blanco, K.G. Gebremedhin, A. Martin-Meizoso, Assessment of phenomenological failure criteria for wood, European Journal of Wood and Wood Products. 70 (2012) 871–882. https://doi.org/10.1007/s00107-012-0638-3.
[35] C. Sandhaas, Mechanical behaviour of timber joints with slotted-in steel plates, 2012.
[36] M. Dorn, Investigations on the Serviceability Limit State of Dowel-Type Timber Connections, 2012.
[37] R. Lemaitre, J.F. Bocquet, M. Schweigler, T.K. Bader. Beam-on-foundation modelling as an alternative design method for timber joints with dowel-type fasteners: Part 1: Strength and stiffness per shear plane of single-fastener joints. In5th INTER Meeting, 13-16 August, 2018, Tallin 2018. Karlsruher Institut für Technologie. URN:http://urn.kb.se/resolve?urn=urn%3Anbn%3Ase%3Alnu%3Adiva-77867
[38] R. Lemaitre, J.F. Bocquet, M. Schweigler, T.K. Bader. Beam-on-Foundation Modelling as an Alternative Design Method for Timber Joints with Dowel-Type Fasteners: Part 2: Modelling Techniques for Multiple Fastener Connections. In6th meeting of INTER (International Network on Timber Engineering Research), Tacoma, USA, August 26-29, 2019 2019. Timber Scientific Publishing, KIT Holzbau und Baukonstruktionen. URN:http://urn.kb.se/resolve?urn=urn%3Anbn%3Ase%3Alnu%3Adiva-89340
[39] R. Lemaître, F. Epinal, J.F. Bocquet, M. Schweigler, T.K. Bader. Beam-on-foundation modelling as an alternative design method for single fastener connections. Design connections in timber structures. 2018;207.
[40] J. Joint Committee On Structural Safety, Risk Assessment in Engineering: Principles, System Representation & Risk Criteria, 2008.
[41] EN 1990: 2002, “Eurocode – Basis of structural design”, European Committee for Standardization, CEN, Brussels, April 2002.

https://doi.org/10.52202/069179-0362

World Conference on Timber Engineering Oslo 2023

EFFECTS OF CONSTANT AND ELF STRENGTH PROFILES ON THE PERFORMANCE OF WOOD FRAME SHEAR WALL STRUCTURES

Francisco X. Flores[1] [2], Philip Line[3], Finley A. Charney[4]

ABSTRACT: Prior numerical studies to evaluate the sensitivity of modeled collapse performance of wood-frame wood structural panel shear wall structures have been limited to the 1- to 5-story index building models used in the FEMA P695 study. Investigated parameters included inherent damping, hysteretic behavior, P-delta effects, and strength profiles. Results showed that greater overstrength and a tapered strength profile from small at the roof level to large at the 1st story level had better collapse performance (i.e., lower collapse risk) and helped to support changes to design requirements in AWC SDPWS-2021. Sensitivity studies performed on 3-, 4- and 5-story building models reported herein expand on the prior evaluation of overstrength and strength profile effects. In addition, results from the study of a 6-story building model are also reported. Structural performance was evaluated using the probability of collapse per the FEMA P-695 methodology, and additional performance metrics such as energy dissipation and maximum story drift were investigated. The results of this investigation show the importance of the strength profile in Light Frame Shear Walls where a Constant strength profile along the building's heights displays the worst performance.

KEYWORDS Wood-frame shear wall, seismic analysis, collapse performance, FEMA P-695

1 INTRODUCTION

The collapse performance of wood-frame wood structural panel (WF/WSP) shear wall structures has been numerically investigated in the past [1-6]. Different parameters, such as inherent damping, hysteretic behavior, P-delta effects, and vertical strength profile, have been modified to evaluate the collapse performance using the FEMA P-695 methodology [7]. This study was conducted to expand previous studies on 3-, 4- and 5-story building models [1] and, for the first time by the authors, to evaluate a 6-story WF/WSP shear wall building model. Vertical strength profile is studied more in-depth by looking at different results, such as the sequence of yielding during a pushover analysis, energy dissipation at different intensity levels, earthquakes, and collapse performance. In addition, the influence of Rayleigh damping was quantified in terms of the probability of collapse and energy dissipation. Counterintuitively it was found that a constant strength profile along the building's height worsens the performance instead of being a conservative design.

2 NUMERICAL MODELS

The 1- to 5-story building models were taken from the FEMA P-695 wood-frame models. These systems were designed using ASCE/SEI 7-22 [8] and AWC Special Design Provisions for Wind and Seismic (SDPWS-2021) [9] requirements. The 6-story building model was developed assuming the same basic principles used for the 1- to 5-story building models.

Numerical WF/WSP shear models were created by modeling the load-deformation response at each level as a shear spring. The shear spring at each level was made using the CUREE-SAWS [10] model, which represents the nonlinear hysteretic behavior that accounts for pinching, stiffness, and strength degradation and is governed by ten different parameters [10-11].

Since diaphragms were idealized as flexible, torsion was not considered, and 2D numerical models developed in OpenSees were deemed sufficient to represent the buildings [12]. The shear wall response was modeled

[1] Manager, Engineering Technology, American Wood Council, 222 Catoctin Circle SE Suite 201, Leesburg, VA, 20174. fflores@awc.org
[2] Professor, Dept. of Civil Engineering, University of Azuay, Cuenca Ecuador. fflores@uazuay.edu.ec,
[3] Senior Director, Structural Engineering, American Wood Council, 222 Catoctin Circle SE Suite 201, Leesburg, VA, 20174. Email: PLine@awc.org
[4] Professor Emeritus, Dept. of Civil and Environmental Engineering, Virginia Tech, 200 Patton Hall, Blacksburg, VA, 24061. Email: fcharney@vt.edu

https://doi.org/10.52202/069179-0363

using the SAWS 10-parameter hysteresis model with the backbone used in this study shown in Figure 1 as "Reference Backbone." The reference backbone, representing low-aspect ratio shear wall behavior, was used at all stories except with different scaling employed that varied peak strength to assess strength profile effects while preserving the backbone load-deformation shape.

In addition to the material nonlinearities incorporated in the numerical models, geometric nonlinearities (P-delta effects) were included explicitly. P-delta effects were modeled using a leaning column with no flexural capacity and significant axial stiffness carrying the gravity load.

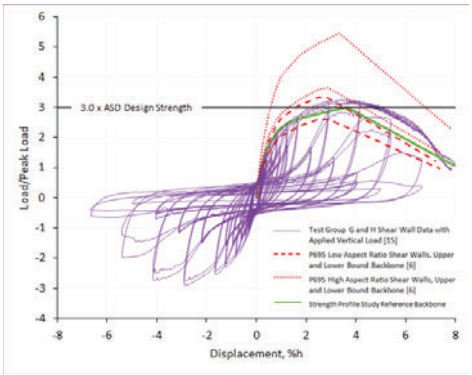

Figure 1 Reference Backbone Curve (green) vs. Test Data (purple) and FEMA P695 Wood Example (red) [1]

The strength profiles to be investigated herein are two for each structure. A "Constant" strength profile where the first story lateral force computed using the equivalent lateral force procedure is assigned as the strength along the building's height. The second strength profile ("ELF") is considered to be the same as the lateral forces computed using the equivalent lateral force procedure.

The shear walls were designed using allowable stress design (ASD) in accordance with SDPWS-2021 [9] and the seismic demands in accordance with ASCE 7-22. Based on test data, each shear wall's overstrength per story (Fu/VASD) was considered equal to 3. F_u is the maximum lateral strength shear wall capacity modeled using the ten parameter material within OpenSees. V_{ASD} is the allowable stress design story shear. In the case of the Constant profile, the maximum lateral strength capacity F_u was constant along the building's height. On the other hand, the F_u in the ELF profile follows the seismic demands at each story in accordance with ASCE 7-22 (Figure 2).

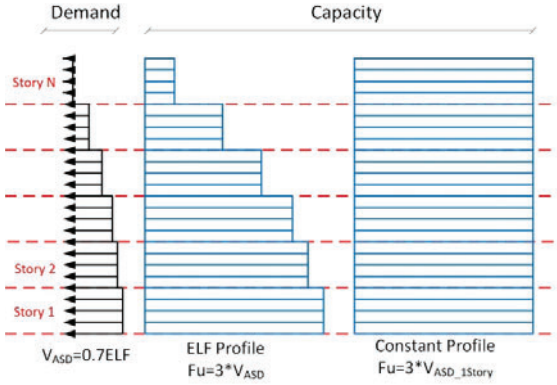

Figure 2 ELF vs. Constant Profile

Finally, Rayleigh damping was incorporated using three different percentages 1%, 2%, and 5% of critical damping. Damping was considered proportional to the building's mass and initial stiffness.

3 METHODOLOGY

The FEMA P695 methodology was used for this parametric study. The numerical models were subjected to static pushover and incremental dynamic analyses to evaluate their collapse performance. Static pushover analyses were performed to quantify overstrength and period-based ductility (μT) parameters. Before assessing the collapse performance of both strength profiles, the dynamic performance at MCE level was quantified using displacement time history and energy dissipation per story.

Incremental dynamic analyses were performed using 44 Far Field ground motions where spectral accelerations were increased until collapse was determined, defined as when the structure could no longer resist lateral loads (dynamic instability) such as from side-sway collapse or exceedance of a specified story drift of 8%. From these results, the probability of collapse for the maximum considered earthquake (MCE) was computed and compared among models.

4 NONLINEAR STATIC PUSHOVER ANALYSES

Nonlinear static pushover analysis was performed using the load pattern proposed in FEMA P695, based on the building's fundamental mode shape. All the structures using both strength profiles, Constant and ELF, were subjected to a lateral load until failure. The pushover curves, in conjunction with analyzing the sequence of yielding along the building's height, provide important insight into the structure's behavior under lateral loads.

Figure 3 displays the pushover curves, including P-Delta obtained for the 4-story model using both strength profiles, Constant and ELF. These curves show how both profiles have the same lateral strength with an overstrength (**Ω**) equal to 1.86. However, the

https://doi.org/10.52202/069179-0363

displacement capacity is significantly more significant for the ELF profile reaching a roof drift of 0.029 compared to 0.012. While the Constant profile has a ductility of 5.75, the ELF profile has a ductility of 8.66. This difference is important, and the reason behind the better performance is that yielding is concentrated in the first story in the Constant profile. On the other hand, yielding for the ELF profile when subjected to the same lateral load used for the Constant strength case is better distributed along the building's height.

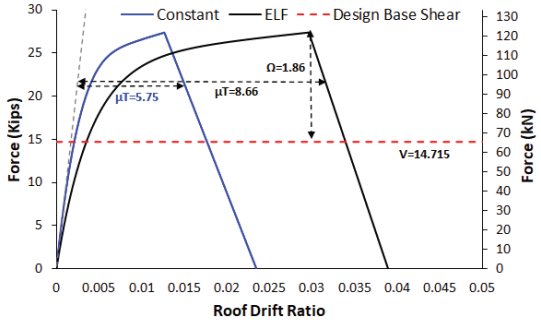

Figure 3 4-Story Pushover Curves

Figure 4 illustrates the performance of the 6-story models when subjected to the increasing lateral load. It can be seen once again that the maximum strength is the same for both strength profiles. However, the displacement capacity of the ELF profile is significantly larger (roof drift=0.011) than the Constant profile (roof drift=0.029). The ductility for the Constant profile is 5.06, while the ELF has a ductility equal to 8.40.

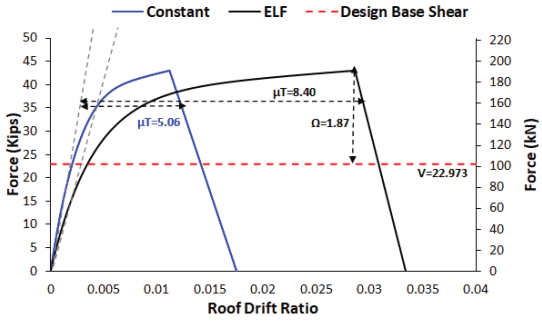

Figure 4 6-Story Pushover Curves

Even though pushover curves for the 4- and 6- story models are presented, the same trends were seen for the 3- and 5-story models.

5 GROUND MOTIONS

The ground motions used in this study were taken from the Far-Field set provided by the FEMA P-695 methodology. The Far-Field record set is twenty-two horizontal component pairs of records (44 in total) from sites located at a distance equal to or greater than 10 km from the fault rupture.

The methodology used to scale the ground motions was also taken from the FEMA P695 methodology and involved two steps: normalizing the individual ground motions with respect to the peak ground velocity and scaling the median acceleration spectrum to the MCE acceleration spectrum at the structure's natural period of vibration. The ground motions were also normalized by the 5-percent damping spectral acceleration at the building's period (S_{MT}). In this way, a scale factor of 2/3 and 1.0 represents the Design Basis Earthquake and Maximum Considered Earthquake (MCE), respectively.

6 DYNAMIC TIME HISTORY RESPONSE AT MCE

Before performing an Incremental Dynamic Analysis where the ground motions are amplitude scaled until the structure collapses, the seismic performance of the models is evaluated at the MCE level earthquake (Scale factor equal to 1). The performance quantification compares the roof drift ratio for both strength profiles. To further understand the complete behavior of the building model with a different strength profile when subjected to a ground motion, the hysteretic energy dissipated per shear wall at each story is computed. The hysteretic energy is calculated integrating the area under the Force (kN) vs. deformation (mm) curve. The results presented herein are for the 2% damping case.

Figure 5 illustrates the roof drift ratio for the 4-story model caused by one of the ground motions scaled at the MCE level. While results for only one ground motion are shown, the trend was the same for other ground motions that caused large displacements. It can be seen that the Constant profile has a residual roof drift ratio of around 0.0159 (roof drift = 7.65in, 194.36mm), while the ELF strength profile shows a residual roof drift equal to 0.048 (roof drift = 2.31in, 58.75mm). The larger residual deformation in the Constant strength profile case is from concentrated yielding in the first story.

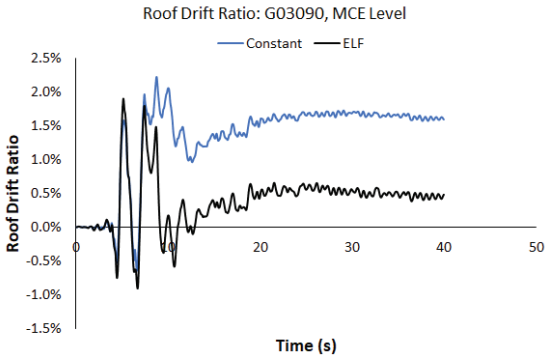

Figure 5 4-Story Roof Displacement Time History Analysis (G03090 MCE, 2% Damping)

Figure 6 and Figure 7 display the hysteretic energy dissipated by the Constant and ELF strength profile when the structure is subjected to the same ground motion (G03090) that caused the roof drift response shown in Figure 5. The dissipation is computed in time as the integral between the story force and story drift [13]. From

Figure 6 for the Constant profile, it can be seen how the first story shear wall is the one that dissipates energy the most (87.2%), meaning that this wall yields the most. This is a straightforward consequence of having first story drift concentrations. This figure also indicates that the last two stories remained elastic because they barely dissipated energy.

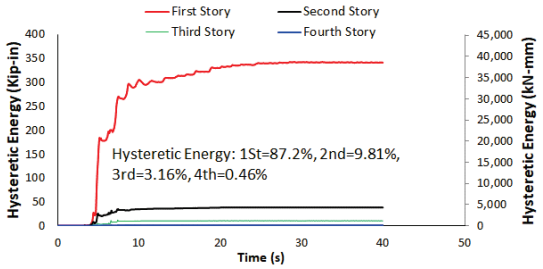

Figure 6 4-Story Energy Dissipation Per Story (Constant Profile, G03090 MCE, 2% Damping)

On the other hand, Figure 7 illustrates the hysteretic energy dissipated by each shear wall per story when the 4-story model has an ELF strength profile. The percentage of the energy dissipated by the first story is 69%, meaning yielding was distributed better along the building's height. Even though yielding distributes more uniformly in comparison to the Constant strength profile, more investigation is required to evaluate the effect of strength profiles that are intermediate between ELF and Constant as well as strength profiles based on targeted strengthening of lower stories to distribute better yielding in the first 2 or 3 stories.

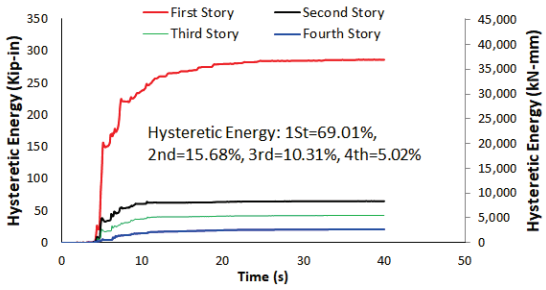

Figure 7 4-Story Energy Dissipation Per Story (ELF Profile, G03090 MCE, 2% Damping)

Figure 8 presents one of the results obtained from the 44 ground motions scaled at the MCE level to which the 6-story model was subjected. This figure shows that the Constant profile strength presents a residual roof ratio of around 0.79% (roof drift = 5.69in, 144.62mm). On the other hand, the ELF strength profile shows a residual roof drift ratio equal to 0.064% (roof drift = 0.46in, 11.68mm). The residual drift ratio is typically dominated by first story deformations, which could be confirmed by looking at the hysteretic energy dissipated by the shear walls.

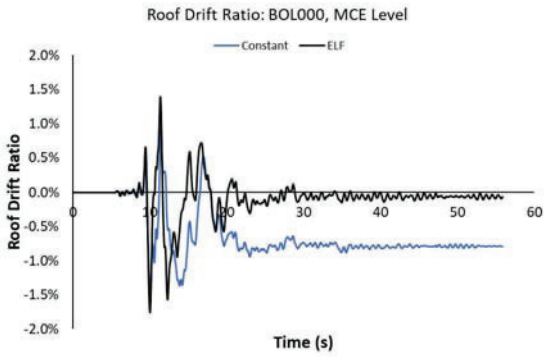

Figure 8 6-Story Roof Displacement Time History Analysis (MCE, Zi=0.02 Ko)

Figure 9 and Figure 10 show the hysteretic energy dissipated by the shear walls along the building's height when subjected to the same ground motion (BOL000) that caused the roof drift response shown in Figure 8. It can be seen how 89% of the dissipated energy, when the Constant profile is used, concentrates in the first two stories. On the other hand, around 71% of the dissipated energy, when the ELF profile is used, focuses on the first two stories. The reduction of the energy dissipated in the first story is around 18% when the ELF profile is used. As a result of having a more uniform distribution of yielding along the building's height, residual deformations decrease when the ELF strength profile is used, and the seismic performance is improved.

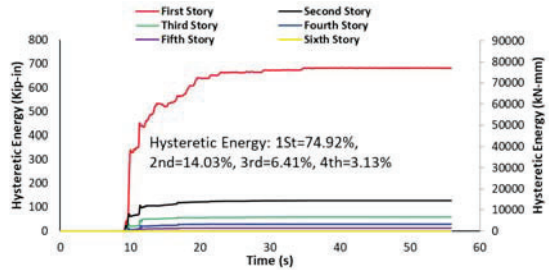

Figure 9 6-Story Energy Dissipation Per Story (Constant Profile, BOL000 MCE, 2% Damping)

https://doi.org/10.52202/069179-0363

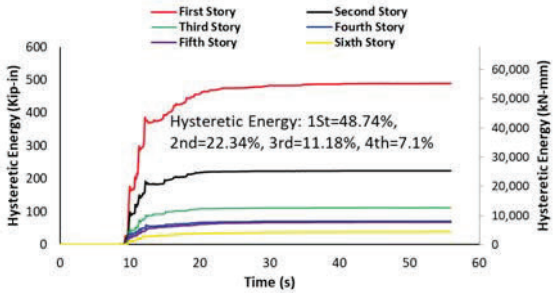

Figure 10 6-Story Energy Dissipation Per Story (ELF Profile, BOL000 MCE, 2% Damping)

7 INHERENT DAMPING ENERGY DISSIPATION

Inherent damping in structures considers energy dissipation from components not explicitly modeled using nonlinear inelastic hysteretic models. It would be challenging to account for all the energy dissipated by all the elements in a structure during an earthquake and the energy dissipated by the lateral resisting system. Therefore, the percentage of the total energy dissipated during an earthquake is typically assigned to inherent damping using either modal damping or Rayleigh damping. Inherent damping evaluated in this study uses Rayleigh damping.

Inherent damping is assigned as an imaginary linear viscous damper within the building using a damping value that is a percentage of the critical damping. The commonly used values assumed vary from 1% to 5%. For instance, FEMA P-695 proposes that the value of inherent damping should be between 2% and 5%.

When Rayleigh damping is used, the damping matrix is formed by considering this matrix proportional to the stiffness and mass matrix. However, the stiffness matrix could change during a seismic analysis when the material and geometric nonlinearities are included in the model. Therefore, there are mainly two options when proportional stiffness damping is considered: initial and tangent stiffness.

In this investigation, 1%, 2%, and 5% proportional to the initial stiffness were considered, leaving the same analyses to be performed using tangent stiffness for future research. However, less energy is expected to dissipate when the tangent stiffness is used because the model's stiffness reduces when yielding occurs. Therefore, this section of the paper shows the amount of energy compared to the total energy taken by the inherent damping. Even though there is nothing proposed for how much energy inherent damping should dissipate as a percent of the total energy dissipated, this type of result could help inform future recommendations.

It was found that the percentage of energy dissipated by inherent damping compared to total energy dissipated for the 44 ground motions scaled to the MCE level depended mainly on the amount of damping assigned and not on the number of stories or the strength profile. The amount of energy dissipated by the inherent damping varies between 10% and 12% for 1% damping, 16% and 20 % for 2 % damping, and 30% and 38% for 5% damping. As previously mentioned, there is no proposed value on how much energy should be dissipated by inherent damping. In the case of wood-frame shear wall structure, this energy represents non-modeled components which, for this study, could potentially represent stucco and gypsum wallboard finish materials, partition walls, and diaphragms that will dissipate energy during an earthquake.

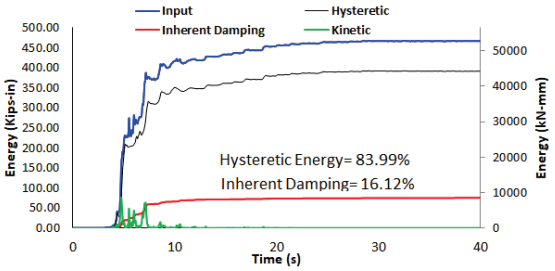

Figure 11 4 Story Energy Balance (Constant profile, 2% Damping)

Figure 11 and Figure 12 show the energy balance using 2% and 5% inherent damping for the 4-story Constant profile. The analyzed ground motion is again the G03090. It can be seen how energy dissipated by the inherent damping increases from 17% to 30.9%. Note that the hysteretic energy shown herein is taken by all the shear walls along the building's height. However, as previously described, the way it distributes depends on the strength capacity profile.

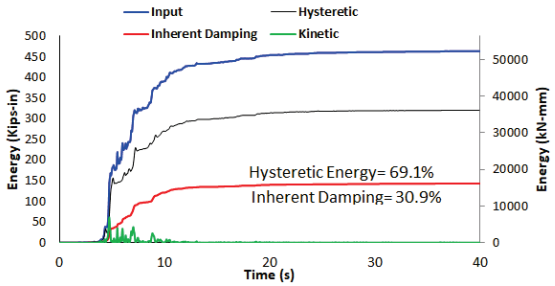

Figure 12 4 Story Energy Balance (Constant profile, 5% Damping)

8 COLLAPSE EVALUATION

The collapse performance of the models is evaluated following the FEMA P-695 procedure. Each building model is subjected to 44 Far-Field ground motions where Incremental Dynamic Analysis [13] is used to assess the model's collapse. Based on previous studies, the collapse is assumed to occur when story drift reaches a value of 8%, or dynamic instability occurs [1]. Once the scale factor that causes the collapse per ground motion is computed, the collapse margin ratio (CMR) is calculated.

https://doi.org/10.52202/069179-0363

The CMR is the ratio between the spectral acceleration that causes the median collapse (22 out of the 44 ground motions) to the spectral acceleration at the MCE level.

The probability of collapse is used as the metric to compare the performance among the building models and strength profiles. The ACMR is a ratio, as described by P-695, that adjusts the CMR with the Spectral Shape Factor (SSF), This accounts for the differences between the spectral shape of rare ground motions in California with the design spectrum or a uniform hazard spectrum. The probability of collapse is computed at the MCE level using as mean the lognormal of ACMR and as standard deviation the uncertainties (β=0.5) [15].

Figure 13 shows the probability of collapse for all the building models using both strength profiles and for different damping ratios. The Constant profile performs in all cases worse than the ELF profile. This could be counterintuitive if one thinks that constant strength at each story along the building's height would be beneficial. The performance worsens with the Constant strength profile because it is prone to drift concentrations in the first story. On the other hand, the ELF profile distributes yielding along the building's height, improving the performance by delaying the first story yielding, contributing to the modeled collapse.

Another important property is inherent damping and how it influences performance. For instance, the 4-story ELF profile modeled probability of collapse varies from 13.1% with 1% damping to 3.6% with 5% damping and is related to the amount of dissipated energy by the inherent damping compared to the total energy dissipated considering both inherent damping and structural system yielding.

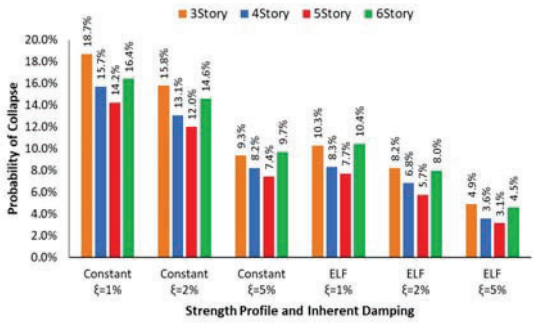

Figure 13 Probability of Collapse Evaluation

9 CONCLUSIONS

This study analyzed different building models ranging in height from 3 to 6 stories. Two different ways these buildings could be designed were considered: a Constant profile where the strength remains constant along the building's height and an ELF profile where a tapered strength from small at the roof to large at the 1st story level is used. In addition, three different values of inherent damping were considered, 1%, 2%, and 5%, proportional to the initial stiffness.

Findings from studies presented herein are summarized as follows:

- The pushover curves showed how the ELF profile improves the displacement capacity and ductility compared to the Constant profile.
- The analyses performed at MCE level earthquakes illustrate the difference in the residual deformations when both profiles are used. Furthermore, evaluating energy dissipated helps explain the extent of concentrated yielding on the first story in the Constant profile.
- A Constant strength profile is more prone to have drift concentrations in the first story resulting in a higher probability of collapse when compared to the ELF strength profile.
- Even though the ELF profile delays drift concentrations in the first story to higher scaling factors compared to the Constant profile, the failure mechanism is still the first story.
- The amount of inherent damping used in analysis directly affects the modeled performance. Therefore, this paper includes data on the amount of energy dissipated based on the damping assigned in the analysis.
- Inherent damping is related to the amount of unknown energy dissipated during an earthquake. However, there is no consensus regarding the amount of energy that should be dissipated by inherent damping. In the case of wood structures, there is likely a wide range given that there is a varied make-up of buildings and multiple components that dissipate energy that is not included in the mathematical model.

10 RECOMMENDATIONS

This study shows the importance of the strength profile on the seismic performance of Light Frame Shear Walls. The trends were the same for all building models from 2- to 6 stories, where the Constant profile performed worse than the ELF profile. In addition, damping was studied using an energy perspective that could help establish a recommended damping ratio value in the future. Even though important conclusions were obtained from this study, the following are recommendations for future research:

- Study profiles vary from the Constant to the ELF profile.
- Investigate profiles that strengthen only the first two stories to move yielding to the upper stories.
- Expand this type of study to other lateral resisting systems.
- Study more in-depth the energy dissipated when tangent stiffness is used instead of initial stiffness.

https://doi.org/10.52202/069179-0363

11 REFERENCES

[1] Line, P., Charney, F. And J. Linville : Influence of story lateral strength profile on modeled seismic response of wood-frame shear wall buildings. WCTE 2020.

[2] Jayamon, J., Line, P., and Charney, F.: Sensitivity of Wood-Frame Shear Wall Collapse Performance to Variations in Hysteric Model Parameters, Journal of Structural Engineering, 145(1): 04018236, 2019.

[3] Jayamon, J., Charney, F., Flores, F., and Line, P.: Influence of Wall Load-Displacement Shape on Seismic Performance of Wood-frame Shear Wall Structures. WCTE 2016

[4] Jayamon, J., Charney, F., and Line, P.: Evaluation of Damping in Wood-Frame Shear Wall Buildings. WCTE 2016.

[5] Perry, L. Line, P., and Charney, F.: Influence of varying strength, from story to story, on modeled seismic response of wood-frame shear wall structures. WCTE 2018.

[6] Line, P., Charney, F., Linville, J.: Influence of story lateral strength profile on modeled seismic response of wood-frame shear wall buildings. WCTE 2021.

[7] FEMA P695: Quantification of Building Seismic Performance Factors, Federal Emergency Management Agency, Washington, D.C., 2009.

[8] ASCE/SEI 7-22: Minimum Design Loads for Buildings and Other Structures, American Society of Civil Engineers, Reston, VA., 2022.

[9] AWC SDPWS-21: Special Design Provisions for Wind and Seismic, American Wood Council, Leesburg, VA 20175.[9] Folz, B., and Filiatrault, A. A Computer program for Seismic Analysis of Woodframe Structures. CUREE Publication No. W-21, Consortium of Universities for Research in Earthquake Engineering, Richmond, CA, 2001.

[10] Folz, B., & Filiatrault, A. . “Cyclic analysis of wood shear walls.” Journal of Structural Engineering, 127(4), 433-441, 2001.

[11] Folz B., Filiatrault A.: Seismic Analysis of Woodframe Structures I: Model Formulation, Journal of Structural Engineering, 130:1353-1360, 2001.

[12] McKenna, F. and Fenves, G.L.: Open System for Earthquake Engineering Simulation (OpenSEES), Pacific Earthquake Engineering Research Center, University of California, Berkeley, CA., 2017.

[13] Uang, C. M., & Bertero, V. V. (1990). Evaluation of seismic energy in structures. Earthquake engineering & structural dynamics, 19(1), 77-90.

[14] D. Vamvatsikos, C.A. Cornell, Applied incremental dynamic analysis, Earthquake Spectra 20 (2004) 523.

[15] G.G. Deierlein, A.B. Liel, C.B. Haselton, C.A. Kircher, K. Principal, ATC-63 methodology for evaluating seismic collapse safety of archetype buildings, ASCE-SEI Structures Congress, Vancouver, BC 2008, pp. 24–26.

World Conference on Timber Engineering Oslo 2023

AN ANALYTICAL MODEL TO INVESTIGATE THE EFFECT OF DIAPHRAGMS ON THE ELASTIC BEHAVIOUR OF MULTI-STOREY COUPLED-PANEL CLT SHEARWALLS

Damian Oliveira[1], Ali Mikael[2], Daniele Casagrande[3], Ghasan Doudak[4]

ABSTRACT: This study develops an analytical model to describe the behaviour of multi-storey multi-panel CLT shearwalls, specifically accounting for cumulative loads between storeys and the effect of the diaphragm. The analysis considers the contribution of hold-downs, wall-to-floor connections, and panel-to-panel joints, as well as loads transferred from storeys above. The analysis has been developed for shearwalls acting as a series of coupled panels (CP) each individually rotating about a corner. Force transfer between storeys is implemented by distributing reactions through the upper floor diaphragm and a direct force from the upper storey's hold-down. Structuring the equations this way allows for a simplified formulation while including several components of the system's complex behaviour. Two-dimensional finite element modelling is used to verify the accuracy of the developed model.

KEYWORDS: CLT, Lateral Design, Modelling, Earthquake, Mid-rise, Derivation, Diaphragm Effect

1 INTRODUCTION

Lateral Load Resisting Systems (LLRS) in Cross Laminated Timber (CLT) used in platform-type buildings typically consist of two types of shearwalls; namely monolithic shearwalls made with a single panel or multi-panel shearwalls comprised of segments connected with vertical joints. The behaviour of multi-panel CLT shearwalls is primarily related to the properties of the vertical joints and mechanical anchors (e.g., hold-down and angle brackets), while the CLT panels generally behave as rigid bodies [1]. Depending on the relative stiffness between vertical joints and hold-down as well as the magnitude of vertical loads, three kinematic modes may be developed in single-storey multi-panel shearwalls, namely a mode consisting of individual panel rotation (coupled panel, or CP), a mode consisting of a global wall rotation (single wall, or SW) and an intermediate mode (IN) comprised of both CP and SW modes [2,3]. Several analytical methods have been developed to predict the elastic behaviour of single-storey multi-panel CLT shearwalls. Flatscher and Schickhofer [4] developed analytical expressions through displacement-based methods while Masroor et al. [5] proposed an analytical methodology taking into account the bi-directional behaviour of angle-brackets [6,7]. Studies on the mechanical behaviour of multi-storey multi-panel CLT shearwalls, including the structural interaction between floor and wall panels have been limited. D'Arenzo et al. [8] developed an analytical model to investigate the interaction between a two-panel shearwall and the upper floor but such model was limited to single-storey shearwall.

This paper seeks to expand the existing single-storey approach by developing analytical expressions to account for the behaviour of multi-storey multi-panel CLT shearwalls, focusing on the CP kinematic mode. In order to replicate the effects of multi-storey behaviour in a single-storey analysis, the resulting reactions of a storey are used to modify the loads applied to the lower storey. Accordingly, the storeys are analyzed sequentially, beginning from the uppermost storey and transferring reaction forces to the next, lower storey. Due to this transfer of forces between stories, the effect of floor diaphragms between the CLT walls is also investigated and incorporated into the method.

The analytical method incorporates the cumulative effects of force transfer from one storey to another, as well as more flexible formulations to describe the connections between the wall panels and the upper and lower floor diaphragms. The proposed equations are verified against the results of two-dimensional finite element modelling using the Dlubal RFEM software.

2 ANALYTICAL METHODOLOGY

Following the methods developed in [2], analytical equations are developed using the method of virtual work and static equilibrium. Due to the rigid nature of CLT panels, the lateral resistance of the wall is assumed to be

[1] Damian Oliveira, Canadian Wood Council, Canada, doliveira@cwc.ca
[2] Ali Mikael, Canadian Wood Council, Canada, amikael@cwc.ca
[3] Daniele Casagrande, National Research Council of Italy, Italy, daniele.casagrande@ibe.cnr.it
[4] Ghasan Doudak, Professor, University of Ottawa, Canada, gdoudak@uottawa.ca

https://doi.org/10.52202/069179-0364

governed by the properties of the hold-downs, floor to wall connections and vertical joints used to connect the individual panels [5], as illustrated in Figure 1. The connection to the lower floor diaphragm is most commonly provided by angle brackets, while the connection to the upper floor diaphragm is often provided by self-tapping screws or angle brackets.

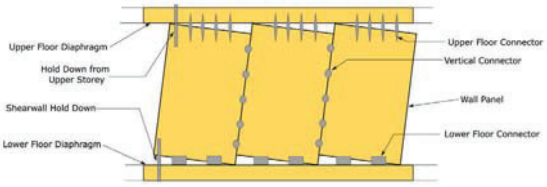

***Figure 1**: Displaced CLT shearwall and connection types*

The local stiffness of the connections between the CLT wall panels and the upper or lower floor diaphragms is distributed linearly along the panel edge, in order to broaden the applicability of the analytical method to various connection locations. The distribution of connection stiffness along the edge of CLT panels has been previously investigated in literature as a method to develop elastic analysis and modelling guidelines suitable for practicing engineers, and the method has achieved good agreement with experimental seismic responses [9].

The distributed stiffness of the wall-to-diaphragm connections, k_a when considering the connection to the lower floor or k_t when considering the connection to the upper floor, was calculated for several potential layouts. The equivalent stiffness was determined by equating the sum of work for a layout of connections with an integration of continuous forces representing the distributed stiffness. Illustration of the methodology with an arbitrary connector stiffness k_{br} is presented in Figure 2, with example stiffnesses presented in Table 1.

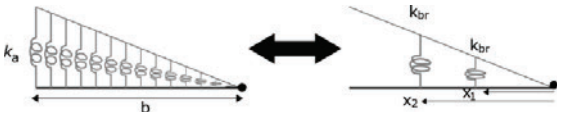

***Figure 2:** Equivalency illustration for two point-stiffnesses*

***Table 1:** Example distributed stiffness equations*

Bracket or Connector Layout	k_a or k_t
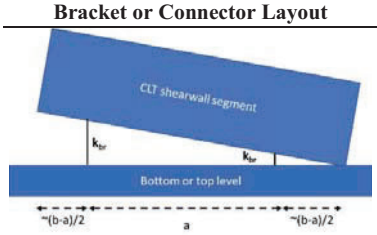	$\frac{3}{2}k_{br}\frac{b^2+a^2}{b^3}$
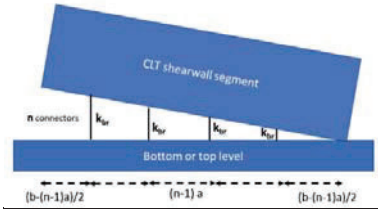	$\frac{n}{4}k_{br}\frac{3b^2+(n^2-1)a^2}{b^3}$

The analytical equations for the CP kinematic mode were determined using the principles of virtual work. The external work acting on the system was contributed to by the applied loads: lateral force F, uplift tension force T and downward vertical loads P_j from the upper floor (Figure 3). The internal work of the system includes contributions from the hold-down, vertical joints, and distributed connections to the upper and lower floor diaphragms. The expressions of external and internal work are presented in Equation (1) and Equation (2), respectively.

$$\sum W_{ex} = Fh\theta + Tb\theta - \sum \mathrm{P_i} b\theta \quad (1)$$

$$\sum W_{int} = \tfrac{1}{2}k_h b^2\theta^2 + \tfrac{1}{2}(m-1)(nk_c)b^2\theta^2 + \tfrac{1}{6}m(k_a+k_t)b^3\theta^2 \quad (2)$$

where m= number of panels, n= number of connectors in the vertical joints, k_h= hold-down stiffness, k_a= distributed lower floor-to-wall stiffness, k_t= distributed upper floor-to-wall stiffness and k_c= vertical connector stiffness.

The CP kinematic mode is defined by the behaviour during lateral displacement, where each panel within the shearwall rotates about a local corner as shown in Figure 3. Due to the equalized rotation across the panels, it is assumed the upper floor remains horizontal, as does the lower floor. The hold-down tensile force, T, and the vertical point loads P_j provide a different representation of the inter-storey load transfer compared to previous work [2].

https://doi.org/10.52202/069179-0364

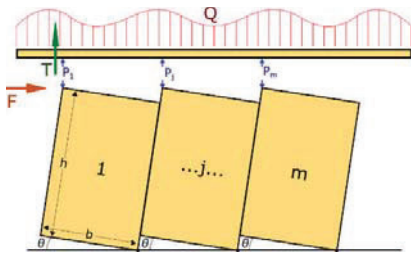

Figure 3: *Illustration of the coupled panel kinematic mode and applied load distribution*

The displacement of the wall causes tension in the hold down of the first panel (j=1), which is transferred as a vertical point load to the storey below. The load is applied upward at the corner of the first panel in the lower storey, as the walls are assumed to be vertically aligned for the transfer of force. The downward vertical load is transferred to the wall through the upper floor diaphragm and applied on the panel corners as point loads P_j. The method utilizes a beam analogy (Figure 4), which includes gravity loads and the net reactions of the storey above in the equivalent vertical load Q. While any pattern of loading can be applied to the beam analogy, the vertical loads and reactions for the panel corners and floor connections above are uniformly distributed along the length of the wall. This distribution of bearing reactions and connection forces is performed according to Equation (3) for storey under consideration (labelled s in the equation), where q_s is the gravity load applied on the floor in kN/m and $R_{cj,(s+1)}$ is the reaction force from the j-th panel of the upper ($s+1$) storey.

$$Q_s \cong q_s + \frac{\sum_1^m R_{cj,(s+1)} - m \times \left(\frac{k_a b^2 \theta}{2}\right)_{(s+1)}}{m \times b} \tag{3}$$

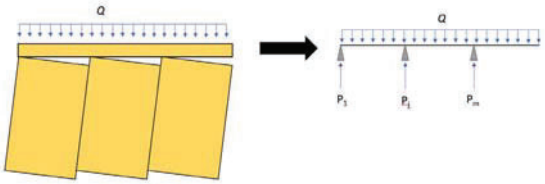

Figure 4: *Illustrated beam analogy for an example isolated shearwall acting in the CP kinematic mode*

Numerical models have shown that distributing the loads uniformly achieves equivalent P_j results as the individually applied reactions for CP analysis, and therefore uniform Q loads are used to simplify the analysis.

Within the analogous system, the contacting point of a panel with the upper floor is treated as a pinned support for a continuous simply-supported beam. This continuous beam represents the upper floor diaphragm above the wall, including an extra length cantilevering over the last supporting panel.

The extent of deflection in a CLT shearwall acting in the CP mode can be described using the angle of rotation θ, as defined in Equation (4), which is also critical in deriving expressions for the connection forces. The connection stiffness to the lower floor k_a, connection stiffness to the upper floor k_t, hold-down stiffness k_h, and the total stiffness of n fasteners in vertical joints nk_c are presented in Equation (5) to describe the combined stiffness k^*.

$$\theta = \frac{1}{k^*}\left(\frac{Fh}{b^2} + \frac{T}{b} - \frac{\sum_1^m P_j}{b}\right) \tag{4}$$

$$k^* = k_h + (m-1) * n * k_c + \frac{mb}{3}(k_a + k_t) \tag{5}$$

The displacement of any point along the wall can be calculated using the angle of rotation. The key displacements to describe the position of the wall panels can generally be defined as the displacement of the panel corners. These displacements include the lateral deflection Δ_h (equal to θ x h) and hold-down elongation v_0 (equal to θ x b).

The elastic resistance of the shearwall is governed by the resistance of the vertical joints and hold-downs, due to the high in-plane rigidity of CLT panels. The equations for the forces in the hold-down and individual vertical connectors, respectively, are presented in Equation (6) and Equation (7). While the stiffness of the connections to the floor diaphragms contributes to the behaviour of the system, they are assumed to not govern the elastic resistance of the wall. The angle of rotation and the location of the wall-to-floor connections can be used with methods of mechanics to calculate the forces in the discrete connectors and ensure adequate capacity.

$$R_h = \frac{k_h}{k^*}\left(\frac{Fh}{b} + T - \sum_1^m P_j\right) \tag{6}$$

$$F_{cy} = \frac{k_c}{k^*}\left(\frac{Fh}{b} + T - \sum_1^m P_j\right) \tag{7}$$

The equations for elastic resistance of the shearwall are derived from Equations (6) and (7), resulting in the set of expressions presented in Equations (8)-(10). Equation (9) provides the wall resistance in the scenario where the hold-down reaches its elastic limit before the connectors in the vertical joint, while Equation (10) provides the resistance where the vertical connectors yield before the hold-down. Due to the nature of the CP kinematic mode, all vertical joints in the wall are exposed to the same magnitude of force.

$$R_w = \min\{R_{wc}, R_{wh}\} \tag{8}$$

https://doi.org/10.52202/069179-0364

$$R_{wh} = r_h \frac{k^* b}{k_h h} + \frac{\sum_1^m P_i \times b}{h} - \frac{Tb}{h} \quad (9)$$

$$R_{wc} = r_c \frac{k^* b}{k_c h} + \frac{\sum_1^m P_i \times b}{h} - \frac{Tb}{h} \quad (10)$$

The defining boundary for the CP kinematic mode is that all panels remain in contact with the floor surface. As such, the boundary for the validity of the analysis can be defined as when the first panel's reaction force (R_{c1}, as calculated in Equation (11)) is greater than or equal to 0. This results in the condition presented in Equation (12), in terms of the applied uplift tension force T at that storey.

$$R_{c1} = R_h + \frac{b^2\theta}{2}(k_a - k_t) - nF_{cy} + P_1 - T \geq 0 \quad (11)$$

$$T < \frac{k_h - nk_c - \frac{b}{2}(k_a - k_t)}{mnk_c + \frac{mb}{3}(k_a + k_t) - \frac{b}{2}(k_a - k_t)} \left(\frac{Fh}{b} - \sum_1^m P_i\right) + \frac{P_1 k^*}{mnk_c + \frac{mb}{3}(k_a + k_t) - \frac{b}{2}(k_a - k_t)} \quad (12)$$

Equation (12) provides the maximum uplift tension force T a given wall can resist while maintaining CP behaviour, which indicates that the effect of hold-down forces from upper storeys on CP kinematic behaviour is significant. Figure 5 presents the limiting condition for CP behaviour, above which the wall is expected to act in the CP kinematic mode and below which it trends towards the SW kinematic mode. As the ratio of overturning moments changes, which includes uplift tension force T and lateral forces F, the boundary line raises such that a shearwall requires increased hold-down stiffness (or higher counteracting gravity load) to maintain CP behaviour. This is a considerable change from the case without uplift forces from upper storeys, represented by the solid line, where a stiffness ratio of 1 or greater is sufficient to ensure CP behaviour regardless of loading.

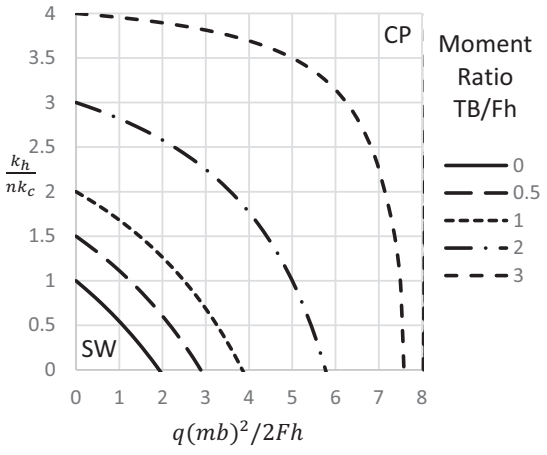

Figure 5: *Effect of uplift tension on behavioural boundary*

3 MODELLING METHODOLODY

Finite element models of both single-storey and stacked multi-storey shearwalls were developed and used to verify the proposed mathematical approaches. The single storey models were used to investigate the assumptions made within the analytical method, as well as verify the accuracy of the final equations. The single-storey models were analyzed sequentially, representing isolated storeys transferring forces to the wall below similarly to the analytical method. The stacked shearwall model is constructed to verify the accuracy of the analyses, as the multi-storey effects would inherently occur during the solution of the model.

The models consist of two-dimensional (i.e. area) rigid elements representing the CLT panels, connected with distributed springs (referred to as linear releases in the software) representing the connections between adjacent CLT panels and between the wall and the upper and lower floors. The floor diaphragms are modelled using properties representing a CLT floor system over an interior wall. Hold-downs are represented by spring elements between the first panels of adjacent storeys (Figure 6), and between the bottom of the lowest first panel and foundation. Dlubal RFEM is used to construct the models and analyze the results.

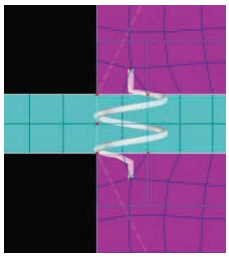

Figure 6: *Modelled hold-down element, in white, between shearwall panels, in purple*

Panel dimensions of 3 m in height and 1.5 m in width are used throughout the modelled walls for consistency. The four-storey model also includes an extended diaphragm, to better represent a shearwall as part of a larger structural system (Figure 7).

https://doi.org/10.52202/069179-0364

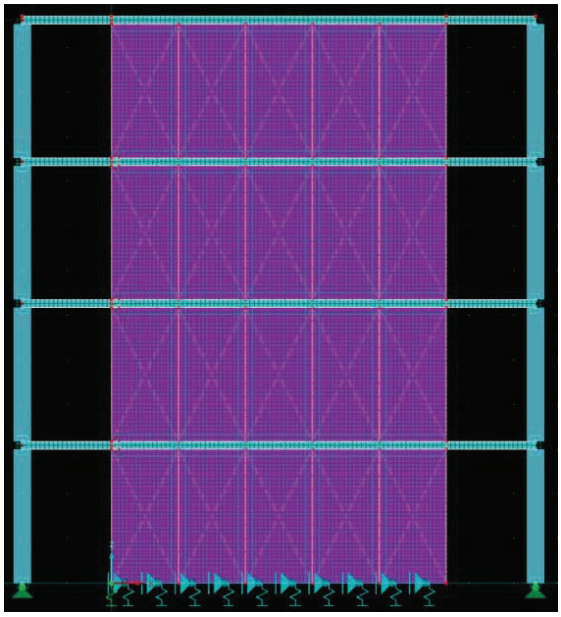

Figure 7: *Four-storey stacked CP model*

The finite element model considers a four-storey stacked five-panel shearwall loaded according to high seismic demands in Victoria (Canada). The load and connection properties are summarized in Table 2. The connection properties are based on manufacturer data for commercial products, and the same stiffnesses are used to connect the wall to both floors.

Table 2: *Coupled Panel modelling properties*

Storey	1	2	3	4
Applied Lateral Load (kN)	42.9	85.7	128.6	96.1
Distributed Gravity Load (kN/m)	20	20	20	10
Number of Vertical Connectors	24	24	15	15
Vertical Connector Stiffness (kN/m)	700	700	700	700
Hold-Down Stiffness (kN/m)	13136	13136	9973	9973
Distributed Floor Connection Stiffness (kN/m/m)	5147	5147	3823	1323

The modelled diaphragm for all cases is 175 mm thick, with an elastic modulus of 9348 MPa and width of 5 m.

4 MODELING RESULTS AND DISCUSSION

The results of the finite element models, as well as the analytical equations, are presented and compared in the following sections. The results of the stacked shearwall model are presented primarily as a target response for the other analyses. The single-storey models are used to investigate the assumptions used in the development of the analytical equations, and the results are compared between assumptions and against the stacked model. The calculated results from the analytical equations are compared against the stacked model result, to evaluate accuracy, as well as the single-storey model results to evaluate consistency.

A sensitivity analysis varying the properties of the floor diaphragm, both within the beam analogy and the finite element modelling, is also presented to investigate the sensitivity of the method.

4.1 STACKED MODEL RESULTS

The stacked shear wall model serves as the target values for verifying the analytical equations and benchmark for the behaviour of the single-storey models used to evaluate the analytical assumptions. The critical results for comparison between the analyses are lateral displacement, panel rotation, and hold-down tension.

The results for the four-storey stacked model indicated a decreasing level of rotation in lower storeys, due to the accumulated gravity load counteracting the lateral forces (Figure 8). While the floor diaphragms between storeys developed curved shapes, the overall surfaces generally remained level between the shearwalls. The results of the analysis are presented in Table 3, indicating inter-storey drift (Δ_h) as well as the total lateral displacement at each floor.

Table 3: *Four-storey stacked model results*

Storey	Δ_h (mm)	Total Lateral Displacement (mm)	θ (mrad)	R_h (kN)
4	3.75	10.37	1.25	15.4
3	3.88	6.56	1.29	19.2
2	1.62	2.64	0.550	16.5
1	0.98	0.98	0.330	6.85

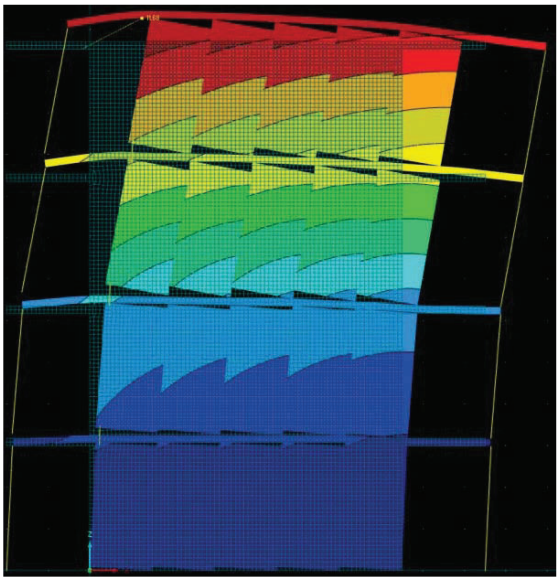

Figure 8: *Displaced shape of four-storey model, 140x deformation*

https://doi.org/10.52202/069179-0364

4.2 SINGLE-STOREY RESULTS

The single storey-models were analyzed sequentially, as in the approach used in the mathematical analysis. A model of the uppermost storey was analyzed first, and the reaction and hold-down results were used to modify the loads applied to the model of the lower storey.

The properties of the connections to the upper floor will influence the behaviour of the CLT shearwall, similarly to the connections between the wall and the lower floor. However, the inclusion of am upper floor diaphragm into the shearwall analysis does not only alter the system response through the connection to the wall panels. The addition of an upper diaphragm alone will modify how the vertical loads are distributed to the wall panels.

Two sets of single-storey models investigated the load distribution effect of floor diaphragms during CP behaviour. One set applies the vertical loads directly to the wall panels (Figure 9) (i.e. without considering a diaphragm), while the other model includes a modelled upper floor diaphragm which will distribute the applied vertical load to the wall panels (Figure 10).

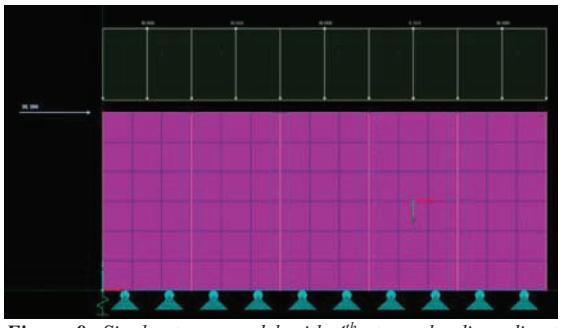

Figure 9: *Single storey model with 4th storey loading, direct panel loading*

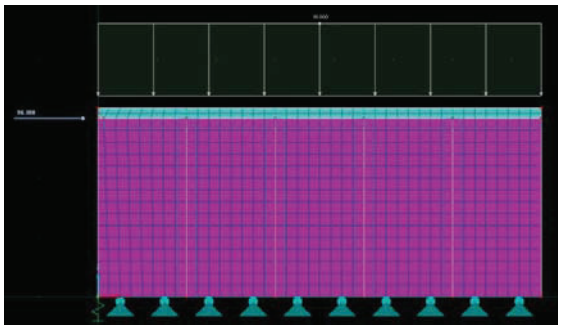

Figure 10: *Single storey model for 4th storey, with diaphragm*

Both models consist of five-panel shearwalls, and as indicated in Table 4, no floor connections were implemented in either model to maintain a valid comparison. Furthermore, the loading was identical between the models, despite differences in reaction values between the analyses which would cause cumulative differences as the forces are transferred to the analysis of the lower storeys. This overall harmonization between the models allows for a direct comparison between the single-storey models and isolates the effect of the floor's distributive properties.

Table 4: *Single storey model information for floor diaphragm comparison*

Storey	1	2	3	4
Lateral Load (kN)	353.3	310.4	224.7	96.1
Gravity Load (kN/m)	95	65	35	10
Uplift Force (kN)	40	35	20	0
Number of Vertical Connectors	24	24	15	15
Vertical Connector Stiffness (kN/m)	700	700	700	700
Hold-Down Stiffness (kN/m)	13136	13136	9973	9973

The model results are presented in Table 5, where it can be observed that the inclusion of the modelled floor diaphragm drastically reduces the lateral deflection for a given loading. This difference can be attributed to the increased moment arm that more directly counteracts the rotation of the panel when the gravity load is applied via a point load on the panel corner rather than distributed over the top edge.

Table 5: *Modelling results for single storey comparison of floor effect*

Storey	Q Loading			Diaphragm Loading		
	Δ_h [1]	θ [2]	R_h [3]	Δ_h [1]	θ [2]	R_h [3]
4	5.96	1.98	29.7	4.52	1.47	22.4
3	13.04	4.33	64.9	7.93	2.58	42.2
2	10.29	3.41	67.4	4.35	1.40	29.4
1	9.76	3.23	63.8	1.64	0.51	10.6

1: mm 2: mrad 3: kN

In order to compare against the four-storey stacked model, and therefore provide storey-be-storey equivalent analysis for comparison with the analytical equations, two additional models were analyzed using the same properties as listed in Table 2. The first set included a floor only above the wall panels, while the second model set extended the upper floor diaphragm to match the construction of the stacked model more closely (Figure 11).

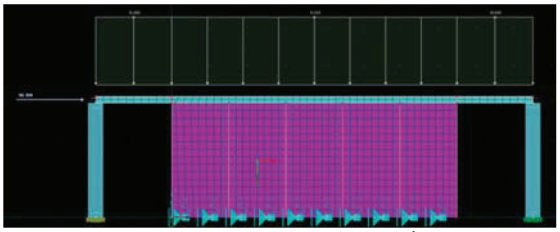

Figure 11: *Extended single storey model for 4th storey*

The accumulated gravity load applied to each single storey model is adjusted by distributing the net reactions from the storey above, using the same methodology presented in Equation (3). The resulting loads applied to

each non-extended single storey model are presented in Table 6, and the results of the analysis are shown in Table 7.

Table 6: *Loading cases for non-extended single storey model*

Storey	1	2	3	4
Lateral Load (kN)	353.3	310.4	224.7	96.1
Gravity Load (kN/m)	74.7	54.3	32.3	10
Uplift Force (kN)	33.7	32.3	17.2	0

Table 7: *Non-extended single storey modelling results*

Storey	Δ_h (mm)	θ (mrad)	R_h (kN)
4	3.45	1.12	17.2
3*	6.36	2.05	32.3
2*	4.71	1.51	33.7
1*	3.46	0.99	25.0

*: Uplift observed in first panel

While the single-storey results in Table 7 follow the same general pattern of diminishing rotation in lower storeys as those in the stacked model results (Table 3), several cases of the single storey analysis exit CP mode by exhibiting uplift in the first panel.

The extension of the floor increases the gravity load on each storey, as shown in Table 8. As a result, all extended single storey models remain in the CP kinematic mode. However, the extended model for the lowest storey does not meaningfully display rocking behaviour due to the accumulated gravity load, as shown in Table 9.

Table 8: *Loading cases for extended single storey model*

Storey	1	2	3	4
Lateral Load (kN)	353.3	310.4	224.7	96.1
Gravity Load (kN/m)	108.5	68.4	29.2	10
Uplift Force (kN)	9.23	20.7	16.4	0

Table 9: *Extended single storey modelling results*

Storey	Δ_h (mm)	θ (mrad)	R_h (kN)
4	3.30	1.07	16.4
3	4.18	1.35	20.7
2	1.44	0.44	9.23
1	0	0	0

Comparing the displacement results of both extended and non-extended models to those of the stacked four-storey model, it can be observed that the addition of the extended floor generally improves accuracy to within 10% of the stacked model results (represented by the solid line in Figure 12). As such, the specific distribution of forces from the floor diaphragm has significant influence on the overall behaviour of the shearwall. The tendency for the non-extended model to overestimate displacement is also noteworthy for the purposes of design conservatism and simplicity of implementation. The two primary factors contributing to this are the lesser amount of gravity load within the system as well as an altered load distribution associated with limiting the upper diaphragm length to only remain above the wall panels.

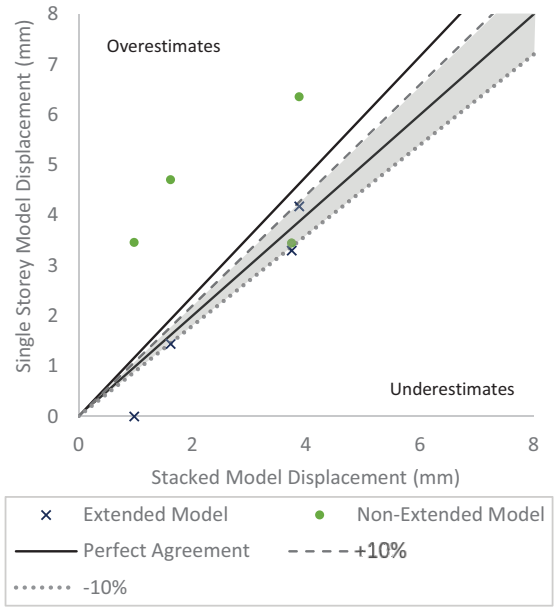

Figure 12: *Lateral displacement comparison between single storey models, against stacked CP models*

4.3 COMPARISON WITH ANALYTICAL RESULTS

The four-storey stacked shearwall was also analyzed using the analytical equations presented section 2. Given the observations regarding the importance of the extended floor diaphragm to the single storey CP models, a beam analogy including extensions equivalent to the stacked model was applied to better reflect the conditions within the stacked model (Figure 13).

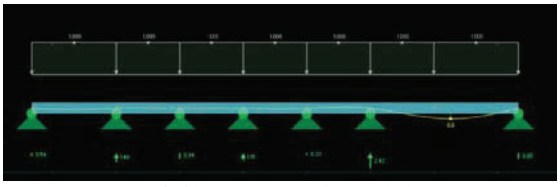

Figure 13: *Extended beam analogy for CP behaviour*

The elastic modulus used within the beam analogy is as presented in Table 2. Table 10 presents the equivalent vertical loads used in combination with the beam analogy, which includes adjustments based on the net reactions from the upper storey (Equation (3)).

https://doi.org/10.52202/069179-0364

Table 10: *Analytical vertical distributed loads*

Storey	Q (kN/m)
4	10
3	33.5
2	57.9
1	87.8

The results of the analysis of the four-storey shearwall acting in the CP kinematic mode are presented in Table 11, where similarly to the extended single storey model no rotation was obtained for the bottom storey. The analytical equations performed similarly to the extended single storey model, with overall good agreement with the four-storey stacked model (Figure 14).

Table 11: *Analytical results for four-storey CP shearwall*

Storey	Δ_h (mm)	θ (mrad)	R_h (kN)	Total Lateral Displacement (mm)
4	3.40	1.13	16.9	9.78
3	4.38	1.46	21.9	6.38
2	2.00	0.67	13.2	2.00
1	0	0	0	0

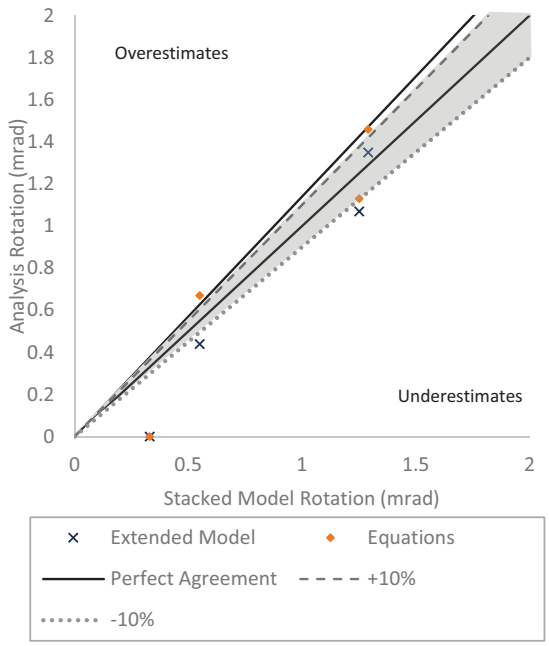

Figure 14: *Rotation angle comparison of proposed analytical expressions and extended model (single-storey), against stacked model*

4.4 FLOOR DIAPHRAGM EFFECT

In order to investigate the sensitivity of the analytical assumptions and finite element model, properties of the diaphragm were varied in both the beam analogy and the finite element model to evaluate the consistency of the results.

The beam analogy, evaluated via one-dimensional modelling, showed no variations in load distribution as elastic modulus of the diaphragm changed. Small variations were observed when changing the depth of diaphragm section, but as shown in Table 12 the discrepancies were minimal within the range of common CLT panel thicknesses. In this analysis, the beam analogy was applied to an isolated five-panel shearwall assumed to have a rotationally fixed boundary condition beyond the last panel, to simulate the effect of continuity on the modelled part (Figure 15).

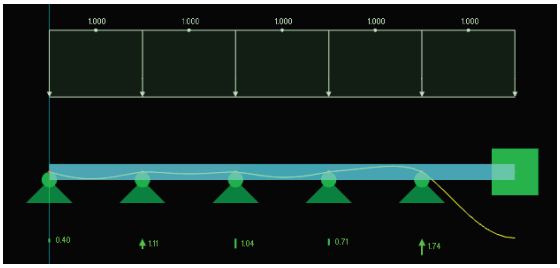

Figure 15: *Beam analogy used in section depth study*

Table 12: *Variation in load factor with diaphragm depth*

Section Depth (mm)	P_1 Factor	P_2 Factor	P_3 Factor	P_4 Factor	P_5 Factor
105	0.40	1.11	1.04	0.70	1.74
175	0.40	1.11	1.04	0.71	1.74
245	0.40	1.11	1.04	0.72	1.73

The sensitivity to floor diaphragm properties was further investigated by varying the effective bending modulus of the modelled floor within the finite element model. As presented in Figure 16, the model results remain consistent until the upper floor bending stiffness is significantly lowered, with only a 3% difference in displacement observed at an 89% reduction. At this point, the diaphragm remains in significant contact with the top surface of the wall panel during displacement and the transfer of forces extends beyond the corner of the modelled panel. As a result, the rotational resistance due to gravity load is reduced by shortening the moment arm and the system displacement begins to increase.

https://doi.org/10.52202/069179-0364

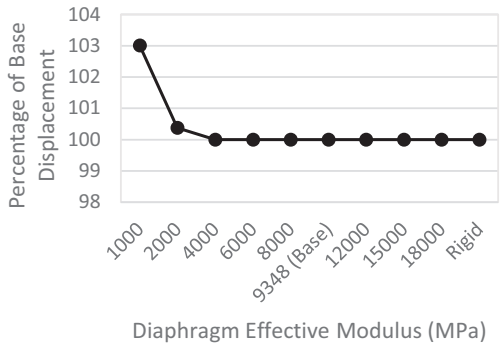

Figure 16: *Variation in model displacement with upper diaphragm stiffness*

While this behaviour contradicts the assumptions of the analytical equations, a floor diaphragm of reasonable stiffness for a CLT panel acting out of plane is expected to be sufficient for the assumed behaviour to remain valid.

These results indicate that the beam analogy for load distribution is reliably applicable to diaphragms in multi-storey platform-type CLT construction, and strengthens the assumptions used in the analytical method for wall behaving in the CP kinematic mode.

5 CONCLUSIONS AND FUTURE WORK

The analytical equations developed in this paper expand upon previous work and provides an approach to calculate displacements and forces in multi-storey CLT shearwall systems while including the effect of floor diaphragms. The results have shown reasonable accuracy when compared against finite element modelling, and the underlying assumptions simplify the individual contributions of the resisting elements while maintaining the complexity of the response. The assumptions regarding the distributive effect of the floor have been shown to be reliable at practical stiffnesses.

Future developments on the topic include expanding the analytical method to include SW kinematic behaviour. Additional modelling analysis can also be used to study and verify equations for more complex systems of shearwalls.

REFERENCES

[1] I. Gavric, M. Fragiacomo and A. Ceccotti, "Cyclic behviour of CLT wall systems: Experimental tests and analytical prediction models.," *J. Struct. Eng.,* vol. 141, no. 11, p. 04015034, 2015.

[2] D. Casagrande, G. Doudak, L. Mauro and A. Polastri, "Analytical Approach to Establishing the Elastic Behaviour of Multipanel CLT Shear Walls Subjected to Lateral Loads," *Journal of Structural Engineering,* vol. 144, no. 2, p. 04017193, 2018.

[3] A. Polastri and D. Casagrande, "Mechanical behaviour of multi-panel cross laminated timber shear-walls with stiff connectors," *Construction and Building Materials,* vol. 332, p. 127275, 2022.

[4] G. Flatscher and G. Schickhofer, "Displacement-based determination of laterally loaded cross laminated timber (CLT) awll systems," in *3rd International Network on Timber Engineering Research Meeting*, Graz, Austria, 2016.

[5] M. Masroor, G. Doudak and D. Casagrande, "The effect of bi-axial behaviour of mechanical anchors on the lateral response of multi-panel CLT Shearwalls," *Engineering Structures,* vol. 224, p. 111202, 2020.

[6] G. D'Arenzo, W. Seim and M. Fossetti, "Experimental characterization of a biaxial behaviour connector for CLT wall-to-floor connections under different load directions," *Construction and Building Materials,* vol. 265, p. 123666, 2021.

[7] G. D'Arenzo, D. Casagrande, A. Polastri, M. Fragiacomo and W. Seim, "CLT Shear Walls Anchored with Shear-Tension Angle Brackets: Experimental Tests and Finite-Element Modeling," *Journal of Structural Engineering,* vol. 147, no. 7, p. 04021089, 2021.

[8] G. D'Arenzo, S. Schwendner and W. Seim, "The effect of floor-to-wall interaction on the rocking stiffness of segmented CLT shear-walls," *Engineering Structures,* vol. 249, p. 113219, 2021.

[9] I. Christovasilis, L. Riparbelli, G. Rinaldin and G. Tamagnone, "Methods for practice-oriented linear analysis in seismic design of Cross Laminated Timber buildings," *Soil Dynamics and Earthquake Engineering,* vol. 128, p. 105869, 2020.

https://doi.org/10.52202/069179-0364

World Conference on Timber Engineering Oslo 2023

DEFLECTION OF CANTILEVER CROSS-LAMINATED TIMBER DIAPHRAGMS UNDER IN-PLANE LOAD

Bibek Bhardwaj[1], Weichiang Pang[2], Michael Stoner[3], Douglas Rammer[4], Steve Pryor[5]

ABSTRACT: Diaphragms are used to transmit lateral loads to the vertical elements (e.g., shear walls) of the lateral force resisting system of a structure. The extent of deflection in diaphragms can determine what mechanism needs to be considered during design for transfer of forces to the vertical elements. Current design specifications do not provide equations that engineers can use to determine the deflections in cantilever Cross-Laminated Timber (CLT) diaphragms. In this paper, the CLT shear wall equation prescribed by 2021 Special Design Provisions for Wind and Seismic (SDPWS) was adapted to get an equivalent analytical equation for cantilever CLT diaphragm deflection. A full scale 6.1 m x 6.1 m (20 ft. × 20 ft.) cantilever CLT diaphragm was tested using displacement controlled cyclic protocol and the deformations at various regions of the diaphragms were measured. Analysis of test results suggests that the modified shear wall deflection equation for a cantilever CLT diaphragm based on SDPWS overpredicts the contribution due to bending and shear deformations.

KEYWORDS: CLT Diaphragm, Diaphragm Deflection, Cantilever, Deflection equation

1 INTRODUCTION

Deflection in diaphragms is an essential consideration for structural design. Excessive deflection in diaphragms is often undesirable as the stiffness of diaphragms can affect storey drifts [1]. The U.S. standard for Minimum Design Loads and Associated Criteria for Buildings and Other Structures (ASCE 7-22) [2] section 12.12.1 sets criteria for allowable design story drift limits. To quantify the distribution of shear forces to the vertical elements, diaphragms are often idealized to be completely flexible or rigid. Section 12.3.1.3 of ASCE 7-22 permits diaphragms to be idealized as flexible if the maximum in-plane diaphragm deflection is greater than twice the average deflection of adjoining elements of the vertical lateral force resisting system (VLFRS). For flexible diaphragms, shear forces are distributed to the VLFRS based on tributary area while for rigid diaphragms, shear forces are distributed based on the relative lateral stiffness of the elements of VLFRS. For light frame diaphragms, section 4.2.4 of the 2021 Special Design Provisions for Wind and Seismic (SDPWS) [3] provides three-term equations for determining in-plane deflections of cantilever diaphragms of cases of uniformly distributed load and concentrated load at the end of the diaphragm. Cross Laminated Timber (CLT) was introduced in the 2015 version of the National Design Specification for Wood Construction (NDS) [4] but such provisions are not yet available for cantilever CLT diaphragms. In this research, the equation for CLT shear walls provided by SDPWS was utilized to get an equivalent expression for deflections in a cantilever CLT diaphragm. The analytical equation was evaluated by comparing its predictions to the observations made during a full-scale test of a 6.1 m x 6.1 m (20 ft. × 20 ft.) cantilever CLT diaphragm.

2 BACKGROUND

In case of light frame diaphragms, the SDPWS provides a three and four-term equation for determining the end deflection of a simply supported diaphragm (equations C4.2.3-2 and C4.2.3-1 respectively) for uniformly distributed load case. For cantilever diaphragms, SDPWS provides three-term equations for determining in-plane deflections for both uniformly distributed and concentrated load at the end cases (equations 4.2-2 and 4.2-3 respectively).

The equation provided by SDPWS for deflection at the free end of a cantilever light frame diaphragm under concentrated point load (4.2-3) is as follows:

$$\delta_{dia} = \frac{8vL'^3}{EAW'} + \frac{vL'}{1000G_a} + \frac{\sum x'\Delta_c}{W'} \qquad (1)$$

Where,

δ_{dia} = deflection at free end of the diaphragm, in.
v = unit induced shear, plf
L' = length of diaphragm, ft.
E = modulus of elasticity of diaphragm chords

[1] Bibek Bhardwaj, Clemson University, USA, bibekb@clemson.edu
[2] Weichiang Pang, Clemson University, USA, wpang@clemson.edu
[3] Michael Stoner, Clemson University, USA, mwstone@clemson.edu
[4] Douglas Rammer, Forest Products Laboratory, USA douglas.r.rammer@usda.gov
[5] Steve Pryor, Simpson Strong-Tie, USA spryor@strongtie.com

https://doi.org/10.52202/069179-0365

G_a = apparent diaphragm shear stiffness from nail slip and panel shear deformation, kip/in.
x' = distance from chord splice to free end of diaphragm
Δ_c = diaphragm chord splice slip, in.
W' = total width of the diaphragm, ft.

The principal modes of deflection for equation 1 are assumed to be deflection due to bending (of the chords, excluding slip), shear deformation (of the panels, excluding slip), shear deformation due to nail slip in the panels and deformation due to anchorage slip. In case of CLT diaphragms, one of the early attempts at quantifying deflections was carried out by Spickler et al. [5] in a horizontal CLT diaphragm deflection design example. The equation presented in the design example was expanded from the four-term diaphragm deflection equation for light frame diaphragms. Unlike light frame diaphragms, where the flexural and shear members are distinct (the flexural deformation is considered only for the chord members while shear deformation is considered only for the sheathing material), for CLT diaphragms, the CLT panels themselves were designed as chord and shear members, capable of withstanding both bending and shear.

In the 2021 version of the SDPWS, section 4.5.2 suggests determining the deflection in a CLT diaphragm using principles of engineering mechanics without explicitly providing an equation. To help engineers and design practitioners come up with an estimate for diaphragm deflection for different layouts and configurations, Lawson et al. [6] have provided recommendations to estimating the various components of deflections in a CLT diaphragm.

Section 4.6.2 of SDPWS suggests determining deflection in CLT shear walls using principles of engineering mechanics as well but provides an equation for calculating the deflection in appendix B.4. Commentary on appendix B.4 provides further insights to the equation and its assumptions. Due to the similarity in layout between a CLT shear wall and a cantilever CLT diaphragm, an equivalent expression for CLT diaphragms can be determined based on the equations for CLT shear walls in the SDPWS.

The equivalent expression for free end deflection in a CLT diaphragm under concentrated point load at the end, generalized for different fastener types (not just nailed spline connection) is given as follows:

$$\delta_{dia} = \frac{576 v P_w L^3}{EI_{eff(in-plane)}} + \frac{vL}{GA_{eff(in-plane)}} + n_0 e_0 + e_{90}\frac{L}{P_W} + \frac{\Delta_a}{W} L \qquad (2)$$

Where,

δ_{dia} = deflection at free end of the diaphragm, in.
v = unit induced shear, plf
P_W = individual panel width, ft.
L = length of diaphragm, ft.
$EI_{eff\ (in\text{-}plane)}$ = effective in-plane bending stiffness of CLT panel, lbs-in^2
$GA_{eff\ (in\text{-}plane)}$ = effective in-plane shear stiffness of the CLT panel, lbs/in. of panel length
n_0 = number of locations for longitudinal (parallel to load) shear fasteners
e_0 = deflection at each fastener location in., (= 0 for single panel diaphragm)
e_{90} = transverse fastener slip, in.
Δ_a = slip at the anchorage, in.
W = total width of the diaphragm, ft.

It should be noted that equation 2 uses customary units used in the US and includes an implicit unit conversion factor in the first term for calculating the deformation due to in-plane panel bending. Modification of equation 2 for SI units would require a modification to that factor.

Figure 1 shows all the deformation modes considered for the equation 2.

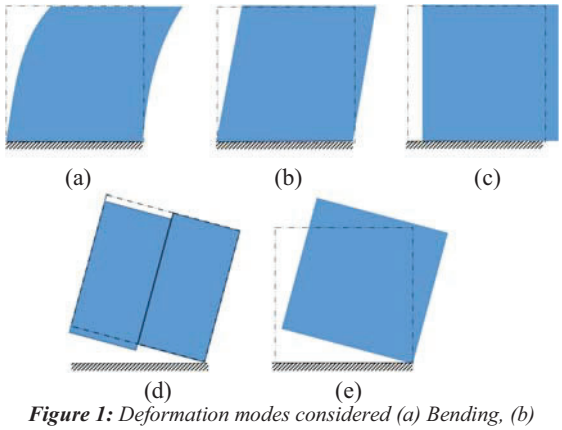

Figure 1: *Deformation modes considered (a) Bending, (b) Shear, (c) Longitudinal shear fastener slip (d) Transverse shear fastener slip, and (e) Anchorage slip.*

This paper takes results from an experimental test conducted on a cantilever CLT diaphragm and compares the deflections observed to the predictions made by the SDPWS based equation (equation 2).

3 EXPERIMENTAL SETUP

3.1 LAYOUT

A 6.1 m × 6.1 m (20 ft. × 20 ft.) CLT diaphragm was tested destructively using displacement-controlled loading based on CUREE (Consortium of Universities for Research in Earthquake Engineering) [7] cyclic protocol [8]. The diaphragm was composed of four 1.5 m × 6.1 m (5 ft. × 20 ft.) panels resting on three 6.1 m (20 ft.) long 17.1 cm (6.75 in.) wide and 34.9 cm (13.75 in.) deep glulam beams along the short edges of the panels as shown in Figure 2. The long edges of the panels were connected using a 2.5 cm (1 in.) thick plywood surface spline using 16d common nails at 7.6 cm (3 in.) c/c as shown in Figure 2. The detailing for the surface spline

https://doi.org/10.52202/069179-0365

connection is shown in Figure 3. The CLT panels were connected to the glulam beams underneath using Simpson strong Tie's SDWS22800DB screws at 15.2 cm (6 in.) c/c on the two outside glulam beams and 20.3 cm (8 in.) c/c on the middle glulam beam (Figure 2). Custom made Simpson Strong Tie hold-downs were installed 25.4 cm (10 in.) from the edges on both sides (Figure 2).

The load was applied using a hydraulic actuator attached to the free end glulam beam.

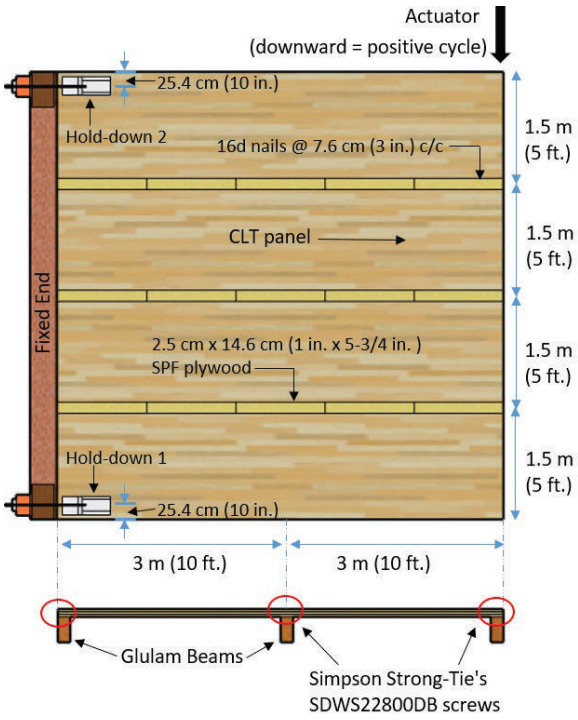

Figure 2: *Layout for the diaphragm test*

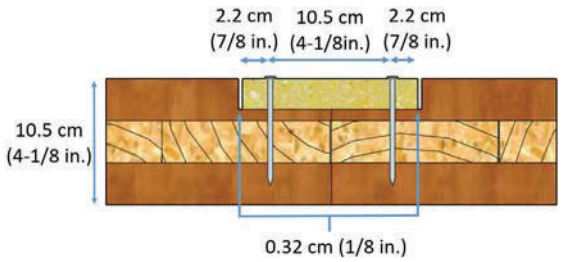

Figure 3: *Surface spline detail*

3.2 DESIGN OF CLT DIAPHRAGM

The diaphragm was designed (for seismic considerations) using recommendations from a design example [5] and SDPWS 2021. The diaphragm had a Load and Resistance Factor Design (LRFD) in-plane shear capacity of 98.3 kN (22.1 kip) based on the strength of the surface spline nailed connection. The Allowable Stress Design (ASD) capacity of the diaphragm was 70.2 kN (15.8 kip). The CLT-glulam screws were designed to have an additional 61% capacity over the design forces expected at the CLT glulam interface. All other components of the diaphragm were design to have at least two times the capacity compared to the design level forces at the respective component per the requirements of SDPWS 2021. The LRFD capacity summary for the diaphragm components is given in Table 1 [8].

Table 1: *LRFD capacities of Diaphragm Components (seismic design)*

Component	Required Capacity*	Design Capacity	Strength Ratio**
	kN (kip)	kN (kip)	
Panel-Panel nailed surface spline	98.3 (22.1)	98.3 (22.1)	1:1
Panel-Glulam screws	98.3 (22.1)	158.4 (35.6)	1.6:1
Tension Chord	222.4 (50)	323.8 (72.8)	2.9:1
Compression Chord	222.4 (50)	327.4 (73.6)	2.9:1
Hold-downs	222.4 (50)	560.5 (126)	5:1

*required capacity for non-shear elements is twice the capacity obtained using design shear forces

**ratio of design capacity to capacity obtained using design shear forces

3.3 INSTRUMENTATION SETUP

Figure 4 and Figure 5 show the location of the various string potentiometers used in the diaphragm test to track component deformations [8]. The load deformation response on the free end glulam beam was captured by the sensors in the hydraulic actuator. Figure 4 also shows the two load cells (LC1 and LC2) used to capture the uplift force experienced by the diaphragm at the hold-down location.

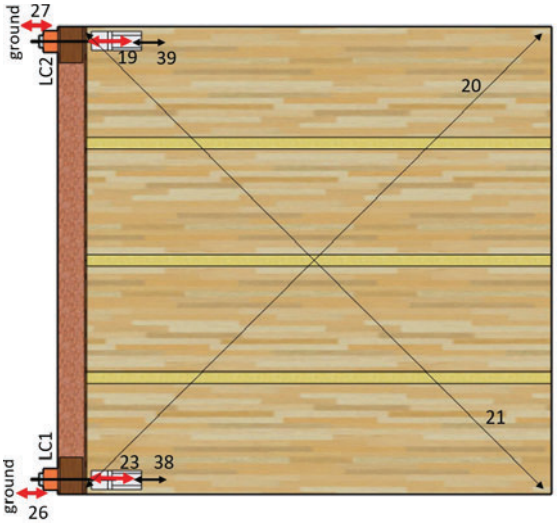

Figure 4: *String pot and hold-down layout on the top of the diaphragm*

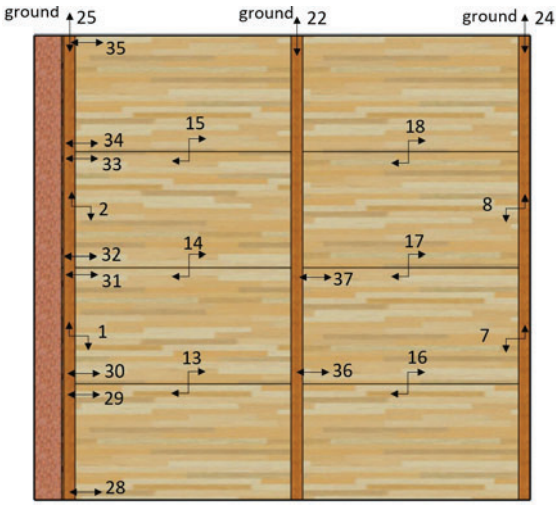

Figure 5: *String pot layout on the bottom of the diaphragm*

It should be noted that the instrumentation was not setup to capture the bending and shear deformations (described in Figure 1a and Figure 1b).

4 RESULTS AND OBSERVATIONS

4.1 OVERALL BEHAVIOUR OF DIAPHRAGM SETUP

Figure 6 shows the hysteresis for the applied displacement vs force observed for the diaphragm test setup [8]. The summary of the test results is shown in Table 1 [8]. The diaphragm setup displayed a relatively symmetrical behaviour for positive and negative cycles. The average initial stiffness of the setup was 24.1 kN/cm (13.8 kip/in.). The peak capacity of the diaphragm exceeded its LRFD capacity by a factor of 1.7. Through the observation of deformations during the test, it was inferred that the peak capacity of the diaphragm was primarily governed by the capacity of its surface spline nailed connection which was consistent with the design detail. Deformations could be visually observed on the surface spline nailed connection, the CLT-glulam screw connection and in the hold-down connection. No significant bending and shear deformation of the panels could be visually observed during the test. Thus, the primary energy dissipation mechanism was concluded to be governed by the various mechanical fasteners utilized in the diaphragm setup, with the CLT panels acting as rigid members. The mechanical fasteners also induced ductility to the diaphragm.

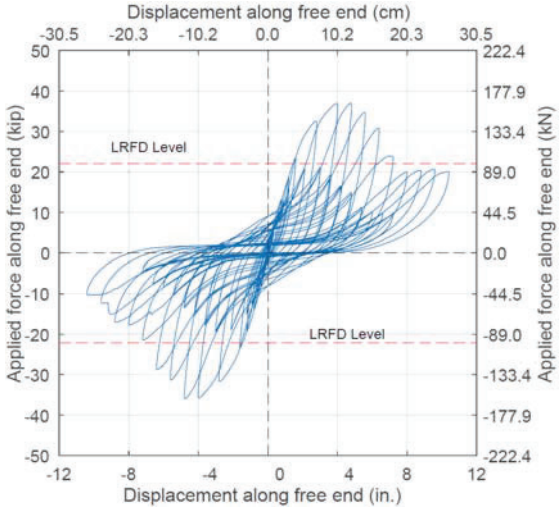

Figure 6: *Force vs displacement hysteresis for the diaphragm test*

Table 2: *Summary of the Diaphragm test*

Design LRFD load	98.3 kN (22.1 kip)
Peak positive load	164.5 kN (37 kip)
Peak positive displacement	11.4 cm (4.47 in.)
Initial stiffness (positive)	22.4 kN/cm (12.8 kip/in.)
Peak negative load	160 kN (36 kip.)
Peak negative displacement	11.2 cm (4.41 in.)
Initial stiffness (negative)	25.6 kN/cm (14.6 kip/in.)
Average peak/LRFD strength	1.7

4.2 DEFLECTIONS AT VARIOUS FORCE LEVELS

Figure 7 and Figure 8 show the contribution of fastener deformation to total diaphragm deflection at various force levels for positive and negative cycles respectively. The force level values in the figures indicate the first time those values were reached during the diaphragm test. The diaphragm level deformations were calculated from the fastener level deformations for nailed surface spline slip (transverse shear fastener), screw slip (longitudinal shear fastener) and slip in the hold-down assembly (anchorage) using the equation 2. The bending and shear deformations which were back calculated by subtracting all other deformations from observed diaphragm deflection. This was done because the test setup did not have sufficient instrumentation to properly isolate contribution due to bending and shear deformations.

Figure 7 and Figure 8 also show the SDPWS based (theoretical) estimates for total bending and shear deformations while Table 3 shows the numerical values.

Table 3: *SDPWS based estimates for bending and shear deformations at various force levels.*

Force level kN (kip)	Bending Def. cm (in.)	Shear Def. cm (in.)
22.2 (5)	0.208 (0.082)	0.107 (0.042)
44.5 (10)	0.417 (0.164)	0.213 (0.084)
70.3 (15.8) - ASD	0.658 (0.259)	0.337 (0.133)
98.3 (22.1) - LRFD	0.921 (0.362)	0.472 (0.186)

https://doi.org/10.52202/069179-0365

The plots suggest that SDPWS based calculation overpredicts the contributions due to bending and shear deformations in a cantilever CLT diaphragm.

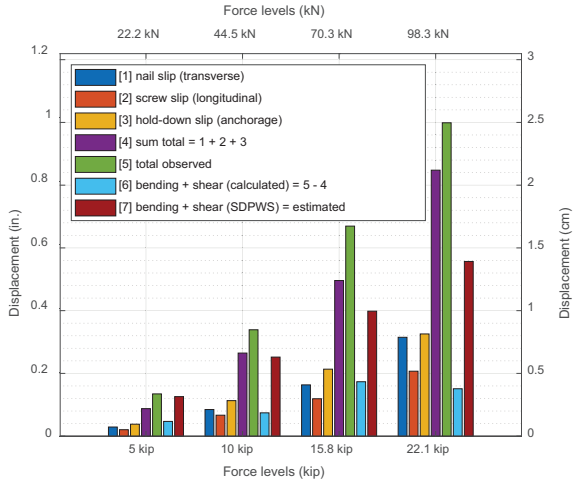

Figure 7: *Contribution of fastener deformation to total diaphragm deformation for positive cycle, ASD = 70.3 kN (15.8 kip), LRFD = 98.3 kN (22.1 kip)*

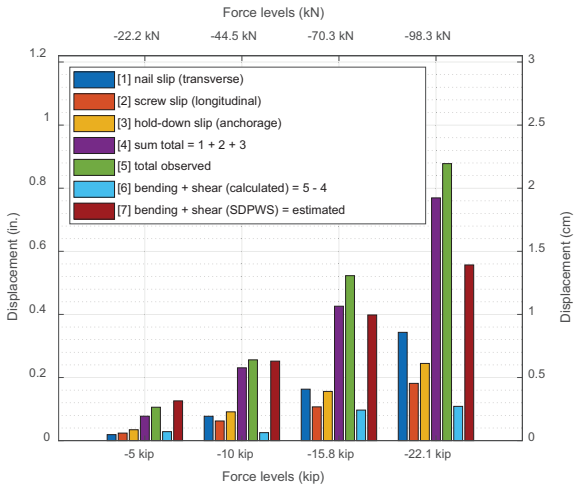

Figure 8: *Contribution of fastener deformation to total diaphragm deformation for negative cycle, ASD = 70.3 kN (15.8 kip), LRFD = 98.3 kN (22.1 kip)*

The back calculated values for bending and shear deformations were 34.8% and 26.8% of the total diaphragm deflections at force level of 22.2 kN (5 kip) for positive and negative cycles respectively. At LRFD level of 98.3 kN (22.1 kip), the back calculated values for bending and shear deformations were 15.1% and 12.4% of the total diaphragm deflection for positive and negative cycles respectively. The bending and shear deformation predicted by SDPWS would have been 93.6% and 119% (i.e., exceed observed diaphragm deflection value) at 22.2 kN (5 kip) for positive and negative cycles respectively. Similarly, bending and shear deformations predicted by SDPWS would have been 55.8% and 63.4% of the total predicted deflection at LRFD level for positive and negative cycles respectively.

The deformations also suggest that the bending and shear deformations were more significant at smaller load levels. It is speculated that as the load levels increased, the bending and shear deformation increased linearly while the other deformations increased non-linearly (at a higher rate), thus leading to lower contribution of bending and shear deformation at higher load levels as the fasteners which have started to deform and yield begin to experience more deflection relative to the CLT panels in bending and shear.

5 CONCLUSIONS

During design, the ratio of deflection in diaphragm to the adjoining components of the VLFRS can be utilized to idealize flexible, rigid or semi rigid diaphragm behaviour which governs the mechanism for force transfer to the vertical elements. The various mechanisms contributing to deflections in cantilever CLT diaphragms were investigated. Observation of deflection data from the test suggested that the equation derived using the in SDPWS equation for CLT shear wall over predicts the contribution of bending and shear deformations. Further experimental testing with instrumentation setup for capturing bending and shear deformations seems necessary to develop equations capable of providing a more accurate prediction for those terms.

ACKNOWLEDGEMENT

The material present in this paper is based on work supported in part by the US Department of Agriculture (USDA) Forest Services and the US Endowment for Forestry and Communities Grant No. E17-96. Any opinions, findings, conclusions, and recommendations presented in this paper are those of the authors and do not necessarily reflect the views of the USDA and the US Endowment for Forestry and Communities. The authors would also like to thank Lancelot Reres, Sovanroth Ou, Harsh Bothra and Jayson Leonard for their help and assistance throughout the project.

REFERENCES

[1] D'Arenzo, G., Casagrande, D., Reynolds, T., & Fossetti, M. (2019). In-plane elastic flexibility of cross laminated timber floor diaphragms. Construction and Building Materials, 209, 709-724. doi: 10.1016/j.conbuildmat.2019.03.060.

[2] Structural Engineering Institute: Minimum design loads for buildings and other structures. ASCE 7, Reston, VA. 2022

[3] American Wood Council: Special Design Provisions for Wind and Seismic, 2021.

[4] American Wood Council: National Design Specification for Wood construction. 2018

[5] Spickler, K., Closen, M., Line, P., and Pohll, M. (2015),. Cross Laminated Timber Horizontal Diaphragm Design Example. Structurlam-CrossLam.

[6] Lawson, J., Breneman, S., & Lo Ricco, M. (2023): Wood Diaphragm Deflections. Part I: Generalizing Standard Equations Using Mechanics-Based

Derivations for Panel Construction. ASCE Journal of Architectural Engineering
[7] Krawinkler, H., Parisi, F., Ibarra, L., Ayoub, A., & Medina, R. (2001): Development of a Testing Protocol for Woodframe Structures. Department of Civil and Environmental Engineering, Stanford University.
[8] Bhardwaj, B., Pang, W., & Stoner, M. (under review). Experimental Characterization of Cantilever Cross-Laminated Timber Diaphragms under In-plane Shear Load. Journal of Structural Engineering.

https://doi.org/10.52202/069179-0365

World Conference on Timber Engineering Oslo 2023

EXPERIMENTAL ANALYSIS OF THE INFLUENCE OF OPENINGS IN THE DEFLECTION OF CROSS-LAMINATED TIMBER PLATES LOADED OUT OF PLANE

Pablo González-Serna[1], Miguel Yurrita[2], José Manuel Cabrero[3]

ABSTRACT:

This paper presents a series of experimental tests that were conducted to investigate the effect of openings on the deformation of cross laminated timber (CLT) floor panels. A comparison is made between the tests results and different FE shell models and simplified beam models developed for prediction. The research aims to provide new design criteria and user-friendly models to enhance the predictability of CLT structures and increase its versatility as a building material.

KEYWORDS: CLT, cross-laminated timber, mass timber, floors, openings, experimental investigation, modelling

1 INTRODUCTION

Cross Laminated Timber (CLT) is increasingly gaining recognition and popularity in the construction industry. This technological timber product combines crosswise oriented layers of timber bonded together by adhesives, resulting in large panels (of maximum sizes around 3m wide and 15 m long) that allow to develop mass prefabricated structures based on timber wall and floor panels. The combination of prefabricated walls and floors enables to a fast erection of many types of constructions, from small structures such as dwellings to very tall buildings. Full size wall and floor panels can be manufactured on demand, and easily installed on site. This includes the possibility to include cut-outs in the panels, such as windows or doors in wall elements. In the case of floors, these openings can be part of staircases, service conduit shafts or skylights.

Knowing the influence of such openings in the mechanical behavior and distribution of forces within the panels is key to seize the capabilities of the material, and design rules and verification methods are in demand among practitioners [1].

1.1 MODELS

Different studies have investigated the influence of openings on CLT shear walls, such as Shanewaz et al. [2], Casagrande et al. [3] and Awad et al. [4]. Stress concentrations around openings on CLT column-slab connections have been studied by Muster [5]. However, there is limited research on the influence of openings on CLT slabs under bending, which is the most usual demand/case.

A simplified approach to predict the behaviour of and verify openings on CLT slabs are grillage models. In this method, the slab geometry is divided into a system of longitudinal and transversal beams that can be analysed independently to determine forces and displacements around holes in the two main directions of the panel. Wallner-Novak et al. [7] describe the application of this method to centered openings in simply-supported longitudinal slabs with uniform distributed load. In this model, a beam width equal to one tenth of the span length is assumed.

Hast and Fatemi [6] compared the results of the grillage model from [7] with finite element models and found that the grillage model provided very conservative results in all cases, and required further adjustments. The possible influence of stress concentrations around the perimeter of the holes was not addressed in the study.

In practice, the most common approach to model CLT are finite element models (FEM) with two-dimensional shell components. This type of model combines Mindlin-Reissner thick plate theory and membrane theory [8], allowing to render axial, bending and shear stiffness, as well as the in-plane and twisting stiffness of panels. All these stiffness components are described by the material stiffness matrix, which can be derived from the orthotropic properties of the different timber layers, through the application of the laminate theory.

[1] Pablo González-Serna, UNAV University of Navarra, Spain, glezsernapablo@gmail.com
[2] Miguel Yurrita, UNAV University of Navarra, Spain, myurrital@alumni.unav.es
[3] José Manuel Cabrero, UNAV University of Navarra, Spain, jcabrero@unav.es

https://doi.org/10.52202/069179-0366

1.2 AIM AND OBJECTIVES

The presented research aims at bringing new insights into the influence of openings in CLT slabs on both ultimate limit state (ULS) and serviceability limit state (SLS), with the goal of making the use of CLT more efficient and user-friendly [9].

This paper, presented in companion with [10], describes a portion of the results obtained from the conducted test campaign, along with a description of the various analytical models utilized to predict the elastic behaviour of the panels. The experimental outcomes are presented and compared with the predictions made by the different models.

2 EXPERIMENTAL TESTS

2.1 TEST CONFIGURATION AND MATERIAL

To study the influence of openings in the behaviour of the panels, two series of panels were tested, one for analyzing the behaviour of the opening under bending and the second under shear, as depicted in Figure 1.

All specimens were made with a similar layup, a 5-layer composition with outers and mid layer in the parallel direction and odd layers crosswise bonded (0º-90º-0º-90º-0º) and a total panel height of 100 mm. Lamellas were made of European spruce (*Picea Abies*) graded as C24 (strength grade according to EN 338 [11], which corresponds to a bending strength of 24 MPa). Lamellas were 20mm thick, 230mm width, and non-edge glued. Individual lamellas with finger joints were fabricated according to EN 14080 [12].

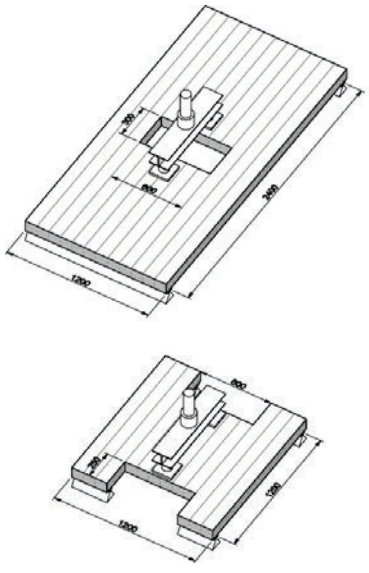

Figure 1: *Bending and shear test series.*

Test configurations were designed based on EN 16351 and EN 408 normalized tests [13]. Panel length, distance between supports and load application distance were set as a proportion of the panel height. Panel width was set to 1200 mm, so that openings of different widths could be tested, and bending in the secondary direction could be activated. Load was applied on two points, to induce bending in the two main directions. Square-shaped pinned pressure plates of 200 mm width were used.

The conducted experimental campaign involved testing full panels (without holes) within the elastic range, followed by testing the same panels with a 300 mm wide opening, also within the elastic range, and finally testing the panels with a 600 mm wide opening until failure. This paper presents the result of the non-destructive tests, which were conducted to evaluate the displacement predictions of different models.

2.1.1 Preliminary tests and material properties

Different material properties were evaluated experimentally before doing the cut-outs on the panels. Density of the panels was measured following the standard EN 408 [13]. The density was corrected to a reference moisture content of 12%, following the procedure of EN 384 [14]. Modulus of elasticity was determined on bending tests on panels without openings, following the test configuration from EN 16351 Annex C [15]. For these tests, a panel width of 1200mm was used. After testing all panels, rolling shear tests were conducted, according to EN 16351 [15] and EN 789 [16]. Rolling shear test specimens, as the one shown in Figure 2, were obtained from the opening cut-outs. Table 1 presents a summary of the obtained results.

Table 1: *Material properties obtained during the preliminary tests.*

Preliminary tests		
Property	Mean value	COV [%]
Density ρ [kg/m^3]	438,40	1,78
Full Cross-Section MOE $E_{CL,net}$ [N/mm^2]	13.578,59	5,53
Effective Shear Modulus G_{eff} [N/mm^2]	554,00	22,62
Longitudinal Shear Modulus G_0 [N/mm^2]	895	-
Rolling Shear Modulus G_R [N/mm^2]	41	19

https://doi.org/10.52202/069179-0366

Figure 2: *Rolling shear test.*

2.1.2 Bending series

Bending series was designed according to the configuration described in the bending test with load perpendicular to the plane from EN 16351 [15]. Distance between supports was set to 2400 mm, and the load application points were separated 600 mm. The overall size of the panels was 2500 x 1200 mm.

Figure 3: *Bending test.*

Openings were cut in the centre of the panel, following a symmetric configuration in the two main directions. Panels were tested within the elastic range. First, without any opening, then with an opening of 300 x 300 mm and lastly with an opening of 300 x 600 mm. Table 2 presents the various opening geometries that were tested on each specimen.

Table 2: *Test iterations on bending series.*

Bending series		
Test iteration	Opening width w_h (mm)	Opening length l_h (mm)
1	0	0
2	300	300
3	600	300

During the three tests, vertical displacement was measured around the opening, under the load application point and at the center of the panel edges, following the pattern illustrated in Figure 4.

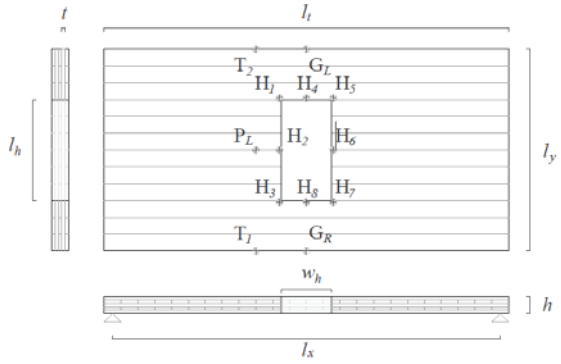

Figure 4: *Measuring points for vertical displacement in bending test series.*

2.1.3 Shear series

Shear series was designed according to the configuration of the bending test for determination of shear strength and stiffness from EN 16351 [15]. The overall size of the panels was 1300 mm long and 1200 mm wide. The distance between supports was set to 1200 mm, and the two load application points were separated 600 mm, the same as in the bending series.

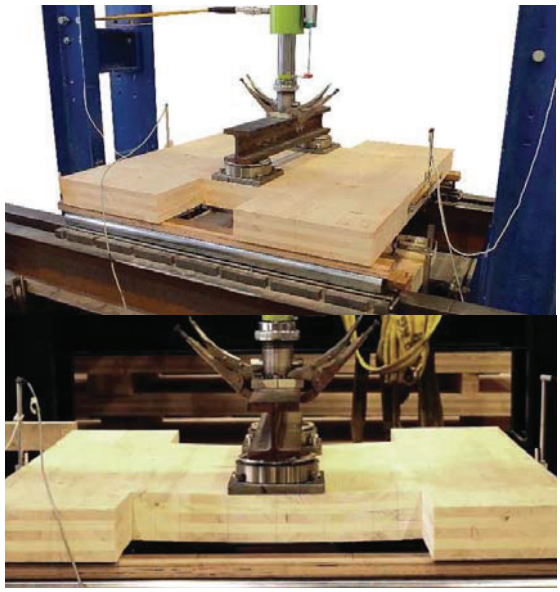

Figure 5: *Shear tests.*

Openings were cut at the supported edges of the panels, following a symmetric configuration in the two main directions. Panels were tested without any opening, then with two openings of 250 x 300 mm and lastly with an opening of 300 x 600 mm.

Table 3: *Test iterations on shear series.*

Shear series		
Test iteration	Opening width w_h (mm)	Opening length l_h (mm)
1	0	0
2	300	250
3	600	250

Vertical displacements were measured around one of the openings, in the central point of the panel, and at the center of the panel edges.

3 MODELS

3.1 ANALYTICAL MODELS

Beam grillage models [7] simplify the analysis by decomposing the floor slab with an opening into a grillage system composed of six beams. Each beam can be analysed independently and later combined with the rest to determine the deflection of the slab. Wallner-Novak et al. [7] describe this system for a rectangular slab with supports in two sides with a central rectangular opening. This method assumes a minimum strip width between the opening and the slab edge of one tenth of the span length l_x must remain.

Since the beam model proposed by Wallner-Novak [7] is for distributed load, a direct comparison with the test results, where point loads were applied, is not possible. Thus, two alternative assumptions have been considered for the validation.

In the first beam model (BM 1) the force is applied as a point load on both transverse beams 3 and 4. The second beam model (BM 2) considers an equivalent uniform distributed load obtained by redistributing the force around the panel surface. The equivalent distributed load is obtained by dividing the reference force F by the surface area of the slab A, as follows:

$$q = \frac{F}{A} = \frac{F}{(l_x l_y) - (l_h w_h)}$$

In both cases, an extra load equal to the self-weight of the panel is considered, obtained from the thickness of the slab h and the density of the panel ρ. The bending stiffness of the beams was assessed with the Modified Gamma Method [17], an adaptation to CLT of the method for composite structural elements included in the Eurocode 5 Annex B [18], originally proposed by Blass and Görlacher [19]. In the herein case of a CLT panel, the rolling shear stiffness of the transverse layers is considered, instead of the stiffness of the connectors. By including the shear influence, the corresponding deformation is increased.

$$(EI)_{ef} = E_{0,mean} \cdot I_{ef,net}$$

$$I_{ef,net} = \sum_{i=1}^{n} (I_i + \gamma_i \cdot A_i \cdot a_i^2)$$

The scheme of the load application and distribution in the two models is given in Figure 6.

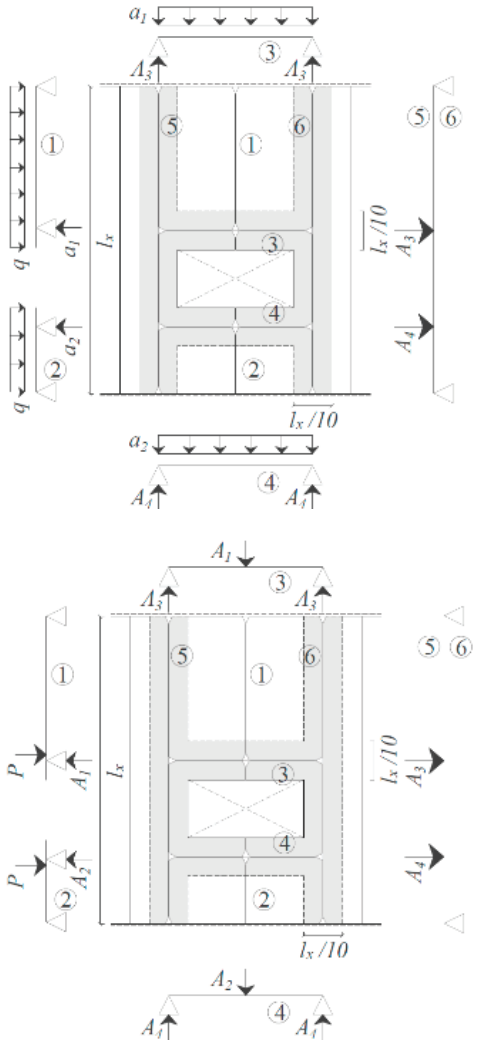

Figure 6: *Load application in beam model with distributed load (top) and beam model with punctual load (bottom).*

In the beam models with distributed load (BM 2), the force was applied to the transverse beams 3 and 4 as a distributed load equal to the reaction force of beams 1 and 2. Longitudinal beams 5 and 6 included both a distributed load and the reaction forces of the transverse beams. In the models with punctual load (BM 1), beams 1 and 2 were neglected, and the load was directly applied to the transverse beams 3 and 4 as punctual forces at their centers, and transferred to beams 5 and 6 as reaction forces. Both models assumed pinned beams. Additionally, to adapt the model with distributed load to the shear series, beams 1 and 2 were replaced by a single loaded beam connecting the center of beams 3 and 4.

https://doi.org/10.52202/069179-0366

3.2 FINITE ELEMENT MODELS

Linear finite element (FE) analyses have been performed using the software RFEM DLUBAL [20]. A parametric study has been carried, analyzing configurations with different opening widths, from 0 to 900 mm with steps of 100 mm.

The FE models were made with 2D shell elements, with stiffness matrix components derived from the individual layer properties according to the lamination theory [8]. Layers were modelled as non-edge glued by neglecting the stiffness in the transverse direction (E_y=0). Correction factors were applied to the torsional and membrane stiffness of the shell elements, according to Austrian National Annex of the Eurocode 5 [21]. The reduction factors for torsional stiffness D_{33} and membrane stiffness D_{88} were set to 0,59 and 0,68 respectively.

A quadrangular mesh with a density of 50 mm was implemented, so that there were always at least 4 elements within the width of the edge of the opening. Displacements were measured at the same points as the recorded displacement in the experimental tests and correspond also to the calculated points in the beam grillage model .

A first set of models (FE 1) was created using the mechanical properties declared in the ETA-06/0138 [22]. In the second set (FE 2) the material model was defined from the properties obtained experimentally in the peliminary tests. The FE models are shown in Figure 7.

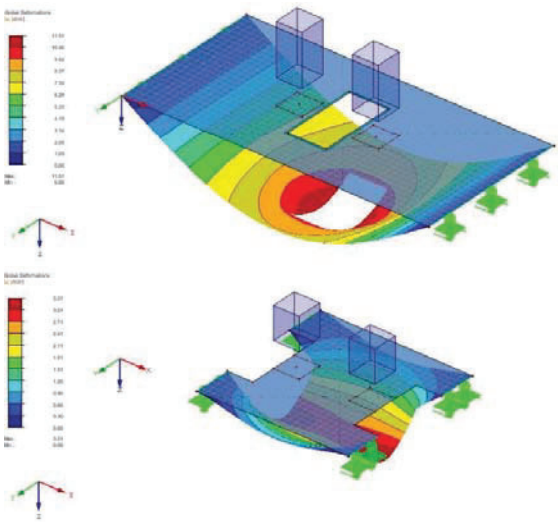

Figure 7: *FE models: bending series (top) and shear series (bottom).*

4 RESULTS AND DISCUSSION

The following graphs show a comparison of displacements from the tests, the FE models and the beam models. The displacement of three representative points is studied, whose location is based on those easily obtained from the beam models. These points are (A) the center of Beam 3, (B) center of Beam 5, and (C) the point where Beam 3 is supported by Beam 5. Points are shown in the diagrams in Figure 6. These points were directly studied on the FE models. However, in the case of the test results, some adjustments were required to do the comparison, since the measuring points were fixed for the three openings studied.

The comparison of the test results and the four cases derived from the analytical models is plotted for bending and shear specimens, respectively. The displacements for the three already described points are plotted separately: the center of Beam 3 (A) is presented in Figure 8 and Figure 11, the center of Beam 5 (B) is studied in Figure 9 and Figure 12, and the support of Beam 3 (C) is given in Figure 10 and Figure 13.

In all the graphs, the abscissas axis accounts for the width of the hole(s) of the slab, while the ordinates axis displays the displacement of the corresponding point. The results of the tests, which consider three cases of holes of widths 0, 300 and 600 mm, are plotted as single values. The behaviour of each of the four models is plotted with curves that consider an opening width range between 0 and 900 mm (when possible), and therefore allow to observe the trend in the response of each case.

The performance of the models clearly differs when considering bending or shear tests. The accuracy of the models is much higher in the bending series, while the displacements predicted for the shear cases are generally lower than the experimental results. It can also be clearly seen that, in all the graphs, the influence of the hole's width is not linear. This trend is reflected in the test results, the FE curves, and the beam models with distributed loads (BM 2). However, the beam model with point loads (BM 1) sometimes exhibits a linear behavior, as noticed for the case of support of beam 3, and in beam 5, for both bending and shear tests. This is due to the assumption of pinned beams, resulting in consistent reaction forces from beams 3 and 4 to beams 5 and 6 being in all hole width scenarios. Despite that, this model tends to predict higher deformations, leading to a more conservative model. No big difference is found between the FE models when considering different material properties.

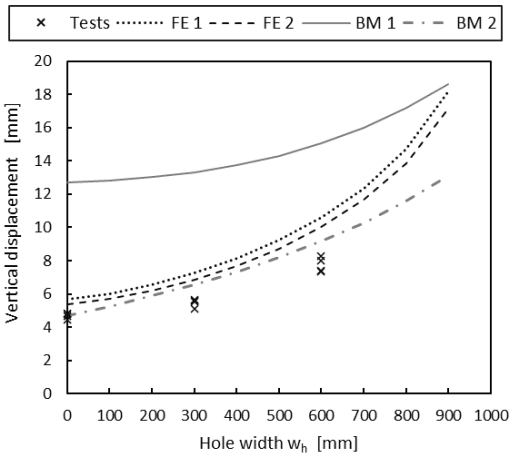

Figure 8: *Bending series. Displacements at reference point A (center of Beam 3).*

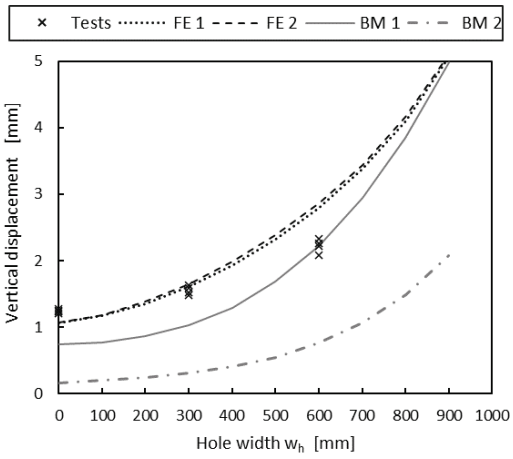

Figure 11: *Shear series. Displacement at reference point A (center of Beam 3).*

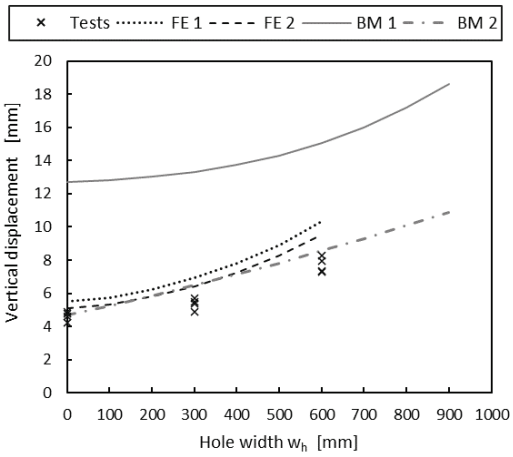

Figure 9: *Bending series. Displacement at reference point B (center of Beam 5).*

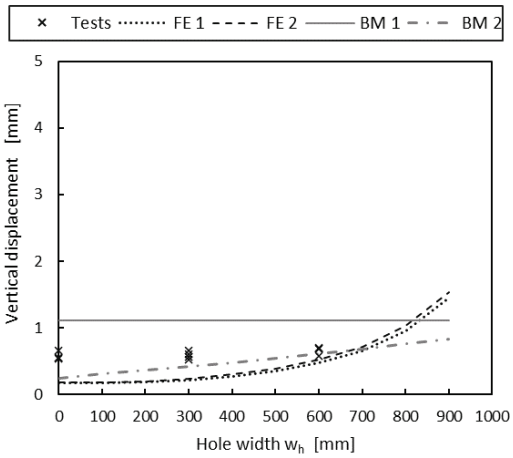

Figure 12: *Shear series. Displacement at reference point B (center of Beam 5).*

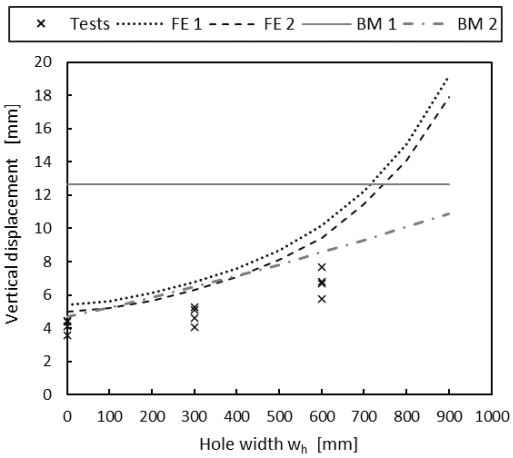

Figure 10: *Bending series. Displacement at reference point C (support of Beam 3).*

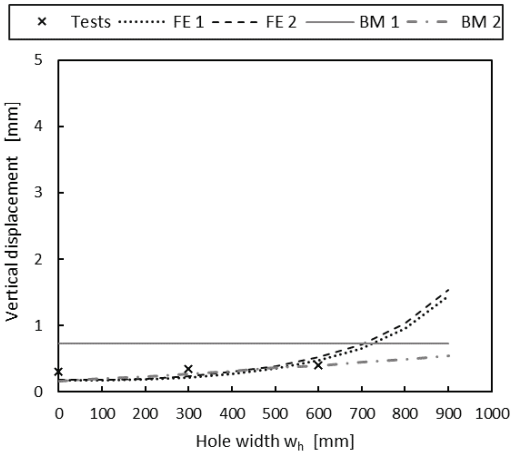

Figure 13: *Shear series. Displacement at reference point C (support of Beam 3).*

https://doi.org/10.52202/069179-0366

5 ACKNOWLEDGEMENTS

Project InnoCrossLam is supported under the umbrella of ERA-NET Cofund ForestValue by MIZŠ, VINNOVA, FORMAS, STEM, BMLFUW, FNR and MINECO-AEI and has received funding from the European Union's Horizon 2020 research and innovation programme under grant agreement N° 773324.

The financial support provided by the Spanish Ministerio de Ciencia, Innovación y Universidades – Agencia Estatal de Investigación under contract PCI2019-103591 AEI and by Fachagentur Nachwachsende Rohstoffe e. V. (FNR) of the German Federal Ministry of Food and Agriculture (BMEL) is gratefully acknowledged.

Special thanks to the staff from Technical University of Munich and their laboratories for the invitation to use their facilities and the personal support. Also, to KLH Massivholz GmbH for supporting the research with test specimens.

REFERENCES

[1] Schenk M., Hübner C., Cabrero J.M.: Cross-laminated timber: A survey on design methods and concepts in practice. CivilEng 3, 610-629, 2022. Doi:10.3390/civileng3030036.

[2] Shahnewaz M., Tannert T., Alam M. S., Popovski M.: In-plane stiffness of cross laminated timber panels with openings. Structural Engineering International 27, 2017, pp. 217-223. Doi:10.2749/101686617Z14881932436131.

[3] Casagrande D., Fanti R., Doudak G., Polastri A.: Experimental and numerical study on the mechanical behaviour of CLT shear walls with openings. Construction and Building Materials 298, 2021, 123858. Doi:10.1016/j.conbuildmat.2021.123858.469.

[4] Awad V., Giresini L., Koshihara M., Puppio M. L., Sassu M.: Experimental analyses and numerical models of CLT shear walls under cyclic loading. Wood in Civil Engineering, IntechOpen, 2017, pp. 223-240. Doi:10.5772/65024.

[5] Muster M.: Column-Slab Connection in Timber Flat Slabs. Doctoral thesis. Swiss Federal Institute of Technology in Zurich (ETH Zurich), 2020.

[6] Hast C., Fatemi D.: Behaviour of cross laminated timber elements with openings at out-of-plane loading conditions. Master Thesis. Lund University, Sweden, 2020.

[7] Wallner-Novak M., Augustin M., Koppelhuber J. Pock K.: Cross-Laminated Timber Structural Design Volume 2. proHolz. Austria, 2017.

[8] Dlubal Software GmbH.: Add-on Module RF-Laminate – Design of Laminate Surfaces – Program Description. Tiefenbach, Germany, 2016.

[9] Azinović B. et al.: InnoCrossLam – adding knowledge towards increased use of cross laminated timber (CLT). In: World Conference on Timber Engineering (WCTE), Oslo, Norway, 2023.

[10] Schenk M., Husel A., Winter S.: Cross-laminated timber floors with openings – Serviceability verifications. In: World Conference on Timber Engineering (WCTE), Oslo, Norway, 2023.

[11] EN 338: Structural timber – Strength classes. Comité Européen de Normalisation (CEN), Brussels, Belgium, 2016.

[12] EN 14080: Timber structures – Glued laminated timber and glued solid timber – Requirements. Comité Européen de Normalisation (CEN), Brussels, Belgium, 2006.

[13] EN 408: Timber structures - Structural timber and glued laminated timber - Determination of some physical and mechanical properties; + AC:2019. Comité Européen de Normalisation (CEN), Brussels, Belgium, 2019.

[14] EN 384: Structural timber – Determination of characteristic values of mechanical properties and density. Comité Européen de Normalisation (CEN), Brussels, Belgium, 2016.

[15] EN 16351: Timber structures - Cross laminated timber - Requirements + AC:2017. Comité Européen de Normalisation (CEN), Brussels, Belgium, 2017.

[16] EN 789: Timber structures – Test methods – Determination of mechanical properties of wood based panels. Comité Européen de Normalisation (CEN), Brussels, Belgium, 2006.

[17] Bogensperger T., Silly G., Schickhofer G.: Comparison of methods of approximateverification procedures for Cross Laminated Timber. Holz.bau forschuungs gmbh, Institute for Timber Engineering and Wood Technology. Graz, Austria, 2012.

[18] EN 1995-1-1:2004 Eurocode 5: Design of timber structures – Part 1-1: General – Common rules and rules for buildings. Comité Européen de Normalisation (CEN), Brussels, Belgium, 2014.

[19] Blass H., Görlacher R.: Bemessung im holzbau – brettsperrholz. Berechnungsgrundlagen, Holzbaukalender, 2003, pp. 1-6.

[20] Dlubal Software GmbH.: RFEM 5 User Manual. Tiefenbach, Germany, 2020.

[21] ÖNORM B 1995-1-1:2019-06: Eurocode 5: Design of timber structures – Part 1-1: General – Common rules and rules for buildings. – Consolidated version with national specifications, national comments and national supplements for the implementation of ÖNORM EN 1995-1-1.

[22] ETA-06/0138 based on EAD 130005-00-0304: Solid wood slab element to be used as a structural element in buildings. Österreichisches Institut für Bautechnik (OIB). Vienna, Austria, 2021.

World Conference on Timber Engineering Oslo 2023

PHENOMENOLOGICAL MODEL FOR SEISMIC DESIGN OF MULTI-STOREY CLT BUILDINGS: CALIBRATION OF INPUT PARAMETERS

Luca Pozza[1], Stefano Pacchioli[2], Andrea Polastri[3] , Valentino Nicolussi[4], Diego A. Talledo[5], Ian Smith[6]

ABSTRACT: A numerical modelling approach for the prediction of the seismic response of multi-storey CLT buildings is proposed. The approach is based on a simplified phenomenological model where the behaviour of the CLT system is reproduced by means of an equivalent elastic modulus assigned to the CLT wall in order to account for both the connections and panel deformability. Phenomenological modelling aims to reproduce faithfully the global response of the structural system in terms of principal elastic period, internal forces in the connection elements and inter-storey drifts. Results of a multy-parametric analyses carried out on different CLT walls, deigned considering increasing level of seismic intensity, are presented and discussed. A design abacus that allows designers for a direct implementation of the proposed phenomenological model and therefore an easy and efficient seismic analysis of a CLT building is finally proposed.

KEYWORDS: Cross-Laminated Timber, CLT building, numerical model, phenomenological modelling approach, seismic design, Timber structures

1 INTRODUCTION

Cross-laminated timber (CLT) is a material suitable to realize multi-storey earthquake-resistant buildings, characterized by timber lightness and by high in-plane strength and stiffness of the massive cross-laminated panel. For these reasons and due to simplicity and rapid execution, CLT buildings have become increasingly common over the last few years [1-2]. However, how to model the CLT buildings, especially under seismic actions, is still an open issue. Several researches study CLT panels mechanical behaviour under cyclic and seismic actions [3-4]; another important discussed topic is related to the panels assembling [5-9] and the presence of openings [10-11]. Connection characterization is a crucial aspect in order to obtain proper input data for the numerical models [12-13]. Results of the different modelling approaches available in literature demonstrate to be quite heterogeneous and do not allow to draw reliable outcomes especially for the case of linear analyses of buildings. Two main modelling approaches are typically adopted in literature for linear analyses of CLT buildings: the first one is a *component model* (*CM*), which adopts elastic springs for connections and elastic elements for the CLT panel generally represented as a lattice grid or as a 2D continuum, while the second one is a simplified *phenomenological model* (*PM*), where the behaviour of the system is reproduced by means of a conventional equivalent elastic stiffness assigned to the CLT wall and capable of accounting for the deformability of the CLT panel and connections assembly [14]. *CM* is typically adopted in the research field and involves a high computational effort since each component of the CLT system must be modelled and properly calibrated. After proper calibration, CM allows to account for the tension-shear behaviour of the connection elements [15-16]. Differently, the *PM* is easier and faster to use respect to the *CM* and is typically adopted by practitioners since commercial software permits to implement the letter straightforward. The aim of the present work is to suitably calibrate the equivalent stiffness that has to be assigned to CLT panels in a *PM* in order to reproduce the seismic behaviour of the entire CLT building. To provide reliable estimation of the equivalent stiffness for the *PM*, different case study configurations have been analysed varying the significant parameters controlling the building response such as number of storeys, connection pattern, geometry, wall slenderness. Results of the performed analyses are used to propose a design abacus that permits an easy implementation of a phenomenological models of a real CLT building by practitioners.

[1] Luca Pozza, DICAM - Structural Engineering, University of Bologna, Italy, luca.pozza2@unibo.it

[2] Stefano Pacchioli, STP Company – Predaia (TN), Italy, stefano.pacchioli@alpenos.it

[3] Andrea Polastri, Institute for Bioeconomy - National Research Council of Italy (CNR-IBE), Italy, andrea.polastri@ibe.cnr.it

[4] Valentino Nicolussi, Institute for Bioeconomy - National Research Council of Italy (CNR-IBE) & DICAM, University of Bologna, Italy, valentino.nicolussi@studio.unibo.it

[5] Diego A. Talledo, IUAV University – Venice, Italy, diego.talledo@iuav.it

[6] Ian Smith, Professor Emeritus, UNB, Canada, ismith@unb.ca

https://doi.org/10.52202/069179-0367

2 CALIBRATION PROCEDURE

Numerical response spectrum analyses have been conducted, comparing results of *CM* and *PM* in order to calibrate the correct equivalent stiffness (E_{eq}) to be assigned to CLT panels in the simplified phenomenological approach (Figure 1). Component-level (CM) modelling approach requires the calibration of constitutive laws for each component (CLT and connections) [17]. In detail CLT panels are modelled as an isotropic material (modulus of elasticity given by the weighted mean values of modulus in the parallel and perpendicular direction to the grain [18]) while connections are implemented as elastic springs (stiffness obtained from experimental tests).The PM modelling approach, at the opposite, disregards the contribution to the structural response given by each component of the system. Connection elements are not directly included in FE model and CLT panels are modelled assigning an equivalent elastic stiffness (i.e. modulus of elasticity) able to account for the deformability contributions of the connections and the panel itself.
In this work the equivalent elastic stiffness to be assigned to different configuration of CLT panels of the *PM* has been calibrated with an iterative procedure. In particular it was minimized an objective function which accounts for the difference between the value of certain control parameters (e.g. principal vibration period T_1, top displacement, inter-storey drift etc..) obtained with the *CM* and those obtained with the correspondent *PM* for the different building configurations.

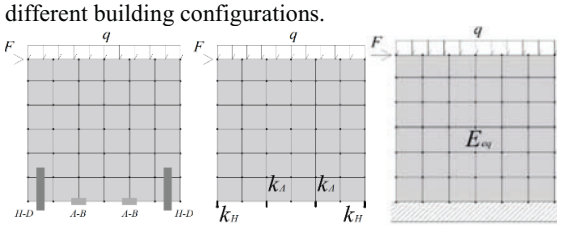

Figure 1: *Real configuration (left) component-level approach (centre) and phenomenological approach (right)*

A multi-parametric analysis was performed and an ad-hoc iterative procedure was implemented in order to provide a reliable definition of the equivalent modulus of elasticity (E_{eq}) to use in the modelling phase.
The iterative procedure starts selecting a certain shear-wall configuration characterized from a given geometry (length, height and thickness of the walls) and a given seismic mass and seismic intensity. The numerical-based approach consists in the iterative calibration procedure described below and schematized in Figure 2.

STEP 1 - definition of the connection pattern necessary to satisfying the different shear-walls configuration in terms of strength and deformability requirement;

STEP 2 - implementation of CM according to Polastri and Pozza [19]. Execution of the linear dynamic analysis to define the values of key parameters to be used for the subsequent calibration of the PM: principal vibration period (T_1^{CM}), base shear (V^{CM}), top displacement (δ^{CM}) and inter-storey drifts ($drift^{CM}$).

STEP 3 - consisted in the setting of the equivalent E_{eq} modulus of the CLT walls at each floor. It has been done thanks an implementation of PM performed with a linear dynamic analysis. The parameters taking into consideration in this analysis are: principal vibration period (T_1^{PM}), base shear (V^{PM}), top displacement (δ^{PM}) and nter-storey drifts ($drift^{PM}$).

ITERATIVE STEP - in the end the goal of this iterative calibration is the evaluating of equivalent modulus of elasticity (E_{eq}) in order to minimize the difference between the selected control parameters ($\Delta_j = Xj^{CM} - X_j^{PM}$). The iterative procedure ended when the comparison is acceptable ($\Delta_j < \Delta_{j\_LIMIT}$) providing a reliable estimation of the equivalent elastic module E_{eq} to be used in the phenomenological approach.

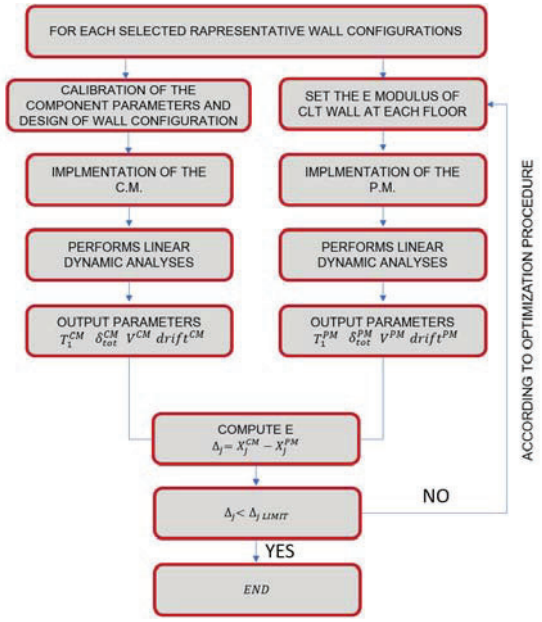

Figure 2: *Scheme of the conceptual iterative procedure for calibration of Eeq.*

The proposed methodology permit to overcome the inaccurate way of the behaviour evaluation of a simplified PM approach giving to a practitioner an extremely easier procedure of modelling thanks a calibration of a E_{eq} suitable for linear seismic analysis.

3 MULTI-PARAMETRIC FE ANALYSES

Numerical models of CLT walls were created using SAP2000 [20] Finite element code, Figure 3. A multi-parametric analysis was conducted considering the following variables: number of floors (3-5-7), base length of CLT panels (L=2,0m; 4,0m; 6,0 m), inter-storey height (assumed equal to 3m), seismic zone and seismic mass. All CLT wall configurations were modelled in 2-D

https://doi.org/10.52202/069179-0367

according to both a component-level approach and a phenomenological approach.

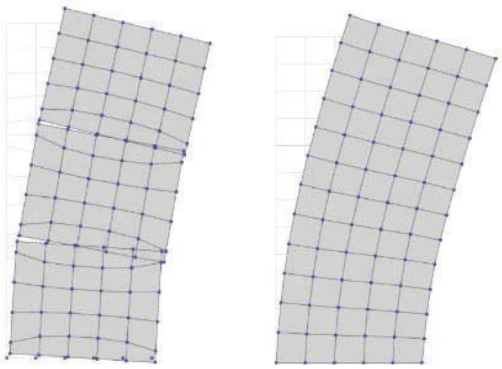

Figure 3: *Example of 3 storeys CLT wall implemented with CM (left) and PM (right)*

The earthquake action was calculated according to Eurocode 8 [9], using design spectra obtained with C soil type, a force modification factor q equal to 1.6. Two increasing levels of seismic intensity have been considered, respectively represented by PGA=0,25g (Low PGA) and 0,35g (High PGA).

Table 1 reports, for each considered configuration, the seismic mass on the wall at different floors.

Table 1: *Seismic mass at each level for each configuration.*

	L=2m		*L=4m*		*L=6m*	
Level	*High Mass* [t]	*Low Mass* [t]	*High Mass* [t]	*Low Mass* [t]	*High Mass* [t]	*Low Mass* [t]
Intermediate floors	3,8	5,6	7,6	11,3	11,4	16,9
Roof floor	1,9	2,8	3,8	5,65	5,7	8,45

Considering the two mass levels and the two seismic zones, a total of 32 different configurations were analysed.
Different pattern of connection specifically designed with regard to both resistance and deformability limit states characterized the different studied configurations. In the design the following connections were considered: WHT340-WHT620 and TTF200-TCF200, Hold-Down and Angle Bracket connection type, respectively. Table 2 reports the mechanical characteristics of the connections in terms of strength and stiffness. It is worth nothing that, for increasing number of storeys and for increasing level of seismic intensity it is necessary to use a larger the number of connectors in order to verify the structure.

Table 2*: Strength and stiffness of metal connection used in the analysis.*

Metal connector	WHT340	WHT620	TTF200	TCF200
Elastic siffness (kN/mm)	5,70	13,25	8,21	8,48
Design force (kN)	46,20	93,70	39,10	39,10

CLT panels were modelled with iso-parametric four-node quadrilateral membrane F.E. in both modelling approaches. In component-level approach (CM) the adopted values for elastic parameters, E=6600 MPa, v=0,35, were given by the weighted mean values of modulus in the parallel and perpendicular direction to the grain [8]. Connection elements (Hold-Down and Angle bracket) were modelled as linear elastic springs with stiffness derived from available experimental tests [ref]. In the *PM*, elastic stiffness of CLT walls was iteratively varied (i.e. reduced respect to the one used for the *CM*) in order to fit the global behaviour obtained with the *CM* by minimizing an objective function including the following control parameters: first vibration period T_1, top displacement, inter-storey drift and base shear force.

4 RESULTS AND DISCUSSION

Results obtained from the CM approach for all the considered configurations are presented in terms of fundamental elastic period (T_1), peak base shear forces at the Ultimate Limit State (ULS), maximum inter-story drift and top displacements at the Serviceability Limit State (SLS). These results are used as reference values for the calibration of the PM according to the proposed calibration procedure.

Figure 4 depicts the peak base shear forces on angle brackets at the ULS for each configuration. It is possible to observe how in several configurations, as the number of floors increases, the shear forces at the base varies slightly.

Figure 5 reports for all the examined shear-wall configurations the values of the principal elastic period. It is possible to observe how wall configurations with short walls and with a connections pattern related to low PGA, have high principal elastic periods T_1. Another parameter that greatly influences the period is represented by the slenderness of the wall. In fact, walls with high slenderness show greater periods of vibration than walls with less slenderness.

Figure 6 shows how an increase in the height of the building leads to high top displacements. For this reason the design requires the use of multiple Hold-Downs (more than two Hold Downs placed one-near-to the other at a corner of a CLT panel)in order to stiffen the structure and to reduce lateral displacements and inter-storey drifts (Figure 7).

Results assessed using the CM approach, on parametric wall configurations (results reported from Figure 4 to Figure 7), have been used in order to calibrate a set of E_{eq} following the optimization procedure previously described. The maximum errors on the significant control parameters ($\Delta_j=X_j^{CM}-X_j^{PM}$), obtained from the iterative procedure, are always lower than 5% confirming the effectiveness of the obtained equivalent modules E_{eq}.

https://doi.org/10.52202/069179-0367

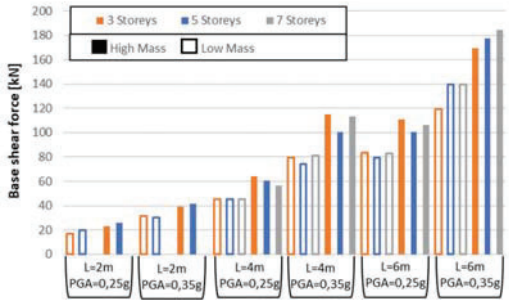

Figure 4: *Base shear force for each configuration*

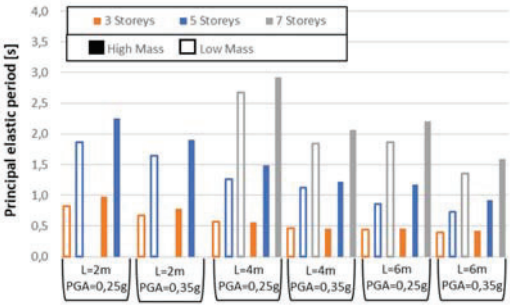

Figure 5: *Principal elastic period T1 for each configuration*

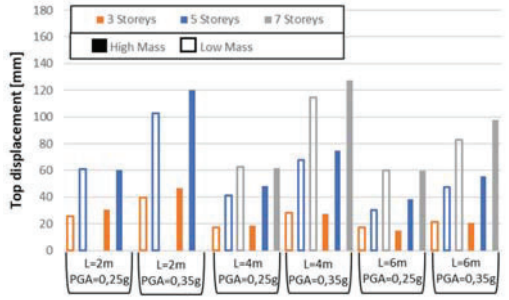

Figure 6: *Top displacement for each configuration*

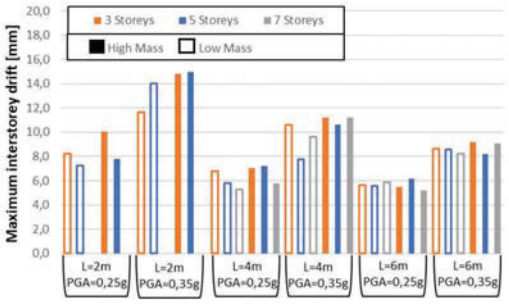

Figure 7: *Maximum inter-storey drift for each configuration*

Results were processed to define the suitable equivalent E modulus (E_{eq}) of the CLT wall as a function of: building geometry, seismic mass and seismic intensity. Obtained equivalent E modulus values (times the wall thickness), to be assigned to the wall of first floor (E_1) in case of a 3-storey building, are reported in Figure 8.

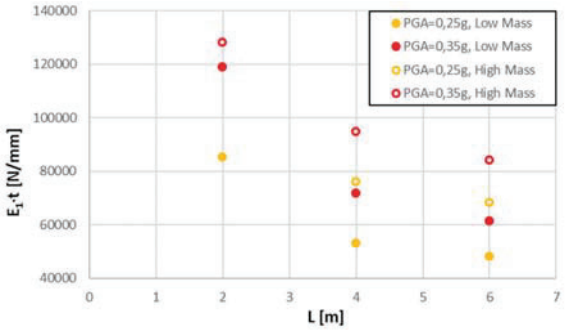

Figure 8: *Example of equivalent module to be assigned to the wall of first floor (E_1) for 3 storeys CLT structure*

A preliminary analysis of the results demonstrates the possibility to adopt a linear correlation between the equivalent stiffness of the wall at the level zero ($E_{eq,0}$) and the geometric proprieties of the shear-wall in terms of slenderness (λ) that is defined as the ratio between the height (H) and the base length (L) of the wall λ=H/L. The aforementioned linear correlation, for the two previously defined level of mass and level of seismic intensity considered in the parametric study, is shown in Figure 9.

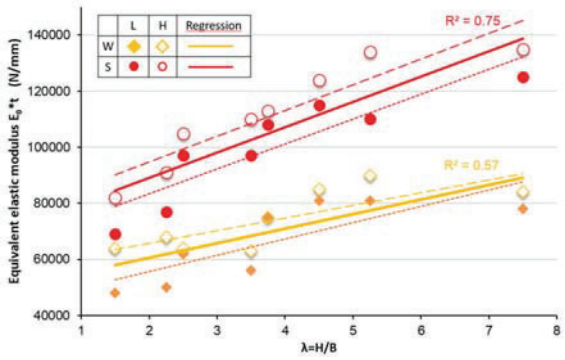

Figure 9*: Correlation between equivalent elastic modulus E_0 and slenderness of wall for different PGA, for different level of mass (Low: dotted lines and High: dashed lines) and level of seismic intensity (Weak: orange lines and Strong: red lines)*

The equivalent stiffness E_{eq0} assign to the wall of the level zero increases as the slenderness increases and is define as:

$$E_{eq0} \cdot t = a \cdot \lambda + b \quad (1)$$

Where: a=9044 and b=70987 for strong seismicity (continuous red line of Figure 8) while a=5184 and b=50325 for weak seismicity (continuous orange line of Figure 8). Based on the obtained results, the following function is proposed to correlate the Elastic module at the base level E_{eq0} and the elastic module at the i-th level $E_{eq,i}$.:

$$E_{eq,i} = E_{eq0}(1 - 0{,}31 \cdot n^{0.12}) \quad (2)$$

Where: n represent the floor number.

https://doi.org/10.52202/069179-0367

Figure 10 reports the mean and predicted values of equivalent stiffness of the upper floors ($E_{eq,i}$) scaled with respect to those of the ground floor ($E_{eq,0}$), at each level in case of a 3-storey building. It is possible to notice a knee adjustment in the stiffness values that can precisely predicted thanks to Equation 2.

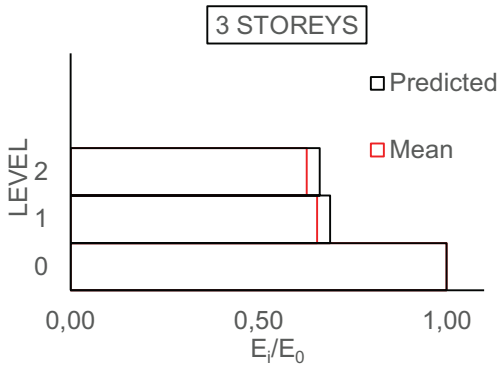

Figure 10*: Equivalent stiffness trend and prediction for 3 storey's structures.*

5 CONCLUSIONS

This study proposes a design-oriented numerical modelling approach for the prediction of the seismic response of multi-storey CLT buildings. It was proposed with the aim of faithfully reproduce the seismic behaviour of multi-storey CLT wall systems. The originality of the proposed phenomenological approach was the adoption of a properly calibrated wall equivalent stiffness accounting for both connections and panel deformability resulting in a real alternative to the more complex component modelling approach.
Results of the multi-parametric analyses and of the calibration procedure allowed the definition of a design abacus useful for a direct implementation of the phenomenological model in the analyses and design of a CLT building.

6 ACKNOWLEDGEMENTS

The Authors would like also to thank the company STP Srl for the support. A special thank goes to Lucia Bettelli for her help in the running of numerical analyses.

REFERENCES

[1] Ceccotti, A., (2008). New technologies for construction of medium-rise buildings in seismic regions: the XLAM case. Structural Engineering International, 18(2), 156-165.

[2] Ceccotti, A., Sandhaas, C., Okabe, M., Yasumura, M., Minowa, C. and Kawai, N. (2013). SOFIE project – 3D shaking table test on a seven-storey full-scale cross-laminated timber building. Earthquake EngStruct. Dyn., 42: 2003-2021.

[3] Pozza, L., Scotta, R., Trutalli, D., Polastri, A. and Smith, I., (2016) Experimentally based q-factor estimation of cross-laminated timber walls. Proceedings of the Institution of Civil Engineers-Structures and Buildings, 169(7), pp. 492–507.

[4] Pozza, L., Savoia, M., Franco, L., Saetta, A., Talledo, D., (2017). Effect of different modelling approaches on the prediction of the seismic response of multi-storey CLT buildings. Int. J. Comp. Meth. and Exp. Meas.

[5] Pozza, L. and Scotta, R., Influence of wall assembly on behaviour of cross-laminated timber buildings. Proceedings of the Institution of Civil Engineers - Structures and Buildings, 168(4), pp. 275–286.

[6] Pacchioli S., Pozza L., Trutalli D., Polastri A., (2021). Earthquake-resistant CLT buildings stiffened with vertical steel ties. Journal of Building Engineering.

[7] Polastri, A., Izzi, M., Pozza, L., Loss, C., Smith, I. Seismic analysis of multi-storey timber buildings braced with a CLT core and perimeter shear-walls. Bull Earthq Eng 2019;17:1009–28. doi:10.1007/s10518-018-0467-9.

[8] Loss, C., Pacchioli, S., Polastri, A., Casagrande, D., Pozza, L. and Smith, I., (2018) Numerical study of alternative seismic-resisting system for CLT buildings. Buildings 2018, 8, 162.

[9] Casagrande, D., Doudak, G., Vettori, M., Fanti, R., (2021), Proposal for an equivalent frame model for the analysis of multi-storey monolithic CLT shearwalls; Engineering Structures, 2021, 245, 112894

[10] Mestar, M., Doudak, G., Caola, M., Casagrande, D., (2020) Equivalent-frame model for elastic behaviour of cross-laminated timber walls with openings; Proceedings of the Institution of Civil Engineers: Structures and Buildings, 2020, 173(5),

[11] Mestar, M., Doudak, G., Polastri, A., Casagrande, D., (2021), Investigating the kinematic modes of CLT shear-walls with openings; Engineering Structures, 2021, 228, 111475

[12] Gavric, I., Fragiacomo, M., Ceccotti, A., (2015) Cyclic behaviour of typical metal connectors for cross-laminated (CLT) structures. Materials and Structures (2015) 48:1841-1857.

[13] Talledo, D., Pozza, L., Saetta, A. and Savoia, M., Coupled shear-tension numerical model for modelling of CLT connections. WCTE 2016, Vienna, Austria, 2016.

[14] Polastri, A., Giongo, I., Angeli, A., Brandner, R. (2018) Mechanical characterization of a pre-fabricated connection system for Cross Laminated Timber structures in seismic regions. Eng Struct 167:705–715.

[15] Pozza, L., Massari, M., Ferracuti, B., and Savoia, M., (2016) Experimental campaign of mechanical CLT connections subjected to a combination of shear and tension forces. Structures and Architecture Beyond their Limits, Edited by Paulo J. da Sousa Cruz, CRC Press, pp. 110–118.

https://doi.org/10.52202/069179-0367

[16] Rinaldin, G., Amadio, C., andFragiacomo, M., (2013) A component approach for the hysteretic behaviour of connections in cross-laminated wooden structures. Earthquake Engineeringand Structural Dynamics, 42(13), pp. 2023–2042, 2013.

[17] Dujic, B., Strus, K., Zarnic, R. and Ceccotti, A., (2010) Prediction of dynamic response of a 7-storey massive X-lam wooden building tested on a shaking table. Proceedings of World Conference on Timber Engineering (WCTE), Riva del Garda, Italy.

[18] Pei, S., van de Lindt, J.W. and Popovski, M. Approximate R-factor for cross-laminated timber walls in multistory buildings. Journal of Architectural Engineering, 19(4), pp. 245–255.

[19] Polastri, A. and Pozza, L., Proposal for a standardized design and modeling procedure of tall CLT buildings. International Journal for Quality Research, 10(3), pp. 607–624.

[20] Computers and Structures I. SAP2000 v20 2018.

[21] CEN European Committee for Standardization. (2009) Design of timber structures—Part 1-1: General—Common rules and rules for buildings. Eurocode 5, CEN, Brussels, Belgium, 2009.

World Conference on Timber Engineering Oslo 2023

AN ACCURATE FINITE ELEMENT MODEL TO STUDY THE PROGRESSIVE COLLAPSE OF POST-AND-BEAM MASS TIMBER BUILDINGS

Chunhao Lyu[1], Benoit P. Gilbert[2], Hong Guan[3], Hassan Karampour[4], Shanmuganathan Gunalan[5], William Leggate[6]

ABSTRACT: The structural behaviour of mass timber buildings under the removal of a load bearing element is complex. To well understand this phenomenon and ultimately develop scientifically based design guidelines against progressive collapse for this type of buildings, there is a need to develop Finite Element models which accurately capture the non-linear structural responses of such buildings. This paper presents how mass timber post-and-beam systems can be accurately modelled using Finite Element under edge and corner column removal scenarios. The model was validated against published 3D experimental tests performed on scaled-down substructures. Results show that the model accurately replicated non-linear behaviour, load redistribution mechanisms, ultimate loads, failure modes, and strain developments. The use of the model was then illustrated by running parametric studies to quantify (i) the influence of the Cross Laminated Timber (CLT) floor panels layout and (ii) one alternative load path, typically ignored in design, on the progressive collapse resistance capacity.

KEYWORDS: Numerical simulations, Finite element, Mass timber post-and-beam buildings, Progressive collapse, Disproportionate collapse, Floor CLT panels layout

1 INTRODUCTION

Progressive collapses of buildings are triggered by abnormal loads, such as explosions, vehicle impacts, construction and design errors, fire and natural disasters [1]. These loads induce a local damage which may propagate throughout the building in a chain reaction, leading to its partial or entire collapse [2, 3]. While these events are rare, they result in significant economic losses, especially for tall buildings, and potential human casualties.

Mid-rise to tall mass timber buildings, i.e. buildings assembled from engineered wood products, such as Laminated Veneer Lumber (LVL), Glued laminated timber (Glulam) and Cross Laminated Timber (CLT) [4], are increasingly gaining international popularity. As these buildings become taller, commonly reaching six storeys and more, the consequences of a potential progressive collapse event also significantly increase. Studying the progressive collapse of mass timber buildings is still a relatively new research topic, and the structural response of various types of mass timber buildings to resist such events has been researched so far, through experimental [5-9], analytical [10, 11] or numerical [12-15] methods. However, the accuracy of the developed numerical models has not yet been verified against experimental tests, or only on component tests [15]. To improve design guidelines, such as the US Department of Defence (DoD) [16], the General Services Administration (GSA) [17], the Institution of Structural Engineers (IStructE) [18] and WoodSolutions technical guides [19, 20], there is a need to develop Finite Element (FE) models which are proven to accurately replicate the structural behaviour of mass timber buildings under a load bearing element removal scenario. Such FE models have been widely used in reinforced concrete and steel structural systems [21-28] to gain in-depth understanding on the structural behaviour through parametric studies and identify the key factors affecting the ability of the structures to resist progressive collapse. Mass timber buildings differ from their concrete [29-32], steel [33-35] and composite-steel [36, 37] counterparts, due to the lack of structural continuity (as built from prefabricated structural elements), the brittle failure mode of the material [38], and the typical lack of ductility of timber-to-timber connections [6, 39]. These characteristics result in mass timber buildings deemed to have fewer possibilities to redistribute the load after the loss of a load bearing elements [19], outlining the necessity to develop an accurate model specific to mass timber buildings.

Consequently, this paper presents how post-and-beam mass timber buildings can be accurately modelled using FE. The proposed numerical model was validated herein against quasi-static 3D experimental tests, performed by

[1] Chunhao Lyu, Griffith University, Australia, c.lyu@griffith.edu.au
[2] Benoit P. Gilbert, Griffith University, Australia, b.gilbert@griffith.edu.au
[3] Hong Guan, Griffith University, Australia, h.guan@griffith.edu.au
[4] Hassan Karampour, Griffith University, Australia, h.karampour@griffith.edu.au
[5] Shanmuganathan Gunalan, Griffith University, Australia, shanmuganathanguna.gunalan@griffith.edu.au
[6] William Leggate, Griffith University, Australia, william.leggate@griffithuni.edu.au

https://doi.org/10.52202/069179-0368

the authors, on scaled-down substructures subjected to edge and corner column removal scenarios, totalling three different tests [7, 8]. As the layout of the CLT floor panels plays a critical role in redistributing the load through the building [7, 8], the influence of various CLT floor panels layouts on the progressive collapse resistance was numerically investigated through parametric study. The influence of the beam-to-column connections of the beams connected to the removed column on the ability of the building to redistribute the load was also studied.

2 FE MODEL OF 3D TESTS

2.1 GENERAL

The commercial finite element software package ABAQUS 6.14 [40] was used to simulate the 3D experimental tests. The beams and columns were modelled using beam elements B31. The 3-ply CLT panels were modelled using four-node general-purpose layered shell elements S4R. The *Composite Layup* tool was employed to define the material properties, thickness and orientation of each ply. Specifically, two types of *Lamina* materials were defined based on the properties provided by the manufacturer [41], namely 20 mm thick external (referred to as "*G8*") and 35 mm thick internal (referred to as "*G6*") laminae. A transversely isotropic material was used for each lamina, with the inputted longitudinal (*L* – parallel to the grain) and transverse (*T* – perpendicular to the grain) material properties summarised in Table 1. The two outer laminae were parallel to the face boards direction while the middle lamina was perpendicular to the two outer laminae. All connector properties were obtained from testing individual components and detailed in [42].

Table 1: *Material properties used in the numerical simulation*

Element	Moduli of Elasticity		Poison ratio	Shear moduli	
	E_L (MPa)	E_T (MPa)	μ_{LT} (-)	G_{LT} (MPa)	G_{TT} (MPa)
Beam/Column	14,100	-	-	800	-
CLT (outside layers)	9,000	450	0.3	700	90
CLT (inside layer)	6,000	300	0.3	400	60

Note: $_L$ – Longitudinal, parallel to the grain direction
$_T$ – Transverse, perpendicular to the grain direction (i.e., in both tangential and radial directions)

2.2 LOADING TREE

The two triangular steel plates and the six rectangular loading pads of the six-point loading tree (see [7] for more details) were simulated with four-node general-purpose shell elements S4R. The spreader beam linking the two plates was modelled with first-order beam elements B31. All these elements were assigned rigid material properties. Three-dimensional CONN3D2 connector elements were employed to connect the different elements together. The detailed model and the connector properties are shown in Figure 1. This model enabled the loading tree it to freely deform without resisting the applied load as in [7, 8]. The four corner nodes of each loading pad were connected to the CLT panels with only the translations restrained, the elements were therefore free to rotate relative to each other. Additionally, the contact between the six rectangular loading pads and the CLT panels was simulated using the "*hard contact* + *Rough*" surface-to-surface contact property, enabling pressure transmission without penetration in the normal direction and no sliding in the tangential directions.

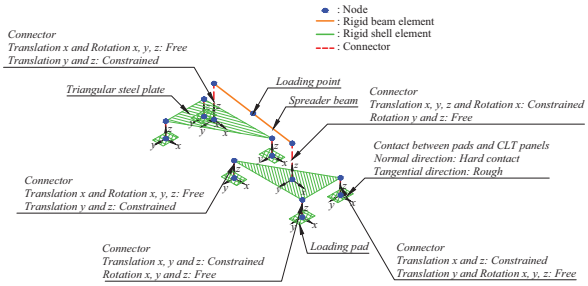

Figure 1: *Six-point loading tree details with local coordinate systems*
(Note: (i) connectors have a nil length in the model but are shown apart in the figure to clarify; (ii) the connector properties shown for the right triangular plate also apply to the left plate)

2.3 BOUNDARY CONDITIONS AND APPLIED LOADS

The overview of the FE model simulating Test EM-1 (and its repeat Test EM-2), with the boundary conditions, is shown in Figure 2. In reference to the global coordinate system *X*-*Y*-*Z*, the displacements of the bottom node of the eight permanent columns were restrained along all axes, while all rotations were released. To simulate the horizontal restraints provided to the substructure (See [7]): (i) the displacement along the *X*-axis of the six peripheral columns shown in Figure 2 was restrained at the elevation of the centreline of the beams and (ii) the edge nodes of the CLT panels shown in Figure 2 had their displacement along the *Z*-axis restrained. The same principles applied to Tests CM-1 and CM-2, but with the locations of the horizontal restraints given in [8].
In the analyses, the same loading sequence as in [7, 8] was simulated and consisted of:

- *Step 1:* Applying the self-weight of (i) the CLT panels of 0.37 kPa (average measured value on 27 panels) as an UDP, (ii) the weights, loaded on the bays not adjacent to the removed column, of 4.8 kPa as an UDP, and (iii) the loading tree (weighing 10.3 kN for Tests EM-1 and EM-2, and 9.4 kN for Tests CM-1 and CM-2) as a point load applied at mid-span of the spreader beam of the tree (see Figure 1). Note that the bottom node of the column stub of the removed column was constrained in displacement along the three degrees of freedom to simulate an undamaged structure during this step.
- *Step 2:* Removing the boundary conditions at the bottom node of the removed column.
- *Step 3:* Displacing along the negative *Y*-axis the node at mid-span of the spreader beam of the loading tree (see Figure 1) to simulate the applied load, maintaining the load applied in *Step 1*.

https://doi.org/10.52202/069179-0368

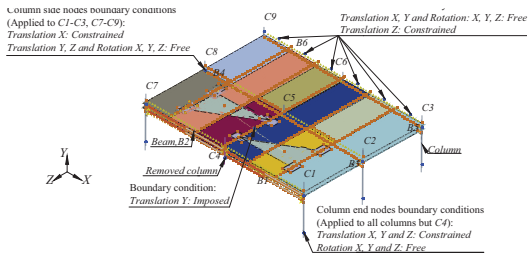

Figure 2: *Numerical model overview with boundary conditions shown for Test EM-1*

2.4 CONNECTIONS AND TIMBER FAILURE MODELLING

Connector elements CONN3D2, with the connector type *"Cartesian + Rotation"*, i.e., allowing all degrees of freedom to be entered by the user, were employed to connect the different components of the structure together, as described in [42].

Bending failure of the beams was observed experimentally in [7, 8] and while the beams were modelled elastically, bending failure of the beams was included in the model with connectors, used as fuses. The region of the maximum bending moment of the critical beams, i.e., the mid-span region of the middle row of beams, was modelled in 10 beam elements of 100 mm each. Adjacent segments were connected together by rigid connectors of zero length, therefore not affecting the elastic mechanical behaviour of the beams. The "*failure*" criteria option was used in the connectors to release the rotational stiffness when the bending moment reached the experimentally measured moment capacity of 13.7 kNm [7], therefore simulating the bending failure. The principle is illustrated in Figure 3 and was found (not shown herein) to correctly model the bending failure of the beams.

As the failure of the CLT panels was not explicitly observed experimentally, failure of the CLT panels was not modelled.

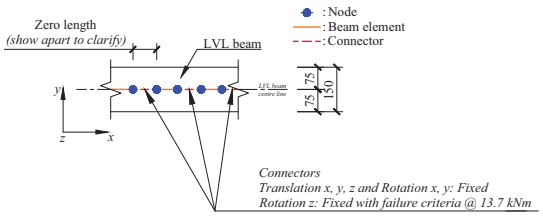

Figure 3: *Modelling bending failure of LVL beams (unit: mm)*

3 3D MODEL VALIDATION

3.1 LOAD-DISPLACEMENT CURVES AND FAILURE MODES

Figure 4 compares the experimental and numerical applied load in *Step 3* (see Section 2.3) versus the removed column displacement, under an edge column removal scenario. Note that the weight of the loading tree was included in the figure by offsetting the curves along the vertical axis as in [7]. Two numerical simulations were run with the shear capacity of the beam-to-column connections either inputted from the values obtained with or without the CLT panels, as discussed in [42]. Ignoring the contribution of the CLT panels in the shear capacity of the beam-to-column connections resulted in the FE analysis underestimating the ultimate load by 26% due to the premature failure of these connections in the second row of beams. It is therefore important to consider this contribution to accurately reproduce the overall structural behaviour and is now considered in this study.

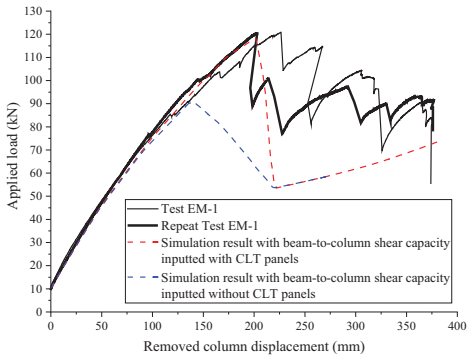

Figure 4: *Load – displacement curves from tests and numerical simulations (Edge column removal scenario only)*

Table 2 compares the experimental and numerical initial stiffness and ultimate loads for the edge column removal scenarios. The FE model accurately (within 3%) replicated both the initial stiffness and ultimate load.

Table 2: *3D FEA results comparison*

Specimen	Initial stiffness (kN/mm)			Ultimate load (kN)		
	Test	FE	Test/FE	Test	FE	Test/FE
EM-1	0.61	0.64	0.95	120.8	118.0	1.02
EM-2	0.66		1.03	120.4		1.02
CM-1	0.21	0.22	0.95	59.9	68.3	0.88
CM-2	0.75	0.63	1.19	97.3	105.7	0.92
		Average	1.03		Average	0.96
		COV	11%		COV	8%

In terms of failure modes, the FE model predicted shear failure to occur at the beam-to-column connectors linking both beams *B3* and *B4* to the interior column *C5* (see Figure 2 for element numbering). This failure mode corresponds well to the one experimentally observed for which shear failure occurred at beam *B3*-to-column *C5* connection. The difference of having two connections failing numerically, when compared to one connection failing experimentally, can be explained by the variability in the connection capacity. As the two connections are loaded similarly and have the same numerical capacity, they fail at the same time in the FE model. Experimentally, one connection will be statistically stronger that the other one, fail first and allow the load to redistribute before the second connection fails.

Note that the maximum load was reached due to bending failure of beam *B4* when repeating Test EM-1 (dotted line in Figure 4). This failure mode was also observed in Test EM-1 but after shear failure of the connection occurred. Bending failure was not observed numerically due to the

https://doi.org/10.52202/069179-0368

connections failing first in shear, and consequently unloading the beams due to the total applied force dropping.

Figure 5 plots the applied load versus the removed column displacement under the two different corner column removal scenarios. Regarding Test CM-1, the initial stiffness matched well with the experimental test, and the predicted ultimate load was 14.0% higher than the experimental test. The beam *B4* bending failure, which was predicted in the FE model was also observed in the experimental test. In the simulation, after the load dropped due to bending failure of beam *B4*, the load steadily increased, likely because the interaction between the bending moment and shear force in the behaviour of the beam-to-column connectors was not considered. Indeed, this allowed the applied load to be fully transferred to columns *C4* and *C8* in shear through the beam-to-column connectors, despite these connections completely failing in bending and likely having a reduced shear capacity. Also see Section 3.2 on the load transfer.

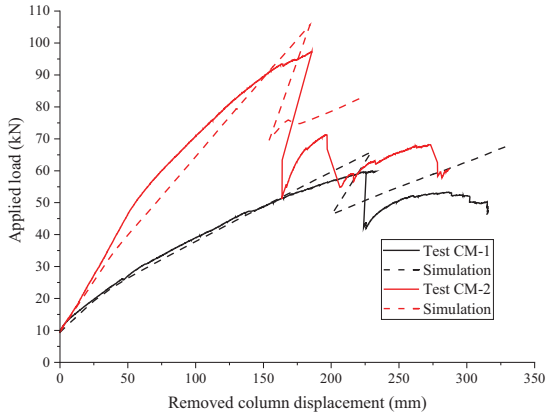

Figure 5: *Load – displacement curves from tests and numerical simulations (Corner column removal scenario only)*

For Test CM-2, the initial stiffness was 20% different between the experimental test and the simulation results, but the overall trend of the load-displacement curve was well captured. Regarding the ultimate load, the experimental and numerical ratio was equal to 0.92. The FE model predicted failure to occur in bending at beam *B3*, matching well with the failure observed in Test CM-2. The numerical model stopped when the removed column displacement reached 220 mm, corresponding to the beam-to-column connector linking beam *B3* and column *C2* reaching its ultimate bending capacity.

3.2 LOAD REDISTRIBUTION

Figure 6 compares the experimental and numerical load redistribution through the system, taken as the column reaction forces, versus the removed column displacement. As the results for Test EM-1 and its repeat Test EM-2 were similar [7], only the results from Test EM-1 are plotted in the figure for clarity. The figure shows that up to reaching the ultimate load, corresponding to a removed column displacement of 122 mm, the numerical model accurately reproduced the load redistribution through the system. After failure, the numerical column reaction force for column *C5* dropped significantly more than the experimental tests due to the two beam-to-column connectors at column *C5* failing numerically against only one experimentally. The load redistribution after failure was however correctly captured for all other columns.

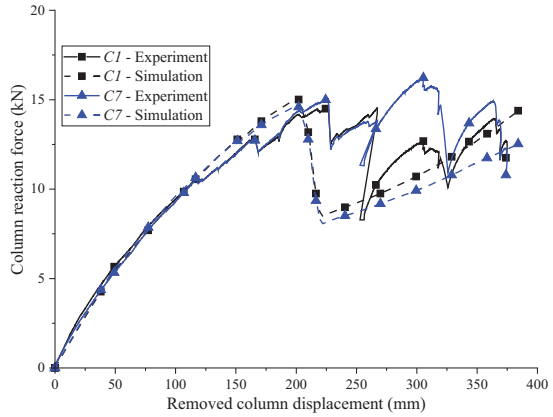

(a) Adjacent columns to removed column

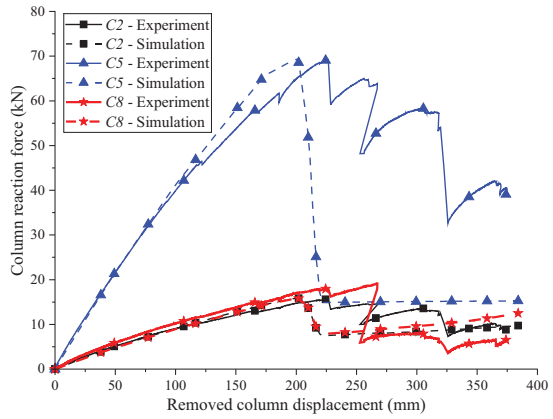

(b) Interior and 2nd-row side columns

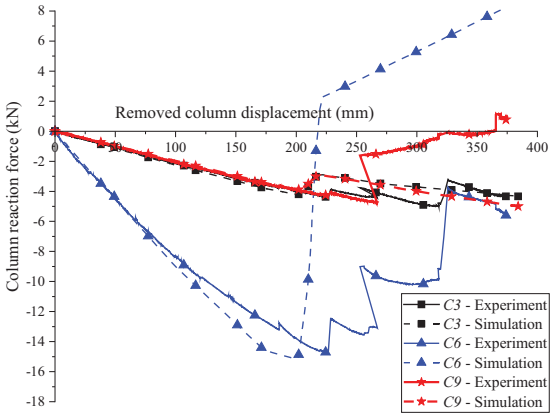

(c) 3rd-row column (back row)

Figure 6: *Load redistribution for edge column removal scenario (shown for Test EM-1)*

Figure 7 plots the experimental and numerical column reaction forces versus the removed column displacement for Test CM-1. Overall, the load redistribution was predicted well for all columns as outlined in the figure. The column reaction forces from Test CM-2 and simulation results are now compared in Figure 8. Similarly to the other two tests, the load redistribution was well captured by the numerical model for Test CM-2.

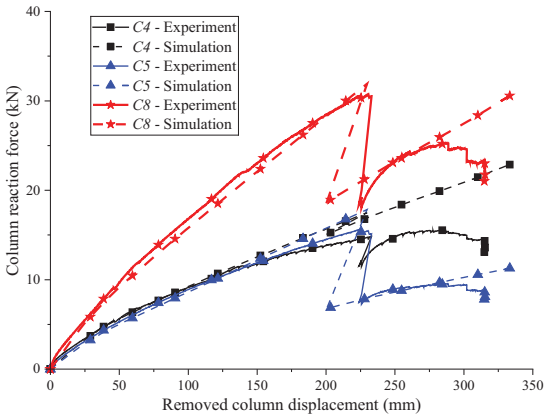

(a) Adjacent columns to removed column and interior column

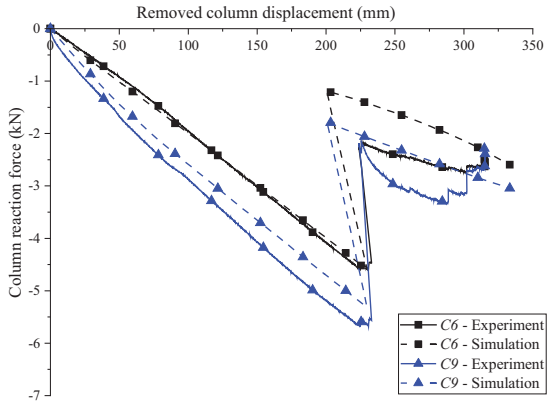

(b) 3rd-row columns (back row)

***Figure 7:** Load redistribution for corner column removal scenario (shown for Test CM-1)*

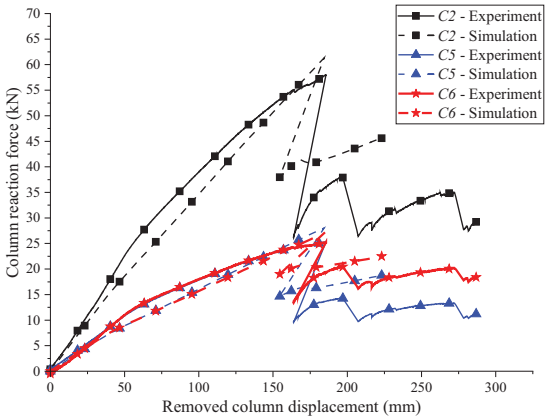

(a) Adjacent columns to removed column and interior column

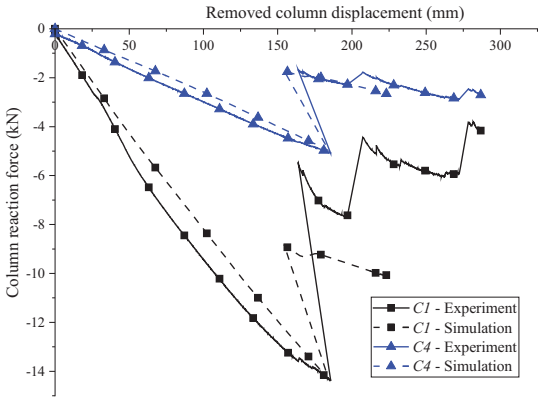

(b) 1st-row columns (front row)

***Figure 8:** Load redistribution for corner column removal scenario (shown for Test CM-2)*

4 PARAMETRIC STUDIES

The validated 3D numerical models are used in this section to perform parametric studies by evaluating the influence of (i) the CLT floor panels layout and (ii) one alternative load path typically not considered in design, on the ability of the building to resisting progressive collapse. In total, eleven additional models were run as part of this section.

4.1 INFLUENCE OF VARIOUS CLT PANEL LAYOUTS

To cover different design practices than the staggered CLT panels from the validated model in Section 3, two additional layouts of the CLT floor panels were considered in this section. In the first and second additional layouts, all floor panels spanned one and two bays, respectively. Analyses were run for both edge and corner columns removal scenarios.

4.1.1 Edge Column Removal Scenario

Figure 9 (a) compares the numerical applied loads in *Step 3* (see Section 2.3) versus the removed edge column displacement for the three different layouts of the CLT panels. Results showed that the initial stiffness was significantly influenced by the CLT panel layouts, with the stiffness when all panels spanned two bays being 4.6 times greater than when all panels spanned one bay. However, the capacity of the staggered and all two-bay long panels was within 3.5% of each other. The failure mode for these two configurations was the shear failure of the beam-to-column connectors on both side of interior column *C5*. For the all one-bay long panels, no specific failure mode was numerically observed. All configurations allowed to withstand an accidental design load of 8.95 kPa in the DoD [16], i.e. corresponding to an applied load of 53.7 kN.

4.1.2 Corner Column Removal Scenario

Figure 9 (b) compares the numerical applied load in *Step 3* versus the removed column displacement for the four

https://doi.org/10.52202/069179-0368

panel layouts, i.e., staggered (Tests CM-1 and CM-2), all two-bay long panels and all one-bay long panels. The initial stiffness of the all two-bay long panels was similar to the one of simulated Test CM-2. However, and while the same failure mode was encountered for these two layouts (i.e., bending failure of beam *B4*), due to different load distributions of the beam, the ultimate load of the all two-bay long panels was 10% lower. Similar to the edge column removal scenario, the model for all one-bay long panels showed the lowest initial stiffness and no specific failure mode was numerically observed. All configurations allowed to withstand an accidental design load of 8.95 kPa in the DoD [16], i.e. corresponding to an applied load of 26.9 kN.

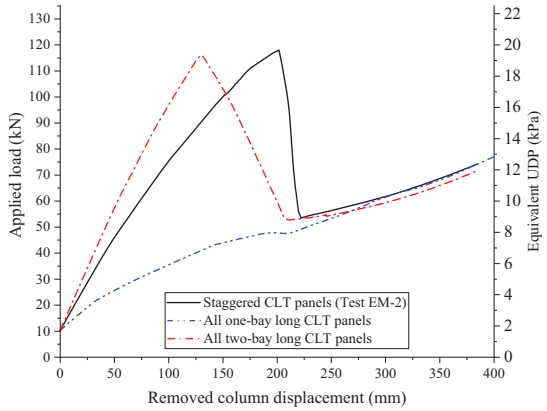

(a) Edge column removal scenario

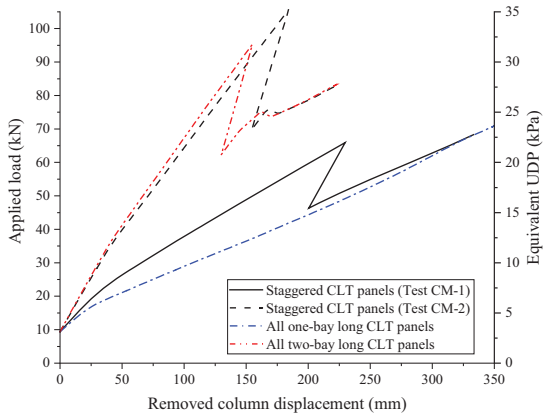

(b) Corner column removal scenario

Figure 9: *Numerical applied force versus removed column displacement for different CLT panel layouts*

4.2 INFLUENCE OF THE BEAM-TO-COLUMN CONNECTORS OF THE FRONT FRAME

During the experimental investigations [7, 8], and as captured by the previous numerical investigations, the beam-to-column connections of the beams connected to the removed column, but located at the opposite end of this column, provided a local support to the CLT panels above. This alternate load path allowed to transfer about 29% of the applied load to the columns directly connected to the removed one by these beams [7]. This local support can be seen in Figure 6 (a), Figure 7 (a) and Figure 8 (a), in which despite experiencing large rotation, the beam-to-column connections did not fail in shear and transferred load to the columns adjacent to the removed one. However, in a design situation and as no data would typically be available on the shear capacity of the beam-to-column connections experiencing large rotation, this alternative load path would be ignored. In other words, all beam-to-column connections of the beams attached to the removed column would be assumed to have failed and not carrying load.

To investigate the influence and the importance of the alternate load path mentioned above to the response of the building, another seven models were analysed with the same CLT layouts as in Section 4.1. In these models, (i) under the edge column removal scenario, the beam-to-column connectors of both beams *B1* and *B2* were ignored and removed from the models, and (ii) for the corner column removal scenario, the beam-to-column connectors of both beams *B2* and *BP3* were similarly removed from the models. The results, in terms of applied load versus removed column displacement, are plotted in Figure 10.

For the model with all one-bay long panels and edge column removal scenario, the structure was not able to carry its self-weight and loading tree when removing the column in *Step* 2 (see Section 2.3), so the response was not plotted in Figure 10 (a). This result shows the importance of the alternative load path offered by the beam-to-column connectors providing local support to the CLT panels above.

Still for the edge column removal scenario, the maximum load was reached for both staggered and two-bay long panels due to shear failure of the beam-to-column connectors linking beams *B3* and *B4* to column *C5*. The former and latter layouts reached a capacity 8.5 and 10.7 times higher, respectively, than the accidental design load of 8.95 kPa in the DoD [16]. In both scenarios, the models were not able to converge after the shear failure of the connectors, due to the sharp decrease of the load.

For the corner column removal scenario, the layout corresponding to one-bay long panels did not reached the accidental design load of 8.95 kPa in the DoD [16], while all other configurations reached a capacity at least 2.2 times greater than this accidental design load.

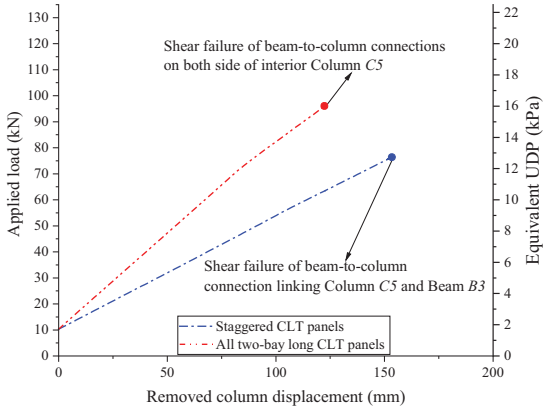

(a) Edge column removal scenario

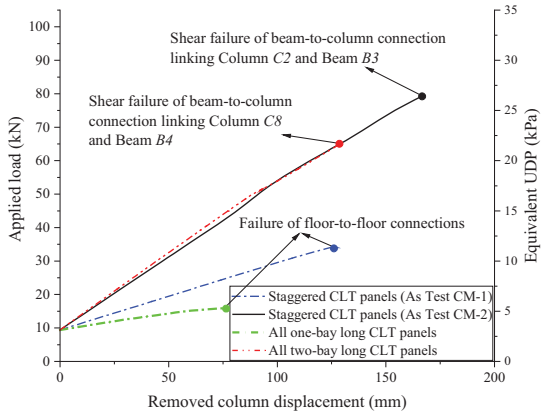

(b) Corner column removal scenario

Figure 10: *Numerical applied force versus removed column displacement when ignoring the beam-to-column connectors linked to the removed column*

5 CONCLUSIONS

This paper presented and validated FE models of post-and-beam mass timber buildings under various column removal scenarios. Parametric studies using the validated numerical model were conducted. The main conclusions of this paper can be summarised as follow:

1. The FE model of the 3D substructures was found to accurately replicate the experimentally observed ultimate loads, initial stiffness, failure modes, load redistributions, deformed shapes and strain developments. The experimental-to-numerical initial stiffness and ultimate load were 1.03 and 0.96, respectively, with associated coefficients of variation less than 0.11.
2. When performing component tests, it was found that the CLT panels could significantly influence the shear capacity of the beam-to-column connections by delaying the failure. An increase in 30% in the shear capacity was attributed to the presence of the CLT panels. This behaviour needs to be considered to accurately capture the structural behaviour of post-and-beam mass timber buildings.
3. Parametric studies showed that if two-bay CLT panels are used: (i) for an edge column removal scenario, staggering or not does not influence the ultimate load, however, (ii) for a corner removal scenario, staggering the panels was found to influence the ultimate by up to 60.3%, when compared to non-staggered panels.
4. Parametric studies also showed that the alternative load path providing by the beam-to-column connectors of the frames connected to the removed column, and locally supporting the CLT panel above, is essential to achieve robustness when only one-bay long CLT panels are used. If this alternative load path cannot be relied on, post-and-beam mass timber buildings with one-bay long CLT panels are not able to resist the accidental design load under a column removal scenario.
5. The validated model can be used to eventually (i) quantify all parameters influencing the behaviour of post-and-beam mass timber buildings to resist progressive collapse, (ii) characterise the properties of timber-to-timber connections required to ensure robustness, (iii) evaluate the alternative load paths in an entire building and (iv) provide data to develop design guidelines.

ACKNOWLEDGEMENT

This study was funded by the School of Engineering and Built Environment, the Griffith University Sciences group and the Australian Research Council (ARC) Industrial Transformation Research Hub IH150100030 on tall timber buildings.

REFERENCES

[1] Adam, J. M., Parisi, F., Sagaseta, J., Lu, X.: Research and practice on progressive collapse and robustness of building structures in the 21st century. Engineering Structures, 173:122–149, 2018.
[2] Ellingwood, B. R.: Mitigating risk from abnormal loads and progressive collapse. Journal of Performance of Constructed Facilities, 20(4):315–323, 2006.
[3] American Society of Civil Engineers, Minimum design loads for buildings and other structures, *(ASCE/SEI 7–10)*, 2013.
[4] Connolly, T., Loss, C., Iqbal, A., Tannert, T.: Feasibility study of mass–timber cores for the UBC tall wood building. Buildings, 8(8), 2018.
[5] Mpidi Bita, H., Tannert, T.: Experimental study of disproportionate collapse prevention mechanisms for mass–timber floor systems. Journal of Structural Engineering, 146(2):04019199, 2020.
[6] Lyu, C. H., Gilbert, B. P., Guan, H., Underhill, I. D., Gunalan, S., Karampour, H., Masaeli, M.: Experimental collapse response of post-and-beam mass timber frames under a quasi-static column removal scenario. Engineering Structures, 213:110562, 2020.
[7] Lyu, C. H., Gilbert, B. P., Guan, H., Underhill, I. D., Gunalan, S., Karampour, H.: Experimental study on the quasi-static progressive collapse response of post-and-beam mass timber buildings under an edge column removal scenario. Engineering Structures, 228:111425, 2021.
[8] Lyu, C. H., Gilbert, B. P., Guan, H., Underhill, I. D., Gunalan, S., Karampour, H.: Experimental study on the quasi-static progressive collapse response of post-and-beam mass timber buildings under corner column removal scenarios. Engineering Structures, 242:112497, 2021.
[9] Cheng, X., Gilbert, B. P., Guan, H., Underhill, I. D., Karampour, H.: Experimental dynamic collapse response of post–and–beam mass timber frames under a sudden column removal scenario. Engineering Structures, 233:111918, 2021.
[10] Mpidi Bita, H., Tannert, T.: Tie-force procedure for disproportionate collapse prevention of CLT

https://doi.org/10.52202/069179-0368

platform–type construction. Engineering Structures, 189:195–205, 2019.
[11] Voulpiotis, K., Köhler, J., Jockwer, R., Frangi, A.: A holistic framework for designing for structural robustness in tall timber buildings. Engineering Structures, 227:111432, 2021.
[12] Mpidi Bita, H., Currie, N., Tannert, T.: Disproportionate collapse analysis of mid–rise cross–laminated timber buildings. Structure and Infrastructure Engineering, 14(11):1547–1560, 2018.
[13] Mpidi Bita, H., Tannert, T.: Disproportionate collapse prevention analysis for a mid–rise flat–plate cross–laminated timber building. Engineering Structures, 178:460–471, 2019.
[14] Huber, J. A. J., Ekevad, M., Girhammar, U. A., Berg, S.: Finite element analysis of alternative load paths in a platform–framed CLT building. Proceedings of the Institution of Civil Engineers: Structures and Buildings, 173(5):379–390, 2020.
[15] Huber, J. A. J., Mpidi Bita, H., Tannert, T., Berg, S.: Finite element analysis of alternative load paths to prevent disproportionate collapse in platform-type CLT floor systems. Engineering Structures, 240:112362, 2021.
[16] Department of Defence, Design of buildings to resist progressive collapse *(UFC 4–023–03)*, 2016.
[17] General Services Administration, Alternate path analysis and design guidelines for progressive collapse resistance, Washington, DC: General Services Administration, 2016.
[18] Institution of Structural Engineers, Practical guide to structural robustness and disproportionate collapse in buildings, London, UK. Institution of Structural Engineers Limited, 2010.
[19] Hewson, N., Technical design guide #39: Robustness in structures, Melbourne, VIC. Forest & Wood Products Australia Limited, 2016.
[20] Woodard, A., Jones, A., Technical design guide #50: Mid–rise timber building structural engineering, Melbourne, VIC. Forest & Wood Products Australia Limited, 2019.
[21] Bao, Y., Kunnath, S. K., El-Tawil, S., Lew, H. S.: Macromodel-based simulation of progressive collapse: RC frame structures. Journal of Structural Engineering, 134(7):1079–1091, 2008.
[22] Han, Q., Li, X., Liu, M., Spencer, B. F.: Performance analysis and macromodel simulation of steel frame structures with beam-column joints using cast steel stiffeners for progressive collapse prevention. Thin–Walled Structures, 140:404–415, 2019.
[23] Khandelwal, K., El-Tawil, S., Kunnath, S. K., Lew, H. S.: Macromodel–based simulation of progressive collapse: Steel frame structures. Journal of Structural Engineering, 134(7):1070–1078, 2008.
[24] Yang, B., Tan, K. H.: Robustness of bolted–angle connections against progressive collapse: Experimental tests of beam–column joints and development of component–based models. Journal of Structural Engineering, 139(9):1498–1514, 2013.
[25] Fu, Q., Tan, K. H., Zhou, X. H., Yang, B.: Numerical simulations on three-dimensional composite structural systems against progressive collapse. Journal of Constructional Steel Research, 135:125–136, 2017.
[26] Kunnath, S. K., Bao, Y., El-Tawil, S.: Advances in computational simulation of gravity-induced disproportionate collapse of RC frame buildings. Journal of Structural Engineering, 144(2):03117003, 2018.
[27] Xue, H., Guan, H., Gilbert, B. P., Lu, X., Li, Y.: Simulation of punching and post–punching shear behaviours of RC slab–column connections. Magazine of Concrete Research, 73(22):1135–1150, 2021.
[28] Xue, H., Guan, H., Gilbert, B. P., Lu, X., Li, Y.: Comparative and parametric studies on behavior of RC–flat plates subjected to interior–column Loss. Journal of Structural Engineering, 146(9):04020183, 2020.
[29] Ma, F., Gilbert, B. P., Guan, H., Xue, H., Lu, X., Li, Y.: Experimental study on the progressive collapse behaviour of RC flat plate substructures subjected to corner column removal scenarios. Engineering Structures, 180:728–741, 2019.
[30] Ma, F., Gilbert, B. P., Guan, H., Lu, X., Li, Y.: Experimental study on the progressive collapse behaviour of RC flat plate substructures subjected to edge–column and edge–interior–column removal scenarios. Engineering Structures, 209:110299, 2020.
[31] Xue, H., Gilbert, B. P., Guan, H., Lu, X., Li, Y., Ma, F., Tian, Y.: Load transfer and collapse resistance of RC flat plates under interior column removal scenario. Journal of Structural Engineering, 144(7), 2018.
[32] Brunesi, E., Nascimbene, R., Parisi, F., Augenti, N.: Progressive collapse fragility of reinforced concrete framed structures through incremental dynamic analysis. Engineering Structures, 104:65-79, 2015.
[33] Yang, B., Tan, K. H.: Experimental tests of different types of bolted steel beam–column joints under a central–column–removal scenario. Engineering Structures, 54:112–130, 2013.
[34] Chen, J., Huang, X., Ma, R., He, M.: Experimental study on the progressive collapse resistance of a two–story steel moment frame. Journal of Performance of Constructed Facilities, 26(5):567–575, 2012.
[35] Li, H., Cai, X., Zhang, L., Zhang, B., Wang, W.: Progressive collapse of steel moment-resisting frame subjected to loss of interior column: Experimental tests. Engineering Structures, 150:203–220, 2017.
[36] Tan, Z., Zhong, W. H., Tian, L. M., Zheng, Y. H., Meng, B., Duan, S. C.: Numerical study on collapse-resistant performance of multi-story composite frames under a column removal scenario. Journal of Building Engineering, 44:102957, 2021.
[37] Mucedero, G., Brunesi, E., Parisi, F.: Progressive collapse resistance of framed buildings with partially encased composite beams. Journal of Building Engineering, 38:102228, 2021.
[38] Thelandersson, S., Honfi, D., "Behaviour and modelling of timber structures with reference to robustness," *Proceedings of the Joint Workshop of*

COST Actions TU0601 and E., J. Köhler, H. Narasimhan and M. Faber, eds., 2009.
[39] Masaeli, M., Gilbert, B. P., Karampour, H., Underhill, I. D., Lyu, C. H., Gunalan, S.: Scaling effect on the moment and shear responses of three types of beam–to–column connectors used in mass timber buildings. Engineering Structures, 208:110329, 2020.
[40] Abaqus/CAE, Analysis user's manual version 6.14, 2014.
[41] XLam, Designing with XLam Cross Laminated Timber, *New Zealand Design Guide Version 2.1*, 2016.
[42] Lyu, C. H., Gilbert, B. P., Guan, H., Gunalan, S., Karampour, H.: Finite element modelling of the progressive collapse of post-and-beam mass timber building substructures under edge and corner column removal scenarios. Journal of Building Engineering, 49, 2022.

https://doi.org/10.52202/069179-0368

World Conference on Timber Engineering Oslo 2023

TIMBER STRUCTURES IN SUBTROPICAL CLIMATE ON DESIGN: BOIS DURAMHEN programs for Guadeloupe, Martinique and Guyane

Paul Quistin[1], Eric Fournely[2], Joseph Gril[3], Gael Godi[4], Luc Cador[5], Thierry Lamadon[6], Laurence Romana[7], Jacques Beauchêne[8], Rostand Moutou Pitti[9],

ABSTRACT: Mainly due to a lack of information on the local climate and its consequences on timber buildings, and regarding Eurocode standard, French West Indies islands and French Guiana remain considered as a service class 3 (SC3). Based on Meteo France (MF) data and moisture content measurements on more than 300 sites in the three departments, on local surrounding air humidity and temperature, the three programs Bois Duramhen 971 (European Synergîle), 972 and 973 (PACTE) are devoted to give answers on the impact of this climate on soft and tropical woods integrated in traditional or new timber structures. Data acquisition and analysis are described. Measurements are performed during more than one year, they are compared and completed by Meteo France data. The analysis is divided in two phases: equilibrium moisture content (EMC) calculated from HR(%) - T(°C) with NFEN1995-1.1/NA moisture diagram and direct measurement of instantaneous MC. Monitoring approaches are performed on, at least few members of two real buildings. In Guiana, drying element are also monitored in order to analyse this natural drying phase. Results obtained by the different approaches, comparison of measurements, calibration of measurement equipment, led to a wide data base and proposals of mapping have been deduced.

KEYWORDS: Service class, Moisture content, Equilibrium moisture content, durability

1 INTRODUCTION

Regarding Eurocode standard dedicated to timber structures, French West Indies islands and French Guiana are often considered as a service class 3 area (the most severe environmental conditions). This decision is partly based on the “severe” climate of these departments, but also mainly on a lack of information on the real local climate and its consequences on timber elements of buildings. A European project, *Synergîle-Bois Duramhen971:BD971*, is devoted to the study of environmental effects on timber structures in Guadeloupe island and two French national projects, *PACTE-Bois Duramhen972: BD972, and Bois Duramhen973: BD973,* propose the same approach for Martinique and French Guiana. The aim of these three programs is to produce a reliable data base and to build a map of service class zones (*SC2 & SC3)* whenever possible. The present work is the results of these studies related to Guadeloupe, Martinique and French Guiana. The chosen strategy is for each [1-3]:

- identification of available meteorological data;
- choice of different buildings or "sites" (≈ 100 for each department);
- 18-months measurement period: temperature (*T*) and relative humidity (*RH*) of surrounding air on the sites, and moisture content (*MC*) on timber elements;
- continuous analysis of the exploitation of data and measurements.

In order widen the data set, different axes of information were investigated (Figure 1). Data provided by Meteo France (MF), the National weather forecast agency, covered large period such as few decades but are limited to available MF stations. Project data covered narrow periods (12 months for the different sites) but a wide area with a large number of sites and buildings. They integrated environmental data but also *MC*.

To complete these measurements, two other main actions were conducted for each department:

- two sites were equipped with 3 monitoring sensors (*HR*%, *T*°C, *MC*%) for 10 months;
- specimens of wood were collected on site and studied for species identification and physical parameters determination on the one hand, tested in environmental chamber to obtain adsorption-desorption characteristics and validate (or not) the equilibrium moisture content (*EMC*) diagram, on the other hand.

[1] Paul Quistin, ANCO Baie Mahault Guadeloupe, France, p.quistin@ancogroupe.fr
[2] Eric Fournely Université Clermont Auvergne, CNRS, Clermont Auvergne INP, Institut Pascal, Clermont-Ferrand, France, eric.fournely@uca.fr
[3] Joseph Gril Université Clermont Auvergne, CNRS, Institut Pascal and INRAE, PIAF, Clermont-Fd, France, joseph.gril@uca.fr
[4] Gael Godi Université Clermont Auvergne, CNRS, Clermont Auvergne INP, Institut Pascal, Clermont-Fd, France, gael.godi@uca.fr
[5] Luc Cador S3CB, Baie Mahault Guadeloupe France, direction.cadrybat@cadrybat.com
[6] Thierry Lamadon BUREAU VERITAS CONSTRUCTION Paris, France, thierry.lamadon@bureauveritas.com
[7] Laurence Romana Université Antilles UA Pointe à Pitre Guadeloupe, France, laurence.romana@univ-antilles.fr
8 Jacques Beauchêne CIRAD UMR EcoFoG, Cayenne, France, jacques.beauchene@cirad.fr
[9] Rostand Moutou Pitti, Université Clermont Auvergne, CNRS, Clermont Auvergne INP, Institut Pascal, Clermont-Fd, France, rostand.moutou_pitti@uca.fr

https://doi.org/10.52202/069179-0369

Figure 1 illustrates the complementarity of these investigations.

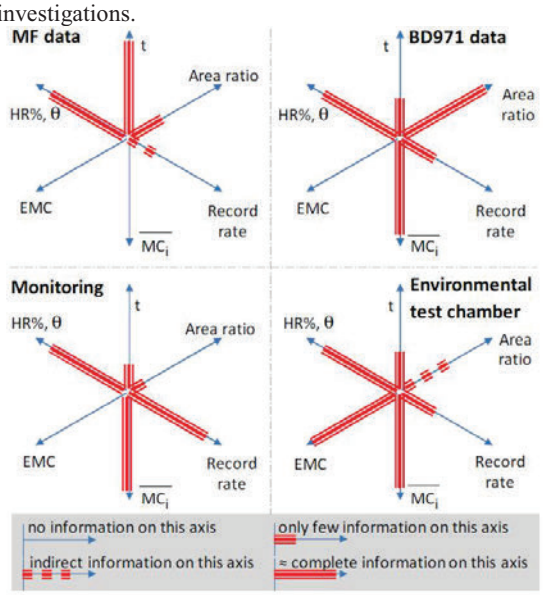

Figure 1: *Complementarity of investigations of projects BOISDURAMHEN [1-3]*

This paper will present successively the specificity of the tropical situation of French departments, the chosen strategy, experimentation on natural drying in Guiana and some results for BD971 (Guadeloupe), BD972 (Martinique) and BD 973 (French Guiana) regarding the sorption behaviour of local species typically used in construction.

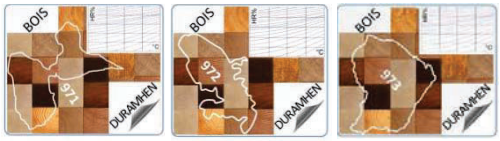

2 SPECIFIC SITUATION OF FRENCH CARIBBEAN ISLANDS AND GUIANA

Guadeloupe (16-17°N, 61-62°W) is composed of a main island with two parts and few smallest islands; Martinique (14-15°N, 60-61°W) is one island [4], French Guiana is included in the South American continent.

The climate is a tropical marine one with a wet hot period and a slightly dryer one for the Caribbean islands [4]. French Guiana is located in the Eastern part of the Guiana Plateau, North of the Amazon basin. More than 90% of its territory is covered by humid equatorial forest [5]. The relief is a vast plateau of average altitude between 100 and 200 meters, with some massifs culminating at 800 meters. It is close to the equator (3-5° North latitude). For the study of the BOIS DURAMHEN projects, MF data (*T*, *RH*) were collected over 10 years for 10 to 16 MF stations per department [4-5]; they are positioned on the maps of Figures 2 and 3. The average *RH* history measured in French Guiana is shown in Figure 4.

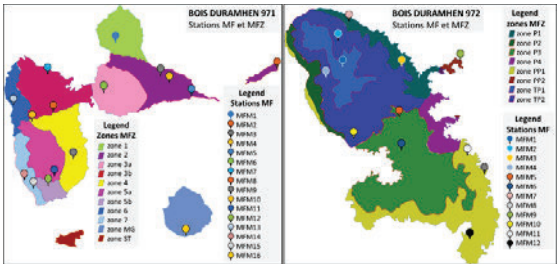

Figure 2: *Location of local meteorological measurement equipment in Guadeloupe and Martinique [4]*

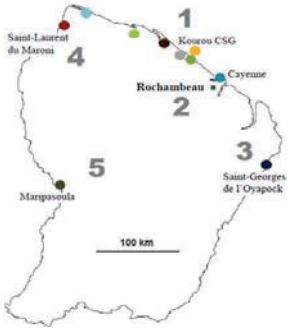

Figure 3: *Location of local meteorological measurement equipment in French Guiana [5]*

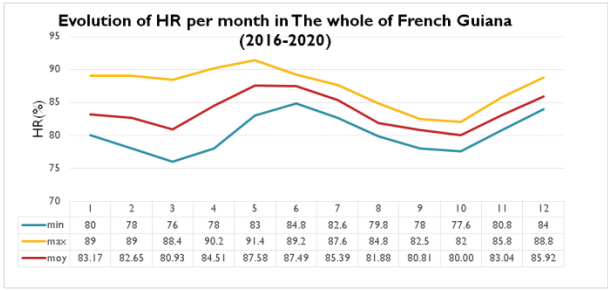

	1	2	3	4	5	6	7	8	9	10	11	12
min	80	78	76	78	83	84.8	82.6	79.8	78	77.6	80.8	84
max	89	89	88.4	90.2	91.4	89.2	87.6	84.8	82.5	82	85.8	88.8
moy	83.17	82.65	80.93	84.51	87.58	87.49	85.39	81.88	80.81	80.00	83.04	85.92

Figure 4: *Extreme values of monthly relative humidity of the air for several years, 10 French Guiana weather stations [5]*

3 DATA ACQUISITION

3.1 MONITORING OF CLIMATE AND MOISTURE CONTENT

For the 3 projects, the acquistion of data was based on two sources:

- data sets provided by Meteo France stations, principaly *HR* (%) and *T* (°C) of the surrounding air,
- on-site measurements of the same parameters and also *MC* (%), twice à month during 13 months with a manual measurement equipement (wood moisture meter with digital display, hand-held, non-destructive).

Some of the sites were chosen to be very close to MF station (less than 800 m) in order to compare *HR* and *T* coming from MF measurements records. In French Guiana, to complete the acquisition data and validate the measurements, 2 sites in different towns (Cayenne and Kourou) were equipped with monitoring sensors (3 per site) recording continuously *HR* and *T*, as well as *MC* of

https://doi.org/10.52202/069179-0369

the wood element (outdoor location). This equipment and its set up are presented on Fig. 5.

Figure 5: *Monitoring 3 wood elements (softwood and hardwood) equipped with sensors in Cayenne.*

3.2 MONITORING OF NATURAL DRYING

To study the natural drying of hardwood under the humidity conditions of French Guiana, the moisture loss down to below fibre saturation point (*FSP*) was monitored for two Guyanese wood species, Angelique (*Dicorynia guianensis*) and Gonfolo (*Qualea rosea*) (Figure 6).

Figure 6: *Natural drying tests: left,* D. guianensis*; right, 8 wood elements (*D. guianensis *and* Q. rosea*) equipped with sensors.*

3.3 MEASUREMENT OF SORPTION ISOTHERMS

The expected *EMC* of wood in a given climate defined by *HR*% and *T*°C, used to define the service class of a zone, is commonly based on the abacus provided by the National Appendix to Eurocode 5- part 1.1 [12-13]. In order to check its applicability to the local context, specimens from 5 typical tropical species used for construction in French Guyana were prepared in Kourou and sent to Clermont-Ferrand, France. Table 1 shows the species designation and the measured specific gravity of the samples.

Table 1 *Species used for sorption isotherm tests*

Species	ID	Specific gravity
Handroanthus serratifolius	EBE	1.071 +/- 0.014
Goupia galbra	GOU	0.883 +/- 0.007
Dicorynia guianensis	ANG	0.816 +/- 0.036
Qualea rosea	GON	0.657 +/- 0.008
Sextonia rubra	GRI	0.590 +/- 0.016

Wood plates 20x20x5mm3 were tested at 28°C in a MKF 240 climatic chamber, with mass measurement at each change of set point. Two samples per species were measured, one oriented TL, one RT. The sequence of *RH* steps, desorption followed by adsorption, is given in Table 2. The *RH* value was previously checked by means of a mirror hygrometer and the set values adapted accordingly [14].

Table 2 *Conditions of sorption isotherms*

Date	*HR* %	*T*°C	Date	*HR* %	*T*°C
01/4/21	93,8	Desorption, 28°C	19/4/21	10,0	Adsorption, 28°C
02/4/21	90,0		20/4/21	20,0	
06/4/21	80,0		21/4/21	30,0	
07/4/21	70,0		22/4/21	40,0	
08/4/21	60,0		23/4/21	50,0	
09/4/21	50,0		26/4/21	60,0	
12/4/21	40,0		27/4/21	70,0	
13/4/21	30,0		28/4/21	80,0	
14/4/21	20,0		29/4/21	90,0	
15/4/21	10,0		30/4/21	93,8	
16/4/21	7,7		03/5/21	0	103°

As the starting state of the wood was unknown, the first point could not be located between the adsorption and desorption isotherms. To clarify this point, a complementary campaign was carried out for the maximum RH level, imposing beforehand a saturation of the same samples by immersion in water for 72h. On this occasion, the hygrometer was recalibrated.

4 RESULTS AND DISCUSSION

4.1 SORPTION ISOTHERMS

The measured sorption isotherms at 28°C are shown in Fig. 7. For each species, the initial desorption is shown in blue and the subsequent adsorption in red. The prediction of the National Appendix [13] for this temperature is shown is dashed line, and the point measured a second time at high humidity, after resaturation, is indicated by the + sign.

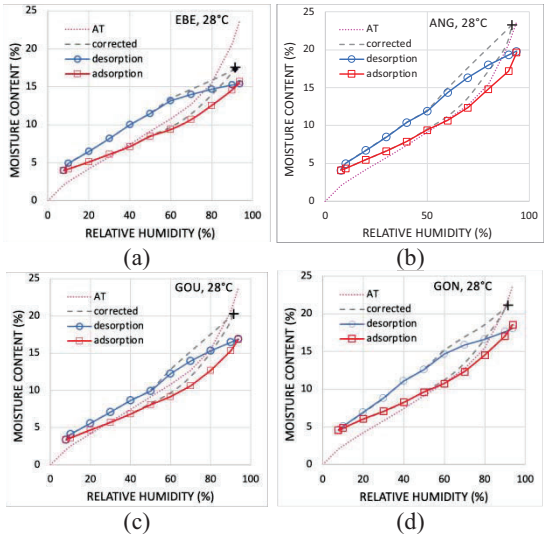

Figure 7: *Sorption isotherms at 28°C: (a)* H. serratifolius*; (b)* G. Galbra*; (c)* D guianensis*; (d)* Q. rosea*; (e)* S. rubra*. Dotted line: abacus from the National Appendix (AT). Dashed line: correction from new measurements after re-saturation.*

https://doi.org/10.52202/069179-0369

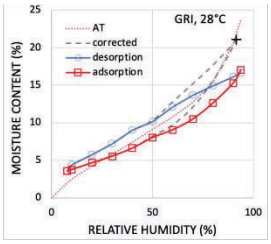

(e)

In the curves of the first campaign, a strong hysteresis between adsorption and desorption can be observed, which can be explained in part by the fact that the duration of the humidity steps is too short to reach a true equilibrium. In view of these results [14], a good agreement with the predictions of the Appendix appears for 40<*HR*<75%, these being placed in an intermediate position between the adsorption and desorption curves. At low humidities, the values are systematically slightly higher. This can also be explained by the slow diffusion process at low humidities. On the other hand, at high humidities the measured values were much lower, suggesting that these tropical woods are less hygroscopic than the temperate woods on which the Appendix charts are based. The measurements of the second campaign led us to question this analysis, as the points obtained, indicated by a cross on the graphs, were, on the contrary, very close. In addition to the correction on the mass allowed by the prior saturation, the more precise measurement of the hygrometry suggests that it had been slightly overestimated during the first campaign. The lower value observed for *H. serratifolius* could be explained by the high density (higher than 1) of this wood, which might have resulted in incomplete saturation. Independent observations [15] (J. Beauchêne, personal communication) suggest, however, that this species is really less hygroscopic than normal; it could be, especially for this species, that the bias on the slow diffusion applies to the whole isotherm, which would be globally overestimated. This reservation could also apply, to a lesser extent, to *G. galbra* which comes behind *H. serratifolius* in density and reputation for lower hygroscopicity [8, 10, 11, 14].

4.2 EQUILIBRIUM MOISTURE CONTENT EMC%

For each country, *EMC* was derived from climatic data, and *MC* was measured. A monthly average value is firstly considered to define service classes; an example of results is shown in Figure 8 for French Guaina.

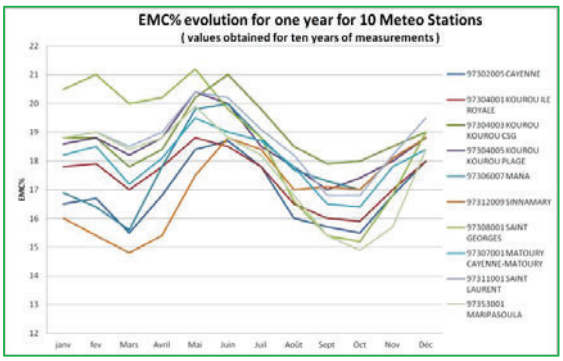

Figure 8: *French Guiana: calculated wood equilibrium moisture content (*EMC*, %) over 12 months [10]*

The average values of EMC and the difference between the minimum and the maximum during one year are taken into account. The results for 12 months can be illustrated in maps for each department (Figures 9-11).

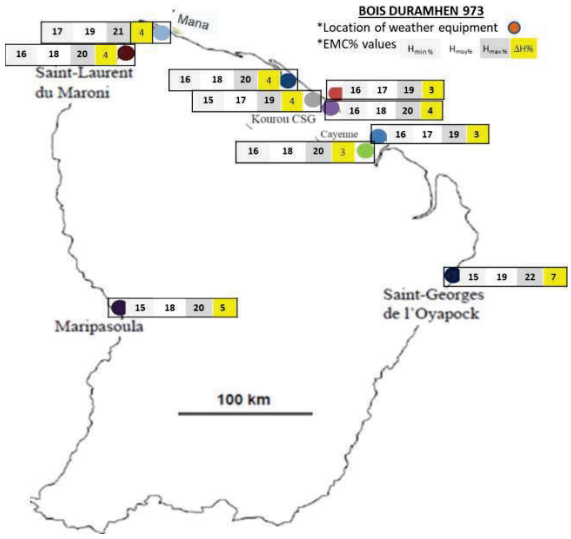

Figure 9: *12-months maps in French Guiana: extreme values of wood equilibrium moisture content (*EMC*, %) obtained for 10 weather stations [10]*

https://doi.org/10.52202/069179-0369

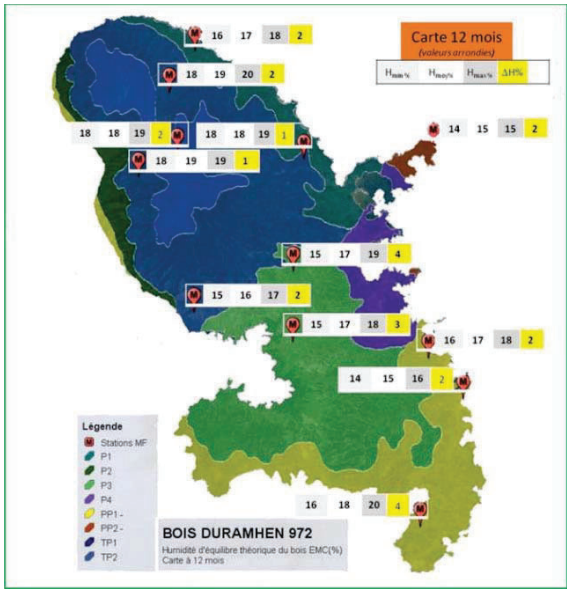

Figure 10: *12-months maps in Martinique: extreme values of wood equilibrium moisture content (*EMC*, %) obtained for 11 weather stations [9]*

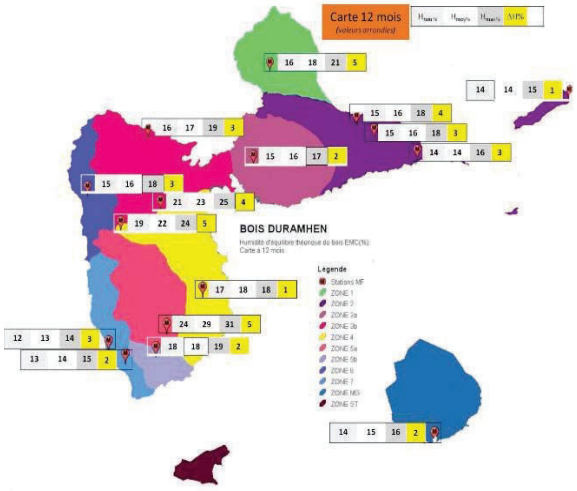

Figure 11: *12-months maps in Guadeloupe: extreme values of wood equilibrium moisture content (*EMC*, %) obtained for 16 weather stations [8]*

On most of the MF stations and different sites, the calculated and measured moisture content values fitted well within the MF Zone. In this case, service class zone could be clearly defined. In other zone(s), the service class determination had to be more detailed in order to propose a more precise mapping. The altitude is an important parameter, as well as the forest environment.

4.3 NATURAL DRYING WOOD AND MONITORING

Variations in *MC* below *FSP* are shown in Figure 12 for natural drying.

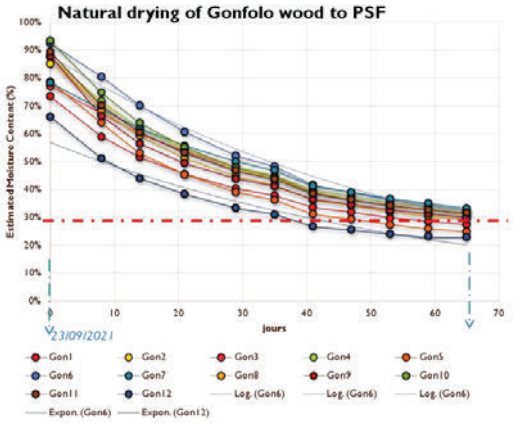

Figure 12: *Moisture loss tracking curves of Gonfolo (Q. rosea) wood (Cayenne) [10]*

Monitoring the humidity at different depths of the samples give information that can be used to monitor the drying of the wood below *FSP* (Figures 13, 14).

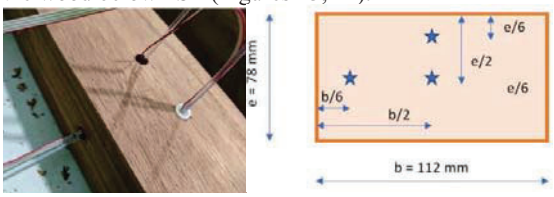

Figure 13: *Natural drying - Geometry, sensor position*

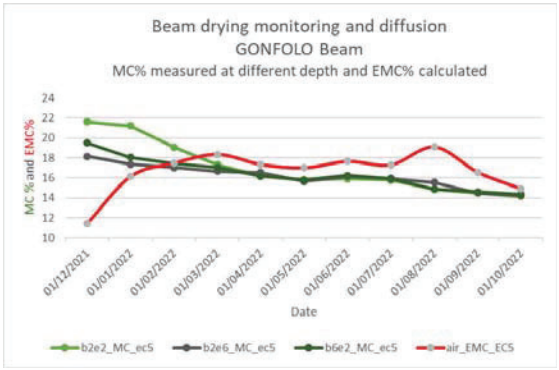

Figure 14: *Moisture content (*MC*, %) tracking curves of Gonfolo (Q. rosea) wood drying – equilibrium moisture content (*EMC*, %) calculated from local air sensor data.*

5 CONCLUSIONS

Results obtained by the different approaches, comparison of measurements, calibration of equipment led to a wide data base and gave interesting projections.

The work carried out confirmed the relevance of the abacus provided by the national appendix to Eurocode 5-part 1.1, to estimate the equilibrium water content of the woods most likely to be used for structural uses in the Guyanese context. However, a reservation must be made for the Ipe (*H. serratifolius*): because of its very high

density this wood had probably not reached the hygroscopic balance: the reputation it has of being less hygroscopic than the usual species could not be invalidated by our tests. Independent observations at CIRAD Kourou nevertheless suggest a lower hygroscopicity of Ipe, as well as Goupi (*Goupia galbra*) but to a lesser extent, whose high density is likely to slow down the achievement of hygroscopic balance. Measurements by dynamic sorption method, with analysis of the kinetics of mass change to extrapolate equilibrium values, could be carried out in order to verify the results obtained.

For the 3 French departments thanks to the results obtained by the BOIS DUR-AMHEN projects, maps were built allowing wood builders to know the humidity conditions of their construction, Figures 9-11.

Professional rules will allow these results to be used and disseminated. Especially for French Guiana, the calculated and measured moisture content values show that certain areas can be considered with conditions of a class of service 2 (SC2), but some towns present conditions of a class of service 3 (SC3).

ACKNOWLEDGEMENT

These works were supported for Martinique island and French Guiana by PACTE and for Guadeloupe island by FEDER Guadeloupe certified by the competitivity cluster Synergîle. Part of this work is based on Meteo France data base.

REFERENCES

[1] Quistin P. et al: Bois Duramhen 972 – Technical report, methodology of study, Août 2017

[2] P. Quistin, E. Fournely, L. Cador, et L. Romana, « Impact of environment on timber structures, BOIS-DURAMHEN

[3] Lamadon Th.: Taux d'humidité et panneaux dérivés en service, Note de cadrage-Bois Duramhen 971, 5pages, 2017

[4] Christian Brévignon: Atlas climatique, l'environnement atmosphérique de la Guadeloupe de Saint-Barthélemy et Saint-Martin. Météo France, 92 pages, 2005

[5] Météo France Atlas Guyanais –Le climat guyanais

[6] P. Quistin, E. Fournely, L. Cador, et L. Romana, « Impact of environment on timber structures, BOIS DUR-AMHEN971, The case of Guadeloupe (FWI) », WCTE 2018 Séoul, Corée, 2018

[7] P. Quistin, et al "Timber Structures In French Caribbean Islands, Impact Of Subtropical Climate On Design : BOIS DURAMHEN PROGRAMS" 2021 WCTE Aug, 9-12, 2021 Santiago, CHILE "

[8] P. Quistin, et al « BOIS DUR-AMHEN971 - Technical report, Results of investigations and measurements », 2019.

[9] P. Quistin, et al « BOIS DUR-AMHEN 972 - Technical report, Results of investigations and measurements », 2019

[10] Quistin P. et al: BOIS DUR-AMHEN 973 - Technical report, REX and methodology of study, January 2023

[11] E. Fournely, Joseph Gril « BOIS DUR-AMHEN 973 Technical Report n°2 / environmental test chamber / adsorption- Study of equilibrium water content », January 2023

[12] Eurocode 5/NA AFNOR, NF EN 1995-1-1/NA, « Eurocode 5, Conception et calcul des structures en bois - Partie 1-1 : généralités - Règles communes et règles pour les bâtiments, Annexe nationale à la NF EN1995-1-1 : 2005 », 2005.

[13] Eurocode 5 (2005) CEN TC 250 SC5, NF EN 1995-1-1. Eurocode 5, Conception et calcul des structures en bois, part. 1-1 : généralités, règles communes et règles pour les bâtiments, 141 p.

[14] Lefranc T. (2021) Effets de l'humidité sur les propriétés hygroscopiques et mécaniques des bois guyanais, Mémoire de projet recherche et développement, Polytech Clermont, 147p.

[15] J. Beauchêne « BOIS DUR-AMHEN 973 Technical Report n°6 / Characteristics of hardwood Guyanese», 2023

https://doi.org/10.52202/069179-0369

World Conference on Timber Engineering Oslo 2023

FRACTURE ANALYSIS OF CROSS LAMINATED TIMBER SHEAR-WALLS WITH OPENINGS

Martina Sciomenta[1]

ABSTRACT:

Strength capacity and deformation contributions of Cross Laminated Timber shearwalls with no openings are primarily governed by the behaviour of the connections. However, a considerably different behaviour and failure mechanism can be expected when openings are cut out of the shearwall panels – i.e. Monolithic Shear Walls. This paper aims to investigate the contribution of lintels and parapets on the mechanical behaviour of monolithic CLT shearwall assemblies with openings. The Abaqus software package was used to numerically investigate the racking resistance by using the extended finite element method (XFEM). A parametric study was performed on different configurations of two-storey CLT shearwalls with openings. The failure conditions related to either the CLT panels or mechanical anchors were taken into account in the analyses. The results showed that the strength and stiffness of shearwalls where openings are cut off the panel are significantly greater than those obtained for shearwalls assembled with separated elements – i.e. Segmented Shear Walls. The increase in strength and stiffness is particularly pronounced in the case of window openings.

KEYWORDS: Walls with Openings, Monolithic Shear Wall, Lintels, XFEM

1 INTRODUCTION

Connections strongly influence the strength capacity and strains of Cross Laminated Timber (CLT) shear-walls without openings but their behaviour and failure mechanism drastically change when openings are cut-out of Monolithic Shear Wall (MSW) panels (Figure 1a).
The opening could cause a significant increase in the shear deformation contribution of the CLT panel. This condition could led to high stress concentration around the corners of the opening, with a consequent possible premature and undesired brittle failure mode.
Openings can alternatively be realized by joining lintel and parapet elements to wall segments, denoted as Segmented Shear Walls (SSW) (Figure 1b). Following this construction method, no moment continuity is ensured between the timber members, so the wall segments could be assumed to behave as cantilevered beams.
Research on the mechanical behaviour of CLT shear-walls with openings has been quite limited, with some studies focussing on the determination of reduction factors on the stiffness of the CLT [1-2] or simplified modelling strategies [3-4]. Available literature on experimental tests indicates potential for brittle failure modes in the CLT panels [5-6], emphasizing the need to better quantify the conditions in which such failure mechanisms occur.
Investigating brittle failures in CLT shear-walls is quite challenging due to three main different aspects: the first one concerns the large scale and the complexity of the problem. In fact, shear-walls are characterized by the presence of both mechanical anchors (variable in number, type and position) and different geometrical properties of timber lintels and parapets

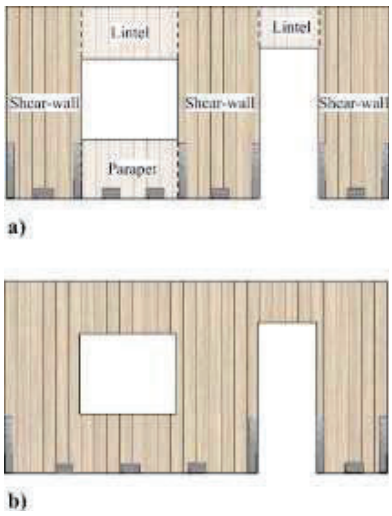

***Figure 1**. a) Monolithic (MSW) shear wall, b) Segmented (SSW) shear wall Fracture modes*

Up to now, instead, most studies involving the crack formation in timber were mainly performed at beam scale (such as LVL beams [7] and notched beams [8-9]), and to resolve detail issues (i.e joint bonding [10-11] and connection [12]).
The second aspect concerns the choice of either 2D or 3D analysis. Most of the FE timber fracture analyses have been carried out via 3D modelling; this latter is a powerful

[1] Martina Sciomenta, University of L'Aquila (DICEAA), Italy, martina.sciomenta@univaq.it

https://doi.org/10.52202/069179-0370

strategy to perform accurate fracture analyses on small scale components but, on the other way, makes the analysis time-consuming for large scale problems.
Finally, the modelling of structural elements with an existing sharp crack/notch allowed, in fracture analysis, the application of the classic finite element (FE) as well as the linear elastic fracture mechanics (LEFM) methods such as the Virtual Crack-Closure Technique (VCCT) or the Cohesive Zone Models (CZM).
However, the crack initiation and its propagation path is unknown a-priori in analysis of full scale walls due to the complex shear-walls mechanical behaviour.
The extended finite element method (XFEM) does not require to know a-priori the crack location and to re-mesh the crack surfaces (typical of the aforementioned classic FE, LEFM-based methods). The XFEM assesses the presence of discontinuities in a material by using special enriched functions in conjunction with additional degrees of freedom. It was first introduced by Belytschko and Black [13] and represents an extension of the conventional finite element method based on the concept of partition of unity introduced by Melenk et Babuska [14], which allows local enrichment functions to be easily incorporated into a finite element approximation.
The XFEM is a well-established method that does not require to know a priori crack path. This method, which is available with both 2D and 3D models, was used to model fracture mechanics problem on different structural materials such as steel [15], concrete [16] and composites [17], however just little was done in the field of timber and wood-based composites.
In this paper, the possibility to apply the XFEM procedure for the crack detection on CLT walls with opening is investigated. The aforementioned benefits of XFEM combined with a 2D analysis will be exploited to provide a novel CLT shear-walls modelling which furthermore allows the crack detection.
The two main aims of this paper are: *i)* to validate the proposed procedure for the cracks initiation and propagation in CLT shear-walls with openings and *ii)* to investigate the contribution of lintels and parapets on the mechanical behaviour of multi-storey CLT shear-wall assemblies.

2 STATE OF THE ART

2.1 FRACTURE MECHANICS

The solution to crack and defect problems can be achieved in the framework of the linear elastic fracture mechanics (LFEM), which is the basic theory of fracture that dealing with the initiation and propagation of cracks in elastic bodies. It was originally developed by Griffith [18] and completed in its essential form by Irwin [19] and Rice [20].
The fracture resistance is the ability of materials to withstand flaws that initiate failure, and usually these properties could be assessed by estimating the fracture toughness (based on Griffith's approach) or the critical value of energy release rate (based on Irwin's approach). These parameters measure the severity of the stress field around crack tips and determine the fracture criteria [21].
A material fracture resistance value varies depending on the loading mode. There are three fracture modes depending on the loading conditions for a crack, Mode I, II and III, representing fracture induced by pure tensile stress perpendicular to the crack plane and that induced by shear stresses, respectively. A mixed mode of Mode I and Mode II is the most common combination in structural applications [22].
The study of brittle failures in timber elements is challenging due to both to the nature of the material and the geometric complexity of some problems. In fact, being timber an orthotropic material, it is far more complicated than for isotropic materials due to the relevance of crack orientation, material stiffness and strength properties, which can all have an impact on the direction and load level at which cracks propagate [23].
However, the fast development of the finite element methods (FEM) allow the user to extended the LEFM concepts and crack criteria to problems with complex geometries and loading conditions [24].
For this purpose, the most common methods used are the Virtual Crack Closure Technique (VCCT) and the Cohesive Zone Model (CZM). VCCT theory assumes that when a crack is extended, the energy required to open the crack is the same required to close it. In the CZM, the equations needed to analyse the fracture process are simplified and focused only on the tip region of the crack, which considers the characteristics of this region with a traction-separation law. In the FEM, the traction-separation law is assigned to cohesive elements defined in the crack path [25].
Modelling stationary discontinuities, such as a crack, with the conventional finite element method requires that the mesh conforms to the geometric discontinuities. Therefore, considerable mesh refinement is needed in the neighbourhood of the crack tip to properly capture the singular asymptotic stress and the strain fields.
It is also required to establish a priori the path crack.
The extended finite element method (XFEM) alleviates these shortcomings as it assess the presence of discontinuities in a material by introducing specially enriched functions in conjunction with additional degrees of freedom.
To simulate crack propagation in wood by FEM, a crack initiation and a crack propagation criterion needs to be specified.
The damage initiation refers to the beginning of degradation of the material response in a certain point. Several damage initiation criteria are available: maximum nominal stress/strain, quadratic nominal stress or maximum principal stress/strain. In each case, damage is assumed to initiate when the stress/strain satisfy the input damage criteria.
The damage propagation specifies how the response (cohesive stiffness) of the material changes (degrade) once the initiation criterion is reached. The overall damage could be accounted by a scalar parameter D which ranges from 0 (no damage) to 1 (complete failure).

https://doi.org/10.52202/069179-0370

The stress that would be measured without damage is multiplied by (1-D) to calculate the stress after damage has occurred. Without damage (D=0), this leads to the undamaged response; with complete failure (D=1), the stress is 0; and in between a fraction of the stress will remain (Figure 3).

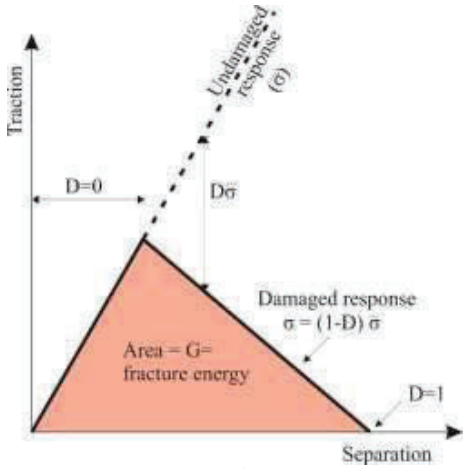

***Figure 3**. Damage initiation and evolution*

3 NUMERICAL ANALYSES

At first, the proposed XFEM procedure was validated for the crack detection on CLT walls with opening. The numerical results from FEM analyses were compared with the experimental ones obtained from a full-scale test performed by Casagrande et al [26] on a single-storey CLT shearwalls with single opening.

3.1 MODELLING STRATEGY

Abaqus software package [25] was used to carry out the numerical analysis.

In this work, 2D planar element were used to model the CLT panel and non-linear link elements were adopted to represent the behaviour of mechanical anchors (Figure 4). By using partitions, the shear-walls lintels and parapets were properly identified in the model. This procedure was particularly useful for our purposes since it allows the user to attribute different material features and enrichments (damage) to portions of mesh which can either experience damage (lintels and parapets) or not.

The elastic orthotropic material behaviour is accounted by considering the effective modulus of elasticity along the vertical, $E_{eff,v}$ (Eq. 1) and horizontal, $E_{eff,h}$ (Eq. 2) directions, as and the shear modulus, G_{eff} (Eq. 3) in accordance with Bogensperger et al. [27] and Brandner et al. [28].

$$E_{eff,v} = \frac{E \cdot t_v}{t_{tot}} \tag{1}$$

$$E_{eff,h} = \frac{E \cdot t_h}{t_{tot}} \tag{2}$$

$$G_{eff} = \frac{G}{1 + 6 \cdot \alpha_T \cdot \left(\frac{t_{mean}}{w_b}\right)^2} \tag{3}$$

being E the elastic modulus parallel to the grain, t_{tot} the total thickness of the CLT panel, t_v and t_h are the sum of thethicknesses of the vertical and horizontal layers, respectively, G is the board'sshear modulus, t_{mean} is the average thickness of boards, w_b is the width of boards and α_T is reported in Eq.4.

$$\alpha_T = p_B \cdot \left(\frac{t_{mean}}{w_b}\right)^{q_B} \tag{4}$$

where q_B is equal to -0.79 and p_B and is equal to 0.53 and 0.43 for 3 and 5 layers CLT panel, respectively, as reported in Brandner et al. [28].

For members not involved in the damage detection (i.e. wall segments), timber was defined as an elasto-plastic orthotropic material to take into account the local plasticization of wood in compression (Figure 4).

The Hill anisotropic yield criterion was adopted and based on the panel orientation, the reference resistance value was assumed equal to the CLT compressive strength parallel to grain: $f_{c,0}$. The corresponding anisotropic stress ratios (R_{ii} with i=1..3; j=1..3) for the other principal directions of interest were properly calculated (Equations 5 and 6).

$$R_{ii} = \frac{\bar{\sigma}_{ii}}{\sigma^0} \tag{5}$$

$$R_{ij} = \frac{\bar{\tau}_{ij}}{\sigma^0 / \sqrt{3}} \tag{6}$$

where $\bar{\sigma}_{11} = f_{c,0}$, $\bar{\sigma}_{22} = \bar{\sigma}_{33} = f_{c,90}$ and $\bar{\tau}_{12} = \bar{\tau}_{13} = \bar{\tau}_{23} = f_v$ are the measured yield stress value and $\sigma_0 = f_{c,0}$ is the reference yield stress specified for the plasticity definition;

The failure conditions related to either the CLT lintels and parapets or mechanical anchors were taken into account in the model analyses.

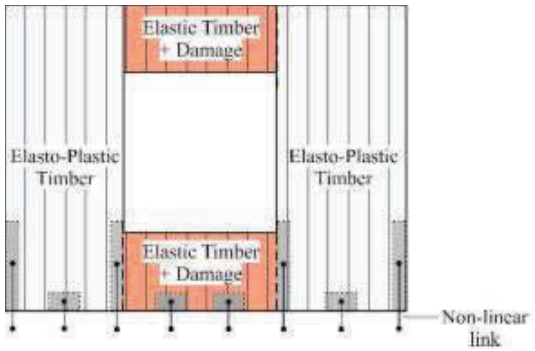

***Figure 4:** Schematic partitions, materials and mechanical anchors definition in Abaqus models*

https://doi.org/10.52202/069179-0370

Damage initiation is defined in the material properties by using a traction-separation law with the maximum nominal stress criterion – (MAXS). With this option, damage will initiate when the maximum stress ratio exceeds the unit (Eq. 7).

$$\max\left\{\frac{\sigma_n}{\sigma_n^0}, \frac{\sigma_s}{\sigma_s^0}\right\} = 1 \quad (7)$$

Being the CLT shear-walls lintels subjected primarily to bending and shear, the peak values of the nominal stresses, σ_n^0 and σ_s^0, are set equal to the effective bending strength in the horizontal direction $f_{m,h,eff} = \frac{f_m \cdot t_h}{t_{tot}}$ and the effective shear strength $f_{v,eff} = \frac{f_v \cdot min(t_h; t_v)}{t_{tot}}$, respectively.

The Wu crack propagation criterion was defined to compute the equivalent fracture energy release rate. It can be expressed in terms of energy release rate as in the following:

$$\left(\frac{G_I}{G_{IC}}\right)^{a_m} + \left(\frac{G_{II}}{G_{IIC}}\right)^{a_n} \geq 1 \quad (8)$$

where G_{IC} and G_{IIC} are the critical fracture energies required to cause failure in the normal and the shear directions, respectively, and G_I and G_{II} are the strain energy release rates which refer to the work done by the traction and its conjugate relative displacement in the normal and shear directions, respectively.

3.2 VALIDATION

A validation of the proposed FE model was carried out by comparing the model results with those obtained from experimental tests conducted by Casagrande et al [26] on single-storey CLT shear-walls with single opening (i.e. Wall 1).

The wall was made with a 3-layered 90 mm thick (30v-30h-30v) CLT panel .

The mechanical properties of the CLT panels are assumed from [26] and are E_0=13411 MPa, G=690 MPa, f_m=48.5 MPa, and f_v= 9.1 MPa. The wall height was equal to 2380 mm and the length was equal to 3300 mm. The geometrical dimensions of the door opening were (b x h / 600 mm x 2040 mm), while the lintel height was equal to 340 mm.

The test was carried out by using a commercially available hold-down anchors (WHT620) to connect the wall to the foundation. Each hold-down was connected to the wall panel using fifty-five 4x60 mm ring shanked nails, while the connection to the steel base beam was achieved using an M20 bolt. Additional blocking systems were adopted [26]. The mechanical anchor was modelled as a non-linear link accounting for its load-displacement curves obtained from Casagrande et al [26]. The blocking systems were modelled by applying a displacement boundary conditions with the component u_1=0 (Figure 5).

The critical values of the energy release needed for describing the fracture criterion were selected to be equal to $G_{IC} = 176\ N/m$ and $G_{IIC} = 734\ N/m$, according to the experimental evidences presented by Haller and Putzger [28], achieved by performing double cantilever beam (DBC) fracture tests and assumed by Kováčiková et al. [29] to study studies related to C24-graded elements fracture.

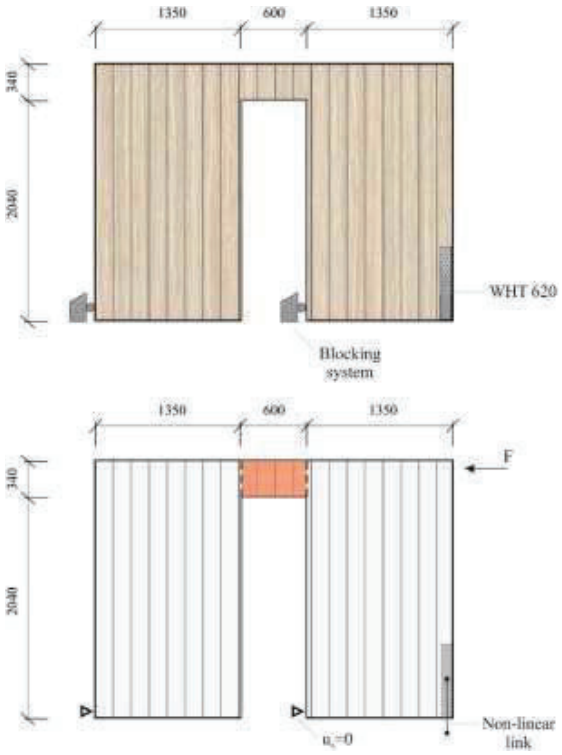

Figure 5: *Wall 1: Test setup (top) and schematic plan of partitions and mechanical anchors definition in Abaqus models (bottom) (measures in mm)*

The empirical parameters a_n and a_m are assumed as 0,5 and 1 respectively, according to [30].

A push-over analysis was carried out by increasing the lateral load applied at the top of the shear-wall.

In Figure 6 the comparison between the experimental and the FEM model curves proved a reasanable match, while in Figure 6 the position and the path of the crack reveal the same propagation observed in the test.

https://doi.org/10.52202/069179-0370

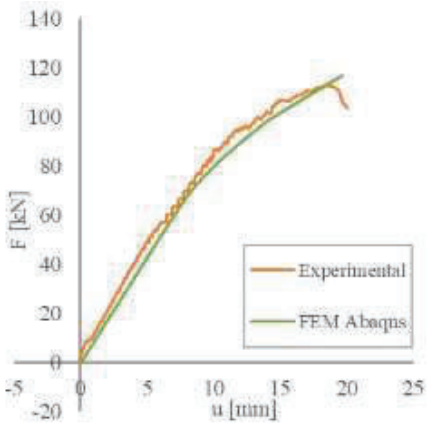

Figure 6. *Model validation with crack opening*

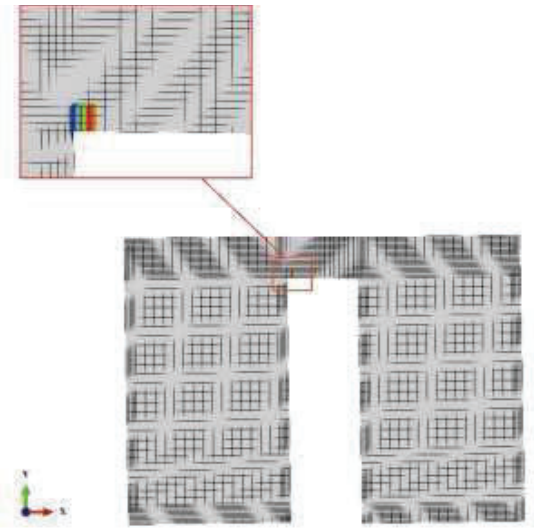

Figure 7. *Model validation with crack opening*

4 MULTI-STORY SHEAR-WALL CONFIGURATIONS

The validated model strategy was applied to two configurations of two-storey and multi-openings shear-walls.

Push-over analyses are carried out by applying a triangular distribution of horizontal forces on the top of the shear-wall.

For these configurations, the lateral stiffness, strength capacity and failure modes were documented and compared for shear-walls with openings either cut of out of the panels (MSW) or constructed with separate elements (SSW) (Figure 8).

The geometrical dimensions as well as the layout of mechanical anchors are reported in Figure 9 for Configuration #1 and in Figure 10 for Configuration #2, respectively.

For Configuration #1, the CLT panels have the same geometrical and mechanical properties of those of the wall described in the previous section. A vertical load equal to 15 kN/m was applied at each storey. The shear walls are anchored using ABR105 angle brackets spaced at 300mm and WHT620 hold-downs at each end of wall segments. The angle brackets are connected to the CLT panel using ten 4,2x89mm spiral nails and the hold-down are attached to the panels using fifty-five 4x60mm ring shanked nails.

For Configuration #2, the CLT panel is a 5-layered 100mm thick boards (20v-20h-20v-20h-20v) CLT shear-wall made of Spruce boards of C24 grade.

The mechanical properties of the CLT panels are assumed from [28] and are E_0=13878 MPa, G=690 MPa, f_m=50,2 MPa, and f_v= 11.0MPa.

The WHT 620 hold-downs and the angle bracket BMF 90x116x48x3 with 11 nails [31] were accounted. No vertical load was applied on Configuration #2 shear-walls

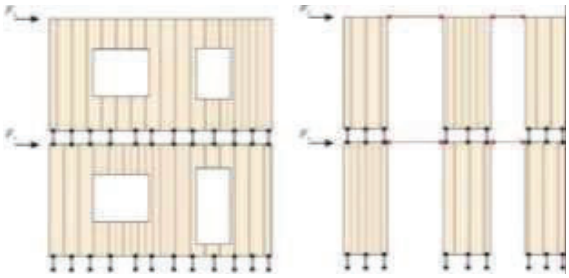

Figure 8: *left) MSW model; right) SSW model*

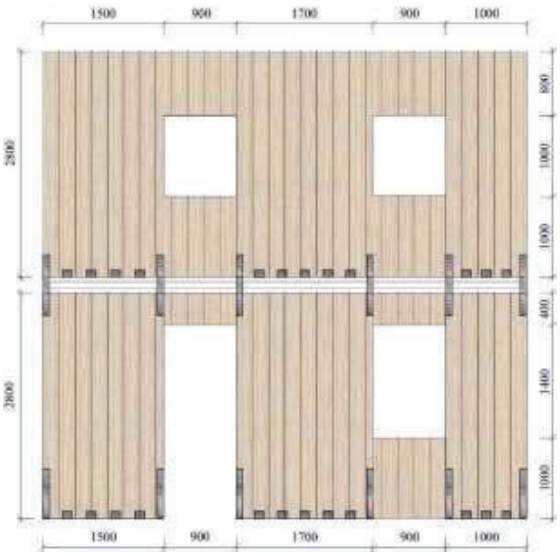

Figure 9: *Shear-wall Configuration #1 (measures in mm)*

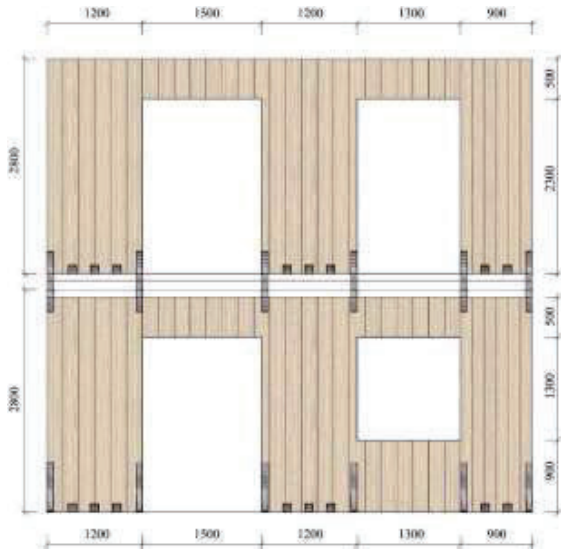

Figure 10: *Shear-wall Configuration #2 (measures in mm)*

The results from the two Configurations are significantly different both for in terms of strength and stiffness. In particular, the evidences from MSW are greater than those obtained for SSW, as displayed in Figure 11 and 12. The increase in strength and stiffness is particularly pronounced in the cases of window openings. The fracture analysis confirmed an high concentration of stress around opening leads to brittle failure modes in CLT lintels, which cannot be ignored in the design of such structural systems.

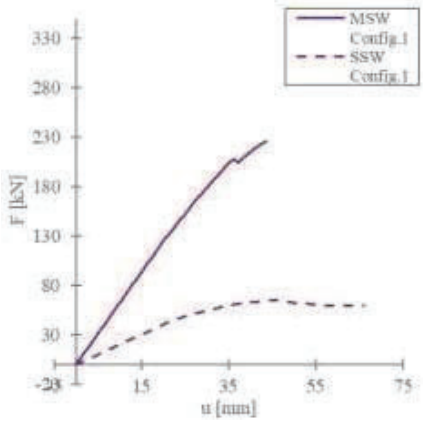

Figure 11: *MSW vs SSW models of cases shown in Figure 9 (Configuration #1)*

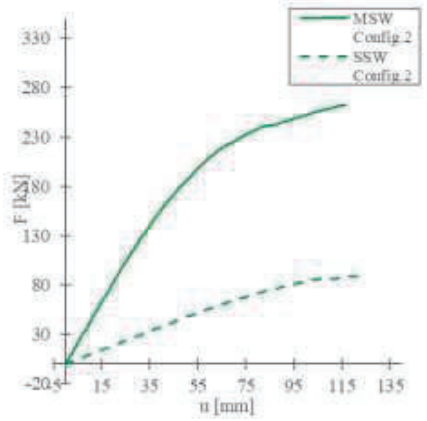

Figure 12: *MSW vs SSW models of cases shown in Figure 10 (Configuration #2)*

Moreover, the fracture mechanisms are also clearly highlighted for Configuration #2 (Figure 13).

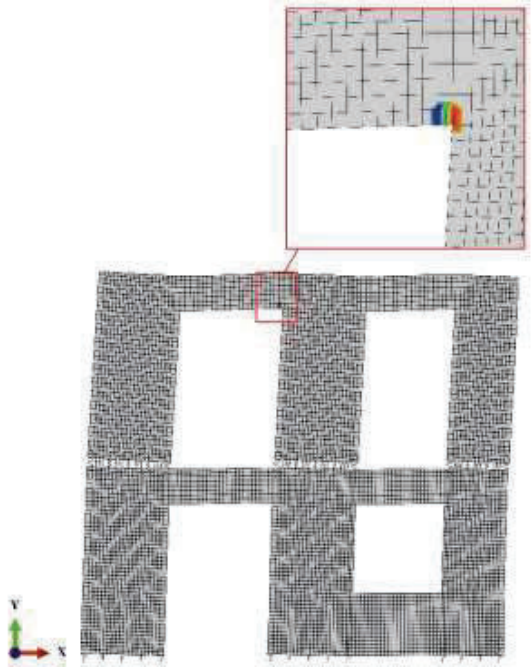

Figure 13: *Fracture mechanisms for Configuration #2.*

5 CONCLUSIONS

In this work a proposal for the crack detection in CLT shear-walls with openings is provided. The Abaqus software package was used to numerically investigate both the crack propagation by using the extended finite element method (XFEM) as well as the contribution of lintels and parapets on the mechanical behaviour of multi-storey CLT shear-wall assemblies.

https://doi.org/10.52202/069179-0370

The proposal was validated on shear-walls experimental evidences and highlighted an excellent matching both in terms of load-displacement curve as for position and path of the crack. Later, two different configurations of two-storey and multi-openings shear-walls were carried on. In addition, in this case the proposal was effective for the crack detection; it was also highlighted the great influence of lintel and parapets in terms of shear-walls global mechanical behaviour.

REFERENCES

[1] Dujic B, Klobcar S, Zarnic R (2015) Influence of openings on shear capacity of wooden 675 walls, *NZ Timber Design Journal,* Volume 16 Issue 1.

[2] Pai S G, Lam F, Haukaas T (2017) Force Transfer Around Openings in Cross Laminated Timber Shear Walls. *Journal of Structural Engineering*, Volume 143, 4.

[3] Mestar, M., Doudak, G., Polastri, A., Casagrande, D.Investigating the kinematic modes of CLT shear-walls with openings (2021) *Engineering Structures*, 228, art. no. 111475. doi: 10.1016/j.engstruct.2020.111475

[4] Mestar, M., Doudak, G., Caola, M., Casagrande, D.Equivalent-frame model for elastic behaviour of cross-laminated timber walls with openings (2020) *Proceedings of the Institution of Civil Engineers: Structures and Buildings*, 173 (5), pp. 363-378.

[5] Shahnewaz M, Tannert T, Alam M S, Popovski M (2017) In-plane stiffness of cross laminated timber panels with openings (2017) *Structural Engineering International,* 27 (2), 681 pp. 217-223.

[6] Yasumura M, Kobayashi K, et al. (2016) Full-scale tests and numerical analysis of low-rise CLT structures under lateral load-ing. Journal of Structural 635 *Engineering Volume* 142 (4), April 2016.

[7] Ardalany, M., Deam, B. & Fragiacomo, M. Experimental results of fracture energy and fracture toughness of Radiata Pine laminated veneer lumber (LVL) in mode I (opening). *Mater Struct* 45, 1189–1205 (2012). https://doi.org/10.1617/s11527-012-9826-1

[8] Jockwer R. Structural behaviour of glued laminated timber beams with unreinforced and reinforced notches, (2014), Published by ETH-Zürich.

[9] Nakao T., Susanti C.M.E, Yoshihara H. Examination of the failure behavior of wood with a short crack in the radial–longitudinal system by single-edge-notched bending test, *J Wood Sci* (2012) 58:453–458, DOI 10.1007/s10086-012-1266-6.

[10] Blackman BRK, Hadavinia H, Kinloch AJ, Williams JG. The use of a cohesive zone model to study the fracture of fibre composites and adhesively-bonded joints. *Int J Fracture* 2003;119:25–46. 3.

[11] Andersson T, Stigh U. The stress-elongation relation for an adhesive layer loaded in peel using equilibrium of energetic forces. *Int J Solids Struct* 2004;41:413-434.

[12] Schoenmakers J.C.M. (2008) Elementary and advanced modelling of the splitting strength of timber connections, *Heron*, Vol.1, pages 58-84.

[13] Belytschko T., Black T., Elastic crack growth in finite elements with minimal remeshing International *Journal for Numerical Methods in Engineering* Volume 45, Issue 5 p. 601-620, 1999.

[14] Melenk J.M., Babuška I.,The partition of unity finite element method: Basic theory and applications, *Computer Methods in Applied Mechanics and Engineering*, Volume 139, Issues 1–4,1996, Pages 289-314, ISSN 0045-7825, https://doi.org/10.1016/S0045-7825(96)01087-0.

[15] Lin, M, Agbo, S, Cheng, JJR, Yoosef-Ghodsi, N, & Adeeb, S. "Application of the Extended Finite Element Method (XFEM) to Simulate Crack Propagation in Pressurized Steel Pipes." Proceedings of the ASME 2017 Pressure Vessels and Piping Conference. Volume 3B: Design and Analysis. Waikoloa, Hawaii, USA. July 16–20, 2017. V03BT03A024. ASME.

[16] Ferretti D., Michelini E., Rosati G., Cracking in autoclaved aerated concrete: Experimental investigation and XFEM modeling, *Cement and Concrete Research*, Volume 67, 2015, Pages 156-167, ISSN 0008-8846,

[17] Zhao L, Zhi J., Zhang J., Liu Z., Hu N., XFEM simulation of delamination in composite laminates, Composites Part A: *Applied Science and Manufacturing*, Volume 80, 2016, Pages 61-71, ISSN 1359-835X, https://doi.org/10.1016/j.compositesa.2015.10.007.

[18] Griffith A.A. “The Phenomena of Rupture and Flow in Solids” Trans. Roy. Soc. A221 163-198 Philosophical Transactions of The Royal Society *A Mathematical Physical and Engineering Sciences* 221(582-593):163-198 (1921). DOI: 10.1098/rsta.1921.0006.

[19] Irwin G. R. “Analysis of Stresses and Strains Near End of a Crack Traversing a Plate” *Journal of Applied Mechanics* 24(24) (1956). DOI: 10.1115/1.4011547.

[20] Rice J. R, "Mathematical Analysis in the Mechanics of Fracture", Chapter 3 of Fracture: An Advanced Treatise (Vol. 2, Mathematical Fundamentals) (ed. H. Liebowitz), Academic Press, N.Y., pp. 191-311(1968).

[21] Liu YP, Li TJ. Application of the virtual crack closure technique (VCCT) using tetrahedral finite elements to calculate the stress intensity factor, *Engineering Fracture Mechanics*, Volume 253, 2021.

[22] Schoenmakers JCM Fracture and failure mechanisms in timber loaded perpendicular to the grain by mechanical connections, Thesis, Eindhoven University of Technology, 2010.

[23] Boone T. J., Wawrzynek P. A., Ingraffea A.R., Finite element modelling of fracture propagation in orthotropic materials, *Engineering Fracture Mechanics*,Volume 26, Issue 2, Pages 185-201, 1987.

[24] Heidari-Rarani M., Sayedain M., Finite element modeling strategies for 2D and 3D delamination propagation in composite DCB specimens using VCCT, CZM and XFEM approaches, *Theoretical and Applied Fracture Mechanics*, Volume 103, 2019, 102246,https://doi.org/10.1016/j.tafmec.2019.102246.

[25] ABAQUS (Version 2023, Dassault Systemes Simulia, Inc)

[26] Casagrande D, Fanti R, Doudak G. Polastrci A (2021) Experimental and numerical study on the mechanical behaviour of CLT shearwalls with openings. *Constr Build Mater* ;298(6):123858, 2021

[27] Bogensperger T, Moosbrugger T, Silly G. Verification of CLT-Plates under loads in plane. WCTE; 2010.
[28] Brandner R, Dietsch P, Droscher J, Schulte-Wrede M, Kreuzinger H, Sieder M. Crosslaminated timber (CLT) diaphragms under shear: Test configuration, properties and design. *Constr Build Mater* 2017;2017(147):312–27.
[28] Haller P., Putzger R., "Fracture Energy in Mode I and Mode II of Reinforced Wood" in Proceedings of the 2nd Colloquium on Textile Reinforced Structures, (Technische Universität Dresden: Eigenverlag, 2003. (CTRS2)), pp. 247-258.
[29] Kováčiková J., Ivánková O., Berg S., Ekevad M., and Klas T., Computational and experimental analysis of timber beams with different types of flaws, AIP Conference Proceedings 2309, 020036 (2020); https://doi.org/10.1063/5.0034413
[30] Qiu, L.P., Zhu, E.C. & van de Kuilen, J.W.G. Modeling crack propagation in wood by extended finite element method. *Eur. J. Wood Prod.* 72, 273–283, 2014.
[31] Gavric I, Fragiacomo M, Ceccotti A. Cyclic behavior of CLT wall systems: experimental tests and analytical prediction models. American Society of civil engineers. *J Struct Eng* 2015;141(11).

https://doi.org/10.52202/069179-0370

World Conference on Timber Engineering Oslo 2023

EMBEDMENT STRENGTH AND STIFFNESS FOR LARGE DIAMETER MECHANICAL FASTENER

Krunoslav Pavković[1], Dean Čizmar[2], Mislav Stepinac[3], Nina Pospiš[4]

ABSTRACT: The paper presents a parametric numerical analysis of the mechanical fastener developed for large span truss girder. The joint has already been presented in previous papers as well as the experimental tests made on the prototype of the truss girder with this type of joint. In this paper previously obtained experimental tests were used to calibrate the numerical model for parametric analysis. Numerical models are made in the Abaqus / CAE software package. Hill's and Tsai-Wu yield criteria, defined by UMAT subroutine, were used to model the wood yield criteria. Fasteners 49 mm, 59 mm, 69 mm and 79 mm in diameter and the angle between applied load and the grain 30°, 45°, and 60° were researched and results were carried out. From the results obtained by numerical models, expressions for stiffness and embedment strength were carried out and presented in the paper.

KEYWORDS: truss girder, large diameter, mechanical fastener, parametric analysis, UMAT, stiffness, embedment strength

1 INTRODUCTION

The growing presence of timber structures in the construction of large facilities, such as bridges and multi-storey buildings, requires development of the new joints with improved and increased strength and ductility. Since 80% of all timber structure damage has been noticed in the connections [1], it is necessary to develop new generation of joints that will ensure greater durability and ductility of the structure.

Joints in timber structures are commonly made with screws, dowels, and nails or dowel-type fasteners. Extensive research has been conducted on embedment strength parallel to the grain, with several proposed expressions for embedment strength [2–4]; however, most of these are limited to small diameter fasteners. One of the well-known design criteria is defined by Johansen [2], which includes the embedment strength and the appearance of a plastic joint in the fastener. Mentioned criteria are part of the Eurocode 5 (EC5) design fastener protocol and will be only satisfied if the minimum distances between the fastener and the loaded edge of the timber element are respected to ensure ductile behaviour of the joints.

Ensuring the ductility of the large diameter fasteners, often requires increasing the timber element dimensions to unrealistic proportions, which is not economically justified. Another solution is to determine the resistance of the joint to brittle failure mode [5,6] or to locally reinforce the zone around the fastener [7–10] in order to ensure ductile behaviour.

1.1 JOINT DESIGN AND FAILURE MODES

The design of a joint made with fasteners can be divided into two criteria: the first criterion involves the local design of each individual fastener, and the second criterion involves the design of the entire joint.

The first criterion involves using the limit state method and equations based on K.W. Johansen's work [6] which are already mentioned. According to this theory, joint failure occurs when the pressure in the timber around the fastener reaches the embedment strength or if the plastic moment resistance in the fastener is reached. The mode of failure that will be critical in each joint depends on the thickness of the timber elements, the diameter and material quality of the fastener, the number of share planes, and the boundary conditions of the connection. Figure 1. shows three characteristic failure modes of wood-wood joints with two share planes, and each failure mode can be expressed by the following equation for joint design resistance (R_d):

Mode failure I

$$R_d = f_{h,\alpha,d} \cdot t \cdot d \tag{1}$$

Mode failure II

[1] Krunoslav Pavković, Department for Civil Engineering, University of Applied Sciences, Zagreb, Croatia, e-mail: kpavkovi1@tvz.hr
[2] Dean Čizmar, Department for Civil Engineering, University of Applied Sciences, Zagreb, Croatia, e-mail: dcizmar@tvz.hr
[3] Mislav Stepinac, Faculty of Civil Engineering, University of Zagreb, Croatia, e-mail: mstepinac@grad.hr
[4] Nina Pospiš, Department for Civil Engineering, University of Applied Sciences, Zagreb, Croatia, student, e-mail: nina.pospis@tvz.hr

https://doi.org/10.52202/069179-0371

$$R_d = f_{h,\alpha,d} \cdot t \cdot d \left[\sqrt{2 + \frac{4M_{y,d}}{f_{h,\alpha,d} \cdot d \cdot t^2}} - 1 \right] \quad (2)$$

Mode failure III

$$R_d = \sqrt{4 \cdot M_{y,d} \cdot f_{h,\alpha,d} \cdot d} \quad (3)$$

Where d is the fastener diameter, t is the thickness of the timber element, $f_{h,\alpha,d}$ is design embedment strength for the load at the angle α regarding to the grain and $M_{y,d}$ is a fastener design plastic moment resistance.

Results obtained using equations (1, 2, and 3) are presented by graphs in Figure 2. and Figure 3. for a joint with one embedded steel plate in the middle of the timber element. Graphs are displayed as a relation between the width of the timber element and the diameter of the fastener. Two graphs are obtained, one for fasteners up to 30 mm in diameter (Figure 4.) and other for fastener larger than 30mm (Figure 5.) on which above mentioned equation according to Eurocode 5 (EC 5) [11], does not apply. Reason for diameter restriction for which formulas can be used, is shown on diagrams where can be seen that 49 mm diameter fastener has a larger design resistance than 79 mm diameter fastener.

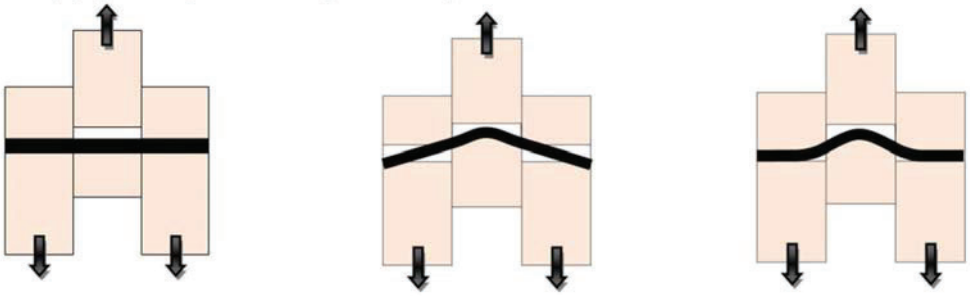

Figure 1. *Connection failure modes, from left to right: Mode I, Mode II and Mode III*

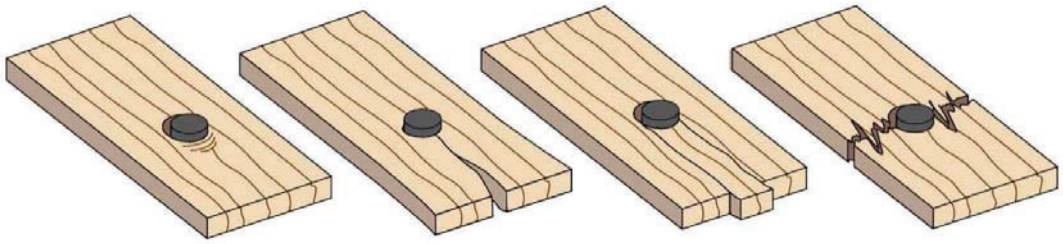

Figure 2. *Failure modes in timber joints* [9]

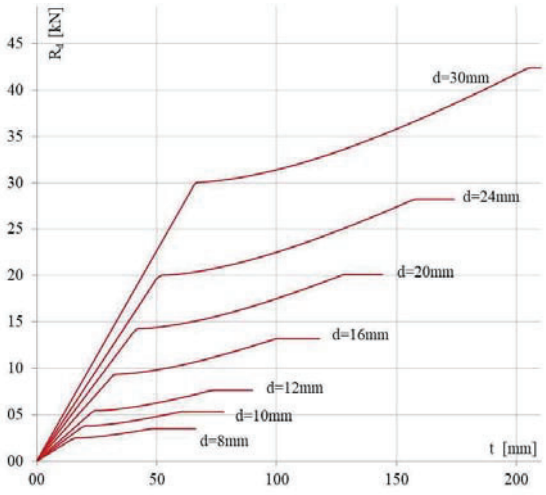

Figure 4. *Fastener resistance in relation to the timber width and fastener diameter up to 30mm*

The second criterion for the joint design is guidelines for the minimum distances between fasteners and the minimum distance between fasteners and the element edge. These given minimum distances prevent the timber element brittle failure modes and enable the ductile behaviour of the joint. In Figure 2. are presented failure modes including the first ductile mode (left picture) which are mentioned above and can be expressed with Johansen equations and followed by three pictures of brittle failure modes occurred due to: splitting, row shear, block, and plug shear or net tension.

The low deformation capacity of the brittle failure modes does not allow any redistribution of forces and causes an immediate failure of the entire connection and at the end of the entire structure [12].

Minimum distances between connectors that fall within the range of 3d to 7d usually require a large surface area for the connection. If the minimum distances are applied to dowels type fasteners with a diameter of 30 mm or more, then the problem arises on how to ensure the

https://doi.org/10.52202/069179-0371

minimum distance between the fastener and the element edge which becomes unsolvable without increasing the timber element's dimensions and increasing the wood consumption in the entire structure.
The connection analyzed in this study by using parametric finite element (FE) analysis does not have any problems with brittle failure modes due to its geometry. Since the joint concept within the truss structure ensures ductility and the large diameter tube (fastener) prevents bending of the fastener itself, the only failure mode that needs to be considered and researched is the embedment strength which is expressed by Equation 1.

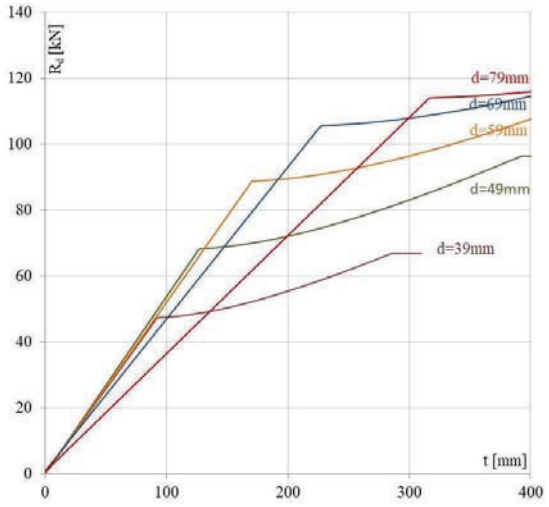

Figure 5. *Fastener resistance in relation to the timber width and fastener diameter above 30 mm*

2 EXPERIMENTAL REASERCH

Previous experimental studies on the joint with a large diameter mechanical fastener were conducted on 12 small samples, in which the load was applied perpendicular, parallel, and at the 45° angle to the grain. In small samples, failure modes were complex and were mostly caused due to cracking under tensile force perpendicular to the grain which was presented in previous papers [8,9,13].
On four large truss girders experimental research was conducted and presented in paper [14].
The truss girder joint consists of the fastener which is a large diameter pipe mounted in the cord of the truss girder and threaded rods glued in the web elements.
Load transfer from the cord to the web is carried out through high-grade bolts that connects the pipe and the connection nut mounted at the end of the threaded glued-in rod. This type of joint design for truss girders provided very ductile behaviour, unlike small samples where failure modes were mostly brittle due to cracking and block tearing. Measurements conducted during experimental research provided a good basis for calibrating finite element models (FEM) and conducting parametric FE analysis to determine a more suitable expression for large diameter fastener embedding strength.
The results obtained from experimental testing on the truss girder are shown in the graph in Figure 7 (grey lines) together with the results obtained from the FEM (black line).

Figure 6. *Joint monitoring during experimental research on a prototype of truss girder*

From the processed experimental results, mechanical characteristic values were determined: maximum force F_{max} = 333 kN, yielding force $F_{y,A}$ = 240.87 kN, $F_{y,B}$ = 191.09 kN, stiffness K_s = 52, and ductility D = 7.02.

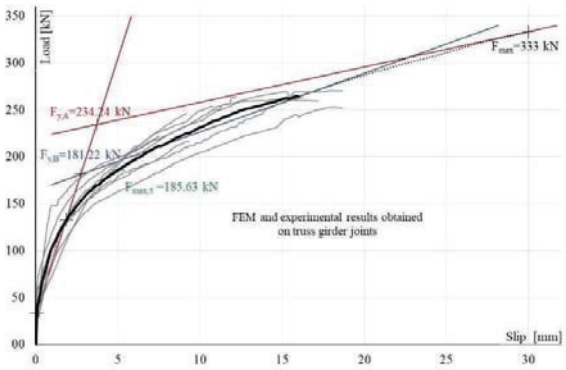

Figure 7. *Results obtained from experimental and FEM results*

3 PARAMETRIC FINITE ELEMENT MODEL ANALYSIS OF THE JOINT

FEM of the truss girder joint were modelled in Abaqus/CAE software package. C3D4 FE were used for modelling timber and steel elements. Considering that only the local behaviour of the joint is researched, a small part of the timber element (500 mm) around the fastener is modelled. Furthermore, for extra CPU time save, one half of the connection was modelled, as shown in Figure 9.
Within the parametric analysis, a total of 12 FEM were made to obtain results for joint stiffness and embedment strength in relation to the fastener diameter. Parametric numerical analysis was made for fasteners 49 mm, 59 mm,

https://doi.org/10.52202/069179-0371

69 mm, and 79 mm in diameter. Also, for each fastener diameter, three models were made with applied load at the angle of 30°, 45°, and 60° to the grain.
The mechanical properties and yield criteria of the wood were defined in the UMAT subroutine, i.e., Tsai-Wu for the connection zone and Hill for the rest of the timber element, as shown in Figure 8. The UMAT subroutine was described in detail in previous research [8].

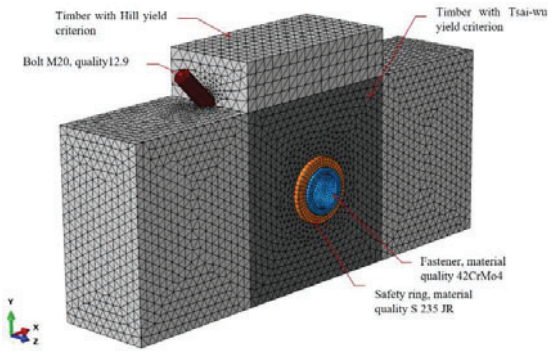

Figure 8. *Assigned yield criteria to joint FEM*

Absolute stiffness for normal stresses was used to model the contact surfaces, as well as the ability of two surfaces to experience tangential sliding with a friction coefficient. The friction coefficient applied for steel-steel contact was adopted as 0.2, and for wood-steel contact, 0.25.
FEM analyses were carried out using nonlinear analysis with included geometric and material nonlinearity. As in previous research papers [8,14], the Newton method with automatic step control was adopted for force control. The maximum load increment step was limited to 0.25t, with an initial setting of 0.1t, and the load increment was linearly set to 1.0 kN per unit time t.
The loading was modeled as a pressure on the bolt cross section in direction parallel with the axes. The given pressure on the surface was 4.40567 N/mm^2, which corresponds to the force of 1000 N on a surface of 226.98 mm^2. The force increment was linearly guided by the amplitude ratio as a function of time.

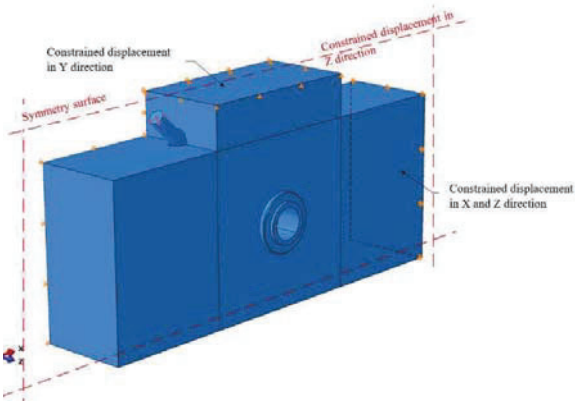

Figure 9. *FEM boundary conditions*

4 RESULTS AND DISCUSSION

As previously mentioned, a total of 12 FEM were analysed. Results of the joint load-slip behaviour were obtained for each model, and some of the results are shown in Figure 10.
The obtained results were processed according to EN 12512 standard [15], using both recommended methods (Method A and B) for determination of yield force and maximal force of the joint.
According to this standard, the maximum force is determined as the smaller value of the following three conditions: the force at the point of joint failure, 80% of the maximum force reached within a displacement of 30 mm if there is a descending branch in the load-slip curve, and the maximum force at a displacement of 30 mm.

Table 1. Joint characteristic values obtained from load-slip graphs

d [mm]	α [°]	$F_{y,A}$ [kN]	$F_{y,B}$ [kN]	K_s [kN/mm]	D	$F_{max,5}$ [kN]	$f_{h,0}$ [N/mm^2]
49	60	224.41	174.03	38.88	5.64	166	31.37
	45	240.87	191.09	52.00	7.02	195	31.34
	30	276.72	226.93	73.20	8.38	238	31.53
59	60	278.68	205.24	43.87	5.06	187	30.79
	45	300.96	224.94	57.37	6.04	218	30.15
	30	306.53	243.85	83.59	8.49	253	28.31
69	60	292.47	214.42	51.01	5.60	204	30.14
	45	327.58	239.66	63.79	6.17	230	28.21
	30	365.68	261.84	85.74	7.31	266	25.95
79	60	339.66	222.91	56.22	5.29	221	29.91
	45	366.77	247.99	70.92	6.10	244	27.13
	30	424.47	283.70	99.09	6.95	304	26.46

https://doi.org/10.52202/069179-0371

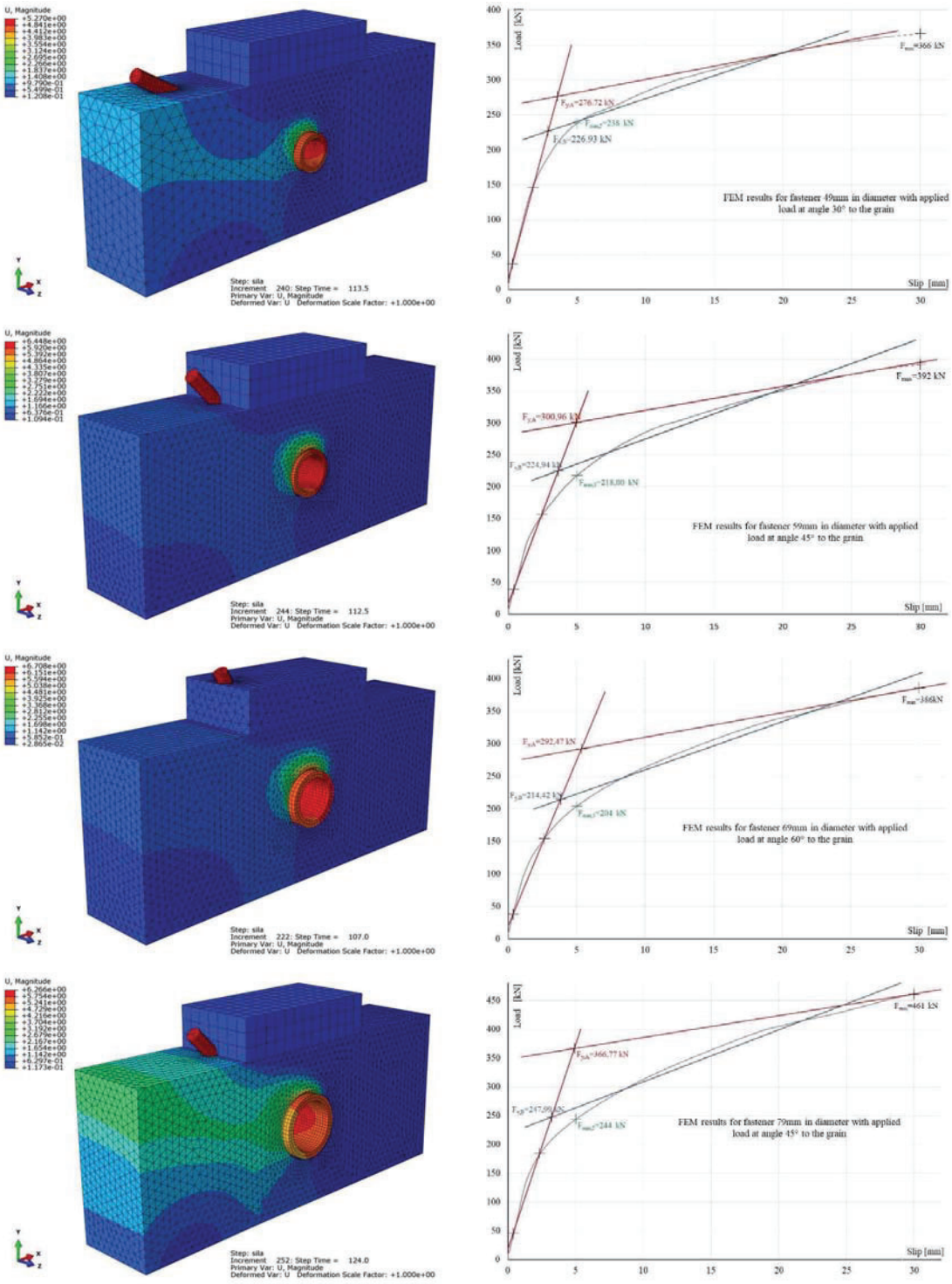

Figure 10. *Representation of joint displacement and load-slip graphs obtained by FEM*

Yield force according to the method A is determined by the intersection of the two lines; the first line is defined by the values of 10% and 40% of maximal load and the second line is defined by 1/6 inclination of the first line and maximal load. Method B is carried out by replacing the plastic region of the load-slip diagram from the yield force obtained from method A to the maximum force with a line defined by the least-squares method. The obtained

values from both methods are presented in Table 1. Also, the obtained results are analysed according to EN 12512 for determining the stiffness of the joint, according to the expression:

$$k_s = \frac{0.4F_{max} - 0.1F_{max}}{\delta_{0.4} - \delta_{0.1}} \quad (4)$$

For each FEM fastener embedment strength is determined according to EN 383 [16]. According to this standard, the characteristic embedment strength is obtained by dividing the force which corresponds to a 5 mm slip values ($F_{max,5}$) by the fastener diameter and thickness of the timber element in which the fastener was mounted. These embedment strengths were converted to embedment strength parallel to the grain, and the obtained values are presented in Table 1.

The obtained stiffness results of all 12 FEM were presented in the graph in Figure 11. Using the least-squares method, formulas for the joint stiffness were obtained for each applied load angle separately. Since the graph shows that all three angles of applied load have similar slopes, the main slope was adopted as the unique stiffness equation:

$$K_S = 0{,}673 \cdot d + 66{,}71\cos\alpha - 24{,}59 \quad (5)$$

The described procedure yielded a unique Equation (5) for determining the stiffness of the researched joint. Since the interception of the results with the y-axis depends on the applied load angle to the grain, and generally on the elastic modulus parallel and perpendicular to the grain, it is necessary to introduce the elastic modulus into the equation. According to the literature [17], the dependence of the three elastic modulus in softwood can be put in a relationship as E_L:E_R:$E_T \approx 20$:1.6:1.

$$K_S = 0{,}718 \cdot d + (2{,}713\cos\alpha - 1) \cdot 2{,}173 \cdot E_L \quad (6)$$

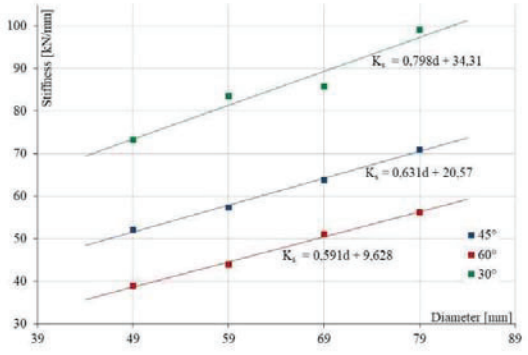

Figure 11. *Joint stiffness in relation to the fastener diameter*

Taking this into consideration, it can be concluded that introducing one elastic modulus is sufficient for defining unique Equation (6) which covers the type of timber, the fastener diameter, and the applied load according to the grain.

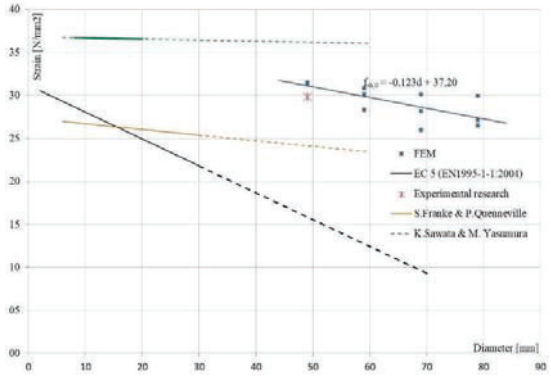

Figure 12. *Embedment strength in relation to fastener diameter*

The embedment strength for the load parallel to the grain is graphically shown in Figure 12. The results were approximated by a straight line obtained by the method of least squares and the equation of the obtained straight line is given by:

$$f_{h,0} = -0{,}123 \cdot d + 37{,}20 \quad (6)$$

From this equation, an expression for the characteristic embedment strength depending on the characteristic density of timber and fastener diameter can be derived as follows:

$$f_{h,0.k} = 0{,}084(1 - 0{,}0033d)\rho_k \quad (7)$$

This equation in comparison to the equation for embedment strength in the EC 5 norm gives a more precise embedment strength for large diameter fasteners loaded parallel to the grain.

5 CONCLUSIONS

The connection designed for large span truss girders with large diameter fastener, as presented in this paper, has shown great ductility and resistance. The geometry of the connection ensures failure due to exceeding the embedment strength. Such a designed joint with a large diameter fastener has served as a good basis for determining the expression for the embedment strength. From the parametric analysis, expressions for the embedment strength for fastener larger than 30 mm in diameter were derived. A comparison of the results showed that the proposed expression falls within the limits of previously obtained expressions and has good overlap with the results obtained from experimental research.

The experimental tests and parametric analysis showed that the expression for the embedment strength found in

https://doi.org/10.52202/069179-0371

Eurocode 5 loses accuracy with increasing diameter of the fastener and requires further adjustment through extensive research. Additionally, it is necessary to consider incorporating an expression for embedment strength for fasteners larger than 30 mm in diameter; because this paper, along with several others, has shown that large-diameter fasteners can ensure joints with ductile behavior, high resistance, and stiffness.

REFERENCES

[1] Santos C, de Jesus A, J. L. Morais J, Louzada J. Quasi-static mechanical behaviour of a double-shear single dowel wood connection. Constr Build Mater, 171–82, 2009.

[2] Johansen KW. Theory of timber connections. International Association of Bridge and Structural Engineering; 249–62, 1949.

[3] Sawata K, Yasumura M. Determination of embedding strength of wood for dowel-type fasteners. Journal of Wood Science, 138–146, 2002.

[4] Franke S, Quenneville P. Bolted and dowelled connections in radiate pine and laminated veneer lumber using the European yield model, 13–28, 2011.

[5] Jensen J, Girhammar UA, Quenneville P. Brittle failure in timber connections loaded parallel to the grain. Proceedings of the Institution of Civil Engineers - Structures and Buildings,168:760–770, 2015.

[6] Jockwer R, Fink G, Köhler J. Assessment of the failure behaviour and reliability of timber connections with multiple dowel-type fasteners. Eng Struct, 172:76–84, 2018.

[7] Haller P, Birk T, Offermann P, Cebulla H. Fully fashioned biaxial weft knitted and stitch bonded textile reinforcement for wood connections. Composites Part B-Engineering - COMPOS PART B-ENG, 37:278–85, 2006.

[8] Pavković K, Rajčić V, Haiman M. Large diameter fastener in locally reinforced and non-reinforced timber loaded perpendicular to grain. Eng Struct, 74:256–65, 2014.

[9] Pavković K, Stepinac M, Rajčić V. Brittle failure modes in reinforced and non-reinforced timber joint with large diameter fastener loaded parallel to grain. Eng Struct, 222:111104, 2020.

[10] Pavković K, Rajčić V, Čizmar D. Parametric Analysis of Large Diameter Mechanical Fastener in Reinforced Glulam. Tehnicki Vjesnik, 21:843–852, 2014.

[11] CEN:EN 1995-1-1 :2004. Eurocode 5: Design of timber structures - Part 1-1: General - Common rules and rules for buildings. 2004.

[12] Jockwer R, Fink G, Köhler J. Assessment of the failure behaviour and reliability of timber connections with multiple dowel-type fasteners. Eng Struct, 172:76–84, 2018.

[13] Pavković K, Čizmar D, Rajčić V. Parametric analysis of large diameter mechanical fastener in reinforced glulam. Tehnicki Vjesnik, 21:843–852, 2014;.

[14] Pavković K, Haiman M, Meštrović M, Rajčić V. Truss girder joint with a large diameter mechanical fastener. Građevinar, 65:869–878, 2013.

[15] EN 12512:2006 Timber Structures - Test Methods - Cyclic Testing of Joints Made with Mechanical Fasteners, Comite Europeen de Normalisation. Brussels. 2006.

[16] EN 383: 2007 Timber Structures - Test Methods - Determination of embedding strength and foundation values for dowel type fasteners , Comite Europeen de Normalisation. Brussels. 2007.

[17] Borgin KB, Loedolff GF, Saunders GR. Laminated wood beams reinforced with steel strips. ASCE Journal of the Structural Division, 94:1681–1705, 1968.

World Conference on Timber Engineering Oslo 2023

NUMERICAL MODELLING OF MASS TIMBER BEAM-COLUMN CONNECTIONS

Labuwatte Manathum Milindu B Jayasekara[1], Robert M Foster[2]

ABSTRACT: Multi-storey timber buildings are becoming increasingly popular due to advancements in engineered timber technology. Sophisticated timber connections in such buildings play a critical role in both the performance and safety of the structure, particularly in accidental and earthquake situations. Therefore, a thorough understanding of timber connection behaviour is necessary for safe and efficient building design. However, few existing studies capture timber connection behaviours in a sufficiently comprehensive manner to be applied to the complex loading conditions that can occur in accidental situations. This study develops a computational modelling approach that can predict intricate pre- and post-failure behaviours of timber beam-column connections under various loading conditions. First, the commercially available Finite Element software package Abaqus was used to model a timber beam-column connection. Then, nonlinear quasi-static analyses were performed under shear and moment conditions. Finally, sensitivity analyses were conducted to ensure that the model produces consistent results. The computational results obtained agree well with experimental results available in the literature. The developed numerical modelling approach is thus shown to have potential for simulating the complicated behaviour of timber connections under loads and, hence, for the design of safe, efficient timber connections.

KEYWORDS: Disproportionate collapse, Computational mechanics, Damage modelling, Timber connections, LVL

1 INTRODUCTION

Engineered timber is built up from mechanically or adhesively connected timber lamellae to form larger, more homogeneous structural sections suitable for the construction of larger timber structures. Engineered timber is increasingly seen as an alternative to conventional construction materials such as concrete and steel for reducing CO_2 emissions in the construction sector [1] - [2]. As a result, engineered timber is now being used extensively in multi-storey building construction [3].

Commonly used engineered timber products are glued laminated timber (glulam), laminated veneer lumber (LVL) and cross-laminated timber (CLT) [4]. These materials are predominantly used in three main building types [5]: Light-timber frame structures, composed of dimensional lumber and engineered timber that are regularly spaced and fastened together to create floor and wall cassettes: CLT buildings, composed of solid CLT floor and wall panels in a platform-type construction arrangement: and post-and-beam structures, consisting of continuous vertical posts and horizontal beams that are, usually, pin-connected to each other. Post-and-beam structures are thought to offer the greatest potential for realising timber buildings taller than 10 storeys [6] and the heights of such buildings are rapidly increasing [7].

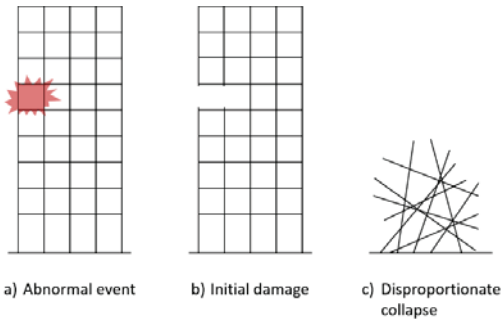

Figure 1: *Disproportionate collapse*

The greater the heights of timber buildings, the more acute the need for thoughtful consideration of abnormal conditions such as fire [8] or disproportionate collapse in design. Disproportionate collapse is a structural collapse in which there is a pronounced disproportion between the initial damage caused by an abnormal event and the extent of the ensuing collapse [9]. A graphical representation of

[1] Labuwatte Manathum Milindu B Jayasekara, PhD Student, Department of Engineering, University of Cambridge, United Kingdom, lmmbj2@cam.ac.uk
[2] Robert M Foster, University Assistant Professor, Department of Engineering, University of Cambridge, United Kingdom, rmf41@cam.ac.uk

https://doi.org/10.52202/069179-0372

this concept is depicted in Figure 1. The key design strategy against this phenomenon is to ensure adequate resistance against failure propagation, i.e., robustness. By limiting the initial damage progression from (b) to (c) in Figure 1, a sufficiently robust structure can be obtained.

Timber beam-column connections, which are often made of steel or aluminium, play a vital role in ensuring reliable robustness of multi-storey timber buildings. These connections provide ductility and continuity to buildings, and with sufficient strength and deformation capacities, they can allow the formation of alternative load paths (ALPs) during initial damage [10] - [11]. These ALPs bridge or bypass a local failure zone; preventing failure propagation throughout the structure and hence averting disproportionate collapse. Examples of such ALPs are catenary, arching and membrane actions [12]. Understanding connection performance under load is thus crucial for achieving a robust building design. However, limited literature is available on timber post-beam connection behaviour [13] - [14].

Computational methods can be a cost-effective and efficient approach for capturing connection behaviours. With recent developments in computational mechanics and failure theories, it may be possible to simulate isotropic metals, anisotropic timber and their combined behaviour in timber connections beyond initial failure. The majority of existing studies are limited to linear elastic-plastic behaviour [15] or simple dowel-type connections [16] or one material/parameter performance [17]. Some studies employ pre-defined failure surfaces to initiate failure [18] - [19] but these may not be suitable for all types of loading because of the need to predefine failure. In addition, the numerical solving methods used in these studies may not be suitable to simulate complex pre- and post-failure material behaviour in timber connections [20]. Therefore, a comprehensive modelling technique is required to capture the behaviours of timber connections under any mechanical loading condition.

This research project aims to develop a computational modelling technique that can capture complex pre- and post-failure behaviour of timber beam-column connections under various loads. This paper presents the initial stages of building the complete computational model. First, material properties and connector details are outlined. Second, the modelling approach and results are discussed. Third, a parametric study is demonstrated. Finally, the conclusions of the study so far are presented.

2 TIMBER CONNECTION

A T-section connector tested by Masaeli et al. [21] and shown in Figure 2 was selected from the literature as an initial experimental benchmark for the development of the computational modelling technique. Full experimental details are provided by Masaeli et al [21] with key properties reproduced here. The tests used Douglas fir LVL timber column and beam sections of sizes 360 × 360 mm^2 and 600 × 252 mm^2 respectively. The T-section was made of AW 6005-A aluminium alloy, and the connection was composed of two rows of six 16 mm (M16 grade 8.8) bolts and ten 16 mm steel dowels (S355). The connector was tested experimentally under shear and moment quasi-statically [21], and the testing arrangements adopted are illustrated in Figure 3. These experimental results are used in this paper to evaluate the performance of the Finite Element (FE) model.

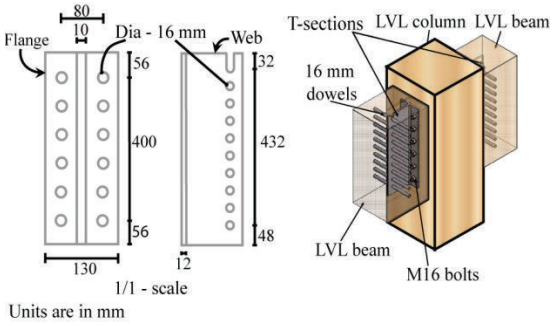

Figure 2: *T-connector details, redrawn after Masaeli et al. [21]*

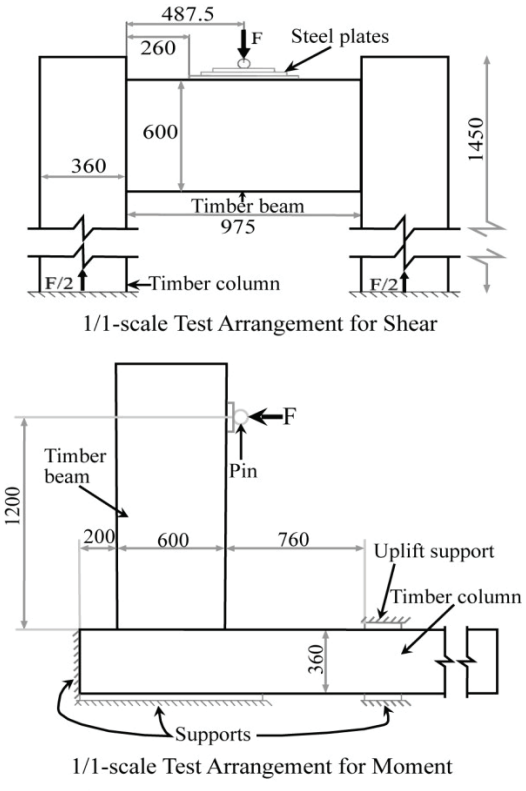

Figure 3: *Experimental testing setups, redrawn after Masaeli et al. [21]*

Material properties adopted in the FE analyses are given in Table 1 and Table 2 for timber and metals respectively.

The majority of these material properties including Young's modulus (E), Poisson's ratio (υ), shear modulus (G) and shear strengths (f_v) are those reported by Masaeli et al. [21]. Strains (ε) for metals are obtained from the wider literature [22]. Steel and aluminium are considered as isotropic materials whereas timber is modelled as an orthotropic material. Principal material directions for timber are depicted in Figure 4.

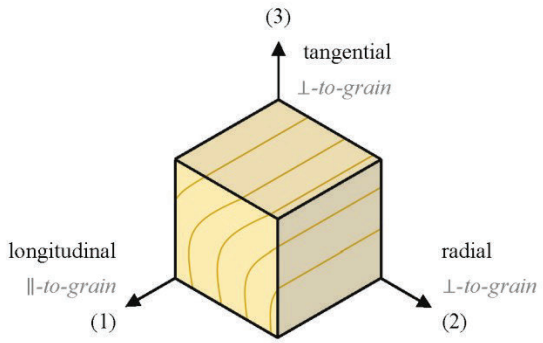

Figure 4: *Timber material directions*

Numerical subscripts for each timber material property represent these principal directions. Subscripts "c", "v", "y" and "m" denote compression, shear, yield and maximum respectively. "f", "σ", "ε_m" and "ε_{tf}" refer to strength, stress, engineering strain at maximum stress and true fracture strain respectively.

Table 1: *Material properties for LVL timber [21]*

Parameter	Unit	Value
E_{11}	MPa	15500
$E_{22} = E_{33}$	MPa	470
$\upsilon_{12} = \upsilon_{13}$		0.37
υ_{23}		0.38
$G_{12} = G_{13}$	MPa	660
G_{23}	MPa	132
f_{c11}	MPa	46.4
$f_{c22} = f_{c33}$	MPa	8.8
$f_{v12} = f_{v13}$	MPa	7
f_{v23}	MPa	1.4

Table 2: *Material properties of metals [21] - [22]*

Parameter	Unit	Bolt	Dowel	Connector
Density	kg/m^3	8050	8050	2710
E	GPa	207	209	70
υ		0.3	0.3	0.23
σ_y	MPa	861	556	187
σ_m	MPa	956	597	221
ε_m		0.09	0.1	0.0553
ε_{tf}		1.03	0.90	1.10

3 FINITE ELEMENT MODEL

All the parts of the connection were drawn separately and assembled as depicted in Figure 5 using the FE software package Abaqus [23].

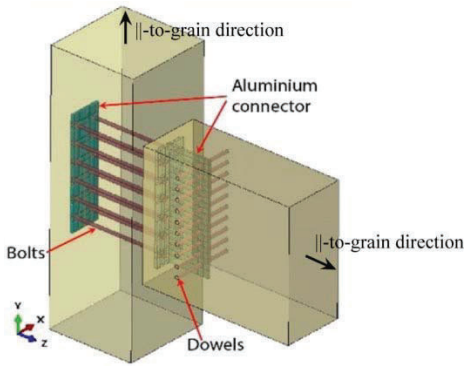

Figure 5: *FE model of the timber beam-column connection*

For the aluminium connector, small 8 mm chamfers were introduced at 90^0-degree corners to avoid numerical singularities. To define relationships between the components, 35 separate contact interactions were defined and constitutive models for metals and timber were specified to simulate their individual behaviour under loads. After performing a mesh sensitivity analysis for each component, boundary conditions and loadings were applied to simulate both shear and moment behaviour of the connector. These are discussed in detail in this section.

3.1 HILL CRITERION FOR TIMBER

The constitutive relationship for timber is defined in this study assuming orthotropic material properties. Only the ductile behaviour of timber under compression was considered in this paper. An elastic-perfectly plastic material model based on the Hill criterion with anisotropic yielding was employed using the properties given in Table 1. The Hill criterion has been successfully used in timber modelling to define plastic yielding [24]. Equation (1) shows the Hill criterion. Yielding occurs when the function reaches the value of 1.

$$f(\sigma) = [F(\sigma_{22} - \sigma_{33})^2 + G(\sigma_{33} - \sigma_{11})^2 + H(\sigma_{11} - \sigma_{22})^2 + 2L\sigma_{23}^2 + 2M\sigma_{31}^2 + 2N\sigma_{12}^2] \quad (1)$$

where:

$$F = \frac{1}{2}\left(\frac{1}{R_{22}^2} + \frac{1}{R_{33}^2} - \frac{1}{R_{11}^2}\right)$$

$$G = \frac{1}{2}\left(\frac{1}{R_{33}^2} + \frac{1}{R_{11}^2} - \frac{1}{R_{22}^2}\right)$$

$$H = \frac{1}{2}\left(\frac{1}{R_{11}^2} + \frac{1}{R_{22}^2} - \frac{1}{R_{33}^2}\right)$$

$$L = \left(\frac{3}{2R_{23}^2}\right), M = \left(\frac{3}{2R_{13}^2}\right), N = \left(\frac{3}{2R_{12}^2}\right)$$

$$R_{11}^2 = \frac{f_{c11}}{f^0}, R_{22}^2 = \frac{f_{c22}}{f^0}, R_{33}^2 = \frac{f_{c33}}{f^0}$$

$$R_{12}^2 = \frac{f_{v12}}{\tau^0}, R_{13}^2 = \frac{f_{v13}}{\tau^0}, R_{23}^2 = \frac{f_{v23}}{\tau^0}$$

https://doi.org/10.52202/069179-0372

where f^0 is the reference yield stress and $\tau^0 = f^0/\sqrt{3}$.

3.2 PLASTICITY MODEL FOR DUCTILE MATERIALS

An elastic-plastic material model was applied for ductile metals. Material properties given in Table 2 were utilised to obtain the engineering stress-strain curves for bolts, dowels and aluminium connector. Yielding was defined using the Von Mises yield surface with isotropic hardening. This criterion has shown promising results in the literature [22]. Von Mises yield criterion is given in Equation (2) and yielding occurs when $\sigma_v \geq \sigma_y$:

$$\sigma_v^2 = \frac{1}{2}[(\sigma_{aa} - \sigma_{bb})^2 + G(\sigma_{bb} - \sigma_{cc})^2 + (\sigma_{cc} - \sigma_{bb})^2 + 6(\sigma_{bc}^2 + \sigma_{ca}^2 + \sigma_{ab}^2)] \quad (2)$$

where σ_v is the Von Mises (equivalent) stress and a, b, c are the principal material directions.

Abaqus requires an equivalent stress-strain curve as input to simulate this yielding of metals. Therefore, engineering stress-strain curves were first converted to true stress-strain curves using Equation (3) and Equation (4):

$$\sigma_t = \sigma_e(1 + \varepsilon_e) \quad (3)$$

$$\epsilon_t = ln(1 + \varepsilon_e) \quad (4)$$

where σ_t is the true stress, σ_e is the engineering stress, ϵ_t is the true strain and $\varepsilon_e$is the engineering strain. As these equations are valid only up to necking, Hollomon's extrapolation method [25] was used to obtain the full curve. The true stress-strain curves were then converted to equivalent stress-strain curves, noting that the true stress-strain curve and equivalent stress-strain curve up to necking are the same. After necking, the Gromada correction factor was applied to account for the tri-axial stress state [25]. The resulting equivalent stress-strain curves are presented in Figure 6. Continuum damage modelling techniques were also employed after necking to simulate the ductile failure of materials [23].

3.3 MESH

Separate mesh sensitivity analyses were conducted for each component of the connection. From these, a suitable mesh arrangement was chosen for each component to maintain accuracy. A total of 268502 8-node linear hexahedral elements (C3D8R) are used in this model. Reduced integration and relax-stiffness hourglass options were included in these elements to minimise shear locking, computational effort and zero-energy deformation modes.

3.4 CONTACTS AND BOUNDARY CONDITIONS

The general contact algorithm in Abaqus was utilized with element-based surface definitions to define contacts in the connection model. These element-based contact surface pairs were specified individually to avoid numerical problems and unwanted energies. To simulate the sliding behaviour of these contacts, a friction coefficient of 0.3 was applied for the tangential direction. For the normal direction, a generalised Lame function proposed by Dorn [26] was employed to characterise pressure-overclosure (resistance to penetration) behaviour of surfaces. This accounts for the softening of timber near bolts and dowel holes.

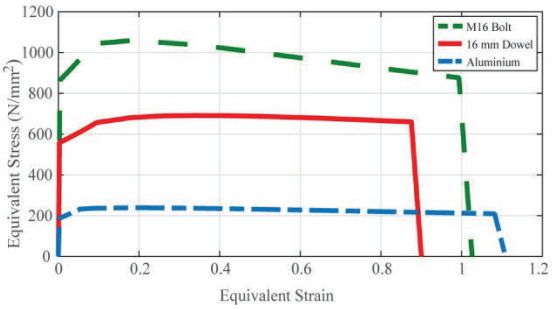

Figure 6: *Equivalent stress-strain curves of bolts, dowels and aluminium connector*

For numerical efficiency, finite sliding with balanced contact weighting was used. This is beneficial for simulating large deformations and for minimising unrealistic node penetrations in contact surfaces. Furthermore, a penalty constraint was also applied to allow these small penetrations in contacts and, therefore, to reduce artificial resisting forces that can cause numerical instabilities. This is particularly useful when circular shapes, such as bolts and dowels, are included in the model.

Boundary conditions were also employed to replicate both shear and moment loading conditions for the connection. The top and bottom surfaces of the column were fixed as shown in Figure 7. A distance of 250 mm between the connector and the fixed boundary conditions was kept to eliminate influence from the fixity to the connector. For the shear analysis, translational degrees of freedom (DOFs) in x- and y-directions at the end of the beam were restrained to resemble the shear behaviour.

3.5 LOADING

For all the numerical analyses conducted, only displacement-based loads were specified to capture moment and shear responses. First, a small displacement of 10 nm was applied to all the parts near contacts for initiating the contacts and eliminating numerical problems. This imposed displacement was then removed while enforcing new vertical displacements to simulate the required responses of the connector.

These vertical displacements were assigned to reference points using a fifth-order polynomial function until failure occurs [23]. The location of the reference point changes depending on the behaviour the numerical model tries to capture: moment or shear. In the case of the moment test, the end of the beam was constrained to a reference point

using coupling constraints with continuum distribution as illustrated in Figure 8. This constrains the DOFs of the nodes in the connecting surface to the DOFs of the reference point. By doing so, imposed displacement to the reference point is distributed in an average sense to the connecting nodes by producing realistic results. A similar procedure was followed for the shear test, but now the connecting surface is at the top of the beam as shown in Figure 8. Accordingly, from the results of numerical models tested in moment and shear, moment-rotation and load-displacement curves were extracted respectively.

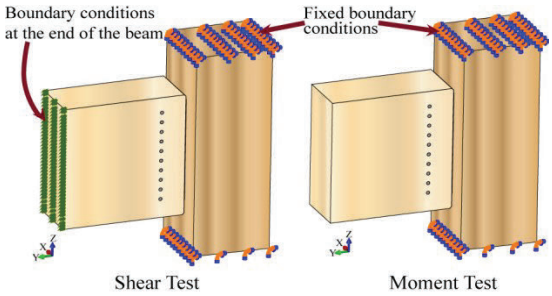

Figure 7: *Boundary conditions of FE models*

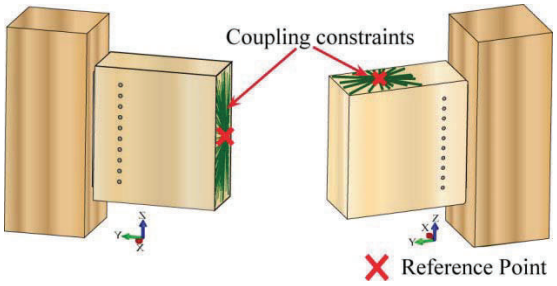

Figure 8: *Coupling constraints and reference points for the moment (left) and shear (right) simulations*

3.6 SOLVER

Owing to the complexities of the behaviour modelled, the commonly used Abaqus standard solver is not suitable for analysing such timber connections. The reason is that this solver solves for equilibrium [23], which means that problems become difficult to solve when a large number of contacts, failure mechanisms and non-linearities are involved. Abaqus explicit solver, on the other hand, solves equations of motion, which means that the calculation remains straightforward, and the overall analysis is efficient. However, this method is more commonly applied for dynamic analyses.

In order to perform a quasi-static analysis using the explicit solver, two sensitivity analyses have to be conducted to keep the kinetic energy acceptably low. One analysis is to identify a load rate that produces zero kinetic energy. It is impractical, even with high-power computing, to recreate the actual load rate used in the experimental tests due to the large number of time increments needed for the analysis. Therefore, a computationally less expensive load rate must be selected. However, increasing the load rate alone may not be sufficient to achieve a computationally efficient analysis.

Mass scaling is another parameter used to aid quasi-static analyses. This speeds up the analysis by increasing the time increment of the solver. However, by doing so, the kinetic energy of the system increases. Therefore, a sensitivity analysis must be performed to find a mass scaling factor. Both these sensitivity analyses are trial-and-error processes. Therefore, a separate dynamic analysis was performed to find the natural frequency of the model, and this was used to decide an initial trial value for the load rate. The resulting selected load rates are 0.25 m s^{-1}, 0.5 m s^{-1} and 1 m s^{-1} and the chosen mass scaling factors are 5, 10 and 20.

The model developed for the moment test was utilised in these two sensitivity analyses. Displacements were applied as described in Section 3.5 using the three different load rates and mass scaling factors. The moment vs rotation plots are shown in Figure 9.

Kinetic energies for each test were also compared to ensure that the kinetic energy is less than 5% of the internal energy. It can be seen that the results converge when the load rate and the mass scaling factor decrease, meaning that kinetic energy is low. Therefore, considering computational cost and kinetic energy, a load rate of 0.25 m s^{-1} and a mass scaling factor of 10 were chosen. The rest of the analyses were conducted using these selected parameters.

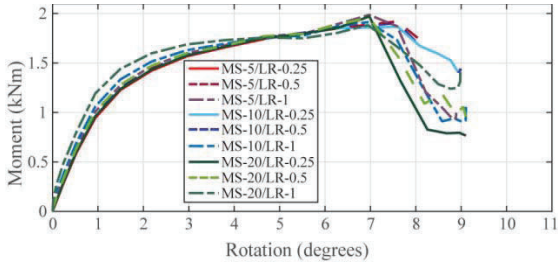

Figure 9: *Sensitivity analysis for mass scaling and load rate*

4 RESULTS AND DISCUSSION

The developed numerical connection model was analysed under shear and moment. Displacement-based loads were applied as described in Section 3.5 with the load rate and mass scaling factor obtained in Section 3.6.

Figure 10 illustrates the moment-rotation prediction in contrast to experimental results in [21]. The computational model captures the moment-rotation response of the connector including post-failure behaviour with good accuracy. The predicted initial stiffness, rotational capacity and maximum moment capacity agree well with the experimental results. It should be noted that, for the maximum moment capacity, there is a deviation of 1% from the average experimental

https://doi.org/10.52202/069179-0372

result. This distinction, however, lies within the experimental envelope and is due to the insignificant dynamic behaviour after elements start to fail. The predicted failure mechanism shown in Figure 11 matches well with the experimental observations of Masaeli et al. [21] – tearing near bolt holes and fracturing at the flange-web interface of the aluminium connector. However, in the FE model, the fracture at the interface is partial in contrast to the experimental fracture.

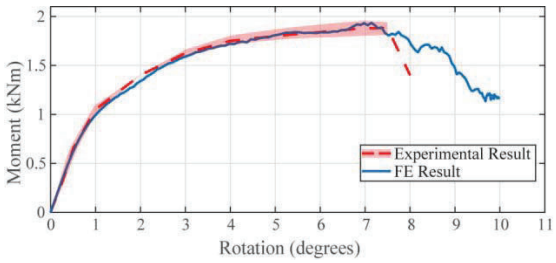

Figure 10: *Experimental [21] and numerical moment vs rotation response*

The shear response of the connector was also estimated and is presented in Figure 12. Overall, the load vs displacement behaviour is similar to the experimental behaviour. However, FE values over-predict the force response and under-predict the displacement response with a maximum variation of 28% and 65% from the average experimental result for the forces and displacements respectively. This may be primarily because of the exclusion of timber brittle failure under tension in these FE models.

As seen in Figure 13, experimentally observed tensile failure perpendicular to grain [21] was not captured in FE simulations. Instead, the applied loads primarily concentrated on the aluminium connector leading to higher resistance and lower displacement capacity. Hence failure occurred in the connector in simulations. Despite this, the numerical model captures the maximum strength capacity well, with a deviation of 2.4%.

In all these analyses, energy outputs of the FE models such as artificial energy, kinetic energy, contact penalty energy, etc., were checked against the recommended limits to ensure that the results are accurate [23].

5 PARAMETRIC STUDY

Parametric studies were conducted to identify the effects of three different parameters. These are discussed in detail in this section.

5.1 BEAM-COLUMN GAP

In the computational models, a small gap between the column and the beam was kept, as displayed in Figure 14. The gap of 23 mm represents the weakened hollow portion of the beam due to machine cut – since this is a concealed connector – and was set to provide 4 mm initial clearance between the bolt nut and the timber. The inclusion of the gap is beneficial in avoiding complicated contacts and reducing computational effort. To explore the influence of this gap, another FE model was developed in which the beam touches the column by fully enclosing the connector. The moment-rotation and load-displacement responses are plotted in Figure 15 and Figure 16 for both models.

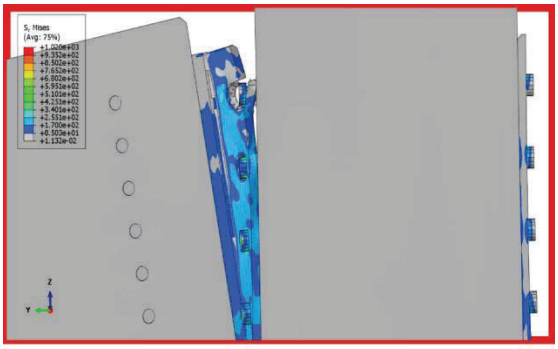

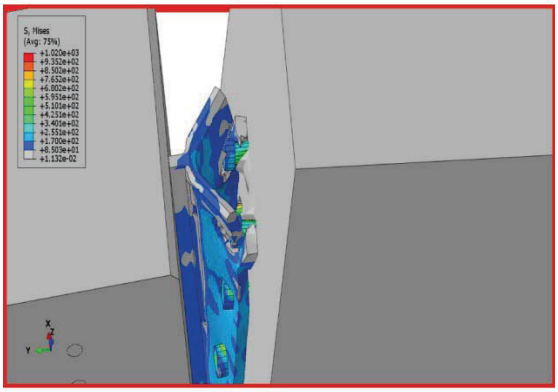

Figure 11: *Failure mode under moment test*

From Figure 15, it can be seen that the results of the FE model without the gap deviate significantly from the experimental results. The maximum moment capacity predicted has a variation of 14.3%. Furthermore, the rotational capacity is under-predicted by approximately 1°. This indicates that if the weakened hollow portion of the beam is not appropriately modelled artificially high resistance against rotation may be observed.

The shear response of the model without the gap shows similar peak resistance but less ductility than the FE model with the gap. For FE models without the gap, a 2.6% higher peak shear resistance and a 30% lower deformation capacity compared to the FE model with the gap were noted, and these may be a result of increased contact area between the connector and the timber beam. Failure modes of both moment and shear simulations are similar to the original FE models. These results suggest that a gap between the column and the beam can be employed to minimise the above-mentioned discrepancies in modelling these types of timber connections.

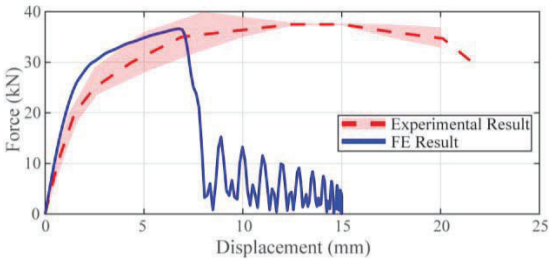

Figure 12: *Experimental [21] and numerical load vs displacement response*

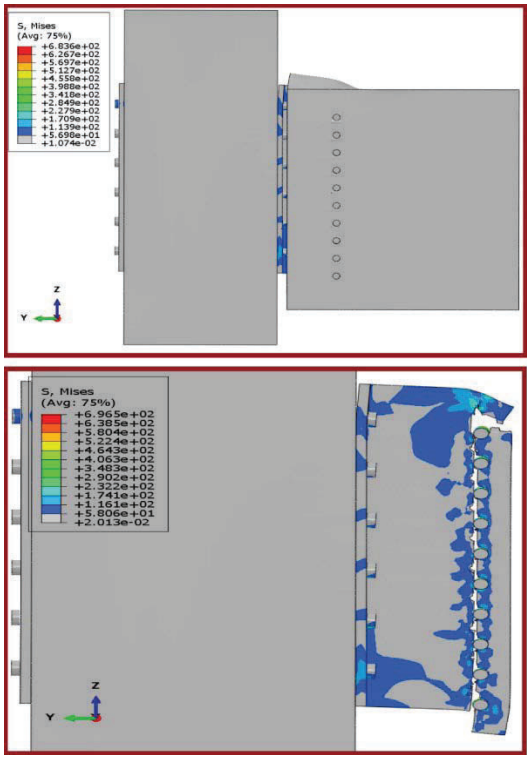

Figure 13: *Failure mode under shear test*

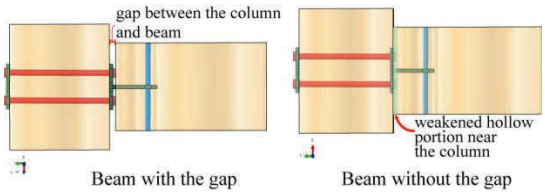

Figure 14: *Column-beam gap*

5.2 CHARACTERISTIC ELEMENT LENGTH

In continuum damage modelling, a total plastic deformation parameter is defined to simulate ductile damage of metals [23]. This parameter is constant for a particular material, and when an element reaches the specified total plastic deformation, element deletion occurs. Total plastic deformation (U^p) is given in Equation (5).

$$U^p = L_c\left(\varepsilon_{tf}^p - \varepsilon_{tn}^p\right) \tag{5}$$

where L_c is the characteristic element length, ε_{tf}^p is the true plastic strain at fracture and ε_{tn}^p is the true plastic strain at necking. ε_{tf}^p and ε_{tn}^p are material properties and are independent of element properties.

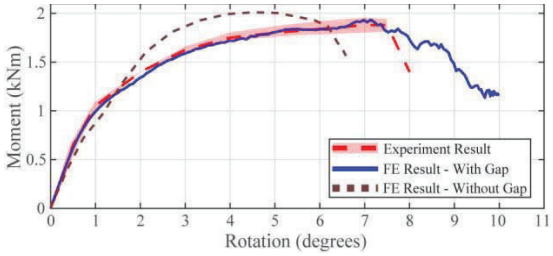

Figure 15: *Experimental [21] and numerical moment vs rotation response of models with and without the gap*

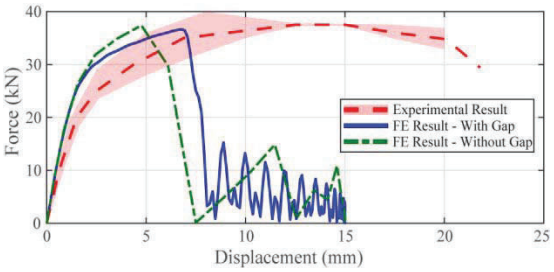

Figure 16: *Experimental [21] and numerical load vs displacement response of models with and without the gap*

Characteristic element length depends on the element geometry and formulation. Same-size elements with an aspect ratio of unity are usually recommended to achieve a uniform L_c in the mesh. If the L_c of elements in the mesh varies significantly from that specified in the damage model, damage behaviour can be different from that defined. As the mesh varies near the holes and the T-joint of the aluminium connector, a sensitivity analysis was conducted for the connector to investigate the impact of L_c on the analysis.

In the original FE model, a value of 2.34 mm was used as L_c for modelling damage in the connector. This value was determined based on the average dimensions of elements in the connector mesh. Another two L_c values were selected for U^p keeping the mesh constant; L_c = 2.10 mm and L_c = 2.60 mm. These two values adequately represent possible element sizes in the mesh. The moment-rotation curves obtained using each L_c value are illustrated in Figure 17.

All three plots follow the same experimental moment-rotation response until approximately 6° of rotation. However, considerable differences between the plots start to appear near the failure point. For L_c = 2.6 mm the analysis over-predicts the maximum moment capacity by 6%, whereas for L_c = 2.1 mm the analysis under-predicts

https://doi.org/10.52202/069179-0372

by 5%. In terms of rotational capacity, L_c = 2.6 mm shows good agreement with the experimental value while L_c = 2.1 mm shows about 1° lower rotational capacity.

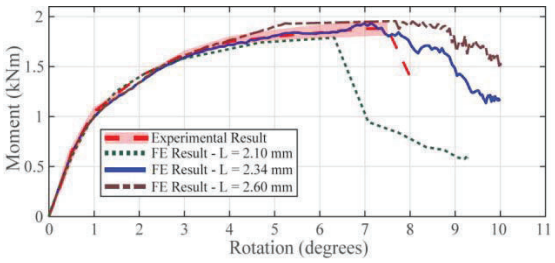

Figure 17: *Experimental [21] and numerical moment vs rotation response for characteristic element length analysis*

Failure modes for L_c = 2.1 mm, L_c = 2.34 mm and L_c = 2.6 mm are shown in Figure 18, Figure 11 and Figure 19 respectively. Three different failure modes were identified. FE models with L_c = 2.1 mm and L_c = 2.34 mm exhibit tearing of aluminium as was seen in experiments, and in the L_c = 2.1 mm model, even the complete fracture near the web-flange interface can be observed. When L_c = 2.6 mm, failure first occurs in the bolts near the column as presented in Figure 19. Failure modes for the shear tests were similar for all three cases as the actual failure occurred in the timber beam.

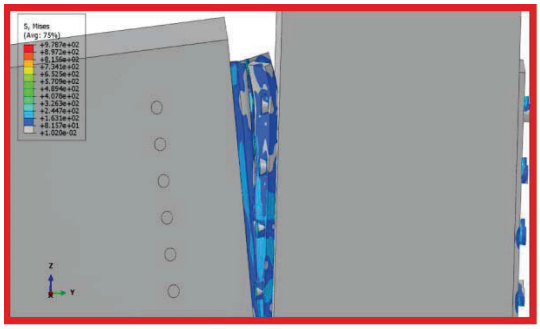

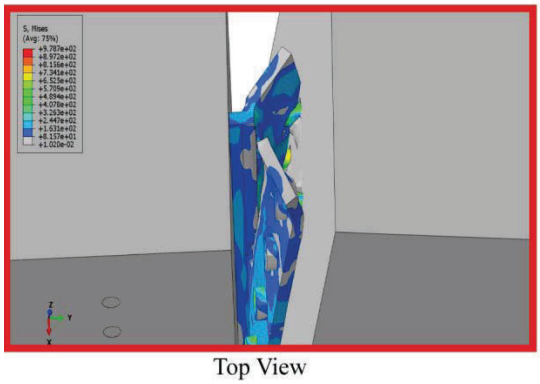

Figure 18: *Numerical failure mode of FE models with L_c = 2.1 mm*

The three failure behaviours observed – tearing and partial fracture, tearing and complete fracture, and bolt failure – are possible alternatives for this connection under moment loading. Therefore, one should consider all such possible mechanisms in order to make predictions and designs if a mesh size of a part varies. In such cases, it is advisable to conduct a parametric study for L_c. This will also take into account the material property variability indirectly in the simulations. Nevertheless, the FE model with average element length may yield overall good results for moment and shear responses.

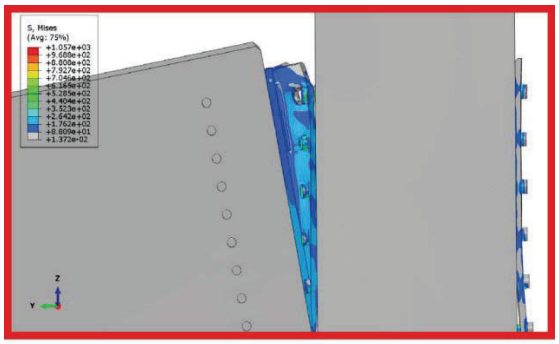

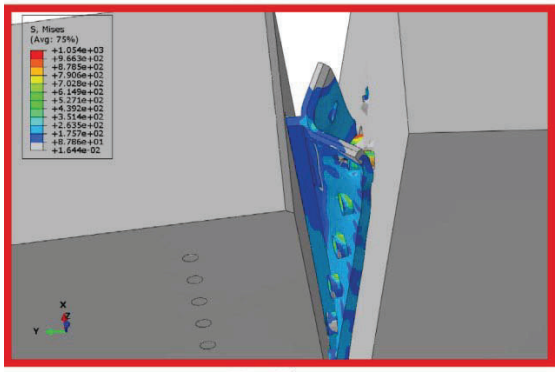

Figure 19: *Numerical failure mode of FE models with L_c = 2.6 mm*

5.3 SYMMETRY OF THE MODEL

To reduce the computational cost, the symmetry of the connection was considered. Based on that, half-models as shown in Figure 20 were created for both moment and shear simulations.

In addition to the boundary conditions and constraints discussed in Section 3.4, symmetric boundary conditions were employed as depicted in Figure 20. Note that, these are applied to the boundary surface excluding the nodes that are involved in contact definitions. This eliminates over-constraint issues. For symmetric boundary conditions, translational DOF in the x-direction and rotational DOFs in the y- and z-directions were restrained. Then, the models were analysed under shear and moment loading conditions to investigate the effectiveness of taking symmetry into account. Moment-rotation and load-displacement curves are shown in Figure 21 and Figure 22, respectively.

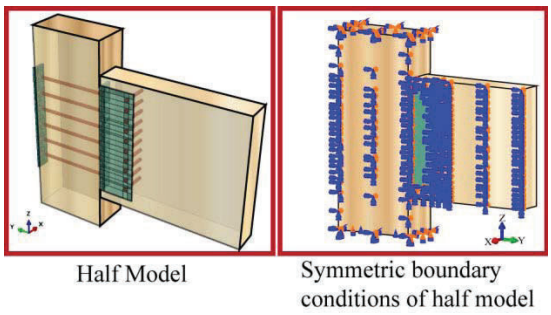

Figure 20: *Half-model and symmetric boundary conditions*

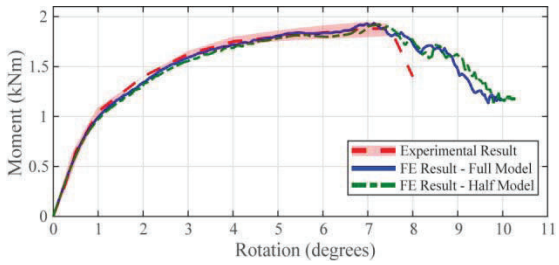

Figure 21: *Experimental [21] and numerical moment vs rotation response of full and half models*

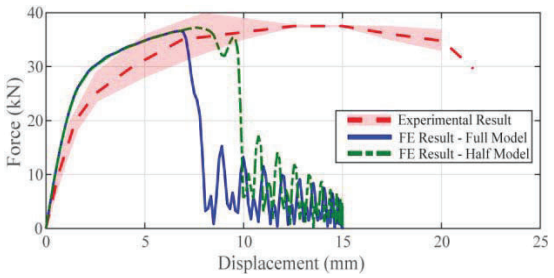

Figure 22: *Experimental [21] and numerical load vs displacement response of full and half models*

The results of the half-model for both moment and shear match closely with the full-model predictions. Therefore, symmetry can be utilised in simulating such timber connections, and this also reduces the computational cost.

6 CONCLUSIONS

This study aims to develop a computational modelling technique that can capture complex pre- and post-failure behaviour of timber beam-column connections under various loads. This paper presents the initial stages of building the complete computational model. A numerical modelling technique was developed using the FE package Abaqus. This technique was then used to analyse a T-section connector under shear and moment to demonstrate the performance of the method. A parametric study was also conducted to increase the accuracy of the model predictions and to evaluate the consistency of the modelling approach adopted. The following conclusions can be drawn:

1. The developed numerical model demonstrates potential in capturing complex pre- and post-failure behaviours of timber connections through large deformations and under different loading situations.
2. For concealed connections, introducing a suitable gap between the column and the beam in the FE models to account for weakening of the hollow portion may provide more realistic results.
3. A sensitivity analysis for the characteristic element length is needed if damage modelling for ductile metals is employed with non-uniform meshes. This is particularly important for FE predictions and designs. An average element length, however, was found to yield overall good results.
4. The symmetry of connections can be taken into account in numerical modelling of connections of this type to improve computational efficiency.

This technique has potential to support design and optimisation of timber connections, especially for robustness. Future works will develop this model to include tensile failure of timber.

ACKNOWLEDGEMENTS

The first author would like to acknowledge Cambridge Commonwealth European and International Trust for the financial support of the Jafar Cambridge Studentship. The authors would also like to thank Prof. Benoit Gilbert and his team at Griffith University, Australia for generously sharing the additional experimental data used in this study.

REFERENCES

[1] R. Sathre, J. O'Connor. Meta-analysis of greenhouse gas displacement factors of wood product substitution. *Environmental Science Policy*, 13(2):104–114, apr 2010.

[2] A. Himes, G. Busby. Wood buildings as a climate solution. *Developments in the Built Environment*, 4:100030, nov 2020.

[3] R. M. Foster, T. P. S. Reynolds. Light weighting with Timber: An Opportunity for More Sustainable Urban Densification. *Journal of Architectural Engineering*, 24(1):02518001, mar 2018.

[4] The Structural Engineer. Engineered wood products and an introduction to timber structural systems. The Institution of Structural Engineers, 2013.

[5] J. A. J. Huber, M. Ekevad, U.A. Girhammar, S. Berg. Structural robustness and timber buildings – a review. *Wood Material Science Engineering*, 14(2):107–128, Mar 2019.

[6] R. Abrahamsen. Mjøstårnet-18 storey timber building completed. In 24. *Internationales Holzbau-Forum IHF*, 2018.

[7] R. M. Foster, M. H. Ramage. Tall Timber. *Nonconventional and Vernacular Construction*

https://doi.org/10.52202/069179-0372

Materials: Characterisation, Properties and Applications [2nd ed.], edited by K. Harries, and B. Sharma, 467–489, 2020. Cambridge: Woodhead Publishing.

[8] A. Law, R. Hadden. We need to talk about timber: fire safety design in tall buildings. *The Structural Engineer*, 3, 2020.

[9] U. Starossek and M. Haberland. Disproportionate Collapse: Terminology and Procedures. *Journal of Performance of Constructed Facilities*, 24(6):519–528, dec 2010.

[10] The Institution of Structural Engineers. Practical guide to structural robustness and disproportionate collapse in buildings. 2010.

[11] P. H. Kirkegaard, J. D. Sørensen, D. Cizmar, and V. Rajˇci´c. System reliability of timber structures with ductile behaviour. *Engineering Structures*, 33(11):3093–3098, nov 2011.

[12] U. Starossek. Progressive Collapse of Structures. London: Thomas Telford Limited, 2009.

[13] C. H. Lyu, B. P. Gilbert, H. Guan, I. D. Underhill, S. Gunalan, H. Karampour, and M. Masaeli. Experimental collapse response of post-and-beam mass timber frames under a quasi-static column removal scenario. *Engineering Structures*, 213:110562, jun 2020.

[14] C. H. Lyu, B. P. Gilbert, H. Guan, I. D. Underhill, S. Gunalan, and H. Karampour. Experimental study on the quasi-static progressive collapse response of post-and-beam mass timber buildings under an edge column removal scenario. *Engineering Structures*, 228, 111425, 2021.

[15] G. D'Arenzo, G. Rinaldin, M. Fossetti, and M. Fragiacomo. An innovative shear-tension angle bracket for Cross-Laminated Timber structures: Experimental tests and numerical modelling. *Engineering Structures*, 197:109434, oct 2019.

[16] A. Hassanieh, H.R. Valipour, M.A Bradford, C. Sandhaas. Modelling of stee-timber composite connections: validation of finite element model and parametric study. *Engineering Structures*, 138:35-49, Feb 2017.

[17] M. Gharib, A. Hassanieh, H. Valipour, and M. A. Bradford. Three-dimensional constitutive modelling of arbitrarily orientated timber based on continuum damage mechanics. *Finite Elements in Analysis and Design*, 135:79–90, nov 2017.

[18] T. Geˇcys, A. Daniunas, T.K. Bader, L. Wagner, J. Eberhardsteiner. 3D finite element analysis and experimental investigations of a new type of timber beam-to-beam connection. *Engineering Structures*, 86:134–145, Mar 2015.

[19] X. Cheng, B. P. Gilbert, H. Guan, D. Dias-da-Costa, and H. Karampour. Influence of the earthquake and progressive collapse strain rate on the structural response of timber dowel type connections through finite element modelling. *Journal of Building Engineering*, 57, 104953, 2022.

[20] M. Wang, X. Song, X. Gu, J. Tang. Bolted glulam beam-column connections under different combinations of shear and bending. *Engineering Structures*, 181:281-292, Dec 2018.

[21] M. Masaeli, B. P. Gilbert, H. Karampour, I. D. Underhill, C. H. Lyu, and S. Gunalan. Scaling effect on the moment and shear responses of three types of beam-to-column connectors used in mass timber buildings. *Engineering Structures*, 208:110329, Apr 2020.

[22] E. L. Grimsmo, A. Aalberg, M. Langseth, and A. H. Clausen. Failure modes of bolt and nut assemblies under tensile loading. *Journal of Constructional Steel Research*, 126:15–25, nov 2016.

[23] Dassault Systèmes Simulia Corp. ABAQUS User's Manual, Version 6.14, 2014.

[24] R Hill. A theory of the yielding and plastic flow of anisotropic metals. Proceedings of the Royal Society of London. Series A. *Mathematical and Physical Sciences*, 193(1033):281–297, may 1948.

[25] S. Tu, X. Ren, J. He, Z. Zhang. Stress-strain curves of metalic materials and post-necking stress strain hardening characterization: A review. *Fatigue & Fracture of Engineering Materials and Structures*, 43:3-19, 2020.

[26] M. Dorn, K. Borst, J. Eberhardsteiner. Experiments on dowel-type timber connections. *Engineering Structures*, 47:67–80, Feb 2013.

World Conference on Timber Engineering Oslo 2023

A NEW MULTI-SPRING ELEMENT TO SIMULATE CLT CONNECTIONS UNDER COMBINED LOADINGS

Matías F. Chacón[1], Pablo Guindos[2], Jairo Montaño[3]

ABSTRACT: A new numerical model of five uncoupled spring elements is proposed to simulate the panel-to-panel Cross-Laminated Timber (CLT) connections made of discrete fasteners. The model accurately simulates the main phenomenological effects in the translational and rotational directions of connections: asymmetrical axial gap (open/closure), in-plane and out-of-plane sliding of panels, and radial/bending stiffness/strength of fasteners. Linear/non-linear spring elements with different constitutive material models for each phenomenological effect are considered. For instance, a modified Richard–Abbott model is used for the radial/bending hysteresis of fasteners. The model is implemented in the ANSYS software through user elements and material routines. An illustrative example under different loading conditions is elaborated to show the main capabilities of the proposed model. Finally, the model is validated with two experimental monotonic in-plane CLT slab tests, where the initial/hardening stiffness, strength capacity, and failure mechanism of both specimens are correctly predicted.

KEYWORDS: CLT connection models, non-linear finite elements, phenomenological-based models, hysteretic models.

1 INTRODUCTION

1.1 OVERVIEW

Nowadays, with the arrival of new mass timber products, such as glue-laminated timber and Cross-Laminated Timber (CLT), the incorporation of efficient and innovative high-ductile connectors, and elaboration of high-precision and faster-prefabricated components, provide a viable option to build mid- to high-rise residential/non-residential buildings under a severer seismic hazard [1]. Particularly, CLT panels can be used in either floor and wall elements or as the material for the entire building.

The most critical and vulnerable part of CLT buildings is their connections, which must be designed with extreme care. Moreover, connections' mechanic capabilities (strength, stiffness, ductility, and dissipated energy) typically govern the whole structure's behaviour, particularly under seismic loads [2]. Those connections can be strengthened with an adequate layout of special straight or inclined fasteners (e.g., nails, screws), special steel parts, or slot connectors, which, together with the connection panel type (e.g., butt, half-lap, single or double surface spline) define mainly their hysteretic behaviour [3]. Several tests have been performed to characterize most of these configurations [3,4].

Complex physical effects are present in the interaction of CLT connections, such as opening/closing of panels, friction, withdrawal extraction of fasteners, large deformation and buckling of fasteners, local compression of wood, and fracture and local separation of pieces of their panels [5]. Hence, it is necessary to consider an adequate numerical model to predict the complex response of these connections and provide a more robust design process for CLT buildings.

1.2 CLT CONNECTIONS MODELING

Generally, Finite Element (FE) macro-models are used to simulate CLT connections, where each component is modelled separately, i.e., timber panels with shell elements and discrete fasteners with a set of nonlinear uniaxial or muti-directional coupled/uncoupled springs based on a mechanical and/or phenomenological material approach (e.g., walls [6] or slabs [7]). Uniaxial elements with uncoupled directional springs consider a specific model for each direction [6,8], while multi-directional coupled several directions [9]. Generally, uniaxial FEs are the most controllable and can generate a combined effect that fits well with experimental tests [10].

Phenomenological-based hysteretic models used for spring elements of CLT connections can be divided into the type of constitutive equations (e.g., algebraic [11] or first-order ordinary differential equations [12]) or in their shape (i.e., smooth [12,13] or polygonal [11,14]). The unloading/reloading paths and pinching effect are simulated in all these models with different precision levels. Moreover, some models include stiffness/strength cyclic degradation [13,14].

[1] Centro Nacional de excelencia para la industria de la Madera (CENAMAD) & Department of Structural and Geotechnical Engineering, Pontificia Universidad Católica de Chile (PUC), mfchacon@uc.cl
[2] CENAMAD & Centro UC de Innovación en Madera (CIM UC-CORMA), PUC, pguindos@ing.puc.cl
[3] CENAMAD & CIM UC-CORMA, PUC, jamontano@uc.cl

https://doi.org/10.52202/069179-0373

1.3 GOAL AND SCOPE

This article summarizes the main results of another recent publication by authors, which provides a new robust non-linear FE model to simulate the CLT connections made of discrete fasteners under different loading conditions. More details can be obtained in the article of Chacón *et al*., 2023 [15]. Section 2 describes the numerical connection model, including its spring elements and material models. Moreover, an illustrative example is added to show the proposed model's capabilities. Also, Section 3 shows the results of two simulated experimental in-plane monotonic CLT slab tests with the considered FE model. Finally, the conclusions are listed in Section 4.

2 NUMERICAL CONNECTION MODEL

Five uncoupled spring elements were considered to simulate a generic discrete-fastener CLT connection. User-element and user-material FORTRAN77 subroutines of FEs and their materials were computationally implemented into the ANSYS software [16], respectively.

2.1 FINITE ELEMENTS

Two bar elements were implemented: (i) a uniaxial straight element of two nodes with one translational or rotational Degree Of Freedom (DOF) per node, called hereafter E1; and (ii) a radial 2D straight element of two nodes with two translational DOFs per node and a Lagrangean co-rotational formulation with radial strain, called hereafter RE2.

2.1.1 E1 element

This bar element has two nodes with one translational (U_x, U_y, or U_z) or one rotational DOF per node (Θ_x, Θ_y, or Θ_z), and one integration point at centroid of the element. It has a non-zero initial length l_o, and due to external forces/moments, the bar suffers a small displacement/rotation in each node $\aleph_i$ with $i \in [1,2]$. Considering a small engineering strain metric, the updated element tangent stiffness $\boldsymbol{K}_{n+1} \in \mathbb{R}^{2\times2}$ is given by

$$\boldsymbol{K}_{n+1} = v_o \frac{\partial \sigma_{n+1}}{\partial \varepsilon_{n+1}} (\boldsymbol{B} \otimes \boldsymbol{B}), \tag{1a}$$

$$\boldsymbol{B} = \frac{1}{l_o}[-1 \quad 1], \tag{1b}$$

where $v_o = Al_o$ is the initial element volume, with A being the cross-section element area, and $\frac{\partial \sigma_{n+1}}{\partial \varepsilon_{n+1}}$ is the consistent material tangent stiffness. Moreover, the updated internal force vector $\boldsymbol{F}_{\text{int}_{n+1}} \in \mathbb{R}^{2\times1}$ is expressed as

$$\boldsymbol{F}_{\text{int}_{n+1}} = v_o \boldsymbol{B}^T \sigma_{n+1}, \tag{2}$$

where σ_{n+1} is the updated material stress. Figure 1a shows two of the six cases that this element can adopt, where the U_x and Θ_y DOFs are shown. It cannot consider a zero-length element due to software restraints.

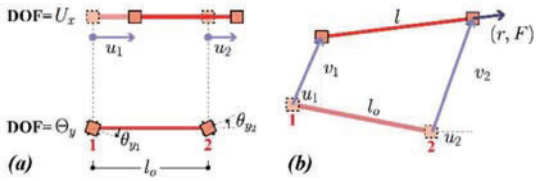

Figure 1: *Definition of the two bar finite elements implemented: (a) E1 (U_x and Θ_y DOFs cases); and (b) RE2.*

2.1.2 RE2 element

This bar element has two nodes, with two translational DOFs per node (U_x and U_y) and one integration point at the centroid of the element. Given some initial position of their nodes $\boldsymbol{x}_i = (x_i, y_i)$, with $i \in [1,2]$, due to external forces, the bar suffers a large arbitrary displacement in each node $\boldsymbol{u}_i = (u_i, v_i)$ (see Figure 1b), which elongates the bar from l_o to l length. Then, considering the Lagrangean co-rotational formulation with engineering strain metric (i.e., $\varepsilon = (l - l_o)/l_o$), the total updated tangent stiffness $\boldsymbol{K}_{n+1} \in \mathbb{R}^{4\times4}$ of this element is expressed as

$$\boldsymbol{K}_{n+1} = v_o \frac{\partial \sigma_{n+1}}{\partial \varepsilon_{n+1}} (\boldsymbol{B}_1 \otimes \boldsymbol{B}_1) + v\sigma_{n+1} (\boldsymbol{B}_2 \otimes \boldsymbol{B}_2), \tag{3}$$

where $v_o = Al_o$ and $v = Al$ are the initial/current element volume; and $\boldsymbol{B}_1$ and $\boldsymbol{B}_2$ are vectors given by

$$\boldsymbol{B}_1 = \frac{1}{l_o}[-\Delta x/l \quad -\Delta y/l \quad \Delta x/l \quad \Delta y/l\,], \tag{4a}$$

$$\boldsymbol{B}_2 = \frac{1}{l}[\Delta y/l \quad -\Delta x/l \quad -\Delta y/l \quad \Delta x/l\,], \tag{4b}$$

with $\Delta x = \Delta x_o + u_2 - u_1$, $\Delta y = \Delta y_o + v_2 - v_1$, $\Delta x_o = x_2 - x_1$, and $\Delta y_o = y_2 - y_1$. The initial/current length l_o and l can be obtained, respectively, as

$$l_o = \sqrt{\Delta x_0^2 + \Delta y_0^2}, \tag{5a}$$

$$l = \sqrt{\Delta x^2 + \Delta y^2}. \tag{5b}$$

The first term of Equation 3 represents the material tangent stiffness, while the second one the geometric stiffness. Moreover, the updated internal force vector $\boldsymbol{F}_{\text{int}_{n+1}} \in \mathbb{R}^{4\times1}$ is given by

$$\boldsymbol{F}_{\text{int}_{n+1}} = v_o \boldsymbol{B}_1^T \sigma_{n+1}. \tag{6}$$

Their element response is studied with a displacement-controlled rotation loop $\theta \in [0, 2\pi]$ and a constant stretching Δl_0, i.e., the displacement load vector $\boldsymbol{u}$ is

$$\boldsymbol{u}(\theta) = (l_o + \Delta l_0) \begin{bmatrix} \cos(\theta) \\ \sin(\theta) \end{bmatrix} - l_o \begin{bmatrix} 1 \\ 0 \end{bmatrix}. \tag{7}$$

A J_2 von Mises material model with a bi-linear isotropic hardening law is assumed. Figure 2 compares their response with the well-known two-node bar element with two translational DOFs per node. Note that only the RE2 element predicts the overall angle's response well, where a constant force and radial to the element direction independent of rotation is observed.

https://doi.org/10.52202/069179-0373

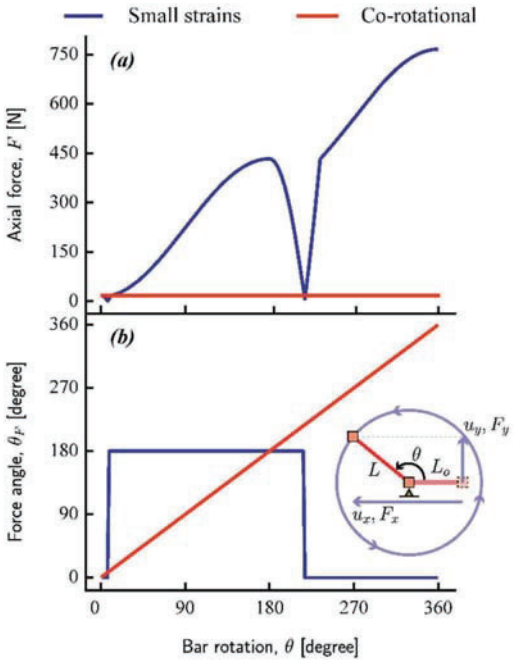

***Figure 2**: Comparison of the RE2 element response between small-strain and co-rotational formulations for a rotation loop $\theta \in [0,2\pi]$ with a constant stretching Δl_0: (a) force-rotation $F(\theta)$; and (b) angle force-rotation $\theta_F(\theta)$.*

2.1.3 Spring elements

To simulate the discrete CLT connections, five uncoupled springs are considered: (i) axial E1 element with asymmetric tensile/compressive model to include the gap of panels; (ii) in-plane shear E1 element with linear-elastic behavior to simulate the lateral slip between panels; (iii) out-of-plane shear E1 element with linear-elastic behavior to include the vertical slip between panels; (iv) radial RE2 element with the Richard–Abbott (RA) model [17] model to add the fastener capacity; and (v) bending E1 element with the RA model to represent the out-of-plane rotation of panels. Figure 3 and Table 1 summarize these elements' main properties and functions.

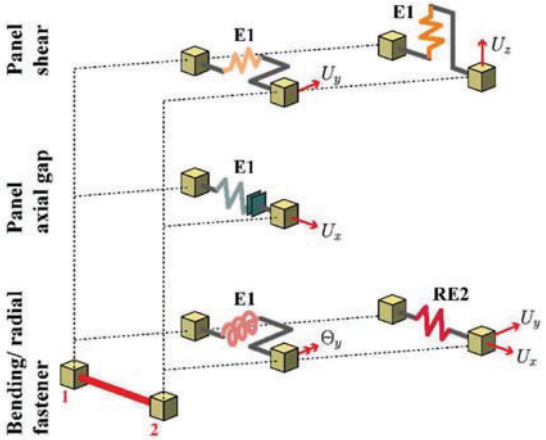

***Figure 3**: Spring elements to simulate a discrete CLT fastener connection. Figure extracted from Chacón et al., 2023 [15].*

***Table 1:** Springs elements for the CLT connection model.*

Id	Function	FE type	DOFs	Material
S1	Panel gap	E1	U_x	Gap
S2	In-plane shear panel	E1	U_y	Linear elastic
S3	Out-of-plane shear panel	E1	U_z	Linear elastic
S4	Radial fastener	RE2	U_x, U_y	Richard–Abbott
S5	Bending fastener	E1	Θ_y	Richard–Abbott

2.2 MATERIAL MODELS

2.2.1 Gap model

A simple and robust asymmetric model simulates the closure/opening gap of CLT panels. It is assumed the following gap force-displacement $F_g(u)$ relation

$$F_g(u) = \langle u \rangle^+ K_g^+ + \langle u \rangle^- K_g^-, \tag{8}$$

where $K_g^{\pm}$ are the Positive/Negative (P/N) (opening/closure) gap stiffness, and $\langle \blacksquare \rangle^{\pm}$ are the P/N Macauley functions (i.e., $\langle \blacksquare \rangle^{\pm} = (\blacksquare \pm |\blacksquare|)/2$). Note that this relation gives a discontinuous slope at zero displacement, which can generate some convergence problems at the FE level.

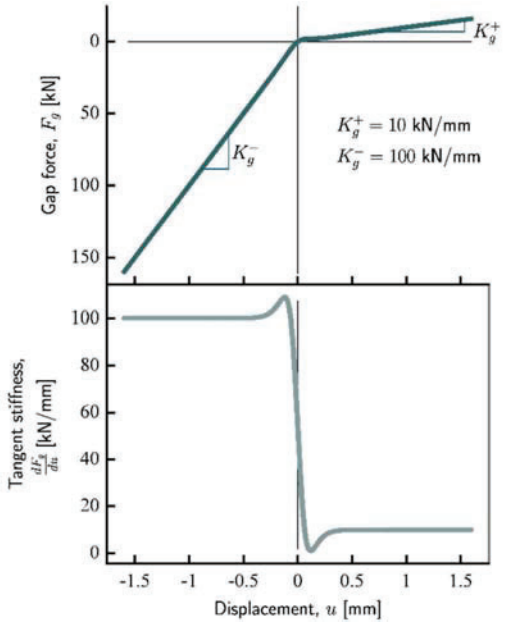

***Figure 4**: Response of gap model: (a) force-displacement $F_g(u)$; and (b) tangent stiffness-displacement $\frac{dF_g(u)}{du}$.*

Then, Equation 8 can be rewritten in terms of some approximated smoothed (C_1-class) P/N Heaviside functions $\widetilde{\mathrm{H}}^{\pm}(u)$ as

$$F_g(u) = \left(\widetilde{\mathrm{H}}^+(u) K_g^+ + \widetilde{\mathrm{H}}^-(u) K_g^-\right) u. \tag{9}$$

Hence, they derivative $\frac{dF_g(u)}{du}$ can be obtained as follows

https://doi.org/10.52202/069179-0373

$$\frac{dF_g(u)}{du} = \sum_{\aleph}\left(\frac{d\widetilde{\mathrm{H}}^{\aleph}(u)}{du}u + \widetilde{\mathrm{H}}^{\aleph}(u)\right)K_g^{\aleph}, \tag{10}$$

where symbol $\aleph$ denotes the '+' and '-' superscript, respectively. For the sake of simplicity, it is considered here the following approximated P/N Heaviside functions $\widetilde{\mathrm{H}}^{\pm}(u)$

$$\widetilde{\mathrm{H}}^{\pm}(u) = \frac{1}{2}[1 \pm \tanh(ku)], \tag{11}$$

where k is an arbitrary parameter such as $\lim_{k\to\infty}\widetilde{\mathrm{H}}^{\pm}(u) = \mathrm{H}^{\pm}(u)$, with $\mathrm{H}^{\pm}(\blacksquare)$ are the P/N stepped Heaviside functions. Figure 4 shows an illustrative example of the gap force-displacement $F_g(u)$ relation and their derivative $\frac{dF_g(u)}{du}$. Note that the slope continuity in both functions is satisfied in the overall displacement range.

2.2.2 Fastener model

A modified version by authors of the Richard–Abbott model [17] is considered to simulate the stiffness/strength fastener capacity. This model was first proposed to simulate the hysteresis of steel connections and can also adequately simulate the cyclic behaviour of timber connections. The model includes the pinching effect, symmetric/asymmetric behaviour, and low-cycle fatigue phenomena.

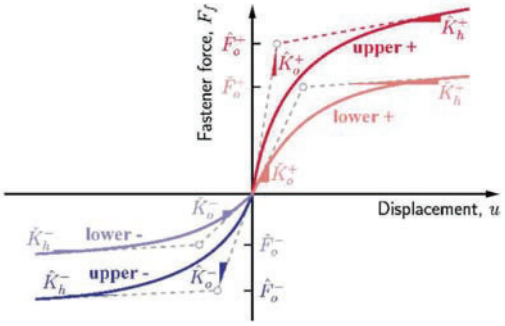

Figure 5: *Definition of parameters for the Richard-Abbott fastener model.*

First, the P/N generalized force-displacement $F_f^{\pm}(u)$ curves (e.g., force or moment and displacement or rotation, respectively) are stated as a combination of an upper $\hat{F}^{\pm}(u)$ and lower $\check{F}^{\pm}(u)$ P/N curves (see Figure 5), and are defined as

$$F_f^{\pm}(u) = f_r^{\pm} - \left(\frac{K_{et}^{\pm}}{\psi_t^{\pm}} + K_{ht}^{\pm}\right)z, \qquad \text{with} \tag{12a}$$

$$\psi_t^{\pm} = \left(1 + \left|\phi_t^{\pm}\right|^{n_t^{\pm}}\right)^{1/n_t^{\pm}}, \qquad \phi_t^{\pm} = \frac{K_{et}^{\pm}z}{f_{1t}^{\pm}} \tag{12b}$$

where $K_{et}^{\pm} = K_{ot}^{\pm} - K_{ht}^{\pm}$, $f_{1t}^{\pm} = f_{ot}^{\pm} + |f_r^{\pm}|$, $z = u_r^{\pm} - u$; $(u_r^{\pm}, f_r^{\pm})$ are the P/N reversal point of curves; $f_{ot}^{\pm}$ are the P/N initial force; $K_{ot}^{\pm}$ and $K_{ht}^{\pm}$ are the P/N initial/hardening stiffnesses, respectively; and $n_t^{\pm}$ are the P/N factor that control the shape of curves. The parameters $f_{ot}^{\pm}$, $K_{ot}^{\pm}$, $K_{ht}^{\pm}$, and $n_t^{\pm}$ are expressed as

$$K_{ot}^{\pm} = \hat{K}_o^{\pm} - (\hat{K}_o^{\pm} + \check{K}_o^{\pm})t, \tag{13a}$$
$$K_{ht}^{\pm} = \hat{K}_h^{\pm} - (\hat{K}_h^{\pm} + \check{K}_h^{\pm})t, \tag{13b}$$
$$f_{ot}^{\pm} = \hat{f}_o^{\pm} - (\hat{f}_o^{\pm} + \check{f}_o^{\pm})t, \tag{13c}$$
$$n_t^{\pm} = \hat{n}^{\pm} - (\hat{n}^{\pm} + \check{n}^{\pm})t, \tag{13d}$$

where $\hat{\blacksquare}$ and $\check{\blacksquare}$ are upper and lower parameters, respectively. The parameter $t \in [0,1]$ is a transition factor that combines the upper and lower parameters linearly and is given by

$$t = \left(\frac{v^{\pm}}{1+v^{\pm}}\right)^{t_2^{\pm}}, \qquad \text{with} \qquad v^{\pm} = \left|\frac{u-u_r^{\pm}}{t_3^{\pm}\left(u_{\max}-u_r^{\pm}\right)}\right|^{t_1^{\pm}} \tag{14}$$

where $t_3^{\pm} \in [0,1]$ are P/N displacement factors that control the shape of pinching curves. Note that the definition of P/N variables $v^{\pm}$ varies from the original RA model to give a symmetric response under symmetric displacement loads. The variable $u_{\max}$ is the maximum displacement at the loading direction, which is defined as

$$u_{\max} = \mathrm{H}^{+}(\zeta)r^{+} + \mathrm{H}^{-}(\zeta)r^{-}, \qquad \text{with} \tag{15a}$$
$$r^{+} = \max_{\tau\in[0,t]}(r^{+}(\tau), \langle u\rangle^{+}), \tag{15b}$$
$$r^{-} = \min_{\tau\in[0,t]}(r^{-}(\tau), \langle u\rangle^{-}), \tag{15c}$$

where $\zeta = \mathrm{sgn}(\dot{u})$ is the loading direction, and $r^{\pm}$ are the P/N displacement thresholds. Note that variables $r^{\pm}$ grow monotonically according to obtained displacements and are independent in both directions.

Second, the model also includes a strength/stiffness degradation phenomenon (fatigue effect), where the degraded generalized force $F_{\omega}^{\pm}$ and the degraded hardening stiffness $K_{h\omega}^{\pm}$ are evaluated according to respective relations

$$F_{\omega}^{\pm} = (1-\omega_f)F_f^{\pm}, \tag{16a}$$
$$K_{h\omega}^{\pm} = (1-\omega_k)K_h^{\pm}, \tag{16b}$$

where $\omega_f \in [0,1]$ and $\omega_k \in [0,1]$ are the strength/stiffness damage variables, respectively, given by

$$\omega_f = 1 - \exp(-J_f\Upsilon), \tag{17a}$$
$$\omega_k = 1 - \exp(-J_k\Upsilon), \tag{17b}$$

with J_f and J_k are the strength/stiffness degraded factor, respectively. Both variables are dependent on the hysteretic dissipated energy Υ (i.e., $\Upsilon(t) = \int F(t)du$). The damage variable ω_f and ω_k does not distinguish the P/N regime, taking the accumulation in both directions. Moreover, Equations 17a-b do not require the completion of cycles to increase the damage as occurs with other proposed models [13,14].

Additionally, the choice of P/N parameters and variables $\theta^{\pm}$ are determined according to loading direction ζ, i.e.,

$$\theta = \mathrm{H}^{+}(\zeta)\theta^{+} + \mathrm{H}^{-}(\zeta)\theta^{-}. \quad (18)$$

Finally, it is essential to note that this model considers a generalized force-displacement (or moment-rotation) relation, whereas the two material models inside of the user-implemented FEs work in the stress-strain space. Then, converting from the force-displacement to stress-strain relation is necessary to give the same FE response as the theoretical point level. Since this model has physical-based parameters, the conversion is explicit and only requires the conversion of three types of parameters: (i) P/N stiffnesses $K_o^{\pm}$ and $K_h^{\pm}$ (or $K_{\theta o}^{\pm}$ and $K_{\theta h}^{\pm}$) for the upper/lower cases; (ii) P/N strengths $F_o^{\pm}$ (or $M_o^{\pm}$) for the upper/lower cases; and (iii) energy-based strength degradation factor J_f. Then, for a force-displacement and moment-rotation relations, their respective above parameters require the following factors

$$\varphi_K = \frac{l_o}{A}, \quad \varphi_F = \frac{1}{A}, \quad \varphi_Y = l_o A, \quad (19a)$$

$$\varphi_K = \frac{l_o}{I_o}, \quad \varphi_F = \frac{1}{I_o}, \quad \varphi_Y = l_o I_o, \quad (19b)$$

where l_o is the element length, A is the cross-section element area, and I_o is the cross-section inertia of element with respect to their centroid. Note that the gap model also requires the conversion of their P/N stiffnesses $K_g^{\pm}$ from force-displacement to stress-strain space, which is used the factor φ_K of Equation 19a.

In summary, the model uses four quadruplets of parameters to define the upper and lower curve ($K_o^{\pm}$, $K_h^{\pm}$, $F_o^{\pm}$, and $n^{\pm}$), three pairs of parameters to state the transition parameter t ($t_2^{\pm}$, $t_2^{\pm}$, and $t_3^{\pm}$), and two parameters to control the fatigue (J_f and J_k). Hence, the model has a total of 24 parameters. An explicit numerical integration scheme for the updated force of this model is performed, where six state variables are considered $\boldsymbol{q} = \{\zeta, \Upsilon_d, r^{+}, r^{-}, u_r, f_r\}$.

Three illustrative examples are considered to show the capabilities of this model. The first two are illustrative examples, where it is used a set of symmetrical and asymmetrical P/N parameters, respectively. In contrast, the third example is a validation of the experimental in-plane cyclic CLT connection test of Gavric *et al.* [5]. Table 2 lists all parameters considered for the three cases. Figure 6 shows the first two cases, whereas Figure 7 the third one. Four increased amplitude loading displacement cycles are applied in the first two cases (see Figure 6). The same displacement pattern as the experimental test is considered for the third case.

***Table 2**: Parameters for the three examples of the RA fastener model.*

	Example		
Parameter	E1	E2	E3
K_o [kN/mm]	[2, 2, 2, 2][(a)]	[3, 2, 3, 2]	[1, 1, 3, 3]
K_h [N/mm]	[30, 30, 10, 10]	[70, 20, 10, 10]	[220, 200, 60, 60]
F_o [kN]	[10, 10, 1, 1]	[10, 5, 3, 1]	[7, 6, -1, 2]
n [-]	[1.5, 1.5, 1.5, 1.5]	[1.5, 1.5, 1.5, 1.5]	[4, 4, 4, 4]
t_1 [-]	[10, 10][(b)]	[15, 15]	[40, 40]
t_2 [-]	[0.9, 0.9]	[0.9, 0.9]	[0.1, 0.1]
t_3 [-]	[0.9, 0.9]	[0.9, 0.9]	[1, 1]
J_f [-]	0	9×10^{-4}	5×10^{-7}
J_k [-]	0	1×10^{-4}	1×10^{-8}

[(a)] P/N upper and P/N lower values, respectively; [(b)] P/N values, respectively.

First, Figure 6a shows the force-displacement hysteresis using symmetrical P/N parameters, where symmetry is preserved regarding the force/stiffness of the envelopes and pinching curves. Second, Figure 6b shows the response of the second case, where a notable strength asymmetry and stiffness/strength degradation is observed. Third, a good fit in terms of envelopes and pinching paths is kept for the third case (see Figure 7a), where an error less than 1% is measured for the peak strength and respective displacement in both directions, and a coefficient of determination η_{det} (R^2) for the force history of 93.25 is calculated. Moreover, the model reproduces with considerable precision the low-cycle fatigue phenomena.

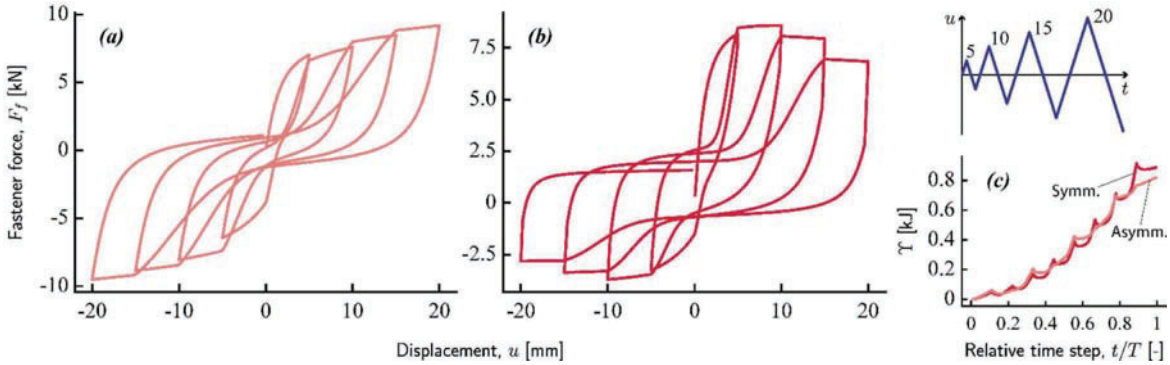

***Figure 6:** Force-displacement hysteresis $F_f(u)$ of the RA fastener model for two illustrative examples with different set of parameters: (a) symmetrical P/N parameters; (b) asymmetrical P/N parameters; and (c) hysteretic dissipated energy of both cases.*

https://doi.org/10.52202/069179-0373

Moreover, Figures 6c and 7b show the history of dissipated energy $\Upsilon(t)$ for all cases. A more significant amount of energy is dissipated in the second case than in the first one due to the incorporation of the stiffness/strength degradation factors in the model. For the third case, an excellent fit is observed concerning the experimental test, where a coefficient of determination η_{det} of 99.02 is estimated. Nevertheless, some minor differences exist, showing a moderate underestimation at 0 to 0.6, while an overestimation from 0.8 to the end is noted.

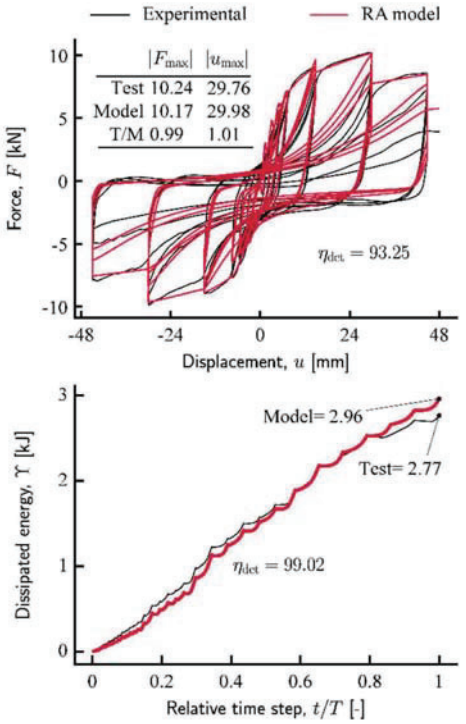

Figure 7: *Third example of the RA fastener model validated with the in-plane cyclic CLT connection test of Gavric et al. 2015 [5]: (a) force-displacement $F(u)$; and (b) dissipated energy-relative time step $\Upsilon(t/T)$.*

2.3 CONNECTION MODEL RESPONSE

To show the response of connection FE model under different loading conditions, an illustrative example is elaborated (see Figure 8a). Two generic square 3-layered CLT panels (t=100 mm) with a width of 1200 mm are joined with nine generic fasteners (ϕ=6 mm), equally spaced along the edge, and are loaded with different independent cyclic loads: axial, in-plane shear, and out-of-plane bending. Displacement-controlled load is applied at right edge of right panel, whereas a fixed support is considered at left edge of left panel. A gap separation of 5 mm between panels is imposed to get a more realistic response and to consider a non-zero length for the spring elements.

A Three-Dimensional (3D) FE model is generated in ANSYS, as shown in Figure 8b. On the one hand, the CLT panels are simulated with a four-node layered-shell element SHELL181 with a linear-orthotropic material model for each lamella, whose material X-axis is oriented parallel-to-grain direction of each lamella. This element accounts for the shear distribution using the Mindlin-Reissner first-order shear-deformation theory and can adequately represent the mechanical behaviour of orthotropic plates since their stiffness depends on the loading situation. On the other hand, each fastener is simulated with the proposed set of five two-node spring elements USER300 and their materials of Sections 2.1 and 2.2, respectively.

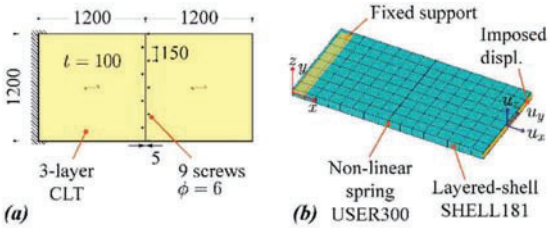

Figure 8*: Connection model example: (a) 2D plan view of setup; and (b) 3D view of FE model. Units in millimetres.*

Table 3*: Material parameters for the connection model example.*

Parameter	Value
CLT	
E_x, E_y, E_z [GPa]	11, 0.37, 0.37
ν_{xy}, ν_{xz}, ν_{yz} [-]	0, 0, 0
G_{xy}, G_{xz}, G_{yz} [GPa]	0.65, 0.185[(a)], 0.185[(a)]
Radial spring (S4)	
K_o [N/mm]	[500, 500, 500, 500][(b)]
K_h [N/mm]	[50, 50, 20, 20]
F_o [kN]	[3, 3, 1, 1]
n [-]	[4, 4, 4, 4]
t_1 [-]	[40, 40][(c)]
t_2 [-]	[0.1, 0.1]
t_3 [-]	[1, 1]
J_f [-]	5×10^{-7}
J_k [-]	3×10^{-8}
Bending spring (S5)	
$K_{\theta o}$ [kN-mm/rad$\times 10^3$]	[1, 1, 1, 1][(b)]
$K_{\theta h}$ [kN-mm/rad]	[50, 50, 10, 10]
M_o [kN-mm]	[10, 10, 1, 1]
n [-]	[4, 4, 4, 4]
t_1 [-]	[40, 40][(c)]
t_2 [-]	[0.1, 0.1]
t_3 [-]	[1, 1]
J_f [-]	0
J_k [-]	3×10^{-1}
Gap spring (S1)	
K_g^+ [kN/mm]	0.13
K_g^- [kN/mm]	3.30

[(a)] $G_{xz} = 0.5E_x/(1+\upsilon_{xz})$ and $G_{yz} = G_{xz}$; [(b)] P/N upper and P/N lower values, respectively; and [(c)] P/N values, respectively.

Table 3 lists the material parameters for the CLT panels and three of the five spring elements (radial, bending, and

gap). Moreover, for the two shear springs (in-plane and out-of-plane), it is assumed a linear-elastic material, where Young's modulus equal to XZ-shear modulus of CLT panels G_{xz} is considered for both springs for simplicity. Also, for the in-plane shear spring, a shear area of $A_{vy} = 5/6A_{\text{fast}} \times 10^{-5}$, with A_{fast} is the fastener cross-section area, is assumed to simulate quasi-null in-plane friction and to avoid singularity (null pivot) at stiffness matrix. In contrast, for the out-of-plane shear spring, a shear area of $A_{vz} = 5/6A_{\text{fast}}$ is taken because no out-of-plane slip is assumed.

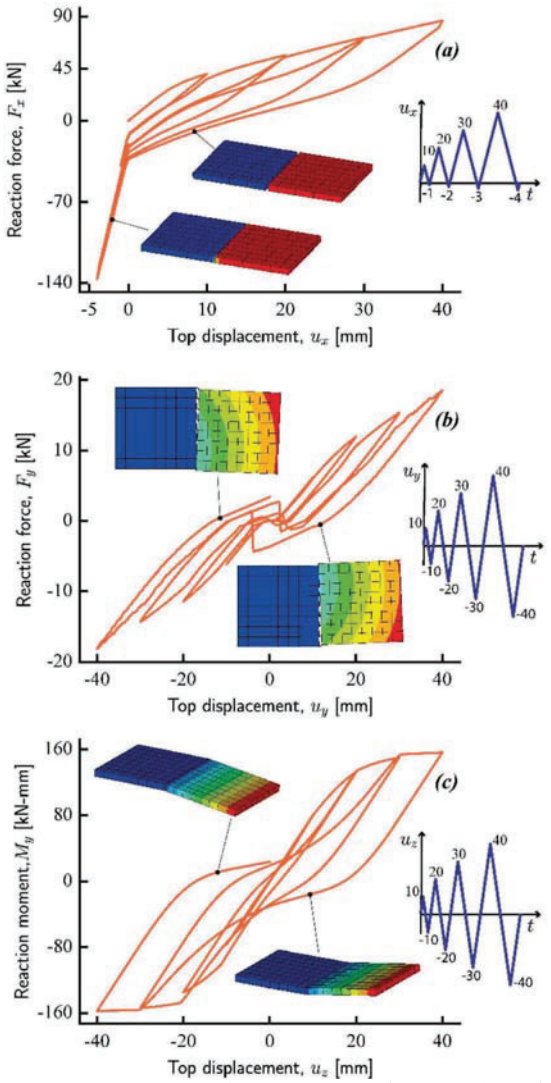

Figure 9: *Response of connection model example under different loadings conditions: (a) axial; (b) shear; and (c) bending. Figures include the displacement field of the FE model for a P/N loading condition at some unspecific time step.*

Figure 9a shows the axial reaction force-axial top displacement $F_x(u_x)$ curve of this FE model under a cyclic axial displacement load. An asymmetric displacement load pattern with four cycles of increased magnitude is considered, where positive (tensile) displacements values are larger than negative (compressive). The gap effect of panels is correctly simulated, where a cyclic behaviour with stiffness degradation and pinching is present in the tensile regime. In contrast, a marked linear-elastic behaviour is noted in the compressive one.

Figure 9b presents the in-plane reaction shear-lateral top displacement $F_y(u_y)$ relation of this FE model under a cyclic in-plane lateral displacement load. Conversely to the axial case, a symmetric P/N displacement load pattern with four cycles of increased magnitude is applied. A symmetric response is observed, with a larger amount of hardening in their envelopes, a significant pinching at the unloading/reloading paths, and an initial gap displacement of approx.—5 mm associated with the length of spring elements. Moreover, a snap-through behaviour is observed at relatively small displacements (around 5 to 10 mm), which is more pronounced at larger displacements. This phenomenon can be attributed to coupling gap/radial fastener springs. Note that this class of load test is scarce in literature (with free panel rotation) and that the shear capacity is lower than the axial one, contrary to several experimental CLT joint tests [4,5].

Figure 9c shows the bending reaction moment-vertical top displacement $M_y(u_z)$ curve of this FE model under a cyclic vertical displacement load. An identical symmetric displacement load pattern to the second case is applied vertically. A hysteretic response is observed, similar to the pure RA fastener response, like in Figure 6a, that no other coupling effects are present for this load case.

3 VALIDATION EXAMPLES

To experimentally validate the proposed numerical connection FE model, the two in-plane monotonic CLT slab test specimens of Veliz *et al*., 2023 [18] are simulated (see Figure 10a). The first specimen, called hereafter Slab1, is composed of three 5-layered CLT panels elaborated with C24-class Chilean radiate pine (t=165 mm) and two top surface spline connections, each made of plywood (t=18.5 mm) and 11 Simpson SDWS22600 (ϕ5.6x150 mm) screws [19] alternated placed. The second specimen, called hereafter Slab2, is composed of four 3-layer CLT panels of identical wood specimen and quality (t=99 mm) and three top butt joint connections, each made of stainless-steel plate (t=3 mm) and 18 Simpson SDS25312 (ϕ6.4x89 mm) screws [19] orthogonally placed. A gap separation of 5 mm between panels was imposed initially in both specimens to avoid an undesirable compression failure between panels and neglect friction forces into the response.

Figure 10b shows the 2D plan view of both specimens and their loading setup. First, a displacement-controlled load is applied in both specimens using two actuators positioned at the middle panels (see Figure 10b). Then, a monotonic load is applied up to reach the complete failure of each slab.

https://doi.org/10.52202/069179-0373

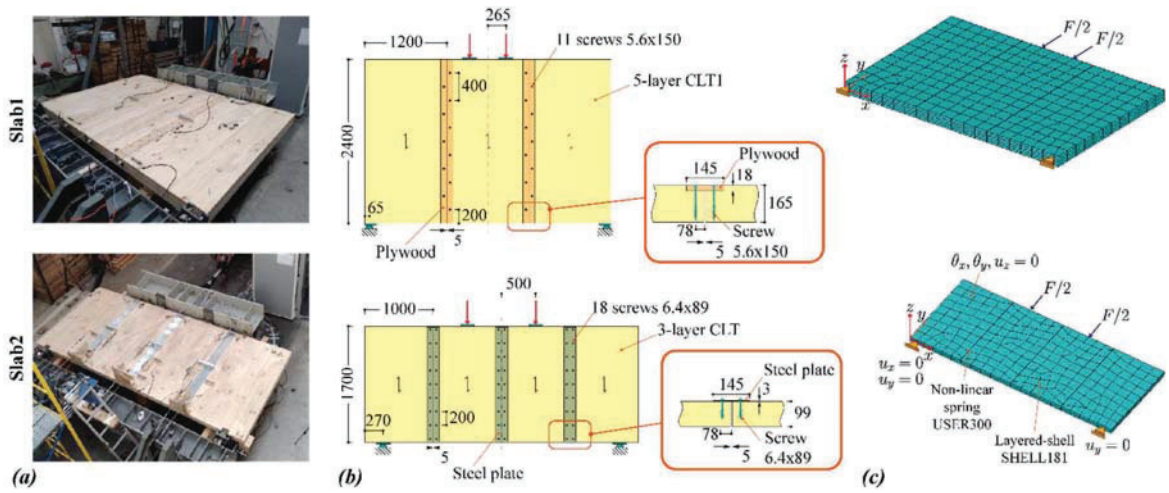

Figure 10: *In-plane monotonic CLT slabs tests of Veliz et al., 2023 [18]: (a) 3D view photograph; (b) 2D plan view of setup; and (c) 3D view of FE model. Figure extracted from Chacón et al., 2023 [15].*

Experimentally, both specimens showed a moderate ductile behaviour, with a ductility of approx. 3.5 and 2.5, respectively (see Figure 12). On the one hand, the failure mechanism of Slab1 was due to the damage of 10 screws (22 in total), which had a mixed failure mode (i.e., 4 ductile and 6 shear brittle). Moreover, fibre densification of CLT around all hole screws and penetration of almost head screws inside plywood were observed. Also, a rigid body motion of panels (without significant damage) with a moderate beam effect was observed, which generates an important shear slip of the central panel, a rotation of both lateral panels, and, consequently, a moderate lateral aperture of both connections. On the other hand, a similar failure mechanism occurred with the Slab2 due to the shear failure of 34 screws (54 in total) and tensile perpendicular-to-fibre failure at central edge panels. In addition to the fibre densification around all hole screws, the steel plates suffer a partial global buckling between each screw span and plastic deformation around screw holes. Furthermore, a more pronounced beam effect than Slab1 was viewed for this specimen due to a larger aspect ratio, where a considerable lateral aperture of connections and a less shear slip of the two central panels were noticed. Finally, note that all these observations explain why Slab2 is stiffer, stronger, and less ductile than Slab1.

Like example of Section 2.3, a 3D FE model is generated in ANSYS for each specimen, as shown in Figure 10c. On the one hand, the CLT panels are simulated with three/four-node layered-shell element SHELL181, where a linear-orthotropic material model is considered for each layer. On the other hand, each fastener is simulated with three of the five proposed spring elements and their respective materials (see Sections 2.1 and 2.2). The three springs considered are panel gap (S1), out-of-plane panel shear (S3), and radial fastener (S4). The other two springs were not required due to that was experimentally observed a significant gap separation between panels (in-plane spring S2) and a negligible out-of-plane rotations (bending fastener spring S5). Note that the out-of-plane spring S3 was included exclusively to avoid a null pivot in the vertical direction of the element stiffness matrix. Moreover, the panel gap springs (S1) were placed only at the nearest node at the top/bottom panel edges. Table 4 lists the material parameters for the panels and two spring elements (radial and gap). Also, same spring element S3 as the example of Section 2.3 is considered here because no significant out-of-plane slip was measured. A monotonic displacement-controlled load pattern is applied equally at the two nodes where the actuators were positioned and using 300-time steps for both specimens.

Table 4: *Material parameters for the two simulated CLT slabs.*

	CLT slab	
Parameter	Slab1	Slab2
CLT		
E_x, E_y, E_z [GPa]	11, 0.37, 0.37	11, 0.37, 0.37
ν_{xy}, ν_{xz}, ν_{yz} [-]	0, 0, 0	0, 0, 0
G_{xy},G_{xz},G_{yz} [GPa]	0.69, 0.345[(a)], 0.345[(a)]	0.69, 0.345, 0.345
Radial spring (S4)		
K_o [kN/mm]	[0.5, 0.5, 0.5, 0.5][(b)]	[0.8, 0.8, 0.8, 0.8]
K_h [N/mm]	[50, 50, 20, 20]	[70, 70, 20, 20]
F_o [kN]	[2.3, 2.3, 1, 1]	[7, 7, 1, 1]
n [-]	[4, 4, 4, 4]	[4, 4, 4, 4]
t_1 [-]	[40, 40][(c)]	[40, 40]
t_2 [-]	[0.1, 0.1]	[0.1, 0.1]
t_3 [-]	[1, 1]	[1, 1]
J_f [-]	5×10^{-7}	1×10^{-7}
J_k [-]	3×10^{-8}	3×10^{-8}
Gap spring (S1)		
K_g^+ [kN/mm]	2.99	1.74
K_g^- [kN/mm]	74.80	43.56

[(a)] $G_{xz} = 0.5E_x/(1+\upsilon_{xz})$ and $G_{yz} = G_{xz}$; [(b)] P/N upper and P/N lower values, respectively; and [(c)] P/N values, respectively.

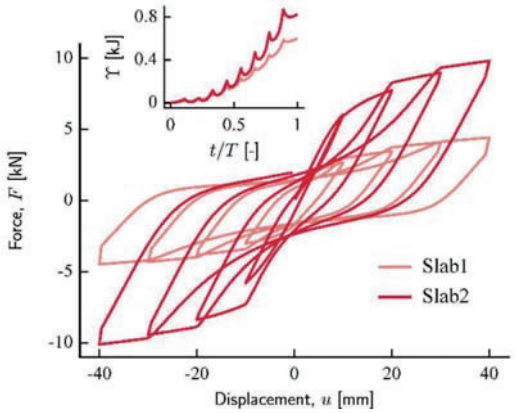

***Figure 11**: Force-displacement hysteresis $F(u)$ of the S4 radial fastener spring element for the two simulated CLT slabs. The figure includes the respective dissipated energy-relative time step $\Upsilon(t/T)$ relation.*

Figure 11 depicts the force-displacement hysteresis of the S4 spring element (radial fastener) with the RA model for the two simulated CLT slabs. Note that the fastener springs of Slab2 have more strength/stiffness than used in Slab1, which is according to the admissible strength capacity of each screw [19]. The traditional inverse iterative approach is considered to calibrate the parameters of springs S1 and S4 for both specimens, where the force-lateral displacement curve $F_y(u_y)$ of each entire FE model is used to minimize the error concerning the experimental test (see Figure 12). Additional experimental CLT connection tests under monotonic/cyclic axial and in-plane shear loads can be required to directly calibrate the spring elements (S1 and S4) to avoid this iterative process. During this process, it was observed that the tensile gap stiffness of spring S1 plays a key role in the failure mechanism of the entire model, especially at the hardening phase. Small values of this parameter give a more CLT panel rotation, whereas large values generate a quasi-pure panel translation.

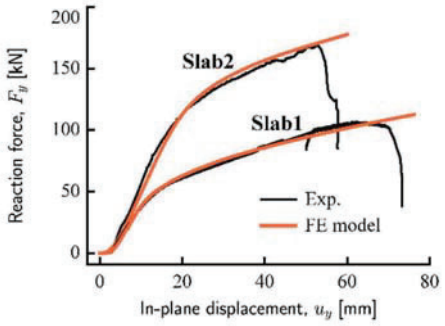

***Figure 12:** Comparison of reaction force-displacement $F_y(u_y)$ for the two tested and simulated CLT slabs.*

Figure 12 compares the experimental measurements concerning the reaction force-lateral in-plane displacement $F_y(u_y)$ curve of each simulated CLT slab. It should be noted that for Slab 1, it was necessary to add an offset displacement of 2.5 mm to the experimental data due to an initial gap separation of 5mm in the model. Nevertheless, it was observed in both slab models a good fit for the elastic and hardening phase concerning experimental results. Although the RA model includes strength degradation, the complete FE model cannot adequately simulate both tests' abrupt softening failure phase.

Figure 13 shows the equivalent von Mises stress (i.e., $\sigma_{eqv} = \sqrt{3/2\boldsymbol{s}:\boldsymbol{s}}$, with $\boldsymbol{s} = \boldsymbol{\sigma} - (\sigma_x + \sigma_y + \sigma_z)I/3$ is the deviatoric stress tensor and $\boldsymbol{\sigma}$ is the Cauchy stress tensor) of the two simulated CLT slabs at the final time step. The maximum value of this field in both specimens is observed to be lower than the allowable compressive strength parallel-to-fibre of panels obtained from the current timber code designs, i.e., $f_{c,0}$=8 MPa [20]. Moreover, the images also show the displacement field, which agrees with the failure mechanism of both experimental tests [18].

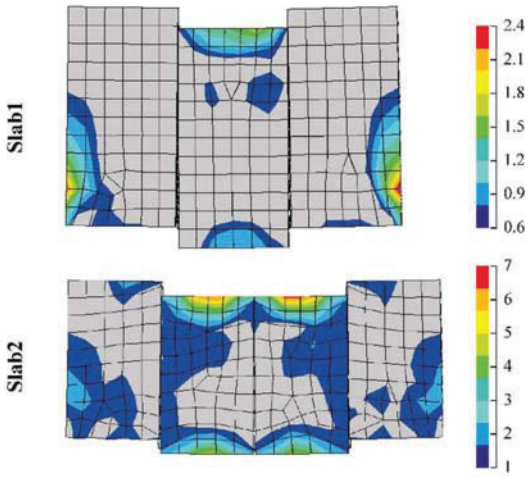

***Figure 13**: Equivalent von Mises stress field σ_{eqv} of the two simulated CLT slabs. Units in MPa. Note: the images also include the displacement field amplified by 3 times.*

4 CONCLUSIONS

A new Finite Element (FE) model is proposed to simulate the discrete-fastener panel-to-panel CLT connections. A set of five linear/non-linear uncoupled spring elements are considered, where each of them simulates the main phenomenological effect of connections under different loading conditions: (i) gap of panels with an axial element and asymmetrical tensile/compressive (gap) model; (ii) in-plane and out-of-plane slip of panels with two linear-elastic uniaxial elements; and (iii) radial and out-of-plane bending stiffness/strength capacity of fastener with a respective radial and uniaxial element using both the modified Richard-Abbott hysteretic model. The main conclusions are:

- On one hand, the gap model adequately simulates the axial behaviour (closure/opening) of CLT panels. On the other hand, the modified Richard-Abbott model

https://doi.org/10.52202/069179-0373

predicts well the contribution of discrete fasteners for the CLT connections. In addition, this model accurately simulates the hysteresis of a generic timber connection, including pinching, asymmetric positive/negative loading, and stiffness/strength degradation phenomena.

- The FE connection model simulates three satisfactory loading conditions: axial, in-plane shear, and out-of-plane bending. The gap effect (open/closure) is correctly simulated at axial loads, where a hysteretic tensile/linear compressive regime is stated. Moreover, at in-plane shear loads with a free panel rotation, a snap-trough behaviour at small displacements is observed due to the coupling of gap and radial fastener springs. Also, at bending loads, the pure bending fastener spring is represented in the overall response of the model.
- The FE model is correctly validated with the experimental results of two CLT slabs under in-plane monotonic loads. Furthermore, the 3D FE models generated agree with the experimental tests regarding initial/hardening stiffnesses, strength capacity, and failure mechanism. Also, it is observed that a critical role plays in the tensile stiffness of the gap spring in predicting the failure mechanism of the entire specimen, where smaller values give larger panel rotations.

ACKNOWLEDGEMENT

Financial support was provided by Centro Nacional de excelencia para la industria de la Madera (CENAMAD), ANID/ BASAL/ FB210015; and FONDEF project, ANID/ FONDEF/ IDeA I+D/ ID20I10312.

REFERENCES

[1] Pei S., Rammer D., Popovski M., Williamson T., Line P., van de Lindt J.W.: An overview of CLT research and implementation in North America. In: *14th WCTE*, Vienna, Austria, 2016.

[2] Sullivan K., Miller TH., Gupta R.: Behavior of cross-laminated timber diaphragm connections with self-tapping screws. *Engineering Structures*, 168: 505–524, 2018.

[3] Hossain A., Popovski M., Tannert T.: Cross-laminated timber connections assembled with a combination of screws in withdrawal and screws in shear. *Engineering Structures*, 168: 1–11, 2018.

[4] Gavric I., Fragiacomo M., Ceccotti A.: Strength and deformation characteristics of typical X-lam connections. In: *12th WCTE*, Auckland, New Zealand, 2012.

[5] Gavric I., Fragiacomo M., Ceccotti A.: Cyclic behaviour of typical metal connectors for cross-laminated (CLT) structures. *Materials & Structures*, 48: 1841–1857, 2015.

[6] Rinaldin G., Amadio C., Fragiacomo M.: A component approach for the hysteretic behaviour of connections in cross-laminated wooden structures. *Earthquake Engineering & Structural Dynamics*, 42 (13): 2023–2042, 2013.

[7] Ávila F., Dechent P., Opazo A.: Seismic behaviour evaluation of CLT horizontal diaphragms on hybrid buildings with reinforced concrete shear walls. *Engineering Structures*, 244: 112698, 2021.

[8] D'Arenzo G., Casagrande D., Reynolds T., Fossetti M.: In-plane elastic flexibility of cross laminated timber floor diaphragms. *Construction and Building Materials*, 209: 709–724, 2019.

[9] Pozza L., Saetta A., Savoia M., Talledo D.: Coupled axial-shear numerical model for CLT connections, *Construction and Building Materials*, 150: 568–582, 2017.

[10] Izzi M., Rinaldin G., Fragiacomo M., Polastri A.: Numerical modelling of steel-to-timber joints and connectors for CLT structures. In: *14th WCTE*, Vienna, Austria, 2016.

[11] Stewart WG.: The seismic design of plywood sheated shear walls, Ph.D. thesis, *University of Canterbury*, Christchurch, New Zealand, 1987.

[12] Ismail M., Ikhouane F., Rodellar J., The hysteresis Bouc-Wen model, a survey. *Archives in Computational Methods Engineering*, 16: 161–188, 2009.

[13] Pang WC., Rosowsky D., Pei S, van de Lindt JW.: Evolutionary parameter hysteretic model for wood shear walls. *Journal of Structural Engineering*, 133 (8): 1118–1129, 2007.

[14] Ibarra LF., Medina RA., Krawinkler H.: Hysteretic models that incorporate strength and stiffness deterioration. *Earthquake Engineering & Structural Dynamics*, 34: 1489–1511, 2005.

[15] Chacón MF., Guindos P., Montaño, Jara A., Benedetti F., Lagos J., Veliz F. Finite element formulation for modelling cross-laminated timber diaphragm connections. Submitted to *Construction and Building Materials*, 2023.

[16] ANSYS. ANSYS Academic Research, Release 20.0, *ANSYS, Inc.*, Canonsburg, Pennsylvania, 2022.

[17] Nogueiro P., da Silva LS., Bento R., Simões R. Numerical implementation and calibration of a hysteretic model with pinching for the cyclic response of steel and composite joints. *Advances in Steel Structures*, 1: 767–774, 2005.

[18] Veliz F., Guindos P., Montaño J., Lagos J.: Experimental monotonic in-plane behavior of high-capacity light-frame and cross-laminated timber diaphragms. Submitted to *Engineering Structures*, 2023.

[19] Strong-Tie S. Fastening Systems Technical Guide. *Simpson Strong-Tie Company Inc*., Canada, 2023.

[20] NCh1198. Wood–Wood Construction–Calculation (in Spanish). *Instituto Nacional de Normalización*. Santiago, Chile, 2014.

World Conference on Timber Engineering Oslo 2023

EXPERIMENTAL AND NUMERICAL ASSESSMENTS OF A LONG-SPAN MASS TIMBER FLOOR SYSTEMS SUBJECTED TO FOOT-FALL INDUCED VIBRATION

Christian Slotboom[1], Carla Dickof[2], Tobias Fast[3]

ABSTRACT: The following paper presents a series of experimental and numerical vibration assessments completed on the long-span floor system of Fast+Epp's home office. Measurements were taken on the building throughout different stages of construction to understand the impact of non-structural elements on floor vibration. Factors considered are partitions, concrete toppings, and screws between the glulam beam and CLT topping. Finite element models are also created for the structure, and predictions from these numerical models are compared to experimental data. The model used simplified models, similar to those practicing designer would make, and several parameters in these are varied to understand their impact on vibration. It was found that non-structural elements had a significant effect on the vibration performance of the system, changing both the fundamental frequency and reducing the overall accelerations.

KEYWORDS: Vibration, Mass Timber, Long-span floor, Footfall loads.

1 INTRODUCTION

Long-span floor systems are preferred for many types of buildings such as office and commercial buildings because they allow for flexible open floor plans suitable to any tenant. However, long-span floors are generally more susceptible to serviceability constraints such as footfall vibration. Human-induced vibration on a floor is the result of periodic excitation (i.e. steps at a regular frequency); this periodic force will cause the floor to vibrate, and if that vibration is too large it may cause occupant discomfort.

Floor vibration is of particular concern to mass timber floor systems. Mass timber's high strength-to-weight ratio makes it an appealing material for use in long-span floor system. However, the lower mass means it is more susceptible to footfall excitation and vibration will more often govern the size of the floor structural elements. As mass timber continues to grow as a building material, it is important to have both accurate structural models and a body of research and in-situ data on vibration performance.

Guidance for designing structure for vibration and completing vibration assessments is established in many well-known documents such as the CCIP design guide for footfall vibration, or the US Mass Timber Floor Vibration Design Guide [1-4]. However, an area of uncertainty that often arises is how non-structural elements in a building, such as the partitions or concrete topping, impact vibration. Some physical testing has noted that non-structural elements have a large impact on floor behaviour [5]. However, the impact of non-structural elements has not been quantified for many in-situ mass timber floors, and few studies have been completed on long-span mass timber floor systems.

As Fast+Epp recently constructed a new home office, an opportunity arose to study some of the uncertainties affecting vibration during the construction of that office. A research program was developed to conduct vibration tests on a full-scale mock-up, and the Fast+Epp home office itself. Assessment of the floor system in Fast+Epp's home office was completed in two phases. In phase one, a physical mock-up of the floor plate used in the office was built and assessed for vibration. A summary of the first phase is provided in Slotboom et al. [6].

The second phase of testing would occur on the home office, and is presented in the following study. Of particular interest for the second phase was how the vibration performance of the structure would change throughout construction. Testing was therefore set up to understand:

- The overall vibration performance of the long span floor system in the building.
- The impact of various structural and non-structural components on the floor's vibration performance.
- How predictions from finite element models compare to actual measurements of the floor system, and how modelling of future floors can be improved.

The results are used to recommend some practical guidelines for modelling practices.

2 EXPERIMENTAL PROGRAM

2.1 BUILDING OVERVIEW

The Fast+Epp home office, as shown in Figure 1, is a four-story structure with a 35m long by 12m wide floor plate and 3mx12m structural grid. The office features a long span mass timber floor system, consisting of 3ply CLT panels supported on glulam beams that span up to 11.5m

[1] Christian Slotboom, Graduate Engineer, Fast+Epp, cslotboom@fastepp.com
[2] Carla Dickof, Associate Principle, Fast+Epp, cdickof@fastepp.com
[3] Tobias Fast, Partner, Fast+Epp, tfast@fastepp.com

https://doi.org/10.52202/069179-0374

between steel columns and a CLT wall. The floor panels are V2M1.1, 105mm SPF CLT, that span perpendicular to the beams and continuously across 2 or 3 bays. The beams used were made of grade 24f-E 608mm deep Douglas Fir Glulam, with width that varies between 265mm, 315mm, and 365mm depending on the floor and location. On the west side of the building, the glulam beams are connected to a series of steel HSS columns with a bolted knife plate connection. A similar detail is used to connect the beams to a CLT wall on the north side of the building. Figure 2 below summarizes floor grid building, while Figure 3 shows the knife plate connection used.

Figure 1: *The Vancouver home office of Fast+Epp.*

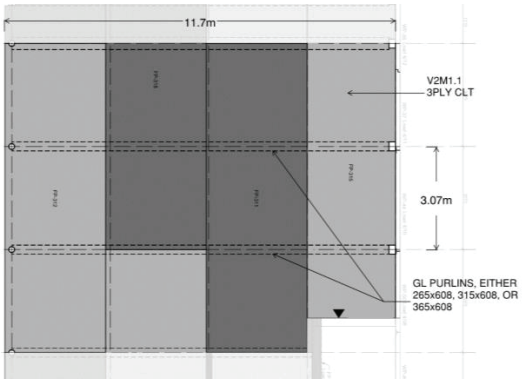

Figure 2:*Summary of the floor grid*

The CLT panels were connected at panel joints plywood splines. These consisted of a 140 mm x 25 mm thick D.Fir strip of plywood along the CLT panels full length. Splines were connected to the panel with 4x60 ring shank nails spaced at 64mm on centre. CLT panels were connected to beams using 6Øx220 partially threaded screws with counter sunk heads, spaced at 400mm. The screw spacing was informed using studies performed on the mock-up [6], where it was found adding additional screws had diminishing returns on stiffness. After the panel was installed, a 50mm concrete topping was applied over an acoustic layer on top of the CLT panel. The concrete had a compressive strength of 32Mpa, and no supplementary connectors were used to join the concrete floor with the CLT panel.

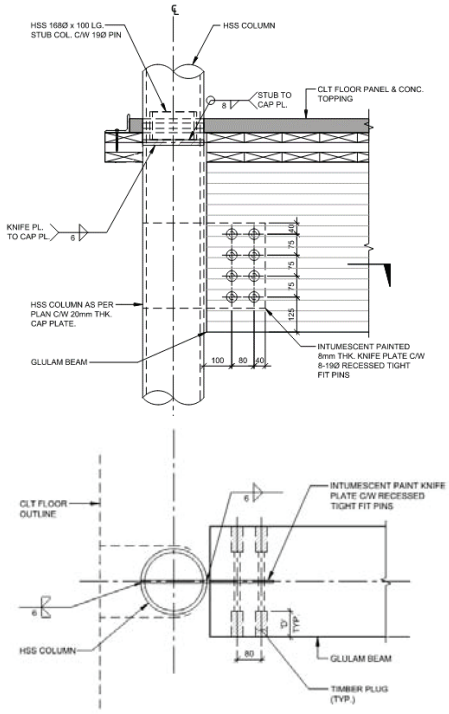

Figure 3: *Colum to beam connection detail.*

2.2 EXPERIMENTAL PROGRAM

Vibration testing on the office was completed at several points during construction to both gauge the performance of the building, and understand the effect of non-structural components on it. A total of four building states were measured:

1. B1: bare superstructure,
2. B2: post concrete topping,
3. B3: post partition installation, and
4. B4: with full building furniture fit-out.

For each building condition, three types of vibration tests were run: ambient vibration, heel-drop, and walking vibration. Vibration was measured with a Crystal Instruments Spyder Analyzer vibration sensor and two accelerometer sensors used to measure vertical accelerations. Most of the testing used a recording increment of 0.002s. Tests were run in a suite, where a receiving location was chosen, and a series of walking trials were completed. Note that because testing occurred during construction, it was not always possible to test all floors of the building, or use the exact same test locations between each test, due to material on site. In particular, testing on L4 was not completed in B1, because the level had not been constructed on the test day.

Walking tests were completed by recording the acceleration response of the floor while a single tester walked along specific walking paths at specific frequencies. Figure 4 provides an overview of the recorder location and typical paths used for the walking tests on the structure. For each receiver location chosen, a

https://doi.org/10.52202/069179-0374

total three walking paths were chosen, and four walking frequencies were tested for each path.

Table 1: *Walking test suite designations.*

Building State	Level	Receiver Locations
B1	L2	R1, R2, R5
	L2	R1, R2, R5
B2	L3	R1
	L4	R1, R2, R5
B3	L4	R1, R2, R5
B4	L3	R1
	L4	R1, R2, R3

Figure 4 also shows typical walking paths and heel drop locations taken for the structure. For each receiver location, several walking paths are walked. The walking paths were chosen and named as follows:

- W1: Walking transverse to the primary beam span, along the centre of the outermost panel.
- W2: Walking parallel to the primary beam span, at the mid-point of the panels.
- W3: Walking parallel to the primary beam span, directly over the beam.

For each walking path, walking tests were completed using four walking frequencies. These were named as follows:

- F1: 1.25 Hz (75 Steps per min).
- F2: Hz (95 Steps per min).
- F3: Hz (110 Steps per min).
- F4: Hz (125 Steps per min).

In heel-drop tests, one vibration sensor was placed at the location of the heel-drop, and another was placed far from them. A tester performed a heel-drop near the accelerometers and the floors acceleration response to that impact was recorded. The heel-drop tests were completed in a grid of points across the floor, where the main sensor location remained in the same place, and second sensor moved with the heel drop location. These tests were used to get a more accurate measurement on the frequencies floor modes were responding at, as walking vibration tests do not have a clear signal decay. Table 2 overviews the heel drop grids that were completed on the floor.

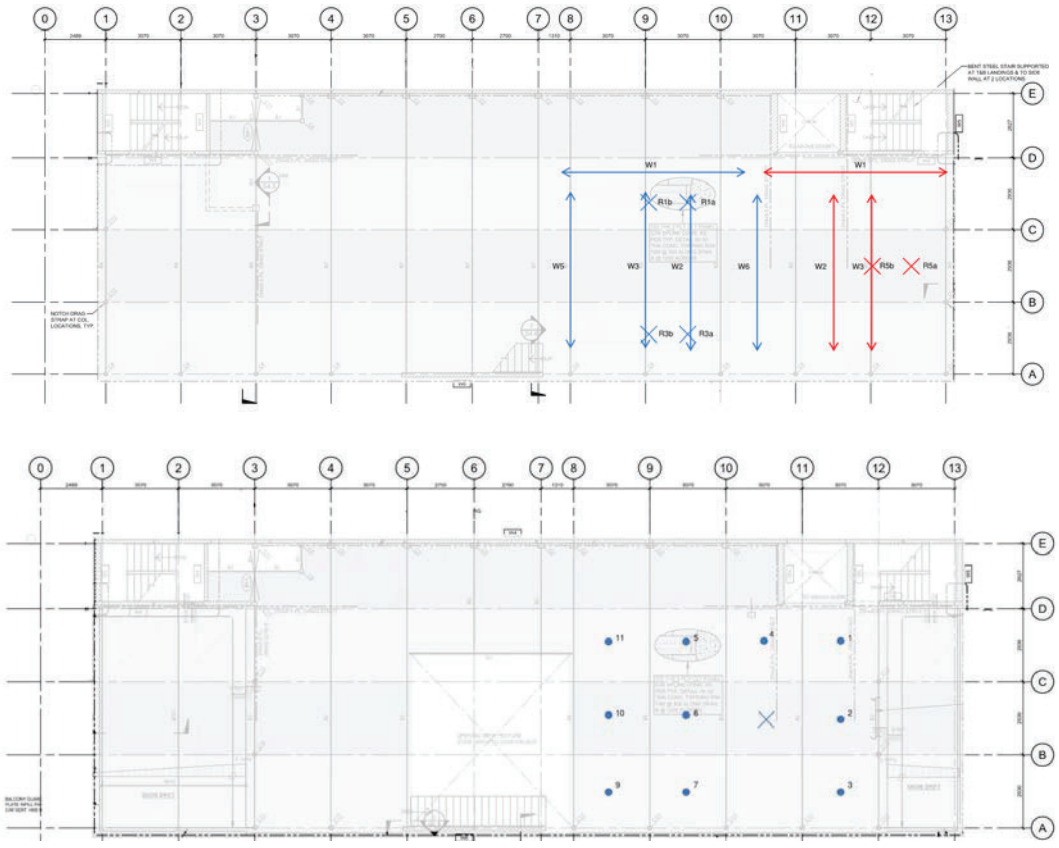

Figure 4: *Summary of walking paths (Wi) and receiving locations (Rj) for testing on 3rd floor, and the heel drop locations on the fourth floor.*

https://doi.org/10.52202/069179-0374

Table 2: *Heel Test Suite Designations.*

Building State	Level	Receiver Location	Heel drop Locations
B2	L3	R6	H1-H9
B3	L4	R6	H1-H11
B4	L3	R6	H1-H11
	L4	R6	H1-H8

Combined, the above naming convention can be used to give each test a designation, based on a test's building state and location. Each walking suite is given a representation based on where it was completed, Ba-Lb-Rc-Wd-Fe, where:

- "a" represents the building state,
- "b" represents the level testing occurred at,
- "c" represents the receiver location chosen,
- "d" represents the walking path taken,
- "e" represents the walking speed used.

Similarly, heel drop experiments were given a designation Ba-Lb-Rc-Hd, where parameters "a", "b", "c" are as described above, and "d" is the number of the heel drop test used.

2.3 EVALUATION METHODOLOGY

There are two significant outputs from each vibration measurement: a signal of the raw acceleration over time, and a frequency spectrum of the Fourier transform that shows which frequencies are dominant in the vibration. The time-acceleration response is used to measure the magnitude of vibration that occurs in the floor, as well as qualitative gauge the response of the floor. Qualitative measurements were completed by visual inspection of vibration signals, to determine if the floor has resonate response to loads and can be characterized as a low frequency floor. The magnitude of vibration is measured by calculating the Root mean Square (RMS) of the vibration signal. Recommendations from CCIP-016 [2] were used to calculate the RMS, including using an averaging time of 1s, and applying a band pass filter to the raw data.

The results frequency domain data were largely used to predict the fundamental frequency of the floor, and estimate changes in system stiffness. The fundamental frequency of the floor was estimated using the frequency of the lowest local peak in the frequency response spectrum. Changes in frequency between building states estimated using first principles, as frequency (ω) is known to be proportional to system stiffness (k) and mass (m) per equation (1).

$$\omega \sim \sqrt{\frac{k}{m}} \qquad (1)$$

Damping measurements for the floor were also measured using the results of heel-drop tests. A logarithmic decrement method was used to measure damping, where peaks from the damped signal were extracted and then an exponential function was fit to those peaks. The resulting function was used to estimate damping in the system.

3 EXPERIMENTAL PROGRAM RESULTS

Testing was completed. Due to issues accessing the site during construction, different testing locations were used between the L3 test on B1, and L3 tests on B2/B4. The effect of this change in location is discussed in Section 4.3.

3.1 ACCELERATION RESULTS

Raw acceleration signals were examined qualitative assess if the floor behaved like a low frequency floor, where response is governed by a resonant build-up of vibration, or a high frequency floor, where response is governed by impulse. Based on the data collected, the floor had a mixed response but mostly behaved as a high frequency floor. However, for many tests it was also observed that the vibration did not fully decline between footfalls. This indicates that there was some resonant response, and the floor did not behave purely as a high frequency floor. Figure 5 shows summarize typical vibration signals seen at walking speed F4. Some resonant behaviour is observed in the second signal, while the first signal is governed by transient response.

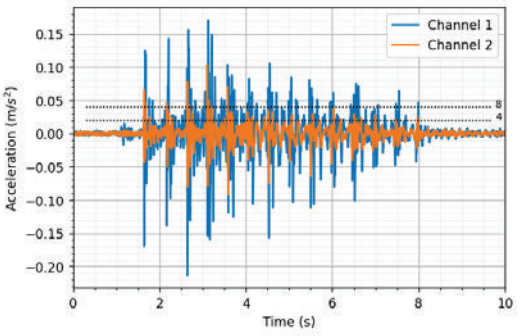

B2-L4-R1-W2-F4

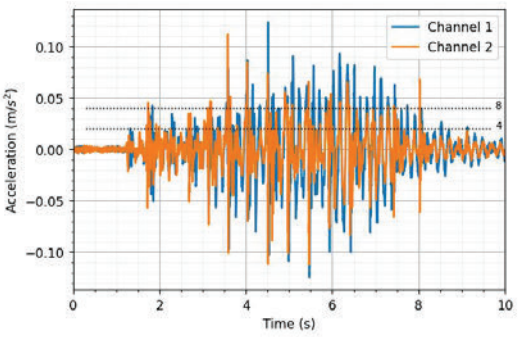

B2-L4-R2-W3-F4

Figure 5: *Acceleration observed in for different walking paths in B2-L4.*

To gauge the comfort of the floor for vibration, the RMS for each acceleration signal was calculated, and the peak value was extracted from the RMS plot. Figure 6 overview the peak RMS and R value recorded by each

channel for mock-up one and two, respectively. R values were determined by dividing the RMS acceleration by a baseline value of 0.005m/s^2. Also included in each figure is a line of the median data observed in the experiment. There is generally an upward trend in response factors as walking speeds increase, and the median RMS acceleration generally decreased as the building became more complete. The median R value in each suite of tests is recorded experiment in Table 3. The same trend from Figure 6 is observed, with decreasing RMS accelerations as the structure progresses through construction.

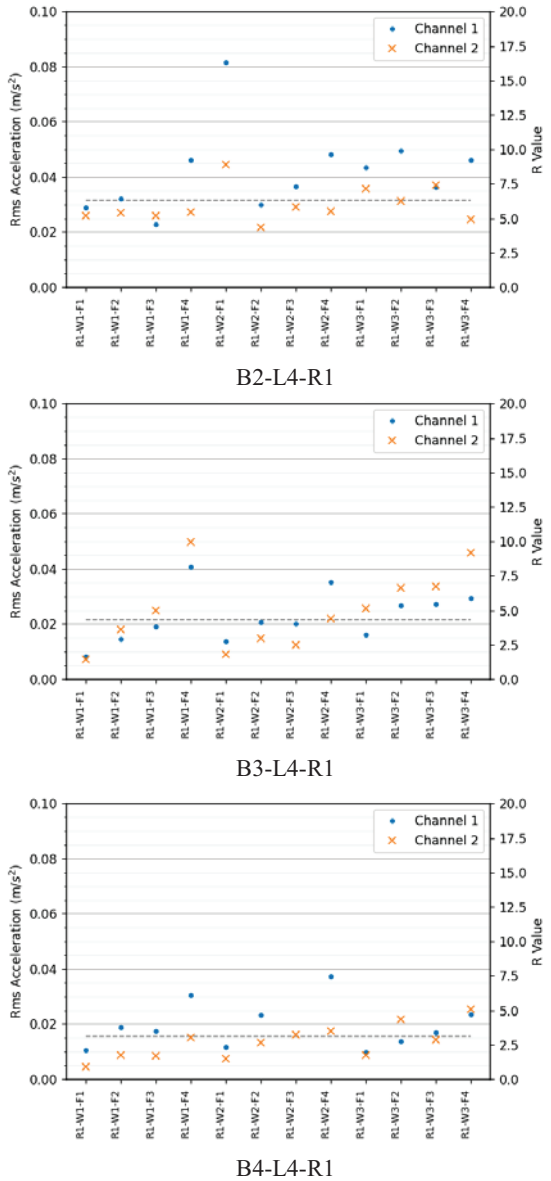

B2-L4-R1

B3-L4-R1

B4-L4-R1

Figure 6: *Peak RMS acceleration for the test series path L4-R1 for conditions B2-B4*

Table 3: *RMS Acceleration vibration results for L3 and L4*

Floor	State	Suite	Median R-Value
L3	B1	R1	16
		R2	8
		R5	16
	B2	R2	5
	B4	R1	6
L4	B2	R1	6
		R2	4
		R5	6
	B3	R1	4
		R2	5
		R3	6
		H	7
	B4	R1	3
		R2	3
		R3	3

For office occupancy, a response factor in the range of 4-8 is a typical acceptable limit. The observed response factors were generally within the range of 5-20, showing the floor was on the edge of what would be considered commercially acceptable.

3.2 FREQUENCY RESULTS

The frequency response of the structure was characterized by an initial peak in the range of 5-10Hz, followed by various local peaks between 15Hz and 30Hz. Based on experience from phase one of testing on the full-scale mock-up, it's expected that the lower peak corresponds to vibration modes from exciting the beams, and the higher frequency peaks come from modes where the panel between beams is excited. To allow for easy comparison, the frequency response plots have been normalized by dividing each graph by its peak response. Figure 7 show typical frequency responses observed for a walking test, and a heel drop test.

Like RMS acceleration, the frequency where the peak occurs is extracted in each test, with a sample plot shown in Figure 8. Table 4 summarize the predicted fundamental frequency of the floor observed in each test, based on figures similar to Figure 8. Here the fundamental frequency of the system is estimated as approximately the lowest frequency peak observed during testing for all channels.

https://doi.org/10.52202/069179-0374

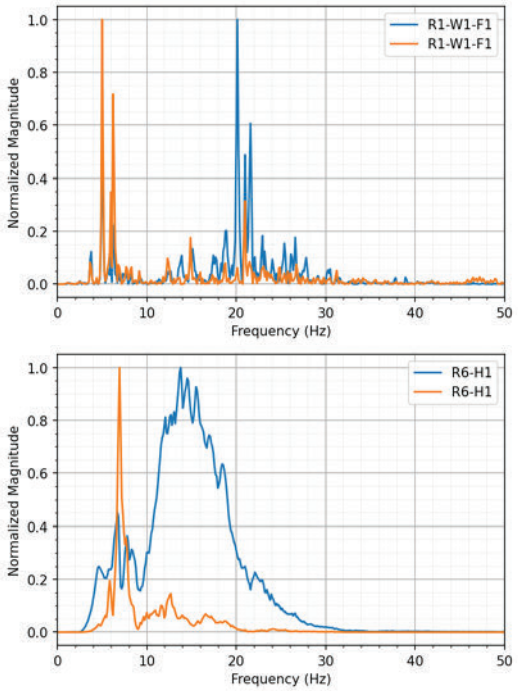

Figure 7: *Sample frequency response plots for Channel 1 (blue) and Channel 2 (orange) from Building condition 4 on the 4th floor. Channel 1 is centred on a beam on the, while Channel 2 is centred between beams in the middle of the CLT panel.*

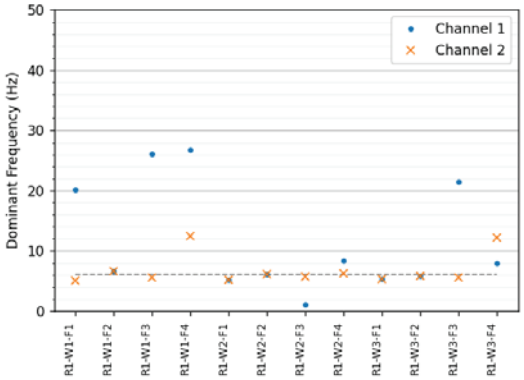

Figure 8: *Peak frequencies observed for walking experiments at R1 in B4-L4.*

Table 4: *Estimated fundamental frequency results for L3 and L4*

Floor	State	Suite	Fundamental Frequency
L3	B1	R1	8
		R2	9
		R5	11.5
	B2	R2	7.5
		H	7
	B4	R1	8
		H	8
L4	B2	R1	5.5
		R2	5.5
		R5	8
	B3	R1	6.5
		R2	16
		R3	7.5
		H	7
	B4	R1	6
		R2	6.5
		R3	7
		H	7

Comparing results between B1 and B2 for L3, a smaller decrease in frequency was noted than expected. When the topping was added to the building, the weight of the system increases from approximately 0.75kPa to 1.95kPa – more than doubling. Based on equation (1), the additional weight of concrete should have decreased the fundamental frequency approximately 40% however, a drop in frequency of about 15% was observed. This effect is discussed further in section 4.3.

3.3 EQUIVALENT VISCOUS DAMPING

The equivalent viscous damping of the floor was also estimated using the heel drop test data. It was generally found that there was a high variance in the predicted damping. This is likely due to vibration not decaying in a cleanly exponential decay, with instead a large drop occurring in the signal after the initial peak. While there is a large spread in the observed values, the damping generally increase in the building through construction.

Table 5: *Damping measurement in the floor system.*

Floor	Condition	Mean (%)	S.D. (%)
L3	B2	3.0	1.0
	B4	4.7	1.3
L4	B2	1.6	0.5
	B3	2.2	1.2
	B4	3.6	1.8

3.4 COMPARISON WITH MOCK-UP

Comparisons were also made between the frequency of the mock-up observed in phase one of testing [6] and the building in condition B1 on L3. Results were used for the mock-up model in condition M1c, which used 6Øx220 screws between the CLT panel and glulam column spaced at 300mm. Table 6 summarizes median frequency observed in both experiments. A higher fundamental frequency was observed in the building compared to the mock-up, indicating that the building was stiffer. The mock-up rested directly on supports in bearing, so an explanation for this increase in stiffness is that the knife plate connectors used have more stiffness than a simple bearing connector.

Table 6: *Observed frequency in Mock-up vs. in the building.*

Test Location	Test Designation	Median Frequency (Hz)
Mock-up	M1c	7.5
Building	B1-L3	8.5

4 NUMERICAL STUDIES

To understand how well Finite Element Model (FEM) predictions compared to observations in experimental data, a set of simplified numerical models were created of the floor in the software package RFEM [9]. The goal of this analysis was not to create highly detailed FEM models; it's known that a sufficiently detailed finite element model can closely match experiment. Instead, the numerical models were built to understand how typical models used by a designer might compare to experimental data. Therefore, only information that designers are likely to have during design was considered, for example, the stiffness from partitions was neglected as this is not typically known. First, baseline models are made and compared to experimental results, then parameters in those models are varied to assess the impact on the dynamic properties of the floor.

4.1 MODEL OVERVIEW

The models considered the whole floor plate for L3, and the right portion of the floor plate on L4. The structural elements considered were as described in section 2.1, and material properties of the elements were estimated from CSA 086.6 [8] for timber and CSA A23.3 [9] for concrete. Figure 9 provides an overview of the baseline models for the first and fourth floor respectively. The CLT using 2D shell elements and RFEM's RF-laminate module [10] while beams were simple beam elements.

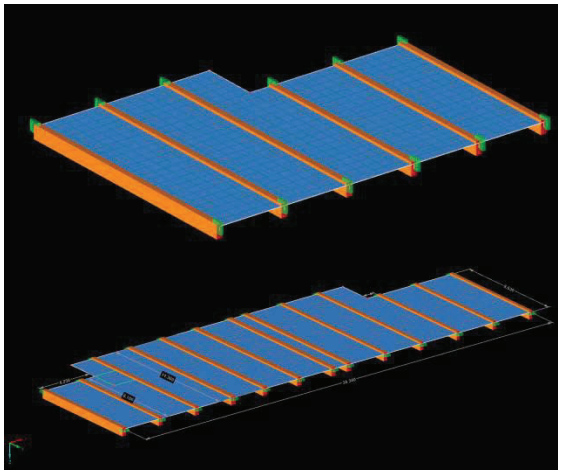

Figure 9: *The FEM model for L4 (top) an L3 (bottom).*

The mass in the model is estimated based on the site conditions observed for each test. Table 7 summarizes the total loads considered, broken down by load source for dead load (DL), superimposed dead load (SDL), and live load (LL). Loads are reported in kPa and converted by RFEM into an appropriate mass. Note that DL has been reported as an equivalent uniform load, however, in the model it assigned to elements as a self-weight. To account for moisture uptake of the members, a self-weight of 4.6kN/m3 is used for the CLT, while 5.3 kN/m3 is used for glulam. In B1, only the self-weight of the structure is considered, while in B2 a 50mm concrete topping is also included in the analysis. For B2, B3 and B4, the weight of the mechanical systems and furnishings are estimated based on the state of the building when tested. No change in mass was noted between B2 and B3 because a similar amount of construction material was on site for each study.

Table 7: *Vibration loads applied to model.*

Condition	DL (kPa)	SDL (kPa)	LL (kPa)
B1	0.7	-	-
B2	0.7	1.2	-
B3	0.7	1.2	-
B4	0.7	1.5	.2

How connections and boundary conditions are modelled will generally have a big impact on system stiffness and the fundamental frequency. For the Yukon office floor there are three main connection fixities to consider: fixity of the panel-to-panel spline connection, fixity of the beam-to-panel, and fixity of the beam to column/wall connection. In the base model a fixed connection was used between the beams, which is also the boundary condition for the model. Because the fixity of beam to column connection has a large impact on system stiffness, both a fixed and pinned connector were studied.

The beam to panel connection will affect composite action of the system. Findings from the mock-up were used to estimate the degree of composite action, with a predicted increase in system stiffness of 40%. Composite included in the model using an offset between the slab and the beam that would increase the system's EI by the appropriate amount. The effect of spline connections is not considered in the assessment, and it is assumed that the concrete toping transfers vibration between with an unobstructed load path.

4.2 COMPARISON ON OF MODELS

Once the base model was finished, several parametric studies were run on typical model assumptions. These studies are used to understand what parameters are most important to include in the model. The parameters considered include: beam stiffness, CLT stiffness, degree of composite action, stiffness from concrete topping, and boundary connection.

Variations of beam and CLT stiffness were completed by applying a stiffness modifier of 0.75 or 1.25 to the system. increasing and decreasing stiffness by 25%. These studies were run to understand how the uncertainty in timber

https://doi.org/10.52202/069179-0374

material might change observed results, and only run on L3. Degree of composite action was measured by running models that had no offset between the CLT and glulam beam, and thus no composite action. The effect of boundary condition and composite action assumptions were also examined. In the pin-connected model, the moment restraint was released at each column to beam connection.

Stiffness from concrete topping was included by adding the concrete stiffness to the CLT stiffness. Including the stiffness this way assumes no composite action between the two layers. Table 8 summarizes the change in stiffness of the CLT in each direction, where EI_x and GA_x are in the strong axis, and EI_y and GA_y are the weak axis. It can be observed that the concrete topping significantly increases the weak axis bending and shear stiffness.

Table 8: *Stiffness per unit meter of bare CLT and topped CLT.*

Condition	EI_x	EI_y	GA_x	GA_y
	($Nmm^2/m \times 10^9$)		($N/m \times 10^6$)	
CLT	883	34	7.5	7.5
CLT & Topping	1230	386	682.5	682.5

Table 9 and Table 10 summarizes the changes made to the base model, as well as the resulting changes to fundamental frequency. These can be compared to the in-situ experimental data to understand how accurate the trends are. For each model and test, the mode shape is extracted from the FEM models at the input location of vibration testing. The effect of concrete topping was examined in the base model, the model using no composite action, and the model using a pin connection. It was found that including the concrete topping increased system stiffness in the range of 5-10%. For variations in stiffness, it was found that variations in CLT stiffness had a low impact on the total stiffness of the system, while variations in beam stiffness affected the frequency on the order of 10-15%. Changes to the composite action also had a moderate effect on the system, on the order of 5-10%. Finally, it was noted that boundary condition had a large influence on the systems stiffness, where the fundamental frequency decreased in the range of 30-40% for models with a pin connection.

Table 9: *Measurements of on L3.*

Model	Condition	Level 3		
		B1 (Hz)	B2 (Hz)	B4 (Hz)
In-situ Experimental Data	-	8.5	7	8
Base Model	No topping	14.4	10	8.7
	Topping	-	10.6	9.3
Beam Stiffness	0.75	12.9	8.9	7.8
	1.25	15.7	10.8	9.5
CLT Stiffness	0.75	14.1	9.8	8.4
	1.25	14.7	10.1	8.8
Non-composite	No topping	13.5	9.4	8.3
	Topping	-	10	8.9
Pin Connection	No topping	9.1	6.3	5.6
	Topping	-	6.5	5.8

Table 10: *Measurements of on L4.*

Model	Condition	Level 4		
		B1 (Hz)	B3 (Hz)	B4 (Hz)
In-situ Experimental Data	-	-	5.5	6.5
Base Model	No topping	14.2	8.6	7.6
	Topping	-	9.0	8.2
Non-composite	No topping	13.3	8.1	7.2
	Topping	14.1	8.7	7.7
Pin Connection	No topping	8.9	5.5	4.9
	Topping	9.2	5.7	5.1

4.3 IMPACT OF NON-STRUCTUAL ELEMENTS

Results from FEM data can be used to predict the effect of non-structural elements on the system. In all numerical models considered, a downward trend in fundamental frequency is observed. Figure 10 provides an overview of the FEM base and pinned model predictions, compared to the experimentally observed data in experiment B1 to B4 on the third floor. The experimental frequencies reported are approximately the lowest from all test groups in Table 4. FEM results are taken from Table 9, and the mode used corresponds to the lowest mode active at the testing location. Results for the experimental data were closer to the pinned model in the bare floor condition, and closer to the fixed model in the final building condition.

A different trend in the observed frequencies was also noted between the FEM data and experimental response. The FEM models had their fundamental frequency decrease by approximately 30% from B1 to B2, and B2 to B4. This contrasts with the experimental model that decreased by only 10% from B1 to B2, and increased marginally between B2 to B3.

Based on Table 9, it's expected that the FEM would predict frequencies approximately 5% higher if the concrete topping is included in the model in a non-composite way. This difference is not enough to explain the differences observed between FEM predictions and experimental data, indicating that some other factor increased the system stiffness between both building

conditions. This suggests that the non-structural concrete topping and other elements had a larger impact on stiffness than expected.

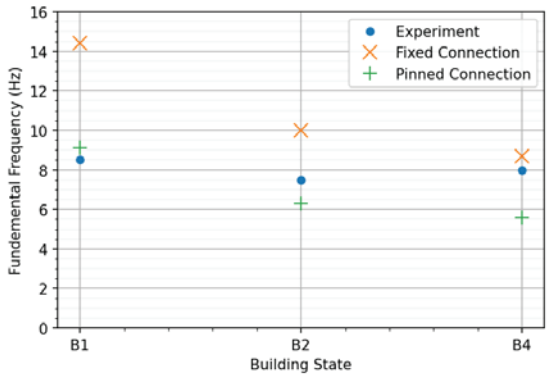

Figure 10: *Comparison of FEM and experimentally observed frequencies.*

The FEM data can also be used to assess the effect changing locations had on the experimental fundamental frequency. As noted prior, different testing locations were used between B1 and B2/B3. A prediction of the frequency at the original testing location can be made based on FEM data. In the models, it was noted that a different mode was active at L3 for the test location used in B2 and B4. This mode had a frequency approximately 20% higher than the base mode shape used in L1. The frequency can therefore be adjusted to approximately 6Hz at B3, and 6.5 Hz at B4.

The fundamental frequency decrease of 25% between B1 and B2 is more closely in line with the expected 40% reported in section 3.2, but still less than expected. This suggests that the concrete topping, or another factor had a larger than expected impact on the stiffness of the system. Some possible reasons for the increases in stiffness in B2 include: additional composite action occurring in the CLT to beam system due to clamping from the concrete weight; or contribution of the concrete slab to the floor stiffness, in either composite or non-composite action.

Similarly, the increase in frequency between B2 and B4 observed in experiment suggests that the non-structural elements such as partitions had a significant effect on the stiffness of the system for vibration.

5 CONCLUSIONS

A series of vibration tests were performed on Fast+Epp's new home office during its construction. In the final state of the building, it was found that the long-span floor system of Fast+Epp's home office was within vibration tolerances for office building. Most observed acceleration signals during walking tests had a response value less than 8. It was also found that non-structural elements had a large impact on the vibration performance of the floor. Based on experimental data normalized with FEM results, on the third floor, the fundamental frequency changed from to 8.5Hz to a 6Hz going from bare floors to floors with topping. This was less than the decrease of approximately 40% that would have been expected with no additional stiffness. The fundamental frequency increased as partitions and furnishings were added, to the building, indicating that these elements added enough stiffness to the floor to overcome the additional mass added.

Finally, during numerical modelling of the floor it was found that the parameter with the largest effect on the floor system was the boundary condition used. It was found that the floor in its final built condition was most accurately described using a fixed connection. It was also found that the trend of frequencies observed during construction in FEM modelling did not match the trend of data from experiments. The inclusion of non-composite stiffness from the concrete topping was not enough to account for the change in stiffness expected. Both trends suggest that non-structural components added more stiffness to the system than expected.

ACKNOWLEDGEMENT

The authors would like to thank Natural Resources Canada (NRC) for their funding support through the GCWood program.

REFERENCES

[1] The Steel Construction Institute (SCI). (2009). SCI P354 – Design of Floors for Vibration: A New Approach.

[2] The Concrete Centre. Willford, M.R., Young, P. (2007). CCIP-016 – A Design Guide for Footfall Induced Vibration of Structures.

[3] Woodworks. Breneman S., Zimmerman R, Gerber A, Epp L, Dickof C, Taylor A, Loasby W., McDonnel E, Slotboom C, McCutcheon J, Vischer R - U.S. Mass Timber Floor Vibration Design Guide

[4] American Institute of Steel Construction (AISC). (2016). Design Guide 11 – Vibrations of Steel-Framed Structural Systems Due to Human Activity (Second Edition).

[5] Hamm, P., Richter, A., Winter, S. (2010). Floor Vibrations – New Results. World Conference on Timber Engineering. Riva del Garda, Italy.

[6] Slotboom C., Dickof C., Fast T., Evaluation of a Long Span Mass Timber Floor Under Footfall Vibration Loads, CSCE 2022

[7] Dubal Software GmbH, RFEM-5: Spatial Models Calculated According to Finite Element Method, 2020

[8] Canadian Standards Association (CSA), Engineering Design in Wood, CSA Standard O86-19, Toronto, ON, Canada: CSA, 2019.

[9] Canadian Standards Association (CSA), Design of Concrete Structures, CSA Standard A23.3-19, Toronto, ON, Canada: CSA, 2019.

[10] Dubal Software GmbH, RF-LAMINATE: Design of Laminate Surfaces, 2016

https://doi.org/10.52202/069179-0374

World Conference on Timber Engineering Oslo 2023

STRUCTURAL PERFORMANCE OF TWO-PANEL CLT SHEAR WALL WITH BOLTED CONNECTION

Daiki Hinata[1], Jun Kubota[2], Takashi Shima[3], Shinji Takatani[4], Masanori Hisada[5], Naohiro Haneda[6]

ABSTRACT: The increasing demand for using timber structures as building structures has led to the development of many cross-laminated timber (CLT) shear wall systems including details on connecting the walls. However, these details are still not sufficient for quick and easy installation purposes. Therefore, ways of improving the installation productivity on site are required. In this study, we propose installing a pair of CLT panels as a single shear wall, i.e., a two-panel CLT shear wall, with bolted connections as a solution. The heavier CLT panels are, the more difficult on-site installation work becomes. If the panels are divided into two, they would be easier to handle as each panel is lighter. Furthermore, a bolted connection is one of the easiest on-site installation connections. This paper presents the structural performances of a two-panel integrated CLT shear wall with bolted connection, which was investigated in element tests on bolted connections and full-scale wall tests. An FE analysis was also conducted to investigate the stresses on the CLT panels and the ultimate behaviors. The results indicated that this system has a high lateral resisting strength and ductility.

KEYWORDS: CLT shear wall, Two-panel CLT wall, Structural test and FE analysis, High productivity

1 INTRODUCTION

The demand for timber components for building structures has been increasing around the world, leading to the development of many cross-laminated timber (CLT) shear wall systems which include connection details [1-3]. However, the connections for CLT shear walls are difficult to install quickly and efficiently. When installing CLT shear wall panels in a steel moment-resisting frame, steel plates are typically inserted into the CLT panel with a slit at the top and bottom, integrating it by driving in drift pins, and bolting the inserted steel plate to a gusset plate pre-installed on a column or beam [3]. This method has two connections between the CLT panel and steel frame, CLT panel-to-steel plate and steel plate-to-gusset plate, which causes low productivity of construction due to the work for installing both connections. Moreover, drift pin connections must be fabricated extremely precisely because the bores for drift pins need to match that on the steel plates, due to the minimum tolerance requirement. It is crucial to find ways of improving installation efficiency on site. Thus, we propose installing a pair of CLT panels as a single shear wall, i.e., a two-panel CLT shear wall, with a bolted connection as a solution. Figure 1 shows sketches of this system in which two sheets of CLT panels are installed on both sides of the gusset plates. The heavier CLT panels are, the more difficult on-site installation work becomes. If the CLT panels are divided into two panels, they can be easier to handle because each panel is lighter. In addition, a bolted connection is one of the easiest to install on site. This paper presents the structural performance of the two-panel integrated CLT shear wall with the bolted connection, which is investigated through element tests for the bolted connections and full-scale wall tests. We also conduct an FE analysis to investigate the stresses in the CLT panels and ultimate behaviors.

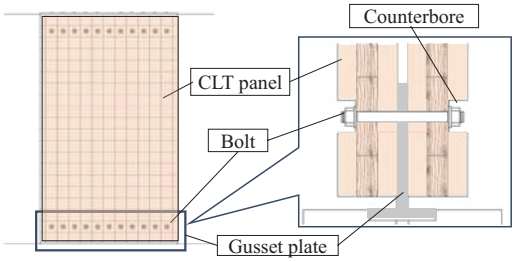

Figure 1: *Sketches of two-panel CLT shear wall*

2 ELEMENT TEST FOR BOLTED CONNECTION

2.1 TEST OVERVIEW

To verify the structural performances of the developed two-panel CLT shear walls with bolted connections and

[1] Daiki Hinata, Kajima Technical Research Institute, Kajima corporation, Japan, hinata@kajima.com
[2] Jun Kubota, Kajima Technical Research Institute, Kajima corporation, Japan, jkubota@kajima.com
[3] Takashi Shima, Kajima Technical Research Institute, Kajima corporation, Japan, shimata@kajima.com
[4] Shinji Takatani, Architectural Design Division, Kajima corporation, Japan, takatani@kajima.com
[5] Masanori Hisada, Architectural Design Division, Kajima corporation, Japan, hisadam@kajima.com
[6] Naohiro Haneda, Architectural Design Division, Kajima corporation, Japan, haneda@kajima.com

https://doi.org/10.52202/069179-0375

determine an appropriate bolt configuration on the CLT shear wall, we conducted element tests for the bolted connections. The tested connections consist of steel plates, assumed to be gusset plates, a pair of CLT panel pieces, and bolts. The bolted connections are shown in Table 1 and Figure 2. In this study, seven types of bolted connections were tested. The parameters were the grade and lamina composition of the CLT, the loading direction of the CLT, and the bolt diameter and arrangement. We used S60 grade 3-ply 3-layer CLTs with a lamina width of 120 mm and thickness of 90 mm, without edge bonding, and S60 grade 5-ply 5-layer CLTs with a lamina width of 122 mm and thickness of 150 mm, with edge bonding. We also conducted tests on M20 series connections with two rows of bolts in the major direction.

It was previously found that the placement of the bending connections, such as drift pins and bolts, between the laminae on the CLT panel can degrade shear strength [4]. Therefore, to eliminate these effects, bolted connections were placed at the center of the lamina width for the CLT shear wall in our study. Accordingly, the CLT panel width of the test area on the element tests is the same as that of the single lamina. Although the structural performance of the bolted joints has been shown to be sufficient in previous experimental results [5], in our study, the CLT panel includes counterbores to prevent the bolt heads from protruding from the face of the CLT panels, for the sake of visibility.

The tests were carried out by applying a tensile force to the upper and lower steel plates attached to the connection, using a universal testing machine. The relative displacements between the steel plate at the position of bolted connections and CLT panels at the same level were measured by LVDTs. We used average relative displacements of the right and left for the following evaluations.

2.2 TEST RESULTS

The relationship between force and displacement is shown in Figure 3, the representative failure mode in Figure 4, and the ultimate strength and initial stiffness derived based on perfect elasto-plastic modeling [6] in Table 2. The bolted connection is not expected to deform more than 40 mm in the CLT shear wall connections because this only occurs when the CLT shear wall drift angle is over 1/20 radians. Therefore, only element test data up to a displacement of 40 mm were used for the evaluation. In Figure 3, the force-displacement curves were shifted to eliminate the influence of the initial slip, which is within approximately 1.5 mm, due to the bolt-hole clearance according to the perfect elasto-plastic modeling rule [6] so that the straight lines between 0.1 Pmax and 0.4 Pmax match zero force / zero displacement point.

At the beginning of all tests, the strength increased almost linearly; however, the slope of the force-displacement curve decreased due to the pop-out failure at the inner lamina (the side in contact with the steel plate) with the width of the bolt diameter in the major direction loading tests, as well as split failure of the inner orthogonal lamina in the minor direction loading tests. The strength was still maintained, mainly due to the resistance of the outer lamina. As the deformation increased, the bolt heads and washers appeared to be significantly embedded in the CLT. After the tests, we observed that all bolts were bent at the center.

The M12 series demonstrated stable structural behavior, regardless of the loading direction, and no significant decrease in strength was observed. Because the M20 series contained thicker CLT panels (5-layer and 5-ply), the major direction tests showed stable structural performance up to a displacement of 40 mm even in the connection with two rows of bolts. However, in the minor

Table 1: *Details and parameters of bolted connection element tests*

ID	Bolt				CLT			Direction	Number of tests
	Diameter [mm]	Yield Point [N/mm^2]	Number @Pitch	Bore Dia. [mm]	Grade Layer-ply	Thickness [mm]	Counterbore Dia × Depth [mm]		
90-M12S	12	400	1	13	S60-3-3	2×90	φ 36×29	Major	6
90-M12W								Minor	6
90-M16S	16	400	1	17	S60-3-3	2×90	φ 50×29	Major	6
90-M16W								Minor	6
150-M20S	20	490	1	21	S60-5-5	2×150	φ 55×50	Major	6
150-M20W								Minor	6
150-2xM20S			2-@120					Major	6

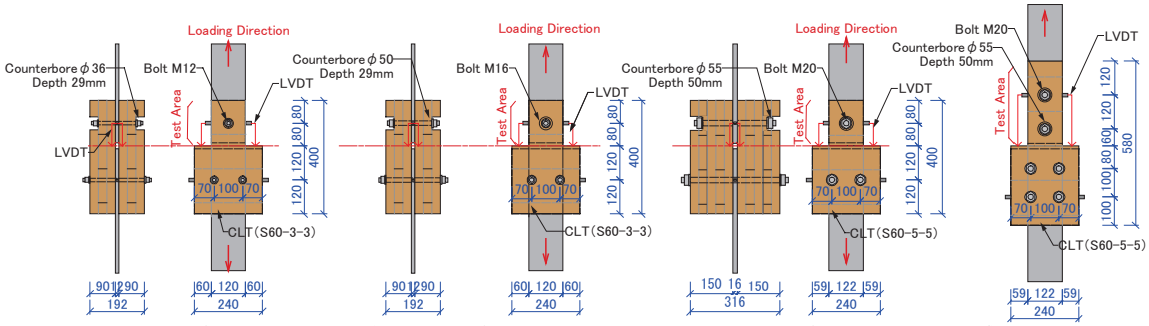

(a) 90-M12S / W *(b) 90-M16S / W* *(c) 150-M20S / W* *(d) 150-2xM20S*

Figure 2: *Configuration of bolted connection element tests*

https://doi.org/10.52202/069179-0375

direction tests, damage to the laminae led to ultimate failure when the deformation was approximately 5 mm. For the six specimens in all tests, the behaviors were approximately similar.

The ultimate strength and initial stiffness tend to be larger for larger bolt diameters and connections arranged in the major direction. Although the strength of the two rows of bolts connection was expected to be less than twice the strength of a single bolt connection due to the group effect, within the scope of this test, the connections with two rows of bolts had approximately the same failure mode as that of the single bolt type, and its strength was slightly higher than that of the single bolt ones.

Thus, we verified that this bolted connection with CLT placed in the major direction is sufficiently ductile with little decrease in strength even after exceeding the elastic limit. Meanwhile, the minor direction connections demonstrated fewer deformation capacities compared with the major direction specimens, indicating that providing a sufficient margin for the bolt connection strength in the CLT minor direction of the shear wall is important for the structural design.

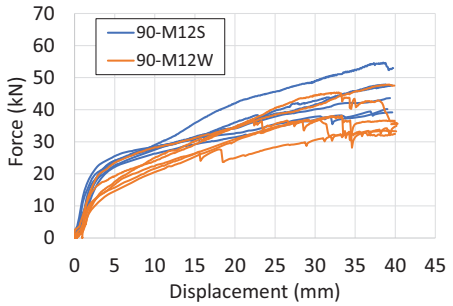

(a) Bolt M12 series

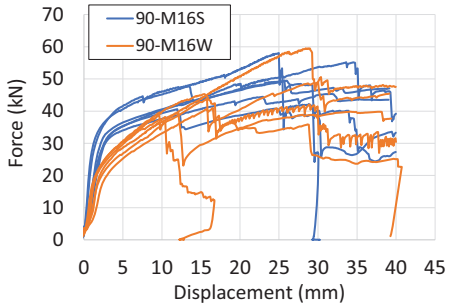

(b) Bolt M16 series

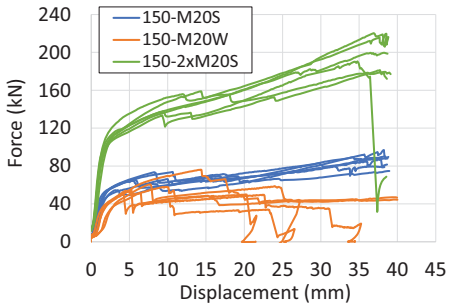

(c) Bolt M20 series

Figure 3: *Relationship between tensile force and average displacement in bolted connection element tests*

Table 2: *Ultimate strength and initial stiffness from bolted connection element tests*

ID	Mean Ultimate Strength [kN]	Mean Initial Stiffness [kN/mm]
90-M12S	36.9	5.2
90-M12W	32.1	3.3
90-M16S	44.0	13.4
90-M16W	38.3	8.8
150-M20S	71.3	17.5
150-M20W	51.2	17.7
150-2xM20S	160.7	37.9

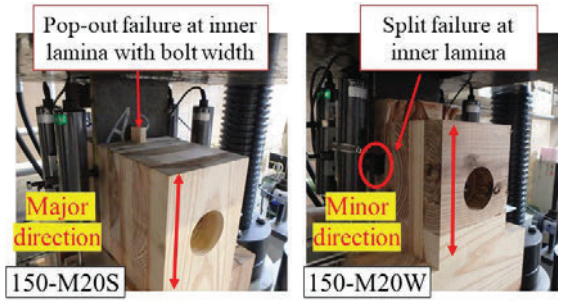

Figure 4: *Representative failure mode*

3 FULL-SCALE CLT SHEAR WALL TEST AND ANALYSIS

3.1 STRUCTURAL TEST OUTLINE

A list of full-scale two-panel CLT shear walls is shown in Table 3, the diagrams are shown in Figure 5, and photos of the test setup are shown in Figure 6. The CLT test walls consist of a gusset plate attached to a steel stub, a pair of CLT panels, and bolts. The parameters were the vertical and horizontal dimensions, CLT composition, and bolt configuration. The combination of bolt diameter and CLT compositions in the CLT wall are the same as the element test detail, and as with the element specimens, bolts were arranged at the center of each CLT lamina width. A clearance of 40 mm was provided between the CLT edge and the upper and lower steel stubs to avoid generating friction forces and compression struts when deformation increased. During the tests, lateral forces were applied to the top of the specimens, and the vertical jacks kept the steel stubs horizontal while allowing them to move vertically. The loading protocol was as follows: ±1/600, ±1/450, ±1/300, ±1/200, ±1/150, ±1/100, ±1/75, and ±1/50 radians for three cycles and ±1/30 and ±1/20 radians for two cycles.

In the S-M12 and S-M16 tests, no damage to the CLT panels was observed while the loading. In the S-M20, a failure of the inner lamina near the outermost bolt was observed at the -1/20 radians peak, as in the element tests. M-M20, with two rows of bolts, also showed no strength reduction, although there were two pop-out failures at the edge of the CLT panels at 1/50 radians and three at 1/20 radians due to bolt deformation. The reason the CLT panels were not damaged was that the average shear stress of the CLT panels at ultimate strength was about 0.66 N/mm^2, which was less than the standard shear failure stress of CLT panels. The strength and initial stiffness of

https://doi.org/10.52202/069179-0375

Table 3: *Dimensions and parameters of full-scale CLT shear walls*

ID	Dimension		Bolt				CLT		
	W [mm]	H [mm]	Dia.	Yield Point [N/mm^2]	Configuration Row-Number	Bore Dia. [mm]	Grade Layers	Thickness [mm]	Counterbore Dia × Depth [mm]
S-M12	1440	2400	M12	400	1-11	13	2x S60-3-3	2×90	φ36×20
S-M16	1440	2400	M16	400	1-11	17	2x S60-3-3	2×90	φ50×27
S-M20	1220	3150	M20	490	1-9	21	2x S60-5-5	2×150	φ55×50
M-M20	1220	3150	M20	490	2-9	21	2x S60-5-5	2×150	φ55×50

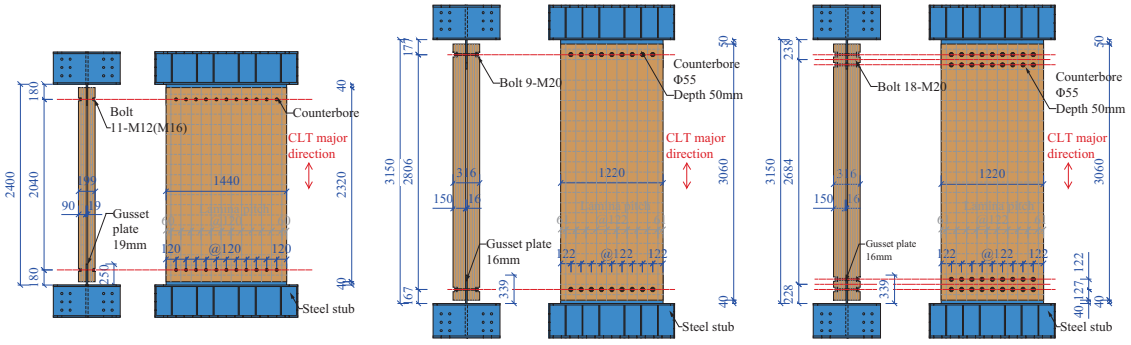

(a) S-M12(M16) *(b) S-M20* *(c) M-M20*

Figure 5: *Configuration of full-scale CLT shear walls*

M-M20 with two rows of M20 bolts tended to be slightly higher than twice the strength of S-M20.

After the test, the CLT walls were decomposed to determine the internal damage on the CLT panels. The inside of the CLT panel of S-M16 is shown in Figure 7. We observed bolt tracks in the diagonal direction with a length of 40 mm in total in the outermost position, as well as bent bolts.

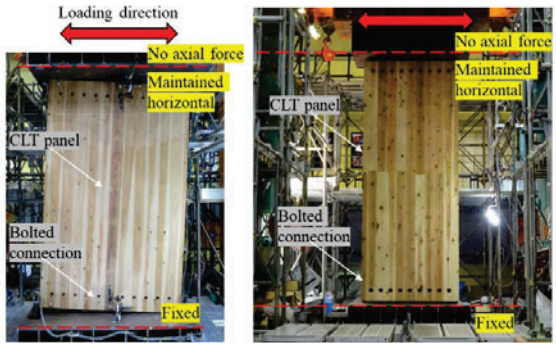

(a) S-M12 *(b) S-M20*

Figure 6: *Full-scale CLT shear wall test setup*

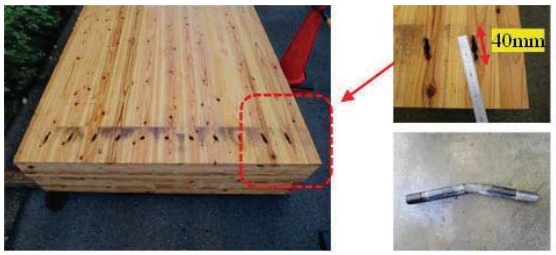

Figure 7: *Inside of S-M16 CLT panel (left: back side of CLT panel, top right: bolt track, bottom right: bent bolt)*

3.2 SIMULATION ANALYSIS OUTLINE

To establish an analysis method for this two-panel CLT shear wall, we compared the test results with the simulation results obtained from an FE analysis. In addition, we also investigate the stress states of the CLT shear walls. The analysis was performed using the MSC Nastran 2019.0 software with monotonic loading. In the analytical model, the gusset plates and CLT panels were modeled with elastic shell elements, and the bolted connection was modeled with nonlinear spring elements in two directions (vertical and horizontal) connecting the gusset plates and CLT panels. Elastic orthogonal anisotropy was applied to the shell elements of the CLT panels as material properties, and the elastic moduli in the major direction, minor direction, and shear were determined by the values of standard [7]. The nonlinear characteristics of the spring elements were assumed to be perfect elasto-plastic. The yielding point and initial stiffness were calculated from the element test results of the major and minor CLT panel directions by using Hankinson's equation shown in equation (1). An outline of the calculation methods is shown in Figure 8. The ultimate strength (P0, P90) and initial stiffness (K0, K90) from the CLT element tests on the major and minor directions are inserted into Hankinson's equation, and the characteristic values (Pθ, Kθ) in the θ direction are then separated into vertical and horizontal components (Pθ_0, Pθ_90, Kθ_0, Kθ_90) by applying a trigonometric function. However, it is necessary to determine the deformation angles of each connection, as observed in the tested CLT wall, because the structural properties depend on the loading direction in practice. Thus, a convergence calculation was used to obtain the deformation angle θ. As shown in the procedure in Figure 9, the deformation angle θ was calculated so that all CLT panel elements and the

https://doi.org/10.52202/069179-0375

springs of bolted connections are satisfied with equilibrium of the deformation and stress.

$$P_\theta = \frac{P_0 \cdot P_{90}}{P_0 \cdot \sin^2\theta + P_{90} \cdot \cos^2\theta} \quad (1)$$

Where P_θ=strength in the θ direction, θ=deformation angle. This equation can be used for stiffness K instead of strength P.

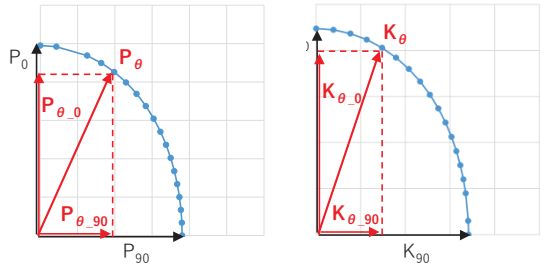

Figure 8: *Calculation method for spring properties at a specific angle*

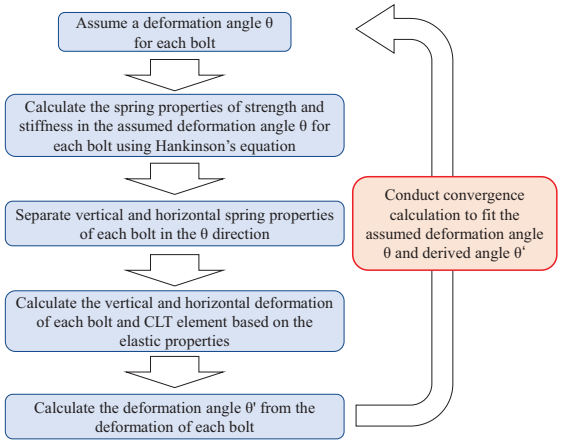

Figure 9*: Convergence calculation process*

3.3 DISCUSSION OF TEST AND ANALYSIS RESULTS

The ultimate strength and initial stiffness calculated by perfect elasto-plastic modeling are listed in Table 4, and Figure 10 shows the relationship between shear force and drift, and its skeleton curves from the full-scale CLT wall tests and simulation. The drift angle on hysteresis curves was calculated by dividing the horizontal displacement between the top and bottom steel stubs by the height between them.

In all specimens, the strength continued to increase up to 1/20 radians, and no significant reduction in strength was observed, indicating that the CLT shear wall exhibited a substantially high deformation capacity. Furthermore, a clearance of +1 mm at the bores on the CLT panel and gusset plates for the bolted connection did not cause slip behavior throughout the tests.

The shear force-drift relationship from the simulation for each CLT shear wall is largely consistent with the test skeleton curves. Because the yielding point of the outermost bolts in the analysis coincides with the elastic limit on the tests, we conclude that the specimens reached the maximum strength through a gradual reduction in stiffness due to the yielding of the bolts. Moreover, from the above, it can be said that the bolt strengths in the analysis were set at a reasonable value. In the S-M16, S-M20, and M-M20 tests, the initial stiffness in the test and the analysis were almost identical. However, in the S-M12 test, the initial stiffness of the analysis was lower than in the test results. One reason for this may be that the initial stiffness obtained by the perfect elasto-plastic modeling of the element tests for the M12 series was evaluated to be lower than the actual values. In the modeling, the initial stiffness is calculated based on the slope connecting the points at 0.1 Pmax and 0.4 Pmax. The evaluation of the test result with the M12 bolt seemed to be affected when the stiffness had already decreased at the 0.4 Pmax point because the maximum strength is much higher than the elastic limit. As a result, it is possible to estimate the initial stiffness of this CLT shear wall from the element test results, but it also illustrates the importance of using the appropriate initial stiffness for the connection.

Hankinson's equation used to calculate the stiffness and strength at an angle was originally devised for materials with a constant wood grain direction, such as lumber and glued laminated wood, and is not intended to be applied to composite materials with orthogonal wood grain directions in each layer, such as CLT. However, we found that the bolted connection showed similar behavior to that of glued laminated timber as the laminae located close to the gusset plate mainly resisted the bolt deformation. This suggests that Hankinson's equation can be used to estimate the spring properties at a specific angle in the bolted connection.

Figure 11 shows the vertical and shear strain contour and the maximum and minimum strain at +1/20 radians for the S-M16 and M-M20 FE analyses, which contain larger values in the same dimension of the CLT shear wall. The shear strain contour indicates that the strain is concentrated at the center of the CLT panel, and the maximum strain in M-M20 at a large deformation is over 3500 μ, which is beyond an allowable value. However, the strain in the surrounding area was kept small, which is consistent with the full-scale test results that showed no damage to the CLT panels.

In conclusion, although there are some issues in the evaluation of stiffness, this simulation method can be used to evaluate the structural performance of the CLT shear wall with sufficient practical accuracy.

Table 4: *Ultimate strength and initial stiffness of CLT shear walls*

ID	Ultimate Strength [kN]		Stress		Initial Stiffness [kN/×10^{-3}rad]	
			Flexural [N/mm^2]	Shear [N/mm^2]		
	Positive	Negative	Absolute mean	Absolute mean	Positive	Negative
S-M12	97.8	-88.6	1.53	0.36	9.0	8.8
S-M16	132.3	-128.5	2.14	0.50	14.4	14.9
S-M20	114.4	-110.2	2.12	0.31	8.7	9.2
M-M20	249.6	-235.5	4.67	0.66	18.4	18.2

https://doi.org/10.52202/069179-0375

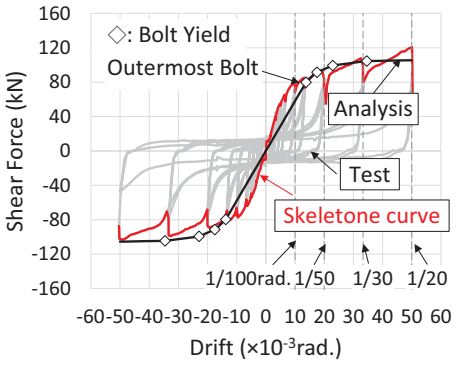

(a) S-M12

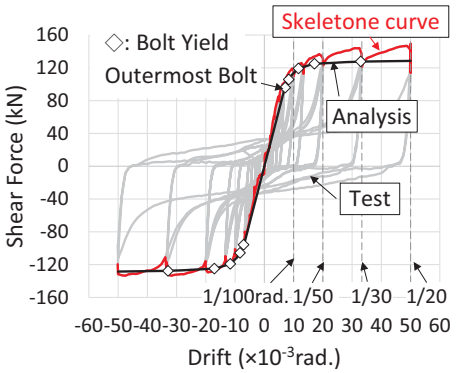

(b) S-M16

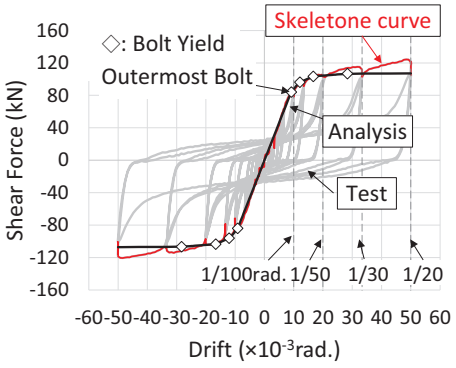

(c) S-M20

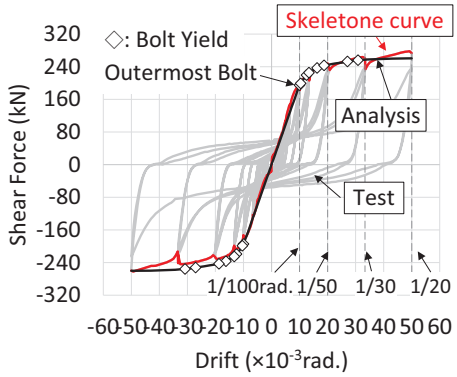

(d) M-M20

Figure 10: *Relationship between lateral shear force and drift angle from test and analysis results of CLT shear wall*

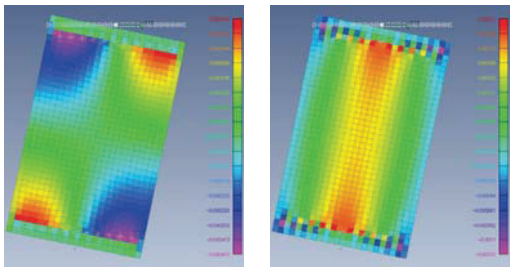

(a) S-M16

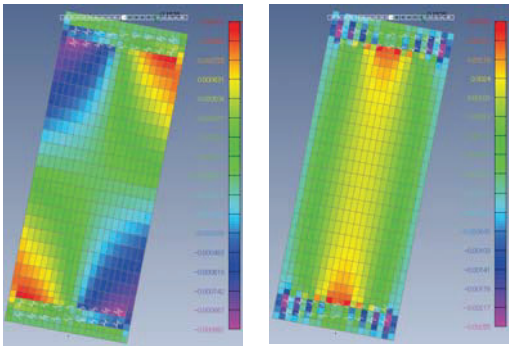

(b) M-M20

Figure 11: *Strain contour of CLT panel obtained by FE analysis at 1/20 radians (right: Vertical strain, left: Shear strain)*

4 CONCLUSION

To improve on-site productivity, we have developed a two-panel CLT shear wall system with a novel bolted connection in which a steel plate is sandwiched between a pair of CLT panels. In the study, we conducted element tests on the bolted connection, a full-scale shear wall test, and an FE analysis. The results showed that this system has a high lateral resisting strength and ductility. Our findings are summarized as follows.

The bolted connections showed high deformation capacities even beyond the elastic limit when the force was subjected to the CLT major direction within the range of the tests.

The full-scale CLT shear wall tests showed that the CLT panels were not damaged up to a large deformation of 1/20 radians in all specimens and the CLT panels had high deformation capacity with no reduction in strength.

For the FE analysis, Hankinson's equation was applied to the element test results to estimate the spring properties of the bolted connection. The simulation results showed that the analytical results were highly consistent with the test results, except for some initial stiffness. Thus, we can conclude that the analytical method is feasible for simulating the structural behaviors of the two-panel CLT shear wall.

REFERENCES

[1] E. J. Baas, G. Granello, A. R. Barbosa, M. Riggio, Post-Tensioned Timber Wall Buildings: Design & Construction Practice in New Zealand & United

https://doi.org/10.52202/069179-0375

States. World Conference on Timber Engineering 2020, Santiago, 2021.
[2] M. Popovski, Z. Chen, A. Iqbal, Performance of Post-Tensioned CLT Shear Walls with Energy Dissipators under Lateral Loads. World Conference on Timber Engineering 2020, Santiago, 2021.
[3] K. Kanazawa: Structural Performance of Composite Structure with CLT Infilled in Steel Frames Using Joint of Drift-pin with Steel Plate. Summaries of Technical Papers of Annual Meeting Architectural Institute of Japan, C-2, Structures IV, pp. 331-334, 2019.9. (in Japanese)
[4] K. Nakatsuji, H. Yamazaki, H. Sakata, N. Toba, Y. Nonaka, A Study on Shear Performance of CLT Connection Using Drift Pins and Insert-steel Gusset Plate, J. Struct. Constr. Eng., AIJ, Vol. 83 No. 754, pp. 1811-1820, Dec. 2018 (in Japanese)
[5] J. Kubota, D. Hinata, Y. Tanaka, S. Takatani, N. Haneda, Evaluation of Structural Properties of Bolt Joint between CLT and Steel Plate. Summaries of Technical Papers of Annual Meeting Architectural Institute of Japan, C-2, Structures IV, pp. 311-312, 2021.9. (in Japanese)
[6] Architectural Institute of Japan: AIJ Standard for Structural Design of Timber Structures, Tokyo, Japan, Maruzen, 2006. (in Japanese)
[7] Japan Housing and Wood Technology Center: Design and construction manual on CLT building version 2016, Tokyo, Japan, 2016. (in Japanese)

World Conference on Timber Engineering Oslo 2023

FORCED RESPONSE MEASUREMENTS ON A SEVEN STOREY TIMBER BUILDING IN SWEDEN

Andreas Linderholt[1], Pierre Landel[1,2], Marie Johansson[2]

ABSTRACT: Forced vibration tests have been conducted on the seven-storey timber building Eken in Mariestad in Sweden. The main objective is to estimate the building's dynamic properties from test data. The eigenfrequencies, mode shapes and their scaling are useful to calibrate numerical models. However, the most important outcomes are the estimates of the modal damping values. The reason is that the damping impacts the acceleration, and thus the serviceability of the building, and at the same time, it is very hard to model damping. So, during the design phase, one must rely on previous test data (of which very few exist for taller timber buildings) or rule of thumbs. It is therefore important to gain knowledge about the damping for timber buildings in order to enable good designs of future and taller timber buildings. The test data shows that the modal damping is roughly equal to 2% of the critical viscous ones for the eigenmodes extracted. The test campaign on Eken is made as a part of the project Dyna-TTB in which vibrational tests have been performed on eight high-rise timber buildings, in Europe, of which Eken is one.

KEYWORDS: Forced vibration, timber building, damping, eigenmodes, experimental modal analysis, Dyna-TTB

1 INTRODUCTION

Within the project Dyna-TTB, measurements on eight multi-storey timber buildings around Europe have been conducted to gain more knowledge on their dynamic performance at serviceability level. The dynamic response of a structure is governed by four quantities: the mass, the damping, the stiffness, and the dynamic load. The damping is the one that is hardest to predict; reliable models are rare and most often the damping is taken from tests or as one value of modal viscous damping taken from rule of thumbs. One of the primary objectives of the Dyna-TTB project is to broaden the knowledge base regarding damping in timber buildings. Such a data base is useful during the development of future, possibly even taller than the tallest today, high rise timber buildings. For modelling purposes, it is also important to have information regarding resonance frequencies, mode shapes and modal masses. The Swedish case study in the DynaTTB project was the seven-storey building Eken (the Oak in English), see Figure 1. For more information on the DynaTTB project see [1]. Examples of other measured buildings in the DynaTTB project can be found in [2]–[5].

The purpose of vibration tests is to get measures of resonance frequencies, to estimate damping, mode shapes and modal masses. The test set-up answers the questions how to excite a structure as well as how and where to measure responses.

The models used to calculate accelerations due to wind loads, in the serviceability limit states, vary between different codes [6]. However, all of them are based on the same concept; only the first bending mode is included. If one assumes the shape of the first bending mode to be known and that the first resonance frequency is associated with the first bending mode, one accelerometer is sufficient to get the desired information. More sensors are beneficial but not necessary. However, to get data for model calibration, several spatially resolved mode shapes are needed or at least most desired. Furthermore, there are many ways of exciting a structure. Forced response measurements have the advantage that they enable scaling of the mode shapes. Shaker excitations are commonly used in forced vibration measurements. It is important that all the excitations stem from the shaker or shakers in the intended directions and that the stimuli are measured. Among different signals that can be used for the shaker excitations, stepped sine testing has the advantage of focusing all the energy in one frequency at the time, which is beneficial when large structures are excited by limited forces.

When creating an FE-model, here representing a multi-storey timber building, important input parameters are the

[1]Andreas Linderholt, Linnaeus University, Department of Mechanical Engineering, 351 95 Växjö, Sweden andreas.linderholt@lnu.se,

[2] Marie Johansson, RISE Research Institutes of Sweden, Wood Building Technology, 501 15 Borås, Sweden. marie.johansson@ri.se

[1,2] Pierre Landel, Linnaeus University, Department of Mechanical Engineering, 351 95 Växjö, Sweden and RISE Research Institutes of Sweden, Wood Building Technology, 501 15 Borås, Sweden, pierre.landel@ri.se

https://doi.org/10.52202/069179-0376

stiffnesses and masses of the different parts of the building system. One example of important parameters is the stiffnesses of connections. This has also been studied in the DynaTTB project [5], [7], [8].

This paper describes the forced vibration test campaign on the building Eken in Sweden. The measurement campaign was performed in the spring of 2022. The paper also presents some of the test results in the form of frequency response functions (FRFs) and modal properties for some of the extracted modes.

2 THE BUILDING EKEN

The building Eken was finished in 2019 and contains 31 rental apartments. It is in the city of Mariestad in the south part of Sweden, see Figure 1. The height, width and depth of the building are 24, 27 and 19 m respectively. The building was built by the company Stenmarks Bygg and it is owned by Mariehus.

2.1 THE BUILDING SYSTEM

Half of the bottom floor is made of concrete whereas the other half, the other storeys and the elevator shaft are made of timber. The building is built using the Moelven Trä 8 system [9]. The load bearing system consists of glued laminated timber (glulam) beams and columns whereas glulam trusses form the stabilizing elements, see Figure 1. In total the structure consists of 12 glulam trusses, four in the weak direction of the building and eight in the strong direction of the building. The glulam trusses are, in principle, symmetrically located in the building and the trusses in the middle go through all seven storeys of the building.

The floor system is made of strengthened LVL sheets acting as a diaphragm system. The connections in the glulam trusses are slotted-in-steel-plates fastened with steel dowels. The other glulam beams are fastened using steel hangers screwed to the gluelam members. These glulam building components are manufactured and assembled by the company Moelven Töreboda.

The apartments are vibrationally isolated from each using a thin concrete screed resting on sound insulation on top of the LVL floors. The floors are separated in all apartment separating walls. The internal walls and ceilings consist of gypsum wall boards on acoustic studs.

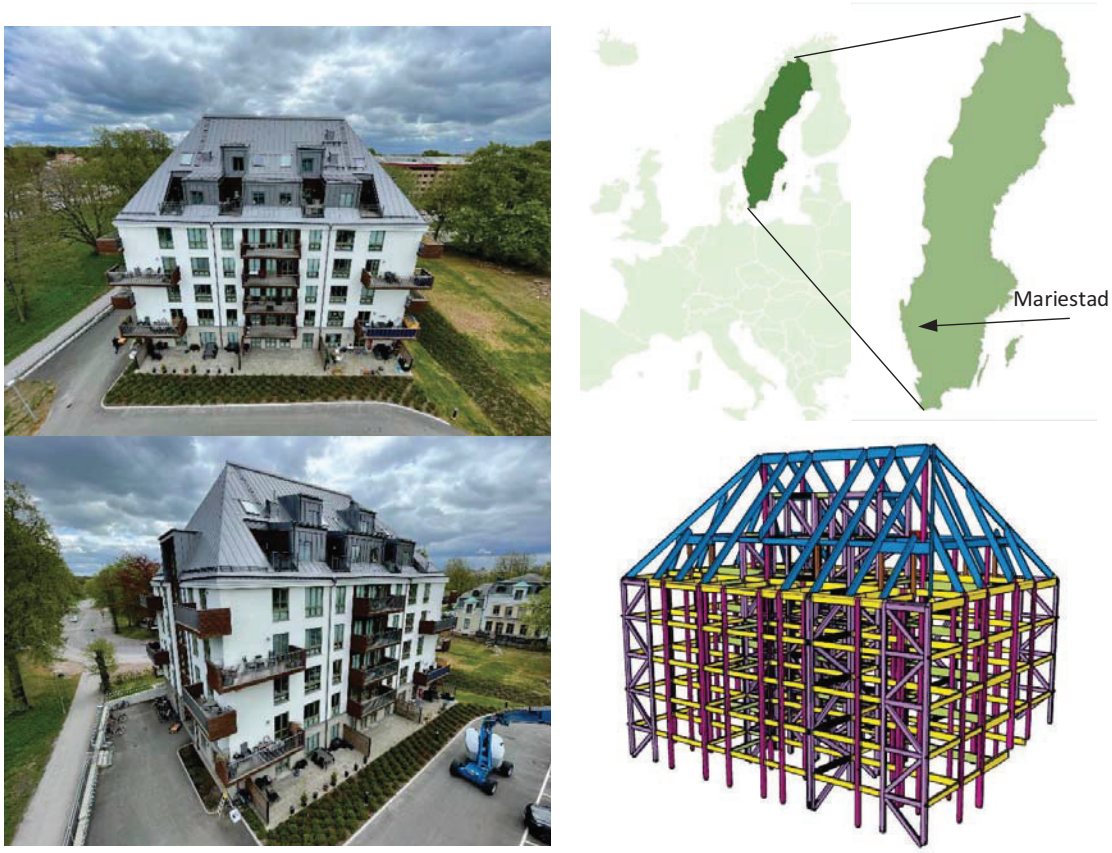

Figure 1. *The Eken building in Mariestad with images of the finished building, its location in Sweden and the glulam parts of its structural system.*

https://doi.org/10.52202/069179-0376

2.2 The test set-up

The dynamic performance of the building Eken has been studied during the measurement campaign using a forced vibration set-up. Forced vibration tests have the benefit of enabling more precise damping estimates than ambient vibration tests. It also renders in e.g., scaled accelerances. Mass inertia forces can be used to excite buildings in forced vibration tests. For that purpose, an APS 420 shaker was used in the Eken measurement campaign, see Figure 2. The shaker was placed in the ventilation room on the top (seventh) floor. Due to the heavy weight (140 kg) of the shaker, it had to be lifted using a crane through a roof window, see Figure 6. To properly excite the building structure, the shaker was bolted to a specially produced steel plate, that was screwed through the floor to one of the main glulam beams and clamped around one of the main glulam columns that runs vertically through the whole building, see Figure 2. The steel plate was prepared to allow for three positions of the shakers to excite the building along its main axis, perpendicular to its main axis and at 45º.

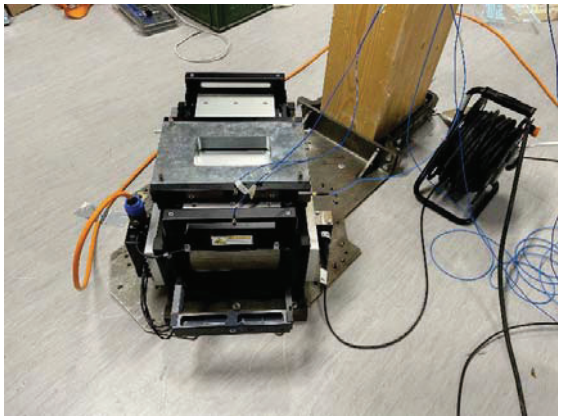

Figure 2. *Excitation by mass inertia, using an APS 420 shaker, used for stepped sine excitation, fastened to a steel plate fastened to the main glulam structure using screws. In this set-up the shaker is placed in a 45° angle to the buildings main axis.*

In total 45 accelerometers: PCB 393B12 and PCB 393M62, with the sensitivity 10V/g, were used to measure the response of the building at different places and different directions. The main configuration of the accelerometers was two accelerometers, mounted on small steel cubes, placed on the building to measure the responses in two orthogonal directions, see Figure 3. The steel cubes with the accelerometers were screwed directly on the structure of the building at four different levels at each of the four corners of the building, under the balconies, see Figure 4, and two positions under the main roof beam at the top of the building. There were also accelerometers placed on the top floor close to the shaker and in the staircase.

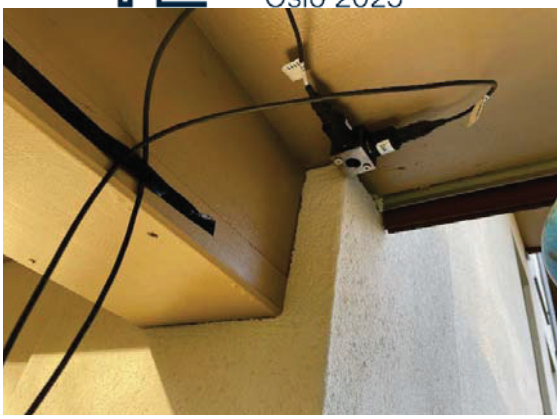

Figure 3. *Two PCB-39 accelerometers positioned under a balcony at one of the corners of the building.*

Three Siemens Scadas data acquisition (DAQ) units, connected via fiber-optic cables, were used to control the excitation and to collect measurement data. One of the boxes was placed in the room where the shaker was located, and it controlled the other two boxes located at the ground outside the building. Each DAQ was put into a plastic box for weather protection and the boxes communicated with the accelerometers via cables, see Figure 5. The accelerometers, cables and the Siemens Scadas data acquisition cables were installed using a 25 m tall skylift, see Figure 7.

Figure 4. *Positioning of sensors, with four accelerometer positions along the height in the four corner of the building and two accelerometer positions under the roof (red boxes) and the shaker at the attic room attached to one of the glulam columns.*

Figure 5. *One of three Siemens Scadas Acquisition boxes.*

https://doi.org/10.52202/069179-0376

2.3 The forced vibration test of the building

The forced vibration test was performed using a stepped sine test set-up. Stepped sine testing has the advantage of focusing all the energy in one frequency at the time. Here, an APS 420 (APS Dynamics) inertia shaker was used for stepped sine testing from 2 Hz to 20 Hz. The excitations were made in 0, 45 and 90 degrees in relation to the axis along the width of the building. The steel plate, under the shaker, was used to connect the shaker directly to the load-bearing structure. The accelerometers were also placed directly to the main glulam structure. Thus, the force was made likely to excite the global modes of the building.

The total recording time for a stepped sine test, going from 2Hz to 20 Hz with a step size of 0.01 Hz took about four hours. Thereafter the direction of the shaker was changed to another angle and the test was repeated. This was made to make sure that all modes in the frequency range were captured.

Figure 6. *Lift off the 140 kg shaker from the ground to the top floor position through a small attic window.*

Figure 7. *Installation of cables and accelerometers in progress using a 25 m sky-lift.*

3 RESULTS

The test data were evaluated using the software Siemens Test Lab. The evaluated parameters in this first basic evaluation were:

- resonance frequencies,
- modal damping,
- mode shapes and
- modal masses.

The data evaluated were in the form of FRFs from which the modal properties were estimated. The quality of the estimates was examined by a comparison between the measured FRFs and the synthesized counterparts. The part of the direct point receptance for excitation in the Y-direction (the flexible direction) that includes the first three resonance frequencies, is shown in Figure 8.

The first bending mode in the weak direction was found to have a frequency of 2.4 Hz. The next mode is a torsional mode at 2.7 Hz.

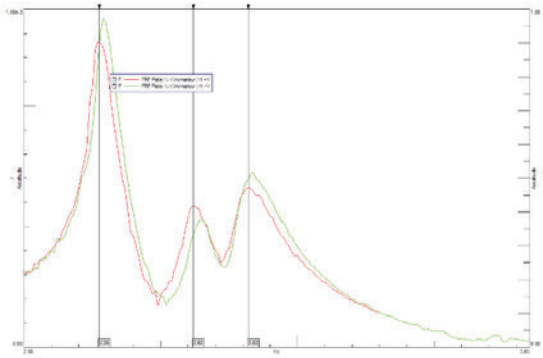

Figure 8. *An FRF stemming from excitation in the Y-direction (the flexible direction). The first three resonances are shown, x-axis scale 2-3 Hz.*

To verify that a sufficient frequency resolution is used, a Nyquist plot is useful, see Figure 9. The plot shows the frequency range including the first three resonance frequencies.

The damping could be evaluated for these modes. A preliminary estimation showed that the relative viscous damping was 1.6% for the first bending mode in the weak direction (at 2.4 Hz). The first torsional mode was found to have a relative viscous damping of 1.9% (at 2.7 Hz). The second bending in the flexible direction had 1.6% damping at 7.0 Hz.

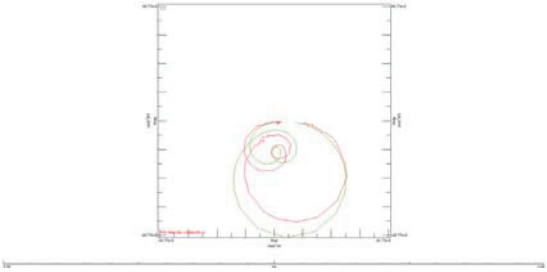

Figure 9. *Nyquist plot for an FRF stemming from excitation in the Y-direction (the flexible direction). The first three resonances are shown.*

Scaled mode shapes were also extracted from test data. An AutoMAC was calculated, and it shows that the mode shapes extracted from the test data are very close to orthogonal. The modal parameters will be used to calibrate an FE-model representing the building. It was possible to find fifteen distinguishable modes in the frequency range 2-20 Hz when exciting the building in the Y-direction (the flexible direction), see Figure 10.

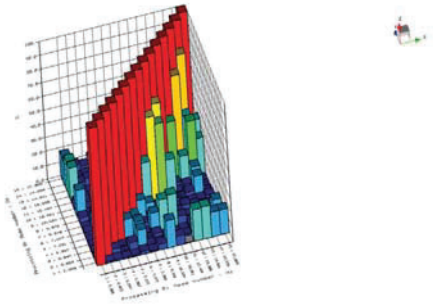

Figure 10. *AutoMAC for modes stemming from excitation in the Y-direction (the flexible direction). There are fifteen distinguishable modes in the frequency range 2-20 Hz.*

When exciting the building in the X-direction (the stiff direction), there were ten distinguishable modes in the frequency range 2-20 Hz, see Figure 11. Some of the

https://doi.org/10.52202/069179-0376

modes are the same in the sets stemming from excitation in the X- and Y-directions. In total around twenty separate modes could be seen in the data.

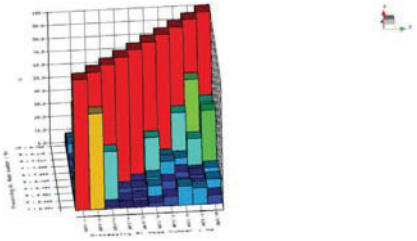

Figure 11. *AutoMAc for modes stemming from excitation in the X-direction (the stiff direction). There are ten distinguishable modes in the frequency range 2-20 Hz.*

The plots of mode shapes, see Figure 12, Figure 13 and Figure 14, show the first bending mode in the Y-direction, the first torsion mode and the second bending mod in the Y-direction. The first bending mode is very symmetric and shows an almost pure bending of the building.

The torsion mode shows a mode shape that is almost symmetric but with the rotation center moved slightly from the center of the building. This is due to that the trusses are not placed perfectly double symmetrical.

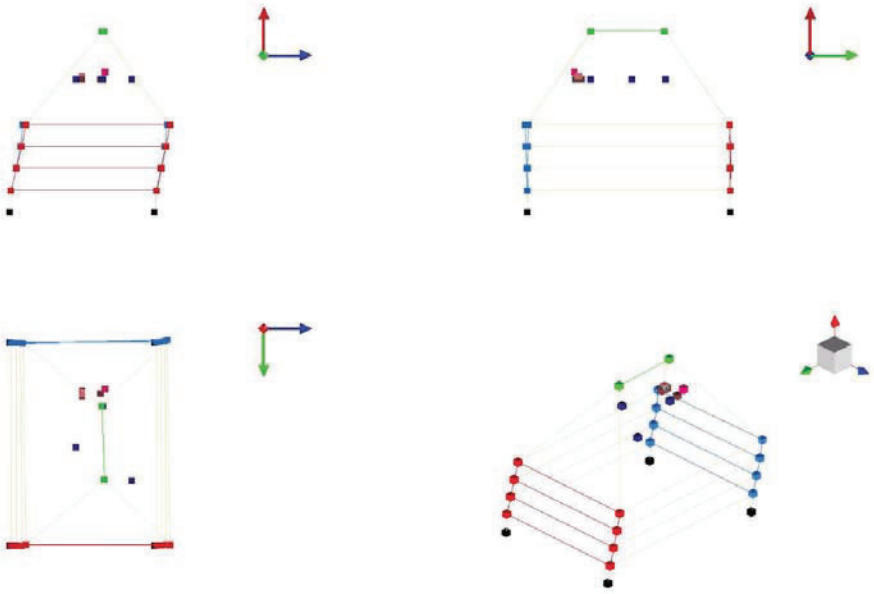

Figure 12. *The first bending mode in the Y-direction (the flexible direction).*

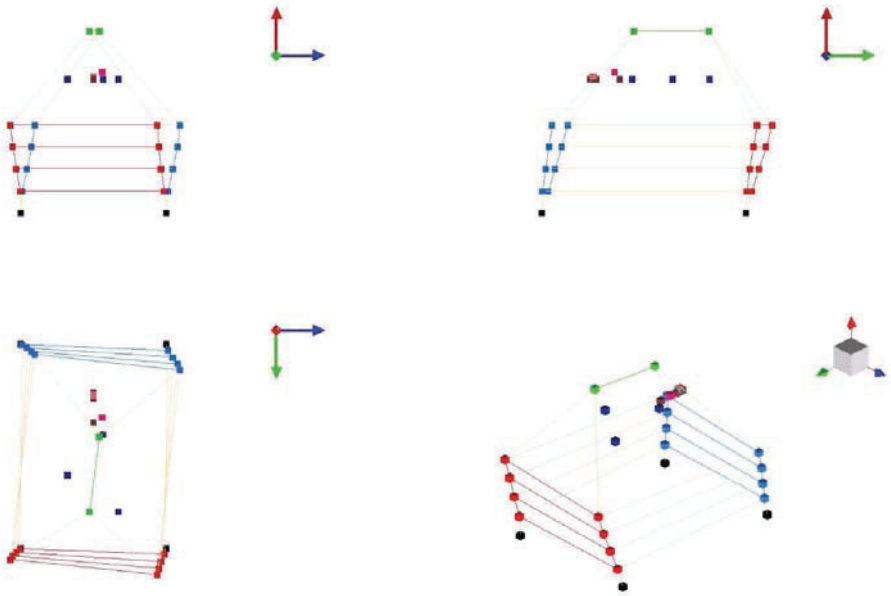

Figure 13. *The first torsion mode.*

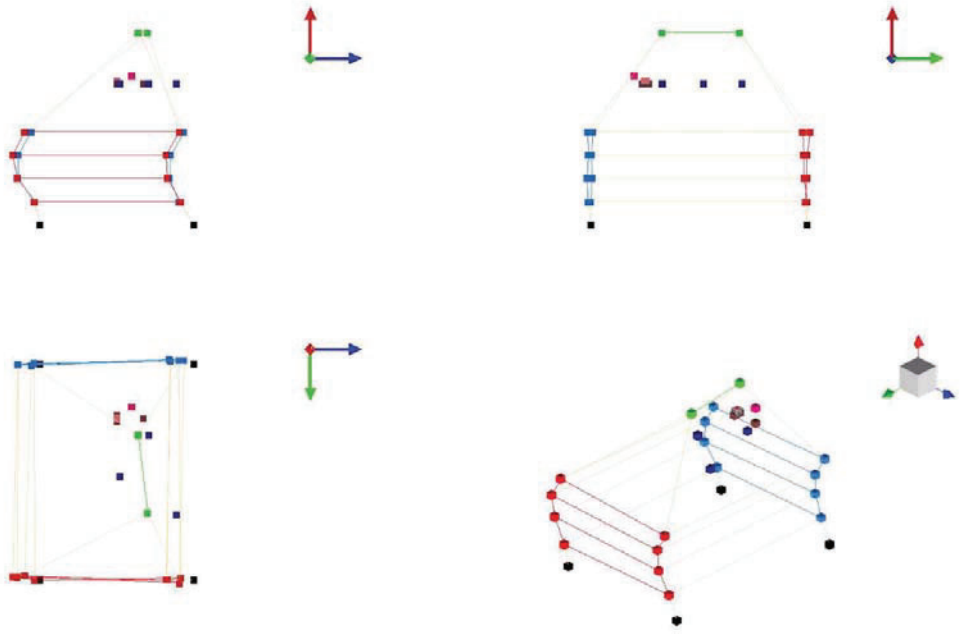

Figure 14. *The second bending mode in the Y-direction (the flexible direction).*

https://doi.org/10.52202/069179-0376

The most important outcome is the contribution to the knowledge base regarding damping in high-rise timber buildings. The damping values are roughly 2% for the modes extracted, see examples in Table 1. That knowledge is valuable in the design work of future and taller timber buildings.

Table 1. *Resonance frequency and relative viscous damping for three vibration modes.*

Mode	Resonance frequency	Damping relative viscous
1st bending, flexible direction	2.4 Hz	1.6%
1st torsion	2.7 Hz	1.9 %
2nd bending, flexible direction	7.0 Hz	1.6 %

4 CONCLUSIONS

In this paper, the vibrational test campaign made on the seven-story timber building Eken in Mariestad in Sweden is presented. By using mass inertia forces generated by an APS 420 shaker in combination with sensitive accelerometers, 10 mV/g, the fundamental and global modes were successfully extracted from test data even when the excitation force amplitude was low. The estimated damping values agree with estimated damping values from other test campaigns within the project Dyna-TTB. The results contribute to the knowledge base regarding damping in high-rise timber buildings and are thus useful for future design of tall timber buildings.

ACKNOWLEDGEMENT

The research leading to these results has received funding from the ForestValue Research Programme which is a transnational research, development and innovation programme jointly funded by national funding organisations within the framework of the ERA-NET Cofund 'ForestValue – Innovating forest-based bioeconomy'".

REFERENCES

[1] R. Abrahamsen, M. A. Bjertnaes, J. Bouillot, B. Brank, and L. Cabaton, "Dynamic response of tall timber buildings under service load-the dynattb research program," Nov. 2020. [Online]. Available: http://urn.kb.se/resolve?urn=urn:nbn:se:lnu:diva-99080

[2] B. Kurent, B. Brank, and W. K. Ao, "Model updating of seven-storey cross-laminated timber building designed on frequency-response-functions-based modal testing," *Structure and Infrastructure Engineering*, 2021, doi: 10.1080/15732479.2021.1931893.

[3] B. Kurent, N. Friedman, W. K. Ao, and B. Brank, "Bayesian updating of tall timber building model using modal data," *Eng Struct*, vol. 266, p. 114570, Sep. 2022, doi: 10.1016/J.ENGSTRUCT.2022.114570.

[4] M. Manthey, O. Flamand, A. Jalil, A. Pavic, and W. K. Ao, "Effect of non-structural components on natural frequency and damping of tall timber building under wind loading," *World Conference on Timber Engineering 2021, WCTE 2021*, 2021.

[5] S. Tulebekova, K. A. Malo, A. Rønnquist, and P. Nåvik, "Modeling stiffness of connections and non-structural elements for dynamic response of taller glulam timber frame buildings," *Eng Struct*, vol. 261, Jun. 2022, doi: 10.1016/J.ENGSTRUCT.2022.114209.

[6] P. Landel, M. Johansson, and A. Linderholt, "Comparative study of wind-induced accelerations in tall timber buildings according to four methods," in *World Conference on Timber Engineering 2021, WCTE 2021*, 2021.

[7] P. Landel, "Wind-induced vibrations in tall timber buildings : Design standards, experimental and numerical modal analyses," Licentiate Thesis, Linnaeus University, Växjö, 2022.

[8] P. Landel and A. Linderholt, "Reduced and test-data correlated FE-models of a large timber truss with dowel-type connections aimed for dynamic analyses at serviceability level," *Eng Struct*, vol. 260, Jun. 2022, doi: 10.1016/J.ENGSTRUCT.2022.114208.

[9] Moelven, "Flervåningshus Trä8." https://www.moelven.com/se/produkter-och-tjanster/allt-om-limtra/flervaningshus-tra8/ (accessed Feb. 02, 2023).

World Conference on Timber Engineering Oslo 2023

SYSTEM IDENTIFICATION OF TALL MASS TIMBER STRUCTURES EMPLOYING AMBIENT VIBRATION TEST AND FE MODELLING

Samira Mohammadyzadeh[1], Jianhui Zhou[2], Lin Hu[3], Fei Tong[4]

ABSTRACT: Despite the recent rapid development in dynamic characteristics identification of structures, lack of knowledge in dynamic properties of tall mass timber buildings is still an open issue for researchers and designers. There are ongoing international efforts to develop a comprehensive database for predicting the vibration performance of timber structures for serviceability and seismic design. This paper discusses an ambient vibration test (AVT) that was conducted on a six-storey mass timber building known as Wood Innovation and Design Centre (WIDC) located in Prince George, Canada. The test results including the experimental natural frequencies and damping ratios were compared with a three-phase test program undertaken in 2014, 2015, and 2017 by FPInnovations. In addition, a numerical modal analysis was conducted on the same building, using both simplified and complex finite element (FE) models. A sensitivity analysis was carried out considering various assumptions of connection types to investigate its effect on the natural frequencies of the structure. The results of current AVT showed minor changes in frequencies over the service time in comparison to previous tests. According to the numerical results, the simplified FE model poorly matched with the results from AVT, while the complex model showed a better agreement with the measured fundamental frequency; however, significant discrepancies were observed in the second and third modes. The sensitivity analysis indicated low impact of different connection type assumptions on the natural frequencies of the case building obtained from the FE models.

KEYWORDS: System identification, Timber buildings, Dynamic properties, Ambient vibration test, Numerical modelling

1 INTRODUCTION

With the use of mass timber products, interest in constructing more high-rise timber buildings has increased recently. However, due to the lightweight and high flexibility of tall timber buildings, they are susceptible to dynamic lateral loads that are induced by wind and earthquakes [1]. To understand their structural behaviour under lateral loads, prediction of the building dynamic properties is of great importance in the design stage. The National Building Code of Canada (NBCC) allows designers to estimate the fundamental period of timber buildings by an empirical formula which was not developed specifically for timber buildings [2].

To address the lack of data, there is an ongoing research campaign on vibration testing of timber buildings to extract the dynamic properties of these structures to form a database [3-6]. Feldmann et.al studied nine timber towers and three tall timber buildings by ambient vibration testing. The results verified the efficiency of this type of experiments and contributed test data on low-amplitude wind vibration of tall timber structures [1]. Reynolds et al. investigated the difference in dynamic properties between two similar 5-storey timber buildings with the same layout and a concrete core. The difference was in walls and floors, the first was made of a light wood frame and the second was made of cross laminate timber (CLT). The results showed high similarity between the dynamic properties of these two buildings [7]. Hafeez et al. studied dynamic properties of 32 light wood frame buildings and concluded that it was inaccurate to take the height of structures as the sole variable in determining the fundamental period of timber structures [8]. Recently, more mass timber buildings in Canada [3-5] and Europe [9] have been tested under dynamic loads at the serviceability level.

Having an experimental database of modal parameters, FE models with increased accuracy can be developed by engineers in practical design [10]. However, certain details of modelling such as connection types and material properties are still open issues in frequency calculations

[1] Samira Mohammadyzadeh, University of Northern British Columbia, Canada, mohammady@unbc.ca
[2] Jianhui Zhou, University of Northern British Columbia, Canada, jianhui.zhou@unbc.ca
[3] Lin Hu, FPInnovations, Canada, Lin.Hu@fpinnovations.ca
[4] Fei Tong, University of Northern British Columbia, Canada, fei.tong@unbc.ca

https://doi.org/10.52202/069179-0377

and overall dynamic behaviour of timber building. Reynolds et al. reported, for the two 5-storey buildings, that the FE modelling of just concrete core provided lower fundamental natural frequencies than the measured values [7]. Larsson et al. investigated a nine-storey concrete-timber hybrid building and found that dynamic properties were highly sensitive to the selected elastic properties of CLT walls, but insensitive to the connection properties [10]. Aloisio et al. modelled eight-storey CLT student apartments building located in Norway. The calibration of their model based on AVT results indicated that the impact of connectors under serviceability conditions is negligible [11]. In this regard, Tulebekova et al. had different findings that the stiffness of connections of the glulam frame in modelling the Mjosa tower were a governing parameter [12]. Kurent et al. updated FE model of a seven-storey CLT building based on an input-output vibration test result. Good agreement was observed between the numerical and experimental frequencies in the first six modes. However, the results showed that frequencies matched better in lower modes than in higher modes. [13].

In this study, an AVT was conducted on Wood Innovation and Design Centre (WIDC) building located in Prince George, Canada, to determine its experimental natural frequencies, damping ratios, and mode shapes. The test results were compared with the existed three-phase test program undertaken in 2014, 2015, and 2017 by FPInnovations [5]. The present study contributes to the assessment of dynamic properties change of a mass timber building during different time of its service life. Furthermore, to investigate the efficacy of commercial structural analysis FE software for modal analysis of tall mass timber buildings, two simplified and complex FE models were developed respectively for sensitivity analysis of different connection properties assumptions, and the results were compared with the experimental data. The test results were compared with predicted fundamental frequency from the NBCC equation.

2 MATERIALS AND METHODS

2.1 BUILDING DESCRIPTION

WIDC is a 29.5-meter tall, six-storey (with a mezzanine and a penthouse) mass timber building located in Prince George, British Colombia, Canada (Figure 1). The main structure consists of an innovative combination of post-and-beam construction and built-up cross-laminated timber floor panels. A balloon-type CLT core around the staircase and elevator shaft serves as the lateral load resisting system. WIDC was built in 2014 and was the tallest modern timber structure in Canada at the time of its construction.

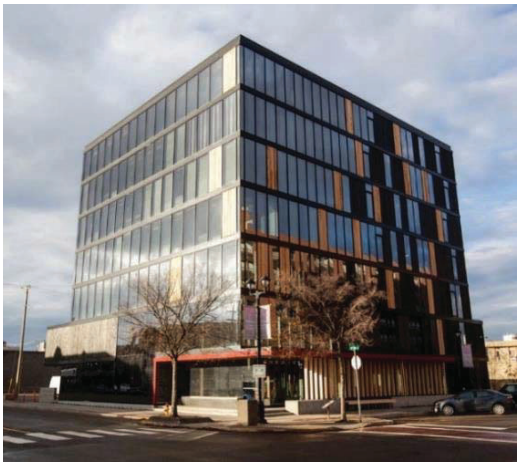

Figure 1: *Wood Innovation and Design Centre [14].*

2.2 AMBIENT VIBRATION TESTS

In 2014, while the building was about to complete with only the structural components and no enclosures, an AVT was conducted to determine its natural frequencies and damping ratios. After the building was completed with all non-structure components and fully occupied in 2015, Phase-II AVT was carried out.

Phase-III AVT was conducted in 2017, to check if the natural frequencies and damping ratios changed from the values measured in 2015. In these three phases, two reference sensors were fixed in the 5th floor level (Phases I and II) and the 6th floor level (in Phase-III). Six sensors with 500 mV/g sensitivity were roved between stories 2-6, 4-6, and 5 to 6 in the three tests, respectively. The location of the sensors is shown in Figure 2.

The results of these previous tests are listed in Table 1 [5]. The first and second vibration modes of the building are the first translational modes along the principal directions, X and Y, respectively, as shown in Figure 2, while the third mode is the first torsional mode.

Table 1: *Frequency and damping ratios of previous phases [5]*

Modes	Natural Frequency (Hz)			Modal Damping Ratio (%)		
	Phase I	Phase II	Phase III	Phase I	Phase II	Phase III
Translation in X	1.1	1.4	1.4	3.0	3.0	2.0
Translation in Y	1.3	1.6	1.6	2.0	2.0	2.0
Torsion	1.5	1.9	1.9	2.0	2.0	3.0

https://doi.org/10.52202/069179-0377

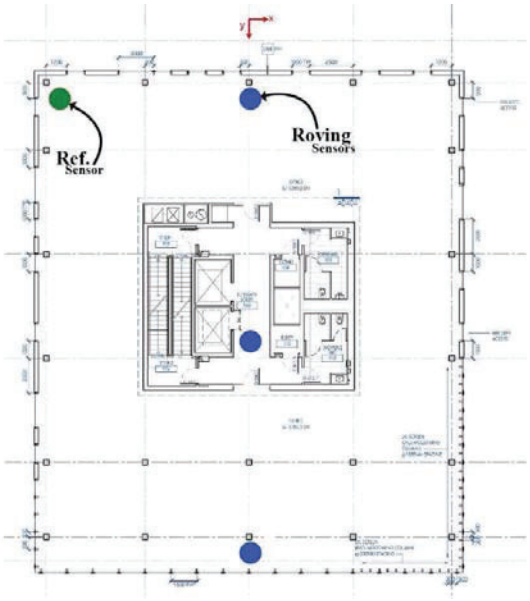

***Figure 2**: Location of the sensors (privious study [5])*

Aiming to monitor the dynamic properties of WIDC at the 9th year of its service life, Phase-IV tests were conducted in January 2023, as discussed subsequently. For the current AVT protocol, a 24-channel SEIMENS SCADAS dynamic data analyser with 10 uniaxial PCB accelerometers of 100 mV/g sensitivity and a sampling frequency of 200 Hz is used for data collection. The time duration for each setup was considered 240 sec. Two accelerometers were mounted on the roof level as the reference accelerometers in X and Y directions of the building and 8 accelerometers were roved between storeys 2-6 for measuring natural frequencies, mode shapes, and damping ratios. The second-floor plan is different from the above floors. However, the sensors were installed at all the floor levels at the same location in plan. No measurements were conducted at the mezzanine floor, which was anticipated not to affect the expected first three mode shapes. Figures 3 and 4 illustrate the locations of the sensors in the building and the overall view of test setup, respectively.

Post-processing of the operational modal analysis (OMA) was carried out using Simcenter Testlab using the OMA add-in. After correlation of time domain measurements, PolyMAX option, which is a curve fitter or modal parameter analyser, was used for producing cross power spectra to estimate the dynamic parameters of the desired system. In this process, all the cross powers functions were visualized along with their sum. Using the sum which is a complex average of all the included cross powers allows the identification of amplitude peaks [15].

2.3 NUMERICALL MODELLING

The experimental results were used to verify the FE model that was developed for modal analysis. For this purpose, the structure was modelled using RFEM 5.25 software in two stages. In the first stage, only the CLT core walls were modelled with lumped seismic inertia assigned at floor levels. The lumped mass was determined based on the actual mass of the materials and effective floor loads of the building. In the second stage, a complex model was developed including glulam beams and columns, CLT shear walls, and CLT floors. The details of modelling (the used material, structural element size, and layout of the elements) is according to the existing technical drawing of the building.

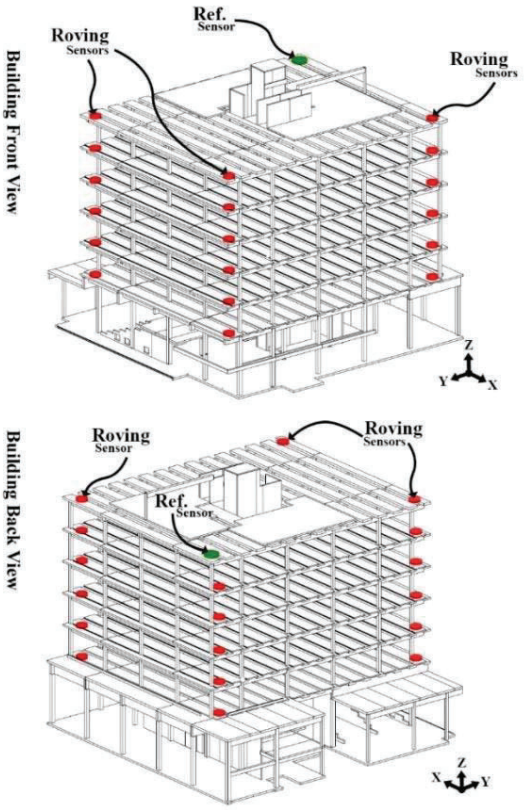

***Figure 3**: Locations of the sensors (phase IV)*

According to available information, the CLT panels used in wall construction are E1 grade 5-ply (175mm) sprue-pine-fir (SPF), and the staggered CLT floors were constructed with E1 grade 5-ply (175mm) and 7-ply (245mm) SFP CLT panels. These floors were modelled as an equivalent 6-ply CLT panel in the complex model. The 24f-EX Douglas Fir glulam beams and 16c-E Douglas Fir glulam columns were used throughout the building. Non-structural elements such as partition walls, façade, claddings, etc were not included in the complex model. The CLT walls and floors were modelled using the RF-Laminate add-on module in RFEM.

A pinned condition was assumed at the base of the columns and walls. As the post and beam were not designed to carry moments, beam-to-post connections were assumed as being pinned. The connections of floor-to-wall and wall-to-wall panels were considered as being fixed. Figures 5 and 6 show the simplified and complex FE models, respectively.

https://doi.org/10.52202/069179-0377

For the sensitivity analysis, floor-to-walls and wall-to-wall panels connection type assumptions were changed to pinned condition while columns and walls connections to the foundation were switched to fixed. This was to investigate the impact of various joint conditions on natural frequencies of the building.

***Figure 4**: Overall view of test setup*

2.4 NBCC PERIOD EQUATION

NBCC (2020) provides empirical equations to estimate the fundamental period of buildings. These equations are applicable to structures with various lateral resistance systems such as reinforced concrete moment resisting frames, steel moment resisting frames, for shear walls, etc.

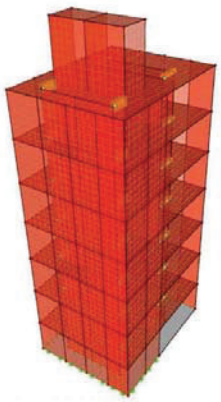

***Figure 5**: Simplified FE model*

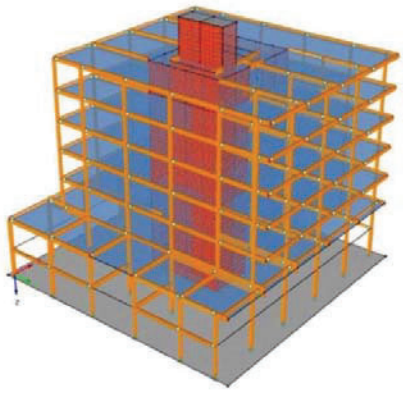

***Figure 6**: Complex FE model*

However, no equation is provided specifically for timber structures. In this paper, the equation for 'shear wall buildings and other structures' was adopted, as follows:

$$T_S = 0.05(h_n)^{3/4} \quad (1)$$

where, T_S and h_n are the fundamental period and the height of structure, respectively [2].

3 RESULTS AND DISCUSSION

3.1 EXPERIMENTAL TEST RESULTS

As listed in Table 2, the results indicate minor changes in the fundamental frequencies of the building over time. Figure 7 shows the cross-power function obtained from OMA. Comparing the test results of Phase III and IV, only 7.1% and 5.2% increase can be seen in the first and third natural frequencies, respectively, while the natural frequency of the second mode remains nearly the same. The relatively small discrepancy in the first and third mode frequencies may result from the differences in test setups used in Phase III and IV. Though accelerometers with different sensitivity (500 mV/g and 100 mV/g respectively) were used in the previous and present study tests, respectively, the sensors' sensitivity in both tests are adequate enough for capturing low frequencies required for this case study.

The consistency of natural frequencies during the time indicates no stiffness degradation in both connections and elements of the building. It should be mentioned that the occupancy of the building is still the same as the previous test, meaning negligible changes of the total mass of WDIC. Damping ratios of the first three modes of the structure at serviceability load level are listed in Table 2. It is well known that the measurement of damping ratios could have high degree uncertainty. Although, some changes can be seen between the values of damping ratios in this study and phase III of the previous study, rounding of the measured damping ratios in phase IV to the integer leads to the same results as previous phase test.

Table 2: *Comparison of natural frequencies (Hz) and damping ratios (%) of the first three modes*

Index	Modes	Values		
		Phase III [5]	Phase IV	Change (%)
Natural Frequencies (Hz)	Translation in X	1.4	1.5	7.1
	Translation in Y	1.6	1.6	0.0
	Torsion	1.9	2.0	5.2
Damping Ratios (%)	Translation in X	2.0	1.5	-25.0
	Translation in Y	2.0	2.0	0.0
	Torsion	3.0	1.5	-50.0

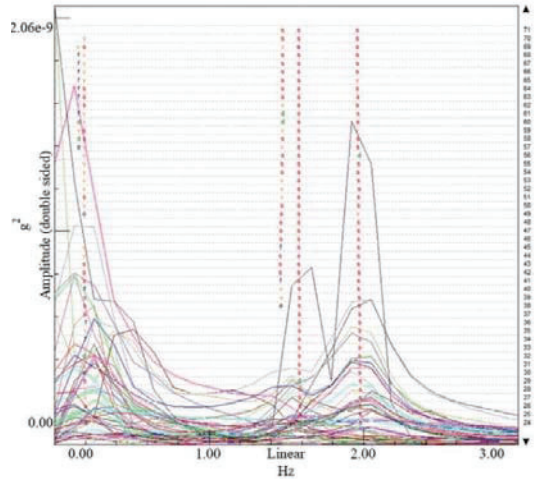

Figure 7*: Typical cross-power function obtianed from phase-IV test*

3.2 FE Modelling Results

The other dynamic property investigated in this study is the mode shapes. As mentioned before, in AVT's the first three mode shapes are the first bending in X direction, the first bending in Y direction, and the torsional mode, respectively. The results of the FE models show good agreement with the finding from AVT. Three first mode shapes of the simplified FE model are shown in Figure 8. Furthermore, the results of the structures mode shapes for phase-IV test and complex numerical FE model are shown in Figure 9.

The comparison between frequency of the first mode in the phase-III AVT, phase-IV AVT, the simplified model, and the complex FE model of the building along with NBCC formulation is shown in Figure 10. As it is clear in Figure 10, there is a significant discrepancy of about 47% between the first natural frequency of the simplified model and the result of Phase-IV AVT. Modelling only CLT core of the building could not predict the building frequencies accurately in this case study, as the first frequency of this model is not well-matched with the measurement. It is worth noting that difference between fundamental natural frequency of the complex model and phase-IVAVT is about 10.8%.

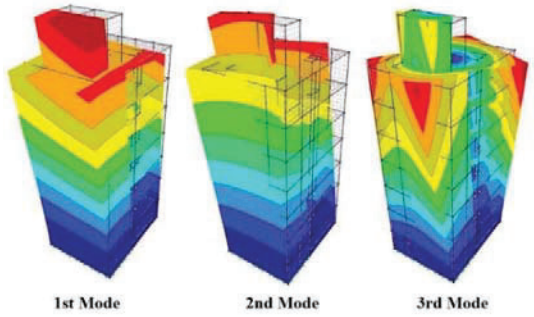

Figure 8*: First three mode shapes of the simlified model*

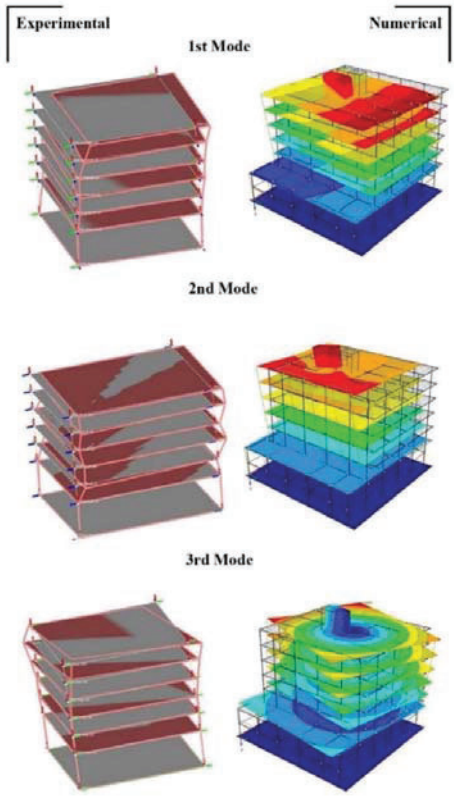

Figure 9*: First three mode shapes of the complex model both numerically and experimentally*

Because the first three measured frequencies of the building are close to each other, the discrepancy of 10.8% between first frequency of the FE model and experiment data cannot be considered as a good match between FE model and test data, though, this discrepancy is lower in comparison with the simplified model. Besides, it is interesting to find that first natural frequency of the

https://doi.org/10.52202/069179-0377

building estimated using the NBCC equation matched the measured value reasonably well from designer's point of view based on the data measured on 19 buildings [16] and close the predicted by the complex model. The results of the first three natural frequencies of the simplified and complex model are listed in Table 3. It is clear that the simplified model provided overestimated frequencies for all the three modes. Moreover, the differences between the measured and FE modelled frequencies are larger in higher modes. This finding agrees with the results found in [13] that matching higher modes of the FE modelling with the test results is more difficult than the lower modes.

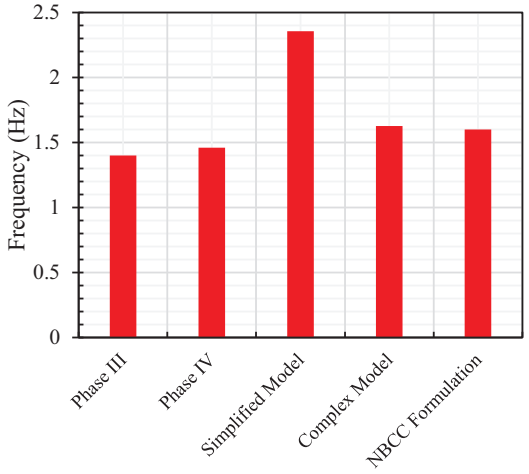

***Figure 10**: Comparision between avt, FE modelling, and nbcc equation for prediction of the first natural frequency*

***Table 3:** Frequencies of the simplified and complex model*

Modes	Simplified model (Hz)	Complex model (Hz)	Discrepancy (%)
Translation in X	2.3	1.6	35.9
Translation in Y	4.3	2.6	49.3
Torsion	6.0	5.0	18.2

3.3 SENSITIVITY ANALYSIS

A sensitivity analysis was carried on both the simplified and complex numerical models to investigate the sensitivity of the frequencies to different assumptions of connection types. The initial models are based on the assumptions mentioned in section 2.3. As shown in Figure 11, by changing wall and columns base connections from pinned to fixed in simplified model, less than 0.3% soar in all three frequencies is observed. Altering wall-to-wall connections from fixed to hinged leads to a reduction of less than 0.6% in all frequencies. Considering wall-to-floor connections hinged as an alternative for fixed assumption, caused 2.6% decrease in the frequencies.

The sensitivity analysis of the complex model yields similar results to the simplified model. By changing floor-to-wall and panel-to-panel wall connections from fixed to hinged, less than 0.7% reduction is observed. Considering fixed connections instead of pinned in the base supports leads to less than 0.5% increase in all frequencies. Details of the sensitivity analysis of the complex model is shown in Figure 12 for the complex model. The results agree well with the findings in [10,11] that indicates low sensitivity of the FE model developed in RFEM to the different assumptions of connection types in structural elements (fixed, pinned or hinged).

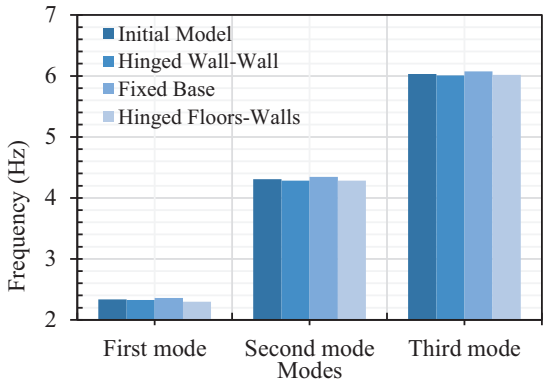

***Figure 11**: Details of the sensitivity analysis of the simpified model.*

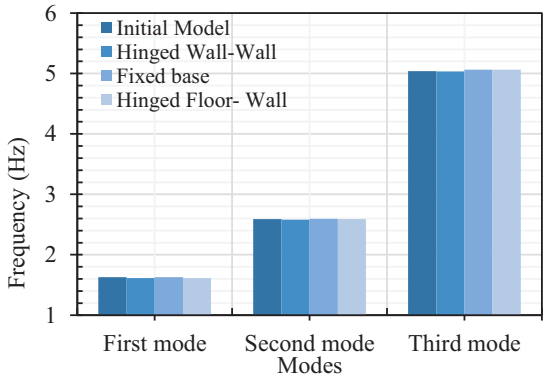

***Figure 12**: Details of the sensitivity analysis of the complex model.*

4 CONCLUSIONS

The dynamic properties of a 29.5-m mass timber building was investigated through both AVT and FE modelling. An ambient vibration test was carried out on the building to assess the differences of the dynamic properties after 9 years of its srvice time, as the result of three-phase AVT is already available from the building construction time. Then, two types of FE modelling were developed in RFEM software and the results of both numerical models were compared with the measured frequencies. Finally, a sensitivity analysis was performed to see the effect of different connection type assumptions on the building frequencies.

https://doi.org/10.52202/069179-0377

A summary of the results and recommendations limited to the current case study can be concluded as follows:

1. According to the experimental test, the first natural frequencies of the structure did not have a significant change in comparison to the last performed AVT in 2017. Frequency change between the first three phase is due to the fact that phase-I testing was performed on the building under construction with only frame and structural components without enclosure. The second phase testing was performed on the finished building with all components that added stiffness and mass, which increased the building frequencies.
2. The results of simplified FE model poorly matched with results of AVT and the complex FE model. Though, the complex model shows a better agreement in the first frequency with the measured frequency values. However, a significant discrepancy can be observed in higher modes. The modal parameters in FE model shows a low sensitivity to the type of connection assumptions (fixed, pinned or hinged), and requires experimental verifications.
3. It is recommended that in the absence of a reasonable reliable FE model, for the design purpose, the NBCC simple equation can be considered to estimate the first natural frequency of mass timber buildings with only shear walls. It is also recommended that for design purpose, for such type of wood construction, 2-3% damping for the occupied building may be used. Besides, if FE modelling is used for design, caution, verification, and calibration is needed.

ACKNOWLEDGEMENTS

The financial support from BC Forest Innovation Invest - Wood First program and the Natural Sciences and Engineering Research Council of Canada (NSERC) is greatly acknowledged.

REFERENCES

[1] A. Feldmann, H. Huang, W. Sh. Chang, R. Harris, P. Dietsch, M. Gräfe, and C. Hein. Dynamic properties of tall timber structures under wind-induced vibration. *World Conference on Timber Engineering*. Pages 6301, 2016.

[2] National Building Code of Canada, National Research. National Research Council of Canada. Volume 1, 2020.

[3] L.Hu. Serviceability of next generation wood buildings: case study of three innovative mid-rise wood buildings. FPInnovations. November 2011.

[4] L. Hu, and S. Cuerrier Auclair. Advanced wood-based solutions for mid-rise and high-rise construction: in-Situ testing of the Origine 13-storey building for vibration and acoustic performances. FPInnovations. March 2018.

[5] L. Hu and S. Cuerrier Auclair. In-Situ testing of the wood innovation and design centre for serviceability performance. FPInnovations. April 2018.

[6] I. Mugabo1, A. R. Barbosa, and M. Riggio. Dynamic characterization and vibration analysis of a four-Storey mass timber building. Frontiers in Built Environment. 5:86, 2019.

[7] T. Reynolds, D. Casagrande, R. Tomasi. Comparison of multi-storey cross-laminated timber and timber frame buildings by in situ modal analysis. Construction and Building Materials. 102: 1009–1017, 2016.

[8] G. Hafeez. Dynamic characteristics of light-frame wood buildings. Ph.D. Dissertation. University of Ottawa. May 2017.

[9] R. Abrahamsen, M. A Bjertnæs, J. Bouillot, B. Brank, L. Cabaton, R.C. cetti, O. Flamand, F. Garains, I. Gavric, O. Germain, L. Hahusseau, S. Hameury, M. Johansson, T. Jo-hansson, W. K. Ao, B. Kurent, P. Landel, A. Linderholt, K. Malo, M. Manthey, P. Nåvik, A. Pavic, F. Perez, A. Rönnquist, H. Stamatopoulos, I. Sustersic, S. Tulebekova. Dynamic response of tall timber buildings under service load- the DynaTTB research program. *EURODYN Conference.* Pages 4900-4910, 2020.

[10] C. Larsson, O. Abeljaber, M. Dorn. Dynamic Evaluation of a Nine-Storey Timber- Concrete Hybrid Building during construction, Research Square, January 25th, 2023.

[11] A. Aloisioa, D. Pascab, R. Tomasib, M. Fragiacomoa. Dynamic identification and model updating of an eight-storey CLT building, Engineering Structures 213:110593, 2020.

[12] S. Tulebekova, K. A. Malo, A. Rønnquist, P. Nåvik. Modeling stiffness of connections and non-structural elements for dynamic response of taller glulam timber frame buildings. Engineering Structures 261:114209, 2022.

[13] B. Kurenta, B. Branka, W. K. Aob. Model updating of seven-storey cross-laminated timber building designed on frequency-response-functions-based modal testing. Structure and Infrastructure Engineering, 19(2):178-196, 2023.

[14] Anonymous, Construction Canada, (2014 Nov.), https://www.constructioncanada.net/wood-innovation-and-design-centre-unveiled-in-b-c/widc/

[15] S. MacDonald, (2020 July), OMA in Simcenter Testlab, https://community.sw.siemens.com/s/article/OMA-in-Simcenter-Testlab

[16] L. Hu, A. Omeranovic, S. Gagnon, M. Mohammad. Wind-induced vibration of tall wood buildings – Is it an issue? *Paper in proceedings of WCTE,* 2014. Quebec City.

https://doi.org/10.52202/069179-0377

World Conference on Timber Engineering Oslo 2023

ON FINITE ELEMENT MODELLING AND MODEL UPDATING OF MULTI-STOREY TIMBER BUILDINGS

Blaž Kurent[1], Boštjan Brank[2], Wai Kei Ao[3], Aleksandar Pavic[4], Manuel Manthey[5]

ABSTRACT: The results of three case studies of timber and hybrid timber buildings have been reviewed. For each case study, experimentally obtained modal data was available. A detailed numerical finite element (FE) model of each building has been developed and used to carry out sensitivity analysis on the uncertain FE modelling parameters and model updating of the most influential input parameters. The importance of several modelling parameters and assumptions is discussed: perpendicular to the grain deformations of floor slabs, connections between cross-laminated timber panels, floor slab deformability, vertical foundation stiffness, and stiffness effect of the façade.

KEYWORDS: tall timber buildings, case studies, finite element model, model updating, modal properties

1 INTRODUCTION

In the last decades, there has been a large increase in the use of timber for multi-story buildings. One of the reasons is that it shows a potential for being a sustainable alternative to mineral-based materials [1]. This has been found through LCA studies showing significant reductions in embodied emissions when substituting timber for concrete [2] [3] [4]. Due to its light weight, timber might play an important role in sustainably densifying the cities [5], mainly by refurbishing existing buildings by adding new storeys or building new and taller buildings onto the existing foundation.

The structural design of a building is often governed by serviceability criteria [6]. For tall timber buildings, a key limitation regarding the serviceability is wind-induced vibrations [7] [8]. To satisfy current comfort criteria (e.g. ISO 10137 [9]) for wind-induced vibration an estimate of the fundamental frequency is needed. A simplistic estimation of the first natural frequency as $46/h$, where h is the height of the building in meters, is offered by Annex F of Eurocode 1 [10]. However, if wind-induced vibrations are governing design criterium, a more accurate estimation method might be desired. Often a finite element (FE) model is built, but there are some uncertainties when it comes to decisions about modelling assumptions.

Connections between CLT panels have been found to govern the behaviour of CLT buildings under seismic loads [11], however, there is no evidence to support similar claims for wind loads. Another uncertainty is connected to the contribution of non-structural elements to the global stiffness of the building. It was often found that for standard steel and concrete multi-storey buildings such non-structural elements increase the first natural frequency of the building [12] [13] [14] [15]. Additionally, for 3-storey OSB sheathed light-frame timber building it was found that non-structural elements increase the natural frequency of the building. It was also found that with increasing amplitude of excitation of the building contribution of the non-structural elements is smaller. Another study on laboratory-based 6-storey light timber-framed building [16] showed that both plasterboards and masonry façade significantly increase the natural frequency of the building. However, how to take them into account in the modelling of timber building is not clear. A large uncertainty is also attributed to the material properties of timber. For the shear modulus of CLT panels mean values of 450 MPa and 650 MPa have been proposed, based on whether narrow sides of boards are glued or not and whether cracks are present [17]. Besides the high variance of material properties of wood by itself, there is a large dependency of material properties on moisture content [18] which initially decreases after construction but then also changes seasonally [19].

[1] Faculty of Civil and Geodetic Engineering, University of Ljubljana, Ljubljana, Slovenia. (bkurent@fgg.uni-lj.si)
[2] Faculty of Civil and Geodetic Engineering, University of Ljubljana, Ljubljana, Slovenia. (bbrank@fgg.uni-lj.si)
[3] University of Exeter, Vibration Engineering Section, College of Engineering, Mathematics and Physical Sciences, North Park Road, Exeter EX4 4QF, UK. (wka203@exeter.ac.uk)
[4] University of Exeter, Vibration Engineering Section, College of Engineering, Mathematics and Physical Sciences, North Park Road, Exeter EX4 4QF, UK. (a.pavic@exeter.ac.uk)
[5] Manuel MANTHEY, Centre Scientifique et Technique du Bâtiment (CSTB), France. (manuel.manthey@cstb.fr)

https://doi.org/10.52202/069179-0378

2 CASE STUDIES

Three case studies were conducted to learn about the as-built stiffness characteristics of the buildings. They followed a similar procedure.

In each, forced vibration tests were carried out, identifying modal properties (natural frequencies, mode shapes and damping ratios). For each of the three buildings, a numerical FE model was built to calculate the modal properties of the building. The FE natural frequencies and mode shapes were compared against the experimental. As a measure of mode shape correlation modal assurance criterion (MAC) was used. The model was then changed by adopting different modelling assumptions to see how the model can be improved. The influence of different modelling parameters was tested with the sensitivity analysis. The more influential parameters were then chosen to be updated in order to find the best match with the experiments. The objective function consisted of measures for comparing natural frequencies and mode shapes. After the model updating the updated parameter values were informative about the modelling error of the initial model. Individual findings and implications will be presented in the next section.

The first case study is Yoker (see Figure 1a) – a seven-storey timber building located in Glasgow, UK [20] [21]. It is fully constructed out of CLT in platform frame type. It has a distinct irregular shape of the building that strongly determines the dynamic properties of the building. The modal testing resulted in eight identified modes of vibration [22], though only the first six were successfully connected with the FE model.

The second observed building is Trinity College student residential five-storey building (see Figure 1b), located in Cambridge, UK [23]. It is a timber-concrete hybrid building with the basement and ground floor constructed out of reinforced concrete and the remaining four floors of the superstructure out of CLT. The building is cladded with a 100 mm self-supporting masonry wall, which is connected with the CLT load-bearing structure with steel horizontal ties. The building is located in a tight urban environment and is being in contact with the abutting building on one end. Modal testing identified three modes of vibration.

The third one is the Hyperion tower in Bordeaux (see Figure 1c), France, with a height of 56 m and 16 storeys. The first three levels are made of concrete and the 13 upper ones are composed of a concrete core, steel peripheral columns with infilled pre-manufactured timber-frame façade, CLT floors, and glue-laminated beams. Three modes of vibration have been identified with forced vibration tests.

3 FINDINGS FROM CASE STUDIES

The three buildings are substantially different in regard to their structural systems, heights and shapes. Each case study was a very unique investigation work to find a model that matches the experiments well. The most difficult was to obtain good MAC values and in each building, a different set of effects were identified that were crucial to obtaining good results. However, two effects had repeated:

1. Vertical stiffness is lower than what is anticipated when the foundation is modelled as rigid and the load-bearing structure is modelled with mean material properties. Not only compliance of the foundation is a possible cause for that, but also perpendicular to the grain deformations of floor slabs in platform frame type buildings could be a reason.

2. The shear stiffness of the CLT walls is higher than what is anticipated when only load-bearing structure is modelled and mean stiffness material properties are adopted. The most probable reason for that is a significant contribution of non-structural elements (such as façade, partition walls, plasterboards etc.), but also the uncertainty of material properties could play an important role. This effect was not found in the hybrid building with concrete core - Hyperion.

In regard to those two effects, several modelling assumptions are discussed below.

Figure 1 Three studied buildings: (a) Yoker, (b) Trinity, and (c) Hyperion.

https://doi.org/10.52202/069179-0378

3.1 PERPENDICULAR TO THE GRAIN DEFORMATION

The two main types of framing for timber buildings are balloon and platform frame type. A well-known limitation of a platform frame are perpendicular to the grain deformations. Due to orthotropic material properties, with elastic modulus perpendicular to the grain being much lower than along the grain elastic modulus, floor slabs are being squeezed between the walls, as illustrated in Figure 2. The large weight of the building acting on a small area under the walls causes local deformations that might result in a damaged façade or plasterboards if the vertical differential movement is not allowed for in the design of those elements.

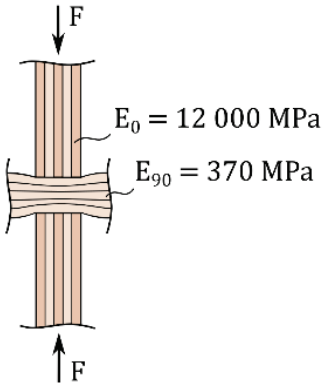

Figure 2 Perpendicular to the grain deformations of CLT floor slabs.

The same effect is observed when the global stiffness of the building is considered. Despite the almost negligible thickness of floor slabs, their vertical deformations are of comparable magnitude to those of the walls. The effect is explained more in detail in [20]. Calculations estimated that a reduction of up to 50 % in overall stiffness in the vertical direction is possible.

These local softening effects are difficult to model accurately when using shell elements. In Yoker and Trinity, this effect was modelled as a reduction of the elastic modulus of vertical layers of CLT walls (while horizontal layers remain unchanged).

Model updating of Yoker resulted in a 40-50% reduction of elastic modulus in the vertical direction, which parallels well with the simplified estimates of this effect's influence. However, reducing the stiffness of the foundation in the vertical direction causes a similar change in the model and, therefore, it is not certain which effect plays a more important role or how their influences are distributed.

This effect was also modelled for Trinity, but no conclusive results were obtained. The reason for that is the low influence of this parameter on the modal properties of the building as was shown with sensitivity analysis. Trinity is not as slender building and its fundamental modes are characterized more by shear rather than bending of the structure.

This effect was not present in Hyperion as loads of columns are not transferred over CLT floor slabs. The columns are stacked directly on top of each other.

Further research in a controlled environment is needed to more clearly understand the effect of perpendicular to the grain deformations on the overall stiffness of the building.

3.2 CONNECTIONS BETWEEN CLT PANELS

Connections between CLT panels pose a large uncertainty when it comes to their contribution of the dynamic properties of the building. In seismic design, connections seem to be the weakest link, however, when exposed to small amplitude excitation they might not contribute as much to the stiffness of the structure. The distinction here should be made between the connections that conjoin CLT walls and floors (in platform frame building), where large friction forces are to be exceeded before the connections are engaged and connections where no large axial forces help join CLT panels (e.g. in-plane connections between floor slab panels).

The stiffness of the connections between CLT walls (in Yoker and Trinity) was not directly modelled, rather a rigid bond was assumed. The contribution of the connections to the modal properties of the building is expected to be found indirectly from model updating. If the in-plane shear modulus of the CLT walls results in a lower value than what is proposed by its producers, connections might be responsible for such a reduction of stiffness. However, both case studies (Yoker and Trinity) concluded that the in-plane shear stiffness of the walls is higher than what was anticipated based on the mean material properties. In Yoker, the in-plane shear modulus was found to be around 60% higher than anticipated. In Trinity, shear stiffness was found to be at least 25% higher. This suggests that connections do not significantly reduce the overall stiffness of the building for small amplitude vibration.

In Hyperion, CLT panel are only used for floor slabs. They will be discussed in the following section.

3.3 FLOOR SLAB IN-PLANE DEFORMABILITY

Floor slabs being modelled as rigid diaphragms is a common assumption, but it may not always be suitable. For all three case studies, it was tested on the models and compared with the assumption of deformable CLT panels. The latter is considered as a more accurate model.

In Yoker, the assumption of a rigid diaphragm gives sufficiently good results for the first three modes (bending and torsion modes), however, to obtain higher modes, modelling floor slabs as deformable was necessary. Namely, higher modes consisted of substantial in-plane deformations of floor slabs. The study of Yoker also suggested that the connections between CLT panels of floor slabs might reduce the stiffness of the floor slabs,

https://doi.org/10.52202/069179-0378

which differs from what has been discussed about the connections between walls and floor slabs in the previous section. Perhaps due to lower axial forces not offering strong friction between floor slab panels.
In Trinity, even the first modes needed floor slabs to be modelled as deformable. This was expected due to its low height.

In Hyperion, the assumption of rigid diaphragm doesn't change the first three natural frequencies significantly. It seems that the assumption is suitable for slender structures.

3.4 FOUNDATION MODELLING

Boundary condition that models soil structure interaction has a paramount influence on the dynamic properties of the building. Commonly, only a rigid foundation is assumed due to a lack of information and large uncertainty connected to the properties of the soil. For timber buildings, which are normally significantly lighter than reinforced concrete buildings, also significantly less material is used to form foundation. Its effect might be far from negligible. For the three observed buildings, the influence of the foundation was studied.

In Yoker, reducing the vertical stiffness of the building was necessary to improve the matching of the model to the experiments. Besides perpendicular to the grain deformations, which were discussed in Section 3.1, soil-structure interaction could be the reason behind the reduced stiffness of the building. In model updating, both vertical and horizontal stiffnesses of the foundation were included. Updated values suggested a rigid boundary condition for horizontal stiffness, but slightly compliant in the vertical direction.

In Trinity, modelling of foundation as flexible in the vertical direction was crucial to obtain a good match with the experimental modal properties. The updated value of the foundation stiffness reduced the stiffness of the building by at least 7% and 26% in the x and y directions, respectively.

Model updating of Hyperion also suggested that the foundation should be modelled as flexible in the vertical direction, whereas, constrained horizontal deflections do not worsen the accuracy of the model. If accurate modelling is desired, the stiffness of the foundations should not be neglected.

3.5 INFLUENCE OF FAÇADE

There is a variety of different façade solutions. Their stiffness properties and mounting to the load-bearing structure vary greatly, therefore, general conclusion for the façade are not possible. However, the three case studies may present an illustrative example.

In Yoker, the in-plane shear modulus of the walls was updated to a 60% higher value that the one proposed by the producers. Façade (together with other non-structural elements) could be the reason for this increase. Though the façade – acrylic brick slips – is quite thin and might not offer significant support.

In contrast, the façade of Trinity consists of 100 mm thick masonry cladding (self-supported masonry wall, connected to the load-bearing structure by horizontal steel ties). It was shown that the inclusion of the masonry cladding was needed and an important contribution to the modal properties of the building. Even when masonry cladding was modelled as an additional rigidly-bonded layer to the CLT, the in-plane shear modulus was updated to a value between 125 % and 210 % of the initial value (proposed by the producer). If the masonry façade was neglected almost a 400 % increase of CLT in-plane shear modulus was obtained from the model updating. This suggests a significant influence of masonry cladding on modal properties of the building.

Prefabricated elements are used for the façade of Hyperion. They are made of 10 mm cladding, 12 mm and 18 mm layers of OSB and 12 mm gypsum panels. The layers are connected with battens to make space for almost 0.5 m insulation and ventilation layers. Model updating of Hyperion did not provide definite conclusions on whether such a façade influences dynamic properties significantly. The governing structural system defining dynamic properties was a reinforced concrete core.

4 CONCLUSIONS

Three case studies of timber and hybrid timber buildings have been reviewed, and their findings are compared. In each, forced vibration testing has been performed to obtain at least 3 modes of vibration, finite element model has been constructed and updated based on the experimental results.

All three case studies showed that modelling foundation as slightly compliant in the vertical direction offers a more accurate prediction of modal properties. The updated stiffness of the foundation differed between the case studies. Two case studies of CLT buildings updated the shear stiffness of the walls higher than initially anticipated based on the assumption of mean material properties of the CLT (and neglecting non-structural elements such as plasterboards, façade, and partition walls). One of the case studies of a platform frame CLT building found a significantly reduced vertical stiffness due to perpendicular to the grain deformations of floor slabs. Case studies showed that the modelling assumption of the rigid diaphragm for floor slabs was suitable for tall and slender buildings in predicting the first three modes. The lower building was not successfully modelled with such an assumption.

The model updating of such complex systems can only be used to obtain such broad findings. For more precise conclusions (perhaps about the effect of connections between CLT panels), testing in a more controlled environment should be performed.

https://doi.org/10.52202/069179-0378

ACKNOWLEDGEMENT

The support of ERA-NET Cofund Forest Value and the corresponding funding bodies (Ministry of Education, Science and Sport of the Republic of Slovenia for Kurent and Brank, and Forestry Commission GB for Ao) is gratefully acknowledged (DynaTTB project). Kurent and Brank also acknowledge the financial support of the Slovenian Research Agency (J2-2490). Manthey also acknowledge the financial support of the ANR and the company Eiffage for the access to the Hyperion building.

REFERENCES

[1] G. Churkina and A. Organschi, "Will a Transition to Timber Construction Cool the Climate?," *Sustainability (Switzerland),* vol. 14, no. 7, pp. 1-8, 2022.

[2] A. M. Moncaster, F. N. Rasmussen, T. Malmqvist, A. Houlihan Wiberg and H. Birgisdottir, "Widening understanding of low embodied impact buildings: Results and recommendations from 80 multi-national quantitative and qualitative case studies," *Journal of Cleaner Production,* vol. 235, pp. 378-393, 2019.

[3] T. Malmqvist, M. Nehasilova, A. Moncaster, H. Birgisdottir, F. Nygaard Rasmussen, A. Houlihan Wiberg and J. Potting, "Design and construction strategies for reducing embodied impacts from buildings – Case study analysis," *Energy and Buildings,* vol. 166, pp. 35-47, 2018.

[4] J. L. Skullestad, R. A. Bohne and J. Lohne, "High-rise Timber Buildings as a Climate Change Mitigation Measure - A Comparative LCA of Structural System Alternatives," *Energy Procedia,* vol. 96, no. 1876, pp. 112-123, 2016.

[5] R. M. Foster and T. P. S. Reynolds, "Lightweighting with Timber: An Opportunity for More Sustainable Urban Densification," *Journal of Architectural Engineering,* vol. 24, no. 1, 2018.

[6] J. Orr, M. P. Drewniok, I. Walker, T. Ibell, A. Copping and S. Emmitt, "Minimising energy in construction: Practitioners' views on material efficiency," *Resources, Conservation and Recycling,* vol. 140, no. June 2018, pp. 125-136, 2019.

[7] M. Johansson, A. Linderholt, Å. Bolmsvik, K. Jarnerö, J. Olsson and T. Reynolds, "Building higher with light-weight timber structures - The effect of wind induced vibrations," *INTER-NOISE 2015 - 44th International Congress and Exposition on Noise Control Engineering,* 2015.

[8] R. Abrahamsen, M. A. Bjertnæs, J. Bouillot, B. Brank, L. Cabaton, R. Crocetti, O. Flamand, F. Garains, I. Gavric, O. Germain, L. Hahusseau, S. Hameury, M. Johansson, T. Johansson, W. K. Ao, B. Kurent, P. Landel, A. Linderholt, K. Malo, M. Manthey, P. Nåvik, A. Pavic, F. Perez, A. Rönnquist, H. Stamatopoulos, I. Sustersic and S. Tulebekova, "Dynamic Response of Tall Timber Buildings under Service Load - the DynaTTB Research Program," *Proceedings of the International Conference on Structural Dynamic , EURODYN,* vol. 2, no. 14, pp. 4900-4910, 2020.

[9] ISO 10137, Bases for design of structures—Serviceability ofbuildings and walkways against vibrations, Geneva: International Organization for Standardization, 2007.

[10] EN 1991-1-4, Eurocode 1: Actions on structures Part 1-4: General actions - Wind actions, Brussels: European committee for Standardization (CEN), 2010.

[11] I. Gavric, M. Fragiacomo and A. Ceccotti, "Cyclic behaviour of typical metal connectors for cross-laminated (CLT) structures," *Materials and Structures,* vol. 48, pp. 1841-1857, 2015.

[12] S. Soyoz, E. Taciroglu, K. Orakcal, R. Nigbor, D. Skolnik, H. Lus and E. Safak, "Ambient and Forced Vibration Testing of a Reinforced Concrete Building before and after Its Seismic Retrofitting," *Journal of Structural Engineering,* vol. 139, no. 10, pp. 1741-1752, 10 2013.

[13] K. Güler, E. Yuksel and A. Kocak, "Estimation of the Fundamental Vibration Period of Existing RC Buildings in Journal of Earthquake Engineering," *Journal of Earthquake Engineering,* vol. 12, pp. 140-150, 2008.

[14] A. Memari, A. Aghakouchak, M. Ghafory Ashtiany and M. Tiv, "Full-scale dynamic testing of a steel frame building during construction," *Engineering Structures,* vol. 21, no. 12, pp. 1115-1127, 12 1999.

[15] M. Manthey, O. Flamand, A. Jalil, A. Pavic and W. K. Ao, "Effect of non-structural components on natural frequency and damping of tall timber building under wind loading," *World Conference on Timber Engineering, WCTE 2021,* 2021.

[16] B. R. Ellis and A. J. Bougard, "Dynamic testing and stiffness evaluation of a six-storey timber framed building during construction," *Engineering Structures,* vol. 23, no. 10, pp. 1232-1242, 2001.

[17] R. Brandner, G. Flatscher, A. Ringhofer, G. Schickhofer and A. Thiel, "Cross laminated timber (CLT): overview and development," *European Journal of Wood and Wood Products,* vol. 74, no. 3, pp. 331-351, 2016.

[18] A. Gülzow, K. Richter and R. Steiger, "Influence of wood moisture content on bending and shear stiffness of cross laminated timber panels," *European Journal of Wood and Wood Products,* vol. 69, no. 2, pp. 193-197, 2011.

[19] C. Larsson, O. Abdeljaber, Å. Bolmsvik and M. Dorn, "Long-term analysis of the environmental effects on the global dynamic properties of a hybrid timber-concrete building," *Engineering Structures,* vol. 268, no. February, p. 114726, 2022.

[20] B. Kurent, B. Brank and W. K. Ao, "Model updating of seven-storey cross-laminated timber building designed on frequency-response-

functions-based modal testing," *Structure and Infrastructure Engineering,* 2021.

[21] B. Kurent, N. Friedman, W. K. Ao and B. Brank, "Bayesian updating of tall timber building model using modal data," *Engineering Structures,* vol. 266, p. 114570, 9 2022.

[22] W. K. Ao, A. Pavic, B. Kurent and F. Perez, "Novel FRF-based fast modal testing of multi-storey CLT building in operation using wirelessly synchronised data loggers," *Journal of Sound and Vibration,* vol. 548, p. 117551, 2023.

[23] B. Kurent, W. K. Ao, A. Pavic, F. Perez and B. Brank, "Modal testing and finite element model updating of full-scale hybrid timber-concrete building," *Engineering Structures,* p. [Submitted], 2023.

https://doi.org/10.52202/069179-0378

World Conference on Timber Engineering Oslo 2023

AMBIENT VIBRATION TESTS AND MODAL ANALYSIS OF A SIX-STORY LIGHTWEIGHT TIMBER FRAME BUILDING

Carmen Amaddeo[1], Michael Dorn[2]

ABSTRACT: This paper describes the in-situ ambient vibration tests of a lightweight timber frame building, performed in order to obtain its modal properties. Our case study is a six-story lightweight timber frame building in Varberg, Sweden. Five battery-driven wireless data acquisition units with a total of 14 uni-axial accelerometers were used to perform the in-situ measurements. Accelerations along the two horizontal directions were recorded with a duration of approximately 40 minutes. Two different only-output frequency and time domain Operational Modal Analysis (OMA) methods were used to evaluate the dynamic properties of the building. The modal parameters obtained from the in-situ measurements, such as natural frequencies and mode shapes, were compared with the parameters obtained from the Finite Element (FE) model of the structure. To perform a detailed numerical analysis of the light-frame timber building, all lateral-load resisting system components were modelled. The FE model was calibrated in function of the results obtained from the OMA of the building. Based on the obtained results from the calibrated FE model, it was possible to conclude that the non-structural elements have an influence on the global dynamic response of the building.

KEYWORDS: Timber, multi-story lightweight timber frame building, operational modal analysis, finite element modeling

1 INTRODUCTION

The realization of multi-story residential and commercial timber buildings is rapidly increasing all around the world. Timber structures are, in general, cost efficient, easy to transport, and quickly built on-site due to the high level of prefabrication. Light-frame timber systems have frequently been used to realize multi-story buildings. For this reason, it is important to understand their in-situ dynamic behavior to verify that such a typology of structures meets the design requirements in terms of structural safety as well as serviceability.

Ambient vibration tests are performed in order to obtain the in-situ modal parameters of the building. The results obtained from in-situ measurements can be used to validate and calibrate the Finite Element (FE) model of the building [1]. Calibrated FE models can be used to optimize the design of similar structures under ultimate and serviceability limit state load conditions.

Tests on lightweight timber frame multi-story buildings have not been extensively conducted with the exception of a few cases. The stiffness of a six-story timber frame building, during the construction stages, using dynamic testing has been evaluated by Ellis et al. [2]. Shake table tests on a full-scale two-story lightweight timber frame structure have been conducted by Filiatrault et al. [3, 4], in order to evaluate the dynamic parameters of the building and its seismic performance. In addition, shake table tests on a three-story lightweight timber frame building have been performed by Sartori et al. [5], focusing on the seismic performance of a prefabricated light-frame timber building and on the interaction of structural components.

In our study, to identify the dynamic parameters of the building, the Enhanced Frequency Domain Decomposition (EFDD) [6], and the Stochastic Subspace Identification (SSI) [7] methods have been used. Operational Modal Analysis (OMA) is considered an effective, non-destructive method to assess the actual operational condition of an existing structure.

This paper presents the in-situ dynamics tests carried out at the so-called, Hus 35 in Varberg, Sweden (Figure 1).

Figure 1: *East view of Hus 35 in Varberg, Sweden (picture by the author).*

[1] Carmen Amaddeo, Linnaeus University, Sweden, carmen.amaddeo@lnu.se
[2] Michael Dorn, Linnaeus University, Sweden, michael.dorn@lnu.se

https://doi.org/10.52202/069179-0379

The structure was subjected to small ambient vibrations induced by wind. The results obtained in this study will be used as a benchmark for a more extensive test campaign that will be conducted on this building as well as on a second neighboring light-frame timber building in Varberg, Sweden, realized with the exact same design.
The modal parameters obtained from the in-situ test were compared to the one obtained from the FE model of the building. Simplified FE models have been widely used because they are numerically efficient and they demand a low computational effort [8, 9, 10]. Recent studies have focused on developing non-linear FE models including a larger number of deformation mechanisms such as: the detailed modeling of each connection, the individual timber frame stud elements, and the sheathing boards [11]. A detailed modeling strategy was developed by Kuai et al. [12] in order to analyze the deformation behavior of light-frame walls. Due to the high computational demand in modeling all connections, this work will include only the spring connections between different panels in the calibration phase of the FE model of the building. A preliminary study of the same building was developed by Amaddeo and Dorn [13] using a simplified modeling approach.

1.1 BUILDING DESCRIPTION

The Pilgatan block in Varberg consists of four six-story buildings all realized with the same light-frame system and built consecutively from 2020 to 2022. Each building has four apartments at each floor with the staircase and elevator shaft in the middle of the building along the East side (see Figure 2).

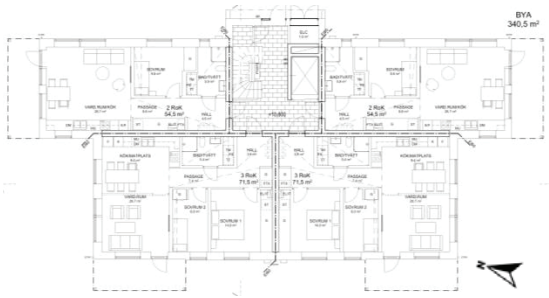

Figure 2: *Plan of a typical story.*

The load bearing system is composed of lightweight timber frames elements. The timber-framed wall panels of the external walls are made of timber studs, 45 mm x 170 mm, and a double layer of Oriented Strand Board (OSB) sheeting panel, 11 mm thick (see Figure 3.a and 3.b). The timber-frame internal walls are made of timber studs, 45 mm x 220 mm and 45 mm x 95 mm, and particle board sheeting panel 38 mm-thick. The elevator shaft and staircase are made with the same system. The load-bearing wall elements are prefabricated and assembled directly on-site. For horizontal stabilization, diagonal steel rods have been used.

This study will focus on the dynamic characterization of one of the buildings in the Pilgatan block, refer to as Hus 35, using ambient vibration tests.

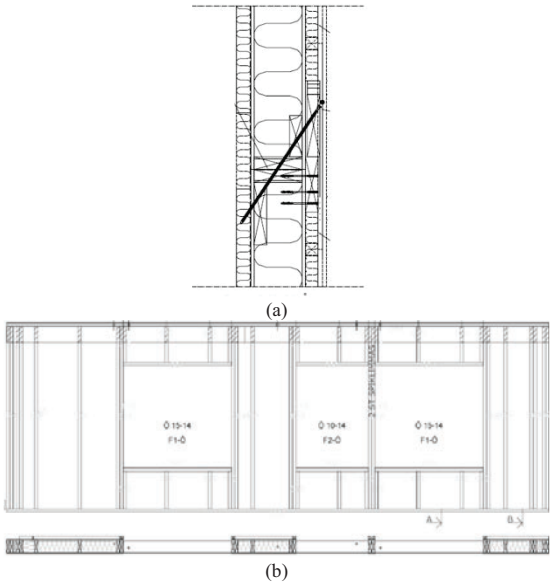

Figure 3: *External wall: (a) Detail of the load-bearing section of a timber-framed wall, (b) Front view of one of the lightweight timber frame panels.*

2 EXPERIMENTAL TESTING PROCEDURE

A first ambient vibration test was carried out in May 2021 [13], using only two data acquisition systems and four accelerometers. During this preliminary test a total of 9 measurements, with a duration of approximately 30 minutes each, were performed. During each measurement, the sensors at the first floor were used as a reference. The extracted natural frequencies of the building were used to validate the sensor layout for the presented study.

Figure 4: *Test setup: two of the total five portable data acquisition systems during the synchronization phase.*

https://doi.org/10.52202/069179-0379

A more extensive ambient vibration test campaign has been conducted starting in October 2022. During this second phase, five wireless data-acquisition systems (see Figure 4) with 14 uni-axial accelerometers, model PCB 393B12 with a sensitivity of 0.5 V/g, were used during the ambient vibration tests.

This type of accelerometers allows us to record low acceleration values also at a low frequency. The sensors were connected to a steel cube element to ensure the orthogonality of the recorded accelerations. The cubes with the accelerometers were connected to a steel plate which secured the placement against sliding, as shown in Figure 5.

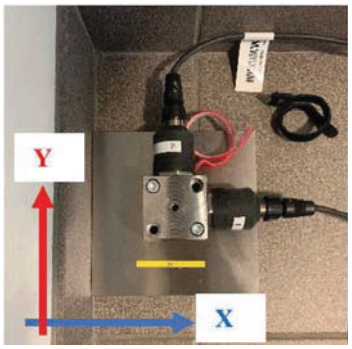

Figure 5: *Detail of the sensors at the first floor, location #1 with the direction of the recorded acceleration.*

Ambient vibration tests are sensitive to the presence of noise, so that both the sensors' location and duration of the test are important parameter during the testing campaign. A thorough placement and proper time synchronization reduces measurement noise and ensures the accuracy of the results.

Three accelerometers were placed on each floor as well as on the roof, except at the third floor where no accelerometers were placed, as shown in Figure 6.

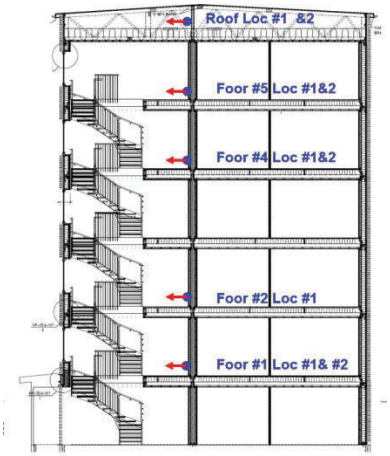

Figure 6: *Building section along the EW direction showing the sensor layout at each level.*

The accelerometers were used to measure the wind and traffic induced ambient vibrations. To minimize the interference with the occupants as well as the input from human induced vibration, the dynamic tests were conducted during the less crowded hours of the day during a work week.

The accelerometers were placed in the area next to the staircase and elevator shaft (see Figure 7). The layout of the sensors for the typical floor level is shown in Figure 7.a, and for the roof level is shown in Figure 7.b, where the sensors are placed farther apart from each other along the longitudinal direction (x-direction).

Measurements were conducted using three accelerometers per floor: one along the longitudinal (x-direction) and two along the transversal (y-direction) direction except at the second floor where only two accelerometers, one along the longitudinal and one along the transversal direction were used (see Figure 6).

The ambient vibration data were recorded for approximately 40 minutes, with a sampling frequency of 120 Hz. The five data-acquisition systems were cable synchronized at the beginning of each test in order to have the same time stamp (see Figure 4). Thereafter, each system was moved to its respective floor and the sensors were connected to each data acquisition system. Actual useable measurement time was reduced by approximately 5 minutes.

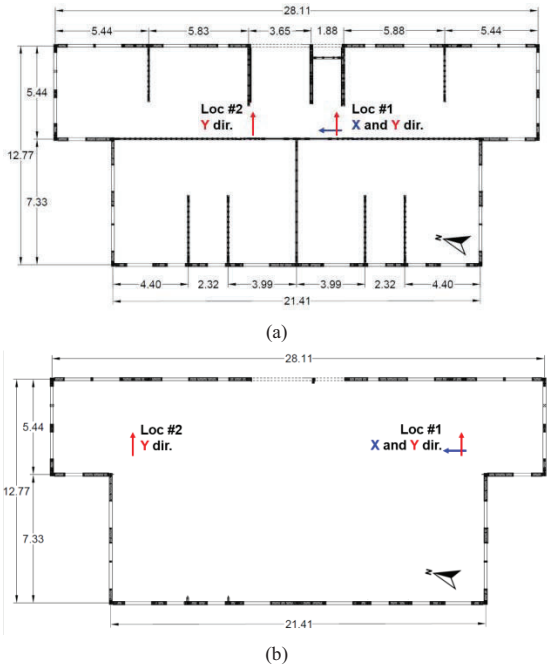

Figure 7: *Sensor layout with the location and direction of the accelerometers. (a) Typical floor level, and (b) Roof level.*

Three different tests were performed on the building in the period between October 2022 and January 2023, to see if any variation of the modal parameters had occurred under different environmental conditions.

https://doi.org/10.52202/069179-0379

The tests were performed respectively on: October 5th, 2021 (Test #1); November 23rd, 2022 (Test #2); and January 10th, 2023 (Test #3). Monthly tests will be performed for a full year in total.

3 EXPERIMENTAL RESULTS

Modal parameters of the building were identified using the EFDD, and SSI methods, respectively a frequency-domain, and a time-domain system identification method. These OMA techniques are available in the software ARTeMIS [14], that was used to analyze the recorded data.

The recorded data were post-processed in order to eliminate corrupted data from the analysis as well as the high-noise signals. A Butterworth filter between 0 and 6 Hz was used to better identify the natural frequencies of the building. This frequency range includes the first three mode shapes of the building in the two translational and torsional directions.

An example of the recorded acceleration at the roof level along the x-direction for a 20 second segment is shown in Figure 8, in which the periodicity of the response can be seen.

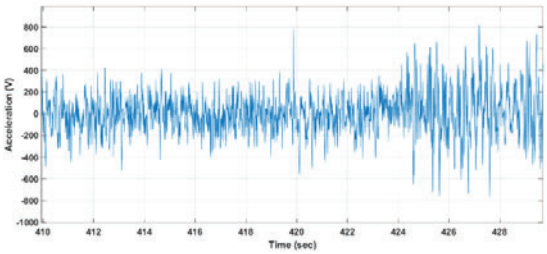

Figure 8: *Acceleration time-history for a 20 second fragment of the 40 minutes data recorded on January 10th, 2023.*

The auto Modal Assurance Criterion (autoMAC) values were calculated [15] and used to measure the degree of correlation and consistency between the mode shape pairs evaluated with one set of collected data. The autoMAC value is defined by Equation (1) as:

$$MAC_{rs} = \frac{|\{\varphi_r\}^T\{\varphi_s^*\}|^2}{\{\varphi_r\}^T\{\varphi_r^*\}\{\varphi_s\}^T\{\varphi_s^*\}} \quad (1)$$

where φ_r and φ_s are the modal vector for the frequency r and s respectively.

3.1 Enhanced Frequency Domain Decomposition (EFDD)

In the EFDD method, in order to evaluate the spectral matrix, the Power Spectral Density (PSD) of a single-degree-of-freedom systems is transformed into the time domain using an inverse discrete Fourier transform [6].

The Singular Value Decomposition (SVD) obtained for the three performed tests is shown in Figure 9. For all measurements, three well defined peaks can be observed at a frequency range between 2 - 4.0 Hz (see Table 1).

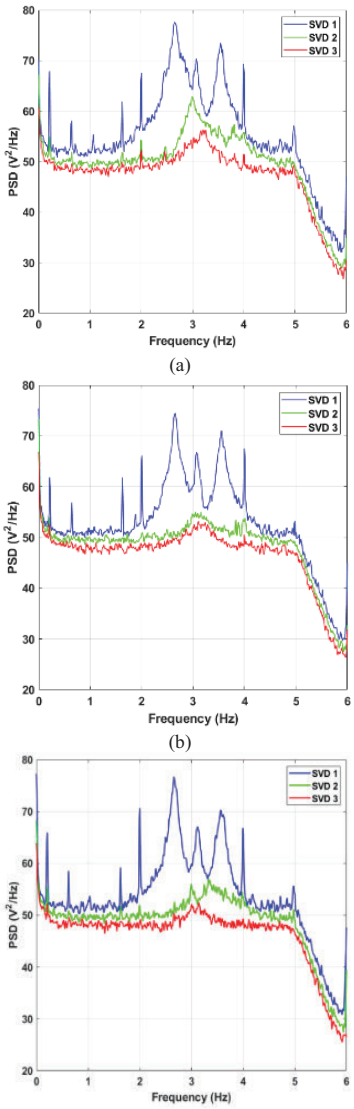

Figure 9: *Singular Value Decomposition (SVD) plot for the EFDD method: (a) Test #1, (b) Test #2, (c) Test #3.*

3.2 Stochastic Subspace Identification (SSI)

The second used system identification method is a time-domain approach. The SSI method is a parametric system identification method that allows the construction of stabilization diagrams. A stabilization diagram is a useful tool for evaluating stable modes and eliminating noise and unstable modes [7, 17].

The state space models' stabilization plots for the three performed tests are shown in Figure 10. The maximum model order is shown by a green horizontal line in Figure 10. In particular, for Test #1, the model order is equal to 23 (see Figure 10a), for Tests #2 and #3 it is equal to 18 (see Figure 10b and 10c).

https://doi.org/10.52202/069179-0379

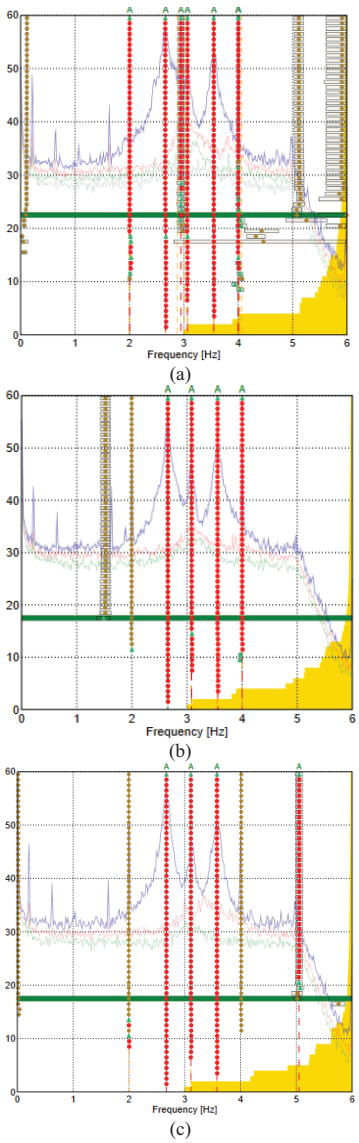

Figure 10: *State space models for the SSI method: (a) Test #1, (b) Test #2, (c) Test #3.*

The vertical red dots in Figure 10 indicate the stable modes within a frequency range between 0 and 6 Hz. The total number of stable modes is changing between the performed tests. Considering that some of the identified frequency values were very close, only the modes with a low value of complexity were considered as real structural modes (see Table 1).

3.3 Results comparison

Table 1 shows the results obtained from the three tests in terms of natural frequencies and damping ratios using the two OMA method, EFDD and SSI method respectively. Three modes of vibration were identified using both system identification methods.

Table 1: *Natural frequencies and damping ratios identified by the EFDD and SSI methods.*

EFDD Method			
	Test #1	Test #2	Test #3
Mode 1	$f_1 = 2.664$ Hz	$f_1 = 2.648$ Hz	$f_1 = 2.673$ Hz
	$\zeta_1 = 2.799$ %	$\zeta_1 = 1.344$ %	$\zeta_1 = 1.549$ %
Mode 2	$f_2 = 3.072$ Hz	$f_2 = 3.075$ Hz	$f_2 = 3.121$ Hz
	$\zeta_2 = 1.143$ %	$\zeta_2 = 0.821$ %	$\zeta_2 = 0.975$ %
Mode 3	$f_3 = 3.546$ Hz	$f_3 = 3.551$ Hz	$f_3 = 3.577$ Hz
	$\zeta_3 = 1.423$ %	$\zeta_3 = 1.707$ %	$\zeta_3 = 1.657$ %
SSI Method			
	Test #1	Test #2	Test #3
Mode 1	$f_1 = 2.658$ Hz	$f_1 = 2.652$ Hz	$f_1 = 2.671$ Hz
	$\zeta_1 = 2.399$ %	$\zeta_1 = 1.627$ %	$\zeta_1 = 1.375$ %
Mode 2	$f_2 = 3.064$ Hz	$f_2 = 3.084$ Hz	$f_2 = 3.110$ Hz
	$\zeta_2 = 1.754$ %	$\zeta_2 = 1.347$ %	$\zeta_2 = 1.449$ %
Mode 3	$f_3 = 3.550$ Hz	$f_3 = 3.557$ Hz	$f_3 = 3.577$ Hz
	$\zeta_3 = 1.452$ %	$\zeta_3 = 1.522$ %	$\zeta_3 = 1.547$ %

It is possible to observe a small variation in terms of natural frequencies identified during the three different tests with both methods. For the natural frequency evaluated with the EFDD method it can be seen a maximum variation equal to 1.5%, for the second identified mode. For the natural frequency evaluated with the SSI method, it can be seen a maximum variation equal to 1.47%, for the second identified mode. Only minor differences in the values of the natural frequencies between both methods are seen.

The SSI method, in general, gives more accurate results while evaluating the damping ratio also for highly complex data, and when there are closely spaced modes as in our case (see Figure 10).
The damping ratio variations between the performed tests are more significative. In particular, it is possible to observe a minimum variation equal to 16.6%, and a maximum variation of 51% for the evaluated damping ratios extracted using the EFDD method. For the SSI method, it can be seen a minimum variation equal to 6.1%, and a maximum variation of 43% for the evaluated damping ratios.
The identified mode shapes, using both OMA methods, for Test #3, performed on January 10th, 2023, are shown in Figure 11.

The first mode shape, shown in Figure 10.a and 10.b, is a translational mode along the transversal direction (y-direction). The second identified mode, shown in Figure 10.c and 10.d, is a torsional mode. The third mode, shown in Figure 10.e and 10.f, is a translational mode along the longitudinal direction (x-direction). Same results in terms of mode shape are visible also for the other performed tests.

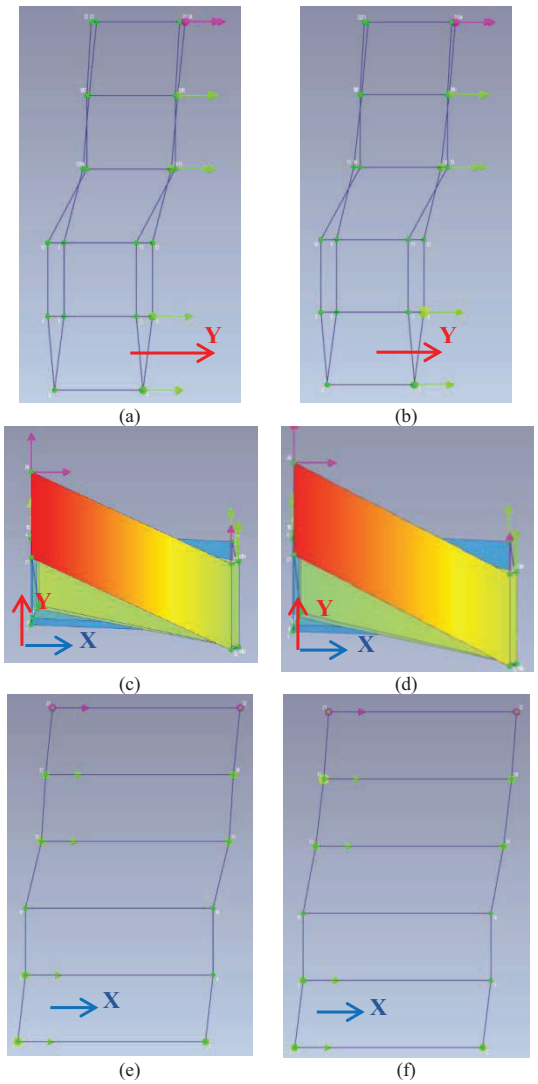

Figure 11: *Identified mode shapes for the Test #3: (a) Mode #1 - EFDD method; (b) Mode #1 - SSI method; (c) Mode #2 - EFDD method; (d) Mode #2 - SSI method; (e) Mode #3 -EFDD method; and (f) Mode #3 - SSI method.*

The autoMAC values for the three performed tests on Hus 35 are shown in Figure 12. Each bar represents the autoMAC value for a specific mode extracted with the SSI method, the values between 0 and 1.0 are proportional to the degree of correlation. The autoMAC value is equal to 1.0 if the mode shape pairs are exactly a match and equal to 0 if those pairs are completely independent or unrelated. Based on the values of the autoMAC, it can be seen that some of the modes are correlated. For this reason, the closed spaced modes with a low value of complexity were considered to be structural modes (see Table 1).

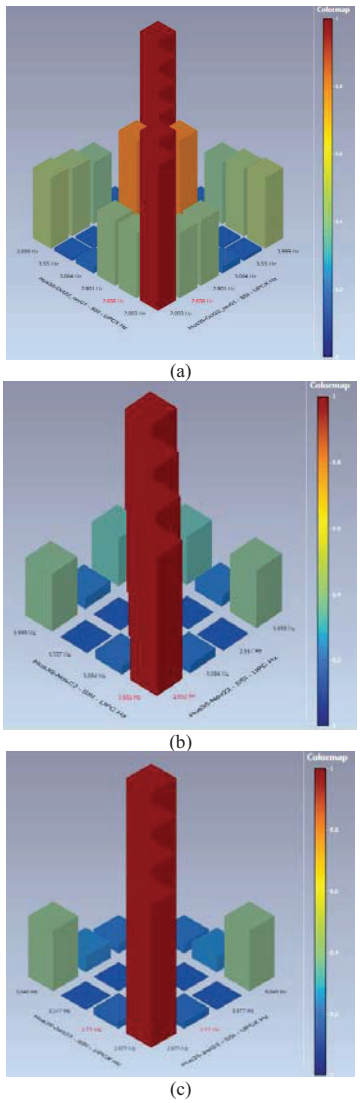

Figure 12: *AutoMAC values for the identified modal parameters with the SSI method: (a) Test #1; (b) Test #2; and (c) Test #3*

4 STRUCTURAL MODELLING

In this study, the FE model of the building was developed using SAP2000 [14]. The FE model was developed to validate the results obtained from the in-situ test in terms of modal parameters as well as to understand the role of non-structural elements in the changes of fundamental frequencies for lightweight timber frame structures.

Every component of each lightweight wall was included in the FE model. In particular, beam elements were used for the timber frame members (studs), shell elements were used for the sheeting boards (OBS panel for the external walls and particle boars panel for the internal walls) and two joint link connections were used for the panel's connections. The detail model for one of the wall panels is shown in Figure 13.

https://doi.org/10.52202/069179-0379

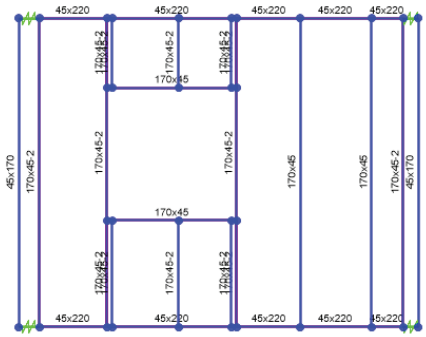

Figure 13: *Lightweight timber frame wall modeled components.*

Table 2 shows the material properties used for the FE model for each different element.

Table 2: *Modeling properties of the elements.*

Element	Characteristics	Properties
Studs (C24 timber)	45 x 170 mm 45 x 220 mm 45 x 95 mm	E = 10200 MPa G = 690 MPa
Sheeting boards	11 mm OSB	E = 6000 MPa G = 1574 MPa
Sheeting boards	38 mm particle board panel	E = 4480 MPa G = 1670 MPa

In order to reduce the computational effort, the floor and roof structural elements, such as joists and floorboards, are not modelled, but only their mass and gravitational loads are included. The FE model developed in SAP2000 is shown in Figure 14.

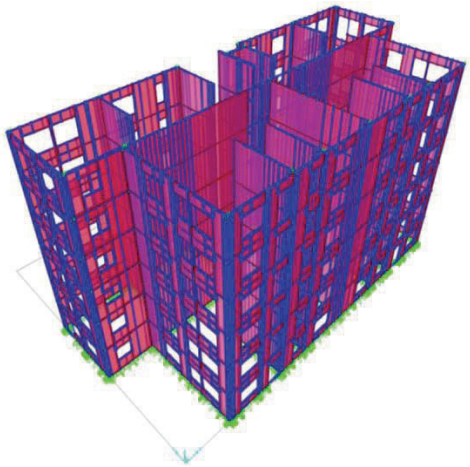

Figure 14: *View of the FE model of the building developed in SAP2000.*

In a first stage, the FE model was developed considering only the gravitational loads from the load bearing system and the slabs (Stage 1). After the ambient vibration tests were performed, in order to calibrate the modal parameters, the load of the non-structural wall components and the façade were added (Stage 2). The façade is a freestanding but horizontally connected to the structure.

The first three modes of the building obtained from the calibrated FE model are shown in Figure 15.

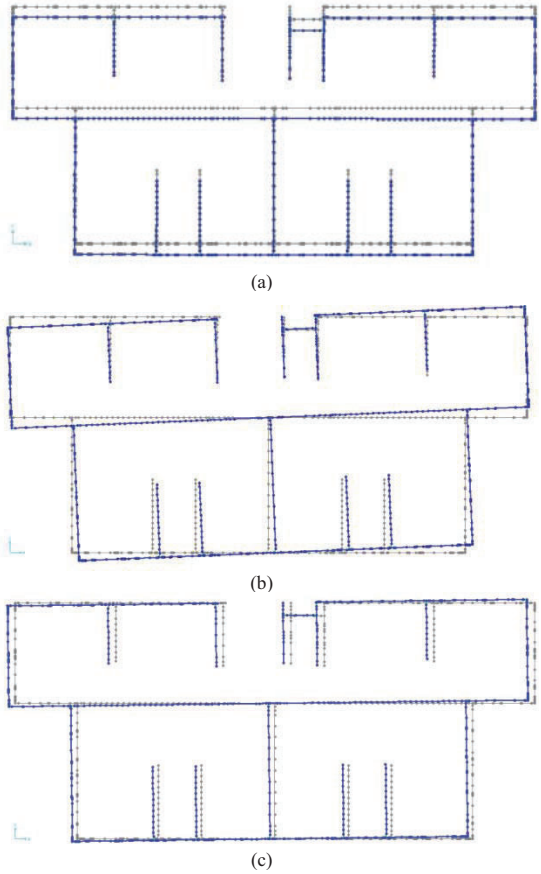

Figure 15: *Mode shapes obtained with the FE model of the building: (a) 1st Mode: f_1=2.80 Hz; (b) 2nd Mode: f_2=3.38 Hz; and (c) 3rd Mode: f_3=4.732 Hz.*

The frequencies identified in Stage 1 were lower than the ones obtained from the ambient vibration tests. The changes in the computed natural frequencies between Stage 1 and 2 are equal to 16% for the translational mode along y-direction, 13.5% for the rotational mode, and 15% for the translational mode along the x-direction.

Figure 16 shows that the frequencies identified in the first stage where higher than the frequencies identified with the updated FE model (Stage 2). These last ones are consistent with the frequencies identified with the OMA for the three performed tests.

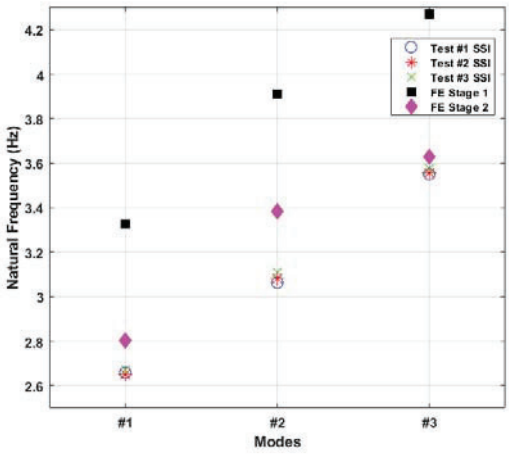

Figure 16: *Comparison between the natural frequencies obtained with the SSI method and the FE model at different stages.*

The higher values of natural frequencies in Stage 1 are compatible with what has been identified in previous studies on a similar building [18]. In particular, for low amplitude wind induced vibrations, ignoring the contributions of non-structural components will lead to an overestimation of the natural frequencies of the building.

5 CONCLUSIONS

The dynamic properties of building Hus 35, part of the Pilgatan block, were identified using frequency and time domain only-output OMA methods. Multiple ambient vibration tests were performed between October 2022 and January 2023. The aim of the testing campaign was to estimate the fundamental natural frequencies, damping ratios and mode shapes of the building and compare them with the one obtained from the FE model.

Three structural modes were identified using the two OMA methods: two translational and one rotational mode. The FE model of the building was developed using elastic beam elements for the studs, elastic isotropic shell elements for the sheeting boards of the external walls and internal walls, and joint link connections for the wall panels connections.

The FE model was calibrated in order to match the results from the in-situ tests in terms of natural frequencies. In particular, the weight on the non-structural elements was added during Stage 2. The mass of the building is a critical parameter while performing the modal analysis of a building. The weight of the exterior wall panels of the façade is an important aspect in calibrating the modal frequencies of the lightweight timber-frame analyzed building.

Further work is necessary in order to develop a more detailed model. In the next stage, the calibrated model should take into account the mechanical behavior of the connections. This will include the sheathing-to-framing connection and the friction and contact interaction between the slabs and the lightweight frame panels. Due to the high computational demand, the implementation and calibration of the mechanical behavior of the connections will be a challenging step.

For low vibrations amplitudes, compatible with the vibrations at the serviceability limit states, the non-structural elements, such as the façade, contribute to the global stiffness of the buildings. For this reason, neglecting the non-structural components in the FE model will overestimate the natural frequencies of the investigated building.

This study is part of a project plan to perform monthly measurements in two identically realized buildings like the one shown in this study. The aim of the project is to relate the possible changes in dynamic properties to the changes in the environmental conditions. Such variations will be implemented also in the FE model of the building to study how such changes can influence the lateral stiffness of the building and its global responce.

Acknowledgements

The authors acknowledge Stiftelsen Nils och Dorthi Troëdssons forskningsfond (project number 1057/22) for the financial support for this project. The authors would like to thank the building owner, Derome, for their interest, easy courteous collaboration, and permission to access the property.

REFERENCES

[1] Mugabo, I., Barbosa, A. R., and Riggio, M.: Dynamic characterization and vibration analysis of a four-story mass timber building. *Frontiers in Built Enviroment*. 5:86, 2019.

[2] Ellis, B. R., and Bougard, A. J.: Dynamic testing and stiffness evaluation of a six-storey timber framed building during construction. *Engineering Structures,* 23(10): 1232-1242, 2001.

[3] Filiatrault, A., Christovasilis, I. P., and Wanitkorkul, A.: Experimental seismic investigation of a full-scale woodframe building. In: *Structures Congress 2008: Crossing Borders*, Vancouver, British Columbia, Canada, April 24–26, 2008.

[4] Filiatrault, A., Christovasilis, I. P., Wanitkorkul, A., and van de Lindt, J.W.: Experimental seismic response of a full-scale light-frame wood building. *Journal of Structural Engineering*, ASCE, 136:246–254, 2010.

[5] Sartori, T., Casagrande, D., Tomasi, R., and Piazza, M.: Shake table test on 3-storey light-frame timber buildings. In: *12th World Conference on Timber Engineering WCTE*, Auckland, New Zealand, 16–19 July 2012.

[6] Brincker, R., Zhang, L., and Andersen, P.: Modal identification of output only systems using frequency domain decomposition. *Smart Material and Structures,* 10: 441–445, 2001.

[7] Brincker, R., and Andersen, P.: Understanding stochastic subspace identification. In: *Proceedings of the 24th International Modal Analysis Conference,* St. Louis, (MO), pages 461–466, 2006.

https://doi.org/10.52202/069179-0379

[8] Pei, S., and van de Lindt, J.W.: Coupled shear-bending formulation for seismic analysis of stacked wood shear wall systems. *Earthquake Engineering and Structural Dynamics*, 38, 1631–1647, 2009.
[9] Pei, S., and van de Lindt, J.W.: Seismic Numerical Modeling of a Six-Story Light-Frame Wood Building: Comparison with Experiments. *Journal of Earthquake Engineering*, 15, 924–941, 2011.
[10] Pang, W., Ziaei, E., and Filiatrault, A.: A 3D model for collapse analysis of soft-story light-frame wood buildings. In: *Proceedings of the World Conference on Timber Engineering*, Auckland, New Zealand, 15–19 July 2012.
[11] Di Gangi, G., Demartino, C., Quaranta, G., and Monti, G.: Dissipation in sheathing-to-framing connections of light-frame timber shear walls under seismic loads. *Engineering Structures*, 208, 110246, 2020.
[12] Kuai, L., Ormarsson, S., Vessby, J., and Mahatjam, R.: A numerical and experimental investigation of non-linear deformation bahaviours in light-frame timber walls. *Engineering Structures*, 252, 113599, 2022.
[13] Amaddeo, C., and Michael, D.: Dynamic characterization of a six-story light-weight timber-frame building. In: 6th *International Conference on Structural Health Assessment of Timber Structures*, Prague, 7-9 September 2022.
[14] ARTeMIS Modal. Available online at: http://www.svibs.com/products/ARTeMIS_Modal.aspx (accessed April 15, 2018), 2017.
[15] Pastor, M., Binda, M., and Harcarik, T.: Modal assurance criterion. *Procedia Eng.* 48, 543–548, 2012.
[16] CSI (Computers and Structures, Inc). SAP2000: Integrated Software for Structural Analysis and Design, Ver. 19. Berkeley, CA: CSI, 2017.
[17] Van Overschee, P., and De Moor, B.: Subspace identification for linear systems. *Norwell, MA: Kluwer Academic Publishers*, 1996.
[18] Steiger, R., Feltrin, G., Weber, F., Nerbano, S., and Motavalli, M.: Experimental modal analysis of a multi-storey light-frame timber building. *Bull Earthquake Engineering* 15, 3265–3291, 2017.

World Conference on Timber Engineering Oslo 2023

DYNAMIC RESPONSE OF TALL TIMBER BUILDINGS UNDER SERVICE LOAD – RESULTS FROM THE DYNATTB RESEARCH PROGRAM

Rune Abrahamsen[1], Magne A. Bjertnæs[2], Jacques Bouillot[3], Boštjan Brank[4], Roberto Crocetti[5], Olivier Flamand[6], Fabien Garains[7], Igor Gavrić[8], Ludwig Hahusseau[3], Alan Jalil[6], Marie Johansson[9], Thomas Johansson[5], Wai Kei Ao[10], Blaž Kurent[4], Pierre Landel[9, 11], Andreas Linderholt[11], Kjell Malo[12], Manuel Manthey[6], Petter Nåvik[2], Alex Pavic[10], Fernando Perez[13], Anders Rönnquist[12], Iztok Šušteršič[8], Saule Tulebekova[12]

ABSTRACT: Wind-induced dynamic excitation is a governing design action determining size and shape of modern Tall Timber Buildings (TTBs). The wind actions generate dynamic loading, causing discomfort or annoyance for occupants due to the perceived horizontal sway, i.e. vibration serviceability problem. Although some TTBs have been instrumented and measured to estimate their key dynamic properties (eigenfrequencies, mode shapes and damping), no systematic evaluation of dynamic performance pertinent to wind loading had been performed for the new and evolving construction technologies used in TTBs.

The DynaTTB project, funded by the ForestValue research program, mixed on site measurements on existing buildings excited by mass inertia shakers (forced vibration) and/or the wind loads (ambient vibration), for identification of the structural system, with laboratory identification of building elements mechanical features, coupled with numerical modelling of timber structures. The goal is to identify and quantify the causes of vibration energy dissipation in modern TTBs and provide key elements to finite element models. This paper presents an overview of the results of the project and the proposed Guidelines for design of TTBs in relation to their dynamic properties.

KEYWORDS: Timber building, wind load, forced vibration, discomfort, modelling, damping, full scale.

1 INTRODUCTION

1.1 Background

The complexity of the design and the construction of buildings increases with their height and the number of storeys. Tallness is relative to experience, situation, or context so the definition of a Tall Timber Building (TTB) cannot be universal. Complexity is found in the production on the construction site due to a high building's height but also in the need for extra technical systems and control. The increased height means higher vertical loads caused by higher weight but also significantly higher horizontal wind loads. For taller structures, the wind load can generate dynamic effects on the structure which must be included in the serviceability design.

1.2 Building system for TTBs

The studies in the Dynamic Response of Tall Timber Buildings Under Service Loads (DynaTTB www.dynattb.com) project show that TTBs, due to their low masses compared to steel and/or concrete buildings, are sensitive to wind loads in the serviceability limit state. The building height where sway is necessary to consider in the design of the structural system is lower than for other building materials such as steel or concrete. The number of storeys where wind-induced vibrations govern the design vary dependent on the building system, building shape and wind speed in the actual location. In zones with high wind velocity and buildings with a larger height to width ratio, it can be a good practice to check the acceleration levels at the highest floor for buildings as low as six storeys in order to check the serviceability limit state criteria [1], [2].

TTBs can be built with several different building systems introducing different difficulties during design and construction. The most common building systems for TTBs are planar elements, beam-column systems with trusses and hybrid systems utilising a combination of materials for the load bearing structure, see Figure 1.

[1]Moelven Limtre, rune.abrahamsen@moelven.no, [2]Sweco, magne.bjertnaes@sweco.no, petter.navik@sweco.no, [3]Eiffage, jacques.bouillot@eiffage.com, ludwig.hahusseau@eiffage.com, [4]University of Ljubljana, Bostjan.Brank@ikpir.fgg.uni-lj.si, bkurent@fgg.uni-lj.si, [5]Moelven SE, crocetti@kth.se, thomas.johansson@moelven.se, [6]CSTB, olivier.flamand@cstb.fr, alan.jalil@cstb.fr, manuel.manthey@cstb.fr, [7]Arbonis, fgarains@arbonis.com, [8]InnoRenew CoE, gavric.igor@gmail.com, iztok.sustersic@innorenew.eu, [9]RISE, marie.johansson@ri.se, pierre.landel@ri.se, [10]Uni Exeter, wka203@exeter.ac.uk, A.Pavic@exeter.ac.uk [11]LNU, andreas.linderholt@lnu.se, [12]NTNU, kjell.malo@ntnu.no, anders.ronnquist@ntnu.no, saule.tulebekova@ntnu.no [13]Smith&Wallwork, fernando.perez@ibk.baug.ethz.ch

https://doi.org/10.52202/069179-0380

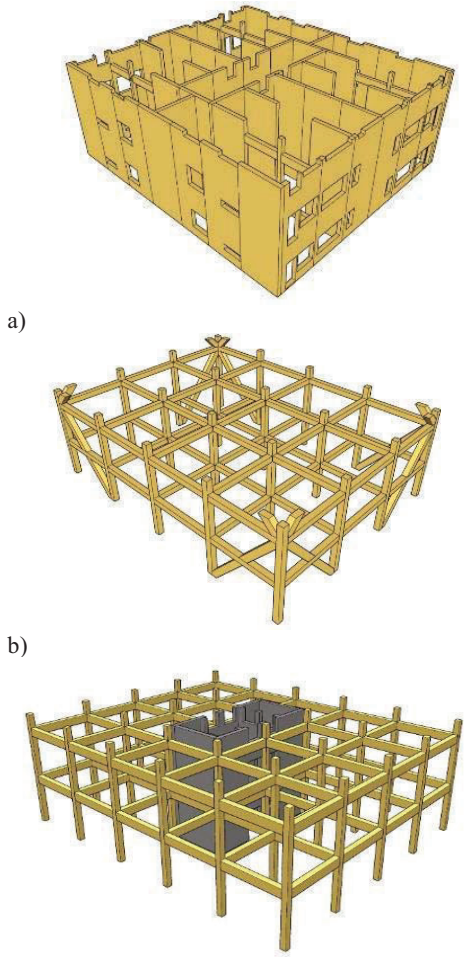

a)

b)

c)

Figure 1: *Typical building systems for TTBs; a) planar elements, b) beam-column systems with trusses and c) hybrid systems using a combination of materials in the load bearing structure.*

1.3 Acceleration and code calculations

The limiting factor in serviceability limit state (SLS) design is in most codes the peak acceleration at the top floor of the building. Often the limit for the acceleration defined in ISO 10137 [1] as the maximum peak acceleration, caused by a wind velocity level with a one-year recurrence period is used. The recommended upper acceleration limits are higher for office buildings than for residential buildings. The maximum acceleration limit is an SLS requirement and is therefore an issue that should be agreed upon in the contract between the property owner and the engineers/contractor.

The codes provide recommendations for how to calculate the along-wind accelerations, as for example in annex B and annex C in Eurocode [2]. These calculation models are built on four types of parameters:

i) the wind velocity and terrain,
ii) the geometry of the building giving the force coefficient,
iii) the aerodynamic properties of the building, and
iv) the mechanical properties of the building.

Some of these parameters are related to the properties of the structure of the building. These parameters are necessary for the actual building and are estimated using a simulation model, often a finite element (FE) model. These structural parameters are:

- the natural frequencies for the bending modes in the two main directions of the building,
- their mode shapes and
- their related modal masses.

The last parameter necessary for the calculation of the along-wind accelerations is a value for the modal damping, which is difficult to model. Therefore, an estimated/measured value must be used. Within the DynaTTB project the modal damping values of eight timber buildings with different structural systems in several European countries have been measured and evaluated, see Table 1.

1.4 The DynaTTB project

The project DynaTTB; Dynamic Response of Tall Timber Buildings under Service Load, ran between 2019 and 2022 with partners from France, Norway, Slovenia, Sweden, and the UK. The main objective of the project was to experimentally identify a number of full-scale TTB structures (finished or currently being built) and, based on these, develop representative FE models for predicting the vibration response of TTBs exposed to wind-induced dynamic loading. The project represents the first systematic evaluation of dynamic performance pertinent to wind loading in the world for TTBs using, in addition to ambient vibration tests, also forced vibration tests. The main results have been included in a Guideline for practicing engineers on how to design TTBs subjected to wind loads in the Serviceability Limit State (SLS). Results have also been disseminated through scientific journals and seminars/conferences. This paper presents an overview of the results and the main structure of the guidelines. More detailed results can be found in [3]–[6] which will be presented at the WCTE 2023 conference. Other results can be found in for example [7]–[15].

2 DESCRIPTION OF BUILDINGS

In the project, a total of eight buildings, see Figure 1, have been tested using, in addition to preliminary ambient vibration tests, also forced vibrations to estimate their dynamic properties: eigenfrequencies, normalized modes shapes and damping. One more building has been tested using Ambient excitation and three of the buildings have also been equipped with long-term monitoring equipment.

The buildings vary in height from four to eighteen storeys with several building systems to represent TTBs in Europe today.

https://doi.org/10.52202/069179-0380

Figure 2: *The buildings tested and their location in Europe.*

Table 1: *Description of the tested buildings.*

	Building 1	**Building 2**	**Building 3**	**Building 4**	**Building 5**	**Building 6**	**Building 7**	**Building 8**
Name	Trinity round church	Flower valley	Inno Renew	Eken	Yoker[2]	Treed-it	Hyperion	Mjøstårnet
Location	UK	Slovenia	Slovenia	Sweden	UK	France	France	Norway
Number of storeys	4	4	4	6	7	12	17	18
Building system	Planar elements	Planar elements	Planar elements	Beams and columns+ trusses	Planar elements	Hybrid	Hybrid	Beams and columns+ trusses
Building height [m]	16 m	12.7 m	16.7 m	24.4 m	22 m	36 m	57 m	85.4 m
Height to highest habituated floor [m]	~12 m	8.9 m	12.5 m	18.0 m	18 m	33 m	50 m	68.2 m
Building width [m]	14 m	14.5 m	23.6 m	27 m	31 m	47.4 m	30.6 m	36.8 m
Building depth [m]	33 m	21.2 m	38.7 m	19 m	28 m	18.6 m	19.1 m	16.3 m

3 CASE STUDIES

This section shortly presents results from three case studies, built with different building systems and of different heights. The presented results include the first natural frequencies, an example of a captured mode shape and a damping value. The three buildings are:

- the seven storey, full CLT building Yoker in UK,
- the seven storey, glulam post and beam structure Eken in Sweden,
- the seventeen storey, hybrid building Hyperion in France.

3.1 Yoker building, UK (CLT structural system)

The building Yoker is located in Glasgow, UK. The building is designed by Smith and Wallwork Ltd and it is built using cross-laminated timber (CLT) from Stora Enso company. The characteristic dimensions of the building are: 31m by 28m in plan, 22m in height above the ground floor slab, 3745m^2 gross floor area, and 550m^2 footprint area. The building is T-shaped with three “wings” and a centrally located stair and elevator shaft. The building was designed using CLT panels in a platform building system, see Figure 3. Five different types of CLT panels were used, varying in thickness from 100mm to 140 mm (except for the stair half-landing with 200mm CLT

[2] The building consist of three wings and the measurement gives the maximum extreme points of the building.

https://doi.org/10.52202/069179-0380

panels), having either 3 or 5 layers were used. The external walls (as well as some internal walls) consist of large CLT panels which have the height of the storey and the length of the building edge, with pre-cut openings for windows. The CLT panels in the Yoker building are typically connected using a combination of angle brackets and wood screws. For more details of the buildings, see [14].

Figure 3. *The main structure of the Yoker building, showing the distribution of the CLT panels in the external walls.*

The dynamic testing of the building was performed using three synchronised APS Model 400 electrodynamic shakers with a total moving mass of 68.85 kg, which were installed on the 6th floor. Altogether 13 sensor locations were chosen with 2 sensor locations on each floor and an additional one on the 6th floor as a reference sensor near the shakers. Each sensor location measured accelerations in two horizontal directions. At the time of the measurements, the building was operational, so installation of the sensors was limited to the corridors in the core of the building. The measurements were performed by researchers from University of Exeter.

An FE-model was built for the structure using the following assumptions: (i) the foundation is rigid and fixed, (ii) the connections were not explicitly modelled, and (iii) the floors are flexible (i.e. the assumption of the rigid-diaphragm is not used). The initial shape for the first bending mode is shown in see Figure 4. The model was updated based on the measurement results in the next phase. The updating showed that shear stiffness of the CLT walls is higher than anticipated by the initial model. Furthermore, the analysis showed that vertical stiffness of the building is lower than initially estimated. The modelling was performed by researchers from University of Ljubljana, for more details of the modelling see [14].

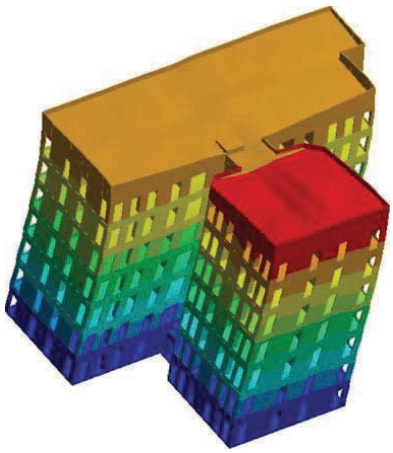

Figure 4. *First mode shape from the FE-analysis.*

The modal properties from the measurement on the Yoker building showed that the first bending mode (including some torsion) had a natural frequency of 2.85 Hz with a relative viscous damping of 1.4%, see [16]. The results also showed that the damping was frequency dependent.

3.2 Eken building, Sweden (Glulam truss structural system)

The building Eken was finished in 2019 and contains 31 rental apartments. The height, width and depth of the building are 24 m, 27 m and 19 m, respectively. The building was built by the company Stenmarks Bygg, and it is owned by Mariehus. The building is built using the Moelven Trä 8 system [17]. The load bearing system consists of glued laminated timber (glulam) beams and columns whereas trusses form the stabilizing elements, see Figure 5Figure 1. The total structure consists of 12 glulam trusses, four in the weak direction and eight in the strong direction of the building. The glulam trusses are in principle symmetrically located in the building and in the centre of the building they stretch from the concrete foundation through all seven storeys of the building. The floor system is made of strengthened LVL sheets acting as a diaphragm system. The connections in the glulam trusses are slotted-in-steel-plates fastened with steel dowels. The other glulam beams are fastened using steel hangers in the glulam beams. These glulam building components are manufactured and assembled by the company Moelven Töreboda.

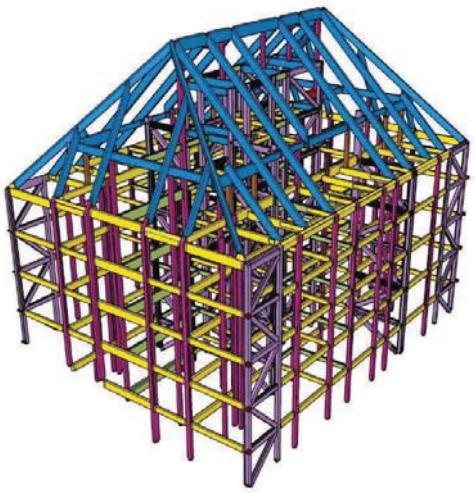

Figure 5. *Glulam structure of the building Eken.*

The dynamic performance of the building Eken has been studied during the measurement campaign using a forced vibration set-up. For that purpose, APS 420 shaker was used, and it was placed on the top (seventh) floor in the ventilation room. In total 45 accelerometers were used to measure the response of the building at different places and directions. The accelerometers were placed at four different levels at each of the four corners of the building, under the balconies, and two positions under the main roof beam at the top of the building. The first bending mode in the weak direction was found to have a frequency of 2.4 Hz. The measurements were performed by Linnaeus University.

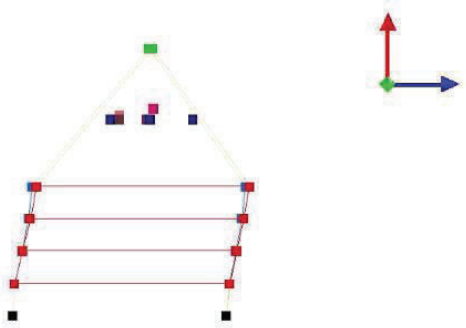

Figure 6. *Modes shape for the first bending mode.*

The first mode was a pure bending mode in the weak direction of the building, see Figure 6. The damping could be evaluated for each resonance frequency. A preliminary evaluation showed that the relative viscous damping was 1.6% for the first bending mode in the weak direction. More details of the measurements can be found in [3].

3.3 Hyperion, France (Hybrid structural system)

The Hyperion Tower, located in Bordeaux, is one of the tallest mass timber buildings in France with 57m height and 17 storeys. It was built by the Eiffage Construction company following a design by Jean-Paul Viguier architect and SETEC structural design office. It is a private housing which is distinguished by its 141 large balconies, made of steel. As for the majority of French buildings using timber it is a hybrid structure, i.e. a central concrete core gives the main resisting part to horizontal loads and satisfies the local fire safety requirements. In Hyperion Tower all floors and horizontal beams are made of CLT, the façade itself uses wood panels as stiffeners.

Mode shapes, frequencies and damping have been measured using excitation by a heavy mass shaker [11], [12] with a 550 kg moving mass allowing large amplitude displacements, used for the evaluation of damping at various stages of amplitude. The first natural frequency of the building was 0.91 Hz with a mode shape as shown in Figure 7.

An FE model was built with ANSYS [13] and used to prepare the testing session as well as checking that the shaker would not overload the structure.

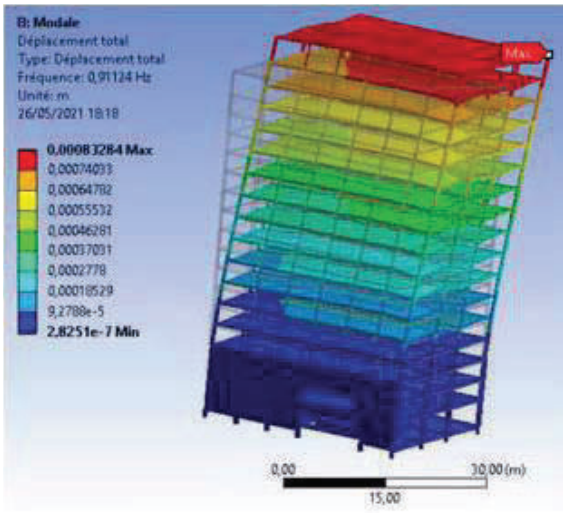

Figure 7. *Mode shape for the first bending mode from the FE-model.*

The FE-model was improved to match the results from the on-site testing, providing a reliable digital twin of the real building. The building was finally equipped with a long-term monitoring system including the measurement of wind 10 m above the roof, in order to check the dynamic behaviour under strong wind. The modelling and measurements were performed by CSTB.

4 GUIDELINES FOR SLS DESIGN OF TTBs

4.1 Overview of the Guidelines

The aim of the guideline is to give recommendations to structural engineers designing TTBs, but is also aimed at manufacturers of timber building systems, property developers interested in building taller with wood and researchers dealing with dynamic effects on TTBs. The focus is on the design for the serviceability limit state (SLS) of tall buildings with timber structures, their

https://doi.org/10.52202/069179-0380

dynamic properties and how wind-induced vibrations can be mitigated. There are several books that describe general design of TTBs, especially with focus on ultimate limit state [18], [19] as well as guides for modelling timber structures [20].

The results of the project will be collected into a written guideline with the tentative title: **Dynamic Properties of Multi-Storey Timber Structures for Wind-Induced Vibrations: Case Studies of Full-Scale Testing and Modelling.**

The general structure of the guidelines will be:

1. Guidelines on calculation of wind-induced vibrations
2. State-of-the-art
   - 2.1 Tall timber building systems
   - 2.2 Wind loads requirements in serviceability limit state
   - 2.3 Dynamic testing of tall timber buildings
   - 2.4 Modelling of tall timber buildings for dynamic response in SLS
3. Building case studies
   - 3.1 Building A
   - 3.2 Building B
   - 3.3 Building …
   - 3.N Building N

4.2 Recommendations for FE-modelling of TTBs

The FE-models established for evaluating the SLS response should provide as a minimum result at least the following parameters: the first natural frequency in bending in the two main lateral directions of the building, their associated mode shapes and the equivalent, or modal, masses.

Based on the project outcomes, the following recommendations can be given when creating an FE-model of a TTB for SLS design:

- Use mean values for density of materials and nominal dimensions of structural elements.
- Use mean values for stiffness of material.
- Masses of non-structural elements should be included in as accurate location as possible.
- Most probable value for live load should be included in the model. Actual live load can be significantly lower than the values recommended in building codes, such as Eurocode 1 [21].
- For structures using planar wood elements, walls and floors are recommended to be modelled including openings.
- For buildings designed using a platform structural system, perpendicular to the grain flexibility of floor slabs is recommended to be included in the model.
- Connections that exhibit semi-rigid behavior in SLS in both translational and rotational directions should be included in the model. As a starting point connection stiffnesses calculated according to Eurocode 5 [22] can be used.
- For hybrid buildings with concrete cores and/or timber concrete floors, average material values representative for the concrete elements are considered. Assumptions made for dynamic seismic models (cracked concrete, etc.) are not relevant.
- For composite timber-concrete floors, the rigid diaphragm assumption can be considered provided that the minimum concrete thickness required for this assumption is verified (see ETA document of considered floor system).
- The horizontal and vertical stiffnesses of the foundation can have a large impact on the results. Soil parameters such as stiffness, damping, etc. are strain rate dependent. Reference values from seismic analysis should be adjusted for SLS verifications.
- Contribution of stiffness of non-structural elements should be explored as their impact on the modal response of the building has been observed.

In general, it is on the safe side to assume conservative mass and stiffness values for the building when creating the model. There are large uncertainties in the FE-models, especially regarding the effect of stiffness of connections, foundation, and the contribution from non-load bearing elements. It is therefore advised to do a sensitivity study for the effect of these parameters on the results.
An FE-model can also be used to estimate the acceleration levels directly if the model can include a representative wind load model.

4.3 Recommendations for on-site measurements

The current number of TTBs completed in the world is still relatively low. Hence, there is still a lot of uncertainties in the modelling, design and construction of these kinds of structures. It is therefore important to measure and evaluate completed structures to investigate the accuracy of the models and update the recommendations and the best practice for modelling TTBs in SLS. The current codes and standards used today also have very limited information on how to model TTBs and on values to be used for example for modal damping in tall timber structures in SLS. To create a statistical basis for a recommended value for damping to be used in the codes, it is necessary to evaluate the modal damping in more completed TTBs. Natural frequencies and mode shapes give a good basis for checking the simulation models used in the design. Further development of the models to simulate the real behaviour of TTBs subjected to wind loads is needed.

For evaluating the dynamic properties of a structure, it is necessary to measure the response (for example accelerations) of the building to a varying force. The building response is normally measured using accelerometers. The force can be imparted to the structure using three principal approaches:

- Ambient vibration (AVT) – Excitation with unknown external force which is assumed to have a frequency spectrum which is broadly flat across the frequency range of interest.
- Free Vibration Test (FreeVT) – The structure is first set into motion by applying known initial conditions,

e.g., by a pull followed by a sudden release or by some unmeasured artificial excitation, such as synchronized swaying of one or more humans or shaker, and then left to vibrate freely on its own.

- Forced vibration test (FVT) – excitation with a known force, for example from a shaker imparting an excitation force to the structure that can be measured, or an impact hammer instrumented with a force sensor.

These methods have benefits and drawbacks for measuring different dynamic properties and are suitable for establishing different properties. Depending on the property of interest, different test methods are most suited, see Table 2.

Table 2: *Dynamic properties and recommended method to use for evaluation.*

	Suitable testing methods		
Property of interest	AVT	FreeVT	FVT
Natural frequency	X	X	X
Modes shapes	X	X	X
Modal damping		X	X
Modal mass			X
Frequency response function			X

For measuring mode shapes, it is necessary to use several sensors along the height of the building. Strong amplitude-dependent behaviour is to be expected for TTBs. To address this in detail, dynamic testing techniques that can cope with such structural features, such as FVT or FreeVT, are required. Accelerometers must follow the motion of the TTB structure they are attached to. Timber floors in TTBs are often covered by acoustic layers. If horizontal shakers are used, such layers can prevent direct transmission of the shaker force to the TTB structure by introducing unwanted flexibility.

5 SUMMARY

This paper presents an overview of the most important results from the DynaTTB project. The results are gathered in a Guideline for engineers and researchers interested in designing and evaluating TTBs.

The results show that it is possible to measure the dynamic properties of the buildings. The results also show that to make an FE model that is valid in its representation of a building's dynamic behaviour in SLS, in terms of eigenfrequency and modes shapes, it is important to take the effect of stiffness in the connections, the foundation and in some cases also non-loadbearing structures such as partition walls, screeds and curtain walls into account.

The results also show that in most cases TTBs exhibit non-linear damping behaviour, which in some cases might be important to consider. In general, the damping is in the range of 1.5-3% of the critical viscous damping depending on the amplitude of the vibrations.

6 ACKNOWLEDGEMENT

The research leading to these results has received funding from the ForestValue Research Programme which is a transnational research, development and innovation programme jointly funded by national funding organisations within the framework of the ERA-NET Cofund 'ForestValue – Innovating forest-based bioeconomy'".

7 REFERENCES

[1] ISO 10137, *Bases for design of structures – Serviceability of buildings and walkways against vibration*, no. Approved: 2008-03-17.

[2] EN 1991-1-4, *EN 1991-1-4 Eurocode 1: Actions on structures -Part 1-4: General actions -Wind actions*. 2005.

[3] A. Linderholt, P. Landel, and M. Johansson, "Forced response measurements on a seven storey timber building in Sweden," in *World Conference on Timber Engineering (WCTE 2023), Oslo 19-22 June*, 2023.

[4] B. Kurent, B. Brank, W. Kei Ao, A. Pavic, and M. Manthey, "On finite element modelling and model updating of multi-storey timber buildings," in *World Conference on Timber Engineering (WCTE 2023), Oslo 19-22 June*, 2023.

[5] K.-A. Malo, H. Stamatopoulos, F. Mikro Masaro, and S. Tulebekova, "Serviceability stiffness for timber connections with dowels and slotted-in steel plates," in *World Conference on Timber Engineering (WCTE 2023), Oslo 19-22 June*, 2023.

[6] R. Abrahamsen, M. A. Bjertnaes, J. Bouillot, B. Brank, and L. Cabaton, "dynamic response of tall timber buildings under service load-the dynattb research program," Nov. 2020.

[7] S. Tulebekova, K. A. Malo, A. Rønnquist, and P. Nåvik, "Modeling stiffness of connections and non-structural elements for dynamic response of taller glulam timber frame buildings," *Eng Struct*, vol. 261, Jun. 2022.

[8] P. Landel, "Wind-induced vibrations in tall timber buildings: Design standards, experimental and numerical modal analyses," Licentiate Thesis, Linnaeus University, Växjö, 2022.

[9] P. Landel and A. Linderholt, "Reduced and test-data correlated FE-models of a large timber truss with dowel-type connections aimed for dynamic analyses at serviceability level," *Eng Struct*, vol. 260, Jun. 2022.

[10] P. Landel, M. Johansson, and A. Linderholt, "Comparative study of wind-induced accelerations in tall timber buildings according to four methods," in *World Conference on Timber Engineering 2021, WCTE 2021*, 2021.

[11] O. Flamand and M. Manthey, "Wind shaking of high rise timber buildings," in *8th European African Conference on Wind Engineering (8EACWE), Bucharest, September 20-23*, 2022.

[12] O. Flamand and M. Manthey, "Improving the modelling of tall timber buildings," in *Current*

https://doi.org/10.52202/069179-0380

Perspectives and New Directions in Mechanics, Modelling and Design of Structural Systems, 2022.

[13] M. Manthey, O. Flamand, A. Jalil, A. Pavic, and W. K. Ao, "Effect of non-structural components on natural frequency and damping of tall timber building under wind loading," *World Conference on Timber Engineering 2021, WCTE 2021*, 2021.

[14] B. Kurent, B. Brank, and W. K. Ao, "Model updating of seven-storey cross-laminated timber building designed on frequency-response-functions-based modal testing," *Structure and Infrastructure Engineering*, 2021.

[15] B. Kurent, N. Friedman, W. K. Ao, and B. Brank, "Bayesian updating of tall timber building model using modal data," *Eng Struct*, vol. 266, p. 114570, Sep. 2022.

[16] W. K. Ao and A. Pavic, "Novel wirelessly synchronised modal testing of operational buildings using distributed OCXO high-precision data loggers," in *Proceedings of the 39th IMAC, A Conference and Exposition on Structural Dynamics 2021IMAC XXXIX* , 2021.

[17] Moelven, "Flervåningshus Trä8," 2022. https://www.moelven.com/se/produkter-och-tjanster/allt-om-limtra/flervaningshus-tra8/ (accessed Nov. 16, 2022).

[18] M. Green, *The case for Tall Wood Buildings*. 2012.

[19] E. Karacabeyli and C. Lum, *Technical Guide for the Design and Construction of Tall Wood Buildings in Canada Special Publication SP-543E*. 2022.

[20] Z. Chen, D. Tung, and E. Karacabeyli, *Modelling Guide for Timber Structures 2022-First Edition*. 2022.

[21] EN 1991-1-1, *Eurocode 1: Actions on structures - Part 1-1: General actions – Densities, self-weight, imposed loads for buildings*. Approved 2002-06-28.

[22] EN 1995-1-1, *Eurocode 5: Design of timber structures – Part 1-1: General – Common rules and rules for buildings*, no. Approved 2004-12-10.

World Conference on Timber Engineering Oslo 2023

QUANTIFYING ROBUSTNESS IN TALL (TIMBER) BUILDINGS: A CASE STUDY

Konstantinos Voulpiotis[1], Styfen Schär[2], Andrea Frangi[3]

ABSTRACT: Robustness research has become popular, however very little is known on its explicit quantification. This paper summarises a quantification method previously published by the main author and proceeds in demonstrating its step-by-step application with a case study tall timber building. A hypothetical 15-storey timber building is designed for normal loads and four improved options are designed to account for abnormal loads in order to increase the building's robustness. A detailed, nonlinear dynamic Finite Element model is set up in Abaqus® to model three ground floor column removal scenarios, and a Random Forest classifier is set up to propagate uncertainties and efficiently calculate the probability of certain collapse classes occurring and the importance of each input parameter. The results show how design improvements at the whole building scale (e.g., strong floors) have a higher impact on robustness performance than just improving the strength and ductility of some selected connections, although these results are exclusive to the building studied. The whole procedure is put in context of the practicing engineer, with a suggestion for a calculation-free, purely qualitative robustness framework. The case study reinforces the importance of a sound conceptual design for achieving robustness in tall timber buildings.

KEYWORDS: Disproportionate collapse, Finite Element Analysis, Random Forest classification, machine learning

1 INTRODUCTION

Our profession is seeing a paradigm shift towards buildings of lower carbon footprint: tall timber buildings are a fine example of this shift. Any departure from the "familiar waters" of the common structural typologies runs a higher risk of not having identified or anticipated certain structural behaviours: similar to the scaling issues that led to the partial collapse of the Ronan Point in London in 1968 [1], we must understand how timber buildings scale to the new heights constructed in the last 10 years, particularly regarding their disproportionate collapse behaviour.

Structural robustness, or disproportionate collapse resistance, is the ability of a structure to withstand damage without disproportionate further consequences, and it is an important and yet not so widely understood quality of our building stock. While a lot of work has been put into understanding structural robustness at a qualitative level and regarding concrete and steel buildings, little is known on the robustness of timber buildings and even less on how to specifically quantify how robust is a building, and whether this is enough or not.

In this paper, we build on the framework presented by Voulpiotis et al. [2] on robustness quantification followed by a case study tall timber building. How to connect this complex work to design in practice is presented in the end. Only essentials are discussed here – for more details and the literature review on the topic please refer to the doctoral thesis of Konstantinos Voulpiotis [3].

2 QUANTIFICATION FRAMEWORK

Since it belongs to the category of extreme (rare) events, disproportionate collapse is best studied in a probabilistic manner. Of the frameworks that have been proposed to quantify robustness in the last 30 years [4–7], the robustness index is a common measurement of the disproportionality of risk: the importance of secondary, or indirect consequences (C_{Ind}) compared to the direct ones (C_{Dir}) given the probability of them occurring following a damage scenario ($P(C|D)$):

$$I_{Rob} = \frac{C_{Dir}}{C_{Dir} + P(C|D) \times C_{Ind}} \quad (1)$$

According to Voulpiotis et al. (2021) [2,8], the consequence can be measured in terms of extent of collapse area ($C_{Dir/Ind} \rightarrow A_{Fail,Dir/Ind}$). Since a damaged building can fail in different ways (let us assume n different "collapse classes"), we calculate the robustness index for a given damage scenario by summing the indirect risk occurring from each collapse class i:

$$I_{Rob} = \frac{A_{Fail,Dir}}{A_{Fail,Dir} + \sum_{i=0}^{n}(P(C_i|D) \times A_{Fail,Ind,i})} \quad (2)$$

Given several damage scenarios, we can obtain a weighted robustness index which is unique to that building design. Assuming several building design

[1] Dr. Konstantinos Voulpiotis, Institute of Structural Engineering, ETH Zurich, Switzerland, voulpiotis@ibk.baug.ethz.ch
[2] Styfen Schär, Institute of Structural Engineering, ETH Zurich, Switzerland, styfen.schaer@ibk.baug.ethz.ch
[3] Prof. Dr. Andrea Frangi, Institute of Structural Engineering, ETH Zurich, Switzerland, frangi@ibk.baug.ethz.ch

https://doi.org/10.52202/069179-0381

improvements, we can use the increase (or decrease) of the average robustness index to decide on the best design solution to increase robustness. This is demonstrated in the case study below.

3 CASE STUDY ANALYSIS

3.1 BUILDING DESIGN

A hypothetical 15-storey timber building skeleton structure for offices in Zürich, Switzerland, is designed to the Swiss standards to quantify its robustness using the method described in the previous section. The design is kept as simple as possible to focus on the collapse performance (Figures 2 & 3): post-and-beam construction with glulam timber beams and columns, and timber-concrete composite floors, all designed for category B loads (office) in service class 1 and also checking for fire, buckling, deflections, and creep. The loads are assumed to go back to a CLT core which functions are a vertical cantilever (not explicitly designed). The materials used are GL32h glulam timber (SIA 265:2012) [9], C25/30 concrete with B500B rebar (SIA 262:2013) [10], and 5.6 connector steel for screws and dowels (SIA 263:2013) [11]. The substructure has not been designed.

The main design focus has been put on the connections, as there is evidence that they play a significant role in increasing structural robustness [12]. We used dowelled connections with slotted-in steel plates for the beam-column connections, glued-in rods for the column-column connections and screwed steel angle brackets for the floor-floor connections. They are all assumed to be pinned for the design of the building, however, their actual stiffness and resistance on all degrees of freedom have been estimated using first principles. An idealized elastic-plastic curve has been assumed for each degree of freedom, defined by only four values: elastic stiffness (K_e), yield load (F_y), plastic deformation (δ_p), and ultimate load (F_u). Full details are in Voulpiotis [3].

Four improved versions of the building have also been designed for comparison: options 2 & 3 employ a diagonally-braced "strong floor" at the 15th or both 7th and 15th floor respectively with the columns designed to work in tension should a support be compromised. Options 4 & 5 employ an increase in the ductility of the beam-column and column-column connections respectively. This increased the size of the connections, which in turn also affected the size of the columns. The buildings have been parametrically defined in Abaqus® and studied in ground floor column removal scenarios using both implicit and explicit solver to consider dynamic and nonlinear effects.

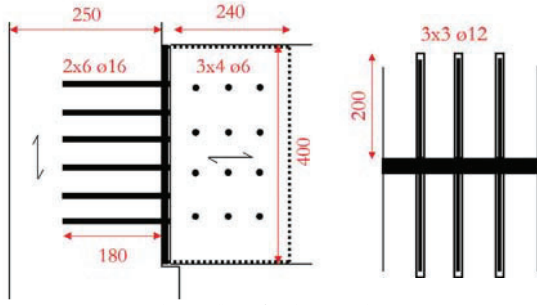

Figure 1: *Beam-column (l) and column-column (r) connections*

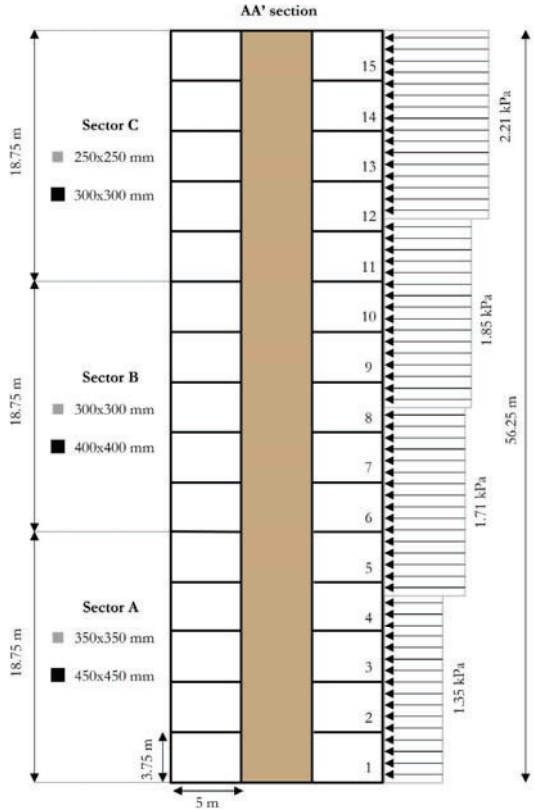

Figure 2*: Case study building section*

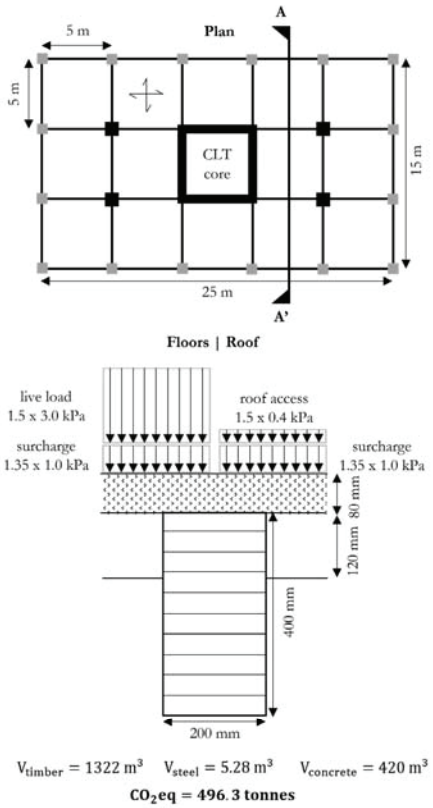

Figure 3: *Case study building plan and detail*

https://doi.org/10.52202/069179-0381

3.2 SURROGATE MODELLING

A surrogate model is a simplified, computationally cheap-to-evaluate mathematical representation of the complex finite element model, necessary to calculate the probabilities of each collapse class occurring in a reasonable amount of time.

Three independent damage scenarios were studied: the removal at the corner, edge, and internal ground floor columns with a removal time of 2 ms:

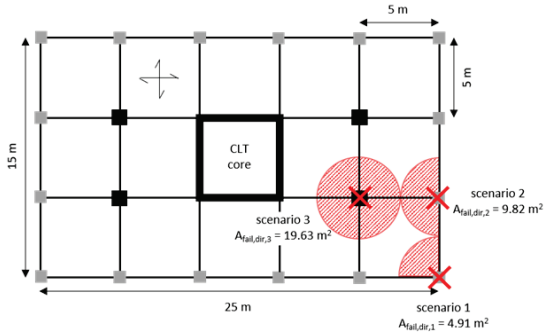

Figure 4: *The three damage scenarios studied*

A probabilistic input vector was set up for each building design and used to train a Random Forest classifier [13], later enriched in the domains of the minority classes using synthetic sampling (SMOTE) [14]. This way the probability of each collapse class occurring (for a given damage scenario) could be calculated with only around 1,500 model runs for each building design. Performance scores (accuracy and macro F1 score) of the classifiers were obtained using k-fold cross-validation [15] and sensitivity analyses were carried out using the Impurity-Based Importance (IBI) [16]. Everything was set up in Python®, using the Scikit-learn [17] and Imbalanced-learn [18] modules. Full details of the algorithm setup and hyperparameter optimisation are provided in Voulpiotis [2]. This learning algorithm can efficiently find patterns in computationally expensive models with chaotic tendencies and is opening up new horizons in the numerical analysis of large, complex structures, such as highly nonlinear analyses of tall timber buildings.

3.3 RESULTS

All analyses were run on the "EULER" High Performance Computer Cluster of ETH Zürich [19]. Using master scripts in Python and a batching system, Abaqus input files and job submissions were performed in parallel by both Intel® and AMD® compute nodes. The model deformations were extracted at the 1.3 second timestamp before the results showed chaotic tendencies (a small change in the inputs led to large, inconsistent changes in the outputs). It is assumed that capturing the initial collapse stages using the method from section 2 suffices to explore cost-effective robustness solutions. Further collapse does occur beyond 1.3 seconds, however, modelling this is both unreliable and also unnecessary.

3.3.1 Design option 1

The code-compliant design option 1 partially collapses in all of the three damage scenarios shown in Figure 4. Additionally, a dominant collapse class is always present (375 m^2 for scenario 1; 1,100 m^2 for scenario 2; and 2,200 m^2 for scenario 3, see Figure 5). The extent of the collapse is increasingly worse by scenario: a corner column removal causes the entire corner of the building to collapse, an edge column removal causes the entire edge of the building to collapse, and an internal column removal causes half the building to collapse (until the assumed rigid core).

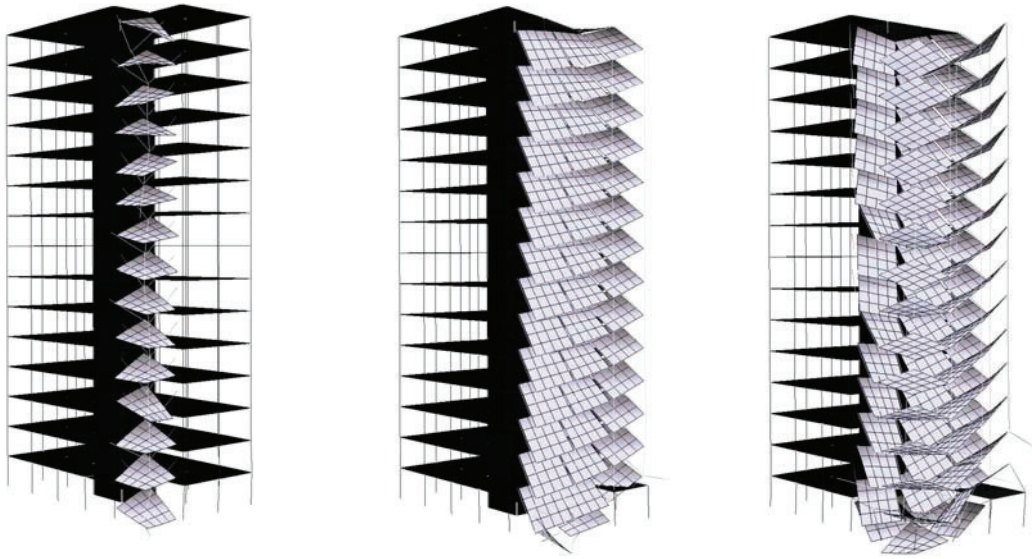

Scenario 1, severity = 375 m^2 Scenario 2, severity = 1,100 m^2 Scenario 3, severity = 2,200 m^2

Figure 5: *Abaqus® images and severity ($A_{Fail,Ind,i}$) values for the dominant collapse classes for design option 1*

The mechanics of the collapses in design option 1 are simple to explain by scenario:

Scenario 1: The load of the 14 unsupported floors is initially transferred towards the neighbouring columns via the beams in cantilever action, and via the floors in in-

https://doi.org/10.52202/069179-0381

plane shear action. The beam-column and floor-beam connections break very quickly, and the entire corner of the building, with the floor slabs detached, is accelerating towards the ground.

Scenario 2: The mechanism is similar to scenario 1, however this time the unsupported area is double in size and the forces are carried by three beams and two slabs per storey. The horizontal forces developing in the edge beams pull on the adjacent corner column, causing it to buckle and collapse too.

Scenario 3: With an even larger initial failure (four times that of scenario 1), a larger portion of the internal frame spreads loads to its surrounding beams and slabs in the same manner as scenarios 1 & 2. However, horizontal resistance is only provided from one side, the core, causing everything on the outer side of the building to buckle and collapse as well.

3.3.2 Design option 2

No collapse was observed for damage scenario 1 in design option 2, where the top floor is a trussed "strong floor". Although to a significantly lesser extent than in design option 1, the failure of an edge or an internal column again caused a progressive collapse. The truss structure is unable to carry the weight of the unsupported building when its area exceeds half a bay. It is therefore not surprising that scenario 3 leads to a collapse, albeit of lower initial extent than in the original design option. Upon removal of the column, the column-column connection breaks axially, and the membrane action that develops in the slabs is pulling the surrounding structure inward (Figure 6). Since stiffness is asymmetric (the core side is much stiffer), the edge of the building buckles and a substantial collapse initiates.

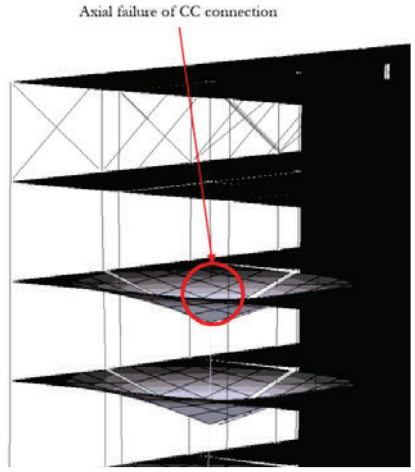

Figure 6: *Scenario 3 of design option 2 @0.5 s, column connection axial failure*

Scenario 2 is more marginal in that it could have supported the weight of the collapsing building had dynamic factors been included in the sizing of the stronger connections. However, the design of the strong floor was static, and the fast column removal speed is causing larger, dynamic force reactions. The failure that caused the collapse was the column-column connection in shear at the floor below the truss (Figure 7). This indicates that the strong floor is not stiff enough to prevent large deformations that will induce very large forces in the surrounding connections. Also, even the much stronger column-column connections are not particularly strong in shear: an alternative for this degree of freedom is an option worth exploring.

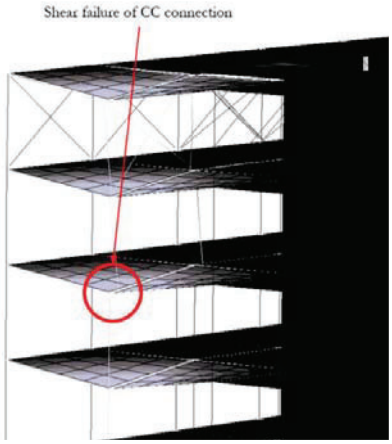

Figure 7: *Scenario 2 of design option 2 @0.4 s, column connection shear failure*

3.3.3 Design option 3

Design option 3 was similar to design option 2 in that scenario 1 was fully arrested. Scenario 2, however, showed a wider and more severe response spectrum (severities up to 1,300 m^2 compared to 950 m^2 for design option 2). The mechanics of the collapse in scenario 2 are similar to design option 2, with the difference that shear failure occurred both above and below the truss strong floor in the middle of the building and destabilised the edge of the building. Collapse very quickly spreads to the lower half. Scenario 3 showed mixed results: in most cases the building survived. No axial failure at the column connections was observed. There were, however, cases where again the shear failure of the column-column connection under the middle strong floor caused the initially contained collapse to spread downward. Unlike design option 1, the horizontal connectivity with the truss reduced the initial spread of the damage to the adjacent corner column in both design options 2 & 3.

3.3.4 Design option 4

No resistance improvement compared to design option 1 was observed for design option 4: although scenario 1 sometimes survived the damage, the spread of collapse classes was much wider with the majority collapse class still being the corner bay as with design option 1, with similar mechanics described earlier and shown in Figure 5. Damage scenarios 2 & 3 showed very consistent behaviour despite the variability of the probabilistic inputs. A possible explanation is that although alternative load paths changed with the improved connections, they could not find their way back to the core. A closer look at the simultaneous improvement of the floor slab design and connectivity, together with the beam and column connectivity, is a worthwhile investment.

3.3.5 Design option 5

Finally, in design option 5, the small change of the column-column connection to increase its ductility did not

improve the robustness performance at all. Collapse mechanics were also similar to option 1.

3.3.6 Robustness indices

The results show that the performance of the original design is disappointing ($I_{Rob,av}$ close to zero) and so is the performance of options 4 & 5 with an improved connection ductility. On the other hand, options 2 & 3 perform much better, although at a higher cost in terms of embodied carbon due to the substantially larger columns and connections to accommodate the strong floor forces. Option 4 performs equally well as option 1, but it also costs more, therefore it is not a cost-effective solution.

The summary of the results is clear in the following table which compares the robustness indices for each damage scenario in each design option, as well as their cost in terms of CO_2-equivalent based on the volume of the structural materials. Surrogate modelling performance scores are also provided below.

Table 1: *Robustness comparison between all design options, including accuracy and marco F1 scores*

	$I_{Rob,sc1}$	$I_{Rob,sc2}$	$I_{Rob,sc3}$	CO_2eq (t)
Concept 1 scores	0.0129 (0.94 / 0.75)	0.0088 (0.73 / 0.40)	0.0088 (0.90 / 0.63)	**496.3**
Concept 2 scores	1.00 (0.83 / 0.36)	0.0182 (0.58 / 0.46)	0.0144 (0.76 / 0.71)	**519.6 (+4.7%)**
Concept 3 scores	1.00 (1.00 / 1.00)	0.0133 (0.56 / 0.43)	0.0274 (0.70 / 0.49)	**520.8 (+5.0%)**
Concept 4 scores	0.0119 (0.68 / 0.49)	0.0091 (1.00 / 1.00)	0.0090 (1.00 / 1.00)	**505.4 (+2.4%)**
Concept 5 scores	0.0095 (0.69 / 0.63)	0.0059 (0.33 / 0.33)	0.0088 (1.00 / 1.00)	**496.27 (-0.002%)**
Average	0.4069	0.0110	0.0137	
$A_{Fail,Dir}$	4.91	9.82	19.63	

With a 34-fold increase in the average robustness index, design options 2 & 3 with structural improvements in the whole building scale ("strong floors") are much better solutions for this particular building. They owe this improvement due to the full arrest of collapse in scenario 1 ($I_{Rob,sc1} = 1.0$) and the marginal, but insufficient improvement of collapse in scenarios 2 and 3 ($I_{Rob,sc2/3} < 0.03$, which is practically not different from zero).

This result is in line with the observations of Mpidi Bita et al. (2019) [20], who also proved the benefit of designing a strong floor from which columns can hang the floors below in case of damage. The benefit of the conceptual design is evident despite their study being on a different structural typology (flat-plate CLT building). Design option 4, equally robust as option 1, requires more steel in the connections and thus becomes uneconomic in the given assumptions. This is not to say that an improvement in the connections cannot increase robustness; rather, the specific solution implemented does not provide sufficient alternative load paths. Design option 5 is marginally worse than the starting option in terms of performance. These results are in line with the alternative load paths and collapse mechanisms discussed in the previous paragraphs. They highlight once again the significance of understanding how alternative load paths are formed, and making sure they lead to the ground. Increasing the ductility of only two connections (e.g. beam-column and column-column in option 4) allows loads to better redistribute in these parts of the structure, however, collapse resistance is also dependent on the floor-beam and floor-floor connections, global stiffness symmetry, and the buckling of columns. One should have a clear understanding of the flow of loads in a structure at the global scale (conceptual design) in order to make the right decisions regarding connection and component detailing.

3.3.7 Sensitivity studies

The properties of the columns and the column-column connections dominate the importance for external damage (scenarios 1 & 2), while the properties of the beams and floors dominate the importance for internal damage (scenario 3). However, the spread of importance values throughout the Random Forest is high, and the importance values themselves are neither high, nor very different from each other. This indicates an absence of an overall dominant feature, which reflects the observations in the collapse mechanisms, and explains why design options 4 & 5 do not perform better in terms of robustness. Collapse is arrested by the structure functioning as a large, complex system and an improvement on many variables, rather than just a few, is necessary to achieve an overall better robustness performance. Full details of the sensitivity study with figures is provided in Voulpiotis [3].

4 FROM RESEARCH TO PRACTICE

4.1 QUALITATIVE DESIGN (SCALE APPROACH)

The procedure outlined so far and the example case study are fairly complex, time-consuming activities. We do not suggest that practicing engineers must go through all this to ensure robustness; rather, simplified, qualitative techniques shall be used for simple or well-established structural typologies, and the full quantification procedure shall only be used for new, unknown typologies (of any material) whose collapse would have very serious consequences to the society.

A reinforced concrete, cast in-situ midrise building is a simple, known structure where robustness can be implicitly assumed. A method to assess its robustness more rigorously without performing any calculations is detailed in Voulpiotis et al. (2021) [2] and is based on considering structural robustness on different levels of the scale (Figure 8): whole building, compartments, components, connections, connectors, and material microstructure. What is important to understand is that current robustness design methods are largely based on preventing collapse to propagate from the component to the whole building level. If we are able to prevent collapse propagation also from connections to components, and from components to building compartments, the disproportionate collapse probability dramatically decreases. This is demonstrated by an example "stacked compartment" structure in Figure 9.

The qualitative approach may of course be also used for complex, unknown structures such as midrise timber buildings like the one studied in this paper. In

https://doi.org/10.52202/069179-0381

combination with advanced quantitative techniques, collaborative work of researchers and practitioners can

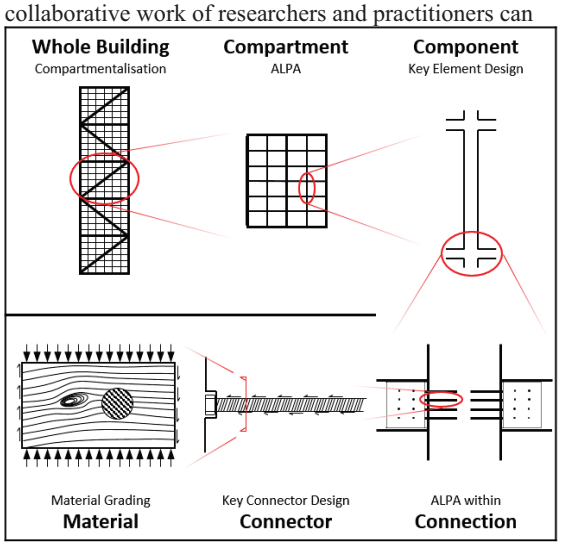

Figure 8: *Robustness can be qualitatively achieved by assessing the load redistributions at different levels of the scale*

lead to a much better understanding of the structural behaviour of new typologies in an implicit fashion, that is, the expert will be able to have a "gut feeling" of a sufficiently robust structure in the exact same way the experienced engineer knows if a beam or column cross section is sufficient in size to serve its purpose without performing any calculations. We may thus be able one day to decide on robustness design improvements based on tabulated design data or using simplified equations, like it is currently done with component design in the building codes.

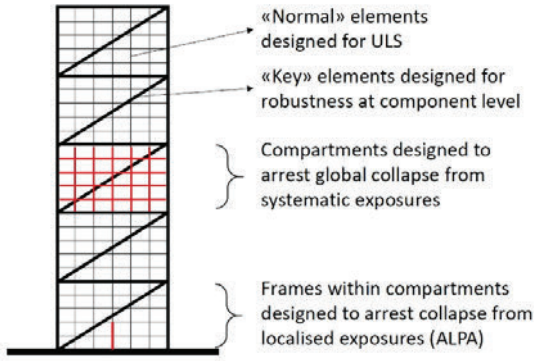

Figure 9: *Proposal of a theoretically "holistically robust" building according to Voulpiotis et al. (2021)* [2]

4.2 RELEVANCE OF BUILDING CODES

As we are aspiring for the building codes to be able to guide practitioners in more detail when it comes to robustness (whether a step-by-step guidance is truly feasible is a debate outside the scope of this paper), we hope to see a shift in the current approach, which offers little more than vague requirements without guidance. The work of Mpidi Bita, et al. (2019) [21] summarises the existing approaches of building codes in various regions (Canada, USA, Europe, Australia/New Zealand) and presents the results from a 171 participant survey. The survey asked practitioners whether they consider robustness in their design and to what extent this is affected by building codes. By looking at the different approaches in concrete, steel, and timber in each of the studied regions, the authors identify key improvements which can be made to existing codes and guidelines, such as the inclusion of specific recommendations for structural robustness, and a performance-based approach, rather than prescriptive requirements.

One of the most important findings of the survey is that robustness is practiced more consistently in regions or materials where the building codes provide more detailed help. With the case study in this paper, we hope to have started a necessary contribution of modelling data, such that timber-specific building codes can adapt and include more detailed guidance on designing robust tall timber buildings.

5 CONCLUSIONS

In this paper we presented an application of the quantification methodology originally presented by Voulpiotis et al. (2021) [2] in the previous world conference (WCTE 2021).

A case study, 15-storey timber building is designed to the Swiss building codes and is run through the quantification methodology using high-fidelity Finite Element Modelling and an adaptive surrogate modelling approach based on Random Forest Classifiers.

The results demonstrate how a sound conceptual design is more important to achieve robustness than localised strength or ductility improvements.

We finally paint a bigger picture of a qualitative-quantitative robustness approach, where the designer considers robustness on different levels of the structural scale, hoping that eventually we will be able to understand robustness intuitively for tall timber buildings as we currently do for simpler structures, such as cast-in-situ reinforced concrete midrise buildings.

The quantification framework and its application are valid for structures of any material and make an important step towards a better understanding of the collapse behaviour – and hence safety – of new structural typologies such as tall timber buildings.

ACKNOWLEDGEMENTS

The financial support of the Albert Lück Stiftung in Switzerland and the technical support of Prof. Dr. Jochen Köhler at the NTNU in Norway have been essential for the successful outcome of this research.

REFERENCES

[1] Bussell MN, Jones AEK. Robustness and the relevance of ronan point today. Struct Eng 2010;88:20–5.

[2] Voulpiotis K, Köhler J, Jockwer R. Robustness of tall timber buildings: an improved framework. Proc World Conf Timber Eng (WCTE 2021) 2021.

[3] Voulpiotis K. Robustness of Tall Timber Buildings. Swiss Federal Institute of Technology (ETH), 2021.

https://doi.org/https://doi.org/10.3929/ethz-b-000526211.
[4] Frangopol DM, Curley JP. Effects of damage and redundancy on structural reliability. J Struct Eng 1987;113:1533–49. https://doi.org/10.1061/(ASCE)0733-9445(1987)113:7(1533).
[5] Fu G, Frangopol DM. Balancing weight, system reliability and redundancy in a multiobjective optimization framework. Struct Saf 1990;7:165–75. https://doi.org/10.1016/0167-4730(90)90066-X.
[6] Baker JW, Schubert M, Faber MH. On the assessment of robustness. Struct Saf 2007;30:253–67. https://doi.org/10.1016/j.strusafe.2006.11.004.
[7] André J, Faber MH. Proposal of guidelines for the evolution of robustness framework in the future generation of Eurocodes. Struct Eng Int 2019;29:433–42. https://doi.org/10.1080/10168664.2019.1599706.
[8] Voulpiotis K, Köhler J, Jockwer R, Frangi A. A holistic framework for designing for structural robustness in tall timber buildings. Eng Struct 2021;227. https://doi.org/10.1016/j.engstruct.2020.111432.
[9] SIA 265: Swiss Society of Engineers and Architects (SIA). SIA 265: Holzbau. Zürich: 2012.
[10] SIA 262: Swiss Society of Engineers and Architects (SIA). SIA 262: Betonbau. Zürich: 2013.
[11] SIA 263: Swiss Society of Engineers and Architects (SIA). SIA 263: Stahlbau. Zürich: 2013.
[12] Dietsch P. Robustness of large-span timber roof structures — Structural aspects. Eng Struct 2011;33:3106–12. https://doi.org/10.1016/j.engstruct.2011.01.020.
[13] Breiman L. Random forests. Mach Learn 2001;45:5–32.
[14] Chawla N V., Bowyer KW, Hall LO, Kegelmeyer WP. SMOTE: Synthetic Minority Over-sampling Technique. J Artif Intell Res 2002;16:321–57. https://doi.org/10.1613/jair.953.
[15] Kohavi R. A study of cross-validation and bootstrap for accuracy estimation and model selection. Proc. 14th Int. Jt. Conf. Artif. Intell. - Vol. 2, Montreal, Quebec, Canada: Morgan Kaufmann Publishers Inc.; 1995, p. 1137–43.
[16] Scornet E. Trees, forests, and impurity-based variable importance. 2020.
[17] Pedregosa F, Varoquaux G, Gramfort A, Michel V, Thirion B, Grisel O, et al. Scikit-learn: Machine Learning in Python. J Mach Learn Res 2011;12:2825–30. https://doi.org/10.1289/EHP4713.
[18] Lemaître G, Nogueira F, Aridas C. Imbalanced-learn: A Python Toolbox to Tackle the Curse of Imbalanced Datasets in Machine Learning. J Mach Learn Res 2017;18:1–5.
[19] ID SIS HPC. Euler Cluster 2021. https://scicomp.ethz.ch/wiki/Euler (accessed August 30, 2021).
[20] Mpidi Bita H, Tannert T. Disproportionate collapse prevention analysis for a mid-rise flat-plate cross-laminated timber building. Eng Struct 2019;178:460–71. https://doi.org/10.1016/j.engstruct.2018.10.048.
[21] Mpidi Bita H, Huber JAJ, Voulpiotis K, Tannert T. Survey of contemporary practices for disproportionate collapse prevention. Eng Struct 2019;199. https://doi.org/10.1016/j.engstruct.2019.109578.

https://doi.org/10.52202/069179-0381

World Conference on Timber Engineering Oslo 2023

LONG-TERM MONITORING OF TALL MASS TIMBER BUILDINGS – EVALUATION OF DYNAMICS PROPERTIES

Samuel Cuerrier Auclair[1], Christian Dagenais[2], Girma Bitsuamlak[3]

ABSTRACT: Due to the lightweight nature of wood construction, wind excitation induces vibration with a larger amplitude when compared to buildings built with heavier materials, such as steel and concrete. The design method provided in the National Building Code of Canada requires buildings' natural frequencies and damping ratios as input. However, there is little data available for mid-to high-rise timber buildings. Therefore, FPInnovations launched a research project to measure mid-to high-rise timber buildings' natural frequencies and damping ratios in attempt to expand the database and validate or adapt the existing equations to estimate the natural frequencies. Two high-rise timber buildings were equipped with an anemometer and accelerometers and are constantly monitored to study how the wind excites high-rise timber buildings. The measurements suggest that the Arbora building and the Origine building have a modal damping ratio of about 2.5%.

KEYWORDS: Tall wood building, Wind-induced vibration, Damping ratio, Empirical mode decomposition (EMD), ambient-vibration test (AVT)

1 INTRODUCTION

Mass timber construction is known to be lightweight and has lower lateral stiffness in comparison to steel or concrete construction. These properties make the building more susceptible to wind-induced vibration in high-rise construction [1, 2]. Excessive vibration of buildings can cause occupants discomfort and damage to finish materials, services, and equipment in the building [3, 4]. These kinds of vibrations are not safety-related issues but may affect the market acceptance of mid- to high-rise timber buildings. Despite the challenge that comes with designing high-rise mass timber (MT) buildings, there is an international interest in building with wood, as it is more sustainable compared to concrete or steel [5]. However, there are still some unknowns regarding the dynamic properties of tall MT buildings under wind-induced vibration.

To evaluate the building response to wind loads, Davenport [3] has developed a process named wind load chain, illustrated in Figure 1, which laid the foundation of modern wind engineering and provides a theoretical basis for many building codes and standards.

Figure 1: *Wind loading chain of Davenport [3]*

As shown in Figure 1, the first step is to study the climate of the target site to define the design wind speed. This design wind speed could be directly taken from the climatic table in the National Building Code (NBC) in Canada [6], or it could be estimated from reliable anemometers. The wind flow around the building site is influenced by the terrain which is, in general, characterized by the roughness (e.g., vegetation, buildings, etc.) and the local topography. The third element of the wind load chain is the aerodynamic effect which is directly influenced by the building shape. This element is generally studied in boundary layers wind tunnels or with computational fluid dynamics (CFD). CFD can only be used for pre-design or for research since the NBC directly states that CFD cannot be used independently of boundary layers wind tunnel procedures. The fourth element of the wind load chain is the dynamic effect. This element is influenced by the dynamic characteristic of the wind and the dynamic properties of the structures. Since tall MT structures are a relatively new type of structure, there are several unknowns regarding its dynamic properties, especially the modal damping ratio [2]. The last element is the criteria which are generally defined by codes and standards.

The study of Bezabeh et al. [2] illustrated the impact of different modal damping ratios on the top floor acceleration caused by induced wind vibration. Several building heights from 10 to 40 storeys were studied with damping ratios from 1% to 10% in different exposure conditions, such as open country, suburban, and urban. The results of this study have shown the importance of the damping ratio on the evaluation of the top floor acceleration.

To fill the knowledge gap in the modal damping ratio of high-rise MT buildings, several European universities and

[1] Samuel Cuerrier Auclair, FPInnovations, Canada, samuel.cuerrier-auclair@fpinnovations.ca
[2] Christian Dagenais, FPInnovations, Canada, christian.dagenais@fpinnovations.ca
[3] Girma Bitsuamlak, University of Western Ontario, Canada, gbitsuam@uwo.ca

https://doi.org/10.52202/069179-0382

institutions launched the DynaTTB initiative in attempt to quantify these properties [7]. In Canada, FPInnovations started a similar research project aiming at quantifying the acceleration and damping ratio under different wind conditions of two existing high-rise MT buildings. As such, two high-rise MT buildings have been equipped with an anemometer and accelerometers to study how the wind excites the buildings. The first building is named Origine and is located in Québec City, and the second is named Arbora and is located in Montreal, both in the province of Québec.

2 BUILDING DESCRIPTION

2.1 ORIGINE BUILDING

Origine is a 13-storeys with a height of 40.0 metres completed in 2018 and designed by Nordic Structures. It is located in Quebec City in Canada and its near surroundings are a green park on the north side, a river on the west side, and low-rise buildings or no buildings on the south and east side, as shown in Figure 2.

The first level consists of a concrete podium, while the twelve other levels are made of MT elements (glulam and CLT). The gravity system consists of a post-and-beam glulam frame and 175 mm 5-ply CLT floor slabs. The typical clear span of the floor is 5.5 m. This type of floor can be considered as a semi-rigid diaphragm.

The lateral load resisting system (LLRS) consists of balloon framed CLT shear walls with vertical glulam elements at the ends of the shear wall. CLT and glulam extend from the concrete podium floor to the roof. The CLTs are either 9-ply 291 mm, 7-ply 244 mm, or 5-ply 175 mm panels, depending on the location and magnitude of the lateral force. For that type of LLRS, the lateral load is essentially taken by the CLT, and the uplift load is resisted by the glulam. The hold-down connectors consist of steel plates with dowels fastened into the wood. The horizontal joints between the CLT panels are connected with steel plates and dowels fastened into the wood. The vertical joints are connected with shear keys, as shown in Figure 3. These connectors are stiffer and stronger compared to traditional fasteners, such as nails, screws, or dowels. To ensure good contact between the two panels, self-tapping screws were inserted diagonally in addition to the shear keys. Several architectural and gravity CLT panels were also installed in the building which certainly contributes to stiffening the building laterally.

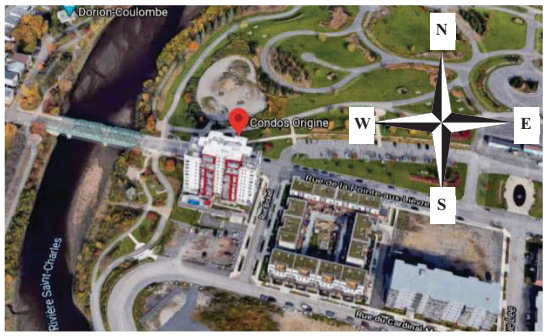

Figure 2: *Surrounding of the Origine building*

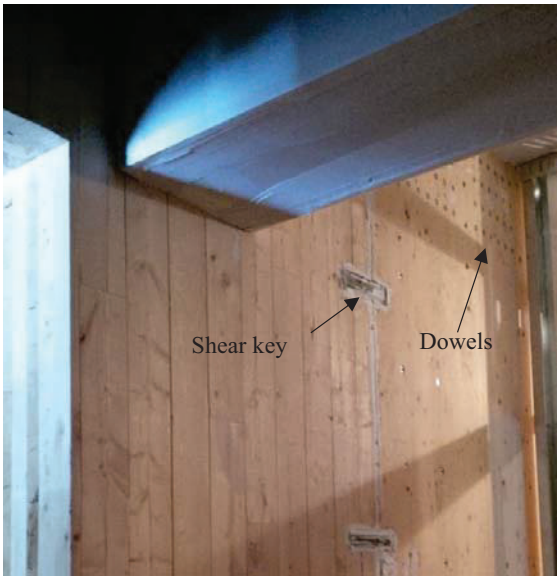

Figure 3: *Shear wall with shear keys and a hold-down with dowels*

2.2 ARBORA BUILDING

Completed in 2017, Arbora building is 8 storeys tall with a height of 24.5 metres and designed by Nordic Structures. It is located downtown Montreal in Canada and its near surroundings are buildings with a similar height except on its south side where it is a large one storey industrial building as shown in Figure 4.

The first level is a concrete podium, and the seven subsequent levels are made of MT (Glulam and CLT). The gravity system consists of a post-and-beam glulam frame and 175 mm CLT floor slabs. The typical floor clear span is 5.5 m. As with Origine, this type of floor creates a semi-rigid diaphragm effect. The LLRS are balloon framed CLT shear walls and elevators cores that extend from the concrete podium floor to the roof. The CLT shear walls are made of either 7-ply 244 mm or 5-ply 175 mm panels, depending on the location and magnitude of the lateral force. The uplift force is resisted by steel plates anchored to the CLT using ring shank nails, as shown in Figure 5. The vertical and horizontal joints between panels were designed with steel plates with ring shank nails. This kind of connection forms a flexible connection between CLT panels.

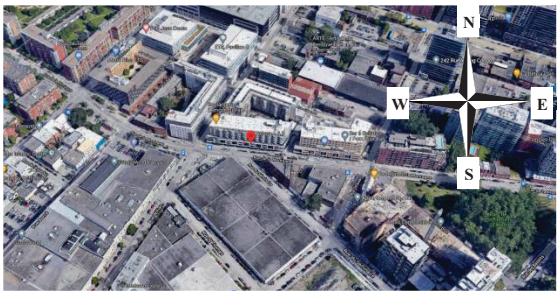

Figure 4: *Surrounding of the Arbora building*

https://doi.org/10.52202/069179-0382

Figure 5: *Shear wall with hold-down connected to the concrete mezzanine*

3 APPROACHES

3.1 Position and location of the devices

Both buildings are being constantly monitored with a set of accelerometers fixed on the ceiling of the top storey and an anemometer located on the roof of the building to roughly estimate the wind speed experienced by the buildings. The monitoring started in 2018 and is still ongoing.

The anemometer on both buildings is from Young Company, and the model used is 05103VK, which offer an output signal voltage output from 0 to 5V for wind speed from 0 km/h to 200 km/h (0 m/s to 55.5 m/s). The anemometer also has a mechanical range of 360° for the wind direction and an output signal of 0 V to 5 V. The location of the anemometer is shown on Figures 6 to 8. It must be understood that the wind flow around a building can be greatly influenced by the structure itself [8, 9]. This means the wind speed measurement cannot be taken as a precise value of the wind speed experienced by the building, namely if the anemometer is in a turbulent region. The analysis of the acceleration responses of the building with respect to the wind speed and direction needs to be made with precautions. Thus, the value measured by the anemometer only gives an indication of how much wind the building experiences. In attempt to limit the turbulence effect, the anemometers were positioned at about 2.5 m above the roof stair entrance (Figure 8).

Figure 6: *Location of the anemometer on the Origine building*

Figure 7: *Location of the anemometer on the Arbora building*

Figure 8: *Photo of the anemometer installed on the Origine building*

The accelerometers used to monitor the building acceleration are model 626B02 from PCB Piezotronics that uses the ICP® signal technology. The main benefit of an ICP® signal in this project is the low output impedance (<100 Ohms) which allows signals to be transmitted over long cables through harsh environments with minimum loss in signal quality [10]. The model 626B02 has a low frequency sensitivity ranging from 0.2 Hz to 6000 Hz and a measuring acceleration range of ± 10 g (± 98 m/s^2). The output signal of the accelerometer range is ± 5 V which gives a sensitivity of 500 mV/g (51 mVs^2/m).

Figures 9 and 10 show the plan locations where a pair of accelerometers have been fixed to measure the acceleration in the x and y directions. They have been fixed on the ceiling of the top floor. Ideally, these accelerometers should have been installed at the corners of the building, but this location would have been within a unit, and if for any reasons these accelerometers would have needed to be accessed, it would have been impossible. Therefore, the accelerometers were installed in a common area hidden in the ceiling.

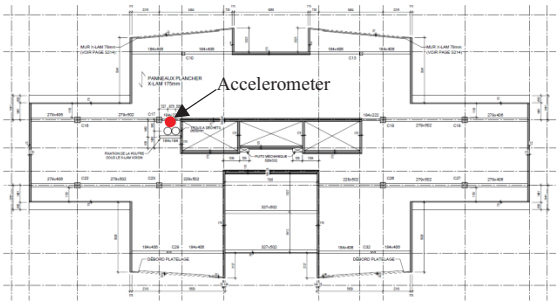

Figure 9: *Location of the accelerometers on the ceiling of the top floor for the Origine building*

https://doi.org/10.52202/069179-0382

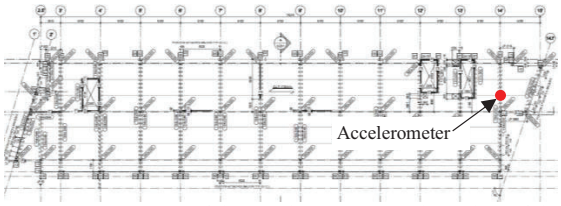

Figure 10: *Location of the accelerometers on the ceiling of the top floor for the Arbora building*

3.2 Data analysis

The data from the accelerometers and the anemometers are acquired at a frequency of 100 Hz permanently. The data are saved in a binary format in blocks of 6 hours. All the acquired data are then screened with a python script to extract meaningful 2-minute data. The trigger to extract the 2-minute window data is based on the 3 seconds average wind speed. The following rules are followed to extract the data for the Origine buildings:

1. If the maximum 3 seconds average wind speed of the 6 hours data block is below 10 m/s, no data are extracted;
2. If the maximum 3 seconds average wind speed of the 6-hour data block is between 10 and 15 m/s, one 2-minute data block is extracted;
3. If the maximum 3 seconds average wind speed of the 6-hour data block is between 15 and 20 m/s, three 2-minute data blocks are extracted unless if the maximum 3 seconds average wind speed of the subsequent data blocks is lower than 15 m/s for which no block is extracted;
4. If the maximum 3 seconds average wind speed of the 6-hour data block is higher than 20 m/s, five 2-minute data blocks are extracted unless if the maximum 3 seconds average wind speed of the subsequent data blocks is lower than 20 m/s for which only three blocks are extracted, or if the maximum 3 seconds average wind speed is lower than 15 m/s for which no data block is extracted.

For the Arbora building, the following rules are used:

1. If the maximum 3 seconds average wind speed of the 6-hour data block is below 10 m/s, no data are extracted;
2. If the maximum 3 seconds average wind speed of the 6-hour data block is between 10 and 15 m/s, two 2-minute data blocks are extracted;
3. If the maximum 3 seconds average wind speed of the 6-hour data block is between 15 and 20 m/s, ten 2-minute data blocks are extracted unless if the maximum 3 seconds average wind speed of the subsequent data blocks is lower than 15 m/s for which only two blocks are extracted;
4. If the maximum 3 seconds average wind speed of the 6-hour data block is higher than 20 m/s, 2-minute data blocks are extracted with no limit on the quantity until the maximum 3-seconds average wind speed of the subsequent data blocks is lower than 20 m/s for which the previous rule applies.

Two different extraction rules were used to have sufficient data for both buildings. The Arbora building is less exposed to wind compared to the Origine building. Therefore, less data during high wind speed events is available.

As described in the previous subsection, the sensitivity of the accelerometers used for the acquisition is 500 mV/g. These accelerometers are considered very sensitive but much more sensitive accelerometers exist at 10,000 mV/g. With the current accelerometers, if the maximum acceleration experienced by the building is the limit prescribed by the NBC for the residential building, 15 milli-g, the actual measurement over the measuring capacity will only be 0.15%. Therefore, noise in the measurement is almost inevitable in this case. In order to extract reliable dynamic properties of the building, the method to analyse the data needs to be carefully chosen.

The load experienced by the building is unknown, thus the modal identification technique used to process the signal of the accelerometer needs to be able to analyse output data only. Over the past decades, different time-frequency methods, including wavelet transform (WT) [11, 12], blind source separation (BSS) [13], and empirical mode decomposition (EMD) [14] have been used as modal identification techniques for large-scale civil infrastructure. Of all methods, EMD has the capability of using only a single channel of measurement.

There are different derivatives of the EMD method, such as the variational mode decomposition (VMD) [15], the multivariate empirical mode decomposition (MEMD) [16], and the time varying filtering-based EMD (TVF-EMD) [17]. This study utilizes the TVF-EMD method, since it can be used with only a single-channel measurement without causing mode-mixing or end effects under the presence of closely spaced modes or measurement noise. This is an important property of this technique, since the signal-to-noise ratio is small for the measurement performed in this study. Additionally, each channel is analysed independently, since the two accelerometers at the top of the building are placed orthogonally and the accelerometers at the ground are not considered during the analysis as the excitation from the ground is negligible in comparison to wind.

The EMD method decomposes the signal into a set of oscillatory waveforms known as intrinsic mode functions (IMFs). Then, the time varying filtering-based EMD (TVF-EMD) [17, 18] performs local cut-off filtering where the signal is successively filtered into local high-pass and low-pass components to decompose it into narrowband signal components (i.e., IMFs). Each IMF has a specific energy and frequency. To determine the modal damping ratio of the structure, an IMF with high energy (high RMS value) around the natural frequencies of the structure is chosen, which is represented by a red "x" and a red circle in Figures 11 and 12. This IMF is then analysed into the time domain by performing an autocorrelation to extract the damping ratio, as shown in Figure 13. The equation shown in Figure 13 is of the following form:

$$E(\tau) = Ae^{-\zeta f_n 2\pi\tau} \quad (1)$$

https://doi.org/10.52202/069179-0382

where ζ is the modal damping ratio, f_n the natural frequency of the IMF, τ is the time lag, A is the amplitude and $E(\tau)$ is the envelope of the autocorrelation.

This method is performed for every 2-minute extracted data. As such, a statistical analysis of the evaluated modal damping ratio for each extracted IMFs can be performed. When extracting modal damping ratio with ambient load, the level of confidence with the modal damping ratio is generally quite low since this is a parameter difficult to evaluate [19]. The level of confidence for every single data of modal damping ratio in this study is in the same order. However, one of the originalities of this study is to have performed that analysis more than 1000 times to obtain a statistical distribution of the modal damping ratio. Therefore, the modal damping ratio of the monitored structure could be based on the average, the median, or the mode in which we have a much better degree of confidence due to the quantity of data.

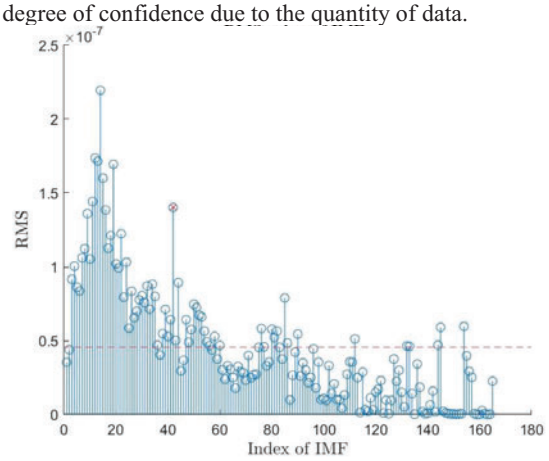

Figure 11: *RMS value of the IMFs*

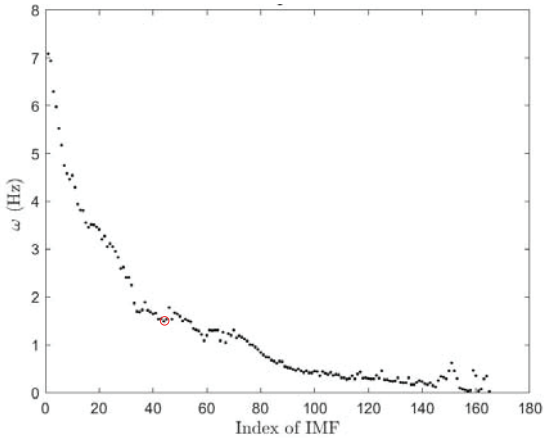

Figure 12: *Frequencies of the IMFs*

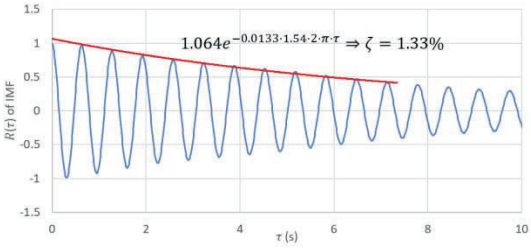

Figure 13: *Autocorrelation of the chosen IMF to evaluate the damping ratio*

4 RESULTS AND DISCUSSION

This section presents the results from the statistical analysis of the extracted modal damping ratio. The monitored buildings are equipped with two uniaxial accelerometers fixed on the ceiling of the top floor. One accelerometer is measuring the acceleration along the short axis of the building, while the other is measuring the acceleration in the orthogonal direction, i.e., along the long axis.

From the monitored data, several 2-minute window data are analysed to extract the damping ratio with a TVF-EMD algorithm [17]. Figures 14 to 17 show the probability density of the extracted damping ratio. It should be noted that, since evaluating the modal damping ratio under ambient loading is very difficult, the reliability of a single measurement for the modal damping ratio is relatively low [19] and therefore, using this method in which there is a statistical distribution of the modal damping ratios is recommended. Analysing more data and then performing statistical analysis of these data is a way to increase the reliability of the damping ratio value assigned to the building, as long as there is no systematic error in the method employed to extract the damping ratio.

It can be observed from Figures 14 to 17 that the lognormal distribution fits the measured damping ratio distribution very well. As a property of lognormal distribution, the probability density below the mode, i.e., highest probability density, decreases rapidly. It means that a very low modal damping ratio is less probable than a high damping ratio. Therefore, the average and the median are always higher than the mode. Tables 1 and 2 provide these estimated values for all the data points and for high wind events. The threshold for high wind events has been chosen only to have enough 2-minute window data under relatively high wind events. Since Origine is more exposed to wind, there is more data available for this building under these wind events. Consequently, threshold value is 18 m/s for Origine and 15 m/s for Arbora. From those tables, it can be observed that the extracted modal damping ratio under high wind speed is similar to the damping ratio extracted under wind speed higher than 10 m/s. This is an important observation, since it indicates that the building is still experiencing a linear behaviour under different wind conditions. Buildings are designed to remain elastic under wind load, but the connections between panels generally exhibit non-linear behaviour even under low load. The non-linear behaviour

https://doi.org/10.52202/069179-0382

of these connections does not seem to influence the damping ratio of the structures under wind loads noticeably.

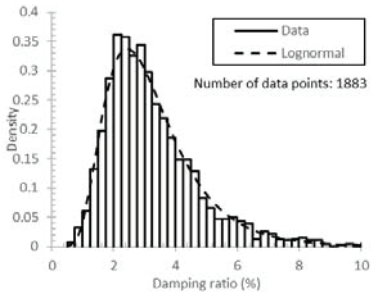

a) Along the short side of the building

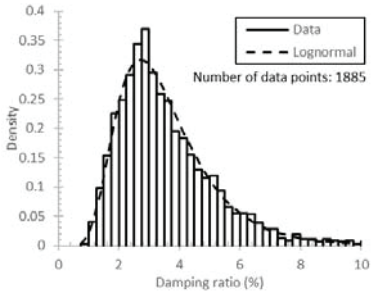

b) Along the long side of the building

Figure 14: *Statistical distribution of the modal damping ratio for wind speed higher than 10 m/s for the Origine Building*

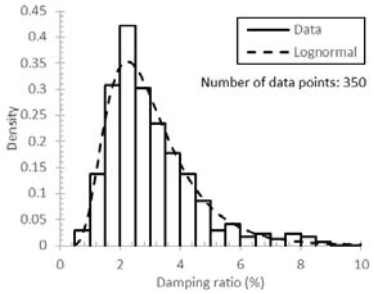

a) Along the short side of the building

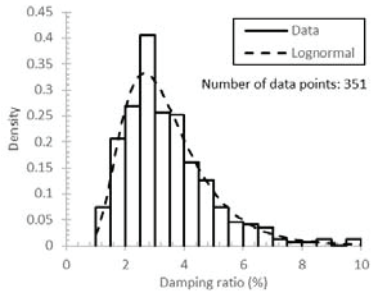

b) Along the long side of the building

Figure 15: *Statistical distribution of the modal damping ratio for wind speed higher than 18 m/s for the Origine Building*

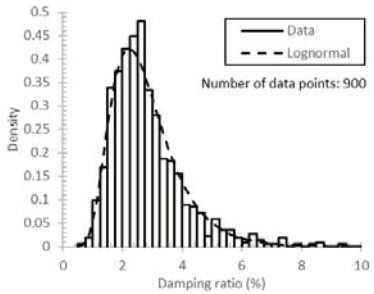

a) Along the short side of the building

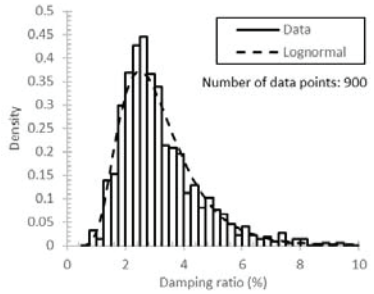

b) Along the long side of the building

Figure 16: *Statistical distribution of the modal damping ratio for wind speed higher than 10 m/s for the Arbora Building*

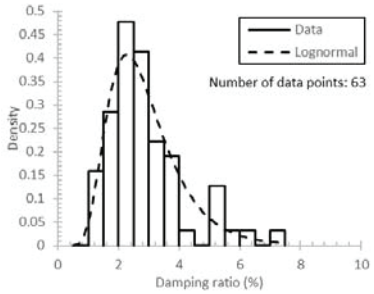

a) Along the short side of the building

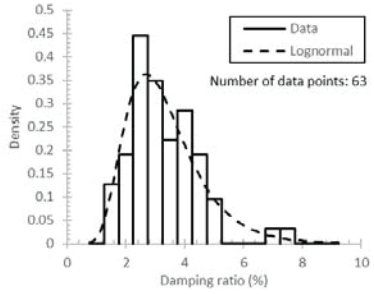

b) Along the long side of the building

Figure 17: *Statistical distribution of the modal damping ratio for wind speed higher than 15 m/s for the Arbora Building*

https://doi.org/10.52202/069179-0382

As mentioned in commentary A of the NBC when defining the stiffness of new material, such value should be based on a 50% exclusion, i.e., the median. Material stiffness is generally used for serviceability limit state verification. Top floor acceleration limitation is a serviceability limit state verification. Therefore, it is believed that the damping ratio of the Arbora and Origine building could be considered as 2.5% which is found to be slightly lower than the median under high wind speed for the fundamental frequency of both buildings. Table 1 and Table 2 present the statistical parameter of the modal damping ratio for both buildings.

Arbora and Origine have similar construction systems. The LLRS are made with balloon frame CLT, and the floors are made with CLT. However, the shape of the buildings is different. Origine has more a tower shape by being almost square, while Arbora is rectangular, and its length is much longer than its height. Since these two buildings have a similar construction material but different shapes, it seems that MT buildings with CLT balloon-framed shear walls have a damping ratio of about 2.5%.

Table 1: *Statistical parameter of the modal damping ratio for the two first natural fundamental frequency for the Origine building*

	Wind > 10 m/s		Wind > 18 m/s	
Statistical Parameter	f_1	f_2	f_1	f_2
Number of data	1883	1885	350	351
Average	3.26	3.56	3.05	3.44
Median	2.96	3.25	2.75	3.15
Mode	2.44	2.71	2.23	2.65

Table 2: *Statistical parameter of the modal damping ratio for the two first natural fundamental frequency for the Arbora building*

	Wind > 10 m/s		Wind > 15 m/s	
Statistical Parameter	f_1	f_2	f_1	f_2
Number of data	900	900	63	63
Average	2.80	3.15	2.88	3.34
Median	2.59	2.91	2.66	3.11
Mode	2.22	2.48	2.27	2.69

5 CONCLUSIONS

This study investigated the modal damping ratio value of the Origine and Arbora mass timber buildings under wind-induced vibration. The Origine building is 13 storeys with a roof height of 40.0 m, and the Arbora building is 8 storeys with a roof height of 24.5 m. These buildings were designed through the development of alternative solutions conforming to the National Building Code of Canada. Although the height of these buildings is not enough to raise serious concerns regarding the wind-induced vibration behaviour of the buildings, they can give relevant and critical data, such as modal damping ratio, that can only be evaluated on real-size buildings. This variable is critical when evaluating the dynamic behaviour of the building under wind-induced vibration.

To extract this dynamic property of the Origine and Arbora buildings, they were equipped with accelerometers fixed on the ceiling of the top floor and an anemometer fixed on the roof to almost permanently monitor the acceleration experienced by the buildings. These data were then screened to extract meaningful 2-minute data windows. These 2-minute data windows were then analysed with a time varying filtering-based empirical mode decomposition (TVF-EMD) algorithm to extract the modal damping ratio of the analysed data. A statistical analysis of the damping ratio was then performed to increase the reliability of the extracted damping ratio, since evaluating such parameters under ambient load with a single measurement has limited reliability. From these analyses it was found that the Origine and Arbora buildings have a damping ratio of about 2.5% for their fundamental natural frequencies. Therefore, for future high-rise mass-timber (MT) buildings with lateral load resisting systems (LLRS) made of cross-laminated timber (CLT), the damping ratio could be assumed around 2.5% or below. Currently, damping ratio for wind-induced vibration is usually assumed to be 1% for MT buildings. Such value is now believed to be overly conservative for high-rise MT buildings with CLT shear walls.

The next steps of this research project will be to estimate the top floor acceleration of different designs of high-rise MT buildings and then to iterate on different structural parameters to optimize the structure for reducing the wind-induced vibration. Usually, for very tall buildings such as skyscrapers, this optimization is made along with shape optimization. However, going through a shape optimization process for high-rise MT buildings may not be the most efficient and economical way, since the height in comparison to conventional steel or concrete skyscrapers is still small and only structural optimization may be sufficient. Such a study will allow defining the best strategies to reduce wind-induced vibration for MT buildings.

ACKNOWLEDGEMENT

Authors would like to thank Natural Resources Canada (Canadian Forest Service) and British Columbia Forestry Innovation Investment for their financial support of this work.

REFERENCES

[1] M. Johansson, A. Linderholt, B. Åsa, K. Jarnerö and T. Reynolds, "Building higher with light-weight timber structures - the effect of wind induced vibrations," in *inter.noise*, San Francisco, California, USA, 2015.

[2] M. A. Bezabeh, G. T. Bitsuamlak, M. Popovski and S. Tesfamariam, "Dynamic Response of Tall Mass-Timber Buildings to Wind Excitation," *Journal of Structural Engineering,* vol. 146, no. 10, 2020.

[3] M. Bezabeh, G. Bitsuamlak, M. Popovski and S. Tesfamariam, "Probabilistic servability-performance assessment of tall mass-timberm buildings subjected to stochastic wind loads: Part I - structural design and wind tunnel testing," *Journal of Wind Engineering & Industrial Aerodynamics,* vol. 181, pp. 85-103, 2018.

[4] M. Popovski, M. Mohammad, C. Ni, M. Rezai, K. Below, R. Malczyk and J. Sherstobitoff, "Design and construction of tall wood buildings: Input data, testing and advanced analysis," *World Conference on Timber Engineering,* 10-14 August 2014.

[5] B. Grann, "A Comparative Life Cycle Assessment of Two Multistory Residential Buildings. Cross-Laminated vs. concrete slab and Column and Light Gauge Steel Walls," FPInnovations, Vancouver, 2013.

[6] Canadian Commission on Building and Fire Codes, "National Building Code of Canada: 2020," National Research Council of Canada, 2022.

[7] DynaTTB consortium, "DynaTTB - Dynamic Response of Tall Timber Buildings under Service Load," 2019. [Online]. Available: https://www.dynattb.com/. [Accessed 21 10 2021].

[8] A. Elshaer, H. Aboshosha, G. Bitsuamlak, A. E. Damatty and A. Dagnew, "LES evaluation of wind-induced responses for an isolated and a surrounded tall building," *Engineering structures,* vol. 115, pp. 179-195, 2016.

[9] G. Bitsuamlak, A. K. Dagnew and J. Erwin, "Evaluation of wind loads on solar panel modules using CFD," *The Fifth International Symposium on Computational Wind Engineering,* 23-27 06 2010.

[10] PCB Piezotronics, "Signal conditioning basics," [Online]. Available: https://www.pcb.com/resources/technical-information/signal-conditioning-basics. [Accessed 20 12 2021].

[11] Z. Hou, M. Noori and R. Amand, "Wavelet-based approach for structural damage detection," *Journal of Engineering Mechanics,* vol. 126, no. 7, pp. 677-683, 2000.

[12] Y. M., S. A. and L. K., "Condition assessment of structure with tuned mass damper using empirical wavelet transform," *Journal of Vibration and Control,* vol. 24, no. 20, pp. 4850-4867, 2018.

[13] A. Sadhu, S. Narasimhan and J. Antoni, "A review of output-only structural mode identification literature employing blind source separation methods," *Mechanical Systems and Signal Processing,* vol. 94, p. 415431, 2017.

[14] N. E. Huang, Z. Shen, S. R. Long, M. C. Wu, H. H. Shih, Q. Zheng, N.-C. Yen, C. C. Tung and H. H. Liu, "The empirical mode decomposition and the Hilbert spectrum for nonlinear and non-stationary time series analysis," *Proc. R. Soc. Lond. A,* vol. 454, pp. 903-995, 8 3 1998.

[15] A. Bagheri, O. E. Ozbulut and D. K. Harris, "Structural system identification based on variational mode decomposition," *Journal of Sound and Vibration,* vol. 417, pp. 182-197, 2018.

[16] N. U. Rehman, S. Ehsan, S. M. U. Abdullah, M. J. Akhtar, D. P. Mandic and K. D. McDonald-Maier, "Multi-Scale Pixel-Based Image Fusion Using Multivariate Empirical Mode Decomposition," *Sensors,* vol. 15, no. 5, pp. 10923-10947, 2015.

[17] M. Lazhari and A. Sadhu, "Decentralized modal identification of structures using an adaptive empirical mode decomposition method," *Journal of Sound and Vibration,* vol. 447, pp. 20-41, 2019.

[18] L. Heng, L. Zhi and W. Mo, "A time varying filter approach for empirical mode decomposition," *Signal Processing,* vol. 138, pp. 146-158, 2017.

[19] F. Magalhães, Á. Cunha, E. Caetano and R. Brincker, "Damping estimation using free decays and ambient vibration tests," *Mechanical Systems and Signal Processing,* vol. 24, no. 5, pp. 1274-1290, 2010.

https://doi.org/10.52202/069179-0382

World Conference on Timber Engineering Oslo 2023

DIFFERENTIAL MATERIAL MOVEMENT IN TALL MASS TIMBER STRUCTURES

Richard McLain[1], Josephine Racine[2], Bryce Lumpkin[3]

ABSTRACT: As mass timber buildings reach unprecedented heights, not to be overlooked in the design and detailing of these structures is the effects of vertical movements, particularly due to their cumulative. Glulam column shrinkage, joint settlement, and creep can affect vertical mechanical systems, exterior enclosures, and interior partitions, as well as differential create challenges where timber framing systems move relative to other structural systems such as concrete core walls. This paper analyzes the reasons for vertical movement (both short and long term), provides methods of calculating anticipated movement, compares calculated movement to on-site verified movement, highlights detailing options, and discusses vertical movement strategies implemented on tall mass timber projects completed in North America.

KEYWORDS: Creep, Settlement, Shrinkage, Crushing, Movement, Deflection, Columns, Monitoring, High-Rise

1 INTRODUCTION

As the height of mass timber buildings continues to grow, a new set of design and detailing challenges arises, creating the need for new engineering solutions to achieve optimal building construction and performance. One necessary detailing consideration is vertical movement, which includes column shrinkage, joint settlement, and creep.

2 TALL MASS TIMBER

U.S. interest in tall timber buildings, i.e., buildings that exceed height and area limits prescribed in the 2018 and previous versions of the International Building Code (IBC), has steadily increased over the past several years. With the introduction of three new construction types in the 2021 IBC—Types IV-A, IV-B and IV-C, which allow up to 18, 12 and nine stories of mass timber construction respectively—these projects are also getting built. Currently, more than 10% of the mass timber buildings in design or built in this country exceed the 2018 prescriptive height limits. Tall projects such as Heartwood in Seattle, 1510 Webster in Oakland, Ascent in Milwaukee, INTRO in Cleveland, 11 E Lenox in Boston, and 80M in Washington DC are either under construction or completed and occupied. At the time of writing, several others are set to break ground.

As the height of mass timber buildings continues to grow, a new set of design and detailing challenges arises, creating the need for new engineering solutions to achieve optimal building construction and performance. One necessary detailing consideration is vertical movement, which includes column shrinkage, joint settlement, and creep. The main concerns are the impact of deformations on vertical mechanical systems, exterior enclosures, and interior partitions, as well as differential vertical movement of timber framing systems relative to other building features such as concrete core walls and exterior façades. This paper analyzes the reasons for vertical movement (both short and long term), provides methods of calculating anticipated movement, compares calculated movement to on-site verified movement, highlights detailing options, and discusses vertical movement strategies implemented on tall mass timber projects completed in North America.

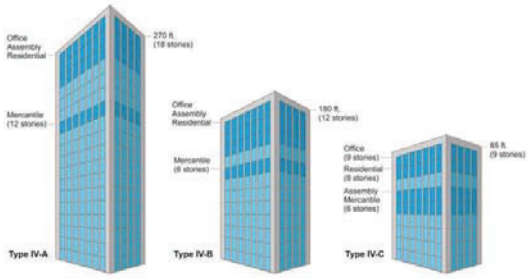

Figure 1: *Introduced with the 2021 IBC, Types IV-A, IV-B, and IV-C construction allow up to 18, 12 and nine stories of mass timber (respectively). Credit: WoodWorks*

3 SOURCES OF VERTICAL MOVEMENT

Vertical movement occurs in all buildings, regardless of height and structural materials used. The key to mitigation is to understand all potential sources of movement, calculate the sum of the ones predicted, and provide connection details that minimize movement and its effects while allowing for field adjustability. Most tall mass timber projects use a structural system of timber beams and columns supporting mass timber floor and roof panels. The columns and beams are usually glue-

[1] Ricky McLain, PE, SE, WoodWorks – Wood Products Council, Cabot, VT, USA, ricky.mclain@woodworks.org
[2] Josephine Racine, EIT, Fast + Epp, Vancouver, BC, CA, jracine@fastepp.com
[3] Bryce Lumpkin, PE, Fast + Epp, Seattle, WA, USA, BLumpkin@fastepp.com

https://doi.org/10.52202/069179-0383

laminated timber (glulam), though structural composite lumber (SCL) can also be used, and options for the panels include cross-laminated timber (CLT), nail-laminated timber (NLT) and dowel-laminated timber (DLT), among others. It is common for the vertical lateral force-resisting systems to be non-wood—e.g., concrete shear walls and steel braced frames. As the primary vertical elements in a tall mass timber building, the timber columns have a significant impact on the net vertical movement of the building. However, the connections of column to column, beam to column and floor panel to column can also play a significant role. Not only should the net vertical movement of the timber columns and connections be considered, so too should the movements of these elements relative to other building systems which may not be moving to the same degree or in the same direction (e.g., timber column movement relative to concrete core wall movement).

The main sources of vertical movement in tall mass timber structures, all of which are addressed in this paper, include:

- Column axial shortening
- Column creep
- Column, beam and panel shrinkage
- Beam and panel crushing perpendicular to grain
- Settlement at connections

Figure 2: *Example column and beam connection at 80M in Washington DC, designed by Hickok Cole*
Credit: WoodWorks

4 BUILDING CODES AND STANDARDS

Applicable building codes and standards vary based on the project's location, the jurisdiction's adopted building code, and any relevant amendments. The following codes and standards commonly apply to tall mass timber buildings.

International Building Code (IBC)
The IBC is a model building code developed by the International Code Council (ICC). Adopted as a base code by most jurisdictions in the U.S., it addresses health and safety concerns for buildings based on prescriptive and performance requirements. This document refers to the 2021 IBC unless otherwise noted.

Chapter 35 of the IBC provides a list of referenced standards, which represent consensus on how a material, product or assembly is to be designed, manufactured, tested or installed to achieve a specified level of performance. Standards that address vertical movement topics are noted below. Additionally, IBC Section 2304.3.3 requires that wood-framed projects greater than three stories include an analysis of the effects of shrinkage. It stipulates that shrinkage in a wood building not have adverse effects on systems such as roof drainage, electrical, mechanical, or other equipment.

National Design Specification® (NDS®) for Wood Construction
Published by the American Wood Council (AWC), the NDS defines the methods to be used in the structural design of wood members and connections. It contains information related to the design of mass timber products including CLT, glulam and SCL. Topics in the NDS that can impact vertical movement include creep and wood crushing when loaded perpendicular to grain.

Product Standards such as ANSI/APA PRG 320 Standard for Performance-Rated Cross-Laminated Timber and ANSI 190.1 Standard for Wood Products – Structural Glued Laminated Timber
Standards for mass timber products typically include dimensional tolerances. For example, PRG 320 requires that the actual width of a CLT panel be within +/- 3.175 mm (1/8-in.) of the specified width, and actual panel length be within +/- 6.35 mm (1/4-in.) of the specified length. Glulam columns up to 6.1 m (20 ft) long must have an actual length within +/- 1.59 mm (1/16-in.) of the specified length. These tolerances can impact vertical movement, particularly at connections.

Note that the abovementioned codes and standards do not contain explicit information on some aspects of vertical movement in tall timber structures. For example, calculations for determining shrinkage in wood members are not detailed in codes and standards, nor is the creep factor for column axial shortening. As such, engineering judgement is necessary and other sources of information are relied on. As with any circumstance requiring the use of engineering judgement, it is the responsibility of the engineer to use the most current information, research, test results, etc. to inform or validate assumptions made. The following sections note several *possible* methods of quantifying vertical movement in tall timber buildings. This information is intended to demonstrate options for quantifying these movements; it is not intended to cover all the options or solutions.

5 QUANTIFYING VERTICAL MOVEMENT

5.1 COLUMN AXIAL SHORTENING

Axial forces on any structural column, be it timber, steel or concrete, cause shortening of the member. Using the

https://doi.org/10.52202/069179-0383

principles of mechanics of materials, the axial shortening of a column is calculated with the equation:
$\Delta_{as} = PL/(AE)$

Where:

- Δ_{as} = column axial shortening (mm or in.)
- not including creep effects
- P = axial load supported by the column (N or lbs)
- L = length of the column (mm or in.)
- A = cross-sectional area of the column (mm^2 or in^2)
- E = modulus of elasticity of the column (kPa or psi)

Following is an example axial column shortening calculation. Note that this is an arbitrary design example and is not related to the actual project examples in the on-site verification information contained in the full document.

- Axial load of 200.2 kN (45,000 lbs) of which 89 kN (20,000 lbs) are dead load, and 111.2 kN (25,000 lbs) are live load, duration of load factor = 1.0
- Assume a 222 mm x 229 mm (8-3/4-in. x 9-in.) Douglas-fir glulam column, layup combination 2
- Column length = 4.6 m (15 feet)
- F'c = 13,445 kPa (1,950 psi)
- E = 11,031,612 kPa (1,600,000 psi)

$\Delta_{as} = PL/AE = (200.2)(4600)/((222*229)(11,031,612/1000^2) = 1.6$ mm
Or $(45,000)(15*12)/((8.75*9)(1,600,000)) = 0.06$ in.

Section 3.5 of the NDS discusses creep effects of long-term loading on deflection of bending members. Although this section of the NDS is directly applicable to bending members, it is not uncommon to also apply creep calculations to axial column deformations (shortening). Equation 3.5-1 in the NDS provides a method of quantifying the deformation effects of long-term loading on bending members.
$\Delta_{as,T} = K_{CR}\,\Delta_{LT} + \Delta_{ST}$, where:

- $\Delta_{as,T}$ = column axial shortening including creep effects (mm or in.)
- K_{CR} = time-dependent deformation creep factor
  - If we assume the creep factor for axial compression is the same as for bending,
- K_{CR} = 1.5 for seasoned timbers, glulam or SCL used in dry service conditions.
- Δ_{LT} = immediate deformation due to long-term loading (mm or in.)
- Δ_{ST} = deformation due to short-term loading (mm or in.)

For the column in the above example, the 89kN (20,000 lbs) axial dead load on the column is the long-term load, and the 111.2 kN (25,000 lbs) axial live load is the short-term load. If one applies this creep deformation equation to axial column shortening, accounting for long-term creep effects, the total anticipated axial column shortening in this example would be:
$\Delta_{as,T} = (1.5)(1.6)(89/200.2) + (1.6)(111.2/200.2) = 1.9$ mm
Or $(1.5)(0.06)(20{,}000/45{,}000) + (0.06)(25{,}000/45{,}000) = 0.07$ in.

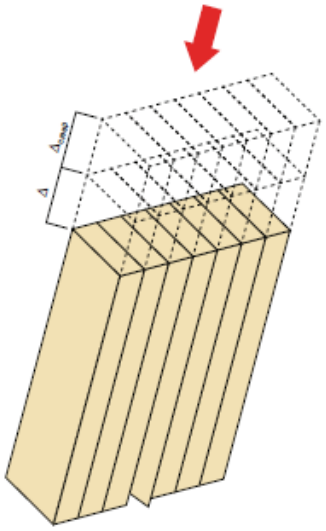

Figure 3: *Shortening of glulam columns*

5.2 SHRINKAGE

Simplistically, wood's cellular structure can be imagined as a bundle of drinking straws held together with a rubber band, with each straw representing a longitudinal cell in the wood. As noted, water can be free water stored in the straw (cell) cavity or bound water absorbed by the straw (cell) walls. At high moisture contents, water exists in both locations. As the wood dries, the free water is released from the cell cavities before the bound water is released from the cell walls. When wood has no free water and yet the cell wall is still saturated, it is said to be at its fiber saturation point (FSP).

The FSP of different species of wood varies but for most common softwoods is around 28-30%. The MC of lumber in service is typically 7-14%, much lower than the FSP. Wood remains dimensionally stable above the FSP, i.e., it doesn't change in dimension with an increase or decrease of moisture as long as it remains above the FSP at all times. This is because the water being absorbed or released is largely free water, not bound water. Once the moisture content drops below the FSP (i.e., bound water is being removed), the wood starts to change dimensionally.

Wood moisture content (MC) is the weight of water in wood as a percentage of the completely dry wood weight. During the life of a tree, its MC can exceed 200%, meaning the total water weight in a given volume of wood makes up two thirds or more of the total weight.

https://doi.org/10.52202/069179-0383

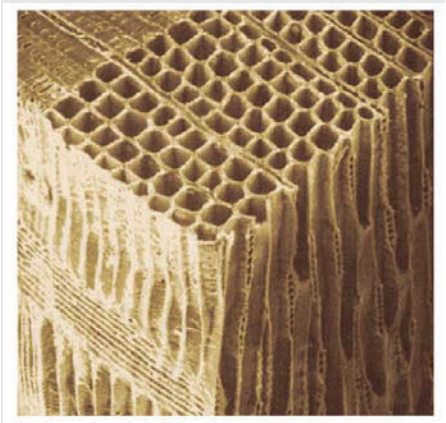

Figure 4: *Southern yellow pine cellular makeup*
Photo: USDA Forest Service Agricultural Handbook

Average shrinkage values from FSP to oven dry are approximately 5% and 7% (radial and tangential shrinkage, respectively), while longitudinal is approximately 0.1% to 0.2% for most species of wood. However, columns in mass timber construction are installed well below the FSP and maintain some residual moisture greater than oven dry. Since only a range of longitudinal shrinkage is provided, the engineer should use engineering judgement when determining the appropriate shrinkage coefficient to use. One method of calculating glulam column longitudinal shrinkage would be to assume an average shrinkage of 0.15% from fiber saturation point (FSP) to oven dry. Assuming that FSP is 28% MC, this allows one to calculate a coefficient of 0.15% / 28 = 0.000054, which equals the amount of longitudinal shrinkage per mm (or inch) of column length per % of MC change.

Using the column from the example earlier in this document, assume a 222 mm x 2229 mm (8-3/4-in. x 9-in.) column, 4.6 m (15 ft) long, with installed MC of 19% and EMC of 12%. Calculated longitudinal column shrinkage is:

$\Delta_{shrinkage}$ = (4600 mm)(0.000054)(19-12) = 1.7 mm
Or (15 ft)(12 in./ft)(0.000054)(19-12) = 0.07 in.

Detailing the column-to-beam connections should also include shrinkage consideration. Cross-grain shrinkage is much more significant than longitudinal shrinkage. A common coefficient used to calculate the cross-grain shrinkage of wood members is 0.0025 in. per inch of cross-sectional dimension for every 1% change in MC. Recall the common range of radial and tangential shrinkage discussed previously, 5% to 7% from FSP to oven dry, and we can see how this 0.0025 coefficient is derived. Assume a worst case of 7% shrinkage and an FSP of 28%, and the cross-grain shrinkage coefficient = 7% / 28 = 0.0025.

For example, a 222 mm x 610 mm (8-3/4-in. x 24-in.) glulam beam with an installed MC of 19% and EMC of 12% would have an anticipated shrinkage of:

Beam Depth: $\Delta_{shrinkage}$ = (610)(0.0025)(19-12) = 10.7 mm
Or (24 in.)(0.0025)(19-12) = 0.42 in.

Beam Width: $\Delta_{shrinkage}$ = (222)(0.0025)(19-12) = 3.9 mm
(8.75 in.)(0.0025)(19-12) = 0.15 in.

If this beam depth shrinkage occurs at each level, the overall effects on a 12- or 18-story mass timber building would be significant, resulting in multiple centimetres of building shrinkage. This is one reason why detailing the beam-to-column connections in multi-story mass timber structures such that beam shrinkage is isolated from impacting the overall building height is a key method of minimizing the impacts of vertical movement.

Consider the relative differences in the following column-to-beam configurations:

Option 1: An upper column bears directly on the mass timber floor panel, which bears directly on the support beam which bears on the lower column. This is essentially a platform-frame detail; because the shrinkage zone per floor is relatively deep (equaling the depth of the floor panel plus depth of the beam), shrinkage per floor is high. In the example above, the shrinkage in the depth of the beam would be approximately 10.7 mm (0.42 in.) per level, in addition to approximately 3 mm (0.12 in.) of panel thickness shrinkage, assuming a 175 mm (6-7/8-in.) deep panel. The total shrinkage per floor due only to beam and panel shrinkage is 13.7 mm (0.54-in.).

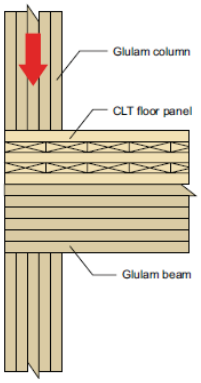

Figure 5: *Example column and beam connection; beam bears directly on column with beam shrinkage accumulation sub-optimal*

Option 2: beams and panels are isolated from the shrinkage zone by connections in which the beams do not bear directly on top of the columns below and similarly, the upper columns do not bear directly on top of the beams or panels. Detailing strategies involve either notching the column to allow the beam to bear on a shelf or creating a

https://doi.org/10.52202/069179-0383

vertical load path where columns above bear directly on columns below, in some cases involving beam hangers. These options essentially eliminate all cross-grain shrinkage zones.

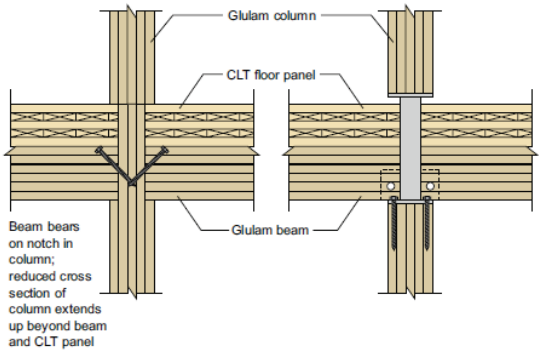

Figure 6: *Example column and beam connections, with beam shrinkage isolated from cumulative building shrinkage*

As the connections in Option 2 illustrate, it is possible (and preferable) to completely isolate beam depth shrinkage from impacting the overall building shrinkage. This is not to say that beam depth shrinkage will not occur—it will. However, keeping the beam depth shrinkage isolated from the continuous vertical load path of the columns minimizes the impacts, which are realized at each individual level without being transferred from one level to the next.

For additional connections and detailing options, browse the WoodWorks CAD/Revit tool and accompanying *Index of Mass Timber Connections* [4].

5.3 PERPENDICULAR-TO-GRAIN CRUSHING

Not only do column, beam and floor panel connection details impact vertical movement because of shrinkage potential, they can add to vertical movement due to crushing of the wood members. When loaded perpendicular to grain, wood members are prone to isolated crushing. NDS Section 3.10.2 provides general guidance on bearing perpendicular to grain, and the NDS Supplement provides allowable perpendicular-to-grain stresses. For softwood species commonly used in mass timber products, the typical range for allowable perpendicular-to-grain stresses is 2758 to 5516 kPa (400 to 800 psi.). Even when keeping actual perpendicular-to-grain stresses at or below allowable levels, some crushing does occur.

For steel-on-wood bearing conditions with the wood member loaded perpendicular to grain, the equations for calculating wood crushing are below. Note that crushing at 73% of allowable perpendicular-to-grain stress is 0.5 mm (0.02 in.) and crushing at 100% of allowable perpendicular-to-grain stress is 1 mm (0.04 in.).

Where: $f_{c\perp} \le F_{c\perp 0.02\ in}$

$$\Delta = 0.02 \times \left(\frac{f_{c\perp}}{F_{c\perp 0.02\ in.}} \right)$$

Where: $F_{c\perp 0.02\ in.} < f_{c\perp} < F_{c\perp 0.04\ in.}$

$$\Delta = 0.04 - 0.02 \times \frac{1 - \left(\frac{f_{c\perp}}{F_{c\perp 0.04\ in.}} \right)}{0.27\ in.}$$

Where: $f_{c\perp} > F_{c\perp 0.04\ in.}$

$$\Delta = 0.04 \times \left(\frac{f_{c\perp}}{F_{c\perp 0.04\ in.}} \right)^3$$

Assume the column in this design example bears on top of a 222 mm x 610 mm (8-3/4-in. wide x 24-in.) deep glulam beam. $F'_{c,perp}$ = 4482 kPa (650 psi.). The perpendicular-to-grain stress on top of the beam is:

$Fc_{,perp}$ = 200.2 kN/(222/1000)(229/1000) = 3940 kPa
Or 45,000 lbs/(8.75)(9) = 571 psi

And the resulting crushing is:
Stress ratio = 3940/4482 = 0.88
Or 571/650 = 0.88. Therefore, use equation 2.0 to calculate crushing:

$\Delta_{crushing}$ = (0.04 - (0.02)((1-(571/650))/0.27)) = 0.03 in. = 0.8 mm

Note that this is the crushing at one of the column-to-beam interfaces (top or bottom of beam surface). The same crushing occurs twice in this instance, essentially doubling the cumulative beam crushing (1.6 mm or 0.06 in total).

Similar to the discussion in the *Quantifying Wood Shrinkage* section above, where beam-to-column connections can be detailed in such a manner as to isolate beams from impacting cumulative building movement, the same is true for beam crushing. By utilizing details where upper columns do not bear directly on top of beams below, and beams do not bear directly on top of columns below, crushing of the wood members is isolated or eliminated and therefore does not contribute to overall building shrinkage. Additional discussion on effective detailing strategies for minimizing shrinkage and crushing effects at beam and column connections is included below.

One place where beams bearing on top of columns may be desired is at cantilevers. When columns are held back from the exterior wall, with the beams and floor panels cantilevering out to support the exterior wall, it might be assumed that the beams need to run directly over the column, which is undesirable from a beam crushing and shrinkage perspective. Rather, a double beam system with

each beam straddling the column, supported by partial bearing on a notch into the column, would allow the beam cantilever while avoiding cumulative effects of both. An example of this detail is shown in Figure 7.

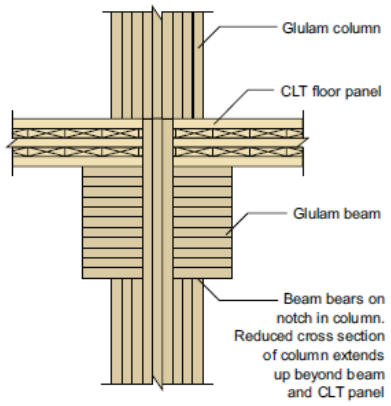

Figure 7: *Double beam system with each beam straddling the column, supported by partial bearing on a notch into the column*

5.4 JOINT SETTLEMENT AT CONNECTIONS

Small amounts of vertical settlement can occur at mass timber connections such as column base and column cap conditions. In addition to mass timber member tolerance allowances (i.e., the length of a column could be +/- 1.6 mm (1/16-in.) of its specified length) the steel hardware at these connections also has tolerance limits that may result in small amounts of settlement. Some engineers include this additional movement in total building shrinkage calculations (1.6 mm or 1/16-in. per floor could be an assumption for this settlement amount) while others choose to ignore it.

6 NET VERTICAL COLUMN MOVEMNT

Summing all of the vertical movements noted above, the net vertical column movement for the design example is calculated as:

$$\Delta_{column} = \Delta_{as,T} + \Delta_{shrinkage} + \Delta_{crushing} + \Delta_{settlement}$$

Using the detail shown in Figure 5 where the beam **is not** isolated from the shrinkage and crushing zone, the net vertical movement per level is:

Δ_{column} = 1.9 + 10.7 + 1.7 + 1.6 + 1.6 = 17.5 mm
Or 0.07 + 0.42 + 0.07 + 0.06 + 0.06 = 0.68 in.

Using the detail shown in Figure 6 where the beam is isolated from the shrinkage and crushing zone, the net vertical movement per level is:

Δ_{column} = 1.9 + 0 + 1.7 + 0 + 1.6 = 5.2 mm
Or 0.07 + 0 + 0.07 + 0 + 0.06 = 0.2 in.

The difference between the two detailing options is significant, further emphasizing the importance of providing details that isolate beam shrinkage and crushing from the overall building movement. Even when doing so, the net vertical column movement for this example, in a 12-story building, would be approximately 62 mm (2.4 in.). Some of this net vertical movement could be reduced with vertical adjustment in connections via shims or other elements placed during construction. This method is described below.

7 DIFFERENTIAL MOVEMENT

The above sections note the potential sources of vertical movement in mass timber framing systems, particularly columns and connections. In most instances, this vertical movement is a downward movement. It is also important to consider how mass timber framing systems interact with other building materials and building components. Other materials may exhibit significantly different vertical movement characteristics. For instance, some materials:

1. Expand due to moisture or thermal changes (brick veneer, masonry shaft walls)
2. Do not shrink due to moisture change but may move with thermal changes (steel framing, and steel/cast iron/PVC piping)
3. Shrink much less than mass timber (concrete core walls)

It is this differential movement that can create issues with the function and performance of finishes, openings, enclosures, mechanical/electrical/plumbing (MEP) systems, structural connections, and more. One of the primary ways to avoid negative impacts is to limit vertical movements of the timber structure as noted in the sections above, while also using detailing strategies discussed in the sections below. It is also important to monitor differential movement during construction, adjusting as necessary. Construction documents and details that provide guidance on how field adjustments should be made at material interfaces are important pieces of the long-term performance solution.

https://doi.org/10.52202/069179-0383

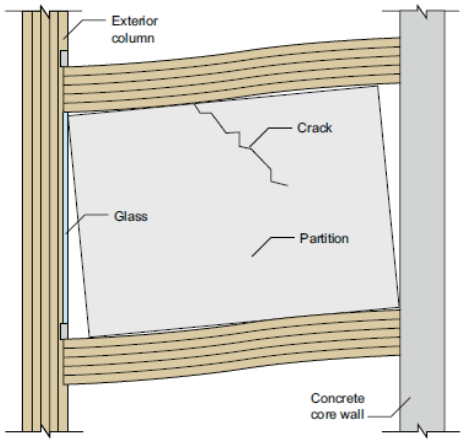

Figure 8: Effects of structure shortening on a glazed façade if differential movement is not accounted for in design and detailing

7.1 EFFECTIVE STRATEGIES AND DETAILING TO MINIMIZE AND ACCOMMODATE MOVEMENT

Several detailing options for beams to columns and columns to columns are shown in Figure 6. Particularly for tall mass timber buildings, where it might be desirable or necessary to make vertical adjustments at the column connections during construction based on real-time feedback (i.e., vertical elevation monitoring), using a detail like the ones in Figure 10 can be effective. In addition to isolating the panels and beams from the shrinkage and crushing zone, these steel connections, which often utilize tube or pipe sections fitted together, can be adjusted by inserting steel shims. For example, the 18-story Brock Commons Tallwood House project discussed later in this document utilized a series of 1.6 mm (1/16-in.)-thick steel shim plates at the column-to-column connections on three strategic levels (8, 12, and 16).

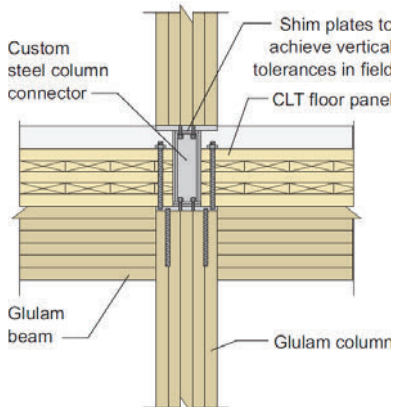

Figure 9: *Column-to-column connection details, with vertical load path isolated from beams and panels*

At connections between different materials, such as a mass timber beam or panel connecting to a concrete core wall, allowances for horizontal and vertical adjustability should be included. One example from the INTRO, Cleveland project is shown in Figure 10. A steel embed plate was cast with the concrete core wall, oversized relative to the steel ledger angle that was later attached to it. The connecting CLT panel was fabricated to allow a small gap between the end of the panel and face of the wall, sized as a function of the tolerance limits for the panel length and wall face location. Vertical adjustability was provided by the oversized embed plate, allowing the steel angle to be field welded to the plate once final elevations were determined (and ideally once some initial shrinkage and settlement had occurred). A similar condition can be used at a beam-to-core wall connection.

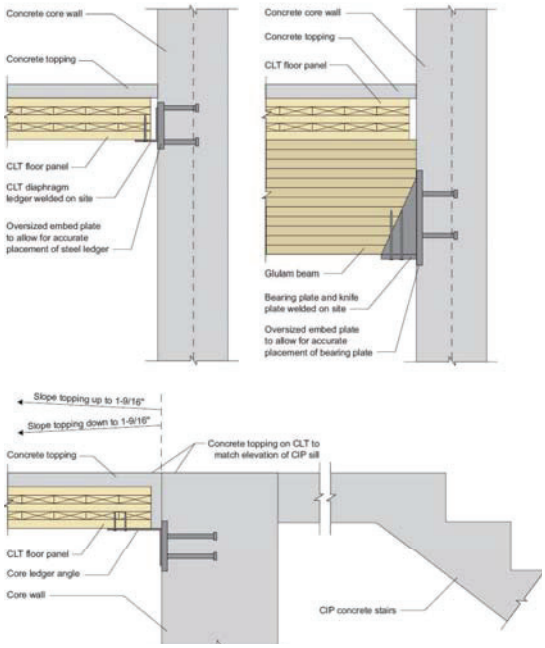

Figure 10: *Options for accommodating differential movement at timber to concrete walls*

Differential movements must also be accounted for in other elements of the building such as vertical MEP runs and exterior wall assemblies. Flex connections within MEP distribution lines (e.g., ductwork, drainage piping, conduit) at each level or every few floors may be prudent. Discussion with the mechanical and electrical engineer is recommended to determine the appropriate steps.

https://doi.org/10.52202/069179-0383

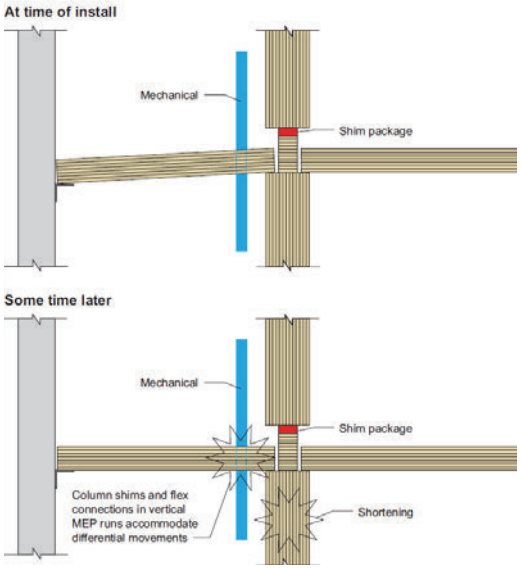

Figure 11: *Potential negative impacts of vertical movements on vertical MEP runs*

Since tall mass timber projects primarily use post-and-beam structural systems, the exterior walls are usually non-load bearing. As such, slip connection details at head of wall conditions not only allow the structure to deflect under gravity loads without loading the walls, but can also function as flex connections that account for vertical differential movements.

7.2 MOISTURE PROTECTION AS A MEANS TO MINIMIZE VERTICAL MOVEMENT

Moisture protection cannot be overemphasized for mass timber, and it is critical that all parties understand the potential effects of moisture on vertical movement potential. It is common on a mass timber project for the architect or engineer, through their specifications, to require a moisture management plan from the contractor. Although on-site material protection is usually considered a means and methods item for the contractor, mass timber is typically both structure and exposed finish. As a result, the design team may have more input on construction moisture management practices than on a non-mass timber project. The design team and owner may choose to require a preconstruction meeting with the contractor to review on-site moisture management techniques.

Key elements of effective construction-phase moisture control in mass timber buildings include:

- Coverings and other means of bulk water deflection/diversion
- Adequate ventilation to promote drying
- Removal of any standing water as soon as possible
- Coatings to protect the mass timber elements, particularly the end grain
- Installation of exterior enclosures in tandem with erection of the timber structure (off-site panelized exterior wall assemblies can aid in this regard)

For additional information on moisture control for mass timber projects, see the WoodWorks publication *U.S. Mass Timber Construction Manual*.

8 SITE VERIFICATION AND HEALTH MONITORING

Structural health monitoring involves the measurement, observation, and analysis of a structure to determine its status over time. These results can be used to determine necessary maintenance, and to ensure intended behaviour of the structure is reflected in the field. Measurements are taken by sensors at regular intervals to provide a numerical history of the structure. The data allows engineers to make observations about the loading and short-term behaviour, draw conclusions about the current state of fatigue, and forecast changes over time.

Once data has been acquired, it must be post-processed to remove noise, normalize variability from environmental effects, and reach meaningful results. Cleansing of data is also important to remove unreliable data, which can result from faulty installation or operation of a sensor.

To monitor short-term and long-term vertical movements in tall mass timber buildings, sensors can be installed throughout the structure to capture specific behaviours of interest. String potentiometers (string pots) can be used to determine vertical movements. These devices use a measuring cable and spring coupled to a spool and rotational sensor. The cable is attached to the point of interest, which will deform relative to the potentiometer. The spring works to maintain tension in the cable, while the sensor determines how much vertical movement has taken place based on the rotation of the spool. String pots can achieve accuracy ±0.0025% of the full scale of the string pot.

8.1 CASE STUDY – BROCK COMMONS TALLWOOD HOUSE

The following is an analysis of one of the first tall mass timber projects in North America to benefit from years of in-service performance feedback and monitoring data.

Located in Vancouver, Canada, Brock Commons Tallwood House is an 18-story hybrid building that includes 17 stories of mass timber construction over a single-story above-grade concrete podium, and two full-height concrete stair cores. The floor system consists of 5-ply CLT panels supported on glulam columns, and the roof is made of prefabricated sections of steel beams and metal decking. As of this writing, the building has five

https://doi.org/10.52202/069179-0383

years of in-service life and has been monitored for vertical movement and moisture content since construction started in 2016.

For the design of a 53 m (174-ft)-tall hybrid building, it was critical to consider differential movement between the timber structure and concrete cores. A specific concern was the potential impact of vertical movement on the mechanical services running through the CLT floor panels adjacent to the concrete cores.

Cumulative differential movement between mass timber members due to fabrication tolerances was minimized by the relatively low probability of occurrence. Glulam columns are typically manufactured with a tolerance of +/- 1.6 mm (1/16-in.) along their height. The probability of having all the shortest members on one side of the panel span and longest on the other is low and was compensated by surveying column datums and using shims as required. Another way to mitigate this risk is to utilize proper truck loading and column identification number tags, such that longer columns are installed above shorter ones and vice-versa.

The following vertical movements for Brock Commons were assessed using structural analysis methods prior to construction and represent cumulative totals at the roof of the building.

- Column shrinkage: 11 mm (0.43-in.)
- Column elastic shortening (short term loading): 25 mm (1-in.)
- Column shortening (creep): 12 mm (0.47-in.)
- Concrete core shrinkage: 12 mm (0.47-in.)
- Concrete core elastic shortening (short term loading): 2 mm (0.08-in.)
- Concrete core shortening (creep): 3 mm (0.12-in.)
- Foundation differential settlement: No critical impact on this project
- Tolerances intra-material: Mitigated by truck sequencing, column marking
- Tolerances extra-material: Interface details between timber and concrete allowing for movement

The anticipated concrete core movement was mainly due to shrinkage, as elastic shortening was negligible. Construction sequencing allowed the design team to minimize this discrepancy because the concrete core was cast in full prior to the erection of timber elements; most of the shortening had already occurred and therefore did not impact the final differential movement between materials.

Based on discussions with the design and construction team, most of the shortening and joint settlement was mitigated by adding a series of 1.6 mm (1/16-in.)-thick steel shim plates at the column-to-column connections on three strategic levels (eight, 12, and 16). The top of the first level column was surveyed and adjusted with leveling nuts at the base to mitigate any differential between columns due to concrete tolerances.

The total shim package thickness varies based on assumed loads and a varying elastic modulus. Due to the general level of uncertainty surrounding these two parameters, only 50% of the calculated values were mitigated, while details were designed to accommodate the other 50% if they were to occur. It is important to maintain this level of flexibility at critical locations so as not to overcompensate for calculated differential movement that does not occur because certain assumptions weren't realized.

The design and construction team also defined a moisture management plan that limited exposure to weather and water accumulation. This plan relied on the following:

- Fast erection pace of one story per week
- Prefabricated enclosure panels installed as soon as each level was built
    - For tall buildings, wall enclosure is a more effective way to reduce exposure to weather than temporary roof enclosure.
- Erection of the timber structure during summer
- Use of sealant and tapes to limit water penetration in the timber
    - With non-edge-glued CLT, this was not sufficient to stop water transfer from the active deck to lower floors; as the CLT panels dried and shrank, some of the lamination lines opened, creating passages for water.
- Use of concrete topping to create an effective water barrier
    - Concrete topping was placed four levels below the active deck, acting as a temporary roof and preventing water transfer to the floors below.
- Fans strategically placed to avoid moisture accumulation

Recording of moisture content across the thickness of CLT panels began at the manufacturing plant, continued through transportation and installation, and is ongoing today. Data showed that panels were kept at a consistent and relatively low moisture content at the factory and during transportation (<19% MC) but that many panels were subject to a large increase on site, especially in the top lamination, exceeding in some cases the fiber saturation point at their surface. Rapid increase and decrease during and after a rain event demonstrated the drying ability of the CLT, such that within a few days the exposed layer was back to an MC below 16%. Data generated from the CLT moisture monitoring was also used to understand the MC of glulam columns.

Throughout construction, strategies were developed to limit water exposure and transfer to lower floors to ensure

that the MC of timber elements could decrease to acceptable ranges as each story was partially enclosed. Once that occurred, the average moisture level during construction was kept below 20%, decreasing to below 15% once the building was complete. After the first two years of use, the MC had settled to between 8% and 15%.

If a proper water management plan is established (and followed), higher moisture content readings during construction should not significantly affect the level of shimming or material interface connections. Real data from Brock Commons confirmed that the variation of moisture content from factory to the project's in-service condition is close to the ranges assumed in the initial column shrinkage calculations.

As part of the Tall Wood Building Demonstration Initiative, Brock Commons benefited from 338 sensors located throughout the structure to measure vertical compression of the timber columns, moisture content, temperature, and humidity. Implemented by SMT Research, instrumentation of the building was deemed important to provide a better understanding of the behavior of tall mass timber structures. This also allowed better tracking of potential issues during construction and a documented comparison of expected vs. actual differential movement.

The timber columns were instrumented to record data for vertical displacement at the first four stories, except for a few columns that were monitored through the roof level. The displacement on the outer columns was about half that of the inner columns, as expected due to the smaller loads. The most recent published shortening record was between 2 mm (5/64-in.) and 4 mm (5/32-in.) per column between levels two and seven, and 0.25 mm (0.01-in.) to 1 mm (0.04-in.) per column between level seven and the roof. Based on this, cumulative column shortening can be assumed to be 22 mm (0.87-in.) total at the roof.

In addition to vertical displacement sensors, the elastic modulus of the lam stock used to manufacture the glulam columns was collected. The average elastic modulus was 20% higher than the design value, which implies 20% less elastic shortening and creep. The values used for elastic modulus, live load, creep, joint settlement, and moisture variation can compel designers to overestimate the total shortening and lead to over-shimming. Engineering judgement and experience in mass timber buildings are important to balance theoretical study. The theoretical study for Brock Commons resulted in 48 mm (1.89-in.) of total shortening compared to 22 mm (0.87-in.) from site monitoring; therefore, the safeguard of shimming up to 50% of the calculated shortening was deemed appropriate for this design. Slight shortening is still expected to occur in the future due to creep.

9 CONCLUSION

The Brock Commons Tallwood House data confirms that it is critical to consider axial column shortening in tall mass timber buildings and that precautions should be taken to address estimated shortening due to the uncertainties that lie within assumptions. It is critical to understand where a designer should allow for flexibility and how to protect other components from structural movements. When properly accounted for, shortening should not negatively affect the construction, use, or long-term performance of the building. Negative impacts can be avoided through a combination of proper detailing and effective moisture management strategies that involve coordination and discussion among all members of the design and construction team.

In addition to regular, on-site observation and movement monitoring, third-party inspections to review movement-accommodating details as installed, and to check items such as shims, will help to ensure that performance matches design intent. To have successful vertical movement performance, proper detailing must lead to proper installation. Education may also be necessary for the building owner, contractor and subcontractors to understand potential issues and how to avoid them. Once fully understood, accommodating vertical movement simply becomes another design criteria.

REFERENCES

[1] McLain, R., Breneman, S., Fire Design of Mass Timber Members, WoodWorks, 2019
[2] U.S. Mass Timber Construction Manual, WoodWorks, 2021
[3] McLain, R., Steimle, D., Accommodating Shrinkage in Multi-Story Wood-Frame Structures, WoodWorks, 2019
[4] WoodWorks CAD/Revit tool and Index of Mass Timber Connections, 2021
[5] Jackson, R. Brock Commons Student Residence, 2016
[6] Fast, P., Jackson, R., BROCK COMMONS A Case Study in Tall Timber. Structure magazine, 2017
[7] Mustapha, G., Khondoker, K., and Higgins, J., Structural Performance Monitoring Technology and Data Visualization Tools and Techniques – Featured Case Study: UBC Tallwood House, SMT Research Ltd., RDH Building Science, 2018

https://doi.org/10.52202/069179-0383

World Conference on Timber Engineering Oslo 2023

SERVICEABILITY PERFORMANCE OF TIMBER DUAL FRAME-WALL STRUCTURAL SYSTEM UNDER WIND LOADING

Osama Abdelfattah Hegeir[1], Haris Stamatopoulos[2], Kjell Arne Malo[3]

ABSTRACT: Due to the moderate stiffness and low mass of timber multi-storey buildings, wind-induced accelerations and displacements usually govern the design. Moment-resisting timber frames (MRTFs) are structural systems that can provide open space and architectural flexibility. However, in regions with moderate to high wind velocities, MRTFs can be used for up to 8 storeys with small out-of-plane spacing between frames (C/C distance of the order of 2-3 m). In this paper, a dual frame-wall structural system is investigated. A parametric study using 2D linear elastic Finite Element Analysis (FEA) is performed to explore the feasibility of the system in regions with moderate wind velocities, considering serviceability requirements (lateral displacements and wind-induced accelerations). Floor vibrations are also taken into account. A 3D FEA model is used to verify the results of the 2D FEA model. Although the focus of the paper is devoted to serviceability requirements, some ultimate limit state considerations are discussed. The results highlight the possibility of using the dual system for multi-storey buildings, with up to 12 storeys and 5 m C/C distance in regions with basic wind velocities up to 26 m/sec.

KEYWORDS: Moment-resisting frames, serviceability, deflections, CLT, glulam, wind-induced accelerations, human-induced vibrations

1 INTRODUCTION

Timber has a very good strength/weight ratio due to its light weight compared to other building materials such as concrete and steel. Moreover, timber can be considered a more environment-friendly construction material than concrete and steel in terms of greenhouse gas emissions [1, 2]. Due to the lightweight nature and moderate stiffness of wood, timber structures are prone to serviceability problems such as excessive accelerations and displacements [3, 4]. Excessive accelerations can cause discomfort to the occupants, and excessive displacements can cause damage and therefore should be kept within acceptable limits.

There exist several structural systems that can provide lateral stiffness to a building. A common structural system used for tall timber buildings is diagonal bracing, such as Treet [4] and Mjøstårnet [5] in Norway. However, these buildings require huge bracing elements running along the height of the structure, which may compromise the architecture flexibility. Cross laminated timber (abbr. CLT) can also be used as a Lateral Load Resisting System (abbr. LLRS). An example of timber building with CLT walls is Stadthaus in London [6]. However, such structures are material-intensive, cellular, and can impose space limitations.

Open and flexible architectural design of buildings is a desirable property, which can be achieved by use of Moment-Resisting Timber Frames (abbr. MRTFs) as a LLRS. In MRTFs, the lateral stiffness relies largely on the stiffness of beam-to-column connections. A feasibility study of glulam MRTFs has been carried out by Vilguts et al. [3], showing that in high-wind regions, glulam MRTFs can hardly be used for more than 8 storeys. The study [3] assumes a prefabricated floor with a small 2.40 m out-of-plane spacing between adjacent frames (abbr. C/C). These limitations are due to wind-induced accelerations and lateral displacements [3].

To overcome the limitations on the number of storeys and achieve larger C/C distance, it is necessary to use larger columns and beams compared to standard glulam dimensions. CLT panels are currently produced with standard dimensions up to 3.5x16.0 m, and therefore can be used to achieve these larger dimensions.

In this paper, the feasibility of using dual frame-wall structural system to build up 12 storeys with C/C distance of 5 m considering a basic wind velocity of 26 m/sec is explored. The system consists of CLT walls, glulam columns and beams, and semi-rigid connections between beams and columns/walls. The feasibility of the system is evaluated, mainly, in terms of Serviceability Limit State (abbr. SLS). However, some Ultimate Limit State (abbr. ULS) considerations are also presented.

2 STRUCTURAL SYSTEM

In this section, the dual frame-wall structural system is explained. Both the LLRS and floor system are described in two different subsections.

[1] Osama Abdelfattah Hegeir osama.a.s.a.hegeir@ntnu.no
[2] Haris Stamatopoulos haris.stamatopoulos@ntnu.no
[3] Kjell Arne Malo kjell.malo@ntnu.no
Department of Structural Engineering, Norwegian University of Science and Technology (NTNU)

https://doi.org/10.52202/069179-0384

2.1 LATERAL LOAD RESISTING SYSTEM

An example of the structural system is shown in Figure 1 (a). In this paper, the focus is given to the structural system in X direction (marked with dotted red box in Figure 1 (a)) where the dual system is used. It consists of continuous CLT walls, continuous glulam columns, and glulam beams. Semi-rigid connections using threaded rods are assumed between beams and walls/columns (see Figure 1 (b)). More details on the connections using threaded rods can be found in [7]. In Y direction, the building may be stabilized by use of diagonal bracing. The LLRS is discussed in more detail in section 4.

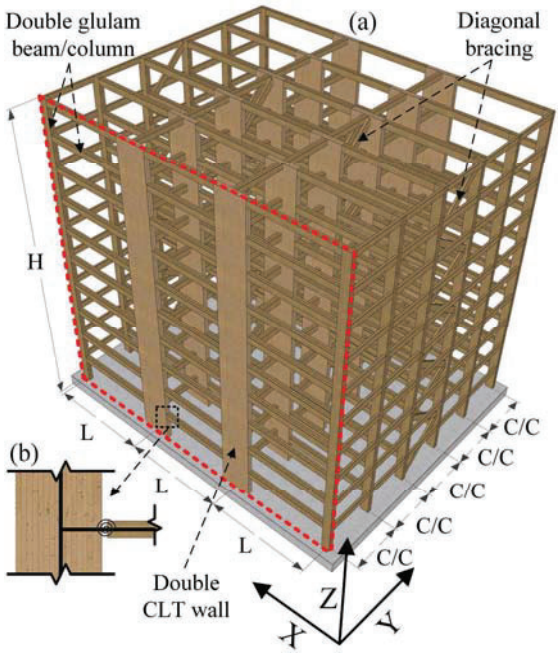

Figure 1: *(a) 3D view of the structural system, (b) semi-rigid moment connection*

2.2 FLOOR SYSTEM

In this paper, a ribbed slab floor system is assumed, see Figure 2. The system consists of CLT panels resting on simply supported secondary beams (glulam). The secondary beams are supported on the main LLRS working in X direction. The floor system is one way with load bearing parallel to Y axis. For better acoustic performance, double beams, columns, and walls are considered. Analysis of floors is discussed in section 3.

3 ANALYSIS OF FLOORS

Human-induced vibrations can be decisive in the design of timber floors [8, 9]. This section explores the serviceability performance of the floor system shown in Figure 2, which includes satisfying deflection limits and human-induced vibrations. However, the vibrations were found to be more critical than deflections. Therefore, the performance was only evaluated with respect to human-induced vibrations.

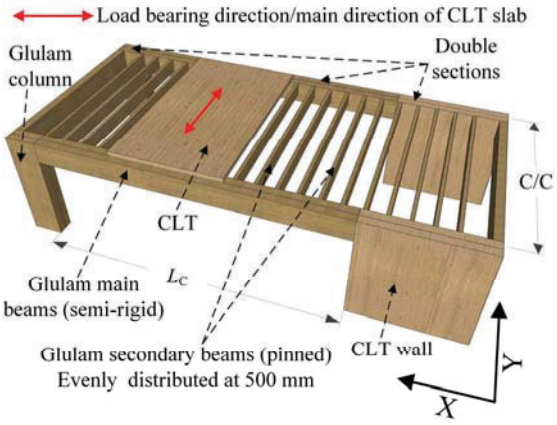

Figure 2: *Floor system*

Linear elastic Finite Element Analysis (abbr. FEA) was used to calculate the fundamental frequency and the deflection of the floor under unit load. The clear span L_C (confer Figure 2) and the stiffness of main beams' connections (confer Figure 2) were varied. The vibration performance of the floor was evaluated using the simplified Hu and Chui criterion [8].

3.1 MATERIALS

The glulam beams used in the floor is assumed of strength class GL30c as defined by EN 14080 [10]. The boards constituting the CLT panels are assumed of strength class C24 as defined by EN 338 [11]. In this paper, it was assumed that (2/3) of the boards are parallel to the main direction of CLT panels (confer Figure 2). The remaining (1/3) are orthogonal to the main direction. Table 1 summarizes mean stiffness properties for GL30c and C24, and the corresponding material axes are illustrated in Figure 3.

Table 1: *Mean stiffness properties for floor elements*

	GL30c	C24	Unit
E_1	13000	11000	N/mm^2
E_2	300	370	N/mm^2
E_3	300	370	N/mm^2
G_{12}	650	690	N/mm^2
G_{13}	650	690	N/mm^2
G_{23}	65	69	N/mm^2

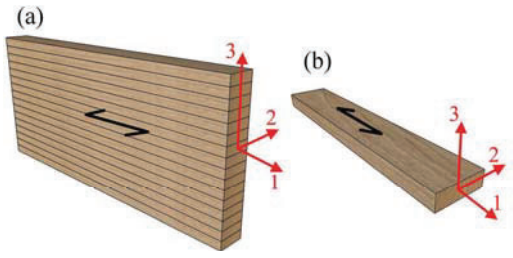

Figure 3: *Material axes for (a) glulam GL30c, (b) C24 boards*

https://doi.org/10.52202/069179-0384

3.2 FINITE ELEMENT MODELLING

CSI SAP2000 [12] was used for FEA. The software can be automated using Open Application Programming Interface (abbr. OAPI). The FEA model of the floor is shown in Figure 4. The main beams (glulam) are modelled using linear beam elements. The ends of the main beams are partially released with respect to bending moment to consider the semi-rigid connections. The secondary beams (glulam) are modelled using shell elements (shown in blue in Figure 4). The CLT slabs are modelled using layered shell elements (shown in red in Figure 4). The connections between the CLT slab and secondary beams, and the connections between the secondary beams and the main beams are modelled using link elements with only axial and shear stiffness (no rotational stiffness).

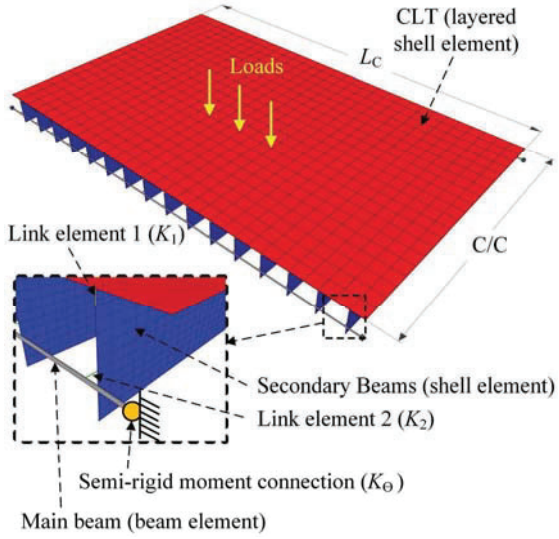

Figure 4: *FEA model of the floor*

3.3 ACCEPTANCE CRITERIA

Several design criteria exist for assessing floor vibrations caused by human activity (e.g. [8, 13]), each taking into account different factors and making different assumptions. In this paper, the simplified criterion proposed by Hu and Chui [8] is used:

$$\frac{(f_{n,1}/18.7)^{2.27}}{w_{1\ kN}} \geq 1.0 \qquad (1)$$

Where $f_{n,1}$ and $w_{1\ kN}$ are the fundamental frequency and the static deflection due to 1.0 kN.

The criterion [8] was developed based on testing of more than one hundred timber floors. Although this criterion [8] was developed in Canada, it is based on physical and subjective evaluations of floors with damping properties comparable to wooden floors found in Norway [14].

3.4 PARAMETRIC STUDY

A parametric study was performed to evaluate the performance of the floor. The parameters varied are summarized in Table 2. Two load scenarios are investigated, namely: heavy load, and light load, see Table 3. The heavy floors represent a case where additional mass is added to improve the performance of the building with respect to wind-induced accelerations (discussed in section 4).

The fundamental frequency $f_{n,1}$ used in evaluating human-induced vibration (see equation (1)) is calculated assuming only the dead load is applied to the CLT slab.

The connections between the CLT slab and the secondary beams, as well as the connections between the secondary beams and the main beams are assumed of equal translational stiffness K_1 and K_2 respectively, confer Figure 4 and Table 2. The main beams connection stiffness K_Θ is reasonably assumed based on the experimental work performed by Vilguts et al. [7] and the analytical work done by Stamatopoulos et al. [15]. Two sets of beams cross-sections and CLT layups are used depending on the load scenario, see Table 4. In total, 60 3D linear elastic analyses were performed.

Table 2: *Parameters used in the parametric study of the floors*

	Value(s)	Unit
Clear span L_C	7−9	m
C/C	5	m
K_Θ	0−15,000	kN·m/rad
K_1*	10	kN/mm
K_2	20	kN/mm
Damping ratio (ξ)	2	%

* Evenly distributed at 250 mm

Table 3: *Load scenarios*

	Heavy load	Light load	Unit
Dead load G_k*	2.0	1.0	kN/m^2
Live load Q_k	3.0**	2.0***	kN/m^2

* Including the own weight of beams and slabs
** Office buildings as defined by EN 1991-1-1 [16]
*** Residential buildings as defined by EN 1991-1-1 [16]

Table 4: *Beams cross-sections and CLT layups used in the parametric study of the floors*

	Load scenario	Cross-section/layup	Unit
Main beam	Heavy/light	$215 \cdot 585$	mm^2
Sec. beam	Heavy	$115 \cdot 450$	mm^2
CLT slab	Heavy	30/30/30	mm
Sec. beam	Light	$90 \cdot 450$	mm^2
CLT slab	Light	40/40/40	mm

Figure 5 shows the performance of the floor according to Hu and Chui [8] as function of the clear span L_C. As shown in Figure 5, for $K_\Theta = 15{,}000$ kN·m/rad, light floors with clear span up to 8.5 m and heavy floors with clear span up to 7.5 meet the acceptance limit. For $K_\Theta = 0$ (pinned), only light floors with clear span of 7.0 m meet the limit.

According to EN 1995-1-1 [17], special investigation is needed for residential timber floors with fundamental frequency less than 8 Hz. Modal analysis is used to calculate the fundamental frequency assuming only dead

load is applied to the CLT slab. The frequencies of light and heavy floors are shown in Figure 6. For floors with $K_\Theta = 15{,}000$, the frequencies of all light floors meet the acceptance limit (8 Hz), while only heavy floors with clear span ≤ 7.5 m meet the limit. For floors with $K_\Theta = 0$, only light floors with clear span ≤ 8.5 m meet the frequency limit.

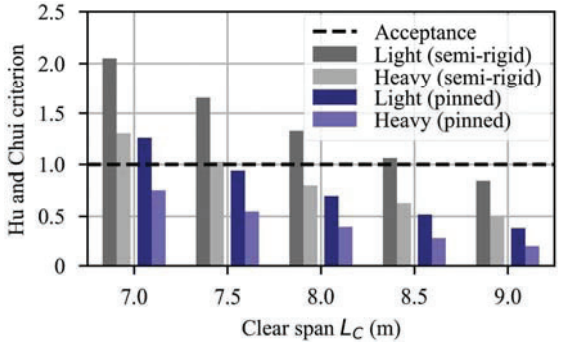

Figure 5: *Hu and Chui [8] criterion for human-induced vibrations (pinned: $\mathbf{K}_\Theta$=0, and semi-rigid: $\mathbf{K}_\Theta$=15,000 kN·m/rad)*

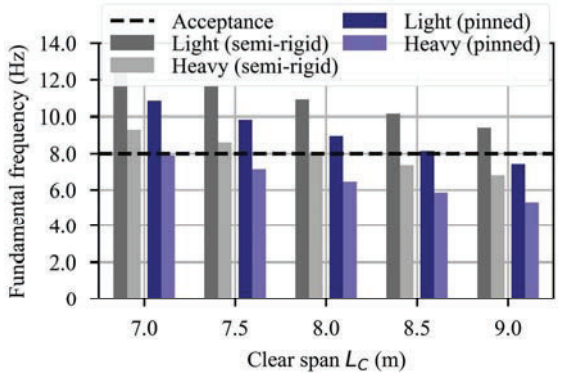

Figure 6: *Fundamental frequencies of floors (pinned: $\mathbf{K}_\Theta$=0, semi rigid: $\mathbf{K}_\Theta$=15,000 kN·m/rad, and only the dead load is considered)*

According to Hu and Chui criterion [8], and in compliance with EN 1995-1-1 [17] requirement of a minimum frequency of 8 Hz, some conclusions can be drawn from the parametric study (see Table 2):

- Light floors with clear span ≤ 8.5 m satisfy the requirements given that $K_\Theta \geq 15{,}000$ kN·m/rad.
- Heavy floors with clear span ≤ 7.5 m satisfy the requirements given that $K_\Theta \geq 15{,}000$ kN·m/rad.
- If pinned connections are used ($K_\Theta = 0$), only light floors with clear span ≤ 7 m meet the requirements.

The influence of main beam connection stiffness (K_Θ) on frequency and vibration performance is shown in Figure 7, where the rotational stiffness (K_Θ) is varied from 0 (pinned) to 15,000 kN·m/rad for a light floor with a clear span of 8 m. As depicted in Figure 7, an increase in K_Θ results in a higher floor frequency and improved vibration performance, owing to the increased floor stiffness.

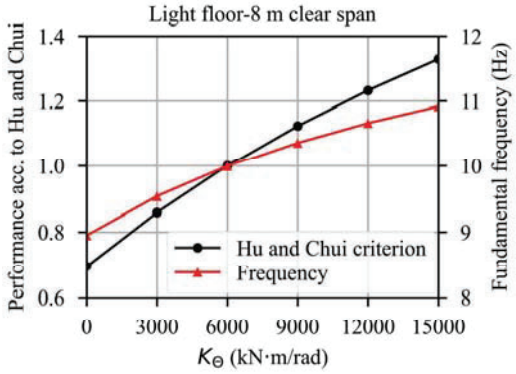

Figure 7: *Influence of main beams connections' stiffness on frequency and vibration performance as per Hu and Chui [8]*

4 ANALYSIS OF LATERAL LOAD RESISTING SYSTEM

Figure 1 shows a 3D structural system with X and Y directions perpendicular to each other. In this section, a small parametric study is performed to evaluate the feasibility of the dual frame-wall LLRS (in X direction) using 2D linear elastic FEA. Although the feasibility is evaluated primarily with respect to SLS, some ULS considerations are discussed. To validate the conclusions drawn from the 2D FEA, a 3D linear elastic FEA model was prepared, and the results were compared with those of the 2D FEA model.

Intuitively, higher connections' stiffness is required at lower storeys. The possibility of using lower connections' stiffness at the higher storeys is also explored.

4.1 MATERIALS

The LLRS in X direction consists of glulam beams, glulam columns, and CLT walls. The stiffness properties of glulam are the same as the floor (see Table 1).

A simplified modelling approach of CLT is to model CLT using equivalent stiffness properties assuming homogeneous cross-section with grain direction of all layers parallel to stress direction as proposed by [18]. This simplified modelling of CLT has shown good accuracy for CLT loaded in-plane [19]. Similar to the floors, 2/3 of the boards are assumed parallel to the main direction of CLT panels and the remaining 1/3 are orthogonal to the main direction. Equivalent stiffness properties of CLT walls are summarized in Table 5. The corresponding material axes are shown in Figure 8. Since linear elements were used to model the CLT walls (explained in 4.2 in this paper), only E_1 and G_{12} are relevant (confer Figure 8). E_1 affects the vertical axial stiffness and the bending stiffness of the CLT walls, and G_{12} affects their in-plane shear stiffness.

Table 5: *Equivalent stiffness properties of CLT walls*

	Equivalent stiffness	Unit
E_1	7457	$\mathrm{N/mm^2}$
G_{12}	518	$\mathrm{N/mm^2}$

https://doi.org/10.52202/069179-0384

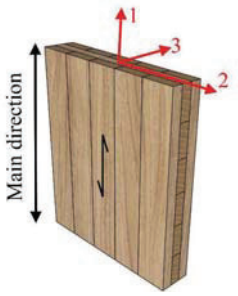

Figure 8: *Material axes for CLT walls*

4.2 FINITE ELEMENT MODELLING

Figure 9 shows the FEA model of the dual frame-wall system (X direction). CSI SAP2000 [12] was used to perform 2D linear elastic FEA. Glulam columns and beams were modelled using linear beam elements with the stiffness properties in Table 1. The CLT walls were also modelled using linear beam elements with the equivalent properties in Table 5. The linear beam elements representing the CLT walls were verified against the layered shell elements available in CSI SAP2000 [12] under in-plane loading. The verification was done on both stresses and displacements and the difference was less than 5%. Hence, linear beam elements were deemed to have sufficient accuracy for the purpose of this study.

All connections (beam-column/wall, wall-foundation, and column-foundation) were modelled using moment partial release available in CSI SAP2000 [12], and were considered semi-rigid with respect to moment and rigid with respect to translation.

Columns and walls have finite heights (in-plane dimension of the cross-section), therefore, when modelled using linear elements, beams' spans are increased. To account for this increase, end-length offset available in CSI SAP2000 [12] is used, see Figure 9. At each end of the beam, a length equal to half the column/wall height is assumed rigid for bending and shear deformations.

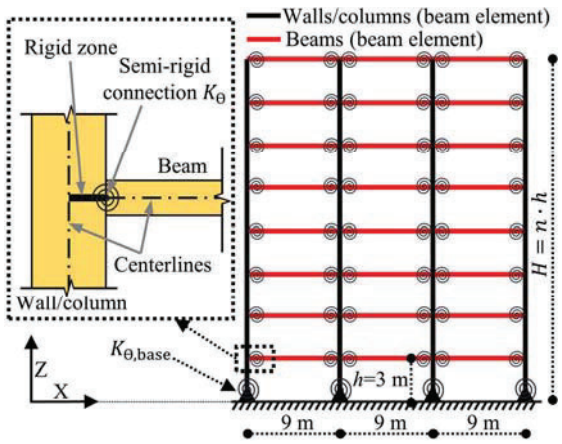

Figure 9: *2D FEA model of LLRS in X direction*

4.3 PARAMETRIC STUDY

In this parametric study, two variations of the LLRS in X direction shown in Figure 9 are considered, namely: exterior CLT walls, and interior CLT walls, see Figure 10. Both heavy and light loading scenarios are considered (see Table 3). The dead load in Table 3 includes the weight of the floor, while the own weight of LLRS is automatically calculated by CSI SAP2000 [12]. The parameters of the parametric study are summarized in Table 6 (total of 520 analyses).

The cross-sections of walls and columns, and the stiffness of their connections to the foundation were varied according to the number of storeys n, see Table 7. All beams, columns, and walls are double sections, confer Figure 2. The cross-sections and stiffness values in Table 6 and Table 7 are for single cross-section.

Table 6: *Parameters of the parametric study of the LLRS*

Parameter	Value(s)
Number of storeys (n)	4/6/8/10/12
Number of bays (n_b)	3
Gravity loads	Light/heavy
Variation	Interior/exterior CLT
C/C (Figure 1)	5 m
Basic wind velocity	26 m/sec
Beams	$215 \cdot 585$ mm^2
Beam-column/wall connection stiffness (K_Θ)	2,500-15,000 kN·m/rad

Table 7: *Cross-section of columns and walls and the stiffness of their connection to foundation (n: number of storeys)*

	n	Cross-sec. (mm^2)	$K_{\Theta,base}$ (kN·m/rad)
Glulam columns	12	$215 \cdot 720$	5,000
	10	$215 \cdot 630$	3,750
	8	$215 \cdot 540$	2,500
	6	$215 \cdot 450$	1,250
	4	$215 \cdot 450$	1,250
CLT walls	12	$215 \cdot 3500$	200,000
	10	$215 \cdot 3000$	150,000
	8	$215 \cdot 2500$	100,000
	6	$215 \cdot 2000$	60,000
	4	$215 \cdot 1500$	30,000

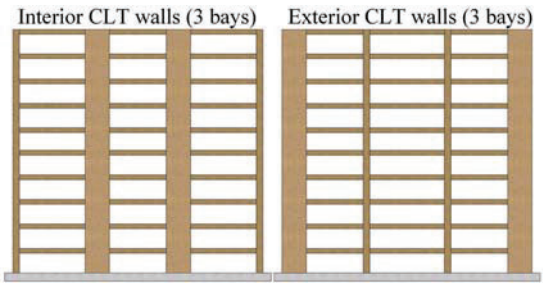

Figure 10: *Two variations of LLRS in X direction*

4.3.1 Serviceability performance

The serviceability performance of LLRS is evaluated in terms of wind-induced accelerations, top floor displacement (abbr. Disp.), and inter-storey drift (abbr. IDR). For the calculation of lateral displacements (Disp. and IDR) due to wind loading (W_k), the characteristic load

combination as defined in EN 1990 [20] with wind as a leading variable was used:

$$E_{\mathrm{d}} = G_{\mathrm{k}} + W_{\mathrm{k}} + \psi_0 \cdot Q_{\mathrm{k}} \quad (2)$$

The combination factor ψ_0 was set to 0.70 according to EN 1990 [20].

Some recommendations of deflections limits are provided by EN 1995-1-1 [17]. According to these recommendations, deflections in simple beams under characteristic load combination defined in EN 1990 [20] should be limited to $1/300 - 1/500$ of the span. No recommendations are given on structure level. As an approximation, the limits for simple beams are used for both lateral displacement at the top of the building (Δ) and relative displacement between two successive storeys (δ):

$$\Delta \leq {}^{H}/_{300}, \delta \leq {}^{h}/_{300} \quad (3)$$

Where h is the height of a storey and H is the total height of the building.

For the calculations of wind-induced accelerations, procedure 1 in Annex B of EN 1991-1-4 [21] was used. The procedure is based on gust factor approach. For the calculation of wind-induced accelerations according to EN 1991-1-4 [21], the mode shape, and the fundamental frequency are required. To obtain both the mode shape and the fundamental frequency, modal analysis using CSI SAP2000 [12] was performed. In the modal analysis, the mass is calculated using the quasi-permanent load combination defined in EN 1990 [20]:

$$E_d = G_k + 0.3 \cdot Q_k \quad (4)$$

Damping is an important input to the wind-induced acceleration calculation. Little research has been done on damping of timber structures, see e.g. [22]. In this paper, 2% damping ratio (ξ) was assumed based on [22]. Basic wind velocity of 26 m/sec and urban environment (IV) as defined by EN 1991-1-4 [21] were assumed for the calculation of wind loads and wind-induced accelerations. Relevant parameters used in the calculation of wind-induced accelerations are summarized in Table 8.

Table 8: *Relevant parameters for calculation of wind loads and wind-induced accelerations*

Parameter	Value
Directional factor C_{dir}	1.0
Seasonal factor C_{season}	1.00
Probability factor C_{prob}	0.73
Orography factor $C_{0(\mathrm{z})}$	1.00
Turbulence factor k_{I}	1.00
Terrain category	IV
Reference height Z_{t}	200
Reference length L_t	300
Structural damping ξ	2%
Width of the building ($C/C \cdot 5$)	25 m

In this paper, the wind-induced acceleration acceptance criterion of ISO 10137 [13] is used. The criterion covers the range from a fundamental frequency of 0.063 to 5 Hz for a maximum wind velocity with a return period of one year, for both residential and office buildings.

Figure 11 shows the wind-induced accelerations against ISO 10137 criterion [13] for all frames (see Table 6). Figure 12 shows the maximum and minimum lateral displacements and IDR for all frames (see Table 6), where maximum and minimum correspond to a set of frames with common parameters and K_Θ =2,500 kN·m/rad and 15,000 kN·m/rad respectively. Light and heavy frames have the same lateral displacements since gravity loads have no influence on lateral displacements.

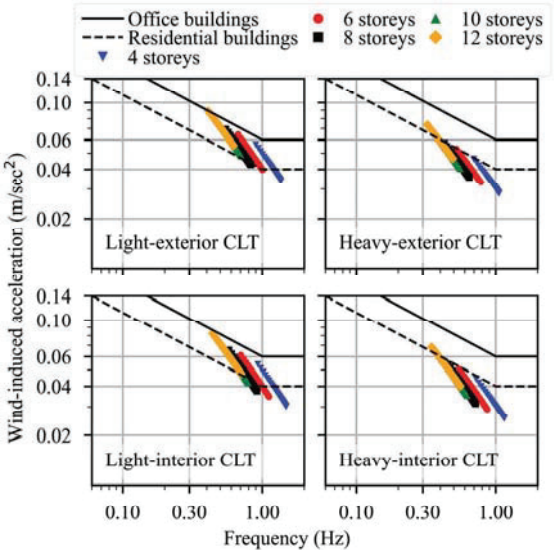

Figure 11: *Wind-induced accelerations against ISO 10137 [13] criterion*

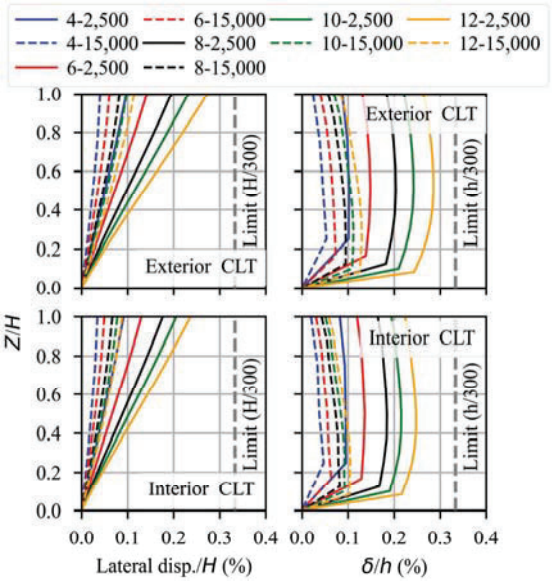

Figure 12: *Lateral displacements and inter-storey drift (Legend: number of storeys-K_Θ, and Z: height above ground)*

As shown in Figure 11 and 12, the variation with interior CLT walls is slightly outperforming the variation with exterior CLT walls. The variation with interior CLT walls has 5-10% lower wind-induced accelerations and 5-15%

https://doi.org/10.52202/069179-0384

lower lateral displacements. Frames with heavy loads have 20% lower wind-induced accelerations.
Observing Figure 11 and Figure 12, some conclusions can be made:

- All frames satisfy the requirements of top floor displacement and IDR by a good margin.
- Heavy frames up to 12 storeys meet the requirement of residential buildings provided that $K_\theta \geq 2 \cdot 5{,}500$ kN·m/rad (5,500 for single cross-section).
- Light frames up to 10 storeys meet the requirement of residential buildings provided that $K_\theta \geq 2 \cdot 11{,}500$ kN·m/rad (11,500 for single cross-section).
- Light frames of 12 storeys do not meet the requirement of residential buildings.
- Light and heavy frames up to 12 storeys meet the requirement of office buildings provided that $K_\theta \geq 2 \cdot 2{,}500$ kN·m/rad (2,500 for single cross-section).

4.3.2 Stiffness reduction in higher storeys

Connections with high stiffness are intuitively required at lower storeys, and connections with lower stiffness may be used in upper storeys. To verify such hypothesis, a 10-storey frame, with interior CLT walls and light gravity loads, is selected as a benchmark. All other parameters remain the same (see Tables 5-7).
A rotational stiffness (K_θ) of 5,000 kN·m/rad is assigned to all beam-to-column/wall connections, this is referred to as the reference case. High stiffness of (K_θ) 15,000 kN·m/rad is then assigned to all connections of one floor at each step starting from the bottom up (total of 10 steps). At the final step, all connections have a stiffness (K_θ) of 15,000 kN·m/rad. The case of all connections being rotationally rigid is also shown. In total, 12 analyses were performed. Figure 13 shows the top floor displacement, maximum IDR, and wind-induced acceleration, all normalized to the reference case (K_θ = 5,000 kN·m/rad). In Figure 13, a value of 0 at the horizontal axis represents all connections with stiffness of 5,000 kN·m/rad (reference case), while a value of 10 represents all connections with a stiffness of 15,000 kN·m/rad.

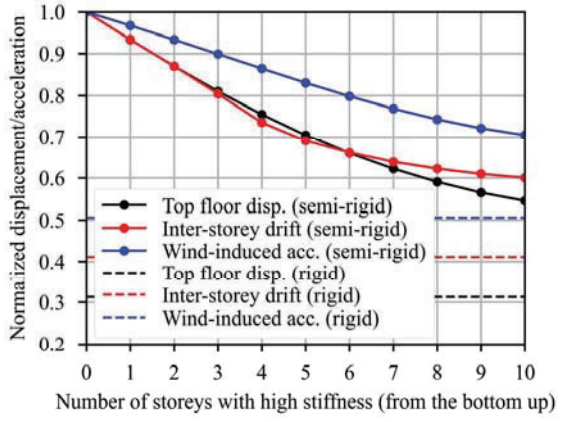

Figure 13: *Top floor displacement, maximum IDR, and wind-induced acceleration with variable K_θ (higher at lower storeys) normalized to the reference case (K_θ = 5,000 kN·m/rad).*

As shown in Figure 13, IDR shows the fastest convergence, followed by top floor displacement and wind-induced acceleration. Using high stiffness (K_θ =15,000 kN·m/rad) for the bottom 5-6 storeys results in 70-90% of the reduction in lateral displacements (top floor displacement and IDR) compared to the case with all connections of high stiffness (10 at the horizontal axis of Figure 13). Using high stiffness for the bottom 5-6 storeys results in 60-70% of the reduction in wind-induced acceleration compared to the case with all connections of high stiffness.

4.3.3 Ultimate limit state considerations

The results of the parametric study (520 analyses) are used to perform design checks for beams, columns, and CLT walls. For the calculation of forces used in the design, the fundamental ULS combination defined in EN 1990 [20] with wind as leading variable action was used:

$$E_d = \gamma_G \cdot G_k + \gamma_Q \cdot W_k + \gamma_Q \cdot \psi_0 \cdot Q_k \quad (5)$$

Where $\gamma_G = 1.20$, $\gamma_Q = 1.50$, $\psi_0 = 0.70$.
The structural design was performed in accordance with EN 1995-1-1 [17]. Since no CLT design checks are included in EN 1995-1-1 [17], the design checks of CLT walls were performed according to [23]. The buckling length was evaluated using linearized buckling analysis. The utilization ratios for beams, columns, and CLT walls are shown in Figure 14 for a total of 520 analyses. As shown in Figure 14, all utilization ratios of beams, columns, and walls are well below unity.

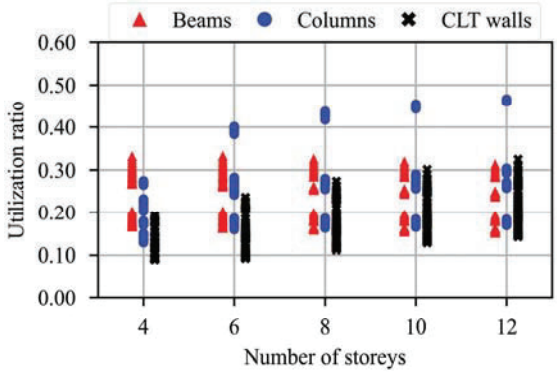

Figure 14: *Utilization ratio for beams, columns, and CLT walls*

Another important consideration is the beam-column/wall connection capacity. For each analysis case (out of the 520), bending moments are calculated at all connections in the frame, the maximum absolute value is then selected, the results are shown in Figure 15.
As shown in Figure 15, all moments are below 70 kN·m. An experimental work performed on moment resisting connections based on threaded rods [24] reported capacity up to 130 kN·m with glulam beams and columns of dimensions ($140 \cdot 450$ mm^2). Based on the calculated bending moments (see Figure 15), and the results in [24], the connections in the dual frame-wall system seem feasible. However, the reported testes in [24] were performed on glulam beam-column connections. Moreover, the limited number of experiments performed

on such connections does not allow the estimation of characteristic capacity. Therefore, further experimental work on moment resisting connections using threaded rods and CLT is needed.

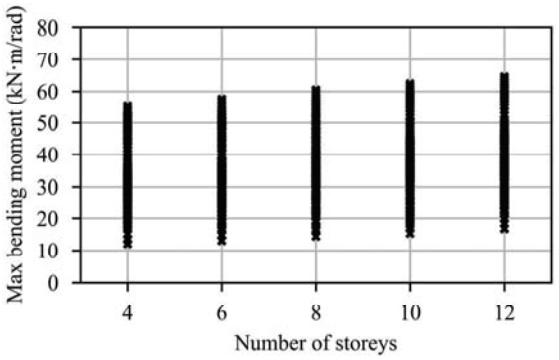

Figure 15: *Maximum absolute bending moment at all beam-to-column/wall connections*

4.4 3D STRUCTURE

To verify the results of the 2D FEA analysis performed in the parametric study, the dual frame-wall system is analysed in 3D. A 3D FEA model of an 8-storey building is analysed using CSI SAP2000 [12].

In X direction, the building is stabilized using the dual frame-wall system with interior CLT walls (confer Figure 1 and Figure 9). The beam-to-column/wall connection stiffness (K_θ) is set to $2 \cdot 12{,}500$ kN·m/rad (double cross-section), see Figure 9.

In Y direction, the building is stabilized using diagonal bracing (confer Figure 1 and Figure 16). The diagonals are modelled using link elements with axial stiffness only. The axial stiffness of each link element representing a diagonal is assumed to be 100 kN/mm (see Figure 16). This value takes into account the axial stiffness of both the diagonal member and the connections at each end of the member. The secondary beams (parallel to Y direction) are modelled using pinned beam elements. Similar to the FEA model of the floor, the CLT slab is modelled using layered shell elements.

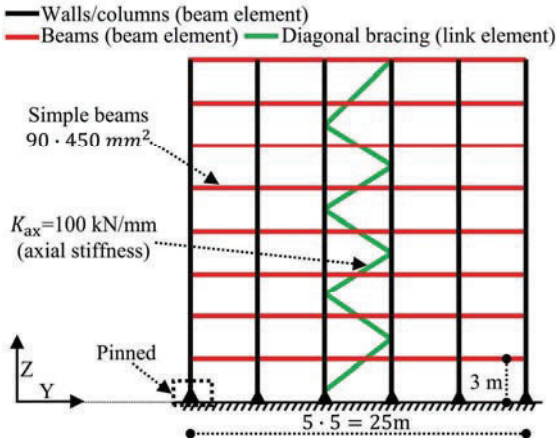

Figure 16: *2D FEA model of LLRS in Y direction*

Figure 17 shows the FEA model of the 3D structure (combining the structural systems in both X and Y). Light loads are applied to the CLT slab (Table 3). Wind loads, load combinations, parameters used for wind-induced accelerations, and cross-sections are the same as the parametric study (section 4.3, Tables 6-8).

Modal analysis of the 3D FEA model showed that the first 2 mode shapes are translational (no torsional modes). Wind-induced acceleration is calculated in X and Y directions. Figure 18 shows the accelerations against the ISO10137 [13] criterion based on 2D and 3D analyses. Wind-induced acceleration in X and Y directions meet the requirement for residential buildings.

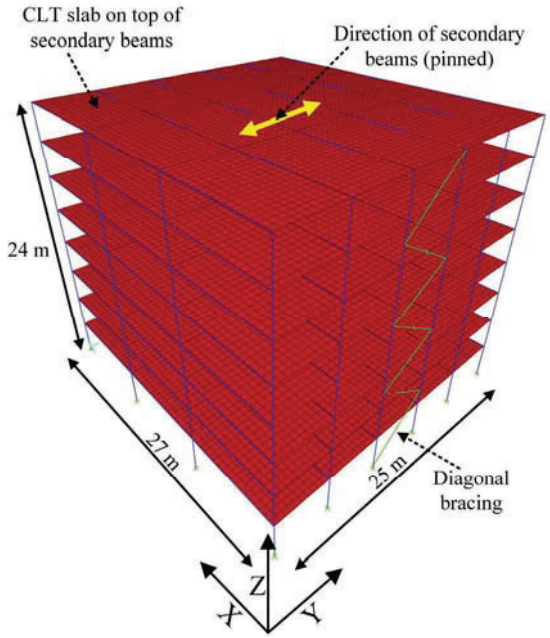

Figure 17: *3D FEA model*

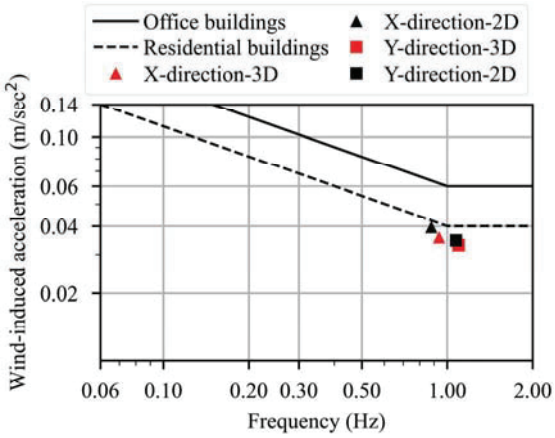

Figure 18: *Wind induced accelerations in X and Y directions of the 3D and the 2D FEA models against ISO 10137 [13] criterion*

The fundamental frequency, top floor displacement, inter-storey drift, and wind-induced accelerations of the 3D

https://doi.org/10.52202/069179-0384

model are summarized in Table 9 (both in X and Y direction). The results of the 2D counterpart model in X direction (results from section 4.3 in this paper) and Y direction are also summarized in Table 9 for comparison. The results of both 3D model and the 2D counterparts show that 2D analysis provides reasonable accuracy with the 3D model being slightly stiffer.

Table 9: *Frequency, lateral displacements, and wind-induced accelerations for the 3D FEA model and the 2D counterpart*

Direction	Property	2D	3D
X	Frequency (Hz)	0.88	0.94
	Top floor disp. (mm)	17.67	14.98
	IDR (mm)	2.61	2.18
	Acceleration (m/sec^2)	0.040	0.036
Y	Frequency (Hz)	1.07	1.10
	Top floor disp. (mm)	13.14	11.81
	IDR (mm)	2.39	2.29
	Acceleration (m/sec^2)	0.035	0.033

5 CONCLUSIONS

In this paper, a dual frame-wall structural system used as a lateral load resisting system in multi-storey timber buildings is studied. Parametric study using 2D linear elastic FEA was performed to evaluate the feasibility of the lateral load resisting system. The vibration performance of floors with respect to human-induced vibration is also discussed using linear elastic FEA. Although the main focus of the paper is on serviceability limit state, some ultimate limit state considerations are presented. To validate the results obtained from the 2D FEA model, a 3D FEA model was also prepared, and the results of both models were compared. The following conclusions are drawn (assuming wind speed of 26 m/sec and urban environment):

- Wind-induced acceleration is more critical than lateral displacements.
- Ultimate limit state is less critical than serviceability limit state. The utilization ratios of all structural elements are well below unity.
- Construction of multi-storey buildings up to 10 storeys with an out-of-plane spacing of 5 m and light flooring system is feasible if the stiffness of the beam-to-column connections is $\geq 2 \cdot 11{,}500$ kN·m/rad ($11{,}500$ for single cross-section).
- Construction of multi-storey buildings up to 12 storeys with an out-of-plane spacing of 5 m and heavy flooring system is feasible if the stiffness of the beam-to-column connections is $\geq 2 \cdot 5{,}500$ kN·m/rad ($5{,}500$ for single cross-section).
- The use of stiff connections can be optimized in such a way that stiffer connections are used in the lower storeys.
- Stiff beam-to-column connections improve the performance of the lateral load resisting system. Moreover, they also improve the performance of the floors with respect to human-induced vibration.
- The use of simplified 2D FEA modelling approach seems to give reasonable accuracy compared to 3D FEA modelling.

REFERENCES

[1] J. L. Skullestad, R. A. Bohne, and J. Lohne, "High-rise timber buildings as a climate change mitigation measure–A comparative LCA of structural system alternatives," *Energy Procedia,* vol. 96, pp. 112-123, 2016.

[2] O. A. Hegeir, T. Kvande, H. Stamatopoulos, and R. A. Bohne, "Comparative Life Cycle Analysis of Timber, Steel and Reinforced Concrete Portal Frames: A Theoretical Study on a Norwegian Industrial Building," *Buildings,* vol. 12, no. 5, p. 573, 2022. [Online]. Available: https://www.mdpi.com/2075-5309/12/5/573.

[3] A. Vilguts, H. Stamatopoulos, and K. A. Malo, "Parametric analyses and feasibility study of moment-resisting timber frames under service load," *Engineering Structures,* vol. 228, 2021, doi: 10.1016/j.engstruct.2020.111583.

[4] K. A. Malo, R. B. Abrahamsen, and M. A. Bjertnæs, "Some structural design issues of the 14-storey timber framed building "Treet" in Norway," *European Journal of Wood and Wood Products,* vol. 74, no. 3, pp. 407-424, 2016, doi: 10.1007/s00107-016-1022-5.

[5] R. Abrahamsen, "Mjøstårnet-Construction of an 81 m tall timber building," in *Internationales Holzbau-Forum IHF*, Garmisch-Partenkirchen, Germany, 2017, vol. 2017.

[6] M. Wells, "Stadthaus, London: raising the bar for timber buildings," in *Proceedings of the Institution of Civil Engineers-Civil Engineering*, 2011, vol. 164, no. 3: Thomas Telford Ltd, pp. 122-128.

[7] A. Vilguts, S. Ø. Nesheim, H. Stamatopoulos, and K. A. Malo, "A study on beam-to-column moment-resisting timber connections under service load, comparing full-scale connection testing and mock-up frame assembly," *European Journal of Wood and Wood Products,* vol. 80, no. 4, pp. 753-770, 2022, doi: 10.1007/s00107-021-01783-2.

[8] L. J. Hu and Y. Chui, "Development of a design method to control vibrations induced by normal walking action in wood-based floors," in *World Conference on Timber Engineering (WCTE2004)*, Lahti, Finland, 2004, vol. 2, pp. 217-222.

[9] P. Hamm, A. Richter, and S. Winter, "Floor vibrations–new results," in *Proceedings of 11th World Conference on Timber Engineerig (WCTE2010), Riva del Garda*, 2010.

[10] CEN, "NS-EN 14080: Timber structures-Glued laminated timber and glued solid timber-Requirements," *European Committee for Standardization: Brussels, Belgium,* 2013.

[11] CEN, "NS-EN 338: Structural timber–Strength classes," *European Committee for Standardization: Brussels, Belgium,* 2016.
[12] *CSI SAP2000 Structural analysis and design*. Computers and Structures. [Online]. Available: https://www.csiamerica.com/products/sap2000
[13] ISO, "ISO10137: Bases for design of Structures - Serviceability of Buildings and Walkways against Vibrations," *International Organization for standardization,* 2007.
[14] A. Homb and S. T. Kolstad, "Evaluation of floor vibration properties using measurements and calculations," *Engineering Structures,* vol. 175, pp. 168-176, 2018.
[15] H. Stamatopoulos, K. A. Malo, and A. Vilguts, "Moment-resisting beam-to-column timber connections with inclined threaded rods: Structural concept and analysis by use of the component method," *Construction and Building Materials,* vol. 322, 2022, doi: 10.1016/j.conbuildmat.2022.126481.
[16] CEN, "NS-EN 1991-1-1: 2002+ NA: 2019: Actions on Structures–Part 1-1: General Actions–Densities, self-weight, imposed loads for buildings," *European Committee for Standardization: Brussels, Belgium,* 2019.
[17] CEN, "NS-EN 1995-1-1:2004+A1:2008+NA:2010: Design of timber structures–Part 1-1: General–Common rules and rules for buildings," *European Committee for Standardization: Brussels, Belgium,* 2010.
[18] H. J. Blass and P. Fellmoser, "Design of solid wood panels with cross layers," in *8th world conference on timber engineering*, 2004.
[19] M. Follesa, I. Christovasilis, D. Vassallo, M. Fragiacomo, and A. Ceccotti, "Seismic design of multi-storey CLT buildings according to Eurocode 8. Ingegneria Sismica," *International Journal of Earthquake Engineering, Special Issue on Timber Structures,* vol. 30, no. 4, pp. 27-53, 2013.
[20] CEN, "NS-EN 1990:2002+A1:2005+NA:2016: Basis of structural design," *European Committee for Standardization: Brussels, Belgium,* 2016.
[21] CEN, "NS-EN 1991-1-4:2005+NA:2009: Actions on Structures–Part 1-4: General Actions–Wind Actions " *European Committee for Standardization: Brussels, Belgium,* 2009.
[22] A. Feldmann *et al.*, "Dynamic properties of tall timber structures under wind-induced vibration," in *World Conference on Timber Engineering (WCTE 2016)*, 2016.
[23] A. Gustafsson, *The CLT Handbook: CLT structures-facts and planning*, First ed. Swedish Wood, 2019.
[24] H. Stamatopoulos and K. Malo, "Wood frame solutions for free space design in urban buildings (WOODSOL)," in *Proceedings of the 7th Forum Wood Building Nordic, Växjö, Sweden*, 2018, pp. 27-28.

 https://doi.org/10.52202/069179-0384

World Conference on Timber Engineering Oslo 2023

INVESTIGATION OF LONG-TERM MODAL PROPERTIES OF A TALL GLUE-LAMINATED TIMBER FRAME BUILDING UNDER ENVIRONMENTAL VARIATIONS

Saule Tulebekova[1], Kjell Arne Malo[2], Anders Rønnquist[3], Petter Nåvik[4]

ABSTRACT: Evaluation of long-term modal properties, such as natural frequencies and damping ratios, is important for tall timber buildings, which can be prone to environmental variations. However, in long-term operational modal analysis, the estimation of modal properties, especially damping ratios can be subject to significant uncertainty due to requirement of stationarity of the input data. Therefore, a combined variational mode analysis and data-driven stochastic subspace identification method was used for modal identification to reduce the potential errors related to the input data. The method was employed to investigate the long-term modal properties of an 18-story glulam frame building using ambient vibration data of 18 months. The observed natural frequencies exhibit seasonal behaviour with an average variation of ±0.02 Hz. Damping ratios do not show a seasonal relationship as opposed to the natural frequencies. The identified natural frequencies tend to have an inverse relationship with the mean temperature, while a positive correlation between the natural frequencies and the relative humidity is observed.

KEYWORDS: dynamic identification, ambient vibrations, tall timber building, VMD, SSI, modal properties.

1 INTRODUCTION

Tall timber buildings are relatively new in the construction industry, and as a result, there is still much research being conducted to understand their dynamic response under different loads, including service loads [1]. In general, tall timber buildings tend to have a lower natural frequency compared to traditional steel and concrete buildings due to inherently low stiffness and mass properties. This means that they are more susceptible to vibrations caused by external forces such as wind or human activities, and this can affect their performance and occupant comfort [2]. Excessive vibrations during strong winds might lead to discomfort for building occupants, particularly on the higher floors, if the design is incorrect.

Modal identification is a process used to determine the natural frequencies, damping ratios, and mode shapes of a structure. It is an important step in evaluating the dynamic response of a structure, as it provides information about the behaviour of the structure under different loading conditions.

Different techniques and methods can be used for modal identification of structures. For example, the operational modal analysis (OMA) method, which relies on ambient vibrations induced by natural events, can be used to identify the dynamic properties of the structure under real-life operating conditions. Other techniques such as impact testing or shaking table tests can also be used to identify the dynamic properties, but they require significant planning and labour and can be quite costly. In comparison to other techniques, OMA is a cost-effective and relatively easy method, which is suitable for long-term measurements.

Data-driven stochastic subspace identification (SSI-DATA) is an OMA technique used to extract dynamic models from ambient vibration data. SSI techniques involve constructing a mathematical model of the structure using the measured response data. This model can then be used to estimate the properties of the structural system. One of the limitations of ambient vibration techniques for modal identification, such as SSI, is the assumption of stationarity. This assumption requires that the ambient vibration signals remain constant over time, which is not always the case in practice. Non-stationarity can occur due to changes in the ambient conditions, such as wind or temperature, or due to changes in the dynamic behaviour of the structure itself. To overcome this issue, the variational mode decomposition (VMD) can be used, which decomposes the initial signal into a set of oscillatory components containing the modes of the structure.

The modal identification of timber buildings presents some additional challenges that are unique to this type of construction. For example, timber structures are more susceptible to environmental factors such as temperature

[1] Saule Tulebekova, NTNU Norwegian University of Science and Technology, Norway, saule.tulebekova@ntnu.no
[2] Kjell Arne Malo, NTNU Norwegian University of Science and Technology, Norway, kjell.malo@ntnu.no
[3] Anders Rønnquist, NTNU Norwegian University of Science and Technology, Norway, anders.ronnquist@ntnu.no
[4] Petter Nåvik, NTNU Norwegian University of Science and Technology, Norway, petter.r.navik@ntnu.no

https://doi.org/10.52202/069179-0385

and humidity, which can cause changes in their material properties over time. In addition, timber buildings tend to have a more complex and variable behaviour compared to traditional steel and concrete structures, which can make their modal identification more challenging.

Several studies investigating the effects of environmental variations on the dynamic properties of timber buildings are available [3,4]. However, no previous studies on the relation between the environmental factors and the dynamic response of tall glulam frame building were conducted.

Considering these challenges, this paper investigates the modal properties of a tall glue-laminated timber (glulam) frame building under long-term ambient and operational variations using combined VMD/SSI technique. The effect of the variational environmental conditions on the identified dynamic properties is investigated using the meteorological data from the nearby weather station.

2 FIELD MEASUREMENTS SETUP

2.1 BUILDING DESCRIPTION

Mjøstårnet is an 18-storey tall glulam (glue-laminated timber) frame building located in Brumunddal, Norway (Fig.1). As of March 2023, Mjøstårnet is considered the tallest residential timber building in the world [5]. The load-bearing system of the building consists entirely of structural timber elements. The building height is 88.8 meters and the structural system consists of glulam trusses connected with slotted-in steel plates [6]. Cross-laminated timber (CLT) is used in the elevator and staircase shafts and the floors are made of prefabricated timber decks (floors 1-10) and concrete decks (floors 11-18). The concrete decks are added purely as additional mass due to occupational serviceability requirements. The pergola truss is mounted at the top of the building for architectural appearance.

(a) Building location (b) The Mjøstårnet building view

Fig.1. The Mjøstårnet building

2.2 EXPERIMENTAL SETUP

A long-term ambient vibration monitoring system was installed inside the building (Figs.2-4). The hardware in the system consists of three Kistler K-Beam® accelerometers, model 8395A2D0 [7], one CompactRIO controller by National Instruments, and connecting wires and cables. The accelerometers have sensitivity of 2000 mV/g and the sampling rate for data was 400 Hz. The building has been in full operational condition, therefore, the placement options for the long-term monitoring setup were quite limited. After the discussion with the building manager, the setup was installed in the emergency staircase shaft. This staircase could only be accessed in emergency cases only, therefore, it was not obstructing the normal operations of the building. Prior to the current accelerometer setup, the accelerometers were installed at the roof of the building. Therefore, to ensure that the captured modes from the current setup were representative of the global structural behaviour, the identified modes were compared against their counterparts from the setup on the roof. More details regarding the comparison of the two setups can be found in [8].

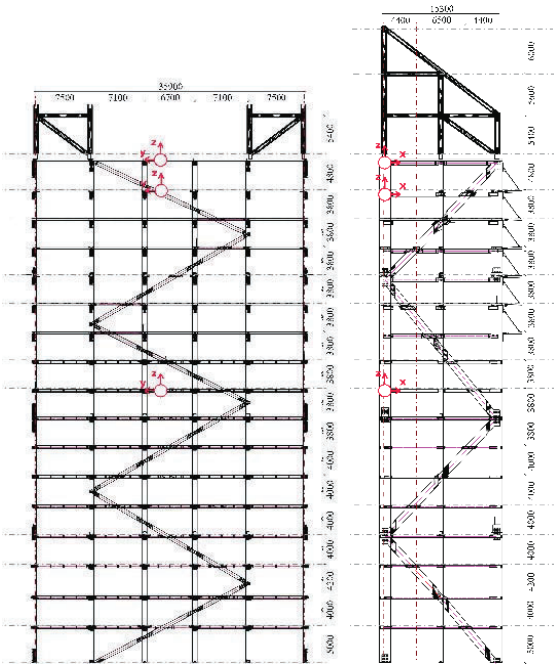

Fig.2. Accelerometer setup inside the building.

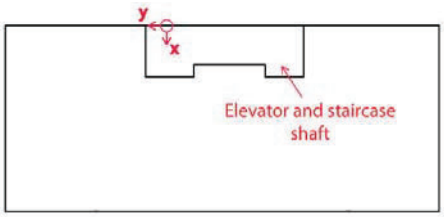

Fig.3. Plan view of accelerometer setup.

https://doi.org/10.52202/069179-0385

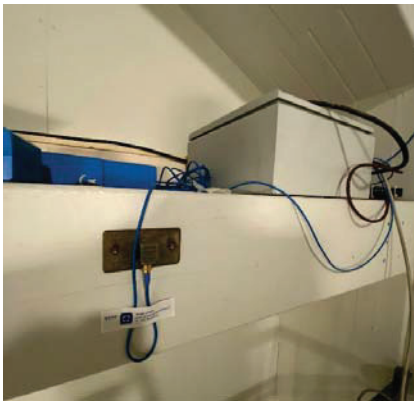

Fig.4. Long-term monitoring setup with the control box.

3 METHODOLOGY

The combined VMD and SSI-DATA methodology is outlined in the Fig.5. First, the initial ambient vibration data is decomposed into a set of modal components using the VMD technique. These identified modal components are then evaluated using the spectral analysis and the modes containing the structural behaviour are selected for further analysis. Then, the SSI-DATA technique is applied separately on each structural mode and the corresponding natural frequencies and damping ratios are identified. The following sections present the methodology in more detail.

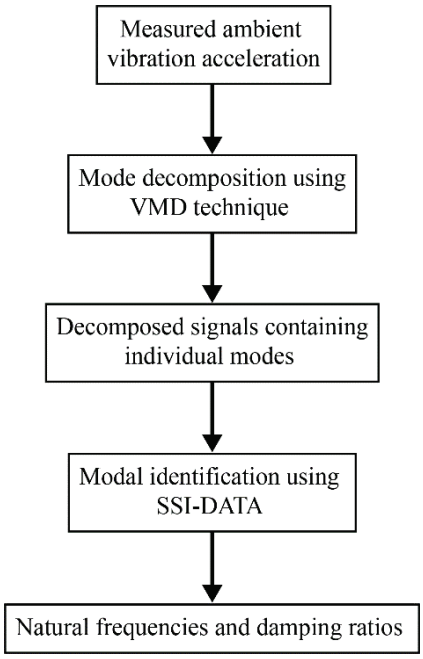

Fig.5. Combined VMD/SSI-DATA methodology.

3.1 VARIATIONAL MODE DECOMPOSITION (VMD)

VMD is a signal decomposition method that aims to decompose a complex signal into a set of intrinsic mode functions (IMFs) or oscillatory components [9]. Each IMF represents a distinct oscillation mode in the signal, which is characterized by a particular frequency and amplitude modulation. The VMD algorithm is based on an optimization problem that seeks to minimize the total power of the signal subject to a set of constraints. The constraints ensure that the extracted IMFs are spatially and temporally localized and are well-separated in the frequency domain. A more detailed description of the technique can be found in [9]. The VMD algorithm can be briefly described as follows:

- Obtain frequency spectrum of each mode by applying the Hilbert transform.
- Shift the frequency spectrum of the mode to the estimated centre frequency using the exponential tune.
- Solve the following minimisation problem to estimate the bandwidth of each mode using the Gaussian smoothness of the demodulated signal:

$$\min_{\{u_k\},\{\omega_k\}} = \left\{ \sum_k \left\| \partial_t \left[\left(\delta(t) + \frac{j}{\pi t} \right) * u_k(t) \right] e^{-j\omega_k t} \right\|_2^2 \right\}$$

$$s.t. \quad x(t) = \sum_{k=1}^{K} u_k(t)$$

where $u_k(t)$ are the decomposed modes, ω_k are the corresponding central frequencies, $\|.\|_2$ is the L2 norm, ∂_t is the derivative with respect to time, $\delta(t)$ is the Dirac delta function, $x(t)$ is the original signal.

After application of the VMD the initial signal is decomposed into a set of modes compacted around the central frequency. The signals containing structural modes are then selected for further analysis.

3.2 STOCHASTIC SUBSPACE IDENTIFICATION (SSI)

Once the signals containing structural modes were identified, thee data-driven stochastic subspace identification (SSI-DATA) technique is applied on each signal separately. The procedure for the SSI-DATA method is explained in detail in [10-12], and a brief description of the method is presented here. In SSI-DATA, the dynamic system is assumed to be described by the discrete state-space model:

$$\mathbf{x}_{k+1} = \mathbf{A}\mathbf{x}_k + \mathbf{w}_k \qquad (1)$$

$$\mathbf{y}_k = \mathbf{C}\mathbf{x}_k + \mathbf{v}_k \qquad (2)$$

where x is a state space vector, which holds the current state of the system at time instant t, y is a measured output at a specified sampling rate, w and v are system noise and measurement noise, respectively, A is a state matrix, and C is an output matrix.

The state-space model of order i is used to identify the eigenvalue μ_i, from which the corresponding pole λ_i can

be obtained at a sampling period t_s. Then, the frequency and damping values, ω_i and ξ_i, can be calculated for each pole. The expressions for the calculation process of the values mentioned above are as follows:

$$\lambda_i = \ln(\mu_i)/t_s \quad (3)$$

$$\omega_i = Im(|\lambda_i|) \quad (4)$$

$$\xi_i = -Re(\lambda_i)/|\lambda_i| \quad (5)$$

Stabilization diagram is then plotted with the stability criteria for natural frequency and damping ratio of 1% and 5% respectively, and the vertically aligned poles on the stabilization diagram indicate a stable frequency.

4 RESULTS

4.1 MODAL DECOMPOSITION

The acceleration time series were processed separately in the x- and y-direction (see Fig.3 for coordinate reference). Acceleration time series were resampled to 8 Hz sampling rate and the band-pass filter between 0.2 Hz - 1.0 Hz was applied to remove the noise and response outside the range of interest. In total three fundamental frequencies were identified: mode 1 at 0.5 Hz (first bending in the x-direction), mode 2 at 0.54 Hz (first bending in the y-direction), and mode 3 at 0.84 Hz (torsion). Fig.6(top) shows the original acceleration time series containing noisy data in the x-direction with the corresponding Fourier spectrum, where the peaks at 0.5 Hz (mode 1, bending) and 0.84 Hz (mode 3, torsion) can be seen.

Below the original data series are the two decomposed signals, which are called the intrinsic mode functions (IMFs) using VMD method, which show only one peak at their respective frequencies, indicating that the signals containing fundamental modes have been successfully separated. Similarly, Fig.7 shows the original acceleration time series containing noisy data in the y-direction (top) and its decomposed IMFs containing the fundamental modes along with the Fourier spectra indicating the fundamental frequencies in y-direction: mode 2 (bending) and mode 3 (torsion). These intrinsic mode functions containing the modes of interest were further processed using the SSI-DATA technique to identify the natural frequencies, damping ratios and mode shapes. Each mode-containing signal was processed separately. The methodology was applied continuously over the entire monitoring period (Jan.2021-Jun.2022) on 1-hr data segments to investigate the variation of the identified modal properties with time.

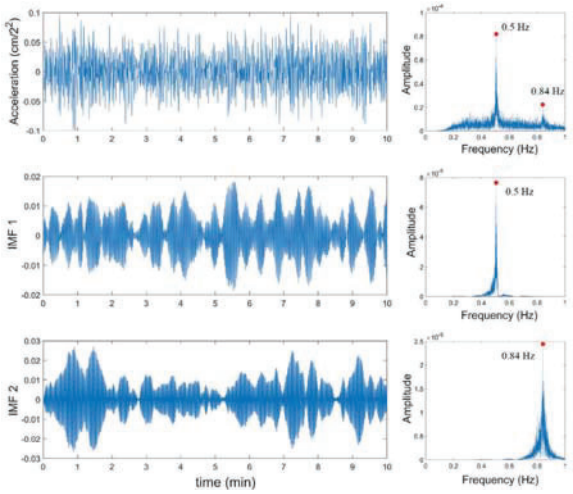

Fig.6. Input signal in x-direction (top) and its decomposed intrinsic mode functions (IMFs) with the corresponding Fourier spectra.

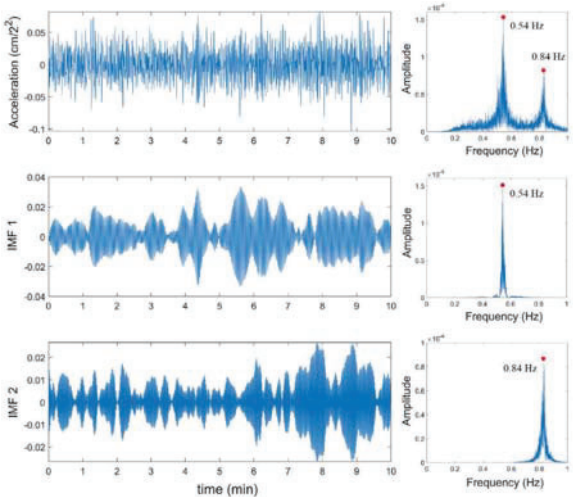

Fig.7. Input signal in y-direction (top) and its decomposed intrinsic mode functions (IMFs) with the corresponding Fourier spectra.

4.2 LONG-TERM MODAL PROPERTIES

The long-term monitoring records of the total of 18 months (Jan.2021-Jun.2022) were processed using the combined VMD/SSI-DATA methodology. Fig.8 shows the variation of the identified natural frequencies with time and the corresponding statistical distributions using 1-hour increments of the acceleration response for the first three modes of vibration. The torsional mode is plotted in both x- and y-direction. From observation, a seasonal pattern of natural frequencies can be observed. The highest values for natural frequencies are observed in the late winter (January-March), while the lowest values are observed in the late summer (July-September). The total natural frequency variation is ±0.015 Hz for mode 1, ±0.02 Hz for mode 2, ±0.03 Hz for mode 3. A larger scatter of identified values can be observed for mode 3 in

https://doi.org/10.52202/069179-0385

the x-direction compared to the y-direction which might be due to the accelerometer placement: location of accelerometers close to the centreline might not allow for a proper identification of the torsional mode in the x-direction.

Fig.9 shows the variation of the identified damping ratios with time and the corresponding statistical distribution using 1-hour increments of the acceleration response for the first 3 modes. Similarly, a larger scatter is observed for mode 3 in the x-direction compared to the y-direction. Unlike natural frequencies, no seasonal variation of damping ratios can be observed. The mean values for the identified damping ratios seem to be quite stable at values around 1% except for mode 3 in the x-direction, where a larger variation is observed.

From Figs.8 and 9, it can be seen that the natural frequencies and damping ratios can be identified quite stably indicating the effectiveness of the combined VMD/SSI-DATA technique for extraction of long-term modal properties from ambient vibration data.

4.3 EFFECT OF ENVIRONMENTAL CONDITIONS

The meteorological data from the closest weather station was used to investigate the effect of the environmental conditions on the identified dynamic properties. The location of the weather station is approximately 10 km away from the building and the weather statistics for the monitoring period was obtained from the Norwegian Climate Service Centre [13]. The following environmental properties were selected for further analysis: mean air temperature (°C) and mean relative humidity (%).

The building in this study is located in a region with humid continental climate with cold and dry winters and comfortably warm summers. The warmest month of the year is July with mean daily temperature of 17°C and the coldest month of the year is December with daily mean temperature of -4.5°C.

Fig.10 shows the mean daily natural frequencies for the first 3 modes plotted together with the mean daily air temperature. The smoothed variations using 1-month averaging window are plotted to represent the trend of the parameters with time. From observation, for all natural frequencies the variation occurs in a similar seasonal manner. The highest frequencies are observed in the late winter and the lowest frequencies are observed in the late summer, with an exception of the first frequency, where the additional peak can be observed in the early summer period. For modes 2 and 3 (x- and y-direction) an inverse relationship is observed between the natural frequencies and the air temperature. The inverse relationship might be caused by the delay between the variational changes and the structural response. For mode 1, the inverse seasonal relationship can be observed in the winter, however, in summer the frequencies seem to have an increasing trend with increase of temperature.

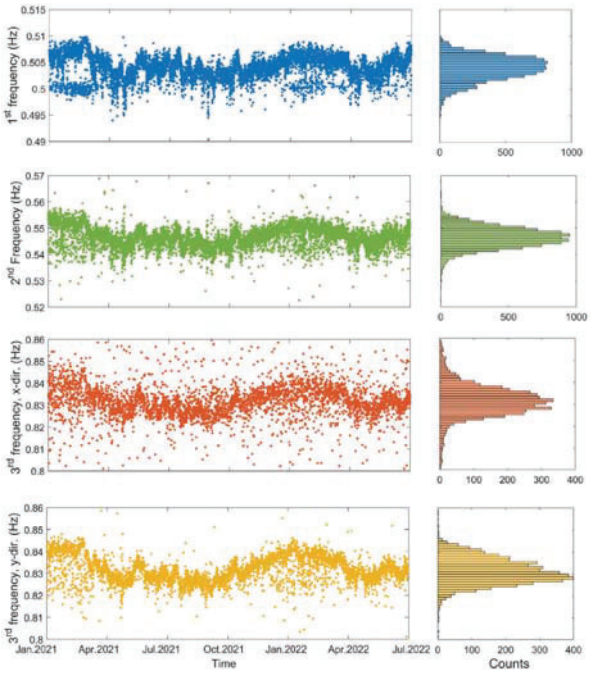

Fig.8. Variation of identified frequencies from 1-hour data segments over time (left) and the corresponding statistical distributions (right) for the first 3 modes of vibration.

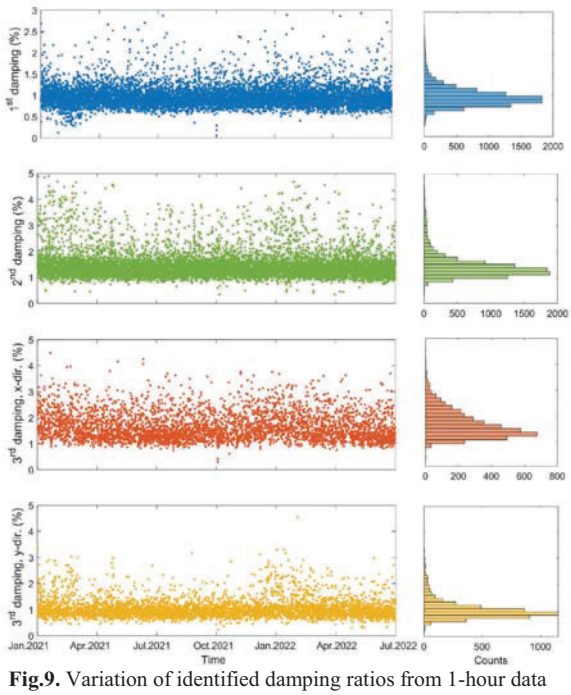

Fig.9. Variation of identified damping ratios from 1-hour data segments over time (left) and the corresponding statistical distributions (right) for the first 3 modes of vibration.

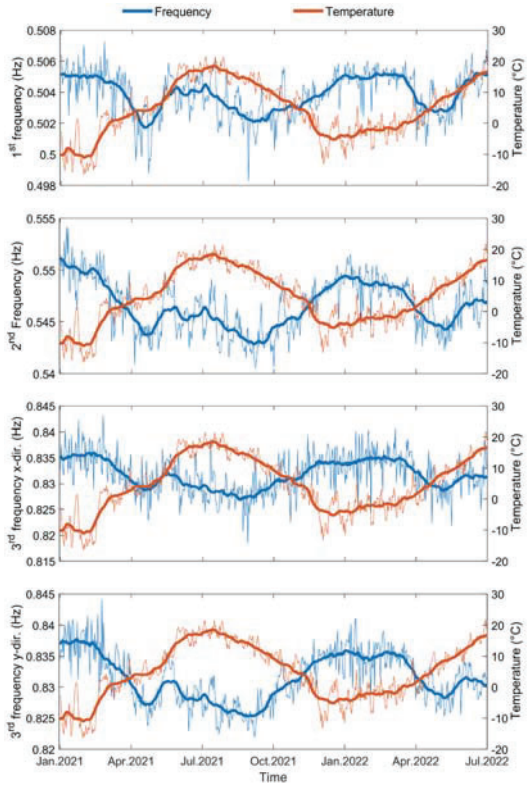

Fig.10. Variation of identified frequencies (1-day mean) and temperature.

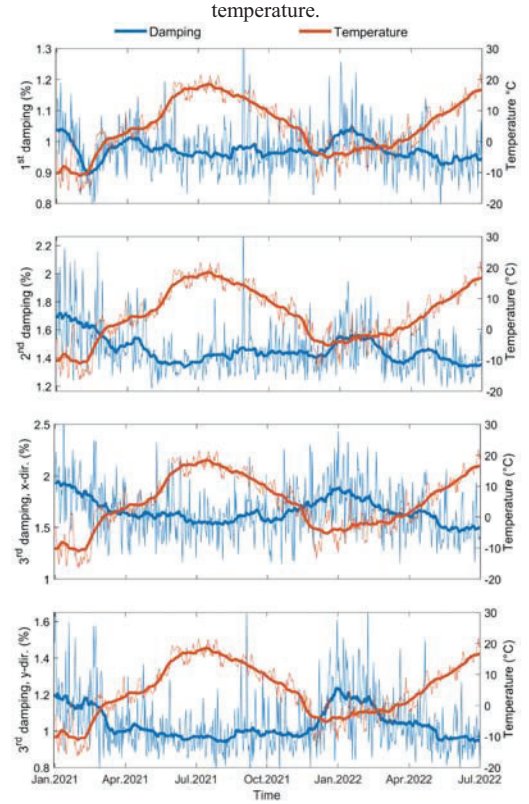

Fig.11. Variation of identified damping ratios (1-day mean) and temperature.

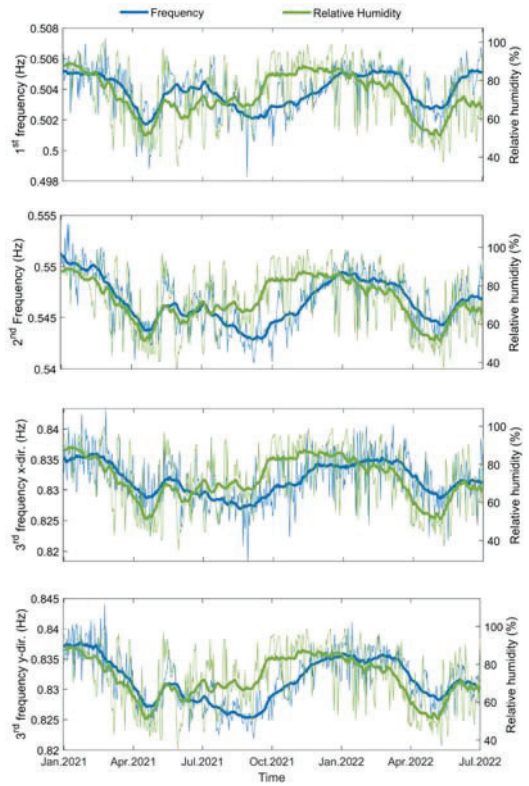

Fig.12. Variation of identified frequencies (1-day mean) and relative humidity.

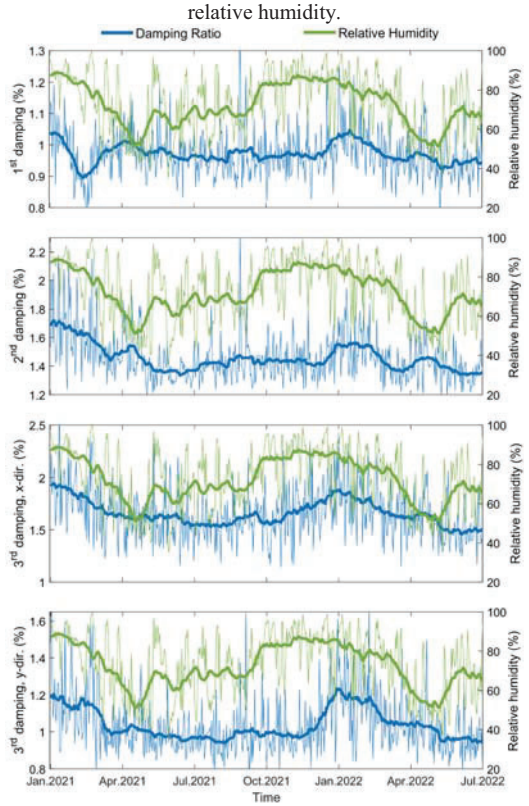

Fig.12. Variation of identified frequencies (1-day mean) and relative humidity.

https://doi.org/10.52202/069179-0385

The variation of mean daily damping ratios is plotted together with the mean daily air temperature as shown in Fig.11. The 1-month smoothed plots are plotted on top of the variations to indicate the trend of parameters with time. No clear relationship is observed between the damping ratios and the seasonal temperature for all three modes of vibration. However, it can be observed that damping ratios are higher in the January-February period compared to the other months for all modes.

Fig.12 shows the variation of the mean daily natural frequencies plotted together with the mean daily relative humidity. The thick smoothed plots (1- month averaging) indicate the trend of the parameters with time. All of the natural frequencies exhibit a positive trend with the relative humidity: with increase of mean relative humidity the natural frequencies increase as well. However, a small delay is observed, indicating that it takes time for the structural properties to respond to the change in relative humidity.

Mean daily damping ratios are co-plotted together with the mean daily relative humidity in Fig.12. From observation no evident effect of the relative humidity on the damping ratios is observed.

For a closer investigation of the effect of environmental conditions on the natural frequencies, 1-month variations of the parameters were co-plotted as shown in Fig.13 for July 2021. Each dot on the figure represents a 1-hour mean value of the parameter. From observation, the relationship between the natural frequency and temperature is not fully clear. A positive relationship between the natural frequency and the relative humidity is observed: increase in the relative humidity results in the gradual increase of the natural frequency with a delay. A similar positive trend between the 1st natural frequency and the relative humidity in Fig.13 was observed for the other two frequencies as well.

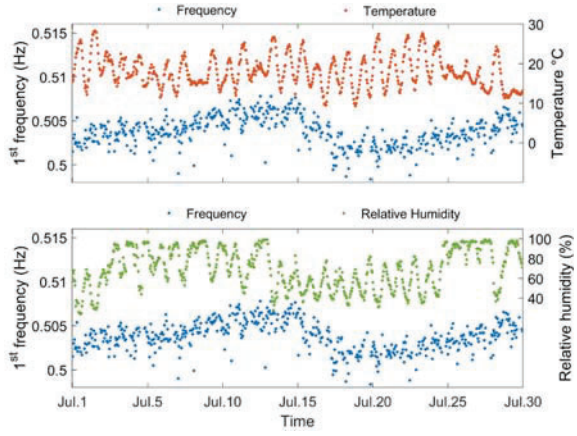

Fig.13. 1-month period (July 2021) variation of identified frequencies co-plotted with mean temperature and mean relative humidity (each dot represents 1-hr segment).

5 CONCLUSIONS

This paper investigated identification of the long-term modal properties under variable environmental conditions of an 18-story glulam frame building in Norway. The combined VMD/SSI-DATA scheme was applied to the measured ambient vibration response. First, the original signal was decomposed with VMD technique into intrinsic mode functions containing the modes; then, the SSI-DATA technique was applied separately on each mode-containing signal to obtain natural frequencies and damping ratios. The identified modal properties were quite stable indicating that the combined methodology can be effectively used for dynamic properties extraction from the ambient vibration data of the tall glulam frame building. The identified natural frequencies for most modes exhibit a similar seasonal behaviour, where highest values for natural frequency are observed in the late winter and the lowest values are observed in the late summer. The identified damping ratios for all modes did not exhibit seasonal variations and have quite stable mean values. From co-plotting the identified frequencies and mean air temperatures, the inverse relationship can be observed for most modes. From co-plotting the natural frequencies and mean relative humidity, a clear positive trend is observed, where the increase in the relative humidity is followed by the increase of the natural frequency for all modes. A delay in response might be caused by the time required for the structural properties of timber to be affected by the environmental conditions. Thus, both temperature and relative humidity impact the natural frequencies: high delay (around 6 months) is observed for temperature variations and a low delay (1-2 months) is observed for the relative humidity.

It is important to note, that in this study analysis of the effect of environmental conditions on the natural frequencies and damping ratios has certain limitations. A longer period of observation is needed to establish a clearer relationship between the seasonal variations and the natural frequencies. Additionally, an on-site weather station measuring both the indoor and outdoor environmental conditions should be installed for a more accurate investigation of the effect of environmental conditions on the dynamic properties of the building.

ACKNOWLEDGEMENT

The research in this paper has been conducted as part of the Dynamic Response of Tall Timber Buildings under Service Load project (DynaTTB). Norwegian Research Council was responsible for providing funding in Norway, grant no.297513.

REFERENCES

[1] Johansson, M., Linderholt, A., Bolmsvik, Å., Jarnerö, K., Olsson, J., and Reynolds, T. Building Higher with Light-weight Timber Structures – the Effect of Wind induced Vibrations. *Proc. Internoise*, San Francisco, 2015.
[2] Heiduschke, A., Kasal, B., and Haller, P. Performance and Drift Levels of Tall Timber Frame Buildings under Seismic and Wind Loads. *Structural Engineering International: Journal of the International Association for Bridge and Structural Engineering (IABSE),* 18(2): 2008.
[3] Leyder, C., Chatzi, E., and Frangi, A. House of natural resources – modal vibration tests and long-term monitoring.

ETH Zurich, Structural Engineering – Timber structures. 2021.
[4] Larsson, C., Abdeljaber, O., Bolmsvik, Å., and Dorn, M. Long-term analysis of the environmental effects on the global dynamic properties of a hybrid timber-concrete building. Engineering Structures, 268 (2022).
[5] The Council on Tall Buildings and Urban Habitat (CTBUH), *CTBUH Ratifies "World's Tallest Timber Building" Following Height Criteria Update*, in *GLOBAL TALL BUILDING NEWS*. 2019.
[6] Abrahamsen, R. Moelven Limtre AS. *Mjøstårnet-Construction of an 81 m tall timber building*. in *International House Forum*. 2017.
[7] Kistler Instrument Corp., *Vehicle Acceleration Measurement*. 2014: 75 John Glenn Drive Amherst, NY14228 USA.
[8] Tulebekova, S., Malo, K.A., Rønnquist, A., and Nåvik, P. *Modeling stiffness of connections and non-structural elements for dynamic response of taller glulam frame buildings.* Engineering Structures, 261 (2022).
[9] Dragomiretksiy, K. and Zosso, D. *Variational mode decomposition.* IEEE Transactions on signal processing 62 (2014).
[10] Van Overschee, P. and B. De Moor, *Subspace identification for linear systems: Theory—Implementation—Applications*. 2012: Springer Science & Business Media.
[11] Kvåle, K.A., Øiseth, O. and Rønnquist, A. *Operational Modal Analysis of an end-supported pontoon bridge.* Engineering Structures, 148:410-423, 2017.
[12] Kvåle, K.A. Operational Modal Analysis toolboxes for Matlab. Available at: https://github.com/knutankv/koma/tree/v.1.0.7.
[13] Norsk Klimaservicesenter (Norwegian Climate Service Centre). Observations and weather statistics. Meterological Institute (MET). Available at: https://seklima.met.no/.

https://doi.org/10.52202/069179-0385

World Conference on Timber Engineering Oslo 2023

INVESTIGATIONS ON SUITABLE LATERAL STIFFENING SYSTEMS FOR TALL TIMBER BUILDINGS

Charles Binck[1], Andrea Frangi[2]

ABSTRACT: As the height of timber buildings continues to increase, the importance of their lateral stiffness concept is growing. At present, the predominant structural system of timber buildings is a timber-concrete hybrid where the lateral stiffness of the building is provided by a reinforced concrete core. However, it is unknown which lateral stiffness concepts for tall timber building are feasible without the use of reinforced concrete. In this paper, five different lateral stiffening systems for tall timber buildings were investigated, with a focus on building heights between 50 and 230 meters. For this purpose, over 12 million building configurations were analysed with different lateral stiffening systems, and a design optimization was performed based on the dynamic response of the buildings subjected to wind loading. The study revealed that the development of semi-rigid connections for moment-resisting timber frames should target a stiffness ratio between 1% and 10% towards a fully rigid joint, to guaranty efficient connection solutions. For such connection stiffnesses, building heights of up to 190m may fulfil the serviceability criteria for cross-sections smaller than 40 x 120 cm.

KEYWORDS: Tall timber buildings, Lateral stiffening systems, Semi-rigid connections, Moment-resisting timber frames, Tube-in-tube systems, Serviceability criteria, Equivalent building stiffness, Height investigations.

1 INTRODUCTION

In the 20th century, buildings in steel and reinforced concrete saw rapid technological and engineering advancements. This enabled the construction of ground-breaking new tall buildings [1]. At present, a similar advancement for tall timber buildings is underway with ever-increasing building heights [2–4]. Two of the world's tallest timber buildings were built in Europe, namely the "HoHo" in Vienna at 84.0m and the "Mjøstårnet" in Brumunddal at 85.4m [5,6]. Since 2022, the tallest timber building is the "Ascent" in Milwaukee at 86.6m [4,7]. However, "Ascent" is constructed on a multi-storey reinforced concrete base [7,8].

As the buildings become taller, wind-induced serviceability vibrations and deflections become the governing design criteria. Here, the importance of the lateral stiffening system grows with increasing building heights. Currently, the predominant structural system is a timber-concrete hybrid where the lateral stiffness of the building is provided by a relatively stiff reinforced concrete core [4,8–10]. However, the use of reinforced concrete is a strong contributor to greenhouse gas emissions [11,12]. Consequently, there is a growing incentive to explore alternative solutions. Besides the promotion of renewable materials, other strong advantages of timber solutions are the lightness of the structures, the potential for a dry construction site and a shorter construction time.

While taller and taller timber buildings are being constructed, the development of feasible alternative lateral stiffness concepts comprising timber components has been stagnant. However, timber has the strength and stiffness to provide feasible solutions. Because of the unparalleled strength-to-weight ratio and similar stiffness-to-weight ratio of timber compared to other conventional building materials, competitive solutions can be provided for both the vertical and lateral load transfer. In Norway, both "Treet" in Bergen and "Mjøstårnet" in Brumunddal, demonstrate options for the lateral stiffening with bracing in the façade [6,13]. However, it is uncertain if other lateral stiffness concepts are feasible for tall timber buildings and which building heights could be achieved with these solutions.

For this purpose, the objective of this paper is to provide a comprehensive analysis of five different lateral stiffening systems, to explore their limits, and to present feasible solutions for building heights up to 190 meters. The systems are examined through more than 12 million simulations of unique building configurations subjected to service-level wind loading. The building configurations comprise different global and local geometries, material properties, mass, structural damping properties, joint stiffnesses, and serviceability criteria. In an analogy to the pioneering work of Fazlur Kahn on the premium for heights for steel and reinforced concrete buildings [14], this paper provides a guideline for current height limits of the lateral stiffening systems for tall timber buildings. The presented investigations of the different systems should be seen as a classification with feasible heights within the range of the chosen parameters and are not intended as boundaries outside this array.

[1] Charles Binck, Institute of Structural Engineering, ETH Zurich, 8093 Zurich, Switzerland, charles.binck@ibk.baug.ethz.ch
[2] Andrea Frangi, Institute of Structural Engineering, ETH Zurich, 8093 Zurich, Switzerland, frangi@ibk.baug.ethz.ch

https://doi.org/10.52202/069179-0386

2 THEORETICAL FRAMEWORK

2.1 STRUCTURAL TYPOLOGIES

Investigations were conducted on a braced inner core (Type I), an external frame tube in the façade (Type II), bracing systems in the façade (Type III and IV) and a tube-in-tube system with an external frame and an internal braced tube (Type V).

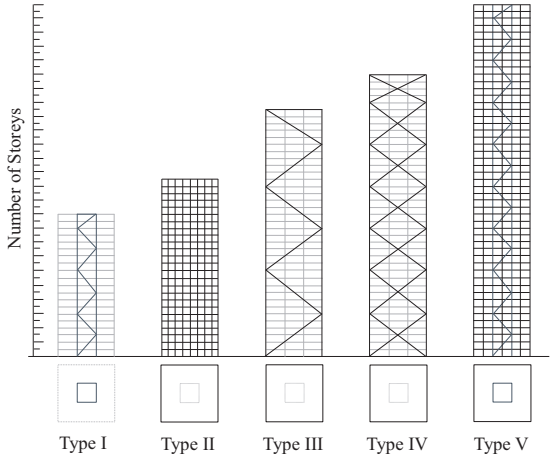

Figure 1: *Overview of the investigated structural typologies based on the work of Fazlur Kahn* [14]

A description of the tube-in-tube concept is given in Binck et al. [15] where the system is illustrated in depth. By introducing moment-resisting connections, the timber parts, which are usually constructed as vertical load-bearing beam-column systems, may contribute substantially to the lateral stiffness. This would enable the beam-column structures to contribute with both vertical and lateral load-transfer.

2.2 PERFORMANCE CRITERIA

To assess the feasibility of the buildings, the serviceability criterion in ISO 10137 [16] based on occupant comfort is used. It is derived from measurements of buildings in vibration use. The serviceability criterion is for peak accelerations of offices or residential uses and is a function of the building's first natural frequency. In this paper, the stricter requirements for residential uses are used.

EN 1994-1-4 [17] provides in Annex B a framework to determine those accelerations and equivalent wind loads based on the gust factor approach for building heights up to 300 m height. In this paper, the basic wind velocity $v_{b,0}$ is 25 m/s. Accelerations are computed with subsequent computations based on a 1-year return period with a probability factor $c_{prob} = 0.73$.

In contrast to the accelerations, the peak deflections are calculated for a corresponding return period of 100 years by the static equivalent loads taking only the first mode into consideration. The higher return period is chosen here for a design criterion where damage on non-structural elements shall be avoided. In literature, there is no consensus or consistency for the criterion to avoid damage to non-structural elements [18,19]. However, current recommendations are in a range between $1/300$ to $1/1000$ of the building height for peak deflections and the inter-storey drifts [18,19]. Here, the performance criteria for peak deflections are set to a maximal global deflection of:

$$u_{peak} \leq \frac{H}{500} \tag{1}$$

for the building and a maximal inter-storey drift of:

$$\delta u_{peak} \leq \frac{h_s}{500}, \tag{2}$$

where H and h_s are the building height and the storey height respectively. The parameters used for the wind actions are summarised in Table 1.

Table 1: *Overview of the parameters for the wind actions according to EN 1991-1-4 (2010).*

Description		a_{peak}	u_{peak} & δu_{peak}
Actions computed according to		EN 1991-1-4 (2010) Annex B	
Basic wind velocity	v_{b0}	25 m/s	
Return period	R	1 year	100 years
Probability factor	c_{prob}	0.73	1.039
Altitude factor	c_{alt}	1.0	
Directional factor	c_{dir}	1.0	
Seasonal factor	c_{season}	1.0	
Turbulence factor	k_1	1.0	
Air density	ρ	1.25	
Reference height	z_t	200 m	
Reference length scale	L_t	300 m	
Minimum height	z_{min}	10 m	
Maximum height	z_{max}	200 m	
Roughness length	z_0	1.0 m	
Orography factor	c_o	1.0	
Design criteria		ISO 10137	$H/500$ $h_s/500$

2.3 METHOD

2.3.1 Finite Element Modelling

The structural analysis and simulations were conducted by adopting and expanding the finite element framework for assessing wind-induced vibrations for planar frames, first developed by Cao & Stamatopoulos [20–22]. In the framework, the trusses and beams use Euler-Bernoulli beam theory, and the columns use Timoshenko beam theory with a shear correction factor of 5/6. The beam-column connections are idealized as linear-elastic rotational springs with a stiffness K_θ, the axial flexibility in the joints of the trusses is neglected, and the column-column joints are assumed to be rigid. More details can be found in Binck et al. [15] and Cao & Stamatopoulos [20–22].

https://doi.org/10.52202/069179-0386

2.3.2 Connection Stiffness

For a rigid beam-column joint, the equivalent rotational joint stiffness $K_{\theta,eq}$ can be derived by static condensation and expressed as:

$$K_{\theta,eq} = \frac{145EI_c}{6h} + \frac{239EI_b}{6l} + \frac{110EI_b^2 \cdot h}{6EI_c \cdot l^2} + 4\frac{EI_c^2 \cdot l}{EI_b \cdot h^2}, \quad (3)$$

where h is the column height, l is the bay length and EI_c is the column stiffness and EI_b is the beam stiffness, clarified in Figure 2. Hence, for a semi-rigid connection, the beam-column connection stiffness K_θ is defined as a fraction α_θ of the equivalent beam-column joint stiffness $K_{\theta,eq}$:

$$K_\theta = \alpha_\theta \cdot K_{\theta,eq}, \quad (4)$$

Where α_θ is the stiffness ratio and varies in the parameter study between 0.1 % and 100%. The connection stiffness K_θ can be illustrated as a reduced cross-section of the beam-column joint, as clarified in Binck et al. [15].

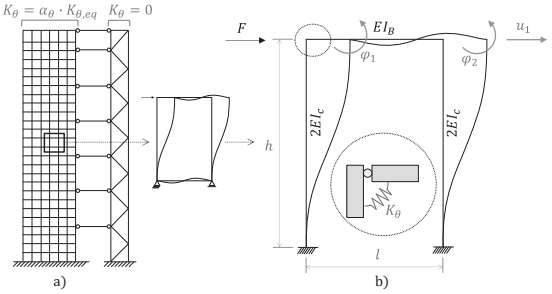

Figure 2: *Structural system (a) and the statically equivalent model for determining the rotational stiffness (b).*

2.3.3 Equivalent Cantilever Stiffness

From a static perspective, a tall building can be illustrated as a vertical, encastered beam. By using this beam, the stiffness of the multi-degree-of-freedom system can be expressed in terms of a simple Timoshenko cantilever beam. This enables an easier expression and comparison of the different structural typologies in relation to the stiffness if an equivalent bending stiffness EI_{eq} and shear stiffness GA_{eq} can be determined. To find EI_{eq}, and GA_{eq}, the deformations can be decomposed as a superposition of the pure bending displacement u_{EI}, and pure shear displacement u_{GA}. Subsequently, the fraction of bending γ_{EI} and shear γ_{GA} contributions can be computed by linear regression.

With this approach, the analytical expression of the predicted displacement $u_{j,pred}$ can be written as:

$$u_{j,pred} = \gamma_{EI} \cdot u_j + \gamma_{GA} \cdot u_j. \quad (5)$$

By solving for γ_{EI} and γ_{GA}, the fraction of bending displacement and shear displacement on the equivalent Timoshenko beam are determined and through the inverse procedure, the equivalent bending stiffness EI_{eq} and shear stiffness GA_{eq} can be derived.

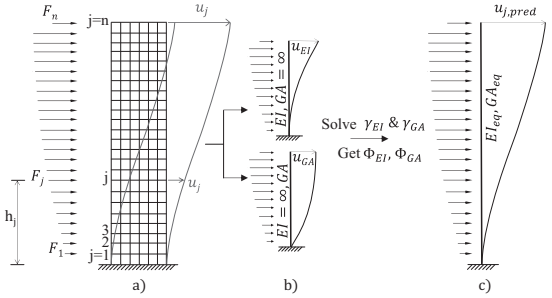

Figure 3: *Model sketch of the mathematical procedure to determine the equivalent beam stiffnesses.*

An appropriate method to determine these stiffnesses for the equivalent cantilever beam, loaded by non-uniformly distributed loads, is the use of the curvature. The building displacements at storey height h_j can be calculated as:

$$u_j = u_{j-1} + \delta u_j, \quad (6)$$

where $u_{j-1}$is the displacement from the storey below and δu_j is the current storey drift, shown in Figure 4. This storey drift δu_j is computed by curvature on the equivalent Timoshenko beam.

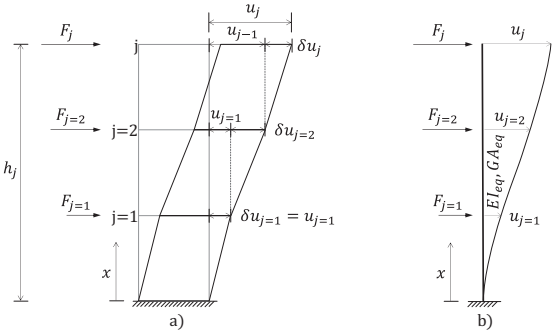

Figure 4: *Calculation method of the deflections for the equivalent cantilever beam.*

For a homogeneous beam with a constant cross-section, the differential equation of a Timoshenko beam is given by:

$$EI_{eq}\frac{\delta^2\phi_y}{\delta x^2} - k_s GA_{eq}\left(\frac{\delta u_z}{\delta x} + \phi_y\right) = 0, \quad (7)$$

where k_s is the Timoshenko shear coefficient, φ_y is the curvature from pure bending, $\gamma_{xz} = -\varphi_y + \phi_y$ is the curvature from pure shear, and ϕ_y is the resulting angle of rotation from both, illustrated in Figure 5.

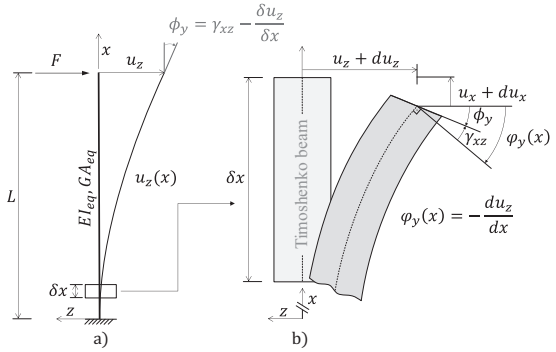

Figure 5: *Applied Timoshenko beam theory.*

Internal forces in a beam are related to the strain, i.e., to the displacement u and the rotation φ_y. For a linear elastic Timoshenko beam, the relations to the bending moment $M_y(x)$ and the shear force Q_z are:

$$M_y(x) = -EI_{eq}\,\frac{\delta\phi_y}{\delta x}, \tag{8}$$

$$Q_z = k_s GA_{eq}\left(\frac{\delta u_z}{\delta x} + \phi_y\right). \tag{9}$$

For the cantilever beam, shown in Figure 5 a), where x gives the positive direction from the clamped end to the free end, the bending moment $M_y(x)$ can be computed from the free-body diagram, as:

$$M_y(x) = F \cdot L - F \cdot x, \tag{10}$$

where F is a point load at position L. Substituting Equation (9) into (7) gives:

$$EI_{eq}\frac{\delta\phi_y}{\delta x} = -F \cdot L + F \cdot x. \tag{11}$$

By integration, the bending curvature is written by:

$$\phi_y(x) = -\frac{1}{EI_{eq}}\left(F \cdot L \cdot x - \frac{1}{2}F \cdot x^2\right) + c_1, \tag{12}$$

where c_1 is a constant. Thus, substituting equation (12) into Equation (9), the total curvature of the Timoshenko beam can be expressed as:

$$\frac{\delta u_z}{\delta x} = \frac{Q_z}{k_s GA_{eq}} + \frac{1}{EI_y}\left(F \cdot L \cdot x - \frac{1}{2}F \cdot x^2\right) + c_1, \tag{13}$$

where the first part of the equation defines the curvature form pure shear and the second part defines the curvature from pure bending.

Equivalent bending stiffness

With Equation (12), the equivalent bending stiffness of a multi-storey building under nonuniform distributed loads can be written as:

$$EI_{eq} = \frac{1}{\frac{\delta u_{j,EI}}{\delta x}} \cdot \left[F_j \cdot \left(h_j \cdot x - \frac{1}{2}x^2\right) + c_{j,EI}\right], \tag{14}$$

where $c_{j,EI}$ is a constant resulting from the curvature at level j as a consequence of the actions below:

$$c_{j,EI} = F_{j-1} \cdot \left(h_{j-1} \cdot x - \frac{1}{2}x^2\right) + c_{j-1}. \tag{15}$$

Equations (14) and (15) show, that the bending curvature at storey j refers to the curvatures and loads from the entire building and indicate the advantage of computer aided calculations. Finally, the inter-storey drift δu_j is written by:

$$\delta u_j = \frac{\delta u_j}{\delta x} \cdot h_j - \frac{\delta u_j}{\delta x} \cdot h_{j-1}. \tag{16}$$

Shear stiffness

In analogy to the bending stiffness, the shear stiffness is derived by Equation (13) to:

$$GA_{eq} = \frac{Q_z \cdot x}{\delta u_{j,GA}}, \tag{17}$$

where Q_z is the shear force and thus the sum of the non-uniformly distributed loads above the height x:

$$Q_z = \sum_{i=j}^{n} F_i. \tag{18}$$

Equivalent cantilever stiffness

With the bending stiffness and shear stiffness, the equivalent beam stiffness can be computed by:

$$K_{B,eq} = \left(\frac{1}{K_{EI,eq}} + \frac{1}{K_{GA,eq}}\right)^{-1}, \tag{19}$$

where:

$$K_{EI,eq} = \frac{3EI_{eq}}{H^3}\ , \quad K_{GA,eq} = \frac{GA_{eq}}{H}. \tag{20}$$

3 PARAMETER STUDY

The parameters are chosen to cover the most realistic variations of the building geometry. Because of the high number of possible configurations, over 12 million simulations are analysed. The varying parameters are the number of stories n_s, number of bays n_b, bay length l_b, column cross-sections $b_c \times h_c$, beam cross sections $b_b \times h_c$, bracing cross-sections $b_{br} \times h_{br}$, rotational stiffness ratio of the beam-column joints α_θ, glued laminated timber strength grades between GL28h and GL75, characteristic storey loads p_s, the internal core ratio β, which is the ratio between the external tube B and the internal tube L_{br}, logarithmic decrement of the structural damping δ_s and the return period R for the basic wind speed. The mass of the building is assumed to be uniformly distributed along the height of the buildings. Figure 6 shows the parameters graphically.

https://doi.org/10.52202/069179-0386

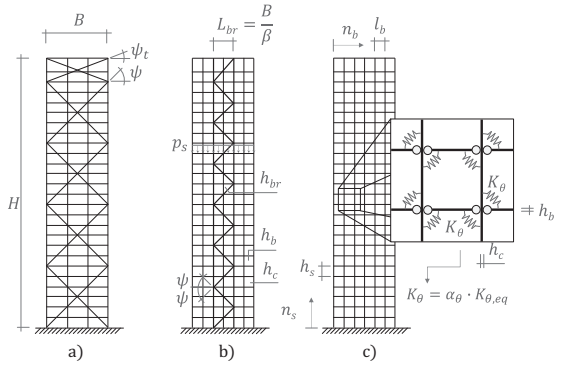

Figure 6: *Illustration of the parameters.*

The constant parameters are the storey height h_s which is fixed at 3.5 m. The bracing angle ψ is variable and determined by the building width and internal core width. However, ψ is approximately 45° and is optimised to find the closest storey, to connect centred to the beam-column-joint. ψ_t is the resulting bracing angle of the top bracing. Table 2 summarises the parameters for the structural investigations. The investigations on the Type II and on the Type V are constant member widths $b_{c,b,br}$, of 0.4m. Here, only the member heights $h_{c,b,br}$ are paramterised and vary between 0.4m and 1.2m. For the braced systems in Type I, III, and IV, the brace cross-sections are square.

Table 2: *Overview of the parameters for the structural investigations*

Structure Typology		Frame (Type II)			Bracing (Type I, III, IV)			Tube-in-Tube (Type V)			
		Min	Max	Step	Min	Max	Step	Min	Max	Step	Unit
Number of bays	n_b	6.00	12.00	2.0	6.00	12.00	2.0	6.00	12.00	2.0	-
Bay width	l_b	2.40	4.20	0.6	2.40	4.20	0.6	2.40	4.20	0.6	m
Number of storeys	n_s	15	65	5.0	15	65	5.0	15	65	5.0	m
Column width	b_c	0.40	0.40	-	0.40	1.20	0.20	0.40	0.40	-	m
Column height	h_c	0.40	1.20	0.20	0.40	1.20	0.20	0.40	1.20	0.20	m
Beam width	b_b	0.40	0.40	-	-	-	-	0.40	0.40	-	m
Beam height	h_b	0.40	1.20	0.20	-	-	-	0.40	1.20	0.20	m
Bracing width	b_{br}	-	-	-	0.40	0.40	-	0.40	0.40	-	m
Bracing height	h_{br}	-	-	-	0.40	1.20	0.20	0.40	1.20	0.20	m
Surface load/storey	p_s	5	10	2.5	5	10	2.5	5	10	2.5	kN/m^2
Rotational stiffness ratio	α_θ	0.1	100	([a])	1	100	([a])	1	100	([a])	%
Material		GL28h[(b)]	GL75[(d)]	GL48h[(c)]	GL28h	GL75	GL48h	GL28h	GL75	GL48h	-
Internal core ratio	β	-	-	-	1	3	0.5	1	3	0.5	-
Structural damping	δ_s	0.1	0.5	0.1	0.1	0.5	0.1	0.1	0.5	0.1	-

([a]) the rotational stiffness of the moment resisting connection is changed unregularly by the following steps: α_θ = 0.1, 0.25, 0.5, 1.0, 2.5, 5.0, 10, 25, 50 100%.
([b]) GL28h according EN 14080 [23] with E=12'600N/mm^2 and G=650N/mm^2
([c]) GL48h for hardwood GLT according Neue Holzbau AG [24] with E=15'000N/mm^2 and G=1000N/mm^2
([d]) GL75 for Pollmeier Baubuche according [25] with E=16'800N/mm^2 and G=850N/mm^2

4 RESULTS AND DISCUSSION

4.1 EQUIVALENT CANTILEVER STIFFNESS

The equivalent stiffness approach in Section 2.3.3, enables the comparison of the different structural systems in terms of the global building stiffness. Independent from the lateral stiffening, the equivalent cantilever beam can quantify the building stiffness. For all the simulations, the coefficient of determination R^2 from the deflections of the finite element results and the predicted deflections of the equivalent cantilever beam is between 0.975 and 1.0. The approach is promising and enables the structural typologies to be assessed in terms of their serviceability.

Based on the results, the varying systems can be analysed towards their bending and shear stiffnesses. Figure 7 shows the scatter of the equivalent bending stiffness EI_{eq} in relation to the equivalent shear stiffness GA_{eq}, where both, horizontal and vertical axis are shown on the base-10 logarithmic scale. In the figure, a set of the results is shown which fulfil the serviceability criteria from Section 2.2 and reveals a slenderness of $H/B > 3.0$. In addition, the plotted results are computed for member grades in GL28h. For the frames and tube-in-tube systems, Figure 7 only presents results for rotational connection stiffness with $\alpha_\theta \leq 1.0$ % and internal core dimensions with $\beta_{br} = 3.0$, i.e. $L_{br} = 1/3 \cdot B$ for Type I and Type V.

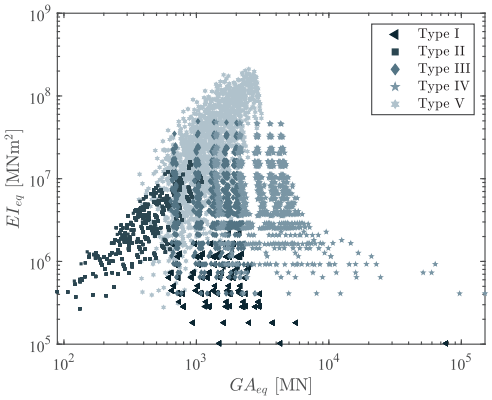

Figure 7: *Behaviour between the equivalent bending stiffness EI_{eq} and shear stiffness GA_{eq}.*

The relation between EI_{eq} and GA_{eq} reveals the strengths and weaknesses of the different systems. Knowing that the frames are more shear compliant than bracings, Figure 7 proves that the tube-in-tube systems as combined configurations achieve bending stiffnesses in the order of braced systems in the façade.

Figure 8 highlights the study resulted building stiffnesses from above in a swarm chart. The figure can be used as a qualitative assessment, to assess the different systems on their global stiffnesses according to the frequency of the results. For all types, the results are visualised in Figure 8 with their distribution of the achieved stiffnesses.

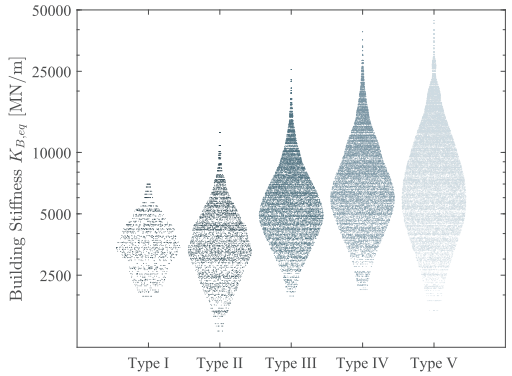

Figure 8: *Equivalent building stiffnesses of the different systems for a set of simulations.*

4.2 ROTATIONAL CONNECTION STIFFNESS

Figure 9 shows the relation of the equivalent rotational joint stiffness $K_{\theta,eq}$ and the bay length l_b, the storey height h_s and varying beam dimensions.

It is apparent from Figure 9 that the storey height h_s becomes less significant with increasing bay lengths l_b. Its impact is smaller in comparison to the bay lengths l_b, the cross-sections of the members $b_b \times h_b$, $b_c \times h_c$, and the young's modulus E. However, the storey height h_s is not negligible, particularly for small bay lengths. For beams which are weaker than the columns, the impact of the bay length l_b diminish and the influence of the storey height h_s is approximately constant for increasing bay lengths. This can be seen in Figure 9.

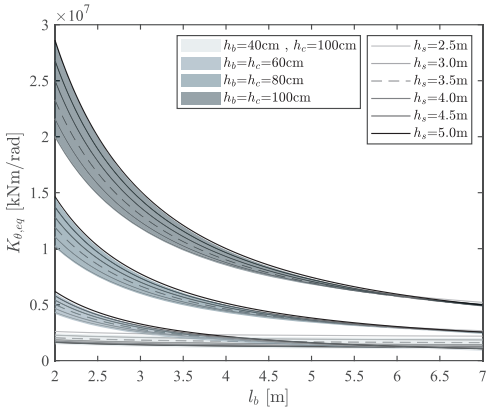

Figure 9: *Relation of the equivalent rotational joint stiffness $K_{\theta,eq}$, bay length l_b, storey height h_s and member cross-sections.*

Since the beam-column connection stiffness K_θ is only a fraction α_θ of the equivalent rotational joint stiffness $K_{\theta,eq}$, as expressed in Equation (4), it is appropriate to identify the impact of the joint stiffness in relation to the building stiffness.

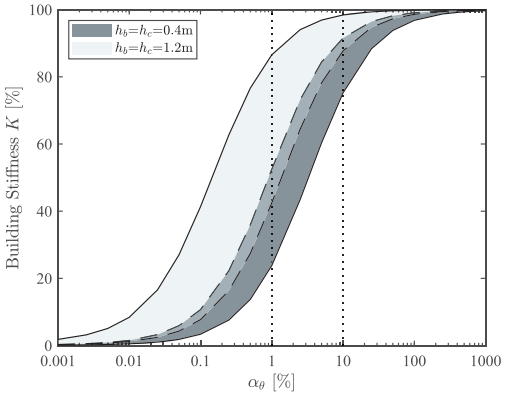

Figure 10: *Impact of the connection stiffness on the global building stiffness. α_θ is plotted on the logarithmic scale to clarify the increase of the building stiffness in the smaller range.*

Figure 10 presents the behaviour of the building stiffness K in relation to the connection stiffness ratio α_θ for a wide range of parameters. The building stiffness K on the vertical axis is here illustrated as the fraction of the equivalent beam stiffness $K_{B,eq}$ towards a fully rigid moment resistant frame to normalise the results. Hence, the building stiffness is expressed in percent:

$$K = \frac{K_{B,eq}(\alpha_{\theta,i})}{K_{B,eq}(\alpha_\theta = 100\%)} \tag{21}$$

The hatched areas in the figure contain all possible combination for the varying parameter configurations,

https://doi.org/10.52202/069179-0386

where configurations with the smallest member cross-sections h_b=h_c=40cm and larges cross-sections h_b=h_c=120cm are subdivided.

Figure 10 reveals, that the beam-column connection stiffness K_θ has a large impact on the building stiffness when the stiffness ratio α_θ is within the range of 0.01% to about 10%. For stiffness ratios α_θ of more than 10%, the impact is smaller because of the exceedingly high values of K_θ and the large number of beam-column joints. A stiffness ratio α_θ of 5% in the beam-column joints results in a global lateral stiffness K between 60% and 98% when compared with an equivalent building with rigid beam-column joints. Whereas slender beams need higher connection stiffnesses than stiffer or larger beams, to achieve maximal building stiffnesses.

So, for instances, achieves a building with a framed tube (Type II) in GL28h with n_b=6 bays, bay lengths l_b=3.6m, n_s=25 storeys, storey height h_s=3.5m, beam and columns cross-sections of $b_b \times h_b$=40×100cm and $b_c \times h_c$=40×60cm a global lateral building stiffness of K=79% for a connection stiffness ratio of α_θ=1.0%. Whereas the same building with a relatively equal stiffness ratio α_θ=1.0%, but with reversed member dimensions, i.e., beam cross-sections $b_b \times h_b$=40×60cm and columns $b_c \times h_c$=40×100cm, only achieves a global building stiffness of K=32%. Figure 11 shows, that only a small α_θ is needed to provide stiff connections as peak accelerations and deflections are only slightly affected after a certain achieved rotational stiffness. For the illustrated 25 multi-storey frame, the gain with connection stiffness ratios α_θ above 1% is marginal.

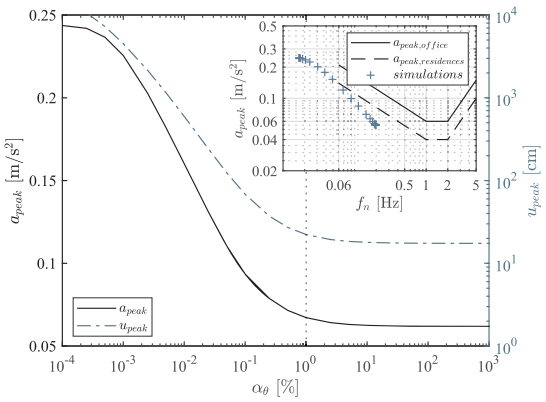

Figure 11: *Behaviour of the peak accelerations and peak displacements related to the rotational connection stiffness for an illustrative external frame (Type II) in GL28h with 25 storeys, 6×3.6m bays, storey height 3.5 m, δ_s=0.1, beam cross-sections 40×100cm and column cross-sections 40×60cm.*

Apart from slender beams, an increase of the stiffness ratio α_θ above 10% is in general not worthwhile. Consequently, the development of semi-rigid beam-column joints should target a stiffness ratio α_θ between 1% and 10% to guarantee efficient solutions. Such stiffness ratios result in stiffnesses, which are high and currently challenging in timber to achieve. However, they are not impossible. Considering the mentioned building above for instances, where beam and column cross-sections are $b_b \times h_b$=40×100cm and $b_c \times h_c$=40×60cm, bay length l_b is 3.6m, storey height h_s is 3.5m, and the elastic modulus E is 12'600N/mm², then, a stiffness ratio α_θ=1% results in a rotational stiffness K_θ of 242'150kNm/rad. Through experimental and analytical considerations Stamatopoulos et al. [26] showed that their current system based on threaded rods results in rotational stiffness ratios α_θ in the order of 2.3%, when the connections would be applied in the mentioned building. Their investigations proved a connection stiffness K_θ in the order of 7618kNm/rad for two threaded rods in plane with members in GL30c and cross-sections of b_b/h_b=14/45cm and b_c/h_c=14/45cm respectively. From an engineering point of view, these results indicate that multi-storey frame structures could enable a new era of tall timber buildings, when combined with an internal core, as will be shown in the following.

4.3 SERVICEABILITY STUDY

The wide-ranging parameter study enables the sensitivity analysis on the significance of the different parameters. The impact and weight of the varying parameters are described in depth in Binck et. al. [15]. Towards the serviceability limit state, the most important parameters of the different systems are the rotational connection stiffness K_θ while stiffness ratios α_θ are under 10%, the member dimensions $b_{b,c,br}$ and $h_{b,c,br}$, the timber grades and the number of bays n_b which have a higher importance than the bay length l_b and storey height h_s. In contrast to the peak displacements, the mass, its distribution, and the damping properties have a pronounced importance on the peak accelerations.

To assess the height limitations of the different stiffening systems, the structures are subjected to the performance criteria, presented in section 2.2. Depending on the varying parameters, the height limit is defined for the tallest structures, which still fulfil all three, the peak acceleration criterion a_{peak}, the peak displacement criterion u_{peak}, and the maximum inter-storey drift δu_{peak} criteria.

For the structural types II, IV and V, Figure 12 shows the structural height limitations with the dashed grey line. The limits are expressed in terms of the maximum storey number and the common parameters. If the peak displacement criteria are the decisive criteria, the height limit is plotted trough the grey circled markers. The grey markers indicate the ultimate storey number for the satisfaction of the displacement criteria. If the acceleration criterion is the decisive criterion, the decision line pass through the black, squared markers. For the latter, the requirements for residential uses according ISO 10137 [16] are assessed.

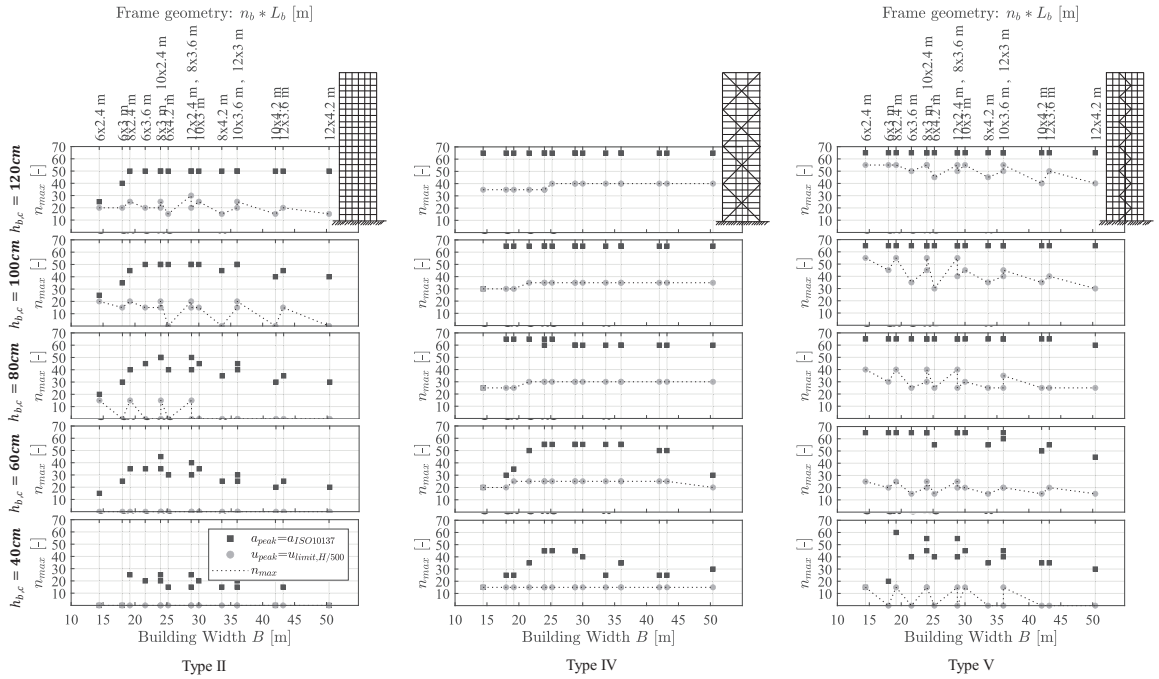

Figure 12: *Height investigations of Types II, IV and V which fulfil the serviceability criteria, expressed in terms of the storey number n_{max}. The common parameters for the shown results are the glued laminated timber strength grades in GL28h for all members, constant characteristic storey loads of p_s=7.5kN/m², storey height h_s=3.5m, structural logarithmic damping decrements of δs=0.1, rotational connections stiffnesses of α_θ=1.0% for the semi-rigid connections and beam and bracing cross-sections of 1) $b_{b,br} \times h_{b,br}$=40×40cm, 2) $b_{b,br} \times h_{b,br}$=40×60cm, 3)) $b_{b,br} \times h_{b,br}$=40×80cm, 4)) $b_{b,br} \times h_{b,br}$=40×100cm, 5)) $b_{b,br} \times h_{b,br}$=40×120cm in the different figures. Type II and V have same column cross-sections. For type IV, the column cross-sections are squared, thus 1) $b_{b,br} \times h_{b,br}$= 40×40cm, 2) $b_{b,br} \times h_{b,br}$=60×60cm, 3) $b_{b,br} \times h_{b,br}$=80×80cm, 4) $b_{b,br} \times h_{b,br}$=100×100cm, 5) $b_{b,br} \times h_{b,br}$=120×120cm.*

Figure 12 reveals the relevance of the displacement criteria for various parameters. In general, three main reasons indicate the relevance of the displacement criteria: first, the small young's modulus E of GL28h leads to relatively weak structures, compared to other materials. This is also a reason for why the height limits for increasing building widths are constant. Regarding the increasing wind contact surface which larger buildings provide, the strains in the extensive large members mount up to large deformations. Only a simultaneous increase of the member cross-sections enables deflection reductions in that case. The second reason is the relatively high storey load for the comparatively weak structures, which is here set to p_s=7.5kN/m² as a characteristic load and corresponds to a building density of about 214 kg/m³ including all dead loads and quasi permanent live loads. For lightweight buildings with storey loads of 5.0 kN/m² for instances, the acceleration criterion becomes frequently the governing criterion. Finally, the third reason is the calculation for the higher return period of 100 years for the displacements.

4.4 HEIGHT INVESTIGATIONS

Based on Figure 12, the determination of the height limits for the structural timber systems is carried out for all parameter configurations. Analogously, Figure 13 summarises the achievable heights for all investigations with varying parameters listed in Table 1 and Table 2. Here the results are valid for the fixed parameters with a constant storey height h_s=3.5m, a logarithmic damping decrement of the structure δ_s=0.1 and constant characteristic storey loads of p_s=7.5kN/m². In Figure 13, the current height limits for GL28h are presented:

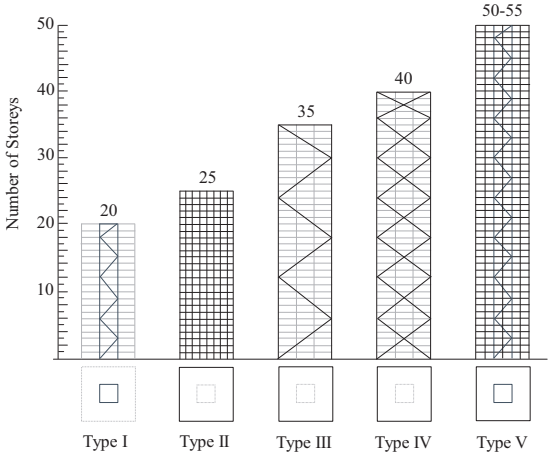

Figure 13: *Height investigations for structural timber systems subjected to wind loading.*

https://doi.org/10.52202/069179-0386

From a serviceability point of view, the results indicate that the braced systems in the façade (Type III and IV) and the tube-in-tube systems (Type V) presents feasible solutions for building heights H>100m. Considering the requirements of $u_{peak} \leq H/500$, $\delta u_{peak} \leq h_s/500$ and the acceleration criterion in ISO 10137 [16] as comfort criteria, the structures perform well up to 140m for Type IV and 175m-190m for Type V with storey heights h_s=3.5m. However, this should be seen more as a guideline than as a stringent boundary. Regarding the serviceability, investigations on higher structures are feasible when larger cross-section will be guaranteed to provide the required stiffnesses.

The advantage of Type V as a tube-in-tube system would be the use of the existing structure from the vertical load transfer while applying simultaneously to the horizontal load transfer, without adding further members in the façade layer. However, high demands are made on the moment-resisting connections as they have to act as key elements to provide the required stiffnesses. At present, these connections are still challenging because of the anisotropic material properties, and their development has just begun. Moment-resisting connections are no common solutions in timber structures but could enable a new field for tall timber buildings.

5 CONCLUSIONS

At present, the predominant structural system for tall timber buildings is a hybrid solution, where a reinforced concrete core provides the lateral stiffness. To assess alternative solutions in timber, five different systems were analysed in this paper to assess the performance of lateral stiffening systems in timber. The main goal was to explore the feasible heights of timber solutions for the presented systems.

Based on a parameter study, the classification of efficient height limits was induced on the lateral stiffness capabilities for wind induced vibrations. The structural typologies have been compared with respect to their stiffness and analysed for peak accelerations and displacement limitations. The height indications have not been analysed and classified according to the ultimate limit state.

With an efficient and well-designed lateral stiffening system, holistic timber buildings can satisfy the acceleration requirements for residential uses according to ISO 10137 and the peak displacement criteria of $u_{peak} \leq H/500$ and $\delta u_{peak} \leq h_s/500$ for a 100 year return period. There is a great potential for timber solutions that will allow buildings to reach heights up to 190m. This potential is dependent by a wide range of parameters and is presented for a certain parameter range in this paper. The key takeaway from the analysed structures should be, that the wind induced deformations are in most cases the decisive requirement while assessing the displacement criteria to $u_{peak} \leq H/500$ at the head deflections and $\delta u_{peak} \leq h_s/500$ for the inter-storey drift.

The comparison can be seen as a fundamental research for height investigations for a new era of timber buildings in terms of different structural systems. This will enable a more global perspective of quantifying the lateral stiffness for tall timber buildings to enforce its structural design. However, a more in-depth study is needed to include the structural analysis on the ultimate limit state in order to provide a holistic assessment on the ultimate height limitations and to identify the “premium for heights”.

ACKNOWLEDGEMENT

This article is written within the framework of the project “Lateral Stiffening Systems For Tall Timber Buildings”. The authors gratefully acknowledge the funding from Innosuisse – Swiss Innovation Agency. Special thanks also go to the project partners Schnetzer Puskas Ingenieure AG and Boltshauser Architekten AG.

REFERENCES

[1] Tamboli AR. Tall and supertall buildings : planning and design. New York: Mcgraw-Hill Education; 2014.

[2] Svatoš-Ražnjević H, Orozco L, Menges A. Advanced Timber Construction Industry: A Review of 350 Multi-Storey Timber Projects from 2000–2021. Buildings 2022;12:404. https://doi.org/10.3390/buildings12040404.

[3] Kuzmanovska I, Gasparri E, Tapias Monne D, Aitchison M. Tall timber buildings: Emerging trends and typologies. World Conference on Timber Engineering (WCTE 2018), Seoul, Korea, Republic Of.: 2018.

[4] Safarik D, Elbrecht J, Miranda W. State of Tall Timber 2022. Council on Tall Buildings and Urban Habitat, CTBUH Research Journal 2022;1:22–9.

[5] Woschitz R, Zotter J. Holzhochhaus HoHo Wien - Das Tragwerkskonzept. Österreichische Ingenieur- Und Architekten-Zeitschrift 2017;162.

[6] Abrahamsen R. Mjøstårnet-18 storey timber building completed. 24 Internationales Holzbau-Forum IHF 2018.

[7] Thornton Tomasetti. Project Ascent 2023. https://www.thorntontomasetti.com/project/ascent (accessed March 14, 2023).

[8] Fernandez A, Komp J, Peronto J. Ascent - Challenges and Advances of Tall Mass Timber Construction. International Journal of High-Rise Buildings 2020;9:235–44. https://doi.org/https://doi.org/10.21022/IJHRB.2020.9.3.235.

[9] Jung P. Suurstoffi BF1 Rotkreuz: 60Meter – 15 Geschosse – 15 Wochen. 24. Internationales Holzbau-Forum IHF 2018, Internationales Holzbau-Forum IHF; 2018, p. 1–12.

[10] Vola M, Verhaegn R, de Jong J. Haut - A 21-storey Tall Timber Residential Building. International Journal of High-Rise Buildings 2020;9:213–20. https://doi.org/https://doi.org/10.21022/IJHRB.2020.9.3.213.

[11] International Energy Agency (IEA). Technology Roadmap - Low-Carbon Transition in the Cement Industry. Paris: 2018.
[12] Bellmann E, Zimmermann P. Klimaschutz in der Beton- und Zementindustrie - Hintergrund und Handlungsoptionen. Berlin: 2019.
[13] Malo KA, Abrahamsen RB, Bjertnæs MA. Some structural design issues of the 14-storey timber framed building "Treet" in Norway. European Journal of Wood and Wood Products 2016;74:407–24. https://doi.org/10.1007/s00107-016-1022-5.
[14] Ali MM, Moon KS. Structural Developments in Tall Buildings: Current Trends and Future Prospects. Archit Sci Rev 2007;50:205–23. https://doi.org/10.3763/asre.2007.5027.
[15] Binck C, Cao AS, Frangi A. Lateral stiffening systems for tall timber buildings – tube-in-tube systems. Wood Mater Sci Eng 2022:1–8. https://doi.org/10.1080/17480272.2022.2086066.
[16] ISO. ISO 10137-2007. Bases for design of structures - Serviceability of buildings and walkways against vibrations. 2007.
[17] CEN. EN 1991-1-4 Eurocode 1: Actions on structures - Part 1-4: General actions -Wind actions. In: European Committee for Standardization, editor., 2010.
[18] Griffis LG. Serviceability Limit States Under Wind Load. Engineering Journal, American Institute of Steel Construction 1993;30:1–16.
[19] Smith R. Deflection Limits in Tall Buildings—Are They Useful? Structures Congress 2011, Reston, VA: American Society of Civil Engineers; 2011, p. 515–27. https://doi.org/10.1061/41171(401)45.
[20] Cao AS. Dynamic response of semi-rigid timber frames subjected to wind loads. Masterthesis. Norwegian University of Science and Technology, 2020.
[21] Cao AS, Stamatopoulos H. A theoretical study of the dynamic response of planar timber frames with semi-rigid moment-resisting connections subjected to wind loads. Eng Struct 2021;240:112367. https://doi.org/https://doi.org/10.1016/j.engstruct.2021.112367.
[22] Cao AS, Stamatopoulos H. Theoretical studies of tall timber buildings subjected to service-level wind loads. World Conference on Timber Engineering (WCTE 2021) 2021:1964–9. https://doi.org/10.3929/ethz-b-000507921.
[23] CEN. EN 14080 Timber structures - Glued laminated timber and glued solid timber - Requirements. 2013.
[24] Neue Holzbau AG. Eigenschaften Brettschichtholz in Laubholz. Lungern: 2020.
[25] Österreichisches Institut für Bautechnik (OIB). ETA-14/0345. Wien: 2021.
[26] Stamatopoulos H, Malo KA, Vilguts A. Moment-resisting beam-to-column timber connections with inclined threaded rods: Structural concept and analysis by use of the component method. Constr Build Mater 2022;322:126481. https://doi.org/10.1016/j.conbuildmat.2022.126481.

https://doi.org/10.52202/069179-0386

World Conference on Timber Engineering Oslo 2023

PERFORMANCE VERIFICATION AND TRIAL DESIGN FOR HIGH-RISE TIMBER FRAME BUILDINGS WITH BUCKLING-RESTRAINED BRACE PART 2: ANALYSIS OF THE TRIAL DESIGN BUILDING

Ryota Minami[1], Toshio Maegawa[2], Taisuke Nagashima[3], Kazuki Tachibana,[4] Hiroki Nakashima,[5] Nobuhiko Akiyama,[6] Yoshihiro Yamazaki,[7] and Takahiro Tsuchimoto[8]

ABSTRACT: Demand has recently emerged for large-scale structures made of timber. In earthquake-prone areas, such structures must feature adequate bearing capacity against major earthquakes. Part 1 of our research in this area entailed studies of methods to strengthen the bearing capacity of timber structures against the forces generated by major earthquakes. The work described in this paper confirms the seismic performance of a 10-story timber building designed by these methods. Analysis confirmed that the suggested methods strengthen the bearing capacity of large timber buildings against the forces generated by major earthquakes.

KEYWORDS: High-rise timber frame building, trial design, nonlinear dynamic analysis, buckling-restrained brace

1 INTRODUCTION

In earthquake-prone areas, structures made of timber tend to suffer significant damage when subjected to earthquake forces. For this reason, in Japan, virtually all medium- and large-scale structures are made of reinforced concrete or steel. However, various recent trends, including environmental issues, have generated demand for medium- and large-scale structures made of timber.

Medium- and large-scale buildings made of steel often incorporate buckling-restrained braces (BRBs) to boost bearing capacity against earthquake forces [1]. BRBs provide significant energy absorption capacity. BRBs incorporated into medium- and large-scale timber frame buildings should shoulder a significant share of the earthquake energy generated and improve building energy absorption capacity. This study assumes a 10-story timber frame building incorporating BRBs in Japan and proposes methods for achieving these design goals. The study also confirms the validity of these methods.

Building a 10-story timber frame building incorporating BRBs also requires sufficiently strong connections between beams or columns and the BRBs. This is due to the considerable strength and stiffness of the BRBs compared to timber constructions. It also requires column base connections with sufficient strength due to the large pull-out forces that can occur at the column base connections of buildings incorporating many braces or shear walls. In Part 1, we proposed multi knife plate steel dowel connections between beams or columns and BRBs (Figure 1) and glued-in rod (GIR) connections for the column base. To confirm the performance of these connections, we performed vertical loading tests of multi knife plate steel dowel connections, cyclic loading tests of timber frames with BRBs, and cyclic loading tests of column base connections with GIR.

This paper describes the trial of a seismic design for a 10-story timber frame building incorporating BRBs and using the connections proposed in Part 1. Our results confirmed their effectiveness, even for a 10-story timber frame building incorporating BRBs. The results reported here confirm the validity of incorporating BRBs in high-rise timber frame buildings.

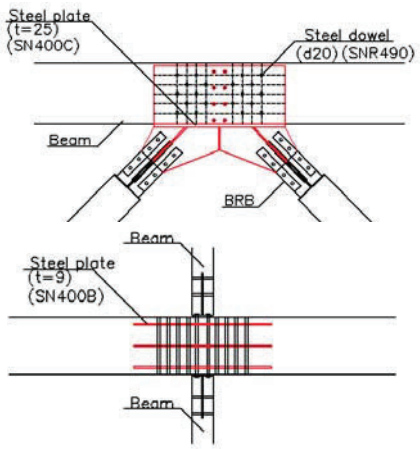

Figure 1: *Multi knife plate steel dowel connection proposed in Part 1*

[1] Ryota Minami, M. Eng., Kumagai Gumi, Japan, ryota.minami@ku.kumagaigumi.co.jp
[2] Toshio Maegawa, Chief Researcher, Kumagai Gumi, Japan, tmaegawa@ku.kumagaigumi.co.jp
[3] Taisuke Nagashima, PhD Eng., Chief Researcher, Sumitomo Forestry, Japan, tsk-naga@sfc.co.jp
[4] Kazuki Tachibana, M. Eng., Sumitomo Forestry, Japan, tachibana_kazuki@star.sfc.co.jp
[5] Hiroki Nakashima, M. Eng., Sumitomo Forestry, Japan, nakashima_hiroki@star.sfc.co.jp
[6] Nobuhiko Akiyama, Dr.Agr., Senior Researcher, Building Dept., NILIM, MLIT, Japan, akiyama-n92rg@mlit.go.jp
[7] Yoshihiro Yamazaki, Dr. Eng., Senior Research Engineer, Building Research Institute, Japan, y_ymzk@kenken.go.jp
[8] Takahiro Tsuchimoto, Dr. Agr., Chief Research Engineer, Building Research Institute, Japan, tutti@kenken.go.jp

https://doi.org/10.52202/069179-0387

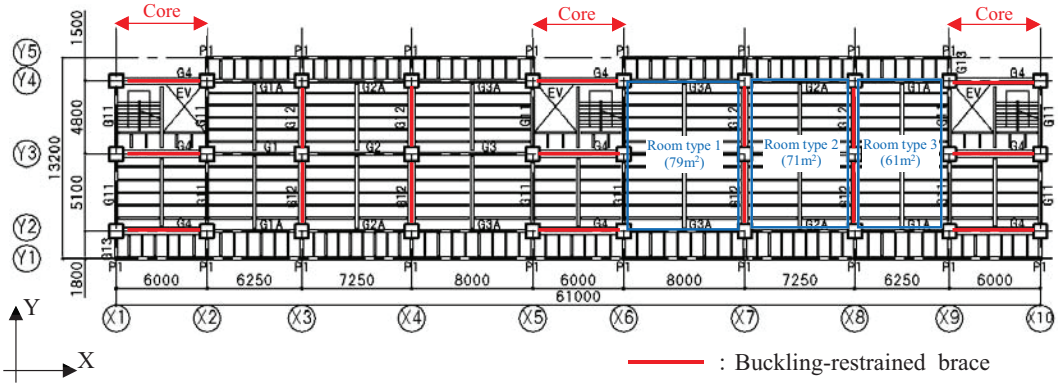

Figure 2: *Plan view of trial design building*

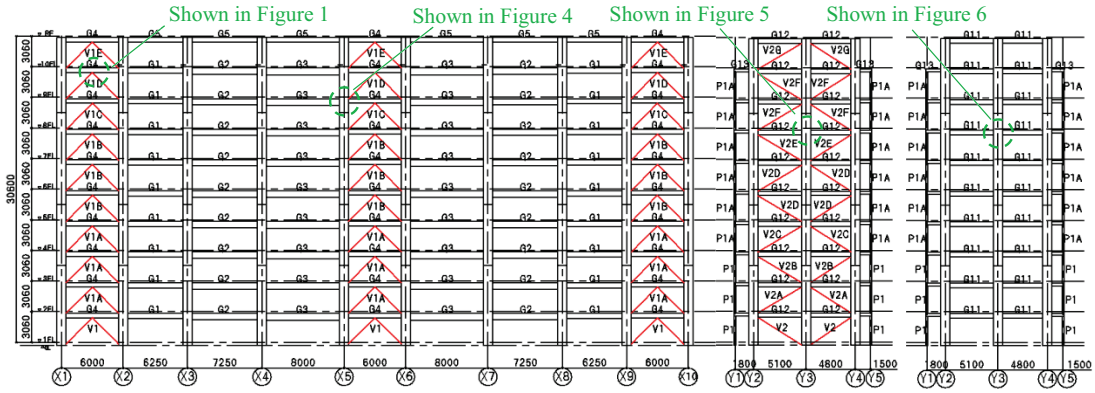

Figure 3: *Frame diagram of the trial design building (Left: Y2, Y3, Y4, Center: X3, X4, X7, X8, Right: other axles)*

2 TRIAL DESIGN BUILDING

2.1 TRIAL DESIGN BUILDING PLANS

Figures 2 and 3 show the plan view and frame diagram of the trial design building. In this paper, only the upper structure is considered. The building is assumed to be used for residential. BRBs are installed in the core (along the X direction) and between the rooms (along the Y direction). Columns and beams are made of glued laminated timber (GLT).

2.2 CONNECTIONS

Figures 4 and 5 show the beam-column connections at which the BRBs are attached. Figure 1 shows the connection between beams and BRBs. In these connections, beams, columns, and BRBs are connected via multi knife plate steel dowel connections. Figure 6 shows other beam-column connections; here, beams and column are connected with bolts and steel dowels due to the perpendicular orientation relative to the connections shown in Figures 4 and 5. In the connections shown in Figures 4 and 5, the steel plate holes of the beams into which the steel dowels are inserted are long. The steel dowels configured parallel to the direction of the grain are not subject to forces perpendicular to the direction of the grain; the steel dowels configured perpendicular to the direction of the grain are not subject to forces parallel to the direction of the grain.

2.3 COLUMN BASE CONNECTIONS

Figures 7 and 8 show the column base connections of the trial design building. Timber column and steel shoes are connected with the GIR connections proposed in Part 1. In this connection, reinforcement bars D29 are inserted and a plasticized section (φ22) is provided to ensure the uniform distribution of forces for the reinforcement bars. Steel shoes and foundations are connected with anchor bolts. In the trial design building, the column base connections in X1, X2, X5, X6, X9, and X10 are Type A (Figure 7). The others are Type B (Figure 8).

2.4 FLOOR SLABS AND CEILINGS

Figure 9 shows the floor slab and ceiling for an apartment in the trial design building. The dead loads are 2,270 N/m^2 (floors 2 to 6) and 1,880 N/m^2 (floors 7 to 10). Figure 10 shows the floor slab and ceiling for the rooftop. Figure 11 shows the floor slab and ceiling for the corridor. The dead load for the rooftop is 1,120 N/m^2; the dead loads for the corridor are 1,930 N/m^2 (floors 2 to 6) and 1,540 N/m^2 (floors 7 to 10).

The design value assumed for the floor slabs and beams live loads on these floor slabs is 1,800 N/m^2. The design value assumed for the frame members is 1,300 N/m^2; and the design seismic load assumed is 600 N/m^2 [2].

https://doi.org/10.52202/069179-0387

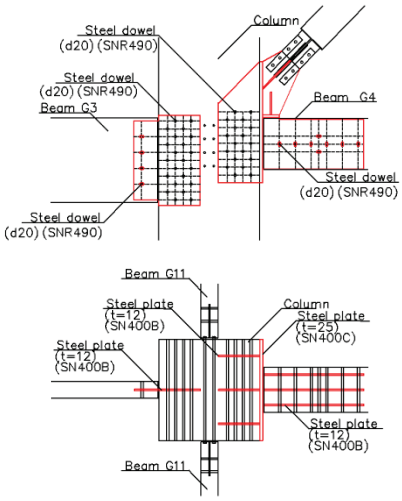

Figure 4: *Beam-column connection at which BRB is attached (X direction)*

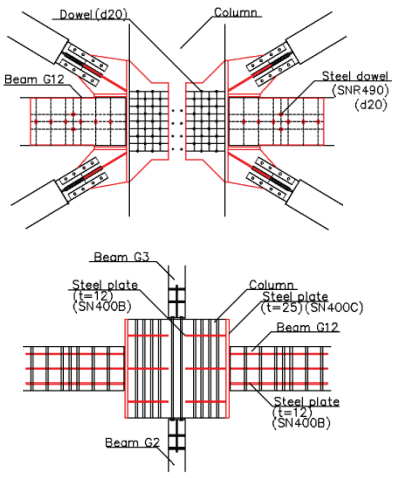

Figure 5: *Beam-column connection at which BRB is attached (Y direction)*

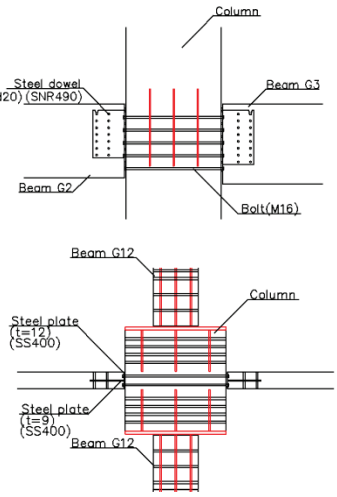

Figure 6: *Beam-column connection at which no BRB is attached*

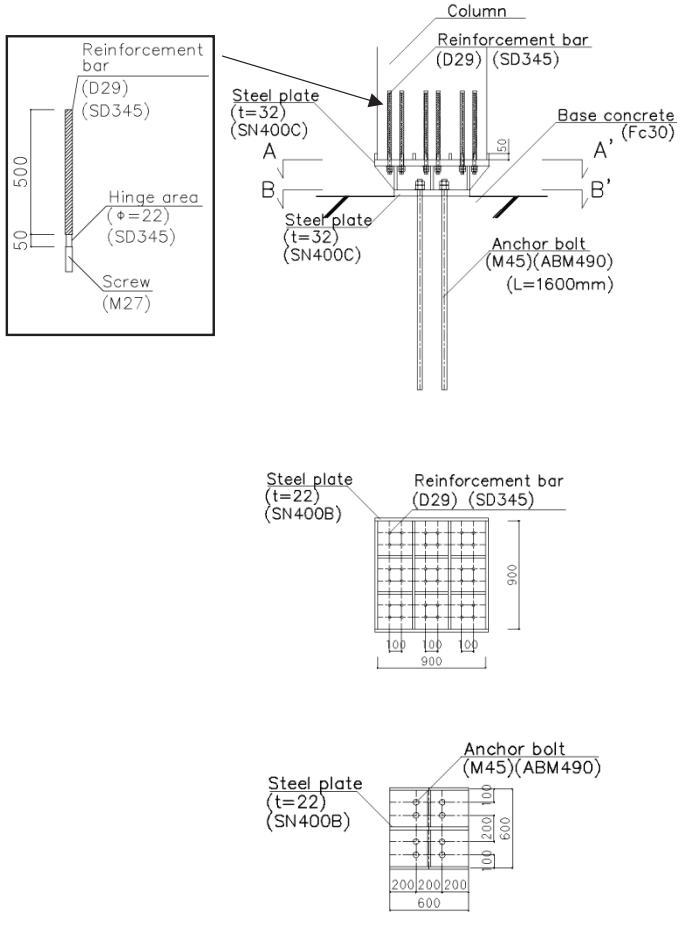

Figure7: *Column base connection (Type A)*

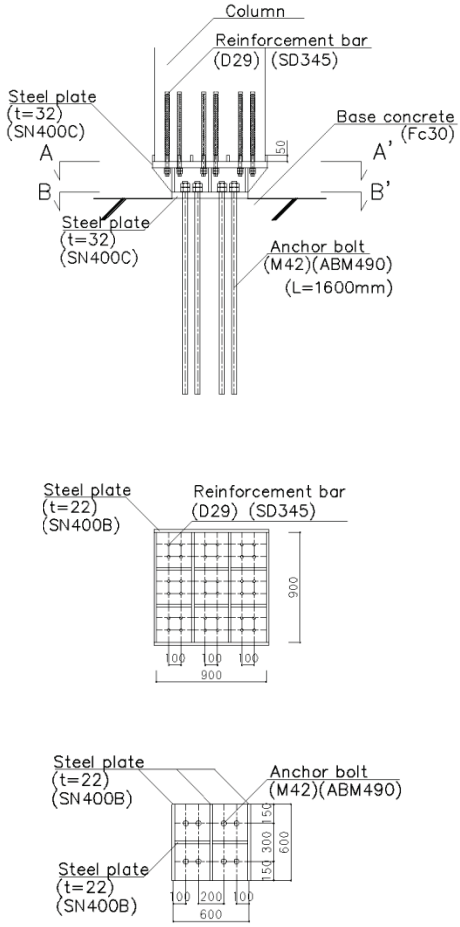

Figure 8: *Column base connection (Type B)*

https://doi.org/10.52202/069179-0387

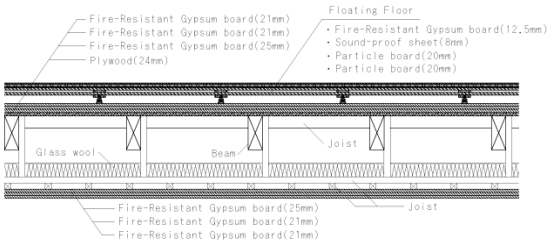

(a) Floors 2 to 6

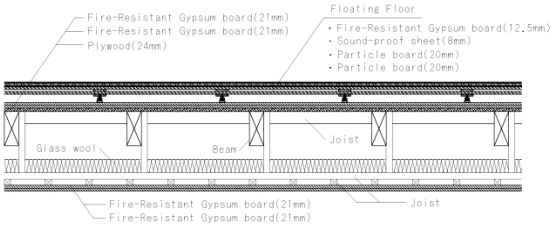

(b) Floors 7 to 10

Figure 9: *Floor slab and ceiling for apartments*

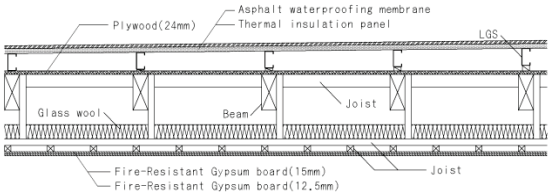

Figure 10: *Floor slab and ceiling for the rooftop*

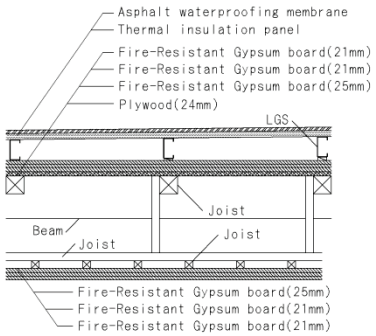

(a) Floors 2 to 6

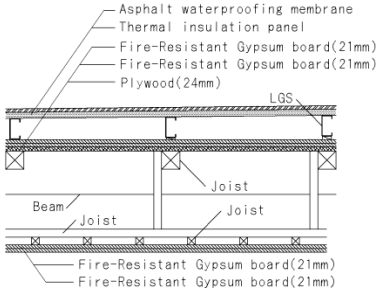

(b) Floors 7 to 10

Figure 11: *Floor slab and ceiling of the corridor*

3 ANALYSIS METHOD

3.1 SEISMIC DESIGN METHOD [3]

The building discussed in this paper is designed to satisfy the structural requirements specified by the Response and Limit Capacity Method, a Japanese code. This code requires verification of dead, live, snow, wind, and seismic loads. This paper considers only seismic loads. Seismic load verification requires drift pushover analysis, a method of nonlinear static analysis that involves increasing lateral loads in increments as shown in Figure 12 and checking the following criteria:

(a) Damage limit

This criterion is used to verify that damage caused by rare large-scale earthquake motions remains within the allowable range. In this paper, the damage limit is defined as the state in which the stress attributable to the lateral seismic load exceeds the temporary allowable stress (2/3 of material strength for timber members and yield strength for steel members) or at which the maximum interstory drift angle exceeds 1/200 rad. The lateral seismic shear force at the damage limit calculated by drift pushover analysis should exceed the lateral seismic shear force given by the following equation:

$$P_{di} = S_d B_{di} Z G_s m_i \quad (1)$$

(b) Safety limit

This criterion is used to verify that the building will not collapse when subjected to extremely rare large-scale earthquake motions. In this paper, the safety limit is defined as the state in which the maximum interstory drift angle exceeds 1/60 rad. The stress attributable to the lateral seismic loads at the safety limit should not exceed the material strength. The lateral seismic shear force at the building safety limit given by drift pushover analysis should exceed the lateral seismic shear force given by the following equation:

$$P_{si} = F\, S_s B_{si} Z G_s m_i \quad (2)$$

where S_d is the acceleration response at the damage limit on engineering bedrock; B_{di} is the acceleration distribution factor at the damage limit (first mode participation vector); Z is the seismic hazard zoning factor,; G_s is the surface soil amplification factor; m_i is weight of the *i*-th story; F is the acceleration reduction factor due to damping at the safety limit; S_s is the acceleration response at the safety limit on engineering bedrock; and B_{si} is the acceleration distribution factor at the safety limit (first mode participation vector).

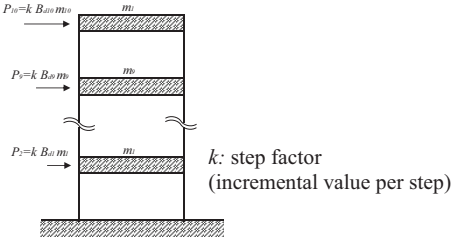

Figure 12: *Distribution of lateral force*

https://doi.org/10.52202/069179-0387

S_d and S_s are as in Figure 13.

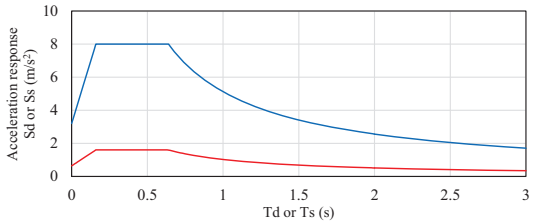

Figure 13: *Acceleration spectrum* $\boldsymbol{S_d}$ *and* $\boldsymbol{S_s}$

G_s is given by the following equation:

$$G_s = \begin{cases} 1.5 \quad for\ T < 0.64 \\ 1.5T/0.64 \quad for\ 0.64 \le T < 0.864 \\ 2.025 \quad for\ 0.864 \le T \end{cases} \qquad (3)$$

where $T = T_d$ when calculating P_{di} and $T = T_s$ when calculating P_{si}.

F is given by the following equation:

$$F = 1.5/(1 + 10\zeta) \qquad (4)$$

T_d and T_s are the response period at the damage limit and safety limit obtained by evaluating story stiffness and mass from the drift pushover analysis results and replacing the building with a 1DOF model, as shown in Figure 14. ζ is the damping ratio of the building given by the following equation:

$$\zeta = (\Delta s \cdot Q_d)/(\Delta d \cdot Q_s) \qquad (5)$$

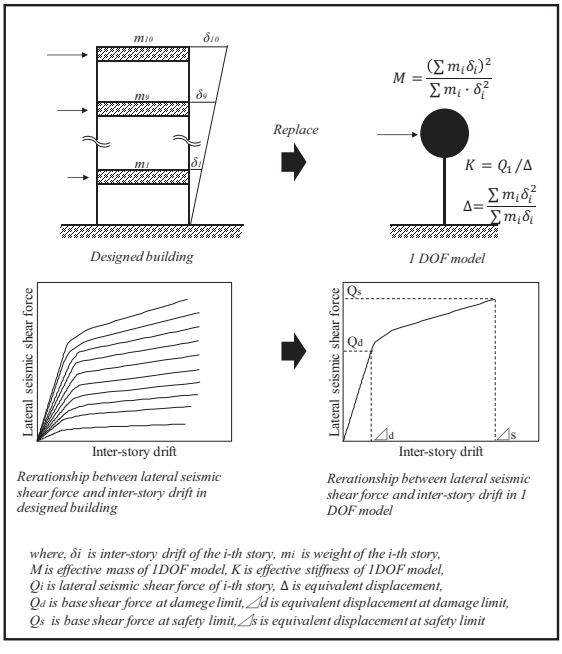

Figure 14: *Method to replace the building with 1DOF*

In addition to verification by the Response and Limit Capacity Method, the building performance upon the input of extremely rare large-scale earthquake motions is confirmed via time history analysis, accounting for P-Δ effects. Figure 15 shows the input earthquake ground motions. These are extremely rare large-scale earthquake motions as defined under Japanese Building Standard Law, which simulates earthquakes using random phase spectra (AW1-L2), the phase spectra specified in HACHINOHE 1968 NS (AW2-L2) and JMA KOBE NS (AW3-L2). The acceleration spectra for the engineering bedrock are shown in Figure 13 (S_s).

The analyses assume a rigid floor assumption and were performed using midas iGen V.920R1x.

3.2 NUMERICAL ANALYSIS MODEL

Figures 16 to 19 show numerical analysis models of the connections shown in Figure 1 and Figures 4 to 8.

In Figures 16 and 17, multi knife plate steel dowel connections are modelled by shear springs (parallel to the direction of the grain and perpendicular to the direction of the grain) and by rotational springs. The stiffness and yield strength values are calculated by the method proposed in Part 1. Knife plate steel dowel connections with long holes are not subject to bending moments and modelled with pin connections. For beam-column connections at which no BRB is attached, the knife plate steel dowel connection in the column is assumed to be rigid due to the negligible influence on building performance during an earthquake.

The connection in Figure 18 is modelled with pin connections since connections incorporating bolts and steel dowels have low stiffness.

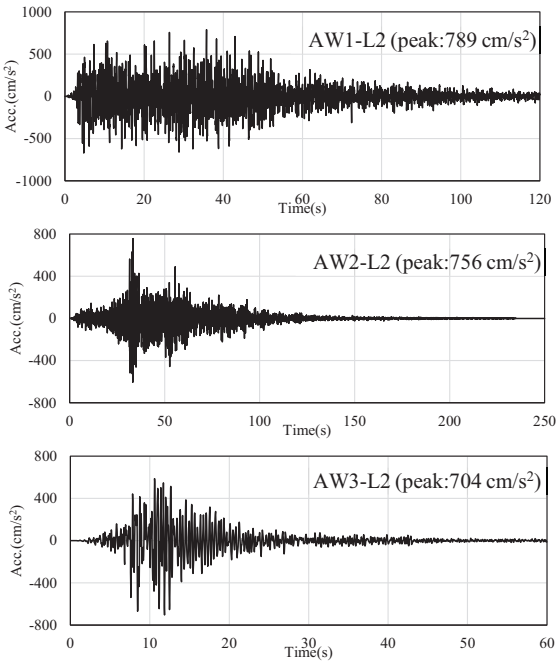

Figure 15: *Accelerations of input earthquakes*

https://doi.org/10.52202/069179-0387

In Figure 19, connections with GIR are modelled by a multi-spring model. (The values for stiffness and yield strength of the spring are given in Part 1.) Connections with anchor bolts are modelled with a multi-spring model. The values for spring stiffness are given by the following equations:

$$k_b = n_b A_b E_b / L \quad (6)$$

$$k_c = B_s \, s \, E_c / L \quad (7)$$

where k_b is the stiffness of the anchor bolt spring; k_c is the stiffness of the base concrete bearing spring; n_b is the number of anchor bolts; A_b is the cross section area of the anchor bolts; E_b is the elastic modulus of the anchor bolts; L is the length of the anchor bolts; B_s is the width of the steel shoe; s is the distance between the springs (= 50 mm); and E_c is the elastic modulus of the base concrete.

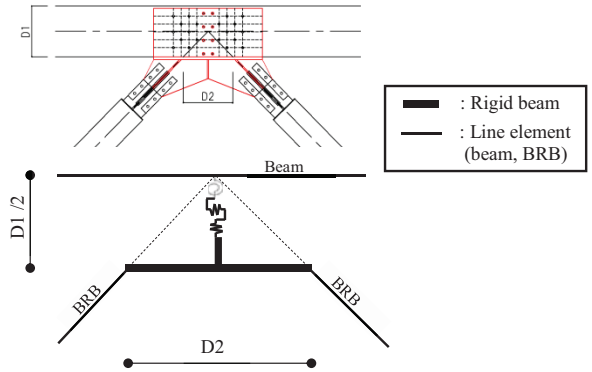

Figure 16: *Numerical analysis model for connection between beam and BRBs*

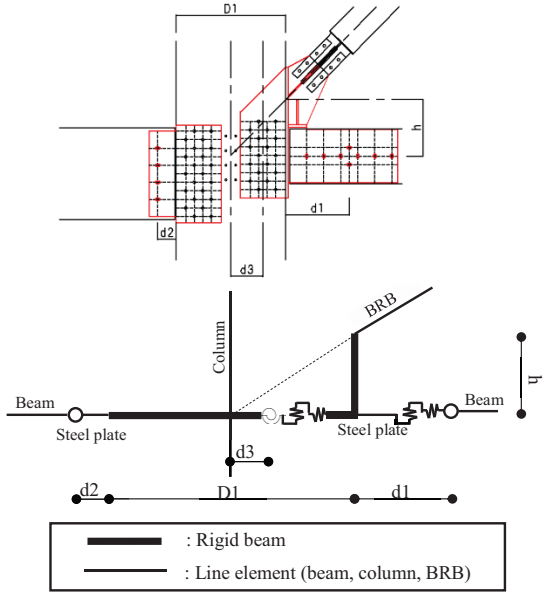

Figure 17: *Numerical analysis model for beam-column connection at which BRB is attached*

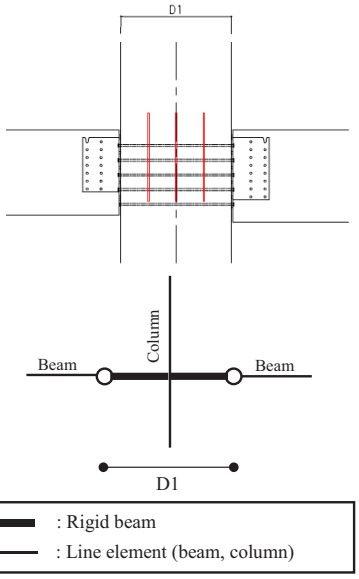

Figure 18: *Numerical analysis model of beam-column connection where BRB is not attached*

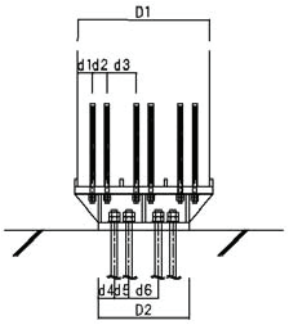

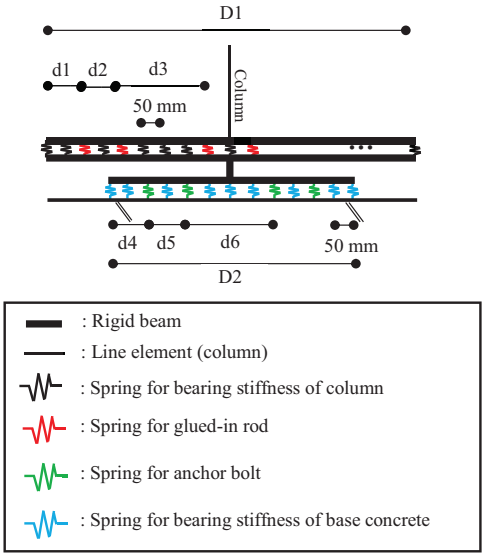

Figure 19: *Numerical analysis model for column base connection*

https://doi.org/10.52202/069179-0387

4 RESULTS OF ANALYSIS

4.1 STRUCTURAL MEMBERS

Tables 1 and 2 present the properties of the structural members of the trial design building as determined by analysis. Figures 2 and 3 show the component layout.

Table 1: *Column and beam properties*

Indicators	Story	Sections	Width × Length (mm)	Strength class in JAS
Column	All	C1	900 × 900	E105-F300 [4]
	1F - 3F	P1	210 × 210	
	4F - 9F	P1A	180 × 180	
Beam	2F - 7F	G1	150 × 600	
		G2	150 × 720	
		G3	150 × 780	
		G1A	150 × 510	
		G2A	150 × 630	
		G3A	150 × 690	
	8F - 10F	G1	150 × 540	
		G2	150 × 690	
		G3	150 × 750	
		G1A	150 × 480	
		G2A	150 × 600	
		G3A	150 × 650	
	RF	G5	150 × 480	
	ALL	G4	400 × 450	
		G11	105 × 480	
		G12	400 × 450	

Table 2: *BRB properties*

Sections	Width × Length (core plate in plastic zone) (mm)	Yield stress of steel materials for core plate (N/mm^2)	Yield load (kN)
V1	12 × 115	235	615
V1A	12 × 100		530
V1B	9 × 110		446
V1C	9 × 90		263
V1D	6 × 100	325	195
V1E	6 × 65		127
V2	9 × 120	355	738
V2A	12 × 128	325	952
V2B	16 × 135	235	955
V2C	19 × 140		1165
V2D	12 × 155		840
V2E	12 × 135		728
V2F	9 × 105	325	307
V2G	6 × 90		176

4.2 RESULTS OF PUSHOVER ANALYSIS

Figures 20 to 23 show the relationship between the interstory drift angle and lateral seismic shear force calculated by drift pushover analysis. In Figures 20 and 21, the damage limit state is the step at which the stress attributable to the lateral load exceeds the temporary allowable stress for the first time. In Figures 22 and 23, the safety limit state is the step at which the maximum interstory drift angle exceeds 1/60 rad for the first time.

From Figures 20 and 21, assuming the cross section shown in Tables 1 and 2, the lateral seismic shear capacity at the damage limit of the trial design building exceeds the lateral seismic shear force in Equation (1); the maximum interstory drift angle does not exceed 1/200 rad. In both the X- and Y- directions, the BRBs are the first structural members to exceed the temporary allowable stress value. From Figures 22 and 23, assuming the cross section shown in Tables 1 and 2, the lateral seismic shear capacity at the safety limit of the trial design building exceeds the lateral seismic shear force given by Equation (2). It was confirmed that the stress attributable to the lateral seismic load in the timber members does not exceed the material strength. Damping ratio ζ in Equation (5) is 15.1% in the analysis for the X-direction and 14.3% in the analysis for the Y-direction. Since the BRBs yielded, significantly high damping was observed. This is consistent with the design philosophy of this building, which is to improve the energy absorption capacity of the building by adopting BRBs.

Figure 24 shows the maximum value of the grain stress at the multi knife plate steel dowel connection between the beam and the BRBs (Figure 1) in this building at the safety limit calculated by pushover analysis for the X-direction. Figure 25 shows the maximum value of the grain stress at the multi knife plate steel dowel connection between the column and the BRBs (Figure 5) in this building at the safety limit calculated by pushover analysis for the Y-direction. They show the stress at multi knife plate steel dowel connections at which the BRBs are arranged in a K-shape does not exceed the temporary allowable stress at the safety limit. In the multi knife plate steel dowel connections used in this building, the greatest stress arises in connections at which the BRBs are arranged in a K-shape. This shows that the connections between the timber structures and the BRBs proposed in Part 1 remain reliable even in a 10-story timber frame building incorporating BRBs.

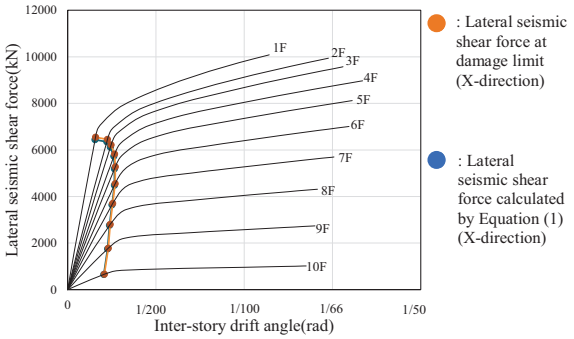

Figure 20: *Relationship between lateral seismic shear force and inter-story drift angle at damage limit in X direction analysis*

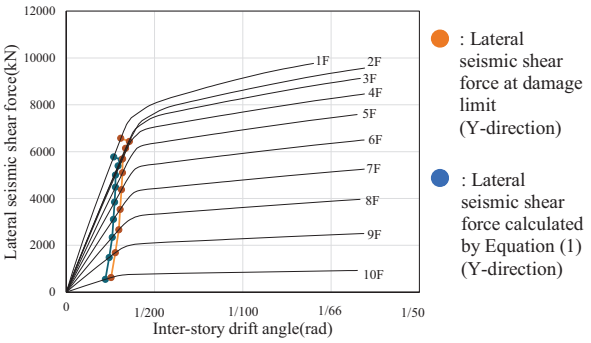

Figure 21: *Relationship between lateral seismic shear force and interstory drift angle at damage limit in Y direction analysis*

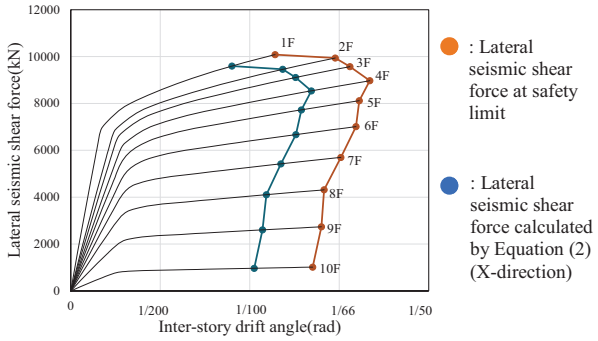

Figure 22: *Relationship between lateral seismic shear force and interstory drift angle at safety limit in X direction analysis*

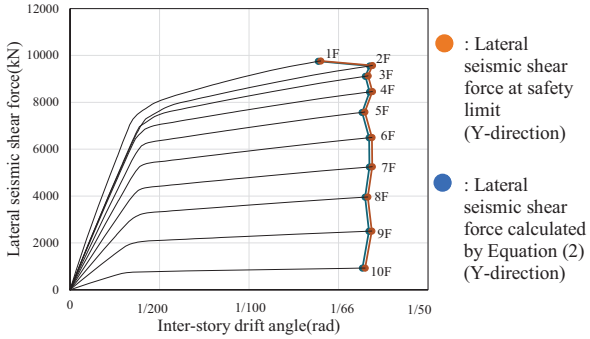

Figure 23: *Relationship between lateral seismic shear force and interstory drift angle at safety limit in Y direction analysis*

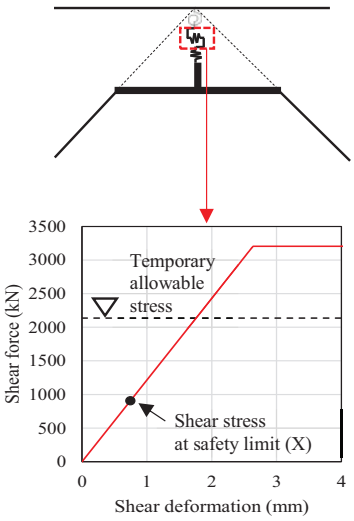

Figure 24: *Maximum grain direction stress at the multi knife plate steel dowel connection between beam and BRBs*

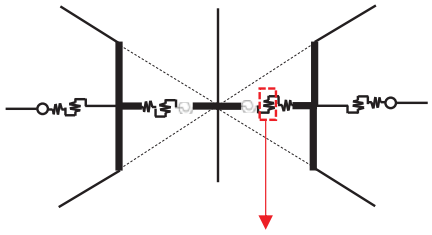

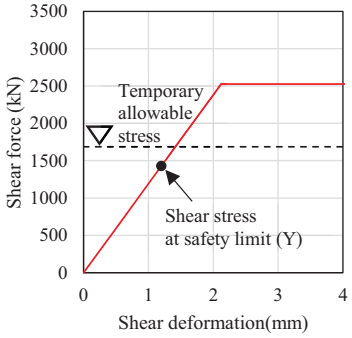

Figure 25: *Maximum grain direction stress at the multi knife plate steel dowel connection between column and BRBs*

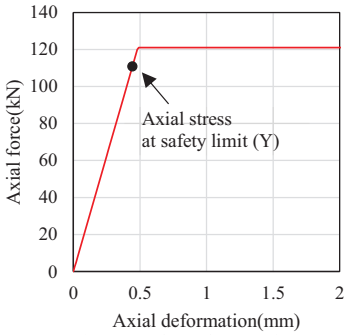

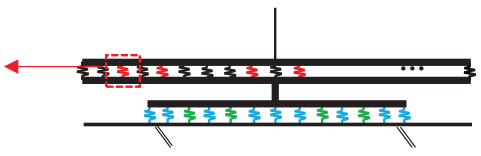

Figure 26: *Maximum axial stress of reinforcing bar in GIR connections*

https://doi.org/10.52202/069179-0387

Figure 26 shows the maximum axial stress for the reinforcing bar in GIR connections (Figures 7 and 8) attributable to the lateral seismic force at the safety limit (in both the X and Y directions). Figure 25 shows that the stress on the reinforcement bar does not exceed the yield strength for the plasticized section at the safety limit. Figure 27 shows M-N interaction curves for GIR and anchor bolt connections (Figures 7 and 8). It indicates that the anchor bolt connections yield before the GIR connection at the column base connection of this building. This means that the GIR connection proposed in Part 1 remains reliable even for a 10-story timber frame building incorporating BRBs in which anchor bolt connections are designed to yield before GIR connections.

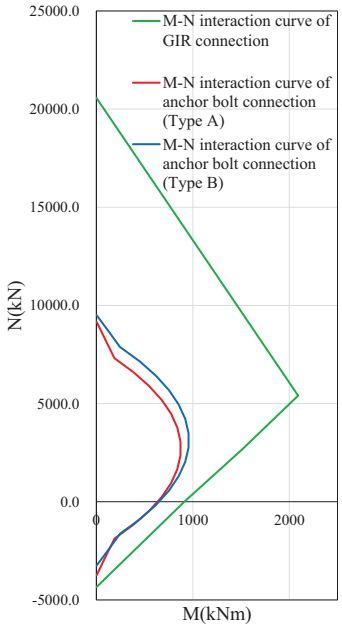

Figure 27: *M-N-interaction curves of GIR connection and anchor bolt connection*

4.3 RESULTS OF TIME HISTORY ANALYSIS

Figure 28 shows the maximum interstory drift angle of the trial design building obtained via time history analysis. Figure 28 shows that the maximum interstory drift angle of the trial design building given by time history analysis does not exceed 1/60 rad, which is assumed to be the interstory drift angle at the safety limit in the drift pushover analysis. It was also confirmed that the stress attributable to the lateral seismic load in the timber member does not exceed the material strength via time history analysis.

Figures 29 and 30 show the maximum value of the grain stress at the multi knife plate steel dowel connection between the beam and the BRBs (Figure 1) and the maximum value of the grain stress at the multi knife plate steel dowel connection between the column and the BRBs (Figure 5). Figure 31 shows the maximum axial stress on the reinforcing bar in the GIR connections, as in the previous section. Figures 29 to 31 show the results of the time history analysis, confirming the effectiveness of the connections proposed in Part 1.

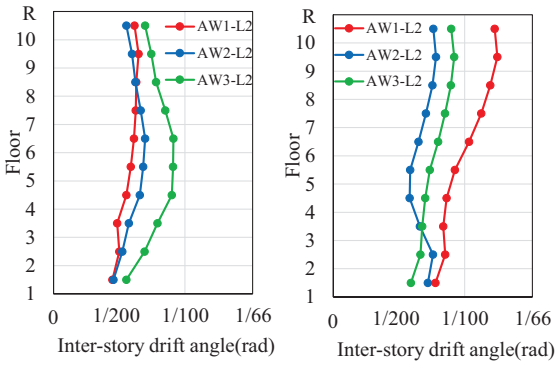

(a) X-direction *(b) Y-direction*

Figure 28: *Maximum inter-story drift angle*

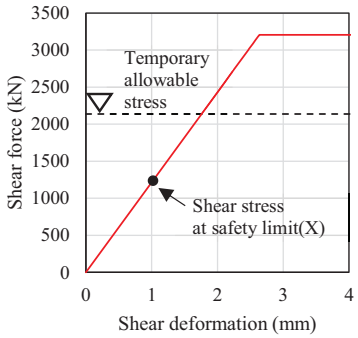

Figure 29: *Maximum grain direction stress at the multi knife plate steel dowel connection between beam and BRBs*

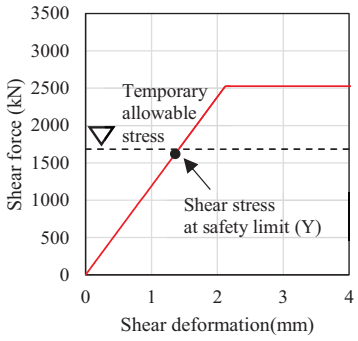

Figure 30: *The maximum grain direction stress at the multi knife plate steel dowel connection between column and BRBs*

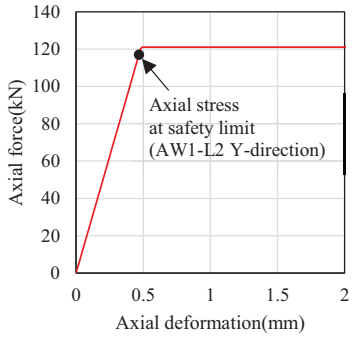

Figure 31: *Maximum axial stress on reinforcing bar in GIR connections*

5 CONCLUSIONS

This paper discusses aspects of trial seismic design for a 10-story timber frame building incorporating BRBs and using the connections proposed in Part 1.

Static analysis based on the Response and Limit Capacity Method and time history analysis confirmed that these BRBs will absorb considerable energy in the event of an earthquake and improve the bearing capacity of high-rise timber frame buildings. Our efforts also confirmed that the stress arising in multi knife plate steel dowel connections between BRBs and beams or columns and in GIR connections of column base connections proposed in Part 1 remains within the experimentally confirmed bearing capacity, thereby confirming the validity of the connections proposed in Part 1.

ACKNOWLEDGEMENTS

This research was conducted as part of “Innovative technology for maintenance and management of construction and infrastructure and for disaster prevention and mitigation” in Public/Private R&D Investment Strategic Expansion Program (PRISM) add-on item “ R&D Project for tall wood building for saving construction site of recovery housing“.

REFERENCES

[1] T. Takeuchi, A. Wada: BUCKLING-RESTRAINED BRACES AND APPLICATIONS, 2017.
[2] Architectural Institute of Japan: Recommendations for loads on buildings (2015), 2015.
[3] National Institute for Land and Infrastructure Management and others: Commentary on Structural Regulations of the Building Standard Law of Japan (2020), 2020.
[4] Architectural Institute of Japan: Standard for Structural Design of Timber Structures (2013), 2013.

https://doi.org/10.52202/069179-0387

World Conference on
Timber Engineering
Oslo 2023

POINT-SUPPORT REINFORCEMENT FOR A HIGHLY EFFICIENT TIMBER HOLLOW CORE SLAB SYSTEM

Cristóbal Tapia[1], Hans Jakob Wagner[2], Simon Treml[3], Achim Menges[4], Simon Aicher[5]

ABSTRACT: The paper presents a new point-supported slab building system concept developed at the Cluster of Excellence on Integrative Computational Design and Construction for Architecture (IntCDC) at the University of Stuttgart. The system uses a hollow-core system with two thin CLT plates acting as flanges and a set of distributed shear web elements in-between. The introduction of point supports induces large shear forces concentrated in the narrow region surrounding the column. This area is reinforced by an LVL core placed in-between CLT flanges, at the column-head position, with discrete web elements connected laterally to introduce the shear forces. Two alternative solutions for this connection are presented, differing mainly in the chosen strategy to bond both components: side bonding of web beams into the LVL core, or only gluing the frontal sloped face of the web beams. An experimental campaign was set, where a total of three specimens of each alternative where manufactured and tested. The results showed a clear superiority of the side-bonded web beams, reaching capacities between four to five times larger than the alternative without side bonding. The paper discusses the relationship of the system with robotic manufacturing processes and presents experimental and corresponding finite element results.

KEYWORDS: multi-storey timber buildings, CLT, LVL, beech LVL, web beam bonding, robotic manufacturing, hybrid composite

1 INTRODUCTION

The last decade has seen a steady increase of multi-storey timber projects [2, 9, 14, 16] enabled by the continuous development of new technologies, including novel connections and structural elements (see e.g. [10, 22]). This trend will foreseeable continue during the next years, as it allows for an efficient use of the already scarce construction area in cities, while offering incentives to reduce CO_2 emissions and improve construction conditions (less noise and shorter build times). Thus, timber is becoming a viable alternative to the presently dominant reinforced concrete (RC) building systems. This is at least true for multi-storey building typologies that afford rigid grids and single span structural systems [16]. However, to achieve similar capabilities as with reinforced concrete or steel buildings in terms of architectural flexibility and long-term (re)-usability, timber-based construction systems must be further developed to increase the possibilities and design freedom of the (re-) distribution and (re-) partitioning of inner spaces. This typically requires relatively long spans, a limited amount of columns that can be freely positioned to optimize flexible use-options and a flat bottom side of the slab to simplify the reinstallation of spatial divisions (inner walls).

Applied to timber structures, such a flexible point-supported slab structure presents several challenges. For example, this concept presupposes a biaxial mechanical behavior of the plate elements, which for the case of timber requires special considerations on the level of edge connections, as plate dimensions are limited by production and transport constraints. Then, since the whole floor plan acts as a monolithic, biaxial plate, large and rather concentrated negative moments form in the immediate proximity and directly above each column, which adds to the high shear stresses in the same region.

These problems constituted important research topics in the last years, where the focus has been placed mainly on the use of cross-laminated timber (CLT) plates. These efforts have lead to the development of several connection concepts for point-supported CLT plates [10, 11, 18, 22], as well as stiff edge connections for CLT plates [3, 17]. Both of these concepts are essential to achieve a slab system with biaxial mechanical behavior, large spans and a flexible arrangement of columns.

However, in terms of material efficiency, the use of CLT

[1]Materials Testing Institute (MPA), University of Stuttgart, Pfaffenwaldring 4b, 70569 Stuttgart, Germany, cristobal.tapia-camu@mpa.uni-stuttgart.de
[2]Institute for Computational Design and Construction (ICD), University of Stuttgart, Keplerstraße 11, 70174 Stuttgart, Germany, hans.jakob.wagner@icd.uni-stuttgart.de
[3]Institute for Computational Design and Construction (ICD), University of Stuttgart, Keplerstraße 11, 70174 Stuttgart, Germany, simon.treml@icd.uni-stuttgart.de
[4]Institute for Computational Design and Construction (ICD), University of Stuttgart, Keplerstraße 11, 70174 Stuttgart, Germany, achim.menges@icd.uni-stuttgart.de
[5]Materials Testing Institute (MPA), University of Stuttgart, Pfaffenwaldring 4b, 70569 Stuttgart, Germany, simon.aicher@mpa.uni-stuttgart.de

https://doi.org/10.52202/069179-0388

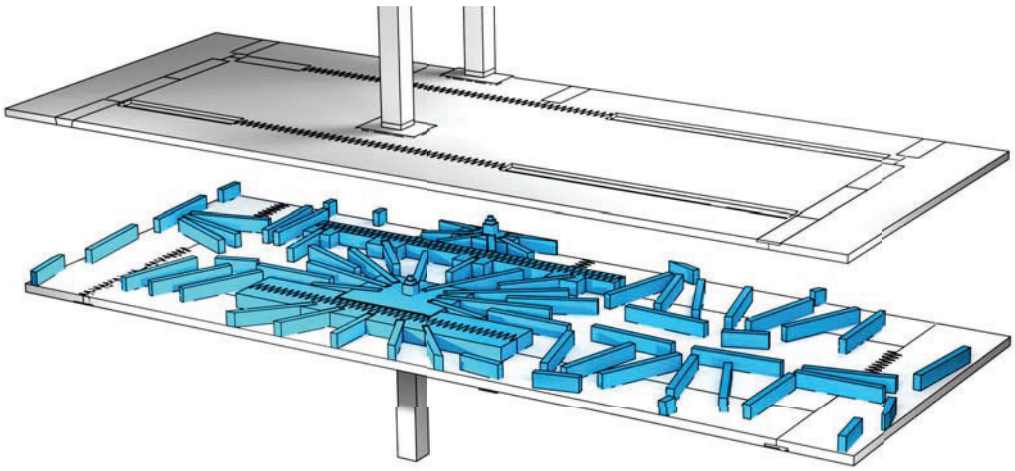

Figure 1: *Illustration of the development of a new hollow-core slab building system based on CLT outer plates with discrete distributed GLT web elements*

for large spans can be regarded as rather wasteful compared to different, more optimized systems. For example, the slab elements used in the building "Mjøstårnet", Norway, were conceived as ribbed elements, thus making a more efficient use of the material [2]. The general concept of ribbed slab elements is appealing in many ways, however, the current implementations—mostly devised as unidirectional elements—restrict the layout of columns to rather strict rectangular grids. Hence, the design space is severely limited [16]. Concepts also exist for computationally designed reinforcing beam networks of timber slabs for flexible column positions [4]. Several questions regarding its structural performance and fire-resistance are not yet answered and in the immediate future this approach seems not economically viable for large-scale building structures.

At the Cluster of Excellence on Integrated Computational Design and Construction for Architecture (IntCDC) of the University of Stuttgart a new slab building system concept is currently being investigated that aims to overcome design limitations of conventional systems in an economically viable manner. This timber building system is conceptualized as a point supported flat slab for large and multi-directional spans without the use of steel and concrete details. An early iteration of the system was presented in [8, 13]. The general concept consists of a hollow-core system with two rather thin CLT plates acting as flanges and a set of discrete, optimally distributed shear web elements in-between. Such a system is naturally very efficient for long spans, however, the introduction of point supports presents demanding challenges, as large shear forces concentrate in one narrow region. Due to the hollow nature of the slab, not enough material is present to resist the highly concentrated shear forces, thus requiring a special solution to reinforce the plate in the region of the supports.

This contribution presents the current development state of a hybrid hard- and softwood solution for the reinforcement of the highly stressed region above the point-supports of a hollow-core slab system. Important aspects of the interrelationship of the system with robotic manufacturing processes are discussed, and first experimental and corresponding finite element results are presented. Finally, the possibilities and limitations for practical applications of the system will be discussed.

2 DESCRIPTION OF THE SYSTEM

2.1 GENERAL

The slab system is composed of two CLT plates acting as biaxial *flanges* and a set of relatively short GLT elements glued between both CLT plates, which take the role of web elements (see Fig. 1). The exact position and orientation of these web elements varies throughout the extension of the floor and is determined by an agent-based model that considers the field of shear forces computed by a finite element (FE) model of the analyzed building [12]. In essence, the web elements are oriented following the shear force trajectories, thus aiming at an efficient utilization of the material. The described build-up of the slab system enables a biaxial behavior with very similar bending stiffness in both principal axes. Depending on the floor plan of the building, the column positions and applied set of loads, regions of high or low *density* of these web elements arise.

2.2 ROBOTIC MANUFACTURING CONCEPT

This differentiated distribution of shear webs within the hollow slab is further enabled by a robotic assembly process of the hollow slab elements. The exact position data of the webs from the computational design methods mentioned above can be directly streamed to a robotic fabrication platform, that assembles the web elements in their exact position. This process was tested for a small scale project presented in [15]. As the robotic platform is digitally controlled the complexity of assembling webs in unique patterns is the same as assembling the webs in standardized positions. Hence the co-design of the slab with optimized web layouts together with digital manufacturing processes allows for optimization potentials in the slab that would be not feasible without the integration of digital design and

https://doi.org/10.52202/069179-0388

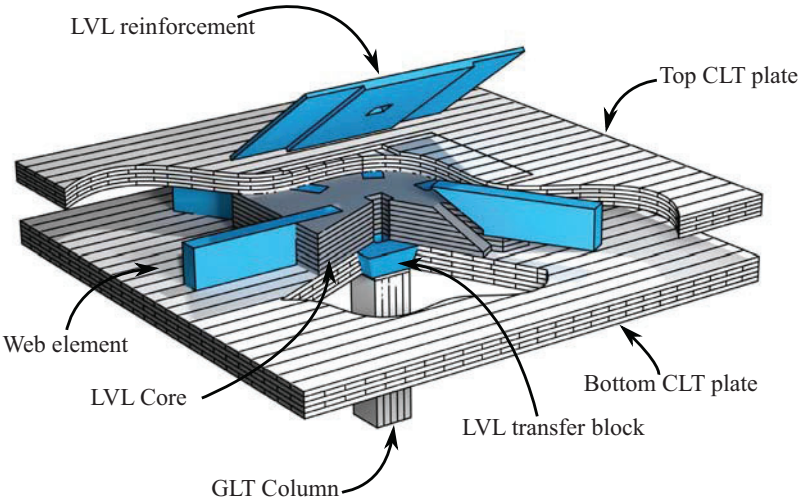

Figure 2: *Concept point-supported hollow-core plate system*

robotic fabrication. The robotic fabrication process nevertheless also has reciprocal requirements to be considered in the internal structural details of the slab. This is especially relevant regarding the structural connection of webs to upper and lower flange and their connection to reinforcement elements inside the hollow slab. The fabrication concept envisions that the robot first selectively applies adhesive on the bottom plate in all areas where webs will be placed. Subsequently webs are placed on the adhesives and pressed with partially-threaded screws. After curing of the bond line between bottom plate and web beams and removal of screws, the plate arrives again at the robotic fabrication setup. Adhesive is applied on top of the webs and the top plate is placed and pressed again using screws. Through this process a structural bond of the inner elements with upper and lower plate can be established completely independent of hydraulic, mechanical or vacuum cramping equipment.

2.3 STRUCUTRAL CHALLENGES AROUND COLUMN SUPPORTS

Intuitively, regions of higher positive moments towards the center of the spanned fields are subject to lower shear forces, thus reducing the density of web elements. On the other side of the spectrum, in the regions surrounding a column the sectional shear forces rapidly increase, requiring a higher amount of material (more webs). Furthermore, the same region will be subjected to highly concentrated negative moments, imposing high biaxial tensile stresses in the plane of the top CLT plate. This is further worsened by the typical presence of a hole, necessary for the transfer of vertical column loads originating in the upper floors of a multi-storey building (see e.g. [10, 14]).

In order to safely handle these unfavorable stresses, a special reinforcement concept is needed. Such concept must consider both, the shear forces and the tensile stresses in the top plate. A possible solution for this is shown in the following.

2.4 COLUMN-HEAD CONCEPT

The proposed solution is composed of three elements, which are illustrated in Fig. 2. Starting from top to bottom the following components are present: (i) an LVL plate on the upper side of the top CLT plate to take care of the reinforcement against high tensile stresses due to negative moments; (ii) a solid LVL block with cavities for the attachment of incoming web elements to help resisting the high shear forces; and (iii) a smaller LVL block inserted in the bottom CLT plate, directly above the column head, to reinforce against failure due to high shear and compressive stresses. These three components are glued to the CLT plates to ensure an efficient load and stress transmission.

The plate for the reinforcement of tensile stresses is the same as presented in [18] for a reinforcement concept for CLT plates, and is therefore not discussed in detail in this paper. The main topic of this paper is the LVL block for the reinforcement of shear forces, where different aspects related to the manufacturing and structural efficiency are covered.

The relatively high shear strength of the spruce LVL block—compared to typical softwood CLT—allows to resists the high shear forces in the region surrounding the column. These forces are mainly coming from the web elements, which raises the question regarding the connection between webs and LVL block.

For the ease of robotic fabrication it would be preferred if a lateral connection between shear web and LVL reinforcement can be avoided. However, for heavily loaded columns this would increase the necessary dimension of the LVL block, as enough surface is required to transfer the shear stresses. In this paper, two alternatives are investigated, resulting from the manufacturing constraints discussed above.

https://doi.org/10.52202/069179-0388

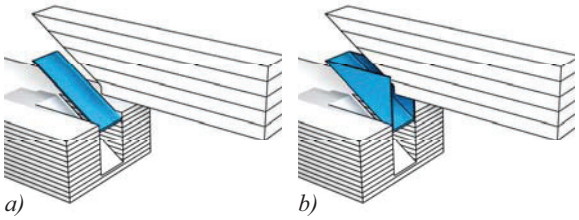

Figure 3: *Alternatives investigated for the application of the adhesive in the connection between GLT web and LVL core elements; (a) Alternative A; (b) Alternative B*

2.5 ALTERNATIVES FOR CONNECTION BETWEEN LVL CORE AND WEB ELEMENTS

2.5.1 Alternative A

The alternative A considers the milling of a wedge-shaped cavity with angle α in the LVL block with a width $w_b > w_w$, where $w_w = 100\,\text{mm}$ is the width of the web element (see Fig. 3a). The end of the web is cut with the same angle α as present in the LVL block. Relatively high tolerances in the horizontal plane need to be considered when large wooden elements are fully robotically assembled. This stems from several factors such as inconsistent dimensional accuracy of GLT beams, manufacturing tolerances of cavity and positioning accuracy of the robotic placement. Between the lateral faces of the GLT and LVL elements a gap with thickness $t_A = 10\,\text{mm}$ is left. This enables a robust robotic placement of the webs into the cavities.

The inclined surface of the web needs to be bonded with the inclined surface of the LVL block. The adhesive that can be applied by the robotic fabrication platform is partially gap-filling up to bond line thicknesses of 1.5 mm. This demands a highly accurate positioning of the web in direction of the longitudinal axis of the web. For this requirement a *locator feature* (see Fig. 4) was included in the web and LVL block geometry, which enables the robot to press the web laterally against the LVL block to ensure precise positioning. Subsequently, the adhesive interfaces between web-bottom plate and web-LVL block are pressed via screws. Further small pockets were included in the design of the LVL cavity and web geometry, to avoid that cured adhesives overruns restrict neither the correct positioning of the web nor that of the top plate.

2.5.2 Alternative B

Alternative B considers a three-sided embedment of the web beam end in the LVL block (see Fig. 3b). This is done by filling the lateral cavities between the LVL block and web beam with a gap-filling, two-component epoxy adhesive, enabling the transfer of shear stresses through these surfaces. From a mechanical perspective, this should be more efficient than alternative A, as more surface is available for the transfer of stresses, and on the side of the web element the surfaces are aligned with the main axis of the GLT element. Compared to alternative A, the gap must be smaller, to avoid using too much adhesive, leading to possible extreme exothermic reactions. Therefore, the gap is set to $t_B = 3\,\text{mm}$. For the fabrication of Alternative B the placement of the web can be achieved within the typical tolerances. Nevertheless, the filling of the gap with the two-component adhesive is a rather laborious task for an automated process. This is mainly because the gap between web and LVL needs to be sealed before glue application, then the glue needs to be filled without impacting the quality of the top web and LVL surface. Finally, the robotic fabrication platform considered for the fabrication of the hollow slab components is not equipped with a two-component epoxy application system. Hence, the fabrication concept for Alternative B considers the robotic placing the web beam into the LVL block, but bonding is performed exclusively to the bottom CLT plate. While the adhesive interfaces between inner elements and bottom plate are stored for curing, the gap between LVL block and web is manually filled with the two-component epoxy adhesive.

3 EXPERIMENTAL CONFIGURATIONS AND MANUFACTURING

3.1 STUDIED CONFIGURATIONS

The shear capacity of the connection was experimentally investigated for both alternatives A and B. The angle α was varied such that the side ratio $r_\alpha = \arctan(\alpha) = 1{:}1$, 1:1.5 and 1:2. The experimental set-up is illustrated in Fig. 5. Here, the LVL core is clamped by pressing a steel plate on the top of the LVL core to a steel I-beam on the bottom by tightening one full-threaded rod at each side. Below the LVL core a set of steel plates were arranged, such that only the area directly below the embedded web beam was allowed to rotate freely (see Fig. 5). The load was applied on a steel plate placed on the top face of the GLT web, at a distance of 20 mm from the edge of the LVL core. The total length of the loading plate varied for each configuration, being $\ell_s = 100\,\text{mm}$ for $r_\alpha = 1{:}1$ and $\ell_s = 220\,\text{mm}$ for $r_\alpha = 1{:}1.5$ and 1:2, respectively.

Self-tapping screws were inserted directly under the loading plate to reinforce this region and to better distribute the shear stresses within the cross-section.

The specimens were tested at the Division of Timber Constructions of the Materials Testing Institute, University of Stuttgart, with a servo-hydraulic universal testing machine with a maximum load capacity of 1.6 MN. The load was applied in displacement-controlled manner with a stroke rate of 0.1 mm/min.

3.2 PROTOTYPE MANUFACTURING

The LVL core was manufactured by bonding six layers of unidirectional spruce LVL plates, where each plate was oriented orthogonally with respect to the adjacent plates. The top-most plate is oriented in the direction parallel to the GLT's main axis. On each LVL block two inclined cavities were milled at the opposite sides, parallel to the main axis of the experimental set-up. This enabled to test connection alternative A on one side and alternative B on the opposite side independently. The cavities in the LVL block were milled with a Kuka Industrial Robot at Züblin Timber GmbH, Aichach, Germany.

https://doi.org/10.52202/069179-0388

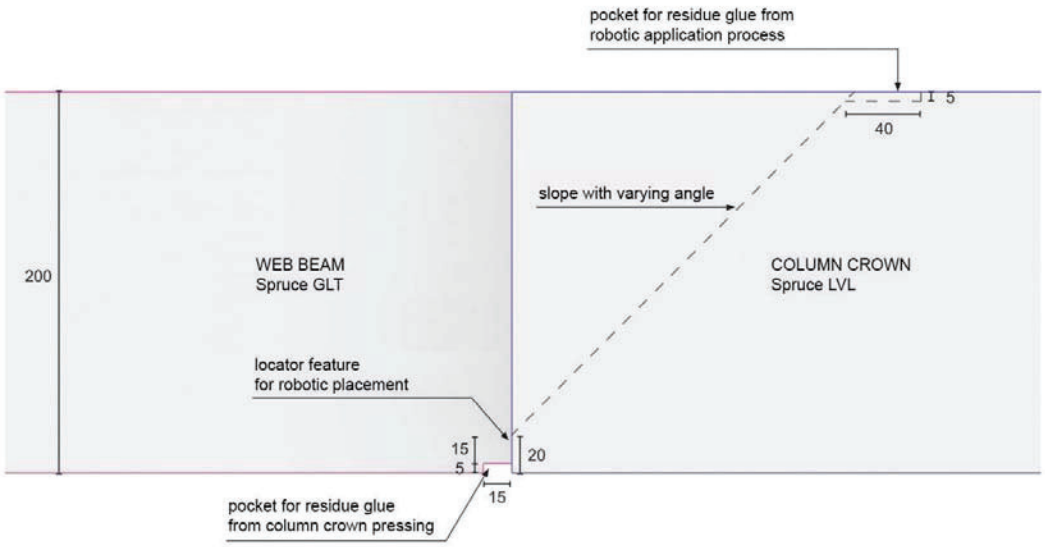

Figure 4: *Locator feature and pockets for residue glue in Alternative A for precise robotic placement*

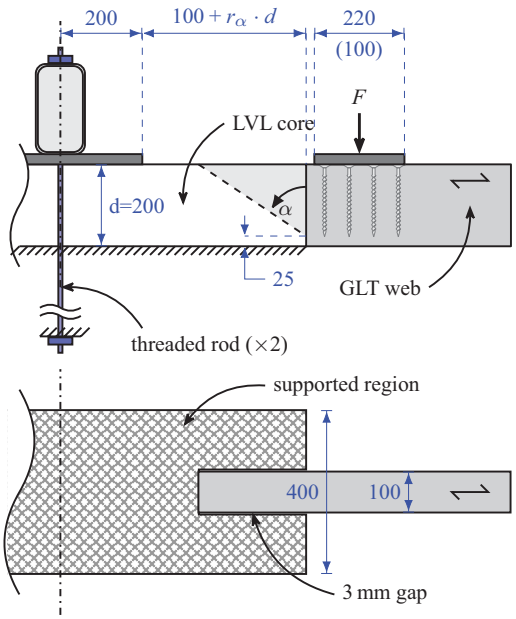

Figure 5: *Experimental set-up used for the study of both alternatives A and B*

Figure 6: *Realized experimental setup*

3.3 BONDING OF SPECIMENS

The bonding of alternative A was performed by applying an aminoplastic melamine-urea-formaldehyde (MUF) adhesive directly on the inclined surfaces of both, the GLT and LVL elements, and then evenly spreading the adhesive with a spatula. Hereinafter, the GLT beam was placed in its intended position, followed by the insertion of two to four partially threaded screws (depending on the geometry) to produce the required pressure. One or two screws were placed vertically, while the others were inserted in a direction perpendicular to the inclined surface. A dummy softwood plate, later removed, was placed below the LVL block in order to provide anchoring material for the threaded screw part.

The procedure followed to bond alternative B consisted on securing the GLT element in its position by means of screws and then sealing the vertical gaps between LVL and GLT by means of a special adhesive tape. Thereafter, the two-component epoxy adhesive was injected through predrilled holes until the gap was completely adhesive-filled.

All specimens were left to cure for at least two days before proceeding with the tests.

https://doi.org/10.52202/069179-0388

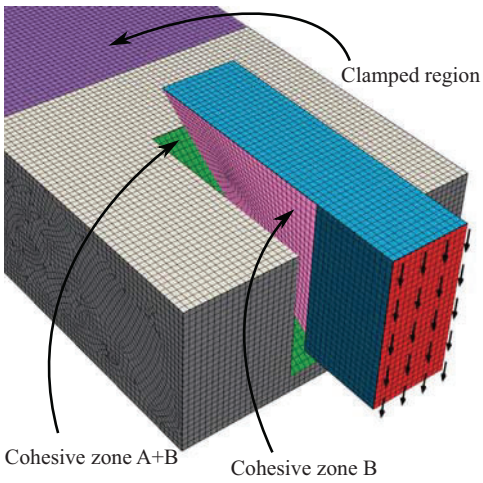

Figure 7: *Geometry, discretization of the implemented finite element model, together with the application of loads and definition of cohesive regions*

4 FINITE ELEMENT MODEL

A 3D finite element (FE) model was implemented with the Python API of the software Abaqus [1]. The model uses linear brick and wedge continuum elements of type C3D8 and C3D6, together with the elastic mechanical properties shown in Table 1. The length of the web beam was defined such that its outer end coincides with the center of the load application point. This reduces the amount of elements in the model and enables the load application in a more evenly distributed manner (see below).

An illustration of the discretization of the model is presented in Fig. 7, where the mesh size is about 20 mm. The bonded interfaces in both alternatives, A and B, were modelled with a cohesive behavior with stiffness parameters $k_n = k_t = 1000\,\mathrm{N/mm^3}$. The cohesive regions used for each alternative are shown in Fig. 7. The clamping condition was simulated by restraining the vertical displacement on a surface at the bottom face, according to Fig. 5, and at the top, while the load application was done by introducing a distributed vertical load on the outer vertical face of the GLT element (see Fig. 7).

The results were saved in the ASCII format (*.fil) and later post-processed with the Python library Pybaqus [19]. The scripts used for this paper are available in [20].

5 EXPERIMENTAL AND NUMERICAL RESULTS

5.1 FEM RESULTS

5.1.1 Shear stresses on the bonded surfaces

The FE model was used to inspect the distribution of shear stresses on the bonded surfaces. Figures 8a and 8b show the shear stresses obtained for r_α = 1:1.5 for alternatives A and B, respectively. It can be seen that the stresses on alternative B (side bonding) are more evenly distributed and reach lower maximum values than for the case of alternative A. Specifically, the stresses on alternative A reach values about two times higher (see Fig. 9). In general, this is an expected result, which is owed to the larger bond surface of alternative B.

Table 1: *Elastic material stiffness properties used for the FEM simulations*

Material	E_0 * [MPa]	E_{90} [MPa]	ν_{12} [–]	ν_{23} [–]	G [MPa]	G_r [MPa]
CLT[1)]	11 000	370	0.2	0.02	690	50
LVL[2)]	12 800	2000	0.2	0.02	430	43

[1)] acc. to values in [6] for softwood boards strength class C24 as indicated in [7]

[2)] acc. to values in [5, 21] (except ν_{ij})

* E_0: MOE parallel to fiber; E_{90}: MOE perpendicular to fiber; G: shear modulus; G_r: rolling shear modulus; $\nu_{12} = \nu_{13}$: Poisson coefficient between the fiber direction and the other two orthogonal directions; ν_{23} Poisson coefficient between both directions perpendicular to the fiber direction.

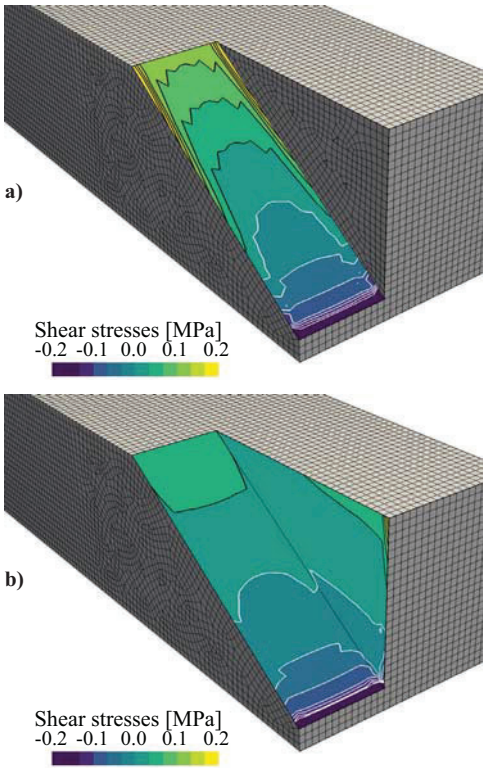

Figure 8: *Shear stresses on the bondfaces for a ratio r_α = 1:1.5; (a) Alternative A; (b) Alternative B*

5.2 EXPERIMENTAL RESULTS

5.2.1 General behavior

The general behavior of the tested specimens can be described with the help of Fig. 10a–c, where the load-displacement curves corresponding to the averaged measurements of front and back LVDT's are presented. These LVDT's measure the relative vertical displacement between GLT and LVL elements (see Fig. 6). The load-displacement responses of the specimens of type A presented mostly a perfectly linear behavior until the maximum load was

https://doi.org/10.52202/069179-0388

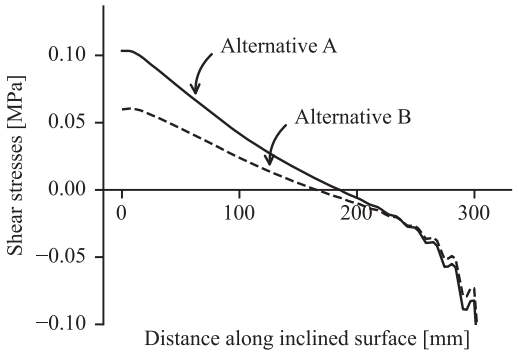

Figure 9: *Shear stresses along the longer dimension of the inclined bonded surface for both alternatives with r_α = 1:1.5 (applied load of* 1 kN*)*

Table 2: *Maximum capacities reached by each specimen*

r_α	Alternative A [kN]	Alternative B [kN]
1:1	20.0	106.1
1:1.5	31.4	122.5
1:2	31.2	119.6

reached, followed by a very brittle failure. The exception was Specimen A-1, which presented a clear stiffness reduction at about 10 kN, thereafter exhibiting a rather nonlinear behavior. The global failure was characterized by the complete de-bonding of the GLT from the LVL element (see Figs. 11a–c).

The behavior of specimens of type B presented a clear nonlinear behavior beyond about 40 % to 50 % of ultimate capacity, then showing a progressively decreasing stiffness for higher loads. The type of post-peak behavior varied for each specimen, where Specimen B-1 (r_α = 1:1) presented the most brittle behavior and Specimen B-3 (r_α = 1:2) showed an almost perfectly plastic behavior. Specimen B-2 (r_α = 1:1.5) lays in-between specimens B-1 and B-3 regarding the post-peak behavior.

Regarding the maximum capacities, Specimens B-2 and B-3 present a similar level ($F \approx 120$ kN), while Specimen B-1 showed a lower value of F = 106 kN. The maximum loads achieved by each specimen are summarized in Table 2. In general, the specimens of type B reached maximum capacities about four to five times larger than specimens of type A. This is an expected results, as the specimens of type B (bonded on the side-faces) not only have a larger bond surface, but also present a more favorable bonding regarding the orientation of the fibers (in type A the fibers are mostly bonded on the end-grain).

5.3 COMPARISON WITH FE RESULTS

The dashed lines in Fig. 10b represent the load-displacement results obtained by the FE model. While a good agreement can be observed for alternative A, the calculated stiffness for alternative B is clearly underestimating the experimental results. This discrepancy might

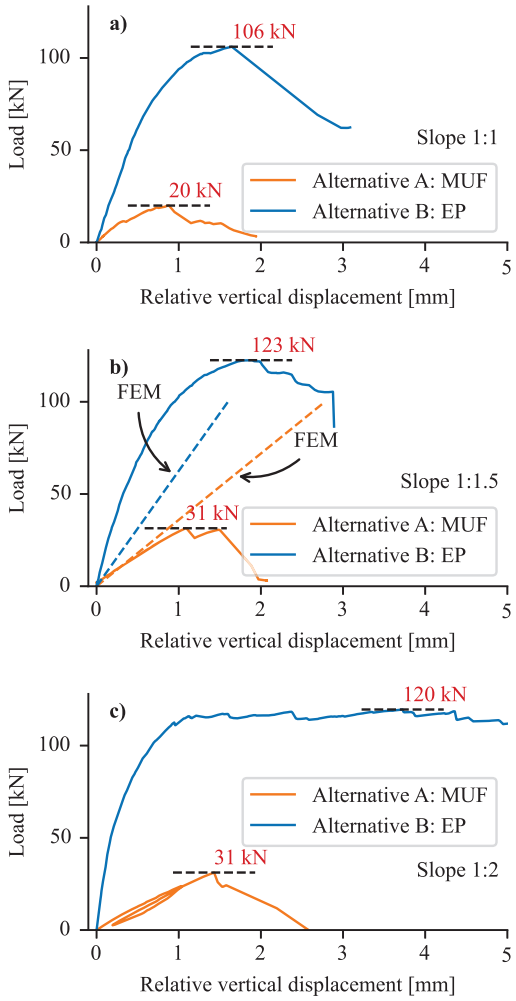

Figure 10: *Load-displacement curves and maximum capacities with data from LVDT's measuring the relative vertical displacement between GLT and LVL for the different investigated alternatives A and B; (a) slope r_α = 1:1; (b) slope r_α = 1:1.5; (c) slope r_α = 1:2*

be explained by the simplification of the load application in the model with respect to the actual load application, as shown in Fig. 5. The numerical corroboration of this effect was left out of this paper due to time constraints.

5.4 ACHIEVED QUALITY OF THE BONDFACES

The bondfaces of the three specimens corresponding to alternative A can be seen in Fig. 11a–c. All surfaces were fully detached immediately after reaching maximum load, as can be suspected from the rather brittle behavior observed. Based on the amount of fiber breakage present, it can be stated that the quality of the bonding was rather poor, as large regions with blunt failures can be seen. This means that the relatively low maximum capacities obtained by the specimens of type A are strongly influenced by the difficulty associated to this kind of bonding.

https://doi.org/10.52202/069179-0388

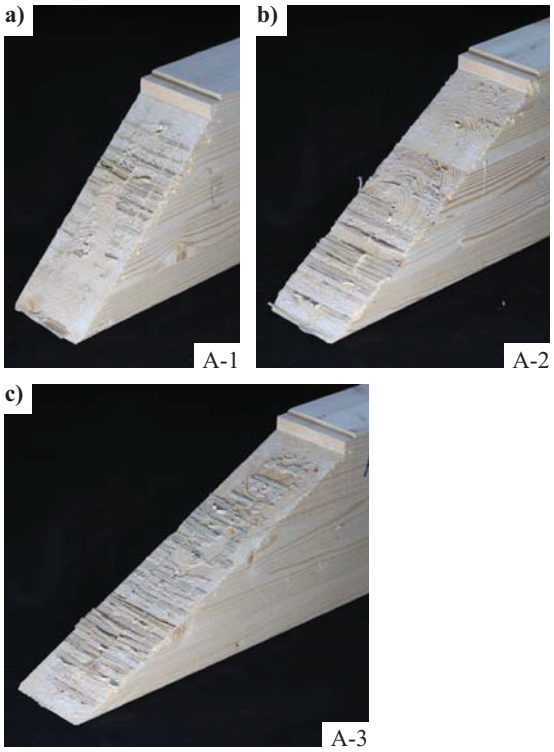

Figure 11: *Bondfaces of specimens of type A after global failure; (a) slope r_α = 1:1; (b) slope r_α = 1:1.5; (c) slope r_α = 1:2*

6 DISCUSSION

6.1 SUITABILITY FOR THE LARGE DEMONSTRATOR BUILDING

Although the connection of type B achieves clearly a better performance than alternative A, the suitability of both alternatives should be assessed based on the requirements for the connection in a real case-study. In this paper, the "Large-Scale Construction Robotics Laboratory" (LCRL)—a building set to apply the different research outputs from the IntCDC Cluster—is used as an example by considering the maximum design loads at the position of the column supports. According to the current state of the design of this building, the column has to resist a maximum design shear force of 753 kN. Considering a total of eight such web elements embedded in a radial pattern around the LVL core element, it is clear that the experimental capacities from alternative A do not reach the needed requirements for the connection. Therefore, alternative B should be preferred in this case.

6.2 GEOMETRY ADJUSTMENTS

Having done the experiments and considering the clearly better results obtained for alternative B, a logical next step is to simplify the connection by removing the inclined bondface altogether. Then, the web would have a typical prismatic shape and would be embedded into the LVL core by means of the same procedure used for alternative B. Experiments to assess this idea are underway and their results will be used to plan a full sized prototype of the slab system.

7 CONCLUSIONS AND OUTLOOK

This paper presented the current state of the slab system developed within the IntCDC Cluster at the University of Stuttgart. In particular, the connection of the shear web elements to the LVL core was investigated by analyzing different geometries and bonding strategies. Based on the experimental and numerical results, as well as on the experience gained from manufacturing the tested specimens, the following conclusions can be stated:

1. The bonding of the lateral faces (alternative B) delivered between four and five times larger maximum capacities in the connection.
2. Based on preliminary design loads for a planned demonstrator building, the rather low capacities exhibited by alternative A do not meet the requirements for the intended use case, thus alternative B should be preferred.
3. The rather low capacities achieved by alternative A, are due to an inferior bonding quality, as could be corroborated in a post-mortem analysis of the specimens.
4. The visualization of the shear stress distribution on the bond faces by means of FE simulations revealed rather uniformly distributed stresses for alternative B, providing additional evidence for the better suitability of side bonded faces for this application.
5. Based on the experimental results, the geometry of the connection will be simplified, removing the inclined surface to increase the lateral bonding surface.

ACKNOWLEDGEMENTS

The presented ongoing research is partially supported by the Deutsche Forschungsgemeinschaft (DFG, German Research Foundation) under Germany's Excellence Strategy – EXC 2120/1 – 390831618. Likewise, the authors would like to thank Thomas Mantzel, Simon Schmid and the team at Züblin Timber (Aichach) for their support.

DATA AVAILABILITY

Some or all data, models, or code generated or used during the study are available in a repository or online in accordance with funder data retention policies. (doi: 10.18419/darus-3381, Ref. [20])

REFERENCES

[1] Abaqus v2020. *ABAQUS/Standard User's Manual, Version 2020*. Providence, RI, USA: Dassault Systèmes, 2020.

[2] R. Abrahamsen. "Mjøstårnet – Construction of an 81 m tall timber building." In: *23. Internationales Holzbau-Forum (IHF)*. Garmisch-Partenkirchen, Germany, 2017.

https://doi.org/10.52202/069179-0388

[3] J. Asselstine, F. Lam, and C. Zhang. “New edge connection technology for cross laminated timber (CLT) floor slabs promoting two-way action.” In: *Engineering Structures* 233 (2021), p. 111777. DOI: 10.1016/j.engstruct.2020.111777.

[4] H. Chai, H. J. Wagner, Z. Guo, Y. Qi, A. Menges, and P. F. Yuan. “Computational design and on-site mobile robotic construction of an adaptive reinforcement beam network for cross-laminated timber slab panels.” In: *Automation in Construction* 142.August (2022), p. 104536. ISSN: 09265805. DOI: 10.1016/j.autcon.2022.104536.

[5] DOP PM–017–2022. *Pollmeier Furnierwerkstoffe GmbH: Laminated veneer lumber made from beech for non-load bearing, load bearing and stiffening elements – Board BauBuche S and BauBuche Q*. Declaration of Performance. 2022.

[6] EN 338. *Structural timber – Strength classes*. Brussels, Belgium: European Committee for Standardization, 2016.

[7] ETA-06/0009. *Binderholz Brettsperrholz – Massives plattenförmiges Holzbauelement zur Verwendung als tragendes Bauteil in Bauwerken*. European Technical Assessment. Berlin, Germany, 2017.

[8] A. Krtschil, L. Orozco, S. Bechert, H. J. Wagner, F. Amtsberg, T.-y. Chen, A. Shah, A. Menges, and J. Knippers. “Structural development of a novel punctually supported timber building system for multi-storey construction.” In: *Journal of Building Engineering* 58.March (2022), p. 104972. ISSN: 23527102. DOI: 10.1016/j.jobe.2022.104972.

[9] K. A. Malo, R. B. Abrahamsen, and M. A. Bjertnæs. “Some structural design issues of the 14-storey timber framed building “Treet” in Norway.” In: *European Journal of Wood and Wood Products* 74.3 (2016), pp. 407–424. DOI: 10.1007/s00107-016-1022-5.

[10] B. Maurer, R. Maderebner, P. Zingerle, I. Färberböck, and M. Flach. “Point-Supported Flat Slabs with CLT-Panels.” In: *Proc. of the World Conference on Timber Engineering (WCTE 2018)*. Seoul, Republic of Korea, 2018.

[11] M. Muster and A. Frangi. “Experimental analysis and structural modelling of the punching behaviour of continuous two-way CLT flat slabs.” In: *Engineering Structures* 205 (2020), p. 110046. DOI: 10.1016/j.engstruct.2019.110046.

[12] L. Orozco, A. Krtschil, L. Skoury, J. Knippers, and A. Menges. “Arrangement of reinforcement in variable density timber slab systems for multi-story construction.” In: *International Journal of Architectural Computing* 20.4 (2022), pp. 707–727. DOI: 10.1177/14780771221135003.

[13] L. Orozco, A. Krtschil, H. J. Wagner, S. Bechert, F. Amtsberg, L. Skoury, J. Knippers, and A. Menges. “Design Methods for Variable Density, Multi-Directional Composite Timber Slab Systems for Multi-Storey Construction.” In: *Proc. of the 39th eCAADe Conference*. Novi Sad (SRB), 2021.

[14] M. Popovski, Z. Chen, and B. Gafner. “Structural behaviour of point-supported CLT floor systems.” In: *Proc. of the World Conference on Timber Engineering (WCTE 2016)*. Vienna, Austria: Vienna University of Technology, 2016.

[15] L. Skoury, F. Amtsberg, X. Yang, H. J. Wagner, T. Wortmann, and A. Menges. “A Framework for managing data in multi-actor fabrication processes.” In: *Design Modelling Symposium - Towards Radical Regeneration*. Berlin: Springer International Publishing, 2022. DOI: 10.1007/978-3-031-13249-0_47.

[16] H. Svatoš-Ražnjević, L. Orozco, and A. Menges. “Advanced Timber Construction Industry: A Review of 350 Multi-Storey Timber Projects from 2000–2021.” In: *Buildings* 12.4 (2022), p. 404. DOI: 10.3390/buildings12040404.

[17] C. Tapia, M. Claus, and S. Aicher. “A finger-joint based LVL connection for the weak direction of CLT plates.” In: *Construction and Building Materials* (2022). (accepted for publication).

[18] C. Tapia, L. Stimpfle, and S. Aicher. “A scalable column-CLT-slab connection for open-plan high-rise timber buildings.” In: *Proc. of the World Conference on Timber Engineering (WCTE 2021)*. Santiago, Chile: Centro UC de Innovación en Madera, 2021.

[19] C. Tapia. *Pybaqus: A Python library for the visualization and post-processing of Abaqus ASCII result files*. Version 0.2.9. 2023. URL: https://github.com/cristobaltapia/pybaqus.

[20] C. Tapia. *Replication Data for: Point-support reinforcement for a highly efficient timber hollow core slab system*. Version V1. 2023. DOI: 10.18419/darus-3381.

[21] Z-9.1-775. *Technical Approval, Brettschichtholz mit dem Keilstoß-System “Hess Limiteless” für tragende Holzkonstruktionen – Approval holder: Hasslacher Holding GmbH*. Berlin, Germany: issued by Deutsches Institut für Bautechnik, 2020.

[22] S. Zöllig, A. Frangi, S. Franke, and M. Muster. “Timber structures 3.0 - new technology for multi-axial, slim, high performance timber structures.” In: *Proc. of the World Conference on Timber Engineering (WCTE 2016)*. Vienna, Austria: Vienna University of Technology, 2016.

World Conference on Timber Engineering Oslo 2023

R&D PROJECT FOR TECHNOLOGIES ABOUT MID- AND HIGH-RISE TIMBER CONSTRUCTION IN JAPAN

Takahito Tsuchimoto[1], Nobuhiko Akiyama[2], and Yoshihiro Yamazaki[3]

ABSTRACT: The share of the timber construction per building area in the low-rise building was increased, but that in the mid- and high-rise building has never grown so much. Then, we conducted the R&D project for the technologies about mid- and high-rise timber construction in Japan. As a results, the performance evaluation method under the load duration of the wood-based composite components and the design method of the semi-rigid glulam frame jointed by drift pins with inserted steel plate were developed. The good results or the effective technical datum for the future implementation of the mid- and high-rise timber construction.

KEYWORDS: Duration of load, CLT panel construction, Design method for ultimate capacity of glulam frame

1 INTRODUCTION

The Act for Wood Use Promotion in Public Buildings was established at 2010 and revised as The Act for Wood Use Promotion to Contribute Realization of Carbon-Free Society at 2021. After 2010, the share of the timber construction per building area in the low-rise building was increased, but that in the mid- and high-rise building has never grown so much. Then, we conducted the R&D project for the technologies about mid- and high-rise timber construction in Japan. The summary of the following 4 themes which the project has focused on are reported in this paper;

1) The performance evaluation method of the wood-based composite components based on the element.
2) The ultimate capacity design of glulam semi-rigid frame and the possibility of the GLT mass timber.
3) The various performance evaluations of the mid-rise wood frame construction using the full-sized 6-story 2x4 testing building.
4) The studies on the simple structural design method for the CLT panel construction and the various performance evaluations using the full-sized test house.

2 PERFORMANCE EVALUATION OF WOOD-BASED COM-POSITE COMPONENT BASED ON ELEMENT

2.1 BACKGROUNDS

The performance evaluation methods for the I-joist which are provided as the designated building materials in Building Standard Law of Japan (hereinafter, "BSL") are specified in the Ministry of Construction Notification No. 1446 of 2000 as the methods based on only tests or that of estimating from the quality of the elements. However, the estimation methods were not clarified and rarely used for the accreditation of Minister of Land, Infrastructure, Transport and Tourism.

It is known that the performance under short-term load can be estimated from the performance of the elements employing the classical strength of materials method. But, it is unknown that those against long-term load can be estimated by the element.

2.2 COEFFICIENT OF DURATION OF LOAD

Therefore, as the one of the typical I-joist, that with 235 mm depth consist of the flange of LVL and the web of OSB were subjected to evaluate the coefficient of duration of load. The flange of 53 x 36 mm LVL, the web of 9.5 mm thick OSB and I-joist were subjected to the creep failure tests, as shown in Photo 1. As a result, the adjustment coefficient with respect to load duration of OSB, LVL and I-joist were 0.62-0.69, 0.73 and 0.72, respectively. The details of test conditions and results would be reported by Dr. R. Takanashi[1]. It was clarified that the adjustment coefficient with respect to load duration might be determined by those of elements whose failure occurred under the static load.

Photo 1: *Tests to evaluate the duration of load for (a) the flange of LVL, (b) the web of OSB and (c) I-joist.*

3. THE ULTIMATE CAPACITY DESIGN OF GLULAM SEMI-RIGID FRAME

3.1 BACKGROUNDS

In the high seismic country Japan, BSL requires that all buildings have to prevent to deform beyond the damage

[1] Takahiro Tsuchimoto, Building Research Institute (BRI), Japan, tutti@kenken.go.jp
[2] Nobuhiko Akiyama, National Institute for Land and Infrastructure Management (NILIM), Ministry of Land, Infrastructure, Transport and Tourism (MLIT), Japan, akiyama-n92rg@mlit.go.jp
[3] Yoshihiro Yamazaki, Building Research Institute (BRI), Japan, y_ymzk@kenken.go.jp

https://doi.org/10.52202/069179-0389

limit under the rarely occurred strong earthquake and that all building have to prevent to collapse under the extremely rarely occurred strong earthquake. In order to design the prevention of collapse, the designer needed to evaluate the ultimate capacity of structure.

3.2 SPECIMENS

Therefore, as one of the typical glulam semi-rigid frames, the estimation formula[2] of the drift pin joint with inserted steel plate was developed and verified in comparison with moment resisting joint tests on them. The specimens had variations in the diameter of pins, arrangements in rectangular or circle and the double or triple layouts, as shown Figure 1.

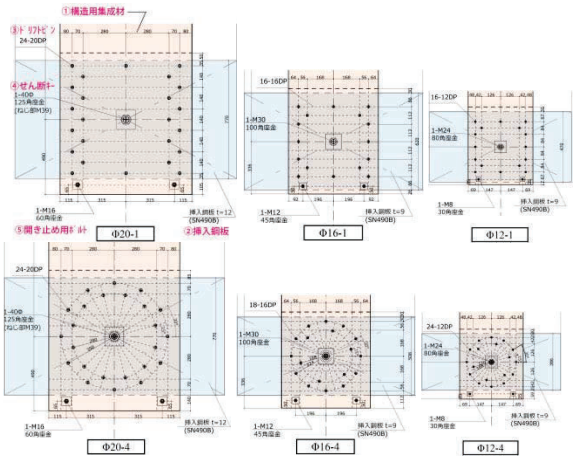

Figure 1: *Specimens of moment resisting joint of drift pins arranged in rectangular with inserted steel plate.*

3.3 TESTS AND RESULTS

The moment tests were conducted to them, as shown Figure 2. The positive and negative alternating load was applied to the top of specimen using an actuator and gradually increased to the failure of specimens. Several examples of the moment-rotational angle relations and typical fracture modes obtained by the tests were shown in Figure 3.

.

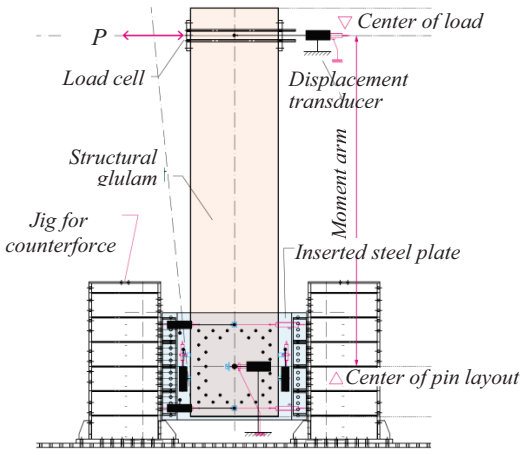

Figure 2: *Schematic diagram of the moment test for joint.*

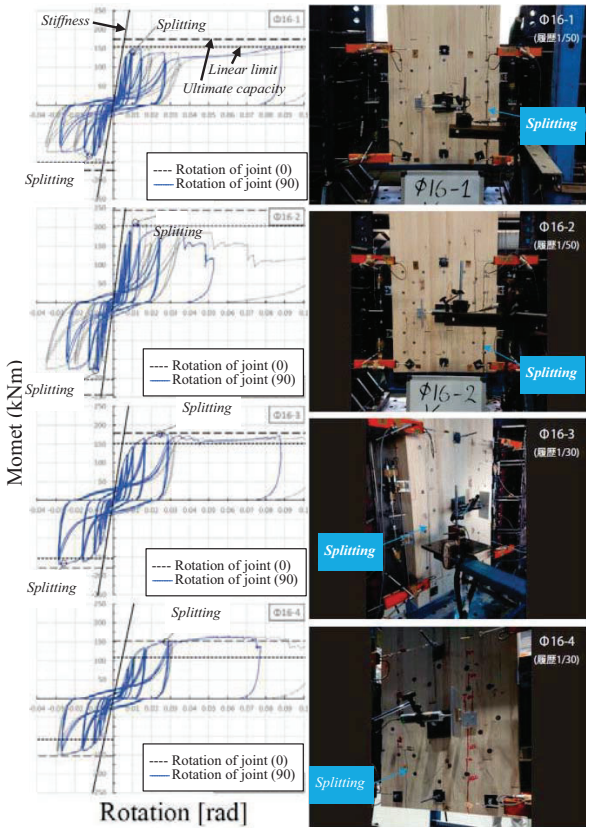

Figure 3: *Examples of* moment-rotational angle relations *and typical fracture modes of the moment test for joint.*

The plasticity factor μ was calculated from moment-rotational angle relations and compared with the depth of beam, as shown in Figure 4. Regarding the plasticity rate, the laminated timber thickness was 6.79 to 8.71 for 750 mm and 4.08 for 500 mm for the double circle, and the laminated timber thickness for the triple circle was 6.78 for 900 mm and 4.61 for 750 mm. Regarding the effect of the number of arrayed circles, the specimens with triple circle array tended to decrease the load earlier than those with double circles, resulting in a lower plasticity factor μ.

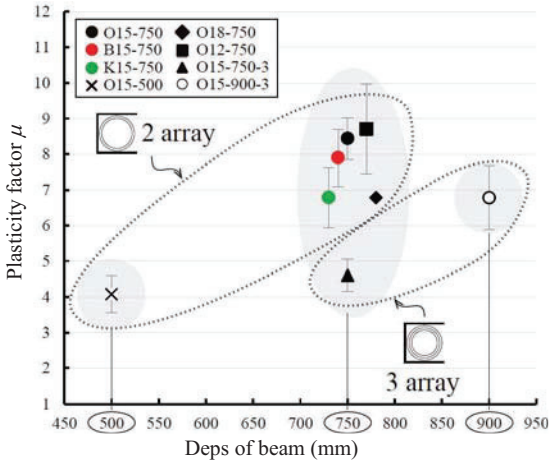

Figure 4: *Relationships between beam depth and plasticity factor μ.*

https://doi.org/10.52202/069179-0389

Then, the stiffness, the yield moment and ultimate moment calculated by the developed estimation formula [2] were compared with those obtained by the tests, as shown in Figure 5, 6 and 7, respectively.

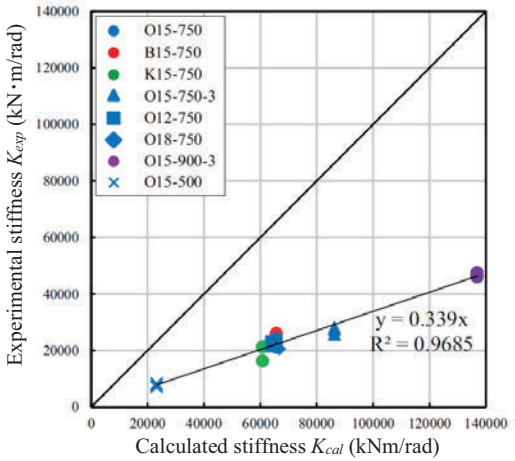

Figure 5: *Relationships between calculated and experimental stiffness.*

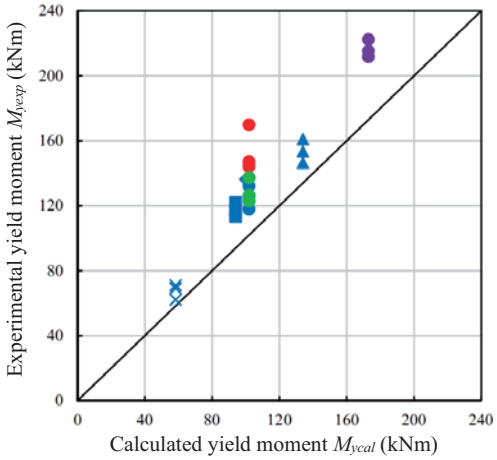

Figure 6: *Relationships between calculated and experimental stiffness.*

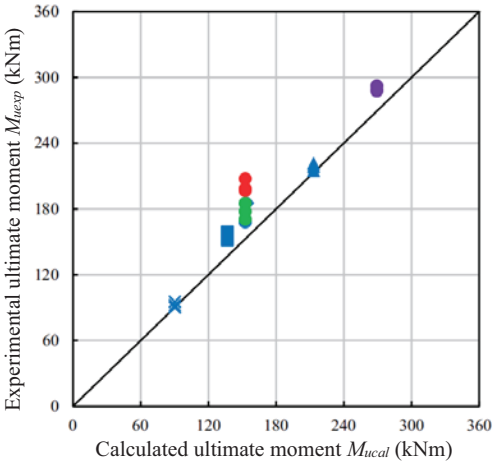

Figure 7: *Relationships between calculated and experimental stiffness.*

Regarding the possibility of estimating the rigidity, the ratio of the experimental value to the estimated value calculated assuming that there is no slip of the steel plate pin diameter + 1 mm tip hole is about 1/3. It was confirmed that the reduction rate indicated in the manuals was insufficient.

Regarding the estimation of yield strength, although Douglas fir was slightly higher, it generally showed high adaptability. It was suggested that a more rational evaluation method can be adopted than the method of setting the short-term allowable strength to 2/3 of the yield strength at which one of the connectors yields, which is written in conventional guidelines and manuals.

In addition, based on them, the evaluation method of the ultimate capacity for the semi-rigid glulam frame jointed by the drift pins with inserted steel plate were derived, and the validity was verified by the full-sized 2-story glulam frame as shown in Photo 2. Details are omitted due to space limitations.

Photo 2: *Tested full-sized 2-story glulam frame jointed by the drift pins with inserted steel plate.*

4 EVALUATION OF DUCTILITY FACTORS FOR TIMBER CONSTRUCTIONS

4.1 BACKGROUNDS

In high seismic country Japan, the ultimate capacity of building over a certain scale must be design under the extremely rarely occurred earthquake. In other words, it need be verified that the applied load or stress on the members, horizontal elements and joints under the base shear of 1.0 is not over the ultimate capacities of them. However, the applied load or stress can be decreased depending on the abilities of deformation. The factor indicating how much they can be decreased is called as Ds and provided in the Notification No.1791 of Ministry of Construction, 1980.

Although the Notification provides Ds according to the specifications of the frame and the L/D of joint, there is little technical knowledge on the relationships between the ductility of the joint or the frame and the Ds of the story. Therefore, these relationships were analysed numerically in this project.

Moreover, the Notification has never shown the Ds of the structure combined by parts with different ductility factor. Therefore, the Ds of the timber constructions combined by parts with different ductility factor were studied analytically in this paper.

https://doi.org/10.52202/069179-0389

4.2 NUMERICAL ANALYSES ON RELATIONS BETWEEN DUCTILITY OF JOINT AND GLULAM STRUCTURES

4.2.1 Analysis models

Three- and five-story semi-rigid frame, the brace and arch structure model in which elastic members are connected by rotation/axial springs were subjected to be analysed. Based on previous experimental data, three cases of high, medium and low capacity were set for the rotation / axial spring, as shown in Figure 8 as an example of a three-layer semi-rigid frame.

4.2.2 Analysis method

For the above-mentioned analysis models, (1) the pushover analyses were carried out, and the ductility factor of the structure, μs1 was obtained by applying the perfect elastoplastic model to the load-story drift curves with. (2) Nonlinear seismic response analyses were carried out, and the ductility factor of the structure, μs2 was obtained by the load-story drift curves. (3) The pushover analyses were applied to the contracted equivalent 1-DOF model of the analysis model, and the ductility factor of the structure, μs3 was obtained by the load-representative story drift curves.

4.2.3 Results and discussion

The relationships between the ductility factors of joint, μj set in the analysis models and those of structure, μs1, μs2, μs3 obtained by the analyses were shown in Figure 9(a), (b) and (c), respectively.

The semi-rigid frame, brace and arch structure model constructed by the joint with the 3-level capacity were subjected to the pushover analysis and others. As results of com-parison of the ductility factor of each structure calculated by the analyses with those of joint, the followings were obtained.

- The ductility factors of structure were usually lower than those of joints.
- The results of analyses on the contracted 1-DOF model were different from other 2 method of analyses.
- If the results of analyses on 3D model and the seismic response analyses were correct, the μ of arch would be lowest, the μ of semi-rigid frame would be relatively high, and the μ of brace would be various.
- Most of μs1 and μs2 were over the 0.5 x μ_j and below the 0.8 x μ_j, so the decreasing factor of seismic load under extremely rarely occurred earthquake may be able to be determined as the value of $(1.5 \times \mu_j - 1)^{-0.5}$ or more.

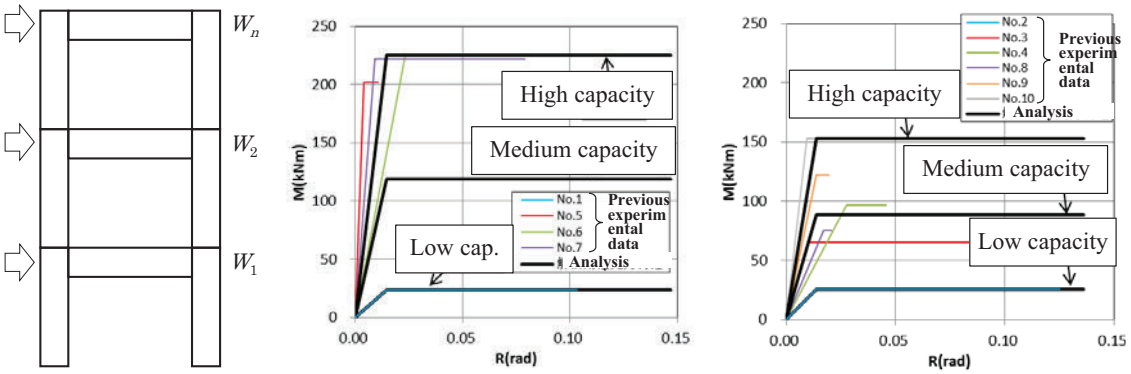

(a) Analysis model *(b) Joint between post and beam* *(c) Joint at bottom of post*

Figure 8: *Analysis model and restoring force characteristic of joints rotation spring.*

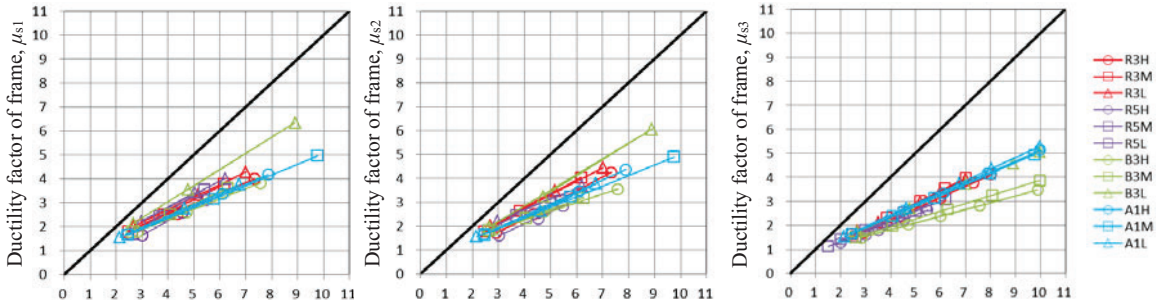

(a) Pushover 3D model *(b) Seismic response analysis* *(c) Pushover of 1-DOF model*

Figure 9: *Relationships between the ductility factors of joint and of structure.*

Notes: The legend of each plot is shown at the right end of (c), and its meaning is as follows. 1st letter shows the structure type of R: semi-rigid frame, B: brace and A: arch structure. 2nd figure shows the story of 3, 5 and 1. 3rd letter shows the joint capacity of H: high, M: medium, and L: low.

https://doi.org/10.52202/069179-0389

4.3 DUCTILITY FACTORS OF TIMBER CONSTRUCTIONS COMBINED BY PARTS WITH DIFFERENT DUCTILITY FACTORS

4.3.1 Analytical model and parametric study

From the past papers, the load-deformation relationships of the semi-rigid glulam frames, the shear walls, the brace systems and arch structure were picked up and modelled, as shown Figure 8. The vertical axis of it was normalised by the allowable capacity, Q_a. The semi rigid glulam frame was assumed as 3 variations with high, medium and low capacity. The shear wall was distinguished between the plywood and gyp-sum board. The brace system was distinguished between the glulam jointed by the drift pins with steel plate and jointed by the bolts. The arch structure was distinguished be-tween the curved glulam without joints and with some joints and straight glulam joint-ed by the drift pins. The ultimate capacity obtained by the bilinear model of the load-deformation relationships was defined as Q_u. The D_s of alone structure is no other than Q_a/Q_u. The D_s of medium glulam frame, SW with plywood and gypsum board and brace jointed by DP and bolts were 0.37, 0.609, 0.707, 0.505 and 0.244, respectively.

The combinations with variable load-deformation relationships, as mentioned above, were applied to the structural model which the summation of allowable capacity, Q_a is 1.0. The mixture ratio of the different load-deformation relationships was defined as β. The summation of the ultimate capacity of the different structure, Q_u was varied from 0.2 to 0.75. The time history response analysis were con ducted to the structural model till the ultimate state.

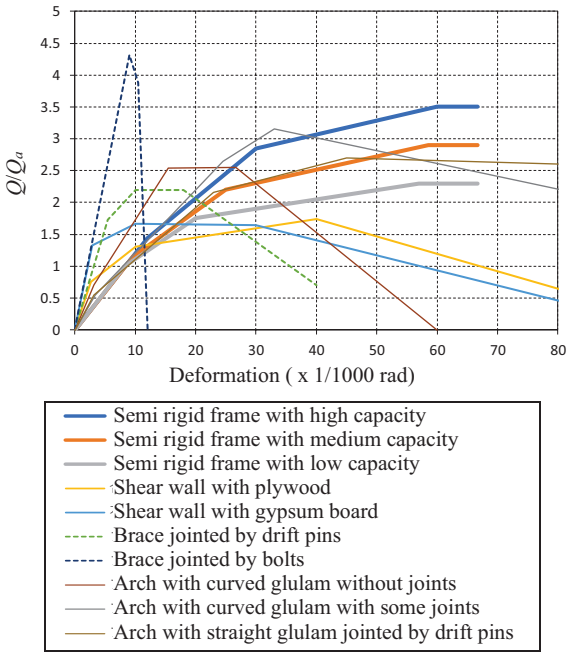

Figure 8: *The picked up and modelled load-deformation relationships.*

4.3.2 Result of parametric study

As a result of the parametric study, the response load-deformation relationships were obtained. When the maximum response deformation agreed with the ultimate deformation, the base shear was calculated by the results and defines as Cu. The Cu is no other than the ductility factor, Ds of combination structure after all. Some samples of Ds were shown in Table 1.

Table 1: *Examples of ductility factor Ds obtained by the analysis*

Glulam frame with medium capacity combined with		Shear wall with plywood	Shear wall with gypsum board	Brace jointed by drift pins	Brace jointed by bolts
Combination ratio β	0	0.34	0.34	0.34	0.34
	0.1	0.34	0.34	0.34	0.29
	0.2	0.34	0.34	0.29	0.29
	0.3	0.31	0.29	0.30	0.52
	0.4	0.29	0.30	0.40	No solution
	0.5	0.29	0.30	0.41	
	0.6	0.29	0.29	0.43	
	0.7	0.29	0.30	0.45	
	0.8	0.30	0.35	0.48	
	0.9	0.35	0.37	0.49	
	1.0	0.35	0.40	0.50	

4.3.3 Conclusion

The ductility factor of timber constructions combined by parts with different ductility factor need to adopt the higher one. However, the case of combination with shear wall had a possibility to decrease the ductility factor still more.

5 6-STORY 2X4 TEST BUILDING

5.1 BACKGROUNDS AND OBJECTIVES

In Japan, there were few construction examples of the mid- and high-rise wood frame construction. High-capacity shear walls and fire-resistant structures have been developed for the mid- and high-rise buildings, however, they have never been constructed actually using them together. In addition, it was necessary to evaluate the performance of each part because the mid- and high-rise buildings were subject to heavy rain and winds, and flat roofs, which had not been implemented for low-rise buildings, were also constructed.

5.2 WORKABILITY

The test building was built in BRI (Photo 3) was completed in 2016 and employed the large amount of gypsum boards in order to satisfy the fire requirement by BSL. The construction of the frame wall construction is to lift and install the frame panels produced in the factory with the crane. The number of man-hours for each process was measured from the number of working days and the number of workers. It took a total of 100 working days and 666 manpower to construct the construction. The number of days and man-hours for each procedure were shown in Table 2. The workability of 0.14 man/m^2 is

https://doi.org/10.52202/069179-0389

about the same as the construction efficiency of a low-rise light frame construction house, but for a medium-rise building, 0.07 man/m^2 is required for marking to ensure construction accuracy. As a result, accuracy of 1 to 1.5/1000 was confirmed both horizontally and vertically after the completion of the framework construction.

This 6-story test building has two-hour fire resistance specifications (triple thick reinforced gypsum boards) on the 1st and 2nd floors, and one-hour fire resistance specifications (double one) on the 3rd to 6th floors. It took 252 man-days to install the large amount of gypsum boards, and they accounted 1/3 of total man-hours, as shown in Figure 10.

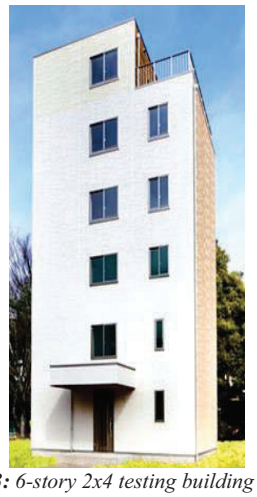

Photo 3: *6-story 2x4 testing building in BRI.*

Table 2: *The number of days and man-hours for each construction procedure*

Procedure	Actual working days	Man-hours	Man-hours required		Remarks
			Per floor area	Per story	
Foundation	26	85	0.42		
Scaffold	6	19	0.09	3.17	Divided into 6 times
Wooden framework		43	0.21	7.17	
Wood framework	13	28	0.14	4.67	
Accuracy management	12	15	0.07	2.50	Marking and others
Fixture working	47	80	0.40	13.33	Stairs, sashes, etc.
Gypsum boards		252	1.25	42.00	
External	17	68	0.34	11.33	
Inside	27	124	0.61	20.67	
Openings	4	4			
Lifting	10	56			9 times*
Sidings		104	0.52	17.33	3 times*
Total	100	666	3.30	111.0	

Note: *: using high place work vehicle

5.3 SINKAGE

The sinkage due to further drying of dimension lumbers or the creep behaviour under the dead and live load is one of the important problems on mid-rise 2x4 construction. It was measured by the displacement transducer set at the end of the wire which was hang from each story to the base, as shown Figure 11.

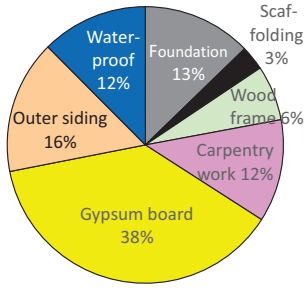

Figure 10: *Distribution of working time of each process.*

Among the measurement results of the sinkage, the measured value of No. 4 is shown as a typical example in Figure 11. It was gradually increased within 1 mm per story, but settled down over 1 year after.

(a) Displacement transducer

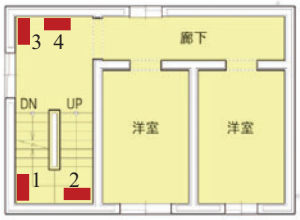

(b) The position of sensors (1-4)

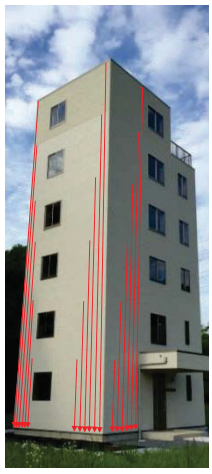

(c) Image of wires

Figure 11: *Measuring methods of sinkage.*

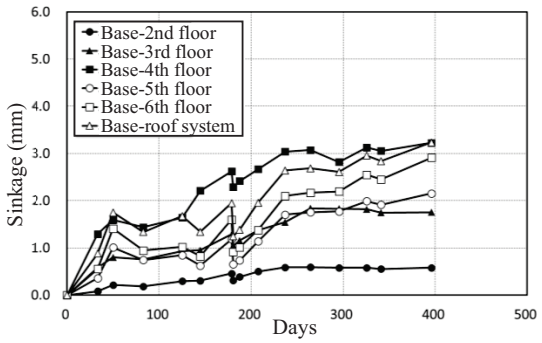

Figure 12: *Sinkage of 6-story 2x4 construction.*

5.4 VERIFICATION OF WATERPROOFING OF FLAT ROOF

The flat roofs are often used for the roofs of mid-rise wooden buildings. Moisture, such as rainwater, acts before waterproofing construction and may be confined by waterproofing layer. Contained moisture conditions that are maintained for long time are likely to cause biodegradation of the structural members.

https://doi.org/10.52202/069179-0389

Therefore, a grid-like ventilation groove was provided in the insulation material to be installed on the roof base material, and this groove was used to discharge moisture from the roof base material to the outside from the deaerator, as shown Figure 13. The water was intentionally sprinkled on the flat roof before waterproof, as mentioned above. The humidity sensors were installed near the grooves of the insulation at every 1 m from the deaerator to measure the humidity continuously. On the other hand, the flat roof balcony without deaerator was subjected to measure the humidity near the grooves of the insulation as a control.

The relative and absolute humidity under the waterproof layer of the flat roofs and the roof balconies decreased regardless of the presence or absence of the deaerator. The humidity of the flat roof with the deaerator reduced faster than the roof balcony without the deaerator. It was clarified that the deaerator installed at the flat roof contributed to the improvement of the moisture emission rate.

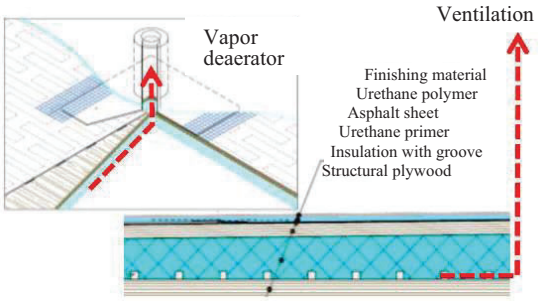

Figure 13: *Vapor deaeration and ventilation system of flat roof*

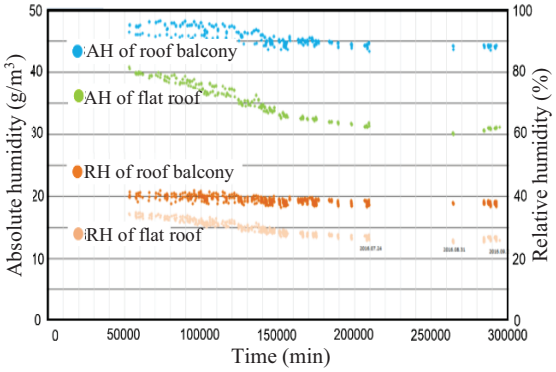

Figure 14: *Time history change of absolute and relative humidity at the flat roof with deaerator and the roof balcony without it.*

5.5 CONCLUSIONS OF 6-STORY 2X4 TEST BUILDING

Through the constructing the 6-story 2x4 test building and the trials to evaluate the various performance, results are summarized as follows:

- The workability of 6-story 2x4 construction is about the same as the construction efficiency of a low-rise light frame construction house.
- The man-hour to install the many gypsum boards accounted 1/3 of the total.
- The sinkage was gradually increased within 1 mm per story, but settled down over 1 year after.
- The deaerator installed at the flat roof contributed to the improvement of the moisture emission rate.

In addition to those, the good results or the effective technical data for the future studies were obtained by the measuring of the seismic response under strong ground motion[3], the water-proof performance of window sash in higher story, the floor impact sound insulation[4] and others.

6 CLT TEST HOUSE

The 2-story CLT test house, as shown in Photo 4, was built in BRI for the experimental construction and the various performance evaluation of the CLT panel construction which had little experienced in Japan. The good results or the effective technical data for the future studies were obtained by the measuring of the dimension stability and the mechano-sorptive deformation of CLT panel, the air tightness, the desorption behaviour of the humid shut in the waterproof layer, the floor impact sound insulation and others.

Photo 4*. 2-story CLT test house in BRI.*

7 CONCLUSIONS

As mentioned above, we have conducted the R&D project for technologies about mid- and high-rise timber construction in Japan in order to grow up the share of the timber construction in the mid- and high-rise building. The results are summarised as follows:

- Through the creep fracture tests on the I-joists and their elements, the adjustment coefficient with respect to load duration of the I-joist might be determined by those of elements whose failure occurred under the static load.
- The developed estimation formula of the yield and ultimate capacities of the moment resisting joint using the drift pin with inserted steel plate was verified by the moment tests on them.
- As the results of the numerical analyses on the relations between ductility factors of joint and glulam structures, it was clarified that the ductility factors of the semi-rigid frame was lower than those of their joints generally, the results of pushover analysis with 1-DOF model were different from those with 3D

https://doi.org/10.52202/069179-0389

model and seismic analysis and the results of the nonlinear seismic response analyses, and others.

- As the results of the ductility factors of the timber constructions combined by parts with different ductility factors, it was clarified that such construction needed to adopt the higher one. However, the case of combination with shear wall had a possibility to decrease the ductility factor still more.
- Through the constructing of 6-story 2x4 test building and the measuring of various performance of it, the results are summarised in section 5.5.

ACKNOWLEDGEMENT

A part of this research was funded by the Public/Private R&D Investment Strategic Expansion Program of Cabinet Office. The studies on 2x4 and CLT testing building were conducted as one of the collaborative research with Japan 2x4 Home Builders Association and Japan CLT Association, respectively. We would like to thank the people concerned.

REFERENCES

[1] R. Takanashi, T. Tsuchimoto, Y. Ohashi, and W. Ishihara: Duration of load under long-term bending load of laminated veneer lumber and wooden i-beam, Proc. of World Conference on Timber Engineering (Oslo), 2023.

[2] N. Akiyama: Case study on high and medium height building in timber construction, Proc. of Panel Discussion "*Where are Japanese middle- and high-rise wooden structures going?*", 12-32, Architectural Institute of Japan, 2021.

[3] T. KASHIMA, T. FUKUBA and H. NAKAGAWA: Strong Motion Instrumentation in a Six-story Wooden Building and Analysis of Its Dynamic Characteristics, Proc. of 16th European Conference on Earthquake Engineering (16ECEE), #10192, 2018.

[4] A. Hiramitsu, R. Tomita, S. Hirakawa, and M. Sato: Floor impact sound insulation of the six-story wood-frame model building, Proc. of the 23rd International Congress on Acoustics, 5007-5012, 2019.

World Conference on Timber Engineering Oslo 2023

A PROPOSAL FOR THE MECHANICAL CLASSIFICATION OF BEAM-TO-COLUMN JOINTS FOR TIMBER STRUCTURES

Giacomo Iovane, Celeste Noviello, Federico M. Mazzolani, Raffaele Landolfo, Beatrice Faggiano

ABSTRACT: The performance of timber structures is greatly influenced by the capacity of the connections, in terms of both strength and stiffness, as well as ductility. Reliable estimations of the structural behaviour of timber buildings is possible through a full understanding of the joint behaviour. At present there is not a standard method that allows to identify the mechanical behaviour of timber connections. To fill this gap, in this paper, a procedure for the classification in terms of strength and stiffness of beam-to-column joints in timber structures is presented. The method is inspired to that one related to steel connections according to Eurocode 3. Then, with reference to a number of experimental studies available in the scientific literature on several timber beam-to-column joints, the proposed classification method is applied on typical configurations, evidencing that common joints can be classified as pinned or semi-rigid.

KEYWORDS: Timber structures, moment resisting frames, beam-to-column joints, joint mechanical classification.

1 INTRODUCTION

In timber constructions, joints have great influence on both local and global structural behaviours. Indeed they realize the constraints and restraints conditions of the structural systems, which the structural models for a reliable estimation of the internal forces and deformations are based on. Therefore a full understanding of the joint mechanical properties, such as strength, stiffness and also ductility, is essential. It is also worth to notice that timber members sizes can be determined by the number and type of connectors rather than by the strength requirements for members.

With regards to Moment Resisting Frames (MRF), several experimental studies have been recently carried out on common timber beam-to-column joints, aimed at evaluating the strength and stiffness capabilities [1-9].

However, both in national and international standards, there is not a method that allows to identify the mechanical behaviour of timber connections. To this purpose the moment-rotation relationship should be characterized.

In this paper, a procedure for the classification in terms of strength and stiffness of beam-to-column joints for timber structures is presented. The method is inspired by the classification procedure for steel connections, consolidated and well described in the Eurocode 3 part 1.8 [10], conveniently adapted according to timber connections characteristics. Then, with reference to several experimental studies available in the scientific literature, common configurations of timber beam-to-column connections, whose experimental moment rotation curves were available, have been classified in terms of stiffness by means of the proposed method.

2 JOINT MECHANICAL CLASSIFICATION ACCORDING TO EUROCODE 3

As indicated in section 6.1 of EC3 part 1-8 [10] for steel constructions, the mechanical model of a joint may be represented by a rotational spring joining the centre lines of the connected members at the point of intersection, for a single-sided beam-to-column joint configuration. The properties of the spring can be expressed in terms of moment-rotation (M-θ) characteristic that describes the relationship between the bending moment $M_{j,Ed}$ applied to the joint and the corresponding rotation θ_{jEd} between the connected members (referring to the j-th member).

The design moment-rotation characteristic should define the following three main structural properties:

- bending moment resistance ($M_{j,Rd}$);
- rotational stiffness (S_j);
- rotational capacity (θ_j,).

The complex mechanical behaviour of joints in terms of strength, stiffness and rotational capacity can be determined through the component method (section 6.1, [10]). The joint is analysed as an assembly of components, whose mechanical behaviour is studied separately, and the design resistance of the joint is assumed as the resistance of the weakest joint component, with reference to all the possible collapse modes.

According to Eurocode 3, part: 1-8 [10], in order to identify the effects of joint behaviour on the global structural analysis, three simplified joint models can be distinguished (Tab. 1): 1) *simple joints*, the joint may be assumed not to transfer bending moments; 2) *continuous*

Giacomo Iovane, giacomo.iovane@unina.it; Celeste Noviello, ce.noviello@gmail.com; Federico M. Mazzolani, fmm@unina.it; Raffaele Landolfo, landolfo@unina.it; Beatrice Faggiano, faggiano@unina.it; University of Naples Federico II, Department of Structure for Engineering and Architecture, Via Claudio 21, 80125, Naples, Italy

https://doi.org/10.52202/069179-0390

joint, the joint may be assumed to transfer the bending moments; 3) *semi-continuous joints*, the joint transfers the bending moments in some extents according to the joint rotational stiffness.

***Table 1**: Type of joint model [10].*

Method of analysis	**Classification of joint**		
Elastic	Nominally pinned	Rigid	Semi-rigid
Rigid-plastic		Full-strength	Partial-strength
Elastic-plastic		Rigid and full-strength	Semi-rigid and partial-strength; Semi-rigid and full-strength; Rigid and partial-strength
	Simple	*Continuous*	*Semi-continuous*
Type of joint model			

With reference to the Moment-rotation (M-θ) relationship, beam-to-column connections can be classified considering three different methods of structural analysis:

a) *elastic analysis*, based on a linear Moment-rotation (M-θ) relationship, where joints are classified according to rotational stiffness S_j (Fig. 1a);
b) *rigid-plastic analysis*, where joints are classified according to strength, provided that they are able to develop suitable plastic rotation (Fig. 1b);
c) *elastic-plastic analysis*, based on a bi-linear M-θ relationship, in which joints are classified according to both stiffness and strength, considering also the rotational capacity (Fig. 1c).

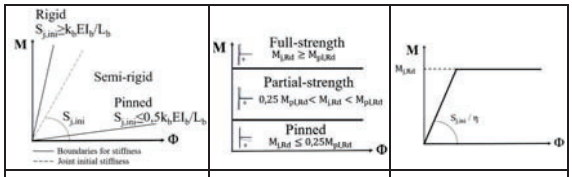

a) b) c)

***Figure 1:** The EC3 joint classification in terms of a) stiffness, b) strength and c) stiffness and strength.*

It is worth noted that the stiffness of the connection should be compared to the stiffness of the connected members. Therefore the joint classification by stiffness can be expressed in terms of a non-dimensional stiffness parameter $\bar{k}$ (eq. 1), depending on the ratio between the initial joint rotational stiffness $S_{j,ini}$ and the bending stiffness of the connected beam (Fig. 1a):

$$\bar{k} = \frac{S_{j,ini}}{\left(\frac{E_S \cdot I_b}{L_b}\right)} \quad (1)$$

where $S_{j,ini}$ corresponds to the elastic bending moment $M_{j,el}$, not exceeding 2/3 $M_{j,Rd}$ ($M_{j,Rd}$ being the design bending strength of the joint), and to the rotation at the elastic limit $\theta_{j,el}$, L_b is the beam span, E_s is the steel elastic modulus and I_b is the beam cross-section moment of inertia. Therefore a joint can be classified as nominally pinned if $\bar{k} \leq 0.5$; semi-rigid if $0.5 < \bar{k} < k_b$; rigid if $\bar{k} \geq k_b$, with $k_b = 8$ for braced frames and $k_b = 25$ for moment resisting frames (Tab. 1). A nominally pinned joint shall be capable of allowing rotations due to design loads and transmitting internal forces, without developing significant bending moments; a rigid joint shall be capable of having a sufficient rotational stiffness to assume the continuity; a joint which does not meet the criteria for a rigid or a nominally pinned joint should be classified as a semi-rigid joint (Fig. 1a).
A joint is classified by strength (rigid-plastic analysis), depending on the ratio between the bending strength $M_{j,Rd}$ of the joint and the bending strength of the connected beam $M_{b,Rd}$ (Fig. 1b; eq. 2), namely the non-dimensional moment resistance parameter (eq. 2):

$$\bar{m} = \frac{M_{j,Rd}}{M_{b,Rd}} \quad (2)$$

Therefore, a joint can be classified as nominally pinned if $M_{j,Rd} \leq 0.25\ M_{b,Rd}$, partial strength if $0.25\ M_{b,Rd} < M_{j,Rd} < M_{b,Rd}$ ($0.25 < \bar{m} < 1$), full strength if $M_{j,Rd} \geq M_{b,Rd}$ ($\bar{m} \geq 1$, Tab. 1).
In a joint classification according to both stiffness and strength (elastic-plastic analysis), as a simplification of the non-linear moment-rotation behaviour, a bi-linear design moment-rotation characteristic may be adopted (Fig. 1c). Therefore, a joint can be classified as semi-rigid and partial-strength; semi-rigid and full-strength or rigid and partial-strength (Tab. 1). As a simplification, the rotational stiffness can be evaluated as $S_{j,ini}/\eta$ (Table 5.2, section 5.1.2 [10]), where η is a coefficient reliant on the connection type.

3 CLASSIFICATION BY STIFFNESS OF TYPICAL TIMBER BEAM-TO-COLUMN JOINTS

3.1 PROPOSED CLASSIFICATION METHOD FOR TIMBER BEAM-TO-COLUMN JOINTS

For the classification of timber joints, it is possible to apply the same method used for steel connections, conveniently modified to consider the timber material characteristics. In particular, the extension of the EC3 classification to timber joints is based on considering the elastic bending strength of the timber beam, $M_{b,el}$, and the timber elastic modulus, E_T.
The steel EC3 formulations for the joint classification in terms of stiffness ($S_{j,ini}$) and strength ($M_{j,el}$) can be suitably revised, by defining the non-dimensional stiffness and strength parameters $\bar{k}$ and $\bar{m}$, as it follows (Eq. 3, 4):

$$\bar{k} = \frac{S_{j,ini} \cdot L_b}{E_T \cdot I_b} \quad (3)$$

$$\bar{m} = \frac{M_{j,Rd}}{M_{b,el}} \quad (4)$$

where $S_{j,ini}$, $M_{j,el}$, $M_{j,Rd}$, $M_{b,el}$ and L_b have been previously defined, E_T is the timber elastic modulus, I_b is the timber beam cross-section moment of inertia.

https://doi.org/10.52202/069179-0390

3.2 APPLICATION OF THE PROPOSED CLASSIFICATION METHOD TO LITERATURE TIMBER BEAM-TO-COLUMN JOINTS

3.2.1 Case studies of beam-to-column joints

From the literature review on experimental campaigns, four recurring types of timber beam-to-column joints can be identified (Fig. 2, 3, 4):

Type 1. Connection with internal or lateral vertical steel plate (rectangular- or T-shaped) and connectors (generally bolts, screws or pins; [3-5, 11-14])

Type 2. Connection with circular arrangement of connectors (generally bolts or screws; [5, 15]);

Type 3. Connection with top and bottom plates or brackets and connectors (generally bolts or screws; [1, 16]);

Type 4. Timber joint equipped with steel link [2, 17, 18].

A total of 46 joints are examined. In particular, for each joint type, the specimens are represented in Figures 2-4 and the number of tests carried out for each type, as well as the beam and column members sizes are provided in Table 2.

Among Type 1 joints, Wang et al. [4] have studied a beam to column joint with internal T-shaped 9.5mm thick steel plate (S235 steel grade) and bolts (M20, 8.8 steel grade), as base specimen S1, specimen S2 reinforced with screws orthogonal to the grains of the beam and column; specimen S3 locally made with cross-laminated glulam timber. The S2 and S3 specimens show increased stiffness and strength as respect to S1. A similar beam to column joint with internal T-shaped 10mm thick steel plate (S235 steel grade) and M16 bolt (8.8 grade), is studied by He and Liu [3], as base specimen S1, specimen S2 reinforced with bars, specimen S3 reinforced with self-tapping screws, in both cases arranged orthogonal to the grains of beam and column. The stiffnesses result quite similar. He et al. [12] analysed the same joint reinforced with hollow PVC tubes in the holes of the timber elements and with screws orthogonal to the grains. These reinforcements led to an increase in strength and stiffness as respect to the non-reinforced specimen. Beltran [5] tested a beam to column joint configuration with internal T-shaped 6.35mm thick steel plate (ASTM A36 steel grade) and connected bolts in a rectangular arrangement (M12, ASTM A325 steel grade). Salem and Petrycki [13] studied a beam to column joint with two external steel plates for evaluating the influence of the number of bolts (M20, ASTM A325 steel grade) and of the edge distance on the strength and stiffness. In particular, four different types of connection have been tested: edge distance equal to 4ϕ (where ϕ is the bolt diameter) and 3x4 bolts (in a rectangular arrangement); edge distance equal to 4ϕ and 3x6 bolts; edge distance equal to 5ϕ and 3x4 bolts; edge distance equal to 5ϕ and 3x6 bolts. The same specimens are tested by using a T-shaped steel plate by Salem [14]. The variation of the edge distance from 4 to 5 ϕ provides a larger increase of bending moment resistance than the variation of the bolts number from 4 to 6. The reverse happens with the internal steel plate. However, in general, from the test results, a low variation of stiffness among the specimen can be observed.

Wang et al. [11] have studied a post-tensioned (PT) energy dissipating beam to column joint, to provide self-centering capacity, connected with a T-shaped steel plate and bolts (M16-20). In particular, two specimens are tested, by varying the post-tensioned force applied to the steel strand (S1=40kN; S2=60kN). The joints shown similar stiffnesses (Fig. 2).

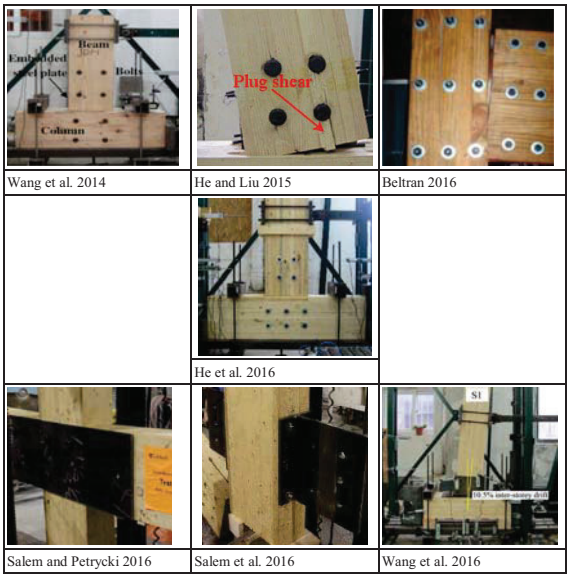

Wang et al. 2014	He and Liu 2015	Beltran 2016
	He et al. 2016	
Salem and Petrycki 2016	Salem et al. 2016	Wang et al. 2016

Figure 2: *Type 1 literature beam-to-column testing joints .*

Among Type 2 joints, Polastri [15] have tested different types of connection: beam to column joint configuration connected with pins (M12, 14, 16) in single (T01) and double (T08, T09) circular arrangements, with glued bars in single (T06) and double (T10) circular arrangements, as well as with a glued connection between timber members (T07). As a result, the glued connections (T06, T10) show higher stiffness and strength as respect to the other connection types. Beltran [5] have tested a beam-to-column joint with two different types of connection: bolts in a circular arrangement (M9, ASTM A307 steel grade); internal T-shaped 6.35mm thick steel plate (ASTM A36 steel grade) connected with bolts with different diameter, steel grade and arrangement (Fig. 3).

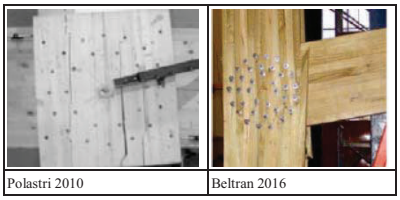

Polastri 2010	Beltran 2016

Figure 3: *Type 2 literature beam-to-column testing joints.*

Among Type 3 joints, Kasal et al. [1, 16] have tested a beam to column joint with two L-shaped aluminium angles located at the beam end top and bottom, connected to the beam through inclined self-tapping screws and to the column with horizontal self-tapping screws (Φ6.5-12mm), and a beam to column joint with two timber

https://doi.org/10.52202/069179-0390

rectangular-shaped plates connected to the beam end top and bottom through inclined self-tapping screws and to the column with horizontal self-tapping screws (Φ6.5-12mm). Both the connections have shown good values of stiffness and strength (Fig. 4).

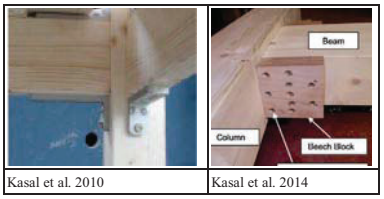

Kasal et al. 2010 | Kasal et al. 2014

Figure 4: *Type 3 literature beam-to-column testing joints .*

Table 2: *Study joints geometrical features.*

Reference studies	Number of tests	Timber member size B x H x L [mm]	
		Beam	Column
Type 1			
Wang et al. 2014	3	130x305x830	272x305x1000
He and Liu 2015	3	200x300x850	250x300x1100
Beltran et al. 2016	2	135x400x1300	200x270x2900
He et al. 2016	3	150x384x1000	240x384x1400
Salem and Petrycki 2016	4	137x318x1541	137x318x1541
Salem 2016	4		
Wang et al. 2016	2	200x300x1500	250x250x1000
Type 2			
Polastri 2010	6	120x600x3410	160x600x3410
Beltran et al. 2016	2	140x400x1300	100x400x3000
Type 3			
Kasal et al. 2010	1	40x120x800	80x80x800
Kasal et al. 2014	1	160x360x1500	200x200x2200
Type 4			
Andreolli 2011	8	120x230x2500	/
Nakatani et al. 2012	3	120x270x1200	120x270x1900
Gohlich and Erochko 2016	4	184x457x2000	184x457x1500
B: Base; H: Height; L: Length			

Type 4 joints have been conceived for seismic dissipative structures to delegate the dissipation capacity to the steel link, avoiding the failure of connections and timber members, which should remain in elastic field in case of earthquake. By integrating the timber technology with steel devices, some authors have proposed different solutions. Andreolli [17] have focused on 8 beam to column joint assemblages equipped with steel link (HE120B profile) connected to the beam by means of 4 glued threaded bars (M16, 6.8 grade, 540mm long), for investigating the joint behaviour with variable end-plate thicknesses (6-8-10-15-20mm). At the end of the tests, joints with large thickness of steel plate have reached higher stiffness and dissipative capacity through the plastic combined tensile-bending deformation of the bars and the bending deformation of the end-plate. Nakatani et al. [2] have tested a beam to column joint equipped with a box steel link connected by means of lag-screw-bolts embedded into the beam parallel to the grain and into the column in 3 different configurations: perpendicular to the grain; perpendicular and with a skew angle as respect to the grain; with a skew angle as respect to the grain. Joints with greater connector inclination have exhibited increased stiffness and strength, with a bolts pull-out failure. Gohlich and Erochko [18] have studied a beam to column joint equipped with steel link connected to the timber members by means of inclined screws, also varying the link profile and the inclination of connectors: dog-bone W250x28 steel profile with 45° inclination screws (Φ10,12mm SWG ASSY); dog-bone W250x28 steel profile with 30° inclination double screws; W200x25 steel profile with 45° inclination screws; W200x25 steel profile with 30° inclination double screws . The joints with dog-bone profile have shown a better performance in terms of both stiffness and ductility than the other connection types (Fig. 5).

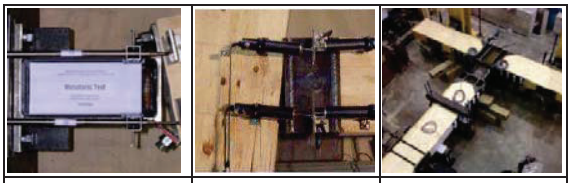

Andreolli 2011 | Nakatani et al. 2012 | Gohlich, and Erochko 2016

Figure 5: *Type 4 literature beam-to-column testing joints .*

3.2.2 Classification of the joint case studies

For the study joints, the initial rotational stiffness ($S_{j,ini}$), the joint elastic bending moment ($M_{j,el}$) and the corresponding rotation ($\theta_{j,el}$) are evaluated starting from the Moment-rotation (M-θ) experimental curves from literature, according to the proposed method. The mechanical parameters are indicated in Table 3.

Moreover, the reference initial rotational stiffnesses for a pinned joint $S_{j,pinned}$ (eq. 5) and a rigid joint $S_{j,rigid}$ of a moment resisting frames (eq. 6) are calculated as it follows and given in Table 3:

$$S_{j,pinned} = \frac{0.5 E_T I_b}{L_b} \quad (5)$$

$$S_{j,rigid} = \frac{25 E_T I_b}{L_b} \quad (6)$$

Therefore, a joint can be classified by comparing the initial rotational stiffness of the joint with the reference ones as it follows:

$S_{j,ini} \leq S_{j,pinned}$ Nominally pinned;

$S_{j,pinned} < S_{j,ini} < S_{j,rigid}$ Semi-rigid;

$S_{j,ini} \geq S_{j,rigid}$ Rigid.

The joint classification by stiffness is also presented in terms of non-dimensional parameters, through the Moment-rotation ($\bar{m}$-$\bar{\theta}$) curves, which are defined based on the following equations (eq. 7, 8):

$$\bar{m} = \frac{M_{j,Rd}}{M_{b,el}} \quad (7)$$

$$\bar{\theta} = \theta_{j,Rd} \frac{E_T \cdot I_b}{L_b \cdot M_{b,el}} \quad (8)$$

where $\theta_{j,Rd}$ is the joint rotation corresponding to $M_{j,Rd}$, evaluated as $M_{j,Rd}/S_{j,ini}$.

The results of the proposed joints classification by stiffness in terms of $\bar{m}$-$\bar{\theta}$ curves are reported in Figure 6.

https://doi.org/10.52202/069179-0390

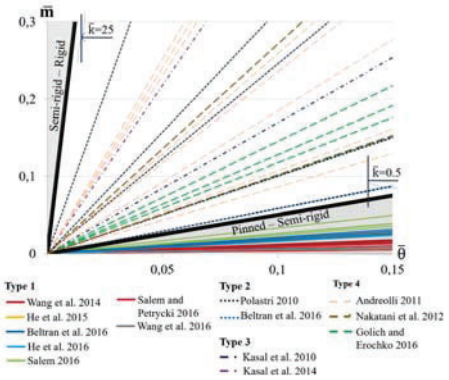

Figure 6: *Classification by stiffness of study joints.*

Table 3: *Classification by stiffness of study joints.*

Reference studies	$S_{j,pinned}$ [kNm/rad]	$S_{j,rigid}$ [kNm/rad]	$M_{j,el}$ [kNm]	$\theta_{j,el}$ [rad]	$S_{j,ini}$ [kNm/rad]
Type 1					
Wang et al. 2014	1759	87953	57.8	0.141	404.1
			35.6	0.101	334.5
			33.9	0.101	329.4
He and Liu 2015	2552	127602	22.2	0.092	256.2
			14.7	0.081	257.4
			27.1	0.113	276.3
Beltrán 2016	2215	110769	42.0	0.040	934.4
	1859	92985	89.6	0.041	2149.7
He et al. 2016	3362	168099	20.0	0.052	382.2
			20.0	0.012	1637.8
			20.0	0.012	1637.8
Salem and Petrycki 2016 Salem 2016	1561	78024	19.0	0.198	95.9
			22.4	0.157	142.5
			20.6	0.101	206.5
			24.0	0.092	260.8
			29.5	0.041	737.5
			16.8	0.021	800.0
			18.6	0.023	810.8
			10.3	0.010	1030.0
Wang et al. 2016	1826	91312	38.3	0.056	677.8
			36.9	0.063	585.7
Type 2					
Polastri 2010	3674	183695	61.4	0.014	4297.0
			80.1	0.004	18033.0
			134.2	0.002	60912.0
			105.7	0.014	7379.0
			134.1	0.018	7345.0
			128.4	0.006	23103.0
Beltrán 2016	2297	114871	55.2	0.072	796.8
	2303	115158	44.0	0.050	905.7
Type 3					
Kasal et al. 2010	43	2160	1.9	0.013	146.15
Kasal et al. 2014	2405	120269	90.2	0.004	20976.7
Type 4					
Andreolli 2011	401	20045	11.1	0.007	1480.0
			8.3	0.012	691.6
			15.08	0.008	1885.0
			10.3	0.011	936.4
			14.8	0.004	3700.0
			18.65	0.009	2072.2
			23.2	0.006	3858.3
			32.3	0.008	4036.3
Nakatani et al. 2012	985	49208	16.0	0.003	5333.3
			16.0	0.008	2000.0
			16.0	0.008	2000.0
Gohlich and Erochko 2016	4792	239643	86.0	0.008	9772.7
			99.1	0.008	11261.4
			110.2	0.009	12244.4
			125.0	0.009	13888.9

Pinned joint
Semi-rigid joint

3.3 ANALYSIS OF JOINTS CLASSIFICATION

As a result of the classification, for a total of 46 joints examined, 22 are pinned, while 24 are semi-rigid.

Among Type 1 joints, most connections are classified as pinned joints [3-5, 11-14], except one specimen [5], characterized by an internal T-shaped steel plate connected to the beam with a circular arrangement of screws and to the column with a rectangular arrangement of bolts, which is classified as semi-rigid joint.

Among Type 2 joints, the connections tested by Polastri [15], characterized by beam with double column and a circular arrangement of pins, or glued bars, or glued connection between timber members, are classified as semi-rigid joints, while the two specimens tested by Beltran [5], characterized by beam with double column and a circular arrangement of bolts, are classified as pinned joint.

Among Type 3 joints, the connection tested by Kasal et al. [1], characterized by two aluminium L-shaped plates and screws, as well as the connection tested by Kasal et al. [16], characterized by two timber rectangular-shaped plates and screws, are both classified as semi-rigid joints.

All timber joints equipped with steel link (Type 4) are classified as semi-rigid joints [2, 17, 18].

In particular, among the semirigid category, for Type 1, the beam-to-column joint tested by Beltran [5] with internal steel plate connected at the beam with a circular arrangement of screws and at the column with a rectangular arrangement of bolts is the only semi-rigid joint. It is worth noticed that it shows the lowest initial stiffness ($S_{C,ini}$=2149.7kNm/rad) than all the other studied semi-rigid joints. For Type 2, the joint with the greatest initial stiffness is the T07 specimen ($S_{T07,ini}$=60912kNm/rad) tested by Polastri [15], which is configured as a glued joint, characterized by the complete gluing of the timber members, confirming the lower deformation of the glued joints compared to the traditional ones. For Type 3, the joint specimen tested by Kasal et al. [16], which has two timber rectangular-shaped plates connected to the beam end top and bottom, shows a higher initial stiffness ($S_{A,ini}$=20976.7kNm/rad) than the joint specimen tested by Kasal et al. [1], which has angles located at the beam end top and bottom ($S_{A,ini}$=146.15kNm/rad). For Type 4, the joint with the greatest initial stiffness is the P20, followed by the P15-10 ($S_{P20,ini}$=4036.3kNm/rad; $S_{P15,ini}$= 3858.3kNm/rad; $S_{P10,ini}$=3700kNm/rad) beam-to-column joints equipped with steel link tested by Andreolli [17], with steel end-plate thicknesses equal to 20-15-10mm respectively and the connecting threaded bars glued in the beam. Next, the beam-to-column joints tested by Nakatani et al. [2], which have a box steel link connected to the timber beam and column with glued threaded rods, follows in the stiffness classification (S_{ini}=2000.0kNm/rad). At last, all beam-to-column joints equipped with steel link profile and dog-bone profile, tested by Golich and Erochko [18] ($S_{MC-1A,ini}$=13888.9; $S_{MC-1B,ini}$=12244.4kNm/rad), are classified as semi-rigid joints, showing high initial stiffness values.

4 CONCLUSIVE REMARKS

The paper focuses on the proposal of a method for the

https://doi.org/10.52202/069179-0390

mechanical classification of timber beam-to-column joints. In particular, the procedure for the mechanical classification of beam-to-column joints in timber MR framed structures is a suitable and efficient adaptation of that one related to steel joints presented in the Eurocode 3 part: 1-8, taking into account the timber structural features. The classification procedure, in terms of stiffness, has been applied to 46 joints studied through experimental tests in the scientific literature. Specifically, four types of joints have been identified: connection with internal or lateral vertical steel plate and connectors (Type 1); connection with connectors in circular arrangement (Type 2); connection with top and bottom plates or brackets and connectors (Type 3); timber joint equipped with steel link (Type 4). The classification of the joints in terms of stiffness has evidenced that 48% of the joints can be classified as pinned joints, while 52% of the joints can be classified as semi-rigid joints.

In particular, in semirigid joints category, beam-to-column joints with glued connection, such as the beam-to-column joint with glued connection between timber members tested by Polastri [15] and the beam-to-column joint equipped with steel link by means of 4 glued threaded bars tested by Andreolli [17], show higher stiffness values than the other joints tested:.

The study is in progress toward the application of the classification method to other beam-to-column joint types and configurations, whose moment-rotation curves have been achieved through experimental tests or even numerical investigations on well refined models, selected from the scientific literature. Moreover where the joints descriptions are completed of every mechanical details, the component method will be applied to better understand the contribution of the connection components features on the mechanical properties of the joints.

ACKNOWLEDGEMENT

The research project DPC–ReLUIS–WP13 – Contribution to standards for timber structures is acknowledged.

REFERENCES

[1] Kasal B., Heiduschke A., Pospisil S., Urushadze S.. Shake table tests of a three-story spatial timber frame with moment connections. In *World Conference on Timber Engineering (WCTE)*, 2010.

[2] Nakatani M., Mori T., Komatsu K.. Development of cross embedded joint using lagscrewbolt. In *World Conference on Timber Engineering (WCTE)*, 2012.

[3] He M.-j. and Liu H.-f.. Comparison of glulam post-to-beam connections reinforced by two different dowel-type fasteners. In *Construction and Building* Materials, 99–108*,* Elsevier Ltd, 2015.

[4] Wang M., Song X., ASCE A.M., Gu X., Zhang Y., Luo L.. Rotational Behavior of Bolted Beam-to-Column Connections with Locally Cross-Laminated Glulam. In *Journal of Structural Engineering*, ASCE, 2014.

[5] Beltran G.- G.. Local energy dissipators for skeleton structures. In *World Conference on Timber Engineering (WCTE),* 2016.

[6] Faggiano B., Iovane G.. First considerations on the design approach and criteria for seismic resistant moment resisting and bracings timber frames. In *World Conf. on Timber Engin.*, 2016. Paper ID1094.

[7] Faggiano B., Iovane G., Tartaglia R., Ciccone G., Landolfo R., Mazzolani F.M., Andreoli M., Tomasi R., Piazza M.. Numerical simulation of monotonic tests on beam-column timber joints equipped with steel links for heavy timber seismic resistant MRF. *16th Inter. Conf. Numerical Analysis and Applied Mathematics (ICNAAM)*, 2116, 2018.

[8] Iovane G., Faggiano B., Noviello C., Mazzolani F.M., Landolfo R., Faggiano B.. Beam-to-column joint with steel link for timber structures: system optimization through numerical investigations and design criteria. In *World Conference on Timber Engineering (WCTE)*, 2020.

[9] Iovane G., Faggiano B.. Timber beam-to-column joint with steel link: design and mechanical characterization through numerical investigation. *8th Intern. Conf. on Computational Methods in Structural Dynamics and Earthquake Engineering* (COMPDYN), 1:2359-2365, 2021.

[10] EN 1993-1-8: 2005: Eurocode 3: Design of steel structures - Part 1-8: Design of joints, CEN, French: Comité Européen de Normalisation.

[11] Wang K., Li Z., He M.. Investigation into the hysteretic performance of selfcentering timber beam-to-column joints. In *World Conference on Timber Engineering (WCTE)*, 2016.

[12] He M., Zhao Y., Ma R.. Experimental investigation on lateral performance of pre-stressed tube bolted connection with high initial stiffness. In *Advances in Structural Engineering*, Vol. 19(5) 762–776, 2016. DOI: 10.1177/1369433215622863.

[13] Salem S. and Petrycki A.. Experimental testing of wood-steel-wood momentresisting bolted connections. In *World Conference on Timber Engineering (WCTE)*, 2016.

[14] Salem S.. Experimental testing of steel-wood-steel glulam frame bolted connections. In *World Conference on Timber Engineering (WCTE)*, 2016.

[15] Polastri A. Caratterizzazione del comportamento di giunti sem-irigidi per strutture lignee in zona sismica. *PhD Thesis*, Supervisor: Prof. Maurizio Piazza, Prof. Ian Smith. University of Trento, University of Brescia, University of Padova, University of Trieste, University of Udine, University of Venezia, 2010.

[16] Kasal B., Asce M., Guindos P., Polocoser T., Asce S.M., Heiduschke A., Urushadze S., Pospisil S.. Heavy laminates timber frames with rigid three-dimensional beam-to-column connections. In *Journal of Performance of Constructed Facilities*, 28(6): A4014014, 2014.

[17] Andreolli M., Piazza M., Tomasi R., Zandonin R.. Ductile moment-resistant steel-timber connections. In Structures and Buildings, 164, SB2, 65-78, 2011.

[18] Gohlich R. and Erochko J.. Development of a heavy timber moment-resisting frame with ductile steel links. In *World Conference on Timber Engineering (WCTE)*, 2016.

World Conference on Timber Engineering Oslo 2023

SECOND GENERATION OF EUROCODE 5-2 ON TIMBER BRIDGES, AN OVERVIEW

Matthias Gerold [1], Hauke Burkart [2]

ABSTRACT: The Eurocodes are design standards published by CEN that are being updated. The first generation was published between 2002 and 2007. Work on the second generation is at different stages, with a common implementation expected in 2027/2028. Design rules on Timber Bridges is published as EN 1995-2.

The second generation implements new knowledge gained the last 20 years. Within timber structures this is quite a fair amount. The mandate given by the European Union, being a large financier of the work, was to improve the structure and clarity of the code, reduction of nationally determined parameters and reduction of alternative equivalent application rules and procedures, removal of rules that are little in use and explanation of the mechanical background of formulas.

Consolidation on design practice has been a great part of the work. Though calculating timber bridges has been conducted in a common way, protecting the timber is as much tradition as it is architectural taste. A timber bridge according to the Eurocode is expected to endure for its design service life independent on being located far south or far north in Europe. The term protected timber bridge is introduced, where weathering is not expected to govern the service life.

All parts of EN 1995-2 have been examined and updated if needed, as here presented.

KEYWORDS: Timber Bridges, Design rules, Eurocode

1 INTRODUCTION

In 2004, the EU and several EFTA states introduced uniform design codes, the so-called EUROCODEs (EC). The goal of the European Committee for Standardization (Comité Européen de Normalisation, CEN) here was to replace the member states' differing or even missing design guidelines by a common set of technical rules that provide the same level of safety and thereby to further minimise barriers within Europe. In 2012, the European Commission issued a mandate for the development of a second generation of the Eurocodes to ensure their long-term applicability and reflect the constant technical developments and knowledge gains (see Figure 1).

Figure 1: *European design codes – Eurocodes*
Source: European Commission, 2021

In the work of 2nd generation Eurocodes updates in Eurocode 0 and 1 forced updates for the other parts. For the series of standards "EN 1995 – Design of timber structures," (EC 5) experts regularly prepare drafts for specific topics in timber construction. To this purpose, six project teams (PT) have been convened from 2015 to 2022. Today, their work is continued by ten working groups (WG), which before the start of project teams conducted a review of existing content of the EC5, in cooperation and coordination with the national standardisation bodies. After extensive revision of the entire Eurocode 5 series, new versions will be available for all members states for enquiry September 2023, following expected formal vote in 2025 and publication around 2027.

2 SUSTAINABLE TIMBER BRIDGE CONSTRUCTION

One of the main topics of editing EN 1995-2 was the implementation of the specifications of EN 1990 and EN 1991-2, in particular requirements for reaching a design service life of 100 years. Since construction professionals speak the language of implementation planning, a new Annex is suggested with simplified figures exemplifies how timber bridges can be protected given proper service. Service is topic in another new suggested annex covering inspection and maintenance of timber bridges. Both

[1] Matthias Gerold, Harrer Ingenieure, Karlsruhe, Germany, m.gerold@harrer-ing.net
[2] Hauke Burkart, Standards Norway, Norway, hbu@standard.no

https://doi.org/10.52202/069179-0391

annexes are informative and may be subject to changes nationally.
Like the building construction code, the code for timber bridges was extended to include requirements and regulations for the durability of structures, taking into account the issues of corrosion protection, deck plates, and timber-concrete composites. The creep factors for concrete in timber-concrete composite bridges are different from those in known building constructions, as the cross-sections are significantly larger. Accordingly, a new normative Annex A of prEN 1995-2 provides relevant conditional equations. prEN 1995-1-1 shall stipulate requirements for numeric analyses (keyword Finite Element Method, or FEM for short).
Eurocode 8, Part 2 ("Design of structures for earthquake resistance"), will in 2nd generation take timber bridges into account. In an Informative Annex, additional hints for the design of bearings are given. It is also relevant to point to the Informative Annex E, which contains suggestions to be considered in view of deformations and dimensional changes of timber constructions under changing environmental conditions such as temperature or timber moisture, and notes on transversely prestressed timber deck plates (among other things for the "cupping" of the deck sides).
Most regulations on deck plates (timber decks) were added to one normative and one informative Annex of prEN 1995-1-1, as these regulations can also be applied to, e.g., nail-laminated timber constructions.
With the technical work basically being done, the document is being translated into German and French before being sent on public Enquiry for 16 weeks starting September 2023. The remaining steps of the standardisation process are shown in [1] and [2].

3 PROTECTION AND SERVICE LIFE

3.1 DURABILITY OF WOODEN MEMBERS

General requirements regarding expected service life, i.e. design service life T_{lf}, form the basis for all bridge design in Eurocodes are given in EN 1990 A.2. Together with requirements on Quality Management are the requirements on Maintenance and Durability that form the basis of bridge building. The latter are defined as:

Maintenance
set of activities performed during the service life of the structure so that it fulfils the requirements for reliability

Durability
Ability of a structure or structural member to satisfy, with planned maintenance, its design performance requirements over the design service life

Based on this, different categories are defined for expected service life. For bridges 100 years is the basic option or choice, and is expected independent of material types. Lower service life may be relevant for simple bridges used for instance in recreational purposes where consequence of failure is very little, but still 50 years are expected. Further lower service life is given for replaceable and temporary structures.
For timber bridges, achieving 50 years, which is the same as building structures and thus the design requirements in the general part of Eurocode 5 are to be used. Requirements for 100 years service life are outlined in the bridge part, comprising:
- Requirements on design;
- Recommendations on structural protection;
- Requirements membranes;
- Requirements on steel protection embedded in timber structures.

Environmental actions, i.e. expected moisture variations and thermal actions, are included in simplified calculation models depending on member size. General information on moisture variations are given in the main part.

For the design of durable timber bridges the term protected and unprotected member are included. Protected member is defined as:

Protected Member
structural member not exposed to direct weathering such as rain, snow, or other sources of moisture ingress

Examples of protected members are given see Figure 2, see also [3]

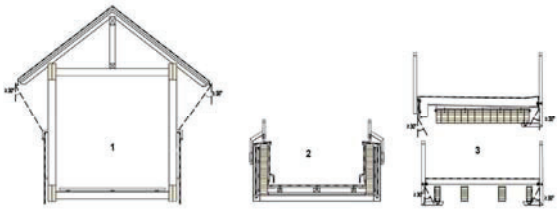

Figure 2: *Examples of protected timber bridges*

Key

membrane or weather-resistant layer

Unprotected member is defined as:

Unprotected Member
structural member that is not protected or partially unprotected from weathering but is within the limits of Service Class (SC) 3

The methodology is that a protected timber bridge is expected to last for 100 years. When parts of a structures are not within the definition of a protected member these must either be easily replaceable, or the expected design service life will be less than 100 years.
Durability and thus sustainability ensure the economic viability of timber structures. Therefore, the following so-called "magic triangle" must be observed:

https://doi.org/10.52202/069179-0391

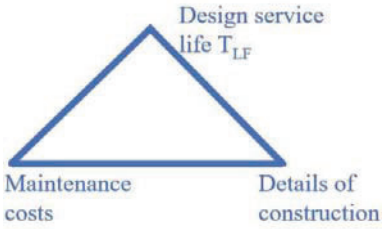

Figure 3: *Important considerations on design*

Requirements on basic structural protection are given in EN 1995-1-1 and EN 1995-2, in some countries with additional national requirements. This leads to a higher robustness of the expected service life, expecting to lower maintenance costs.

2nd generation of EN 1995-2 includes detailing by figures in Annex how timber bridges can generally be protected. Five possibilities for basic structural timber protections are given (see e.g. Figure 4), together with more detailed examples on expansion joints (three methods; see e.g. Figure 5) and bridge caps (2 examples).

Furthermore, a suggested monitoring scheme is included as monitoring timber bridges may be a useful addition to inspection, in some European countries mandatory. Currently an arch bridge is taken as example showing which parts of the bridge are expected to be critical and thus wise instrumenting, also with regard to the Use Class according to EN 355.

Because of translation of European standards all figures are language neutral, creating rather lengthy keys to each figure.

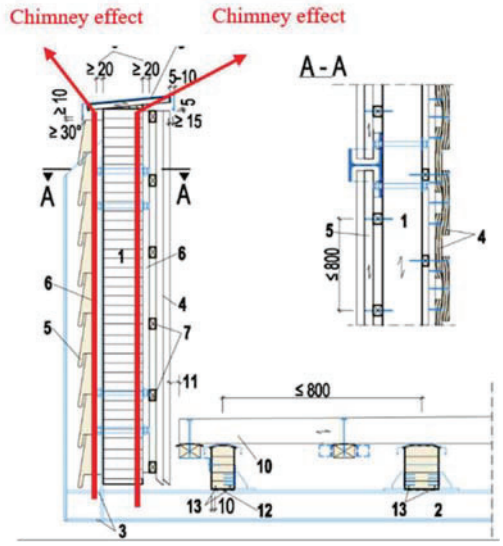

Figure 4: *Example of detailing figure with explanation text on ventilation in red*

Key

A-A	Section A – A
1	Main girder
2	Steel frame
3	Borehole in top and bottom flange
4	Cladding (generally outside)
5	Vertical weather boarding (outside)
6	Vertical battens
7	Horizontal battens
8	Ventilation openings, horizontal ≥ 100 cm²/m, vertical ≥ 50 cm²/m
9	Aluminium plate or equivalent
10	Grooved planks (e.g.)
11	Gap with: 15 mm if floor-cover shuttering, 30 mm if cover stripe, groove and tongue
12	Rubber or elastomer mat
13	Weather groove (notch)

The ventilation openings for such a detail should be the following:

- Horizontal ≥ 100 cm^2 / m
- Vertical ≥ 50 cm^2 / m
- Minimum width 20 mm

https://doi.org/10.52202/069179-0391

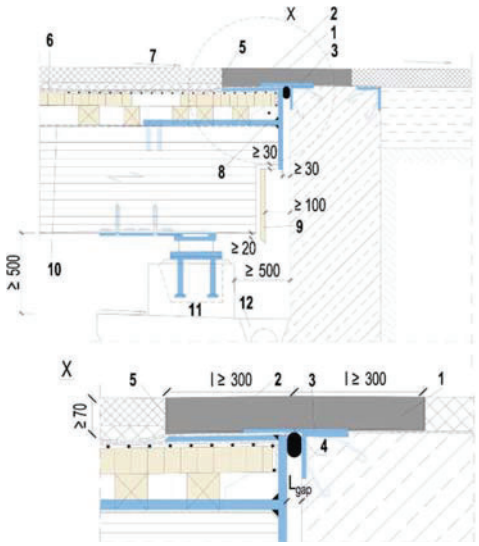

Figure 5: *Example of detailing on a closed transition between bridge and abutment*

Key

X	Detail "X"
1	Trough filling
2	Surface seal
3	Cover strip
4	Fixing peg
5	Trough flank
6	Sealing system
7	Longitudinal gradients
8	Closing profile (steel)
9	Face board
10	Permeable protection layer with glued overlapping
11	Pier
12	Drainage

3.2 DURABILITY OF STEEL MEMBERS

For steel members the updated standard gives requirements of protection of steel members in wooden structures by declaring a timber exposure category class T_E. Different protection levels depending on atmospheric exposure C_E, service class SC and expected design service life results in different recommendations of minimum protection either by steel grade or zinc coverage. Requirements of protection of steel in general is covered by Eurocode 3.

Situation	*Timber exposure category* [a] T_E	*Atmospheric exposure category* [b] C_E	*Typical atmospheric exposure* [c] *(informative)*	*Examples of minimum*	
				zinc thickness [d]	*stainless steel grade (type)* [e]
Protected outdoor with access of pollution (SC2 and SC3)	T_E3/T_E4	C_E2	L_{sea} > 10 km L_{street} > 100 m and/or low polluted area (< 5 µg/m³ of SO_2)	T_R3: 40 µm [f] (n/a [g]) if T_E4) [20 µm [f] (55 µm if T_E4)] [h]	CRC II (e.g. 1.4301)
	T_E3/T_E4	C_E3	10 km > L_{sea} > 3 km 100 m > L_{street} > 10 m and/or medium polluted area (5 µg/m³ ≤ SO_2 ≤ 30 µm/m³)	C_R3: 110 µm [80 µm] [h]	CRC III (e.g. 1.4401)
	T_E3/T_E4	C_E4	3 km > L_{sea} > 0,25 km L_{street} < 10 m and/or high polluted area (30 µg/m³ < SO_2 ≤ 90 µm/m³)	C_R4 [b]: n/a [g] [110 µm] [h]	CRC III (e.g. 1.4401)
	T_E3/T_E4	C_E5	L_{sea} < 0,25 km and/or very high polluted area (90 µg/m³ < SO_2)	C_R5 [b]: n/a [g]	CRC III (e.g. 1.4529)
Permanent in contact with ground- or fresh-water (SC4) [i]	T_E5	n/a [g]	For T_E5/SC4 especially in case of seawater each case should evaluated individually.	C_R5 [b]: n/a [g]	CRC III to CRC V

[a] *Timber exposure categories T_E3, T_E4 and T_E5 are according to prEN 1995-1-1:202x, Table 6.1*

[b] *Atmospheric exposure categories C_E2, C_E3, C_E4 and C_E5 are according to prEN 1995-1-1:202x, Table 6.2 and Table 6.3*

[c] *The specified values for SO_2 are references values only and may vary.*

L_{sea} indicates distance from the sea. The actual exposure depends on the prevailing wind direction and the topography of the coast to saltwater seas e.g. Atlantic Ocean, North Sea, Baltic Sea, Mediterranean See, Black Sea, Irish Sea

L_{street} indicates distance from roads with heavy traffic with de-icing salt

[d] *pure zinc coating and hot-dipped galvanized coating*

T_R3 is the timber resistance class according to prEN 1995-1-1:202x, 6.3

C_R are the resistance classes for metal fastener or connector made of carbon steel to corrosion according to prEN 1995-1-1:202x, 6.3

Figure 6: *Current proposal on protection of steel members embedded in timber in prEN 1995-2. Numbers in red are for 50 years, other values 100 years.*

4 TIMBER DECK PLATES

Timber deck plates comprise decks made of solid-wood beams arranged side by side in the direction of span, clamped together. As a result, the (punctual) wheel loads can be distributed over several beams (see prEN 1995-1-1 Figure U.3). Nowadays, these deck plates (timber decks) are largely used in Scandinavian and Baltic states often using glued laminated timber (GL) as beams and stressed together with steel rods. Requirements regarding these structures have been updated representing state of the art including newer research on the topics. This also includes requirements on modelling of the bridge decks using Finite Elements Software (see prEN 1995-1-1 Annex V) as well as updated recommendations on friction coefficients and requirements to minimum stress forces.

https://doi.org/10.52202/069179-0391

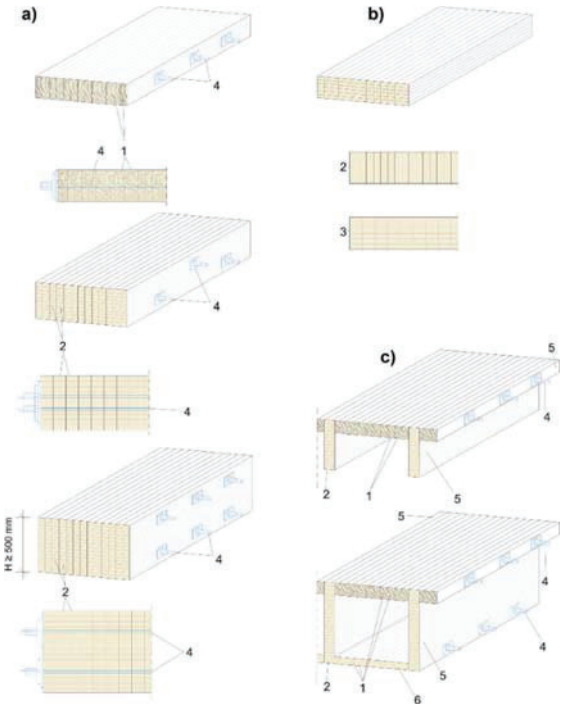

Figure 7: *Examples of timber bridge decks covered in prEN 1995-2*

5 TIMBER-CONCETE COMPOSITE (TCC) AND INTEGRAL ABUTMENTS

TCC decks are included in the updated bridge standard, giving requirements on design and recommendations on durability and design. Creep must be evaluated carefully and as such this is also topic in the updated draft. For a more detailed presentation on the topic see [5] presentation from Mr. Prof. Dr.-Ing. Jörg Schänzlin

Integral timber bridges, bridges with a flexural connection to a concrete abutment, have gained some experience and are also included in the timber bridge code.

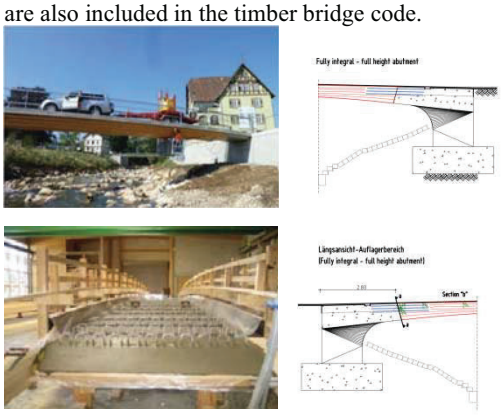

Figure 8: *Examples of integral timber bridge designs.*

6 SERVICE LIMIT STATE

6.1 DEFLECTIONS AND DEFORMATIONS

Requirements on deflections due to traffic-load and wind-force have been updated. These actions should be verified and limited in order to prevent unwanted dynamic impact due to traffic, infringe of required clearances and cracking of surfacing layer, ensuring also sufficient run-off from standing water (see [2]).

6.2 OSCILLATIONS AND DAMPING

A rather large update has been conducted on the subjects oscillations and damping. Simplification regarding requirements given in other parts of Eurocodes are introduced in the timber bridge part. An example is shown in figure 9, where different requirements are gathered in one requirement, see black line in figure 9.

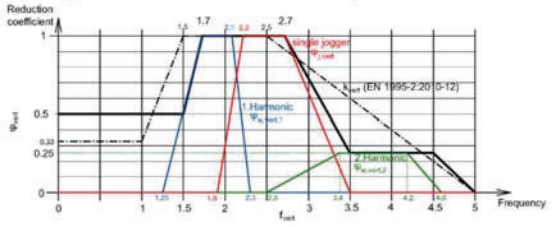

Figure 9: *Examples of integral timber bridge designs.*

For further reading see [4] presentation by Mrs. Prof. Dr.-Ing. Patricia Hamm

7 FATIGUE

It was decided to move fatigue requirements into the general part as these may be necessary also for buildings with cyclic loads, such as crane structures, wind turbine tower, highway traffic sign posts, or bell towers. This means that in EN 1995-2, only those parts were kept that are relevant for timber bridges, in particular:

- some general parts concerning the fatigue assessment of timber structures;
- parts of the document that deal with fatigue load models;
- a simplified fatigue verification model especially for bridges.

Basis in fatigue verification is the stress ratio R_T as the arithmetical minimum stress to the maximum stress of a particular stress cycle in timber design. Since the factor representing the reduction of fatigue strength with number of load cycles k_{fat} values depend on RT, a simplification is also required to offer a real advantage over the 'full' k_{fat} verification. Therefore, it is proposed to consider only whether the fatigue loading is alternating or not and to use the k_{fat} values for $R_T = 0$ or $R_T = -1$, respectively.

The k_{fat} values were evaluated for two lanes and 2*106 cycles (trucks), giving anticipated 100 years design service life using an ß-factor equal to 3 (substantial consequences). This yields a design load cycle number of $1.2*10^9$.

https://doi.org/10.52202/069179-0391

8 PERSPECTIVE

The completion of the work on the European timber construction standards is scheduled for 2026/2027, which still seems far-off. Current status for the timber bridge code is that it is made ready for public Enquiry by september 2023 together will all other parts on timber structures (i.e. part 1-1 General rules and rules for buildings, part 1-2 Fire design and part -3 Execution). After Enquriry no new technical content will be added, only changes to what is suggested will be made, thus most of the essential changes are already known. The scope of the standard will inevitably grow, as new timber construction products need to be considered and known design approaches need to be extended and optimised. The update is guided by the central interest of increasing the user-friendliness – not only by profiting from digital availability and efficient search options but also by restructuring, homogenising, and simplifying the regulations. Nevertheless, as with the adjustment of the first generation of Eurocode 5, an additional process of learning, training, and education will be necessary, with this process starting already prior to the final publication. In conclusion, it may be stated: the second generation of Eurocode 5 is not a revolution but an evolution that consistently builds on the experiences and principles of the previous version.

ACKNOWLEDGEMENT

The authors would like to acknowledge the work done by members of both project team 6 and working group 6 of CEN/TC 250/SC 5 to their contributions over a very long period. In total more than 30 experts have contributed to this work.

REFERENCES

[1] Schenk, M.; Werther, W.; Gerold, M.: The Next Generation – Die Weiterentwicklung der Holzbaubemessung nach Eurocode 5. Quadriga, H. 6, p. 16–19, 2022

[2] Müller, A.; Schiere, M.; et al.: Details for timber bridges with asphalt wearing surfaces. 4th International Conference on Timber Bridges ICTB2021PLUS, Biel (Switzerland), 2022

[3] Gerold, M.: The further Development of the Design of Timber Structures according to Eurocode 5 – Part 2: Timber Bridges. Overview EN 1995-2 and Annex D Examples for Detailing. 4th International Conference on Timber Bridges ICTB2021PLUS, Biel (Switzerland), 2022

[4] Hamm, P: Vibration, Deflections. 4th International Conference on Timber Bridges ICTB2021PLUS, Biel (Switzerland), 2022.

[5] Schänzlin, J.; Dias, A.: TCC and Integral Bridges. 4th International Conference on Timber Bridges ICTB2021PLUS, Biel (Switzerland), 2022.

World Conference on Timber Engineering Oslo 2023

TALL WOOD BUILDINGS WITHIN THE 2020 NATIONAL BUILDING CODE OF CANADA

Marc Alam[1], Rodney McPhee[1]

ABSTRACT: In the past decade, many examples have been seen where large and tall buildings of mass timber construction have been built around the world, including here in North America. This paper summarizes the approved provisions within the 2020 National Building Code of Canada (NBC) to allow tall wood buildings up to 12 storeys. The paper will include discussion about the historical precedent of moving away from the NBC prescriptive approach of recognizing only two primary types of construction ─ combustible and noncombustible construction ─ and provide details introducing a new third type of construction called 'encapsulated mass timber construction' (EMTC), which is required to be used for these tall wood buildings. This includes details on current fire research on mass timber construction and the proposed new prescriptive fire protection requirements introducing EMTC within the 2020 NBC.

KEYWORDS: Tall wood buildings, 2020 National Building Code of Canada, Encapsulated mass timber construction

1 INTRODUCTION

The Canadian Commission on Building and Fire Codes (CCBFC), approved changes in the 2020 National Building Code (NBC) to allow construction of tall wood buildings up to 12 storeys in height. This proposal includes a new construction type called 'encapsulated mass timber construction' (EMTC). EMTC is generally defined as a type of construction where a degree of safety is attained through a combination of prescribed minimum sizes of structural mass timber elements and a minimum time for these elements to be protected from fire (encapsulated) using a noncombustible protective membrane.

2 NBC CONSTRUCTION TYPES

2.1 EXISTING CONSTRUCTION TYPES

The 2015 NBC contained two primary construction types: noncombustible and combustible construction. These construction types have been in the NBC since the 1960s. 'Noncombustible construction' means '*that type of construction in which a degree of fire safety is attained by the use of noncombustible materials for structural members and other building assemblies*' [1] (e.g., concrete, steel, masonry). 'Combustible construction' means '*that type of construction that does not meet the requirements for noncombustible construction*' [1] (e.g., wood frame, masonry joist, etc.). There is a subset of combustible construction referenced in the NBC known as 'Heavy Timber Construction' that is defined as '*that type of combustible construction in which a degree of fire safety is attained by placing limitations on the sizes of wood structural members and on the thickness and composition of wood floors and roofs and by the avoidance of concealed spaces under floors and roofs*' [1].

Buildings of noncombustible construction can be of unlimited height and unlimited area when they are designed with a 2-hour structural fire-resistance rating and sprinklered throughout. Buildings of combustible construction are limited to a maximum building height of six storeys, with a maximum six storey building area of 1,500 m^2 (16,145 ft^2) for residential occupancies or 3,000 m^2 (32,290 ft^2) for business and personal services occupancies, when they are designed with a 1-hour structural fire-resistance rating and sprinklered throughout.

2.2 NEW CONSTRUCTION TYPE

The Canadian Wood Council submitted a Code Change Request (CCR) package to the CCBFC in 2016 to introduce provisions in the NBC permitting tall wood buildings above six storeys when constructed with a new construction type called 'Encapsulated Mass Timber Construction' (EMTC). The CCR package was reviewed by the CCBFC Standing Committee on Fire Protection (SC-FP). The SC-FP is made up of volunteers chosen for their fire protection expertise to represent all facets of the construction industry from across Canada. Following lengthy discussions and analysis, the SC-FP developed revised wordings for the proposed changes, which were posted for review and comment as part of three public reviews in 2017, 2018, and 2019. In resolving the public comments, the final wording of the changes were

[1]Marc Alam, Canadian Wood Council, Canada, malam@cwc.ca
[1]Rodney McPhee, Canadian Wood Council, Canada, rmcphee@cwc.ca

https://doi.org/10.52202/069179-0392

approved by the SC-FP and recommended to the CCBFC to be included in the 2020 NBC.

EMTC means '*that type of construction in which a degree of fire safety is attained by the use of encapsulated mass timber elements with an encapsulation rating and minimum dimensions for the structural timber members and other building assemblies*' [2]. In simple terms, EMTC is defined as the combination of two components: encapsulation rating and minimum dimensions of structural mass timber members.

2.2.1 Encapsulation Rating

The first component of EMTC, the 'encapsulation rating', is defined as '*the time in minutes that a material or assembly of materials will delay the ignition and combustion of encapsulated mass timber elements when it is exposed to fire under specified conditions of test and performance criteria, or as otherwise prescribed by this Code*' [2]. The encapsulation rating is determined using a new standard fire test method, CAN/ULC-S146 "*Standard Method of Test for the Evaluation of Encapsulation Materials and Assemblies of Materials for the Protection of Mass Timber Structural Members and Assemblies*" [3]. The fire exposure conditions used in this new test method is the same as the standard time-temperature curve (see Figure 1) from CAN/ULC-S101, "*Standard Methods of Fire Endurance Tests of Building Construction and Materials*" [4]. This is the same time-temperature curve from ASTM E119, "*Standard Test Methods for Fire Tests of Building Construction and Materials*" [5], and similar to time-temperature curve from ISO 834, "*Fire-Resistance Tests*" [6] (see Figure 1).

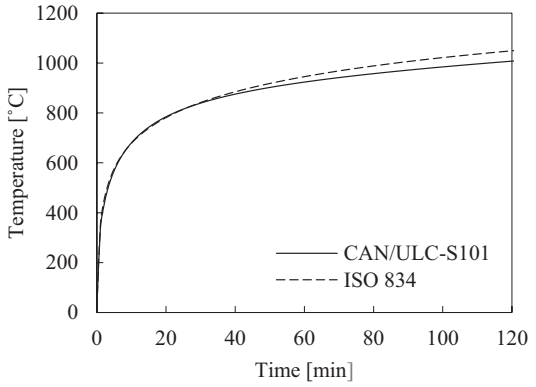

Figure 1: *CAN/ULC-S101 and ISO 834 standard time-temperature curves*

In CAN/ULC-S146, the encapsulation material or assembly of materials are applied to a timber substate and tested within a horizontal furnace with a minimum specimen size of 3.66 m (12 ft) x 3.66 m (12 ft). Unless otherwise prescribed, the encapsulation material or assembly of materials must be noncombustible and is assigned an encapsulation rating that relates to the lesser of the times at which an average temperature rise of 250°C (482°F) or a maximum temperature rise of 270°C (518°F) is recorded at the interface (see Figure 2) of the encapsulation material(s) and the wood substrate that is part of the test specimen.

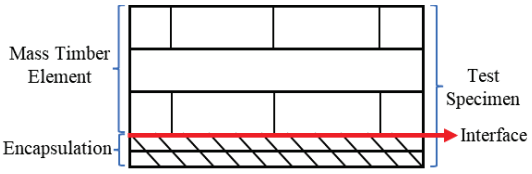

Figure 2: *Temperature interface location in the test specimen*

The minimum encapsulation rating prescribed by the NBC for EMTC is 50 minutes, but in some special cases, a 25-minute rating is permitted. The 2020 NBC provisions also include specifications that describe generic materials that are otherwise deemed to meet the 50-minute encapsulation rating: 2 layers of not less than 12.7 mm (1/2 in) thick Type X gypsum board and not less than 38 mm (1-1/2 in) thick gypsum-concrete or concrete topping. Type X gypsum board, conforming to ASTM C1396 "*Standard Specification for Gypsum Board*" [5], is a fire-resistant board that is manufactured with glass fibre reinforcements and other additives to help limit thermal degradation due to fire exposure [8].

2.2.2 Minimum Dimensions for Timber Members

The second component of EMTC, the minimum dimensions required for the structural mass timber members are shown in Table 1:

Table 1: *Minimum dimensions of mass timber elements*

Structural Wood Elements	Minimum Thickness, mm	Minimum Width × Depth, mm × mm
Wall that is a fire separation or exterior wall (1-sided exposure)	96	-
Wall that requires a fire-resistance rating but is not a fire separation (2-sided exposure)	192	-
Floors and Roofs (1-sided exposure)	96	-
Beams, columns and arches (2- or 3-sided fire exposure)	-	192 × 192
Beams, columns and arches (4-sided fire exposure)	-	224 × 224

Note: Fire separation means a construction assembly that acts as a barrier against the spread of fire [2].

These minimum dimensions are prescribed to increase the likelihood that the timber elements, once they are burning, will exhibit the fire performance characteristics of mass timber rather than of lightweight, small-dimensioned wood elements. This means that after initiation of charring, the timber elements will still be thermally thick for the required fire-resistance rating period [7].

3 CODE REQUIREMENTS

3.1 HEIGHTS AND AREA

The 2020 NBC provisions prescribe the height and area limits for buildings constructed of EMTC. Building height (in storeys) is defined as '*the number of storeys contained*

https://doi.org/10.52202/069179-0392

between the roof and the floor of the first storey.' [1] The building height limit is 12 storeys, with a 42-meter (138-foot) physical height limit (see Figure 3) that is also mandated for the building, which is measured between the floor of the first storey and the uppermost floor level. The first storey is defined as '*the uppermost storey having its floor level not more than 2 m (6.5 ft) above the lowest of the average levels of finished ground adjoining each exterior wall of the building.*'

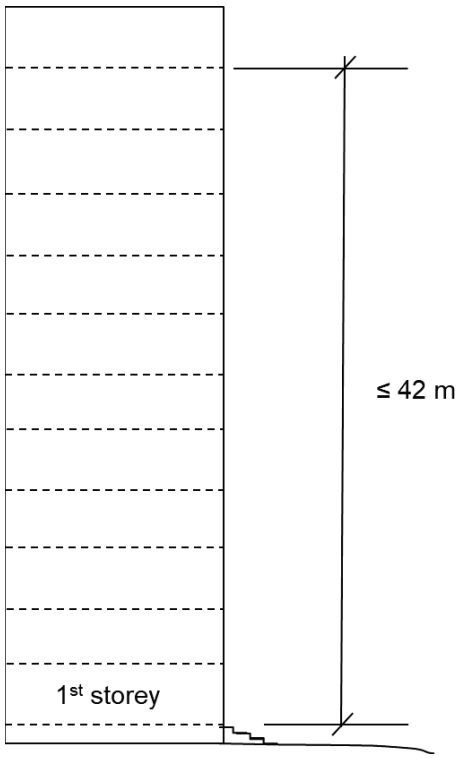

Figure 3: *Physical height limit of EMTC buildings*

Building area means '*the greatest horizontal area of a building above grade within the outside surface of exterior walls or within the outside surface of exterior walls and the centre line of firewalls'* [1]. For buildings constructed of EMTC, the maximum building area for any building height is 6,000 m^2 (64,585 ft^2) for a residential occupancy and 7,200 m^2 (77,500 ft^2) for a business and personal services occupancy.

3.2 FIRE-RESISTANCE AND SPRINKLERING

Fire-resistance ratings within the NBC are determined on the basis of results of standard fire tests conducted in conformance with CAN/ULC-S101 [4]. Within buildings constructed of EMTC, floor assemblies are required to be fire separations, with a fire-resistance rating of not less than 2 hours, and mezzanines shall have a fire-resistance rating of at least 1 hour. Loadbearing walls, columns and arches shall have a fire-resistance rating not less than that required for the supported assembly.

Buildings constructed of EMTC are required to be sprinklered throughout, with the automatic sprinkler system designed in accordance with NFPA 13, "*Standard for the Installation of Sprinkler Systems*" [8].

3.3 OCCUPANCY TYPES

The NBC classifies occupancy (building use) types within 6 different Groups. The main occupancy types permitted on all storeys in buildings constructed of EMTC are Group C, residential and Group D, business and personal services occupancies. Other occupancy types are permitted on the lower storeys as follows: Group E, mercantile occupancy, on the first and second storey, Group A2, assembly occupancy, up to the third storey, and storage garages up to the fourth storey. In addition, Group F2 and F3, medium- and low-hazard industrial occupancies are permitted on the first and second storeys of buildings with a Group D occupancy (See Figure 4).

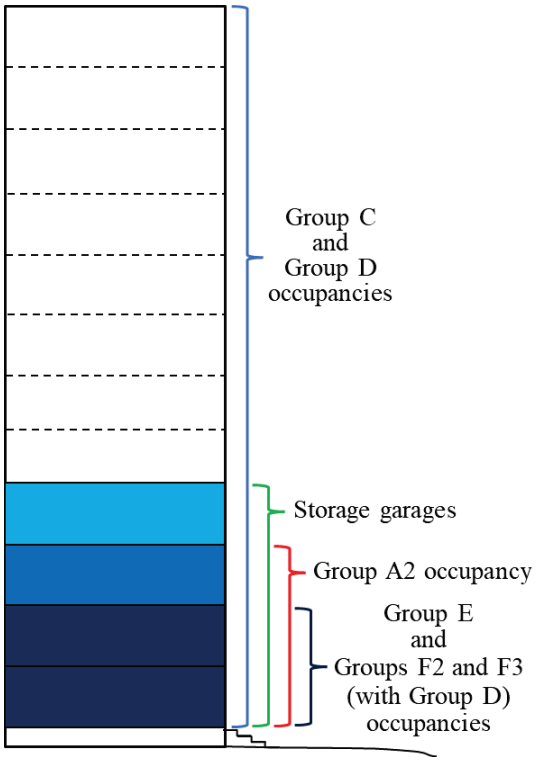

Figure 4: *Allowable occupancy type locations*

3.4 COMBUSTIBLE MATERIALS PERMITTED

Combustible materials are permitted within buildings of EMTC. These include combustible roofing materials, window sashes and frames, exterior cladding, components in exterior walls, nailing elements, stairs, interior finishes, elements in partitions, raised wood floors, concealed spaces, and non-loadbearing wood frame partitions. The provisions regarding combustible components that require more detail are explained below.

3.4.1 Exterior Cladding

Generally, exterior walls and cladding on a building constructed of EMTC shall be noncombustible. Cladding on wall assemblies tested in accordance with CAN/ULC-

https://doi.org/10.52202/069179-0392

S134, "*Fire Test of Exterior Wall Assemblies*" [11] is also permitted, along with some very limited amounts of combustible cladding that are arranged in accordance with three specific design approaches.

CAN/ULC-S134

The CAN/ULC-S134 methodology is a full-scale standard fire test for exterior walls. This fire test evaluates fire spread on the exterior of buildings that have combustible cladding or other combustible components within the exterior wall.

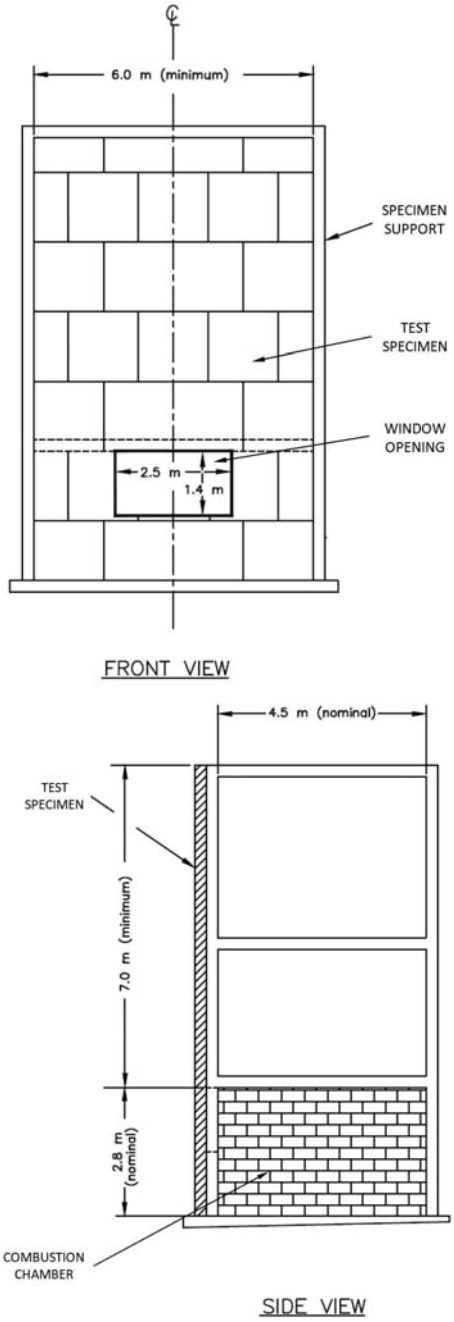

Figure 5: *Typical CAN/ULC-S134 test facility* [11]

The test facility (see Figures 5 and 7) consists of a façade with a minimum 6 m (19.7 ft) width and 9.5 m (31.2 ft) height. The burn room located on the lowest level is 6 m (19.7 ft) wide by 4.5 m (14.8 ft) deep by 2.8 m (9.2 ft) high with a 2.5 m (8.2 ft) wide by 1.4 m (4.6 ft) high window opening. The mass flow rate of gas (shown in Figure 6) shall be adjusted throughout a period of 25 min followed by an observation period of 35 min. From the start of the test (ignition), the gas flow is increased linearly for 5 min, followed by a 15 min steady state period, followed by another 5 min period of linear decrease to zero.

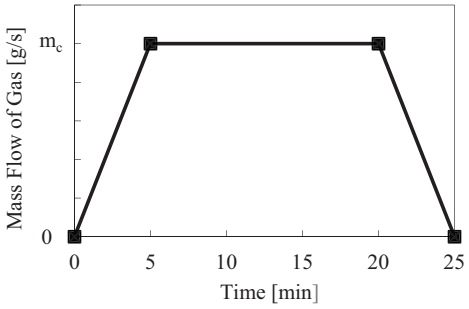

Figure 6: *Mass flow of gas vs time* [11]

The steady mass flow rate of gas, m_c, consists of flames emerging from the opening exposing the outer face of the wall to a heat flux density of 45 ± 3 kW/m^2 at 0.5 m above the top of the opening and 27 ± 2 kW/m^2 at 1.5 m above the top of the opening.

Figure 7: *Example CAN/ULC-S134 test*

Exterior combustible cladding and combustible exterior wall assemblies tested in accordance with CAN/ULC-S134 shall be permitted in buildings constructed of EMTC if they satisfy the following criteria: flaming on or in the

https://doi.org/10.52202/069179-0392

wall assembly does not spread more than 5 m (16.4 ft) above the opening and the heat flux during the flame exposure on the wall assembly is not more than 35 kW/m^2 measure at 3.5 m (11.5 ft) above the opening [1]. The 2020 NBC will include descriptions of generic exterior wall assemblies deemed to satisfy the criteria. These assemblies are shown in Table 2.

Table 2: *Generic CAN/ULC-S134 exterior wall assemblies* [2]

Structural Members	Absorptive Material	Sheathing	Cladding
38 mm × 89 mm wood studs spaced at 400 mm o.c.	89 mm thick rock or slag fibre in cavities formed by studs	-	12.7 mm thick fire-retardant-treated plywood siding
140 mm thick rock or slag fibre in cavities formed by studs	140 mm thick rock or slag fibre in cavities formed by studs	Gypsum sheathing ≥ 12.7 mm thick	Noncombustible exterior cladding
38 mm × 140 mm wood studs spaced at 400 mm o.c.	140 mm thick rock or slag fibre in cavities formed by studs	15.9 mm thick fire-retardant-treated plywood	Noncombustible exterior cladding
38 mm × 140 mm wood studs spaced at 600 mm o.c. attached CLT wall panels ≥ 38 mm thick	140 mm thick glass, rock or slag fibre in cavities formed by studs	Gypsum sheathing ≥ 12.7 mm thick	Noncombustible exterior cladding
89 mm horizontal Z-bars spaced at 600 mm o.c. attached to CLT wall panels ≥ 105 mm thick	89 mm thick rock or slag fibre in cavities formed by Z-bars	-	Noncombustible exterior cladding attached to 19 mm vertical hat channels spaced at 600 mm o.c.

Combustible Cladding

As noted earlier, along with noncombustible cladding and cladding on walls tested in accordance with CAN/ULC-S134, the 2020 NBC will permit three approaches to allow the use of combustible cladding on exterior walls of buildings constructed of EMTC.

The first approach allows for not more than a 10% portion of the exterior cladding on each storey to be combustible and any such portion shall not be contiguous over more than 4 storeys. With this approach, each contiguous combustible cladding portion shall have a maximum width of 1.2 m (3.9 ft). They must also be separated from other portions on the same storey by a horizontal distance of not less than 1.2 m (3.9 ft) and from other portions on the adjacent storeys by a horizontal distance of not less than 2.4 m (7.9 ft). The combustible cladding shall have a flame-spread rating of 75 when tested to CAN/ULC-S102, "*Standard Method of Test for Surface Burning Characteristics of Building Materials and Assemblies*" [12]. Flame-spread rating means '*an index or classification indicating the extent of spread-of-flame on the surface of a material or an assembly of materials as determined in the standard fire test*' [1].

The second approach also allows for not more than a 10% portion of the exterior cladding on each storey to be combustible, and does not impose the 1.2 m width limit, but any such portion shall not be contiguous across adjacent storeys. As such, the maximum total width of any portion (aggregate width for multiple portions on the same storey) is limited to 10% of the storey width. For portions on adjacent storeys, they shall be separated by a distance of not less than 2.4 m (7.9 ft). Similarly, the combustible cladding shall have a flame-spread rating of 75 when tested to CAN/ULC-S102.

The third approach allows for up to 100% of the cladding on exterior walls of the first storey, provided all of the combustible cladding can be directly accessed and are located not more than 15 m (49.2 ft) from a street or access route, measured horizontally from the face of the building [2].

These approaches can be applied individually or in combination as shown in Figure 8. All other portions of cladding that are not combustible are required to be noncombustible or tested in accordance with CAN/ULC-S134.

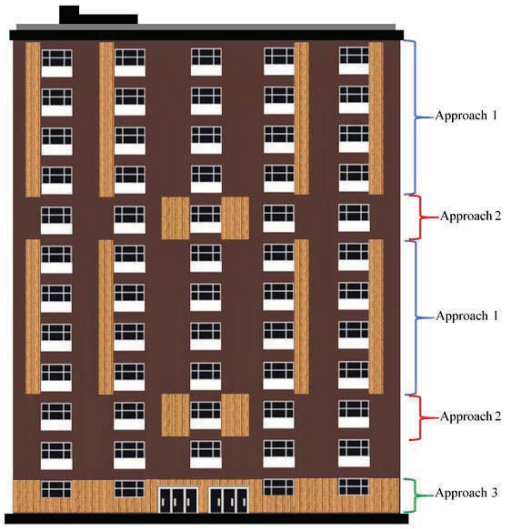

Figure 8: *Example of combustible cladding approaches on buildings constructed of EMTC*

3.4.2 Concealed Spaces

Concealed spaces within structural mass timber elements are permitted in buildings constructed of EMTC. For one example, see Figure 9, where the two mass timber floor slabs are separated by mass timber beams creating a concealed space.

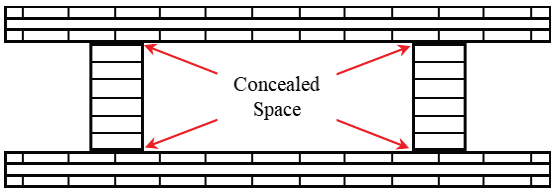

Figure 9: *Example of concealed space in mass timber elements*

These concealed spaces shall be provided with one of the following protective measures set out in the 2020 NBC [2]:

https://doi.org/10.52202/069179-0392

1. Sprinklered and divided into compartments by fire blocks.
2. Completely filled with rock or slag fibre insulation conforming to CAN/ULC-S702, "*Mineral Fibre Thermal Insulation for Buildings*," [13] and having a density of not less than 32 kg/m^3.
3. If horizontal (e.g., floor element), lined with not less than one layer of 12.7 mm (1/2 in) Type X gypsum board or noncombustible material providing an encapsulation rating of not less than 25 min.
4. If vertical (e.g., wall element), lined with not less than one layer of 12.7 mm (1/2 in) Type X gypsum board or noncombustible material providing an encapsulation rating of not less than 25 min and vertically divided into compartments by fire blocks.

Concealed spaces are also permitted where wood nailing elements are used for the attachment of a material or assembly of materials to provide an encapsulation rating in a building constructed of EMTC, provided the concealed space created by the wood nailing elements is not more than 25 mm (1 in) deep as shown in Figure 10.

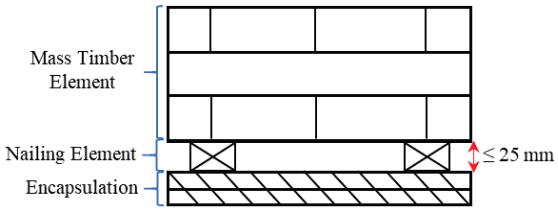

Figure 10: *Maximum depth of concealed space created by wood nailing elements*

Unlike any concealed spaces found within mass timber elements, these concealed spaces will not need to be protected.

3.4.3 Combustible Elements in Partitions

Combustible partitions, which do not enclose exits or vertical service spaces, are permitted in buildings constructed of EMTC. The partitions shall consist of solid lumber not less than 38 mm (1.5 in) thick or wood framing. Protection shall be provided on each face of the partitions. The protection shall consist of one layer of 12.7 mm (1/2 in) thick Type X gypsum board, with all joints either backed or taped and filled, or one layer of 19 mm (3/4 in) thick fire-retardant-treated wood. If fire-retardant-treated wood is used on partitions containing wood framing, the wood stud cavities shall be filled with noncombustible insulation.

3.5 DAMAGE OR REMOVED ENCAPSULATION MATERIAL

In the 2020 National Fire Code of Canada (NFC) [14], there is a new requirement for buildings constructed of EMTC for encapsulation material or assembly of materials if they are damaged or removed such that their integrity is compromised. The 2020 NFC requires that these damaged or removed encapsulation materials or assembly of materials be repaired or replaced in conformance with the 2020 NBC to restore their encapsulation rating.

3.6 PROTECTION DURING CONSTRUCTION

To address safety during construction, the 2020 NFC requires that protective encapsulation be installed in different locations within buildings constructed of EMTC. The encapsulation material or assembly or materials will need to provide an encapsulation rating of not less than 25 min. This rating can be met with one layer of not less than 12.7 mm (1/2 in) thick Type X gypsum board.

The encapsulation will be required to be installed on 100% of the interior side of mass timber stairways and vertical service spaces, and on each face of solid lumber, mass timber or wood framing partitions. In addition, 80% of the area of the underside of the mass timber floor assembly on each storey and 65% of the total area of structural mass timber within the storey will need to be encapsulated during construction [14].

To allow for quick construction of buildings of EMTC, the NFC permits that not more than the four uppermost contiguous storeys to be unprotected during construction. For example, for a 7 storey EMTC building under construction, the first 3 storeys would need to be encapsulated and top 4 storeys can be unprotected. To be able to construct the 8th storey, the first 4 storeys would be protected.

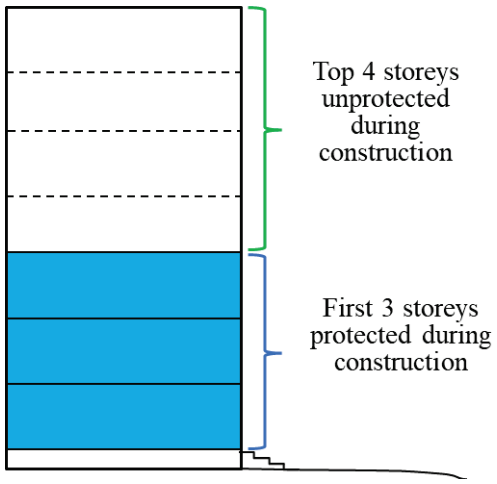

Figure 11: *Example of protection during construction*

3.7 EXPOSED MASS TIMBER

Exposed mass timber elements are permitted in buildings constructed of EMTC. There are limits to the percentage of exposed mass timber walls, beams, columns, arches, and ceilings that may be within either suites or fire compartments within the buildings. A suite means "*a single room or series of rooms of complementary use, operated under a single tenancy, and includes dwelling units, individual guest rooms in motels, hotels, boarding houses, rooming houses and dormitories as well as individual stores and individual or complementary rooms*

https://doi.org/10.52202/069179-0392

for business and personal services occupancies" and a fire compartment means "*an enclosed space in a building that is separated from all other parts of the building by enclosing construction providing a fire separation having a required fire-resistance rating*" [1].

For exposed surfaces of mass timber walls within a suite, they need not be protected if their aggregate surface area does not exceed 35% of the total wall area of the perimeter of the suite in which they are located and each exposed surface faces the same direction [2]. An example of a residential suite with exposed mass timber walls is shown in Figure 12. The surrounding blue rectangle is considered the perimeter of the suite and the total wall area around the perimeter would be used to find the percent of exposed mass timber permitted within the suite. The green lines are the location of the exposed walls within the suite. They represent less than 35% of the total wall area of the perimeter of the suite. Also, the exposed surfaces all face the same direction, as represented in Figure 12 where the green lines are drawn on the right side of each wall.

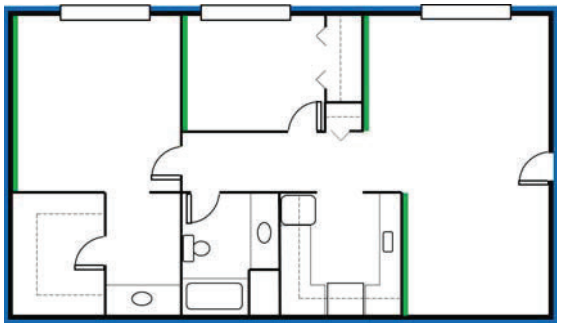

Figure 12: *Example of residential suite with exposed mass timber walls*

The exposed mass timber walls will also be required to have a flame-spread rating not more than 150.

Similarly, exposed surfaces of mass timber beams, columns, and arches within either a suite or fire compartment can be unprotected if their combined aggregate surface area does not exceed 10% of the total wall area of the perimeter of the suite or fire compartment [2]. They also will be required to have a flame-spread rating not more than 150.

The combined exposed surfaces of mass timber walls, beams, columns, and arches within a suite shall not exceed 35% of the total wall area of the perimeter of the suite. For example, if the suite has exposed mass timber beams, columns, and arches that represent the maximum 10% of the total wall area of the perimeter of the suite, then exposed mass timber walls are only permitted to have the remaining 25% of the total wall area of the perimeter of the suite be exposed, for a total of 35%.

Exposed surfaces of mass timber ceilings will have two options to allow for them to be unprotected within suites. The first option for exposed surfaces of mass timber ceilings is where the aggregate area does not exceed 10% of the total ceiling area of the suite and the exposed surfaces have a flame-spread rating not more than 150. In this case, mass timber walls, beams, columns, and arches within the suite are permitted to be exposed as described. The second option for exposed surfaces of mass timber ceilings is where the aggregate area does not exceed 25% of the total ceiling area of the suite and the exposed surfaces have a flame-spread rating not more than 75. With the higher percent of exposed ceilings, no mass timber walls are permitted to be exposed, but exposed beams, columns, and arches are still permitted [2].

A summary of exposed mass timber requirements for buildings constructed of EMTC is shown in Table 3.

Table 3: *Summary of exposed mass timber elements* [2]

Exposed mass timber element	Max aggregate surface area as a percentage of the total		Flame spread rating	Other requirements
	Wall area of the perimeter of the suite	Ceiling area of the suite		
Walls	35%	-	150	Surfaces face the same direction
Beams, columns, and arches	10%	-	150	Also permitted in a fire compartment
Combined walls, beams, columns, and arches	35%	-	150	Wall surfaces face the same direction
Ceilings (option 1)	-	10%	150	Exposed W/B/C/A permitted
Ceilings (option 2)	-	25%	75	No exposed walls

The exceptions to allow surfaces of mass timber elements to be exposed within buildings constructed of EMTC is, in part, based on cross-laminated timber (CLT) room burn research conducted at Carleton University in 2013 [13] and 2014 [14]. In the CLT room burn tests, without automatic sprinkler protection, the fire duration was influenced by the amount of exposed mass timber, the re-radiation between opposing/facing walls, and the char fall-off of CLT. This research limited the percent of exposed mass timber and required all exposed wall surfaces to face the same direction in buildings constructed of EMTC.

In 2018, after the 2020 NBC EMTC exposed mass timber percentages were initially accepted by the SC-FP of the CCBFC, the National Research Council Canada (NRC) undertook two research projects on fire testing of mass timber compartments without sprinkler systems and with exposed mass timber surfaces:

1. Fire Testing of Rooms with Exposed Wood Surfaces in Encapsulated Mass Timber Construction [15]
2. Nail Laminated Timber Compartment Fire Tests [16]

In the first NRC research project, the walls and roof of the test compartment were built from second generation CLT, which meets the 2018 version of ANSI/APA PRG 320, "*Standard for Performance-Rated Cross-Laminated Timber*" [17]. The adhesives used in the CLT conform to

https://doi.org/10.52202/069179-0392

the elevated temperature performance requirements in the standard, which exclude the use of adhesives that permit premature CLT char layer fall-off resulting in fire regrowth during the cooling phase of fully developed fire [17]. In the second NRC research project, the walls and roof of the test compartment were built from nail laminated timber (NLT) made on site at NRC. Several of the compartments in both research projects also included some percentage of exposed glued laminated timber beams and columns.

In most cases, the exposed surfaces of mass timber walls, beams, columns, and ceilings within the compartments exceeded the maximum allowances that have been chosen and approved for buildings constructed of EMTC in the 2020 NBC. These research projects show that the percentages of the acceptable exposed mass timber within EMTC buildings are conservative and can be increased. A new CCR has been submitted to increase these percentages in the 2025 edition of the NBC and is under review by the SC-FP.

4 CONCLUSIONS

This paper summarizes the code changes that were proposed to allow for the construction of tall wood buildings up to 12 storeys within the 2020 National Building Code of Canada. A description of the new construction type used for these tall wood buildings called encapsulated mass timber construction (EMTC) was also introduced. Details of the two main components of EMTC, encapsulation rating and minimum dimensions for timber members were explained. Detailed information about the code requirements on the different components of these tall wood buildings within the 2020 National Building and Fire Codes were shown. Specifics on current research projects on fire testing of mass timber compartments with exposed mass timber surfaces are included.

REFERENCES

[1] National Research Council of Canada, National Building Code of Canada 2015, Ottawa, 2015.

[2] National Research Council of Canada, National Building Code of Canada 2020, Ottawa, 2022.

[3] Underwriters Laboratories of Canada, "CAN/ULC-S146 Standard Method of Test for the Evaluation of Encapsulation Materials and Assemblies of Materials for the Protection of Mass Timber Structural Members and Assemblies," Standards Council of Canada, Ottawa, 2019.

[4] Underwriters Laboratories of Canada, "CAN/ULC-S101 Standard Methods of Fire Endurance Tests of Building Construction and Materials," Standards Council of Canada, Ottawa, 2014.

[5] ASTM International, "E119 Standard Test Methods for Fire Tests of Building Construction and Materials," ASTM International, West Conshocken, 2022.

[6] International Organization for Standardization, "ISO 834 Fire-Resistance Tests," ISO/TC 92/SC 2 Fire containment, Geneva, 2021.

[7] ASTM International, "ASTM C1396 Standard Specification for Gypsum Board," ASTM International, West Conshohocken, 2017.

[8] CertainTeed, "What is fire rated gypsum?" https://www.certainteed.com/drywall/what-fire-rated-gypsum/. [Accessed 4 February 2022].

[9] CHM Fire Consultants Ltd., "Defining Mass Timber for Tall Buildings," Canadian Wood Council, Ottawa, 2016.

[10] National Fire Protection Association, "NFPA 13 Standard for the Installation of Sprinkler Systems," NFPA, Quincy, 2019.

[11] Underwriters Laboratories of Canada, "CAN/ULC-S134 Standard Method of Fire Test of Exterior Wall Assemblies," Standards Council of Canada, Ottawa, 2018.

[12] Underwriters Laboratories of Canada, "CAN/ULC-S102 Standard Method of Test for Surface Burning Characteristics of Building Materials and Assemblies," Standards Council of Canada, Ottawa, 2018.

[13] Underwriters Laboratories of Canada, "CAN/ULC-S702 Mineral Fibre Thermal Insulation for Buildings," Standards Council of Canada, Ottawa, 2021.

[14] National Research Council of Canada, "National Fire Code of Canada," Ottawa, 2022.

[15] C. J. McGregor, "Contribution of Cross Laminated Timber Panels to Room Fires. Masters Thesis," Carleton University, Ottawa, 2013.

[16] A. R. M. Hevia, "Fire Resistance of Partially Protected Cross-Laminated Timber Rooms. Masters Thesis," Carleton University, Ottawa, 2014.

[17] Joseph Su et al, "Fire Testing of Rooms with Exposed Wood Surfaces in Encapsulated Mass Timber Construction," National Research Council Canada, Ottawa, 2018.

[18] Joseph Su et al, "Nail Laminated Timber Compartment Fire Tests," National Research Council Canada, Ottawa, 2019.

[19] American National Standards Institute, "Standard for Performance-Rated Cross-Laminated Timber," APA - The Engineered Wood Association, Tacoma, 2018.

World Conference on Timber Engineering Oslo 2023

BEARING SUPPORTS REINFORCED WITH SCREWS: EXPERIMENTAL INVESTIGATION AND DISCUSSION OF THE DESIGN MODELS IN EUROCODE 5

Roberto Tomasi[1], Angelo Aloisio[2], Ebenezer Ussher[1], Kari Ryen Thunber[1], Eldbjørg Aaraas Hånde[1], Harald Liven[3]

ABSTRACT: This experimental investigation has been undertaken with the aim to discuss the current model for compression perpendicular to grain (CPG) proposed in the new Eurocode 5 draft. The current draft present two approaches proposed to assess load-carrying capacity of timber members subjected to CPG with reinforcement (Proposed reinforcement approach) and without reinforcement (New Model). The predictions of existing capacity models are compared to the experimental results of 39 timber specimens, distinguished by different load, screw and geometric configurations. Current capacity models for CPG with reinforcement assume two failure mechanisms, mainly characterized by their location, i.e. the contact area of the applied load (first mode) or the screw tips (second mode). However, the experimental tests reveal that the second mode never occurs despite the model predicting the occurrence of the second mode in more than half of the tested specimens. Additionally, the experimental tests show the fallacy of existing models in accurately estimating the capacity associated with the second failure mode. Parallelly, the model appears to be relatively conservative for the first failure mode.

KEYWORDS: Compression perpendicular to the grain, reinforcement with screws, experimental test

1 INTRODUCTION

The direction of the grain influences mechanical properties of wood, e.g. perpendicularly to the grain it presents considerable lower strength and stiffness [1]
Compression perpendicular to grain (CPG) failure leads to a collapse of the cellular tubes and acts as a failure transversely to the tubular layers.
Therefore, the CPG failure is a crucial problem, especially in the case of permanent deformation in the structures [2], even in the case when they do not cause structural failure.
In the case of CPG without reinforcement, the design approach proposed for the current draft of the new Eurocode 5 is based on the yield slip-line model, see Leijten [3].
Studies have also identified various techniques in improving the member strength in compression perpendicular to the grain (CPG) such as glued-in threaded rods and glued-on plywood plates. Alternatively, screws with uninterrupted threads have been observed to be economically viable in improving CPG capacity of timber members.
Therefore, the current draft of the consolidated version of the new Eurocode 5 on the table for discussion provides additional guidelines for implementing CPG with reinforcement [4].
The proposed design approach is based on the investigation made by Bejtka in 2005 [5], who observed three failure modes in timber subjected to CPG with reinforcement:

- the first failure mode is associated with pushing the reinforcing screws into the timber. It is observed with supports enhanced with short screws and the pushing-in capacity is assumed equal to the withdrawal capacity;
- the second failure mode occurs when slender screws are employed in reinforcing a member against CPG and it is characterised by buckling of the screws;
- the third failure mode is also associated with short screws in which a deformation is observed in a plane formed by the tips of the screws.

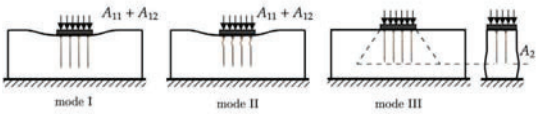

Figure 1: *Failure modes for CPG with reinforcements*

The minimum predicted value is considered to be the limit state to which the demand on a member in CPG may be compared for design. The candidate design approach still presents some gaps in knowledge concerning the test data that strengthen and validate the calculation model. Thus, Tomasi et al [6] experimentally investigated the CPG of

[1] Faculty of Science and Technology, Norwegian University of Life Sciences, P. O. Box 5003 Ås 1432, Norway
[2] Università degli Studi dell' Aquila, L'Aquila, 67100, Italy
[3] Moelven Industri, Norway

https://doi.org/10.52202/069179-0393

reinforced specimens, with the object of validating the standards approach, whose findings are summarized in this paper.

2 STANDARDS PROPOSAL

2.1 CGP WITHOUT REINFORCEMENT

The CPG model presented in [3] is based on the assumption that the compressive stresses spread as in an isotropic material with a degree depending on the deformations. The standard version of the model is given in Table 1.

Table 1: *Design model of non-reinforced members under CPG*

$$\sigma_{c,90,d} \leq k_p \cdot k_{c,90} \cdot f_{c,90,d} = B_1 \quad (1)$$

$$k_{c,90} = \sqrt{\frac{l_{ef}}{l_c}} \leq 4 \quad (2)$$

Where $k_{c,90}$ is a load arrangement factor, l_{ef} is the effective spreading length of the compressive stresses estimated by assuming a 45° diffusion angle, l_c is the contact length of the applied force, k_p takes into account the material behaviour and the deformation perpendicular to the grain (the factor accounts for the increased stiffness when the deformation increases).

2.2 CGP WITH REINFORCEMENT

Based on the failure modes described above, the capacity model proposed by Bejtka and Blass for CPG with reinforcement [7], is formulated as the minimum resistance associated with two following failure mechanisms (see Table 2):

- The first failure mode, labelled A_1, corresponds to the specimen failure by the contact area of the load. It is obtained by adding the timber and screw contributions, named A_{11} and A_{12} respectively. A_{11} accounts for the crushing of wood member at the support contact surface, adopting an effective length $l_{ef,1}$ higher than the contact length of the applied force, and k_{pr} for the material behaviour and the deformation perpendicular to the grain. A_{12} accounts for the pushing-in capacity of the screw including buckling effect.
- Second failure mode labelled A_2, considers failure of wood member with an effective length along a plane at the tip of the screws, which is determined adopting an effective length $l_{ef,2}$ calculated assuming a 45° diffusion angle.

The wood contribution A_{11} is coherent with the current guidelines in the Eurocode 5 for assessing unreinforced CPG in a member, which depends on the loading situation and the effective contact loading length due to the rope effect of contributing fibres adjacent to the loaded area.

Table 2: *Design model of reinforced members under CPG*

$$F_{c,90,Rk} = min\begin{cases} A_{11} + n \cdot A_{12} = A_1 \\ A_2 \end{cases} \quad (3)$$

where

$$A_{11} = k_{pr} \cdot b_c \cdot l_{ef,1} \cdot f_{c,90,k}$$

$$A_{12} = min\{F_{w,k}, F_{c,k}\}$$

$$A_2 = b \cdot l_{ef,2} \cdot f_{c,90,k}$$

$$l_{ef,1} = l_c + \min\{30\text{mm}, l_c\} + \min\{30\text{mm}, l_c, l_e\} \quad (4)$$

$$l_{ef,2} = l_r + (n_0 - 1) \cdot a_1 + \min\{l_r, a_{3,c}\} \quad (5)$$

The screw withdrawal strength can be calculated in function of the shear strength $f_{w,k}$ distributed along the screw surface areas according to this formula:

$$F_{w,k} = \pi \cdot d \cdot l_w \cdot f_{w,k}, \quad (6)$$

Where $f_{w,k}$ can be assumed as:

$$f_{w,k} = 8.2 \cdot k_w \cdot k_{mat} \cdot d^{-0.33} \cdot \left(\frac{\rho_k}{350}\right)^{k_\rho} \quad (7)$$

The screw buckling resistance is determined in function of an instability coefficient κ_c based on the model of a Winkler elastic beam in an elastic subgrade.

$$F_{c,k} = \frac{\gamma_R}{\gamma_{M1}} \cdot \kappa_c \cdot N_{pl,k} \quad (8)$$

where $N_{pl,k} = \pi \cdot \frac{d_1^2}{4} \cdot f_{y,k}$ and $\frac{\gamma_R}{\gamma_{M1}} \approx 1.18\ (*)$

*) $\frac{\gamma_R}{\gamma_{M1}}$ can be assumed equal to one for estimating the mean value of the buckling resistance.

3 EXPERIMENTAL CAMPAIGN

3.1 MATERIAL AND METHODS

The test specimens are glue-laminated timber of service class GL30 C, with dimensions of 800 × 140 × 225 or 1200 × 140 × 540 mm (length × width × height) with screw reinforcement produced by Rothoblaas and SFS. Figure 3 shows the considered load cases, tested with and without reinforcement, following the EN408 and ISO 6891 recommendations. The test procedure agrees with the one followed by Leijten [2], who investigated similar load cases without reinforcement.

Figure 2 show a schematic overview of the different screws, with the effective screw length applied in the design model. The screws are fully threaded self-tapping screws, except for the WT-T screw, which is double-threaded (in this case an effective screw length of 130 mm is used in the calculation). Each specimen is labelled with a unique name composed of its screw arrangement, screw

diameter, screw length, load case, and test number, see right Figure 2. All specimens were pre-drilled with a diameter 4.5 mm in a length of approximately 50 mm by using a bench pillar drill machine. The pre-drilling ensured having a straight hole, following the producer's recommendations for the diameter and length.
The screws are used in four arrangements according to Figure 4.

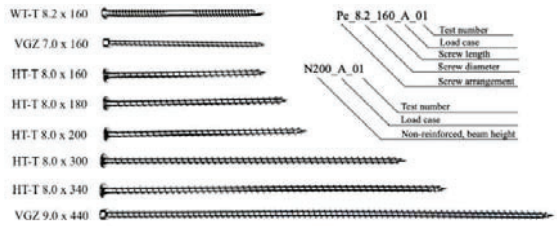

Figure 2: *Screws geometry and description of the labels for reinforced and non-reinforced test specimens.*

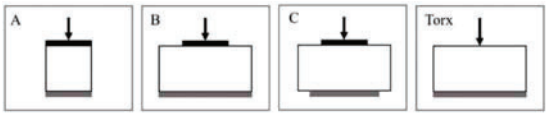

Figure 3: *Load cases*

It must be remarked that the experimental values cannot be compared with the characteristic resistance $F_{c,90,k}$ proposed in Equation (3). This is because the authors did not repeat each configuration multiple times to achieve a statistical description of the specific case. Therefore, an unbiased comparison with the experimental data requires estimating the predicted mean of the capacity. Hence, the mean of the resistance perpendicular to grain and yielding steel strength replaced the formulation's characteristic values in Table 2. The mean CPG timber strength is considered equal to $F_{c,90,m} = 3\,MPa$, following [8]. Conversely, the mean yielding strength of steel is set equal to 1000 MPa, based on separate experimental tests on the screws. The mass density of timber is assumed equal to $\rho_m = 390\ kg/m^3$. The load cases are graphically described in Figure 3.

- **Load case A** represents the block test of the specimens according to EN 408. For the reinforced samples, the predicted failure mode is the second, i.e. collapse by the screws' tips. Conversely, in the case of non-reinforced samples, the failure appears right below the load application area following to the first mode.
- **Load case B** considers a uniformly distributed load and corresponds to the case of the beam on continuous support (see left case in Figure 3).
- **Load case C** has direct loading on the opposite face. The support is a loading area of 140 x 180 mm (width x length). The goal is to investigate the failure in the reinforced area. Hence, the loading area is greater compared to the support (360 x 140 mm).
- **Torx:** This test directly loads the screw head and achieves the failure of the screw alone. The predicted failure mode is buckling for all screws, except for the shorter screws, where the effective screw length equals 130 mm. According to the theory of an elastic beam in elastic subgrade, the buckling capacity is not dependent on the screw length [9].

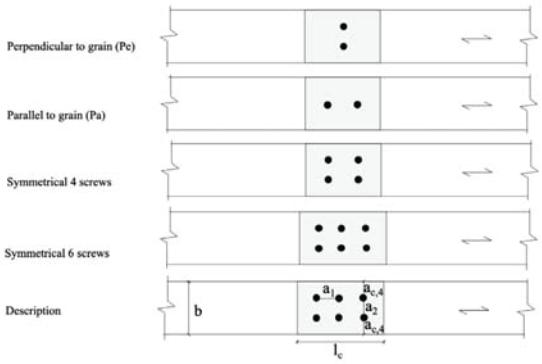

Figure 4: *Screw arrangement.*

3.1.1 Specimen preparation

The specimens were delivered as long beams by Moelven Limtre. The specimens were stored at the laboratory of wood technology at the material test laboratory of the Norwegian University of Life Sciences (NMBU). The relative humidity and the temperature during the storage are equal to 50% and 20° respectively. In a second step, the beams were cut into smaller pieces with a chainsaw to get the correct dimensions. The pre-drilling and insertion of the screw were done using electric drills produced by Bosch and Makita. The screws were drilled with a right angle, and the head was in all cases flush with the timber surface.

3.1.2 Testing procedure

The specimens are subjected to a compressive force by the load cell of the ZwickRoell Z1200 UTM (Universal Testing Machine). The deformation is measured by an integrated sensor in the load cell and external sensors. During the test execution, two horizontal and two vertical sensors are used, see Figure 5. The horizontal sensors are placed on each long side of the specimen corresponding to the screw tip. All estimations are carried out following EN408 and ISO6891 recommendations.

3.1.3 Loading protocol

There is no standard procedure for testing members subjected to CPG with screw reinforcement. However, the tests are executed on the basis of EN408 and ISO6891. In the ISO6891 procedure of loading the estimated load, F_{est} is determined as the minimum between A_1 and A_2. In the case of non-reinforced members for load cases B and C, the force is estimated with k_p equal to 1.0.
The test consists of four phases. Phases 1,2 and 3 are based on load rates, while the fourth is displacement-driven. Phases 1 and 2 follow the ISO6891 and aim to avoid residual initial deformations and stabilize the

https://doi.org/10.52202/069179-0393

loading area. The specimen is loaded up to 40% of the estimated resistance F_{est}, held for 30 seconds before the load decreases to 10% of F_{est}, and then held for 30 seconds. The load rate in phases 1 and 2 is determined as the ratio between 40% and 10% of F_{est} respectively, and 60 seconds. The actual load-displacement curves used in the analyses correspond to phase 3. Phase 3 follows the EN408. Hence, the maximum force will be reached within 300 ± 120 seconds. Phase 4 has a 1mm/min deformation rate, following Dietsch [10]. The test will stop automatically if the load reduces to 20% or the level of deformation reaches 12%.

In load cases A and Torx, the tests are executed with the first three phases, while load cases B and C are executed following the entire protocol. The Torx test is executed by connecting a Torx bit to the load cell through a steel plate. The mean moisture content of the specimens measured by a Delmhorts RDM3 instrument was 12.3%.

3.1.4 Estimation of the experimental capacity

The failure load for non-reinforced specimens has been estimated using an iterative procedure similar to the one described in EN 408 to estimate the compressive strength. Based on the load-displacement curves the line referring to the plausible elastic range between 10% and 40% of the estimated capacity is translate in a new parallel line, with 1% offset to the gauge length. The intersection between this second line 2 and the load-deformation curve determines the estimated capacity (F_{est}). If this value is within 5% of the predicted one $F_{c,90,est}$, it is considered valid. Otherwise, the process is repeated until the value is within the 5% tolerance.

3.2 EXPERIMENTAL RESULTS

he authors reported 31 tests with eight different screws in four loading conditions. The load-displacement curves exhibit an initial linear elastic behaviour, see Figure 5. The slope of the curves reduces when the load approaches the maximum load. After this point, the load decreases. This range corresponds to the failure of the screws and the local crushing of timber. After the screw failure, there is a slight increase in capacity after a certain point. This growth is related to the activation of the timber contribution. In the elastic range, the load-displacement curve has the same trend. Beyond the plastic range, the load-deformation curve depends on the specific failure mode. The horizontal expansion is below 2 mm for all cases, except for load case A, although it does not represent a design situation.

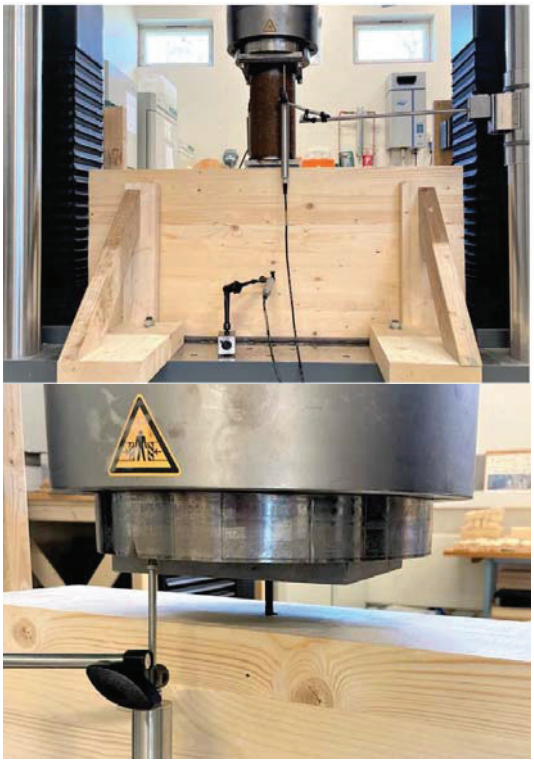

Figure 5: *Setup of specimen with height 540 mm in ZwickRoell Z1200- Setup of Torx test.*

Figure 6 plots all experimental results for load cases A (block test) B and C for the specimen with H = 225 mm, while Figure 7 plot the torx test results. The relevant experimental outcomes are resumed in ***Table 3*** and Table 4. The tables collects the test label, the failure mode, the maximum force (for torx test) and that corresponding to 1% deformation. The column 'increase' reports the percentage increment in capacity due to the presence of screws compared to the specimen without reinforcement.

The major aspects are:

Case A: The capacity increases slightly with the reinforcement. The observed failure mode is the timber failure, despite the significant deformation of the screws. The load-displacement curves are close to each other. As expected, the elastic stiffness of the reinforced model is higher. Theoretically, the effective diffusion length of the reinforced specimen is not fully exploited due to the specimen's geometry.

Case B: The failure modes are buckling and withdrawal. The horizontal displacement is below 1 mm for all cases, except for S6_7.0_160_B, where the horizontal displacement is 1.50 mm. Test Pa_7.0_160_B and Pe_7.0_160_B exhibited the same resistance at 1% deformation. The difference between the configurations is the screw arrangement. The curves of the reinforced specimens have a peak and then decrease, while those of the non-reinforced ones monotonically increase. As expected, the reinforcement causes a higher stiffness. The configuration S6_7.0_160_B shows a significant increase

in capacity. However, the configuration has a considerable number of screws, and the contact area is increased to 140 x 360 mm (width x length). For the configuration S6_9.0_440_B, the horizontal displacement is greater than 1 mm; otherwise, the horizontal displacement is below 1 mm. In the configurations with a 540 mm height, the predicted failure mode, A_1, is confirmed by the test results, except for S6_9.0_440_B. The capacity model yields a 20% overestimation of the test results. Interestingly, no differences emerged between the two configurations with different orientations of the screws (perpendicular or parallel to the grain direction). The predicted failure mode of the screws in the 540 mm specimen is buckling, except for the screw WT-T 8.2 x 160 mm, where withdrawal is reported.

In contrast to the predictions, all screws with a 160 mm length failed due to withdrawal.

In the case of 2 x HT-T 8.0 x 180 mm screws, the failure mechanism is both withdrawal and buckling.

4 x HT-T 8.0 x 180 mm has an apparent withdrawal failure. Similarly, HT-T 8.0 x 200 mm changes the failure mode with the number of screws. Considering a constant load area, the capacity variation between the load configurations may be due to screw length, diameters, and timber imperfections.

Case C: A steel plate with dimensions 360 x 140 mm (length x width) is applied on the non-reinforced side. The capacity of the test specimens increases with the reinforcement. The horizontal displacement is approximately 1-2mm for all cases. The configuration with 2x VGZ 7.0 x 160 mm had a higher capacity than 2 x WT-T 8.2 x 160 mm. The curves of reinforced specimens have a peak and then decrease. The capacity increases with the number of screws. For 225 mm specimens, the failure mode is withdrawal, despite the predictions. The distinction in capacity between A_1 and A_2 is minor.

Torx: The failure modes of the screws are withdrawal and buckling, see Figure 8. The load increases with the length of the screw, except when the size of the screw is 200 mm. In this case, the capacity decreases. All curves exhibit a clear peak. With the VGZ 7.0 screw, the capacity is higher compared to the HT-T 8.0 screw. However, the failure is reached at a smaller displacement. Contrary to the previously reviewed tests, the maximum force achieved is estimated. The predicted failure mode corresponds to the test results, except for VGZ 7.0 x 160 mm, where the failure mode is withdrawal. The design model's decisive capacity is consistently lower than the test results. The mean ratio between the test results and the predicted capacity is 1.55. The impact of the slenderness is considered by testing the HT-T screw with a constant diameter and different lengths. In all cases, the screw failed due to buckling.

3.3 DISCUSSION

The screw and timber contribution to the capacity of the reinforced specimens can be isolated using the outcomes of the Torx tests. Since the timber contribution in the Torx test can be assumed negligible, the Torx tests provide the contribution of a single screw. Accordingly, the role of timber can be estimated by subtracting from the force associated with 1% deformation the capacity obtained from the Torx test multiplied by the number of screws. The timber contribution to the capacity according to the failure mechanism A_1 , named A_{11}, reads:

$$A_{11} = \left(F_{1\%,def} - n \cdot F_{max}\right) \quad (9)$$

Parallelly, the average screw contribution to the capacity, named A_{12}, can be obtained from the $F_{\max}$ of the Torx tests as follows:

$$A_{12} = F_{max} \quad (10)$$

The main aspects emerging from the experimental results are the following:

- The timber contribution to the capacity of the reinforced specimen is approximately 73% and 51% for the samples with two and four screws, respectively. This fact proves that using four rather than two screws reduces the timber contribution by nearly 20%.
- The timber contribution moderately varies if the screw length increases from 160 mm to 440 mm. The A_{11} contribution is on average, 110 for 160 mm screws and 137 for 440 mm.
- The model significantly underestimates the screw contribution by 42% on average. Conversely, the disparity in terms of timber contribution is lower. On average, it is 2% for the two-screws specimens and -22% for the four screws. On the contrary, in this case, the design model overestimates the timber contribution for the four screws specimens. The mean timber contribution from test results is 72% and 51% with two and four screws, respectively. In the design model is 72% and 45%, with two and four screws.
- According to the standard proposal, k_{pr} should be 1.5 for load case B and 1 for load case C. Still, the experimental data contradict these assumptions. The test results for load cases B and C with identical screw arrangements (except for the size of the steel plates) are within the same range of capacity. The dissimilarity is insignificant and lower than 10% in most cases and on average 2%. Therefore, this fact proves that the capacity of the two load cases can be predicted with the same k_{pr} coefficient.

https://doi.org/10.52202/069179-0393

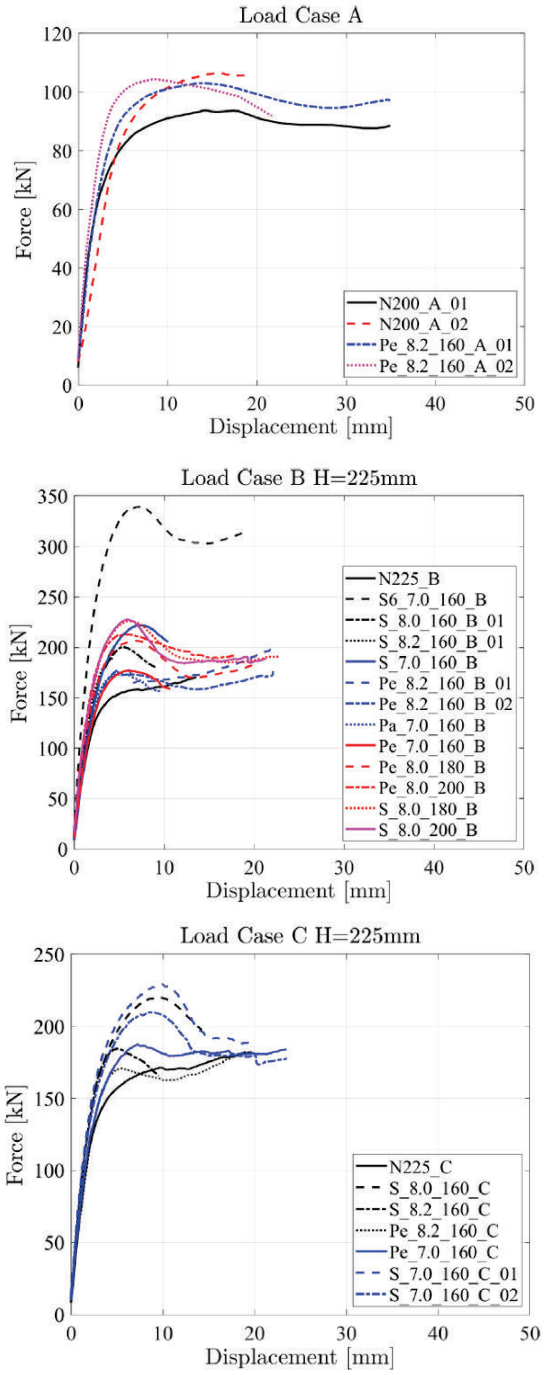

Figure 6: *Force–displacement curves for load case A, load case B, and load case C.*

Table 3: *Main results of the experimental tests and corresponding predictions according to the capacity model.*

Type			Failure mode	
	$F_{1\%,\,def}$	Incr.*	Exp.	Th.
	[kN]	[%]		
Load Case A				
N200_A	88	/	B_1	/
Pe_8.2_160_A	96	9.10	A_2	A_2
Load Case B				
N225_B	152	/	B_1	/
N540_B	182	/	B_1	/
Pe_7.0_160_B	172	13.20	A_1 $F_{w,k}$	A_2
Pa_7.0_160_B	172	13.20	A_1 $F_{w,k}$	A_2
Pe_8.2_160_B	174	14.50	A_1 $F_{w,k}$	A_2
Pe_8.0_180_B	196	28.90	A_1 $F_{w,k}$/ $F_{c,k}$	A_2
Pe_8.0_200_B	205	34.90	A_1 $F_{c,k}$	A_2
S_7.0_160_B	210	38.20	A_1 $F_{w,k}$	A_2
S_8.2_160_B	189	24.30	A_1 $F_{w,k}$	A_2
S_8.0_160_B	194	27.60	A_1 $F_{w,k}$	A_2
S_8.0_180_B	217	42.80	A_1 $F_{w,k}$	A_2
S_8.0_200_B	217	42.80	A_1 $F_{w,k}$	A_2
S6_7.0_160_B	311	104.6	A_1 $F_{w,k}$	A_2
Pe_8.0_300_B	234	41.40	A_1 $F_{c,k}$	A_1 $F_{c,k}$
Pe_9.0_440_B	230	39.40	A_1 $F_{c,k}$	A_1 $F_{c,k}$
Pa_9.0_440_B	225	36.70	A_1 $F_{c,k}$	A_1 $F_{c,k}$
S_8.0_300_B	256	55.20	A_1 $F_{c,k}$	A_1 $F_{c,k}$
S_8.0_340_B	271	64.20	A_1 $F_{c,k}$	A_1 $F_{c,k}$
S_9.0_440_B	292	77.00	A_1 $F_{c,k}$	A_1 $F_{c,k}$
S6_9.0_440_B	455	175.80	A_1 $F_{c,k}$	A_2
Load Case C				
N225_C	165	/	B_1	A_1 $F_{c,k}$
N540_C	182	/	B_1	/
Pe_7.0_160_C	173	11.60	A_1 $F_{w,k}$	A_2
Pe_8.2_160_C	169	9.00	A_1 $F_{w,k}$	A_1 $F_{c,k}$
S_7.0_160_C	192	23.90	A_1 $F_{w,k}$	A_2
S_8.2_160_C	183	18.10	A_1 $F_{w,k}$	A_2
S_8.0_160_C	191	23.20	A_1 $F_{w,k}$	
Pe_9.0_440_C	229	25.80	A_1 $F_{w,k}$	A_1 $F_{c,k}$
S_9.0_440_C	235	29.10	B_1	A_1

*) increase with respect to the unreinforced specimen

https://doi.org/10.52202/069179-0393

Table 4: *Main results of the experimental torx tests and corresponding predictions according to the capacity model.*

Type			Failure mode	
	F_{max}	F_{max}/A_1	Exp.	Th.
	[kN]			.
Torx test				
T_7.0_160	21.9	1.6	A_1 $F_{c,k}$	A_1 $F_{w,k}$
T_8.2_160	21.3	1.3	A_1 $F_{w,k}$	A_1 $F_{w,k}$
T_8.0_160	28.3	1.5	A_1 $F_{w,k}$	A_1 $F_{c,k}$
T_8.0_180	29.2	1.6	A_1 $F_{c,k}$	A_1 $F_{c,k}$
T_8.0_200	27.5	1.5	A_1 $F_{c,k}$	A_1 $F_{c,k}$
T_8.0_300	26	1.4	A_1 $F_{c,k}$	A_1 $F_{c,k}$
T_8.0_340	28.5	1.6	A_1 $F_{c,k}$	A_1 $F_{c,k}$
T_9.0_440	40.8	1.8	A_1 $F_{c,k}$	A_1 $F_{c,k}$

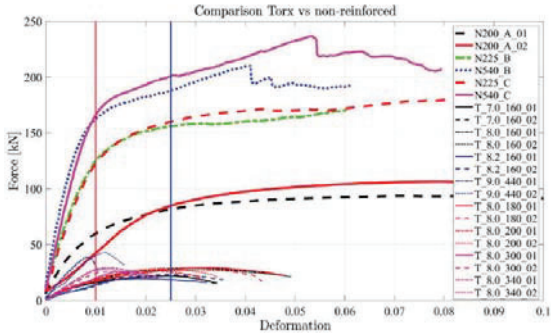

Figure 7: *Comparison between the torx tests on the single screws and those on non-reinforced specimens.*

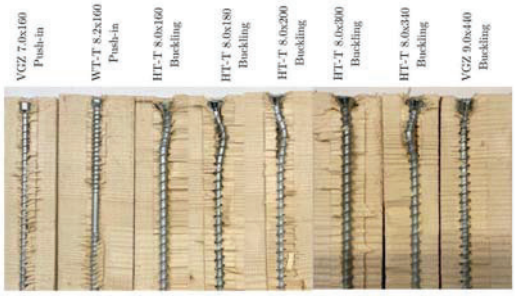

Figure 8: *Failure modes of the tested screws.*

Figure 9 plots the experimental capacity ($F_{1\%,def}$) and A_1, A_2 obtained from the design model. The most relevant aspect is that while A_1 and the experimental capacity are in good agreement, except for case C, A_2 is mostly lower than $F_{1\%,def}$ and exhibits a high scatter.

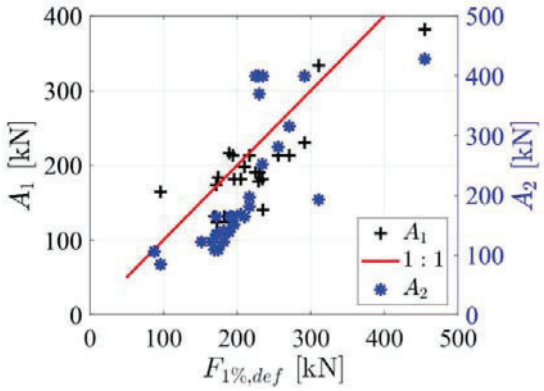

Figure 9:*. Experimental vs model predictions for the first (A1) and second (A2) failure mechanism,*

The failure mode achieved for all tests is according to A_1 for load cases B and C. However, some of the predicted failure modes appear to be different from the results of the experimental campaign. For example, in the event of shorter screws, the expected failure mode is mostly buckling, while the achieved failure mode is withdrawal. This evidence further proves that the specimen's failure corresponds to the A_1 mechanism. Additionally, it suggests that the A_2 model might be inaccurate and possibly underestimate the timber contribution by the screw tips. Consequently, it can be assumed that the capacity of A_2 is higher than the test results for load cases B and C. This fallacy possibly originates from the definition of the spreading length.

This failure mode A_2 is observed by Bejtka with small loading areas and short screws[5]. At the end of the screw, the force is transferred to the timber. The maximum pressure in the timber emerges at the screw tip and depends on the effective dispersion length and width. The effective length depends on the length of the screws, the screw arrangement, and the design situation.

This experimental outcome encourages researchers to study this aspect further to derive a reliable expression for the spreading length in predicting the capacity associated with the A_2 failure mechanism. Notably, the predictions for load case C are biased. The model underestimates the capacity, as a consequence of assuming $k_{pr} = 1$, as above remarked.

The timber contribution to resistance corresponds to the 1% deformation, while the screw contribution corresponds to the screw resistance, taken as the minimum between the buckling and the push-in resistances. However, this hypothesis is valid if the resistance of the screws is approximately reached at 1% deformation. Yet, the main difficulty behind this verification is the correct computation of the deformation in the Torx tests. While the specimen deformation in the non-reinforced specimens can be estimated as the ratio between the vertical displacement and the specimen height, this calculation might not be correct in the case of the Torx. During the push-in or buckling of the screws, the measured displacement does not result in the deformation of the entire specimen since only the

https://doi.org/10.52202/069179-0393

cylindrical layer wrapping the screw is affected by the deformation.

Therefore, the timber deformation associated with the Torx tests could be defined as the ratio between the vertical displacement and the screw length. Figure 7 compares the force-deformation curves of the non-reinforced and Torx tests, where the deformation in the non-reinforced specimens is computed as the ratio between the measured vertical displacement of the timber plate and the specimen height. The force-deformation curves of the non-reinforced samples are almost alike, showing a bend almost to the 1% deformation. The Torx tests exhibit a similar behaviour since the plastic branch approximately occurs between 0.01 and 0.02 deformation. Therefore, given the excellent estimation of the screw contribution A_{12} highlighted in the previous paragraphs, the authors conclude that the additivity hypothesis can be considered a reasonable assumption for a Standard. It must be remarked that the comparison in Figure 7 is only based on non-reinforced specimens to exclude all possible interaction phenomena occurring in the reinforced samples. The timber and screw contribution are already summed in the reinforced specimens. Thus, it is challenging to divide them and verify the additivity hypothesis.

4 CONCLUSIONS

This paper discusses experimental tests of timber specimens with screw reinforcement under compression perpendicular to the grain (CPG). In detail, the CPG tests comprise 31 structural arrangements different for the number and placement of the screws, specimens geometry and load pattern. The experimental capacities are used to validate the accuracy of the design model proposed in the next generation of Eurocodes. The experimental results show that using threaded screws as reinforcement effectively increases the capacity of timber subjected to CPG. However, the measured capacities do not entirely agree with the design model predictions. The current predictive model assumes two failure mechanisms, mainly distinguished by their location: the applied load's contact area (first mode A_1) or screw tips (second mode A_2). The first model is based on the mere summation of the timber and screw contributions. The failure modes achieved in the tests confirm the accuracy of the A_1. These tests ascertain the additivity hypotheses behind the predictive model. The experimental tests reveal that the second mode never occurs despite the model predicting the occurrence of the second mode in more than half of the tested specimens.

Conversely, the estimates corresponding to the failure mechanism A_1 agree with the test results. Yet, the predicted capacity is a bit lower for load case C. This might depend on the k_{pr} coefficient, assumed 1.5 and 1 for load cases B and C, respectively. The overall predicted failure mode of A_1 is mainly confirmed, except for the shorter screws.

The paper shows that the model predictions significantly improve if the same $k_{pr} = 1.5$ is assumed for all load configurations. Nonetheless, the additivity hypotheses for the A_1 failure mode can be considered sufficiently accurate for standards.

REFERENCES

[1] Porteous J, Kermani A. Structural timber design to Eurocode 5. John Wiley & Sons; 2013.

[2] Leijten AJM, Larsen HJ, der Put T. Structural design for compression strength perpendicular to the grain of timber beams. Constr Build Mater 2010;24:252–7.

[3] Leijten AJM. The bearing strength capacity perpendicular to grain of Norway spruce - Evaluation of three structural timber design models. Constr Build Mater 2016;105:528–35. https://doi.org/10.1016/j.conbuildmat.2015.12.170.

[4] Dietsch P. Reinforcement of timber structures - Standardization towards a new section for EC5. Proceedings of the 5th International Conference on Structural Health Assessment of Timber Structures (SHATiS) 2019, 25-27th September 2019.

[5] Bejtka I. Verstärkung von Bauteilen aus Holz mit Vollgewindeschrauben. Band 2 Der Reihe Karlsruher Berichte Zum Ingenieurholzbau, Doctoral Thesis, Fakultät Für Bauingenieur-, Geo- Und Umweltwissenschaften, Universität Fridericiana Zu Karlsruhe 2005;2. https://doi.org/10.5445/KSP/1000003354.

[6] Tomasi R, Aloisio A, Hånde EA, Thunberg KR, Ussher E. Experimental investigation on screw reinforcement of timber members under compression perpendicular to the grain. Eng Struct 2023;275. https://doi.org/10.1016/j.engstruct.2022.115163.

[7] Blass HJ, Bejtka I. Reinforcements perpendicular to the grain using self-tapping screws. Proceedings of the 8th World Conference on Timber Engineering 2004;1:233–8.

[8] Bogensperger T, Augustin M, Schickhofer G. Properties of CLT-panels exposed to compression perpendicular to their plane. At the Conference International Council for Research and Innovation in Building and Construction, Working Commission W18-Timber Structures 2011:1–15.

[9] Timoshenko SP, Gere JM. Theory of elastic systems 1961.

[10] Dietsch P, Rodemeier S, Blaß HJ. Transmission of perpendicular to grain forces using self-tapping screws. International Network on Timber Engineering Research INTER, Meeting 6, 2019.

World Conference on Timber Engineering Oslo 2023

MODIFICATION OF PARTIAL SAFETY FACTORS FOR A SEMI-PROBABILISTIC EVALUATION OF EXISTING TIMBER STRUCTURES

Maria Loebjinski[1], Wolfgang Rug[2/3], Hartmut Pasternak[4]

ABSTRACT: The evaluation of the load-bearing capacity of existing structures is a central and important part in the work of structural engineers. At state, engineers are confronted with the challenge of applying design rules developed for new structures in the evaluation of existing ones as no specific recommendations exist on a European level. This task needs to be addressed in the development of common codes and standards. As a contribution, a first step of this study is the evaluation of the reliability level of timber elements subjected to common limit states. Based on these analyses, a modification of the target reliability for existing structures is discussed and a suggestion for different levels is given. In another step, this contribution presents a proposal for a stepwise procedure for the evaluation of the load-bearing capacity of structural timber in existing structures considering different levels of available information. Focus is set on the provision of a flexible semi-probabilistic evaluation concept; modified partial safety factors are calibrated on the resistance side for selected limit states. Additionally, options to consider updated material parameters from a survey on site supported by technical devices are discussed and further need for research is identified.

KEYWORDS: existing timber structures, evaluation, partial safety factor, code calibration

1 INTRODUCTION

Eurocodes form the basis of design and verification of structures. At state, rules for the design of new structures are applied for the evaluation of the load-bearing capacity of existing structures. The newly introduced Technical Specification *CEN/TS 17440:2020-10* [1] as a first common specification for the evaluation of existing structures offers new paths: qualitative evaluation, quantitative evaluation or a combination of both. A qualitative evaluation is based on past performance of the structure. For a quantitative evaluation, the *Partial Factor Method* is recommended, reliability-based methods and risk-informed methods can be applied additionally. The assessment should verify that the structure has adequate reliability. Target values can be taken from *EN 1990* [2] or may be defined in National Annexes. As the target reliability is defined based on an optimisation of failure consequences and efficiency of safety measures (see *ISO 2394:2015* [3] or *SIA 269/2011* [4]), an altered definition for existing structures is possible. Annex C of [1] formulates that "The target reliability level for existing structures can be lower than that for new structures as the relative cost of safety measures to increase the reliability of an existing structure is greater than that for a new structure." (C.3.(4) Note 2). Thus, *CEN/TS 17440:2020-10* [1] opens new ways for the adjustment of the well-proven semi-probabilistic verification format of the Eurocodes for their application on the special demands in the evaluation of existing structures. Basis for an evaluation of the load-bearing capacity of an existing structure is a careful and detailed investigation including an assessment in situ. For existing structures, different national recommendations, on an international level *ISO 13822:2010* [5] and with special focus on existing timber structures *EN 17121:2019* [6] provide the basis for a qualified assessment. Updated information from an assessment on site should be considered in the modified semi-probabilistic evaluation. Results are always specific for the structure at hand what complicates standardisation. Thus, a structured process including options to modify safety elements is needed to systematize the use of updated information in the evaluation.

2 METHODOLOGY

Loads and material parameters are subjected to a natural variability. Besides, model uncertainties have to be considered. Thus, the resulting reliability of different limit states varies depending on the input variables. Hence, a standard cannot provide a reliability level that is most optimal for all kinds of limit states [7], safety elements are defined by optimisation. What is more, [8] emphasizes that reliability indices can hardly serve as indicators without direct link to the model parameters used to calculate them. The calculation of the implicit safety level of current design is hence a good and goal-oriented option to produce reliable values. This approach presupposes that

[1] Maria Loebjinski, Technical University of Braunschweig, Germany, m.loebjinski@tu-braunschweig.de
[2] Wolfgang Rug, University of Sustainable Development, Eberswalde, Germany
[3] Laboratory for timber construction and ecological building technology, Eberswalde, Germany
[4] Hartmut Pasternak, Brandenburg University of Technology, Germany, hartmut.pasternak@b-tu.de

https://doi.org/10.52202/069179-0394

built structures satisfy public safety requirements [9]. The reliability index β is thus a comparative value of the actual analysis and should not be used separated from the underlying model assumptions.

Based on these considerations, the following path is chosen: Timber members in common limit states are designed for a 100% utilisation of the semi-probabilistic design-check equations with current partial safety factors (PSF) from EC 1 [10] and EC 5 [11] ($\gamma_G = 1.35$ for permanent loads, $\gamma_Q = 1.5$ for variable loads, $\gamma_M = 1.3$ for structural timber strength properties) and evaluated by reliability analyses. The resulting reliability level is determined for a set of limit states, load ratios and a range of the coefficient of variation (*cov*) of the material strength. Based on the obtained reliability level, PSF are calibrated for chosen limit states aiming for an optimised verification of existing timber structures with dominating limit states clearly defined. Besides, options to update PSF based on new information are discussed. Finally, a proposal for a stepwise evaluation procedure is presented. Selected limit states for the analyses are given in Figure 1. The numbering is used in the presentation of results.

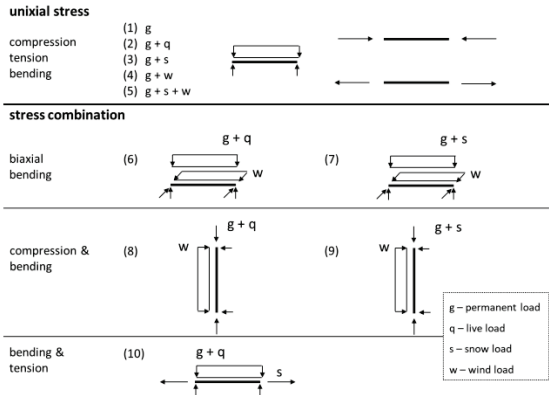

Figure 1: *Loads, load directions and stresses*

The general formulation of the limit state function (LSF) is given by eq. (1)

$$g_i(R, G, Q_1, Q_2, \theta_R, \theta_G, \theta_{Q1}, \theta_{Q2}) = z_d \theta_R R - LA_G \theta_G G - (1 - a_G)\left(LA_{Q1}\theta_{Q1}E_1 \cdot (1 - LA_{Q1})\theta_{Q2}E_2\right) \stackrel{!}{=} 0 \quad (1)$$

with R the resistance variable and θ_G its model uncertainty, G the permanent action and θ_G the model uncertainty associated with it. Q_1 and Q_2 are two variable actions, θ_{Q1} and θ_{Q2} their model uncertainty variables. LA_G is the load ratio of the permanent action and LA_{Q1} is the load ratio of the first variable action in relation to the total variable load. Variable loads are combined using the *Ferry Borges & Castanheta* combination rule [12]. What is more, z_d is the design parameter to ensure a one-hundred percent utilisation of the semi-probabilistic design equation, see [13]. It can be calculated by eq. (2) for one an eq. (3) for two variable actions

$$z_d \frac{k_{mod} \cdot f_k}{\gamma_M} - \gamma_G LA_G g_k - \gamma_Q (1 - LA_G) q_k \stackrel{!}{=} 0 \quad (2)$$

$$z_d \frac{k_{mod} \cdot f_k}{\gamma_M} - \gamma_G LA_G g_k - \gamma_Q (1 - LA_G)\left(LA_{Q1} q_{1,k} + (1 - LA_{Q1}) q_{2,k}\right) \stackrel{!}{=} 0 \quad (3)$$

with k_{mod} the modification factor for load duration and service class, f_k, g_k and q_k the characteristic values for the material strength, permanent and variable loads respectively. Limit states have been formulated according to EC 5-1 [11]. Probabilistic parameters are given in Table 1. The *cov's* of the material strength are based on [14] and a broad literature study in [15]. The influence of alterations of the material *cov* are studied. *Cov's* for live loads are based on own calculations applying [16, 17], see [15]. Parameters for snow and wind loads are based on [17] (wind) and [18] (snow). Load change rates have been oriented on [13] and adopted for German climatic conditions. Please note that in the current version of the JRC documentation "*Reliability background in the Eurocodes*" (unpublished) a higher variability of snow and wind loads has been documented. This especially affects the time-invariant part (taken here with $V_\theta = 0.10$). Besides, the variability of the bending strength is lower in the mentioned report ($V_{fm} = 0.20$) than in the present study ($V_{fm} = 0.25$). As the report was not published at the time of preparation of this contribution, values have been assumed based on the official background documentation of *DIN 1055-100* [18] and the *JCSS PMC* [14, 17].

Table 1: *Probabilistic parameters,* $T_{ref} = 50\ years$

		Variable		Distr.	μ	V
R	Timber[1]	Bending strength	f_m	LN	1.00	0.25
		Comp. strength parallel to grain	$f_{c,0}$	LN	1.00	0.20
		Tension strength parallel to grain	$f_{t,0}$	LN	1.00	0.30
E	**Permanent loads[2]**		G	N	1.00	0.10
	Live Load[3]					
	Small room (A ≤ 20m²)		N	GUM	1.00	0.40
	Large room (A > 20m²)				1.00	0.25
	Snow load[4]		S	GUM	1.00	0.25
			n_p	det.	50·60	-
			n_r	det.	10	-
	Wind load[4]		W	GUM	1.00	0.16
			n_p	det.	50·365	-
			n_r	det.	50·365	-
Model[5]	**Resistance**		θ_f	N	1.00	0.07
	Load	Permanent load	θ_G	N	1.00	0.05
		Live load	θ_N	N	1.00	0.10
		Snow load[6]	θ_S	N	1.00	0.10
		Wind load[6]	θ_W	N	1.00	0.10

[1] Indicative from [14], analyses for a range of values; [2] Based on [14]; [3] T_{ref} = 50a, based on own calculations; [4] T_{ref} = 50a, based on [13, 17, 18]; [5] Multiplicative, attached to variable

The reliability analyses are performed by *First Order Reliability Method (FORM)* [19] in MATLAB® [20]. Calculations have been double-checked by exemplary hand calculations with the help of [21] and a selection of *Monte Carlo Simulations* (*MCS*) in MATLAB® [20]. To study the influence of the variables on the calculated reliability, sensitivity factors for selected configurations are shown. Based on the results, a proposal for the target reliability is worked out. γ_M is then calibrated for a set of limit states by *FORM*. As permanent loads can be updated on site, an update of permanent actions as suggested in *SIA 269/2011* [4] is considered in the modification of γ_G and an adjustment of the stochastic properties in the calibration. To avoid systematic programming errors, the

verification is done by *Monte Carlo Simulation* (*MCS*). All calculations have been performed on single structural components. Calibrated PSF and a suggestion for the update of γ_M based on a reference property are structured in an evaluation procedure for practical application. All calculations have been performed for $T_{ref} = 50\ years$.

3 RESULTS

3.1 Reliability analyses

3.1.1 Permanent loads (1)

Figure 2 and Table 2 show the results for permanent load with three different *cov's*. The blue line indicates the target of EN 1990 Annex C ($T_{ref} = 50\ years$) and consequence class (CC) 2. The sensitivity factors confirm the dominating influence of the structural resistance on the reliability. Please note that $\sum \alpha^2 = 1$; an α-value close to 1 shows a great influence of the considered value on the calculated reliability. For $V_G \geq 0.10$ the calculated reliability is lower than the target from EC 0, Annex C.

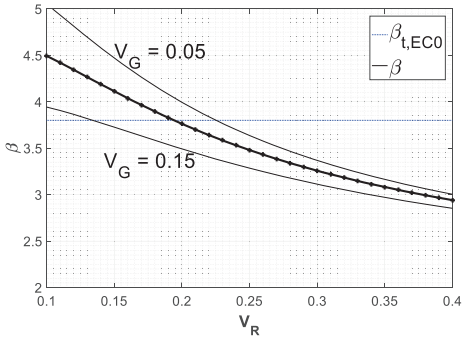

Figure 2: *Reliability index for permanent loads (1)*

Table 2: *Exemplary sensitivity factors*

V_R	f	G	θ_f	θ_G
		$V_G = 0.05$		
0.20	-0.89	0.21	-0.35	0.21
0.25	-0.92	0.18	-0.28	0.18
0.30	-0.95	0.16	-0.24	0.16
		$V_G = 0.10$		
0.20	-0.84	0.37	-0.33	0.21
0.25	-0.89	0.32	-0.27	0.18
0.30	-0.92	0.29	-0.23	0.15
		$V_G = 0.15$		
0.20	-0.80	0.48	-0.30	0.19
0.25	-0.85	0.43	-0.26	0.17
0.30	-0.88	0.38	-0.22	0.15

3.1.2 Permanent and one variable load (2), (3) & (4)

The analyses have been performed for one variable load with $V_Q = 0.25$ (Figure 3, Table 3). The reliability analyses show lower reliabilities than the target. Sensitivity factors reveal the increasing influence of the variable load with increasing load ratio.

Further analyses have been performed for one variable load (wind load) with $V_W = 0.16$ (Figure 4, Table 4). Recent analyses on wind load modelling can be found in [22]. Further studies indicate that the total wind load could be modelled using *cov's* in the range $V_{W,50} = 0.20...0.25$, see e.g. [23, 24]. For further calculations in this study $V_{W,50} = 0.16$ for the time invariant part based on the calculation applying the coefficients in [17] as indicated above and with regard to studies in [25, 26] and $V_{W,\theta} = 0.10$ for the time-invariant part is assumed.

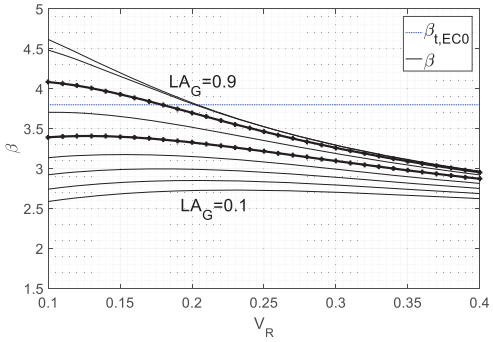

Figure 3: *Reliability index for permanent and one variable load with* $V_Q = 0.25$*, (2)/(3)*

Table 3: *Exemplary sensitivity factors,* $V_Q = 0.25$

V_R	f	G	Q	θ_f	θ_G	θ_Q
			$LA_G = 0.3$			
0.20	-0.80	0.16	0.45	-0.30	0.12	0.15
0.25	-0.87	0.15	0.35	-0.26	0.11	0.13
0.30	-0.91	0.14	0.29	-0.23	0.10	0.11
			$LA_G = 0.5$			
0.20	-0.68	0.08	0.64	-0.26	0.06	0.21
0.25	-0.77	0.08	0.55	-0.23	0.06	0.19
0.30	-0.84	0.08	0.47	-0.21	0.06	0.17
			$LA_G = 0.7$			
0.20	-0.61	0.04	0.72	-0.22	0.03	0.24
0.25	-0.70	0.04	0.65	-0.21	0.03	0.22
0.30	-0.77	0.04	0.58	-0.19	0.03	0.20

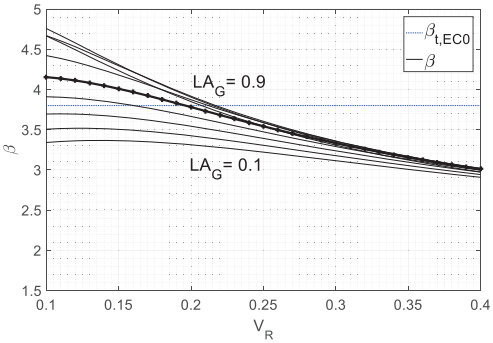

Figure 4: *Reliability index for permanent and one variable load with* $V_Q = 0.16$ *(4)*

Table 4: *Exemplary sensitivity factors,* $V_Q = 016$

V_R	f	G	W	θ_f	θ_G	θ_W
			$LA_G = 0.3$			
0.20	-0.86	0.19	0.26	-0.33	0.14	0.14
0.25	-0.91	0.17	0.20	-0.28	0.12	0.12
0.30	-0.93	0.15	0.17	-0.23	0.11	0.10
			$LA_G = 0.5$			
0.20	-0.79	0.11	0.47	-0.30	0.08	0.22
0.25	-0.86	0.10	0.37	-0.26	0.07	0.19
0.30	-0.90	0.09	0.30	-0.23	0.07	0.16
			$LA_G = 0.7$			
0.20	-0.71	0.05	0.60	-0.27	0.04	0.26
0.25	-0.80	0.05	0.50	-0.24	0.04	0.23
0.30	-0.85	0.05	0.42	-0.21	0.03	0.21

https://doi.org/10.52202/069179-0394

3.1.3 Permanent, snow and wind load (5)

Figure 5 illustrates the reliability for flexural stress from combinations of permanent, snow and wind load. An analysis for Germany showed that for roof angles 30° < α < 75° the load ratio of permanent loads is approximately 50% for normal roof weights (comparison of mean values, coastal areas excluded). Thus, exemplary sensitivity factors for $LA_G = 0.5$ and two different *cov's* of the material strength are given in Table 5**.** Due to the assumed low variability of the wind load its influence on the reliability is rather small. Note that these values are exemplary for $LA_G = 0.5$ and the influence of variable loads increases with greater load ratio.

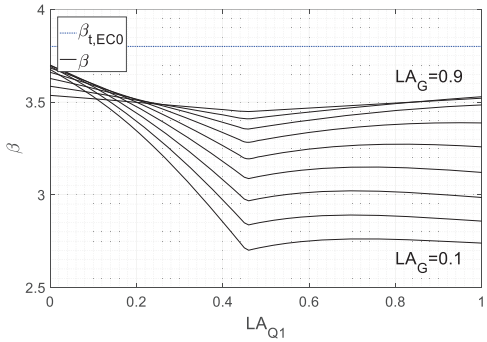

Figure 5: *Reliability index for permanent and variable load 1 (snow) and variable load 2 (wind) with $V_R = 0.25$, uniaxial stress (5)*

Table 5: *Exemplary sensitivity factors, $V_R = 0.25$, $LA_G = 0.5$*

V_R	f	G	S	W	θ_f	θ_G	θ_S	θ_W
				$LA_{Q1} = 0.3$				
0.20	-0.88	0.21	0.18	0.00	-0.34	0.11	0.07	0.14
0.25	-0.92	0.18	0.14	0.00	-0.28	0.09	0.06	0.12
				$LA_{Q1} = 0.5$				
0.20	-0.84	0.19	0.34	0.00	-0.32	0.10	0.12	0.09
0.25	-0.90	0.17	0.26	0.00	-0.27	0.09	0.10	0.08
				$LA_{Q1} = 0.7$				
0.20	-0.78	0.16	0.50	0.00	-0.30	0.08	0.17	0.04
0.25	-0.85	0.15	0.39	0.00	-0.26	0.08	0.14	0.04

3.1.4 Biaxial bending (6) & (7)

Biaxial flexural stress from permanent load and snow (6) or live (7) load in one direction and wind load in the other direction, as relevant for e.g. purlins or half-timber walls, have been analysed, considering different load presence time n_p and load change rate n_r. Flexural strengths in both directions are correlated with $\rho = 0.8$. The ratio of width and height has been assumed $b/h = 1/2$; a ratio was needed to calculate the design parameter z_d. However, the influence of the latter has been turned out to be rather small. A load distribution factor $k_m = 0.7$ for rectangular cross sections has been applied according to EC 5-1 [11]. Figure 6 and Figure 7 show the results. It has turned out that the difference to one-axial bending is rather small for the considered configurations. Sensitivity factors are very similar to Table 5 and thus not repeated here, details can be found in [15].

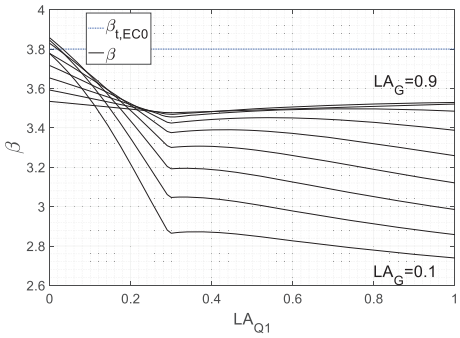

Figure 6: *Reliability index for permanent and variable load 1 (snow) and variable load 2 (wind) with $V_R = 0.25$, biaxial bending (6)*

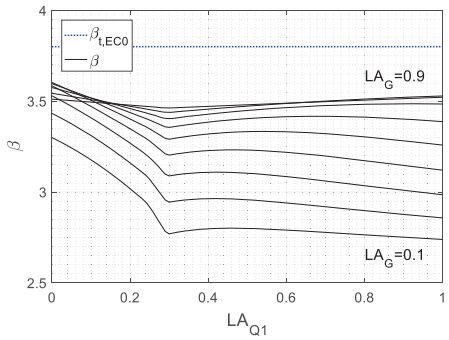

Figure 7: *Reliability index for permanent and variable load 1 (live load) and variable load 2 (wind) with $V_R = 0.25$, biaxial bending (7)*

3.1.5 Compression + bending (8) & (9)

The combination of compression and flexural stress has been analysed for compression from permanent and snow load (8) / live load (9) and bending from wind load as e.g. relevant for struts in roof structures of half-timbered walls. Strength properties are correlated with $\rho = 0.8$. The ratio of width and height is $b/h = 1/2$. Figure 8 and Figure 9 show the reliability. The analyses show that for LA_{Q1} the reliability is rather constant for an increasing ratio of variable load one (snow in (8); live load in (9)). Table 6 and Table 7 sensitivity factors for $LA_G = 0.5$.

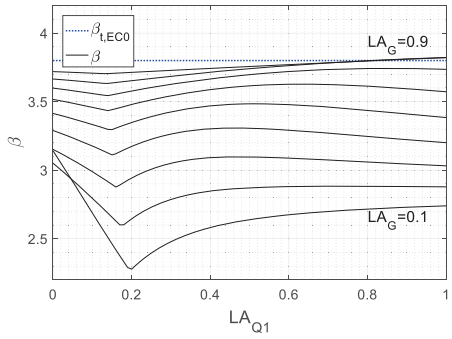

Figure 8: *Reliability index for compression from permanent and variable load 1 (snow load) and bending from variable load 2 (wind) with $V_{R,m} = 0.25$, $V_{R,c} = 0.20$ (8)*

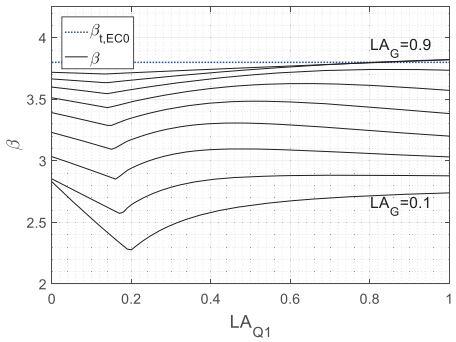

Figure 9: *Reliability index for compression from permanent and variable load 1 (live load) and bending from variable load 2 (wind) with $V_{R,m} = 0.25$, $V_{R,c} = 0.20$ (9)*

Table 6: *Exemplary sensitivity factors, $V_{R,m} = 0.25$, $V_{R,c} = 0.20$, $LA_G = 0.5$ (8)*

f_m	f_c	G	S	W	θ_f	θ_G	θ_S	θ_W
$LA_{Q1} = 0.3$								
- 0.74	- 0.44	0.26	0.23	0.00	- 0.33	0.14	0.09	0.06
$LA_{Q1} = 0.5$								
- 0.68	- 0.44	0.21	0.41	0.00	- 0.31	0.11	0.14	0.04
$LA_{Q1} = 0.7$								
- 0.61	- 0.43	0.16	0.54	0.00	- 0.28	0.09	0.18	0.02

Table 7: *Exemplary sensitivity factors, $V_{R,m} = 0.25$, $V_{R,c} = 0.20$, $LA_G = 0.5$ (9)*

f_m	f_c	G	S	W	θ_f	θ_G	θ_S	θ_W
$LA_{Q1} = 0.3$								
- 0.74	- 0.44	0.26	0.23	0.00	- 0.33	0.14	0.09	0.06
$LA_{Q1} = 0.5$								
- 0.68	- 0.44	0.21	0.41	0.00	- 0.31	0.11	0.14	0.04
$LA_{Q1} = 0.7$								
- 0.61	- 0.43	0.16	0.54	0.00	- 0.28	0.09	0.18	0.02

3.1.6 Tension + bending (10)

The combination tension and flexural stress has been analysed for tension from permanent/snow load and bending from live load (e.g. tension beams in collar beam roof structures). Strength values are correlated ($\rho = 0.8$). The ratio of width/height is $b/h = 1/2$. Figure 10 shows the reliability, Table 8 shows exemplary sensitivity factors, that reveal the dominating influence of the combination of snow load and tension stress. The reliability has been found out to be comparatively low, which is due to the disadvantageous combinations of variables with a high variability. However, it has to be noted that in existing roof structures this limit state for the mentioned elements is commonly not characterised by a utilisation of 100 %.

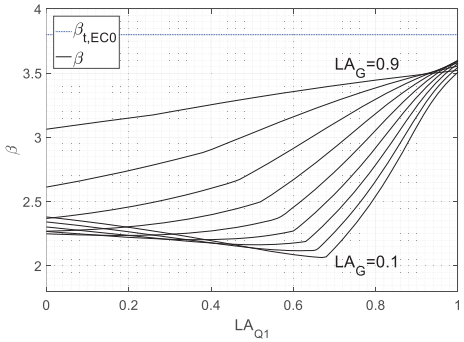

Figure 10: *Reliability index for tension from permanent and variable load 1 (snow) and bending from variable load 2 (live load) with $V_{R,m} = 0.25$, $V_{R,t} = 0.30$ (10)*

Table 8: *Exemplary sensitivity factors, $V_{R,m} = 0.25$, $V_{R,t} = 0.30$ (10)*

f_m	f_t	G	N	S	θ_f	θ_G	θ_N	θ_S
$LA_{Q1} = 0.3$								
- 0.62	- 0.34	0.06	0.01	0.65	- 0.19	0.03	0.02	0.19
$LA_{Q1} = 0.5$								
- 0.68	- 0.32	0.07	0.01	0.60	- 0.21	0.04	0.03	0.17
$LA_{Q1} = 0.7$								
- 0.77	- 0.26	0.10	0.03	0.50	- 0.23	0.05	0.07	0.14

3.2 Summary and discussion of target reliability

The analyses of these rather simple limit states result in significant lower reliability indices than the target from *EC 0 Annex C* [2] for consequence class CC2 ($\beta = 3.8$, $T_{ref} = 50\ years$). The aim of the present study is to work out a proposal for an adjusted semi-probabilistic verification format for existing timber structures. As a basis it is assumed that current design fulfils public safety requirements and can thus serve as a basis to define target values. This assumption is justified as no increased number of failure events has been documented for these common limit states. Thus, it is suggested to take the average reliability level from the presented analyses as a target value. The combination of tension and bending can be excluded as these members mostly do not show a utilisation of 100%; verification is often governed by connections which is not in the focus of this work. Based on the presented analyses $\beta_{t,exis} = 3.2$ is suggested.

According to [27] two levels are needed for the evaluation of existing structures: a minimum level and a target level. For the evaluation of existing members in structures not affected by structural changes and supposed to clearly defined dominating limit states it is suggested to apply a target reliability, that considers aspects of economic optimisation. [28] suggest to apply $\Delta\beta = -0.5$ for a target reliability of existing structures and $\Delta\beta = -1.5$ for a minimum reliability. [29] suggests to move one line higher for the relative costs of safety measures from *ISO 2394:2015* [3] what results in $\Delta\beta = -0.2 \ldots -0.9$. Based on the results of the analyses, $\beta_{t,eval} = 2.9$ is suggested as a target for members in service ($T_{ref} = 50\ years$) that

https://doi.org/10.52202/069179-0394

are not affected by damages or major changes. During calibration of partial safety factors, a scatter around the target will occur. During the calibration for the defined target, the reliability should not fall below the minimum level $\beta_0 = 2.5$. which is the minimum reliability level under economic optimisation in [30]. Alterations of structural members should be verified using the same safety elements as for new structures.

3.3 Calibration of partial safety factors

3.3.1 Method

The major work in engineering practice is performed applying the semi-probabilistic safety format using partial safety factors (PSF). For the limit states (1) – (9) (Figure 1) and the target reliability levels proposed above the PSF $\gamma_{M,opt}$ for the material strength has been calibrated. The general optimisation procedure is described in [3, 31, 32] and given in eq. (4)

$$min\, D\,(\gamma_M) = \sum_i w_i w_{pen} (\beta_i - \beta_t)^2 \qquad (4)$$

with w_i the weighting factor for the LSF and w_{pen} a penalty factor, penalising a reliability lower than the target more than a higher one [9]. Different penalty functions have been investigated in [13]. For this work, penalty factors from eq. (5) have been applied.

$$w_{pen} = \begin{cases} 1 & for \quad \beta_i \geq \beta_t \\ 1 + (\beta_i - \beta_t) & for \quad \beta_i < \beta_t \end{cases} \qquad (5)$$

All considered load combinations of snow and wind load have been weighted equally, as studies indicated that they vary a lot depending on location and roof angle and no clear weighting could be identified [15]. For permanent and live load, the weighting factors in Table 9 have been considered and compared to results assuming $LA_G = 0.5$ and $V_N = 0.25$ only. Results of the three options have turned out to lead to similar results.

Table 9: *Weighting factor w_i for permanent and live loads*

	V_N	LA_Q	w_i		Remarks
			a	**b**	
1)	0,25 (A > 20m²)	0,3	0,50	0,35	*Live load categories office, lobby and living room with A > 20m², and hotel and class rooms.*
2)	0,25 (A > 20m²)	0,5	0,40	0,50	*Live load categories office, lobby and living room with A > 20m², and hotel and class rooms.*
3)	0,40 (A ≤ 20m²)	0,5	0,10	0,15	*Live load categories office, lobby and living room with A ≤ 20m², and hospital rooms.*
			$\Sigma = 1$	$\Sigma = 1$	

During calibration the PSF for permanent and variable loads have been fixed to $\gamma_G = 1.20$ and $\gamma_Q = 1.50$, respectively. The value $\gamma_G = 1.20$ takes into account a reduced variability of permanent loads obtained in a survey on site and is chosen based on [4]. The reduced variability is also considered by a reduced variability of permanent actions of 7% instead of 10% to consider an investigation on site. The results are based on a load ratio of permanent loads of $LA_G = 0,5$ and further statistical parameters given in Table 1.

3.3.2 Results

Table 10 and Table 11 show the results for the suggested reliability index for the evaluation level. In [15] results for further reliability indices can be found.

Table 10: *Calibration results $\gamma_{M,opt}$ for the proposed evaluation level and uniaxial stresses*

	permanent load (1)	live load (2)	snow load (3)	wind load (4)	snow + wind load (5)
V_R	$\gamma_{M,opt}$	$\gamma_{M,opt}$	$\gamma_{M,opt}$	$\gamma_{M,opt}$	$\gamma_{M,opt}$
0.18	1.14	1.19	1.19	1.11	1.15
0.20	**1.16**	**1.19**	**1.19**	1.13	**1.17**
0.22	1.18	1.21	1.21	1.15	1.19
0.25	**1.22**	**1.23**	**1.23**	**1.19**	**1.22**

Table 11: *Calibration results $\gamma_{M,opt}$ for the proposed evaluation level and simple stress combinations*

	two-axial bending (6)	two-axial bending (7)	comp. + bending (8)	comp. + bending (9)
$V_{R,m}$	$\gamma_{M,opt}$	$\gamma_{M,opt}$	$\gamma_{M,opt}$	$\gamma_{M,opt}$
0.18	1.15	1.16	1.19	1.18
0.20	1.17	1.17	1.20	1.19
0.22	1.19	1.19	1.21	1.20
0.25	**1.22**	**1.22**	**1.23**	**1.22**

$V_{R,m}$ – coefficient of variation (cov) of the bending strength. cov of compression strength correlated by $\rho = 0.8$

3.3.3 Summary and Proposal

Keeping in mind practical applicability, the number of PSF should be limited. Thus, a simplified set of optimised PSF $\gamma_{M,opt}$ is proposed that considers the inhomogeneity and anisotropy of timber as structural material but keeps the intended ease of use of the semi-probabilistic design / evaluation format, (Table 12). As $\gamma_Q = 1.5$ for all variable loads, $\gamma_{M,opt}$ also depends on the considered loads. The application of different PSF for different variable loads to consider their statistical properties properly would help to reach a more uniform reliability level.

Table 12: *Proposal for a set $\gamma_{M,opt}$ for the evaluation level*

stress	**loads**	
	perma-nent	combinations with variable loads
compression parallel to grain	1.15	1.20
bending, two-axial bending, comp.& bending	1.20	1.20
tension parallel to grain	1.30	1.30

Remarks: Calibration for $\beta_{t,eval} = 2{,}9$, live load categories A and B, snow and wind loads, load ratio of permanent load $LA_G \geq 0.5$, $\gamma_{G,up} = 1.20$, $\gamma_Q = 1.50$

In order to apply the results (Table 10, Table 11) for an updated material variability from material tests, a sufficient number of tests has to be considered. A proposal in [26] introduces a conversion factor to account for a limited number of tests. For rehabilitation measures PSF as for new structures should be applied in accordance with [33] where it is stated that structural members directly affected by changes should be verified applying the same requirements as for new structural members.

3.3.4 Verification of PSF

The verification of results is an important part of scientific work. While the calibration of modified PSF has been performed with *FORM*, the verification has been performed by *MSC* (crude *Monte Carlo Sampling*) to avoid systematic programming errors. Results have been double checked with *FORM* analyses. Exemplary results are presented in Figure 11 to Figure 16 (graphs produced applying *FORM* after double check with *MCS)*. All analyses are performed for $T_{ref} = 50\ years$. All figures are based on a 100% utilisation of the semi-probabilistic design-check equation. PSF are $\gamma_{G,up} = 1.20$, $\gamma_Q = 1.50$, $\gamma_{M,opt} = 1.20$.

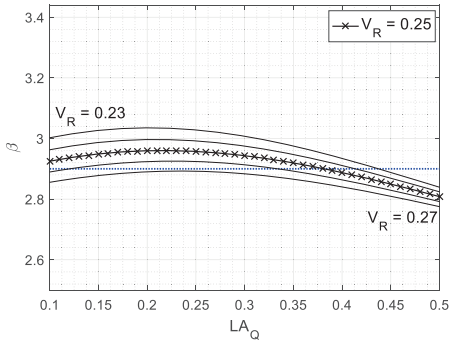

Figure 11: *Reliability index for uniaxial stress, permanent and one variable load with* $V_Q = 0.25$

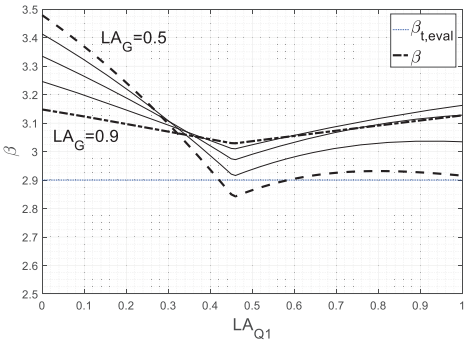

Figure 12: *Reliability index for uniaxial stress, permanent, snow and wind load,* $V_R = 0.20$

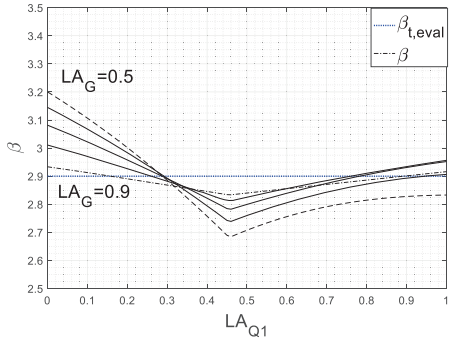

Figure 13: *Reliability index for uniaxial stress, permanent, snow and wind load,*$V_R = 0.25$

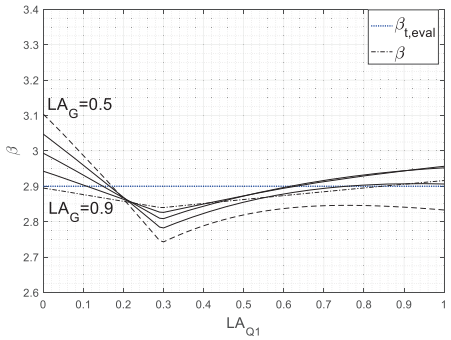

Figure 14: *Reliability index for two-axial bending, permanent, snow and wind load,* $V_R = 0.25$

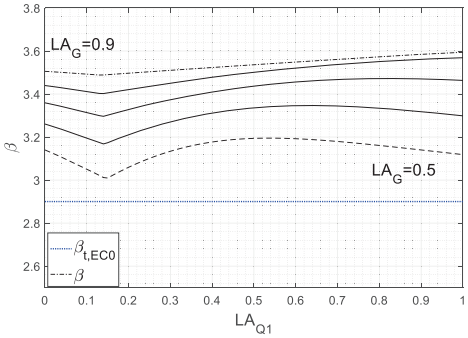

Figure 15: *Reliability index for compression and bending, permanent, snow and wind load,*$V_{R,m} = 0.25$, $V_{R,c} = 0.20$

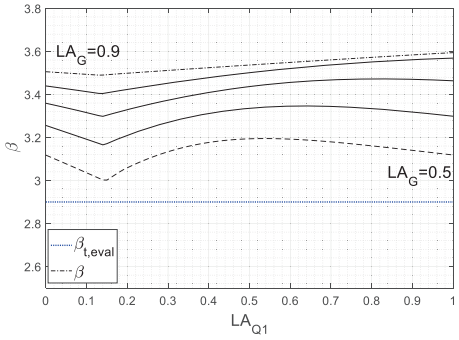

Figure 16: *Reliability index for compression and bending, permanent and live and wind load,*$V_{R,m} = 0.25$, $V_{R,c} = 0.20$

Neglectable differences between results of FORM and MCS have been identified. Thus, for the investigated limit states a sufficient accuracy of the approximation by FORM is given and systematic errors are not present.

The results show that the calibration target $\beta_{t,eval} = 2.9$ (indicated by blue horizontal line) has kept in the majority of analyses. The scatter results from the selection of a limit number of PSF. Thus, the calibration has been successful for the chosen target. However, the target reliability index is chosen based on the analyses presented and needs further discussion by the scientific community and relevant authorities. Results for further targets in the range $2.5 \leq \beta \leq 3.2$ can be found in [15].

https://doi.org/10.52202/069179-0394

3.4 Update of Partial Safety Factors based on Material Update

A great potential when analysing the load-bearing capacity of an existing structure is that it exists in tangible form. Updated material models can be built combining on-site tests and analyses in the laboratory, see e.g. [34]. Different options for the consideration of updated material properties in the semi-probabilistic safety format can be described. One is the application of an improved strength grading supported by technical means, see e.g. [35]. This is, however, not in the focus of this work.

Another option is the consideration of reduced uncertainties due to a detailed investigation in situ by adjusted safety elements. Here also two options can be discussed. The first one is the modification of PSF based on a reduced material variability by direct update of the variable. Adjusted PSF can be calculated applying the *Design Value Method* (DVM) or the *Adjusted Partial Safety Factor Method* (APFM) as described in [36]. Additional to knowledge concerning the special material variability at hand, a target reliability that has been agreed upon and sensitivity factors are needed. Simplified sensitivity factors can be taken from [2]. However, sensitivity factors are factors considering the influence of the change of a certain variable in the limit state on the reliability. Thus, the application of simplified sensitivity factors ignores the advantage of the availability of more detailed information concerning the actual load and material properties at hand and the governing limit state. Hence, updated sensitivity factors for certain limit states as outcome of the presented reliability analyses can be applied. Note that these sensitivity factors are only applicable if updated PSF are also applied for the loads by updated sensitivity factors to keep the intended reliability.

The second option is the update of the PSF on the material side using an updated reference variable. A proposal is described in [37] and presented shortly hereinafter.

The mean value $\mu_{y|x_{meas}}$ and the standard deviation $\sigma_{y|x_{meas}}$ of a target property y dependent on a reference variable x are defined by eq. (6) and (7), respectively, see [38]. $\mu_{y,code}$ and $V_{y,code}$ are the mean value and the *cov* of the target variable as defined in prior information (e.g. a code), respectively. $\mu_{x,code}$ and $V_{x,code}$ are the mean value and the *cov* of the reference variable as defined by prior information, $\rho_{x,y}$ is the correlation coefficient.

$$\mu_{y|x_{meas}} = \mu_{y,code} \cdot \left(1 + \rho_{x,y} \cdot V_{y,code} \cdot \frac{x_{meas} - \mu_{x,code}}{\mu_{x,code} \cdot V_{x,code}}\right) \quad (6)$$

$$\sigma_{y|x_{meas}} = V_{y,code} \cdot \mu_{y,code} \cdot \sqrt{1 - \rho_{x,y}^2} \quad (7)$$

Eq. (8) is derived from eq. (6) and (7).

$$V_{y|x_{meas}} = \frac{\sigma_{y|x_{meas}}}{\mu_{y|x_{meas}}} \quad (8)$$

$$V_{y|x_{meas}} = \frac{V_{y,code} \cdot \sqrt{1 - \rho_{x,y}^2}}{\left(1 + \rho_{x,y} \cdot V_{y,code} \cdot \frac{x_{meas} - \mu_{x,code}}{\mu_{x,code} \cdot V_{x,code}}\right)}$$

with eq. (9) for the PSF of a lognormal distributed resistance variable, the updated PSF $\gamma_{m,\mathrm{up}}$ can be calculated according to eq. (10). Here α_R is the sensitivity factor of the resistance variable, β is the target reliability and q is the quantile of the distributed used to define the characteristic value for semi-probabilistic design.

$$\gamma_m = exp\left(V_R \cdot \left(\alpha_R \cdot \beta + \Phi^{-1}(q)\right)\right) \quad (9)$$

$$\gamma_{m,\mathrm{up}} = exp\left(\frac{V_{y,code} \cdot \sqrt{1-\rho_{x,y}^2}}{\left(1+\rho_{x,y} \cdot V_{y,code} \cdot \frac{x_{meas}-\mu_{x,code}}{\mu_{x,code} \cdot V_{x,code}}\right)} \cdot \left(\alpha_R \cdot \beta + \Phi^{-1}(q)\right)\right) \quad (10)$$

The model uncertainty factor γ_{Rd} is considered by eq.(11).

$$\gamma_{M,\mathrm{up}} = \gamma_{Rd} \cdot \gamma_{m,\mathrm{up}} \quad (11)$$

Application examples can be found in [38, 39]. Please note that uncertainties determining the reference variable, e.g. measurement errors are not considered in this approach. An option is the consideration of an additional error term as described in [40] and left to further work.

3.5 Suggestion of a stepwise evaluation procedure

An evaluation procedure for existing structures needs to be flexible in terms of applicability for the actual circumstances at hand. That includes availability of information, consequences of failure and economic considerations. Thus, a procedure is needed that embraces levels with lower degree of information and an evaluation more on the safe side and different options to include updated information that comes along with higher efforts in terms of time and costs. A proposal has been presented in [41]. The stepwise evaluation procedure embraces three *Knowledge Levels* (terminology based on [30]) including an evaluation without update (*KL 1*), a level including a modified semi-probabilistic evaluation divided into three sublevels (*KL 2*) and a level for advanced probabilistic methods (*KL 3*), see Table 13. With increasing level, the information becomes more detailed as well as the evaluation format does. These levels are connected to a proposal for strength grading levels (*SGL*), see [35]. An application example can e.g. be found in [39].

Table 13: *Proposal for a stepwise evaluation procedure*

<table>
<tr><th colspan="3">semi-probabilistic <u>without</u> update - KL 1</th></tr>
<tr><td colspan="3">visual grading in situ
partial safety factors from
EN 1990, EN 1995-1-1, EN 1995-1-1/NA</td></tr>
<tr><th colspan="3">semi-probabilistic <u>with</u> update - KL 2</th></tr>
<tr><td>KL 2a)</td><td>KL 2b)</td><td>KL 2c)</td></tr>
<tr><td colspan="3">update of permanent loads: $\gamma_{G,up} = 1{,}20$ (unfavourable)</td></tr>
<tr><td colspan="3">variable loads: $\gamma_Q = 1{,}50$</td></tr>
<tr><td>visual grading in situ</td><td>grading supported by tech. devices</td><td>update of material parameters</td></tr>
<tr><td>strength grade: visual grading</td><td>strength grade: grading supported by tech. devices</td><td>update of material properties by material tests</td></tr>
<tr><td colspan="2">PSF on resistance side as optimised $\boldsymbol{\gamma_{M,opt}}$ for actual limit states</td><td>PSF on resistance side for updated property $\boldsymbol{\gamma_{M,up}}$</td></tr>
<tr><th colspan="3">probabilistic - KL 3</th></tr>
<tr><td colspan="3">grading supported by technical devices /
update of material parameters</td></tr>
<tr><td colspan="3">probabilistic evaluation by approximation or simulation
update of material model based on material tests</td></tr>
</table>

Please note that the calibration results for $\gamma_{M,opt}$ are only applicable under the given requirements and the intended limit states and load ratios. As results are given depending on the *cov* of the material strength, an updated of material properties leading to e.g. a reduction of the scatter can be considered by choosing the results for the adjusted value. Note that for the update of material properties a sufficient number of tests and strong correlation of target and reference variable are required. As a first orientation, correlation coefficients should be $\rho > 0.6$.

4 CONCLUSION

A responsible use of energy and resources are important elements of the development of a sustainable economy. The preservation of existing structures plays a central role that has never been more important than today. Thus, code calibration cannot only focus on the necessary further development of codes in the context of the design of structures and their application on innovative structural materials. The evaluation of existing structures needs to be integrated in the concept of Eurocodes considering the special requirements that come along with this challenge. In this context, rules and requirements need to be flexible so that they can be adopted for different structural tasks.

The presented works contains analyses of the reliability of timber members according to current standards. The analyses show a scatter of the reliability depending on the considered LSF. Sensitivity factors indicate a great influence of the material strength on the calculated reliability. Based on these results, the target reliability is discussed and modified PSF depending on the LSF and, as a second option, considering an update of material properties are presented.

However, more studies considering further and more complex limit states and further detailing concerning the update of target properties based on in situ measured reference properties have to carried out to enlarge the concept for a wider range of practical cases. Besides, further studies need to embrace the reliability of historic connections, also carpenters' connections. What is more, new information on the modelling of variable actions should be considered, see e.g. [23, 24] for wind loads. Calculating the implicit reliability level of design codes, this might have an influence on the resulting reliability level. However, as the target value for the calibration has been defined based on this calculated implicit level, the evaluation of the influence on the calibration of PSF is left to further work. However, a centrals task in the development of codes and standards for existing structures, it has to be discussed how the target reliability has to be be defined for a calibration of PSF for existing structures.

ACKNOWLEDGEMENT

A major part of the content has been developed in a funding period of *The German Federal Environmental Foundation* (*DBU*, project no. 20015/409, 2016-2018). The authors thank the institution for the generous support.

REFERENCES

[1] *Assessment and retrofitting of existing structures*, TS 17440:2019 (E), CEN/TC 250, Oct. 2020.

[2] *Basis of structural design*, DIN EN 1990:2010-12, CEN, Dec. 2010.

[3] *General principles on reliability for structures*, ISO 2394:2015(E), ISO, Schweiz, 2015.

[4] *Grundlagen der Erhaltung von Tragwerken*, SIA 269:2011, SIA, Zürich, Jan. 2011.

[5] *Bases for design of structures - Assessment of existing structures*, ISO 13822:2010(E), ISO, Aug. 2010.

[6] *Conservation of cultural heritage – Historic Timber Structures – Guidelines for the On Site Assessment*, EN 17121:2019-12, CEN, 2019.

[7] C. J. Turkstra, *Theory of Structural Design Decisions: Study No. 2*. Ontario, Canada, 1970.

[8] R. E. Melchers, *Structural reliability analysis and prediction,* 2nd ed. Chichester: Wiley, 1999.

[9] M. Baravalle and J. Köhler, "A framework for estimating the implicit safety level of existing design codes," in *12th International Conference on Structural Safety and Reliability (ICOSSAR)*, Vienna, 2017, pp. 1037–1046.

[10] *Eurocode 1: Actions on structures – Part 1-1: General actions – Densities, self-weight, imposed loads for buildings*, EN 1991-1-1:2010-12, CEN, Dec. 2010.

[11] *Design of timber structures – Part 1-1: General – Common rules and rules for buildings*, EN 1995-1-1:2010-12, CEN, Dec. 2010.

[12] J. Ferry Borges and M. Castanheta, *Structural Safety,* 2nd ed. Lisbon, 1971.

[13] M. Baravalle, "Risk and Reliability Based Calibration of Structural Design Codes," Dissertation, Norwegian University of Science and Technology, Trondheim, 2017.

[14] JCSS, "Probabilistic Model Code: Part 3 - Resistance Models," Joint Committee on Structural Safety, 2006. Accessed: Mar. 8 2016. [Online]. Available: http://www.jcss.byg.dtu.dk/

[15] M. Loebjinski, *Bewertung der Tragfähigkeit von Holzkonstruktionen beim Bauen im Bestand: Ein Beitrag zur substanzschonenden Erhaltung von bestehenden Gebäuden*. Dissertation, Schriftenreihe des Lehrstuhls für Stahl- und Holzbau, Band 19. Brandenburgische Technische Universität, Cottbus, 2021. [Online]. Available: http://d-nb.info/1241545375/34

[16] CIB, "Actions on Structures: Live Loads in Buildings," CIB Report W81, 1989.

[17] JCSS, "Probabilistic Model Code: Part 2 - Load Models," Joint Committee on Structural Safety, 2001. Accessed: Mar. 29 2016. [Online]. Available: http://www.jcss.byg.dtu.dk/Publications/Probabilistic_Model_Code

[18] J. Grünberg, *Grundlagen der Tragwerksplanung - Sicherheitskonzept und Bemessungsregeln für den konstruktiven Ingenieurbau: Erläuterungen zu DIN 1055-100,* 1st ed. Berlin: Beuth, 2004.

https://doi.org/10.52202/069179-0394

[19] A. M. Hasofer and N. C. Lind, “An Exact and Invariant First-Order Reliability Format,” *American Society of Civil Engineers/ Engineering Mechanics Division*, vol. 100, no. 1, pp. 111–121, 1974.
[20] MathWorks, *MATLAB*, 2016. [Online]. Available: https://www.mathworks.com/products/matlab.html
[21] G. Spaethe, *Die Sicherheit tragender Baukonstruktionen,* 2nd ed. Wien: Springer-Verlag, 1992.
[22] J. Botha, Retief, Johan, V., and C. Viljoen, “Hierarchical Bayesian wind load models for reliability assessment and calibration of standards,” in *12th International Conference on Structural Safety and Reliability (ICOSSAR)*, Vienna, 2017, pp. 2470–2479.
[23] M. Holický and M. Sýkora, “Probabilistic Models for Wind Actions,” in *2016 Second International Symposium on Stochastic Models in Reliability Engineering, Life Science and Operations Management (SMRLO)*, Beer Sheva, Israel, Feb. 2016 - Feb. 2016.
[24] T. P. McAllister, N. Wang, and B. R. Ellingwood, “Risk-Informed Mean Recurrence Intervals for Updated Wind Maps in ASCE 7-16,” *J. Struct. Eng.*, vol. 144, no. 5, p. 6018001, 2018, doi: 10.1061/(ASCE)ST.1943-541X.0002011.
[25] S. Glowienka, “Zuverlässigkeit von Mauerwerkswänden aus großformatigen Steinen: Probabilistische Analyse von großformatigem Mauerwerk aus Kalksandstein und Porenbeton mit Dünnbettvermörtelung,” Dissertation, Technische Universität Darmstadt, 2007.
[26] A. M. Fischer, “Bestimmung modifizierter Teilsicherheitsbeiwerte zur semiprobabilistischen Bemessung von Stahlbetonkonstruktionen im Bestand,” Dissertation, Technische Universität Kaiserslautern, 2010. Accessed: Mar. 29 2016. [Online]. Available: https://kluedo.ub.uni-kl.de/frontdoor/index/index/docId/2259
[27] D. Diamantidis, M. Holický, and M. Sýkora, “Reliability and Risk Acceptance Criteria for Civil Engineering Structures,” in Vol. 16, No. 2, paper #8, *Transactions of the VŠB – Technical University of Ostrava: Civil Engineering Series*, 2016.
[28] D. Diamantidis, M. Holický, and M. Sýkora, “Target Reliability Levels Based on Societal, Economic and Environmental Consequences of Structural Failure,” in *12th International Conference on Structural Safety and Reliability (ICOSSAR)*, Vienna, 2017, pp. 644–653.
[29] T. Vrouwenvelder, “Developments towards full probabilistic design codes,” *Structural Safety*, vol. 24, pp. 417–432, 2002.
[30] Joint Research Centre, “New European technical rules for the assessment and retrofitting of existing structures,” European Commission, Luxembourg, EUR, Scientific and technical research series, 2015.
[31] J. D. Sørensen, “Code Calibration and Timber Experience,” Institute of Building Technology and Structural Engineering, Aalborg University, Aalborg, COST Action E24, 2001.
[32] T. Vrouwenvelder, “Reliability Based Code calibration - The use of the JCSS Probabilistic Model Code,” JCSS, Workshop on Code Calibration, Zürich, 2001.
[33] Fachkommission Bautechnik der Bauministerkonferenz (ARGEBAU), “Hinweise und Beispiele zum Vorgehen beim Nachweis der Standsicherheit beim Bauen im Bestand,” Apr. 2008. Accessed: Jan. 15 2016. [Online]. Available: http://www.bvpi.de/bvpi-content/aktuelles/argebau.htm
[34] H. S. Sousa, J. M. Branco, and P. B. Lourenço, “A Holistic Methodology for Probabilistic Safety Assessment of Timber Elements Combining Onsite and Laboratory Data,” *International Journal of Architectural Heritage*, vol. 10, no. 5, pp. 526–538, 2015, doi: 10.1080/15583058.2015.1007177.
[35] G. Linke, W. Rug, and H. Pasternak, “Strength grading of timber in historic structures – methodology and practical application,” in *6th International Conference on Structural Health Assessment of Timber Structures (SHATiS)*, 2022.
[36] FIB, *Partial factor methods for existing concrete structures: Recommendation*. Lausanne, Switzerland: Fédération internationale du betón, 2016.
[37] M. Loebjinski, J. Köhler, W. Rug, and H. Pasternak, “Development of an optimisation-based and practice orientated assessment scheme for the evaluation of existing timber structures,” in *6th International Symposium on Life-cycle Analysis and Assessment in Civil Engineering (IALCCE)*, London: CRC Press, 2019, pp. 353–360.
[38] J. Köhler, “Die Aktualisierung als zentrales Element in den Erhaltungsnormen - Aspekte der Probabilistik,” in *Dokumentation SIA*, D 0240, *Erhaltung von Tragwerken - Vertiefung und Anwendung: Unterlagen zu den Einführungskursen*, H. Bahnholzer, Ed., Zürich, 2011, pp. 33–36.
[39] M. Loebjinski, G. Linke, W. Rug, and H. Pasternak, “Redevelopment of a wooden roof construction under preservation order,” in *5th International Conference on Structural Health Assessment of Timber Structures (SHATiS)*, 2019, pp. 912–921.
[40] S. Pöhlmann and R. Rackwitz, “Zur Verteilungsfunktion von Werkstoffeigenschaften bei kontinuierlich durchgeführten Sortierungen,” *Materialprüfung*, vol. 23, no. 8, pp. 277–278, 1981.
[41] M. Loebjinski, W. Rug, and H. Pasternak, “The Influence of Improved Strength Grading In Situ on Modelling Timber Strength Properties,” *MDPI buildings*, vol. 10, no. 2, p. 30, 2020, doi: 10.3390/buildings10020030.

World Conference on Timber Engineering Oslo 2023

REVIEW OF THE CODE DEVELOPMENT EFFORTS FOR TALL MASS TIMBER BUILDINGS IN THE US

Lori Koch[1], Matthew Hunter[2], M. Omar Amini[3]

ABSTRACT: The 2021 International Building Code (IBC) is the current edition of the predominant model building code adopted for use in the United States. For the first time in the history of US model code development, the 2021 IBC recognizes tall mass timber buildings. With the addition of three new types of construction, US designers can design tall mass timber structures up to 18 stories in height. These provisions are the culmination of a nearly five-year effort by stakeholders participating in the code development process. A brief history of this effort is presented in this paper, including the formation of the International Code Council's (ICC) Tall Wood Ad Hoc Committee. Four (4) work groups, namely, Definitions and Standards, Fire, Structural, and Codes were convened to formulate science-based code change language that led to the current provisions. Analysis of the fire testing completed in support of the code changes is presented and a brief discussion of current research and testing, as well as proposed code changes for future editions of the IBC is also discussed.

KEYWORDS: Cross-laminated Timber, Building Codes, Tall Mass Timber

1 INTRODUCTION

1.1 IBC/IRC

Structural building design in the United States most commonly falls under the jurisdiction of one of two model codes developed by the International Code Council (ICC): the International Residential Code® (IRC®) or the International Building Code®(IBC®). The IRC addresses the design and construction of one- and two-family dwellings and townhouses not more than three stories above grade. The IBC is applicable to all buildings, apart from structures designed to meet the requirements of the IRC. States or other localities across the US regularly adopt updated versions of these standards as their building code – sometimes without alterations, other times with deletions or amendments as the locality deems necessary. The process of code adoption varies from state to state, as evidenced by the map in Figure 1. Some states use a statewide adoption process, while others allow local authorities to adopt updated codes at their discretion. The IBC and IRC both have top-to-bottom provisions for the design and construction of buildings of various structural materials and systems. This paper focuses on the IBC provisions related to structural design and fire safety for mass timber structures.

1.2 NDS/SDPWS

Within the IBC and IRC are dozens of referenced standards produced by relevant organizations. The referenced standard for structural design of wood buildings is the *National Design Specification*® (NDS) *for Wood Construction*. Lateral force resisting systems in wood structures subject to wind or seismic loads are governed by the provisions of the *Special Design Provisions for Wind and Seismic*® (SDPWS), also a referenced standard in the IBC and IRC. Both the NDS and SDPWS are published by the American Wood Council (AWC), a not-for-profit trade association representing North American wood products manufacturers. AWC is accredited by the American National Standards Institute (ANSI) and develops state-of-the-art engineering data, technology, and standards on structural wood products for use by design professionals and building officials.

The NDS is AWC's longest tenured standard, providing structural and fire design provisions for solid sawn and engineered wood products as well as connections in these wood products. In the 2015 edition [1] of the NDS, structural and fire design provisions for cross-laminated timber (CLT) were added. Codified lateral design provisions for CLT diaphragm and CLT shear wall systems were subsequently introduced in the 2021 edition of SDPWS [2].

[1] Director, Educational Outreach, American Wood Council, United States, lkoch@awc.org.
[2] Northeast Regional Manager, American Wood Council, United States, mhunter@awc.org.
[3] Manager, Wind and Seismic, American Wood Council, United States, oamini@awc.org.

https://doi.org/10.52202/069179-0395

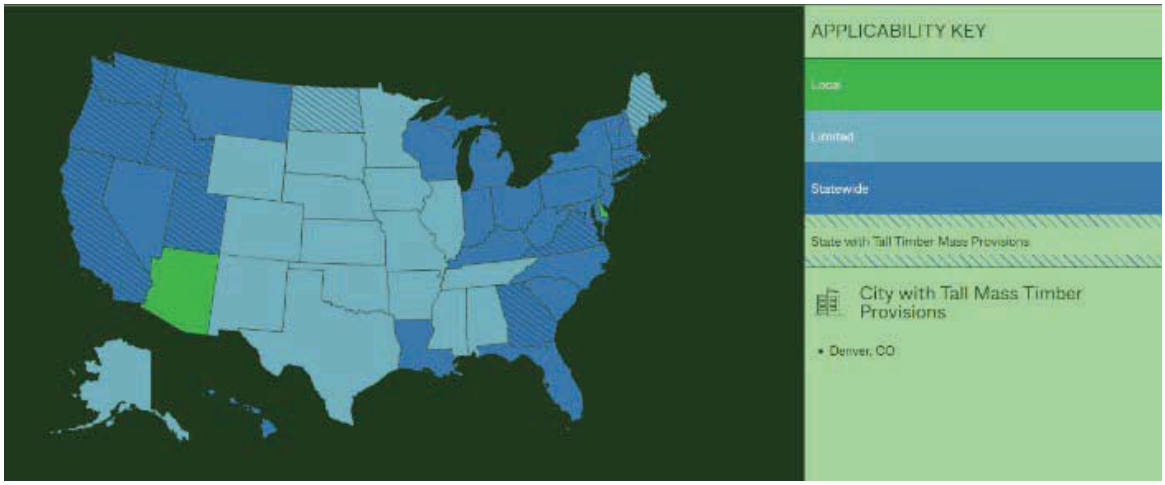

Figure 1. *Code Adoption Map*

2 WOOD BUILDING CODES PRIOR TO 2015

Type IV-HT Heavy Timber construction (referred to as Type IV prior to the adoption of the 2021 IBC [3] Tall Mass Timber provisions) have been present not only through the entire history of the IBC, but also in the historic "legacy" codes used prior to 2000 throughout the US. The definition of Type IV-HT is as follows: "*Type IV construction (Heavy Timber, HT) is that type of construction in which the exterior walls are of noncombustible materials and the interior building elements are of solid wood or laminated wood without concealed spaces…Minimum solid sawn dimensions are required for structures built using Type IV construction (HT)…"* [4].

The story and height limits for Type IV-HT - Heavy Timber construction under the 2015 IBC [4] (and previous editions) is 6 stories and 26m (85 ft) height. Buildings classified as Type IV construction have non-combustible exteriors, and the timber primary structural frame is required to meet minimum dimensional criteria (nominal 6" x 8"/153mm x 203mm for columns and nominal 6" x 10"/153mm x 254mm for beams or joists).

In historic heavy timber buildings (Figure 2a), the robust cross sections of the members stand in stark contrast to the smaller members used in conventional repetitive light-frame wood construction (Figure 2b). Repetitive light-frame buildings in the US can refer to both Type III or Type V construction. Type III construction is defined in the IBC as follows: "*Type III construction is that type of construction in which the exterior walls are of non-combustible materials and the interior building elements are of any materials permitted by this code. Fire-retardant treated wood framing and sheathing complying with Section 2303.2 shall be permitted within exterior wall assemblies of a 2-hour rating or less."* Type V construction is defined as: *Type V construction is that type of construction in which the structural elements, exterior walls and interior walls are of any materials permitted by this code* [4].

In some instances, Type III-A can match the building height of Type IV-HT buildings (85' feet/26m) but may permit fewer stories due to occupancy type restrictions and sprinkler system configurations. Additionally, until all the passive and active fire protection and fire-resistance rated construction is complete, repetitive light frame buildings are typically more susceptible to threats from fire than Type IV-HT structures. The inherent structural mass of Heavy Timber imparts fire resistance to the primary structural frame because of the ability of wood to slowly char over time, versus sudden catastrophic structural collapse of other construction materials that are exposed to fire.

The term *cross-laminated timber* appears for the first time in the US codes in the 2015 edition of the IBC [4]. It is defined therein as: *a prefabricated engineered wood product consisting of not less than three layers of solid-sawn lumber or structural composite lumber where the adjacent layers are cross oriented and bonded with structural adhesive to form a solid wood element*. The manufacturing standard for cross-laminated timber, ANSI/APA PRG-320 [5] also makes its first appearance in the 2015 IBC. This permitted the use of CLT as a building element in Type III, IV and V construction. These two changes in the 2015 IBC were instrumental towards the eventual adoption of Tall Mass Timber/Tall Wood Building changes in the 2021 IBC [3].

Following the definition of cross-laminated timber and the manufacturing standard in the 2015 IBC, changes to the 2018 IBC were more intended as a reorganization of terms, content, and referenced standards associated with wood construction. Content describing Heavy Timber that was originally contained within Chapter 6 (Types of Construction) was relocated to Chapter 23 (Wood chapter). Chapter 23 received many new entries specific to cross-laminated timber. A Table was created to call out dimensions for heavy timber structural components comprised of solid sawn lumber, structural glued laminated timber (Glulam), and structural composite lumber (SCL) for column, floor, beam, girder, and roof framing members. Prior to the adoption of the 2021 IBC terms like *mass timber* and *tall mass timber* were not defined.

https://doi.org/10.52202/069179-0395

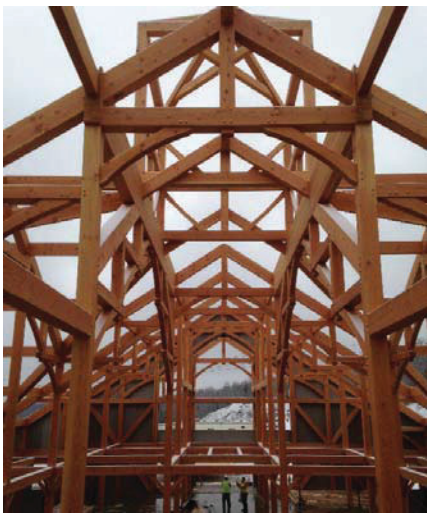

(a)

(b)

Figure 2. *(a) Traditional Heavy Timber, Type IV-HT, (b) a repetitive light-frame podium building*

3 ICC TALL WOOD BUILDING AD-HOC COMMITTEE

In late December of 2015, industry members and other interested parties petitioned the ICC to explore the science of tall wood buildings and take action to develop the necessary code changes to support this new construction type. The ICC determined this effort was valid and formed an Ad-Hoc Committee to evaluate the potential for new mass timber construction types in the IBC. The Tall Wood Building Ad-Hoc Committee, or TWBAH as it became known, was formed under the leadership of ICC [6]. Over eighty individuals volunteered to serve on the TWBAH, and this consensus-based committee was comprised of representatives from building material industries (including members from concrete, steel, and masonry industries), respected building and fire officials, registered professional architects and structural engineers, fire protection experts, and other industry related stakeholders.

Due to the tremendous volume of data that required review, the TWBAH appointed four work groups: Definitions and Standards, Fire, Structural, and Codes. These work groups immediately identified several key performance objectives that guided their development of any proposed code changes:

- No collapse under reasonable scenarios of complete burn-out of fuel without automatic sprinkler protection being considered.
- No unusually high radiation exposure from the subject building to adjoining properties to present a risk of ignition under reasonably severe fire scenarios.
- No unusual response from typical radiation exposure from adjacent properties to present a risk of ignition of the subject building under reasonably severe fire scenarios.
- No unusual fire department access issues.
- Egress systems designed to protect building occupants during design escape time, plus a factor of safety.
- Highly reliable fire suppression systems to reduce risk of failure during reasonably expected fire. Degree of reliability proportional to evacuation time (height) and risk of collapse.

The TWBAH worked for almost 5 years to analyze data and research from across the globe on CLT and mass timber buildings. The Fire Work group had arguably the most challenging task of identifying realistic fire test scenarios to validate the increased story and overall heights proposed by the TWBAH. Fortunately, several notable fire tests of cross-laminated timber had been conducted prior to the formation of the committee [7]. In 2012, an ASTM E119 [8] test was conducted on a 5-ply CLT wall panel assembly that was loaded with 87,000 pounds (39,462 kg). The intent of the test was to have the assembly obtain a two-hour fire-resistance rating. The test was concluded when flame front penetration was observed through the assembly at three-hours and six minutes.

Additional compartment fire testing was conducted at the Southwest Research Institute (SWRI) in 2015 [9], the research and fire test labs at NIST (National Institute of Science and Technology) in the National Research Council of Canada in 2017[10]. Follow-up testing of heat resistant adhesives to ensure the layers of CLT did not delaminate during fire conditions were also conducted at SWRI in 2017 [11]. All the data from previous fire tests was taken into consideration to design the fire tests that were conducted on the two-story test structure at the US ATF (Bureau of Alcohol, Tobacco, Firearms and Explosives) laboratory in direct support of the proposed Tall Mass Timber code change proposals in the 2021 IBC.

The five fire test scenarios conducted at ATF [7, 12] are described in Table 1.

https://doi.org/10.52202/069179-0395

Table 1: *Summary of ATF Fire Tests*

Test	Description	Date	Duration
1	All mass timber surfaces protected with 2-layers of 15.9 mm (5/8 in.) Type X GWB – establishes baseline	5/23/17	3 hours
2	30% of CLT ceiling area in living room and bedroom exposed – represents maximum exposure in Type IV-B	5/31/17	4 hours
3	Two opposing CLT walls exposed – one in bedroom and one in living room (there is a partition wall) – Type IV-B	6/20/17	4 hours
4	All mass timber surfaces fully exposed in bedroom and living room. Sprinklered – normal activation	6/27/17	6 minutes
5	All mass timber surfaces fully exposed in bedroom and living room (except bathroom). Sprinklered – 23 min delayed activation	6/29/17	30 minutes

Figure 3: *Fire Test 1 test progression photos*

All the fire tests conducted at the ATF laboratory were designed to replicate the actual conditions as permitted under the proposed Tall Mass Timber code change proposals. These fire tests validated the fire performance of CLT and the ability of the material to withstand flame and sustained high temperatures (over 1000°C and 18 and 23 megawatts of energy release) generated by the room and contents fire without any contribution of the fire sprinkler system.

It should be noted that the CLT panels tested at the ATF were not manufactured with adhesives that are required under the most current CLT manufacturing standard, ANSI/APA PRG320-18 [5]. The use of fire-resistant adhesives only increased the robust fire performance of CLT as proven in follow on testing conducted at the Research Institute of Sweden (RISE) in 2020 [13].

A total of five additional compartment tests were conducted at RISE [13], all with the primary objective of exposing increasing amounts of exposed CLT ceiling surfaces. A secondary objective was to model the performance of exposed ceiling and wall intersections.

The robust fire resistance of CLT panels manufactured in accordance with ANSI/APA PRG 320-18 [5] was again validated during the RISE tests. The testing proved that CLT constructed with heat-resistant adhesives did not lead to fire regrowth conditions or result in elevated ceiling temperatures greater that 600°C after the decay phase.

4 CLT SHEAR WALL DESIGN REQUIREMENTS

Seismic design based on the equivalent lateral force procedure in the IBC relies on factors from referenced standard ASCE/SEI 7 – *Minimum Design Loads and Associated Criteria for Buildings and Other Structures* [14]. The design requirements are provided in ANSI/AWC *Special Design Provisions for Wind and Seismic* 2021 edition (SDPWS-21) [2]. The SDPWS-21 is referenced in the 2021 IBC [3], and both SDPWS-21 and ASCE 7-22 will be referenced in the 2024 IBC.

The two defined CLT shear wall system types in SDPWS-21 are: (a) *CLT shear wall system* and (b) *CLT shear wall system with shear resistance provided by high aspect ratio panels only*. Both have seismic design factors (i.e., R, Ω_0, C_d) provided in ASCE 7-22 Table 12.2-1. Seismic performance factors and structural height limits appearing in ASCE 7-22 are summarized in Table 2.

Individual CLT panels of CLT shear walls are expected to exhibit rocking, as shown in Figure 4, with the strength of the system controlled by nailed connections. Typical CLT shear wall configurations with the corresponding components are shown in Figure 5. Prescribed nailed connectors are shown at the bottoms and tops of panels and at adjoining vertical panel edges. For multi-panel configurations, free-body diagrams for the tension end panel and compression end panels are shown in Figure 6.

To ensure rocking behavior, as shown in Figure 4, and development of the nailed connection strength, design requirements include: (1) use of CLT panels of prescribed aspect ratios; (2) use of prescribed nailed connectors at bottoms of panels, tops of panels, and adjoining vertical edge(s) of multi-panel shear walls; (3) strength requirements for overturning tension devices (e.g., hold-downs); and (4) compression zone length requirements. Design requirements also include equations for calculating nominal unit shear capacity provided by the prescribed nailed connectors and for calculating the CLT shear wall deflection. The structural design of the CLT panels for resistance to tension, compression, bending, and shear, as well as the design of connections to CLT panels, is required to be in accordance with the NDS. Requirements for the design of CLT diaphragms are also provided in SDPWS.

https://doi.org/10.52202/069179-0395

Table 2: *Design Coefficients and Factors for CLT Seismic Force-Resisting Systems (appearing in ASCE/SEI 7-22 Table 12.2-1)*

Seismic Force-Resisting System	Detailing Requirements, ASCE/SEI 7-22 Section	R	Ω_0	C_d	Structural Height, h_n, Limit Seismic Design Category B, C, D, E & F
Cross-laminated timber shear walls	14.5	3	3	3	20 m [65 ft]
Cross-laminated timber shear walls with shear resistance provided by high aspect ratio panels only	14.5	4	3	4	20 m [65 ft]

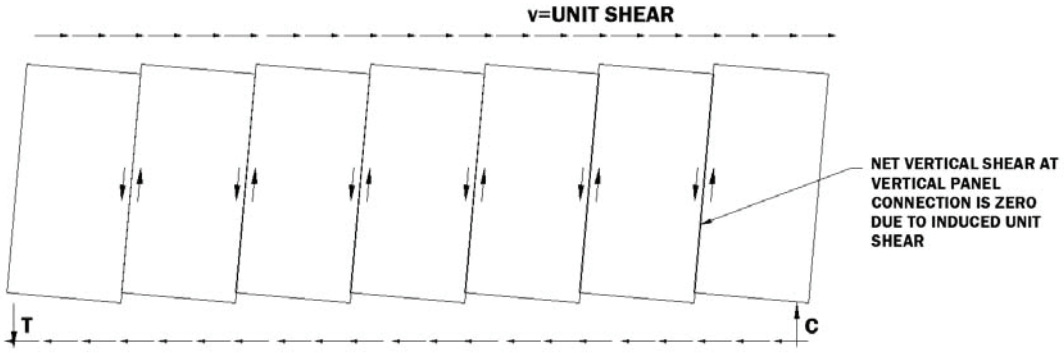

Figure 4: *Illustration of Rocking Behavior of Seven Individual Panels in a Multi-panel CLT Shear Wall*

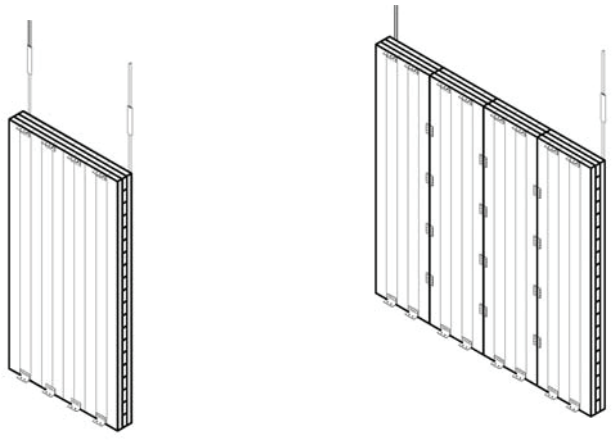

(a) (b)

Figure 5: *Typical CLT shear wall for a) single-panel configuration and b) multi-panel configuration*

https://doi.org/10.52202/069179-0395

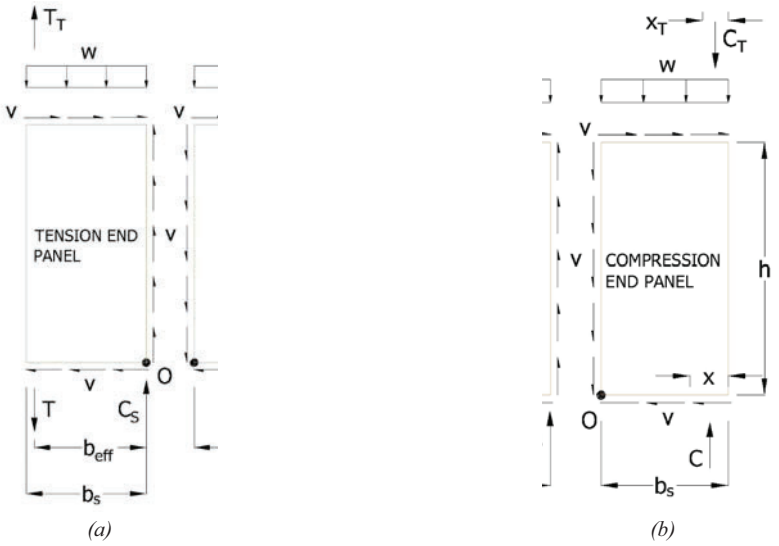

Figure 6: *Free-body Diagram for (a) the Tension End Panel and (b) the Compression End Panel of the CLT Multi-panel Shear Wall*

Additional Resources for Seismic Requirements

Background information on the development of the CLT shear wall system is available in General Technical Report FPL-GTR-281 *Determination of Seismic Performance Factors for Cross-Laminated Timber Shear Walls Based on the FEMA P695 Methodology* [15]. The report includes testing, modeling, and archetypes that led to the development of seismic design coefficients for the CLT shear wall system.

The NEHRP Recommended Seismic Provisions for New Buildings and Other Structures, Volume I: Part 1 Provisions and Part 2 Commentary, 2020 Edition, FEMA P-2082-1 [16] includes design requirements for CLT shear walls. As a predecessor to requirements in ASCE 7-22 and SDPWS, the NEHRP requirements are similar but not identical to those appearing in SDPWS. The 2020 NEHRP *Recommended Seismic Provisions: Design Examples, Training Materials, and Design Flow Charts*, FEMA P-2192 [17], contain design examples based on the 2020 NEHRP Provisions. FEMA P-2192 includes an approximate 25-page example of the CLT shear wall system following the requirements of ASCE 7-22 and SDPWS. The example features the seismic design of cross-laminated timber shear walls used in a three-story, six-unit townhouse cross-laminated timber building of platform construction.

5 2021 IBC FINAL PRODUCT – CODE CHANGE SUMMARY (Type IV-A, IV-B, IV-C)

5.1 2021 IBC

The efforts led by the TWBAH Committee resulted in the inclusion of tall mass timber provisions in the 2021 IBC [3]. Three new building types were added to the IBC, called Type IV-A, IV-B, and IV-C construction, permitting the tallest ever code accepted wood construction in the US. A brief summary of the maximum story limits and building heights allowed in the 2021 IBC is presented in Table 3.

Table 3: *New 2021 IBC Building Types and Height Limits*

Building Type	IV-A	IV-B	IV-C
Maximum # Stories[1]	18	12	9
Maximum Building Height	82m/ 270ft	55m/ 180ft	26m/ 85ft

[1] Based on Occupancy Use of the building

These building code provisions have already been adopted by several state and local jurisdictions, and will continue to be adopted by municipalities across the US.

5.2 2018 NDS

A product chapter for CLT was introduced in the 2015 NDS and updated in the 2018 NDS [18]. Reference to the 2018 NDS was updated in the 2018 IBC and is retained in the 2021 IBC. The NDS specifies that the design procedures for CLT are only applicable to materials manufactured in accordance with production standard ANSI/APA PRG-320 [5] and includes provisions on structural design, connection design, and fire design. The NDS allows designers to choose one of two design methods, Allowable Stress Design (ASD) or Load and Resistance Factor Design (LRFD) for CLT structural and connection designs. However, it limits fire design provisions to ASD designs only.

5.3 2021 SDPWS

The 2021 SDPWS [2] is the first edition of the standard to include provisions for CLT-based lateral-force resisting systems (LFRS). Coupled with the previously discussed seismic factors published in ASCE 7-22 [11], designers

can use CLT diaphragms and shear walls to resist loads due to wind and seismic forces. SDPWS allows for designs using both ASD and LRFD.

6 FUTURE PLANS

6.1 2024 IBC Approved Code Change

The TWBAH Committee established early on during the 2021 IBC development process that only criteria based upon actual tests would be utilized to evaluate the fire performance of CLT. Over 600 data collection points were utilized during the ATF Fire Tests. This extensive data collection was done in part, to facilitate additional follow-up testing. The conservative, relatively small, unprotected portions of both walls and ceilings were justified under the testing criteria performed at the ATF laboratory because the CLT utilized for all five tests was not fabricated with fire-resistant adhesives per the ANSI/APA PRG320-18 standard [5]. In fact, the standard had not even been drafted in 2017 during the time of the ATF tests. The fire-resistant adhesive requirements of ANSI/APA PRG320-18 prevent failure at the glue line of the CLT within the test compartment. Pursuant to the previous fire tests at ATF, recorded compartment temperatures decayed below the point at which reignition of exposed CLT would occur (572°F/300°C). A successful test meant that the compartment temperature dropped below 300°C prior to the conclusion of testing at 240 minutes.

Based on recent RISE tests, a code change proposal, submitted and approved under the ICC governmental consensus process for the development of the 2024 IBC, will permit mass timber ceilings to be exposed for ceiling areas not to exceed 100% of the floor area in Type IV-B Construction. For design professionals to take advantage of this provision, the walls must retain the non-combustible sheathing requirements (typically a minimum of two layers of 5/8 in. or 16mm Type X gypsum board) for the Type IV-B Construction. Additionally, all other stringent active and passive fire protection requirements would apply for these structures which are permitted to be up to twelve (12) stories and one-hundred and eighty feet (180 ft/55 m). This code change permits design professionals to showcase the aesthetically pleasing properties of wood, without sacrificing any reduction in fire performance.

REFERENCES

[1] American Wood Council (ANSI/AWC). "National Design Specification (NDS®) for Wood Construction." Leesburg, VA, (2015).

[2] American Wood Council (ANSI/AWC). "Special design provisions for wind and seismic." Leesburg, VA, (2021).

[3] International Code Council. "International Building Code." Country Club Hills, IL., 2021.

[4] International Code Council. *"International Residential Code."* Country Club Hills, IL., 2015.

[5] APA - The Engineered Wood Association, Standard for Performance-Rated Cross Laminated Timber, ANSI/APA PRG 320. Tacoma, Washington, US, 2011.

[6] International Code Council, https://www.iccsafe.org/products-and-services/i-codes/code-development/cs/icc-ad-hoc-committee-on-tall-wood-buildings/

[7] American Wood Council (ANSI/AWC), https://awc.org/resource-hub/?gsearch=&gtag=tmt-fire-testing

[8] ASTM International, Standard, ASTM E119-20: Standard test methods for fire tests of building construction and materials., (2020).

[9] Southwest Research Institute (SwRI), "Full-scale Tests in a Furnished Living Room to Evaluate the Fire Performance of Protected Cross-Laminated and Nail Laminated Timber Construction.", prepared for American Wood Council (2015). https://awc.org/wp-content/uploads/2022/02/AWC-NLT_CLT_Compartment_Fire-Final_Report.pdf

[10] National Research Council of Canada (NRC) and National Institute of Standards and Technology (NIST), "Fire Safety Challenges of Tall Wood Buildings - Phase 2: Task 2 & 3 – Cross Laminated Timber Compartment Fire Tests." (2018).https://tsapps.nist.gov/publication/get_pdf.cfm?pub_id=925297

[11] Southwest Research Institute (SwRI), "Development of Fire Performance Assessment Methodology for Qualifying Cross Laminated Timber Adhesives.", prepared for American Wood Council, (2017). https://awc.org/wp-content/uploads/2022/02/TMT-SwRIFinalReportonAdhesiveQualificationTests-180409.pdf

[12] Zelinka, Samuel L.; Hasburgh, Laura E.; Bourne, Keith J.; Tucholski, David R.; Ouellette, Jason P. 2018. "Compartment fire testing of a two-story mass timber building." General Technical Report FPL-GTR-247. Madison, WI: U.S. Department of Agriculture, Forest Service, Forest Products Laboratory. 1-480.

[13] Research Institute of Sweden (RISE) "Fire Safe Implementation of Visible Mass Timber in Tall Buildings-Compartment Fire Testing", 2021.

[14] American Society of Civil Engineers (ASCE), "Minimum Design Loads for Building and Other Structures." ASCE Standard ASC/SEI 7-22, Reston, Virginia, 2021.

[15] van de Lindt, J., Rammer, D., Amini, M. O., Line, P., Pei, S., and Popovski, M. "Determination of Seismic Performance Factors for Cross-Laminated Timber Shear Walls Based on the FEMA P695 Methodology." General Technical Report FPL-GTR-281, Madison, WI: US Department of Agriculture, Forest Service, Forest Products Laboratory, (2021).

[16] Federal Emergency Management Agency, NEHRP Recommended Seismic Provisions for New Buildings and Other Structures, Volume I: Part 1 Provisions and Part 2 Commentary, FEMA P-2082-1, prepared by the Building Seismic Safety Council of the National Institute of Buildings Sciences. (2020).

https://doi.org/10.52202/069179-0395

[17] Federal Emergency Management Agency NEHRP Recommended Seismic Provisions: Design Examples, Training Materials, and Design Flow Charts, FEMA P-2192, prepared by Building Seismic Safety Council of the National Institute of Buildings Sciences (2020).

[18] American Wood Council (ANSI/AWC) "National Design Specification (NDS®) for Wood Construction." Leesburg, VA (2018).

World Conference on Timber Engineering Oslo 2023

IMPROVEMENT OF THE DURABILITY OF TIMBER BRIDGES BY INTELLIGENT DESIGN AND RESPONSIBLE MAINTENANCE

Antje Simon[1], Markus Jahreis[2], Johannes Koch[3]

ABSTRACT: Timber bridges may contribute to climate protection due to their carbon sink capability and substitutional effect. One basic requirement for the increased application of timber as an ecological and sustainable construction material is long-term durability. This can only be achieved by consistently using structural protection measures in all stages of planning, construction and service life. The paper presents sample drawings for the design of structurally protected timber bridges and provides recommendations for useful maintenance measures. Using standardized drawings increases effectiveness and efficiency in engineering offices and reduces the danger of serious errors in planning. Regarding their ecological and sustainable advantages, a significant increase in the market share of timber bridges is to be expected in Germany. Aesthetic, well-protected and durable timber bridges of a high-quality standard will characterise the landscape in the future.

KEYWORDS: timber bridges, durability, design, sample drawings, details, maintenance

1 INTRODUCTION

Timber bridges have a centuries-old tradition. A few very old, well-protected bridges demonstrate the potential of timber as a natural structural material (Figure 1). However, the specifics of this orthotropic and hygroscopic material need to be considered in general timber construction and that of bridges in particular. Careful observance to the structural details is required. The material must be protected against moisture ingress. The strength and stiffness of wood decrease with increasing moisture content. Timber starts to swell and shrink with changing moisture, causing internal stress and cracks. Furthermore, a higher moisture content enables insects and fungi to attack and destroy the structure.

Figure 1: *Old covered bridge in Aarberg (Switzerland), built in 1568 (photo: A. Simon)*

If the specific requirements are ignored, there is high-risk potential for destruction, and the maintenance costs significantly increase. Inspections of several bridges in Germany have confirmed that most defects are caused by faulty design and a lack of protection and maintenance measures. The long-term durability of timber bridges can only be achieved by consistently using structural protection measures in all stages of planning, construction and service life. Therefore, the research project "Protected timber bridges (ProTimB)" was initiated to define a new standard for durable timber bridges. The results of the project have been published in a research report [1].

2 THE RESEARCH PROJECT PROTIMB

2.1 OVERVIEW

The outcome of the project is a set of technical guidelines for the design, construction and maintenance of protected timber bridges (Figure 2). Formally, it is inspired by the existing sets of rules for other materials established by the German Federal Highway Research Institute (BASt) to facilitate their application in practice.

The design rules [2] consist of references for planning, samples for structural analysis and 36 new sample drawings (MuZ-HolzBr). In addition, "Recommendations for technical contractual terms for timber bridges (ETV-HolzBr)" have been developed for construction [3].

[1] Antje Simon, University of Applied Sciences Erfurt, Germany, antje.simon@fh-erfurt.de
[2] Markus Jahreis, University of Sustainable Development Eberswalde, Germany, markus.jahreis@hnee.de
[3] Johannes Koch, University of Applied Sciences Erfurt, Germany, johannes.koch@fh-erfurt.de

https://doi.org/10.52202/069179-0396

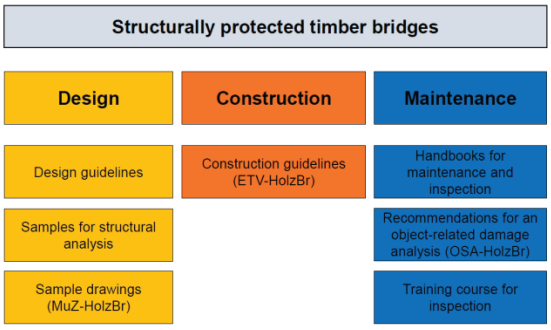

Figure 2: *Overview of the new guidelines and project results*

Sample handbooks have been written for the maintenance and inspection of timber bridges and recommendations for an object-related damage analysis (OSA-HolzBr) have been compiled. Furthermore, an advanced training course has been conceptualised for timber bridge inspectors. Additionally, nine protected timber bridges crossing rivers were comprehensively monitored [4]. The most important guidelines for design and maintenance will be presented in the following. For further details see [1].

2.2 DESIGN

2.2.1 Overview

A set of new sample drawings [5] has been developed for the design of timber bridges. It is based on older drawing sets [6] and [7], which it updates and extends. The 36 new drawings illustrate durable and proven solutions for special structural details (Table 1).

Table 1: *Contents of the sample drawings for protected timber bridges*

Drawing	Contents
H-Belag 1-4	Variants of decks and their mounting (closed surfaces as asphalt sealings, concrete- and natural stone slabs and open surfaces using wooden planks)
H-Dicht 1-3	Design of sealings for the timber-superstructure
H-Gel 1-5	Variants of parapets and their fastening
H-Kap 1-2	Mounting of concrete caps on timber structures
H-Lag 1-3	Details for bearings
H-Schutz 1-8	Structural protection measures (covering, cladding, ventilation distances, protrusion)
H-Trog 1-2	Design of cross frames and bracing structures for trough bridges
H-Übe 1-4	Transition structures and expansion joints
H-Was 1-3	Details for drainage and dewatering
H-Zug 1	Accessibility of substructure

They are closely related to the familiar drawings of the German Federal Highway Research Institute (BASt) [8]. Annex D of the new version of the European Code for Timber Bridges EC5-2 [9] also shows sample drawings inspired by the results of the ProTimB project.

The drawings focus on the critical points of timber bridges such as decks, sealings, parapets, bearings and expansion joints. Special attention was paid to the structural protection measures including recommendations for covering, cladding, ventilation distances and protrusion. In Germany, structural protection takes precedence over chemical treatment. All load-bearing members must be structurally protected. Secondary structural members may remain unprotected but should then be regarded as "maintenance elements" with a lower service life of 10 to 20 years.

This strategy is also followed by the next edition of Eurocode [9].

According to this new code, timber bridges will be divided into four categories to define their design service life. For protected timber bridges in category 1, a design service life of 100 years is expected. To achieve this design service life analogously to bridges made of other materials, the main structural components shall be designed with structural protection. Category 2 includes timber bridges whose main structural members are protected for a 50-year design service life. Replaceable structural parts of protected bridges (category 3) should achieve a design service life of 25 years. For temporary structures (category 4), a maximum design service life of 10 years is expected. Unprotected timber bridges belong to category 4.

As a basis for planning protection measures, the use class (UC) has to be defined for every single timber member (Figure 3) according to [10].

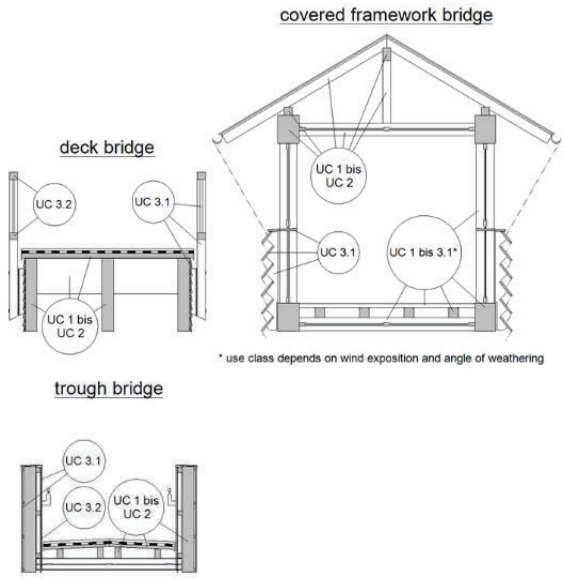

Figure 3: *Assignment of timber members to use classes (UC) in different exposure situations*

Appropriate structural protection measures and wood species, based on their durability class, should be derived from the use class. Analogously to the procedure according to [11], the main objective is to achieve use class 0 to avoid chemical treatment. For every single timber member, the classifications and protection measures should be summarised in a separate design plan as shown in Table D.1 of [9].
One special feature of the sample drawings is the definition of maintenance elements. If non-load-bearing or easily replaceable timber components are exposed to weathering (e.g. railings, cladding and planks), a significantly shorter service life is to be assumed for these components compared to the service life of the protected main load-bearing structure. Weathered timber components must be regularly maintained and replaced if their stability, traffic safety or durability is impaired. Therefore, these components are explicitly marked as maintenance elements.
The following will offer important design advice and present and explain examples of the drawings.

2.2.2 Bridge deck surfaces and sealings

In principle, a closed deck is preferable to an open deck, as the main girders located under the deck are structurally well protected by a dense layer. Bridges over roads and railway lines should generally be provided with a closed deck.
For a closed deck, an under-ventilated construction is recommended. In contrast to the direct arrangement of the sealing on the main supporting structure, an under-ventilated structure enables direct checking for leaks, creates a second sealing level and reduces blistering during asphalt paving. An under-ventilated construction can also be more easily repaired. The following setup should be used (H-Belag 1 (Figure 4) in connection with H-Dicht 1):

- Top layer: mastic asphalt, 25 – 45 mm thickness,
- Protection layer: mastic asphalt, 25 mm thickness, mounting temperature 180 – 200°C,
- Sealing: polymer-bitumen water-proofing membrane fixed to timber deck,
- Epoxy resin-based primer,
- Wood-based panel on squared timber as spacer for under-ventilation, minimum surface inclination 2.5 %,
- Protective layer, diffusion-open,
- Timber deck, minimum surface inclination 2.5 %.

In the case of open decks, the planks must be fastened to a separate decking beam placed next to the main beam (H-Belag 3 and H-Belag 4). Direct fastening of the planks to the main girder is not permissible, as the fasteners penetrate the sealing arranged above the main girder and thus impair structural timber protection. The decking planks and the decking beam are maintenance elements with a shorter service life, as they are exposed to direct weathering and dirt through use. A sheet metal cover on the top side and a nail sealing strip (H-Belag 3) or a plastic membrane extend the service life of the separate decking beam. In the case of open decks, the joint between the end of the superstructure and the chamber wall must be closed to prevent dirt, grit, leaves or similar from falling through and remaining on the support bench (H-Belag 3 and H-Übe 4).

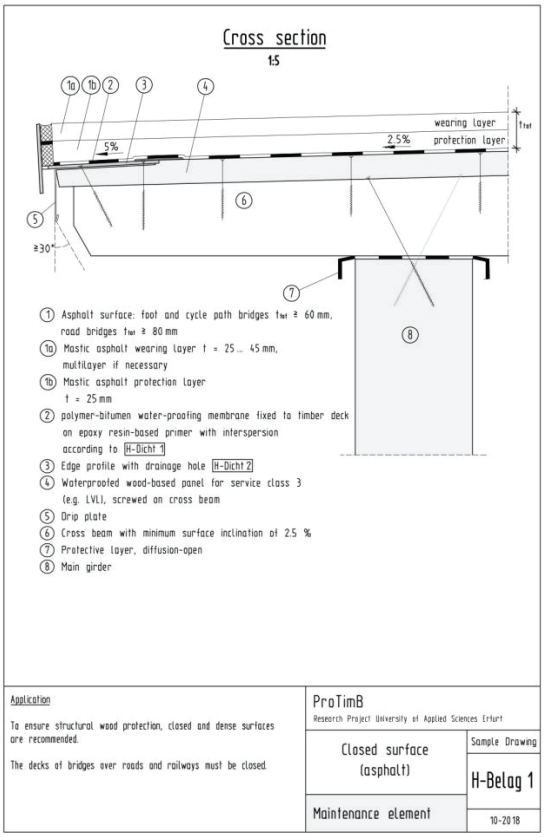

Figure 4: *Sample drawing H-Belag 1 showing the surface layers and the sealing*

2.2.3 Railings

Weathered wooden railings are maintenance elements with a shorter service life. They need to be replaced after 10 to 20 years.
Knots on the surfaces of wooden planks and handrails can lead to break-outs and increase rotting. Therefore, the components of wooden railings should contain as few knots as possible.
Architecturally interesting alternatives to wooden railings are steel railings with wooden handrails. For the handrail, the use of acetylated or other modified wood is recommended due to its higher durability and low tendency to crack and deform.
When fixing the railing to the main beam, it is important to make sure that the structural wood protection of the main beam is maintained. Water must not be led to the main girder via the fastening elements (pos. 5 of H-Gel 5, see Figure 5).

https://doi.org/10.52202/069179-0396

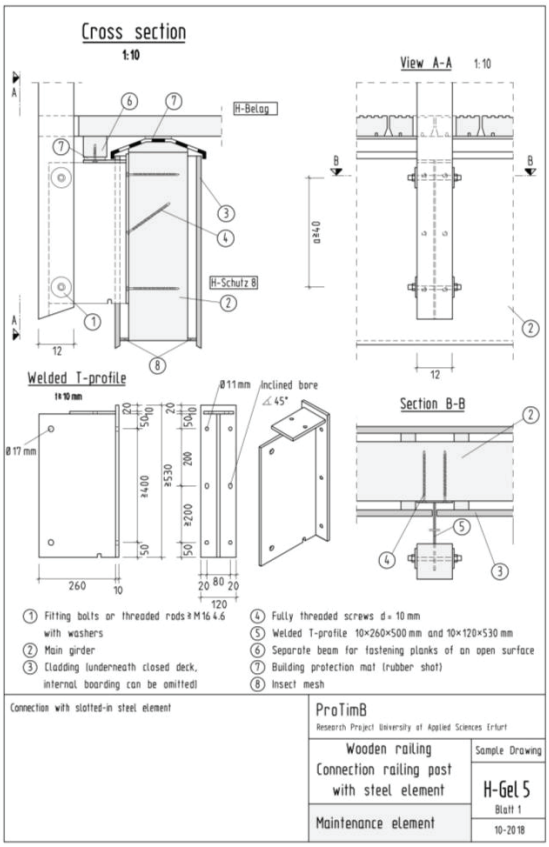

Figure 5: *Sample drawing H-Gel 5 explaining the connection of a railing post by a steel element*

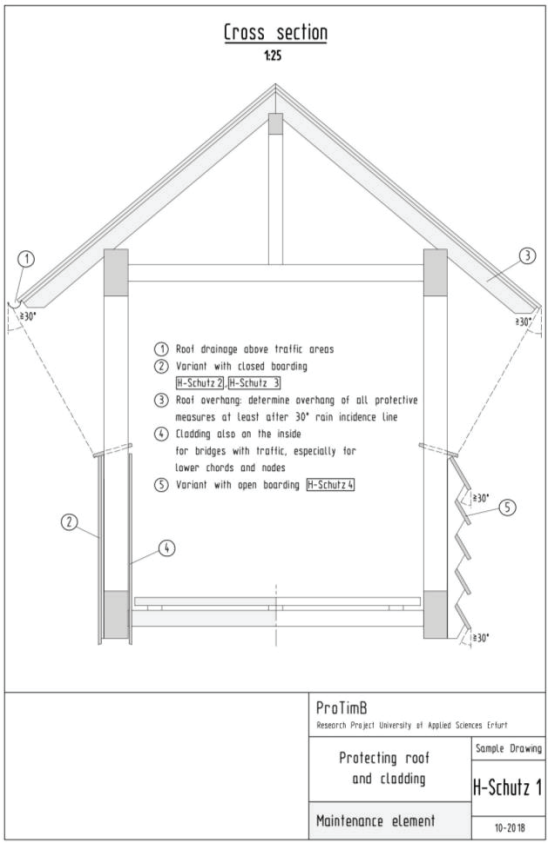

Figure 6: *Sample drawing H-Schutz 1 explaining general structural protection measures*

For pedestrian bridges, the minimum height of the railings is 1.00 m. If bridges are used by cyclists, the railings must be at least 1.30 m high.

2.2.4 Structural protection measures

The sample drawings in H-Schutz regulate details of structural timber protection as the most important basis for durability.

Structural timber protection can be attained by using a closed surface or a sufficient roof overhang and/or by cladding. Any covering must protrude at least far enough to prevent rain falling at an angle of 30° from the vertical from reaching the load-bearing timber structure (H-Schutz 1, see Figure 6). At wind-exposed locations, a significantly larger angle of rain incidence can occur. In this case, the protective measures must be extended. Lower chords of trusses are particularly at risk, as water can penetrate the connecting details, nodes and horizontal cracks and cannot run off. If wind exposure is unknown, it is recommended to plan load reserves in the static calculation for the subsequent installation of additional cladding. Alternatively, it is possible to calculate the main structure with reduced strength in service class 3 (as necessary for unprotected members) instead of service class 2 (as permitted for protected members).

Construction with a sufficient lateral overhang is preferable to cladding, as hands-on inspection of the main structure is easier. Open claddings (H-Schutz 4) facilitate hands-on inspection (Figure 7).

Figure 7: *Swiss timber bridge structurally protected by a roof and an open cladding (photo: A. Simon)*

Closed cladding should be easily removable or hinged to improve the inspection of the construction behind (H-

Schutz 6, see Figure 8). Due to better water drainage, vertical cladding is preferred to horizontal cladding (H-Schutz 2). Inside trough bridges, horizontal boards can be advantageous, as individual horizontal lamellas could be more easily replaced in the splash water area.

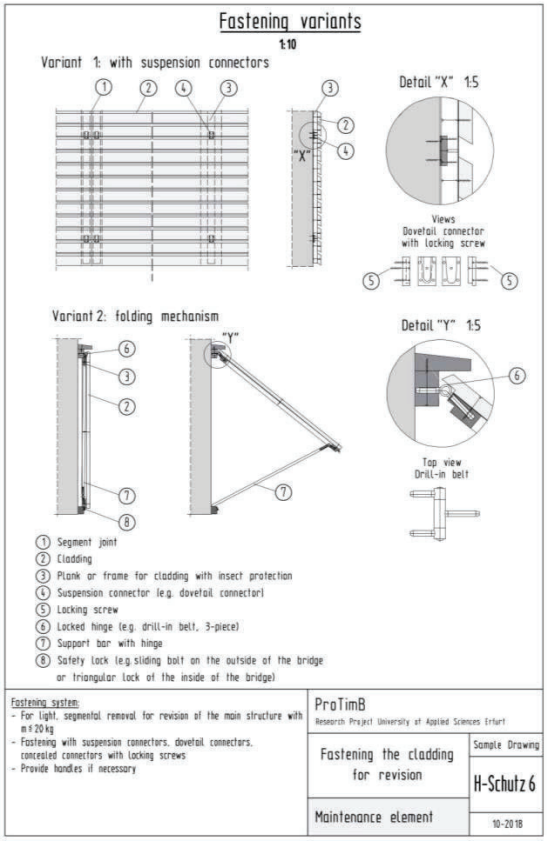

Figure 8: *Sample drawing H-Schutz 6 showing a removable cladding for inspection*

The following basic and special measures for structural timber protection should be observed in timber bridge construction:

- Wooden bridges should be designed for low-maintenance (e.g. by integral structures, watertight expansion joints, closed surfaces) or in a maintenance-friendly manner (facilitation of cleaning and inspection by sufficiently large distances between the components).
- During assembly, the moisture content of the wood should correspond to the expected moisture content on site (approx. 16 to 18 M%).
- Wooden components and their connections must always be designed in such a way that precipitation is deflected by weather protection. Alternatively, it has to be drained away so fast that no increase in wood moisture can occur and no moisture accumulation takes place. Timber components shall be installed with air circulation at an appropriate distance from other building components and from the terrain to avoid moisture transfer or moisture accumulation and to allow rapid drying. Direct weathering must be effectively prevented during transport, storage and the construction phase (e.g. by covering with foil).
- Insect infestation must be precluded (e.g. by using kiln-dried timber, insect-impermeable covers, coloured heartwood with sapwood content $\leq$ 10 % or open arrangement of timber members with regular inspection).

2.2.5 Accessibility

In order to facilitate the bridge-inspection, minimum distances should be maintained between the superstructure and the substructure as well as the surrounding terrain (H-Zug 1, see Figure 9). Sufficient distances also guarantee air ventilation and prevent the influence of spray water and vegetation.

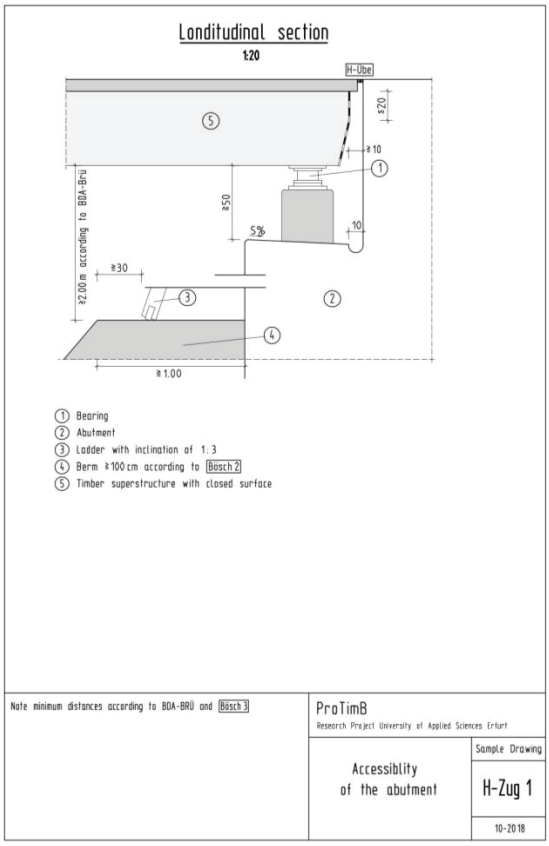

Figure 9: *Sample drawing H-Zug 1 showing minimum distances for good ventilation and easy inspection*

Special protection of the end-grain surfaces is necessary, e.g. by arranging waterproof transition joints, arranging rear-ventilated sheets or boards or by means of diffusion-open paint or membrane. Ventilation and accessibility of the end-grain surfaces can be ensured by chamfering the beam's ends and maintaining a distance to the chamber wall of at least 0.10 m.

https://doi.org/10.52202/069179-0396

A clear distance between the superstructure and the support bench of at least 0.50 m enables the bearings to be easily checked. In addition, the wooden main beams are prevented from being affected by water and dirt on the support bench. Manual cleaning of the support bench is also facilitated. A sufficiently wide and plane area in front of the abutment and a clear height of at least 2 m enable the inspection of the superstructure's underside (Figure 10).

Figure 10: *Bottom view of a timber-concrete composite bridge (Birkbergbridge, Germany) showing a sufficient distance between superstructure, support bench and ground for good ventilation and easy inspection (photo: A. Simon)*

2.3 CONSTRUCTION

"Recommendations for technical contractual terms for timber bridges (ETV-HolzBr)" have been developed for construction [3]. This document defines basic material requirements for the timber, engineered wood products, thermally and chemically modified wood, adhesives and steel components. Specifications are given for minimum dimensions, surface qualities and limits for deformation due to shrinkage and swelling. The production, storage, delivery, quality control and assembly of structural timber elements are regulated. For the purposes of quality control, the document defines limits for dimensional and moisture tolerances, cracks and surface qualities at the factory and at the construction site. Furthermore, it contains necessary measures to be taken for structural timber protection and the corrosion protection of steel components in timber bridges. Suggestions for the design of timber-concrete composite bridges and of wildlife bridges complete these guidelines. With the extension of the Eurocode for timber structures [11], execution rules will also be normatively regulated in the future.

2.4 MAINTENANCE

Respecting the principles of structural protection is mandatory but not sufficient for durable timber bridges. Their intended service life of 60 to 100 years can only be achieved in combination with regular maintenance and inspection. Manuals for maintenance and inspection have been developed within the ProTimB project [1].

The maintenance manual explains useful service measures, their necessary intervals, the required technical equipment and means of access to facilitate economical maintenance. Service measures include:

- the cleaning of the superstructure, benching, road surface, bridge drains and drainage channels,
- the removal of vegetation all around the bridge in a radius of at least 2 m,
- the renewal of coatings, sealants, joints,
- the repair of planks, asphalt layer, cladding, cover plates and parapet members.

An interval is recommended for every measure, taking the structural element's service life and seasonal weathering and pollution into account. In addition, a continuous monitoring of the timber moisture content is advised.

2.5 BRIDGE INSPECTION

Independently of maintenance, bridges must be regularly inspected in Germany. Every bridge has to be visited twice a year and checked once a year. Additionally, the basic inspection and main inspection have to be performed alternately every three years. The main inspection requires a hands-on check of every structural component and is therefore the most complex and expensive. For special types of timber bridges such as framework bridges, cable-stayed bridges or bridges for wildlife, an inspection manual supplements the maintenance manual. The inspection manual explains the tasks for continuous observation (usually twice a year) and the annual survey as well as for the basic and the main inspection in detail.

It is recommended to use the checklists for continuous observation and survey, which are part of the inspection manual, in parallel to the maintenance manual. The following aspects have to be checked during the annual observation:

- All structural protection measures have to be checked for functionality (covering, sealings, cladding).
- All accessible members have to be checked for sufficient protection from moisture and dirt (marks of running water, timber with earth contact, growth of moss and algae).
- The timber moisture content has to be measured in damp and vulnerable areas.
- All accessible members have to be checked for wood-destroying fungi, incipient rot and wood-destroying insects.
- Protruding connectors have to be observed (screws in planks, dowels in knot areas).

https://doi.org/10.52202/069179-0396

It is recommended to record damage and compare it with the condition of the previous observation. On this basis, necessary conservation measures can be derived to ensure economical bridge maintenance and to achieve long durability.

The inspection manual contains the recommended measuring methods and provides special hints for organisation, accessibility, documentation and traffic security during the inspection. Regarding individual structural characteristics, the regular inspection of every timber bridge can be optimised and performed economically. If a regular inspection reveals complex damage of unclear cause or unclear dimension of defects, further recommendations are given for the implementation of an object-related damage analysis.

3 CONCLUSIONS

Technical guidelines guarantee professional state of the art design and construction standards.

The sample drawings for timber bridges describe recommended structural details for the planning, calculation and execution of timber bridges. They represent proven and durable solutions for recurring technical tasks and reflect the respective state of the art. Intelligent design and responsible regular maintenance improve the durability of timber structures, enabling bridges made of timber to achieve the service lives of concrete and steel bridges.

Aesthetic, well-protected and durable timber bridges of a high-quality standard will characterise our landscape in the future.

ACKNOWLEDGEMENT

The new guidelines for protected timber bridges were developed within the research project “Protected Timber Bridges (ProTimB)”. The research has been supported and funded by the Federal Ministry of Education and Research of Germany, the companies of the Qualitätsgemeinschaft Holzbrückenbau e. V. (Schaffitzel Holzindustrie GmbH + Co. KG, Schmees & Lühn Holz- und Stahlingenieurbau GmbH, Grossmann Bau GmbH) and Setzpfandt Beratende Ingenieure GmbH & Co. KG. The authors thank all partners and supporters for their technical and financial support.

REFERENCES

[1] Simon, A.; Arndt, R.; Jahreis, M.; Koch, J. (2019) Entwicklung einheitlicher Richtlinien für den Entwurf, den Bau, die Überwachung und Prüfung geschützter Holzbrücken – Protected Timber Bridges (ProTimB). Final research report. University of Applied Sciences Erfurt, Germany.

[2] Simon, A.; Jahreis, M.; Koch, J.; Arndt, R. W. (2020) Moderne Holzbrücken planen, bauen, erhalten - Teil 1: Bauwerksentwurf. Bautechnik 97 (2020), Heft 02, Ernst & Sohn, Berlin.

[3] Simon, A.; Koch, J.; Jahreis, M.; Arndt, R. W. (2020) Moderne Holzbrücken planen, bauen, erhalten - Teil 2: Bauausführung und Erhaltung. Bautechnik 97 (2020), Heft 02, Ernst & Sohn, Berlin.

[4] Koch, J.; Simon, A.; Jahreis, M. (2022) Effectiveness of structural protection measures for timber bridges – results of long-term moisture monitoring. In *ICTB 2021 plus*, Biel, Switzerland.

[5] Informationsdienst Holz [Hrsg.] (2019) Musterzeichnungen für Holzbrücken, holzbau handbuch Reihe 1, Teil 9, Folge 3.

[6] Gerold, M. (2006) Musterzeichnungen Holzbrücken (Sample drawings to the German standard ZTV-ING 9-3 Timber Bridges). Final research report, DGfH Innovations and Service Ltd. Munich.

[7] Qualitätsgemeinschaft Holzbrückenbau (2012) Detailzeichnungen Holzbrücken, 03/2012.

[8] Federal Highway Research Institute (2022) Richtzeichnungen für Ingenieurbauten (RiZ-ING). 01/2022.

[9] Draft prEN 1995-2 (2023) Eurocode 5 - Design of timber structures – Part 2: Bridges. 2023-01.

[10] DIN EN 335 (2013) Durability of wood and wood-based products – Use classes: definitions, application to solid wood and wood-based products. German version EN 335:2013-06.

[11] DIN 68800 (2019) Wood preservation – Part 1: General. 2019-06.

[12] Draft prEN 1995-3 (2022) Eurocode 5 - Design of timber structures – Part 3: Execution rules. 2022-10.

https://doi.org/10.52202/069179-0396

World Conference on Timber Engineering Oslo 2023

WOOD DURABILITY BASED IN THE NEW BRAZILIAN TIMBER STRUCTURES CODE ABNT NBR 7190: 2022

Leandro Dussarrat Brito[1], Everaldo Pletz[2], Carlito Calil Junior[3].

ABSTRACT: The ABNT NBR 7190:1997 standard has recently undergone a revision process. Thus, this paper treats of the Chapter 12 wood durability of the standard revision project Brazilian, Design of Timber Structures code ABNT NBR 7190: 2022. Wood is an organic material and it must receive a prior analysis of the conditions in which it will be applied to identify the need for specific preservative treatment, seeking to obtain durability and resistance to wood biodeterioration agents, such as fungi, xylophagous insects and marine bores. Similar to Chapter 12 Wood durability of the ABNT NBR 7190: 2022 standard revision project, ABNT NBR 16143: 2013 complements regarding the wood preservation treatment, where it also establishes the system with six Use Categories for wood, with an emphasis on treatment preservative to increase the durability of construction systems. A very important aspect that must be considered is the elaboration of a project in which the durability is assured. Thus the purpose of the Use Categories System is to offer a simplified tool for decision making regarding the rational and intelligent use of wood, through a systemic approach to the producer and user, which ensures greater durability of constructions.

KEYWORDS: Brazilian Design of Timber Structures code, Timber structures, Wood durability.

1 INTRODUCTION

Wood is an organic material that can have biodeterioration.

To develop the design of a timber structure, it is necessary to ensure a minimum durability compatible with its purpose and with the investment to be made (ABNT NBR7190: 1997) [1].

Usually a good performance of the structural member is expected throughout its useful life. The key element to identify wood performance over time is durability (CALIL et al, 2006; CALIL JUNIOR & BRITO 2010) [2, 4].

Thus, durability is the capacity of a product to maintain its performance above pre-established minimum values in line with users under expected conditions of use (CALIL JUNIOR et al, 2006) [2].

2 BRIEF HISTORIC

The first Brazilian Code of Timber Structures was published in 1951 under the name of NB 11 - Design and Construction of Timber Structures [5], with a deterministic design method.

In February 1982 it was renamed ABNT NBR 7190:1982 without any modification.

As of 1992, a new study of this standard was started using the semi-probabilistic method of dimensioning in limit states.

As long as the research and scientific work evolved in the country, starting from the Technical Bulletin BT/PEF/9602/USP Fusco et al (1996)[6] updated the published standard revision project to version ABNT NBR 7190:1997 [1] with emphasis in the use of noble woods. In this version of the standard, topics on wood durability were introduced according to the Biodeterioration Risk Classes.

When developing the design of a timber structure, it is necessary to ensure a minimum durability compatible with its purpose and with the investment to be made.

The structural members of a timber construction can be exposed to different Risk Classes of biodeterioration depending of the biotic organisms present in the local and the environmental conditions that may favor the attack (FUSCO et al 1996)[6].

From the draft standard carried out by Fusco et al (1996) [6], Annex D of the ABNT NBR 7190: 1997 [1] was added, which is informative and deals with recommendations on the durability of wood.

In this Annex D of NBR 7190:1997 [1], five situations of Biodeterioration Risk Classes were presented to be considered in the design of timber structures (CALIL JUNIOR et al, 2003) [7].

Brazolin et al (2004) [8] proposed the elaboration of a standard of wood preservation to help producers and users of the civil construction sector to increase the durability of timber construction systems. In this work, a systematic approach was presented on the subject of biodeterioration and wood preservative treatment called the System of Risk Classes, which now has six situations of these classes (BRAZOLIN et al 2004) [8].

Calil Junior et al (2006) [2] presented six Risk Classes, when from Brito (2010) [3] it started to be called Use Classes. The term “risk” was replaced by “use” in order not to depreciate the use of wood.

[1]Leandro Dussarrat Brito, LaMEM/SET/EESC/USP University of São Paulo, Brazil, dussarrat@sc.usp.br
[2]Everaldo Pletz, Department of Structures, UEL State University of Londrina, Brazil, pletz@uel.br
[3]Carlito Calil Junior, LaMEM/SET/EESC/USP University of São Paulo, Brazil, calil@sc.usp.br

https://doi.org/10.52202/069179-0397

In 2013, a new revision of NBR 7190 began, based on new research and work carried out by the CB-002 committee and in parallel with the revision project of this standard, ABNT NBR 16143:2013 Wood Preservation – Use Categories System [9] was prepared, when the term Use Categories was officially changed.
Thus, in the NBR 7190:2022 standard revision project, it now has the six Use Categories [10].
It is worth noting that the ABNT NBR 16143:2013 was prepared by the Brazilian Wood Committee (ABNT/CB-31), by the Wood Preservation Study Committee (CE-31: 000.15) [9].
While the revision of the ABNT NBR 7190-1:2022 standard was elaborated in the Brazilian Civil Construction Committee (ABNT/CB-002), by the Commission for the Study of Timber Structures (CE-002:126.010)[10].

3 WOOD DURABILITY

The Chapter 12 of the new version of the ABNT NBR 7190:2022 treat with the theme "Durability of wood".
Among the various materials intended for civil construction, wood has exceptional qualities that elect it, in many respects, especially under the criterion of sustainability, as a high-performance building material (ABNT NBR 7190:2022).
However, wood is an organic material and must receive prior analysis of the conditions in which it will be applied, in order to identify the need for specific preservative treatment, seeking to obtain the best result in terms of durability and resistance to biodeteriorating agents of wood, such as fungis, xylophagous insects and marine borers (NBR 7190:2022).
The structural classification provides a connection between the timber structural members and their expected performance when they come into service (CALIL JUNIOR. et al, 2003; CALIL JUNIOR et al, 2006; CALIL JUNIOR & BRITO, 2010; CALIL JUNIOR et al, 2015) [2, 4, 7, 11].
Usually, good performance is expected over the entire useful life of the structural member (CALIL JUNIOR. et al, 2003; CALIL JUNIOR et al, 2006; CALIL JUNIOR & BRITO, 2010; CALIL JUNIOR et al, 2015) [2, 4, 7, 11].
The key element for this prediction is its durability, defined as the ability of a product to maintain its performance above pre-established minimum values, on consonance with users, under the intended conditions of use (CALIL JUNIOR. et al, 2003; CALIL JUNIOR et al, 2006; CALIL JUNIOR & BRITO, 2010); (CALIL JUNIOR et al, 2015) [2, 4, 7, 11].
A large number of biotic agents and abiotic agents have the potential to reduce wood performance over time (CALIL JUNIOR. et al, 2003; CALIL JUNIOR et al, 2006; CALIL JUNIOR & BRITO, 2010; CALIL JUNIOR et al, 2015) [2, 4, 7, 11].
The structural designer, however, can guarantee durability using a combination of three factors [2, 4, 7, 11]:

- Better design detailing;
- Preservative treatment;
- Inspection, maintenance and repairs.

An important aspect is to always record the works carried out for later verifications (CALIL JUNIOR. et al, 2006) [2].

4 WOOD PRESERVATION – USE CATEGORIES SYSTEM

According to the ABNT NBR 7190: 2022 wood preservation is the set of preventive and curative recommendations adopted to control biological agents (fungi, xylophagous insects and marine bores), physical and chemical that affect the properties of wood, adopted in the development and maintenance of wood components in the built environment.
Initially proposed by Brazolin et al (2004) [8] as Risk Category System, currently the normative term of ABNT NBR 7190:2022 becomes Use Category System.
The purpose of the Use Categories System is to offer a simplified tool for decision making regarding the rational and intelligent use of wood, through a systemic approach to the producer and user, which ensures greater durability of constructions.
The creation of the set of use categories was based on the principle of valuing the project as the first and most important preventive tool to be used with the objective of obtaining a wooden construction endowed with durability.
The system consists of establishing six Use Categories based on the conditions of exposure or use of the wood, on the expected performance of the component and on the possible biodeteriorators agents present (ABNT NBR 16143: 2013; ABNT NBR 7190: 2022) [9, 10].
In the design of timber structures, the following use categories should be considered [9, 10]:

- **Use Category 1:** Inside buildings, out of contact with the soil, foundations or masonry, protected from weathering, internal sources of moisture and local free from access by subterranean termites or arboreal.

- **Use Category 2:** Interior of buildings, in contact with the masonry, without contact with the soil or foundations, protected from the weather and indoor sources of moisture.

- **Use Category 3:** Interior of buildings, out of contact with the soil and protected from the weather, which can, occasionally be exposed to sources of moisture.

- **Use Category 4:** Outside use, out of contact with the soil and subject to the weathering.

- **Use Category 5:** Contact with soil, fresh water and other situations favorable to deterioration, such as setting in concrete and masonry.

- **Use Category 6:** Exposure to salt water or brackish.

Thus, in the current Brazilian standard ABNT NBR 7190: 2022, depending on the service condition in which the wood of the structure will be exposed, each corresponding

https://doi.org/10.52202/069179-0397

use category is susceptible to attack by biodeteriorating organisms, as listed [9, 10]:

- **Use Category 1:** drywood termite, wood borer beetle;
- **Use Category 2:** drywood termite; wood borer beetle; subterranean termite, arboreal termite;
- **Use Category 3:** drywood termite; wood borer beetle; subterranean termite; arboreal termite; mold fungis; stain fungis; decay fungis;
- **Use Category 4:** drywood termite; wood borer beetle; subterranean termite; arboreal termite; mold fungis; stain fungis; decay fungis;
- **Use Category 5:** drywood termite; wood borer beetle; subterranean termite; arboreal termite; mold fungis; stain fungis; decay fungis;
- **Use Category 6:** marine borers; mold fungis; stain fungis; decay fungis.

The figure 1 illustrates some examples of biodeterioration risk situations for each corresponding use category, taking a residence as an example.

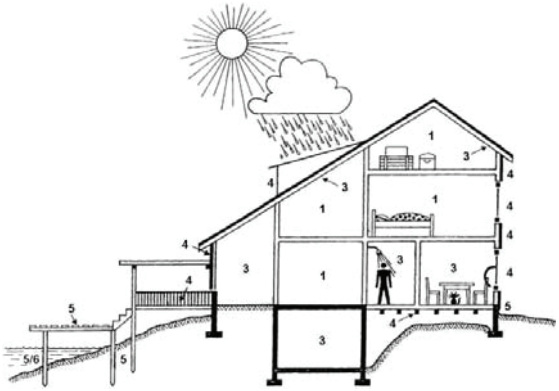

Figure 1: *Use Categories, depending on the situation of biodeterioration risk in a residence. Source: (BRITO (2010); CALIL & BRITO (2010); BRITO (2014)[3,4,12].*

Due to the chemical nature of the preservative products recommended for the treatment of wood, in the construction components of structures, which may be in direct contact with people or animals, it is recommended to use suitable finishes, such as "stains", varnishes and/or paints, to prevent migration and/or leaching of the preservative product. (CALIL JUNIOR. et al, 2006) [2].

5 APPLICATION OF THE USE CATEGORIES SYSTEM

The Use Category System defines recommendations that must be adopted during the design phase of a construction with wooden components, helping to choose the preservative treatment of wood - product and process (ABNT NBR 16143: 2013; ABNT NBR 7190: 2022) [9, 10]. This decision process is represented by the Flowchart 1 of the Figure 34 in ABNT NBR 7190: 2022 [10].

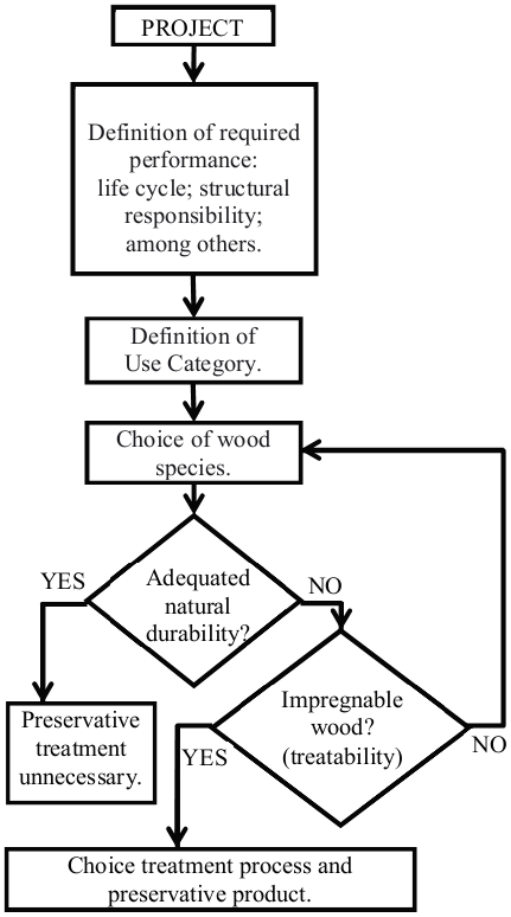

Flowchart 1: *Choice of treatment and wood species in the project. Fonte:* ***Figure 34 in ABNT NBR 7190:2022****.*

Thus, when using wood as an engineering material, the following steps must be considered mandatory (ABNT NBR 16143: 2013; ABNT NBR 7190: 2022) [9,10]:

a) Definition of the required performance level for the wooden component or structure, such as: useful life, structural responsibility and commercial and legal guarantees;

b) Evaluation of the biological risks to which the wood will be subjected during its useful life – attack by fungis, xylophagous insects and/or marine borers;

c) Definition of the wood species suitable for use and the need for preservative treatment considering: natural durability of the species, treatability, treatment process and available preservative products. The preservative

treatment is necessary if the chosen species is not naturally durable for the category of use considered and/or if the wood contains sapwood, a portion naturally susceptible to attack by xylophagous organisms;

d) Selection of the appropriate wood treatment process and preservative product.

6 USE CATEGORIES: TIMBER STRUCTURAL AND CONSTRUTIVE ELEMENTS

With a focus on preservative treatment to increase durability in the useful life of structural member and constructive wooden, ABNT NBR 16143:2013 Wood Preservation - Use Categories System [9] - complements the system of six use categories of the current version of ABNT NBR 7190: 2022 Projects of Wooden Structures [10].
Tables 1 to 4 list the possible applications of lumber wood, roundwood, glulam, and wood panels as engineering material, with the six use categories of probable, according to ABNT NBR 16143: 2013 [9].

Table 1: *Lumber wood. Fontes: BRASOLIN et. al (2004); ABNT NBR 16143:2013; [8, 9].*

Application	**Probable Use Category**
Floor	2 e 3
Doors and Windows	2, 3 e 4
Floor beam	2 e 3
Door Jambs	2, 3, 4 e 5
Reel	1, 2, 3 e 4
Fences	4 e 5
Columns	2, 3, 4, 5 e 6
Handrail	2, 3 e 4
Crossarm	4
Bridge defense	5 e 6
Deck planks	3 e 4
Railway sleeper	5
Reusable wooden based packaging	1, 2, 3 e 4
Stairs	2, 3, 4 e 5
Piles	5
Roof structure	2, 3 e 4
Ceiling	2 e 3
Foundation	5 e 6
Railing	2, 3 e 4
Kerb	4 e 5
Door trim	2, 3 e 4
Window	1, 2, 3 e 4
Wainscoting	2 e 3
Strut	2 e 3
Furnitures	1, 2, 3 e 4
Ornaments	2, 3 e 4
Pergola	4 e 5
Playground	4 e 5
Bridge/ Footbridge	4, 5 e 6
Door	1,2 e 3
Wall	2, 3 e 4
Baseboard	2, 3 e 4
Window sill	2, 3 e 4
Fascia	4
Tiles shingles	4
Cooling tower	5
Beam	2, 3 e 4
Baldrame beam	5

https://doi.org/10.52202/069179-0397

Table 2: *Roundwood. Fontes: BRASOLIN et. al (2004); ABNT NBR 16143:2013; [8, 9].*

Application	Probable Use Category
Fences	4 e 5
Columns	2, 3, 4 e 5
Crossarm	4
Bridge defense	5 e 6
Railway sleeper	5
Roof structure	2, 3 e 4
Foundation	5 e 6
Kerb	4 e 5
Fence posts	5
Furniture	1, 2, 3, 4 e 5
Playground	4 e 5
Bridge/ Footbridge	4, 5 e 6
Post (energy and telephony)	5
Wooden board bridge	4

Table 3: *Glulam. Fontes: BRASOLIN et. al (2004); ABNT NBR 16143:2013; [8, 9].*

Application	Probable Use Category
Arch	2, 3 e 5
Columns	2, 3, 4, 5 e 6
Bridge/ Footbridge	4, 5 e 6
Post (energy and telephony)	5
Beam	2, 3 e 4

Table 4: *Wood panels. Fontes: BRASOLIN et. al (2004); ABNT NBR 16143:2013; [8, 9].*

Application	Probable Use Category
Floor	2, 3, 4 e 5
Packaging (non-disposable)	1, 2, 3, e 4
Furnitures	1, 2, 3 e 4
Wall	2, 3 e 4
Tiles shingles	4
Roof (undercover)	2 e 3
Plywood box beam	2, 3 e 4

7 CONCLUSIONS

The Use Categories System defines the indications that must be taken in the design phase of a construction with wooden elements, thus helping to choose the most appropriate treatment for wood preservation.

Once the Use Categories are defined at the design step, the structural designer resorts to the ABNT NBR 16143:2013 standard and defines which will be the most appropriate preservative treatment to be used for each timber structural members.

The Annex D (informative) of ABNT NBR 7190:1997 dealt with recommendations on the durability of wood.

In the revised version of the ABNT NBR 7190:2022 standard, the content ceases to be informative and becomes normative and mandatory, available in Chapter 12 Durability of wood.

ACKNOWLEDGEMENT

The authors thanks to Department of Structures Engineering SET, to Postdoctoral Research Committee CPq/EESC/USP of the University of São Paulo, and to National Council of Scientific and Technological Development CNPq.

REFERENCES

[1] ASSOCIAÇÃO BRASILEIRA DE NORMAS TÉCNICAS. ABNT NBR 7190:1997. Projeto de Estruturas de Madeira. Rio de Janeiro. Rio de Janeiro, 1997.

[2] CALIL JUNIOR, C. et al. Manual de projeto e construção de pontes de madeira. ISBN: 85-98156-19-1. Suprema, São Carlos, 2006.

[3] BRITO, L. D. Recomendações para o Projeto e Construção de Estruturas com Peças Roliças de Madeira de Reflorestamento. 339 págs. Dissertação (Mestrado) Departamento de Engenharia de Estruturas, Escola de Engenharia de São Carlos, Universidade de São Paulo. São Carlos, 2010.

http://sistemas.set.eesc.usp.br/static/media/producao/2010ME_LeandroDussarratBrito.pdf
[4] CALIL JUNIOR, C.; BRITO, L. D. Manual de Projeto e Construção de Estruturas com Peças Roliças de Madeira de Reflorestamento. LaMEM/SET/EESC/USP. ISBN: 978-85-8023-000-0. São Carlos, 2010. https://ibramem.files.wordpress.com/2011/05/manualdeprojetoeconstruc3a7c3a3odeestruturascompec3a7asrolic3a7asdemadeiradereflorestamento.pdf
[5] ASSOCIAÇÃO BRASILEIRA DE NORMAS TÉCNICAS. NB 11: Cálculo e execução de estruturas de madeira. Rio de Janeiro, 1951.
[6] FUSCO, P. B.; CALIL JUNIOR, C.; ALMEIDA, P. F. O. Norma de projeto de estruturas de madeira. Universidade de São Paulo. BT/PEF/9602. ISSN 0103-9822. São Paulo, 1996.
[7] CALIL JUNIOR, C.; LAHR, F. A.; DIAS, A. A. Dimensionamento de Elementos Estruturais de Madeira. , Editora Manole, Barueri, SP, 2003.
[8] BRAZOLIN. S; LANA, L. E.; MONTEIRO, M.B.B; LOPEZ, G.A.C e PLETZ, E. Preservação de madeiras – sistema de classe de risco. Revista Madeira: arquitetura e engenharia, ano 5, nº 13. EESC, IBRAMEM. ISSN 1806-6097. São Carlos, SP. mai/ago 2004.
[9] ASSOCIAÇÃO BRASILEIRA DE NORMAS TÉCNICAS. ABNT NBR 16143:2013. Preservação de Madeiras – Sistema de Categorias de Uso. Rio de Janeiro, 2013.
[10] ASSOCIAÇÃO BRASILEIRA DE NORMAS TÉCNICAS. CB-02 Projeto de Revisão da ABNT NBR 7190:2022. Projeto de estruturas de madeira. Rio de Janeiro, 2022.
[11] CALIL JUNIOR, C. et al. Manual of Design and Construction of timber bridges. Structural Engineering. LAP – LAMBERT Academic Publishing. ISBN: 978-3-659-71734-5. Germany, 2015.
[12] BRITO, L. D. Patologia em estruturas de madeira: metodologia de inspeção e técnicas de reabilitação. Tese (Doutorado) Departamento de Engenharia de Estruturas, Escola de Engenharia de São Carlos, Universidade de São Paulo. São Carlos, 2014. http://sistemas.set.eesc.usp.br/static/media/producao/2014DO_LeandroDussarratBrito.pdf

https://doi.org/10.52202/069179-0397

World Conference on Timber Engineering Oslo 2023

UPDATING EUROCODE 5 – DESIGN GUIDANCE FOR INCREASING THE ROBUSTNESS OF TIMBER STRUCTURES

Pedro Palma [1], Jørgen Munch-Andersen [2], and Philipp Dietsch [3]

ABSTRACT: The European structural timber design standard EN 1995-1-1 *Eurocode 5* is currently under an extensive revision and the latest draft includes a new Informative Annex on *Additional guidance for increasing the robustness of timber structures*. The design rules in this new Annex are focused on direct design methods that provide explicit verifications for specific scenarios of assumed local failure: i) design for resistance to removal of load-carrying elements and; ii) design for segmentation using fuse elements. Dynamic effects related to a sudden loss of a load-carrying element are considered through dynamic amplification factors, which are provisionally prescribed as $\gamma_{dyn} = 2.0$. The design of fuse elements is based on limiting their load-carrying capacity, ensuring that they fail under certain damage scenarios. The upper values of the load-carrying capacity of connections are very dependent on the specific type of connection, but a over-strength factor $4 = R_{k,0.95}/R_{k,0.05}$ is provisionally prescribed.

KEYWORDS: robustness, progressive collapse, EN 1995-1-1, Eurocode 5, element-removal analyses, fuse elements

1 INTRODUCTION

1.1 BACKGROUND

Twenty years after their initial publication, the structural Eurocodes are currently under revision. A new topic that is now explicitly considered in the latest draft version of FprEN 1990:2022 *Eurocode 0 Basis of structural design* [1] is resistance to disproportionate collapse. This draft includes an Informative Annex E with additional guidance for enhancing the robustness of buildings and bridges. This Annex E, however, provides only very general guidance and does not provide a clear hierarchy of design strategies to prevent disproportionate collapses. The European standardisation committee CEN/TC 250/SC 5, responsible for EN 1995-1-1 *Eurocode 5 Design of timber structures* [2] took on the task of developing specific design guidance for increasing the robustness of timber structures. This work has been carried out by members of its Working Group 10 and the outcome is a new Informative Annex to the latest draft of prEN 1995-1-1 Eurocode 5.

1.2 SCOPE AND OBJECTIVES

This paper presents the new Annex A *Additional guidance for increasing the robustness of timber structures* of prEN 1995-1-1 Eurocode 5. It gives an overview of design strategies to increase resistance to disproportionate collapse, focusing on timber structures [3–5] and including lessons learned from past accidents [6,7]. Advantages and shortcomings of the different strategies are discussed. The design rules in the new Annex A are presented, alongside with their background. Aspects that need to be further investigated are also highlighted

1.3 DISCLAIMER

The opinions expressed in this paper are those of the authors and do not necessarily represent the official position of the Technical Committee CEN/TC 250/SC 5 or the opinion of its other members.

2 DEFINITIONS

FprEN 1990:2022 Eurocode 0 [1] defines *robustness* as the "ability of a structure to withstand adverse and unforeseen events without being damaged to an extent disproportionate to the original cause". The Swiss standard SIA 260:2013 *Basis of Structural Design* [8] uses a somewhat different formulation and defines robustness as the "ability of a structure and its members to keep the amount of deterioration or failure within reasonable limits in relation to the cause". These definitions of robustness coincide with what has been more broadly defined as *resistance to disproportionate collapse* or *collapse resistance* [9,10,3]. The definition of robustness adopted in this paper is instead *insensitivity to initial damage*, which is one of the aspects of *collapse resistance* (Figure 1), alongside with *vulnerability* (susceptibility of a structural component to be damaged

[1] Pedro Palma, Empa, Structural Engineering Research Lab, Switzerland, pedro.palma@empa.ch
[2] Jørgen Munch-Andersen, Aalborg University, Department of the Built Environment, Denmark, jcma@build.aau.dk
[3] Philipp Dietsch, Timber Structures and Building Construction, Karlsruhe Institute of Technology (KIT) Germany, dietsch@kit.edu

https://doi.org/10.52202/069179-0398

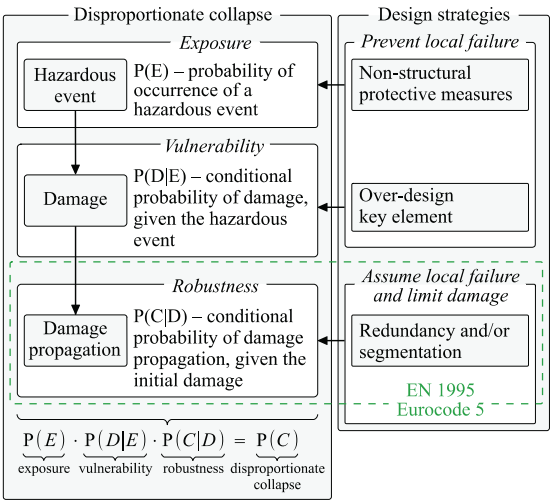

Figure 1: *Disproportionate collapse prevention strategies and robustness-focused scope of prEN 1995-1-1 Eurocode 5 (based on Starossek and Haberland [10] and Palma et al. [4]).*

by an abnormal event) and *exposure* (abnormal events, not explicitly considered in ordinary design) [11]. A robust structure is, therefore, less prone to disproportionate collapses. Finally, a disproportionate collapse might not be *progressive*, as statically determinate structures will most likely collapse after the failure of a single component.

The main difference between design for robustness and design for accidental situations [12] is that the latter assumes identified and quantified abnormal actions (e.g. far-field blasts or vehicle impacts), against which the structure can be explicitly designed, so that a specified reliability level is reached. Design for robustness, on the other hand, deals with exposures that cannot be identified and/or quantified. These can be errors in the design, construction, or use of the structure that lead to structural deficiencies, or external man-made (e.g. accidental or deliberate blast, impact, or fire) or natural events (e.g. extreme snow or wind loads, or degradation of the structure)Design for robustness deals mostly with threat-independent scenarios that assume an initial notional damage (e.g. sudden removal of a load-carrying member). The corresponding robustness-related design strategies are focused on limiting damage propagation through redundancy and/or segmentation.

3 DESIGN FRAMEWORK FOR RESISTANCE TO DISPROPORTIONATE COLLAPSE

Starossek's [11] design framework for resistance to disproportionate collapse (Figure 2) can be divided into the following main parts [13]:

i) risk assessment/classification of the structure;
ii) specification of hazard scenarios;
iii) specification of performance objectives;
iv) selection of design strategies
v) carrying out of verification procedures.

The level of *design requirements* should be based on the risk assessment of building. This can be achieved by undertaking the risk assessment and building classification frameworks described, e.g. in Section 4.1. The specification of *hazardous scenario*s, such as threat-specific (e.g. impact of a car in a ground-floor column) or non-threat-specific events (e.g. notional damage such as a sudden removal of a structural component), and *performance objectives* (i.e. the acceptable level of damage/consequences) should involve other stakeholders besides the owner and the design team, namely the relevant civil and building authorities and even insurance companies. For major projects, the specification of hazardous scenarios requires some experience, since the creation of general rules is difficult due to the many possible scenarios and the project-specific nature of many of them. Once the hazard scenarios are considered and the performance objectives are set, the structural design team then selects the *design strategies* (e.g. protection or overdesign measures to prevent local damage, robustness measures to limit damage propagation) and the *design verification procedures* (e.g. based on structural analysis models or even testing). A schematic overview of this design framework for resistance to disproportionate collapse is given in Figure 2.

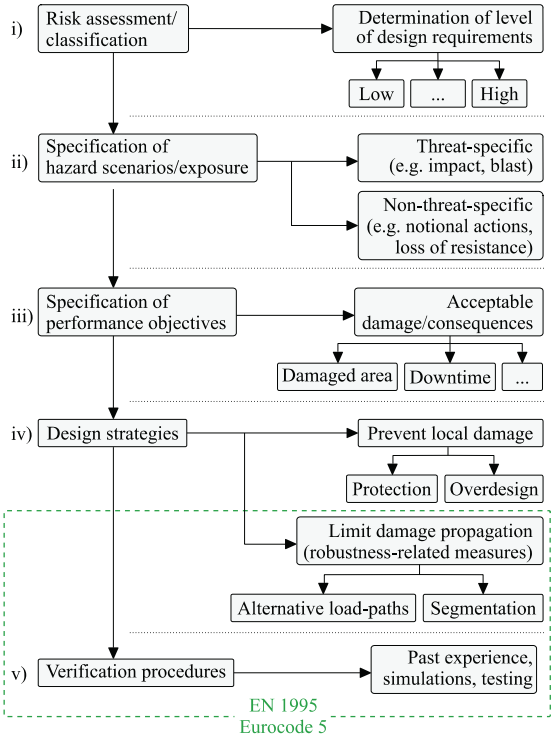

Figure 2: *Design framework for resistance to disproportionate collapse, based on Starossek [11], and the scope of prEN 1995-1-1 Eurocode 5.*

https://doi.org/10.52202/069179-0398

For buildings with low importance and exposure, it should be possible to achieve an adequate level of resistance to disproportionate collapse without any explicit design verifications. However increasingly complex verifications are often required for buildings of high importance and/or exposure.

4 DESIGN IN ACCORDANCE WITH THE STRUCTURAL EUROCODES

4.1 APPROACH

The structural Eurocodes in their current and upcoming versions, as well as most other current structural design codes, adopt a limit-state design approach, based on a probabilistic representation of the design parameters so that predefined appropriate reliability levels are reached. EN 1990 *Eurocode 0* establishes the design principles, based mostly on the partial factor method, EN 1991 *Eurocode 1* specifies the actions and their values, and timber-specific aspects are addressed in EN 1995 *Eurocode 5*. (Figure 3).

FprEN 1990:2022 *Eurocode 0* [1] recommends that structures "be designed to have an adequate level of robustness" and states that "for most structures, design in accordance with the Eurocodes is assumed to provide an adequate level of robustness without the need for any additional design measures". This statement might be based on the fact that not so many disproportionate collapses have been observed [14] and that it has been traditionally accepted that "structural codes may consider these [progressive collapse] requirements satisfied if all other requirements can be fulfilled" [15,16]. However, assuming that designing in accordance with the Eurocodes automatically provides an adequate level of robustness is a rather "optimistic" view and has been shown not to be true in some cases, as some studies on multi-storey timber buildings have shown [17].

As other design frameworks for resistance to disproportionate collapse [18,19], FprEN 1990:2022 *Eurocode 0* [1] starts by assessing the *importance* of the building, i.e. the *direct* and *indirect* risks or consequences of a collapse, and its *exposure*, i.e. the probability of occurrence of a hazardous event (e.g. accident, malicious or unintentional actions). FprEN 1990:2022 Eurocode 0 [1] establishes five consequence classes (Table 1), based on an indicative qualification of consequences (loss of human life or personal injury and economic, social or environmental consequences). The exposure of the structure, i.e. the level of threat, is not explicitly accounted for (or it is assumed to be proportional to the importance of the building) [13].

FprEN 1990:2022 Eurocode 0 [1] then allows for the design method for "providing enhanced robustness" to be selected based on the consequence class (CC) of the structure (Table 2).

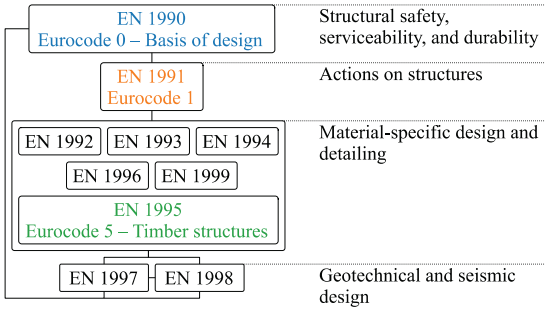

Figure 3: *Links between the Eurocodes (https://eurocodes.jrc.ec.europa.eu/showpage.php?id=13)*

4.2 SHORTCOMINGS

One of the shortcoming regarding resistance to disproportionate collapse is that design verifications are made only on the local (component) level, following an element-by-element approach.It is hereby assumed that the reliability of the structure is not much smaller than the reliability of each member or connection [20]. However, the response of a structure to an initial local damage is dependent not only on the behaviour of its components in

Table 1: *Qualification of consequence classes (FprEN 1990 2022* ***[1]****). Assignment of structures to consequences classes is a Nationally Determined Parameter (NDP), i.e. it can be defined at a national level by regulatory authorities in each Member State.*

Consequence class (CC)	Indicative qualification of consequences	
	Loss of human life or personal injury [a]	Economic, social or environmental consequences [a]
CC0 – Lowest	Very low	Insignificant
CC1 – Lower	Low	Small
CC2 – Normal	Medium	Considerable
CC3 – Higher	High	Very great
CC4 – Highest	Extreme	Huge

[a] The consequence class is chosen based on the more severe of these two columns.

Table 2: *Indicative design methods for "enhancing robustness" taken from FprEN 1990 2022 [1].*

Consequence class	Design methods
CC1 – Lower	No design methods to provide enhanced robustness need be applied.
CC2 – Normal	When specified by the relevant authority or as agreed for a specific project by the relevant parties, either: a) For buildings: use of prescriptive design rules for ties to provide integrity, ductility and alternative load paths; or b) Design of particular structural members as 'Key members'; and/or c) Segmentation.
CC3 – Higher	Satisfy the requirements for CC2 appropriately adapted and in addition consider, where appropriate: a) potential initial failure events; b) propagation of failure; c) resulting consequences; d) risks.

https://doi.org/10.52202/069179-0398

isolation, but on their arrangement and connectivity to the structure and the requirements for the reliability of the components should depend on the characteristics of the structure [20].

Another issue of the current approach regarding design for resistance to disproportionate collapse is the difficulty in dealing with extreme risks, i.e. low probability/high consequence events, such as a disproportionate collapse, due to the lack of statistical data [11]. Strategies to enhance resistance to disproportionate collapse are "not generally associated with a target level of reliability as in structural member design against identified actions and could involve consideration of a conditional reliability" [1]. Therefore, these events cannot easily be handled within the current reliability-based framework, even though target reliability levels have been set in the past for ultimate limit states corresponding to progressive collapse [15,16].

As mentioned above, it is difficult to judge the resistance of a structure to disproportionate collapse simply based on the individual behaviour of its elements and neglecting the structure's sensitivity to initial damage. Tests on a medium-rise multi-storey platform-frame building, with structural walls and floors constructed from small section timber studs and cladded with wood-based panels, showed that such buildings had "significant inherent robustness and capacity to span over removed panels" [21–23]. On the other hand advanced mechanical simulations, which also took into account the variability of mechanical properties, of a medium-rise cross-laminated timber building showed that simple compliance with building codes [4] (both the Eurocodes and the *National Building Code of Canada* and CSA O86-09:2010) led to a probability of disproportionate collapse as high as 32% after removal of a load-carrying element [17].

Finally, the indicative design methods for "enhancing robustness" prescribed by FprEN 1990:2022 *Eurocode 0* [1] (Table 2) are not actually focused on increasing robustness, i.e. insensitivity to initial damage, and can hence be misleading. Strategies such as the overdesign of "key members" reduce the local *vulnerability* of the structure, but do not necessarily lead to increased *robustness* (Figure 1). Prescriptive design rules (e.g. providing ties or imposing failure modes with sufficient ductility in the connections) might, in some cases, promote rather than prevent collapse progression [7,11].

5 DESIGN STRATEGIES AGAINST DISPROPORTIONATE COLLAPSE

Given that different structures are vulnerable to disproportionate collapse in different degrees, design for resistance to disproportionate collapse cannot be completely independent of the specifics of each project. Hence, it should be considered in the early (i.e. conceptual) stages of the design process [4,5]. For structures in higher consequence classes, resistance to disproportionate collapse should be based on more detailed analyses that include explicit *direct* design verifications for specific scenarios (e.g. element-removal analyses). This *direct* approach is more compatible with architectural complexity and design procedures that allow evaluating the global structural behaviour as a function of the behaviour of single elements. It can give valuable insights regarding resistance to disproportionate collapse of the structure. However, the required time, skill, and computational effort is greater than with the *indirect* approach. In any case, design for resistance to disproportionate collapse should not be interpreted as "simply applying rules" as this could lead to these aspects being addressed too late in the design process, hence limiting the applicable strategies or involving considerable costs. Rather should design for resistance to disproportionate collapse be addressed in the conceptual design of the structures.

Resistance to disproportionate collapse can be achieved at different levels (Figures 1 and 2):

- preventing local failures by
  - *adopting protective measures* to reduce the probability, extent or mitigate the exposure of the structure to abnormal events, or by
  - *overdesigning key elements* to reduce the probability of damage in case of a hazardous event, i.e. reduce the vulnerability of key elements and increase safety against initial failure;
- assuming local failure and limiting damage propagation (robustness-related measures to increase insensitivity to initial damage), through
  - *redundancy*, e.g. through alternative load paths and/or
  - *segmentation*, e.g. ensuring that collapsing parts are isolated from the rest of the structure.

Design strategies based on adopting *protective measures* often fall outside the scope of structural design (e.g. vehicle barriers, access control, active fire protection). Strategies based on *overdesigning key elements* should be a last resort [3,5,25,26], used only in cases where other alternatives are not viable or too costly. Design of key elements follows the common design procedure, even if the considered hazards and assumed actions are anything but common, like blast and impact, and the corresponding structural design can often be done in accordance with available guidance [4,12].

The *redundancy* strategy is based on providing an alternative load path (ALP) for the forces previously transmitted through load-carrying components that are assumed to have failed. It is based on assessing the behaviour of the remaining structure after an initial notional damage. A commonly assumed initial damage is the notional removal of one or several components of the structure. Then a so-called *element-removal analysis* is performed, with the objective of evaluating if the

[4] The building was not designed for earthquake resistance, only for a 1.0 kPa horizontal wind action. Explicit design for earthquake resistance could have indirectly increased the resistance to disproportionate collapse.

https://doi.org/10.52202/069179-0398

remaining structure is able to accommodate the damage. Redundancy on its own might not be suitable to avoid disproportionate collapse. In the case of repetitive structures, systematic design or execution errors can compromise the ability of a structure to redistribute loads and lead to progressive collapse [6,7], as the alternative load paths are all affected by a common-cause failure.

In these cases, *segmentation* can be an adequate design strategy. The objective of this strategy is to compartmentalise the structure in a way that collapse progression after an initial damage is halted at predefined locations, i.e. at the segment's borders, either through fuse-type elements or by having control joints at which the segments are physically separated. Most common solutions for *vertical segmentation* rely on providing shock-absorbing zones with high energy dissipation capacity. Examples of vertical segmentation are scarce, however, the 14-storey timber building "Treet", in Norway, includes a paradigmatic example [27]: this building has two "power storeys" that carry a prefabricated concrete slab on top of which four levels of residential modules are stacked; these "power storeys" should be able to halt a progressive collapse of the stacked residential modules, limiting the extent of collapse.

6 DESIGN FOR ROBUSTNESS IN prEN 1995-1-1 EUROCODE 5

6.1 SCOPE

As already discussed in Section 2, mistaking robustness with resistance to disproportionate collapse is a common misconception. Robustness-related strategies assume that damage has occurred and focus on limiting the extent of the damage, whereas increasing resistance to disproportionate collapse can be achieved through other strategies that are not related to robustness. Two other common misconceptions on the scope of prEN 1995-1-1 Eurocode 5 are that it should specify: i) *hazardous scenarios*, e.g. impact of a car in a ground-floor column, or a notional removal of a load-carrying component; and ii) *performance objectives*, e.g. allowed collapsed/ damaged area. However, as discussed in Section 3, these aspects are not to be addressed by the structural design team alone and must involve other stakeholders, such as the owner, the authorities, and other relevant parties.

The simple application of prescriptive design rules does not imply that performance requirements are met [11], hence they are therefore not addressed in prEN 1995-1-1 Eurocode 5. Preventing local failures by adopting protective measures also falls outside of the scope of structural design codes. Overdesigning key elements can be done within the normal design framework of the Eurocodes [4,12], even if the design actions are arbitrarily determined instead of statistically assessed (Section 5). In addition, even if overdesigning identified key elements contributes to increasing the resistance to disproportionate collapse, it is mostly unrelated to increasing robustness.

Ensuring robustness cannot simply be based on "applying rules". Choosing an adequate structural concept is as important for robustness as it is for seismic design. The new Annex A of prEN 1995-1-1 Eurocode 5 is focused on direct design methods, in which robustness can be explicitly demonstrated for specified initial damage scenarios (e.g. loss of one or more columns) and performance requirements (e.g. acceptable extent of collapse as a percentage of floor area, volume, or costs). This can only be achieved for design strategies based on *assuming local failure* and limiting the damage that follows, namely *redundancy* through alternative load paths and/or segmentation through fuse elements.

6.2 DRAFT CLAUSES IN prEN 1995-1-1

6.2.1 Overview

The members of Working Group (WG) 10 *Basis of design and materials*, of the European standardisation Technical Committee CEN/TC 250/SC 5 *Eurocode 5* have drafted robustness-related clauses for the upcoming revised version of Eurocode 5. A note in the main part of the standard highlights that designing for robustness is more related to the structural concept, redundancy, adequate choice of structural materials, and structural detailing than to complex analyses. More detailed provisions are given in informative Annex A *Additional guidance for increasing the robustness of timber structures*.

Annex A contains provisions for design strategies to increase robustness based on limiting the total damage following assumed scenarios of initial local failure (Figures 2 and 4), namely:

i) creation of alternative load paths (*redundancy* strategy); and
ii) segmentation of the structure into distinct parts that are able to collapse without inducing structural failures in other parts, by means of fuse elements.

Annex A is based on the assumption that the design will be based on linear-elastic structural analyses, as the other parts of Eurocode 5. Therefore, non-linear and dynamic effects have to be considered through adequate factors imposed on actions, resistances, and stiffnesses. It is not yet clear if enough data is available to derive all these factors, or if its application will be limited specific types of elements and connections.

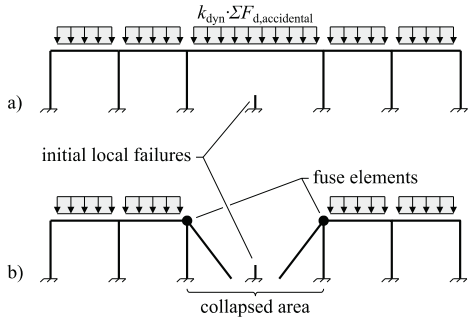

Figure 4: *Design strategies in the latest draft of Annex A of the prEN 1995-1-1 Eurocode 5: a) design for removal of load-carrying elements; b) design for segmentation using fuse elements.*

https://doi.org/10.52202/069179-0398

6.2.2 Design for removal of structural elements

The design verifications for *resistance to removal of load-carrying elements* includes two scenarios:

i) failure of a structural element including dynamic effects and impact of falling debris; and
ii) remaining structure, without the failed structural element.

In the first scenario, the dynamic effects corresponding to the sudden failure of a load-carrying element are considered by applying a partial factor γ_{dyn} on the actions. Different values have been proposed for such dynamic amplification factors. Grantham and Enjily [23] propose a modification factor of 2.0 (for timber-frame walls). Mpidi Bita et al. [17] state that for a 12-storey CLT building the forces from the dynamic simulation were about 1.5 times higher than the outcome from static analysis. Dietsch and Kreuzinger [28] determine dynamic amplification factors due to brittle failures in timber elements with shear reinforcement in form of self-tapping screws around 1.2. Cheng et al. [29] performed dynamic element-removal experiments on small-scale beam-column frames and report dynamic amplification factors between 1.3 and 1.7 for frames with ductile connections and above 2.0 for frames with brittle connections. Stevens et al. [30,31] present results that show a range of dynamic amplification factors from 1.20 to 1.85 for steel buildings and from 1.00 to 1.40 for concrete buildings. In the current draft of Annex A, a single provisional value $\gamma_{dyn} = 2.0$ is recommended, but it is still under discussion whether different values should be given depending on the type of structure and connections.

In this first scenario, the prescribed mechanical properties are those corresponding to an *instantaneous* load-duration class in EN 1995-1-1:2004 Eurocode 5 [2]. The prescribed combination of actions is that for accidental design situations [1].

Some element-removal scenarios might not impose dynamic effects on the structure (e.g. gradual loss of an element during a fire, excessive settlement of a foundation). In such cases, only the second design scenario is relevant. It is also important to note that whenever an alternative load path is mobilised, the failure might go unnoticed if the structure does not exhibit visible deflections or extensive cracking. Such a situation can eventually lead to a progressive collapse. This is particularly important in the case of very stiff secondary systems [6,7].

6.2.3 Design for segmentation using fuse elements

Robustness can be increased by designing for segmentation, e.g by isolating collapsing parts of the structure. Segmentation by interrupting the structural continuity is particularly important to limit the extent of damage in the case of systematic flaws that reduce the resistance of the structure at many locations, namely in repetitive structures.

Design for segmentation may be achieved by limiting the upper value of the load-carrying capacity of fuse elements, which are structural elements that are presumed to fail under certain damage scenarios in order to halt a progressive collapse. Given the large variability exhibited by the mechanical properties of timber, the fuse elements should be connections and the upper design value of their load-carrying capacity $R_{d,sup}$ should be smaller than the design effect of the action that it will carry in the case of a collapse $E_{d,fuse}$

$$R_{d,sup} \leq E_{d,fuse}. \quad (1)$$

In the current draft of Annex A, the upper design value of the load-carrying capacity of the fuse element $R_{d,sup}$ is calculated using the 95th-percentile value $R_{k,0.95}$ of the load-carrying capacity. Partial safety factors γ_M or γ_R are those for accidental design situations. The strength modification factor k_{mod} to be used is that for actions assigned to the *instantaneous* load duration class.

The values of $R_{k,0.95}$ are very dependent on the specific type of connection. In the absence of more ac-curate information, it is proposed that $R_{k,0.95} = 4 \cdot R_{k,0.05}$ is used. In a more recent experimental study on nailed and screwed steel-to-timber connections, Munch-Andersen [32] found an over-strength factor (ratio between the 95th-and the 5th-percentile values) of about 2.2. Connections with laterally-loaded dowel-type fasteners are prone to have considerable over-strength due to a possible pronounced rope-effect, which might complicate their use as fuse elements.

The design effect of the action $E_{d,fuse}$ is typically based on analyses of specific scenarios of initial local failure and includes relevant dynamic effects. In many cases, $E_{d,fuse}$ is mainly dependent on the self-weight of the part of the structure that is assumed to collapse. The fuse elements can also be conceptualised as in the example given in Figure 5 (not applicable in seismic regions), in which the rotations during failure lead to the detachment of failing and attached member.

It is in any case important to ensure that the remaining structure is able to carry relevant horizontal loads and that its members are adequately braced.

Design for segmentation and design for removal of structural elements can be used in combination, e.g. the structure can be segmented and alternative load paths can be provided within the segments.

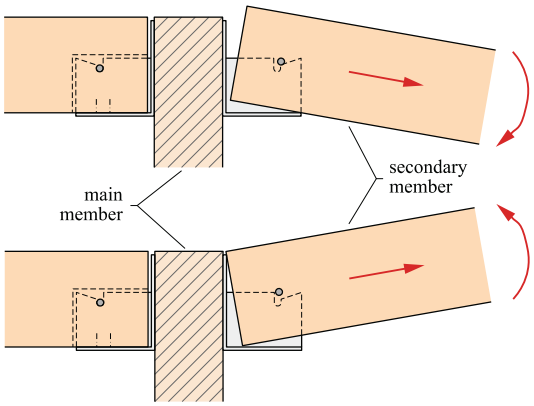

Figure 5: *Example of fuse element by Waidelich [33].*

https://doi.org/10.52202/069179-0398

7 CONCLUSIONS

Codification of resistance to disproportionate collapse of timber structures within the framework of the Eurocodes is not straightforward, in particular due to the lack of well-established design procedures. Designing for robustness (which is a part of the resistance to disproportionate collapse) shall primarily be considered in the early stages of design, e.g. by choosing an adequate structural concept, materials, and detailing.

The new Annex A of prEN 1995-1-1 Eurocode 5 is focused on direct design methods, in which *robustness* can be explicitly demonstrated for specified initial damage scenarios and performance requirements. Annex A contains provisions for design strategies to increase robustness based on limiting the total damage following assumed scenarios of initial local failure, namely the creation of alternative load paths and segmentation using fuse elements. Dynamic effects related to a sudden loss of a load-carrying element are considered through dynamic amplification factors, which are provisionally prescribed as $\gamma_{dyn} = 2.0$. The design of fuse elements is based on limiting their load-carrying capacity, and an over-strength factor $4 = R_{k,0.95}/R_{k,0.05}$ is provisionally recommended.

ACKNOWLEDGEMENT

The authors thank the members of Working Group (WG) 10 *Basis of design and materials*, of the European Standardisation Committee TC 250/SC 5 *Eurocode 5*, for the very insightful discussions. The authors also thank COST Action CA 20139 *Holistic design of taller timber buildings (HELEN)*.

REFERENCES

[1] FprEN 1990:2022. Eurocode – Basis of structural and geotechnical design. Brussels: European Committee for Standardization (CEN); 2022.

[2] EN 1995-1-1:2004. Eurocode 5: Design of timber structures – Part 1-1: General – Common rules and rules for buildings. Brussels: European Committee for Standardization (CEN); 2004.

[3] Huber JAJ, Ekevad M, Girhammar UA, Berg S. Structural robustness and timber buildings – a review. Wood Material Science & Engineering 2018.

[4] Palma P, Steiger R, Jockwer R. Addressing design for robustness in the 2nd-generation EN 1995 Eurocode 5. INTER/52-22-2, Proceedings of the International Network on Timber Engineering Research, Meeting Fifty-two, Tacoma, USA, 2019, p. 16+6.

[5] Mpidi Bita H, Huber J, Palma P, Tannert T. Prevention of disproportionate collapse for multi-story mass timber buildings: review of current practices and recent research. Journal of Structural Engineering 2022;148:04022079.

[6] Dietsch P. Robustness of large-span timber roof structures — Structural aspects. Engineering Structures 2011;33:3106–12.

[7] Munch-Andersen J, Dietsch P. Robustness of large-span timber roof structures – Two examples. Engineering Structures 2011;33:3113–7.

[8] SIA 260:2013. Basis of Structural Design. Zurich: Schweizerischer Ingenieur- und Architektenverein (SIA); 2013.

[9] Ellingwood B, Smilowitz R, Dusenberry D, Duthinh D, Lew H, Carino N. Best Practices for Reducing the Potential for Progressive Collapse in Buildings | NIST. National Institute of Standards and Technology (NIST); 2007.

[10] Starossek U, Haberland M. Disproportionate collapse: terminology and procedures. Journal of Performance of Constructed Facilities 2010;24:519–28.

[11] Starossek U. Progressive collapse of structures. ICE Publishing; 2018.

[12] EN 1991-1-7:2006. Eurocode 1 - Actions on structures - Part 1-7: General actions - Accidental actions. Brussels: European Committee for Standardization (CEN); 2006.

[13] Palma P, Felicita M, Vojnovic L. Structural robustness – Design framework for resistance to disproportionate collapse. Design for robustness, adaptability, disassembly and reuse, and repairability of taller timber buildings: a state of the art report, 17-21: COST Action CA 20139 Holistic design of taller timber buildings (HELEN); 2022.

[14] Frühwald Hansson E. Analysis of structural failures in timber structures: Typical causes for failure and failure modes. Engineering Structures 2011;33:2978–82.

[15] Brynildsen O. Proposal for safety codes for load-carrying structures – code and recommendation concerning safety methods. CIB-W18/4-16, Proceedings of the International Council for Research and Innovation in Building and Construction, Working Comisson W18 – Timber Structures, Paris, France, Meeting 4, p. 56.

[16] Brynildsen O. Comments to proposal for safety codes for load-carrying structures. CIB-W18/4-18, Proceedings of the International Council for Research and Innovation in Building and Construction, Working Comisson W18 – Timber Structures, Paris, France, Meeting 4, 1975, p. 31.

[17] Mpidi Bita H, Currie N, Tannert T. Disproportionate collapse analysis of mid-rise cross-laminated timber buildings. Structure and Infrastructure Engineering 2018;14:1547–60.

[18] GSA. General Services Administration (GSA) Alternate Path Analysis and Design Guidelines for Progressive Collapse Resistance. U.S.A.: U.S. General Services Administration; 2013.

[19] UFC 4-023-03. Design of buildings to resist progressive collapse. Department of Defense (DoD); 2016.

[20] JCSS Probabilistic Model Code. Part I – Basis of design. JCSS Probabilistic Model Code, Joint Committee on Structural Safety; 2001, p. 62.

[21] Milner M, Edwards S, Turnbull D, Enjily V. Verification of the robustness of a six-storey timber-frame building. The Structural Engineer 1998;76.
[22] Enjily V. The performance of timber structures, elements and components. COST Action E24 Copenhagen Meeting, Denmark: COST Action E24; 2001.
[23] Grantham R, Enjily V. UK Design Guidance for multi-storey timber frame buildings. Proceedings of the 8th World Conference on Timber Engineering (WCTE2004), vol. 1, Lahti, Finland, 2004, p. 1001–5.
[24] CSA O86-09. Engineering Design in Wood. Ontario, Canada: Canadian Standards Association; 2010.
[25] Arup. Review of international research on structural robustness and disproportionate collapse. Arup; 2011.
[26] Hewson N. Robustness in structures. Forest and Wood Products Australia; 2016.
[27] Abrahamsen RB, Malo KA. Structural design and assembly of "Treet" - a 14-storey timber residential building in Norway. Proceedings of the World Conference on Timber Engineering 2014 (WCTE 2014), Quebec City, Canada, 2014, p. 8.
[28] Dietsch P, Kreuzinger H. Dynamic effects in reinforced beams at brittle failure – evaluated for timber members. Engineering Structures 2020;209:110018.
[29] Cheng X, Gilbert BP, Guan H, Underhill ID, Karampour H. Experimental dynamic collapse response of post-and-beam mass timber frames under a sudden column removal scenario. Engineering Structures 2021;233:111918.
[30] Stevens D, Crowder B, Sunshine D, Marchand K, Smilowitz R, Williamson E, et al. DoD research and criteria for the design of buildings to resist progressive collapse. Journal of Structural Engineering 2011;137:870–80.
[31] Stevens D, Martin E, Williamson E, McKay A, Marchand K. Recent developments in progressive collapse design 2015.
[32] Munch-Andersen J. Upper and lower resistance of small steel-to-timber connections and comparaision with revised EYM. Submitted to the World Conference on Timber Engineering (WCTE 2023), Oslo, Norway, 2023.
[33] Waidelich M. Konstruktive Ausbildung von Primär- und Sekundärtragwerken in weitgespannten Holztragwerken im Hinblick auf Robustheit und Kollapsverhalten. Masterarbeit. Technischen Universität München (TUM), 2011.

https://doi.org/10.52202/069179-0398

World Conference on Timber Engineering Oslo 2023

THE NEW BRAZILIAN TIMBER STRUCTURES CODE NBR7190: 2022

Carlito Calil Junior[1], Felipe Hideyoshi Icimoto[2], Leandro Dussarrat Brito[3]

ABSTRACT: The first Brazilian Timber Structures Code was published in 1951 under the name of NB11: Design and construction of timber structures, with a deterministic design method and composed of 16 pages without annex. In February of 1982, it was renamed NBR7190: 1982 without any modifications. In 1992 start the new study of this code using the limit states design method. This version, using the load and resistance factored design (LRFD), was published in 1997 by the Brazilian Association of Technical Standards with the emphasis on the utilization of hardwoods. A new study started in 2013 in order to consider all the new wood composite industrialized materials and connections. Considering the huge amount of hardwoods in Brazil, new test methods were developed in order to calibrate the new materials. This paper aims to present the New Brazilian Code for Timber Structures Design, NBR7190: 2022, relating the new revision for structural grading recommendations for softwoods and hardwoods planted in Brazil. Details of structural and constructive systems, Glulam, CLT, fire and preservation recommendations for design and new types of connections are also presented.

The New Brazilian Timber Structures Design Code NBR7190: 2022 is composed of 7 parts, that are: Part 1: Design criteria; Part 2: Test Methods for visual and mechanical grading of structural lumber; Part 3: Test Methods for characterization of defect-free specimens for native timber; Part 4: Test Methods for characterization of structural lumber; Part 5: Test Methods for determination of strength and stiffness of connections; Part 6: Test Methods for characterization of glued laminated timber; Part 7: Test Methods for characterization of cross laminated timber.

These six test methods for structural properties, grading, quality control of Glulam and CLT, and connections are also presented in related papers. Part of these codes is based on international codes such as EUROCODE and ISO.

KEYWORDS: Brazilian timber design code, timber structures, timber structural properties

1 INTRODUCTION

The Brazilian Timber Design Code is based on the Limit States Design concept used with the partial factor method, moving from an Allowable Stress Design of 1982 to a Probabilistic Limit States Design in 1997 using a calibration coefficient to convert tabulated medium strength properties to characteristic 5% values of load effects and resistances.

This paper aims to present the New Brazilian Code for Timber Structures Design, NBR7190: 2022, relating the new revision for structural grading recommendations for softwoods and hardwoods planted in Brazil. Details of structural and constructive systems, Glulam, CLT, fire and preservation recommendations for design and new types of connections are presented.

The global objective of the code is to fix the general conditions that must be followed in the design, construction and control of current timber structures, namely: bridges, buildings, roofs, decks and formworks.

2 MATERIAL PROPERTIES

The properties to consider in the design of timber structures are: density, strength, stiffness and moisture content. The specified properties of strength and stiffness correspond to the class of moisture content of 12%, that is 20 degrees Celsius and 65% of relative humidity.

2.1 CHARACTERIZATION OF TIMBER PROPERTIES

The new code considers two types of characterization of material properties based on defect-free specimens for native wood and structural samples for reforestation and

[1] Carlito Calil Junior, LaMEM/SET/EESC/USP, University of São Paulo, São Paulo, Brazil, calil@sc.usp.br
[2] Felipe Hideyoshi Icimoto, Urbem, São Paulo, Brazil, felipeicimoto@urbembr.com
[3] Leandro Dussarrat Brito, LaMEM/SET/EESC/USP, University of São Paulo, São Paulo, Brazil, dussarrat@sc.usp.br

https://doi.org/10.52202/069179-0399

native species. The second type corresponds to the characterization of structural lumber based on the commercial lumber with all the defects like knots, fissures, slope of grain, warp, etc.

2.2 STRENGTH CLASSES

The two types of strength classes are simply a group of species/strength grade combinations that have similar properties. For native hardwoods five classes are defined: D20, D30, D40, D50 and D60. These numbers represent the characteristic value of compression parallel to grain stress for each strength class based on the characterization of small defect-free specimens. These strength classes represent the values of the strength and stiffness properties of forty-two tropical hardwood timbers grown in Brazil with adequate statistical analysis according to researches since 1980's to define the five classes for hardwoods, as we can observe in Table 1.

Table 1: *Strength classes of native wood defined with clear samples.*

Classes	$f_{c0,k}$ MPa	$f_{v0,k}$ MPa	$E_{c0,m}$ MPa	Density (12%) kg/m³
D20	20	4	10 000	500
D30	30	5	12 000	625
D40	40	6	14 500	750
D50	50	7	16 500	850
D60	60	8	19 500	1 000

Source: ABNT NBR 7190: 2022

For reforestation species, the strength classes are based on tests of structural lumber as an alternative for native timber. The strength classes are based on bending strength with 12 strength classes for softwoods and 8 strength classes for hardwoods according to Table 2 and Table 3.

Table 2: *Strength classes for C14 to C24 softwoods.*

Softwoods C14 a C24						
	C14	**C16**	**C18**	**C20**	**C22**	**C24**
Resistance properties (MPa)						
$f_{m,k}$	14	16	18	20	22	24
$f_{t,0,k}$	8	10	11	12	13	14
$f_{t,90,k}$	0,4	0,4	0,4	0,4	0,4	0,4
$f_{c,0,k}$	16	17	18	19	20	21
$f_{c,90,k}$	2,0	2,2	2,2	2,3	2,4	2,5
$f_{v,k}$	3,0	3,2	3,4	3,6	3,8	4,0
Stiffness properties (GPa)						
$E_{0,med}$	7	8	9	9,5	10	11
$E_{0,05}$	4,7	5,4	6,0	6,4	6,7	7,4
$E_{90,med}$	0,2	0,3	0,3	0,3	0,3	0,4
G_{med}	0,4	0,5	0,6	0,6	0,6	0,7
Density (kg/m³)						
ρ_k	290	310	320	330	340	350
ρ_{med}	350	370	380	390	410	420

Source: ABNT NBR 7190: 2022

https://doi.org/10.52202/069179-0399

Table 3: *Strength classes for C27 to C50 softwoods.*

Softwoods C27 a C50						
	C27	**C30**	**C35**	**C40**	**C45**	**C50**
Resistance properties (MPa)						
$f_{m,k}$	27	30	35	40	45	50
$f_{t,0,k}$	16	18	21	24	27	30
$f_{t,90,k}$	0,4	0,4	0,4	0,4	0,4	0,4
$f_{c,0,k}$	22	23	25	26	27	29
$f_{c,90,k}$	2,6	2,7	2,8	2,9	3,1	3,2
$f_{v,k}$	4,0	4,0	4,0	4,0	4,0	4,0
Stiffness properties (GPa)						
$E_{0,med}$	12	12	13	14	15	16
$E_{0,05}$	7,7	8,0	8,7	9,4	10	11
$E_{90,med}$	0,4	0,4	0,4	0,5	0,5	0,5
G_{med}	0,7	0,8	0,8	0,9	0,9	1,0
Density (kg/m³)						
ρ_k	370	380	400	420	440	460
ρ_{med}	450	460	480	500	520	550

Source: ABNT NBR 7190: 2022

Table 4: *Strength classes for D18 to D70 hardwoods.*

Hardwoods D18 a D70								
	D18	**D24**	**D30**	**D35**	**D40**	**D50**	**D60**	**D70**
Resistance properties (MPa)								
$f_{m,k}$	18	24	30	35	40	50	60	70
$f_{t,0,k}$	11	14	18	21	24	30	36	42
$f_{t,90,k}$	0,6	0,6	0,6	0,6	0,6	0,6	0,6	0,6
$f_{c,0,k}$	18	21	23	25	26	29	32	34
$f_{c,90,k}$	7,5	7,8	8,0	8,1	8,3	9,3	11	13,5
$f_{v,k}$	3,4	4,0	4,0	4,0	4,0	4,0	4,5	5,0
Stiffness properties (GPa)								
$E_{0,med}$	9,5	10	11	12	13	14	17	20
$E_{0,05}$	8	8,5	9,2	10	11	12	14	16,8
$E_{90,med}$	0,6	0,7	0,7	0,8	0,9	0,9	1,1	1,33
G_{med}	0,6	0,6	0,7	0,8	0,8	0,9	1,1	1,25
Density (kg/m³)								
ρ_k	475	485	530	540	560	620	700	900
ρ_{med}	570	580	640	650	660	750	840	1080

Source: ABNT NBR 7190: 2022

2.3 DESIGN CRITERIA

The new code adopts the stability design criteria based on the EUROCODE 5 EN 1995-1-1:2009: Design of timber structures.

Representative Strength and Stiffness Values

The design values X_d of one wood property is obtained from the characteristic value X_k by the following formulae:

$$X_d = K_{mod} \frac{X_k}{\gamma_w} \quad (1)$$

Where γ_w the partial safety is factor of wood properties and K_{mod} is the modification factor that considers the influences that are not accounted in factor γ_w.

Modification Factors
The global modification factors K_{mod} is composed by the product of two partial modification factors, that is:

$$k_{mod} = k_{mod1} \cdot k_{mod2} \quad (2)$$

The partial modification factor number $K_{mod,1}$ consider the load classes and types of materials used, according to Table 5.

Table 5: *Values of* k_{mod1}.

Load class	Load duration	Wood type: Sawn wood Roundwood Glulam CLT LVL	Wood type: Recomposed wood
Permanent	More than 10 years	0,60	0,30
Long duration	Six months to 10 years	0,70	0,45
Medium duration	One week to 6 months	0,80	0,65
Short duration	Less one week	0,90	0,90
Instantaneous	Momentary	1,10	1,10

Source: ABNT NBR 7190: 2022

The partial modification factor number K_{mod2}, consider the classes of moisture content and types of materials used, according to Table 6.

Table 6: *Values of* K_{mod2}.

Wood moisture class	Wood type: Sawn wood Roundwood Glulam CLT LVL	Wood type: Recomposed wood
(1)	1,00	1,00
(2)	0,90	0,95
(3)	0,80	0,93
(4)	0,70*	0,90

*It is not allowed to use MLCC for humidity class 4.

Source: ABNT NBR 7190: 2022

2.3.1 Partial strength coefficients for Ultimate Limit States

The partial coefficient γ_w for Ultimate Limit States due the normal stresses has the basic value $\gamma_w = 1,4$. The partial coefficient for Ultimate Limit States due to shear stresses has the basic value $\gamma_w = 1,8$.

2.3.2 Partial coefficient for Serviceability Limit States.

The partial coefficient for Serviceability Limit States has the basic value $\gamma_w = 1,0$.

Partial Safety Factors for Ultimate Limit States: - the partial factor for compression parallel and normal to grain is $\gamma_{wc} = 1,4$, - the partial factor for tension parallel to grain is $\gamma_{wt} = 1,8$, - the partial factor for shear is $\gamma_{wv} = 1,8$, Stiffness The design analysis that the safety depends of wood stiffness like the instability in compression elements the elasticity modulus parallel to grain must be taken as:

$$E_{co,ef} = k_{mod1} \cdot k_{mod2} \cdot E_{o,med} \quad (3)$$

And the transversal modulus as:

$$G_{med} = \frac{E_{co,med}}{16} \quad (4)$$

https://doi.org/10.52202/069179-0399

Design Considerations in Stability of Compression Elements

In the compression design process, slenderness structural elements, may be subject of accidental eccentricity loads and geometrical lumber imperfections and this situation is considered in the code by applying an accidental eccentricity value of L/300. This mean that all the compression members with $\lambda > 40$ must be designed for bending and compression forces, where the bending forces appeared by eccentricity of L/300 multiply by the normal load. The formulas to be applied in the design of compression members are:

$$\sigma_{\mathrm{Nc,d}} = \frac{\mathrm{N}_{c,d}}{A} < \mathrm{f}_{\mathrm{co,d}} \quad (5)$$

3 TIMBER CONNECTIONS

The old code considers only two models for the design of connections using steel dowels, that is, embedment and bending.
The proposed code adopt the models used in EUROCODE 5 EN 1995-1-1:2009: Design of timber structures.
The modes for one and two shear sections using wood-wood and one and two shear sections using steel plate-wood and wood-steel plate-wood.
The main types of connections presented are nails, bolts and steel rings.

4 TEST METHODS

The New Brazilian Timber Structures Design Code NBR7190: 2022 is composed of 6 tests methods, that is:

Test Methods for visual and mechanical grading of structural lumber;

This Part 2 of the code establishes the criteria for visual and mechanical grading of lumber pieces of softwood and hardwood from planted forests for structural use. It aims to assign a strength class to each of the pieces that make up the batch of wood to be used classification by piece. This Part applies to wood pieces whose maximum dimensions of the cross section do not exceed the limits of 60 mm for the smallest dimension and 300 mm for the largest dimension.

Test Methods for characterization of defect-free specimens for timber of native timber;

This Part 3 of the code specifies the test method for characterizing defect-free specimens for wood from native forests. This Part applies to the determination of strength and stiffness properties in order to design of timber structures of native wood, related to complete, minimal and simplified characterization of sawn wood from native forests. Include the clear wood tests of bending, compression parallel and perpendicular, tension parallel and perpendicular, shear, toughness and embedment parallel and perpendicular to grain.

Test Methods for characterization of structural lumber;

This Part 4 of the code specifies test method for sampling and characterization of structural lumber for determining the medium and characteristic values of the structural properties of sawn timber of rectangular cross-section. Includes the tests of bending, compression parallel and perpendicular, tension parallel and perpendicular, shear and the determination of the transversal elasticity G value

Test Methods for determination of strength and stiffness of connections;

This Part 5 of the code specifies methods for the determination of the strength and stiffness of joints with mechanical fasteners used in timber structures (metal-dowel, timber dowel, screws, nails, stamped connectors and rings). It does not apply to the detailed procedures for each type of mechanical connector.

Test Methods for characterization of glued laminated timber;

This Part 6 of the code presents the test methods for the characterization of glued laminated timber (Glulam). The tests available are delamination tests for external and internal exposure, shear test of glue line, tensile strength parallel to the grain of the finger joints, and the amount of adhesive applied. In addition, provides some guidance for the production of finger joints. The delamination and shear of the glue line tests were based on the EN 14080 [4] with some adaptations. On the other hand, the tensile strength parallel to the grain test was based on EN 408 [5], whereas the failure mode of the finger joints was based on ASTM D4688/D4688 [6].

Test Methods for characterization of cross laminated timber

This Part 7 of the code presents the tests for CLT panels, its concepts and fundamental bases, that in part, was based in international codes like European Norms and ISO. Aiming at international standardization of quality control and characterization of CLT panels, some tests were based on established methodologies in the literature and European standards, the most advanced on the subject. Several academic works have been carried out to use international testing methods for Brazilian products, thus validating such methods. The main tests of this part are: strength and effective stiffness to bending perpendicular to the plane test and delamination test.

https://doi.org/10.52202/069179-0399

5 TIMBER STRUCTURES IN FIRE SITUATION

The new version considers the normal fire that represents the temperature elevation as a function of time defined by the Brazilian Code NBR 5628 given by the expression:

$$\theta g = \theta o + 345 \log (8t + 1). \quad (6)$$

The structural safety related to the limit states of fire will be imposed by the safety analysis given by:

$$S_{fi,d} \leq R_{fi,d} \quad (7)$$

Where $S_{fi,d}$ is obtained by exceptional combinations of actions defined by ABNT NBR 8681 or may be designed considering 60% of the design actions in normal situations (20 °C), that is, $S_{fi,d}$ = 0,60 Sd. The value of $R_{fi,d}$ is determined according to:

$$R_{fi,d} = k_{mod,fi} \frac{R_{0,2}}{\gamma_{w,fi}} \quad (8)$$

$k_{mod,fi}$ is 1,0 and includes the effects of the strength reduction and stiffness of wood; $\gamma_{w,fi}$ is 1,0 and $R_{0,2}$ must be designed by the normal design at normal temperature, however considering the area reduction and the mechanical properties substituted by the amount of 20% (20 percentile), that is:

$$f_{0,2} = k_{fi} f_k \quad (9)$$

$$E_{0,2} = k_{fi} E_{0,05} \quad (10)$$

Where k_{fi} is given in a table.

6 WOOD DURABILITY: USE CATEGORIES

According to the ABNT NBR 7190: 2022 wood preservation is a set of preventive and curative measures adopted to control biological agents (fungi, xylophages insects and marine bores), physical and chemical that affect the properties of wood, adopted in the development and maintenance of wood components
in the built environment.

In the design of timber structures, the following use categories should be considered:

Use Category 1: Inside buildings, out of contact with the soil, foundations or masonry, protected from weathering, internal sources of moisture and local free from access by subterranean termites or arboreal.

Use Category 2: Interior of buildings, in contact with the masonry, without contact with the soil or foundations, protected from the weather and indoor sources of moisture.

Use Category 3: Interior of buildings, out of contact with the soil and protected from the weather, which can, occasionally be exposed to sources of moisture.

Use Category 4: Outside use, out of contact with the soil and subject to the weathering.

Use Category 5: Contact with soil, fresh water and other situations favorable to deterioration, such as setting in concrete and masonry.

Use Category 6: Exposure to salt water or brackish.

In this way depending on the service condition in which the wood of the structure will be exposed, each corresponding use category must be considered and the susceptibility of attack by bio deteriorating organisms.

Each use category of durability has the correspondent treatment process and preservative product recommended.

7 CONCLUSIONS

The New Brazilian Code for Timber Structures Design, NBR7199: 2022, a load and resistance factored design (LRFD) code considers the structural grading recommendations for softwoods and hardwoods planted in South America with special attention for the production and design for Glulam structural elements. Rules for grading and gluing with the reforestation species are also presented. This new version adopts the connections models design used in EUROCODE 5 EN 1995-1-1:2009: Design of timber structures. The principal idea was to have a very similar code for all the countries of South America.

ACKNOWLEDGEMENT

The authors thanks of the São Paulo University for their support.

https://doi.org/10.52202/069179-0399

REFERENCES

[1] ASSOCIAÇÃO BRASILEIRA DE NORMAS TÉCNICAS. ABNT NBR7190: 2022 – Part 1: Design of Timber Structures

[2] SALES, A.. Hardwood strength classes. Ph.D. thesis Universidade de São Paulo, SP, 2006.

[3] ASSOCIAÇÃO BRASILEIRA DE NORMAS TÉCNICAS. ABNT NBR7190: 2022 Timber Structures - Part 2: Test Method; Structural timber. Grading. Requirements for visual and mechanical grading standards

[4] ASSOCIAÇÃO BRASILEIRA DE NORMAS TÉCNICAS. ABNT NBR7190: 2022 Timber Structures – Part 3: Test Method for clear samples.

[5] ASSOCIAÇÃO BRASILEIRA DE NORMAS TÉCNICAS. ABNT NBR7190: 2022 Part 4: Design of Timber Structures –Test Method - Structural timber. Strength classes.

[6] ASSOCIAÇÃO BRASILEIRA DE NORMAS TÉCNICAS. ABNT NBR7190: 2022 Timber Structures – Part 5: Test Method for structural timber. Grading. Requirements for mechanical connections.

[7] ASSOCIAÇÃO BRASILEIRA DE NORMAS TÉCNICAS. ABNT NBR7190: 2022 Timber Structures – Part 6: Test Method Structural Glulam members. Requirements delamination, shear glue line strength, finger joint strength.

[8] ASSOCIAÇÃO BRASILEIRA DE NORMAS TÉCNICAS. ABNT NBR7190: 2022 Timber Structures – Part 7: Test Method Structural cross laminated timber..

[9] ASSOCIAÇÃO BRASILEIRA DE NORMAS TÉCNICAS. ABNT NBR 16143:2013. Preservação de Madeiras – Sistema de Categorias de Uso. Rio de Janeiro, 2013.

World Conference on Timber Engineering Oslo 2023

EVALUATION OF CLT SHEAR WALLS FOR INCREASED STRUCTURAL HEIGHT LIMIT AND FOR EFFECT OF VARYING PANEL ASPECT RATIO

M. Omar Amini[1], Philip Line[2], John W. van de Lindt[3], Doug Rammer[4], Francisco Flores[5]

ABSTRACT: In the US, two CLT shear wall systems are defined in SDPWS 2021 and ASCE 7-22, *CLT shear wall* with CLT panel aspect ratio ranging from 2:1 to 4:1 (*CLT-R3*) and *CLT shear wall with shear resistance provided by high aspect ratio panels only* (*CLT-R4*). Both of these systems are applicable up to a structural height of 19.8 meters [65 feet] in Seismic Design Categories B through F, thus limiting some applications. To increase usability of this system, two analytical study cases are presented in this paper: Study Case 1, increase in structural height limit for *CLT-R3* and *CLT-R4* systems in moderate seismic regions (i.e., SDC C_{max}); and Study Case 2, panel aspect ratio range for *CLT-R4* system. This evaluation was performed using the FEMA P695 methodology on several archetypes that were prototypical representation of the CLT shear wall system. For both study cases the archetypes passed the collapse performance objective of FEMA P695 indicating that *CLT-R3* and *CLT-R4* systems up to and including 8 stories can be used in SDC C_{max} and *CLT-R4* system with CLT panel aspect ratio ranging from 3.5:1 to 4.5:1 can be used in SDC D_{max}.

KEYWORDS: Cross-laminated timber (CLT), seismic performance factors, FEMA P695

1 INTRODUCTION

There has been a recent increase in the number of studies geared towards investigating CLT system behavior and performance under cyclic and dynamic loading. Most of these studies originated in Europe (e.g., Dujic et al. [1]; Ceccotti [2]; Hristovski et al. [3]), in North America (e.g., Popovski et al. [4]; Pei et al., 2013 [5]; Popovski and Gavric [6], van de Lindt et al. [7]) and in Japan (e.g., Okabe et al. [8]; Tsuchimoto et al. [9]). While some studies aimed to provide a novel contribution to the developing body of knowledge in this new area of engineering and construction, some of the studies have adopted a systematic approach to investigating seismic behavior of CLT with the eventual goal of obtaining seismic performance factors or codification of some kind. A review of some of these studies is provided in Pei et al. [10] and a more recent comprehensive review of seismic behavior of CLT can be found in Izzi et al. [11].

In the US, the cross-laminated timber (CLT) shear wall seismic force resisting system was recognized in building code reference standards for the first time with inclusion of seismic design requirements in 2021 Special Design Provisions for Wind and Seismic (SDPWS) [12] and in ASCE 7-22 Minimum Design Loads and Associated Criteria for Buildings and Other Structures [13].

Seismic performance factors, namely, the response modification factor, R, deflection amplification factor, C_d, and overstrength factor, Ω, were developed by applying the FEMA P695 [14] methodology to the CLT shear wall system [7, 15, 16]. The evaluation process is summarized in Figure 1 with the details explained in Amini et al. [15]. The methodology consists of experimental testing, development of a design methodology, archetype development, numerical modelling, nonlinear analyses, and peer panel review. The process was applied to a number of archetypes that were prototypical representations of the seismic force resisting system. These analyses resulted in computing the so-called "margin against collapse" of each archetype and hence the CLT shear wall system with specific requirements dictated by FEMA P695. The methodology takes into account uncertainties inherent in the test data and modelling methods as well as inherent variability in the suite of ground motion records.

Two CLT shear wall systems are defined and recognized by SDPWS and ASCE 7; *CLT shear wall* with CLT panel aspect ratio ranging from 2:1 to 4:1 with R=3, C_d=3, and Ω = 3; and *CLT shear wall with shear resistance provided by high aspect ratio panels only* with CLT panel aspect ratio equal to 4:1 with R=4, C_d=4, and Ω = 3; hereafter referred to as *CLT-R3* and *CLT-R4*, respectively. Both

[1] Manager, Wind and Seismic, American Wood Council, 50 Catoctin Circle NE, Suite 201, Leesburg, VA 20175, USA. E-mail: oamini@awc.org

[2] VP, Codes and Regulations, American Wood Council, 50 Catoctin Circle NE, Suite 201, Leesburg, VA 20175, USA. E-mail: pline@awc.org

[3] Harold Short Endowed Chair Professor, Department of Civil and Environmental Engineering, Colorado State University, Fort Collins, CO 80523, USA. E-mail: jwv@engr.colostate.edu

[4] Research General Engineer, Forest Products Laboratory, One Gifford Pinchot Drive, Madison, WI 53726, USA. E-mail: douglas.r.rammer@usda.gov

[5] Manager, Engineering Technology, American Wood Council, 50 Catoctin Circle NE, Suite 201, Leesburg, VA 20175, USA. E-mail: fflores@awc.org

https://doi.org/10.52202/069179-0400

systems have a structural height limit of 19.8 meters [65 feet] in Seismic Design Category (SDC) B through F. Seismic performance factors and structural height limits appearing in ASCE 7-22 [13] are summarized in Table 1. This paper summarizes results of application of the FEMA P965 method to increase usability of the CLT shear wall systems defined in SDPWS. In one study, an increase in the structural height limit beyond the current limit of 19.8 meters [65 feet] in moderate seismic hazard areas (i.e., SDC C_{max}) is evaluated. In a separate study, an expanded aspect ratio range between 3.5:1 and 4.5:1 is evaluated for *CLT-R4* as a replacement for the existing exact limit of 4:1.

2 DESIGN METHODOLOGY

The design of the CLT shear wall system in accordance with SDPWS [7] includes requirements for use of CLT panels meeting aspect ratio requirements, prescribed connections (i.e., nails and connectors) at the bottom and top of the walls and at vertical edges of multi-panel shear walls, and tie-downs to transfer overturning induced tension forces. These requirements result in combined bending yield and pull-out of the nails from the CLT panels which exhibit rocking and sliding behaviour under in-plane shear loading. Example single-panel and multi-panel CLT shear wall configurations are shown in Figure 2.

Table 1: *Design Coefficients and Factors for CLT Seismic Force-Resisting Systems (appearing in ASCE/SEI 7-22 Table 12.2-1)*

Seismic Force-Resisting System	Detailing Requirements, ASCE/SEI 7-22 Section	*R*	Ω_0	C_d	Structural Height, h_n, Limit Seismic Design Category B, C, D, E & F
Cross-laminated timber shear walls	14.5	3	3	3	19.8 meters [65 feet]
Cross-laminated timber shear walls with shear resistance provided by high aspect ratio panels only	14.5	4	3	4	19.8 meters [65 feet]

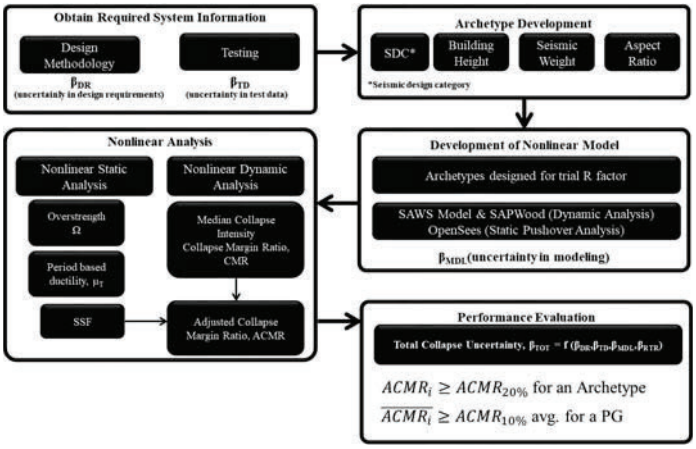

Figure 1: *CLT Shear Wall System Evaluation Process (van de Lindt et al., 2020)*

3 ARCHETYPES

A floor plan for an example index building with the extracted archetypes highlighted in red dashed lines is shown in Figure 3. While prior studies [7, 16] evaluated 72 archetypes (extracted from index buildings) for a full comprehensive study on CLT shear wall system, a reduced number of archetypes is analysed for this study based on prior findings that collapse probabilities are correlated to pushover strength (V_{max}/W) with superior collapse performance associated with increased strength. This study conservatively evaluated archetypes associated with smaller values of pushover strength. Study cases are shown in Table 2. For increased structural height limit for

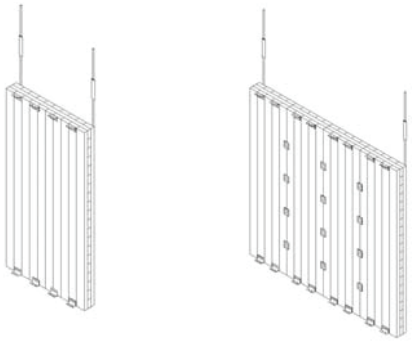

Figure 2: *(a) Single panel configuration (b) Multi-panel configuration*

https://doi.org/10.52202/069179-0400

CLT-R3 system, 8-story archetypes are considered and designed for SDC C_{max}. These were then grouped into two performance groups, PG-1 and PG-2 based on the CLT panel aspect ratio. For the evaluation of aspect ratio range for *CLT-R4* system, archetypes of 2-6 stories were considered and designed for SDC D_{max}. These were also grouped into two performance groups, PG-3 and PG-4 based on the CLT panel aspect ratio. Both study cases were with high gravity load and shear wall line length of 6.1m-18.3m extracted from the index buildings. In total 18 archetypes were considered in this study.

Table 2: *Study cases*

	CLT shear wall system	**Seismic Design Load Level**
Increased structural height limit (25.91 meters [85 feet])	*CLT-R3* *CLT-R4*	SDC C_{max}
Expanded aspect ratio range (3.5:1 – 4.5:1)	*CLT-R4*	SDC D_{max} /SDC D_{min}

The FEMA P-695 methodology requires archetypes to be designed for the Design Earthquake (DE) and then evaluated for the Maximum Considered Earthquake (MCE). Seismic loads are defined in terms of seismic design category (SDC) and occupancy category of the structure. Based on the methodology, structures are considered Occupancy Category I or II and receive an importance factor equal to 1.0. For Study Case 1 (increased structural height limit) the archetypes were designed for the Design Earthquake (DE) in SDC C_{max}, S_s= 0.55g, S_1=0.132g, F_a=1.36 and F_v=2.28. For Study Case 2 (expanded aspect ratio range) the archetypes were designed for SDC D_{max}, S_s= 1.50g, S_1=0.6g, F_a=1 and F_v=1.5, since the highest SDC governs the performance.
The building period was calculated in accordance with FEMA P-695 where it was taken as the product of coefficient for the upper limit (Table 12.8-1, ASCE 7-16 [17]) and the approximate fundamental period, Section 12.8.2.1 of ASCE 7-16. Designs were based on the ELF procedure explained in Sec 12.8 of ASCE 7-16 using R of 3 and 4 for Study Cases 1 and 2, respectively.
The selected archetypes were designed to ensure over-strength (i.e., provided shear capacity over shear demand) was minimized. After the design, the as-designed archetypes were then evaluated via numerical modeling for a set of predefined ground motions. Performance groups, archetypes and their corresponding seismic design parameters are provided in Table 3.

4 NUMERICAL MODELLING

In order to match prior study analysis methods, CLT shear wall behavior is characterized using the phenomenological CUREE-SAWS model [18]. This 10-parameter model defines force, stiffness and degradation as part of the hysteretic behaviour. The 10-parameters used for CLT shear walls are based on CLT shear wall test results which incorporated tension rods for overturning, and the prescribed shear connections in accordance with the design method in SDPWS 2021 [12]. This hysteretic fitting is discussed in van de Lindt et al. [7] and an example of the SAWS model fitted to the test data is shown in Figure 4. In Study Case 2, for CLT panels with aspect ratios of 3.5:1 and 4.5:1, parameters were scaled based on test data for CLT shear walls with panel aspect ratio of 2:1 and CLT shear wall with panel aspect ratio of 4:1. The effect of this scaling was seen in terms of peak strength and deformation capacity. An example for the two panel multi-panel configuration is shown in Figure 5. Looking at Figure 5, the lower aspect ratio (3.5:1) configuration has a larger strength but smaller deformation capacity while the higher aspect ratio panel case (4.5:1) has a lower strength but a gentler slope for the post peak behavior.
Nonlinear static pushover and incremental dynamic analysis (IDA) (Vamvatsikos and Cornell [19]) were performed in OpenSees [20] assuming that the structure is composed of rigid diaphragms attached to shear walls that are represented by nonlinear hysteretic springs. P-Delta effects were also included using a leaning column.
Static pushover was performed for each archetype to determine maximum base shear resistance, V_{max}, and ultimate displacement, δ_u. The results of these analyses were then used to determine overstrength factor, Ω, and period-based ductility, μ_T. The former is defined as the ratio of maximum base shear over design base shear and the latter is obtained from the pushover analyses using the following equation.

$$\mu_T = \frac{\delta_u}{\delta_{y,eff}} \quad (1)$$

where δ_u is the roof displacement corresponding to 80% post peak load ($0.8V_{max}$) and $\delta_{y,eff}$ is the effective yield roof displacement.

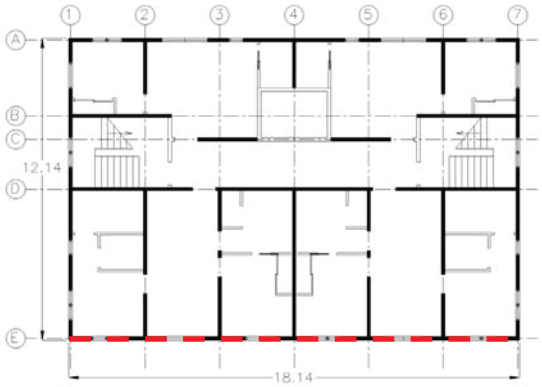

Figure 3: *Example index building floor plan (dimension in meters)*

https://doi.org/10.52202/069179-0400

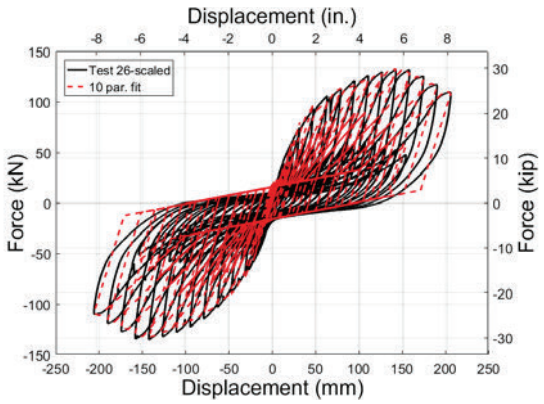

Figure 4: *Four panel multi-panel configuration scaled data and hysteretic fit*

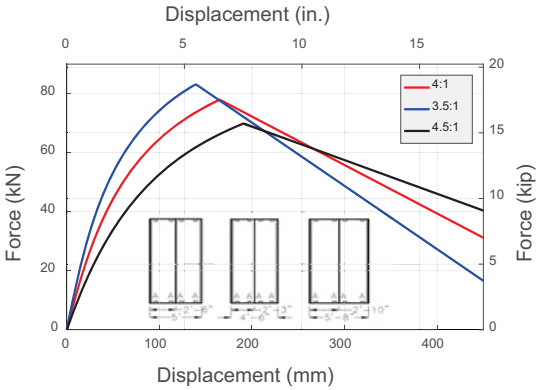

Figure 5: *Two panel multi-panel configuration with different aspect ratios*

Table 3. *Performance groups*

Study Cases	Performance Group	Aspect Ratio	Seismic Design Category	Archetype No.	Number of stories	T (sec)	T_1 (sec)	V_b, kN (kip)	W, kN (kip)	S_{MT} (g)
Study Case 1, Increased structural height limit	PG-1	Low aspect ratio panels, R=3	SDC D_{min}/C_{max}	1	8	0.802	1.72	166.13 (37.35)	1999.82 (449.6)	0.374
				2	8	0.802	1.26	185.3 (41.66)	2229.34 (501.2)	0.374
				3	8	0.802	1.12	299.08 (67.24)	3598.97 (809.12)	0.374
	PG-2	High aspect ratio, R=4		4	8	0.802	1.90	124.54 (28)	1999.82 (449.6)	0.374
				5	8	0.802	1.76	139 (31.25)	2229.34 (501.2)	0.374
				6	8	0.802	1.57	224.31 (50.43)	3598.97 (809.12)	0.374
Study Case 2, Expanded high aspect ratio range	PG-3	3.5:1 aspect ratio, R=4	SDC D_{max}	7	3	0.36	0.56	86.69 (19.49)	330.04 (74.2)	1.50
				8	2	0.26	0.50	77.35 (17.39)	309.58 (69.6)	1.50
				9	3	0.36	0.54	264.34 (59.43)	1003.91 (225.7)	1.50
				10	6	0.60	0.77	182.72 (41.08)	733.92 (165)	1.49
				11	6	0.60	0.62	203.76 (45.81)	819.77 (184.3)	1.49
				12	6	0.60	0.63	328.89 (73.94)	1323.72 (297.6)	1.49
	PG-4	4.5:1 aspect ratio, R=4		13	3	0.36	0.76	86.69 (19.49)	330.04 (74.2)	1.50
				14	2	0.26	0.69	77.35 (17.39)	309.58 (69.6)	1.50
				15	3	0.36	0.74	264.34 (59.43)	1003.91 (225.7)	1.50
				16	6	0.60	1.05	182.72 (41.08)	733.92 (165)	1.49
				17	6	0.60	0.86	203.76 (45.81)	819.77 (184.3)	1.49
				18	6	0.60	0.63	328.89 (73.94)	1323.72 (297.6)	1.49

IDA [19] was performed for a set of 22 bi-axial ground motions (44 records) termed "Far-Field" in FEMA P695 [14]. The ground motion scaling was performed in accordance with the FEMA P695 methodology where a record set is scaled by a single factor such that the median response spectrum of the normalized set matches the spectral acceleration of interest at the fundamental period of the building. According to the FEMA P695 methodology, the damping can be in the range of 2% to 5% of critical damping and for the purpose of this study the conservative lower bound of 2% critical damping was assumed. This damping was applied based on classic Rayleigh damping using the mass matrix and the initial stiffness matrix.

IDA results were used to generate fragility curves which were then used to determine median collapse spectral acceleration ($\hat{S}_{CT}$) defined as the spectral acceleration at which half the ground motions cause collapse (Ibarra et al. [21]). The non-simulated collapse criteria based on an inter-story drift ratio of 4.5% and 5.5% (specified limit

https://doi.org/10.52202/069179-0400

state) were used for cases of low aspect ratio panels (2:1) and high aspect ratio panels (4:1), respectively. These are discussed in detail in van de Lindt et al. [7]. A sample fragility obtained based on the CLT shear wall collapse criteria is shown in Figure 6. For Study Case 2, the non-simulated collapse criteria were scaled to reflect the corresponding deformation capacities. Inter-story drift ratio of 5.25% and 5.75% were used for the two high aspect ratio panel cases of 3.5:1 and 4.5:1, respectively.

5 PERFORMANCE EVALUATION

Collapse Margin Ratio (CMR) for each archetype was calculated as the ratio of median collapse intensity, $\hat{S}_{CT}$, to MCE ground motion intensity, S_{MT}. CMR was then adjusted to an Adjusted Collapse Margin Ratio (ACMR) using the Spectral Shape Factor (SSF) to account for the effects of spectral shape.

$$ACMR = CMR * SSF \quad (2)$$

SSF was determined based on the SDC for which the archetype was designed, and the period-based ductility obtained from the pushover analysis. ACMR is then compared with the acceptable ACMR that is calculated considering the uncertainties corresponding to the record-to-record variability (β_{RTR}), design requirements (β_{DR}), test data (β_{TD}), and modelling (β_{MDL}). The methodology accounts for these uncertainties using total system collapse uncertainly, β_{TOT}, given by the following equation:

$$\beta_{TOT} = \sqrt{\beta_{RTR}^2 + \beta_{DR}^2 + \beta_{TD}^2 + \beta_{MDL}^2} \quad (3)$$

These β values are based on qualitative ratings that are then translated to quantitative values. The ratings used for evaluation in this study are provided in Table 4. Considering the completeness of design requirements, β_{DR} of 0.10 was used in this study which is smaller than 0.20 used in the original study [7]. A detailed discussion on consideration of uncertainties on collapse evaluation is provided in Chapter 7 of FEMA P695 [14] and van de Lindt et al. [7]. The effect of total system collapse uncertainty on the fragility curve is demonstrated in Figure 6 shown earlier. While the median remains unchanged, additional uncertainty flattens the curve resulting in higher probability of collapse at MCE spectral intensity.

For performance evaluation all the individual archetypes needed to pass the $ACMR_{20\%}$ criteria (FEMA P695 criteria for an individual archetype to pass) and the average of the performance groups exceed the $ACMR_{10\%}$ criteria (FEMA P695 criteria for a performance group) for the performance groups. The results are provided in Table 5. Looking at the table, all the individual archetypes and performance groups for both study cases pass their respective collapse criteria. Performance groups results are also summarized in Figure 7 showing all the performance groups passing their corresponding criteria.

6 CONCLUSIONS

The evaluation of increased structural height limit for both CLT shear wall systems defined in SDPWS, namely *CLT-R3* and *CLT-R4*, showed that archetypes up to and including 8 stories met the collpase performance objective of FEMA P695 for use in SDC C_{max}. The evaluation of expanded aspect ratio for *CLT-R4* system, showed that archetypes of 1-6 stories with CLT panel aspect ratio ranging from 3.5:1 - 4.5:1 met the collapse perfromance objective of FEMA P695 for use in SDC D_{max}.

Table 4: *Quality ratings used for evaluation*

Uncertainty	Quality rating value	Description
Record-to-record (β_{RTR})	0.40	$\beta_{RTR} = 0.1 + \mu_T \leq 0.40$
Design requirements (β_{DR})	0.10	Superior: High in completeness and robustness and high confidence
Test data (β_{TD})	0.20	Good: Medium in completeness and robustness and high confidence
Modeling (β_{MDL})	0.20	Good: Medium in completeness and robustness and high confidence

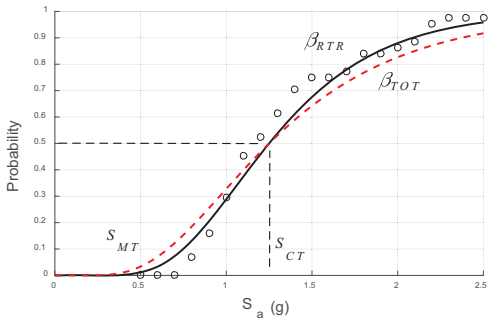

Figure 6: *Archetype 1 collapse fragility curve with lognormal fit*

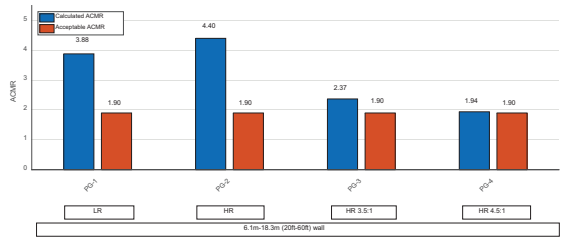

Figure 7: *Summary of ACMR for performance groups, ξ=0.02 (damping ratio), NSC (Non-simulated collapse);*
Study Case 1=4.5% Inter-story drift for LR (Low aspect Ratio) (2:1) and 5.5% for HR (High aspect Ratio) (4:1),
Study Case 2=5.25% Inter-story drift for HR (High aspect Ratio) (3.5:1) and 5.75% for HR (High aspect Ratio) (4.5:1)

https://doi.org/10.52202/069179-0400

Table 5: *Collapse Evaluation Parameters*

Study Case	No.	Collapse Margin Parameters					Acceptance Check		
		Ω	μ_T	$\hat{S}_{CT}$	CMR	SSF	ACMR	Acceptable ACMR	Pass/Fail
Study Case 1, Increased structural height limit					**PG-01**				
	01	3.10	2.08	1.25	3.33	1.17	3.89	1.52	PASS
	02	3.53	2.46	1.28	3.42	1.19	4.09	1.52	PASS
	03	2.58	3.18	1.11	2.96	1.23	3.65	1.52	PASS
	PG	**3.07**			**3.24**		**3.88**	**1.90**	**PASS**
					PG-02				
	04	3.48	2.52	1.30	3.47	1.20	4.16	1.52	PASS
	05	3.04	3.15	1.40	3.73	1.23	4.60	1.52	PASS
	06	2.62	3.80	1.32	3.53	1.26	4.45	1.52	PASS
	PG	**3.05**			**3.58**		**4.40**	**1.90**	**PASS**
Study Case 2, Expanded aspect ratio range					**PG-03**				
	7	3.72	3.31	2.71	1.80	1.20	2.16	1.52	PASS
	8	4.04	3.88	2.67	1.78	1.22	2.16	1.52	PASS
	9	3.40	3.83	3.01	2.01	1.22	2.44	1.52	PASS
	10	3.66	2.71	2.96	1.99	1.18	2.35	1.52	PASS
	11	3.78	3.61	3.27	2.19	1.22	2.68	1.52	PASS
	12	2.76	4.18	2.93	1.96	1.24	2.44	1.52	PASS
	PG	**3.56**			**1.96**		**2.37**	**1.90**	**PASS**
					PG-04				
	13	3.12	3.02	2.31	1.54	1.18	1.82	1.52	PASS
	14	3.40	3.51	1.97	1.31	1.20	1.58	1.52	PASS
	15	2.86	3.43	2.63	1.75	1.20	2.10	1.52	PASS
	16	3.07	2.48	2.24	1.50	1.17	1.76	1.52	PASS
	17	3.18	3.21	2.74	1.84	1.21	2.22	1.52	PASS
	18	2.30	3.67	2.64	1.77	1.23	2.17	1.52	PASS
	PG	**2.99**			**1.62**		**1.94**	**1.90**	**PASS**

REFERENCES

[1] Dujic B., Aicher S., Zarnic R. Racking Behavior of Light Prefabricated Cross-Laminated Massive Timber Wall Diaphragms Subjected to Horizontal Actions. Otto Graf Journal, Materialprüfungsanstalt Universität, Otto-Graf-Institut, Stuttgart. 2006; (17).

[2] Ceccotti A. New Technologies for Construction of Medium-Rise Buildings in Seismic regions: The XLAM Case. Structural Engineering International 2008; 18 (2): 156-165.

[3] Hristovski V, Dujic B, Stojmanovska M, Mircevska V. Full-scale shaking-table tests of XLam panel systems and numerical verification: Specimen 1. Journal of Structural Engineering. 2012 Oct 13;139(11):2010-8.

[4] Popovski M, Schneider J, Schweinsteiger M. Lateral load resistance of cross-laminated wood panels. In World Conference on Timber Engineering 2010 Jun (pp. 20-24).

[5] Pei, S., van de Lindt, J. W., and Popovski, M. (2013). "Approximate R-factor for Cross Laminated Timber Walls in Multi-story Buildings." *J. Archit. Eng.*,19(4), 245–255

[6] Popovski, M., & Gavric, I. (2015). "Performance of a 2-story CLT house subjected to lateral loads." *Journal of Structural Engineering*, *142*(4), E4015006.

[7] van de Lindt, J. W., Amini, M. O., Rammer, D., Line, P., Pei, S., & Popovski, M. (2020). Seismic performance factors for cross-laminated timber shear wall systems in the United States. *Journal of Structural Engineering*, *146*(9), 04020172.

[8] Okabe M, Yasumura M, Kobayashi K, Haramiishi T, Nakashima Y, Fujita K. Effect of vertical load under cyclic lateral load test for evaluating Sugi CLT wall panel. InWorld Conference on Timber Engineering, Auckland, New Zealand 2012 Jul (pp. 15-19).

[9] Tsuchimoto, T., Kawai, N., Yasumura, M., Miyake, T., Isoda, H., Tsuda, C., Miura, S., Murakami, S., Nakagawa, T. Dynamic and static lateral load tests on full-sized 3-story CLT construction for seismic design. In 13th World conference on timber engineering WCTE, Quebec 2014 Aug (Vol. 1014).

[10] Pei S, Van De Lindt JW, Popovski M, Berman JW, Dolan JD, Ricles J, Sause R, Blomgren H, Rammer DR. Cross-laminated timber for seismic regions: Progress and challenges for research and implementation. Journal of Structural Engineering. 2014 Nov 6; 142(4).

[11] Izzi, M., Casagrande, D., Bezzi, S., Pasca, D., Follesa, M., & Tomasi, R. (2018). "Seismic behaviour of Cross-Laminated Timber structures: A state-of-the-art review." *Engineering Structures*, *170*, 42-52.

[12] American Wood Council (ANSI/AWC). (2021). "Special design provisions for wind and seismic." *Leesburg, VA*.

[13] ASCE. Minimum Design Loads for Building and Other Structures. ASCE Standard ASC/SEI 7-22, American Society of Civil Engineers, Reston, Virginia; 2021.

[14] FEMA. Quantification of building seismic performance factors: FEMA P695. Federal Emergency Management Agency, Washington, D.C.; 2009.

[15] Amini, M. O., van de Lindt, J. W., Rammer, D., Pei, S., Line, P., & Popovski, M. (2018). Systematic experimental investigation to support the development of seismic performance factors for cross laminated timber shear wall systems. *Engineering Structures*, *172*, 392-404.

[16] van de Lindt, J., Rammer, D., Amini, M. O., Line, P., Pei, S., and Popovski, M. (2021) "Determination of Seismic Performance Factors for Cross-Laminated Timber Shear Walls Based on the FEMA P695 Methodology." General Technical Report FPL-GTR-281, Madison, WI: U.S. Department of Agriculture, Forest Service, Forest Products Laboratory, (In press).

[17] ASCE. Minimum Design Loads for Building and Other Structures. ASCE Standard ASC/SEI 7-16, American Society of Civil Engineers, Reston, Virginia; 2016.

[18] Folz B, Filiatrault A. Cyclic analysis of wood shear walls. Journal of Structural Engineering. 2001 Apr; 127(4):433-41.

[19] Vamvatsikos, D. and Cornell, C. A. (2002), "Incremental Dynamic Analysis", *Journal of Earthquake Engineering and Structural Dynamics.* 31(3), 491-514.

[20] McKenna, F. et al. (2011). "Open system for earthquake engineering simulation (OpenSees) (2.3.2 ed.)." Berkeley, CA: Pacific Earthquake Engineering Research Center, University of California.

[21] Ibarra L., Medina R., Krawinkler H. (2002). "Collapse assessment of deteriorating SDOF systems" *Proceeding of the 12th European Conference on Earthquake Engineering, London, UK, Paper reference 665, Oxford: Elsevier, September 9-13.*

https://doi.org/10.52202/069179-0400

World Conference on Timber Engineering Oslo 2023

BEAVER: A PARAMETRIC DESIGN FRAMEWORK FOR TIMBER ENGINEERING

Renan Prandini[1], João Tavares Pini[2], Márcio Sartorelli Venâncio de Souza[3]

ABSTRACT: Developments in digital modelling tools and requirements for low-carbon buildings have produced increased complexity in the field of timber structural engineering. This paper presents advancements and applications of the on-going development of Beaver, an open-source plugin for Rhino3D and Grasshopper environment, which allows live-fed parametric analysis and design of timber structures (elements and connections) according to "Eurocode 5 – Design of Timber Structures". With the help of Grasshopper and finite element analysis plugins such as *Karamba3D*, structural data can be fed to Beaver for integrated timber ULS and SLS analysis allowing a Performance-Based Design (PBD) and therefore integrates structural conception and timber structural engineering in a single decision-making step.

Case studies are presented using the proposed framework to discuss about how timber engineering practice can benefit from a computational engineering toolbox when integrated to a variety of design methods such as form-finding, genetic algorithms and spatially associative problems to explore various design possibilities and while ensuring structural safety.

KEYWORDS: parametric design, timber engineering, Eurocode 5, engineering software, beaver, grasshopper, karamba3d, moment-stiff, semi-rigid, timber design, timber connections, performance-based design, structural optimization, genetic algorithm, form-finding.

1. INTRODUCTION

Generative processes have marked the current avant-garde experimentations in architecture and engineering. Contemporary tools have allowed designers to explore new spatial tectonics in architecture, which is also presented as an added layer of geometrical complexity to the physical behaviour of structures. To deal with these non-standard solutions, engineers have increasingly adopted parametric tools for the design and analysis of structures. Although many computational methods are available for handling complex geometry, timber-engineering design is still identified as setback on the interdisciplinary design-to-production process to data exchange [1].

In that context, a commonly used tool for dealing with early-stage design validation is Karamba3D [2], a Grasshopper finite element analysis plug-in used to analyse structures such as: spatial trusses, frames or shell structures. With a simple algorithm, it allows the designer to explore a range of structural arrangements and instantly have structural feedback on the design. The live-fed structural output is one of the key features of Karamba which allow for further spatial explorations and information-aided design, such as cost or environmental impact of the designed structure.

Although the structural data output from Karamba and other visual programming tools are decisive for validation of concepts, it also relies on the experience of the structural designer to develop further parametric routines to evaluate if the output renders a valid result in terms of building structural safety codes.

In a previous paper [3], the authors proposed a beta version of Beaver: a Grasshopper plugin developed to evaluate the necessary safety Eurocode 5 checks, which assists the design of feasible timber-framed structures and the exploration of optimal solutions in terms of topology, aesthetics, costs and global structural behaviour.

Beaver is now presented in its first official version, with an improved workflow that allows a more straightforward usage of the tool as it is now completely integrated with Karamba3d, requiring minimal steps to connect both tools. Beaver software architecture was recreated to enable coupling of Beaver functionality not only inside Grasshopper, but also any other .NET application. The tool is now open sourced to promote the collaboration between professionals on the field as well as for research and educational purposes.

[1] Renan Prandini, MSc. Arch. Eng. Politecnico di Milano, Structural Engineer, renan.pran@gmail.com
[2] João Tavares Pini, Arch. Eng. University of São Paulo, Brazil. Head of Engineering at Ita Construtora, www.itaconstrutora.com.br, joao@itaconstrutora.com.br
[3] Márcio Sartorelli Venâncio de Souza, PhD candidate in Structural Engineering, University of São Paulo, Brazil. Software Developer at StructureCraft, Canada, msouza@structurecraft.com

https://doi.org/10.52202/069179-0401

2. BOUNDING STRUCTURAL ENGINEERING AND SOFTWARE DEVELOPMENT

One of the main issues in the practical field of structural engineering and design is mainly due to compatibility between computational models. It is difficult or almost impossible to find end-to-end solutions to design, analysis and detail buildings. Common practice is to transfer models between different software applications specialized to their needs, which can be detailing, structural analysis, thermal analysis, and so on. This is a well know issue of CAD (Computer Aided Design) and CAE (Computer Aided Engineering) systems. Most of integration issues relate to loss of data, compatibility during the process and lack of automation [4]. Those issues arise due the different characteristics between the processes. A CAD model is mainly a computational representation of the geometry, not necessarily having attributes and properties. These features are crucial inside CAE environment, as it needs data such as material properties, physical interfaces, and element types.

Grasshopper3d appeared as a good candidate to enable integration between CAD/CAE systems. It offers a convenient way to create scripts for geometry processing and automation in a powerful CAD environment, and many research is being applied in developing CAE systems inside it, such as Karamba3D [2], Kiwi3D [5] and BATS [6] for structural analysis, Ladybug [7] for Thermal/Solar Analysis, Butterfly [7] and Eddy3d [8] for CFD analysis.

Beaver first conception was to overcome one of the limitations of structural design inside of Grasshopper which was the lack of structural design tools according to valid design codes [3]. Its beta version was composed of a series of Grasshopper components that worked based on element internal forces and displacements provided by a structural frame analysis software. Generic routines were conceived in C# in order to evaluate the Limit States according to Eurocode 5 procedures [9]. As inputs, along with internal forces and displacements, the nominal strength, modification coefficients for load duration, service class and material uncertainties are considered. As outputs one can access actions and resistance ratios and considered analysis information such as failure mode of elements or fasteners, along with specific evaluation reports.

However, this implementation has shown some limitations. All design check routines were implemented individually in a series of Grasshopper components that communicate thought the connection of many individual parameters, which made quite challenging to transfer data between components as well as to implement new features, such as new design codes and direct integration with Grasshopper structural analysis plugins. The lack of structured data also made it demanding to filter values such as utilization data, based on combination and/or design check type, making it difficult to select data to display in colour and display graphs.

Also, while parametric design environments display great advantages for integrated structural design and analysis, the development of a C# library for the design of timber structures could also be beneficial to many other .NET applications. This is particularly important since many modern engineering companies are promoting in-house software development teams, both by dedicated software engineers but also by use of structural engineers with software development skills. This also may support the extension and creation of structural analysis software for academic purposes.

To overcome those limitations, a full refactor of Beaver software architecture was made. The first decision was to make Beaver functionality independent from Rhino and Grasshopper API's, creating a .NET Standard library named *BeaverCore* [10]. This library provides an object-oriented-model to assign and evaluate structural design checks.

On top of that layer sits BeaverGrasshopper [11], which is the actual Grasshopper plug-in. It provides data wrappers to pass BeaverCore objects between Grasshopper components, making the design process simpler and with less Grasshopper components. Also, a Beaver object-oriented model enables the conversion of structural analysis models, such as Karamba3d models, into an evaluated Beaver model in a simple straight-forward manner.

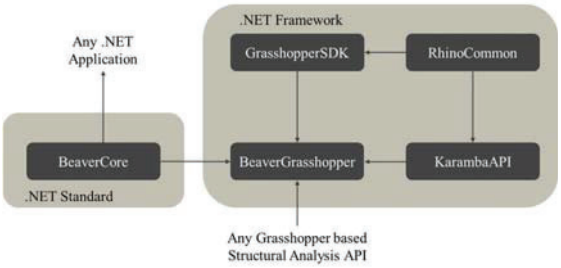

Figure 1: *Beaver dependencies flowchart*

1.1 BeaverCore: A open-source .NET library for structural timber engineering design

BeaverCore is a .NET library that contains an object model to properly assign structural members and its internal forces to apply the desirable design checks for timber members and connections.

Beaver functionality was split from the original GH plug-in to easen the development of additional features on design checks and proper structural models independent from any platform. This enables the use of BeaverCore in any other .NET application, such as FEA software and web/cloud-based platforms. BeaverCore has its code totally open-sourced, in a wish to assist designers to potentially enhance its functionality for other design codes, national annexes and further developments regarding other timber-based structural materials. The reliability of the tool is promoted by the development of unit tests that assures that the results provided by Beaver

https://doi.org/10.52202/069179-0401

can be verified by the community and allow awareness of the methods and algorithms used in its formulation.

1.2 BeaverGrasshopper: A Grasshopper plugin for parametric timber design

BeaverGrasshopper is a Grasshopper layer built on top of BeaverCore library to fulfil the original Beaver purpose of enabling parametric structural timber design according to official structural codes. The Grasshopper plug-in now only deals with managing BeaverCore object data between the Grasshopper components, that just queries data from BeaverCore object model. With this object model it is also possible to integrate Beaver fully with third-party FEA plug-ins such as Karamba3d by translating their API object model to BeaverCore model. This makes the use of Beaver way simpler since you can define all properties in your FEA model and automatically check the results of the Eurocode checks.

The presented workflow is integrated to *Karamba3D* by assigning element-related parameters of *Eurocode 5* such as span length, cantilever considerations, service classes, buckling lengths and other necessary parameters to *Karamba* beam elements.

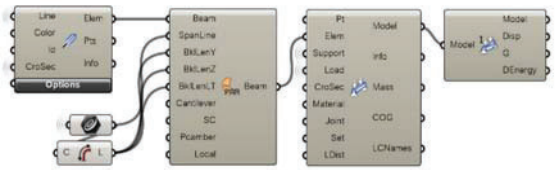

Figure 2: *Typical model setup for Beaver consists in using native Karamba elements and including necessary inputs for EC5 calculations.*

After the FEA analysis is performed by *Karamba*, all Beaver input data can be retrieved directly from *Karamba's* model to allow the final limit state timber analysis and further result displays. It is also possible to filter the load-case and bending direction to be displayed.

Figure 3: *A Karamba3D analysed model can be directly fed into Beaver components for displaying the limit state analysis.*

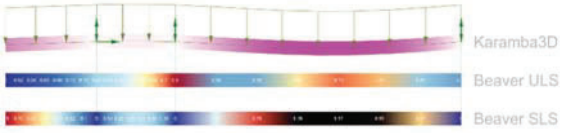

Figure 4: *Example of the ULS and SLS displayed results for a loaded beam with two spans and a cantilever.*

In addition, calculation reports are now available for result checking of Beaver analysis of elements and connections, which avoids the "black-box" perception of users, allows better benchmarking processes and promotes an educational usage of the software.

Figure 5: *A parametric dowel-type moment-stiff connection can be generated and verified in real time*

Having a generic solver for timber structure validation allows for exploration of new tectonics of construction and experimentation on problems whose physical properties are directly associated with geometrical constraints. This is all done through a live-fed calculation with intuitive outputs.

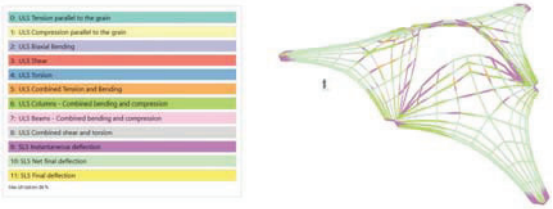

Figure 6: *Dealing with complex geometry requires deeper understanding of the governing checks of the structural analysis.*

Also, parametric processes are generally very useful for designers which perform specific design methods on multiple projects which are not necessarily complex structures. Grasshopper, along with *Karamba3D*, have shown to be increasingly used by the industry in all stages to fasten design processes from the concept to documentation, and a complete timber limit state analysis is also beneficial is this perspective.

https://doi.org/10.52202/069179-0401

3. APPLIED PROBLEM-SOLVING

Three study cases are presented in order to highlight the benefits of computational design approach to timber engineering and to illustrate how specific designs can be achieved through topological optimizations, form finding and integration between connection detailing and global structural behaviour.

1.3 Fishbelly trussed beam form-finding

This structure was designed Ita construtora, Brazil, to be a competitive alternative to typical steel and precast concrete structures usually employed for Boat Hangars located in tropical areas. With modular spans of 6 by 20 meters, permeable façades and lightweight steel sandwich panel roofs, the structural arrangement will mainly be affected by low permanent load case, low imposed load cases, high wind load cases and no earthquake or snow consideration.

To achieve this product, the structural concept goals were:

- *Minimal timber volume*
- *Minimal use of steel*
- *100% CNC machining*

The project started with the intuition that those goals would be achievable with a trussed beam for the long span and secondary beams for the short spans, where the roof sandwich panels are to be attached. Considering critical variable wind load scenarios, all structural elements were conceived in timber, in order to allow both tension and compression resistance.

A Grasshopper algorithm was written to generate multiple trussed beam arrangements. Karamba3D and Beaver were used to allow an on-time Eurocode 5 analysis considering all load case scenarios.

The variable structural arrangement parameters where:

- *Main beam division ratio*
- *Truss height*
- *Elements cross sections*

In terms of main beam division ratio, from a one-post trussed beam to a multiple posts fish-belly beam, there is an optimal cross section for each arrangement in order to employ minimal timber volume. Less posts scenarios generate larger buckling lengths and larger spans on upper chord, resulting in larger cross sections. In the other hand, multiple posts scenarios will allow smaller buckling lengths and chord cross sections, but the volume of the added posts and the number of timber connections will also be incremental.

Also, minimal beam division ratios will generate obtuse angles on lower chord that demand timber segmentation and steel connections, while higher beam division ratios will allow straighter angles that may allow lower chord continuity with the use of a curved glulam beam.

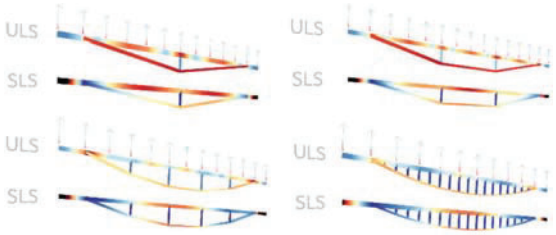

Figure 5: One to multiple posts trussed beam geometries with adjusted acceptable cross sections.

In terms of truss height, considering ULS analysis, a higher truss will allow smaller cross sections by reducing normal forces on upper and lower chords, but will also increment the lower chord length. Considering SLS analysis, higher truss heights will result in less deformation and SLS may be critical, demanding cross sections with higher bending resistance.

Figure 6: *Different truss heights with adjusted acceptable cross sections.*

Based on the presented parameters, this Grasshopper script allows multiple acceptable solutions in terms of structural safety, and the genetic algorithm [12] was used to generate and compare those arrangements in terms of timber volume and safety, resulting in the optimal arrangement bellow.

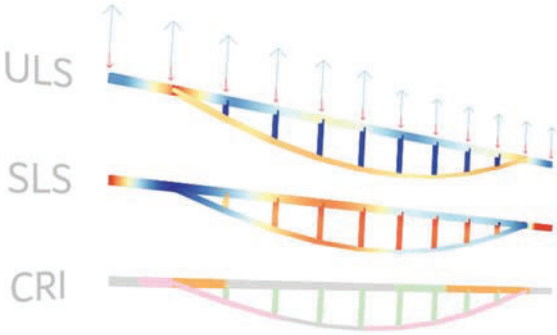

Figure 7: *Optimal genetic algorithm solution considering asymmetrical wind load cases*

Considering the main project goals presented above, minimal timber usage would be achieved with this solution. In the other hand, the minimal use of steel would only be achieved if the lower chord is made of a continuous beam, resulting in only two main connections between lower and upper chord, and this would be easily possible by considering a curved continuous glulam beam.

In the other hand, the third project goal is develop a 100% CNC machined timber structure, and for most production plants this allows only straight timber elements.

https://doi.org/10.52202/069179-0401

Considering those goals, the best concept would be to develop the correct geometry to allow both upper and lower chords to be continuous and also straight members, pretensioned together in pre-assembly process, in a way that curvature will be generated by posts lengths.

Karamba3D is a parametric tool that allows the consideration of imposed curvature strain loads, developed to allow the analysis of timber grid shells, for example. With the of this method, it is possible do model the structure correctly, considering the bending moments generated by the initial imposed curvature. This pretension adds permanent bending moment to both chords, which must be considered at the ULS analysis, and will result in a too high pre-camber that will affect SLS analysis.

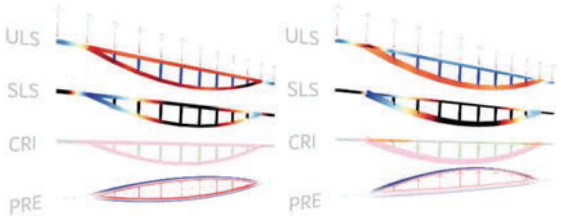

Figure 8: *Imposed curvature bending moment and pre-camber are governed by the inertia relation between upper and lower chords and the overall truss height.*

With this new script that includes pretension forces and deformations for the Beaver ULS and SLS analysis, Grasshopper genetic algorithm should converge to an optimal solution that will meet the main project goals of minimal timber volume, minimal use of steel and 100% CNC machining.

What is interesting about this study-case is that we realized that a very a large spectrum of the inputs will result in not acceptable structures, and depending on the imposed loads the form-finding process will never converge to a possible safe result, because of three main reasons:

- *Higher truss heights will simultaneously result in better SLS ratios and worse ULS ratios due to incremental imposed curvature bending moments.*
- *To generate acceptable imposed pre-camber, the Y-axis inertia relation between upper and lower chord must be drastically different, while section areas tend to be similar due to axial loads.*
- *Incrementing cross sections will not necessarily minimize ULS ratios, since they also increment bending moments due to the imposed curvature loads.*

Thankfully to the minimal loads of this typical scenario, the genetic algorithm found a small spectrum of possible results and could finally reach the optimal relation for the main beam division ratio, truss height and element cross sections.

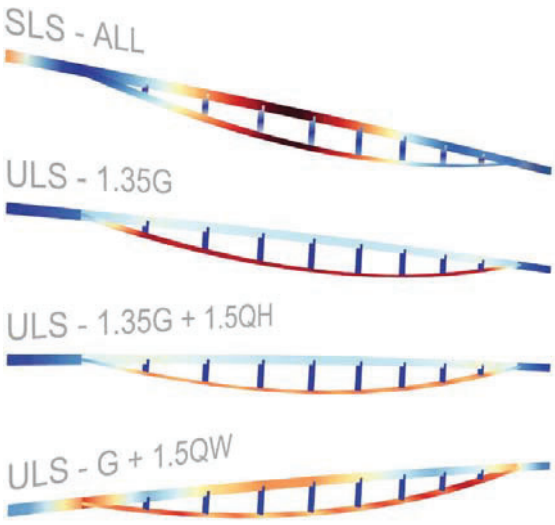

Figure 9: *Design ratios from critical load-cases displayed at the optimal structural arrangement generated by the algorithm. Imposed curvature strain load bending moment and precamber considered, along with and asymmetrical wind load cases.*

But there was one more topic that could be developed for a last optimization. The script was built based on a parabolic curvature, ant that is not perfect since it generates a peak bending moment at the first and last fish belly posts, and this affects directly the lower chord ULS analysis.

A last script was written to allow a fine manipulation of truss height and curvature for the now defined division ratio and cross sections, in order to find the optimal curvature. After this last analysis, a greater safety margin was achieved without incremental production costs.

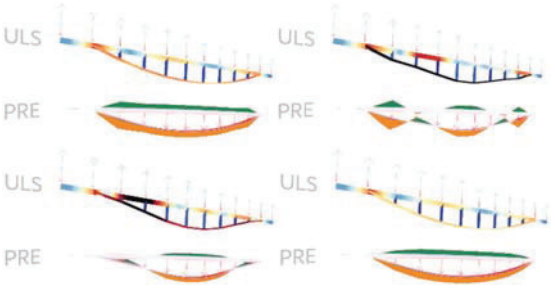

Figure 10: *Genetic algorithm playing with curvature to find the minimal peak bending moment, generated by the imposed curvature strain load.*

With the help of Karamba3D and Beaver, the final structural arrangement was achieved. In the next steps, before reaching the final product, a double check on the structural safety will be made along with the connection detailing. Later, a 1:1 mock-up will be produced to allow an evaluation of pre-assembly process and to be load-tested in order to verify that safety standards are met as expected.

https://doi.org/10.52202/069179-0401

1.4 Doubly curved roof with straight elements

Reciprocal beams have an intimate relationship with structural behaviour and the spatial arrangement of beams. Defining the correct pattern for a structurally sound structure can be a calculation-intensive process with many design possibilities. The roof in Franz Masereel Centre has undergone several topology optimizations based solely on global deflections because workflows regarding structural verifications according to code were be too time-consuming for an integrated design approach [13].

Applying Beaver into a geometrical formulation within Grasshopper will immediately offer feedback on the structural feasibility of the structure, while also allowing for topological optimizations. This is essentially true to reciprocal systems where each element is dependent on each other for achieving global stability and thus have no structural hierarchy between elements.

In the example below, a doubly curved surface is subdivided in a diagrid subdivision to form a reciprocal grid where two subsequent lines of the diagrid are joined together to form one continuous element. A script for moving each start and end node of these joined lines to the middle of the next continuous line was built so that an iterational procedure can occur until a geometrical convergence is reached. This allowed for an approximation of the double curvature surface while maintaining strictly straight elements connecting at middle points of the next element on the reciprocal grid.

A design exploration can take place where the reciprocal grid can vary in terms of subdivision in the u and v domains of the NURBS surface. Different designs are then tested against code in Beaver and a structurally sound solution can be chosen where a balance between number of connections and suitable cross section sizes is achieved.

Figure 11: *Design explorations are possible where the structural arrangement is critical to the final solution.*

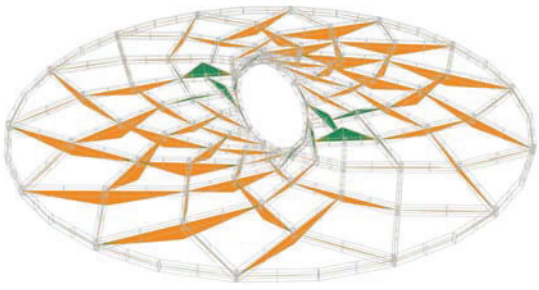

Figure 12: *Bending moment around the y-y axis of each member.*

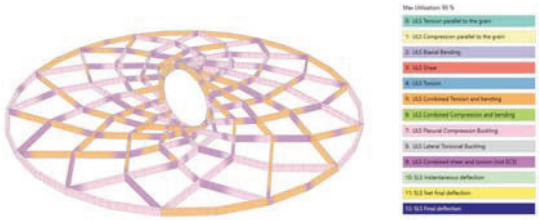

Figure 13: *A Color-coded plot shows the critical SLS or ULS verification according to code for each FE node of the structure.*

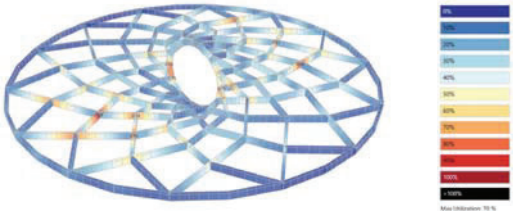

Figure 14: *ULS utilizations according to EC5.*

1.5 Integrated calculation of semi-rigid moment stiff connection

Since serviceability requirements often determine element sections in timber structures, optimization processes can occur by implementing semi-rigid connections in early design stages. On the other hand, engineering practice often neglects the effects of semi-rigid timber connections due to the several iterations needed to ensure proper structural behaviour.

The implementation of rotational stiffness on FE models represent a time-intensive task of the detail design since the resulting moment affects not only the forces acting the connection but also the resistance of each fastener due to a change in the angle between the acting force and the relative angle to the grain in the timber element.

Beaver proposes an integrated process of semi-rigid connection design where the rotational stiffness can be live verified and fed back to the finite element software, resulting in an automated iterative approach on the design of the timber structure and its connections. This integration is particularly important because every change made on the connection design affects the bending moment acting upon it. Since the resistance of each fastener depends on the angle between the grain direction and the fastener force, it is difficult to infer whether a change in the connection design is conservative or not. In most cases, a recalculation of the connection is necessary.

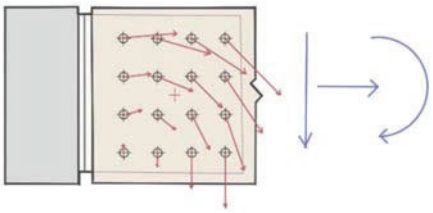

Figure 15: *The resistance of each fastener is calculated separately since the vectorial sum of forces affects the angle between force and grain.*

https://doi.org/10.52202/069179-0401

Designers can often oversee the effects of semi-rigidity of the connections especially when they are designed for pure shear and tension. The choice in arrangement and type of fasteners and number of shear planes affect deeply the behaviour of the connection, which may lead to an undesirable moment-stiffness in the connection. An integration between a global model and the connection detailing is desired to ensure the compliance of the connection to standards.

Figure 16: *Calculated fastener utilization on a simple-span beam for a steel-to-timber connection adopting hinged (left) and semi-rigid (right) hypothesis*

In the previous paper [3], the authors presented another geometrical optimization of a truss system where Beaver was used for an early stage engineering design of a 40m span roof for a horse arena, designed and executed by Ita Construtora, Brazil, in 2020. A benchmark is presented to demonstrate how Beaver is able to produce reliable results also at later-design stages.

Not only optimizations in truss geometry and member cross-section design have been optimized but also the connection design was considered in early stages. Fasteners geometry at the critical multiple shear plane tensile connections affected greatly on section design due to possible block shear failure and there was a concern that the effect of moment semi-rigidity and sliding of the dowels would effect on deformations and on the integrated design of each fastener.

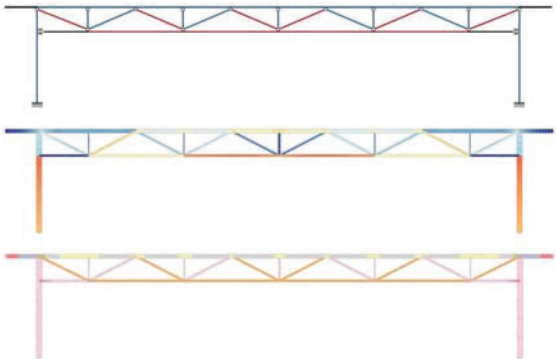

Figure 17: *Structural principles, Beaver utilizations and critical check according to code.*

A high number of fasteners and steel plates were needed to take tensile forces on the connections of the truss, inherently creating a semi-rigid moment-stiff connection between elements. This affects not only global deformations and actions on each member but also the design of the connection, leading to an iterative process on the engineering design.

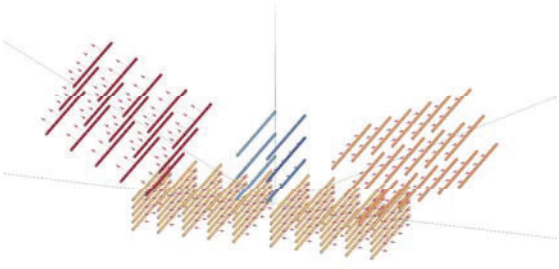

Figure 18: *The connection nodes of the structure were modelled in 3D and verified according to EC5 in real time.*

The workflow adopted integrates both timber engineering member design, connection design and 3D model documentation into one single interface, making sure the fastener arrangement is compatible with the cross-section and facilitates the coordination between draftsmen, engineers and builders.

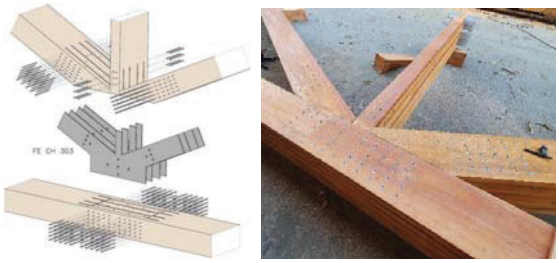

Figure 19: *Project and pre-assembly of one of the multiple shear connections used as a benchmark in Beaver.*

Figure 20/21: *Final structure after truss geometry and section optimization along with connection design.*

https://doi.org/10.52202/069179-0401

4. CONCLUSIONS

The framework and case studies presented in this paper display an integration between computational design tools – i.e., evolutionary solvers, multi-objective optimizations and form-finding processes – and timber engineering calculations, allowing for a broad variety of design methods and its associated performance in relation to current standards.

The improved integration with *Karamba3D* allows the designer to evaluate its results easily by performing a structural safety evaluation. By managing *Karamba*'s data directly from a back-end integration, Beaver is able to perform live limit state evaluations, which suits well with computational design workflows and early design phases. Furthermore, Beaver combines the limit state analysis for timber elements and its respective connections in a live-fed calculation, assisting designers to consider a variety of spatially associative problems such as the effects of semi-rigid stiffness and fastener arrangements on global structural behaviour and member design.

After all, Beaver aims to assist designers to integrate geometrical formulations, finite element analysis, safety structural checks and solver algorithms in order to simplify structural design in a parametric environment. The latest improvements of the tool deliver a better user experience of the tool, as well as invite the field to use and collaborate with it by making its core logic open-source, and independent from Grasshopper. The authors hope that this step will provide a tool to develop new systems as well to help improve its features either by professional collaboration as well inside scientific research in the areas of structural engineering and software development.

5. REFERENCES

[1] Apolinarska A. Complex Timber Structures from Simple Elements. Computational Design of Novel Bar Structures for Robotic Fabrication and Assembly. Doctoral thesis ETH Zürich, 2018.

[2] Preisinger, C. Heimrath, M. Karamba – A Toolkit for Parametric Structural Design. Structural Engineering International, 24(2):217-221, 2014.

[3] De Souza, M.S.V. Pini, J. Beaver: A computational parametric approach for conception, analysis and design of timber structures. WCTE 2020, Santiago, Chile.

[4] Gujarathi, G.; MA, Y.-S. Parametric CAD/CAE integration using a common data model. Journal of Manufacturing Systems, v. 30, p. 118–132, 2011.

[5] Bauer, A. et al. Exploring Software Approaches for the Design and Simulation of Bending Active Systems. International Association for Shell and Spatial Structures (IASS) Symposium, 2018.

[6] De Souza, M.S.V. and Pauletti, R.M.O.. "An overview of the natural force density method and its implementation on an efficient parametric computational framework" Curved and Layered Structures, vol. 8, no. 1, 2021, pp. 47-60. https://doi.org/10.1515/cls-2021-0005

[7] Roudsari, M.; Pak, M. Ladybug: A parametric environmental plugin for Grasshopper to help designers create an environmentally-conscious design. In: PROCEEDINGS of BS 2013: 13th Conference of the International Building Performance Simulation Association, 2013.

[8] Kastner, P.; Dogan, T. A cylindrical meshing methodology for annual urban computational fluid dynamics simulations. Journal of Building Performance Simulation, Taylor & Francis, v. 13, n. 1, p. 59–68, 2019

[9] EN-1995-1-1. Eurocode 5: Design of Timber Structures – Part 1-1. European Committee for Standardization, Bruxels, 2004.

[10] BeaverCore. Available at https://github.com/beaverstructures/Beaver.

[11] BeaverGrasshopper. Available at https://www.food4rhino.com/en/app/beaver

[12] Rutten, David. Galapagos: On the Logic and Limitations of Generic Solvers.

[13] Bergis L., de Rycke K. Reciprocal frame for the roof of the Franz Masereel Centre. IASS Annual Symposium, 2017

https://doi.org/10.52202/069179-0401

World Conference on Timber Engineering Oslo 2023

STRUCTURAL CHARACTERIZATION OF NATIVE SPECIES ACCORDING TO THE NEW BRAZILIAN STANDARD ABNT NBR 7190: 2022 – PART 4

Fabiana Yukiko Moritani[1], Felipe Hideyoshi Icimoto[2], Rodrigo de Souza Nogueira[3], Carlito Calil Junior[4], Lorenzo Lube dos Santos[5], Adriano Wagner Ballarin[6]

ABSTRACT: Timber is a heterogeneous material with high variability in its physical and mechanical characteristics. Therefore, whenever possible, it is essential to grade timber members using results from tests of structural size specimens that better express its structural quality to meet the design requirements. The Brazilian Standard ABNT NBR 7190: 2022 – Part 4, introduced test methods for mechanical characterization and strength grading of sawn timber in structural sizes. This study aimed to perform these mechanical tests for assign strength class for three native species of the Amazon rainforest obtained from trees under sustainable forest management (Caixeta (*Simarouba amara* Aubl.), Cedrinho (*Erisma uncinatum* Warm.), and Goiabão (*Planchonella pachycarpa* Pires.)). The Goiabão species had the highest characteristic value of bending strength and was graded as D60, Cedrinho D24, and Caixeta D18. Results also showed a high correlation ($R^2 = 0.94$) between modulus of elasticity in dynamic and static bending tests.

KEYWORDS: Structural timber, Strength grading, Mechanical properties, Native species.

1 INTRODUCTION

Wood is one of the most used materials in civil construction and it is essential to know the physical and mechanical properties for the best use of the material in timber structures design, mainly alternative species with potential for use in a rational way.

Extraction of wood in the Amazon rainforest is only allowed through forest management (planning practices and conservation principles which ensures the forest's capacity to continuously supply a product or service plans [1]) and authorization of sustainable exploitation. The awareness of the use and preservation of natural resources from Brazilian tropical forests has been applied with the dissemination of sustainable forest management concepts and the marketing of certified wood.

Several native species from forest management are not recognized for commercialization as raw or engineered timber due mainly to the lack of research on its properties or the correct dissemination of knowledge. The main studies on Brazilian native species can be found in [2-4].

The new Brazilian Standard ABNT NBR 7190 [5] for the design of timber structures, has seven parts and presents new topics and concepts, as mechanical tests for connections and detailed design methods and quality control procedures for engineered wood products (*e.g.* glulam and CLT). Following the initiative of other international standards and trying to express the structural quality of wood better, preconizes mechanical characterization and strength grading of sawn timber using structural size specimens, although, in special situations, allows this characterization using small clear specimens. Part 1 of the standard [5] specifies that strength and stiffness properties of timber are, in general, attributed to batches considered homogeneous – classification by batch - and presents the strength classes. ABNT NBR 7190 - Part 4 [6], based on ISO 13910 [7] details the experimental tests for structural size specimens: density, 4-point bending, tensile and compression parallel to the grain, tensile and compression perpendicular to the grain, shear parallel to the grain and, transversal modulus of elasticity.

This study aimed to characterize and grade three native wood species from Amazon rainforest using this new standard: *Simarouba amara* Aubl., *Erisma uncinatum* Warm., and *Planchonella pachycarpa* Pires.

[1] Fabiana Yukiko Moritani, ISISE, Department of Civil Engineering, University of Coimbra, SerQ – Innovation and Competence Forest Centre, Portugal, fabianamoritani@gmail.com
[2] Felipe Hideyoshi Icimoto, URBEM, Brazil, felipe.icimoto@urbembr.com
[3] Rodrigo de Souza Nogueira, University of São Paulo, Brazil, rodrigosouzan@usp.br
[4] Carlito Calil Junior, University of São Paulo, Brazil, calil@sc.usp.br
[5] Lorenzo Lube dos Santos, University of São Paulo, Brazil, lls@alumni.usp.br
[6] Adriano Wagner Ballarin, Sao Paulo State University – UNESP, Brazil, adriano.ballarin@unesp.br

https://doi.org/10.52202/069179-0402

2 MATERIALS AND METHODS

2.1 MATERIALS

Three native species from Amazon rainforest were characterized (Figure 1): Caixeta (*Simarouba amara* Aubl.), Cedrinho (*Erisma uncinatum* Warm.) and, Goiabão (*Planchonella pachycarpa* Pires.). These timber boards were obtained from trees under sustainable forest management. Table 1 presents their apparent densities, nominal section and the sample size of the experimental program.

Figure 1 – Species tested

Table 1 – Experimental program - species and sample size (N)

Species	*Scientific names*	Density (kg/m³)	N	Nominal section (cm)
Goiabão	*Planchonella pachycarpa* Pires.	902	57	4x12
Cedrinho	*Erisma uncinatum* Warm.	606	55	4x12
Caixeta	*Simarouba amara* Aubl.	424	62	4x14

2.2 TEST METHODS FOR MECHANICAL CHARACTERIZATION OF STRUCTURAL TIMBER

The characterization was carried out by mechanical tests in structural size specimens according to the new Brazilian Standard NBR 7190 – Part 4 [6], based on ISO 13910 [7]. Additionally, nondestructive test through 3-point bending test was carried out to obtain the reference static modulus of elasticity, as well as the transverse vibration method was used to determine the dynamic modulus of elasticity.

2.2.1 Nondestructive tests

The dynamic modulus of elasticity in bending was obtained for each timber board with a nondestructive grading through Metriguard model 340. The Metriguard Technolgies Inc. provided and calculated the dynamic modulus of elasticity by Equation (1).

$$E_{dyn} = \frac{f_n^2 . W . L^3}{K . b . h^3} \qquad (1)$$

Where: E_{dyn} is the dynamic bending modulus of elasticity, f_n is the undamped natural frequency, W is weight of the specimen, L is the span length, K is the constant of equipment, b is the width of specimen, and h is the thickness of the specimen.

The nondestructive bending test was carried out through 3-point static bending test (see Figure 2) to obtain the static modulus of elasticity. The boards was placed in flatwise position and loaded at center-point. The modulus of elasticity was determined in linear elastic regime (normally in 10% to 40% to ultimate load). The deflection measurement was taken at the center point while applying incremental load until the deflection reached 40% of ultimate load. The modulus of elasticity was calculated from Equation (2):

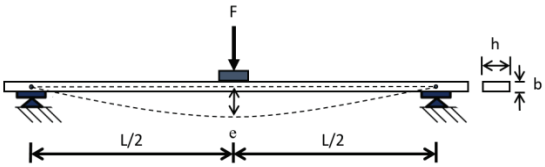

Figure 2 - Non-destructive static bending test [8]

$$E = \frac{1}{4} \cdot \left(\frac{L}{b}\right)^3 \cdot \left(\frac{\Delta F}{\Delta e}\right) \cdot \frac{1}{h} \qquad (2)$$

Where, L (mm): span length; h (mm): height of cross-section; b (mm): width of cross-section; F_{ult}: ultimate load; ΔF (N): incremental load; Δe (mm): incremental deflection.

2.2.2 Characterization tests

Mechanical characterization tests were carried out in structural boards according to the new Brazilian standard ABNT NBR 7190 – Part 4: 2022 [6], which was based on ISO 13910: 2005 [7]. The experimental program consists of: 4-point static bending, tension parallel and perpendicular to the grain, compression parallel and perpendicular to the grain and shear parallel to the grain.

4-point static bending

The 4-point static bending test (see Figure 3) was performed to obtain the static modulus of elasticity and bending strength of structural timber boards. The boards were loaded at two points, spaced *6h* between the ends of each support. To determine the modulus of elasticity in bending (E), the deflection measurement at the center-point was taken while applying incremental load until the deflection reached $L/300$. The bending strength (f_m) was determined by increasing the applied load until the maximum load was reached. The modulus of elasticity and bending strength were calculated from Equations (3) and (4):

https://doi.org/10.52202/069179-0402

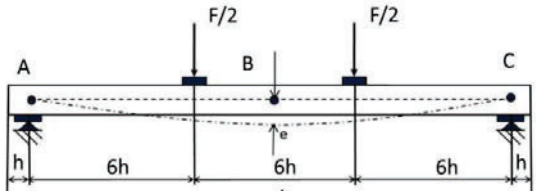

Figure 3 – Bending test [6]

$$E = \frac{23}{108} \cdot \left(\frac{L}{h}\right)^3 \cdot \left(\frac{\Delta F}{\Delta e}\right) \cdot \frac{1}{b} \quad (3)$$

$$f_m = \frac{F_{ult} \cdot L}{b \cdot h^2} \quad (4)$$

Tension parallel to the grain

The tension parallel to the grain test (see Figure 4) was carried out using the Metriguard 422 Tension Proof Testers, which has an 800 kN load capacity. The boards were subjected gradually increasing the applied load until the failure. The tension strength parallel to the grain was determined using Equation (5):

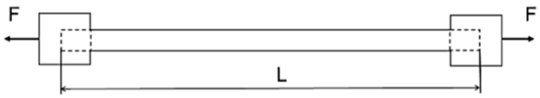

Figure 4 – Tension strength parallel to the grain test [6]

$$f_{t,0} = \frac{F_{ult}}{b \cdot h} \quad (5)$$

Where, $f_{t,0}$ (MPa): tension strength parallel to the grain; F_{ult} (N): ultimate load; h (mm): height of cross-section; b (mm): width of the cross-section.

Tension perpendicular to the grain

The tension perpendicular to the grain test was carried out using alternative method with the EMIC universal testing machine (see Figure 5), which has a load capacity of 30 kN. The specimen was comprised of the full cross-section that was cut the length L_h equal to *h/3* of the timber board. The specimen was submitted to a 3-point bending test and loaded gradually until it failed. Equation (6) was used to calculate the tension strength perpendicular to the grain:

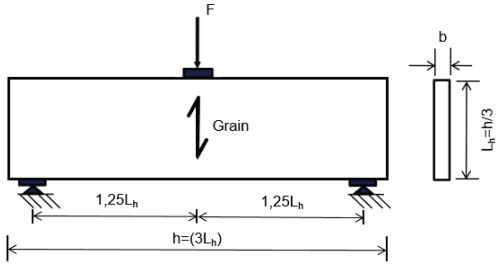

Figure 5 – Tension perpendicular of the grain strength test [6]

$$f_{t,90} = \left(\frac{3{,}75 \cdot F_{ult}}{b \cdot L_h}\right) \cdot \left(\frac{0{,}03 \cdot b \cdot {L_h}^2}{800^3}\right)^{0,2} \quad (6)$$

where, $f_{t,90}$ (MPa): tension strength perpendicular to the grain; F_{ult} (N): ultimate load; h (mm): height of cross-section; b (mm): width of cross-section; L_h (mm): length cut from the specimen; $\left(\frac{0{,}03 \cdot b \cdot {L_h}^2}{800^3}\right)^{0,2}$: a factor that normalized the tension strength to the equivalent value for a timber cube of side length equal to 800 mm.

Compression parallel to the grain

The compression parallel to the grain test (see Figure 6) was executed using the AMSLER universal testing, which has a load capacity of 25000 kgf. Two specimens with *6b* length were compressed axially until failure. The ultimate load F_{ult} was the lower value of the applied load at failure for the two specimens. The compression strength parallel to the grain was calculated from Equation (7):

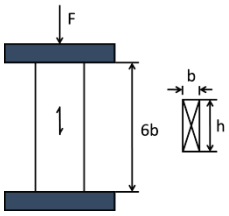

Figure 6 – Compression parallel to the grain test [6]

$$f_{c,0} = \frac{F_{ult}}{b \cdot h} \quad (7)$$

Where, f_{c0} (MPa): compression strength parallel to the grain; F_{ult} (N): ultimate load; h (mm): height of cross-section; b (mm): width of the cross-section.

Compression perpendicular to the grain

The compression strength perpendicular to the grain was obtained using the AMSLER universal and the setup shown in Figure 7. The specimen was cut to a length of *6h*, and then loaded until it either failed or reached a maximum deformation of 0.1 mm. The compression strength perpendicular to the grain was calculated from Equation (8):

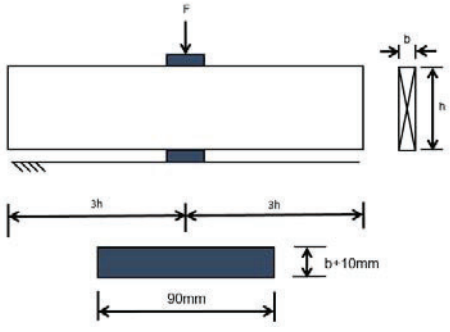

Figure 7 – Compression perpendicular to the grain test [6]

$$f_{c,90} = \frac{F_{ult}}{90 \cdot b} \text{ or } f_{c,90} = \frac{F_{0,1h}}{90 \cdot b} \quad (8)$$

Where f_{c90} (MPa): compression strength perpendicular to the grain; F_{ult} (N): ultimate load; $F_{0,1h}$ (N): load at a deformation of 0.1h mm; b (mm): width of the cross-section.

Shear parallel to the grain

The shear parallel to the grain test was performed according to the setup shown in Figure 8. The specimen was cut to a length of *7h*, and then loaded until it either failed that presented shear failure mode or bending failure mode. However, all results were used to calculate shear strength, regardless of failure mode. The shear strength parallel to the grain was determined from Equation (9):

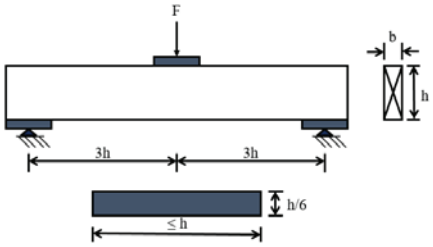

Figure 8 – Shear parallel to the grain test [6]

$$f_v = \frac{0{,}75 \cdot F_{ult}}{b \cdot h} \quad (9)$$

Where, f_v (MPa): shear strength parallel to the grain; F_{ult} (N): ultimate load; h (mm): height of cross-section; b (mm): width of cross-section.

2.2.3 The characteristic value of the strength

The characteristic value of strength properties of each species was calculated assuming they are logarithmically normally distributed according to EN 14358: 2016 [9]. Thus, the mean value, standard deviation and characteristic value were obtained from Equations (10), (11) and (12), respectively:

$$\bar{y} = \frac{1}{n}\sum_{i=1}^{n} \ln m_i \quad (10)$$

$$s_y = max\left\{\sqrt{\frac{1}{n-1}\sum_{i=1}^{n}(\ln m_i - \bar{y})^2};\ 0{,}05\right\} \quad (11)$$

$$m_k = \exp(\bar{y} - k_s(n)s_y) \quad (12)$$

Where: $\bar{y}$ is the mean sample value, n is the number of test values, m_i is the individual test value i of stochastic variable m, s_y is the standard deviation, m_k is the 5-percentile value of stochastic variable m, $\bar{y}$ is the sample mean value, s_y is the standard deviation, and $k_s(n)$ is the factor used to determine characteristic value. The factor $k_s(n)$ was calculated from Equation (13):

$$k_s(n) = \frac{6{,}5\ n + 6}{3{,}7\ n - 3} \quad (13)$$

Where: n is the number of test values.

3 RESULTS

3.1 Experimental data

Table 2 presents the maximum, minimum and mean value, standard deviation, and coefficient of variation of physical and mechanical properties for "Caixeta".

Table 2 – Density and mechanical properties of Caixeta

Properties	Min.	Max.	Mean	Std.	CoV (%)
ρ_{ap} (kg/m³)	351	498	424	32	7.54
E_{dyn} (GPa)	7.65	13.44	10.62	1.24	11.63
E_{flat} (GPa)	8.02	13.38	10.70	1.22	11.39
E_{edge} (GPa)	8.03	11.78	9.74	1.00	10.23
f_m (MPa)	41.13	80.92	56.80	9.80	17.25
f_{t0} (MPa)	24.07	65.10	40.97	13.72	33.50
f_{t90} (MPa)	0.35	1.13	0.64	0.21	32.35
f_{c0} (MPa)	34.33	50.16	40.59	4.17	10.27
f_{c90} (MPa)	6.54	7.97	7.42	0.68	9.20
f_{v0} (MPa)	3.17	5.42	4.56	0.75	16.55

Table 3 presents the maximum, minimum and mean value, standard deviation, and coefficient of variation of physical and mechanical properties for "Cedrinho".

Table 3 – Density and mechanical properties of Cedrinho

Properties	Min.	Max.	Mean	Std.	CoV (%)
ρ_{ap} (kg/m³)	550	672	606	31	5.19
E_{dyn} (GPa)	7.52	19.76	12.45	2.37	19.01
E_{flat} (GPa)	8.05	15.13	11.97	1.73	14.46
E_{edge} (GPa)	6.91	15.13	12.39	1.90	15.36
f_m (MPa)	29.85	90.31	60.17	18.27	30.37
f_{t0} (MPa)	36.74	64.53	50.93	11.80	23.17
f_{t90} (MPa)	0.33	0.68	0.51	0.11	20.84
f_{c0} (MPa)	35.21	58.10	45.57	5.89	12.92
f_{c90} (MPa)	7.96	11.86	10.00	1.49	14.88
f_{v0} (MPa)	4.89	7.26	5.87	0.83	14.08

https://doi.org/10.52202/069179-0402

Table 4 presents the maximum, minimum and mean value, standard deviation, and coefficient of variation of physical and mechanical properties for "Goiabão".

Table 4 – Density and mechanical properties of Goiabão

Properties	Min.	Max.	Mean	Std.	CoV (%)
ρ_{ap} (kg/m³)	776	1018	902	56	6.26
E_{dyn} (GPa)	14.53	30.24	20.92	3.41	16.28
E_{flat} (GPa)	13.47	28.15	20.19	3.45	17.09
E_{edge} (GPa)	14.89	22.94	18.55	1.81	9.75
f_m (MPa)	76.68	123.16	99.34	15.24	15.35
f_{t0} (MPa)	50.65	105.00	74.97	19.82	26.44
f_{t90} (MPa)	0.30	1.78	0.67	0.42	62.52
f_{c0} (MPa)	46.98	88.48	70.61	11.14	15.78
f_{c90} (MPa)	20.37	31.54	25.45	4.41	17.32
f_{v0} (MPa)	6.93	9.68	8.44	1.11	13.20

Table 5, 6 and 7 present the characteristics values and a comparison to the properties values of strength class assigned for each species.

Table 5 – Characteristic values and strength class of Caixeta

Properties	Caixeta	D18	Diff (%)
ρ_{ap} (kg/m³)	424	570	-25.6
E_{dyn} (GPa)	10.6	9.5	11.8
E_{edge} (GPa)	9.7		2.5
E_{flat} (GPa)	10.7		12.6
f_m (MPa)	40	18	112.2
f_{t0} (MPa)	18	11	63.6
f_{t90} (MPa)	0.3	0.6	-43.3
f_{c0} (MPa)	33	18	83.3
f_{c90} (MPa)	5.7	7.5	-24.0
f_{v0} (MPa)	3.0	3.4	-11.7

Table 6 – Characteristic values and strength class of Cedrinho

Properties	Cedrinho	D24	Diff (%)
ρ_{ap} (kg/m³)	606	580	4.5
E_{dyn} (GPa)	12.4	10.0	24.0
E_{edge} (GPa)	12.4		24.0
E_{flat} (GPa)	12.0		20
f_m (MPa)	29	24	20.8
f_{t0} (MPa)	26	14	85.7
f_{t90} (MPa)	0.3	0.6	-50.0
f_{c0} (MPa)	35	21	66.6
f_{c90} (MPa)	7.1	7.8	-9,0
f_{v0} (MPa)	4.3	4.0	7.5

Table 7 – Characteristic values and strength class of Goiabão

Properties	Goiabão	D60	Diff (%)
ρ_{ap} (kg/m³)	902	840	7.4
E_{dyn} (GPa)	20.9	17.0	22.9
E_{edge} (GPa)	18.6		9.4
E_{flat} (GPa)	20.2		18.8
f_m (MPa)	72	60	20.0
f_{t0} (MPa)	38	36	5.6
f_{t90} (MPa)	0.2	0.6	-66.7
f_{c0} (MPa)	49	32	53.1
f_{c90} (MPa)	17.5	11.0	59.1
f_{v0} (MPa)	6.1	4.5	35.6

Piter *et al.* (2003) [10] presented mechanical characterization and visual grading of Argentinean *Eucalyptus grandis* with specimens in structural size. The growth characteristics had greater influence reducing strength and stiffness, and obtained different mechanical properties in comparison with strength class system established in EN 338 [11].

When considering the characteristic value of bending strength, mean density, and modulus of elasticity of the "Caixeta" species, the mechanical properties and density of the strength class assigned has significantly lower than the characteristics values of "Caixeta" species. Although the characteristic bending strength was 40 MPa, the low values of modulus of elasticity and density resulted in class D18, which have the lowest strength class in ABNT NBR 7190 [5]. "Cedrinho" species presented characteristics values higher than the properties of the strength class assigned to it, except for the tension strength perpendicular to the grain and shear strength parallel to the grain. It is worth mentioning that "Goiabão" species, with the highest mechanical properties and density, was included in strength classes D60 and also showed characteristics values higher than the mechanical properties of the assigned strength class, except for the tension strength perpendicular to the grain.

Therefore, it is recommended that industries should performed characterization tests for each species they plan to use in their production line, according to well-defined standards. Based on the results of these tests, appropriate strength classes for each species should be established.

3.2 Comparison between dynamic and static modulus of elasticity

Figure 9 shows the association between dynamic and 4-point static modulus of elasticity data for the three species, that the coefficient of determination value (R^2) was 0.9394. Generally, the correlation between the static and dynamic modulus of elasticity is considered high if above 90%. The ABNT NBR 7190 – Part 2 requires that this correlation be above 90%. Morin-Bernard *et al.* (2020) [12] compared the dynamic and static modulus of elasticity of two hardwood species that showed the

coefficient of determination for white ash ($R^2 = 0.94$) and yellow birch ($R^2 = 0.87$).

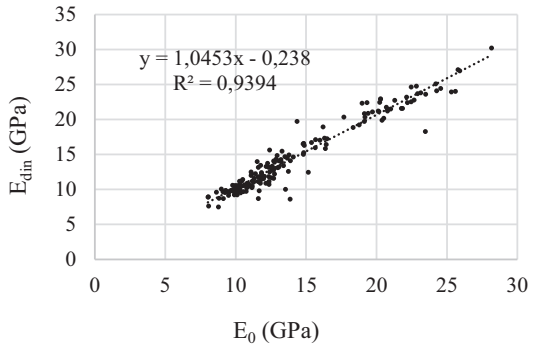

Figure 9 – Dispersion graphic of the static (E_0) and dynamic (E_{din}) modulus of elasticity

Table 8 presents the mean values, the coefficient of variation (%) of the static and dynamic modulus of elasticity for each species and comparative ratios, $\mathbf{E_{flat}/E_{dyn}}$ and $\mathbf{E_{edge}/E_{dyn}}$. The dynamic modulus of elasticity was higher than the static modulus of elasticity for "Cedrinho" and "Goiabão" species. Furthermore, the $\mathbf{E_{edge}/E_{dyn}}$ ratio obtained greater differences, mainly for the "Caixeta" and "Goiabão" species. Sales *et al.* (2009) [13] performed structural grading though nondestructive methods, *i.e*. ultrasound and transverse vibration, and compared to static bending results. The authors evaluated structural members of *Eucalyptus grandis* and *Pinus sp*. The transverse vibration method allowed for modulus of elasticity closer to the values obtained by the static modulus of elasticity that the average percentile variations were 4.42% for *Eucalyptus grandis* and 4.33% for *Pinus sp*.

The modulus of elasticity in flatwise position was closer than edgewise position. The edgewise position is required by ABNT NBR 7190 – Part 4 [5] for the characterization of the 4-point static bending test. However, the dynamic modulus of elasticity through transverse vibration method have been carried out in the flatwise position, the same position required by the Brazilian standard ABNT NBR 7190 – Part 2 [7], for the nondestructive test of the 3-point static bending.

Table 8 – Modulus of elasticity in bending (static and dynamic) and comparison ratio between dynamic and static modulus of elasticity

Properties	Caixeta	Cedrinho	Goiabão
$\mathbf{E_{dyn}}$ **(GPa)**	10.62	12.45	20.92
	11.63%	19.01%	16.28%
$\mathbf{E_{flat}}$ **(GPa)**	10.70	11.97	20.19
	11.39%	14.46%	17.09%
$\mathbf{E_{flat}/E_{dyn}}$	1.01	0.96	0.97
$\mathbf{E_{edge}}$ **(GPa)**	9.74	12.39	18.55
	10.23%	15.36%	9.75%
$\mathbf{E_{edge}/E_{dyn}}$	0.92	0.99	0.87

4 CONCLUSIONS

Mechanical characterization tests were performed in structural size specimens for three native species of the Amazon rainforest obtained from trees under sustainable forest management, *i.e.* Caixeta (*Simarouba amara* Aubl.), Cedrinho (*Erisma uncinatum* Warm.) and, Goiabão (*Planchonella pachycarpa* Pires.). The experimental campaign followed the new Brazilian Standard ABNT NBR 7190 – Part 4 [6] Additionally, non-destructive tests were carried out 3-point static bending test to determine modulus of elasticity and transverse vibration test to determine the dynamic modulus of elasticity. Main highlights are:

- Static and dynamic modulus of elasticity were analysed and the regression presented a high coefficient of determination ($R^2 = 0.9394$).
- The comparison of the static and dynamic modulus of elasticity showed that E_{flat} had closer values to E_{dyn} than E_{edge}, since transverse vibration through Metriguard model 340 requires flatwise position to determine the dynamic modulus of elasticity.
- The species were classified into strength classes by the characteristic value of bending strength and, mean values of static modulus of elasticity and density. "Goiabão" was graded as D60, "Cedrinho" D24, and "Caixeta" D18. However, it was observed that the tension strength perpendicular to the grain and the shear parallel to the grain did not achieve the values presented by the strength classes assigned to these species.

ACKNOWLEDGEMENT

The authors would like to thank WWF-BRASIL (World Wide Fund for Nature), and Wood and Timber Structures Laboratory (LaMEM) of the Department of Structural Engineering (SET) of the São Carlos Engineering School (EESC) - University of São Paulo (USP) for making this work possible. This study was partly financed by FIPAI (Foundation for the Increase of Research and Industrial Improvement), and the Coordenação de Aperfeiçoamento de Pessoal de Nível Superior – Brasil (CAPES) under Finance Code 001.

REFERENCES

[1] PEREIRA, D., SANTOS, D., VEDOVETO, M., GUIMARÃES, J., & VERÍSSIMO, A. *Forest Facts***.** Belém: Imazon. 2010.

[2] ZANGIÁCOMO, A. L *Employment of alternative tropical timber species in glued laminated timber structural elements production.* São Carlos, 2003. 78p. Dissertation (Master degrees) – São Carlos School of Engineering of University of São Paulo.

https://doi.org/10.52202/069179-0402

[3] DIAS, F. M., & LAHR, F. A. R. Estimation of wood strength and stiffness properties through apparent density. *Scientia Forestalis*, 65(2), 102-113. 2004.
[4] WOLENSKI, A. R. V., PEIXOTO, R. G., AQUINO, V. B. D. M., CHRISTOFORO, A. L., LAHR, F. A. R., & PANZERA, T. H. (2020). Evaluation of mechanical strengths of tropical hardwoods: proposal of probabilistic models. *Eur. J. Wood Wood Prod*., 78(4), 757-766.
[5] BRAZILIAN ASSOCIATION OF TECHNICAL STANDARDS *ABNT NBR 7190* – Design of Timber Structures. 2022.
[6] BRAZILIAN ASSOCIATION OF TECHNICAL STANDARDS *ABNT NBR 7190* – Design of Timber Structures – Part 4: Test Methods for Characterization of Structural Timber. 2022.
[7] INTERNATIONAL ORGANIZATION FOR STANDARDIZATION. ISO 13910. Timber structures - Strength graded timber - Test methods for structural properties. Switzerland. 2014.
[8] BRAZILIAN ASSOCIATION OF TECHNICAL STANDARDS *ABNT NBR 7190* – Design of Timber Structures – Part 2: Test methods for visual and mechanical grading of structural lumber. 2022.
[9] CEN. 2016. *EN 14358: Timber structures - Calculation and verification of characteristic values*. Bruxelles, Belgium: European Committee for Standardization.
[10] PITER, J. C., ZERBINO, R. L., & BLAß, H. J. (2004). Visual strength grading of Argentinean Eucalyptus grandis: Strength, stiffness and density profiles and corresponding limits for the main grading parameters. *Holz als Roh-und Werkstoff*, 62, 1-8.
[11] CEN. 2012. *EN 338*: Structural timber – Strength classes. Brussels.
[12] MORIN-BERNARD, A., BLANCHET, P., DAGENAIS, C., & ACHIM, A. (2020). Strength grading of northern hardwood species for structural engineered wood products: identification of the relevant indicating properties. *BioResources*, 15(4), 8813.
[13] SALES, A.; CANDIAN, M.; DE SALLES CARDIN, V. Nondestructive evaluation of timber: the new Brazilian code for the design of timber structures. *Mater Struct*, v. 43, n. 1-2, p. 213, 2010.

World Conference on Timber Engineering Oslo 2023

PREFABRICATED TIMBER CONCRETE COMPOSITES

Sam Winder[1], Dan Chapman[2], Panayiotis Papastavrou[3], Simon Smith[4], Allan McRobie[5]

ABSTRACT: Timber-concrete composite floor panels offer a lightweight structural floor system that can be used with a panelised construction method. Currently, prefabricated timber-concrete composite (TCC) floor solutions are rare. This is partly due to a lack of knowledge regarding the shear connectors that join the timber and concrete elements and the impact of additional interlayers between the timber and concrete elements is even less well understood. This research project was undertaken as part of the broader work being done for the GenZero initiative by the UK's Department for Education (DfE) working with industrial partners Smith and Wallwork Engineers, Ecosystems Technologies, Thorp Precast, and several others. In particular, the impact of two different shear connectors on the proposed 8m by 1.8m TCC slabs was investigated: a concrete notch and a steel dowel. Full-scale slab and small-scale shear experiments were carried out, supplemented by computational analysis, to establish the properties of specific connectors and their impact on whole slab dynamic and static performance. The inclusion of any interlayer immediately reduced structural performance, but varying the interlayer thickness and build up only had a small impact. A critical feature of shear connector design was found to be the extent to which a connector is vertically restrained.

KEYWORDS: Timber-concrete composites, Off-site manufacturing, Vibration performance, Finite Element modelling

1 INTRODUCTION

Timber-concrete composite floor panels offer a relatively lightweight structural floor system that can be used with a panelised construction method. Currently, prefabricated timber-concrete composite (TCC) floor solutions are rare. This is in part due to a lack of knowledge regarding the shear connectors that join the timber and concrete elements, and the impact of additional interlayers between those timber and concrete elements, which is even less well understood.

This research project was undertaken as part of the broader work being done for the GenZero initiative [1] by the UK's Department for Education (DfE) working with industrial partners Smith and Wallwork Engineers, Ecosystems Technologies, and Thorp Precast.

1.1 GENZERO

The DfE have identified the need to build up to 200 new secondary schools each year in the 2030s. The GenZero initiative looks at how future secondary schools could be designed to meet this demand while aligning with the government's commitment to net zero carbon emissions by 2050. The key aims of the initial GenZero research project was to develop a flexible secondary school design system which could be applied to multiple sites and achieve net zero carbon in both construction and operation.

The DfE aim to pioneer a new method to build these secondary schools, using the principles of Design for Manufacture and Assembly (DfMA) to design a kit of high-performance parts from which new schools can be developed, and then quickly assembled onsite.

An initial prototype of a single classroom was displayed at the COP26 Glasgow summit, which gave the opportunity for testing and improving the understanding of the floor slab solution. Other prototyping projects are ongoing.

1.2 GENZERO FLOOR SLAB

For the majority of the GenZero design a high-performance timber concrete composite floor panel was proposed. These prefabricated panels aimed to meet the structural requirements, as well as provide benefits for fire separation between floors, acoustic separation and thermal mass. The concrete would also provide a hard-wearing architectural finish, reducing the number of on-site trades and would minimise whole life carbon compared to finishes that need to be replaced every few years.

The floor panels span 8m and are 1.8m wide. The panel build-up, Figure 1, is made of a 75mm concrete slab, on top of an acoustic resilient layer (~5mm) supported on a timber boarding layer (24mm) which also acts as a permanent formwork. The concrete then acts compositely with the glulam ribs below. There is one central rib of 200x400mm with two half ribs (100x400mm) at each edge to create a continuous appearance underneath while helping to protect the concrete edges. The glulam is made using UK grown timber with a material grade of GL16+.

[1] Sam Winder, Smith and Wallwork Engineers, sam.winder@smithandwallwork.com
[2] Dan Chapman, Mott Macdonald, daniel.chapman@mottmac.com
[3] Panayiotis Papastavrou, Smith and Wallwork Engineers, panayiotis.papastavrou@smithandwallwork.com
[4] Simon Smith, Smith and Wallwork Engineers
[5] Prof. Allan McRobie, University of Cambridge

https://doi.org/10.52202/069179-0403

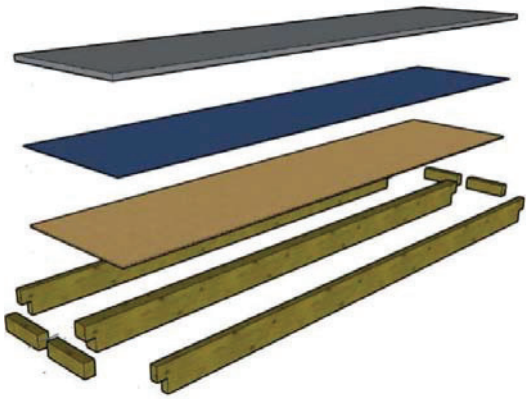

Figure 1: *Exploded view of floor GenZero slab.*

1.3 TECHNICAL MOTIVATION

The structural performance of timber or concrete is already well understood. What is less well understood are the methods of joining these materials to form a composite, especially with the inclusion of interlayers. The properties of these connectors have a significant impact on the performance of the overall structure, as the connectors dictate to what extent composite action occurs. This in turn determines the global stiffness of the slab. Then under large loads, the design of the shear connectors will govern the failure mode and the failure load. The key metrics of performance for a shear connector are its slip modulus and failure load, which can then be used to calculate the global slab properties.

There are evidently many methods to join timber and concrete to make a composite connector. The original GenZero research (a literature review and design exercise) identified two connector types to take forward from a literature review: a 20mm flanged steel dowel and a notch 50mm into the timber. See Figure 2. The assessment was based on a balance of structural performance, manufacturability and an attempt to limit the number of connectors for manufacturing ease and reduced noise transmission.

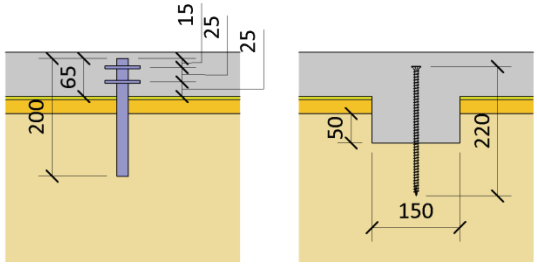

Figure 2: *Composite connectors, flanged dowel on the left, concrete notch on the right*

The two types of composite connector have been researched and tested before. However, the effect of adding interlayers between the concrete and the timber members is not adequately understood. Previous research has given flat reduction factors for strength and slip modulus values for interlayers. Table 1 shows the reduction factors put forward from the 2018 COST report "Design of timber-concrete composite structures" [2], which summarised available research.

Table 1: Reduction factors due to interlayers [2]

	Strength R.F. (%)	Stiffness R.F. (%)
Dowels	8	35
Notches	16	34

It is important to note that the reduction factors given in Table 1 are not a function of the interlayer thickness or interlayer material. It is intuitive to expect a thicker interlayer will have a greater impact on stiffness. The original GenZero prototype includes an interlayer of two materials with a thickness of ~ 30mm. More recent guidance published in March 2022 'Design of Timber Structures. Structural design of timber-concrete composite structures.' [3] is also limited on detail. For example, if the interlayer is as stiff as the timber "The Slip Modulus of dowel-type fasteners may be taken as that for a similar configuration without an interlayer with a reduction factor of 30%." Otherwise "the slip modulus should be determined by tests", which is what this report aims to provide for the GenZero design.

Previous research has typically used higher grade glulam timber, with greater stiffness and strength properties. The GenZero design differs by using softer UK grown glulam timber elements with a grade of GL16+. GL16+ was proposed by Edinburgh Napier University specifically for UK grown timber. Material properties for GL16+ are given in Table 2.

Table 2: *GL16+ timber properties*

Bending strength	$f_{m,g,k}$	22.5	N/mm^2
Tensile strength	$f_{t,0,g,k}$	18.0	N/mm^2
	$f_{t,90,g,k}$	0.5	N/mm^2
Compressive strength	$f_{c,0,g,k}$	22.5	N/mm^2
	$f_{c,90,g,k}$	2.5	N/mm^2
Shear strength	$f_{v,g,k}$	3.5	N/mm^2
	$f_{r,g,k}$	1.2	N/mm^2
Modulus of Elasticity	$E_{0,g,mean}$	8,400	N/mm^2
	$E_{0,g,0.05}$	7,000	N/mm^2
	$E_{90,g,mean}$	300	N/mm^2
Shear modulus	$G_{g,mean}$	650	N/mm^2
	$G_{r,g,mean}$	65	N/mm^2
Density	$\rho_{g,k}$	363	kg/m^3
	$\rho_{g,mean}$	400	kg/m^3

Dynamic performance typically governs the design of long-span timber floors such as the GenZero design. This research focuses on the small strain and dynamic behaviour of the composite shear connectors and full slab, with the aim of informing the development of prefabricated timber-concrete floor panels. This is done by analytical methods, finite element modelling of the shear connectors and the slab unit, small-scale lab testing

https://doi.org/10.52202/069179-0403

comparing different shear connectors and interlayers, and full-scale lab testing of a complete slab focusing on its dynamic properties under footfall excitation.

2 CONNECTOR BEHAVIOUR

This section aims to establish the performance of the individual composite connectors identified for the GenZero prototype and explore the effect of the proposed interlayer. This is done through small scale tests of the connectors and through computational analysis.

2.1 EXPECTED VALUES FROM LITERATURE

The anticipated failure load and stiffness from the literature is given in Table 3. The flanged dowel values are based on existing research [4], with stiffness scaled with the timber density to power of 1.5. Values for the notch are based off guidance in the COST report [2], which gives a flat stiffness value based on notch width, with no relation to timber properties.

Table 3: *Predicted connector properties*

Connector	Predicted failure load, kN	Slip modulus, kN/mm
Flanged dowel	27	109
Flanged dowel w/ interlayer	25	71
Notch	29	120
Notch w/ interlayer	24	76.8

2.2 CONNECTOR SPECIMEN DESIGN

Four test specimens were constructed to cover both connectors and three different interlayers build ups, see Table 4 for a summary. The number of specimens was limited by the availability of UK grown glulam.

Table 4: *Small-scale test specimens (SF = Rothoblaas Silent Floor)*

Test	Shear connector	Interlayer depth, mm	Interlayer Composition
1	Dowel	0	None
2	Dowel	24	OSB
3	Dowel	29	SF + OSB
4	Notch	29	SF + OSB

The specimens were designed for symmetric shear tests with two connectors in each side, so that no additional moments would be placed on the shear connectors.
The geometry of each specimen was designed to replicate the full size GenZero slab, with the same timber dimensions as an outside rib and the same concrete thickness. Where the interlayer thickness is varied the dowel embedment depth is kept the same. The key variation from the full-scale slab is the concrete is unreinforced and has the same width as the beam.

2.2.1 CONCRETE

The GenZero design specified a concrete grade of RC30/37 with a 70% GGBS replacement mix. The concrete mix used for the tests did not include GGBS due to availability, however this should only affect curing times. Concrete test results are given in Table 6, showing the strength requirements were met.
The mix was relatively dry, making it harder to compact leading to concerns that voids may have formed in or near the connectors.

Table 5: *Concrete mix used in shear test specimens.*

Test type	Number of tests	Mean failure load (MPa)
Cube	3	42.4
Cylinder	2	32.7

2.3 SMALL SCALE TESTING METHOD

The small-scale shear tests were completed in accordance with BS EN 26891:1991 [5] to ensure relevance to all stakeholders. The loading regime is shown in Figure 3, specimens are loaded elastically, unloaded, and then loaded to failure. This allows connectors to embed and shows a hysteresis loop for the cycle. Testing was completed with an Instron machine using load control for the initial cycle then displacement control to prevent any sudden failure; Figure 4 shows a photo of the test set up.

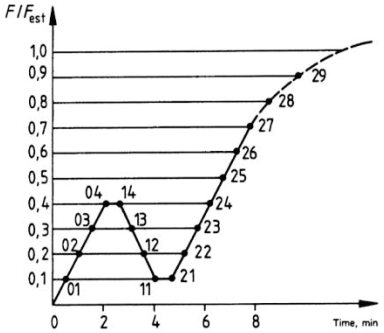

Figure 3: *Loading protocol [5]*

Figure 4: *Test set up, with specimen 1 after failure*

https://doi.org/10.52202/069179-0403

The standard also provides the method to calculate the slip modulus from experimental results. This required calculating an estimate of the failure load for each specimen, which was typically done using values from literature. Test 4 was the exception, which was subjected to the same regime as Test 3 in order for the performance of the two different shear connectors to be better compared.

2.3.1 DIGITAL IMAGE CORRELATION

Digital Image Correlation (DIC), also called Particle Image Velocity (PIC), was used to measure strain in the specimens during testing. This is done by spray painting dots onto the specimen then comparing digital images to track deformations and calculate the strain field.

2.4 COMPUTATIONAL ANALYSIS

SIMSOLID was used to create a Finite Element Model of individual connections to extend the parameter field covered. FEA models were developed for the two connector types. This was proposed by the full-scale slab fabricator as it simpler to manufacture.

The interlayer was modelled as an air gap, to make a lower bound estimate where the interlayer material does not contribute to the stiffness, through friction or restraint.

2.5 RESULTS AND DISCUSSON

2.5.1 EXPERIMENTAL

Table 6 shows the characteristic connector properties calculated using BS EN 26891:1991 for each specimen with four connectors. The results for a single connector are then compared to the expected values from literature in Table 7. Initial impressions of the results show both the capacity and stiffness of the dowel connector drop significantly as the interlayer increases. Also, the notch connector slightly outperforms the dowel connector for the same interlayer.

Compared to the literature the strength values are relatively similar. However, the experimental stiffness values are generally lower by a factor of 10, this is discussed later.

For the flanged dowel the literature gave a stiffness reduction of 35% where the experimental results show reductions of 51% and 62% for the OSB interlayer and the combined OSB and resilient layer interlayer respectively. This shows a flat reduction factor for any interlayer is unsuitable.

Table 7: *Predicted vs experimental connector properties*

Test	1	2	3	4
Predicted failure load, kN	27	25	25	24
Experimental failure load, kN	27	20	17	27
Predicted slip modulus, kN/mm	109	71	71	77
Experimental slip modulus, kN/mm	13.4	6.5	5.1	6.8

However, there is a significant discrepancy between the slip moduli of the experimental and literature values. This discrepancy can't be explained by the interlayer build-up as test 1 which had no interlayer is also significantly lower than the literature, suggesting something is wrong with the specimen design. None of the shear test specimens failed in the shear connectors. In each case there was bearing failure at the base of the specimen first. For example, Figure 4 show the cracking patterns of the concrete in failure of Test 1; note cracking at the base. The onset of this cracking may have reduced the stiffness of the shear connectors in the specimen. Therefore, the results from the small-scale tests are indicative of the relative performance of the shear connectors with given interlayer but are not reflective of the true absolute values of the slip moduli and shear strength.

Table 6: *Experimental specimen properties (4 connectors)*

	Property	Notation	Unit	Test			
				1	2	3	4
1	**Maximum Load**	**F_{max}**	**kN**	**107.5**	**78.9**	**69**	**108**
2	estimated maximum load	F_{est}	kN	100	90	80	80
3	initial slip	v_i	mm	0.88	1.54	1.54	1.41
4	modified initial slip	$v_{i,mod}$	mm	0.74	1.40	1.57	1.19
5	joint settlement	v_s	mm	0.14	0.14	-0.03	0.22
6	elastic slip	v_e	mm	0.57	0.76	1.01	0.45
7	initial slip modulus	k_i	kN/mm	45.3	23.4	20.7	22.7
8	**slip modulus**	**k_s**	**kN/mm**	**53.7**	**25.8**	**20.4**	**27.0**
9	slip at 60% F_{est}	$v_{0.6}$	mm	1.31	2.23	2.51	1.77
10	modified slip at 60% F_{est}	$v_{0.6,\ mod}$	mm	1.15	1.94	2.49	1.49
11	slip at 80% F_{est}	$v_{0.8}$	mm	2.06	2.95	3.91	2.12
12	modified slip at 80% F_{est}	$v_{0.8,\ mod}$	mm	1.90	2.66	3.89	1.83

https://doi.org/10.52202/069179-0403

Only a narrow strip of concrete was used in each specimen, rather than having the concrete overhang to replicate a larger part of the slab. A larger concrete area would increase the crushing failure load. The use of a dry mix, resulting in voids inside the specimen (Section 2.3.6) will have exacerbated this problem. Finally, the concrete was completely un-reinforced. Including a reinforcement mesh would be more representative.

2.5.2 COMPUTATIONAL

The absolute values for slip modulus the FEA produced were substantially higher than the literature and experimental values, see Table 8. This is potentially the result of imperfections in real world samples. For example, within a concrete notch, the concrete face in unlikely to be perfectly smooth, meaning protruding elements are likely to bed into the timber until a sufficient surface area is in contact with the timber, effectively reducing the initial slip modulus. Similarly, this could happen with hole tolerances with the dowel connector.

Table 8: *FEA slip moduli*

Interlayer Thickness, mm	Slip Modulus, kN/mm (Normalised)		
	Rectangular notch	Flanged dowel	Dowel Experimental
0	363 (1.0)	297 (1.0)	13.4 (1.0)
5	225 (0.62)	144 (0.48)	6.5 (0.49)
29	206 (0.57)	93 (0.31)	5.1 (0.38)

More interesting is the normalised slip modulus for each connector type. These are shown for a variety of interlayer thickness in Figure 5. Each connector shows a significant drop in slip modulus as the gap first starts, then a more steady, approximately linear reduction. This indicates a flat reduction factor is suitable for thin interlayers approx. <5mm. However, for larger interlayers the linear drop does become pronounced, showing the limitations of the current literature.

The FEA models and experimental values also show a larger initial reduction compared to the literature values, in particular the dowel reduction is substantially larger. This suggests a larger experimental set with the improvements discussed in Section 2.5.1 is required to fully characterise the behaviour of these connectors.

3 FLOOR SLAB BEHAVIOUR

Two full size GenZero floor slabs were constructed for structural testing as part of the prototype build. Testing included impact vibration tests, and a 3-point bend test with cyclic loading. These tests aimed to verify whether the original design met the structural requirements and to explore the properties of the composite connectors through back calculation of the whole slab's behaviour.

3.1 SLAB DESIGN AND MANUFACTURE

Each slab has the same dimensions and build up with the full interlayer (24mm OSB and 5mm resilient layer), shown in Figure 6. Connector spacing was kept the same for both slabs to ensure a direct comparison. Along each rib connectors were spaced at 1m intervals. In the wider central rib, two dowels were used at each interval and double width notch was used.

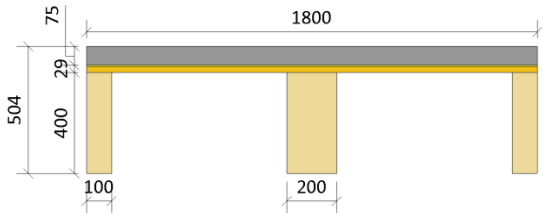

Figure 6: *GenZero slab cross-section*

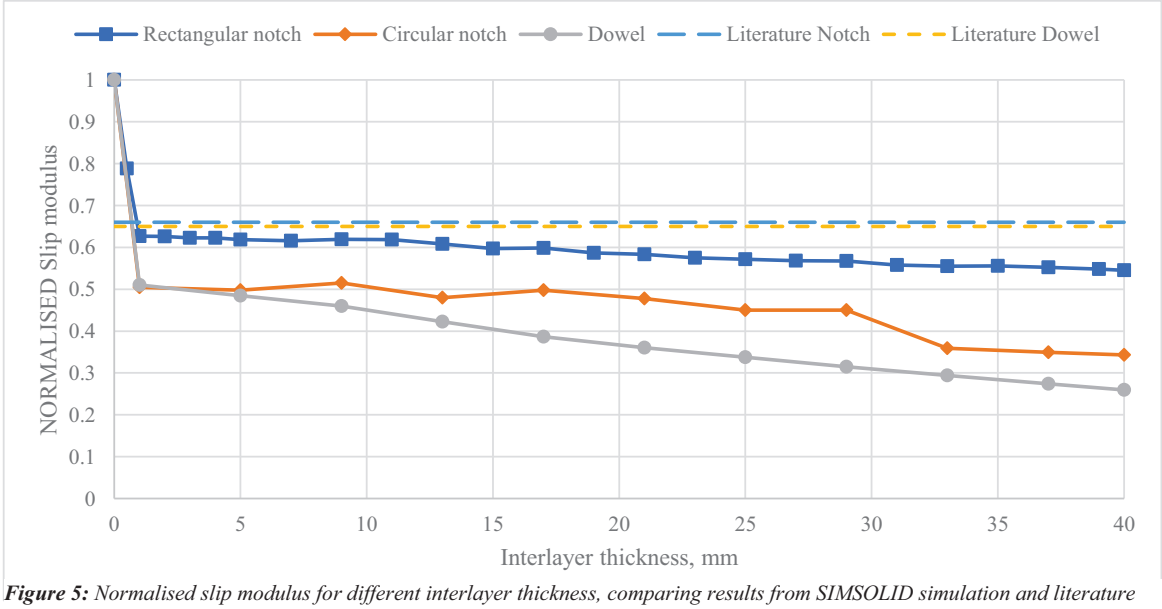

Figure 5: *Normalised slip modulus for different interlayer thickness, comparing results from SIMSOLID simulation and literature*

https://doi.org/10.52202/069179-0403

ECOSystems Technologies fabricated the timber elements, connectors and applied the resilient layer, then the slabs were transported to Thorp Precast to pour and polish the concrete.
The C16+ timber that made up the glulam beams of the prototype outperformed initial expectations of stiffness. Research from Edinburgh Napier University demonstrated that the timber performed closer to a C24 classification, since the modulus of elasticity of the glulam was 11GPa rather than the initially assumed 8GPa. The high GGBS content of the concrete slab made power floating more difficult. The prototype slabs had a slightly curved profile on their surface, with more cover at the edges than in the middle. This meant a few of the steel dowel shear connectors were visible. Variation in the slabs' mass can be seen in Table 9.
The dowel connectors were intended to be glued in; however the epoxy was missed, which could have a significant impact on performance.

Table 9: *Prototype slab masses*

Prototype shear connector	Weight (kN)
Notch	33.28
Dowel	33.33

3.2 VIBRATION TESTING

3.2.1 TEST METHOD

Dynamic testing was completed using an instrumented hammer, see Figure 7, with accelerometers glued to the floor slab. The hammer was used to excite the slab vertically while it was simply supported at each end. This would enable measurement of the fundamental frequency of the slab, which is the most relevant for excitation from walking. The fundamental frequency of the slab is a property of the slab and therefore would be independent of where the hammer blow is struck and where the receiving accelerometer is placed. However, the exception is that a mode will neither be excited by the hammer nor received by the accelerometer if either of those two points on the slab coincide with a nodal point of the vibration in that mode. Therefore, data was collected from a variety of locations to help produce confidence in the nature of the resonant peak being detected. Numerous off-centre impacts from the instrumented hammer and off-centre accelerometer measurements were taken to avoid mistaking any torsional or minor axis flexural modes of vibration for the fundamental mode.

Figure 7: *Instrumented hammers on test slab*

3.2.2 DYNAMIC RESULTS

Figures 8 to 10 show the key frequency data for each slab. Figures 11 and 12 show a spiral plot for the notched connector slab based on the equation of motion:

$$F = m.\ddot{x} + v.\dot{x} = k.x$$

The accelerometer glued to the slab, records the acceleration of the slab, which can be numerically integrated to find the velocity and position. After the initial impact the external force, F = 0. Therefore, if each of the exponents are constant (the slabs' mass, stiffness and damping factor) the equation of motion defines a plane in space on which the oscillations of the slab create an ellipse. As the oscillations decay this ellipse decays into a spiral.
Table 10 shows the key results from these figures, showing the notch connector performs better than the dowel. From these values and the slab masses response factors for a range of input walking frequencies were calculated, using the method from "A Design Guide for Footfall Induced Vibration of Structures" [6], the results are shown in Figures 13 and 14.

Table 10: *Experimental dynamic values*

	Natural Frequency (Hz)	Damping Factor (% critical)
Dowel	8.6	2
Notch	10.2	4.5

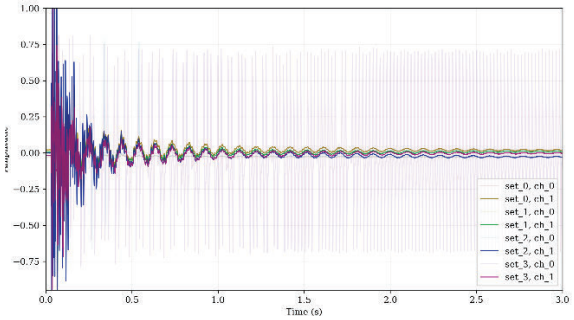

Figure 8: *Time domain data of notch connector slab*

https://doi.org/10.52202/069179-0403

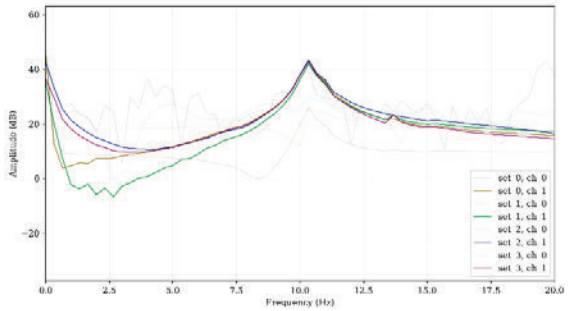

Figure 9: *Frequency domain data for notch connector slab*

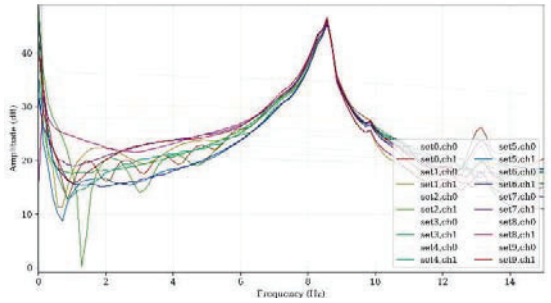

Figure 10: *Frequency domain data for the dowel connector slab*

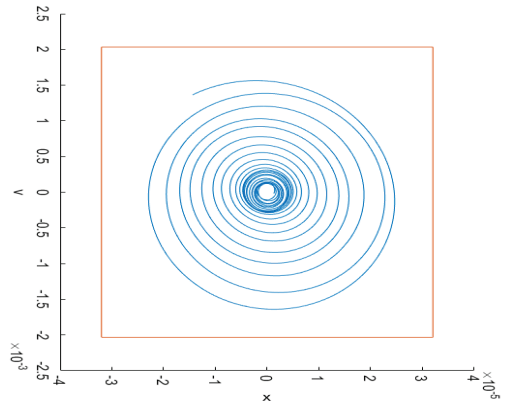

Figure 11: *Vibration decay spiral of notch connector slab*

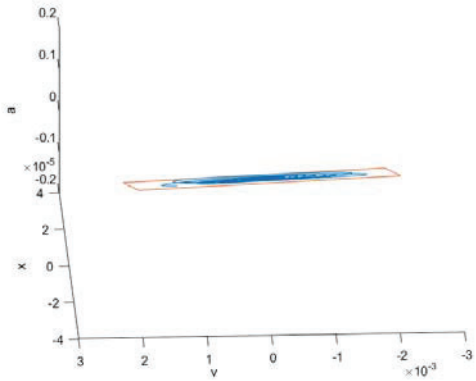

Figure 12: *Vibration decay spiral of notch connector slab*

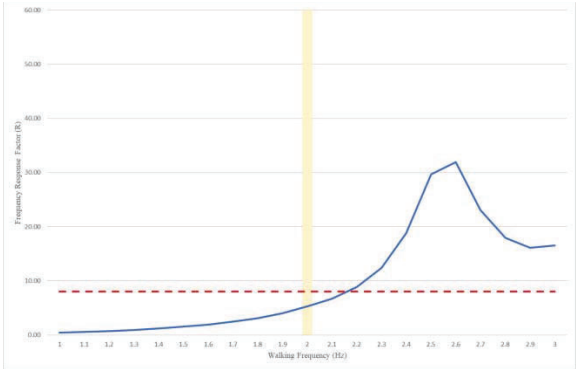

Figure 13: *Response factors for different walking frequencies of the notched connector slab, the yellow line indicates the max expected walking frequency in a classroom, the red line indicates the max permissible response.*

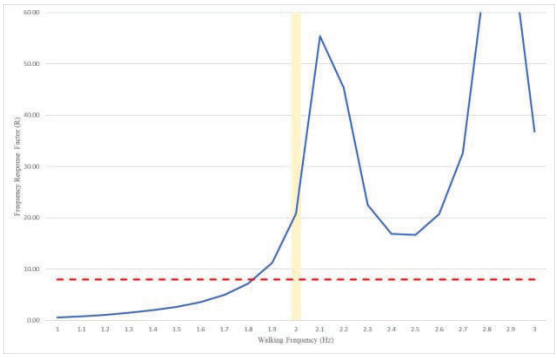

Figure 14: *Response factors for different walking frequencies of the dowel connector slab, the yellow line indicates the max expected walking frequency in a classroom, the red line indicates the max permissible response.*

3.2.3 DISCUSSION OF RESULTS

There is a clear difference between the appearance of the fundamental resonant peak of the notch slab and the equivalent resonant peak in the dowel slab, compare Figures 9 and 10. The clean resonant peak in the notched slab is what one would normally expect to see. The shape of the resonant peak in the dowel slab indicates that there are in fact two resonant peaks at very similar frequencies superimposed on top of one another. One possible explanation would be to suggest that there were two modes present with similar natural frequencies, for example a bending mode and a torsional mode that were both excited at the same time. However, this would be very unlikely given that torsional modes should only occur at higher frequencies due to the long thin shape of the slab. This was confirmed by impacting the slab at different locations. By impacting the slab near the edge, one would expect to excite a torsional mode, whereas impacting the slab along at centre line should excite no torsional modes. In all the above cases the same 8.6Hz peak was present with the same shape, and no torsional modes in the considered frequency range were observed. Instead, the shape of the peak is indicative of an asymmetric slab. If the left half of the slab and the right

https://doi.org/10.52202/069179-0403

half of the slab were built slightly differently, with subtly different masses and stiffnesses, then the left half of the slab would have a subtly different resonant frequency to the right half. Then the two resonant peaks would superimpose and join into one resonant peak with a shape similar to what was observed. This is the most likely explanation since it is consistent with the defects recorded, for example one of the glulam ribs was 10mm thinner in width than specified.

Often a linear damping factor is assumed to simplify analysis, Figures 11 and 12 demonstrate that damping was linear in both slabs. As discussed in Section 3.2.2, if the damping factor, v, was linear the spiral would lie on a plane, as can be seen. However, if the damping factor was non-linear a 'bowl' shape would be observed instead.

The notch shear connected slab performed better than the dowel slab. However, this is not due to the performance of the shear connector alone. The dowel slab had more issues with its manufacture and the dowel connectors were not glued into the timber.

3.3 3-POINT BEND TEST

3.3.1 TEST METHOD

There is no specific standard for testing TCC slabs, therefore a test method was developed based on the protocol for steel concrete composites (SCC). "Design of composite steel and concrete structures" [7] lays out methods for testing both shear connectors and composite slabs. This uses a four-point bend test with an initial cyclic loading phase before the slab is taken to failure.

To test the TCC slabs, a 3-point test is used with an initial phase of 25 cycles to 30% of the estimated failure load. A 3-point bend test was justified as the primary interest of this test is the slab stiffness, and it would make a shear failure more likely which is of greater interest to evaluate the shear connectors. The number of cycles is reduced from the SCC test as steel fatigue is less of an interest here, this is also seen in the small-scale test method where timber connections require a single cycle and SCC connectors require 25.

To collect the data, multiple techniques were used. DIC imaging was used to monitor the slab by the supports. LED monitoring was used to track relative movement of different regions of the slabs. Transducers were placed under each rib, to measure deflection.

3.3.2 RESULTS

Table 11 shows key results from the test. There was a hydraulic fault in the actuator during testing of the notch prototype slab. There was a control error with the hydraulic actuator, resulting in a sudden impact on the notch slab. This made a loud sound, including cracking from the slab. This impact recorded a maximum load of 105kN. However, this value is likely to be an overestimate due to the water hammer pressure excited within the actuator as a result of this sudden load.

The remainder of the test on the notch slab was conducted in displacement control, but the need to adjust the program led to interrupted data acquisition from the actuator.

The initial failure mode of the notch slab was in the shear connectors. The initial failure mode of the dowel slab was in bending.

Table 11: *Experimental slab performance.*

Prototype slab	**Notch**	**Dowel**
Elastic limit (kN)	93	100
Peak load (kN)	117	104
Bending stiffness (N/mm^2 $x10^{12}$)	59.3	23.7

Both slabs had significant post failure strength and ductility. The notch slab was able to resist the full extension of the actuator of approximately 160mm. When the load was removed the slab rebounded, but not to its original height. The dowel slab did not rebound after its final failure at its peak load near the maximum extension of the actuator.

3.3.3 DISCUSSION OF RESULTS

Using the methods of built-up sections, from EC5 [8] it is possible to back-calculate the slip modulus of the shear connectors in a slab from the experimental values of central deflection in bending as shown in Table 12.

Given that a negative slip modulus is impossible, the result indicates that the dowel slab is performing worse than would be expected if no composite action was occurring at all. This cannot be a consequence of the performance of the shear connector alone. Nevertheless, the result demonstrates that the dowel performed very poorly. The calculation was based on the design dimensions of the slab, but as discussed in Section 3.1 the prototype slabs contained defects.

Table 12: *Connector slip moduli calculated from bend test*

Prototype shear connector	Slip modulus (kN/mm)
Notch	45.0
Dowel	-1.1

Table 13: *Revised connector slip moduli calculated from bend test, to account for manufacture*

Prototype shear connector	Slip Modulus (kN/mm)
Notch	69.5
Dowel	1.0

A revised calculation was then performed, reducing the cross-section to match the as built dimension and accommodate for imperfections in manufacture. Specifically, Table 13 was produced by reducing the concrete depth by 10mm to 65mm, as some dowels were partially exposed from the polishing and assuming each rib had been planned by 10mm each on average, reducing to total width of glulam from 400mm to 360mm.

However, this does not account for the fact that the slab with dowel shear connectors was generally in a poorer condition with more defects before the test than the slab with notch shear connectors. This brings the slip modulus value of the notch more in line with the literature value. Due to the construction defects of the dowel slab, in particular the missing glue in the dowel connector, these full-scale results are disregarded.

3.4 DYNAMIC VS BENDING STIFFNESS

The bending stiffness of the two full scale slabs can be back calculated from both the vibration tests and the 3-point bend tests to show the effects of load duration, these are shown in Table 14. As is typically expected both slabs are stiffer during the dynamic tests, by 23% and 119% for the notch and dowel respectively. The greater drop in stiffness of the dowel connector slab suggests it is more susceptible to degradation over time, this may be from increased cracking in the concrete or greater embedment of the dowels into the timber.

Table 14: *Slab bending stiffness*

	Bending stiffness (N/mm^2 $x10^{12}$)
Full composite action	122.3
No composite action	25.4
Notch (static)	59.3
Notch (dynamic)	73.2
Dowel (static)	23.7
Dowel (dynamic)	52.1

3.5 COMPUTATIONAL ANALYSIS

An ABAQUS FEA model of the full-scale slab was created to explore the internal forces acting within the slab to understand what elements are affecting the performance of the concrete slabs.

3.5.1 MODELING UNCERTAINTIES

The glulam was modelled as a homogenous anisotropic material rather than as a built-up section of lamina. The material properties assigned in the test were based on Eurocodes [7] in the case of concrete, this causes some uncertainty as the actual value as is dependent on cracking. Values for the glulam were based on recent research from Edinburgh Napier University, while mean values are used in the model there is still significant natural variation within timber causing more uncertainty.

3.5.2 MODELING INSIGHTS

The key insight provided from modelling was the importance of vertical restraint to the composite connectors. If a shear connector is allowed to lift, it provides much less resistance to shear than if it is held down. Figures 15 and 16 show the normal stress distributions in a TCC slab, for a notch shear connector both with vertical restraint, replicating the fully threaded screw in the connection, and without vertical restraint, no additional screw. When there is no restraint, the connectors lift and the slab provides virtually no structural contribution, Figure 16. In comparison Figure 15 shows the slab stressed, in a pattern consistent with the connector locations.

This also helps explain the particularly poor performance of the experimental dowel slab, because the glue was missed from the dowels meaning there was limited vertical restraint.

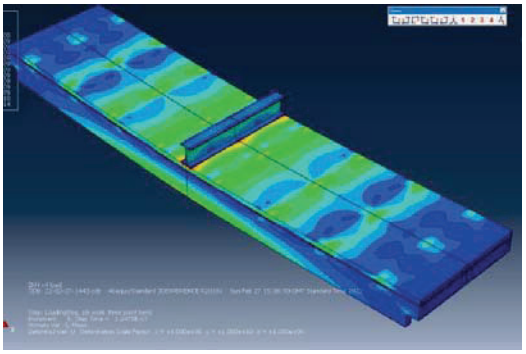

Figure 15: *Notch connector slab with vertical restraint*

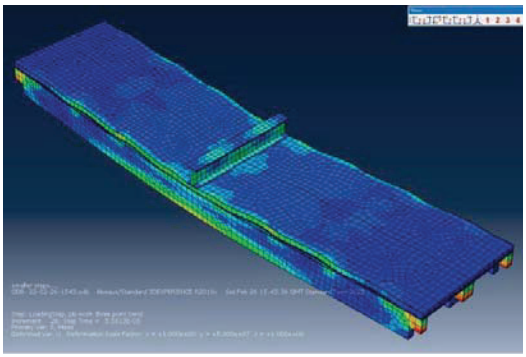

Figure 16: *Notch connector slab without vertical restraint*

4 GENZERO DESIGN EVALUATION

4.1 STRENGTH PERFORMANCE

To meet ULS requirements (G_k =0.5kN/m^2, Q_k=3.8kN/m^2) both slabs must be able to resist an equivalent central point load for bending strength: $P = 46$ kN, and an equivalent central point for shear strength: $P = 92$ kN. Shear failure is the limiting parameter and both slabs pass.

Table 15: *Satisfaction of strength criteria*

	Required Maximum load (kN)	Achieved Maximum load (kN)	Result
Notch	92	117.5	**PASS**
Dowel	92	100.2	**PASS**

https://doi.org/10.52202/069179-0403

4.2 DEFLECTION PERFORMANCE

Under SLS loading, the equivalent central point load, P = 38.9 kN. The instantaneous deflection limit = $span$ / 250 = 32.2mm. Both slabs pass.

Table 16: *Satisfaction of deflection criteria*

	Permitted deflection (mm)	Deflection under load (mm)	Result
Notch	22.4	7.9	**PASS**
Dowel	22.4	12.1	**PASS**

4.3 VIBRATION PERFORMANCE

GenZero put forward two vibration performance criteria, a minimum natural frequency of 8Hz with 10% live load applied, noting however vibration tests were completed with no live load. Then a maximum frequency response of 8 for excitation walking frequencies up to 2Hz as suggested in [6]. Both slabs pass the basic natural frequency test, only the notched connector passes the frequency response test.

Table 17: *Vibration criteria and results*

	Minimum resonance (Hz)	Natural frequency (Hz)	Result
Notch	8.00	10.22	**N/A**
Dowel	8.00	8.56	**N/A**

	Allowable FR	Maximum FR	Result
Notch	8	6.8	**PASS**
Dowel	8	22.1	**FAIL**

5 CONCLUSIONS

There was no case where an interlayer improved structural performance. Each connector saw a large initial drop off before a reduced linear decline. Therefore, in design an interlayer should be avoided. If absolutely required, the thickness of the interlayer should be minimised.

A key attribute of a composite connector is vertical restraint. The full-scale slab modelling and the missing epoxy of the dowels showed the significant impact of removing this restraint.

The notch connector outperformed the dowel in all tests completed. Future work could investigate the effect of notch shape to help simplify manufacture, circular notches are typically easier to cut. Initial modelling of a circular notch with similar dimensions to the rectangular notch produced a less stiff connector.

The GenZero slab design was shown as viable. The full-scale tests can be taken as a lower bound of performance due to the manufacturing imperfections. Key to making this solution a reality would be manufacturing consistency.

ACKNOWLEDGEMENTS

Phil McLaren, Martin Touhey, Dave Layfield (CUED Structures Lab Technicians)
Pieter Desnerck (Department of Engineering, UoC)
Beverly Quinn, Ian Naylor (DfE)
Matt Stevenson (Ecosystems Technologies)
Harvey Thorp (Thorp Precast)
Santi Davi (Rothoblaas)
Wojciech Plowas, Robert Hairstans (Edinburgh Napier)

REFERENCES

[1] www.genzero.co.uk
[2] A. Dias, J. Schänzlin, P Dietsch. Design of timber-concrete composite structures. Table 6: Test data on the influence of the interlayer in the load carrying capacity and stiffness of timber-concrete connections. COST (European Cooperation in Science and Technology) Germany, 2018
[3] 'Design of Timber Structures: Structural Design Of Timber-Concrete Composite Structures.' [PD CEN/TS 19103:2021] March 22, 2022
[4] E. Lukaszewska, H Johnsson, L. Stehn. Connections for Prefabricated Timber-Concrete Composite Systems. Luleå University of Technology, 2006
[5] BS EN 26891:1991
[6] Concrete centre. A Design Guide for Footfall Induced Vibration of Structures, 2006
[7] Eurocode 4. Design Of Composite Steel And Concrete Structures. General rules and rules for buildings BS EN 1994-1-1:2004 Annex B
[8] Eurocode 5 BS EN 1995-1-1-2004 Annex B pg. 110
[9] M. Fragiacomo, D. Yeoh. Design of timber-concrete composite beams with notched connections, 2010

World Conference on Timber Engineering Oslo 2023

NUMERICAL MODELLING OF A CROSS-LAMINATED TIMBER-TO-CONRETE DOWEL-TYPE CONNECTION USING THE BEAM-ON-FOUNDATION MODEL

Joan W. Gikonyo[1], Eva Binder[2], Michael Schweigler[3], Thomas K. Bader[4]

ABSTRACT: The aim of the research presented herein is to investigate the mechanical behaviour of cross-laminated timber (CLT)-to-concrete dowel-type connections. For reliable timber-concrete-composite structures, mechanical connections between the two construction materials are of great importance. This paper investigates the nonlinear load-displacement behaviour, giving access to the stiffness and strength, as well as ductile connection failure modes, of a CLT-to-concrete composite connection using a Beam-on-Foundation (BoF) model. The latter is a numerical model that utilizes non-linear springs for the interaction between the fastener and the surrounding CLT and concrete materials. The influence of: (i) fastener diameter, (ii) initial slip, (iii) concrete embedment properties, and (iv) axial fastener resistance due to friction, on the connection shear capacity and slip modulus, was investigated in a parameter study. The nonlinear load-displacement response, connection stiffness and strength predicted by the BoF model were moreover compared to laboratory tests and the European Yield Model (EYM), which supported the validity of the BoF model. In addition, it was shown that the BoF model could enhance the prediction of the slip modulus compared to the current design regulations in Eurocode 5.

KEYWORDS: Beam-on-Foundation Model, CLT-to-concrete composite connections, connection stiffness

1 INTRODUCTION

The need for energy efficiency in construction has propelled the popularity of timber structures. Apart from exceptionally high mechanical properties in relation to the low weight of the material, timber has low mechanical properties under certain loading conditions and timber structures are prone to vibrations due to the lightweight nature of the material. The use of timber in combination with other construction materials in hybrid structures or structural composite elements, such as Timber Concrete Composites (TCC), can considerably improve the mechanical performance and stability as compared to conventional timber structures [1]. In TCC elements, timber and concrete elements are placed strategically in the tension and compression zones, respectively. Some of the benefits associated with TCC structures compared to timber structures are increased stiffness and load bearing capacity, improved sound insulation, reduced sensitivity to vibrations and improved structural bracing. In order to make use of the composite action in structural elements, efficient shear connections between the tension and compression-resisting components, i.e., between timber and concrete elements, are critical for the realization of the aforementioned benefits [2].

Most of the comprehensive experimental and numerical analyses of timber-concrete composite structures have been carried out with structural timber or glued laminated timber employed as the tension element. In recent years, studies on Cross Laminated Timber (CLT)-concrete composite structures have become increasingly popular. CLT is a pre-engineered timber product with an orthogonal laminar structure composed of an odd number of layers, usually with a maximum of seven layers. The popularity of CLT-to-concrete composite structures is attributed to improved mechanical properties in both longitudinal and transverse directions of CLT. CLT is attractive in development of full-scale wall and floor elements. CLT–concrete hybrid floor systems improve the bending capacity of the pure CLT floor elements by 3-5 times [3]. The suitability of common types of connectors such as, dowel-type fasteners [4], adhesive connections [5] and even novel types of connections [6] for CLT-to-concrete connections have been investigated by various researchers. Though adhesive connections provide an effective way to ensure a rigid shear connection between the concrete and CLT, shrinkage induced deflections of the composite connection render dowel-type connectors more suitable [1]. The stiffness of dowel-type connections in TCC elements depends on the deformation that takes place at the joint. Therefore, design of TCC connections assumes partial composite action, due to the difficulty in achieving full rigidity due to deformation at joints [7]. Ductility of dowel-type steel fasteners used in TCC connections increases the load-bearing capacity as well as the ultimate deformation capacity, because typically the connection shear capacity activates before the member ultimate load is reached [8]. However, ductile behaviour of the connection may not necessarily lead to ductile behaviour of the composite element if the stiffness of the

[1] Joan W. Gikonyo, Linnaeus University, Sweden, joan.gikonyo@lnu.se
[2] Eva Binder, Linnaeus University, Sweden, eva.binder@lnu.se
[3] Michael Schweigler, Linnaeus University, Sweden, michael.schweigler@lnu.se
[4] Thomas K. Bader, Linnaeus University, Sweden, thomas.bader@lnu.se

https://doi.org/10.52202/069179-0404

connection is higher than predicted, as the timber may exhibit brittle failure [2]. This emphasizes the importance of accurately predicting the slip modulus of TCC connections. Dias et al. [9] carried out a comparison between experimental tests on the load-bearing capacity of timber-to-concrete composite connections and the European Yield Model (EYM) by Ehlbeck and Larsen [10] in Eurocode 5 [11] (EC5) for i) timber-to-timber, ii) steel-to-timber and iii) timber-to-timber with a gap. The experimental results showed good agreement with all three EYM models. However, the EYM for steel-to-timber connections showed the best fit with the experimental results. Moreover, Dias et al. [12] compared experimental results for the slip modulus to i) analytical models based on beam-on-elastic foundation, and ii) the Eurocode-based empirical design equation for timber-to-timber connections, multiplied by a factor of two, as suggested in the code. The results showed that both models overestimated the slip modulus obtained in the experiments. Nonetheless, the experimental results showed better agreement with the Eurocode design equation.

The strength and slip modulus of TCC connections is experimentally determined according to EN 26891 [13]. However, Dias [14] showed that the connection slip modulus determined as per EN 26891 was inaccurate due to the pronounced non-linear response of TCC connections. Dias notes that the maximum slip observed in TCC connections is usually less than 8 mm, thus significantly lower than 15 mm indicated in EN 26891 [13], thereby, overestimating the shear capacity. Furthermore, it turns out that factors such as, initial slip [15], dowel diameter [6], concrete stiffness and strength [16] and connector inclination [4], influence the strength and slip modulus of CLT-to-concrete connections. The extent to which such factors influence the global response of CLT-to-concrete connection is largely unknown, which emphasizes the need for suitable design models for the prediction of both slip modulus and load bearing capacity of CLT-to-concrete connections.

The aim of this study is to validate a Beam-on-Foundation (BoF) model of CLT-to-concrete connections, by means of comparing model predictions with experimental results. The model is then applied to investigate the influence of various factors on the shear capacity and slip modulus of CLT-to-concrete connections. The outcome of this study provides experimental and numerical results that can be useful for creating structural design codes for CLT-concrete composite structures.

2 MATERIALS AND METHODS

2.1 Materials

The cross-laminated timber (CLT) elements, produced with boards of strength class C24 according to EN 338 [17], were stored in a climate room under standard climate conditions of 20°C and 65% RH for more than a year and it was assumed that an equilibrium moisture content of approximately 12% was established. The corresponding mean density of the CLT elements was 493 kg/m^3 (CV= 22%, 3 specimens). The prefabricated concrete elements were stored for at least 28 days before the tests, which leads to a stiffness of at least 33 GPa, with a mean density of 2371 kg/m^3 (CV= 1%, 3 specimens). The threaded rods for the connection had an ISO metric thread M24 and a quality of at least 8.8 grade steel.

2.2 Experimental tests on CLT-to-concrete shear connections

CLT-to-concrete connections were tested in a double shear push-out test configuration, see Figures 1 and 2. The tests were performed in a test frame, mounted with a hydraulic piston with a load capacity of up to 500 kN (MTS 210.45 G2, Flex test 60, MTS System Corporation, Sweden). In the test setup, the concrete element in the middle was connected by a threaded rod to two CLT side elements, kept together by a washer (d_{out}= 44 mm and d_{in}= 25 mm) and nut at each end, see Figure 1. The threaded rod was inserted into pre-drilled holes (d= 25 mm) in the timber and a casted hole in the concrete (d= 25 mm). A displacement-controlled load was applied to the concrete at a rate of 3 mm/min. Through a hinge included in the steel loading device, pure vertical loading and an even load distribution was ensured. The loading was stopped when the machine displacement reached 30 mm. The local displacement between concrete and CLT was measured with four linear variable differential transformers (LVDTs) – two on each side of the specimen. The mean local displacement of the LVDT measurements between the concrete and timber, the displacement, and the applied force from the testing machine over time were further processed and considered for the validation of the numerical model.

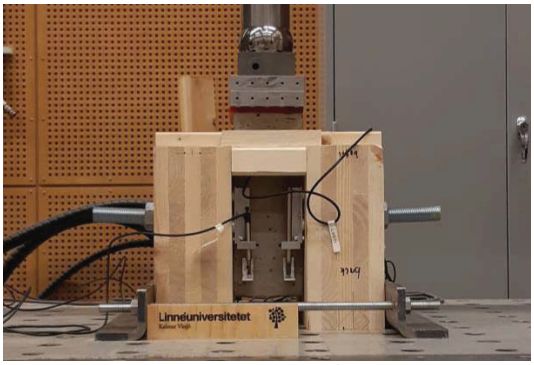

Figure 1: *Experimental test set-up used to carry out the shear test for the CLT-to-concrete connection.*

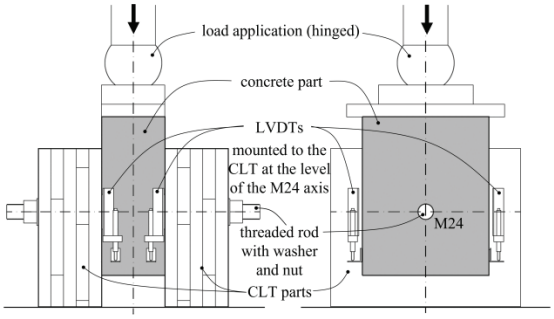

Figure 2: *Illustration of the experimental push-out test set-up for the CLT-to-concrete connection.*

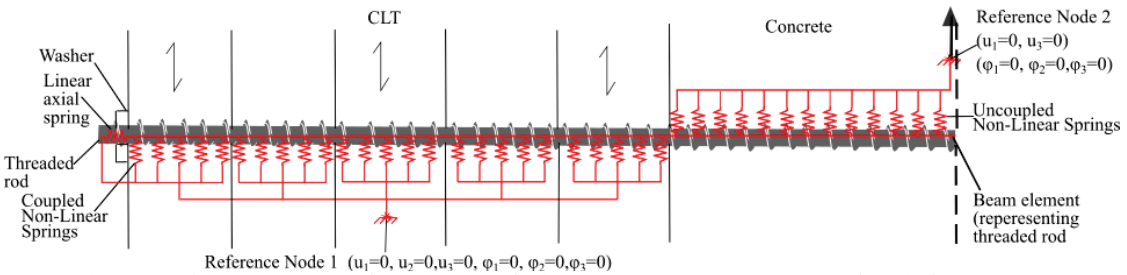

Figure 3: *Illustration of the Beam-on-Foundation (BoF) model for the CLT-to-concrete connection described in Section 2.2. The BoF model was created by considering symmetry and applying appropriate boundary conditions along the symmetry line.*

2.3 Numerical modelling of CLT-to-concrete connection using the BoF model

The 2-dimensional beam-on-foundation (BoF) model, illustrated in Figure 3, was used to simulate the CLT-to-concrete shear connection in the research presented herein. The model has been utilized by various researchers such as, Lemaitre et al. [18] and Schweigler et al. [19] to predict steel-to-timber connection behaviour, while considering non-linear embedment and elasto-plastic steel material behaviour. The model is composed of a deformable beam element that represents the steel fastener and rigid beams that host non-linear springs. These springs describe the local interaction between the steel fastener and the surrounding timber and concrete materials.

The model has four main inputs, a) the geometry of the connection, b) the non-linear load-slip data used to define the interaction between the steel dowel and, the i) concrete and ii) timber, c) the local interaction between washer and timber, and d) the mechanical properties of the steel fastener. Boundary conditions as regards the specimen support and the loading of the connection, as well as a possible lateral support at the washer or for symmetry conditions are specified at the reference nodes of the rigid elements and the fastener, see Figure 3.

2.3.1 Lateral embedment and axial withdrawal behaviour of timber

The non-linear load-slip data for the springs between the steel fastener and the CLT is defined using embedment load-slip data. The 2-dimensional BoF model considers two in-plane force components i) parallel to the fastener, related to the axial withdrawal capacity of the fastener and ii) perpendicular to the fastener, related to the lateral embedment behaviour of the fastener. The BoF model utilizes embedment load-slip data for both loading directions with respect to the grain direction of the timber, parallel and perpendicular to the grain, in the corresponding layers of the CLT. In lieu of experimentally determined embedment data for the connection materials, the analytical formula from Richard and Abbott [20] was used to determine the embedment stress, σ_h, in [MPa] at a particular displacement, u, in [mm] as,

$$\sigma_h(u) = \frac{(k_{f,el} - k_{f,pl}) \cdot u}{\left[1 + \left[\frac{(k_{f,el} - k_{f,pl}) \cdot u}{f_{h,inter}}\right]^a\right]^{\frac{1}{a}}} + k_{f,pl} \cdot u, \quad (1)$$

with the embedment parameters $k_{f,el}$ as the elastic foundation modulus in [N mm^{-3}] , $k_{f,pl}$ as the plastic foundation modulus in [N mm^{-3}], $f_{h,inter}$ as the intersection of the line defined by $k_{f,pl}$ with the y-axis in [MPa], and a as a transition parameter between $k_{f,el}$ and $k_{f,pl}$. The embedment parameters were determined using analytical formulas from a database [21] that includes several timber products, i.e., structural timber, Laminated Veneer Lumber (LVL), plywood and glulam, loaded both parallel and perpendicular to the grain as

$$f_{h,inter,0} = 0.1253 \cdot \rho - 20.32, \quad (2a)$$
$$f_{h,inter,90} = 0.1108 \cdot \rho - 28.47, \quad (2b)$$
$$k_{f,el,0} = 0.1374 \cdot \rho - 12.90, \quad (2c)$$
$$k_{f,el,90} = 0.0922 \cdot \rho - 18.20, \quad (2d)$$
$$k_{f,pl,0} = 0.0047 \cdot \rho - 2.0, \quad (2e)$$
$$k_{f,pl,90} = 0.0084 \cdot \rho - 2.21, \quad (2f)$$

where, ρ is the density of the timber in [kg m^{-3}]. In this study, the mean density of the CLT of 493 kg m^{-3} (see Section 2.1) was used to determine embedment parameters. It should be noted that the embedment parameter, $f_{h,inter,}$ in Equations (2a-b) was determined using the proposed formula for $f_{h,5mm}$ in [21]. Assuming the same dependence of the two parameters ($f_{h,inter,0}$ and $f_{h,inter,90}$) on the density, as for $f_{h,5mm,0}$ and $f_{h,5mm,90}$, might lead to a slight overestimation of the behaviour perpendicular to the grain. Figure 4 illustrates the embedment stress-displacement curves generated from Equations (2a-b) with consideration of the large displacement effect according to Schweigler et al. [19] when coupling the springs parallel and perpendicular to the fastener's axis. Only the component parallel to the loading direction of the connection, for loading parallel and perpendicular to the grain is shown in Figure 4. The non-linear stress-displacement data describing the axial capacity in between the fastener and the wood, was determined according to Schweigler et al. [19] with consideration of a friction coefficient, $\mu = 0.3$.

Once the stress displacement curves for both the embedment and axial (withdrawal) behaviour were determined, the corresponding forces of one embedment element in the model, $F(u)$, at a particular displacement, u, was calculated as,

$$F(u) = \sigma_h(u) \cdot d_{major} \cdot \Delta t \quad (3)$$

with the embedment stress, $\sigma_h(u)$ at that particular displacement, the major diameter of the threaded rod,

https://doi.org/10.52202/069179-0404

d_{major}, and the distance between adjacent springs, Δt. A single linear spring, positioned at the end of the fastener, simulated the axial resistance due to the washer. The stiffness of the axial spring of 3.9 kN/mm was determined, by considering the area of the washer of 994 mm^2 and the characteristic compression strength of the wood, $f_{c,90k}$, of 2.9 MPa, assuming a yield displacement of slightly less than 1 mm. The compressive strength was chosen equivalent to that of timber with an average density of 490 kg m^{-3} as per EN 338 [17], matching the mean density of the CLT. In dowel-type shear connections, and especially for fasteners inserted into pre-casted and pre-drilled holes, a clearance between the fastener and the surrounding material can be observed, which typically leads to an initial slip in the connection's load-displacement behaviour. Moreover, the indentation of the threaded part of the rod into the pre-drilled hole, leads to an initially softer behaviour, before full contact with the surrounding material is established. To consider this, the embedment stress-displacement curve is offset by a certain displacement representing the initial slip. The stiffness of the embedment curve up to the initial slip displacement was assumed to be 1% of the elastic foundation modulus, $k_{f,el}$.

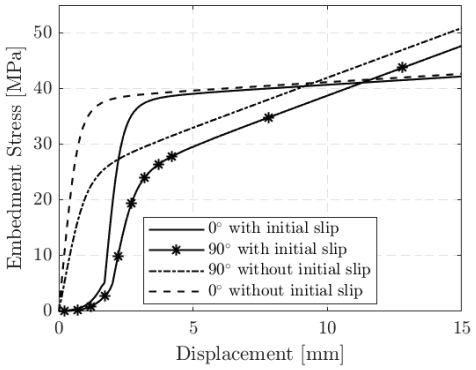

Figure 4: *Embedment stress-displacement curves of timber derived from embedment parameters using Equations (1) and (2).*

2.3.2 Concrete behaviour

The non-linear load-slip data for the interaction between the steel fastener and the concrete was determined as a multiple of the embedment parameters for the parallel loaded layer in the CLT. The values for $f_{h,inter}$ and $k_{f,el}$ were increased threefold, to account for the higher stiffness and compression strength of concrete, while for $k_{f,pl}$ the same values as for timber were used. Additionally, unlike the connectors between the steel fastener and the timber that were coupled, the connector elements parallel and perpendicular to the fastener's axis were uncoupled, since only small displacements were expected in the concrete, and thus, large displacement effects were neglected. In addition, connectors were only specified for the force resistance perpendicular to the fastener's axis, neglecting any possible axial resistance. Equations (1) and (2) were used to determine the stress-displacement curve for these non-linear spring connector elements. Subsequently, Equation (3) was used to determine the corresponding force-displacement data applied in the model.

2.3.3 Steel fastener

For the yield strength, the nominal values for steel quality 8.8 were increased by about 25%, since frequently higher yield and ultimate strength as compared to declared values were observed in connection tests. The remaining material properties of the threaded rod used in the BoF models presented herein were based on the properties of a dowel applied in [22]. Figure 5 shows the stress-strain relationship used in the model. Based on this stress-strain data, moment-rotation (bending angle) curves for various threaded steel rod diameters were determined using a numerical model of a 3-point bending test setup. In this study, consideration was made for both the major and minor diameter. The major diameter includes the depth of the thread while the minor diameter excludes the depth of the thread and thus is the diameter of the shank of the rod. The yield moment, $M_{y,R}$, was determined for a specific bending angle according to EN 409 [23] and further used in the analytical formulas provided in Eurocode 5 to determine the shear capacity of the CLT-to-concrete connections. In cases where the BoF model simulates threaded fasteners, the diameter of the threaded rod in the bending behaviour is specified as the minor diameter.

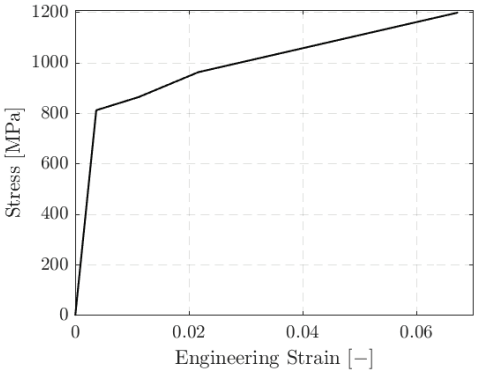

Figure 5: *Elasto-plastic response of the threaded steel rod.*

2.3.4 Evaluation of connection behaviour

After displacement-controlled loading at the reference node 2 in, shown in Figure 3**,** and the calculation of corresponding reaction forces at the support, the output from the BoF model is a force-displacement curve. The shear capacity and the slip modulus were determined according to EN 26891 [13]. Therefore, the shear capacity was defined as the maximum force up until 15 mm displacement. The slip modulus was determined as the gradient between the points at 10% and 40% of the shear capacity.

The results from the BoF model were compared to predictions of the European Yield Model (EYM) given by analytical formulas for the design of timber shear connections in Eurocode 5 (EC5) [11], for connections with a thick steel plate in steel-to-timber connections loaded in shear. This assumes a clamping of the fastener in the concrete (like in the steel) as compared to the considerably weaker behaviour of timber. EC5 determines the shear capacity, $F_{v,R}$, per shear plane for the

three failure modes associated with a thick steel plate for laterally loaded steel-to-timber connections as,

$$F_{v,R,mode1} = f_h t d_{major}, \quad (4a)$$

$$F_{v,R,mode2} = f_h t d_{major}\left(\sqrt{2+\frac{4M_{y,R}}{f_h t^2 d_{major}}}-1\right)+\frac{F_{ax,R}}{4}, \quad (4b)$$

$$F_{v,R,mode3} = 2.3\sqrt{2M_{y,R}f_h d_{major}}+\frac{F_{ax,R}}{4}, \quad (4c)$$

where, f_h is the embedment strength of timber or CLT in [MPa], $M_{y,R}$ is the yield moment of the fastener in [N mm], t is the thickness of the timber or CLT, d is the major diameter of the threaded rod in [mm] and $F_{ax,R}$ is the withdrawal capacity of the fastener. The contribution due to the rope effect, $F_{ax,R}/4$, representing the friction in the shear planes, was neglected as the friction in the shear plane was prevented in the experiments and BoF model. The yield moment, $M_{y,R}$, was determined at a particular angle of rotation, α, in [°] defined in EN 409 as,

$$\alpha = \alpha_1\left(\frac{2.78\cdot\rho}{f_t}\right)^{0.44}+\alpha_2, \quad (5)$$

where α_1 is the rotation angle in [°] dependent on the diameter of the dowel-type fastener, ρ is the density of the timber where the fastener is applied in [kg m^{-3}], f_t, is the tensile strength of the fastener in [MPa] and α_1 is 0° for dowels and bolts. In the standards, Equations (4) and (5) are based on characteristic values in a semi-probabilistic design concept. However, in this study mean values were applied to allow for a comparison with the experimental data and the BoF model predictions. The connection's serviceability slip modulus per shear plane, K_{ser} was determined as proposed in EC5 as,

$$K_{ser} = \frac{\rho_m^{1.5} d_{major}}{23} \quad (6)$$

where d_{major} is the major diameter of the threaded rod in [mm] and ρ_m is the mean density of wood in [kg m^{-3}]. EC5 proposes that for concrete (steel)-to-timber connections K_{ser} be multiplied by two as Equation (6) was derived for timber-to-timber connections.

3 RESULTS AND DISCUSSION

3.1 Model Validation

To validate the BoF model described in Section 2.3 it was used to predict the shear capacity and slip modulus of the experimentally investigated CLT-to-concrete shear connection detailed in Section 2.2. Symmetry and appropriate boundary conditions were used to create the BoF model, illustrated in Figure 3. A comparison of the shear capacity and slip modulus of the connection to i) the EYM and ii) the BoF model, was carried out. Figure 6 summarizes the results from the comparison also indicating the deformed shape of the fastener from the BoF simulations. The global force-displacement behaviour of the connection as predicted by the BoF model showed good agreement with the experimental results. Both the experiments and the BoF model illustrated ductile failure with substantial hardening past the yield point. Figure 6 shows the results from the BoF model, EYM and experiments. The slip modulus and shear capacity from the experiments and the BoF model were determined according to EN 26891 [13], as detailed in Section 2.3.4.

Meanwhile, for comparison to the EYM the embedment strength of CLT, f_h, was determined as the average embedment stress of the parallel and perpendicularly loaded layers (with initial slip from Figure 4) at 15 mm displacement, 44.8 MPa. The major diameter of the steel rod, 24 mm, was used to calculate the embedment force-displacement data of wood. Similarly, when determining the shear capacity according to the EYM, the major diameter was used. However, the minor diameter of the steel rod, 20.3 mm, was assumed to determine the moment resistance of the threaded steel rod, which yielded a plastic moment of $M_{y,R} = 1169$ kN mm. The contribution from the rope effect was neglected as the test set-up ensured no friction occurred between the concrete and CLT surfaces.

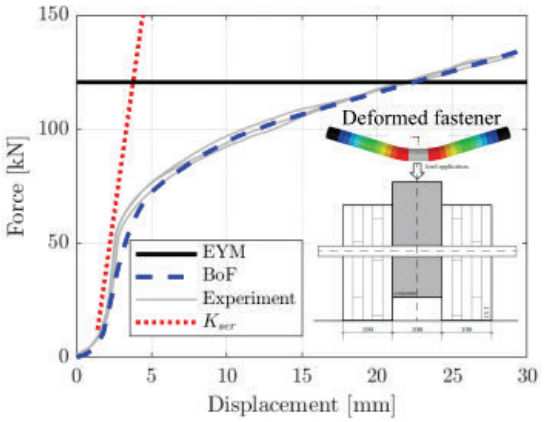

Figure 6: *Comparison of the global force-displacement results from the experiments to the BoF prediction and the EYM according to Eurocode 5.*

The results, summarised in Table 1, revealed that the EYM overestimated the shear capacity of the connection by 13%. On the contrary, the BoF model predicted the shear capacity rather accurately. The EYM assumes full utilization of the plastic moment of the fastener and ideal plastic behaviour of the wood embedment, which in the experiments and BoF model is not reached for all areas along the fastener. The BoF model underestimated the slip modulus by 20%. On the contrary, K_{ser} overestimated the slip modulus by 29%. The overestimation of K_{ser} is similar to what Dias et al. observed in [14]. The underestimation from the BoF model was attributed to the use of the minor diameter instead of the major or effective diameter of the threaded steel rod which results in a lower embedment stiffness and lower yield moment, $M_{y,R}$, of the threaded steel rod, and thus, lower shear capacity and slip modulus. The deformed shapes of the fastener from the BoF model and experiment agreed well with failure mode 2 from EYM, characterized by clamping of the fastener in the concrete with a deformation of the fastener in the CLT.

https://doi.org/10.52202/069179-0404

Table 1: *Comparison of BoF model and the EYM predictions to the experimental results of the CLT-to-concrete connection.*

Shear capacity [kN]			Slip Modulus [kNmm^{-1}]		
EYM	BoF	Experiment	K_{ser}	BoF	Experiment
120.6	106.5	107.2	45.7	28.4	35.5

3.2 Parameter study

A preliminary parameter study was carried out to investigate the influence of dowel diameter, initial slip, concrete stiffness, friction along the fastener, and axial resistance due to the washer on the global force-displacement response of the BoF model prediction discussed in Section 3.1. In this parameter study, only one parameter alteration was done per study, as compared to the reference connection. The results, shown in Figure 7, indicate that altering any of these five parameters resulted in a change in the global force-displacement response of the connection, thereby influencing the connection shear capacity and slip modulus.

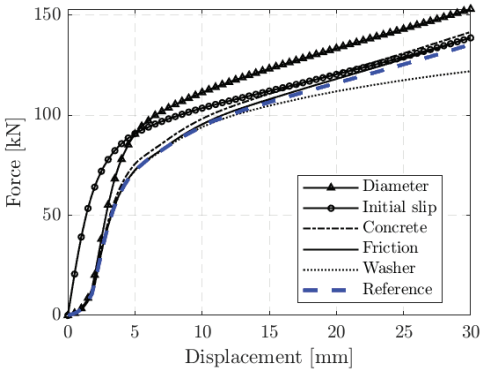

Figure 7: *Initial parameter study of various factors that influence the force-displacement behaviour of the CLT-to-concrete reference shear connections.*

The results from this preliminary parameter study are summarised in Table 2. The slip modulus and shear capacity of the connection were assessed according to EN 26891 [13]. This investigation revealed that assuming the major instead of the minor diameter of the rod yielded the highest increase in shear capacity of the reference connection by up to 16%. Additionally, neglecting initial slip, assuming stiffer and stronger concrete and a higher friction coefficient resulted in 5%, 4% and 1% increase in shear capacity, respectively. However, neglecting the washer yielded a reduction of the shear capacity by 2%. Moreover, the study of the aforementioned parameters shows that, neglecting the initial slip resulted in the highest increase in the slip modulus of 28%. Furthermore, assuming the major instead of the minor diameter, stiffer and stronger concrete and a higher coefficient of friction caused 18%, 6% and 1% increase in the slip modulus, respectively. Neglecting the washer had negligible influence on the slip modulus. However, upon further assessment it was evident that the influence of the washer and friction were more important for the behaviour beyond 15 mm displacement. Furthermore, the effect of the washer is overlaid with the effect of the friction along the fastener between fastener and CLT. A 1% increase in the force due to an increased friction coefficient was found at 9 mm displacement. The force further increased with increased fastener displacement, finally yielding 3% higher force than the reference connection at 30 mm displacement. Similarly, the influence of the withdrawal capacity due to the washer was observable beyond a displacement of 13 mm, where the force was 1% lower than in the reference connection. Increased displacement showed a marked increase of the influence of the washer. At a maximum displacement of 30 mm, neglecting the washer yielded a 10% lower force.

Table 2. *Influence of various parameters on the shear capacity and slip modulus of the reference connection.*

Parameter	Reference Value	New value	Shear capacity	Slip modulus
Diameter	20.3 mm	24 mm	+16%	+18%
Initial slip	2 mm	0 mm	+5%	+28%
Concrete	$3 \cdot f_{h,inter}$ $3 \cdot k_{f,el}$	$4 \cdot f_{h,inter}$ $4 \cdot k_{f,el}$	+4%	+6%
Friction	0.3	0.4	+1%	+1%
Washer	Included	Neglected	-2%	~0%

With these findings, an in-depth parameter study was done to look further into the influence of four out of the five aforementioned parameters. The influence of the washer capacity on the connection shear capacity is not presented since a similar behaviour as for the coefficient of friction was seen. As a reference, the connection illustrated in Figure 3 was used. Three important items should be noted to guide the discussion hereafter regarding the reference connection: i) embedment stress-displacement data was used without the initial slip, see Figure 4, ii) the washer was neglected, and iii) the threaded rod was modelled using the major diameter. All other properties of the BoF model, the elasto-plastic behaviour of the threaded rod and concrete embedment properties were used as specified in Section 2.

3.2.1 Diameter of threaded rod

The diameter of a fastener influences its mechanical properties as the moment resistance increases with increase in the diameter. Therefore, it follows that using the major diameter of the threaded rod will result in increased shear capacity and slip modulus. However, assuming the major diameter, d_{major}, implies that the shank of the threaded rod is larger. To investigate the influence of assuming the yield moment for the minor or major diameter, i.e., d_{minor} or d_{major} for modelling the threaded steel rod, several BoF models were created for various threaded steel rods major diameters, 10 mm $\leq d_{major} \leq$ 30 mm. The ratio of d_{minor} to d_{major} ranged between 0.88 and 0.83. For the BoF simulations, firstly, the threaded steel rod was modelled using d_{major}, like in the reference model, and secondly, variant models of the reference connection were created with the threaded steel rod modelled using the d_{minor}. For both models, the force-displacement data used for the wood in the CLT, determined according to Equation (5), was calculated using the d_{major}. Furthermore, the results were compared to the EYM. In the latter, the rope effect, representing the friction in the shear planes, was neglected as the friction

in the shear plane was prevented in the experiments and BoF model. The yield moment applied in the EYM was determined for the maximum bending angle, α, using i) d_{minor} and ii) d_{major} according to EN 409 [23].

The results showed that assuming the yield moment from d_{minor} resulted in reduced shear capacity and slip modulus for both the BoF model and the EYM, see Figure 8. This was attributed to the reduced mechanical properties of the fastener. A comparison between the BoF model predictions showed that assuming d_{minor} resulted in up to 21% reduction in shear capacity for the 10 mm threaded rod. The reduction in shear capacity was lower for larger diameters of the threaded rod. The BoF model for the 30 mm threaded rod showed 14% reduction in shear capacity.

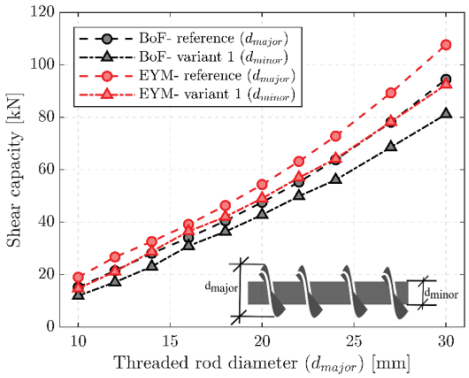

Figure 8: *Comparison of the BoF model and EYM predictions for shear capacity of a CLT-to-concrete connection, per shear plane, while using the minor and major diameter.*

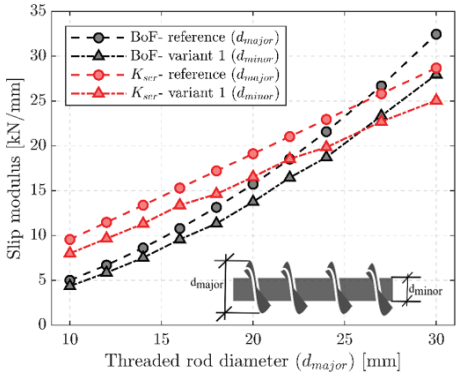

Figure 9: *Comparison of the BoF model and K_{ser} predictions for slip modulus of a CLT-to-concrete connection, per shear plane, while using the minor and major diameter.*

A comparison of the results from the BoF models to the EYM showed that shear capacity predicted from the EYM was on average 15% and 17% higher than the equivalent BoF model predictions utilizing the d_{major} and d_{minor}, respectively. The difference was highest at smaller diameters of the threaded rod with up to 20% and 19% higher shear capacity in the EYM than the BoF model with d_{major} and d_{minor}, respectively. The difference between EYM and BoF model could be because the EYM assumes full utilization of the plastic moment of the fastener and ideal plastic behaviour of the wood embedment, which in the BoF model is not reached for all areas along the fastener. Thus, the EYM will give an upper limit for the connection capacity if the input for the embedment strength is used as assumed in this study. An analysis of the connection's slip modulus showed that BoF models that utilized d_{major} yielded on average 13% higher slip modulus compared to equivalent BoF models that utilized d_{minor}, see Figure 9. The comparison between K_{ser} and BoF model predictions for connection slip modulus showed that K_{ser} yielded higher slip modulus. The difference was highest for small dowel diameters with up to 48% and 56% higher K_{ser} as compared to equivalent BoF models that utilized d_{major} and d_{minor}, respectively. The difference reduced with increased dowel diameter, with models utilizing threaded rod major diameters, d_{major}, ranging between, 24 mm < d_{major} < 26 mm, showing rather good agreement with K_{ser}. However, for threaded rods with diameters, d_{major} > 26 mm, K_{ser} yielded a lower slip modulus of the CLT-to-concrete connection as compared to the BoF model. These findings highlight the disadvantage of K_{ser} being defined independent of the connection failure mode, resulting in a substantial simplification for certain connection layouts.

3.2.2 Initial slip

Initial slip refers to the displacement that occurs between fastener and borehole before full contact is achieved with the surrounding timber matrix. This phenomenon leads to a reduced initial elastic foundation modulus, $k_{f,el}$, for the wood as detailed in Section 2.3.1. Therefore, this parameter study investigates the influence of the initial slip on the shear capacity and slip modulus of CLT-to-concrete connections. Several models of the CLT-to-concrete connection were created for various threaded rod diameters from 10 mm to 30 mm, using the BoF model with embedment stress-displacement data i), without initial slip (reference) and ii) with initial slip (Variant 1), illustrated in Figure 4. The results showed that BoF models of the reference CLT-to-concrete connection with initial slip yielded on average 4% lower shear capacity in comparison to equivalent BoF models without initial slip, see Figure 10. A similar difference was found for the EYM predictions. This was attributed to the reduced embedment strength for the models with the initial slip. Accounting for the initial slip leads to a shift of the embedment curve. Thus, same absolute displacement values give lower embedment stress for the models with initial slip, especially for embedment loading perpendicular to the grain, which shows an increase in embedment stress after yielding. This effect is reflected also in the embedment strength definition, where f_h was determined at 15 mm displacement according to EN 26891 [13]. The comparison of the BoF model with the EYM showed that the EYM yielded a higher connection shear capacity for both models, i.e. variant 1 and reference, on average 16% and 15%, respectively. The EYMs with smaller threaded rod diameters when compared to their equivalent BoF models showed up to 20% higher shear capacity. Similar to the previous study on the diameter of the threaded rod, the difference reduced with increased diameter. The effect of the initial slip on the connection slip modulus was similar to that on the shear capacity, as the initial slip resulted in a reduced slip

https://doi.org/10.52202/069179-0404

modulus, see Figure 11. In addition to an initial weaker overall response of the connection, the lower slip modulus is also given due to reduced shear capacity that determined the points at 10% and 40% of the shear capacity, between which the slip modulus was determined. The lower point at 10% of the shear capacity was found to be located in the initial softer part of the load-displacement curve, which resulted in a reduced slip modulus of the connection. Consideration of the initial slip caused on average 28% reduction in slip modulus. Moreover, an analysis of variant 1 BoF models, that considered initial slip, showed that K_{ser} prediction yielded a higher slip modulus of all variant 1 BoF models of the CLT-to-concrete connection for various threaded rod diameters. The results for the comparison of the reference BoF models and their equivalent EYMs is as detailed in Section 3.2.1.

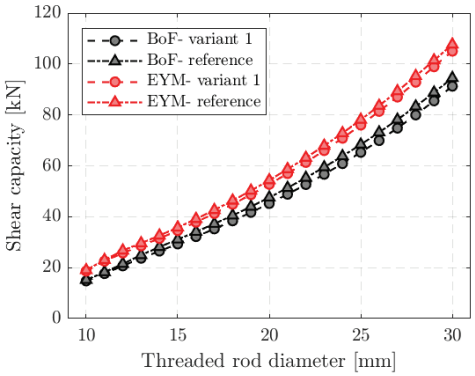

Figure 10: *Comparison of the BoF model and EYM predictions for shear capacity of a CLT-to-concrete connection, per shear plane, to investigate the influence of initial load slip.*

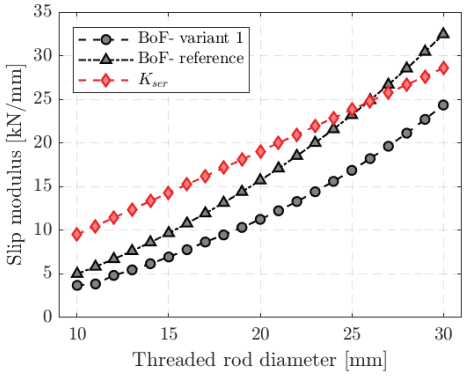

Figure 11: *Comparison of the BoF model and K_{ser} predictions for slip modulus of a CLT-to-concrete connection, per shear plane, to investigate the influence of initial load slip.*

3.2.3 Embedment stiffness and strength of concrete

The stiffness and strength parameters used to determine the load-displacement data for the interaction between the threaded steel rod and the concrete, detailed in Section 2.3.2, were based on the wood properties parallel to the grain and multiplied by a factor of 2 (BoF model variant 1), factor of 3 (reference BoF model) and factor of 4 (BoF model variant 2). The results from this study showed that there was on average 3% increase in shear capacity of the reference connection when the strength and stiffness of the concrete was increased, see Figure 12. Conversely, the shear capacity decreased on average by 6%, with decrease in the concrete strength and stiffness. This difference in the shear capacity due to altering the concrete strength and stiffness was most pronounced for BoF models with diameters less than 13 mm. A comparison of the BoF models with the EYM showed that the EYM yielded a higher shear capacity of 19%, 15% and 12%, than for variant 1, reference connection and variant 2 BoF models, respectively.

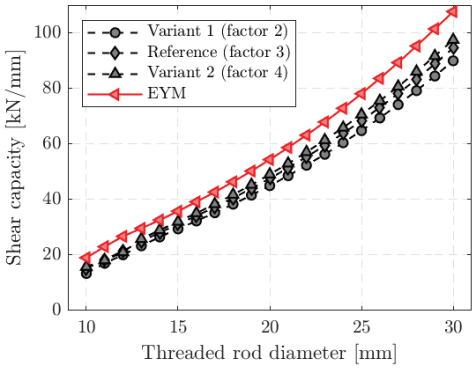

Figure 12: *Comparison of the BoF model and EYM predictions for shear capacity of a CLT-to-concrete connection, per shear plane, to investigate the influence of concrete stiffness and strength.*

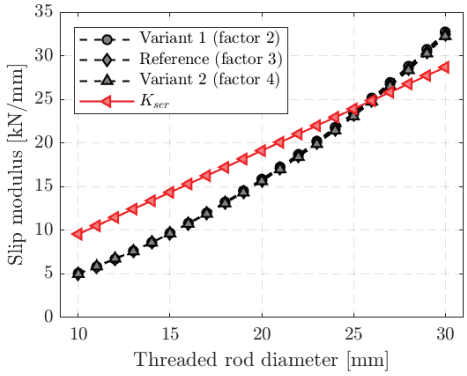

Figure 13: *Comparison of the BoF model and K_{ser} predictions for slip modulus of a CLT-to-concrete connection, per shear plane, to investigate the influence of concrete stiffness and strength.*

The reduction in the difference in the shear capacity between the EYM and the BoF models with increase in concrete strength and stiffness was attributed to increased bending deformation of the fastener within the CLT due to increased clamping. The EYM highlights that the shear capacity is directly linked with the corresponding failure modes [11]. If the side member thickness, in this case concrete, is larger than that of the diameter, failure mode 2 characterized by development of a single plastic hinge in the side member is observed according to the EYM. Therefore, Equation 4(b) was used to determine the shear capacity of the connection. The yield moment associated with this connection was determined for a certain bending angle, α, according to EN 409 [23]. Increasing the concrete stiffness and strength increased the clamping of

the fastener within the concrete whilst increasing the rotation of the fastener in the CLT. Increased fastener rotation led to activation of more spring connector elements in the CLT, and in addition to a larger resistance per spring, due to the larger spring connector displacements, hence increasing the shear capacity. Contrary to the findings on shear capacity, increasing the strength and stiffness of concrete had negligible effect on the slip modulus of the connection, see Figure 13. A comparison of the results from BoF models, variant 1 and variant 2, to equivalent BoF models of the reference connection for varying diameters, showed less than 1% difference. Similar to previous studies, K_{ser} yielded higher slip modulus for most of the BoF models considered. The results were similar to the comparison of reference BoF model to equivalent EYM detailed in Section 3.2.1.

3.2.4 Friction

The influence of friction between the rod and the wood on the shear capacity and slip modulus of CLT-to-concrete connections was investigated for various diameters of the threaded rod. The friction coefficient, μ. was altered, such that for each threaded steel rod considered for this study, two variants of the reference BoF model (μ=0.3), were created. BoF model variant 1 assumed μ=0 and BoF model variant 2 assumed μ=0.6.

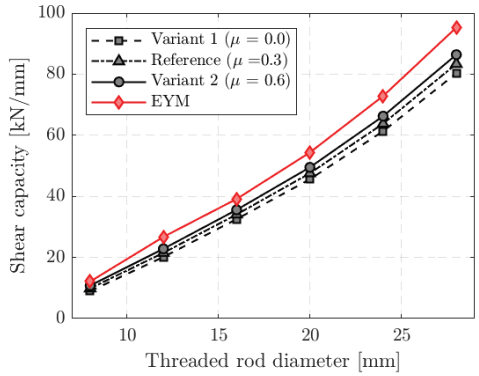

Figure 14: *Comparison of the BoF model and EYM predictions for shear capacity of a CLT-to-concrete connection, per shear plane, to investigate the influence of friction.*

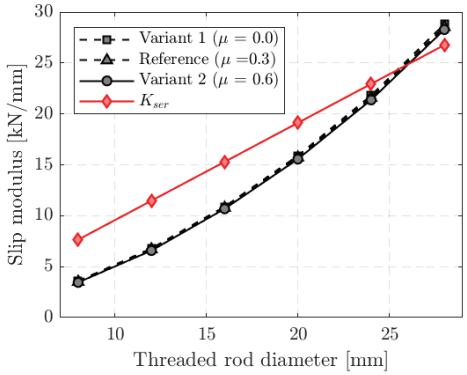

Figure 15: *Comparison of the BoF model and K_{ser} predictions for slip modulus of a CLT-to-concrete connection, per shear plane, to investigate the influence of friction.*

A comparison of the reference BoF model with variant 1 and 2 was carried out. The results showed that increasing the friction coefficient in BoF model variant 2 led to a subsequent increase in the shear capacity. On average, this increase was 5%, with higher relative increase for smaller threaded rod diameters, see Figure 14. Similarly, assuming no friction, i.e., μ=0 in BoF model variant 1 led to a 5% reduction in shear capacity when compared to the reference model. As discussed for the preliminary parameter study in Section 3.2, a considerable large connection displacement is needed to cause a substantial inclination of the fastener, to take an effect of the axial force component caused by friction on the connection shear resistance. The EYM prediction was not influenced by a change in the friction coefficient. On average, the EYM recorded, 18%, 13% and 9% higher shear capacity than BoF model variant 1, reference BoF model and BoF model variant 2, respectively. Similar to the findings in the parameter study on the influence of concrete stiffness and strength, in Section 3.2.3, there was negligible influence of the friction coefficient on the slip modulus of the connection, see Figure 15. These findings are similar to results from a parameter study on the influence of the axial fastener behaviour on the shear capacity of steel-to-timber connections in [19].

4 CONCLUSIONS

The beam-on-foundation (BoF) method was applied herein to predict the shear capacity and slip modulus of CLT-to-concrete connections. The parameter study rests on a validation of the BoF model with experiments on a CLT-to-concrete connection with a single threaded rod. Results indicated validity of the BoF model for this application by a good agreement of the nonlinear load-displacement behaviour, and thus of the shear capacity and slip modulus, between simulations and experiments. From the comprehensive parameter study, it can be concluded that:

- Shear capacity and slip modulus are substantially influenced by the choice of either using the minor or major diameter of the threaded rod for BoF simulations and EYM predictions.
- Consideration of the initial slip in the BoF model results in reduced shear capacity and slip modulus of CLT-to-concrete connections, determined according to EN 26891.
- Varying the friction coefficient between rod and wood between 0-0.6 and varying the embedment properties of concrete had negligible influence on the slip modulus, and only a minor influence on the shear capacity of the investigated CLT-to-concrete connections.
- K_{ser} proposed in EC5 was found to give simplified slip modulus predictions for CLT-to-concrete connections, since the influences of parameters like e.g. the fastener slenderness, are not considered in the design equation, but their impact was shown by the BoF model.

The BoF model was found to be useful in determining both the slip modulus and shear capacity of the connection. Application of the model in engineering

https://doi.org/10.52202/069179-0404

design can lead to more reliable and economic connections in CLT-to concrete composite slabs.

5 ACKNOWLEDGEMENT

The authors would like to acknowledge the support from the Knowledge Foundation through the project 'Improving the competitive advantage of CLT-based building systems through engineering design and reduced carbon footprint' (project number 20190026).

6 References

[1] A. Siddika, M. A. A. Mamun, F. Aslani and Y. Zhuge, "Cross-laminated timber–concrete composite structural floor system: A state-of-the-art review," *Engineering Failure Analysis,* vol. 130, 2021.

[2] A. Ceccotti, "Composite concrete-timber structures," *Progress in Structural Engineering and Materials,* vol. 4, no. 3, pp. 264-275, 2002.

[3] K. Quang Mai, A. Park, K. T. Nguyen and K. Lee, "Full-scale static and dynamic experiments of hybrid CLT–concrete composite floor," *Construction and Building Materials,* vol. 170, pp. 55-65, 2018.

[4] K. Mai, A. Park and K. Lee, "Experimental and numerical performance of shear connections in CLT–concrete composite floor," *Materials and Structures,* vol. 51, 2018.

[5] V. Bajzecerová, J. Kanócz, M. Rovňák and Maroš Kováč, "Prestressed CLT-concrete composite panels with adhesive shear connection," *Journal of Building Engineering,* vol. 56, 2022.

[6] A. Samuel C., S. Luca and S. Alexander, "A new composite connector for timber-concrete composite structures," *Construction and Building Materials,* vol. 112, pp. 84-92, 2016.

[7] Y. Jiang and R. Crocetti, "CLT-concrete composite floors with notched shear connectors," *Construction and Building Materials,* vol. 195, pp. 127-139, 2019.

[8] D. Alfredo M.P.G. and J. Luís F.C., "The effect of ductile connectors on the behaviour of timber–concrete composite beams," *Engineering Structures,* vol. 33, no. 11, pp. 3033-3042, 2011.

[9] A. M. P. G. Dias, S. M. R. Lopes, J. W. G. V. d. Kuilen and a. H. M. P. Cruz, "Load-Carrying Capacity of Timber–Concrete Joints with Dowel-Type Fasteners," *Journal of Structural Engineering,* vol. 133, no. 5, pp. 720-727, 2007.

[10] J. Ehlbeck and H. Larsen, "Eurocode 5 - Design of timber structures: Joints," in *International Workshop on Wood Connectors*, 1993.

[11] EN 1995-1-1, Design of timber structures—Part 1-1: General—Common rules and rules for builidngs., Brussels: (CEN), European Committee for Standardization, 2011.

[12] A. Dias, H. Cruz, S. Lopes and J. van de Kuilen, "Stiffness of dowel-type fasteners in timber-concrete joints," *Proceedings of the Institution of Civil Engineers - Structures and Buildings,* vol. 163, no. 4, pp. 257-266, 2010.

[13] EN 26 891: 1991 Timber structures - Joints made with mechanical fasteners - General principles for the determination of strength and deformation characteristics, Brussels: (CEN), European Committee for Standardization, 1991.

[14] A. M. P. G. Dias, Mechanical behaviour of timber-concrete joints, (doctoral thesis), Delft University of Technology, 2005.

[15] J. Cao, H. Xiong, Z. Wang, Chen and Jiawei, "Mechanical characteristics and analytical model of CLT-concrete composite connections under monotonic loading," *Construction and Building Materials,* vol. 335, 2022.

[16] J. Luis Filipe Carvalho, S. M. Rodrigues, Lopes and C. and Helena Maria Pires, "Interlayer Influence on Timber-LWAC Composite Structures with Screw Connections," *Journal of structural engineering,* vol. 137, no. 5, 2011.

[17] EN 338:2016 Structural timber – Strength classes, Brusssels: (CEN), European Committee for Standardization, 2016.

[18] R. Lemaitre, J. Bocquet, M. Schweigler and T. Bader, "Beam-on-foundation modelling as an alternative design method for timber joints with dowel-type fasteners: Part 1: Strength and stiffness per shear plane of single-fastener joints.," in *International Network on Timber Engineering Research (INTER) , Meeting 51*, Talllinn, Estonia, 2018.

[19] M. Schweigler, M. Vedovelli, R. Lemaître, J.-F. Bocquet, C. Sandhaas and T. K. Bader, "Beam-on-Foundation Modeling as an Alternative Design Method for Timber Joints with Dowel-Type Fasteners –Part 3: Second Order Theory Effects for Considering the Rope Effect," in *International Network on Timber Engineering Research*, 2021.

[20] R. M. Richard and B. J. Abbott, "Versatile Elastic-Plastic Stress-Strain Formula," *Journal of the Engineering Mechanics Division,* vol. 101, 1975.

[21] M. Schweigler, T. K. Bader, J.-F. Bocquet, R. Lemaître and C. Sandhaas, "Embedment test analysis and data in the context of phenomenological modeling for dowelled timber joint design," in *International Network on Timber Engineering Research*, Tacoma, WA, USA, 2019.

[22] ADIVbois, "Technical report – experimental characterization of connection stiffness (in French, not published yet)".

[23] EN 409 Timber Structures - Test methods - Deyermination of the yield moment of dowel type fasteners, Brussels: (CEN), European Committee for Standardization, 2009.

World Conference on Timber Engineering Oslo 2023

EXPERIMENTAL AND NUMERICAL STUDY OF MOULDED WOOD TECHNOLOGY WITH FIBRE-PLASTIC COMPOSITE NODE ELEMENTS

Siavash Namari[1], Peer Haller[1]

ABSTRACT: The reduction of CO2 emissions and the enhancement of resource efficiency have emerged as significant motivators for research and development activities. One particular area of interest in sustainable building materials is moulded wood tubes, which offer the benefits of wood as a renewable resource and the material efficiency of composite construction. These tubes are well-suited for lightweight structures that are subject to dynamic and static loading. This paper proposes a method for joining thin-walled wooden elements with node elements composed of fibre-reinforced plastic (FRP) that incorporates integrally manufactured multilayer 3D fabrics that are adaptable to the component geometry. The investigation includes both experimental and numerical approaches to establish the load-bearing capacity of such connections. Experimental tests were conducted on specimens of different sizes under tension, while numerical models were developed to assess the load-bearing behaviour of small and large scale tests, as well as perform static verifications. The proposed solution has potential applications in the fabrication of a solar roof demonstrator. The results suggest that the use of FRP for connecting moulded wood tubes is a viable approach.

KEYWORDS: Connections, Composite structure, Moulded wood, Compressed wood, Fibre-reinforced plastics (FRP)

1 INTRODUCTION

The Federal Republic of Germany's industrial policy goals of reducing CO2 emissions and enhancing resource efficiency have served as a catalyst for research and development efforts. These endeavours necessitate the utilization of sophisticated and expensive tools, but the structural mechanical performance remains suboptimal [1].

Besides the use of sustainable building material such as wood, the use of high-performance composite materials instead of traditional metallic construction materials is an efficient way of improving material and energy efficiency while decreasing carbon dioxide consumption. The potential of moulded wood technology in combination with fibre composite materials is particularly relevant in spatial structures which static systems primarily transmit normal forces. Recent studies have shown that the cellular structure of wood can be compressed under the influence of moisture and heat due to its thermo-hydro-mechanical properties [2]. This process is used by researchers to create moulded wooden construction elements formed from thin compressed wood panels, with a tubular cross-section being the simplest form. A tubular cross-section represents the simplest form, combining high structural strength for compression with very low material consumption [3]. Compared to massive solid wood cross-sections typically used in timber construction, moulded wooden tubes combine high structural strength for compression with very low material consumption, enabling a weight-efficient application of the material and saving up to 70% of the raw material [4]. Moulded wooden tubes can be reinforced with high-performance fibres such as carbon or glass to create resource-efficient, high-performance composite wood components [5]. The positive properties of wooden tubes are especially useful in three-dimensional load-bearing structures, where compressive forces predominate due to the static system. These tubes have been used as rod-shaped construction elements in truss or lattice structures, including a 30m high truss structure built as a support for a 10kW wind power plant (see Figure 1) [6], [7].

Figure 1: *Left: Moulded wooden tubes with reinforcements using glass, carbon or aramid fibres, Right: Wind power plant made of moulded wood tubes and steel connecting elements*

Previously, steel joining solutions for construction required heavy castings or expensive, multi-step sheet metal forming. However, this project aims to develop a more efficient manufacturing and assembly process for lightweight timber construction systems. The paper will use moulded wood tubes and fibre-reinforced plastic composite as connection means, which are made of multilayer 3D fabrics. The adhesive connection of the node elements with the shaped wood profiles offers

[1] Siavash Namari, Peer Haller, Technische Universität Dresden (TU Dresden), Institute of Steel and Timber Construction, siavash.namari@tu-dresden.de

https://doi.org/10.52202/069179-0405

constructive advantages compared to mechanical fasteners, which imply a weakening of the cross-section. The combination of moulded wood and fibre-reinforced plastic enables versatile modular construction solutions that meet architectural and structural requirements. This innovative approach aims to remove the significant barriers to sustainable, lighter and architecturally diverse construction methods. After completion, a solar roof will be built as a technology demonstrator. The demonstrator will be characterized by high prefabrication, low dead weight with high load-bearing capacity and material efficiency. The construction should also be able to be implemented in a short assembly time. The final design is a pavilion with a roof made of solar modules that functions as a solar charging station, supported by two moulded wood elements (Figure 2).

Figure 2: *Design of the technology demonstrator*

Tensile testing has been performed on test specimens with varying geometries based on a design featuring 33, 25 and 17 cm long glass fibre-reinforced plastic (GRP) slats. These tests will be modelled using finite element method (FEM) software and compared against the test results. Subsequently, the demonstrator will be modelled in FEM software to showcase the performance of the lightweight wood support system. The load-bearing behaviour of the developed modules will be evaluated under site-typical load scenarios, providing valuable insights into their practical application. Any necessary design optimizations will be identified and incorporated accordingly. Ultimately, a comprehensive recommendation for structural implementation in lightweight timber construction support systems will be presented.

2 MATERIAL

2.1 Thermo-Hydro-Mechanical Treatment

In mechanical wood technology, it is well known that low strength and durability can be improved by treatment with increased temperature and humidity. These processes are known as Thermo-Hydro-Mechanical (THM) processes. Under THM conditions, the amorphous building blocks of the wood structure soften, which enables shaping, compression and bending. The viscoelastic behaviour of the wood is utilized, whereby at low temperatures and low moisture content, the wood behaves like glass, while at high temperatures and high moisture content, it shows entropy-elastic behaviour.

Thermo-hydro-mechanical compression can reduce the cavities in the wood cells, especially in hardwood. Theoretically, wood can be compressed in all directions (longitudinal, tangential, or radial), but compression in the radial direction is the most practical. Due to the porous cell structure, it is possible to contract the cell structure in the compression process with an appropriate process regime without causing microscopic damage to the cell structure. The process of compressing wood typically occurs in a hot press with a constant displacement rate at high temperatures ranging between 120 to 160 ◦C. If the press is opened immediately after the compression process, compressed wood (CW) may exhibit partial springback or return to its original shape. To counteract this, it is necessary to cool the CW specimens down to below 80 ◦C while in the compressed state. Post-treatment may be required subsequently to limit this effect and ensure dimensional stability. Recovery, a characteristic of CW whereby it achieves partial or complete recovery of its original dimensions when exposed to water or high humidity, is known as shape memory. In this project, to avoid CW springback, specimens were cooled to 40 ◦C after compression, thereby ensuring stable dimensions. The research results show that CW and CW connectors offer a significant increase in the strength and stiffness properties compared to normal softwood or hardwood [8].

2.2 Moulded Wood Production

Wood has numerous advantages as a building material, including its eco-friendly properties and environmental friendliness. While wood performs well in most areas, some materials may outperform it in terms of specific properties such as density and Young's modulus. To make the most of wood as a building material, it is crucial to consider both its advantages and disadvantages. For example, wood has lower strength, is anisotropic and is vulnerable to weathering [9]. To maximize wood's positive attributes, it is often used in combination with other materials such as steel, concrete, glass and textiles in sustainable construction methods. Softwood is the most commonly used type of wood in construction because of its straight, long trunks. The development of moulded wood technology also opens up new possibilities for using deciduous trees in construction, contributing to a more sustainable building industry.

In addition to mechanical properties, the structural and economic performance of a cross-section is also important. The sawmill, as the primary step in the value-added chain, plays a crucial role in the provision of full cross-sections from a grown tree. However, the process results in significant material losses and a lack of competitiveness, as only about 60% of the stem wood remains of value [10]. To improve efficiency, material savings must be made during cross-section formation. The yield of raw wood and waste significantly affect the price structure of wood products, favouring tree species with long and straight trunks, such as softwoods like spruce, over hardwoods with branched crowns like beech or oak. The manufacturing of rectangular cross-sections involves traditional machining methods, including sawing, milling,

planning and sanding with minimal energy and force, followed by joining with synthetic binding agents.
The use of round and rectangular solid cross-sections in wood-based materials is commonly accepted in the construction industry [9]. However, compared to other technical profiles made of metal or plastic, the full cross-sections created by traditional processing methods have a lower second-degree moment of Inertia. The compression process creates deformation reserves in the wood, which are later used for bending. With a suitable process regime, depending on temperature, humidity and compression speed, the compression process is reversible and fixable with almost no damage to the cell structure. The compression direction runs in the plane of the plate. In the subsequent moulding process for the production of thin-walled tubular cross-sections, the solid wood panel is shaped into profiles with the addition of heat and moisture and then fixed, as can be seen in Figure 3.

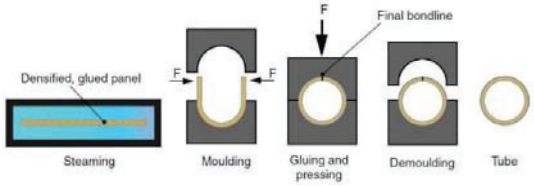

Figure 3: *Schematic production of a wooden tube by shaping* ***[11]***

The ability of cell walls to recall memory means that the folding is reversible and the radius of curvature of the moulded wood tubes depends on the intensity of the previous compression. All open and closed profile shapes with any length and thickness can be produced using this technique. The successful process for manufacturing moulded wood profiles is patented by the Technical University of Dresden. The numerous investigations and derived properties of the moulded wood profiles have shown decisive advantages, including a lower weight compared to the full cross-section, small shrinkage, the use of all types of wood, including deciduous wood of lower quality, low waste in the sawmill, forming instead of machining and the high synergy of the bond with fibres. Product-specific evaluations in comparison with sawn, glued and glued laminated timber have demonstrated the technology's biggest advantages.

2.3 Fibre-Plastic Composite Node Elements

As mentioned, this paper aim to develop new node elements for lightweight structural systems made of moulded wood elements. The aim is to ensure a correct and constructive connection between the moulded wood profiles to transfer stresses caused by load between them. The node elements will be produced from multi-layer fabric and resin systems. Previous material models will be used to calculate the material parameters and the appropriate polymeric resin of the matrix will be selected based on simulations.
The fibre-reinforced plastic node elements offer a multitude of advantages over existing metal connections. For successful use in lightweight support systems, the advantages must be put into practice. The decisive advantages are, among other things, the significantly reduced weight of a node element made of fibre plastic compared to steel alternatives and the resulting lower assembly effort due to the unnecessary use of heavy equipment. This results in the possibility of realizing new supporting structures. A symbolic node element is shown in Figure 4.

Figure 4: *Node element made of carbon fibre* ***[12]***

The connection of moulded wood profiles with fibre-plastic composite node elements is a relatively new field and as such, there is no established calculation method to evaluate the material behaviour of the structural adhesive connection. Therefore, previous material characteristics of glued wooden surfaces must be adapted to the structural adhesive connection. The load-bearing capacity of a structural adhesive connection primarily depends on the shear and transverse tensile stresses occurring in the adhesive surface.

3 EXPERIMENTAL PROGRAM

3.1 Material and methods

The aim of these tests was to use force-displacement diagrams to quantify the load-bearing behaviour and characterize the failure mechanisms. Proportionally reduced test specimens were produced for the uniaxial tensile test and three different test specimen series with different dimensions were produced. Spruce glued laminated timber compressed by around 25% was used as the material and five test specimens were produced per series.
The test specimens were designated according to the length of the lamination and the GRP lamellae. The designation of the test specimen of GRP-H33 shown in Figure 24.

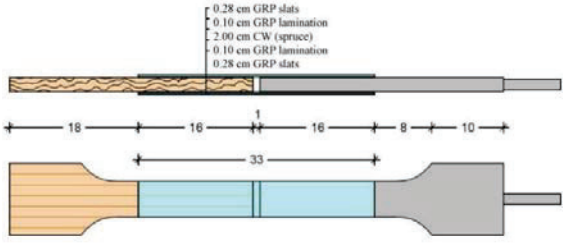

Figure 5: *Test specimen GRP_H33*

Tensile test specimens made of compressed spruce wood, fibreglass lamination, Plexus MA300 adhesive and two Glass Reinforced Plastic (GRP) lamellas. The test

https://doi.org/10.52202/069179-0405

specimens were assembled by sanding and applying a spacer and an adhesive layer, followed by the GRP lamella set. The elastic adhesive connection was used to absorb tensile shear loads that primarily occur in the tensile test. Three different test series with different dimensions were produced for the tensile tests. The results were evaluated based on the force-displacement diagrams.

Table 1 summarizes the properties of the materials used in the test specimens, including the density, tensile strength and Young's modulus of the compressed wood, glue and GRP.

Table 1: *Properties of the materials of the test specimens*

Characteristic		CW	Glue	GRP
density ρ	[g/cm³]	0.61	0.97	1.76
tensile strength R_m	[N/mm²]	55.9	20.7-27.6	319
Young's modulus E	[N/mm²]	15600	931-1137	20500

The tensile test was conducted at room temperature of 20°C and 65% relative humidity, in accordance with ISO 554:1976-07 and The test run corresponds to the loading procedure DIN EN 26891:1991-07. The test setup, involved hanging the test specimens in the testing machine with a steel connector. The ALMEMO 2890-9 precision measuring device and data logger, together with two displacement sensors, were used to measure the applied force and displacement.

3.2 Experimental setup and results

The samples showed a linear load-displacement behaviour until sudden and brittle failure of the fibre reinforcement and wood cross-section, with the specimens failing at an average load of 65 kN.

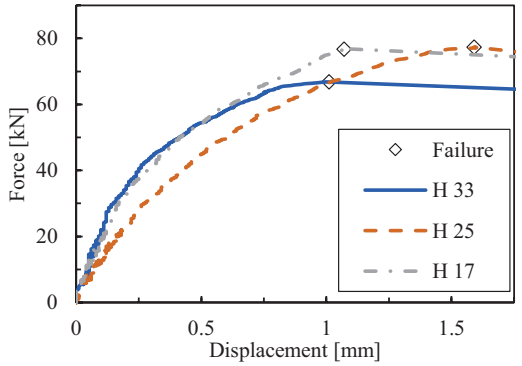

Figure 6: *Force-displacement diagram for the tensile test series*

Test series consists of three test bodies with GRP lamellae of different lengths, one for each previously described test body series. Table 9 summarizes all relevant properties of the test body series for the main conclusions, with values obtained from the mean values of all considered test specimens. The maximum load is greater for the test specimen series with a GRP lamella length of 25 cm, while the displacement is larger for the 33 cm specimens with wooden components. The steel component values have only marginal differences. The smallest displacements at the highest possible maximum loads are achieved for the test specimen series with a GRP lamella length of 17 cm. Although the maximum load and displacement are of secondary importance due to the different test specimen geometries, the expected maximum load of 55.9 kN is exceeded for all test specimen series with wooden components, indicating that the wooden body has a higher tensile strength in the composite.

Table 2: *Maximum loads, displacements of the test series*

Test specimen	H 33	H 25	H 17
F_{max} [kN]	64.79	77.48	73.79
u_{max} [mm]	1.24	1.45	1.05
k_s [kN/mm]	85.50	78.44	99.60

The displacement modulus, denoted as K_s, is a measure of the stiffness of a timber connection and is used to assess its load-bearing capacity and serviceability. It represents the force required to produce a displacement of 1 mm. The DIN EN 26891:1991-07 test procedure is used to determine the displacement modulus for mechanical fasteners. However, since there is no standard for adhesive connections in Euro code 5, this procedure is also used to evaluate the stiffness values of adhesive wood connections, enabling comparison of the test specimens' stiffness values. For mechanical fasteners, the displacement modulus is determined by the load application, structural conditions, connection type, load-bearing capacity and accuracy of fit, characterizing the displacement of the fastener. However, for adhesive connections, determining the displacement modulus is more challenging as it depends on the displacement of the entire adhesive surface and, therefore, the test specimen. The force-displacement relationship is used to derive the stiffness of adhesive connections.

Four different failure modes were identified, with the failure of the lamination being the most critical. For the failure of the lamination, two different failure modes were observed: either the lamination detaches from the wood surface or the wood-side lamination detaches from the adhesive bond but remains attached to the wood surface. The exact differentiation between these two possibilities is not possible due to the overall failure of the lamination. Another type of failure is the breakage of the GRP lamella, which mainly occurs at the connection to the steel member and occurs both vertically and horizontally. The failure of the splice and the fracture of the wooden body are also observed. The irregular fractures of the wooden specimens can be due to irregularities in the wood or knots. Figure 7 shows an example of the failure mechanism of the tensile test.

https://doi.org/10.52202/069179-0405

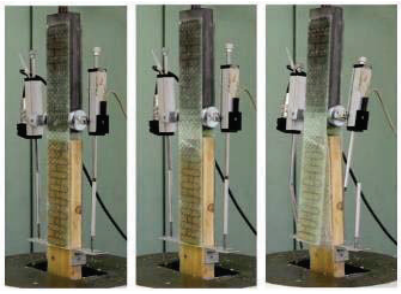

***Figure 7:**, An example of failure mechanism of tensile test*

The lamination failure is evident in almost every test specimen and can be identified as a critical failure. In the test specimen series H33, the failure of the GRP lamella is also identified for all test specimens. There are occasional breaks in the wooden body across all series, but failure mode (d) is not decisive.

For all test specimens of the series with steel components, the breakage of the GRP lamellae is recognizable as the decisive failure. The failure of the adhesive connection only occurs once and can be explained by the insufficient processing of the adhesive and the resulting weak points.

In summary, while the lack of video recordings makes it difficult to fully understand the failures, the images of the test specimens allow for the assessment of the relevant failure mechanisms. The failure of the lamination and the breakage of the GRP lamellae are identified as the critical failures.

4 NUMERICAL MODEL

The modelling of wood is a complex and challenging task due to the many structural parameters and the variable environmental conditions that influence the mechanical properties of the material. Moisture, in particular, has a significant impact on the mechanical behaviour, along with the type of load, duration and temperature. Natural features such as density, knots, aging and orthotropic also affect the material properties.

For Finite Element Method (FEM) models, no universal model exists that can fully and precisely describe the constitutive relationships of wood. Different models and approaches are used, depending on the type of problem to be solved. Fracture mechanics approaches are used for brittle problems, while a combination of the classical flow theory of plasticity with a criterion according to Hill, Hoffman, or Tsai-Wu is used for ductile problems. Physical, mathematical-static and hybrid model approaches can also be used and simplifications related to damage and failure may be applied to ensure reliability.

This article focuses on a mathematical-static model, which has a high degree of reliability but limited scope. The material properties used in the model are selected based on the load and are divided into the elastic range, the transition from elastic to plastic with the associated yield condition and the plastic range with the hardening law. According to the theory of material behaviour modelling, there are four essential building blocks for creating a reliable model. These include a valid material model, loading condition, a hardening law and reliable material data [13], However, modelling materials realistically can be challenging due to various factors. For instance, the yield surface only describes the moment when failure occurred but not the type of failure.

Despite these difficulties, the approaches described serve as a simplified assumption for understanding the material behaviour and subsequent finite element (FE) modelling. Modelling wood as a material is a complex subject influenced by various factors such as moisture, viscoelasticity and so on in addition to elastic and plastic deformation [13]. The ANSYS software, which is a finite element software used to solve linear and nonlinear problems in structural mechanics, is employed to model tensile tests and later the demonstrator. The simulation process used an extensive trial-and-error method until the simulation results matched the experimentally performed tensile tests.

4.1 Material Parameters

The materials of the components and their properties are defined in the technical data. The material properties of the GRP slats are taken from the material data sheet provided. The density, modulus of elasticity and maximum tensile strength are given and a bilinear isotropic hardening model is selected. The yield point and tangent modulus are required to characterize the bilinear isotropic hardening, but there is no data for either property, so assumptions were made and continuously improved during the simulation process. The values summarized in Table 10 are assumed as material properties.

***Table 3:** Material properties of the GRP slats*

Characteristic	Value	Unit
density ρ	1760	kg/m²
Young's modulus E	20500	MPa
Poisson's ratio v	0.18	-
bulk modulus K	10677.08	MPa
shear modulus G	8686.44	MPa
Stretch limit R_p	75	MPa
tangent modulus E_T	8000	MPa
Max Tensile Strength R_m	319	MPa

Similar to the GRP slats, the lamination of wood is made up of a fibre material and resin. The material properties are summarized in Table 4

***Table 4:** Material property of the lamination of the wood*

Characteristic	Value	Unit
density ρ	1760	kg/m²
Young's modulus E	18000	MPa
Poisson's ratio v	0.18	-
bulk modulus K	9375	MPa
shear modulus G	7627.12	MPa
Stretch limit R_p	65	MPa
tangent modulus E_T	5000	MPa
Max Tensile Strength R_m	250	MPa

https://doi.org/10.52202/069179-0405

The wood component of the test specimen consists of compressed spruce wood with a degree of compressionV of about 25%. Due to the orthotropic, the orthotropic elasticity is used with three Young's modules, Poisson's ratios and shear moduli. The same values are used for the values in the tangential and radial directions, as these differ only minimally in the specified directions and only the properties perpendicular to the fibre were determined in the tests.

Table 5: *Material properties of the compressed wood (V = 25%) (Sources:* ***[8]****;* ***[14]****;* ***[15]****)*

Characteristic	Value	Unit	Ref.
density ρ	610	kg/m²	[8]
Young's mod. Long. E_L	770	MPa	[8]
Mod. elasticity radial E_R	770	MPa	[8]
Mod. elasticity tang. E_T	15600	MPa	[8]
Poisson's ratio ν_{RT}	0.43	-	[14]
Poisson's ratio ν_{TL}	0.025	-	[14]
Poisson's ratio ν_{RL}	0.04	-	[14]
shear modulus G_{RT}	50	MPa	[15]
shear modulus G_{LR}	840	MPa	[8]
shear modulus G_{LT}	840	MPa	[8]
compressive strength $f_{c,L}$	66.7	MPa	[8]
compressive strength $f_{c,R}$	7.5	MPa	[8]
compressive strength $f_{c,T}$	7.5	MPa	[8]
tensile strength $tf_{t,L}$	55.9	MPa	[8]
tensile strength $tf_{t,R}$	0.5	MPa	[8]
tensile strength $tf_{t,T}$	0.5	MPa	[8]
shear strength τ_{LT}	8.8	MPa	[8]
shear strength τ_{RT}	8.8	MPa	[8]
shear strength τ_{LR}	8.8	MPa	[8]
Stretch limit R_p	55.9	MPa	-
yield stress ratioR_{11}	1	-	-
yield stress ratioR_{22}	0.11	-	-
yield stress ratioR_{33}	0.11	-	-
yield stress ratioR_{12}	0.23	-	-
yield stress ratioR_{13}	0.23	-	-
yield stress ratioR_{23}	0.23	-	-

In the model used here, the mesh for all 8 components of the test specimen consists of tetrahedrons, as this was the only way to find a solution due to the geometry of the shoulder stick shape used and the size of the mesh.. Overall, the geometry shown in Figure 8 is meshed with 8938 elements and 20657 nodes.

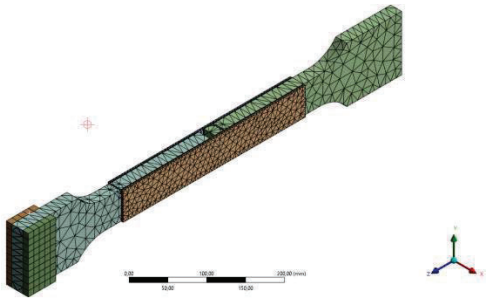

Figure 8: *Meshed geometry of the tensile sample*

4.2 Comparison of the numerical and experimental results

With the described material and simulation parameters, as well as mesh refinement, the force-displacement diagram shown in Figure 9 was obtained. This diagram shows all curves of the tests and the ANSYS model. The model curve is almost identical to that of the tests.

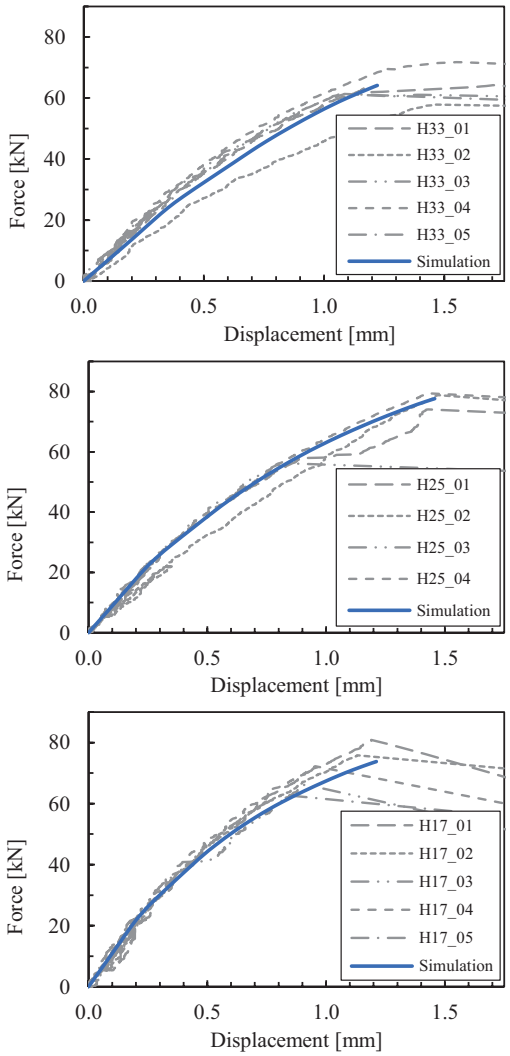

Figure 9: *Comparison of the force-displacement diagrams of test specimen with the numerical model*

For the model of the test specimen with a GRP length of 33 cm, the yield strength of the of the wood was set at 66 MPa based on the test data. To evaluate the model further, the displacement modulus of the tests is compared with that of the model. The displacement modulus is evaluated similarly to the calculation of the displacement modulus of the tests. For a direct comparison, the displacement modulus is evaluated analogously to the expected maximum load of 55.9 kN of the tests.

Figure 10 shows the maximum main stresses of the entire component. The principal normal stress hypothesis is used to predict the failure of brittle materials without yielding.

https://doi.org/10.52202/069179-0405

Positive values indicate tensile stresses and negative values indicate compressive stresses. The highest tensile stress is 305.01 MPa and the highest compressive stress is 59.64 MPa. The exact locations of the maximum stresses are evaluated separately and the GRP lamellae in the transition area from wood to steel components have the highest stress values on the surface.

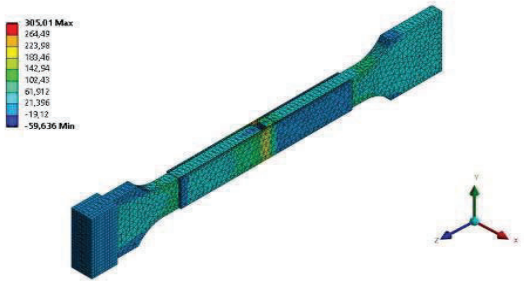

Figure 10: *Maximum principal stresses (MPa) of the entire component H33*

Figure 11 shows the maximum principal stresses of the wood components, which are analysed separately as the weakest part of the composite. Due to the lack of damage in the model, the tensile stresses in the model are compared with the maximum tensile strength or yield point.

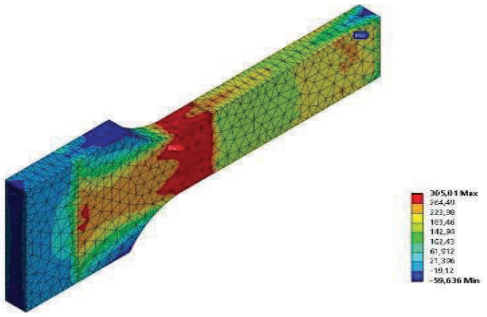

Figure 11*: Maximum principal stresses (MPa) of the timber member H33*

In the positive Z-direction, the maximum stresses over the entire cross-section develop into two stress peaks, which are illustrated in Figure 12. The crack of test specimen 02 of the test specimen series H33 is shown. It is located exactly where the curve of the shoulder stick shape begins and coincides with the edge of the red area of the stress distribution. The maximum tensile stress within the wood component is 66.4 MPa, which exceeds the material's specified yield strength of 66 MPa, causing the wood component to fail.

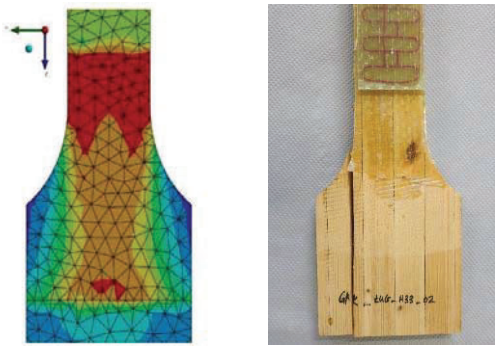

Figure 12: *(left) Stress distribution of the wood on the shoulder stick shape H33, (right) Fracture of the wooden body of the test specimen H33*

Figure 13 (left) shows the stresses curve in the horizontal direction, while Figure 13 (right) shows it in the vertical direction, with the cutting plane at the level of the maximum value. The greatest tensile stress was found to be within the steel component at the edge of the lamination layer.
However, the theory of maximum principal stress only applies to brittle materials and the steel component is the only component exhibiting ductile material behaviour. Therefore, the values of the maximum tensile stresses on the steel component must be interpreted with caution. Furthermore, the stress must be treated with care due to the high stress gradient in the direction of the negative X-axis.

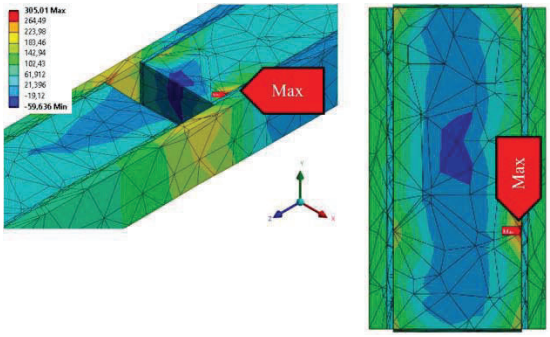

Figure 13: *(left) Stresses in the horizontal section plane H33, (right) Stresses in the vertical section plane H33*

Comparing the stress distribution of the maximum tensile stresses in the wood component and the adjacent slats provides insight into an optimal GRP slat length. The lamellas in the three models show the highest tensile stresses, with decreasing lamella length resulting in an increase in stress despite lower maximum loads. The stress distribution in the wooden component is similar in all models, with stresses increasing from the middle of the test specimen to the end of the GRP lamella.

5 Model of the Demonstrator

The demonstrator will consist of circular-shaped wood profiles and fibre-reinforced plastic node elements. The purpose of this modelling is to evaluate the performance

https://doi.org/10.52202/069179-0405

of the fibre-reinforced load-bearing systems made of wood.

The purpose of the demonstrator is to showcase the aesthetics and performance of moulded wood profiles reinforced with fibre-reinforced plastic node elements, while also serving a practical function. As a result, the building must meet certain construction requirements. To meet these requirements, a pavilion was built with a high enough roof to allow for space underneath and with solar modules as the roof to allow for the generation of solar energy. This energy could then be used to power a charging station for electric bicycles or scooters while also protecting them from the weather.

The pavilion was designed with a bar structure supported by two moulded wood supports that are 3 meters apart, with the node profiles fixed symmetrically to the supports for both sides. The roof was initially planned as an inward sloping barrel roof with innovative curved solar modules, but due to issues with module procurement and unpredictability, the roof shape was changed to a straight through roof. The roof has a surface area of 4.95 meters in length and 3 meters in width, with a one-sided inclination of 3° to ensure water drainage. The solar modules are attached to the edge and centre rails using different aluminium profiles, which are then connected to the moulded wood profiles via steel plates negligible.

The moulded wood supports have a circular ring cross-section with an outer diameter of 23 cm and a wood thickness of 2 cm. The branches connected to the supports have the same dimensions for both supports, with the lower branch connecting to the support at an angle of 55° and a maximum length of 2.022 meters. The upper branch is at an angle of 65° to the support and is 1.788 meters long. The node elements are identical for both columns, with a height of 37.2 cm and a gap between the elements.

The materials used in the model include moulded wood profiles for the supports and branches, fibre-reinforced plastic for the node elements, steel for the edge and centre supports and aluminium for the edge and middle rail. Glass was used for the roof construction, with a high modulus of elasticity of 70,000 MPa and a density of 29.85 kg/m³. The load-bearing behaviour of the wood profiles would be improved with lamination for protection against the weather, but this was not modelled. The calculation model developed for the demonstrator is based on the reliable orthotropic material properties of the wood determined by compression tests on moulded wood pipes. The model assumes an ideal bond between the wood and fibre-reinforced plastic.

The models were based on six possible wind load positions and their respective load combinations. Due to the large number of models and the similarity in the truss structure's behaviour under load, not all models are described. It was observed that a two-sided wind load, regardless of the direction of action, had a more favourable effect on the entire supporting structure than a one-sided load. Due to the loading on both sides, the deformations in the upper and lower branches of the columns were of the same magnitude on both sides. The composite roof had a stiffening effect that prevented major deformations on both sides. The deformations were specified separately for each direction of the coordinate system and Figure 14 provided an overview of the order of magnitude of the total deformation of the demonstrator, showing that the greatest deformations were in the centre of the roof area. The low deflection when the load was introduced at a point indicated that the roof construction was very stiff and could be neglected for the evaluation.

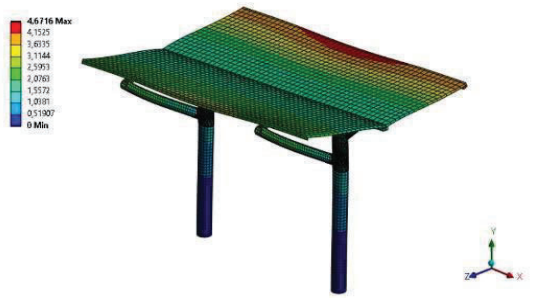

Figure 14: *Total displacement of the model with the load position bilateral wind pressure*

The deformation behaviour of the construction differs between wind pressure and wind suction. Under two-way wind suction and load combination 1, which results in a total uplift load, the structure is displaced in the negative X-direction, while under two-way wind suction the displacement takes place in the positive X-direction. This deformation behaviour can be explained by the longitudinal roof pitch. The normal vector of the wind load points in the same direction as the resulting displacement. Under wind suction, the upper and lower branches deform in the Z-direction in the same amount. Both are pulled upwards as a result of the suction. Under wind pressure, the lower branch deforms more than the upper branch due to its greater length.

The serviceability limit state was checked using the displacements. In order to be able to assess the ultimate limit state, a stress evaluation is required. In the models with wind pressure loading, the largest tensile and compressive stresses occur at the same location. Both maximum values are reached on the inside in the rear upper node element (Figure 15).

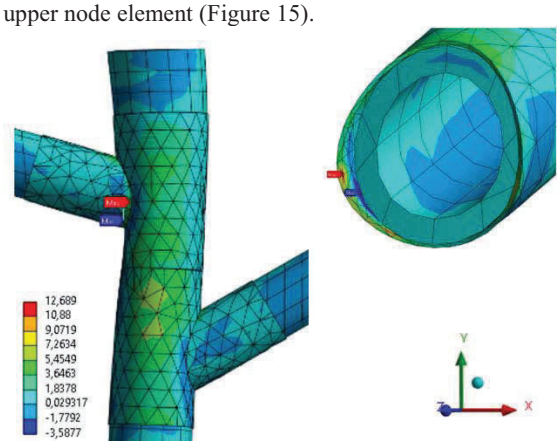

Figure 15: *Maximum principal stresses in model 1 (values in MPa)*

All tensile and compressive stresses that occur in the models are significantly lower than the maximum strengths of the individual materials of the components. The demonstrator model results show that the truss structure is stable enough to withstand maximum external loads.
The deformation behaviour of the bar structure is accurately represented and the maximum displacement values are within permissible limits. The stress evaluation of the supporting structure is consistent with the expected stress distribution and heavily stressed areas. Stress levels in the model are relatively low, but the roof structure has a significant impact on the load-bearing behaviour of the truss structure.

6 CONCLUSIONS

In this paper, the importance of advancing innovative constructions in timber technology was emphasized. While wood has clear advantages in construction, it also has technical limitations that must be addressed. The development of moulded wood profiles has demonstrated great potential for use in architecture, construction, lightweight construction and plant construction, as it improves weak points in technical applications of wood. Additionally, the use of technical fibres and textiles has increased efficiency and lowered material costs in timber construction. The combined use of moulded wood and fibre-reinforced plastics is developed coherent and modular construction solutions that meet a variety of architectural and structural requirements and enable a broad range of applications.
Test programme and the numerical models are being used in an attempt to provide sound knowledge for moulded wood tubes connecting with fibre-plastic composite node elements. The lightweight wood construction system developed features a high degree of prefabrication, extremely low dead weight with high load-bearing capacity, material efficiency and durability. Based on the moulded wood technology, a technology demonstrator in the form of a solar roof will be built.
In summary, the models used in this study were found to reliably represent tests to failure, despite simplifications and idealizations. Results of tensile tests showed that mechanical properties of wood components can be improved in combination with fibre-reinforced plastics, particularly in terms of optimal lamella length. The joining technology of shaped wood profiles and node elements using adhesive technology was found to offer an optimally adaptable force transmission surface, which is an advantage over mechanical connection means. Further testing is needed to ensure functionality under fluctuating mechanical loads and climatic conditions.

ACKNOWLEDGEMENT

The authors gratefully acknowledge the funding provided by the ZIM via Federal Ministry for Economic Affairs and Climate Action of Germany. The authors also thank the project partners Institute of Textile Machinery and High Performance Material Technology of TU Dresden, Korropol GmbH and Niemeier Fahrzeugwerke GmbH for their collaboration.

REFERENCES

[1] F. M. o. F. (Germany), „Immediate climate action programme for 2022," 2022. [Online]. Available: https://www.bundesfinanzministerium.de/Content/EN/Standardartikel/Topics/Priority-Issues/Climate-Action/immediate-climate-action-programme-for-2022.html. [Zugriff am 2023 02 01].

[2] G. F. Navi P, „Effects of thermo-hydro-mechanical treatment on the structure and properties of wood," *Holzforschung,* pp. 287-293, 2000.

[3] J. Hartig, J. Wehsener und P. Haller, „Experimental and theoretical investigations on moulded wooden tubes made of beech (Fagus sylvatica L.)," *Construction and Building Materials,* 2016.

[4] J. Wehsener, T. Werner, J. Hartig und P. Haller, „Advancements for the structural application of 19 fiber-reinforced moulded wooden tubes," *Materials and Joints in Timber Structures, Springer,* Nr. 20, pp. 99-108, 2014.

[5] P. Haller, „Concepts for textile reinforcements for timber structures," *Materials and Structures,* Nr. 40, p. 107–118, 2007.

[6] T.-E. Werner, „Profil aus Holz und Verfahren zu seiner Herstellung". Germany Patent 102007015018A1, 2007.

[7] B. Hahn, T. Werner und P. Haller, „Experimental and numerical investigations on adhesively bonded," *Construction and Building Materials,* 2019.

[8] S. Namari, L. Drosky, B. Pudlitz, P. Haller, A. Sotayo, D. Bradley, S. Mehra, C. O'Ceallaigh, A. M. Harte, I. El-Houjeyri, M. Oudjene und Z. Guan, „Mechanical properties of compressed wood," *Construction and Building Materials,* 2021.

[9] P. Haller, Structural wood engineering handbook, 2009: Verlagsgesellschaft Rudolf Müller, Stuttgart.

[10] P. Haller, A. Ringhofer und G. Schickhofer, „Wood, timber and structural elements: economic, mechanical and technological aspects," *Wood Material Science & Engineering,* pp. 261-267, 2015.

[11] A. Kuntar, D. Sandberg und P. Haller, „Compressed and moulded wood from processing to products," *Holzforschung(,* Nr. 7, p. 885–897.

[12] ITM, „Institute of Textile Machinery and High Performance Material Technology," 03 29 2022. [Online]. Available: https://tu-dresden.de/ing/maschinenwesen/itm.

[13] P. Niemz und W. U. Sonderegger, Eigenschaften, Prüfung und Kennwerte, Hanser, 2021.

https://doi.org/10.52202/069179-0405

[14] R. Ross, Wood handbook: Wood as an engineering material, U.S. Department of Agriculture, Forest Service., 2021.

[15] C. Sandhaas, Mechanical behviour of timber joints with slotted-in steel plates, Wöhrmann, 20212.

World Conference on Timber Engineering Oslo 2023

MECHANICAL BEHAVIOUR OF NOTCH CONNECTION FOR MARITIME PINE CLT-CONCRETE COMPOSITE

Carlos Albino[1], Carlos Martins[2], Cláudio Ferreira[3], Renato Augusto[4], Alfredo Dias[5]

ABSTRACT: Cross Laminated Timber (CLT) is one of the most representative Engineered Wood Products, especially for low- and mid-rise timber buildings. Although in the 2000s, its use in Europe increased significantly, Portugal is still at a starting point and Spain needs a boost for its dissemination. Aiming promotion and dissemination of this type of buildings in SUDOE region, Eguralt project promotes research and innovation capacity for its sustainable growth. As a partner, one of SerQ's objectives is to promote the production of CLT solutions with wood from local species. The advantages of CLT are well known. However, the use of CLT in composite solutions requires the study of the overall performance, namely: stiffness; strength; dynamics and acoustic performance. Continuing recent studies in these areas, this paper presents an experimental campaign on the assessment of CLT-concrete connections and its comparison with the design models available.

CLT was produced at SerQ's facilities with local maritime pine (*Pinus pinaster* Ait.) wood. In situ concrete casting and precast concrete processes were a study variable. Notch shear connectors with different geometries and screws or U-shape rebar cages to prevent uplift, gives the system its composite behaviour. The load capacity of the connectors was theoretically predicted and validated with shear tests, and the experimental results were then compared with those. The results of the specimens cast in situ were satisfactory, while the results of the precast specimens were below expectations.

KEYWORDS: CLT-concrete composite, composite floor, connection, experimental testing, maritime pine, shear test.

1 INTRODUCTION

Both Glued Laminated Timber (glulam) and CLT are the most common used Engineered Wood Products (EWPs) for timber construction (rehabilitation and new buildings) all over the world [1,2]. They are mainly produced by softwoods, namely Spruce (*Picea abies* L.) and Scots pine (*Pinus sylvestris* L.) [3,4]. The current challenge of using timber structures in construction, is due to their positive environmental impact since they have significantly less embodied energy, and associated carbon emissions than equivalent steel and concrete structural systems [5].

The increasing demand for EWPs requires the study of alternative species, also facing some issues related to the environmental and economic impacts due to long-distance transport. Iberian Peninsula has a small number of CLT producers whose focus is the use of local species, namely Radiata pine (*Pinus radiata* D. Don) and Maritime pine (*Pinus pinaster* Ait.). Bonding and mechanical performance of both species, both for glulam and CLT, have already been validated for different adhesives [6,7].

The performance of CLT buildings by itself is recognized. However, adding a layer of concrete on the floor elements significantly increases their ultimate and serviceability performance throughout the increase of stiffness, load carrying capacity, vibration frequencies, and acoustics [8,9]. The key factor for an effective behaviour of both materials is the connection. Within the scope of Eguralt project, an experimental campaign intends to characterize the mechanical performance of CLT-concrete notched connections aiming to obtain an effective solution for medium/long spans (second phase of the study). In addition, focused on sustainability, the main goal is to develop prefabricated solutions that allow easy decoupling. The results are then compared with design methods namely those specified in the Eurocode 5 [10] and in the Technical Specification CEN/TS 19103 [11].

2 MATERIALS AND METHODS

The specimens were prepared in two different stages: S1 (May 2022) and S2 (January 2023). CLT specimens using three layers of maritime pine were produced at SerQ's facilities. In stage S1 the timber was selected according to density, ensuring the class was higher than C18. After planning, the boards had a final thickness of 30 mm and 100 mm wide. In stage S2 the timber was selected according to the dynamic modulus of elasticity, ensuring

[1] Carlos Albino, University of Coimbra, ISISE, Department of Civil Engineering, Coimbra, Portugal, capa@uc.pt
[2] Carlos Martins, University of Coimbra, ISISE, Department of Civil Engineering, Coimbra, Portugal, carlosmartins@gmail.com
[3] Cláudio Ferreira, SerQ, Sertã, Portugal, cferreira@serq.pt
[4] Renato Augusto, SerQ, Sertã, Portugal, raugusto@serq.pt
[5] Alfredo Dias, University of Coimbra, ISISE, Department of Civil Engineering, Coimbra, Portugal, alfgdias@dec.uc.pt

https://doi.org/10.52202/069179-0406

the class was equal to or higher than C24, and the boards had a final thickness of 30 mm and a width of 200 mm. A layer of concrete (maximum aggregate dimension of 14 mm) with 60 mm thickness was considered and reinforced with an electro-welded steel mesh (AQ50; 100 mm by 100 mm) placed at mid depth of concrete to prevent cracking. Table 1 shows the material properties in each stage, where *MC* is the moisture content, ρ is the density and E_{dyn} is the dynamic modulus of elasticity of the timber; f_{cm} is the concrete mean value of the compressive strength. The timber properties shown in this table are related to the lamellae at the interface with the concrete layer.

Table 1: *Material properties.*

Stage	Timber			Concrete	
	MC [%]	ρ [kg/m³]	E_{dyn} [MPa]	f_{cm} [MPa]	Class
S1	14 ± 2	580 ± 80	12000 ± 4800	46.8	C35/45
S2	16 ± 2	620 ± 60	15500 ± 1500		

Nine connection configurations are considered (see Table 2) based on the concept of a perpendicular/inclined notch and with/without screw to resist uplift stresses. Research on inclined notches is not recent [12]. However, the used shape follows the pattern referred to in Ouch *et al*. (2021) [13]. For those connections with a screw, SPAX 8x120 mm full threaded and washer head screw is installed in the centre of the notch. The connector design using these screws is covered by the European Technical Assessment ETA-12/0114 [14].

Table 2: *Notch configurations.*

Specimen ID	Notch [mm]			Stage	
	Top Length	Bottom Length	Depth	Timber	Concrete
MrP20	150	150	20	S1	S1
MiP20	90	90	20	S1	S1
MiI20	90	114	20	S1	S1
MiP45	90	90	45	S1	S1
MiI45	90	144	45	S1	S1
MrpP20	150	150	20	S2	S1
MrpI20	150	174	20	S2	S1
MpP20	90	90	20	S2	S1
MpI20	90	114	20	S2	S1

Meaning of the specimen ID:
M – wood species: maritime pine.
r – reference (150 mm notch top length); i – in situ concreting; p – prefabricated concrete.
P – perpendicular notch; I – inclined notch.
20 and 45 – notch depths in mm.

Three groups of two specimens 500 mm long, 200 mm wide and 90 mm thick were fabricated for each configuration. To comply with the symmetrical system indicated by Annex C of the Technical Specification CEN/TS 19103 [11], each specimen is composed of two CLT panels glued to each other and placed between two reinforced concrete (RC) slabs (see Figure 1). The assembly of each individual layer of RC with the respective specimen of CLT is previously performed. On reference specimens (MrP_) and in situ specimens with perpendicular notch (MiP_), a screw is installed in the centre of the notch – see Figure 2 (a). A U-shape rebar cage is installed on specimens with an inclined notch (MiI_) – see Figure 2 (b).

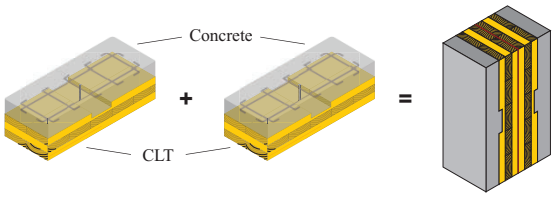

Figure 1: *Specimens bonding.*

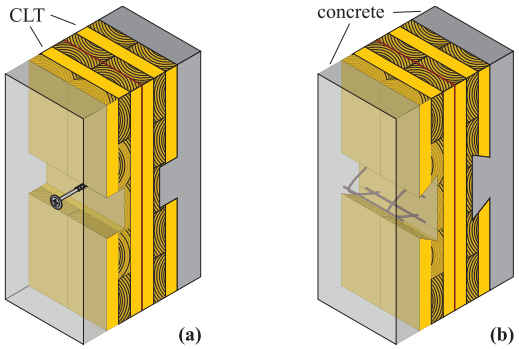

Figure 2: *Notch configurations: (a) perpendicular and (b) inclined notch.*

Precast reinforced concrete panels (Mrp_ and Mp_) are manufactured with a 90 mm square hole in the centre. The assembly is carried out by filling the notch with grout SikaGrout®-218 [15]. In specimens with perpendicular notch (MrpP20 and MpP20), the connection is reinforced with a screw to prevent uplift, while in inclined notch specimens (MrpI20 and MpI20), no steel connector is installed (see Figure 3).

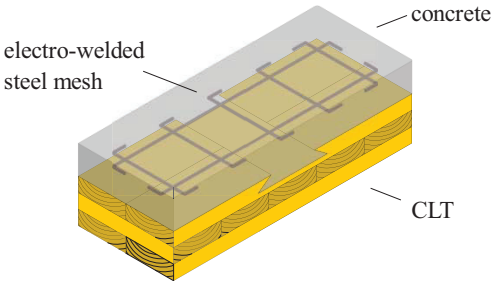

Figure 3: *Inclined notch without steel connector.*

3 EXPERIMENTAL APPROACH

For the CLT-concrete composite connections characterization, the push-out test is used. The test setup is made conform to the push-out test given in EN 26891 [16] – see Figure 4– where the dashed line represents a simulation as the graph behaviour depends on the specimen being tested. To design the loading procedure, the maximum loading must be known or estimated. Table 3 shows the estimated load-carrying capacity for some of

the specimens by Clause 10.3.4.3 of the Technical Specification CEN/TS 19103 [11]. The estimate was made considering timber strength class C24 and concrete strength class C35/40.

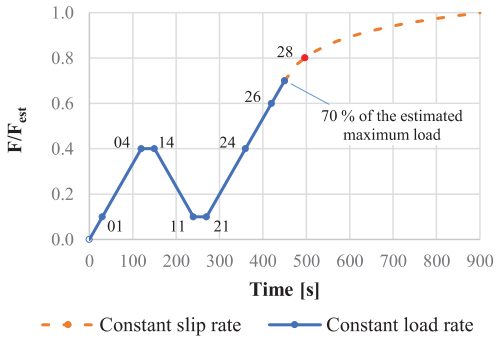

Figure 4: *Loading procedure given in EN 26891* [16].

Table 3: *Estimated maximum load for each stage S1 notch configuration based on characteristic values.*

Specimen ID	Load-carrying capacity $F_{Rd,shear\ plan}$ [kN]	Slip modulus k_{ser} [kN/mm]	Failure mode
MrP20	52	200	Crushing of timber
MiP20	52	200	Crushing of timber
MiI20	52	200	Crushing of timber
MiP45	107	300	Shear of concrete
MiI45	116	300	Crushing of timber

Test setup consisted of a force jack with a capacity of 500 kN that applied a uniform vertical load on the top surface of the CLT block through a steel plate that distribute the load across the timber, a symmetrical specimen of CLT-concrete connection, and two reaction steel plates (high enough to allow the timber section to move freely vertically within the limits of the standard: at least 15 mm) to support the reinforced concrete plates. To avoid a dangerous collapse of the specimen, it is restrained at the top and bottom without prestressing, as shown in Figure 5 (a).

To measure relative displacement (slip) between the CLT and concrete panels four LVDTs are placed, at half height, two for each shear plan – see Figure 5 (b).

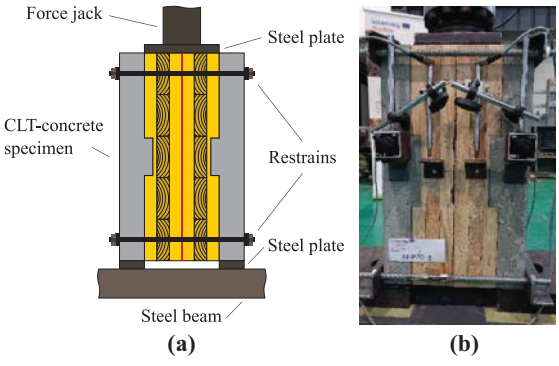

Figure 5: *(a) test setup and (b) LVDT positions.*

Load and slips were recorded at 0.1 s and all tests were filmed by two cameras, one positioned at the front and other at the back and photographed from all sides for later evaluation and clarification of doubts related to failure modes.

4 RESULTS AND DISCUSSION

4.1 RESULTS

Figure 6 shows the load (F_{appl}) *versus* joint slip of the representative shear planes of each perpendicular notch configuration, and Figure 7, of the inclined notches. Generally, the specimen reaches its maximum load-carrying capacity (collapse of the first shear plane) before a differential displacement between the CLT and the reinforced concrete of 2 mm in the notch area. After that, most specimens reach about half their maximum load-carrying capacity (collapse of the second shear plane) for slips greater than 5 mm. The specimens with notches 150 mm long, cast in situ, (reference specimens) have the highest load-carrying capacity and a ductile behaviour was observed. Specimens with a 90 mm long notch have an intermediate load-carrying capacity and prefabricated specimens have a lower load-carrying capacity.

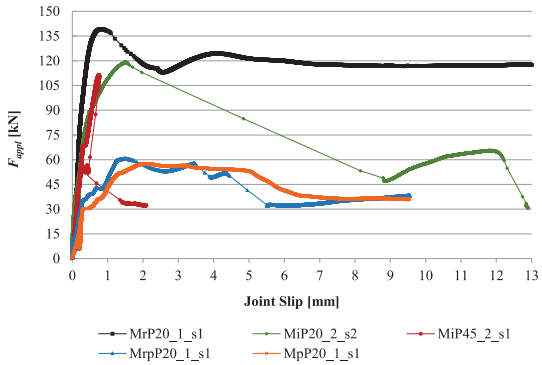

Figure 6: *Force per shear plane versus joint slip (perpendicular notch).*

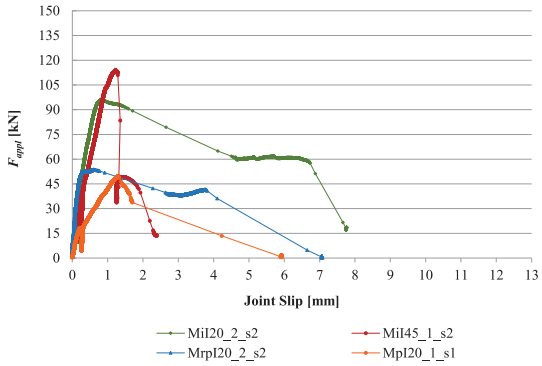

Figure 7: *Force per shear plane versus joint slip (inclined notch).*

To complement the above, see Table 4 that shows the load-carrying capacity (F_{max}), and the stiffness of the connections in the service limit state quantified by the slip

https://doi.org/10.52202/069179-0406

modulus (K_s). These values are provided by the average (μ), standard deviation (σ) and coefficient of variation (relative standard deviation, *RSD*).

Table 4: *Mean values of shear strength and slip modulus per shear plane.*

Specimen	F_{max} [kN]			K_s [kN/mm]		
	μ	σ [-]	*RSD* [%]	μ	σ [-]	*RSD* [%]
MrP20	140.6	6.9	4.9%	376.0	111.0	29.5%
MiP20	117.3	4.7	4.0%	302.4	78.0	25.8%
MiI20	100.7	5.3	5.3%	206.8	66.7	32.2%
MiP45	109.0	5.2	4.8%	251.1	76.0	30.3%
MiI45	109.6	10.1	9.2%	177.7	37.4	21.1%
MrpP20	57.3	5.4	9.4%	162.3	37.7	23.2%
MrpI20	52.9	6.4	12.2%	194.4	62.6	32.2%
MpP20	61.0	6.1	10.1%	228.4	147.9	64.7%
MpI20	49.8	4.8	9.7%	252.4	188.5	74.7%

Table 5 shows the maximum mean slips at maximum load (δ_{Fmax}) and just before collapse ($\delta_{Collapse}$). Generally, the reference specimens (MrP20) show a greater slip at maximum load. Higher values were only observed at similar configuration, for pre-cast connection (3.7 mm at maximum load). This happened very close to the collapse which occurred on average at 51 kN per shear plane.

Table 5: *Mean slip values on connections.*

Specimen	δ_{Fmax} [mm]			$\delta_{Collapse}$ [mm]		
	μ	σ [-]	*RSD* [%]	μ	σ [-]	*RSD* [%]
MrP20	1.50	0.38	25.41%	2.59	1.08	41.66%
MiP20	1.09	0.32	29.46%	1.25	0.39	30.85%
MiI20	1.46	0.66	44.88%	1.87	0.76	40.76%
MiP45	0.63	0.22	34.98%	0.71	0.32	45.58%
MiI45	1.12	0.31	27.33%	1.24	0.39	31.86%
MrpP20	3.69	4.14	112.39%	5.11	4.14	80.98%
MrpI20	0.61	0.28	46.67%	2.24	1.91	84.93%
MpP20	1.44	0.44	30.27%	6.10	1.56	25.61%
MpI20	1.14	0.26	23.08%	1.63	0.96	59.04%

Prefabricated specimens all collapsed due to shear of grout at the interface between the concrete and CLT plates. Precast reinforced concrete panels were manufactured with a 90 mm square hole in the centre. Despite the specimens' preparation having been carried out to ensure good adhesion between grout and concrete, in some areas it was found the grout had detached from the concrete. Figure 8 shows a shear plane after the failure. It can be seen areas where the grout was properly connected to the concrete and areas where grout has detached the concrete.

4.2 DISCUSSION

The specimens with a reference notch equally presented two collapse failure modes: shear and crushing of timber. In these specimens, the collapse has a ductile behaviour. It is possible to see shear of concrete, which may have been limited by the electro-welded steel mesh. Two of the reference specimens presented both failure modes in the same shear plane (see Figure 9).

Figure 10 shows the top of MrP20_1 CLT specimen where the growth rings of the two lamellae are shown and identified. It can be seen the lamellae with wider growth rings collapsed by crushing parallel to grain and lamellae with more compact growth rings collapsed by shear parallel to grain.

In the remaining configurations, the collapse was due to shear of concrete. Collapse was governed by a brittle behaviour instantly decreasing the load-carrying capacity of the connection.

Figure 8: *Shear of grout in MrpI20_2 specimen.*

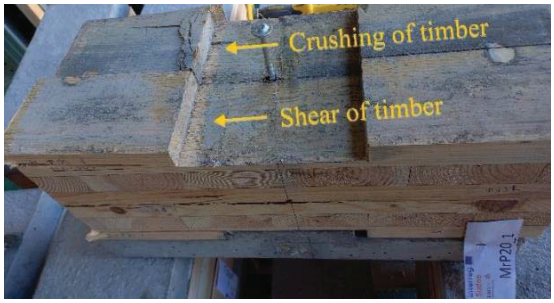

Figure 9: *MrP20_1 specimen with shear and crushing of timber in the same shear plane.*

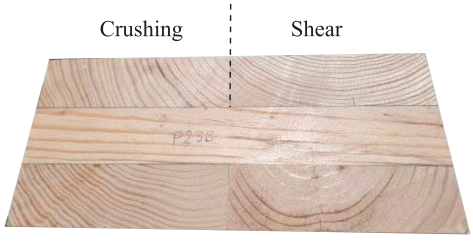

Figure 10: *MrP20_1 specimen with shear and crushing of timber in the same shear plane.*

Regarding the prediction of the connections load-carrying capacity, results given by the Technical Specification are lower than the experimental results. Nevertheless, connections with a 45 mm deep notch showed similar results. Technical Specification assumes slip modulus increase with the depth of the notch. On the opposite, tests revealed a decrease, comparing the 20 mm and 45 mm deep notches. Technical specification predictions related to failure modes only matched in specimens MrP20 (even with maximum load carrying capacity underestimated) and MiP45.

To evaluate the results of the prefabricated specimens, half of their width (100 mm) was considered to disregard some areas where the grout detached from the concrete. Table 6 presents the average load-carrying capacity and connection stiffness values, per millimetre, of the specimens cast in situ, considering a total width of 200 mm. The values for the prefabricated specimens are also presented, per millimetre, considering the width of 100 mm.

Table 6: *Load-carrying capacity and connection stiffness values per millimetre.*

Specimen	F_{max} [kN/mm]	K_s [kN/mm/mm]
MrP20	1.41	1.88
MiP20	1.17	1.51
MiI20	1.01	1.03
MrpP20	1.15	1.62
MrpI20	1.06	1.94
MpP20	1.22	2.28
MpI20	1.00	2.52

Figure 11 shows the notch length influence on results. MrP20 and MiP20 specimens were compared. Additionally, results of configurations A1 and A2 by Yeoh *et al.* (2008) [17] were also compared. In this analysis, MrP20 and A1, by Yeoh *et al.* (2008), specimens were taken as reference. The longer the notch, the higher the load-carrying capacity, slip modulus, and slip at the maximum load capacity value.

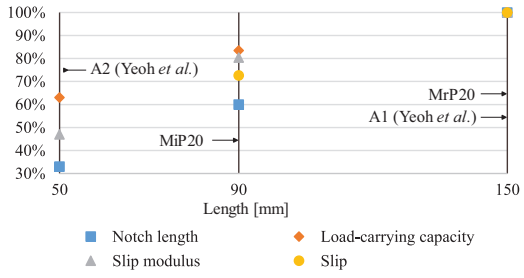

Figure 11: *Influence of notch length on results.*

Figure 12 shows the perpendicular notch depth influence on results. MiP20 and MiP45 specimens were compared. Additionally, results of configurations A1 and A3 by Yeoh *et al.* (2008) [16] were also compared. In this analysis, MiP20 and A1, by Yeoh *et al.* (2008), specimens were taken as reference. In the MiP_ specimens, it was found that increasing the notch depth by 125 %, decreased both the load-carrying capacity and slip modulus by 20 %. The slip at the maximum load capacity value decreased about 40 %. In Yeoh *et al.* (2008) study, with a 50% decrease in the notch depth, slip modulus increased by 40 %, and load-carrying capacity was kept similar.

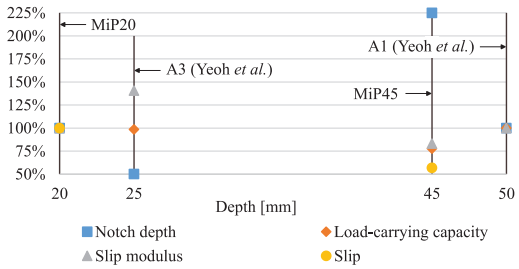

Figure 12: *Influence of perpendicular notch depth on results.*

Figure 13 shows the inclined notch depth influence on results. MiI20 and MiI45 specimens were compared. Comparison with results from literature references was not possible. MiI20 specimen was taken as reference. It was found that increasing the notch depth (125 %), decrease both the slip (20 %) and slip modulus (15 %). The load-carrying capacity increased around 10 %.

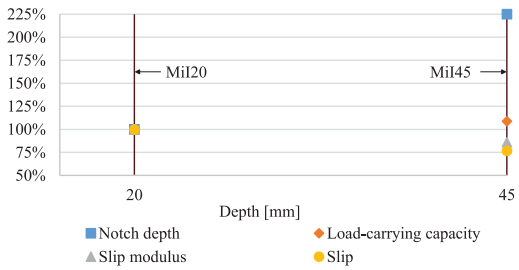

Figure 13: *Influence of inclined notch depth on results.*

Figure 14 shows the inclined notch influence on results. MiI20/MiP20 (20 mm deep) and MiI45/MiP45 (45 mm deep) specimens were compared. MiP20 and MiP45 specimens were taken as reference. Inclination in the 20 mm deep notches resulted in 15 % loss of load-carrying capacity and 30 % of stiffness (slip modulus) of the connection. In the 45 mm deep notches, there was a loss of connection stiffness similar to that of the 20 mm notches, nevertheless, the inclination had no effect on the load-carrying capacity.

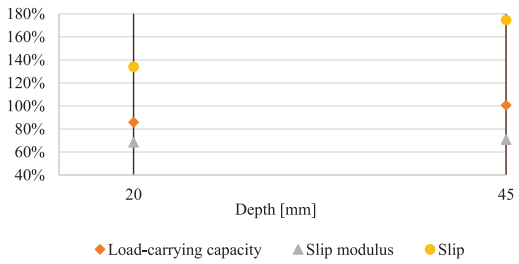

Figure 14: *Influence of inclined notch on results.*

https://doi.org/10.52202/069179-0406

The 150 mm long prefabricated specimens lose load-carrying capacity (about 20 %) compared to those cast in situ. When the notch is inclined the loss is higher (20 %). In the 90 mm long notches, the prefabricated specimens with perpendicular notches have a higher load-carrying capacity compared to inclined notches. The specimens with inclined notch maintain similar load-carrying capacity despite the length of the notch. The reference notch has less connection stiffness on the prefabricated specimens.

5 CONCLUSIONS

Connections between CLT produced with local maritime pine wood and reinforced concrete (cast in-situ and precast) were tested to study the composite system behaviour. The experimental results and the design results provided by the standards were compared.

The load-carrying capacity of the cast-in-situ concrete connection is greater than that of precast concrete, nevertheless, generally, the slip modulus is lower. The notch depth has no significant influence on results. The notch length is the most important factor affecting the connection performance both at mechanical properties and ductile behaviour. More tests must be carried out to increase the reliability of results.

ACKNOWLEDGEMENT

This work was partly financed by FCT/MCTES through national funds (PIDDAC) under the R&D Unit Institute for Sustainability and Innovation in Structural Engineering (ISISE), under reference UIDB/ 04029/2020, and under the Associate Laboratory Advanced Production and Intelligent Systems ARISE under reference LA/P/0112/2020 and Interreg Sudoe Programm (FEDER funds) through EGURALT project (SOE4/P1/E1115).

REFERENCES

[1] M. Mohammad, S. Gagnon, B.K. Douglas, L. Podesto, Introduction to Cross Laminated Timber, Wood Des Focus. 22 (2012) 3–12.

[2] J. Hildebrandt, N. Hagemann, D. Thrän, The Contribution of Wood-Based Construction Materials for Leveraging a Low Carbon Building Sector in Europe, Sustain Cities Soc. 34 (2017) 405–418. https://doi.org/https://doi.org/10.1016/j.scs.2017.06.013.

[3] R. Brandner, Production and Technology of Cross Laminated Timber (CLT): A state-of-the-art Report, in: Graz, 2013.

[4] G. Fink, J. Kohler, R. Brandner, Application of European Design Principles to Cross Laminated Timber, Eng Struct. 171 (2018) 934–943. https://doi.org/https://doi.org/10.1016/j.engstruct.2018.02.081.

[5] C.A.S. Hill, The Environmental Consequences Concerning the Use of Timber in the Built Environment, Front Built Environ. 5 (2019). https://doi.org/10.3389/fbuil.2019.00129.

[6] C. Martins, A.M.P.G. Dias, H. Cruz, Bonding performance of Portuguese Maritime pine glued laminated timber, Constr Build Mater. 223 (2019) 520–529. https://doi.org/https://doi.org/10.1016/j.conbuildmat.2019.06.143.

[7] S. P., C. J.R., G. L., D. A.M.P.G., D. A., Bonding quality assessment of cross-layered Maritime pine elements glued with one-component polyurethane adhesive, Constr Build Mater. 211 (2019) 571 – 582. https://doi.org/10.1016/j.conbuildmat.2019.03.064.

[8] C. Martins, P.G. Santos, P. Almeida, L.M.C. Godinho, A.M.P.G. Dias, Acoustic performance of timber and timber-concrete floors, Constr Build Mater. 101 (2015) 684–691. https://doi.org/https://doi.org/10.1016/j.conbuildmat.2015.10.142.

[9] A.M.P.G. Dias, J. Skinner, K.I. Crews, T. Tannert, Timber-concrete-composites increasing the use of timber in construction, European Journal of Wood and Wood Products. 74 (2016). https://doi.org/10.1007/s00107-015-0975-0.

[10] EN 1995-1-1:2004+A1:2008, Eurocode 5: Design of Timber Structures, Part 1-1: General - Common Rules and Rules for Buildings, CEN - European Committee for Standardization, Brussels, 2008.

[11] CEN/TS 19103:2021, Eurocode 5: Design of Timber Structures – Structural design of timber-concrete composite structures – Common rules and rules for buildings, CEN - European Committee for Standardization, Brussels, 2021.

[12] M. Brunner, J.H.J.O. Negrão, K. Rautenstrauch, K.-U. Schober, Timber Concrete Composites, in: 2008: pp. 9–15.

[13] V. Ouch, P. Heng, Q.H. Nguyen, H. Somja, T. Soquet, A Notched Connection for CLT-Concrete Composite Slabs Resisting to Uplift Without Metallic Connectors: Experimental Investigation, in: Fib Symposium 2021: Concrete Structures: New Trends for Eco-Efficiency and Performance, Lisbon, Portugal, 2021. https://hal-univ-rennes1.archives-ouvertes.fr/hal-03254979.

[14] SPAX International GmbH & Co. KG, European Technical Approval ETA-12/0114, (2012). www.spax.com.

[15] Sika Portugal SA, SikaGrout®-218, (2020). https://prt.sika.com/pt/solucoes-para-construcao/ref-colagem-estrutural/grout-cimenticio/sikagrout-218.html (accessed February 24, 2023).

[16] EN 26891:1991, Timber Structures - Joints Made With Mechanical Fasteners -General Principles For the Determination of Strength and Deformation Characteristics, Technical, CEN - European Committee for Standardization, Brussels, 1991.

[17] D. Yeoh, M. Fragiacomo, P. Aldi, M. Mazzilli, U. Kuhlmann, Performance of notched coach screw connection for timber-concrete composite floor system, 1 (2008) 294–301.

World Conference on Timber Engineering Oslo 2023

EXPERIMENTAL INVESTIGATION OF AN INNOVATIVE BEAM-TO-COLUMN CONNECTION UNDER CYCLIC LOADING.

Ahmed Mowafy[1], Ali Imanpour[2], Ying Hei Chui[3], Hossein Daneshvar [4]

ABSTRACT: The mechanical behaviour of steel is crucial in hybrid steel-timber systems, especially in areas prone to seismic activity. This paper presents a study of a novel semi-rigid connection that employs U-shaped steel plates as seismic fuses in a beam-to-column connection. The connection aims to introduce self-centring steel braced frames as lateral systems, combined with mass timber structures as a gravity load-resisting system, to enhance their structural performance against earthquakes. The fuses are designed to yield in axial compression or tension, with a bending combination that enables the connection to produce yielding at a specific moment level. The study focuses on the results obtained from cyclic fuse testing, connection testing, and comparing the connections to existing solutions to demonstrate their potential as a reliable and resilient option for mass timber buildings in seismic areas. The findings indicate that the developed connections provide reliable ductile behaviour, and timber elements can be protected from damage through the capacity protection provided by the fuses and their yielding mechanism.
KEYWORDS: Hybrid Structures, Mass Timber buildings, U-shaped plates, Semi-Rigid Connections, Seismic fuses, lateral load resisting systems (LLRS).

1 INTRODUCTION

Timber mass buildings face a unique design challenge due to the need for high-performance connections. In recent years, researchers have focused on improving the behaviour of these connections to enhance the seismic resilience of timber structures. One solution to this issue is to use a pure hinge connection for timber structures that can accommodate drift during seismic events, and steel frames can provide ductility to dissipate seismic energy [1]. Alternatively, the connection itself could dissipate the energy by introducing a steel component with reasonable ductile behaviour. Various types of connections that can dissipate seismic energy have been proposed, such as perforated plates [2], top and seat angle connections[3], wooden elements connected to steel stubs [4], Glulam post-to-beam connections reinforced by dowel-type fasteners [5], connections with three separate steel box sections [6], and prestressed timber beam-column connections[7]. Despite these solutions, the ideal type of connection for timber mass buildings would have replaceable sacrificial elements to reduce downtime and rehabilitation costs, as a lesson learned from the 2010-2011 Christchurch earthquake series [8]. One example is the proposed hybrid moment resisting frame connection with replaceable steel links [9]; however, there are few examples of these advanced replaceable-fuse connections.

This paper presents an innovative beam-to-column connection that uses replaceable U-shaped plates as a source of ductility during an earthquake. U-shaped plates were first introduced by Kelly et al. to provide energy dissipation between structural walls [10]. Incorporating U-shaped plates into the developed connection offers several advantages, including cost-effective fabrication, simple installation and replacement, as well as exceptional inelastic characteristics such as high energy dissipation capacity and fatigue performance [10,11]. The developed connection, shown in Figure 1, consists of two main parts: a pin mechanism located at the centre and replaceable U-shaped fuses situated above and below it.

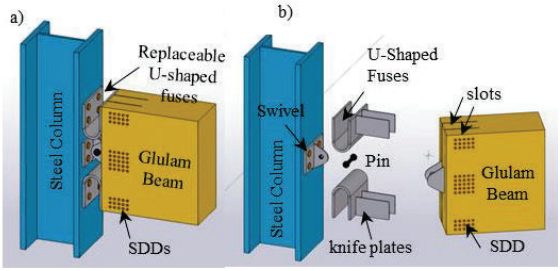

Figure 1: *Developed Beam-to-column Connection: a) Assembled connection b) Disassembled connection.*

All components are connected to the timber beam using two knife steel plates embedded in the timber and attached using self-drilling dowels (SDDs), which are widely used in these forms of connections due to their mechanical properties, including high tensile and shear strength, excellent corrosion resistance, and ductility, as well as their architecturally pleasing appearance. Then the components are connected to the steel column using regular high-strength bolts with ASTM A490 grade [13].

[1] Ahmed Mowafy, University of Alberta, Canada, mowafysa@ualberta.ca
[2] Ali Imanpour University of Alberta, Canada, imanpour@ualberta.ca
[3] Ying Hei Chui, University of Alberta, Canada, yhc@ualberta.ca
[4] Hossein Daneshvar, University of Alberta, Canada, Hossein.daneshvar@ualberta.ca

https://doi.org/10.52202/069179-0407

The research aims to test the seismic performance of this innovative connection and compare it with other existing solutions to demonstrate its potential as a reliable and resilient option for timber mass buildings in seismic areas.

2 EXPERIMENTAL PROGRAM

Two testing programs, the Fuse-Testing (FT) and Connection Testing (CT) have been developed. The FT program (Figure 2) assesses the inelastic properties of the seismic fuses used in the connection, while the CT program (Figure 3) tests the capacity-protected items in the connection and determines the overall hysteresis response of the connection under cyclic loading. The testing setups, loading procedures, and specimens used for both programs are discussed in this section.

2.1 Fuse Test setup

The FT setup shown in Figure 2 examines two symmetric specimens to avoid introducing eccentric loading to testing machine. The setup includes two identical testing fixtures connected to the uniaxial machine via its grips. Two back-to-back angles are welded to an intermediate plate that is attached to the machine arm for each fixture. The load from the machine is distributed evenly to the fuse legs by distributing plates. The specimens are connected to the distribution plate and ultimately to the horizontal leg angle by four pre-tensioned high-strength steel bolts. Scissor Displacement, which is the relative vertical displacement between the two fuse legs, was measured using four Linear Variable Differential Transformers (LVDTs). The front face and the outside curved surface of the left specimen were monitored through non-contact strain field measurements utilizing Digital Image Correlation (DIC).

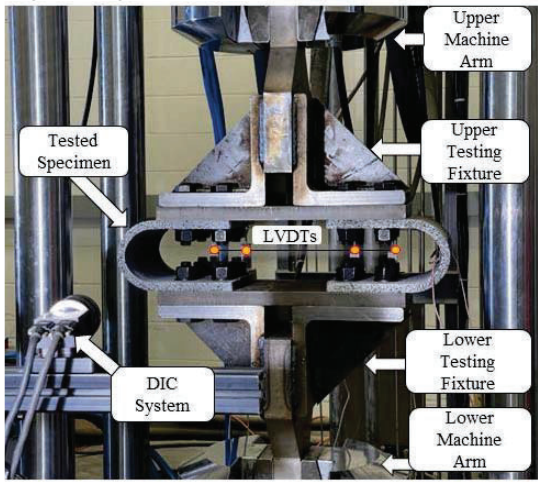

Figure 2: *Fuse-Testing Setup*

2.2 Connection Test setup

The connection testing was carried out at C-FER Technologies, Alberta, Canada, using a reaction wall made of reinforced concrete and a hydraulic actuator with a 300 kN maximum load capacity. A steel beam fastened to a reinforced concrete floor with steel anchors served as a representation of the column component. A load cell in the actuator was used to measure the load, and inclinometers, LVDTs, and potentiometers were installed to quantify connection, rotation, displacement, and lateral movement. DIC technology was used to assess the non-contact strain field.

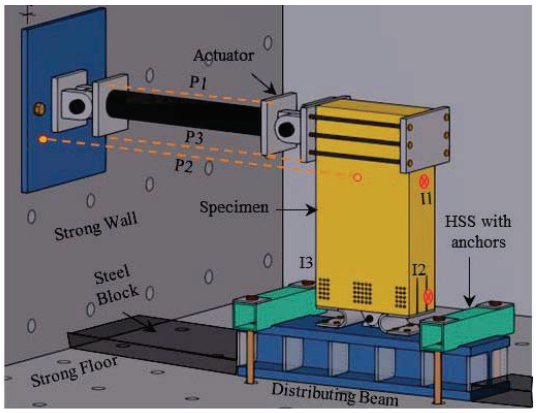

Figure 3: *Proposed Connection-Testing Setup*

2.3 Loading Procedure

Both sets of specimens were tested using the displacement control protocol recommended in FEMA 461 [14] as shown in Figure 4. This involved 26, where each pair of consecutive cycles shares the same amplitude, followed by a gradual increase in amplitude. This protocol was used to induce a 3% storey drift in a hybrid steel-timber structure. For the fuse testing, the cyclic displacement history consisted of 26 cycles to achieve a maximum displacement of 6 mm between the legs, followed by ten additional cycles to reach 20 mm. The maximum scissor displacement was limited to 20 mm to avoid bolt contact. Similarly, cyclic loading protocols were employed for connection testing, consisting of 26 cycles up to 54 mm displacement and ten additional cycles up to 140 mm or until failure. The maximum beam displacement was limited to 144 mm to avoid bolt contact and a 150 mm actuator stroke limit.

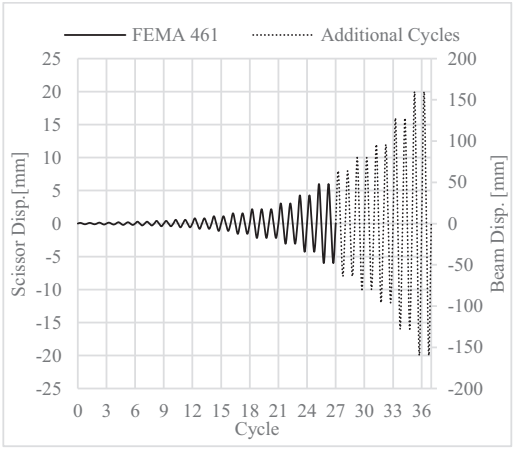

Figure 4: *Loading Protocol*

https://doi.org/10.52202/069179-0407

2.4 Specimens

The U-shaped plates used as the test specimens for fuses were made of CSA G40.21 300W steel and came in four different thicknesses: 13 mm, 16 mm, 19 mm, and 22 mm for Specimens FT-S1, FT-S2, FT-S3, and FT-S4, respectively. The plates were shaped using a bespoke bender without any heat treatment. For the connection testing, four identical glulam beams with dimensions of 265x608x1150 mm were produced, each to be utilized for a different fuse thickness, as shown in Table 1. The only aspect of the beams that varied was the quantity of Self Drilling Dowels (SDD) employed at the top and bottom portions of each specimen. The predicted maximum shear force during cyclic loading was intended to be supported by the intermediate pin SDDs, with a total number of 25.

Table 1. *Connection Testing (CT) Specimens*

Specimen	Fuse thickness	SDD number per top or lower part
CT-S1	13 mm	20
CT-S2	16 mm	28
CT-S3	19 mm	40
CT-S4	22 mm	50

3 INSIGHT FOR THE TESTING PROGRAM RESULTS

This section describes the results of experimental testing and analysis of timber connections and fuses for seismic-resistant structures. The testing involved the use of fuse and connection specimens, and the results were analyzed based on deformation hysteresis curves, Von Misses strain measurements, and moment-rotation hysteresis responses. This section also includes a discussion of the behaviour of the fuses and connections in tension and compression and a comparison between the behaviour of the fuses in connection testing and fuse testing.

3.1 Fuse Testing

Figure 5 illustrates a deformation hysteresis curve for a chosen fuse specimen 3 (a 19-mm fuse). The fuses exhibited high ductility, enabling them to effectively dissipate seismic energy. Furthermore, the fuses were able to compress up to the expected yielding strength, and all specimens could move their scissor legs up to a maximum distance of 20 mm without fracture. However, the behaviour of the fuses in compression was not identical to that in tension due to the varying boundary conditions. Under tension, the fuse reached a maximum force of 250 kN, while under compression, it reached an even higher maximum force of 340 kN.

Figure 6 illustrates the Von Misses strain measurements at the front face of the fuse at maximum tension (Point a) and maximum compression (Point b). The scale range was set to show the strain values that go beyond yielding, enabling the detection of the plastic zones. During testing, a gap in tension was observed between the fuse leg that ends at the outer bolt edge and the horizontal plate of the testing fixture that applies the loads [Figure 6. a]. On the other hand, complete contact between the plate and the fuse leg occurred during compression [Figure 6. b]. The unloaded fuse seemed to yield at the same load level until full contact was achieved. At this point, the fuse started to accommodate more stiffness until the yielding zone occurred near the full contact edge. Overall, the results suggest that the behaviour of the fuses in compression was not the same as in tension due to various boundary conditions that affected the fuses in each situation. The findings have implications for understanding the behaviour of the fuses and their potential use in seismic-resistant structures.

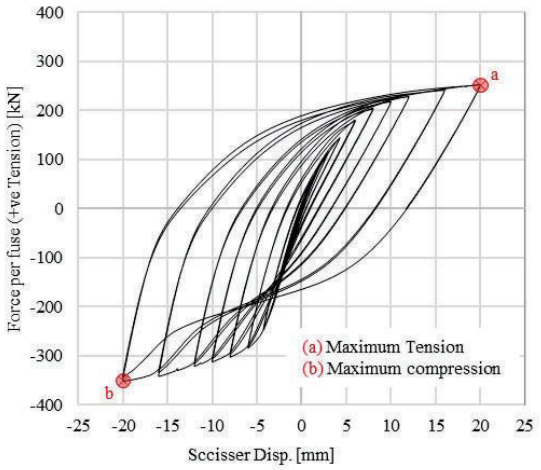

Figure 5: *Fuse Testing - Sample hysteresis response: FT- S3*

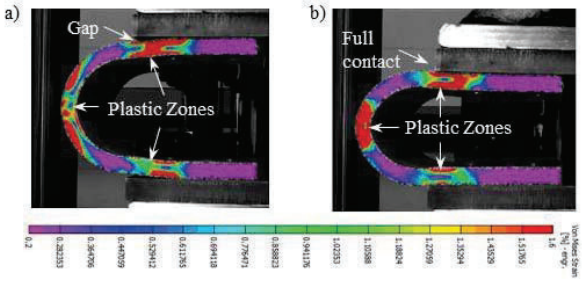

Figure 6: *Fuse Testing – Von Misses Strain measures for Specimen FT-S3: a) Maximum Tension (Point a); b) Maximum Compression (Point b).*

3.2 Connection Testing

In Figure 7, the moment-rotation hysteresis response of the CT-S3 specimen is shown, demonstrating high ductility, good energy dissipation, and no strength degradation in the connections. The overall connection stiffness did not reduce nor exhibit pinching, which suggests that even better ductility could have been achieved if the beam had undergone higher displacement during testing. All specimens followed a consistent pattern and were able to reach the maximum rotation level

https://doi.org/10.52202/069179-0407

without global failure. No significant out-of-plane deformations were captured. The ultimate moment for CT-S1, CT-S2, CT-S3, and CT-S4 specimens as 32, 48, 72, and 92 kN, respectively.

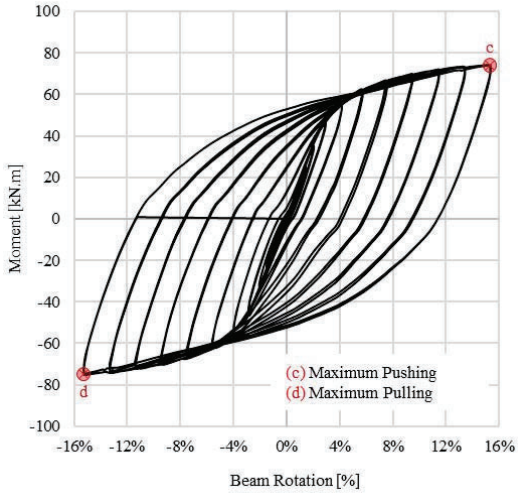

Figure 7: *Connection Testing – Sample hysteresis response: CT- S3*

Figure 8.and Figure 8.b showcase the CT-S3 specimen at maximum pushing (Point c) and pulling (Point d) during testing, respectively. As demonstrated, no splitting cracks emerged in the glulam beam specimens during testing. In Figure 9, the DIC strain measurements at the front view of both fuses in tension and compression utilized in the connection at maximum pushing (Point c) are presented. The plastic zones, in this case, were more concentrated at the mid-bent of the fuse rather than the legs.

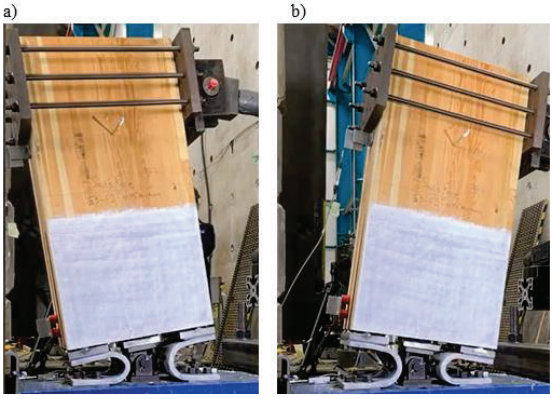

Figure 8: *Connection Testing – Specimen CT-S3 deformations: a) maximum rotation at pushing (Point c); b) maximum rotation at pulling (Point d).*

3.3 Comparison between Fuse behaviour in Fuse testing and connection testing

On analyzing the behaviour of fuses in connection testing (Figure 10.a) and fuse testing (Figure 10.b) under compression, a significant difference was observed. In connection testing, the fuse leg is allowed to rotate, while in fuse testing, it is fixed. Consequently, the plastic zones in connection testing (Figure 10.c) are more prominently concentrated at the mid-bent of the fuse than at the contact points of the fuse leg end. On the other hand, in fuse testing (Figure 6), the legs are more actively engaged due to the testing fixture forcing the legs to remain straight.

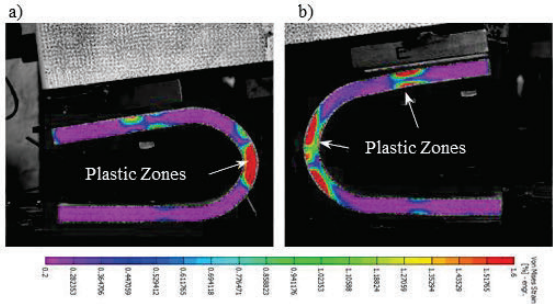

Figure 9: *DIC Von Misses Strain measures at maximum pushing (point c): a) Compressive Fuse; b) Tensile Fuse.*

This difference arises because the connection rotation matches the deformed shape of the fuse if it is compressed freely in the perpendicular direction to its legs. However, in fuse testing, the legs are constrained, and thus the deformation pattern is different. Moreover, the gap that was observed during tension in the connection testing fuses did not completely close during compression due to the residual deformations introduced in the fuse leg during tension. Therefore, the inelastic properties of the tensile fuse dominate the overall hysteresis performance of the connection, and a symmetric hysteresis response can be easily developed, which is not the case in fuse testing.

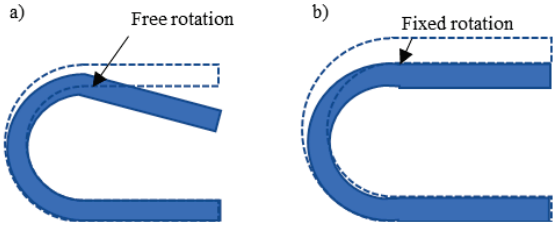

Figure 10: *Deformed shapes of fuses: a) Connection Testing; b) Fuse Testing.*

In conclusion, the testing results demonstrate the importance of considering the effects of connection rotation and leg deformation when evaluating timber connection performance. The observed ability of the fuse leg to rotate freely during connection testing resulted in a distinct deformation pattern and a concentrated plastic zone at the mid-bend of the fuse. This, combined with the inelastic properties of the tensile fuse, facilitated the development of a symmetric hysteresis response. However, using the results of fuse testing to ensure the capacity design of the connection remains valid is a more conservative approach. These findings have significant implications for the design and evaluation of timber connections, potentially leading to the development of more efficient and reliable structural systems.

https://doi.org/10.52202/069179-0407

4 Connection Evaluation

The connection evaluation is done by comparing its characteristics to some of the existing solutions. These characteristics include ductility factor, μ, ultimate moment, M_u and failure mode. Table 2 shows the tests used in this comparison along with the beam cross-section and the failure mode shown in each one.

Table 2. *Comparison test results with previous connection tests*

Connection	Beam Cross Section	Failure mode
Developed connection (2023)	608×265	Ductile U-shape yielding
Dong et al (2021) [15]	450×315	Ductile Dowel Yielding
Karagiannis et al.(2017) [16]	280×140	a bolt-row shear failure
He et al.(2017) [17]	260×130	Wood Splitting
He and Liu(2015) [5]	300×200	Ductile rod yielding
Lam et al.(2010) [18]	304×130	Splitting

Figure 11 provides a visual representation of the relationship between two critical factors in connection design. The chart is divided into several zones, each representing a different type of connection performance based on the compromise between ductility and ultimate moment. The horizontal axis represents ductility, a measure of how much a material can deform before fracturing. The vertical axis represents the strength ratio, which is the ultimate moment divided by the yielding moment of a connection used to measure the connections' ability to resist external loads and stresses without failing. The chart is divided into several regions or zones, each representing a different type of connection performance. The zone in the upper right corner represents the ideal connection design, characterized by high ductility and high ultimate moment. Other zones represent various levels of compromise between ductility and strength ratio, such as connections with lower ductility but a higher strength ratio or vice versa. The chart provides a valuable tool for engineers and designers to optimize connection design based on their specific needs and constraints.

The ductility factor(μ) plays a crucial role in determining the behaviour of a structural element under seismic loading conditions. As per the EN12512 [19] guidelines, μ is calculated using Equation (1):

$$\boldsymbol{\mu = \theta_u / \theta_y} \quad (1)$$

Where θ_u represents the rotation at ultimate moment capacity, and θ_y is the rotation at yielding. Based on the value of μ, the structural element is categorized as brittle (μ ≤ 2), low ductility (2 < μ ≤ 4), moderate ductility (4 < μ ≤ 6), or high ductility (μ > 6), according to Smith et al.'s categorization of Timber connections [20]. This classification helps in selecting the appropriate connection design for seismic-resistant structures based on the desired ductility and ultimate moment capacity. the ductility factor is calculated based on the average of tested specimens. In cases where there are multiple groups, the average of the strongest group is considered. For determining the ultimate moment capacity, the average value of tested specimen is used, except for the cases with no replicates, where the most robust specimen represents each study, as is the case for our developed connection.

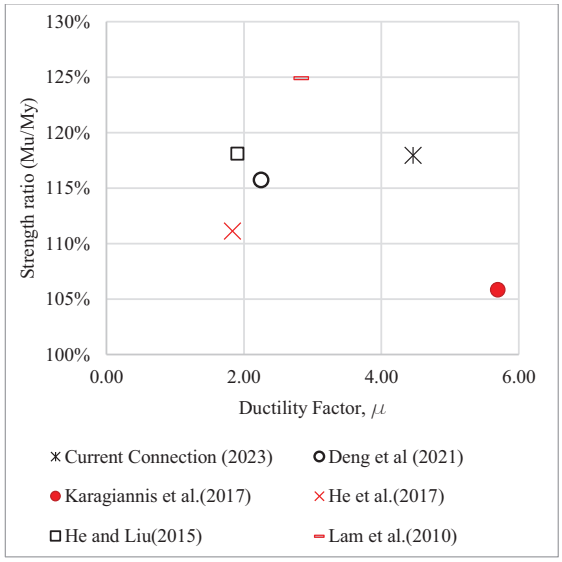

Figure 11: *Optimization chart used in the comparison between the developed connection and samples from existing solutions.*

The chart (Figure 11) clearly indicates that the developed connection is located in a favourable position. It exhibits higher ductility than the connection with the highest strength ratio presented by Lam et al. (2010) [18] and a higher strength ratio than the connection with the highest ductility factor introduced by Karagiannis et al. (2017) [16]. It is noteworthy that all the connections with a red colour legend in the chart have a brittle failure mode, such as plug shear, splitting, or bolt-row shear failure. Thus, by excluding these connections that failed in a brittle manner from the chart, the developed connection would be an ideal solution. Moreover, the developed connection offers a unique advantage in that it is the only one among the represented solutions that feature easy-to-replace fuses. This feature sets it apart from other connections and makes it a superior choice for multiple applications.

5 SUMMARY AND CONCLUSIONS

This study describes the experimental program developed to evaluate the cyclic response of a steel timber beam-to-column connection for seismic-resistant design. The testing program includes fuse testing and connection testing, which are used to determine the inelastic

https://doi.org/10.52202/069179-0407

mechanisms of seismic fuses and the connection. The results of the experimental testing are presented, including overall connection response, von Misses strain demands, and moment-rotation hysteresis responses. The fuses demonstrated a high capacity for dissipating seismic energy, and the connections were capable of resisting significant cyclic demands (in the order of 8% drift ratio) without brittle failure. The proposed connections demonstrated a comparative performance in terms of overstrength and deformation capacities in comparison with similar timber connections developed in the past. Overall, the experimental program provides valuable insight into the cyclic behaviour of U-shaped fuses implemented into beam to column connections of timber structures in tension and compression and provides a basis for future research in this field.

ACKNOWLEDGEMENT

The authors gratefully acknowledge the generous support provided by the Natural Sciences and Engineering Research Council of Canada, Advanced Research in Timber Systems (ARTS), and the Canadian Institute of Steel Construction Centre for Steel Structures Education and Research at the University of Alberta, whose financial assistance was instrumental in enabling this research. In addition, we extend our heartfelt appreciation to PAALID ENG, Western Archrib, Alberta Innovates, the I.F. Marison Lab, and C-FER Technologies for their invaluable contributions to this study. Their provision of materials, preparation of specimens, testing operations, and hosting of the test operation were integral to our research efforts. Special thanks are due to C-FER Technologies for their partnership and commitment to advancing our understanding of this field.

REFERENCES

[1] A. Mowafy, A. Imanpour, and Y. H. Chui, “Evaluation of the Seismic Response of an Innovative Hybrid Steel-Timber Structure,” *Ce/Papers*, vol. 4, no. 2–4, pp. 1864–1873, 2021, doi: 10.1002/cepa.1497.

[2] H. Daneshvar, J. Niederwestberg, C. Dickof, R. Jackson, and Y. Hei Chui, “Perforated steel structural fuses in mass timber lateral load resisting systems,” *Eng. Struct.*, vol. 257, no. March, p. 114097, 2022, doi: 10.1016/j.engstruct.2022.114097.

[3] L. F. Sirumbal-Zapata, C. Málaga-Chuquitaype, and A. Y. Elghazouli, “Experimental assessment and damage modelling of hybrid timber beam-to-steel column connections under cyclic loads,” *Eng. Struct.*, vol. 200, no. August, p. 109682, 2019, doi: 10.1016/j.engstruct.2019.109682.

[4] M. Andreolli, M. Piazza, R. Tomasi, and R. Zandonini, “Ductile moment-resistant steel-timber connections,” *Proc. Inst. Civ. Eng. Struct. Build.*, vol. 164, no. 2, pp. 65–78, 2011, doi: 10.1680/stbu.9.00098.

[5] M. J. He and H. F. Liu, “Comparison of glulam post-to-beam connections reinforced by two different dowel-type fasteners,” *Constr. Build. Mater.*, vol. 99, pp. 99–108, 2015, doi: 10.1016/j.conbuildmat.2015.09.005.

[6] H. Yang, W. Liu, and X. Ren, “A component method for moment-resistant glulam beam-column connections with glued-in steel rods,” *Eng. Struct.*, vol. 115, pp. 42–54, 2016, doi: 10.1016/j.engstruct.2016.02.024.

[7] a Iqbal, S. Pampanin, and a Buchanan, “Seismic Performance of Prestressed Timber Beam-Column Sub-Assemblies,” *New Zeal. Soc. Earthq. Eng.*, no. 27, 2010.

[8] S. Pampanin, “Reality-check and renewed challenges in earthquake engineering: Implementing low-damage systems - From theory to practice,” *Bull. New Zeal. Soc. Earthq. Eng.*, vol. 45, no. 4, pp. 137–160, 2012, doi: 10.5459/bnzsee.45.4.137-160.

[9] R. Gohlich, J. Erochko, and J. E. Woods, “Experimental testing and numerical modelling of a heavy timber moment-resisting frame with ductile steel links,” *Earthq. Eng. Struct. Dyn.*, vol. 47, no. 6, pp. 1460–1477, 2018, doi: 10.1002/eqe.3025.

[10] J. M. Kelly, R. I. Skinner, and A. J. Heine, “Mechanisms of Energy Absorption in Special Devices for Use in Earthquake Resistant Structures.,” *Bull. New Zeal. Soc. Earthq. Eng.*, vol. 5, no. 3, pp. 63–73, 1972, doi: 10.5459/bnzsee.5.3.63-88.

[11] M. J. N. Priestley, “The PRESSS program - Current status and proposed plans for Phase III,” *PCI J.*, vol. 41, no. 2, pp. 22–40, 1996, doi: 10.15554/pcij.03011996.22.40.

[12] A. Baird, T. Smith, A. Palermo, and S. Pampanin, “Experimental and numerical Study of U-shape Flexural Plate (UFP) dissipators,” *NZSEE Conf.*, no. January 2021, pp. 1–9, 2014, [Online]. Available: http://db.nzsee.org.nz/2014/poster/2_Baird.pdf.

[13] ASTM, “Standard Specification for Structural Bolts , Alloy Steel , Heat Treated , 150 ksi Minimum,” no. January 2004, pp. 7–12, 2010, doi: 10.1520/A0490-12.2.

[14] FEMA; and ATC, “461/Interim Testing Protocols for Determining the Seismic Performance Characteristics of Structural and Nonstructural Components,” no. June. Applied Technology Council, Redwood City, CA 113, 2007.

[15] W. Dong, M. Li, M. He, and Z. Li, “Experimental Testing and Analytical Modeling of Glulam Moment Connections with Self-Drilling Dowels,” *J. Struct. Eng.*, vol. 147, no. 5, pp. 1–18, 2021, doi: 10.1061/(asce)st.1943-541x.0002977.

[16] V. Karagiannis, C. Málaga-Chuquitaype, and A. Y. Elghazouli, “Behaviour of hybrid timber beam-to-tubular steel column moment connections,” *Eng. Struct.*, vol. 131, pp. 243–263, 2017, doi: 10.1016/j.engstruct.2016.11.006.

[17] M. He, J. Zhang, and Z. Li, “Influence of cracks on the mechanical performance of dowel type glulam bolted joints,” *Constr. Build. Mater.*, vol. 153, pp. 445–458, 2017, doi: 10.1016/j.conbuildmat.2017.07.095.

[18] F. Lam, M. Gehloff, and M. Closen, “Moment-

resisting bolted timber connections," *Proc. Inst. Civ. Eng. Struct. Build.*, vol. 163, no. 4, pp. 267–274, 2010, doi: 10.1680/stbu.2010.163.4.267.
[19] CEN, "Standards Europe. EN 12512:2001 Timber structures - Test methods," Brussels, Belgium, 2001.
[20] I. Smith, A. Asiz, M. Snow, and Y. . Chui, "Possible Canadian/ISO Approach to Deriving Design Values from Test Data," 2006.

https://doi.org/10.52202/069179-0407

World Conference on Timber Engineering Oslo 2023

AN EXPERIMENTAL STUDY ON THE SAFETY PERFORMANCE OF A WOOD MASONRY STRUCTURE

Daiki Iwamoto[1], Joichi Nakakuki[2], Waikong Lam[3], Hiro Kawahara[4], Masamichi Sasatani[5]

ABSTRACT: This paper presents the experimental results conducted to evaluate the mechanical properties and safety of a wood masonry structure called "Mirika no Ki" (Mirika) used in a complex cultural facility in Japan. Mirika is designed to prioritize the use of locally sourced wood and emphasizes its potential reusability during disasters or emergencies. The wood is stacked in 36 layers with a section size of 105 mm x 170 mm, and full-threaded screws are utilized for joints. The study evaluates the horizontal resistance of Mirika through an in-plane horizontal loading test on a wood masonry wall. Additionally, two further experiments were conducted to verify the structural integrity and functionality of the joints. The objective of this study is to provide fundamental data for designing wood masonry structures to promote the recycling of wood materials.

KEYWORDS: Wood masonry structure, Screw joint, Pull-out resistance of screws, In-plane shear test, Out-of-plane shear test

1 INTRODUCTION

Forests have multiple functions such as preserving national land and supplying forest products, so proper maintenance and preservation are necessary. In Japan, there is a movement to promote wood recycling through the establishment of laws related to the promotion of wood utilization. As part of the active use of wood, the renovation plan of a complex cultural facility in Nakagawa City, Fukuoka Prefecture, utilized a locally manufactured wood masonry structure "Mirika no Ki" (Mirika) with the concept of emphasizing space and gathering people under the tree (Figure 1).

The design of Mirika prioritizes the use of raw wood harvested in Nakagawa City to emphasize its importance and provide the ability to reuse it in case of disaster or emergency. The lumber used to construct Mirika has a section size of 105 mm x 170 mm and is stacked in 36 layers by varying the length of the members. The joints between each piece of lumber are made from the top layer using full-threaded screws (Figure 2), which have high reproducibility, are easy to construct, and allow for freedom in shaping. Therefore, the development of Mirika is expected to greatly contribute to the promotion of wood material recycling. However, there are few similar structures, so data to design from is limited. Therefore, in this research, experiments are conducted to obtain basic data to design wood masonry structures. The forces acting on the joints are thought to arise in the screw in tension and shear directions and the wood in compression direction and are carried by the tension of the screw and the compression of the wood in the bending direction. This study aimed to evaluate the safety and mechanical properties of Mirika, a material used in wood masonry structures. In-plane wall experiments were conducted as well as joint pull-out and joint bending tests to validate the structural integrity and functionality of the joints. The

Figure 1: *Wood Masonry Structure" Mirika no Ki"*

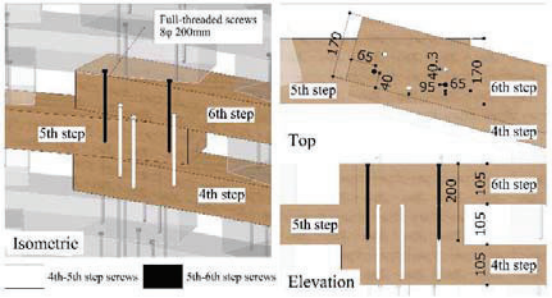

Figure 2: *Detailed image of the joint*

[1] Daiki Iwamoto, Tokyo Denki University, Japan, 21fma06@ms.dendai.ac.jp
[2] Joichi Nakakuki, Tokyo Denki University, Japan, 18fa081@ms.dendai.ac.jp
[3] Waikong Lam, Noot Engineering Consultant, Japan, waikong.lam@noot.engineer
[4] Hiro Kawahara, Tokyo Denki University, kawahara@mail.dendai.ac.jp
[5] Masamichi Sasatani, Tokyo Denki University, sasatani@mail.dendai.ac.jp

https://doi.org/10.52202/069179-0408

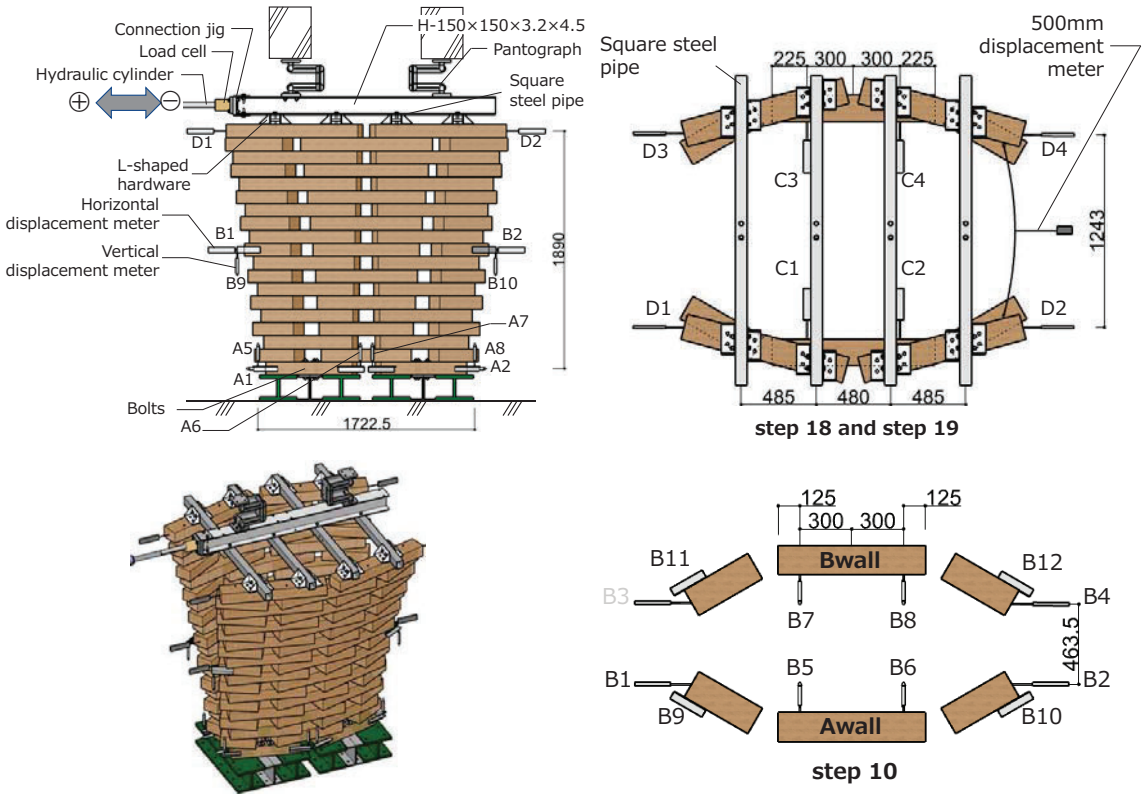

Figure 3: *Shear wall test specimen and setup*

results of these experiments provided fundamental data for the design of Mirika.

2 SHEAR WALL TEST

2.1 SPECIMENS AND SETUP

In Japan, elastic design is usually performed with a base shear coefficient of 0.2 to 0.3. However, since Mirika is thought to be unstable due to its high center of gravity, the base shear coefficient was set to 0.5. Therefore, Mirika's self-weight 0.5 times (15kN) was set as the target for horizontal resistance, and an in-plane horizontal loading test was conducted on a wood masonry wall. An experiment was conducted on the application of horizontal forces within the wall of the wooden assembly structure. The shape and dimensions of the test body in the wall test and the position of the displacement meter are shown in Figure 3.

The test body cuts out 1/6 of Mirika from the top and uses up to the 19th step, which is the height of the opening. Two test bodies were joined back-to-back, with the top of the two bodies were constrained by steel.

This is to consider the impact of stress on the surface and stabilize the test body shape and reproduce the resistance mechanism under the same condition where force is applied in the direction of the opening as Mirika. The sections of 105 mm x 170 mm cedar lumber were stacked vertically, and full-threaded screws 8Φ200 mm were used with 3 screws at each joint for the lower 5th step and 2 screws at each joint for the 6th step and above.

The loading schedule was implemented according to the literature and the apparent shear deformation angle was

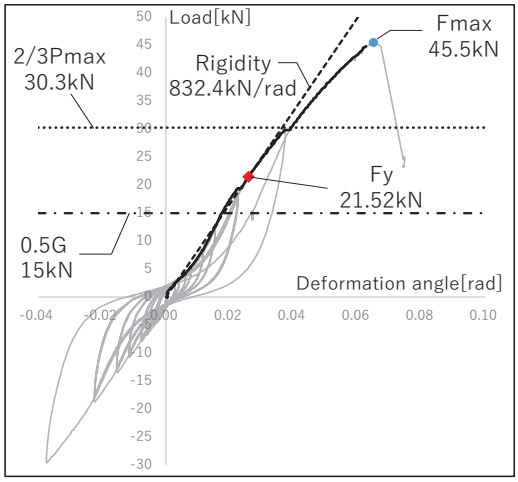

Figure 4(a): *Load deformation angle curve*

tested 3 times at various radian values (1/450, 1/300, 1/200, 1/150, 1/100, 1/75, and 1/50) in positive and negative alternation, with a single repetition at 1/30 rad. The loading was increased to reach the maximum load and then continued until it decreased to 80% of the maximum load.

2.2 RESULTS

Load deformation angle curve and final failure condition in Figure 4. The graph uses a true shear deformation angle. The horizontal displacement of the beam material was measured using a 500 mm displacement transducer

https://doi.org/10.52202/069179-0408

Figure 4(b): *Ultimate Fracture Properties (Left), pulling out of screws (Right)*

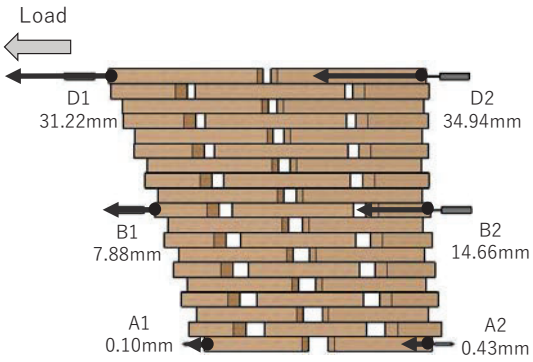

Figure 5: *Awall horizontal displacement*

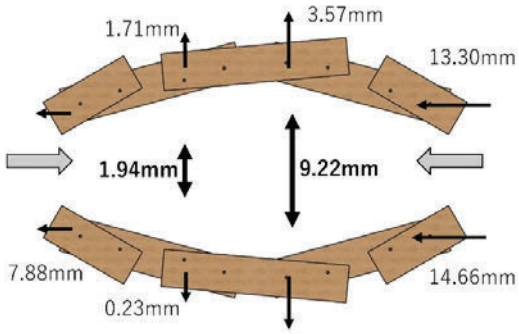

Figure 6: *10th step horizontal displacement*

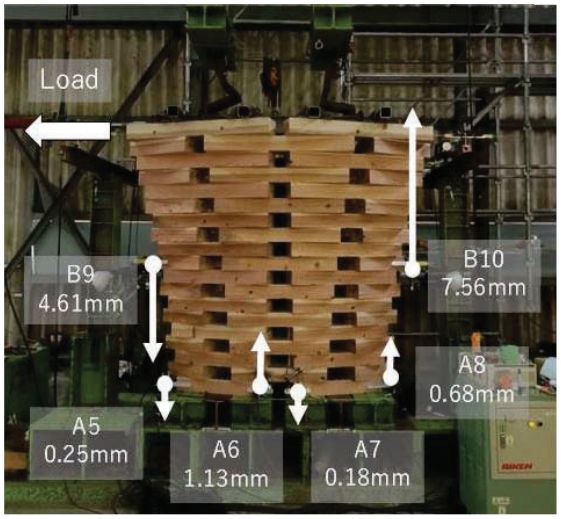

Figure 7: *Awall Vertical displacement*

attached to the shaft of the 19th step. For the horizontal displacement of the foundation, the average value of the horizontal displacement meters A1 to A4 of the 1st step is used.

For the vertical displacement of the column foot, the average value of the vertical displacement meters A5 and A9 of the first section and the average value of A8 and A12 are used to calculate. The characteristic value was calculated based on reference 4). The final fracture behavior was the pullout of screws at the 5th and 6th steps when the horizontal displacement of the 19th step was 140 mm and the maximum bearing capacity was 45.45kN, and the maximum pullout of about 70 mm was observed after the fracture. Figure 5 shows the horizontal deformation of Awall at 0.5G, and Figure 6 shows the horizontal displacement at the 10th step, which is the middle of the w all. The deformation on the right side is larger than that on the left side at the 10th step. Also, at the 10th step, both the deformation in the direction outside the surface and the deformation in the direction inside the surface are larger on the right side compared to the left side. Therefore, while the 10th step undergoes shear deformation in the direction of the applied force, it collapses in the direction inside the surface and deforms in the direction outside the surface. Figure 7 shows the vertical displacement at 0.5G (15kN). On the tenth floor, the deformation on the left side of Awall is 4.61mm vertically downwards and on the right side it is 7.56mm vertically upwards, which means it is rocking in the left direction. The safety of the wall as Mirika has been confirmed from the results exceeding the target of this structure's 0.5G in terms of buckling strength and 2/3Pmax.

https://doi.org/10.52202/069179-0408

3 PULL-OUT TESTS

3.1 SPECIMENS AND SETUP

A pull-out test was conducted to confirm the characteristics of the joint part when subjected to tension force in this structure. The test body consisted of cedar wood (density: 411.7kg/m3 (avg.), moisture content: 14.7% (avg.)) with dimensions of 105 mm x 170 mm × 250 mm and was fastened using 8φ200 mm full-threaded screws (Figure 8). The number of full-threaded screws was varied in two ways, 1 screws (S1) and 2screws (S2), with each variation resulting in 6 test bodies for a total of 12 test bodies. The load was applied at a uniform speed of 1mm/min using a universal testing machine (2000kN). The measurement item was the average value obtained from two displacement gauges, which were placed on the wood in the vertical direction and measured the bolt pull-out amount δ. The load was increased until the maximum strength was exceeded by 0.8Pmax or the wood was cracked, ending the experiment.

3.2 RESULTS

The load-deformation curve of the pull-out test is shown in Figure 9. The calculation of characteristic values was based on the manual for designing wooden joints 1). The final failure mode of the S1 test specimen was screw head embedment for 1 of the 6 specimens, and destruction by pulling out the tip of the screw for 5 specimens (Figure 10). The average ultimate strength of S1 was 6.16kN, which was 37% higher than the calculated value assuming a wooden screw in the "Standard for structural design of timber structures" (AIJ standard[1]). The final endurance was over the calculated value for 5 out of 6 bodies and had a higher distribution than the calculated value overall. Defects may have affected it, as there were knots and cracks of around 4d size in the vicinity of the screw within 7d from the screw location of the used lumber. The large variation in test results may be due to the high-density variability (CV) of 12% in the lumber and instability in the shape of the test body. The final destructive properties of the S2 test bodies were that 1 out of 6 bodies had the tip of the screw pulled out and 5 bodies were broken by cracking along the fibers of the wood (Figure 11). The test bodies that were broken by cracking had almost linear stiffness increases until the yielding and cracking of the wood occurred around 0.8mm and the load dropped once. The average final resistance per screw in S2 was 6.38kN, which was 42% higher than the calculated value assuming

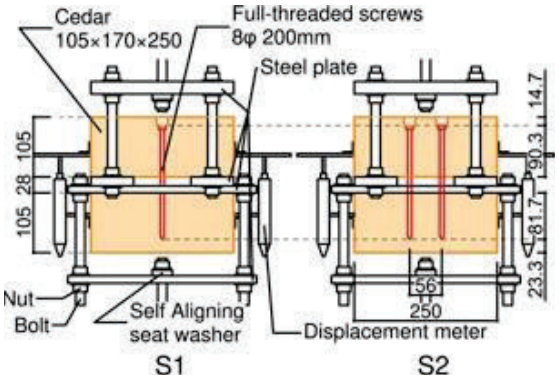

***Figure 8(a)**: Specimen configuration and set-up*

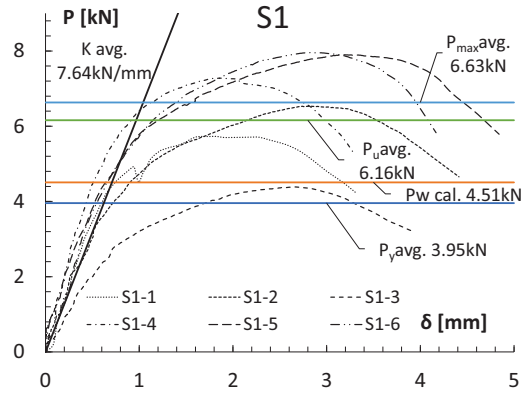

***Figure 9(a)**: S1 load-deformation curve*

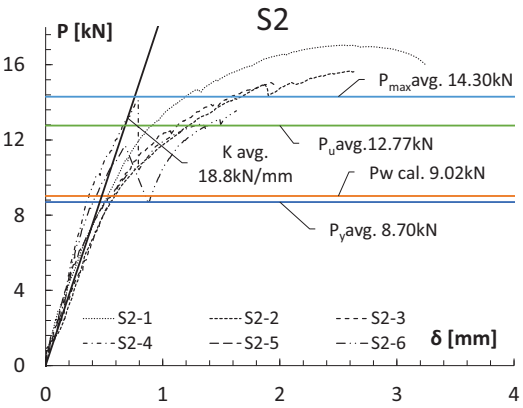

***Figure 9(b)**: S2 load-deformation curve*

***Figure 8(b):** Picture of pull-out test*

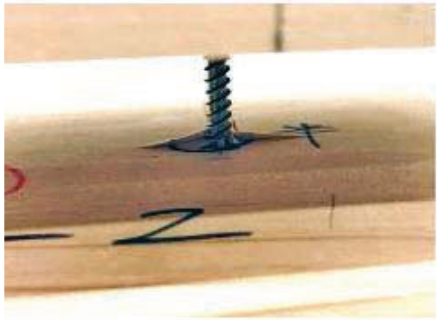

***Figure 10:** S1 pulling out the tip of the screws*

***Figure 11:** S2 cracking along the fibers*

https://doi.org/10.52202/069179-0408

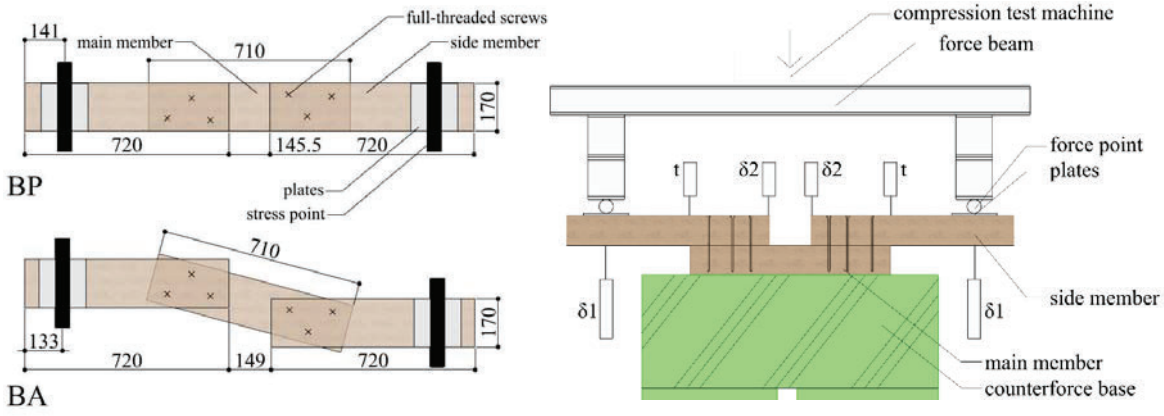

***Figure 12**: Joint test specimen shapes and installation*

wood screws using AIJ standards. When compared with the yielding resistance of S1, S2 demonstrated more than 2 times the yielding resistance. From this, it can be said that there is no reduction in withdrawal resistance due to multiple screws in the joint.

4 JOINT TEST

4.1 SPECIMENS AND SETUP

The experiment outline and test body dimensions are shown in Figure 12. The purpose of the bending experiment of the joint is to understand the mechanical characteristics when the locking deformation by the horizontal force causes the overturning moment in Mirika. The test body was shaped to reproduce the shape of the joint's 1st-2nd steps, which was considered to generate the most bending stress in Mirika.

The test body was made by layering two Sugi timber materials with main timber dimensions of 105 mm x 170 mm × 710 mm and side timber with the same cross-sectional length of 720 mm in the fiber direction parallel (BP) or rotated 15 degrees in the plane (BA), and with a water content of 16.3% (avg.), the density of 412kg/m3 (avg.), and Young's modulus of 6892.2N/mm2 (avg.). Three full-threaded screws 8Φ 200 mm were driven vertically.

The shape of the test body was layered symmetrically left and right to consider stability during loading. The rotation angle of BA is the same as that of Mirika. The screw insertion position was determined by the edge distance and spacing based on the AIJ standard for lag screw joints. Both BP and BA were arranged similarly to the first and second sections of Mirika. The number of test bodies was 6 for BP and 7 for BA. The measurement items were vertical displacement δ1 [mm] at the applied force point, compression amount t [mm] at the main member mouth position, and vertical displacement δ2 [mm] at the side member end.

The test body was placed on a counterforce base, plates for preventing compressive strain, and cylindrical fixtures were installed at both applied force points, and a uniaxial compression test machine with 2000kN was used to apply vertical force through an applied force beam. The applied force schedule was to reach the maximum strength in about 10 minutes, and the force was applied

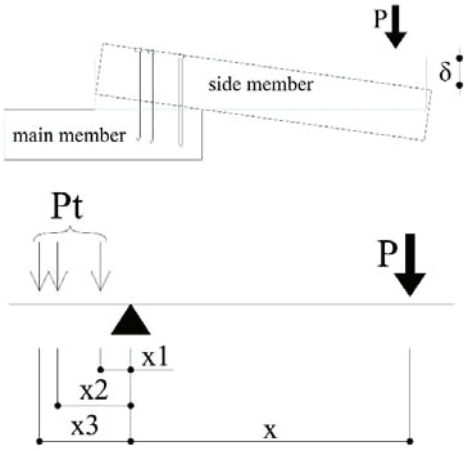

***Figure 13**: Joint dynamics model*

$$P = P_t \cdot \frac{x_1 + x_2 + x_3}{x} \qquad (1)$$

P: Estimated Bending Strength P_t: Screw Pull-out Strength
x: Distance from the bottom of the timber to the point of application
x_1, x_2, x_3: Distance from timber edge to screw core

until it reached 0.8Pmax after reaching the maximum strength. The estimated maximum strength was calculated by assuming the wood to be a rigid body and using the balance Equation of the pulling strength of the screw and the moment depending on the insertion position based on Equation (1) (Figure 13)

4.2 RESULTS

The load-deformation curve is shown in Figure 14, the experimental conditions are shown in Figure 15, and the characteristic values are shown in Table 1. The vertical axis of Figure 14 is the load on the side that broke among the left and right of 1 test body, and the horizontal axis is the vertical displacement of the point where the load was applied on the side that broke. The calculation of the characteristic values is the same as for the pull-out test.

The final fracture behaviour is dominated by the pull-out of the screws in both BP and BA, and the fracture is accompanied by wood compressive displacement. Brittle fractures were not observed in all test specimens, and the load gradually decreased after the maximum strength. In BA, rotational deformation in the direction of twisting of

https://doi.org/10.52202/069179-0408

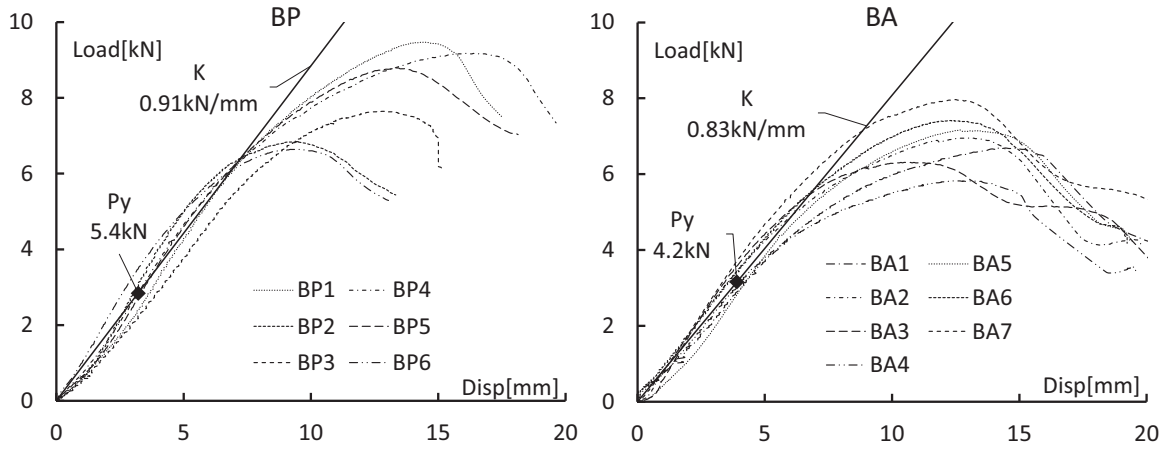

Figure 14: *Joint test load-deformation curve*

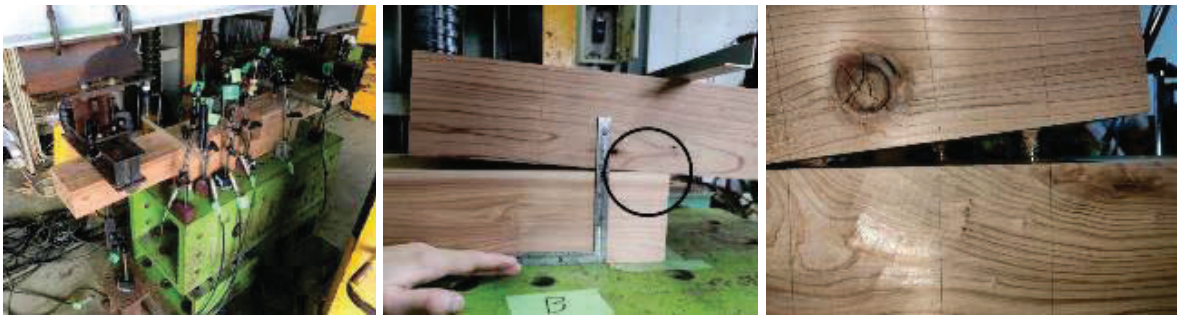

Figure 15: *Joint test process (Left), wood compressive displacement (Middle), pulling out of screws (Right)*

Table 1: *Joint test characteristic value*

		Initial stiffness K [kN/mm]	Yield strength Py [kN]	Maximum capacity Pmax [kN]	Ultimate strength Pu [kN]
BP	Average	0.92	5.40	8.09	7.45
	Lower limit	0.88	2.84	5.49	5.16
	Equation (1)	—	6.37	—	—
	Equation (2)	—	2.84	—	—
BA	Average	0.83	4.23	6.90	6.35
	Lower limit	0.81	3.16	5.37	4.75
	Equation (1)	—	6.02	—	—
	Equation (2)	—	3.02	—	—

the side member also occurred due to the angle of the material. The average yield strength obtained from the experiment was lower than the predicted strength calculated by equation (1), with 85% for BP and 70% for BA. This is the effect of the moisture content of the wood used and the compression between the woods. The average moisture content of the wood used in both series was about 22%, exceeding the recommended value of the AIJ standard, so there is a possibility of a decrease in screw withdrawal resistance and an increase in compression amount. And the compression between the wood pieces resulted in a triangular compression that maximizes the end of the main member. This causes the rotation center of the main member during the bending deformation of the joint to move from the end of the main member to the center of gravity of the triangular compression, resulting in experimental values lower than

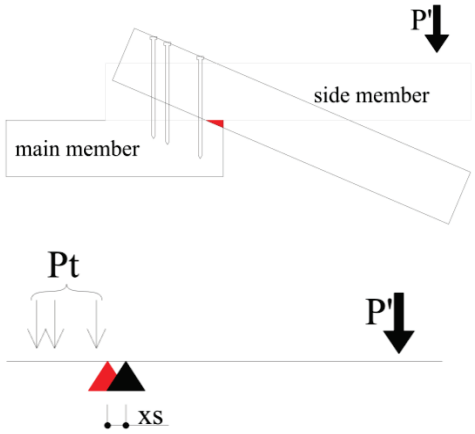

Figure 16: *Joint dynamics model considered compression*

$$P' = P_t \cdot \frac{x_1 + x_2 + x_3 - 3x_s}{x + x_s} \qquad (2)$$

P': Estimated Bending Strength $x_s : x_p/3$
x_p : Main material compression length

the bending resistance assumed in Equation (1) when the wood is assumed to be a rigid body.
Therefore, there is a possibility that the estimated value will be closer to the experimental value by modelling the support point that considers the compression of the wood. Considering the above factors, the lower limit of the bending-yield capacity of this joint was calculated using Equation (2) (Figure16), which was developed from

https://doi.org/10.52202/069179-0408

Equation (1) using the wood-screw pullout capacity equation in the AIJ Standard and the penetration equation in the Design Manual for Wood Structural Joints. Here, it is assumed that the dominant area of wood compression is near the edge of the main member, based on the extra-length condition and the experimental results. The bending capacity was estimated by applying the fulcrum reaction force of Figure 16 to ΣN in the denting equation to obtain x_p and using the moment balancing equation if the center of rotation moves to one-third of that value. Comparing the estimated values calculated above with the experimental values, the BP series and BA series are -0.3% and -4.3%, respectively, and the bending-yield capacity of the joints in this test specimen shape can be estimated on the safe side using Equation (2).

5 CONCLUSION

The mechanical properties of wooden composite structures were verified through experiments. The following are the results obtained from this study.

1. The mechanical properties of the joints in Mirika were experimentally understood.
2. In the pull-out experiment, the average ultimate strength of the S2 series was 2.07 times that of the S1 series, and it is considered that there was no reduction in initial rigidity in the wooden joint shape in the scope of this experiment.
3. When considering the rotation of the joint, there is compression between the wooden materials, and it is necessary to consider the movement of the rotation center in estimating the strength.
4. In the wall inside the surface experiment, the yielding strength was 21.5kN and 2/3Pmax was 30.3kN, and the safety as a structural body of the wall was confirmed as the result exceeded the target weight of the bookshelf (15kN).

ACKNOWLEDGEMENT

We thank Mr. Furumori Koichi (Furumori Koichi architectural design studio), Mr. Sugioka Toshikuni (Sugioka Sawmill), Mr. Ikeo Taku (Sumai koubou), and Mr. Kenzo Nagasako, Mr. Masaya Funakoshi (undergraduate students in Tokyo Denki University) for their cooperation in conducting this research. We gratefully acknowledge their support.

REFERENCES

[1] Architectural Institute of Japan. Standard for structural design of timber structures in Japan. October 2002.

[2] D. Iwamoto, J. Nakakuki, H. Kawahara, M. Sasatani. Experiment on the structural performance of timber masonry joints Part 1: Outline of large wooden bookshelf structure and experimental study of pull-out test. AIJ Hokkaido Chapter Architectural Research Meeting, pp. 421-422, September 2022.

[3] J. Nakakuki, D. Iwamoto, H. Kawahara, M. Sasatani. Experiment on the structural performance of timber masonry joints Part 2: Joint bending tests. AIJ Hokkaido Chapter Architectural Research Meeting, pp. 423-424, September 2022.

World Conference on Timber Engineering Oslo 2023

STRUCTURAL PERFORMANCE OF REINFORCED GLULAM BEAMS

Laith I. Gharaibeh[1], Ghasan Doudak[2]

ABSTRACT: The performance of wood glulam beams is generally characterized by brittle behaviour with little to no post-peak strength. Attempts to enhance the post-peak behaviour of glulam beams have included principles of reinforcing the tension face, while promoting more ductile compression-side failure. In the current study, Near-Surface Mounted (NSM) rebars are utilized to reinforce glulam beams in order to enhance their performance when subjected to static and dynamic loading. The reinforcement rebars are installed inside grooves at the tension face of the beam, using epoxy adhesive. The reinforced glulam beams were tested statically in four-point bending and with simply supported boundary conditions. Another set of reinforced glulam beams was tested under simulated blast loads using a shock-tube device. Similar loading and boundary conditions were also applied during the dynamic tests. An analytical approach was developed, verified, and used to investigate glulam beams reinforced with steel, GFRP, and CFRP rebars. The result of this comparison indicated a significant enhancement in the maximum peak strength and stiffness of the reinforced beams using steel and CFRP rebars, while beams reinforced with GFRP rebar exhibited lower increases in strength and stiffness.

KEYWORDS: Reinforced Glulam, Steel reinforcement, NSM, Blast load, Shock-tube device.

1. INTRODUCTION

Glued laminated timber (Glulam) has been successfully used for decades in heavy timber construction, with recent examples including the Brock Commons building in B.C. Canada and the headquarters of the Swiss media corporation in Zurich, Switzerland. The behaviour of glulam in flexure is generally characterized as linear-elastic brittle, under both static and dynamic loading [1]. The ultimate flexural failure typically occurs on the tension face at a defect (e.g. knots) or in some instances at finger joints [2]. Several research studies have been conducted to enhance the post-peak performance of timber beams in order to produce a more ductile failure mode. Examples of these attempts include reinforcing the tension face of the beam in order to delay the development of cracks at the tension side. This also helped initiate crushing failure mode at the compression face which in turn facilitated the increase in the overall energy-dissipation capabilities of the beam elements. Lacroix and Doudak [3] reinforced glulam beams using fiber-reinforced polymers (FRP) and reported an increase of 20% to 40% in the moment capacity depending on the reinforcement configuration. Yang et al, [4] reinforced a series of glulam beam specimens by applying steel reinforcing rebars at the beam tension face using reinforcement ratios of 0.5%, 1%, and 1.7%. The study reported increases in the range of 32% to 45% in moment capacity. Kliger et al. [5] investigated a wide range of reinforcement ratios of steel and carbon fiber plates. The study found that a maximum reinforcement ratio of 2% was appropriate to avoid shear failure before the ultimate flexural capacity of the beam was reached. The study also reported an increase in moment capacity in the range of 57% to 96%, when compared to the reference unreinforced beam. The behaviour of structural elements under blast loading is also greatly affected by high strain rates, resulting from the short duration of the loading. Research in the field of blast effects on timber elements has generally focussed on individual components with idealized simply supported boundary conditions, including light-frame stud walls [6,7], glulam beams and columns [1], as well as cross-laminated timber (CLT) elements [8]. Although some attempts have been made to address timber-composite assemblies, these studies have been limited to FRP sheets [3], steel straps [9], and corrugated steel panels [10]. Different types of reinforcing materials can be used to strengthen glulam beams using rebars, such as steel, glass fiber-reinforced polymer (GFRP), and carbon fiber-reinforced polymer (CFRP). In addition to providing sufficient strength and stiffness, steel can also add a significant amount of ductility, which in turn enhances the structural response of the glulam elements under blast loading. In the current study, epoxy is used as a bonding agent as well as a coating material to protect the steel. One of the disadvantages of GFRP is its low stiffness, which reduces its efficiency as a reinforcement material. CFRP material has high stiffness,

[1] Laith I. Gharaibeh, University of Ottawa, Canada, Lghar082@uottawa.ca
[2] Ghasan Doudak, University of Ottawa, Canada, gdoudak@uottawa.ca

https://doi.org/10.52202/069179-0409

but it is also associated with a high cost. The current study aims to investigate possible retrofit techniques to reinforce glulam beams using the near-surface-mounting (NSM) method. The structural behaviour of reinforced glulam beams using steel, GFRP and CFRP rebars will also be examined analytically.

2. EXPERIMENTAL PROGRAM

2.1 METHODOLOGY

The overarching goal of the experimental program is to validate analytical approaches that would facilitate the analysis of composite timber-reinforcement elements using the NSM reinforcement method. The experimental program includes subjecting full-scale beam specimens to static and blast-simulated dynamic testing under similar loading configurations and boundary conditions. The NSM method involves hollowing out grooves in the perimeter of the beam, placing the reinforcements inside the grooves, and then applying the epoxy over the reinforcement and initiating the curing process. The installation process of the NSM rebar method is illustrated in Figure 1.

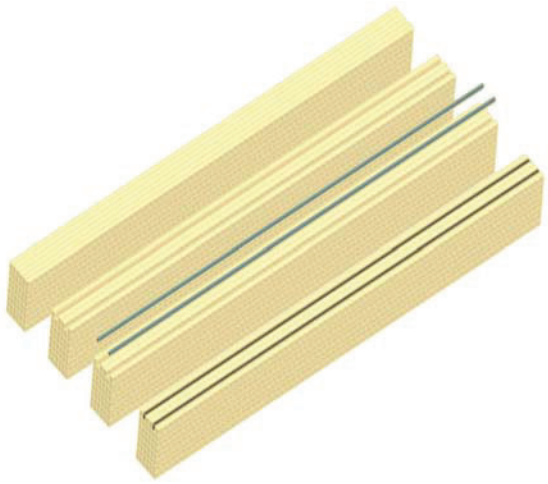

Figure 1: *NSM installation process*

The fact that the reinforcement is embedded inside the wood and surrounded by epoxy increases the contact surface area, unlike external reinforcement. Moreover, the reinforcement can be easily applied at the bottom or the side of the beam, unlike the external fabric reinforcements that have to be applied at both the bottom and side faces of the beam to provide suitable confinement and avoid debonding. The aesthetic appearance of the reinforcement could also be enhanced by adding a thin strip of wood to cover the groves after applying the reinforcement with the epoxy materials.

2.2 SPECIMENS AND TEST SETUP

Glulam beams with NSM reinforcement were tested statically and dynamically under a four-point bending. The procedure and configuration for the static and dynamic tests are presented in the following sections.

2.2.1 Static test

A set of glulam beams reinforced with 10M, 15M, and 20M steel rebars were tested statically. The beams consisted of a cross-sectional dimension of 137 mm x 191 mm and a length of 2.5 m. The beam grade was 24F-ES/NPG, produced by Nordic Structures. Wire gauge sensors were used to measure the displacement at the middle and one-third points of the beam span length. Strain gauges were also attached at the perimeter of the wood glulam section as well as along the steel reinforcements to measure the strain distributions. Furthermore, lateral supports were used at both ends of the beams to prevent out-of-plane buckling. The loads were applied to the beam specimens using a hydraulic jack, through an I-steel section. Load cells were placed at the supports to measure the reaction forces, as shown in Figures 2 and 3.

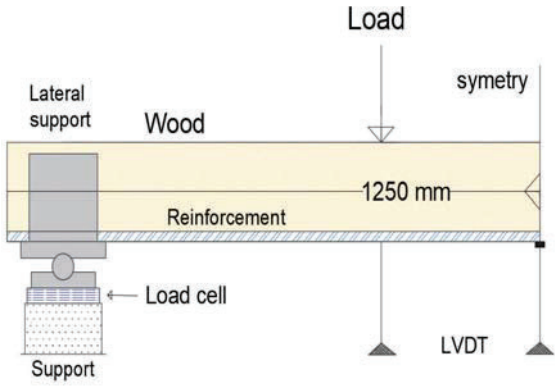

Figure 2: *Half-beam view for the static test.*

Figure 3: *Static test for glulam beam*

2.2.2 Dynamic test

A matched set of reinforced beams was tested under simulated blast loading using the shock-tube apparatus located at the University of Ottawa. Similar loading and boundary conditions to those described in the static loading tests were employed for the simulated blast tests, with the exception that the beam specimens were placed vertically, and the loads were applied horizontally. The shock-tube apparatus uses air pressure to create different

combinations of pressure and impulse to simulate the effect of far-field explosions. The device consists of three components: the driver, spool, and expansion sections. The driver section length can range from 305 mm to 5185 mm. Different combinations of pressures and impulses can be generated by changing the driver length. The shock-tube device is capable of generating a maximum pressure of 100 kPa and impulse of up to 2200 kPa-ms, as well as a positive phase duration of up to 70 ms. Aluminium foil layers are placed at the front and back of the spool, and when the desired air pressure in the spool is reached, the air pressure in the driver is drained, rupturing the aluminium foils and allowing the compressed air to propagate along the expansion section and interact with the test specimen. A load transfer device (LTD) mounted at the end-frame was used to collect the pressure and transfer it to the mounted specimen. The main components of the shock-tube device are shown in Figure 4.

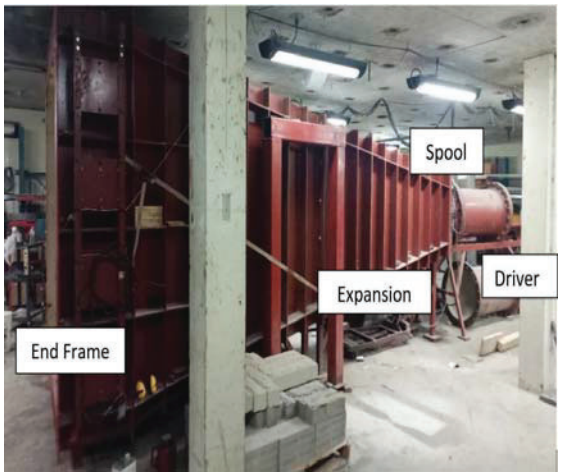

Figure 4: *Shock-tube device*

The displacement of the beam at mid-span was measured using linear variable displacement transducers (LVDTs) with the high-speed capability to capture the dynamic blast load. Dynamic load cells were used to measure the force reactions at the ends of the beams. The measurements were recorded using a data acquisition system (DAS) having a sampling rate of 10,000 samples per second. Furthermore, a high-speed camera having a recording rate of 2000 frames per second was used to capture the behaviour of the specimen and detect the failure mode during the test.

3. RESULTS AND DISCUSSION

3.1.1 Experimental Results

An example of the experiment results from the static test is presented in this section. The force-displacement curves for both the unreinforced and reinforced beams with 10M steel rebars are shown in Figure 5.

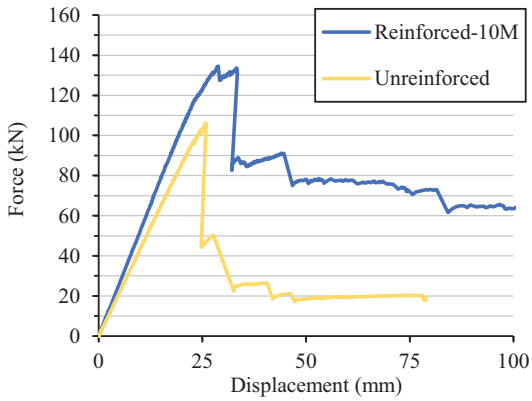

Figure 5: *Force-displacement curve*

From Figure 5 it can be observed that the strength and stiffness of the reinforced beam are significantly increased by the addition of the two steel reinforcement rebars. For this example, the strength and stiffness of the beam were increased by 34% and 23%, respectively, when compared to the unreinforced specimen. More importantly, it can be noted that the post-peak behaviour of the reinforced beam is greatly enhanced. A post-peak load carrying capacity in the range of 47% of the peak load is maintained until displacement levels are in excess of 100 mm.

Figure 6: *Damaged reinforced beam*

As shown in figure 7, cracks were developed and propagated at the tension face of the beam, and the epoxy material was fractured. The wood fibers at top of the beam were crushed due to compression stress. This type of failure mode is preferable since it enhances both the maximum peak strength as well as the post-peak behaviour of the glulam beam.

3.1.2 Analytical Results

The analysis approach used to predict the behaviour of the composite beam is the fiber section method. The analysis is conducted by setting an initial strain value at the top of the beam and selecting an initial position for the neutral axis depth (Z). Then, the strain profile along the depth of the beam is distributed linearly based on the Euler-Bernoulli beam theory by assuming that plane sections remain plane. The strain and stress are calculated at each

https://doi.org/10.52202/069179-0409

fiber based on the material model proposed by Buchanan [11], as shown in Figure 8.

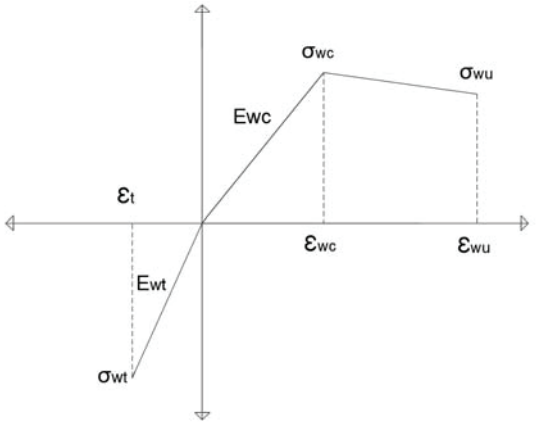

Figure 7: *Material wood model*

The model has been successfully used to simulate wood material behaviour in several previous studies [e.g., 1, 2]. In this model, σ_{wc} and σ_{wu} represents the maximum and ultimate stress in compression, respectively, and σ_{wt} is the maximum tensile stress. E_{wt} and E_{wc} are the modulus of elasticity for wood in tension and compression, respectively. ε_{wc} and ε_{wu} represent the strains at the maximum and ultimate stress in compression, respectively, while ε_{wt} is the failure strain at σ_{wt}. Following the calculation of the stresses at each fiber layer, the tension or compression force is calculated by taking the average stress at that fiber and multiplying it by the area of the fiber. The summation of the tension and compression forces from all fibers must satisfy equilibrium. If the equilibrium is not reached, a new value for depth Z is generated, and the entire procedure is repeated until the equilibrium is satisfied. The fiber moment is obtained by multiplying the force in the fiber by the distance to the neutral axis. The procedure is repeated for a new value of strain increment until the moment-curvature relationship for the beam section is achieved.

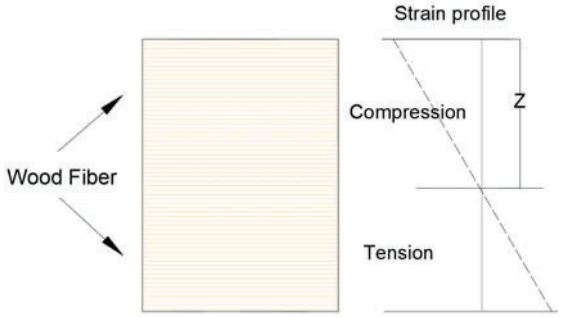

Figure 8: *Fiber section for glulam beam*

A VBA Excel-based code was developed and used to conduct the fiber section analysis and establish the stress-strain relationship along the depth of the beam. The effect of groove size was also considered in the analysis. Finally, the curvature is integrated twice to determine the displacement along the entire beam. The force-displacement curve obtained from this analytical procedure is compared with the experimentally obtained curve, as shown in Figure 10. The figure shows that the theoretical model provided a very good agreement with the experimental result in terms of force and displacement. Work is currently underway to extend the modeling capabilities beyond the peak load and to account for the behaviour of the reinforced beams.

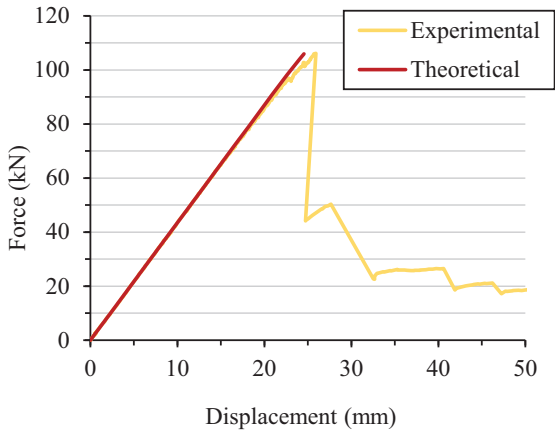

Figure 9: *Static test for glulam beam*

3.1.3 Reinforced beam

The analytical procedure presented in the previous section was used to compare the behaviour of glulam beams reinforced with steel, GFRP and CFRP rebars. For the steel rebar, an elastoplastic material model was used, as shown in Figure 11, where F_y represents the yield stress, E_s is the modulus of elasticity, and ε_y is the yielding strain. For the GFRP and CFRP materials, the stress-strain relationship is assumed to be linear, with E_g and E_c representing the modulus of elasticity, while F_g and F_c are the associated stresses, respectively. ε_c and ε_g are the failure strains for CFRP and GFRP materials, respectively, as shown in Figure 12.

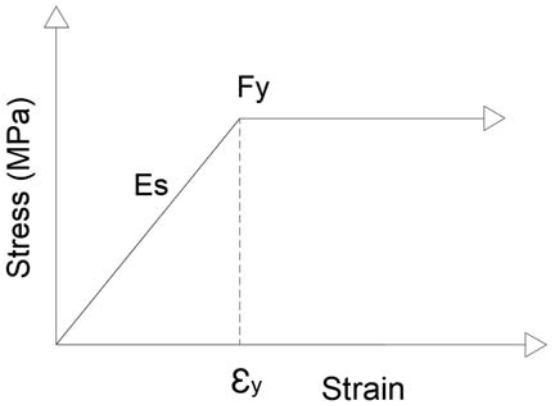

Figure 10: *Steel elastoplastic model*

https://doi.org/10.52202/069179-0409

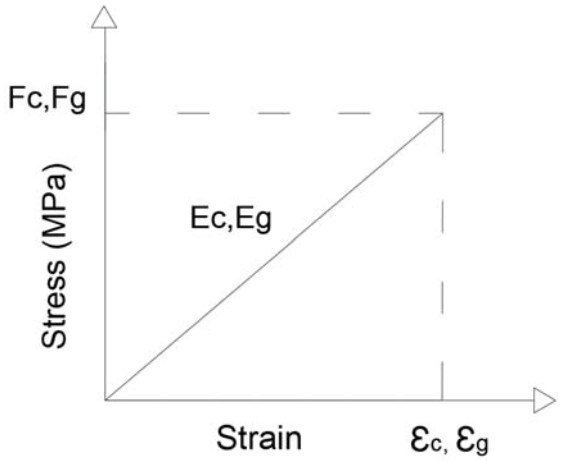

Figure 11: *GFRP and CFRP linear models*

For the reinforced beams, the forces at the reinforcements have to be included in the summation of the forces to satisfy the equilibrium along the cross-section. The reinforcements were assumed as concentrated elements since their cross-sectional area is very small compared to the glulam member. The analytical model was modified to accommodate the effect of the reinforcements in the sectional analysis. Figure 13 shows the wood fiber cross-section for the reinforced glulam beams, including the GRFP, CFRP, or steel rebar reinforcements.

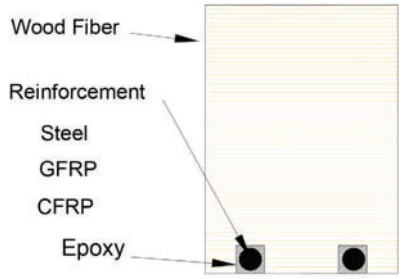

Figure 12: *Fiber-reinforced beam section*

For the purpose of the analytical comparison, US rebar sizes #4, #5 and #6 were used due to their availability in steel, GFRP and CFRP rebar sizes. The material property for the steel rebars was assumed to be according to ASTM 615 [12] with 420 MPa tensile strength and 200 GPa modulus of elasticity. The GFRP rebars were assumed to be consistent with those produced by MST Rebar Inc. in Canada [13], with 60 GPa in modulus of elasticity and 1,000 MPa minimum tensile strength, while the CFRP rebars were assumed to have 124 GPa modulus of elasticity and 2,000 MPa minimum tensile strength, similar to those produced by Hughes manufacturer in US, [14]. An example of a moment-curvature distribution along half the beam length is shown in Figure 14, for reinforced beams with #6 steel reinforcement rebars.

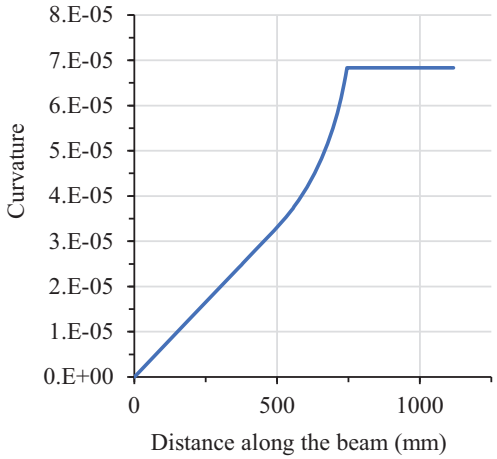

Figure 13: *Moment-curvature distribution*

Using the analytical model, the force-displacement curves obtained for the glulam beams reinforced with steel rebar sizes #4, #5 and #6 are compared, as shown in Figure 15.

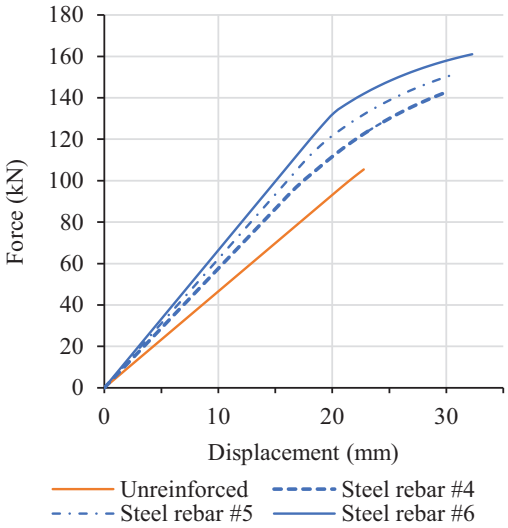

Figure 14: *Reinforced beam with steel rebar*

From this comparison, it can be observed that the strength of the reinforced glulam beams was increased by 35%, 45% and 53% when using rebar sizes #4, #5 and #6, respectively, compared to the unreinforced beam. The corresponding increases in stiffness was 24%, 34% and 53%, respectively. The curves using the GFRP reinforcement rebars are shown in Figure 16. It can be observed that the increase in strength is less than that observed in the beams analyzed with steel reinforcements, while for stiffness, only a minor increase is observed. The non-linear behaviour observed near the peak load in specimens with steel rebars is much less pronounced in GFRP rebars.

https://doi.org/10.52202/069179-0409

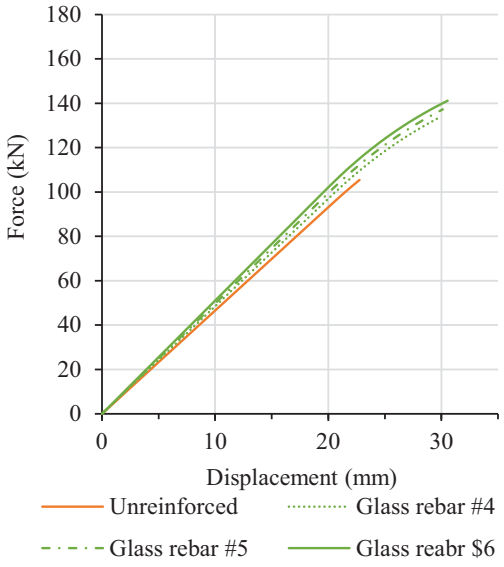

Figure 15: *Reinforced beam with GFRP*

Figure 17 presents the results for the beams with the CFRP reinforcement rebars, and shows increases in strength of 40%, 49% and 56%, using rebar sizes #4, #5 and #6, respectively, while the corresponding stiffness increases were 14%, 20% and 27%. The results show that the general increase magnitude is comparable to the steel rebars when it comes to the beam strength, however, the increase associated with stiffness is less, which can be attributed to the higher modulus of elasticity of the steel rebars.

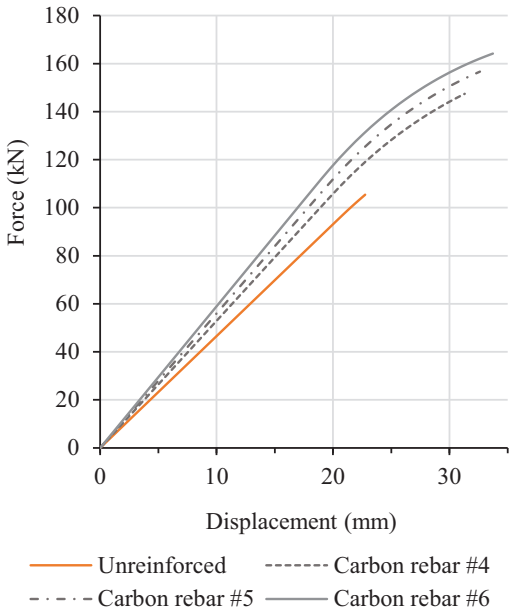

Figure 16: *Reinforced beam with CFRP*

A direct comparison between the three retrofitting options, illustrating the benefit of utilizing steel rebars, is shown in Figure 18 for the same rebar size (i.e., #6).

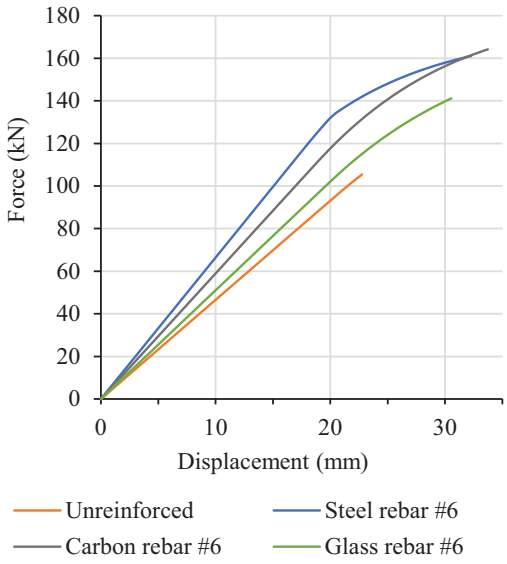

Figure 17: *Glulam beams with reinforcements*

4. CONCLUSIONS

Near-surface mounted rebars were used to enhance the performance of glulam beams, especially in the post-peak region. Reinforcements were embedded inside the beam at the tension face and adhered to the beam using epoxy. The behaviour of the reinforced beams was investigated experimentally, and results showed a significant enhancement in the strength, stiffness as well as post-peak behaviour. An analytical approach, developed based on the fiber method and using available wood constitutive models, was validated using the experimental results. The models were then used to compare the impact of using steel, GFRP and CFRP reinforcement rebars. The result of this comparison showed a significant enhancement in the maximum peak strength when using steel and CFRP rebars, while better enhancement in stiffness was obtained from the steel rebars. For beams reinforced with GFRP rebars, the increase in strength and stiffness was modest.

REFERENCES

[1] Lacroix, D. N., Doudak, G.: Effects of High Strain Rates on the Response of Glulam Beams and Columns. Journal of Structural Engineering, 144(5), 04018029, 2018.

[2] Lacroix, D. N., and Doudak, G. : Determining the Dynamic Increase Factor for Glued-Laminated Timber Beams" *Journal of Structural Engineering*, 144(9), 04018029, 2018.

[3] Lacroix, D.N., Doudak, G.: Experimental and Analytical Investigation of FRP Retrofitted Glued-Laminated Beams Subjected to Simulated Blast

Loading, Journal of Structural Engineering, 144(7), 04018089, 2018.
[4] Yang H., Liu W., Lu W., Zhu S., Geng Q: Flexural behavior of FRP and steel reinforced glulam beams: Experimental and theoretical evaluation. Constr. Build. Mater. 106:550–563, 2016.
[5] R. Kliger, M. Al-Emrani, M. Johansson, R. Crocetti, editors. Strengthening glulam beams with steel and composite plates, *Proceedings of the Asia-Pacific Conference on FRP in Structures,* 2007, Hong Kong.
[6] Lacroix, D., & Doudak, G. (2012). Behaviour of typical light-frame wood stud walls subjected blast loading. World Conference on Timber Engineering: Strength and Serviceability - Extreme Events. Auckland, New-Zealand.
[7] Lacroix, D. N., and Doudak, G. (2015). "Investigation of Dynamic Increase Factors in Light-Frame Wood Stud Walls Subjected to Out-of-Plane Blast Loading." *Journal of Structural Engineering*, 141(6), 04014159.
[8] Poulin, M. et al. (2017) Experimental and analytical investigation of cross-laminated timber panels subjected to out-of-plane blast loads: Journal of Structural Engineering: Vol 144, no 2,
[9] Lopez-Molina, A. and Doudak, G. (2019) "Retrofit techniques for cross-laminated timber (CLT) elements subjected to blast loads," *Engineering Structures*, 197, p. 109450.
[10] Lacroix, D.N., Doudak, G. and El-Domiaty, K. (2014) "Retrofit options for light-frame wood stud walls subjected to blast loading," *Journal of Structural Engineering*, 140(4).
[11]. Buchanan, A., H. (1990). "Bending strength of lumber." Journal of Structural Engineering, 116(5), 17.
[12] ASTM A615 / A615M-09, Standard Specification for Deformed and Plain Carbon-Steel Bars for Concrete Reinforcement, ASTM International, West Conshohocken, PA, 2009.
[13] MST-BAR® Manufactured by MST Rebar Inc., Toronto, Canada.
[14] Aslan™ 200 Carbon fiber reinforced polymer (CFRP) bars for structural strengthening, owens corning, 2018.

https://doi.org/10.52202/069179-0409

World Conference on Timber Engineering Oslo 2023

BENDING TESTS ON TIMBER CONCRETE COMPOSITES WITH PERFOBOND CONNECTIONS

Elif Appavuravther[1], Bram Vandoren[1], José Henriques[1]

ABSTRACT: Long spans in timber concrete composites (TCC) is the next step of improvement that is ambitioned by the industry and designers for more efficient structures. With Perfobond connections, which are originally developed for steel-concrete composites (SCC) constructions, targeting longer spans in TCC is feasible. In this paper, full scale TCC beams are experimentally investigated under four point bending with the use of Perfobond connections. Two sets of experiments are performed with a variation of the concrete type (normal weight concrete vs lightweight concrete). The results indicate that the use of Perfobond connections lead to a linear behaviour until initial local damage. In specimens with lightweight concrete, failure in the most loaded connections is observed, however it did not lead to strength degradation. For specimens with normal weight concrete however, maximum load is obtained with the connection failure which led to significant cracking of timber under bending (tension side) and subsequently, the collapse of the TCC beam. As a result of this experimental campaign, a performant behaviour of the TCC beam implementing the Perfobond connections is observed and therefore, longer spans may be envisaged.

KEYWORDS: Perfobond connector, adhesively bonded connection, timber concrete composite, bending test

1 INTRODUCTION

The use of timber is re-gaining popularity in the construction sector. To comply with the neutral emission regulations in Europe by 2050, the use of timber is one of the solutions that can help since the carbon emission of the wood is much lower when compared to the traditional, commonly used construction materials, such as concrete. To overcome the weaknesses of the structural properties of using bare timber, such as vibration and deflection, the combination of concrete with timber is an innovative solution which is becoming more and more implemented by the construction sector. Besides its reliable structural behaviour, using a concrete slab and timber beam allows a prefabricated solution where the on-site application time can be limited, the quality of the materials and assembly can be controlled due to limited execution on site. Concrete can also be used to rehabilitate and reinforce the existing timber structures. Timber-concrete composite solutions are relatively new and the experimental work on bending behaviour of the beams is limited in the current literature [1, 2].

In a TCC beam, the target is that the concrete slab resists the compression stresses and the timber beam resists the tensile stresses. This optimal case can be obtained once the beam is in a high composite action. Such high composite action is obtained with connections with high stiffness. Traditional connections used in TCC, such as dowel connections, are limited in strength and stiffness [3, 4]. Notch connections lead to a high strength and stiffness, however they do not prevent an uplift (and therefore use of a screw is required) and have a very brittle behaviour [5, 6]. Bonded-in connection is another solution to overcome the limitations on strength and stiffness exhibited by common dowel connections [7]. Even though these connections have been investigated for decades, only recently researchers are coming to an agreement to have requirements in the design codes, such as a sub-section dedicated to bonded-in rods in the version under preparation of the prEN 1995-1-1 [8]. This is an important step to support designers using bonded-in solutions however, it only covers steel rods, and an extension to steel plate connectors is still to be done since they are being experimentally investigated in TCC for the past few decades [9-15].

Once the connection behaviour is determined, it is important to examine the behaviour of the connection in full scale composite beams under bending loading. The bending tests helps to determine how the composite action is achieved, how efficient it is, the distribution of stresses, the impact of the connection behaviour on the mechanical performance of the beam and therefore the capacity to distribute load.

In this work, Perfobond connections commonly used in SCC are adopted into TCC beams. Perfobond is a steel plate connector, originally developed for SCC beams. The steel plate, welded to the steel beam, is embedded in the concrete slab where mechanical interlock is mobilised at

[1] Elif Appavuravther, Hasselt University, Belgium, eliftuba.appavuravther@uhasselt.be
Bram Vandoren, Hasselt University, Belgium, bram.vandoren@uhasselt.be
Jose Henriques, Hasselt University, Belgium, jose.gouveiahenriques@uhasselt.be

https://doi.org/10.52202/069179-0410

the tip of the plate and through a concrete dowel action, obtained through predrilled holes in the plate [16], simultaneously, shear-slip and uplift resistance are mobilised.
In this experimental work, two different configurations are tested, one series with normal weight concrete and one with lightweight concrete. Failure loads and failure modes are compared for the two cases. The results indicate that, with the use different concrete types and strengths, similar behaviour and load capacity are obtained. Then, given the high strength and stiffness of this connection, leading to increased spacing between connectors, the suitability of the Gamma method to predict bending stiffness and load capacity is assessed. Moreover, experimental results are compared with more common solutions, such as rod connections from the literature, to further evaluate on the performance of TCC beams using Perfobond connections. The results show potential for the development of long spans beams.

2 MATERIALS AND METHODS

2.1 TEST SPECIMENS AND DESIGN

In this study, full scale bending tests are performed on 5.2 m long TCC beams. Three replicas of each series are tested. The difference between the two series is the concrete type. The concrete slab cross section was 600 x 70 mm and timber with a cross section of 90 x 270 mm (see Figure 1 (a)). In the timber beams, ten grooves with the dimensions of 110 mm x 55 mm x 10 mm are opened. For each beam, a total of ten connections are used, with spacing of 500 mm. The locations of the connections are presented in Figure 1 (b). The spacing is determined using the Gamma method for residential building and complying to ultimate limit state and service limit state [17].
The timber beam is covered by an adhesive tape to avoid moisture flow from the concrete to the timber and to avoid the friction between the two materials. The adhesive, with approximately 2mm thickness, is applied and dried in an indoor environment and following the recommendations given in the product Technical Documentation [18].
Additionally, a bare timber beam with the same cross-section as those used in the composite solution was tested for sake of comparison.

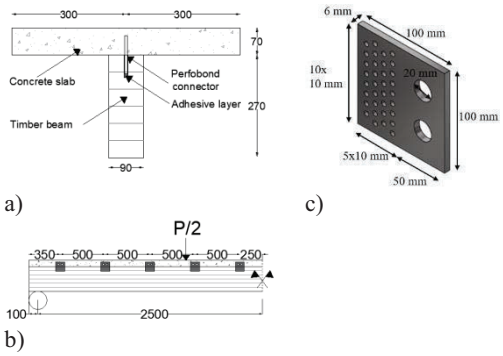

Figure 1 *Test specimens (a) cross section of the TCC beam (b) elevation view of test specimens (c) Perfobond connector dimensions*

2.2 MATERIALS

In the specimens denoted with P-NWC, normal weight concrete with a 28- day cubic compression strength of 41 MPa and density of 2200 kg/m^3 is used. In the series denoted by P-LWC, lightweight concrete with a 28- day cubic strength of 25 MPa and density of 1600 kg/m^3 is used. Minimum reinforcement is used to avoid concrete tension cracks [19]. Glulam timber of strength class 24h (Picea Abies specie) is used. Perfobond connectors with steel grade S355 are used, with cross section dimensions given in Figure 1 (c). The Perfobond is designed using the design model given in the literature [16]. For the bonding between the Perfobond connector and the timber beam, Sika Anchorfix-3030 epoxy-acrylate is used [20].

2.3 TEST SET-UP, MONITORING AND TEST PROCEDURE

The experimental set-up consists of a meccano system (the experimental frame), a hydraulic jack, load cells, supports and LVDTs (Linear Variable Differential Trasformer), as illustrated in Figure 2 (a). In total, eight LVDTs are installed on each beam, seven in the horizontal direction and one in the vertical direction at the midspan. The horizontal ones correspond to either connection location or placed under the loading. The LVDT locations are given in Figure 2 (b).
Each specimen was centred both in longitudinal and transversal direction to avoid eccentricity due to loading. The loading protocol given in EN 26891 is followed [21].

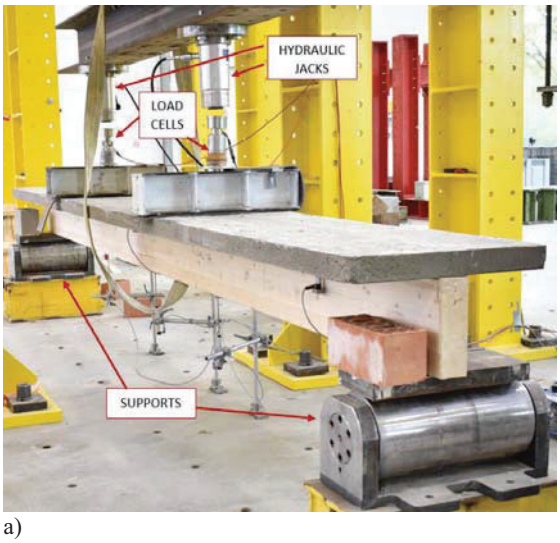

a)

https://doi.org/10.52202/069179-0410

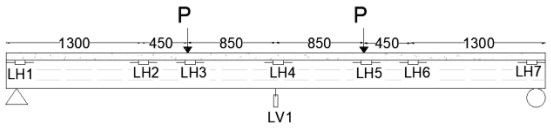

b)

Figure 2 *(a) Test set-up (b) LVDT Locations*

3 RESULTS AND DISCUSSION

3.1 TEST RESULTS

In Figure 3, the force-midspan deflection behaviour of all three replicas of each series and of the bare timber beam under four point bending is given. In Table 1, mean loads, at two different load levels, are given, i) at the initial failure, F_1, where the first failure is observed (during the experiments with the change in the slope of the force-slip behaviour) and ii) the maximum load where sudden loss of resistance is observed, F_{max}.

For the P-NWC series, no initial failure load is recorded as the first peak in the load lead to sudden load decrease.

A steep linear behaviour is obtained until F_{max} and the recorded force is 67.6 kN on average. At this point, the failure is due to the connection failure. In Figure 4 (a), the slip increase at F_{max} can be observed for specimen P-NWC-A (for force-slip behaviour of the beams, only the results of one series is presented for sake of clarity and as other specimens followed a similar trend). The major slip increase occurred at the LH1 and LH2 followed by LH3. The LVDT LH2 is located approximately under the third connection (see Figure 1 (b)), which justifies the connections 1, 2 and 3 failing, causing the significant slip measured at LH1 and LH2. Because of the brittleness of the connection in this case (with this type of concrete, NWC), the redistribution of force does not occur smoothly. The load was distributed among the connections as there are a few spikes of increase in load after a drop, as the slip increases, until the load could no longer be bore by the timber beam. A picture of the failed beam can be found in Figure 5 (a) where the timber failure is clear. Minor cracks at the concrete were observed however, failure of the connections was not extended to a visible form in the concrete and timber.

For the P-LWC series, a very steep behaviour is observed until on average 55.8 kN. At this point, a reduction in the slope of the force-deflection is observed without loss of the load capacity. At this load level, F_1, cracks around the connections are observed. The slip recordings from LH 1 and 2 given in Figure 4 (b), show the first three failed connections. A significant slip increase is recorded on LH 3 and 5 where the 4th connection is located showing that also failure on those connections occurred. The load is distributed among the remaining connections until the load capacity increased on average of 66.2 kN and at this load level, timber cracked, as given in Figure 5 (b), setting to the maximum capacity of these specimens. At the maximum load, the cracks around the connections became more visible and cone shaped failures are observed as the connection rotated with the increased load (see Figure 5 (b & c)). And this behaviour is different from the previous, here, connection failed in a less brittle mode which is seen by the fact that load is still increasing in a smooth way up to maximum load. It should also be noted that no uplifting occurred between the concrete and the timber layer.

One timber beam (90 x 270 mm) is tested under the same conditions to observe the difference with the TCC beams. A linear but rather more flexible behaviour is observed. The beam failed due to bending strength (tension) at 44.8 kN. This force-deflection curve clearly shows how the use of concrete improves the strength and stiffness of a timber beam.

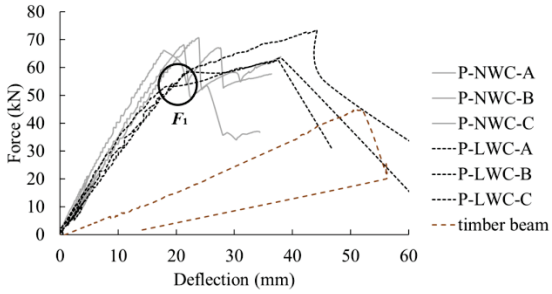

Figure 3 *Force-midspan deflection*

Table 1 *Experimental results (failure loads and failure modes)*

Specimen ID	F_1 (kN)	F_{max} (kN)	Failure at F_1	Global failure
Timber beam	-	44.8	-	Timber tension failure due to bending
P-NWC	-	67.6	-	Connection failure
P-LWC	55.8	66.2	Connection failure	Timber tension failure due to bending

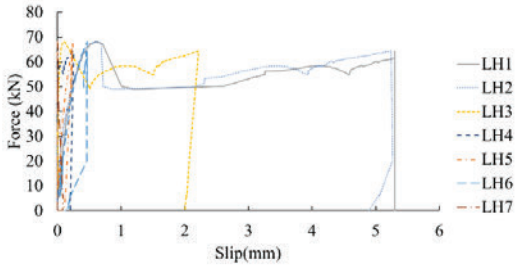

a)

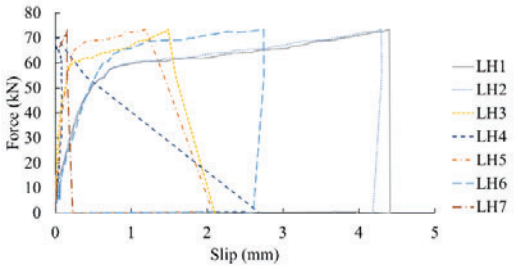

b)

Figure 4 *Force-slip curve (a) P-NWC-A (b) P-LWC-C*

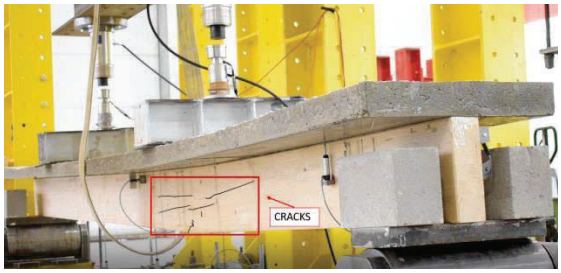

a)

b)

c)

Figure 5 *Failed specimens (a) P-NWC (b) P-LWC (c) P-LWC first connection failure resulting in cone failure in the concrete due to rotation of the connection*

3.2 DISCUSSION

With the change in the type and the strength of the concrete, a few observations can be made;

- The stiffness the TCC beam (Figure 3) is not significantly affected. The use of normal weight concrete lead only to a slightly stiffer behaviour. This increase is due to higher young modulus of this concrete type and of corresponding connection stiffness [22].
- The concrete type had an impact on the pre-peak behaviour due to the different behaviour of the connection with each type. In NWC the connection is stronger but more brittle not allowing a smooth distribution of forces through the connections distributed along the beam.
- As concrete did not govern maximum load capacity, the two series presented similar load capacity governed by the cracking of the timber beam. However, the concrete type played a role in the pre-peak behaviour due the impact of the concrete type at the shear connection level [22].
- The use of concrete and shear connections lead to 24% and 50% increase on load capacity with lightweight concrete and normal weight concrete, respectively.
- The curve (Figure 3) shows a significant difference in the bending stiffness between the composite beams and the bare timber. The bending stiffness increased 3.2 and 2.6 times when normal weight concrete and lightweight concrete and connections are added to the bare timber, respectively.

4 APPLICATION OF THE GAMMA METHOD TO A DISCRETE CONNECTION

Currently, the Gamma method is the analytical approach used for design since it is in the design code prEN 1995-1-1 [17]. Even though the limited range of application can lead to deviations on the prediction of the bending stiffness of the composite beam, and the corresponding stress distribution [23], the method is commonly used due to the simplicity and suitability for the current practical applications of TCC beams. Some of the causes of such deviations is in the fact that the model is developed for sinusoidal loading and the load distribution among connections is assumed to be equal. This assumption is accurate if the connection spacing is small [1]. In this work, however, with four-point bending and connection spacing of 500 mm, this is not the case. The connections outside in the loading zones does have same shear flow, however, the slip is higher further away from the midspan. The slip results showed that not all connections failed at the same load level (specially the series P-NWC – the decrease and increase in the force-deflection curve shows the connections failed gradually).

In Table 2, the comparison of experimental results with the Gamma method are given for the bending stiffness (EI), maximum load (F_{max}) and failure modes. In addition to experiments from this paper, an example from the literature with rod connections are used [23].

The expected failure mode by the Gamma method was the connection failure for the Perfobond connections, and combined bending and axial forces for the rod connections [23], which are in agreement with the experimental results reported. The connection forces are calculated using prEN 1995-1-1 Annex B [17].

The results show in terms of maximum load prediction, 33% and 62% underestimation is recorded for normal weight and lightweight concrete, respectively. The force limit for connections is introduced from the shear test results [22]. In shear tests, for the series with the use of lightweight concrete, failure at the connection level is recorded at less than half in comparison to the series with

https://doi.org/10.52202/069179-0410

the normal weight concrete. This justifies the 100% difference in the expected failure loads. This results clearly show that in the Gamma method, the connection forces are underestimated under bending behaviour. And 21% of underestimation is recorded from the rod connection Again, this underestimation is due to the fact that with the Gamma method, linear force distribution among all connections is assumed, whereas, in this study and the literature [23], it is shown that it does not represent the reality and the underestimation of connection forces. The spacing of connections is however, is expected to cause more deviation, which is also shown in this comparison.

With the Perfobond connections the overestimation of bending stiffness is approximately 5%, however for rod connection this is limited to 13%. The limited deviation for these experiments shows a good accuracy however, overestimation can cause problems in design applications. With bending stiffness, the results are in better agreement with the Gamma method as it is directly dependent on the mechanical and geometric properties of the composite beams.

Table 2 *Bending stiffness comparison between experimental results and Gamma method using Annex B of EN 1995-1-1 [17]*

	EI (kNm²)	**F_{max} (kN)**	**F_{max} mode**
P-NWC	8285.7	67.6	Connection failure
P-NWC_ Gamma method	8703.0	45.3	Connection failure
Difference (%)	-5.0	33.0	
P-LWC	7161.7	55.8	Connection failure
P-LWC_ Gamma method	7613.5	21.5	Connection failure
Difference (%)	-6.3	61.5	
Sebastian et al. [23]	1889.8	40.0	Combined bending and axial force
Sebastian et al._Gamma method	1638.2	31.6	Combined bending and axial force
Difference (%)	13.3	21.0	-

5 CONCLUSIONS

The objective of this work is to investigate the bending behaviour of TCC beams incorporating Perfobond shear connections. As a result of this experimental work, it can be concluded that Perfobond connections lead to a strong behaviour under bending loading. In both series, where the difference was the strength and the type of the concrete, the initial failure was a connection failure, followed by a bending strength (timber tension) failure.

The results indicate that the concrete type and strength had an effect on the load-deflection behaviour of the beam as it impacted the connection behaviour, however, maximum load capacity was not very different since the failure was due to the timber.

When the force midspan deflection of the TCC beam is compared with a (non-composite) timber beam, an increase of 24% and 50% on load capacity with lightweight concrete and normal weight concrete, respectively was recorded.

With the use of the Gamma method from prEN 1995-1-1, the bending stiffness, expected failure load and failure mode are compared. The results show that even though the failure mode was in agreement, Gamma method underestimates the maximum load and overestimates the bending stiffness. The deviation in bending stiffness can be explained with the deviation in the material properties. The deviation in the maximum load capacity depends on a few factors such as loading type, connection spacing and underestimation of the connection forces under bending loads.

This work shows that, with the given parameters, high composite action can be obtained with connection failure, which is targeted in TCC. Especially when lightweight concrete is used, controlled ductile failure is recorded.

ACKNOWLEDGEMENT

The authors would like to acknowledge Sika Belgium and LTS for contribution of materials and technical support. The support of master's students Thomas Sutens, Frédérique Claes and Joris Swinnen from 2020 – 2021 academic year are appreciated.

REFERENCES

[1] COST, *Design of timber-concrete composite structures - A state-of-the-art report by COST Action FP1402 / WG 4*. Shaker Verlag Aachen, 2018.

[2] S. Monteiro, A. Dias, and S. Lopes, "Transverse distribution of internal forces in timber–concrete floors under external point and line loads," *Construction and Building Materials,* 2016.

[3] COST, C. Sandhaas, J. Munch-Andersen, and P. Dietsch, Eds. *Design of Connections in Timber Structures*. 2018.

[4] A. Dias, "Mechanical behaviour of timber-concrete joints," PhD, TU Delft, Delft, Netherlands, 2005.

[5] L. Boccadoro, R. Steiger, S. Zweidler, and A. Frangi, "Analysis of shear transfer and gap opening in timber-concrete composite members with notched connections," (in English), *Materials and Structures,* Article vol. 50, no. 5, OCT 2017 2017, Art. no. ARTN 231.

[6] A. Dias, F. Fragiacomo, R. Harris, P. Kuklic, V. Rajicic, and J. Schanzlin, "Technical Specification – Final Draft - Eurocode 5: Design of Timber Structures - Part 1-3: Structural design of timber concrete composite structures – Final Draft / Project Team CEN/TC 250- SC5.T2," 2019.

[7] G. Tlustochowicz, E. Serrano, and R. Steiger, "State-of-the-art review on timber connections with glued-in steel rods," *Materials and Structures,* vol. 44, pp. 997-1020, 2011.

[8] *Eurocode 5: Design of timber structures (consolidated draft prEN 1995-1-1, formal enquiry)* 2022.

[9] P. Clouston, L. Bathon, and A. Schreyer, "Shear and bending performance of a novel wood-concrete composite system," (in English), *Journal of Structural Engineering,* Article vol. 131, no. 9, pp. 1404-1412, SEP 2005 2005.

[10] E. Lukaszewska, "Development of Prefabricated Timber-Concrete Composite Floors," PhD, Department of Civil, Mining and Environmental Engineering, Lulea University of Technology, Sweden, 2009.

[11] C. Avez, "Design of an adhesively bonded-in steel plate connection for Cross Laminated Timber," PhD in Engineering Science and Technology, University of Mons, Mons, Belgium, 2021.

[12] J. Miotto and A. Dias, "Evaluation of perforated steel plates as connection in glulam-concrete composite structures," (in English), *Construction and Building Materials,* Article vol. 28, no. 1, pp. 216-223, MAR 2012 2012.

[13] D. Otero-Chans, J. Estevez-Cimadevila, F. Suarez-Riestra, and E. Martin-Gutierrez, "Experimental analysis of glued-in steel plates used as shear connectors in Timber-Concrete-Composites," (in English), *Engineering Structures,* Article vol. 170, pp. 1-10, SEP 1 2018 2018.

[14] F. Suarez-Riestra, J. Estevez-Cimadevila, E. Martin-Gutierrez, and D. Otero-Chans, "Perforated shear plus reinforcement bar connectors in a timber-concrete composite solution. Analytical and numerical approach," (in English), *Composites Part B-Engineering,* Article vol. 156, pp. 138-147, JAN 1 2019 2019.

[15] E. Martin-Gutierrez, J. Estevez-Cimadevila, D. Otero-Chans, and F. Suarez-Riestra, "Discontinuous pi-form steel shear connectors in timber-concrete composites. An experimental approach," *Engineering Structures,* vol. 216, no. 110719, 2020.

[16] E. Oguejiofor and M. Hosain, "A parametric study of perfobond rib shear connectors," (in English), *Canadian Journal of Civil Engineering,* Article vol. 21, no. 4, pp. 614-625, AUG 1994 1994.

[17] *EN 1995-1-1 - Design of timber structures - Part 1-1: General rules and rules for buildings,* E. C. f. Standardization, 2004.

[18] Sika, "Technical Documentation Sika Anchorfix - 3030," ed: Sika.

[19] *EN 1992-1-1 Design of concrete structures - Part 1-1: General rules and rules for buildings,* E. C. f. Standardization, 2004.

[20] Sika, "Product Data Sheet Sika Anchorfix - 3030," ed: Sika.

[21] *EN 26891 - Timber Structures - Joints Made with Mechanical Fasteners - General Principles for the Determination of Strength and Deformation Characteristics*, 1991.

[22] E. Appavuravther, B. Vandoren, and J. Henriques, "Push-out tests on adhesively bonded perfobond shear connectors for timber-concrete composites," *Journal of Building Engineering,* 2022.

[23] W. Sebastian, O. Bell, C. Martins, and A. Dias, "Experimental evidence for effective flexural-only stiffnesses to account for nonlinear flexural-slip behaviour of timber-concrete composite sections," (in English), *Construction and Building Materials,* Article vol. 149, pp. 481-496, SEP 15 2017 2017.

https://doi.org/10.52202/069179-0410

World Conference on Timber Engineering Oslo 2023

DESIGN OF ASYMMETRIC FRICTION CONNECTION FOR SESIMIC RETROFITTING OF RC FRAMES WITH CROSS-LAMINATED TIMBER PANELS

Angelo Aloisio[1,2], Francesco Boggian[1], Roberto Tomasi[2]

ABSTRACT: This paper proposes a probabilistic model for predicting the friction coefficient of asymmetric friction connections to be used for the seismic retrofitting of reinforced concrete buildings using Cross-Laminated Timber (CLT) panels. The model has been calibrated on the experimental force-displacement curves of the AFC samples, tested at the Norwegian University of Life Sciences (Norway), within the e-SAFE research project.

KEYWORDS: Cross-Laminated Timber; Passive Dampers; Friction dampers; Seismic retrofitting; Probabilistic models.

1 INTRODUCTION

Among hysteretic devices, friction dampers have been gaining more attention in the last few years. These dampers dissipate seismic energy by mechanical damping through sliding friction with the primary braking rather than breaking principle [1]. There is a wide range of applications of friction dampers, from civil to mechanical and avionic engineering [2]. However, there are still a few attempts to use friction dampers for seismic retrofitting civil structures. Venuti 1976 [3] and Pall et al. in 1980 [4] were the first to add friction devices as additional damping sources in civil structures. The Limited Slip Bolt (LSB), evolved to the Pall Frictional Damper (PFD), exhibited stable, almost rectangular hysteresis cycles [5], [6]. PFD is conceived for X- and K-bracings. Its worldwide success has confirmed the merits of the PFD. Multiple applications and research papers are proving the value and efficiency of the PFD [7]–[10]. The main drawbacks of PFD are the relatively low capacity (less than 10 kips), the need for high precision work for its manufacture, and specialized training for the installation process [11], [12].
In 1989 Fitzgerald et al. [13] devised a friction connection called the Slotted Bolted Connection (SBC), characterized by a more straightforward design than the PFD. The proposed SBC worked by sliding channel bracing plate over a gusset plate interconnected by high strength bolts with washers (Belleville spring) for adjusting the bolt tension.
There are two main classes of SBC: the Symmetric and Asymmetric friction connection [14], [15]. Symmetric Friction Connection (SFC) is a type of SBC that consists of the main plate (with slotted holes), two brass shims, two outer plates, and high strength bolts.
Initially proposed by Clifton [16], Asymmetric Friction Connection (AFC) is another type of SBC [17], [18]. AFCs consist of steel plates and shim layers clamped by the pre-tensioned bolts.
AFC is a crucial component of Sliding Hinge Joints (a low damage beam-to-column connection for the Moment Resisting Frame). AFCs installed in SHJ consist of shims, cleat, cap plate, high strength bolts, and bottom flange of the beam. The friction originates from the sliding between (i) beam bottom flange and upper shim and (ii) cleat and lower shim [16]. Initial developments of AFC were based on brass shims [19]. Subsequent studies by Mackinven [20] extended the application to mild steel and aluminium shims. The AFC is simple to build, cost-effective, and capable of dissipating energy under seismic excitation.
However, the AFC hysteretic stability highly depends on the mutual hardness between the steel and shim layers. In addition, the stability of the hysteretic performance is affected by the interaction between abrasive and adhesive wear and friction phenomena. There are several examples of application of AFC connections in real buildings, see [21], [22]. A few scholars [23]–[27] attempted to verify the consequences of wear and friction on AFC in the past years. They found that a stable cyclic behaviour can be achieved if there is a significant difference in the mutual hardness of the siding surfaces, i.e. shim layer and steel plates. The similarity in sliding surfaces' hardness causes a significant instability of the hysteresis loop mainly due to the large amount of work-hardened wear particles produced during the sliding mechanism. These particles abrade the sliding surfaces in an irregular pattern, thus exhibiting a wear abrasive mechanism defined by Grigorian and Popov [19] and Khoo et al. [18]. The stability of the hysteresis curve, in the case of non-lubricated sliding surfaces, depends on the initial wear of the shim or steel plates. For instance, in the case of the shim layer being less hard than the plates, the initial wear increases the roughness of the shim layer. The wear particles generated in this process create lubrication that

[1] University of L'Aquila, Italy
[2] Faculty of Science and Technology, Norwegian University of Life Sciences, Oslo, Norway

https://doi.org/10.52202/069179-0411

stabilizes the friction coefficient. Therefore, the wear particles generated in the initial phase are crucial to achieving a stable performance of the AFC.
Aluminium shims are among the materials that exhibit the best performance, with the lowest and more stable friction coefficient. Currently the shims to be used in AFC are recommended to be abrasion-resistant, like (high hardness) steel [21]. Nonetheless, AFCs with high hardness cleat and high hardness shims do not provide specific benefit on the seismic performance [28].
There are different typologies of AFCs. The most used and studied is the Sliding Hinge Joint (SHJ). The SHJ is a flexural connection designed to use at the beams' ends in steel moment-resisting frames. It is an AFC where energy is dissipated through sliding in slotted bolted connections in the beam bottom flange [29]. The initial application of friction connections to low-damage moment-resisting joints has been recently extended to pinching-free connections for timber structures [30]. Pinching represents one of the significant weaknesses in timber structures since it is associated with considerable degradation after repeated cycles [31], [32]. Loo et al. [33] investigated the possibility of using SFC instead of hold-down for restraining timber shear walls against uplift, to cap the force transmitted to the wall, and reduce inelastic damage. The subsequent experimental campaigns presented in [15] established the effectiveness of SFC on reducing the degradation and pinching phenomena typical of timber connections. The following studies presented in [34] pointed to a displacement-based design method for multistorey CLT buildings with friction connections. Next to the findings by Loo et al., [35] studied the response of SFC connected to a CLT panel. Zamani and Quenneville proposed a resilient slip friction connection (RSF) as a hold-down connector for CLT panels [36]. So far, no AFC was used as a connection system for CLT panels except for the attempts by Boggian et al. [37]–[39]. Boggian et al. tested AFCs for a hybrid structural system, the e-CLT technology.

2 MECHANICAL RESPONSE OF THE E-CLT

Fig.1 shows the representation of the e-CLT system applied to a building. CLT panels are attached to the beams of each floor with a couple of friction connections (AFC), which can act as rigid connections or slide according to the entity of the horizontal force acting on the building. The basic functioning principle of the AFC is illustrated in Fig.2. When the applied force is below a certain threshold the AFC doesn't activate and stays in the *stick phase*, thus the total resisting force at the i-th story (f_t) is the summation of the resisting forces of the CLT panel (f_{clt}) and the RC frame (f_{rc}). If the reaction of the CLT panel exceeds the slip force (f_s), the AFC activates and transitions to the *slip phase*, and thus the total resisting force is the summation of the resisting force of the RC frame and the slip force of the AFC.

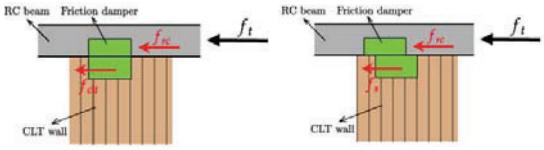

(a) (b)

***Figure 1**: Illustration of the contributions of forces: (a) before the AFC activation and (b) after the AFC activation.*

The e-CLT unit behaves like a parallel system, whose governing equations are:

$$f_t = f_{\mathrm{rc}} + f_{\mathrm{clt}} \quad \text{if} \quad |f_{\mathrm{clt}}| \le |f_s| \tag{1}$$

$$f_t = f_{\mathrm{rc}} + f_s \quad \text{if} \quad |f_{\mathrm{clt}}| > |f_s| \tag{2}$$

The conditional statement on the exceedance of the slip force drives the transition between the two stick and slip phases of the response.

3 EXPERIMENTAL TESTS

The data used in this paper descend from an experimental campaign on AFC specimen at component level. The full campaign is described in [40], and this section will give a synthetic overview of the activity. The specimen, called HYB, is shown in Fig.2, and is composed by an anchor profile (fixed rigidly to the beam of each floor/testing machine during the experiments) and a free profile, which is connected both to the CLT panel, with a screw connection, and to the anchor profile, with two preloaded bolts which allow for sliding in an elongated hole. Both profiles are made of cold bent steel and are 8mm thick. The friction connection is completed by a cap plate and 2 aluminium shim layers to improve the stability of the friction behaviour, which are 2mm thick.

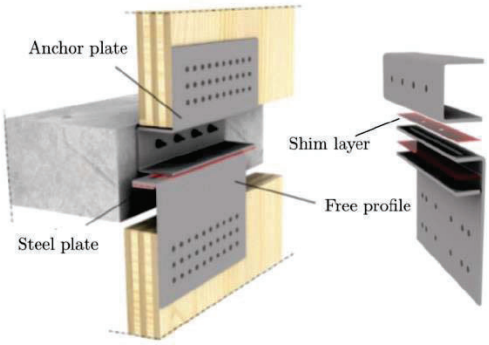

***Figure 2**: Illustration of the tested specimen.*

3.1 OVERVIEW OF THE TESTS

A total of 20 tests was carried out, on 5 different specimens. Every specimen was tested more times and in some cases with different preload forces. The main setup is shown in Fig. 3. The anchor plate is attached to the cross head of the testing machine, which moves up and down, simulating the horizontal movement of a beam subjected to seismic forces. The free profile is connected to a 100mm thick CLT panel with 33 10x80 screws, and to the anchor profile with 2 M16 bolts. The tests were carried out in displacement control method, with a speed of

https://doi.org/10.52202/069179-0411

2mm/s and the following cyclic protocol: 1x5-10mm+3x20-40-60-80-100mm. Fig.3 shows a picture of the main setup and a scheme with the indication of the various sensors acquiring data. The thermocouple was placed directly on the steel plate where friction was occurring.

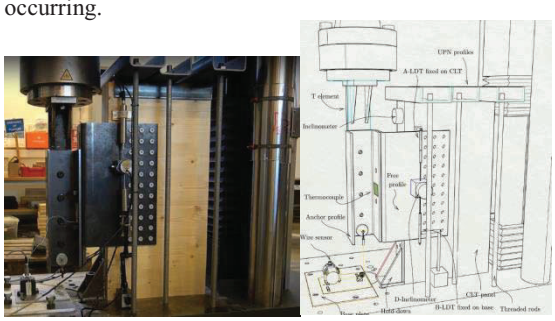

***Figure 3**: Main setup for the testing activity.*

3.2 RESULTS

An extract of the results is shown in Fig.4 for specimen HYB-3. The load displacement graph shows shape that resembles a rectangle, which would be the ideal shape for friction connections hysteresis loops. In this case the shape is not a pure rectangle because it represents the hysteresis of the whole system, which included the deformability of the steel plates and the screw connection. The S-like shape at the branches where the load changes direction is due to the pinching of the timber connection. Full detailed results are presented in [40].

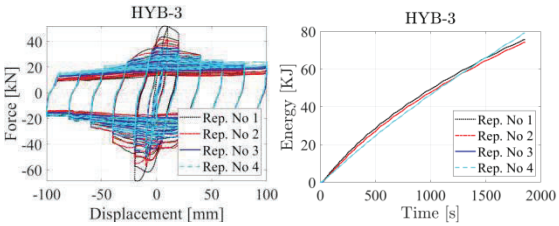

***Figure 4**: Results for specimen HYB-3.*

3.3 ESTIMATE OF THE FRICTION COEFFICIENT

The estimate of the slip force, and thus the friction coefficient, from experimental data is not direct and requires the definition of an approach. This is because the force changes during the tests and the sign changes. The definition of slip force is based on the cumulated dissipated energy, which is a strictly increasing function, as seen in Fig.5. The dissipated hysteretic energy can be defined as follows:

$$E = \sum_{i=0}^{n} E_i = \sum_{i=0}^{n} \left| \frac{F_{i+1}+F_i}{2} \cdot (\delta_{i+1} - \delta_i) \right| \quad (3)$$

where E is the dissipated energy, E_i the dissipated energy at the $i-$th time step, F_i and δ_i are the force and displacement at the same time step, respectively.

The cumulative distance of travel D is the sum of the displacement time steps:

$$D = \sum_{i=0}^{n} |\delta_{i+1} - \delta_i| \quad (4)$$

The slip force is defined as the work per unit of length:

$$F_{\text{slip}} = \frac{E}{D} \quad (5)$$

The experimental friction coefficient μ is finally calculated as

$$\mu = \frac{F_{\text{slip}}}{n_s n_b F_P} \quad (6)$$

where F_{slip} is the slip force calculated in Eq.(5), n_s is the number of shear surfaces equal to 2, n_b is the number of the preloaded bolts equal to 2, and F_P is the preload force. It must be remarked that the above definition of the friction coefficient cannot be entirely interpreted and understood in light of the Amontons laws. Friction in AFC is not just the product of friction between plates mutually sliding. Therefore, the estimated friction coefficient must be considered a system friction coefficient, representing the entire structural performance.

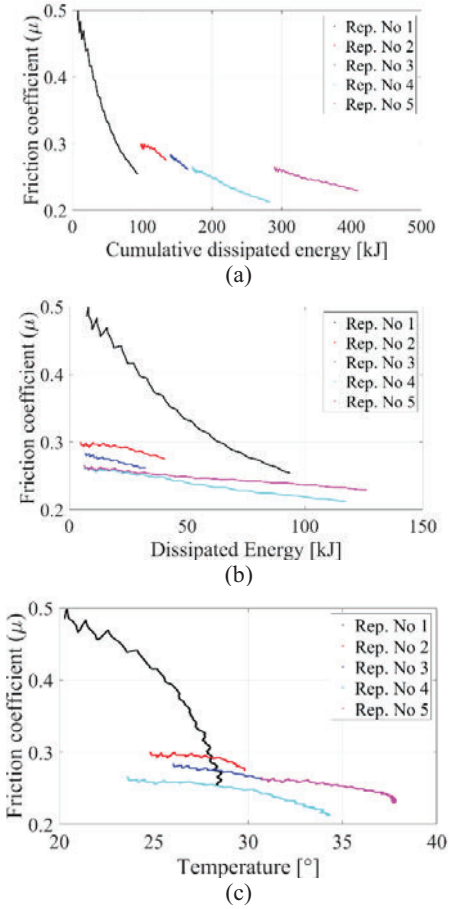

***Figure 5**: Illustration of the contributions of forces: (a) before the AFC activation and (b) after the AFC activation.*

4 PROBABILISTIC FRICTION MODEL

The formulation to predict the friction coefficient can be decoupled into two models. The first model defines the dependence between the value of the friction coefficient estimated at the beginning of each cyclic response μ_0 and its value estimated at the beginning of the first cyclic response from the time of the AFC installation $\hat{\mu}_0$. The second model predicts the value of the friction coefficient μ during each cyclic response starting from the value of

the friction coefficient estimated at the beginning of the response μ_0. The two models will describe two aspects of the friction coefficient evolution. The first will express the dependence of μ on the deformation history. The second will define its evolution during each cyclic response.

Following [40], the model that relates μ_0 to $\hat{\mu}_0$ is formulated as

$$\log(\mu_0) = \log(\hat{\mu}_0) + \gamma_1(\epsilon_p) + \sigma_1\varepsilon \quad (7)$$

where ϵ_p is the dissipated energy accumulated from the past loading tests of the specimen up to the beginning of the cyclic response to be simulated and $\sigma_1\varepsilon$ is the model error, with σ_1 model standard deviation and ε normally distributed random variable. The logarithm is used as variance stabilizing transformation.

The correction term $\gamma_1(\hat{\epsilon}_p)$ is constructed as a polynomial function of ϵ_p. The relevant terms in the polynomial function are selected using the procedure followed in [40]. The selection process (i.e., the removal of explanatory functions from the initial model) stops after a cumulative increase of the model standard deviation greater than 5% that would lead to an excessive loss of accuracy. Although the number of terms in a probabilistic model is often selected in order to balance accuracy and ease of use, in this case, given the limited amount of data available for the calibration, the number of terms is limited to avoid possible over-fitting of the data.The model for μ is formally similar and can be written as

$$\log(\mu) = \log(\mu_0) + \gamma_2(\epsilon_p, \epsilon_d, \hat{\mu}_0) + \sigma_2\varepsilon \quad (8)$$

with ϵ_d dissipated energy estimated from the beginning of the current load test, without the contributions related to the past deformation history. Among the explanatory functions considered for γ_2 there are $\hat{\mu}_0$ and powers of e_p and e_d up to the fourth order. Increasing the order of the powers of e_p and e_d above the fourth is avoided because it would lead to a limited increase in accuracy but would also result in an impractical and less manageable model. The models resulting from the selection processes read

$$\log(\mu_0) = \log(\hat{\mu}_0) + \theta_1{\epsilon_p}^{\frac{1}{2}} + \sigma_1\varepsilon \quad (9)$$

and

$$\log(\mu) = \log(\mu_0) + \theta_2 + \theta_3\hat{\mu}_0 + \theta_4{\epsilon_p}^{\frac{1}{2}} + \theta_5{\epsilon_d}^2 + \theta_6{\epsilon_d}^3 + \sigma_2\varepsilon \quad (10)$$

Both models are calibrated with a Bayesian approach. For all models, the calibration is performed at each stage of the model selection process with the STAN package of the R software that uses a gradient descend method.

Ref provides the statistics of the unknown parameters $\boldsymbol{\Theta} = \{\boldsymbol{\theta}, \boldsymbol{\Sigma}\}$, with $\{\boldsymbol{\theta} = \{\theta_1 \dots \theta_5\}$ and $\boldsymbol{\Sigma} = \{\sigma_1, \sigma_2\}$. The Adjusted R-squared for the two models are Adj-R^2=0.8287 for the model of $\log(\mu_0)$ and Adj-R^2=0.7217 for the model of $\log(\mu)$.

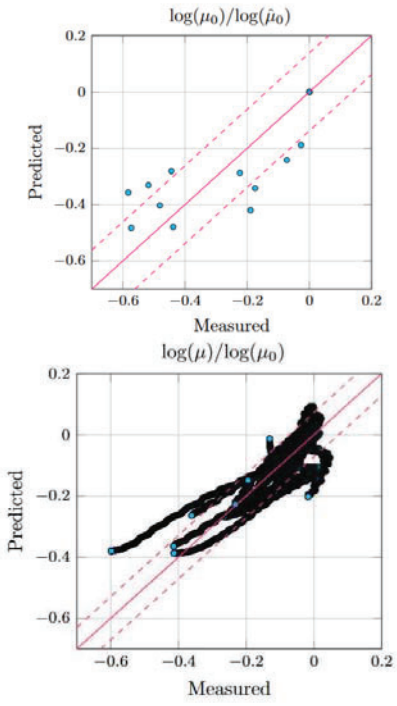

Figure 6: *: Predicted capacity versus measured values of the*

Fig.6 (a) and (b) show the predicted versus measured values of the ratios $\log(\mu_0)/\log(\hat{\mu}_0)$ and $\log(\mu)/\log(\mu_0)$, respectively. The closer the data points are to the 1:1 lines (i.e., the continuous lines in the figure), the more accurate are the predictions. The two figures also show the region within one standard deviation of the median value (i.e., the region between the dashed lines). From Fig. 6(b), it is possible to recognise data from different load tests. The predictions related to some of them exhibit a limited bias that may depends on features that are not captured by the explanatory functions considered in the model selection. A prediction for μ can be obtained combining Eq. (9) and Eq. (10) as

$$\mu = \hat{\mu}_0 e^{\theta_2 + \theta_3\hat{\mu}_0 + (\theta_1+\theta_4){\epsilon_p}^{\frac{1}{2}} + \theta_5{\epsilon_d}^2 + \theta_6{\epsilon_d}^3 + \sigma_t\varepsilon} \quad (11)$$

where $\sigma_t = ({\sigma_1}^2 + {\sigma_2}^2)^{1/2}$. To understand if the temperature can be used as a predictor for the values of μ, the temperature measured during the load test, T, is added into the set of the explanatory functions used to find the correction term for $\log(\mu)$, i.e., $\gamma_2 = \gamma_2(\epsilon_p, \epsilon_d, \hat{\mu}_0, T)$. In this case, the inclusion of T among the explanatory function change the selection process, and T is selected among the significant explanatory functions. The modified model for $\log(\mu)$ has the form

$$\log(\mu) = \log(\mu_0) + \theta_6 + \theta_7{\epsilon_p}^{\frac{1}{2}} + \theta_8\epsilon_p + \theta_9{\epsilon_p}^2 + \theta_{10}{\epsilon_d}^3 + \theta_{11}\epsilon_d + \theta_{12}{\epsilon_d}^4 + \theta_{13}T + \sigma_3\varepsilon \quad (12)$$

https://doi.org/10.52202/069179-0411

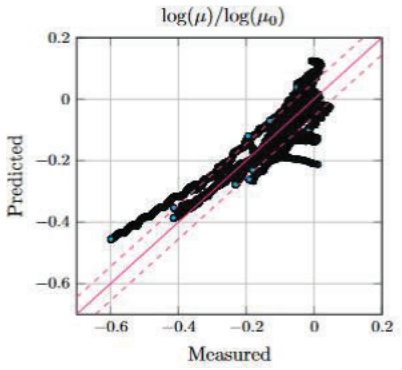

Figure 7: Predicted capacity versus measured values of the friction coefficient.

Fig.7 shows the agreement between the recorded and predicted values of μ, obtained using Eq. (12). The standard deviation of the model error is smaller compared to the model in Eq. (11) and the Adjusted R-squared higher (Adj-R^2=0.8267) . Although the probabilistic friction model dependent on the dissipated energy exhibits a satisfactory performance with an Adj-R^2=0.7217, the inclusion of the temperature as a regressor significantly increases the accuracy of the prediction, leading to an Adj-R^2=0.8267. This increased accuracy does not show the causal link between temperature increment and friction coefficient reduction. Instead, the probabilistic friction model provides evidence of the temperature role without clarifying if it is the cause or the effect of the friction coefficient variation. The experimental results and probabilistic model proved that the proposed structural system based on aluminium shims deserves further improvement to achieve a more stable and reliable hysteretic response.

5 CONCLUSIONS

This research presents the results of quasi-static cyclic tests on Asymmetric Friction Connections (AFC), serving as dissipating devices in the e-CLT system. The e-CLT, proposed under the Horizon 2020 research project e-SAFE, is a seismic retrofitting solution for RC frames based on Cross-Laminated timber (CLT) panels and AFCs. The authors carried out multiple repetitions of the same cyclic load protocol to assess the dependence of the aluminium-steel friction coefficient of the tested AFCs on the temperature, the energy dissipated during the test and that dissipated during the past deformation history of the specimen. The friction coefficient exhibited a significant dependence on both physical quantities. The friction dependence on the dissipated energy during the deformation history might originate from wear phenomena, mainly localized by the bolts, and MPV effects. The mutual sliding between aluminium and steel leads to the abrasive wear of the softer material (aluminium in the current case) and the reduction of the friction coefficient from nearly 0.5 to 0.2 during the first load protocol. Further repetitions of the load protocols on the same specimen also evidenced a dependence on the dissipated energy cumulated during each test. The physical variable possibly responsible for this phenomenon is the increasing temperature during each loading protocol. Following the standard semi-physical approach in hysteresis, the authors developed two probabilistic data-driven friction models calibrated from the experimental data using a Bayesian approach. The data-driven model simulates the evolution of friction without distinguishing between the causes of strength degradation's, like MPV interaction, changes in the properties in the sliding surfaces, and/or prying effects. The first engineering-oriented model depends on the dissipated energy, while the second includes the measured temperature as regressor. The first model exhibits a satisfactory performance with an Adj-R^2=0.7217. However, the presence of temperature as a regressor significantly increases the accuracy of the prediction, leading to an Adj-R^2=0.8267. The higher description capability of the model that includes temperature among the regressors does not show the causal dependence of the friction coefficient reduction on temperature but only the high correlation between the two. Regrettably, the authors do not have multiple tests where the initial temperature of the specimen is varied to rigorously prove the possible dependence of friction on the temperature variation. The first model can predict the friction coefficient in nonlinear analyses of the AFC using a straightforward Coulomb friction model, where the friction coefficient represents an energy-dependent parameter. The authors followed a Bayesian approach for calibrating the coefficients of the friction model, which also provides the complete distributions of the model parameters and allows the update of the model with newly available data.This model can be theoretically extended to different AFCs typologies after proper calibration based on the experimental cyclic response related to multiple load protocols repetitions. Future research efforts, possibly carried out within the Horizon 2020 research grant, will aim to rigorously assess the friction coefficient's dependence on the initial temperature of the specimens.

ACKNOWLEDGEMENT

This paper was carried out in the framework of the Energy and seismic affordable renovation solutions (e-SAFE) project, which has received funding from the European Union's Horizon 2020 research and innovation programme under grant agreement No.893135. Neither the Executive Agency for Small and Medium-sized Enterprises (EASME) nor the European Commission is in any way responsible for any use that may be made of the information it contains.

REFERENCES

[1] A. S. Pall, C. Marsh, and others, Response of friction damped braced frames, *J. Struct. Eng.*, vol. 108, no. 9, pp. 1313–1323, 1982.

[2] L. Pesaresi, M. Stender, V. Ruffini, and C. W. Schwingshackl, DIC measurement of the kinematics of a friction damper for turbine applications, in *Dynamics of Coupled Structures, Volume 4*, Springer, 2017, pp. 93–101.

[3] W. J. Venuti, Energy Absorption of High Strength Bolted Connections, *Test Rep.*, 1976.

[4] A. S. Pall, Energy dissipation devices for aseismic design of buildings, in *Proceedings of a Seminar and Workshop on Base Isolation and Passive Energy Dissipation*, 1986, pp. 223–232.

[5] A. S. Pall and C. Marsh, Friction-damped concrete shearwalls, in *Journal Proceedings*, 1981, vol. 78, no. 3, pp. 187–193.

[6] A. S. Pall, Friction devices for aseismic design of buildings, in *4th Canadian Conference on Earthquake Engineering*, 1983, pp. 475–484.

[7] C. Pasquin, N. Leboeuf, R. T. Pall, and A. Pall, Friction dampers for seismic rehabilitation of Eaton's building, Montreal, in *13th world conference on earthquake engineering*, 2004, pp. 1–2.

[8] R. Chandra, M. Masand, S. K. Nandi, C. P. Tripathi, R. Pall, and A. Pall, Friction-dampers for seismic control of La Gardenia towers south city, Gurgaon, India, 2000.

[9] A. Pall, S. Vezina, P. Proulx, and R. Pall, Friction-dampers for seismic control of Canadian space agency headquarters, *Earthq. Spectra*, vol. 9, no. 3, pp. 547–557, 1993.

[10] B. Wu, H. Li, L. Lin, and M. Shan, Seismic retrofit of a city hall in Northeast China with frictional energy dissipators, *J. Build. Struct.*, vol. 19, no. 5, pp. 28–36, 1998.

[11] B. Wu, J. Zhang, M. S. Williams, and J. Ou, Hysteretic behavior of improved Pall-typed frictional dampers, *Eng. Struct.*, vol. 27, no. 8, pp. 1258–1267, 2005.

[12] A. Filiatrault and S. Cherry, Performance evaluation of friction damped braced steel frames under simulated earthquake loads, *Earthq. spectra*, vol. 3, no. 1, pp. 57–78, 1987.

[13] T. F. Fitzgerald, T. Anagnos, M. Goodson, and T. Zsutty, Slotted bolted connections in aseismic design for concentrically braced connections, *Earthq. spectra*, vol. 5, no. 2, pp. 383–391, 1989.

[14] M. Latour, G. Rizzano, A. Santiago, and L. S. da Silva, Experimental response of a low-yielding, self-centering, rocking column base joint with friction dampers, *Soil Dyn. Earthq. Eng.*, vol. 116, pp. 580–592, 2019.

[15] W. Y. Loo, P. Quenneville, and N. Chouw, A new type of symmetric slip-friction connector, *J. Constr. Steel Res.*, vol. 94, pp. 11–22, 2014, doi: 10.1016/j.jcsr.2013.11.005.

[16] G. C. Clifton, Semi-rigid joints for moment-resisting steel framed seismic-resisting systems, ResearchSpace@ Auckland, Auckland, 2005.

[17] H.-H. Khoo, C. Clifton, G. MacRae, H. Zhou, and S. Ramhormozian, Proposed design models for the asymmetric friction connection, *Earthq. Eng. \& Struct. Dyn.*, vol. 44, no. 8, pp. 1309–1324, 2015.

[18] H.-H. Khoo, C. Clifton, J. Butterworth, G. MacRae, and G. Ferguson, Influence of steel shim hardness on the Sliding Hinge Joint performance, *J. Constr. Steel Res.*, vol. 72, pp. 119–129, 2012.

[19] C. E. Grigorian, Energy dissipation with slotted bolted connections, University of California, Berkeley, 1994.

[20] H. Mackinven, Sliding Hinge Joint for steel moment frames experimental testing, *Unpubl. ENCI493 Proj. Report. Dep. Civ. Eng.*, 2006.

[21] S. Ramhormozian and G. C. Clifton, Optimised Sliding Hinge Joint (OSHJ): Design and Installation Guide for a Low Damage Seismic Resisting System. New Zealand Heavy Engineering Research Association, 2020.

[22] S. Ramhormozian, C. Clifton, and S. Gledhill, The Optimised Sliding Hinge Joint (OSHJ): Overview and First Application to a Project, in *International Conference on the Behaviour of Steel Structures in Seismic Areas*, 2022, pp. 837–843.

[23] G. A. MacRae, G. C. Clifton, H. Mackinven, N. Mago, J. Butterworth, and S. Pampanin, The sliding hinge joint moment connection, *Bull. New Zeal. Soc. Earthq. Eng.*, vol. 43, no. 3, pp. 202–212, 2010.

[24] S. Yeung, H. Zhou, H. Khoo, G. C. Clifton, and G. MacRae, Sliding shear capacities of the Asymmetric Friction Connection, in *2013 NZSEE Conference, April*, 2013, pp. 26–28.

[25] G. W. Rodgers, R. Herve, G. A. MacRae, J. Chanchi Golondrino, and J. G. Chase, Dynamic Friction Coefficient and Performance of Asymmetric Friction Connections, *Structures*, vol. 14, pp. 416–423, 2018, doi: https://doi.org/10.1016/j.istruc.2017.09.003.

[26] J. C. Chanchi Golondrino, G. A. MacRae, J. G. Chase, G. W. Rodgers, and G. C. Clifton, Seismic behaviour of symmetric friction connections for steel buildings, *Eng. Struct.*, vol. 224, p. 111200, 2020, doi: https://doi.org/10.1016/j.engstruct.2020.111200.

[27] A. F. Santos, A. Santiago, M. Latour, and G. Rizzano, Analytical assessment of the friction dampers behaviour under different loading rates, *J. Constr. Steel Res.*, vol. 158, pp. 443–459, 2019.

[28] S. Ramhormozian, G. Clifton, S. Maetzig, D. Cvitanich, and G. MacRae, Influence of the Asymmetric Friction Connection (AFC) ply configuration, surface condition, and material on the AFC sliding behaviour, 2016.

[29] H.-H. Khoo, C. Clifton, J. Butterworth, and G. MacRae, Experimental study of full-scale self-centering sliding hinge joint connections with friction ring springs, *J. Earthq. Eng.*, vol. 17, no. 7, pp. 972–997, 2013.

[30] T. Tannert and C. Loss, Contemporary and Novel Hold-Down Solutions for Mass Timber Shear Walls, *Buildings*, vol. 12, no. 2, p. 202, 2022.

[31] A. Aloisio, A. Contento, R. Alaggio, B. Briseghella, and M. Fragiacomo, Probabilistic assessment of a Light-Timber Frame shear wall with variable pinching under repeated earthquakes, *J. Struct. Eng.*, vol. In press, 2022.

[32] A. Aloisio, M. Pelliciari, A. V. Bergami, R. Alaggio, B. Briseghella, and M. Fragiacomo,

 https://doi.org/10.52202/069179-0411

Effect of pinching on structural resilience: performance of reinforced concrete and timber structures under repeated cycles, *Struct. Infrastruct. Eng.*, pp. 1–17, 2022.

[33] W. Y. Loo, P. Quenneville, and N. Chouw, A numerical study of the seismic behaviour of timber shear walls with slip-friction connectors, *Eng. Struct.*, vol. 34, pp. 233–243, 2012, doi: https://doi.org/10.1016/j.engstruct.2011.09.016.

[34] W. Y. Loo, P. Quenneville, and N. Chouw, Rocking Timber Structure with Slip-Friction Connectors Conceptualized As a Plastically Deformable Hinge within a Multistory Shear Wall, *J. Struct. Eng.*, vol. 142, no. 4, p. E4015010, 2016, doi: 10.1061/(ASCE)ST.1943-541X.0001387.

[35] D. Fitzgerald, T. H. Miller, A. Sinha, and J. A. Nairn, Cross-laminated timber rocking walls with slip-friction connections, *Eng. Struct.*, vol. 220, p. 110973, 2020.

[36] A. Hashemi, P. Zarnani, R. Masoudnia, and P. Quenneville, Experimental testing of rocking cross-laminated timber walls with resilient slip friction joints, *J. Struct. Eng.*, vol. 144, no. 1, p. 4017180, 2018.

[37] A. Aloisio, M. Pelliciari, S. Sirotti, F. Boggian, and R. Tomasi, Optimization of the structural coupling between RC frames, CLT shear walls and asymmetric friction connections, *Bull. Earthq. Eng.*, pp. 1–26, 2022.

[38] F. Boggian, C. Tardo, A. Aloisio, E. M. Marino, and R. Tomasi, Experimental cyclic response of a novel friction connection for seismic retrofitting of RC buildings with CLT panels, *J. Struct. Eng.*, vol. In press, 2022, doi: 10.1061/(ASCE)ST.1943-541X.0003313.

[39] A. Aloisio, F. Boggian, and R. Tomasi, Design of a novel seismic retrofitting system for RC structures based on asymmetric friction connections and CLT panels, *Eng. Struct.*, vol. 254, p. 113807, 2022.

[40] P. Gardoni, A. Der Kiureghian, and K. M. Mosalam, Probabilistic capacity models and fragility estimates for reinforced concrete columns based on experimental observations, *J. Eng. Mech.*, vol. 128, no. 10, pp. 1024–1038, 2002.

World Conference on Timber Engineering Oslo 2023

SHEAR TESTS ON PERFOBOND CONNECTIONS IN TIMBER CONCRETE COMPOSITES

Elif Appavuravther[1], Bram Vandoren[1], José Henriques[1]

ABSTRACT: With an increase in trend to integrate more wood into the construction industry, timber concrete composite (TCC) solutions are an efficient manner to overcome the limitations of timber. In the current literature, there are various connections that have been investigated for TCC systems. One with sufficient performance to target massive constructions is still limited. In this paper the use of the Perfobond connector, originally developed for steel concrete composite (SCC), is explored in TCC. The connection consists of a discrete steel plate with dowel action in the concrete side. For TCC an adjustment of gluing a part of the Perfobond to the timber member is made. Experimental investigation with the variable of a few parameters such as, different types of concrete and surface roughness of the Perfobond (bonded in the timber part) is performed. As a result of this experimental work, it is possible to observe that the Perfobond connector is performant in terms of both strength and stiffness. The results of this work indicate that, by using the most optimal design of a Perfobond connector, a performant connection can be introduced to TCC which makes it possible to target longer spans.

KEYWORDS: Perfobond connector, adhesively bonded connection, timber concrete composite, shear test

1 INTRODUCTION

The use of TCC systems in construction is in an increasing trend as more environmentally friendly solutions are targeted. Therefore, performant shear connections between timber and concrete are needed. The goal is to target a high composite action, by using a stiff shear connection, which minimizes the slip between the members and ideally leading to compression stresses in the concrete and tension stresses in the timber.

In TCC literature, dowel connections, notch connections and recently bonded-in dowel are extensively studied [1]. Bonded-in dowel connections are proven to minimize the strength and the stiffness limitations, of the traditional dowel connections, and to avoid the brittle failure common in notch connections [2]. The major problem with the bonded-in dowels was to come to common design rules for researchers and designers. The use of an adhesive makes a significant difference in the behaviour of the connection [3]. In the recently consolidated version of the prEN 1995-1-1 under preparation for the 2nd generation of Eurocodes, a subsection is devoted to the bonded-in rods [4]. Even though the guidelines are limited, it will support designers. Since the early 21st century, bonded-in steel plates are an ongoing application in TCC. The first patented system is HBV developed in Germany by Bathon [5-7]. This is a continuous steel mesh adhesively bonded to timber and the remainder of the connector is embedded into the concrete. With the mesh on the steel, a bonding is formed with the adhesive in the timber part and with the concrete. The continuous steel mesh is designed to be controlled by the yielding of the steel mesh, which leads to a ductile behaviour of the connection.

Since the success of HBV, multiple researchers worked on continuous or discrete steel plate connections [3, 8-12]. In this paper, a connector commonly used in SCC, the Perfobond connector was used, which was developed to be used in long span bridge constructions [13]. This connector is welded to the steel beam, and inserted into the concrete layer of the SCC member. The part in the concrete has holes, which mobilizes dowel action between the connector and the concrete in addition to the bearing component at the tip of the connector. The application of the connector is slightly modified to be used in TCC. The part welded to the steel profile is now extended to be embedded into the timber element. An adhesive is used to bond the connector to the timber. The plate in the concrete part is designed and used as done in SCC [14].

In this work, an experimental investigation of the Perfobond connector is performed. The impact of concrete type and surface roughness of Perfobond on strength and stiffness is investigated. The results show that a Perfobond is a promising performant connector with high strength and stiffness, however, with limited ductility, which can be further improved to be used in industrial application.

[1] Elif Appavuravther, Hasselt University, Belgium, eliftuba.appavuravther@uhasselt.be
Bram Vandoren, Hasselt University, Belgium, bram.vandoren@uhasselt.be
Jose Henriques, Hasselt University, Belgium, jose.gouveiahenriques@uhasselt.be

https://doi.org/10.52202/069179-0412

2 DESIGN OF TEST SPECIMENS

The use of Perfobond connections are a common application in SCC. They have been developed to replace studs in long span construction and with the optimized design requirements in the literature, strong and stiff connections are obtained in which one Perfobond replaces a significant number of studs [13].

In this work, the connections that are embedded in the concrete part are designed using the experimental work conducted by Oguejiofor and Hosain [14]. The steel plate is designed using EN 1993-1-8 [15]. The part adhesively bonded to timber was slightly more challenging to design as there are no guidelines. Potential failure modes are identified that can occur in the timber part by using examples from the bonded-in literature [2] and application of bonded-in steel plates [3, 8-10]. The final dimensions of the Perfobond can be found in Figure 1 (a) and (b). In both of the plates, the surface of the steel plate is smooth without any treatment. To assess the bond between the steel plate and the adhesive, two different configurations are tested; i) a smooth Perfobond in which the bond with adhesive is directly through the surface of the plate (Figure 1 (a)) and ii) perforations formed in the part embedded in the timber to increase the surface area of the adhesive and with the adhesive filled through the perforations, a mechanical interlock is targeted (Figure 1 (b)).

In this experimental work, two different parameters are investigated; i) the effect of perforations on the connector and ii) the type of the concrete.

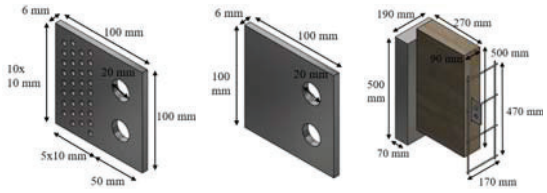

a) b) c)

Figure 1 *Test specimens (a) Perfobond without perforations, (b) Perfobond with perforations, (c) 3D view of the specimens*

3 MATERIALS AND METHODS

3.1 TEST SPECIMENS

Symmetrical shear push-out type tests were conducted with a central timber and concrete layer on both sides. The timber is predrilled with groove dimensions of 110x10x55 mm, and the sides that were in contact with concrete are taped to avoid moisture entering the timber and to avoid the friction between the two materials. The 2/3 of the groove is filled with an epoxy acrylate-based anchoring adhesive, Sika Anchorfix-3030 [16], and the Perfobond is inseerted as soon as the adhesive is applied. The specimens are prepared in an indoor lab environment and were left a minimum of 24h for the adhesive to dry as recommended by the manufacturer [16]. The concrete is casted approximately after 7-days the adhesive was applied. Minimum reinforcement is used to avoid concrete tension failure [17]. Detailed dimensions of the specimens are given in Figure 1 (c) [18].

3.2 MATERIALS

The timber used in this work is GL 24h with a moisture content of 12.34% (Hydromete or oven dry method) and average density of 483 kg/m^3.

The Perfobond connector is steel grade S355 without any surface treatment.

For the concrete, two different concrete types are used: normal weight and lightweight concrete. Physical and mechanical properties of the concrete, determined according to the EN 12390-3 [19], can be found in Table 1 along with the other testing variable, the use or not of perforation in the perforbond connector (Figure 1 a) and b)).

Each specimen is named by the connection name initial (P) – presence of perforations in the bonded part (Y if available, N if not) and by the concrete type used (NWC for normal weight concrete and LWC for lightweight concrete).

Table 1 *Test specimen properties*

Experimental ID	Concrete type & Density (kg/m^3)	Concrete mean cube strength (MPa)	Perforation
P-Y-NWC	NWC 2400	78	Yes
P-N-NWC			No
P-Y-LWC	LWC 1600	25	Yes
P-N-LWC			No

3.3 TEST SET-UP, MONITORING AND TEST PROCEDURE

The experimental set-up (Figure 2), including monitoring system, consists of a test frame, a hydraulic jack, a load cell and LVDTs (Linear Variable Differential Transformer). The specimens are equipped with seven LVDTs, two horizontal and five vertical ones. The horizontal ones are placed at the top and bottom of the specimens to record timber-concrete separation. Four of the vertical ones are placed at the connection level, on both sides of the specimens as recommended by EN 26891 [20], to measure relative slip between materials. The remaining vertical LVDT is placed at the level of the load cell.

The loading procedure from EN 26891 is followed [20].

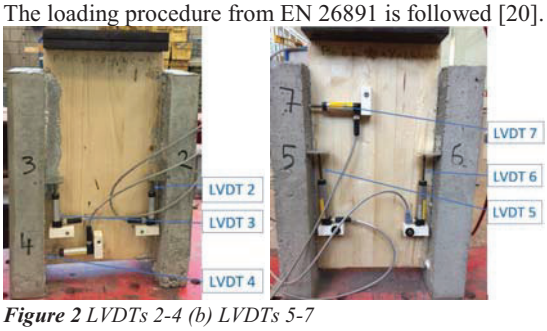

Figure 2 *LVDTs 2-4 (b) LVDTs 5-7*

https://doi.org/10.52202/069179-0412

4 RESULTS AND DISCUSSION

4.1 TEST RESULTS

In Table 2, mean value and coefficient of variation (COV) of the initial damage load (F_1), maximum load capacity (F_{max}) and stiffness (K_{ser}) are given for all four series. Initial damage load is determined by the reduction on the slope of the force-slip curve. The maximum load capacity is determined by the maximum capacity a connection could bear and the stiffness of the connection is determined as recommended in EN 26891 [20] and corresponding to the load-slip curve slope at 10% and 40% of F_{max}. In Figure 3, the load-slip curve for the series with and without perforations are presented. In both figures, F_1 is marked to clearly illustrate the initial damage load.

In series P-Y-NWC and P-Y-LWC, given in Figure 3 (a), the initial reduction in stiffness is caused by the damage between the bondline to the timber at 94.4 kN and 44.4 kN, respectively. With the loss of adhesion, load is transferred through bearing to the timber. Because the concrete was strong enough, crushing of timber started in the specimens with the use of normal weight concrete and governed the load capacity. When the bonding was totally lost, the connection reached its maximum capacity of 117.4 kN. For the specimens with lightweight concrete, with bondline failure, the load is transferred to the concrete through bearing between timber and perfobond connector and due to the lower strength of the concrete, concrete dowel failure is observed at 60.8 kN.

For the series P-N-NWC and P-N-LWC, given in Figure 3 (b), initial damage is due to the bondline failure of the bond to Perfobond connector at 76.7 kN and 38 kN, respectively. After the initial damage, the failure patterns are very similar to cases with the presence of surface roughness.

In all series, a very high stiffness is recorded, ranging between 297 to 442 kN/mm. It should also be noted that the COV is high for this parameter as a small deviations or inaccuracies in measurments as low as 0.1 mm have a significant impact.

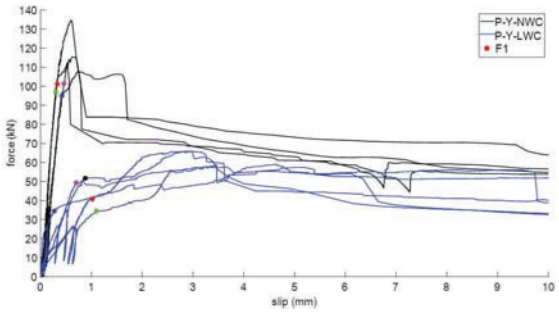

a)

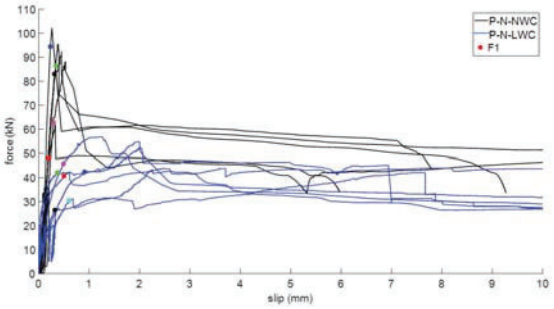

b)

Figure 3 *Force-slip curves (a) for the specimens with perforated connections (P-Y-NWC and P-Y-LWC) and (b) for the specimens without perforated connections (P-N-NWC and P-N-LWC)*

Table 2 *Test results*

Specimen ID		F_1 (kN)	F_{max} (kN)	K_{ser} (kN/mm)
P-Y-NWC	Overall mean	94.4	117.4	441.9
	COV (%)	9.7	18.1	24.0
P-N-NWC	Overall mean	76.7	87.5	419.7
	COV (%)	27.0	17.5	41.3
P-Y-LWC	Overall mean	44.4	60.8	403.4
	COV (%)	16.6	6.5	39.3
P-N-LWC	Overall mean	38.0	48.3	296.9
	COV (%)	20.1	14.7	44.3

4.2 DISCUSSION OF TESTING PARAMETERS

In this experimental work, the effect of concrete type and the connector perforations in the timber part are investigated. In Figure 3, the effect of the concrete type can be clearly observed. In both figures, the series with the use of normal weight concrete have a very stiff behaviour until (almost) the maximum load carrying capacity, after this point, with brittle failure at the bondline, a sudden decrease in the load capacity (30 – 50%) is observed. In the series with the use of lightweight concrete, the behaviour is linear until F_1, with much flexible behaviour due to participation of the concrete. After this load level, the force-slip behaviour shows a nonlinear response until the maximum load capacity is reached. Unlike the series with normal weight concrete, the drop in load capacity is smaller, as the use of lightweight concrete lead to a more ductile behaviour since the participation of the concrete was higher. In terms of maximum load capacity, the use of normal concrete

https://doi.org/10.52202/069179-0412

lead to double capacity in comparison to the lightweight concrete (Table 2).
The use of perforated connections leads to a difference in the mechanics of the connector as the bond between the connector and the timber is efficient. The use of perforations leads to an increased load capacity and stiffness behaviour.

5 COMPARISON WITH THE LITERATURE

In order to contextualize the mechanical performance of the Perfobond connector for TCC, the different types of connections available for use in composite beam floor solutions, and covering different target applications, are here discussed. In Table 3, various connections used in TCC and Perfobond connections used in steel-concrete composites (SCC) are summarized in terms of strength (F_{max}), stiffness (K_{ser}) and ultimate slip (v_u). The ultimate slip is determined by EN 12512 [21], which is the slip value corresponding to the 80% of the force after the maximum load capacity is reached.
Four groups of connections are identified: i) dowel type connections; ii) notch connections; iii) steel plate connections in TCC; iv) Perfobond connections in SCC. The results of the referred mechanical properties are given per connection per shear plane. Details of the experiments can be found in the given references. In Figure 4 the chart provides a comparative overview of the different types of shear connections collected. For each mechanical property (F_{max}, K_{ser} and v_u), values are normalized to the respective maximum reported value, namely: strength and stiffness connection 11 [22] and ultimate slip connection 12 [23]. Then, the mean values of test specimens (normalized) P-Y-NWC and P-Y-LWC are also included (represented by the dots). Only these two type of specimens have been used because, as discussed previously, the use of perforations can delay the failure of the bondline zone and consequently, the connection can perform better.
Though, a quantitative comparison may not be entirely realistic, given the geometrical and material differences between the collected test specimens, however, Figure 4 provides a good perception on their relative mechanical performance. The chart shows that Perfobond in SCC is the strongest, the stiffest and the most ductile [22, 23]. Then, on the other side, screw connections present a lower load capacity and stiffness. Consequently, their application in TCC solutions targets lower load-bearing demands and is mainly due to the easiness and cost of application. Notches are as performant as the connections with steel plates, being the limited ultimate slip the main drawback. However, except for case 7, limited ultimate slip is also a problem in shear connections using plates in TCC due to the brittle behaviour of glue connections. Regarding this mechanical property, connections using Perfobond in SCC and SNP toothed metal plate (case 7) can provide the highest values, even higher than screws [22-24]. The extensive research on Perfobond connections for SCC also demonstrates that, if optimally designed, this type of connections can provide a balanced response, combining high stiffness and load bearing capacity with interesting plastic deformation on the Perfobond connector.
The comparison of the tested connection with the collected connections shows that it is as performant as the connections with bonded-in plates (cases 7 – 10). Case 9 is the case most similar to the configuration investigated in this paper, with a steel plate glued to the timber using an epoxy based adhesive [24]. In the reference (case 9), normal weight concrete is used. The strength of the series P-Y-NWC is in perfect agreement. In terms of stiffness, P-Y-NWC behaves slightly better (due to surface roughness). In terms of slip capacity however, a small reduction is observed. However, given the fact that the connection was design to avoid plastic deformations in the Perfobond connector, there is potential to increase plastic deformations, as it is the case of the Perfobond in SCC.

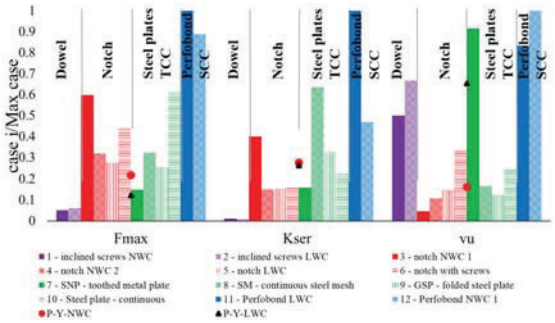

Figure 4 *Comparison of the mechanical performance of the tested Perfobond with the different type of connections available for TCC (including Perfobond in SCC)*

https://doi.org/10.52202/069179-0412

Table 3 *Collection of different type of shear connections for TCC (including Perfobond in SCC)*

Type	ID	Fmax (kN/m)	Kser ((kN/mm)/m)	vu (mm)
Dowel	1 - inclined screws NWC [25]	13	9	6
	2 - inclined screws LWC [25]	15	7	8
Notch	3 - notch NWC 1 [26]	150	305	1
	4 - notch NWC 2 [27]	80	115	1
	5 - notch LWC [27]	69	117	2
	6 - notch with screws [27]	110	125	4
Steel plate (S-TCC)	7 - SNP - toothed metal plate [12]	37	121	11
	8 - SM - continuous steel mesh [12]	81	484	2
	9 - GSP - folded steel plate [12]	64	249	2
	10 - Steel plate – continuous [11]	153	170	3
Perfobond (P-SCC)	11 - Perfobond LWC [22]	**251**	**760**	10
	12 - Perfobond NWC 1 [23]	223	357	**12**

6 CONCLUSIONS

As a result of this experimental work, it can be concluded that Perfobond connection are strong and very stiff therefore a high composite action can be achieved. The concrete type and strength had a significant effect on the load capacity of the connections. Adding surface roughness through the inclusion of perforations had a positive impact on the performance of the connection as the bond between the connector and the timber improved. Moreover, a comparison with commonly used TCC connections has been made and showed that the solution is as performant as notch connections and as similar connections using steel plates. The tested Perfobond connections present high strength and stiffness with relatively low ultimate slip, however, the latter was somehow expected, as the focus was on the performance of the connection depending mainly on the adhesive part. Ductility should be sought with the plastic deformations of the connector and / or by adding a rebar through the holes on the concrete side of the connection, which was not covered in the present study.

ACKNOWLEDGEMENT

The authors would like to acknowledge Sika Belgium and LTS Belgium for their material contribution and Philippe Courtoy (LTS Belgium) for his technical contribution. Hasselt University Master's students from the 2019 – 2020 academic year, Mathias Hendrikx and Stijn Gielis, are gratefully acknowledged for their help and experimental work.

REFERENCES

[1] COST, *Design of timber-concrete composite structures - A state-of-the-art report by COST Action FP1402 / WG 4*. Shaker Verlag Aachen, 2018.

[2] G. Tlustochowicz, E. Serrano, and R. Steiger, "State-of-the-art review on timber connections with glued-in steel rods," *Materials and Structures,* vol. 44, pp. 997-1020, 2011.

[3] C. Avez, "Design of an adhesively bonded-in steel plate connection for Cross Laminated Timber," PhD in Engineering Science and Technology, University of Mons, Mons, Belgium, 2021.

[4] *Eurocode 5: Design of timber structures (consolidated draft prEN 1995-1-1, informal enquiry) [under review]*, 2021.

[5] T. D. HBV-Systems, "Load bearing constructions using wood-concrete-composite technique with glued-in HBV®—Shear connectors.," ed. Goethestr, Germany: TiComTec., 2014.

[6] P. Clouston, L. Bathon, and A. Schreyer, "Shear and bending performance of a novel wood-concrete composite system," (in English), *Journal of Structural Engineering,* Article vol. 131, no. 9, pp. 1404-1412, SEP 2005 2005.

[7] L. Bathon and M. Graf, "A continuous wood-concrete-composite system," in *6th World Conference on Timber Engineering*, Whistler Resort, British Columbia, Canada, 2000.

[8] E. Martin-Gutierrez, J. Estevez-Cimadevila, D. Otero-Chans, and F. Suarez-Riestra, "Discontinuous pi-form steel shear connectors in timber-concrete composites. An experimental approach," *Engineering Structures,* vol. 216, no. 110719, 2020.

[9] F. Suarez-Riestra, J. Estevez-Cimadevila, E. Martin-Gutierrez, and D. Otero-Chans, "Perforated shear plus reinforcement bar connectors in a timber-concrete composite solution. Analytical and numerical approach,"

https://doi.org/10.52202/069179-0412

(in English), *Composites Part B-Engineering,* Article vol. 156, pp. 138-147, JAN 1 2019 2019.

[10] D. Otero-Chans, J. Estevez-Cimadevila, F. Suarez-Riestra, and E. Martin-Gutierrez, "Experimental analysis of glued-in steel plates used as shear connectors in Timber-Concrete-Composites," (in English), *Engineering Structures,* Article vol. 170, pp. 1-10, SEP 1 2018 2018.

[11] J. Miotto and A. Dias, "Evaluation of perforated steel plates as connection in glulam-concrete composite structures," (in English), *Construction and Building Materials,* Article vol. 28, no. 1, pp. 216-223, MAR 2012 2012.

[12] E. Lukaszewska, "Development of Prefabricated Timber-Concrete Composite Floors," PhD, Department of Civil, Mining and Environmental Engineering, Lulea University of Technology, Sweden, 2009.

[13] L. C. Neves, P. Vellasco, and I. Valente, *Shear connectors that use concrete dowels*, 1st Edition ed. (ECCS TC 11 - Composite Sturctures - WG1 - Shear Connectors). 2018.

[14] E. Oguejiofor and M. Hosain, "A parametric study of perfobond rib shear connectors," (in English), *Canadian Journal of Civil Engineering,* Article vol. 21, no. 4, pp. 614-625, AUG 1994 1994.

[15] *EN 1993-1-8: Design of steel structures - Part 1-8: Design of joints,* E. C. f. Standardization, 2005.

[16] Sika, "Product Data Sheet Sika Anchorfix - 3030," ed: Sika.

[17] *EN 1992-1-1 Design of concrete structures - Part 1-1: General rules and rules for buildings,* E. C. f. Standardization, 2004.

[18] E. Appavuravther, B. Vandoren, and J. Henriques, "Push-out tests on adhesively bonded perfobond shear connectors for timber-concrete composites," *Journal of Building Engineering,* 2022.

[19] *EN 12390-3 Testing hardened concrete - Part 3: Compressive strength of test specimens*, 2009.

[20] *EN 26891 - Timber Structures - Joints Made with Mechanical Fasteners - General Principles for the Determination of Strength and Deformation Characteristics*, 1991.

[21] *EN 12512 - Timber structures - Test methods - Cyclic testing of joints made with mechanical fasteners*, 2002.

[22] I. Valente and P. Cruz, "Experimental analysis of Perfobond shear connection between steel and lightweight concrete," (in English), *Journal of Constructional Steel Research,* Article|Proceedings Paper vol. 60, no. 3-5, pp. 465-479, MAR-MAY 2004 2004.

[23] J. Vianna, L. Costa-Neves, P. Vellasco, and S. de Andrade, "Experimental assessment of Perfobond and T-Perfobond shear connectors' structural response," (in English), *Journal of Constructional Steel Research,* Article vol. 65, no. 2, pp. 408-421, FEB 2009 2009.

[24] E. Lukaszewska, H. Johnsson, and M. Fragiacomo, "Performance of connections for prefabricated timber-concrete composite floors," *Materials and Structures,* pp. 1533-1550, 2008.

[25] L. Marchi, R. Scotta, and L. Pozza, "Experimental and theoretical evaluation of TCC connections with inclined self-tapping screws," (in English), *Materials and Structures,* Article vol. 50, no. 3, JUN 2017 2017, Art. no. ARTN 180.

[26] S. Monteiro, A. Dias, and J. Negrao, "Assessment of Timber-Concrete Connections Made with Glued Notches: Test Set-Up and Numerical Modeling," (in English), *Experimental Techniques,* Article vol. 37, no. 2, pp. 50-65, MAR-APR 2013 2013.

[27] Y. Jiang, X. Hu, W. Hong, J. Zhang, and F. He, "Experimental Study on Notched Connectors for Glulam-lightweight Concrete Composite Beams," *Bioresources,* vol. 15(2), pp. 2171-2180, 2020.

World Conference on Timber Engineering Oslo 2023

DELTABEAM® WITH TIMBER FLOOR JOINTS – LOAD BEARING CAPACITY AT AMBIENT TEMPERATURE AND IN FIRE SITUATION

Salla-Mari West[1], Elena Camnasio[2], Simo Peltonen[3]

ABSTRACT: DELTABEAM® Composite Beam represents an excellent solution for creating a slim floor structure with timber slabs. Hybrid structures are nowadays increasingly popular as the combination of steel, concrete and timber enables the optimization of the design by taking advantage of the strong points of each material. However, the combination of different materials and the use of innovative design details set the challenge for assessing the safety and reliability of the solution. Therefore, Peikko investigated the load bearing capacity of the joints between DELTABEAM® and cross-laminated timber slabs both at ambient temperature and in fire situation. Load transfer tests, a charring test and a loaded fire test were carried out in order to prove the effectiveness of the transverse reinforcement, which ties the beam and slab together and secures the load transfer. As far as DELTABEAM®, the fire resistance is ensured by inner rebars so that no additional fireproofing is needed. In particular, the full-scale loaded fire test confirmed the satisfactory performance of both edge and intermediate DELTABEAM®s with cross-laminated timber slabs. The results allowed for developing test-based design recommendations and showed how the typical timber slab details can be used in a new and more efficient way with DELTABEAM® slim floor solution.

KEYWORDS: composite beam, slim floor, hybrid structure, timber slab, fire performance, full-scale tests

1 INTRODUCTION

Innovative construction solutions are nowadays needed to meet a wide range of design requirements, like complex architectural shapes, optimized use of the materials, demanding load conditions, sustainability aspects, and even cost-efficiency, among others. In this regard, DELTABEAM® hybrid timber structures represent a perfect way to tackle these aspects simultaneously [1]. DELTABEAM® slim floor structures [2] have been widely approved and successfully used in projects over the years. Recently, the solution has been adopted in combination with timber slabs as well [3]. Compared to traditional timber structures, the use of a steel and concrete composite beam integrated into the floor allows to achieve longer spans and to avoid load-bearing walls (Figure 1). This gives more architectural freedom, enables smooth ceilings, reduces the volume of the materials, and eases the construction process.

One of the main benefits of DELTABEAM® solution is that additional fireproofing of the beam is not needed. This is particularly convenient for timber structures, where fire design might be critical. DELTABEAM® fire rebars that are embedded in the concrete inside the steel profile guarantee the resistance of the main structural load bearing element in the event of a fire. Such reinforcement is designed depending on project fire rating requirement according to Eurocodes [4] and [5] and its performance has been extensively proved by testing in the past [6].

Figure 1: *DELTABEAM® slim floor structure with mass timber slab.*

However, additional testing is needed for hybrid constructions to give evidence that timber, concrete and steel can satisfy the design demands in overall, as their combination is not yet comprehensively standardized. In order to fill the lack of regulations and give reliable proof at the same time, Peikko conducted a wide research program on DELTABEAM® hybrid timber structures, which took into account not only its behaviour in fire situation but also other design issues, such as the vibration performance [7] and the way how to connect other timber elements and how to ensure the timber-concrete composite action [8].

The part of the research on the load carrying capacity of DELTABEAM® timber floor joints both at ambient temperature and in fire situation is herein presented.

[1] Salla-Mari West, Peikko Group, Finland, salla-mari.west@peikko.com
[2] Elena Camnasio, Peikko Group, Italy, elena.camnasio@peikko.com
[3] Simo Peltonen, Peikko Group, Finland, simo.peltonen@peikko.com

https://doi.org/10.52202/069179-0413

2 DELTABEAM® TIMBER FLOOR JOINTS

Joints and their design usually have a major impact on a structure's properties. In fact, the joints affect its load-bearing capacity, stability and fire performance, thus even influencing the type of failure that can occur. This can be even more critical for timber structures that have many different joints and connecting details [9].
Beam-floor joints have to be designed to prevent the separation between the parts and to transfer the forces from the slab to the supporting structural elements depending on different design conditions. In case of hybrid timber structures, the interaction between concrete and timber at the interface between the composite beam and the floor panel should be considered as well. Moreover, when accounting for the fire situation, beam-floor joints need generally to be protected by concealed connections, fire-rated gypsum boards and/or intumescent paints or seals in order to get the required fire resistance [10].
The above-mentioned design challenges can be effectively solved by using DELTABEAM® with timber slabs. The load bearing capacity at DELTABEAM® floor joint is ensured by a strut-and-tie mechanism that relies on DELTABEAM® inclined web. In fact, in the final composite stage, the loads are transferred to DELTABEAM® through a compression arch against the inclined web (Figure 2). Such mechanism is valid both at ambient temperature and in fire situation.

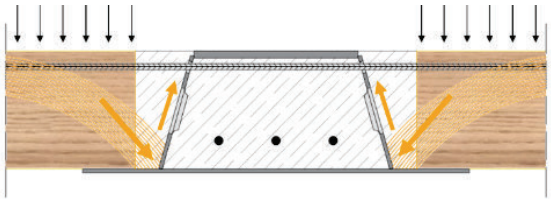

Figure 2: *Load transfer mechanism of DELTABEAM® hybrid timber structure at final stage.*

Compression forces are taken by the concrete surrounding DELTABEAM® steel profile while transverse rebars carry tension forces [3]. This means that the load is supported directly by the steel ledge only at installation stage and not after concrete hardening. During construction, the presence of the ledge allows for fast and easy positioning of the floor elements on the bottom flange of DELTABEAM® and it is suitable for different slab types, such as mass timber slabs, composite timber slabs and beam decks.
The transverse reinforcement is essential in securing the load transfer mechanism at DELTABEAM® floor joint (Figure 3). Rebars are usually placed through DELTABEAM® airholes, web holes, and additional web holes or within the concrete topping in case of composite slabs. In case of solid timber slabs, grooves are cut in the panels for rebar installation. More information about the detailing of DELTABEAM® timber floor joint can be found in [3].

Figure 3: *Transverse reinforcement for solid timber and composite timber slabs.*

3 RESEARCH PROGRAM

As joints are generally the weakest part of a timber structure, especially when exposed to fire, the main scope of the investigation regarded the fire performance of DELTABEAM® floor joints. However, the load carrying capacity of the joint has been first studied by finite elements and then verified by load transfer tests at ambient temperature. Such investigation is important to validate the assumed load transfer mechanism and useful to understand how the fire exposure possibly affects the behaviour.
A charring test and a loaded 90-minute fire test were then carried out on DELTABEAM® and timber slabs as continuation of the load transfer tests at ambient temperature. Cross-laminated timber (CLT) floor panels were used for all the tests, as being one of the main representatives of mass timber products [11].

3.1 LOAD TRANSFER TESTS

Load transfer tests were carried out on full-scale specimens of both timber and composite timber slabs supported by DELTABEAM® Composite Beam. Aim of the test was to prove that the failure would eventually take place in the slab, either in timber or in concrete, but not at DELTABEAM® support with load level well above the practical loads in projects. In the purpose of investigating the load capacity of the floor joint only, the beam behaviour was excluded by supporting the central part of DELTABEAM® bottom flange along its length. Thus, only the steel ledge was left unsupported and free to deform under the load.
The specimens were grouped by type as shown in Figure 4. The depth of DELTABEAM® standard profile was selected to match the thickness of the slab, which was built with 5-layer assembly CLT panels. In particular, composite timber slabs had a concrete topping thickness equal to 1/3 of the total thickness, as it occurs in most of the real cases. The shear connection between the timber

https://doi.org/10.52202/069179-0413

panel and the concrete topping was a notched one with large head screws inside the notches [12].
Each specimen had a different detailing of the interface between the timber panels and the outer concrete of DELTABEAM® to cover possible cases that are used in projects. The end face of the timber panel was cut either vertical or inclined so to be parallel to the web of the beam. In case of the inclined end cut, additional details that consisted in pockets or chamfers along the end face were introduced to check the improvement of the resistance of the joint given by such tailored geometry (Figure 4). More information can be found in [1] and [13].
A preliminary check of the load transfer capacity of the joint in a simulated fire situation was performed during this phase of the research program by removing the supporting ledge in three of the specimens with the inclined end cut. This represents the worst-case scenario by assuming the complete loss of stiffness and resistance of the ledge, which in reality occurs progressively when exposed to fire. Similar simulated fire situation was even previously tested by removing artificially the bottom part of a CLT panel and performing bending tests on a simply supported single span timber slab with edge DELTABEAM® [3].

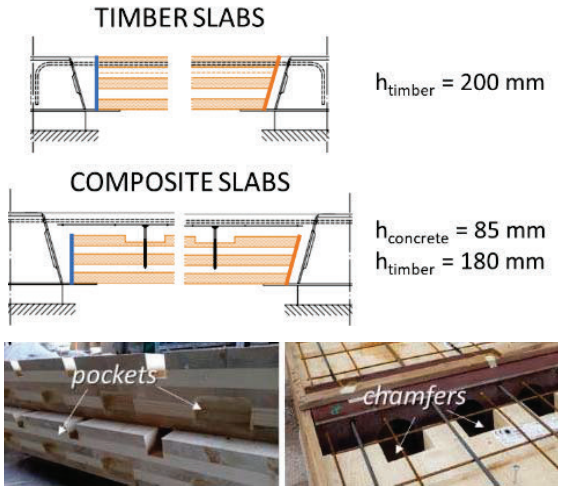

Figure 4: *Types of the tested specimens and close up-view of the panel end faces with tailored geometry.*

The test setup consisted of two symmetric 3-meter long CLT spans supported by one intermediate DELTABEAM® and by roller supports at the ends (Figure 5). The slabs were loaded with a line load and slab deflections were measured below, at a distance from the centre line of DELTABEAM® that equals three times the thickness of the slab. Compared to distributed load in normal design conditions, this is an unfavourable condition, which maximizes the shear and forces the failure in the area close to the beam. Test results can be then assumed on the safe side with respect to standard design loads.

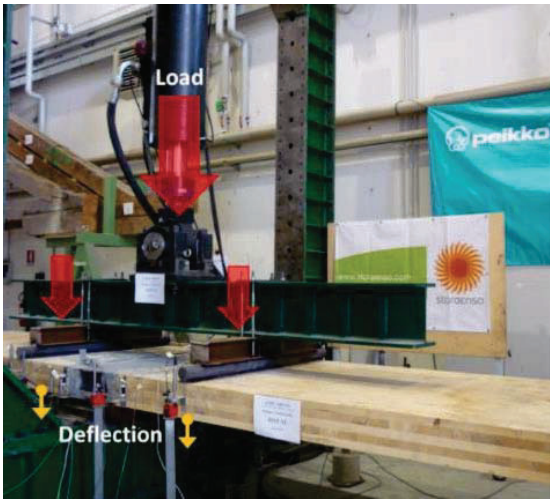

Figure 5: *Test setup of the load transfer tests.*

3.1.1 Timber slabs

Specimens with timber slabs exhibited a rolling shear failure in the slab area between the applied load and the support, as expected (Figure 6). In fact, timber exhibits limited resistance to shear forces that act orthogonal to grain direction, which determines the low rolling shear capacity of the CLT panels and may trigger the failure in circumstances such as concentrated loads and short spans like the ones in the tests.
Despite the severe test conditions that induced high shear stresses in the panel area close to DELTABEAM®, the load bearing capacity of the support was kept until the end of the tests, although the steel ledge deflected up to 20 mm, which was due to a significant rotation of the slab end.

Figure 6: *Rolling shear failure and ledge deflection in timber specimens.*

The satisfactory performance of the joint was observed even in the specimens without the supporting ledge. This proves that the ledge does not support the load directly and that the assumed load transfer mechanism is actually established. However, the presence of the ledge is favourable for the confinement of the bottom part of the slab, thus preventing the tensile failure due to the stresses orthogonal to the fibres of the longitudinal bottom layer.
On the contrary, such failure type occurred in the two specimens representing the simulated fire condition (Figure 7) even though it did not hinder a satisfactory load carrying capacity. These specimens had both the inclined end cut of the panel and one of these had the pockets along

https://doi.org/10.52202/069179-0413

the end face. In this case, the joint was stiffer, and the bearing resistance was even higher thanks to the concrete parts inside the pockets that can offer back-up support to the slab. Such detail is useful to improve the performance of the joint especially when the edge of the timber panel is cut vertically.

Figure 7: *Timber panel failure in specimens without DELTABEAM® ledge.*

Figure 8 shows the load-deflection curves of the timber slab specimens. The load represents the support reaction on both DELTABEAM® sides, which was about 80% of the total load applied on the slabs in all cases. This is due to the test setup with concentrated load close to the beam support, but it also shows that DELTABEAM® floor joint can provide a higher degree of fixity to the slab end compared to the simply supported condition that is usually assumed for timber slabs.

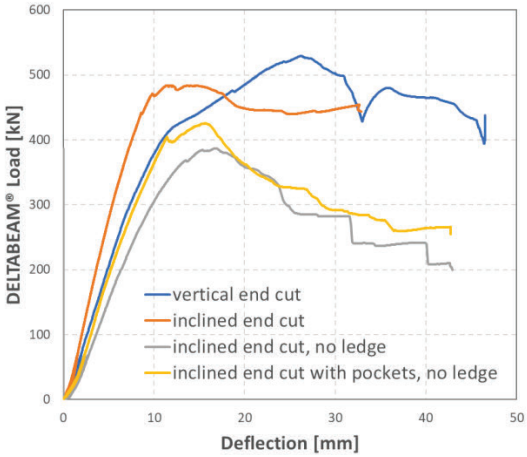

Figure 8: *Load-deflection curves of timber slab specimens.*

The peak loads were significantly high. Even in the simulated fire condition that showed the lowest load carrying capacity, the applied force corresponded to a load of about 130 kN/m on one side of the beam. This is far beyond standard design loads. Moreover, the results showed that the load carrying capacity of the support was maintained even for a slab deflection up to about 40 mm for all cases, which is above usual design deflection limits.

3.1.2 Composite slabs

The failure type of the composite timber slabs was mainly the cracking of the topping, which started from the separation between timber and concrete in the area close to the beam that had no connectors to take the tensile forces. The crack pattern clearly indicated the direction of tensile stresses, which were orthogonal to the orientation of compression forces pointing from the applied load to the notches (Figure 9).

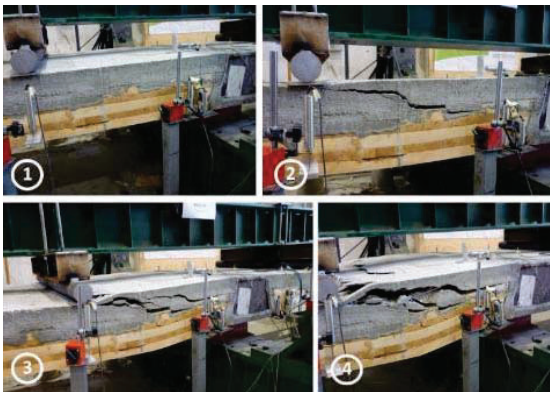

Figure 9: *Concrete topping crack pattern development in composite timber slabs.*

Rolling shear in timber and/or bending failure of the slab occurred as well. The latter one usually develops in CLT panels when the composite action between concrete and timber is lost. Slight pull-out failure of the large head screws was also observed, as the actual failure load exceeded the expected one (Figure 10). In fact, such failure modes occurred at load levels that were far higher than the standard design ones. The simulated fire condition, i.e. DELTABEAM® with no ledge, was tested in case of composite slab as well. Similarly to what observed with solid timber slabs, the bottom layers of the timber panel failed due to tension orthogonal to the grain. The support was anyhow able to carry the load without failing.

Figure 10: *Failure modes in composite timber specimens: bending, rolling shear, screw pull-out and tension orthogonal to the grain (clockwise).*

Figure 11 shows the load-deflection curves of the composite timber slab specimens. The load carried by DELTABEAM® was about 74% of the total load applied

on the slabs in all cases. Composite timber slabs are generally stiffer and more resistant than timber slabs of equal height, when concrete is properly connected to the timber panel. That is why the composite specimens showed greater stiffness and higher peak load values than the solid timber ones.
In particular, the specimen with inclined end cut of the timber panel and chamfers cut along the edge reached the maximum load capacity of the actuator (100 tons) without failing. The failure occurred then by keeping the load constant for few minutes. The improvement of the bearing capacity, which is due to the development of concrete struts close to DELTABEAM® web holes, shows the effectiveness of the tailored geometry and supports the assumptions of the model of the load transfer mechanism.

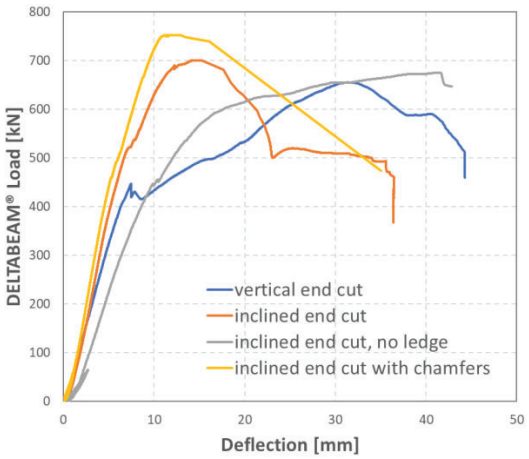

Figure 11: *Load-deflection curves of composite timber slab specimens.*

3.2 FIRE TESTS

The charring test and the 90-minute loaded fire test concerned DELTABEAM® Composite Beam with solid timber slabs without any top concrete. Composite timber slabs are usually stiffer and performed better in load transfer tests in ambient temperature. Because of this, solid timber slab structure was selected for the two fire tests to test the most unfavourable situation.

3.2.1 Charring test

Due to the fall of charred layers, the carbonization of the CLT board is not linear and progresses at several carbonization rates [14]. To design CLT slabs against fire, it is recommended to use the reduced cross-section method described in EN 1995-1-2 [15]. In the reduced cross-section method, the parts of the cross-section with assumed zero strength and stiffness are removed and no longer contribute to the resistance of the cross-section. The charring depth is the distance between the bottom surface of the original member and the position of the char-line and should be calculated from the time of fire exposure and the relevant charring rate. The position of the char-line should be taken as the position of the 300-degree isotherm [15].
The two-hour charring test concerned DELTABEAM® with commonly used timber slab details adapted for a slim floor structure. Based on the load transfer tests in ambient temperature, experience and performed fire design calculations, the most suitable joint details were selected for the test. The specimen for the charring test had seven different details, which were equipped with thermocouples. DELTABEAM® Composite Beam was not fireproofed in any of the seven cross-sections. CLT 200 L5s and CLT 280 L7s timber slabs were placed on the DELTABEAM® Composite Beam ledges or downstands. The DELTABEAM® and the CLT 200 L5s slabs had equal depth. In Figure 12 the finished specimen for the charring test is presented. The temperature data from the charring test proved that the charring depth is smaller in the joint area between DELTABEAM® Composite Beam and CLT slab than in the middle of the CLT slab area, without any additional fireproofing.

Figure 12: *Specimen for the two-hour charring test without loading.*

There are different options for the edge geometry of the timber slab, like vertical or inclined end cut shown in Figure 4. The geometry of the CLT slab end does not affect the load-bearing capacity of the structure or joint. Figure 13 shows the temperatures in the joint area between DELTABEAM® and CLT slabs without any additional fireproofing under the beam or under the CLT slabs. The charring rate with the vertical end cut is higher in the beginning, but in the end, the effective charring depth is about the same for both end cuts. At a distance of 100 mm from the CLT soffit the temperature has settled to 100 degrees for both end cuts.
Before the charring test, the effective charring depth was calculated for the CLT slab without any additional fireproofing. The effective charring depth would be 108 mm according to [15] and the CLT product charring rate [16]. After the test, the effective charring depth was calculated according to [15] and the temperature data. Figure 13 shows that the 300-degree char-line at 120 min is between 60 mm and 80 mm. To be on the safe side, 80 mm will be selected. By adding the thickness of material close to the char line with zero strength and

https://doi.org/10.52202/069179-0413

stiffness according to [15], the effective charring depth for both end cuts is then 87 mm. With both CLT end cuts, the effective charring depth proves to be less in the joint area between DELTABEAM® and CLT slab than the calculated effective charring depth at the midspan of the CLT using CLT product charring rate.

In conclusion, both vertical and inclined end cuts are safe to be used in CLT slabs in fire situation. Moreover, based on the extensive measurement data from the various details, it could be clearly seen that DELTABEAM® Composite Beam had no negative impact on the charring rate of the CLT panel in any of the investigated details.

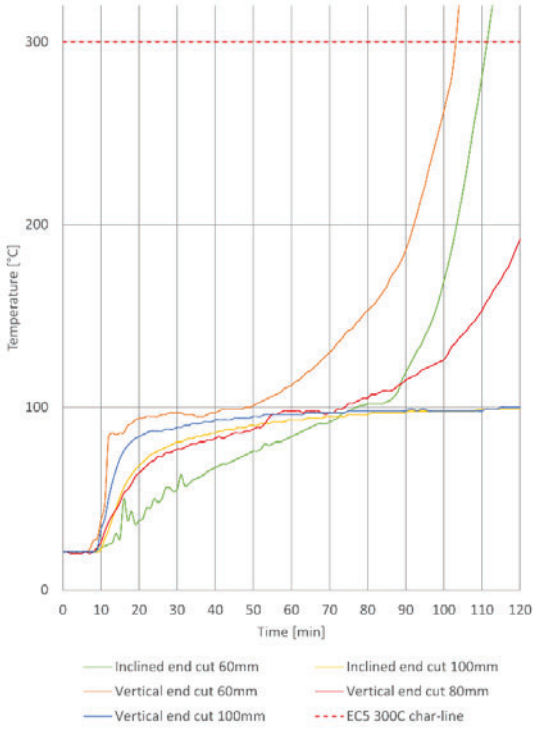

Figure 13: *Temperature in the CLT slab in the joint area, 60-100 mm from the CLT soffit.*

3.3 90-MINUTE LOADED FIRE TEST

In the REI90 fire test, CLT 200 L5s timber slabs were placed on the DELTABEAM® Composite Beam ledges. The specimen consisted of DELTABEAM®s and CLT slabs which all had an equal depth of 200 mm. No additional fireproofing was used in DELTABEAM®s or in CLT slabs. In Figure 14 the finished specimen for the 90-minute fire test is presented.

The load was constant during the entire 90-minute fire test. The load arrangement simulated DELTABEAM® and CLT slab structure with 8 m CLT span, 1.7 kN/m^2 permanent load and 5 kN/m^2 live load (ψ_1=0.7). Therefore, the support reaction in the joint area between DELTABEAM® Composite Beam and CLT slab was equal to 20.8 kN/m on each side. This corresponds to only the 16% of the maximum support reaction measured in the simulated fire condition (Paragraph 3.1.1). This shows that standard design conditions are well on the safe side when compared to the maximum load carrying capacity of the joint, that was evaluated at ambient temperature with no ledge.

Figure 14: *Specimen for the 90-minute loaded fire test consisting of two edge beams, an intermediate beam and two CLT panels.*

Rebars with 12 mm diameter and 600 mm spacing were used in DELTABEAM®s. At the intermediate beam, the transverse reinforcement passes through the air holes at the top end of DELTABEAM® web plates. At the edge beams the transverse reinforcement passes through the web holes (Figure 15).

Figure 15: *Reinforcement in edge beam situation.*

The 90-minute loaded fire test proved that the interface between DELTABEAM® Composite Beam and timber floor can sufficiently transfer loads from the floor to the beam in both edge and intermediate beams during a fire situation. Due to the protecting effect of the DELTABEAM® ledge the charring depth in the joint area was not as deep as in the middle of the CLT span. After the 90-minute loaded fire test, the specimen was demolished to investigate the charring of the structure. Figure 16 shows that the charred timber above the DELTABEAM® ledge stays in place. This is due to the presence of the steel ledge, which prevents the spalling of the charred parts and the possible tensile failure orthogonal to the remaining timber fibres (Paragraph

https://doi.org/10.52202/069179-0413

3.1.1), despite having completely lost its strength and stiffness after 90-minute exposure. In addition, this charred timber keeps protecting the joint area after the bottom lamella of the CLT slab has fallen along the span.

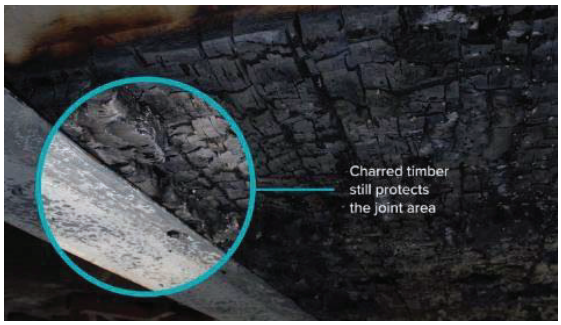

Figure 16: *Specimen from below after 90-minute loaded fire test.*

3.3.1 Load bearing capacity, integrity, and insulation

In the case of fire, structures shall be designed and constructed in such a way that they can maintain their load-bearing capacity during the relevant fire exposure. Where fire compartmentation is required, the elements forming the boundaries of the fire compartment, including joints, shall be designed and constructed in such a way that they maintain their separating function during the relevant fire exposure. The criteria for integrity and insulation must be fulfilled when relevant [15]. In the 90-minute fire test with loading, all REI90 requirements for load-bearing capacity, integrity and insulation were met.

Deflections were measured in the middle of the CLT elements, in the middle of the intermediate DELTABEAM® and in the middle of the edge DELTABEAM®s. The deflections at 90-minute were between 40 mm and 50 mm for DELTABEAM®s and CLT slabs, which are less than $L^2/400d$ mm = 136 mm (depth of the specimen d is 200 mm, and the span L is 3300 mm). The deflection rate was less than $L^2/9000d$ mm/min = 6.05 mm/min. Therefore, the criteria of the load-bearing capacity R were met.

The average temperature rise for the whole structure at 90 min was 62 degrees. This value is smaller than the value of 140 degrees, which is the limit temperature of the insulation criterion. The highest temperature rise was equal to 92 degrees at 90 min. The highest temperature rise was less than 180 degrees, which fulfils the insulation criteria at any point of the specimen. Based on the high number of measured temperature values in the joint area between DELTABEAM® Composite Beam and CLT slabs, the insulation I criteria for average and the highest temperature rise were met.

There were no flames on the unexposed surface and no gaps in the specimen. Based on the visual observations, the integrity E criteria were met.

3.3.2 Load transfer

Figure 17 shows how the loads are transferred to DELTABEAM® through a compression arch against an inclined web in a fire situation. The angle of inclination of the compression arch slightly changes during fire exposure and the support shifts to the bottom corner of DELTABEAM® profile. As a result of the compressive stresses path, the charred timber part remains in the confined space between the beam ledge, the concrete grout and the uncharred timber slab. This provides an insulation to the joint area during fire and slows down the charring of the portion of the timber panel above the ledge.

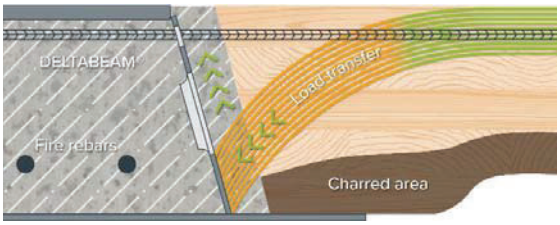

Figure 17: *Load transfer in a fire situation.*

Based on visual observations of the REI90 fire test, the charring happens only at the bottom of the timber slab, as expected. The joint concrete is clean without any damage. The fire has not burned through the joint. After the fire test, when the specimen had cooled down, the specimen was cut into three pieces at mid-spans of the CLT parallel to the beam. Finally, a section of the CLT slab next to the edge and intermediate DELTABEAM® was removed to investigate the charring in the joint area.

Figure 18 and Figure 19 present that there is about half of the second lamella remaining in the joint area, while in the middle of the CLT span the second lamella is already fully charred. The depth of the uncharred timber in the middle of the CLT span was between 120 mm and 135 mm, meaning that about 70 mm of the CLT slab depth was charred. On the contrary, about 50 mm of the CLT slab depth was charred in intermediate and edge beam cases at the joint area. The specimen continued to burn during disassembling the load arrangement and lifting the specimen. Due to this, the measured remaining timber slab depth is on the safe side. The charring depths measured during demolition support the temperature data measurements and prove that the calculated effective charring depth is conservative.

All displacement transducers were set on DELTABEAM® as a reference. The relative displacement between the top end corner of CLT slab and the top plate corner of DELTABEAM® was measured in vertical and horizontal direction (Figure 20). The measured relative displacement values show that the joint area performs well during a fire situation, as no major slip was observed. The results prove that the transverse reinforcement effectively ties DELTABEAM® Composite Beam and CLT slab together, thus securing the load transfer.

https://doi.org/10.52202/069179-0413

Figure 18: *Charring in the DELTABEAM® and CLT slab joint, next to the joint concrete.*

Figure 19: *Charring in the middle of the CLT span.*

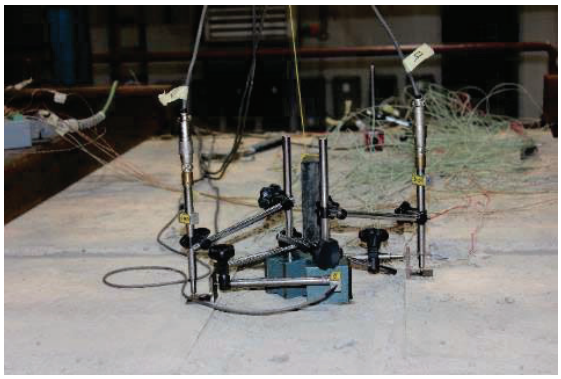

Figure 20: *Assembled displacement sensor in the joint area at mid beam span in vertical and horizontal direction.*

3.3.3 Normal stresses in transverse reinforcement

In Figure 21 the normal stresses in the transverse rebars in edge and intermediate beam situations during the 90-minute loaded fire test can be seen. The normal stresses were highest in an edge beam situation due to the unsymmetric load. Based on the stress-strain curves of the transverse rebars, the normal stress increases linearly and then decreases linearly following the same path. This shows that the transverse rebars do not yield since there are no permanent deformations according to the stress-strain curves.

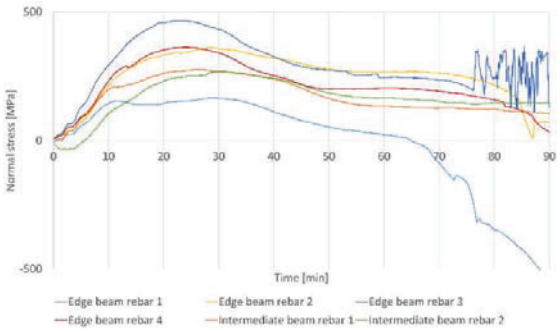

Figure 21: *Normal stresses vs time in the transverse rebars.*

In Figure 22 the changes of the bending stiffness of DELTABEAM® Composite Beam during the 90-minute loaded fire test are presented. The highest reduction of the bending stiffness can be observed during the first 30 minutes. At the same time, the normal stresses in the transverse rebars increase the most.

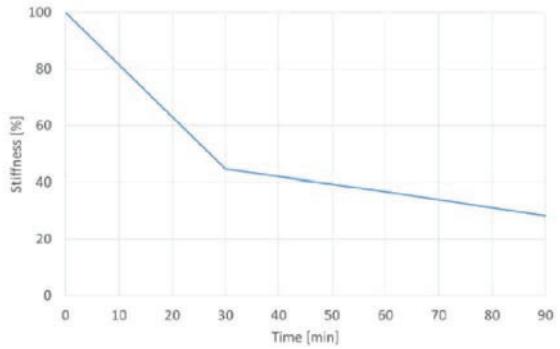

Figure 22: *Bending stiffness of DELTABEAM® Composite Beam vs time during the 90-minute loaded fire test.*

4 TIMBER FLOOR JOINTS DESIGN RECOMMENDATIONS

Relevant design recommendations for DELTABEAM® timber floor joints can be drawn based on test evidence. The load transfer mechanism is safely established regardless the shape of the end face of the timber panel. In fact, the results showed that both the vertical and inclined end cut of the timber panel give adequate resistance to the joint. However, the inclined end cut can provide higher peak values of the load capacity, as friction reaction forces that develop between the outer concrete of DELTABEAM® and the inclined side of the panel are in favour of the strut-and-tie mechanism. The additional details such as pockets and chamfers proved to be effective as well and are therefore recommended. In any case, proper concrete filling of the gap between the beam and the timber panel should be ensured.

https://doi.org/10.52202/069179-0413

The use of transverse reinforcement is essential to carry the tensile forces that develop through the joint. The effectiveness of the tying system was proved by the performance of the specimens at ambient temperature, where any rebar failure such as pull-out or blow-out failure occurred despite the high load level and severe test condition.
The results of the load transfer tests also confirmed that joints of the composite slabs are stiffer and more resistant compared to timber ones with same thickness. Moreover, the reinforced concrete topping provides continuity between adjacent slabs, is favourable to reduce floor vibrations and allows for easy installation of the transverse rebars through or above DELTABEAM® steel profile.
On the contrary, grooves need to be cut in solid timber slabs for the installation of the transverse reinforcement. The required length of the grooves depends on the needed amount of notches to secure the load transfer from timber slabs to DELTABEAM®. In fact, grooves are filled in with concrete so that compressive stresses between concrete and timber develop at the locations of the notches (Figure 23). The distance between the notches has to be designed in a way that it will not fail in shear. In order to transfer the total force properly, the tie rebar shall also extend beyond the last notch up to the end of the groove. Therefore, the rebar length depends on either the required length of the grooves or the required anchorage length according to [4], whichever the maximum. For example, for the REI90 fire test specimen, the anchorage length of the rebars was determined by the design of the grooves. The minimum concrete cover according to [4] should be also guaranteed.

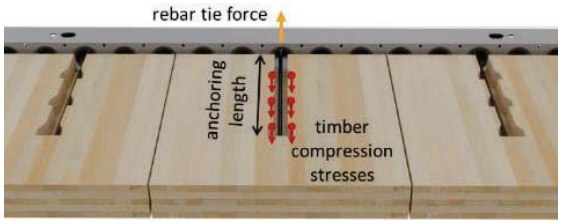

Figure 23: *Force in transverse rebar creates pressure in the notches.*

It is important to have wide enough grooves especially when the transverse rebar is not only securing the load transfer but also carrying an unsymmetric load, for example. In fact, having a wide enough concrete block, along with a sufficient amount of reinforcement, prevents the concrete from cracking, which might occur when tensile stresses get higher. For example, the grooves in the fire test specimen for the edge beam situation were two times wider than in the intermediate beam. Moreover, the load eccentricity causes compressive stresses to the topmost part of the timber panel (Figure 24). Such compression must not exceed the design compressive strength of timber along the grain.

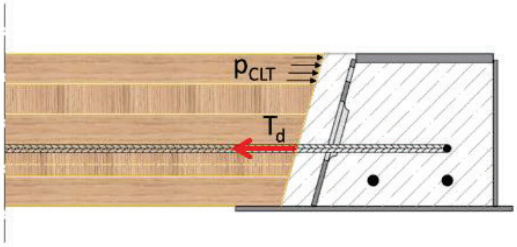

Figure 24: *Unsymmetric load in the edge beam situation.*

In case of unsymmetric load, which occurs in the edge beams, the transverse rebars should be located as low as possible in order to maximize the lever arm between tension and compression resultants. Deeper grooves are then needed and rebars are generally placed through the web holes or through additional lower holes depending on the project. However, the progression of the charring in the timber panels and the temperature increase in the slab at fire exposure have to be considered. In fact, transverse rebars should be placed satisfactorily above the area affected by the major temperature increase so as to limit the steel strength reduction that shall be accounted for according to [5].
After the timber under the groove has charred away, the concrete would heat up following the standard fire exposure. According to the measurement data at 90-minute fire exposure, this design assumption is on the safe side. In fact, the temperature on the bottom of the groove was 100 degrees, while the temperature in the transverse rebar was 114 degrees in the joint area. According to [5], rebar steel strength reduction is 80% at 200 degrees. This proves that the mechanical properties of the transverse rebars were reasonably not affected by the temperature increase during the entire test, which confirms the satisfactory performance of DELTABEAM® timber floor joints in fire situation.

5 CONCLUSIONS

The extensive research program, which included load transfer tests at ambient temperature, a charring test and a 90-minute fire test with loading, assessed that timber floor joints equipped with proper transverse reinforcement can safely transfer the load from the slab to DELTABEAM® Composite Beam. In particular, it has been proved that the assumed strut-and-tie design model is established and effective in fire situation too without any additional fireproofing under the beam or the timber slab, so to achieve a slim floor structure that can be left exposed and used together with various common timber floor details used in real-life projects.
Peikko is nowadays continuing the research on DELTABEAM® hybrid timber structures in order to optimize the solution even more, provide reliable design information and give engineering support to customers. Future investigations will concern shear connection tests and beam tests, among others.

https://doi.org/10.52202/069179-0413

ACKNOWLEDGEMENT

The authors would like to thank Stora Enso for providing the technical support and the CLT slab elements. Peikko also greatly acknowledges Eurofins Expert Services Oy (Finland) and the University of Trento (Italy) for performing the tests.

REFERENCES

[1] Camnasio E., Peltonen S.. Load transfer tests on DELTABEAM® with hybrid timber floors. *Proceedings of the Italian Concrete Conference (ICC)*, Napoli, Italy, 12th-15th October, 2022.

[2] Peikko Group. *DELTABEAM® Composite Beams – Slim Floor Structure with integrated fire proofing*. Technical Manual, 2021.

[3] Peikko Group: *DELTABEAM® Slim Floor Structure with timber construction*. Technical Manual, 2023.

[4] CEN European Committee for Standardization. *SFS-EN 1992-1-1 - Eurocode 2: Design of concrete structures. Part 1-1: General rules and rules for buildings*, Brussels, 2004.

[5] CEN European Committee for Standardization. *SFS-EN1994-1-2 - Eurocode 4: Design of composite steel and concrete structures. Part 1-2: General rules - Structural fire design*. Brussels, 2004.

[6] Beckmann O., Klein-Holte R.. *Design recommendations for hollow core slabs supported on DELTABEAM® – Position of support reaction forces*. White Paper, www.peikko.com, 2022.

[7] Yrjölä J., Salonen J.. *Performance of DELTABEAM®-CLT floors in human-induced vibration*. White Paper, www.peikko.com, 2021.

[8] Peikko Group. *Hybrid solutions*. https://www.peikko.com/products/hybrid-solutions/overview/, 2022.

[9] Swedish Wood. *The CLT Handbook. CLT structures – facts and planning*. Stockholm, 2019.

[10] McLain R., Breneman S.. *Fire Design of Mass Timber Members*. WoodWorks, www.woodworks.org, 2019.

[11] Stora Enso. CLT by Stora Enso, Technical Manual. https://www.storaenso.com/en/products/wood-products/massive-wood-construction, 2021.

[12] Yeoh D., Fragiacomo M., De Franceschi M., Heng Boon, K.. State of the art on timber-concrete composite structures: Literature review. *Journal of structural engineering*, *137*(10), 1085-1095, 2011.

[13] Camnasio E.. *DELTABEAM® with hybrid timber floors load transfer tests*, White Paper, www.peikko.com, 2022.

[14] Puuinfo: PALOTURVALLINEN PUUTALO Asuin- ja toimitilarakentaminen, 2021. https://puuinfo.fi/suunnittelu/ohjeet/paloturvallinen-puutalo-asuin-ja-toimitilarakentaminen/

[15] CEN European Committee for Standardization. *SFS-EN1995-1-2. Eurocode 5: Design of timber structures - Part 1-2: General - Structural fire design*. Brussels, 2004.

[16] Stora Enso: Cross-laminated timber (CLT). https://www.storaenso.com/en/products/mass-timber-construction/building-products/clt, 2022.

World Conference on Timber Engineering Oslo 2023

MECHANICAL BEHAVIOUR OF TIMBER-STEEL COMPOSITE CONNECTION SYSTEMS

Alireza Shahin[1], Craig J.L. Cowled[2], Henri Bailleres[3], Sabrina Fawzia[4]

ABSTRACT: Although timber is an ideal building material offering significant structural, environmental, and economic advantages, restrictions on the supply of high-quality timber is a limiting factor for the construction industry. To manage this problem, this study investigated an innovative approach to develop a sustainable and economical composite section with improved structural performance by combining low-grade timber and steel using advanced manufacturing technologies. In this paper, 20 specimens with 2 different configurations of this novel adhesive-free Timber-Steel Composite (TSC) connection system were designed, manufactured, and tested. By conducting standard pull-out tests on these new types of composite systems, the influences of factors such as type, pattern and spacing of the fasteners on the shear performance of these systems were evaluated and discussed. Test results demonstrated a significant difference between failure mode and nonlinear behaviour of nailed and screwed TSC connections. Screwed TSC connections showed on average 40% more shear capacity but 12% less stiffness compared to nailed TSC connections. A FE model of this composite system was developed and verified against test results. The FE model could accurately predict the nonlinear load-slip behaviour of this composite system. This model will be used in further work to develop an optimised full-scale TSC beam.

KEYWORDS: Timber-Steel Composite (TSC) connection system; Shear connectors; Static pull-out tests; Load-slip curves; Finite element modeling

1 INTRODUCTION

Timber is a strong, safe, and sustainable building material that offers significant structural, environmental, and economic advantages compared to other traditional building materials like concrete [1-3]. However, two significant reasons that are endangering the growing interest in timber construction are the high costs of manufacturing existing engineered mass timber products and limitations on the supply of high-quality timber [4]. One practical solution to address this problem is to combine low-grade timber with another building material like steel and manufacture a cost-efficient and sustainable composite section that would benefit from the structural advantages of both materials. Prior studies focused mostly on the potential for combining wood with other materials such as hot-rolled steel or concrete to create composite sections with better structural performance [5-8]. A literature review showed that even though the performance of some of these composite sections showed considerable improvement, the majority of them failed commercially because they used expensive materials or required a labour-intensive, and complex manufacturing methods [9, 10]. Therefore, the primary objective of this study is to develop a sustainable and economical composite connection system using low-grade timber and sheet steel and evaluate the performance of these novel adhesive-free components by conducting experimental studies and numerical modeling.

2 EXPERIMENTAL STUDY

2.1 MATERIALS AND METHODS

Timber material was provided from the Southern Queensland pine resource, which includes *pinus elliottii* var. *elliottii* (a.k.a. slash pine), *pinus caribaea* var. *hondurensis*, and a hybrid of the two species with F5 stress grade in accordance with AS 2858 [11]. F5 is the lowest grade of timber used in structural components with a nominal average modulus of elasticity of 6.9 GPa. All timber boards used for building TSC samples were cut with the same cross-section dimensions of (35 × 90) mm and length of 460 mm. Grade 250 structural steel plates with 1.6 mm thickness were utilised for manufacturing the composite specimens. All steel plates used for manufacturing specimens were cut with similar cross-

[1] Alireza Shahin, Queensland University of Technology, Faculty of Engineering, Australia, a2.shahin@hdr.qut.edu.au
[2] Craig J.L. Cowled, Queensland University of Technology, Faculty of Engineering, Australia, craig.cowled@qut.edu.au
[3] Henri Bailleres, Scion, Forests to Timber Products, New Zealand, henri.bailleres@scionresearch.com
[4] Sabrina Fawzia, Queensland University of Technology, Faculty of Engineering, Australia, sabrina.fawzia@qut.edu.au

https://doi.org/10.52202/069179-0414

section dimensions of (1.6 × 90) mm and length of 340 mm. To fabricate each TSC specimen, a steel plate was placed in between two (2) F5 timber pieces in a symmetrical arrangement and all three layers were connected using mechanical fasteners. While smooth shank D-head nails with 2.87 mm diameter and 65 mm length were used for manufacturing of nailed TSC configurations, fully threaded self-drilling screws with 4.8 mm diameter and 70 mm length were used to fabricate screwed TSC configurations. The main advantage of using gun-driven D-head nails and self-drilling screws was increasing the speed of fabrication by elimination of pre-drilling timber and steel components.

Figure 1 shows the function and details of the self-drilling screws used for fabrication of TSC specimens of this study. The twist shaped point of this type of screw acts as a drill and eliminates the necessity of pre-boring timber and steel elements. To prevent threads from engaging the upper timber piece, wings of this type of screw help by making a clearance hole through the timber that is wider than the threads. At final stage, the wings hit the steel and break off and threads then begin to engage. In this way, application of this type of self-drilling screw creates a solid connection between the steel and timber layers.

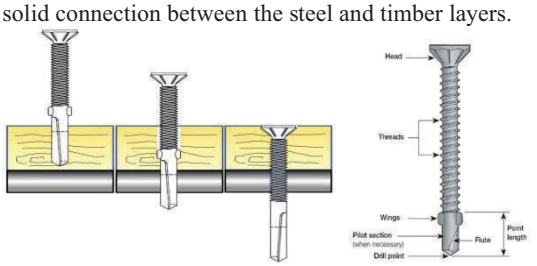

(a): Function *(b): Details*

Figure 1: *Self-drilling screws for developing TSC specimens*

Besides using simple, fast, and cost-effective fabrication method for developing these novel TSC connection systems, a unique testing setup and arrangement were fabricated to carry out the standard pull-out experiments of this study (Figure 2(a)). The pull-out tests were conducted on 20 TSC specimens with two (2) different configurations (Figure 2(b)) based on testing procedure provided by BS EN 26891 [12] standard to evaluate the effects of key parameters such as connector type, number, and patterns on the shear performance of these systems. The lower part of each specimen was held with three (3) bolts and the upper part was gripped in the jaws of the machine. As shown in Figure 2(b), specimens of group A were manufactured with three (3) fasteners with staggered pattern, while group B samples were built with four (4) fasteners with linear pattern. To evaluate the performance and effects of using different types of fasteners, all samples of each different group were fabricated using both D-head nails and self-drilling screws.

(a): Test setup

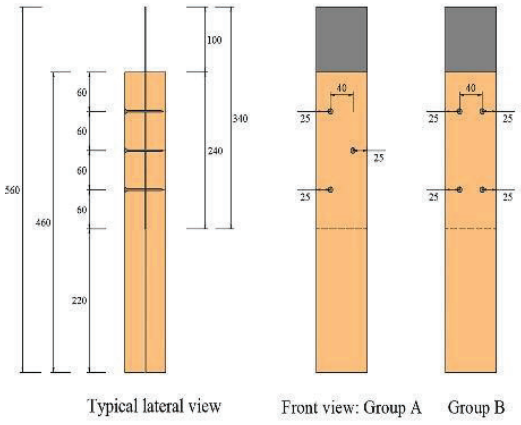

(b): Different TSC configurations

Figure 2: *Pull-out test on TSC connection systems*

2.2 CONFIGURATIONS, LOADING PATTERN AND INSTRUMENTATION

To make a direct comparison between different TSC configurations with various fasteners' pattern and spacing, the connectors end, and edge distances of all specimens were considered the same. Table 1 shows details of each TSC configuration of this study.

Table 1: *TSC configuration details and characteristic*

Group name	Config. ID	Type and size of connector	Spacing (mm)	Number of specimens
Group A	TSCA1	D-head Nail (Ø = 2.87, L= 65)	60	5
	TSCA2	Self-drilling Screw (Ø = 4.8, L= 70)	60	5
Group B	TSCB1	D-head Nail (Ø = 2.87, L= 65)	120	5
	TSCB2	Self-drilling Screw (Ø = 4.8, L= 70)	120	5

All specimens were loaded parallel to the grain direction until total failure. The pull-out loading protocol was based on a modified approach presented by the BS EN 26891 [12] standard with initial loading and unloading to remove any internal looseness between timber and steel elements. The load-slip curve of each specimen was obtained using two laser extensometers placed at both side of each sample.

3 TEST RESULTS AND DISCUSSION

To compare the performance of various TSC configurations, the average nonlinear load-slip curves of all tested specimens of each configuration were plotted.

To evaluate the effects of different types of connectors on the shear performance of TSC connection systems, Figure 3 illustrates the average load-slip curves of TSC connections with staggered and linear connectors' patterns each of them built with both self-drilling screws and D-head nails.

As the load-slip curves clearly show, the major difference between nailed and screwed TSC connections is their failure modes and nonlinear behaviour of the connections after reaching their yield load. While nailed TSC connections experienced ductile behaviour with gradual failure, screwed TSC connections showed brittle behaviour with sudden failure. After reaching their ultimate load, nailed connections still had remarkable residual capacity left and this trend continued until total failure of the system, while the screwed connections suddenly failed with no residual capacity left in the system.

According to the test results and obtained nonlinear load-slip curves of all tested specimens, self-drilling screws showed greater load-carrying capacity in comparison to D-head nails used in TSC connections with both staggered and linear fasteners patterns. Using self-drilling screw instead of D-head nail for manufacturing TSC connections improved the yield, ultimate, and maximum load-carrying capacity of TSC configurations with staggered fasteners' pattern on average by 60%, 40%, and 40%, respectively. In contrast, due to this replacement the stiffness of the TSC connection reduced on average by 12%. Similarly, screwed TSC connections with linear connectors' pattern showed on average 40% more load-carrying capacity and 17% less stiffness compared to nailed ones with the same fasteners' pattern.

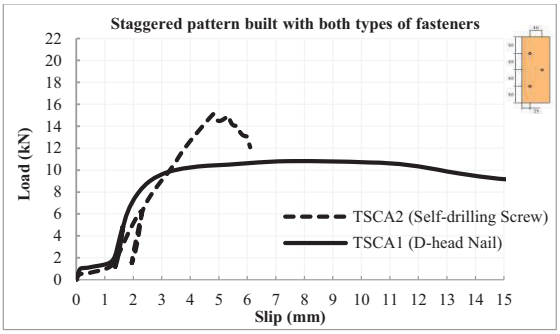

(a): Staggered pattern

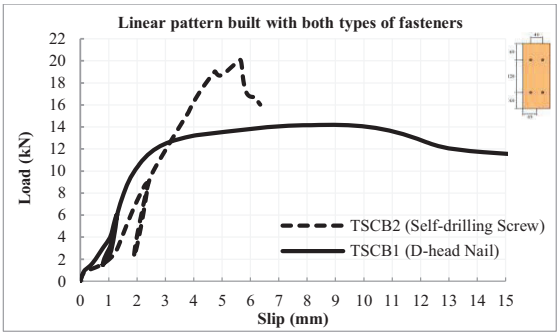

(b): Linear pattern

Figure 3: *Average load-slip curves of TSC connections with various connectors' patterns built with both types of fasteners*

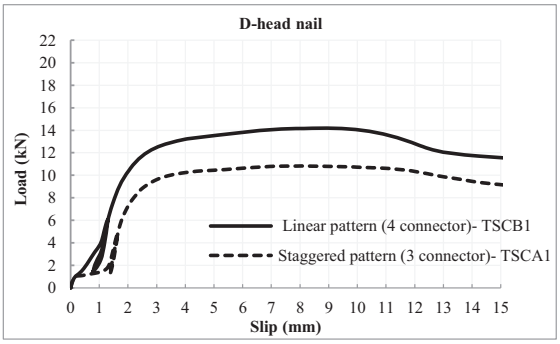

(a): D-head nail

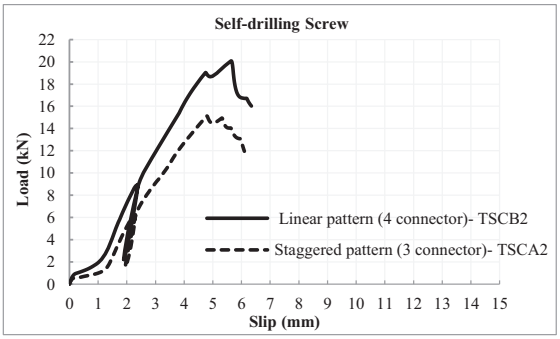

(b): Self-drilling Screw

Figure 4: *Average load-slip curves of nailed (top) and screwed (bottom) TSC connections with staggered and linear patterns*

https://doi.org/10.52202/069179-0414

Figure 4 shows the influences of number and patterns of the fasteners on shear performance of the TSC connection systems.

According to the test results, the shear capacity and stiffness of both nailed and screwed TSC connections significantly improved by one fastener addition. We expect to see an improvement of 33% with the addition of an extra connector.

For nailed TSC connections, the shear capacity and stiffness of the specimens with linear pattern improved on average by 31% and 36%, respectively compared to nailed samples with staggered pattern. This aligns with expectations.

For screwed TSC connections, the shear capacity and stiffness of the specimens with linear pattern increased on average by 33% and 28%, respectively compared to in comparison with screwed specimens with staggered pattern. This aligns with expectations.

4 NUMERICAL MODELING

A nonlinear 3D finite element (FE) model of nailed TSC connection with linear connectors' pattern was developed and analysed using CSI SAP [13] structural analysis software (Figure 5). The result of the nonlinear load-slip of the numerical FE model was compared and validated with experimental results.

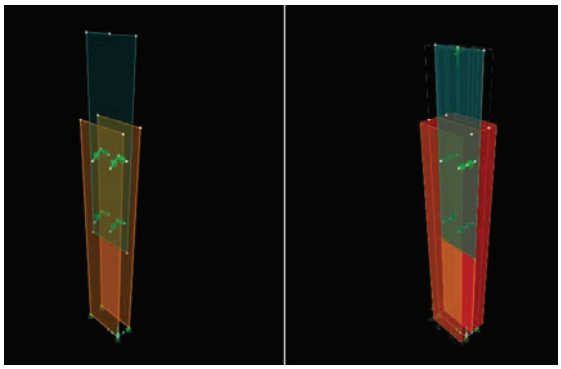

Figure 5: *FE model of nailed TSC connection in SAP program*

4.1 MATERIAL MODELLING

Timber was modelled as a nonlinear orthotropic material. To define the behaviour of F5 timber in the elastic zone, the material properties were obtained by conducting standard tests according to AS/NZS 4063.1:2010 [14] as presented in Table 2.

To define the nonlinear behaviour of timber under loading in plastic zone, the stress-strain curves of timber obtained by conducting standard compression and tension material tests on F5 timber specimens were used as shown in Figure 6.

Grade 250 structural steel was modelled as a nonlinear isotropic material with modulus of elasticity and Poisson's ratio equal to 200100 MPa and 0.3, respectively. Thanks to information obtained from the manufacturing company, the stress-strain curve of G250 steel plate was defined, as shown in Figure 7, to consider the actual behaviour of steel plate under loading.

Table 2: *Elastic Material properties and parameters for developing numerical models of F5 timber*

Description	Value
Longitudinal modulus of elasticity	6447 MPa
Tangential modulus of elasticity	290 MPa
Radial modulus of elasticity	477 MPa
Poisson's ratio for deformation along the tangential axis	0.444
Poisson's ratio for deformation along the radial axis	0.392
Poisson's ratio for deformation along the tangential axis	0.447
The modulus of rigidity based on shear strain in the LT plane	341.7 MPa
The modulus of rigidity based on shear strain in the LR plane	354.6 MPa
The modulus of rigidity based on shear strain in the RT plane	64.5 MPa

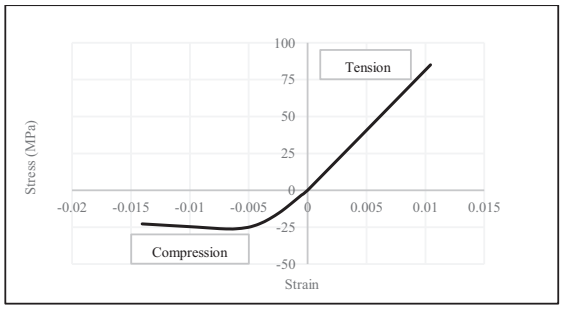

Figure 6: *Nonlinear stress-strain curve of F5 timber material in compression and tension zone*

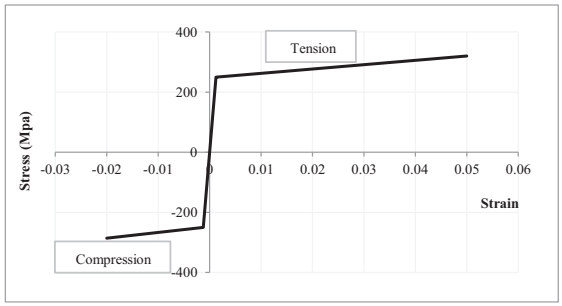

Figure 7: *Bilinear stress-strain curve of Grade 250 structural steel in compression and tension zone*

4.2 SHEAR CONNECTORS MODELLING

Fasteners can be modelled in CSI SAP software [13] using nonlinear two-joint link elements to connect timber and steel components as illustrated in Figure 8. This element has six controllable degrees of freedom (DOF) including three translational springs (U1, U2, and U3) and three rotational springs (R1, R2, and R3). U1 is an axial spring, U2 and U3 are shear springs, R1 is a torsional spring, and R2 and R3 are pure bending springs.

https://doi.org/10.52202/069179-0414

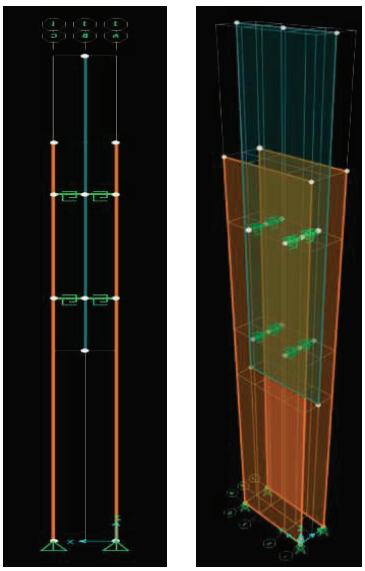

(a): Developed FE model in SAP

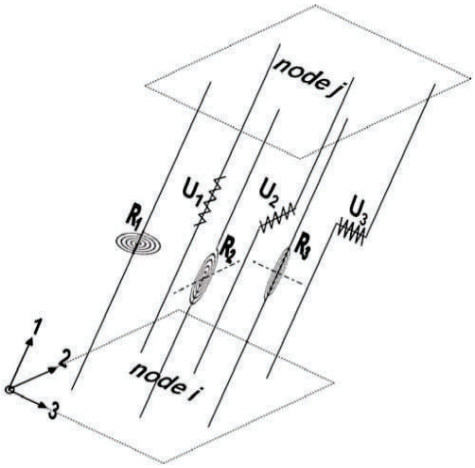

(b): Six DOF of link element

Figure 8: *Nonlinear two-joint link element used for modeling fasteners in CSI SAP software*

In actual testing condition, the compression of the fasteners is negligible. Therefore, to avoid the link elements being compressed or elongated during analysis, the U1 axial spring was fixed. The pure bending springs R2 and R3 were also fixed to avoid any relative rotation of the steel plates and timber boards during analysis. Torsional spring R1 represents the actual spinning of the nail inside the wood components. To consider this behaviour a stiffness of zero was assigned to this spring to enable the free torsional rotation of the link elements. The accurate nonlinear behaviour of the connectors was considered in the FE model by defining and assigning the nonlinear load-slip curve obtained by conducting pull-out tests on TSC connections to U2 and U3 shear spring as shown in Figure 9. Since the responses of the link elements in the U2 and U3 DOF are independent, they were defined uncoupled.

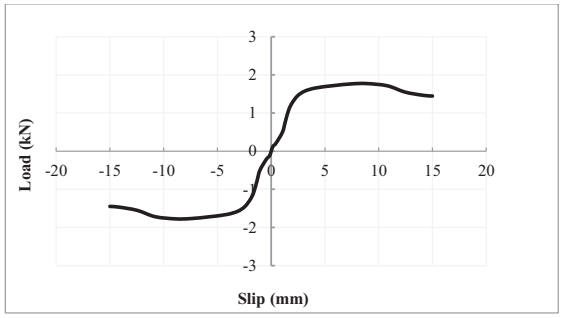

Figure 9: *Nonlinear load-slip response of each link element*

SAP software offers several options to define the nonlinear features of the link element among which the multi-linear Takeda plasticity property was chosen since it allowed the precise definition of the load-slip data even with this capability to consider stiffness degradation under cyclic loading condition.

Each connector was modelled by two link elements at each side of the steel plate so that the sum of the forces of two link elements were equal to the force of each fastener.

4.3 FE MODELLING PROCEDURE

Both timber boards as well as steel plate were modelled by Thick Shell Element. By assigning the nonlinear material properties that were defined in section 4.1 to these elements, the actual nonlinear behaviour of these elements was considered.

Eight points were defined on the middle steel plate and four points were defined on each timber board at the exact location of the fasteners to assign the nonlinear two-joint link element at these places for connecting timber and steel plates. All points on each shell element were constraints as a full body to move and rotate as a uniform element. To model restraint effects of steel brackets in actual testing condition, the end of each timber board was restrained as a pinned support to prevent translation in three (3) directions.

Unit loads at locations of loading points were assigned to the steel plate. This load was incrementally increased and pulled the steel plate upward until the control point at the top of the steel plate reach the target displacement. Nonlinear displacement controlled static pull-out analysis were then performed by considering P-Delta effects to fully monitor large displacement due to nonlinear behaviour of the connectors.

4.4 ANALYSIS RESULTS

Figure 10 shows the comparison between the average experimental load-slip curve obtained by conducting pull-out tests on nailed TSC connections (grey line) with linear connectors' pattern and the simulated load-slip curve obtained from the developed FE model of this TSC configuration in CSI SAP software (black line). Clearly, the FE model closely simulates the load-slip response of the connection system. The model could precisely predict the behaviour and stiffness of the connection in the elastic zone and closely determine the yield point and maximum

https://doi.org/10.52202/069179-0414

load-carrying capacity of the system (Table 3). More importantly, the developed FE model could accurately reflect the real nonlinear behaviour of the connection system by simulating the strength reduction and stiffness degradation after reaching its peak shear capacity. It should be noted that since the FE model was analysed under uniform loading condition, it did not reflect the initial slip of the system that was monitored in the actual tests due to applying ISO loading pattern with initial loading and unloading steps.

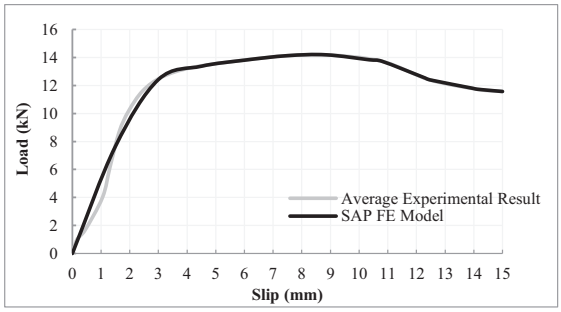

Figure 10: *Comparison between experimental and numerical load-slip curves of nailed TSC connection*

Table 3: *Comparison of experimental and FE results*

Config. ID	F_{Exp} (kN)	F_{FE} (kN)	V_{Exp} (mm)	V_{FE} (mm)	$\frac{F_{Exp}}{F_{FE}}$	$\frac{V_{Exp}}{V_{FE}}$
TSCB1	14.19	14.18	8.85	8.86	1.0007	0.9988
Standard Deviation	1.17	-	1.21	-	-	-

Note: F denotes maximum load and V is the joint slip corresponding to the maximum load.

5 CONCLUSION

Several pull-out tests on different configurations of a novel TSC connection system were conducted to monitor the shear performance and capacity of the specimens and evaluate the impacts of key variables such as various type, pattern and spacing of the fasteners. In addition, FE model of this composite system was developed in CSI SAP software and the analysis result of the model was compared and verified against experimental load-slip curve.

The test results showed critical difference between failure mode and nonlinear behaviour of nailed and screwed TSC connections under loading condition. While nailed TSC connections showed ductile behaviour with gradual failure, screwed TSC connections experienced brittle behaviour with sudden failure. Self-drilling screws showed 40% more shear capacity compared to D-head nails used in TSC connections. However, screwed TSC connections had on average 12% less stiffness compared to nailed ones. TSC connections with linear pattern of fasteners showed on average 30% more load-carrying capacity compared to the TSC configurations with staggered pattern.

The developed FE model could simulate the nonlinear load-slip response of the nailed TSC connection with great accuracy. This modeling approach offers a simple means to investigate the influences of key variables such as a greater number of fasteners or different thickness of steel and timber elements on shear capacity of the TSC connection system. The calibrated FE model will be refined with additional test results of various configurations and used to develop optimised full-scale TSC beams. Furthermore, to further investigate the effects of various variables, a comprehensive parametric study will be conducted in future research.

ACKNOWLEDGEMENT

The work presented here was supported by an Australian Government Research Training Program Scholarship and a top-up scholarship provided by Craig Cowled and the School of Civil and Environmental Engineering at Queensland University of Technology to AS.

Materials were kindly provided by Hyne Timber and QUT.

We also wish to thank QUT technical staff who assisted with preparation of the specimens and experimental testing. Frank De Bruyne, Barry Hume, Benjamin Brownlee and Zeph Kadel have all made this project possible and their contribution is highly valued.

REFERENCES

[1] Hyne Timber. *CLT and GLT: A perfect combination for many structural building solutions*. Maryborough, Australia, 2019.

[2] A. Rahai, A. Shahin, F. Hatami.: Progressive collapse resisting capacity of reinforced concrete load bearing wall structures. *Journal of Central South University*, 22(7):2730-2738, 2015.

[3] T. Żmijewki, and D. Wojtowicz-Jankowska. Timber - Material of the Future - Examples of Small Wooden Architectural Structures. In: *IOP Conference Series: Materials Science and Engineering*, 245:082019, 2017.

[4] H. Bailleres, D.J. Lee, C. Kumar, S. Psaltis, G. Hopewell, and L. Brancheriau. *Improving returns from southern pine plantations through innovative resource characterisation*, Forest & Wood Products Australia, Project No: PNC361-1415, 2019.

[5] A. Hassanieh, H.R. Valipour, M.A. Bradford. Load-slip behaviour of steel-cross laminated timber (CLT) composite connections. *J. Const. Steel Res.*, 122:110-121, 2016.

[6] M. Chybiński, Ł. Polus. Theoretical, experimental and numerical study of aluminium-timber composite beams with screwed connections. *Constr. Build. Mater.*, 226:317-330, 2019.

[7] G. Schiro, I. Giongo, W. Sebastian, D. Riccadonna, M. Piazza. Testing of timber-to-timber screw-connections in hybrid configurations. *Constr. Build. Mater.*, 171:170-186, 2018.

[8] J. Cao, Y. Liu, Y. Wang, Y. Zhang. Load-slip performance of timber-to-concrete connections with U-steel connectors under push-out test. *J. Build. Eng.*, 45:103527, 2022.

[9] F. Riola-Parada. *Timber-Steel Hybrid Beams for Multi-Storey Buildings* [Dissertation]. Vienna University of Technology, Vienna, Austria, 2016.

[10] A. Shahin, C. Cowled, H. Bailleres, F. Sabrina. Experimental study on shear performance of layered timber-steel composite and timber-timber connection systems using low-grade timber and mechanical fasteners. In preparation for submission to *Constr. Build. Mater*.

[11] AS 2858:2008. *Timber - Softwood - Visually stress-graded for structural purposes*. Standards Australia, Sydney, Australia, 2008.

[12] EN 26891:1991. *Timber Structures - Joints made with mechanical fasteners - General principles for the determination of strength and deformation characteristics*. European Committee for Standardization, Brussels, Belgium,1991.

[13] CSI. *SAP2000 Integrated Software for Structural Analysis and Design*. Computers and Structures Inc., Berkeley, California, 2020.

[14] AS/NZS 4063.1:2010. *Characterization of structural timber, Part 1: Test Methods*. Standards Australia, Sydney, Australia, 2010.

https://doi.org/10.52202/069179-0414

World Conference on Timber Engineering Oslo 2023

FINITE ELEMENT MODELLING OF HYBRID WOOD/ALUMINIUM ASSEMBLY WITH WOOD-FILLED ALUMINIUM AND STEEL DOWELS

Gotre Bi Djeli Bienvenu. BOLI [1, 2], Marc. Oudjene [2], Daniel. Coutellier [3], Hakim. Naceur [4]

ABSTRACT: This paper presents a Finite Element modelling procedure for hybrid structures made of confined wood within a thin aluminium envelope using the explicit dynamic analysis through the use of LS-DYNA® software. The primary use of hybrid structures will be for highway bridge safety barriers in order to assess the energy absorption capabilities during an impact due to a car accident. The mechanical behaviour of the wood was modelled using the built-in material model MAT-143 in LS-DYNA. The comparison of the numerically predicted failure behaviour and the global response expressed as force-displacement responses of the studied hybrid structures to those reported in the literature, has shown the ability of the model to simulate the failure behaviour of such hybrid structures.

KEYWORDS: Wood, Aluminium, Finite Element, Hybrid structures, wood-filled aluminium composites.

1 INTRODUCTION

Timber is known as one of the oldest and longest standing building materials in existence, with evidence showing homes built over 10,000 years ago used wood as a primary source for construction materials [1]. In the last two decades, the used of wood in the construction sector has increased due to the development of engineered wood products (EWPs) such as cross-laminated timber (CLT), laminated veneer lumber (LVL) and glued laminated timber (glulam), which offer improved and homogenous mechanical properties for their use as structural materials. Massive timber construction requires suitable connections in order to join the different elements of the building. The most common connection in contemporary timber structures are manufactured using steel plates and laterally loaded metal dowel-type fasteners (Figure 1). The benefits of these types of connections are the ease of manufacturing, design, and assembly, in addition to their high load carrying capacity and ductility. However, the use of metallic connections in timber structures can reduce the fire resistance of the structure as metallic components increase the heat transfer in the connection [2]. In addition, the weight of the steel elements (plate, dowels, bolts) in the connection can be regarded as drawbacks during the operating phase. In fact, the high stiffness of steel in comparison to wood can increase the stress in the wood, thus increasing the probability of brittle failure in the timber members, which is undesirable in timber construction. In this respect, the use of lightweight et competitive connection systems by reducing the amount of metal used within the timber structure would be most advantageous in terms of the improvement of the fire resistance, the corrosion resistance and the reduction of the weight of the connection.

Figure 1: *Metal fasteners in timber construction [3]*

Glued connection is also used in the category of non-metallic connection in timber structures. However, the use of adhesives has some drawbacks as they can produce volatile organic compounds (VOCs) and reduce the recyclability of the wood products. In this context, a

[1,2] Bienvenu BOLI, LAMIH, UMR CNRS 8201, Université Polytechnique Hauts-de-France (UPHF), gotre-bi-djeli-bienvenu.boli.1@ulaval.ca
[2] Marc Oudjene, Department of Civil and Water Engineering, Laval University, Quebec, Canada
[3] Daniel Coutellier, LAMIH, UMR CNRS 8201, UPHF
[4] Hakim Naceur, LAMIH, UMR CNRS 8201, INSA Hauts-de-France, UPHF

https://doi.org/10.52202/069179-0415

research program called: "Towards Adhesive-Free Timber Buildings (AFTB)" and funded by the North-West-European Interreg program was born. The aim was to develop ''green" and adhesive free EWPs and connection systems using compressed wood dowels as a joining fastener to substitute the traditional adhesives (or metallic fasteners) [4]. In the same context, El-Houjeyri et al. [4] have designed some novel adhesive free engineered Wood Products by using compressed wood dowels (CWD) as a joint element to connect timber laminates and members. The strength and stiffness properties of the CWD were characterized based on three-point bending tests and compared to the values obtained from uncompressed wood specimens. The CWD were used as connection elements in timber-to-timber connections in double shear push-out tests and the results were compared to those of a timber-to-timber connection with a steel dowel. The authors [4] have found that, in terms of load-carrying capacity, the joints assembled using compressed wood dowels compared well to their counterparts assembled using a steel dowel, but have a strength and stiffness characteristic values lower than to the joints assembled using a steel dowel. In this respect, an optimization of the CWD could be achieved for better structural performance.

As some countries in Europe, some countries in North America like Canada have shown also interest in using those EWPs and lightweight materials in the construction sector. For example, the government of Quebec published in 2013 the Wood Charter [5] and in 2015 the Quebec Aluminium Development Strategy (SQDA) [6], which aim to promote the use of EWPs and aluminium in the construction sector. In fact, these two materials (wood and aluminium) have low environmental impact in comparison to steel et concrete, are recyclable, sustainable and are locally produced in Québec. In this context, Rollo et al. [7] have investigated a solution of a hybrid dowel by confining a CWD in an aluminium tube in order to improve the mechanical characteristics of the CWD developed by El-Houjeyri et al. [4]. Following the work of El-Houjeyri et al. [4] and Rollo et al. [7], Tétreault et al. [8] have proposed a novel hybrid timber-to-aluminium connection by using hybrid wood-filled aluminium dowels and steel dowels. However, due to the novelty of these hybrid structures using wood and aluminium, they are not yet considered in calculation standards like the CSA-O86 (National Standards of Canada: Engineering design in wood). Thus, to obtained reliable and safe application of these products, experimental tests are needed and the tests need to cover as many scenarios as possible. In contrast, the use of numerical simulation means of the finite element (FE) method appears to be a good alternative in order to reduce the number of experimental tests. In this study, it is proposed to investigate and evaluate a numerical procedure for the design and the analysis of hybrid structures with confined wood. We investigate the capability of the wood material formulation (*MAT_143/*MAT_WOOD) available in LS-DYNA for simulating the mechanical behaviour and the failure response of hybrid assembly (Wood/Aluminium) using either wood-filled aluminium hybrid dowels or steel dowels.

2 FINITE ELEMENT MODELLING

Different hybrid wood/aluminium structures including confined wood available in the literature were selected to evaluate the performance of the built-in material model **MAT_143/*MAT_WOOD*. Three-Point Bending test on densified wood dowel and on hybrid wood-filled aluminium dowel (Figure 2) were carried out by Rollo et al. [7]. Double shear tests on hybrid systems (timber-to-aluminium connections) assembled using wood-filled aluminium hollow tube dowel and steel dowel were carried out and analysed experimentally by Tétreault et al. [8]. This section presents the different material models used in the FE model, the FE modelling techniques used to simulate the different loading and geometric conditions.

2.1 MATEIRAL MODELLING

2.1.1 Wood material model: MAT-143

At macroscopic scale, wood material is commonly assumed to be orthotropic as its properties vary in the three directions: longitudinal (L or 1), radial (R or 2) and tangential (T or 3). Wood material model MAT-143 [9] in LS-DYNA considers the wood as a transversely isotropic. Parallel direction represents longitudinal (L) axis and perpendicular direction refers to radial (R) or tangential (T) axis of timber. The strength criteria are defined using Hashin's formulation with different analytical forms for the parallel $f_{||}$ and perpendicular $f_{\perp}$ criteria according to equations (1) and (2) respectively:

$$f_{||} = \frac{{\sigma_{11}}^2}{X^2} + \frac{({\sigma_{12}}^2 + {\sigma_{13}}^2)}{{S_{||}}^2} - 1 \qquad (1)$$

$$f_{\perp} = \frac{(\sigma_{22} + \sigma_{33})^2}{Y^2} + \frac{{\sigma_{23}}^2 - \sigma_{22}\sigma_{33}}{{S_{\perp}}^2} - 1 \qquad (2)$$

where σ_{11}, σ_{22}, σ_{33}, σ_{12}, σ_{13}, σ_{23} are the stress components; X and Y are the tensile or compressive strength in parallel and perpendicular to the grain direction respectively. $S_{||}$ and $S_{\perp}$ are the shear strength in parallel and perpendicular to the grain direction respectively. Failure occurs in parallel to the grain direction when $f_{||} > 0$ and in perpendicular to the grain direction when $f_{\perp} > 0$.

The evolution of the damage parameter *d* follows separate rules for parallel and perpendicular to the grain directions. In parallel direction, failure is often considered to be catastrophic and failure in this direction renders the wood useless. When failure occurs in parallel direction, all six stress components are degraded uniformly and wood cannot carry any load after failure. However, if failure occurs in perpendicular to the grain direction, only the perpendicular stress components are degraded. The two expressions of the damage are given by equations (3) and (4) for parallel and perpendicular modes respectively:

https://doi.org/10.52202/069179-0415

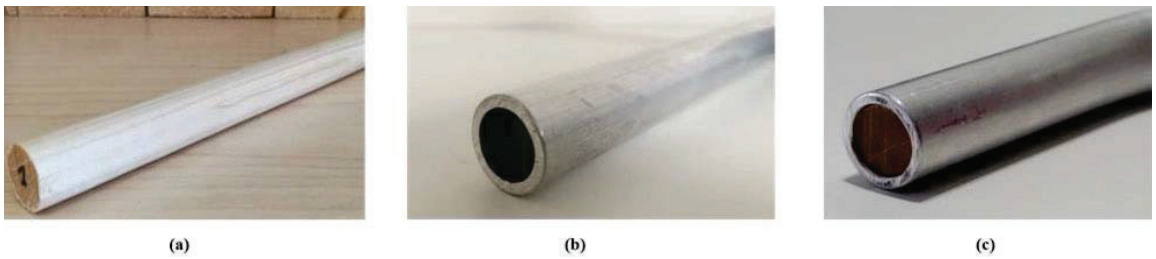

(a) (b) (c)

Figure 2: *Different parts of the hybrid wood-filled aluminium dowel: (a) compressed wood dowel; (b) aluminium tube; (c) hybrid wood-filled aluminium dowel [7]*

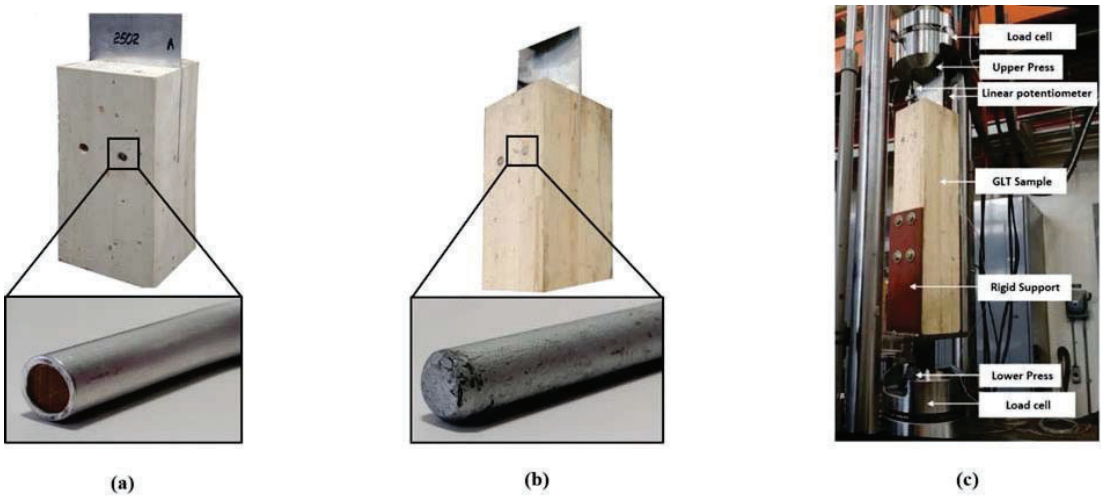

(a) (b) (c)

Figure 3: *Hybrid wood/aluminium system: (a) assembled with hybrid wood-filled aluminium dowel; (b) assembled with galvanized steel dowel; (c) experimental setup [8]*

$$d(\tau_{\parallel}) = \frac{d_{max\parallel}}{B}\left[\frac{1+B}{1+Be^{-A(\tau_{\parallel}-\tau_{0\parallel})}} - 1\right] \quad (3)$$

$$d(\tau_{\perp}) = \frac{d_{max\perp}}{D}\left[\frac{1+D}{1+De^{-C(\tau_{\perp}-\tau_{0\perp})}} - 1\right] \quad (4)$$

where B and D are the softening parameters obtained from experimental data. A and C are internally calculated based on the value of fracture energy G_f according to equations (5) and (6):

$$A = \tau_{0\parallel} L\left(\frac{1+B}{BG_{f\parallel}}\right) log(1+B) \quad (5)$$

$$C = \tau_{0\perp} L\left(\frac{1+D}{BG_{f\perp}}\right) log(1+D) \quad (6)$$

The laminated stock used during the experimental test for the Glued Laminated Timber (GLT) were made of Spruce-Pine-Fir. The wood dowel used for the manufacturing of the hybrid wood-filled aluminium dowel were made of French spruce. The material properties as applied for MAT-143 in this study are summarized in Table 1. The mechanical parameters are either identified based on the mean experimental values or by means of the well-known inverse approach.

Table 1: *Material properties for the compressed spruce and for the Glued Laminated Timber used in the FE model for MAT-143 (LS-DYNA parameters in parentheses)*

Mechanical property	Compressed spruce	GLT
$\boldsymbol{\rho = \rho_{wood}}$ [kg/m^3]	1174	560
$\boldsymbol{E_L\,(EL)}$ [MPa]	30000	1200
$\boldsymbol{E_T\,(ET)}$ [MPa]	2000	480
$\boldsymbol{G_{LT}\,(GLT)}$ [MPa]	1750	720
$\boldsymbol{G_{TR}\,(GTR)}$ [MPa]	1000	130
$\boldsymbol{\upsilon_{LT}\,(PR)}$ [-]	0,41	0,26
$\boldsymbol{f_{t,L}(XT)}$ [MPa]	125	60
$\boldsymbol{f_{c,L}(XC)}$ [MPa]	120	50
$\boldsymbol{f_{t,T}(YT)}$ [MPa]	12,5	3,5
$\boldsymbol{f_{c,T}(YC)}$ [MPa]	104	13,5
$\boldsymbol{f_{v,L}(SXY)}$ [MPa]	85	6,5
$\boldsymbol{f_{v,T}(SYZ)}$ [MPa]	120	6,5
$\boldsymbol{G_{f,L,I}(GF1\parallel)}$ [MPa.mm]	40,5	25
$\boldsymbol{G_{f,L,II}(GF2\parallel)}$ [MPa.mm]	291,5	90
$\boldsymbol{G_{f,T,I}(GF1P)}$ [MPa.mm]	1,35	0,24
$\boldsymbol{G_{f,T,II}(GF2P)}$ [MPa.mm]	2,75	0,7
$\boldsymbol{B(BFIT)}$	300	30
$\boldsymbol{D(DFIT)}$	300	30
$\boldsymbol{d_L(DMAX\parallel)}$	0,9999	0,9999
$\boldsymbol{d_T(DMAXP)}$	0,9900	0,9900

https://doi.org/10.52202/069179-0415

2.1.2 Material model for the aluminium: MAT-024

The mechanical behaviour of aluminium was modelled with MAT-024 material model in LS-DYNA. MAT-024 describes an elastic-plastic material with an arbitrary stress versus strain response and arbitrary strain rate dependency can be defined. Strain rate may be accounted for using the Cowper and Symonds model. The stress-strain curve of the aluminium is given using the Ramberg-Osgood law using equation (7):

$$\varepsilon = \frac{\sigma}{E} + K\left(\frac{\sigma}{E}\right)^{n} \quad (7)$$

where $\boldsymbol{E}$ is the Young's modulus and K and n the hardening parameters. Equation (7) represents the evolution of the engineered strain as a function of the engineered stress. Material model MAT-024 requires the true stress as a function of the true strain. The curve of the engineered stress as a function of the engineered strain is transformed into a curve representing the true stress as a function of the true strain and is given through the material model MAT-024. The material properties used in the FE were defined as:

- Density: 2700 kg/m^3
- Young's modulus: 70 000 MPa
- Poisson's ratio: 0,33
- Yield stress: 210 MPa
- Hardening parameters for aluminium A6061-T6: n = 45 for an ultimate strain of 8% as prescribed by Eurocode 9.

2.1.3 Material model for the steel dowel: MAT-003-Plastic Kinematic

The material behaviour of the steel dowel was modelled with the material model MAT-003 representing an elastic-plastic isotropic material behaviour with the option of including rate effects by using the Cowper and Symonds model. The material properties used in the FE were defined as:

- Density: 7877 kg/m^3
- Young's modulus: 210 000 MPa
- Poisson's ratio: 0,33
- Yield stress: 450 MPa

2.2 FE MODELLING OF THE THREE-POINT BENDING TEST ON HYBRID WOOD-FILLED ALUMINIUM DOWEL

The FE model of the Three-point bending test was done first for the compressed wood dowel and then for the hybrid wood-filled aluminium dowel. Figure 4.b shows the FE model of the three-point bending test and Figure 4.a shows the experimental set up used by Rollo et al. [7]. Constant stress eight-node solid elements (LS-DYNA ELFORM 1) and fully integrated shell elements (LS-DYNA ELFORM 16) are applied to represent the geometrical setup of the test. The wood dowel is meshed using solid elements and the loading cylinder and support are meshed using shell elements. The material behaviour of the loading cylinder and the supports is modelled with the rigid material model MAT-020 with a Young's modulus $E = 207\,000\ MPa$ and a Poisson's ratio of $\nu = 0{,}3$. All nodes of the supports are fully clamped and a velocity control was applied to the rigid loading cylinder using an explicit time integration. A rate of $5mm/min$ was used during the experimental tests, which is like a quasi-static test.

The FE model of the hybrid wood-filled aluminium dowel was done by inserting under compression the wood dowel inside the aluminium tube. Constant stress eight-node solid elements are used to mesh the aluminium tube. The boundary conditions used for the hybrid wood-filled aluminium dowel are the same as those used for the compressed wood dowel. The contact between the wood dowel and the aluminium tube was defined using the AUTOMATIC_SURFACE_TO_SURFACE contact with a friction coefficient of 0,3. Figure 5 shows the FE model of the Three-Point Bending test on the hybrid wood-filled aluminium dowel.

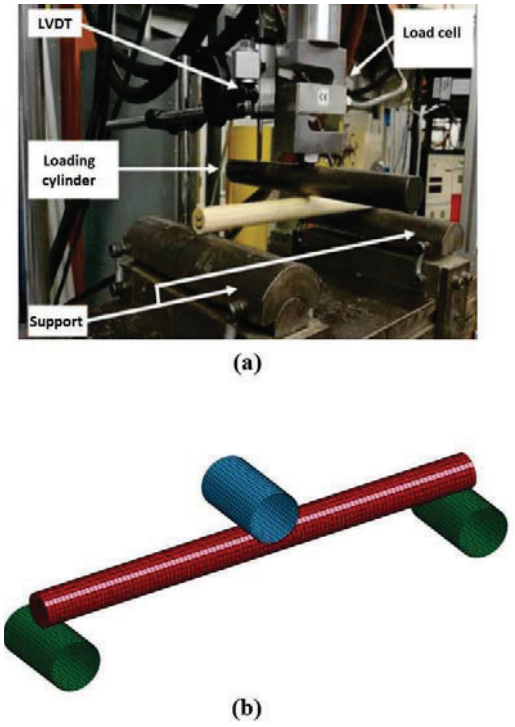

Figure 4: *Three-Point Bending test on compressed wood dowel: (a) experimental setup [7]; (b) FE model*

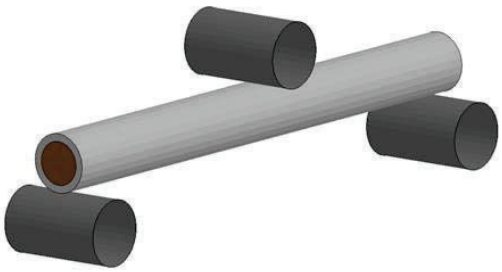

Figure 5: *FE model geometry for the Three-Point Bending test on hybrid wood-filled aluminium dowel*

https://doi.org/10.52202/069179-0415

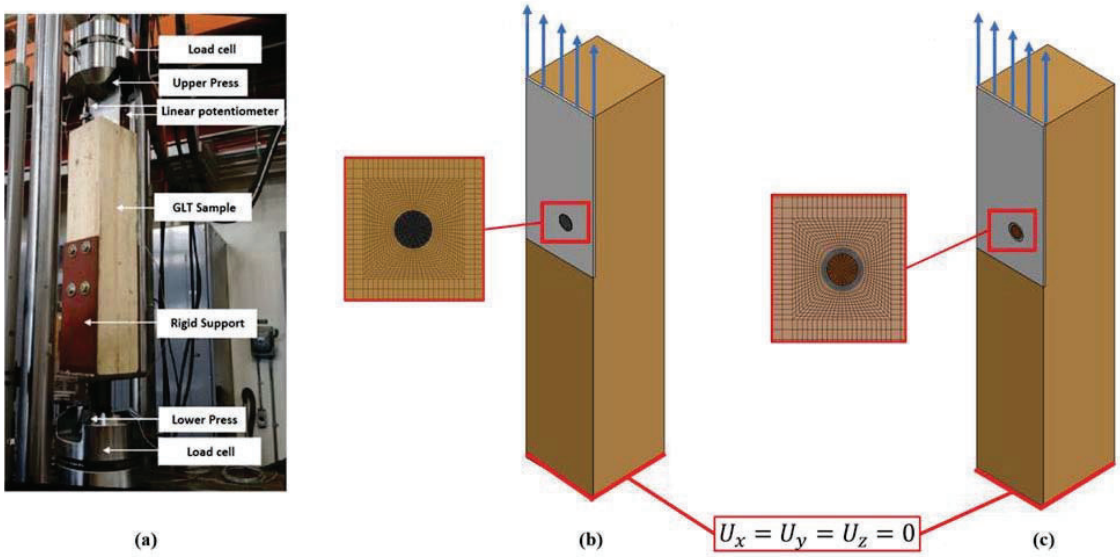

Figure 6: *Double shear tensile test on hybrid wood/aluminium assembly: (a) Experimental setup [8]; (b) FE model of the assembly with galvanised steel dowel; (c) FE of the assembly with hybrid wood-filled aluminium dowel*

2.3 FE MODELLING OF THE DOUBLE SHEAR TESTS ON HYBRID SYSTEMS (TIMBER-TO-ALUMINIUM CONNECTIONS)

Two series of experimental tests were conducted on structural timber-to-aluminium assemblies. The first series of tests were carried out on hybrid timber-to-aluminium assemblies connected with galvanised steel dowels (Figure 3.b). The second series of tests were done on hybrid timber-to-aluminium assemblies connected with wood-filled aluminium dowel (Figure 3.a). For the two series of tests, the hybrid assembly is made of Glued Laminated Timber with a groove in which an aluminium plate is inserted and hold with the dowels. The assembly is hold on the bottom with screws on a rigid support and the aluminium plate is given a displacement at a rate of $2mm/min$.

The FE model of the two types of assemblies was done using eight-node constant stress solid elements (LS-DYNA ELFORM 1) with hourglass control type 6 (which use the Belytschko-Bindemann approach) for the Glued Laminated Timber, the aluminium plate, the galvanised steel dowel, as well as for the wood-filled aluminium dowel. The presence of two symmetry planes allows to modelled only one-quarter of the model by applying symmetry boundary conditions in the two symmetry planes. The mesh was refined in the vicinity of the dowel's holes in the Glued Laminated Timber (Figure 6.b and 6.c). In the FE model, only the part of the assembly above the rigid support is modelled by assuming that the dowels used to assembly to the rigid support stay undeformed during the test and so no failure happens in the part of the Glued Laminated Timber in contact with the rigid support.
The nodes on the bottom surface of the Glued Laminated Timber are all constrained ($U_x = U_y = U_z = 0$) and a velocity control is applied on the top nodes of the aluminium plate (Figure 6.b and 6.c) using an explicit time integration.
All contacts in the FE model, either existing at the beginning or developing during the simulation are set to be automatically detected by the software by using the AUTOMATIC_SURFACE_TO_SURFACE contact algorithm.

3 RESULTS

3.1 THREE-POINT BENDING TEST ON WOOD FILLED ALUMINIUM DOWEL

The results of the Three-Point Bending test on the wood-filled aluminium dowel were analysed in terms of the global response expressed as force-displacement curves and the failure predictions. Figure 8 compares the numerically obtained Force-Displacement curve (red dashed curve line) to those reported experimentally (black curves) in literature by Rollo et al [7]. All experimental responses showed a first drop of load, which corresponds to the failure of the confined wood into the aluminium tube. The load is then carried by the aluminium tube until the occurrence of the final failure in the aluminium tube. These results show the ability of the aluminium tube in reducing the brittle failure of the wood material by improving the ductility of the entire hybrid wood-filled aluminium structure. The experimental curves showed also some variations in the peak force as well as in the failure of the confined wood which results from the natural bio-composite characteristic of the wood material. However, with the calibrated material parameters, it can be seen through Figure 8 that the FE model was able to predict the mean value of the experimental responses. Figure 7.a shows the fracture pattern of the FE model which is in good agreement with the experimental observations. The failure occurred in tension on the bottom side of the hybrid dowel and propagated through it.

https://doi.org/10.52202/069179-0415

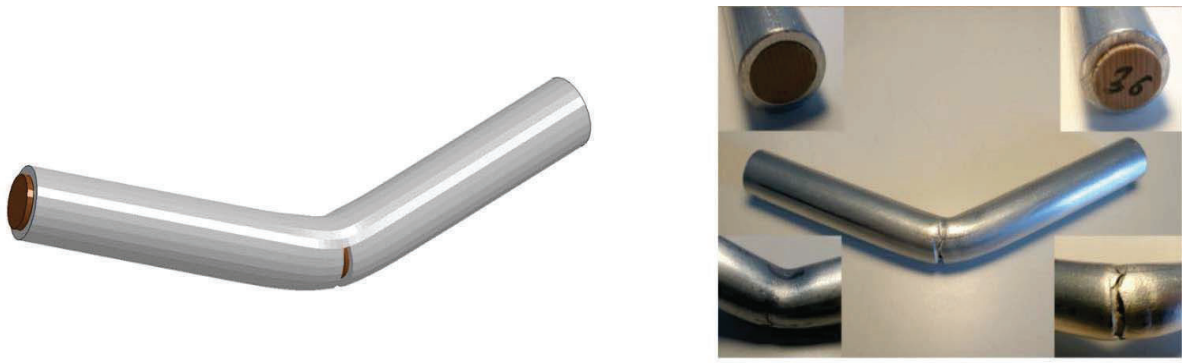

(a) (b)

Figure 7: *Failure modes during the Three-Point Bending test on hybrid wood-filled aluminium dowel: (a) Numerical; (b) Experimental*

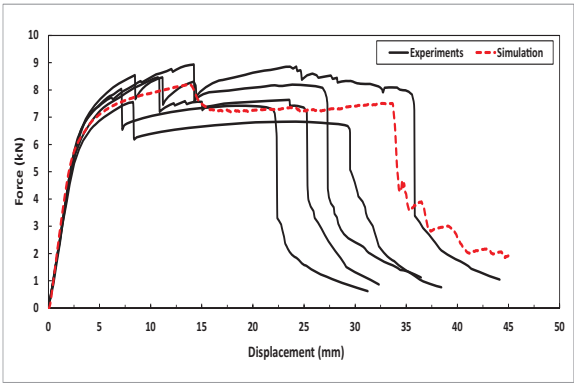

Figure 8: *Force-Displacement curves on the Three-Point Bending test on hybrid wood-filled aluminium dowel*

3.2 DOUBLE SHEAR TEST ON HYBRID WOOD/ALUMINIUM ASSEMBLY

The failure modes observed during the first series of experimental tests on the hybrid assembly connected with galvanised steel dowel was observed in the Glued Laminated Timber. Figure 9.a depicts the experimentally observed failure. The cracks observed along the grain direction in the Glued Laminated Timber members are probably caused by tension load perpendicular to the grain direction resulting from the displacement of the dowels. The predicted failure modes and cracks propagation with the FE analysis are presented in Figure 9.b. A good correlation can be seen between the predicted failure modes and the crack growth and the experimental inspection. The failure starts in the vicinity of the dowels and propagates in the Glued Laminated Timber in transverse tension. A comparison of the load-deflection curves between the numerical prediction and experiments is displayed in Figure 10, in which a good agreement can be seen for the global linear and non-linear behaviour and for the peak load at failure.

The failure behaviour during the second series of the experimental tests with the hybrid wood/aluminium assembly connected with the hybrid wood-filled aluminium dowel is displayed in Figure 11.a. The failure happens in the Glued Laminated Timber in the location of the aluminium plate, resulting from the deformation of the hybrid wood-filled aluminium dowel which fits into the groove of the Glued Laminated Timber due to the displacement of the aluminium plate. It can be seen on Figure 11.b that the predicted failure mode is in good agreement with the experimental observations. The comparison of the numerically obtained Force-Displacement curves to the experiments as presented in Figure 12 shows a good agreement in the non-linear behaviour as well as the load-carrying capacity and the failure. It is worth noting that the failure in perpendicular tension along the grain direction in the Glued-Laminated Timber as observed during the first series of test with the galvanised steel dowels initiates also in the Glued Laminated Timber during the second series of the test with the hybrid wood-filled aluminium dowels, but this failure modes do not propagate because of the premature failure of the hybrid dowel. Thus, an optimization of the hybrid wood-filled aluminium dowel is necessary in order to reach the performance of the galvanised steel dowel.

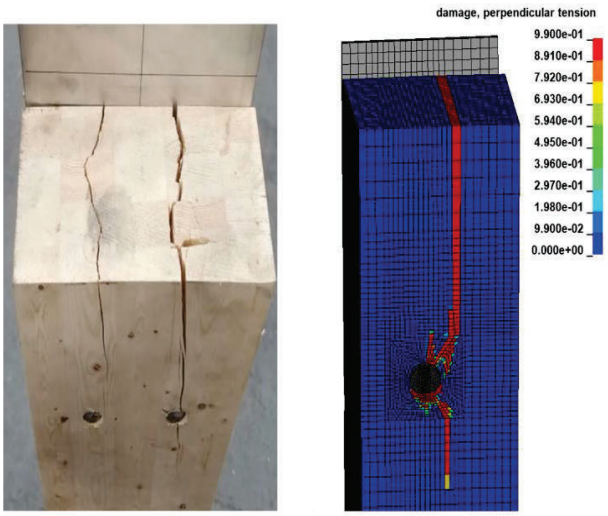

(a) (b)

Figure 9: *Perpendicular tension failure for the hybrid assembly with galvanized steel dowel*

https://doi.org/10.52202/069179-0415

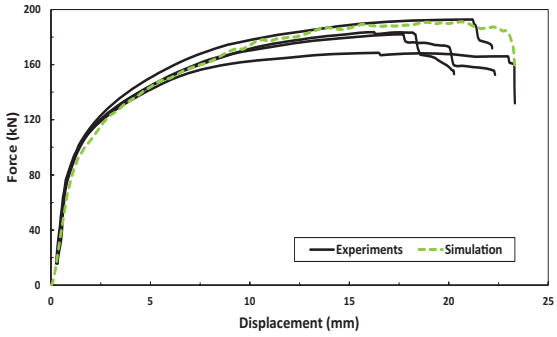

Figure 10: *Force-Displacement curves for the hybrid assembly with galvanised steel dowel*

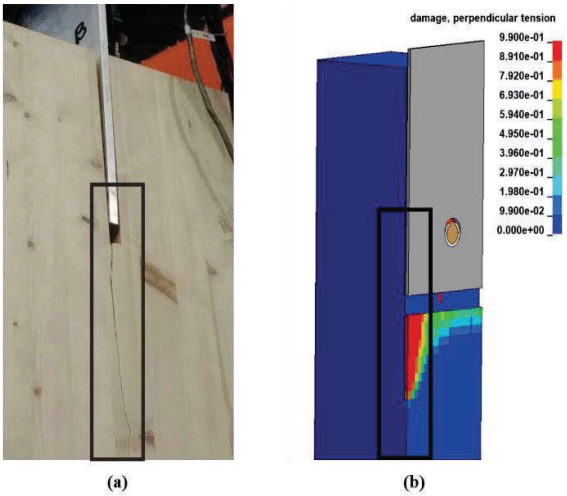

Figure 11: *Perpendicular tension failure for the hybrid assembly with hybrid wood-filled aluminium dowel*

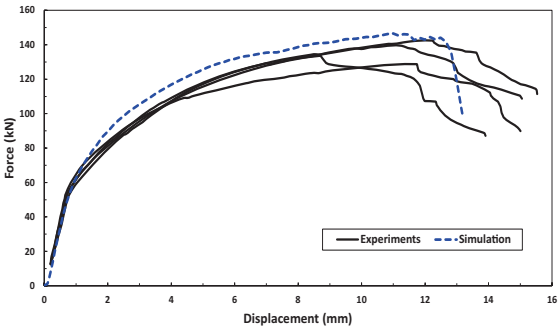

Figure 12: *Force-Displacement curves for the hybrid assembly with hybrid wood-filled aluminium dowel*

4 CONCLUSION

In this study, the ability to predict the mechanical behaviour of wood and confined wood by using the FE method and the built-in LS-DYNA material model MAT-143 was investigated. This material model performs well in simulating the global mechanical behaviour of the confined wood under quasi-static loading condition and the initiation and propagation of the fracture in timber. Though the numerical results are in good agreement with the experimental ones, works are needed in order to asses results of the numerical model, to become a real alternative for predicting the failure of safety barriers for highway bridges.

ACKNOWLEDGEMENT

The financial supports of the Natural Sciences and Engineering Research Council of Canada (NSERC/CRSNG) and “La region Hauts-de-France” are gratefully acknowledged.

REFERENCES

[1] Woods S., *A History of Wood from the Stone Age to the 21st Century*, the journal of the American institute of architects, accessed 13 February 2023 https://www.architectmagazine.com/technology/products/a-history-of-wood-from-the-stone-age-to-the-21st-century_o

[2] EN 1995-1-2:2004 Eurocode 5: Design of timber structures – Part 1-1: General – Structural fire design European Committee for Standardization (CEN), Brussels, 2004.

[3] Mocabois. (2022). Bâtiment industriel [online image, accessed 13 February 2023]. https://mocabois.fr/batiment-industriel/

[4] El-Houjeyri, I., Thi, V. D., Oudjene, M., Khelifa, M., Rogaume, Y., Sotayo, A., & Guan, Z. *Experimental investigations on adhesive free laminated oak timber beams and timber-to-timber joints assembled using thermo-mechanically compressed wood dowels*. Construction and Building Materials, 222, 288-299, 2019.

[5] MRN. *Charte du Bois* ; Ministère des Forêts, de la Faune et des Parcs : Montréal, QC, Canada, 2013.

[6] Gouvernement du Québec, Ministère de l’Économie, de la Science et de l’Innovation. *Stratégie Québécoise de Développement de l’aluminium 2015–2025* ; Gouvernement du Québec, Ministère de l’Économie, de la Science et de l’Innovation : Montréal, QC, Canada, 2015.

[7] Rollo G. *Étude expérimentale et numérique d’un nouveau goujon hybride bois-aluminium pour les assemblages bois*. Master’s thesis, University Laval, 2021.

[8] Tétreault M. G. *Étude et modélisation de nouveaux assemblages hybrides en bois aluminium*. Master’s thesis, University Laval, 2022

[9] Murray Y. D. *Manual for LS-DYNA wood material model 143*. No. FHWA-HRT-04-097. United States. Federal Highway Administration, 2007.

World Conference on Timber Engineering Oslo 2023

EXPERIMENT ON AXIAL CAPACTY-BENDING CAPACITY RELATIONSHIP OF STEEL BAR-TIMBER COMPOSITE COLUMN

Keisuke Hayata[1], Motohiro Mukai[2], Shinich Shioya[3]

ABSTRACT: In light of the current climate crisis, there has been much recent interest in using timber structural members in large buildings, because timber is as renewable natural resource, and moreover, in severe earthquake prone, such as Japan, they are more desired on the grounds of light weight of timber members. We are developing a frame system formed by timber members reinforced by deformed steel bars, i.e., rebars using epoxy resin adhesive and have already developed a technique for the connection between column of ground floor and reinforced concrete foundation. Performance of the column was reported in the previous WCTE2021. We have planned an experiment to investigate bending characteristic of the other portion except hinge of the column bottom. This paper reports the experiment, its results, and comparison of experiment result and calculation on bending moment capacity.

KEYWORDS: Composite timber, Column, Deformed steel bar, Bending moment capacity, Yield moment

1 INTRODUCTION

S.Shioya, (author [3]), has proposed a structural system for building construction, adopting Hybrid Glulam Timber members using Steel bars (HGTSB, nicknamed "Samurai" in Japan) and has developed the structural design methodology [1]. Our team is now developing more refined and more competitive and commercial structural system for buildings adopting HGTSB and its structural design methodology.

2 BACKGROUND AND TARGET

S.Shioya has already developed a technique for rigid connection of rebars inside the composite timber, using carbon fiber plastic sleeve (CFS) and epoxy resin adhesive with works similarly to work process of the glued-in-rod, and reported performance of the column adopted the technique [1]. And then his group testified the application of the technique to the connection between column of ground floor and reinforced concrete foundation, by loading test of column specimens [1,2].

Figure 1(a)-(b) illustrate cross-section and side view of one specimen of an experiment [2], which is modelled for mid-rise buildings with a half-sized scale. Figure 1(c) and (d) show horizontal force-deformation angle relationship of a specimen and bending moment-rotation relationship of its footing's hinge. Yellow line relationship indicates one calculated for a conventional glulam timber column with no rebar, same cross-section, and rigid-fixed end. Light black line indicates experimental loops. The connection is found to produce high bending capacity and abundant-energy dissipation up to large deformation. Red line indicates skeleton curve calculated by the method mentioned in the previous literature [2]. The method has accurately estimated yielding moment and bending capacity of bending hinge of HGTSB column. On the other hand, the method for estimating those moment and capacity for the portion except the hinge in column, also is required. The aim of this study is to develop the method for estimating bending characteristic of the portion and the column of story above second story in building.

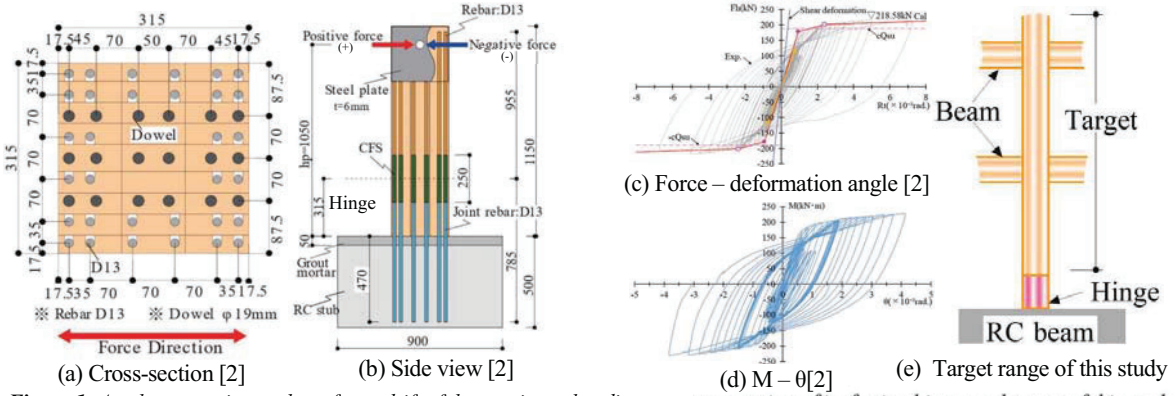

(a) Cross-section [2] (b) Side view [2] (c) Force – deformation angle [2] (d) M – θ[2] (e) Target range of this study

Figure 1: *A column specimen, shear force-drift of the specimen, bending moment-rotation of its footing hinge, and target of this study*

[1]Keisuke Hayata, Department of Architecture, Kagoshima University, Japan, k2923135@kadai.jp
[2] Motohiro Mukai, Department of Architecture, Kagoshima University, Japan
[3] Shinichi Shioya, Department of Architecture, Kagoshima University, Japan, k7347039@kadai.jp

https://doi.org/10.52202/069179-0416

3 COMPRESSION TEST

3.1 SPECIMEN

Figure 2 illustrates cross-section and side views of specimen. The scale was 1/4. Area ratio of rebars/ 8-D13 to column's gross-area/150mm x 150mm was 4.5%.
The number of specimens was to be 5 for conventional glulam timber column and 5 for the composite column. Glulam timber was prepared according to Japanese Ceder, E65-F225, in Japanese Agriculture Standard (JAS); its laminas had no joint such as finger joint. Table 1 lists mechanical properties of lamina by tests; bending strength of the lamina was 49.0N/mm^2. Rebar grade was SD345; tensile yielding strength was 384N/mm^2; ultimate tensile strength was 553N/mm^2. The adhesive for the rebar was epoxy resin adhesive with allowable upper temperature of 110℃. The process of embedding rebars adhered to the same way as Literature [3].

3.2 LOADING AND MEASUREMANT

Figure 4 illustrates set-up for loading and measurement. Monotonic compression was loaded using Amsler compression testing machine (Capacity=2MN). Axial compression force, axial deformation of overall of specimen, and axial strain of timber surface were measured.

3.3 RESULTS

Table 3 lists experimental and calculated results.

3.3.1 **Failure**

Figure 5 illustrates final failures; Figures 5(a)-(c) are WO specimens and Figures 5(d)-(f) are HW specimens.

i) Glued laminated timber specimen (WO)

In WO-4 in Fig. 5(b), vertical cracks appeared in wood at an axial force of 570 kN and after then the cracks developed along the wood grain. Eventually, the wood grain was crushed in middle region of specimen height, resulting in grain bending. In WO-5 in Fig. 5(c), portion of fracture was at the top, but the fracture was similar to that of WO-4.

ii) Composite timber specimen (HW)

The fracture condition of HW-3 is shown in Figure 5(e). Vertical crack occurred at axial force of 959 kN and then the crack developed along the rebar as the force increased. Portion of fracture was at the top. The fracture of HW-5 is shown in Fig. 5(f). Fracture was at the bottom. It can be seemed that location of local defects due to wood heterogeneity would be starting point of the fracture.

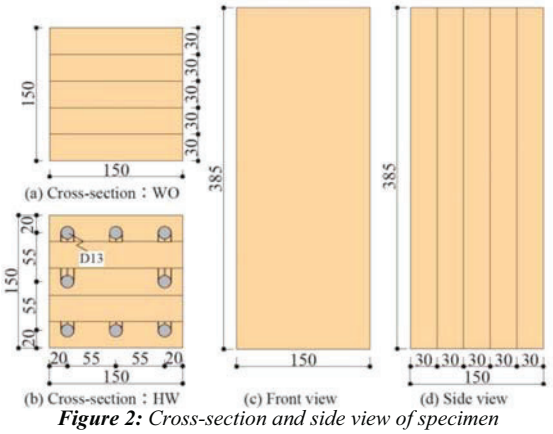

Figure 2: *Cross-section and side view of specimen*

Table 1: *Mechanical properties of lamina*

Unit: N/mm^2

Grade	Compression		Tension		Bending	
	Ec	Fc	Et	Ft	Eb	Fb
L50	5421(6)	25.2(11)	5640(5)	32.3(10)	6396(6)	49(11)

Ec,Et,Eb: Young's modulus, Fc, Ft, Fb: Strength, ( ): The number of testpeice

Table 2: Mechanical properties of rebar

Unit: N/mm^2

Diameter	a_o *in mm*^{2}	E	σ_y	σ_B
D13	126.7	1.88x10^5	384	553

a_0: Nomial cross-sctional area of rebar
E: Young's modulus, σ_y : Yielding strength
σ_B: Braking strength

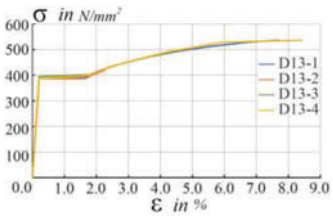

Figure 3: *Rebar in tension*

Photo1: *Experiment situation*

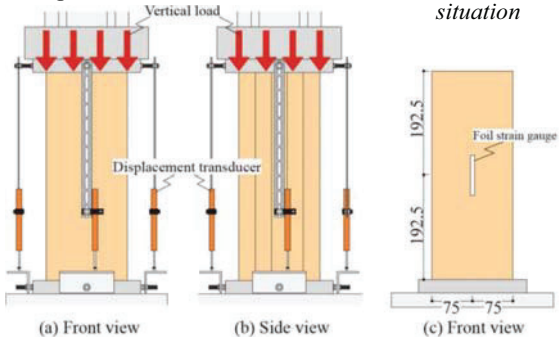

Figure 4: *Set-up for loading and measurement*

Table 3: *Specimens, experimental results, and calculation results of Compression loading test for column*

Specimen	B: Witdh	D: Depth	Height	The number and diameter of rebar	P_g	$_eF_m$	$_e\sigma_c$	$_cF_m$	$_c\sigma_c$	eFy	ε_p	ε_m	ε_{90}	ε_u	E	Failures
	in mm				%	*in kN*	*in N/mm^2*	*in kN*	*in N/mm^2*	*kN*	*in ×10^{-6}*	*in ×10^{-6}*	*in ×10^{-6}*	*in ×10^{-6}*	*in N/mm^2*	
WO-1	150.6	150.5	385.3	–	0.00	579	25.6			324	3028	10563	12661	16866	4900	
WO-2	150.7	150.5	384.6	–	0.00	579	25.6			334	2998	9047	13845	17363	5450	
WO-3	150.7	150.4	385.6	–	0.00	579	25.6	581 of average	25.6 of average	339	3352	10649	13779	15125	5200	Cruching of wood
WO-4	150.7	150.4	384.8	–	0.00	579	25.6			350	3247	10496	22164	26705	5150	
WO-5	150.7	150.2	385.3	–	0.00	586	25.9			351	3010	9126	17574	28369	5900	
HW-1	150.7	150.2	382.9	8-D13	4.48	890	39.3			654	2291	16087	16665	18462	14150	
HW-2	151.0	150.0	382.3	8-D13	4.48	952	42.1			670	2544	10711	25422	29166	13900	
HW-3	150.7	150.2	383.1	8-D13	4.48	963	42.6	944	41.7	679	2554	13062	23592	22358	14100	Cruching of wood and buckling of rebar
HW-4	150.9	150.0	381.5	8-D13	4.48	941	41.6			659	2375	8347	18422	24897	14100	
HW-5	150.6	150.3	382.8	8-D13	4.48	949	41.9			649	2435	12128	22805	23957	14100	

P_g:Aria ratio of total rebar to b-D, $_eF_m$: Axial capacity in experiment, $_e\sigma_c$: Axial stress as $_eF_m$ divided by b-D, $_cF_m$: Axial capacity caculated, $_c\sigma_c$: Axial stress as $_cF_m$ divided by b-D, $_eF_y$:Yeilding load in experient, ε_p: Strain at proportional limit, ε_m: Strain at maximum capacity, ε_{90}: Strain at reaching 90% of $_cF_m$ after maximum capacity, ε_u : Starin at finish of laoding, where these starin were calculated from data by displacement transducer.

https://doi.org/10.52202/069179-0416

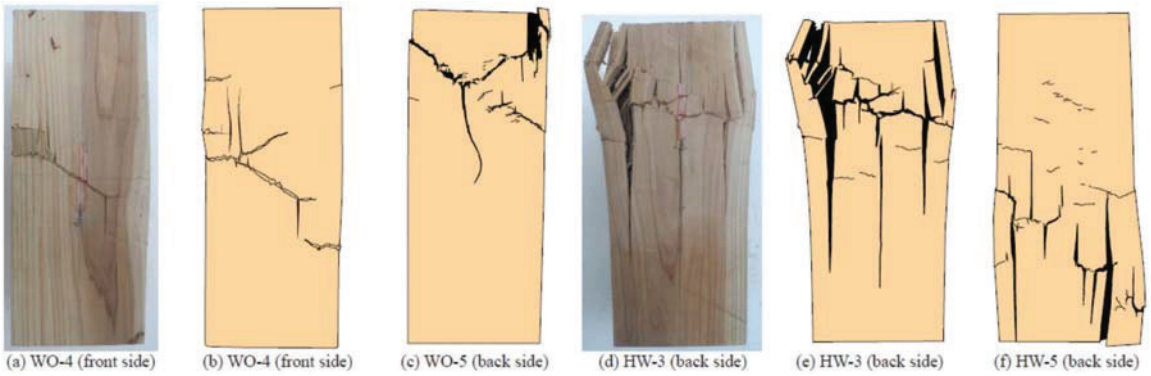

Figure 5: *Final failures*

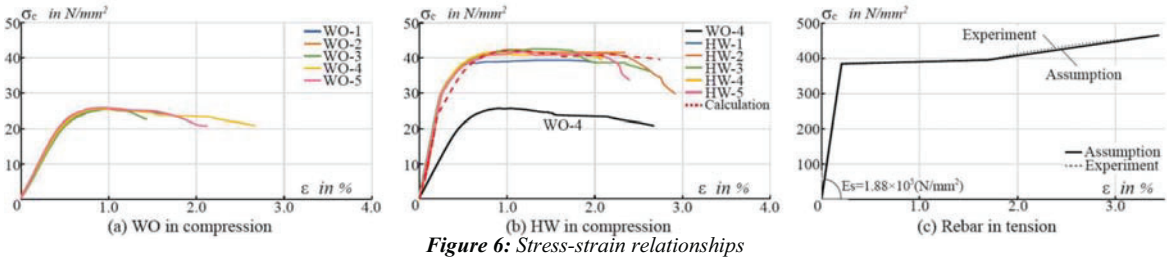

Figure 6: *Stress-strain relationships*

3.3.2 Compression stress-strain curve

The stress-strain relationship is shown in Figure 6. Vertical axis is taken as the compressive force divided by gross area of column (150x150mm), while horizontal axis is taken as the average deformation of the displacement transducers divided by height of column (385mm).

i) Glulam timber specimen (WO)

Figure 6(a) shows compressive stress-strain relationship of WO specimen is shown; those of the five specimens was similar stress-strain relationship.

ii) Composite timber specimen (HW)

Figure 6(b) shows compressive stress-strain relationships of HW specimen in comparison with that of WO-4, where the HW specimen had significantly increased elastic stiffness, compressive strength, and limit strain at which the compressive strength can be maintained (hereafter referred to as limit strain) in comparison with those of WO-4. Compressive strength increased by a factor of nearly 1.7 and was maintained up to a range of 2.0-3.0% in compressive.

3.4 ESTIMATION of COMPRESSIVE STRESS-STRAIN RELATIONSHIP

In Figure 6(b), a red dash line indicates a stress-strain relationship calculated, by assuming stress-strain curve for wood being the same as that of WO-4 and that for rebar as a curve shown in Figure 6(c) based on the results of Table 2 and Figure 3. The calculated stress-strain relationship is seen to estimate initial stiffness and compressive strength of experimental result. The point at which experimental capacity start to decrease against calculated one might be thought to be that at which buckling of rebars within column occurred. It might be thought that axial force of rebar increased as the capacity of the timber decreased, causing the rebar to buckle. The amount of decrease in the capacity of timber is thought to be a key to identifying the point at which buckling of the rebar occurs.

4 BENDING TEST

4.1 SPECIMEN

Figure 7 illustrates configuration of specimen. Scale, cross-section, and material were the same as the compression test mentioned above. Direction of bending was selected to be parallel to gluing layer of lamina, i.e.,

Table 4: *List of specimens*

Specimen	η	N *in kN*
HW(NM)-0.0	0.00	0.0
HW(NM)-0.0-B	0.00	0.0
HW(NM)-0.1-B	0.10	57.6
HW(NM)-0.2-A	0.20	115.2
HW(NM)-0.4-A	0.40	230.4
HW(NM)-1.04-B	1.04	600.0

η : Ratio of axial force N : Axial force

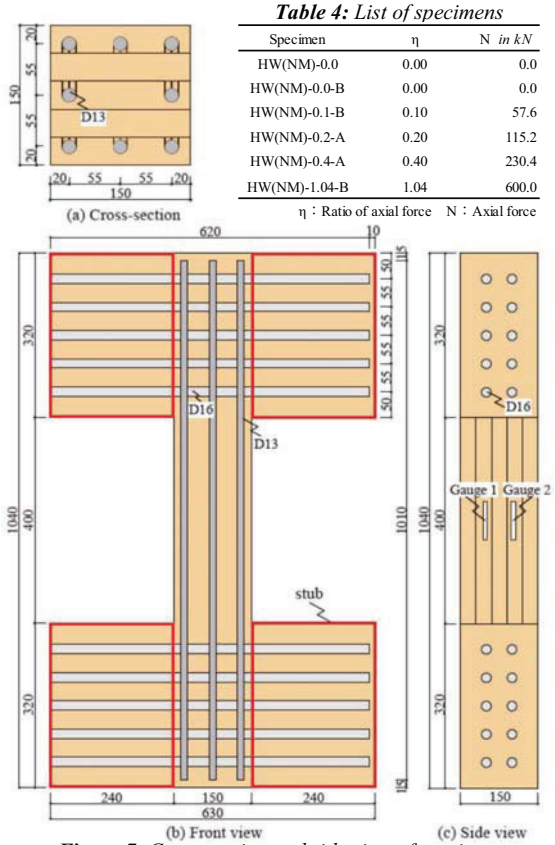

Figure 7: *Cross-section and side view of specimen*

https://doi.org/10.52202/069179-0416

weak-axis direction. Upper and lower portions of the specimen were bound to four timber stubs, with a connection using Glued-in-rod. The section between the upper and lower stubs was tested.

Table 4 lists specimen names, ratios of axial force to compressive capacity assumed, and axial forces acted. The specimen was one type of steel bar-timber composite column and the number of it was 6. Variable of specimen was magnitude of axial force, i.e., vertical force. The name of specimen was HW(NM), charged with a numerical value 'η' representing axial force ratio.

As described in later Section 4.4.1, consideration of failure of the first specimen led to adhesion of steel plate A or steel plate B to both sides of the stubs. The same adhesive as that used for the rebar was also used for these plates. Names of specimen to which the steel plates were bonded were additionally marked with the symbol 'A' or 'B' for the steel plate.

The axial force ratio was assumed to be ratio of the constant vertical load divided by average compressive capacity of the composite specimens of the compression test mentioned above. The specimens were manufactured at the same time as the specimens of the compression test.

4.2 LOADING AND MEASUREMANT

Figure 8 and Photo 2 illustrate set-up for loading of combing compression with bending. The stub was fixed with high-tension PC bar, to upper or lower H-shaped steel beam. The apparatus including a specimen was placed into other Amsler compression testing machine (Capacity=2MN) for long column. The loading was conducted to be exert a specified constant compression and to exert bending moment on it by both oil jacks up to ultimate capacity while maintaining the magnitude of the axial force. One-way pin was connected to connections between testing machine and the upper and lower H-shaped beams. Lateral braces were connected between upper stub and lower stub to prevent specimen from being out of plane. Figure 9 illustrates positions of foil strain gauges and measuring sections of deformation by displacement transducers. Foil strain gauges (measuring length: 60 mm) were adhered to surface of the wood. Two strain gauges were adhered to both surface in tensile and compressive surface; one strain gauge was adhered to side surfaces. The position of displacement transducers was changed between the upper and lower stubs in relation to

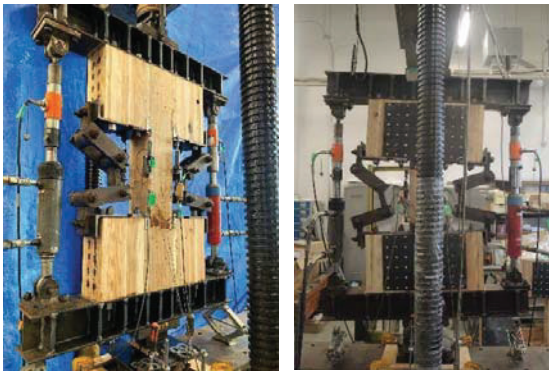

Photo2: *Set-up for loading*

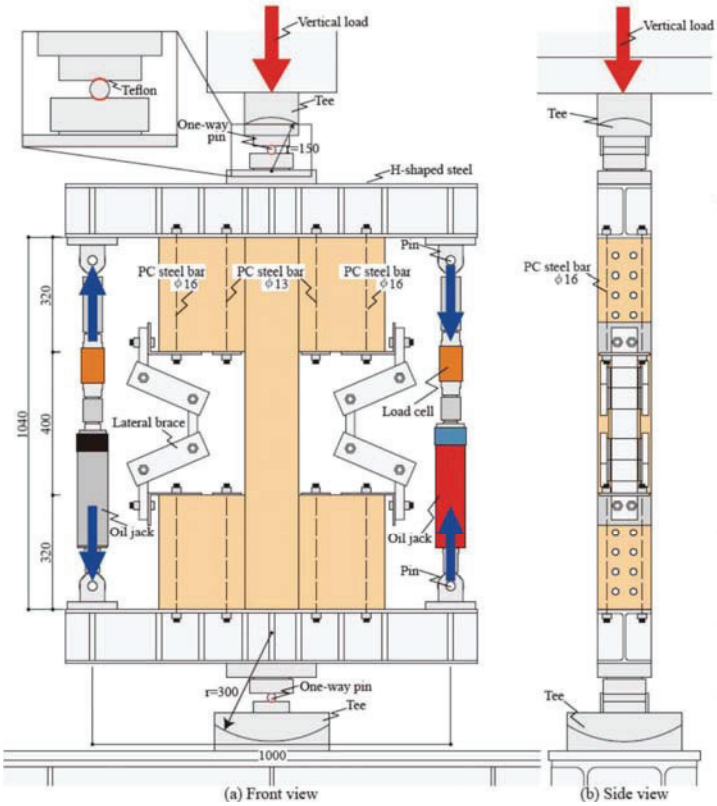

Figure 8: *set-up for loading*

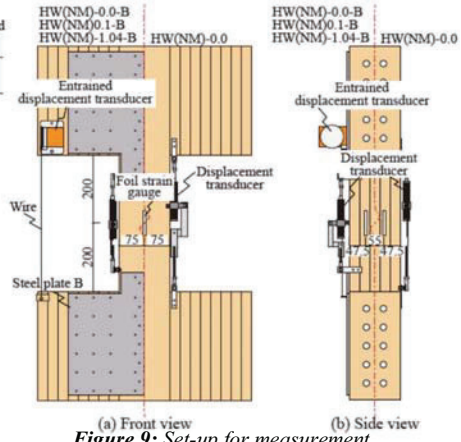

Figure 9: *Set-up for measurement*

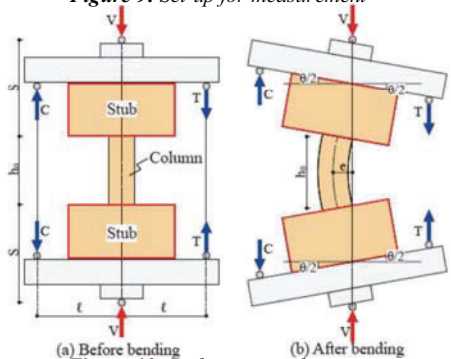

Figure 10: *Deformation of specimen under bending force*

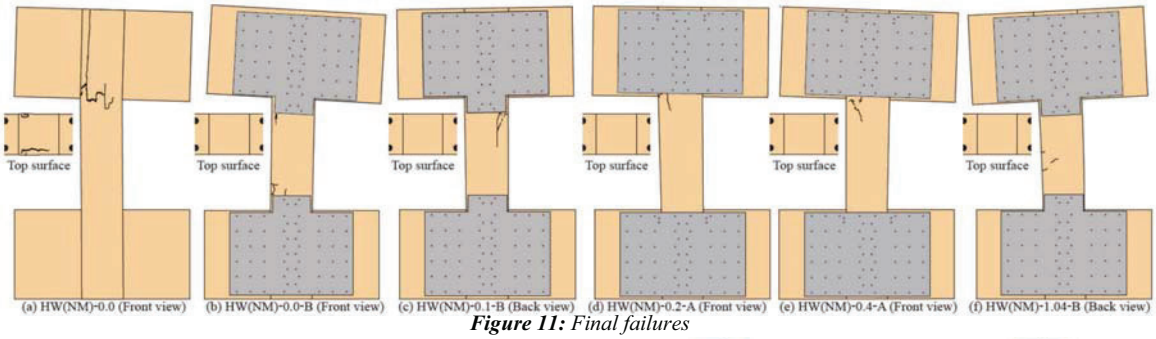

Figure 11: *Final failures*

the steel plates reinforcing the stubs. For the specimens adopting steel plate B, which will be described in Section 4.4.3, in addition to the displacement transducers, two entraining-displacement transducers were installed at both ends of the stub so that deformation due to cracks by bending could also be measured to be included.

4.3 BENDING MOMENT OF COLUMN

Figure 10 illustrates deformation of specimen under bending force. When moment is exerted on the section between the pins, cross-section at the middle height of column moves horizontally from its initial position. The horizontal distance is designated as eccentricity distance/e. An additional moment/ V・e also acts on the section due to the vertical force/V. The maximum moment/M_u is expressed as Equation (1), and the additional moment increases as the vertical force/V is increased.

$$M_u=C\cdot(\ell-e)+T\cdot(\ell+e)+V\cdot e \quad (1)$$

where C: compressive force of the oil jack for bending force, T: tensile force of the oil jack for bending force, ℓ : horizontal distance from the one-way pin to the oil jack, e: horizontal distance from line of action of the vertical load to centroid of cross-section at the middle height of the column, V: vertical force.

As the eccentricity distance/e was not measured in this experiment, it was calculated from the curvature by strain of wood or the angle of rotation between the upper and lower stubs. The curvature was taken as value by the foil strain gauge on wood and the angle of rotation was taken as value from the displacement transducer. Section/S in Figure 10(a) from center of rotation of the one-way pin to the border of column was assumed to be as rigid. Because the column is under bending and axial force, the eccentricity distance/e is expressed in Equation (2) using curvature/ϕ and in equation (3) using rotation angle/θ, on the basis of deformation of specimen.

$$e_s=S\cdot\phi\cdot h_o/2+(\phi\cdot h_o/2)\cdot(h_o/4) \quad (2)$$

$$e_d=S\cdot\theta/2+(\theta/2)\cdot(h_o/4) \quad (3)$$

4.4 RESULTS

4.4.1 Failure and strengthening of stub

Figure 11(a) illustrates failure of specimen HW(NM)-0.0 with zero axial force. This is the first specimen which was tested. Vertical cracks progressed along tensile rebars

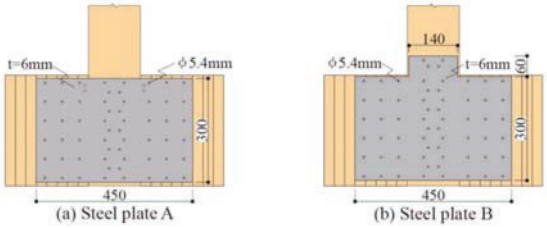

Figure 12: *Shape and dimensions of steel plate*

within the stub at near maximum load capacity; finally, anchorage failure of rebar occurred. Split cracks were observed on top surface of column after having removed the specimen from the apparatus, as shown in Figure 11(a). In buildings, the anchorage length of rebar is significantly ensured because columns are continuous in several stories. Because purpose of this study is to estimate bending capacity, steel plate A shown in Figure 12 (a) was bonded to side surface of the stubs in order to prevent the crack along rebar. It was employed for specimens with axial force ratios of 0.20 and 0.40. These specimens were named as HW(NM)-0.2-A and HW(NM)-0.4-A. Figures 11(d) and 11(e) illustrate final failures of specimens/HW (NM)-0.2-A and HW(NM)-0.4-A. The cracks along rebar occurred slightly and no cracks were observed at the top and bottom surface of column. Considering of these failures, the shape of steel plate was further modified as shown in Figure 12(b). These three specimens were HW(NM)-0.0-B, HW(NM)-0.1-B, and HW(NM)-1.04-B with axial force ratios of 0.00, 0.10 and 1.04, respectively. Figure 11(b) illustrates failure of specimen HW(NM)-0.0-B bonded with steel plate B. Cracks by bending occurred and reached maximum capacity of higher amount. Figure 11(f) illustrates failure of HW(NM)-1.04-B, in which the axial force was increased up to an axial force ratio of 1.04. No crack was observed in tensile surface, and a slight swelling was observed in wood portion in compression.

4.4.2 Moment-curvature relationship

Figure 13 shows moment-curvature relationship. The moments according to Equation (1) and (3) are shown as a solid line, and the case where the eccentricity distance 'e' is set to zero is shown as a dotted line. The assumption of e=0, after reaching the maximum bending moment, was selected on the ground of those failures which were concentrated near the borders between the stub and the column section. The moment of the solid curve increases as the axial force increases, against the dotted curve. It can be confirmed that the additional moment due to the vertical force should be taken into account in the moment of action.

https://doi.org/10.52202/069179-0416

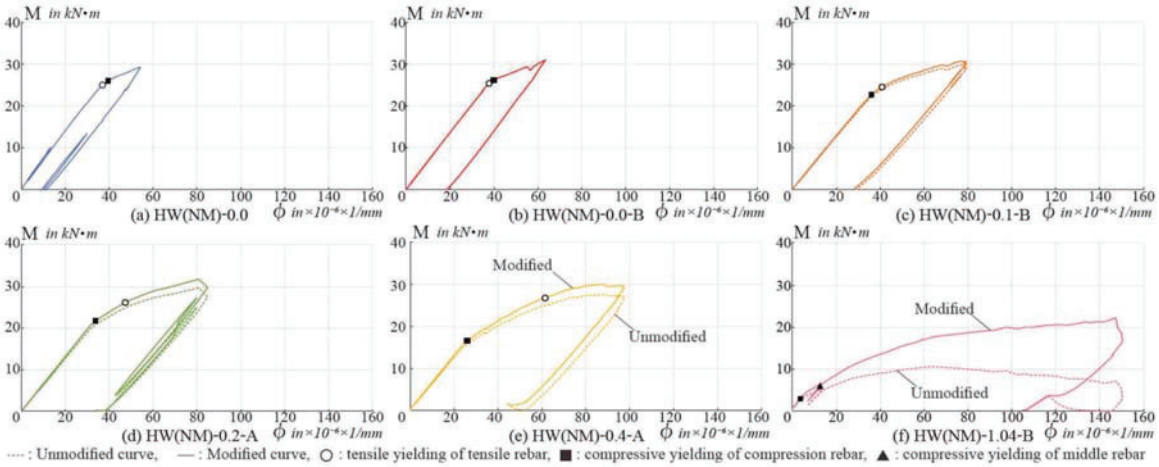

Figure 13: *Moment-curvature relationship*

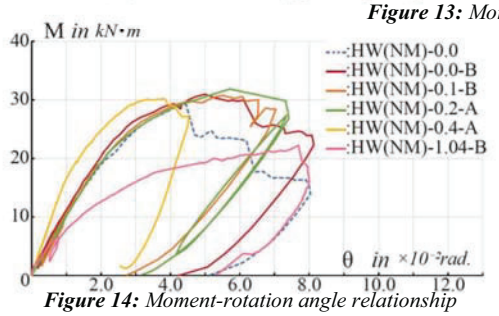

Figure 14: *Moment-rotation angle relationship*

Table 5: *Specimens, and experimental results of bending loading test for column*

Specimen	η	N	E	eMy	eMm
		in kN	*in N/mm²*	*in kN-m*	
HW(NM)-0.0	0.00	0.0	16041	25.0	29.3
HW(NM)-0.0-B	0.00	0.0	15903	25.4	30.9
HW(NM)-0.1-B	0.10	57.6	14990	22.7	30.7
HW(NM)-0.2-A	0.20	115.2	15202	21.8	31.9
HW(NM)-0.4-A	0.40	230.4	15087	16.6	30.1
HW(NM)-1.04-B	1.04	600.0	14775	3.0	22.3

η:Ratio of axial force, N:Axial force, E:Young's modulus, $_eM_y$:Yeilding moment, $_eM_m$:Bending capacity

Hereafter, the moments are described in terms of the additional moment.

The curvature was calculated from strain in the gauges on wood surface. The strain for curvature used average of the two strain gauges on a surface. The two values were in close agreement. The symbols '△',etc. indicate timings at which the strains at positions of tensile rebar, compression rebar, and middle rebar reached yielding strain of rebar, by using linear interpolation from values of the strain gauges on tensile and compressive surfaces.

The tensile rebar is indicated by symbol '○'; the compression rebar by symbol '□'; the middle rebar by symbol '△'. Tensile yield is indicated by white paint and compression yield by black paint. It was confirmed that when the axial force ratio was 0.00, yielding of tensile rebar or compressive rebar was almost simultaneous. However, as the axial force ratio increased, compressive yielding of the compression rebar preceded and yielding of the tensile rebar delayed. In the case of HW(NM)-1.04-B, of which the axial force was the highest of them, the tensile rebar did not yield and the middle rebar yielded in compression. Yielding of rebar is seen to decrease the stiffness. Bending moment at yielding decreased as the axial force increased, but the bending capacity tended to increase up to an axial force ratio of 0.2 and to decrease above that value. Table 5 lists experimental values of Young's modulus of column. The Young's modulus tended to decrease with increasing axial force. The maximum decrease is 8.9%, but it should be noted that yielding moment decreases significantly.

4.4.3 Moment-rotational angle relationship

Figure 14 shows moment-rotation angle relationship. HW(NM)-0.0, which was not reinforced with steel plates, is indicated by dotted line. HW(NM)-0.0 had the largest reduction of capacity after reaching maximum capacity because it accompanied rebar slip within the stub and wood split around rebar. HW(NM)-0.2-A and HW(NW)-0.4-A produced a less increase in rotation angle after the bending cracks. In HW(NM)-0.2-A and HW(NW)-0.4-A, the displacement transducer was fixed to the inner of the column section and deformation of bending cracks near the inner could not be included in the deformation, so the curves had less increase in the rotation angle after the bending crack. In the specimens reinforced with steel plate/B, two entrained displacement transducers (sensitivety:1 /10 mm) were installed to measure elongation and contraction between top stub and bottom stub, and the rotation angle was calculated from deformation by them.

5 BENDING TEST OF BEAM

5.1 AIM

Only material tests of the lamina were conducted in the column bending tests, and no bending tests of column of Glulam timber was conducted. Because bending strength of the Glulam timber could not be specified, experimental capacities of the column bending capacity could not be validated. Bending test by Glulam timber beams was conducted to capture relative relationship between strength of lamina and bending strength of Glulam timber in the column (cross section:150x150 mm).

5.2 CAUSE OF REDUCTION OF BENDING CAPACITY OF COLUMN SPECTIMN

As described in Section 4.4.1, failures were concentrated at the boundary between column and stub. The cause for this will be holes (diameter: 20mm) for the Glued-in-rod

to connect column to the stubs (hereinafter referred to as "insertion hole") drilled in column, and insertion holes close to the failure zone may have reduced bending capacity of Glulam timber.

5.3 SPECTIMN

Figure 15 shows shape and dimensions of beam specimen. Two types of specimens were employed: one Glulam timber beam and two Glulam beams with rebar inserted and glued at mid-span of the beam. The former was named as BWO and the latter as BWR-1 and BWR-2. The details of rebar and the insertion hole (diameter:20mm) were the same as those of the column specimen mentioned in Section 4.1. The lamina of the specimen also was the same species and grade, i.e., cedar/L50. However, the timing of fabrication of these specimens differed from that of the column specimens.

5.4 LOADING AND MEASUREMANT

Figure 16 illustrates set-up for loading and measurement. 4-point bending test was employed. Direction of bending was selected to be parallel to gluing layer of lamina as that of the column. Vertical deformation at the mid-span of beam, sinking deformations at left and right support points, and wood strain on upper and lower surfaces near the mid-span (length of inspection: 60 mm) were measured.

5.5 RESULTS

Figure 17 shows vertical force-deflection relationship at mid-span. The deflection was subtracted by deflection of both supports. The reduction in stiffness by inserted rebar is not clear, but maximum forces were reduced to 77.5% and 87.3% for BWR-1 and BWR-2 beams with rebar compared to that of Glulam timber beam (BWO). Figure 18 shows moment-curvature relationship of mid-span. The curvature was calculated from strain of foil strain gauges on upper and lower surfaces of timber. Figure 19 s hows positions of the foil strain gauges. Curvature in Figure 18(a) employed that of strain gauge away from the rebar/ (Location I). Bending stiffness of position away from the insert hole of rebar was hardly affected. The curvature in Figure 18(b) employed that of the location II close to the rebar. At the location, bending stiffness was reduced by the insert hole. Photo 4 shows final failures. Specimens with rebar had tensile cracks on at lower tensile surface as if connecting the insertion holes, whereas compressive portion by bending was never affected by the insertion holes because rebar and its adhesive produce compressive resistant. Figure 20 shows the relationship between moment and strain of foil strain gauges. Solid line indicates strain on lower tensile surface and dashed line dose strain of that on upper compression surface. In lower tensile surface, strain near the rebar was larger, while, in upper compression surface, strain was not affected by the rebar.

From these results, it can be concluded that, in compression zone by bending, bond interface between rebar and wood can resist compression, but, in tensile zone, the adhesive for rebar peels off at that of insertion hole and only wood's width excluding the sum of diameter of the hole can resist, resulting in a decrease in maximum bending capacity of Glulam timber beam.

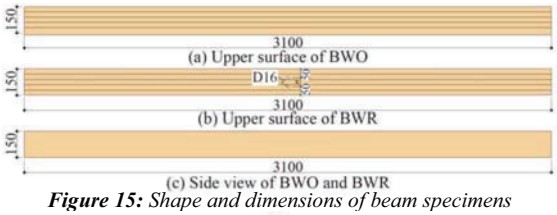

Figure 15: *Shape and dimensions of beam specimens*

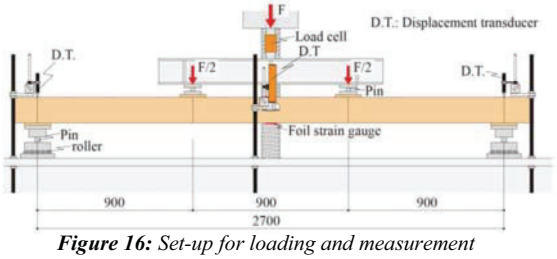

Figure 16: *Set-up for loading and measurement*

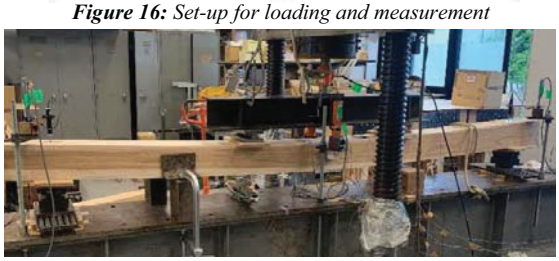

Photo 3: *Experiment situation*

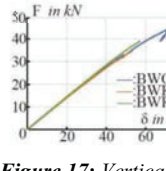

Figure 17: *Vertical force-deflection relationship of mid-span*

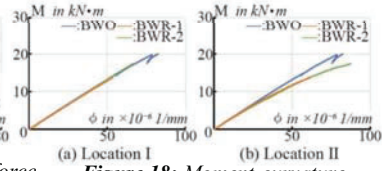

Figure 18: *Moment-curvature relationship*

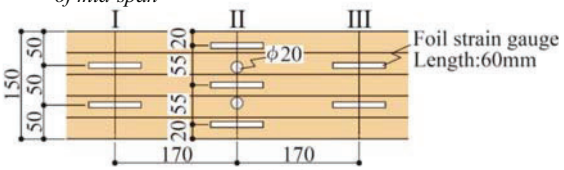

Figure 19: *Locations of the foil strain gauges*

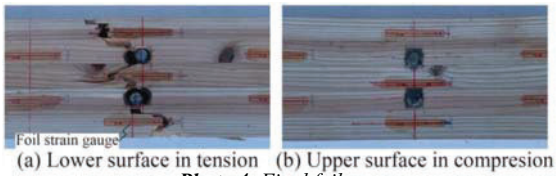

Photo 4: *Final failures*

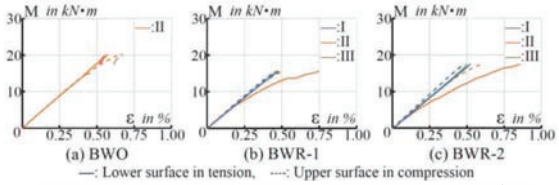

Figure 20: *The relationship between moment and strain of foil strain gauges*

5.6 BENDIG STRENTHS OF GLULAM TIMBER AND LAMINA

Figure 21in the next page shows resisting cross-section of beam for calculation of bending strength of timber at Location II. In BWR-1 and BWR-2, width equal to

https://doi.org/10.52202/069179-0416

diameter of the insertion hole was assumed to be unresisting over range from the neutral axis to lower tensile surface, and then the sectional modulus was calculated: the bending strength was calculated by dividing maximum moment using the modulus. Sectional modulus for BWO was calculated as a rectangular cross-section. The bending strength based on these calculations are indicated as horizontal lines in Figure 22. The bending strengths of BWO (solid line) and BWR-1 (dotted line) were almost the same, while that of BWR-2 (dashed line) was 1.11 times greater than BWO. The maximum force of BWR-1 was 0.78 times as much as that of BWO, and that of BWR-2 was 0.87 times as much as that of BWO. Therefore, it can be considered that bending strength of glulam timber can be identified more accurately by using the sectional modulus for effective cross-section in Figure 21. In the same figure, data of bending strength are plotted as symbol '△' and data of tensile strength are done as symbol '○' , by material tests of lamina. Figure 23 illustrates shapes and dimensions of the lamina testpiece. The numbers of bending and tensile specimens was 15 each. Tensile strength of BWO was 0.67 times as much as average of bending strengths and 1.20 times as much as average of tensile strengths.

It is well known that bending strength of glulam timber approaches tensile strength as its depth increases, and their magnification ratios correspond to this tendency. Figure 24 shows distribution of data of bending strength and tensile strength from material test of lamina testpieces of the column specimen described in Section 4.1.

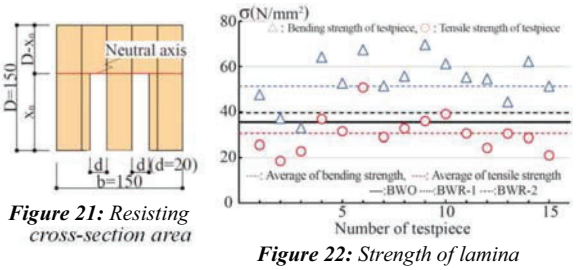

Figure 21: *Resisting cross-section area*

Figure 22: *Strength of lamina*

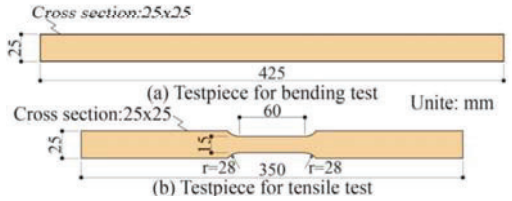

Figure 23: *Shapes and dimensions of the lamina testpiece*

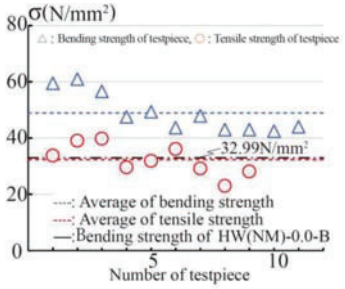

Figure 24 *Strength of column lamina by testpiece*

Similarly, comparing the mean values, tensile strength was 0.66 times as much as that of the bending strength. The bending strength of the Glulam timber calculated from HW-(NM)-0.0-B with zero axial force using the sectional modulus for Figure 21 is shown as a horizontal one dot chain line in Figure 24. In the calculation, Young's modulus of rebar was assumed to be the standard value of 2.05×10^5 N/mm^2, the yield strength of the rebar was done to be test value (384 N/mm^2), and Young's modulus of timber was done to be average/5530 N/mm^2 of Young's modulus by tensile and compression tests of lamina. Bending capacity was calculated using Equation (18) described later. In Figure 24, the horizontal one dot chain line is seen to be within range of data of tensile strength of lamina.

From above discussion, it can be concluded that it is reasonable to assume bending strength of Glulam timber to be 32.99 N/mm^2, which is the bending strength calculated from HW(NM)-0.0-B by Young's modulus of average of experimental values of the tensile testpieces and the sectional modulus for Figure 21.

6 AXIAL FORCE-BENDING CAPACITY CORRELATION CURVE

6.1 EXPERIMENTAL RESULTS

Figure 25 plots data of axial force and yielding moment with symbol '○' and data of axial force and bending capacity with symbol '●'. The experimental values for compression test of column were plotted with bending capacity being zero. Yielding moment employed bending moment at which rebar yielded on the moment-curvature relationship in Figure 13. Bending capacity employed maximum bending moment. HW(NM)-0.0 without steel plate reinforcement is indicated by symbols '△' or '▲'. The yield moment decreases linearly with increasing axial force. On the other hand, the bending capacity increases over range of axial force ratio/ η of 0.0-0.2, but rather increases and decreases when η is 0.4 or higher.

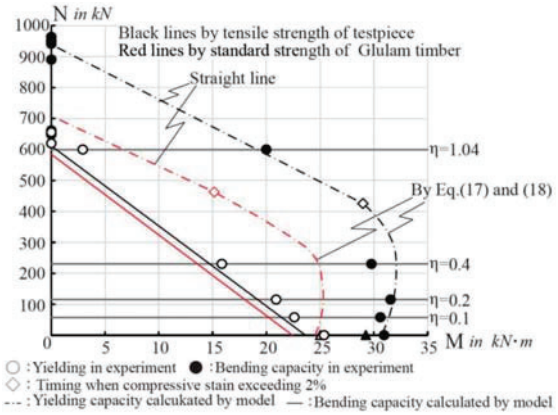

Figure 25: *Axial forth-bending capacity correlation curve*

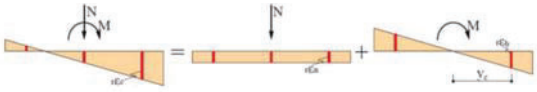

Figure 26: *Model of bending strain distribution*

https://doi.org/10.52202/069179-0416

6.2 ESTIMIATION FOR YIELD MOMENT

Figure 26 illustrates a model of bending strain distribution in a column section. Except when axial force is zero, compression rebar yields first because axial force/N and bending moment/M act simultaneously. The moment can be estimated as moment at which compression rebar yields. Even if axial force is zero, yielding moment can be estimated on the assumption that tensile yielding of tensile rebar and compressive yielding of compression rebar occur simultaneously in a symmetrical cross-section. Strain ${}_r\varepsilon_c$ of compression rebar is the sum of the strain ${}_r\varepsilon_n$ by axial force and the strain ${}_r\varepsilon_b$ by bending moment. ${}_r\varepsilon_n$ and ${}_r\varepsilon_b$ are expressed by Equations (2) and (3) .

$$ {}_r\varepsilon_c = {}_r\varepsilon_n + {}_r\varepsilon_b \quad (1) $$

$$ {}_r\varepsilon_n = N/A_e \cdot 1/E_w \quad (2) $$

$$ A_e = b \cdot D + (n-1) \cdot \Sigma a_r $$

$$ {}_r\varepsilon_b = \phi \cdot y_c $$

$$ = M/(E_w \cdot Ie) \cdot y_c \quad (3) $$

where, b: column width, D: column depth, n: Young's modulus ratio (=E_r/E_w), E_r: Young's modulus of rebar, E_w: Young's modulus of timber, a_r: area per rebar, ϕ : curvature, y_c: distance from neutral axis to compression rebar, I_e: sectional secondary moment of column including effect of rebar.

Strain ${}_r\varepsilon_y$ of rebar which reaches the yield stress/σ_y can be expressed by dividing σ_y by the Young's modulus/E_r of the rebar by using Equation (4).

$$ {}_r\varepsilon_y = \sigma_y/E_r \quad (4) $$

Substituting this ${}_r\varepsilon_y$ into ${}_r\varepsilon_c$ in Equation (1), yield moment/M_y in which stress in the rebar reaches yielding stress/σ_y is finally expressed as Equation (5).

$$ M_y = (\sigma_y/n - N/A_e) \cdot I_e/y_c \quad (5) $$

6.3 ESTIMATION FOR BENDING CAPACITY

6.3.1 Rapture strain of wood in bending capacity

Figure 27 shows bending moment-strain relationship of the column specimen. Moments were assumed to be moments taking axial force into account. The strain was taken as foil strain gauge value.

For HW(NW)-0.0 and HW(NW)-0.0-B with zero axial force, the magnitude of compressive strains on compression surface and tensile strains in tensile surface at the maximum bending moment were almost identical: the former was -0.40% and the latter was 0.55%.

For HW(NM)-1.04-B, where the axial force was the greatest of them and its wood did never fail in tension by bending, the strain at the compression surface increased up to -1.80 to -1.95%, but the strain at the tensile surface was only 0.42%. The maximum strain at the tensile of HW(NM)-0.0, where the rebar slip-failed at the stub without steel plates, was still only 0.42%.

From these results, it can be concluded that if bending capacity is determined by tensile rupture by bending, the tensile strain of wood of the tensile surface by bending can be assumed to be 0.5%.

6.3.2 Stress-strain relationship of wood

Figure 28 shows stress-strain curves for compression and tensile tests for testpiece of lamina of the column specimen. In only one testpiece of compression test, compressive strength was maintained up to approximately 2% of strain after compressive yielding. However, as seen in Figure 6, rebar boosts the strain up to approximately 2%. Roughly, the relationship can be assumed to be fully elastoplastic. In tensile test, wood ruptures immediately when the tensile strength is reached.

On the basis of these results, stress-strain relationship of wood in compression and tension, adopted as a model for estimation of bending capacity, are shown in Figure 29(a).

6.3.3 Equation for estimation of bending capacity

Figure 29(b) illustrates an assumed stress distribution of column at bending capacity. Timing when strain of tensile surface by bending reaches 0.5% is assumed to be timing of bending capacity. The distance/x_n from the compression surface to neutral axis is expressed in Equation (6).

$$ x_n = -\varepsilon_c/(\varepsilon_t - \varepsilon_c) \cdot D \quad (6) $$

where ε_c: strain on compression surface by bending, ε_t: strain on tensile surface, D: column depth

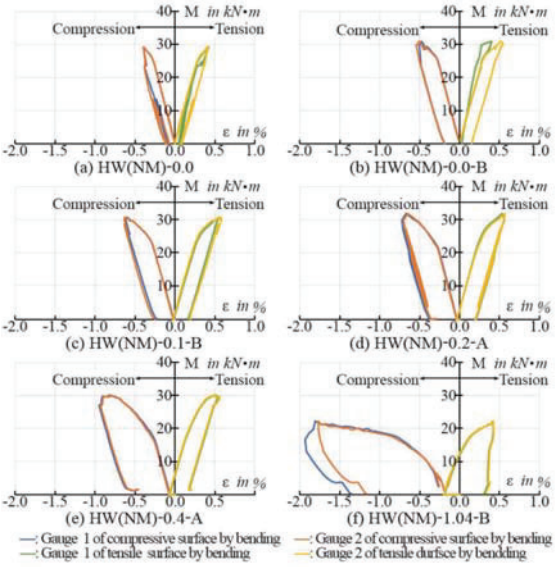

Figure 27: *Bending moment-strain relationship*

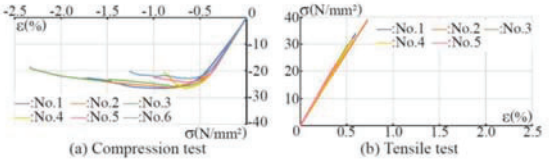

Figure 28: *Stress-strain relationships of lamina*

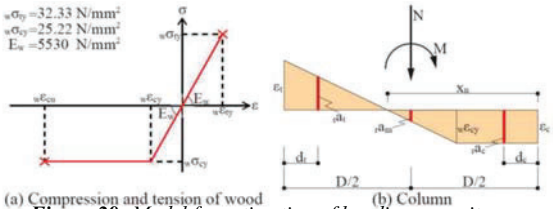

Figure 29: *Model for estimation of bending capacity*

https://doi.org/10.52202/069179-0416

Strain/$_r\varepsilon_c$ of rebar on the compression, strain/$_r\varepsilon_t$ of rebar on the tension, and strain $_r\varepsilon_m$ of middle rebar at column depth are expressed by Equations (7)-(9), respectively.

$$_r\varepsilon_c=\varepsilon_c\cdot(x_n-d_c)/x_n \quad (7)$$

$$_r\varepsilon_t=\varepsilon_t\cdot(D-x_n-d_t)/(D-x_n) \quad (8)$$

$$_r\varepsilon_m=\varepsilon_c\cdot(x_n-0.5\cdot D)/x_n \quad (9)$$

where d_c: distance from compression surface to its near rebar, d_t: distance from tensile surface to its near rebar.

Resultant force/$_rT$ of rebars in tension, resultant force/$_rC$ of rebars in compression, and resultant forcer/$_rC_m$ of rebars in the middle at column depth are expressed by equations (10)-(12), respectively.

$$_rT=E_r\cdot{}_r\varepsilon_t\cdot{}_ra_t \quad (10)$$

$$_rC=E_r\cdot{}_r\varepsilon_c\cdot{}_ra_c \quad (11)$$

$$_rC_m=E_r\cdot{}_r\varepsilon_m\cdot{}_ra_m \quad (12)$$

where $_ra_t$: cross-sectional area of tensile rebar
$_ra_c$: cross-sectional area of compression rebar
$_ra_m$: cross-sectional area of middle rebar

Resultant force/$_wT$ of wood in tension and resultant force/$_wC$ of wood in compression are expressed by Equations (13) and (14).
The compression range can be divided into a constant section and the other section like a triangle because there is a section where stress level is constant within assumed stress-strain relationship of wood.

$$_wT=0.5\cdot{}_w\sigma_{ty}\cdot b\cdot(D-x_n) \quad (13)$$

$$_wC={}_wC_1+{}_wC_2 \quad (14)$$

$$_wC_1=0.5\cdot{}_w\sigma_{cy}\cdot b\cdot{}_w\varepsilon_{cy}/\varepsilon_c\cdot x_n \quad (15)$$

$$_wC_2={}_w\sigma_{cy}\cdot b\cdot(\varepsilon_c-{}_w\varepsilon_{cy})/\varepsilon_c\cdot x_n \quad (16)$$

where $_w\sigma_{ty}$: tensile strength of wood, $_w\sigma_{cy}$: compressive strength of wood, $_w\varepsilon_{cy}$: strain of wood at its compressive strength

Axial force balance is given by Equation (17), and bending capacity/M_u is given by Equation (18).

$$N+{}_rT+{}_wT={}_rC_m+{}_rC+{}_wC \quad (17)$$

$$\begin{aligned}Mu={}&{}_rT\cdot(0.5\cdot D-d_t)+{}_wT\cdot(0.5\cdot D-1/3\cdot(D-x_n))\\&+{}_rC\cdot(0.5\cdot D-d_c)+{}_wC_1\cdot(0.5\cdot D-(1/3\cdot x_n\\&\cdot{}_w\varepsilon_{cy}/\varepsilon_c+x_n\cdot(\varepsilon_c-{}_w\varepsilon_{cy})/\varepsilon_c))\\&+{}_wC_2\cdot(0.5\cdot D-0.5\cdot x_n\cdot(\varepsilon_c-{}_w\varepsilon_{cy})/\varepsilon_c)\end{aligned} \quad (18)$$

6.4 COMPARISON OF CALCULATION AND EXPERIMENTAL VALUES

In Figure 25, correlation curves of axial force-yield moment by solid line and axial force-bending capacity by single-dotted curve are shown. The black curves were calculated on the basis of strength and resisting cross-section mentioned in Section 5.6. However, as the axial force increases, the strain of the compression surface exceeds the limit of strain (2.0%). For higher axial forces, the curve was assumed to be approximated by a straight line connecting the point and the point of uniaxial compression capacity with bending being zero. Yield moment tends to decrease linearly as axial force increases, and bending capacity curve has a maximum value at an axial force ratio/ η of approximately 0.3, which is consistent with experimental trend. Calculated curves are generally in agreement with experimental values. Red curves using standard values for rebar (SD345) and cedar laminated wood (E65-F225) are evaluated on the safe side. For wood, compressive strength on compressive zone was assumed as compressive strength, whereas tensile strength on tensile zone was assumed as bending strength.

7 SUMMARY

In order to develop estimation method of yield moment and bending capacity for the steel bar-timber composite column subjected to axial compression and bending moment for column of story above second story in building, compression test and bend test of column, and bend loading test of Glulam timber beam were conducted by specimens scaled as 25%. The results are summarized as followings:

i) Compression capacity and stiffness of column increase as the amount of rebar increases. Also, ductility of compression increases slightly and become stable.
ii) Yield bending moment decreases linearly as axial force increases whereas bending capacity varies as a curve with a peak at axil force ratio being approximately 0.3.
iii) Bending capacity of column was estimated more accurately when duct of wood in column due to joint rebar for connection stub to column was taken account. This suggests that column-beam connection in building should also take account for the duct by bolts or glued-in rod used in the connection.
iv) Formula for estimation of bending yield moment and bending capacity of column with increasing axial force were proposed, and the correlation curve by using the formulas and tensile properties of lamina estimated accurately experimental data. By using standard values of Glulam timber, the curve estimated the experimental data on the safe side.
v) The ratios of tensile strength, compressive strength of lamina, and bending strength of glulam timber were identified. Tensile strength of timber by bending of glulam timber can be estimated to be close to the tensile strength of lamina and the compressive strength of the wood in the compression zone by bending can be done to be close to the compressive strength of lamina.

ACKNOWLEDGEMENT

This project was funded as Grants-in-Aid for Scientific Research 'A' by Japan Society for the Promotion of Science, 2022.

REFERENCE

[1] S.Shioya, et al. : An innovative hybrid timber structure in Japan: performance of column and beam, WCTE 2016.
[2] M. Mukai, et al. : Horizontal-loading test of steel bar-timber composite column for mid-rise building, WCTE 2021.
[3] K. Mori, S. Shioya: Stiffness and strength of full-scale steel bar-timber composite beams with comparative small-depth, WCTE 2021.
[4] N. Fukutomi, S. Shioya: Design method to estimate stiffness and strength of hybrid timber-steel bar beams, WCTE 2018.

World Conference on Timber Engineering Oslo 2023

FINITE ELEMENT ANALYSIS OF BUCKLING BEHAVIOR OF TIMBER ENCASED STEEL COMPOSITE COLUMNS SUBJECTED TO AXIAL LOAD

Ying Gao[1], Feiyang Xu[2], Minghao Geng[3], Qibin Hu[4], Xinmiao Meng[5]

ABSTRACT: Timber encased steel composite (TESC) columns provide a feasible application to large-scale and high-rise structures. This paper investigates the axial load distribution and buckling behavior of TESC columns with embedded H-section steel through finite element (FE) analysis combined with parametric studies. The numerical results revealed that increasing the slenderness ratio could enhance the confinement effect of the timber in improving the maximum load. A larger proportion of timber area provided a more significant confinement effect in enhancing the ductility of the steel, and then a minimum area ratio for TESC columns considering the confinement effect of timber was determined.

KEYWORDS: Finite element analysis, Steel-timber composite column, Load distribution, Parametric study

1 INTRODUCTION

The use of wood for construction purposes has increasingly been the subject of investigations in past decades due to its significant sustainability superiorities such as carbon sequestration and low environmental impact [1]. Timber-steel composite structures have been demonstrated as effective structural solutions for modern timber structures. Benefiting from the composite systems with reasonable design, the disadvantages of wood can be minimized to some extent, while the advantages of steel and timber can be fully utilized.

Timber encased steel composite (TESC) column is a steel-timber composite member with remarkable potential for multi-story timber buildings that have been increasingly needed in recent years. Typically, the steel is fully embedded in the glulam and connected through adhesives, [2]. The use of steel, on the one hand, can effectively improve the stiffness and strength of the column without increasing or not significantly increasing the column size, which is beneficial to structural design such as indoor space utilization. On the other hand, it alleviates the issue of the shortage of wood resources in China and is conducive to the promotion and application of timber in construction. Meanwhile, the outer timber not only provides lateral confinement on the inner steel to enhance the strength but also offers anti-corrosion and fire-retardant coating for the inner steel. The TESC column has been applied as fire-resistant structural columns in timber structures such as the Wood Square Building [3]. TESC columns could be prefabricated in the factory, ensuring product quality and on-site assembly efficiency. Although the cost of the TESC column will increase compared with the glulam column, it is expected that the improvement of the structural performance of TESC columns can offset this increase.

Several experimental studies have been conducted to investigate the mechanical behavior of TESC columns with different configurations. [2, 4-7] Significant improvements in the stiffness and load-carrying capacity of TESC columns were observed. However, the application of TESC columns is inhibited to some extent due to the lack of design methods. A choice should be made between the steel and the timber design methods or made based on both methods. The root of the choice lies in an insightful evaluation concerning the load distribution of each component in the composite column and the interaction at the interface, which is critical for structural design. In this regard, more efforts are needed to gain insight into the structural responses and establish relevant design methods. Nonetheless, the load distribution and interaction are difficult to monitor during the tests. Thus, performing numerical studies to fill the gaps is an available and significant approach to structural analysis [8].

In this paper, a numerical investigation on the axial load distribution and buckling behavior of TESC columns with embedded H-section steel is described. The proposed FE models are built via ABAQUS and validated through experimental results from previous studies [2]. Parametric studies are then performed to evaluate the effects of variations in geometric parameters and material strengths on the compressive behavior of the encased steel column by analyzing the axial load distribution on steel and timber of TESC columns.

[1] Ying Gao, BFU Beijing Forestry University, China, gaoying@bjfu.edu.cn
[2] Feiyang Xu, BFU Beijing Forestry University, China, xufeiyang1996@bjfu.edu.cn
[3] Minghao Geng, BFU Beijing Forestry University, China, gmh7210406@bjfu.edu.cn
[4] Qibin Hu, UA University of Alberta, Canada, qibin@ualberta.ca
[5] Xinmiao Meng, BFU Beijing Forestry University, China, mengxinmiao@bjfu.edu.cn

https://doi.org/10.52202/069179-0417

2 AXIAL COMPRESSION TESTS OF TYPICAL TESC COLUMNS

Axial compression tests of TESC columns were performed by Hu et al. [2]. The glulam of the column was made of first-grade Douglas-fir. The moisture content of the tested samples was approximately 12%. The mean density was 480 kg/m^3. The inner steel was wide flange hot-rolled H-section steel (Q235B class) with sectional dimensions of 125 × 125 × 6.5 × 9 mm. The resorcinol adhesive was used to produce the glulam and the two-component epoxy adhesive was applied to connect the glulam and steel. The width (D) of the square TESC column was 226 mm. The manufacturing process of the TESC column is shown in Figure 1(a). A total of 6 TESC specimens were tested with lengths of 1100 mm, 1700 mm and 2300 mm. The loading protocol was according to standard GB/T 50329–2012 [9], and the test setup is displayed in Figure 1(b). The axial compression tests were conducted with the same moisture content. The support conditions of the specimen were fixed at the bottom and hinged at the top. Strength failure of 1100 mm long specimens and global buckling of 1700 and 2300 mm specimens was observed. as shown in Figures. 1(c). The load–axial displacement curves are shown in Figure 1(d) The load-axial strain behavior, initial stiffness, load-carrying capacity and ductility were determined (see Hu et al. [2]). The previous test results provide a basis for the calibration of the FE models.

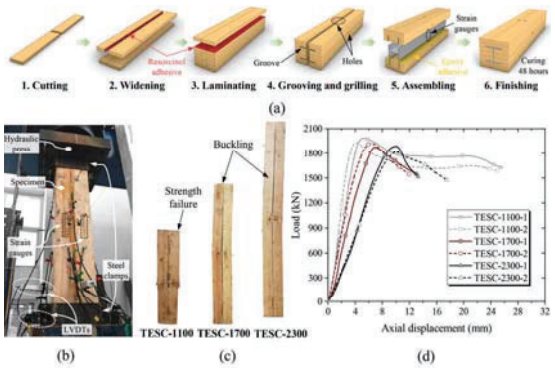

Figure 1: *Summary of axial compression tests: (a) fabrication of the TESC column, (b) test setup, (c) typical failure modes and (d) load-axial displacement curves [2]*

3 FINITE ELEMENT ANALYSIS

3.1 MATERIALS

The elasto-plastic constitutive law was adopted for timber [10]. The elastic behavior of timber was defined as orthotropic through the Engineering Constants in ABAQUS, and the properties are listed in Table 1. The compressive MOE E_L and strength f_{ct} parallel to the grain of timber were determined by axial compression tests on two short full-scale glulam columns. The plastic behavior was characterized by the Hill yield criterion for anisotropic materials [11].

Table 1: *Material properties of timber*

Property		Timber	CoV (%)
Elastic Modulus (MPa)	E_L	13600	3.12
	E_R [7]	577.9	16.70
	E_T [7]	424.2	9.01
Poisson's Ratio [13]	u_{LR}	0.292	
	u_{LT}	0.449	
	u_{RT}	0.390	
Shear Modulus (MPa) [13]	G_{LR}	870.4	
	G_{LT}	1060.8	
	G_{RT}	95.2	
Compressive strength (MPa)	Parallel	26.32	7.45

Note: L, R and T represent the axial, radial and tangential directions of timber, respectively.

The material properties of the steel were obtained through tensile tests. The average MOE E_s and yield strength f_y were taken as 206 GPa and 280 MPa, respectively. The elastic-plastic isotropic behavior was considered and a multilinear stress-strain relationship was adopted in FE models. The Poisson's ratio was set to 0.3.

3.2 MODELING

The FE models were built using the software ABAQUS. The 8-node linear brick element with reduced integration (C3D8R) was selected to simulate the steel and timber. For simplicity, the following steps were adopted: the arc at the flange-web junction of the H-section steel was taken as the right angle due to the negligible effect on the simulation results. However, the six pre-drilled holes (diameter = 20 mm) for threading through the strain gauges in actual TESC columns were considered, given that it significantly affected the failure modes of the specimens [7]; each glulam was regarded as an entirety without glue delamination [14]; the tie constraint was set to simulate the contact between steel and timber due to a near full composite action before reaching the maximum load observed in the tests [2, 5, 7].

The boundary conditions and meshing are shown in Figure 2. A reference point coupled with the top surface of the column was established for applying the load and boundary conditions. The top and bottom surface of the specimen was constrained as a hinge end and a fixed end, respectively.

A mesh convergence test was carried out by element refinement. The global size of the characteristic element varied from 20, 15 and 10 mm. Considering the computational accuracy and efficiency, the global size of the characteristic element was set as 15 mm. The FE models were loaded using a displacement-control procedure in a quasi-static state. The displacement was directly applied to the reference point at the top surface.

The first buckling mode obtained from the eigenvalue buckling prediction was adopted as the initial geometric imperfection distribution, and its magnitude was taken as 1/1000 of the column length.

https://doi.org/10.52202/069179-0417

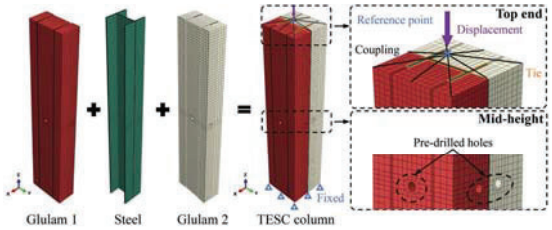

Figure 2: *Geometric modeling of the TESC column*

3.3 SIMULATION VALIDATION

The numerical results were compared and discussed with the experimental results. The numerical failure modes exhibited good agreement with the test observations, as shown in Figure 3. The local damage caused by the pre-drilled holes at the mid-height of the column was well simulated by FE models. It should be noted that the pre-drilled holes increase the influence of the geometry of the TESC column on its buckling performance, thus weakening the ability of FE models to verify the correctness of the material properties of timber to a certain extent. Nevertheless, the built FE models remain reliable since the pre-drilled holes affect the buckling capacity of the TESC column to the same extent. If the strength of the timber is too large or too small, it will lead to significant errors. In addition, the FE model could not predict the cracking at the post-peak stage since the adhesive layers were neglected. The numerical load-axial displacement curves displayed a relatively good trend with test results, as displayed in Figures 4(a) to (c). Nevertheless, the initial slope of numerical curves in the elastic stage was slightly higher, which was commonly observed [15, 16]. The initial differences between FE models and physical specimens, as well as the relatively large deformation at the specimen end, may cause the higher axial displacement recorded from the LVDTs, thus exhibiting a lower initial stiffness in the experimental curves. The load-axial strain relationships of timber were further used to validate the FE modeling methods, especially the elastic behavior, as shown in Figures 8(b) to (f). It was found that the numerical results showed excellent consistency with the experimental results.

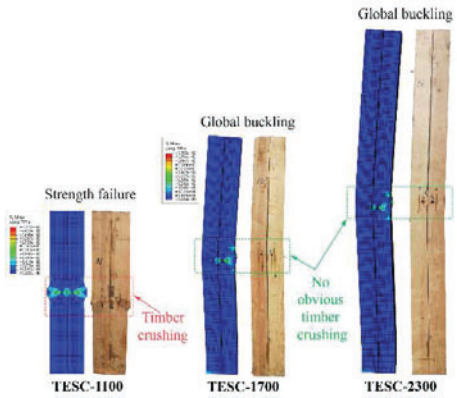

Figure 3: *Comparison of deformation and damage of TESC specimens observed in experiments and FE models.*

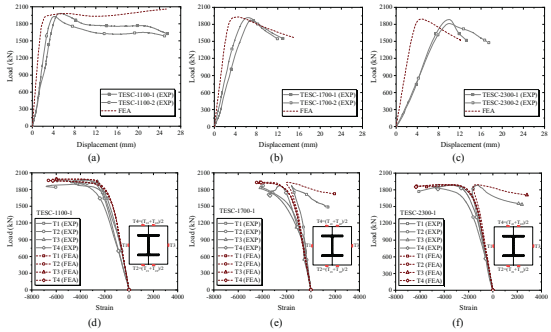

Figure 4: *Comparison between numerical and experimental results: (a), (b) and (c) load-axial displacement curves; (d), (e) and (f) load-axial strain curves of timber*

The authors also performed a finite element analysis on the axial compressive behavior of 16 L-shaped TESC columns with the same materials in this paper but a different cross-sectional shape [7]. The differences between numerical results and experimental results are basically within 10% and the reliability of FE models was validated. Although the section of the simulated TESC column is different, the same modeling methods were adopted. Therefore, it can be further proved that The proposed modeling approaches show to be sufficiently accurate in predicting the axial compressive behavior of the TESC columns.

3.4 LOAD DISTRIBUTION

The validated FE models were used to analyze the load distribution on individual components of the TESC column. The load on each component was extracted through the function of "Free body cut" in ABAQUS. Figure 5 shows the load-axial displacement curves of TESC columns and components. 'IS' and 'OT' respectively represent the inner steel and outer timber in the TESC column, and 'TESC' represents the composite column. The yield point was determined by the farthest-pointing method [17].

The failure sequence of steel and timber was shown from the analysis of load distribution on components. The steel yielding occurred earlier than the timber and TESC column, with a load level of approximately 40% of the load-carrying capacity. It results from the relatively small steel ratio (5.77%) of the TESC column, even though the steel yield strength is much larger than the timber compressive strength. The specimen TESC-1100 entered the yield stage almost synchronously with the timber. In contrast, the yield displacement of specimen TESC-2300 was closer to that of the steel. It implies that with an increasing slenderness ratio, the crucial component that determines the yield of the TESC column changes from timber to steel. It is worth noting that both the timber and steel components almost simultaneously reached their maximum load with the TESC column, indicating a

https://doi.org/10.52202/069179-0417

perfect composite effect with the full utilization of different materials being achieved. The residual load-carrying capacity of steel in the specimen TESC-1100 was kept stable due to the sufficient lateral restraint provided by the timber. However, the load allocated on components in specimens TESC-1700 and TESC-2300 gradually decreased after reaching the maximum load due to the global buckling.

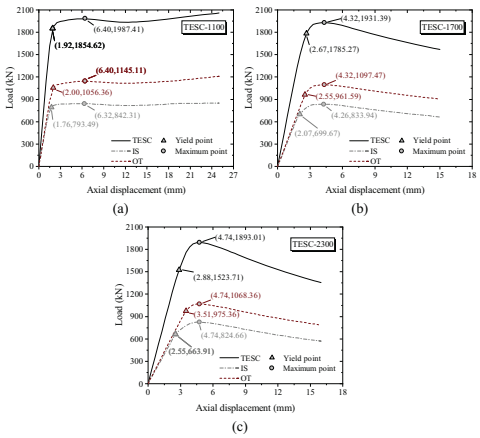

Figure 5: *Load distribution on components of specimens: (a) TESC-1100, (b) TESC-1700 and (c) TESC-2300*

To assess the confinement effect provided by the timber on steel, the load-axial displacement curves of each component in the TESC column and the bare parts were compared, as shown in Figure 6. “S” and “T” represent the bare steel column and bare timber column, respectively. Take specimens with a length of 2300 mm as an example. It was found that the confinement effect provided by the timber on steel was primarily reflected in enhancing the load-carrying capacity and ductility. The confinement effect was activated after the yielding of the steel component, allowing the steel component in the TESC column to exhibit a smoother yielding stage and a higher maximum load than the bare steel column. The bare steel column reached the maximum load of approximately 713 kN at 3.20 mm, while the steel component reached the maximum load of approximately 825 kN at 4.80 mm. Furthermore, the outer timber suppressed the post-buckling behavior of the inner steel, thus leading to a substantially higher residual load-carrying capacity than that of the bare steel column. However, the load-carrying capacity of the timber component was lower than the bare timber column. The bare timber column reached the maximum load of approximately 1195 kN at 5.80 mm, while the timber component of the TESC column reached the maximum load of approximately 1068 kN at 4.80 mm. It is because the timber component is in the field of axial compression and lateral pressure, which weakened the load-carrying capacity of the timber.

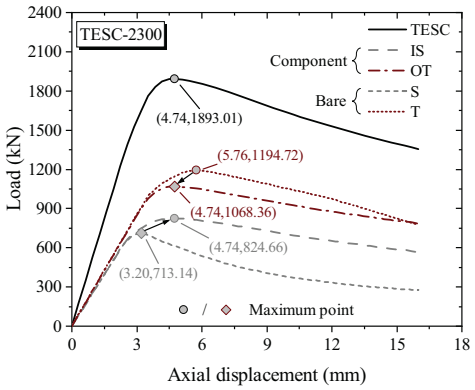

Figure 6: *Comparison of load on components and individual loaded parts*

4 PARAMETRIC STUDY

Based on the validated FE modeling, a parametric study was conducted to evaluate the influence of geometric and material parameters on the compressive behavior of TESC columns and the load distribution on components. The parameters were categorized into two groups. The first group A focused on the strength-related parameters, including the steel yield strength and the compressive strength parallel to the grain of timber. The second group B regarding the geometric-related variables, including the steel area, timber area and slenderness ratio.

The details of the parameters are listed in Table 2. The steel yield strengths changed from 235, 345, 460, and 960 MPa. According to [13], three commonly used wood species of Engelmann Spruce (*Picea engelmannii*), Red Pine (*Pinus resinosa*) and Western Larch (*Larix occidentalis*) were selected. The average compressive strengths parallel to the grain are 30.9 MPa, 41.9 MPa and 52.5 MPa, respectively. Five types of H-section steel with different steel areas were chosen from the standard GB/T 11263—2017 [18]. The steel ratio (A_s/A_{TESC}) by the steel sectional area A_s and the TESC column sectional area A_{TESC} was used to describe the specimen with the same composite area but different steel areas. The area ratio (A_{TESC}/A_s) was used to describe the specimen with different timber areas but the same steel area. The value of A_{TESC}/A_s was determined by the cross-section width D (ranging from 125 mm to 260 mm) of the TESC column or the width t (ranging from 0 mm to 50 mm) of the encased timber between the H-section steel shown in Figure 10(b). The slenderness ratio λ changed from approximately 5 to 200. The corresponding column lengths L were taken as 500, 1100, 1700, 2300, 2900, …, and 16300 mm. The increment of the length was 600 mm. The λ was calculated as follows.

$$\lambda = \frac{KL}{i} \tag{1}$$

$$i = \sqrt{\frac{I_t + I_s E_s / E_t}{A_t + A_s f_y / f_{ct}}} \quad (2)$$

where K represents the effective length factor. Since the top end of the TESC column was hinged and the bottom end was fixed, the value of K was set to 0.7. The radius of gyration of the cross-section i was calculated by Eq. (2) according to [19], where I_s and I_t were the moments of inertia of the steel and timber components around the minor-axis of H-section steel, respectively. The column TESC-2300 was selected as the control specimen of the parametric study considering that the column length of 2300 mm was common in practical applications. A total of 140 FE models, including the corresponding bare steel columns and timber columns, were built and analyzed. It should be noted that the predrilled holes at the mid-height specially designed for the strain measurement of the inner steel in tests, were not considered in the parametric study.

Table 2. *Investigated parameters in the parametric study*

Group	Steel yield strength f_y (GPa)	Timber strength f_{ct} (MPa)	Steel ratio (Steel sectional dimensions, $b \times d \times t_w \times t_f$, mm)	Width t/D (mm)	Area ratio A_{TESC}/A_s	Length L (mm)
A	235 345 460 690 960	26.32	5.77% (125 × 125 × 6.5 × 9)	226	17.34	2300
	280	26.32 30.9 41.9 52.5	4.12% (100 × 100 × 6 × 8)	226	24.28	2300
		26.3 30.9 41.9 52.5	5.77% (125 × 125 × 6.5 × 9)		17.34	
		26.3 30.9 41.9 52.5	7.66% (150 × 150 × 7 × 10)		13.06	
B	280	26.32	4.12% (100 × 100 × 6 × 8) 5.77% (125 × 125 × 6.5 × 9) 7.66% (150 × 150 × 7 × 10) 9.78% (175 × 175 × 7.5 × 11) 12.15% (200 × 200 × 8 × 12)	226	24.28 17.34 13.06 10.22 8.23	2300
	280	26.32	5.77% (125 × 125 × 6.5 × 9)	0 40 125 140 160 185 226 260	1.00 3.91 5.30 6.65 8.69 11.62 17.34 22.95	2300
	280	26.32	4.12% (100 × 100 × 6 × 8)	226	24.28	500, 1100, 1700, …, 16500
			5.77% (125 × 125 × 6.5 × 9)		17.34	500, 1100, 1700, …, 16500
			7.66% (150 × 150 × 7 × 10)		13.06	500, 1100, 1700,

https://doi.org/10.52202/069179-0417

Note: The steel ratio was calculated as $A_s/A_{TESC} \times 100\%$; When the value of t/D is less than 125, it represents t, otherwise it represents D.

To evaluate the confinement effect provided by the timber on steel, the maximum load enhancement N_{ens} and the ductility enhancement μ_{ens} of the steel component were defined and calculated as follows.

$$N_{ens} = \frac{N_{IS}}{N_S} \tag{3}$$

$$\mu_{ens} = \frac{\mu_{IS}}{\mu_S} \tag{4}$$

where N_{IS} and μ_{IS} represent the maximum load and ductility of the steel component, respectively. N_S and μ_S denote the maximum load and ductility of the bare steel column under axial loading, respectively. The ductility μ was calculated as follows.

$$\mu = \frac{d_u}{d_y} \tag{5}$$

where d_y and d_u are the displacements corresponding to the yield load and ultimate load, respectively. The ultimate load of the steel was the load when the load dropped to 85% of the maximum load.

4.1 STEEL YIELD STRENGTH

The load-axial displacement curves of TESC columns and their components with different steel yield strengths are shown in Figure 7. It was assumed that the constitutive relationship of the steel was less influenced by the strength grade, so the consistent stress-strain relationship was adopted for the steel. The trends of curves shown in Figure 7(a) indicate that although steel contributed a small percentage of the total sectional area, increasing the steel yield strength could remarkably enhance the maximum load of the composite column. A significant strength enhancement of 73.07% is achieved when the steel yield strength increased from 235 MPa to 960 MPa. Moreover, it could be seen from Figures 7(b) and (c) that the load-carrying capacity of the composite column was mainly provided by the steel component when the steel yield strength was larger than 460 MPa. An interesting finding was observed in Figure 7(c) that increasing the steel yield strength led to a higher maximum load of the timber. It can be explained by the fact that the yield of the TESC column is delayed when the steel yield strength increases, thus can fully utilize the compressive strength of the timber. Nonetheless, the TESC column with a higher steel yield strength exhibited a slightly less ductile response, even though the higher residual load-carrying capacity at the end of the analysis was observed.

The enhancement of maximum load and ductility of the steel component is shown in Figure 7(d). When the steel yield strength increased from 235 MPa to 960 MPa, the value of N_{ens} and μ_{ens} decreased in general, indicating that the confinement effect is insufficient for the higher grade steel. In other words, reducing the strength differences between timber and steel can receive a better confinement effect for the steel. Furthermore, the value of μ_{ens} was much higher than that of N_{ens}, showing that the confinement effect provided by timber influences the ductility of the inner steel more than the strength.

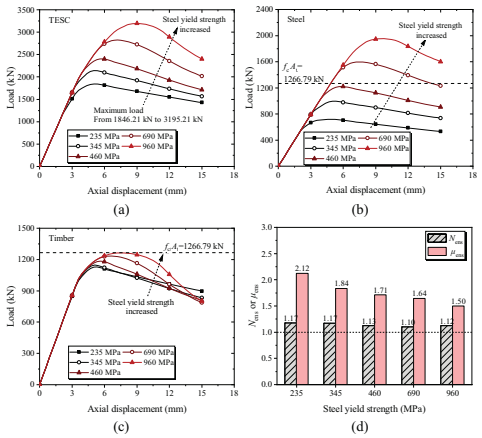

Figure 7: *Comparison of load-axial displacement relationships with different steel yield strengths: (a) TESC column, (b) steel component, (c) timber component and (d) enhancement of maximum load and ductility*

4.2 STEEL AREA

The load-axial displacement curves of TESC columns with different steel ratios are shown in Figure 8. As expected, the larger steel ratio contributed to the higher stiffness and load-carrying capacity of the TESC column, as shown in Figure 8(a). When the steel ratio increased from 4.12% to 12.15%, the initial stiffness and maximum load were enhanced by 72.01% and 56.23%, respectively. It can be seen in Figure 8(b) that such enhancement results from the contribution of the steel component. Meanwhile, Figure 8(c) shows that the stiffness and maximum load of the timber component decreased when the steel ratio increased due to the relative decrease in the timber area.

The comparison of maximum load enhancement and ductility enhancement of the steel component and the individual part is shown in Figure 8(d). With the increase of the steel ratio from 4.12% to 12.15%, the values of N_{ens} and μ_{ens} decreased, indicating that the higher steel ratio leads to the lower confinement effect provided by timber, and the steel ratio should be less than 12.15% in the proposed TESC columns. Furthermore, it can also be seen that the ductility showed higher sensitivity to the steel ratio than the maximum load.

https://doi.org/10.52202/069179-0417

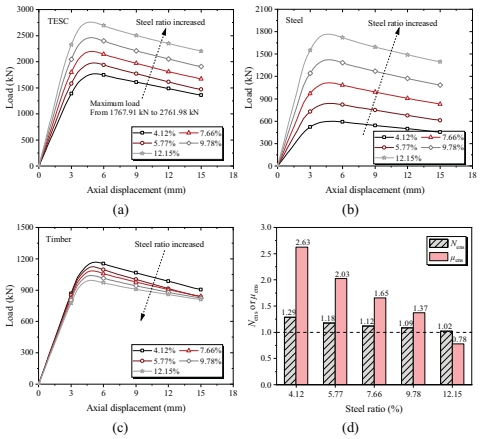

Figure 8: *Comparison of load-axial displacement relationships with different steel ratios: (a) TESC column, (b) steel component, (c) timber component and (d) enhancement of maximum load and ductility of steel*

4.3 TIMBER STRENGTH

The maximum load of TESC columns with different compressive strengths parallel to the grain of timber and steel ratios are compared in Figure 9(a). Similar to the effects of the steel yield strength, the higher value of f_{ct} also led to the higher maximum load of TESC columns. Using a higher grade of timber is an effective method to enhance the capacity of the composite column due to the much larger sectional area proportion of the timber component. For the TESC column with a larger steel ratio, however, a lower enhancement of the load-carrying capacity of the TESC column was observed. It indicates that the TESC column with high timber compressive strength and a large steel ratio may not be economic in terms of load-carrying capacity. It was also found that the effect of increasing timber compressive strength on improving the steel component capacity was not significant. Take specimens with a steel ratio of 5.77 % as an example. The load-axial displacement curves of the steel component are shown in Figure 9(b). Only less than 6% of the enhancement of maximum load was gained. It may result from the steel already reaching its yield strength. In this regard, increasing the compressive strength of timber allows the steel to experience a more pronounced yield plateau accompanied by a larger maximum displacement. In conclusion, it is reasonable to consider that the response of improving timber compressive strength on the steel component is mainly reflected in the hardening effect after the yielding of the steel.

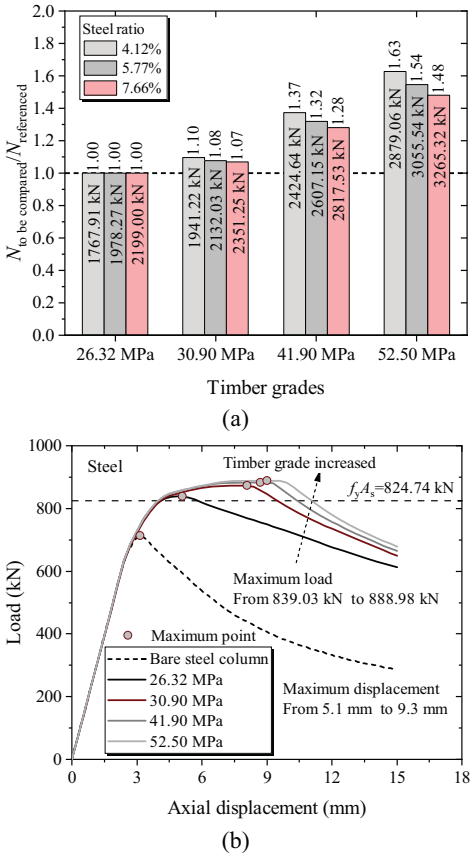

Figure 9: *The influence of timber compressive strength: (a) enhancement of maximum load of TESC columns and (b) load-axial displacement curves of the steel component in TESC columns with the steel ratio of 5.77%*

4.4 AREA RATIOS A_{TESC}/A_S

The effects of timber area on the steel component are discussed and analyzed in this section, as shown in Figure 10. It should be noted that when $A_{TESC}/A_S < 5.30$, the steel component is partially covered by timber, while the steel is fully coated by timber when $A_{TESC}/A_S > 5.30$.

Figure 10(a) shows that the influence of an increasing timber area followed a similar trend to the decrease of the steel ratio, with the enhanced maximum load and the ductile response of the steel. In the case of $A_{TESC}/A_S < 5.30$, increasing timber area slightly improved the load-carrying capacity and ductility of the steel component, as shown in Figure 10(b). It is because the buckling of the steel flanges is not well restrained since the steel is not fully covered. For $A_{TESC}/A_S > 5.30$, the mechanical performance of the steel component, especially ductility, was significantly improved. More than twice times enhancement of ductility was obtained when A_{TESC}/A_S was increased to approximately 23, whereas the value of the strength was only enhanced by approximately 20%. It is noteworthy that the steel could reach the yield strength when the value of A_{TESC}/A_S was 11.62. A slight enhancement of strength was observed when $A_{TESC}/A_S > 11.62$. The results revealed

https://doi.org/10.52202/069179-0417

that before reaching the steel yield strength, increasing the timber area greatly improves both the load-carrying capacity and the ductility of the steel component. After that, the effects of such an increase are mainly reflected in suppressing the post-buckling behavior of the steel component.

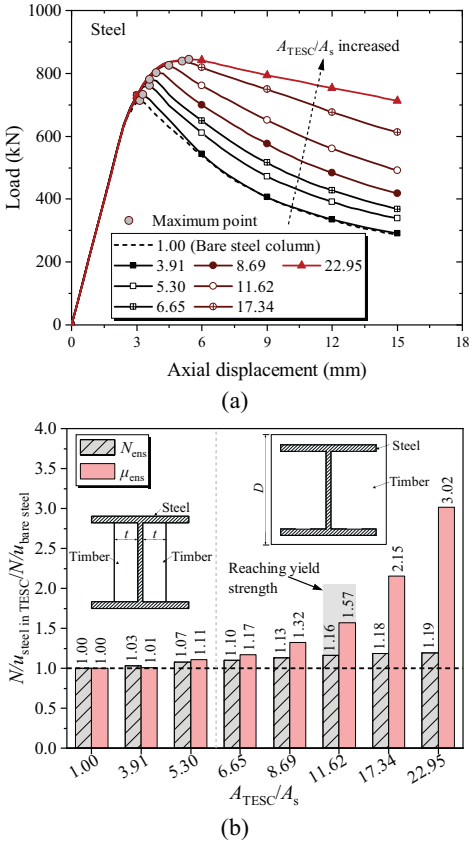

Figure 10: *Comparison of the steel component and the bare steel column: (a) load-axial displacement curves and (b) enhancement of maximum load and ductility*

The results mentioned above imply that the strength of the steel component might not be fully utilized with a relatively thin timber coating. Consequently, there is a minimum ratio of A_{TESC}/A_S (ξ_{min}) to ensure the steel component could reach the strength capacity under axial compression [20]. A parametric study was conducted to identify the value of ξ_{min}. The length-to-width ratio (L/d) of the steel component was defined, where d was the flange width of the H-section steel and was set to 125 mm (sectional dimensions of the steel: 125 × 125 × 6.5 × 9 mm) in this case. The column length L changed from 1000 mm to 3500 mm. Three steel yield strengths, namely 235, 280 and 345 MPa, were adopted. The relationship between ξ_{min} and L/d is shown in Figure 11(a). It was found that as L/d increased, a larger ξ_{min} was needed to provide enough lateral confinement. Subsequently, linear relationships are proposed to calculate the ξ_{min} as follows.

$$\xi_{min} = k\left(L/d - r_0\right) + s_0 \quad (6)$$

where k is the slope of the design curve, r_0 is the smallest L/d to ensure that the bare steel column could reach the yield strength under axial compression, and s_0 is the minimum ξ_{min} related to the sectional area of the steel component, which is taken as 5.30 in this work. The recommended values of parameters in Eq. (6) are shown in Figure 11(b). The ratios of calculation to simulation results were within the range of 0.85 to 1, indicating that the proposed design curves are safe. Meanwhile, it avoids material waste due to overly conservative calculation results.

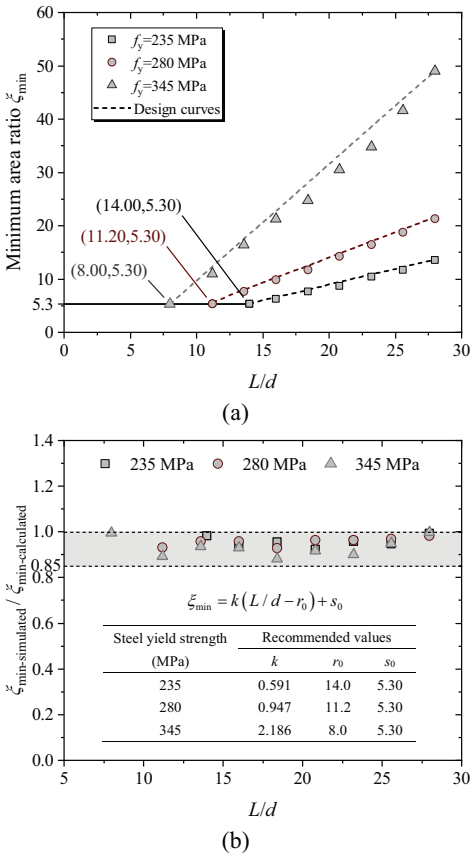

Figure 11: *Calculation results: (a) design curves and (b) comparison between calculation and numerical results*

4.5 SLENDERNESS RATIO

The influences of the slenderness ratio on the load-carrying capacity of the steel component were investigated. The TESC columns with steel ratios of 4.12%, 5.77% and 7.66% were selected in this section. The sectional dimensions of TESC columns were 226 ×

226 mm. The non-dimensional slenderness λ_n was used and calculated as follows.

$$\lambda_n = \sqrt{\frac{N_p}{N_{cr}}} = \frac{KL}{\pi}\sqrt{\frac{f_y A_s + f_{ct} A_t}{E_s I_s + E_t I_t}} = \frac{\lambda}{\pi}\sqrt{\frac{f_{ct}}{E_t}} \quad (7)$$

$$N_p = f_y A_s + f_{ct} A_t \quad (8)$$

$$N_{cr} = \frac{\pi^2 (E_s I_s + E_t I_t)}{(KL)^2} \quad (9)$$

Considering that the steel was converted into timber in Eq. (2), only the parameters of timber (f_{ct}/E_t) were adopted in Eq. (7). Relationships between the enhancement of the maximum load of the steel component and the non-dimensional slenderness are shown in Figure 12(a). The maximum load was nonlinearly enhanced with an increasing slenderness ratio. Three distinctive stages are observed. In stage A ($\lambda_n < \lambda_b$), the TESC column exhibited strength failure and the maximum load increased slowly. In stage B ($\lambda_b < \lambda_n < \lambda_{cr}$), the elasto-plastic instability dominated the failure mode of the composite column. A substantial amount of the load-carrying capacity recovered owing to the lateral restraint of timber, thus remarkably improving the maximum load when the slenderness ratio increased. In stage C ($\lambda_{cr} < \lambda_n$), the increase rate of the maximum load enhancement slowed down and tended to be stable since the elastic instability governed the failure mode. In addition, the smaller steel ratio of the TESC column contributed to the higher load enhancement of the steel component.

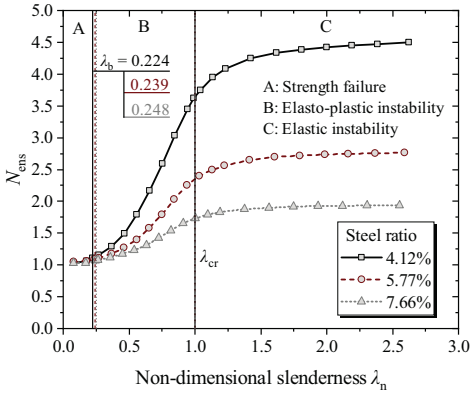

(a)

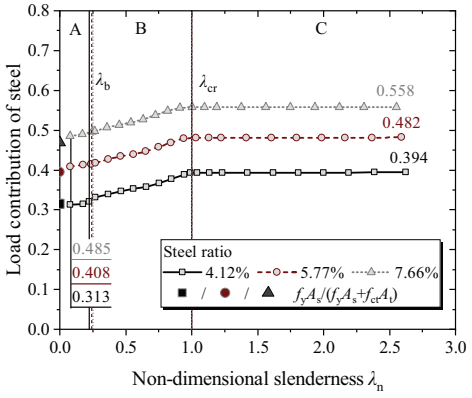

(b)

Figure 12: *Influence of slenderness ratios on the steel component: (a) enhancement of maximum load and (b) load contribution of steel*

The load contribution of the steel component when the TESC column reached the maximum load was compared, as shown in Figure 12(b). It was observed that the larger steel ratio led to the higher load contribution of the steel component. Owing to the confinement effect, the minimum load contribution ratio of the steel in the investigated slenderness ratios is slightly higher than the value of $f_yA_s/(f_yA_s+f_{ct}A_t)$. When it entered stage B, the elasto-plastic instability occurred and the curves almost linearly increased. After that, the load contribution of the steel component kept stable with a negligible improvement. It is due to the occurrence of elastic instability, the much high second-order effect results in the load-carrying capacity of the slender TESC column being independent of the material strength. In conclusion, the steel component carries an increasing percentage of the maximum load of the TESC column when the slenderness ratio increases.

5 CONCLUSIONS

The axial load distribution and buckling behavior of TESC columns with embedded H-section steel were investigated via a thorough numerical investigation in this work. The proposed FE modeling approaches of TESC columns reasonably simulated the experimental responses. The numerical results showed that the steel influenced the yield of the TESC column more than timber under a large slenderness ratio. Additionally, the increase in column length also led to a large load enhancement of the steel component compared with the bare steel column.

Parametric studies revealed that the geometry parameters exhibited more influence than the material strength on the compressive behavior of TESC columns and the encased steel. For a TESC column with a certain slenderness ratio, the maximum load of steel increased significantly with a larger area ratio when the minimum area ratio was not reached. While the ductility of the steel increased remarkably with a larger area ratio when the minimum area ratio was reached. For a TESC column with a certain

https://doi.org/10.52202/069179-0417

area ratio, either reducing the steel yield strength or enhancing the timber compressive strength could benefit the compressive performance of the steel. In addition, increasing the slenderness ratio led to a larger load contribution of the steel when the TESC column reached the maximum load.

The minimum area ratio of the TESC column was determined considering the inner steel could reach the yield strength. A thicker timber coating was required with an increase in either yield strength or length-to-width ratio of the inner steel. The proposed design curves regarding the area ratio and length-to-width ratio of the steel could be used for determining the scale of the TESC column.

ACKNOWLEDGEMENT

The authors gratefully acknowledge the National Natural Science Foundation of China under Grant [number 51908038] and the National Key R&D Program of China under Grant [number 2021YFB2301602] for supporting this research.

REFERENCES

[1] Churkina G, Organschi A, Reyer CPO, Ruff A, Vinke K, Liu Z et al. Buildings as a global carbon sink. *Nature Sustainability*, 3:269-76, 2020.

[2] Hu Q, Gao Y, Meng X, Diao Y. Axial compression of steel–timber composite column consisting of H-shaped steel and glulam. *Engineering Structures*, 216:110561, 2022.

[3] Quintana GP, Carradine DM, Bazaez R. State of the art and practice of seismic-resistant hybrid timber structures. *European Journal of Wood and Wood Products*,79:5-28, 2020.

[4] Mikio K, Hiroshi I, Shuitsu Y. The design and installation of a five-story new timber building in Japan. *Proceedings of the Summaries of Technical Papers of Annual Meeting Japan Society for Finishing Technology*, Tokio, Japan, 2005.

[5] Kia L, Valipour H.R. Composite timber-steel encased columns subjected to concentric loading. *Engineering Structures*, 232:111825, 2021.

[6] Kusumoto S, Shioya S, Kawabe R, Inomoto K. Innovative Hybrid Timber Structure in Japan Beam-To-Beam Moment Resisting Connection. *World Conference on Timber Engineering. Vienna*, Austria, 2016.

[7] Xu F, Xuan S, Li W, Meng X, Gao Y. Compressive performance of steel-timber composite L-shaped columns under concentric loading. *Journal of Building Engineering*, 48:103967, 2022.

[8] Tao Z, Wang Z, Yu Q. Finite element modelling of concrete-filled steel stub columns under axial compression. *Journal of Constructional Steel Research*. 89:121-31, 2013.

[9] GB/T 50329-2012. Standard for test methods of timber structures. Ministry of Housing and Urban-Rural Development of the People's Republic of China, Beijing, China Architecture Publishing Press, 2012.

[10] Li Z, He M, Wang X, Li M. Seismic performance assessment of steel frame infilled with prefabricated wood shear walls. *Journal of Constructional Steel Research*, 140:62-73, 2018.

[11] Hill R. The mathematical theory of plasticity. London: Oxford University Press, 1950.

[12] Navaratnam S, Thamboo J, Poologanathan K, Roy K, Gatheeshgar P. Finite element modelling of timber infilled steel tubular short columns under axial compression. *Structure*, 30:910-24, 2021.

[13] Ross RJ. Wood handbook—Wood as an engineering material. Madison, WI: U.S.: General Technical Report FPL-GTR-190, Department of Agriculture, Forest Products Laboratory; 2010.

[14] Ehrhart T, Steiger R, Palma P, Gehri E, Frangi A. Glulam columns made of European beech timber: compressive strength and stiffness parallel to the grain, buckling resistance and adaptation of the effective-length method according to Eurocode 5. *Materials and Structures*, 53:1-12, 2020.

[15] Liang H, Li W, Huang Y, Lu Y. Axial behavior of CFST stub columns strengthened with steel tube and sandwiched concrete jackets. *Thin-Walled Structures*, 155:106942, 2020.

[16] Aslani F, Uy B, Tao Z, Mashiri F. Behavior and design of composite columns incorporating compact high-strength steel plates. *Journal of Constructional Steel Research*, 107:94-110, 2015.

[17] Feng P, Cheng S, Bai Y, Ye L. Mechanical behavior of concrete-filled square steel tube with FRP-confined concrete core subjected to axial compression. *Composite Structures*, 123:312-24, 2015.

[18] GB/T 11263—2017. Hot rolled H and cut T section steel. Beijing, China Standardization Administration, 2017.

[19] CECS 159:2004 Technical specification for structures with concrete-filled rectangular steel tube members. Beijing, China Association for Engineering Construction Standardization, 2004.

[20] Wang Z, Feng P, Zhao Y, Yu T. FRP-confined concrete core-encased rebar for RC columns: Concept and axial compressive behavior. *Composite Structures*, 222:110915, 2019.

World Conference on Timber Engineering Oslo 2023

EFFECTS OF ELEVATED TEMPERATURE ON BENDING CAPACITY OF STEEL BAR-TIMBER COMPOSITE BEAM

Tsukasa Ueno [1], Nao Matsuoka [2], Shinichi Shioya[3]

ABSTRACT: We have been developing a rigid frame system formed by timber members strengthened by deformed steel bars using epoxy resin adhesive. Buildings may often suffer from elevated temperature in Summer , such as 45.3℃ ever reported in Japan or approximately 65℃ in the attic space. On the other hand, when buildings suffer fire, the composite members also be required to resist against Dead load by using fireproof coating or burning marginal layer (i.e. charring layer). The resisting portion may be mainly lower than 100℃. We planned an experiment to reveal effects of those elevated temperatures on bending capacity of the composite beam. This paper reports the test, its results and discussion.

KEYWORDS: Composite timber, High temperature, Beam, Deformed steel bar, Bending capacity, Fire

1 INTRODUCTION

We have been developing a rigid frame system formed by timber members strengthened by deformed steel bars using epoxy resin adhesive [1]. Buildings may often suffer from elevated temperature in Summer, such as 45.3℃ ever reported in Japan or approximately 65℃ in the attic space. On the other hand, when buildings suffer fire, the composite members also be required to resist against Dead load by using fireproof coating or burning marginal layer (i.e. charring layer). Its portion resisting to dead load will be designed to be mainly lower than 100℃. We planned an experiment to reveal effects of those elevated temperatures on bending capacity of the composite beam. This paper reports the test, its results and discussion.

2 BACKGROUND AND AIM

Little research on heat resistance of timber mixed with different kind of materials, has been reported. Elevated temperatures in building in Japan is such as mentioned above; in an attic space, the maximum temperature may be approximately 75℃. These increase of temperature needs to be considered in design for steel bar(rebar) - timber composite member because of their deference in thermal expansion. We have already revealed creep of the composite beam under elevated temperature of 80-110℃ and reported that the rebar can reduce dramatically the creep of bending deformation of the beam and the proposed method can estimate the creep [2].

However, effects of elevated temperature on bending capacity of the beam were not revealed because of limit of loading apparatus capacity.

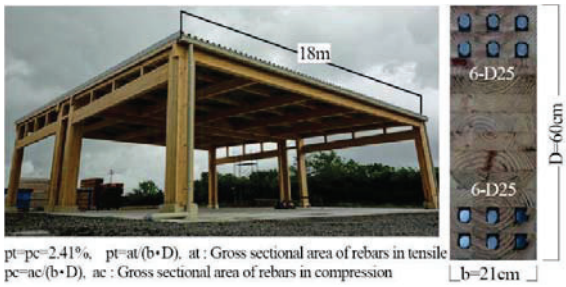

Figure 1: *Prototype building utilizing hybrid beam and column proposed in this study, designed by S. Shioya with approval from authorities and constructed in July 2014*

We planned an experiment of loading the composite beam under the elevated temperatures to reveal the capacity. This paper reports the experimental test and its results.

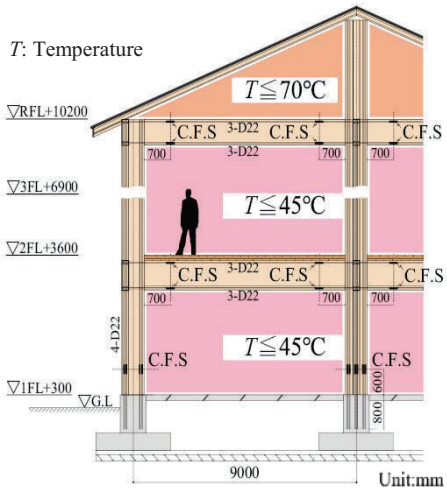

Figure 2: *Elevated temperatures in building assumed in this research*

[1] Tsukasa Ueno, Department of Architecture and Architectural Engineering, Kagoshima University, Japan, k3241487@kadai.jp
[2] Nao Matsuoka, Department of Architecture, Kagoshima University, Japan.
[3] Shinichi Shioya, Department of Architecture, Kagoshima University, Japan, k7347039@kadai.jp

https://doi.org/10.52202/069179-0418

3 EXPERIMENTAL TEST

3.1 SPECIMEN

Figure 3 shows cross-sections of beam specimens which are conventional Glulam timber and the composite timber. Those sizes were adjusted to testing space inside electric heating furnace. Scale ratio of depth of beam was 1/5 and that of width was 1/3 to full-scale beam expected. Area ratios of upper rebar to gross area of beam was 2.54%. The ratio of lower rebar was, also, the same as the upper rebar. Glulam timber employed all low-grade laminas of L50 in Japanese Agriculture Standard to prevent excessive increase in bending capacity because upper limit of the apparatus. The laminas were bonded with resorcinol resin adhesive. Manufacturing process of specimens was the same as that in previous paper [2]. Figure 4 illustrates side views. Furthermore, finger joints were, also, made to be located at its mid-span range in order to prevent excessive increase in load. Properties of rebar, adhesive for rebar, and lamina are listed in Table 1-Table 3.

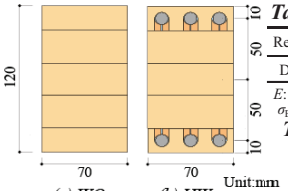

Figure 3: Cross section of beam

Table 1: *Tensile properties of rebar*

Rebar	Grade	E	σ_y	σ_B
D10	SD345	1.96×10^5	403	577

E: Young's modulus, σ_y : Yield strength, σ_B : Breaking strength (Unit: N/mm^2)

Table 2: *Properties of Epoxy adhesive*

E	F_c	F_{cs}
2700	110	60

E: Young's modulus (Unit: N/mm^2)
F_c: Compressive strength
F_{cs}: Shearing strength by compression

Table 3: *Properties of lamina*

Test	Lamina Grade	Lamina Type	The number of testpieces	E in N/mm^2	F_b in N/mm^2
Bending	L50	with joint	5	5501	36.7
		Pure lamina	10	5166	50.3
Tensile		with joint	5	4269	21.9
Compression		Pure lamina	10	4961	32.9

E: Young's modulus, F_c: Bending strength, with joint: testpiec with one finger joint, Pure lamina: testpiec with no finger joint

3.2 SETUP AND LOADING

Figure 4(a) illustrates setup for loading and heating in electric furnace. Photo 1(a) shows loading system against specimen when it is not yet installed within the furnace.; Photo 1(b) shows an outside view of the furnace. The loading was conducted under hanging in mid-air from reaction frame. Specimen was loaded under 4-point bending; upper H-shaped steel beam was subjected to vertical force/F at its mid-span, by oil jack as shown in Figure 4(a) and Photo 1. Shear-span and mid-span lengths were selected so that the specimen will fail in bending.

To prevent the lateral buckling of beam, four steel plates to bind specimen, were connected to the reaction frame, at both supports and near mid span.

Figure 5 shows measuring positions for deformation, strain, and temperature. The deflection at the mid-span was measured with two displacement transducers. The curvature was calculated from foil strain gauges on timber at mid-span and shear strain was done with rosette gauge on both shear spans. Temperatures were measured with thermocouples at three positions: at the top bar, at the bottom bar, and at middle of beam depth.

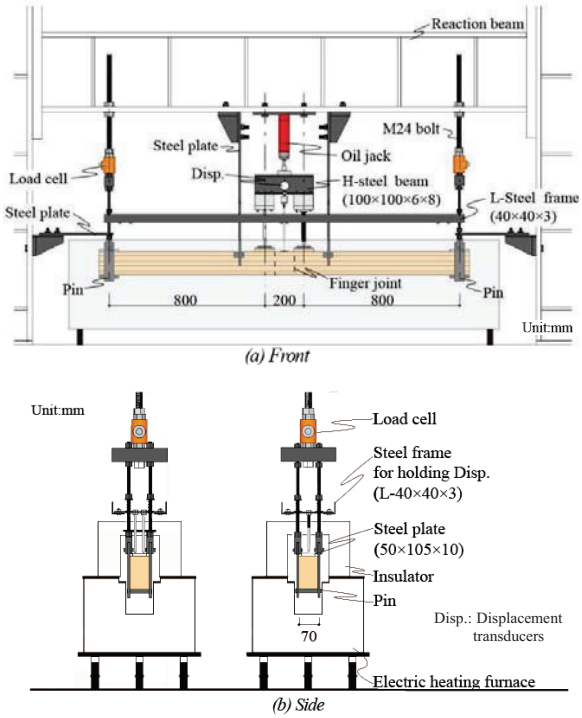

Figure 4: *Setup for loading and heating*

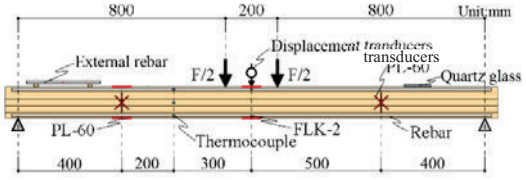

Figure 5: *Arrangement of foil strain gauges and displacement transducers*

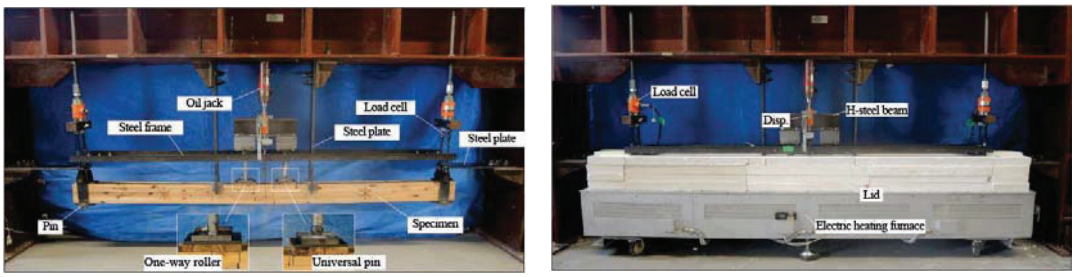

(a)Loading and measuring system after furnace was removed *(b)Heating and loading in electric furnace*

Photo 1: *View of a specimen hanged with bolts connected by loadcell from reaction beam and setup it in furnace*

https://doi.org/10.52202/069179-0418

Table 4: *The number of beam specimen*

Member	Name	Temperature				Total
		RT	45℃	70℃	90℃	
Timber	WO	3	2	2	2	9
Hybrid timber	HW	3	2	3	1	9

RT: Room temperature

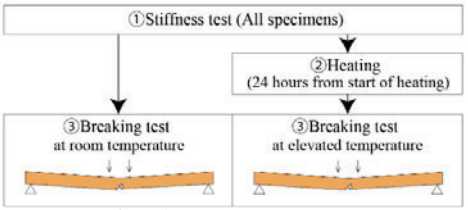

Figure 6: *Procedures for testing*

3.3 HEATING PROGRAM AND TEST PROCEDURE

Table able 4 shows the number of specimens for each target temperature. The temperature levels were assumed as following: room temperature/29.3℃-31.2℃, maximum temperature of the general floor of building/45℃, maximum temperature of the attic of building/70℃, and maximum temperature of steel bar-timber composite beam with fireproof cladding for 2-hour fire resistance/90℃. Figure 6 illustrates procedure for test. First, loading to measure stiffness of each specimen for deflection was conducted at room temperature, and then the specimens were heated up to the target temperature and then was maintained at the temperature for about 24 hours from the start of the heating, and finally, loading was conducted up to fracture under the temperature. On the other hand, unheated specimens were also prepared for loading up to fracture at room temperature. Symbols in the specimen name represents cross section, target temperature, and the order tested within specimens at each target temperature.

3.4 CALIBRATION OF VALUE OF FOIL STRAIN GAUGE

Table 5 lists types of foil strain gauges used for each material. Figure 7 shows condition of gauge attached on test piece of rebar, and Figure 8 shows conditions of foil strain gauge attached on quartz glass with thickness of 10 *mm*. In order to capture behavior of strain gauges due to elevated temperature, strain gauges were attached to quartz glass which is hardly affected by temperature change. In addition, strain change of one external rebar in Figure 7, which was not externally restrained, was prepared for comparison with that of internal rebars within specimen. Quartz glass and external rebar were placed on top of the specimen within the furnace. Only four specimens: HW45-1, HW45-2, HW70-1, and HW70-2 were measured axial strain of the internal rebar. Figure 9 shows behavior of strain gauges attached to the quartz glass as temperature change from the start of heating. The horizontal axis is amount of temperature increase at top of specimen in the furane. As the temperature elevates, the strain of the gauge progresses toward the compression side. This is a characteristic of the strain gauge's self-temperature compensation. The straight line for the data is shown by a pink one dot chain line. The strain value based on the approximate straight line was, in this paper,

Table 5: *Type and measuring length of foil starin gauge*

Material	Type	Length
Rebar	FLK-2	2 *mm*
Timber	PL-60	60 *mm*

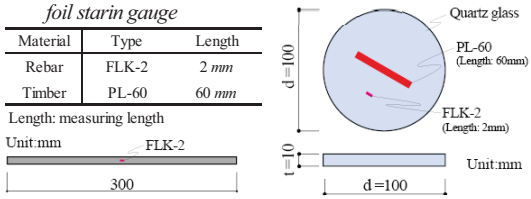

Figure 7: *Location of foil strain gauges on external rebar(D10)*

Figure 8: *Foil strain gauges bonded to quartz glass*

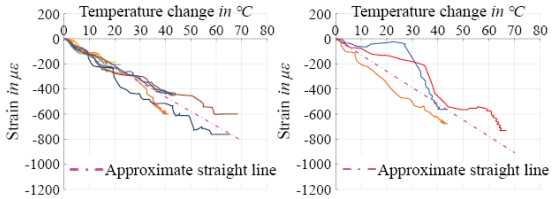

Figure 9: *Foil strain gauge behavior due to elevated temperature*

assumed to be subtracted from value direct-measured on specimen to cancel effect of the self-temperature compensation.

3.5 DIFINITION OF REDUCTION OF MECHANICAL PROPETIES AND ITS EXPRESSION

Effects of moisture content on mechanical properties of wood at elevated temperature was investigated by Kaku and Hasemi et al. by means of bending tests on small specimens of Japanese cedar and zelkova wood [3].

As well as the paper, to investigate effects of temperature rise on mechanical properties of the composite beam, Young's modulus in bending, shear modulus, and bending strength of Glulam timber beam are first expressed as E_{wt}, G_{wt}, and F_{wt}, respectively, with elevated temperature/t. When assuming t=R at room temperature, Young's modulus in bending for Glulam timber beam can be expressed as E_{wR}, E_{w45}, E_{w70}, and E_{w90} at each temperature. Furthermore, residual modulus ration is defined as an index of change in mechanical property with elevated temperature. The residual modulus ratio of Young's modulus/E_{wt} in bending of a Glulam timber beam is expressed as E_{wt}/E_{wR}. Residual modulus ratio of other properties is expressed in the same way.

As Young's modulus in bending and shear modulus can be measured by non-destructive test, E_{wt} and E_{wR}, G_{wt} and G_{wR} can be determined for one same specimen, and the residual modulus ratio can be measured for each specimen. On the other hand, for one same specimen, it is impossible to compare values of bending strength, proportional limit moment, yield moment, and bending strength at different temperatures, for example, 45℃ against room temperature at the same specimen, because the specimen will be subjected up to failure at room temperature.

Therefore, their residual ratios were calculated by dividing experimental value at each target temperature/t by average of an experimental value for specimens that were tested up to failure at room temperature.

https://doi.org/10.52202/069179-0418

Table 6: *Room temperature at starting of heating test* *in ℃*

Specimen	RT			45℃		70℃			90℃	
No.	1	2	3	1	2	1	2	3	1	2
WO	30.8	30.8	29.3	27.7	27.0	30.2	29.6	-	28.2	23.9
HW	31.2	31.0	30.1	26.4	28.8	29.4	29.7	27.3	27.1	-

3.6 HISTROY OF HEATING

Table 6 lists room temperature at the time of the non-destructive stiffness test for each specimen. Figure 10 shows history of heating temperature of specimens. Figure 10(a) and Figure 10(b) are those by thermocouple at upper and lower rebar positions in specimens except HW70-1 and WO70-1; Figure 10(c) is by those of HW70-1 and WO70-1.

For the two specimens shown in Figure 10(c), fluctuating heating was used in order to investigate stress variation in wood and rebar by temperature changing. Heating system of electric furnace caused difference in temperature at upper and lower positions of beam. The temperature in test was controlled by that of thermocouple at upper rebar within specimen.

3.7 EXPERIMENTAL RESULTS

3.7.1 Mechanical properties at room temperature

Table 7 lists experimental results of each specimen by destructive test at room temperature. Figure 11(a) shows moment/M – curvature/ ϕ relationship/M- ϕ for Glulam timber specimen/WORT, Figure 11(b) shows force/F – deflection/δ relationship/F-δ, and Figure 11 (c) shows maximum shear stress/τ_{max} – shear strain/γ relationship /τ_{max} – γ. In Figure 11(a) and (c), average value of three slopes of elastic stiffness is shown by a pink dashed line. Figure 12 shows results for the composite speceimens/HWRT. Averages of experimental bending

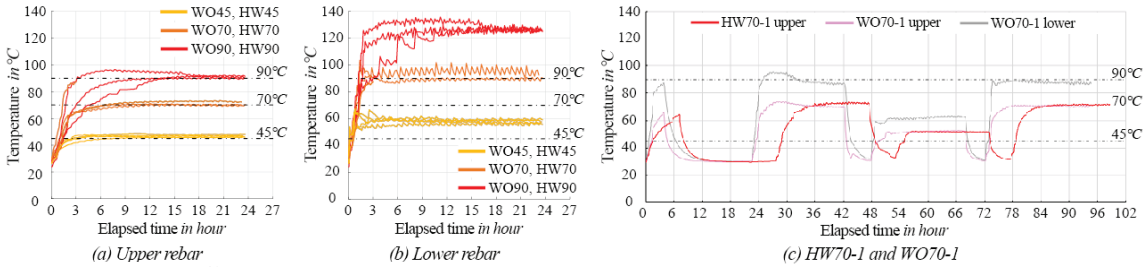

(a) Upper rebar *(b) Lower rebar* *(c) HW70-1 and WO70-1*

Figure 10: *Histories of heating temperature*

Table 7: *Experimental results of specimen at room temperature*

(a) Timber beam

Specimen	E_{wR}	G_{wR}	$E_{wR}\cdot I_{wR}$	$M_{m,wR}$	$F_{b,wR}$
	in N/mm^2		in $N\cdot mm^2$	in $kN\cdot m$	in N/mm^2
WORT-1	4266	712	4.30×10^6	4.19	24.97
WORT-2	4993	742	5.03×10^6	4.00	23.80
WORT-3	5357	734	5.40×10^6	3.81	22.69
Average	4872	729	4.91×10^6	4.00	23.82

(b) Steel bar-timber composite beam

Specimen	E_{hR}	G_{hR}	$E_{hR}\cdot I_{hR}$	$M_{p,hR}$	$M_{y,hR}$	$M_{m,hR}$	$F_{b,hR}$
	in N/mm^2		in $N\cdot mm^2$	in $kN\cdot m$			in N/mm^2
HWRT-1	4748	806	25.80×10^6	9.23	10.40	13.79	82.07
HWRT-2	4830	876	26.25×10^6	8.65	10.40	13.94	82.95
HWRT-3	4723	923	25.67×10^6	9.10	10.75	13.13	78.17
Average	4767	868	25.91×10^6	8.99	10.52	13.62	81.07

E: Young's modulus, G: Shearing elastic modulus, $E\cdot I$: Bending stiffness, M_p: Bending moment at proportional limit M_y: Yield moment, M_m: Bending moment, F_b: Bending strength

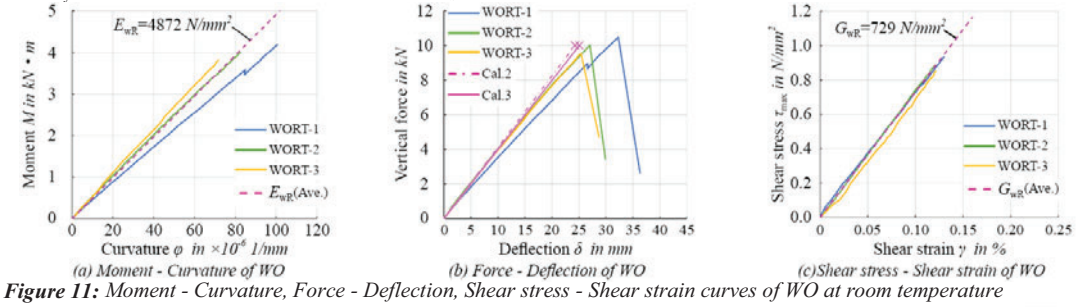

(a) Moment - Curvature of WO *(b) Force - Deflection of WO* *(c)Shear stress - Shear strain of WO*

Figure 11: *Moment - Curvature, Force - Deflection, Shear stress - Shear strain curves of WO at room temperature*

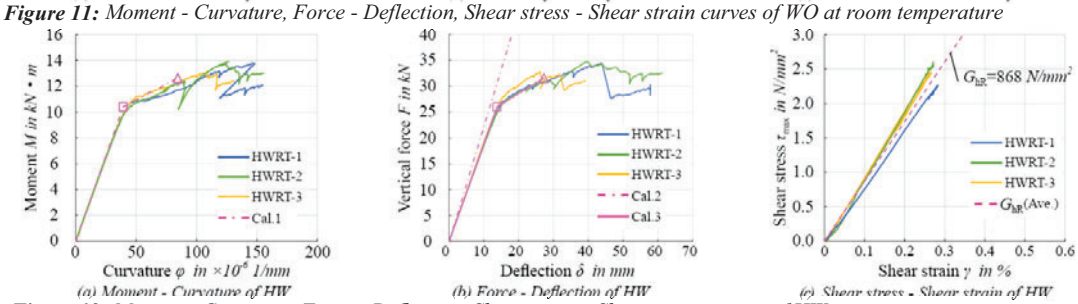

(a) Moment - Curvature of HW *(b) Force - Deflection of HW* *(c) Shear stress - Shear strain of HW*

Figure 12: *Moment - Curvature, Force - Deflection, Shear stress - Shear strain curves of HW at room temperature*

https://doi.org/10.52202/069179-0418

stiffness and bending capacity of the composite specimens/HWRT were 5.28 and 3.40 times higher than those of Glulam timber specimens/WORT, —using Young's modulus of wood in bending of Glulam timber specimen and Young's modulus and yield strength of rebar are shown by a pink one dot chain line by Cal.1 and Cal.2. Calculation process was refered to previus papers[4,5]. Equation for estimation of bending capacity of the composite beam is discribed as following.

$$M_u = {}_wM_u + {}_sM_y \quad (1)$$

where ${}_wM_u$: ultimate moment capcity of timber except the rebars, *i.e.* product of the section modulus and bending strength of timber, ${}_sM_y$: yield moment capacity by only rebar within beam section.

$${}_sM_y = a_t \cdot f_y \cdot j \quad (2)$$

where a_t: gross cross-area of upper or lower rebar
f_y: yield strength of rebar, j: distance from lower the rebar to the upper rebar.

In the composite beam, it can be thought that as yielding and plastic flow occures in rebar befor the beam reaches bending capacity, internal stress due to elevated temperature will decay after its yielding. Therefore Equation (1) can estimate bending capaity of the composite beam by ignoring the internal stress and by considering only decrease of Young's modulus and bending strength of timber owing to elevated temperature. In Figure 11(b) and Figure 12(b), elastic stiffness relationship based on the beam theory (Cal. 2), which considers only flexural deformation is shown by a pink one dot chain line. The relationship (Cal. 3) calculated up to bending fracture by addition of shear deformation is shown by a pink solid line. Point at yield moment is indicated by '□' and point at bending capacity is done by '△'. For shear deformation, a shear modulus of elasticity of 729 *N/mm*^{2} was assumed to be the average of experimental values for Glulam timber specimens /WORT, and the shape factor was assumed to be 1.2 from the energy method for calculating the shear deformation. In the calculated values for the composite specimen, the stiffness of only timber within the composite specimen was assumed to be exhibited, after yielding of rebar. As seen in Figure 12(b), Cal. 3 which considers shear deformation, roughly estimates elastic stiffness, yield moment, secondary stiffness and bending capacity of the composite specimens.

3.7.2 Correction of strain by foil strain gauge

As described in Section 3.4, it is necessary to correct foil strain gauge reading. Figure 13 shows relationship between change in strain of wood and quartz of WO45-1 from heating start and heating elapsed time; Figure 13(a) shows change in measured value, and Figure 13(b) shows change in the corrected value. The time at which target temperature was reached is indicated by black vertical one dot chain line; Figure 14 shows change in strain in wood of HW70-2, and Figure 15 shows change in strain in rebar of the same specimen. Positions and number of the gauge are shown in Figure 16. The strains of wood and rebar need to be corrected on the basis of the approximate straight line shown in Section 3.4 by a pink one dot chain line.

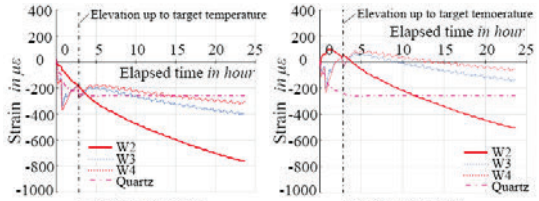

Figure 13: *Strains of wood before and after correction for WO45-1*

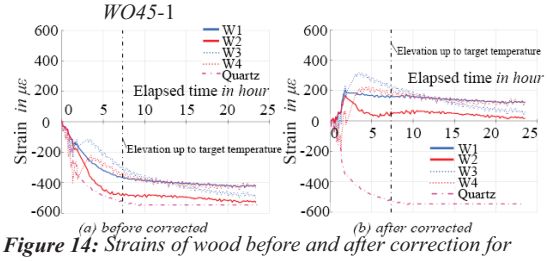

Figure 14: *Strains of wood before and after correction for HW70-2*

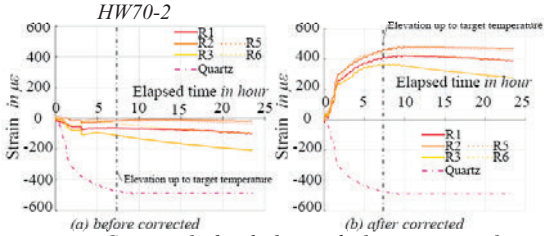

Figure 15: *Strains of rebar before and after correction for HW70-2*

Table 8: *Experimental results of specimen at elevated temperatures represented as average value of each type of specimens*

(a) Timber beam

Specimen	E_{wR}	E_{wt}	$\gamma_{Ew(t)}$	G_{wR}	G_{wt}	$\gamma_{Gw(t)}$	F_{bwt}	$\gamma_{Fbw(t)}$
	in N/mm^2		$=E_{wt}/E_{wR}$	*in N/mm*^{2}		$=G_{wt}/G_{wR}$	*in N/mm*^{2}	$=F_{bwt}/F_{bwR}$*
WORT	4872	-	-	729	-	-	23.82*	1.00
WO45	4229	3890	0.92	758	726	0.96	18.80	0.79
WO70	4464	4146	0.93	845	811	0.96	16.80	0.70
WO90	5053	4774	0.95	784	-	-	15.50	0.65

(b) Steel bar-timber composite beam

Specimen	E_{hR}	E_{ht}	$\gamma_{Eh(t)}$	G_{hR}	G_{ht}	$\gamma_{Gh(t)}$	M_{ph}	$\gamma_{ph(t)}$	M_{yh}	$\gamma_{yh(t)}$	M_{mht}	$\gamma_{mh(t)}$	F_{bht}
	in N/mm^2		$=E_{ht}/E_{hR}$	*in N/mm*^{2}		$=G_{ht}/G_{hR}$	*in kN·m*	$=M_{pht}/M_{phR}$*	*in kN·m*	$=M_{yht}/M_{yhR}$*	*in kN·m*	$=M_{hmt}/M_{hmR}$*	*in N/mm*^{2}
HWRT	4767	-	-	868	-	-	8.99*	1.00	10.8*	1.00	13.64*	1.00	82.07
HW45	4748	4325	0.91	812	718	0.89	8.20	0.91	9.75	0.90	12.16	0.89	72.38
HW70	4714	4176	0.89	841	775	0.92	8.91	0.99	10.3	0.95	11.48	0.84	68.33
HW90	4808	3815	0.79	886	-	-	6.16	0.69	8.76	0.81	10.28	0.75	61.19

E: Young's modulus
G: Shearing elastic modulus
M_p: Bending moment at proportional limit
M_y: Yield moment, M_m: Bending moment
F_b: Bending strength
γ: Ratios at elevated temperatures

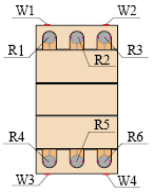

Figure 16: *Gauge's number*

https://doi.org/10.52202/069179-0418

The quartz strain is negative and shrinking over the entire range. This means effect of the self-temperature compensation of foil strain gauge. Measured strains of wood and rebar are negative as the temperature rises, but the corrected strains of wood and rebar are positive until the target temperature was reached, which can be explained by phenomenon of thermal expansion of material. By using the corrected values of strain, discussion hereafter is done.

3.7.3 Degrade in mechanical properties with elevated temperature

Table 8 in the previous page lists mechanical properties and the residual modulus ratios from the loading tests. Figure 17 shows comparison of moment-curvature and force-deflection relationships for Glulam timber specimen and composite specimen. Numbers in the figures indicate the number of specimen name. Compared to Glulam timber specimen, the composite specimen maintained extremely high stiffness and bearing capacity even at high temperatures. Stiffness and bending capacity of both the Glulam timber specimen and the composite specimen decreased with elevated temperature, against those at room temperature.

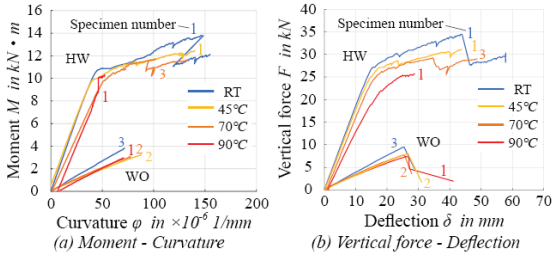

(a) Moment - Curvature (b) Vertical force - Deflection

Figure 17: *Comparison of experimental property at each temperature*

Figure 18 shows variation of residual modulus ratio of the initial bending stiffness. Coloured symbols indicate experimental values for the composite specimen; uncoloured symbols indicate those for the Glulam timber specimen. Red solid line and blue solid line indicate average of those experimental values for each type, respectively.

The residual modulus ratio of initial stiffness in bending of Glulam timber shown in Figure 18 hardly decrease above 45°*C* and increases at 90°*C*. This tendency is also observed in the residual modulus/$\gamma_{wG(t)}$ and $\gamma_{hG(t)}$ of elasticity in shear, as seen in Table 8 (a) and (b).

It is considered that moisture in wood might have been removed as temperature rising and this phenomenon would mitigate the decrease in stiffness.

On the other hand, it should be noted that the residual modulus ratio of bending stiffness of the composite beam

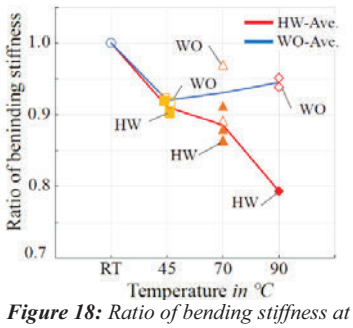

Figure 18: *Ratio of bending stiffness at elevated temperature to stiffness at room temperature*

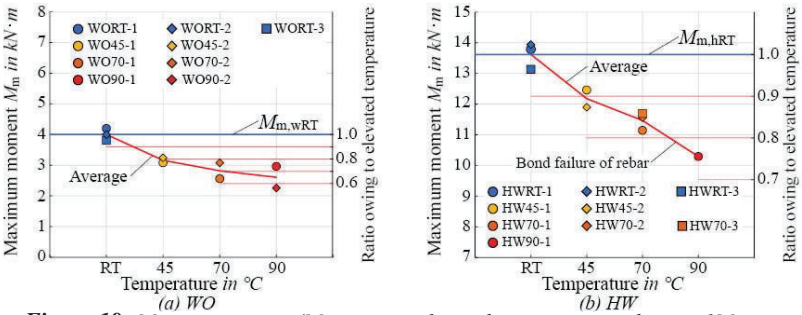

(a) WO (b) HW

Figure 19: *Maximum moment/M_m owing to elevated temperature and ratio of M_m at elevated temperature to $M_{m,RT}$ at room temperature*

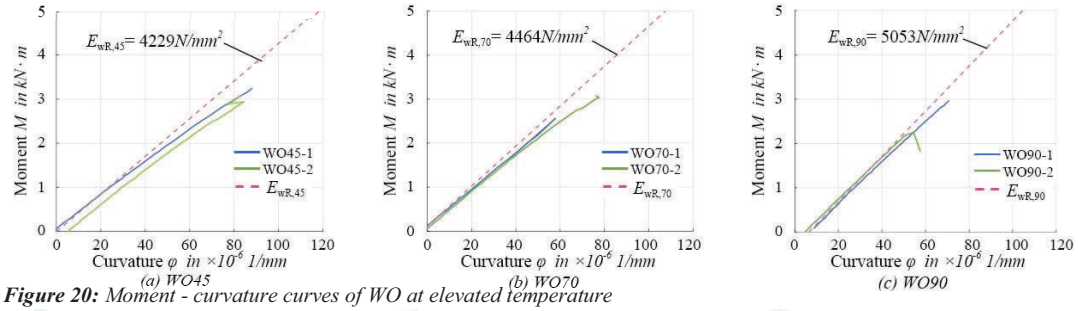

(a) WO45 (b) WO70 (c) WO90

Figure 20: *Moment - curvature curves of WO at elevated temperature*

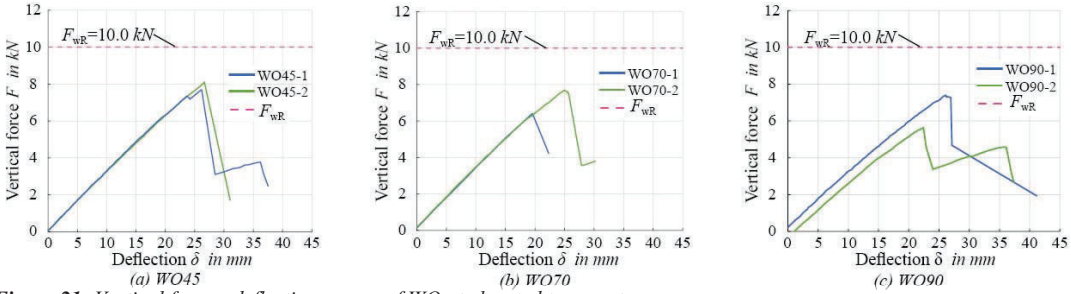

(a) WO45 (b) WO70 (c) WO90

Figure 21: *Vertical force - deflection curves of WO at elevated temperature*

https://doi.org/10.52202/069179-0418

decreased as temperature rising as seen in Figure 18. In addition, the performance of rebar bonded in timber under high temperature might have decayed due to softening of the adhesive of rebar at elevated temperature.

Figure 19 shows variation of the residual ratio of bending capacity. Compared to Glulam timber specimen, the composite specimen performed a smaller percentage loss of performance. The decrease was more pronounced as temperature rising in both specimen types. It can be confirmed that the decrease in bending capacity of the composite specimens is limited to be 20% or less at temperatures below 70°C. Figure 20 shows moment-curvature relationship for Glulam timber specimen at elevated temperatures. Pink dashed line is average of bending stiffness at room temperature. Figure 21 shows force-deflection relationship of Glulam timber specimen at different temperatures. Horizontal pink dashed line is average of maximum force of the Glulam timber specimen/WORT at room temperature. Stiffness and maximum capacity of the Glulam timber specimen is seen to decrease at elevated temperatures compared to room temperature.

3.7.4 Failures after loading test

Figure 22 shows failures of specimens after destructive loading test. All specimens showed tensile fracture at lower portion of wood near mid-span. Those cracks progressed from finger joints. For the Glulam timber specimens, there was no significant difference in failure between at room temperature and at 90°C. On the other hand, for the composite specimens, bond failure around lower rebar was observed in addition to the finger joint fracture in HW90-1. The fracture is shown in Figure 22(d), (e), and Photo 2. Its Cracks were observed along the lower rebar in the axial direction of it. This failure was not observed in the other composite specimens. The upper temperature limit of the epoxy adhesive for bonding rebar is 110°C based on the results of a push-through test under elevated temperature [5]. As shown in Figure 10(a) and (b), owing to heating system of electric furnace, temperature at

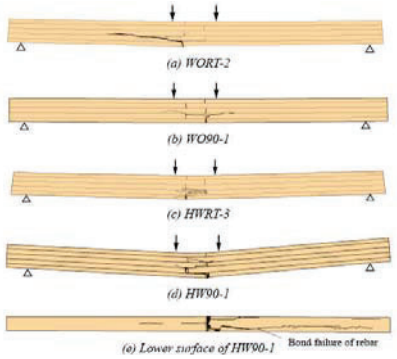

Figure 22: *Failures of specimens after loading test*

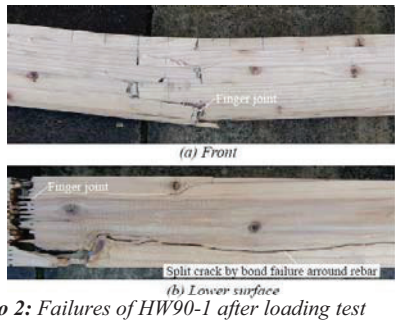

Photo 2: *Failures of HW90-1 after loading test*

position of the lower rebar exceeds 120°C when heated to 90°C at the upper rebar. The excessive temperature rising might have resulted in a decrease in rigidity of Epoxy adhesive around the lower rebar.

3.7.5 Estimation of mechanical properties of composite beam

Figure 23 and Figure 24 show moment-curvature and force-deflection relationships of the composite specimens at different temperatures, respectively.

As curvature, deflection, and strain were generated during heating, there was a residual component due to its heating at the start of loading immediately after heating program was completed.

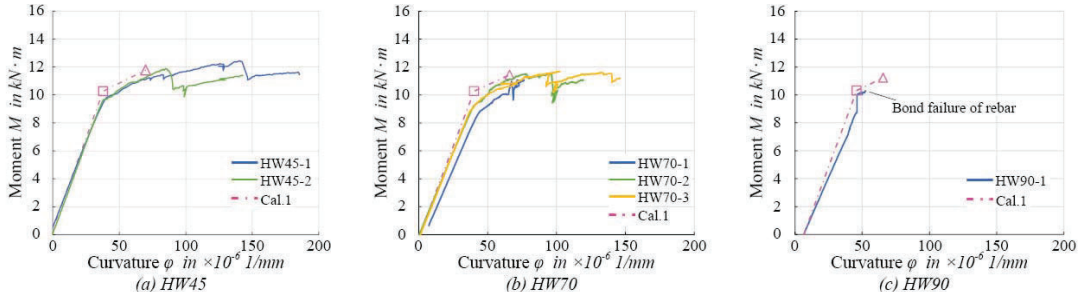

Figure 23: *Moment - curvature curves of HW at elevated temperature*

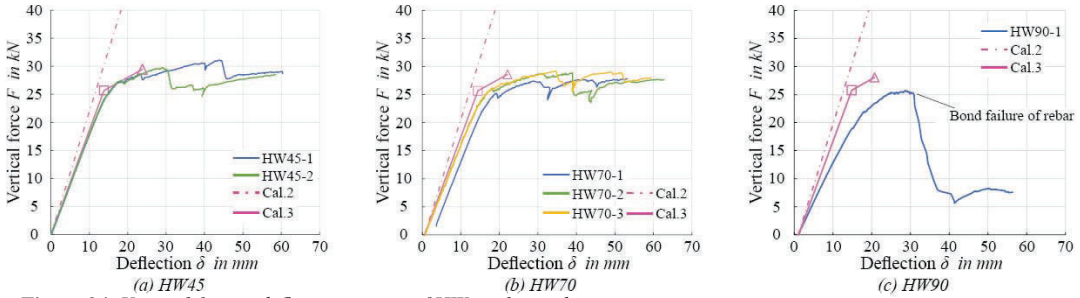

Figure 24: *Vertical force - deflection curves of HW at elevated temperature*

https://doi.org/10.52202/069179-0418

Cal.1, Cal.2 and Cal.3 in the same figure are the same as those in Section 3.7.1, but as modulus of elasticity and bending strength of timber decrease with elevated temperature, the decrease ratios were considered in the calculation. In Figure 24, except for the bending strength at 90°*C*, the bending stiffness and bending capacity are generally estimated by the calculated values.

On the other hand, the variation of temperature and moisture content might have caused internal stress and decreased the yield moment. The fact that none of the calculated values considers the amount of variation in the stress may have resulted in overestimation of yield moment. In Figure 23(c) and Figure 24(c), those of the specimen at 90°*C* have overestimated bending capacity. As mentioned above, bond stiffness around rebar is considered to have decreased with the elevated temperature. The decrease in bond stiffness is considered to have led to a decrease in bending capacity because contribution of the rebar is reduced.

Figures 25(a) and (b) show moment-strain relationships for wood and rebar of the composite specimens during stiffness tests at 45°*C*. Figures 25(c) and 25(d) and 25(e) and 25(f) show moment-strain relationships at 45°*C* and 70°*C*, respectively, during destructive loading. Solid yellow and red lines represent strain of upper and lower surface of timber and strain of rebar, respectively, calculated based on the assumption of plane of cross-section. To the increased strain by loading, the residual strain after the heating was added. In calculated values, degradation of wood's performance due to elevated temperature was considered. In the figure, '□' is experimental strain of wood and ○ is experimental strain of rebar. For 70°*C*, experimental value of wood strains on the bending-tension side were larger than the calculated values. Temperature at lower rebar position reached 90°*C* or higher when heated at 70°*C* as reason of electric furnace mentioned above. This is considered to cause a decrease in wood performance or adhesion stiffness. The horizontal pink dashed line in the figure represents calculated yield moment. This calculated value is the same as '□' symbols shown in Figures 23 and 24, which only consider the reduction in wood performance. As mentioned above, it can be seen here that the calculated values provided an overestimation of yield moment.

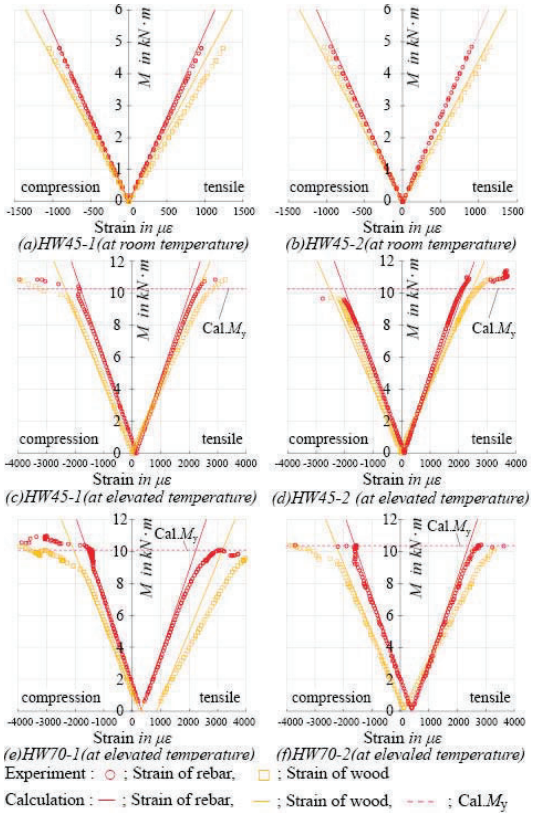

Figure 25: *Comparison of calculation to experiment of bending moment-strain curves on rebar and timber surface*

3.7.6 Strain of rebar outside and wood within specimen

Figure 26 and Figure 27 show variations of strains of external rebar and surface of timber with heating time passing. Timing at which is reached the target temperature is represented by a vertical one dot chain line. In WO45-1, the gauge at point W1 on the upper surface of beam was defective. Strain on the external rebar was almost constant after it reaching target temperature. Assuming that coefficient of thermal expansion of rebar is 10 μ/°*C*, i.e., a common value, amount of the coefficient multiplied by the amount of temperature increased from initial temperature of heating is shown by thin blue line/Cal.R.

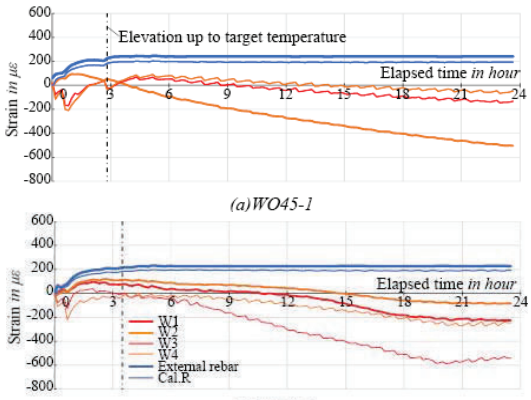

Figure 26: *Variation of axial strains of wood and external rebar in WO45-series specimen heated up to 45 °C*

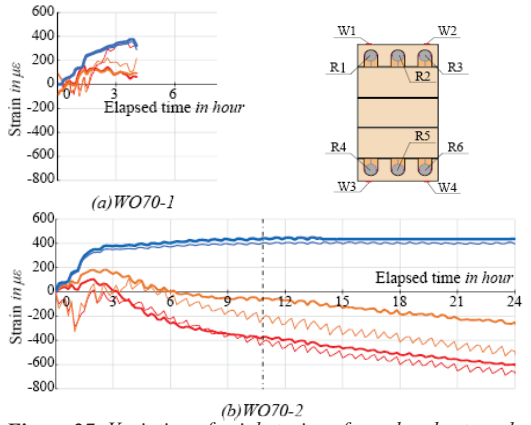

Figure 27: *Variation of axial strains of wood and external rebar in WO70-series specimen heated up to 70 °C*

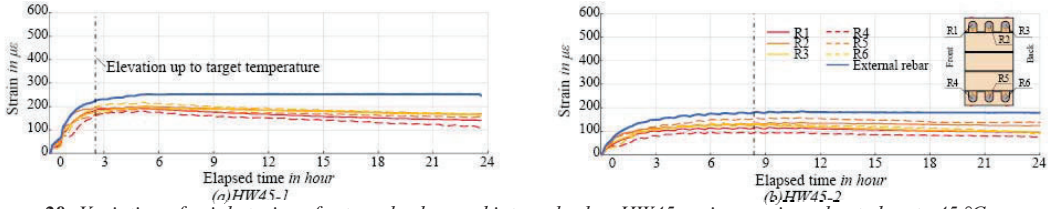

Figure 28: *Variation of axial strains of external rebar and internal rebar HW45-series specimen heated up to 45 ℃*

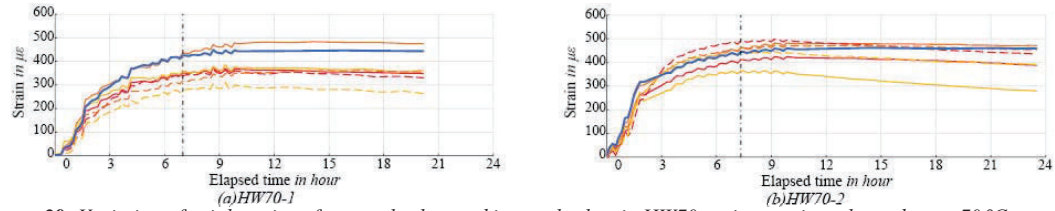

Figure 29: *Variation of axial strains of external rebar and internal rebar in HW70-series specimen heated up to 70 ℃*

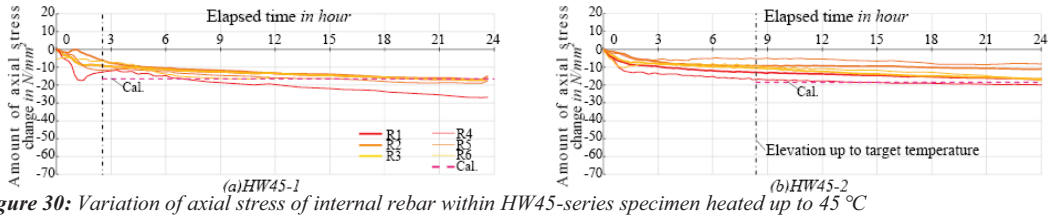

Figure 30: *Variation of axial stress of internal rebar within HW45-series specimen heated up to 45 ℃*

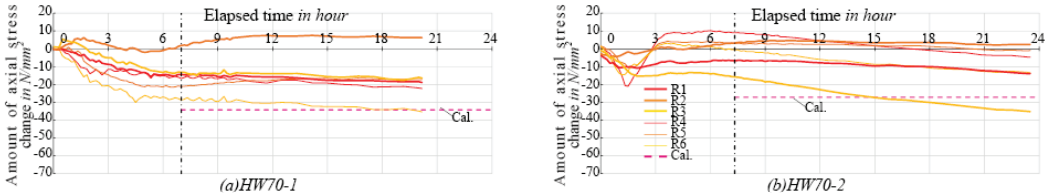

Figure 31: *Variation of axial stress of internal rebar within HW70-series specimen heated up to 70 ℃*

As the external rebar was located on the upper surface of specimen, temperature at the upper rebar was assumed to be temperature of the external rebar. For heating temperatures of 45°*C* and 70°*C*, amounts of elongation strain (thick blue line) of the external rebar generally agreed with the calculated values (thin blue line) of the elongation strain of the external rebar.

On the other hand, strain of wood in Glulam timber specimens increased positive at the beginning of heating, but began to decrease before the target temperature was reached, and then became negative and shrank after the target temperature was reached. This phenomenon is considered to be caused by dehumidification of wood during heating and shrinkage in grain direction of wood because humidity was not controlled in the electric furnace. This is more pronounced at the higher heating temperature of 70°*C*. It can be confirmed that shrinkage due to decrease in moisture content is larger than thermal expansion of wood due to elevated temperature. This suggests that internal stresses in attic of actual buildings need to be estimated taking into account both the shrinkage of wood due to decrease in moisture content and elongation of rebar due to increase in temperature, because of repeative high temperature environment in the attic.

3.7.7 Strain of rebar within specimen

Figure 28 and Figure 29 show variations of strains of the external rebar and the internal rebar. The point at which it reached the target temperature as well, is indicates by a vertical one dot chain line. For the specimens at 45°*C*, strain of the internal rebar was smaller than that of the external rebar, and strains of upper and lower bars were similar. In HW70-1 at 70°*C*, strain of internal rebar was also smaller than that of the external rebar, but in HW70-2, strains of the external and internal rebars were close. As strain of the external rebar was stable at the same level in the two specimens, it is considered that variation of wood may have some influence, but the increase in strain of internal rebar in HW70-2 cannot be explained. The reason for the smaller strain in the internal rebar relative to the external rebar is that the internal rebar is restricted by wood around itself. All strains of the internal rebar decreased as heating time passing. No such decrease occurs in the external rebar. Therefore, the decrease in strain of the internal rebar can be attributed to the shrinkage of timber due to the dehumidification of wood.

3.7.8 Stress of internal rebar based on strains of external rebar and timber

Figure 30 and Figure 31 show variation of amount of axial stress of rebars in the composite specimens during heating. The amount of stress variation is the amount of variation of the difference in strain between the external and the internal rebar in Figure 28 and Figure 29 multiplied by Young's modulus of rebar (experimental value). Equation (3) shows an equation for estimation of yield moment.

https://doi.org/10.52202/069179-0418

$$M_y = \sigma_y / n(I_e / y_s) \quad (3)$$

where y_s: distance from the neutral axis to rebar, σ_y: yield strength of rebar, n: ratio of Young's modulus of rebar to bending Young's modulus of timber, I_e: sectional secondary moment considering rebar

Equation (3), which estimates yield moment when the rebar yields, is affected by ratio/n of Young's modulus in bending between rebar and timber. As shown in Table 1, Young's modulus of timber in bending with increasing temperature was captured by force tests on Glulam timber specimens. Using Young's modulus from non-destructive test before heating and Young's modulus from loading after heating test, yield moments in each case are calculated using Equation (3), and difference between the former and latter calculated values may be regarded to be component of yield moment due to only the reduction in Young's modulus of timber.

Figure 32 shows variation of calculated yield moment with increasing temperature as indicated by pink dashed line/Cal.M_y, where Cal.M_y can be seen to estimate experimental value of HWRT at room temperature.

Average of the experimental values at room temperature is shown by a blue horizontal line/$M_{y,hRT}$.

Difference of Cal.M_y with respect to $M_{y,hRT}$ means amount due to the reduction of Young's modulus in bending of timber. Magnitude of those difference ranges only 4-8% of calculated yield moment at room temperature. The difference between Cal.M_y and experimental value indicated by red solid line means amount due to the difference in expansion and contraction between rebar and timber.

The reduction/ΔM in moment can be evaluated by replacing yield stress/σ_y in Equation (3) with amount /$\Delta\sigma_T$ of increase or decrease in axial stress of rebar, and the equation can be given as Equation (4).

$$\Delta M = \Delta\sigma_T / n(I_{eT} / y_s) \quad (4)$$

$\Delta\sigma_T$ in Equation (4) can be back-calculated by ΔM. Assuming that ΔM is equal to amount of Cal.M_y subtracted by average values of experimental yield moments at each temperature, $\Delta\sigma_T$ can be obtained by using Equation (4).

Results of $\Delta\sigma_T$ calculated are shown in Figure 30 and Figure 31 by horizontal a pink dashed line (Cal.). Cal. estimated roughly the experimental value of stress in internal rebar in HW45-1 and 2, but, in HW70-1 and 2, Cause of tend to overestimate those in compression is unknown currently.

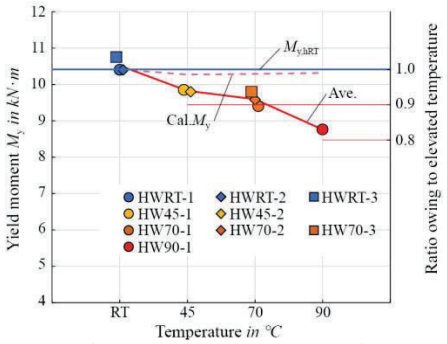

Figure 32: *Yield moment/M_y owing to elevated temperature and ratio of M_y at elevated temperature to $M_{y,RT}$ at room temperature*

On the basis of above discussion, equation for estimation of yield moment of steel bar-timber composite beam that takes temperature rise into account can be summarized as following.

$$M_y = (\sigma_y - \Delta\sigma_T) / n(I_{eT} / y_s) \quad (5)$$

where σ_y, $\Delta\sigma_T$, y_s: previous definition, n_T: ratio of Young's modulus of rebar to Young's modulus of timber in bending at elevated temperature, I_{eT}: cross-sectional secondary moment of the composite beam considering elevated temperature

In the future, it is necessary to estimate variation of the internal stress of rebar.

4 SUMMARY

Bending test of beams under high temperature with uncontrolled moisture absorption and dehumidification of wood were conducted to investigate effect of temperature rising on mechanical properties of the steel bar-timber composite beam. The results are summarized as the followings:

i) Although Young's modulus in bending, shear modulus and bending strength of timber decrease with temperature rising, the decrease is mitigated by loss of moisture in timber.

ii)Bending stiffness and bending capacity of the composite beam could be estimated from room temperature to 70°C, by the proposed estimation method considering the decrease in Young's modulus and bending strength of timber due to temperature rising, ignoring internal stress caused by the temperature.

iii) Yield moment of the composite beam should take into account effect of the internal stress in addition to decrease in mechanical performance of timber owing to temperature rising. In the future, we plan to develop a method for estimating the internal stress on safe side.

ACKNOWLEDGEMENT

This project was funded by Grant-in-Aid for Challenging Research in Japan and its experiment was conducted by all staffs of Shioya's laboratory. The authors gratefully acknowledge their work.

REFERENCE

[1] S.Shioya, et al.: An innovative hybrid timber structure in Japan: performance of column and beam, Vienna, WCTE 2016.

[2] N. Matsuoka, K. Fukudome, S. Shioya: Heat resistance of steel bar -timber composite beam, Santiago, WCTE 2021.

[3] C. Kaku, Y. Hasemi, et al.: Influence of moisture content on the structural properties of wood under high temperature, Vienna, WCTE 2016.

[4] N. Fukutomi, S. Shioya: Design method to estimate stiffness and strength of hybrid timber-steel bar beams, Seoul, WCTE 2018

[5] Mori, S. Shioya: Stiffness and strength of full-scale steel bar-timber composite beams with comparative small-depth, Santiago, WCTE 2021

World Conference on Timber Engineering Oslo 2023

THE ADHESIVE SHEAR CONNECTION OF TIMBER AND CONCRETE SLABS IN HUMID ENVIRONMENT

Viktória Bajzecerová[1], Ján Kanócz[2], Viktor Karľa[3], Miroslava Javoríková[4]

ABSTRACT: The paper analyzes the influence of humidity and temperature changes on the normal and shear stresses in timber-concrete composite (TCC) panels with an adhesive shear connection. Three TCC panels were placed into an air-conditioned climate chamber and subjected to an environment typical of swimming-pool areas. Within the test, strains in two orthogonal directions were measured. A FEM model of the TCC specimens was created and validated against the measured strains. Using the FEM model, both normal and shear stresses were evaluated. The results show that the highest normal stresses occurred near the shear connection. In addition, increased timber moisture content by 2.1% caused achieving the flexural tensile strength of concrete perpendicular to the timber grain direction.

KEYWORDS: Timber-concrete composite slab, Adhesive shear connection, Hygrothermal load, shear stress

1 INTRODUCTION

Timber-concrete composites (TCC) are widely applied today as footbridge and/or bridge slabs [1,2], as well as the floor slabs of multi-story buildings [3,4]. For rapid construction, prefabricated TCC panels are especially useful, for which it is advantageous to use mass timber panels, such as vertically-laminated timber and cross-laminated timber plates [5–7]. There are numerous ways to ensure the concrete and timber layers' composite action, such as mechanical fasteners, notches, perforated steel strips, glued-in rods, and adhesives [8–11].

In comparison to mechanical fasteners, adhesive shear connections provide many advantages: rigid connection providing full interaction of timber and concrete slabs, a more uniform shear flow distribution, so no local stress concentrations occur, and a relatively simple calculation model since it is not necessary to consider the slip between timber and concrete parts of composite slab. While the glued-in rods method is well established and is becoming more common for the joining of timber structures, adhesive shear connections for TCC slabs still need to be studied in more detail from several aspects regarding its long-term behaviour, such as the creep, ageing of mechanical properties, as well as the effects of humidity, thermal changes and fire exposure [12].

The long-term bending tests of timber-concrete composite slabs with adhesive shear connection [13–15] showed that the adhesive might not be the weak link in their long-term behaviour. The composite action was unaffected by long-term loading. Results, however, indicated that the humidity and temperature conditions significantly impact the stress and deflection of the TCC over time. Furthermore, the effects of the ambient humidity and temperature changes are manifested increasingly with the growing rigidity of the shear connection between the timber and the concrete [16].

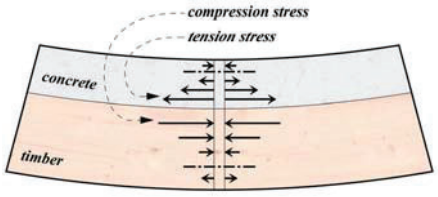

Figure 1: *The effect of restrained timber deformation in adhesively bonded TCC panel with increasing moisture content*

2 INFLUENCE OF HYGROTHERMAL LOAD

Due to uneven thermal and humidity deformations of concrete and timber in orthogonal directions, normal stress in composite members occurs, which can cause

[1] Viktória Bajzecerová, Technical University of Košice, Faculty of Civil Engineering, Košice, Slovak Republic. viktoria.bajzecerova@tuke.sk
[2] Ján Kanócz, Technical University of Košice, Faculty of Art, Slovak Republic. jan.kanocz@tuke.sk
[3] Viktor Karľa, Technical University of Košice, Faculty of Civil Engineering, Košice, Slovak Republic. viktor.karla@tuke.sk
[4] Miroslava Javoríková, Technical University of Košice, Faculty of Art, Slovak Republic. miroslava.javorikova@tuke.sk

https://doi.org/10.52202/069179-0419

defects of timber or concrete or the failure of the adhesive shear connection [17]. The effect of hygrothermal load on TCC is explained in Figure 1.

The increasing moisture content of the timber causes the elongation of the timber slab, which is limited by the adhesive concrete board and results in deflection and normal and shear stress near the glue line of TCC.

Using TCC panels as structural elements of roofs and walls of buildings with wellness, sauna or swimming pools may use the accumulation ability of the concrete and thus reduce the energy required for heating. On the other hand, the humid environment can cause unwanted deformations or possible failure of the glued joint. The presented study discusses the potential use of TCC with adhesive shear connection in such humid environmental conditions.

The research performed [19] dealt with the behaviour of TCC panels with an adhesive shear connection solely under the hygrothermal load and without other impacts, such as creep from gravity load or concrete shrinkage. The specimen loading was performed in a climate chamber. The test included temperature, moisture content, and strain measurements in two orthogonal directions. This paper presents evaluations of the measured results using the numerical FEM model. The aim was to analyse the normal and shear stresses caused by the humid environment typical of swimming-pool areas.

3 EXPERIMENTAL INVESTIGATION

3.1 SPECIMENS

Three specimens of TCC with adhesive shear connection were prepared to conduct the test (Figure 2).

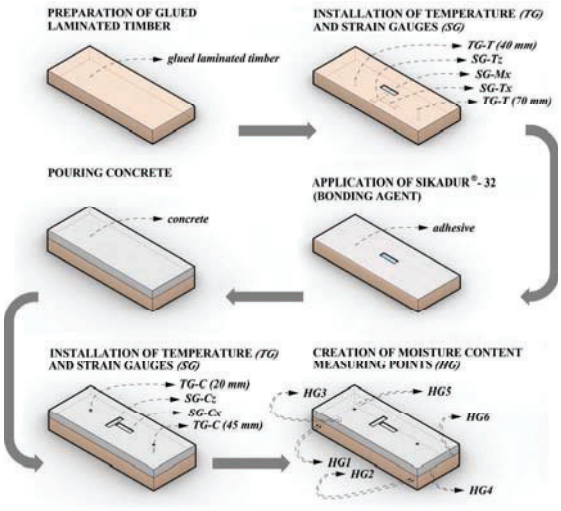

Figure 2: *Illustration of specimens' preparation*

First, strain gauges (SG) were installed on the top of the 750 mm long, 300 mm wide and 80 mm deep glued laminated timber slabs. After that, the 2-component epoxy adhesive Sikadur 32 was applied on top of the timber slabs. Subsequently, the 50 mm thick fresh concrete layer was cast on the wet adhesive on the timber slabs with no structural reinforcement. The prepared specimens were stored in lab conditions for about two years. Before the test, temperature (TG) and strain gauges (SG) were installed, as well as moisture content measure points (HG) were created. The final setup of specimens in the climate chamber is photographed in Figure 3, along with inset dimensions.

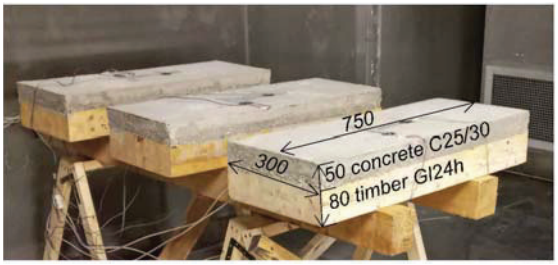

Figure 3: *Specimens in climate chamber; dimensions in mm*

3.2 MATERIAL PARAMETERS

For the test specimens, concrete C25/30 was chosen. Its real mechanical properties were defined according to EN standard 12390 [20]. Its cylinder and cube compressive strength 371 days after concreting were 55 MPa and 67 MPa, respectively. Its modulus of elasticity was determined as 26 GPa, flexural tensile strength as 8 MPa, and density as 2295 kg.m^{-3}. The mechanical parameters of the concrete are listed in Table 1.

Table 1: *Mechanical parameters of 371-day concrete*

Mechanical parameter	Value	Unit
Cylinder compressive strength	55	MPa
Cube compressive strength	67	MPa
Flexural tensile strength	8.1	MPa
Modulus of elasticity	26	GPa
Density	2295	kg.m^{-3}

The properties of glued laminated timber used for TCC panels were defined according to EN standard 408 [21]. Its modulus of elasticity parallel to the grain was determined as 13.9 GPa and bending strength as 50 MPa. The density of timber used was 425 kg.m^{-3}. The mechanical parameters of the timber are listed in Table 2.

Table 2: *Mechanical parameters of timber*

Mechanical parameter	Value	Unit
Bending strength	50.0	MPa
Modulus of elasticity parallel to the grain	13. 9	GPa
Density	425	kg/m^3

The modulus of elasticity and coefficient of thermal expansion of bonding agent Sikadur®-32, provided by the manufacturer [22], were 4.0 GPa, and 8.2x10^{-5} °C^{-1}, respectively. The shear strength of the adhesive connection with a value of 4.0 MPa was evaluated from 5 shear specimens of the same material used [7].

3.3 TES SET UP AND MEASURING METHODS

The three specimens (TC1, TC2 and TC3) were exposed to an environment with varying relative humidity and temperature by being placed in one chamber of air-conditioned climate chamber Thermotron WP-2(527)-2(THCM1-5) (Thermotron Industries, Holland, MI) (Figure 3).

Data acquisition system ALMEMO 5690-2 (Ahlborn, Holzkirchen, Germany) was used to store the data of ambient temperature, ambient relative humidity, and temperature gauges at various depths of the specimens (TG in Figure 2) at 15 min intervals.

Strain gauges with a length of 100 mm were placed in the x-direction and z-direction on top of the concrete and at the bottom of timber slabs (SG in Figure 2) to measure strains. Before concreting, another strain gauge was fixed on top of the timber slabs in the x-direction, which was 50 mm long (SG-Mx in Figure 2). Quantum MX 840 (HBM, Darmstadt, Germany) universal measurement amplifier module acquired data from strain gauges at 50 s intervals.

Moisture content in timber was monitored at six measuring points created on each specimen (HG in Figure 2) using a two-pins moisture content resistance meter WHT 770 (ELBEZ, Czech Republic).

3.4 HYGROTHERMAL LOAD

The hygrothermal load chosen for the analysis of humid conditions that are typical of that in swimming-pool areas are given in Table 3. The thermal and humidity conditions are similar to the measured data published in [18].

Table 3: *Considered environmental conditions*

Environment	T (°C)	RH (%)
0 - Initial conditions	20.0	65.0
1 – Swimming pool hall without mechanical ventilation	20.3	88.5
2 – Swimming pool hall with mechanical ventilation	34.3	51.8
3 - Shower room	34.6	71.9

T – temperature; RH – relative humidity

The initial conditions against which all further environmental changes were compared were a temperature (T) of 20°C and relative humidity (RH) of 65% (Environment 0). The initial conditions took 12 days, and the timber moisture content stabilised at 14%. The following environment settings were initiated only after stabilising the measured strains, the temperature in the whole depth of specimens and timber moisture content. Under humid Environment 1, warm and dry Environment 2, and warm Environment 3, the moisture content was stabilised at 16.1%, 11.4% and 14%, respectively.

3.5 THERMAL AND HUMIDITY EXPANSION COEFFICIENTS

Within the test, two segments of timber and concrete slab with dimensions of 300 mm × 450 mm were subjected to environmental changes. The same materials as for the TC specimen were used. Thermal and humidity expansion coefficients were calculated as the ratio of the measured strains and differences in temperature or moisture content of the timber slabs. These coefficients for concrete were calculated similarly, but the differences in relative humidity of the environment were used for the humidity expansion coefficient. More can be found in [19].

Table 4: *Thermal expansion Coefficients*

Thermal Expansion Coefficient	$\times 10^{-6}$ (1/°C)
Concrete	17.15
Timber parallel to grain	1.93
Timber perpendicular to grain	54.43

Table 5: *Humidity expansion Coefficients*

Humidity Expansion Coefficient	$\times 10^{-3}$ (-)
Concrete*	0.26
Timber parallel to grain	3.78
Timber perpendicular to grain	96.04

* *In relation to the change in RH (-)*

4 THEORETICAL INVESTIGATION

4.1 FEM MODEL GEOMETRY

The theoretical analysis of the specimens was performed by a finite element method (FEM) using ANSYS software [19]. The geometry of the model corresponded to real specimens. The depth of the adhesive layer was neglected, and the adhesive connection was defined as a bonded contact region between the timber and concrete. Regarding boundary conditions, zero displacements were set in 3 points, according to Figure 4. The mesh element size was set to 5 mm.

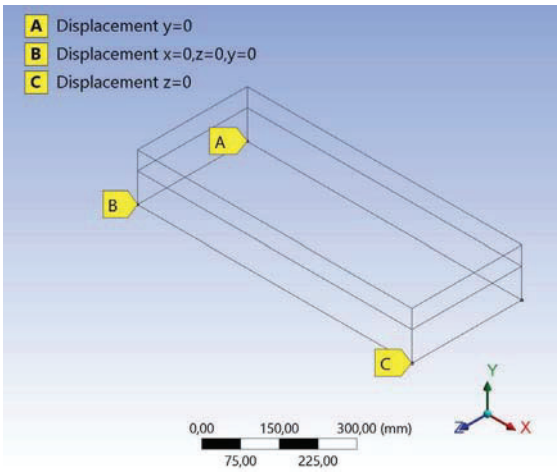

Figure 4: *FEM model – boundary conditions*

https://doi.org/10.52202/069179-0419

4.2 MATERIAL SETTINGS

The concrete was considered a linear elastic isotropic material. The mechanical parameters of the concrete were set according to Table 1. Poisson's ratio of concrete was assumed to be 0.18.
The timber was defined as linear elastic orthotropic material with the grain orientation in the x-axis, according to Figure 5.

Orthotropic Elasticity		
Young's Modulus X direction	13900	MPa
Young's Modulus Y direction	463	MPa
Young's Modulus Z direction	463	MPa
Poisson's Ratio XY	0	
Poisson's Ratio YZ	0	
Poisson's Ratio XZ	0	
Shear Modulus XY	690	MPa
Shear Modulus YZ	690	MPa
Shear Modulus XZ	69	MPa

Figure 5: *FEM model – the timber material parameters setting*

The reliable values of Poisson's ratios of timber were not possible to define due to a large discrepancy in available data [24]. Therefore, Poisson's ratios were set to zero because they were assumed to have a negligible effect on the results. A similar assumption was declared in [25].
Thermal and humidity expansion coefficients were set according to the measured values in Tables 4 and 5.

4.3 HYGROTHERMAL LOAD

In the FEM analysis, the temperature and humidity changes were modelled as a change in Thermal Conditions relative to the initial temperature.
Regarding the specimens' relatively small depth and the long duration of the hygrothermal load test step, it was assumed that the diffusion laws could be neglected. An instant adaptation of the temperature and humidity of both volumes of the FEM model was considered.

5 RESULTS

5.1 STRAINS

Strains parallel to the timber grain (x) and perpendicular to the timber grain (z) in the middle parts of the panels were analysed. The strain differences between each of the three environments (Table 3) and the initial environment were evaluated. In Figures 6 to 8, the strain differences over the cross-section of the TCC panel calculated from the measured (TC1, TC2, TC3) and calculated (FEM) data are plotted.
Although the calculation model did not consider the uneven temperature and humidity profiles in the cross-section and neglected the diffusion laws, it predicted the measured strains relatively well. Therefore, based on this comparison, the model was considered valid and suitable for the following analyses of normal and shear stresses.

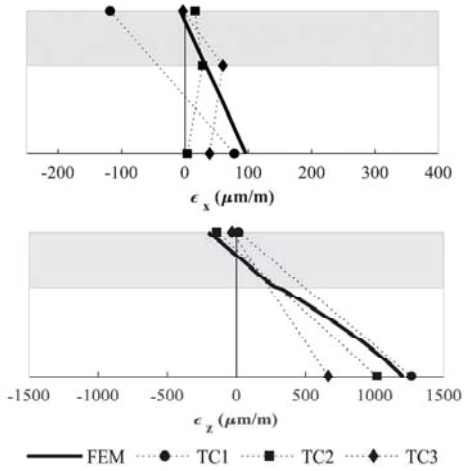

Figure 6: *Measured (TC1, TC2, TC3) and calculated (FEM) strains in x- (ε_x) and z- direction (ε_z) in Environment 1*

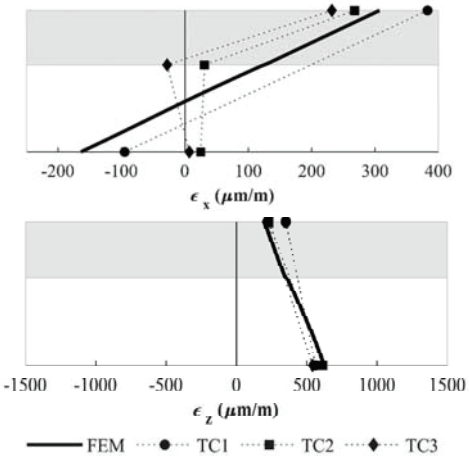

Figure 7: *Measured (TC1, TC2, TC3) and calculated (FEM) strains in x- (ε_x) and z- direction (ε_z) in Environment 2*

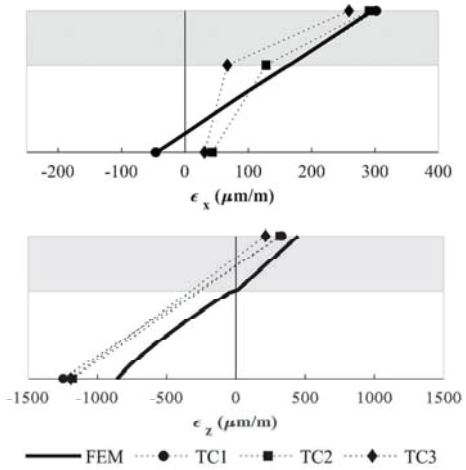

Figure 8: *Measured (TC1, TC2, TC3) and calculated (FEM) strains in x- (ε_x) and z- direction (ε_z) in Environment 3*

https://doi.org/10.52202/069179-0419

5.2 NORMAL STRESSES

Due to uneven and resisted deformation of the timber and concrete slab of the TCC panel, normal stresses occur (Figure 1). Therefore, the higher the differences in inelastic thermal and humidity strains, the higher stress can be expected. The normal stresses evaluated using FEM analysis are presented in Figures 9 to 13 and listed in Tables 6 and 7.

The tension in the concrete seems to be the weakest part of TCC slabs in humid Environment 1. The growth of the timber moisture content (MC) causes an increase in the tension stresses on the bottom surface of concrete up to +2.1 MPa in the x-direction (Figure 9), and in the z-direction increased almost to a value of the tensile strength of the concrete used with the value of +7.5 MPa (Figure 10). It should be noted that the tension strength of standard concrete is lower than that of the concrete used. The tension stresses usually bear the reinforcement in the concrete slabs, but the tension stress in the case of hygrothermal load occurs near the glued line and might cause the local failure of the adhesive connection.

The humid Environment 1 caused only a small increase in timber normal stresses with a value of less than 1 MPa.

The highest values of the normal stresses were expected in the middle part of the TCC slabs in both directions. Based on this expectation, the strain gauges were placed in the middle of the TCC slab span. However, as resulted from the FEM analysis of the warm Environment 3, the highest values of normal stresses were observed not in the middle part of the specimens, as previously expected in [19], but at the edges of specimens (Figures 13 and 14).

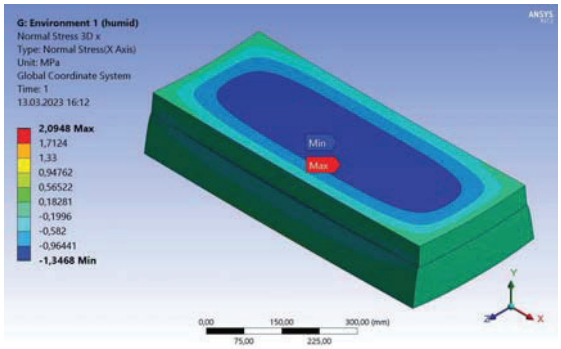

Figure 9: *Humid Environment 1 - normal stress in x direction*

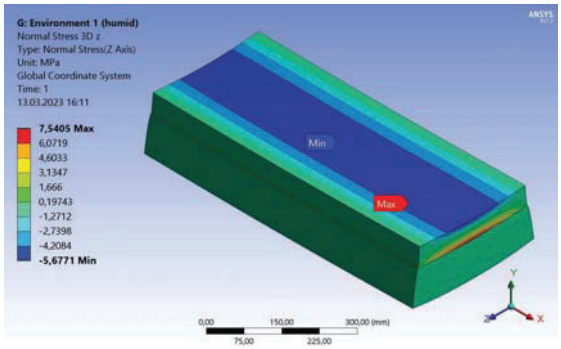

Figure 10: *Humid Environment 1 - normal stress in z direction*

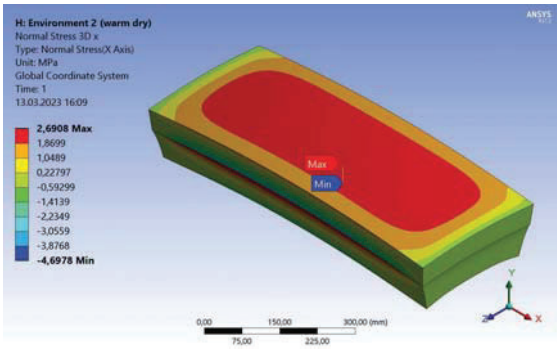

Figure 11: *Warm and dry Environment 2 - normal stress in x direction*

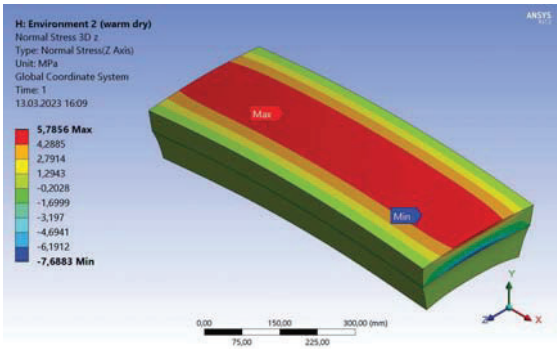

Figure 12: *Warm and dry Environment 2 - normal stress in z direction*

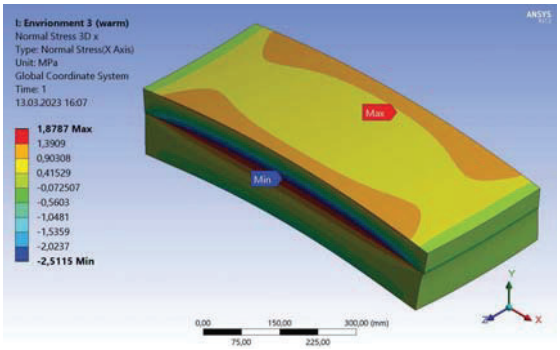

Figure 13: *Warm Environment 3 - normal stress in x direction*

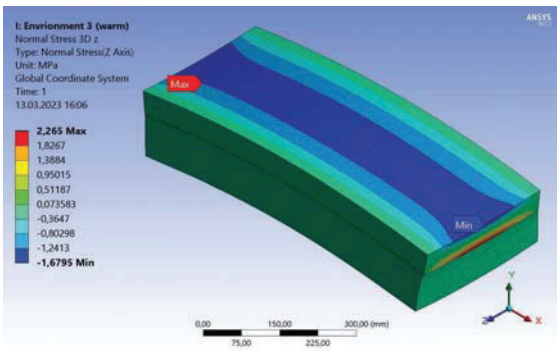

Figure 14: *Warm Environment 3 - normal stress in z direction*

https://doi.org/10.52202/069179-0419

The thermal expansion coefficient of concrete is almost 9-times higher than that of the timber parallel to the grain (in the x-direction), but on the contrary, it is 0.32-times lower than that of the timber perpendicular to the grain (in the z-direction). The orthotropic behaviour of the timber leads to a complex 2-dimensional problem of TCC slabs. From the Figure above, the highest stresses in all environments occurred solely in the concrete. Therefore, Tables 6 and 7 list the maximum stress values in timber and concrete parts separately.

Table 6: *Maximum values of normal stresses in x direction*

Env.	Concrete		Timber	
	compress. (MPa)	tension (MPa)	compress. (MPa)	tension (MPa)
1	-1.35	2.09	-0.69	0.25
2	-4.70	2.49	-1.33	2.69
3	-2.51	1.16	-1.02	1.88

Table 7: *Maximum values of normal stresses in z direction*

Env.	Concrete		Timber	
	compress. (MPa)	tension (MPa)	compress. (MPa)	tension (MPa)
1	-5.68	7.54	-0.90	0.07
2	-7.69	5.79	-0.07	0.91
3	-1.68	2.27	-0.25	0.02

In the case of the warm and dry conditions of Environment 2, the increase in temperature and the decrease in timber moisture caused an increase in compressive stresses on the bottom surface of the concrete in the z-direction, with a value of -7.7 MPa (Figure 12 and Table 7), which is about 14% of the cylinder compressive strength (Table 1).

From all considered environments, the timber slab was subjected to the highest stresses in Environment 2. On the other hand, the tension stress on the top of the timber surface and the compression stress on the bottom surface would reduce the normal stress due to possible future positive bending due to an external load.

It can be concluded that based on the FEM analysis, the normal stresses in the TCC panels caused by the chosen hygrothermal load did not exceed the strength values of the timber or concrete used. On the other hand, standard concrete with a lower value of flexural tensile strength will possibly crack near the glued line and can lead to the failure of the adhesive shear connection.

5.3 SHEAR STRESSES

Figures 15 to 17 show the shear stress diagram on the bottom surface of the concrete since higher values than on the top of the timber were observed (Table 8). According to FEM analysis, the shear stress in the glue line reached the value of the shear strength of the adhesive connection in Environment 2. This may explain the thin cracks in the glue line at the edges of the panels that were observed after the test.

Table 8: *Maximum values of shear stress*

Environment	Concrete (MPa)	Timber (MPa)
1	3.77	1.33
2	4.02	1.51
3	1.99	1.27

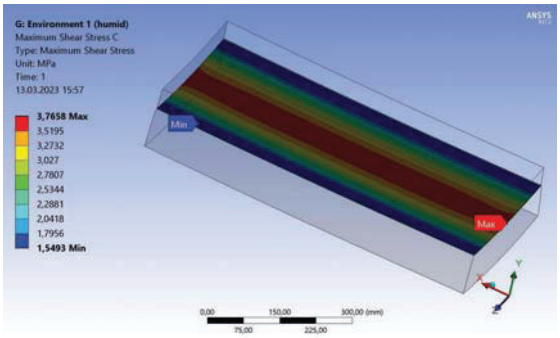

Figure 15: *Humid Environment 1 - Maximum shear stress on the bottom of the concrete*

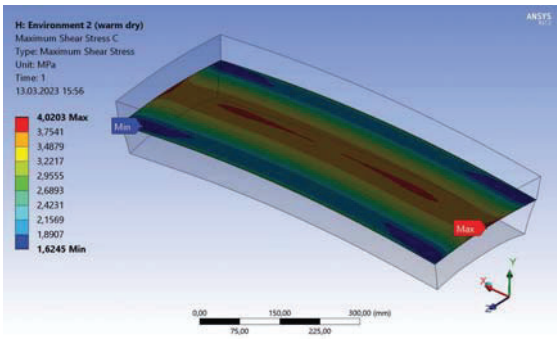

Figure 16: *Warm and dry Environment 2 - Maximum shear stress on the bottom of the concrete*

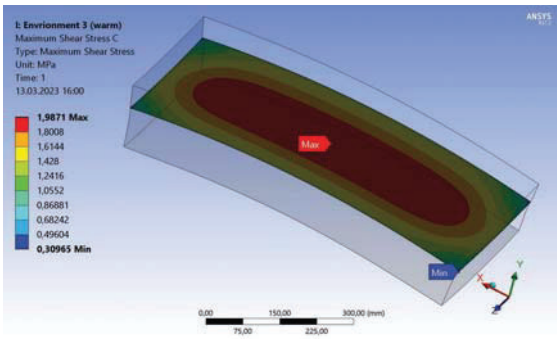

Figure 17: *Warm Environment 3 - Maximum shear stress on the bottom of the concrete*

6 CONCLUSIONS

The hydrothermal stresses near the glue line can limit the use of TCC panels with adhesive shear connections in humid environmental conditions. Therefore, in the experimental analysis, three various environments typical of swimming-pool areas were considered. Based on the measured data, a numerical FEM model was validated and used for the stress evaluation.

From the results, it can conclude that the weakest point of adhesively bonded TCC is the tension stress in the concrete layer. Concrete with a lower value of flexural tensile strength will possibly crack near the glued line and can lead to the failure of the adhesive shear connection. For a humid environment, therefore, high-strength concrete could be more suitable. The shear stress at the edges of the specimens possibly caused the thin cracks in the glued line observed after the test.

The geometrical dimensions of the specimens were relatively small; only fragments of real panels were used in the analysis. But it can assume that the hygrothermal deformations of panels with the same concrete-to-timber ratio cause the same curvature, regardless of the width and length, causing similar normal stresses. On the other hand, the shear stress at the real-size panel edges could possibly be more significant. The size effect will be studied in more depth in future.

Ongoing research focuses on the shear strength differences in the glued line of TCC panel specimens subjected to hygrothermal load over the entire contact surface of the timber and concrete parts of the panels. In addition, further research is still needed to fully comprehend the complex topic of the adhesive connection of TCC, especially in the field of ageing.

ACKNOWLEDGEMENT

This work was supported by the Scientific Grant Agency of the Ministry of Education, Science, Research and Sport of the Slovak Republic and the Slovak Academy of Sciences under Projects VEGA 1/0626/22, VEGA 1/0307/23, and KEGA 030TUKE-4/2022.

REFERENCES

[1] Rodrigues J.N., Dias A., Providência P.: Timber-concrete composite bridges: State-of-the-art review. BioResources 8(4):6630-6649, 2013.

[2] Fragiacomo M., Gregori A., Xue J., Demartino C., Toso M.: Timber-concrete composite bridges: Three case studies. Journal of Traffic and Transportation Engineering (English Edition), 5(6):429-438, 2018.

[3] Naud N., Sorelli L., Salenikovich A., Cuerrier-Auclair S.: Fostering GLULAM-UHPFRC composite structures for multi-storey buildings. Engineering Structures, 188:406-417, 2019.

[4] Estévez-Cimadevila J., Martín-Gutiérrez E., Suárez-Riestra F., Otero-Chans D., Vázquez-Rodríguez J.A.: Timber-concrete composite structural flooring system. Journal of Building Engineering, 49:104078, 2022.

[5] Zhang L., Zhou J., Chui Y.H.: Development of high-performance timber-concrete composite floors with reinforced notched connections. Structures, 39:945-957, 2022.

[6] Pang S.J., Ahn K.S., Jeong S.M., Lee G.C., Kim H.S., Oh J.K.: Prediction of bending performance for a separable CLT-concrete composite slab connected by notch connectors. Journal of Building Engineering, 49:103900, 2022.

[7] Bajzecerová V., Kanócz J., Rovňák M., Kováč M.: Prestressed CLT-concrete composite panels with adhesive shear connection. Journal of Building Engineering, 56: 104785, 2022.

[8] Suárez-Riestra F., Estévez-Cimadevila J., Martín-Gutierrez E., Otero-Chans D.: Perforated shear + reinforcement bar connectors in a timber-concrete composite solution. Analytical and numerical approach. Composites Part B: Engineering, 156:138-147, 2019.

[9] Al-Sammari A.T., Clouston P.L., Breña S.F.: Finite-element analysis and parametric study of perforated steel-plate shear connectors for wood-concrete composites. Journal of Structural Engineering, 144(10):04018191, 2018.

[10] Dias A.M.P.G., Kuhlmann U., Kudla K., Mönch S., Dias A.M.A.: Performance of dowel-type fasteners and notches for hybrid timber structures. Engineering Structures, 171:40-46, 2018.

[11] Nemati Giv A., Fu Q., Yan L., Kasal B.: Interfacial bond behavior of adhesively-bonded timber/cast in situ concrete (wet bond process). Acta Polytechnica CTU Proceedings, 33:398-403, 2022.

[12] Dias A., Schänzlin J., Dietsch P.: Design of timber-concrete composite structures: A state-of-the-art report by COST Action FP1402/ WG 4. Berichte aus dem Bauwesen, Shaker, 2018.

[13] Bajzecerová V., Kanócz J.: Long-term bending test of adhesively bonded timber-concrete composite slabs. In: Advances and Trends in Engineering Sciences and Technologies III, 15-20, 2019.

[14] Eisenhut L., Seim W., Kühlborn S.: Adhesive-bonded timber-concrete composites – Experimental and numerical investigation of hygrothermal effects. Engineering Structures, 125:167-178, 2016.

[15] Tannert T., Endacott B., Brunner M., Vallée T.: Long-term performance of adhesively bonded timber-concrete composites. International Journal of Adhesion and Adhesives, 72:51-61, 2017.

[16] Bajzecerová V., Kanócz J.: The Effect of Environment on Timber-concrete Composite Bridge Deck. Procedia Engineering, 156:32-39, 2016

[17] Ginz A., Seim W.: Moisture-induced internal stress within adhesive-bonded timber-concrete composites. In: *WCTE 2018*, 1-6, 2018.

[18] Jorge L., Dias A., Costa R.: Performance of X-Lam panels in a sports center with an indoor swimming-pool. Journal of Civil Structural Health Monitoring, 5:129-139, 2015.

[19] Bajzecerová V., Kanócz J., Kormaníková E., Karľa V., Orolin P., Vranay F.: Normal Stress Distribution of Timber-Concrete Composite Panels with an Adhesive Shear Connection under Thermal and Humidity Loadings. BioResources, 16(3):4862-4875, 2021.

https://doi.org/10.52202/069179-0419

[20] EN 12390. Testing hardened concrete. European Committee for Standardization, Brussels, Belgium, 2013.
[21] EN 408. Timber structures. Structural timber and glued laminated timber. Determination of some physical and mechanical properties. European Committee for Standardization, Brussels, Belgium, 2013.
[22] Sika, A. G. Product Data Sheet Sikadur®-32 Normal, Sika AG, Baar, Switzerland, 2017.
[23] Ansys Workbench Release 17.2.
[24] Bartolucci B., De Rosa A., Bertolin C., Berto F., Penta F., Siani A. M.: Mechanical properties of the most common European woods: a literature review, Frattura ed Integrità Strutturale, 14(54):249-274, 2020.
[25] Turesson J., Berg S., Björnfot A. et al.: Shear modulus analysis of cross-laminated timber using picture frame tests and finite element simulations. Materials and Structures, 53:112, 2020.

World Conference on Timber Engineering Oslo 2023

CYCLIC TESTS ON AN INNOVATIVE FRICTION DISSIPATIVE DEVICE FOR SEISMIC RETROFIT WITH CLT PANELS

Francesco Boggian[1,2*], Angelo Aloisio[1,3], Roberto Tomasi[1]

ABSTRACT: Seismic renovation is a topic of crucial importance for many countries in the southern part of Europe, where the high levels of seismic hazard, combined with the presence of old RC frame structures, poses a severe risk to the lives of many. The e-CLT system, part of the European project e-Safe, proposes a seismic retrofit system for existing RC frame buildings by attaching CLT panels to the facade and connecting them to the existing structure with innovative friction dissipative devices. The authors conducted an experimental campaign at component level for this novel connector, with two different setups, with and without a CLT panel. This paper presents the cyclic test results on these friction devices, with particular attention to the influence of the timber connection on friction behaviour.

KEYWORDS: seismic renovation, Friction connector, experimental test, energy dissipation

1 INTRODUCTION

Up to 60% of residential buildings in Italy were built between 1946 and 1990, and 25% before 1946 [1], when proper seismic building codes were not available (the first codes were presented in the 1980s), and are therefore in great need of retrofitting. Many retrofit systems are available, directed either at reinforcing the existing structure, or providing extra energy dissipation Some systems can offer both. Traditional systems include steel jacketing, FRP, but are often cumbersome and expensive. The dissipation approach uses three different types of dissipation devices: active, semi-active and passive [2]. This paper will focus on friction dampers, a particular type of passive dissipation device that is becoming more studied in recent years for application in buildings. In its simplest form, a friction device is composed of three plates clamped together by preloaded bolts [3]. The middle plate has an elongated bolt, the outer plates have round holes, so there can be relative slip between the plates when the applied force reaches the friction limit. The system proposed by the authors is called e-CLT (Fig.1)[4], [5]: CLT panels are attached from the outside of existing buildings without disturbing the users' lives during renovation work. The main novelty of the system lies in the connection between the timber panel and the existing building: a Friction Connection, capable of offering a stiff joint for low levels of horizontal actions whilst sliding and dissipating energy via friction when subjected to higher loads like earthquakes. This paper presents an experimental study on a prototype of this novel connection, following the first phase presented in [5]. In the first phase, the friction connection was tested by itself, focusing solely on the friction behaviour, while the novelty of this paper is a new testing setup that includes a CLT panel. The goal is to study the performance of the interaction between friction connection and timber connection.

2 E-CLT

The system tested in this paper is part of an ongoing European project called e-SAFE (Energy and Seismic AFfordable rEnovation solutions) [5]. The project was financed in the Horizon 2020 framework of "decarbonizing the EU building stock", and proposes a multi-faceted approach to building renovation [4]. Different disciplines are involved, with to obtain better performances both regarding energy efficiency and structural behaviour. One of the systems proposed for seismic retrofit of existing RC frame buildings with masonry infill is called e-CLT, shortly illustrated in Figure 1.

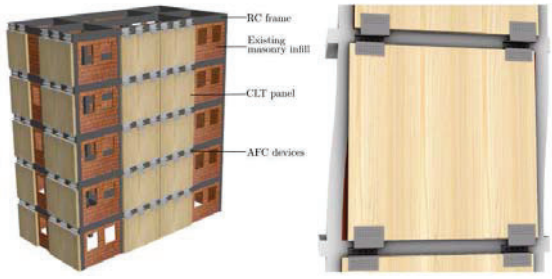

Figure 1: *e-CLT seismic retrofit system* [5].

* corresponding author: francesco.boggian@nmbu.no
1 Faculty of Science and Technology, Norwegian University of Life Sciences, Norway
2 WSP Norge, Norway
3 Department of Civil, Construction-Architectural and Environmental Engineering, University of L'Aquila, Italy

https://doi.org/10.52202/069179-0420

The renovation system e-CLT entails the application of a CLT panel from the outside of a building, on the bays without any openings, thus without disturbance for the residents. The main novelty lies in the connection system between the CLT panel and the existing structures: friction connections link the CLT panel to the beams of every floor. The friction connection is composed of two steel plates: the anchor profile is rigidly connected to the RC beam of a floor and the CLT panel of the floor above, while the free profile is connected to the CLT panel of the floor below and the anchor profile via preloaded bolts that can slide in an elongated hole. In this way, by setting the desired preload in the bolts, it is possible to choose the activation force of the sliding mechanism. For lateral force levels below the activation threshold the connection will behave as stiff. In contrast, for higher load levels, such as in the event of an earthquake, the system will start to slide and dissipate energy via friction. This paper will describe of one of the prototypes of this novel friction connection and the results from some cyclic tests.

3 MATERIALS AND METHODS

3.1 SPECIMEN

Different shapes and configurations of the specimen were modelled and tested in various phases, as seen in Figure 3. In the first testing phase, presented in [5], the research focused on two main designs: STD (standard) and ALT (alternative), seen in Figures 3 and 4. STD is composed of two steel plates: the anchor profile is rigidly connected to the beam of a floor and the CLT panel above, while the free profile has an elongated hole and is connected to the anchor profile and to the CLT panel below. In this case the screw connection the CLT panel is on the front of the system, offering easy access and inspection. Initial modelling and tests highlighted weaknesses in the 3-bend shape and high eccentricity between friction bolts and free profile, as seen in Fig.4, which brought to the conceiving of the ALT profile [6]. In this case, both CLT-to-steel screw connections are moved to the back, which means simpler L shapes for the plates and reduced eccentricity. This brought better mechanical performances at the expense of reduced accessibility of the screw connection. A further elaboration of the ALT is the ALT-AS, seen in Fig.5. In this prototype the free profile is composed of two separate pieces, connected by lateral bolts in elongated holes, which offer the additional benefit of vertical adjustability in the mounting phase [6], [7]. The third phase of testing, addressed in this paper, used a design called HYB (hybrid), which attempts to keep the positive aspects of STD and ALT: front mounting possibility and more straightforward L shape [8].

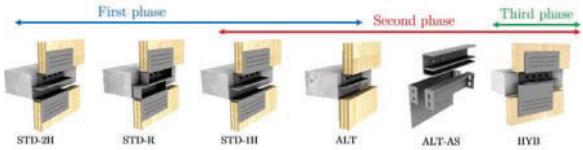

Figure 2: *Evolution of the dissipator shape.*

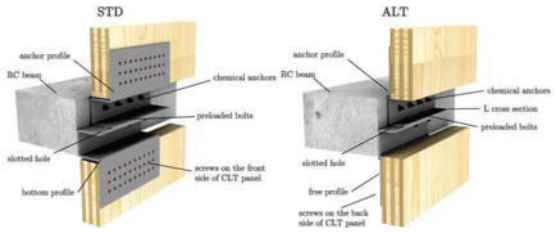

Figure 3: *Main features of the initial STD and ALT shapes* [5].

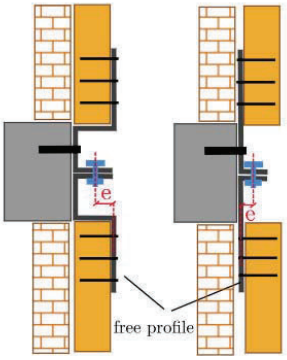

Figure 4: *Section illustration of STD and ALT shapes* [5].

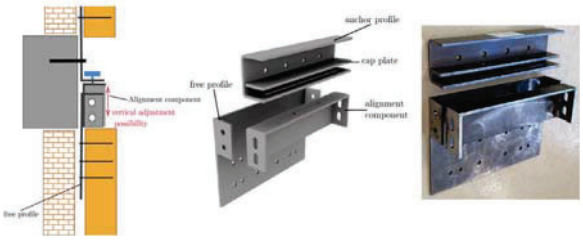

Figure 5: *Illustration of the ALT-AS shape* [7].

The HYB specimen, seen in Fig.6, is composed of two 8mm thick cold bent steel plates: the anchor profile is attached to the beam of the existing building and the CLT panel of the upper floor, while the free profile is attached to the CLT panel of the lower floor and the anchor profile with two high strength M16 bolts. The connection to the CLT panel is made with 33 10x80 screws. The free profile presents an elongated hole, which permits relative sliding, with a clearance of movement of 100mm in both directions. The friction connection is completed by a cap plate and two aluminium shim layers, which improve the friction behaviour. Four specimens were tested, as seen in Tab. 1. HYB 2 and HYB 3 were identical, HYB_e had a slightly reduced eccentricity, HYB_s was tested on a different steel setup. Multiple repetitions were performed on each specimen, with different preloads according to Tab.1.

https://doi.org/10.52202/069179-0420

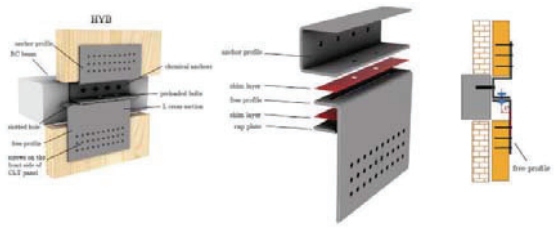

Figure 6: *Illustration of the HYB specimen* [8].

3.2 SETUP AND LOAD PROTOCOL

Two different setups were used for testing. The main setup is seen in Fig.3, where the free profile is connected with screws to a 100mm thick CLT panel. The anchor profile, simplified to a C shape for testing purposes, was connected to the actuator of the press, which simulated the movement of beam in a real building by moving up and down. One specimen was tested on a different setup, without the CLT panel, seen in Fig.8, to study the influence of the screw connection on friction behaviour. All the tests were carried out in displacement control with a speed of 2mm/s and the same cyclic protocol: 1x5-10mm+3x20-40-60-80-100mm.

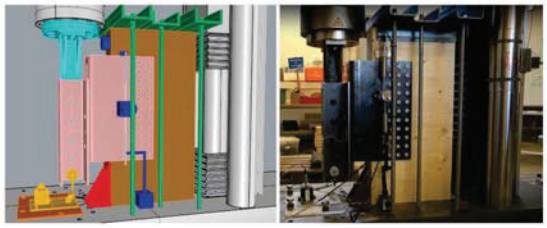

Figure 7: *Setup with CLT panel* [8].

Figure 8: *Setup without CLT panel* [8].

Tab.1 shows the list of the specimen that were tested, and the repetition performed on each specimen.

Table 1: *Test list.*

Specimen	Rep.	Preload kN	Setup
HYB-2	1	25	CLT
	2	25	
	3	25	
	4	25	
HYB-3	1	25	CLT
	2	25	
	3	25	
	4	25	
HYB_e-1	1	25	CLT
	2	25	
	3	37.5	
	4	37.5	
	5	37.5	
HYB_s-1	1	25	no CLT
	2	25	
	3	37.5	
	4	37.5	
	5	37.5	

4 RESULTS AND DISCUSSION

This section will give a brief overview of the experimental results; the complete outcome is presented in [8]. Figures 9 to 12 show results of the tests in term of force-displacement graphs. The first three pictures refer to the specimens tested on the main setup, with the CLT panel. The shape of the hysteresis loops closely resembles that of a rectangle, which is the ideal shape for a rigid-plastic system. The shape is not precisely a rectangle since the system is not a pure friction connection, but it's influenced by the deformability of the steel plates and of the timber screw connection. The influence of the screw timber connection on the friction system is primarily visible in the initial cycles and at the change of directions: the graphs present a slight S shape, typical of the pinching phenomena of timber connections, which causes a loss in energy dissipation. In all the tests, the force value reaches peaks at initial cycles and then stabilizes to lower constant values, this was also observed in the previous campaign and is due to both the static vs dynamic friction behaviour and to wear degradation phenomena of the friction surfaces.

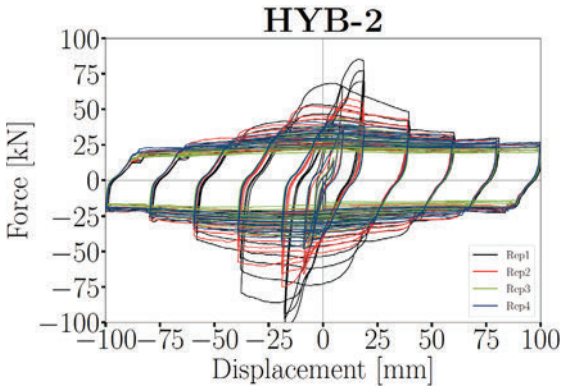

Figure 9: *Results of specimen HYB-2.*

Specimen HYB_e doesn`t present a drastically different behaviour from specimens HYB-2 and HYB-3, suggesting that the reduced eccentricity doesn`t play a key role in the stable friction behaviour. Figure 12 presents the results from the specimen that was tested on the second setup, which was made only of steel and used a bolted connection instead of a screw connection. The immediate difference in the graphs is that the shape is more

https://doi.org/10.52202/069179-0420

rectangular, and the load inversion branches are more vertical, given the higher stiffness of the bolted connection. Additionally, the steel setup offers a more stable friction behaviour, with minor fluctuations in the slip force value, suggesting that a stiffer connection system is preferable to exploit the full potential of the friction connection.

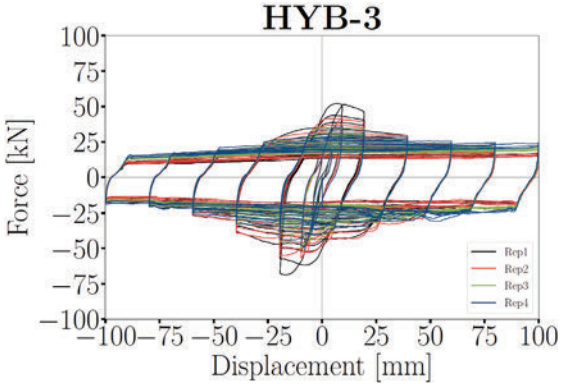

Figure 10: *Results of specimen HYB-3.*

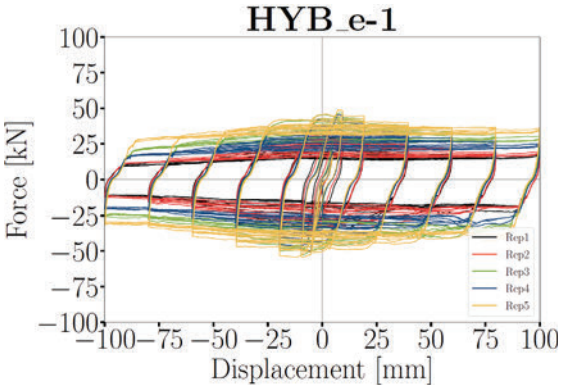

Figure 11: *Results of specimen HYB_e-1.*

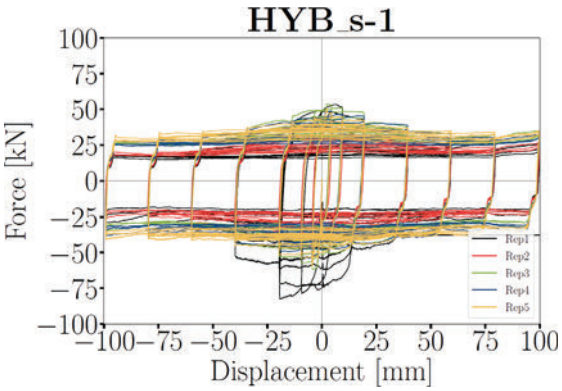

Figure 12: *Results of specimen HYB_s-1.*

Results in terms of slip force and friction coefficient are presented in Table 2. The definition of the slip force from the experimental data is not immediate, as the value fluctuates throughout the test, changes sign and is influenced by the initial phenomenon of changing from static to dynamic friction. The authors decided, therefore, to use the same approach adopted by [9]. The definition of slip force is based on the total dissipated energy and the cumulated displacements, both values are positive and strictly increasing functions. The dissipated hysteretic energy is defined by the following:

$$E = \sum_{i=0}^{n} E_i = \sum_{i=0}^{n} \left| \frac{F_{i+1}+F_i}{2} \cdot (\delta_{i+1} - \delta_i) \right| \quad (1)$$

where E is the dissipated energy, E_i the dissipated energy at the $i-$th time step, F_i and δ_i are the force and displacement at the same time step, respectively.
The cumulative distance of travel D is the sum of the displacement time steps:

$$D = \sum_{i=0}^{n} |\delta_{i+1} - \delta_i| \quad (2)$$

The slip force is thus calculated as the energy per unit of length:

$$F_{\text{slip}} = \frac{E}{D} \quad (3)$$

The experimental friction coefficient μ is calculated as

$$\mu = \frac{F_{\text{slip}}}{n_s n_b F_P} \quad (4)$$

where F_{slip} is the slip force calculated in Eq.((4)), n_s is the number of shear surfaces equal to 2, n_b is the number of the preloaded bolts equal to 2, and F_P is the preload force from Tab.1.

Tab. 2 shows the friction coefficient values as an average for the repetitions on every specimen with the same preload force. The global average of the testing campaign is 0.21, which aligns with literature values for friction coefficients of aluminium vs steel. [10]. Aluminium is also a good choice for the friction system for its ease of sourcing, manufacturing, and price, when compared to other possible materials for the shim layers of the friction connection.

Table 2: *Test results: slip force and friction coefficient.*

Tests	Preload [kN]	F_{slip} [kN]	μ
HYB-2(r1234)	25	25.9	0.26
HYB-3(r1234)	25	20.5	0.21
HYB_e-1(r12)	25	18.2	0.18
HYB_s-1(r12)	25	21.2	0.21
HYB_e-1(r345)	37.5	29.9	0.20
HYB_s-1(r345)	37.5	32.2	0.22
mean			0.21

Tab. 3 attempts to clarify the most critical aspect of the difference between the two setups: energy dissipation. When testing a simple friction connection, composed of a basic system of 3 plates with relative sliding, the expected mechanical behaviour is a perfectly plastic system, producing rectangular hysteresis loops, as seen in Fig.13a. The friction device tested in this campaign is more complex than a basic friction connection, it has a complex

https://doi.org/10.52202/069179-0420

shape and it`s asymmetric, thus introducing additional deformational contribution to the system. These components then reduce the energy dissipation compared to the ideal rectangular behaviour, see Fig.13b. Moreover, if a connection with screws is added to the system, then it acts as an additional deformation component, which also causes a loss of energy dissipation and a more unstable friction behaviour, see Fig.13c. This concept is summarised in Tab. 3 where some values of dissipated energy are presented. In the first part of the table, the dissipated energy is the average as the tests on the CLT setup vs the test on the steel setup for a preload of 25kN, while in the second part, the same dissipated energy value is presented but referred to the tests with 37.5kN preload. The percentage of difference in dissipated energy summarises the contribution of the screw connection to the friction system. On average it causes a 12% energy loss when compared to a system without the CLT connection.

Table 3: *Test results: dissipated energy.*

Test	F_{slip} [kN]	Energy [MJ]μ
HYB-2; HYB-3; HYB_e-1 (r12)	21.8	78.5
HYB_s-1(r12)	21.2	89.4
Diff %		12.2
HYB_e-1(r345)	29.9	100.5
HYB_s-1(r345)	32.2	118.6
Diff.%		11.4

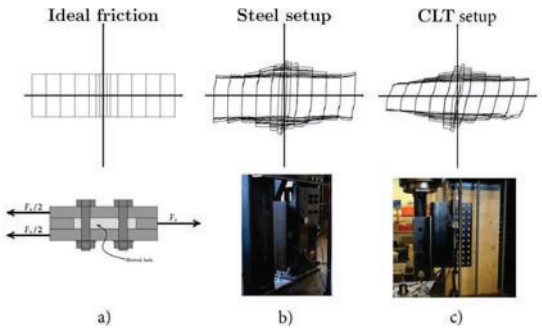

Figure 13: *Scheme illustrating how the addition of more components to the friction connection influences the behaviour: a)single ideal friction connection; b)specimens tested on the steel setup in* [5], [8]*; c) specimens tested on the CLT setup in* [8].

5 CONCLUSIONS

This paper presents the results of an experimental campaign on a novel friction connection for seismic retrofit purposes. The retrofit system, part of the European project e-Safe, is called e-CLT and consists of applying a CLT panel to the outside of existing RC-framed buildings by using a special connector that acts as a friction damper. The experimental campaign presented in this paper, following the first phase presented in [11], aims at studying the interaction between the friction behaviour and the presence of a screw connection between the steel plate and a CLT panel. Four different specimens were tested on two setups: one with a CLT panel and one without a CLT panel, and the main conclusions are:

- The system works and dissipates energy with a rectangular-like shaped hysteresis loop, while not being a perfect rigid-plastic system because of the many components of the system;
- Aluminium represents a good choice for the shim layers, and the friction coefficient values that were obtained are in line with literature values;
- The main effect of adding a steel-to-timber screw connection to the system is a loss of dissipation capacity due to the added deformability component: on average the system with CLT connection dissipates 12% less energy.

Following the promising results of the testing campaign at component level, a new series of tests at frame level is being planned. A 3x4 m RC frame with masonry infill will be tested with and without the e-CLT retrofit system.

FUNDING

This paper was carried out in the framework of the "Energy and seismic affordable renovation solutions" (e-SAFE) project, which has received funding from the European Union's Horizon 2020 research and innovation programme under grant agreement No.893135. Neither the Executive Agency for Small and Medium-sized Enterprises (EASME) nor the European Commission is in any way responsible for any use that may be made of the information it contains.

REFERENCES

[1] ISTAT, *ISTAT. Annuario statistico italiano*, vol. 1. 2015.

[2] D. S. Priya, A. Cinitha, P. K. Umesha, and N. R. Iyer, "A critical review on enhancing the seismic response of buildings with energy dissipation methods," *J. Struct. Eng.*, vol. 42, no. 3, pp. 78–88, 2015.

[3] T. F. Fitzgerald, T. Anagnos, M. Goodson, and T. Zsutty, "Slotted bolted connections in aseismic design for concentrically braced connections," *Earthq. spectra*, vol. 5, no. 2, pp. 383–391, 1989.

[4] G. Margani, G. Evola, C. Tardo, and E. M. Marino, "Energy, seismic, and architectural renovation of RC framed buildings with prefabricated timber panels," *Sustain.*, vol. 12, no. 12, p. 4845, 2020.

[5] F. Boggian, C. Tardo, A. Aloisio, E. M. Marino, and R. Tomasi, "Experimental Cyclic Response of a Novel Friction Connection for Seismic Retrofitting of RC Buildings with CLT Panels," *J. Struct. Eng.*, vol. 148, no. 5, 2022.

[6] M. R. Hatletveit, "Mechanical assessment of a steel dissipating system for RC buildings retrofitting with CLT panels," Norwegian University of Life Sciences, 2020.

https://doi.org/10.52202/069179-0420

[7] A. Aloisio, A. Contento, F. Boggian, and R. Tomasi, “Probabilistic friction model for aluminium–steel Asymmetric Friction Connections (AFC),” *Eng. Struct.*, vol. 274, p. 115159, 2023.

[8] F. Boggian, A. Aloisio, and R. Tomasi, “Experimental and analytical study of Friction Connection for seismic retrofit with Cross-Laminated Timber (CLT) panels,” *Earthq. Eng. \& Struct. Dyn.*, vol. 51, no. 14, pp. 3304–3326, 2022.

[9] D. Fitzgerald, A. Sinha, T. H. Miller, and J. A. Nairn, “Axial slip-friction connections for cross-laminated timber,” *Eng. Struct.*, vol. 228, p. 111478, 2021.

[10] J. C. Chanchi Golondrino, G. A. MacRae, J. G. Chase, G. W. Rodgers, and G. C. Clifton, “Asymmetric Friction Connection (AFC) design for seismic energy dissipation,” *J. Constr. Steel Res.*, vol. 157, pp. 70–81, 2019.

[11] F. Boggian, C. Tardo, A. Aloisio, E. Marino, and R. Tomasi, “Experimental cyclic response of a novel friction connection for seismic retrofitting of RC buildings with CLT panels,” *J. Struct. Eng.*, 2022.

World Conference on Timber Engineering Oslo 2023

NAIL-LAMINATED TIMBER-CONCRETE COMPOSITE BEAMS WITH NOTCHED CONNECTIONS AND STEEL FIBRE REINFORCEMENT

Hamidreza Chaboki [1], Lei Zhang [2], Thomas Tannert [3], Jianhui Zhou [4]

ABSTRACT: The utilization of timber-concrete composite (TCC) floors, which involves connecting a wood beam or panel to a concrete layer via shear connectors, has experienced a surge in popularity in recent years. Although notched connections have proven to be cost-effective shear connections, without proper concrete reinforcement, cracks can develop in the notched area and ultimately lead to brittle shear failure. In this paper, we present research aimed at mitigating crack growth in concrete and preventing notch shear failure in concrete by employing steel fibre reinforcement. Eight groups of nail-laminated TCC beams with varying notch depth, location and number of notches, and thickness ratio of concrete to timber were tested under third-point bending. The results demonstrated that the number of notches and thickness ratio had the greatest impact on beam bending properties, while the influence of notch location and depth was marginal. Furthermore, the steel fibres effectively delayed crack propagation in the concrete notches, resulting in timber failure in all tested specimens. The notches cut on NLT and filled with concrete affect the modulus of elasticity of NLT and need to be considered for the calculation of composite efficiency and effective TCC beam bending stiffness.

KEYWORDS: Timber-concrete composite floor, Bending performance, Notched connection, Steel fibres

1 INTRODUCTION

1.1 Background

Timber-concrete composite (TCC) floors exhibit enhanced bending stiffness and load-carrying capacity compared to pure timber floors of the same depth, enabling longer spans. The combination of a concrete layer to resist compression and timber to resist tension results in efficient utilization of the mechanical properties of both materials. In addition, TCC floors offer superior fire resistance, vibration damping, and acoustic performance compared to bare timber floors [1-5].

Shear connections are integral to generating composite action between the materials in TCC. Various types of connections have been tested, including self-tapping screws and glued-in steel mesh plates [5]. However, these metal fasteners can be disadvantageous in terms of constructability, cost, and labour intensity. Notched connections, prefabricated using computer numerical control machines, offer a potential solution, as they allow for precise, rapid, and cost-effective production with minimal use of metal fasteners [4]. However, the reduction of the cross-sectional area due to the notches impacts the bending capacity and stiffness of the TCC floors [6]. The TCC floor bending stiffness and strength are also influenced by the number and locations of notches, as well as the presence of additional steel fasteners [7]. Up to date, the notched connections are not standardized in the TCC floor design.

Zhang et al. [7] conducted a parametric study to investigate the impact of various geometry-related factors such as depth and number of notches, timber shear length, and concrete thickness on the bending stiffness of TCC floors. Their findings suggest that optimizing the number, location, and size of notches can lead to high composite efficiency in the TCC system. Shi et al. [6] examined the shear behavior of notched connections and observed that when the length of the notch increased from 150 mm to 250 mm, the failure mode changed from shear failure of concrete in the notch to compression failure of timber in front of the notch. Zhang et al. [8] developed an analytical method involving a simple release-and-restore procedure to predict stress distribution and slip between timber and concrete while considering the discrete and semi-rigid features of the notched connections.

The high stiffness of notched connections allows the notches to be spaced along the beam at a large distance, making the concrete layer susceptible to cracking due to stress concentration at the notches. The cracking of concrete can lead to brittle failure and a reduction in beam load-carrying capacity, especially in the absence of reinforcement [9,10]. To address these issues, additional screws are often used to take the tensile forces and restrict crack opening and uplifting [11,12]. Alternatively, micro-notches with millimetre dimensions can be milled into the timber surface to improve continuous shear transfer and reduce uplifting forces [13]. Müller and Frangi [13] showed that micro-notches can achieve close-to-full

[1] Hamidreza Chaboki, University of Northern British Columbia, Canada, chaboki@unbc.ca
[2] Lei Zhang, University of Northern British Columbia, Canada, lzhang2@unbc.ca
[3] Thomas Tannert, University of Northern British Columbia, Canada, thomas.tannert@unbc.ca
[4] Jianhui Zhou, University of Northern British Columbia, Canada, jianhui.zhou@unbc.ca

https://doi.org/10.52202/069179-0421

composite action and sufficient shear strength for common residential and office buildings.

In concrete structures, steel fibres are often used as reinforcement to reduce crack formation and control propagation. These fibres connect and bridge gaps in the concrete during hardening, delaying crack growth and reducing crack width [14]. It is advantageous to strength the concrete layer in TCC with steel fibres to restrict the crack opening and prevent shear failure of notched connections.

1.2 OBJECTIVES

In this study, the bending performance of nail-laminated timber-concrete composite beams with notched connections and steel fibre reinforcement was investigated. Third-point bending tests were conducted on eight groups of nails-laminated TCC beams, each featuring varying notch depth, location, and number of notches, as well as thickness ratios of concrete to timber layers, to investigate the variation of notches on the bending performance of the beams, as well as the efficacy of steel fibres in mitigating brittle failure of notched connections. The effect of notches on the modulus of elasticity of NLT for calculating the composite efficiency of TCC was also evaluated.

2 EXPERIMENTAL INVESTIGATIONS

2.1 SPECIMEN CONFIGURATIONS

A total of 24 TCC beams, divided into eight groups, with three replicates in each group, were constructed and tested. The beams had a width of 190 mm, a length of 3.06 m (span of 2.9 m), and a total thickness of 150 mm. The number, depth, and location of notches varied among the groups are shown in Table 1 and illustrated in Figure 1. The notches were symmetrically positioned about the mid-span of beams.

To prevent layer separation, three self-tapping screws with a diameter of 8 mm were inserted into each specimen at the mid-span and two ends, as illustrated in Figure 2. The screws, which had an embedment length of 50 mm in both wood and concrete, were made of carbon steel with a zinc coating. In the case of SP7, the thicker timber layer required a longer embedment length of 60 mm into the wood.

Table 1: *Specification of specimens*

Group	Concrete to timber thickness ratio	Number of notches	Notch depth (mm)
SP1	2:3	2	20
SP2	2:3	2	20
SP3	2:3	4	20
SP4	2:3	4	30
SP5	2:3	4	40
SP6	2:3	4	15-25
SP7	1:2	4	20
SP8	1:1	4	20

The reference group SP3 had a concrete thickness of 60 mm and a timber thickness of 90 mm, with four notches that were 20 mm deep and 150 mm long. To explore the impact of the number of notches on the stiffness and strength of the TCC beams, SP1 and SP2 featured only two notches that were 20 mm deep and spaced 1800 mm and 1200 mm apart, respectively. The location and length of notches in SP4 and SP5 were identical to those of the reference group, but the depths of the notches were 30 mm and 40 mm deep, respectively. In SP6, the notch depth varied along the beam length, with a depth of 25 mm near the supports and 15 mm near the mid-span. Finally, SP7 and SP8 were similar to the control group but differed in their timber-to-concrete thickness ratios. The thickness of timber and concrete in the specimens ranged from 75-100 mm and 50-75 mm, respectively.

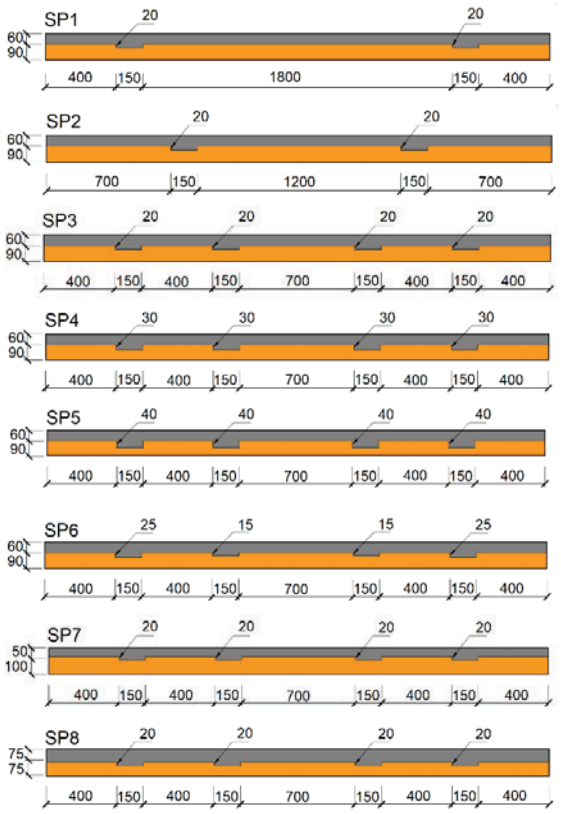

Figure 1: *Nail-laminated timber-concrete composite beam configurations (dimensions in mm)*

2.2 MATERIALS

Five 38 mm thick spruce-pine-fir (SPF) lumber planks of grade No. 2 were nailed together (6d, 3 inches long, one row @ 120 mm spacing) to fabricate the nail-laminated timber (NLT) beams. The lumber had an average density of 444 kg/m^3 and a moisture content of 13% before testing. The notches on NLT were cut using a router. The moduli of elasticity (MOE) of the NLT beams were measured before (E_t) and after ($E_{t,notched}$) cutting the notches by non-destructive centre-point bending tests.

https://doi.org/10.52202/069179-0421

The average measured MOE values of each NLT group are listed in Table 2, which indicates different levels of MOE reduction after notching (11% to 62%). SP5 with the deepest notches showed the highest drop in MOE while SP1 with the minimal number of notches showed the lowest reduction. The choice of MOE on the composite efficiency and the bending stiffness of TCC are discussed in the results section.

Table 2: *Average MOE values of NLT beams*

Group	E_t (MPa)	$E_{t,notched}$ (MPa)	$E_{t,n\&c,FEM}$ (MPa)
SP1	7802	6907	7027
SP2	9618	7291	7921
SP3	7931	5941	6855
SP4	7900	4451	5488
SP5	8615	3311	4685
SP6	7677	6208	6622
SP7	8316	6493	6605
SP8	9790	6460	7925

Note: E_t is the MOE of NLT tested without notches; $E_{t,notched}$ is the MOE of NLT tested with notches; $E_{t,n\&c,FEM}$ is the MOE of NLT determined from the finite element model.

Figure 2: *Specimen preparation A) NLT with notches and screws B) Formwork for concrete casting C) After concrete curing*

The specimen preparation process is shown in Figure 2. To avoid the formation of voids around the corners of notches, the nominal maximum coarse-aggregate size in concrete was chosen as 10 mm. All the specimens were made from the same batch of concrete. To reinforce the concrete layer, HE-4550 steel fibres with 50 mm length and two bend ends were used in a volume reinforcement ratio of 0.5%. Three cylinders with a nominal diameter of 100 mm and a height of 200 mm were cast at the same time and tested according to ASTM C39/C39M-20 [15] after 28 days. The average compressive strength of concrete cylinders was 39.3 MPa, with a coefficient of variation of 1%. Concrete cylinders had a density of 2,325 kg/m^3. The Young's modulus of concrete was estimated as 28027 MPa based on the 28-day compressive strength (f_c') and density (γ_c) applying Eq. (1) [16]:

$$E_c = (3300\sqrt{f_c'} + 6900)(\frac{\gamma_c}{2300})^{1.5} \quad (1)$$

2.3 FINITE ELEMENT MODELS

2D finite element models of the NLT beams were developed in the general-purpose finite element software ABAQUS [17] to numerically evaluate MOE of the notched NLT with concrete filled in notches ($E_{t,n\&c,FEM}$). The contact between timber and concrete in the tangential direction was defined as penalty with a coefficient friction of 0.6 [18] and a hard contact in the normal direction. The model was verified for both solid and notched NLT beams. The results of MOE for the notched NLT filled with concrete are shown in Table 2. Compared to NLT without notches, the reduction of MOE with notches filled with concrete ranges from 10% to 46% depending on the notch configurations.

2.4 METHODS

The TCC beams were tested under three-point bending based on ASTM 198-15 [19], as illustrated in Figure 3. The supports were 100 mm wide to avoid indentation of wood. Two string potentiometers were used to measure the mid-span deflection, and four LVDTs were installed at two ends of each beam on both sides to measure the relative slip between timber and concrete. The deflection and load were recorded for calculating the bending stiffness and moment capacities. The displacement-controlled load was applied at a rate of 3 mm/min to ensure the specimens failed in roughly 20 minutes.

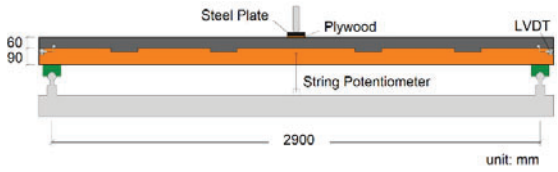

Figure 3: *Schematic of the bending test setup*

The serviceability bending stiffness (referred to as bending stiffness herein) of the floors was determined from Eq. (2) [19]:

$$EI = \frac{PL^3}{48\Delta} \quad (2)$$

where L is span and P/Δ is the slope of the load-deflection curve between 10% and 40% of peak load, regarded as the load level at serviceability limit states [20].

Eq. (3) was used to determine the ultimate bending stiffness of the beams [19]:

$$EI_{ult} = \frac{L^3}{48}\frac{0.8P_{max}}{\Delta_{0.8}} \quad (3)$$

https://doi.org/10.52202/069179-0421

where $\Delta_{0.8}$ indicates the mid-span deflection at 80% of the peak load [20].

The composite efficiencies of the tested TCC beams were evaluated by comparing them with non-composite and full composite TCC beams. The theoretical bending stiffness of a non-composite floor can be calculated using Eq. (4), where E_c and E_t are the concrete and timber moduli of elasticity, respectively; and I_c and I_t are the concrete and timber second moments of area, respectively [21].

$$EI_{no} = E_c I_c + E_t I_t \tag{4}$$

The bending stiffness for the theoretical full composite floor is determined according to Eq. (5) [21]

$$EI_{full} = E_c I_c + E_t I_t + \frac{\left(\frac{h_c + h_t}{2}\right)^2}{\frac{1}{E_c A_c} + \frac{1}{E_t A_t}} \tag{5}$$

where A_c and A_t are the cross-section areas of concrete and timber, respectively; and h_c and h_t are the concrete and timber depths, respectively.

The deflection-based composite efficiency [21] is calculated according to Eq. (6):

$$\lambda = \frac{\Delta_{no} - \Delta}{\Delta_{no} - \Delta_{ful}} = \frac{\frac{1}{EI_{no}} - \frac{1}{EI}}{\frac{1}{EI_{no}} - \frac{1}{EI_{full}}} \tag{6}$$

where Δ_{no}, Δ_{ful}, and Δ are the deflections of the non-composite, full composite, and tested beams under the same load (10% - 40% of peak load).

3 RESULTS AND DISCUSSION

3.1 LOAD-DEFLECTION RELATIONSHIPS & FAILURE MODES

The load-deflection curves and failure modes for each group are presented in Figures 4 and 5, respectively. As the load increased, the TCC beams deformed elastically at the beginning and then exhibited nonlinear deformation after surpassing certain load levels. Concrete shear cracks formed around notches and propagated diagonally or nearly vertically after reaching certain load levels, but the steel fibers limited the extent of crack opening. Since the NLT beams were attached using nails, the lumber planks failed individually, causing multiple peaks and drops in the load-deflection curves.

The failure modes of the specimens are summarized in Table 3. The majority of TCC beams failed in the timber layer due to tension or combined bending and tension, as shown in red circles in Figure 5. Notched connection configurations and the relative thicknesses of timber and concrete in TCC beams did not significantly impact the failure patterns.

In terms of concrete failure, almost all specimens had diagonal concrete cracking at the notched corners (shear cracks) that started in a diagonal or almost vertical orientation, then spread horizontally. Once the first timber bending failure happened, a gap between timber and concrete was formed. With more lumber failure and an increase in deflection, the notched connections in the concrete portion were sheared off, starting with one external notch near the support and then the internal notch on the same side. The failure of the notches caused the failure of the concrete layer.

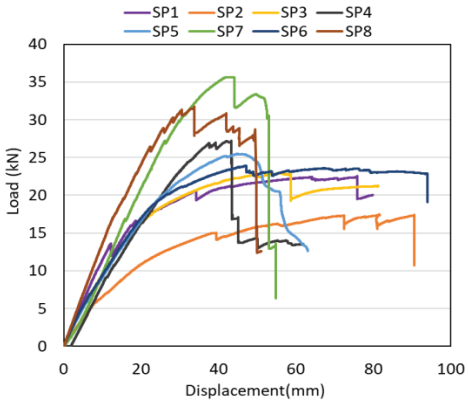

Figure 4: *Typical load-deflection curves of each group*

Figure 5*: Failure patterns of NLTCC beams under bending*

The specimens SP1, SP7, and SP8 with the same notched connections but different concrete-to-timber thickness

ratios exhibited slightly different failure patterns. SP1 experienced timber bending failure at mid-span without visible damage to the concrete layer. SP7 was able to withstand a higher load even after two lumber planks failed by bending. The steel fibres controlled the crack width in the concrete, resulting in higher loads and buckling failure of the concrete. In SP8, after the timber failure, concrete was buckled under compression. It is worth noting that the steel fibres limited the crack width and provided ductility. The progressive failure in NLT and the reinforcement of concrete using steel fibres are believed to be the reasons for the ductile behaviour observed in these groups.

Table 3: *Nail-laminated TCC beam failure modes*

Group	Failure mode
SP1	Timber combined bending and tensile failure
SP2, SP3 SP4, SP5 SP6	Timber combined bending and tensile failure & notch shear failure in concrete
SP7 SP8	Timber combined tensile and bending failure, notch shear failure in concrete & concrete buckling

3.2 BENDING PROPERTIES

The bending properties including the average peak load (P_{max}), bending stiffness (EI), ultimate bending stiffness (EI_{ult}), and bending stiffness reduction are listed in Table 4. Comparing load-carrying capacities among different groups, groups SP1 and SP2 exhibited similar load-carrying capacities, approximately 18.5 kN; Groups SP3-6 exhibited similar load-carrying capacities at around 24.0 kN; Groups SP7 and SP8 exhibited the highest load-carrying capacities of 32.5 kN. Comparing groups SP1-6, all of which had the same total beam thickness and concrete-to-timber thickness ratio, it is apparent that the number of notches had a positive impact on the floor load-carrying capacity. Interestingly, the depth of notches between 15 mm and 40 mm did not affect the load-carrying capacity when comparing groups SP3-6. No clear trend can be observed concerning the impact of the thickness ratio of concrete to timber on the strength properties of beams.

The notch configuration had slightly different effects on the serviceability and ultimate bending stiffness of beams. SP1,3-5 have similar serviceability bending stiffness values from 438 to 458 kNmm^2, while those of SP2 and SP6 had lower values from 382 to 398 kNmm^2. Although the NLT beams had higher bending stiffness in SP2 and SP6 (shown in Table 2), the lower connection stiffness in the two specimen series resulted in lower bending stiffness of composite beams. SP8 has the highest bending stiffness owing to the highest concrete-to-timber thickness ratio. However, the second-highest bending stiffness was observed in SP7 which had the lowest concrete-to-timber thickness ratio. It should be noted that small cracks can happen in concrete while moving the TCC beams before testing, and workmanship was not the same in all the specimens. SP7 seems to be the group with the highest quality, making it difficult to investigate the effect of notch configurations on beam bending stiffness.

The reduction of stiffness from serviceability state (EI) to ultimate state (EI_{ult}) varies among the groups from 1.4% to 28.0% without a clear pattern. Further analysis of the slip between the two layers in each group is required, as the notch configurations may have an impact on the actual connection stiffness in each group.

Table 4: *Summary of peak load and bending stiffness*

Group	P_{max} (kN)	EI (kNm^2)	EI_{ult} (kNm^2)	Reduction of stiffness
SP1	19.0	439	432	1.4%
SP2	18.0	382	274	28.0%
SP3	23.7	458	343	26.1%
SP4	25.5	458	394	13.8%
SP5	23.4	438	383	12.6%
SP6	25.3	398	382	3.6%
SP7	33.4	578	533	8.0%
SP8	31.9	684	581	15.2%

3.3 COMPOSITE EFFICIENCY

The calculated deflection-based composite efficiencies of the composite beams according to Eq. (6) are presented in Figure 6. The values are computed with different MOE values of NLT beams listed in Table 2. The values in blue are calculated based on the measured E_t of NLT beams without notches; values in red were based on the measured $E_{t,notch}$ of NLT beams with notches; and values in grey were based on $E_{t,n\&c,FEM}$ of NLT beams with notches filled with concrete determined from finite element models. The trend of composite efficiency among groups is similar to that of the serviceability bending stiffness. Groups SP7 and SP8 had higher composite efficiencies than the rest of the groups, while group SP2 has the lowest composite efficiency.

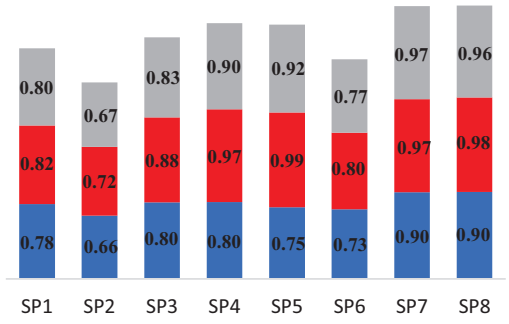

Figure 6: *Composite efficiency of deflection using different timber modulus of elasticity*

Not surprisingly, the higher the MOE used, the lower the composite efficiency was determined. The choice of MOE values of NLT beams can lead to different judgments of composite efficiency and composite action. For instance, for group SP5, the composite efficiency using the measured $E_{t,notch}$ is 24% higher than that using the

https://doi.org/10.52202/069179-0421

measured E_t, and is 7% higher than that using the $E_{t,n\&c,FEM}$. The same issue of choosing MOE of timber will arise when it comes to the prediction of bending stiffness of TCC beams with notches, which should be considered in the design practice.

4 CONCLUSIONS

The bending properties of 24 NLT-concrete composite beams with varied notched configurations and steel fibre reinforcement were investigated experimentally in this work. The following conclusions can be derived: 1) The notch number and concrete-to-timber ratio had major impacts on the beam bending performance, while notch location and depth had marginal impact. 2) The use of steel fibres can postpone shear failure in concrete and ensure a more controllable timber bending failure. 3) The effect of notches on the MOE of timber can lead to different interpretations of composite efficiency and prediction of bending stiffness of composite beams.

ACKNOWLEDGEMENT

This project was supported through an NSERC Discovery Grant and the BC Forestry Innovation Investment –Wood First program. The authors appreciate the technical support from the technicians at the Wood Innovation Research Laboratory at UNBC.

REFERENCES

[1] Higgins, C., Barbosa, A. R., Blank, C. 2017. Structural tests of concrete composite-cross-laminated timber floors. Rep. No. 17-01. Corvallis, OR: Oregon State University.

[2] Martins, C., Santos, P., Almeida, P., Godinho, L., Dias, A. 2015. Acoustic performance of timber and timber-concrete floors. Construction and Building Materials, 101: 684–691.

[3] Mai, K. Q., Park, A., Nguyen, K. T., Lee, K. 2018. Full-Scale Static and Dynamic Experiments of Hybrid CLT–Concrete Composite Floor. Construction and Building Materials, 170: 55–65.

[4] Zhang L., Chui Y. H., Tomlinson D. 2020. Experimental investigation on the shear properties of notched connections in mass timber panel-concrete composite floors. Construction and Building Materials, 234: 117375.

[5] Yeoh, D., Fragiacomo, M., De Franceschi, M., Heng Boon K. 2011. State of the Art on Timber-Concrete Composite Structures: Literature Review. Journal of Structural Engineering, 137(10): 1085-1095.

[6] Shi, D., Hu, X., Du, H., Xie, Z., Meng, Y. 2021. Study on shear performance of notched connections for glulam-concrete composite beams under fire. Fire Safety Journal, 126: 103482.

[7] Zhang, L., Zhou, J., Zhang, S., Chui, Y. H. 2022. Bending stiffness prediction to mass timber panel-concrete composite floors with notched connections. Engineering Structures, 262: 114354.

[8] Zhang, L., Zhang, S., Chui, Y. H. 2021. Analytical evaluation to the timber-concrete composite beam connected with notched connections. Engineering Structures, 227: 111466.

[9] Jiang, Y., Crocetti, R. 2019. CLT-concrete composite floors with notched shear connectors. Construction and Building Materials, 195: 127-139.

[10] Dias, A., Schänzlin, J., Dietsch, P. 2018. Design of timber-concrete composite structures. COST Action FP1402/WG 4, Shaker Verlag Aachen.

[11] Boccadoro, L., Steiger, R., Zweidler, S., Frangi, A. 2017. Analysis of shear transfer and gap opening in timber-concrete composite members with notched connections. Materials and Structures, 50(5): 1–15.

[12] Boccadoro, L., Zweidler, S., Steiger, R., Frangi, A. 2017. Bending tests on timber-concrete composite members made of beech laminated veneer lumber with notched connection. Engineering Structures, 132: 14–28.

[13] Müller, K., Frangi, A. 2021. Micro-notches as a novel connection system for timber-concrete composite slabs. Journal of Engineering Structures, 245: 112688.

[14] Ghalehnovi, M., Karimipour, A., de Brito, J., Chaboki, H. 2020. Crack width and propagation in recycled coarse aggregate concrete beams reinforced with steel fibres. Applied Sciences, 10(21): 75-87.

[15] ASTM. 2020. Standard test method for compressive strength of cylindrical concrete specimens. ASTM C39/C39M-20. West Conshohocken, PA: ASTM.

[16] CSA. 2019. Design of concrete structures. CSA A23.3-19. Mississauga, ON, Canada.

[17] ABAQUS/CAE. 2017. User's Manual. Dassault Systeme Simulia.

[18] Jaaranen, J., Fink, G. 2020. Friction behaviour of timber-concrete contact pairs. Construction and Building Materials, 243: 118273-118282.

[19] ASTM. 2015. Standard test methods of static tests of lumber in structural sizes. ASTM D198-15. West Conshohocken, PA: ASTM.

[20] CEN. 1991. Timber structures — Joints made with mechanical fasteners — General principles for the determination of strength and deformation characteristics. EN 26891. Brussels, Belgium: CEN.

[21] Zhang, L., Zhou, J., Chui, Y. H., Tomlinson, D. 2022. Experimental Investigation on the Structural Performance of Mass Timber Panel-Concrete Composite Floors with Notched Connections. Journal of Structural Engineering, 148: 04021249.

World Conference on Timber Engineering Oslo 2023

PUSH-OUT TESTS OF WET-PROCESS ADHESIVE-BONDED BEECH TIMBER-CONCRETE AND TIMBER-POLYMER-CONCRETE COMPOSITE CONNECTIONS

Matthias Füchslin[1,2], Philippe Grönquist[1,3,4]*, Sandro Stucki[5,6], Tim Mamie[7], Steffen Kelch[7], Ingo Burgert[5,6], Andrea Frangi[1]

ABSTRACT: For timber-concrete composite (TCC) elements, a stiff and rigid connection results in an enhanced shear stress transfer at the timber-concrete interface, and thus, reduces the necessary cross-section height. A full composite action can hypothetically be achieved using an adhesive connection. In this study, an adhesive system developed for a wet-process gluing of concrete to European beech glued-laminated timber (GLT) is investigated by means of push-out tests. The tests were conducted on a specimen series with three different sizes of varying shear length, and evaluated using digital image correlation (DIC). The bondline shear strengths showed a pronounced size dependency, while the connection stiffness remained similar but showed a very large variability. These findings challenge the interpretation of bondline connection properties derived from push-out tests of glued TCC elements. In addition to the wet-process adhesive system with cement-based concrete, bonding between timber and a polymer concrete was investigated as an alternative possibility for TCC.

KEYWORDS: Adhesive connection, Digital image correlation, Polymer concrete, European beech GLT

1 INTRODUCTION

For the design of timber concrete-composite (TCC) structures, reliable knowledge of the specific connection behaviour is important. While annex B of Eurocode 5 [1] provides the "γ-method" in order to approximate the composite's flexural rigidity, the value of γ itself is to be derived from the connection stiffness K, which in turn, is to be determined for each specific type of connection. For the determination of K, usually, one of two types of push-out tests is commonly used: (1) a symmetric double-shear push-out test, such as suggested in annex C of CEN/TS 19103 [2], or (2) a single-shear push-out test with asymmetrical samples. Both methods possess specific advantages and disadvantages, such as potential prevailing asymmetry due to variability in timber material properties in test (1) when both side parts are timber, or high friction forces between timber and concrete for test (2). Additionally, in both tests, due to the load path, moments are induced and the resulting stress state does not reflect pure shear. Nonetheless, both methods tend to result in reliable values of K for most of the available TCC connection types, i.e., prevalently for the different metallic fastener and notch types.

To maximize composite action, and thus maximize the static efficiency of the TCC cross-section, a glued connection can be used. In this case, for the design of slabs, a value of $\gamma = 1$ (fully rigid connection) is usually assumed without the need for more precise analysis of K [3,4]. In fact, a handful of previous studies analysed the load-bearing behaviour of adhesively bonded TCC using building component scale sized push-out tests [5-13]. In most of the cases, the push-out tests were solely used for the purpose of verification of the load bearing capacity of the adhesive bond, whereas the connection stiffness K was not investigated. An exception is the study by Tannert et al. [13] who reported $K \approx 1'160 - 1'340$ kN/mm for a two-component epoxy adhesive (*Sikadur-32 Hi-Mod*). However, the aforementioned drawbacks of the testing methods do not necessarily permit to derive reliable values of K and of the shear strength, especially in the case of a glued connection, due to the non-local but dispersed and complex force flow.

In this study, European beech glued-laminated timber (GLT) was bonded in a wet process to self-compacting concrete using a newly developed hybrid adhesive combining epoxy and silane-terminated polymers. In order to assess a size-dependency of the connection properties, symmetric double-shear push-out tests were conducted on three specimen series with different shear length each. Surface strain fields were measured using digital image correlation (DIC), and bondline connection stiffness K was determined from surface displacement fields. In addition, two specimen series using a directly-bonding polymer concrete were tested to provide a benchmark and assess the bonding behaviour of polymer concrete on beech timber.

2 MATERIALS AND METHODS

2.1 Specimen series design

Three pushout specimen series with different shearing lengths were designed. In the case of the adhesive-bonded

[1] ETH Zurich, Institute of Structural Engineering, Switzerland
[2] B3 Kolb AG, Switzerland
[3] University of Stuttgart, Institute of Construction Materials, Germany
[4] University of Stuttgart, Materials Testing Institute, Germany
[5] Empa, Cellulose & Wood Materials, Switzerland
[6] ETH Zurich, Institute for Building Materials, Switzerland
[7] Sika Technology AG, Switzerland
* Correspondence: philippe.groenquist@iwb.uni-stuttgart.de

https://doi.org/10.52202/069179-0422

concrete in a wet process, the series were denoted as follows:

- **CL** (concrete large) with shearing length of 2 x 240 mm,
- **CM** (concrete medium) with shearing length of 2 x 180 mm, and
- **CS** (concrete small) with shearing length of 2 x 120 mm.

The shearing depth, and depth of all specimen components, was chosen as 240 mm. The detailed sample design is depicted in Figure 1. For series CL, CM, and CS, the predicted failure mode was a shear failure of the adhesive, while the probability of a shear failure of the concrete near the adhesive bond could not be entirely excluded. For the benchmark series using directly bonding polymer concrete, two series were chosen:

- **PM** (polymer concrete medium) with shear length of 180 mm, and
- **PS** (polymer concrete small) with shear length of 120 mm.

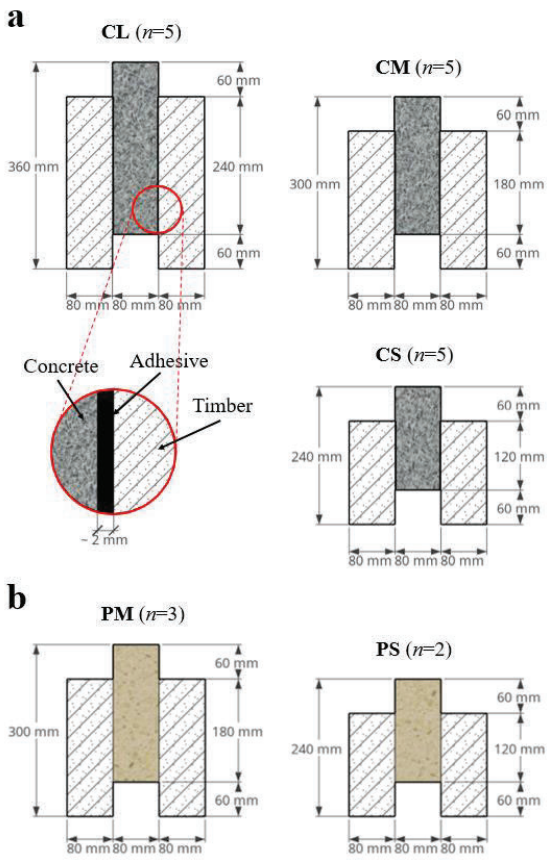

Figure 1: *Push-out specimen series with dimensions and number of tested specimens (n). Specimens have a constant depth of 240 mm (out of plane dimension).* ***a****: Series CL, CM, and CS for adhesively-bonded concrete in wet process.* ***b****: Series PM and PS for directly bonded polymer concrete.*

2.2 Specimen production

Defect-free GLT blocks of strength class GL48h were obtained from *Fagus Suisse SA*, made of European beech (*Fagus sylvatica*) wood of Swiss origin [14]. The blocks, were cut and planed to match the dimensions as shown in Figure 1. Their density was recorded as 722±20 kg/m^3, at an initial wood moisture content of approx. 8±0.5%. For the series CL, CM, and CS, for 5 specimens per series, a two-component silane-terminated polyurethane epoxy-hybrid (STP-E) adhesive, developed by *Sika Technology AG,* was evenly applied to both the timber side-parts of the pushout specimens. An amount of 1500 g/m^2 was applied on cleaned timber surfaces. After an initial phase of 25 minutes in horizontal position to allow for the adhesive to reach an optimal viscosity, see Figure 2a, the coated blocks were inserted into the formwork. *Sikacrete-16 SCC* [15], a self-compacting ready-mix concrete from *Sika Schweiz AG* of approx. grade C30/37 and maximal grain size of 16 mm, was cast in between the blocks, see Figure 2b. The specimens were left in the formwork for 5 days, and were tested after 28 days, meanwhile being covered by plastic foil during curing of the concrete to avoid drying.

For the series PM and PS, with 2 specimens each, the timber blocks were directly inserted into the formwork. *Sikadur 42 HE* [16], an epoxy-based grout from *Sika Schweiz AG*, in combination with quartz sand of grain size of < 4 mm, was cast. The specimens were left in the formwork for 5 days, and were tested after 28 days.

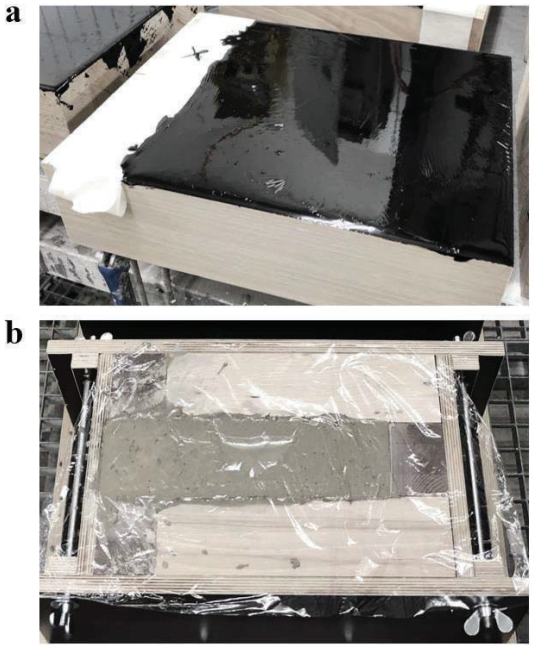

Figure 2: *Preparation of concrete specimens (CL, CM, CS).* ***a****: Application of controlled amount of STP-E adhesive (black).* ***b****: Casted self-compacting concrete mixture in formwork containing beech GLT with applied adhesive.*

2.3 Pushout testing

The specimens were tested using a displacement-controlled servo-hydraulic testing machine of type *Schenck 1600*, with a maximal capacity of 1600 kN (see Figure 3). Compressive forces were continuously recorded by a load cell. In addition to the machine displacement, redundant displacement measurements were conducted by three linear variable differential

transducers (LVDT) between the loading plates and surrounding the pushout specimens. Furthermore, a camera recorded an applied speckle pattern on the specimen sides in order to compute surface displacements and strain fields by means of digital image correlation (DIC). The specimens were initially loaded and unloaded twice until 30% of their estimated carrying capacity, and then ultimately loaded until failure.

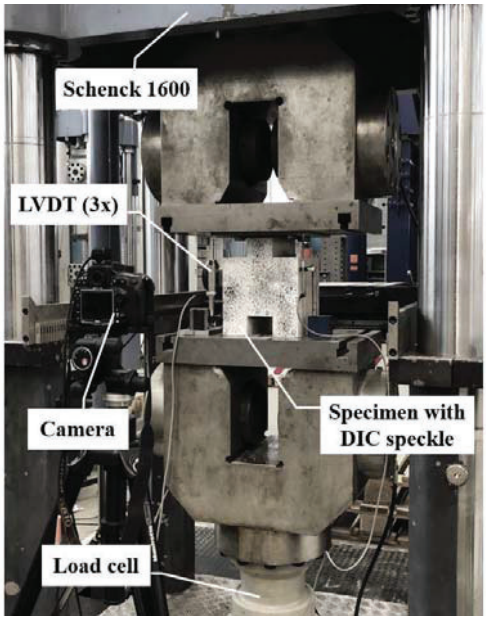

Figure 3: *Testing setup. Compressive Force applied by a displacement-controlled servo-hydraulic testing machine (Schenck 1600). Additional displacement measurements by three linear variable differential transducers (LVDT), and by digital image correlation (DIC).*

2.4 Determination of properties

The bondline shear strengths f_v were determined by dividing the maximum recorded forces F_{max} by the shearing area A_v:

$$f_v = \frac{F_{max}}{A_v}$$

The bondline connection stiffness K was determined for each of the two shearing lengths (right and left) per specimen separately, by dividing half of the applied force ΔF (force difference in a linear range of force-displacement) by the resulting average differential displacement between the timber and the concrete ($v_{m,t} - v_{m,c}$) parts:

$$K = \frac{\Delta F}{2(v_{m,t} - v_{m,c})}$$

The separate timber ($v_{m,t}$) and concrete ($v_{m,c}$) displacements were calculated locally for each of the parts near the bondline, but as averages over the whole shearing lengths, from computed displacement fields using the DIC technique. For DIC processing, *Ncorr*, an open source 2D DIC *Matlab*-based program was used [17].

3 RESULTS

Obtained results for shear strengths and bondline connection stiffnesses are shown in Figure 4 and Figure 5 as single data points, and summarized in Table 1 as mean values. An exemplary load vs. displacement curve is shown in Figure 6. A pronounced size-dependency in the shear-strengths across the different series CL (0.55 N/mm^2), CM (1.32 N/mm^2), and CS (2.22 N/mm^2) can be observed. However, these reported bondline shear strengths do not necessarily reflect the shear strength of the adhesive bond itself. As shown in Figure 7, the failure modes for the C-series (CL, CM, and CS) could be characterized as cohesive shear failure of the concrete near the bondline. For the same series, the connection stiffness shows no size-dependency, but instead, a very high scattering, as standard deviations surpass or are in the range of the mean values, see Table 1. Across all wet-process adhesive-bonded series, a mean value of 1.36 ± 0.72 N/mm^2 for the bondline strength at the moment of concrete cohesive failure at the bondline, and a mean value of 1'182 ± 1'469 kN/mm for the bondline connection stiffness can be reported.

The directly-bonded polymer concrete P-series (PM and PS) showed much better performances of the bondline, with overall mean values of 12.24 ± 3.34 N/mm^2 and 19'235 ± 25'202 kN/mm for the stress acting on the bondline at the moment of failure, and the bondline connection stiffness, respectively. Here, two failure modes were exclusively observed: Tensile-shear failure of polymer concrete and subsequent shear failure of timber, see Figure 7d. No size-dependency of the shear strengths is visible from the four tested specimens. However, an even higher standard deviation than for the adhesive-bonded specimens is reported for the bondline connection stiffness.

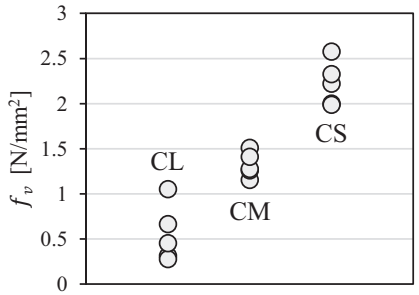

Figure 4: *Bondline shear strength (concrete cohesive failure) data points of series CL, CM, and CS, displaying size-dependency.*

https://doi.org/10.52202/069179-0422

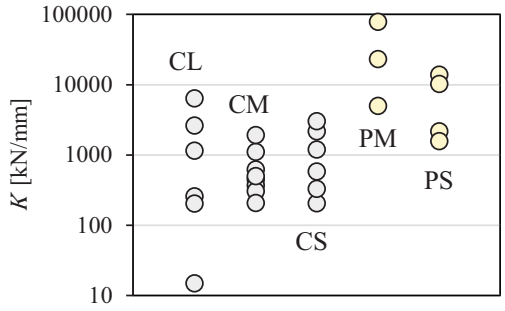

Figure 5: *Bondline connection stiffness (K) calculated from DIC data of both shearing lengths for each specimen of series CL, CM, CS, PM, and PS (note: Some data points missing due to DIC processing not possible).*

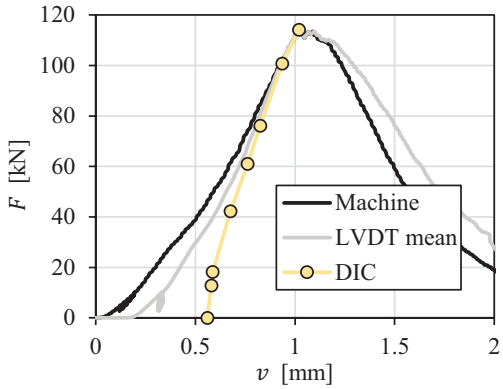

Figure 6: *Exemplary load (F) vs. displacement (v) curves of a specimen from series CS as measured by machine displacement, mean value of 3 LVDT curves, and displacement computed by DIC (markers represent images taken by camera). Curves were horizontally shifted to reach F_{max} simultaneously.*

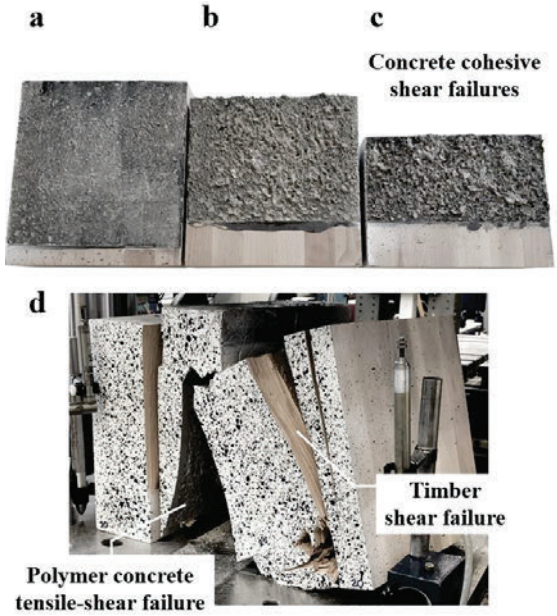

Figure 7: *Observed failure modes. a: Series CL: Concrete cohesive shear failure. b: Series CM: Concrete cohesive shear failure. b: Series CM: Concrete cohesive shear failure. d: Series PM and PS: Polymer concrete tensile-shear failure and timber shear failure.*

Table 1*: Results of push-out tests (mean values ± standard deviations of single series): n: Number of specimens, l_v: Shearing length, A_v: Shearing Area, F_{max}: Force at failure, f_v: Shear strength of bondline, K: Bondline connection stiffness calculated using DIC fields.*

	n	l_v[mm]	A_v[mm^2]	F_{max} [kN]	f_v [N/mm^2]	K [kN/mm]
CL	5	2 x 240	115'200	63.5 ± 32.8	0.55 ± 0.28[a]	1'175 ± 2'465
CM	5	2 x 180	86'400	114.1 ± 10.7	1.32 ± 0.12[a]	685 ± 569
CS	5	2 x 120	57'600	128.0 ± 12.7	2.22 ± 0.22[a]	1'253 ± 1'130
				ø:	1.36 ± 0.72[a]	1'182 ± 1'469
PM	2	2 x 180	86'400	1'025.0 ± 360.0	>[7.05; 14.26][b,c]	31'754 ± 30'554[d]
PS	2	2 x 120	57'600	795.9 ± 170.2	>[11.73; 15.91][b,c]	6'965 ± 6'064[d]
				ø:	>12.24 ± 3.34[b]	19'235 ± 25'202[d]

[a]: Shear stress acting on bondline at the moment of concrete cohesive failure at/near the adhesive bondline.

[b]: Shear stress acting on bondline at the moment of polymer concrete failure.

[c]: Data points of both tested specimens.

[d]: Interfacial zone stiffness (polymer concrete and timber), no observed bondline compliance (see Figure 10).

https://doi.org/10.52202/069179-0422

4 DISCUSSION

From the exemplary load displacement curves obtained by the three different methods (machine, LVDT, and DIC displacements) as shown in Figure 6, it can be seen that the measured DIC fields can be validated well by the LVDT measurements in regions of higher loads, after the curves are horizontally shifted to match at F_{max}. Therefore, justifying the use of DIC in order to calculate bondline stiffness values K. It can also be seen, that there is a pronounced stiffness difference between the three displacement-recording techniques, showing that both machine and LVDT displacements appear too compliant in comparison to DIC displacements, until ~70% of the maximal load.

Exemplary DIC fields are shown in Figure 8 for a specimen of series CS. From this data, it is clearly visible that for the C-series, a distinct bondline behaviour can be identified: The vertical displacements shown in Figure 8a differ significantly between concrete and timber, meaning that deformation happens primarily at the bondline. This is supported by the shear strains shown in Figure 8c, and in turn, supports the determination attempt of a bondline connection stiffness K in the case of wet-process adhesively-bonded pushout specimens, as presented in Table 1.

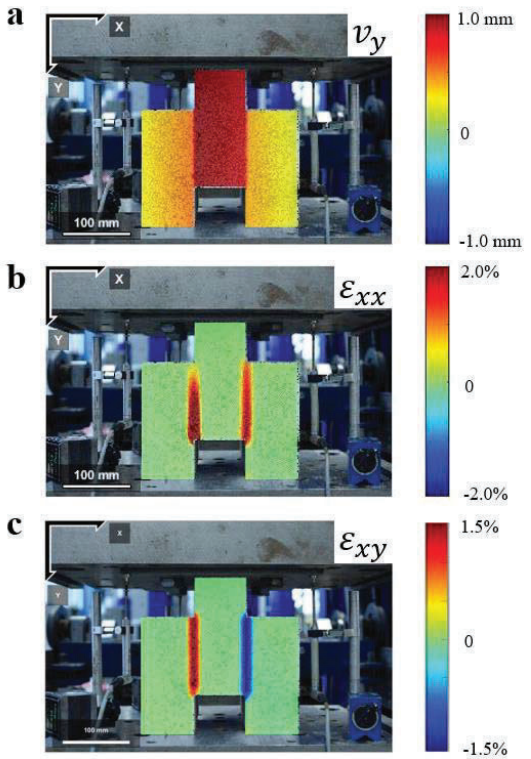

Figure 8: *Exemplary DIC analysis of a specimen of series CS at a force value close to failure of $F \approx F_{max}$ (133 kN).* ***a****: Vertical deformations (v_y), used for determination of bondline connection stiffness K.* ***b****: Horizontal strains (ε_{xx}).* ***c****: Shear strains (ε_{xy}).*

The observed size-dependency in the bondline shear strength may have been influenced by the superposition and interrelations of the following stresses acting at the bondline:

- Stresses induced by concrete shrinkage during hardening,
- possible stresses induced by timber swelling or shrinkage, caused by influences of the concrete water during hardening and subsequent testing hall climate,
- tensile stresses induced by the moment of eccentricity due to the load path inherent to the double-shear push-out setup ($\sigma_{ecc.} \propto b_t / l_v^2$, where b_t is the in-plane width of the timber side parts, and l_v is the shearing length).

These stresses tend to induce undesirable peeling stresses on the bondline, negatively influencing the obtained shear strengths. In addition, the fact these stresses, together with the main shear stresses from the vertical load, are typically shear-lag distributed over their respective shearing lengths, certainly affected the obtained values. In fact, size effects, supposedly stemming from such influences, are a well know phenomenon in testing of structural adhesives [18]. In standards where shear testing of adhesive bondlines with variable possible specimen sizes is possible, e.g. as in annex D of EN 14080 [19], corrections factors of shear strength are recommended for size deviations with respect to a reference size. However, in the present study and within its intents, it is not clear what specimen size could be considered as a suitable reference size.

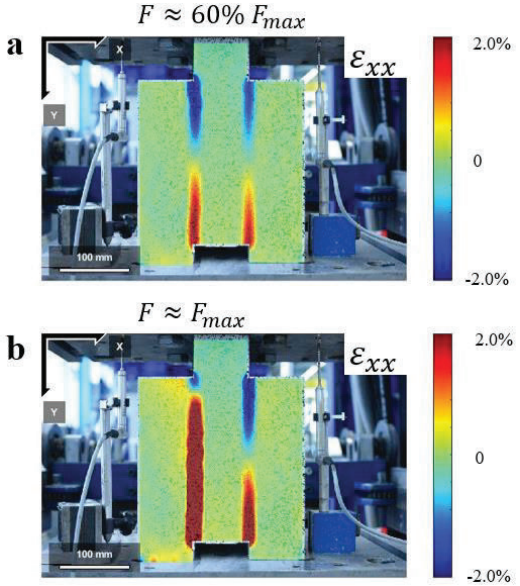

Figure 9: *Example of obtained horizontal strain (ε_{xx}) evolution for a specimen of series CL at two different load levels.* ***a****: At a force of $F \approx 60\% F_{max}$ (30 kN).* ***b****: At a force close to failure $F \approx F_{max}$ (51 kN).*

Moreover, additional influences such as friction at the bottom of the side timber parts between wood and metal plate, as well as slight but possible unevenness of the timber side parts may also have, and even to a greater extent, influenced the results. An example is shown in Figure 9: Here, the horizontal strain evolution at the bondline is shown for a specimen of series CL. While still

https://doi.org/10.52202/069179-0422

symmetrical at the lower load level, the horizontal strain is not symmetrical anymore across the two bondlines at the higher load level close to failure. In contrast, this behaviour could not be observed in the case of the CS specimen shown in Figure 8b. It is to be expected, that the horizontal stresses at the bondline highly affect the bondline performance, as e.g. they may directly reflect the amount of perpendicular tensile stress acting at the bondline. A symmetrical behaviour would a priori result in a better bondline performance.

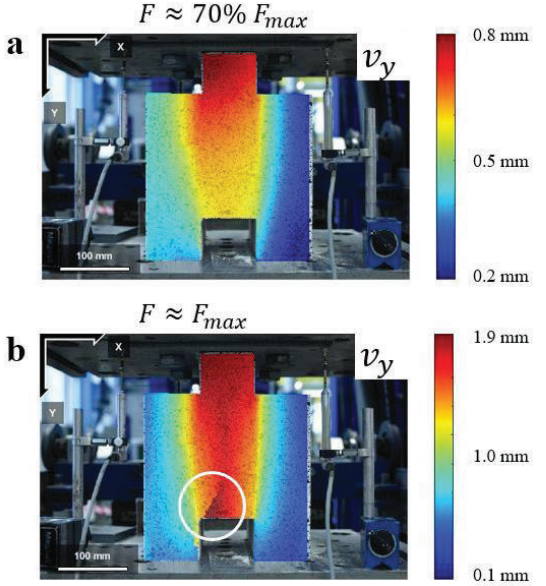

Figure 10: *Example of obtained vertical deformation (v_y) evolution for a specimen of series PM at two different load levels used for determination of bondline connection stiffness K.* ***a****: At a force of $F \approx 70\% F_{max}$ (890 kN).* ***b****: At a force close to failure $F \approx F_{max}$ (1230 kN), white circle shows polymer concrete tensile-shear failure.*

Furthermore, an additional aspect with high potential impact is the production process of the specimens. As can be seen in studies at small scale [20,21], slight variability in adhesive pot or open time, or concrete mixture (e.g. water to cement ratio), may influence measured values. A hint towards the latter influence can be seen in the shear failure surfaces shown in Figure 7. A rather smooth shear failure was consistently observed for the samples CL, while more rough surfaces were observed for the series CM and CS, which cannot be explained otherwise. Herewith, the series CS, with the highest bondline strength, displayed the roughest surface, where the roughness appears to be characterized by the size of the concrete aggregates. It should also be noted, that in particular for a brittle material such as concrete, the concept of pure shear failure can be questioned, as the shear strength (or as in this case a cohesive shear strength at the bondline) is not the result of a pure shear stress state, but always involves tensile stresses. Therefore, the strength values provided in Table 1 should be interpreted accordingly, meaning that the shear strength of the adhesive connection itself could in theory be higher. The reported values rather represent the acting shear stresses in the bondline at the moment of cohesive concrete failure, which is, as said above, to be considered specific for this pushout tests situation. Therefore, the problematics and relevance of the observed size effect for design can safely be relativized.

From a bondline strength perspective, the P-series proved to significantly outperform the adhesive bond of the C-series. This is explained by the fact that polymer concrete, in contrast to cement-based concrete, possesses a rather high tensile (cohesive) strength. The herein reported overall mean value for the push-out strength of 12.24 N/mm^2, at the moment of polymer concrete failure, is slightly higher than comparable polymer concrete alternatives bonded to softwood and tested in a push-out manner [22,23].

While the high variability obtained for the bondline connection stiffness of the C-series can be attributed, as the variability in bondline strength, to the overall variability of load-deformation behaviour (caused by the above mentioned effects), this is not entirely the case for the P-series. Here, as can be seen from the vertical deformation exemplarily shown in Figure 10 for a PM specimen, a distinctive bondline deformation behaviour cannot be identified. Instead, the whole interface region appears to deform continuously, as the vertical deformations happen in the timber and in the polymer concrete. Therefore, the bondline stiffness values of Table 1 for PM and PS do not possess any physical meaning, and for design, $\gamma = 1$ can be assumed straightforwardly. Note that this is also the case for the wet-process adhesive-bonded C-series, since for most specimens $K \gtrsim 1'000$ kN/mm. However, and in contrast, the physical meaning of K can be supported by the DIC fields shown in Figure 8a.

Finally, while pushout tests assessed by DIC were certainly insightful in these cases of continuous rigid connections, they proved to produce values that are difficult to be fully understood and interpreted. Therefore, alternative or additional testing methods, e.g. bending tests, can be recommended in order to characterize adhesive bonds for TCC elements.

5 CONCLUSIONS

The study showed that in the case of adhesive-bonded TCC connections produced in wet process, results of push-out tests need to be interpreted and used with caution. Shear strengths were found to be strongly size-dependent, and do not directly reflect adhesion strength, but rather cohesive strength of concrete at the bondline. Furthermore, and even though DIC proved to be a powerful characterization tool, a reliable derivation of connection stiffness K was hardly possible. However, for most specimens, $K \gtrsim 1'000$ kN/mm could still be reported, justifying the prevalent assumption of $\gamma = 1$ in the case of a continuous adhesively-bonded TCC connection. Finally, an alternative to the classical adhesive bonding of cement-based concrete to beech wood was demonstrated in the form of directly-bonding polymer concrete. Here, pushout tests showed a far superior performance of the bondline compared to wet-process glued cement-based concrete.

ACKNOWLEDEGEMTS

We sincerely thank Thomas Schnider for the preparation of the casting formwork and Dominik Werne and Pius Herzog for help with the testing setup. Furthermore, we would like to express our gratitude to the further involved project partners from *Fagus Suisse SA* and *Sika Technology AG*. This project was funded by *Innosuisse - Swiss Innovation Agency* (37233.1 IP-ENG *'Verklebter Holz-Beton-Verbund - Mit Buchenholz und Polymerbeton zu innovativen Lösungen'*).

REFERENCES

[1] EN 1995-1-1:2004, Eurocode 5: Design of timber structures - Part 1-1: General - Common rules and rules for buildings.

[2] CEN/TS 19103:2021, Eurocode 5: Design of Timber Structures — Structural design of timber-concrete composite structures — Common rules and rules for buildings.

[3] Dias, A., Schänzlin J., Dietsch P.: Design of timber-concrete composite structures: A state-of-the-art report by COST Action FP1402 WG 4. Shaker Verlag, Aachen, 2018.

[4] Koch S., Grönquist P., Monney C., Burgert I., Frangi A.: Densified delignified wood as bio-based fiber reinforcement for stiffness increase of timber structures. Composites Part A, 163, 2022.

[5] Negrão J. H., Oliveira F. M., Oliveira C. L.: Investigation on Timber-Concrete Glued Composites. 9th World Conference on Timber Engineering (WCTE), Portland US, 2006.

[6] Brunner M., Romer M., Schnüriger M.: Timber-concrete-composite with an adhesive connector (wet on wet process). Materials and Structures, 40:119–126, 2007.

[7] Kanócz J., Bajzecerová V.: Timber - Concrete composite elements with various composite connections part 3: Adhesive connection. Wood Research, 60(6): 939-952, 2015.

[8] Eisenhut L., Seim W., Kühlborn S.: Adhesive-bonded timber-concrete composites – Experimental and numerical investigation of hygrothermal effects. Engineering Structures, 125, 2016.

[9] Kostić S., Meier S., Cabane E., Burgert I.: Enhancing the performance of beech-timber concrete hybrids by a wood surface pre-treatment using sol-gel chemistry. Heliyon, 4(9):e00762, 2018.

[10] Frohnmüller J., Fischer J., Seim W.: Full-scale testing of adhesively bonded timber-concrete composite beams. Materials and Structures, 54:187, 2021.

[11] Kästner M., Rautenstrauch K.: Polymermörtel-Klebverbindungen für Holz-Beton-Verbundbrücken Teil 1. Bautechnik, 98, 2021.

[12] Arendt S., Sutter M., Breidenbach M., Schlag R., Schmid V.: Neue Forschungsergebnisse zu Nass-in-Nass geklebten Holz-Beton-Verbunddecken. Bautechnik, 99, 2022.

[13] Tannert T., Gerber A., Vallee T.: Hybrid adhesively bonded timber-concrete-composite floors. International Journal of Adhesion and Adhesives, 97, 2020.

[14] Fagus Suisse SA. Fagus Stabschichtholz - Bemessungswerte für Buche. 2021.

[15] Sika Schweiz AG: Produktdatenblatt Sikacrete®-16 SCC. Version 01.05, July 2020.

[16] Sika Schweiz AG: Produktdatenblatt Sikadur®-42 HE. Version 02.04, August 2020.

[17] Blaber J., Adair B., Antoniou A.: Ncorr: Open-Source 2D Digital Image Correlation Matlab Software. Experimental Mechanics, 2015.

[18] Okkonen E. A., River B. H.: Factors affecting the strength of block-shear specimens. Forest Products Journal, 39(1), 1988.

[19] EN 14080:2013: Timber structures – Glued laminated timber and glued solid timber – Requirements.

[20] Fu Q., Yan L., Thielker N.A., Kasal B.: Effects of concrete type, concrete surface conditions and wood species on interfacial properties of adhesively-bonded timber – Concrete composite joints. International Journal of Adhesion & Adhesives, 107, 2021.

[21] Nemati Giv A., Fu Q., Yan L., Kasal B.: Interfacial bond strength of epoxy and PUR adhesively bonded timber-concrete composite joints manufactured in dry and wet processes. Construction and Building Materials, 311, 2021.

[22] Becker W., Schober K., Weber J.: Vergussknotenlösungen im Ingenieurholzbau. Bautechnik 93, 2016.

[23] Jahreis M.: Zur Entwicklung von Polymerverguss-Kopplungselementen für den Holzbau. Dissertation, Bauhaus-Universität Weimar, 2019.

https://doi.org/10.52202/069179-0422

World Conference on Timber Engineering Oslo 2023

SEISMIC FRAGILITY OF A NEW MASS TIMBER-STEEL HYBRID BUILDING SYSTEM EQUIPPED WITH CLT FLOOR DIAPHRAGMS

Chaoyue Zhang[1], Cristiano Loss[2]

ABSTRACT: An essential step in analysing a Seismic Force-Resisting System (SFRS) is to ascertain how lateral loads distribute within the structure in-between horizontal systems, such as roof and floor diaphragms, and vertical members, such as shear walls and bracings. Clear identification of load paths requires a proper assessment of the in-plane stiffness of floor diaphragms. Nevertheless, in the context of designing SFRS with diaphragms made of wood, neither comprehensive code provisions nor accurate computational methods exist to account for its in-plane flexibility. This shortage of knowledge becomes even more obvious if compared to the common reinforced concrete flooring systems. To investigate influences of the actual in-plane stiffness of diaphragms on the global response of the SFRS, this research performs incremental dynamic analysis (IDA) on a new mass timber-steel hybrid building system via the OpenSees platform and compares its collapse fragility to that of an ideal building model with rigid diaphragms. The SFRS of hybrid building entails concentrically X-braced steel frames, whose nonlinear responses are explicitly simulated, including global buckling, tensile yielding, and post-buckling behaviours. Overall, the fragility analysis concluded that the adoption of the proposed hybrid floor system, with the reinforcement of panel-to-panel connections that contributes to sufficient in-plane stiffness, can facilitate a comparable seismic performance as the building with the fully rigid diaphragm.

KEYWORDS: Mass timber-steel hybrid building, In-plane diaphragm flexibility, IDA, OpenSees modelling

1 INTRODUCTION

1.1 HYBRID MASS TIMBER CONSTRUCTION

Hybrid mass timber construction refers to structural assemblies that combine engineered wood products, such as cross-laminated timber (CLT), with concrete and/or steel. By leveraging the prefabrication method, massive production off-site and speedy assembly on-site of large timber members can be readily attained. With previous research mostly focusing on the lateral behaviour of CLT shear walls and bracing systems, attention is shifting to high-performance earthquake-resistant systems equipped with CLT floor diaphragms.

1.2 IN-PLANE DIAPHRAGM FLEXIBILITY

Floor diaphragms are designed to resist gravity loads and transmit lateral loads to adjoining vertical members of the Seismic Force-Resisting System (SFRS). As a convention in seismic design, rigid diaphragms distribute applied lateral shear forces by the relative rigidity of the SFRS, whereas flexible diaphragms distribute forces based on tributary area. Consequently, to properly assess diaphragm flexibility is imperative to quantify the lateral force demands and, as such, produce economic proportion and sizing of structural members of an SFRS. In terms of the dynamic response, the diaphragm's flexibility plays a pivotal role in affecting the global dynamic behaviour of buildings as well as the local distribution of inertia forces, shears, and bending moments along the edges of the diaphragm [1]. However, most building codes lack the criteria for specifying the actual in-plane stiffness of wood and mass timber diaphragms by explicitly specifying reduction factors used for seismic design. Practitioners must confront inevitable challenges when attempting to incorporate mass timber floor assemblies into a high-performance hybrid building system.

2 HYBRID TIMBER-STEEL BUILDING

2.1 DESCRIPTION OF THE BUILDING

Figure 1 shows the architectural view of the 4-story timber-steel building prototype that entails a Special Concentrically Braced Frame (SCBF) with repeatable modules of innovative CLT-steel floor diaphragms.

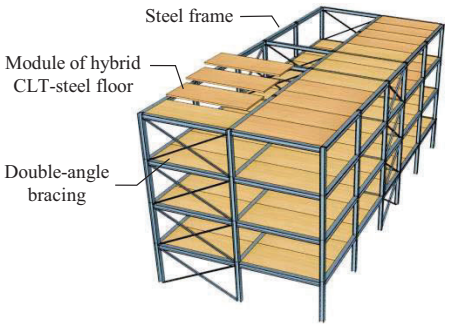

Figure 1: *Mass timber-steel hybrid building archetype*

[1] Chaoyue Zhang, Sustainable Engineered Structural Solutions Laboratory, The University of British Columbia, Canada, chaoyuez@mail.ubc.ca

[2] Cristiano Loss, Sustainable Engineered Structural Solutions Laboratory, The University of British Columbia, Canada, cristiano.loss@ubc.ca

https://doi.org/10.52202/069179-0423

The building has a 28.5 m long by 12 m wide footprint, with a 3.2 m inter-story height. Structural novelties of the hybrid floor modules are attributed to the composite action engaged between the CLT panels and steel beams. From the structural perspective, the high strength-to-weight ratio of CLT panels can impart the overall hybrid system with sufficient in-plane stability when subjected to horizontal forces. When subjected to severe earthquake excitations, the lightness of mass timber-based floors can effectively reduce the demands of the induced inertia forces acting upon each story.

2.2 DESIGN CONSIDERATIONS

The proposed CLT-steel hybrid building archetype was designed for residential usage, and located in Bucchianico, Chieti, Italy [2]. For the gravity design, a specified dead load (G_2) of 3 kN/m^2 plus a live load (Q) of 2 kN/m^{2}was adopted, factored by 0.3 (Ψ_2) according to the load combination parameters defined in the Italian Building Code [3] for multi-story residential buildings. The estimated total gravity load for stories 1 to 3 was 3.6 kN/m^2; the total gravity load for story 4 was 3 kN/m^2. The seismic design of the hybrid building followed the equivalent linear elastic force procedure of Eurocode 8 [4] with reference to "other" structure types. The design response spectrum was drawn given the soil class type C, typographical category type "t1", and a building life span of 50 years. The code-based fundamental period of the building was estimated at 0.34 seconds, based on the total height of the superstructure. Considering the local seismic hazard having a 10% probability of exceedance, corresponding to the life safety performance level defined in Eurocode (2004), the design base shear force for the 4-story building archetype was calculated as 1200 kN after applying a reduction factor *q* of 4 to account for system overstrength and ductility of typical braced steel frame structures.

Table 1: Selection of steel elements

Elements	Sections	Steel
Beams	IPE 360	S355
	IPE 300	S355
	IPE 220	S275
Columns	HEB 220	S275
	HEB 300	S275
	HEB 280	S275
	HEB 220	S275
Braces	2L 110X70X12	S275
	2L 100X65X10	S275
	2L 60X60X8	S275

The steel structs, including beams, girders, columns, and braces, of the SCBF employed parallel flange I-shaped (IPE), wide flange H-shaped (HEB), and L-formed hot rolled profiles with steel in S275 and S355 strength class [4], respectively. Table 1 lists the selected cross sections and materials of beams, columns, and braces. Notice that a stockier section (2L 110X70X12) is used for braces at the first and second story considering potential greater demands of seismic force and deformation at the lower stories during earthquake ground shakings. The SFRS of the four-story building adopted dissipative SCBFs, with steel struts and connections sized and detailed to enforce major inelastic deformation of bracing diagonals and maintain elastic deformation of beams and columns. Properly capacity-designed SFRSs provide the building with outstanding lateral strength and stiffness. Considering large and infrequent seismic events, the compressive buckling and yielding tensile behaviour of the bracing elements can offer incredible ductile deformability to accommodate the induced large inelastic drift demands and assure the satisfaction of intended performance levels. The beam-to-column joints of the unbraced frame consisted of shear tabs, while the beam-to-column-brace joints of the braced frame were reinforced by welding gusset plates.

2.3 HYBRID CLT-STEEL FLOOR DIAPHRAGMS

Figure 2 details the key components of the innovative hybrid CLT-steel floor module, which can be demounted into two main parts: the CLT panel and two customized cold-formed U-shaped beams. The 85 mm thick CLT panel of one floor module is 2.4 m in width and 5.83 m in length. Two U-shaped steel beams that attach to the CLT panel are 5.815 m long and are manufactured by 4 mm thick S355 steel sheets [4]. Moreover, the four 140 mm wide perforated steel plates at each end of the U-shaped beam are bounded to the CLT panel by pouring an epoxy-based resin into precut slots (A-A). In the middle section of the U-shape beam (B-B), 80 mm long full-threaded self-tapping screws (STSs) are driven into predrilled holes at a spacing of 500 mm to connect with the panel.

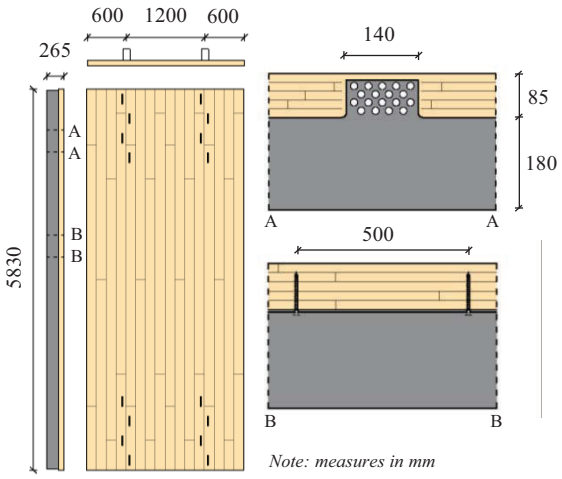

Figure 2: *Hybrid CLT-steel floor diaphragm module*

Each prefabricated hybrid floor module is installed into the braced steel frames by bolting special steel links to the ends of the U-shaped beams. Figure 3a shows the configuration of the beam-to-beam special links. Multiple pairs of STSs oriented at the designated angle, as shown

https://doi.org/10.52202/069179-0423

in Figure 3b, are used to fasten the edges of the CLT panels in order to create a continuous slab. Application of those special steel links between the steel frame and hybrid floor modules not only accommodates potential structural misalignment or imperfections but also allows for rapid replacement of any damaged components after major earthquake events. Furthermore, the prefabricated floor modules can greatly accelerate on-site assembly and, as such, effectively save total fabrication time and labour costs. Large-scale implementation of the proposed hybrid system can conceivably leverage most prefabrication techniques.

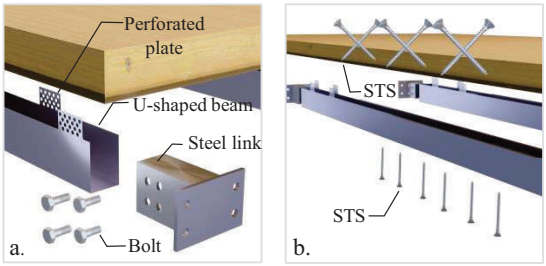

Figure 3: *Beam-to-beam and panel-to-panel connections*

3 NUMERICAL INVESTIGATION

3.1 MODEL OF FLOOR DIAPHRAGM

Finite-element (FE) sub-modelling approach aims to reproduce the in-plane shear stiffness and failure mechanisms recorded in the full-scale experiment of the hybrid CLT-steel floor diaphragm performed by [5]. Figure 4 shows features of the constructed test specimen assembled by staggering the hybrid prefabricated CLT-steel floor modules. The dimensions of the specimen were 6 m in width and 12 m in length. The location of the applied in-plane shear load, *F*, is also annotated in Figure 4. To highlight the contributions of the panel-to-panel connections to the in-plane shear stiffness of the diaphragm, to tests were performed on the same floor specimen by installing and removing the STSs at the edges of the CLT panels.

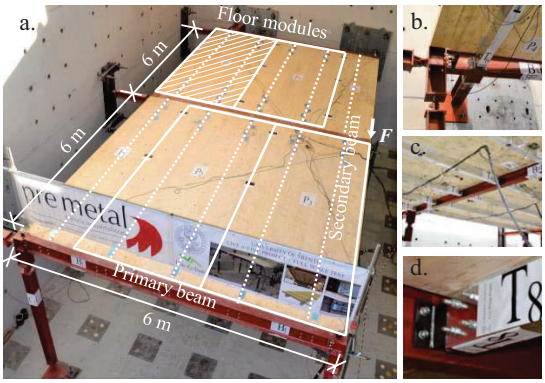

Figure 4: *Floor subassembly of the full-scale in-plane test*

3.1.1 Component modelling

It has been shown that the ductile and dissipative behaviour of the connections governs the performance of the tested hybrid steel-timber floor diaphragm. No damage in the 5-layer CLT panels was observed after each of the three in-plane shear tests performed. In OpenSees [6], CLT is thus modelled by the *ShellMIT4* element with the *PlateFiber* section and *ElasticOrthotropic* material. According to Loss and Frangi [5], the observed deterioration mechanism demonstrated superior composite actions between timber and steel elements together with weak component joints. Significant ductile deformation was found to concentrate at the beam-to-beam connections. The local shear-tension breakage of the bolts that fastened the outstanding flanges of the steel link outlined the ultimate failure point of the floor system. To replicate the distinctive nonlinear behaviour of the beam-to-beam connection, the numerical representation of the steel link consists of four parts linked in series: (i) a *ZeroLength* element that represents the bolt contact gap, (ii) a short hollow tube that slots in the U-shaped beam, (iii) outstanding flanges that are welded to the hollow tube, and (iv) bolts connected to the primary beam, as shown in Figure 5b. Both the steel tube with hollow section and the flange segment with rectangular section are modelled by the *forceBeamColumn* element with discretized fibre section and *Steel02* material. The two ends of the flange are connected to the primary beam by two nonlinear axial springs using the *ZeroLength* element. Figure 5a illustrates the boundary restraints of the floor subassembly, which are modelled as rollers with translative DOFs constrained only.

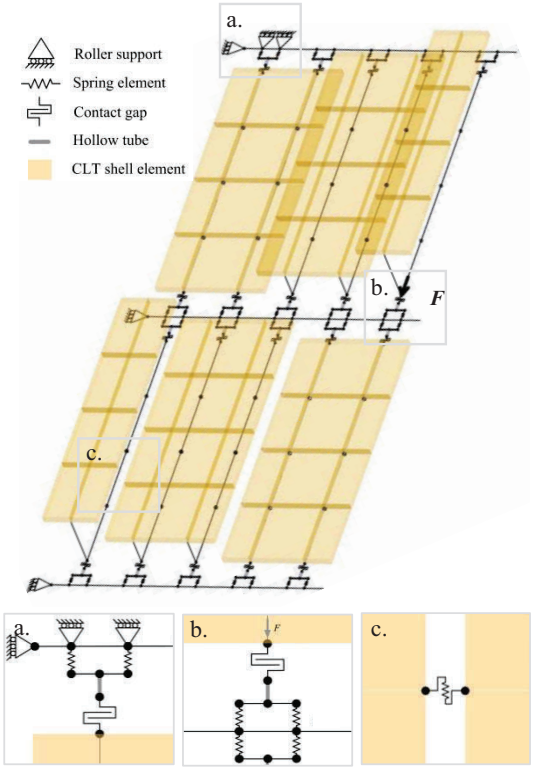

Figure 5: *OpenSees model of the hybrid floor subassembly*

In addition, under seismic actions, the induced in-plane shear transferred between CLT panels could place significant slip demands on the STSs. Datasets retrieved from cyclic tests of panel-to-panel STS connections performed by Loss et al. [7] were used to represent their hysteretic behaviour. In OpenSees, the *Pinching4* material was used to simulate the strength and stiffness degradation of the pane-to-panel connections in the in-plane shear direction.

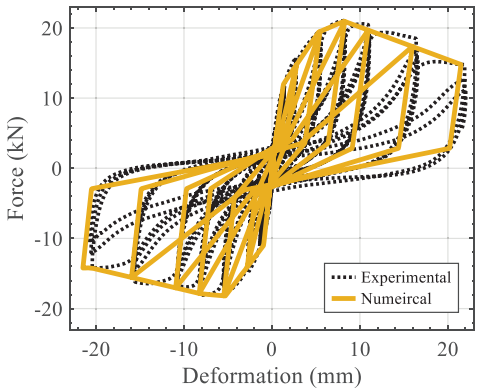

Figure 6: *Calibrated behavior of panel-to-panel connections*

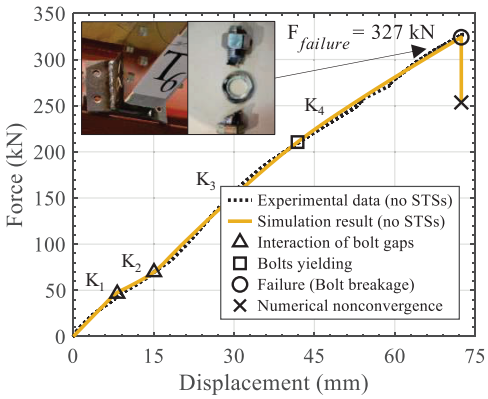

Figure 7: Validated response of floor model without STSs

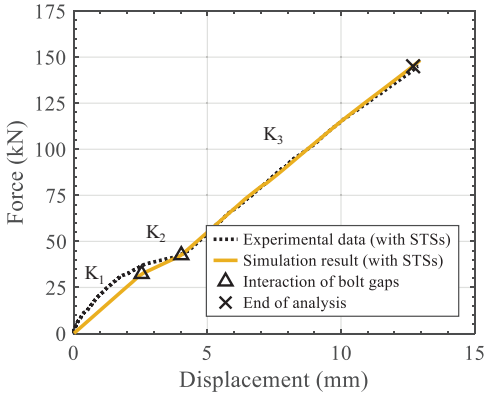

Figure 8: Validated response of floor model with STSs

Figure 6 shows the calibrated hysteretic response of the STS, which is characterized by a severe loss in stiffness in reloading. Such known pinching behaviour is not uncommon for steel mechanical connectors embedded in timber due to the crushing the wood fibers underneath the connector surface. Consequently, the calibrated material was assigned to the nonlinear translational spring using a *ZeroLength* element, as shown in Figure 5c. For simulating the test specimen without the panel-to-panel connections, the physical contact between panels was idealized by embedding the *ElasticPPGap* material into the *ZeroLength* element. High compressive stiffness and strength with zero tensile resistance were added to the material to prevent mutual penetration of CLT shell elements.

3.1.2 Model validation

Model validation of the CLT-steel hybrid floor diaphragm subassembly was accomplished by simulating T_2 and T_3 in-plane shear tests published in [5]. For the specimen subjected to a destructive monotonic test (T_3), the CLT panels were not tied together with STSs. Figure 7 plots the well-matched simulated results of the numerical model versus the experimental data, with a maximum error of about 13% in values in terms of in-plane stiffness K_2. The initial drop of stiffness, from K_1 to K_2, when displacement reaches about 7 mm, is attributed to the interaction of bolt-hole gaps between the hollow steel tube and the U-shaped beam. After the gap is closed, the in-plane stiffness restores to the initial level before the beam-to-beam connections bolts yield, which signifies a further small reduction of the overall shear stiffness. When the applied in-plane load increases up to approximately 327 kN, the deformation of the beam-to-beam connections reaches the maximum, which results in the breakage of bolts under combined effects of shear and tension, as annotated by the detached flange in Figure 7. In the numerical model, only the axial tensile resistance of the bolt is considered, and its ultimate capacity is ascertained by calibrating to the test result by warping *Steel02* material with *fatigue* material, which can trigger failure based on a predefined maximum deformation.

Figure 8 shows the simulation results of T_2 test, including the panel-to-panel connections. The simulated K_1 and K_2 have a relatively large deviation from the measured in-plane stiffness with a maximum error beyond 30%. It should be noted that the results of the original cyclic test program (T_2) published in [5] did not display a distinctive hysteretic or deteriorated response as for the in-plane shear force and displacement relationship. A marginal reduction in stiffness occurred during the unloading phase with a maximum relative residual deformation equal to 2 mm only. This slight offset from the original position was mostly due to the friction between the steel-to-steel surfaces of the beam-to-beam connections. No degradation of stiffness and strength was observed during the reloading phase. Therefore, the numerical model of the hybrid floor subassembly, inclusive of the panel-to-panel connections, was shown to capture the overall behaviour of the system and its members.

https://doi.org/10.52202/069179-0423

3.2 MODEL OF STEEL FRAME

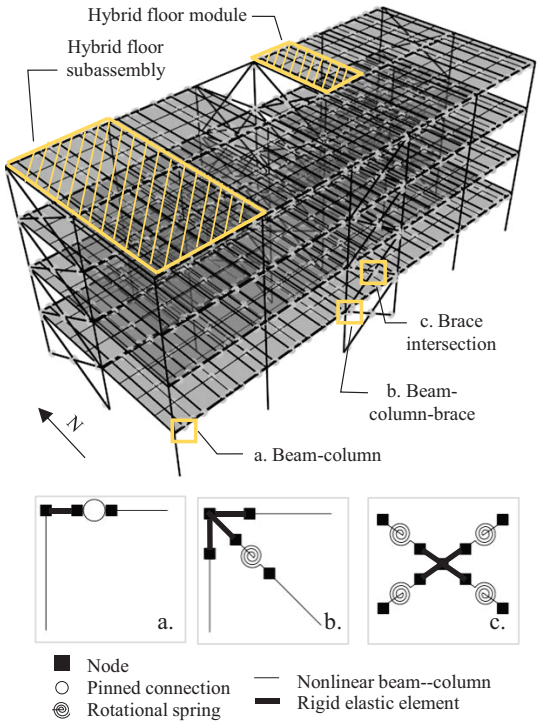

Figure 9: *OpenSees model of the hybrid building archetype*

To accurately predict the building's seismic performance throughout varying limit states, a reliable FE model should explicitly capture critical nonlinear deterioration modes and failure mechanisms of structural components. Numerical models of steel structs of the braced frame implemented in this paper, such as brace, beam, and column, take advantage of the state-of-art nonlinear frame elements in OpenSees [8]. Such frame element was created to explicitly simulate the nonlinear material response due to the post-yielding behaviours of the steel members, such as strain hardening. Being a fibre-type model, it applies the distributed plasticity theorem through numerical integrations of stress resultants over discretized sections along the member length.

3.2.1 Component modelling

Characteristic deterioration modes of braces include buckling in compression, yielding in tension, and post-buckling behaviour. In this work, multiple *forceBeamColumn* elements with finely meshed fibre cross sections were used to produce those highly nonlinear responses, as suggested by Uriz and Mahin [9]. This verified method applies to a range of cross-section shapes of braces, such as hollow circular, hollow square, I wide flange, and double angles. To account for geometric nonlinearities when brace buckles with substantial axial deformation under compression, the *forceBeamColumn* elements were assigned with *Corotational* transformation with exact nonlinear transformation of element displacement and forces between the global and local coordinate systems [10].

Large rotational and axial forces concentrated in bracing members also attract great nonlinearities to their adjacent components. Hsiao et al. [11] indicated that local yielding in beams and columns was significant based on previous experiments. To simulate the nonlinear behaviour of the beams and columns, the *dispBeamColumn* element was used.

Connections between beams and columns of unbraced bays were designed using shear tabs. The actual bending stiffness of shear tab connections along the strong axis of beams does not evidently contribute to the moment resistance of beam-to-column joints. Hence, it was simplified as a pin connection plus a short-length element equal to the half depth of the column, as shown in Figure 9a. The idealized pin connection was modelled by implementing the *EqualDOF* constraint with the designated rotational degree-of-freedom (DOF) released. For the braced bays, the presence of gusset plates provides additional reinforcement to the beam-to-column connection and, meanwhile, serves as the critical boundary condition for the brace. Yoo [12] suggested that the out-of-plane rotational stiffness of the gusset plate plays an important role in affecting brace buckling and post-bulking behaviours, given the considerable rotation demands. Therefore, the analytical model proposed by Hsiao et al. [11] was adopted, which is characterized by a combination of a nonlinear rotational spring located at the physical end of the brace and several rigid elements that represent regional enhanced stiffness, as shown in Figure 9b. Figure 9c shows the center part where four brace diagonals are connected by the gusset plate. The FE model adopts a similar approach by linking four nonlinear rotational springs with rigid elements intersecting at the centroid of the middle gusset plate.

3.2.2 Model validation

Validation of the numerical model of the double-angle L-shaped bracing strut intends to reproduce the hysteretic performance of specimen strut 8 tested under cyclic loading by Black et al. [13]. The simulated hysteretic response of the brace against the experimental data is presented in Figure 10. Considerable deterioration of strength and stiffness under compression is shown if compared to the stable performance in tension.

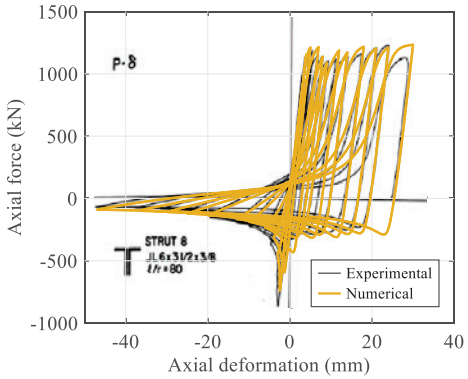

Figure 10: Validated hysteretic response of double-angle brace

https://doi.org/10.52202/069179-0423

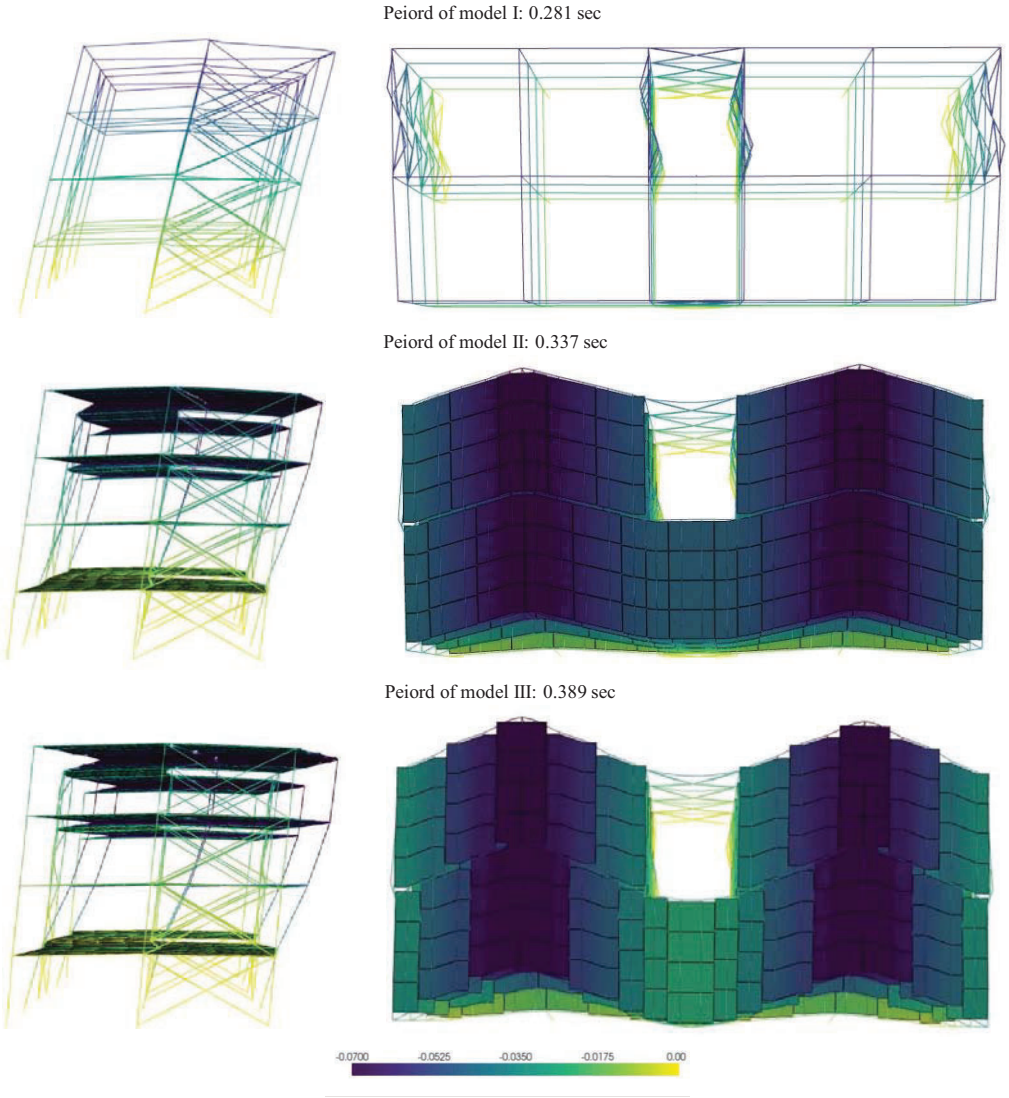

Figure 11: Mode shape 2 (translation in the south-north direction) of three building models

Three FE models of the building were analyzed. The building model with fully rigid floor diaphragms is denoted as Model I. With the hybrid CLT-steel floor system and panel-to-panel connections the building model is denoted as Model II. The companion model without the panel-to-panel connections is denoted as Model III.

4 MODAL RESPONSE

Table 2: Periods (sec) of first three mode shapes

Model	Mode 1	Mode 2	Mode 3
I	0.408	0.281	0.242
II	0.454	0.337	0.312
III	0.571	0.389	0.384

Modal analysis was conducted to calculate periods of the first three mode shapes: horizontal translation in the east-west direction, horizontal translation in the south-north direction, and torsion, as shown in Table 2. Figure 11 depicts the translational mode shape 2 of three building models. Specifically, the first two periods of Model II are both about 0.05 s longer than those of Model I. In case of hybrid CLT diaphragms without the panel-to-panel STS connections, the model has 40% higher periods, if compared to Model I, regarding the two translational mode shapes. For torsion, Model III has a period of 0.384 s and that is approximately 60% higher than that of Model I. It can be noted that the reinforcement of STSs between CLT panels conspicuously reduces the overall in-plane flexibility of diaphragms. Besides, the lack of restraints between CLT panels underpins the aggregated behaviour of in-plane shear deformation and rotation of individual

https://doi.org/10.52202/069179-0423

hybrid floor modules, which conceivably elongates the translational and torsional periods of the building archetype.

5 FRAGILITY ANALYSES

To retrieve a comprehensive evaluation of the seismic performance of different building models through IDA, a total of 20 ground motion records were selected from the Pacific Earthquake Engineering Research Center Shallow Crustal Earthquakes database [14], scaled to a minimum mean square error with respect to the target spectrum over a period range from 0 seconds to 2.5 seconds, which is determined by the period of dominance according to the local disaggregation results retrieved from the software REXEL [15] for site Bucchianico, Chieti, Italy. Figure 12 plots the uniform hazard spectrum, which corresponds to a hazard level of 10% probability of occurrence in 50 years, and the selected records.

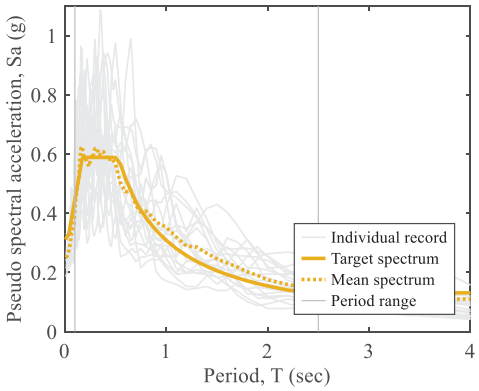

***Figure 12**: Target response spectrum and selected records*

Three damage states (DSs) are of interest when evaluating their exceeding likelihoods given a certain level of ground shaking intensity, as expressed by a cumulative distribution function and plotted by a fragility curve. Particularly, DS1 identifies the transition point between the model's elastic behaviour and the first nonlinearity. DS2 refers to a 2% maximum inter-story drift ratio (ISD), which is associated with the collapse prevention performance level for braced steel frames specified in FEMA 356 [16]. In addition, DS3 is determined by either the simulated collapse point, where a single IDA curve reaches a plateau due to deteriorating mechanisms or the last converged time-integration step.

Figure 13 shows the probability of exceeding different DSs as a function of the intensity measure (IM), which is represented by the 5%-damped spectral acceleration at the structure's fundamental period Sa (T_1, 5%).

By comparing three fractiles of IM, Model II has the highest spectral acceleration to exceed DS1. To be specific, 16% of records need to reach Sa $\geq$ 0.95g, 50% of records need to reach Sa $\geq$ 1.27g, and 84% of records need to reach Sa $\geq$ 1.70g. This suggests that implementation of the proposed hybrid CLT diaphragm enables the building to sustain a median intensity of ground motion up to approximately two times the intensity of the design uniform hazard (i.e., 0.59g), before any structural nonlinearity arises. The median Sa of Model II is 0.1g and 0.18g greater than those of Model I and III.

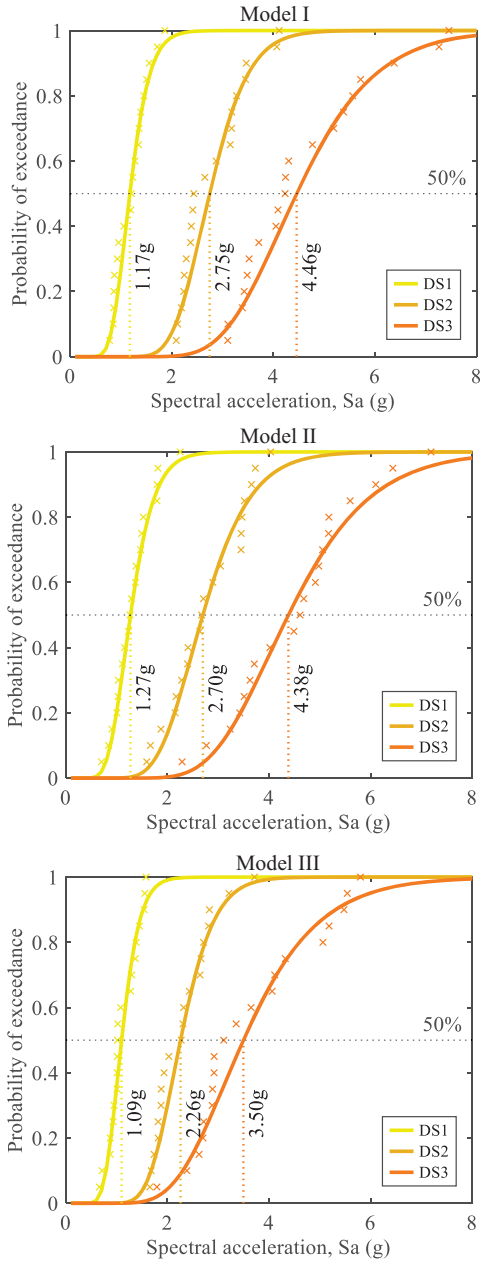

***Figure 13:** Fragility curves under three damage states*

In case of exceeding DS2, the 16% Sa capacity of Model I is approximately 8% and 23% higher than that of Models II and III. A trivial difference is observed in the median value between Model I and Model II. The intensity value at which 84% of the records need to be scaled to produce the demand δ = 2% is 3.54 g for Model II, which is significantly higher than the value of Model III, while

https://doi.org/10.52202/069179-0423

close to that of Model I. A similar trend was found concerning the global collapse limit state; and no major difference was observed in all three fractiles of IM between Models I and II. Compared to Model III, however, Model II has a 25% (i.e., 4.38 g) and 21% (i.e., 5.84 g) larger value at the 50% and 84% percentile, respectively. Consequently, it can be summarized that the required intensity for Model I and Model II to exceed DS2 and DS3 are comparatively similar; and that shaking level needs to be reduced by more than 20% for Model III to reach both DSs.

6 CONCLUSIONS

The seismic fragilities of an innovative mass timber-steel hybrid building archetype equipped with prefabricated CLT-steel composite floor diaphragms were presented. The 3D numerical model developed in OpenSees entailed critical nonlinearities primarily contributed by deteriorating behaviours of steel structs, such as the low cycle fatigue behaviour and section fracture mechanism of the bracing member. Particularly, the local failure modes were incorporated explicitly into the calibrated sub-models of the CLT-steel floor diaphragms, including the beam-to-beam connections. Building archetype assembled by the validated sub-models was subjected to the incremental dynamic analysis, assuming a suite of 20 ground motion records that were scaled up to the global collapse of the building. The building's seismic performance was assessed using fragility curves. Based on the probabilistic analysis results, it can be concluded that the overall seismic performance of Model II is comparatively similar to that of Model I in terms of the conditional probability of exceeding all three damage states, given any level of ground motion intensity. In the context of adopting the proposed CLT-steel floor diaphragm module, careful considerations should be placed on the panel-to-panel connections, as they are contributors to the overall in-plane stiffness of floor subassemblies.

ACKNOWLEDGEMENT

This research was financed by the Natural Sciences and Engineering Research Council (NSERC) of Canada through the Discover Program, grant number RGPIN-2019-04530, and Discovery Launch Supplement, grant number DGECR-2019-00265. The Donald S. McPhee Fellowship and Robert and Averil Kennedy Wood Science Graduate Scholarship awarded to Chaoyue Zhang are also acknowledged. Free access to the Digital Research Alliance of Canada computer cluster is also acknowledged (https://alliancecan.ca/en).

REFERENCES

[1] J. Humar and M. Popovski, "Seismic response of single-storey buildings with flexible diaphragms," *Can. J. Civ. Eng.*, vol. 40, no. 9, pp. 875–886, 2013, doi: 10.1139/cjce-2012-0493.

[2] A. Roncari, F. Gobbi, and C. Loss, "Nonlinear static seismic response of steel frame buildings equipped with hybrid cross-laminated timber floor diaphragms," *Front. Built Environ.*, 2020.

[3] Italian Ministry of Infrastructure and Transport, "Istruzioni per l'applicazione delle «Nuove norme tecniche per le costruzioni» di cui al decreto ministeriale 14 gennaio 2008," *Gazzetta Ufficiale della Repubblica italiana*, 2009.

[4] C. Eurocode, "8: Design of structures for earthquake resistance—Part 1: General rules, seismic actions and rules for buildings (EN 1998-1: 2004)," *Eur. Comm. Norm. Brussels*, 2004.

[5] C. Loss and A. Frangi, "Experimental investigation on in-plane stiffness and strength of innovative steel-timber hybrid floor diaphragms," *Eng. Struct.*, 2017, doi: 10.1016/j.engstruct.2017.02.032.

[6] F. McKenna, M. H. Scott, and G. L. Fenves, "Nonlinear Finite-Element Analysis Software Architecture Using Object Composition," *J. Comput. Civ. Eng.*, vol. 24, no. 1, pp. 95–107, 2010, doi: 10.1061/(asce)cp.1943-5487.0000002.

[7] C. Loss, M. Piazza, and R. Zandonini, "Connections for steel–timber hybrid prefabricated buildings. Part II: Innovative modular structures," *Constr. Build. Mater.*, 2016, doi: 10.1016/j.conbuildmat.2015.12.001.

[8] M. H. Scott, G. L. Fenves, F. McKenna, and F. C. Filippou, "Software Patterns for Nonlinear Beam-Column Models," *J. Struct. Eng.*, vol. 134, no. 4, pp. 562–571, 2008, doi: 10.1061/(asce)0733-9445(2008)134:4(562).

[9] P. Uriz, F. C. Filippou, and S. A. Mahin, "Model for Cyclic Inelastic Buckling of Steel Braces," *J. Struct. Eng.*, vol. 134, no. 4, pp. 619–628, 2008, doi: 10.1061/(asce)0733-9445(2008)134:4(619).

[10] M. H. Scott and F. C. Filippou, "Response Gradients for Nonlinear Beam-Column Elements under Large Displacements," *J. Struct. Eng.*, vol. 133, no. 2, pp. 155–165, 2007, doi: 10.1061/(asce)0733-9445(2007)133:2(155).

[11] P. C. Hsiao, D. E. Lehman, and C. W. Roeder, "Improved analytical model for special concentrically braced frames," *J. Constr. Steel Res.*, vol. 73, pp. 80–94, 2012, doi: 10.1016/j.jcsr.2012.01.010.

[12] J. H. Yoo, "Analytical Investigation on the Seismic Performance of Special Concentrically Braced Frames," 2006.

[13] G. Black, W. A. B. Wenger, and E. P. Popov, "Inelastic Buckling of Steel Struts Under Cyclic Load Reversals," Berkeley, CA, 1980.

[14] "PEER Ground Motion Database - PEER Center." https://ngawest2.berkeley.edu/ (accessed Feb. 20, 2023).

[15] I. Iervolino, C. Galasso, and E. Cosenza, "REXEL: Computer aided record selection for code-based seismic structural analysis," *Bull. Earthq. Eng.*, 2010, doi: 10.1007/s10518-009-9146-1.

[16] ASCE, "American Society of Civil Engineers, FEMA 356 Prestandard and Commentary for the Seismic Rehabilitation of Building," *Rehabilitation*, no. November, 2000.

https://doi.org/10.52202/069179-0423

World Conference on Timber Engineering Oslo 2023

STRUCTURAL BEHAVIOR OF TIMBER-STEEL-JOINTS WITH EITHER DOWEL-TYPE FASTENERS OR CONTINUOUS JOINTS

Simon Aurand[1], Jakob Boretzki[2], Peter Haase[2], Thomas Ummenhofer[2], Philipp Dietsch[1]

ABSTRACT: For the development of a new hybrid construction method combining the materials steel and timber for linear load-carrying elements subjected to bending loads, different joining methods were investigated. The joining methods were 1) dowel-type fasteners, partly in combination with higher friction in the shear plane and 2) continuous joints, mainly by bonding with adhesives. Tests were carried out to investigate the maximum load-carrying capacity as well as the stiffness of the joints, aiming to transfer the results to the linear load-carrying elements. Where applicable, nominal shear stresses were evaluated. The tests with dowel-type fasteners were mainly carried out to create reference values to compare to the other joining methods. The results with the modified surfaces to increase friction in the shear plane were quite promising regarding the initial stiffness, however, further research of the surface modification has to be carried out. The specimens with continuous joints can be regarded analytically as fully bonded. Bonded specimens with additional bolts combine high stiffness with a residual load-carrying capacity after shear failure of the timber of 30-40% of the maximum load.

KEYWORDS: timber-steel composite beams, dowel-type fasteners, adhesive bonding, continuous joints

1 INTRODUCTION

The results presented in this paper were determined as part of an ongoing research project. Its main objective is the development of a hybrid construction method by combining the materials steel and timber for linear load-carrying elements subjected to bending loads, similar to [1, 2]. The hybrid construction method is characterized by the shear-resistant embedment of a steel profile in a compact timber cross-section, see Figure 1. The bond between the steel profile and the timber cross-section is achieved either by dowel-type fasteners, by a continuous joint or by a combination of the two methods. In this way, the specific advantages of the two materials can be utilized in an optimized manner and the weaknesses of the materials can be compensated for by the composite partner. These hybrid members enable a significant increase in the possible spans, in comparison with conventional timber structures, as they result in a considerable increase in bending stiffness. All this while maintaining compact cross-sectional dimensions. In return, the timber profiles laterally support the thin steel profile and hence prevent its buckling failure. Also, the timber encapsulates and hence protects the steel profile in case of fire.

2 MATERIAL COMBINATIONS

By analytical investigation, suitable material pairings of timber and steel were identified, that are best utilized for different geometric configurations of the cross-section. In particular, a vertically embedded flat steel profile as well as two horizontally embedded profiles were investigated (see Figure 1). To calculate the degree of utilization of the two composite partners, a 4-point-bending test according to EN 408 [3] was chosen as static system. For simplification, full bond between the timber and steel was assumed, and that the cross-sections remain even. Characteristic values were applied in the investigation.

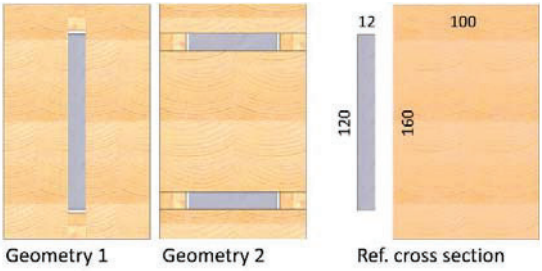

Figure 1: *Exemplary timber-steel hybrid cross-sections*

A variety of material combinations and cross-sections was analyzed. The investigation showed that for a low timber grade, a low steel grade is appropriate and high timber grades require high steel grades to realize equal degrees of utilization. Also, the availability of the used materials was considered. Based on the degree of utilization and the material's availability, two suitable pairings were chosen:

[1] Karlsruhe Institute of Technology (KIT), Timber Structures and Building Construction, Germany, mail: aurand@kit.edu, dietsch@kit.edu

[2] Karlsruhe Institute of Technology (KIT), Steel and Lightweight Structures, Germany, mail: jakob.boretzki@kit.edu, peter.haase@kit.edu, thomas.ummenhofer@kit.edu

https://doi.org/10.52202/069179-0424

First, commonly available glulam GL24h combined with normal steel S355, and second, common softwood LVL with only parallel layers (LVL48P according to [4]) combined with high-strength steel S460. For both combinations, the degree of utilization in both composite partners was nearly identical. For the combination GL24h+S355, the timber was decisive with a utilization of 100% compared to the steel with 93%. For the combination LVL48P+S460, the steel was decisive with a utilization of 100% compared to the timber with 92% (see Table 1).

Compared to the reference cross-section of only the timber part (100 x 160 mm²), the increase in stiffness of geometry 1 with one vertical steel profile was 87% for glulam and 72% for LVL. For geometry 2 with two horizontal steel profiles, the increase in stiffness was 213% for glulam and 176% for LVL (see Table 1). The decrease of deflection at mid-span, applying the same load level as the reference cross-section, was 47% for glulam and 42% for LVL for geometry 1 and 68% for glulam and 64% for LVL for geometry 2. The results for geometry 1 were also compared to a hypothetic cross-section consisting only of the vertical steel component (12 x 120 mm²), see Table 1. Buckling failure was excluded and not further considered for the analysis.

Table 1: *Exemplary results of analytical investigation*

Reference cross-section	Geometry 1		Geometry 2	
	GL24h + S355	LVL48P + S460	GL24h + S355	LVL48P + S460
	Degree of utilization			
Timber:	100%	92%	100%	92%
Steel:	93%	100%	93%	100%
	Stiffness			
Timber:	+87%	+72%	+213%	+176%
Steel:	+103%	+123%	-	-
	Deflection			
Timber:	-47%	-42%	-68%	-64%
Steel:	-51%	-37%	-	-

3 JOINING METHODS AND THEIR MANUFACTURE

The studied joining methods can be categorized in two main groups:

- Dowel-type fasteners
- Continuous joints

3.1 Dowel-type fasteners

The idea behind the use of dowel-type fasteners was the wide availability of such fasteners and their ease-of-application. Especially self-tapping screws offer potential. Additionally, the possibility to increase the load-carrying capacity and especially the stiffness by modifying the steel surface was investigated.
Dowel-type fasteners commonly used in timber construction were chosen. All fasteners had a uniform outer diameter of 10 mm.

The following fasteners were investigated:

- Galvanized dowels for comparative tests
- Galvanized bolts with large washers (Ø = 50 mm)
- Partially threaded screws with a washer head (Ø = 22.5 mm) as well as a countersunk head (Ø = 17.0 mm)
- Fully threaded screws with a countersunk head (Ø = 18.5 mm)

The holes for the fasteners were drilled with a special twist drill, which allowed to drill through both materials, timber and steel without changing the drill bit. However, while drilling through the steel, the drill had to be constantly removed from the hole to allow for the clearing of the metal shavings. This resulted in a slightly greater hole diameter in one of the two side members, which was clearly noticeable when inserting the dowels, bolts, and screws. The fit of the fasteners was always tighter in the second timber side member. Also, the use of the timber-steel twist drill had the disadvantage of leaving one timber side member with a hole the size of the screws' outer diameter instead of the screws' shank diameter (for partially threaded screws) or the screws' core diameter (for fully threaded screws). This also resulted in a more loose fit of the fastener in one of the two side members. The second timber part of the specimens with screws was not pre-drilled for tests with GL24h. However, for tests with LVL48P, the second timber part was pre-drilled with 7 mm, according to their product specification [5, 6].

As mentioned before, the possibility of a surface modification in terms of higher friction in the shear plane was investigated. In [7], various surface modifications were studied, of which two surface modifications were tested in this project:

- Milled circular pattern
- Coated with quartz sand

The milling of the circular pattern into the steel surface was done by using a face mill with replaceable inserts, of which every second insert was removed. The rotational speed as well as the feed rate of the milling tool were both set quite high in order to achieve a rough circular pattern, as can be seen in Figure 2. To obtain a satisfying result, various pairings of rotational speed and feed rate were tested.

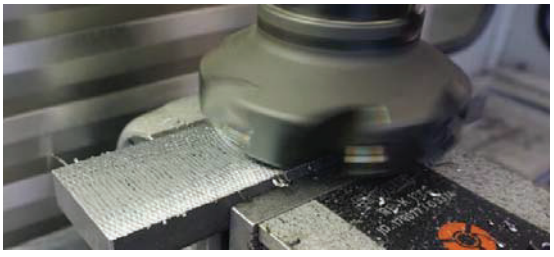

Figure 2: *Milling process of circular pattern*

https://doi.org/10.52202/069179-0424

For the coating of the steel with quartz sand a two component epoxy resin (2K EP [8]) was applied onto the steel surface. The surface was sandblasted and degreased with butanone. The adhesive layer had a thickness of ca. 0.5 mm and the quartz sand had a maximum grain size of 1 mm with about 90% of the grain size between 0.5-0.8 mm. The quartz sand was then pressed by hand into the resin and the resin cured according to the manufacturer's specification. Extracts from the manufacturing process and the final surface can be seen in Figure 3.

Figure 3: *Manufacturing process of coated specimens*

3.2 Continuous joints

The continuous joining was achieved by two different methods:

- Pressing in punched metal plate fasteners (nail plates)
- Adhesive bonding

The nail plates used consisted of 1 mm steel sheets with a nail length of 8.5 mm [9]. The nail plates were adhesively bonded to the steel surface, see Figure 4. Here, the same 2K EP was used as for the coated surface. Again, the steel and the nail plates were sandblasted and degreased before the adhesive was applied. The nail plates with the steel parts were then pressed into the timber parts. A pressing power of around 5 N/mm² was applied, partly exceeding the compressive strength perpendicular to the grain of the timber side members. This resulted in either deformed timber parts or only partially pressed-in nail plates. Therefore, the manufacturing order was changed and the nail plates were first pressed into the timber and afterwards the steel was bonded to the nail plates. Better results could also be achieved when placing the timber parts “edgewise”, i.e. pressing the nail plates in the side surface in multiple laminations/veneers.

Figure 4: *Bonding of nail plates to steel parts*

For the adhesive bonding of steel and timber, two different adhesives were chosen, a two component epoxy resin (2K EP [10]) and a two component polyurethane adhesive (2K PU [11]). For each combination, the respective pull-off adhesion strength was determined, see Figure 5 left. During these tests, a perpendicular force was applied to separate the bonded loading fixture from the surface. This easy and standardized test (e.g. [12]) allowed for a comparison of the adhesion properties of adhesives. Furthermore, different tools for their application were tested for both adhesives. Two requirements were pursued: an even and defined spread of the adhesive and a shape of the applied adhesive, which results in a preferably bubble-free adhesive layer. The best results were obtained with a notched spatula with 4 mm notches.

For the manufacturing of the composite test specimens, the steel parts were all sandblasted and cleaned with butanone before bonding. For the PU adhesive, a primer [13] had to be applied additionally. The timber parts were all planed directly before bonding. The bonding of the specimens was done in normal climate 20°C/65%rH.

All tests with continuous joints were performed with and without additional bolts. For the tests with additional bolts, the bolts were already used in the manufacturing process to apply the contact pressure.

A more detailed description of the selection of the adhesives and the manufacturing process of the adhesively bonded composite specimens is given in [14].

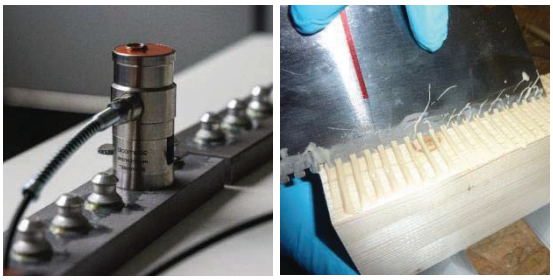

Figure 5: *Pull-off adhesion tests prior to final material selection (left) and spreading of adhesive with notched spatula (right)*

4 TESTS WITH STEEL-TIMBER JOINTS

4.1 TEST SETUP AND PROGRAM

Joint tests were performed to determine the joint properties. The test specimens were designed based on Johansen’s yield theory [15] with two shear planes for each fastener (see Figure 6). The timber parts were dimensioned in such a way, e.g. with an end distance $a_{3,t} = 7d = 70$ mm, that failure of the fasteners occurred with two plastic hinges per shear plane. The density of both timber side members was equal. An overview of the performed tests is given in Table 2. In total, 100 tests were performed of which an excerpt is presented in the following.

https://doi.org/10.52202/069179-0424

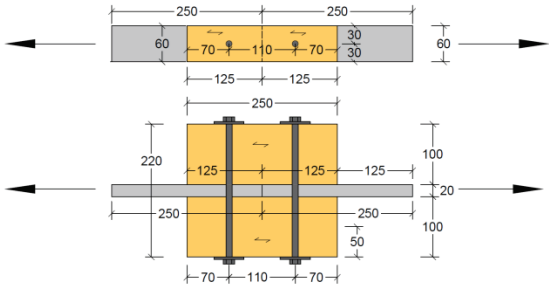

Figure 6: *Test specimens*

The joint tests were performed according to EN 26891 [16] with an unloading loop. Each test was stopped after failure of the specimen or after reaching a displacement of 15 mm in one of the shear planes. For all specimens and all shear planes, the relative displacement between the timber and the adjacent steel part was measured continuously. For this, a digital image correlation (DIC) system [17] was used, see Figure 7. The DIC system repeatedly took pictures of the test specimen with applied markers and the software calculated the displacement of the markers in each frame.

Table 2: *Number of tests for different joining methods and two different timber grades*

No.	Joint	GL24h	LVL48P
1	Dowels	3	3
2	Bolts	4	-
3	Bolts + milled surface	3	-
4	Bolts + coated surface	5	-
5	Screws A[1)] (countersunk head)	3	-
6	Screws B[2)] (washer head)	3	3
7	Screws C[3)] (countersunk head)	3	3
8a	Nail plates	3	3
8b	Nail plates + bolts	2	-
9a	2K EP	5	5
9b	2K EP + bolts	5	5
10a	2K PU	5	5
10b	2K PU + bolts	5	5

[1)] partially threaded screws with countersunk head
[2)] partially threaded screws with washer head
[3)] fully threaded screws with countersunk head

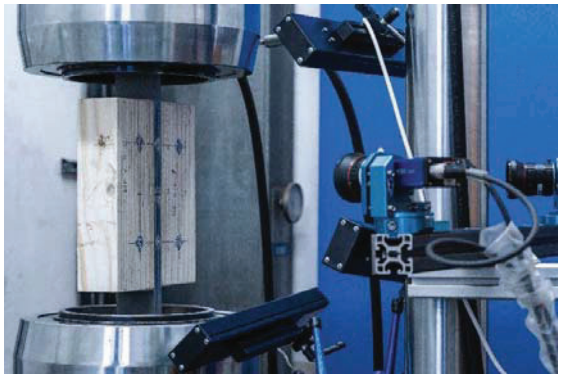

Figure 7: *Test setup with digital image correlation (DIC) system*

4.2 TEST RESULTS AND DISCUSSION

4.2.1 General

For each specimen, the maximum load F_{max} per shear plane was evaluated. The stiffness k_s was evaluated separately for all four shear planes in the range between 10-40% of F_{max}, unless otherwise stated. In order to take into account the influence of the manufacturing process as well as the surface treatment, the stiffness k_i was additionally evaluated in the range of 0-40% of F_{max}. On the one hand, the influence of the larger borehole diameter is shown for the test specimens with screws, and on the other hand, the influence of the surface treatment is taken into account for the test specimens with the roughened surfaces. The results for all tests with dowel-type fasteners are given in Table 3 and the exemplary load-displacement curves in Figure 10. For all tests with continuous joints, the results are given in Table 4 and exemplary load-displacement curves in Figure 14. The force F_{max} is the mean value of all three to five tests of one series per fastener and shear plane. The stiffness k_i and k_s is the mean value of all four shear planes and all tests of one series. For the specimens with continuous joints, a nominal shear stress f_v was evaluated. The shear stress was calculated with the mean value of F_{max} of all tests of one series and the generalized area of the shear plane, i.e. 60 mm x 125 mm less the hole diameter, for tests with fasteners. To better compare the different joining methods, the nominal shear stress was also evaluated for the specimens with dowel-type fasteners, although no shear failure occurred. The timber parts were stored at normal climate 20°C/65%rH and mean moisture contents of $u = 10\%$ for glulam and $u = 8.7\%$ for LVL were evaluated. The density of the glulam specimens varied between 388 and 488 kg/m³ and for LVL between 483 and 643 kg/m³ (see Table 3 and Table 4).

4.2.2 Tests with dowel-type fasteners

The reference tests with GL24h+S355 and dowels reached a mean load of 10.6±0.47 kN and a mean stiffness k_i of 3.97±1.16 kN/mm and with LVL48P+S460 a mean load of 14.9±0.33 kN and a mean stiffness k_i of 8.32±1.21 kN/mm. The stiffness k_s was evaluated between 20-50% of F_{max} and k_i between 0-50%. The specimens failed by splitting of one of the timber side members, before reaching a relative displacement of 15 mm in any of the four shear planes. The designed failure with two plastic hinges per shear plane was reached. However, for some dowels, the plastic hinges were barely visible. This leads to the assumption that the end distance $a_{3,t} = 7d = 70$ mm was not large enough.

The tests with bolts and large washers reached a mean load of 14.6±1.59 kN and a mean stiffness k_i of 5.85±1.65 kN/mm. The stiffness k_s was evaluated between 30-60% of F_{max} and k_i between 0-60%. Here, the two plastic hinges were clearly visible. Splitting of the timber occurred as well, however, did not result in a decrease of the load. Whereas the tests with dowels showed some initial slip, the tests with bolts and washer showed no slip at all because of the pre-stressing from tightening the nut. The slightly higher stiffness k_s of the dowel joints (see Table 3) might be due to the fact, that

https://doi.org/10.52202/069179-0424

the actual dowels' diameter was measured with $d = 10.0$ mm, while the bolts' actual diameter was only 9.4 mm, thus resulting in a tighter fit of the dowel joint.

The tests with bolts and modified surfaces both reached slightly higher results with $F_{max} = 17.1 \pm 0.60$ kN for the milled surface and 18.3±2.58 kN for the coated surface. The stiffness amounted to $k_i = 4.82 \pm 0.80$ and 5.80±1.06 kN/mm, respectively. For the tests with the milled surface, the stiffness k_s was evaluated between 40-60% of F_{max} and k_i between 0-60%. For the tests with the coated surface, the stiffness k_s was evaluated between 30-50% of F_{max} and k_i between 0-50%. The load-displacement curves showed a significantly higher initial stiffness, due to the increased friction between steel and timber. The tests with the milled surface remained in stick state up to almost one third of the total load, which is quite astonishing as there is almost no visible damage to the timber surface, as can be seen on the left in Figure 8. This was not the case for the tests with the coated surface, where large deformations were needed to properly press the quartz sand into the timber surface, which then led to high abrasion of timber fibers, as can be seen on the right in Figure 8. However, the tests showed that a surface modification in combination with laterally loaded fasteners is not as promising as in combination with mainly axially loaded fasteners, see [7].

Figure 8: *Milled surface with almost no abrasion and no damage to the timber surface (left) and coated surface with high abrasion of timber fibers (right)*

The tests with partially threaded screws reached the lowest loads with $F_{max} = 9.89 \pm 0.39$ kN for the screws with a countersunk head and 11.2±0.98 kN for the screws with a washer head. The stiffness was also quite low with $k_i = 1.27 \pm 0.10$ (countersunk head) and 1.29±0.15 kN/mm (washer head). The stiffness k_s was evaluated between 20-50% of F_{max} and k_i between 0-50%. The low results can be explained with the manufacturing process of the specimens, where a 10 mm hole was drilled through one timber side member and through the steel. So for the smooth shank to be in contact with the timber, approximately 1.5 mm displacement had to be reached first. This also resulted in the formation of only one plastic hinge per shear plane on the side of the shank, as can be seen in Figure 9.

The fully threaded screws performed better with a mean load of 16.5±0.41 kN for GL24h and 18.9±1.60 kN for LVL48P and a mean stiffness k_i of 2.90±0.39 kN/mm and 4.35±0.84 kN/mm, respectively. The stiffness k_s was evaluated between 10-35% of F_{max} and k_i between 0-35%.

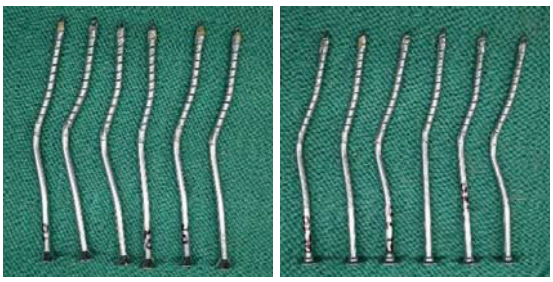

Figure 9: *Partially threaded screws after tests with countersunk head (left) and washer head (right)*

The coefficient of variation (COV) of the resulting maximum loads is within the expected range with 2% to 14% for GL24h and 2% to 8% for LVL48P. The COV of the evaluated stiffness values is significantly higher with 7% to 35% for GL24h and 12% to 26% for LVL48P, again as expected. In general, the tests showed that screws are not able to provide the desired composite properties in this project. The maximum loads are mainly reached at large displacements of 15 mm, see also Figure 10. The stiffness is correspondingly low and feature a large scatter, see also Figure 11.

Table 3: *Maximum load F_{max}, stiffness k_i and k_s, and shear stress f_v per fastener and shear plane for joints with dowel-type fasteners (incl. standard deviation and COV in %)*

No.	F_{max}	k_i	k_s	f_v	ρ
	kN	kN/mm	kN/mm	N/mm²	kg/m³
GL24h					
1	10.6	3.97	6.36	1.43	446
	0.47	1.16	1.30	0.06	7.14
	4%	29%	20%	4%	2%
2	14.6	5.85	4.37	1.97	466
	1.59	1.65	1.05	0.21	11.4
	11%	28%	24%	11%	2%
3	17.1	4.82	3.97	2.31	452
	0.60	0.80	1.15	0.08	4.21
	3%	17%	29%	3%	1%
4	18.3	5.80	5.65	2.46	431
	2.58	1.06	1.80	0.35	19.1
	14%	18%	32%	14%	4%
5	9.89	1.27	1.68	1.33	440
	0.39	0.10	0.59	0.05	1.00
	4%	7%	35%	4%	0%
6	11.2	1.29	1.76	1.50	443
	0.98	0.16	0.12	0.13	1.50
	9%	12%	7%	9%	0%
7	16.5	2.90	2.60	2.22	478
	0.41	0.39	0.33	0.06	-
	2%	13%	13%	2%	-
LVL48P					
1	14.9	8.32	9.56	2.01	641
	0.33	1.21	1.15	0.04	1.26
	2%	15%	12%	2%	0%
6	13.7	1.72	1.99	1.85	625
	0.92	0.29	0.49	0.12	20.3
	7%	17%	25%	7%	3%
7	18.9	4.35	4.14	2.54	613
	1.60	0.84	1.06	0.22	7.03
	8%	19%	26%	8%	1%

https://doi.org/10.52202/069179-0424

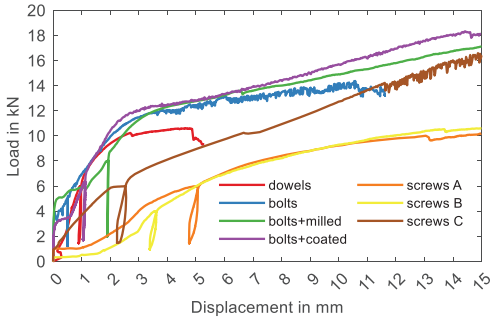

Figure 10: *Load-displacement curves for all tests with dowel-type fasteners and material combination GL24h + S355J2*

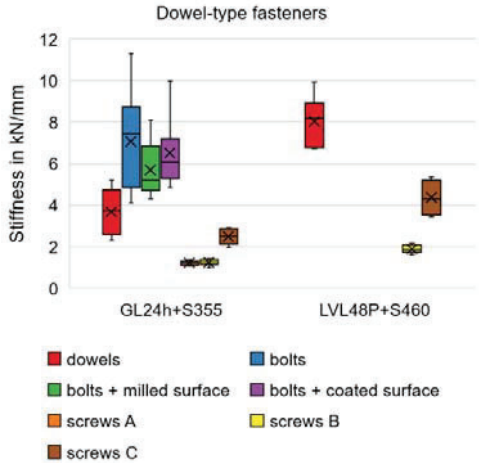

Figure 11: *Stiffness for all tests with dowel-type fasteners and both material combinations*

4.2.3 Tests with continuous joints

The tests with the nail plates resulted in a higher maximum load F_{max} = 21.3±0.47 kN and a significantly higher stiffness k_i = 116±46.2 kN/mm. The specimens failed brittle by shear failure in the timber, in the plane of the nail tips, see Figure 12. A nominal shear stress of f_v = 2.84±0.06 N/mm² was evaluated. For the tests with additional bolts, the maximum load increased to F_{max} = 26.2±3.78 kN, the stiffness however decreased to k_i = 84.1±21.7 kN/mm. This might be due to the fact, that the size of the nail plates decreased by the bolt's cross-section, thus decreasing the joined area. Again, the specimens failed by shear failure of the timber side members. Here, the evaluated shear stress was 3.53±0.51 N/mm². The lower shear stress for the tests without bolts might be due to the fact that these were the first specimens, where the nail plates were not properly pressed in, thus reducing the area to transfer loads. After initial failure, the load-carrying capacity dropped to about half the maximum load. Splitting of the side members occurred, but was regarded as secondary failure. Exemplary tests showed that the load-carrying capacity could be further increased if the timber parts were oriented "edgewise" thus pressing the nail plates in multiple laminations/veneers.

Figure 12: *Failed specimen of test with nail plates, glulam and additional bolts (left) and test with nail plates and LVL (right)*

The tests with bonded specimens reached the highest loads with F_{max} = 24.8±4.19 kN for the 2K EP and 29.3±4.38 kN for the 2K PU. Stiffness values of k_i = 655±166 kN/mm and 464±63.3 kN were evaluated. The displacements at the time of failure were very small with only 0.2 mm. Shear failure occurred in the timber mainly very close to the contact surface with the steel (see Figure 13). Shear stresses of 3.31±0.56 N/mm² and 3.90±0.58 N/mm² were evaluated for the two adhesives. Again, for the tests with additional bolts, the load-carrying capacity dropped to about 30 kN after the shear failure occurred, which approximately was the maximum load of the tests on solely bolted joints. The load level then only slightly increased with increasing displacement. At a displacement of 15 mm, the tests were terminated.

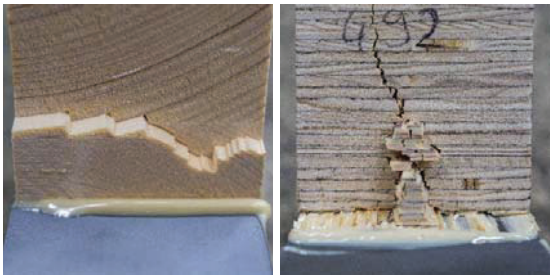

Figure 13: *Failed specimen of test with 2K EP and glulam (left) and test with 2K PU, LVL and bolt (right). Splitting was secondary failure and occurred after sudden shear failure*

In general, no differences of the used adhesives could be observed in the test results. In Figure 14, load-displacement curves for the tests with continuous joints are given. Because of the very small displacements at the time of failure of the adhesively bonded specimens paired with the ductile behavior and large deformations of the specimens with additional bolts, the scale of the x-axis is split into two sections with different intervals.

The COV of the resulting maximum loads is within the expected range with 2% to 17% for GL24h and 8% to 11% for LVL48P. The COV of the evaluated stiffness values is significantly higher for GL24h with 6% to 40%, as expected and rather low for LVL48P with 8% to 19%, see also Figure 15. Because of the very small displacements at the time of failure, the measurement uncertainty has to be considered and will be evaluated in future steps.

https://doi.org/10.52202/069179-0424

Table 4: *Maximum load F_{max}, stiffness k_i and k_s, and shear stress f_v per fastener and shear plane for continuous joints (incl. standard deviation and COV in %)*

No.	F_{max}	k_i	k_s	f_v	ρ
	kN	kN/mm	kN/mm	N/mm²	kg/m³
GL24h					
8a	21.3	116	106	2.84	448
	0.47	46.2	35.2	0.06	8.37
	2%	40%	33%	2%	2%
8b	26.2	84.1	72.3	3.53	466
	3.78	21.7	15.0	0.51	31.1
	14%	26%	21%	14%	7%
9a	24.8	655	610	3.31	423
	4.19	166	176	0.56	1.14
	17%	25%	29%	17%	0%
9b	33.0	464	435	4.44	425
	3.74	63.3	35.4	0.50	21.3
	11%	14%	8%	11%	5%
10a	29.3	584	589	3.90	427
	4.38	47.2	77.8	0.58	16.3
	15%	8%	13%	15%	4%
10b	32.7	552	556	4.41	425
	2.51	33.2	46.2	0.34	6.25
	8%	6%	8%	8%	1%
LVL48P					
8b	24.2	311	284	3.26	630
	2.61	59.4	40.9	0.35	1.28
	11%	19%	14%	11%	0%
9a	27.6	514	492	3.72	492
	2.95	42.8	50.1	0.40	3.6
	11%	8%	10%	11%	1%
9b	32.0	506	480	4.26	492
	2.87	51.8	46.3	0.38	3.87
	9%	10%	10%	9%	1%
10a	28.8	489	464	3.89	491
	2.45	48.6	49.9	0.33	5.13
	8%	10%	11%	8%	1%
10b	30.1	457	432	4.02	490
	2.73	51.7	54.8	0.36	4.57
	9%	11%	13%	9%	1%

An in-depth presentation of the test results and subsequent discussion is given in [14].

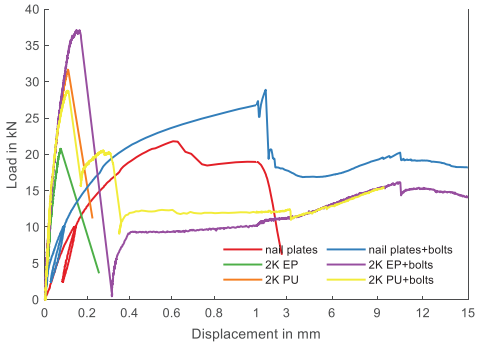

Figure 14: *Load-displacement curves for all tests with continuous joints and material combination GL24h+S355J2*

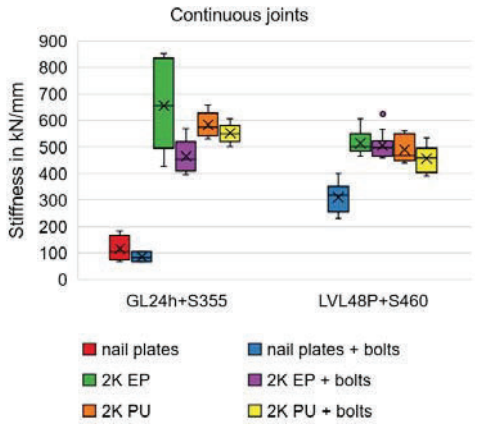

Figure 15: *Stiffness for all tests with continuous joints and both material combinations*

5 SUMMARY AND OUTLOOK

The test results give a comprehensive overview of the different joining methods studied in this research project on hybrid timber-steel beams. All tests were carried out with the same sized specimens. The outer diameter for all dowel-type fasteners was the same, as well as the bonded area for the tests with continuous joints. The tests showed that dowel-type fasteners are not suitable for the desired purpose. Also, both surface modifications did not have the desired effect and only slightly increased the results. For the joining methods with continuous joints, fully bonded hybrid beams under bending load can be assumed. The tests also revealed valuable information about the use of bolts with bonded joints and the ductile behavior after initial shear failure of the timber.

In a further step, the behavior of the joining methods under varying environmental conditions is to be investigated. In future tests, the specimens are subjected to changing climatic conditions while simultaneously being loaded with a percentage of the load established in the here presented tests. Here, the climatic conditions of service class 1 (dry conditions, indoor environment) as well as service class 2 (more humid conditions, protected outdoor environment) are of interest.

For adhesives, the surrounding temperature is also of great importance. Each adhesive has its own specific glass transition temperature, which characterizes the range of temperature above which the glassy, brittle adhesive becomes rubbery and ductile. Once the glass transition temperature is reached, the adhesive's mechanical properties are reduced significantly. Also, the material properties of timber decrease with increasing temperature. Therefore, tests with high temperatures and adhesively bonded specimens will be performed in future tests.

Following the small scale tests with the different joining methods, full scale tests of timber-steel-composite beams are planned. In this realm, the two geometries presented in chapter 2 will be tested. The cross-sections and the dimensions of the beams will be analogous to the analytical investigation. The four-point bending tests will be performed according to EN 408.

https://doi.org/10.52202/069179-0424

REFERENCES

[1] Winter W., Riola-Parada F.: Timber-Steel Hybrid Beams for Multi-Storey Buildings: Final Report. In: *World Conference on Timber Engineering WCTE 2016*. Vienna, Austria; 2016.

[2] Tsai M.-T., Le T.: Determination of Initial Stiffness of Timber–Steel Composite (TSC) Beams Based on Experiment and Simulation Modeling. *Sustainability* 10(4):1220; 2018.

[3] EN 408:2012-10: Timber structures - Structural timber and glued laminated timber - Determination of some physical and mechanical properties; German version; 2012.

[4] Finnish Woodworking Industries Federation: LVL Handbook Europe. Helsinki; 2020.

[5] ETA-19/0553: HECO-TOPIX-plus (or HTP or HT-plus), HECOTOPIX-plus-T (or HTP-T or HT-plus-T) and HECOTOPIX-plus-CC (or HTP-CC or HT-plus-CC) screws; ETA-Danmark A/S; 2021.

[6] ETA-11/0190: Würth self-tapping screws; Deutsches Institut für Bautechnik (DIBt); 2018.

[7] Aurand, S., Blass, H.-J.: Connections with inclined screws and increased shear plane friction. Proceedings of: *International Network on Timber Engineering Research INTER 54.* Paper 54-7-5. Online; 2021.

[8] Product data sheet: Sikadur®-370 (Provisional); Sika Services AG, Zurich, Switzerland; 2016.

[9] Allgemeine bauaufsichtliche Zulassung Z-9.1-761: Nagelplatte M 20 H als Holzverbindungsmittel; Deutsches Institut für Bautechnik (DIBt); 2015.

[10] Technical data sheet: Jowat® Epoxidharz 692.30; Jowat SE, Detmold, Germany; 2019.

[11] Technical data sheet: LOCTITE CR821 PURBOND; Henkel AG & Co. KGaA, Düsseldorf, Germany; 2022.

[12] EN ISO 4624:2016-08: Paints and varnishes - Pull-off test for adhesion (ISO 4624:2016); German version; 2016.

[13] Technical data sheet: BONDERITE M-NT 1455-W; Henkel AG & Co. KGaA, Düsseldorf, Germany; 2017.

[14] Haase, P., Boretzki, J., Albiez, M., Aurand, S., Sandhaas, C., Ummenhofer, T., Dietsch, P.: Influence of the joining technique on the structural behaviour of hybrid timber-steel components. Under review for *Wood Material Science & Engineering*; 2023.

[15] Johansen, K.W.: Theory of timber connections. *International Association for Bridge and Structural Engineering*. 9, 249-262; 1949.

[16] EN 26891:1991-07: Timber structures; joints made with mechanical fasteners; general principles for the determination of strength and deformation characteristics (ISO 6891:1983); German version; 1991.

[17] Q400 DIC Digital Image Correlation – non contact 3D deformation sensor; LIMESS Messtechnik und Software GmbH, Krefeld, Germany; 2023.

https://doi.org/10.52202/069179-0424

World Conference on Timber Engineering Oslo 2023

SEMI-INTEGRAL FULL-SCALE STUTTGART TIMBER MODEL BRIDGE

Simon Aicher[1], Kai Simon[2]

ABSTRACT: This paper reports on the on-set, design and realization of the Stuttgart Timber Model Bridge (STMB), which represents worldwide the largest full-scale demonstrator of a novel concept for timber bridges. The demonstrator bridge, erected at the Campus of University of Stuttgart in 2016, has been developed within two consecutive EU-research projects. It comprises several so far novel solutions concerning supports and superstructure. All derived novelties aim at a new generic type of robust timber bridges being significantly superior vs. premature degradation experienced at many of today´s timber bridges. In pursuing of the project aim first an extensive assessment of present deficiencies of mostly untreated timber bridges including a field study at 120 bridges has been performed. Based hereon, new construction concepts and detailing for the supports and the superstructure were derived. Major novelties are the realization of an integral fully rigid timber-reinforced concrete (RC) joint and of detached member-embankment connections. The build-up of the superstructure includes a double-water shielding and the implementation of a most advanced remote-controlled moisture monitoring system. The robustness of the novel bridge concept has been positively evaluated for a period of seven years with planed partly over-excessive mechanical and water loadings.

KEYWORDS: timber bridge, integral timber-RC-joint, detached cantilever support, novel robustness concept, superstructure with double water-shielding, advanced remote moisture monitoring

1 INTRODUCTION

The aim of the research task, pursued within two consecutive EU-research projects at Timber Department of MPA University Stuttgart consisted in the development of a visionary, robust timber bridge of highest possible durability. The novel design should overcome the weakness of the existing bridges significantly without implementation of any wood preservative treatments. In order to achieve the envisaged goal in a first step a thorough analysis and field study was conducted at 120 timber bridges of different build-ups and ages. Based hereon in total 16 recurring damage scenarios were identified and attributed to different generic bridge types such as e.g. truss, trough and deck bridges [1], [2].

Based on the classification and understanding of the damage on-sets a novel bridge type was conceived, detailed, designed and finally a full-scale prototype, the so-called Stuttgart Timber Model Bridge (STMB) was built (Figure 1). The demonstrator, representing the world´s largest research demonstrator bridge, erected at the Campus of Stuttgart University, was inaugurated in June 2016 by the state minister of rural affairs and is publicly accessible since then. The bridge serves for continued extensive measurements of strains, displacements, forces and moisture evolution based on latest measurement technology. The bridge can also be used on request by external researchers for specific investigations, e.g. regarding static and dynamic loading or advanced sensorics.

Figure 1: *Rendering view of the Stuttgart Timber Model Bridge (STMB)*

2 INTEGRAL AND SEMI-INTEGRAL BRIDGES

2.1 GENERAL

So-called integral structures, here in specific integral bridges, are designed without joints and bearings as defined e.g. in the German guideline for the design, construction and equipment of civil engineering structures, part 2, section 5 [2]. According to the definitions in [2], the superstructure of an integral bridge is continuous without joints along the entire length of the bridge and is not separated from the piers, abutments and pillars by joints or bearings. All components are monolithically connected to each other. Figures 2 a) – c) [3] schematically illustrate the essential differences of a common bridge structure with bearings and expansion

[1] Materials Testing Institute (MPA), Department Timber Constructions, University of Stuttgart, Germany, Head of Department

[2] Materials Testing Institute (MPA), Department Timber Constructions, University of Stuttgart, Germany, Kai.Simon@mpa.uni-stuttgart.de

https://doi.org/10.52202/069179-0425

joints in the super-structure-abutment-transition as well as in the sliding pillar-superstructure connection (Figure 2a) vs. a frame-like integral bridge structure (Figure 2b).

The definitions for semi-integral bridge constructions are not throughout consistent in North America and Europe. Here the definition acc. to [3] is used whereby a semi-integral bridge features a monolithic connection of the super structure with the middle support(s) whilst the end supports rest on bearings and can slide as in a usual bridge construction (Figure 2c). This definition can be extended, when e.g. looking at the symmetry conditions at the middle pillar, to a semi-integral bridge construction where abutment and superstructure are rigidly connected at one (end) pier whilst the other end and eventual intermediate supports allow expansion and sliding in longitudinal direction and partly orthogonal hereto. The latter definition can then be immediately applied to the constructed Stuttgart Timber Model Bridge (STMB). The fact that the STMB comprises two sliding supports is owed to the curvature of the bridge in the ground elevation.

Integral bridge structures, which up to now are constructed almost exclusively in reinforced concrete and steel composite construction show a number of significant advantages over conventional bridges with sliding bearings and joints, whereby some specifics apply when using timber for the superstructure. It should be mentioned that the concept of integral and semi-integral bridges is (almost) not considered in the present or newly drafted timber bridge design codes EN 1995-2 [4], [5]. Draft EC5-2 mentions integral abutment bridges in chapter 7.5, hereby referring exclusively to draft EC0 [6], which addresses soil aspects. However, integral timber-concrete joints being a prerequisite for integral and semi-integral timber bridges are not addressed at all.

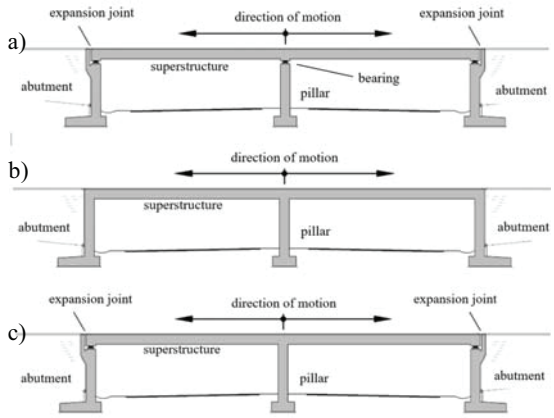

Figure 2: *Bridge construction concepts a) standard bridge superstructure with bearings and expansion joints, b) integral bridge with monolithic connections of superstructure, pillar and abutments, c) semi-integral bridge with rigid connection at the middle pillar*

2.2 ADVANTAGES OF INTEGRAL BRIDGES

The most important advantage of an integral bridge consists in the complete elimination of bearings and expansion joints, which are particularly susceptible to damage and are highly maintenance-intensive. For this aspect precise data is available for the area of steel and concrete construction. The maintenance costs of the two groups of components mentioned are about 10% of the total maintenance costs, while their share of the pure construction costs is only 3% [7]. Furthermore, bearings and expansion joints often cause damage to the overall structure, too, which also applies to a considerable extent to timber bridges [1]. A second significant advantage resulting from the monolithic connection between superstructure and the abutments consists in the significantly smaller section forces due to the clamping effect, which enable very slender, more aesthetic and more cost-effective constructions.

The magnitude of section force reductions of integral and semi-integral bridges can be illustrated in approximative manner by a comparison of a both- or one-sided clamped beam vs. a simple supported (bridge) beam. It should be noted that the comparison of rigid clamping vs. sliding supports represents a theoretical limit case as the abutment shows a finite rotational stiffness depending on soil conditions and abutment wall height. In the following a uniform loading is assumed.

In case of a both-sided clamped beam (i.e. integral bridge) the extreme moment ($ql^2/24$) at the support is 1,5 times smaller as compared to the field moment ($ql^2/8$) of a simply supported beam. In case of the semi-integral substitute model (one-sided clamped, opposite side simply supported) the clamping moment equals the field moment of the simply supported situation. However along most of the beam length a significantly reduced moment exists, whereby the extreme field moment ($ql^2/14,2$) reduces by a factor of 1,8. Additionally to section forces from external gravity loading (self-weight, traffic, …) stresses from constrained internal forces, not occurring in simply supported bridges have to be considered, what is regarded below.

Irrespective of the mentioned superimposed eigenstress-related forces integral structures are more robust overall and have significant load redistribution reserves as a result of the static overdetermination.

2.3 DISADVANTAGES OF INTEGRAL BRIDGES

For integral RC and steel composite bridge structures, the constrained internal forces resulting from concrete shrinkage, temperature and non-uniform lowering of the supports, which interact to a large extent with the ground conditions, i.e. the ground stiffness, have a disadvantageous effect. In the case of integral bridges, a realistic consideration of the soil parameters is therefore of significantly greater importance than for bridges with sliding bearings. Hereby it is not sufficient to work with characteristic lower parameters [2], [8]. Depending on the respective foundation and pier stiffnesses, integral structures suffer comparable longitudinal deformations as

https://doi.org/10.52202/069179-0425

bridges with sliding bearings. These displacements and rotations are passed on directly to the backfill via the monolithically connected abutments. In the Northern Hemisphere the annual climate change results in positive and negative constrained internal forces. This leads to monotonic and cyclic deformations of the abutment wall that act on the backfill (see Figure 3). In case of integral timber bridges the constrained internal forces result from a superposition of changes in temperature but most important from moisture variations.

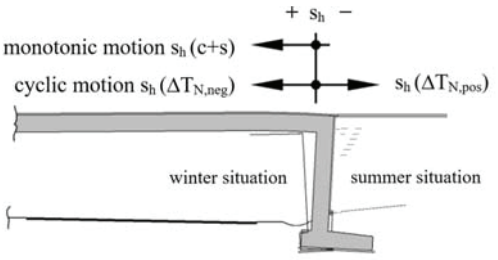

Figure 3: *Displacements of an integral abutment during seasonal change*

2.4 INTERNAL FORCES FROM TEMPERATURE AND MOISTURE CHANGES

In the design of timber structures, the effect of temperature induced movement (expansion / contraction) as opposed to the moisture induced movement (swelling / shrinking) is rarely considered. However, in structures with hindered movment possibilities as in case of integral bridges this feature has to be taken into consideration as being beneficial.

The temperature expansion coefficient of softwoods (spruce and fir) parallel to fiber can be roughly assumed as $\alpha_{T,0} = 0{,}4 \cdot 10^{-5}$ [1/K], hence being about one third as compared to steel. The moisture expansion coefficient parallel to fiber is generally taken as $\alpha_{u,0} = 10 \cdot 10^{-5}$ [1/1%Δu]. Although this value is 25 times higher as $\alpha_{T,0}$, this is partly compensated by the much higher temperature ΔT than moisture Δu changes.

In case of integral RC bridges the two general design scenarios of a uniform and linearly varying temperature distribution along cross-section depth of the superstructure are regarded. In a well-ventilated timber pedestrian bridge, it is considered sufficient to assume a rather symmetric parabolic temperature and moisture distribution over the beam cross-section as illustrated in Figure 4 (see also [9]).

For an exemplary illustration of the temperature-moisture expansion interaction in a timber bridge the parabolic distribution is approximated by a linearly stepped function. It is assumed (common for climate in Germany) that the conditions at bridge erection are: $T_0 = 10°C$ and $u_0 = 12\%$. In the summer load case the outer 1/6 of the cross-section depth d experience at the centroid a reduced moisture content of 8% (Δu = 4%) while in the center part comprising 4/6 of d the reduced moisture content amounts to 10% (Δu = 2%). The Temperature the centroid of the outer parts is assumed to be 30°C (ΔT = 20°C) and at the center at 25°C (ΔT = 15°C). The ratio of the restrained normal forces resulting from temperature (N_T) vs. moisture (N_u) generally reads

$$\frac{N_T}{N_u} = \frac{\varepsilon_T}{\varepsilon_u} = \frac{\alpha_T \, \Delta T_N}{\alpha_u \, \Delta u} \tag{1}$$

For the outer beam parts the summer situation then delivers

$$\left[\frac{N_T}{N_u}\right]_{Sommer} = \frac{0{,}4 \cdot 10^{-5} \cdot 20}{10 \cdot 10^{-5} \cdot (-4)} = -0{,}2 \tag{2}$$

which means that the tension force at the joint location induced by the moisture depended wood shrinkage is reduced by the counteracting temperature extension by 20%. The resulting restrained normal force of the outer cross-section parts then reads

$$\begin{aligned} N_{T,u,summer} &= (\alpha_T \Delta T + \alpha_u \Delta u)\, EA \\ &= (0{,}4 \cdot 20 + 10 \cdot (-4)) \cdot 10^{-5} \cdot EA \\ &= |-32 \cdot 10^{-5}| \cdot EA \quad \text{(tensile force)} \end{aligned} \tag{3}$$

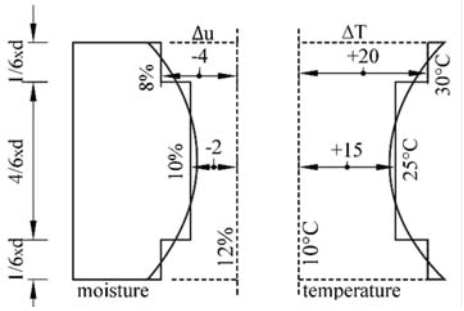

Figure 4: *Assumed moisture and temperature gradient of the timber (GLT) superstructure member in the summer period (erecting state: T = 10°C, u = 12%)*

3 THE STUTTGART TIMBER MODEL BRIDGE

3.1 DURABILITY ORIENTED DESIGN AND DETAILING APPROACH

Architecturally driven the Stuttgart Timber Model Bridge (STMB) was developed as a so-called deck-bridge, i.e. an open construction without a weather sheltering roof, considered outdated in modern architecture. The structural concept and the details of the build-up of the STMB was then in particular driven by an intention to avoid any of the previously identified 16 generically different durability damage scenarios ([1] and [10]). To do so and to deliver a trustworthy, reliable show case of the effectiveness of all newly or stringent consistently pursued ideas it was considered inevitable to verify all detailing in a full-scale demonstrator building with dimensions immediately transferable to practical use. In more detail, the following constraints were considered mandatory for the bridge layout:

- No penetration of covering and superstructure by any mechanical fastener from top to lower or bottom surfaces. This aims to avoid an extremely often

https://doi.org/10.52202/069179-0425

occurring damage / decay situation where water penetrates – gravity wise – along the periphery of nails, screws, dowel type fasteners as the surrounding hole in the wood gets enlarged over time. The interacting mechanical, moisture and temperature loading causes small cavities which enable unhindered and hardly to detect water penetration.

- Avoidance of any access and accumulation of decay generating greenery, dirt, split, water and snow at the supports. This necessitates a revision to the typical bridge end-support-abutment detailing shown in Figure 5, where the end-grain face(s) of the superstructure beam(s) or plate ends close to the rear wall of the abutment. The cavity between the timber end grain face and the abutment rear wall, unless cleaned frequently, fills with greenery or dirt over time causing numerous bridge damages. An enlargement of the cavity width *a* to a sufficiently high distance of about 0,5 to 1 m is in general considered being uneconomic as this necessitates a much larger support bank / bridge benching of the abutment. In order to overcome the sketched decay prone support situation two new on-sets were developed, outlined below.
- Realization of a redundant two-layer water shielding of the main superstructure beam
- Segmented, easy demountable and repairable bridge pavement elements made from durable wood species. Note: Due to funding issues Douglas fir boards of rather low durability (class 3-4 according to EN 335 [11]) were used in the STMB.
- Enabling of easy inspection access especially of the superstructure from the narrow faces by shutters which can be opened by hinges.
- Continuous monitoring of the moisture evolution at discrete points.
- Segmented linear sensors for leakage detection at the lower sealing layer.

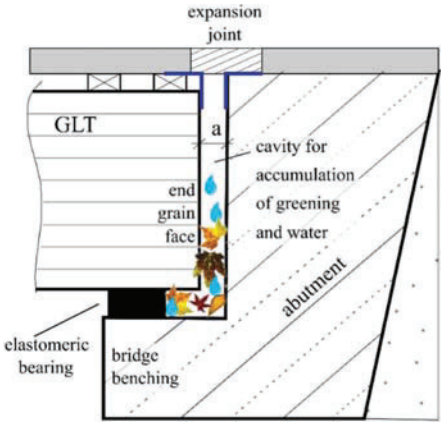

Figure 5: *Frequent damage / decay prone detail of superstructure – abutment transition of bridges with sliding end supports where the narrow cavity between GLT end grain face and abutment wall is subject to accumulation of greening and water*

3.2 BASIC CONSTRUCTION DETAILS

The Stuttgart Timber Model Bridge (STMB) was realized as a pedestrian and cycling bridge, but the principle is applicable to heavy traffic purposes, as well. Generically, the bridge can be termed a semi-integral deck bridge. The bridge is curved in plan view with a length of 22 m. The clear width of the superstructure is 2 m (see Figures 6, 7 and 8). The main load carrying member is a block-glued GLT beam (GL 24h) with a cross-section of 40 cm x 120 cm, which is supported at both ends and at mid-span at the location of highest curvature.

The bridge design considered a uniformly distributed characteristic load of 5 kN/m^2, a characteristic point load of 10 kN as well as front and rear axle loads of a service/rescue car of 40 kN and 80 kN, respectively.
At the north-east (NE) end the GLT superstructure member is rigidly clamped to the concrete abutment by a novel integral joint, specified in more detail below. The abutment is backfilled with a paved sloping ramp enabling car access to the bridge.

The supports at mid-length and at the south-east (SE) end are constructed as sliding supports with two rubber bearings, each. At the mid-span support sliding is unrestricted in any horizontal direction whilst at the SE support the sliding is prevented normal to beam longitudinal axis. The rubber bearings which are positioned at the quarter-points of the cross-sectional width of the GLT member rest on a horizontal steel frame which itself is supported by four steel screw piles at the mid-span and at the SE end support, respectively. It should be mentioned that screw piles present excellent options for cheap but robust sustainable foundations of light-weight (timber) bridge structures which can be erected and remounted very fast.

The SE end support was constructed in view of the above outlined end-support decay scenario by a so-called detached transition from the embankment to the bridge superstructure.

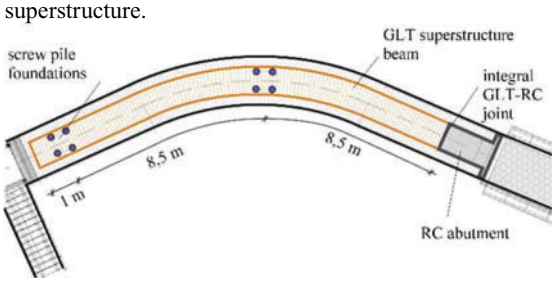

Figure 6: *Plan view of the Stuttgart Timber Model Bridge*

4 DETAILS OF SUPPORT CONSTRUCTIONS

4.1 INTGRAL RIGID TIMBER-CONCRETE ABUTMENT JOINT

The north-east (NE) support was realized for the first time in timber bridge construction as a fully integral - moment, torsion, shear force rigid timber-reinforced concrete (RC) joint (see also [10] and [12]). The connection is based on rebars (n = 34, d_{rod} = 16 mm, strength grade B500) glued

https://doi.org/10.52202/069179-0425

into the GLT beam with an epoxy resin, then protruding by about 1,2 m from the end grain face (see *Figure 7* a) – c)). The GLT rebars were aligned/connected with the rebars of the reinforcement cage cased by the concrete formwork and then the assembly of the GLT and the cage bars was cast in a single step to form a rigid connection without any gap. This novel support construction, fully apart from mechanical considerations, provides the possibility to overcome in conjunction with a continuous decking the present onsets of timber decay starting from the GLT end grain face through greenery/earth and hence moisture accumulation between GLT and abutment wall as illustrated schematically in Figure 5.

The load capacity of such a joint has been verified in previous investigations reported in [13]. These tests demonstrated a superior moment and shear force transfer. The bending stiffness and capacity results in a first conservative assumption exclusively from the normal forces in the rods glued-in parallel to grain at distance e = 284 mm. This holds entirely true for the rebars located at the bending tension side, here located at the top side, due to the negative bending moment at the clamped joint, at the top. At the bending compression side, however, it is reasonable to assume an additional load transfer via contact compression between the GLT end grain face and the concrete abutment. The load sharing between rod and contact forces can in first instance be assessed by a parallel system model which undergoes significant variations over time depending on moisture changes and relaxation. This aspect is quantified separately.

The shear force transfer evolves somewhat more complicated as outlined below. As a full understanding of the mechanism and hence of a reliable capacity assessment of the shear force transfer in the GLT was on-going at time of the bridge construction, the shear force transfer was realized in redundant manner via two complementary approaches A and B:

Mechanism A is represented by the behaviour of a ribbed dowel type fastener glued-in parallel to grain and loaded laterally. The capacity may then be assessed by a Johansen model for a dowel type fastener loaded in single shear between GLT and a thick steel plate. For a laterally loaded dowel type fastener a high risk of splitting parallel to fiber and premature failure of the total joint exists in case the dowel / rebar is positioned close to the tension loaded GLT edge $a_{4,t}$. This, however, cannot be avoided in the given case as a high moment capacity necessitates a large internal lever arm e (see Figure 7 c) of the rebars glued-in the GLT cross-section. In the STMB the edge distances of the rebars (d = 16 mm) were chosen as $a_{4,t}$= 58 mm = 3,6 · d. To overcome the splitting risk the surrounding wood was reinforced by fully threaded self-tapping screws inserted from the bottom side, i.e. bending compression edge of the superstructure GLT.

The second shear force transfer mechanism B was based on some rebars at the bending tension and bending compression edge which were bonded-in with an inclination angle of 20°. These inclined bears then transfer the shear force by tension in the bar and embedment compression stresses in the timber. A details analysis of both shear force transfer mechanism is presented in a separate contribution.

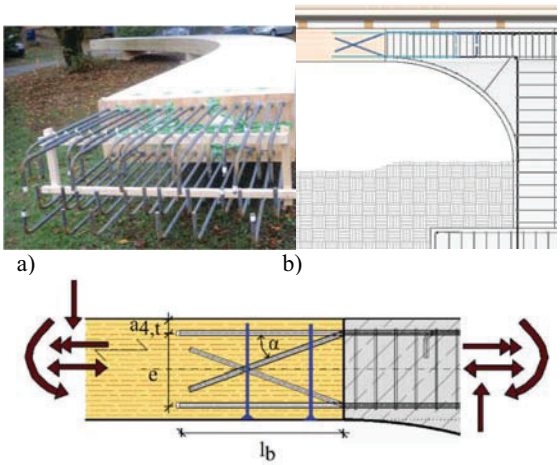

Figure 7: *Integral GLT-RC support embankment a) primary superstructure GLT beam with glued-in rebars; b) scheme of the integral joint/support solution, c) detail section of the integral joint*

4.2 DETACHED CANTILEVER-TYPE BRIDGE-EMBANKMENT TRANSITION AND CENTER SUPPORT

The SE end support consists of a plain rubber bearing where a translation displacement is restricted only in direction perpendicular to the bridge axis. The bridge related novelty consists in the fact that the GLT-RC joint exceeds the NE support cantilever-like by about 1,5 m. At the SE end the transition to the embankment is fully decoupled by means of a perforated steel grid plate supported by L-shaped steel brackets fixed to the pier front. This solution again enables a full detachment of the end grain face of the timber / superstructure from the embankment and hence exclusion of biodegradation.

The mid-span and the SE flexible supports consist of screw-piles, which are especially apt for light-weight, easily demountable sustainable foundations.

5 CROSS-SECTIONAL-BUILD UP OF THE BRIDGE

The cross-sectional-build-up of the superstructure is shown in Figure 8 a). In brief, two decoupled water shielding planes were constructed (Figure 8 b) and c)). The cross-ply LVL plate was then covered by a bonded fiber reinforced roofing membrane layer inclined at a small angle (6°) vs. the horizontal plane to enable a water drainage to the lower bridge edge. The inclination is then compensated with regard to a horizontal plane by tapered support beams for the pavement. An important feature of the superstructure build-up is that no mechanical fastener penetrates any structural and water proofing component / layer from top. The connection of the cross-ply LVL plate as well as for the hand rail is realized by angle brackets connected to the narrow faces of the structural GLT beam.

https://doi.org/10.52202/069179-0425

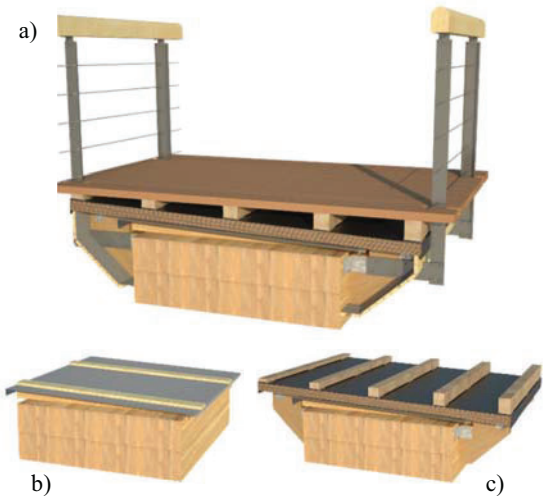

Figure 8: *build-up of STMB a) total cross-section, b) lower water shielding, c) upper water shielding*

6 INSTALLED MONITORING SYSTEMS

The monitoring of the bridge comprises the mechanical aspects (displacements, strains, forces) and hygro-thermal issues such as moisture and temperature evolutions. All data are sampled at multiple points within the cross-section and along the bridge length and are recorded continuously remote. Special novel line sensors are applied to register eventual water penetration despite the double water proof shielding.

The detailing of the Stuttgart Timber Model Bridge (STMB) results from above mentioned research project [1]. To ensure and prove the function of the implemented construction preservation measures a monitoring concept with the following components was installed (see Figure 9):

- 16 sensors for punctual moisture content (u) measurement in different depths (electrical resistance method)
- 3 sensors for climate (cli) located beside and under the GLT superstructure beam and between the GLT structure and the sealing layer
- 3 sensors for wood temperature (T_{timber})
- 11 sensors for leakage detection at the second sealing layer (L)
- 1 displacement transducer for temperature and moisture dependent length variation of the GLT (d_L)
- 5 displacement transducers for vertical and horizontal relative displacements at the integral GLT-concrete abutment connection (d_v, d_h)
- 8 strain gauges on the surface of the GLT beam to obtain the stresses at the integral support (ε_{Timber})
- strain gauges on 8 of the glued-in rods at the integral GLT-concrete connection (ε_{rod})

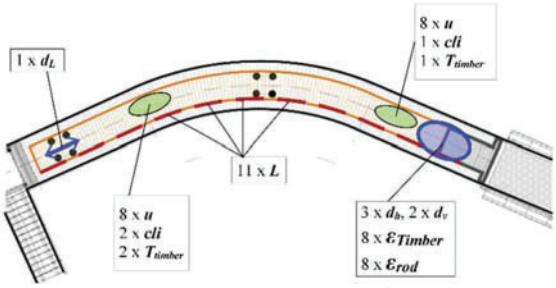

Figure 9: *Overview and locations of the different monitoring sensor-types*

All systems are running continuously and send wireless their data in a regular interval to a server. A big challenge of the combination of five different data logging systems consists in the consolidation and evaluation of the data. Five data loggers of different manufacturers are necessary for the functioning of the of the installed systems. Every system has its own method to record, transcript and send the data to the web. Some are sending the files via email protocol, others are using the File Transfer Protocol (FTP) to a local server and others are sending the data via FTP to a remote server of the manufacturer. At the homepage related to STMB (www.stuttgarter-bruecke.de) results of the monitored values are shown and updated continuously. Further investigations [14] at MPA University Stuttgart aim to compile a monitoring system with one centralised logger and computing unit which can handle all of the installed sensors.

7 RESULTS

7.1 CLIMATE AND MOISTURE MEASUREMENTS

In a rough summary of the climate measurements throughout seven years it can be stated that the temperature (daily mean values) varied over a year's season in the range of -5°C and +26°C. The relative humidity daily mean values varied from 45% in summer to 90% in winter. Based on the climate recordings the resulting surface moisture content derived by [15]

$$u(T,rH) = 10^{-2}\left[\frac{-T\cdot\ln(1-rH)}{0{,}13\cdot\left(1-\frac{T}{647{,}1}\right)^{-6{,}46}}\right]^{\frac{1}{110\cdot T^{-0{,}75}}} \quad (4)$$

is shown in Figure 10. It can be summarized that the calculated surface moisture (daily means) varied from 8% to 20% with a mean value over seven years of about 14,5%.

https://doi.org/10.52202/069179-0425

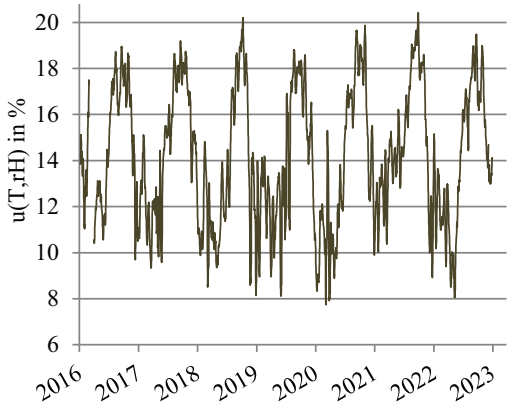

Figure 10: *Theoretical surface moisture content calculated from monitored air temperature and humidity by Eq. (4)*

The recording of the moisture content in different locations of the superstructure GLT beam by electrodes positioned at different depths of 1 cm, 3 cm and 6 cm is depicted exemplary in Figure 11. The graph shows that the moisture in 1 cm depth conforms rather well with computed surface moistures presented in Figure 10. Further it can be seen that the moisture amplitudes closer to mid-depth are significantly reduced. In a rough approximation the moisture contents vary in the cross-sectional center part in the range of 13,5 % to 16 % with a mean value of roughly 15 %. Further details and improvements regarding the moisture monitoring are presented in [14].

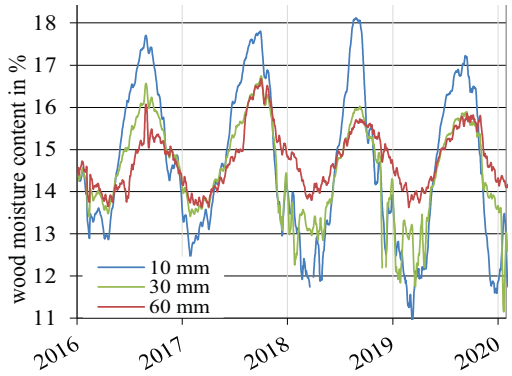

Figure 11: *Results of wood moisture monitoring of the GLT superstructure beam in cross-sectional depths of 10 mm, 30 mm and 60 mm*

7.2 MECHANICAL LOAD TESTS

In order to acquire a thorough understanding and experimental verification of the load carrying mechanisms of the integral joint of GLT and RC-abutment different static and dynamic load tests of the STMB were conducted. Due to page limitations, here one exemplary test is presented.

To activate a high bending moment in the rigid integral joint, a dead load in form of steel plates and concrete blocks were located at the mid-point of the first bridge field for a long-term test lasting six months. The 8.000 kg dead load was carried up in eight steps by a fork lift with an empty weight of 2.000 kg, shown in Figure 12.

Figure 12: *Load application for a long-term test with a fork lift*

The results of the measurements during this step-wise load application represented by rod forces calculated from strain gauges applied on the glued-in rebars are given in Figure 13. The correlation of strain and force was calibrated for all of the monitored rebars in a test machine before bonded into the GLT. The graph shows the results of four rebar forces, whereby two rebars are located at the upper bending tension edge and two at the lower bending compression edge of the joint. The tension rebar forces after full load application amount to 12,7 kN and 11,2 kN whereby the difference of the values results from the additional torsion moment because of the curved geometry of the GLT superstructure (Figure 13). In contrast hereto, the compressive forces show a much lower value of 4,3 kN in both cases being roughly 35% of the tension forces. The reason for the significantly smaller compression rebar forces can be attributed to the superimposed contact pressure of the GLT end-grain face to the RC-abutment whereas the tensile forces have to be transferred exclusively via the rebars. Figure 13 also shows the force peaks of the additional weight of the fork lift itself. The characteristic load carrying capacity in tension of a single rebar glued into the GLT is about 80 kN hence much higher than the forces resulting of the here applied bending moment.

A detailed analytical and numerical analysis of the integral joint, presented separately, reveals a satisfactory agreement between calculated and measured rebar forces.

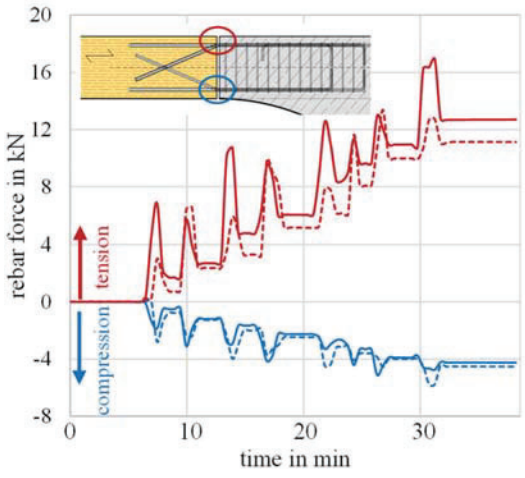

Figure 13: *Tensile and compressive forces in the rebars of the integral joint during stepwise application of 8.000 kg dead load*

https://doi.org/10.52202/069179-0425

8 EXPERIENCE AFTER SEVEN YEARS OF SERVICE LIFE

So far, all recorded mechanical and hygro-thermal results conformed well to the expectations/calculations. The agreements of the measurements are in all cases superior to the anticipated values [3]. In the follow-up of the STMB three public pedestrian bridge with both-sided integral timber-RC joints were realized and are monitored by MPA University of Stuttgart.

9 ACKNOWLEDGEMENT

The financial support of the research in two consecutive research projects RWB-EFRE No 051203 and 051303 by EU and state of Baden-Wuerttemberg is gratefully acknowledged. Many thanks are owed to the co-funding of University of Stuttgart enabling the continuous monitoring.

Special thanks to the sponsors listed below without whose support the construction of the "Stuttgart Timber Model Bridge" would not have been possible:

- Adolf Würth GmbH & Co. KG
- GODEL-BETON GmbH
- HECO-Schrauben GmbH & Co. KG
- Forum Holzbau
- Holzwerk Gebr. Schneider GmbH
- IB Rief, Ingenieurberatung
- KRINNER Schraubfundamente GmbH
- MERK Timber GmbH
- Metsä Wood Deutschland GmbH
- Paul Bauder GmbH & Co.KG
- Rettenmaier Holzindustrie Hirschberg GmbH
- Schaffitzel Holzindustrie GmbH + Co. KG
- SIMPSON STRONG-TIE GmbH
- Ulrich Lübbert Warenhandel GmbH & Co. KG

REFERENCES

[1] S. Aicher und N. Leitschuh: Wooden pedestrian and bicycle bridges - results and consequences from 100 bridge inspections (in German), Proceedings: *3rd Stuttgarter Holzbau Symposium*, Germany, 2015.

[2] Federal Ministry for Digital and Transport: RE ING: Guideline for the Design, Construction and Equipment of Civil Engineering Structure, Germany: Federal Highway Research Institute (BASt), 2022.

[3] M. Plötzl, J. Schlaich und K. Schäfer: Grundlagen für den Entwurf, die Berechnung und konstruktive Durchbildung lager- und fugenloser Brücken, Bd. Part 461, G. C. f. R. Concrete, Hrsg., Berlin, Germany: Beuth Verlag, 1996.

[4] EN 1995-2:2004: Eurocode 5: Design of timber structures - Part 2: Bridges, Brussels, Belgium: European Committee for Standardization (CEN).

[5] prEN 1995-2:2023: Eurocode 5: Design of timber structures - Part 2: Bridges, Brussels: CEN/TC 250/SC 5/WG 6 N 405, European Committee for Standardization (CEN).

[6] FprEN 1990:2022, Final Draft: Eurocode - Basis of structural and geotechnical design, Brussels: NA 005-51-01 AA N 1697, European Committee for Standardization (CEN).

[7] S. Schiefer, M. Fuchs, B. Brandt, G. Maggauer und A. Egerer: „Particularities in the Design of Semi-integral Prestressed Concrete Bridges (in German), *Beton- und Stahlbetonbau, Volume 101*, Issue 6, pp. 790-802, 2006.

[8] D. Berger, C.-A. Graubner, E. Pelke und M. Zink: Design tools for integral road bridges (in German), Jointless construction - *Publication series of the Hessian Road and Traffic Administration* (Germany), 2004.

[9] S. Aicher: Robust durable timber bridges - the possibilities of semi- and full-integral constructions (in German), Proceedings: *Karlsruher Holzbautage*, Germany, 2016.

[10] S. Aicher, N. Leitschuh und J. Hezel: Stuttgarter Holzbrücke (in German), Research Report EFRE research project Nr: 051203, MPA University of Stuttgart, 2015.

[11] EN 335:2013: Durability of wood and wood-based products - Use classes: definitions, application to solid wood and wood-based products, Brussels, Belgium: European Committee for Standardization (CEN).

[12] J. Hezel und S. Aicher, „The Stuttgart bridge - a novel robustness on-set (in German),“ Proceedings: *4th International Timber bridge days*, Filderstadt, Germany.

[13] J. Hezel, S. Aicher und T. Helbig: Integral, bonded Timber-Concrete-Abutment-Connection (in German), Proceedings: *3rd Stuttgarter Holzbau-Symposium, Stuttgart* (Germany), 2015.

[14] K. Simon, J. Hezel und S. Aicher: Advanced data logging system for moisture monitoring of timber bridges – background and large-scale application, Conference Proceedings: *4th International Conference on Timber Bridges (ICTB)* in Biel, Switzerland, 2022.

[15] S. Avramidis: Evaluation of three variable models for the prediction of equilibrium content of wood, *Wood Science and Technology 23*, pp. 251-258, 1989.

https://doi.org/10.52202/069179-0425

World Conference on Timber Engineering Oslo 2023

LIMBERLOST PLACE: A 10-STOREY SLAB-BANDED STRUCTURE

Md Shahnewaz[1], Robert Jackson[2]

ABSTRACT: The $150M Limberlost Place (previously known as "The Arbour") is a 10-storey, 16,250 m^2, exposed tall wood building located on George Brown College's waterfront campus in Toronto, Canada. This project will serve as an educational hub for George Brown College, housing the Tall Wood Research Institute, a childcare centre in addition to a significant amount of teaching and social spaces for their architectural program. Fast + Epp developed an innovative large span beamless structural system that is comprised of CLT timber-concrete composite (TCC) slab bands with perpendicular CLT infill panels supported on glulam columns. This long-span flat plate system allows for flexibility in architectural programming and unobstructed mechanical distribution. An extensive testing program on the TCC slab bands was completed at the University of Northern British Columbia in 2020, which has provided valuable engineering information to the design community for future tall wood projects and composite systems. To facilitate innovation, the project received funding through the National Resources Canada Green Constriction Wood Program, alongside other partners.

KEYWORDS: Timber concrete composite, cross-laminated timber, connections, tall timber, slab band

1 INTRODUCTION

The 10-storey 52.5m tall Limberlost Place is poised to transform Toronto's skyline with the construction of a mass timber tall wood, net-zero carbon emission building (Figure 1). The building name was inspired by a nearby forest the "Limberlost Forest and Wildlife Reserve", Huntsville, ON, Canada. The building is located on George Brown College's waterfront campus in the East Bayfront district of Toronto, Canada. The building will facilitate classrooms and lecture halls, and host The Tall Wood Institute.

Figure 1: *Rendering of Limberpost Place*

To reflect the purpose of the building and to develop economic and environmental structural solutions, a holistic design approach with mass timber as the primary structural material was chosen. The building has a footprint of 62m×37m and was designed for load conditions as required by the 2017 edition of the Ontario Building Code (OBC) [1] and the 2015 edition of the National Building Code of Canada (NBCC) [2]. The 9.2m long timber concrete composite (TCC) slab bands will be exposed from the underside in some locations, for architectural expression. These floors will be supported on glulam columns from the ground floor to the upper roof (Figure 2). The typical glulam columns were designed to provide additional distribution areas for shear stresses and reduce the weak-axis bending in the panels. This project is one of the first tall timber buildings to proceed with "assembly" occupancy in Canada – where many of the existing tall timber buildings are for commercial or residential occupancies.

The structure was designed for a two-hour fire event, with all structural timber designed for full exposure. A char analysis was completed with the provisions given in Annex B of CSA O86 [3]. In addition to this char analysis, supplemental calculations were also undertaken using the Ministry of Municipal Affairs and Housing Supplementary Standard, SB-2 Fire Performance Ratings, in subsection 2.11 of the OBC for glue-laminated timber beams and columns. The structural steel also met the requirements to achieve a two-hour fire-resistance rating and through detailing with drywall encapsulation. The fire rating and associated alternative solutions were a

[1] Md Shahnewaz, Specialist Engineer, P.Eng., M.A,Sc., PhD., Fast+Epp, Vancouver, Canada, mshahnewaz@fastepp.com Robert Jackson,
[2] Partner, P.Eng., Struct.Eng., P.E., S.E., MIStructE, Fast+Epp, Vancouver, Canada, rjackson@fastepp.com

https://doi.org/10.52202/069179-0426

significant part of this project, undertaken by GHL Code Consultants Ltd, alongside CHM Fire Consultants Ltd.

2 SUPERSTRUCTURE

The ground floor structure consists of a 300 mm thick reinforced concrete slab supported on concrete columns and walls below. The transition from concrete columns to glulam columns is made 500 mm above the ground level slab, jacketing the steel column bases in concrete. From level 2 to 8, the TCC slab bands serve as the primary floor structure and eliminate the need for deep glulam beams, providing more headroom and space for mechanical and electrical components. The 244 mm thick 7-ply CLT panels act compositely with 150 mm concrete topping spanning 9.2 m in the north-south direction and support the non-composite 191 mm thick 7-ply CLT infill panels between them, as shown in Figure 2a. A photo of the slab bands and infill panels can be seen in Figure 2b.

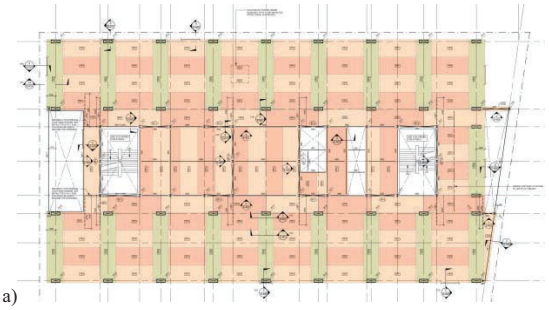

a)

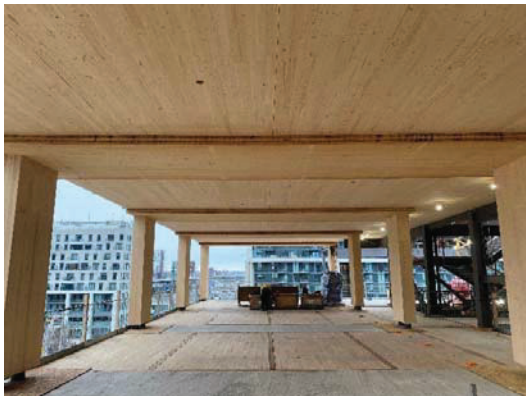

b)

Figure 2: *a) Typical floor plan, b) Typical slab bands.*

The TCC slab bands are supported by 422 × 1210 mm glulam columns, designed and positioned beneath the slab-bands to resist the effects of unbalanced loading. The column connection (Figure 3) is configured to provide direct load transfer between the vertical elements rather than transmitting forces through the TCC floor panels. Glulam columns arrived on-site with a steel connecting plate and Hollow Structural Section (HSS) stubs, secured to the end-grain of the column with glued-in rods. The glulam column above had a a similar connection with smaller diameter HSS stubs allowing a 'sleeve in' connection. Stubs are connected using bolts, which allow for simple installation and act as a tension connection in the extreme event where a column below is eliminated, according to progressive collapse principles. CLT floor panels were notched around the HSS tubes and bear directly on the column below.

The CLT roof panels support additional loading from the weight of the green roof and the snow, however public access is restricted at those green roofs on the north and south side of Level 9, in order to match the design loading with that of the floors below. At the south green roof, however, there will be additional double glulam beams underneath each TCC band to support the column loads above. The columns above, which partially support the roof, are anchored to the top of the TCC bands at the mid-span. The typical "wallumns" are terminated at this level. Where the building continues up to Level 10 and the upper roof, the "wallumns" transition into smaller 430 x 456 mm glulam columns.

At Level 10, a 245 mm thick 7-ply CLT deck spans north-south between glulam purlins abd steek beams, supported by columns below. The structural steel members in the core area are the same as the floor below. All structural components within this space have been designed for a 2hr fire rating. The same glulam columns supporting Level 10 will continue up to support the roof. There, 245 mm thick 7-ply CLT panels span between purlins, along the slope of the roof. On the west and east sides of the upper roof, side roofs will also be made of 7-ply CLT panels supported on a series of steel purlins. In the middle of these side roofs, large louvred openings are to be created to serve as solar chimneys.

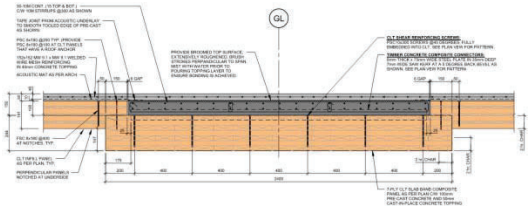

a)

b)

Figure 3: *a) Typical slab band section, b) Mock-Up*

https://doi.org/10.52202/069179-0426

3 LATERAL SYSTEM

The primary means of lateral stability consists of a long central core of concentric limited ductility steel braced frames coordinated with the stairs, elevators, and mechanical spaces in the center of the building (Figure 4). Several timber options, including CLT shear walls and glulam braced frames were explored, as was a conventional concrete core system. Ultimately, a steel braced frame system (Figure 4) was found to be the best fit for the project due to the following reasons. Firstly, the steel braces are much more slender than a glulam equivalent, allowing for greater flexibility for wall openings for architectural and required services. Secondly, the steel braced frame cores add more ductility and overstrength to the overall structure in comparison to a timber braced frame system, allowing for a more efficient seismic force-resisting system. Thirdly, the de-centralized mechanical rooms require a significant number of services into the 'core' space, meaning many holes in the walls which would be practically feasible. Fourthly, the steel components can be erected simultaneously with the timber components, resulting in a faster erection period sharing the hook of one crane. The steel braces HSS, while the beams and columns within the cores are various sizes of wide-flange sections. These steel components are concealed, thus requiring no further fire protection. The design of the steel core members is governed by wind versus seismic forces in both E-W and N-S directions.

a)

b)

Figure 4: *a) Steel braced frames, b) Steel braced frame erection sequence in 2-storey lifts.*

4 STRUCTURAL TESTING

A comprehensive experimental testing program was conceived and executed on the TCC slab bands to inform the project design. The CLT specimens were prepared by Structurlam, in Penticton, BC and the concrete for slab bands was poured by Datoff Bros Construction Ltd, Prince George. All tests were conducted at the University of Northern British Columbia's Wood Innovation and Research Laboratory in Prince George, BC.

4.1 MATERIALS

The tested CLT panels for the slab bands were 245 mm thick 7-ply, grade E1M5 [3]. The panels were manufactured as per PRG320 [4] with Spruce-Pine-Fir (SPF) 2100 Fb-1.8E machine-stress rated and No.3 grade for the major and minor strength axis laminations, respectively. Two-thirds of the slab bands were reinforced at two intensity levels (high level: 9 rows of screws spaced at 75 to 225 mm and low level: 6 rows screws spaced at 300 mm). The concrete topping on the slab bands is 150 mm with a minimum specified strength of 35 MPa. The concrete was reinforced with 10M longitudinal rebar spaced at 150 mm top and bottom, and stirrups were 10M spaced at 300 mm.

Three types of composite connectors were used. Type A: Fully threaded self-tapping screws (ø11×250 mm) installed at an angle of 45º; Type B: perpendicular steel plates 2100mm x 75mm x 6.4 mm (length x depth x thickness) hammered into a 7mm saw kerf, and Type C: parallel 90mm x 2mm HBV plates glued into saw kerfs using a polyurethane-based adhesive.

4.2 CONNECTOR TESTS

A total of 18 small-scale shear tests were conducted to investigate the capacity, stiffness, and failure mechanisms of steel kerf plates as TCC shear connectors with varying embedment depths. Steel kerf plates of 6 mm thick and 200 mm wide were installed in the CLT in a 7 mm wide saw kerf at 5^0 back bevel as shown in Figure 5a-c. The steel plate embedment depths into the CLT were varied: i) 35 mm deep, ii) 70 mm deep, and iii) 90 mm deep. The specimens were tested under in-plane shear by rotating 12°, similar to the procedure suggested in EN-408 [5]. The loads were applied according to EN-26891 [6] with a displacement-controlled protocol at a rate of 5 mm/min as shown in Figure 5d.

https://doi.org/10.52202/069179-0426

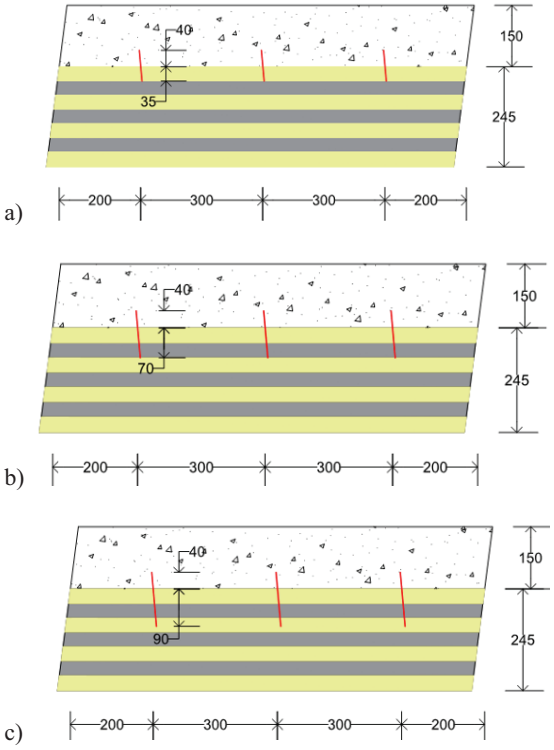

Figure 5: *a-c) Specimens including steel kerf plate embedment variations, d) Small-scale test setup.*

4.3 HALF-SCALE TESTS

The half-scale TCC slab bands were tested to assess their shear capacity and failure pattern at high shear zones with different levels of CLT shear reinforcements, to evaluate the performance of the TCC floors with different shear connectors and shear reinforcing. The test series are summarized in Table 1. The floors were connected to 430×1,178 mm glulam columns by 12-ø16×250 mm glued-in rods.

Table 1: Overview of Test Series

Series		ID	Reinf.	Connector	Test Type	#of tests
half-scale	S2	S2-UR	-	NA	B	2 each
		S2-HR	low			
		S2-FR	high			
	S3	S3-UR-A	-	Type A	B	2 each
		S3-HR-A	low			
		S3-FR-A	high			
	S4	S4-UR-B	-	Type B	B	2 each
		S4-HR-B	low			
		S4-FR-B	high			
	S5	S5-UR-C	-	Type C	B	2 each
		S5-HR-C	low			
		S5-FR-C	high			
full-scale	S6	S6-HR-A	low	Type A	B	2 each
		S6-HR-B		Type B		
		S6-HR-C		Type C		
	S7	S7-HR-A	low	Type A	T	1 each
		S7-HR-B		Type B		
		S7-HR-C		Type C		

Note: B – bending, T-torsion

Test series S2 is the control series, consisting of 5030 mm long raw CLT panels (no concrete topping) (Figure 6). Test series S3 to S5 (Figures 7 to 9) are TCC slab bands consisting of 5030 mm long CLT panels with 150 mm concrete topping. The three different connector layouts (Type A to C) are shown in Figure 7 to Figure 9. Two replicates from each unreinforced, low-reinforced, and high-reinforced CLT panels and TCC slab bands were provided, for a total of 6 raw CLT panels on the control side, and 18 TCC slab bands.

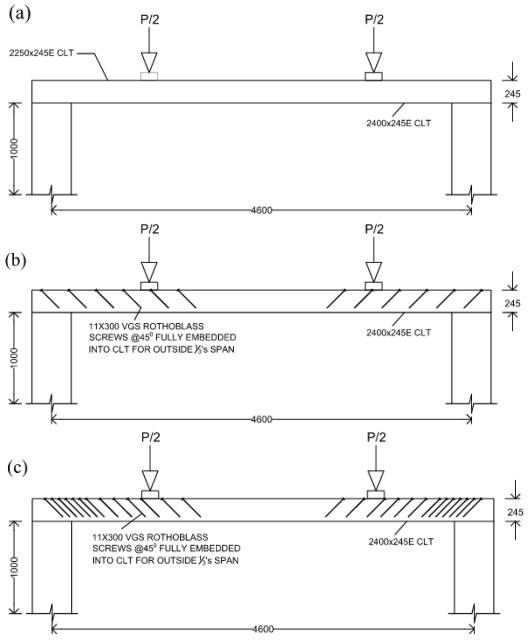

Figure 6: *Test series S2- half-scale raw CLT panels: a) unreinforced, b) low, and c) high reinforced CLT panels.*

https://doi.org/10.52202/069179-0426

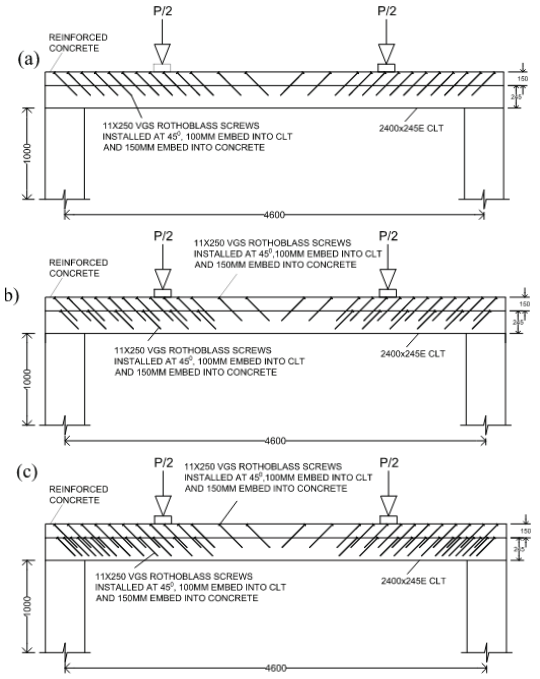

Figure 7: *Test series S3: half-scale TCC with screw connectors: a) unreinforced, b) low reinforced, and c) high reinforced CLT panels.*

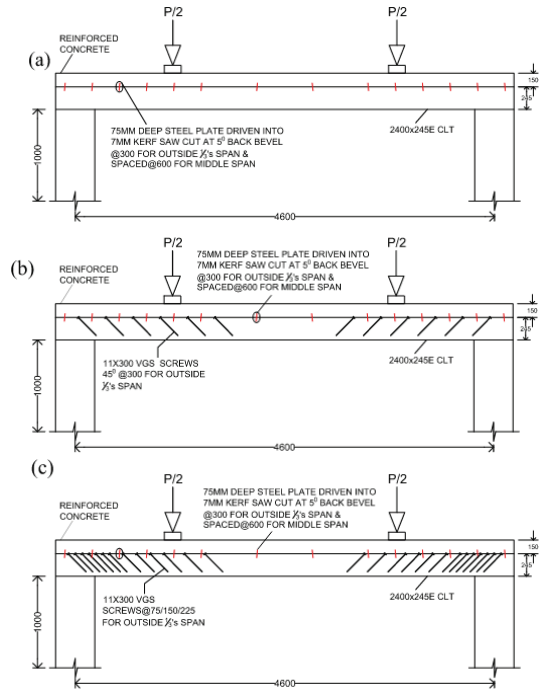

Figure 8: *Test series S4: half-scale TCC with kerf plate connectors: a) unreinforced, b) low, and c) high reinforced CLT panels.*

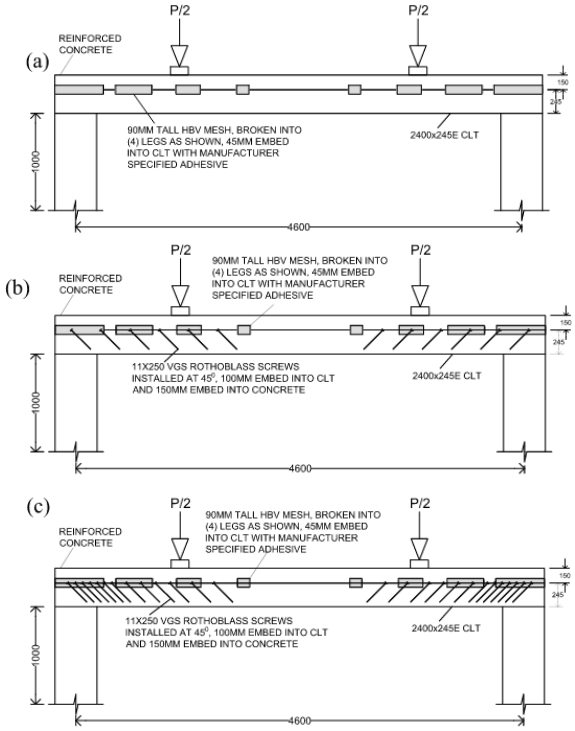

Figure 9: *Test series S5: half-scale TCC with HBV connectors: a) unreinforced, b) low, and c) high reinforced CLT panels.*

The tests on half-scale specimens were conducted under 4-point bending as shown in Figures 10a and 10b on raw CLT panels (Series S2) and TCC slab bands (Series S3-S5), respectively. The loads were applied at one-third points using two 500 kN and two 250 kN actuators for a total maximum load of 1,500 kN, and were distributed at the third-point lines using steel spreader beams. When the specimens did not fail after reaching the 1500 kN maximum actuator load, the spreader beam was moved to mid-span to re-test the specimen under three-point loading. All specimens were tested under displacement-controlled loading at a constant rate of 15 mm/min.

Figure 10: *Schematic of 4-point bending tests.*

4.4 FULL-SCALE TESTS

Similar to the half-scale, all full-scale specimens were comprised of 245 mm thick, 7-ply CLT panels with 150 mm concrete topping connected with self-tapping screws, steel kerf plates, and HBV shear connectors (Type A, B, C respectively, as laid out in Table 1). These specimens were tested under four-point bending (Series S6) and torsional loading (Series S7). Series S6-S7 consisted of 9.6 m long, low-reinforced CLT panels with 150 mm concrete topping, with three specimens of each connector type, as shown in Figure 11.

Similar to half-scale specimens, the loads in series S6 were applied at one-third points using two 500 kN and two 250 kN actuators, for a total of 1500kN maximum, and were distributed at the third-point lines using spreader beams. The torsional specimens were tested with edge loading using one 500 kN and two 250 kN actuators, for a total of 1500kN maximum. All specimens were tested under displacement-controlled loading at a constant rate of 15 mm/min. The CLT panels of all full-scale slab bands specimens in S6 and S7 were low-reinforced. Two replicates of S6 and one replicate of S7 from each connector types were tested, a total of 6 and 3 TCC slab bands from series S6 and S7, respectively.

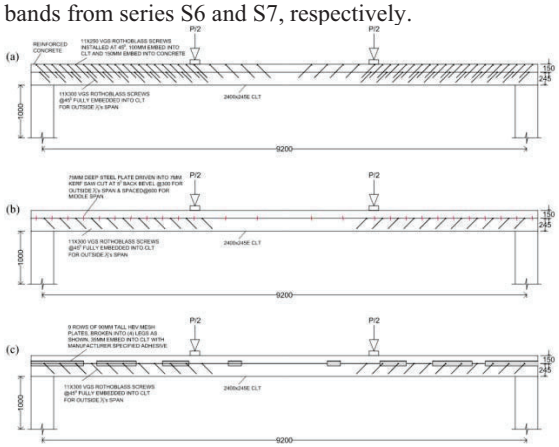

Figure 11: *Test series S6 and S7: full-scale TCC self tapping screw connections, kerf plates, and HBV.*

5 TEST RESULTS AND DISCUSSION

5.1 CONNECTOR TESTS RESULTS

From the small-scale tests, the connector performance was evaluated at the maximum load F_{max}, displacement at maximum load d_{Fmax}, serviceability stiffness K_{ser}, and ultimate stiffness K_u. The mean values of various metrics from the in-plane tests are listed in Table 2. The detailed analysis results were reported in a previous publication [8]. The load-deflection from small-scale series S1 tests are shown in Figure 12. Typical failure patterns are shown in Figure 13. The post-yield behaviours of the connectors with three different embedment depth were different. Connector type S1-A with 35 mm embedment resulted the highest deformation capacity, while connector Type S1-C with 90 mm embedment resulted the lowest deformation capacity with a steep decrease in load after reaching its maximum. Type S1-A connectors had the lowest load-carrying capacity, yield, and ultimate strengths (F_{max} = 350 kN), while Type S1-B and Type S1-C connectors' capacities were slightly higher, i.e. on average 7% and 5%, respectively higher compared to Type S1-A. All connector types had started yielding at similar range deformations of between 0.8 to 0.9 mm. Results showed that there are some reductions in deformation capacity when the kerf plates were embedded beyond the first layer of CLT. The stiffnesses observed both at serviceability and ultimate loads for Type S1-A, Type S1-B connectors, and Type S1-C connectors were similar (Table 2). In sum, with deeper the embedment depth beyond first layer of the CLT panel did not provide any improvement in the connection performance, therefore, the floor specimens for the full-scale testing were manufactured with Type S1-A steel plate connectors.

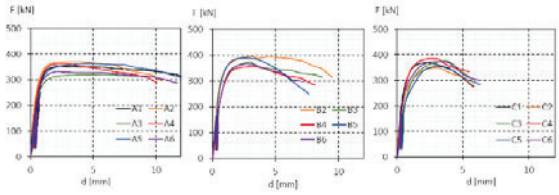

(a) (b) (c)

Figure 12: *Typical failure pattern in small-scale tests: a) S1-A, b) S1-B, and c) S1-C*

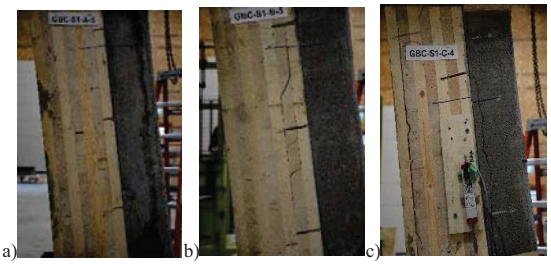

a) b) c)

Figure 13: *Typical failure pattern in small-scale tests: a) S1-A, b) S1-B, and c) S1-C*

Table 2: Results from series S1-small-scale

Series	CLT embedment	#of tests	F_{max}	d_{Fmax}	K_{ser}	K_u
			[kN]	[mm]	[kN/mm]	
S1-A	35 mm deep	6	350	3.3	416	444
S1-B	70 mm deep	6	376	2.9	395	354
S1-C	90 mm deep	6	368	3.0	438	453

5.2 HALF-SCALE TESTS RESULTS

Half-Scale CLT Panels

The load-deflection curves from series S2 on CLT panels shows three segments until failure, ascending elastic and elastic-plastic segments, and descending segment from peak loads to failure (Figure 14). Typical failure patterns from series S2 in unreinforced, low and high-reinforced panels are shown in Figure 15. The unreinforced CLT panels failed in a sudden brittle manner due to rolling shear failure near the support (Figure 15a) at an average load of 885 kN. The low-reinforced panels also failed in shear (Figure 15b), at a higher load of on average 968 kN. The failure mechanism in the high-reinforced panels pushed from shear to bending (Figure 15c).

https://doi.org/10.52202/069179-0426

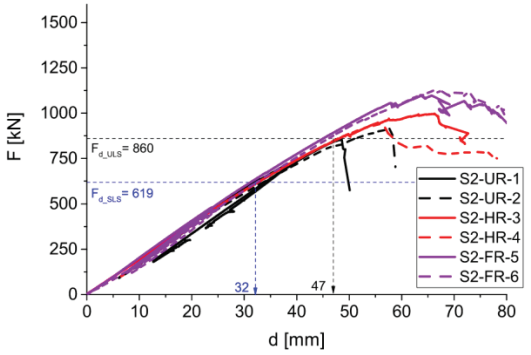

Figure 14: *Load-deflection curves for series S2- CLT panels*

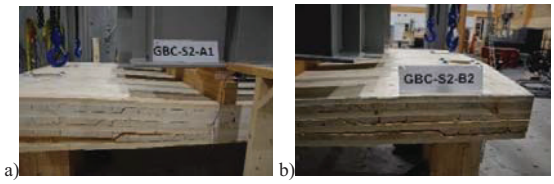

Figure 15: *Typical series S2 failures on CLT: a) unreinforced, b) low-reinforced specimens,*

Half-Scale TCC Slab Bands

Typical failure pattern in slab bands with screws are shown in Figure 16. The unreinforced specimens S3-UR failed in shear as seen in Figure 15a at an average load of 1,445 kN. One of the low-reinforced panel S3-HR slab band failed in shear (Figure 17b) at an average load of 1,487 kN. The other low-reinforced slab did not fail in 4-point bending tests as it reached actuators capacities, therefore, after retest under 3-point loading, it failed in bending at mid-span (Figure 17c). Similarly, both high reinforced slab S3-FR only failed after being re-tested in a three-point bending (Figure 17d) at an average load of 1,968 kN.

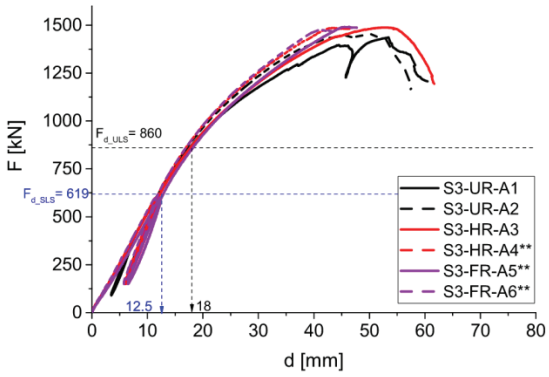

Figure 16: *Load-deflection curves for series S3- half-scale TCC bands with screw connectors*

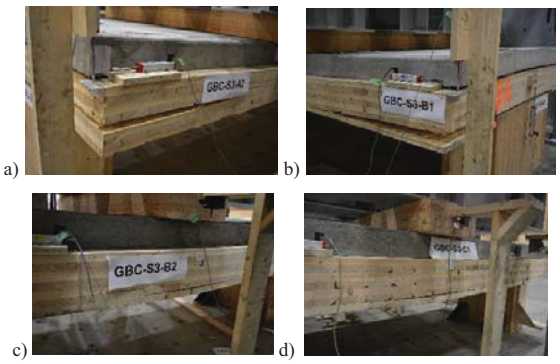

Figure 17: *Typical series S3 failures on TCC slab bands with screws connectors: a) unreinforced, b-c) low-reinforced specimens, and d) high-reinforced specimen*

Failure patterns in series S4 slab bands with kerf plates are shown in Figure 18. The unreinforced specimens S4-UR failed in shear as seen in Figure 19a at an average load of 1,482 kN. Both low S4-HR and high reinforced S4-FR slabs were failed at mid-span bending after being re-tested in a three-point loading (Figure 19 b-c) at an average load of 2,586 kN and 2,441 kN, respectively.

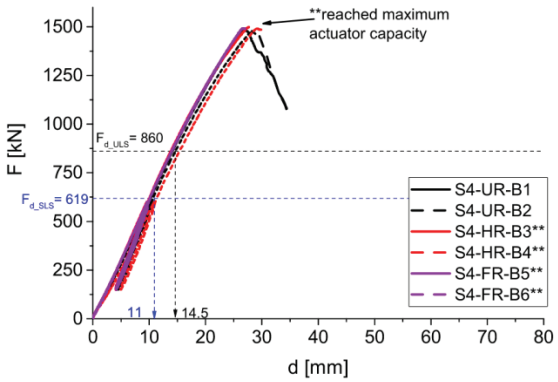

Figure 18: *Load-deflection curves for series S4- half-scale TCC bands with kerf plates connectors*

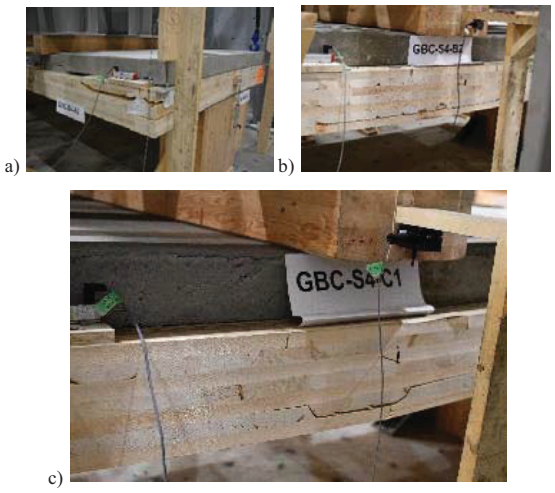

Figure 19: *Typical series S5 failures on TCC slab bands with HBV connectors: a) unreinforced, b) low-reinforced specimens, and c) high-reinforced specimens*

https://doi.org/10.52202/069179-0426

Failure patterns in series S5 slab bands with HBV are shown in Figure 20. All series S5 TCC slab bands with HBV failed in shear (Figure 21 a-c) at support at an average load of 1,261 kN, 1,316 kN and 1,493 kN, in S5-UR, S5-HR, and S5-FR, respectively.

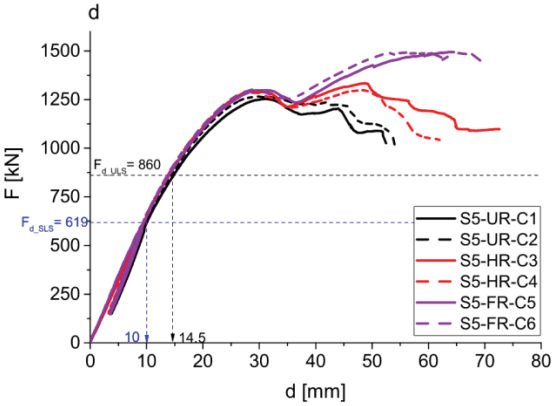

Figure 20: *Load-deflection curves for series S5- half-scale TCC bands with HBV connectors*

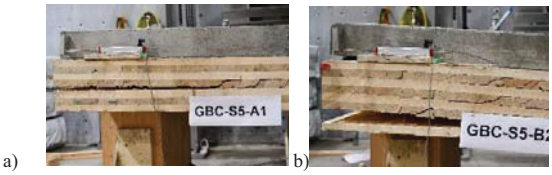

Figure 21: *Typical series S5 failures on TCC slab bands with HBV connectors: a) unreinforced, b) low-reinforced specimens*

5.3 FULL-SCALE TESTS RESULTS

The mid-span load-deflection curves of the full-scale TCC slab bands in series S6 are shown in Figure 22 and typical failure patterns are illustrated in Figure 23. The slabs bands with screws composite connector failed in bending at mid-span at an average load of 706 kN and estimated bending moment capacity of M_{max} = 1,100 kNm. Similarly, slab bands with Type B kerf plates connector also failed in mid-span bending, however, at 47% higher loads compared to Type A screw connectors. The average failure load was observed 1,040 kN and estimated bending capacity of M_{max} = 1,619 kNm. The TCC slab bands with Type C composite connector HBV failed in connector shear at an average load of 670 kN which was the lowest among the three connector types and the estimated bending capacity was M_{max} = 1,043 kNm. Although HBV connectors in TCC slab bands failed initially, the final subsequent failure occurred at mid span due to bending.

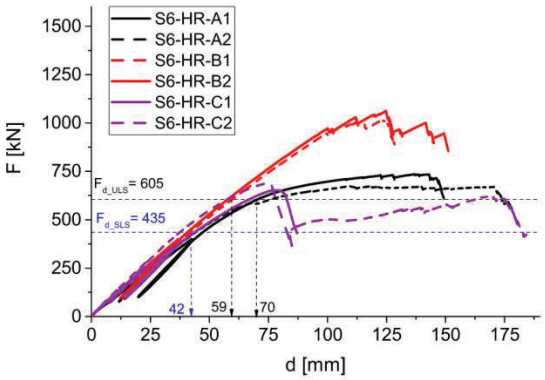

Figure 22: *Load-deflection curves for series S6- full-scale TCC bands -under 4-point bending tests*

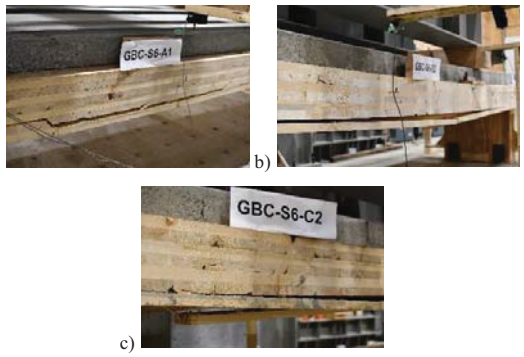

Figure 23: *Typical series S6 failures under 4-point bending on full-scale TCC slab bands with: a) screw connectors, b) kerf plates connectors, and c) HBV connectors*

The mid-span load-deflection curves of the full-scale TCC slab bands in series S7 under torsional loading are shown in Figure 24 and typical failure patterns are illustrated in Figure 25. The TCC slab bands with Type A screws composite connector reached first failure at 285 kN, and a maximum load of 442 kN at a deflection of 255 mm. The TCC slab bands with Type B kerf plates composite connector reached first failure at 234 kN and a maximum load of 489 kN at a deflection of 261 mm. The TCC slab bands with Type C HBV reached first failure at 257 kN, and a maximum load of only 413 kN at a deflection of 159 mm. Under torsional loading in series S7, the first failure was always triggered by the pull-out of the glued-in rod from the column support as shown in Figure 25c followed by failure in bending at mid-span on the loaded side at ultimate loads (Figure 25a). Therefore, in the final project design phase, all glued-in rods are capacity protected using 15 ø16×400 mm glued-in threaded rods were used instead of 12 ø 16×250 mm rods used in tests, see Figure 25c.

https://doi.org/10.52202/069179-0426

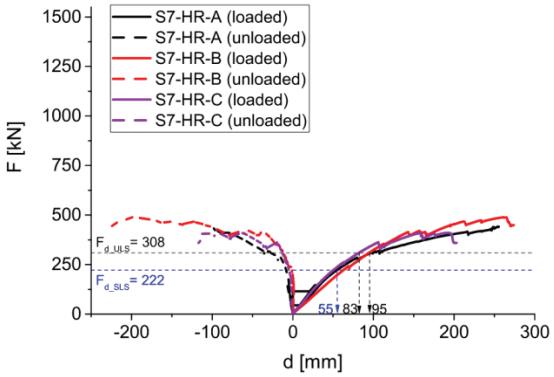

Figure 24: *Load-deflection curves for series S7- full-scale TCC bands -under torsional tests*

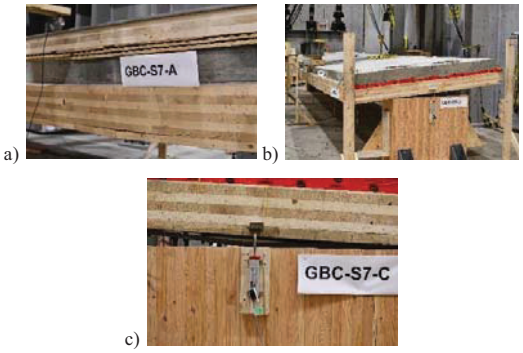

a) b) c)

Figure 25: *Typical series S7 failures under torsion on full-scale TCC slab bands with: a) screw connectors, b) kerf plates connectors, and c) HBV connectors*

6 CONCLUSIONS

Fast + Epp initiated an ambitious design approach to one of Toronto's tallest timber buildings. The innovative 'slab banded' gravity system allows for flexibility in architectural programming and unobstructed mechanical distribution. By coupling this timber gravity system to a steel braced frame core, the superstructure can be erected as a prefabricated 'kit of parts', alongside the envelope system.

The extensive testing program evaluated the performance and efficiency of TCC slab bands with various composite connectors. The screw reinforcement in the CLT significantly increased the shear capacity of the panels. The failure modes also shifted shear to bending failure in some heavy reinforcing specimens. The 150 mm concrete topping compositely connected to the CLT panel improved the out-of-plane shear capacity by up to 167% when compared to bare CLT panels. Weak-axis shear failure was observed in some TCC specimens due to warping over the glulam columns and this can be avoided by adding diagonal reinforcing screws in transverse direction at the end of slab bands, which was incorporated in the final design phase (as seen in Figure 26a). TCC with steel kerf plates exhibited the highest capacity and stiffness and were priced by multiple suppliers to be the most economical option, therefore, final design was moved forward with this solution (Figure 26b). Torsion tests showed pull-out failure of glued-in rods, which must be avoided, so lengthening of the rods and increasing the number of rods was deployed in final design.

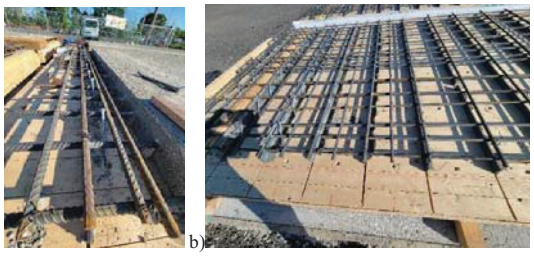

a) b)

Figure 26: *a) Diagonal screws at 45^0 in weak axis, b) typical slab band reinforcement before concrete pour*

The structural testing program allows a low-cost timber composite system, provide invaluable design information to the engineers. It is currently under construction, with structural completion targeted for late 2023.

ACKNOWLEDGEMENT

The project was supported by Natural Resources Canada (NRCAN) through the Green Construction Wood (GCWood) program. The CLT specimens were prepared by Structurlam, in Penticton, while the concrete was poured by Datoff Bros Construction Ltd, Prince George. The support by the UNBC technicians Michael Billups and Ryan Stern and undergraduate research assistant Anthony Bilodeau is greatly appreciated.

REFERENCES

[1] Ontario Building Code (OBC) [online]. Available: https://www.buildingcode.online
[2] NBCC. National Building Code of Canada 2015. Institute for Research in Construction, National Research Council of Canada, Ottawa, ON, 2015.
[3] CSA O86-19. Engineering design in wood. Canadian standards association, Mississauga, ON, 2019.
[4] ANSI/APA PRG 320. Standard for Performance-Rated Cross-Laminated Timber. American National Standards Institute. New York, USA, 2017.
[5] EN 408, Timber structures—Structural timber and glued laminated timber—Determination of some physical and mechanical properties, European Committee for Standardization (CEN), 2010, Brussels, Belgium.
[6] EN 26891, Timber structures—Joints made with mechanical fasteners—General principles for the determination of strength and deformation characteristics, European Committee for Standardization (CEN), 2013, Brussels, Belgium.
[7] Shahnewaz, M., Jackson, R., Tannert, T.: CLT concrete composite floors with steel kerf plate connectors. Construction and Building Materials, 319, 126092, 2022.

World Conference on Timber Engineering Oslo 2023

STRUCTURAL DESIGN OF HYBRID STRUCTURE WITH CLT SEISMIC PANELS AND STEEL FRAME

Kouji Fukumoto [1], Marina Koda[2], Hiroshi Isoda[3]

ABSTRACT: We have developed a new hybrid structural system with fire-resistance performance, combining CLT infill panels and a steel frame, for middle- and high-rise buildings. This structural system draws out the potential structural performance of CLT panels by holding them in the steel frames. Steel frames, without considering CLT panels, can support gravity loads of a high-rise building during fires so that it may be possible to omit the fireproof covering of the CLT panels and to specialize CLT panels to support seismic forces. This paper shows the details of the developed hybrid system as well as the seismic design and fire resistance experimental result, with an actual example project.

KEYWORDS: CLT, Steel frame, Hybrid structure, Seismic panel, Seismic performance, Fire-resistance performance

1 INTRODUCTION

Since the Japanese government notification related to CLT (Cross Laminated Timber) was enforced in 2016, the manuals on design have been developed [1], and the buildings using CLT are becoming more and more in use in Japan as well as in other countries. The high-rise buildings utilizing CLT (for example, Reference [2]) have been already constructed in Europe and North America where CLT is in widespread use prior to other countries. In Japan as well, the efforts to apply timber structures to middle- and high-rise buildings have become active. Although CLT is expected to be usable as leading structural material for that purpose, currently, its use for middle- and large-scale buildings has not been widespread partly because of the needs to meet higher seismic standards and fire protection standards than in other countries.

Under the circumstances, the authors had an opportunity, in 2018, to design the structure of the Hyogo Forestry Hall, a five-story office building aimed at becoming a model for encouraging broad use of CLT by making effective use of CLT.

However, in case of using a CLT panel construction method in an urban central area like Kobe City, fireproof covering for timber structural members to meet the requirement for ensuring the one-to-three-hour fire resistance performance according to the application area and scale of the building as specified in the Building Standards Act of Japan not only conflicts with the architectural request for representing wood in a space but also raises issues of labour and cost for installing fireproof covering. Thus, securing the fire-resistance performance of a timber structure involves multifaceted issues. Furthermore, large-section glued laminated timber is required to achieve a large span exceeding 10 meters necessary for a work space of office with a timber structure. If fire resistive glued laminated timber is used for that purpose, it would be more disadvantageous in terms of cost.

Besides, application of CLT to high-rise buildings is difficult because if CLT is used as seismic structural elements in a timber frame as has been before or if a structure is assembled only with CLT panels, the surrounding timber frame will fail before CLT exhibits its strength to the full as shown in Figure 1. Moreover, with the CLT panel construction method or a structural system in combination with the conventional timber structure, it will be difficult to rationally attain high axial force retention and a large span frame which are indispensable to a high-rise building, with consideration for economical efficiency as well.

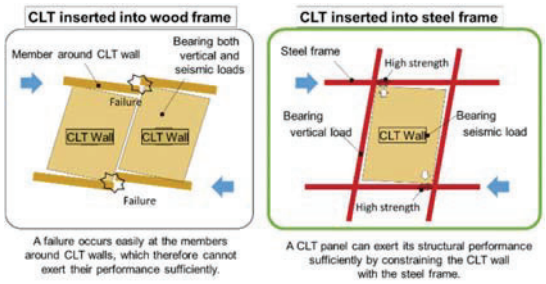

Figure 1: *CLT panels inserted into steel frame*

Therefore, the authors had an eye on a structural system with CLT as seismic structural elements built in a steel

[1] Kouji Fukumoto, Associate Professor, Okayama University, Japan, k.fukumoto@okayama-u.ac.jp (Former position: Structural Engineering Section, TAKENAKA Corporation, Japan)
[2] Marina Koda, Structural Engineering Section, TAKENAKA Corporation, Japan, marina.kouda@takenaka.co.jp
[3] Hiroshi Isoda, Professor, Research Institute for Sustainable Humanosphere, Kyoto University, Japan, hisoda@rish.kyoto-u.ac.jp

https://doi.org/10.52202/069179-0427

structure as reported in [3], which was aimed at achieving high axial force retention and a large span rationally and economically through a steel structural frame by constraining CLT with the steel frame and thereby letting CLT exhibiting its inherent structural performance. Additionally, we specialized CLT panels as seismic structural elements and eliminated the need for fireproof covering to improve the design, workability and economic efficiency.

This paper presents the structural design method taking an actual project, and also shows the verification results of the effect of the combustion of CLT on the fire-resistance performance of the surrounding steel in case without fireproof covering for CLT seismic panels in order to ensure the fire-resistance performance of the structural system. Furthermore, the paper reports the construction condition focused on the joints.

2 STRUCTURAL DESIGN METHOD IN "HYOGO FORESTRY HALL"

2.1 OUTLINE OF STRUCTURAL SYSTEM

Figure 2 shows the outline of the Hyogo Forestry Hall, a case of the authors' design, and Figure 3 shows a structure rendering of the same building. As shown in Figure 4, the

Designed by	: Takenaka Corporation
Built by	: Takenaka Corporation and Daiwa House Industry (Special Construction JV)
Building area	: 310.49 sq. m
Gross floor area	: 1567.10 sq. m
Scale	: 5 above ground floors and one penthouse floor
Structure	: CLT and Steel
Construction period	: March 2018 to January 2019 (10 months)

Figure 2: *Outline of Hyogo Forestry Hall*

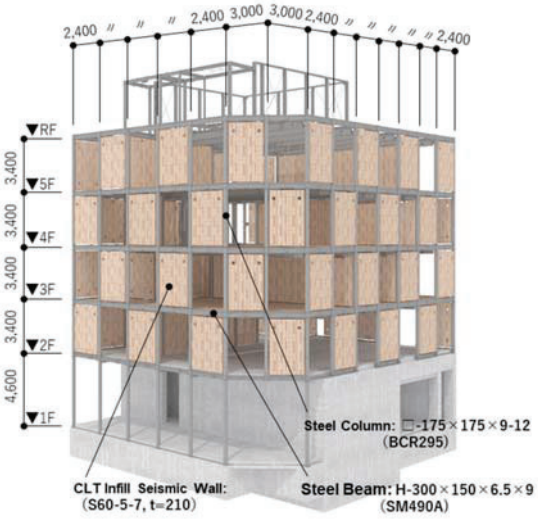

Figure 3: *Structure rendering*

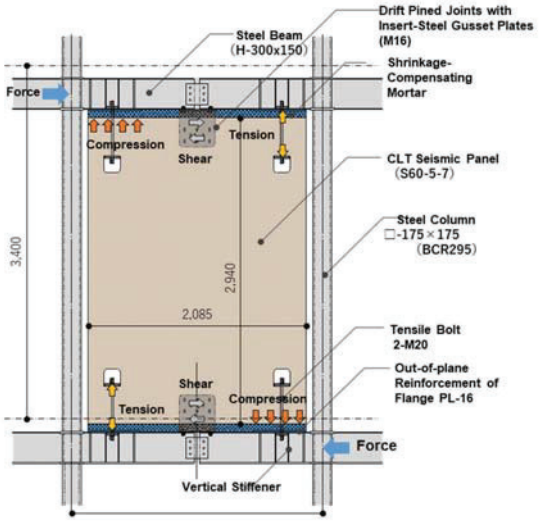

Figure 4: *CLT panel inserted in steel frame*

standard configuration consists of a CLT infill seismic wall S60-5-7 (210 mm thick with 5 layers and 7 plies), steel columns (□-175x175x9, BCR295) and steel beams (H-300x150x6.5x9, SM490A). A CLT seismic panel, 2.940 m high and 2.085 m wide (H/L =1.41), is placed on a steel grid at the floor height of 3.4 m with columns arranged at a spacing of 2.4 m. Tensile bolts 2-M20 (ABR400) are placed at four corners of a CLT panel for the tensile joints, while the drift pined joints with insert-steel gusset plates (drift pin diameter 16 mm) are provided at the center for the shear joints. We also filled the space between CLT panels and steel beams with shrinkage-compensating mortar to make sure of the later described fire-resistance performance and stress transmission.

2.2 RELATIONS BETWEEN JOINT STRENGTH AND SHEAR FORCE BORNE BY CLT INFILL SEISMIC WALL

Table 1 shows the relations between the joint strength and the shear force borne by CLT panels in the above structural system. The horizontal strength depends upon the equilibrium between the moment by the couple of vertical forces due to the yield tension strength of tensile bolts (T_y) and the bearing strength of the upper and lower bearing area (C_c) and the moment by the couple of shear forces (Q_j) in upper and lower shear joints caused by horizontal forces as shown in Figure 5. The CLT panel was S60-5-7 (210 mm thick), however the compressive strength of the bearing area was assumed to be S60-5-5 (150 mm thick) by not considering the outermost plies since the beam flange was 150 mm wide.

The analytical result indicated that the transmission of the compression stress in the bearing area of CLT panels that depends upon the shear yield strength of boundary beams (Q_v) was 56% of that in case of depending upon the bearing strength of CLT panels (C_c). In that case, assuming that the tensile bolts have tensile-yielded simultaneously, the shear stress of CLT panels (τ) is 0.62 N/mm^2. However, the tensile yield strength was set for tensile bolts to prevent prior failure at the position around

https://doi.org/10.52202/069179-0427

a square hole in a CLT panel as shown by the dotted line in Figure 6. Its contribution rate to the whole horizontal force ($M_{Ty}/\Sigma M_R$) is 23.3% when calculated using the rotational resistances in Table 1.

This project is also intended to minimize steel members by utilizing the structural performance of CLT panels. However, the section of steel beams can be increased to further increase the bearing force of CLT. Although the steel beam flanges receive the out-of-plane force due to the bearing force from CLT panels, vertical stiffeners are installed on the beams as shown in Figure 4. The compression stress from CLT panels is designed to allow the shear yield of steel beams. These vertical stiffeners also help prevent the steel beam web plates from shear buckling.

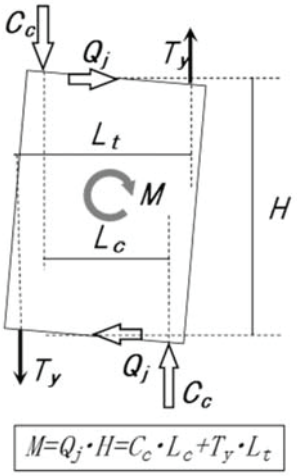

Figure 5: *Conceptual diagram of rotational resistance*

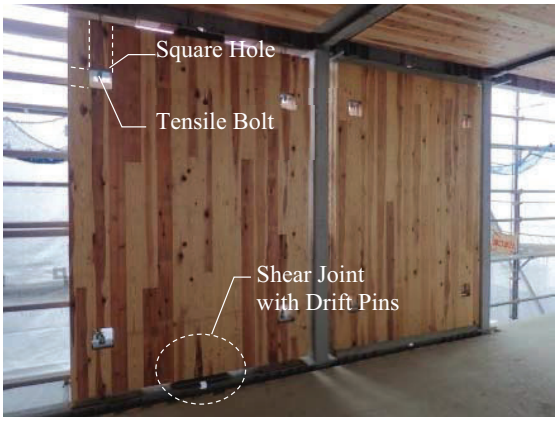

Figure 6: *Joints of CLT panels*

2.3 DESIGNING OF SHEAR JOINTS

The drift pined joints with insert-steel gusset plates were applied for the shear joints. The hybrid structure with CLT seismic panels and a steel frame can account for the frictional force effectively because the structure system makes the compression stress predominant by constraining CLT panels.

Thus, this study considers the horizontal resistance force caused by frictional force with the coefficient of 0.3.

Table 1: *Rotational resistances of CLT infill seismic walls in Hyogo Forestry Hall*

CLT wall	Height	H	2940	(mm)
	Width	L	2085	(mm)
	Thickness	t	210	(mm)
	Strength Classification		S60-5-7	
	In-plane bending strength	F_b	11.6	(N/mm^2)
	In-plane shear strength	F_s	2.3	(N/mm^2)
	Apparent Strength Classification		S60-5-5	
	Compressed area thickness	t_c	150	(mm)
	In-plane compressive strength	F_c	9.72	(N/mm^2)
Steel beam	Section		H-300x150x6.5x9	
	Tensile yield point strength	F_t	357.5	(N/mm^2)
	Shear yield strength	F_s	206.4	(N/mm^2)
	Shear sectional area	A_s	1833	(mm^2)
Tensile bolt	Material		ABR400	
	Yield point strength	σ_y	235	(N/mm^2)
	Diameter		M20	
	Quantity	n	2	(pcs.)
	Sectional area	a_t	490	(mm^2)
Tensile bolt position		d_t	230	(mm)
$L-d_t$		d	1855	(mm)
Bearing area width[1]		0.25d	463.8	(mm)
Compression resultant force position		d_c	231.9	(mm)
Bearing area effective sectional area		A_e	69563	(mm^2)
Distance between couple of compression forces		L_c	1621	(mm)
Distance between couple of tensile forces		L_t	1625	(mm)
Bearing strength of CLT wall		C_c	676.1	(kN)
Compressive strength of beam inclined to grain		C_{cv}	–	(kN)
Shear strength of beam		Q_v	378.3	(kN)
Min. strength of CLT bearing area		C_u	378.3	(kN)
Yield strength of tensile bolt		T_y	115.2	(kN)
Rotational resistance due to Ccu		M_{Ccu}	613.4	(kN·m)
Rotational resistance depending on Ty		M_{Ty}	187.1	(kN·m)
Full rotational resistance		ΣM_R	800.5	(kN·m)
CLT horizontal strength		Q_R	272.3	(kN)
CLT shear stress		τ_R	0.622	(N/mm^2)
CLT shear reference strength		F_S	2.700	(N/mm^2)

The structural performance of drift pins was designed by using the results of the previous joint experiment [4] using CLT panels (S60-5-5) and drift pins, 16 mm in diameter. In addition, considering the strength reduction coefficient 0.8 for arrangement of one row of several pins, the yield shear force per piece of drift pin, 16 mm in diameter, (q_{dpy}) was set to 22.7 kN per piece, and the initial stiffness (K_s) was set to 13.0 kN/mm per piece.

The design had an enough allowance for the primary design stage. The number of drift pins was determined so that the displacement of shear joint element springs under

https://doi.org/10.52202/069179-0427

the horizontal load-carrying capacity might not exceed the ultimate displacements at the shear joints as later described. The authors have reached the conclusion, through the above described designing process, that the shear stress (τ) that the CLT seismic panels can bear is 0.62 N/mm^2.

2.4 FLOW OF STRUCTURAL DESIGN

Figure 7 shows the structural design flow of the Hyogo Forestry Hall. For this building, the allowable stress for sustained loading was designed without CLT seismic panels to specialize them as seismic structural elements. On that condition, we went through the following processes in a sequential order in compliance with the Seismic Calculation Route 3 as a steel structure under the Building Standards Act of Japan: Designing of the allowable stress for sustained and temporary loading; checking of the story deformation angles, modulus of eccentricity and story stiffness ratio; calculation of the horizontal load-carrying capacity; and checking of the ultimate displacements at the joints. Since the required horizontal load-carrying capacity has not been calculated in the previous studies, this study reduced the whole building to an equivalent single-degree-of-freedom system and then used a method of calculating the reduction rate of the required horizontal load-carrying capacity (structural characteristics factor: D_s) from the ductility factor on the assumption of the property of energy conservation.

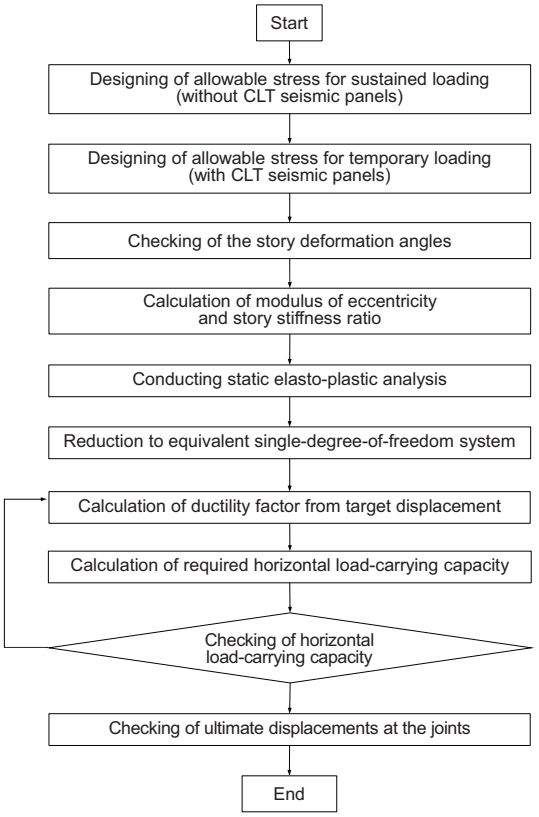

Figure 7: *Flow of structural design*

2.5 STRESS ANALYSIS MODEL

Figure 8 shows a stress analysis model of the Hyogo Forestry Hall. CLT panels were replaced by equivalent linear materials, which were analyzed as elastic bodies. The upper and lower ends of the wall had rigid beams as wide as the wall, and tension and compression springs at the wall joints on the ends and shear springs in the center were placed as nonlinear elements.

As regards the tension springs at tensile bolts, the springs of the following three elements in series were used as the initial stiffness (K_{CTB}) for calculation in accordance with the Japanese CLT Manual: the initial stiffness caused by the bearing stress of the timber immediately under the washers for the tensile bolts (K_C), the initial stiffness caused by the tension of the timber at the both ends of notches (K_T) and the tensile axial stiffness of the tensile bolts (K_B), where they are arranged so that the strength might depend upon the tensile yield of tensile bolts without causing the prior tensile or shear failure of CLT to occur around the square holes. The elastic-plastic properties were modelled to be bilinear.

The compression springs in the bearing area were modelled to be bilinear, by calculating the bearing spring stiffness (K_P) on the assumption that the bearing stiffness per unit area (k_c) was 15.6 N/mm^3 for the bearing area of $0.25d \times t$ and then calculating the compression stress (P_{PY}) from the compressive strength (F_c), in compliance with the Japanese CLT Manual [1].

The shear springs at the shear joints, using the yield strength per piece of drift pin shown in Section 2.3, were considered to be rigid (K_{S1}) until the frictional force (P_F) based on the assumption that the friction coefficient was 0.3 against the compressive strength of the bearing area. After that, the stiffness according to the number of drift pins (K_{S2}) was given, and they became trilinear type with a break point at the strength (P_{SY}) as a result of adding the yield strength of drift pins (P_{DPY}) to P_F. Although the tensile and compression spring elements were placed at the nodes of corners of wall panels for the sake of simplicity, the spring stiffness and strength require corrections (reduction) in consideration for the effect of the actual stress positions. By referring to the Japanese CLT manual [1], we set the correction factor (R) to $0.83d/D$, and multiplied the stiffness by R^2 and the strength by R.

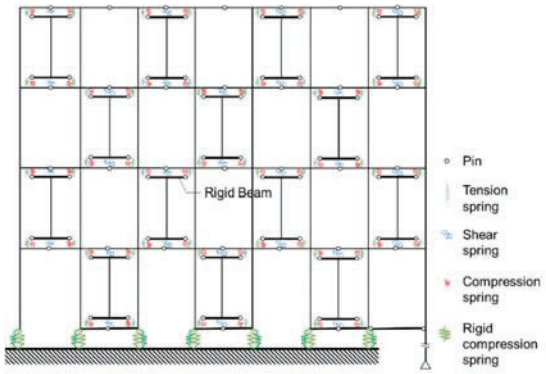

Figure 8: *Overview of stress analysis model*

https://doi.org/10.52202/069179-0427

Table 2 shows the calculation results for the joint springs in the standard configuration in Figure 4 by using the above procedure. A steel frame was modelled with linear elements, and the bilinear elastic-plastic properties were defined at the member ends. Although the shear yield of steel beams occurs due to the features of CLT panel layout in this structural system, the authors referred to the Reference [5] for the restoring force characteristics against the shear yield of steel plate reinforced by stiffeners and set the decreasing rate of the shear stiffness from the initial stiffness after the shear yield to 0.015.

Table 2: *Joint element springs*

Compression spring			Tension spring			Shear spring		
k_C	(N/mm^3)	15.6	K_C	(kN/mm)	101.9	μ		0.3
d	(mm)	1855	K_T	(kN/mm)	1767.8	P_F(=μ·P_{PY})(kN)		202.8
0.25d	(mm)	464	K_{CT}	(kN/mm)	96.3	DP		φ16
t	(mm)	150	Tensile bolt diam.		M20	n_S	(pcs.)	11
F_C	(N/mm^2)	9.72	A_B	(mm^2)	260	q_{dPY}	(kN/pc.)	22.7
K_P	(kN/mm)	1085.2	n_B	(pcs.)	2	k_S	(kN/mm/pc.)	13.00
P_{PY}	(kN)	676.1	L_B	(mm)	478	P_{DPY}	(kN)	249.7
			K_B	(kN/mm)	223.0	K_{S1}	(kN/mm)	10000.0
			K_{CTB}	(kN/mm)	67.3	K_{S2}	(kN/mm)	143.0
			P_{BY}	(kN)	115.1	P_{SY}	(kN)	452.5

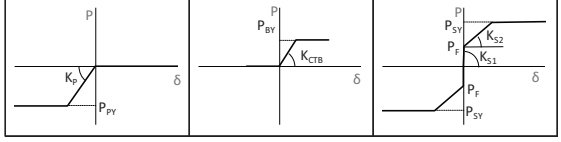

Table 3: *Stress analysis results*

Direc-tion	Story deformation angle (rad)	Modulus of eccentricity	Story stiffness ratio	Shear force sharing rate of CLT (%)	Mean shear stress of CLT (N/mm^2)
X-direc-tion	1/494 (FL level 4)	0.13 (FL level 4)	0.74 (FL level 4)	79.1 (FL level 2)	0.36 (FL level 2)
Y-direc-tion	1/469 (FL level 2)	0.12 (FL level 3)	0.74 (FL level 2)	84.9 (FL level 2)	0.40 (FL level 2)

2.6 STRESS ANALYSIS RESULTS

Table 3 shows the stress analysis results. In the primary design, the shear force sharing rate of a CLT infill seismic wall is as high as about 80%, the story deformation angle could be also reduced to slightly less than 1/500, smaller than the target value 1/200. Thus, the results indicated that the stiffness of a CLT infill seismic wall was fully contributory.

2.7 HORIZONTAL LOAD-CARRYING CAPACITY CALCULATION

For the Hyogo Forestry Hall, the authors developed the above stress analysis model, and then performed static elasto-plastic analysis and calculated the horizontal load-carrying capacity as shown by the flow diagram in Figure 7, where the problem was how to set the required horizontal load-carrying capacity. There were no experimental findings about the deformation performance and energy absorption of a hybrid structure with CLT seismic panels and a steel frame. Therefore, we reduced the building to an equivalent single-degree-of-freedom (SDOF) system (Figure 9) and then calculated the reduction rate of the required horizontal load-carrying capacity (structural characteristics factor: D_s) from the equation on the assumption of the property of energy conservation with ductility factor. The seismic force based on the Building Standards Act of Japan was caused to act on each floor (P_i), which was followed by static elasto-plastic analysis, where the horizontal displacement distribution on each floor in each step was reduced to the representative displacement Δ and acceleration A of an equivalent single-degree-of-freedom system (Equations (1) and (2)). If you set a freely-selected target displacement Δn against this $A-\Delta$ curve and establish an energy-equivalent, perfect elasto-plastic model, then that determines the ductility factor (μ), and the value of structural characteristics factor (D_s) to calculate the required horizontal load-carrying capacity (Q_{un}) will be calculated in Equation (3) based on the property of energy conservation (Equations (3) and (4)). From this relationship between a freely-selected target displacement Δn and the D_s value, the acceleration (A_n) equivalent to the required horizontal load-carrying capacity converted into acceleration can be obtained. The intersection between this $A_n-\Delta n$ curve and the $A-\Delta$ curve becomes a point to determine the horizontal load-carrying capacity.

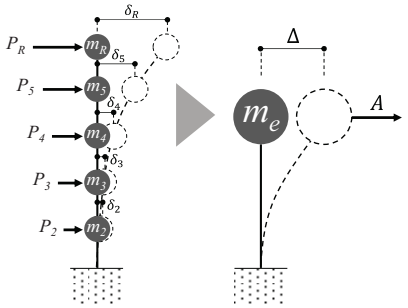

Figure 9: *SDOF System*

$$A = Q_B \cdot \frac{\sum m_i \cdot d_i^2}{(\sum m_i \cdot d_i)^2} \quad \cdots(1)$$

$$\Delta = \frac{\sum m_i \cdot d_i^2}{\sum m_i \cdot d_i} \quad \cdots(2)$$

$$D_s = \frac{1}{\sqrt{2\mu - 1}} \quad \cdots(3)$$

$$\mu = \frac{\Delta_u}{\Delta_y} \quad \cdots(4)$$

$$Q_{un} = D_s \cdot F_{es} \cdot Q_{ud} \quad \cdots(5)$$

where Q_B = story shear force of the lowest floor, m_i = mass of the level-i floor, d_i = displacement of the level-i floor, Δ_y, Δ_u = yield displacement and ultimate displacement of perfect elasto-plastic model, bilinear (refer to Figure 12), Q_{un} = required horizontal load-carrying capacity, F_{es} = shape factor (1 in this case) and Q_{ud} = story shear force when the base shear coefficient is 1.

Figures 10 and 11 respectively show the moment diagram and hinge diagram under the horizontal load-carrying capacity. Figure 12 shows the story shear force - story deformation relationship by floors in the +X direction, and Figure 13 illustrates the acceleration – representative displacement curve of an equivalent SDOF system obtained from Figure 12.

https://doi.org/10.52202/069179-0427

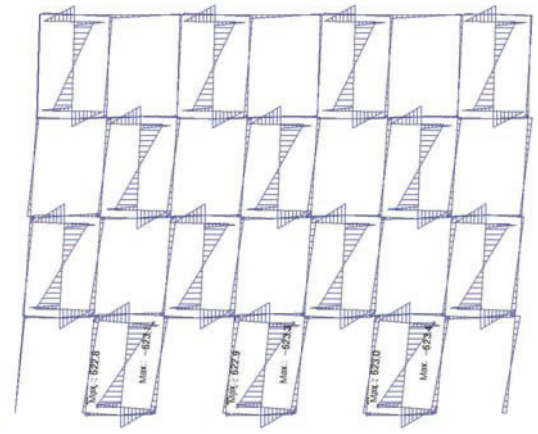

Figure 10: *North plane stress diagram (moment diagram) (under horizontal load-carrying capacity, in +X direction)*

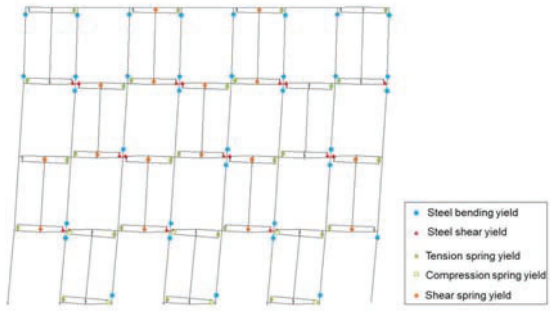

Figure 11: *North plane hinge diagram (under horizontal load-carrying capacity, in +X direction)*

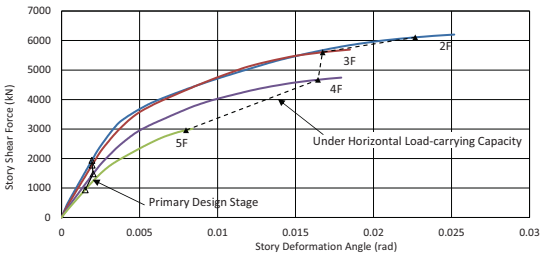

Figure 12: *Story shear force - story deformation angle relationship (in +X direction)*

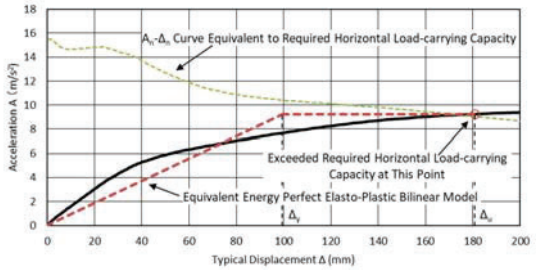

Figure 13: *Acceleration - representative displacement relationship (in +X direction)*

Table 4: *Horizontal load-carrying capacity calculation results*

Direc-tion	Story defor matio n angle (rad)	Ds	Fes	Qud (kN)	Qun (kN)	Qu (kN) (Qu/Qun)	Shear force sharing rate of CLT (%)	Mean shear stress of CLT (N/mm^2)
+X-direc-tion	1/44 (FL level 2)	0.616	1.0	9698	5972	6110 1.02	68.9 (FL level 2)	1.05 (FL level 2)
-X-direc-tion	1/48 (FL level 2)	0.627	1.0	9698	6077	6110 1.01	68.9 (FL level 2)	1.05 (FL level 2)
+Y-direc-tion	1/46 (FL level 2)	0.571	1.0	9698	5534	5722 1.03	76.6 (FL level 2)	0.99 (FL level 2)
-Y-direc-tion	1/44 (FL level 2)	0.606	1.0	9698	5876	5916 1.01	77.1 (FL level 2)	1.02 (FL level 2)

The result of performing the horizontal load-carrying capacity calculation for all the cases by the above method was as shown in Table 4, which indicates that the D_s values were between 0.57 and 0.63. The replacement by a bilinear type with an equivalent area has resulted in the calculation result larger than 0.55, the maximum D_s value of RC constructions that is specified in the Building Standards Act of Japan, because of the displacement (Δ_y) increased at yield, preventing the ductility factor (μ) from increasing.

The yields of joints, bending yields of steel columns and shear yields of steel beams occurred as shown by the hinge diagram in Figure 10. Generally, there is a concern of the web buckling in response to the shear force at the steel beam ends. However, as they are reinforced with stiffeners at a spacing of 100 to 140 mm in this case, the shear deformation performance can be expected. As a whole, the behavior with deformation performance is considered to be indicated. Therefore, the D_s values higher than those of strength type RC constructions are slightly unreasonable calculation results, which lacks evidence data to support them in the current situation. Accordingly, performance verification by such means as structure experiments is required in the future.

Furthermore, the sharing rates of the CLT seismic panels under horizontal load-carrying capacity were 68.9 to 77.1%, as shown by the horizontal load-carrying capacity calculation results in Table 4, which shows lower percentages than in the primary design stage. Still, the mean shear stress (τ) was approximately 1.0 N/mm^2. Finally, it was confirmed that the deformations of the spring models of joint elements at the joints did not exceed the ultimate deformation (δ_u). For the tensile joints, the ultimate displacement was considered to take place at the time when the tensile strain of tensile bolts was 10%. As for the shear joints by the drift pined joints with insert-steel gusset plates, the ultimate deformation (δ_u) was set to 32 mm in accordance with the experimental results in Reference [4].

3 SECURING FIRE-RESISTANCE PERFORMANCE

Even if used in a fireproof building, CLT seismic panels are not required to have fire-resistance performance under

https://doi.org/10.52202/069179-0427

the Building Standards Act of Japan because they do not support sustained loads but bear only horizontal forces. However, there is a possibility that the CLT seismic panels will continuously self-burn even after the end of fire, and the steel frame to which the panels are installed may be subjected to heating beyond the legally required fire-resistance performance. Hence, the authors performed the full-scale heating test on this structural system to verify the fire-resistance performance.

Figures 14 to 16 show the diagram and photos of the full-scale heating test specimens, and Table 5 shows a list of specimens. In the standard configuration shown by Figure 4, the upper part of the vertically divided panel was called the Specimen No. 1, and the lower part was called the Specimen No. 2. The Specimen No. 1 included the assumed CLT floor, which was covered on the upper and lower surfaces with reinforced gypsum boards for fireproofing and installed up to about one meter from the frame center. The space between a CLT seismic panel and a steel beam was filled with 80 mm thick shrinkage-compensating mortar both to transmit compression stress and to cover the beam flanges for fireproofing. We used calcium silicate boards as fireproof covering for the steel of these specimens and gypsum boards for the floor.

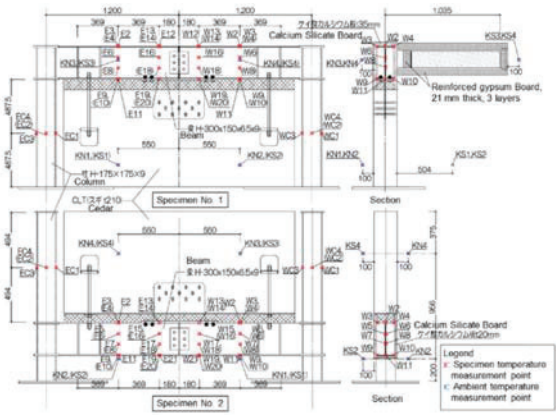

Figure 14: *Full-scale heating test specimen diagram*

Table 5: *List of full-scale heating test specimens*

Specimen No.	Steel column	Steel beam	Fireproof covering (Calcium silicate board)
No. 1	□-175x175x9 (STKR400)	H-300x 150x6.5x9 (SS400)	Column: 1 hr. (20 mm) Beam: 2 hrs. (35 mm)
No. 2			Column: 1 hr. (20 mm) Beam: 1 hr. (20 mm)

Figures 17 to 20 show the temperature histories at the measuring points of the specimens (the measuring points with the W-codes shown in Figure 14 represent the beam measurement results). It was confirmed that the CLT seismic panels of the both specimens reburned two to four hours after the end of heating and that the ambient temperatures of the specimens rose again up to about 700 degrees Celsius, and the CLT seismic panels burned down about one hour after that. This re-increase of the ambient temperatures after the end of heating is considered to have been attributable to the fact that the continuous burning from the both sides of the CLT seismic panels even after the end of heating turned into violent reburning when penetrating the CLT seismic panels. For the Specimen No. 1, we reinforced the fireproof covering of the beams to achieve 2-hour fire rating against the temperature rise of the CLT seismic panels due to reburning, which resulted in reducing the beam steel temperature to about 230 degrees Celsius. Consequently, the temperature dropped after reaching the peak 360-420 minutes after the start of heating. Though a temporary rise in the temperature was observed immediately after 60 minutes have passed since the start of heating, that was caused by the hot air that entered through the corners of the floor's butt ends which normally were not heated surfaces. The tensile bolts and shear joints that join CLT seismic panels to steel beams become thermal bridges and cause the steel temperatures to rise. However, keeping 80 mm thick shrinkage-compensating mortar limits the temperatures near the joints (W19 and W20 of No. 1 and W13 and W14 of No. 2) to about 250 degrees Celsius and consequently reduces the effect of the thermal bridges to be minor.

Figure 15: *Test specimen No. 1*

Figure 16: *Test specimen No. 2*

As described above, the maximum temperature of steel after heating for 60 minutes becomes about 450 degrees Celsius, which is considered to have the remaining strength beyond this building's stress due to sustained loading.

https://doi.org/10.52202/069179-0427

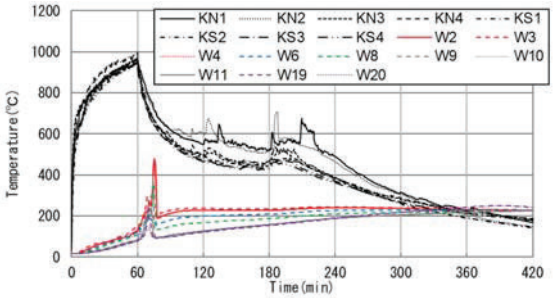

Figure 17: *Heating test results (Beam, Specimen No. 1)*

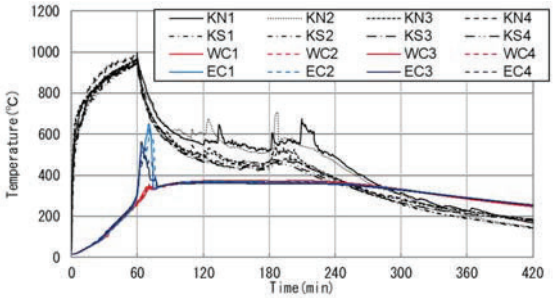

Figure 18: *Heating test results (Columns, Specimen No. 1)*

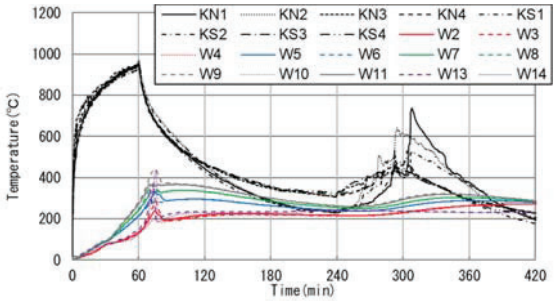

Figure 19: *Heating test results (Beam, Specimen No. 2)*

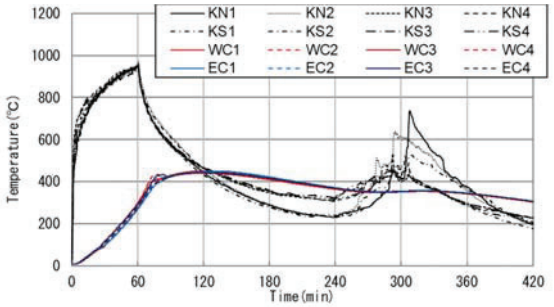

Figure 20: *Heating test results (Columns, Specimen No. 2)*
**For the codes showing the measurement points in the specimens in Figures 16 to 19, refer to Figure 13.*

4 CONSTRUCTION OF JOINTS

4.1 JOINTS TO TRANSMIT TENSION STRESS (TENSILE BOLT JOINTS)

Figure 21 shows the joint detail of a CLT and steel hybrid structure. Tensile bolts are placed at the four corners of the CLT infill seismic wall to transmit the tension stress generated due to the bending stress of the wall, and joined to the steel beam flanges.

As shown in Figure 22, the upper and lower surfaces of a CLT panel are filled with shrinkage-compensating mortar to transmit the compression stress and to provide steel beams with fire-resistance performance against the burning of CLT in case of fire as described in Chapter 3. A preliminary execution test was performed on the filling properties of shrinkage-compensating mortar, which verified that the mortar enabled the filling close to 100%.

Figure 21: *Tensile bolt joint*

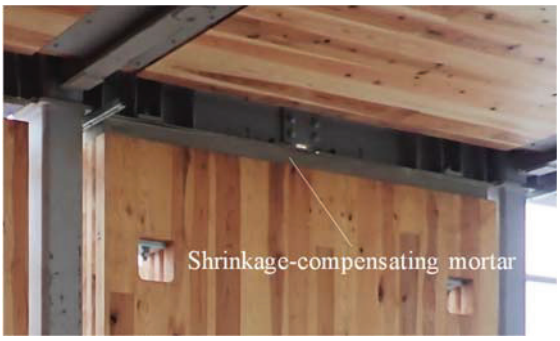

Figure 22: *Shrinkage-compensating mortar*

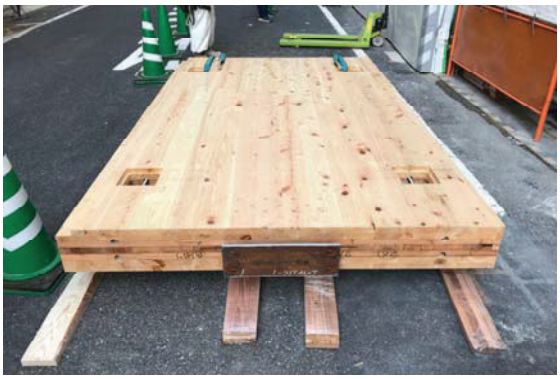

Figure 23: *Shear joint*

https://doi.org/10.52202/069179-0427

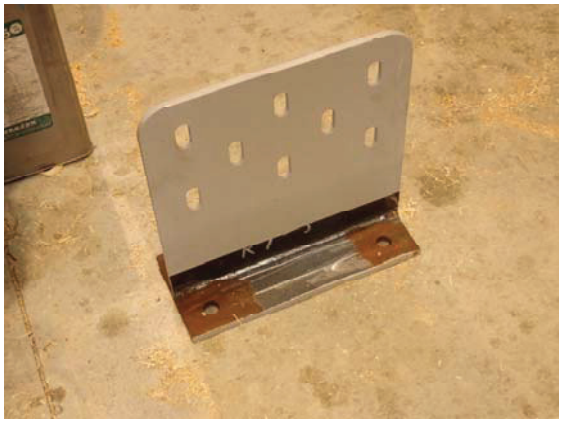

Figure 24: *Shear joint*

4.2 JOINTS TO TRANSMIT SHEAR STRESS (SHEAR JOINTS)

Refer to Figures 23 and 24. The drift pined joints with insert-steel gusset plates are used to transmit the shear stress. The insert-steel gusset plates are joined to the steel beam flanges through baseplates with high strength bolts. The drift pin holes in the insert-steel gusset plates are vertically loose so as not to be affected by the rotational deformation caused by the bending of a CLT panel and to allow level adjustments during construction.

4.3 JOINTS OF CLT FLOOR PANELS

Figures 25 and 26 show the joints of the CLT floor panels to the steel beams. The CLT floor panels are placed on the angle brackets installed on the steel beam webs and fixed with wood screws from the underside of the angles. Installation of angle brackets enables alignment of the CLT floor panels with the top level of the steel beams, which contributes to an increase in the effectiveness to the floor height. Besides, since wood screws do not require prepared holes, there is no need for strict precision management during construction. Hence, use of wood screws brings a great improvement in the construction efficiency during erection, compared with the cases of using drift pins or bolts.

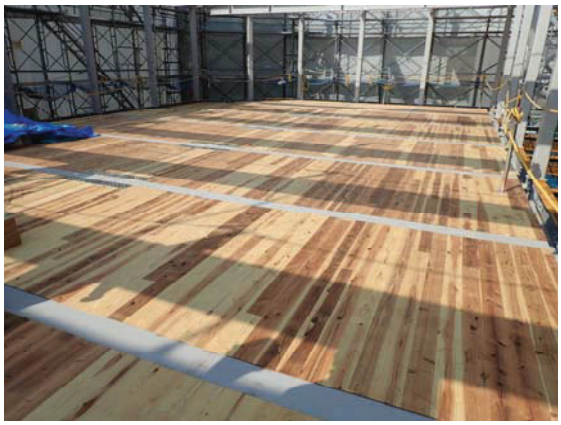

Figure 25: *CLT floor panels*

Figure 26: *CLT-floor-panel to steel-beam joint*

Thus, the joints between the CLT panels and steel frame of this building have contributed to the establishment of joining methods in consideration of fire-resistance performance and workability as well as the enhancement of the structural performance.

5 CONCLUSIONS

The above discussion shows that incorporation of CLT seismic panels into a steel frame makes it possible to exhibit the structural performance of the CLT panels efficiently. Additionally, this paper presents a series of structural design method including horizontal load-carrying capacity calculation through an actual case of design and confirms the usefulness of this structural system including fire-resistance performance.

REFERENCES

[1] Japan Housing and Wood Technology Center: Design and construction manual of building using CLT, 2016. 10 (in Japanese)

[2] Naturally wood and Forestry Innovation Investment. :Brock Commons Storyboards Factsheet.(online), available from <https://www.naturallywood.com/wp-content/uploads/2020/08/brock-commons-storyboards_factsheet_naturallywood.pdf> (accessed 2021.4.19)

[3] Bezabeh, M. Tesfamariam, S. and Stiemer, S.: Equivalent viscous damping for steel moment-resisting frames with cross-laminated timber infill walls, Journal of Structural Engineering, ASCE, DOI: 10.1061/(ASCE)ST.1943-541X.0001316. 2015

[4] Nakashima, S., Masuda, H., Fujishiro, A., Nonaka, H., Morimoto, T., Otsuka, K.: Development of CLT Drift Pinned Connection for Low-rise Timber Structure, Summaries of Technical Papers of Annual Meeting, Architectural Institute of Japan, Structures III, pp. 417-418, 2018.7 (in Japanese)

[5] Takahashi, Y. and Shinabe, Y.: Experimental Study on Restoring Force Characteristics of Shear Yielding Thin Steel Plate Elements, Buildings, Journal of Structural and Construction Engineering (Transactions of AIJ), Vol. 62, No. 494, pp. 107-114, 1997.4 (in Japanese)

https://doi.org/10.52202/069179-0427

World Conference on Timber Engineering Oslo 2023

TECHNICAL CONCEPT AND FEASIBILITY OF STEEL SHEET REINFORCED SYNTHETIC WOOD BEAM

Shogo Oda[1], Chikako Tabata[2], Yoshito Tomioka[3]

ABSTRACT: This paper is intended to explain the technical concept of steel sheet reinforced synthetic wood (SSRW). SSRW focuses on improving the integrity of wood and steel to increase the strength and toughness of hybrid materials. The composition includes laminated wood inserted with thin steel sheets prepared with adhesive holes and dowels. We conducted scale-model experiments to evaluate the feasibility of SSRW. We found that the vertical insertion of steel sheets demonstrated notable gains in rigidity and strength. Further, we observed that SSRW achieves 1.9 to 2.1 times greater bending rigidity as well as gains in strength than the unreinforced specimen.

KEYWORDS: Laminated wood, Adhesive opening, perforated steel metal

1 INTRODUCTION

Steel sheet reinforced synthetic wood (SSRW) is a wood-steel-hybrid-material for structural members, with a steel sheet reinforcement inserted in the cross-section of synthetic wood, as shown in Figure 1.

The purpose of SSRW is to compensate for the discontinuity of potential defects. Inserting the steel sheets between adhesive surfaces of wood can mitigate inconsistency in material strength.

In addition, this can moderate the localized stress concentration at the joint, which tends to be a critical part of structure design.

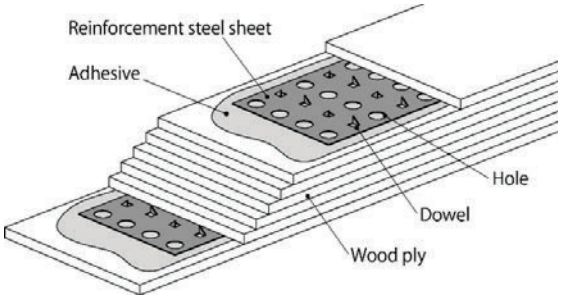

Figure 1: *Composition of SSRW*

Figure 1 shows the composition of SSRW.

Thin steel sheets are inserted and sandwiched between the adhesive layer of engineering wood.

The steel sheet has holes through which the adhesive penetrates and dowels that bite into the wood for temporary mechanical fixing and alignment.

2 PREVIOUS INVESITIGATIONS

Here, we discuss two recently proposed wood-steel hybrid beams.

Tanaka et al. (2007) prepared synthetic wood specimens with a 200 mm × 100 mm cross-section and added 6 mm-steel plates.

There were two specimens: plates on the bottom sides only, and on both the top and bottom. This was done using lag screws without adhesive.

They conducted a 3-point bending test with a span of 4 m and found that in both specimens, the maximum strength was approximately 1.2 times greater than that of plain wood.

The fracture behaviour of the specimens showed cracks in the wood material stressed by lag screws.

This is significant, especially on the tension side (bottom), where the wood was separated with a gap because the stretch of wood material could not follow that of the steel plate.

Winter et al. (2012) prepared 360 mm × 160 mm cross-section of synthetic wood inserted with cold formed or welded H shaped 4 mm-thick steel plate in wood material grooves by four threaded rods.

They conducted 4-point bending tests with a span of 6 m and found that the maximum loads of cold-formed and welded sheets were similar.

The fracture behaviour of both specimens was wood material rupture on the tension side.

This fracture occurred because the wood material could not follow the bending of the steel plate inside the beam.

These previous investigations were generally aimed at achieving high rigidity and high strength in hybrid beams. The hybrid material was wood with thick steel plates, which had low integrity.

[1] Shogo Oda, Undergraduate Student, Div. Archi., Graduate School of Eng., Mie Univ., Japan, 419744@m.mie-u.ac.jp
[2] Chikako Tabata, Associate Prof., Graduate School of Eng., Mie-Univ., Japan, tabata@arch.mie-u.ac.jp
[3] Yoshito Tomioka, Prof., Graduate School of Eng., Mie-Univ., Dr. Eng., Japan, tomioka@arch.mie-u.ac.jp

https://doi.org/10.52202/069179-0428

Additionally, beam fractures were caused by the rupture of the wood on the tension side of the hybrid material.
In SSRW, a very thin steel sheet is used as the reinforcing material to obtain uniform rigidity with wood.
We focused on improving the cross-sectional integrity and bending performance of wood material and steel plates.
This hybrid beam aims to improve toughness rather than rigidity.

3 EXPERIMENT OUTLINE

We conducted 3-point and 4-point bending tests in three phases. The bending tests were performed until the specimen fractured.
A scale-model was used for the specimens to comprehensively study many experimental parameters in a short time and at a low cost.
We observed the maximum proof strength, initial rigidity and fracture behaviour in the bending tests.

3.1 TEST SETTING

1) Phase 1 and Phase 2
Phase1 and 2 were 3-point bending tests.
The span of each specimen was 600 mm.
Figure 2 shows the test setting.

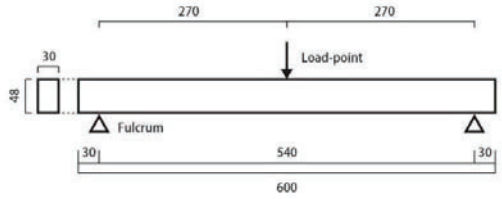

Figure 2: *Test setting in phase 1 and phase 2*

2) Phase 3
Phase 3 consisted of 4-point bending tests.
The span of the specimen was the same as that used in the previous phase.
Figure 3 shows the test setting in phase 3.

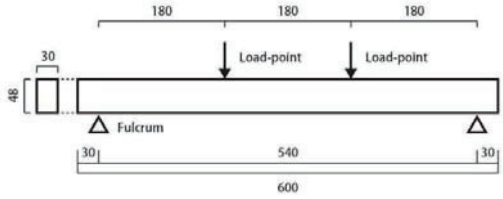

Figure 3: *Test setting in phase 3*

3.2 SPECIMEN PREPARATION

Figure 4 shows the specimen production process.
The specimens were 30 mm × 48 mm in cross-section and 600 mm in length and were made of 6 mm thick falcata laminated wood bonded with an epoxy resin adhesive.
Galvalume steel sheets 0.27 mm thick were used as the reinforced steel sheets.

The test specimen fabrication method:
(a) Markings were made directly on the steel sheet where the hole was drilled.
(b) Steel sheets of 0.27 mm thick were cut to 680 mm × 36 mm size.
(c) Holes were punched along the markings.
(d) The holes and cutting edges of the steel sheet were planar compensated using a plastic hammer.
(e) The surface of the steel sheet was degreased with ethanol.
(f) Steel sheets were placed along the markings of the lamina, and the lamina and buck sheets were laminated.
(g) The specimen was temporally fixed with a clamp.

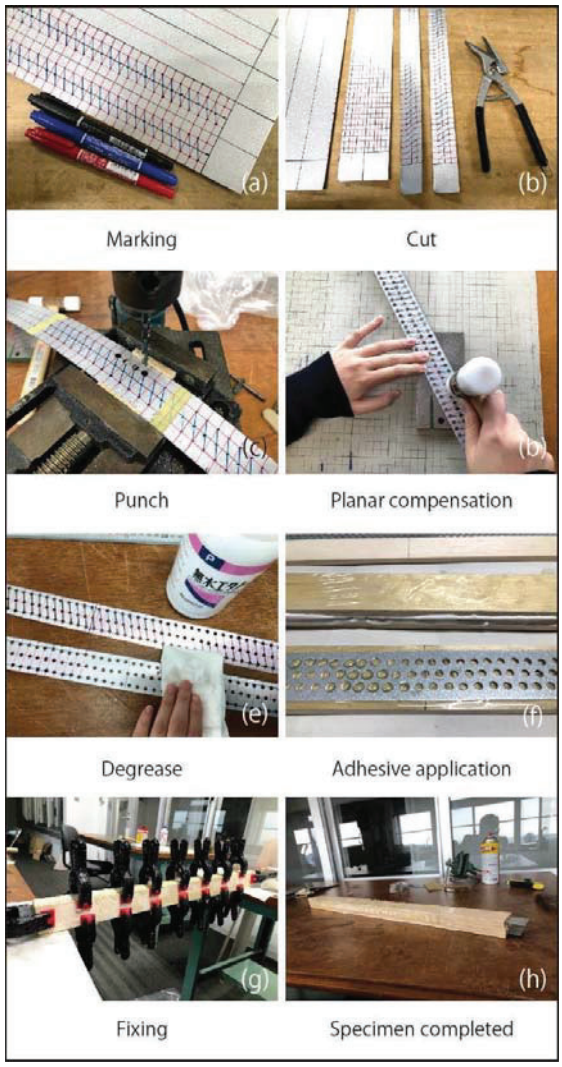

Figure 4: Specimen preparation

https://doi.org/10.52202/069179-0428

4 EXPERIMENTS

The experiment was conducted in three phases.

4.1 [PHASE 1]: EFFECT OF INSERTION DIRECTION

In phase 1, specimens with steel sheets inserted vertically and horizontally were prepared, as shown in Figure 5 and 7.
The main parameter of phase 1 was the cross-sectional insertion direction to confirm its effect on the performance of the specimen.
The parameter was also prepared to examine the effect of dowels.

1) Specimen parameters
In phase1, we used 7 specimen types.
One laminated wood beam with only lamina stacked vertically in cross-section was prepared.
Three specimens were prepared with steel sheets inserted vertically, and three specimens were prepared with steel sheets inserted horizontally.

2) Results: Load-deflection relationship
Figure 6 shows the load deflection relationship in the vertical insertion group.
This group of specimens significantly outperformed the unreinforced specimens in terms of initial rigidity and maximum proof strength in all the tests.
The initial rigidity was 1.9 to 2.1 times higher, and the maximum proof strength was 1.3 to 1.5 times higher.
The V-N specimens exhibited the highest initial rigidity, but the lowest maximum proof strength.
The lack of holes in the steel sheets caused premature delamination of the lamina and steel sheets.
V-4Hm-3.3 with holes showed the greatest maximum proof strength.
V-3Dm-4 with dowels applied to the holes performed worse than V-3Hm-3.3 in terms of both, initial rigidity and maximum proof strength.
Figure 8 shows the load deflection relationship in the horizontal insertion group.
These specimens behaved similarly to the unreinforced specimens.
The superiority of openings and dowels was not clear in these specimens.

3) Fracture behaviour
Figure 9 shows the fracture behaviour of vertical series.
The cross-section of the specimen with the wood cut away is shown.
The beam fractured in bending tension from the centre of the beam.
In V-4Hm-3.3, the facture shape shows that the wood fracture progress roughly along the rupture of the steel sheets.
V-3Dm-4 showed a similar fracture shape.
Figure 10 shows the fracture behaviour of H-N.
Bending and tensile fracture from the centre of the beam.
The steel sheet on the tension side was broken from the band.

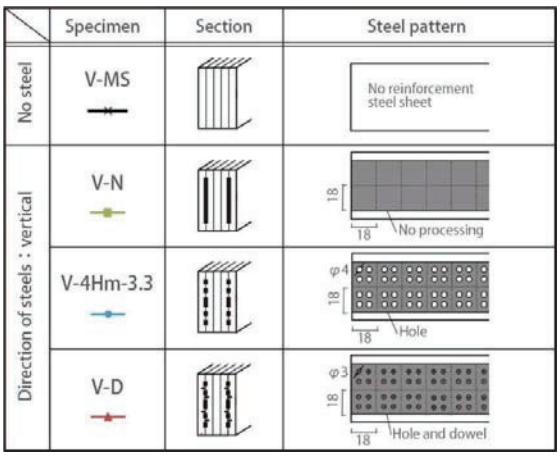

Figure 5: *Specimen parameters of vertical series in phase 1*

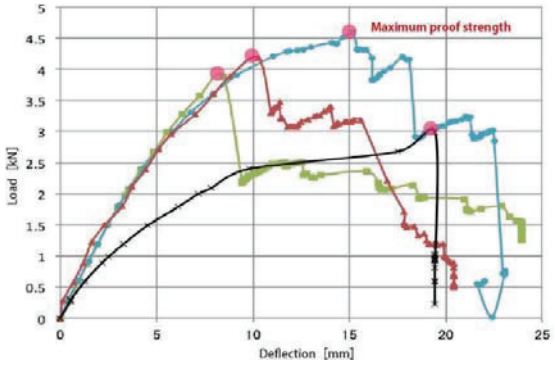

Figure 6: *Load-deflection relationship in vertical series*

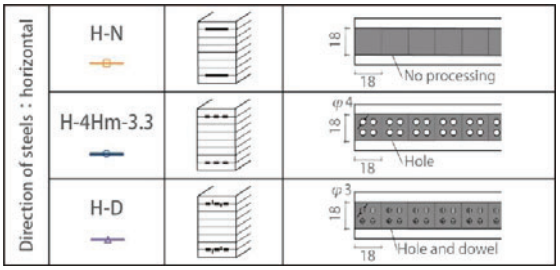

Figure 7: *Specimen parameters of horizontal series in phase 1*

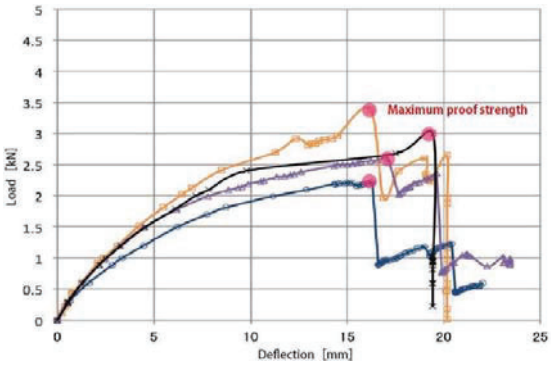

Figure 8: *Load-deflection relationship in horizontal series*

https://doi.org/10.52202/069179-0428

4) Discussion
The specimens with vertically inserted steel sheets had better initial rigidity and maximum proof strength.
Specimens V-4Hm-3.3 and V-3Dm-4, in the load-deflection diagram showed an increase in toughness with repeated load decreases and recovery after the maximum proof strength.
The progression of the fracture from the outermost band to the next band of the steel sheet on the tension side was repeated, and the wood followed the fracture.
The thin steel sheet and its holes resulted in a highly integrated cross-section of wood and steel.
V-3Dm-4 with dowels applied to the holes performed worse than V-3Hm-3.3 in both, initial rigidity and maximum proof strength.
This experiment did not confirm the superiority of dowels. The reason for this is thought to be a defect in the processing method of the dowel section, inferred from the V-3Dm-4 fracture developed from the v-cut section at the base of the dowels.

4.2 [PHASE 2]: EFFECT OF HOLE PLACEMENT

In this phase, specimens were limited to a group of vertically inserted steel sheets.
The main parameters of phase 2 were the placement and size of holes in the steel sheet to confirm if they affected bending performance.

1) Specimen parameters
Figure 11 shows specimen parameters in Phase2.
Specimens were prepared in 6 types.
Three different hole sizes (5.5 mm, 6.5 mm, and 7.5 mm) were prepared.
One specimen had a grid arrangement of holes in the steel sheet (V-5Hg-6.5) and three had staggered holes.
V-MS and V-N had the same configuration as the specimens in phase 1.

2) Results: Load-deflection relationship
Figure 12 shows the load deflection relationship in phase 2.
Initial rigidity was improved for all specimens over that of simple laminated wood beams.
Almost all the specimens had higher maximum proof strength than simple laminated wood beams. Only V-5Hg-6.5 was inferior.
V-5Hg-6.5 was likely defective because the behaviour of the load-deflection diagram was unstable during the early stages of loading.
V-N had the largest initial rigidity and maximum proof strength, but low toughness.

3) Fracture behaviour
Figure 13 shows the fracture behaviour of V-N.
The specimen fractured in the middle of the beam so that the fibres of the tension side wood were severed.
The steel sheet band lifted approximately 3 mm from the wood.
Figure 14 shows the fracture behaviour of V-5Hg-6.5.
The specimen fractured in bending tension from the centre of the beam.

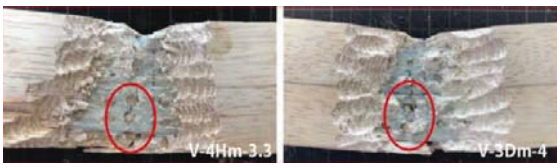

Figure 9: *Fracture behaviour of vertical series*

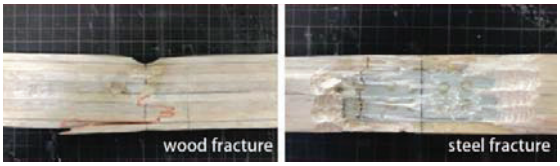

Figure 10: *Fracture behaviour of H-N*

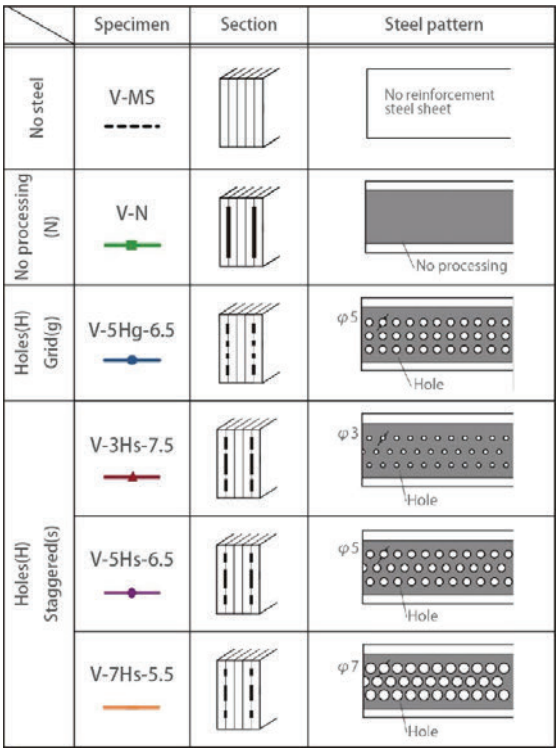

Figure 11: *Specimen parameters in phase 2*

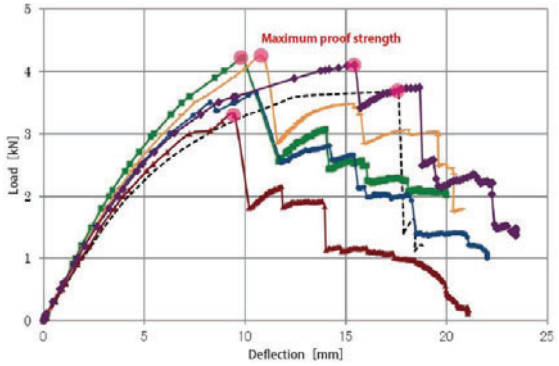

Figure 12: *Load-deflection relationship in phase 2*

https://doi.org/10.52202/069179-0428

The steel sheet band lifted approximately 0.9 mm from the wood.

4) Discussion
Apart from V-5Hg-6.5, the initial rigidity and maximum proof strength of the specimens were higher than those of simple laminated wood beams.
The insertion of steel sheets improves bending performance.
The specimen reinforced with a steel sheet without holes showed the greatest initial rigidity and maximum proof strength, but the steel was lifted from the wood up to the neutral axis after unloading.
The specimens reinforced with steel sheets with holes showed better toughness.
Hole size showed a trend towards improved performance for larger sizes.

4.3 [PHASE 3]: EFFECT OF BANDWIDTH

Specimens were limited to a group of vertically inserted steel sheets in phase 3.
The main parameter was steel sheet bandwidth, which was tested to see if it affected bending performance.

1) Specimen parameters
Figure 15 shows specimen parameters in phase 3.
Specimens were prepared in 6 types.
Steel sheets were prepared with holes in a staggered arrangement (V-5Hg-6.5, V-5Hs-4, V-5Hs-3, and V-4Hs-3) and modular arrangement.
V-5Hs-6.5 and V-4Hm-3.3 had the same composition as the specimens in phases 1 and 2.

2) Results: Load-deflection relationship
Figure 16 shows the load-deflection relationship in phase 3.
V-5Hs-4 had the greatest initial rigidity.
The specimen with the greatest maximum proof strength and toughness was V-4Hs-3.

3) Fracture behaviour
Figure 17 shows the behaviour of V-4Hs-3.
The tension side of the wood fractured near the loading point.
In the tension side, the band lifted1.2 mm out of plane.
Figure 18 shows the behaviour of V-5Hs-4.
V-5Hs-4 also showed a similar fracture shape to V-4Hs-3.

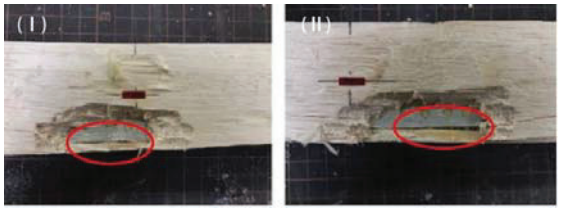

Figure 17: *Fracture behaviour of V-4Hs-3*

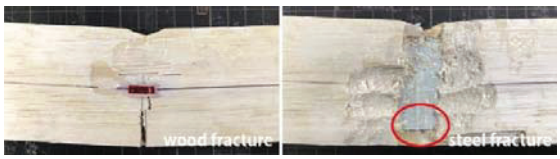

Figure 13: *Fracture behavior of V-N*

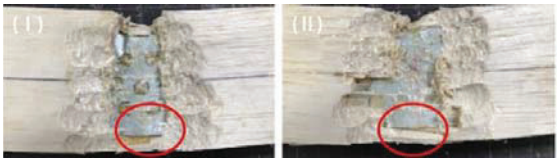

Figure 14: *Fracture behavior of V-5Hg-6.5*

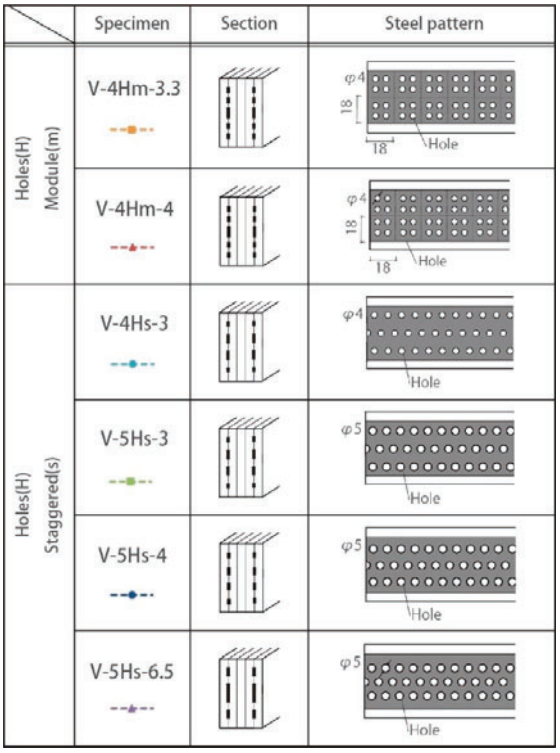

Figure 15: *Specimen parameters in phase 3*

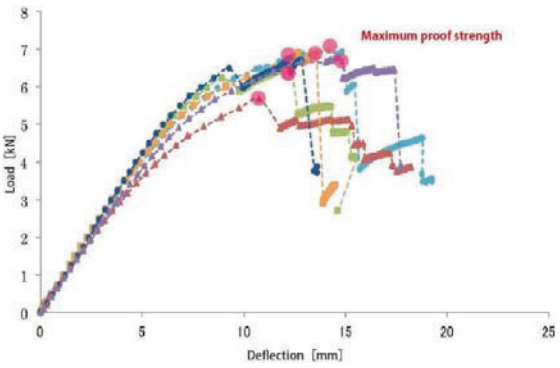

Figure 16: *Load-deflection relationship in phase 3*

https://doi.org/10.52202/069179-0428

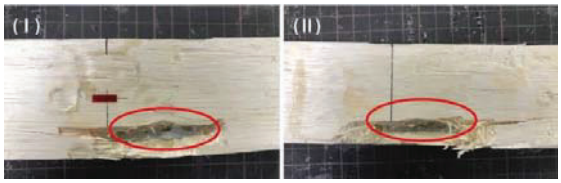

Figure 18: *Fracture behaviour of V-5Hs-4*

4) Discussion
No clear effect of the bandwidth parameter on bending performance could be observed.
Regarding the placement of holes, there was a slight performance improvement trend towards staggered placement.
The staggered arrangement may be due to the homogenisation of stress transmission in the cross-section, as the bands of the steel sheets intersect at an angle.

5 GENERAL OBSERVATION

The insertion of steel sheets was observed to improve bending performance.
Specimens with vertically inserted steel sheets had better initial rigidity and maximum proof strength than those with steel sheets inserted horizontally.
This result suggests that the vertical reinforcement of steel sheets with wood materials is a more effective than the horizontal reinforcement.
The hole size parameter showed a trend towards improved performance for larger sizes.

6 CONCLUSION

The observations from our study can be summarised as follows:
1) Bending performance is improved by inserting steel sheets into the laminated wood.
2) Vertical insertion of the steel sheet is more effective than horizontal insertion.
3) Holes in the steel sheet improve the integrity of the steel and wood sections.

ACKNOWLEDGEMENT

The results of this research are greatly attributed to the efforts of Ms. Yoko Aoyama.

REFERENCES

[1] Tanaka, H., & Ono, T. (2007). Evaluation of stiffness and strength for hybrid timber beams reinforced with steel plates and carbon fiber sheets. J. Struct. Constr. Eng., AIJ, NO.621, 89-96.
[2] Winter, W., Tavoussi, K., Pixner, T., & Parada, F., (2016). Timber-steel-hybrid beams for multi-storey buildings: Final report, in WCTE 2016 – World Conference on Timber Engineering – Vienna, Austria.
[3] Technical Concept and Expected Applications of Perforated Steel Sheet Reinforcement Applied to Synthetic Wood, Kagaku Kogyo, Vol.71, No.11, Kagaku-Kogyosha, 2020,11.
[4] Patent # 6784381, October 27, 2020, Japan Patent Office.

https://doi.org/10.52202/069179-0428

World Conference on Timber Engineering Oslo 2023

TIMBER-CONCRETE-COMPOSITE BEAMS WITH DISCRETE PERFORATED STEEL PLATE SHEAR CONNECTORS

Dolores Otero-Chans[1], Javier Estévez-Cimadevila[2], Emilio Martín-Gutiérrez[3], Félix Suárez-Riestra[4], José A. Vázquez-Rodríguez[5]

ABSTRACT: This paper describes an experimental research on timber-concrete-composite (TCC) beams made with discrete perforated steel plates shear connectors. The research included shear tests on different connectors made with perforated steel plates glued with epoxy in timber ribs and short and long-term test on beams with 8.88 meters of span. An unbonded tendon along with a self-tensioned system was used to limit the deflections of the beams on some of the short-term tests. A locked tendon was also used in long-term tests.

The different proposals of shear connectors made with discrete perforated glued steel plates showed a great strength and stiffness, with almost negligible slip between timber and concrete in service. This shear connectors, were used to design 8.88-meter span beams that showed a behaviour close to the full composite action in short-term tests, indicating a great potential to design medium and long-span beams and floors.

Some of the beams have been subjected to long-term loads for more than two years in an interior and uncontrolled environment. After that, the stiffness of the beams was evaluated under different test configurations and they were finally tested until failure.

KEYWORDS: long-span floors, timber-concrete composite, discrete shear connector, glued steel plates.

1 INTRODUCTION

Extensive research has been carried out in recent years around TCC systems, due to the enormous advantages they offer compared to only wood or only concrete solutions. The efficiency of these systems lies in the design of the shear connections between both materials, which must limit the relative slip in order to achieve a composite action as full as possible.

Traditionally, these connection systems have been classified into three large groups: notched connections, screwed connections and glued connections [1]. Within glued solutions, it can also be distinguished between direct glued solutions, in which the adhesive is the only connecting element between the wood and the concrete; and solutions with bars or plates glued into the wood, these being the ones that act as connectors with the concrete layer.

A considerable number of experimental studies have been carried out on connectors made with glued bars. Some studies have been carried out with continuous glued steel meshes used as shear connector, most of them linked to the system HBV® [2]. The studies carried out with short steel sheets placed discreetly along the length of beams or floor elements to constitute TTC systems are much smaller.

This paper summarizes the studies carried out by our team on the behaviour of a system based on the use of discrete perforated steel plates as shear connectors. The study carried out includes the experimental study of various arrangements of the perforated plates and the bending test of pieces with spans of 8.88 m in both short-term and long-term configurations. The effect of a unbonded but locked tendon was studied in short- and long-term tests. In some of the short-term bending tests, a tensioning system has been used to improve the behaviour of the floor in service.

2 SHORT-TERM TESTS ON SHEAR CONNECTORS

The specimens consisted of a fibre-reinforced concrete slab with 80 mm thickness and a rib of glued laminated timber with a cross-section of 120x160 mm and GL28h strength class. The Fibre-reinforced concrete, made from CEM II/B-M (V-L) 32.5N cement with a content of 350 kg/m3 and polyolefin macro-fibres Sika-Fiber48, was used to minimize the effect of shrinkage. The shear connectors were made from hot-galvanised 5-mm

[1] Dolores Otero-Chans, School of Architecture, University of A Coruña, Spain, dolores.otero.chans@udc.es
[2] Javier Estévez-Cimadevila, School of Architecture, University of A Coruña, Spain, javier.estevezc@udc.es
[3] Emilio Martín-Gutiérrez, School of Architecture, University of A Coruña, Spain, emilio.martin@udc.es
[4] Félix Suárez-Riestra, School of Architecture, University of A Coruña, Spain, felix.suarez@udc.es
[5] José Antonio Vázquez-Rodríguez, School of Architecture, University of A Coruña, Spain, jose.vazquez@udc.es

https://doi.org/10.52202/069179-0429

thickness steel plates, with 10-mm staggered holes every 15 mm. Two 8-mm thickness slots were made on the upper face of the wooden ribs to place the perforated galvanized steel plates glued using a two-component epoxy adhesive with a thickness of 1.5 mm.
Two batches of tests were carried out to evaluate different shapes of the connectors. In the first batch tests were carried out on 3 types of connectors: only with the plate, including transverse reinforced bars passing through the holes in the plates, including longitudinally welded reinforced bars on the plates (Figure 1).

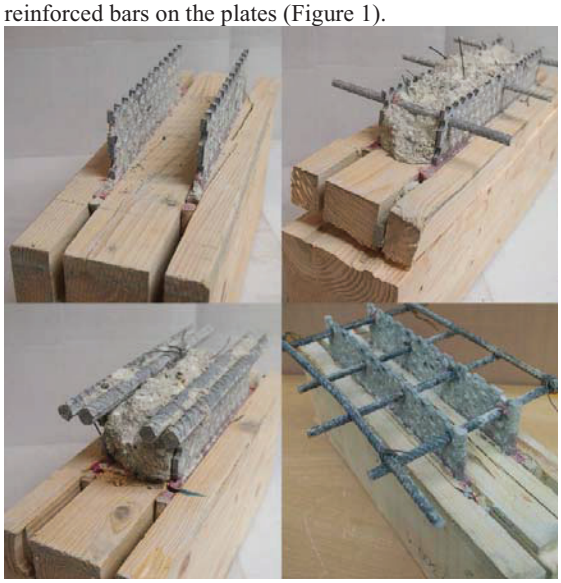

Figure 1: *Shear test specimens open after failure to check gluelines.*

Two connector lengths, 180 and 300 mm, were studied for each type of specimen. 18 specimens of 6 different types were subjected to failure in a shear test, obtaining the failure values, failure modes, and relative slip between the wood and the concrete [3]. All the specimens failed mainly by shear in timber (Figure 1).
Failure load ranged from 157.1 to 195.1 kN (average 179.1 kN) for 180-mm specimens and from 232.9 to 326.4 kN (average 260.4 kN) for 300-mm specimens. Specimens with longitudinally welded bars obtained, in average, the better results, although the difference between the three types was small. The load-slip behaviour of the connections lead to slip moduli between 707.5 and 1164.3 kN/mm for 180-mm specimens and between 2301.9 and 4298.1 kN/mm for 300-mm specimens.
In the second batch 6 new types of specimens were tested including vertically welded reinforced bars at the ends of the plates that were inserted a longer length in pre-drilled holes in the timber member (Figure 2). The types tested included three different configurations of bars and plates, varying the height of the plates and the anchorage length of the bars. For each of these configurations, two connector lengths, 180 and 300 mm, were tested again [4].

Figure 2: *Gluing of shear test specimens with plate+rods arrangement.*

All the specimens failed mainly by shear in timber again. Those made with plates+rods showed a greater ductility because of the anchorage of the rods although there was not significant difference for ultimate failure load when comparing specimens with the same length of the connector. In this case, failure load ranged from 175.1 to 213.6 kN (average 194.7 kN) for 180-mm specimens and from 213.6 to 318.6 kN (average 265.6 kN) for 300-mm long specimens. Slip moduli ranged between 959.8 and 1259.4 for 180-mm specimens and between 2103.0 and 3407.3 kN/mm for 300-mm specimens.
From these results, a simple predictive analytical model was proposed to determine the ultimate capacity of the shear connection [5].
Given that all the connectors tested showed high resistance and k_{ser} values, the simplest system was used for the elaboration of specimens for the full-scale beam tests.

3 SHORT-TERM TESTS ON TCC BEAMS

Eight beams with a total length of 8.88 meters and a T-section were made. The upper concrete slab had a dimension of 720x60 mm and the lower wooden rib had a section of 180x210 mm. An additional 30-mm thickness formwork board makes up a total height for the beam of 300 mm and a slenderness L/30. The characteristics of the materials were similar to those used in the previous shear tests. A 30x60 mm longitudinal groove was made on the underside of the wooden rib to house a tendon in some of the test configurations (Figure 3).
Four of the eight beams housed a tendon of 20 mm in diameter and the other four of 26.5 mm in diameter. Tendons were Y1100H Steel Dywidag threaded bars (with ultimate tensile strength 1100 MPa, and yield strength 900 MPa). The tendons were not adhered to the timber joists. Figure 3 shows the temporary blocks used solely for the purpose of positioning the tendons within the grooves.
Perforated S235 grade galvanized steel plates with dimensions 300x105x5 mm were used as shear connection between timber and concrete The pattern of the holes in the plates was similar to that of the previous shear push-out tests. A two-component epoxy adhesive was used to glue the plates to the timber joist. The perforated plates were arranged with variable spacing along the beam, as can be seen in figure 4. The minimum distance between them was 450 mm and the maximum 650 mm. In the area of the centre of the span, section

https://doi.org/10.52202/069179-0429

without shear, a distance between connectors of 1390 mm was disposed.

Figure 3: *Geometrical configuration of 8.88-m long beams.*

Four different test configurations were carried out, with the aim of evaluating the difference in deflections between them: test of pieces without tendons (test 1); test with non-adherent tendons and no pretensioning force, but with the tendons affixed at the ends of the beams (test 2); test with non-adherent tendons and a pretensioning force of 30 kN (test 3) and test with non-adherent tendons fixed to a self-tensioning system patented by the authors (test 4) [6].

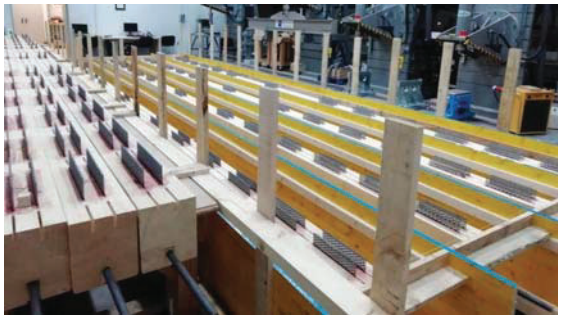

Figure 4: *Arrangement of the beams previous to the pouring of the concrete.*

For tests 2 to 4, four results were available for each of the tendon diameters studied. Tendon washer-type load cells were place at both end of tendons in tests 2 to 4 to record the loads reached in the tendons.

Figure 5: *Short-term test on 8.88-meter span beams.*

Beams were tested under a four-point bending test. Two load hypotheses were studied in each type of test: a quasi-permanent load hypothesis (with a value of 4.0 kN/m^2) and another full load hypothesis (with a value of 7.5 kN/m^2). For all tests the relationship between load and displacement at the midpoint was recorded. Additionally, a measurement was made in the central area of the beam corresponding to the relative deformation of two points separated 2 meters from each other, with the aim of determining the local stiffness (EI_{local}) in the area where there is only flexion since the shear is null. For this, a rigid aluminum bar was arranged as shown in Figure 5. Finally, six of the eight beams were tested until failure, reserving the remaining two for long-term tests. All the beams failed due to tension in the lower fibre of the wooden rib (Figure 6). No significant damage or cracks were observed in the concrete slab.

Figure 6: *Tensile failure in the lower fibre of the timber joist.*

Discreetly placed glued plate connections (at variable distances along the beams) resulted in a composite action close to 99% in all cases. Additionally, the use of non-adherent tendons allows reducing the deflection of the beams. The reduction in deflection was around 10% in the case of non-prestressed tendons and reached values close to 30% when the self-tensioning system was used [7].

https://doi.org/10.52202/069179-0429

In any case, the timber-concrete composite section proved to be very efficient in bending even in non-tensioned solutions, with deflections lower than 1/400 of the span for a ratio span/height of 30.
Finally, thebeams were tested until failure keeping the tendons locked.
Failure loads ranged from 69.3 to 122.2 kN, with no significant differences between the mean failure load of the beams with 20 or 26 mm diameter tendons.
The analysis of the two proposed service load hypotheses showed practically linear load-displacement curves in all cases.

4 LONG-TERM BEHAVIOUR OF TCC BEAMS

Two 8.88m-spam beams were subjected to long-term loads for more than two years (823 days), from October 2019 to December 2021, in an interior and uncontrolled environment (in Lugo, Spain). The test protocol during that period included the measurement of the environmental conditions (relative humidity and temperature), the humidity content of the beam components and the deflection at different moments of the process. The environmental conditions were continuously recorded by a thermo-hygrometer model LASCAR EL-USB-2 that collects data at half-hourly intervals. Periodically, the moisture content of the wood was recorded with a moisture meter model GANN Hydromette RTU 600.

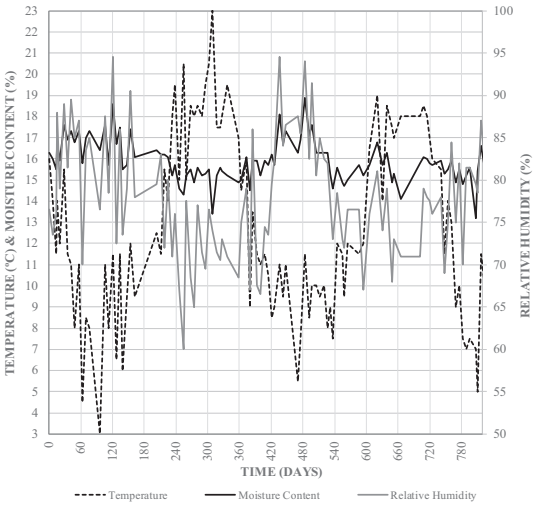

Figure 7: *Variation of the environmental conditions and the moisture content of the wood during the test period.*

The ambient temperature varied during this period between a minimum of 3.0 and a maximum of 23.0º Celsius (average value 13.5ºC), and the relative humidity between 60.0 and 94.5% (average value 76.5%). The average moisture content of the wood (determined from the measurement made at various points on the beams) ranged from a minimum of 13.2% to a maximum of 18.9%, with an average value of 16.5% (Figure 7).

Figure 8: *Arrangement of the long-term test.*

The beams were arranged as simply-supported. One of them had the Dywidag tendon affixed at the ends, without any pre-tensioning force. Washer-type load cells were arranged to record the variation in tendon load over time. The other beam was completely free, the cross-section only with timber and concrete, without any tendon blockage.
The self-weight of the beams was evaluated in 1.44 kN/m. The imposed load was applied by boxes filled with water which represents a uniform imposed load of 1.60 kN/m and an equivalent load of 5.0 kN/m^2, including self-weight (Figure 8).
Figure 8 shows the deflection values recorded throughout the entire period. The instantaneous deflection values, 13 and 11.3 mm for the beam without and with tendon, respectively, correspond only to the imposed load. The deflection values throughout the period respond to the total load (including self-weight), and respond both the deflection due to creep and the deflection derived from environmental variations. Considering the ratio between the self-weight and the imposed load, the instantaneous deflection corresponding to the total load would be about 24.7 and 21.5 mm, respectively. Figure 8 also represents the load value recorded in the blocked tendon and the moisture content of the wood. The relationship between deflection variations, tendon load, and moisture variation are evident.
Figure 9 shows the difference in deformation of the beam with a blocked tendon and the beam with an unblocked tendon. The instantaneous deflection of the beam with a locked tendon is 86% of that of the one without the locked tendon. This proportion remains substantially constant throughout the process, varying between 79 and 95%. The difference between both deformations decreases as time progresses, until reaching that 95% towards the end of the period.

https://doi.org/10.52202/069179-0429

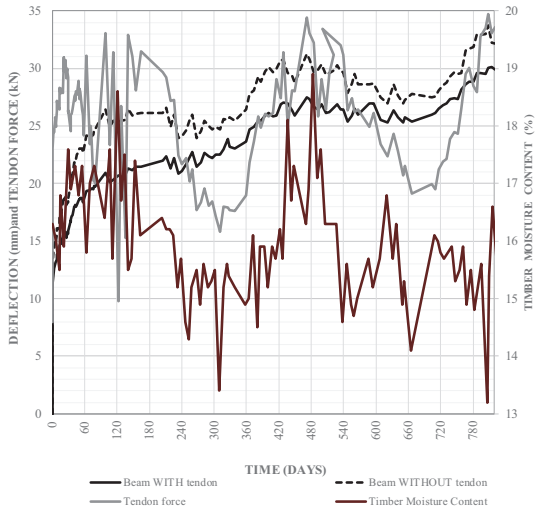

Figure 9: *Evolution of the total deflection during the long-term test along with the force in the tendon and the timber moisture content.*

In Figure 10 only the creep deformation is represented, also related to the moisture content and the force in the tendon. In this figure, it is more evident how the creep deformation of the two beams tends to equalize over time. Figures 9 and 10 also shows the relationship between the increase in deformation and the increase in the moisture content of the wood. The efficiency of the tendon is greater when the moisture content of the wood increases, since in the Figures 8 and 9 it can be seen that in these cases the difference between the creep deflections of the two beams also increases.
The creep deformation after two years is somewhat lighter than the instantaneous deformation (the total deformation is slightly below than twice the instantaneous).

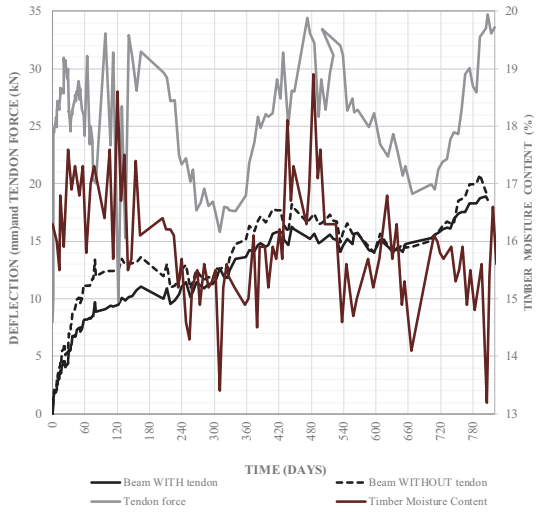

Figure 10: *Evolution of the creep deflection during the long-term test along with the force in the tendon and the timber moisture content.*

5 SHORT-TERM TESTS OVER PRELOADED BEAMS

After the long-term test, the beams were unloaded and remained supported along their entire length for about 60 days. Then, the beams were tested again in short-term. Two types of test were carried out: type A and type B.
In test type A the beams were arranged as simply-supported with two cantilevers, with a span between supports of 6.90 meters. In test type B the beams were arranged as simply-supported with a span equal to 8.7 m. A schematic representation of the load arrangement can be seen in Figure 11.

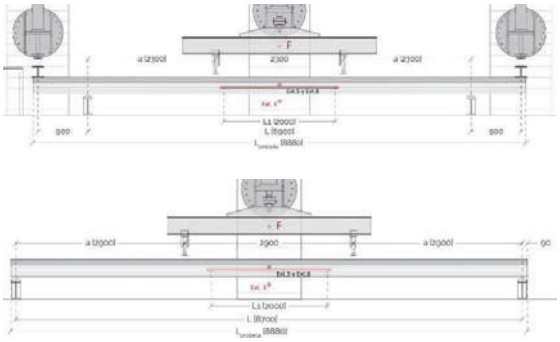

Figure 11: *Type A and type B arrangements for the short-term tests made after long-term tests.*

In test type A, the beams were loaded three times. The first load is carried out with the tendon unlocked and without any restriction at the ends of the cantilevers. The beams are loaded to a maximum of 7.5 kN and the deflection at the midpoint is recorded. Subsequently, the ends of the beams were blocked at a distance of 0.9 meters from the supports, generating a reaction to the upward vertical displacement of the ends. To achieve this blocking, loads were applied by means of two load cells located at the ends of the cantilevers that remained in a fixed position after applying a load of 1 kN. In this situation, the beam was again loaded to a maximum of 7.5 kN in two different situations, the first without locking the tendons and the second locking the tendons by means of end locking nuts. In both cases, the descent of the midpoint and the load at the ends were recorded (Figure 12).
Given that a very linear load-deflection behaviour had been observed in the previous tests, low-magnitude loads were applied in this case to measure the bending stiffness in order not to damage the pieces in the different configurations tested. The load was applied by constant speed according to EN 408:2010+A1. A hydraulic testing machine equipped with a 600 kN load cell was used. In the same way as in the previous short-duration tests, a deflection measurement was carried out in the central area of the beam of the relative deformation of two points separated 2 meters from each other, with the aim of determining the local stiffness (EI_{local}), using a rigid aluminium bar as indicated in Figure 11.

https://doi.org/10.52202/069179-0429

Figure 12: *Type A test arrangement, with cantilevers at the end of the beam.*

In the type B test, the beams are arranged as simply supported with a span of 8.7 meters. In this case, a first load phase is carried out with a maximum value of 9.8 kN and the deformation of the pieces with the tendons not locked and with the tendons locked is recorded. Finally, the pieces are tested until failure with the tendons not locked.

The type A test allows verifying the ability of the fibre-reinforced concrete slab to withstand small-magnitude tensions without cracking, which would allow the design of continuous elements over several spans.

Table 1 shows the mean values of breaking load and flexural stiffness (EI) for the tests carried out before and after long-term tests.

Table 1: *Failure loads of simply-supported beams.*

Tests	Locked tendon	Average failure load [kN]	Average bending stiffness EI [kN·m]
First short-term tests	No	-	11660
	Yes	93.7	12680
Second short-term tests (after long-term load)	No	68.9	10660
	Yes	-	12580

The increase in the global bending stiffness of the beams with the tendon locked with respect to the tendon without locking is between 9% and 32%. The difference between the beams that have been subjected to long-term tests and those that have not undergone long-term tests is bigger for beams without tendon. The result is practically the same in the case of tests performed with the tendon locked. To this regard, it is necessary to remember that in the case of beams from long-term tests, only two specimens are available, so conclusions must be taken with caution.

The failure load is not comparable between the two tests, since in one case the beams were tested until failure with the tendon locked and in the other without it. But, considering the little difference in behaviour observed in terms of stiffness, it could be concluded that the arrangement of a locked tendon (without pre-stressing) could increase the bending strength of the beam by up to 27%.

6 CONCLUSIONS

Discrete perforated glued steel plates constitute a very effective solution for the development of timber-concrete-composite systems.

Shear connection with perforated steel plates between timber and concrete can be improved by using additional steel bars. However, the improvement in performance is slight, so the use of additional bars must be justified by other design criteria.

Full scale short-term tests were made on TCC beams with 8.88-meter span. The use of perforated plates as shear connector showing a composite action close to 100%.

The use of non-adherent tendons allows to reduce de deflections in beams between 10 and 30%, depending on the pre-tensioning force of the self-tensioning device used.

The use of non-prestressed tendons can also reduce long-term deflections, especially when the moisture content of the wood is high.

ACKNOWLEDGEMENTS

This study is part of the research project ‘‘High-performance timber-concrete-composite hollow-core floors for sustainable and eco-efficient construction (AlveoTCC)”, ref. PID2019-107859RB-100. The study developed was funded by MCIN/ AEI /10.13039/501100011033.

This research is alsopart of the research project “Self-tensioning high performance structural floors with glued laminated timber-fibre reinforced concrete composite section” (BIA2016-77184-P) financed by the Spanish Ministry of Economy and Finance and the European Regional Development Fund (ERDF).

REFERENCES

[1] Yeoh D., Fragiacomo M., Franceschi M., Boon K.H. State of the Art on Timber-Concrete Composite Structures: Literature Review. *Journal of Structural Engineering*, pages 1085-1095. ASCE, USA, 2011.

[2] Naud N., Sorellia L., Salenikovich A., Cuerrier-Auclair S. Fostering GLULAM-UHPFRC composite structures for multi-storey buildings. *Engineering Structures*, pages 406-417. Elsevier, England, 2019.

[3] Otero-Chans D., Estévez-Cimadevila J., Suárez-Riestra F., Martín-Gutiérrez E. Experimental analysis of glued-in steel plates used as shear connectors in Timber - Concrete - Composites. *Engineering Structures*, pages 1-10. Elsevier, England, 2018.

[4] Martín-Gutiérrez E, Estévez-Cimadevila J., Otero-Chans D., Suárez-Riestra F. Discontinuous π-form steel shear connectors in timber-concrete composites. An experimental approach. *Engineering Structures*, 110719. Elsevier, England, 2020.

[5] Suárez-Riestra F., Estévez-Cimadevila J., Martín-Gutiérrez E., Otero-Chans D. Perforated shear + reinforcement bar connectors in a timber-concrete composite solution. Analytical and numerical

https://doi.org/10.52202/069179-0429

approach. *Composites Part B: Engineering*, pages 138-147. Elsevier, England, 2019.

[6] Otero-Chans D., Estévez-Cimadevila J., Suárez-Riestra F., Pérez-Valcárcel J. Application of a New System of Self-Tensioning to the Design of Large-Span Wood Floor Framings. *Journal of Structural Engineering*. ASCE, USA, 2016.

[7] Estévez-Cimadevila J., Otero-Chans D., Martín-Gutiérrez E., Suárez-Riestra F. Testing of different non-adherent tendon solutions to reduce short-term deflection in full-scale timber-concrete-composite T-section beams. Journal of Building Engineering, 101437. Elsevier, England, 2020.

[8] Suárez-Riestra F., Estévez-Cimadevila J., Martín-Gutiérrez E, Otero-Chans D. Timber-Timber-Composite (TTC) beam long-term behaviour. Full scale experimental campaign and simplified analytical model *Jconstruction and Building Materials*, 129649. Elsevier, England, 2022.

World Conference on Timber Engineering Oslo 2023

A NEW BUILDING STRUCTURAL SYSTEM USING TIMBER-CONCRETE-COMPOSITE MEMBERS

Javier Estévez-Cimadevila[1], Dolores Otero-Chans[2], Emilio Martín-Gutiérrez[3], Félix Suárez-Riestra[4], José A. Vázquez-Rodríguez[5]

ABSTRACT: This paper presents a novel system for the construction of building structures based on the use of timber-concrete-composite pieces (floors, beams and columns). Beams and floors are composed of a prefabricated lower glued laminated timber (GLT) flange glued to one or more plywood ribs that are linked to an upper concrete slab poured in situ using an efficient timber-concrete connection of holes made on the ribs.

An extensive experimental campaign was carried out to validate the solution: shear tests of wood-wood and wood-plywood glue line; delamination tests of wood-wood and wood-plywood glued planes; shear tests of the timber-concrete connection with different configurations; finally, full scale four-point bending tests of simple supported beams and three-point bending tests of pieces in an overhanging configuration.

In order to know the performance of the system, sizing curves using the Gamma Method were developed. Results indicates a light, slender and high stiffness structural solution very suitable to be used in building construction.

KEYWORDS: Timber-concrete-composite, structural building systems, timber flooring, mixed beams, shear connection

1 INTRODUCTION

The advantages of the timber-concrete structural solutions are well known and are referenced in many papers [1-3]. A suitable design of timber-concrete composite (TCC) sections allows to take advantage of the properties of both materials to achieve a more efficient structural solution than only-timber structures with lower self-weight than only-concrete solutions.

The behaviour and performance of these systems fundamentally depends on the efficiency of the shear connection between both materials. This efficiency is based on achieving a high strength against shear forces with low slip of the connection; thus achieving a high composite effect and a ductile behavior. The state of the art includes different timber-concrete connection systems such as steel fasterners and plates, glued solutions, or the mechanical transmission of forces through the use of notches, grooves or slots in the wood [4-7]. These connections show very different characteristics in strength, stiffness and ductility of the joint.

This paper describes a complete solution for the construction of building structures using perforated plywood or laminated veneer lumber (LVL) as timber-concrete connection. The paper contains a summary of the different experimental campaigns carried out to validate the behaviour of the system. This includes not only the experimental analysis of the connection but also bending full-scale tests of simply supported beams and pieces in a an overhanging configuration. Results obtained allow to conclude the high strength and stiffness behaviour of the system proposed.

2 DESCRIPTION OF THE SYSTEM

The system is based on the use of prefabricated timber pieces complemented with concrete poured in situ [4]. The system is composed of the following elements:

Floors. The floor is formed by prefabricated T or π shaped pieces composed by a lower flange of glued laminated timber (GLT) glued to one or more perforated plywood or LVL ribs (Figure 1). The connection between this pieces and the upper concrete slab is made using the holes filled by the in situ poured concrete.

Beams. The beam solution is very similar to flooring pieces. A π-shaped piece composed by a lower GLT flange glued to two perforated plywood or LVL ribs which ends are machined to conform the connection to the columns. The use of reinforcement bars makes it possible

[1] Javier Estévez-Cimadevila, University of A Coruña, Spain, javier.estevezc@udc.es
[2] Dolores Otero-Chans, University of A Coruña, Spain, dolores.otero.chans@udc.es
[3] Emilio Martín-Gutiérrez, University of A Coruña, emilio.martin@udc.es
[4] Félix Suárez-Riestra, University of A Coruña, Spain, felix.suarez@udc.es
[5] José A. Vázquez-Rodríguez, University of A Coruña, jose.vazquez@udc.es

https://doi.org/10.52202/069179-0430

to create an efficient semi-rigid connection with the columns.

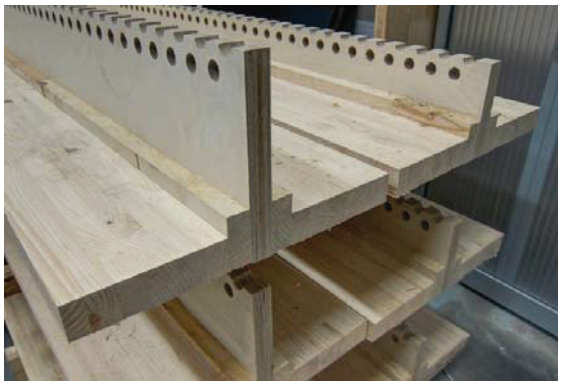

Figure 1: *Prefabricated T-shaped flooring pieces with different heights*

Columns. The columns are composed of a perforated plywood box section that satisfied two objectives: formwork of the concrete and support the flooring structure during the period in which the concrete is not sufficiently strong.

Figure 2 shows a computer-generated image of the complete system using cardboard blocks as infill formwork during the concrete pouring.

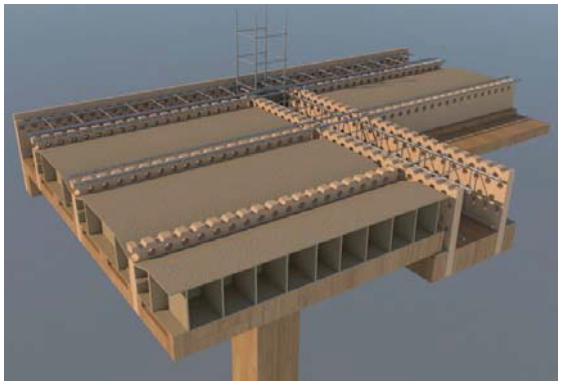

Figure 2: *Image of the complete system*

3 TEST CAMPAIGN

In order to validate the solution five test campaigns were carried out.

3.1 SHEAR TEST IN THE GLUE LINE

96 glue lines (72 wood-wood and 24 wood-plywood) of 8 samples of 390x50x50 mm, consisted of 7 *Picea abies* wood layers, strength class GL28h, and 2 birch plywood layers glued at both ends, were tested according to the UNE-EN 14080:2013 (Figure 3).

The results showed the efficacy of the connection in terms of strength with an average value of shear resistance of 9.63 N/mm^2 for wood-wood glue line and 7.16 N/mm^2 for wood-plywood glue line [8].

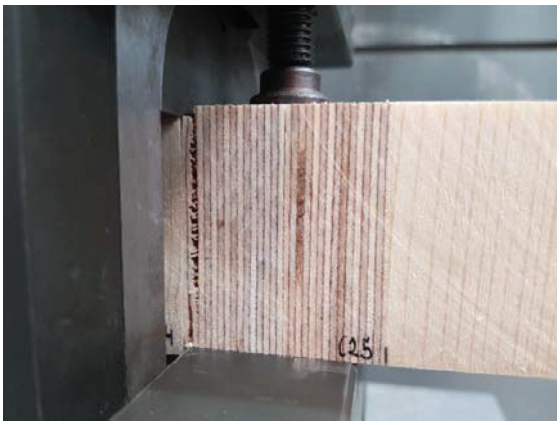

Figure 3: *Shear test in the glue line*

3.2 DELAMINATION TEST IN THE GLUE LINE

32 glue lines (24 wood-wood and 8 wood-plywood) of 8 samples of 195x75x77 mm were tested according to the UNE-EN14080:2013 (Figure 4). In 79.2% of wood-wood lines and in 62.5% of wood-plywood lines no delamination occurs. In the other lines average delamination was of 8%. Consequently, the results guaranteed the integrity of the glue lines [8].

Figure 4: *Delamination test in the glue line*

3.3 SHEAR TEST OF TIMBER-CONCRETE CONNECTION

An experimental analysis of the shear connection was carried out using push-out shear test according to EN 26891:1992 (Figure 5).

https://doi.org/10.52202/069179-0430

Figure 5: *Push-out shear test of timber-concrete connection*

Twelve samples of 480x300x300 mm were tested in a first campaign. Six of specimens were constituted with two 15 mm thick birch plywood boards joined to a 50–120 mm thick concrete slab. In the other six specimens the thickness of the boards was increased to 21 mm. 3 reinforcement bars of 8 mm, B500S steel grade, were placed in concrete slab crossing the upper file of holes of the board.

A second campaign was carried out with 45 samples of nine types of specimens in which different parameters were analysed: configuration of boards (one of 42 mm thick or two of 21 mm thick each one), holes disposition and diameter (2 rows, 20 mm diameter and 50 mm spacing or 1.5 rows, 30 mm diameter and 62 mm spacing), and use or not of B500S grade steel reinforcement bars.

Tests results show a very high stiffness and consequently a favourable composite action with k_{ser} values from 283.5 to 887.7 kN/mm per unit length depending of different configurations analysed [8, 9]. Moreover, load-slip curves for each tested showed a ductile failure that is a very positive characteristic in TCC solutions (Figure 6).

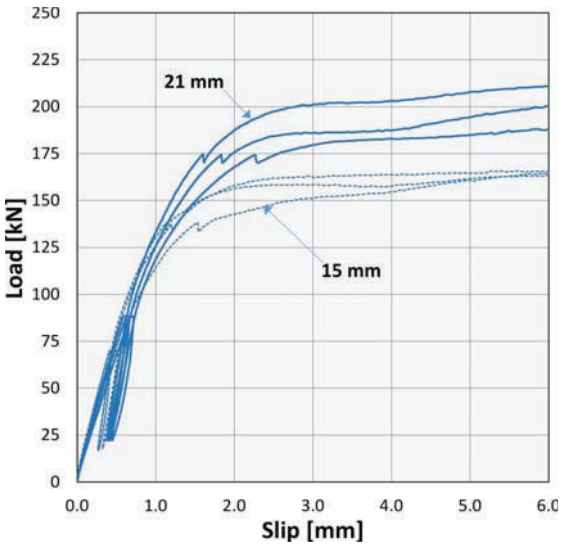

Figure 6: *Load-slip curves of specimens with two birch plywood boards of 15 mm and 21 mm thick.*

3.4 FULL SCALE FOUR-POINT BENDING TESTS OF SIMPLE SUPPORTED TCC BEAMS

Based on the results obtained in the shear test connection analyzing different parameters, the solution of a single 40 mm thick board with 1.5 rows of 30 mm diameter roles and 62 mm spacing has been chosen. This configuration combines efficiency and simplicity.

Full scale four-point bending tests of nine simple supported TCC beams according to standard EN 408:2010+A1:2012 were carried out with 3 different configurations: 3 samples of 6 m span and a height of 25 cm; 3 of 7.2 m and 30 cm; 3 of 8.4 m and 35 cm. In all cases the slenderness ratio was L/24 (been L the span of the beam).

The specimens consist of an inverted T-shaped piece formed with a 600x60 mm glulam flange made with *Picea abies* GL24h and a 40 mm thick birch plywood board with 30 mm diameter perforations. This board is joined to an upper concrete slab of 600x50 mm with polyolefin macrofibres added. Compression test of concrete specimens provided a mean strength value of 39.9 N/mm^2 at 28 days. 8 mm diameter and 120 mm long rebars were inserted through every three perforations of the boards (Figure 7). Additionally, a 200x200 mm ϕ6 mm steel mesh was placed to control cracking caused by shrinkage of concrete. Light cardboard blocks were designed to acting as lighten infill and formwork during the concrete pouring.

https://doi.org/10.52202/069179-0430

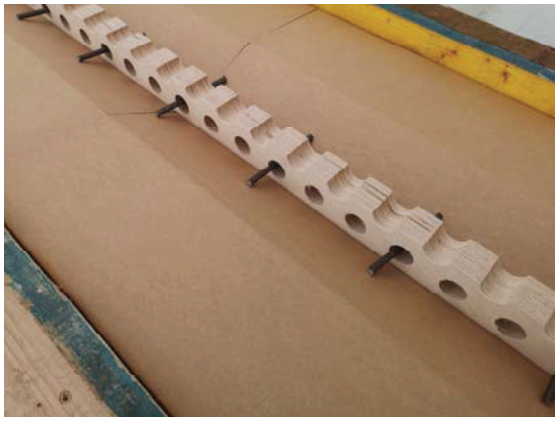

Figure 7: *Specimen with carboard bloks and rebars positioned previously the concrete pouring of 50 mm thick upper slab. In the photograph, the steel mesh has not yet been placed.*

Figure 8: *Bending test of a 7.20 m span specimen*

The lowest ultimate load value obtained in the tests corresponds to a total equivalent surface load of 39.04 kN/m^2, which represents a value 7.8 times higher than the total load of floors for residential use (self-weight+light partitions and finishes+ variable load=5.0 kN/m^2) [10].

Failure occurs suddenly, affecting the glulam flange of the central part of the beam in areas of knots or finger joints and extending due to longitudinal shear failure up to the beam supports (Figure 9).

The most unfavorable relative deflection obtained for service load of all samples tested was L/1069 for a total service load of 5.00 kN/m^2 and L/573 for a load of 9 kN/m^2 (been L the span of the beam), that would correspond to a building for public use. Therefore, the results indicate a high bending stiffness of the pieces and the effectiveness of the composite action despite the high slenderness of the pieces (L/24) and the unfavorable configuration that represents, from the point of view of the deformations, the simply supported beams condition [10].

Figure 9: *Longitudinal failure of the glulam flange*

3.5 FULL SCALE THREE-POINT BENDING TESTS OF TCC PIECES IN A AN OVERHANGING CONFIGURATION

One of the outstanding advantages of the developed system is that it allows the construction of floors and beams with pieces serving several spans or in an overhanging configuration. This results in a more efficient use of materials thanks to a more favorable distribution of bending moments and better behaviour in service at the deformation level. Three–point bending tests were carried out of eight specimens to evaluate the behavior against negative bending. 3 with a height of 250 mm an a overhanging span of 1.5 m; 3 with a height of 300 mm an a overhanging span of 1.8 m and 2 with a height of 350 mm an a overhanging span of 2.1 m. A slenderness ratio of L/6 was adopted in all cases.

Figure 10: *Specimen with the steel mesh and the rebars positioned in the area of negative bending moments.*

The specimens tested have the same section and material characteristics as those already described for the four-point bending tests, with the only difference being that

https://doi.org/10.52202/069179-0430

there is a reinforcement in the area of negative bending moments made up of two 12 mm diameter rebars (Figure 10).

Figure 11: *Test of 1.80 m overhanging span specimen*

Figure 12: *Cracking process in the concrete upper slab*

Two types of failure modes have been observed in the tests: tensile failure of plywood rib in three of the specimens and shear failure at the glulam joint between flange and plywood rib in the remaining five pieces. In all cases, when load is approaching to the ultimate load value, an important cracking process of concrete slab occurs (Figure 11).

The lowest value of ultimate load obtained for all specimens tested was 8.03 times the design load considered for residential buildings (5.0 kN/m^2). Attending to service state limitations, a relative deflection of 1/358 of overhanging span was obtained for a design load of 5.0 kN/m^2.

Both results obtained, ultimate load and relative deflection, indicates a very favourable behaviour of the structural system proposed.

4 SYSTEM PERFORMANCE

With the aim to know the performance of the floor system preliminary sizing curves were developed using the Gamma Method, usually recommended for the analysis of TCC structures [11]. These curves are no final sizing solutions but simply establish the appropriate range of use of the floor system developed and its possibilities [8].

Gamma Method is highly accurate for simply supported beams but its error increases significantly in pinned-clamped beams and clamped-clamped beams as Girhammar pointed in [12]. However, the error can be significantly reduced by applying the Gamma Method but using effective beam length la distance between points of zero moment.

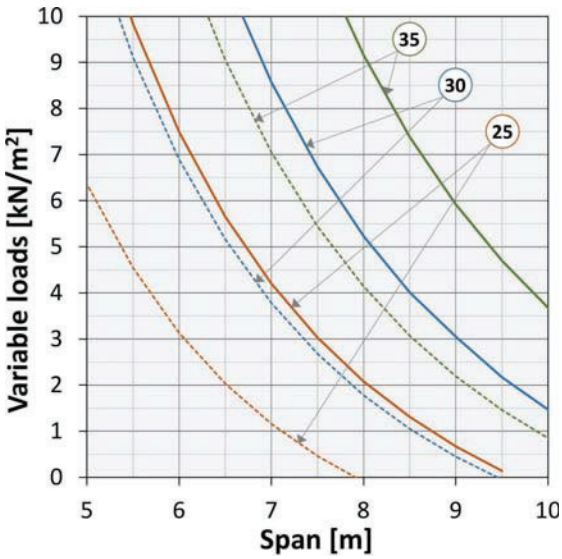

Figure 13: *Floor sizing curves.*
Symply supported pieces. Permanent load 2.5 kN/m^2.
Deformation: L/300-continuous line; L/500-dashed line

Figure 13 shows the most unfavorable case at the dimensioning level of the floor, since it corresponds to simply supported pieces. Creep deformation was considered with the total permanent load and a 30% of the variable load. The results indicate that for residential use and a deflection limit of L/500, a floor with a slenderness of L/24 has adequate sizing for a permanent service load of 2.5 kN/m^2 and an additional variable load slightly

https://doi.org/10.52202/069179-0430

higher than 3.0 kN/m^2. This range of slenderness increases to L/30 and L/35 for extreme and internal spans, respectively.

These results indicate the efficient use of mechanical qualities of the materials of the system thanks to the high composite action and, consequently, its suitability for the execution of building structures.

5 CONCLUSIONS

Timber-concrete-composite system developed show very interesting properties for the construction of building structures: low self-weight of 1.80 kN/m^2, high stiffness, slender flooring solutions, semi-rigid connections between elements and an easy construction process.

The system is based on an efficient timber-concrete connection characterized by the use of boards perforated in their entire length crossed by the in-situ poured concrete. Shear test results show a very favourable combination of high stiffness and efficient composite action with a ductile failure, desirable characteristic in TCC solutions.

Full-scale four and three-point bending test results indicate a very strength and stiff behaviour of the system proposed.

ACKNOWLEDGEMENT

This study is part of the research project ''High-performance timber-concrete-composite hollow-core floors for sustainable and eco-efficient construction (AlveoTCC)", ref. PID2019-107859RB-100. The study developed was funded by MCIN/ AEI /10.13039/501100011033.

REFERENCES

[1] M. Knauf, Market potentials for timber-concrete composites in Germany's building construction sector, *European Journal of Wood and Wood Products* 75 (2017) 639-649. https://doi.org/10.1007/s00107-016-1136-9.

[2] A. Dias, J. Skinner, K. Crews, T. Tannert, Timber-concrete-composites increasing the use of timber in construction, *European Journal of Wood and Wood Products* 74 (2016) 443-451. https://doi.org/10.1007/s00107-016-1136-9.

[3] D. Yeoh, M. Fragiacomo, M. De Franceschi, K. Heng Boon, State of the Art on Timber-Concrete Composite Structures: Literature Review, *Journal of Structural Engineering* 137 (2011) 1085-1095. https://doi.org/10.1061/(ASCE)ST.1943-541X.0000353.

[4] [9] S. Di Nino, A. Gregori, M. Fragiacomo, Experimental and numerical investigations on timber-concrete connections with inclined screws, *Engineering Structures* 209 (2020), 109993. https://doi.org/10.1016/j.engstruct.2019.109993.

[5] [21] M. Fragiacomo, C. Amadio, L. MacOrini, Short- and long-term performance of the ''Tecnaria'' stud connector for timber-concrete composite beams, *Materials and Structures* 40 (2007) 1013-1026. https://doi.org/10.1617/s11527-006-9200-2.

[6] [22] B. Shan, Y. Xiao, W.L. Zhang, B. Liu, Mechanical behavior of connections for glubam-concrete composite beams. *Construction and Building Materials* 143 (2017) 158–168. https://doi.org/10.1016/j.conbuildmat.2017.03.136.

[7] J. Kanócz, V. Bajzecerová, Š. Šteller, Timber–Concrete composite elements with various composite connections Part 2: Grooved connection. *Wood Research* 59 (2014) 627-638.

[8] J. Estévez-Cimadevila, E. Martín-Gutiérrez, F. Suárez-Riestra, D. Otero-Chans, J.A., Vázquez-Rodríguez. Timber-concrete composite structural flooring system. *Journal of Building Engineering* 49 (2022) 104078. https://doi.org/10.1016/j.jobe.2022.104078.

[9] D. Otero-Chans, J. Estévez-Cimadevila, F. Suárez-Riestra, E. Martín-Gutiérrez. Perforated board shear connector for timber-concrete composites. *Wood Material Science & Engineering* (2022). https://doi.org/10.1080/17480272.2022.2089594.

[10] E. Martín-Gutiérrez, J. Estévez-Cimadevila, F. Suárez-Riestra, D. Otero-Chans. Flexural behavior of a new timber-concrete composite structural flooring system. Full scale testing. *Journal of Building Engineering* 64 (2023) 105606. https://doi.org/10.1016/j.jobe.2022.105606.

[11] A. Dias, J. Schänzlin, P. Dietsch (eds.), Design of timber-concrete composite structures: *A state-of-the-art report by COST Action FP1402* / WG 4, Shaker Verlag Aachen, 2018.

[12] U.A. Grihammar, A simplified analysis method for composite beams with interlayer slip, International Journal of Mechanical Science 51 (2009) 515–530. https://doi.org/10.1016/j.ijmecsci.2009.05.003

World Conference on Timber Engineering Oslo 2023

STUDY ON FAILURE MECHANISMS OF HYBRID STRUCTURE OF REINFORCED CONCRETE FRAME WITH CLT INFILL

Hamood Alwashali[1], Ahmad Ghazi Aljuhmani[2]

ABSTRACT: The objective of this study is to clarify the possible failure mechanisms and strength of RC frames with CLT infill, and to investigate the CLT panel compression strut width. Five failure mechanisms and a simplified strength evaluation method were proposed based on a literature review of the RC frames with different material infills. Experimental tests of diagonal compression of CLT panels were conducted and results were used in finite element analysis to evaluate the change of failure mechanisms based on strut width and relative stiffness for the RC frame and CLT.

KEYWORDS: Hybrid structures, Reinforced concrete buildings, CLT infill panels, Seismic capacity

1 INTRODUCTION

Hybrid reinforced concrete (RC) and timber structures are getting much attention, and their numbers are increasing rapidly as an eco-friendly solution to contribute towards the sustainable societies prescribed in the UN's Sustainable Development Goals (SDGs). Cross-laminated timber (CLT) has relatively high shear strength, is lightweight, and has low carbon emissions. Using CLT panels as shear walls in RC or steel structures can increase the seismic capacity of the building with also securing lower seismic demand due to CLT's low mass. In addition, CLT walls have relatively greater deformation capacity than RC shear walls, resulting in improving not only the lateral strength of the structure but also its ductility. However, the insertion of CLT panels in the RC frames could also lead to unwanted failure mechanisms (e.g., brittle failure). Therefore, it is essential to understand and investigate the possible failure mechanisms and seismic behaviour of these structures.

Recently in Japan, RC frames or steel frames with CLT infill buildings were constructed, as shown in Figure 1. Worldwide, several researchers have started investigating the effect of CLT infill on RC or steel frames. A parametric study on different types of steel frames with CLT infill using static pushover analysis was carried out by Dickof et al. [1] to clarify the ductility and overstrength values. It was found that CLT infill is effective in the case of lower ductility frames, whereas it does not have much influence in the case of ductile frames. [1] focused only on the influence of CLT infill on the ductility factor and the increase of strength for the RC frame. However, the possible failure mechanism, as well as an evaluation method, were not considered in [1]. Another numerical simulation has been carried out by Stazi et al. [2] to understand the effect of CLT infill on RC frames. This study also focused only on the overall influence of the CLT panel on the increase of the strength and stiffness of the RC frame. Several experiments on five 1/3 scale RC frames with different CLT infill types were conducted by Haba et al. [3]. In [3], even though several specimens with the same RC frame and different CLT panels' specifications were tested, only one failure was observed, which is a shear failure in the RC columns. As for Steel structures with CLT infill, there have been few recently constructed buildings in Japan [4] and several experiments tested by Fukumoto et al. [5]. However, there is a lack of research on RC buildings with CLT shear walls, and in the previous studies[1-3], researchers have only investigated the increase in strength and ductility of the frame due to the insertion of the CLT panel. In addition, research on the different possible failure mechanisms of such structures is still lacking, and evaluation guidelines and standards for engineering practice are still unavailable.

Therefore, the objectives of this study are: first, clarify the possible in-plane failure mechanisms of RC frames with CLT panels infill. Finally, Investigate the effect of different parameters (e.g., compression strut width and CLT-to-RC connections) on the expected failures.

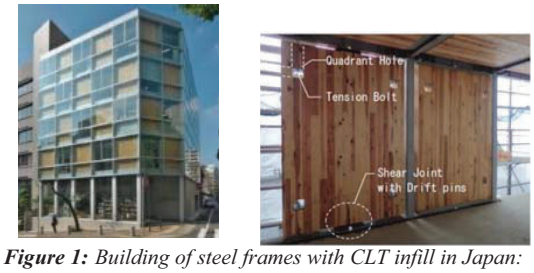

Figure 1: *Building of steel frames with CLT infill in Japan: Hyogo Forestry Hall [4](left figure). Details of CLT panel with steel frame (right figure) [5]*

[1] Hamood Alwashali, Okayama University, Japan, hamood@okayama-u.ac.jp
[2] Ahmed Ghazi Aljuhmani, Tohoku University, Japan, aljehmani@rcl.archi.tohoku.ac.jp

https://doi.org/10.52202/069179-0431

2 EXPECTED FAILURE MECHANISMS

Although CLT Infill in RC frames is a new concept, infill walls or post-installed walls are common practices, such as masonry infill walls and steel braces. The main difference is that the material properties of the CLT panel are different, which may completely alter the RC frame performance compared to other conventional methods, and this has not been investigated in past studies. Possible failure mechanisms and evaluation methods of lateral strength capacity were investigated. In this section, the possible failure mechanisms of RC frames with CLT infill systems are investigated based on previous research or based on comparisons with other infill materials.

2.1 COLUMN SHEAR FAILURE

This failure was observed in experiments by Haba et al. [1] and is shown in Figure 2 and illustrated in Figure 3. 1/3 scale specimen with CLT panels along the entire width of the frame (1540 mm) was tested. The height of the CLT infill was 840 mm, and it was fixed with the RC frame using epoxy resin. Two panels of Japanese Cedar CLT (Mx60b-3-3 grade) were used with 60 mm thickness (30 mm for each panel). In this case, the RC columns are shear-critical columns (the shear capacity for the RC columns is less than the flexural capacity). Thus, the frame does not have enough deformation capacity for the CLT infill to fail first, and the dominant failure will be column shear failure.

In this case, A simple estimation of the maximum strength capacity is proposed to be calculated by adding three components: the strength of the two RC columns and the strength of connections at the top of the CLT panel, and is shown in Equation (1), with reference to Figure 3.

$$Q_{sh} = 2 \times Q_{su} + Q_{joint} \quad (1)$$

Where Q_{su} is the column shear strength calculated as prescribed in the Japanese AIJ code [6], or it can be calculated using any other adequate standards or method. The Q_{joint} is the strength of the CLT to RC joint on top, in the test by [1], it was estimated using the strength of the epoxy material injected between the RC frame and CLT infill. If there are no connections between the CLT panel and the RC frame, then Q_{joint} can be ignored.

Figure 2: *Column shear failure as observed in [3]*

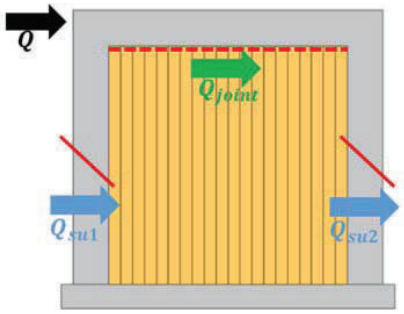

Figure 3: *Column shear failure for RC frame with CLT*

2.2 PUNCHING SHEAR FAILURE

Having relatively strong and very stiff walls within an RC frame could cause a punching shear failure, which is observed in RC frames with strong steel braces as in Ishimura et al. [7], as shown in Figure 4 and in Figure 5 in Japanese seismic evaluation standard JBDPA [8]. Punching shear failure of RC frame is also observed with other types of infill walls such as masonry infill that were retrofitted by ferrocement, mentioned by Sen et al. [9]. This failure could happen in the case of a very strong CLT infill relative to the surrounding RC frame.

In this case, maximum strength capacity can be estimated by adding three components. The first component is the RC column (windward) which has punching shear failure. The second component is the connections at the top of the CLT panel and RC beam. The third component is the leeward RC column, which could fail in either shear or flexural, and can be calculated by Equation (2), with reference to Figure 6.

$$Q_{pun} = PQ_{c1} + Q_{joint} + min(Q_{su}, Q_{mu}) \quad (2)$$

Where PQ_{c1} is the punching shear capacity of the first column as prescribed in JBDPA [8], Q_{su} is column shear strength, and Q_{mu} is column flexural strength.

Figure 4: *Punching shear failure as observed in [7]*

https://doi.org/10.52202/069179-0431

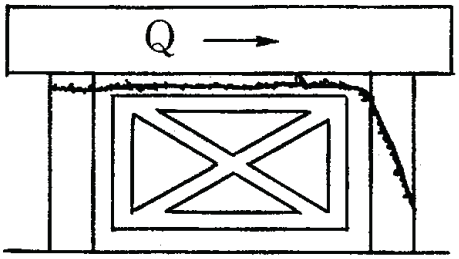

Figure 5: *Punching shear failure illustrated in JBDPA [8]*

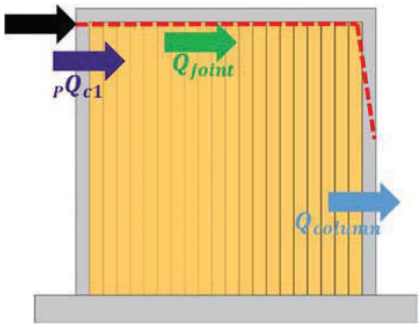

Figure 6: *Punching shear failure for RC frame with CLT*

2.3 FRAME OVERALL FLEXURAL FAILURE

Figure 7 shows the overall flexural failure that could occur when the CLT infill is stiff relative to the RC frame and the CLT panel is strongly connected to the RC frame.

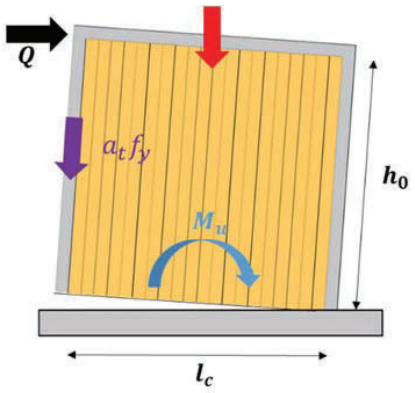

Figure 7: *overall flexural failure of the composite structure*

In this case, the RC frame and CLT panel will act as a single component similar to a cantilever flexural wall. There are no experimental tests of RC frames with CLT infill having an overall flexural failure. However, similar behaviour is observed with other infilled walls, such as tests by Laughery et al. [10] on RC frames with post-installed RC walls shown in Figure 8. It can occur as well with masonry infills such as tests by Sen et al. [9]. In this failure, maximum strength capacity can be estimated by the overall flexural capacity (Q_{fl}) as a cantilever flexural wall as shown in Figure 8. The maximum strength could be calculated using Eq. 3 and Eq. 4 which are adopted from JBDPA [8] with reference to Fig.7.

$$Q_{fl} = M_u / h_0 \quad (3)$$

$$M_u = a_t f_y l_c + 0.5 N l_c \quad (4)$$

Where M_u is moment capacity, h_0 is the clear height of the column, a_t is longitudinal reinforcement area for one column, f_y is the yield strength of the column's longitudinal reinforcement, l_c is the distance between the centers of the boundary columns, and N is the total axial load applied on the entire frame. It should be noted here that the maximum strength is calculated entirely based on the RC frame strength. There is no contribution for the CLT panel by assuming there are no tension connections between the CLT panel and the RC frame at the bottom. If connections are added at the bottom of the CLT panel, then the tensile of the CLT panel could also contribute to the flexural capacity and need to be added to Eq. 4.

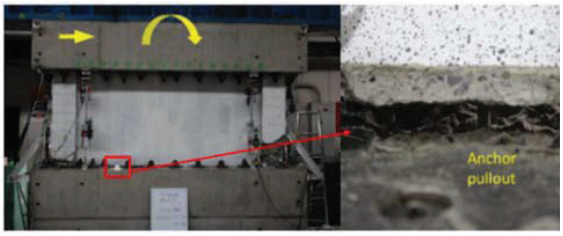

Figure 8: *Overall flexural failure as observed in [10]*

2.4 CLT PANEL SHEAR FAILURE

No experimental studies are showing the shear failure of CLT walls in RC frames. However, other infill materials such as masonry infill walls in RC frames had a shear failure, such as those shown in Figure 9. For CLT infill, it could occur in a ductile RC frame with relatively lower stiffness for CLT. In this case, the columns are flexural columns (the flexural capacity of the column is less than the shear capacity of the column). Thus, the frame has enough deformation capacity for the CLT infill to deform, and the dominant failure will be CLT failure. Capacity can be calculated by adding the flexural strength of the two columns to the shear strength of the CLT panel itself, as shown in Equation (6) and Equation (7) with reference to Figure 10. It should be noted here that Q_{mu} needs to be calculated assuming the clear height h_0 to be around half of the column clear height.

$$Q_{CLT-s} = Q_{mu1} + Q_{mu2} + S_{CLT} \quad (6)$$

$$S_{CLT} = \tau_{CLT} \times L_{CLT} \times t_{CLT} \quad (7)$$

Where Q_{mu1} and Q_{mu2} are windward and leeward column capacity, S_{CLT} is CLT panel shear capacity, and τ_{CLT}, L_{CLT}, and t_{CLT} are CLT panel shear strength, length, and thickness, respectively.

https://doi.org/10.52202/069179-0431

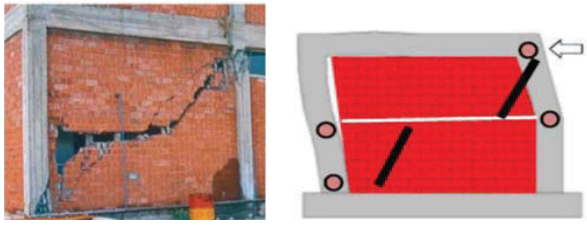

Figure 9: *Masonry shear failure in 1999 Turkey EQ (left figure) [11], and as observed in Sen et al. [9] (right figure)*

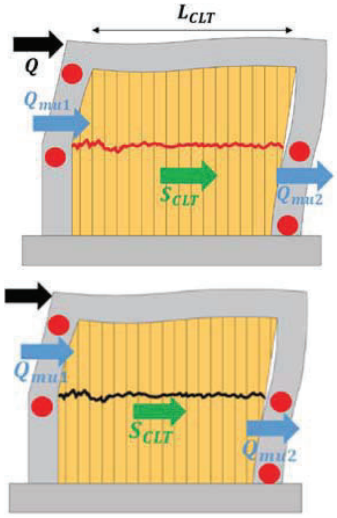

Figure 10: *CLT shear failure for RC with CLT infill*

2.5 CLT PANEL COMPRESSION FAILURE

There are no experimental studies yet showing the failure of CLT diagonal compression failure in RC frames but there are recent tests of steel frames with CLT infill such as experimental tests by Fukumoto et al. [5] and shown in Figure 11. However, Fukumoto`s tests are of steel frames without any boundary columns attached to CLT infill as shown in Figure 11, which is different from the concept investigated here of RC frames confining the CLT infill. In addition, other infill materials in RC frames, such as masonry walls, had a shear failure considering diagonal compression failure, which was observed in the experiment done by Alwashali et al. [12] on masonry infill, as shown in Figure 12. It is thought that CLT infill could also have a similar failure mechanism.

This failure is similar to the CLT panel shear failure; however, in this case, CLT compression capacity (C_{CLT}) is less than CLT shear capacity (S_{CLT}).

This failure capacity can be calculated by Equation (8) and Equation (9) with reference to Figure 13.

$$Q_{CLT-c} = Q_{mu1} + Q_{mu2} + C_{CLT} \quad (8)$$

$$C_{CLT} = \sigma_{CLT} \times W_{strut} \times t_{CLT} \times \cos\theta \quad (9)$$

Where C_{CLT} is CLT panel shear capacity, σ_{CLT} is CLT panel compressive strength, W_s is compression strut width with, θ is the angle between the RC base and the strut with reference to Figure 13. The estimation of the strut width (W_s) is a complex topic that has not been studied previously for CLT infills. The following section will investigate the strut width based on simple diagonal compression tests and finite element analysis.

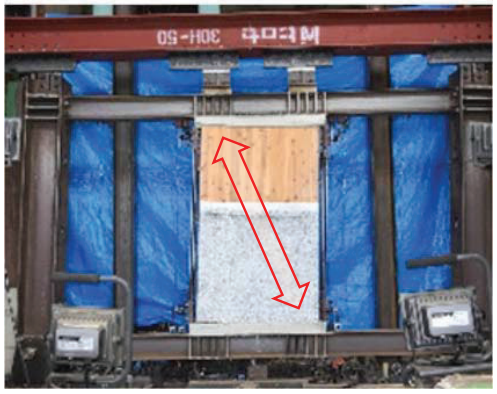

Figure 11: *Experiments of Steel frame with CLT infill tested by Fukumoto et al. [5]*

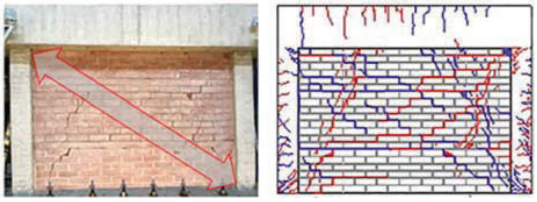

Figure 12: *Compression strut failure of RC frame with masonry infill [12]*

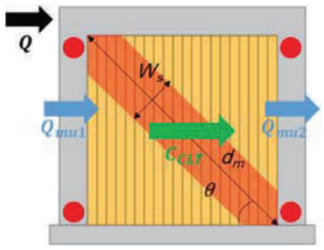

Figure 13: *overall flexural failure of the composite structure*

3 COMPRESSION STRUT MECHANISM

The capacity evaluation for all the failure mechanisms mentioned above, except CLT compression strut failure, is relatively well understood and thought that could be directly applied. However, the failure of the compression strut of CLT infill as well as its width is still poorly understood. Thus, in this section, we investigated the strut width based on conducting diagonal compression tests on CLT walls and then model the CLT infill using finite element analysis to investigate the strut width.

https://doi.org/10.52202/069179-0431

3.1 DIAGONAL COMPRESSION STRUT

In the case of CLT infill, no calculation approaches nor empirical equations were proposed for strut width. One simple approach is to assume the methods used for masonry infill might also be applicable to CLT infill. In this study, the two methods by FEMA-306 [13] and Sen et al. [9] only are compared. The values of strut width to the diagonal length that are calculated by the two methods for different flexural relative stiffness (frame flexural stiffness divided by CLT panel flexural stiffness) are shown in Figure 13. The calculations of strut width by [9] and [13] showed large variations, as can be seen in Figure 14. This could lead to uncertainty in estimating strength by the failure mechanism of the strut.

In order to adequately estimate the strut width of CLT infill in the RC frame, simple diagonal tests were conducted, and then finite element models were developed and validated by the diagonal test. The FE analysis is then used to simulate the CLT infill in the RC frame to estimate the compression strut width.

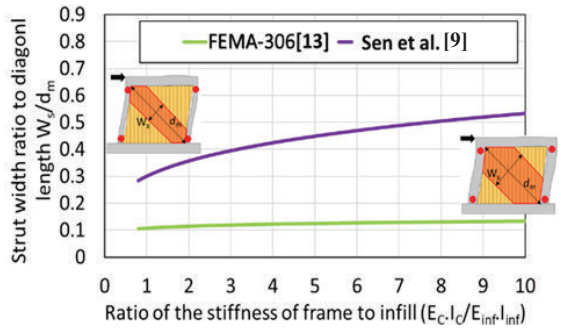

Figure 14: *Strut width relation with relative flexural stiffness of RC frame to CLT infill*

3.2 DIAGONAL COMPRESSION EXPRIMENT

The interaction between the CLT infill panel and the RC frame under lateral forces is shown in Figure 15. The transmitted forces to the CLT panel at the corner of the actual RC frame could be reproduced using a diagonal compression test configuration, as shown in Figure 15. Therefore, this test-set up was used to obtain the characteristics of CLT panels under compression forces.

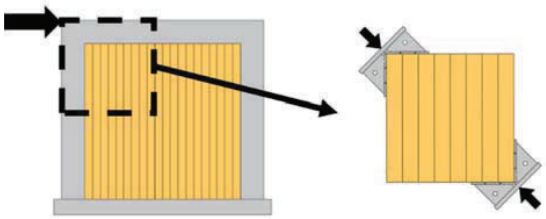

Figure 15: *Behaviour of CLT panel under lateral load*

A hydraulic Jack was used to apply a monotonic vertical downwards force on a 1200 mm by 1200 mm CLT panel (loading rate in the range of 0.15~0.2 mm/s). Three replicates were tested, and all the panels were 5-layer 150 mm thick panels made from Japanese cedar with Mx-60-5-5 grade. Each panel was installed vertically between two steel 'shoe' caps as shown in Figure 16 and Figure 17, which were designed to distribute the load such that local bearing failure of the CLT panel does not occur.

LVDTs were attached along the two diagonals of the CLT panel to calculate shear deformation. Shear deformation was calculated using Equation (10) with reference to Figure 18.

$$\gamma = \frac{\Delta x + \Delta y}{900 \times \sqrt{2}} \qquad (10)$$
$$\delta = \gamma \times 1200$$

Where Δx and Δy are the values obtained from the horizontal and the vertical overall LVDTs, respectively.

In addition, digital image correlation (DIC) was also used in the tests and the properties and details of the DIC setup are shown in Figure 19, and data were analyzed using the DIC Software OPTECAL [14].

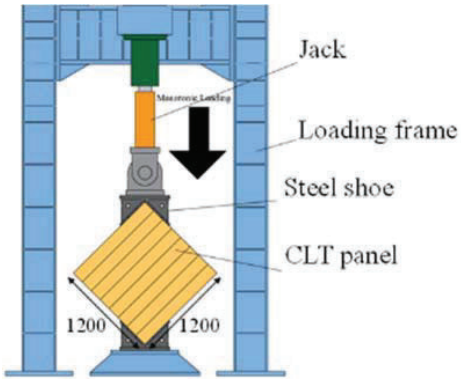

Figure 16: *Loading set-up of the compression test*

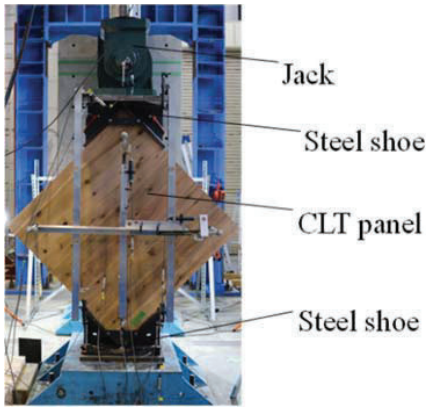

Figure 17: *photo of Loading set-up of the test*

https://doi.org/10.52202/069179-0431

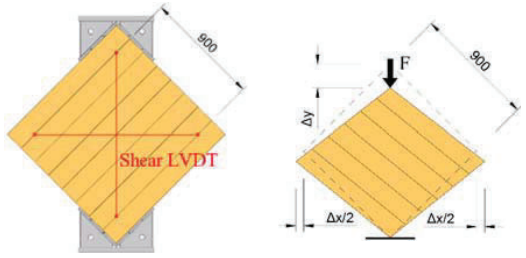

Figure 18: *LVDTs set-up and shear deformation*

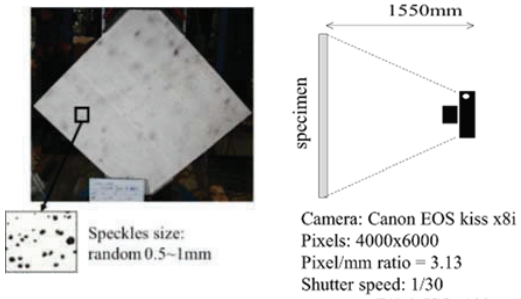

a) The painted side of the specimen for DIC

b) Location of the camera

Figure 19: *The details of the DIC set-up*

3.3 SIMULATION USING FEM MODEL

A numerical model was created using the FEM software Abaqus [15]. The CLT panel was modelled as a solid element. The model consists of five layers, and the interaction between each CLT layer was assumed to be a tie constraint with no slip. Each layer was modelled as an elastic orthotropic material with three directions (L, R, T): longitudinal (in the direction of the grain), radial, and tangential as shown in Figure 20. Each CLT layer has an axis orientation perpendicular to the adjacent layers. The mechanical properties of each layer are shown in Table 1, which was taken from the Japanese Wood Handbook [16].

Table 1: *Japanese Cedar material properties [16]*

Species	Young modulus (MPa)			Shear modulus (MPa)			Poisson ratio		
	E_L	E_R	E_T	G_{LT}	G_{LR}	G_{RT}	ν_{LT}	ν_{LR}	ν_{RT}
Japanese cedar	8700	620	260	460	650	15	0.58	0.405	0.901

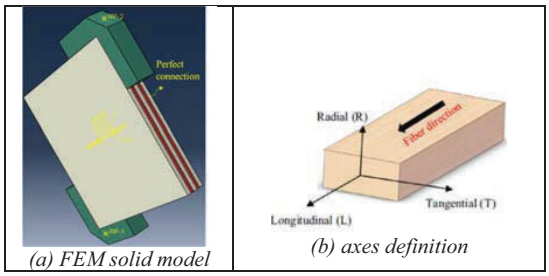

(a) FEM solid model

(b) axes definition

Figure 20: *CLT panel FEM model properties*

A comparison between shear displacement-shear force curves for the FE model and experiment is shown in Figure 21. The stiffness obtained from the FE model (100.4 kN/mm) was relatively close values to the average value from the experiment (106.3 kN/mm).

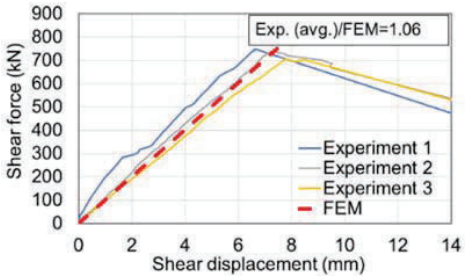

Figure 21: *Comparison between FEM and experiments*

A comparison between the strain obtained from the experiment by DIC and FEM results is shown in Figure 22. In this case, horizontal (ε_x) and vertical (ε_y) axial strain distribution were compared at the point just before maximum load P_{max}. Overall, the strain distribution is similar in both FEM and DIC, showing that the response is governed by one main compressive strut, indicating that FEM can capture the general stress paths and give close strain values.

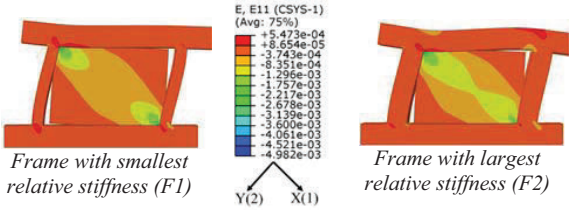

Frame with smallest relative stiffness (F1)

Frame with largest relative stiffness (F2)

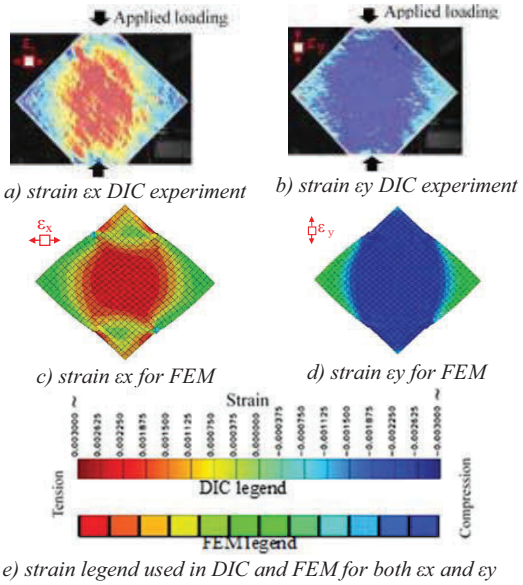

a) strain εx DIC experiment

b) strain εy DIC experiment

c) strain εx for FEM

d) strain εy for FEM

e) strain legend used in DIC and FEM for both εx and εy

Figure 22: *Comparison between FEM and DIC*

3.4 FEM MODEL FOR RC FRAME WITH CLT INFILL

FEM software Abaqus [15] was used to model the RC frame with CLT infill. Only concrete was modeled with elastic solid elements for simplicity, since the main focus is the strut width in the CLT infill. Young's modulus and Poisson's ratio for RC were taken as 23000 MPa and 0.2, respectively. The CLT model was the same as the model used in the diagonal compression model (section 3.3). The frame was fixed in all directions at the bottom and free at the top. The interaction between the CLT panel and the RC frame was assumed as hard contact with no penetration between the CLT and RC elements with no friction interaction. A total of 10 frames was modelled, and the difference between each model is the relative flexural stiffness between the RC columns and the CLT infill (infill thickness was fixed, and the RC columns' dimensions were increased).

Regarding stiffness increase due to the CLT infill, the initial stiffness of bare frame F1 (the frame with the smallest relative stiffness) was 17.5 kN/mm, and stiffness increased to 75.4 kN/mm after adding the CLT infill with an increase of about 4.3 times. The initial stiffness of bare frame F2 (the frame with the largest relative stiffness) was 121.9 kN/mm, and stiffness increased to 185.9 kN/mm after adding the CLT infill with an increase of about 1.5 times. The results of strain in the diagonal strut direction for the F1 frame and F2 frame are shown in Figure 23. Although the strain values differ slightly between these two frames, the strut width almost does not vary much. In order to compare quantitative values of the strut width, a method proposed by Jin et al. [17] was used. In this FEM analysis, a total of 12 sections were taken, and, for each section, the average strain was calculated by taking the equivalent strain area for the actual strain curve as shown in Figure 24.

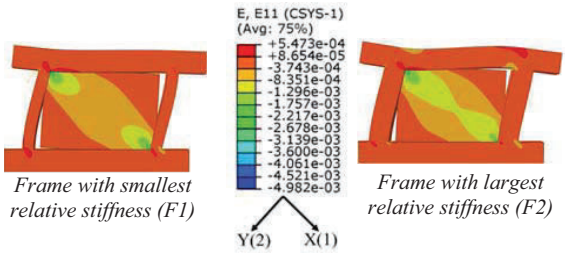

Figure 23: *Normal strain in X-direction (strut direction)*

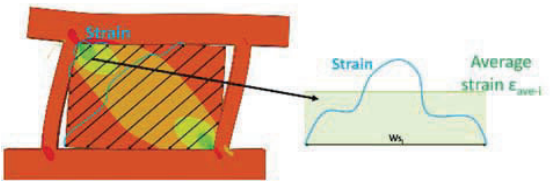

Figure 24: *Strut sections and average strain calculations*

The strut width obtained from the FEM analysis for different relative RC to CLT stiffness is shown in Figure 25. In Figure 25, The strut width ranges between $0.34d_m$ and $0.36d_m$ with different relative RC to CLT stiffness. When also compared to the two masonry infill methods [9,13], it was found that FEM analysis has a similar tendency with FEMA-306 [13] for masonry infill; however, FEM analysis gave larger strut width values.

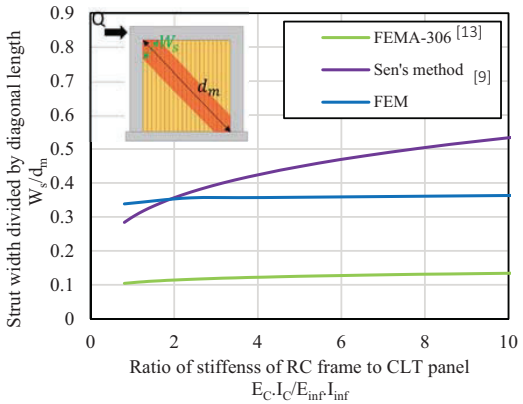

Figure 25: *Comparison of strut width obtained by FEM modelling CLT versus other methods*

3.5 EXAMPLE OF STRENGTH EVALUATION

In this study, the lateral strength of the RC frame with CLT infilled (Q_{cal}) is proposed to be calculated by taking the minimum of the calculated lateral capacity based on the five different failure mechanisms discussed previously in section 2, as shown in Equation (11).

$$Q_{cal} = min\left(Q_{sh}, Q_{pun}, Q_{fl}, Q_{CLT-c}, Q_{CLT-s}\right) \qquad (11)$$

A case study of the RC frame tested by Alwashali et al. [12] with masonry infill (specimen F-1.5) will be presented to understand the failure mechanisms well. This RC frame will be used here, assuming CLT infill as shown in Figure 26. The thickness of the CLT panel is assumed to be 60 mm, and shear and compression strength for CLT are assumed to be 4.1 MPa and 174 MPa, respectively. These values are based on the material tests conducted based on the diagonal compression test presented in section 3.2.

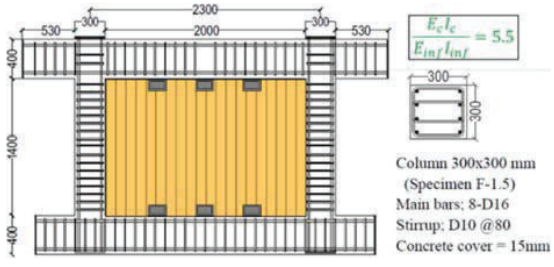

Figure 26: *A case study on RC frame for capacity evaluation (from Alwashali et al. [12])*

https://doi.org/10.52202/069179-0431

A comparison between several methods for only the compression failure strength of the case study frame is shown in Figure 27. It should be noted that deformation capacity evaluation is out of the scope of this paper and thus the story drift axis in Figure 27 and Figure 28 is used for illustration only. As shown in Figure 27, there is a large variation between the estimation of maximum strength for the diagonal compression failure considering previous studies for different materials. The FE analysis investigated in this study gives around 2 times (1037kN) the value estimated using the FEMA 306 method (548kN). This uncertainty and the lack of CLT strut width experiments will lead to significant variations in the expected strength capacity and failure mechanisms.

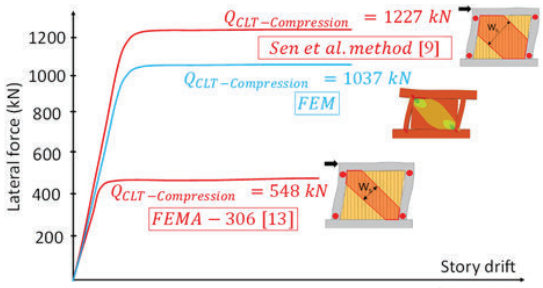

Figure 27: *Failure strength for the case study frame*

The expected lateral strength capacity of the case study frame for all the five expected failure mechanisms is as shown in Figure 28.

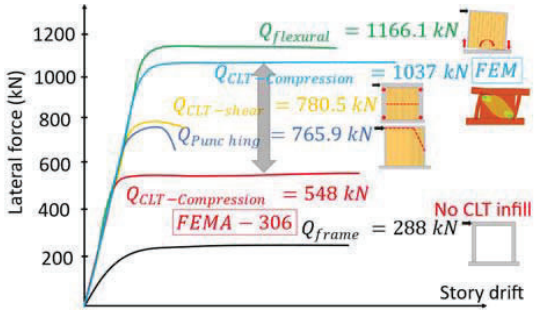

Figure 28: *Calculated capacity of the case study frame*

Three shear connections were assumed at the top and at the bottom of the CLT infill to make the example shown here more practical. This number was also assumed to avoid punching shear failure. Each shear connection has a shear strength of 80 kN (total of 240 kN as Q_{joint} in Eq(2). For CLT compression strut failure, the FEMA 306 [13] (for masonry) and FE analysis results (presented in this study) were used to calculate the strut width. As shown in Figure 28, compression failure gives the minimum strength value and is expected in a case assuming the strut width of masonry as in FEMA-306 [13]. However, in the case of strut width obtained from the FE analysis, the capacity of compression failure increased, and thus punching shear failure becomes the most probable failure type. The influence of the strut width is crucial in seismic design since it affects not only the maximum capacity but also the expected seismic behaviour, which could change the behaviour from desirable ductile failure to undesirable brittle punching shear failure. Experimental verification and investigation to understand the behaviour of CLT infills are still needed.

4 CONCLUSIONS

This study presented different expected failure modes for hybrid structures of Reinforced concrete (RC) frames with CLT infill based on previous studies and observations for RC frames with other infills. Also, a FEM model was developed and verified by component compression test to study the effect of CLT compression strut width on the expected failure. The main conclusions are as follows:

1. Five different possible failure modes for RC frames with CLT infill were studied based on the literature review for RC frames with other material infills.
2. The seismic capacity and in-plane failure mechanism of RC frames with CLT infill could be predicted based on the evaluation method presented in this paper.
3. Compression strut width methods for RC frames with masonry infill have big variations when used with CLT.
4. FEM analysis showed that the compression strut width does not change much by changing the relative stiffness of the RC frame and the CLT infill (the margin was between 0.34 and 0.36 of the strut length).
5. CLT compression strut width and CLT-to-RC shear connections could significantly affect the probable failure mechanisms, changing it from ductile to brittle failure. Therefore, further experimental investigations are needed to predict the probable failure mechanism.

ACKNOWLEDGEMENT

The study was partly supported by the agency of Japan Society for the Promotion of Science (JSPS) and project KAKENHI Grant Number 21K14283 (Principal investigator: Hamood Alwashali, Okayama University).

REFERENCES

[1] Dickof, C., Stiemer, S.F., Bezabeh, M.A. and Tesfamariam, S., 2014. CLT–steel hybrid system: Ductility and overstrength values based on static pushover analysis. Journal of Performance of Constructed Facilities, 28(6), p.A4014012.

[2] Stazi, F., Serpilli, M., Maracchini, G. and Pavone, A., 2019. An experimental and numerical study on CLT panels used as infill shear walls for RC buildings retrofit. Construction and building materials, 211, pp.605-616.

[3] Haba, R., Kitamori, A., Mori, T., and Fukuhara, T., 2016. Development of clt panels bond-in method for seismic retrofitting of RC frame structure. J. Struct. Constr. Eng, 81, pp.1299-1308.
[4] Xtech 2019, accessed 30 December 2021, <https://xtech.nikkei.com/atcl/nxt/mag/na/18/00076/100200003/>.
[5] Fukumoto K., Kouda M., Kubo K., Usami T., Kitamori A., Miyauchi Y., and Isoda H., 2021 Experimental study on CLT seismic panel infilled within steel frame. J. Struct. Constr. Eng., AIJ, Vol. 86, No.787, 1345-1356, Sep., 2021
[6] AIJ, 2016. AIJ Standard for Lateral Load‑Carrying Capacity Calculation of Reinforced Concrete Structures.
[7] Ishimura, M., Sadasue, K., Miyauchi, Y., and Yokoyama, T., 2012, September. Seismic performance evaluation for retrofitting steel brace of existing RC building with low-strength concrete. In Proc. of the 15th World Conf. on Earthquake Engineering, 15th WCEE (pp. 24-28).
[8] JBDPA/The Japan Building Disaster Prevention Association, 2001. Standard for seismic evaluation of existing reinforced concrete buildings.
[9] Sen, D., Alwashali, H., Tafheem, Z., Islam, M. S., and Maeda, M., 2020, September. Experimental investigation and capacity evaluation of Ferro-cement laminated masonry infilled RC frame. In Proc. of the 17th WCEE.
[10] Laughery, L., Ichinose, T., Maeda, M., Alwashali, H., Takahashi, H., Hanzawa, M., Okada, T., Ide, A. And Sonn, K., A Potential Vulnerability In High-Strength Reinforced Concrete Shear Wall Retrofits.
[11] Bachmann, H. and Suisse. Office fédéral de l'environnement, 2003. Seismic conceptual design of buildings: basic principles for engineers, architects, building owners, and authorities. SDC.
[12] Alwashali, H., and Sen, D., 2019. Experimental investigation of influences of several parameters on seismic capacity of masonry infilled reinforced concrete frame. Engineering Structures, 189.
[13] Federal Emergency Management Agency, 2013. Evaluation of earthquake damaged concrete and masonry wall buildings. FEMA.
[14] Optical: Digital Image Correlation software 2020.
[15] Dassault Systemes Simulia Corp., Abaqus software.
[16] Basic theory of wood structure: Architectural Institute of Japan: Wood Industry Handbook.
[17] Jin, K., Choi, H. and Nakano, Y., 2016. Experimental study on lateral strength evaluation of unreinforced masonry-infilled RC frame. Earthquake Spectra, 32(3), pp.1725-1747.

https://doi.org/10.52202/069179-0431

World Conference on Timber Engineering Oslo 2023

PRELIMINARY STUDY ON THE TENSION-ONLY BRACED SELF-CENTERING STEEL-TIMBER HYBRID FRAME

Fei Chen[1], Minghao Li[2], Minjuan He[3], Zheng Li[4]

ABSTRACT: A lateral load resisting system called tension-only braced self-centering steel-timber hybrid frame (TOB-SCSTHF) is proposed. The system utilizes the self-centering steel-timber hybrid joints to provide the self-centering action to the frame. Tension-only braces (TOBs) are used to increase the lateral strength and stiffness of the system. Experimental results on the hybrid joints were taken as the basis to develop the numerical model of the beam-column joints. The model was then extended to the frame model, which was used to explore the hysteretic behavior of TOB-SCSTHF. It was found that the combined use of steel angles in the beam-column joints and the TOBs was efficient in enhancing the structural performance, including the strength, stiffness, energy-dissipation, and the self-centering capability.

KEYWORDS: Steel-timber hybrid joints, Self-centering, Tension-only braces, Lateral performance

1 INTRODUCTION

With the development of engineered wood products (e.g., glued laminated timber, GLT) [1], heavy timber frames have been increasingly used in multi-story buildings. However, heavy timber moment frames are often found to have low stiffness under wind and seismic loads [2]. To increase the lateral stiffness, timber braces can be added to form braced frames. Despite increased stiffness, research has shown braced frames have significant reduction in system ductility and the permanent deformations due to the potential failure of the timber braces and significant residual deformations in the brace end connections. Researchers also attempted to add buckling-restrained braces (BRBs) to GLT frames [3]. Test results revealed that both the stiffness and the ductility of the GLT frames were enhanced. However, the residual deformations of the BRB braced frames were significant.

In this paper, as shown in Figure 1, a lateral load resisting system, TOB-SCSTHF, is proposed. The system consists of two critical components: the self-centering steel-timber hybrid joints (hereafter referred to as hybrid joints) and the tension-only braces. The self-centering capability and lateral stiffness of the system are provided by the hybrid joints and TOBs, respectively. Quasi-static loading tests on two joint specimens were conducted. Further, a numerical model for the hybrid joint was developed within the OpenSees platform. The model was extended to explore the hysteretic response of the TOB-SCSTHF.

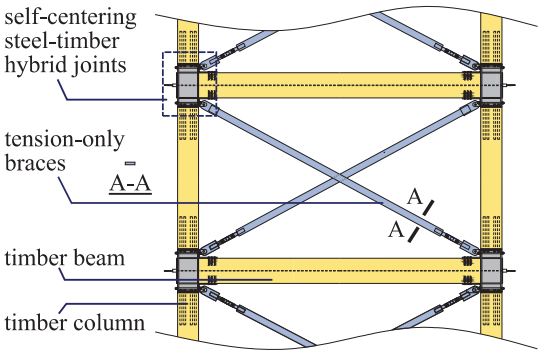

Figure 1 : Tension-only braced self-centering steel-timber hybrid frame (TOB-SCSTHF)

2 CYCLIC TEST ON HYBRID JOINTS

Two hybrid joints were prepared for the cyclic loading test. The details of the test results are available in [2]. A brief introduction of the tests is provided as follows. Two hybrid joint specimens were named Imp-S1 and Imp-S2, respectively. Different from conventional self-centering timber beam-column joints, the hybrid joint used a steel panel in the beam-column interface, as shown in Figure 2 (a). After the post-tensioning of steel tendons, the steel panel resisted the compression from the beam. Glued-in rod (GIR) connections were used to connect the steel panel to the GLT columns. Two-component epoxy resin and grade 4.8 M16 steel rods (each with a slenderness ratio of 25) were used to fabricate the GIR connections. To make a fair comparison, the size of the hybrid joints

[1] Fei Chen, Tongji University, China, chen_fei@tongji.edu.cn
[2] Minghao Li, University of British Columbia, Canada, minghao.li@ubc.ca
[3] Minjuan He, Tongji University, China, hemj@tongji.edu.cn
[4] Zheng Li (Corresponding author), Tongji University, China, zhengli@tongji.edu.cn

https://doi.org/10.52202/069179-0432

was kept the same as that of self-centering timber joint specimens reported in [5]. The initial post-tensioning force for Imp-S1 and Imp-S2 was 54.87 kN and 76.20 kN, respectively. The CUREE loading protocol was used in the test. The moment-rotation curves of the two specimens are shown in Figure 2 (b) and (c). With the use of the steel panel, the gap opening was easy to form in the beam-column interface. As a result, the final failure of two specimens was the fatigue failure of steel angles. Compared with conventional self-centering timber joints, the hybrid joint had higher stiffness, energy-dissipation capability, and connection ductility [4]. The development of the numerical model for the hybrid joint is desired to facilitate further investigation of hybrid joints.

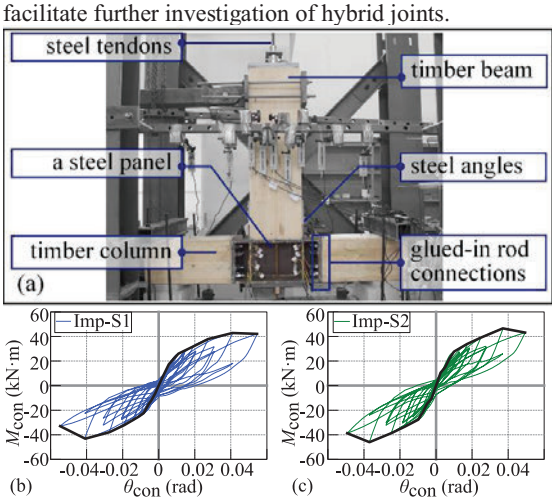

Figure 2 : Cyclic loading test on hybrid joints

3 NUMERICAL SIMULATION ON HYBRID JOINTS

3.1 DETAILED MODEL

The hybrid joint was simulated in OpenSees. There were three key points in the simulation: 1) the modeling of the gap-opening at the timber beam to steel panel interface; 2) the moment-rotation behavior of the GIR connections; and 3) the slip behavior of the self-tapping screws connecting steel angles to the beam.

3.1.1 Modeling of the gap-opening mechanism

As per [6], for self-centering timber joints, the gap-opening mechanism can be simulated with a series of compression-only springs at the beam-column interface. These springs are placed in parallel after being assigned with the Elastic-No Tension (ENT) material property. After post-tensioning, these springs are evenly compressed. The beam-column interface is opened when the edge spring resists zero compression. However, the distributed spring modeling technique might not be ideal in the simulation of the self-centering steel-timber hybrid joint. The reason is that the accumulative damage at the beam end for a hybrid joint is unable to be considered. During the cyclic loading test, permanent compression deformation was observed at the end of the timber beam. After the test, the compression deformation was most obvious at two toes of the beam end. After the gap opening, the compression force was concentrated into the toe which acted as a rocking pivot. The wood crushing occurred when the GLT compression strength was reached. As a result, the compression stiffness was different for laminations along the height of the beam. The stiffness of the top and bottom laminations degraded faster than that of the inner laminations. The distributed springs with the ENT material however assumed that the springs remained elastic and had no degradation of stiffness, which was different from the test observations. In the paper, the Hyperbolic Gap (HG) material was used for the distributed springs. The HG material is also compression-only. But given compression yield strength F_{ult}, accumulative damage can be considered by HG. The compression stiffness is zero upon a larger compression deformation required for the element with the HG material. Both the strength and stiffness parameters are required in defining the HG material. To determine the strength parameter F_{ult}, the principle of strength equivalence was used. The compression resisted by all springs equaled the compression capacity of the timber beam. Given the rectangular cross-section for the beam, F_{ult} is given by Equation (1). To determine the initial stiffness of the HG material K_{max}, the principle of stiffness equivalence was used with consideration of the end-effect at two ends of the timber beam. As illustrated in Figure 3, the compression stiffness of TB1 was set the same as that of TB2. TB1 corresponded to the beam with two end-effect zones. It can be modelled as three springs in serial. To consider the end effect, two side springs have a reduced axial stiffness represented by $k_{gap}E_{para}/l_e$. TB2 was the beam used in the detailed model for the hybrid joint. TB2 was the beam with only one end-effect zone. One spring connected with a distributed spring model can be used to represent TB2. Assuming the axial stiffness of TB1 equals that of TB2, the initial stiffness K_{max} is obtained with a consideration of the end-effect, as given by Equations (2)-(4).

$$F_{ult} = \frac{f_{para} b_b h_b}{N A_1} \tag{1}$$

$$K_{max} = k_{end} E_{para} \tag{2}$$

$$k_{end} = \frac{L_0}{\frac{\lambda+2}{\lambda} \cdot \frac{L_b - 2l_e}{A_b} - \frac{L_b^*}{A_b}} \tag{3}$$

$$\lambda = \frac{k_{gap}\left(L_b - 2l_e\right)}{l_e} \tag{4}$$

where F_{ult} = yielding compression stress, f_{para} = wood strength parallel to the grain, b_b = beam width, h_b = beam section height, N = number of springs in parallel, A_1 = tributary section area of each spring, A_b = beam section area, k_{end} = reduction factor, k_{gap} = end-effect factor, E_{para} = elastic modulus parallel to the grain, L_0 = length of the offset region, L_b = length of TB1, L_b^* = length of TB2, and l_e = length of the end-effect zone.

https://doi.org/10.52202/069179-0432

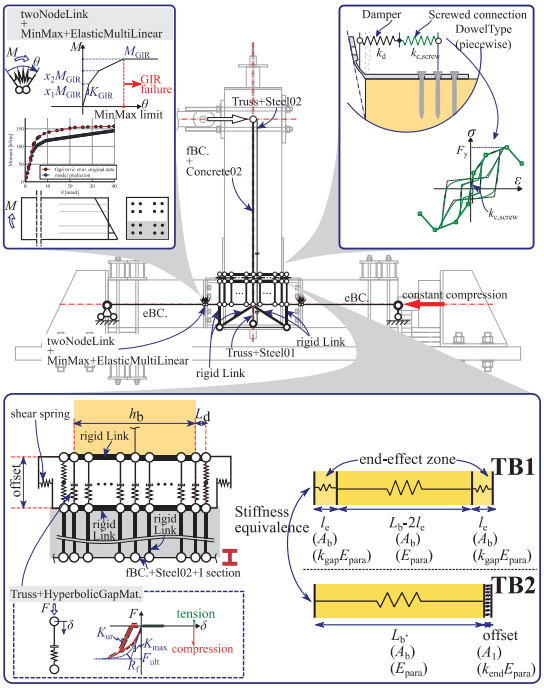

Figure 3 Stiffness equivalence and model illustration

3.1.2 Modeling of the GIR connection

To model the GIR connection, the twoNodeLink element was used to link two overlapped nodes and their degrees of freedom (DOFs) were controlled with the EqualDOF command in OpenSees. Except for the rotational DOF, two translational DOFs of the two nodes were kept the same because only the moment-rotation behavior was modelled. The twoNodeLink element was assigned with ElasticMultiLinear material wrapped with the MinMax material. ElasticMultiLinear material model represented the rotational behavior of GIR connections as a polyline model. The analytical prediction of the GIR connections was conducted based on the model proposed by Ogrizovic et al [7]. The prediction result was in the polyline form and was used as the input for the ElasticMultiLinear material model. The design of GIR connections aimed to ensure that GIR connections had the moment capacity over the possible demand. While the MinMax material was still used to simulate the possible failure of GIR connections. The maximum rotation was specified in the MinMax material. When the relative motion between the two nodes exceeded the limit specified, the MinMax material was activated to fail the ElasticMultiLinear material.

3.1.3 Modeling of the connector between steel angles and beam

The mechanical behavior of self-tapping screws (STSs) connecting steel angles to the timber beam was considered to ensure that the connection stiffness was not overestimated. During the test, the relative slip between one leg of the steel angle and the side face of the timber beam was observed when the gap opening was large. The DowelType model [8] was used to simulate the behavior of STS connections. The Bezier envelope was used as the backbone curve. Based on the European Yield Model, strength of each STS connection was calculated and used as the input for the DowelType model. The initial stiffness of the STS connections was taken as the minimum value obtained from different STS stiffness models. As per Dong et al. [3], there was a uniform model for the prediction of the shear stiffness k_{ser} of a single inclined STS, as given by Equation (5). The formula was originally proposed by Mirdad et al. [9] for the STS connection between concrete and solid timber. Dong et al. [10] further proved that with the proper selection of the embedment stiffness K_h and the withdrawal stiffness K_{ax} per unit area, the equation was also applicable in calculating the stiffness of the STS connection between the steel member and the GLT member. As per Equation (5), the contribution of the withdrawal stiffness to the total lateral stiffness of STS connections is zero when the angle between the axis of a single STS and the grain direction is 90 degrees. As given by Equations (6)~(8), three different formulas of K_h were used to calculate the lateral stiffness of STS connections. The lowest value among the three prediction results was taken as the input for the initial stiffness of the DowelType model. k_{ser} was calculated to be 992 N/mm. Other material parameters were adopted as the values suggested in [8].

$$k_{ser}=\frac{3E_{STS}Id\left[2\left(3l_f+2l_{ef}\right)K_{ax}\pi l_{ef}\left(\cos^2\theta+0.5\mu_f\sin 2\theta\right)\right]}{6E_{STS}I\left(3l_f+2l_{ef}\right)+K_h dl_{ef}^2 l_f^3\sin^2\theta}+\frac{3E_{STS}IdK_h l_{ef}^2\left(\sin^2\theta-0.5\mu_f\sin 2\theta\right)}{6E_{STS}I\left(3l_f+2l_{ef}\right)+K_h dl_{ef}^2 l_f^3\sin^2\theta} \quad (5)$$

$$K_h=\frac{0.00011\rho_m^{2.443}d^{-0.956}}{7.663\cos^2\theta+2.645\sin^2\theta} \quad (6)$$

$$K_h=\frac{\left(0.22+0.014d\right)\rho_m d^{-1}}{1.17\sin^2\theta+\cos^2\theta} \quad (7)$$

$$K_h=\frac{2\rho_m^{1.5}\dfrac{d_{ef}}{23}}{dl_{ef}} \quad (8)$$

where E_{STS} = elastic modulus of STS, $I=\pi d^4/64$ the moment of inertial of the STS, d = nominal diameter of the STS, l_f = free length of the STS, l_{ef} = effective penetration length of the STS, θ = angle between the axis of STS and the direction of the wood grain, μ_f = friction coefficient, ρ_m = mean value of the wood density, d_{ef} = effective diameter of the STS.

3.1.4 Comparison against experimental results

The comparison between the numerical simulation results and experimental results was shown in Figure 4. The hysteretic curves from the simulation and the test recording are overlapped in the first two subfigures. The model prediction agreed well with the test results in terms of both the strength and the residual deformation. However, the decompression point of the model was lower than that of the test. One possible reason was that the stiffness degradation of the springs at the beam-column interface was severe than in the real situation. After a few cycles of loading, the two side springs had significant stiffness degradation and could not support the rocking of the beam. Inner springs then picked up the load

and acted as the rocking pivot. As a result, the decompression point was slightly lower than the test results. The numerical model also performed well in predicting the variation of the post-tensioning force and energy dissipation, as shown in Figure 4 (c)~(f).

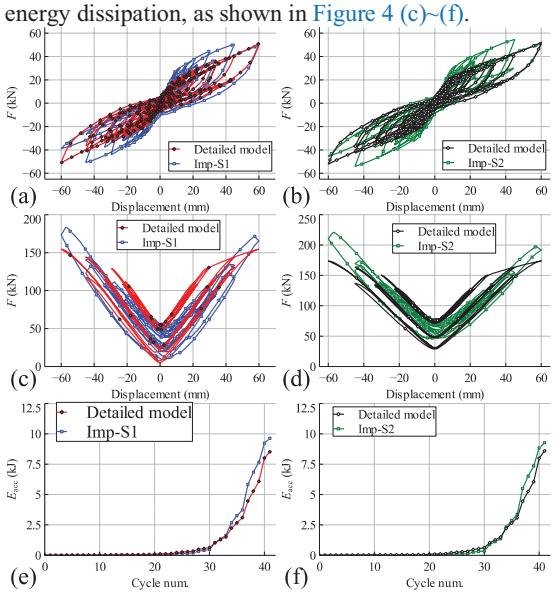

Figure 4 : Numerical simulation against experimental results

3.2 PHENOMENOLOGICAL MODEL

The integration of the aforementioned detailed model into the frame model might be difficult due to the complexity of the joint model. To avoid the convergence problem, a phenomenological model was further developed for the hybrid joints. To mimic the hysteretic behavior of hybrid joints, SelfCentering and DowelType materials were combined in parallel as the candidate material for the phenomenological model. The number of parameters required for SelfCentering and DowelType material was 4 and 17, respectively. The genetic algorithm was used to build the automatic calibration process for the phenomenological model. NSGA-II [11] was selected to conduct the multi-objective optimization. One of the desirability functions is given by Equation (9). The function F_1 was used to ensure that the force-displacement curve of the simulation results match the test results. In addition, the second desirability function F_2 was defined in terms of energy dissipation, as given by Equation (10). Constrained by F_2, the model error of the accumulative energy dissipation was expected to be controlled.

$$F_1 = \sum_{i=1}^{n} \omega_i \left(F_{it} - F_{im}\right)^2 \tag{9}$$

$$F_2 = \sum_{i}^{n} \frac{\left|E_{it} - E_{im}\right|}{\left|E_{it}\right|} \tag{10}$$

where ω_i,i=1~n = the weight factor for the ith data point, F_{it} = target force of the ith data point, F_{im} = model force of the ith data point, E_{it} = target energy dissipated upon the ith data point, E_{im} = model energy dissipated upon the ith data point.

The flowchart of the parameter calibration process is shown in Figure 5. To ensure that the optimized parameters can be obtained, the number of generations was 20. It means that the set of parameters was obtained after 20 times of evolution. Within each round of evolution, the number of candidates was 5000. For each candidate, the value of each model parameter was randomly set within the rational range. The final results were obtained after the comparison between 10000 (20 times 5000) combinations of parameters. More than one set of parameters was available after the multi-objective optimization. All the final outputs were non-dominated solutions, which meant each of them, i.e., one set of parameters, was a suitable compromise to minimize both desirability functions.

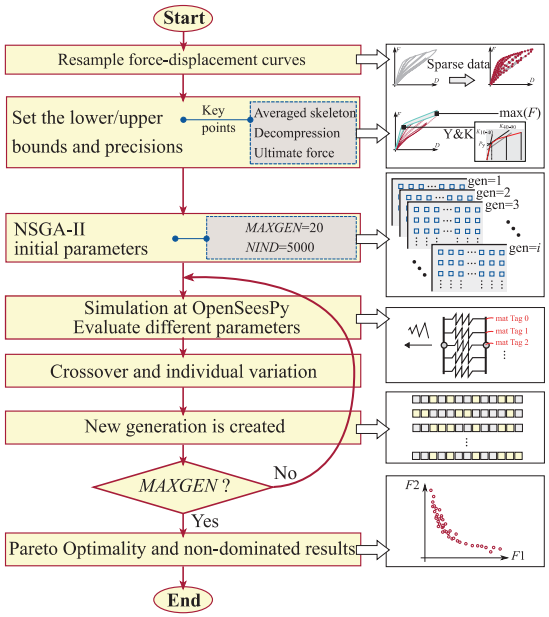

Figure 5 : Flowchart for determining the optimized parameters for the phenomenological model

Taking one of the non-dominated solutions to make the simulation in OpenSees, the prediction from the phenomenological model was presented in Figure 6, together with the results from the detailed model. The comparison validated the accuracy of the phenomenological model. The model was then integrated into the frame model in the next section.

https://doi.org/10.52202/069179-0432

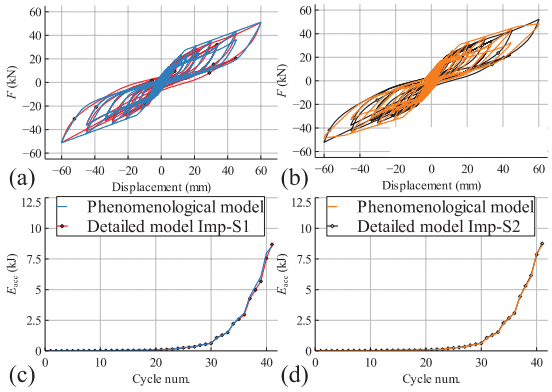

Figure 6 : Flowchart for determining the optimized parameters for the phenomenological model

4 NUMERICAL SIMULATION OF TOB-SCSTHF

The hysteretic behavior of TOB-SCSTHF was explored based on the phenomenological model of the hybrid joint. The modeling method of TOBs is first introduced and validated against theoretical solutions. It is then followed by the numerical simulation on TOB-SCSTHF with or without steel angles installed at the beam-column joints.

4.1 MODELING OF TOBs

Compared with common steel braces, TOB is characterized as a steel brace with negligible compression resistance. It is expected that TOBs provide zero resistance to the self-centering frame during the load reversal. An equivalent model was proposed for TOBs by Ying et al. [12] in ABAQUS. The modeling technology was recreated within OpenSees. As shown in 错误!未找到引用源。, the model has four truss elements connected end to end.

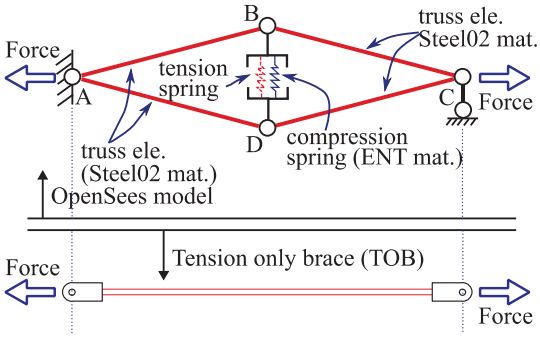

Figure 7 : OpenSees model for a single TOB

Nodes A and C are the two ends of a single TOB. When the TOB is in tension, nodes A and C depart from each other, and element BD is under compression. When the TOB is in compression, nodes A and C are getting closer and the element BD is in tension. Element BD is assigned with two materials in parallel: ENT and Elastic material. ENT material is a compression-only material and Elastic material has a close to zero tension stiffness. So element BD can resist compression only. When the TOB model is under tension along the AC axis, element BD resists the compression, so the TOB model has the tension stiffness. The TOB model has no compression resistance because the BD element has zero tension stiffness.

The TOB with the flat bar was simulated by using the TOB model. Under the reversed cyclic loading, the hysteretic curves of TOBs with three different thicknesses (4/6/8 mm) were obtained. The simulation results are shown in Figure 8. The analytical prediction on the yielding force and the initial stiffness of a single TOB were also annotated in Figure 8. The satisfactory agreement validated the modeling method for TOBs.

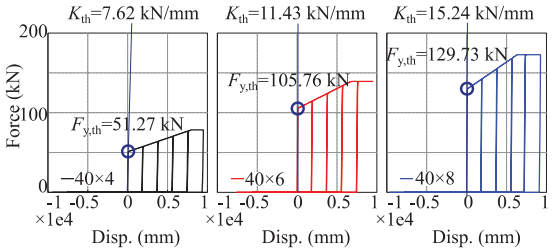

Figure 8 : Numerical predictions on the TOBs with different thickness

4.2 MODELING OF TOB-SCSTHF

Both the hybrid joint model and the TOB model were integrated into the OpenSees model for TOB-SCSTHF. The basic geometry and material information of the frame are listed in Figure 9.

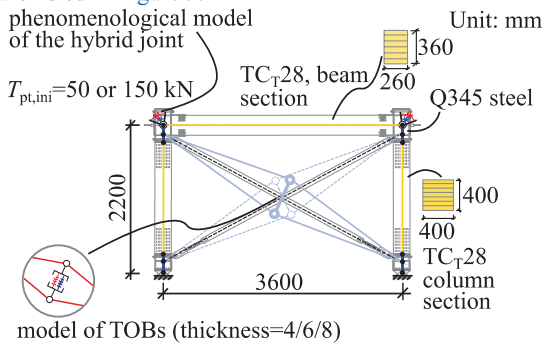

Figure 9 : Numerical model of TOB-SCSTHF

Five numerical models were built corresponding to the five TOB-SCSTHFs listed in Table 1.

Table 1 : Information of five TOB-SCSTHF models

Model ID	TOB[a]	$T_{pt,ini}$ (kN)	Steel angles at beam-column joints
M1	40×4	50	w/o
M2	40×6	50	w/o
M3	40×8	50	w/o
M4	40×4	150	w/[b]
M5	40×6	150	w/[c]

[a] Numbers represent cross-sections of TOB in mm;
[b] The steel angles had reduced thickness of 7 mm;
[c] The steel angles had reduced thickness of 5 mm.

https://doi.org/10.52202/069179-0432

TOBs with three thicknesses were used in the same SCSTHF ($T_{pt,ini}$=50 kN, without steel angles). The hysteretic curves of the three TOB-SCSTHFs are shown in Figure 10 (a). The hysteresis of the TOB-SCSTHF was in a flag shape and almost zero residual deformation was found when the lateral force was zero. The stiffness and strength of the SCSTHF were enhanced along with the increase in the thickness of TOBs. At the same time, the difference in TOBs used in the frame didn't change the residual deformation. All three frames had a full re-centering after the cyclic loading. Without the degradation of the self-centering capability, TOBs can be used when SCSTHF has insufficient lateral strength or stiffness. The introduction of TOBs into SCSTHF also changed its energy dissipation capability. As shown in Figure 10 (b), there is a plateau on the curve of accumulative energy. When no beam-column dampers are used in the SCSTHF, TOBs are the only component dissipating energy. The plastic deformation and the related energy dissipation can only happen within the first loading cycle if multiple loading cycles with the same loading amplitude was applied to the TOBs. After the first loading cycle, the TOB is elongated due to plastic deformation. It means that a larger deformation is required to make the TOB under tension again. To increase the energy dissipation of TOB-SCSTHF, steel angles were installed at the beam-column joints. Two models with steel angles were simulated and their responses are shown in Figure 10 (c). Their hysteretic curves were still in the flag shape and an increase in the residual deformation was also noticed. The increase was due to the use of steel angles. Since the use of TOBs had no influence on the self-centering performance of the frame, the installation of the steel angles was a compromise solution to the frame. The accumulative energy dissipation curves of the two new frames were shown in Figure 10 (d). Owing to the energy dissipation by the steel angles, a continuous increase is observed in the two curves. It means that the combined use of steel angles and TOBs in SCSTHF is a promising solution when there is a requirement for different structural aspects, including strength, stiffness, energy-dissipation, and residual deformations.

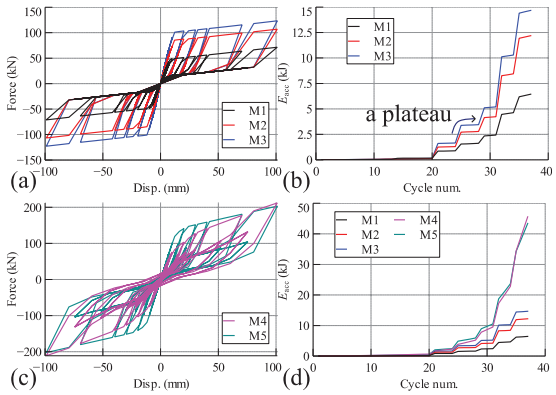

Figure 10 **:** Hysteretic responses of TOB-SCSTHF with or without steel angles

5 CONCLUSIONS

This paper presents a preliminary study on the hysteretic performance of a new lateral load resisting system called TOB-SCSTHF for heavy timber frames. The cyclic test on the hybrid beam-column joints proved their capability to provide sufficient re-centering action to the frame. Based on the experimental results, both detailed and phenomenological models were developed for the hybrid joints. The joint model was then integrated into the numerical model of TOB-SCSTHF. The simulation results showed that the introduction of TOBs increased the lateral resistance and stiffness of the frames. Being different from the BRBs, the use of TOBs did not impair the self-centering capability.

ACKNOWLEDGEMENT

The authors gratefully acknowledge the support from National Natural Science Foundation of China (Grant NO. 52222802), Shanghai Rising Star Program (21QA1409300), Sichuan Science and Technology Program (Grant NO. 2021YFH0117), and China Scholarship Council (Grant No. 202206260172).

REFERENCES

[1] Sun X., He M., and Li Z. Novel engineered wood and bamboo composites for structural applications: State-of-art of manufacturing technology and mechanical performance evaluation. Construction and Building Materials, 249, 118751, 2020.

[2] Shu Z., Ning B., Chen J., Li Z., He M., Luo J., and Dong H. Reinforced moment-resisting glulam bolted connection with coupled long steel rod with screwheads for modern timber frame structures. Earthquake Engineering & Structural Dynamics, 2022.

[3] Dong W., Li M., Lee C. L., MacRae G., and Abu A.: Experimental testing of full-scale glulam frames with buckling restrained braces. Engineering Structures, 222, 111081, 2020.

[4] Li Z., Chen F., Sun X., Shu Z., and He M.: Hysteretic performance of self-centering glulam beam-to-column connections with steel core panel zone. *International Conference on Green Building, Civil Engineering and Smart City*, pages 893-900. Springer, Singapore, 2023.

[5] Li Z., He M., and Wang K.: Hysteretic performance of self-centering glulam beam-to-column connections. Journal of Structural Engineering, 144(5), 04018031, 2018.

[6] Granello G., Palermo A., Pampanin S., Pei S., and Van De Lindt J.: Pres-lam buildings: state-of-the-art. Journal of Structural Engineering, 146(6), 04020085, 2020.

[7] Ogrizovic J., Wanninger F., and Frangi A.: Experimental and analytical analysis of moment-resisting connections with glued-in rods. Engineering Structures, 145, 322-332, 2017.

[8] Dong H., He M., Wang X., Christopoulos C., Li Z., and Shu, Z.: Development of a uniaxial hysteretic

https://doi.org/10.52202/069179-0432

model for dowel-type timber joints in OpenSees. Construction and Building Materials, 288, 123112, 2021.
[9] Mirdad M. A. H., and Chui Y. H.: Stiffness prediction of mass timber panel-concrete (MTPC) composite connection with inclined screws and a gap. Engineering Structures, 207, 110215, 2020.
[10] Dong W., Li M., Lee C. L., and MacRae G.: Numerical modelling of glulam frames with buckling restrained braces. Engineering Structures, 239, 112338, 2021.
[11] Deb K., Pratap A., Agarwal S., and Meyarivan, T. A. M. T.: A fast and elitist multiobjective genetic algorithm: NSGA-II. IEEE transactions on evolutionary computation, 6(2), 182-197, 2002.
[12] Yin H., and Shi G.: Finite element analysis on the seismic behavior of fully prefabricated steel frames. Engineering Structures 173: 28-51, 2018.

World Conference on Timber Engineering Oslo 2023

DEVELOPMENT OF HYBRID RIGID FRAME STRUCTURE METHOD USING SEMI-RIGID TIMBER BEAMS

Akihiko Miyake,[1] Ryoma Murata[2]

ABSTRACT: The authors are working to develop a construction method that incorporates semi-rigid timber beams into a steel frame structure to form a rigid frame structure. In structures constructed by this method, the joints of the semi-rigid timber beams, consisting of drift pins inserted into steel plates, resist seismic moments, generating a bending yield at the root end of the inserted U-shaped steel plates. We believe this explains the specified bearing strength and deformability achieved. We performed experiments and analysis to verify the structural performance of structures incorporating CLT semi-rigid beams. This paper describes the results of full-size in-plane bending tests performed on semi-rigid beam joints; tensile tests performed on individual drift pin joints; and the finite element method analysis used to assess the experimental results.

KEY WORDS: Medium- and large-scale timber building, hybrid structure, CLT, semi-rigid beam, inserted steel plate and drift pin joints

1 INTRODUCTION

There has been growing interest in recent years in using timber—particularly for medium- and large-scale buildings—to promote a low-carbon society and to make more effective use of domestic forestry resources. In Japan, growing numbers of medium- and high-rise buildings feature timber construction or hybrid construction incorporating timber.

This study discusses the development of a rigid frame construction method that incorporates timber beams into a steel structure (Figure 1).

This method involves connecting semi-rigid timber beams to steel columns. The inserted steel plate and drift pin joints at the ends of the beams function as rigid frame beams and resist lateral forces during an earthquake. The timber beams bear the bending moments and shear forces generated by an earthquake, while the steel beam located nearby bears the vertical loads associated with the slabs and interior and exterior materials, so that the timber beams are not subject to constant loading.

Figure 2 shows the joint. Cross laminated timber (CLT) is used for the semi-rigid timber beams. Slits are cut into the center, into which U-shaped steel plates are inserted, allowing joints using drift pins. The steel columns have brackets welded to them. Friction joints incorporating high-strength bolts between the brackets and attached plates allow the transmission of bending moments and shear forces during an earthquake. In the event of a major earthquake, it is expected that both the drift pin joints and the roots of the U-shaped steel plates will yield, ensuring deformability.

As part of this study, we performed full-size in-plane bending tests on the end of a semi-rigid beam removed from a joint between a semi-rigid timber beam and a steel column. We also performed tensile tests of individual drift pin joints to determine their characteristic values and assessed the results via finite element method analysis. This paper presents the test results, comparisons of the test results and analytical modeling results.

Figure 1: *Three-dimensional view of the construction*

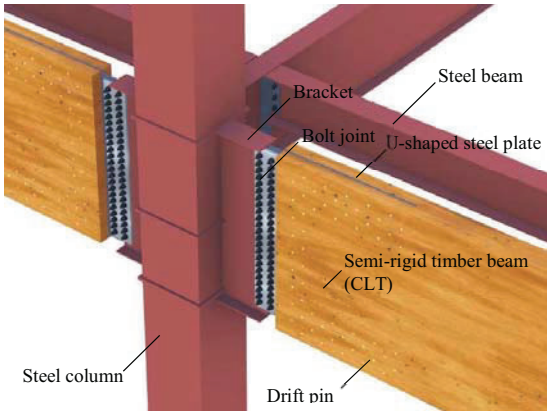

Figure 2: *Outline of the joint*

[1] Akihiko Miyake, Kumagai Gumi Co.,Ltd., Japan, akihiko.miyake@ku.kumagaigumi.co.jp

[2] Ryoma Murata, The University of Tokyo, Japan, murata@murataryoma.com

https://doi.org/10.52202/069179-0433

2 BEAM END JOINT FULL-SIZE IN-PLANE BENDING TEST

2.1 TEST AIMS

To confirm the behavior, load deformation relationship, and failure characteristics of a joint at the end of a semi-rigid timber beam subject to lateral forces during an earthquake, we extracted the section of a semi-rigid timber beam from the end to the center of the span. We then performed in-plane bending tests of the joint by repeatedly applying alternating positive and negative loads.

2.2 TEST PIECE OVERVIEW

Figure 3 shows the test piece. The CLT used for the test piece was S60-5-7 (in JAS) Japanese cedar (with the joints of the two outer-layer side-by-side plies shifted by half). One test piece was cut from each of the three parent boards. Table 1 gives the specifications for the CLT used in the tests. The test pieces here are referred to as "Cn-F," with the "n" indicating parent board number 1, 2, or 3. The inserted steel plate was made of SN400B (in JIS G3136, yield strength from 235 to 355 N/mm^2 and tensile strength from 400 to 510 N/mm^2) machined into a U-shape. The drift pins were made of SNR400B (in JIS G3138, yield strength from 215 to 335 N/mm^2 and tensile strength from 400 to 510 N/mm^2), with 55 pins arranged as shown in Figure 3. Table 2 gives the mechanical properties of the drift pins and the inserted steel plate. The holes in the CLT have a clearance of 0 mm with respect to the 16 mm diameter drift pins; the holes in the inserted steel plate have a clearance of + 1 mm; and the slit in the CLT has a clearance of + 2 mm with respect to the 19 mm thickness of the inserted steel plate.

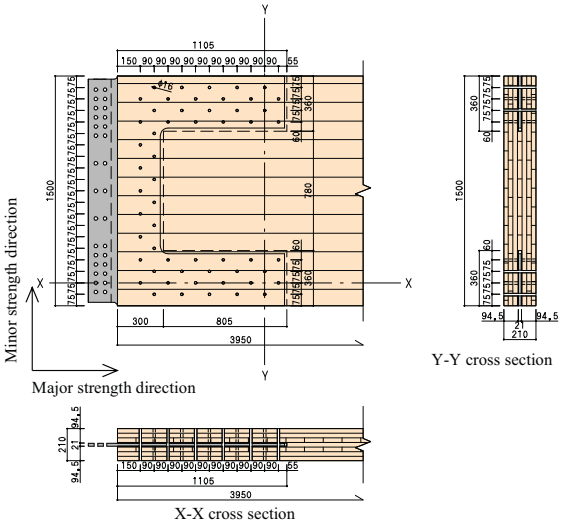

Figure 3: *Test piece for semi-rigid beam end joint full-size in-plane bending test*
(Dimensions are machined CLT dimensions.)

Table 1: *CLT specifications*

Specimen	Density [kg/m^3]	M.C. [%]
C1-F	414	10.4
C2-F	408	10.8
C3-F	424	10.8
Ave.	415	10.7

Table 2: *Mechanical properties of steel used in the tests*

Material	σ_y [N/mm^2]	σ_{max} [N/mm^2]	Yield strain [μ]
Driftpin	326 (0.9%)	459 (0.3%)	-
Steel plate	297 (1.2%)	429 (0.5%)	1434 (0.6%)

* Figures in parentheses are standard deviation values.

2.3 TEST METHOD

Figure 4 shows an overview of the test setup. The test piece was set up by rotating the semi-rigid beam by 90°, clamping the lower end to the test bed with a bracket jig, and applying a force at the point assumed to be the center of the span (the reflexion point of the anti-symmetric bending moment attributable to the seismic force). The force was applied by pushing and pulling the side of the semi-rigid beam using a bearing plate attached to an actuator. To keep the bearing plate from becoming embedded in the timber, we secured steel plates ($t \times H$ = 12 × 225) of identical thickness as the specimen on both sides of the test piece using 60 screws with a diameter of

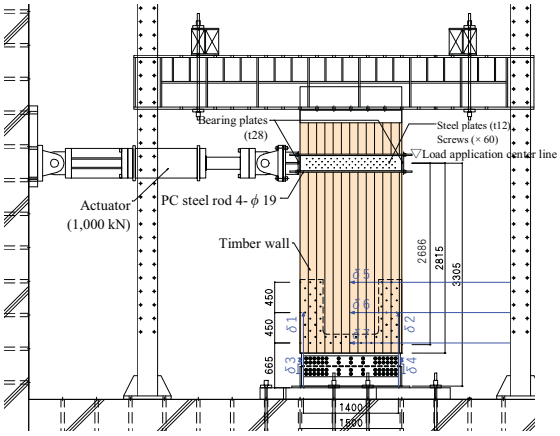

(a) Loading diagram

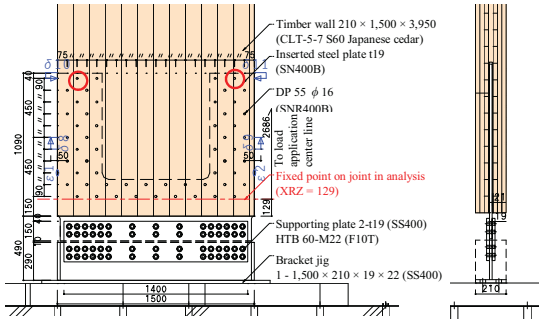

(b) Joint vicinity

Figure 4: *Overview of vertical wall end joint full-size in -plane bending test*

https://doi.org/10.52202/069179-0433

8 mm and length of 90 mm. We applied the loading by rotating the joint by 1/600, 1/450, 1/300, 1/200, 1/150, 1/100, 1/75, and 1/50 rad three times in succession in the positive and negative directions, and then by 1/30 rad once in the positive and negative directions. We then applied this same loading until the joint had turned by 1/15 rad in the positive direction or until the load declined to 0.8 times of the maximum load. We used Equation (1) to calculate the angular rotation of the joint from the displacement.

$$\theta = \frac{(\delta_2 - \delta_4) - (\delta_1 - \delta_3)}{1{,}400} \quad (1)$$

Here, δ_1 and δ_2 are the displacements (absolute vertical displacement for the CLT) for the 1st and 2nd displacement meters, while δ_3 and δ_4 are the displacements (relative vertical displacement for the CLT and bracket jig) for the 3rd and 4th displacement meters (see Figure 4 (a)). Moment M at the joint is obtained by multiplying the shear force Q measured by the load cell inside the actuator connected to the jack by the distance 2.686 m from the load application point to the fixed point on the joint in the analysis (129 mm from the CLT end; refer to Section 4.4.2 for the definition of the fixed point on the joint in the analysis). Strain gauges (ε1 and ε2) were also attached to the sides of the U-shaped root of the inserted steel plate.

2.4 TEST RESULTS

Figure 5 shows the relationship between the joint moment and rotation angle for all three test pieces. Table 3 lists the characteristic values obtained from the tests. Here, we calculated rotational stiffness K_θ as the mean secant stiffness at the first peak on the positive and negative sides for a control deformation angle of 1/300 rad. We calculated the yield strength of the drift pin joint by setting the mean value of the positive and negative loads as drift pin joint yield strength ${}_{DP}M_y$ for the yield moment of the joint at the point at which the individual drift pin joint on which the greatest stress acts reaches the mean yield point displacement value of 2.65 mm discussed in Section 3. Here, based on the analysis in Section 4, the individual drift pin joint subject to the most severe stress was determined to be the drift pin circled in Figure 4 (b). The corresponding displacement δ_{FDP} was obtained using Equation (2).

$$\delta_{FDP} = \frac{1}{2}\left(\sqrt{\left(\frac{600}{800}\cdot\delta_8\right)^2 + {\delta_{10}}^2} + \sqrt{\left(\frac{600}{800}\cdot\delta_9\right)^2 + {\delta_{11}}^2}\right) \quad (2)$$

Here, δ_8 and δ_9 are the displacements (relative vertical displacement for the CLT and inserted steel plate) for the 8th and 9th displacement meters (see Figure 4 (b)), while δ_{10} and δ_{11} are the displacements (relative lateral displacement for the CLT and inserted steel plate) for the 10th and 11th displacement meters (see Figure 4 (b)).

We calculated the yield strength of the inserted steel plate by setting the mean value of the positive and negative loads as the inserted steel plate yield strength ${}_{PL}My$ for the joint moment at the point at which the strain gauges (ε1 and ε2) mounted on the root of the U-shape of the inserted steel plate reach the tensile yield strain of 1,434 μ (see Table 2) for the inserted steel plate.

We calculated ultimate strength as the mean of the positive and negative loads for moment M_u for which the area of the trapezoid for the elastic perfectly plastic model in which the moment is M_u with the rotational stiffness as the primary gradient within the range up to 1/50 rad is equivalent to the area enclosed by the experimental joint moment and joint rotation angle plot and the X axis.

Behavior was virtually identical for all three test pieces up to a joint rotation angle of 1/30 rad, with none exhibiting significant failure. When the C3-F test piece was pulled beyond 1/30 rad, group shear failure occurred at the drift pin joint under tension at around 1/20 rad. The load dropped to approximately 60%, accompanied by a breaking sound, at which point we stopped the test. The C1-F and C2-F test pieces reached 1/15 rad with no significant reductions in load or group shear failure; we stopped the tests at this point. Figure 5 shows that the drift pin joint yield (${}_{DP}M_y$) and inserted steel plate yield (${}_{PL}M_y$) occurred almost simultaneously.

Figure 6 shows the condition of test piece C1-F after disassembly. Each drift pin is deformed at one or three hinge points along its length. The deformation of the drift pin is more severe in the area framed in red in Figure 6 (a-1) and less severe in the area framed in blue, clearly indicating that the extent of the deformation varies with location. This appears to be because the magnitude of the stress occurring in each drift pin differs with distance from

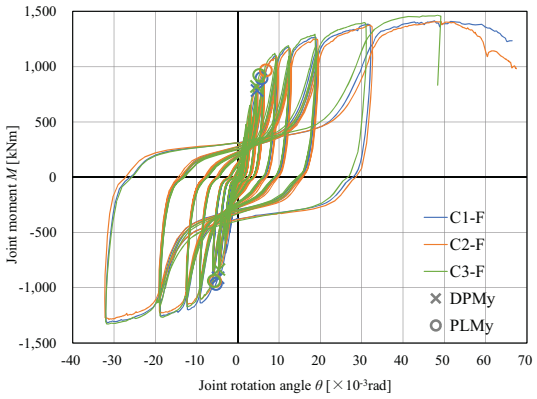

Figure 5: *Relationship between joint moment and rotation*

Table 3: *List of characteristic values obtained from tests*

Test piece	Rotational stiffness K_θ [kNm/rad]	Joint fixed point x_{RZ} [mm]	Drift pin joint yield strength ${}_{DP}M_y$ [kNm]	Steel plate yield strength ${}_{PL}M_y$ [kNm]	Maximum strength M_{max} [kNm]	Ultimate strength M_u [kNm]	
			${}_{DP}\theta_y$ [×10⁻³rad]	${}_{PL}\theta_y$ [×10⁻³rad]	θ_{max} [×10⁻³rad]	θ_v [×10⁻³rad]	θ_u [×10⁻³rad]
C1-F	201,620	107	847	930	1,411	1,127	
			4.7	5.5	47.7	5.7	20.0
C2-F	204,578	136	829	953	1,407	1,103	
			4.5	6.1	49.3	5.3	20.0
C3-F	204,529	130	880	932	1,463	1,125	
			5.0	5.5	48.4	5.5	20.0
Ave.	203,576	124	852	938	1427	1119	
			4.7	5.7	48.5	5.5	20.0

https://doi.org/10.52202/069179-0433

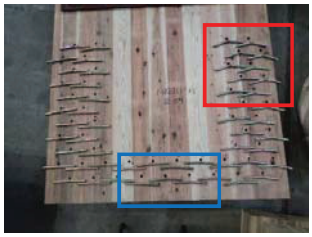

(a-1) Drift pins after disassembly

(a-2) Enlarged view of area framed in red

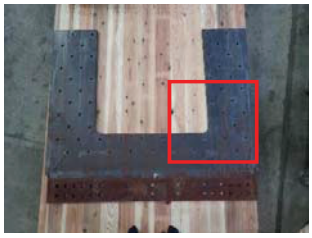

(b-1) Inserted steel plate after disassembly

(b-2) Enlarged view of area framed in red

Figure 6: *Condition of vertical wall end joint full-size in-plane bending test piece after disassembly*

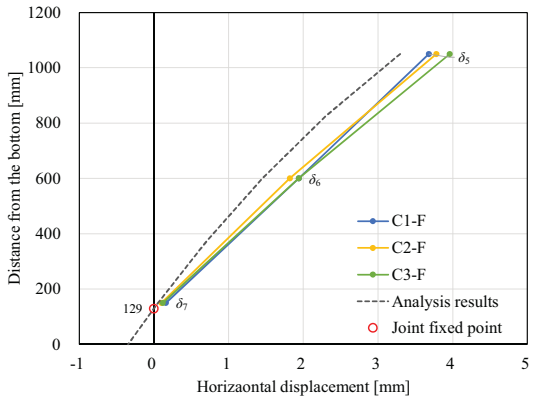

Figure 7: *Test piece horizontal displacement and fixed point*

the center of rotation of the joint. The inserted steel plate is deformed in the direction of the stress acting on the drift pin joint. The root area of the U-shape exhibits delamination of the blackened layer, demonstrating that residual deformation starts at the root area. In conjunction with the state of the test piece, this led us to conclude that the inserted steel plate had yielded at the drift pin joint and the root area of the U-shape.

Figure 7 shows the horizontal displacement (δ_5 to δ_7 in Figure 4 (a)) of the test piece at the positive initial peak in the 1/300 rad cycle. The horizontal axis represents lateral displacement, while the vertical axis represents the distance from the semi-rigid beam end. The fixed point of the joint indicates the distance from the CLT end at which the length of the section is 0 (the horizontal displacement is 0) when a regression line is plotted from the horizontal displacement for each test piece at the corresponding peak. Section 4.4.2 provides more information on the joint fixed point.

3 INDIVIDUAL JOINT TENSILE TEST

3.1 TEST AIMS

With this construction method, drift pins joined to the CLT in the inserted steel plate configuration provide bending resistance, which ensures the specified strength, rigidity, and deformability. A thorough understanding of the performance of the drift pin joint is required to predict the actual rigidity and strength of the joint. At the same time, it is not possible to use the same equations to calculate rigidity [1] and strength [2], as CLT features a laminar configuration with mixed and perpendicular fiber directions. Since the angle θ between the direction of the stress from the drift pin and the direction of the strong axis of the CLT varies depending on the position of the drift pin, it is necessary to identify the effects due to θ.

Thus, we performed tensile tests on individual drift pin joints to confirm individual drift pin joint performance and the effects due to θ.

3.2 TEST PIECE OVERVIEW

The test pieces were manufactured by cutting out pieces of CLT measuring 300 mm in width for each of the four angles, as shown in Figure 8. The CLT used the same parent board as used for the full-size test described in Section 2 (see Table 1 for specifications). The test pieces are referred to as "Cn-Eθ," with "n" indicating parent board number (1, 2, or 3) and "θ" indicating the angle of the applied load with respect to the strong axis of the CLT (0, 30, 60, or 90). The inserted steel plate was made of SN400B, and the drift pins were made of SNR400B. We used two drift pins of each. Table 4 presents the mechanical properties of the drift pins and inserted steel plates. We prepared three test pieces for each of the four angles, with one piece cut out from each parent board. As in Section 2, the holes in the CLT had a clearance of 0 mm with respect to the drift pins, while the holes in the inserted steel plates had a clearance of + 1 mm. The slit in the CLT had a clearance of + 2 mm with respect to the inserted steel plate.

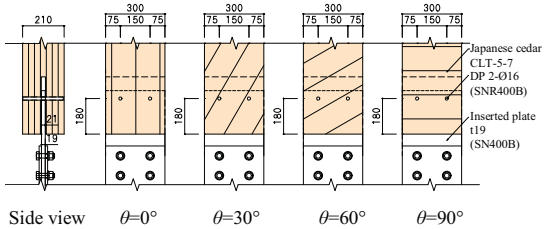

Figure 8: *Overview of individual joint tensile test pieces*

Table 4: *Mechanical properties of steel used in tests*

Material	σ_y [N/mm^2]	σ_{max} [N/mm^2]
Driftpin	326 (0.9%)	459 (0.3%)
Steel plate	312 (2.0%)	431 (0.4%)

* Figures in parentheses are standard deviation values.

https://doi.org/10.52202/069179-0433

3.3 TEST METHOD

Figure 9 shows the loading configuration. Loads were applied using 1,000 kN center hole jacks for tensioning and compressing. Axial forces were measured using pressure transducers connected to each jack. We measured the relative displacement between the inserted steel plate and the CLT at two points (on the front and back) and used the mean value as the joint displacement. We performed positive and negative loading three times and treated tensile loading as positive loading. These loads were applied by repeatedly applying displacements of $\delta pt \times 1/2$, 1, 2, 4, 6, 8, 12, and 16, based on the yield displacement of δpt = 1.55 mm in the preliminary test done at θ = 0°, until the load declined to 0.8 times of the maximum load or until the displacement reached 30 mm.

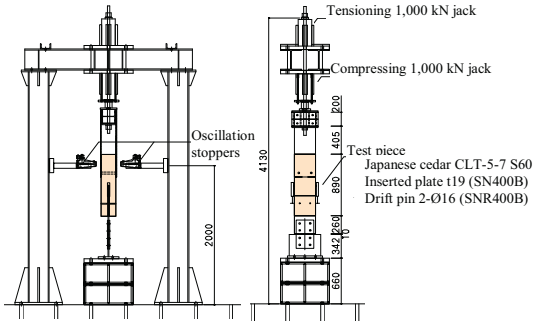

Figure 9: *Individual joint tensile test loading configuration*

3.4 TEST RESULTS

Figure 10 shows the relationship between load per drift pin and deformation for each angle. Table 5 shows the mean characteristic values (θ = 0, 30, 60, and 90 values are mean values for three test pieces; ALL values are mean values for all 12 test pieces) obtained in the tests. We calculated characteristic values such as yield strength and initial stiffness by the method described in reference [3]. The red lines in Figure 10 indicate the mean values for the tri-linear models with test pieces corresponding to each specification. Here, the first breakpoint of the tri-linear model is the point (P_y, δ_y), and the second breakpoint of the tri-linear model is the point (P_{max}, δ_{max}). After testing, we removed the drift pins, assigning those showing zero bending points to Yield Mode I, those with one bending point to Yield Mode III, and those with three bending points to Yield Mode IV. Figure 11 shows some of the disassembled test pieces.

The load-displacement relationship shown in Figure 10 confirmed that stiffness for all test pieces begins to decline at a relative displacement of approximately 2 mm. When the test pieces were disassembled, the drift pins demonstrated behavior corresponding to Yield Mode III or IV. This suggests that drift pin yield occurred and that bearing yield occurred in timber parts in contact with the drift pins. Ultimately, the load declined with each repetition for 16 × δ_{pt} cycles. Examination of the drift pins after disassembly showed that many had failed from the area at which they were in contact with the inserted steel plate near the center. We estimate that fatigue fracture occurred at 16 × δ_{pt} cycles.

When we compared the direction θ of the stress acting from the drift pin, we found no obvious differences due to θ for initial stiffness or joint yield strength. Based on this, we conclude that the effects on individual drift pin performance due to the direction θ of the stress acting from the drift pin are negligible.

Table 5: *Characteristic values obtained from tests*

Actual angle [°]	Yield strength P_y [kN] / Yield displacement δ_y [mm]	Maximun strength P_{max} [kN] / Displacement at Pmax δ_{max} [mm]	Initial stiffness K_1 [kN/mm]	Secondary stiffness K_2 [kN/mm]	Mode
0	31.6 / 2.79	47.0 / 24.3	11.6	0.72	IV,IV,IV
30	29.4 / 3.05	44.9 / 22.7	10.0	0.79	IV,IV,IV
60	31.4 / 2.21	46.3 / 24.8	14.4	0.66	IV,IV,IV
90	32.6 / 2.56	45.7 / 24.4	13.3	0.60	III,III,IV
ALL	31.3 / 2.65	46.0 / 24.0	11.8	0.69	-

θ=0° θ=60°

Figure 11: *Condition of joint tensile test pieces after disassembly*

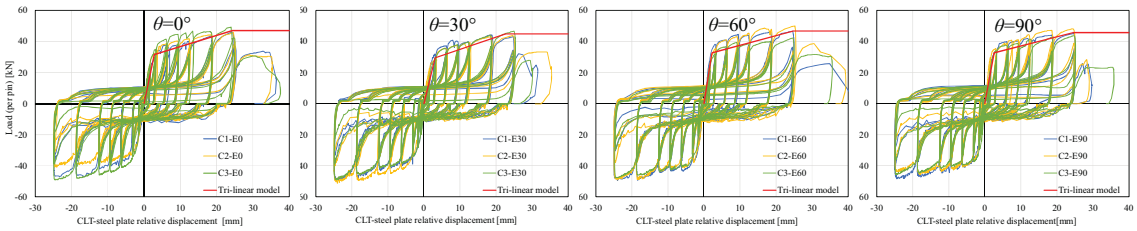

Figure 10: *Individual joint tensile test load displacement relationship*

https://doi.org/10.52202/069179-0433

4 FINITE ELEMENT METHOD ANALYSIS

4.1 ANALYSIS AIMS

We performed our analysis by the finite element method for the semi-rigid beam end joint full-size bending test performed in Section 2. We then compared the analysis results to the test results. Here, we drew on the measurements obtained in the tests described in Section 3 to assess individual drift pin joint and material strength for the inserted steel plate.

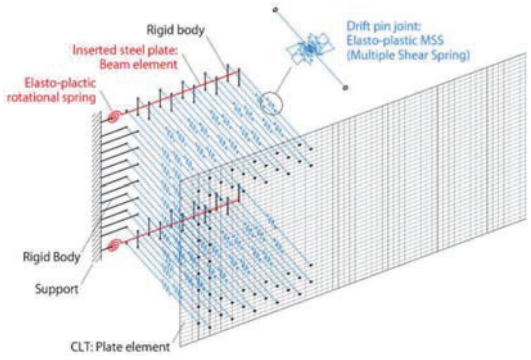

Figure 12: *Overview of analysis model*

Table 6: *Analysis model details*

Element	Element type	Details
CLT	Plate element	t=210mm, E_0=4,285kN/mm^2, E_{90}=1,714N/mm^2, G=0.5kN/mm^2
Drift pin	MSS (n=4)	k_1=5.90kN/mm, p_1=10.52kN k_2=0.342kN/mm, p_2=15.45kN
Inserted steel plate	Beam element	B×D = 19mm×340mm Elasto-plastic spring for root area (See Figure 13.)

* E_o : Young's modulus in strong axis direction,
E_{90} : Young's modulus in weak axis direction
G : Elastic shear modulus
k_1,k_2: Stiffness of each shear spring
p_1,p_2: Strength of each shear spring

4.2 ANALYSIS MODEL

Table 6 lists the details of the analysis model. Figure 12 provides an overview of the model. CLT stiffness is specified as described in reference [4]. We modeled the inserted steel plate individual drift pin joint as a tri-linear model using a multiple shear spring (MSS, with number of partitions n = 4). We calculated individual shear spring stiffness value k_1 and k_2 and yield load p_1 and p_2 by applying the following equations, as in reference [5].

$$k_1 = {K_1}\Big/{\sum_{i=1}^{n} \sin^2 \frac{1}{n}\pi} \quad (3)$$

$$k_2 = {K_2}\Big/{\sum_{i=1}^{n} \sin^2 \frac{1}{n}\pi} \quad (4)$$

$$p_1 = {P_y}\Big/{\sum_{i=0}^{n-1} \sin \frac{1}{n}\pi} \quad (5)$$

$$p_2 = {P_{max}}\Big/{\sum_{i=0}^{n-1} \sin \frac{1}{n}\pi} \quad (6)$$

Here, k_1 is the initial stiffness of each shear spring [kN/mm], p_1 is the first yield load for each shear spring [kN], k_2 is the secondary stiffness of each shear spring [kN/mm], p_2 is the second yield load for each shear spring [kN], K_1 is the initial stiffness of the individual joint [kN/mm], K_2 is the secondary stiffness of the individual joint [kN/mm], P_y is the yield strength of the individual joint [kN], and P_{max} is the maximum strength of the individual joint [kN]. Each Characteristic value of the individual joint are treated as independent of angle based on the test results described in Section 3, in which we observed no obvious differences due to angle for either. Thus, we used the mean values of the test results for all 12 test pieces (see Table 5 for values).

We modeled the inserted steel plate root area as a rotational spring with tri-linear restoring force properties, as shown in Figure 13. The initial stiffness was set to K_0 = 135,912 kNm/rad, derived from the elastic analysis of the U-shaped steel plate. With the rotational spring, we replaced the skeleton curve obtained from the results of equations (7) to (13) while reducing the stiffness by the ratio of the cross-sectional moment of inertia of the residual elastic region to the cross-sectional moment of inertia of the entire cross section with a tri-linear model.

$$M_y = Z \cdot \sigma_y \quad (7)$$

$$M_p = Z_p \cdot \sigma_y \quad (8)$$

$$M_i = M_y + (M_p - M_y)i/m \quad (9)$$

$$x_i = \sqrt{\frac{3D^2}{4} - \frac{3M_i}{B\sigma_y}} \quad (10)$$

$$I_i = \frac{B(2x_i)^3}{12} \quad (11)$$

$$K_i = I_i / I_0 \, K_0 \quad (12)$$

$$\theta_i = \theta_{i-1} + \frac{(M_p - M_y)/m}{(K_i + K_{i-1})/2} \quad (13)$$

Here, M_y is the yield moment [kNm]; Z is the section modulus [mm^3]; σ_y is the inserted steel plate yield stress (= 297) [N/mm^2]; M_p is the fully plastic moment [kNm]; Z_p is the plastic section modulus [mm^3]; i is the number of steps; m is the number of divisions (= 10); M_i is the bending moment for step i [kNm]; x_i is the non-plasticized part thickness for step i [mm]; D is the steel plate thickness (= 340) [mm]; B is the steel plate width (= 19) [mm]; I_i is the cross-sectional moment of inertia for step i [mm^4]; K_i is the rotational stiffness for step i [kNm/rad]; and θ_i is the rotation angle for step i [rad].

The first break point with the tri-linear model occurs when the yield moment M_y is reached. The second break point occurs when the fully plastic moment M_p is reached. These were determined so that Area 1 and Area 2 in Figure 13 are identical. The calculations here for M_y and M_p assume the inserted steel plate yield stress of 297 kN/mm^2 (see Table 2) used in Section 2 for the inserted steel plate yield stress.

https://doi.org/10.52202/069179-0433

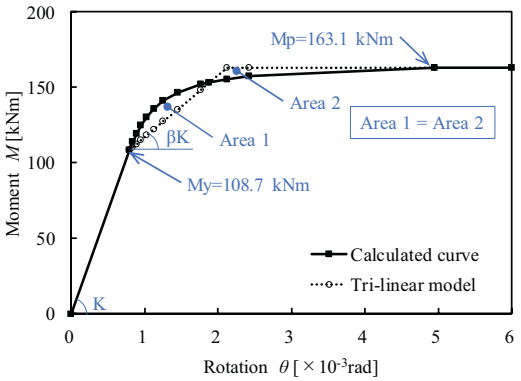

Figure 13: *Rotational spring of inserted steel plate root area*

4.3 ANALYSIS CONDITIONS

The model set was subjected to static incremental loading analysis. Figure 14 shows the analysis conditions. Incremental loading analysis was performed by positioning the load 2,815 mm from the end of the CLT in the same way as in the full-size tests, with the 41 nodes at that position connected to rigid beam elements. A nodal load was applied to the uppermost node.

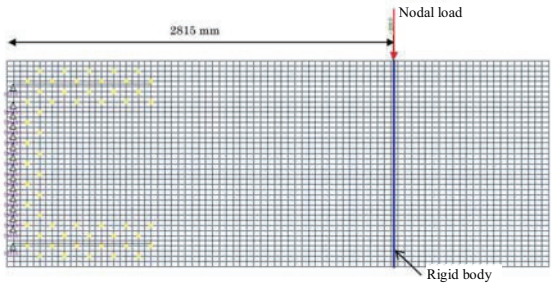

Figure 14: *Analysis conditions*

4.4 ANALYSIS RESULTS

4.4.1 Moment-rotation angle relationship

Figure 15 shows the relationship between moment and rotation angle for the joint. Joint moment M is defined as the value obtained by multiplying the shear force applied to the model by the moment arm length (described later) of 2.686 m. The solid lines indicate the results for the three test pieces. The dashed lines indicate incremental analysis results. The "×" symbols (M = 785 kNm, $\theta = 3.91 \times 10^{-3}$ rad) on the dashed line indicate the point at which the displacement of the first drift pin reaches the yield displacement δ_y 2.65 mm of the individual joint in the incremental analysis. The joint load moment at this point is defined as the yield moment ${}_{DP}M_y$ of the drift pin joint obtained from the analysis. The "○" symbols (M = 917 kNm, $\theta = 4.99 \times 10^{-3}$ rad) indicate the point at which bending yield occurs at the root of the inserted steel plate in the incremental analysis (when M_y in Figure 13 is reached). The joint load moment at this point is defined as the yield moment ${}_{PL}M_y$ of the drift pin joint obtained from the analysis. Figure 15 shows that the drift pin yield and inserted steel plate bending yield in the analysis relatively near-simultaneously.

Table 7 compares the mean test results and analysis results for the rotationnal stiffness, yield strength, and ultimate strength of the joint. Ultimate strength M_u in the analysis results is defined as the joint moment when a bi-linear curve is drawn so that the initial gradient is the rotational stiffness and the area is equivalent to the joint moment-rotational angle relationship in the range up to 1/50 rad.

From Figure 15, the finite element method analysis was able to track the experimental results with good accuracy. The load increase after yielding can be reproduced by inputting the spring of the drift pin joint and the inserted steel plate at root area of the U-shaped part with a tri-linear type. The difference between the analysis results and the experimental results is large in the range of after 1/50 rad, but this is considered to be because the decrease in strength after reaching the maximum strength of each element was not reproduced in the analysis.

4.4.2 Joint fixed point position

This paper defines as the joint fixed point the point on a semi-rigid beam joint at which no displacement occurs when a load results in rotational deformation. The distance from the point at which the force is applied to the fixed point of the joint is used as the moment arm length for the calculation of the joint moment.

Figure 7 shows the 1/300 rad cycle positive peak for the semi-rigid beam end joint full-size in-plane bending test, together with the analysis results for the same load conditions. The analysis results at this point are within the elastic range. Figure 7 confirms that the joint fixed point generally coincides with the test results. Based on these results, we defined the y-intercept (= 129 mm) of the analysis results (dashed line) as the joint fixed point position. Based on the dimensional relationship shown in Figure 4, we calculated the moment arm length to be 2,686 mm (= 2,815 mm - 129 mm).

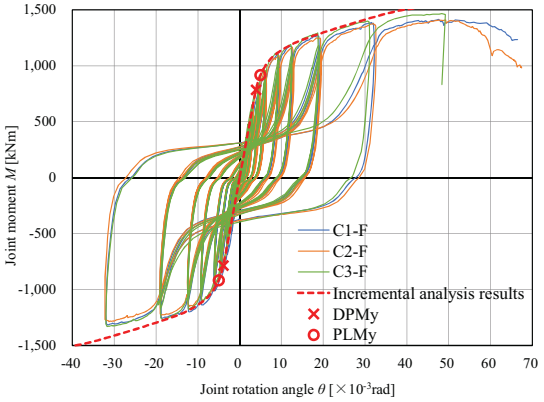

Figure 15: *Joint moment-rotation angle relationship (Comparison of test results and analysis results)*

Table 7: *Comparison of test data and analysis data*

Test Ppiece	Rotational stiffness K_θ [kNm/rad]	Driftpin joint yield strength ${}_{DP}M_y$ [kNm]	Steel plate yield strength ${}_{PL}M_y$ [kNm]	Ultimate strength M_u [kNm]
Test data (mean of 3 values)	203,576	852	938	1,119
Analysis data	202,716	785	917	1,168
Analysis data/Test data	1.00	0.92	0.98	1.04

https://doi.org/10.52202/069179-0433

5 CONCLUSIONS

We carried out full-size in-plane bending tests on the end joint, and finite element method analysis to verify the performance of joints on semi-rigid timber beams using CLT. Our findings are presented below.

- Full-size in-plane bending tests on the end joint of semi-rigid timber beams using CLT demonstrated the capacity to achieve the specified strength and deformability.
- The bending yield of individual drift pin joints and the bending yield of the U-shaped inserted steel plate root area may improve the deformability of semi-rigid timber beam joints.
- Both individual joint initial stiffness and joint strength had minimal dependence on angle, given the specifications used in the individual joint tensile tests.
- The results confirm that an analysis model based on the finite element method can accurately evaluate the experimental values.
- The position of the point at which displacement does not occur (joint fixed point) was determined from the analysis results. The results for the joint fixed point were generally consistent with test results.

ACKNOWLEDGEMENTS

This study was carried out using materials kindly provided by Meiken Lamwood Corp. We are grateful for the support of all those involved.

REFERENCES

[1] Kuenzi EW : Theoretical design of a nailed or bolted joint under lateral load, USDA, No.D1951, March 1955

[2] Johansen K. W.: Theory of timber connections, Int. Assoc. Bridge and Struct. Eng 9 : pp.249-262, 1949

[3] Japan 2×4 Home Builders Association : Structural Calculation Guideline for Platform Frame Wall Construction, 2007.

[4] Japan housing and Wood Technology Center : Design and Construction Manual for Timber Structures using Cross Laminated Timber (CLT), 2016.

[5] Architectural Institute of Japan : Recommendation for the Design of Seismically Isolated Buildings, 2013.

World Conference on Timber Engineering Oslo 2023

AN EXPERIMENTAL AND NUMERICAL INVESTIGATION ON A DOVETAIL NOTCHED CONNECTION FOR CROSS-LAMINATED-TIMBER-CONCRETE COMPOSITE SLABS

Vanthet Ouch[1], Piseth Heng[2], Hugues Somja[3], Thierry Soquet[4]

ABSTRACT: A specific dovetail notched connection has been proposed for CLT-concrete composite slabs. The particularity of this notched connection is its dovetail shape that provides a mechanical locking to limit the uplift without metallic screws. The experimental pushout results showed high stiffness and resistance. However, low ductility was obtained due to the failure by rolling shear of CLT. The performance and failure mechanism of the notched connector can be influenced by numerous variables. This paper presents a numerical study on the effect of different parameters related to the geometry and material properties, on the performance of the notched connection. First, an advanced 3-dimensionnal finite element model of the experimental test considering the nonlinear properties of the materials and the orthotropic behaviour of the CLT has been developed. The results of this model were validated against the experimental ones obtained from static pushout tests. A good agreement of the force-slip curves was obtained, and the model was able to reproduce the failure observed in the tests. Having validated the FE model, the parametric study was conducted to better understand the notched connector under the influence of variations in geometrical and material properties. Two different failure modes were obtained : the concrete shear at the notch and the rolling shear of the cross-layer of the CLT panel. The rolling shear failure of the CLT panel should be avoided in order to improve the post peak-performance of the notched connector. Reducing the notch length and increasing the heel length provoke the concrete shear failure of the notch, which improves the ductility of the connector if sufficient V-shape rebars are placed inside the notch. The stiffness of the connector can be influenced by changing the parameters such as the concrete resistance, the thickness of the concrete panel, the amount of V-shape rebars, the notch length and the heel length.

KEYWORDS: Dovetail notched connector, Pushout test, Parametric study, CLT-concrete composite slabs.

1 INTRODUCTION

Being responsible for around 39 percent of all carbon emissions around the world, the building and construction sectors are considered as the main contributor to the climate change [1]. The devastating consequences of climate changes urge the involved organizations to revolutionize building materials and construction methods in order to achieve 100 percent net zero emissions buildings by 2050. With such an objective, sustainable solutions for buildings have been widely studied. As an alternative to the traditional concrete or timber structures, Timber Concrete Composite (TCC) slabs might be an interesting solution that balance environmental impacts with structural and economical performances. A TCC slab is formed by laying a concrete panel on top of a timber panel and connecting them together using shear connection systems. This combination benefits the high performances of concrete in compression and of timber in tension. The structural response of the composite system is ordinarily governed by the strength, stiffness, and ductility performance of the connection system.

Different types of shear connection systems have been developed in the past including steel fasteners, notches, and glue in order to enhance structural performance and cost-efficiency of TCC structures [2]. Among them, notched connection might be considered as the most effective system due to its high strength, stiffness as well as construction convenience. However, for this notched connection, steel fasteners are in general inserted in the timber and connected to the concrete notch to improve the shear strength and ductility of the connection as well as the uplift resistance between the concrete and timber. These steel fasteners are expensive and time-consuming in the construction process.

In response, a dovetail notched connection for CLT-concrete composite slabs has been proposed by T. Soquet and investigated by the authors [3]. The particular shape

[1] Vanthet Ouch, LGCGM/Structural Engineering Research Group, INSA de Rennes, France and Department of Civil Engineering, Institute of Technology of Cambodia, vanthet.ouch@insa-rennes.fr
[2] Piseth Heng, LGCGM/Structural Engineering Research Group, INSA de Rennes, France, piseth.heng@insa-rennes.fr
[3] Hugues Somja, LGCGM/Structural Engineering Research Group, INSA de Rennes, France, hugues.somja@insa-rennes.fr
[4] Thierry Soquet, Architecture Plurielle agency, Rennes, France, t.soquet@archi-plurielle.com

https://doi.org/10.52202/069179-0434

of the proposed notch configuration provides a geometrical constraint to limit the uplift without the need for metallic elements (see Figure 1). Experimental pushout tests have been conducted to determine the mechanical properties of the notched connection. It was found that the connection system showed high strength and stiffness with brittle failure due to the limited rolling shear resistance of the cross-layers of the CLT panel.

This paper presents a numerical study on this notched connection using Abaqus/Explicit [4] in order to determine the influence of selected parameters on the behaviour of the notched connection. First, a 3D FE model of the pushout test was developed and validated against the experimental results. Then, a parametric study on the variables defining the geometry and the materials was carried out.

2 SUMMARY OF THE EXPERIMENTAL WORK

2.1 MATERIAL CHARACTERISATION

The concrete was tested to determine the actual properties on the same day as pushout tests. Two series of three-cylinder specimens with a dimension of 11×22cm were tested for compressive strength f_{cm} and tensile strength f_{ct}. Table 1 presents the results obtained from concrete characterisation.

Table 1: *The results obtained from the concrete test*

Test	f_{ct} [MPa]	f_{cm} [MPa]
1B-1	3.20	34.51
1B-2	2.56	29.12
1B-3	3.39	39.51
Average (Var.)	3.05 (0.36)	34.38 (4.24)

CLT panels TOT'm X [5] were used. They are constituted of wooden planks with a thickness of 33 mm each, stacked in crossed layers at 90° and glued together over their entire surfaces (except the edge surfaces). Small-scale characterisation tests including longitudinal compression tests and rolling shear tests were conducted. The longitudinal compression tests were carried out in accordance with EN 408 [6] on 12 samples while the rolling shear tests using a configuration proposed in previous research [7] were carried out on 5 samples with three lamination layers (one cross layer sandwiched by two longitudinal layers). These samples had dimensions of 99 mm thick by 140 mm large by 269 mm long. Table 2 presents the value of longitudinal compression strength $f_{c,0}$,rolling shear strength f_v, and rolling shear modulus G_r obtained from characterisation test.

Table 2: *The results obtained from the timber test*

Test	$f_{c,0}$ [MPa]	G_r [MPa]	f_v [MPa]
Avg.	31.26	127	1.49
(Var.)	(5.33)	(25)	(0.17)

Steel rebars for the concrete panel and the notch connector have a nominal yield strength of 500 MPa.

2.2 RESULTS OF PUSHOUT TESTS

A series of three identical symmetrical pushout tests (1B-1, 1B-2 and 1B-3) were performed in order to determine the shear resistance, the stiffness, the deformation capacity and the failure mode of the dovetail notched connectors. The dimensions of the three specimens are presented in Figure 1. Specimen 1B-1 has a width of 500 mm, whereas specimens 1B-2 and 1B-3 have a width of 400 mm. The specimen was placed vertically on a support table, and the load was applied on the top surface of the CLT panel using a force jack with the capacity of 1500 kN (see Figure 2a). The test procedure described in Annex B of Eurocode 4 part 1-1 (2004) [8] was followed. The relative slip at the contact layer between concrete and timber panel was measured using Digital Image Correlation method with a precision of ± 0.1 mm. Two cameras were employed to record the relative displacements in the back face and the front face of the tested specimens.

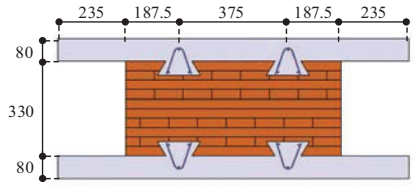

(a) Pushout specimen

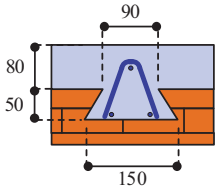

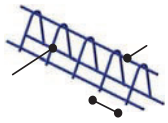

(b) Notched connector *(c) V-shape rebar cage*

Figure 1: *Configuration of pushout specimen (unit in mm)*

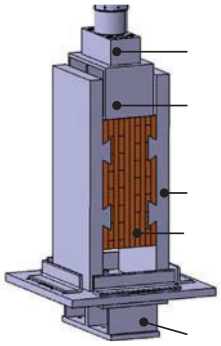

(a) Test setup *(b) Failure mode*

Figure 2: *Description of pushout test setup and failure mode*

Figure 3 and Table 3 present the force-slip curves and the results obtained from the pushout tests, respectively. The test results showed high shear resistance and stiffness for all the three tested specimens. However, a low ductility

was obtained, as the failure mode was governed by the shear failure of one cross-layer of the CLT panel (see Figure 2b). The maximum relative slip obtained from the experimental tests ranged between 0.8 mm and 1.6 mm. The maximum loads attained per connector per meter width (F_{max}) were 420 kN/m, 428 kN/m and 464 kN/m for test 1B-1, 1B-2 and 1B-3, respectively. The slip modulus to be used at serviceability limit state (SLS) K_s and ultimate limit state (ULS) K_u reported in Table 3 were computed following the method proposed by Ceccotti [9].

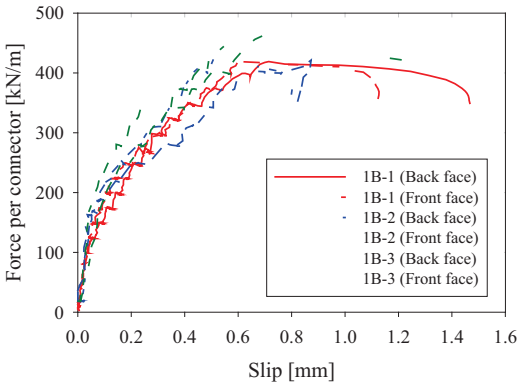

Figure 3: *Load-slip curve of pushout tests*

Table 3: *The results for one connector per one meter linear*

Test	F_{max} (kN/m)	$\delta_{F_{max}}$ (mm)	K_s (N/mm/m)	K_u (N/mm/m)
1B-1	420	0.79	1.81×10^6	1.41×10^6
1B-2	428	1.02	1.38×10^6	0.85×10^6
1B-3	464	0.90	1.29×10^6	1.10×10^6
Avg.	437		1.49×10^6	1.03×10^6

3 NUMERICAL STUDY

As mentioned above, the numerical study is divided into two steps. The first step consists of developing a 3D FE model of the experimental pushout test using ABAQUS/Explicit. The results of this model are validated against the experimental results. In the second step, the validated model serves to carry out a parametric study on the influence of various parameters on the behaviour of the notched connection.

3.1 MODEL ESTABLISHMENT

3.1.1 Geometry and boundary condition

To improve the computation speed, only one fourth of the test configuration was considered by taking advantages of the symmetric disposition and boundary conditions. All the components of the specimen as well as the steel loading block were modelled (see Figure 4a). The symmetric boundary conditions were applied at the highlighted surfaces in red and in blue colour (See Figure 4b), constraining the displacements in X-direction and Z-direction, respectively.

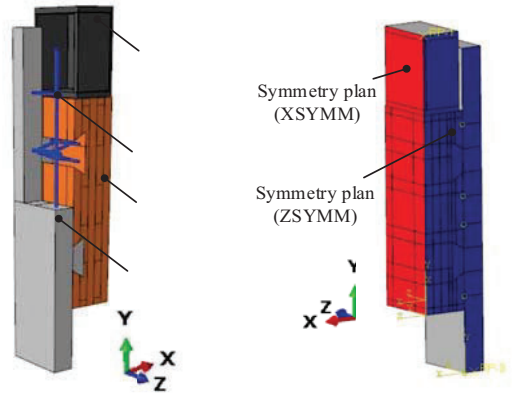

(a) Geometry *(b) Symmetry condition*

Figure 4: *Geometry and symmetry condition of the FE model*

The support was modelled by applying a rigid constraint to the bottom surface of the concrete panel that rigidly follows the movement of a reference point (see Figure 5a). All the degrees of freedom of this reference point were fixed.

The loading was simulated by applying an imposed displacement to another reference point that governs a rigid displacement of the top flange of the loading block HEA-300 (see Figure 5b).

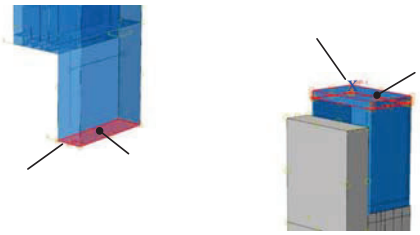

(a) Support *(b) Loading*

Figure 5: *Support and Loading condition of the FE model*

3.1.2 Material modelling

Concrete was considered as a non-linear isotropic material [10]. The concrete damaged plasticity (CDP) model available in Abaqus/Explicit was adopted [11] to reproduce properly the two main behaviours of concrete (compression crushing and tensile cracking). The actual concrete strength obtained from cylinder tests was used. Moreover, the parameters to define the flow potential and the yield surface including the dilatation angle Ψ, the eccentricity ϵ, the ratio of biaxial compressive strength to uniaxial compressive strength f_{b0}/f_{c0}, the shape factor for yield surface K_c, and the viscosity parameter μ were defined as in Table 4.

Table 4: *Parameters of concrete damaged plasticity model*

Ψ [^{0}]	ϵ	f_{b0}/f_{c0}	K_c	μ
40	0.1	1.16	0.67	0

Timber was considered as an orthotropic material using the assumption that the stiffness and the strength in radial

https://doi.org/10.52202/069179-0434

and in tangential directions were identical. The mechanical stiffnesses were derived from the technical specification [5] except the rolling shear modulus G_r. The latter was taken from a specific shear test (see Table 5).

Table 5: *Mechanical stiffnesses of the timber*

E_1 (MPa)	$E_2=E_3$ (MPa)	$G_{12}=G_{13}$ (MPa)	G_{23} (MPa)	ν (-)
11000	370	690	127	0

Note: The subscription 1,2,3 refer to longitudinal, transversal, and radial directions, respectively.

The plasticity of the timber was defined using the orthotropic yield criteria proposed by Hill [12]. This criterion is an extension of Von-Mises yield criterion that consider the orthotropic behavior of the material. The stress potentials are related to the compressive strength parallel to grain $f_{c,0}$ and the shear strength of the timber f_v [13]. The timber strength was adopted from the characterization tests with $f_{c,0}=31$ MPa and $f_v=1.49$ MPa. Therefore, the six input parameters in ABAQUS were determined and are presented in Table 6.

Table 6: *Stress potentials adopted in the FE model*

R11	R22	R33	R12	R13	R23
1	0.0965	0.0965	0.22	0.22	0.084

Steel rebars were considered to be an isotropic material and to exhibit a bilinear elastic-plastic behaviour in the FE model. Properties based on experimental tests from literature [14] were used and are summarized in Table 7.

Table 7: *Tensile properties of steel reinforcement*

f_y (MPa)	f_u (MPa)	E (GPa)	ε_y [-]	ε_u [-]
500	635	200	0.00317	0.14559

3.1.3 Mesh definition and contact interaction

The concrete panel, the CLT panel and the HEA-300 loading block were meshed using hexahedral element with reduced integration and hourglass control (C3D8R) while the steel rebars were modelled using two-node beam element, B31. A finer mesh (5 mm) was generated in the neighbouring region of the connection system (see Figure 6). The rest had a size of 10 mm.

Surface-to-surface contact between concrete panel and CLT panel as well as between loading block (HEA 300) and CLT panel (see Figure 7) had to be considered. The contact properties were defined by hard contact and friction penalty formulations for the normal and tangential behaviours, respectively. In this study, the friction coefficient for the contacts between concrete and timber, and between steel and timber were 0.62 [15] and 0.50 [16], respectively. Apart from that, an embedded constraint was adopted for the interaction between the steel reinforcement and the concrete panel.

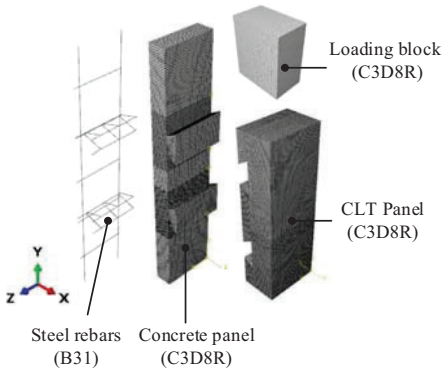

Figure 6: *The mesh of components in the FE model*

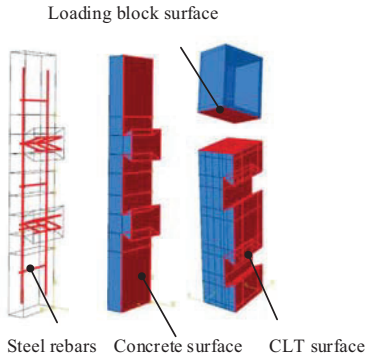

Figure 7: *Contact surface of each component in the FE model*

3.2 MODEL VALIDATION

The failure mode from the simulation was governed by the rolling shear failure of the CLT panel, reproducing the same failure mode as in experimental tests. Figure 8a,b illustrates the deformed shape and rolling shear stress at a maximum load obtained in FE model. Due to the configuration of the loading block that covers all the top surface of the CLT panel, a part of the load was transferred directly to the concrete notch in form of compressive force in the longitudinal layer and the rest was transmitted via rolling shear action of the cross-layers (see Figure 8c). Therefore, the real rolling shear resistance should be lower than the maximum force obtained in the test.

Figure 9a presents the comparison of force-slip curves obtained from the FE model and from the experimental tests. It can be seen that the FE model estimated a peak load at around 431 kN that is in good agreement with the experimental value, with approximately 2 percent difference. However, the behaviour of the notched connector in the FE model is stiffer, as smaller slip was obtained at the peak load compared to the experimental results. In fact, during the experimental tests, several cyclic loadings were applied, and rather frequent pauses were taken to observe the cracking in the concrete. This has generated additional slips due to additional creep strains. In order to be able to compare the results with the ones from the FE model, the slips caused by the cyclic loadings and the pauses were removed from the results. Figure 9b presents the new load-slip curves. A better

https://doi.org/10.52202/069179-0434

agreement of the curves was obtained. The comparison between the results obtained from FE model and the ones from experimental tests are summarized in Table 8. The differences of maximum force F_{max} and corresponding slip $\delta_{F_{max}}$ were respectively 2 percent and 3 percent while higher discrepancies of slip modulus were noticed with 22 percent and 8 percent for the values at SLS and at ULS, respectively. The precision of the Digital Image Correlation technique adopted in the pushout tests was 0.1 mm. Hence, it is difficult to obtain accurate experimental values of the slip modulus, as the connection is very stiff.

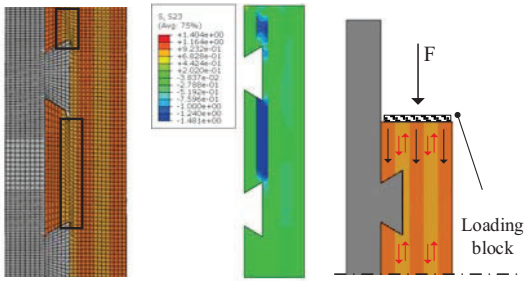

(a) Deformed shape *(b) Rolling shear stress* *(c) Load transfer from loading block*

Figure 8: *Deformed shape of the cross-layer, rolling shear stress, and load transfer mechanism from loading block in the FE model*

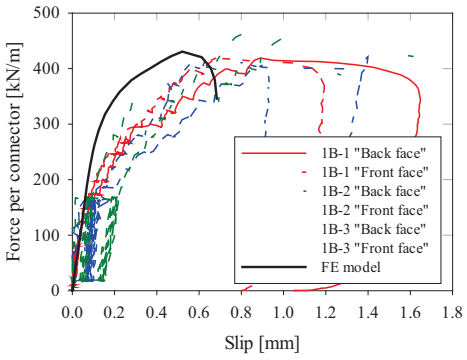

(a) Original experimental load-slip curves

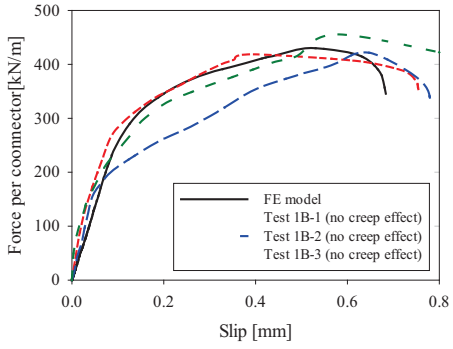

(b) Modified Load-slip curves

Figure 9: *Comparison of load-slip curves*

Table 8: *Results of the FE model and experimental tests*

Test	F_{max} [kN/m]	$\delta_{F_{max}}$ [mm]	K_s [N/mm/m]	K_u [N/mm/m]
1B-1	420	0.39	3.92×10^6	3.22×10^6
1B-2	428	0.65	3.13×10^6	1.40×10^6
1B-3	464	0.50	3.38×10^6	2.08×10^6
Avg.	437	0.54	3.48×10^6	2.24×10^6
FEM	431	0.52	2.73×10^6	2.43×10^6
Diff.	2%	3%	22%	8%

Note: Diff.=(Avg.-FEM)/FEM

3.3 PARAMETRIC STUDY

3.3.1 Parameters investigated

To gain a thorough understanding of the mechanical behaviour and to predict the possible mechanisms of the notched connection system, a parametric study was conducted using the validated FE model. The investigated parameters were divided into two groups. The first group of parameters involved general parameters, including the concrete strength f_c, the thickness of the concrete panel h_c, and the heel length of the CLT panel l_t (see Figure 10a). On the other hand, the second group of parameters (see Figure 10b) were associated with the notched connector, including notch length l_n, notch depth d_n, and cross-sectional area of the V-shape reinforcement inside the notched connection A_s. However, the material and geometrical properties of the CLT (mechanical properties and thickness of the CLT panel) is invariable since they are fixed in the industrialized solution. Additionally, the notched angle of 59.04^0 is fixed to maintain the notched shape, while the V-shape rebars can be adjusted to fit inside the notched connector.

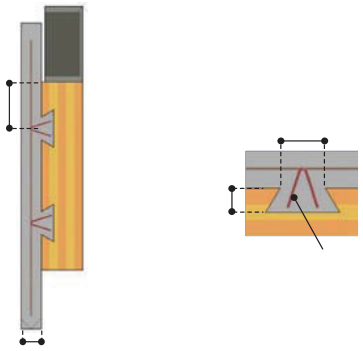

(a) First group of parameters *(b) Second group of parameters*

Figure 10: *Geometrical parameters studied*

3.3.2 First group of parameters

Table ***9*** describes the details of the first group of parameters. C1, C2, and C3 simulations investigated the parameter of concrete strength, thickness of the concrete panel, and heel length of the CLT panel, respectively. In Case C3-1, the heel length of the CLT panel was increased from 187.5 mm to 375 mm.

https://doi.org/10.52202/069179-0434

Table 9: *The details of the first group of parameters*

Parameter		f_c [MPa]	h_c [mm]	l_t [mm]
Reference		35	80	187.5
C1	C1-1	25	80	187.5
	C1-2	45		
C2	C2-1	35	50	187.5
	C2-2		100	
C3	C3-1	35	80	375

The force-slip curves of all the cases in the first group of parameters are drawn in Figure 11. The results obtained from the numerical simulation are presented in Table 10. The value in bracket refers to the difference of peak loads in the different cases to the one in the reference case.

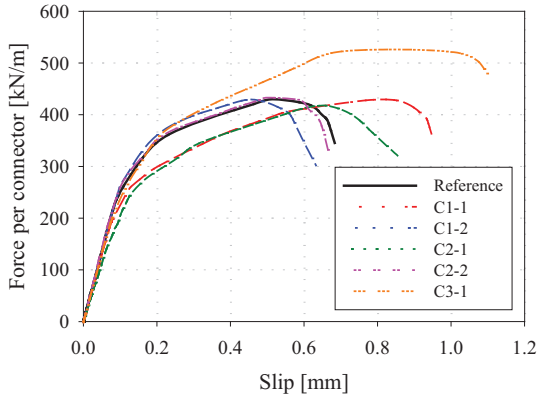

Figure 11: *Force-slip curve of numerical study of C1/C2/C3*

Table 10: *Results obtained from numerical study of C1/C2/C3*

Test	F_{max} [kN/m]	δ_{Fmax} [mm]	K_s [N/mm/m]	K_u [N/mm/m]	Failure mode
Ref.	431 (1.00)	0.52	2.73×10^6	2.43×10^6	RS
C1-1	429 (1.00)	0.78	2.58×10^6	2.03×10^6	RS
C1-2	430 (1.00)	0.45	2.73×10^6	2.63×10^6	RS
C2-1	419 (0.97)	0.66	2.17×10^6	1.96×10^6	RS
C2-2	435 (1.00)	0.48	2.87×10^6	2.62×10^6	RS
C3-1	526 (1.22)	0.72	2.51×10^6	1.95×10^6	CS

Note: RS refers to Rolling shear of the CLT while CS refers to Concrete shear of the concrete panel.

Except for Case C3-1, the failure of the notched connector was governed by the rolling shear failure of the cross-layer of the CLT panels. The maximum force ranged from 419 kN to 435 kN and was logically not influenced by the parameters related to the concrete. The maximum difference was approximately 3 percent compared to the reference case. In Case C3-1, the failure was governed by the concrete shear in the lower notched connector, even if the rolling shear stress was large in the cross-layer of the CLT panel. Figure 12 illustrates the tensile damage in the concrete panel, rolling shear stress of the CLT panel, and V-shape rebars stresses under the maximum load. The damage in the critical shear plane in the concrete was close to 1.0, while the V-shape rebars were experiencing the yielding stress (of 500 MPa) in the lower notched connector at the maximum load. It can be inferred that the simulation of Case C3-1 provides an estimation of the connection resistance on the concrete side. A 22 percent increase in the maximum force was observed compared to reference case.

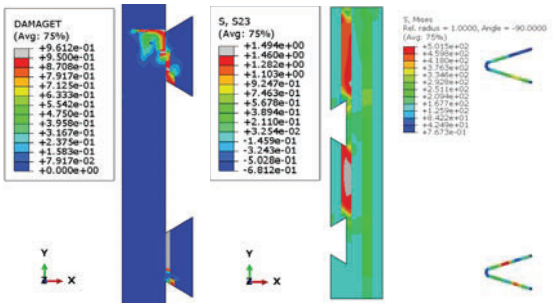

(a) Tensile damage *(b) Rolling shear stress* *(c) Stress of the rebars*

Figure 12: *Tensile damage in concrete and rolling shear stress of the CLT at the maximum load in Case C3-1*

In terms of the force-slip relationship, the curves exhibit similar trends in linear elastic region until a load level of approximately 270 kN. From this load level, Cases C1-1 and C2-1, which adopt lower concrete strength and smaller concrete thickness, respectively, show larger slips than other cases for the same load. The change of the parameters in these cases led to an earlier tensile damage of the concrete panel (see Figure 13). Regarding Case C3-1, a plateau of force-slip curve was noticed, starting from 0.72 mm of slip, where the first failure of the lower notched connector was obtained and ending at 0.99 mm of slip, where the other connector failed and the V-shape rebars in both notches experienced the yielding stress.

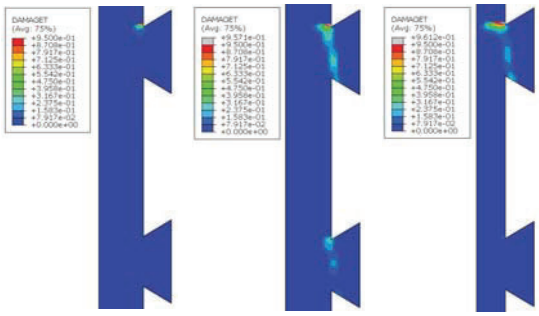

(a) Reference case *(b) Case C1-1* *(c) Case C2-1*

Figure 13: *Tensile damage of the concrete panels at the load level of 270 kN*

In addition, high stiffness was observed in both service and ultimate conditions in all cases, and slips at the maximum load of the first group ranged from 0.45 mm to 0.78 mm. In cases where the failure was related to rolling shear of the CLT panel, the ductility was limited. In case C3-1, as the maximum load was governed by the shear failure in the concrete, a higher slip of approximately 1.1 mm was achieved in Case C3-1.

Regarding other cases, it can be assumed that the concrete strength and the thickness of the concrete slab had little influence on the load bearing capacity of the notched connector since the connector behaviour was limited by the rolling shear resistance of the CLT panel. It is worth to remind that the real rolling shear resistance is lower than the experimental maximum load due to the loading

block configuration that resulted in some loading being transferred directly to the concrete panel via longitudinal compression of the CLT panel. However, lower concrete strength and smaller thickness of the concrete panel reduced the stiffness of the notched connector due to the early damage of the concrete panel.

3.3.3 Second group of parameters

The details of the parameters in the second group are described in Table 11. C4, C5, and C6 simulations investigated the influence of the notch length l_n, the notch depth d_n, and the cross-sectional area of V-shape rebar A_s, respectively. In the reference case, 5 V-shape 6-mm rebars with 90-mm spacing were used in the notched connection, corresponding to a section of 141.37 mm^2. For Case C6-1, no V-shape rebar was used in the notch, whereas 2 6-mm V-shape rebars were included in the notch for Case C6-2.

Table 11: *The details of the second group of parameters*

Parameter		l_n [mm]	d_n [mm]	A_s [mm^2]
Reference		90	50	141.37
C4	C4-1	40	50	141.37
	C4-2	140		
C5	C5-1	90	25	141.37
C6	C6-1	90	50	0
	C6-2			56.55

Figure 14 presents the force-slip relationships for all the cases in the second group of parameters. The results obtained from the numerical simulation are summarized in Table 12. The same two types of failure modes were observed: rolling shear of the CLT panel and concrete shear.

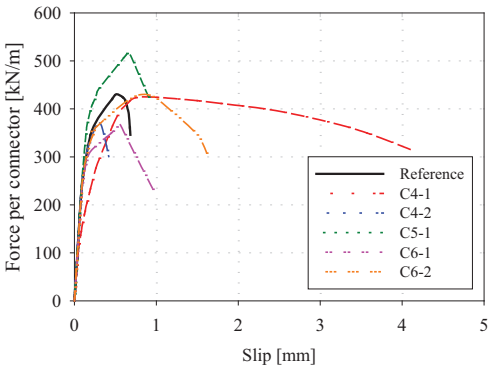

Figure 14: *Force-slip curve of numerical study of C4/C5/C6*

Table 12: *Results obtained from numerical study of C4/C5/C6*

Test	F_{max} [kN/m]	δ_{Fmax} [mm]	K_s [N/mm/m]	K_u [N/mm/m]	Failure mode
Ref.	431 (1.00)	0.52	2.73×10^6	2.43×10^6	RS
C4-1	425 (0.99)	0.85	1.51×10^6	1.11×10^6	CS
C4-2	370 (0.86)	0.30	2.88×10^6	2.80×10^6	RS
C5-1	516 (1.20)	0.65	2.78×10^6	2.54×10^6	CS
C6-1	364 (0.84)	0.53	2.63×10^6	2.60×10^6	CS
C6-2	427 (0.99)	0.75	2.68×10^6	2.36×10^6	RS+CS

Note: RS refers to Rolling shear of the CLT while CS refers to Concrete shear of concrete panel.

In cases C4, the change of notch length resulted in modifying the area of the cross layer of the CLT panel. The decrease of the notch length from 90 mm to 40 mm in Case C4-1 contributed to the higher rolling shear resistance of CLT panel and to the lower shear resistance and stiffness in the concrete. In this case, the failure was governed by the shear failure of concrete in notched connector with a maximum force of 425 kN and a corresponding slip of 0.85 mm. Figure 15 shows the damage in tension of the concrete panel and yield stress of the V-shape rebars inside the notched connection at the maximum load. From force-slip curves, Case C4-1 exhibits higher slip in the elastic region compared to other cases.

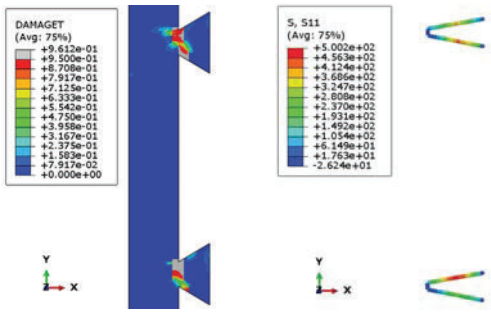

(a) Tensile damage *(b) Stress in tension*

Figure 15: *Concrete shear failure and stress of V-shape rebar in Case C4-1 at maximum load*

Besides, Case C4-2 resulted in rolling shear failure at the maximum force of 370 kN and a corresponding slip of 0.30 mm. In this case, the increase of notched length (140 mm) led to the decrease of approximately 14 percent in rolling shear cross-section (resistance) while the corresponding slip decreased nearly two-fold. As shown in force-slip curves, the behaviour of the notched connector remained in the elastic region when the brittle failure happened in the cross-layer of CLT panel.

Decreasing the notch depth from 50 mm to 25 mm, which is smaller than the first longitudinal layer's thickness (33 mm), increases the working rolling shear section of the CLT panel in Case C5-1. This resulted in a failure that was limited by the shear failure of the concrete at a maximum force of 516 kN and a corresponding slip of 0.65 mm. It can be seen that the load bearing capacity increased by 20 percent compared to that in the reference case. The failure started from the lower notched connector, followed by the upper one as shown in Figure 16a. At the maximum load, high rolling shear stresses were found from the loading surface to the lower notched connector (blue colour) with a maximum rolling shear stress of approximately 1.49 MPa (see Figure 16b).

It should be noted that the failures in Case C5-1 of second group parameters and Case C3-1 of first group parameters, both with the same notch length, were governed by concrete shear. The maximum force in Case C3-1 was 2 percent higher compared to Case C5-1. However, the ductility of Case 3-1 is slightly better than

https://doi.org/10.52202/069179-0434

that of Case C5-1, possibly due to the different anchorage length of the V-shape rebars placed inside the notches.

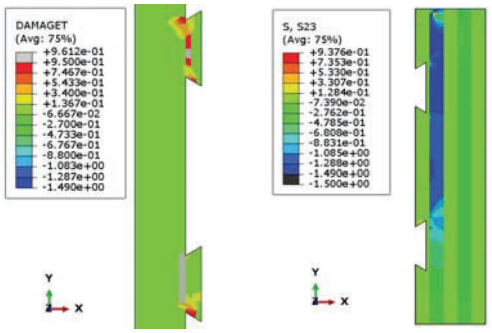

(a) Tensile damage *(b) Rolling shear stress*

Figure 16: *Tensile damage in concrete and rolling shear stress of the CLT at the maximum load in Case C5-1*

The number of V-shape rebars was investigated in Case C6-1 and Case C6-2. It was found that the maximum force decreased when the amount of V-shape rebars was reduced.

The failure mode of Case C6-1 was governed by the concrete shear at the maximum force of 364 kN with a corresponding slip of 0.53 mm. The load bearing capacity decreased by 16 percent, compared to the reference case. When no shear reinforcement was placed inside the notched connector, the concrete damage started earlier, at a load level of approximately 300 kN as shown in force-slip curve (see Figure 14). At the maximum load, the upper notched connector failed first and was followed by the lower one. For the CLT panel, the highest rolling shear resistance obtained was approximately 1.43 MPa (see Figure 17).

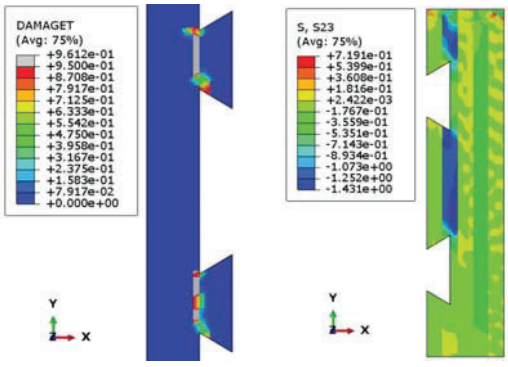

(a) Tensile damage *(b) Rolling shear stress*

Figure 17: *Tensile damage in concrete and rolling shear stress of the CLT at the maximum load in Case C6-1*

In Case C6-2, the failure was initiated by concrete shear failure of the notched connector. The maximum load was obtained at 427 kN with a corresponding slip of 0.75 mm, when the upper notched connector failed. At this point, a high rolling shear stress was obtained in the cross-layer of the CLT panel.

The V-shape rebars were subjected to a tensile stress of 478 MPa at the maximum load and experienced the yield stress shortly after when the concrete of the upper notched connector failed. The tensile damage of the concrete and the rolling shear stress of the CLT panel can be visualized in Figure 18.

In terms of stiffness, the studied parameters have minimal influence, except for the Case C4-1, in which the stiffness decreased more than half compared to the reference case. However, the notched connector in Case C4-1 can be still considered as stiff, as its stiffness is higher than the suggested value of the design slip modulus of 1.00×10^6 N/mm/m proposed in the recommendations for the design of TCC beams with notched connectors given in BNTEC [17].

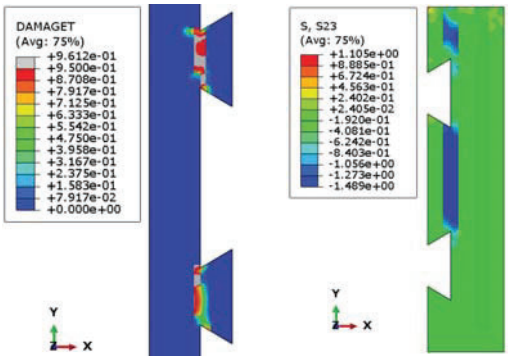

(a) Tensile damage *(b) Rolling shear stress*

Figure 18: *Tensile damage in concrete and rolling shear stress of the CLT at the maximum load in case C6-2*

Regarding the ductility, no improvement was obtained by changing the values of the parameters in the second group, except for Cases C6-2 and C4-1 where ultimate slips of around 1.5 mm and 4.2 mm, respectively, were obtained.

4 CONCLUSION

This paper presents the experimental and numerical investigations on a novel notched connector for CLT-concrete composite floor systems. The pushout tests showed high shear resistance and stiffness of the connector, but low ductility, as the failure was governed by rolling shear failure of the cross-layer of the CLT panel. In addition, a full FE model of the pushout tests using ABAQUS/Explicit was established and validated against the experimental results. The simulation was capable of reproducing the failure mode of the experimental tests and giving a good agreement of force-slip curve with the results from pushout tests. The validated model was then used for a parametric study to investigate the influence of various parameters of the geometries and the materials. The following results are obtained from the parametric study:

- If not changing the notch dimensions, the strength and the thickness of the concrete panel had no significant influence on the strength, as it was governed by the rolling shear failure in cross-layer of the CLT panel. However, they had a slight effect on the stiffness of the connector, as earlier damage in the concrete notches was obtained in these cases.

- An increase of the heel length led to a larger cross-layer area of the CLT panel, and the failure was then governed by concrete shear of the notched connector. A small improvement of the post-peak behaviour was obtained. An estimation of the load provoking the concrete failure in shear was obtained. It was 22 percent larger than the mean of the experimental results.
- Decreasing the notch length from 90 mm to 40 mm was able to provoke a concrete shear failure, resulting in the improvement of the ductility of the system. Lower stiffness was found when adopting a notch length of 40 mm, but it was larger than the value suggested in BNTEC [17] for notched connections.
- A reduction of the notch depth to a value smaller than the thickness of the first longitudinal layer of the CLT panel increased the cross-section of the rolling shear of the CLT panel. This led to a higher strength and stiffness. However, low ductility was still observed.
- A higher amount of V-shape rebars increased the strength and stiffness of the notched connection.

In conclusion, based on the numerical results, it is possible to improve the ductility of the present notched connection by prioritizing the shear concrete failure of the notch, if a sufficient number of V-shape rebars are placed inside the notch. This prioritization can be obtained by increasing the spacing between the connectors, in order to increase the rolling shear resistance. The concrete failure should happen for a load 22 percent larger than the experimental resistance obtained by pushout tests. However, these conclusions need to be confirmed by additional experimental investigations.

REFERENCES

[1] F. Schreyer, G. Felix, et al. Common but differentiated leadership: strategies and challenges for carbon neutrality by 2050 across industrialized economies. Environmental Research Letters 15.11 (2020): 114016.

[2] A. Ceccotti, Timber-concrete composite structures Timber Eng., 2 (1) (1995)

[3] V. Ouch, P. Heng, Q. H. Nguyen, H. Somja, T. Soquet, a notched connection for CLT-concrete composite slabs resisting to uplift without metallic connectors: experimental investigation. Fib Symposium 2021, Jun 2021, Lisbon, Portugal.

[4] ABAQUS computer software, v.6.14, Simulia, Dassault Systemes.

[5] Avis-Technique. 3.3/17-925 v1, Panneaux bois à usages structurel – mur et plancher, Wood structural panels, 2017.

[6] EN 408:2003-08. Timber structures – Structural timber and glued laminated timber – Determination of some physical and mechanical properties. CEN European Committee for Standardization (2003)

[7] M. Gong, Y. H. Chui, Evaluation of Planar Shear Properties of Cross Layer in Massive Timber Panel. Report, University of New Brunswick, Fredericton, Canada, 2015.

[8] European standard EN 1994-1-1, Eurocode 4: Design of composite steel and concrete structures - Part 1-1: General rules and rules for buildings, CEN, Brussels (2004).

[9] A. Ceccotti, Composite concrete–timber structures. In: Progress in structural engineering and materials, Nethercot D et al. editors. vol. 4, No. 3; 2002. p. 264–75.

[10] L. Cedolin, Y.R.J. Crutzen, S.D. Poli Triaxial stress–strain relationship for concrete. ACI J, 103 (1977), pp. 423-439

[11] B. Alfara, F. López-Almansa, S. Oller, New methodology for calculating damage variables evolution in Plastic Damage Model for RC structures. Eng Struct 2017;132:70–86.

[12] R. Hill, The Mathematical Theory of Plasticity, Clarendon Press, Oxford, 1950.

[13] A. Dias, J.W. Van de Kuilen, S. Lopes, et al., A non-linear 3D FEM model to simulate timber–concrete joints, Adv. Eng. Softw. 38 (8–9) (2007) 522–530.

[14] T. Kartheek, T. V. Das, 3D modelling and analysis of encased steel-concrete composite columnusing ABAQUS. Materials Today: Proceedings, 27, 1545-1554. using ABAQUS. Materials Today: Proceedings, 27 (2020), 1545-1554.

[15] J.R. Aira, F. Arriaga, G. Íñiguez-González, J. Crespo Static and kinetic friction coefficients of Scots pine (Pinus sylvestris), parallel and perpendicular to grain direction Mater Constr, 64 (315) (2014), p. e030

[16] J.W.G. Van de Kuilen, M. Dejong, 3D-numerical modelling of DVW-reinforced timber joints. In: Proceedings of WCTE 2004 – World Conference on Timber Engineering, Espoo Finland (CD Rom); 2004.

[17] Bureau de normalisation (BNETC), BNTEC P21A N376 Projet final TS Mixte Bois béton, BNTEC, 2020.

https://doi.org/10.52202/069179-0434

World Conference on Timber Engineering Oslo 2023

A 3D DUCTILE-NOTCHED CONNECTION FOR TIMBER-CONCRETE COMPOSITE BEAM : EXPERIMENTAL INVESTIGATION

Adham Al Rahim[1], Piseth Heng[2], Clemence Lepourry[3], Hugues Somja[4], Franck Palas[5]

ABSTRACT: A 3D ductile-notched connection for timber concrete composite beams is proposed in this study. The innovation of the proposed connector is the particular geometry of the notch. This configuration on one hand generates three shear planes instead of one as typical notched connection and on the other hand provides a mechanical locking to limit the uplift without the need for metallic screws. This paper presents an experimental investigation on the behaviour of the newly proposed notched connector. Three pushout tests were performed. The results show high strength and stiffness as well as ductility, as the failure mode was governed by local crashing of the timber. In addition, one flexural test was carried out on the beam specimen. The mode of failure was governed by flexural failure of the timber beam. The analysis of the slip and the uplift demonstrated the effectiveness of the connectors.

KEYWORDS: 3d ductile-notched connection, Timber-concrete composite beam, Pushout tests, Inversed flexural tests

1 INTRODUCTION

The new environmental regulations such as the RE2020 [1] in France stimulate the interest of using structural timbers in the construction within the last few years. However, timber slabs fulfil hardly all the criteria for serviceability. In this case, timber-concrete composite members represent a great compromise by associating timber with concrete. This association can improve the flexural strength and stiffness of the members as well as the sound insulation, the vibration performance, and the thermal insulation properties [2]. Several configurations of shear connectors have been proposed for timber-concrete composite members [3]. For instance, ordinary smooth nails of 70 mm with a diameter of 3.4 mm, arranged in pair, have been used as timber-concrete connectors [4]. 12 mm and 16 mm lag screws have been employed for their hybrid failure mode related to the steel's plastic deformation [5]. The first research on tooth plates was conducted in 1984. This technology was used in the construction of timber-concrete composite wall in Sweden [6]. The use of adhesive and epoxy resin within the connection system has been also investigated [7]. Although notched connections perform well in term of strength and stiffness, poor ductility is obtained when the failure is governed by shear rupture of the concrete notch [8]. Steel screws placed inside the concrete notches are sometimes added to improve the post-peak behaviour [9], but the installation of these steel fasteners increases the construction cost. In this context, a novel composite floor technology, called Bobé, is proposed (see Figure 1a). It combines a reinforced concrete slab and an inverted T-shaped wooden beam, which are joined by means of 3D notch connectors with three shear planes. The particular shape of the notch provides a geometrical locking for limiting the uplift, and the rebars (Figure 1b) improve the post-peak behaviour of the connection.

This paper presents an experimental study on the behaviour of the proposed notched connectors for timber-concrete composite beams. In this study, a series of three symmetrical pushout tests were performed in order to determine the strength, stiffness, ductility and failure of the connection system. In addition, a six-point bending test has been made to verify the effectiveness of the notched connection for timber-concrete composite beams.

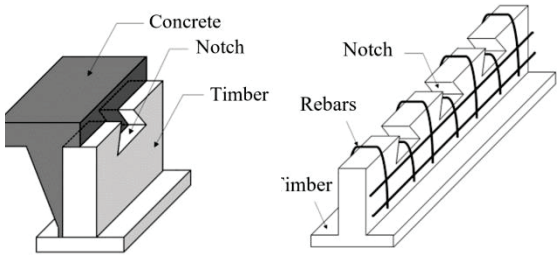

Figure 1: *3D notched connectors for timber-concrete beams.*

[1] Adham Al Rahim, LGCGM/Structural Engineering Research Group, INSA de Rennes, France, adham.al-rahim@insa-rennes.fr
[2] Piseth Heng, LGCGM/Structural Engineering Research Group, INSA de Rennes, France, piseth.heng@insa-rennes.fr
[3] Clemence Lepourry, INGENOVA, France, clemence.lepourry@ingenova-lab.fr
[4] Hugues Somja, LGCGM/Structural Engineering Research Group, INSA de Rennes, France, hugues.somja@insa-rennes.fr
[5] Franck Palas, Concept Technique Design R & D, France, franck.palas@ctdconseils.com

https://doi.org/10.52202/069179-0435

2 PUSHOUT TESTS

2.1 SPECIMENS AND TEST SETUP

The pushout test program included three identical specimens, noted by S1, S2 and S3. The specimens are made of two glued timber panels of solid pine (Spruce) with a grade of C24, measuring 1020 mm in height, 360 mm in width, and 70 mm in thickness, embedded between two concrete slabs (see Figure 2a). The compressive strength of timber, has been tested on 10 compressive pieces, parallel to the grain, with a cross section of 75 x 200 mm and length of 450 mm, according to EN 408 guideline [10]. An average resistance of 34.30 MPa, with a standard deviation of 3.19 MPa, was obtained. The average moisture content was found to be 13.05%, with a standard deviation of 1.27%.

Regarding the pushout specimens, two shear connectors, with a spacing of 326 mm, are made on each timber panel, as illustrated in Figure 2b. The concrete slabs were 450 mm in width, 1120 mm in length, and 80 mm in thickness (Figure 2c). The concrete strength grade was C25/30. The real average strength, obtained from compressive tests on cylindrical specimens, with a diameter of 110 mm and a length of 220 mm, was 27.7 MPa, with a standard deviation of 1.58 MPa. In turn, the notches are reinforced with B500B grade U-shaped rebars, with a diameter of 6 mm.

In order to reduce the friction, and to ensure a smooth contact between the materials, the timber panels were painted before concrete casting. For all specimens, the first of the two concrete slabs were cast on the same day in a horizontal position. Two days after, the specimens were lifted and turned over for the second casting. The timber panel and concrete slabs had an offset of 100 mm in length.

The test setup is described in Figure 3a. The compression load is imparted on the wooden panel by means of a hydraulic jack with 1000 kN capacity and a stroke length of 200 mm, and transferred to the concrete slabs through the connectors. Subsequently, the load is counterbalanced by the reaction forces provided by the rigid supporting system.

The monotonic loading protocol, derived from EN 26891, started with an initial ramp up to 40% of the estimated failure load, followed by a discharge and then a steady increase up to failure. The estimated capacity (F_{est}) of the specimen, with four connectors, was estimated to be 188 kN referring to the BNTEC guidelines [12]. The loading is sustained until the specimen failure is reached.

The measurement devices for the push out tests are illustrated in Figure 3b. The relative slip and uplift between timber and concrete were recorded by linear variable displacement transducers (LVDTs). On each side of the specimen, four uplift LVDTs with a stroke length of 2.5 mm and 6 mm, and four slip LVDTs with a stroke length of 25 mm, were attached.

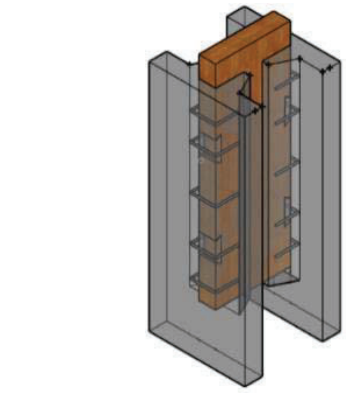

(a).

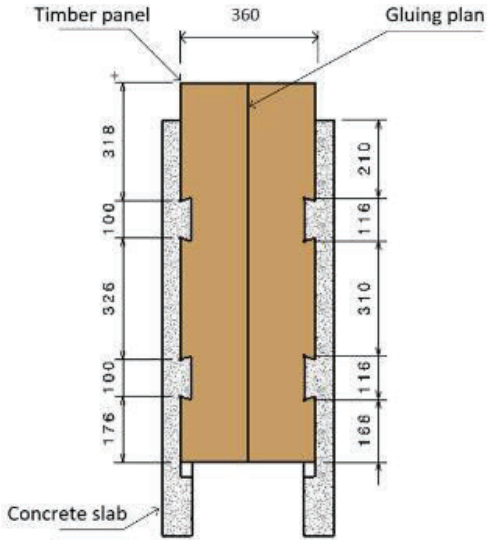

(b).

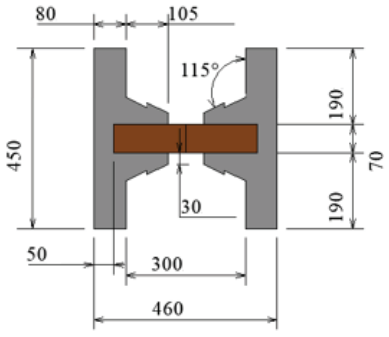

(c).

Figure 2: *(a) 3D view. (b) Front view. (c) Top view.*

https://doi.org/10.52202/069179-0435

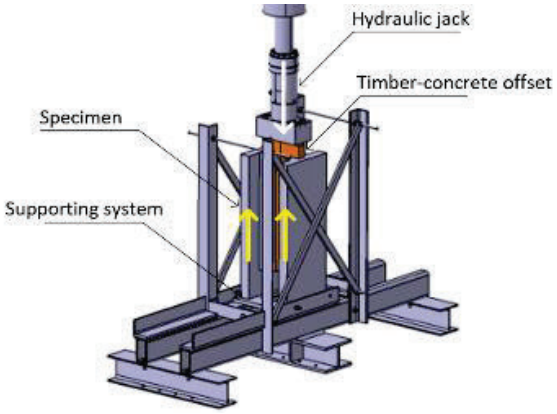

(a).

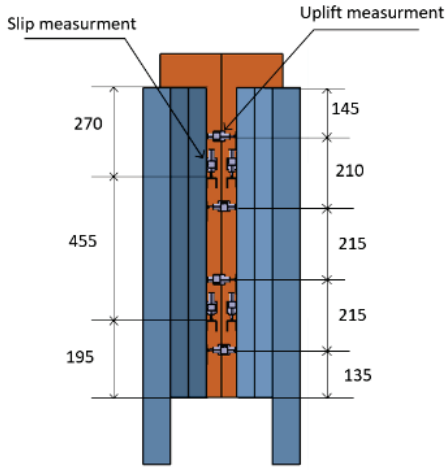

(b).

Figure 3: *(a) Test setup. (b) Measurement devices.*

2.2 RESULTS

Figure 4a and Figure 4b exhibit the evolution of the applied force as a function of the mean slip and the mean uplift, respectively. A high ductility of the connection was obtained, as the failure mode in the three tests was governed by the local crushing of the timber. The specimens were cut after tests to allow for an assessment of large compressive deformation of timber at the position of the notch connections (Figure 5). The maximum forces (F_{max}) obtained are 206.8 kN, 170.1 kN, and 198.5 kN for tests S1, S2 and S3, respectively. Adopting the method proposed by Ceccotti [13], the mean stiffness at serviceability limit state (K_s) and at ultimate limit state (K_u) are 184.8 kN/mm with a standard deviation of 19.3 kN/mm and 167.3 kN/mm with a standard deviation of 15.5 KN/mm, respectively.

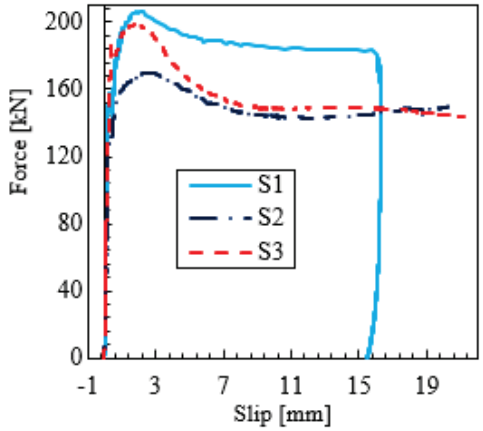

(a).

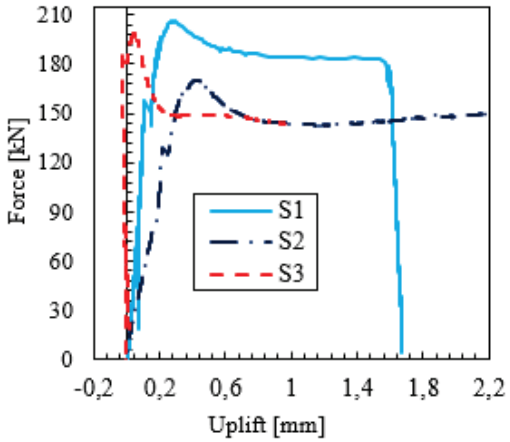

(b).

Figure 4: *(a) Force-slip curves. (b) Force-uplift curves.*

(a).

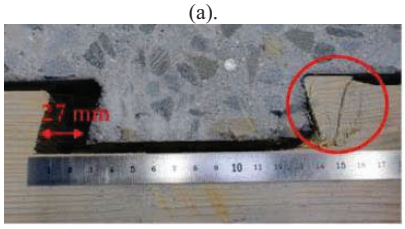

(b).

Figure 5: *(a) Local crushing of timber. (b) Zoom version.*

3 SIX-POINT BENDING TEST

3.1 SPECIMENS AND TEST SETUP

This test aims at studying the flexural behaviour of the timbre-concrete floor system.

Three specimens of the timber concrete composite beam, noted F_1, F_2, and F_3, were designed and fabricated. Each specimen was made of two identical T-shape wooden beams connected to a concrete slab using 14-notched connectors, with a spacing of 426 mm (Figure 7a). The T beam, had a cross section of 175 x 68 mm (height x width) for the web and 58 x 145 mm (height x width) for the flange (Figure 7b). For reducing friction between materials and ensure a smooth interface, the timber beams were coated with paint before concrete casting. The average moisture content in timber beams of the specimens was measured before flexural tests of F_1, F_2, and F_3, at 8%, 9%, and 8%, respectively.

To determine the mechanical properties of the timber beams, ten wooden pieces, with a mean cross section of 68 x 173 mm and a mean length of 397 mm, were tested for their compressive strength parallel to the grain. The average compressive modulus of elasticity (MOE) was 5297 MPa, with a standard deviation of 834 MPa. The flexural modulus of elasticity, tested on ten timber beams at the measured moisture content, was 11166 MPa with a standard deviation of 1445 MPa [14].

The timber beams were embedded in the concrete slab with an insertion depth of 20 mm. The concrete slab was designed with dimensions of 6845 x 920 x 80 mm (length x width x thickness) (see Figure 7b). The concrete slab was reinforced with a rebar mesh ST10 with a rebar diameter of 6 mm and a spacing of 200 mm. The actual average concrete strength was determined on cylindrical samples of 110 x 220 mm (diameter x length), on the same day of each flexural test. The results were 25.26 MPa (27 days age), 47.81 MPa (43 days age), and 23.26 MPa (92 days age), with a standard deviation of 0.124 MPa, 3.25 MPa, and 2.92 MPa, for F_1, F_2, and F_3, respectively.

The test setup consisted of a 1500 kN capacity hydraulic jack, a guidance system for a vertical loading only, two supporting systems, and a spreading system to transfer the applied load to the specimen through four points (Figure 7c).

The flexural performances were investigated via a reversed six-point bending test. In such a configuration, the specimen is invertedly mounted on the testing device, and a vertical pull is exerted by the hydraulic jack (Figure 7a). This specific setup has been developed in order to obtain measurements for loads lower than the weight of the specimen.

For all three specimens, the same loading protocol was respected. It consists of five consecutive phases (Figure 7b): 1. Lifting of the specimen upon contact with the supports, 2. Assembly of the lag screws between the supporting system and the specimen, 3. Quasi-permanent service limit state (SLS) cycling (five to seven cycles), 4. Ultimate limit state (ULS) cycling (one cycle), and 5. Loading to the failure. Service and ultimate limit states correspond to the loads of use category A (floors) in Eurocode 1 [15].

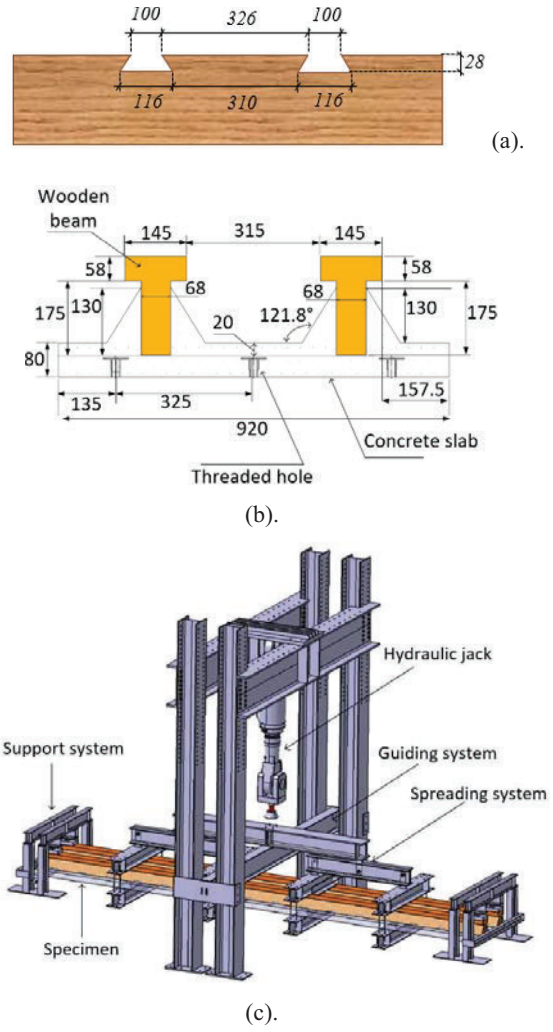

Figure 6: *(a) Notch connectors geometry and spacing. (b) Cross section dimensions of timber concrete floor. (c) 3D test setup. Dimensions in mm.*

Before the test began, the specimen was lifted slowly to make contact with the supports. During this phase, the accuracy of the instrument's operation and data acquisition was checked. Once contact was achieved, the test officially started. A displacement control was adopted, with a speed of 3 mm/min.

To measure the interface slips between the timber and concrete, eighteen linear variable differential transducers (LVDTs) were fixed horizontally on the timber beams with nine being located on front side and nine on the back side of the specimen. For the uplift, ten LVDTs were attached vertically on the timber beams. Five LVDTs were affixed to the front side of the specimen and another five were fixed on the back of the specimen. For both measurements, the pushrod of LVDT was set in contact with a steel plate that was glued on the concrete side. Additionally, five LVDTs are employed to quantify the vertical deflection of the specimen (Figure 8).

https://doi.org/10.52202/069179-0435

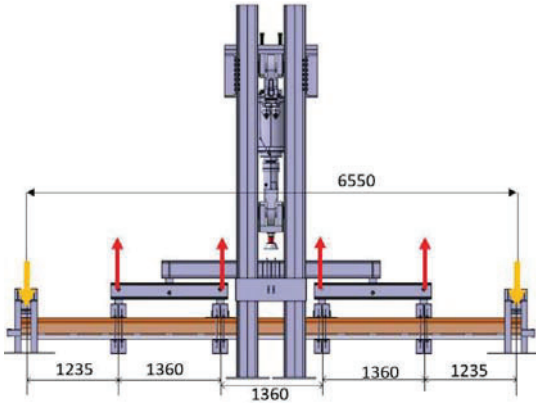

(a).

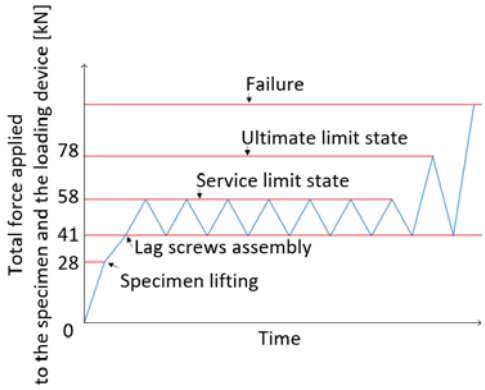

(b).

Figure 7: *(a) 2D test setup. (b) Protocol. Dimensions in mm.*

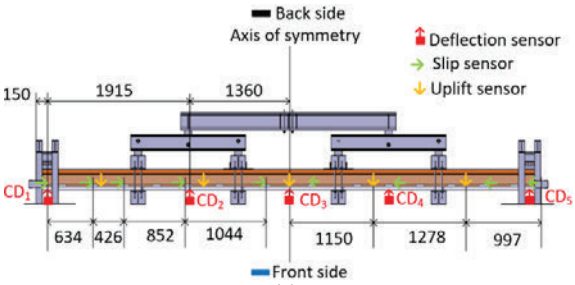

(a).

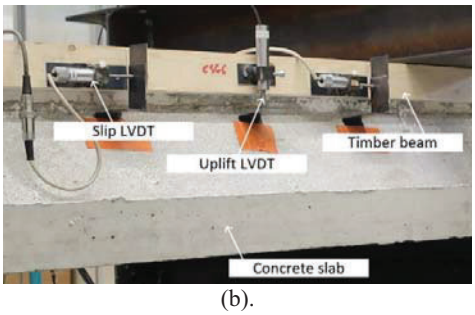

(b).

Figure 8: *(a). Bending test instrumentation. (b). Reel photo of instrumentation.*

3.2 TEST RESULTS

3.2.1 Load capacity and failure mode

In the initial period of loading, at the service limit state compaction, there was no visible cracks in timber beams or concrete slab of the specimens F_1 and F_2, while, some cracks were observed on the concrete drop in the specimen F_3 (see Figure 10a). At the ultimate limit state, as the load was on the increase, invisible fibre breakage of wood were heard and fractures appeared on the concrete drop of F_1, F_2, and F_3. During the loading process to the total collapse, failure occurred at mid-span due to the combination of bending and tensile fractures in the flange of the timber beam. The collapse of F_1, F_2, and F_3 was governed by the rupture of the timber beam (see Figure 10b, Figure 10c, and Figure 10d). The maximum loads reached were 130.2 kN, 123.5 kN, and 128 kN, applied on F_1, F_2 and F_3, respectively. The corresponding mid-span deflection was 61 mm, 47.2 mm, and 68.6 mm, respectively (Figure 9).

However, the examination after collapse uncovered the absence of shear failure at the locations of timber-concrete connectors for all specimens tested. In addition, the uplifts between the concrete and the timber were limited, demonstrating the excellent shear resistance exhibited by the selected connectors.

3.2.2 Experimental bending stiffness

Figure 9 displays the force vs mid-span deflection curves for all the specimens. The experimental bending stiffness was calculated by Eq. (1) based on the elementary beam theory.

$$EI_{exp} = \frac{F}{4w}\left[\frac{1}{2}(2a+b)\left(a+\frac{3}{2}b\right)^2\right] \quad (1)$$

In such expression, a is the distance from the loading point to the support, a = 1235 mm; b is the distance between two loading points, b = 1360 mm; F is the maximum force applied by the hydraulic jack to the specimen during the compaction cycle; w is the corresponding mid-span deflection.

The results of the three tests are collected in the Table *1*.

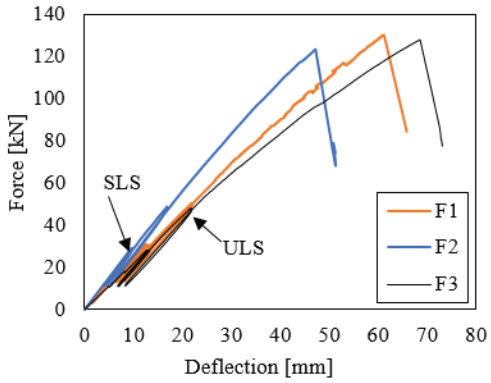

Figure 9: *Load-deflection curves at mid-span of all specimens.*

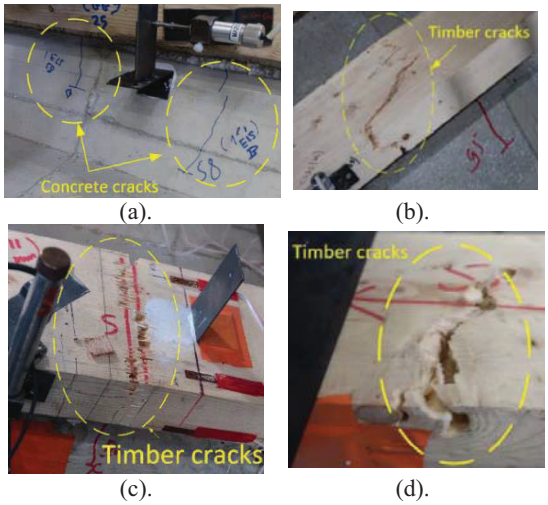

(a). (b). (c). (d).

Figure 10: *(a). Cracks in concrete drop. (b). Failure of F_1. (c). Failure of F_2. (d). Failure of F_3.*

Table 1 Flexural rigidity of the test specimens.

Specimen	$\mathbf{EI_{1-SLS}}$ (10^{13}) Nmm^2	$\mathbf{EI_{ULS}}$ (10^{13}) Nmm^2
F_1	1.22	1.15
F_2	1.57	1.49
F_3	1.14	1.13

Where, EI_{1-SLS} is the flexural rigidity at the 1st cycle of the service limit state, and EI_{ULS} is the flexural rigidity at the ultimate limit state. It can be observed that the flexural stiffness of specimens F_1 and F_3 exhibit a comparable level, while that of the specimen F_2 is relatively higher. The higher concrete strength measured in the F_2 test might be a contributing factor.

3.2.3 Relative slip

The relative slips along the composite beam span were depicted in Figure 11 at different load levels. The three cases have shown the higher relative slips occurred at the both ends of the beam. The maximum relative slips were 0.72 mm, 0.92 mm, and 1.98 mm, recorded for F_1, F_2, and F_3, respectively. However, the relative slips obtained from the bending test do not exceed the plastic resistance of the connector obtained in push-out tests (see Figure 4a).

3.2.4 Interface uplift

Figure 12 shows the distribution of uplift at the interface between timber and concrete layers. It can be noticed that the uplift at the mid-span were much higher than that at the both ends of the specimen. The maximum timber-concrete uplifts were 0.29 mm, 0.5 mm, and 0.55 mm, recorded for F_1, F_2, and F_3, respectively. The test results showed that the geometrical locking of the connector offered an effective resistance to uplift between concrete and timber layers.

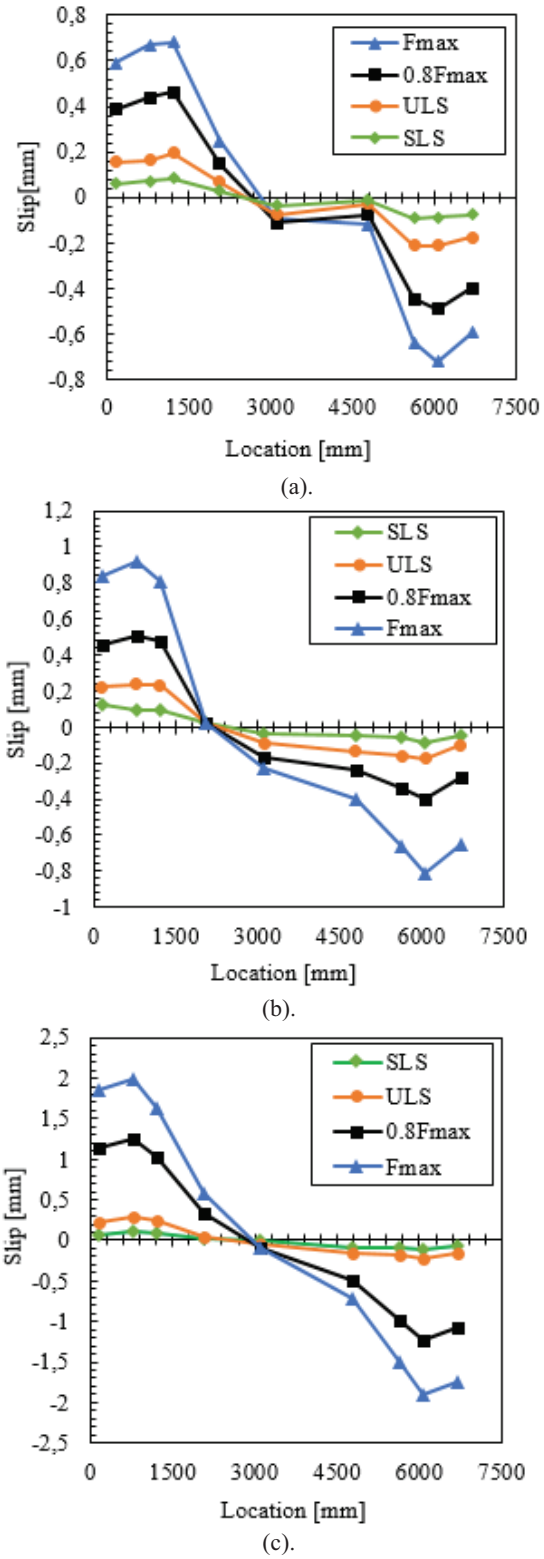

Figure 11: *Load-slip curves of the composite beams. (a) F_1 test. (b) F_2 test. (c). F_3 test.*

https://doi.org/10.52202/069179-0435

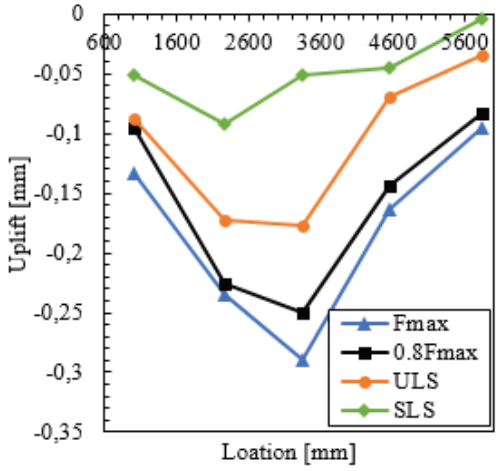

(a).

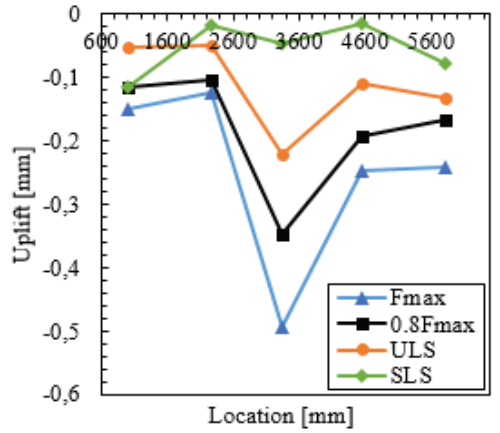

(b).

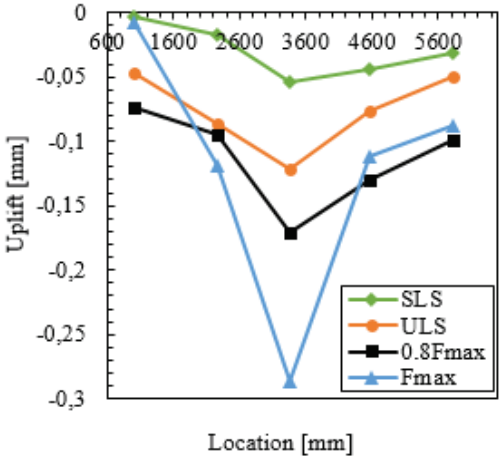

(c).

Figure 12: *Load-uplift curves of the composite beams. (a) F_1 test. (b) F_2 test. (c). F_3 test.*

3.2.5 Analytical evaluation according to Eurocode 5

According to Annex B of the Eurocode 5 guidelines [16], the ϒ-method was employed to assess the flexural performance of the timber-concrete beam. The general effective bending stiffness is expressed as:

$$EI_{eff} = E_1I_1 + E_2I_2 + \gamma_1E_1A_1a_1^2 + \gamma_2E_2A_2a_2^2 \quad (2)$$

For the tested specimens, the Eq.(2) becomes:

$$EI_{eff} = 2(E_1I_1 + E_2I_2 + \gamma_1E_1A_1a_1^2 + \gamma_2E_2A_2a_2^2) \quad (3)$$

In such formula, E_i (MPa), I_i (mm^4), and A_i (mm^2) denote the elastic modulus, the second moment of area, and the cross section of the concrete slab ($i = 1$), and timber beam ($i = 2$), respectively; a_i (mm) represents the distance between the centroid of the component (i) to the overall neutral axis of the composite cross section, given in Eq.(4):

$$a_1 = \frac{\gamma_2E_2A_2}{\sum\gamma_iE_iA_i}d_{1-2}$$

$$a_2 = \frac{\gamma_1E_1A_1}{\sum\gamma_iE_iA_i}d_{1-2} \quad (4)$$

Where, d_{1-2} (mm) is the distance between the centroides of the two components.

Timber was taken as a reference (γ_2=1) and the γ_1 parameter of the shear connector can be written as:

$$\gamma_1 = \frac{1}{1 + \frac{\pi^2A_1E_1s}{KL^2}} \quad (5)$$

Where, K (N/mm) and s (mm) are the stiffness and spacing of shear connectors, respectively, and L (mm) is the beam span.

For the present analytical calculation, the effect of the cracking of concrete is approximated by neglecting the contribution of the concrete drops, except the steel rebars (HA8), while the concrete drops are not taken into account (see Figure 13).

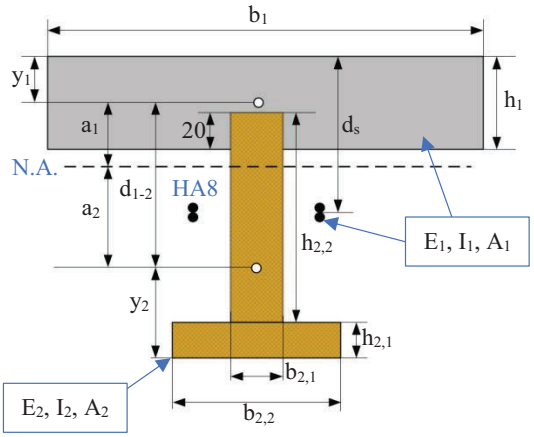

Figure 13: *Composite beam cross section.*

N.A. and d_s denote the overall composite neutral axis and the distance between the steel rebars to the upper slab surface, respectively; and y_i represents the position of the centroid of the element (i).

The geometrical parameters indicated on the Figure 13 were measured and represented in Table 2. While, the

parameters of the analytical method were calculated and provided in Table 3.

Table 2 Dimensions of timber-concrete cross section.

	Parameter	F_1	F_2	F_3
Concrete slab	h_1[mm]	76	83.5	79.5
	b_1[mm]	458.75	457.5	460
	y_1[mm]	41.5	44.1	43.2
	A_1[mm^2]	34875	37982	36614
	I_1[mm^4]	33992832	36126620	37700607
	d_s[mm]	155	159	159.5
Timber beam	$h_{2,1}$[mm]	57.5	59	54.5
	$b_{2,1}$[mm]	68	67.5	68
	$h_{2,2}$[mm]	179	175.5	180
	$b_{2,2}$[mm]	142	140.5	140.5
	y_2[mm]	99.5	98.5	99.4
	A_2[mm^2]	20337	20136	19897
	I_2[mm^4]	103000000	99900000	99700000
	$d_{2,1}$[mm]	151.5	155.4	151.4

Table 3 Effective bending stiffness of test specimens.

	Parameter	F_1	F_2	F_3
	E_1[MPa]	29050	35178	28340
	E_2[MPa]		11166	
	L[mm]		6550	
ELS	K_s[kN/mm]		184.8	
	γ_1	0.65	0.58	0.64
	γ_2		1	
	a_1[mm]	38.8	34.7	37.7
	a_2[mm]	112.7	120.7	113.7
	EI_{eff}[10^{13}Nmm^2]	1.20	1.32	1.20
	EI_{exp}[10^{13}Nmm^2]	1.22	1.57	1.14
	Error (%)	1.6	15.9	5
ELU	K_u[kN/mm]		167.3	
	γ_1	0.63	0.56	0.62
	γ_2		1	
	a_1[mm]	39.9	35.8	38.8
	a_2[mm]	111.6	119.5	112.6
	EI_{eff}[10^{13}Nmm^2]	1.19	1.3	1.19
	EI_{exp}[10^{13}Nmm^2]	1.15	1.49	1.13
	Error (%)	3.3	12.7	5

According to the comparaison results, represented in Table 3, a good accuracy between the analytical and experimental results can be noticed for the specimens F_1 and F_3. Whereas, in case of F_2, the test results were underestimated, at both service and ultimate limit states with an error of 15.9% and 12.7%, respectively.
This approach exhibits an inadequate consideration of concrete cracking, thereby neglecting the beneficial effect of the higher concrete strength in F_2 test on the crack formation.

4 CONCLUSIONS

This paper presents an experimental study on a newly proposed notched connection for timber-concrete composite beams. Three pushout tests were made. The results showed high strength and stiffness of the connector. The high ductility of the connector was obtained as the failure was governed by local crashing of the timber in compression. In order to assess the failure mode, flexural capacity, slip, and uplift of the beam specimens, 6-point bending tests were performed on three timber-concrete specimens. The failure mode was governed by a brittle tensile-flexural rupture of the flange of the timber beam. It must be noted, that after collapse, no failure was observed in either the concrete slab or the notch connectors. The analysis of slips and uplifts revealed the effectiveness of the shear connection without the need of any mechanical elements.
Moreover, the analytical method, proposed in Eurocode 5 guidelines, is used to calculate the effective bending stiffness of the composite beams, with a simple hypothesis to account the concrete cracking. An acceptable accuracy, compared with the experimental results, is reached.
A new methodology, is currently being developed to refine the representation of the concrete cracking in the analytical calculation with the aim of reducing the discrepancy between analytical and test results.

5 REFERENCES

[1] Ministère de la transition écologique et Centre d'études et d'expertise sur les risques, l'environnement, la mobilité et l'aménagement, “Réglementation Environnementale Des Bâtiments Neufs (RE2020),” 2020.

[2] A. Buchanan, Fire performance of timber construction, Prog. Struct. Engng Mater. 2 (2000) 278–289.

[3] A. Dias, Mechanical behaviour of timber-concrete joints, PhD thesis, Technische Universiteit Delft, April 2005.

[4] M; BRANCO, J.S. ; CRUZ et M. PIAZZA : Experimental analysis of laterally loaded nailed timber-to-concrete connections. Construction and Building Materials, 23, 2009.

[5] Bruce L. DEAM, Massimo FRAGIACOMO et Andrew H. BUCHANAN : Connections for composite concrete slab and LVL flooring systems. Materials and Structures, 41(3):495–507, 2008. ISSN 1359-5997.

[6] Ulf Arne GIRHAMMAR : Nail-plates as shear connectors in composite timber and concrete structures. In Congrès de l’AIPC, 1984.

[7] Clouston, P., Bathon, L., and Schreyer, A. (2005). “Shear and bending performance of a novel wood-concrete composite system.” J. Struct. Eng., 131(9), 1404–1412.

[8] Gutkowski R, Brown K, Shigidi A, Natterer J. Laboratory tests of composite woodconcrete beams. Constr Build Mater 2008;22(6):1059−66.

[9] Y. Jiang, X. Hu, W. Hong, J. Zhang, F. He, Experimental study on notched connectors for glulam-lightweight concrete composite beams. BioResources, 15(2020), pp.2171-2180.

[10] AFNOR, NF EN 408 : Bois de structure et bois lamellé-collé, 2012.

[11] CEN. Timber structures – Joints made with mechanical fasteners – General principles for the determination of strength and deformation characteristics, EN 26891: 1991. Brussels; 1991.

https://doi.org/10.52202/069179-0435

[12] Bureau de normalisation (BNETC), XP CEN/TS 19103 Conception et calcul des structures - Calcul des structures mixtes bois-béton - Règles communes et règles pour les bâtiments, BNTEC, 2022.

[13] A. Ceccotti, Structures en bois aux Etats Limites - STEP 2, Chapitre VII-4 : Structures Bois-Béton. Paris : SEDIBOIS / union nationale Française de Charpente, Menuiserie, Parquets, 1997.

[14] S. Fuentes, Flexural test on timber beams, BOIS HD, January 2022.

[15] EN1991-1-1 **:** Eurocode 1 - actions sur les structures - Partie 1-1 : Actions générales — Poids volumiques, poids propres, charges d'exploitation des bâtiments (P 06-111-1:2003-03, NA:2004-06, A1:2009-03).

[16] Eurocode 5, Design of Timber Structures. Part 1-1: General - Common Rules and Rules for Buildings. EN 1995-1-1, Brussels, 2004.

World Conference on Timber Engineering Oslo 2023

HIGH CAPACITY SHEAR CONNECTORS AND APPLICATION FOR TIMBER-CONCRETE BRIDGES

Raitis Lacis[1], Maris Karlsons[2]

ABSTRACT: This paper describes the experimental study of a new hybrid type shear connector for timber-concrete composite systems. The main emphasis of the study is the development and testing of high capacity shear connectors and their use in timber-concrete systems associated with high structural demand for composite interaction such as vehicular and pedestrian bridge structures. Experimental pushout test data of a hybrid shear connector is presented along with the full-scale bridge design and testing using this shear connection system. Shear connection consists of two main parts welded together: a circular hollow section (CHS) and a common steel nail plate. The first part is considered a rigid dowel, but the addition of the nail plate considerably improves the redistribution of the shear forces to a larger area of the timber body, thus minimizing the risks of high concentration shear-induced damage locally if only dowel is used. Based on the test results, a single span timber-concrete vehicular bridge design and load-proof aspects are briefly discussed, including factors of different loading effects and construction methods.

KEYWORDS: Bridge, Timber-concrete composite, Shear connection, Circular hollow section, Nail plate

1 INTRODUCTION

Appropriate choice of the shear connector configuration is crucial in order to provide effective degree of composite action between timber and concrete structural parts such as beams and slabs. Vehicular bridges have to sustain relatively high concentrated loads both in the ultimate state as well as at the service level. As a result, timber-concrete systems require special attention to the shear connection used because of it directly depends the vertical deformations and overall stress state of timber/concrete components.

In order to level up the ability of timber-concrete systems to compete with other structural formulas, it requires to develop shear connectors, that both have high stiffness and high strength so that they not limit the overall design of the structure.

Many types of timber-concrete shear connectors have been tested during the last two decades [1]. These include different combinations of notched, screwed, dowel-type and adhesion based connections generally subtyped as continuous or discrete shear connectors [2]. The purpose of this paper is to present a hybrid type of connection, that employs two of the aforementioned principles by using a large diameter dowel in the form of a circular hollow section (CHS) filled with concrete [3] in combination with a widely known industrial product, punched nail plate (see Figure 1 and 3) representing the semi-continuous part of the connector.

The proposed connector's experimental push-out testing results are presented, including shear stiffness, ultimate strength, failure character, and specific sample preparation aspects that were taken into account to achieve failure, particularly in the shear mode along the wood grain. Particular investigation results were directly used in the design, construction and proof loading of a single span vehicular timber-concrete bridge. A quantitative discussion is given to demonstrate the importance of chosen construction method for the timber-concrete composite bridge, which is already at the design stage. For instance, temporary construction propping or no propping affect the magnitude of shear forces in the connectors, the permanent self weight induced stresses of beams/slabs and overall structural stiffness.

2 MATERIALS AND TEST SETUP

2.1 CONFIGURATION OF THE CONNECTOR

Hybrid connector consists of the steel nail plate and circular hollow section (steel CHS), which are welded together in 90° configuration (Figure 1). Connector is pressed into the predrilled slot of the timber beam and hollow section is consequently filled with the concrete during the deck construction process in such a manner that no steel parts are exposed to the direct environmental impacts. Timber and concrete penetrating part of CHS dowel serves well for the transfer of shear force in the concrete deck and provides stiffness due to its volume and relatively large contact area, but the nail plate effectively distributes these forces in the timber with the help of many small sized but high number of nails. Besides, as the steel CHS element extends also in the timber then it functions as a circular notch and thus providing extra stiffness. (Figure 2b).

[1] Raitis Lacis, Inzenierbuve LTD., Latvia, raitis.lacis@inzenierbuve.lv
[2] Maris Karlsons, JMR-Frame LTD., Latvia, maris.karlsons@jmr-frame.lv

https://doi.org/10.52202/069179-0436

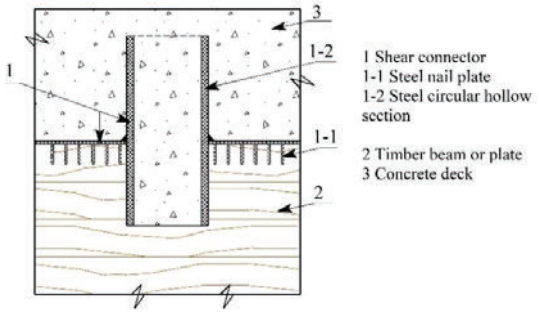

Figure 1: *Cross section of the nail plate/CHS shear connector*

Figure 2: *a) single connector; b) predrilled slots in the timber; c) timber beams with pressed-in shear connectors*

For less demanding shear systems a variation presented in Figure 2 appears to be more practical due to its simpler application, however, research of this layout is outside the scope of this publication and is reserved for future investigations [3].

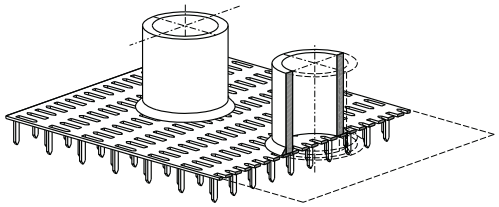

Figure 3: *Variation of shear connector without CHS extension to the wood*

2.2 PREPARATION OF THE SAMPLES AND TESTING PROCEDURE

Samples for the laboratory push-out testing in shear were prepared using symmetrical test layout depicted in Figure 4 and 5. This employs two identical slip surfaces constituting two shear planes each of which characterizes individual shear connector. Shear connectors and sample dimensions were chosen to represent the design of full-scale bridge, which was intended following the current research.

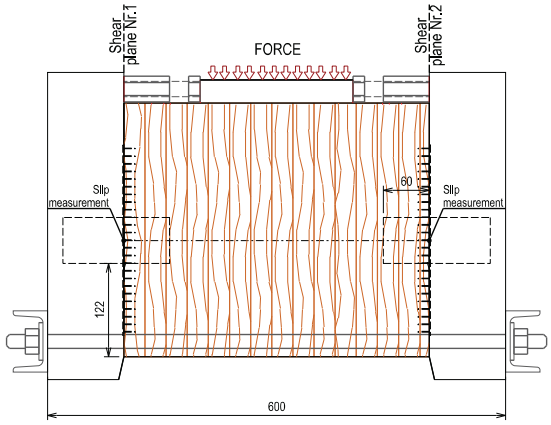

Figure 4: *Layout of the sample*

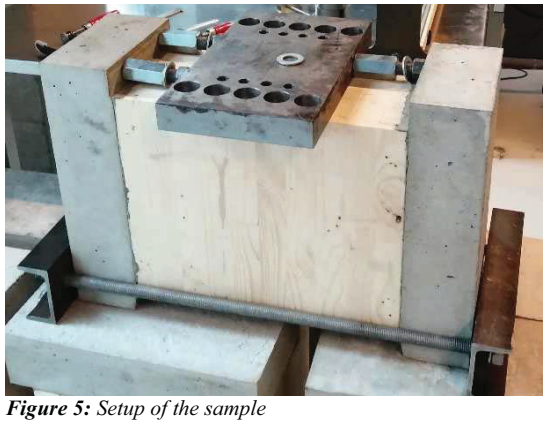

Figure 5: *Setup of the sample*

General characteristics of the materials used:
Timber class GL24h according to [5], moisture content 8-11%;
Concrete class C35/45 [6];
Steel class of circular hollow section S355, diameter 60mm, wall thickness=3mm;
Nail plate Wolf 15N [7], steel class S280, size 175×250mm.
The test timeline and loading schedule followed the routine of EN 26891 [8], see time-load history in Figure 6. Loading machine Zwick/Roell Z600.
Number of specimens: seven (one of which were predamaged).

https://doi.org/10.52202/069179-0436

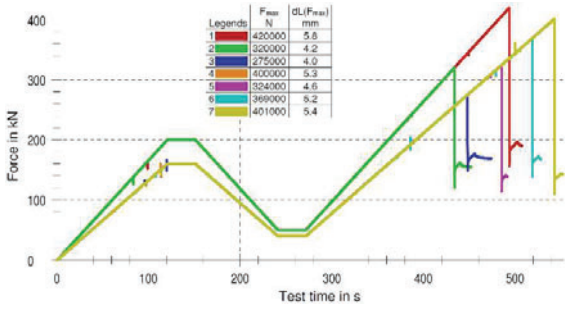

Figure 5: *Time-load history of the samples tested*

Special attention was paid in the sample preparation process in order to avoid unnecessary mechanical restraining effects during the loading. When applying vertical force to the timber upper face, horizontal reactions at the top and bottom of the sample develops, which tend to split the sample at the bottom and push it together at the upper part. As a result, compression fixings were used at the top level and tension rods at the bottom. Steel plate for the force distribution at the top was chosen such that expected failure of the shear plane is not crossed over and failure in pure shear could be objectively expected.

3 RESULTS OF PUSH-OUT TESTS

3.1 Ultimate shear capacity and stiffness

Values of ultimate shear capacity varied from 275kN to 420kN (see Table 1). The lowest value 275kN represents the sample Nr.3, which was predamaged, but still tested for the sake of interest. All of the seven samples failed in a brittle manner (Figure 6).

Table 1: *Shear capacity, slip and stiffness results of push-out tests*

#	F_{max} * [kN]	Slip at $0,6F_{max}$ [mm]	Slip at $0,8F_{max}$ [mm]	Stiffness at $0,6F_{max}$ [kN/mm]	Stiffness at $0,8F_{max}$ [kN/mm]
1	419,8	0,9	1,4	134,7	117,8
2	319,6	0,8	1,1	125,7	119,4
3	274,9	0,6	0,9	134,1	125,5
4	400,0	1,1	1,4	114,3	111,1
5	324,3	0,7	1,1	130,1	115,8
6	369,1	0,8	1,2	138,4	127,3
7	401,0	0,9	1,3	133,7	122,4

*F_{max} results are presented for the symmetric sample layout (two connectors per sample)
**Slip and stiffness values calculated as an average from two of the connectors forming one test sample. In all tests only one side failed

For each sample, the slip values between timber and concrete were measured during the loading. Due to the minor geometrical and material variation the slip values always differed for the two shear connectors of the sample (example in the Figure 6), therefore for all the samples a complete failure only occurred in one of the shear plane, the other in all cases remained intact.

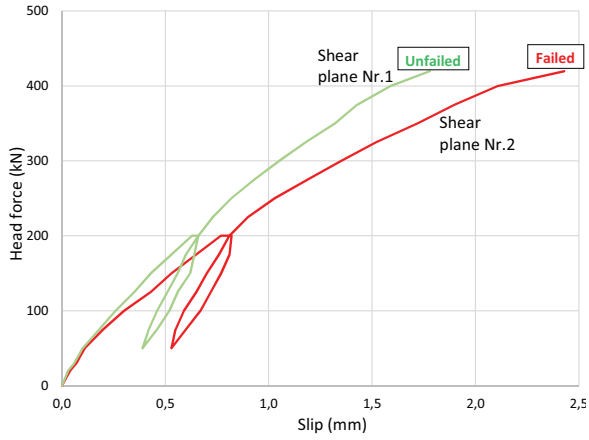

Figure 6: *Slip - load values (example of one sample)*

Failure mechanism observed was in pure shear by the block shear failure in wood depicted in Figure 7 and 8. Extension of the CHS element in the wood demonstrates provision of extra stiffness and strength as the line of the failure copies CHS profile in all of the samples. Physical deconstruction (Figure 9 and 10) of the failed sample indicates some plastic deformation in front of the CHS profile (compression perpendicular to the grain) before wood failure in shear along and mostly between the annual rings takes place. Notably that CHS element is relatively intact and only outer nails of the plate are visibly deformed after the ultimate slip of the shear surface in the wood.

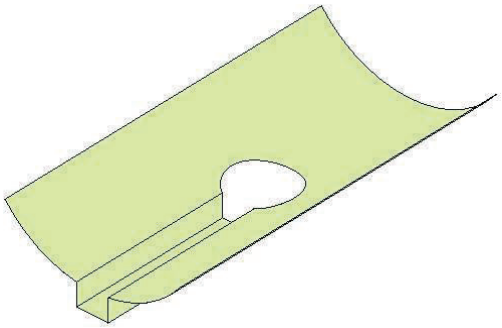

Figure 7: *Typical shear failure plane*

https://doi.org/10.52202/069179-0436

Figure 8: *Top and bottom surface after the failure*

Figure 9: *Condition of the connector after the failure (wood part removed)*

Figure 10: *Compression by the CHS element perpendicular to the grain*

4 APPLICATION OF TEST RESULTS IN THE DESIGN OF TIMBER-CONCRETE BRIDGE

Laboratory tests of the shear connectors were preliminary part of the timber-concrete bridge design process during which all of the necessary data in terms of connectors stiffness and strength were acquired. Once these were established a design of the the full-scale bridge could be carried out. Structural model was build using 2D beam elements following the grillage modelling principles. Timber and concrete cross sectional parts were placed by appropriate eccentricities and interconnected with spring elements [12] characterised by the stiffness values established from the connector's push-out tests.

Figure 11: *Jecupe bridge in a construction stage and in a finished state*

The bridge consists of ten individual laterally braced glulam beams (GL28h 750×220mm) and cast-in situ concrete deck (C35/45). Length of theoretical span is 12,80m (Figure 11, 12); minimal design load is heavy-duty forestry vehicles up to 60t. Concreting of the deck was done using temporary propping beneath the glulam beams. Bridge is named after the river it is crossing (*Jecupe bridge*) - it was successfully built and load-proofed in 2020, location Nica parish, Latvia) proving to a client (Latvia's State Forests) that rationally approached timber-concrete systems can be a competitive option for the bridge inventory.

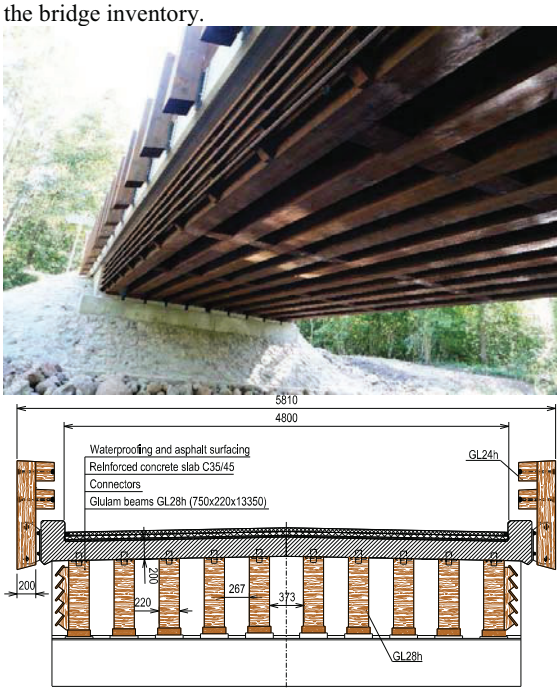

Figure 12: *Cross section of the bridge*

Load-proofing procedure included symmetrical and asymmetrical quasi-static load schemes using 40t five axle vehicle. Load effects were controlled by vertical

https://doi.org/10.52202/069179-0436

deformation measurements and strain gage system installed on the lower face of the timber beams at midspan. Beam stresses were calculated based on the continuous strain measurements (Figure 13), which approved satisfactory load distribution and stiffness across the beams.

Figure 7: *Load-proof with 40t vehicle*

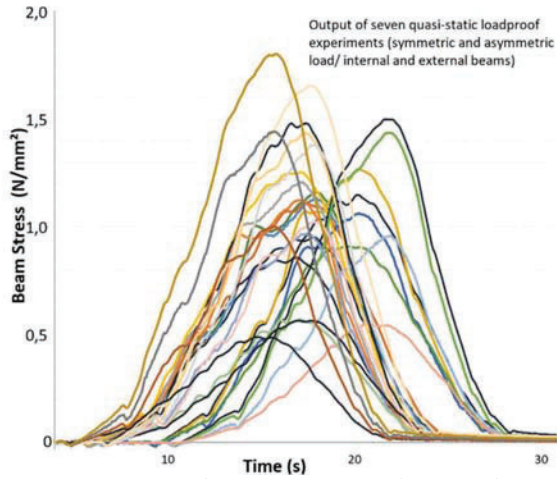

Figure 13: *Calculated beam stresses (based on recordings of strain gages)*

Figures 14, 15, 16, 17 summarises main load effects for different design and load-proof situations. Main differentiation is made between different construction methods (temporary propping and no propping) and different load models including Load model 1 (α=0,8). Also load effects of theoretical non-composite situation is given in order to emphasize the importance of shear connectors in timber-concrete composite systems.

Maximum shear (Figure 14) force in the connectors according to the design model were purposefully kept low due to the brittle character of the connection region as established in the laboratory tests. For instance, maximum value of Eurocode ultimate limit state shear force in the connectors zone using Load model 1 (α=0,8; γ_{LM1}=1,5) did not exceed 56 kN. However, at everyday service levels (60t wood harvester and 40t five axis vehicle) as demonstrated in the calculations and load-proof situation the total self weight and live load connectors shear force maximal range is 14 kN to 28kN depending on the vehicle and live load placement relatively to the longitudinal axis. Highest beam stresses registered in asymmetric load-proofing did not exceed 1,8 MPa. According to the design model stresses of similar category are in the range of 2 MPa.

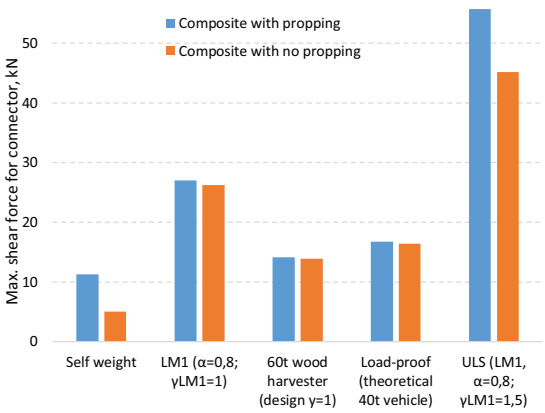

Figure 13: *Comparison of maximal shear forces of connectors*

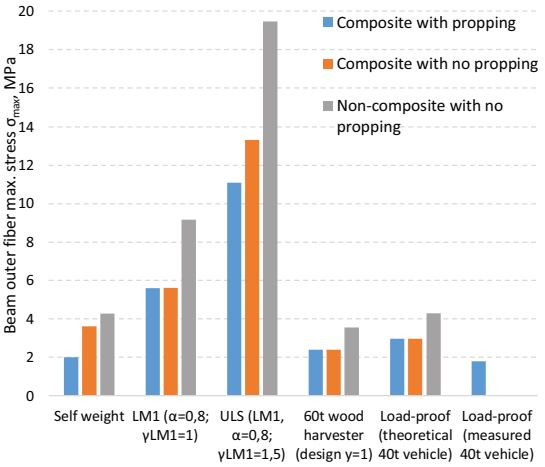

Figure 14: *Maximal beam bending+tension stresses*

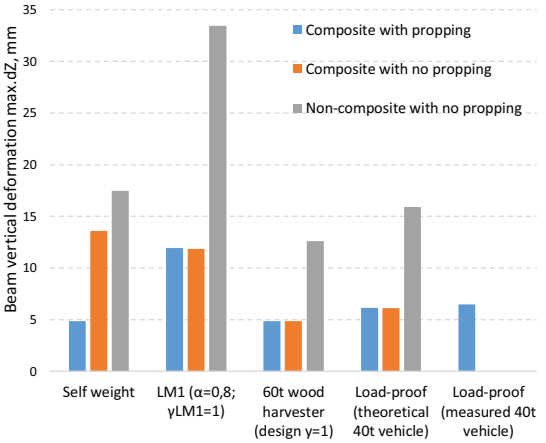

Figure 15: *Comparison of vertical deformations*

https://doi.org/10.52202/069179-0436

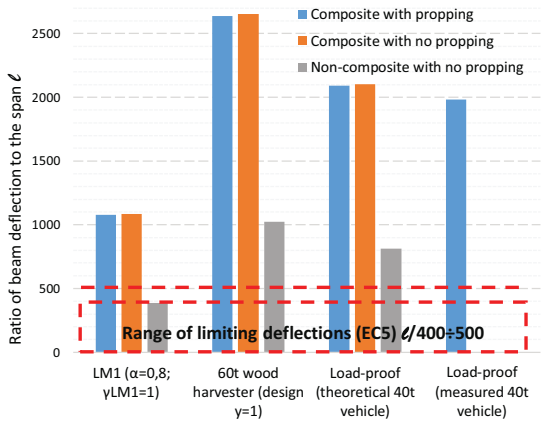

Figure 16: *Serviceability criteria of vertical deformations*

As for the deflection category, the lowest vertical deformations (Figure 15) are achievable using temporary propping construction method naturally on the expense of increased shear forces. Figure 16 represents levels of serviceability for different live load situations. For this shear connection and bridge design a deflection criteria of EC5 serviceability is fully satisfied ranging from 1/1080 for the LM1 and 1/1983 for the load-proof 40t vehicle (Figure 16).

5 CONCLUSIONS

Experimental testing demonstrated high strength and stiffness of the proposed hybrid shear connectors. Their applicability to the road bridges with design loads of up to the Load Model 1 (α=0,8) has been presented. Different construction methods and impact on the shear connectors utilisation and general stress state of the timber-concrete bridge was quantitatively discussed acknowledging potential use of the hybrid shear connectors in other bridge design situations.

REFERENCES

[1] Rodrigues J., Dias A.; Providencia, P.: Timber-Concrete Composite Bridges: State-of-the-Art Review. Bioresources. Vol.8, No.4. 6630-6649. 10.15376/biores.8.4.6630-6649, 2013.

[2] Riestra F.S., Cimadevila J.E., E. Martín-Gutiérrez E.M., Chans D.O.: Perforated shear + reinforcement bar connectors in a timber-concrete composite solution. Analytical and numerical approach. Composites Part B Engineering. 10.1016/j.compositesb.2018.08.074, 2018.

[3] Lacis R.: Shear connector of the timber-concrete composite systems consisting of punched metal nail plate and steel hollow section. Patent office Republic of Latvia. Application Nr.LVP2021000008, 2020.

[4] EN 14080:2013. Timber structures - Glued laminated timber and glued solid timber, 2014.

[5] EN 1992-1-1:2004 Eurocode 2: Design of concrete structures, 2015.

[6] Deutsches Institut für Bautechnik (DIBt): Technical approval Z-9.1-210. Wolf-Nagelplatten Typ15N, 15 NE,15Z und 15 ZE als Holzverbindungsmittel, 1997.

[7] EN 26891:1992 Timber structures - Joints made with mechanical fasteners. General principles for the determination of strength and deformation characteristics, 1992.

[8] EN 1995-2:2005 Eurocode 5: Design of timber structures - Part 2: Bridges

[9] Girhammar U. A.: Nail-plates as shear connectors in composite timber and concrete structures. IABSE 12th Congress, Vancouver, Final Report,pp. 961-968, 1984

[10] [10] Van der Linden M.:. Timber-concrete composite beams. HERON. Vol. 44. No.3 (1999) ISSN0046-7316

[11] [11] Aicher S., Klöck W, Dill-Langer G., Radovic B.: Nails and nailplates as shear connectors for timber-concrete composite constructions, Otto-Graf-Journal Vol. 14, 2003

[12] Midas Civil software manual, 2023

World Conference on Timber Engineering Oslo 2023

DEVELOPMENT OF LVL-CONCRETE COMPOSITE FLOOR SYSTEMS

Alireza Fadai[1], Johann Scheibenreiter[2], Alex Müllner[3], Marie Theres Brunauer[4]

ABSTRACT: The growing enormous number of mid-rise timber buildings in European metropolitan areas leads to the investigation of a possible optimization potential in the use of timber in combination with other building materials. Various timber-based composite floor systems, in particular the combination of laminated veneer lumber products and other conventional building materials, such as conventional or steel fiber reinforced concrete coupled by various sorts of dowel-type or notched connections, are studied. In regard to structural, economical and resource efficiency on overall component level, the extent of interrelationships in the development of multifaceted optimized system solutions can be shown.

This paper shows the results of the feasibility studies and the conceptional design. The objective of the studies is to develop application-optimized multi-layered structural composite floor systems with a special focus on the joint design of the various thereby used connection types between the coupled composite layers. The conceptual feasibility studies illustrate the capabilities in the application of laminated veneer lumber products in composite floor systems. Consequently, the presented results enable engineers, as well as builders and planners, to further strengthen the implementation of timber-based composites within modern building applications. A construction-optimized design with increased resource efficiency can be achieved.

KEYWORDS: Composite structure, Laminated veneer lumber, Steel fiber concrete, Dowel-type connection, Notched connection, Sustainable building

1 INTRODUCTION

In Austria, timber construction has increasingly gained market share over the last twenty-five years. Based on the total constructed usable volume in the building sector, it has increased from 14 up to 24% between 1998 and 2018 [1].
In 2018 (24%) the timber-based building material proportion in housing construction is distributed to 53% (newly built single and multi-family houses as well as extensions and conversions) and 47% in non-residential construction (public, commercial and industrial buildings as well as agricultural buildings). At the residential segment, the proportion of timber-based construction has risen particularly strong with an increase from 10 up to 23% in the mentioned period [1].
Further increases are to be expected, especially for large-volume buildings as residential and public buildings.
The city of Vienna continues to grow and an increasing population means that more living space must be made available. Since land is not available in unlimited quantities and there are some old buildings in Vienna without roof extensions, there is the possibility of extending them and thus creating new living space. As of 2018, it is estimated that approximately 9,300 expandable roofs are available in Vienna [2].
Often, the top floor is designed as a reinforced concrete structure with or without a connect to an existing wooden floor. If steel fiber concrete is used instead of conventional reinforcement concrete, this could lead to a more economical construction method. Thus, with the help of steel fiber concrete and an existing wooden floor, a composite roof can be created in old buildings, which, for example, can be erected economically and increase the structural safety.

Within the framework of the research project the Department of Structural Design and Timber Engineering (ITI) at the Vienna University of Technology (TU Wien) in cooperation with Schmid Schrauben Hainfeld Ltd. developed a multi-layer floor system, composed of concrete connected to timber sections and use advantages of each used building material. Timber-hybrid elements meet modern architecture´s demands and can help to increase the use of timber as building material.

[1] Alireza Fadai, TU Wien, Research Unit of Structural Design and Timber Engineering, Austria, alireza.fadai@tuwien.ac.at
[2] Johann Scheibenreiter, Schmid Schrauben Hainfeld Ltd., Austria, johann.scheibenreiter@schrauben.at
[3] Alex Müllner, TU Wien, Austria, alex.muellner@tuwien.ac.at
[4] Marie Theres Brunauer, TU Wien, Austria, marie-theres.brunauer@tuwien.ac.at

https://doi.org/10.52202/069179-0437

2 EXPERIMENTAL TEST EXECUTION

The research project includes design concepts, feasibility studies and performance assessments of the components in order to improve the overall performance. In addition, the development includes experimental investigations of the components in order to improve the overall performance.

2.1 STEEL FIBER CONCRETE

In Austria and Germany guidelines on the use of fiber-reinforced concrete are available. In Austria, this is the "Fiber-reinforced concrete" guideline published by the Austrian Construction Engineering Association (ÖBV) [3] and in Germany the "Steel-reinforced concrete" guideline published by the German Committee for Reinforced Concrete (DAfStb) [4]. These guidelines, which have been introduced by the building authorities, also permit the use of fiber-reinforced concrete. For the connection of wooden beams and fiber-reinforced concrete, fasteners are used, especially in old buildings in the form of self-tapping screws. For the use of these screws, European Technical Assessments (ETA) are required [5]. In previous investigations [6, 7], compression-shear tests were carried out to show the equivalence of fiber-reinforced concrete to normally reinforced concrete. It was confirmed that the investigated lanyards in fiber-reinforced concrete give equivalent results in terms of load-bearing capacity and serviceability. These tests were carried out for steel fiber reinforced concrete, which was qualified according to the Austrian guideline.

2.1.1 Experimental investigations according to the guidelines for fiber-reinforced concrete

In this chapter, the tests carried out according to the Austrian [3] and German guidelines [4] are described and evaluated. The aim of the tests is to show the difference between the two guidelines using the same fiber-reinforced concrete with 25kg/m³ steel fibers and to find a possible correlation between the test results in order to save multiple tests in the future. The background to this is that fiber-reinforced concrete tests are relatively expensive and time-consuming, one test of a concrete-beam takes about 60 minutes and at least six tests are prescribed to state performance [8].

The 4-point bending test itself lasted 20 min per fiber-reinforced concrete bar (Figure 1). This time results from the deformation rates of 0.1mm/min up to 0.75mm and 0.25mm/min up to 4mm deflection. For a better comparison, all specimens are tested up to 4 mm deflection and then the test is terminated. After that, the specimens are "manually" broken in the middle to count and evaluate the number of fibers in the fracture surface.

In addition to the post-cracking tensile strength in the bending tension zone, the compressive strength is also determined using four cube specimens with an edge length of 15cm.

Figure 1: *Completed fiber-reinforced concrete testing according to DAfStb guideline*

For each specimen, the deflection wis measured using two probes, the applied force and the test time. The bending tests start loading the beams according to the ÖBV guideline [3]. In the first two tests, the measuring frequency is 10Hz, then increased to 20Hz. During the first test, the aluminum angles, which served as stops for the measuring probes, were glued on with a 2-component adhesive. However, one angle came off after the initial cracking, so that control via the displacement transducers was no longer possible and the test had to be aborted. As a result, the aluminum angles are screwed to the bending beams with a 5x30mm dowel in all further tests. Furthermore, in the fifth test according to the ÖBV guideline [3], the test also failed because it was not possible to create a complete force-deflection diagram. In this test, there is a sudden drop in the force after the initial crack and the test is terminated prematurely. For these reasons, only ten complete test results exist carried out according to the ÖBV guideline [3]; for the tests according to the DAfStb guideline [4], all twelve tests are successful. The tests according to the ÖBV guideline [3] are labeled and numbered as sample K1-12 and those according to the DAfStb guideline [4] as sample G1-12.

In general, it can be said that oscillations after the initial crack and the force drop can be observed in the force-deflection diagrams. Figure 2 shows an example of a diagram in which the deviations can be seen.

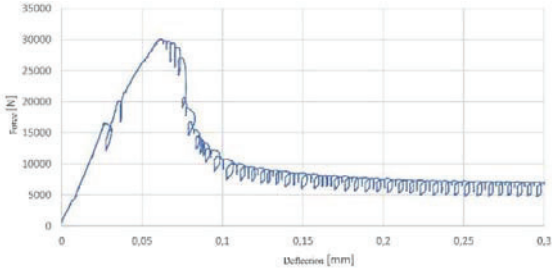

Figure 2: *Evaluation of the force-deflection diagram specimen K8 [8]*

https://doi.org/10.52202/069179-0437

It can be seen that in a range of 0.005 mm the deflection increases very quickly, although the force is slightly reduced. This is a deformation-controlled test with a deformation rate of 0.10 mm/min and it can be seen from the measured data, that within 50 milliseconds the deflection increases by 0.0037 mm and the force decreases by 40.95 N. Therefore, the deformation speed in this range is 4.40 mm/min.
Subsequently, the force is decreased and the deflection consequently becomes less. After that the force is increased again and in a certain range, there is again a sudden increase in the deflection.
This effect occurs in almost all the specimens tested, both the shorter (ÖBV) and the longer (DAfStb) ones. The reason for this effect is the control behavior of the machine. [8].

Based on the tests carried out, the fiber concrete C25/30 XC2 GK8 F52 ZG1 with a steel fiber content of 25kg/m³ corresponds to classes T2 and G1 according to the Austrian ÖBV guideline [3] and L1-0.6 and L2-0.9 according to the German DAfStb guideline [4]. Based on these classifications, the German guideline results in lower design values. Thus, if a fiber-reinforced concrete is classified with classes T2 and G1 according to the Austrian guideline and designed with classes L1-0.6 and L2-0.9 according to the German guideline, sufficient safety is provided. However, this does not apply in the opposite sense, since the design values of the German guideline are significantly lower.
In summary, it can be said that significantly different design values according to German and Austrian guidelines can be expected for the same fiber-reinforced concrete. For both serviceability and ultimate limit state, the characteristic post-cracking tensile strengths differ, in some cases considerably. Therefore, when converting these values into the design values of the post-cracking tensile strengths, the formulas of the guidelines are adapted to the respective test. The evaluation of a test series according to the respective other guideline makes little sense, since the characteristic values of the post-cracking tensile strengths are almost identical, but the design value, which is decisive, is different. Furthermore, the values of the individual tests scatter very strongly, which makes a general correlation of the two guidelines difficult.
In general, the test results of the DAfStb guideline "Steel fiber reinforced concrete" [4] is more conservative than the Austrian guideline [3].

2.2 CONFIGURATION OF THE JOINTS

The load-bearing behavior of the floor element is not only dependent on the properties of the single composite materials, but also on the configuration of the joints between the timber and concrete-based composite layers. This is the subject of numerous experimental Push-Out tests.
Load-bearing capacity of structures can be increased significantly by the usage of semi-rigid or rigid shear connections (e.g. dowel-type or notched connections) between the timber and concrete composites. By the optimized use of composite materials on joint level as well as on overall component level, not only structural performance can be increased, but also resource efficiency.
For this reason, resource-conserving load-bearing composite structures consisting of various types of laminated veneer lumber (LVL), such as spruce or beech LVL, in combination with different types of concrete toppings, such as conventional reinforced concrete (RC) or steel fiber concrete (SFC), coupled by various types of joints (dowel-type fasteners, notches) are being investigated (Figure 3).
The experimental performance assessments are executed by means of small-scaled Push-Out tests. Due to technical and geometrical aspects, the various test series partially differ in terms of the number of shear transmission points per shear joint as well as in terms of the number of shear joints (symmetric assemblies with one shear joint respectively double symmetric assemblies with two shear joints). In order to ensure the comparability of the individual test series, all experimental results are related to a single shear transmission point. Thus, not only conclusions about the various joint typologies become possible, but also values for further structural computations can be gained (Figure 3).

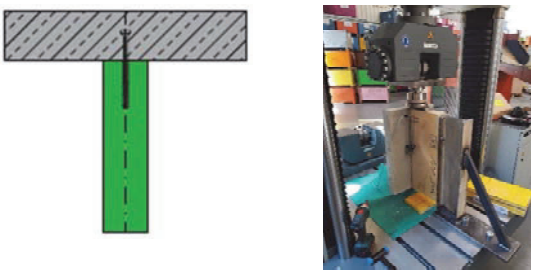

Figure 3: *Examined composite assemblies*

2.2.1 Discussion of experimental test results

Assessing the gained test results with focus on the spruce LVL assemblies' significant diversities, but also similarities within the individual test series can be identified.
Concerning the application of beech LVL assemblies coherent test results in conjunction with the spruce LVL assemblies can be observed. With the initial objective to evaluate the general suitability of hardwood LVL (beech) in comparison to softwood LVL (spruce), the conducted test series are carried out with a smaller amount of respective specimen (3 specimen in each case). As a consequence of this, the gained test results are likely to be less statistically significant and are accompanied by a simultaneously increased scattering compared to the spruce LVL assemblies, but also show the quantitative promising trends as to be expected. The increased material stiffness of hardwood beech LVL further leads to increased mechanical properties of the examined assemblies.

https://doi.org/10.52202/069179-0437

With respect to the application of crossed screw typologies a reduced increase of the load-bearing capacity in comparison to not crossed screw typologies can be observed. In conclusion, the doubling of screws per shear transmission point only leads to a 33% higher maximum load $F_{max,k}$. So, the application of screw typologies with a pure tensile load transfer can be described as the more efficient variation compared to the application of screw typologies with a combined tensile/compressive load transfer.
By the application of notch typologies, the maximum loads $F_{max,k}$ as well as the slip moduli $K_{ser,mean}$ can be increased noticeably. A significant influence of the notch depth cannot be observed thereby.

3 CONCEPTUAL FEASIBILITY STUDIES

Technically, the ribbed timber-concrete composite floor is planned as a prefabricated component. These elements can be installed completely on the construction site or subsequently assembled and concreted on site.
The structural design idea of timber-based composite constructions is founded on the utilization of joints between the single composite layers to reach an optimized application of each used composite material.

The research project includes design concepts, feasibility studies and performance assessments of the components in order to improve the overall performance. Based on the results of the performance assessments and on accompanying computation approaches (shear analogy method according to DIN EN 1995-1-1/NA [9] respectively gamma-method according to ÖNORM EN 1995-1-1 [10]) different types of composite floors are developed and compared with each other.

A comparative parameter study is done with the aim of finding a resource-efficient solution for a single-span floor system with a total length up to 12 meters (between 8m, 10m and 12m) considering fire resistance R90 (see Figure 4 as an example for a span of 8.00m).

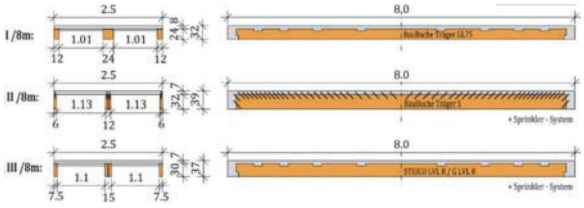

Figure 4: *Optimized LVL-RC composite floor structures for 8m with various connection notches and screws [6]*

The resource efficiency is investigated in terms of the cross-sectional dimensions, the constellation of the materials and the kind of connections including form-fitting notches and fasteners, which can be fixed mechanically [6].

Type I is a floor system without sprinkler, Type II is a system with sprinkler and mechanical fasteners - by hand inserted screwed connection (about 13 pc. /m^2) and type III is a system with sprinkler as well as reduced timber square sections and with notches as very strong and stiff connectors between timber and concrete - notches cut in the timber and filled with concrete.
A significant part in the optimization of the floor systems is using the cost-efficient quantity of timber. This means Beech-LVL ribs instead of the massive cross-laminated timber (CLT) elements. This offers advantages especially in terms of reduced resource consumption.

With regard to the material cost calculation, it should be mentioned that only the material prices are actually calculated. It makes sense to carry out a material cost calculation. The decisive factor here is that only the material costs are evaluated in monetary terms and this is not a detailed cost calculation. Furthermore, the relationship between resource efficiency and cost efficiency for the ranges investigated becomes apparent.
For this purpose, reference values for cubic meter prices of LVL and reinforced concrete are obtained.
With the help of the already determined amount of resources per floor element, it is possible to make a rough cost calculation for a floor element or to roughly determine a price per square meter for a LVL-concrete composite floor of the respective span. It should be noted that additionally required materials after the installation of the individual ceiling elements are not taken into account depending on the constructive system.
Additionally, the material costs for the different solution variants are determined, the most cost-efficient solution can be determined.
Moreover, costs for an active fire protection system (sprinkler system) are included in the calculation, if this is necessary to be able to comply with the fire protection requirements. In this case, the sprinkler system is purely an acquisition cost without the maintenance costs. Although these costs are not directly material costs, they must be taken into account so that all solutions can be considered equal and thus remain comparable with each other [6].
By including a sprinkler system, the amount of timber can be reduced to a minimum, so that just the verifications of the design for the normal state ("cold-state design") are fulfilled. This optimization of the timber cross-section results in the use of narrow but high ribs. However, if the joint between timber and concrete is to be achieved via shear notches, a minimum width of the LVL ribs is required, otherwise the notch verifications according to [11] cannot be fulfilled. Notches are basically suitable for new buildings and an efficient composite variant. No additional resources are required, production is simple and cost efficient, only a small number of notches is needed and no additional personnel is required in the manufacturing process. In the case of screws, the rib width can be further reduced to 60mm if the verification permits. According to the approval, an edge distance of 30mm is required. In the case of fasteners, a large number are

https://doi.org/10.52202/069179-0437

required and the manpower required for setting the screws should not be underestimated either. However, as already mentioned, this is not taken into account in the material cost calculation. But due to the fact that the costs for the LVL ribs make up the main part of the material costs of the floor element and that minimum timber cross-sections are possible due to the joint via screws, a resource- as well as cost-efficient solution is also possible with screws for new buildings (see Figure 5; Solution II/8m). However, it should be mentioned here again that by minimizing the timber cross-section, an extinguishing system is mandatory to meet the fire protection requirements. And the installation of an extinguishing system is, of course, inevitably associated with an expenditure of resources, but it is often a basic requirement in high-rise construction. Comparing the concrete slab, it results for 12m to 10m span-width a reduced thickness of the slab by 3cm (from 11cm to 8cm), comparing a span of 8m, hardly no further reduction is possible. The reason for this is either the minimum thickness of 7cm specified in the approval, as well as the vibration verification according to Eurocode 5 [10] which is no longer fulfilled with a further reduction.

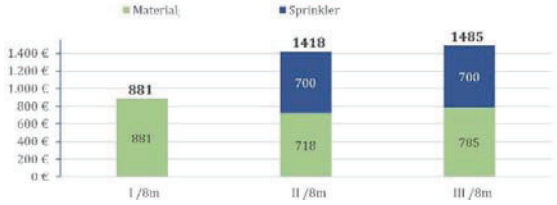

Figure 5: *Comparison of material cost calculation for 8m with various connection notches and screws [6]*

3.1 TIMBER-STEEL FIBER CONCRETE-COMPOSITE

In addition to the studies presented above, the verifications of the load-bearing capacity and serviceability are carried out on modelling bending beam floor [8]. The dimensions are chosen in such a way that the verifications of the load-bearing capacity and serviceability go out with the tests carried out. A brief overview of the most important data for this study of the timber-fiber-reinforced concrete beam floor is below mentioned:

Dimensions of the wooden beams C24: width 16cm, height 26cm, span of the beams: 6m
Height of the concrete layer C25/30: 7cm
Residential building; service class 1
Fasteners Composite screws ACC 8.0 x 165 screwed at an angle of 45°, 3 rows of screws per timber beam, screw-in depth in the timber: 7.1cm
Thickness of the formwork: 2.5cm
The cross-section is shown below, the beam spacing is 65cm, therefore all verifications are carried out for a 65cm wide cross-section.

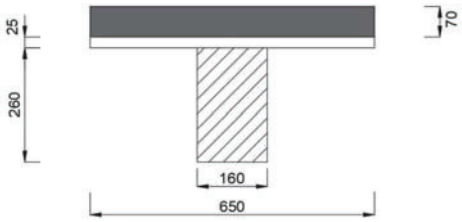

Figure 6: *Composite floor structures connection with screws [8]*

Based on the results, it can be seen that the fiber-reinforced concrete is the most stressed cross-section. Therefore, it is important to ensure that the bending moment in the fiber-reinforced concrete cross-section is reduced to a minimum, if possible, while at the same time increasing the normal force.

In the present example, the verifications of load-bearing capacity (ULS) and serviceability (SLS) are fulfilled for a fiber-reinforced concrete T2 according to the ÖBV guideline [3] and L1-0.6/ L2-0.9.

Finally, different classes of fiber-reinforced concrete will be compared and the effects on utilization or the number of fasteners will be presented. The aim of the study is to keep the number of fasteners as low as possible while maintaining an economical fiber-reinforced concrete class.

First, a reduction of the fiber-reinforced concrete layer thickness of 6cm is investigated. The fastener spacing is 25cm minimum and 80cm maximum. This results in 70 screws, which corresponds to a reduction of 40 screws per meter of slab strip. At the same time, the utilization is 92% according to the German guideline [4], which is authoritative.

In a further step, a fiber-reinforced concrete of class T3 according to the Austrian guideline [3] is considered in more detail. Here, a 7cm thick fiber-reinforced concrete layer is again assumed and a screw spacing of 15cm in the minimum and 60cm in the midspan. The only change compared to the original configuration is the design value of the post-cracking tensile strength of 0.31N/mm². Thus, the use of screws results in a utilization of 84% compared to 86%. A fiber-reinforced concrete of class T4 would produce a utilization of 81%. Thus, the difference in design is not too great when changing the fiber-reinforced concrete class alone.

If the minimum lanyard spacing is increased to 25cm and the maximum to 80cm as well as using a fiber concrete class T4 and increasing the tensile strain in the cross section from 0.9 to 1.5‰, an equilibrium condition with utilization of 98% is obtained. This means that with a fiber concrete two classes higher and a higher utilization, fasteners can be saved, in this case 40 pieces.

As a final optimization step, an increase of the fiber concrete class from L1-0.6 or L2-0.9 to L1-0.9 or L2-1.2 is also investigated when considering the German guideline [4]. Here, the utilization in the fiber-reinforced concrete cross-section also changes from 89 to 87%. Under the same boundary conditions, a saving in

https://doi.org/10.52202/069179-0437

connection material would only be possible with a fiber-reinforced concrete class three classes higher.

Table 1 summarizes the decisive results of the different optimization variants. It should be noted, however, that these results only refer to the example given here.

In summary, increasing the fiber-reinforced concrete class has very little effect on the load-bearing capacity of the fiber-reinforced concrete cross-section. A more effective way to save fasteners, especially screws, is to reduce or optimize the thickness of the fiber-reinforced concrete layer. However, when the concrete thickness is reduced, the compressive stresses are increased. Thus, depending on the application and the given boundary conditions, it must be decided which variant, fiber-reinforced concrete or reinforced concrete, is to be used.

Table 1: *Overview of optimization*

Optimization variant	Number of screws	Change in utilization
Reference example T2 or L1-0.6, L2-0.9	110	0%
Thickness of the fiber concrete layer 6cm	70	+3%
Fiber concrete T3	110	-2%
Fiber concrete T4	70	+12%
Fiber concrete L1-0.9 or L2-1.2	110	-2%

In this study, only a fiber concrete with 25kg/m³ steel fibers is considered. Subsequently, the question is how big the differences are between the two guidelines with a fiber content of 20 or 30kg/m³. Further research questions on this topic would be how the combination of plastic fibers with steel fibers affects the load-bearing capacity and shrinkage behavior. The use of steel fibers in lightweight concrete would also be a useful option when used in timber-fiber-reinforced concrete composite structures in order to reduce the deadweight of the floor. In order to verify the calculations of timber-fiber-reinforced concrete composite floors, both fiber-reinforced concrete tests and tests on timber-fiber-reinforced concrete composite floors with the same fiber-reinforced concrete would be useful in a further step. Thus, a classification of the fiber-reinforced concrete according to Austrian and German guidelines would be available and the effects in the ultimate load of the composite floor would be visible.

4 CONCLUSIONS

The experimental performance assessments of spruce LVL assemblies as well as of beech LVL assemblies generally show promising results for an application of LVL products in composite floor systems. Also concerning the substitution of conventional reinforced concrete (RC) through steel fiber concrete (SFC), a general suitability can be observed.
The conceptual feasibility studies, based on the results of the performance assessments and on accompanying computation approaches, show the capabilities in the application of LVL products in composite floor systems. Consequently, the presented results enable engineers, as well as builders and planners, to further strengthen the implementation of timber-based composites within modern building applications.
A significant part in the optimization of the floor systems is using the cost-efficient quantity of timber. This means Beech-LVL ribs instead of the massive cross-laminated timber (CLT) elements. This offers advantages especially in terms of reduced resource consumption.

ACKNOWLEDGEMENT

The research project is a collaborative effort of the ITI/TU Wien and the Schmid Schrauben Hainfeld Ltd. The authors gratefully acknowledge the support of the Schmid Schrauben Hainfeld Ltd. and the TU Wien, Austria.

REFERENCES

[1] A. Teischinger, R. Sting and G. O. Praxmarer, 15 07 2019. [Online]. Available: http://www.proholz.at/news/news/detail/holzbauanteil-in-oesterreich-ein-viertel-des-hochbau-aufkommens-bereits-aus-holz/. [Accessed 26 10 2019].

[2] Gruber, E., Gutmann, R., Huber, M., & Oberhuemer, L., *Leistbaren Wohnraum schaffen-Stadt weiter bauen: Potenziale der Nachverdichtung in einer wachsenden Stadt: Herausforderungen und Bausteine einer sozialverträglichen Umsetzung,* Kammer für Arbeiter und Angestellte für Wien, 2018.

[3] ÖBV, *Richtlinie: Faserbeton,* Vienna: Österreichische Vereinigung für Beton- und Bautechnik, 2018.

[4] DAfStb, *Erläuterungen zur DAfStb-Richtlinie Stahlfaserbeton,,* Bochum : Deutscher Ausschuss für Stahlbeton, 2014.

[5] "European Technical Assessment 18/0829 Schmid Schrauben RAPID T-Con Wood-concrete composite slab with dowel-type fasteners," EOTA - European Organisation for Technical Assessment, [Online]. Available: https://www.eota.eu/etassessments/8378. [Accessed 11 March 2023].

[6] P. Rädler , *Master's thesis: Resource-efficient timber-concrete composite floors for use in the timber high-rise buildings,* Vienna: Department of Structural Design and Timber Engineering, Vienna University of Technology, 2018.

[7] S. Zahirovic, *Master's thesis: Structural behavior of laminated veneer lumber fiber concrete composite floors,* Vienna: Department of Structural Design and Timber Engineering, Vienna University of Technology , 2019.

[8] A. Blaha, *Master's thesis: Zum Einsatz von Holz-Faserbeton-Verbunddecken: Theoretische und experimentelle Untersuchungen,* Vienna: Department of Structural Design and Timber Engineering, Vienna University of Technology, 2021.

[9] German Institute for Standardisation, "DIN EN 1995-1-1/NA - National Annex – Nationally determined parameters – Eurocode 5: Design of timber structures – Part 1-1: General – Common rules and rules for buildings," 2013.

[10] Austrian Standards, *ÖNORM EN 1995-1-1 - Design of timber structures - Part 1-1: General - Common rules and rules for buildings (consolidated version),* 2019.

[11] Schönborn, F., Flach, M., & Feix, J., "Bemessungsregeln und Ausführungshinweise für Schubkerven im Holz-Beton-Verbundbau," *Beton- und Stahlbetonbau,* vol. 106(6), pp. 385-393, 2011.

https://doi.org/10.52202/069179-0437

World Conference on Timber Engineering Oslo 2023

ANALYTICAL AND EXPERIMENTAL STUDY ON REVERSIBLE STEEL-TIMBER COMPOSITE CONNECTION SYSTEMS

Fabiana Yukiko Moritani[1], Pedro Santos [2], Luís Jorge [3], Alfredo Dias [4]

ABSTRACT: This paper presents a study on the structural behavior of steel-timber composite (STC) with a special focus on reversible connection systems. Particularly, it addresses the research of composite structure floors comprising cold-formed steel (CFS) beams and cross-laminated timber (CLT) panels that allow a highly industrialized and reversible construction as well as high mechanical efficient since it overcomes the inherent limitations of each component. The analysis is based on an experimental campaign carried out to assess the mechanical behavior of the proposed connection systems in terms of stiffness and strength as well as relevant failure modes. A series of new bolted connection systems are proposed and push-out tests on five types of CFS-CLT composite connections were performed to obtain the load-slip curves and failure modes. The test results were compared with those provided by EN 1995-1-1 analytical models. The results showed that bolted joints using special types of nut obtained higher load bearing capacity and slip modulus than screwed joints of similar diameter. The failure modes were, mostly, simultaneous occurrence of embedding strength failure on CLT and slight developing of plastic hinges on connectors.

KEYWORDS: Steel-Timber Composite, Cross-Laminated Timber, Cold-Formed Steel, Connections

1 INTRODUCTION

Composite structures have been used as an effective solution for modern buildings combining the benefits of dissimilar materials to overcome their individual limitations and improve the structural system performance [1-2]. Besides the structural efficiency due to the composite action, the application of steel-timber composite (STC) structures allows to use prefabricated elements and, in some cases, a fully reversible construction system. STC applications for buildings presents many advantages proving their suitability as a structural solution, for instance: lightness, structural in-plan stability, low environmental impact, as well as the possibility of recycling and replace the degraded elements [3].

The engineered wood products with high mechanical performance such as Laminated Veneer Lumber (LVL), Glued Laminated Timber (Glulam) and Cross-Laminated Timber (CLT) are prefabricated structural elements of timber whose use have increased significantly in the construction industry due to lower carbon footprint, relatively high mechanical performance and lower self-weight in comparison with other traditional solutions [4-5]. The association of steel profiles and CLT slabs allows highly industrialized construction, as the elements are connected quickly, precisely, and using full-dry mechanical devices [3]. Comparatively to traditional lightweight timber structures, CLT panels are higher strength-to-weight ratio, and due to its crossed-layers and massive nature, the structural capacity and fire resistance are improved, making it possible to design and build large timber structures that are competitive against steel and reinforced concrete but significantly more sustainable [6-9]. The CFS profiles are attractive options in commercial and residential buildings due to high structural performance, lightweight, ease of prefabrication and quick assembly on site [10-12]. The increasing application of CFS in the construction industry has brought researches to overcome the safety issues and to

[1] Fabiana Yukiko Moritani, University of Coimbra, ISISE, ARISE, Department of Civil Engineering, Coimbra, Portugal, fabianamoritani@gmail.com

[2] Pedro Santos, University of Coimbra, ISISE, ARISE, Department of Civil Engineering, Coimbra, Portugal, psantos@dec.uc.pt

[3] Luís Jorge, Polytechnic Institute of Castelo Branco, Portugal, luisfc@ipcb.pt

[4] Alfredo Dias, University of Coimbra, ISISE, ARISE, Department of Civil Engineering, Coimbra, Portugal, alfgdias@dec.uc.pt

https://doi.org/10.52202/069179-0438

improve the use of CFS elements as primary structures [13].

Therefore, the association of CFS beams and CLT panels can also satisfy requirements in terms of lightweight, prefabrication, modularity, sustainability, on-site installation, and relative manufacturing costs [1]. Navaratnam *et al.* (2021) [14] investigated the structural performance through FEM model of CLT-CFS composite beam for the flooring system. Karki *et al.* (2022) [15] carried out push-out tests of CFS-plywood connections with screws and bolts, as well as the influence of adhesives at the shear interface. Based on the results, the authors recommended using self-drilling screws, M8 nuts and bolts for CFS-timber composite flooring systems. Vella *et al.* (2020) [16] performed experimental tests of CFS and timber panel (*i.e.* plywood and particleboard) connections with inclined screws. This study evaluated the influence of type of timber panel, type and inclination of connector, and the thickness of CFS. The authors showed that the CFS thickness influences significantly the resistance to thread withdrawal failure and degree of rotational restraint of the fastener head.

In this paper, novel connection systems for CFS-CLT composites are presented in order to achieve an efficient mechanical behavior, allowing a simple and quick assembly/disassembly process, requiring fewer connectors, and thus, globally, turning the composite system into a more economical and efficient solution than the current ones found for CFS-CLT composites.

2 CONNECTIONS FOR CFS-CLT COMPOSITE STRUCTURES

The connector types used in this study comprise self-drilling screws and bolts, with 60 mm length and 8 mm diameter. More details are given in Table 1 and Figure 2.

Table 1 - Parameter of connections

ID	Connector	Description
S1	Screw	Self-drilling screws, 8 mm diameter, $f_{y,k}$ = 1000 N/mm²
B1	Bolt + washer + nut	Bolt, 8 mm diameter, grade 8.8, with washer (24 mm external diameter) and nut
B2	Bolt + T-nut	Bolt, 8 mm diameter, grade 8.8, with T-nut for wood (11 mm height, 9 mm external diameter and 22 mm outer diameter)
B3	Bolt + threaded insert	Bolt, 8 mm diameter, grade 8.8, with threaded insert (19 mm height and 12 mm external diameter)
B4	Bolt + threaded insert + T-nut	Bolt, 8 mm diameter, grade 8.8, with threaded insert (same as in B2 connection) and T-nut (same as in B3 connection)

Figure 1 – Connection components (a) Screw; (b) Bolt; (c) Washer and nut; (d) T-nut for wood and, (e) Threaded insert for wood

Connections S1 and B1 ("S" stands for screw and "B" for bolt) are commonly used in timber structures and those were considered as reference connectors to the new solutions B2 (using a T-nut), B3 (using a threaded insert) and B4 (a combination of concepts of connections B2 and B3. Bolted connection systems are considered due to easiness for quick assemble and disassemble (presumably and assuming normal conditions of the use of the structure, i.e., service limit states) as well the possibility of pre-fabrication on factory. Threaded inserts and T-nut were used to provide stiffness to the bolted connections (i.e. to reduce the stiffness lose effect due to the hole clearance) and at the same time keeping the disassemble advantages of the bolted solution. In the bolted connections, 8 mm diameter holes were predrilled and at one of the surfaces of the CLT (solutions B1, B2 and B4), a 28 mm diameter hole was drilled insertion of washer/nuts and avoided the protruding from the outer surface of the CLT panel.

3 EN 1995-1-1 DESIGN RULES FOR CFS-CLT DOWEL-TYPE CONNECTIONS

The design rules for dowel-type that are recommended in EN 1995-1-1 [17] are based on the Johansen's Theory [18]. The method establishes the limit equilibrium equations for timber-to-timber and steel-to-timber connections, assuming the rigid-plastic behavior of the connectors and the timber subjected to crushing by the rigid connector. Two concepts that translate these hypotheses into the calculation are the localized crushing resistance of the timber and the plastic moment of the connector. Depending on the mechanical and geometric characteristics of the elements involved in the connection, the failure can take different forms; however, the friction forces between the connected elements and the withdrawal strength of the fasteners are ignored in Johansen's model [19-20]. The failure modes always imply the localized crushing of the timber, combined or not with plastic hinges in the connector [21].

The characteristic load-carrying capacity of the dowelled connections depends on the yield strength, the embedment strength, and the withdrawal strength of the fastener. EN 1995-1-1 [17] provides equations to determine the load-

https://doi.org/10.52202/069179-0438

carrying capacity of single- and double-shear plane in different connection types [19].

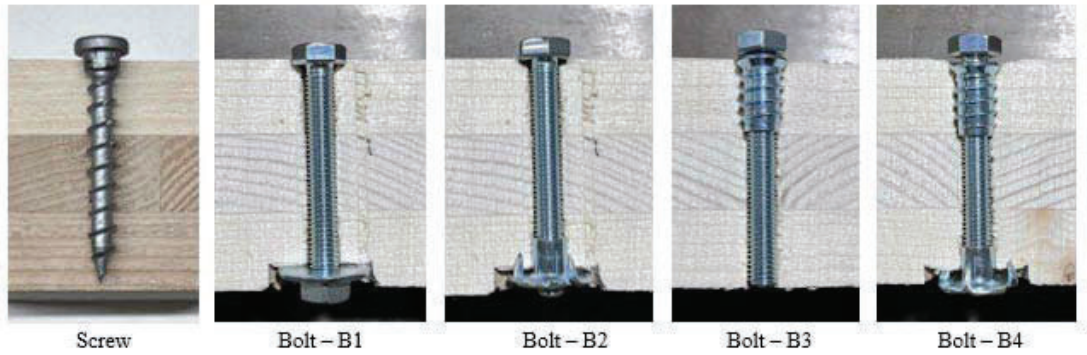

Figure 2 – Types of tested connection systems.

For a thin steel plate in single-shear, the characteristic load-carrying for screws per shear plane per fastener $F_{v,Rk}$, is taken as the minimum value found from Equation (1a):

$$F_{v,Rk} = min\begin{cases} 0.4\, f_{h,k}\, t_1\, d & \text{(1a)} \\ 1.15\sqrt{2\, M_{y,Rk}\, f_{h,k}\, d} + \frac{F_{ax,Rk}}{4} & \text{(1b)} \end{cases}$$

Where, $f_{h,k}$ is the characteristic embedment strength in the timber member; t_1 is the thickness of the timber member or the penetration depth; d is the screw diameter; $M_{y,Rk}$ is the characteristic fastener yield moment; $F_{ax,Rk}$ is the characteristic withdrawal capacity of the screw.

For cold-formed steel profiles, thin-walled sheets are usually considered since their thickness is generally less than half the fastener diameter. In Figure 3, two failure modes are presented for thin steel-timber connection that represent, respectively, the embedment of timber member obtained from Equation (1a) and the same failure plus the plastic moment of the connector from Equation (1b).

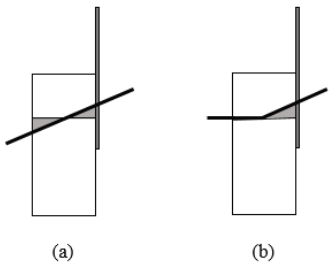

Figure 3 - Failure modes for thin steel-timber connection; (a) embedment of timber member; (b) embedment of timber member plus plastic moment of the connector

Models for determination of the embedment strength in CLT connections were developed in several studies [19-22] and an empirical model for the load-slip behavior of steel-CLT composite connections was proposed by Hassanieh *et al.* (2017) [23].

The value of the characteristic embedment strength in the timber member with pre-drilled is given in EN 1995-1-1 [17] by Equation (2):

$$f_{h,k} = 0.082\,(1 - 0.01\, d)\, \rho_k \qquad (2)$$

Where, d is the screw diameter and ρ_k is the characteristic density of wood.

The characteristic fastener yield moment ($M_{y,Rk}$), according to EN 1995-1-1 [17], is calculated from Equation (3):

$$M_{y,Rk} = 0.3\, f_{u,k}\, d^{2.6} \qquad (3)$$

Where, $f_{u,k}$ is the material characteristic tensile strength.

For bolted connections, according to EN 1995-1-1 [17], the characteristic withdrawal capacity is given by the minimum of the following possible failure mechanisms: maximum bolt tensile capacity ($F_{R,t,k}$), punching of the washer in the timber ($F_{ax,Rk,\ bearing}$) or punching of the bolt in steel plates ($B_{p,Rk}$), as shown in Equation (4).

$$F_{ax,Rk} = min\begin{cases} F_{\mathrm{R,t,k}} \\ F_{ax,Rk,bearing} \\ B_{p,Rk} \end{cases} \qquad (4)$$

The bearing capacity of steel plate should not exceed that an equivalent washer, whose external diameter corresponds to a minimum between *12t* and *4d*.

The slip modulus per shear plane per fastener under service load (K_{ser}) for screws or bolts are given by the Equations (5):

$$K_{ser} = {\rho_m}^{1.5}\, d/23 \qquad (5)$$

For steel-to-timber connections, K_{ser} should be based on ρ_m for timber member and could be multiplied by 2.0.

https://doi.org/10.52202/069179-0438

4 EXPERIMENTAL PROGRAM

Experimental characterization of the developed CFS-CLT composite connections is carried out through push-out tests according to EN 26891 [27]. In total, five types of CFS-CLT connections systems were tested to characterize the shear-slip behavior of the proposed connections.

As result of tests, load-slip curves of CFS-CLT composite connections were obtained to determine the ultimate load capacity and slip modulus.

4.1 MATERIALS

The timber elements used in this study were a CLT panel made from 3-layered of Spruce lamellae of strength class C24 (Table 2). The panel was cut in 350 mm wide x 400 mm long stripes. In the push-out test the CLT panel was loaded in the direction parallel to the external layers' grain. The cold-formed steel profile used was an Omega profile S350GD whose properties are given in Table 3.

Table 2 - Properties of CLT panel

Parameter	
Modulus of elasticity (MPa)	11000
Compressive strength (MPa)	24
Density (kg/m³)	420
Thickness (mm)	3 x 20

Table 3 - Properties of CFS profile

Parameter	
Modulus of elasticity (MPa)	210000
Yield strength (MPa)	350
Ultimate strength (MPa)	420
Thickness (mm)	2.5
Height (mm)	250
Length (mm)	400

4.2 FABRICATION OF SPECIMENS

Five types of CFS-CLT connection (Figure 2) in a total of eighteen specimens (six for S1 and three for each bolted solution) were produced (Table 1). Each specimen was composed of a CLT panel connected to the flanges of two CFS profiles (each with two connectors per shear plane) using a symmetric layout, resulting in two independent shear planes, as shown in Figure 4.

4.3 LAYOUT AND CONFIGURATION OF PUSH-OUT TESTS

The specimens were placed in the testing rig as shown in Figure 5. Four linear variable differential transformers (LVDTs) were used to measure the relative displacement (or slip) between the CLT panel and CFS profile.

The loading procedure was carried out as specified in EN 26891 [27]. The test stop conditions were failure of the specimen, 15 mm of slip or 900 s of test, whatever occurred first. The loading procedure was updated with respect to the ultimate load obtained in the first specimen tested within each solution (pre-test).

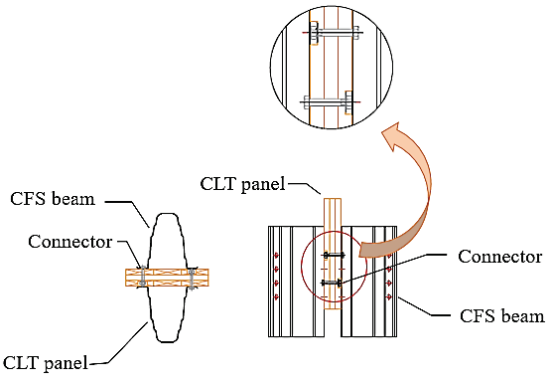

Figure 4 – Scheme of connection tests

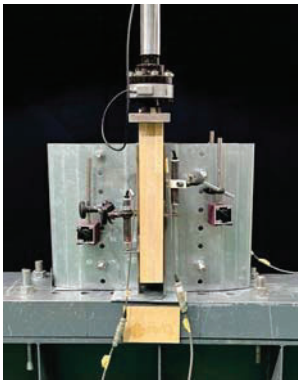

Figure 5 - Layout of push-out test

5 RESULTS AND ANALYSES

5.1 LOAD-SLIP CURVES

The load-slip curves of the CFS-CLT connections with screws and bolted connectors obtained per specimen and per solution are shown in Figures Figure 6 to Figure 10.

With regard to the ultimate load capacity (F_{ult}) of the composite connections it can be observed that the bolted solutions present higher values than joints with screws. Although the solutions B3 and B4 were pre-drilled, the bolts were connected with a nut at the top of the hole, which provided higher initial slip modulus than solutions B1 and B2. Although screwed connection had on average higher stiffness than solutions B1 and B2, the screwed joint showed rapid loss of stiffness with increase on load. All load-slip curves demonstrated ductile behavior. Similar to the results shown in Hassanieh *et al.* (2016) [4], the load-slip curves of the joint solutions with screws (Figure 6) showed close to elastic-perfectly plastic behavior, while the bolted solutions presented some hardening characteristics.

https://doi.org/10.52202/069179-0438

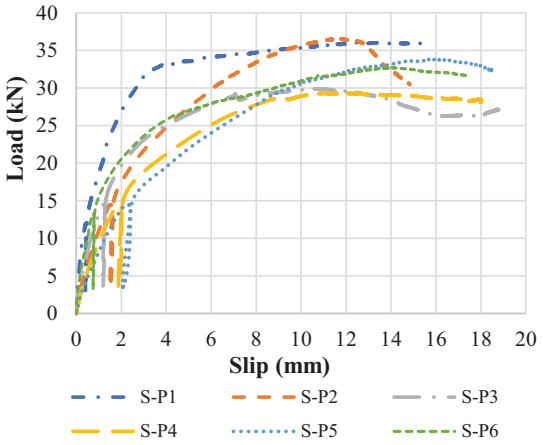

Figure 6 – Screw load-slip curve

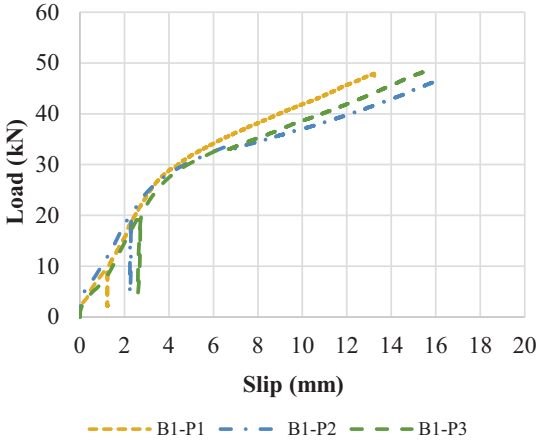

Figure 7 – Bolt-B1 load-slip curve

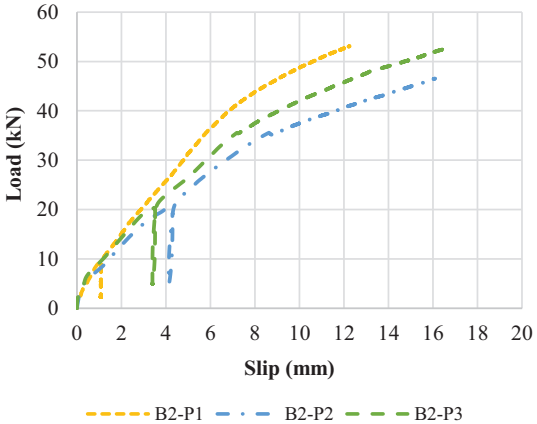

Figure 8 – Bolt-B2 load-slip curve

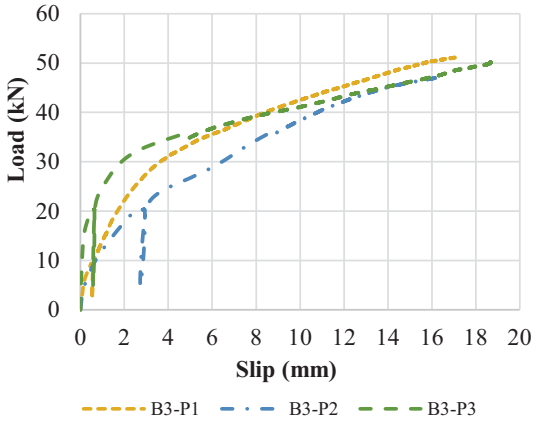

Figure 9 – Bolt-B3 load-slip curve

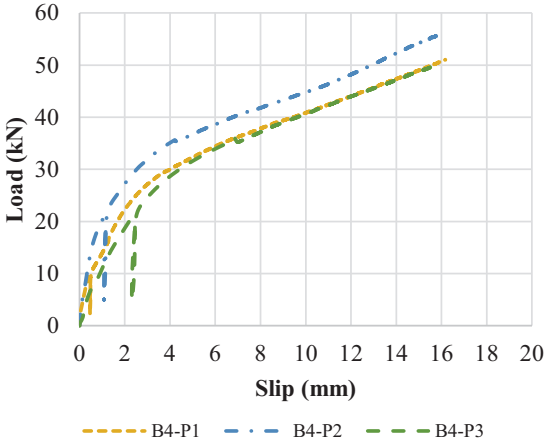

Figure 10 – Bolt-B4 load-slip curve

5.2 TEST RESULTS

The mean values obtained in the tests for the ultimate load capacity (F_{ult}) and slip modulus (k_s) - defined according to EN 26891 [27] - are presented in Table 4, as well the characteristic values calculated according to EN 14358 [28]. The mean ultimate load capacity for the screwed connections was 8.3 kN while for the bolted solutions, in descending order, was: 13.1 kN (B4), 12.7 kN (B2), 12.4 kN (B3) and 11.9 kN (B1). Regarding the mean slip modulus, for screws a value of 2773 N/mm was achieved while for the bolted solutions, in descending order, was: 4413 N/mm (B3), 3604 N/mm (B4), 1737 N/mm (B1) and 1543 N/mm (B2). Overall, the ultimate load capacity of the different bolted connections was quite similar (maximum difference around 1.2 kN). Both B2 and B3 connections presented similar load capacity, however B2 presented the lowest stiffness while B3 the highest. On the other hand, B4 connection (which was a combination of concepts of connections B2 and B3) resulted in a solution with the second highest slip modulus (3604 N/mm) and the highest ultimate load capacity of all solutions (13.1 kN).

https://doi.org/10.52202/069179-0438

Table 4 – Test results per connector, mean and characteristic values, and comparison between EN 1995-1-1 predictions.

Type	Specimen n°	F_{ult}^{*} (kN)	k_s (N/mm)
S1	1	9.0	6044
	2	9.1	1781
	3	7.5	2249
	4	7.3	1465
	5	8.5	1227
	6	8.2	3871
	Mean	8.3	2773
	CoV (%)	9.1	67.0
	Ch. value	6.6	-
	EN 1995-1-1 $F_{v,k}$ | K_{ser}	7.5	5988
	$F_{v,k}/F_{ult}$ | K_{ser}/k_s	1.1	2.2
B1	1	12.0	1604
	2	11.6	1833
	3	12.2	1774
	Mean	11.9	1737
	CoV (%)	2.5	6.8
	Ch. value	10.2	-
	EN 1995-1-1 $F_{v,k}$ | K_{ser}	5.8	5988
	$F_{v,k}/F_{ult}$ | K_{ser}/k_s	0.6	3.5
B2	1	13.3	2003
	2	11.6	1036
	3	13.1	1591
	Mean	12.7	1543
	CoV (%)	7.2	31.5
	Ch. value	10.0	-
	EN 1995-1-1 $F_{v,k}$ | K_{ser}	5.8	5988
	$F_{v,k}/F_{ult}$ | K_{ser}/k_s	0.6	3.9
B3	1	12.8	4015
	2	11.8	1591
	3	12.6	7634
	Mean	12.4	4413
	CoV (%)	4.1	68.9
	Ch. value	10.6	-
	EN 1995-1-1 $F_{v,k}$ | K_{ser}	5.8	5988
	$F_{v,k}/F_{ult}$ | K_{ser}/k_s	0.6	1.4
B4	1	12.8	4428
	2	14.1	4390
	3	12.5	1994
	Mean	13.1	3604
	CoV (%)	6.4	38.7
	Ch. value	10.7	-
	EN 1995-1-1 $F_{v,k}$ | K_{ser}	5.8	5988
	$F_{v,k}/F_{ult}$	0.5	1.7

Note: CoV: Coefficient of variation; Ch. Value – Characteristic value calculated according to EN 14358 [28]; *Ultimate load capacity equally distributed on four connectors.

In general, B1 solution compared poorly against the other bolted ones regarding stiffness and strength. Comparing the bolted solutions with the screwed one, it is found that the firsts performed better in terms of strength while in terms of stiffness only B3 and B4 solutions superseded the S1 connection.

Table 4 shows a comparison of the ultimate load capacity and slip modulus between push-out test results and those estimated according to EN 1995-1-1 [17]. According to the predictions, the characteristic load-carrying capacity per connector and per shear plane was $F_{v,k}$ = 7.5 kN and $F_{v,k}$ = 5.8 kN for the screwed and bolted connections, respectively. The slip modulus under service was K_{ser} = 5988 N/mm for both screws and bolts.

The estimated ultimate load capacity was mostly lower than the value obtained in tests, with a test-to-estimated ratio between 0.5 and 0.6 for bolts. In terms of the estimated slip modulus, the results showed that those were significantly higher than the test values - the mean ratio was 2.2 for the screwed connection and between 1.4 and 3.9 for the bolted connections.

It should be noticed that the coefficient of variation of the results was noticeable (67.0% for screwed joints and between 6.8% and 68.9%), and this may be the reason for the discrepancy found. Likewise, Vella *et al.* (2021) [29] presented the same analysis for CFS and plywood composite connections and reported that the estimated load capacity was significantly lower than that measured from the tests, with a mean test-to-estimated ratio $F_{v,EN}/F_{v,k}$ of 0.55 and even higher ratios of K_{ser}/k_s (around 6.20) on their connections.

Overall, from the novel connections proposed and assessed in this study, solutions B3 and B4 presented the highest and more balanced performance, and thus showing a significant potential to be used in CFS-CLT structures.

5.3 FAILURE MODES

According to EN 1995-1-1 [17], two failure modes are possible for steel-to-timber composite connection with thin steel plate in single shear – (a) embedment of timber and connector rotation; (b) connector bending and plastic hinge.

Figure 11 shows slight developed plastic hinges on a bolt and on a screw (less pronounced in the last). Figure 12 and 16 show local deformations around the CFS holes and rotation of the screws and bolts head at the end of the tests, being more evident in the bolt connections because those were subject to higher loads. Figures 13 to 15 shows the crushing of timber and the embedding of the bolts. In the present study, the CFS sheet of the specimens was unable to significantly restrict the rotation of the connectors, which created a localized deformation around the CFS hole, a large rotation of the connector and excessive crushing in the CLT panel. Therefore, the failure modes obtained in the tests were much closer to mode (a) presented in Figure 3.

https://doi.org/10.52202/069179-0438

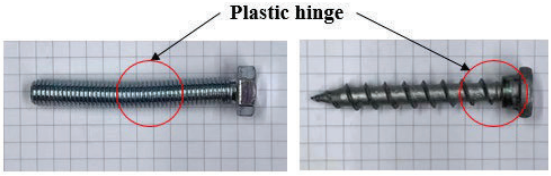

Figure 11 - Failure details of screw and bolt.

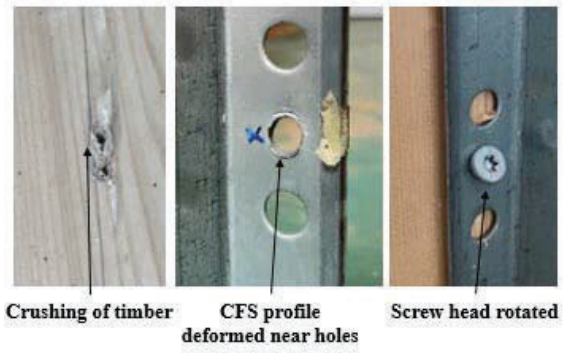

Figure 12 - Failure details of screwed connection.

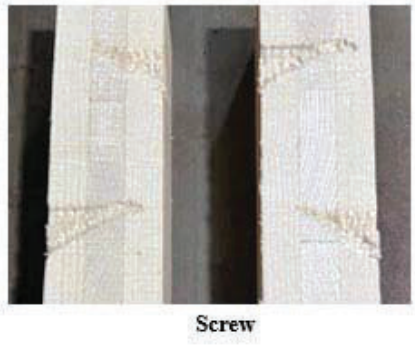

Figure 13 – Failure details of CLT panels (screws).

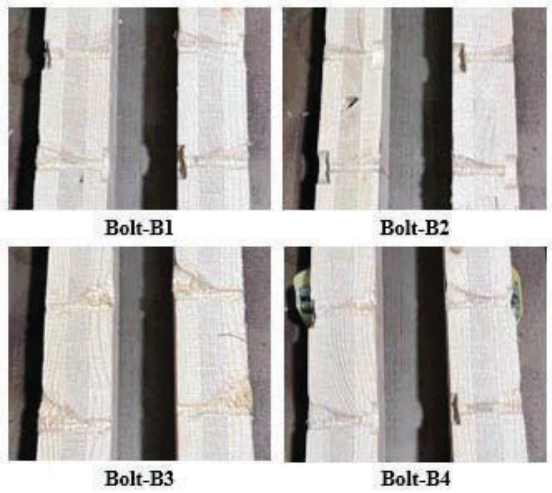

Figure 14 – Failure details of CLT panels (bolts).

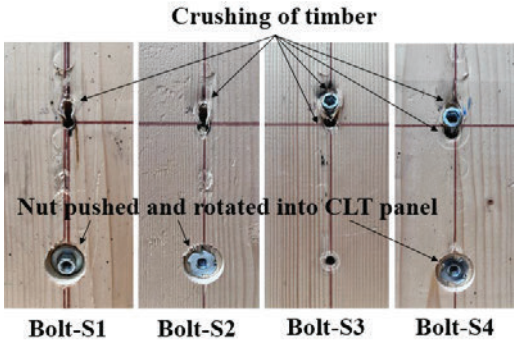

Figure 15 - Failure details of bolted connection (CLT panel side).

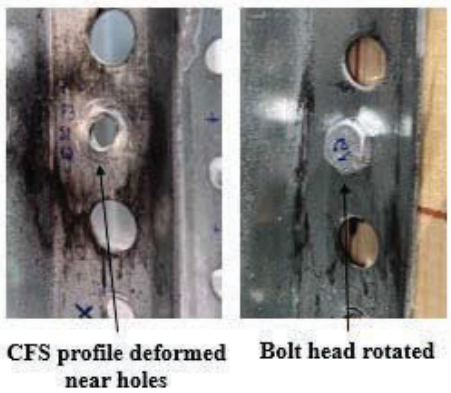

Figure 16 - Failure details of bolted connection (CFS side).

6 CONCLUSIONS

This study presented novel proposed types of connection for CFS-CLT composite solutions and their mechanical behavior. Those solutions include self-drilling screw S1 and bolt B1, which are commonly used in timber structures. In addition, new bolted solutions were proposed, *i.e.* B2 (using a T-nut), B3 (using a threaded insert) and B4 (a combination of concepts of connections B2 and B3.

Push-out tests on CFS-CLT connections were carried out according to EN 26891 [27]. The load-slip curves and failure modes revealed ductile behavior, with failure occurred after a large post-peak branch in the load-slip curve. It can be seen the failure modes were simultaneous occurrence of the embedding strength failure of CLT and slight developing plastic hinges in both connectors, as well as local deformations around the CFS holes and rotations of the screws and bolts.

Overall, the bolted connection solutions B3 and B4 obtained the highest ultimate load capacity and slip modulus, and thus showing a significant potential to be used in CFS-CLT structures.

https://doi.org/10.52202/069179-0438

ACKNOWLEDGEMENT

This work was partly financed by FCT / MCTES through national funds (PIDDAC) under the R&D Unit Institute for Sustainability and Innovation in Structural Engineering (ISISE), under reference UIDB / 04029/2020, and under the Associate Laboratory Advanced Production and Intelligent Systems ARISE under reference LA/P/0112/2020 and financed national funds through FCT – Foundation for Science and Technology, under reference 2021.07651.BD. The authors gratefully acknowledge the University of Coimbra, and SerQ – Innovation and Competence Forest Centre as host institutions.

REFERENCES

[1] LOSS, C. & DAVISON, B. 2017. Innovative composite steel-timber floors with prefabricated modular components. *Eng. Struct.*, 132(695-713).

[2] CECCOTTI, A. 2002. Composite concrete-timber structures. Prog. struct. eng. mater., 4(264-275).

[3] LOSS, C., PIAZZA, M. & ZANDONINI, R. 2016. Connections for steel-timber hybrid prefabricated buildings. Part I: Experimental tests. *Constr. Build. Mater.*, 122(781-795).

[4] HASSANIEH, A.; VALIPOUR, H. R.; BRADFORD, M. A. 2016. Experimental and analytical behaviour of steel-timber composite connections. *Constr. Build. Mater*. 118. (2016). 63-75.

[5] SATHRE, R.O.C.J., A Synthesis of Research on Wood Products and Greenhouse Gas Impacts, Vancouver, BC, 2010.

[6] HASSANIEH, A., VALIPOUR, H. R. & BRADFORD, M. A. 2016a. Experimental and numerical study of steel-timber composite (STC) beams. *J. Constr. Steel Res.*, 122(367-378).

[7] BRADFORD, M. A., HASSANIEH, A., VALIPOUR, H. R. & Foster, S. J. 2017. Sustainable steel-timber joints for framed structures. In: Juozapaitis, A., Daniunas, A. & Zavadskas, E. K. (eds.) Modern Building Materials, Structures and Techniques. Amsterdam: Elsevier Science Bv.

[8] BRANDNER, R., FLATSCHER, G., RINGHOFER, A., SCHICKHOFER, G. & THIEL, A. 2016. Cross laminated timber (CLT): overview and development. *Eur. J. Wood Wood Prod.,* 74(3), pp 331-351.

[9] KARACABEYLI, E., GAGNON, S. *Canadian CLT Handbook*. 2019 Edition. Vol. 1. FPInnovations. Pointe-Claire, QC. Available in: https://web.fpinnovations.ca/clt/

[10] KYVELOU, P., GARDNER, L., NETHERCOT, D. A. 2015. Composite Action Between Cold-Formed Steel Beams and Wood-Based Floorboards. *Int. J. Struct. Stab. Dyn.*, 15(1540029).

[11] AMSYAR, F., TAN, C. S., CHAU KHUN, M., SULAIMAN, A. 2018. Review on Composite Joints for Cold-Formed Steel Structures. *E3S Web of Conferences*, 65(08006).

[12] DAR, M. A., SUBRAMANIAN, N., ANBARASU, M., DAR, A. R., LIM, J. B. P. 2018. Structural performance of cold-formed steel composite beams. *Steel Compos. Struct*. 27(5), pp 545-554.

[13] 13 LEE, Y. H., TAN, C. S., MOHAMMAD, S., MD TAHIR, M., SHEK, P. N. 2014. Review on cold-formed steel connections. *The Scientific World Journal*, 2014.

[14] NAVARATNAM, S., WIDDOWFIELD SMALL, D., GATHEESHGAR, P., POOLOGANATHAN, K., THAMBOO, J., HIGGINS, C. & MENDIS, P. 2021. Development of cross laminated timber-cold-formed steel composite beam for floor system to sustainable modular building construction. *Struct*, 32(2021), pp 681-690.

[15] KARKI, D., AL-HUNAITY, S., FAR, H., & SALEH, A. 2022. Composite connections between CFS beams and plywood panels for flooring systems: Testing and analysis. *Struct*, 40 (2022), pp. 771-785.

[16] VELLA, N., GARDNER, L., & BUHAGIAR, S. 2020. Experimental analysis of cold-formed steel-to-timber connections with inclined screws. *Structures* (Vol. 24, pp. 890-904).

[17] CEN. 2004. *Eurocode 5: Design of timber structures. Part 1-1: General - Common rules and rules for buildings*. Bruxelles, Belgium: European Committee for Standardization.

[18] JOHANSEN, K. W. 1949. Theory of timber connections. *Int Assoc Bridge Struct Eng*, 9, 249-262.

[19] FONSECA, E. M., LEITE, P. A., SILVA, L. D., SILVA, V. S., & LOPES, H. M. 2022. Parametric study of three types of timber connections with metal fasteners using Eurocode 5. *Applied Sciences*, 12(3), 1701.

[20] GOCCÁL, J. "Load Carrying Capacity of Metal Dowel Type Connections of Timber Structures. *Civ. Environ. Eng*. 2014, 10, 51-60.

[21] FARIA, Amorim; NEGRÃO, João. 2009. *Design of timber structures.* Publindústria Technical Editions.

[22] UIBEL, T. & BLASS, H. 2007. Edge joints with dowel type fasteners in cross laminated timber. *Proceedings of the International Council for Research and Innovation in Building and Construction*. Working Commission W18–Timber Structures. 40th meeting, Bled.

[23] UIBEL, T. & BLASS, H. 2013. Joints with Dowel Type Fasteners in CLT Structures. COST Action FP1004 - Focus Solid Timber Solutions - European Conference on Cross-Laminated

https://doi.org/10.52202/069179-0438

Timber (CLT), Graz University of Technology, Graz.
[24] KENNEDY, S., SALENIKOVICH, A., MUNOZ, W., MOHAMMAD, M. 2014. Design equations for dowel embedment strength and withdrawal resistance for threaded fasteners in CLT. *World Conference in Timber Engineering*, Quebec.
[25] DONG, W., LI, Q., ZHANG, H., WANG, Z., ZHOU, J., GONG, M. 2019. Embedment Strength of Cross-Laminated Timber for Smooth Dowel-type Fasteners. *MATEC Web Conf.,* Vol. 275.
[26] HASSANIEH, A., VALIPOUR, H. R., BRADFORD, M. A. 2017. Composite connections between CLT slab and steel beam: Experiments and empirical models. *J. Constr. Steel Res.*, 138(2017), pp 823-836.
[27] CEN. 1991. *EN 26891: Timber structures - Joints made with mechanical fasteners - General principles for the determination of strength and deformation characteristics*. Bruxelles, Belgium: European Committee for Standardization.
[28] CEN. 2016. *EN 14358: Timber structures - Calculation and verification of characteristic values*. Bruxelles, Belgium: European Committee for Standardization.
[29] VELLA, N., GARDNER, L., & BUHAGIAR, S. 2021. Analytical modelling of cold-formed steel-to-timber connections with inclined screws. *Eng. Struct.*, 249, 113187.

World Conference on Timber Engineering Oslo 2023

Experimental and Numerical Investigations on the Usage of CLT Panels to Form Timber-Steel Composite Floor Systems

Hugh Merryday[1], Megan Potuzak[2], David Roueche[3], Kadir Sener[4]

ABSTRACT: This paper presents experimental and numerical results from an ongoing investigation to evaluate the performance of steel-timber composite floor systems. A composite floor system comprised of cross-laminated timber (CLT) made from Southern Yellow Pine species was fastened to a hot-rolled wide flange steel beam using self-tapping wood screws. Experimental evaluations included pushout tests for mechanical fastener characterization and a beam test that was monotonically tested under a four-point bending setup. Beam test results were compared against a steel-timber fiber model, existing equations adapted from steel-concrete composite design, and experimental steel-CLT load-slip response from the pushout testing. Near full-composite behavior was observed in the beam prior to connection slip but reduced to partial-composite behavior as screws began to deform. A substantial increase in strength and stiffness was observed for the composite beam from the non-composite (hybrid) case which was nearly equal to the level of composite action achieved during the test. Both the section fiber model and adapted steel-concrete composite design equations estimated the steel-CLT beam behavior with reasonable accuracy compared to the experimental test.

KEYWORDS: Mass timber, steel-CLT composite beam, self-tapping screws

INTRODUCTION

The recent popularity of mass timber construction as an alternative to traditional materials such as steel, concrete and masonry can be credited to its designation as a renewable resource. Also, mass timber, such as cross-laminated timber (CLT), can improve construction times as modular elements are manufactured off-site and installed with minimal site work. However, due to limitations stemming from strength and serviceability, mass timber elements are not efficient for high-rise construction since deep glue-laminated beams are often required for large spans. Accordingly, Figure 1 depicts a popular design practice to address this challenge in which hybrid construction systems involve the use of mass timber floor panels as decking elements in steel-frame structures. Utilizing this system will enable smaller steel beams and girder sections while maintaining a CLT deck comparable to the more well-established steel-concrete construction. However, unlike steel-concrete construction, there is little to no guidance on the design of steel-timber composite construction. Thus, engineers must oversize steel members to work as floor members alone, ignoring any strength contribution provided by the CLT deck.

This paper presents ongoing experimental and numerical studies to evaluate the performance of steel-CLT composite beams using large diameter self-tapping screws as shear connectors. Previous experimental studies have been conducted on steel-CLT composite beams with the use of heavy-duty wood screws and bolted connections [1]; whereas in the US, self-tapping screws are a preferred choice in the mass-timber industry over other types of connection for their speed of installation (Figure 1). Static pushout tests have been conducted to evaluate the connection strength and to identify possible failure modes associated with three self-tapping screw types used in steel-timber composite construction [2]. This study also presents preliminary results from a large-scale beam test, informed by the pushout test results, conducted to investigate the flexural strength performance of steel-CLT composite using one of the self-tapping screw types. A section fiber model has been developed to predict the flexural behavior of steel-timber beams, accounting for partial composite action at the steel-timber interface. The model obtains both section-level and member-level behavior to provide a holistic summary of the beam's response. Finally, model results are compared with experimental data.

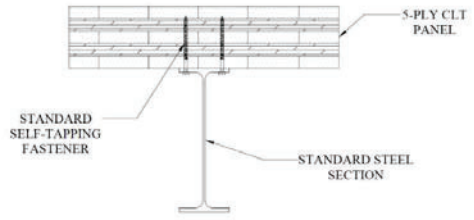

[1] Hugh Merryday, Auburn University, Department of Civil and Environmental Engineering, USA, hcm0044@auburn.edu
[2] Megan Potuzak, Auburn University, Department of Civil and Environmental Engineering, USA, mtp0027@auburn.edu
[3] David Roueche, Auburn University, Department of Civil and Environmental Engineering, USA, dbr0011@auburn.edu
[4] Kadir Sener, Auburn University, Department of Civil and Environmental Engineering, USA, sener@auburn.edu

https://doi.org/10.52202/069179-0439

Figure 1: *Typical cross-section of steel-CLT hybrid construction.*

2 METHODOLOGY

2.1 MATERIALS

CLT used in this study was manufactured from southern yellow pine at a nearby CLT production facility. According to manufacturer specifications, the alternating 5-ply layup consisted of visually graded No. 2 or better lumber in the outermost and middle layers and No. 3 or better in the remaining transverse layers in accordance with the National Design Specification (NDS) for Wood Construction [3]. The specific gravity and moisture content were measured in accordance with ASTM D2395 [4]. The moisture content was measured to be 10.2% and the specific gravity was measured to be 0.46±0.07 (mean and standard deviation) for 20 samples. Steel sections used for pushout and beam testing consisted of hot-rolled W16 x 31 (American designation) made from A992 steel with a measured yield strength of 385 MPa and ultimate strength 495 MPa as provided from the mill test report. Self-tapping screws used to attach CLT to steel are shown in Figure 2 and their geometric and material properties are shown in Table 1. The fastener bending yield strength, F_{yb}, was determined in accordance with ASTM F1575 [5]. In Table 1, L is the screw length, D_n is the nominal diameter, D_s is the shank diameter, and D_r is the root diameter.

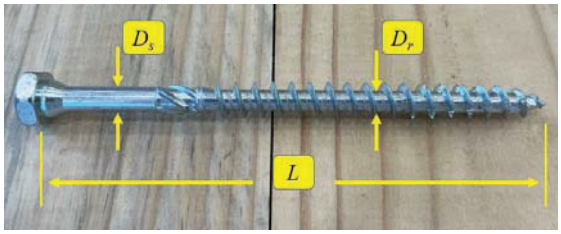

Figure 2: *Self-tapping screw used in beam test.*

Table 1: *Geometric and mechanical properties of self-tapping screws.*

L (mm)	D_n (mm)	D_s (mm)	D_r (mm)	F_{yb} (MPa)
160	12.7	8.1	6.9	1280

2.2 MONOTONIC PUSHOUT TESTS

Pushout tests were conducted using a symmetrical test setup, with two CLT panels fastened to each flange of the steel section with two rows of screws. CLT panels had dimensions of 457 mm wide by 610 mm tall with varying thickness depending on the number of laminations (35 mm per lamination). Steel sections measured 610 mm tall with adequate offset from the end of CLT panels to accommodate displacement. The standard test specimen is shown in Figure 3, with a typical layout of 8 screws. 12.7 mm holes were punched in the steel flange using a hydraulic punch to replicate field conditions. The transverse hole spacing was 102 mm leaving a 19 mm center-to-edge distance on the steel flange. To ensure screws were installed straight, a 6 mm pilot hole was provided, and the self-tapping screws were torqued to 54 N-m in accordance with manufacturers' recommended torque limits. Four potentiometers, one at each specimen corner, were used to measure the relative slip between the steel and CLT panels during testing. The load regime was adapted from ASTM D5652 [6], where load was applied under displacement control at a rate of 2.54 mm/min to reach the maximum load in approximately 10 minutes. Tests were stopped either when screw failure occurred, or 80 percent of the post-peak load was reached. Further details of the pushout tests are available in [2].

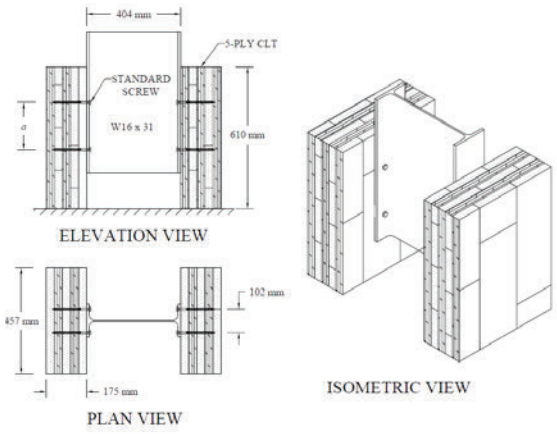

Figure 3: *Standard pushout test specimen.*

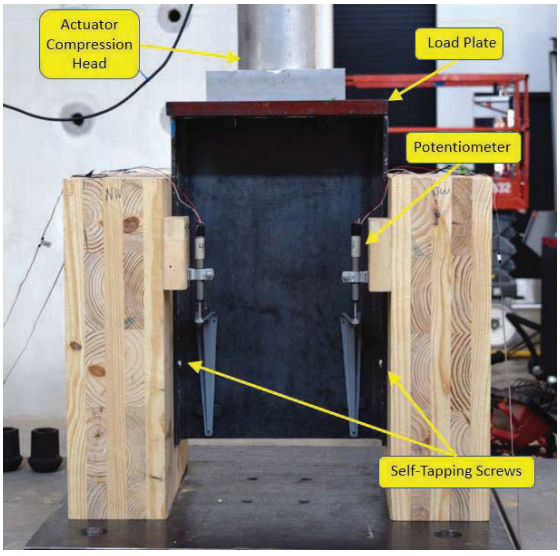

Figure 4: *Pushout test setup.*

2.3 LARGE-SCALE BEAM TEST

The beam test was conducted using a four-point bending test setup as shown in Figures 5 and 6, with a continuous 5-ply CLT panel fastened to a 9.14-meter long W16 x 31 steel member. The CLT deck measured 483 mm wide and was oriented so that the major strength direction was parallel to the length of the beam. Screws were installed at 305 mm spacing using methods outlined for pushout testing, without the use of pilot holes to mimic field application. Six string potentiometers were used to monitor and record vertical displacement at midspan, load points, and at the mid-shear spans. Four inclinometers were placed at mid-height of the steel section at each load point to measure rotation. Eight 25 mm slip sensors were used to measure the relative slip between the steel and CLT along the length of the beam. Strain gauges were attached to the steel and CLT within the constant moment region to capture the strain profile of the cross-section. Figure 7 illustrates the steel and wood strain gauge arrangement at midspan. Load was monotonically applied through a transfer beam under displacement control at a rate of 1.27 mm/min and was increased to 2.54 mm/min in the post-yield region. The test was stopped when the actuator stroke limit was reached. To limit out of plan deflection, Teflon plated bracing was provided at midspan with 3 mm of clearance as shown in Figure 8.

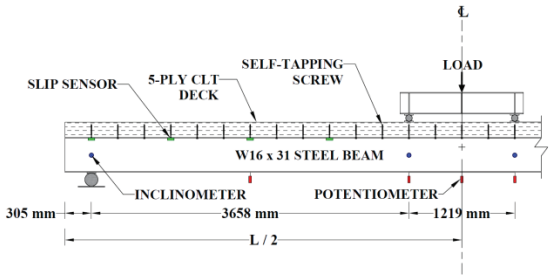

Figure 5: *Steel-CLT four-point bending test setup and instrumentation.*

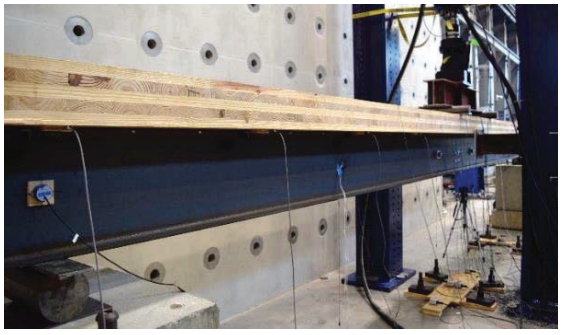

Figure 6: *Steel-CLT four-point bending test setup.*

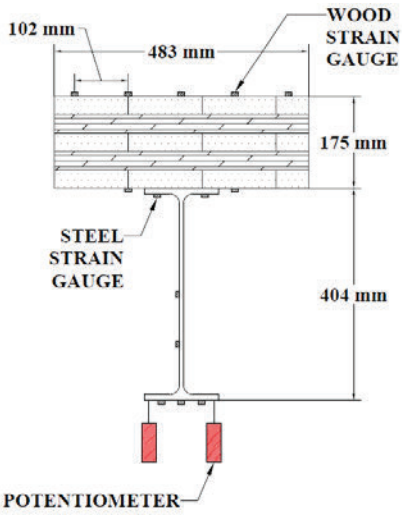

Figure 7: *Midspan instrumentation layout.*

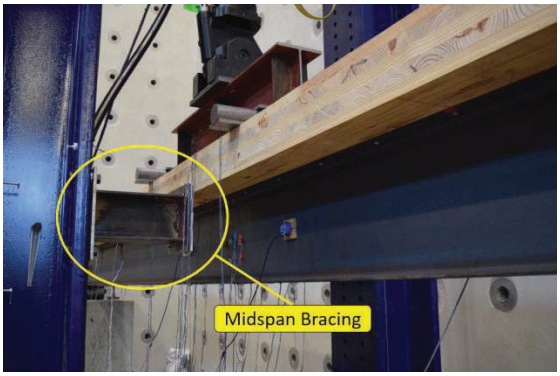

Figure 8: *Steel-CLT beam test specimen at midspan.*

2.4 NUMERICAL MODEL

A 2D section fiber model was developed to analyze the flexural behavior of steel-timber beams, accounting for the degree of partial composite action between the steel and timber, cross-sectional dimensions, mechanical properties, and timber orientation. The model discretizes the cross-section into small horizontal layers, which are assigned with uniaxial material properties and dimensions corresponding to each layer. In steel-CLT beams, different material properties were assigned to each layer of timber based on its orientation. Using fundamental constitutive relationships between stress and strain of each material and establishing force equilibrium, the cross-sectional stress and strain profiles were obtained at increasing curvatures. The percentage composite action incorporated into the strain calculation was obtained through calibration of slip strain measurement from testing, as provided in Equation (1).

$$CA_{strain} = (1 - \varepsilon_{slip\_test} \,/\, \varepsilon_{slip\_non-comp})\% \qquad (1)$$

https://doi.org/10.52202/069179-0439

In Equation (1), CA_{strain} = percentage composite action determined from slip strain, ε_{slip_test} = slip strain measured at curvature φ obtained from experimental test, and $\varepsilon_{slip\_non\text{-}comp}$ = slip strain under non-composite (0% composite) condition at curvature φ obtained from fiber model. The percentage composite action was assumed to be constant throughout the analysis that resulted in a linear relationship between slip strain and curvature.

The section moment was calculated for incrementally increasing curvature levels to develop the moment-curvature response of the cross-section, where equal curvature was assumed for steel and timber elements at the same cross-section. The numerical model steps to achieve the moment-curvature relationship are summarized in Figure 9. Once the moment-curvature relationship was obtained for the section, this response was integrated along the beam length to obtain member-level responses including mid-span deflection, interfacial slip at beam ends, and support rotation. The fiber analysis results were validated against a database of steel-timber beam tests, and the comparisons are discussed in detail elsewhere [7].

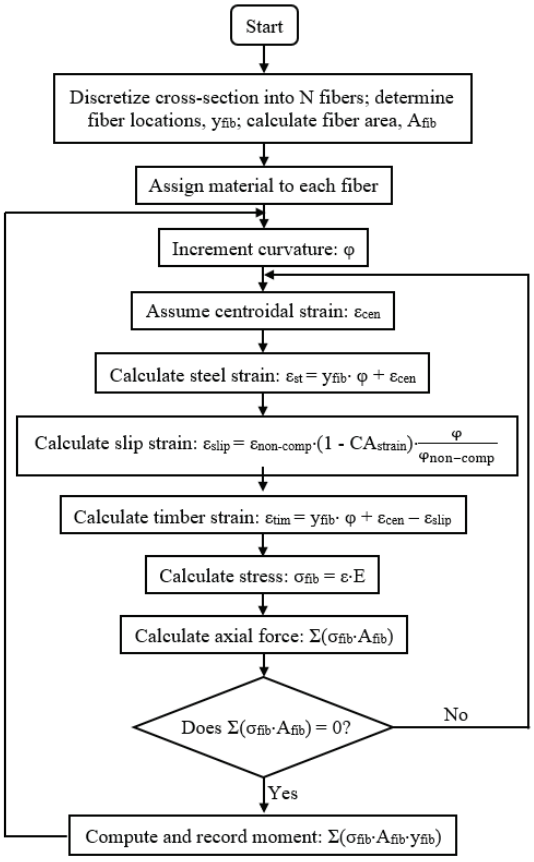

Figure 9: *Flowchart summarizing section fiber analysis model.*

2.5 STRENGTH AND STIFFNESS PREDICTIONS BASED ON AISC APPROACH

Since steel-concrete composite floors are a common structural system, extensive research has been performed to establish design equations to calculate beam stiffness and flexural capacity for these composite systems. Steel-timber composite flooring systems resemble steel-concrete composite systems in that they both pair low-tensile strength materials with structural steel members. Therefore, the applicability of typical steel-concrete composite design equations on steel-timber systems were evaluated. Understanding the correlation between these two structural systems as it pertains to partial composite action would accelerate the adoption of steel-timber composite structures into design provisions.

The design equations analyzed were adopted from the American Institute of Steel Construction (AISC) Specification [8]. The Specification provisions in Chapter I characterize composite action between structural steel members and concrete slabs as a fraction of the combined shear strength of the shear connectors within the shear span of the beam to the minimum strength contribution between the steel and concrete elements. Similarly, Equation (2) emulates the AISC steel-concrete composite system equation by replacing concrete compressive strength and shear stud strength with timber compressive strength and mechanical connector (self-tapping screw) shear strength:

$$CA_{strength} = \frac{\Sigma Q_n}{\min\left(A_s f_y, \Sigma f_{c,tim} A_{tim}\right)} \qquad (2)$$

where $CA_{strength}$ = percentage composite action based on strength, ΣQ_n = total shear strength of mechanical connectors located within the shear span, A_s = cross-sectional area of steel, f_y = steel yield strength, $f_{c,tim}$ = timber compressive yield strength, and A_{tim} = cross-sectional area of timber.

Once the partial composite action percentage is determined from Equation (2), the effective stiffness of each beam is calculated in accordance with the Specification Equation C-I3-3, as shown in Equation (3):

$$EI_{equiv} = E_s * \left[I_s + \sqrt{CA_{strength}}\left(I_{tr} - I_s\right)\right] \qquad (3)$$

where EI_{equiv} = equivalent flexural stiffness of steel-timber composite member, E_s = elastic modulus of steel, I_s = moment of inertia of steel, and I_{tr} = transformed moment of inertia of the steel-timber cross section.

Additionally, the plastic moment capacity was calculated for each steel-timber beam to compare the accuracy of experimental results, as outlined in Section I2a of the Specification. These calculations performed in accordance with the AISC Specification are compared to experimental data to draw conclusions about their applicability to steel-timber composite flooring systems.

https://doi.org/10.52202/069179-0439

3 EXPERIMENTAL RESULTS

3.1 PUSHOUT TESTS

Results of pushout testing for the screws used in this beam test have been previously presented in detail elsewhere, [2], but will be briefly summarized for the type of screw used in the beam testing.

Typical failure of the screws used for beam testing was associated with the formation of a single plastic hinge within the CLT accompanied by a brittle shear/tensile failure at the steel-CLT interface. The cross-section of a typical pushout test specimen with screws spaced at 203 mm is shown in Figure 10. This study concluded that the abrupt transition of the screw geometry between the head and shank disrupted the full development of a double plastic hinge. The representative load-slip response of the screws shown in Figure 11 demonstrated that the screws have an average strength of 29.8 kN/screw corresponding to an average maximum slip of 17.3 mm. The connection was also observed to experience a region of no slip due to torquing during initial parts of the loading, as highlighted in Figure 11.

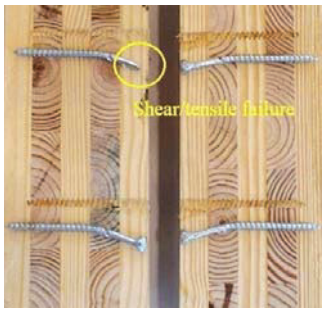

Figure 10: *Failure mode of self-tapping screws loaded parallel to outer lamination in steel-timber pushout setup.*

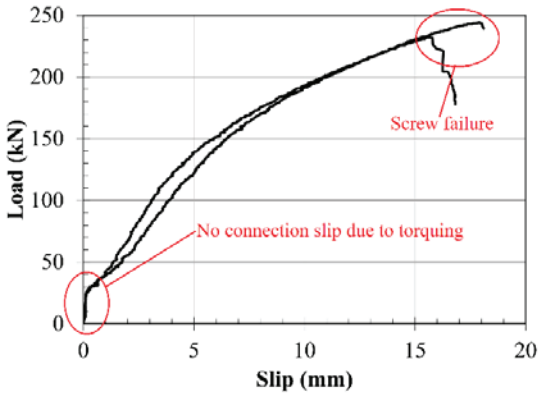

Figure 11: *Load-slip response of steel-CLT connection comprised of eight self-tapping screws.*

3.2 BEAM TEST

No distinct failure mode was observed as the test was stopped due to the constraints of the actuator stroke as shown in Figure 12. Though not a limiting factor for strength, Figure 13 depicts initiation of crushing of timber at a finger joint location on the top surface near midspan. It should also be noted that the beam experienced two instances of support settlement, where the roller/pin setup adjusted to accommodate large rotations.

The load vs. midspan displacement, load vs. support rotation, and load vs. average relative slip between the steel and CLT at the supports are presented in Figures 14, 15, and 16, respectively. The load vs. displacement plot indicated a stiff response until relative slip initiated at the steel-timber interface. The reduced stiffness response was linear until yielding initiated in the steel member at around 150 kN. The load gradually increased in a nonlinear fashion until the actuator stroke limit was achieved (250 mm), and the specimen was unloaded. The load vs. rotation and load vs. slip plots were observed to follow a similar response to the load-displacement, where a reduced stiffness response was followed by a post-yield nonlinear response until stoppage. However, the load slip response depicts a region of no slip between the steel and CLT at the support up to a load of 25 kN when slip initiated. A linear slip response was observed until steel yielding, at which a nonlinear response occurred.

The relative slip between the steel and CLT along the beam corresponding to various load levels is shown in Figure 17. The slip is observed to increase with distance away from load points and indicated a nearly symmetric slip-response in each shear span. The section strain profiles at the initiation of yielding and at ultimate loading conditions is shown in Figure 18, indicating the shifting in each neutral axes observed in CLT and steel with nearly identical curvature in both members. The variation in wood strains across the width of the CLT top surface is shown in Figure 19. The compressive strains in the wood members were observed to be uniform until nearing the ultimate load, where one side experienced more strain.

The service-level stiffness (EI_{eff}), support rotation, and beam end slip corresponding to the ultimate load are provided in Table 2. The service-level stiffness was calculated as the tangent slope of moment-curvature responses between moments corresponding to 80 and 120 kN-m. The yield and ultimate displacements are provided in Table 3, where yielding is defined as the initiation of yielding based on steel tension strain measurements.

https://doi.org/10.52202/069179-0439

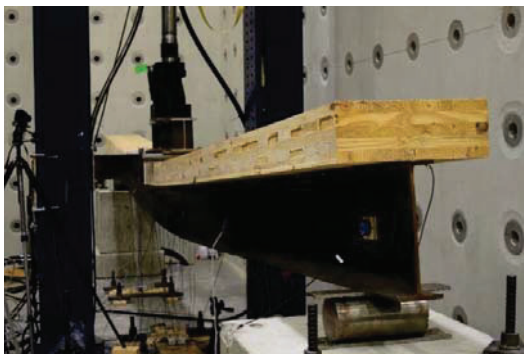

Figure 12: *Beam at ultimate loading condition.*

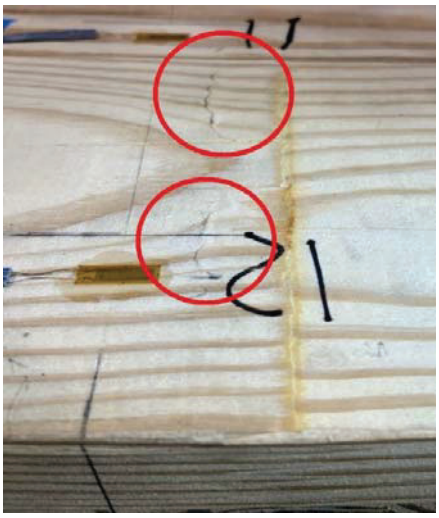

Figure 13: *Crushing of timber lamination at midspan finger joint location.*

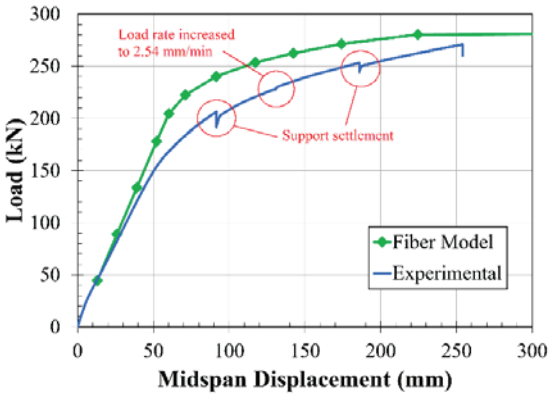

Figure 14: *Experimental midspan displacement compared with fiber analysis results.*

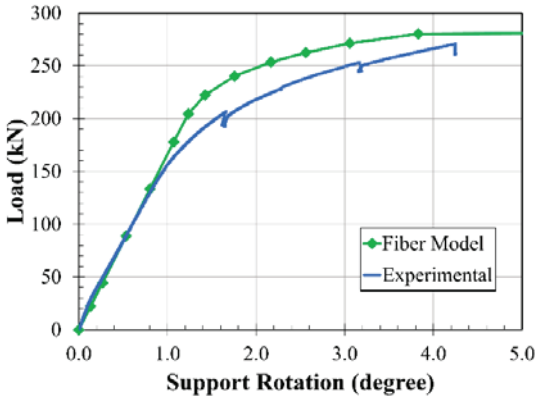

Figure 15: *Average experimental support rotation compared with fiber analysis results.*

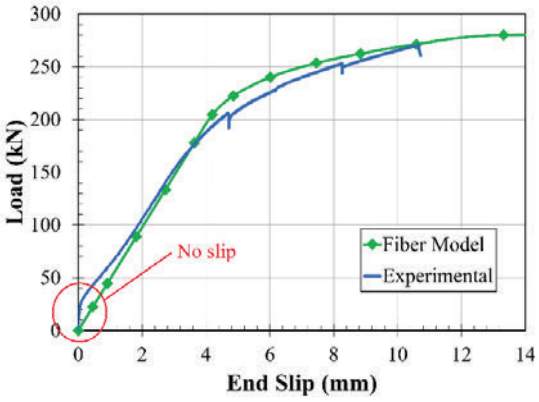

Figure 16: *Average steel-CLT slip at supports compared with fiber analysis results.*

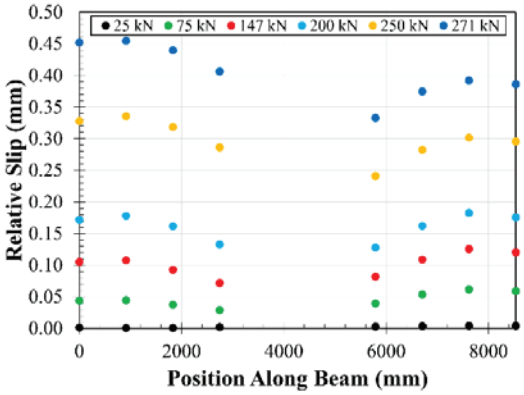

Figure 27: *Measured slip along the length of the beam measured from support-to-support.*

https://doi.org/10.52202/069179-0439

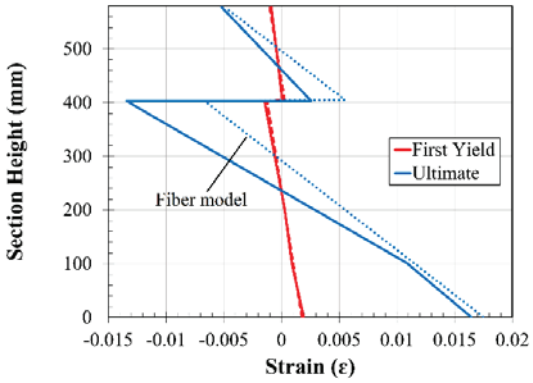

Figure 18: *Experimental yield and ultimate strain profiles compared with fiber analysis results (indicated by dashed lines).*

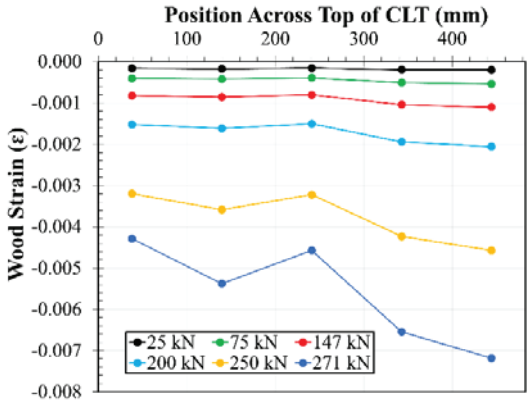

Figure 19: *Midspan strain distribution across the width on top of the CLT.*

Table 2: *Ultimate strength, average maximum rotation, average maximum slip, and relative stiffness.*

	Ultimate Strength (kN)	Support Rotation (degree)	End Slip (mm)	EI_{eff} (10^{12} Nmm^2)
Exp.	271	4.3	10.6	36.0
Fiber Anlys.	280	4.1	14.1	44.5
AISC	283	-	-	54.8

Table 3: *Yield and ultimate strength and midspan displacements.*

	Yield Load (kN)	Yield Disp. (mm)	Ult. Str. (kN)	Ult. Disp. (mm)
Exp.	147	49	271	254
Fiber Anlys.	200	58.7	280	241

4 DISCUSSION OF BEAM TEST RESULTS

The results demonstrate that the steel-CLT beam constructed with self-tapping screws exhibited partial-composite behavior based on the measured slip strain at the steel-CLT interface. However, prior to the initiation of slip, the beam exhibited near full-composite action as indicated by strain continuity at 25 kN shown in Figure 20. Using Equation (1), the composite action was determined to be 91.4% at 25 kN. After overcoming the initial friction provided by screw torquing, it is observed that the strain continuity at the interface was lost, and the slip strain increased with increasing loading as shown in Figure 21. Consequently, the composite action was calculated to be 46.0% and 37.9% at 75 kN and 147 kN, respectively. The increase in slip strain results from the relative slip between the steel and CLT, as pictured in Figure 22, since the self-tapping screws are deforming due to the shear flow occurring at the interface. Thus, it was observed that the composite action between the steel CLT reduces as the load-slip response increases.

The test also produced some notable results that are useful for design purposes. Firstly, it was observed that the CLT was under uniform compression across the width until reaching large displacements, suggesting that there was no major shear lag observed in the CLT deck. This means that the entire width of the CLT can be accounted for in the calculations. Additionally, it was observed that the CLT deck provided adequate support of the steel compression flange against lateral torsional buckling. Since this beam test configuration does not mimic a real floor system application where a much wider panel would typically be used, it is useful to know that the CLT can be relied upon to provide continuous bracing against lateral-torsional buckling even at a relatively narrow slab width.

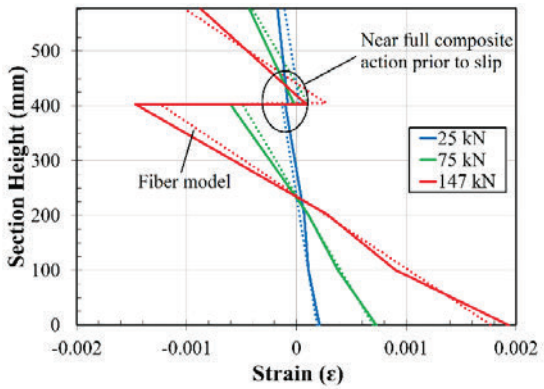

Figure 20: *Experimental service-level strain profile of section compared with fiber analysis results (indicated by dashed lines).*

https://doi.org/10.52202/069179-0439

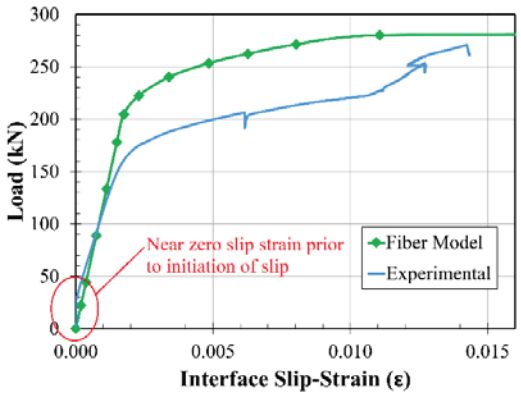

Figure 21: *Experimental slip strain at midspan between the steel flange and CLT slab*

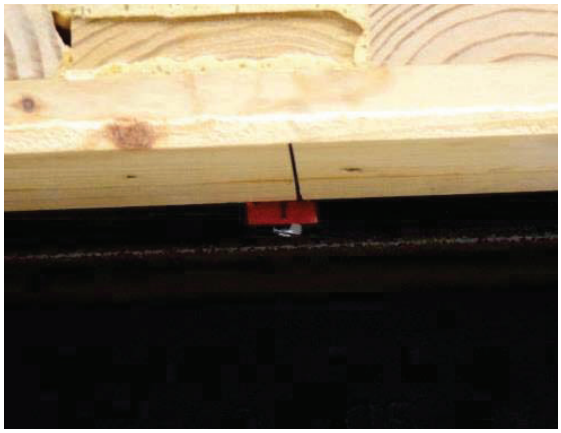

Figure 22: *Relative slip between the steel flange and CLT deck at support location*

Overall, the 2D fiber model predicted the beam behavior with reasonable accuracy compared to the experimental steel-CLT beam, considering the simplicity of the model and various underlying assumptions. From the fiber analysis, the percentage composite action at the steel-CLT interface was determined to be 41 percent at 111.2 kN. This percentage composite action was assumed constant throughout the fiber model analysis. The fiber analysis results yielded accurate ultimate strength, maximum rotation, and strain profiles through the section (Figures 20 and 21). Compared to the experimental steel-CLT behavior, the fiber analysis results predicted the ultimate strength to be 3% greater and the maximum rotation to be 5% lower. However, the fiber analysis results overestimated the maximum slip and initial stiffness by approximately 32% and 20%, respectively. Several limitations exist within the model due to assuming elastic-perfectly plastic behavior of the steel and CLT and assuming constant percentage composite action throughout the analysis.

Furthermore, the AISC calculations adapted from steel-concrete composite beam design predicted the ultimate capacity of the beam within 4 percent accuracy, but overestimated the initial stiffness by about 47 percent, as reported in Table 2 and Figure 23.

Finally, the experimentally obtained moment curvature response is provided in Figure 23 by taking the derivative of measured rotation at load points, and compared against AISC capacity and stiffness, fiber analysis, and 0% composite action (hybrid case). The experimental moment curvature is observed to closely align with the AISC stiffness until initiation of yielding. By accounting for the contribution of composite behavior, the flexural stiffness and moment capacity increased by nearly 40%, from the hybrid case.

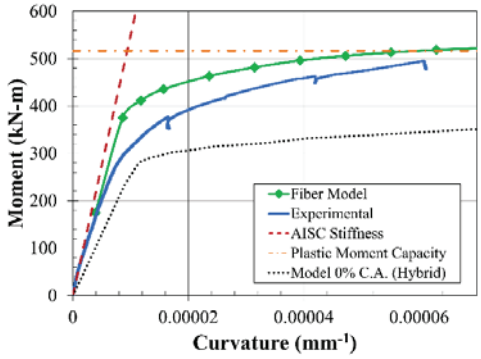

Figure 23: *Moment-curvature relationships for experimental steel-CLT beam and fiber model compared against AISC stiffness and plastic moment capacity.*

5 CONCLUSIONS

As demand increases for mass timber in high-rise construction, there exists a need for design guidance for efficient structural systems such as steel-CLT floor systems. A steel-CLT composite beam constructed with self-tapping wood screws was monotonically tested under a four-point bending setup and compared with analysis results obtained from a fiber model. Test results demonstrate almost full-composite (greater than 90%) behavior prior to connection slip but reducing to partial composite (about 40% prior to steel yielding) behavior with increasing load due to screw deformation. For design purposes, it was observed that the CLT deck was under near uniform compression and the deck provided continuous bracing for the steel against lateral torsional buckling. The fiber analysis model predicted the steel-CLT flexural response with reasonable accuracy, including the ultimate strength, maximum rotation, and strain profiles, but has limitations due to its assumptions and simplicity. Calculations adapted from steel-concrete composite design proved to be accurate for calculating the plastic moment capacity of the beam but overestimated its flexural stiffness.

6 FUTURE RESEARCH

Additional testing will be completed utilizing self-tapping screws in steel-CLT composite beams with the aim to develop a design guide for practicing engineers.

https://doi.org/10.52202/069179-0439

Parameters that will be investigated will include increasing CLT width, adjusting screw spacings, minor strength CLT bending (perpendicular orientation), and the contribution of concrete topping. Furthermore, the steel-CLT beams will be modelled in finite element analysis software to gain a deeper understanding of steel-timber flexural behavior.

ACKNOWLEDGEMENT

This research is financially supported by the United States Department of Agriculture (USDA) under the Wood Innovations Grant, 21-DG-11083150-150, with additional financial and in-kind support from the Softwood Lumber Board, American Institute of Steel Construction, SmartLam, and Simpson Strong-Tie.

REFERENCES

[1] A. Hassanieh, H. R. Valipour, and M. A. Bradford, "Experimental and numerical investigation of short-term behavior of CLT-steel composite beams," *Engineering Structures*, vol. 144, pp. 43–57, May 2017, doi: 10.1016/j.engstruct.2017.04.052.

[2] H. Merryday, K. Sener, and D. Roueche, "Pushout tests on steel-timber connections using self-tapping screws," presented at Structures Congress 2023, New Orleans, United States, May 2023.

[3] American Wood Council (AWC), *NDS-National Design Specification for Wood Construction,* Leesburg, VA., 2017.

[4] ASTM, *Standard Test Methods for Density and Specific Gravity (Relative Density) of Wood and Wood-Based Materials.* ASTM D2395-21. West Conshohocken, PA., 2021.

[5] ASTM, *Standard Test Method for Determining Bending Yield Moment of Nails.* ASTM F1575-21. West Conshohocken, PA, 2021

[6] ASTM, *Standard Test Methods for Single-Bolt Connections in Wood and Wood-Based Products.* ASTM D5652-21. West Conshohocken, PA., 2021.

[7] M. Potuzak, K. Sener, and D. Roueche,"Numerical studies on the flexural behavior of behavior of steel-timber composite floor systems," presented at Structures Congress 2023, New Orleans, United States, May 2023.

[8] American Institute of Steel Construction (AISC), *Steel Construction Manual, Fifteenth Edition*, Chicago, IL, 2017.

https://doi.org/10.52202/069179-0439

World Conference on Timber Engineering Oslo 2023

EXPERIMENTAL TESTING OF SMALL-SCALE TIMBER-CONCRETE COMPOSITE BEAMS UTILIZING ADHESIVE SHEAR CONNECTIONS

Adam Petrycki[1], Osama (Sam) Salem[2], Matthew Leitch[3]

ABSTRACT: Timber-concrete composite (TCC) structural elements have shown desirable mechanical characteristics for use in the structural design of mass timber buildings. Most shear connections used in TCC elements are not perfectly rigid. However, a nearly full composite behaviour can be achieved in TCC sections that utilize adhesive for their shear connections, which significantly increases the stiffness and strength of the resulting sections. Due to the costs and logistics of large-scale studies, an experimental program was conducted to test small-scale TCC beams from a black spruce glulam section. Modulus of Elasticity (MOE), Modulus of Rupture (MOR) and compression tests were conducted on two groups of samples. The first group was for small-size beams with no concrete layer on top, that were taken from a glulam beam section, and consisted of three sub-groups: Group A for beams with no glue line present; Group B for beams with one horizontal glue line at mid-depth between two lamellae; and Group C for beams with one vertical glue line at the beam midspan. The second group was for small-size TCC beams that utilized adhesive for their shear connections and consisted of three sub-groups: Group D for TCC beams with 28-day concrete age that utilized wet-on-dry adhesion process; Group E for TCC beams with 7-day concrete age that utilized wet-on-wet adhesion process; and Group F for TCC beams with 28-day concrete age that utilized wet-on-wet adhesion process. Each sub-group consisted of 10 samples for determining the MOE and MOR and another 10 samples for the compression tests. Additionally, Scanning Electron Microscope images were taken for the adhesive lines between the wood lamellae highlighting how a perfectly rigid connection can be developed using adhesive. The results for the glulam beam specimens were found to have a low coefficient of variability and are close to the results published in the available literature. This suggests similar characteristics of glulam made from small diameter trees on both small and large scales. In contrast, the results of the TCC beam specimens were more variable due to the application of two different adhesion methods (i.e., wet-on-wet, and dry-on-wet methods). Also, all test specimens experienced brittle failures.

KEYWORDS: Timber-concrete composite (TCC) sections, Glulam, Adhesive shear connections, Composite action

1 INTRODUCTION

Timber-concrete composite (TCC) systems have been proven to provide many benefits over conventional timber or reinforced-concrete floor systems [1]. TCC systems have seen increased use in new construction and the rehabilitation of existing timber structures. Such composite systems rely on various shear connectors to develop the composite action between the timber element carrying the tensile forces and the concrete topping layer having the compressive forces. Brittle failure can occur in the timber element and the concrete layer. The type and mechanical characteristics of the utilized shear connectors can influence the failure mode (i.e., brittle, or ductile) of a TCC system [2]. While mechanical shear connectors, such as screws and steel plates, are approved for specific composite systems in the EU, none of these connectors guarantee perfectly rigid composite action. Therefore, initial stiffness for a TCC section is reduced when calculated using the gamma method. TCC systems with adhesive shear connections can achieve perfectly rigid behaviour in both small [3] and large-scale tests [4]. Adhesives connections can be applied either in a dry-on-wet method between a timber element and a cured concrete section or in wet-on-wet method, where a mass timber element has adhesive applied to it and fresh concrete is poured on top before the adhesive sets.

Full-size tests of TCC elements can be costly and time consuming, and storage constraints can limit the number of samples produced in an experimental setting. Small-scale tests can be more cost effective, and the smaller size of elements can allow for a greater number of samples to be produced. A greater number of specimens can increase confidence in the test results and be used as a cost-effective pilot project before committing resources to a large-scale testing program. However, mass timber elements can be difficult to scale down proportionally while maintaining their mechanical properties. For example, glued-laminated timber (glulam) and cross-laminated timber (CLT) elements are stronger than their individual lamina, so using clear samples of the wood

[1] Adam Petrycki, PhD. Candidate, Dept. of Civil Engineering Lakehead University, Ontario Canada, apetryck@lakeheadu.ca
[2] Sam Salem, Professor and Chair, Dept. of Civil Engineering, Lakehead University, Ontario Canada, sam.salem@lakeheadu.ca
[3] Mathew Leitch, Professor and Chair, Faculty of Natural Resources Management, Lakehead University, Ontario, Canada, mathew.leitch@lakeheadu.ca

https://doi.org/10.52202/069179-0440

species in the lamina would not provide the same results as a proportionally scaled down mass timber element. Before committing to a large-scale experimental program on TCC floor slabs with an adhesive connector and in accordance with ASTM-143-14 [5] standard requirements, this study investigated:

- the effect of the adhesive bond line between small-diameter, black spruce glulam wood elements themselves;
- whether these glulam elements could be used to represent the behaviour of a mass timber floor element in a TCC flexure beam, with a perfectly rigid adhesive connection;
- the difference on results between the wet-on-wet and dry-on-wet application process; and
- whether the strength of a small-scale TCCs concrete element was more accurately reflected through conventional sized testing cylinders or compression columns sized to ASTM-143-14.

2 EXPERIMENTAL PROGRAM

2.1 SPECIMENS DETAILS

In accordance with ASTM-143-14 standard, specimens tested for determining the MOE and MOR measured 300 mm in length and 20 x 20 mm cross-sectional dimensions. Whereas the specimens tested in compression had a height of 60 mm and 20 x 20 mm cross-sectional dimensions. Black spruce of 24F-ES stress grade was used from a glulam beam section for the timber elements. The glulam beam was composed of finger-jointed lamina with cross-sectional dimensions of 25 mm x 50 mm made from small diameter black spruce harvested between 80 and 120 years of age. The relevant mechanical properties are summarized in Table 1.

Table 1: *Mechanical properties of black spruce glulam [6]*

Product name	Nordic Lam
Stress grade	24F-ES/NPG
Comp. parallel to grain	33.0 MPa
Tension parallel to grain	20.4 MPa
Modulus of elasticity	13100 MPa

The compressive strength values of the two concrete batches used in the MOE/MOR specimens and compression specimens are summarized in Table 2. Due to the small size of the samples, a regular concrete mixture could not be used, as the maximum aggregate size is typically not greater than 1/3 the depth of the concrete layer so a number 6 sieve, with an opening of 3.35 mm was used to sieve the materials, resulting in a reduced concrete strength, based on the assumption of the concrete element having a slab thickness of 10 mm.

Table 2: *Average compressive strengths of concrete cylinders (MPa)*

Batch No.	1 (dry-on-wet)	2 (wet-on-wet)
7-day concrete age	15.8	15.4
28-day concrete age	19.74	20.1

To cast a TCC element in a wet-on-wet process, mimicking the process of casting a TCC section in place instead of prefabricating it, required the specification of a moisture insensitive adhesive capable of bonding wet concrete to timber. Sikadur®35 Hi-Mod [7] was selected. It is classified as a moisture insensitive, two-component structural epoxy with a 14-day shear strength of 41.0 MPa and a pot life of 30-38 mins. To ensure a proper bond, after the adhesive is applied, the concrete must be poured on top and packed into the form (without disturbing the adhesive) within 30 minutes.

Specimens for flexure bending tests had three different material cross sections: clear black spruce from a glulam beam, two black spruce laminae with an adhesive connection passing through the cross-sections centroid either vertically or horizontally aligned to the load as seen in Figure 1, and TCC elements with equal depths of concrete and black spruce with the concrete element oriented towards the load as seen in Figure 2.

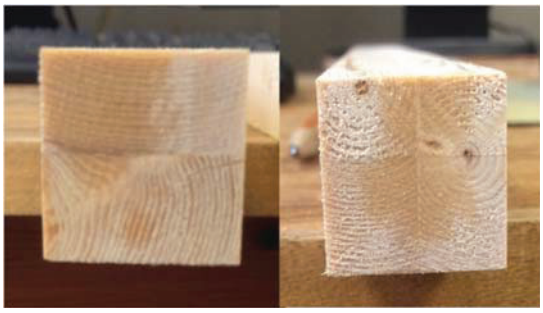

Figure 1: *Sample glue line orientation for MOE and MOR samples, mid-depth (left) and perpendicular to mid-depth (right)*

Figure 2: *TCC flexure specimens*

https://doi.org/10.52202/069179-0440

2.2 SPECIMENS PREPERATION

Pieces of wood were cut from a glulam beam section and sized to be either 10 mm or 20 mm (deep) by 20 mm (wide) and 355 mm long for the bending tests and 60 mm tall for the compression tests. Samples were placed in a conditioning chamber at 20 ˚C and 65% relative humidity for a week, to bring their moisture content to 12% as required by ASTM D4933-16 [8].

For TCC elements, Sikadur®35 Hi-Mod was applied to the 10 mm deep glulam elements and either topped with concrete in a wet-on-wet process and allowed to cure for 7 or 28 days in forms before testing, or applied to previously cast, 10 mm deep, 20 mm wide, 355 long concrete elements in a dry-on-wet process and tested at 28 days. All concrete elements were lightly vibrated, covered with plastic to retain moisture, and lightly misted for the first seven days.

2.3 TEST SETUP

The test program consisted of 60 three-point flexure bending specimens and 70 compression samples, consisting of 10 samples in each of Group A to F and A to G, respectively. The respective test variables of the specimens are summarized in Table 3 for the three-point flexure bending tests and in Table 4 for the compression tests.

The MOE is a measurement of the stress-strain relationship within a material and describes the stiffness of a material with respect to the allowable amount of elastic deformation before full recovery is no longer possible. The MOR is a measurement of the maximum bending capacity of a sample before failure occurs.

Table 3: *MOE and MOR test matrix*

Group	Material (cure time)	Glue line location	Concrete batch No.
A	Glulam	Perp. to mid-depth	N/A
B	Glulam	Mid-depth	N/A
C	Glulam	N/A	N/A
D	TCC (28-day)	Mid-depth	1
E	TCC (7-day)	Mid-depth	2
F	TCC (28-day)	Mid-depth	2

The compression resistance parallel to wood grain was tested as this type of load occurs in both axially loaded columns, as well as the top fibres of beams undergoing flexure bending. Compression tests were done on small-size columns of concrete as well as glulam and TCC sections as the compressive strength of a concrete sample scaled to ASTM-143-14 would more accurately reflect the compressive strength of the concrete element in the TCC sections as opposed to the results of a full-size test cylinder.

TCC elements undergoing three-point flexure bending in groups E and F made with a wet-on-wet process were tested at 7 days in addition to 28 days as in-situ where a wet-on-wet process could be used with a mass timber elements acting as the formwork for the concrete, as the TCC element could reasonably be expected to take some loading at 7 days. Samples in Group D made with the dry-on-wet process reflect a prefabricated TCC section which would not be loaded until the concrete had cured for 28 days or much longer before being bonded to a mass timber element at a factory or on site.

Table 4: *Compression tests matrix*

Group	Material	Concrete batch No.	No of days
A	Glulam	N/A	N/A
B	Glulam	N/A	N/A
C	Glulam	N/A	N/A
D	TCC	1	28
E	Concrete	2	7
F	Concrete	2	28
G	Concrete	1	28

The MOE and MOR tests were conducted using the three-point Tinius Olson H10KT testing machine (Figure 3); while for the compression tests, the Tinius Olsen Universal Testing Machine H50KT was utilized in accordance with ASTM-143-14 testing standard.

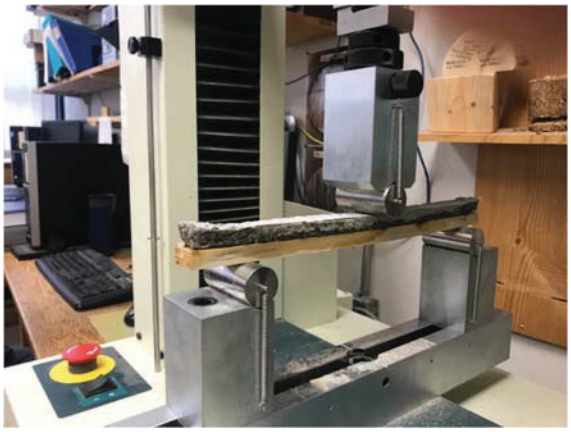

Figure 3: *Three-point flexure bending test with computer registered failure*

Samples were loaded until the machine detected a failure, as shown in Figure 4, during a compression test of a TCC column.

Once loading of a test specimen stopped, failure modes were observed and recorded. Based on the registered load and corresponding deflection, the MOE, MOR, and the compression resistance parallel to wood grain were all determined. Each group had 10 samples to ensure

reasonable consistency and thus, the co-efficient of variation (CV) was calculated to determine the relative consistency of the results.

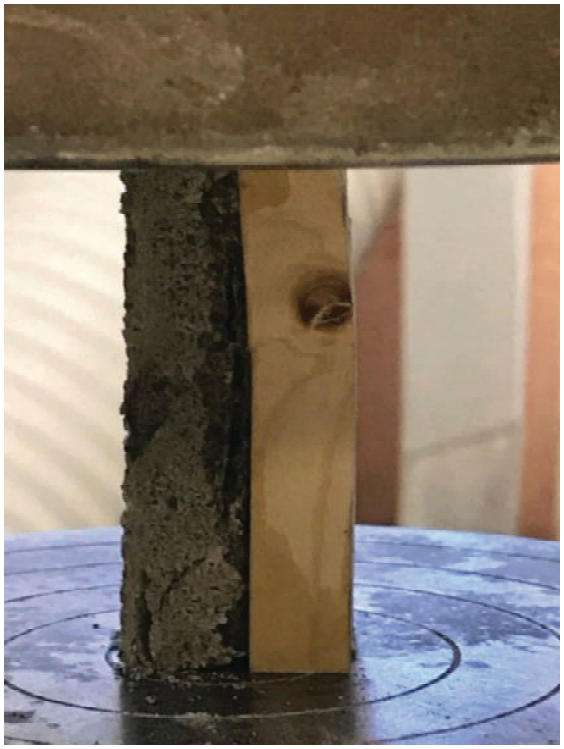

Figure 4: *Computer registered failure of a TCC column under compression*

2.4 MICROSCOPIC STUDY

In addition to the mechanical properties testing, a microscopic study was undertaken to observe the adhesive interface between black spruce lamina from the glulam section and to visually highlight its effectiveness. A Scanning Electron Microscope (SEM) provides high resolution images by using electrons to bombard a sample and interpret the measured results into a digital image. The Hitachi Su-70 Schottky Field Emission SEM used in this study is in the Wood Science and Testing Facility at Lakehead University. Small cubes measuring 1 mm on all sides were cut from the pieces that were used for sectioning with the microtone. The electrical nature of this type of microscope requires biological samples to be coated in gold before being placed in the machine.

Detailed features seen in the cross-sectional plane from the SEM imagery include resin canals, early wood, and latewood tracheid (the latewood cells being particularly small and dense), and the wood-glue-wood interface between laminates is seen in Figure 5.

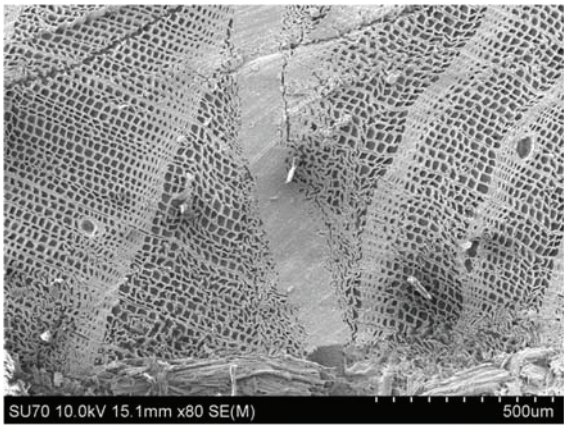

Figure 5: *Glulam SEM cross-section overview*

The SEM microscopy showed that many of the longitudinal tracheid are crushed and broken during the lamination process as can been seen in the cell walls near the glue line and within the glue, as shown in Figures 6 and 7.

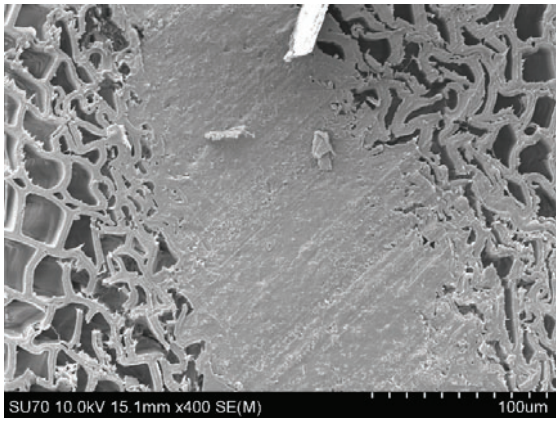

Figure 6: *Glulam SEM cross-section with glue line details*

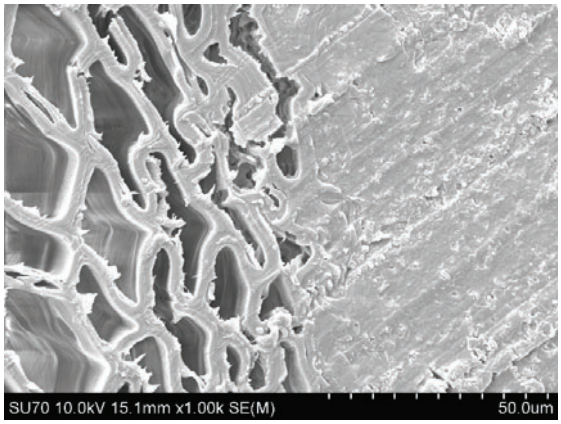

Figure 7: *Glulam SEM cross-section, glue-wood line detail*

The completeness of the wood-glue bond can be seen in Figure 8, where the glue is shown to seamlessly be bonded along the longitudinal tracheid cell walls both between the laminates and away from the glue line.

https://doi.org/10.52202/069179-0440

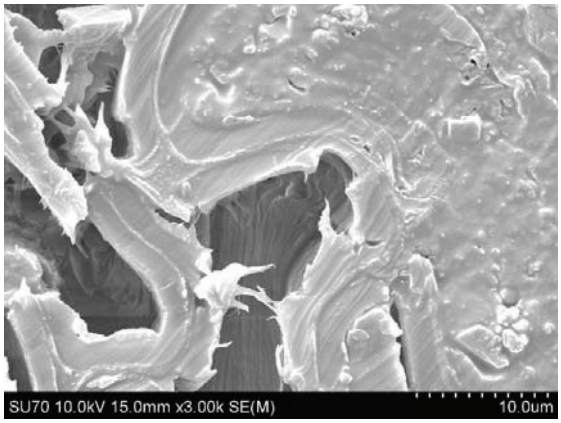

Figure 8: *Glulam SEM cross-section, showing glue-wood bond detail*

3 RESULTS

3.1 MECHANICAL

The MOE and MOR test results are summarized in Table 5; whereas Table 6 shows the compression test results. Test specimens in Group D from Table 5 used concrete from batch No. 1 and specimens in Groups E and F used concrete from batch No. 2.

Table 5: *MOE and MOR test results*

Group ID.	MOE		MOR	
	Value (MPa)	CV (%)	Value (MPa)	CV (%)
A (glulam)	19,990	9.6	95.3	10.6
B (glulam)	17,566	20.7	88.0	19.8
C (glulam)	10,957	12.7	85.8	9.8
D (TCC-dry, 28-day)	8,646	15.7	50.4	28.6
E (TCC-wet, 7-day)	6,327	21.8	31.7	13.4
F (TCC-wet, 28-day)	6,629	28.7	38.7	24.0

Table 6: *Compression column test results*

Group ID.	Value (MPa)	CV (%)
A (glulam)	48.6	5.3
B (glulam)	49.7	11.1
C (glulam)	46.0	9.8
D (TCC, 28-day)	27.2	22.5
E (concrete, 7-day)	7.64	26
F (concrete, batch 2, 28-day)	13.71	19.6
G (concrete, batch 1, 28-day)	20.4	18.7

The compression columns, from Table 6, tested in Groups D and G were made using concrete from batch No. 1, and concrete compression columns in Groups E and F were made using concrete from batch No. 2.

3.2 FAILURE MODES

3.2.1 Three-point flexure bending

In the three-point flexure bending tests, samples from Groups A, B and C all experienced brittle tensile failure in the wood, as shown in Figure 9. Group A had different break patterns than those of Groups B and C. Group A specimens would often see a tensile break across the bottom of only one lamina (half the width of the cross section due to the vertically oriented glue line). Failure in Groups B and C was characterized by a break across the width of the entire singular lamina (Figure 9). Typically, all failures occurred around a defect in the wood, such as a knot or a finger joint.

Figure 9: *Typical tensile failure mode in glulam samples*

Failure in the TCC beams almost always occurred in the concrete and was characterized by very sudden and brittle failure. Occasionally, some of the concrete at the adhesive bond would shear off after vertical or diagonal cracking appeared at the midspan, resulting in a section of the concrete flying away as the wood beam rebounded due to the load being removed by the machine after it detected the failure in the concrete, as shown in Figure 10.

https://doi.org/10.52202/069179-0440

Figure 10: *Sudden and brittle shear failure near the adhesive interface*

Other observed failures modes include local crushing in the top concrete layer near the point load (Figure 11), diagonal shear cracks in the concrete (Figure 12) or vertical separation above the adhesive interface indicating a reduced area of effective adhesive (Figure 13).

Figure 11: *Local crushing from compression near the applied load*

Figure 12: *Diagonal shear crack at failure*

Figure 13: *Shear along adhesive interface (indicative of epoxy quality control) with some shear failure in concrete*

A small number of TCC samples appeared to have failed due to tensile failure in the wood as seen in Figure 14.

Figure 14: *Tensile failure in wood component*

However closer inspection of these samples often showed small cracks in the concrete as seen in Figure 15, suggesting the concrete had failed and transferred the load to the wood, resulting in a tensile splitting failure.

Figure 15: *Shear crack visible in concrete close to tensile failure zone in timber*

https://doi.org/10.52202/069179-0440

3.2.2 Compression

For Groups A, B and C, the wood samples experienced typical compressive failure modes in the wood fibres as shown in Figure 16.

Figure 16: *Compression specimens from Groups A, B and C*

Failure in Group D, the TCC columns, was typically observed in the wood, after some cracking in the concrete, as shown in Figure 17.

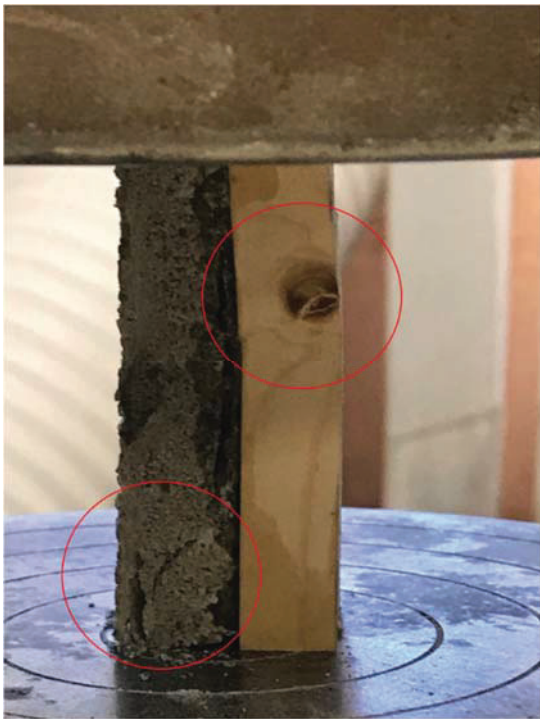

Figure 17: *Failure in timber and concrete in the composite column compression test*

This suggests that the failure of the timber after the concrete stopped contributing to the load-carrying capacity and thus, the load path progressed through the timber element only. The damage in the timber is around the circled knot, a stress concentration area, and the damage in the concrete is at the base, suggesting a bearing failure that crushed the concrete locally.

The small-scale concrete columns, typically failed without cone development and thus, failure predominantly followed vertical lines. This may have been due to the square shapes of the columns and their small size. In some cases, the column crumbled to very small parts as seen in Figure 18. The compressive strength of the small-size compression samples (Figure 18) was a more accurate representation of the concrete's compressive strength in the TCC flexure beams than the strength of the full-size compression test cylinders.

Figure 18: *Failure in timber and concrete in the composite column compression test*

4 DISCUSSION AND RECOMMENDATIONS

From the flexure bending tests results, specimens in Groups A and B had significantly higher MOE values than those in Group C, by a factor of 1.8 and 1.6, respectively. This suggests that adhesive bond between the lamina and orientation of the growth rings allowed for loading to be better distributed around defects in the lamina compared to the specimens in Group C which came from the same glulam section but were clear wood samples. The MOE, MOR, and compression resistance values for the clear black spruce samples in Group C were in line with the values found in literature for the same species of tree and harvest region [9]. The modulus of rupture in all three glulam groups was similar with an increase of 5% and 10% in MOR for Groups B and A, respectively. From the MOE and MOR results from Group A and B, it is shown that the presence of glue lines increased the MOE but not the MOR compared to the clear wood specimens in Group C, suggesting that small diameter black spruce elements glued together and tested at the small scale can model the increased stiffness of built-up timber sections used in full-scale testing.

https://doi.org/10.52202/069179-0440

The timber elements were moisture conditioned prior to application of the adhesive and bonding with fresh or dry concrete in line with previous experimental work on TCC elements [10]. Extensive shear tests have shown that in typical applications, failure will occur in either the timber or concrete elements before the adhesive if enough surface area is covered [11]. From the tests of the present study, it was seen that in all TCC bending tests the concrete elements failed. This was expected as the timber and concrete elements had equal cross-sectional areas under bending; however, the compressive strength of the concrete was appreciably lower than either the tensile or bending strength of the timber elements in the small-scale TCC beams.

While hundreds of samples at the small scale have been tested for shear strength in push-out tests, most large-scale tests of adhesively bonded TCC beams and slabs have a limited number of samples [12-15]. For the TTC elements, the MOE for specimens made with the wet-on-wet process at 7-days (Group E, Figure 19) and 28-day (Group F, Figure 20) were very close, and both values were significantly lower than the MOE for Group D with the dry-on-wet application method (Figure 21). However, the application method most likely did not reduce the MOE of these samples, rather the reduction in strength came from the difference in the concrete batches.

As seen in Figure 19, the samples at 7-days with the lowest strength of concrete, suffered significantly more damage to the concrete layer, with many of the sections separating. Of the 10 samples, 5 failed due to shear cracks in the concrete, followed by local shear failure in the concrete at the bond line, and the other 5 samples failed due to local crushing failure in the concrete.

In Group F (Figure 20), 1 of the 28-day wet-on-wet, specimens exhibited a severe shear crack followed by failure in the concrete at the glue line upon rebound of the wood sample. The 9 other samples failed with minor cracks in the concrete element or due to local crushing. Conversely, in the 28-day, dry-on-wet specimens, 3 exhibited a severe shear crack followed by failure in the concrete at the glue line upon rebound of the wood sample. The 7 other samples failed with minor cracks in the concrete and no local crushing failure in the concrete was seen. This suggests that at the small scale, a better bond was formed with the fresh concrete than the previously cast small-scale strips. As the compressive strength of the batch used in the wet-on-wet specimens was lower than in the dry-on-wet specimens, local crushing in the concrete was an observed failure mode in the former group and not in the latter group which all failed due to shear in the concrete element.

Figure 19: *7-day wet-on-wet MOE-MOR TCC beam specimen*

Figure 20: *28-day, wet-on-wet MOE-MOR TCC beam specimen*

https://doi.org/10.52202/069179-0440

Figure 21: *28-day, dry-on-wet MOE-MOR TCC beam specimens*

In compression tests, the samples with two laminae in the cross-section had an average increase in strength of 5%. The TCC columns had a compressive strength of 27.2 MPa, which was between the 46-49.7 MPa of the glulam groups and the 20.4 MPa of the concrete compression column from batch No. 1. This suggests that the adhesive bond with the wood element, with its higher compressive strength, increased the capacity of the column overall, in comparison to pure concrete columns made from the same batches of concrete. TCC compression samples consistently failed in the concrete elements as seen in Figure 22. The results show that there could be some potential in future programs studying the behaviour of prefabricated TCC wall panels.

Due to the potential for variability between wood elements, large numbers of specimens are required to increase the confidence in results, small scale testing if shown to be accurate with respect to full scale applications can allow for pilot studies to be conducted before a more expansive full scale testing program is designed.

Despite batch No. 1 and 2 of the concrete having similar compressive strength values with standard test size cylinders, the compressive strength values for batch No. 1 and 2 with small-scale compression specimens were 20.4 and 13.7 MPa, respectively. This can explain the reduction in the MOE and MOR values between the 28-day wet-on-wet specimens and the 28-day dry-on-wet specimens. To reduce the CV of the results and increase confidence of these observations, a greater number of samples are required.

Figure 22: *28-day, dry-on-wet compression specimens*

5 CONCLUSIONS

Adhesive can be used to develop a perfectly rigid (full composite action) TCC structural elements. However, quality control during the adhesion application process can be an issue. Also, brittle failure modes exhibited by TCC elements that utilized adhesive for shear connections are not desirable. Using small-diameter wood species and bonding them together with an adhesive can provide mechanical properties in accurate proportion to full-size mass timber elements which have greater mechanical properties than clear wood specimens. Small scale testing of adhesively bonded TCC elements can provide informative data before large scale testing at a reduced resource cost. Small scale concrete compression tests provide a more accurate picture of the compressive behaviour of the concrete in small-scale TCC flexure beams than the results obtained from a standard size concrete tests cylinder. The quality control of the dry-on-wet application method is better due to some potential displacement of adhesive, especially at the small scale, when placing fresh concrete on top of the epoxy.

ACKNOWLEDGEMENT

This research project has been mainly funded using the Discovery Grant awarded to the second author by the Natural Sciences and Engineering Research Council of Canada (NSERC).

REFERENCES

[1] Ceccotti, A. (1995). Timber-concrete composite structures. *Timber engineering, step*, *2*(1).

[2] Fragiacomo, M., & Lukaszewska, E. (2011). Development of prefabricated timber–concrete composite floor systems. *Proceedings of the Institution of Civil Engineers-Structures and Buildings*, *164*(2), 117-129.

[3] H. J. Negrão, M. F. Oliveira and L. C. Oliveira, "Investigation on timber-concrete glued composites," *Proc., WCTE 2006—The 9th World Conference on Timber Engineering*, August 2006.

[4] Tannert, T., Gerber, A., & Vallee, T. (2020). Hybrid adhesively bonded timber-concrete-composite floors. *International Journal of Adhesion and Adhesives*, *97*, 102490.

[5] ASTM D143-14 (2014). "Standard test methods for small clear specimens of timber," ASTM International, West Conshohocken, USA

[6] CCMC (Canadian Construction Materials Centre). 2007. Nordic LamTM. Evaluation Report CCMC 13216-R. CCMC, Ottawa, Ontario

[7] Sika Canada Inc. Product Data Sheet: Sikadur-35 Hi- Mod LV. Point-Claire, QC, Canada, 2017.

[8] ASTM D4933-16 (2021). "Standard Guide for Moisture Conditioning Of Wood And Wood-Based Materials," ASTM International, West Conshohocken, USA

[9] Torquato, L. P., Auty, D., Hernández, R. E., Duchesne, I., Pothier, D., & Achim, A. (2014). Black spruce trees from fire-origin stands have higher wood mechanical properties than those from older, irregular stands. *Canadian Journal of Forest Research*, *44*(2), 118-127.

[10] Youssef, G., Loulou, L., Chataigner, S., Caré, S., Flety, A., Le Roy, R., ... & Aubagnac, C. (2014). Analysis of the behaviour of a bonded joint between laminated wood and ultra high performance fibre reinforced concrete using push-out test. *Construction and Building Materials*, *53*, 381-391.

[11] Negrão, J. H. J. D. O., Leitão de Oliveira, C. A., Maia de Oliveira, F. M., & Cachim, P. B. (2010). Glued composite timber-concrete beams. I: Interlayer connection specimen tests. *Journal of Structural Engineering*, *136*(10), 1236-1245.

[12] Negrão, J. H. J. D. O., Maia de Oliveira, F. M., Leitão de Oliveira, C. A., & Cachim, P. B. (2010). Glued composite timber-concrete beams. II: analysis and tests of beam specimens. *Journal of Structural Engineering*, *136*(10), 1246-1254.

[13] Le Roy, R., Pham, H. S., & Foret, G. (2009). New wood composite bridges. *European journal of environmental and civil engineering*, *13*(9), 1125-1139.

[14] Brunner, M., Romer, M., & Schnüriger, M. (2007). Timber-concrete-composite with an adhesive connector (wet on wet process). *Materials and structures*, *40*, 119-126.

[15] Frohnmüller, J., Fischer, J., & Seim, W. (2021). Full-scale testing of adhesively bonded timber-concrete composite beams. *Materials and Structures*, *54*, 1-21.

https://doi.org/10.52202/069179-0440

World Conference on
Timber Engineering
Oslo 2023

EFFECT OF DIFFERENT TESTING METHODS ON THE STRUCTURAL PERFORMANCE OF WOODEN SHEAR WALLS

Yua Kosuge[1], Satoshi Onishi[2], Hideyuki Nasu[3]

ABSTRACT: The purpose of this study was to verify the effect of different testing methods on structural performance evaluation in in-plane shear tests with high-strength bearing walls. The results obtained from tie-rod type tests were used to verify the effects of axial force and placement of tie-rod on the performance evaluation of bearing walls. As a result, it was verified that axial force has almost no effect on the performance evaluation of bearing walls in general strength bearing walls. In the future, we will verify the effects of axial force and placement of tie-rod on the performance evaluation of bearing walls by changing the test specimen specifications.

KEYWORDS: Shear wall test, Column-base fixed type, Tie-rod type, Placement of tie-rod, Axial force of tie-rod

1 INTRODUCTION

In Japan, performance evaluation of bearing walls in wooden buildings is based on in-plane shear tests. There are two types of test methods: column-base fixed type and tie-rod type.

The column-base fixed type is a method of restraining lifting by attaching hold-down hardware to the legs of a bearing wall (Fig.1.1). This is currently the most used test method. However, when used for high-strength bearing walls, there is concern that the column-leg joints may fail prior to the end state of the bearing wall.

The tie-rod type is a method of restraining the lifting of bearing wall legs by using tie-rods (steel rods) (Fig.1.2). This test method is suitable for evaluating the performance of the bearing wall itself. This test method is often used for high-strength bearing walls.

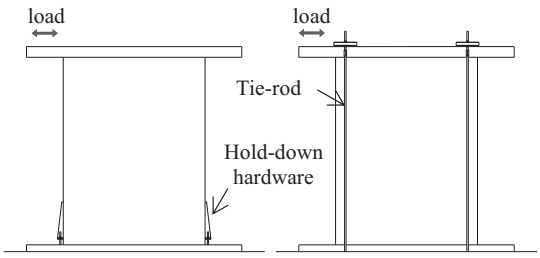

Fig 1.1: *Column-base fixed*

Fig 1.2: *Tie-rod type*

In recent years, high-strength bearing walls have been developed to promote the use of medium to large scale wooden buildings. Accordingly, the tie-rod type is increasingly used. However, it is not clear how different testing methods affect the performance evaluation of such high-strength bearing walls. The purpose of this study was to compare the results of tests conducted with column-base fixed type and tie-rod type, and to determine the effect of the different test methods on performance evaluation.

In the tie-rod type test method, it is common knowledge the restraint by the tie rods is such that no load is applied. The tie rods are often placed along the column core, but this depends on the test equipment and the test specimen specifications. It was thought that different axial forces and placements would affect the performance evaluation, but it was not clear how much they would affect it. Therefore, in the tie-rod type, the effects of tie-rod axial force and placement on performance evaluation were also examined.

2 SUMMARY OF RESEARCH

The purpose of this study was to verify the effect of different testing methods on structural performance evaluation in in-plane shear tests with high-strength bearing walls. In terms of the effect of restraint force on performance evaluation, differences in restraint force and left-right differences in restraint force have a slight effect on structural performance but almost no effect. Controlling the restraining force through torque management or other means would have less effect on performance evaluation. In terms of the effect of the different placements on the performance evaluation, the structural performance of the specimens with 200 mm different tie-rod placements was compared, and the results were almost the same, so there was no effect with differences in placement. In terms of the effect of the different test methods on the performance evaluation, the determinants of allowable shear strength were different, but the values were the same, so there was no effect of the final evaluation on the wall strength.

[1] Yua Kosuge, Graduate School, Nippon Institute of Technology, JAPAN, yua.kosuge@gmail.com
[2] Satoshi Onishi, Asst., Mr.Eng., Nippon Institute of Technology, JAPAN, onishi.satoshi@nit.ac.jp
[3] Hideyuki Nasu, Prof., PhD. in Eng., Nippon Institute of Technology, JAPAN, hideyuki.nasu@nit.ac.jp

https://doi.org/10.52202/069179-0441

3 EFFECT OF AXIAL FORCE ON THE STRUCTURAL PERFORMANCE

3.1 VERIFICATION WITH GENERAL STRENGTH BEARING WALLS

First, the effect of the axial force of the tie rods on the performance evaluation of the bearing walls was verified. The specimens were compression braced load-bearing walls (Fig. 3.1,3.2). A total of four tie rods were placed along the column cores. The left front and left back tie rods restrained the uplift of the left leg, and the right front and right back tie rods restrained the uplift of the right leg. Initially, to understand the relationship between the tightening angle and the axial force of the tie rods, the axial force was measured when the nuts of the tie rods were tightened by hand and when they were tightened half a turn each using a tool. The results are shown in Fig. 3.3 and Table 3.1. The total axial force for both the left and right sides was less than 1kN when hand tightened. At 1260- degree, the left axial force was about 36kN and the right axial force was about 44kN, with the right axial force tending to be higher. This is considered due to the distortion of the specimen and the order of tightening.

Next, in-plane shear tests were performed with the tie-rods tightened to the limit (1260-degree). The test results are shown in Table 3.2. While the wall magnification was equivalent to 2.5, the result was 2.8. Considering that a total axial force of about 80kN was applied, the axial force has almost no effect on the performance evaluation of bearing walls.

Fig 3.1: *Before the test*

Fig 3.2: *After the test*

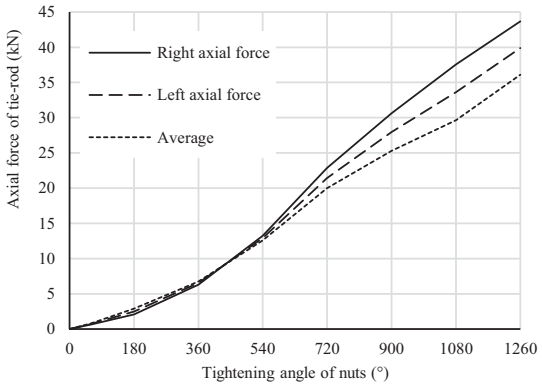

Fig 3.3: *Test results (Axial force)*

Table 3.1: *Test results (Axial force)*

Tightening angle	Axial force of tie-rod (kN)					
	Left front	Left back	Left total	Right front	Right back	Right total
By hand	0.48	0.32	0.80	0.48	0.16	0.64
180˚	1.45	1.45	2.90	1.13	0.97	2.10
360˚	3.22	3.55	6.77	3.55	2.74	6.29
540˚	5.80	6.77	12.57	6.77	6.45	13.22
720˚	9.67	10.32	19.99	11.93	10.96	22.89
900˚	12.42	12.89	25.31	15.15	15.47	30.62
1080˚	14.99	14.67	29.66	18.70	18.86	37.56
1260˚	18.05	18.05	36.10	21.44	22.24	43.68

Table 3.2: *Test result (Shear wall test)*

	Hand-tightened	Half-turn	Axial force 20kN
K [kN/rad.]	5622.49	7576.65	7610.97
Pmax [kN]	55.57	54.37	54.07
Py [kN]	34.99	33.44	30.15
Pu [kN]	49.26	48.09	48.13
δv [rad.]	0.0087	0.0063	0.0063
δu [rad.]	0.0340	0.0339	0.0331
μ	3.8806	5.3487	5.2379
Ds	0.3846	0.3211	0.3248
Py [kN]	34.99	33.44	30.15
Pu*(0.2/Ds) [kN]	25.62	29.95	29.63
2/3Pmax [kN]	37.05	36.25	36.05
Pγ [kN]	36.17	38.64	38.75
Pa [kN]	25.62	29.95	29.63

3.2 VERIFICATION WITH HIGH-STRENGTH BEARING WALLS

The test specimens were two specifications. One is framework construction method bearing walls and the other is framed wall construction method bearing walls (Fig.3.4,3.5). Three specimens were used for each.

For the framework construction method bearing walls, 9mm plywood (JAS A class 2) was attached using CN50 nails at a pitch of 150mm in the middle passage and 75mm in the perimeter. For the framed wall construction method bearing walls, 9mm plywood (JAS A class 2) was attached using CN50 nails at a pitch of 200mm in the middle passage and 50mm in the perimeter.

https://doi.org/10.52202/069179-0441

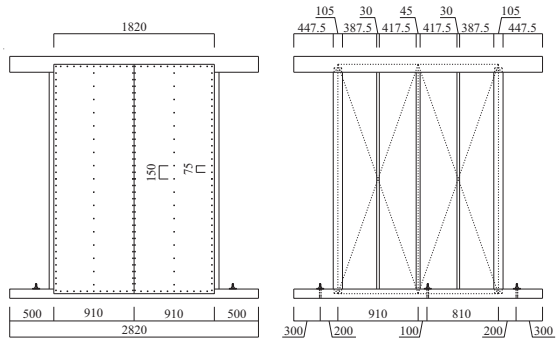

Fig 3.4: *Framework construction method bearing wall*

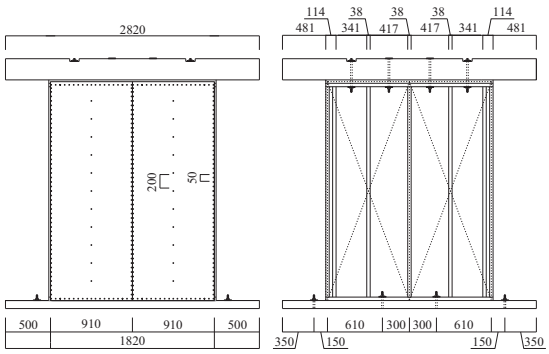

Fig 3.5: *Framed wall construction method bearing wall*

Table 3.3: *Measured results of restrained axial force*

		Left axial force [kN]	Right axial force [kN]	Left-Right differences [kN]
Framework construction	1. Hand-tightened	3.63	3.74	0.11
	2. Half-turn	14.80	16.86	2.06
	3. Axial force 20kN	20.91	20.61	0.30
Framed wall construction	1. Hand-tightened	3.19	2.59	0.60
	2. Half-turn	17.86	12.83	5.03
	3. Axial force 20kN	22.51	21.62	0.89

Installation for tie rod type is shown in Fig.3.6,7. There are three test conditions. One is when the tie rods are hand-tightened, another is when they are hand-tightened and then tightened a half-turn using a tool, and the third is when they are tightened until the axial force per column reaches 20 kN (the long-term design axial force for a typical Japanese house). Table 3.3. shows the measured results of the restrained axial force at each condition.

The tie rod type in-plane shear test was performed using a load frame tester in Nippon Institute of Technology (Fig.3.6,7). The loading method is repeated three times in alternating positive and negative, and the loading cycle is apparent shear deformation angle 1/600, 1/450, 1/300, 1/200, 1/150, 1/100, 1/75, 1/50, 1 / 30 rad. (Only 1/30 rad was repeated once). The tie rod test was repeated when the true shear deformation angle, which is the apparent shear deformation angle minus the deformation angle due to the rotation of the leg, reached each specific deformation angle.

Fig 3.6: *Framework construction method bearing wall*

Fig 3.7: *Framed wall construction method bearing wall*

Table 3.4,3.5 and Fig 3.8,3.9 shows the test results for each specification.

The load-displacement curve for the three conditions for the framework construction method bearing wall were almost identical. All allowable shear strengths (Pa) were determined by Pu (0.2/Ds). Compare the hand-tightening case with the half-turn and 20 kN cases. Compared the allowable shear strengths (Pa), the hand-tightening with half-turn and 20 kN cases. The value was 20% lower in the hand-tightening case. This is because Pu had the highest value, but Ds had unfavorable values. Compared to the fracture properties, the plywood peeling was total for the half-turn and 20 kN cases, whereas it was partial for the hand-tightened case. Compared the allowable shear strengths (Pa), the half-turn and 20 kN cases. The values were equivalent. The fracture properties were both plywood peeling, and the degree of plywood peeling was similar. Compared with hand-tightening and half-turn, 20 kN cases shows that the difference in initial restraint force affects the performance evaluation. Although there was a difference of approximately 10 kN in the restraint force between the half-turn and 20 kN, the allowable shear capacity was equivalent. Therefore, we believe that above a certain level of restraint force, there is no significant difference in performance.

https://doi.org/10.52202/069179-0441

The load-displacement curves for the framed wall construction method bearing walls were almost identical for the hand-tightened and 20 kN cases but differed for the half-turn case. All allowable shear strengths (Pa) were determined by Pu (0.2/Ds). In the case of half-turn, both Pu and Ds showed unfavorable values, resulting in lower values of allowable shear strengths (Pa) than during the other conditions. In the half-turn case, there was nail penetration but little damage to the plywood. In the case of hand-tightened and 20 kN, nail pull out and punching out occurred, and damage to the plywood was significant. The reason why the half-turn case resulted differently from the other conditions was due to the balance between the left and right restraining axial forces. In the case of half-turn, there was a relatively large left-right difference in restraint force, with a lower value for the right restraint force, which affects the time of final failure. The load-bearing wall tended to lift during other conditions, and the load-bearing wall rotated as one piece. Therefore, the allowable shear capacity showed low values due to low initial stiffness and unfavorable toughness.

Table 3.4: *Result of framework construction method bearing*

	Hand-tightened	Half-turn	Axial force 20kN
K [kN/rad.]	5622.49	7576.65	7610.97
Pmax [kN]	55.57	54.37	54.07
Py [kN]	34.99	33.44	30.15
Pu [kN]	49.26	48.09	48.13
δv [rad.]	0.0087	0.0063	0.0063
δu [rad.]	0.0340	0.0339	0.0331
μ	3.8806	5.3487	5.2379
Ds	0.3846	0.3211	0.3248
Py [kN]	34.99	33.44	30.15
Pu*(0.2/Ds) [kN]	25.62	29.95	29.63
2/3Pmax [kN]	37.05	36.25	36.05
Pγ [kN]	36.17	38.64	38.75
Pa [kN]	25.62	29.95	29.63

Table 3.5: *Result of framed wall construction method bearing*

	Hand-tightened	Half-turn	Axial force 20kN
K [kN/rad.]	5622.49	7576.65	7610.97
Pmax [kN]	55.57	54.37	54.07
Py [kN]	34.99	33.44	30.15
Pu [kN]	49.26	48.09	48.13
δv [rad.]	0.0087	0.0063	0.0063
δu [rad.]	0.0340	0.0339	0.0331
μ	3.8806	5.3487	5.2379
Ds	0.3846	0.3211	0.3248
Py [kN]	34.99	33.44	30.15
Pu*(0.2/Ds) [kN]	25.62	29.95	29.63
2/3Pmax [kN]	37.05	36.25	36.05
Pγ [kN]	36.17	38.64	38.75
Pa [kN]	25.62	29.95	29.63

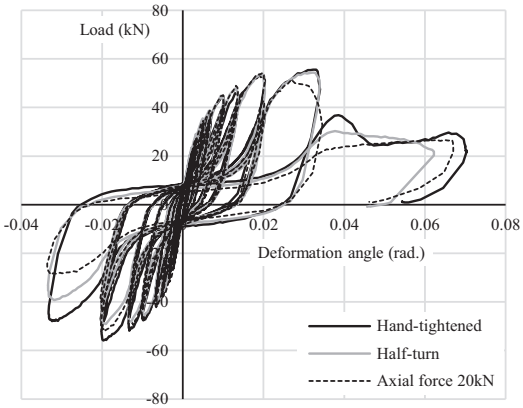

Fig 3.8: *Load-displacement curve*
Framework construction method bearing wall

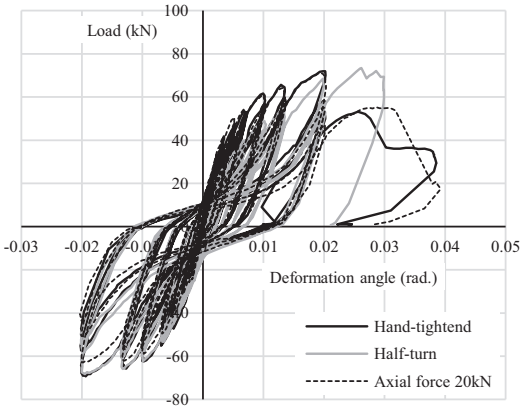

Fig 3.9: *Load-displacement curve*
Framed wall construction method bearing wall

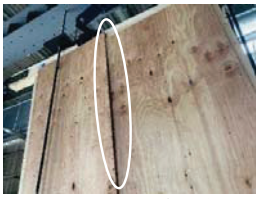

Fig 3.10: *Plywood peeling half-turn and 20 kN cases*

Fig 3.11: *Plywood peeling hand-tightened case*

Fig 3.12: *Nail penetration half-turn case*

Fig 3.13: *Nail punching out hand-tightened and 20 kN*

4 EFFECT OF TIE-ROD PLACEMENT

4.1 TEST OVERVIEW

The effect of the placement of the tie rods on the performance evaluation of the bearing walls was verified. In-plane shear tests had different tie-rods placement. The test results of the previous research were compared again,

https://doi.org/10.52202/069179-0441

and a new perspective on the effect of the placement of the tie rods on the performance evaluation of the bearing walls was verified.

4.2 TEST SPECIMENS AND TEST METHODS

The tie rod type in-plane shear test was performed using a load frame tester in Nippon Institute of Technology (Fig.4.1,4.2). The loading method is repeated three times in alternating positive and negative, and the loading cycle is apparent shear deformation angle 1/600, 1/450, 1/300, 1/200, 1/150, 1/100, 1/75, 1/50. The tie rod test was repeated when the true shear deformation angle, which is the apparent shear deformation angle minus the deformation angle due to the rotation of the leg, reached each specific deformation angle.

Fig 4.1: *Placement of tie rod (First and second specimens)*

Fig 4.2: *Placement of tie rod (Third specimens)*

4.3 TEST RESULTS

Table 4.1 shows the test results and Figure 4.3 shows the load-displacement curves. The allowable shear strengths (Pa) were determined by the yield strength, Py, for the first specimen, and by the toughness value, Pu (0.2/Ds), for the second and third specimens. The load-deformation angle curves at ultimate failure were different for the first, second, and third specimens. These differences were due to different factors of fracture properties. Since the results of the first specimen were different from those of the other specimens, a comparison of the second and third specimens was conducted to verify the effect of the different placements on the performance evaluation. The load-displacement curves were almost identical. The allowable shear strengths (Pa) showed 11.6 for the second and 10.2 for the third, a difference of about 10%. The left and right restraints at 1/600 rad. were generally in agreement. The left restraint force at 1/50 rad. was generally consistent. The right restraining force showed approximately 167 kN for the second body and 212 kN for the third body, a difference of about 20%. However, the differences in determinants and allowable shear strengths (Pa) were all about 10%, and the load-displacement curves and fracture characteristics were almost identical, suggesting that the differences in tie-rod placements had little effect on the performance evaluation of the bearing walls.

Table 4.1: *Test results*

	First	Second	Third
K [kN/rad.]	13084.3	12331.8	12972.2
Pmax [kN]	87.9326	83.58	82.24
Py [kN]	50.00	44.56	50.34
Pu [kN]	82.03	73.78	78.69
δv [rad.]	0.0038	0.0036	0.0038
δu [rad.]	0.0062	0.0059	0.0060
μ	6.4797	4.6553	3.3386
Ds	0.2891	0.3468	0.4196
Py [kN]	50.00	44.56	50.34
Pu*(0.2/Ds) [kN]	56.74	42.54	37.50
2/3Pmax [kN]	58.62	55.72	54.82
Pγ [kN]	67.08	68.03	70.53
Pa [kN]	50.00	42.54	37.50

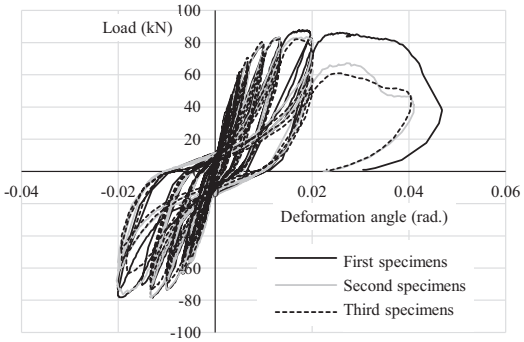

Fig 4.3: *Load-displacement curve*

5 EFFECTS OF DIFFERENT TEST METHODS

5.1 TEST SUMARY

The effects of different testing methods for in-plane shear tests on the performance evaluation of load-bearing walls. The influence of the different test methods is verified by comparing the results of in-plane shear tests using the fixed column leg and tie-rod methods.

https://doi.org/10.52202/069179-0441

5.2 TEST METHODS

The tie rod type in-plane shear test was performed using a load frame tester in Nippon Institute of Technology (Fig.5.1,5.2). The loading method is repeated three times in alternating positive and negative, and the loading cycle is apparent shear deformation angle 1/600, 1/450, 1/300, 1/200, 1/150, 1/100, 1/75, 1/50. The tie rod test was repeated when the true shear deformation angle, which is the apparent shear deformation angle minus the deformation angle due to the rotation of the leg, reached each specific deformation angle.

Fig 5.1: *Specimen installation state (Column-base fixed type)*

Fig 5.2: *Specimen installation state (Tie-rod type)*

5.3 TEST RESULTS

The load-displacement curves are shown in Figure 5.3 and the test results are in Table 5.1,5.2. The allowable shear strengths (Pa) were 10.21 kN and 10.47 kN for the column-base fixed type and tie-rod type, respectively, with the tie-rod type showing a slightly higher value. The allowable shear strengths (Pa) were determined by 0.2Pu $\sqrt{(2\mu-1)}$ for the fixed column leg method and Py for the tie-rod method, and the determining factors differed depending on the test method. Comparing the determinants, only 0.2Pu$\sqrt{(2\mu-1)}$ is higher for the tie-rod type. The other determinants were higher for the column-base fixed type. Since the column-base fixed type showed more favorable performance in terms of bearing capacity and the tie-rod type showed more favorable performance in terms of toughness, the different test methods are considered to have an influence on the performance evaluation. However, since the allowable shear strengths (Pa) values were comparable, we believe that the different testing methods have little effect on the final evaluation.

Table 5.1: *Test results*

	Column-base fixed type	Tie-rod type
K [kN/rad.]	1395.30	1696.49
Pmax [kN]	17.37	16.02
Pu [kN]	16.05	14.55
δv [rad.]	0.011	0.008
δu [rad.]	0.063	0.062
Ds	0.314	0.270

Table 5.2: *Determinants of allowable shear strengths*

	Column-base fixed type	Tie-rod type
Py	11.20	10.47
Pu*(0.2/Ds)	10.21	10.75
2/3Pmax	11.58	10.68
Pγ	11.42	11.01
Pa (kN)	10.21	10.47

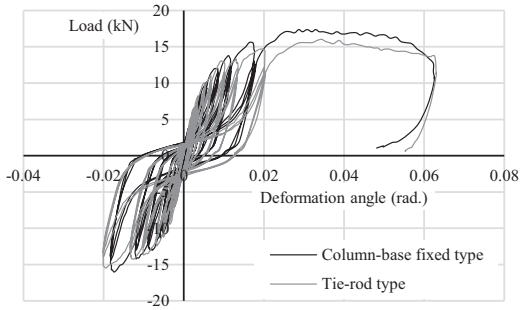

Fig 5.3: *Load-displacement curve*

5.4 SUMMARY

Although the determinants were different, the allowable shear strengths (Pa) were almost identical. Therefore, the differences in test methods affect the performance evaluation but have little effect on the final allowable shear strengths (Pa) evaluation.

6 CONCLUSION

In terms the effect of restraint force on performance evaluation, differences in restraint force and left-right differences in restraint force have a slight effect on structural performance but almost no effect. Controlling the restraining force through torque management or other means would have less effect on performance evaluation. In terms of the effect of the different placement on the performance evaluation, the structural performance of the specimens with 200 mm different tie-rod arrangements was compared, and the results were almost the same, so there was no effect with differences in placement. In terms of the effect of the different test methods on the performance evaluation, the determinants of allowable shear strength were different, but the values were the same, so there was no effect of the final evaluation on the wall strength.

REFERENCES

[1] Japan 2×4 home builders association.: Guidelines for calculating the structure of framed wall construction methods, 2018.

[2] Japan Housing and Wood Technology Center.: Allowable Stress Design for Wood Frame Houses, 2017.

https://doi.org/10.52202/069179-0441

World Conference on Timber Engineering Oslo 2023

DEVELOPMENT OF HIGH STRENGTH BEARING WALLS FOR FRAMEWORK CONSTRUCTION METHOD USING 2X4 LUMBER AND PLYWOOD MADE OF JAPANESE TIMBER

Hideyuki Nasu[1], Kenji Aoki[2], Hiro Kawahara[3]

ABSTRACT: The purpose of this research is to develop a high strength bearing wall for the framework construction method using Japanese frame material and Japanese plywood. To achieve this, it is necessary to consider the combination, or balance, of plywood thickness, wood species, frame materials and type of nails. At first, single shear tests were performed on the nail joints, then the optimum combination was determined by modelling. After that, the performance of the walls was verified with in-plane shear tests using full-scale bearing walls. It was found that when the wall legs are joined to the ground with metal joints, a brittle fracture has occurred at the metal joint. Therefore, by changing the test method from the column fixed type to the tie rod type without using metal joints, column base breakage was prevented and the high strength performance of the shear wall itself was confirmed.

KEYWORDS: Framework construction method, Single shear tests, In-plane shear tests, Fixed column base, Tie rod

1 INTRODUCTION

Wooden public buildings are increasing popularity. In public buildings, a large space is often required, and research on load-bearing walls using structural plywood that can produce a high-strength load-bearing walls with easy construction has been promoted. At present, a lot of Japanese timber is being harvested and it is thought that effective utilization of this timber and the additional higher value will stabilize Japan's supply and demand of timber and stimulate forestry. However, most of the frame materials are imported materials, such as SPF, and domestic materials are rarely used. Therefore, one of the effective uses for domestic large-diameter materials is the use of the frame wall construction method for frame materials.

2 SUMMARY OF RESEARCH

We intend to develop a type of high strength frame wall construction bearing wall using domestic frame material and domestic plywood for public buildings. In order to realize this, it is necessary to consider the plywood thickness, the combination of the tree species, the frame material, and the type of nails. Therefore, after examining the optimum combination for the bearing walls from single shear tests with nail joints, in-plane shear tests (column base fixed type and tie rod type) were conducted on the actual bearing walls. The target performance is 10 times the wall strength ratio of the Japanese building code regulations, 1.96 kN/m horizontal allowable load/length of wall performance.

3 SINGLE SHEAR TESTS

3.1 SUMMARY OF EXPERIMENTS

Test bodies were made using 2×6 cedar as the center materials and plywood as the side materials (Fig. 1). The number of test specimens were 54 in total, 6 in each of 9 specifications with varying plywood thickness and tree species. Three types of plywood were selected: cedar (C), larch (L), and cedar-larch mixed plywood (M). The combination of plywood and nails were CN50 nails for 12 mm thick, CN65 nails for 15 mm thick, and CN75 nails for 24 mm thick for the purpose of exhibiting excellent one-side shear performance. The tests were performed monotonically using a 50 kN universal testing machine at Nippon Institute of Technology. The loading time was such that the time to reach the maximum load was 5 minutes ± 2 minutes. The displacement was determined by measuring the relative displacement between the frame material and the both side of plywood for recording the average.

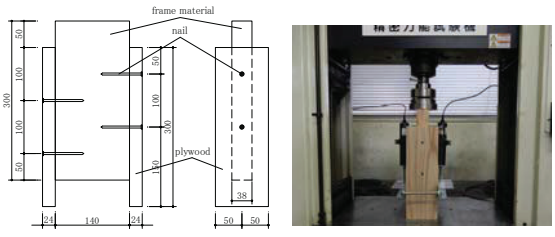

Fig. 1 *Single shear specimens*

[1] Hideyuki Nasu, Prof., PhD in Eng., Nippon Institute of Technology, Japan, hideyuki.nasu@nit.ac.jp
[2] Kenji Aoki, Associate Prof., PhD in Agr., The University of Tokyo, Japan, aoken@g.ecc.u-tokyo.ac.jp
[3] Hiro Kawahara, Assistant Prof., PhD in Agr., Tokyo Denki University, Japan, kawahara@mail.dendai.ac.jp

https://doi.org/10.52202/069179-0442

3.2 EXPERIMENTAL RESULTS

Table 1 shows the average and standard deviation of the experimental results of each specification, and Fig. 2 to 4 show graphs of the experimental results. Note that the test results are values for one nail. For the cedar plywood and the mixed plywood, the average value of maximum loads and allowable test stress were increased in proportion to the thickness of plywood (Table 1). The results were as follow. With larch plywood the test specimen with 15 mm thickness had similar load and maximum stress to the specimen with 24 mm thickness. In the case of cedar and composite plywood, there were many indentations and punching out of nail heads (Fig. 5 and 6). In larch plywood, bending deformation of nails was common (Fig. 7).

Table 1 *Average test results*

Specimen name	K (kN/mm)	S.D.	Py (kN)	S.D.	δ y (mm)	S.D.	Pmax (kN)	S.D.	δ max (mm)	S.D.
C-12	1.04	0.14	3.17	0.28	3.08	0.39	5.50	0.32	20.75	2.34
C-15	1.66	0.28	3.80	0.51	2.42	0.82	6.94	0.52	21.18	5.92
C-24	1.97	0.27	5.38	0.49	2.81	0.60	10.02	0.73	23.85	4.11
L-12	1.58	0.18	4.31	0.38	2.75	0.31	7.93	0.46	20.07	1.30
L-15	2.40	0.47	6.13	0.50	2.69	0.66	12.00	0.34	25.50	7.21
L-24	2.43	0.59	6.74	0.26	2.97	0.83	11.42	0.59	26.69	1.77
M-12	1.48	0.23	3.70	0.14	2.56	0.32	6.58	0.23	21.04	1.38
M-15	1.95	0.38	4.12	0.48	2.22	0.60	7.62	0.44	20.13	7.91
M-24	2.49	0.27	7.23	0.94	2.94	0.55	12.27	1.43	25.98	3.93

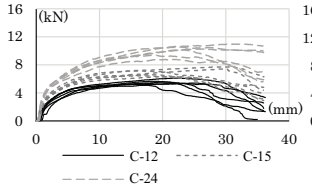

Fig. 2 *C specification load-displacement curve*

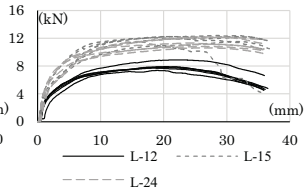

Fig. 3 *L specification load-displacement curve*

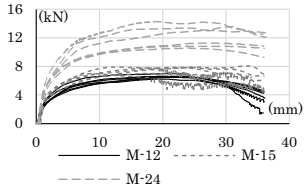

Fig. 4 *M specification load-displacement curve*

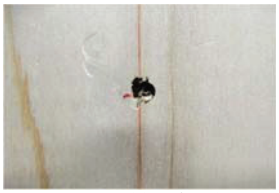

Fig. 5 *Nail head sinking*

Fig. 6 *Nail punching out*

Fig. 7 *Bending deformation of nails*

4 MODELING BEARING WALLS

Assuming a wall panel with a width of 1820 mm and a height of 2460 mm, the calculation was performed assuming that the nail distance of the face material was 50 mm and 75 mm. The yield strength of one nail was determined from the test average value obtained in the experiment in 3 SINGLE SHEAR TESTS, and the allowable shear strength as a load-bearing wall was determined therefrom (Fig. 8 and 9). The wall magnification is obtained by multiplying the allowable shear strength of the load-bearing wall by the reduction factor due to toughness as the short-term allowable shear strength. Among these, the C-24, L-15, L-24, and M-24 specifications with each nail distance of 50 mm and the L-24, M-24 specifications with each nail distance of 75 mm are predicted to be high strength bearing walls (Table 2).

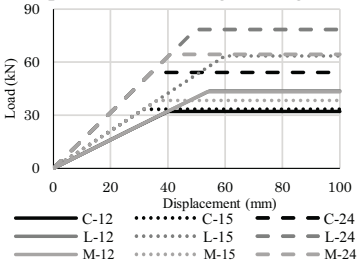

Fig. 8 *Nail 50 mm distance elastic-plastic model*

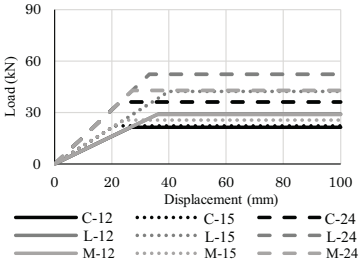

Fig. 9 *Nail 75 mm distance elastic-plastic model*

Table 2 *Modeling wall magnification*

Specimen name	Nail distance	Wall magnification
C-12	@75mm	4.66
	@50mm	6.40
C-15	@75mm	5.50
	@50mm	7.57
C-24	@75mm	7.89
	@50mm	10.85
L-12	@75mm	6.33
	@50mm	8.49
L-15	@75mm	9.02
	@50mm	10.62
L-24	@75mm	10.05
	@50mm	13.81
M-12	@75mm	5.52
	@50mm	7.59
M-15	@75mm	6.00
	@50mm	8.25
M-24	@75mm	10.48
	@50mm	14.41

5 COLUMN BASE FIXED TYPE IN－PLANE SHEAR TESTS

5.1 OUTLINE OF TEST SPECIMEN

The dimensions of the test specimen were 1820 mm (2P) in wall length and 2400 mm in wall height for wooden surface materials (Fig. 10). The framing material used was 204 cedar wood (JAS A class 2). Normally, there is only one vertical frame between panels, but with high strength load-bearing walls, the spacing between nails for holding plywood is narrow, and the vertical frame may be damaged. Therefore, the vertical frames between the panels were joined together and fastened with CN75 nails in a 300 mm distance staggered arrangement. In the same way, the orientation of the torso was changed to horizontal use to make it harder to break. The specifications of the bearing wall are 3 of C-24 specification using cedar 24 mm plywood material, L-15 specification using larch 15 mm plywood material, and L-24 specification using 24 mm larch plywood material. In the L-15 and L-24 specifications, the each nail distance for securing the vertical frames were changed to double-rows with CN75 nails 100 mm distance. For the joint connectors, HD metal joints with the short-term reference strength of 60 kN were used for the column pedestal, and HD metal joints with the short-term reference strength of 40 kN were used for the column base fixed type tests.

https://doi.org/10.52202/069179-0442

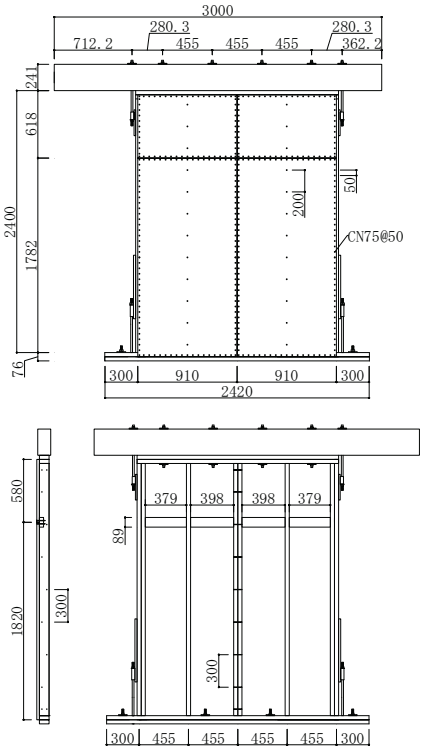

Fig. 10 *C-24 specification test body*

5.2 TESTS METHOD

The column-base fixed type in-plane shear tests were performed using a load frame tester in Nippon Institute of Technology (Fig. 11). The loading method was repeated three times in alternating positive and negative, and the loading cycle was apparent shear deformation angle 1/450, 1/300, 1/200, 1/150, 1/100, 1/75, 1/50, 1 / 30 rad. (only 1/30 rad. was repeated one time).

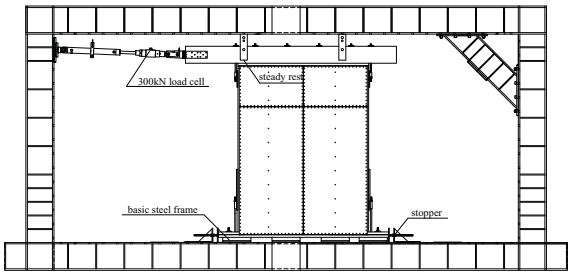

Fig. 11 *Specimen installation state*

5.3 EXPERIMENTAL RESULTS

Tables 3 and 4 show the experimental results for each specification, and Fig. 12 shows a graph of the test results. Comparing the structural performance of the three specifications, the initial stiffness and maximum load were in the order of L-15, L-24, and C-24. However, when compared by wall magnification, the C-24 specification, L-15 specification, and L-24 specification were in descending order. In the case of the C-24 specification, in which the nails of the vertical frame were placed as usual, the vertical frame between the panels was greatly displaced, and the outer vertical frame caused bending failure at the time of tearing (Fig. 13, 14). In L-15 and L-24, because the number of nails between panels was increased, the displacement of the vertical frame was suppressed, but aggregated shear failure of the vertical frame was induced at the wall legs (Fig. 15, 16).

Table 3 *Test results*

	C-24	L-15	L-24
K (kN/mm)	1.39	1.91	1.60
Py (kN)	32.50	36.59	32.22
Pmax (kN)	52.88	64.26	57.07
δu (mm)	210.46	100.82	132.98
Pu (kN)	48.18	57.22	48.90
δv (mm)	34.62	29.96	30.52
μ	6.08	3.37	4.36
Ds	0.30	0.42	0.36

Table 4 *Calculation result of wall magnification*

	C-24	L-15	L-24
P_Y (kN)	28.91	39.05	33.17
2/3Pmax (kN)	35.25	42.84	38.05
(0.2/Ds)×Pu (kN)	32.18	27.25	27.16
Py (kN)	32.50	36.59	32.21
P_0 (kN)	28.91	27.25	27.16
Wall magnification	8.10	7.64	7.61

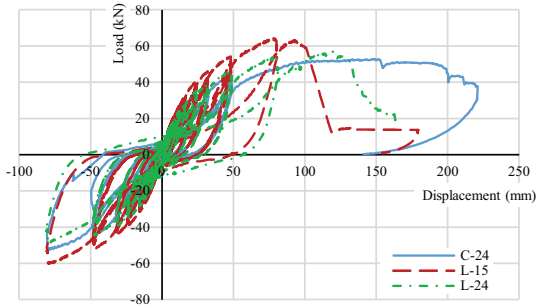

Fig. 12 *Load-displacement curve*

Fig. 13 *Misalignment between vertical frames*

Fig. 14 *Bending deformation of vertical frame*

Fig. 15 *Suppression of vertical frame displacement*

Fig. 16 *Collective shear failure*

5.4 COMPARISON OF TEST RESULTS AND MODELING

A comparison of the modeling and test results showed that all specifications were below the wall magnification of the modeling (Table 5). It is considered that the wall magnification of the test was lower than the estimated value due to the occurrence of brittle collective failure and the sinking at the upper and lower ends of the vertical frame, which was ignored in the calculation. In addition, in the modeling, it is assumed that the joint is destroyed, but in the experiment assuming high magnification, such as in this study, the frame material was destroyed.

https://doi.org/10.52202/069179-0442

Therefore, when the wall magnification was calculated from the yield load that was not affected by the fracture and compared with the estimated results, the results were almost similar.

Table 5 *Comparison of wall magnification*

Specimen name	C-24	L-15	L-24
Nail distance	CN75 @50mm	CN65 @50mm	CN75 @75mm
Modeling wall magnification	10.85	10.62	10.05
Wall magnification calculated from P_0	8.10	7.64	7.61
Wall magnification calculated from Py	9.11	10.25	9.03

5.5 SUMMARY OF COLUMN BASE FIXED TYPE IN-PLANE SHEAR TESTS

When more nails were struck into two vertical frames, the force concentrated on the metal joint, causing collective destruction of the metal joint. In order to achieve a wall magnification of 10 times, it is necessary to consider the number of nails that hold the panels together and the metal joint that suppresses collective destruction.

6 TIE ROD TYPE IN-PLANE SHEAR TESTS

6.1 SUMMARY OF EXPERIMENTS

When the degree of fixation of the vertical frame increased from the destructive properties in Fig.16, collective destruction of the outer vertical frame occurred. It is considered that the stress is concentrated on the wall bases due to the increased wall strength. The performance of the bearing wall itself could not be verified with the fixed column base, and there was concern that the wall strength would be determined by the performance of the metal joint. In order to grasp the performance of the load-bearing wall itself, it is necessary to conduct an experiment that does not break the column base metal joints before the wall itself. Therefore, a tie rod type in-plane shear test was carried out in which the lifting of the load bearing wall legs was suppressed with a tie rod. The tie rod type in-plane shear test is suitable for evaluating the shear performance of the load-bearing wall.

6.2 OUTLINE OF TEST SPECIMEN

From the modeling of wall magnification in 4 MODELING BEARING WALLS, tie rod type tests were performed with C-24 specification, L-15 specification and L-24 specification. In the case of the tie rod type, it is described as TC-24 specification, TL-15 specification, TL-24 specification, and the number of test specimens was one each.

6.3 TEST METHOD

The tie rod type in-plane shear test was performed using a load frame tester in Nippon Institute of Technology (Fig. 17). The loading method was repeated three times in alternating positive and negative, and the loading cycle is apparent shear deformation angle 1/600, 1/450, 1/300, 1/200, 1/150, 1/100, 1/75, 1/50, 1 / 30 rad. (only 1/30 rad. was repeated one time). The tie rod test was repeated when the true shear deformation angle, which is the apparent shear deformation angle minus the deformation angle due to the rotation of the leg, reached each specific deformation angle.

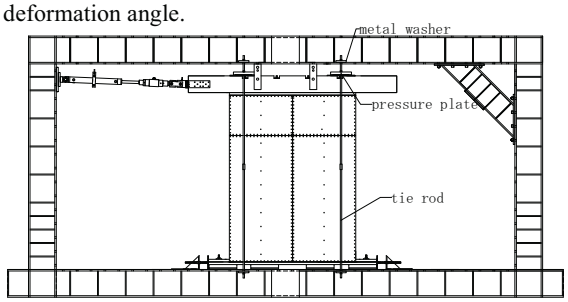

Fig. 17 *Specimen installation state*

6.4 EXPERIMENTAL RESULTS

Tables 6, 7 show the experimental results for each specification, and Fig. 18 shows a graph of the test results. In the TC-24 and TL-15 specifications, measurement was not possible until the end due to measurement failure. In TL-24, the wall magnification was determined by Py, and the value was 8.61 times. Comparing the TL-24 with the other two specifications, the one with the highest rigidity and maximum load was the TL-24 specification, so it is considered that the other two specifications will not perform any better. When confirming the fracture properties, the entire bearing wall showed rocking behaviour, cracks occurred in the lower frame from deformation after 1/50 rad. (Fig. 19, 20). In all specifications, cracks were caused by nails hit into the lower frame at the final failure. This failure could reduce the ultimate performance of the walls.

Table 6 *Test results*

	TC-24	TL-15	TL-24
K (kN/rad.)	3536.12	3700.01	5980.68
Py (kN)	30.80	27.20	30.70
Pmax (kN)	53.33	49.73	56.92
δu (rad.)	0.0406	0.0512	0.0650
Pu (kN)	47.55	44.67	53.01
δv (rad.)	0.0134	0.0121	0.0089
μ	3.02	4.24	7.34
Ds	0.45	0.37	0.27

Table 7 *Calculation result of wall magnification*

	TC-24	TL-15	TL-24
P_T (kN)	26.51	26.81	34.90
2/3Pmax (kN)	35.55	33.15	37.95
(0.2/Ds)×Pu (kN)	21.35	24.15	39.20
Py (kN)	30.80	27.20	30.70
P_0 (kN)	21.35	24.15	30.70
Wall magnification	5.99	6.77	8.61

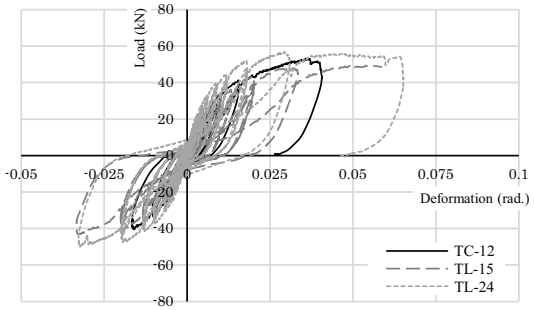

Fig. 18 *Load-deformation angle curve*

https://doi.org/10.52202/069179-0442

Fig. 19 *Crack of lower frame*

Fig. 20 *Cracking progress*

6.5 OVERVIEW OF ADDITIONAL TEST

An additional test was performed to find a specification that can exceed the wall magnification by 10 times, because the target specification did not exceed the target wall magnification of 10 times. The nails were placed in one low frame material, thus the nail interval became shorter, then frame material was broken. Therefore, it was thought that cracking of the framed material could be prevented by staggering the nails between the vertical frames. In addition, since the frame material can be connected not only with nails but also with plywood, it is considered that rigidity and strength can be improved. We set the TL-24W specification (Fig. 21). The TL-24W specification uses a zigzag arrangement of 75 mm nails to hold the plywood, so that more nails can be hit than a 50 mm distance single row arrangement, while keeping the gaps between nails and preventing the nail spacing from becoming shorter. Since there were originally two vertical frames between panels, nails were struck in one vertical frame in a staggered arrangement. As a result of estimating the wall magnification by the method described in 4 MODELING BEARING WALLS before starting the final version of test, wall magnification was estimated 19.33 times. The test method was the same as in Section 6.3.

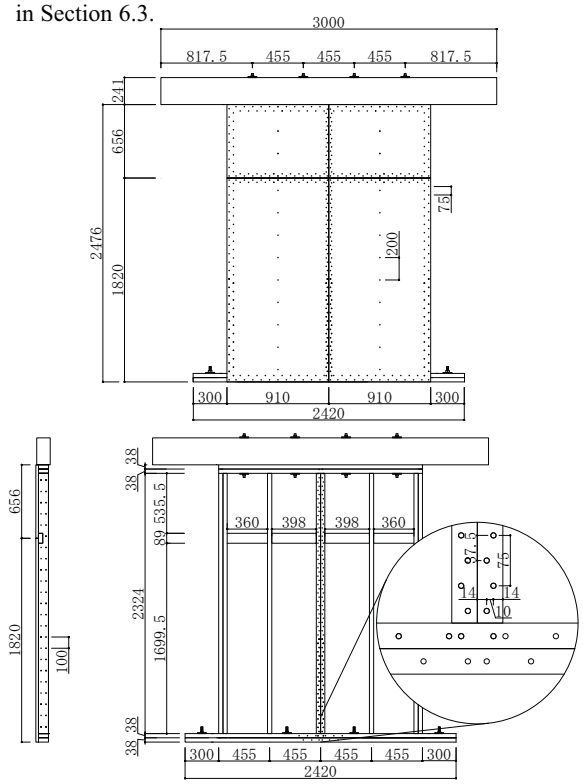

Fig. 21 *TL-24W specification test body*

6.6 ADDITIONAL TEST RESULTS

Tables 8, 9 show the experimental results for each specification, and Fig. 22 shows a graph of the test results. The TL-24W specification showed higher structural performance than the TL-24 specification from the beginning of deformation. This is considered to be due not only to an increase in the number of nails, but also to an increase in rigidity caused by connecting the frame members with plywood. When the fracture properties were confirmed, the vertical frame protruded from the minute deformation (1/450 rad.) because the bearing wall exhibited rocking behavior (Fig. 23). This is probably because the rigidity of the wall itself has increased and the legs have been rotated without deforming the wall. When the interlaminar deformation angle reached 1/50 rad., cracks occurred in the lower frame, although slightly less than before (Fig. 24). It is considered that the reason why the wall magnification of the experiment was lower than that of the modeling is that the deviation between the vertical frames from the initial stage of deformation is more remarkable than before, even though the vertical frame sinks (Fig. 25 and 26). However, the structural performance reached 12.39 times, exceeding the target wall magnification of 10 times.

Table 8 *Test results*

	TL-24	TL-24W
K (kN/rad.)	5980.68	8274.40
P_y (kN)	30.70	44.21
Pmax (kN)	56.92	77.00
δu (rad.)	0.0650	0.0556
Pu (kN)	53.01	70.46
δv (rad.)	0.0089	0.0085
μ	7.34	6.53
Ds	0.27	0.29

Table 9 *Calculation result of wall magnification*

	TL-24	TL-24W
P_γ (kN)	34.90	48.54
2/3Pmax (kN)	37.95	51.33
(0.2/Ds)×Pu (kN)	39.20	48.59
P_y (kN)	30.70	44.21
P_0 (kN)	30.70	44.21
wall magnification	8.61	12.39

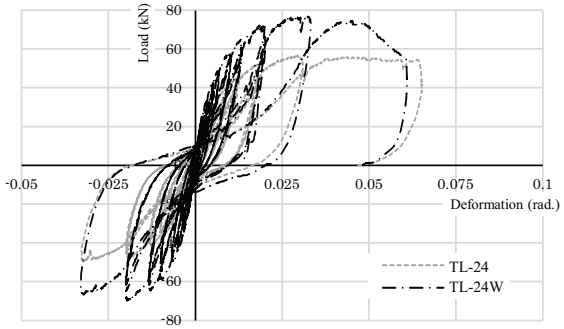

Fig. 22 *Load-deformation angle curve*

Fig. 23 *Lift of vertical frame*

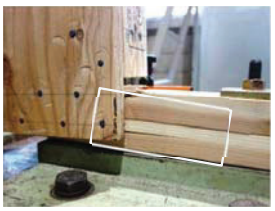

Fig. 24 *Cracking of the base*

https://doi.org/10.52202/069179-0442

Fig. 25 *Vertical frames misalignment*

Fig. 26 *Sinking of vertical frame*

6.7 SUMMARY OF TIE ROD TYPE IN-PLANE SHEAR TESTS

Even in the case of a shear wall test with a wall magnification of about 10 times, which was the target in this study, the performance of the shear wall itself could be evaluated by changing the test method to a tie rod type. In actual design, it is conceivable to prevent breakage in the vertical frame by increasing the number of vertical frames according to the pulling force acting on the vertical frame and installing appropriate HD metal joints.

7 CONCLUSION

Through this research, it was possible to realize a high-strength framework construction method wall (equivalent to a wall magnification of 10 times the wall strength ratio of the Japanese building code) using domestic Japanese cedar framing materials and Japanese plywood that are commercially available, without using special tools or special materials. Also, within the scope of this research, to make higher structural or fully effective performance of the surface material, two vertical frames between the panels were joined, nailing to the head joint and base through plywood, it is necessary to increase the degree of fixing between the vertical frames between panels. The tie rod type test method is better than the column base fixed type test method for verifying higher performance wall, such as 10 times the wall strength ratio of the Japanese building code regulations using Japanese timber.

ACKNOWLEDGEMENT

This research was carried out by the “Innovative Technology Creation Promotion Project in JAPAN through Field for Knowledge Integration and Innovation”. These experiments were conducted by Mr. Daiki Kato, a master's course student at Nippon Institute of Technology. We would like to thank all those involved.

REFERENCES

[1] Kenji Aoki, Ken-ichi Sugimoto, Fumio Kamiya : Development of high load carrying capacity shear wall with thick plywood sheathing. AIJ J. Technol. Des. Vol.20, No.44, 111-114, Feb., 2014

[2] Junji Toda, Tatsuya Shibusawa, Hirofumi Nagao, Kenji Aoi, Yasushi Ono, Shiro Nakajima : The embedment properties parallel to and perpendicular to the grain of Sugi, Hinoki and Karamatsu dimensional lumber. Wood industry, Vol.70, No.12, 578-583, 2015

[3] Junji Toda, Tatsuya Shibusawa, Hirofumi Nagao, Kenji Aoki, Yasushi Ono, Shiro Nakajima : The nail-joint shear properties of Sugi, Hinoki and Karamatsu dimensional lumber. Wood industry, Vol.71, No.3, 95-100, 2016

[4] ⓒ JAPAN 2×4 HOME BUILDERS ASSOCIATION: Guidelines for calculating the structure of framed wall construction methods, 2011.

https://doi.org/10.52202/069179-0442

World Conference on Timber Engineering Oslo 2023

IMPACT OF EXTERIOR SIDING WALLS AND THE CONNECTING METHODS IN WOODEN HOUSES: COMPARATIVE VERIFICATION FOR STRUCTURAL PERFORMANCE WITH DIFFERENT CONNECTION METHODS OF WALL SIDINGS

Kouta Matsumoto [1], Kiyotaka Terui [2], Hideyuki Nasu [3]

ABSTRACT: In recent years, siding has been widely used for the exterior walls of Japanese houses. There are two methods of installation: nailing (hereinafter referred to as "nailed SD") and hooking with metal fittings (hereinafter referred to as "hooked SD"). Previous research [2] shows that nailing bears about 10% of the external force, but it is not clear how much external force is borne by the hooked SD. In this study, we will examine the extent to which a hooked SD bears the external force in terms of wall magnification. The objective was also to elucidate the contribution of the SD itself to the wall magnification. The specimens were subjected to static force tests to extract the structural performance of each load-bearing element. Static force tests revealed the following results compared to the nailed SD, which was the mainstream method at the time. The present mainstream hooked SD was found to have reduced bearing capacity.

KEYWORDS: Wooden Houses, Exterior Materials, Sidings, Static Force Tests, Non-structural Members

1 INTRODUCTION

There are two methods of finishing the exterior walls of wooden houses: wet methods, such as mortar exterior walls, and dry methods, such as siding (hereinafter referred to as "SD"). Wet methods have been commonly used in the past, but in recent years, dry methods have been widely used in order to shorten the construction period and to address the shortage of skilled workers. There are two types of installation methods for ceramic-SD: Nailed SD (Figure 1) and Hooked SD (Figure 2).

In the past, nailed SD was the most common method, but cracks and defects occur around the nails due to inter-story deformation caused by external forces such as earthquakes. However, since hooked SD does not cause major visible damage such as cracks and defects like nailed SD, hooked SD is currently the most common type of SD. However, since hooked SD is a method in which the SD is hooked to the joints, it is considered to have almost no ability to restrain the interstory deformation of the frame against external forces such as seismic forces, and there is concern that the actual bearing capacity may be reduced.

The Architechal Institute of Japan [1] states that 2/3 of external forces such as seismic forces are borne by bearing walls and 1/3 by non-bearing walls such as SD. The same style for [2] states that nailed SDs bear about 10% of the external force. The same style for [3] and other full-scale experiments have also been conducted, but it has not been clarified how much external force is borne by hooked SDs.

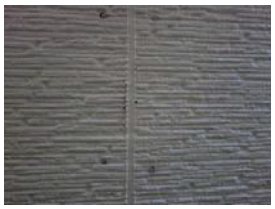

Figure 1: *Nailed SD*

Figure 2: *Hooked SD*

2 OBJECTIVE

The purpose of this study is to determine how much external force is borne by a hooked SD in terms of wall modulus by subtracting the structural performance of the bearing wall itself from the structural performance of the bearing wall to which the SD has been applied. The purpose of this study is to clarify the contribution of the SD itself to the wall ratio.

3 SUMMARY OF RESEARCH

3.1 TEST SPECIMEN SUMMARY

In order to extract the structural performance of each load-bearing element, the test specimens were constructed using the Single-sided fascia (Figure 3) and Single-sided plywood (Figure 4) specifications as load-bearing walls, as well as the Nailed SD (Figure 5) and Hooked SD (Figure 6) specifications with the SD fastened to the frame to grasp the structural performance of the different

[1] Kouta Matsumoto, Graduate Nippon Institute of Technology, JAPAN, Email: kouta.matsumoto.1113@gmail.com
[2] Kiyotaka Terui, POLUS R&D Center of Life-Style Co., Ltd. JAPAN, Email: 01452terui-sz@polus.co.jp
[3] Hideyuki Nasu, Prof., PhD. in Eng, Nippon Institute of Technology, JAPAN, Email: hideyuki.nasu@nit.ac.jp

https://doi.org/10.52202/069179-0443

fastening methods for ceramic SD, a dry construction method.

In addition, in order to understand the bearing capacity of the SD when installed in a load-bearing wall, tests were conducted using six specifications: a Single-sided fascia specification with SD fastened to the Single-sided fascia specification and a Single-sided fascia + nailed SD specification (Figure 7), and a Single-sided fascia specification with SD fastened to the Single-sided fascia + hooked SD specification (Figure 8). The test specimens were conventional wooden walls with a core width of 3640 mm for columns and a core distance of 2730 mm for transverse members, with 105 mm square cross sections for columns and foundations, 105 mm x 30 mm for studs, 180 mm x 105 mm for beams, and 90 mm x 45 mm for braces. In order to suppress bending deformation of the beams and pull out of the columns due to up thrusting of the braces, which bear the compressive force, yamagata plates were attached to the top and bottom ends of the middle columns that are connected to the transverse members on the back of the specimens.

The thickness of SDs was 14 mm for nailed SDs and 15 mm for hooked SDs, and joints were made with joints dedicated to each SD (Figures 9 and 10).

3.2 EXPERIMENTAL SUMMARY

The static in-plane shear static force test was conducted using a force frame tester at the POLUS R&D Center of Life Style with a fixed leg using three repetitive positive-negative alternating cycles of force as described in The same style for [4] (Figure. 11 and 12). The applied force was controlled by displacement, and three push-pull cycles of 1/450, 1/300, 1/200, 1/150, 1/100, 1/75, and 1/50 rad. were performed, and only those that could be applied up to 1/30 rad. were pushed and pulled once. Thereafter, pull-destruction was performed with a target of 1/15 rad. The deformation for each interlaminar deformation angle that was repeated is shown in Table 1.

Table 1: *Deformation for each interlaminar deformation angle*

Interstitial deformation angle (rad.)	1/450	1/300	1/200	1/150
Amount of deformation (㎜)	6.06	9.10	13.65	18.20
Interstitial deformation angle (rad.)	1/100	1/75	1/50	1/30
Amount of deformation (㎜)	27.30	36.40	54.60	91.00

3.3 EVALUATION METHOD

The SD contribution ratio is calculated by dividing the wall ratio of the wall with SD installed by the wall ratio of the single-sided fascia bearing wall specification; the SD contribution ratio is calculated by dividing the wall ratio of the single-sided fascia bearing wall specification with SD installed by the wall ratio of the single-sided fascia bearing wall specification. The burden ratio was calculated by dividing the contribution ratio by the wall ratio of the single-sided fascia bearing wall specification with SD installed.

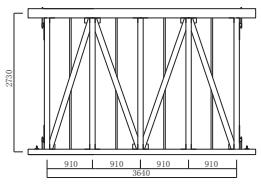

Figure 3: *Single-sided fascia specifications*

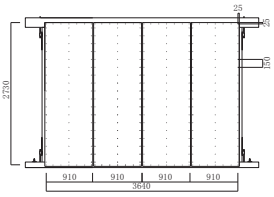

Figure 4: *Single-sided plywood specification*

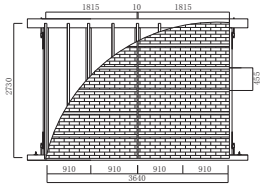

Figure 5: *Nailed SD specification*

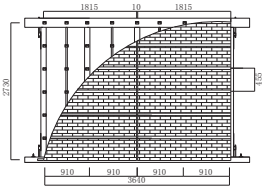

Figure 6: *Hooked SD specification*

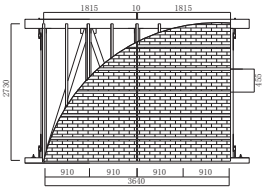

Figure 7: *Single-sided fascia + nailed SD specification*

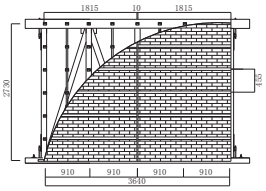

Figure 8: *Single-sided fascia + hooked SD specification*

Figure 9: *Dedicated fittings (stainless steel nails)*

Figure 10: *Dedicated fittings (hooks)*

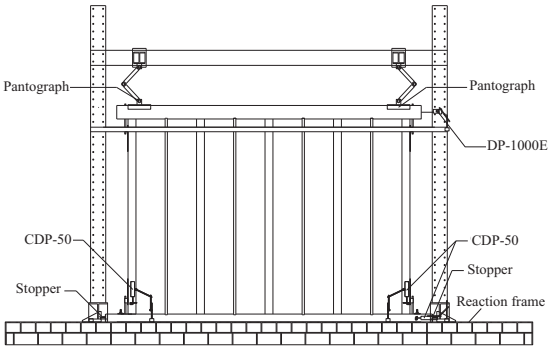

Figure 11: *Test object installation status*

Figure 12: *Actual test unit installation (SD wall)*

https://doi.org/10.52202/069179-0443

4 EXPERIMENTAL RESULTS

The relationship between load and horizontal displacement for each specification is shown in Figures 13~16, and the Pa determinants and calculated wall factors for each specification are shown in Table 2. The wall magnification of the Single-sided fascia specification was 2.18 times compared to the assumed wall magnification (2.00 times), which is almost equivalent. The wall factors for walls with SDs constructed using different fastening methods were 1.14 times for the Nailed SD specification and 0.28 times for the Hooked SD specification. In addition, the wall-to-wall ratio of the Single-sided fascia + nailed SD specification, in which SD was fastened to the Single-sided fascia wall, was 4.08x, which was much higher than the value obtained by adding the wall-to-wall ratios of the Single-sided fascia and nailed SD specifications (3.32x). The value of 2.39 times for the Single-sided fascia + hooked SD specification was almost equal to 2.46 times, which is the value obtained by adding the wall factors for the one-sided rebar and hooked SD specifications. The single-sided plywood specification showed a wall factor of 2.50 times, the same as the assumed wall factor.

The nailing SD itself was converted to a wall factor of 1.90 times and the burden ratio was 46.5%, while the hooking SD itself was converted to a wall factor of 0.21 times and the burden ratio was 8.7%.

Table 2: *The Pa determinants for each specification and the calculated Wall ratio*

	Py(kN)	2/3Pmax(kN)	Pr(kN)	(0.2/Ds)×Pu(kN)	Wall facto
Single reinforcement specification	16.16	18.99	19.44	15.61	2.18
Single-sided plywood specification	17.87	22.50	26.27	18.48	2.50
Nailed SD specification	12.16	15.59	8.68	8.19	1.14
Hooked SD specification	4.62	5.83	2.16	2.00	0.28
Single-sided fascia + nailed SD specification	29.15	36.35	30.23	30.36	4.08
Single-sided fascia + hooked SD specification	20.54	22.18	21.19	17.11	2.39

※Paint sections are Pa determinants

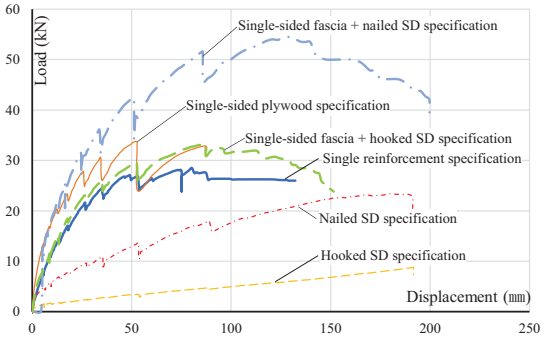

Figure 13: *The relationship between load and horizontal displacement*

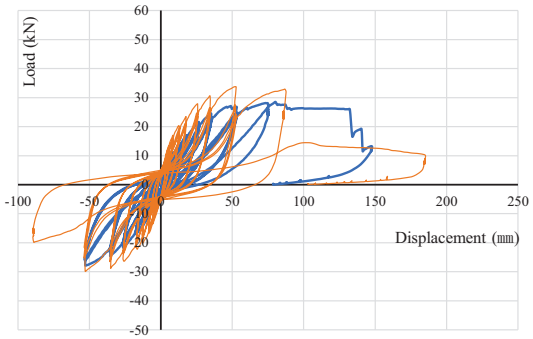

Figure 14: *Relation between load and horizontal displacement of load-bearing walls*

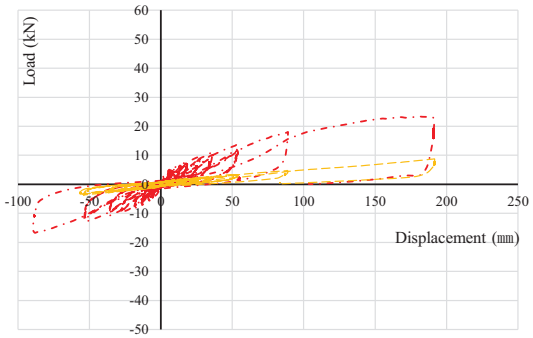

Figure 15: *Relationship between load and horizontal displacement of SD walls with different fastening methods*

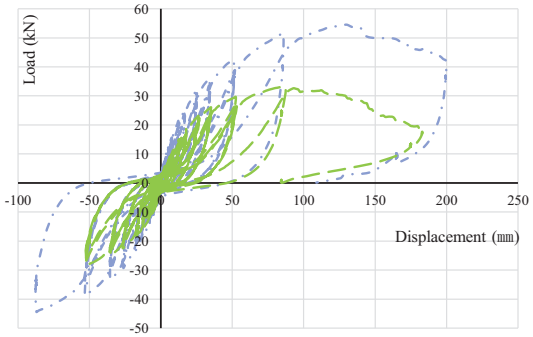

Figure 16: *Relation between load and horizontal displacement of SD walls with different fastening methods when SD is installed in a Single-sided fascia bearing wall.*

5 COMPARISON AND DISCUSSION

5.1 SINGLE-SIDED FASCIA SPECIFICATION AND SINGLE-SIDED FASCIA + NAILED SD SPECIFICATION

The load-horizontal curves are shown in Figure 17 and a comparison of test results in Table 3. The Single-sided fascia + nailed SD specification improved the overall structural performance compared to the Single-sided fascia specification. The yield load and ultimate bearing capacity increased by about 80%, and the maximum bearing capacity and toughness values increased by about 90%. The reason for this improvement is thought to be that nailing the SDs restrained the entire wall, as if it were a face plate load-bearing wall. The nailed SDs were also

https://doi.org/10.52202/069179-0443

considered to be a factor in the increase in the overall restraint of the wall due to the use of the furring strips for ventilation as joints. These factors are thought to have increased the bearing capacity by suppressing bending deformation of the beams and pulling out (Figure 18 and Figure 19) of the columns due to the beams pushing up against the fascia, which bears the compressive force.

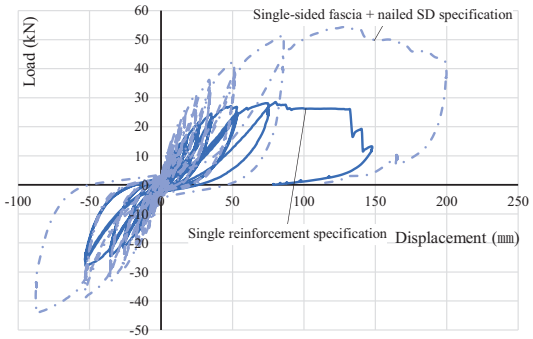

Figure 17: *Relationship between load and horizontal displacement for single-sided fascia specification and single-sided fascia + SD with nails specification*

Table 3: *Test results and ratios for Single reinforcement specification and Single-sided fascia + nailed SD specification*

Structural performance	unit	Single reinforcement specification	Single-sided fascia + nailed SD specification	Ratio※
K	kN/㎜	0.98	1.36	138.7%
Pmax	kN	28.49	54.53	191.4%
E	kN・㎜	3104.95	8466.70	272.6%
Ds		0.33	0.31	93.93%
Pu	kN	26.09	47.63	182.5%
Py	kN	16.16	29.15	180.3%
2/3Pmax	kN	18.99	36.35	191.4%
Pr(1/120rad.)	kN	19.44	30.23	155.5%
(0.2/Ds)×Pu	kN	15.61	30.36	194.4%

※Calculated based on Single Reinforcement Specification

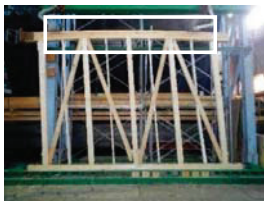

Figure 18: *Bending deformation of beams*

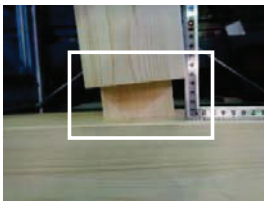

Figure 19: *Pillar pull out*

5.2 SINGLE-SIDED FASCIA SPECIFICATION AND SINGLE-SIDED FASCIA + HOOKED SD SPECIFICATION

A comparison of test results is shown in Table 4 and Figure 20. The Single-sided fascia + hooked SD specification showed a slight improvement in structural performance, except for initial stiffness, compared to the Single-sided fascia specification, but only the initial stiffness was almost the same. From this, we consider that the influence of the hooked SD is almost negligible until 0.4Pmax, when the value of the initial stiffness is determined. The yield load increased by about 30%, and the maximum and ultimate bearing capacity increased by about 20%. The damage check revealed that the joints had scratches where the metal fittings interfered with each other (Figure 21 and 22). This caused a restraining force on the SD, and the resistance force of the SD was transmitted to the frame via the metal fittings.

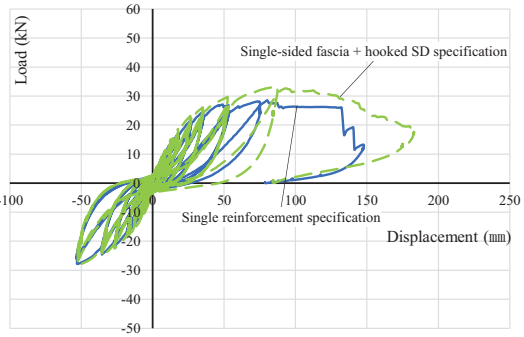

Figure 20: *Relation between load and horizontal displacement for single-sided facia specification and single-sided facia +hooked SD specification*

Table 4: *Test results and ratios for Single reinforcement specification and Single-sided fascia + hooked SD specification*

Structural performance	unit	Single reinforcement specification	Single-sided fascia + nailed SD specification	Ratio※
K	kN/㎜	0.98	0.94	95.9%
Pmax	kN	28.49	33.27	116.7%
E	kN・㎜	3104.95	3871.37	124.6%
Ds		0.33	0.35	106.0%
Pu	kN	26.09	30.15	115.5%
Py	kN	16.16	20.54	127.1%
2/3Pmax	kN	18.99	22.18	116.7%
Pr(1/120rad.)	kN	19.44	21.19	109.0%
(0.2/Ds)×Pu	kN	15.61	17.11	109.6%

※Calculated based on Single Reinforcement Specification

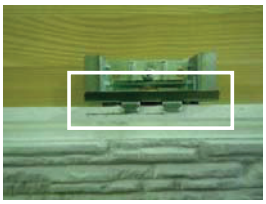

Figure 21: *Gaps created in the topmost joints due to the nearly eliminated gap in the metal fittings (under pressure)*

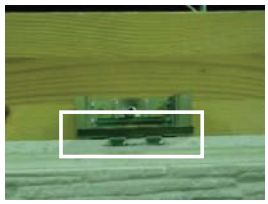

Figure 22: *Gap between fittings and no gap at uppermost joint (0 load)*

5.3 SINGLE-SIDED FASCIA + NAILED SD SPECIFICATION AND SINGLE-SIDED FASCIA + HOOKED SD SPECIFICATION

A comparison of the Single-sided fascia + nailed SD specification and the Single-sided fascia + hooked SD specification is shown in Table 5 and Figure 23. The structural performance of the Single-sided fascia + nailed SD specification was higher than that of the Single-sided fascia + hooked SD specification. A performance difference of about 70% was observed for the wall ratio. Yield load, maximum bearing capacity, and ultimate

https://doi.org/10.52202/069179-0443

bearing capacity increased by approximately 60%. This is due to the fact that the Single-sided fascia + nailed SD specification with nailed SD and nailed furring strips restrained the entire wall like a plywood bearing wall, which suppressed deformation such as the lifting of columns, and thus increased the bearing capacity. The most significant difference in the values was in the amount of energy absorption, which increased by approximately 2.2 times. We believe that the difference in initial stiffness and the difference in the number of joints per SD caused the difference in the ability to distribute the force to the entire wall.

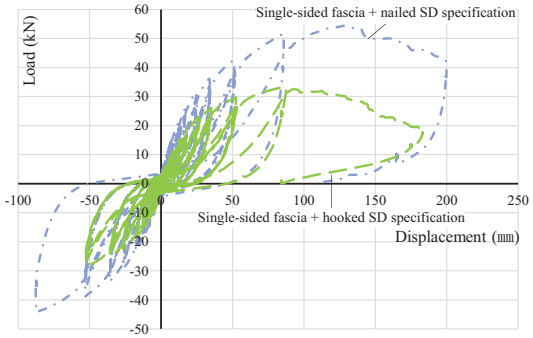

Figure 23: *Relationship between load and horizontal displacement for single-sided fascia + nailed SD specification and single-sided fascia + hooked SD specification*

Table 5: *Difference in performance between SD specification of Single-sided fascia + nailed and SD Specification of single-sided fascia + hooked*

Structural performance	unit	Single-sided fascia + nailed SD specification	Single-sided fascia + hooked SD specification	Ratio※
K	kN/㎜	1.36	0.94	144.6%
Pmax	kN	54.53	33.27	163.9%
E	kN･㎜	8466.70	3871.37	218.7%
Ds		0.31	0.35	88.5%
Pu	kN	47.63	30.15	157.9%
Py	kN	29.15	20.54	141.9%
2/3Pmax	kN	36.35	22.18	163.8%
Pr(1/120rad.)	kN	30.23	21.19	142.6%
(0.2/Ds)×Pu	kN	30.36	17.11	177.4%

※Calculated based on Single Reinforcement Specification

5.4 SINGLE-SIDED FASCIA + NAILED SD SPECIFICATION AND ADDITIVE VALUE OF SINGLE-SIDED FASCIA SPECIFICATION AND NAILED SD SPECIFICATION

Figure 24 shows a comparison of the load-horizontal curves of the measured values (hereafter referred to as "measured values") and the added values (hereafter referred to as "added values") of the Single-sided fascia + nailed SD specification and the Single-sided fascia specification + nailed SD specification. The measured values showed an increase in structural performance compared to the added values. The difference between the measured values and the additive law is considered to be due to the difference in stress transfer to the frame. Looking at the fracture behavior of the nailed SD and Single-sided fascia + nailed SD specifications, both specifications showed cracking of the SD and fracture of the furring strips (Figures 25 and 26), and the damage to the SD was almost the same. However, looking at the backside of the specimens, the Single-sided fascia + nailed SD specification showed greater damage to the frame due to the dislodging of the studs, the penetration of the foundation by the fascia, and the pulling out of the columns due to the rupture of the pile plate (Figs. 27 and 28). No damage to the frame occurred in the nailed SD and Single-sided fascia specifications. The installation of the nailed SDs caused the entire wall to deform as a single unit, which transmitted sufficient force to the fascia and increased the stress transmitted to the frame, resulting in damage to the frame, such as column pull out. This suggests that the difference between the measured and added values was caused by the increase in the maximum bearing capacity.

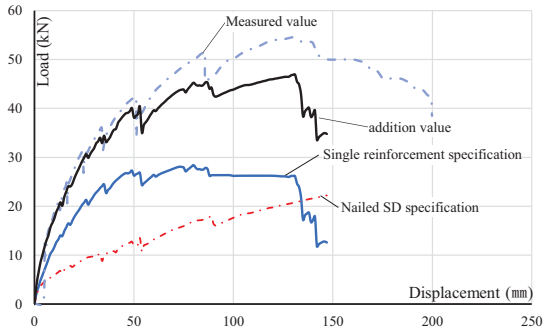

Figure 24: *Relationship between load and horizontal displacement of added values for single-sided fascia + nailed SD specification and single-sided fascia + nailed SD specification*

Figure 25: *Cracks from around nails*

Figure 26: *Cracks in the furring strips*

Figure 27: *Dislodgement of inter-posts*

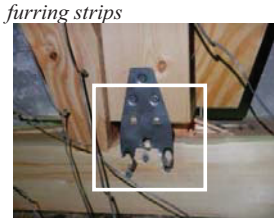

Figure 28: *Rupture of Yamagata Plate*

5.5 SINGLE-SIDED FASCIA + HOOKED SD SPECIFICATION AND ADDITIVE VALUE OF SINGLE-SIDED FASCIA SPECIFICATION AND HOOKED SD SPECIFICATION

A comparison of the Single-sided fascia + hooked SD specification (hereafter referred to as "measured value") and the additive value of the Single-sided fascia

https://doi.org/10.52202/069179-0443

specification + hooked SD specification (hereafter referred to as "additive value") is shown in Figure 29. There is almost no difference between the measured values and the additive values, indicating that the additive law is valid. This is due to the fact that the SDs hardly bear the load-bearing capacity and depend on the load-bearing capacity of the structural members, which is why there is no difference. Also, there is a difference in final failure between the measured value and the added value. In the case of the measured value, the strength was reduced due to the pull out of screws attached to the fascia plate (Figure 30), whereas in the case of the added value, the strength was reduced due to the buckling failure of the fascia (Figure 31), resulting in the difference in the graphs near the endpoint.

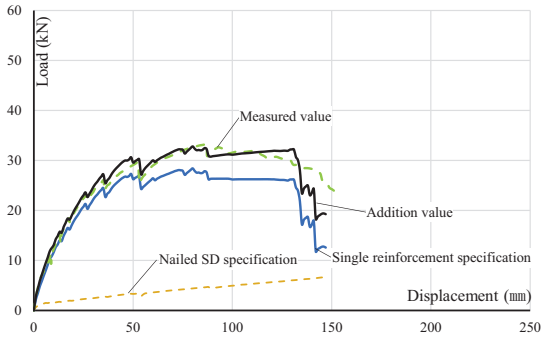

Figure 29: *Relationship between load and horizontal displacement for the added values of single-sided fascia + hooked SD specification and single-sided fascia + hooked SD specification*

Figure 30: *Fascia plate screws missing*

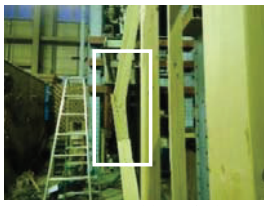

Figure 31: *Buckling failure of Fascia*

6 CONCLUSION

The burden ratio was 46.5% for nailed SD and 8.7% for hooked SD. Although SD exterior walls are not included in the structural design as load-bearing walls, it was found that the wall ratio of the current mainstream "hooked SD" was about 70% lower than that of the nailing SD, which was the mainstream at that time.

ACKNOWLEDGEMENT

The test specimens and test site for this study were provided by POLUS R&D Center of Life Style.

REFERENCES

[1] Architectural Institute of Japan: Design Standard for Wooden Structures and its Commentary - Allowable Stress and Allowable Strength Design Method -, 2006

[2] Watahiki M., Nakano I., Machida K., Ohashi Y., Sakamoto I.: A Study on Additive Law of Horizontal Force Carrying Ratio and Restoration Rate Characteristics in Wood Frame Houses, Journal of the Architectural Institute of Japan, AIJ 2006

[3] Nasu H., Ishiyama H., Noguchi H.: Study on Tensile Force Input to Column-Leg Joints in Wooden Frame Construction, Journal of the Architectural Institute of Japan, AIJ 2004

[4] Japan Housing and Lumber Technology Center: Allowable Stress Design of Wooden Frame Construction Houses, 2017 ed.

https://doi.org/10.52202/069179-0443

World Conference on Timber Engineering Oslo 2023

STUDY ON THE EVALUATION OF THE RESTORING FORCE CHARACTERISTICS OF FLOOR OF TRADITIONAL WOODEN BUILDING IN KYOTO

Rongji Fu[1], Mina Sugino[2], Yasuhiro Hayashi[3]

ABSTRACT: The vibration characteristics and seismic performance of traditional wooden buildings are heavily influenced by the restoring force characteristics of the floor. In this paper, we perform static loading tests on floors of traditional wooden buildings in Kyoto to understand the restoring force characteristics of floors of various specifications (Non-joist floor/ Joist floor). Then, Degrading Slip models (DS models) are used to develop highly accurate restoring force characteristics models of tested floors. In order to build restoring force characteristics models of floors with other specifications, a predictive formula for skeleton curves of floors is established. In addition, to calculate the skeleton curves of floors by using the formula, shear force-deformation models of a single nail are constructed by conducting the loading tests of floorboard-beam joints. The results indicated that 1) There are significant differences in restoring force characteristics of two different floors. 2) DS models can accurately represent the restoring force characteristics of the experiments. 3) Established predictive formula can simulate the skeleton curve of Non-joist floor with the shear force-deformation models of a single nail.

KEYWORDS: Traditional wooden building, Floor, Restoring force characteristics, Static loading test

1 INTRODUCTION

Since the 1995 Southern Hyogo Prefecture Earthquake, Japan has entered a period of seismic activity, and the risk of damaging earthquakes in various regions is increasing. And with the imminent occurrence of the giant Nankai Trough earthquake, inland crustal earthquakes are also said to occur frequently around that time. Meanwhile, there are many traditional wooden buildings in Japan. The promotion of seismic resistance reinforcement of these traditional wooden buildings is an urgent issue. Response obtained from time history response analysis can provide important information and basis for seismic resistance reinforcement.

To evaluate the response of the traditional wooden buildings against ground motions accurately, many static loading tests of structural components have been conducted to develop the analysis models. In this paper, we focused on the restoring force characteristics of floors, which affect the vibration characteristics of traditional wooden buildings.

The floors of Japanese traditional wooden buildings are usually consisted of wooden floorboards and steal nails. These floors have lower initial stiffness and bearing capacity than the floors of plywood is used due to sliding deformation between floorboards. But previous studies have shown that during large deformation angles, friction occurs between the floorboards, resulting in greater shear force [1-3]. Therefore, in this paper, we perform static loading tests on floors of traditional wooden buildings in Kyoto to understand the restoring force characteristics of floors of various specifications (Non-joist floor/ Joist floor) and to develop restoring force characteristics models. The models are aimed to describe the hysteresis characteristics with high accuracy to improve the accuracy of time history response analysis results. Then, to build restoring force characteristics models of floors with other specifications, a predictive formula for skeleton curves of floors is established. In addition, to calculate the skeleton curves of floors by using the formula, shear force-deformation models of a single nail are constructed by conducting the loading tests of floorboard-beam joints.

2 STATIC LOADING TEST

2.1 FLOOR SPECIMENS

The four specimens shown in Figure 1 and 2 are 1910 mm in the beam direction and 2865 mm in the girder direction, corresponding to half of a six-tatami room. The beams (270x120x2870 mm), girders (270x120x2910 mm), and small beams (180x120x1955 mm) of the specimens were all made of Oregon Pine (scientific name: *Pseudotsuga menziesii*). Dovetail joints were used to connect the beams and girders. Dovetail-dado joints were used between the girders and small beams. There were two types of non-joist floor specimens and joist floor specimens: those

[1] Rongji Fu, Kyoto University, Japan, rp-furongji @archi.kyoto-u.ac.jp
[2] Mina Sugino, Kyoto University, Japan, rp-sugino@archi.kyoto-u.ac.jp
[3] Yasuhiro Hayashi, National Institute Technology Maizuru Collage, Japan, y.hayashi@maizuru-ct.ac.jp

https://doi.org/10.52202/069179-0444

without floorboards (TS, TJ) and those with floorboards (FS, FJ). The floorboards of the Non-joist floor specimen FS were 30 mm thick cedar (scientific name: *Cryptomeria japonica*) boards, and two N90 (which means the length of the nail is 90 mm) nails were utilized to fix the floorboards to the beams. Joists (105x45x899 mm) were installed between each beam in joist floor specimens (TJ, FJ). Dado joints were used to connect joists and beams. And at the joint, the joist was fixed to the beam with N75 nails, one on each side. The joist floor specimen FJ was covered with 15 mm thick cedar boards, and floorboards were fixed to the beams with two N45 nails. The nailing interval for both specimens was 110 mm. Details of the floorboard-beam joint are shown in Figure 3.

2.2 LOADING METHOD

The loading system is depicted in Figure 4. The load was applied to the top of the specimens. To prevent the overall rotation of the specimens, a pantograph was used to keep the beam horizontal. The vertical displacement of the top beam of the specimens was not constrained. Two cycles of positive and negative alternating cyclic loading were used for the static loading test. The target displacement of the specimens took the deformation angle R = 1/450, 1/300, 1/150, 1/120, 1/100, 1/75, 1/50, 1/30, 1/20, 1/15, 1/10 and 0.15 rad. Figure 5 shows the specimen FJ under load.

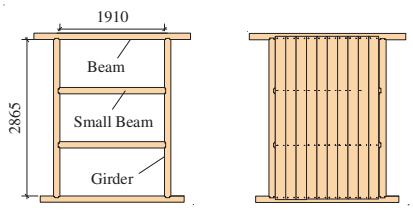

(a) *Specimen TS* (b) *Specimen FS*

Figure 1: *Non-joist floor specimens*

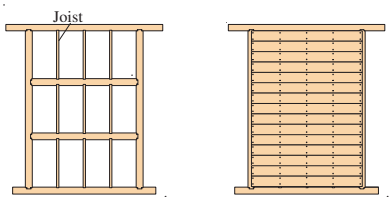

(a) *Specimen TJ* (b) *Specimen FJ*

Figure 2: *Joist floor specimens*

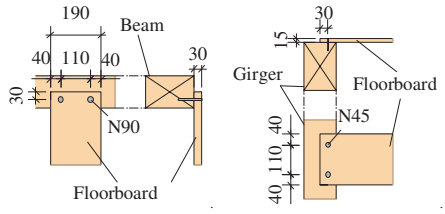

(a) *Specimen FS* (b) *Specimen FJ*

Figure 3: *Floorboard-beam joint*

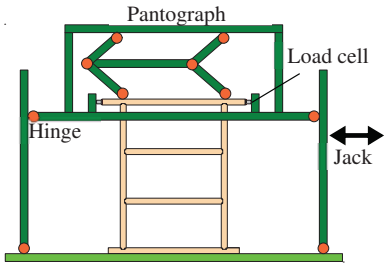

Figure 4: *Loading system of floor specimens*

Figure 5: *Specimen FJ under load (R = 0.15 rad)*

2.3 RESULTS

The restoring force characteristics of the floor specimens are shown in Figure 6. For all the specimens, the additional shear force due to the P-Δ effect was excluded using the method described in Ref [4].

At a target deformation angle R of 1/30 rad, the maximum load of TS and TJ was approximately 2 kN. Subsequently, as shown in Figure 7, the cracking of the dovetail joint developed, and the overall specimen load of the entire specimen decreased. Specimen TJ had slightly higher load at large deformation than Specimen TS due to the bending resistance of the joist.

For the Non-joist floor specimen FS, the load visibly increased about R = 1/15 rad. By R = 0.15 rad, no nail damage was observed.

Specimen FJ produced a shear force of 5.5 kN at 1/30 rad, and the load increased from 1/15 rad. The initial stiffness of specimen FJ was relatively high and the load gradually increased as the target deformation angle progressed. When the target deformation angle was small, the load at 0 rad was relatively high, but the load at 0 rad decreased with the applied load. During the large deformation, the nails of the upper and lower outer edge floorboards were pulled out from the girders as shown in Figure 8.

3 RESTORING FORCE CHARACTERISTICS MODELS

In this paper, the DS model developed by J.Nezaki et al. [5] was used to model the restoring force characteristics of the floor specimens. Degrading Slip model (DS model)

https://doi.org/10.52202/069179-0444

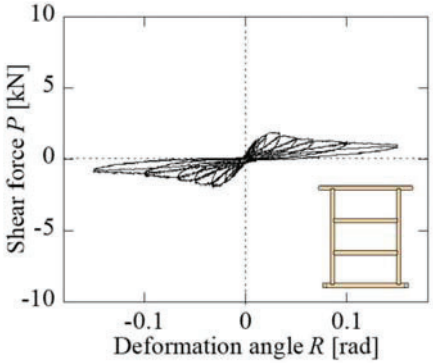

(a) *Specimen TS*

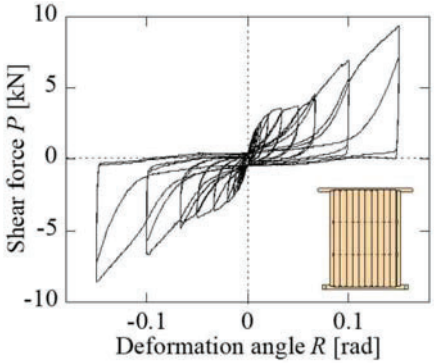

(b) *Specimen FS*

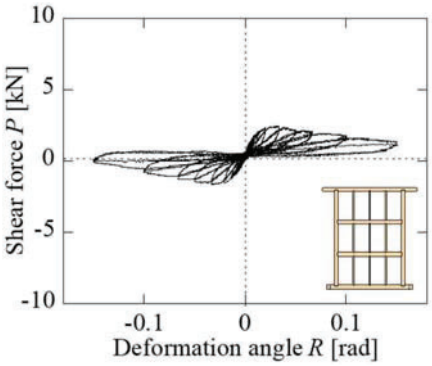

(c) *Specimen TJ*

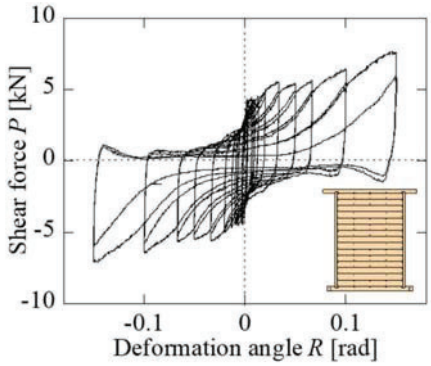

(d) *Specimen FJ*

Figure 6: *Restoring force characteristics*

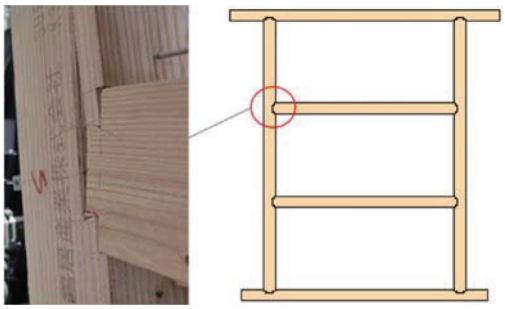

Figure 7: *The crack of the dovetail joint*

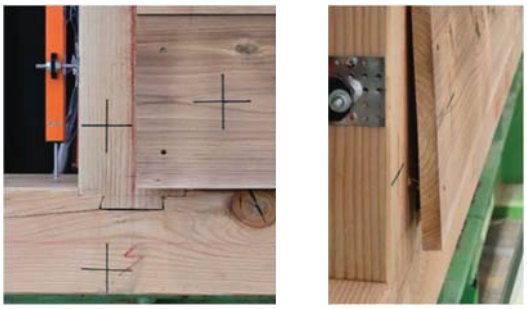

Figure 8: *Pulled out nail*

can describe the lowering slip stiffness around zero deformation angle as the maximum experienced deformation angle increases.

Figure 9 shows a comparison between the experimental data with the DS models. The figure illustrates that the DS models accurately represented the restoring force characteristics of the experiments. The initial stiffness of the TS, TJ specimens differed insignificantly. When the boards were applied, the initial stiffness of the Non-Joist floor increased by a factor of two, while that of the joist floor increased by a factor of eight. Furthermore, for specimen TS and FS the shear force Q_0 at the deformation angle of 0 rad of the hysteresis loop was 0.2-0.4 kN, which was not much different between the two specimens. While the shear force Q_0 at the deformation angle of 0 rad of FJ was much higher than Q_0 of TJ. Therefore, the area of the hysteresis loop of specimen FJ was larger than that of the TJ.

4 MECHANICAL MODEL

In Chapter 3, the restoring force characteristics models of the floor specimens were built. However, in actual traditional wooden buildings, the results obtained from experiments cannot be used directly in design because the specifications vary widely from building to building. Since the parameters of the DS models are mostly decided

https://doi.org/10.52202/069179-0444

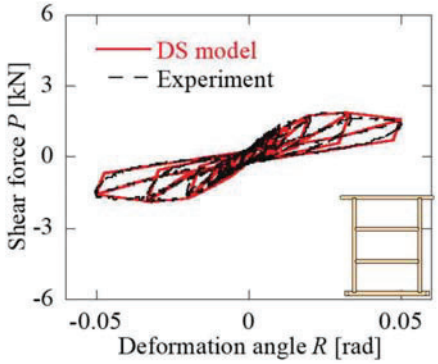

(a) *Specimen TS*

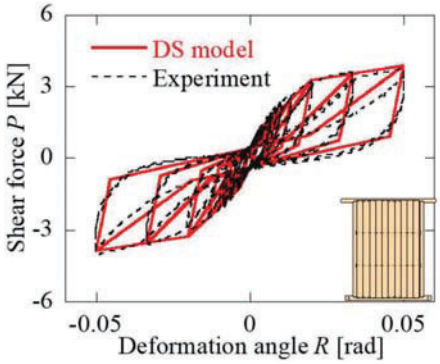

(b) *Specimen FS*

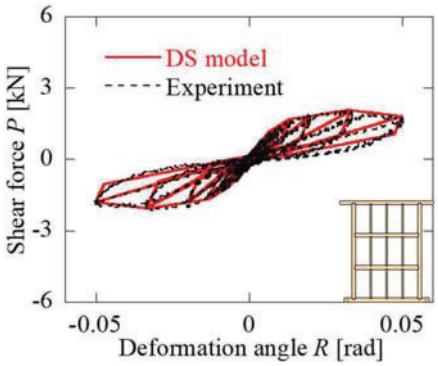

(c) Specimen TJ

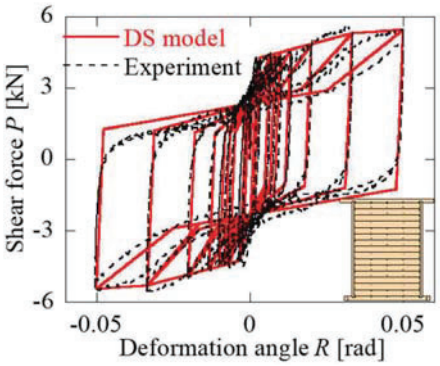

(d) *Specimen FJ*

Figure 9: *Restoring force characteristics models*

according to the skeleton curve of floors, it is necessary to estimate the skeleton curve in developing restoring force characteristics models for floors with varying specifications, such as the number of nails and floorboard orientation. In this chapter, we started by building a shear force-deformation models for a single nail joint. The shear force-deformation models were then used to create a prediction formula that can simulate the skeleton curve of the entire floor.

4.1 SHEAR FORCE-DEFORMATION MODELS OF NAIL JOINT

Figure 10 shows the specimens simulating the floorboard-beam joint. At the floorboard-beam joint, the boards' movement causes the nails to bend in the same direction. The direction of movement of the boards is random because of the seismic load. Therefore, the effect of the direction of movement of the board on the nails' resistance characteristics needs to be confirmed by experimentation. As shown in Figure 10, there were 3 types (PV, PP, VP) of floorboard-beam joint. The fiber orientations of the floorboard and beam were different for each of the 3 types of floorboard-beam joint. To correspond to the floor specimens FS and FJ described in the Chapter 2, each type of floorboard-beam joint had two specimens with the same length of nails (N45 and N90) and thickness of the floorboard (15 mm and 30 mm) as specimens FS and FJ.

The loading systems are shown in Figure 11. The beam was fixed and positive and negative cyclic forces were applied to the floorboard side. The target displacement δ of the nails were 1, 2, 4, 6, 8, 10, 15, 20, 25 mm.

The skeleton curves of shear force-deformation characteristics of a single nail are shown in Figure 12. The figure shows that the maximum load of the single N90 nail in PV specimen was about 15% lower than that of the single nail of other specimens. On the other hand, the single N45 nail in PV specimen had a higher maximum load than the single nail in the other specimens. The differences between specimens with nails of the same length were likely due to specimen variability rather than fiber direction effects. Since no significant fiber direction effects were identified, the average of the results from the three types of specimens was used to model the shear force-deformation relationship for a single nail. The results are shown in Figure 13.

4.2 PREDICTIVE FORMULA FOR SKELETON CURVES

In the formula, the floor shear force was divided into three sections: the shear force of the floor frame P_b; the shear force P_n caused by nails; and the shear force P_f due to friction. The skeleton curve of the DS model of the TS, TJ specimens were used to represent the floor frame shear force P_b. The force P_n and P_f were calculated by the formula suggested in Ref [3]. Taking the specimen FJ as an example, the formula is explained as follows.

https://doi.org/10.52202/069179-0444

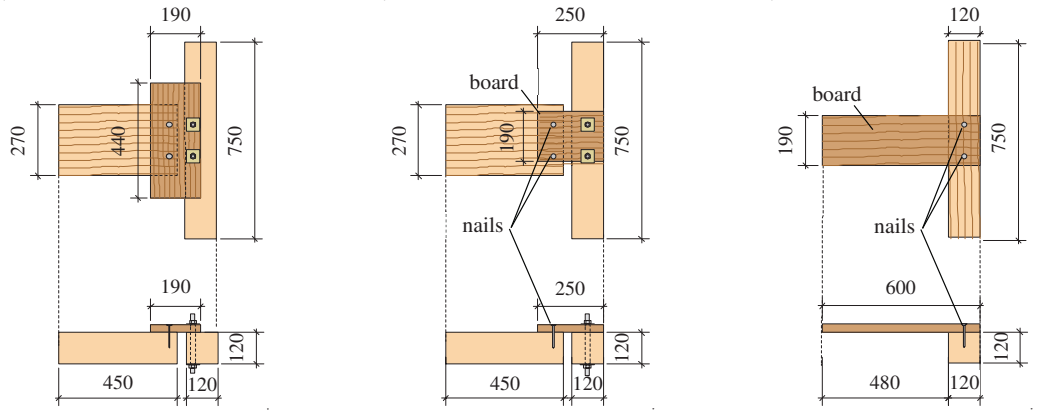

(a) *Specimen PV* (b) *Specimen PP* (c) *Specimen VP*

Figure 10: *Floorboard-beam joint type*

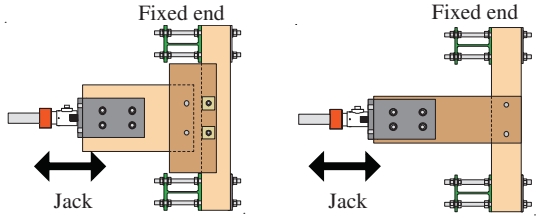

(a) *PV, PP* (b) *VP*

Figure 11: *Loading systems of joint specimens*

The height of floor specimens is H, the deformation angle is R and the number of floorboards is N. As shown in Figure 15 the deformation caused by the rotation of the floorboards δ_x is calculated from Equation (1). When the rotation angle of the specimen occurs, the height of the specimen will shrink relative to the height of all the floorboards. The amount of shrinkage must be symmetrically distributed from the centre of the specimen. Therefore, as shown in Figure 14, when the centre of the girder is considered as the centre of rotation, the shrinkage $\delta_y(i)$ corresponding to the distance $h(i)$ from the centre of

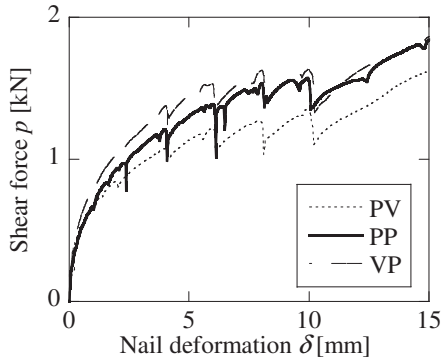

(a) *N90 nail*

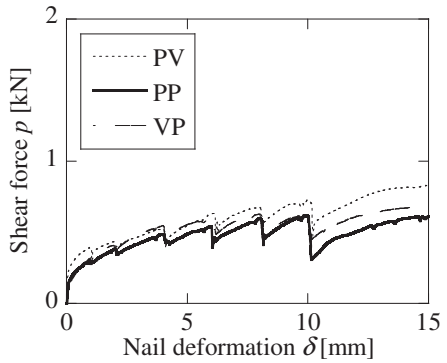

(b) *N45 nail*

Figure 12: *The skeleton curves for a single nail*

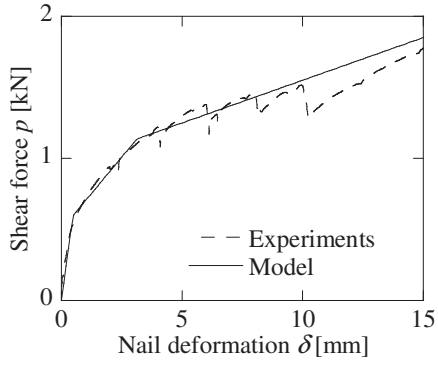

(a) *N90 nail*

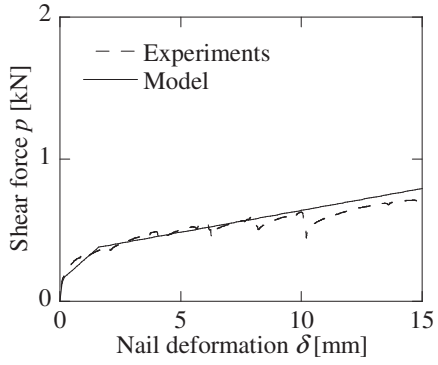

(b) *N45 nail*

Figure 13: *The shear force-deformation relationship for a single nail*

each floorboard to the centre of the specimen can be calculated from Equation (2). The symbol (*i*) represents the *i*-th board. The shrinkage $\delta_y(i)$ can be seen as the y-axis deformation of nails in the i-th floorboard. So, the total deformation δ can be calculated from Equation (3). Substituting the total deformation δ of the nail (*i*) into the nail shear force-deformation relationship constructed in Chapter 4.1, the total shear force of the nail $p_{45}(i)$ can be obtained. The x-axis and y-axis shear force $p_x(i)$ and $p_y(i)$ can be calculated from Equation (4) as shown in Figure 16. Then, the resistance moment M_n of the whole specimen can be obtained from Equation (5). Here, *m* is the number of nail joints per board (*m* = 5 for joist floor specimen FJ). The friction force between the boards is then calculated from the y-component $p_y(i)$ (Equation (4)) and the coefficient of friction. The frictional force $p_f(i)$ acting on the *i*-th plate, as shown in Figure 17, can be obtained from the difference between the upper and lower plate frictional forces from Equation (6). The resisting moment M_f can be obtained from the frictional force $p_f(i)$ and the distance $h(i)$ from the centre of the floor specimen (Equation (7)). The resisting moments M_n and M_f divided by the height of specimen *H* are the resisting forces P_n and P_f (Equation (8)).

The simulation results for a friction coefficient μ of 0.3 are shown in Figure 18. The shear force P_b of the floor frame was the skeleton curve of the restoring force characteristics model of the floor flame specimen TS and TJ built in Chapter 3; the shear force $P_{(model)}$ of the floor specimen was calculated by adding P_b, P_n and P_f.

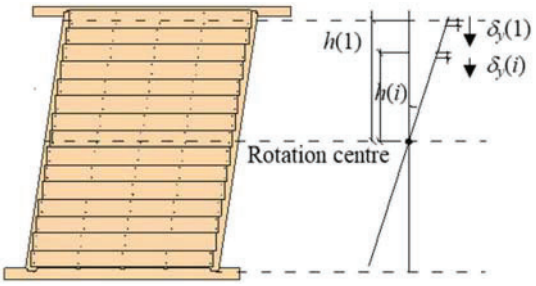

Figure 14: *y-axis deformation*

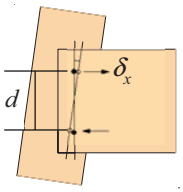

Figure 15: *x-axis deformation*

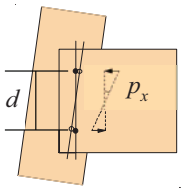

Figure 16: *x-axis force*

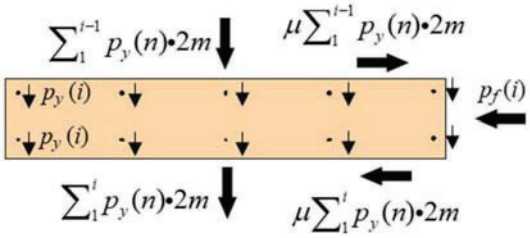

Figure 17: *Friction force caused by y-axis force $p_y(i)$*

$$\delta_x = \frac{d}{2}\sin R \tag{1}$$

$$\delta_y(i) = h(i)\ (1-\cos R) \tag{2}$$

$$\delta(i) = \sqrt{(\delta_y(i))^2 + (\delta_x)^2} \tag{3}$$

$$p_x(i) = p_{45}(i)\ \frac{\delta_x}{\delta(i)} \quad p_y(i) = p_{45}(i)\ \frac{\delta_y(i)}{\delta(i)} \tag{4}$$

$$M_n = m\ \sum_{i=1}^{N} p_x(i)\ \frac{d}{2} \tag{5}$$

$$p_f(i) = 2m \cdot p_y(i)\ \mu \tag{6}$$

$$M_f = \sum_{i=1}^{N} p_f(i)\ h(i) \tag{7}$$

$$P_n = M_n / H \qquad P_f = M_f / H \tag{8}$$

The shear force $P_{(exp)}$ was the skeleton curve of the restoring force characteristics model built in Chapter 3. The figure shows that $P_{(model)}$ and $P_{(exp)}$ of the FS specimen corresponded approximately. The load was carried by the floor flame during micro-deformation. The frictional force P_f increased gradually with increasing deformation angle. From *R* = 1/30 rad, the shear force of the floor flame decreased due to cracks in the dovetail joints, so the shear force of the floor specimens was borne by the nails and frictional forces.

On the other hand, for the specimen FJ, the difference between the model and the experimental result for the initial stiffness was significant. Predictive formula for skeleton curves of Joist floor should take further consideration.

5 CONCLUSIONS

In this research, we have used static loading tests on traditional wooden buildings floors to develop highly accurate models of restoring force characteristics for two types of floors. In addition, the shear force-deformation models of a single nail has been used to build a mechanical model that can estimate the skeleton curve of the floor. The results indicated that

1) There are significant differences in restoring force characteristics of two different floors.
2) DS models can accurately represent the restoring force characteristics of the experiments.
3) Established predictive formula can simulate the skeleton curve of Non-joist floor with the shear force-deformation models of a single nail.

ACKNOWLEDGEMENT

The authors would like to thank Y. Kimoto for his assistance through this research. This research is supported by JSPS Grants-in-Aid for Scientific Research JP19H00793. Part of this work was supported by JST SPRING, Grant Number JPMJSP2110.

https://doi.org/10.52202/069179-0444

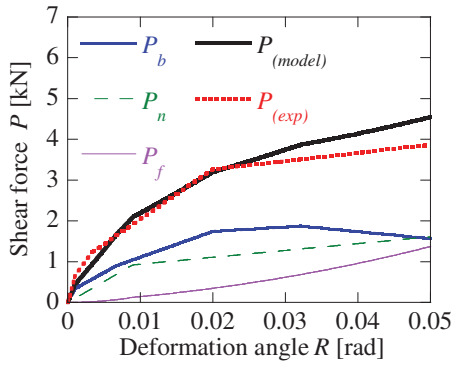

(a) *Specimen FS*

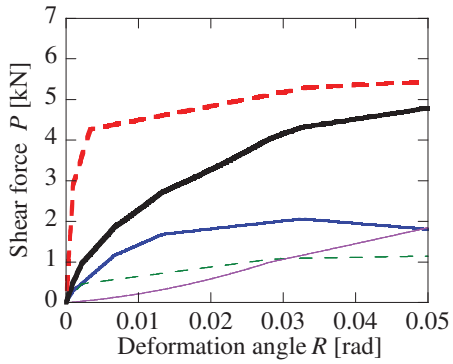

(b) *Specimen FJ*

Figure 18: *Simulation results for a friction coefficient μ of 0.3*

REFERENCES

[1] T. Kamada and D. Fukumori: Bearing Characteristics for Shearing Deformation of Floor Systems of Traditional Wooden Houses. Bulletin of Faculty of Engineering, Fukuyama University, 31:131-138, 2007. (in Japanese)

[2] M. Minami, A. Kitamori, K. Jung and K.Komatsu: Shear Peformances of the Floor System Using Japanese Cedar Planks. Japan's Journal of Structural and Construction Engineering, Vol.74, No.644:1785-1793, 2009. (in Japanese)

[3] A.Takino, Y.Azumi, S.Okamoto, T. Nakagawa, T.Shibutani and M.Murakami: Formula to Predict the Shear Peformance of Floor Construction of Traditional Wooden Structures Considering the Increasing Strength Based on Friction. Japan's Journal of Structural and Construction Engineering, Vol.79, No.703:1329-1336, 2014. (in Japanese)

[4] T.Morii, M.Miyamoto, H.Takahashi and Y.Hayashi, Influence of P-Δ Effects on Deformation Capacity of Wooden Frames Structure. Japan's Journal of Structural and Construction Engineering, Vol.75, No.650:849-857, 2010. (in Japanese)

[5] J.Nezaki, R.Fu, M.Sugino, and Y. Hayashi: Modeling and Respond Analysis of Resilience Characteristics of Traditional Japanese Wooden Frame structure with Earthen Walls Part 1: Modeling Methods for Resilience Characterics. In: Annual Conference Proceedings of the Architectural Institute of Japan, Structure II, 261-262, 2022. (in Japanese)

World Conference on Timber Engineering Oslo 2023

INFLUENCE OF PLASTERBOARD ON THE STRUCTURAL PERFORMANCE OF TIMBER-FRAMED SHEAR WALLS

Craig J.L. Cowled[1], Tom P. Slattery[2], Keith Crews[3], Harrison Brooke[4]

ABSTRACT: Timber-framed shear walls are commonly used in residential buildings to provide lateral strength and stiffness against wind and earthquake loads. Wood-based panel products, such as plywood and oriented strand board, are typically fixed to timber framing with nails or screws to provide the necessary racking resistance of a shear wall. Plasterboard is a panel product used on walls to achieve a smooth finished surface. Plasterboard provides some strength and stiffness to the wall even though its primary function is architectural; however, most shear wall tests ignore the influence of plasterboard. The aim of this study is to quantify the influence of plasterboard on the structural performance of timber-framed shear walls. To achieve this aim, six (6) timber-framed shear walls (groups P1 and P2) were fabricated with 7mm F8 plywood sheathing on one side and 10mm plasterboard on the other side and tested under a monotonic loading protocol. Results were then compared with previous test results of three (3) similar timber-framed shear walls (group M1) without plasterboard. Results show that plasterboard improved the ultimate racking strength of these shear walls by up to 53%, a statistically significant result. Shear wall stiffness and failure modes were not affected by adding plasterboard.

KEYWORDS: Shear wall; Plasterboard; Monotonic loading

1 INTRODUCTION

Timber-framed shear walls do the important work of resisting racking forces from wind and earthquake that act on buildings. These shear wall systems usually comprise wood-based panel products, such as plywood or oriented strand board (OSB), nailed or screw-fixed to the structural timber framing. Shear wall systems then get tested in a laboratory to find their racking strength and stiffness and the data collected in these tests is used to justify their design rating. It is common practice to use only structural elements in a test panel, such as timber framing, sheathing, connectors, tiedowns and anchors. Plasterboard, also known as gypsum board or drywall, is rarely attached to laboratory test panels even though it is ubiquitous in residential construction and known to provide some strength and stiffness (*e.g.*, [1,2]).

Here, we report on our experimental test plan to quantify the influence of plasterboard on the structural performance of timber-framed shear walls. Following a brief literature review, the test method is described. Results are presented and compared to previous work [3] on timber-framed shear walls without plasterboard. Analysis and discussion highlights the additional capacity of timber-framed shear walls due to plasterboard.

2 LITERATURE REVIEW

The contribution of plasterboard to the racking resistance of residential buildings is formally recognised in the Australian Standard AS1684.2:2021 [4] where cl.8.3.6.2 allows for a design racking capacity of 0.45 kN/m if one side of the wall is sheeted and 0.75 kN/m if both sides of the wall are sheeted up to a maximum of 50% of the total racking resistance requirement for the building.

Wolfe [5] conducted an early comparison of walls with solid timber diagonal braces checked into studs. Wolfe found that gypsum wallboard improved the strength of these walls by as much as 300% and improved stiffness by as much as 400%.

Patton-Mallory *et al.* [1] tested several combinations of walls with plywood and gypsum board. They found that walls with plywood on one side and gypsum board on the other side outperformed walls with plywood only on one side by 30% – 40%. They did not report on stiffness.

Of note, both Wolfe [5] and Patton-Mallory *et al.* [1] found that the overall capacity of the shear walls could be predicted accurately by summing the capacity of the component parts of the system.

Liew *et al.* [2] found that walls with plasterboard fixed on one side of the shear wall using screws, but no adhesive, achieved ultimate capacities of 2.0 – 3.5 kN/m. This result is far better than the nominal design capacities in AS1684 [4].

[1] Craig J.L. Cowled, Queensland University of Technology, Faculty of Engineering, Australia, craig.cowled@qut.edu.au
[2] Tom P. Slattery, Queensland University of Technology, Faculty of Engineering, Australia, thomas.slattery@hdr.qut.edu.au
[3] Keith Crews, University of Queensland, Future Timber Hub, Australia, k.crews@uq.edu.au
[4] Harrison Brooke, Engineered Wood Products Association of Australasia, Australia, harrison.brooke@ewp.asn.au

https://doi.org/10.52202/069179-0445

Uang and Gatto [6] found that adding plasterboard to an OSB or plywood sheathed shear wall improved ultimate strength by 6% - 18% and improved stiffness by 30% - 90%. They also found that adding plasterboard altered the failure mode of the shear walls from the sheathing-to-timber connections to the framing timber itself.

Satheeskumar *et al.* [7] conducted simulated wind load tests on a full-size house building. The building was tested in two different conditions: 1) with structural elements only, and 2) with architectural claddings such as plasterboard and cornices. They found that plasterboard and cornices contributed about 40% of rigidity to the building.

This literature review shows that plasterboard does, in fact, contribute to the structural performance of timber-framed buildings; however, further work is needed to quantify the influence of plasterboard on typical shear wall systems that are in use in Australia.

3 DESCRIPTION OF TEST PANEL

Our standard test panel is 2700 (h) × 2400mm (l) with plywood sheathing fixed to one side of the panel and plasterboard fixed to the other side of the panel. Timber framing is kiln dried (KD) MGP10 *pinus radiata* with 90 × 35mm studs at 600mm spacings and 90 × 45mm top and bottom plates. Timber is sorted by density into four groups (*i.e.*, high, medium, low, and very low density). Timber framing for the three (3) P2 test panels is taken from sorted very low-density timber and is representative of the JD5 joint group. Timber framing for the three (3) P1 test panels is taken from sorted low, medium, and high-density timber to ensure that a broad range of densities are represented (nominally JD4 joint group). Joint groups for different species are defined in Australian standards for the purpose of joint design.

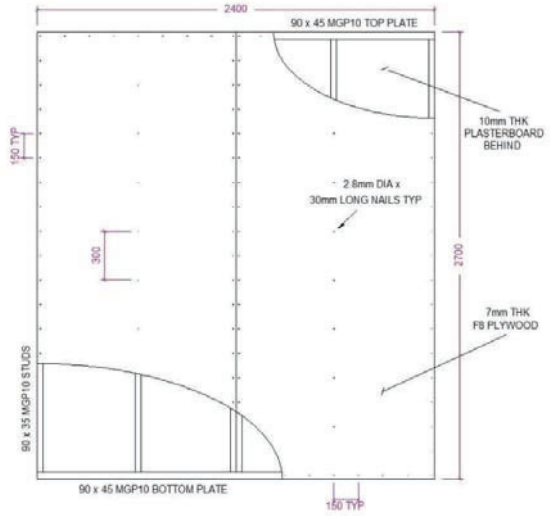

Figure 1: *Typical Test Panel (Plywood side).*

Plywood sheets are 2700 (h) × 1200mm (l) × 7mm thick F8 plywood sheathing consisting of three (3) veneers of radiata pine with a D grade face and back glued together with a phenolic A bond resin. The plywood sheets are connected to the timber framing with 2.8 (ϕ) × 30mm (l) galvanised clouts at 150mm spacings around the edges of the sheets and 300mm spacings at intermediate studs (Figure 1). The nail pattern precisely follows Detail (h) of Table 8.18 in AS1684.2 [4].

Plasterboard sheets are 1350 (h) × 2400mm (l) × 10mm thick randomly selected off the shelf from three (3) different Australian manufacturers. The plasterboard sheets are connected to the timber framing with 6g × 25mm (l) screws (*i.e.*, 3.5mm (ϕ)) at 270mm spacings and no adhesive (Figure 2).

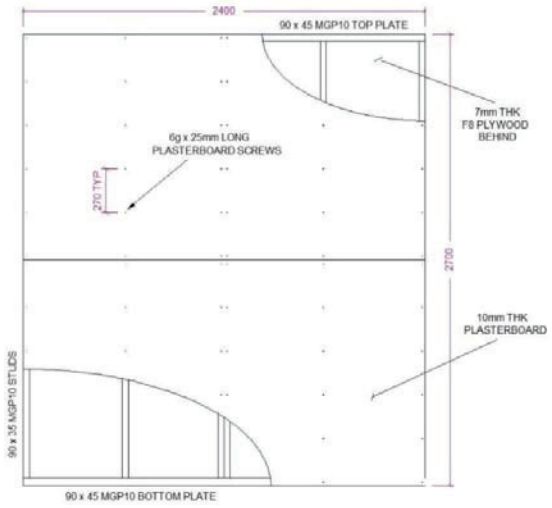

Figure 2: *Typical Test Panel (Plasterboard side).*

To resist sliding, the test panels were anchored to a steel floor beam with 3M12 bolts through the bottom plate at 1200mm spacings. To resist overturning the test panels were secured with an M12 tiedown rod from the top plate nearest the ram end. 50 × 3mm square washers were used with each bolt and tiedown rod.

The test panels in this study are almost identical to the test panels in the loading protocol study by Cowled, Crews, and Gover [3] with two exceptions: 1) plasterboard was not used in the previous study, and 2) the timber framing in the previous study was sourced from the Southern Queensland pine resource, which is either *pinus elliottii* var. *elliottii* (a.k.a. slash pine), *pinus caribaea* var. *hondurensis*, or a hybrid of the two species. Material properties of these species are comparable to those of radiata pine. These timber species have similar strength grades. Slash pine and Caribbean pine have a slightly higher density than radiata pine (*i.e.*, 650 kg/m^3 and 575 kg/m^3 respectively compared to 550 kg/m^3 for radiata pine). Slash pine has a better rated joint group (*i.e.*, nominally JD4 compared to nominally JD5 for radiata pine and Caribbean pine) [8]. All other aspects of the test setup, including tiedowns and anchors are identical to the test setup in [3]. The loading mechanism and loading protocol used in this study is identical to that used on test group M1 in [3].

https://doi.org/10.52202/069179-0445

4 TEST METHOD

Test panels P1.1 and P2.1 were tested with a simple displacement-controlled monotonically ramping load at 10 mm/min similar to the method outlined in EN 594 [9]. Results from testing of P1.1 and P2.1 were used to select a suitable design load of 7.2 kN/m and 6.9 kN/m respectively which were then used to test the remaining panels according to the load-controlled method described in [3] for test group M1, which is consistent with the prototype test method in Appendix D of AS1720.1 [10].

A 500kN MOOG hydraulic actuator was used to apply the load at the top plate. Three (3) linear variable displacement transducers were used to capture sliding at the toe of the wall (Δ_4) and overturning (Δ_2 and Δ_3). Two (2) laser sensors, mounted on an independent steel frame, were used to capture the horizontal displacement at the top of the wall (Δ_1). The test setup is shown in Figure 3.

Figure 3: *Test Panel P2.1.*

Since the data from the laser sensors is not clean, the displacement used for plotting has been measured at the hydraulic actuator and adjusted to match the laser data using a nonlinear least squares optimisation algorithm. Adjusted displacement then is:

$$\Delta_{adj} = \alpha \cdot \Delta_1 \tag{1}$$

where α is the multiplier obtained from curve-fitting using the nonlinear least squares optimisation described above. Racking displacement can also be corrected to remove the sliding and overturning components to obtain the shear component of the displacement:

$$\Delta_s = \Delta_1 - \Delta_4 - (\Delta_2 - \Delta_3) \cdot \frac{h}{l} \tag{2}$$

where, h and l are the height and length of the test panel.

5 RESULTS

Load – adjusted displacement (Δ_{adj}) plots for the P1 (blue lines) and P2 (red lines) groups of test panels are presented in Figure 4 along with those of the M1 group of test panels from [3] (black lines).

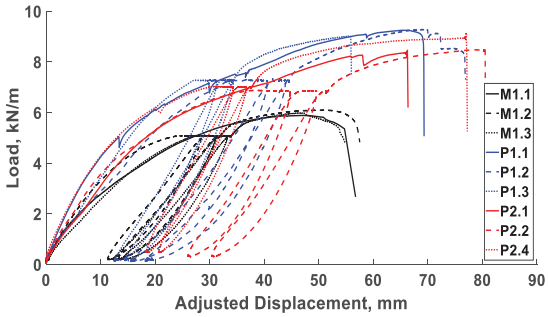

Figure 4: *Load – Adjusted Displacement Plots for Groups M1 (plywood only) [3], P1 (plywood & plasterboard), and P2 (as per P1 except with very low-density timber).*

The clearest observation from this plot is that plasterboard significantly improves the ultimate capacity of plywood braced shear walls. Initial stiffness also appears to be higher in the P1 and P2 groups compared to the M1 group; although, this relationship is not as clear when load is plotted against global displacement or corrected racking displacement.

Structural performance characteristics have been calculated in this paper in accordance with the methods outlined in ASTM E2126 [11]. The maximum load obtained is P_{ULT}. The global secant shear modulus is calculated at $0.4 \times P_{ULT}$:

$$G' = \frac{P}{\Delta_e} \times \frac{h}{l} \tag{3}$$

where P and Δ_e are the load in kN and displacement in mm at $0.4 \times P_{ULT}$ where global displacement is used (*i.e.*, including components of shear, overturning, and sliding). The internal secant shear modulus, calculated at $0.4 \times P_{ULT}$, uses the corrected shear displacement, Δ_s, from (2):

$$G_{int} = \frac{P}{\Delta_s} \times \frac{h}{l} \tag{4}$$

The yield load is found by deriving an equivalent energy elastic-plastic (EEEP) curve from the global load – displacement curve.

$$P_y = \left(\Delta_u - \sqrt{\Delta_u^2 - \frac{2A}{K_e}} \right) K_e \tag{5}$$

where, A is the area under the load – global displacement curve, Δ_u is the ultimate displacement (*i.e.*, corresponding to the last data point on the load – displacement curve where the absolute load is equal to or greater than $0.8 \times P_{ULT}$, K_e is the elastic shear stiffness equal to $(0.4 \times P_{ULT})/\Delta_e$.

https://doi.org/10.52202/069179-0445

The ductility ratio is:

$$D = \frac{\Delta_u}{\Delta_y} \quad (6)$$

where, Δ_y is the global displacement taken from the EEEP curve at P_y.

Structural performance characteristics for the P1 and M1 group of test panels are presented in Table 1 below.

The P1 group of test panels, which were fabricated with plywood on one side and plasterboard on the other side, achieved a mean ultimate strength of 9.18 kN/m and a tight variance (σ = 0.12 kN/m). The P2 group of test panels, which were identical to the P1 group except for having very low-density timber framing, achieved a mean ultimate strength of 8.72 kN/m (σ = 0.39 kN/m). Both results are significantly higher (53% & 46% respectively) than the mean ultimate strength of 5.99 kN/m for the M1 group of test panels in [3] (σ = 0.10 kN/m), which were fabricated without plasterboard and tested in the same laboratory with identical boundary conditions and the same loading protocol. The higher ultimate and yield strength of the P1 and P2 groups of test panels, as compared to the M1 group, is statistically significant with a *p*-value of 0.05 on a one-sided Wilcoxon ranksum test.

Table 1: *Results*

Test Panel	P_{ULT} (kN/m)	P_y (kN/m)	G' (kN/mm)	G_{int} (kN/mm)	D
M1.1	5.89	5.39	1.05	3.15	6.03
M1.2	6.09	5.47	1.01	1.55	3.90
M1.3	5.98	5.36	0.77	2.10	3.03
μ	**5.99**	**5.41**	**0.95**	**2.27**	**4.32**
σ	0.10	0.06	0.15	0.81	1.54
P1.1	9.25	7.87	1.35	2.62	4.57
P1.2	9.29	8.09	0.73	2.04	2.60
P1.3	9.02	7.90	0.95	2.32	2.56
μ	**9.18**	**7.96**	**1.01**	**2.33**	**3.24**
σ	0.12	0.09	0.26	0.24	0.94
P2.1	8.46	7.31	0.87	0.56	3.04
P2.2	8.53	7.11	1.13	2.87	4.89
P2.4*	9.16	7.76	1.34	2.52	5.12
μ	**8.72**	**7.39**	**1.12**	**1.99**	**4.35**
σ	0.39	0.34	0.24	1.24	1.14

* Data unavailable for test panel P2.3, so panel P2.4 was made.

Curiously, plasterboard did not improve the global and internal stiffness of the test panels in this study. This finding contradicts previous studies which found that plasterboard improved stiffness [5,6,7].

The in-group variance of ductility is high enough to make the higher ductility of the M1 group seem unremarkable.

Failure modes were similar between the test panels in this study and the M1 group of test panels. The primary mode of failure in all groups was nail pullout of the plywood-to-timber connection (see Figure 5). Two nail pull-through failures were observed in test panel M1.1 because this panel failed dramatically under load control. Timber fractures were observed in P1.1 (top of the end stud) and P1.2 (bottom plate near the heel of the wall, see Figure 6). Tearing of the plywood was observed at one nail in P1.2 and two nails in P2.4. The plasterboard in the P1 and P2 groups of test panels experienced localised crushing of the plasterboard at the screw holes, pull-through failures, and some tearing of the plasterboard at the corners (see Figure 7).

Figure 5: *Nail Pullout, Test Panel P1.1.*

Figure 6: *Timber Fracture, Test Panel P1.2.*

Figure 7: *Plasterboard Damage, Test Panel P2.1.*

6 DISCUSSION OF LIMIT STATES

The shear wall system in this study is described as Method A of Detail (h), Table 8.1, AS1684.2 [4] and it has a published design capacity of 5.6 kN/m.

A similar shear wall system was originally tested in 1975 by Frodin and Ross [12], following a devastating cyclone in Darwin the previous year. Differences between test panel TP4 in [12] and the M1 group of test panels in [3] include the use of unseasoned hardwood timber framing instead of KD pine, 3.18mm (ϕ) clouts instead of 2.8mm (ϕ) clouts, studs at 450mm spacings instead of 600mm spacings, a panel height of 2.4m instead of 2.7m, a panel length of 2.7m instead of 2.4m, and the use of steel strapping at the corners of test panel. TP4 in [12] achieved an ultimate strength of 9.72 kN/m.

Several decades later, C.G. 'Mick' McDowall [13] tested panel TP2, which differed from the M1 group of test panels from [3] in only one respect; that is, TP2 in [13] was 2.4m high compared to the 2.7m high M1 group of test panels in [3]. TP2 in [13] achieved an ultimate strength of 8.21 kN/m.

It should also be noted that the loading protocols in [12] and [13] differed to the loading protocol used for the M1 group of test panels in [3] with design loads for TP4 in [12] being 2.07 kN/m (held for 5 min) and 2.87 kN/m (held for 5 min) and the design load for TP2 in [13] being 4 kN/m (held only once for 5 min); whereas, test panels M1.2 and M1.3 in [3] held a design load of 5 kN/m twice for 5 min. As argued in [3], the use of different loading protocols may have influenced results.

Adopting Mick McDowall's 2004 methodology [13] for determining limit state design values, also described in [3], the upper limit for the factored design strength of this wall system, based on TP2 from [13], would be:

$$Q^* = 0.8 \times 8.21 = 6.57\ kN/m \tag{7}$$

This result exceeds the design value of 5.6 kN/m in AS1684.2 [4] by 17%; however, the more recent work by Cowled, Crews, and Gover [3] raised concerns because it found that the factored design strength of this system, based on the M1 group of test panels, was 14% lower than the published design value:

$$Q^* = 0.8 \times \frac{5.89 + 6.09 + 5.98}{3} = 4.79\ kN/m \tag{8}$$

The work in the current study reassures us that, when architectural finishes such as plasterboard are considered, the design strength of this system does, in fact exceed the published design values. For this shear wall system an appropriate design load exceeds the published design load of 5.6 kN/m by 28%:

$$Q^* = 0.8 \times \frac{\begin{matrix}9.25 + 9.29 + 9.02 + \ldots \\ \ldots 8.46 + 8.52 + 9.16\end{matrix}}{6} = 7.16\ kN/m \tag{9}$$

7 CONCLUSIONS

We have presented here the findings of our study into the influence of plasterboard on the structural performance of timber-framed shear walls tested in accordance with the monotonic load-controlled test method outlined in AS1720.1 [10]. Test panels were 2700 (h) × 2400mm (l) using MGP10 framing and 7mm thick F8 radiata pine plywood sheathing fixed with 2.8 (ϕ) × 30mm (l) galvanised clouts at 150mm spacings around the edges of each panel and 300mm spacings along the intermediate stud. The P1 ($n = 3$) and P2 ($n = 3$) groups of test panels in this study also had 10mm thick plasterboard fixed to the other side with 6g × 25mm (l) plasterboard screws at 270mm spacings. The P2 group of test panels were fabricated with very low-density timber framing (nominally JD5 joint group) whereas the P1 group of test panels were fabricated with timber from a range of densities (nominally JD4 joint group). Results of this study were compared to the M1 group of test panels in a previous study [3] ($n = 3$) which did not have plasterboard attached. Test conditions, including tiedowns, anchors, and loading protocol, were identical for both the P1 and M1 group of test panels.

We found that plasterboard improves the ultimate and yield strength of timber-framed plywood-braced shear walls by 37% to 53%; however, stiffness and ductility are unaffected by the addition of plasterboard in this study.

Since the published capacities of timber-framed shear walls are primarily based on testing of panels without plasterboard cladding, as is the case for shear wall systems described in Table 8.1 of AS1684.2 [4], our findings provide the construction industry with confidence.

ACKNOWLEDGEMENT

The work presented here was supported by scholarships awarded to TS, including an Australian Government Research Training Program Scholarship and an industry top-up scholarship by Australian Panel Products, Engineered Wood Products Association of Australasia (EWPAA), Pryda Australia, and One Forty One.

Materials were kindly provided by One Forty One, Carter Holt Harvey, and an Advance Queensland A&TSI Research Fellowship awarded to CC, which was funded by the Queensland State Government, the EWPAA, and Queensland University of Technology (ATSIRF00817-18RD3). Test panels were fabricated by Bretts Timber & Hardware.

We also wish to thank the staff at QUT's Banyo Pilot Plant Precinct where the experimental work was done. Frank De Bruyne, Cameron Creevey, Barry Hume, Glenn Atlee, and Zeph Kadel have all made this project possible and their contribution is highly valued.

REFERENCES

[1] Patton-Mallory, M., Gutkowski, R.M., Soltis, L.A.: *Racking Performance of Light-Frame Walls Sheathed on Two Sides* (Research Paper FPL 448). Forest Products Laboratory, Madison, Wisconson, U.S., 1984.

[2] Liew, Y.L., Duffield, C.F., Gad, E.F.: The influence of plasterboard clad walls on the structural behaviour of low rise residential buildings. *Electron. J. Struct. Eng.*, 2:1-16, 2002.

https://doi.org/10.52202/069179-0445

[3] Cowled, C.J.L., Crews, K., Gover, D. Influence of loading protocol on the structural performance of timber-framed shear walls. *Const. Build. Mater.*, 288:123103, 2021.
[4] AS 1684.2:2021. *Residential timber-framed construction – Part 2: Non-cyclonic areas.* Standards Australia, Sydney, Australia, 2021.
[5] Wolfe, R.W. *Contribution of Gypsum Wallboard to Racking Resistance of Light-Frame Walls* (Research Paper FPL 439). Forest Products Laboratory, Madison, Wisconson, U.S., 1983.
[6] Uang, C.-M., Gatto, K. Effect of Finish Materials and Dynamic Loading on the Cyclic Response of Woodframe Shearwalls. *J. Struct. Eng.*, 129(10):1394-1402, 2003.
[7] Satheeskumar, N., Henderson, D.J., Ginger, J.D., Humphreys, M.T., Wang, C.H. Load sharing and structural response of roof-wall system in a timber-framed house. *Eng. Struct.*, 122:310-322, 2016.
[8] Forest and Wood Products Australia Ltd. *WoodSolutions - Wood Species - Softwood*. https://www.woodsolutions.com.au/wood-species/softwood. 2023.
[9] EN 594:2011. *Timber structures – Test methods – Racking strength and stiffness of timber frame wall panels*. European Committee for Standardization, Brussels, Belgium, 2011.
[10] AS 1720.1:2010. *Timber structures – Part 1: Design methods*. Standards Australia, Sydney, Australia, 2010.
[11] ASTM E2126-11. *Standard Test Methods for Cyclic (Reversed) Load Test for Shear Resistance of Vertical Elements of the Lateral Force Resisting Systems for Buildings*. ASTM International, West Conshohocken, PA, 2018.
[12] Frodin, J., Ross, A.H. *CapCiv-2 – A Report on Shear Testing of Plywood Sheathed Wall Panels for the Plywood Association of Australia*. Capricornia Institute of Advanced Education, Rockhampton, Australia, 1975.
[13] McDowall, C.G. *Combined Racking and Uplift Test Results for Panels of DD and Less than DD Grade Plywood & Some Thoughts on Choosing Limit States*. Plywood Association of Australia, Brisbane, Australia, 2004.

World Conference on Timber Engineering Oslo 2023

EXPERIMENTAL CHARACTERIZATION OF CLT SHEAR WALLS CONNECTED TO PERPENDICULAR WALLS

Elisabetta Maria Ruggeri[1], Giuseppe D'Arenzo[2], Denise Li Cavoli[3], Ignazio Casiraro[4], Marinella Fossetti[5]

ABSTRACT: "Box-type" CLT buildings are realized by connecting CLT panels through dowel-type fastener and mechanical anchor connections, which govern the lateral behaviour of these structures. However, while a lot of investigations in literature have been focused on the behaviour of connections placed at the base of CLT shear walls, typically hold downs and angle brackets, less studies have been focused on the behaviour of connections between perpendicular walls and how their affect the lateral response of CLT shear walls. This paper presents some results of a large experimental campaign aimed at investigating the effects of the interaction provided by perpendicular walls on the lateral behaviour of CLT shear walls. The findings of this experimental study showed that the structural interaction due to the presence of perpendicular wall significantly influence the lateral response of a CLT shear wall and increase its lateral performances, such as the lateral stiffness, the lateral capacity and the deformation capacity.

KEYWORDS: CLT shear wall, Perpendicular walls, Experimental tests, Lateral performance, Structural interaction.

1 INTRODUCTION

The Lateral Load Resisting System (LLRS) of Cross-Laminated Timber (CLT) buildings is composed of the CLT shear walls along with their base connections, which are typically realized using hold downs and angle brackets. Several testing programmes have been conducted to explore the lateral performance of CLT shear walls [1–3] and the results of these experimental investigations showed that the wall base connections govern the cyclic behaviour of a CLT shear wall system and provide the necessary ductility and energy dissipation. However, the lateral behaviour of a CLT shear wall is also influenced by other connections that can be found in the perimeter of the CLT panels. In particular, these connections vary depending on the type of construction. In this regard, CLT building construction typologies can be distinguished in "shear wall-type", in which the shear walls are not connected with the perpendicular walls in the corner of the building, and "box-type", in which the shear walls and the perpendicular walls are connected in the corner of the building by means of mechanical connections, see Figure 1.

The mechanical behaviour of CLT "box-type" buildings, especially those erected using the platform method, significantly depend on the effects of interactions between primary and secondary structural elements such as perpendicular walls, floor diaphragms, lintels and their mechanical connections, see for instance [4–9].

Concerning the "box-type" buildings, the influence of the perpendicular walls and the wall-to-wall connections is an issue of special interest. The effect of the interactions between the shear walls and the perpendicular walls on the lateral behaviour of CLT buildings was found in several numerical and experimental studies [10–13]. However, if from one side the effects of these interactions were found to be significative, from the other side no significant efforts were undertaken so far to investigate the effects of the interactions between CLT shear walls and perpendicular walls.

This paper presents an experimental campaign aimed at investigating the lateral response of CLT shear walls connected to perpendicular walls by means of typical screwed wall-to-wall connections. The main objective of this study is to quantify the increase of lateral performances of CLT shear walls as a result of their interactions with perpendicular walls.

[1] Elisabetta Maria Ruggeri, Faculty of Engineering and Architecture, "Kore" University of Enna, Italy, elisabettamaria.ruggeri@unikorestudent.it
[2] Giuseppe D'Arenzo, Timber Structures and Building Rehabilitation, University of Kassel, Germany, giuseppe.darenzo@uni-kassel.de
[3] Denise Li Cavoli, Faculty of Engineering and Architecture, "Kore" University of Enna, Italy, denise.licavoli@unikorestudent.it
[4] Ignazio Casiraro, Faculty of Engineering and Architecture, "Kore" University of Enna, Italy, and Department of Civil Engineering and Architecture, University of Catania, Italy, ignazio.casiraro@unikorestudent.it
[5] Marinella Fossetti, Faculty of Engineering and Architecture, "Kore" University of Enna, Italy, marinella.fossetti@unikore.it

https://doi.org/10.52202/069179-0446

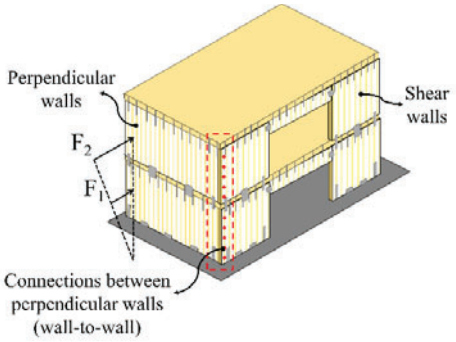

Figure 1: *Representation of a "box-type" CLT building.*

2 EXPERIMENTAL TEST PROGRAM

2.1 MATERIALS AND CONFIGURATIONS

The experimental tests presented in this study were carried out at L.E.D.A. Research Centre of the University of Enna "Kore" (Italy). CLT panels used during the tests consisted of five-layered panels with a total thickness equal to 100 mm and layer thicknesses of **20**-20-**20**-20-**20** mm (in bold the thickness of the layers arranged in the vertical direction). Hold-downs (HDs) type WHT340 [14] were used to anchor the wall panels against rocking displacements. These connectors were fastened in the vertical flange by means of twelve annular ringed nails 4×60 mm [15] and anchored to the foundation through one M16 bolt strength class 8.8. Whereas, angle brackets (ABs) type WBR90110 [14] were used to anchor the shear wall against sliding displacements. These connectors were fastened in the vertical flange by means of thirteen annular ringed nails 4×60 mm [15] and anchored to the foundation by means of two M12 bolts strength class 8.8. Self-tapping screws HBS 10×200 mm [16] were used to join the perpendicular wall with the shear wall. These connections, which were positioned to span across at least two layers of the perpendicular wall panel, were installed with a spacing of 250 mm, resulting in a total number of wall-to-wall connections equal to ten. Hold-downs, angle brackets and self-tapping screws were produced by Rothoblaas. In Figure 2 the connections used for the experimental tests are shown.

Two CLT wall assembly configurations were considered to investigate the lateral performance of CLT shear walls connected to CLT perpendicular walls: single Shear Wall configuration (SW), see Figure 3 (a), which considers a single CLT shear wall subjected to lateral load, and Shear Wall connected to a Perpendicular Wall configuration (SW+PW), see Figure 3 (b), which considers the same CLT shear wall subjected to lateral load connected to a perpendicular wall positioned at the end of the shear wall. All shear wall specimens were made of monolithic wall panels with dimensions equal to 250×250 cm. Each shear wall was anchored at base with two hold-downs located at the extremities of the wall panels and four angle brackets distributed along the shear wall length, see Figure 3 (a) and (b). Whereas, specimens of perpendicular walls consisted of monolithic wall panels with dimensions equal to 50×250 cm, each of which was anchored at the base with one hold-down, see Figure 3 (b).

a) b) c)

Figure 2: *Connections used for the experimental tests:(a) hold-down WHT340, (b) Angle bracket WBR90110, (c) HBS 10×200 mm.*

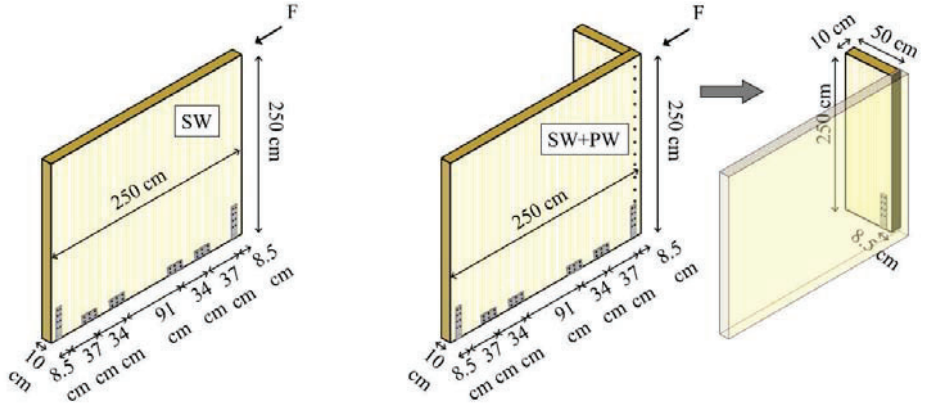

a) b)

Figure 3: *CLT wall assembly configurations and geometries (measures in cm): (a) Single Shear Wall configuration (SW), (b) Shear Wall connected to a Perpendicular Wall configuration (SW+PW).*

https://doi.org/10.52202/069179-0446

In total four experimental tests are presented in this study, including one monotonic and one cyclic test for each configuration. An overview of the experimental tests is given in Table 1.

Table 1: *Overview of the experimental tests*

ID test	Test type
SW_2.50	1 Monotonic
	1 Cyclic
SW+PW_2.50	1 Monotonic
	1 Cyclic

2.2 LOAD PROTOCOLS AND TEST SET UP

Monotonic tests were performed in displacement control with the imposed displacement increasing at a constant rate of 0.10 mm/sec, see Figure 4 (a), according to the standard procedure EN594 [17]. The cyclic tests were also performed in displacement control with a rate between 0.05 and 0.25 mm/sec, depending on the displacement level, according to the standard procedure in EN12512 [18], see Figure 4 (b). In order to study the lateral behaviour of the shear wall-perpendicular wall systems using fewer parameters, all tests were performed by applying the horizontal load without applying any vertical load.

The monotonic and the hysteretic parameters of the shear wall tests were evaluated according to EN12512 [18]. The mechanical parameters evaluated from the load-displacement curves of the monotonic tests are the yielding load F_y, yield displacement V_y, maximum load F_{max}, maximum displacement V_{max}, ultimate load F_{ult}, ultimate displacement V_{ult}, ductility D, and elastic stiffness K_{el}, which was calculated as the slope between 10% and 40% of the maximum load. The same parameters were assessed for backbone curves obtained from the cyclic tests, for both positive and negative displacements. The hysteretic parameters evaluated from the cyclic tests are the dissipated energy E_d, the equivalent viscous damping v_{eq} and the normalised impairment of strength between the first and third cycles $\Delta F_{1\text{-}3}$.

Figure 5 (a) and (b) shows photos of the test set-up for both SW_2.50 and SW+PW_2.50 configurations. The lateral load was applied by means of a 300 kN hydraulic actuator. In particular, the lateral load was distributed on the shear wall panel by means of a steel beam IPE 160 type, properly drilled and fastened to the top of the shear wall panel with 24 10×200 mm self-tapping screws. The CLT walls were anchored, through the hold-downs and the angle brackets described in the previous section, to two steel beams HEB 220 type, properly drilled, used to simulate the foundation (see Figure 5). Linear variable displacement transducers (LVDTs) were used to measure vertical and horizontal displacements at different locations of the specimens. Three LVDTs for measuring uplifts of shear wall and perpendicular wall were placed in lower corners of both shear wall and perpendicular wall. One LVDT was placed in the lower corner of the shear wall for measuring the horizontal base displacement. The horizontal head displacement of the shear wall was measured with an LVDT placed on an external steel structure, while another LVDT was used to monitor the horizontal displacement of the steel beam representing the foundation (HEB 220).

The horizontal displacement at the top of the shear wall was obtained by subtracting the horizontal displacement of the steel beam representing the foundation (HEB 220) from the horizontal displacement measured by the LVDT placed on the shear wall head. In order to avoid the out-of-plane movements of the CLT panels, a steel frame system was used.

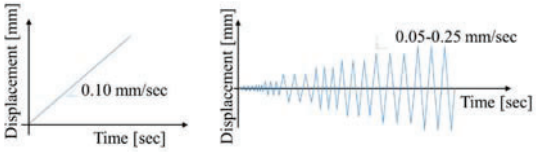

a) b)

Figure 4: *Loading protocol for (a) monotonic and (b) cyclic tests.*

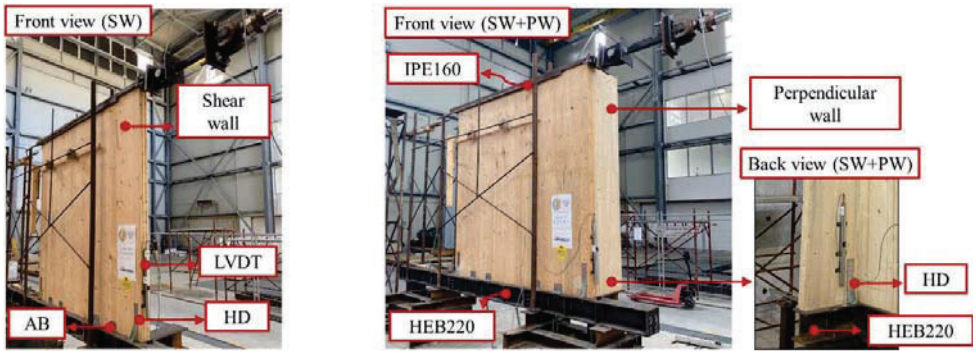

a) b)

Figure 5: *Photos of test set-up: a) SW configuration, b) SW+PW configuration.*

https://doi.org/10.52202/069179-0446

3 EXPERIMENTAL RESULTS

Figure 6 (a) and (b) show some photos of the specimens at the end of the tests, for the two configurations SW_2.50 and SW+PW_2.50, respectively.

During the tests, the top lateral displacement of the systems was mainly governed by a combination of sliding and rocking mechanism with a predominant rocking. In particular, CLT panels behaved almost as rigid bodies and the deformations occurred in the joint between CLT panel and wall base connections.

As shown in Figure 7, deformations were observed at the base of the hold-downs (HDs) with failure mechanisms associated with the embedment of the wooden panel and failure of the nails of the vertical flange, with formation of plastic hinges. Moreover, some nails failed due to tearing of the nail head. As a result, the nail shank remained embedded in the CLT panel. Angle brackets (ABs) were capable of bearing both shear and tensile loads, but failures were observed in some instances in the nails of the vertical flange, resulting in the formation of plastic hinges. In some cases, failures were observed in both nails and bolts, see Figure 7. No failure was observed in the screws of the wall-to-wall connections.

A comparison between the hysteresis loops acquired from the cyclic tests and the load-displacement curves obtained from the monotonic tests for two test configurations, SW_2.50 and SW+PW_2.50, is shown in Figure 8 (a) and (b), respectively. Figure 8 (a) and (b) depict graphs indicating that the outcomes obtained from the cyclic test align with those from monotonic tests. From this figure, it can be observed the typical symmetrical hysteresis loops for positive and negative displacements in case of single shear wall configuration (SW).

a) b)

Figure 6: *Photos of the specimens at the end of the tests: a) SW_2.50, b) SW+PW_2.50.*

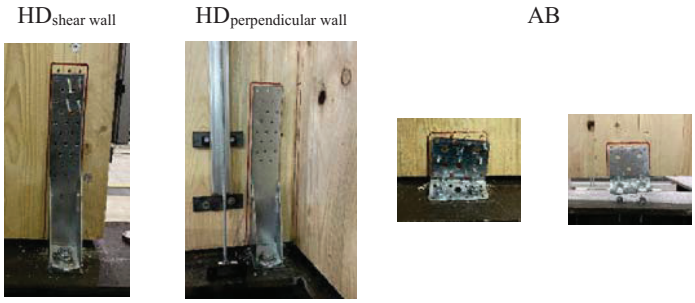

Figure 7: *Some photos of the connection failures.*

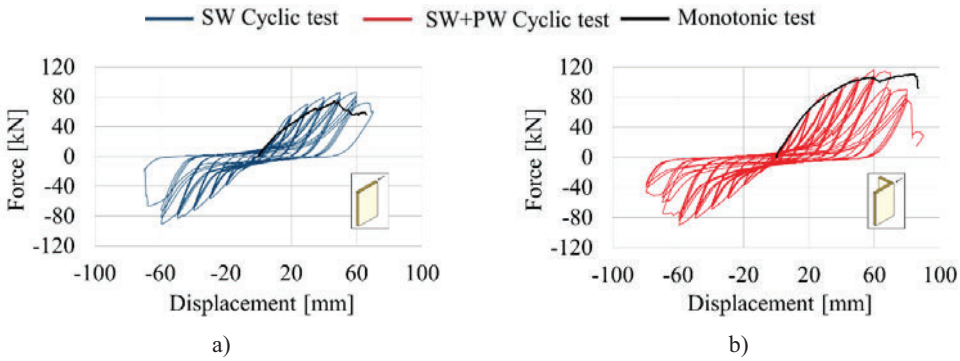

a) b)

Figure 8: *Comparison between hysteresis loops and load-displacement-curves from monotonic tests: a) SW_2.50, b) SW+PW_2.50.*

https://doi.org/10.52202/069179-0446

On the other hand, for the SW+PW configuration, asymmetric hysteresis loops describe a different behaviour of the system for positive and negative displacements. This asymmetric behaviour is due to the asymmetric distribution of the base connections, when the perpendicular wall is taken into account.
Table 2 presents the mechanical parameters evaluated for the load-displacement curves obtained from the monotonic tests, while the mechanical parameters evaluated from the backbone curves of the cyclic tests are shown in Table 3, for both range of positive and negative displacements.
The findings from both monotonic and cyclic tests indicate that the structural interactions due to perpendicular wall contributes to improve the lateral performance of the shear wall. In the next, the percentage of the increments are calculated, considering the average values between the results obtained from the load-displacement curves of the SW test (both monotonic and cyclic tests in the range of positive displacements) and the results obtained from the load-displacement curves of the SW+PW tests (both monotonic and cyclic tests in the range of positive displacements).Specifically, the average increases of the lateral stiffness (K_{el}) and the lateral capacity (F_{max}) of the SW+PW configuration respect to the case of SW configuration, are about 40% and 41%, respectively. Moreover, results show an increment of the deformation capacity (V_{ult}) in case of SW+PW configuration equal to 25%.
Figure 9 shows the displacement paths, evaluated for both monotonic and cyclic tests, of the hold-down placed at the base of the shear wall and of the hold-down placed at the base of the perpendicular wall. The graphs plotted in Figure 9 show that hold downs of shear wall and perpendicular wall are subjected to close vertical displacements, due to the effect of the interaction provided by the wall-to-wall connections. Figure 9 highlights therefore that perpendicular walls may act as a hold-down system and have a significant effect on the behaviour of the lateral load resisting system. This can also be seen from the photo in Figure 9, which shows the uplifts of both shear wall and perpendicular wall.
The outcomes in terms of hysteretic parameters are shown in Figure 10 (a) and (b). Results of the equivalent viscous damping v_{eq} and the normalised impairment of strength ΔF_{1-3} are plotted in graphs, which report in the horizontal axis the cycles and in the vertical axis the hysteretic parameters. The findings of cyclic tests show a maximum impairment of strength ΔF_{1-3} about 16.7% and 27.3% in case of SW and SW+PW configurations, respectively. Moreover, an average equivalent viscous damping v_{eq} of 7.2% and 9.2% was found for the SW and SW+PW configuration, respectively.
The comparison of the dissipated energy E_d between SW and SW+PW configurations, is presented in Figure 10 (c). In both configurations the dissipated energy follows a similar trend for all tests. The maximum values of dissipated energy E_d were equal to 25 and 42 kJ, in case of SW and SW+PW configuration, respectively.

4 CONCLUSIONS

This paper presented an experimental campaign aimed at investigating the lateral response of CLT shear walls connected to perpendicular walls by means of typical screwed wall-to-wall connections. The lateral performance of two configurations was investigated: SW, i.e. single shear wall, and SW+PW, i.e. shear wall connected to perpendicular wall.
The purpose was to compare the results obtained from these two configurations in order to evaluate the increases in lateral performances of the shear wall when the perpendicular wall is taken into account. The results of this study show that shear walls connected to perpendicular walls reach significative higher structural performance in terms of lateral stiffness, lateral capacity and deformation capacity than typical single shear walls.

Table 2: *Mechanical parameters evaluated from the load-displacement curves of monotonic tests*

Test conf.	K_{el} [kN/mm]	F_y [kN]	F_{max} [kN]	F_{ult} [kN]	V_y [mm]	V_{max} [mm]	Vv_{ult} [mm]	D [-]
SW_2.50	2.28	67.67	74.46	59.57	28.03	46.41	64.00	2.38
SW+PW_2.50	3.19	91.69	110.19	88.16	27.66	83.84	86.81	3.14

Table 3*: Mechanical parameters evaluated from the backbone curves of the cyclic test*

Conf. test	Displ.	K_{el} [kN/mm]	F_y [kN]	F_{max} [kN]	F_{ult} [kN]	V_y [mm]	V_{max} [mm]	V_{ult} [mm]	D [-]
SW_2.50	(+)	2.4	79.6	85.9	69.9	33.2	49.9	69.9	2.1
	(-)	2.0	-85.1	-90.0	-72.0	-42.7	-59.4	-65.0	1.5
SW+PW_2.50	(+)	3.4	96.6	115.7	92.6	26.9	59.9	81.0	3.0
	(-)	1.9	-85.1	-90.1	-72.0	-42.7	-59.3	-75.0	1.7

https://doi.org/10.52202/069179-0446

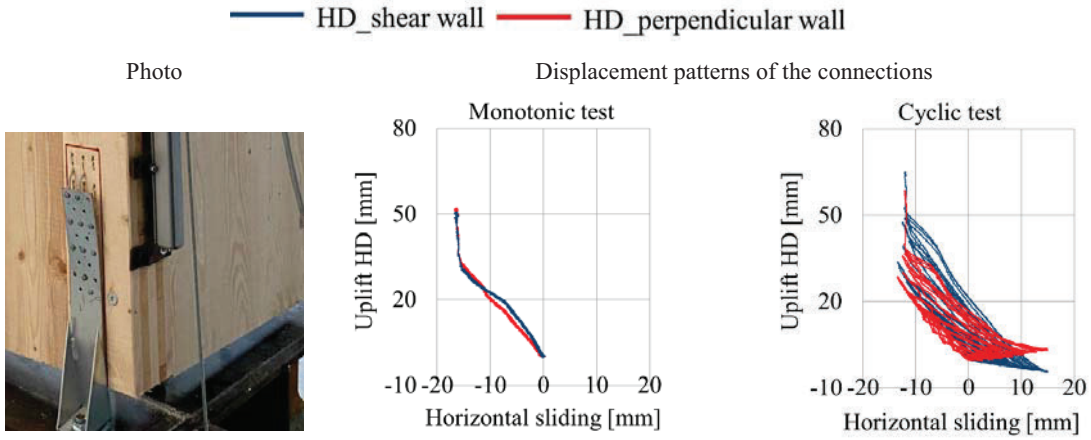

Figure 9: *Photos of the lower corner of the system and displacement path of the hold downs under tension.*

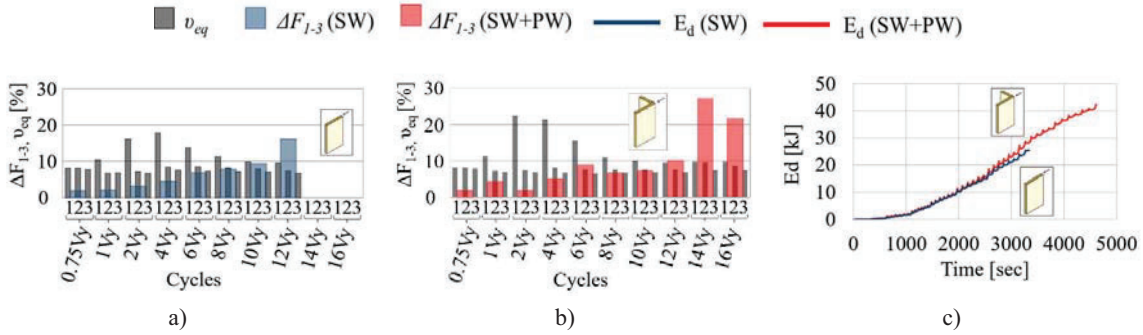

Figure 10: *a) Equivalent viscous damping v_{eq} and the impairment of strength ΔF_{1-3} in case of SW configuration, b) equivalent viscous damping v_{eq} and the impairment of strength ΔF_{1-3} in case of SW+PW configuration, c) comparison of dissipated energy E_d obtained from the cyclic tests of SW and SW+PW configurations.*

Increase of performances is governed by the properties of the wall-to-wall connections as well as the properties of the hold downs used in the perpendicular walls. In this study, in which the same hold downs were used for anchoring the shear wall and the perpendicular wall, increase of lateral stiffness and lateral capacity up to 40% and 41% were found, respectively. Moreover, experimental results show an increment of the deformation capacity in case of SW+PW configuration equal to 25%.

The findings of this experimental study showed that the presence of perpendicular walls provide significative interaction effects with the shear walls, and contribute to the so-called box behaviour of CLT buildings. The results presented in this study provides valuable insights into the interaction between shear walls and perpendicular walls in CLT platform-type buildings, demonstrating that these interactions can significantly modify the lateral response of CLT structures.

ACKNOWLEDGEMENT

The authors would like to thank the companies Rothoblaas S.r.l. and Francesco Mirrione Legnami S.r.l. for providing the material needed for the experimental campaign carried out at the L.E.D.A. Research Center. Part of the activities are also framed within the framework of the CADS Project - Creazione di un Ambiente Domestico Sicuro (Project Code ARS01_00920), co-funded by the MIUR, from PON and FSC funds - Projects for Industrial Research and Experimental Development in the 12 areas of specialization identified in the PNR 2015-2020, Notice No. 1735 of 13/07/2017.

REFERENCES

[1] Hummel J, Flatscher G, Seim W, Schickhofer G. CLT Wall Elements Under Cyclic Loading – Details for Anchorage and Connection. Focus Solid Timber Solut - Eur Conf Cross Laminated Timber 2014:152–65.

[2] D'Arenzo G, Casagrande D, Polastri A, Fossetti M, Fragiacomo M, Seim W. CLT Shear Walls Anchored with Shear-Tension Angle Brackets:

Experimental Tests and Finite-Element Modeling. J Struct Eng 2021;147:1–16. https://doi.org/10.1061/(asce)st.1943-541x.0003008.

[3] Gavric I, Fragiacomo M, Ceccotti A. Cyclic Behavior of CLT Wall Systems : Experimental Tests and Analytical Prediction Models. J Struct Eng 2015;141:1–14. https://doi.org/10.1061/(ASCE)ST.1943-541X.0001246.

[4] Yasumura M, Kobayashi K, Okabe M, Miyake T, Matsumoto K. Full-Scale Tests and Numerical Analysis of Low-Rise CLT Structures under Lateral Loading. J Struct Eng 2016;142:1–12. https://doi.org/10.1061/(asce)st.1943-541x.0001348.

[5] D'Arenzo G, Schwendner S, Seim W. The effect of the floor-to-wall interaction on the rocking stiffness of segmented CLT shear-walls. Eng Struct 2021;249:113219. https://doi.org/10.1016/j.engstruct.2021.113219.

[6] Shahnewaz M, Popovski M, Tannert T. Deflection of cross-laminated timber shear walls for platform-type construction. Eng Struct 2020;221:111091. https://doi.org/10.1016/j.engstruct.2020.111091.

[7] Tamagnone G, Rinaldin G, Fragiacomo M. Influence of the Floor Diaphragm on the Rocking Behavior of CLT Walls. J Struct Eng 2020;146:1–11. https://doi.org/10.1061/(ASCE)ST.1943-541X.0002546.

[8] Lukacs I, Tsalkatidis T, Tomasi R. Structural redundancy in Cross-Laminated Timber buildings. Proc World Conf Timber Eng WCTE2016, August 22-25, Vienna Austria 2016:5779–86.

[9] D'Arenzo G. An elastic model for the prediction of the lateral response of Cross-Laminated Timber shear walls with openings. Eng Struct 2023;274:115055. https://doi.org/10.1016/j.engstruct.2022.115055.

[10] Tamagnone G, Fragiacomo M. On seismic design of structures with CLT walls Sul Progetto in Zona Sismica di Strutture a Pareti Lignee in Xlam 2017:42–51.

[11] Popovski M, Gavric I. Performance of a 2-Story CLT House Subjected to Lateral Loads. J Struct Eng 2015;142:1–12. https://doi.org/10.1061/(asce)st.1943-541x.0001315.

[12] Hummel J, Seim W. Displacement-based design approach to evaluate the behaviour factor for multi-storey CLT buildings. Eng Struct 2019;201. https://doi.org/10.1016/j.engstruct.2019.109711.

[13] Ruggeri EM, D'Arenzo G, Fossetti M, Seim W. Investigating the effect of perpendicular walls on the lateral behaviour of Cross-Laminated Timber shear walls. Structures 2022;46:1679–95. https://doi.org/10.1016/j.istruc.2022.10.141.

[14] ETA - European Technical Assessment. Rotho Blaas WHT hold downs and angle brackets. ETA-11/0086-Danmark A/S 2015:1–26.

[15] ETA-European Technical Assessment. Rotho Blaas Connector Nails LBA. ETA-22/0002-Danmark A/S 2022;5:248–53.

[16] ETA - EuropeanTechnicalAssessment. Rotho Blaas Self-tapping screws and threaded rods. 2022.

[17] EN594. Timber structures. Test methods. Racking strength and stiffness of timber frame wall panels 2011.

[18] EN12512. Timber structures. Test methods. Cyclic testing of joints made with mechanical fasteners. 2005.

 https://doi.org/10.52202/069179-0446

World Conference on Timber Engineering Oslo 2023

FULL-SCALE LATERAL TESTING AND MODELLING OF INDUSTRIALIZED TIMBER DIAPHRAGMS INCLUDING ONLY FRAMING AND NON-STRUCTURAL SHEATHING

Fernando Véliz[1], Xavier Estrella[2], Pablo Guindos[3]

ABSTRACT: Over the last decade, industrialized mid-rise light-frame timber buildings have gained popularity in Chile due to their structural, manufacturing, and environmental advantages. However, structural design aspects and industrialization prescriptions are not thoroughly addressed by national design codes, highlighting the need for developing standards to regulate industrialized earthquake-resistant timber systems. Therefore, this paper presents the outcomes of a large national project aimed at characterizing the lateral performance of a series of full-scale industrialized timber diaphragms employing Chilean materials. Eight 3.6x2.4 m specimens were tested under in-plane lateral load, considering different detailings such as sheathing, nailing, and framing. Besides, bare slabs (no sheathing) were also studied in the campaign. Strength results proved to be consistent with those proposed by international regulations, while chord tensions exceeded 30% of those obtained by principles of engineering mechanics. Additionally, it was found that adding gypsum boards over plywood does not considerably improve the global stiffness, although it considerably increased the in-plane strength. Finally, a finite-element numerical model was developed for the slabs studied in this campaign, proving to be capable of capturing the nonlinear behavior of the specimens under large lateral displacements.

KEYWORDS: Diaphragms, timber buildings, gypsum, I-joist, in-plane testing, numerical modeling

1 INTRODUCTION

Since the 1950s, low-rise wood-frame structures have considerably increased across seismic regions, with recent data [1] showing a bright future for multi-story timber buildings in the years to come. Nevertheless, the lower stiffness of timber structures can produce a detrimental impact on their performance. Such an issue shows the fundamental role of diaphragms in the performance of buildings under seismic loads [2] or wind action, influenced by the local diaphragm's behavior, either rigid or flexible [3] as classified by [4]. Several experimental campaigns [5-10] have proven that both the shear capacity and stiffness of diaphragms are primarily dependent on the sheathing-to-framing connection [6].

Even though a large amount of research has been oriented to the traditional light-frame diaphragms, there is still a lack of studies focused on I-Joist diaphragms. For example, concerns about the validity of applying the same design provisions to conventional and I-joist diaphragms [11], have led designers to challenge such design methods, mainly due to the potential splitting of I-joist flanges, which was not addressed in those codes. Such concerns were partially addressed through I-joist diaphragm tests, such as those conducted by Weyerhaeuser, whose results have been reported by [12]. Among other outcomes, the researchers found that a lower shear strength improvement on I-joist diaphragms was reached when replacing 6d nails with 10d nails (+16% strength), compared to that improvement reached using sawn-lumber joists diaphragms and the same nails (+70% strength), attributable to flange splitting. Furthermore, other investigations such as the one conducted by [13], which considered eight 7.3x7.3 m I-joist diaphragms, proved that wooden I-joist diaphragms meet the design values specified in the Special Design Provisions for Wind and Seismic SDPWS standard [14], whose parameters were originally calibrated based on sawn lumber tests.

The new tendency of building higher timber buildings has raised concerns about the fire resistance of these structures. Such a concern is usually solved using gypsum boards. The structural contribution of gypsum panels has been experimentally assessed, however, putting the focus on gypsum sheathing over shear walls [15-17]. Some studies have tested gypsum sheathing attached to ceilings [18], which was supposed to improve their in-plane strength within the linear range. Such lack of data led authors [19-20] to study the contribution of gypsum sheathing in diaphragms. Then, an experimental campaign shown in [18] assessed the contribution of gypsum over ten full-scale (3.7 x 4.9 m) plywood roof

[1] Fernando Véliz, Centro Nacional de Excelencia para la Industria de la Madera (CENAMAD), Pontificia Universidad Católica de Chile, fdveliz@uc.cl
[2] Xavier Estrella, Ecole Polytechnique Federale de Laussane, Switzerland, edisson.estrellaarcos@epfl.ch
[3] Pablo Guindos, Centro Nacional de Excelencia para la Industria de la Madera (CENAMAD), Pontificia Universidad Católica de Chile, pguindos@ing.puc.cl

https://doi.org/10.52202/069179-0447

diaphragms, including both pitched and flat specimens. Such investigation focused on determining if the diaphragm strength or stiffness was increased by adding a 12 mm thick gypsum board, evaluating also the impact of employing different roof pitches. Tests confirmed that the increase in apparent stiffness for flat roofs is negligible; by contrast, gypsum increased the apparent stiffness of gable roofs by an average of 32% and hip roofs by 21%.

An important lack of houses has been noted in Chile the last decade, estimating a need of 650.000 units [21]. The main alternative chosen by the Housing Ministry to afford this lack is associated with industrialized construction, which can reduce manpower, time and overall cost, while better quality houses are obtained in contrast to using the traditional method [22]. Nowadays, guidelines such as the SDPWS [14] standard used to design timber structures in Chile, since no design recommendations are available in local regulations [21] to date. Therefore, the present investigation aims at contributing with scientific data for the inclusion and regulation of industrialized timber diaphragms in the Chilean code [21], including both experimental and numerical information of different typologies through an experimental campaign.

2 EXPERIMENTAL STUDY

As previously mentioned, this research is mainly focused in providing both experimental and numerical information for timber diaphragms, considering different typologies, including I-Joist framing as well as sawn-lumber framing, and non-structural ceiling panels over the diaphragms, so these contributions can be experimentally measured in terms of strength and stiffness. To address these issues, a set of 8 industrialized full-scale diaphragms 3.6 x 2.4 m were tested as part of the investigation presented in this paper according to ASTM E-455 loading protocol [23], considering a third-point load condition, and the results were used to validate the numerical models presented in a subsequent section of this document. The so-called numerical model was based on M-CASHEW software [24] and following the modeling guidelines proposed by [25].

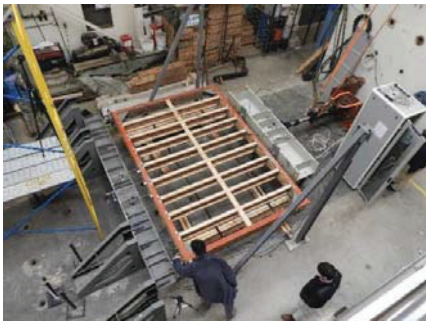

Figure 1: *Layout of the lateral testing of the specimens.*

2.1 DIAPHRAGM SPECIMENS

Different parameters were considered such as using sawn lumber joists as well as I-joists, assessing the contribution of gypsum panels over the structural sheathing and including different type of fasteners. Four diaphragms were constructed using 41 x 185 mm (2'' x 8'') sawn-lumber framing, graded as a C24 Chilean Radiata Pine [26]. The other four specimens were built using LSL as chord-and-end beams, while 241 mm deep LPI18 I-joists were used as interior beams, attached to LSL beams with ITS2.56/9.5 Hangers, and spaced at 407 mm on center.

Sawn-lumber (SL) specimens' chords were attached using Simpson Strong-Tie HRS416Z Straps, thus allowing to install strain gauges more easily, to experimentally obtain the chord tension. Every specimen was attached in their corners with four steel angles – attached by means of 8 shear bolts, 22 mm in diameter and 150 mm in length – to prevent early failures at the chord-to-end beam joint.

The first specimen of each configuration (sawn-lumber and I-joist), consisted of a bare slab, to measure the timber frame's stiffness, and then compared to the stiffness of the sheathed specimens. The sawn-lumber bare specimen was tested to failure, while, the I-joist specimen was tested only up to a design load, aiming at re-using it.

The second specimen of each configuration was designed with the same framing as the bare specimens. Nevertheless, these specimens were reinforced with an 11.1 mm thick APA rated OSB panel as sheathing on one side of the framing. The sawn-lumber diaphragm employed 2.9 x 65 mm smooth shank nails, spaced at 100 mm on center for the edge nailing, and 150 mm at adjoining panel edges parallel to the load direction. The I-joist diaphragms' panels were attached to the framing using 2.5 x 50 mm ring shank nails, spaced at 65 mm on center in the edge of the panels, and 100 mm at the adjoining panel edges parallel to the load direction. In all cases, field nailing was set to 300 mm on center . The third specimen of each configuration was similar to the second one, however, in this configuration the diaphragms were sheathed with a 15.1 mm thick plywood panel instead of 11.1 mm OSB, employing the same nails and nailing patterns for each case.

Finally, the fourth specimen of each configuration was equivalent to the third one, however 15 mm thickness gypsum boards were attached with of 8 x 75 mm drywall screws over the plywood sheathing, to evaluate the contribution of the non-structural sheathings. A brief list of the specimens is presented in Table 1.

Table 1: *Labeling and description of test specimens.*

Label	Nail spacing (mm)		Panel	t	Nail
	Edge	Joint*		mm	(mm)
SL – BARE	-	-	-	-	-
SL – OSB	100	150	OSB	11.1	2.9x65
SL – PLY	100	150	Ply	15.1	2.9x65
SL - PLY/GWB	100 (300)	150 (300)	Ply (Gyp)	15.1 (15)	2.9x65 (8x75)
IJ – BARE	-	-	-	-	-
IJ – OSB	65	100	OSB	11.1	2.5x50
IJ – PLY	65	100	Ply	15.1	2.5x50
IJ - PLY/GWB	65 (300)	100 (300)	Ply (Gyp)	15.1 (15)	2.5x50 (8x75)

https://doi.org/10.52202/069179-0447

(*) Adjoining panel edge parallel to load direction.

2.2 TEST SET-UP

A reinforced-concrete reaction wall and a strong floor were used to carry out the tests. As shown in Figure 2, a H500x500x246 mm steel beam was connected to a 250 kN capacity hydraulic actuator, to distribute the load to the specimens in two points, by means of load-transfer plates, as shown in Figure 1. Rollers were placed under the diaphragms to braced them, avoiding out of plane displacements. Load cells were attached to a 4000 mm long W10x48 reaction beam and placed near to the corners of the unloaded chord of each diaphragm. Four angle brackets supported the 4 meters long reaction beam and were also anchored to the strong floor using post-tensioned steel bars, thus ensuring that the friction between steel plates and strong floor was greater than applied load by the hydraulic actuator.

The adopted set-up was designed to position the specimens in a flat manner, parallel to the strong floor, and placed over steel bars to allow the diaphragm to move under in-plane loads. Each test was instrumented with eleven linear variable displacement transducers (LVDT), to measure different displacements, such as those in the unloaded chord beam, between sheathing panels, displacement in the angle brackets, among others. A system connected to a PC was used to collect the data.

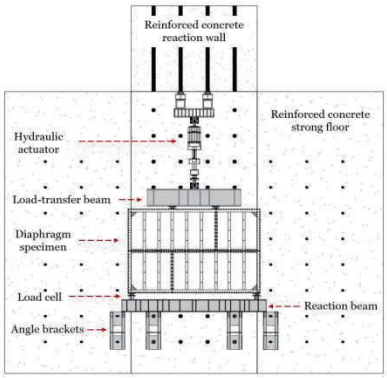

Figure 2: *Plan view of test set-up. Taken from [27].*

2.3 LOADING PROTOCOL

Tests were carried out based on the guidelines provided by the ASTM E455 standard [23]. SL – OSB and SL – PLY specimens were tested according to a loading protocol (force-controlled) based on [9], as shown in Figure 3. Both tests were performed considering a design load of 50 kN, however, to evaluate the stiffness degradation at low/high load levels, the SL – OSB specimen started the loading protocol at the fifth cycle, and loaded to the failure at the end. Conversely, the SL – PLY specimen started the loading protocol at the very first cycle and loaded to the failure after the fourth 1x design load cycles. Stiffness results can be found in [27].

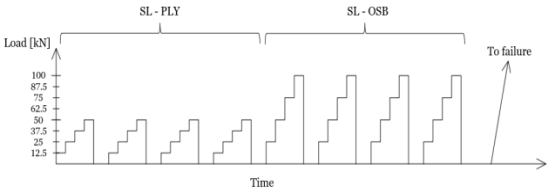

Figure 3: *Loading protocol for SL-PLY and SL-OSB specimens.*

The rest of the specimens were tested under a monotonic loading protocol, all of them displacement-controlled, with a displacement rate of 5 mm per minute. Load was stopped when the peak load dropped by approximately 20%.

3 NUMERICAL MODELING

Numerical models are a valuable tool for researchers when studying the nonlinear response of structures since they provide the means to overcome the physical and resource limitations of lab testing. However, numerical models also require a validation process against real specimens to measure their reliability level, precision, and prove that they meet the minimum requirements for structural engineering, beings this latter especially relevant when unconventional systems or solutions are studied. Therefore, this section presents a nonlinear numerical model for the timber diaphragms tested as part of this research project, validates its results against the test data presented in previous sections, and carries out additional analyses to better understand the nonlinear response of industrialized timber diaphragms. The numerical model has been developed employing the M-CASHEW software built by [24] and following the modeling guidelines proposed by [25].

Timber beams were represented using Euler-Bernoulli frame elements (elastic response) that have 3 degrees-of-freedom at each node. An elasticity modulus E = 11.4 GPa was considered for the sawn lumber model, based on the experimental results reported by [25]. Also, an elasticity modulus of 11.5 GPa were employed for I-joist beams according to [28], and 9.3 GPa for LSL, according to values declared by the manufacturer. Besides, the frame elements employed a corotational approach in the numerical formulation. Nailed connections were modeled employing zero-length spring elements with 3 degrees-of-freedom per node. The so-called MSTEW model proposed by [29] for nonlinear timber connections was employed in the X and Y direction, whereas a zero-stiffness element was considered for rotations. It should be noted that the elements used for the directions X and Y employed the true-oriented approach developed by [24] with the aim of avoiding overestimated values for the diaphragm's capacity and stiffness, as has been found by prior investigations [29,30]. The governing parameters for the MSTEW model were computed by nonlinear minimization techniques from the test data on nailed connections similar to [31].

The sheathing panels were modeled by means of shear rectangular elements with 5 degrees-of-freedom: one for rigid-body rotation, two for in-plane shear deformation, and two for rigid-body translation. Note that panels' rigid behavior consider the bearing between them. Based on the experimental data from [25], a shear modulus G = 1.3 GPa was used when modeling the OSB panels, and G = 0.5 GPa when modeling plywood panels, according to Table C4.2.3A of SDPWS [14]. When conducting analyses with the model, a displacement-controlled approach was employed along with a norm displacement increment test as convergence criteria. Besides, up to 20 iterations were conducted at each load step and the residual tolerance was set as 1e-6 kN. Full details on the modeling approach can be found in [25] and [27].

4 RESULTS AND DISCUSSION

4.1 FAILURE MODE

The diaphragms presented failure modes related to fasteners, as usually shown in the literature [5-13]. All specimens failed due to pull out of the nails in the edges of the panels (Figure 4a, 4c), crushing of OSB panels, cutting of drywall screws (Figure 4d) and a non-expected failure in the loaded chord of SL-PLY specimen (Figure 4b). The frame structure appeared to remain undamaged, particularly in the unloaded chord beam. Steel angles in each specimen prevented undesired end-beam to chord-beam joint failure, allowing them to exhibit typical ductile failure modes.

The smooth shank nail used in SL diaphragms led these specimens to show failure modes associated to pull out of the nails, due to their low friction resistance. In case of SL-PLY/GWB, no shear cracking was seen over the gypsum boards. Conversely, the main failure was due to the cutting of drywall screws and pulling out of the nails attaching the edges of the plywood underneath, as shown in Figure 4d.

Most of the investigations on I-joist diaphragms have considered nail spacings not closer than 102 mm, and employing 10d sheathing nails [11-13], which increased the probability of flanges to split. Thus, this paper attempted to reduce nail spacing, reducing the nail diameter at the same time, minimizing as much as possible the probability of splitting without decreasing shear capacity. As shown in SL specimens, failure modes on IJ specimens were also due to pull out of nails and crushing of panels by nails head. IJ-OSB, IJ-PLY and IJ-PLY/GWB specimens showed ductile failure modes as previously mentioned, although IJ-PLY also presented brittle failures located at blocking, like those reported in [13]. As well as in SL-PLY/GWB, the failure mode of IJ-PLY/GWB was partially due to the cutting of drywall screws, added to local gypsum failures and detachment, as reported in [31]. No cracking of global gypsum panels was reported, as shown in Figure 4e. Further results are available in [27].

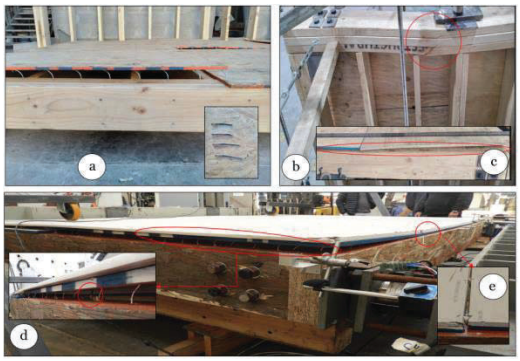

Figure 4: *Typical failure modes of diaphragm specimens.*

4.2 FORCE-DISPLACEMENT RESPONSE

The monotonic and envelope curves are plotted in Figure 5. The y-axis located in the right shows unit shear capacity, which is the peak capacity divided into 2 and then divided into the width of the diaphragm. Initially, the monotonic response was approximately linear up to drift values (midspan displacement divided into half mid-span length) of about 0.2-0.5% for SL specimens, and up to 0.6% for IJ specimens [27]. Bare specimens appeared to behave virtually elastic according to Figure 5.

Beyond the mentioned drifts, the structural response turned to be highly non-linear, mainly due to the local deformation of nails. A summary of the main results is listed in Table 2, which includes peak capacity on each test (F_0), elastic stiffness (K_0), yielding load (F_y), yielding displacement (δ_y) according to ASTM E2126 [33] and ductility ratio (μ), which was obtained as δ_u / δ_y. Note that ultimate displacement δ_u was omitted from Table 2 due to space constraints.

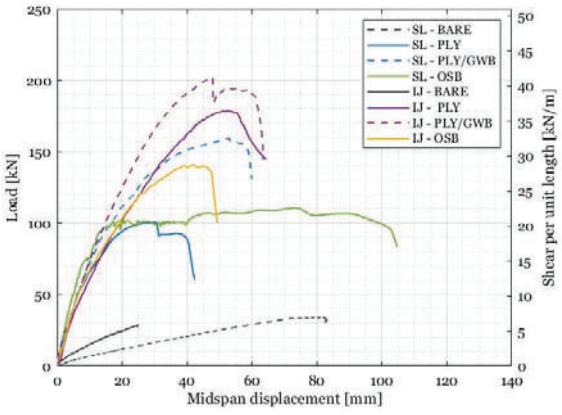

Figure 5: *Force versus mid-span displacement response.*

https://doi.org/10.52202/069179-0447

Table 2: *Summary of experimental results. Adapted from [27].*

Tested Diaphragm	F_0 kN	K_0 kN/mm	F_y kN	δ_y mm	μ -
SL – BARE	33	0.5	-	-	-
SL – OSB*	110	11.4	104	9.8	10.6
SL – PLY*	100	9.3	92	11.2	3.71
SL -PLY/GWB	160	7.5	145	19.2	3.11
IJ – BARE	-	1	-	-	-
IJ – OSB	141	7.6	125	17	2.85
IJ – PLY	179	5.5	156	26.8	2.36
IJ – PLY/GWB	203	6.6	182	25.2	2.5

(*) Envelope curves were used to obtain the parameters presented.

4.3 AXIAL CHORD TENSION EQUATION CHECKING

The most common way for modeling diaphragms analytically, and to estimate their chord tensions comes from principles of engineering, where the diaphragm is assumed as a deep and thin beam, thus the sheathing panels act as the web, supporting the shear, and the chords act as flanges, supporting all the axial tension, which is usually estimated as M/W, where M is the flexural moment diagram along the chord, and W is the width of the diaphragm. Thus, this research included two specimens (SL-OSB and SL-PLY) to assess how well this assumption fits with the experimental results. Both specimens were instrumented at the unloaded chord with one strain-gauge each, as shown in Figure 6. To consider the contribution of both straps, the axial load measured in each strain-gauge was. The comparison was evaluated at the shear allowable design of each specimen: for SL-OSB (4 kN/m), the experimental axial chord tension indicated 7.4 kN, with a theoretical tension of 5 kN, thus showing a 48% of percentage difference. For SL-PLY (shear limit of 4.5 kN/m), the experimental measurement recorded a value of 6.6 kN, in contrast to 5.5 kN from the theoretical estimation, showing a 20% of percentage difference. Such percentage differences confirmed thw well-functioning of such an assumption, and in particular the M/W equation, even though experimental results appear to be slightly higher. These underestimations may be attributable to the axial load duplication, since axial loads at the instrumented strap were probably higher than those at the non-instrumented strap, due to the eccentricity with respect to the shear resistant zone, i.e., the sheathing panel. Further research needs to be carried out on this topic.

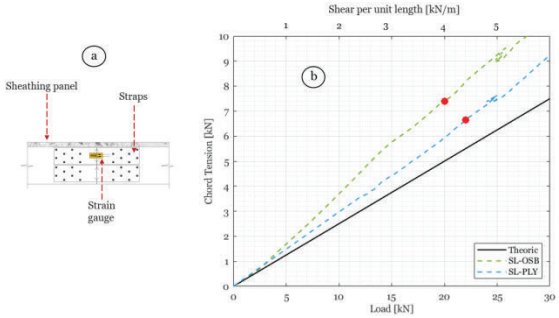

Figure 6: *Chord tension measurements versus theorical M/W estimation: (a) shows the location of strain gauge and in (b) is shown the measurements up to the starred allowable design limit.*

4.4 DESIGN IMPLICATIONS

This section compares the experimental results with the estimations of strength and stiffness provided by SDPWS [14]. This section is intended to evaluate how well code provisions adjust with the experimental results reported in the present investigation. Even though SDPWS standard is only applicable to diaphragms uniformly nailed, and just with one type of sheathing per specimen, PLY/GWB specimens were also Ied in this section, but not deeply discussed.

4.4.1 Strength

The nail sizes and sheathing panels used in this research were chosen for being commonly used in the Chilean industry, however, they were not coincident with North 5merican configurations, then they were not applicable to meet SDPWS [14] available unit shear capacities. Thus, two different methods to obtain unit shear capacities (v_{SDPWS}) were employed in the present research. The first consisted of choosing the more similar configuration from Table 4.2A of the SDPWS [14] standard. Thus, considering 6d common nails (2.87 mm in diameter) and 9.5 mm (⅜ in) sheathing panels, nominal unit shear capacities were taken from 4 – 6 in nailing pattern (785 plf) and 2.5 – 4 in nailing patterns (1175 plf) to compare with SL specimens and IJ specimens, respectively. In contrast, the second method consisted in estimating allowable unit shear capacities for each specimen by means of Johansen's theory [34], as explained in [9]. Following these approaches, experimental and theoretical shear capacities for each specimen were shown in Table 3. Experimental unit shear capacities for SL specimens were between 78-96% larger than those proposed in SDPWS [14], while for IJ specimens the experimental to SDPWS [14] nominal contrast were between 68-114%. Allowable unit shear capacities were obtained by dividing experimental and SDPWS nominal values by 2.8, as suggested in [14]. Conversely, Tissell & Elliot [9] method was chosen to properly estimate allowable unit shear capacity for each specimen, allowing to take into account the accurate variables for every specimen, such as nail size, sheathing thickness, among others. Such a method allowed to calculate the allowable unit shear capacity of

each specimen through their Johansen's yielding mode [34], multiplied by the nails separation. Table 3 shows in its lasts two columns the allowable unit shear capacity derived from [9] method. As it can be highlighted from Table 3, conventional SL specimens reached experimental-allowable unit shear capacities between 61-100% higher than those proposed via [9] method, while conventional IJ specimens exhibited experimental-allowable unit shear capacities between 144-172% higher than those proposed via [9] method. On the other hand, since both experimental and SDPWS nominal results were divided into 2.8, percentage variance are the same as those presented above.

Table 3: *Nominal and allowable unit shear capacity.*

Test	Nominal		Allowable (ASD)		
	v_{exp} kN/m (plf)	v_{SDPWS} plf	v_{exp} plf	v_{SDPWS} plf	$v_{T\&E}$ kN/m (plf)
SL – OSB	22.5 (1540)	785	550	280	4 (275)
SL – PLY	20.5 (1400)	785	500	280	4.5 (310)
SL – PLY/GWB	32.8 (2250)	-	805	-	-
IJ – OSB	28.9 (1980)	1175	710	420	4.2 (290)
IJ – PLY	36.7 (2515)	1175	900	420	4.8 (330)
IJ – PLY/GWB	41.6 (2850)	-	1020	-	-

* T&E: Tissell & Elliot [9].

4.4.2 Stiffness and deflections

The stiffness of a uniformly nailed diaphragms may be indirectly calculated from SDPWS Eq (4.2-1), which is usually employed to calculate the mid-span displacement within linear range. This equation is relevant since it allows to predict whether the diaphragms will behave rigidly or flexibly in contrast to the lateral force resisting system underneath, according to principles such as those published in [4]. The mid-span displacement is calculated as follows:

$$\delta = \frac{5vL^3}{8EAW} + \frac{vL}{4G_v t_v} + 0.188Le_n + \frac{\sum x\Delta_c}{2W} \quad (1a)$$

$$\delta = \frac{5vL^3}{8EAW} + \frac{0.25vL}{1000G_a} + \frac{\sum x\Delta_c}{2W} \quad (1b)$$

Equation (1a) includes bending, panel shear deformation, nail slip, and chord splices slip, while Eq. (1b) eases the use of the first equation by combining both shear flexibilities, generating an apparent diaphragm shear stiffness G_a, which is a function of nail slip in the linear range. Under the same logic as in section 4.4.1, since no SDPWS [14] configurations are exactly coincident with those carried on in this research, G_a values were calibrated with the monotonic and cyclic (envelopes) sheathing-to-framing tests presented in [27], which were used to determine the nail slip e_n in equation C4.2.3-3 in SDPWS [14], and presented here as Equation (2):

$$G_a = \frac{1.4v_{ASD}}{\frac{1.4v_{ASD}}{G_v t_v} + 0.75e_n} \quad (2)$$

where $G_v t_v$ correspond to shear stiffness of wood structural panels. Due to the lack of precisely information, values from Table C4.2.3A from SDPWS [14] were taken, where 14.6 kN/mm (83500 lb/in) and 7.5 kN/mm (43000 lb/in) were considered for 11.1 mm thickness OSB and 15.1 mm thickness plywood, respectively. G_a values were tabulated in Table 4, which also shows all the parameters considered for each of the 4 conventional specimens tested to be used in Equation (1b).

Table 4: *Mid-span displacement comparison at allowable design levels.*

Tested Specimen	SL – OSB	SL – PLY	IJ – OSB	IJ – PLY
L (mm)	3663	3663	3663	3663
L (ft)	12	12	12	12
E (Gpa)	11.4	11.4	9.3	9.3
E (psi × 10^6)	1.65	1.65	1.35	1.35
A_{chord} (in^2)	35.3	35.3	33.2	33.2
W (mm)	2443	2443	2443	2443
W (ft)	8	8	8	8
x (mm)	1831	1831	-	-
x (ft)	6	6	-	-
Δ_c (in)	0.003	0.003	-	-
G_a (kips/in)	7	5	11.5	6.5
v_{ASD} (lb/ft)	275	310	290	330
δ_{SDPWS} (in)	0.12	0.19	0.07	0.15
δ_{SDPWS} (mm)	3.07	4.81	1.94	3.89
δ_{exp} (mm)	1.69	2.56	2.59	3.22
$\delta_{SDPWS}/\delta_{exp}$	1.81	1.87	0.75	1.21

Load-displacement curves were calculated for each specimen presented in Table 4 and were plotted against the corresponding experimental results. As shown in Figure 7, each conventional specimen (uniformly nailed and with one sheathing) was plotted until the corresponding allowable shear limit, defined in Table 3 and Table 4 in the y-axis, while the x-axis was limited to 0.27% drift, equivalent to 5 mm of mid-span displacement. Note that most of specimens behaved

https://doi.org/10.52202/069179-0447

slightly stiffer than their corresponding SDPWS [14] prediction, being the only exception the specimen IJ – OSB, whose percentage difference was about 25%, probably attributable to a poor nailing process. These outcomes may provide a first overview of how conservative this equation is for estimating mid-span displacements inside the linear range for Chilean industrialized diaphragms. Although not a fair comparison, non-conventional specimens which included gypsum boards were included in Figure 7 with the purpose of showing the difference in contrast with conventional systems.

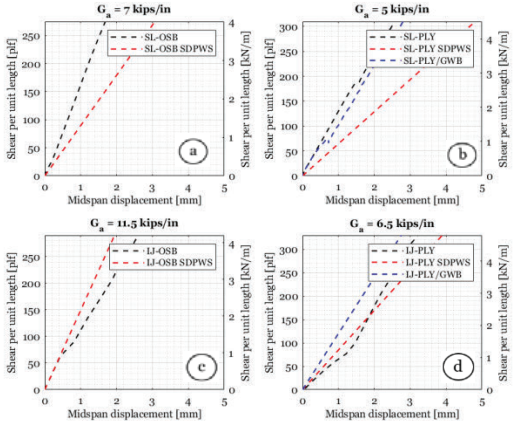

Figure 7: *Measured and calculated mid-span displacement curves for allowable design levels: (a) SL-OSB specimen, (b) SL-PLY and SL-PLY/GWB, (c) IJ-OSB specimen, and (d) IJ-PLY and IJ-PLY/GWB specimens. Adapted from [27].*

4.5 NUMERICAL MODELING

This section had the purpose of confirm the well-functioning of the M-CASHEW [24] software at modeling diaphragms with different configurations, including different types of nails, panel sheathings, among others. To address this purpose, 5 out of the 6 diaphragms experimentally tested – which are presented in Table 5 - were contrasted versus numerical models. Note that SL-OSB specimen was excluded from this comparison, because its loading protocol, as shown in Figure 3, produced notorious creep, mechanism which is not possible to reproduce by M-CASHEW [24]. Thus, this section considered monotonic analyses and one cyclic analysis (SL-PLY) with little to no creep. Loading set-up used in numerical models was to that used in experimental tests, i.e., the protocol suggested by ASTM E455 [23], applying the loads in the north-south direction.

The good agreement between experimental results and numerical models can be appreciated in Figure 8 and Table 5, which shows the comparison between global stiffness, peak capacity, ultimate displacement, and ductility. As previously mentioned, The IJ-OSB specimen showed an unexpected low stiffness, which was confirmed by its numerical model contrast, showing a clearly stiffer behavior within the linear range, although capacity and ductility appeared to be consistent with its corresponding experimental result.

The PLY/GWB specimens, i.e., those sheathed with gypsum over a plywood panel, were modeled only considering the plywood panel, since gypsum board did not appear to add any shear capacity. In this line, drywall screws were modeled directly as springs over plywood panels, attaching them to the framing underneath. These results have proven the feasibility of M-CASHEW to properly model light-frame diaphragms, as shown in Figure 8. It should be highlighted that the deformation of sheathing-to-framing connectors was the main flexibility source, while those attributable to framing were negligible [27].

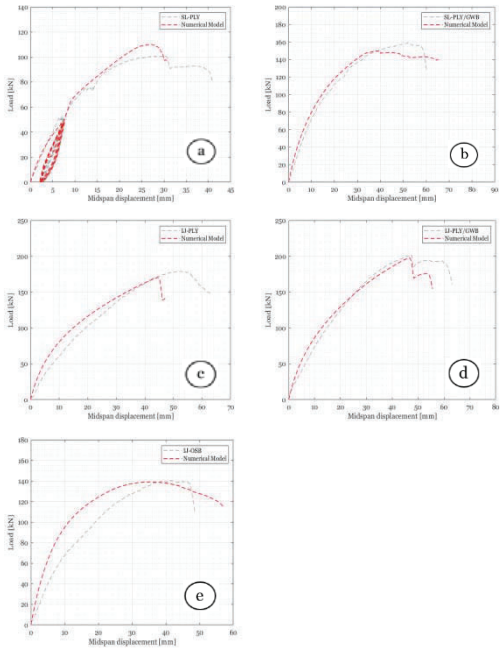

Figure 8: *Experimental and numerical model contrasts: (a)SL-PLY, (b) SL-PLY/GWB, (c) IJ-PLY, (d) IJ-PLY/GWB, I IJ-OSB.*

Table 5: *Structural properties of numerical models.*

Numerical model	F_0 kN	K_0 kN/mm	δ_u mm	μ -
SL – OSB	-	-	-	-
SL – PLY	110	9.8	30.7	2.1
	(1.1)	(1.05)	(0.74)	(0.56)
SL – PLY/GWB	150	8.67	65.2	4.5
	(0.93)	(1.15)	(1.08)	(1.43)
IJ – OSB	140	12.4	56.9	5.98
	(0.99)	(1.63)	(1.17)	(2.09)
IJ – PLY	170	8	47.6	3
	(0.95)	(0.68)	(0.75)	(1.27)
IJ – PLY/GWB	197	8.3	55.5	3.1
	(0.97)	(1.25)	(0.88)	(1.24)

https://doi.org/10.52202/069179-0447

(*) Values in parentheses correspond to the ratio between numerical and experimental results.

5 CONCLUSIONS

An experimental campaign was carried out on 8 full-scale industrialized timber diaphragms, proving its feasibility to withstand in plane shear loads without showing severe damage. The main conclusions of the present investigation are listed below:

Strength results resulted to be consistent with the recommendations provided by SDPWS [14], while experimental chord tension measurements suggest that an enlargement factor of 30% should be applied to chord tension obtained by mechanic principles. Anyway, more research on this topic must be performed to confirm such statement.

Experimental results showed that OSB-sheathed specimens were between 20-40% stiffer than those sheathed with plywood, regardless the framing. Also, I-Joist diaphragms results showed that those sheathed with 15.1 mm thickness plywood performed 27% stronger than those sheathed with 11.1 mm thickness OSB, consistent to Johansen's theory [34]. Likewise, I-Joist diaphragms developed larger peak capacities than sawn lumber diaphragms, which suggests that the more quantity of nails, the larger peak capacity, no matter if these nails have smaller diameters. Conversely, experimental results showed that sawn lumber diaphragms – sheathed with 2.9x65 mm nails - performed stiffer (between 10-70%) than their I-Joist counterparts – sheathed with 2.5x50 nails -. Thus, considering that I-Joist bare frame performed 100% stiffer than sawn lumber bare diaphragm, and that sawn lumber sheathed specimens contained less nail quantity than I-joist sheathed specimens, this leads to the conclusion that in plane stiffness is mainly controlled by nail diameter, while peak capacity is mainly controlled by nail quantity [27].

Peak capacity and in-plane stiffness were increased by using gypsum boards over plywood panels with 8x75 mm drywall screws. In fact, an increase of 15% was reached in the peak capacity, while a 20% improvement was noted in stiffness, particularly considering I-Joist specimens results.

Although the M-CASHEW [24] software had been mainly used to reproduce light-frame walls behavior until this research, with limited investigations attempting to predict diaphragm's structural response, this research proved the feasibility of M-CASHEW [24] to accurately predict mid-span displacements all the way to failure for different monotonically and cyclically loaded diaphragms. A more comprehensive discussion of these results is going to be available in literature soon.

Finally, these experimental results (which are deeply discussed in [27]) will serve as the basis for the inclusion of light-frame diaphragms in the Chilean regulation code [26]. Unit shear capacities, as well as the well-functioning behavior of mid-span displacement equations presented in here will experimentally support their adoption in the mentioned code.

REFERENCES

[1] Follesa, M., Fragiacomo, M., Casagrande, D., Tomasi, R., Piazza, M., Vassallo, D., Canetti, D., & Rossi, S. (2018). The new provisions for the seismic design of timber buildings in Europe. *Engineering Structures*, *168*, 736–747. https://doi.org/10.1016/j.engstruct.2018.04.090

[2] Fuentes, S., Fournely, E., & Bouchaïr, A. (2014). Experimental study of the in-plan stiffness of timber floor diaphragms. *European Journal of Environmental and Civil Engineering*, *18*(10), 1106–1117. https://doi.org/10.1080/19648189.2014.881760

[3] Dolce, M., Lorusso, V. D., & Masi, A. (1994). Seismic response of building structures with flexible inelastic diaphragm. *The Structural Design of Tall Buildings*, *3*(2), 87–106.

[4] ASCE. (2017). Minimum design loads and associated criteria for buildings and other structures. In *Minimum Design Loads and Associated Criteria for Buildings and Other Structures*. American Society of Civil Engineers (ASCE). https://doi.org/10.1061/9780784414248

[5] Bott, J. W. (2005). *Horizontal stiffness of wood diaphragms*. Virginia Tech.

[6] Countryman, D. (1952). Lateral tests on plywood sheathed diaphragms. *Douglas Fir Plywood Association (DFPA), Tacoma, WA*.

[7] Countryman, D., & Colbenson, P. (1954). *Horizontal plywood diaphragm tests: Laboratory Report No. 63*.

[8] Tissell, J. R. (1966). Horizontal Plywood Diaphragm Tests. *Laboratory Report*, *106*.

[9] Tissell, J. R., & Elliott, J. R. (1977). *Plywood diaphragms*.

[10] Zagajeski, S., Halvorsen, G. T., GangaRao, H. V. S., Luttrell, L. D., Jewell, R. B., Corda, D. N., & Roberts, J. D. (1984). Theoretical and experimental studies on timber diaphragms subject to earthquake loads. *Final Summary Report, Department of Civil Engineering, West Virginia University, Morgantown, WV*.

[11] Zhang, S., Daneshvar, H., & Chui, Y. H. (2021). Comparison of Lateral Load Performance of Light Wood Diaphragms Built with Sawn Lumber and Wood I-Joists. *Journal of Materials in Civil Engineering*, *33*(1). https://doi.org/10.1061/(asce)mt.1943-5533.0003544

[12] Waltz, N., & Dolan, J. D. (2010). I-Joist diaphragm systems: Performance Trends Observed with Full-Scale Testing. *Wood Design Focus*. www.dbmcontractors.com

[13] Yeh, B. J., Herzog, B., Skaggs, T., & others. (2016). Performance of full-scale I-joist diaphragms. *Proceedings of 3rd Meeting of International Network on Timber Engineering Research (INTER). INTER*, 15–49.

[14] American Wood Council. (2021). *Special Design Provisions for Wind and Seismic*. www.awc.org.

[15] Filiatrault, A., Christovasilis, I. P., Wanitkorkul, A., & van de Lindt, J. W. (2010). Experimental seismic

https://doi.org/10.52202/069179-0447

response of a full-scale light-frame wood building. *Journal of Structural Engineering*, *136*(3), 246–254.
[16] Mcmullin, K. M., Asce, M., & Merrick, D. S. (2007). *Seismic Damage Thresholds for Gypsum Wallboard Partition Walls*. https://doi.org/10.1061/ASCE1076-0431200713:122
[17] Mcmullin, K. M., & Merrick, D. (2001). *Seismic Performance of Gypsum Walls-Experimental Test Program Chapter 2. Literature Review*.
[18] Kirkham, W. J., Gupta, R., & Miller, T. H. (2015). Effects of Roof Pitch and Gypsum Ceilings on the Behavior of Wood Roof Diaphragms. *Journal of Performance of Constructed Facilities*, *29*(1). https://doi.org/10.1061/(asce)cf.1943-5509.0000490
[19] Walker, G., & Gonano, D. (1984). Experimental investigation of the diaphragm action of ceilings in resisting lateral loads on houses. *Proc., Pacific Timber Engineering Conf*, 543–550.
[20] Alsmarker, T. P. (1991). Structural diaphragms in wood-framed buildings. *Proc., Int. Timber Engineering Conf*, *4*, 4–354.
[21] Ministerio de Vivienda y Urbanismo. (2022). *Plan de Emergencia Habitacional 2022 - 2025*.
[22] Bari, N. A. A., Abdullah, N. A., Yusuff, R., Ismail, N., & Jaapar, A. (2012). Environmental Awareness and Benefits of Industrialized Building Systems (IBS). *Procedia - Social and Behavioral Sciences*, *50*, 392–404. https://doi.org/10.1016/j.sbspro.2012.08.044
[23] ASTM. (2019). ASTM E455-19: Standard Test Method for Static Load Testing of Framed Floor or Roof Diaphragm Constructions for Buildings. *ASTM International, West Conshohocken, PA 19428-2959*. https://doi.org/10.1520/E0455-19
[24] Pang, W., & Hassanzadeh Shirazi, S. M. (2013). Corotational Model for Cyclic Analysis of Light-Frame Wood Shear Walls and Diaphragms. *Journal of Structural Engineering*, *139*(8), 1303–1317. https://doi.org/10.1061/(asce)st.1943-541x.0000595
[25] Estrella, X., Guindos, P., Almazán, J. L., & Malek, S. (2020). Efficient nonlinear modeling of strong wood frame shear walls for mid-rise buildings. *Engineering Structures*, *215*. https://doi.org/10.1016/j.engstruct.2020.110670
[26] Instituto Nacional de Normalización. (2014). *NCh 1198. Madera - Construcciones en Madera - Cálculo*.
[27] Veliz, F., Estrella, X., Lagos, J., & Guindos, P. (2023). Testing and nonlinear modelling of industrialized light-frame timber diaphragms including optimized nailing and nonstructural sheathing. *Engineering Structures (under review)*.
[28] Grandmont, J.-F., Cloutier, A., Gendron, G., & Desjardins, R. (2010). *Wood I-joist model sensitivity to oriented strandboard web mechanical properties*.
[29] Folz, B., & Filiatrault, A. (2001). Cyclic analysis of wood shear walls. *Journal of Structural Engineering*, *127*(4), 433–441.
[30] Judd, J. P., & Fonseca, F. S. (2005). Analytical model for sheathing-to-framing connections in wood shear walls and diaphragms. *Journal of Structural Engineering*, *131*(2), 345–352.
[31] Jara, A., & Benedetti, F. (2017). *Informe No. 14 – Registro de estudio de ensayos de conectores*.
[32] Rizzi, E., Giongo, I., Ingham, J. M., & Dizhur, D. (2020). Testing and Modeling In-Plane Behavior of Retrofitted Timber Diaphragms. *Journal of Structural Engineering*, *146*(2). https://doi.org/10.1061/(asce)st.1943-541x.0002473
[33] ASTM. (2018). ASTM E2126-11: Standard test methods for cyclic (reversed) load test for shear resistance of vertical elements of the lateral force resisting systems for buildings. *ASTM International, West Conshohocken, PA: 2018.*
[34] Johansen, K. W. (1949). *Theory of Timber Connections*.

World Conference on Timber Engineering Oslo 2023

FEASIBILITY STUDY ON LONG-SPAN CLT-GLULAM COMPOSITE FLOORING SYSTEM CONNECTED WITH BAMBOO-TENON SHEAR CONNECTORS

Yue Diao[1], Cristiano Loss[2]

ABSTRACT: The rise of cross-laminated timber (CLT) became a cornerstone for the development of mass timber high-rise buildings and for large applications of timber products in construction. The design of CLT floors is often hinged upon meeting the vibration and deflection requirements under serviceability limit states. As a result, thick and material-intensive sizes of floor members can result from the design to fulfil the minimum stiffness requirements.

A long-span composite flooring system made of CLT panel and glulam ribs is a structurally optimized and cost-effective solution. In this paper, a feasibility study of a 12-meter composite flooring system consisting of CLT slab and glulam ribs jointed through bamboo-tenon shear connectors was conducted. The flooring system was designed to achieve performance objectives per the National Building Code of Canada, focusing on office spaces. Finite element modelling was used to investigate the behaviour of connectors under push-out shear forces. A parametric study of the shear connector was then carried out. Impacts of the material properties of mortise-tenon on the behaviour of the joints were discussed. Further, the structural performance of the composite system was investigated under several case scenarios. Specific design recommendations for adopting bamboo-tenon as the shear connector in composite systems were provided.

KEYWORDS: Bamboo connectors, CLT composites, flooring systems, long-span floors

1 INTRODUCTION

1.1 COMPOSITE FLOORING SYSTEMS

The acceptance of composite flooring systems started with the growth of reinforced concrete-based and concrete-steel composite floors. In Europe, design provisions of such composite floors have been included in Eurocode 4 [1]. More recently, research has been conducted with the aim of replacing concrete slabs with CLT panels. With specific reference to the timber-timber floor composites, general design guidelines of a fully connected CLT-glulam ribbed system have been discussed in the proceeding of the joint Conference of COST Action [2]. Several long-span timber floor solutions using inclined self-tapping screws as shear connectors have been studied in Europe [3]. Research has been conducted to investigate new connection systems; the result of metal fastener combinations employed in timber composite floor structures can be founded in [4]. It has been shown that these mechanically connected composites can be designed assuming full composite action. However, with the increase in floor span, the number of metal fasteners used, the on-site labor costs and the construction time increase along with it, making larger span timber flooring systems less attractive in practice. Therefore, there is an urge to develop high-structural performance connection systems for timber composite floor systems.

1.2 MODERN CARPENTRY JOINTS

The advancement of automation technologies in the wood industry, namely computer-numerically-controlled (CNC) machining technology, increased the level of prefabrication of CLT structures. As a result, CLT panels can be manufactured as wall and floor elements and quickly assembled on-site. These technologies also increased the possibility of using CNC machining carpentry joints to serve as the connection system in mass timber construction. Studies of carpentry joints used in modern timber frame structures have been conducted by Tannert et al. [5] and Claus and Seim [6]. More recently, the castellation CLT joints have been studied by Brown et al. [7]. Schmidt and Blass [8] have investigated the behavior of hardwood connectors serving as in-plane shear connectors for CLT walls.

1.3 ENGINEERED BAMBOO PRODUCTS

Bamboo is a rapidly renewable biomaterial with similar environmental benefits and mechanical properties as timber. Full culm bamboo can be applied as a structural

[1] Yue Diao, Sustainable Engineered Structural Solutions Laboratory, Department of Wood Science, University of British Columbia, Canada, yuediao@mail.ubc.ca

[2] Cristiano Loss, Sustainable Engineered Structural Solutions Laboratory, Department of Wood Science, University of British Columbia, Canada, cristiano.loss@ubc.ca

https://doi.org/10.52202/069179-0448

material in low-rise residential housings in countries with rich bamboo resources, such as the Philippines, Colombia, Ecuador, China, and India. In recent years, significant efforts have been devoted to the characterization of the mechanical properties of engineered bamboo products, such as laminated bamboo lumber (LBL), parallel strand bamboo (PSB), and bamboo laminated veneer lumber (BLVL), aiming to expand their application as load-bearing members in buildings and eventually, incorporate them into the building code. However, other factors of using bamboo material in the built environment must be addressed, such as the fire protection strategy, the connection design approach, and its long-term behaviour.

1.4 OBJECTIVES

Seeing the technological developments in the wood industry and needs for a sustainable building environment, this paper aims to develop an engineered bamboo shear connectors for wood composite floorings. Due to enhanced mechanical properties of engineered bamboo, it is anticipated that such bamboo-tenon connectors are suitable candidates for CLT-glulam floors intended for long-span usage. Besides, the design value of the bamboo-tenons remains in the elastic region, aiming to prevent the irreversible damage in local areas of timer members for future deconstruction and reconstruction purpose.

2 CLT-GLULAM RIBS COMPOSITE FLOORING SYSTEM CONNECTED WITH BAMBOO SHEAR CONNECTORS

2.1 CLT-GLULAM FLOOR

A 12-meter timber composite flooring system consisting of a 3-ply CLT panel and glulam ribs connected by bamboo-tenon shear connectors was designed to fulfil the static performance objectives per the National Building Code of Canada (NBCC) [9]. A non-structural concrete topping was placed on top of the CLT panels and counted as dead load only. The flooring system was modular designed, assumed sitting on continuous mass timber vertical load-bearing elements or hybrid timber-based frameworks. The structural elements are illustrated in Figure 1.

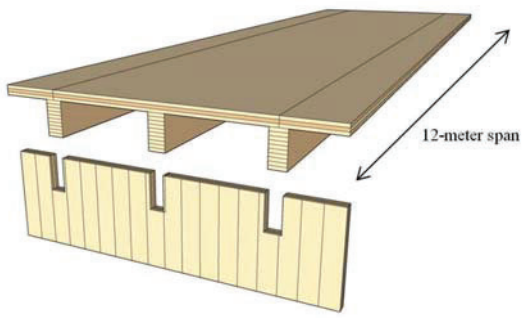

Figure 1: *CLT-glulam composite flooring and its end supports*

2.2 BIO-BASED TENON-TYPE SHEAR CONNECTORS

The three-piece tenon-type shear connector requires grooving into both the CLT and glulam ribs and is made of engineered bamboo products, as shown in Figure 2.

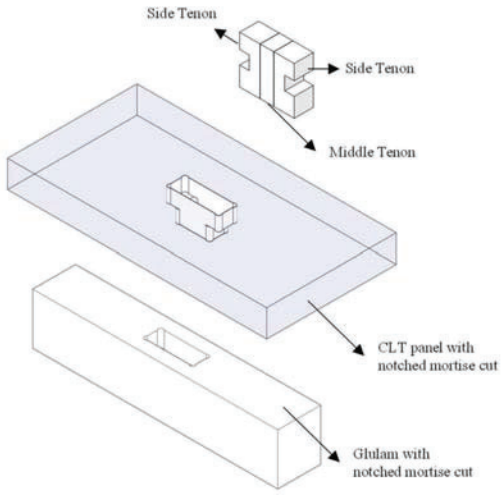

Figure 2: *Three-piece bamboo-tenon shear connector and CLT-glulam with mortise cuts*

The geometry of the tenon was inspired by the traditional joinery technique combined with CNC-machined carpentry joints used in modern timber structures. The sides of the tenon are symmetrical pieces with grooved profiles to accommodate CLT panels. The middle piece is used for tightening the mortise-tenon joint. The entire connector is embedded in mass timber members and covered by non-structural floor components, as described in Section 2.1. The corners of mortises in CLT and glulam were routed as rounded circles (i.e., notches in the figure). It is a feature of modern CNC machine drilling and provides a buffer area at the corner of the mortise-tenon contact region. Two engineered bamboo products were considered for the tenon material in this study, e.g., parallel strand bamboo (PSB) and laminated bamboo lumber (LBL).

3 MODELLING IN ANSYS

3.1 MATERIAL PROPERTIES

Mass timber products in this study., i.e., CLT and glulam, were modelled using solid wood properties and assembled by layer's fibre orientation. Wood is assumed as an orthotropic material. The material properties of PSB and LBL were described using the transversal isotropic and orthotropic models, respectively. This difference is caused by their different processing procedure [10]. The fibre orientation of each material and corresponding axis directions in the modelling space are shown in Figure 3.

https://doi.org/10.52202/069179-0448

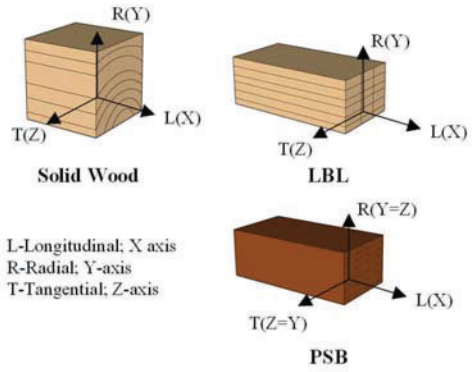

Figure 3: *Biomaterials fibre orientations and their axes in Cartesian coordinate system*

The elastic properties of wood were obtained from Wood Handbook [11]. The species of CLT and glulam are spruce (Sitka) and Douglas-fir, respectively. For details see authors' previous work [12]. The elastic properties of bamboo products are listed in Table 1 and Table 2, while more details can be found in [13, 14] and [15, 16] for PSB and LBL, respectively.

Table 1: *Elastic modulus of engineered bamboo products*

Product	E_x	E_y	E_z	G_{xy}	G_{xz}	G_{yz}
PSB	11890	3066	3066	1361	1361	746
LBL	9391	1440	1149	1365.08	1260.09	461.81

*Unit in Mpa

Table 2: *Poisson ratios of engineered bamboo products*

Product	μ_{xy}	μ_{xz}	μ_{yz}
PSB	0.411	0.411	0.115
LBL	0.25	0.2	0.42

Material properties under compressive and shear forces are the decisive parameters in tenon-type contact joints. Summarizing from [13-17], the constitutional law of wood and bamboo product is illustrated in Figure 4. It should be noticed that the stress-strain relationship of wood material under complex stress was well established for modelling with entire curve behaviour. In contrast, the studies on the stress-strain relationship of bamboo products most focus on describing the curve before failing.

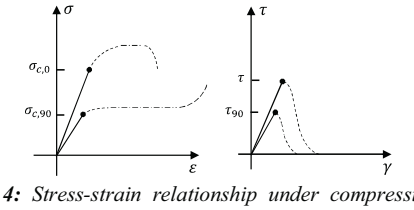

Figure 4: *Stress-strain relationship under compression and shear*

The bilinear isotropic hardening model is assumed to describe the behaviour of wood and engineered bamboo products in the plastic phase. Table 3 lists the tangent modulus of wood in compression, validated by the mean values of clear wood specimens from [18] and [19] for spruce CLT species and Douglas-fir glulam species, respectively. The tangent modulus and strengths of PSB and LBL under compression and shear forces were obtained from the mean value results from [13-14] and [15-16], respectively. σ_{xx}, σ_{yy} and σ_{zz} are the normal stresses; σ_{xy}, σ_{yz} and σ_{xz} are the shear stresses.

Table 3: *Properties in the plastic region (unit in Mpa)*

Item	CLT, Spruce	Glulam, D.-Fir	PSB, Moso	LBL, Moso
$E_{Tangent}$	123.20	149.60	2853.60	93.91
σ_{xx}	37.80	50.00	33.09	46
σ_{yy}	4.1	6.0	7.68	21.63
σ_{zz}	4.1	6.0	7.68	19.62
σ_{xy}	4.08	5.7	23.44	18.13
σ_{yz}	0.93	1.9	3.64	22.59
σ_{xz}	2.85	3.99	23.44	6.58

The Hill criterion, given in Equation (1), was applied as the failure criteria:

$$f(\sigma) = \sqrt{\begin{matrix} F(\sigma_{yy}-\sigma_{zz})^2 + G(\sigma_{zz}-\sigma_{xx})^2 \\ +H(\sigma_{xx}-\sigma_{yy})^2 + 2L\sigma_{yz}^2 + 2M\sigma_{zx}^2 + 2N\sigma_{xy}^2 \end{matrix}} \quad (1)$$

F, G, H, M, and N are material constants from the tests, defined by Equation (2)-(7):

$$F = \frac{1}{2}\left(\frac{1}{R_{yy}^2} + \frac{1}{R_{zz}^2} - \frac{1}{R_{xx}^2}\right) \quad (2)$$

$$G = \frac{1}{2}\left(\frac{1}{R_{zz}^2} + \frac{1}{R_{xx}^2} - \frac{1}{R_{yy}^2}\right) \quad (3)$$

$$H = \frac{1}{2}\left(\frac{1}{R_{xx}^2} + \frac{1}{R_{yy}^2} - \frac{1}{R_{zz}^2}\right) \quad (4)$$

$$L = \frac{3}{2}\left(\frac{1}{R_{yz}^2}\right) \quad (5)$$

$$M = \frac{3}{2}\left(\frac{1}{R_{xz}^2}\right) \quad (6)$$

$$N = \frac{3}{2}\left(\frac{1}{R_{xy}^2}\right) \quad (7)$$

R_{ij} are the yield stress ratios, defined by Equation (8):

$$R_{11} = \frac{\sigma_{xx}^y}{\sigma_y};\ R_{11} = \frac{\sigma_{yy}^y}{\sigma_y};\ R_{11} = \frac{\sigma_{zz}^y}{\sigma_y};\quad R_{11} = \sqrt{3}\frac{\sigma_{xy}^y}{\sigma_y};\ R_{11} = \frac{\sigma_{yz}^y}{\sigma_y};\ R_{11} = \frac{\sigma_{xz}^y}{\sigma_y} \quad (8)$$

https://doi.org/10.52202/069179-0448

Assuming the compressive strength in the main fibre direction as the reference yielding stress, σ_y, the generated yield stress ratios are listed in Table 4.

Table 4: *Yield stress ratios*

Item	CLT, Spruce	Glulam, D.-Fir	PSB, Moso	LBL, Moso
R_{11}	1.00	1.00	1.00	1.00
R_{22}	0.11	0.12	0.23	0.47
R_{33}	0.11	0.12	0.23	0.43
R_{12}	0.19	0.20	1.23	0.68
R_{23}	0.04	0.07	0.19	0.85
R_{13}	0.13	0.14	1.23	0.25

3.2 MODELLING AT THE JOINT LEVEL

One-meter-long solid-type joint models were built in the ANSYS workbench to investigate the joint shear performance under static push-out force. See Figure 5.

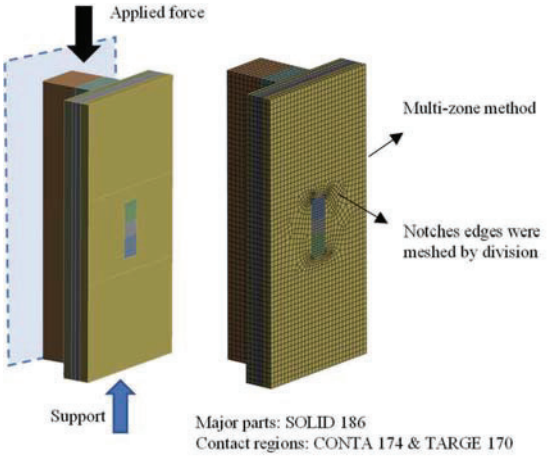

Figure 5: *Joint model*

CLT panel was modelled by layers bonded together. The crosswise layout was defined by a local coordinate system. Glulam was built as one united body and its material properties were defined by the global coordinate system. Both members were split locally to improve the meshing quality around the mortise. The tenon was orientated with the main fibre direction perpendicular to the shear force direction with a specific defined local coordinate system. Solid 186 element was employed in all bodies. The multizone meshing method was applied. To capture the mortise-tenon in detail, the meshing size around the contact area was refined. The mortise notch edges were divided into 5 segments. Face meshing was applied to the tongue of the CLT panel. The global and local meshing sizes were compatible and chosen for a high-quality finite-element meshing result. The overall meshing size of CLT and glulam were set as 18 mm whereas the meshing size of the tenon was set as 15 mm. The meshing quality was 0.94 on the average, with all the components meshed using hex elements.

The surface element was used to evenly distribute applied force to the loading area. Sub-steps were set for convergence after approaching the plastic region of materials. In sub-step 1 to 4, the force increment is 20 kN. After applying 80 kN to the model, 10 kN was applied per sub-step until the finish. Large deformation was allowed. A frictional coefficient of 0.5 was applied to all the contact surfaces within the model [20].

The parametric study was conducted to investigate the joint performance when varying material combinations of tenons and contact characteristics between tenon pieces. The studied schemes are listed in Table 5.

Table 5: *Parametric study scheme*

Scheme No.	Side Tenon	Middle Tenon	Contact
1	PSB	PSB	Bonded
2	PSB	PSB	Frictional
3	PSB	LBL	Frictional
4	LBL	LBL	Bonded
5	LBL	LBL	Frictional
6	LBL	PSB	Frictional

Note: Contact refers to between tenon pieces

3.3 MODELLING AT THE FLOOR LEVEL

The CLT-glulam rib flooring system was modular designed where one floor module consists of one CLT slab with dimensions of $105 \times 1200 \times 12000$ mm (thickness × width × length) and one glulam with dimensions of $175 \times 380 \times 12000$ mm (width × depth × length). Single floor module was built in ANSYS Workbench adjusting the modelling method used for the joint, with minor changes on meshing. The variation of timber products caused by it defects and product assembly process are not considered in this stage of investigation. However, to better capture the structural behaviour at the system level, the meshing size of the fully and not connected composite beams was set as 60 mm. This was compared with the theoretical results of applying the Gamma method to a simply supported CLT-glulam composite floor of the same configuration. Bonded contact was applied between CLT and glulam under fully connected situations, whereas frictional contact was applied for not structurally connected composite floors. The same frictional coefficient as the joint model was used. The proposed bamboo-tenon connected flooring system was built based on geometry imported from SolidWorks. The as-built floor models are shown in Figure 6.

The case study was conducted using the loading conditions listed in Table 6. The impact of supporting systems on the structural behaviour was studied, considering common office space usage; see cases 1 to 3. In these cases, a specified live load of 2.4 kpa is uniformly distributed on the floor. The serviceability of the proposed flooring system was compared under 1.0 DL + 1.0 LL load combinations. Extreme loading conditions, as per Notes A-Table 4.1.5.3 of NBCC, were also studied. Such cases as using proportions of the long-span floor as

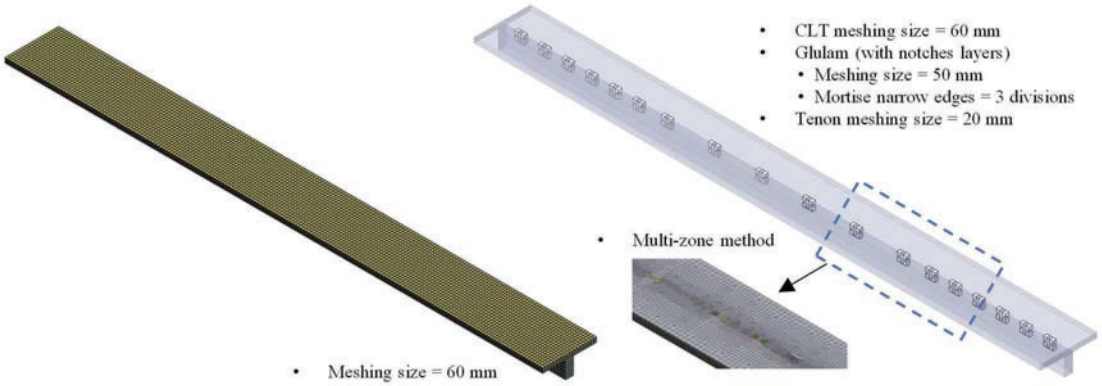

Figure 6: *Finite-element models of one module CLT-glulam composite floor (Left: full and not connected floor; right: proposed floor)*

Table 6: *Case studies of the flooring system*

Loads	Boundary conditions and loading areas
Uniformly distributed loads, q: 1.0 DL +1.0 LL	Case 1: Simply support
	Case 2: Fix-Roller
	Case 3: Fix Ends
Uniformly distributed loads, q: 1.25 DL +1.5 LL	Case 4: Simply support
Uniformly distributed loads, q: 1.25 DL +1.5 LL Partially distributed load, q': 1.5 LL	Case 5: Extra LL in the middle segments
	Case 6: Extra LL at both ends
	Case 7: Extra LL at one end

a temporary storage room for files or furniture. In these cases, an extra live load of 2.4 kpa was partially distributed on segments of the flooring system. See cases 4 to 7. The 12-meter span floor is divided into 4 segments of 3 meters. The flexural behaviour of the proposed composite flooring system under ultimate limit states and extreme loading conditions were investigated.

4 RESULTS AND DISCUSSION

4.1 LOAD-SLIP CURVES OF THE JOINT

Figure 7 shows the load-slip responses of the parametric study results extracted from the joint models at varying of the design scheme. The estimated elastic stiffness of the joints is specified in Table 7.

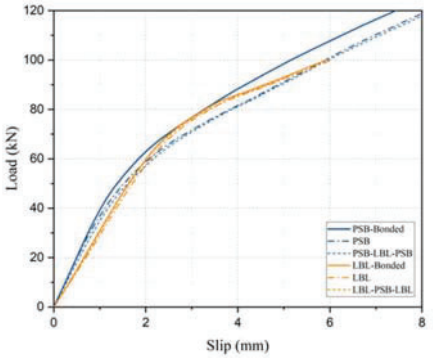

Figure 7: *Extracted load-slip responses*

Table 7: *Stiffness results of tenon joints*

Scheme No.	Tenon Configuration*	Stiffness (kN/mm)
1	PSB-Bonded	39.62
2	PSB	36.73
3	PSB-LBL-PSB	34.46
4	LBL-Bonded	30.89
5	LBL	29.11
6	LBL-PSB-LBL	30.69

*Side-middle-side tenon material

In schemes 1 to 3, PSB is designed to be directly in contact with the timber members. On the contrary, schemes 4 to 6 employ LBL as the side tenons in contact with the CLT and glulam members.

Within the PSB tenon groups, i.e., scheme 1 to 3, the internal bonded group hindered the sliding between tenon components, resulting in an increase of 8% on the overall

https://doi.org/10.52202/069179-0448

stiffness result compared to the pure PSB tenon group. The same effect occurs in the LBL-bonded and LBL groups, which shows a 6% increase of the stiffness. When changing the middle tenon material from PSB to LBL, i.e., from scheme 2 to scheme 3, the joint stiffness reduces by 21 % due to lowering the stiffness of the middle tenon. Interestingly, by changing the middle tenon from PSB to LBL, i.e., from scheme 5 to 6, the stiffness increased by 5%, closing to the boned group (scheme 4). The stress distributions under different loads are plotted in Figure 8.

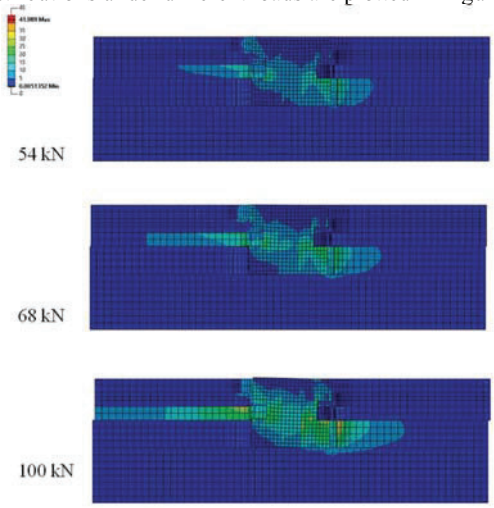

Figure 8: *Von-mises stress distribution of LBL-PSB-LBL tenon*

4.2 IMPLEMENTATION OF BAMBOO-TENON TO THE LONG-SPAN COMPOSITE FLOORING SYSTEM

By analysing the joint response under push-out shear forces, the LBL-PSB-LBL tenon (scheme 6) was selected for the proposed CLT-glulam flooring application. The proportional limit of 54 kN from the load-slip curves was assumed as the joint capacity. The flooring system was divided into three segments assuming different connectors spacing in each, in order to simplify the installation of the shear connectors. The amount and spacing of selected bamboo-tenon shear connectors are illustrated in Figure 9, and details are summarized in Table 8.

Table 8: *Bamboo-tenon distribution along the beam*

Segment	Starting point	Ending point	Amount per meter	Spacing	Edge distance
1	0	3000	2	300	300
2	3000	9000	1	800	400
3	9000	12000	2	300	300

Unit in mm

The composite efficiency of the proposed composite floor was investigated using Equation (9).

$$\eta = \frac{(EI)_{ef} - (EI)_0}{(EI)_\infty - (EI)_0} \quad (9)$$

Where $(EI)_{ef}$, $(EI)_0$ and $(EI)_\infty$ represent the effective bending stiffness from the proposed bamboo-tenon shear connector jointed composite flooring system, not connected composite floor and the fully connected composite floor, respectively.

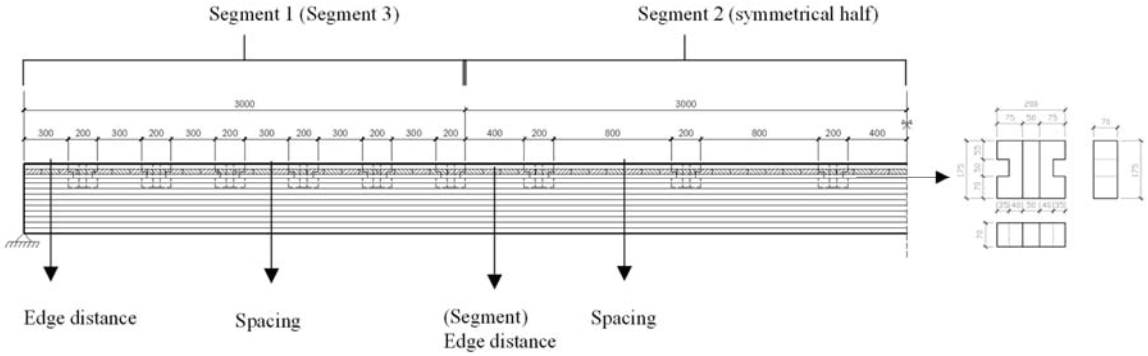

Figure 9: *Bamboo-tenon shear connector connected CLT-glulam composite floor*

4.3 CASE STUDIES OF THE COMPOSITE FLOOR UNDER SERVICEABILITY DEISGN

Figure 10 shows the case study results on the composite flooring system under serviceability loads (case study 1 to 3 in Table 6). All case scenarios were loaded to the prescribed loads. In the simply supported composite floor (case 1), the composite efficiency of the proposed flooring system is 50.79%. The supporting conditions significantly influenced the composite efficiency of the composite floor. Fixed support in this study has limited both the translations and rotations of the floor end elements. By moving into restrained supports, the differences in deflection between the floor with no and full composite action was shown reduced. Specifically, the composite efficiency of floors with fix-roller supports and the fixed ends support were 27.41 % and 14.69%, respectively. These indicate the benefits of implementing shear connectors become less remarkable when increasing the restriction from the supporting system.

A construction path was created on the CLT-glulam interface, going through the central line of the glulam top surface and penetrating through tenons if implemented. The shear stresses on the interface are plotted in Figure 10, (c). With tenons inserted, the shear stress on the interface shows an oscillating pattern, i.e., the stress increases when passing through a tenon, reaches the regional maximum value at the contact surface of mortise-tenon and decreases to zero when moving to the area where no tenon is inserted. For example, in case 1, the regional peak stress value occurs at 500 mm from the edge, which is also the end of the first inserted tenon. Also in case 1, the regional peaks value along the span shows the same decreasing trend as fully connected composite beams, i.e., the regional peak value keeps declining when approaching the mid-span of the floor. By changing the degrees of freedom at the supports, the maximum stress moved from the first tenon area to the 6th and the 5th tenon in the fix-roller and the fixed ends cases, respectively.

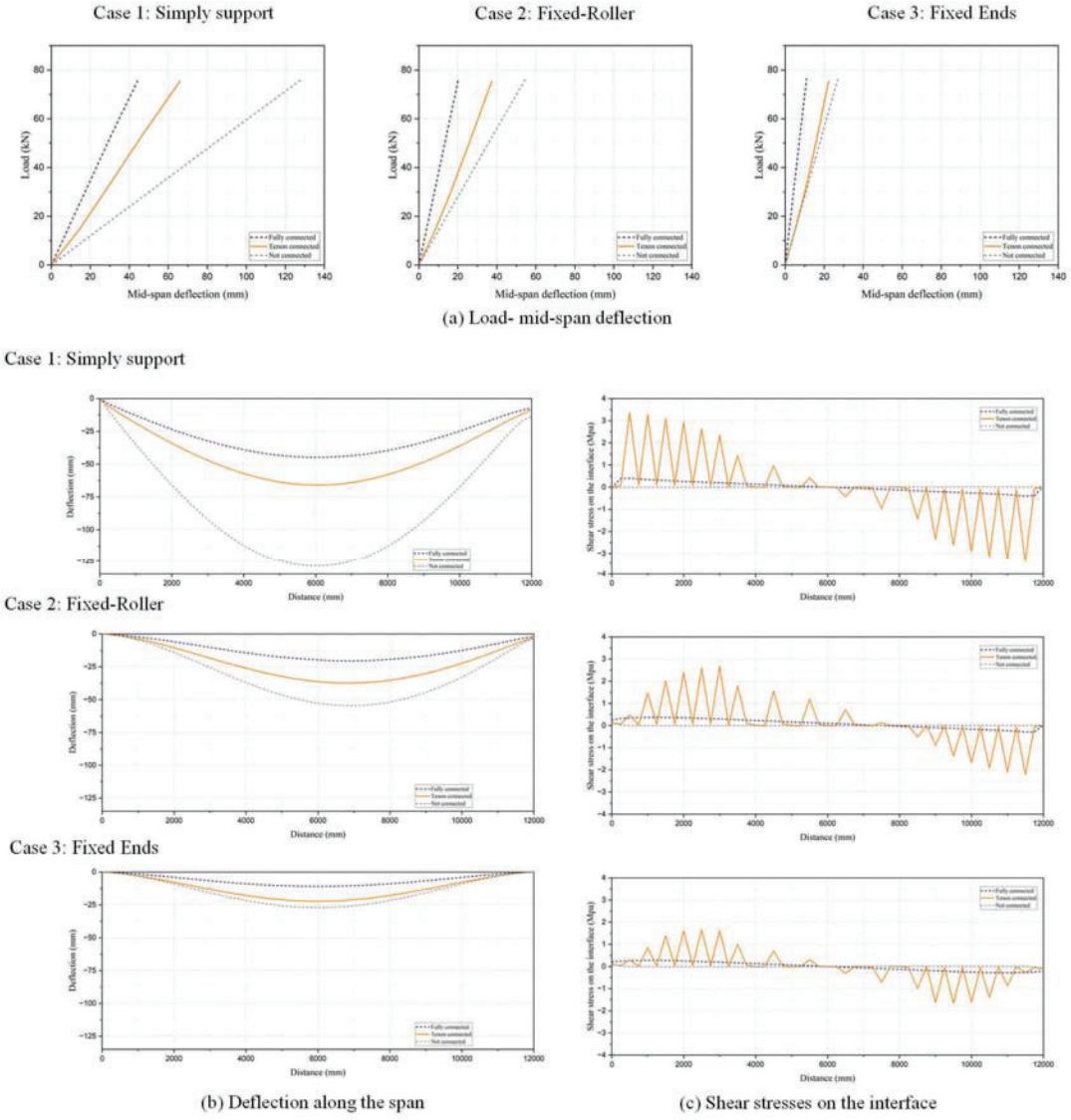

Figure 10: *Comparison on the flexural performance of the composite floors with different boundary conditions under serviceability loading conditions*

Figure 11 shows the case study results of long-span composite floors with extra partially distributed live loads with loading conditions listed in Table 6. The case study models were loaded to the design load as described in Table 6, case 4 to 7. A yielding point can be observed on the load-deflection curves. It should be noticed that this is caused by the deformation near the supporting area. Evidence can be found from the deflection along the beam curves, where a kink appeared near the supports. The stress distribution of the composite flooring system plotted in Figure 12 also illustrates this deformation. Besides, stress results were checked on all structural members. It shows all members remain in their elastic regions under the design value.

https://doi.org/10.52202/069179-0448

Compared to the simply supported with uniformly distributed loads case (case 1), the shear stress increased at the increasing of live load on the floor segments in other cases. For example, when adding an extra 2.4 kpa live load to each end, the peak shear stress increased from 4.16 Mpa in case 1 to 4.42 Mpa in case 6.

Among three extreme loading case scenarios, the extra live loading area on the middle segments causes more deflection of the structure and overall shear stresses on the interface. Therefore, this case scenario should be seen as the least favourable scenario under extreme loading conditions.

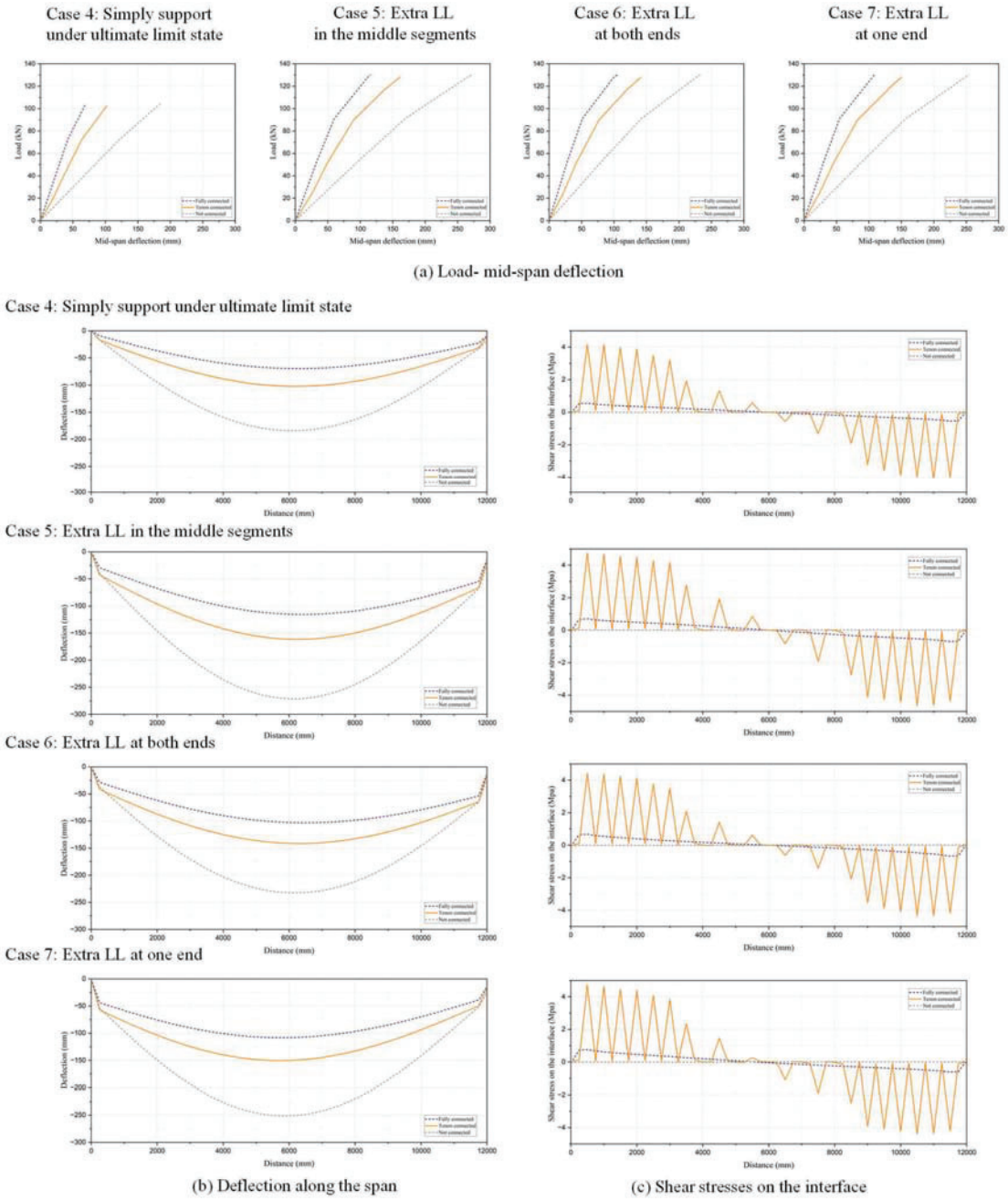

Figure 11: *Comparison on the flexural behaviour of the composite floors under ultimate limit state and extreme loading conditions*

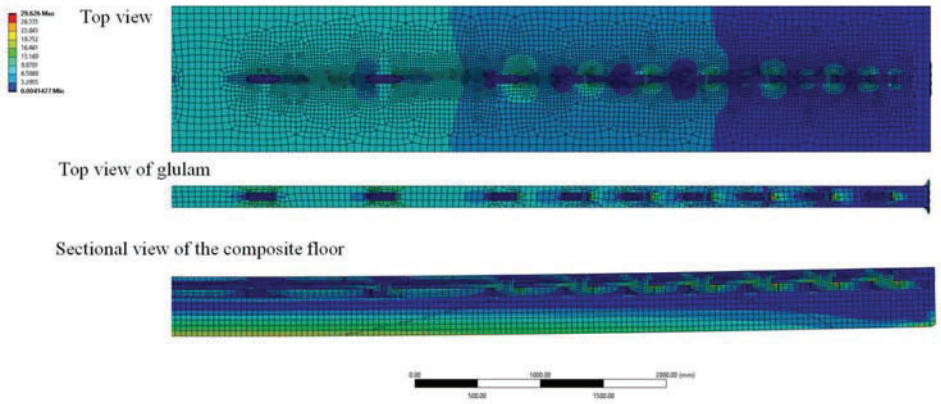

Figure 12: *Von-mises stress distribution of bamboo-tenon connected composite floor under ultimate limit state (half span, case 4)*

5 OVERVIEW

5.1 COMPARISON BETWEEN THE ANALYSIS AT THE JOINT LEVEL AND THE FLOOR LEVEL

The geometric feature of the bamboo-tenon, i.e., the tongue-and-groove cut, was generated for the purpose of quick assembly and disassembly. In one of the preliminary FEM simulations at the joint level, where bonded contact was applied to all the contact surfaces within the mortise-tenon, a quick distortion occurred on the glulam notches edge and the tongue of CLT panels, indicating the potential decrease of the overall joint capacity due to the existence of glue. Within the parametric study scope of this study (Table 5), the comparison between internal glued joint groups and the frictional connected joints showed a limited increase in the joint stiffness by internal bonding. Considering the costs of adhesives and the curing time, the internal glued joint was not chosen for the subsequent floor design.

However, the rotational behaviour of the tenon has a more significant impact on the global flexural behaviour when implemented in the long-span CLT-glulam flooring system. When the composite system undergoes deformation under bending, the rotational behaviour of the tenon leads to a detached mortise-tenon surface at the bottom. Therefore, the proposed tenon-type shear connector failed to efficiently transfer the forces between members as anticipated. A much lower composite efficiency is witnessed when analysing the proposed bamboo-tenon connected long-span composite floor.

This inconsistent results between the joint and the floor models indicates that special attention needs to be drawn to the rotational behaviour of tenon-type connectors. Specifically, tenon geometries and shape can be redefined with a new design to minimize the rotation of the bamboo-tenon under shear forces.

5.2 COMPARISON BETWEEN PROPOSED CONNECTOR AND SELF-TAPPING SCREWS

CLT construction using self-tapping screws as connectors has been studied and well implemented in practice. In the 7-meter CLT ribbed composite system studied by [21], 48 screws were used to engage floors with full composite action. For longer spans, the number of screws rises and can be around 80 to 90 [22]. In general, high level of composite action is guaranteed by reducing spacing of screws, as demonstrated by [23].

Using a specific selection of material combination, the number of shear connectors used to assemble a 12-meter flooring system can be as low as of 18 bamboo-tenons. Besides, the fabrication tolerance can be preciously controlled in the factory. As such, the proposed tenon-type connectors of this study demonstrate a structurally efficient solution.

5.3 LIMITATIONS OF MODELLING

Compared to the well-established knowledge on the behaviour of wood, the lack of harmony material testing methods on engineered bamboo products and reliable dataset of their mechanical properties led to uncertainty in the estimation of the bamboo-tenon connector capacity.

Besides, future modelling will benefit from the experimental test results of the joints, as well as the full-scale flooring tests. Limited by the knowledge and experimental database of the structural behaviour of tenon-type shear connectors, 3D floor models were used in this study. Further study can advance this modelling method by incorporating reliability analysis on the impacts of defects on the mechanical properties of structural members.

6 CONCLUSION

This paper mainly investigated the structural performance of a bamboo-tenon shear connector jointed long-span CLT-glulam ribbed composite flooring system. Specific recommendations for the bamboo-tenon design are concluded as follows:

1. Having a stiffness of 30.69 kN/ mm per tenon per joint and an elastic capacity of 54 kN under shear forces, the LBL-PSB-LBL tenon material combination is recommended for this three-piece tenon design;
2. A total number of 18 bamboo-tenon were implemented by segments in the proposed composite flooring system; however, the

https://doi.org/10.52202/069179-0448

rotational behaviour of the tenon reduced the composite efficiency;

3. By increasing the restrains of supports on the composite flooring system, the variance in the flexural behaviour of floors under full and non-composite action was shown reduced, resulting in less composite efficiency when implementing shear connectors;
4. Under extreme loading conditions, the extra live load partially distributed on the middle segments should be concerned as the worst-case scenario and should be prioritized.

This feasibility study demonstrates the potential of using bamboo-tenon as shear connector in CLT-glulam long-span flooring systems. Further optimization of the bamboo-tenon is needed. This research helps broaden the applications of engineered bamboo products in the future building environment.

ACKNOWLEDGEMENT

This research was financed by the Natural Sciences and Engineering Research Council (NSERC) of Canada through the Discover Program, grant number RGPIN-2019-04530, and Discovery Launch Supplement, grant number DGECR-2019-00265. MOSO® Bamboo company is acknowledged as the engineered bamboo products sponsor in this study. The State Scholarship Fund of China, No. 202006510006, awarded to Yue Diao, is also acknowledged.

REFERENCES

[1] Committee of European Normalisation (CEN). EN 1994-1-1-2004, Eurocode 4: Design of composite steel and concrete structures, Part 1–1 General Rules and Rules for buildings 1994–2005.

[2] A. Thiel, R. Brandner. ULS Design of CLT Elements –Basics and Some Special Topics. In: Joint Conference of COST Actions FP1402 & FP1404 KTH Building Materials, 65-90, 2016.

[3] P. Papastavrou, S. Smith, T. Wallwork, A. McRobie, N. Niem. The Design of Cross-Laminated Timber Slabs with Cut-Back Glulam Rib Downstands-From Research to Live Project. In: WCTE, 2016.

[4] N. Jacquier. U. A. Girhammar. Evaluation of Bending Tests on Composite Glulam–CLT Beams Connected with Double-Sided Punched Metal Plates and Inclined Screws. Constr and Build Mater, 95: 762-773, 2015.

[5] T. Tannert, F. Lam, T. Vallee. Strength Prediction for Rounded Dovetail Connections Considering Size Effects. J. Eng. Mech., 136(3): 358-366, 2010.

[6] T. Claus, W. Seim. Development of the Multiple Tenon Timber Connection Based on Experimental Studies and FE Simulation. Engineering Structures, 173:331-339, 2018.

[7] J. R. Brown, M. Li, F. Sarti. Structural Performance of CLT Shear Connections with Castellations and Angle Brackets. Engineering Structures, 240: 112346, 2021.

[8] T. Schmidt, H. J. Blaß. Contact Joints in Engineered Products. In: WCTE, 2016.

[9] Canadian Commission On Building And Fire Codes. “National Building Code of Canada: 2020,” March 28, 2022, v. 1, 792 p.; v. 2, 708 p.

[10] B. Sharma, A. Gatóo, M. Bock & M. Ramage. Engineered bamboo for structural applications. Construction and Building Materials, 81, 66–73, 2015.

[11] Forest Products Laboratory. Wood handbook—Wood as an engineering material (General Technical Report FPL-GTR-282; p. 543). Department of Agriculture, Forest Service, Forest Products Laboratory, 2021

[12] Y. Diao, & C. Loss. Long-span CLT-glulam composite flooring system connected with bamboo-based shear connectors: Feasibility of design for assembly. CSCE 2021 Annual Conference, Whistler, BC, Canada, 2022

[13] D. Huang, Y. Bian, A. Zhou, & B. Sheng. Experimental study on stress–strain relationships and failure mechanisms of parallel strand bamboo made from phyllostachys. Construction and Building Materials, 77, 130–138, 2015.

[14] H. Li, Z. Qiu, G. Wu, D. Wei, R. Lorenzo, C. Yuan, H. Zhang, & R. Liu. Compression Behaviors of Parallel Bamboo Strand Lumber Under Static Loading. Journal of Renewable Materials, 7(7), 583–600, 2019.

[15] H. Li, Q. Zhang, D. Huang, & A. J. Deeks, Compressive performance of laminated bamboo. Composites Part B: Engineering, 54, 319–328, 2013.

[16] C. Hong, H. Li, Z. Xiong, R. Lorenzo, X. Li, & Z. Wang. Axial compressive behavior of laminated bamboo lumber columns with a chamfered section. Structures, 33, 678–692, 2021.

[17] Z. Chen, E. Zhu, & J. Pan. Numerical simulation of wood mechanical properties under complex state of stress. Chinese Journal of Computational Mechanics, 28(4), 629–634, 2011.

[18] S. Widehammar. Stress-strain relationships for spruce wood: Influence of strain rate, moisture content and loading direction. Experimental Mechanics, 44(1), 44–48, 2004.

[19] S., Ellis, & P. Steiner. The behaviour of five wood species in compression. IAWA Journal, 23(2), 201–211, 2002.

[20] Ansys® Academic Research Mechanical, Release 2021 R1, Ansys Innovation Courses, Contact Mechanics, ANSYS, Inc.

[21] R. Masoudnia, A. Hashemi, P. Quenneville, M. Asce, S. Engineer, & G., Ipenz. Predicting the Effective Flange Width of a CLT Slab in Timber Composite Beams. J. Struct. Eng., 18, 2018.

[22] J. Negrão, & L. Jorge. CLT Structure for Long Span Floors and Roofs—Optimizing the Cross-Section Properties. 41st IAHS World Congress: Sustainability and Innovation for the Future, 10, 2016.

[23] C. Zhang, X. Zheng, & F. Lam. Development of composite action in a new long-span timber composite floor: Full-scale experiment and analytical approach. Engineering Structures, 279, 115550, 2023.

World Conference on Timber Engineering Oslo 2023

STUDY ON FRAME DESIGN OF CONVENTIONAL WOODEN HOUSE

Tomoya Sahata[1], Naohito Kawai[2], Hideyo Tsukazaki[3]

ABSTRACT: This study assesses conventional Japanese architectural methods. Japanese houses constitute a framework with columns and beams. In addition to these structures, braces are installed to provide resistance to earthquakes and wind loads. A brace wall consists of foundations, columns, beams, and braces. Members are produced from standing trees. Therefore, the member length is constrained. For this reason, the lengths of timbers distributed in the market are 3–6 m. For horizontal members such as beams, the ends of the members must be connected to provide the necessary length for the building. For this study, we confirmed the effects on the strength and failure properties when joints were provided on beams that make up the brace wall. Results indicate that the joint of the beam placed on the 910 mm brace wall did not affect the maximum load, but had a slightly reduced initial stiffness.

KEYWORDS: Beam joint, Brace wall, Factual investigation, In-plane shear test, Structural analysis

1 INTRODUCTION

A conventional Japanese wooden house is made up of wooden materials such as columns and beams (Fig. 1). For an average-sized house, a joint is necessary to extend the beam length. As a rule, this joint should not be placed inside the wall to which the brace is to be attached, as presented in Fig. 2 [1]. However, when performing seismic reinforcement work, it might be necessary to install a beam joint on the brace wall [2]. Our drawing survey [3] results revealed that many beam joints in braced walls exist, even in new houses. Reports of past studies have described many findings from examinations of braced walls and beam joints. For braced walls, the effects have been confirmed of different species of braces and different types of joint hardware at the end of the braces on strength properties [4, 5]. Regarding joints, the effects of different species of wood, cross-sectional dimensions, and shapes of the joints on joint performance have been confirmed [6, 7]. However, the effects on brace walls have not been clarified when the beam joint is installed in the brace wall. Therefore, this study was conducted to elucidate the effects of beam joints of braced walls on strength and fracture properties. As described herein, a questionnaire survey related to the arrangement of the joints was administered to frame designers. After the configurations of loading tests and structural analyses were found, the beam joint effects on the strength properties of braced walls were assessed.

[1] Tomoya Sahata, Polytechnic University, Japan (Kogakuin University Doctoral Program) t-sahata@uitec.ac.jp
[2] Naohito Kawai, Kogakuin University, Japan kawai-nk@cc.kogakuin.ac.jp
[3] Hideyo Tsukazaki, Polytechnic University, Japan tukazaki@uitec.ac.jp

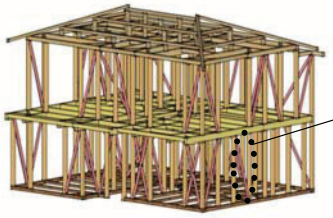

Figure 1: *Shaft assembly model*

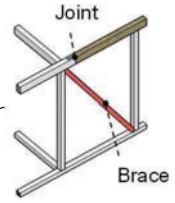

Figure 2: *Joint of beam member in brace wall*

2 FACTUAL INVESTIGATON

2.1 OUTLINE OF THE ACTUAL SURVEY

A questionnaire survey was conducted of frame designers at wood processing (hereinafter, pre-cutting) factories with the aim of identifying trends in the arrangements of joints in beam members. The first survey targeted 108 pre-cutting factories with annual processing area of approximately 100,000 m^2 or more. The second survey was administered to 201 companies (including 64 pre-cutting factories targeted by the first survey) that mainly use software from three major pre-cut CAD manufacturers. The number of newly selected pre-cutting factories was 137. The total number of companies in the first and second surveys was 245. Table 1 presents results of the questionnaire collection. The combined collection rate for the first and second questionnaires was 24.1%. Interviews were conducted with 23 of the 68 respondents to assess their responses.

Table 1: *Questionnaire collection results*

Number	1st time	2nd time	Duplication	Total	Response rate Number of companies responding / Number of companies sent
Shipping companies	108	201	64	245	59 companies/245 companies (%) 24.1 %
Answer companies	24	35	–	59	
Respondents	24	44	–	68	–

2.2 LENGTH OF WOOD TO BE USED

Findings from the survey of the lengths of timber used for horizontal members are depicted in Fig. 3. Because the

https://doi.org/10.52202/069179-0449

same trend was observed for the horizontal structure of the first floor, second floor, and shed structures, they are presented together. As the figure shows, 4 m timber is the most commonly used material, followed by 3 m and 5 m. According to the interview survey, 3 m and 5 m timbers are used in the right places in relation to the positions of the columns and openings, perhaps because of the very low use of lumber longer than 6 m, the high price, and the reduced ease of installation on site.

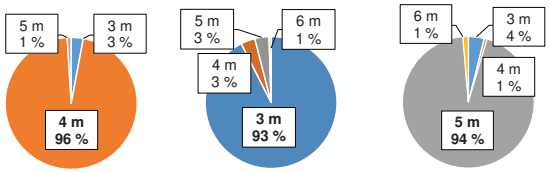

Figure 3: *Priority of specified length of horizontal member to be used*

2.3 TYPES OF JOINTS FOR HORIZONTAL MEMBERS

Results of a survey of the types of connections used for horizontal members are portrayed in Fig. 4 for the first floor, second floor, and shed sections together. Fig. 4 shows that more than 70% use the type B joining method. The type A jointing method is also often used for horizontal structures of the first floor. Type A joints are often used in the horizontal structure of the first floor because the foundation and base are connected by anchor bolts, which require no high bending performance. Furthermore, interviews conducted after the questionnaires were collected also indicate construction-related reasons, such as easier on-site assembly.

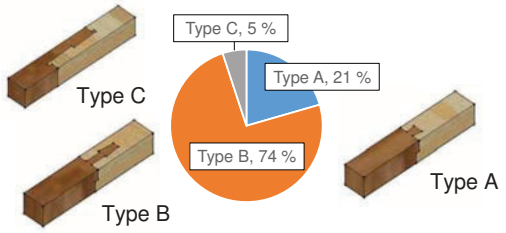

Figure 4: *Types of beam joints in horizontal members*

2.4 JOINT OF HORIZONTAL MEMBERS PLACED IN THE BRACE WALL

A questionnaire survey was administered to ascertain the actual situation of the frame design work. The relative positions of the brace and the beam joints in the brace wall are presented in Fig. 5. Joints of the beam in the brace wall are of three types: push up of the single brace (Fig. 5(i)); the opposite side of the push up portion of the single brace (Fig. 5(ii)); and the push up portion of the double brace (Fig. 5(iii)). Results of these investigations of the beam joints in the brace walls are shown in Fig. 6. The percentages of designers who responded "give special consideration" or "give consideration" were 74% in the case of Fig. 6(i) and 80% in the case of Fig. 6(iii). Those findings indicate that more than 70% of the designers responded that they would "consider" or "give consideration" to the push up portion of the brace in the brace wall. However, the interview survey results suggest that beam joints had to be placed at the push-up of the braces sometimes to prioritize the yield of fixed-length materials (mainly 3 m and 4 m).

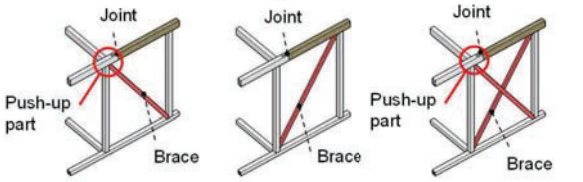

Figure 5: *Positions of beams in joints of a brace wall*

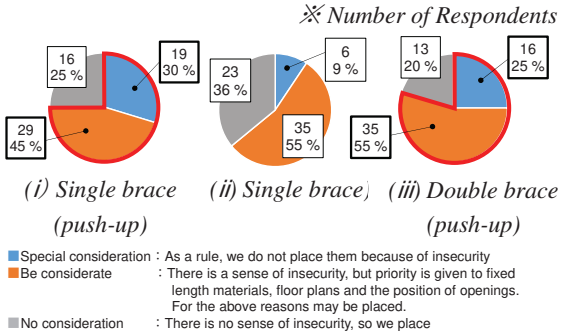

Figure 6: *Awareness of beam joints on the inside of brace walls*

3 IN-PLANE SHEAR TEST

3.1 SPECIMEN AND TEST BODY

Table 2 presents the specifications of members that constitute the test body. Fig. 7 shows the test body configuration: cross-sectional dimensions of the foundation and column are 105 × 105 mm; the beam is 105 × 180 mm; the studs are 30 × 105 mm; and the brace is 45 × 90 mm. The test body dimensions indicate a 910 mm wall length and a 2730 mm wall height. It is noteworthy that the 910 mm test body length is a traditional Japanese unit. The test body parameters reflect how to set the brace and presence and absent joint. The test body name is the following.

[Test body name] A – B

A: How to set a brace

B: Presence or absence of beam joint

Table 2: *List of physical properties of test materials*

Material name	Tree species	Air-dry density (kg/m³)	Moisture content (%)	Average annual ring width (mm)	Young's modulus (kN/mm²)
Foundation	Cedar	482	14	4.3	11.5
Column	RW laminated wood	496	14	–	11.5
Beam	RW laminated wood	471	15	–	10.5
Brace	Cedar LVL	369	11	–	8.3
Stud	WW laminated wood	432	11	–	11.8

Table 3 presents a legend for test body symbols. It lists the test bodies. The number of test bodies was three for each. The total of test bodies was 12.

https://doi.org/10.52202/069179-0449

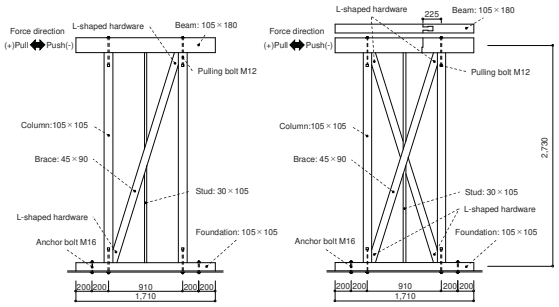

Single brace / joint none *Double brace / joint placed*

Figure 7: *Configuration of In-plane shear test (unit: mm)*

Table 3: *List of test bodies*

Test body symbol	How to set a brace	Presence or absence of beam joint	Number of test bodies
SN	**S**ingle	**N**one	3
SJ	**S**ingle	**J**oint	3
DN	**D**ouble	**N**one	3
DJ	**D**ouble	**J**oint	3

3.2 TEST METHOD

The test method was based on an allowable stress design for wood-frame housing [8]. The historical force was repeated three times with positive and negative alternating forces so that the apparent deformation angle became 1/450, 1/300, 1/200, 1/150, 1/100, 1/75, and 1/50 rad, as presented in Fig. 8. Then it was pulled until the apparent deformation angle became 1/15 rad. As presented in Fig. 9, the relative rotation angle between the upper member and lower member of the beam joint is calculated using the displacement of two electrical displacement meters attached to the beam joint.

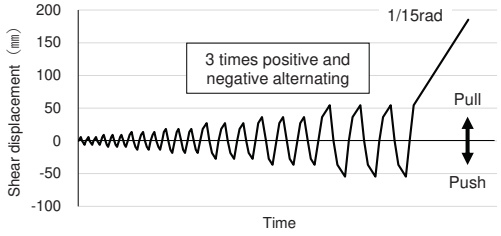

Figure 8: *Loading schedule for in-plane shear test*

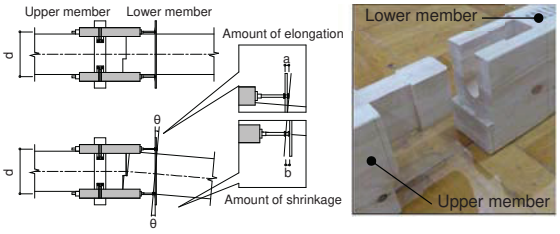

$\theta = (a - b) / d$

θ: Relative displacement angle of two members (rad)

a,b: Displacement by displacement meter (mm)

d: Distance between gauge points (mm)

Figure 9: *Method of rotation angle calculation for beam joint angles of beams joint*

3.3 TEST RESULTS AND DISCUSSION

Fig. 10 shows the relation between the load and the shear deformation angle. Table 4 presents the maximum load and initial stiffness as calculated from the test results presented in Fig. 10. The maximum load and initial stiffness of the test body of the single brace (SN) are greater than those of the SJ. For the test body of the double brace, the maximum load and initial stiffness of DN are comparable to those of DJ. Table 5 shows the rotation angle of the joints at maximum load. From Table 5, it is apparent that the angle of rotation of the joint at maximum load is greater for SJ than for DJ. This greater angle can be attributed to the difference in the magnitude of the moment generated at the beam joint by the brace. In the case of the double brace, because the compression brace is joined to the tension brace at the midpoint of the lengthwise direction of the material, one can infer that the force pushing up the beam is less than that of the single brace because of the relaxation of the compressive force. Fig. 11 shows the test body at 1/15 rad. From the left side of Fig. 11, it is apparent that no marked damage has occurred to the beam joints. This finding suggests that the effect of the beam joints on the maximum load of the braced wall is small. Regardless of the presence or absence of beam joints, the failure of all test bodies terminated in buckling of the compression brace, as shown on the right side of Fig. 11.

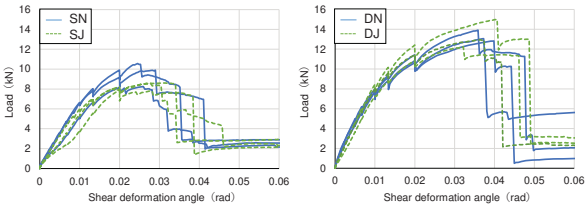

Single brace wall *Double brace wall*

Figure 10 *Relation between load and shear deformation angle*

Table 4: *Structural property values when pulled*

Test body name	Maximum load (kN)					Initial rigidity (kN/rad)				
	No.1	No.2	No.3	Average	Ratio	No.1	No.2	No.3	Average	Ratio
SN	10.6	8.3	9.9	**9.6**	–	663	510	673	**615**	–
SJ	8.0	8.6	8.6	**8.4**	**0.88**	634	477	424	**512**	**0.83**
DN	13.1	12.8	13.9	**13.3**	–	835	799	738	**791**	–
DJ	15.0	12.9	12.2	**13.4**	**1.01**	795	768	695	**753**	**0.95**

Table 5: *Joint rotation angle at maximum load (rad)*

No.	SJ	DJ
No.1	0.002	0.000
No.2	0.008	-0.001
No.3	0.023	0.004
Average	0.011	0.001

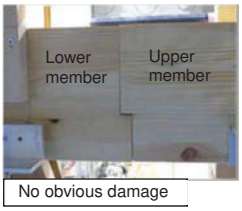

State of the joint *Viewed from the side*

Figure 11: *State of the test body at 1/15 rad(SN)*

https://doi.org/10.52202/069179-0449

4 STRUCTURAL ANALYSIS

4.1 OVERVIEW OF THE ANALYTICAL MODEL

The analytical model is the same as the test body, with SN, SJ, DN, and DJ. An example of an analytical model is portrayed in Fig. 12. The wall has 910 mm length and 2730 mm height. The model replaced the members with wires, with nodal springs placed at each joint. Rotational springs were incorporated at the column-head joints and at the column-leg joints. The braces were placed with axial springs according to the direction of the applied force. Braces were designed so that, because of horizontal loads, the braces would push the beams upward when compression forces were applied. The top edge of the brace was kept close to the right edge of the beam. To reproduce effects of the L-shaped brace fastening metal, shear springs were placed to connect the top end of the brace to the top end of the column. For the SJ and DJ analytical models, rotational springs were set at the beam connections. To simplify the analytical model, the inter-columns were not modeled. Structural analysis was performed using software (Wallstat pro ver. 5.0.0β10) [9].

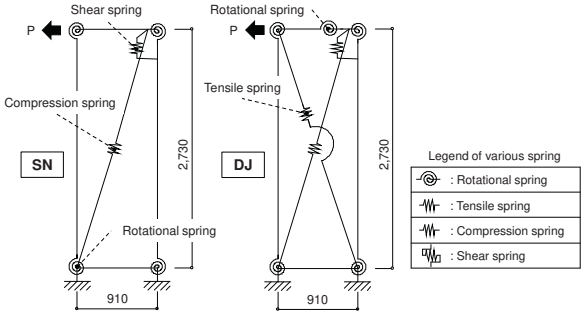

Figure 12: *Analytical model example (unit: mm)*

4.2 JOINT STIFFNESS AND INFLECTION POINTS

In-plane rotation tests were applied to calculate the rotational stiffness of the column head-column leg joint. The test body configuration of the column head is shown at the left panel of Fig. 13. The test body configuration of the column leg is shown in the right panel. Fig. 13 shows that the applied forces were alternating positive and negative. The rotation angle of the joint was calculated from the values of two displacement gauges, as presented in Fig. 14. The number of test bodies was six for both the column head and the column leg joints. The relation between the moments and joint rotation angles of the six bodies and the skeletal curves created based on the test results is presented in Fig. 15. The initial and secondary stiffnesses of the six bodies are presented in Table 6.

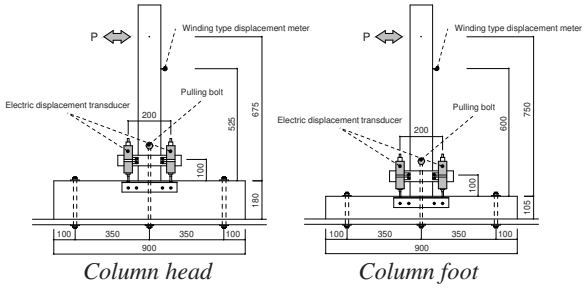

Figure 13: *In-plane rotation test configuration (unit: mm)*

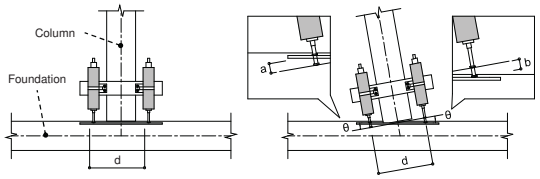

$\theta = (a - b) / d$

θ: Relative displacement angle of two members (rad)
a,b: Displacement by displacement meter (mm)
d: Distance between gauge points (mm)

Figure 14: *Calculation method of rotation angle of column-head and column-foot joint*

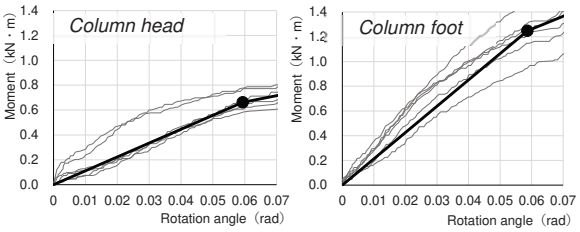

Figure 15: *Relation between moment and rotation angle of column-head and column-foot joint*

Table 6: *List of rotational rigidity in column-head and column-foot joint*

Column head

Test piece number	Primary stiffness (kN・m/rad)	Secondary stiffness (kN・m/rad)
1	11.3	5.7
2	12.0	5.0
3	11.2	4.8
4	9.9	5.1
5	10.9	4.5
6	11.5	5.2
Average	**11.1**	**5.0**
Standard deviation	**0.6**	**0.4**

Column foot

Test piece number	Primary stiffness (kN・m/rad)	Secondary stiffness (kN・m/rad)
1	26.4	12.4
2	22.0	11.0
3	20.1	9.2
4	21.4	8.1
5	21.2	12.1
6	16.5	9.5
Average	**21.3**	**10.4**
Standard deviation	**2.9**	**1.6**

Axial force tests were conducted to elucidate the joint characteristics. The test bodies were constructed as presented in Fig. 16 with six test bodies. The axial force test results are shown in Table 7: the average values of tensile and compressive stiffness were, respectively, 23.0 kN/mm and 45.1 kN/mm. The rotational stiffness of the joint was calculated using the tensile and compressive stiffnesses obtained from axial force test results. The rotational stiffness (mountainous deformation) calculation method is depicted in Fig. 18. In the case of bending deformation of a joint, tension is borne by part A and compression by part B. The stiffness per unit area was calculated by dividing the tensile and compressive stiffnesses shown in Table 7 by the respective bearing area. The calculation results show that the stiffness per unit area was 16.7 N/mm^3 on the tensile side and 2.9 N/mm^3 on the compressive side. The neutral axis was found to be 82.5 mm from the bottom edge by solving the equation of equilibrium between the tension and compression sides. Therefore, the rotational stiffness is calculated as the sum of tensile and compressive forces, 127 kN.m/rad, assuming that the stress level increases uniformly from the neutral axis to the outermost circumference.

https://doi.org/10.52202/069179-0449

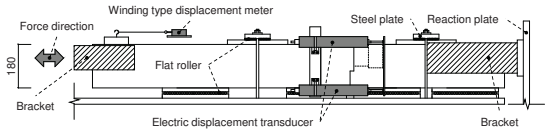

Figure 16: *Axial force test configuration (unit: mm)*

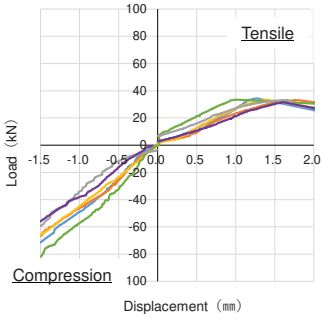

Figure 17: *Relation between load and displacement for axial force test*

Table 7: *List of test results (Tensile and compressive stiffness)*

No.	Tensile stiffness (kN/mm)	Compressive stiffness (kN/mm)
1	26.9	49.4
2	20.1	44.4
3	26.1	44.1
4	27.8	53.8
5	18.0	39.0
6	19.3	40.1
Average	**23.0**	**45.1**
Standard deviation	**4.0**	**5.1**

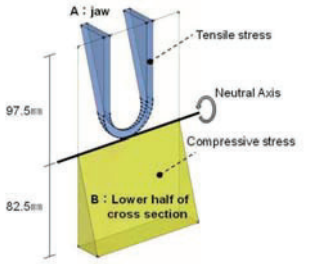

Tensile stiffness: 23.0 kN/mm
Pressure receiving area under tension: 1,381 mm^2
Tensile stiffness per unit area: 23.0 / 1,381 = 16.7 N/mm^3

Compressive stiffness: 45.1 kN/mm
Pressure receiving area under compression: 15,628 mm^2
Compressive stiffness per unit area: 45.1 / 15,628 = 2.9 N/ mm^3

Figure 18: *Method of calculation rotational stiffness of beam joints*

The compressive stiffness of the single brace was ascertained from the load–displacement relation: the results of the analysis of the frame model consisting of rotational spring at the column-head-column-foot joint were subtracted from the in-plane shear test results obtained for the brace wall (average of three bodies) in Chapter 3 (Fig. 19).

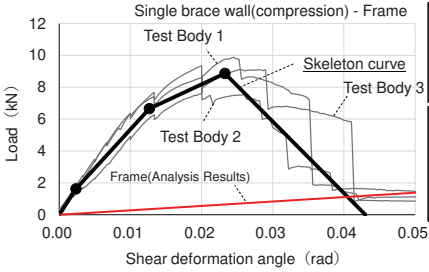

	Stiffness (kN/rad)
1st	687
2nd	489
3rd	208
4th	-450

	Inflection point displacement (rad)
1st	0.002
2nd	0.013
3rd	0.023
4th	0.043

Figure 19: *Skeleton curve of compression brace in a single-braced wall*

The tensile stiffness of the brace portrayed in Fig. 20 was found by subtracting the analytical results obtained for the frame model consisting of rotational spring at the column head-column leg connections from the in-plane shear test results (average of three bodies) of the tensile brace wall shown in the same figure.

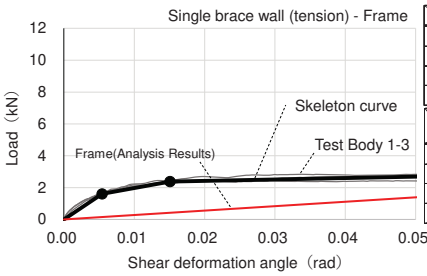

	Stiffness (kN/rad)
1st	296
2nd	80
3rd	9
4th	-79

	Inflection point displacement (rad)
1st	0.005
2nd	0.015
3rd	0.051
4th	0.085

Figure 20: *Skeleton curve of tensile brace*

We calculated the shear stiffness of the L-shaped brace hardware applied to the analytical model from the axial force of the brace and the displacement of the brace end found from results of in-plane shear tests of the brace wall (average of three bodies) (Fig. 21).

Figure 21: *Skeleton curve of L-shaped brace hardware at the top edge of the brace*

The compressive stiffness of the double braces was calculated from the results of the in-plane shear tests described in Chapter 3 and from results obtained for the single braces. A compression brace in a double-braced wall has higher strength performance than a compression brace in a single-braced wall because the tensile brace in a double-braced wall delays buckling of the compression brace. However, the tensile brace performance was assumed to be equivalent to that of the single braces. The skeletal curves of the compression brace of the double-braced wall are presented in Fig. 22. From the in-plane shear test results obtained for the double-braced wall, the relation between the load and shear deformation angle of the frame and tensile bracing was subtracted to obtain the skeleton curve of the compression bracing of the double-braced wall.

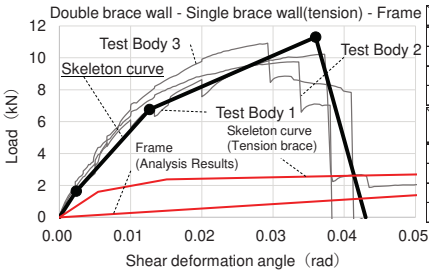

	Stiffness (kN/rad)
1st	687
2nd	489
3rd	208
4th	-1645

	Inflection point displacement (rad)
1st	0.002
2nd	0.013
3rd	0.036
4th	0.043

Figure 22: *Skeleton curve of compression brace in a double braced wall*

https://doi.org/10.52202/069179-0449

4.3 COMPARISON OF ANALYTICAL AND TEST RESULTS

Fig. 23 presents test results for each parameter and the analytically obtained results of the model with the previously described characteristic values. The test results and analysis results show general agreement. The developed analysis model is inferred as reasonable.

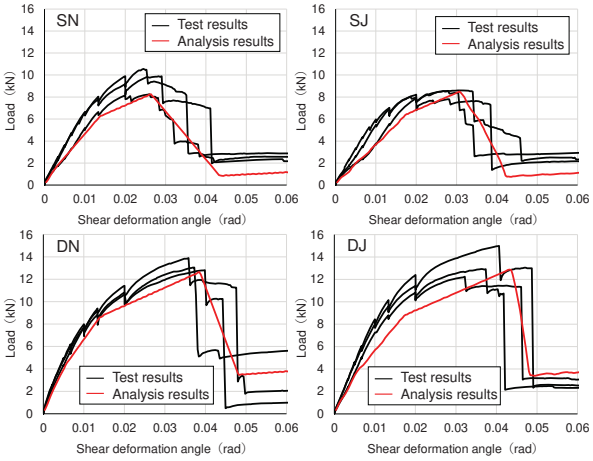

Figure 23: *Relation between load and shear deformation angle in test and analysis*

Fig. 24 presents analytical results obtained for single-braced and double-braced walls. Fig. 25 shows the strength properties obtained from Fig. 24 and the test results. From Fig. 25, the maximum load was almost identical in the test and analytical results. Regarding the initial stiffness, the analytical results showed smaller values than the test results, but the tendency of the initial stiffness to decrease with the joint was similar. The test and analysis results demonstrated that the initial beam stiffness was reduced when the beam joint was placed at the push up of the brace, although it did not affect the maximum load.

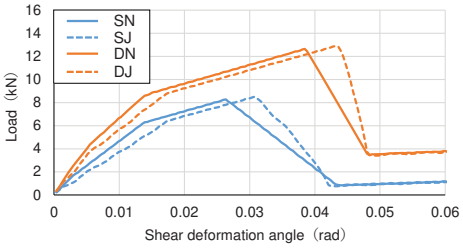

Figure 24: *Relation between load and shear deformation angle in analytical results*

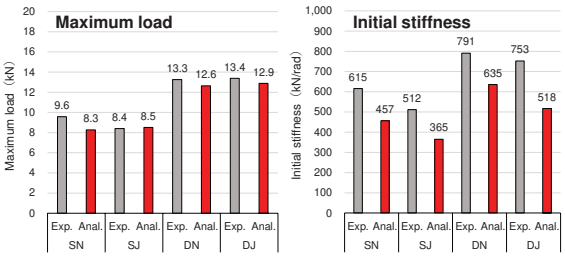

Figure 25: *Maximum load and initial stiffness of analytical and test results*

5 CONCLUSIONS

A survey was administered to frame designers. The responses indicated that more than 70% of frame designers have concerns about a beam joint at the push-up portion of the brace. In-plane shear tests of single-braced and double-braced walls were conducted. The applied force test results indicated reduction of the initial stiffness of the single-braced, 910-mm-long wall by approximately 20% when the beam joint was placed at the push-up portion of the brace. Structural analyses were conducted by creating an analytical model of the braced wall. Those analyses revealed a similar trend to that indicated by the experimentally obtained results, thereby confirming the beam joint influence analytically.

REFERENCES

[1] Independent administrative agency Housing Finance Support Organization, Wooden house construction specifications book, Inoue Shoin, 2016.

[2] City of Yokohama, Architecture Bureau guidance department architecture planning section, Seismic retrofit and construction of existing wooden houses manual (2009 Edition – Second Printing), reference 2023.1.9

[3] T. Sahata, N. Kawai, H. Tsukazaki, H. Maekawa, and S. Matsudome, Study on frame design in wooden house with machined members, Summaries of technical papers of Annual Meeting, Architectural Institute of Japan, pp. 211-212, 2019

[4] A. Nishino, N. Satomura, T. Taguchi, and Y. Ohashi, Study on aseismic repair method of cross wooden brace in the same plane. (Part 2 the difference in strength depending on the tree types of the wooden brace), Summaries of technical papers of Annual Meeting, Architectural Institute of Japan, pp. 535-536, 2019.

[5] Y. Nomura, K. Kanda, Y. Yamazaki, H. Sakata, and H. Isoda, Experimental study on mechanical behavior of wooden brace wall with different types of brace joint Part 1. Outline of experiments and failure mode, Summaries of technical papers of Annual Meeting, Architectural Institute of Japan, pp. 189-190, 2017.

[6] S. Sato, E. Fujino, and Y. Ohashi, A study on tensile strength of conventional wooden joints Part 1. koshikakekama-tsugi, Summaries of technical papers of Annual Meeting, Architectural Institute of Japan, pp. 97-98, 2002.

[7] Y. Kitada, and Y. Owada, A study on strength of conventional wooden joints – A tensile test of koshikakekamatsugite and okkakedaisentsugi-, Summaries of technical papers of Annual Meeting, Architectural Institute of Japan, pp.133-134, 2007.

[8] Public interest incorporated foundation Japan Housing and Wood Technology Center, Allowable stress design of wooden framed houses, 2017.

[9] T. Nakagawa, and M. Ohta,et al. "Collapsing process simulations of timber structures under dynamic loading III: Numerical simulations of the real size wooden houses", Journal of Wood Science, Vol. 56, No. 4, pp. 284-292, 2010.

https://doi.org/10.52202/069179-0449

World Conference on Timber Engineering Oslo 2023

EXPERIMENTAL ANALYSIS OF A SCREW-GLUED SHEAR CONNECTION FOR USE IN MASS TIMBER COMPOSITE PANELS

Tyler Hull[1], Daniel Lacroix[2]

ABSTRACT: Ribbed or box section mass timber composite (MTC) panels offer a potential solution to the floor span limitations of conventional mass timber panels due to vibration. Glued connections have shown to be a viable shear connection in MTCs due to their high strength and stiffness. Investigated herein is the behaviour of a screw-glued connection of commercially available construction adhesive and self-tapping screws, to assess its viability to adequately transfer forces between the flanges and webs of MTCs. Shear tests on four 400mm long dimensional lumber T-sections yielded an average slip modulus of 17.63N/mm per mm^2 of glue, with an average yield stress of 4.59MPa and 3.47MPa from two bilinear data fit models. The connection was used to fabricate six 1.8m long dimensional lumber T-beams which were tested in flexure and used to validate a numerical model capable of capturing the behaviour. The results agreed well, with the average experimental midspan deflection being 0.98 of the average numerical midspan deflection. Overall, when used on a 10m HMT panel, analytical results using the γ-method indicated a nearly fully composite shear connection was achieved, and a vibration-controlled span of 10.4m was possible for the 455mm deep section.

KEYWORDS: Mass timber composite, screw-glued, shear connection, shear testing, experimental analysis

1 INTRODUCTION

1.1 BACKGROUND

Conventional mass timber flat slab floor systems, such as cross-laminated timber (CLT) panels on glulam beams, have difficulty rivalling the column spacing standard achieved by other commercially available floor systems due to the mass timber slab spans being limited by vibration and human comfort [1,2]. To achieve long floor spans using an all-wood system in structures where larger and open floor plans are needed (e.g., office, institutional, and high-end residential), designers have employed mass timber composite (MTC) ribbed (i.e., T-beams) and box (i.e., I-beams/hollowcore) panel floor systems (e.g., Catalyst, Spokane, WA, USA [3]; WoodIn, Waterloo, ON, Canada [4]). Figure 1 shows an example of a MTC ribbed panel consisting of a CLT panel for the flange that is connected to glulam webs through shear connections.

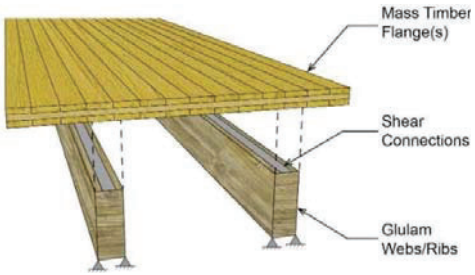

Figure 1: *Mass Timber Composite Ribbed Panel*

MTCs have shown the viability to overcome the current vibration and serviceability limitations of conventional mass timber flat slab floor systems (i.e., exceeding 7-8m), and be a viable all-wood long span floor system solution [5]. However, the shear connection (e.g., glue, self-tapping screws (STS)) has a crucial role in the transfer of forces between the flange(s) and the web. Due to vibration concerns at serviceability limit states often being the governing criteria in the design of MTCs, the shear connection's stiffness is critical to the overall element performance. Research has shown that glued connections [6] exhibit the highest shear connection stiffness; however, little research has been done on the types of glue to use, clamping procedures, and stiffnesses achieved in order to produce commercially viable bonds.

Montgomery [6] conducted a wide-ranging experimental study investigating the performance of 24 different shear connection options for hollowcore mass timber (HMT) panels through uniaxial tests on small-scale components and used the connection stiffness to numerically investigate their effects on, the behaviour of a 12.2 long HMT panel. It was observed that stiffer shear connections were necessary to achieve near fully composite action between the elements, thereby maximizing the efficient use of materials in the HMT panel, in addition to meeting the requirements for a 12.2m span. The identified connections were comprised of STS driven at an angle (30-45°), glue pressed, screw-glued, and perforated metal

[1] Tyler Hull, PhD Candidate, University of Waterloo, Waterloo, Canada, tyler.hull@uwaterloo.ca
[2] Daniel Lacroix, Assistant Professor, University of Waterloo, Waterloo, Canada, daniel.lacroix@uwaterloo.ca

https://doi.org/10.52202/069179-0450

plates with adhesive. Connections such as STS driven vertically (90°) were reported to not produce the needed stiffness to efficiently achieve adequate vibration performance at long spans [6]. Chen and Lam [7] investigated the performance of STS at 90° through numerical modelling and experimental testing on box panels comprised of CLT as top and bottom flanges, and dimensional lumber for the webs. As a result of the connection stiffness, the overall section exhibited minimal composite behaviour resulting in a highly non-linear stress distribution over the depth of the section, and tensile failure in the webs occurring rather than in the bottom flange [7]. While this connection proved to not be optimal for achieving the composite action needed for long span MTCs, good agreement was demonstrated between the numerical model and experimental results, thereby indicating the viability of numerical methods for predicting the behaviour of MTCs [7].

Jacquier and Girhammar [8] investigated CLT-glulam T-beams in bending for the purpose of developing a cassette (i.e., box) composite floor slab for use in multi-storey CLT buildings. In their study, STS driven at 45°, doubled-sided punched metal plates (DSNP), screw-glued, and a combination of STS and DSNP were utilized for the shear connection between the flange and web. The results between the experimental and predicted bending stiffness determined using the gamma (γ)-method, which is introduced in Annex B of Eurocode 5 [9], agreed reasonably well with the experimental results [10], thereby indicating that analytical methods such γ-method can be used to predict the stiffness of MTCs in design. This observation was also confirmed by Hull and Lacroix [11] who compared the results of the γ-method to finite element modelling results. The γ-method was able to reasonably accurately predict the bending stiffness of the MTC panel, with the main difference between the finite element model and γ-method being attributed to shear lag effects observed in the flanges [11].

Despite the fact that initial studies have showcased the potential of MTCs to be designed to meet long floor spans in a laboratory and numerical setting, adoption of mass timber long span floor systems by the industry has been hindered in large part due to the complications associated with implementing viable shear connections in manufacturing processes, particularly glued connections. This is primarily due to the fact that the glue bond can vary greatly depending on the type of glue used, the contact pressure, the glue line thickness, and environmental conditions during the assembly. Screw-gluing was shown to be a viable option for utilizing the high shear stiffness of glued connections without the need for large hydraulic presses [6,12]. However, the practical application of screwed gluing in manufacturing applications has been limited by the lack of knowledge on possible adhesive and screw configurations.

1.2 OBJECTIVES

The overarching aim of the larger research program is to develop fundamental knowledge of mass timber composites (MTCs) and the effects of connection detailing on their behaviour in order to develop design guidelines and aid in their adoption by industry. The research specific objectives of this study are to: 1. investigate the shear behaviour of a screw-glued connection made with a commercially available construction adhesive, 2. establish the flexural behaviour of dimensional lumber T-beams using the screw-glued connection, 3. validate a finite element model capable of capturing the connection behaviour and predict the flexural response of the T-beams, and 4. investigate the potential span capabilities of MTC panels using the screw-glued connection analytically. Due to the limited information on the behaviour of connections and the effects of stiffness on the degree of composite action, as well with relatively higher associated costs with mass timber products, dimensional lumber was chosen to first investigate the behaviour and feasibility of the screw-glued connection in MTC panels.

2 SHEAR PERFORMANCE OF SCREW-GLUED CONNECTION USING DIMENSIONAL LUMBER

2.1 METHODOLOGY

The potential of using screw-glued connections in MTCs is first evaluated on a total of four specimens consisting of dimensional lumber. The shear connection specimens were 400mm in height and consisted of 35mm x 200mm Spruce-Pine-Fir (SPF) No.1/2 flanges connected to 40mm x 160mm Douglas Fir-Larch (D.Fir-L.) webs using a screw-glued connection. The connection consisted of 6mm diameter (dia.) x 100mm long partially threaded self-tapping screws (STS) with washer heads spaced at 133mm centre-to-centre (c/c), as well as a 10mm wide bead of commercially available silane modified construction adhesive (Figure 2). A 10mm wide bead of adhesive to every 40mm wide of web surface area was deemed adequate to provide full-surface coverage and adequate squeeze out.

Figure 2: *Dimensional Lumber Shear Test Specimens*

Additionally, 25mm dia. washers were added beneath the existing washer heads of the screws as a measure to aid in evenly spreading the pressure distribution of the screw-gluing as well as to prevent local wood crushing under the

https://doi.org/10.52202/069179-0450

screw heads (Figure 2). This assembly of partially threaded screw and 25mm dia, washer was able to achieve a load of 4.5kN [13], resulting in an average clamping stress of 0.85MPa. The flanges were sourced from a local Ontario wood supplier whereas the webs were removed from an existing building in Waterloo, Ontario Canada and donated to the University. In their original size, the web members had widths varying from 88 to 90mm to depths of 195-200mm. To maximize the use of wood, each element was planed to the final web dimensions thus yielding two webs per piece of wood donated. It should also be noted that the adhesive used complies with existing regulatory strength and durability requirements as a sub-floor adhesive [14].

A 500kN universal testing machine was used to evaluate the screw-glued bond performance of the four specimens under monotonic loading. The slip between the web and flange was recorded using a linear variable displacement transducer (LVDT) on both sides of the web and the average slip between the LVDTs was used in the stiffness calculation.

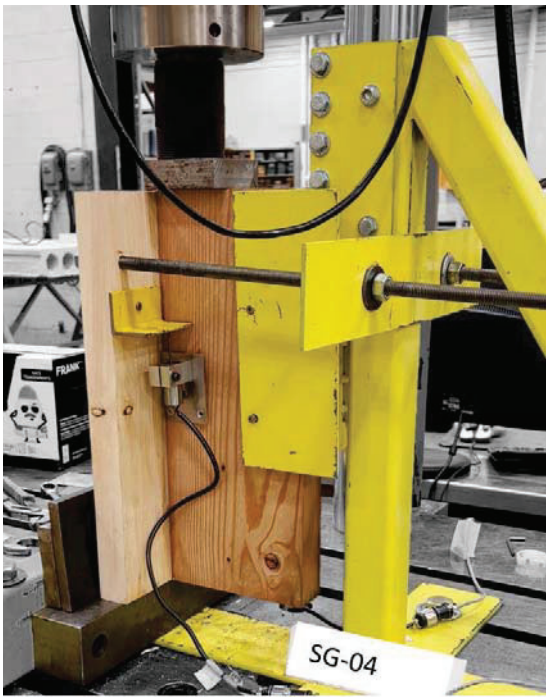

Figure 3: *Shear connection test setup*

The Standard Test Method for Strength Properties of Adhesive Bonds in Shear by Compression Loading (ASTM D905) [15] specifies a uniform loading rate of 5mm/min ± 25%, although the standard also states that there is no apparent effect on the bond strength for loading rates ranging 0.38 to 10.27mm/min. Additionally, the standard Test Methods for Mechanical Fasteners in Wood and Wood-Based Materials (ASTM D1761) [16] proposes a loading rate of 2.54 mm/min ± 25%. Due to the shear connection being comprised of adhesive and screws, a loading rate of 2mm/min was chosen which resulted in times to failures on average of 1.5 to 2 minutes. As shown in Figure 3, the flange of the test specimen rested on a solid steel block that was secured to the testing frame, while a reaction frame (yellow), with a roller along the web, was used to resolve the eccentricity between the load application point and flange bearing location. Two steel bolts with a steel plate were also used to prevent rotation if any local crushing occurred beneath the flange.

Following each test, the moisture of both the flanges and web were determined using a Tramex MRH3 pin-probe moisture and relative humidity meter. The webs and flanges had an average moisture content of 9.2% and 11.2% respectively, with a maximum deviation of ±1% moisture. To determine the specific gravity, smaller clear wood elements were cut off the flange and web of each of the shear specimens. The clear wood specimens were then oven-dried according to Density and Specific Gravity (Relative Density) of Wood and Wood-Based Materials (ASTM D4442) [17] in order to determine the specific gravity of each. The D.Fir-L web elements had an average specific gravity of 0.47 with a coefficient of variation (CoV) of 0.02, while the SPF flange elements had an average specific gravity of 0.40 with CoV of 0.05.

2.2 EXPERIMENTAL TEST RESULTS

From the experimental tests, three key parameters were determined for each specimen: 1. the maximum load averaged over to glue area to determine the glue bond shear strength, 2. the slip stiffness (k_s), and 3. the stiffness up until the maximum load (k_{Fmax}). Table 1 presents the individual and average values of the screw-glued connections as well as their CoV.

Table 1. *Shear connection load-slip results*

Specimen	Shear Strength [MPa]	Slip Stiffness, k_s [N/mm per mm^2]	Connection Stiffness at Max Load, k_{Fmax} [N/mm per mm^2]
SG-01	4.69	19.11	18.78
SG-02	5.85	15.55	13.29
SG-03	3.89	15.94	12.11
SG-04	3.43	19.91	16.29
Avg.	**4.47**	**17.63**	**15.12**
CoV	0.20	0.11	0.17

The slip stiffness (i.e., initial stiffness), which is key when designing MTCs for service level and vibration criteria, was determined as the slope between 10% and 40% of the maximum load as defined by EN 26891 [18,19] for mechanical fastener connections. The connection stiffness at maximum load (k_{Fmax}) was determined as the slope from the origin to the maximum load.

The shear strength of the screw glued bond averaged 4.47MPa, with a CoV 0.20. The high glue bond shear strength is a promising result as it indicates the composite connection can likely be designed for the strength of the wood material. The variation seen in the CoV of the shear

https://doi.org/10.52202/069179-0450

strength was attributed to specimens SG-02 and SG-04 where the difference in failure mode between these two specimens in the post glue bond failure observation can be seen presented in Figure 4. SG-02 (Figure 4a) shows a failure of wood fibre from both the web and flange indicating that the flange had a similar strength to the web, whereas for SG-04, the failure occurred almost entirely in the flange. Additionally, some wood decay was observed in the web at the top of the connection, as highlighted in Figure 4b.

(a) Failure plane of SG-02

(b) Failure plane of SG-04

Figure 4: *Representative failure of screw-glued shear connection*

In general, it is observed from Table 1 that the slip stiffness had less variation than the maximum load and provides encouraging results for the overall repeatability of the screw-glued connection given the number of variables that can influence the overall behaviour (e.g., lumber grade, stiffness, surface planning, glue vs. wood failure, moisture content, curing conditions).

Determining the yield point of timber-timber composites is another key parameter needed for design calculations. Two bilinear load deformations models were data fitted to each specimen and the bilinear models were then averaged together to obtain a representative bilinear model for the screw-glued connection. The first bilinear model used the methodology presented in EN 12512 [20], and although intended for joints made of mechanical fasteners, this method provided good representation for the behaviour of the screw-glued connection. In the EN 12512 model [20], two sloped lines are determined, with their intersection being the yield point. The first line is defined by the slip stiffness from Table 1, while the second line is a tangent with a slope based on Equation (1).

$$\tan\beta = \frac{1}{6}\tan\alpha \tag{1}$$

Where α is the angle formed by the slip stiffness line, and β is the angle formed by the tangent line. The tangent line is drawn on the load-slip curve where the slope of the tangent and load-slip curve are equal. The second bilinear model was proposed for its simplicity and relatively good agreement with the test data. Here, the yield point is determined where the slip stiffness line attains 75% of the maximum load. The second slope is then drawn between the yield point and maximum load point. Both models are demonstrated for specimen SG-04 in Figure 5: Load-slip curve of SG-04 with bilinear models.

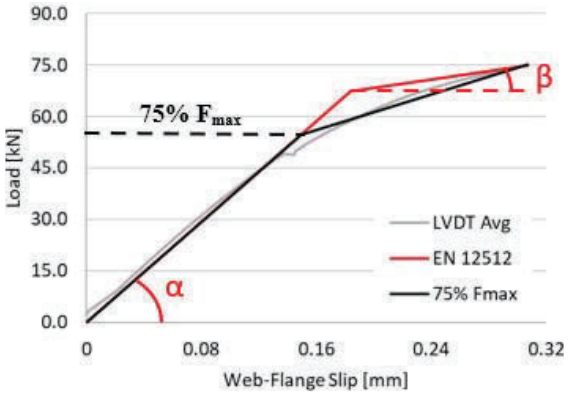

Figure 5: *Load-slip curve of SG-04 with bilinear models*

The average curves for the four specimens are presented in Figure 6, with the yield point results in Table 2. Generally, both models capture the behaviour well, with the EN 12512 [20] having a higher yield stress.

https://doi.org/10.52202/069179-0450

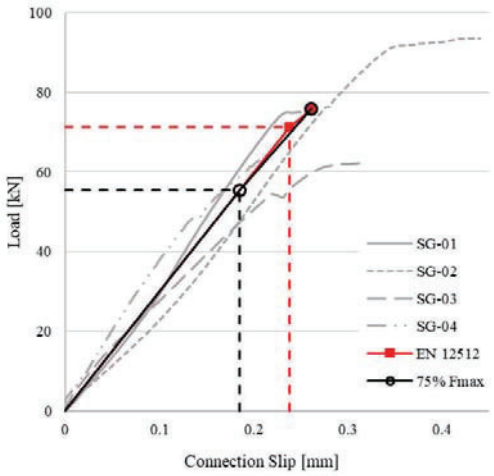

Figure 6: *Load-slip curves and averaged bilinear models*

The yield stress was determined by dividing the data fit yield load for each specimen by the 40mm x 400mm screw-glued area. Some variation is seen in the slip and load of the yielding point. This can be attributed to the variability in wood material shear strength, as well as stiffness, and its influence of the glue bond behaviour. The average yield stresses of 4.59 MPa and 3.47 MPa demonstrate the potential for structural viability of a screw-glued connection using a commercially available bead extruded silane modified adhesive by primarily achieving failure in the wooden elements first, as opposed to a pure glue failure being the dominating failure mode.

Table 2. *Yield point using bilinear models*

Specimen	EN 12512		75% F_{max}	
	Yield Slip [mm]	**Yield Stress** [kN]	**Yield Slip** [mm]	**Yield Stress** [kN]
SG-01	0.222	4.67	0.167	3.52
SG-02	0.336	5.76	0.256	4.39
SG-03	0.234	3.73	0.183	2.92
SG-04	0.184	4.20	0.132	3.04
Avg.	**0.244**	**4.59**	**0.185**	**3.47**
CoV	0.26	0.18	0.24	0.17

3 DIMENSIONAL LUMBER T-BEAM BENDING TESTING

3.1 METHODOLOGY

The dimensional lumber T-beams were 2m in length with a 1.8m clear span and consisted of an identical 35mm x 200mm SPF No.1/2 flange as well as a 40mm x 160mm D.Fir-L. web compositely connected using the screw-glue configuration tested in Section 2. Prior to each of the T-beams being assembled, the web and flange elements were each tested non-destructively to determine the modulus of elasticity, E. This was done by loading the elements in their T-beam orientation (i.e., the flanges on the flat and the webs on edge) in four-point bending and recording the midspan deflection using a string pot. The actuator load was increased up to 10kN and 2kN for the webs and flanges, respectively, to obtain a representative linear load-displacement curve to calculate the modulus of elasticity for each using classical Euler beam theory. However, since the midspan deflections recorded included deformations due to shear which results in the apparent modulus of elasticity, E_{app}. To get the true modulus of elasticity (i.e., shear free), E_{true}, additional analysis was required. Equation (2) was used to remove the shear deformations from the midspan deflection, where E_{true} could then be calculated using classical Euler beam theory.

$$\Delta_{shear} = \frac{\frac{P}{2}L}{3AG} \tag{2}$$

Where P is the actuator load, L is the clear span of the specimen (1.8m), A is the cross-sectional area, and G is the shear modulus taken as $E_{app}/15$ for the webs and $E_{app}/18$ for the flanges based on the lumber species and recommendations from Forest Products Laboratory's Wood handbook [21]. The results from the modulus of elasticity determination are presented in Section 3.2 in Table 3.

A total of six-dimensional lumber T-beams were assembled and loaded in four-point bending using the test setup shown in Figure 7. During the testing, the displacement at midspan was monitored using a string pot which passed through the table, while the slip between the web and flange was recorded using LVDTs located 0.3m and 0.6m from the midspan of the beams. Similar to the modulus of elasticity determination, the midspan deflection was used to determine the apparent and true stiffness of the beams, EI_{app} and EI_{true} respectively, based on the linear portion of the load-displacement curve.

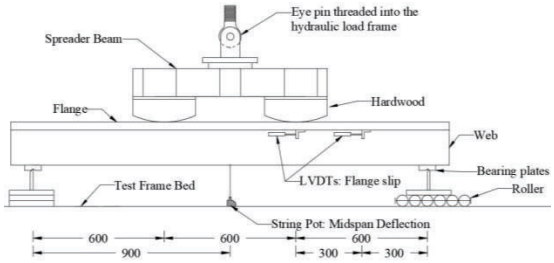

Figure 7: *Four-point bending test setup*

3.2 EXPERIMENTAL TEST RESULTS

The results from the modulus of elasticity determination for the flange and web elements of each beam are presented in Table 3. Overall, the flanges' modulus of elasticity was very consistent was an average E_{true} of 9062MPa, while more variability was seen in the average E_{true} of the webs of 13430MPa. This higher variation is attributed to the fact that the final web size was obtained by planing the original member to their final size, thus affecting the distribution of defects and grain deviation from member to member.

https://doi.org/10.52202/069179-0450

Table 3: *Modulus of elasticity results*

Specimen	Flange*		Web	
	E_{app} [MPa]	E_{true} [MPa]	E_{app} [MPa]	E_{true} [MPa]
SG-01	9219	9268	8485	9350
SG-02	8408	8452	10473	11375
SG-03	9781	9833	11172	12197
SG-04	9748	9800	15600	17409
SG-05	8102	8146	12822	14128
SG-06	8828	8875	14630	16121
Avg.	**9014**	**9062**	**12197**	**13430**
CoV	0.07	0.07	0.21	0.20

*Flange modulus of elasticity measured on flat

Key results describing the properties of each of the T-beams section are presented in Table 4. The maximum bending moment was determined by the maximum load reached in the test after the initial linear-elastic region of the load-displacement response. The average of this was 10.8kNm. However, considerable variation was observed and can primarily attributed to the variable grade of wood in the webs. Due to planing of the donated material into the final web sizes, some of them had less grain deviation and fewer defects as well as knots than others, thus resulting in increased flexure and shear strength in these specimens.

Table 4: *T-beam bending experimental results*

Specimen	Max Bending Load [kNm]	Apparent Stiffness, EI_{app} [Nmm^2]	True Stiffness, EI_{app} [Nmm^2]
SG-01	6.4	3.12E+11	3.96E+11
SG-02	13.7	3.33E+11	4.08E+11
SG-03	9.7	3.12E+11	3.72E+11
SG-04	10.3	4.21E+11	4.99E+11
SG-05	15.3	4.32E+11	5.03E+11
SG-06	9.4	4.07E+11	4.64E+11
Avg.	**10.8**	**3.69E+11**	**4.40E+11**
CoV	0.27	0.14	0.12

Nonetheless, lower CoVs were observed for the apparent and true stiffness of the sections. These are the primary focus of the experimental program as it is used in the comparison to the numerical modelling in Section 4, while also being indicative of the serviceability-level response, a key concern for future application in mass timber composites. The average apparent and true stiffness of the sections were found to be 3.69×10^{11}Nmm^2 and 4.40×10^{11}Nmm^2 respectively. Most of the variability in these results was attributed to the different modulus of elasticity of the webs, as the web modulus of elasticity was generally indicative of the overall stiffness of the assembly (i.e., T-beam). For example, lower modulus of elasticity sections such as SG-01 and SG-02 had lower overall assembly stiffnesses than the ones with higher modulus of elasticity sections such as SG-04 and SG-05. The experimental load-displacement curves of all six specimens are presented in Figure 8.

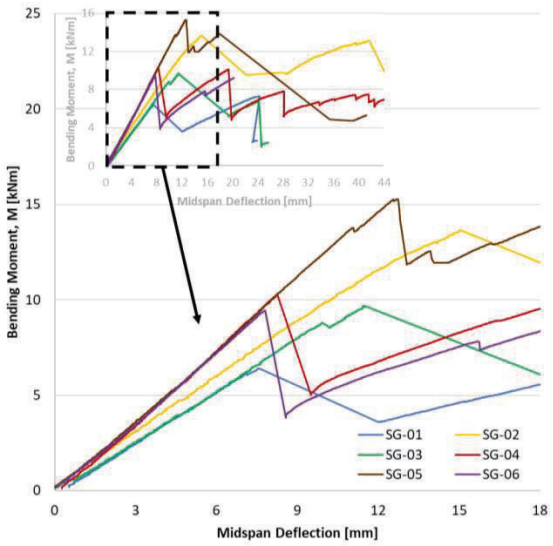

Figure 8: *T-beam load-displacement curves*

In general, due to the relatively short spans and increase section modulus of the T-section, the initial failure mode consisted of shear failure in the webs. This was followed by secondary flexural failures such as simple, splintering, and cross-grain tension in the web, while failure of the flanges was observed to either be due to compression yielding or simple tension. Figure 9 shows a representative T-beam at ultimate failure.

Figure 9: *Representative failure mode of T-beams*

4 NUMERICAL ANALYSIS

4.1 NUMERICAL MODEL DESCRIPTION

A numerical model was developed in *ABAQUS* finite element software [22] to capture the behaviour of the dimensional lumber T-beams and screw-glued connection. The assembly was generated using three separately defined elements; the SPF flange, the D.Fir-L web, and the loading blocks shown in Figure 10. The flange and web were modelled as 3D deformable solids, while the loading blocks were modelled as 3D rigid elements. The contact between the webs and flanges was modelled as a cohesive contact in the sliding direction and a "hard" contact in the normal direction. Boundary conditions were applied at the support locations

https://doi.org/10.52202/069179-0450

restricting all degrees of freedom except in-plane rotation, and in-plane displacement representing the roller end. The slip stiffness of the screw-glued bond, k_s, was used as the in-plane slip of the cohesive bond in the numerical model. Contact between the T-beam and the support blocks was modelled as a "hard" contact in the normal direction and a frictional penalty coefficient of 0.15 [23] in the tangential direction.

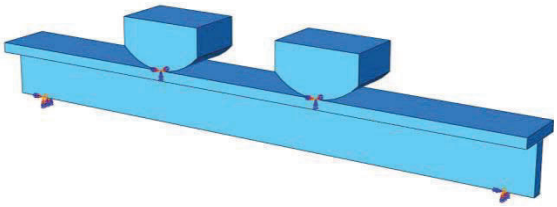

Figure 10: *Finite element model showing T-beam below two loading blocks and boundary conditions applied*

The wood elements are modelled as a linear-elastic orthotropic material using ABAQUS' engineering constants option, where the primary direction (1) represents the longitudinal direction of the wood grain and the two secondary directions (2) and (3) represent the two perpendicular to grain directions (i.e., radial and tangential). The experimentally determined true modulus of elasticity for each web and flange is used for the longitudinal modulus of elasticity, E_1, while the shear modulus G_{12} and G_{13} is taken as $E_{true}/15$ for the webs and $E_{true}/18$ for the flanges based on the lumber species and recommendations from Forest Products Laboratory's Wood handbook [21]. The Poisson ratios were also based on recommendations for each species group from Forest Products Laboratory's Wood handbook [21]. The remaining E_2, E_3, and G_{23} are based on CSA O86 [24] recommended values in term of E_{true}. The material parameters are summarized in Table 5.

Table 5: *Material parameter values used in ABAQUS model*

	Web Element	Flange Element
E_1 (MPa)	$E_{true,web}$	$E_{true,flange}$
E_2 (MPa)[1]	$E_1/30$	$E_1/30$
E_3 (MPa)[1]	$E_1/30$	$E_1/30$
ν_{12}	0.32	0.35
ν_{13}	0.35	0.35
ν_{23}	0.39	0.45
G_{12}[2] (MPa)	$E_1/15$	$E_1/18$
G_{13}[2] (MPa)	E1/15	E1/18
G_{23}[3] (MPa)	$G_{12}/10$	$G_{12}/10$

4.2 COMPARISON OF EXPERIMENTAL AND NUMERICAL RESULTS

The numerical model was run for each T-beam specimen, with the corresponding combination of web and flange true modulus of elastically, in order to validate the numerical results against the experimental results. For each T-beam, a specific bending moment and displacement point corresponding to an initial failure and the transition from linear-elastic to non-linear were carefully selected for comparison to the model. Thus, the loading in the model was increased until it reached the specific bending moment, $M_{specified}$, and then the experimental and numerical displacements were compared. The results of this comparison are summarized in Table 6. It should be noted the numerical model was limited to the linear-elastic stiffness of the T-beams and did not aim to predict ultimate failure.

Table 6: *Comparison of experimental (Exp.) and FE model deflections at midspan based on specified bending moment*

Specimen	**$M_{specified}$** [kNm]	**Exp. Deflection** [mm]	**FE Model Deflection** [mm]	**Exp./FE Model** [-]
SG-01	6.0	6.98	7.06	1.01
SG-02	10.8	11.15	11.27	1.01
SG-03	7.8	8.78	7.42	0.85
SG-04	9.9	7.95	7.30	0.92
SG-05	12.9	10.35	11.58	1.12
SG-06	9.0	7.42	7.18	0.97
			Avg.	**0.98**
			CoV	0.09

The numerical model agreed reasonably well with the numerical model, with the average experimental midspan deflection being 0.98 of the numerical midspan deflection with a CoV of 0.09. The deviation in SG-03 and SG-05 is not uncommon for dimensional lumber and can partially be attributed to the presence of localized defects in the wooden elements, lack of a continuous bond, and appreciable error in the properties (e.g., average slip stiffness used). The load-displacement curve for each of the experiment specimens, along with the numerical model response is presented in Figure 11: Load-deformation curve from experimental and numerical model results. Overall, the numerical model was deemed capable of capturing the screw-glued shear connection behaviour.

https://doi.org/10.52202/069179-0450

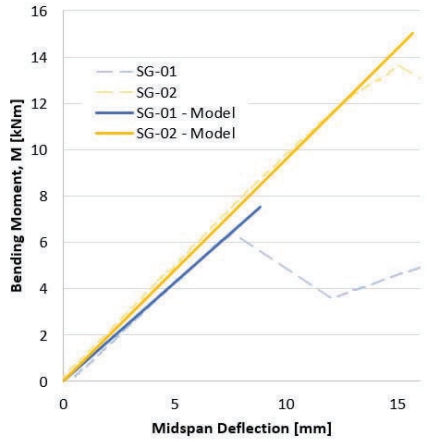

(a) T-beam SG-01 and SG-02

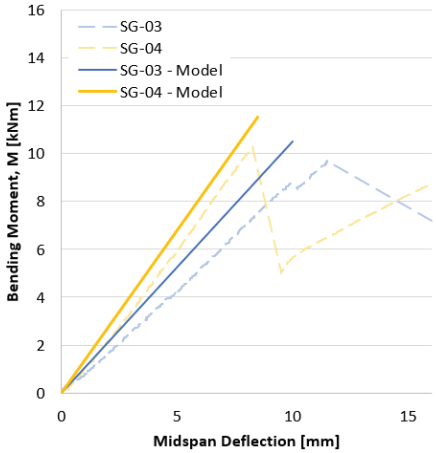

(b) T-beam SG-03 and SG-04

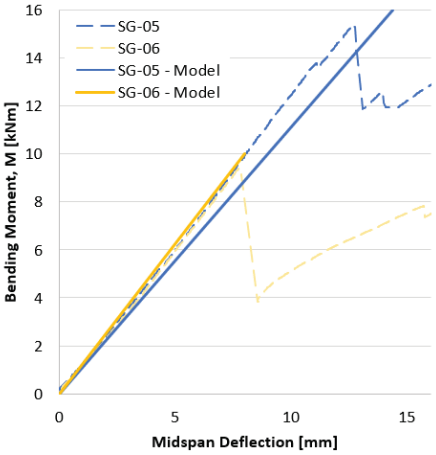

(c) T-beam SG-05 and SG-06

Figure 11: *Load-deformation curve from experimental and numerical model results*

5 IMPLICATIONS ON MASS TIMBER COMPOSITES

To investigate the feasibility of the shear-glued connection studied in the current paper for use in MTC panels, the experimentally determined slip stiffness from Table 1 was analytically applied to a 10m long CLT-glulam HMT panel shown in Figure 12. The HMT panel consisted of four 80 x 245mm SPF 20f-E grade glulam webs and two 105 x 2400mm V2 grade CLT panels, with material properties taken from CSA O86 [24]. The γ-method, which has been shown to be an accurate method for determining the behaviour of MTCs in design [10,11], was used for this analysis.

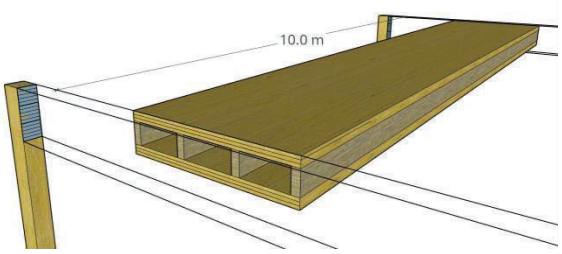

Figure 12: *10m hollowcore mass timber panel*

The results of the analysis are presented in Figure 13 where the screw-glued connection slip stiffness was able to achieve a high degree of composite action (>95%), thus resulting in an HMT panel that was able to meet the design criteria of a 10m span for stiffness requirements due to vibration demands. For comparison, a few select connections experimentally tested on CLT-glulam shear specimens by Montgomery [6] and Jacquier [10] are also presented in Figure 13.

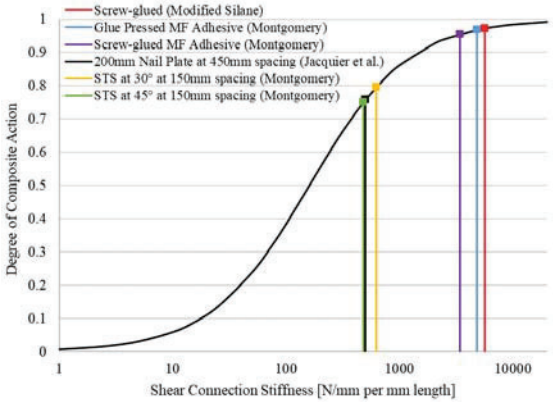

Figure 13: *Degree of composite action in HMT panel based on shear connection stiffness*

For the screw-glued connection, the HMT panel achieved a stiffness of approximately 105 x 10^{12} Nmm^2 which corresponded to a vibration-controlled span, according to the CSA O86 Annex A clause A8.5.3 [24] for the vibration-controlled span of CLT panels, of 10.4m. Overall, this indicated that the commercially available bead extruded silane modified adhesive and partially threaded STS is an easily applied, and structurally viable screw-glued connection for MTC panels, able to achieve high degrees of composite action.

https://doi.org/10.52202/069179-0450

6 CONCLUSIONS AND FUTURE WORK

Presented herein are the results of an experimental study investigating the behaviour of a screw-glued connection, with the goal of justifying it as a structurally viable shear connection for MTC panels. The connection consisted of 6mm dia. x 100mm long partially threaded STS with washer heads spaced at 133mm c/c, as well as a 10mm wide bead of commercially available silane modified construction adhesive on a 40mm wide web. Additionally, 25mm dia. washers were added beneath the existing washer heads of the screws as a measure to aid in evenly spreading the pressure distribution of the screw-gluing, as well as to prevent local wood crushing under the screw heads. The results have shown that the screw-glued connection was able to achieve a slip modulus of 17.63 N/mm per mm^2 of glue with a CoV of 0.11. The lower level of variation in the connection stiffness is encouraging for the overall repeatability of the screw-glued connection given the number of variables that can influence the overall behaviour (e.g., lumber grade, stiffness, surface planning, glue vs. wood failure, moisture content, curing conditions). Overall, when used on a 10m HMT panel, analytical results using the γ-method indicated a nearly fully composite shear connection was achieved and a vibration-controlled span of 10.4m was possible for the 455mm deep section.

Two bilinear models were used to represent the load-slip response and to determine the yield stress of the screw-glued connection. The first, based on EN 12512, provided an average yield stress of 4.59MPa while the second, based on yield occurring at 75% of the maximum load, provided an average yield stress of 3.47MPa.

The average apparent and true stiffness of the sections were found to be $3.69 \times 10^{11} Nmm^2$ and $4.40 \times 10^{11} Nmm^2$ respectively, with most of the variation in stiffness across specimens attributed to the different modulus of elasticity of the webs. Generally, higher webs stiffnesses were proportional to higher T-beam section stiffnesses. The experimental T-beam results were then compared to a FE model created to capture the behaviour. For each T-beam flange and web element, the modulus of elasticity was determined not destructively and used as input for the model. Overall, the numerical model agreed well with the numerical model, with the average experimental midspan deflection being 0.98 of the numerical midspan deflection with a CoV of 0.09. The numerical model was thus deemed likely capable of capturing the screw-glued connection behaviour and will be used on future numerical analysis of MTCs.

The screw-glued connection investigate herein has proven to be a structurally viable and easy to apply shear connection with great potential for use in MTC panels. Future work applies the current screw-glued connection, along with other promising shear connection candidates, to CLT-glulam shear specimens with the goal of determining the optimal connection based on connection stiffness and yield stress, constructability, and cost for use in the production of MTC panels in industry. The optimal three connection configurations are used in the fabrication of 15 CLT-glulam T-beams which, to the author's knowledge, will be one of the largest studies on MTC panels.

REFERENCES

[1] Kirsten Lewis Rijun Shrestha, Keith Crews BB. The Use of Cross Laminated Timber for Long Span Flooring in Commerical Buildings. WCTE 2016 - World Conf. Timber Eng., 2016.

[2] FPInnovations. Canadian CLT Handbook. 2nd Editio. Pointe-Claire, Quebec: 2019.

[3] WoodWorks - Wood Product Council. Case Study: Catalyst. Spokane, Washington, USA: 2020.

[4] Element5 Co. WoodIn 2023. https://elementfive.co/projects/woodin/.

[5] Hull T, Lacroix D. Analytical Investigation of the Potential of Hollowcore Mass Timber Panels for Long Span Floor Systems. In: Walbridge S, Nik-Bakht M, Ng KTW, Shome M, Alam MS, El Damatty A, et al., editors. Can. Soc. Civ. Eng. Annu. Conf. 2021, Singapore: Springer Nature Singapore; 2022, p. 621–33.

[6] Montgomery WG. Hollow Massive Timber Panels: A High-Performance, Long-span Alternative to Cross Laminated Timber. Clemson University, 2014.

[7] Chen Y, Lam F. Bending Performance of Box-Based Cross-Laminated Timber Systems. J Struct Eng 2013;139.

[8] Jacquier N, Girhammar UA. Evaluation of bending tests on composite glulam-CLT beams connected with double-sided punched metal plates and inclined screws. Constr Build Mater 2015. https://doi.org/10.1016/j.conbuildmat.2015.07.137.

[9] European Committee for Standardization (CEN). EN 1995-1-1:2004/A2:2014 – Eurocode 5 – Design of timber structures – Part 1-1: General – Common Rules and Rules for Buildings. Brussels, Belgium: European Committe for Standardization; 2014.

[10] Jacquier N, Girhammar UA. Evaluation of bending tests on composite glulam–CLT beams connected with double-sided punched metal plates and inclined screws. Constr Build Mater 2015;95:762–73. https://doi.org/10.1016/J.CONBUILDMAT.2015.07.137.

[11] Hull T, Lacroix D. Comparative analysis of the feasibility of hollowcore mass timber panels for long span floor systems. World Conf. Timber Eng., Santiago, Chile: 2021, p. 8.

[12] Katarina Bratulic MA. Screw Gluing - Experimental and Theoretical Study on Screw Pressure Distribution and Glue Line Strength. WCTE 2016, 2016.

[13] Rothonblass. Plates and Connectors for Timber Buildings. 2019.

[14] ASTM. Standard Specification for Adhesives for

https://doi.org/10.52202/069179-0450

Field-Gluing Wood Structural Panels (Plywood or Oriented Strand Board) to Wood Based Floor (D3498−19a). vol. i. 2019. https://doi.org/10.1520/D3498-19a.2.
[15] ASTM. Standard Test Method for Strength Properties of Adhesive Bonds in Shear by Compression Loading. ASTM D905-21 2021.
[16] ASTM. Standard Test Methods for Mechanical Fasteners in Wood and Wood-Based Materials. D1761-20 2020.
[17] ASTM. Standard Test Methods for Direct Moisture Content Measurement of Wood and Wood-Based Materials (ASTM D4442). West Conshohocken, PA: 2020.
[18] CEN. Timber Structures - Joints Made with Mechanical Fasteners - General Principles for the Determination of Strength and Deformation Characteristics (EN 26891) 1991:6.
[19] Muños W, Salenikovich A, Mohammad M, Quenneville P. Determination of Yield Point and Ductility of Timber Assemblies: in Search for a Harmonised Approach. World Conf Timber Eng 2008;Volume 1.
[20] CEN. Timber Structures - Test Methods - Cyclic Testing of Joints Made with Mechanical Fasteners (EN 12512) 2001:18.
[21] Forest Products Laboratory. Wood handbook - Wood as an engineering material. Madison, WI: Forest Products Laboratory, USDA Forest Service,; 2010.
[22] Dassault Systemes Simula Corp. ABAQUS [Computer software] 2020.
[23] Koubek R, Dedicova K. Friction of wood on steel. Linnaeus University, 2014.
[24] Canadian Standards Association. Engineering Design in Wood. CSA-O86 2019.

World Conference on Timber Engineering Oslo 2023

LOADING TEST OF CLT-SHEAR WALL CONNECTED WITH STEEL BAR－TIMBER COMPOSITE COLUMN DISSIPATING HIGH-ENERGY

Takumi Suyama [1], Riko Kawasaki [2], Atsuya Kawasoe[3], Tomokazu Yoshioka[4], Shinichi Shioya[5]

ABSTRACT: In light of the current climate crisis, there has been much recent interest in using timber structural members in large buildings, since timber is as renewable natural resource. Moreover, in severe earthquake prone zones, such as Japan, they are more desired on the grounds of light weight of timber members. We are developing a frame system formed by steel bar-timber composite members strengthened by deformed steel bars (i.e., rebars) using epoxy resin adhesive. We are also developing Cross Laminated Timber (CLT)-shear wall for the frame. One of the most excellent mechanical characteristics of CLT are its high shear stiffness and shear capacity. It is most advisable to use one long CLT panel as one continuous wall without cutting it at floor levels. This paper reports the application of the rotating shear plate concept to the CLT wall and experiment of the shear wall dissipating high-energy, by damper installed in a frame consisting of steel bar-timber composite columns and timber beams.

KEYWORDS: Shear wall, Cross-Laminated Timber, Composite timber, Column, Re-centering, Energy-dissipation

1 INTRODUCTION

One of the most excellent mechanical characteristics of Cross Laminated Timber (CLT) is its high shear stiffness and shear capacity. The structural component that can take advantage of that is shear wall. However, it is difficult to utilize fully the characteristics of CLTs, if they are cut and connected at floor level of each story in buildings, and they are also time-consuming and expensive. It is most advisable to use one long CLT panel as one continuous wall. The maximum dimension of one CLT panel available in Japan is 3.0 m x 12.0 m. It is possible to adopt the CLT as one 2-story to 4-story continuous wall. A mechanism is required to transfer the horizontal inertia force generated by the CLT slab during an earthquake to the shear wall. However, if the continuous wall yields in bending or rotates at its wall bottom, rotation, vertical misalignment deformation will occur at the connection between the slab and the wall above the second story. When the deformations are larger, it is currently difficult to transfer shear force between the slab and wall CLTs without damaging the connection during an earthquake. Future seismic design of buildings, on the other hand, will require performance to control damage and residual deformation. To control damage in slab-to-wall joints, a joint method that can only transmit horizontal shear force without restricting the rotation and the vertical deformation is desirable. Shioya has devised a shear key plate (rotational shear key) that allows rotation and transmits only shear forces in steel bar-timber composite column-beam connection [1]. Rocking wall is effective in reducing its residual deformation. Rocking CLT shear walls have already been developed [2], but the level of shear force that can be transmitted is extremely low, approximately 25% of the shear capacity of CLT wall. This paper reports the application of the rotational shear key plate concept to CLT shear wall and experiment of a shear wall dissipating high-energy by dampers, which are installed in a frame consisting of steel bar-timber composite columns and timber beams.

2 ARRANGEMENT AND AIM OF SHEAR WALL

Figure 1 shows a schematic diagram of assumed structure and shear wall, and its arrangement, where 3-story rigid-frame structure is assumed. Shear walls are placed in ridge direction. One-piece type of one CLT panel with a width of 3 m per one span (one-piece type) or two-piece type of two CLT panels can be assumed. Column is to be made of steel bar-timber composite column. The span in the ridge direction of building is assumed to be 3.6-3.8m and are connected with Glued laminated (Glulam) timber beams. The shear wall is assumed not to resist to axial forces from Dead load and Live load of building. Long-term loads are assumed to be resisted by the left and right columns of the shear wall.

The rotational shear key plate is incorporated so that its wall bottom performs as pin and is connected to RC foundation.

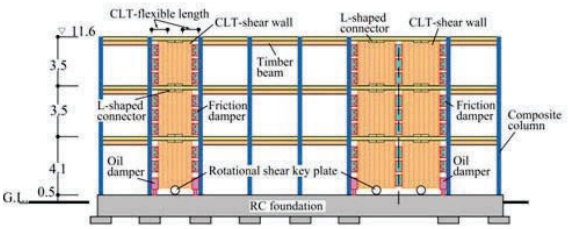

Figure 1: *Shear wall, damper, and rotational shear-key plate in a frame*

[1] Takumi Suyama, Department of Architecture, Kagoshima University, Japan
[2] Riko Kawasaki, Department of Architecture, Kagoshima University, Japan
[3] Atsuya Kawasoe, National institute of technology Kagoshima college, Japan
[4] Tomokazu Yoshioka, Kyusyu University, Japan
[5] Shinichi Shioya, Department of Architecture, Kagoshima University, Japan, k7347039@kadai.jp

https://doi.org/10.52202/069179-0451

Shear wall and CLT slab are connected to each other with L-shaped angle steel and screws (hereinafter referred to as "L-shaped hardware joint") only over center segment of the span.

As the slab is not restrained by the shear wall over section between the L-shaped hardware joint and its columns, the slab is expected to absorb the vertical deformation between the CLT wall and the columns and not to be damaged over the section.

Friction dampers and oil dampers are installed between the CLT wall and the column, dissipating energy using the vertical deformation between them which is caused by the rotation of the CLT wall. The friction damper is expected to dissipate vibration energy mainly during big earthquakes, i.e., after 1/200 rad. and the oil damper is expected to dissipate the vibration energy during frequent small and medium earthquakes and vibrations caused by wind loads to improve the habitability in building.

3 FRICTION DAMPER AND ITS PROPERTY

The shape of the damper is shown in Figure 2. It consists of a steel plate/Part A, T-shaped steel/Part B, two ultra-high strength aluminium plate/Part C for sliding material, two filler steel plate/Part D, two splice plates/ Part E, two thick square washer/Part F and a high-strength bolt/Part G. In the experiment, high-strength bolts with an embedded foil strain gauge were used to accurately measure tension force of the bolts. Part A is inserted into a slit cut in the

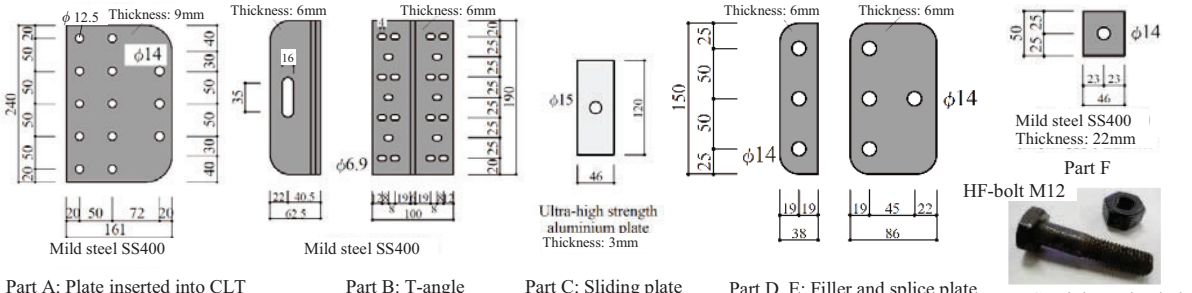

Figure 2: *Parts of proposed friction damper*

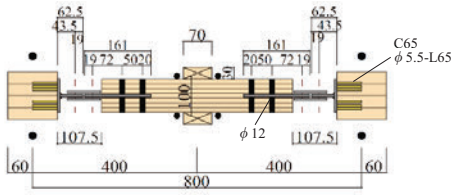

Photo 1: *PC steel bar embedded with a foil strain gauge ϕ 13-M14, Grade: C, Capacity:146^{kN}*

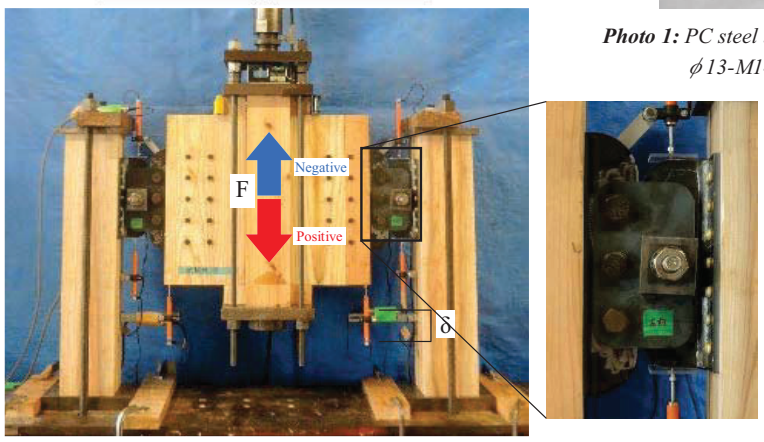

(a) Set-up for loading

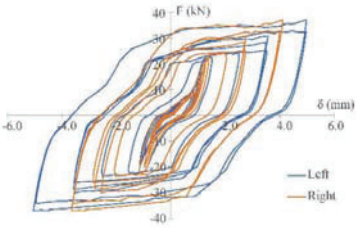

(b) Slip of overall

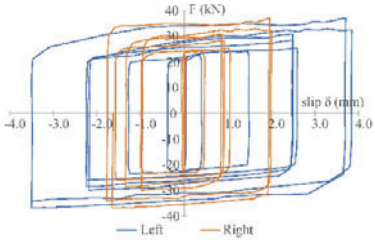

(c) Slip of Plate A – T-angle

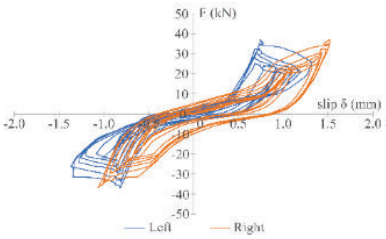

(d) Slip of CLT– Plate A

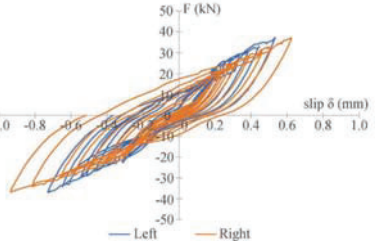

(e) Slip of T-angle–column

Figure 3: *Damper specimen and Vertical force/F-slip deformation/ δ relationships*

https://doi.org/10.52202/069179-0451

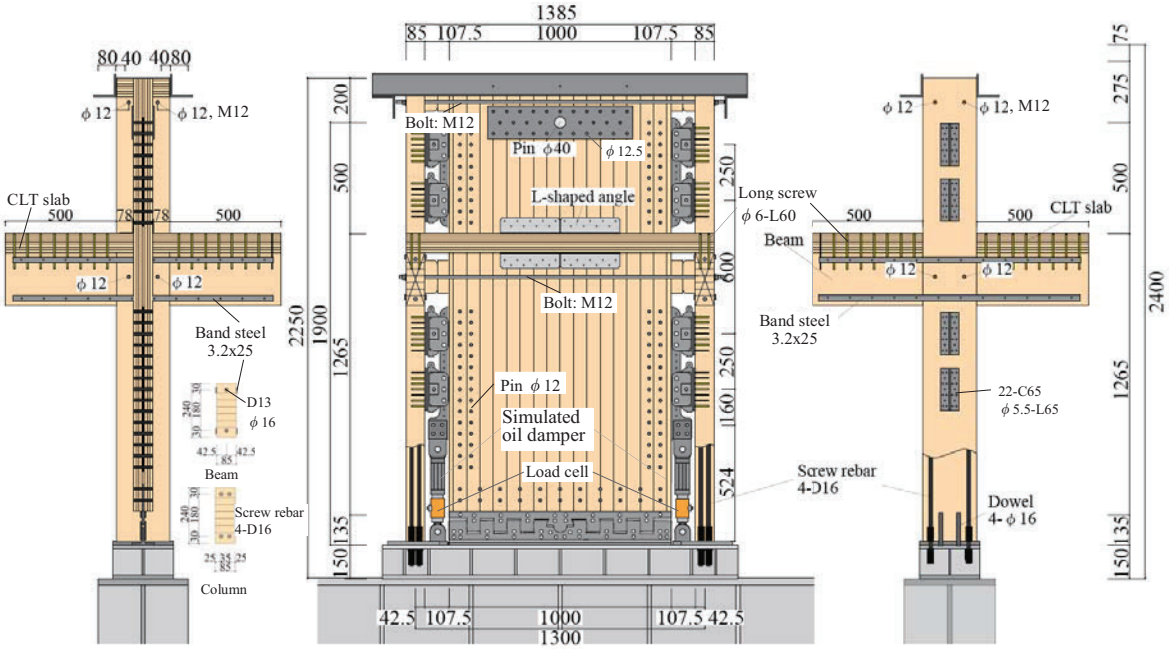

(a) Side view to CLT (b) Front (c) Side view to column

Figure 4: *Shape and dimensions of specimen*

centre of the thickness of the CLT and secured with drift pins. Part B is fixed to the side of the column with self-tapping screws.

Figure 3(a) shows a set-up for cyclic reversed loading test to investigate the frictional characteristics of the damper. In the damper, friction force and energy dissipation generate on two sliding surfaces between web of Part B and ultra-high-strength aluminium plate/ Part C. The aluminium plate is fixed to the splice plate using sand blast. The friction force-deformation relationship is shown in Figure 3(b)-(e). The friction force can be assumed to be 1/2 of the vertical load F. Deformation as horizontal axis in Figure 3(c) is the sliding deformation of the aluminium plate, which means that the initial stiffness is higher than others and there is little slackness. The skeleton curve of the relationship can be seen such as a tri-linear curve and not an inverted S shape curve. Except Figure 3(c), the curves have an inverted S-shaped loop shape with initial slackness caused by clearance around the drift pin or the screw. This characteristic was anxious to lead to a deterioration in horizontal shear force-drift relationship of the shear wall.

4 LOADING TEST OF SHEAR WALL

4.1 SPECIMEN

Figure 4 shows configuration of specimen, which was scaled at 40% and modelled as a range from the first floor to center of the second story height in frame planned such as one CLT panel was to be fitted in one span in the three-story frame consisting of steel rebar-timber composite columns and Glulam timber beams.

The column was rectangular in cross section and made of steel bar-timber composite member, which was selected to be in the weak axis direction of the column in loading direction. CLT panel and the columns were connected by

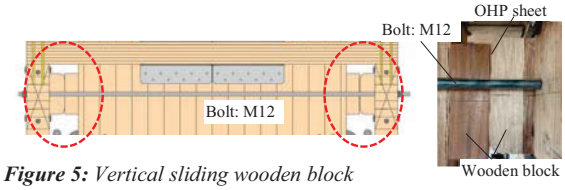

Figure 5: *Vertical sliding wooden block*

the friction damper mentioned in Chapter 3. No beam was employed to connect the left column and the right column. However, as shown in Figure 5, a pair wooden block was fixed to the column between the column and the CLT panel with tapping screws so that the interface of the wooden blocks could allow vertical sliding by being inserted a polyethylene terephthalate sheet. This prevents space between the columns and the CLT panel from closing, and separation between those is prevented by penetrating two long bolts through the columns on both sides and tightening those with washers and nuts.

This connectoin method is planned to be done at each floor, but in this specimen, it was also done near the top loading height.

Bottom of the CLT wall was connected to H-shaped steel flange as foundation by two pair-rotational shear key plates. However, in actual buildings, column bottom is planned to be anchored to reinforced concrete foundation by inserting column rebar into its ducts for the rebar and then grouting into the ducts.

Orthogonal beams were connected by glued-in-rod to the columns. The orthogonal beams were also made of steel bar-timber composite member. The second floor was made of the same CLT as the CLT wall and was connected to the CLT wall with L-shaped hardware joint. This was designed such that shear force could be transmitted from floor to wall. Two CLT slabs were connected by self-tapping screw to the orthogonal beams.

https://doi.org/10.52202/069179-0451

4.2 DETAILS OF SPECIMEN

4.2.1 Cross laminated timber (CLT)

The CLT had 84 mm thickness and consisted of 5 layers of 7 plies with lamina thickness of 12 mm which was width haggled. The strength grade was in accordance with cedar M60B of Japanese Agricultural Standard (JAS).

4.2.2 Column

The column adhered to cedar Glulam timber of E65F225 of JAS. Rebar was screw rebar with nominal diameter of D16 and yield strength level of SD390. The area ratio of tensile bars to column cross-section was 1.94%, and the ratio of the total rebars was 3.88%.

4.2.3 Connection of column bottom

Figure 6 shows detail of column bottom. The screw rebar coupler cut in 1/2 of the lengthwise direction was used as a nut. Nut/A was tightened on the column side with a lock nut. A steel plate was secured by wood screw to basement of the column, and then four dowel holes were drilled to match hole in the steel plate and four dowels were inserted. The column basement was fixed by tightening the screw rebar with nut B by passing the screw rebar and the dowel to upper flange of the H-shaped steel foundation. The steel plate was fixed to the H-beam with high-tension bolts.

4.2.4 Friction damper

Figure 7 shows detail of friction damper. High-strength aluminium plates (thickness=3.0 mm) are placed on both sides of web of T-shaped angle steel such as makes the joint surface slid. The tension of PC steel bar pressing the sliding surface was measured with a strain gauge embedded in the PC-steel bar. Splice plate was blasted on its one side to prevent misalignment with the aluminium plate. In addition, high-strength bolt was used to tighten splice plate to steel plate inserted into CLT panel to form friction joint between the splice plate and the inserted plate. Figure 8 shows shape and dimension of the inserted steel plate into CLT side face. The drift pin was made of hardened steel rod of S45C by heat treatment with a diameter of 12 mm.

4.2.5 Rotating shear key plate

Figure 8 shows a rotational pair-shear key plate (thickness = 9.0 mm). It was made of mild steel of SS400 and cut by laser-cut machine controlled with computer. Figure 10 shows set-up for the rotational shear key plate which consists of upper comb plate and lower comb plate.

Figure 11 shows the process of assembling of rotational shear keys. Upper two shear plates are friction-joined with high-strength bolts to both sides of the steel plate inserted to CLT-wall's bottom. Lower two shear plates are friction-joined with high-strength bolts to both sides of web of T-shaped angle steel secured to H-shaped steel foundation of reaction steel frame with high-strength bolts. The design of the pair shear key plate is based on magnitude of shear force and rotation angles to be allowed. The shear capacity of CLT wall of this specimen in design is 173 kN on the basis of its nominal shear strength and horizontal cross-section area considered wood ducts, and the pair-shear key plate can transmit shear force of approximately 1221 kN (= 9 x 1000/2 x 235/$\sqrt{3}$ x 2). Rotation angles of up to 3.3 x 10^{-2} rad. is to be allowable.

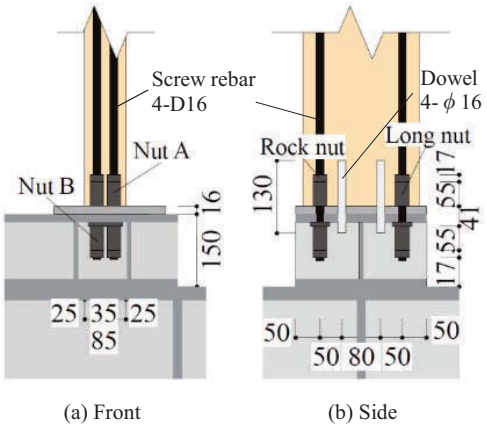

Figure 6: *Detail of connection of column bottom*

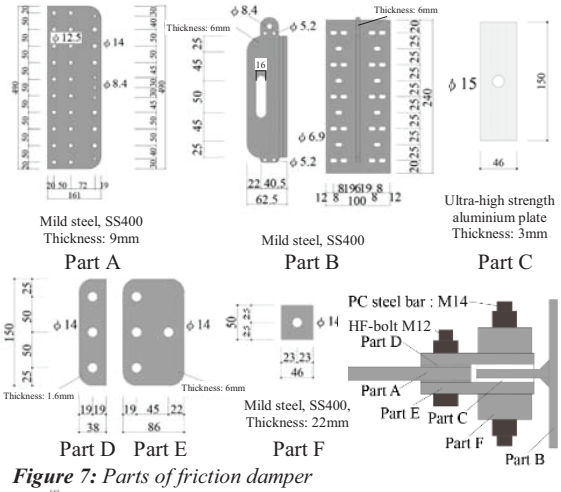

Figure 7: *Parts of friction damper*

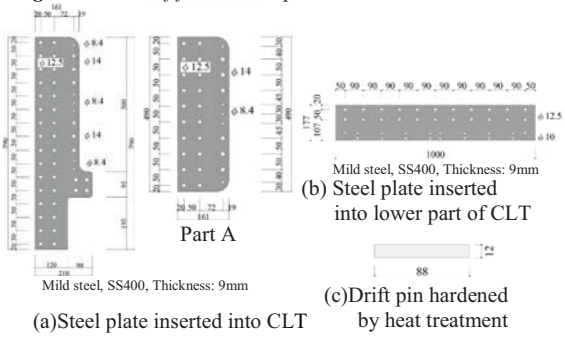

Figure 8: *Shape and dimensions of inserted steel plate*

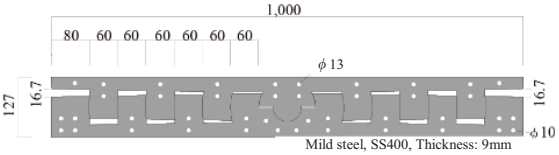

Figure 9: *Shape and dimensions of rotational shear key plate*

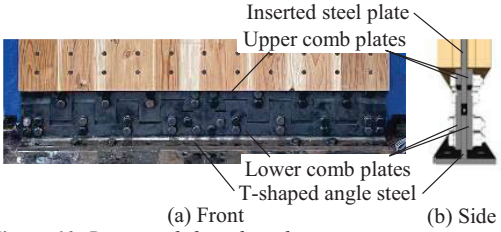

Figure 10: *Rotational shear key plate*

https://doi.org/10.52202/069179-0451

Photo 2: *Simulated oil damper adjusted to stiffness equivalent to oil damper up-down stiffness*

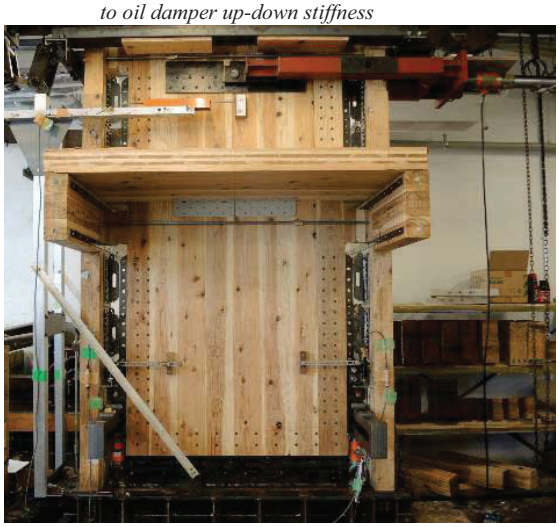

Photo 3: *set-up for loading*

4.3 LOADING

Figure 12 and Photo 3 show set-up for loading. H-beams of foundation were fastened to steel reaction frame with high-strength bolt, and repeated positive and negative cyclic horizontal force was applied at pin position at top of the CLT wall. No vertical load was applied to the columns. To prevent out-of-plane deformation of the top of the wall, two L-shaped steel beams sandwiched both side of the top of the wall, and the L-shaped steel beams and the reaction frame were connected by lateral braces. The lateral braces were joined so that the column heads were not restrained in loading direction. The loading protocol is shown in Figure 14. Orange colour indicates the force applied to check stiffness of specimen installed with each damper, and blue colour represents main protocol for seismic loading. The horizontal displacement at the top of the wall was controlled by deformation angle divided by 1691 mm of the height between the foundation and the displacement transducer. However, the initial 1-2 cycles were controlled by horizontal force.

4.4 MEASUREMENT

Figure 15 shows set-up for measurement of deformation and strain. The horizontal deformation of the wall was measured at the center of the wall width using displacement transducer attached to an aluminium frame fixed to the H-beam of the foundation, close to the height of the force point. Deformations of left and right dampers on the first story and the right damper on the second story, vertical up-down deformation of the CLT wall bottom, and the vertical deformation of CLT slab against the CLT wall were measured with displacement transducers.

Vertical axial strain and shear strain of CLT panel and vertical axial strain of timber near column bottom were measured with foil strain gauge (measuring length: 60 mm, long-term period measurement specification).

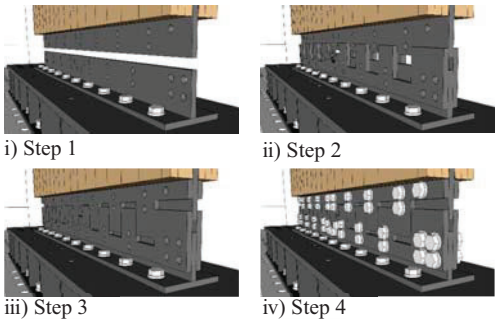

Figure 11: *Process of assembling of rotational shear key plates*

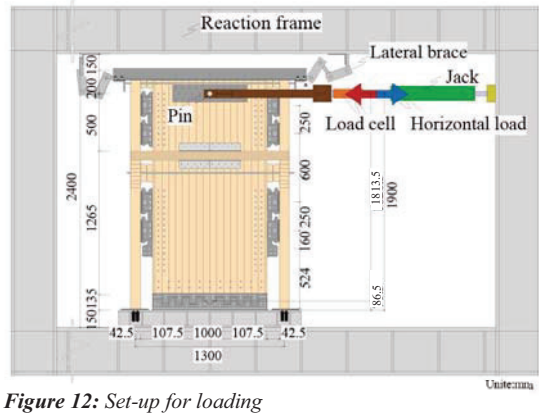

Figure 12: *Set-up for loading*

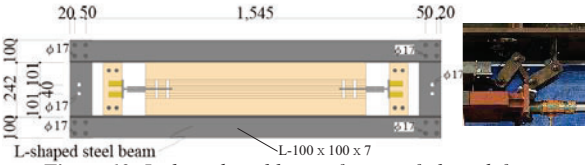

Figure 13: *L-shaped steel beams for out-of-plane deformation prevention*

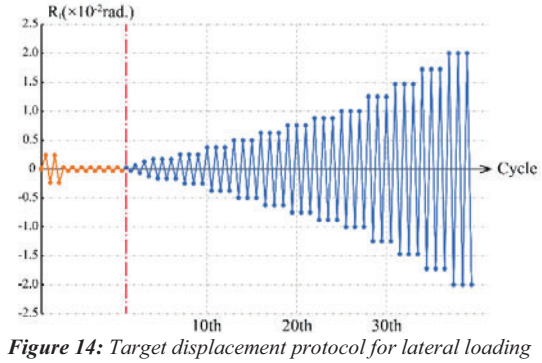

Figure 14: *Target displacement protocol for lateral loading*

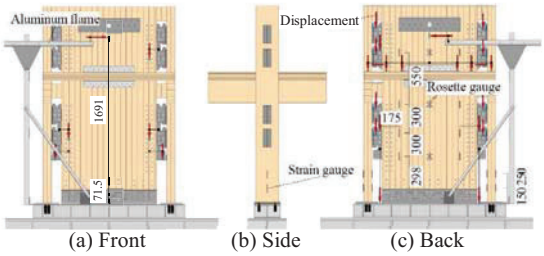

(a) Front (b) Side (c) Back

Figure 15: *Set-up for displacement and strain*

https://doi.org/10.52202/069179-0451

5 EXPERIMENTAL RESULTS

5.1 HORIZONTAL LOAD-HORIZONTAL DISPLACEMENT ANGLE RELATIONSHIP

Figure 17 shows horizontal force - deformation angle relationship. The deformation angle was calculated by dividing average horizontal displacement of the front and back near loading point by height of the displacement meter (1691 mm).

Horizontal force applied as reversed cyclic loading from the 4th cycle, experiencing each target deformation angle three times. The three cycles were observed to follow almost the same loop until the final deformation, and the cyclic loading did not cause any decrease in load capacity. The loops until the 30th cycle is shown in red and loops after the 30th cycle is shown in blue. Owing to loosening of the high-strength bolts of two splice plate of one friction damper connected to the top of wall from the 13th cycle to the 30th cycle, the relationship became loops such as it stiffs again after yielding.

This reason is considered that the stiffness is increased when the damper rotates owing to the loosening and the high-strength bolts strikes the side of hole in the splice plate and the inserted steel plate. After unloading at the time of recognizing the rotation of the splice plate, the friction damper was returned to be vertical and then the high-strength bolts were tightened.

Average shear stress obtained by dividing the maximum horizontal force of +110.4kN and -105.9kN at +1/50 rad. by area of horizontal cross section of CLT panel was 1.28 N/mm2. The average of those forces was 62% of shear capacity of the CLT wall bottom considering the deficiency by the drift pint and the inserted steel plate. As it may be possible to increase the horizontal loading capacity by increasing the tension of the PC steel bar in the friction damper, next work is going to reveal behaviour of the shear wall subjected to higher load levels by increasing the tension.

5.2 BEHAVIOR OF DAMPER

Figure 18 shows relationship of vertical shear force Q_D per a damper and sliding deformation δs between the inserted steel plate and the T-shaped angle steel. Q_D was calculated by the following Equation (1).

$$F \cdot h = 4 \cdot Q_D \cdot \ell \quad (1)$$

where F is horizontal force; h is height (1813.5mm) of the force point from rotational center of the rotational shear key; ℓ is horizontal distance (1100 mm) between the right damper and the left damper.

At first, the right-first damper on the lowest height from the bottom slid and yielded at -16.52kN in the fourth cycle; next, the right-third damper was done at -21.93kN in the seventh cycle; the left-first damper was done at -23.95kN in the tenth cycle, as well as the right-first damper.

As well as the horizontal force - deformation angle relationship, the relationship of damper was observed to

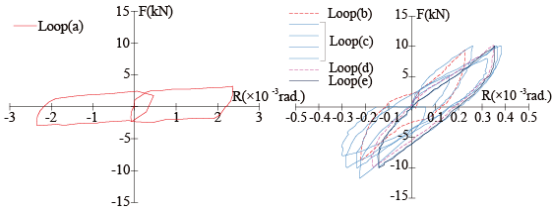

(a) Loop at step adding only rotational shear-key plate (b) Loops at steps adding each damper

Figure 16: *Lateral force-deformation angle Relationship*

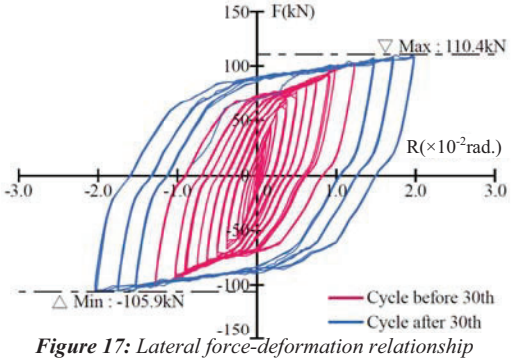

Figure 17: *Lateral force-deformation relationship*

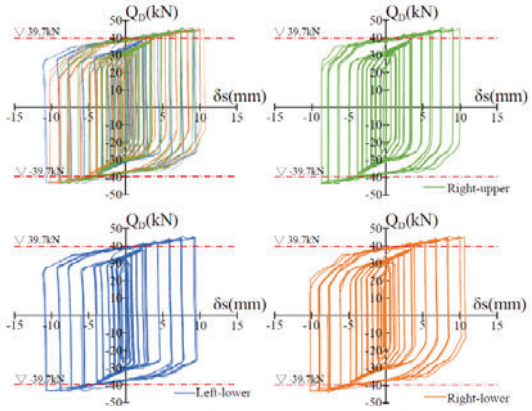

Figure 18: *Friction force/Q_D – slip relationship/δ between Part A –T-shaped angle steel*

be that of an increase in friction force after 1/68 rad. was observed. The maximum of sliding deformation of dampers during the final cycle of loading was+10.75 mm for the right-first damper; -11.22 mm for the left first damper; +9.97 mm for right third damper. The deformation of damper at higher position tended to be smaller, and the deformations of right and left dampers were to be close.

Figure 19 shows the relationship between tension change of the PC steel bar and sliding deformation in the damper. The target initial tension was selected to be 40.0 kN. The damper on the left side of the fourth row is considered to have loosened the PC steel bar due to the loosening of the high-strength bolt. Excluding this damper, the third row has the largest reduction, and the reduction became smaller as it approached the wall foot. It can be inferred that the frictional force might have been greater for the

https://doi.org/10.52202/069179-0451

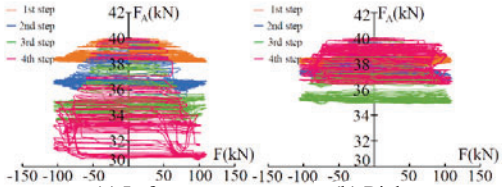

(a) Left (b) Right

Figure 19: *Variation of tension in PC steel bar*

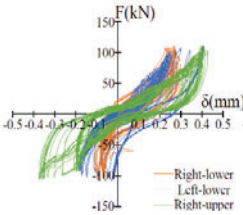

Figure 20: *Lateral force-slip deformation between CLT and Part A*

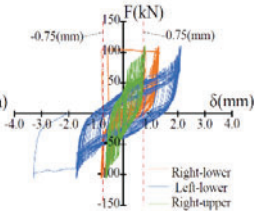

Figure 21: *Load – slip deformation between T-angle and column*

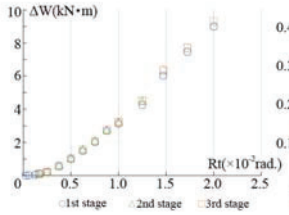

Figure 22: *Dissipation energy*

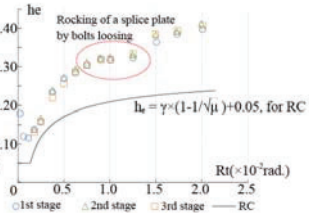

Figure 23: *Equivalent viscous damping factor/he*

right damper for the reason that the left damper has a greater reduction in tension than the right damper.

Figure 20 shows variation of sliding deformation of CLT and inserted steel plate against the horizontal force. It is an inverse S-shaped relationship with stiffness increasing from ±0.2 mm. The explanation of these is that after clearance of steel plate and its drift pin and clearance between drift pin and hole for itself in CLT closing, those resist each other. However, even maximums of sliding were negligible small.

Figure 21 shows variation of sliding deformation of the T-shaped angle steel against column. The maximum deformation in the final cycle was +1.333 mm at the right first damper; the left- first, +2.120 mm and the right third, +0.806 mm. A value of 0.75 mm sliding deformation is shown in the figure as a single vertical line, which roughly correspond clearance of hole in the T-angle steel and the neck of taping-screw. This also can be explained as clearance of those might have closed.

5.3 ENERGY DISSIPATION

Figure 22 shows variation of amount of energy dissipated by loops of each target deformation angle.

Although amount of energy at the same target deformation angle increased slightly in the second and third cycles compared to the first cycle, there was little difference in the amount, and there was no degradation of absorbed energy owing to the repetitive loading.

Figure 23 shows variation of the equivalent viscous damping constant he. The value calculated for reinforced concrete structure are represented by solid black lines.

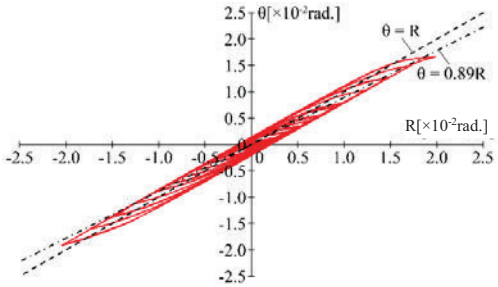

Figure 24: *Rotation angle of CLT– deformation angle relationship*

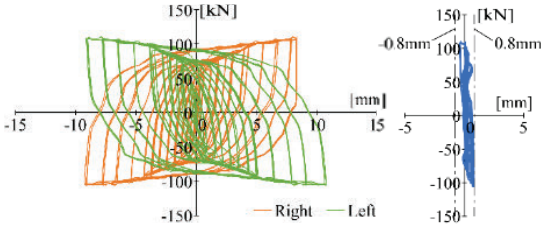

(a) Comparison of left and right (b) Center

Figure 25: *Lateral force – vertical deformation of wall bottom relationship*

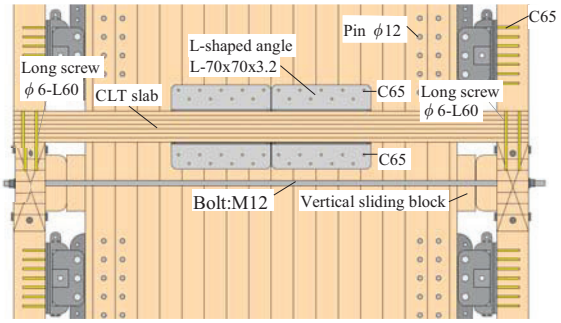

Figure 26: *Connection of CLT floor and CLT wall*

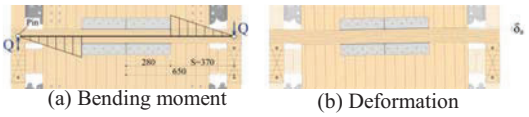

(a) Bending moment (b) Deformation

Figure 27: *Condition of CLT slab as CLT wall rotating*

This shear wall exhibited extremely high energy dissipation performance compared to RC, with performance of more than 10% from the initial deformation level and 40% at 1/50 rad.

5.4 WALL BOTTOM ROTATION

As shown in Figure 15, vertical displacements of CLT wall against the H-shaped steel of the foundation were measured on both left-hand and right-hand of the wall, by using transducers fixed to the lowest steel plate inserted into the CLT. Figure 24 shows variation of rotation angle of the CLT bottom calculated from the displacement, compared to the displacement angle as shear wall, i.e., drift. The rotation angle accounts for approximately 90% of the drift. Figure 25(a) shows variation of up-down displacements versus shear force. Figure 25(b) shows variation in the sum of two displacements at each side. This sum means vertical elongation at the rotation center of the rotating shear plate. Even when the drift increased up to 1/50 rad, the sum was less than ±0.8mm. This

https://doi.org/10.52202/069179-0451

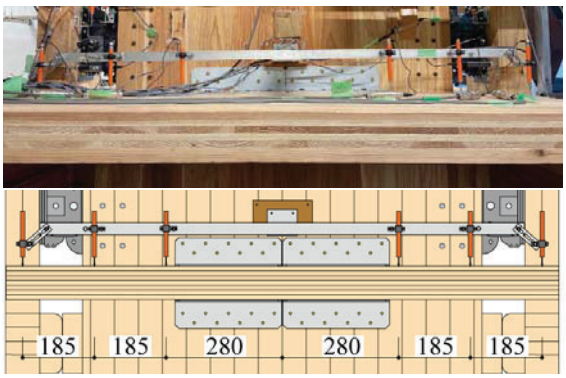

Figure 28: *Set-up for displacement*

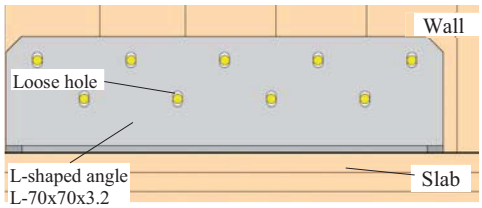

Figure 29: *Rotation-allowing angle steel*

demonstrates that the rotational shear key might have hardly elongated in vertically direction. This suggests that the left-hand dampers and the right-hand dampers might have slid as well, that sum of damper friction forces at each side might have been approximately same, and that the rotational shear key might not have been subjected to great tensile force in vertical.

5.5 VERTICAL DEFORMATION AND DAMAGE OF CLT SLAB

Figure 28 shows setup for measuring vertical displacement of the slab. An aluminium angle with displacement transducers attached were fixed to the CLT wall. The deformation measured is vertical deformation of the slab perpendicular to the aluminium angle.

The vertical deformation of the slab at each measured position against horizontal line passing through the fixed position of the aluminium angle can be approximated by the following Equation (2).

$$y_i = x_i \cdot \theta - \delta_i \quad (2)$$

where y_i and x_i are referred to Figure 30; θ is drift; δ_i is displacement of the transducer.

Figure 30 shows the distribution of the vertical deformation of the slab at a drift of +1/50 rad. The one dot chain line represents an inclination of drift=1/50 rad. This can be regarded as the inclination of the aluminium angle to which the displacement transducers were fixed. Vertical displacements of top surface of the slab can be calculated by using Equation (2), a distribution of which is shown by red solid line.

Even at the positions of the left and right boundaries of the L-shaped angle steel joint, values of the red line are different from those of the one dot chain line.

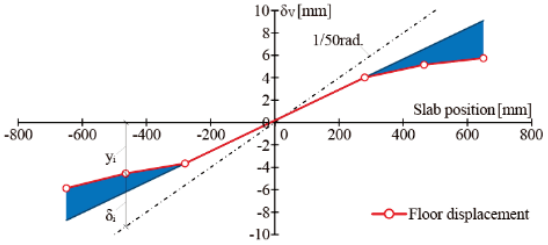

Figure 30: *Vertical displacement of floor*

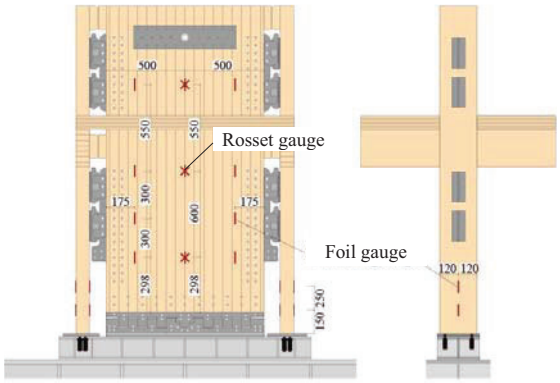

Figure 31: *Set-up for measurement of strain gauge*

This means that sliding deformation occurs between the CLT wall and the CLT slab over range of the angle steel joint. This may result from clearance between the screw holes and screw diameters at the joining angles and torsional deformation between the wall and the slab. The extent that the slab is deformed within range except the angle steel joint can be regarded as blue areas.

If the deformation of the slab is less than allowable value, no damage is expected to occur. The maximum values at drift=1/50. were 2.87 mm on the left side and 3.35 mm on the right side. In this experiment, the slab was not damaged even when the deformation reached 1/50 rad. This argues that this proposed system can significantly absorb the vertical deformation between column and wall, preventing the slab damage.

In the future, it is necessary to develop a method to estimate the deformation and damage deformation of slabs.

5.5.1 ROTATION-ALLOWING ANGLE STEEL

However, it is considered difficult to quantitatively estimate and design those factors. If the screw holes on the wall side of the angle steel are made vertical long holes as shown in Figure 29 so that the rotation of the wall is not restrained at the joint surface between the angle and the wall, the rotation of CLT wall and the vertical deformation caused by the rotation of wall bottom can be absorbed and the damage of CLT slab can be prevented, with transmitting transverse shear force by earthquake motion. Next experiment is planned to adopt the modified angle steel with the long holes.

https://doi.org/10.52202/069179-0451

5.6 SHEAR FORCE OF COLUMN

As shown in Figure 31, column strain was measured using foil gauges. Bending moment of column at each height position can be calculated by multiplying cross-sectional secondary moment of column by its curvature which is calculated using the strain of the foil gauge, as well known[3,4]. Shear force of column can be also calculated as gradient of two bending moments of lower and higher positions of the columns.

In the calculation, it was assumed that Young's modulus of timber is 6500N/mm^2 and that of rebar is 2.05x10^5 N/mm^2, which are nominal values of each. Figure 32 shows shear force vs drift relationship for the columns, comparing the horizontal force of the shear wall. The left and right columns resisted elastically up to 1/50 rad. At 1/50 rad. the positive force on the left column reached 9.5% of the horizontal force, and the negative force on the right column did 7.2%.

5.7 VERTICAL FORCE ON ROTATIONAL SHEAR KEY PLATE

Axial force of column can be calculated from strain of the strain gauges as well as bending moment. Figure 33 shows variation of sum of axial forces of the left and right columns. The sum must have been resisted by the rotational shear key plate. Although there is possibly some error because of Young's modulus of timber assumed as the nominal value, the sum at 1/50rad. is 6.6% of the column axial force calculated from the maximum horizontal load, which is extremely small. From this result, also, it can be seemed that the left and right friction dampers might have slid in good balance.

5.8 SHEAR STRESS-STRAIN RELATIONSHIP OF CLT WALL

As shown in Figure 31, shear strain was measured at three different heights by a rosette gauge (measuring length: 60 mm). Figure 34 shows average shear stress-shear strain relationship. Shear stress was defined as horizontal force divided by horizontal cross-sectional area of CLT wall. Shear strain was calculated from diagonal strain for simplicity; Figure 34(a) shows those up to initial ±3 cycles. Slope of the stiffness at the loop is shown by single-dotted line. The slope is the shear modulus G_W. Figure 34(b) shows those up to the final cycle. The plastic strain is found to be larger in upper part of the wall. This reason cannot have been explained at this time.

The shear modulus of CLT is, in general, 300-500 N/mm^2, but this experimental value is 3.0-4.0 times higher than the values. This is partly because of the assumption that shear forces of column was ignored and horizontal force was resisted by only CLT wall. However, as mentioned above, the shear forces of the column might have accounted for only 8.4% of the total load, so other factors may be responsible.

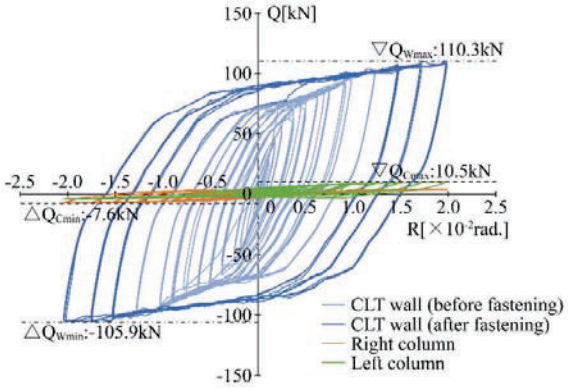

Figure 32: *Lateral shear force – displacement angle*

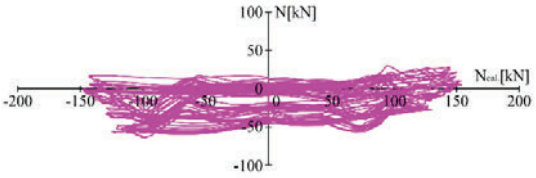

Figure 33: *Sum of axial forces of left-hand and right-hand columns calculated from strain gauge measurings - axial force of column calculated from lateral force relationship*

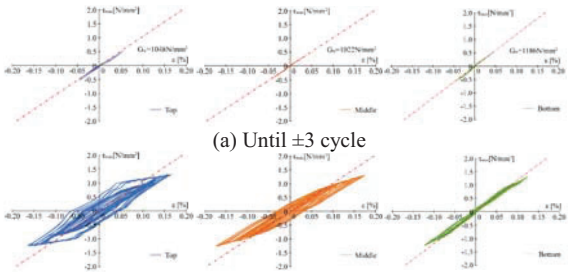

(a) Until ±3 cycle

(b) Until final

Figure 34: *Shear stress – shear strain relationship*

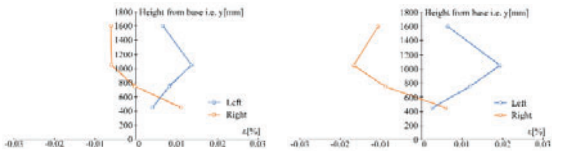

(a) +1/100rad. (b) +1/50rad.

Figure 35: *Distribution of vertical strain of CLT wall by bending*

5.9 DISTRIBUTION OF BENDING MOMENT OF CLT WALL

As shown in Figure 35, vertical axial strain of the CLT wall was measured at four heights with a foil strain gauge (measuring length: 60 mm). Strain values were extremely small, 0.019% at even maximum. Those cannot be analysed in detail considering the variation of wood, but those of the left side indicate tensile strain and those of the right-side do compressive strain. These results are the exact opposite against moment by horizontal force F under positive load. On the other hand, the strains near the rotational shear key and near the loading point will be smaller.

This can be explained as those positions are pins and bending moment is zero. These results can be considered

https://doi.org/10.52202/069179-0451

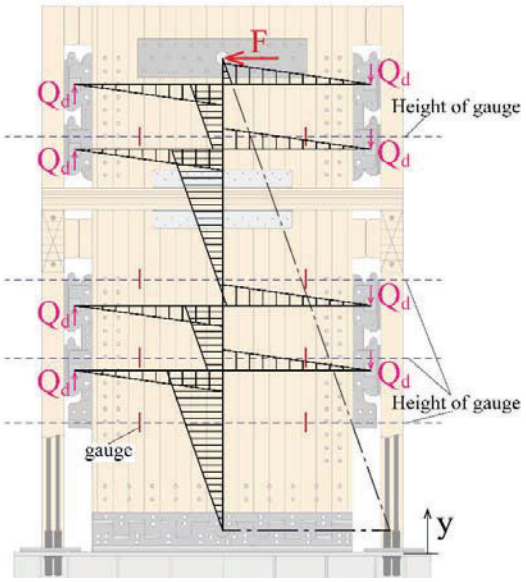

Figure 36: *Bending moment diagram for CLT wall*

to correspond to the distribution of bending moments in the CLT wall shown in Figure 36.

Moment by the horizontal force increases linearly as its height approaches the rotational shear key, as shown in one dot line, but bending moment of the CLT wall hardly increases because vertical friction force of each damper causes bending back. If shear force of columns is ignored because of it being small, horizontal shear force of the CLT wall can be considered constant regardless of height. Thereby, aspect of bending moment distribution of the CLT wall can be captured by assuming that the CLT wall bottom is pin. The heights of each strain gauge are represented by horizontal broken line. The left side is tensile, and the right side is compressive, corresponding to results of the strain in Figure 35.

These results demonstrate that the columns act as flange of wall and its CLT dose as web, similarly to H-shaped steel and that the columns resist against the bending moment of shear wall and the CLT wall dose almost against only the shear force. One of features of this shear wall is that the bottom of the CLT wall is connected to the foundation using rotational shear key plate, which significantly reduces bending moment of the CLT wall and perfectly suppresses damage of the CLT wall. The result of strain mentioned here is one of events supporting the features.

6 SUMMARY

In this paper, we proposed a shear wall system in which CLT panels are incorporated into a rigid-frame structure of steel bar-timber composite members, which authors have been developing, and revealed mechanical characteristic of the shear wall subjected to reversed cyclic lateral loading by a specimen scaled as 40%. The results are summarized as follows.

i) A friction damper so as to be installed between the CLT wall and the column and a connection method were proposed, and then it was confirmed that the damper can be easily joined. Although yield capacity of the damper increased with amount of its sliding deformation and the number of loading iterations, the capacity gradually converged to a constant value as the deformation increasing. Sliding deformation occurred in the joint between the damper and the CLT wall and in the joint between the damper and the column owing to clearance of holes in the drift pin or holes in self-taping screw, but the amount of deformation was almost negligible in the deformation of the shear wall.

ii) The rotational shear key plate was proposed to transmit shear force as the bottom of the CLT wall rotating, and it was confirmed that the plate could be easily joined to the CLT wall and that the incorporated CLT-shear wall allowed the rotation angle as planned.

iii) The shear wall yielded by sliding of friction damper at approximately 1/400 rad., and then produced elastoplastic history loops that generated extremely abundant energy dissipation and hardly degraded with repetitive loading.

iv) The maximum horizontal force in this loading test was 110.3 kN at 1/50 rad. This was 1.31 N/mm^2 at the average shear stress of CLT wall, which was 1.72 N/mm^2 when considering deficiency of joint drift pins and inserted steel plates at the wall bottom.

v) No failures were observed up to 1/50 rad. in this specimen by incorporating friction dampers and a rotational shear key plate and by making the best use of the steel bar-timber composite columns of flame.

vi) As it may be possible to increase the horizontal capacity of the shear wall by increasing tension of the PC steel bars, next work is going to reveal behaviour of the shear wall subjected to higher load levels by increasing the tension.

ACKNOWLEDGEMENT

This project was funded by Grant-in-Aid for Research-A in Japan and its experiment was conducted by all staffs of Shioya's laboratory. The authors gratefully acknowledge their work.

REFERENCES

[1] K. Nagano, et al.: Experiment of a new connection between column and beam producing high-energy dissipation and re-centering, Santiago, WCTE 2021.

[2] Francesco Sarti, et al.: Design and testing of post-tensioned timber wall systems, Quebec City, WCTE 2014.

[3] Kazuya Mori, Shinichi Shioya: Stiffness and strength of full-scale steel bar-timber composite beams with comparative small-depth, Santiago, WCTE 2021

[4] M. Mukai, Takao Ohota, Kazuya Mori, Riko Kawasaki, Shinichi Shioya: Horizontal - loading test of steel bar - timber composite column for mid-rise building, Santiago, WCTE 2021

[5] Kazuya Mori, Shinichi Shioya: Stiffness and strength of full-scale steel bar-timber composite beams with comparative small-depth, Santiago, WCTE 2021

World Conference on Timber Engineering Oslo 2023

TIMBER VAULTS FOR ULTRA-LOW-CARBON BUILDING STRUCTURES

Shane Hossell[1], Will Hawkins[2], Antony Darby[3], Tim Ibell[4], Nicola Lines[5]

ABSTRACT: This paper explores the benefits of using curvature and arching action in timber flooring systems to reduce the embodied carbon and aid in material efficiency. In this paper, the embodied carbon of the proposed timber barrel vault system with granular infill is compared with a more conventional cross laminated timber (CLT) floor. The proposed barrel vault system is constructed out of curved glue-laminated timber that spans between supporting beams. Steel ties are used to restrain the horizontal thrust forces generated by the vault. A two-dimensional parametric optimisation of the barrel vault floor system and the CLT floor in terms of minimising embodied carbon was undertaken using a script written in MATLAB, analysed using matrix stiffness methods and optimised using a genetic algorithm. The analysis was carried out on spans ranging between 4m and 12m with the optimal solution dependent on the interaction between the fabrication stresses, arch height, and rod diameter. The resulting design for 4m to 12m spanning office floors results in a 35% to 41% reduction in embodied carbon compared to an equivalent CLT system.

KEYWORDS: Timber vaults, optimisation, genetic algorithm, embodied carbon, fabrication stresses

1 INTRODUCTION

1.1 SUSTAINABLE MATERIAL EFFICIENCY

Building materials production emits around 10% of global energy-related CO_2 emissions, largely driven by cement and steel manufacturing [1]. To address this, the focus has shifted towards reducing embodied carbon in building materials. Embodied carbon factors are often linked to a unit volume or mass of material and therefore reducing the quantity of material results in concomitant reduction in the environmental impact of the building.

Floors typically account for 50% to 70% of a building structure's material consumption and weight [2]. Adding to this, floor area demand is predicted to increase by 75% between 2020 and 2050, with 80% expected to occur within developing countries [3]. Thus, material reduction in floors while maintaining safety is becoming even more critical to reducing overall embodied carbon in buildings.

Timber has recently re-emerged as an alternative for building structures with the introduction of mass timber products. Designers are increasingly turning to cross-laminated timber (CLT) panels as an environmentally friendly option for constructing buildings [4]. These panels, which are made from orthogonally bonded layers of sawn timber, have enabled faster construction through automated prefabrication, lower material uncertainty, and enabled longer spans made from timber. These benefits have consequently allowed CLT to be used in slab systems and walls. The simple and familiar geometries provided by CLT, and other mass timber products, have made it possible for the risk averse construction industry to adopt the material within their designs. Mass-timber buildings have also been shown to provide lower embodied carbon solutions when compared to steel and concrete [2]-[4] and, with the added advantage of biogenic carbon sequestration, this makes timber a viable solution to support a net-zero building industry.

However, CLT slabs are not optimal in their construction; the core material in a CLT slab does not contribute significantly to the member strength as it merely acts as a spacer between the extreme top and bottom fibres, which does most of the work [4]. Additionally, the cost of using timber in buildings is still seen as more expensive than designs utilising steel and concrete [2]. There are, therefore, numerous motivations for the efficient use of timber to ensure sustainability: to minimise fossil emissions during the construction stage, which are permanently released into the atmosphere; reduce cost; to ensure the sustainable use and distribution of a finite resource, which is under ever increasing demand.

New forests will be required for timber buildings to act as a carbon sink, which will threaten existing biodiversity and will increase competition for land. According to a comprehensive study by Mishra et al. [7] even if there is additional demand for timber in construction, the global

[1] Shane Hossell, University of Bath, United Kingdom, smh95@bath.ac.uk
[2] Will Hawkins, University of Bath, United Kingdom, wh604@bath.ac.uk
[3] Antony Darby, University of Bath, United Kingdom, absapd@bath.ac.uk
[4] Tim Ibell, University of Bath, United Kingdom, abstji@bath.ac.uk
[5] Nicola Lines, University of Bath, United Kingdom

https://doi.org/10.52202/069179-0452

plantation area would need to expand by 100% by 2100 compared to 2020 with this figure increasing to 200% if 90% of all new urban dwellers were to live in timber buildings. Therefore, to ensure a sustainable supply of timber in the future will require a material first approach whereby existing timber designs are optimised for material efficiency based on the actual stress distribution within the member [8]. The challenge is to create flooring systems and design methods that balance low embodied carbon solutions with safety standards, while meeting the performance expectations.

1.2 COMPRESSION VAULTS: STRUCTURAL TIMBER INSPIRED BY NATURE

Unlike concrete and steel structures, timber beams are often governed by serviceability limit states (deflection or vibration) as opposed to strength, since their low mass-to-stiffness ratio results in thick floors and high material consumption. As a result of this, the low span-to-depth ratios required to satisfy serviceability requirements make it difficult to justify using timber beams for long spans.

Trees have evolved to be strong under combined compression and bending forces to support their own weight all while resisting the prevailing winds. This can be taken advantage of by developing vaulted floor systems that act primarily in compression and bending, with the geometric stiffness of the vault compensating for the low timber stiffness. The additional stiffness benefits of using vaults have been demonstrated by Hawkins et al. [9] in previous work on concrete **floors**, where increased structural efficiency resulted in significant reductions in embodied carbon, particularly for longer spans.

Curved timber structures are fabricated by bending initially straight lamellas to the specified curvature, before bonding them with adhesive to lock-in the curvature and enable composite action. Advances in laminating techniques and adhesives have enabled the creation of highly complex geometries, such as the Urbach Tower at the Remstal Gartenschau in Germany [10] and the work by Robeller et.al [11] on curved-folded thin shell CLT structures. During fabrication, high initial stresses can develop in curved timber structures, leading to overstressing under service loads if the lamellas are too thick [12]. However, the viscoelastic behaviour of wood causes the initial bending stresses to decrease over time, a process known as stress relaxation. As shown by Lara-Bocanegra et Al. [12], the initial bending stresses can decrease by 45% to 66% after two years, with the reduction largely depending on the initial curvature of the beam, moisture content and temperature.

1.3 AIMS AND OBJECTIVES

Considering the need for lower embodied carbon structures, this project aims to create a low carbon flooring system using the compression and bending strength properties of timber in combination with the stiffness benefits of vaults. The research compares the embodied carbon of conventional CLT floors with a timber barrel vault design and hypothesises that timber vaults will have the similar efficiency savings as concrete vaults, but with the advantage of simpler design and fabrication and lower embodied carbon. To equilibrate the compression forces in the vault, steel rods acting in tension are provided. This paper describes the preliminary feasibility investigation of using timber vaults as potential embodied carbon saving when compared with cross laminated timber floors.

2 METHODOLOGY

2.1 BASIC PARAMETERS

Two floor systems were adopted during the study with spans ranging from 4m to 12m. The first type of floor investigated in the study was a single span CLT floor designed to Eurocode 5 [13] and shown in Figure 1. The resultant embodied carbon calculated from the CLT floor was then compared to the proposed curved timber floor systems. An optimisation exercise using a genetic algorithm was carried out for the barrel vault flooring system, shown in Figure 2, which comprises of a single spanning parabolic arch supported on two glulam beams with steel ties to counter lateral thrust. Granular fill of earth, gravel or rubble provides a level top surface and is hypothesised to improve vibration and acoustic performance. The material used for all the timber elements was C24, with the properties adopted from EN 338:2016 [14] for sawn timber and EN 14080:2013 [15] for glue-laminated timber.

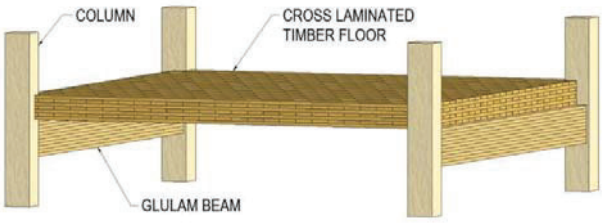

Figure 1: *Cross laminated timber floor*

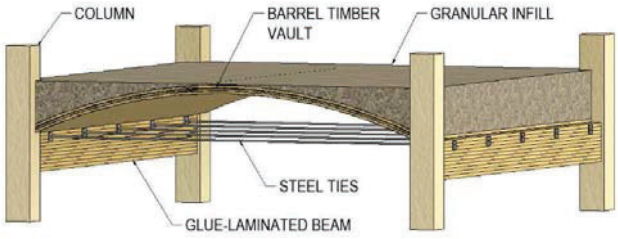

Figure 2: *Barrel vault timber floor*

2.2 DESIGN CRITERIA

Floor loadings were selected to represent a typical office design according to BS EN 1991-1-1 [16]. The design loadings included a live load of 3.5 kN/m^2 (2.5 kN/m^2 office loading and 1 kN/m^2 for movable partitions) and a superimposed dead load of 1 kN/m^2 with ULS partial load

https://doi.org/10.52202/069179-0452

factors of 1.5 and 1.35 respectively. The self-weight of the beams, arch and infill were included as permanent dead load with a ULS load factor of 1.35.

Deflections were calculated under serviceability limit state (SLS) under both short term and long-term loading in accordance with BS EN 1995-1-1 [13]. A limiting instantaneous deflection (ω_{inst}) of Span/300 and long-term deflection (ω_{fin}) of Span/250 was adopted in the designs. A partial load factor of 1 was used for both imposed and dead loads. To account for creep and moisture effects on deflection, a creep factor (k_{def}) of 0.6 was used under service class 1.

Two load patterns were considered, as shown in Figure 3. The first comprises a uniformly distributed imposed load over the full width of the floor to determine the maximum compression in the vault. The second load pattern consists of only applying the imposed load over half the floor to determine the maximum bending moment. The granular infill material was applied proportionally to the height of the vault.

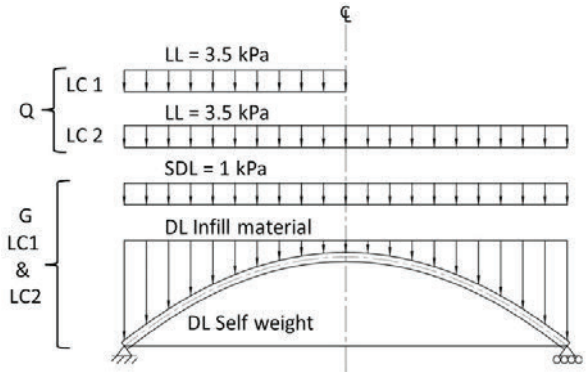

Figure 3: *Applied loading on the barrel-vault floor structure*

2.3 EMBODIED CARBON FACTORS

The focus of the study is limited to cradle-to-gate emissions (Modules A1-A3) and the embodied carbon and density values of the materials presented in **Table 1**. The carbon footprint of each floor design was calculated by summing the products of each material's quantity and its corresponding embodied carbon value.

The embodied carbon value for timber was sourced form an environmental product declaration (EPD 000124) [17] from a UK-based large timber merchant, which covers life cycle stages A1-A3, which includes tree felling, transport, processing, kiln drying, and finishing. The study assumed melamine-urea formaldehyde (MUF) resin, and its embodied carbon value was taken from Wilson [18] with a spread rate of 300 g/m^2 [19]. MUF resin was selected for the study based on consultations with glulam manufactures, as it is commonly used due to its cost-effectiveness and reliable performance [20], [21]. The embodied carbon value for the infill material was obtained from the Inventory of Carbon and Energy Circular Ecology [22].

Table 1: *Embodied carbon factors*

Material	Sawn timber (C24)	Adhesive (MUF)	Steel	Gravel infill
Density (kg/m^3)	420	-	7850	1835
Embodied carbon (kgCO_2e/kg)	115	1.775	1.55	0.00747

2.4 STRENGTH CAPACITY INCLUDING FABRICATION STRESSES

The design moment capacity, including fabrication stresses, shown in Figure 4, was calculated at each point along the length of the parabolic vault. The capacity was calculated at each point to avoid over conservatism, as the minimum fabrication stresses occur at the supports and the maximum occur at the centre of the vault. Equation 1 defines the height, u, of a parabolic vault with maximum height (h) and span (L). Utilising Equation 1 and its first and second derivatives, the curvature (K) and radius of curvature (R) at each point along the vault can be determined from Equation 2. Equation 3 determines the initial fabrication stresses at each point along the length of the beam using the Young's modulus of timber (E) and the moment of inertia of the lamella (I).

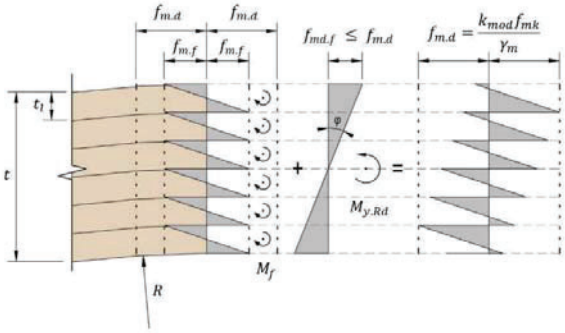

Figure 4: *Design load capacity in bending including fabrication and in-service stresses*

Stress relaxation was considered by reducing the initial fabrication stresses by 20%, which accounts for 1 week of relaxation, as adopted from Lara-Bocanegra [12]. The moment capacity of the section, Equation 4, was determined by limiting the maximum bending stress in the section to the design stress ($f_{md.f}$) as shown in **Figure 4**.

$$u = 4h\left(\frac{x}{L} - \left(\frac{x}{L}\right)^2\right) \quad (1)$$

$$K = \frac{1}{R} = \frac{|u''|}{[1 + (u')^2]^{\frac{3}{2}}} \quad (2)$$

$$f_{m.f} = \frac{KEI}{z_l} \quad (3)$$

https://doi.org/10.52202/069179-0452

The maximum additional stress capacity ($f_{md.f}$) was calculated by varying the curvature (φ) until the maximum design stress (f_{md}) within the timber was achieved. The maximum stress in the section occurs at the interface between the top and bottom lamellas and governs the moment capacity of the section. The utilisation of the section was calculated using Equation 5 using the calculated axial force ($N_{C.0.ED}$) and moment ($M_{0.ED}$) with the respective axial capacity ($N_{c.0.RD}$) and moment capacity ($M_{0.RD}$). The axial capacity incorporates the effect of buckling by including an instability factor (k_c).

$$M_{0.RD} = f_{md.f} Z_{xx} \tag{4}$$

$$\frac{N_{C.0.ED}}{k_c N_{c.0.RD}} + \frac{M_{0.ED}}{M_{0.RD}} \leq 1 \tag{5}$$

2.5 PARAMETRIC DESIGN OPTIMISATION OF THE BARREL VAULT

Optimisation studies date back over 50 years with genetic algorithms (GAs) being widely used and recognised in the optimisation of steel and concrete structures [23]. The optimisation study used in this paper comprises of a number of continuous and discrete variables, and the GA has proven to be a powerful tool when multiple interacting variables are used [24].

A two-dimensional parametric optimisation of the CLT floor and barrel vault in terms of embodied carbon was undertaken using a script written in MATLAB [25]. The vault design was optimised by considering the arch height, lamella thickness and steel rod diameter as continuous variables. The number of lamellas used in the parabolic arch and glulam beams was set as a discrete variable. The vault was discretised into a series of beams and nodes and analysed using matrix stiffness methods.

The genetic algorithm function in MATLAB [25] was used to find the optimal design as it is well-suited to handle both discrete and continuous variables by incorporating a penalty term into the objective function [26]. This penalty term transforms the constrained optimisation problem into an unconstrained one. During the optimisation process, the penalty function effectively penalises individuals in the population that violate the constraints more severely, guiding the search towards feasible solutions [27]. Figure 6 shows the optimisation process that was used for the vaults. The optimisation exercise evaluated a range of lamella thickness, steel rod diameters and arch heights for spans ranging from 4m to 12m.

The optimisation exercise is split into two branches. The first branch entails using the defined geometry for a specific set of input parameters to calculate the volumes and mass of the of each of the floor materials. The resultant mass of material is then multiplied by an embodied carbon factor and summed together to obtain the overall embodied carbon of the system. The second branch of the analyses performs a structural analysis of the system with the applied loading.

The capacity of the section, utilising the input geometry, is calculated, and used to determine the utilisation factors for each of the ultimate and serviceability limit states. With the increase in curvature of the beam there is a concomitant increase in fabrication stresses and therefore, to mitigate these stresses, the lamellas thickness needs to reduce. However, the fabrication of glue-laminated vault requires material to be planed off each of the faces of the lamellas to achieve a smooth surface to ensure adequate bonding between the layers. Conversations with glulam manufactures indicate that approximately 5mm of timber is planed off the top and bottom of the lamellas and 10mm is planed off each side irrespective of lamella thickness as shown in Figure 5. The tighter the radius of the lamellas, the thinner the lamellas need to be, and more material wastage occurs due to planing. This wastage has been included in the optimisation exercise.

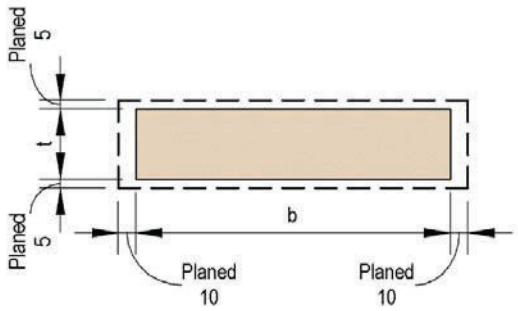

Figure 5: *Material wastage due to planing*

2.6 DESIGN OPTIMISATION OF THE CLT FLOOR

The cross laminated timber (CLT) floor system (Figure 1), was designed according to Eurocode 5 [13] and rests on two glulam beams. The equivalent stiffness was calculated using the gamma method to account for the orthogonal timber layers. The floor thickness was optimised by considering the lamellas thickness and number of lamellas.

The one-way spanning system was designed to meet both the ultimate limit states and serviceability limit states described in Section 2.1. Two CLT floor designs were considered; one that only met the deflection limits and another that satisfied both the deflection and vibration limits, to assess the impact of vibration in longer span designs. The vibration design of the CLT floor limited the natural frequency to 8Hz and satisfied the requirements of Eurocode 5 [13]. The embodied carbon calculation does not include fixings, columns, insulation, and other non-structural elements.

https://doi.org/10.52202/069179-0452

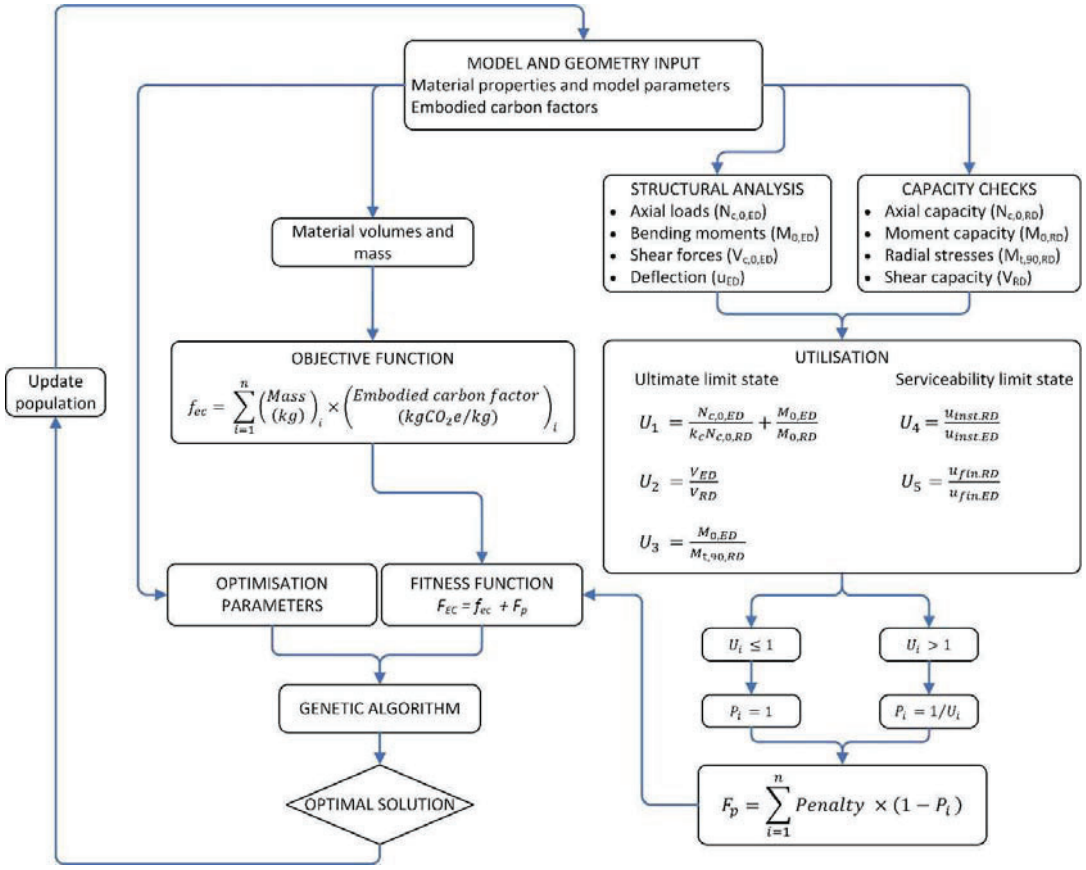

Figure 6: *Constrained optimisation process using Genetic Algorithms*

3 RESULTS AND DISCUSSION

The optimal embodied carbon solution for the vault system depends on the interplay between the arch height, rod diameter, number, and thickness of the lamellas. Figure 8 to Figure 10 shows the embodied carbon for an 8m span barrel vault compared to a CLT design, with and without vibration design. The optimal solution is indicated in the figures. The plots distinguish the embodied carbon contribution per square metre of the primary glulam beams, parabolic barrel vault, gravel infill and steel.

Embodied carbon with fixed arch height

The first investigation determined the impact of arch height on embodied carbon, with the results shown in Figure 8. The optimal arch height has a direct impact on the overall building height and solution feasibility. Using Section 2.5, the variables shown in Figure 8 were optimised for an 8m span and the lamella thickness of the primary glulam beams were fixed at 40mm to minimise material wastage. The CLT floor's embodied carbon, with and without vibration design, is also presented to show the magnitude of embodied carbon savings over the range of vault heights. The lowest carbon design occurs at a height of 0.6m (Span-to-height of 13). Near the optimal solution, there is minimal variation in embodied carbon. For instance, decreasing the arch height to 0.5m results in only a 2.45% increase in embodied carbon.

Embodied carbon savings decrease with increasing arch height, due to material wastage resulting from larger curvature causing higher fabrication stresses, which necessitates thinner lamellas.

For low arch heights, the steel rod diameter must increase significantly to control the horizontal thrust forces and ensure the design is compression governed over bending. Arch heights below 0.26m for the 8m span floor system produces higher embodied carbon than the CLT floor due to need for a large steel rod diameter required to restrain the horizontal thrust force produced by the shallow vault.

Embodied carbon fixed diameter of the steel rod

The second analysis examined the impact of rod diameter on embodied carbon, with the results presented in Figure 9. For an 8m span, when the steel rod diameter is less than 12mm, the system shifts from being compression governed to bending as the steel rod's utilisation is exceeded. At rod diameters exceeding 12mm, the steel rod has sufficient capacity to enable a compression governed vault system to form. Also, with rod diameters exceeding 12mm, the strength utilisation of the steel rod decreases and only the stiffness affects the optimal solution. This shift to a compression system results in a 150mm decrease in vault thickness, as shown in Figure 7(b), and a corresponding reduction in embodied carbon.

https://doi.org/10.52202/069179-0452

Figure 7(a) shows that the optimal solution is achieved at the minimum diameter of the steel rod (greater than 12mm) that results in negligible fabrication stresses. Rod diameters between 12mm and 21mm require vault heights that result in high lamella curvatures, leading to residual fabrication stresses that reduce the bending capacity of the section.

For rod diameters greater than the optimal diameter of 21mm, the vault thickness remains relatively constant with only a minimal variation of 1.7 $kgCO_2e/m^2$ between a rod diameter of 21mm and 70mm. This indicates that increasing the rod diameter beyond 21mm has little effect on the embodied carbon of the vault, which is also seen in Figure 9.

Strength vs Deflection

During this analysis, the optimal solution produced by optimising for strength alone (Combined bending and compression with buckling), and deflection alone, is compared with the optimal solution found by considering both strength and deflection design requirements. The results are shown in Table 2.

Strength and deflection have competing objectives to minimise embodied carbon: strength aims for a solution with low arch height, and large number of lamellas to minimise fabrication stress, while deflection seeks a high arch height to maximise the beneficial properties of the geometric stiffness of the vault but still considers the weight of the fill material. The deflection only optimal solution considers both live load distributions (full live load and half the live load). Additionally, the deflection only solution also aims for a solution with the minimum number of lamellas that results in the lowest possible waste. Therefore, in this problem, the solution tends to the maximum lamella thickness.

To satisfy both strength and deflection requirements, the optimisation compromises between the two solutions. The height of the arch is predominately governed by deflection, while the number of lamellas is determined by the fabrication stresses. The increase in arch height from the strength optimal solution causes the lamella to become thinner resulting in additional material wastage. The optimal solution based solely on the deflection only criteria results in the lowest embodied carbon solution at the optimal rod diameter, due to there being no fabrication stress constraints. The quantity of embodied carbon is then followed by the strength only solution.

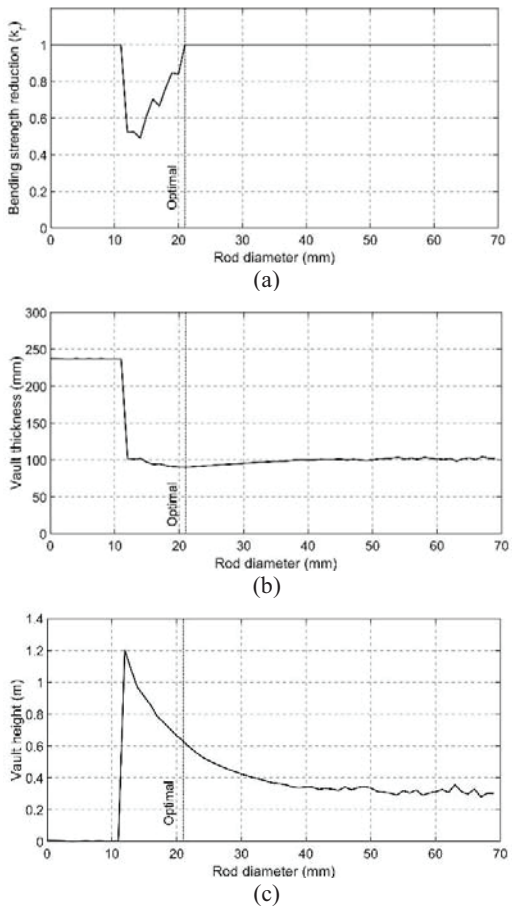

Figure 7: *Results for an 8m span parabolic vault showing, (a) The vault thickness with increasing rod diameter, (b) Vault height, (c) Bending strength reduction*

However, meeting both criteria results in a higher embodied carbon due to the increase in arch height from the strength only optimal solution and number of lamellas from the deflection only optimal solution.

Embodied carbon fixed lamella thickness

Figure 10 presents the results of the optimisation analysis by fixing the lamella thickness and limiting it to between 2mm and 40mm. The analysis indicated that the optimal number of lamellas is 3 with an optimal lamella thickness of 30mm for an 8m span.

Table 2: *Parabolic vault optimisation results for an 8m span barrel vault at the optimal rod diameter*

Optimisation constraint	**Arch height (m)**	**Lamellas (no.)**	**Lamella thickness (t) (mm)**	**Embodied carbon ($kgCO_2e/m^2$)**	**Utilisation**		
					Strength (incl. buckling)	Instantaneous deflection (ω_{inst})	Long term deflection (ω_{fin})
Strength	0.38	3	33	35.19	1	1.93	2.18
Strength + Deflection	0.56	3	30	36.84	1	0.9	1
Deflection	0.60	1	78	29.10	>> 1[1]	0.9	1

1) Fabrication stresses utilises most of the section's capacity

https://doi.org/10.52202/069179-0452

lamellas results in a sudden drop in the embodied carbon due to a reduction in fabrication material wastage. The choice of lamella thickness and number of lamellas is shown to not influence the embodied carbon in the primary beams.

Embodied carbon with increasing span

The analysis was repeated for spans between 4m and 12m with the results presented in Figure 11. Utilising the barrel vault floor system results in a reduction in embodied carbon between 35% and 41%, compared to the equivalent CLT floor when only considering strength design, buckling and deflection. However, at spans exceeding 5m, vibration governs the design of the CLT floor, and therefore it is likely that the barrel vaults will need to be checked and designed for vibration as well. It is worth noting that the diameter of the steel rod is determined by its stiffness rather than its strength. The strength utilisation of the steel rod in all the spans was around 50%, thus using higher strength steel is unnecessary.

Design considerations

The analysis showed that incorporating curvature in the floor design saves embodied carbon when compared to a traditional CLT floor design. However, there are several aspects that have not been considered that could make the floor system more inefficient, which include:

- Vibration. However, adding granular fill to the system is likely to enhance its damping properties and, when combined with the geometric stiffness of the vault, may prove more advantageous than a CLT floor system when vibration dominates the design at long spans.
- Fire design was not considered in the analysis and could result in additional embodied carbon in the design of the vault structure with the addition of a charring layer or other fire-resistant systems. This would also be necessary for the CLT system.
- The fabrication of curved timber members presents several challenges that may impact the feasibility of the floor solution. The production costs of curved timber members may be higher, as the process will be more labour intensive and require more resources compared to CLT floor fabrication. Additional design and fabrication of the connection between the steel rod and the timber beam is required, and the addition of fill entails an additional construction activity on site, which could increase construction time.
- Overall height of the optimal vaulted floor system is typically higher than the equivalent CLT floor and this may impose a constraint on the overall building design.
- Self-weight bending of the steel tie rod has not been considered which may lead to a reduction in geometric stiffness of the tie and therefore the floor as a whole.

However, several aspects which may improve efficiency have also not been considered in this preliminary investigation, including the following:

- Utilising double curvature in the form of groin vaults could eliminate the need for primary beams and provide a more efficient solution. This was demonstrated with concrete groin vaults in the research undertaken by Hawkins et al. [9].
- The addition of prestress. As shown in [28], the addition of prestress reduces the maximum vertical displacement.
- Optimising the form of the vault to reduce the bending moments caused by the gravel infill.

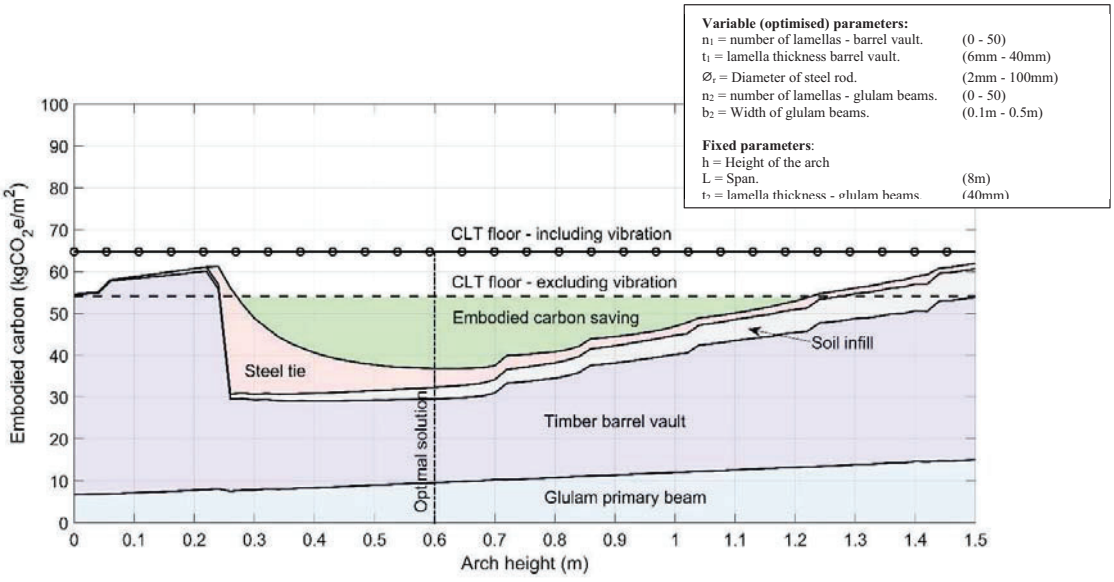

Figure 8: *Embodied carbon optimisation of the barrel vault by fixing the arch height for an 8m span floor*

https://doi.org/10.52202/069179-0452

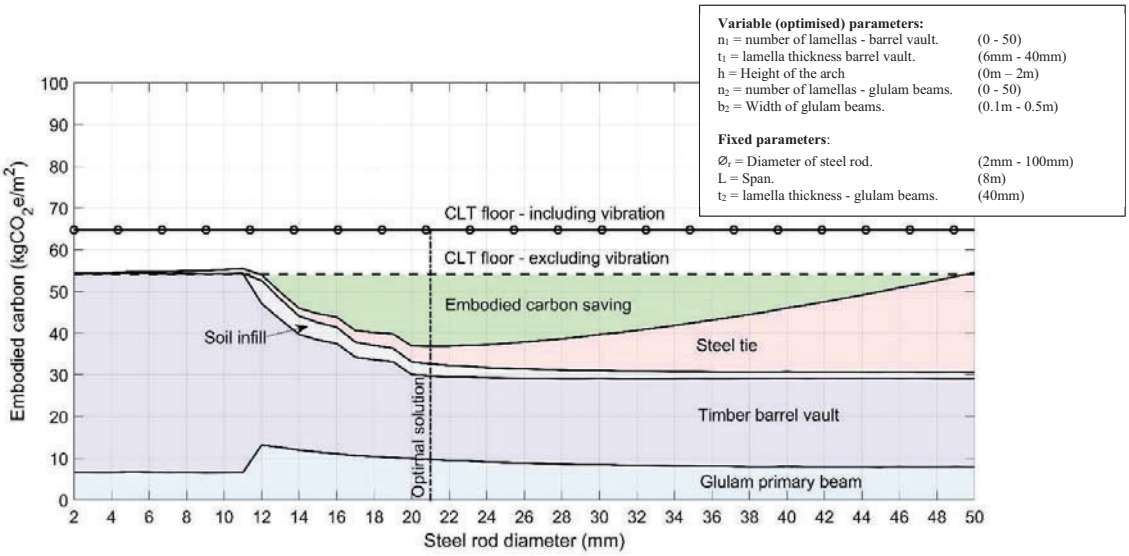

Figure 9: *Embodied carbon optimisation of the barrel vault by fixing the diameter of the steel rods for an 8m span floor*

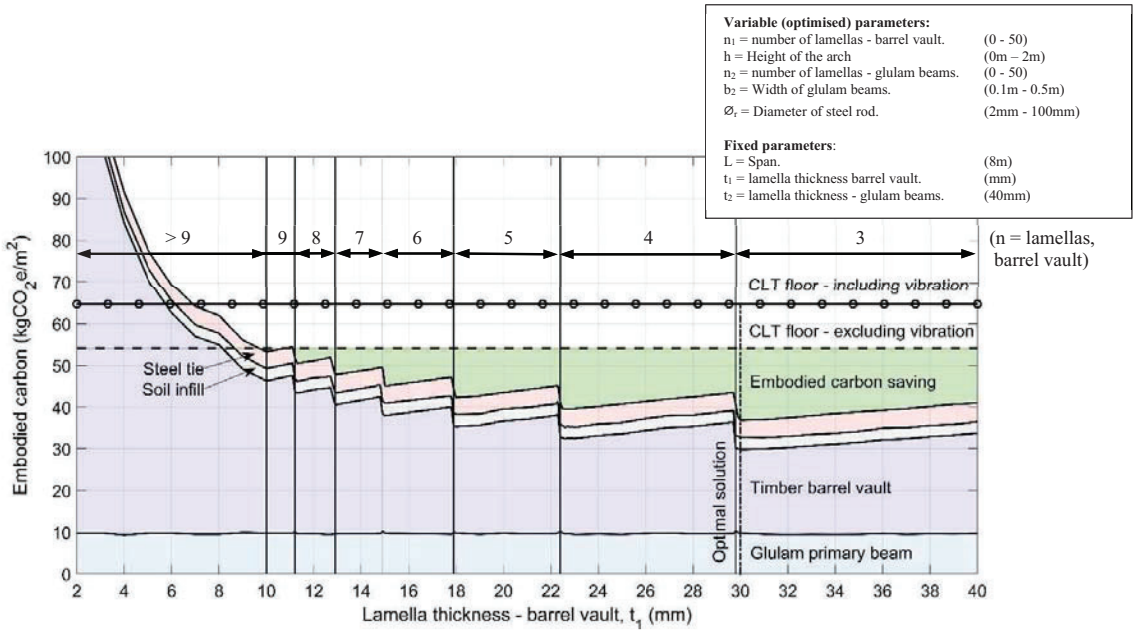

Figure 10: *Embodied carbon optimisation of the barrel vault by fixing the barrel vault lamella thickness*

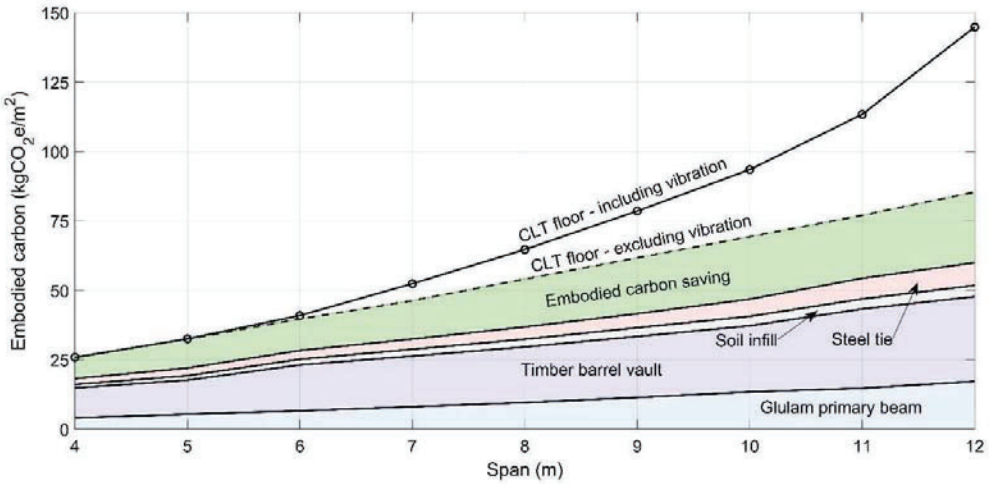

Figure 11: *Embodied carbon optimisation with increasing span*

https://doi.org/10.52202/069179-0452

4 CONCLUSIONS

This paper investigates the potential of using timber barrel vaults as a low carbon alternative to CLT floors, by shifting the primary load resistance from bending to compression. A curved timber barrel vault system with granular infill is proposed, using glued, curved lamellas spanning between straight glulam beams, which span between columns. The horizontal forces generated by the vault is restrained by steel ties. An optimisation exercise using a genetic algorithm with a penalty function was performed, using both discrete and continuous parameters, to evaluate the performance of the system. Finally, the proposed system was compared to a CLT floor for a typical office design with spans between 4 to 12m. The key conclusions of the investigation are as follows:

- Compared with an equivalent CLT floor, the proposed barrel vault system provides a significant embodied carbon saving of between 35% and 41% across the analysed spans.
- The optimal design of the proposed timber vault solution is achieved when both strength and deflection utilisations are equal to one, which occurs at an optimal span-to-height ratio between 13 – 14.
- The arch height is predominantly governed by the deflection criteria with the number of lamellas determined by the fabrication stress.
- The optimal solution is dependent on the balance between the arch height, rod diameter and fabrication stresses. The optimal solution occurs at a maximum arch height that results in no stress reduction due to fabrication stresses, which is balanced by a steel rod with sufficient stiffness.
- The restraint by the tie at the optimal solution is dependent primarily on the stiffness of the material.

This paper shows that introducing curvature into timber floors provides a feasible and efficient solution to lowering embodied carbon. The process followed during the research shows a method that structural engineers can implement to optimise the reduction of their embodied carbon in buildings.

5 FUTURE WORK

To potentially achieve greater savings, the glulam primary beams can be removed by replacing the barrel vault with a doubly curved groin vault system, especially for longer spans. The next step is to analyse groin vaults and optimise their design by including vibration, acoustic performance, and fire design. This includes the form of the vault, the ease of fabrication, connection details, and coordination with building services to develop a cost-efficient solution. The study will also investigate the type and quantity of infill material that is needed to meet vibration and acoustic requirements while reducing the dead load. Furthermore, the potential of vaulted floor systems will be explored by comparing them with other efficient timber flooring systems that are currently on the market.

ACKNOWLEDGEMENT

This research was supported by the EPSRC DTP studentship [Number: EP/T518013/1]

REFERENCES

[1] United Nations Environment Programme, 2020 Global Status Report for Buildings and Construction: Towards a Zero-emission, Efficient and Resilient Buildings and Construction Sector. Nairobi: United Nations, 2020. Accessed: Jan. 16, 2023. [Online]. Available: https://globalabc.org/sites/default/files/inline-files/2020%20Buildings%20GSR_FULL%20REPORT.pdf

[2] H. L. Gauch, C. F. Dunant, W. Hawkins, and A. Cabrera Serrenho, 'What really matters in multi-storey building design? A simultaneous sensitivity study of embodied carbon, construction cost, and operational energy', Applied Energy, vol. 333, p. 120585, Mar. 2023, doi: 10.1016/j.apenergy.2022.120585.

[3] IEA, 'Net Zero by 2050', IEA: Paris, 2021, [Online]. Available: https://www.iea.org/reports/net-zero-by-2050, License: CC BY 4.0

[4] P. Mayencourt and C. Mueller, 'Structural Optimization of Cross-laminated Timber Panels in One-way Bending', Structures, vol. 18, pp. 48–59, Apr. 2019, doi: 10.1016/j.istruc.2018.12.009.

[5] C. De Wolf, F. Yang, D. Cox, A. Charlson, A. S. Hattan, and J. Ochsendorf, 'Material quantities and embodied carbon dioxide in structures', Proceedings of the Institution of Civil Engineers - Engineering Sustainability, vol. 169, no. 4, pp. 150–161, Aug. 2016, doi: 10.1680/ensu.15.00033.

[6] G. Churkina et al., 'Buildings as a global carbon sink', Nat Sustain, vol. 3, no. 4, Art. no. 4, Apr. 2020, doi: 10.1038/s41893-019-0462-4.

[7] A. Mishra et al., 'Land use change and carbon emissions of a transformation to timber cities', Nat Commun, vol. 13, no. 1, Art. no. 1, Aug. 2022, doi: 10.1038/s41467-022-32244-w.

[8] M. Pramreiter, T. Nenning, L. Malzl, and J. Konnerth, 'A plea for the efficient use of wood in construction', Nat Rev Mater, Jan. 2023, doi: 10.1038/s41578-023-00534-4.

[9] W. Hawkins, J. Orr, T. Ibell, and P. Shepherd, 'A design methodology to reduce the embodied carbon of concrete buildings using thin-shell floors', Engineering Structures, vol. 207, p. 110195, Mar. 2020, doi: 10.1016/j.engstruct.2020.110195.

[10] S. Bechert, L. Aldinger, D. Wood, J. Knippers, and A. Menges, 'Urbach Tower: Integrative structural design of a lightweight structure made of self-shaped curved cross-laminated timber', Structures, vol. 33, pp. 3667–3681, Oct. 2021, doi: 10.1016/j.istruc.2021.06.073.

[11] C. Robeller, S. S. Nabaei, and Y. Weinand, 'Design and Fabrication of Robot-Manufactured Joints for a Curved-Folded Thin-Shell Structure Made from CLT', in Robotic Fabrication in Architecture, Art and Design 2014, W. McGee and M. Ponce de Leon,

https://doi.org/10.52202/069179-0452

Eds. Cham: Springer International Publishing, 2014, pp. 67–81. doi: 10.1007/978-3-319-04663-1_5.
[12] A. J. Lara-Bocanegra, A. Majano-Majano, F. Arriaga, and M. Guaita, 'Long-term bending stress relaxation in timber laths for the structural design of lattice shells', Construction and Building Materials, vol. 193, pp. 565–575, Dec. 2018, doi: 10.1016/j.conbuildmat.2018.10.224.
[13] British Standards Institution, 'Eurocode 5: Design of timber structures. General. Common rules and rules for buildings'. London: British Standards Institution, 2004.
[14] British Standards Institution, 'BS EN 338 Structural timber. Strength classes'. London: British Standards Institution, 2016.
[15] British Standards Institution, 'BS EN 14080 Timber structures. Glued laminated timber and glued solid timber.' London: British Standards Institution, 2013.
[16] British Standards Institution, 'Eurocode 1: Actions on Structures. Part 1-1: General Actions — Densities, Self-weight, Imposed Loads for Buildings'. London: British Standards Institution, 2002.
[17] Wood for Good, 'Environmental product declaration for 1 cubic meter of kiln dried planed or machined sawn timber used as structural timber, BRE 000124.' 2017. [Online]. Available: https://woodforgood.com/assets/Downloads/EPD/BREGENEPD000124.pdf
[18] J. B. Wilson, 'Life-Cycle Inventory of Formaldehyde-Based Resins Used in Wood Composites in Terms of Resources, Emissions, Energy and Carbon', Wood and Fiber Science, pp. 125–143, Mar. 2010.
[19] M. Brunetti et al., 'Comparison of different bonding parameters in the production of beech and combined beech-spruce CLT by standard and optimized tests methods', Construction and Building Materials, vol. 265, p. 120168, Dec. 2020, doi: 10.1016/j.conbuildmat.2020.120168.
[20] M. Dunky, 'Urea–formaldehyde (UF) adhesive resins for wood', International Journal of Adhesion and Adhesives, vol. 18, no. 2, pp. 95–107, Mar. 1998, doi: 10.1016/S0143-7496(97)00054-7.
[21] S. Park, B. Jeong, and B.-D. Park, 'A Comparison of Adhesion Behavior of Urea-Formaldehyde Resins with Melamine-Urea-Formaldehyde Resins in Bonding Wood', Forests, vol. 12, no. 8, p. 1037, Aug. 2021, doi: 10.3390/f12081037.
[22] Circular Ecology, 'Inventory of Carbon and Energy v3.0. Circular Ecology [Online].' 2019. Accessed: Dec. 30, 2022. [Online]. Available: https://circularecology.com/embodied-carbon-footprint-database.html
[23] J. R. Villar-García, P. Vidal-López, D. Rodríguez-Robles, and M. Guaita, 'Cost optimisation of glued laminated timber roof structures using genetic algorithms', Biosystems Engineering, vol. 187, pp. 258–277, Nov. 2019, doi: 10.1016/j.biosystemseng.2019.09.008.
[24] J. R. Villar, P. Vidal, M. S. Fernández, and M. Guaita, 'Genetic algorithm optimisation of heavy timber trusses with dowel joints according to Eurocode 5', Biosystems Engineering, vol. 144, pp. 115–132, Apr. 2016, doi: 10.1016/j.biosystemseng.2016.02.011.
[25] MATLAB, 'R2021b Update 3 (9.11.0.1873467)'. The MathWorks Inc, Natick, Massachusetts, 2021.
[26] A. A. Khan and R. N. Mir, 'Optimization of Constrained Function Using Genetic Algorithm', 2017.
[27] M. Gen and R. Mitsuo, A survey of penalty techniques in genetic algorithms. Piscataway, N.J: Institute of Electrical and Electronics Engineers, 1996.
[28] W. Hawkins, J. Orr, P. Shepherd, and T. Ibell, 'Design, Construction and Testing of a Low Carbon Thin-Shell Concrete Flooring System', Structures, vol. 18, pp. 60–71, Apr. 2019, doi: 10.1016/j.istruc.2018.10.006.

World Conference on Timber Engineering Oslo 2023

SEGMENTED COMPOSITE SECTIONS WITH WOOD DOWELS

Matthias Brieden[1]; Max Braun[2], Werner Seim[3]; Kristina Schramm[4], Philipp Eversmann[5]

ABSTRACT: Recent research approaches try to expand the scope of application of timber construction elements. Possibilities to reduce the material consumption and raise the automatization level are also gaining interest to an increasing degree. Segmented sections with wood connectors are predestined for this challenge because of their modular character. Analytical, numerical and experimental investigations are conducted to assess the effects of different geometrical and material parameters. The results provide a strong basis to understand and improve the effectiveness of these sections.

KEYWORDS: segmented sections, elastic composite, modular engineering, robotic fabrication, wood dowels

1 INTRODUCTION

Questions of the consumption of resources, efficient material usage, recyclability and sustainability at large are gaining significant importance within the construction sector. In addition, experts and the public are focusing increasingly on aspects of automatization, modular production and robotic fabrication. Accordingly, civil engineering in general and timber engineering in particular should also take these topics into account. [1]
A current research project at the University of Kassel is being carried out by the Chair for Timber Structures and Building Rehabilitation together with the Chair of Experimental and Digital Design and Construction. The project includes both numerical studies about the effective use of material and experimental studies to develop new types of connections with wood dowels.
The overall objective of this optimization process is to develop new types of slab and wall elements by using beam sections of limited length, which should be taken from reused or recycled materials as far as possible, and addresses all those aspects. Timber engineering can provide here an important contribution to the urgent questions of sustainability and resource consumption. [2]

2 GENERAL SET-UP

The research activities deal with segmented box-type elements. The section is symmetric and composed of two oriented strand board (OSB) panels, forming the upper and the lower layer of the element, and the web beam section, for which structural timber (KVH) C24 is used. Due to the "second-usage approach" of the project, other timber products and different strength classes may also be considered in the future. The connection between the upper and lower OSB panels and the web section is realised by wood dowels. These fasteners can be arranged in several set-ups, including various distances or angles. The general set-up can be seen in Figure 1.

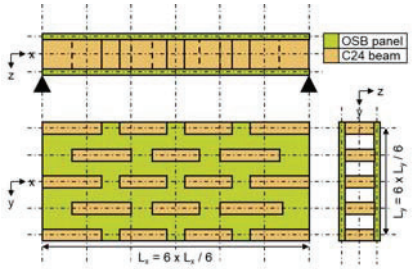

Figure 1: *General set-up*

3 METHODICAL APPROACH AND MODEL DEVELOPMENT

3.1 GENERAL

Both numerical and experimental investigations are part of the research. Whereas the numerical calculations provide the possibility of determining the influences of a huge number of different parameters systematically (e.g. geometry, material combinations, fasteners), the experimental testing should help to validate and calibrate the numerical models.
Analytical methods for composite sections can be found in EC 5 [3]. Several comparative studies with the analytical calculations are performed to check and verify the basic numerical approach. The pros and cons of different types of modelling can be found and assessed by varying the level of composite elasticity (between no and rigid composite). Finally, a numerical model has been developed and validated.

[1] Matthias Brieden, Timber Structures and Building Rehabilitation, University of Kassel, Germany; mbrieden@uni-kassel.de
[2] Max Braun, Timber Structures and Building Rehabilitation, University of Kassel, Germany
[3] Werner Seim, Timber Structures and Building Rehabilitation, University of Kassel, Germany
[4] Kristina Schramm, Experimental and Digital Design and Construction, University of Kassel, Germany
[5] Philipp Eversmann, Experimental and Digital Design and Construction, University of Kassel, Germany

https://doi.org/10.52202/069179-0453

3.2 SET-UP AND PARAMETERS

As a first step, a construction element with a segmented beam was investigated (Figure 2).

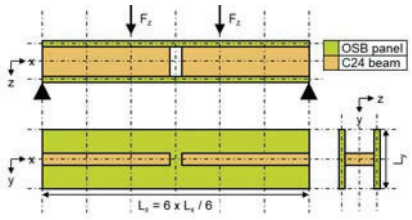

Figure 2: *Set-up for first step*

The materials considered are OSB panels and C24 beams; wood dowels at variable distances and slip moduli are applied for the fasteners. Dimensions and properties are listed in Table 1. The gap length is 2.0 cm.

Table 1: *Geometrical and material parameters*

		OSB	C24
Width	$L_y=b_y$	360 mm	60 mm
Height	$L_z=h_z$	24 mm	200 mm
Moe	$E_{0,mean}$	198 kN/cm^2	1,100 kN/cm^2
Density	ρ_{mean}	600 kg/m^3	420 kg/m^3

The wood dowels have a length of ℓ_{td} = 10.0 cm and a diameter of d_{td} = 1.0 cm; the distance between these fasteners is set to e = 2.0 cm. The static system is a single-span beam with a length of L_x = 2.0 m. The beam is loaded with two vertical forces of F_z = 10 kN. This arrangement represents a four-point bending set-up.

3.3 SELECTED RESULTS AND DISCUSSION

The deformation curve was determined numerically for each variation of the set-up. The results are shown in Figure 3 exemplary for K = 15.00 kN/cm. The curve for a non-segmented element is included as a reference. The other curves represent the three parts of the cross-section.

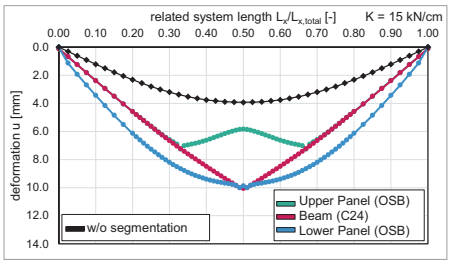

Figure 3: *Selected results*

The points where the load was applied ($L_x/L_{x,total}$ = 0.33; $L_x/L_{x,total}$ = 0.67) can easily be identified because of the contact between the upper panel and the beam. The upper panel separates itself from the beam between these points; the transmission of tensile forces through the dowels was deactivated for this numerical calculation. The deformation curve of the beam – actually, due to the gap, there are two beams – is linear, but it shows a discontinuity at midspan. This discontinuity is caused by the segmentation which is located here. Regarding the lower panel, it can be seen that the curve is not linear. The beam and the lower panel do not act as a composite cross-section because of the deactivated tensile forces. The ends of both beams push against the lower panel at midspan, which initiates the detachment of the lower panel.

Table 2: *Deformation in midspan*

		deformation u	
		absolute	related
Reference		3.938 mm	100 %
Upper panel	*OSB*	5.834 mm	145 %
Beam	*C24*	10.059 mm	255 %
Lower panel	*OSB*	9.869 mm	251 %

The segmentation leads to deformations that are more than 2.5-times higher in relation to the reference curve. The numerical results in midspan can be found in Table 2.

3.4 FURTHER EVALUATIONS AND PARAMETRIC STUDY

In addition to the investigation of construction elements on a macro level, single components were also evaluated on a micro level, for example, the behaviour and load factor of the dowels. As part of this, the optimization of the arrangement of these components was conducted. Effects of inclined dowels, which are about to transfer tension forces, were considered.

The results of these experimental tests and more detailed information are published by Brieden et al. [4]. Against this background, the slip moduli of the different configurations of fasteners was selected for the further investigations.

Investigations into modified set-ups were conducted; in particular, the impact of multisegmented web beams was evaluated. Other types of constructions will be considered to grasp effects such as the warping of the upper layer,.

The approach described previously was transferred to the general set-up. Thus, the opportunity to evaluate different combinations and variations of segmented sections with elastic composite is enabled. The influence of missing web segments at different locations will be determined to outline different effects – such as the rearrangement of the load transfer from web to covering layer – within this step.

4 DESIGN OF TEST SPECIMENS

4.1 GENERAL

Three major layouts are considered to assess the influence of the different configurations.

The arrangement of the fasteners – total number, properties, inclination, distance, *inter alia* – are constant for all layouts. The loads applied are also constant.

https://doi.org/10.52202/069179-0453

4.2 DESIGN PARAMETERS

4.2.1 Geometry and elements

Each layout consists of two OSB panels and five C24 beams; the dimensions can be found in Table 3. The beams are arranged in five axes, all identical.

Table 3: *Dimensions of components*

		dimension [mm]		
		length L_x	width L_y	height L_z
Upper panel	*OSB*	4,600	1,250	25
Beams x)	*C24*	4,600	60	200
Lower panel	*OSB*	4,600	1,250	25

x) L_x for refence variation; otherwise segmented

As described in the previous sections, wood dowels are used to realise the connection between the different elements. The wood dowels have a length of ℓ_{td} = 10.0 cm and a diameter of d_{td} = 1.0 cm.

Table 4: *Slip moduli of fasteners*

	slip modulus K [kN/cm]	
	compression	shear
Perpendicular dowel (1 dowel)	1.25	9.00
Inclined dowel (2 dowels)	5.00	12.50

The slip moduli of the wood dowels depend upon the arrangement (perpendicular or inclined) and the particular direction (tension or shear), see Table 4.

Table 5: *Distance between fasteners*

		distance e [mm]	
		Axes I / III / V	Axes II / IV
Frist segment	X	50	50
	O	3×100|2×150|3×100	4×125
	X	125	125
	total	9 fasteners	5 fasteners
Second segment	X	125	125
	O	4×125	4×125
	X	125	125
	total	5 fasteners	5 fasteners
Third segment	X	125	125
	O	4×125	4×125|3×100|4×125
	X	125	125
	total	5 fasteners	12 fasteners
Fourth segment	X	125	125
	O	4×125	4×125
	X	125	125
	total	5 fasteners	5 fasteners
Fifth segment	X	50	50
	O	3×100|2×150|3×100	4×125
	X	50	50
	total	9 fasteners	5 fasteners

The total number of fasteners for each variation is 326, of which 100 are inclined. The position of the inclined fasteners results from the specimen's layout; they are located at the beginning and end of each single segmented beam and inclined by α = 15°. The detailed distribution can be found in Figure 4 and Table 5.

The distances between the particular dowels varies between e = 5.0 and 12.5 cm and can be found in Table 5. The inclined fasteners here are labelled "X", while the perpendicular ones are named "O". Moreover, the number of fasteners for the particular segment is listed.

More information concerning the wood dowels can be found in Brieden et al. [4].

4.2.2 Loads and load cases

A total of g_k = 1.0 kN/m² is considered for the self-weight of the elements. Furthermore, an additional self-weight, for example, floor construction because of vibrations, thermal or acoustic aspects, of Δg_k = 2.0 kN/m² is taken into account. Regarding the live load, p_k = 2.0 kN/m² is considered.

Two load cases are evaluated. A total load of $q_d^{ULS} = 1.35 \cdot (1.0 + 2.0) + 1.50 \cdot 2.0 = 7.0$ kN/m² is applied for the evaluation of the ultimate limit state, whereas the total load in the serviceable limit state is $q_d^{SLS} = 1.0 \cdot (1.0 + 2.0) + 1.0 \cdot 2.0 = 5.0$ kN/m².

Table 6: *Loads and load cases*

		load [kN/m²]	
		USL	SLS
Self-weight	g	1.35	1.00
Add. self-load	Δg	2.70	2.00
Live load	p	3.00	2.00
Total	q_d	7.00	5.00

Table 6 summarises the loads and load cases.

4.3 REFERENCE ELEMENT

A construction with two OSB panels and five C24 beams is considered for the reference element. An overview of this variation is presented in Figure 4.

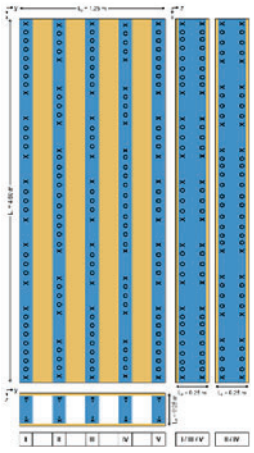

Figure 4: *Reference specimen*

The inclined fasteners in the figures are illustrated as "X" while the perpendicular ones are marked as "O".

The length of the beams is identical for all five axes – L_x = 4.60 m.

https://doi.org/10.52202/069179-0453

4.4 GAP SEGMENTED ELEMENT

The gap segmented element consists of two OSB panels and five segmented C24 beams. An overview of this variation is presented in Figure 5. A pair of inclined fasteners are applied ("X") at the beginning and end of each particular beam. The other (inner) fasteners are arranged perpendicular to the board surface ("O"). The gap between the single segments has a width of 5 cm.

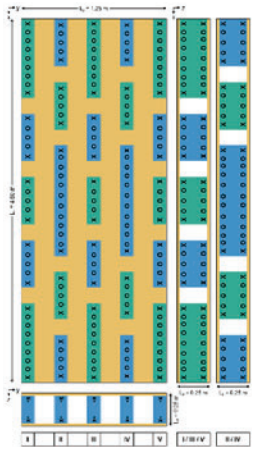

Figure 5: *Gap segmented specimen*

4.5 NOTCHED SEGMENTED ELEMENT

Furthermore, an element with two OSB panels and five notched segmented C24 beams is considered. An overview of this variation is shown in Figure 6. It is already known that a pair of inclined fasteners are applied ("X") at the beginning and end of each particular beam. The other (inner) fasteners are arranged perpendicular to the board surface ("O").

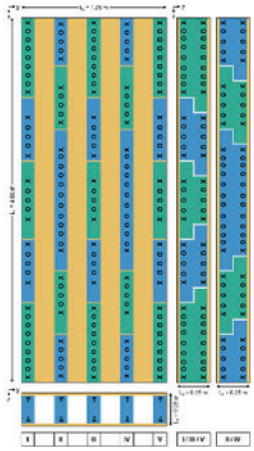

Figure 6: *Notched segmented specimen*

The gap between the single segments has a width of 5 cm, while the length of the notch is 10 cm.

5 NUMERICAL MODELLING

5.1 GENERAL

A numerical model of each variation was created for the investigations. The software RFEM 6 was used [6].
The OSB panels and the C24 beams were modelled as four node shell elements, whereas beam elements were used for the fasteners. An element size of 5.0 cm was chosen for the quadratic elements.

5.2 MODELS

5.2.1 Reference

Figure 7 shows the numerical model of the reference element without the upper panel for a clearer illustration. The support can be seen in addition to the five beams and the lower panel. The support was modelled with steel plates and should help to reduce local stress peaks.

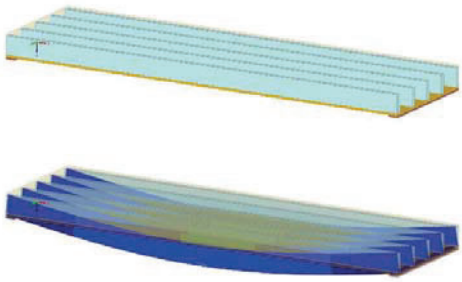

Figure 7: *Reference – model and deformations*

The second part of the figure shows the deformed model for the serviceable limit state (SLS).

5.2.2 Gap segmented

The model of the gap segmented variation is shown in Figure 8 in the same way as described previously. Here, the gaps within the five beams can be seen very well.

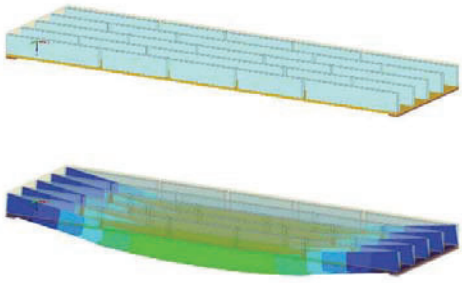

Figure 8: *Gap segmented – model and deformations*

The deformation can also be found in the figure. The relative deformation between the lower panel and the beams can also be seen for the outer edges. As the colours indicate, the deformation is higher for this variation.

5.2.3 Notched segmented

Finally, the numerical model for the notched segmented variation can be found in Figure 9. The notches are also depicted.

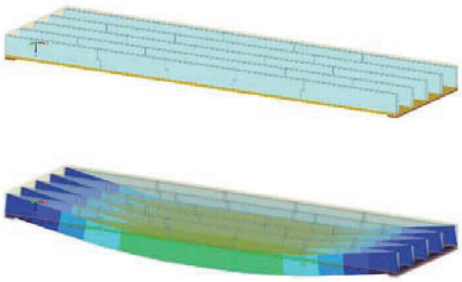

Figure 9 *Notched segmented – model and deformations*

An illustration of the deformed element for the SLS is shown in the second part of the figure.

5.3 RESULTS

5.3.1 General

As mentioned in section 4.2.2, two cases are considered. For the first one – the ultimate limit state – the stresses occurring (bending stress, shear stress and connection force) for the different components of each element are determined and compared. Exemplary, the bending stress in midspan and the connection force are presented in the following. In order to investigate the SLS performance, the deformations of the panels are considered and discussed later on.

5.3.2 Ultimate limit state

Cross-section

The distribution of axial stresses at midspan (L_x = 2.30 m) is illustrated in Figure 10 to Figure 12. The diagrams show the stress as a function of the element height L_z. The different colours of the lines represent the particular axes as labelled in Figure 4 to Figure 6; the axes indicate the position in the y-direction (Axis I: L_y = - 0.625 m to Axis V: L_y = + 0.625 m).

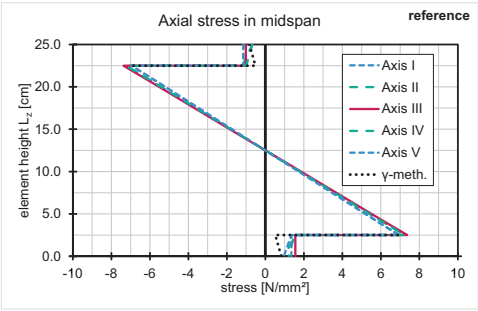

Figure 10: *Ultimate limit state (ULS) – reference – bending stress in midspan*

The different parts of the cross-section, i.e. upper panel, beam, lower panel, can be identified by their dimensions and orientations. The lower panel is located at the bottom of the diagrams (L_z = 0.0 … 2.5 cm); the upper panel can be found at the top of the diagrams (L_z = 22.5 … 25.0 cm); the results for the beams can be seen in between (L_z = 2.5 … 22.5 cm).

In addition, the corresponding bending stresses, which have been determined analytically with "Gamma Method" according to EC 5 [3], are shown for the reference model in Figure 10.

As the diagram illustrates, the stress at the different axes for the reference model only differ very slightly. The maximal stress comes up to $\sigma_{max}^{panel} \approx 1.3$ N/mm² for the panels, and $\sigma_{max}^{beam} \approx 7.4$ N/mm² at the joints (L_z = 2.5 and 22.5 cm) between the panels and the beams for the beams.

Concerning the comparison with the analytical results, some deviations can be found. Regarding the panels, for example, the values do not fit completely. These differences might be caused by the assumptions and simplification that are necessary for the analytical calculation – for example, a homogeneous fastener distance of e = 12.5 cm has been assumed for the "Gamma Method" in contrast to the distances applied for the numerical investigation (see Table 5).

Nonetheless, the agreement between the analytical and the numerical results is obviously good.

Figure 11 shows the stresses occurring for the gap segmented variation. Compared to the reference variation, the stresses in midspan for the beams are significantly lower, while it is vice versa for the panels. This is because of the different load transmission caused by the segmentations of the beams. Considering the illustration in Figure 5, it can be seen that the beam segments in axis I, III and V in midspan are shorter than the ones in axis II and IV. This leads to a higher stress in the latter beam segments, see the green lines in Figure 11. Due to the segmentation of the beams, a load shifting from the beams to the panels occurs.

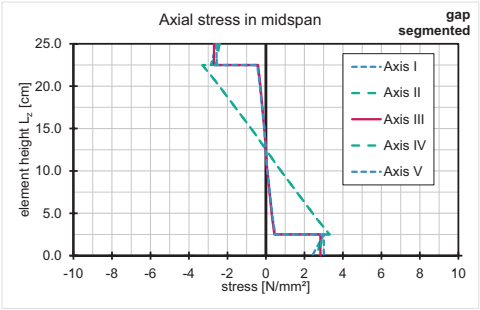

Figure 11: *ULS – gap segmented – bending stress in midspan*

The values of the maximal stress come up to $\sigma_{max}^{panel} \approx 3.0$ N/mm² for the panels, and $\sigma_{max}^{beam} \approx 3.5$ N/mm² at the joints (L_z = 2.5 and 22.5 cm) between the panels and the beams for the beams.

Figure 12 illustrates the axial stresses in midspan for variation notched segmented sections. Again, the load shifting effects can be seen. In comparison with the gap segmented variation, the stress in the panels reduces, whereas for the beams, it increases. Concerning these results, the influence of the notched segmented sections can be seen. The notching of the beams creates a different load transmission.

https://doi.org/10.52202/069179-0453

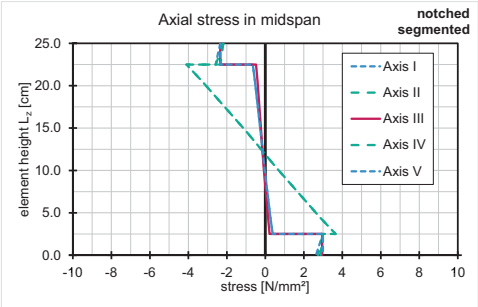

Figure 12: *ULS – notched segmented – bending stress in midspan*

The values of the maximal stress come up to $\sigma_{max}^{panel} \approx 2.5$ N/mm² for the panels, and $\sigma_{max}^{beam} \approx 4.1$ N/mm² at the joints ($L_z = 2.5$ and 22.5 cm) between the panels and the beams for the beams.

Fasteners

In order to evaluate the performance of the fasteners, in spite of considering each single dowel, the total number and the corresponding load was investigated.

These results can be found in Figure 13, which shows the load – here, the normal force – of the fasteners grouped for each variation.

Concerning the results, a distinction between fasteners with tensile force and those with compression force is necessary. As the diagram shows, the maximal tensile force is lower than $F_t = 0.7$ kN, while the compression force goes down to $F_c = -3.0$ kN. This means that the relation of the maximal tensile to the maximal compression load is about one to four.

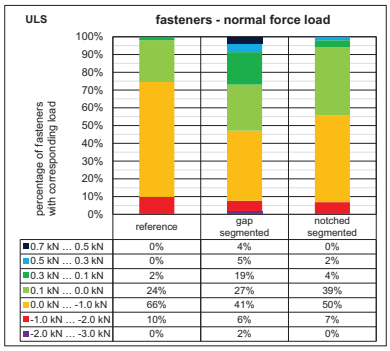

	reference	gap segmented	notched segmented
0.7 kN … 0.5 kN	0%	4%	0%
0.5 kN … 0.3 kN	0%	5%	2%
0.3 kN … 0.1 kN	2%	19%	4%
0.1 kN … 0.0 kN	24%	27%	39%
0.0 kN … -1.0 kN	66%	41%	50%
-1.0 kN … -2.0 kN	10%	6%	7%
-2.0 kN … -3.0 kN	0%	2%	0%

Figure 13: *ULS – fasteners – normal force*

About a quarter of the fasteners are tensile loaded for the reference variation. Although only 45 % and 55 % of the gap and the notched segmented variation, respectively, are under compression, the majority of the tensile loaded fasteners – 46 % and 43 %, respectively – are loaded with less than $F_t = 0.3$ kN.

The main part of the fasteners for all three variations was loaded with $F_c = 0.0 \ldots -1.0$ kN.

5.3.3 Serviceability limit state

Panels

The results of the investigation of the SLS – here, the total deformation of the panels – are presented as surfaces in Figure 14 to Figure 16.

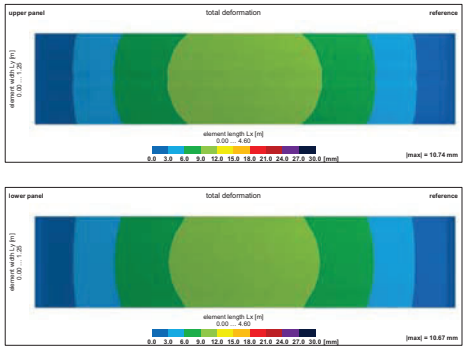

Figure 14: *SLS – reference – panels – total bending deformation*

The diagrams show the deformation of the upper and the lower panel as well as the maximal value. As expected, the difference between both panels is not significant.

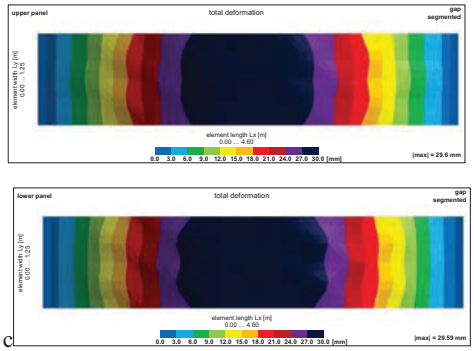

Figure 15: *SLS – gap segmented – panels – total bending deformation*

As the diagrams indicate, the deformation is maximal for the gap segmented element. The relation between the maximal deformation of the variations is 1.0 to 3.0 to 2.5.

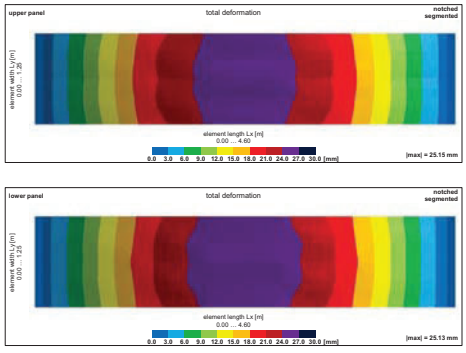

Figure 16: *SLS – notched segmented – panels – total bending deformation*

https://doi.org/10.52202/069179-0453

6 EXPERIMENTAL INVESTIGATIONS

The results of the numerical investigations indicate that this is a promising approach and experimental testing of macro-scaled specimens is actually conducted and evaluated. These tests and the detailed analysis of the measured and documented results are currently being done at the University of Kassel.

7 CONCLUSIONS AND OUTLOOK

Promising results have been achieved to date. Analytical and numerical approaches for different types of segmented beams were used and compared with good compliance. Further investigations were conducted against this background.
The methodology, development and selected results as well as additional information concerning the further investigations are presented within this paper.
The current results and findings in combination with experimental testing on a micro and macro scale will enable new and further application areas for segmented composite sections.

ACKNOWLEDGEMENT

The results presented were achieved within the DFG research project “Additive robotic assembly techniques for timber construction – Computational design and integrated structural joining methods”. This project is funded by “Deutsche Forschungsgemeinschaft”. The work would not have been possible without this support.
The authors would like to thank the funding agencies, colleagues named in the bibliography and representatives of the companies involved in the project, as well as the associated project committees for their contributions.

REFERENCES

[1] Thelandersson, S.; Larsen, H.: Timber Engineering; Wiley, March 2003.
[2] Bissig, D.: Variantenstudium zur Entwicklung einer zweiachsig tragenden Hohlkastendecke aus Holz; Doktorandenkolloquium „Holzbau Forschung + Praxis“, Universität Stuttgart, March 2022.
[3] EN 1995-1-1: Eurocode 5: Design of timber structures – Part 1-1: General – Common rules and rules for buildings; German version EN 1995-1-1:2004 + AC:2006 + A1:2008. European Committee for Standardization, Brussels. December 2010.
[4] Brieden, M.; Braun, M.; Seim, W.: Tension loaded connections with wood dowels, WCTE 2023.
[5] EN 1991-1-1: Eurocode 1: Actions on structures – Part 1.1: General actions – Densities, self-weight, imposed loads for buildings; German version EN 1991-1-1:2002 + AC:2009. European Committee for Standardization, Brussels. December 2010.
[6] RFEM 6: https://www.dlubal.com/.

https://doi.org/10.52202/069179-0453

World Conference on Timber Engineering Oslo 2023

LIGHT-FRAME TIMBER SHEAR-WALLS WITH DIAGONAL BOARD SHEATHING: EXPERIMENTAL AND NUMERICAL INVESTIGATION

Alessandro Setti[1], Daniele Casagrande[2], Andrea Polastri[3], Riccardo Fanti[4], Maurizio Follesa[5], Ezio Riggi[6]

ABSTRACT: The lateral stability of Light-frame timber (LFT) shear-walls is typically ensured by the nailed connection between the wooden frame elements and the sheathing wooden panels, e.g. Oriented Strain Boards (OSB), whereas hold-downs and angle brackets are typically adopted to limit the rigid body rotation and sliding of shear-walls. A valuable alternative to wooden panels in the sheathing of LFT shear-walls is given by diagonal boards. Wooden boards are typically 45° inclined and fastened to frame members, on one or both sides, by means of nails. This paper presents a numerical and experimental study of LFT shear-walls with diagonal board sheathing through extensive experimental campaign and finite element modelling. Monotonic tests were performed on six full-scale LFT shear-walls whereas monotonic shear tests were conducted at connection level to determine the mechanical properties of sheathing-to-framing nailed connections. The results showed that shear-walls sheathed on two sides, with boards which are 90° oriented one to the other, are characterized by significant in-plane shear resistance and can be considered as a feasible alternative to traditional LTF with wooden sheathing panels.

KEYWORDS: Light-frame shear-wall, diagonal sheathing board, lateral load, timber constructions, nailed connection.

1 INTRODUCTION

Light-frame timber (LFT) structures are certainly one of the most spread structural system used for low-to-mid-rise timber buildings worldwide. The lateral load resisting systems in such structural type is typically composed of LFT platform-type shear-walls which are designed to resist both vertical and lateral loads. The lateral stability of LFT shear-walls is typically ensured by nailed connection between wooden frame and sheathing elements, typically wooden panels such as e.g. Oriented Strain Boards (OSB) or plywood. Hold-downs and angle brackets are typically adopted to limit the rigid body rotation and sliding of shear-walls, especially in seismic prone areas, where lateral forces can reach particularly severe intensity.

Several comprehensive studies have been conducted to investigate the mechanical behaviour of traditional LFT shear-wall subjected to lateral loads. The seismic behaviour of shear-walls sheathed with OSB panels was investigated in the CUREE project ([1], [2]) through full-scale shear-wall tests and full-size building shake table tests. Salenikovich and Dolan [3] investigated the monotonic and cyclic behaviour of shear-walls with different aspect ratios showing that sheathing-to-framing connection mechanical properties and connection spacing have large influence on the shear-walls' response. The NEESWood project [4] provided essential outcomes obtained from shake table tests on two-storey and six storey buildings that lead to define the seismic behaviour of low-to-midrise LFT buildings in North America, through the development of a performance-based seismic design approach. Tomasi et al. [5] and Casagrande et al. [6], within the SERIES project, investigated the seismic response of two three-storey LTF buildings braced with LFT shear-walls sheathed with OSB or gypsum panels by means of shaking table tests.

A valuable alternative to wooden panels, for sheathing LFT shear-walls, is given by diagonal boards. Wooden boards are typically 45° inclined and fastened to the frame members by means of nails (Figure 1a). LFT walls with diagonal board sheathing had been largely used for many decades in the construction of low-rise buildings primarily in North America and a revival of such structural type is being observed also in Europe nowadays. However, limited information on their mechanical behaviour is available in literature. Partial designed models have been developed and limited provisions have been included in Standard documents [7] The mechanical behaviour of light-frame timber walls with diagonal board sheathing has been studied since the late 1950.

[1] Alessandro Setti, Institute of Bioeconomy-National Research Council of Italy (CNR-IBE), Italy, alessandro.setti@ibe.cnr.it
[2] Daniele Casagrande, Institute of Bioeconomy-National Research Council of Italy (CNR-IBE), Italy, daniele.casagrande@ibe.cnr.it
[3] Andrea Polastri, Institute of Bioeconomy-National Research Council of Italy (CNR-IBE), Italy, andrea.polastri@ibe.cnr.it
[4] Riccardo Fanti, Institute of Bioeconomy-National Research Council of Italy (CNR-IBE), Italy, riccardo.fanti@ibe.cnr.it
[5] Maurizio Follesa, dedaLEGNO, Firenze, Italy, follesa@dedalegno.com
[6] Ezio Riggi, Institute of Bioeconomy-National Research Council of Italy (CNR-IBE), Italy, ezio.riggi@ibe.cnr.it

https://doi.org/10.52202/069179-0454

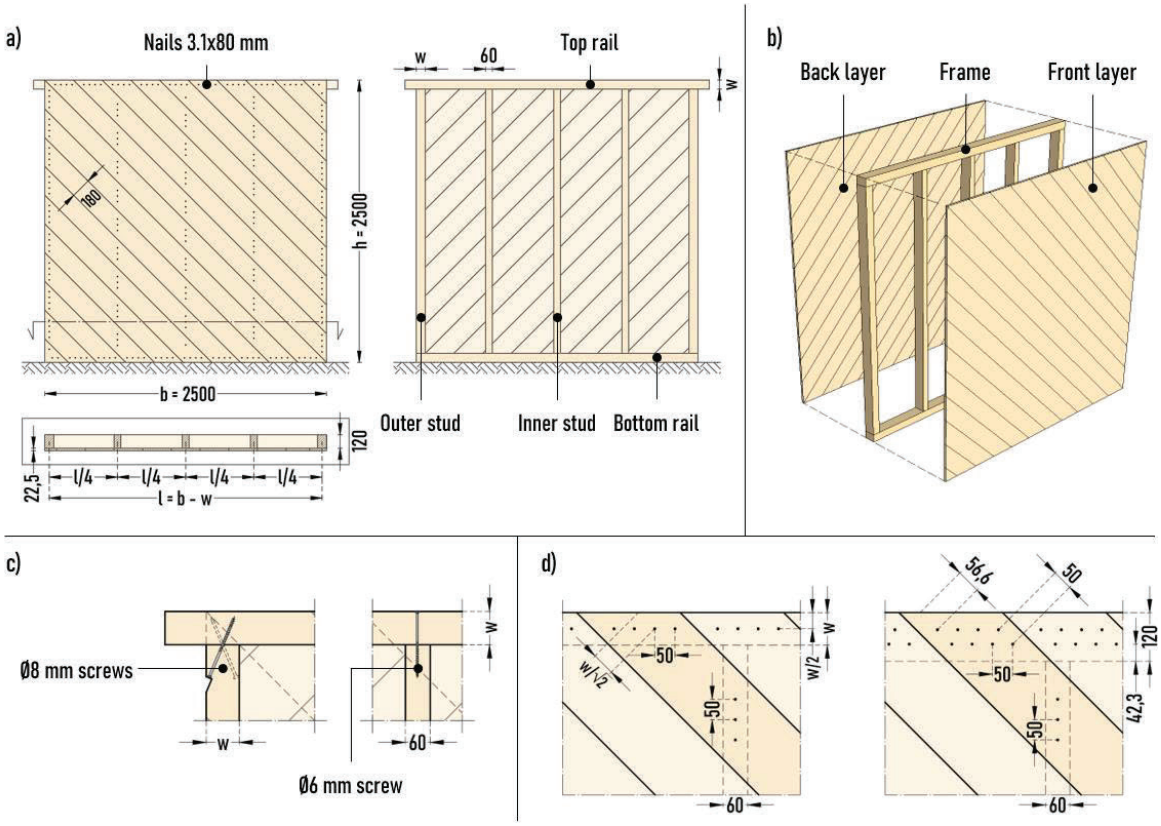

***Figure 1**: Shear-wall types and geometries: a) single sheathing board layer (1s) and general dimensions; b) double crossed sheathing board layers (2s); c) frame member connections; d) sheathing-to-framing nail layouts.*

Doyle [8] conducted an experimental campaign on seventeen shear-walls characterized by: different number of sheathing layer (single or double layers), type of boards (full-length and jointed) and corner with or without reinforcements The results provided by single sheathing layer walls showed that the overall mechanical behaviour depended on stresses which are acting within the boards: shear-walls with boards subjected to tension were stiffer and stronger than shear-walls with boards subjected to compression. Similar outcomes were obtained by Ni and Karacabeyli [9] in Canada by means of both monotonic and cyclic tests on sixteen shear-walls. The influence of different parameters was studied: sheathing layer configurations (either single or double layer), type of mechanical anchor, magnitude of vertical loads and reinforcements.

This paper presents a numerical and experimental study of the mechanical behaviour of LFT shear-walls with diagonal boards sheathing through experimental and numerical analyses. Monotonic tests were performed on six LFT shear-walls whereas monotonic shear tests were conducted at connection level to determine the mechanical properties of sheathing-to-framing nailed connections. Numerical finite element models were implemented to predict the mechanical behaviour of tested shear-walls.

2 EXPERIMENTAL CAMPAIGN

2.1 SHEAR-WALL TESTS

The shear-walls were assembled at the mechanical test laboratory of the Institute of Bioeconomy (formerly Ivalsa) of the National Research Council of Italy. Monotonic tests were carried out on six 2.50x2.50 m LFT shear-walls sheathed with boards (Figure 1a and 1b). Either 80x120 mm (type A) or 120x120 mm (type B) solid wood members were used as frame outer members (rails and outer studs) whereas 60x120 mm members were adopted for inner studs. The specimens were assembled using C24 wooden members; studs were spaced at quarter length of shear-wall (l) defined as the difference between the base of the wall (b) and the width of the frame perimeter member (w). A couple of crossed and inclined semi-threaded screws (8x160 or 8x200 mm) were adopted to ensure connection between rails and outer studs whereas a single semi-threaded screw (6x160 or 6x200 mm) was adopted as connection between rails and inner studs (Figure 1c). C16 boards (width 180±20 mm and thickness 22.5mm) were placed inclined 45° with respect to the timber frame and connected to the frame by means of either four or eight 3.1x80 mm ring nails. Three nails were used to connect the boards to the inner studs (Figure 1d). Sheathing-to-framing nailed connection layouts were adopted in accordance with the provisions reported in Eurocode 5 [10]. Sheathing boards were placed on either one side (1s) or both sides (2s) of the wall frame; this latter

https://doi.org/10.52202/069179-0454

configuration had boards placed on one side 90° oriented from boards on other side of the frame (double crossed layers) as shown in Figure 1. Test set-up used for full-scale shear-wall experimental campaign is shown in Figure 2. Specimens were anchored to the steel foundation by means of a couple of special mechanical anchors designed to fully prevent sliding and rocking of the specimen. Such anchors consisted of 15 mm thick steel plates provided with slotted holes where a special hold-down was connected by a steel dowel in order to allow free rotation of the specimen. These steel plates were bolted to the steel foundation element and the special hold-downs were connected to lateral side of outer studs by means of 5x70 mm LBS screws (30 or 60 screws were used for 1s or 2s shear-wall type respectively). As shown in Figure 2, lateral load was applied by means of a horizontal hydraulic jack through a steel top beam equipped with thick angular steel plates at top wooden rail ends to transfer the load from the hydraulic actuator to the top rail of the wall. Additional restraints were provided at the top of the wall specimen, on both sides, to prevent out-of-plane displacements of the wall and buckling.

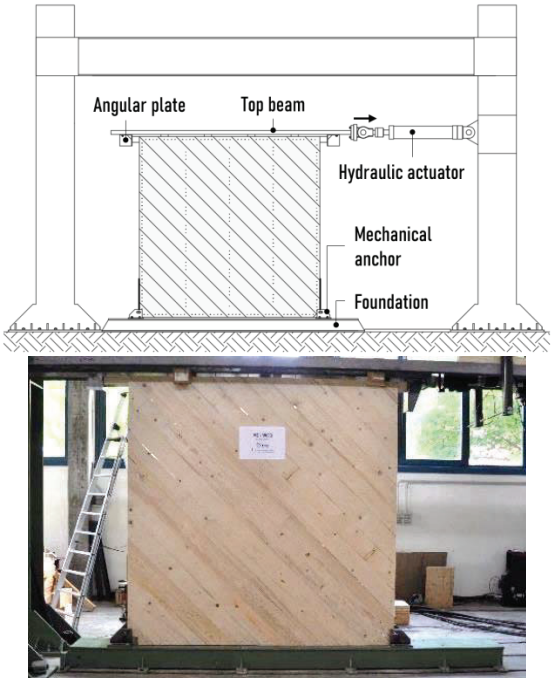

Figure 2: *Set-up of full-scale shear-wall tests.*

The instrumentation layout is represented in Figure 3. Linear Variable Displacement Transductors (LVDT) were used to measure the top horizontal displacement δ_T (M1), and the sliding of the specimen δ_B (M2) at the foundation level; two vertical LVDTs were placed in correspondence of ground anchor to measure the up-lift δ_V (M3 and M4) of the specimen. Finally, two diagonal LVDTs were placed to measure diagonal deformation of the frame (M5 and M6). The list of specimens used for experimental campaign is reported in Table 1.

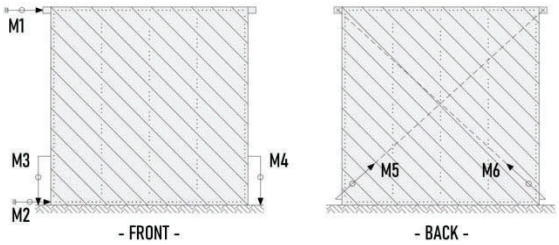

Figure 3: *Instrumentation layout for full-scale shear-wall tests.*

Each specimen reported an alphanumeric label: the sheathing layer configuration (1s or 2s) was identified; the next letter ("C" or "T") depended on stress which was acting within diagonal boards during the test (compression or tension respectively), see Figure 4; the last part identified the sheathing-to-framing nail configuration which depended on both the number of nails adopted (either four or eight) and on the dimensions of frame perimeter members (defined with letters "A" and "B").

With regard to W001b, the specimen used in test W001 was strengthened by means of an angle bracket at the upper corner (Figure 5). The purpose of this solution was to create a corner reinforcement (CR) in order to prevent failure of the perimeter member connection, thereby increasing in-plane strength capacity.

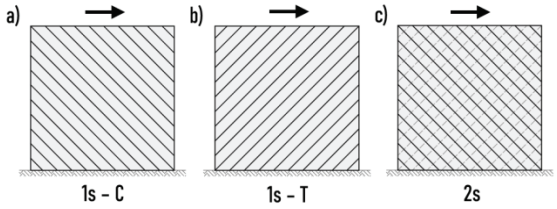

Figure 4: *Laying direction of boards compared to load direction used for W001 and W001b (compression) (a), W002 (tension) (b) and W003, W004 and W005 (c).*

Monotonic test procedure was defined in accordance with EN594. The test protocol consisted in a linear displacement with a constant speed of 0.2 mm/s imposed to shear-wall until 100 mm displacement (measured from hydraulic actuator LVDT) was reached or failure of the specimen occurred.

Table 1: *Full-scale shear-wall tests.*

Test	Label	Frame perimeter members
		width x depth
[-]	[-]	[mm]
W001	1s – C – 4A	80 x 120
W001b*	1s – C – 4A – CR	80 x 120
W002	1s – T – 4A	80 x 120
W003	2s – 4A	80 x 120
W004	2s – 4B	120 x 120
W005	2s – 8B	120 x 120

**specimen W001 stiffened with a further corner reinforcement (CR).*

https://doi.org/10.52202/069179-0454

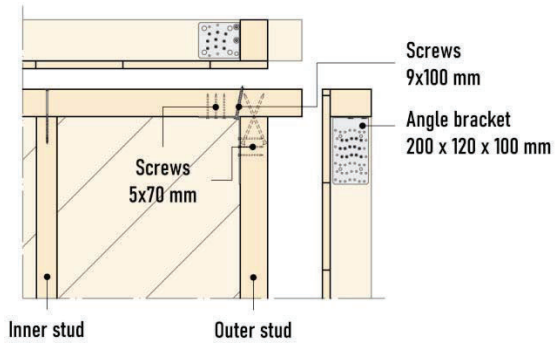

Figure 5: *Details of corner reinforcement used for W001b specimen (1s – C – 4A – CR).*

The results obtained with the experimental campaign are reported in
Table 2. Load-displacement curves are shown in Figure 6. The relative displacement δ was calculated with equation (1); in particular the sliding and the rocking of the specimen (δ_R) were subtracted from the top horizontal displacement.

$$\delta = \delta_T - (\delta_B + \delta_R) \quad (1)$$

The rocking displacement component δ_R is taken equal to δ_V as the aspect ratio of shear-walls is 1:1.
The results obtained from "1s" wall configuration (single sheathing layer) showed that in-plane strength capacity was dependent on the direction of the sheathing boards. As the matter of fact, two completely different behaviours from W001 (1s – C – 4A) and W002 (1s – T – 4A) were observed. During test W001, the shear deformation imposed by the external load was forcing the boards in compression stresses creating a diagonal compressed "strut" within the sheathing layer which led to the failure of the connection at the upper corner (Figure 7a). The concentrated forces caused relative displacements both in vertical and horizontal directions between the outer frame member. In addition, the shear-deformation caused the separation of the boards (Figure 8a).

Conversely, in test W002, the sheathing boards acted in tension. The stress configuration leads the frame perimeter members to compress each other (Figure 7b). Besides, shear deformation caused the contact between each board, generating collateral stresses in perpendicular direction which were acting in opposition to the movement of the specimen and which allowed the shear-wall to reach a maximum force almost four times greater than that obtained for shear-wall with boards subjected to compression (W001) (Figure 8b). The specimen has demonstrated a quite linear behaviour until the end of loading protocol and failure occurred in sheathing-to-framing connection,

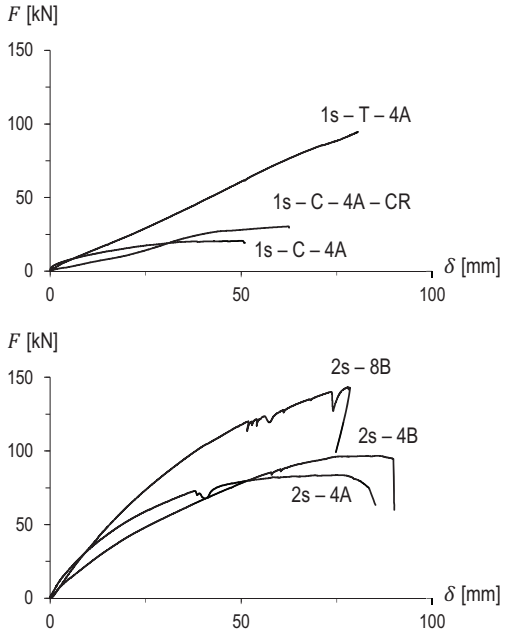

Figure 6: *Load-displacement curves from full-scale shear-wall tests.*

Table 2: *Full-scale shear-wall test results.*

Label	δ_{max}	F_{max}	δ_u	F_u	K	μ
[-]	[mm]	[kN]	[mm]	[kN]	[kN/mm]	[-]
1s – C – 4A	60.1	21.3	64.2	20.0	1.27	n/a*
1s – C – 4A – CR	62.4	30.4	62.5	29.5	n/a*	n/a*
1s – T – 4A	80.5	94.5	80.5	94.5	1.15	1.00
2s – 4A	75.0	83.7	84.6	67.0	3.07	3.98
2s – 4B	85.5	96.7	90.0	77.4	2.00	2.10
2s – 8B	78.1	143.5	78.3	114.8	3.10	1.97

- *δ_{max}, F_{max} peak point of load-displacement curve;*
- *δ_u, F_u ultimate curve point defined as the displacement at 80% of maximum load post peak or displacement limit of test protocol;*
- *K is stiffness assessed as the slope of the straight line passing from the origin of the axes to the yield point that was defined according to provisions reported in EN12512 (intersection between the secant between 10% and 40% of the maximum load and the tangent to the capacity curve with 1/6 slope of the secant line);*
- *μ ductility defined as the ultimate and yielding displacement ratio.*

**not reported as unreliable values (see Table 1).*

https://doi.org/10.52202/069179-0454

It is worth mentioning that specimen W001b (1s – C – 4A – CR, wall with corner reinforcement) increased in-plane strength capacity of almost 50% compared to W001; failure occurred due to angular bracket yielding used to reinforce the corner connection (Figure 7c).
Significantly different responses were obtained from "2s" wall configurations (double crossed sheathing layers) tests compared to "1s" configurations, providing greater strength capacity and stiffness. Double crossed tests provided a strength capacity almost four-to-seven times greater than W001.

Figure 7: *Wall frame corner detail: a) failure of W001 frame perimeter members connection; b) no visible failure occurred for W002; c) failure of W001b by yielding of angle bracket. Pull-out of frame perimeter members connection for W003 (d), for W004 (e) and W005 (f).*

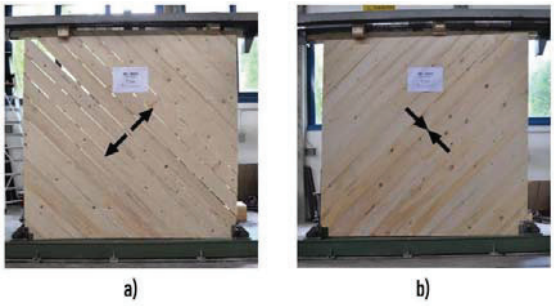

Figure 8: *Shear deformation: a) W001 sheathing boards tend to separate; b) W002 sheathing boards tend to contact.*

Load-displacement curves obtained from "2s" wall configuration tests showed a decreasing trend of the slope due to the progressive withdrawal of the screws which connected frame perimeter members on the left corner during the tests (Figure 7d, 7e and 7f). Similar mechanical behaviour with a decrease of stiffness during the test was observed in "1s" wall configuration with boards subjected to compression stresses. (see Figure 7a).

2.2 CONNECTION LEVEL TESTS

Experimental monotonic tests were carried out at connection-level on sheathing-to-framing nailed connection. These tests were designed and performed in order to characterize the mechanical behaviour of board-to-stud nailed connection and with the aim of collecting input parameters for the numerical model. The three sheathing-to-framing connection configurations used on full-scale shear-wall experimental campaign (see Figure 1d) were tested as reported in Table 3. Three specimens were tested for each configuration. Monotonic tests were carried out in accordance with the loading protocols defined in EN26891 [11].
Test set-up adopted for experimental campaign is represented in Figure 9: four LVDTs were placed to measure relative slip of nails between frame wood element and the two boards. Test protocol consisted in a linear displacement with a constant speed of 0.08 mm/s imposed to top CLT element until failure occurred or 80% of load post peak was reached. Load-displacement curve was drawn through mean displacement and force measured by a 600 kN load.

Table 3: *Sheathing-to-framing connection tests.*

Test	Configuration	Solid wood element		Board	
		width	depth	width	depth
[-]	[-]	[mm]	[mm]	[mm]	[mm]
001	4A	80	120	180	22
002	4A	80	120	180	23
003	4A	77	120	173	21.5
004	4B	120	120	182	22.5
005	4B	120	120	184	22
006	4B	120	120	182	23
007	8B	120	120	180	22.5
008	8B	118	116	170	22
009	8B	118	116	195	22

The results and load-displacement curves are reported per single nail in Table 4 and Figure 10, respectively.
In Table 5 it has also reported the mean values of peak load and load measured at 15 mm displacement on the three sheathing-to-framing configurations. The mean values of the reached maximum strength decrease, increasing both the number of nails and the cross section of frame member. Load-displacement mean curves obtained from connection-level tests were used to characterize sheathing-to-framing connection behaviour for numerical analyses.

https://doi.org/10.52202/069179-0454

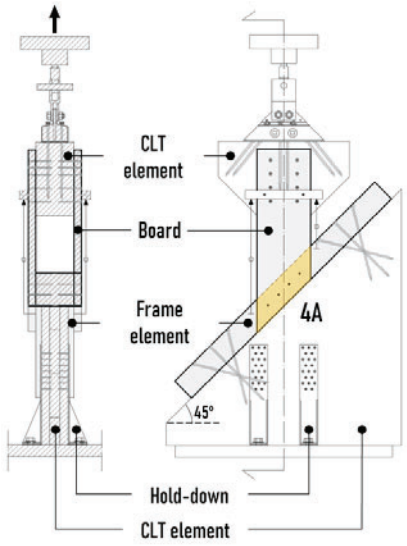

Figure 9: *Sheathing-to-framing connection test setup.*

Table 4: *Connection level test results per single nail.*

Test	Cf.	δ_{max}	F_{max}	δ_u	F_u	K
[-]		[mm]	[kN]	[mm]	[kN]	[kN/mm]
001	4A	17.3	2.16	29.7	1.73	0.22
002	4A	19.0	2.32	30.1	1.90	0.17
003	4A	18.8	1.69	26.9	1.35	0.28
004	4B	17.2	1.66	24.7	1.33	0.42
005	4B	17.3	1.57	28.6	1.26	0.20
006	4B	15.9	1.98	26.3	1.58	0.23
007	8B	18.4	1.65	31.1	1.32	0.32
008	8B	17.4	2.15	30.4	1.72	0.19
009	8B	14.7	2.07	23.4	1.66	0.24

- *δ_{max}, F_{max} peak point of load-displacement curve;*
- *δ_u, F_u ultimate curve point defined as the displacement at 80% of maximum load post peak;*
- *K is stiffness assessed as defined in full-scale shear-wall tests (see Table 2).*

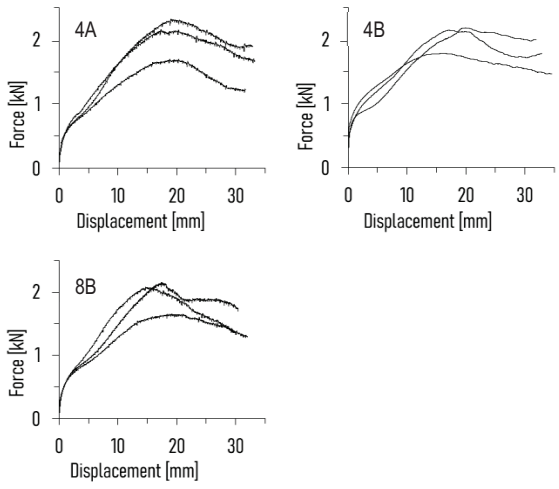

Figure 10: *Load-displacement curve of monotonic tests on sheathing-to-framing connection.*

Table 5: *Sheathing-to-framing configuration mean values and CoV.*

Configuration	F_{max}	CoV	F_{15mm}	CoV
[-]	[kN]	[%]	[kN]	[%]
4A	2.06	16%	1.89	14%
4B	2.03	11%	1.92	7%
8B	1.96	14%	1.96	14%

3 NUMERICAL ANALYSES

Numerical finite element analyses were conducted through the commercial software SAP2000 [13], see Figure 11, in order to predict the mechanical behaviour of LFT shear-walls with diagonal board sheathing.

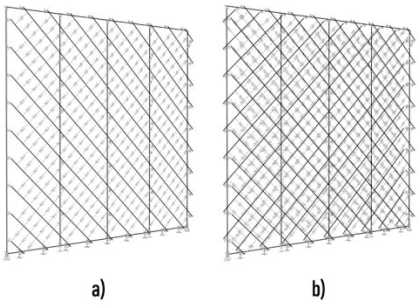

Figure 11: *Numerical model developed for "1s" (a) and "2s" (b) shear-walls.*

Orthotropic material was used to define the properties of wooden members (both frame member and diagonal lumber). The axial and bending stiffness of the solid wood members were set assuming an elastic modulus $E_{0,mean}$ = 12200 MPa .Furthermore, perpendicular to the grain and shear moduli were defined in accordance with EN338 [14]: $E_{90,mean}$ = 390 MPa and G_{mean} = 690 MPa.

Wooden frame and sheathing boards were modelled through "frame" elements. Outer and inner studs were connected to top and bottom rails by means of "non-linear links". Bottom rail was hinged to each end and provided by "line springs" along the frame object and resisting under compression only, in order to simulate the presence of the foundation. Sheathing boards were connected to the frame members by means of "non-linear links" whose mechanical behaviour was obtained by the sheathing-to-framing connection tests. Furthermore, boards were connected each other in perpendicular direction through "gaps" equal spaced in order to simulate the contact between the boards and taking into account the perpendicular to the grain compression forces due to shear-wall deformation.

Lateral increasing force in correspondence of top rail was imposed through non-linear static analyses. As an example, Figure 12 represents the comparison between experimental analysis and numerical results for specimen used in test W003 (2s – 4A).

It is noteworthy to mention that the distribution of stresses within sheathing boards was constant along each single board but with a decreasing trend moving gradually from the diagonal boards to the shorten ones.

https://doi.org/10.52202/069179-0454

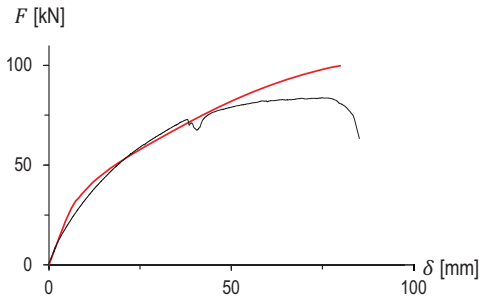

Figure 12: *Comparison between load-displacement curve obtained from test W003 (2s-4A) (black) and numerical result obtained from numerical model (red).*

4 CONCLUSIONS

An experimental campaign and a numerical investigation, on the mechanical behaviour of LFT walls with diagonal sheathing boards was conducted.

Results showed that shear-walls sheathed on one side (1s, single sheathing layer shear-walls) demonstrates a completely different behaviour in terms of resistance and stiffness, based on stresses which acting within sheathing boards, showing how the lateral resistance is strongly ruled by board laying direction. Corner reinforcement could be provided in order to avoid early failure in the connection between perimeter wood members of "1s" shear-wall, the reinforcement increases lateral resistance.

Regarding shear-walls sheathed on two sides with boards placed on one side 90° oriented from boards on other side of the frame (2s, double crossed sheathing layer shear-wall), the results showed that are characterized by significant in-plane shear resistance comparable to traditional LFT walls braced with wooden sheathing panels. The finite element model gave reliable results in terms of capacity curve if compared with these obtained from full-scale shear-wall tests, confirming that the model developed can be used to predict the mechanical behaviour of light-frame timber shear-walls with diagonal board sheathing.

5 ACKNOWLEDGEMENT

This work was carried out within the project "MiaCasa – Moduli Innovativi per Alloggi in Comunità ad Alta Sostenibilità Ambientale", financed by FESR Sicilia 2014/2020, the European Regional Development Fund (ERDF) cofinanced by Sicily Region (Italy).

REFERENCES

[1] Filiatrault A, Uang C, Seible F (2000), Ongoing seismic testing and analysis program in the Curee-Caltech Woodframe project in California. In: Proceedings world conference on timber engineering 2000, Whistler Resort BC, Canada.

[2] Filiatrault A, Fischer D, Folz B, Uang C, Seible F (2001), Shake table test of a two-story woodframe house In: Element 1 research meeting, January 12.

[3] Salenikovich, A.J., Dolan, J.D (2003), The racking performance of shear walls with various aspect ratios. Part I. Monotonic tests of fully anchored walls Forest Products Journal, 53 (10), pp. 65-73.

[4] Van de Lindt JW, Rosowsky DV, Filiatrault A, Davidson RA, Symans MD (2008), Performance-based seismic design of mid-rise light-frame wood buildings: an overview of the neeswood project. In: 10th World Conference on timber engineering.

[5] Tomasi R, Casagrande D, Grossi P, Sartori T (2015), Shaking table tests on a three-storey timber building, Proc Inst Civil Eng Struct Build 168(11):853–867.

[6] Casagrande, D., Grossi, P., Tomasi (2016), R., Shake table tests on a full-scale timber-frame building with gypsum fibre boards, European Journal of Wood and Wood Products, 74 (3), pp. 425-442.

[7] CSA O86-14 (2019), Engineering design in wood. CSA Group, Mississauga.

[8] Doyle D. V. (1969), Diaphragm action of diagonally sheathed wood panels. Forest Products Laboratory, Forest Service, U.S. Department of Agriculture.

[9] Ni C., Karacabeyli E. (2007), Performance of shear walls with diagonal or transverse lumber sheathing. Journal of Structural Engineering, Vol. 133, No. 12.

[10] EN 1995-1-1:2004/A2 (2014) Eurocode 5: Design of timber structures. Part 1-1: General. Common rules and rules for buildings.

[11] EN 594 (1995): Timber Structures - Test Methods - Racking Strength and Stiffness of Timber Frame Wall Panels. CEN, European Committee for Standardization, Brussels.

[12] EN 26891:1991 (1991): Timber structures – Joints made with mechanical fasteners – General principles for the determination of strength and deformation characteristics. CEN, European Committee for Standardization, Brussels.

[13] SAP2000. "CSI – SAP2000 Integrated Software for Structural Analysis and Design." Computers and Structures Inc., Berkeley, California.

[14] EN338:2016 (2016): Timber Structures - Strength Classes. CEN, European Committee for Standardization, Brussels.

World Conference on Timber Engineering Oslo 2023

SEISMIC PERFORMANCE OF CLT SHEAR WALL INFILLED HYBRID STEEL MOMENT FRAME WITH CONCEALED STEEL PLATE AND DRIFT PINS CONNECTIONS

Hiroshi Isoda[1], Richard Yip Je Too[2], Kazumi Kanazawa[3]

ABSTRACT: In Japan, the recent introduction of Cross Laminated Timber (CLT) started gaining attention because of its ability to perform under seismic activities. The increasing of utilization of timber in mid-rise buildings became possible followed by the change in height limit of fire-proofed timber buildings (e.g., Steel-CLT hybridization) in the Building Standard Law. However, the design method of such hybrid structures in Japan has yet to be generalized and it has become an obstacle for structural designers. In this paper, a series of models for hybrid steel moment frame (SMF) CLT shear walls structures are presented for the non-linear incremental displacement analysis. The model was verified by the experiment results and can potentially serve as an appropriate method to design future CLT-Steel hybrid structures.

KEYWORDS: Cross Laminated Timber, Hybrid Structures, Lateral Performance, Cyclic Tests

1. INTRODUCTION

Hybrid systems require an application of 2 or more materials and enable the benefits of each material to be applied to seismic force resisting systems. For instance, in timber and steel hybridization, the ductility of steel provides significant post-yield deflection capability, allowing the structure to dissipate seismic energy during earthquakes. On the other hand, the timber infill can increase the stiffness of the system, which can reduce the fundamental period and drift values in seismic vulnerability. [1]

Recently, many researchers are beginning to focus on research topics regarding steel-timber hybrid buildings. In Canada, research on steel-timber hybrid system was conducted [2]. The proposed system consists of a steel beams with wooden shear wall infills connected to the studs via nails. In China, a hybrid system consisting a steel frame with wooden shear wall infill was proposed, in which nails were also used to connect the wooden shear walls [3]. From the results, it was observed that the timber infill could contribute to the increase of stiffness and strength of the structure significantly. Nonetheless, ultimate failures like panel tear out and bending of nails were observed. The failures show that the stiffness and strength of the connection is inadequate, indicating that the system could resist more load if properly designed with stronger connection, as well as with stronger infills.

To overcome such problems, a new steel-timber hybrid system is proposed in this paper. It utilizes concealed plate with drift pin (DP) connections as the wall-to-frame connection and cross laminated timber (CLT) as the infill wall for better seismic performance. The advantages of using DP connectors is that, it can have high ductility like nails and screws, while also maintaining its high rigidity. In Japan, the research on steel-timber hybrid system utilizing concealed steel plate with DP connection was initially conducted by Fukumoto et. al. [4]. However, the system consists of steel tie bars as well, which are exposed, and fire safety would become an issue. Because of this, newly developed wall-to-frame connection was proposed that consists of only DP connections with concealed steel plate inserted into the pre-opened slit in the CLT panel.

In 2018, Kanazawa et. al. [5] reported the results on this type of hybrid system for the first time. In 2019, 4 new types of specimens were additionally introduced, of which the results have not been reported anywhere else. On top of that, in Japan, the standard seismic design methodology for such hybrid system has not been generalized. Therefore, this paper will compare and discuss the results of all 2018 and 2019 specimens and also to propose an analysis model that can trace the cyclic behaviour of the system. The model could serve as a fundamental design methodology with the aim to accelerate the promotion of such hybrid system. It should be noted that the presented contents in this paper are a part of the journal paper accepted for publication, written by Richard et al [6]. For more information, please refer to the paper listed in the reference.

2. DESCRIPTION OF TEST SPECIMENS

Figure 1 and 2. shows the naming method of the specimens and the detailed figure of the standard hybrid specimen FM-S60-32, respectively. Figure 3 and 4. show the specimen overview of tests conducted in 2918 and 2019, respectively. It should be noted that the CLT-steel hybrid frame experiment was conducted at 1/2 scale. The size of the specimens is 3600mm and 2000mm between

[1] Hiroshi Isoda, Research Institute for Sustainable Humanosphere, Kyoto university, Japan, hisoda@rish.kyoto-u.ac.jp
[2] Richard Yip Je Too, Research Institute for Sustainable Humanosphere, Kyoto university, Japan,
[3] Kazumi Kanazawa, Research and Development Institute, Takenaka Corp., Japan. (former graduate student at Kyoto University)

https://doi.org/10.52202/069179-0455

the center of steel columns and steel beams, respectively. The steel column is SN490B graded with size of RH-300x300x10x15 for all specimens. Column and beam connections are rigidly welded and reinforcing ribs were appropriately placed in
each specimen. The CLT panel used in the experiment is made of Japanese Cedar, which is 1531mm in height (1631mm for FS-S60-32), 1100mm in width (1075mm for FM-S60-32-S) and 105mm in thickness. At the wall-to-frame connection, concealed steel plate and DP connections are applied. To further connect the concealed steel plate to the steel frame, several bolts were used. The length and the DPs were 105mm and 10mm, respectively. The thickness of the concealed steel plate was 6mm. Moreover, non-shrink mortar was also infilled in between the CLT panel and the frame, to increase fire safety as well as to cover the uneven surfaces of the steel beam for better distribution of the compression load from the CLT panel.

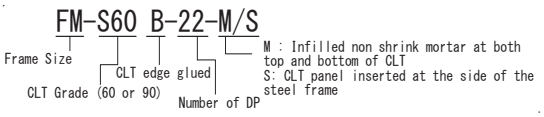

Figure 1: *Naming method of the specimens*

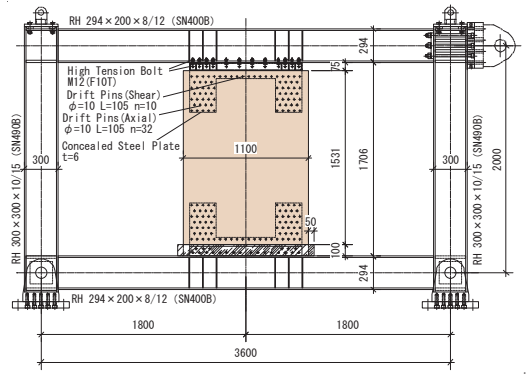

Figure 2: *Detailed figure of FM-S60-32*

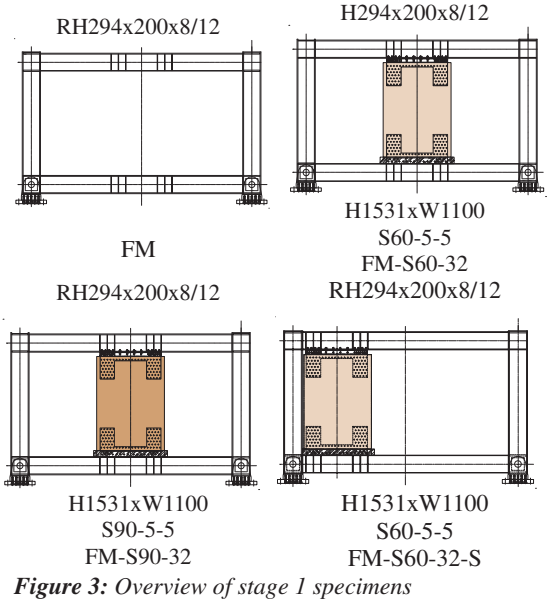

Figure 3: *Overview of stage 1 specimens*

In this paper, a total of 8 specimens, including 2 steel bare frame and 6 CLT-steel hybrid specimens with different configurations were prepared and investigated. The parameters of the hybrid specimens, including the descriptions are listed as follows:
1. Stiffness grading of CLT panel(S60 or S90): Specimen that consists of CLT infill with higher grading (S90) was introduced to investigate its effectiveness in the hybrid system, compared to the lower graded CLT (S60).

2. Edge gluing between the laminas in the CLT panel: To investigate the difference in the amount of contribution to the overall shear resistance due to the increased performance provided by the edge gluing in the CLT shear wall.

3. Positioning of CLT panel: To investigate the effectiveness of the shear force resisted by the infilled
CLT shear wall when it is placed at the side of the steel frame.
4. Number of drift pins (22 or 32): To investigate the influence of the number of drift pins (32+10+32 or 22+14+22 configuration) on the lateral performance of the hybrid system.
5. Position of infill non-shrink mortar: To investigate the effect of a higher stiffness option due to the stronger compressive strut formed in the CLT shear wall.

6. Size of the steel beam (FS:RH-194x150x6x9 or FM:RH-294x200x8x12, both SN490N graded): To investigate the capability in energy dissipation which occurs through the yielding of the steel beam.

3. TESTING METHODS AND DATA ACQUISITION

Figure 5. illustrates the setup of the cyclic loading test and the measuring positions for data acquisition. The test specimen was pushed and pulled by two hydraulic

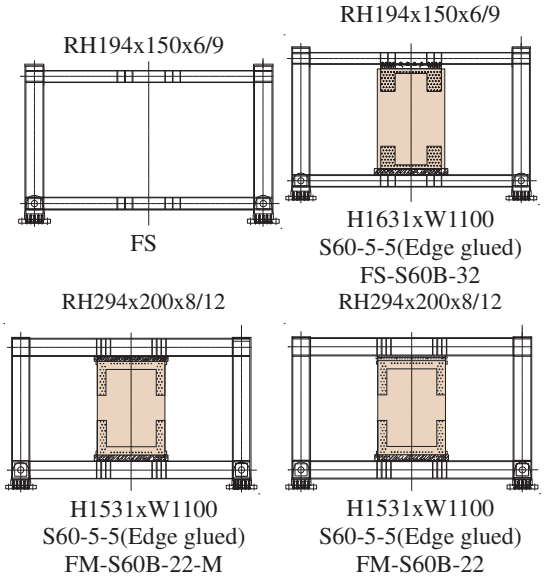

Figure 4: *Overview of stage 2 specimens*

https://doi.org/10.52202/069179-0455

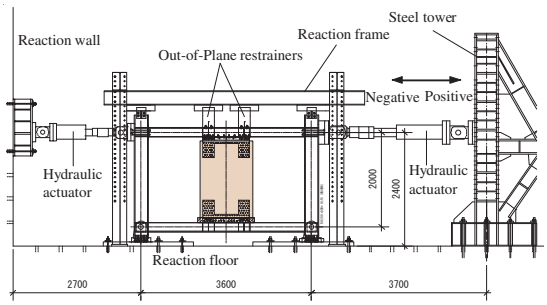

Figure 5: *Configuration of cyclic loading test*

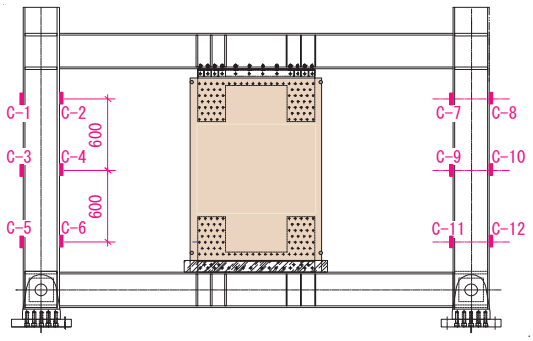

Figure 6: *Position of strain gauges on steel columns*

actuators from both sides of the frame. Out-of-plane restrainers were set above the top of the steel beam to prevent out of plane deformation. The steel frame was also fixed to the reaction floor.

The horizontal displacement δ was measured at the centre of top steel beam. The drift angle R is calculated by δ/H, where H is the distance between centre of the beams (=2000mm).

To evaluate the shear force in each of the steel frame and the CLT infill, the following equations were used. The shear force resisted by the steel frame (Qc) can be obtained by adding the shear forces in the left (Q_{CL}) and right (Q_{CR}) steel columns. The shear force in each steel column was determined using Equation (1).

$$Q_{CL} \text{ or } Q_{CR} = \frac{M_{top} + M_{bottom}}{h} = \frac{(\varepsilon_{top} + \varepsilon_{bottom})EZ}{2h} \quad (1)$$

In Equation (1), M_{top} and M_{bottom} are the bending moments of the top part and bottom part of each steel column, ε_{top} and ε_{bottom} are the strain values recorded using strain gauges located at the top (C-1, C-2 and C-7, C-8) and bottom (C-5, C-6 and C-11, C-12) of the steel columns, respectively, shown in Figure 6. E is the elastic modulus of steel (2.05×10^5 N/mm^2), Z is the section modulus of the steel columns (1.35×10^6 mm^3), and h is the vertical distance between the strain gauges (1,200 mm).

In the CLT-Steel hybrid wall system, the total shear force (Q) was resisted by two components, the steel frame and the CLT shear wall. Therefore, from the load-sharing by the two components, Q_{CLT} can be acquired by using Equation (3).

$$Q_C = Q_{CL} + Q_{CR} \quad (2)$$

$$Q_{CLT} = Q - Qc \quad (3)$$

It should be noted that both stage 1 and 2 test specimens were subjected to different cyclic loading protocol of controlled angular displacement with cycles grouped in phases, as indicated in Figure 7. Even though the loading protocols were different, the obtained results for both stages were essentially the same. The first phase for 1/200 rad contains only 2 full reversed cycles for stage 2 specimens, while others contain 3 cycles. Finally, the loading will be terminated at final pushover at 1/10rad, where the specimens are expected to fail.

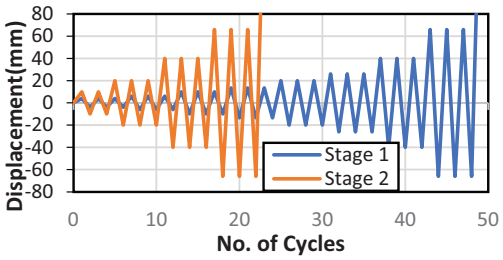

Figure 7: *Loading protocol*

4. RESULTS AND DISCUSSIONS.

4.1 Load-Displacement Properties

Figure 8. summarizes the load-displacement hysteresis curves of all specimens. From the figures, it can be observed that with the exception of FM-S60-32-S, the CLT-infilled specimens with FM beams experienced strength degradation at an angular deformation of around 1/50 to 1/30 rad due to the shear failure of the CLT infill. It can be said that the shear capacity of the CLT infill was fully utilized. As for FS-S60B-32, strength degradation did not occur because one of the two steel beams yielded and buckled markedly at 1/30 rad, which led to out-of-plane deformation of the CLT infill. All the specimens were tested successfully, per the loading schedule, except for specimen FM-S60-32-S, for which the test had to be terminated prematurely because of the large compression flange local buckling of the beam. Overall, almost no slip behaviour was observed among the hysteretic behaviour of the specimens with CLT infill, an outcome that was similar to the hysteretic behaviour of the steel frame specimens. This shows that the steel frame was dominant in terms of the behaviour of the hybrid system.

Table 1 summarizes the specimens' maximum capacity and initial stiffness. The table shows that the installation of the CLT panel significantly increased the maximum load capacity and initial stiffness of the steel bare frame. From Figure 8 and Table 1, the following principal conclusions can be drawn:

1. When comparing specimen FS-S60B-32 and FM Frame to FS frame, the results show that same amount of increase in maximum capacity and initial stiffness were obtained in both cases. Considering that there was no strength degradation occurred in FS-S60B-32, it indicates that by

https://doi.org/10.52202/069179-0455

infilling a CLT panel into a slender frame, the hybrid system is capable of increasing the stiffness while still maintaining the ductility.

2.When comparing FM framed hybrid specimens to FM frame, the results show that the reinforcement effect in maximum capacity and initial stiffness by the CLT infill is lower compared to FS-S60B-32. Although strength degradation occurred in FM framed hybrid specimens, the amount is not large overall, demonstrating that the lateral load was shared by both the steel frame and the infill, which worked closely together to resist lateral load.

4.2 Typical Failure Modes

In this section, the typical failure modes of the hybrid systems are presented. At 1/100rad, noticeable displacement at the DP connections was observed in specimens with fewer DP connectors. Due to the yielding of DP connectors, specimens FM-S60B-22 and FM-S60B-22-M were observed to undergo early failure at the wall-to-frame connection, of a type that involved compressive buckling at the concealed steel plate as shown in Figure 9(a). Between 1/50 and 1/30rad, all specimens except specimen FS-S60B-32 underwent shear failure along the grain of CLT's lamina, as shown in Figure 9(b). Because of the early yielding of DP connectors, specimens FM-S60B-22-M and FM-S60B-22 showed particularly significant failure in the CLT shear wall, which split in half vertically in the middle as shown in Figure 9(c). However, in the case of FM-S60B-22-M, the lateral load was maintained even after the splitting, as the mortar at top and bottom constrained the potential rocking motion of the split CLT, thus enabled each broken section to continue to resist lateral load individually.

At large deformations (1/50 rad~1/10 rad), the steel frame began to display yielding evidence, thereby demonstrating the capability to dissipate energy through plastic deformation. While yielding of the steel frame was observed in all specimens, it is noticeable that the DPs in specimens with 22+14+22 configurations underwent yield deformation before yielding of the steel frame; this proved the capability to dissipate energy at smaller deformations. After the experiments were concluded, almost all the specimens with infilled CLT shear walls were observed to have experienced the separation of a CLT panel from a concealed steel plate at one or more locations, as shown in Figure 9(d). This was because of the repetitive bending deformation of the DPs under a growing angular cyclic displacement.

4.3 Load Sharing Effect

As described above, in the CLT-steel hybrid system, the shear force is jointly resisted by the CLT panel and the columns of the steel frame. In order to evaluate the effectiveness of the hybrid system's lateral load resistance, the percentage of shear force resisted by each of the subsystems was calculated for all specimens using the values of Eqs. (2) and (3); the results are shown in Figure 10. The percentage of utilized CLT shear capacity calculated using Eq. (4) is also shown,

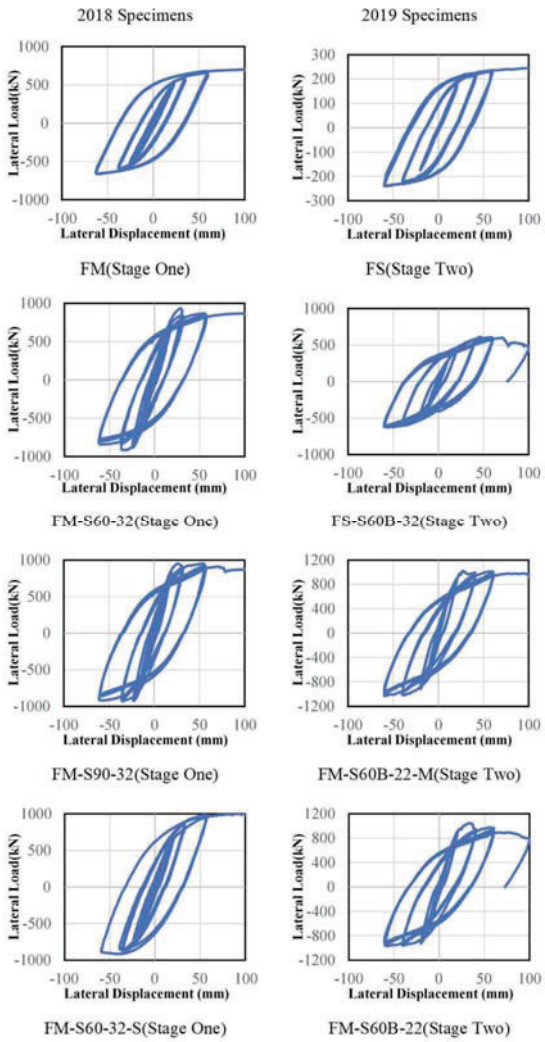

Figure 8: *Load-Displacement Skeleton Curves*

Table 1: Maximum capacity and initial stiffness

Specimen Name	Maximum capacity(kN)		Initial stiffness (kN/mm)	
	P_{max}	Compare to FS* or FM frame	K	Compare to FS* or FM frame
FS	247.5	-	8.5	-
FS-S60B-32	611.5	2.5*	25.6	3.0*
FM	791.3	2.9*	24.32	3.2*
FM-S60-32	931.7	1.2	46.08	1.9
FM-S90-32	931.7	1.2	51.88	2.1
FM-S60-32-S	1003.4	1.3	37.11	1.5
FM-S60B-22-M	1015	1.3	55.74	2.3
FM-S60B-22	1045	1.3	51.56	2.1

https://doi.org/10.52202/069179-0455

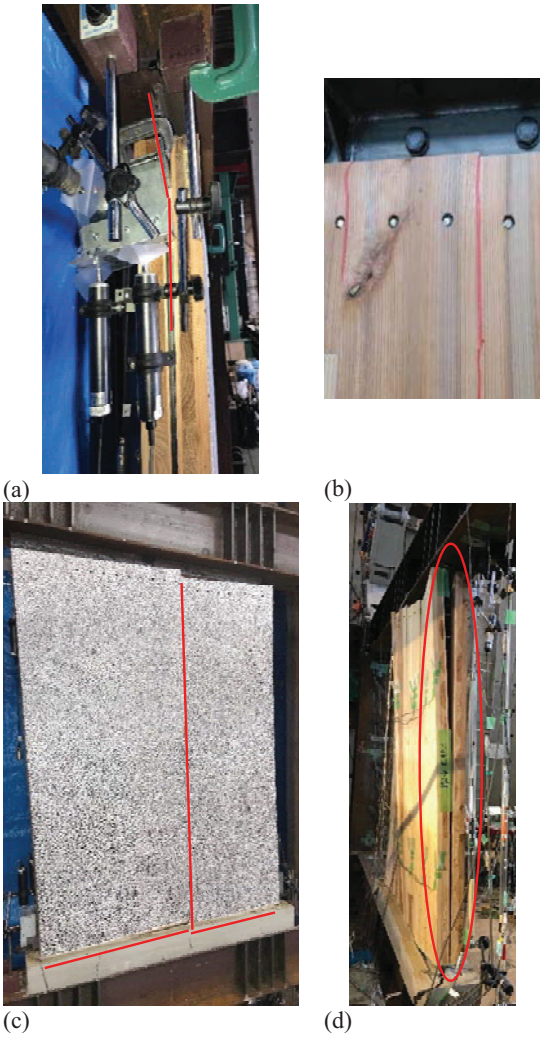

Figure 9: *Failure mechanisms*

$$Q_{CLT(\%)} = \frac{Q_{CLT}}{\min\{Q_s, Q_m\}} \times 100 \quad (4)$$

where, Q_{CLT} is the shear force resisted by the CLT during the test, and $\min\{Q_s, Q_m\}$ is the calculated CLT shear strength (268.9kN for S60 and 311.9kN for S90).

In the case of FS-S60B-32, at the initial cyclic deformation of 1/200 rad, 50% of the shear capacity of CLT was utilized. As the deformation progressed, the shear capacity was utilized up to 127% at peak. In terms of the sharing of resistance between the panel and the frame, the CLT infill resisted more than half of the shear force until almost the end of the experiment without any strength degradation. That was because, as compared with tests based on the FM frame, this specimen used the more slender FS beams. Because of that, this specimen was observed to experience significant torsional buckling at 1/30 rad, which led to the out-of-plane deformation of CLT.

For the other five specimens, a different result was observed. The shear capacity of the CLT was taken

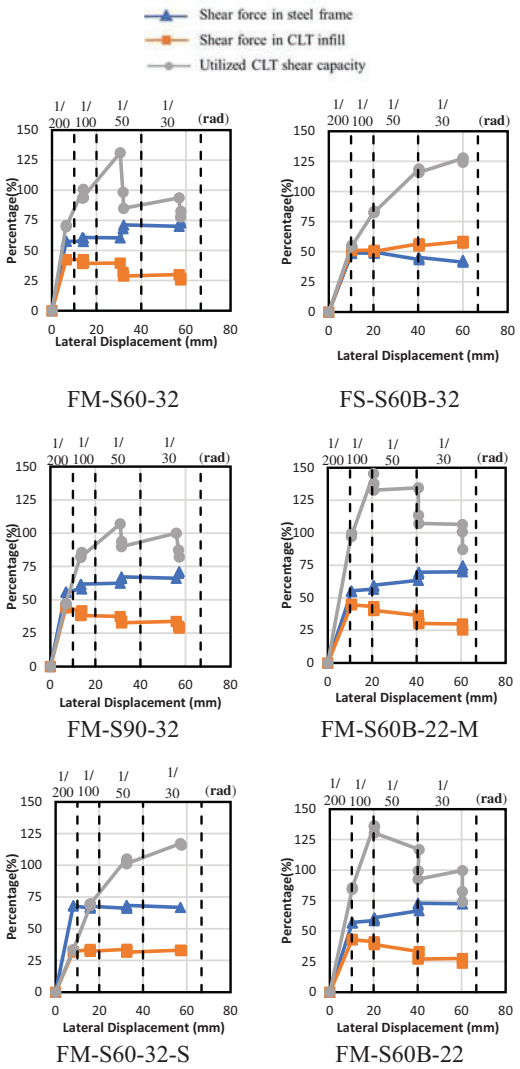

Figure 10: *Load sharing effect between steel frame and CLT infill*

advantage of at a comparatively smaller deformation, especially those specimens that had a 22+14+22 DP configuration. This is because of the early yielding of the DP connectors, which caused the CLT to deform more freely, a fact which also resulted in early shear failure of the CLT. Overall, the shear capacity of the CLT was utilized to beyond 100% (107~145%) in every specimen, proving that the utilization of the shear capacity of CLT infill was maximized. As for the sharing of the load, the steel frame resisted more than 50% of the shear force throughout the experiment because of the more robust beams, which were more capable of transferring the lateral loads to the steel columns. As observed in the discussion of failure mechanisms, the CLT could still resist some shear force even after shear failure. Due to the accumulation of damage, the percentage of force resisted by the CLT infill nonetheless decreased gradually, as shown in Figure 10.

https://doi.org/10.52202/069179-0455

5. NUMERICAL ANALYSIS

5.1 Analysis Model

A hysteresis model that can accurately reflect the hybrid system's behaviour was developed using a commercial software, SNAP V7.0 [7]. The analysis model for specimen FM-S60-32 is shown in Figure 11, as an example for the overall explanation. Figure 12 provides an overview of a series of elemental tests conducted to help define the parameters of each component in the model.

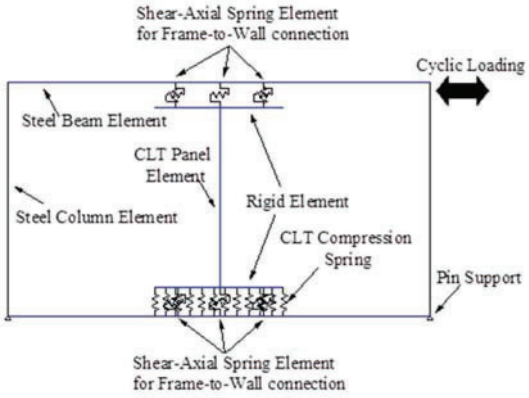

Figure 11: *Analysis model for specimen FM-S60-32*

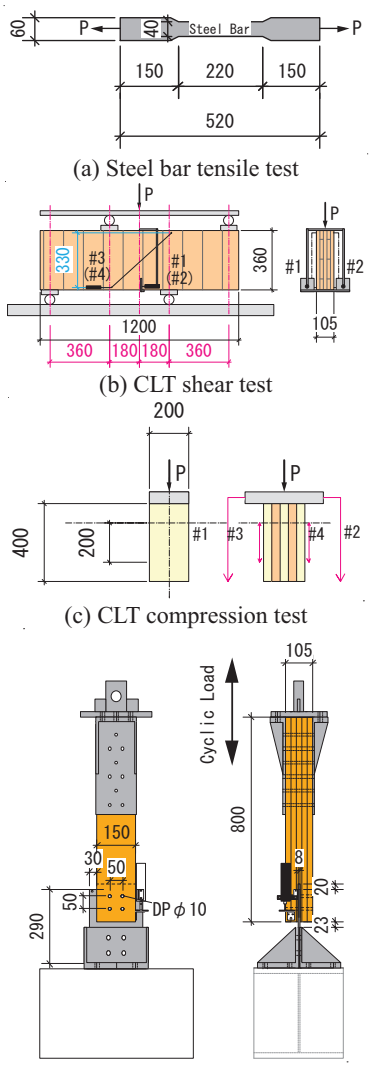

(a) Steel bar tensile test

(b) CLT shear test

(c) CLT compression test

(d) Drift pin cyclic test

Figure 12: *Overview of elemental tests*

Firstly, the hysteretic response of the steel frame was reproduced and confirmed through validation with the test results of the steel bare frame specimens. The bare frame model is basically the same as the example shown in Figure 11, minus the CLT infill elements. The hysteretic response of the steel frame was reproduced using the proposed modified Ramberg-Osgood model [8]. The parameter values used to define the steel frame model were obtained from the steel bar tensile test, illustrated in Figure 10(a). A good agreement between the experimental and analytical results was obtained, as shown in Figure 13.

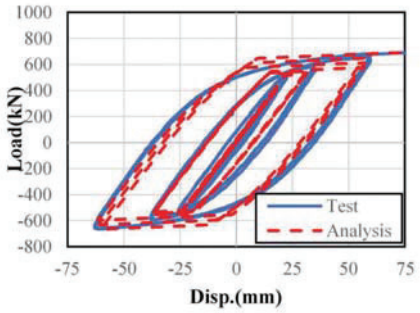

Figure 13: *Comparison between the test and numerical results of FM steel bare frame*

As for the CLT infill, it was modelled as an I shape with a vertical beam element in the middle and horizontal beam elements on the top and the bottom. During the experiments, strength degradation occurred due to the shear failure of the CLT infill. To reproduce such behaviour, the vertical beam element is defined as non-linear with model that allows strength degradation. The shear properties of the CLT infill were obtained from the CLT shear elemental test, illustrated in Figure 12(b). On the other hand, the horizontal beam elements were defined as rigid to allow effective load transfer between the CLT and steel frame through the DP connections in the numerical model. The contact surface between the CLT infill and the non-shrink mortar was modelled using a series of spring elements placed 100mm apart. Each of the bearing spring was adjusted to only resist compression and modelled as an elastic-plastic element, of which the parameter input was obtained from the CLT compression test illustrated in Figure 12(c). However, the bearing springs at the ends were considered to only have half the stiffness and yield strength, as each of the bearing springs is assumed to bear the compression load by a certain area.

Finally, the wall-to-frame connections (drift pin connections) was modelled using a series of axial-shear spring elements, which can resist both axial tensile and compression, as well as shear forces. The hysteretic behaviour of the connection was represented using the

https://doi.org/10.52202/069179-0455

modified NCL model, proposed by Matsunaga et al. [9]. As illustrated in Figure 12(d), the drift pin cyclic test was conducted to obtain the load-deformation relationships for

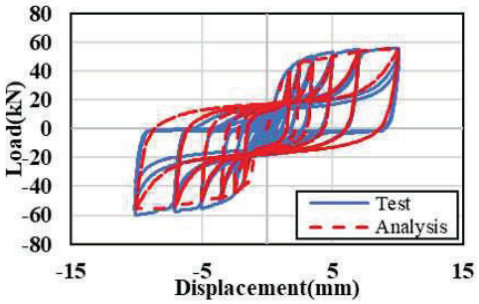

Figure 14: *Comparison between the drift pin cyclic test and calibrated numerical result*

the frame-to-wall connection. The elemental test results were then used for calibration to obtain the parameters of the modified NCL model. It can be seen from the comparison of the analysis result and the test result in Figure 14, the calibration went well as the model is capable of reproducing the slip and pinching behaviour of the DP connection under cyclic loading.

5.2 Modelling Results

The analysis model was subjected to the same loading protocol as the structural experiments. The predicted hysteresis loops, load sharing effect and cumulative energy dissipation (obtained by calculating the area under the hysteresis loops) of the hybrid system are shown in Figure 15, 16 and 17. Since the modelling results are similar for all specimens, only the results for FM-S60-32 specimen are shown.

From Figure 15, it can be observed that the plotting of the yielding of steel beam, shear failure of CLT and yielding of DP from the test and analysis results are in good agreements. Generally, the numerical results were able to reproduce the hysteretic behaviour of the hybrid system; a behaviour that is governed by the steel frame.

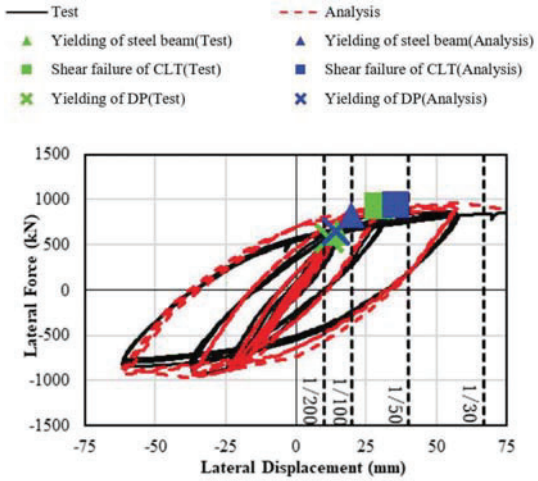

Figure 15: *Predicted hysteresis loops*

From Figure 16 and Figure 17, it can be seen that the model predictions were capable of capturing the trend of the load sharing effect between the two subsystems (steel frame and CLT) and also the cumulative energy dissipation at all test cycles.

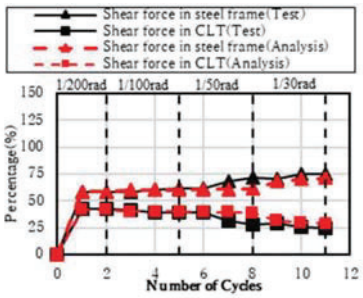

Figure 16: *Load sharing effect (Test vs. Analysis)*

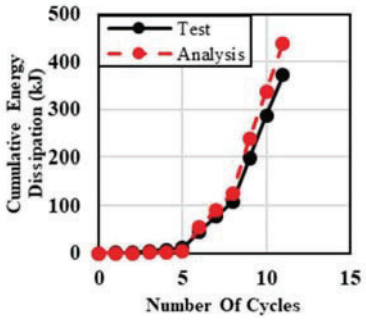

Figure 17: *Cumulative Energy Dissipation (Test vs. Analysis)*

6. CONCLUSIONS

This paper reports the experimentally observed and numerically simulated performance of a CLT-steel hybrid system using concealed steel plates and drift pins as wall-to-frame connections in different configurations. The load-displacement properties, failure mechanisms, equivalent viscous damping factors, and shear force sharing effect between the timber and steel subsystems were observed and discussed.

From the load-displacement properties, it was observed that significant increases in initial stiffness and maximum capacity for the bare steel frame could be obtained by infilling a CLT shear wall. At large deformations, most of the specimens were seen having an ultimate failure at the wall-to-frame connection, for example, shear failure of the bolted connection, buckling failure of the moment-bearing concealed steel plate, and detachment of the CLT panels from the moment-bearing concealed steel plate. As for the sharing of shear force between the CLT panel and the steel frame, the results showed that both of these components worked closely together to resist the lateral load. In general, the burden of resistance increased for the steel frame once damage developed in the CLT infill. Also, when the steel beam size was larger than the two under test (M frames as opposed to S frames), the steel columns could resist most of the lateral load due to the more effective transfer of load from the beam.

https://doi.org/10.52202/069179-0455

After the structural experiments were concluded, a non-linear finite element model was developed using SNAP V7.0 for the purpose of simulating the experimental results and as a basis for making further predictions. Three sub-models were made of the frame, the CLT panels, and the frame-panel connections, respectively, and combined to reproduce the experimental results accurately. The results of the numerical model did reliably agree with the experimental results. Such validation of the numerical model by the experimental results means that the model is a candidate to serve as a tool for designing such wood-steel hybrid structures, intended for applications as lateral load resisting systems for medium- to high-rise buildings in Japan. In addition, for further studies, the numerical model may be used to conduct seismic analyses to determine appropriate R-factors, which are required when designing such structures.

ACKNOWLEDGEMENT

This research was supported by the Forestry Agency under Ministry of Agriculture, Forestry and Fisheries. (Project Title: Development of seismic wall construction technology for wood-based materials such as CLT, 2018)

REFERENCES

[1] Tesfamariam, S., S. Stiemer, C. Dickof, and M. Bezabeh. (2014): Seismic Vulnerability Assessment of Hybrid Steel-Timber Structure: Steel Moment-Resisting Frames with CLT Infill, Journal of Earthquake Engineering, 18:6, 929-944

[2] Stiemer, S. F., S. Tesfamariam, E. Karacabeyli, and M. Propovski. 2012. "Development of steel-wood hybrid systems for buildings under dynamic loads." In *Proc., 7th Int. Specialty Conference on Behaviour of Steel Structures in Seismic Areas (STESSA).* Abingdon, England: CRC Press.

[3] Li, Z., X. Wang, M. He, W. Dong, and H. Dong. 2019. "Seismic performance of timber-steel hybrid structures. I: Subassembly testing and numerical modeling." *J. Struct. Eng.,* 145 (10), 04019113. https://doi.org/10.1061/(ASCE)ST.1943-541X.0002395.

[4] Fukumoto, K., Kouda, M., Kubo, K., Usami, T., Kitamori, A., Miyauchi, Y. and Isoda, H. "Experimental Study on CLT Seismic Panel Infilled within Steel Frame, Buildings, Journal of Structural and Construction Engineering" (Transaction of AIJ), Vol.86, No.787, pp.1345-1356, 2021.9 (in Japanese) https://doi.org/10.3130/ajis.86.1345

[5] Kanazawa, K., Isoda, H., Kitamori, A., Usami, T. and Araki, Y. "Structural Performance of Composite Structure with CLT Wall Infilled In Steel Frames Using Drift-Pin With Steel Plate, Buildings", Journal Of Structural and Construction Engineering (Transaction of AIJ), Vol.86, No.788, pp.1430-1439, 2021.10 (in Japanese) https://doi.org/10.3130/ajis.86.1430

[6] SNAP Ver.7. *Finite Element Structural Analysis Software.* KOZO SYSTEM. https://www.kozo.co.jp/program/kozo/snap/index.html

[7] Richard Yip Je Too and Isoda, H. 2023. "Seismic Performance of CLT Shear Wall Infilled Hybrid Steel Frames with Concealed Steel Plates and Drift Pin Connections." J. Struct. Eng., DOI: 10.1061/JSENDH/STENG-12074

[8] Meng, L., Ohi, K. and Takanashi, K. 1992. "A simplified model of steel structural members with strength deterioration used for earthquake response analysis." *J. Struct. Constr. Eng.*, 437, 115-124. [in Japanese]. https://doi.org/10.3130/ajisx.437.0_115

[9] Matsunaga, Y., Soda, I. and Miyazu, Y. 2008. "Modeling of restoring force characteristics of wooden structures and its application to dynamic analyses," Proceeding of the 78th Architectural Research Meetings, 2007, Architectural Institute of Japan, Kanto Chapter, pp.201-204. [in Japanese]

World Conference on
Timber Engineering
Oslo 2023

INVESTIGATION OF A NOVEL TIMBER-MORTAR CONSTRUCTIVE SYSTEM

Andrea Polastri[1], Riccardo Fanti[2], Pietro Rigo[3], Efrem Demarchi[4]

ABSTRACT: Timber constructions are well-know because are able to guarantee structural safety and easy assembling as well as high level of thermal insulation and living comfort. The new challenge is to enhance the use of local resources and starting to design the whole building in order to permit to dismantle and reuse/recycle the different elements/materials at the end of building-life. A constructive technology that can answer to all the aforementioned requirements is represented by a timber-mortar composite structures recently proposed. The use of timber-masonry structures belongs to the European tradition and different typologies of wooden frame infilled with masonry or with clay/mortar have been used all over the world. This paper analyses the mechanical behaviour of a new concept of timber frame wall infilled with lime mortar: experimental results show that, for low-rising buildings, the presented system is a valuable alternative to timber shear-walls (e.g. Light Frame Timber or Cross Laminated Timber). Furthermore, the studied system permits to use small-section timber elements that can be easily obtained sawing local wood; moreover, indoor air quality and living comfort are guaranteed using, for the whole construction, only few natural row materials such as wood, lime, clay and hemp.

KEYWORDS: Use of local wood, Wooden frame, Timber-mortar wall, Reuse-Recycle, Experimental test.

1 INTRODUCTION

In the last decades the use of timber in constructions has constantly increased, driven by the physical-mechanical properties of wooden products: the very high strength-to-density ratio of wood makes it extremely competitive for buildings constructions in seismic-prone areas. Moreover, the thermal properties of wooden panels can be exploited to improve energy efficiency of new residential buildings. Light-Frame Timber (LFT) and Cross Laminated Timber (CLT) represent the most widely used timber technologies, in particular, LFT give the possibility to prefabricate the entire wall (structure, insulation and also electrical and plumbing systems) while CLT panels are becoming strong engineered and industrialized products. Recently both research institutes and the productive sector have been starting to study and propose timber constructive systems able to ensured structural safety, high level of thermal/acoustic insulation and, at the same time, to improving the living comfort (i.e. optimal thermo-hygrometric indoor conditions and quality of air indoor). Contextually, the main challenge is to re-design the entire building process in order to increase the use of wood grown in areas close to construction site. The use of local resources (e.g. wooden row material) and an appropriate study of the end-of-life phases as the dismantling/disassembling and the reuse/recycle are critical points that have to be considered.

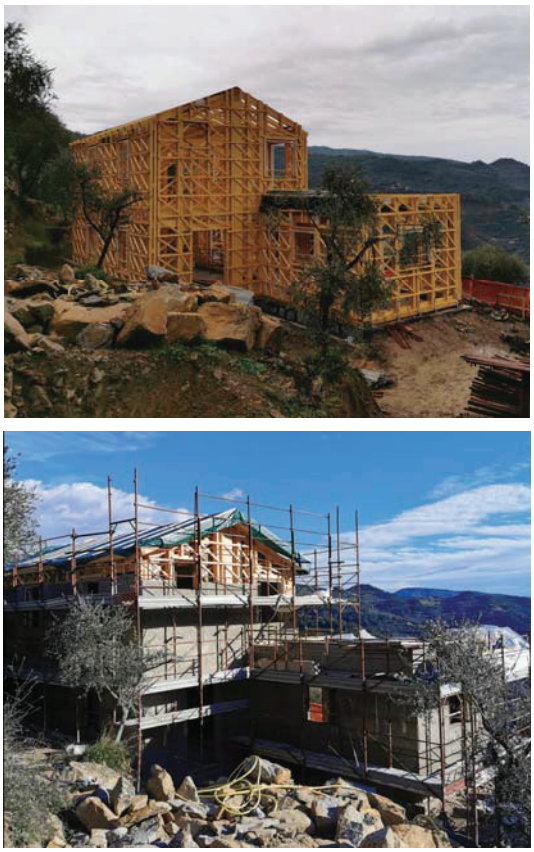

Figure 1: *Example of timber-mortar constructive system use; prefabricated only-timber frames assembled on-site (above) and building during the pouring of lime mortar (below)*

[1] A. Polastri, Institute of Bioeconomy-National Research Council of Italy (CNR-IBE), Italy, andrea.polastri@ibe.cnr.it
[2] R. Fanti, Institute of Bioeconomy-National Research Council of Italy (CNR-IBE), Italy, riccardo.fanti@ibe.cnr.it
[2] P. Rigo, Institute of Bioeconomy-National Research Council of Italy (CNR-IBE), Italy, pietro.rigo@ibe.cnr.it
[3] E. Demarchi, Nidus Srl, Italy, efrem.demarchi@gmail.com

https://doi.org/10.52202/069179-0456

A valuable solution is to distinguish the different function of the building elements adopting engineered materials and high-technology connections for the bracing systems, able to guarantee the stability of the structure even in case of earthquake, while secondary elements could be obtained with timber elements composed by row wooden material. Another way is represented by the use of only-natural material (i.e. wood, mortar, brick, etc…) and, where necessary, steel connections which have to be separated and recycled as used-iron at the dismantle phase. With these materials it is possible to obtain all the building elements both structural/non-structural walls and horizontal floors/roof.

This paper will discuss the possibility to erect low-rising buildings with a novel constructive system named "*Nidus*" that belong to the second category being the whole building composed by timber elements infilled with mortar. More than 20 low-rise buildings (up to 3 storeys) have been realized in Italy in the last decade with this technology. Starting from the state of the art, the new timber-mortar system will be presented and results of an experimental mechanical tests campaign will be discussed.

2 STATE OF THE ART

Timber frame structures with masonry infill, also called "half-timber" buildings, have been used all over the world. The main reasons for this widespread diffusion are certainly the easy access to materials, the simple construction method and the good seismic response. Examples of this kind of structures can be found in many European countries, especially in seismic prone areas: "*fachwerk*" (North-Central Europe), "*gaiola pombalina*" (Portugal), "*casa baraccata*" (South Italy), "*lefkada*" (Greece), "*hatil, himiş* and *bağdadi"* (Turkey). Other examples of timber frames with mansory infill can be found in other regions all over the world: *"taq* and *dhajji-dewari"* (Kashmir, India), "*assam-type structure"* (Himalayan region), *"chuan-dou timber frame"* (Southwest of China), *"kay peyi"* (Haiti) and *"tapial, adobe and quincha"* (South and Centre America).

As pointed out by Langenbach [1], it's relevant to observe that some of these structural systems were specially developed and selected as earthquake-resistant construction. In Lisbon (Portugal), after a disastrous earthquake in 1755, the construction system called "*gaiola pombalina*" was used for the reconstruction of the city. This structural system consists of a three-dimensional wooden frame, braced with wooden elements and filled with stones and bricks. The inspiration for this technique came from the observation that the half-timber type constructions had withstood better the earthquake [1] than the "only" masonry structures, thanks to their deformability. In the southern part of the Calabria Region (Italy), after an earthquake in 1783, a system constituted by masonry reinforced with timber frames, called "*casa baraccata*", was indicated from the government as an essential requirement to ensure safety [2]. An comprehensive collection of articles concerning the seismic behaviour of *half timber buildings* in the Mediterranean area, experimental tests and numerical modelling is presented by Ruggieri et al. [3]

Recent seismic events (Turkey in 1999, Greece in 2003, Kasmir in 1967 and 2005, Haiti in 2010) have highlighted the good seismic response of these mixed constructions. For this reason, some research projects have been conducted in order to improve the knowledge regarding the seismic resistant behaviour of this kind of traditional wood frame structures. Makarios et al. [4] studied the seismic response of the traditional buildings of Lefkas Island in Greece observing a good seismic behaviour. Dogangun et al. [5] and Gülhan et al [6] observed an excellent seismic response of traditional buildings after the earthquake occurred in Kocaeli and Duzcedel (Turkey) in 1999. Kaushik et al. [7] reported about the better behaviour of traditionally constructed timber-masonry structures compared to reinforced concrete structures during the Sumatra earthquake in 2004. Kaushik et al. [8] observed that both masonry and reinforced concrete buildings showed poor performance during the Sikkim (India) earthquake of 2006, while traditionally constructed half-timber houses showed acceptable damage.

Several experimental studies on the behaviour of traditional half-timbered walls are available in literature. Four modules of a timber crossed frame without masonry infill and three identical modules with masonry infill have been tested by Ferreira et al. [9] under horizontal and vertical load and compared with numerical models. Three different types of half-timbered walls (unreinforced, retrofitted with GFRP sheets and filled with brick masonry) have been tested by Vasconcelos et al. [10], the latter showing high values of ductility. Half-timber walls build in real scale were tested under cyclic load by Poletti et al [11] considering two different infill typologies, as well as the possibility of having no infill, showing that the presence of infill increases the cyclic stiffness, as well as the energy dissipation and the ductility. Two full-size of a "*gaiola pambolina*" walls, were tested in a cyclic manner by Dutu et al. [12] showing a good in-plane behaviour of the timber–framed masonry system and significant deformation capacity. Meireles et al. [13] conducted cyclic shear testing to study the hysteretic behaviour of the interior wooden walls of the half-timber "*gaiola pambolina*" building in Portugal, showing non-linear load–displacement responses and high ductility. A full-scale replica of "*casa baraccata*" wall has been tested under quasi-static cyclic load by Ruggieri et al. [14] and Sandak et al. [15], at CNR-IBE laboratory in San Michele all'Adige – Italy. Ali et al. [16] conducted in-plane quasi-static cyclic tests on three full-scale "*dhajji-dewari"* building walls and monotonic tensile and bending tests on connections, showing that the masonry infill does not increase the lateral load capacity, but it has an effect on the energy dissipation capacity of the system. Two distinct geometrical variations of "*quincha*" were tested by Quinn et al. [17] with and without the infill, showing that the infill increases stiffness and capacity, 4.5 and 2 times respectively. Chand et al. [18] conducted an experimental campaign on seven different connections generally adopted in "*assam-type*" houses using cyclic tests and pull-out tests showing high deformability and ductile behaviour. Cyclic tests were

performed by Liang et al [19] on three "*Chuan-dou*" timber frame models with a scale of 1:2 with and without infill. Experimental analysis of seismic resistance of Haitian timber-framed structures with stones-earth infill called "*kay peyi*" were performed by Vieux-Champagne et al. [20] at CNR-IBE Laboratory demonstrating the high ductility of the filled wood structures.
Novel composite wooden-masonry or wooden-mortar walls have been proposed and used in different European countries. Bettini [21] studied the use of partitioned *adobe* infills in association with timber frames. Recent studies have highlighted the possibility to use hemp cement as infill in low-rise timber buildings [22-26].
All the aforementioned studies agree with the fact that the composite timber-masonry or timber-mortar structures lead to an optimal overall behaviour: framed timber structure is loaded by vertical/horizontal loads and, at the same time, confines the masonry/mortar infill which collaborate in order to stiffen the wall and to transmit the vertical/horizontal loads to the foundation; furthermore, the infill element is able to guarantee good thermal performances during the summer season, thanks to the mass given by infilled material.

3 THE COSTRUCTIVE SYSTEM

Nidus timber structure is given by "balloon-frame" prefabricated wooden truss elements (maximum width 2,5m) modules that are assembled at the factory and jointed together at the construction site.

Once defined the architectural concept of the building, timber prefabricated modules, that will compose the different walls, have to be designed. A complete 3D model (Figure 2) have to be implemented and all the wooden elements, needed to assemble the prefabricated truss, have to be drawn and verified.

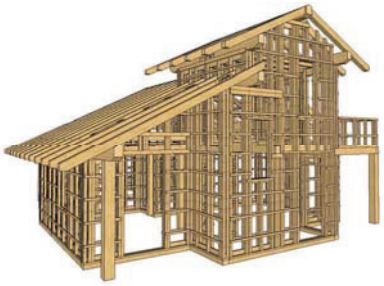

Figure 2: *Nidus constructive system, 3D model*

According to the 3D design, the carpentry/factory can cut manually or through a CAD-CAM process and CNC machines all the small-section wooden elements. Typically, the vertical wooden elements are 80mm x 80mm, while horizontal and diagonal are 80mm x 30mm. An horizontal beam is expected at the inter-storey level in order to support the floor beams (e.g. 160mm x 240mm) that will be inserted and screwed to the continuous vertical elements at the construction site.
Different members are jointed together with 5mm diameter screws according to the assembling drawings (Figure 3): the carpentry/factory can use the well-known steel modular frame developed for LFT prefabrication.

Figure 3: *Nidus balloon-frame prefabricated modules*

The preassembled elements, identified by a numerical code, that clearly indicate the position, can be easily moved by simply use of lifting belts. Once placed in the right position the studs are anchored to the pre-casted concrete foundation with commercial hold-down (uplift forces) and the bottom beams is connected to foundation with standard concrete bolts (shear forces). Modules can be screwed one to each other in order to avoid gap between the vertical elements. Typically the last horizontal closure is a standard timber inclined beams roof (Figure 4). By this doing in a couple of days the whole structure is erected.

Figure 4: *On construction site: Nidus modules assembled*

In order to obtain the complete wall-system, wooden-cement panels have to be stapled on the external faces of the timber frame. Finally, the empty area between panels is infilled with mortar composed by a mix of lime, perlite and hemp (Figure 5) characterized by a density equal to 350÷450 kg/m^3, as the softwood used for the structure.

Figure 5: *Detail of Nidus wall during mortar casting*

Is important to note that, according to the *Nidus* constructive systems, the casted lime mortar creates a continuous layer that wrap the entire building running both on the vertical external surface (walls) both on the external horizontal surface (roof) giving a unique layer of

https://doi.org/10.52202/069179-0456

thermal insulation and natural air tightness (no membrane/tapes are required), see Figure 6.

Figure 6: *Lime mortar casted in the space between floor beams (up) and on the top of the roof (below)*

4 FULL-SCALE TESTS

Full scale tests were carried out to investigate the mechanical behaviour of the timber-mortar wall system in particular *only-timber* frame (Figure 7, left) was tested according to the EN 594:2011 [27] monotonic procedure, furthermore complete *wall-systems* (Figure 7, right and Figure 8) were tested both according to monotonic and cyclic protocols, EN 594:2011 [27] and EN 12512:2001 [28], respectively.

Figure 7: *Full scale tests on only-timber frame (left) and complete-wall system (right)*

The *only-timber* specimen (Figure 7, left) is a timber frame composed by small wooden elements (vertical elements 80mm x 80mm, horizontal elements 100mm x 28mm and diagonal elements 60mm x 28mm) assembled with 5mm diameter screws. In order to realize the complete *wall-system* specimens (Figure 8), the procedure described in Section 2 was applied to two further *only-timber* specimens: external panels were stapled and the mortar was casted; two months later, tests were performed. Specimens were realized respecting exactly the procedure given by *Nidus* constructive system.

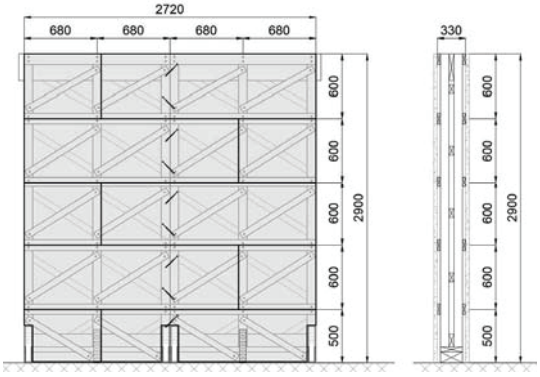

Figure 8: *Complete wall-system, geometry and connections*

Consistently with the provisions reported in EN 594 a series of transducers was applied to the tested specimens, as shown in Figure 9. A Linear Variable Displacement Transducer (LVDT), named LPM057, measured the horizontal displacement at the top corner of the wall. According to [27] these displacements are required to calculate the racking stiffness of the specimen. Two LVDTs (LPM052 and LPM053) measured the diagonal displacements of each module which forms the wall. A LVDT (LFV033) was placed at the centre of the wall in order to measure the relative vertical displacement between the two modules. Two LVDTs, LPM055 and LPM056, measured the uplift of the wall at the hold-downs positions, as shown in Figure 6. In cyclic test the same transducers were applied.

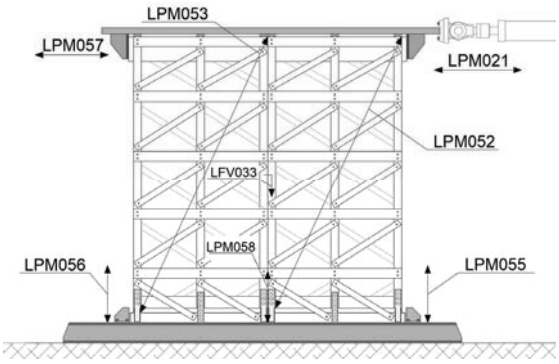

Figure 9: *The complete-wall system at the end the test*

The timber frame was anchored to the steel foundation with 4 couples of hold down (4 hold downs at both side of the wall), in order to avoid rigid rotation due to uplift forces, while the horizontal sliding is prevented by a steel rigid element (bolted to the steel foundation) in contact with the bottom wooden beam (Figure 10).
All the performed tests were stopped once reach the maximum displacement given by EN 594:2011 [27] equal to 100mm. At the end of the test the *only-timber* specimen did not show any failure because the high deformability of the structure given by the large displacements permitted by the ductile behaviour of the timber-timber screwed connections.

https://doi.org/10.52202/069179-0456

Figure 10: *The complete-wall system at the end the test*

Observing *complete-wall* specimens, both in case of monotonic and cyclic test, it was not possible to see any failure because the inner mortar layer was covered by the external panels. At the end of the tests, in order to identify possible local failures a visual analysis was performed removing a couple of panels: it was possible to recognize the cracks developed at the mortar-wood contact surfaces, see Figure 11.

Figure 11: *The specimens after the test: lateral panel removed in order to analyse mortar status*

The results of the experimental campaign were reported in Table 1 in terms of failure mode, stiffness k, maximum load F_{max} and corresponding displacement v_{max}. A comparison between load-displacement curves are reported in Figure 12.

Table 1: *Mechanical parameters of the tested specimens*

ID	wall-system	protocol	k [kN/mm]	F_{max} [kN]	v_{max} [mm]
1	only-timber	monotonic	0,3	21,6	96,6
2	timber-mortar	monotonic	5,9	82,7	87,8
3	timber-mortar	cyclic*	3,1	75,9	99,4

*mechanical parameters are referred to backbone curve of the first quadrant

Experimental results demonstrate, comparing the complete *wall-system* to the *only-timber* specimens, the high contribution to load-carry capacity (+400%) given by the infilled mortar; stiffness increases more than ten times. In particular, monotonic test on timber-mortar wall showed comparable strength and higher stiffness as the double-sheeted LFT, studied by Grossi et al [29,30], characterized by nails 2.8x60mm spaced at 50mm. Is noteworthy that LFTs showed high loss of strength, due to sheeting nail failure, in a range of top displacements between 40mm and 60mm. At the opposite the studied wall showed a continuous increase of strength until the end of the test (at an imposed displacement equal to 100mm).

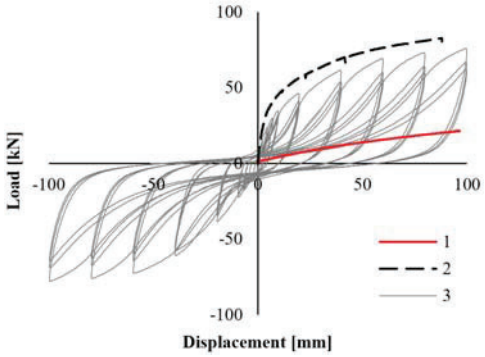

Figure 12: *Load-vs-displacement curves of monotonic and cyclic tests*

Figure 12 showed that the mortar infilled in timber-frame (complete *wall-system*) provided a not negligible contribution, in terms of strength and stiffness, associated with a good capacity of energy dissipation. These contributions are not considered in the design phase yet due to the lacking of a calculation method for *complete-system*. Nowadays practitioners design the timber-mortar walls as *only-timber* frame structure, consistent with EN1995:2004 [31] provisions and so, the contribution of the infilled mortar is neglected. The analytical calculation underestimates the strength, stiffness and energy dissipation capacity of the *complete-system;* hence further studies and tests are required in order to fully-characterize the mechanical properties of the presented constructive system.

5 CONCLUSIONS

This paper presents a new constructive system that uses timber frame structural walls infilled with lime mortar. Results of experimental campaign on a full scale shear walls are presented and discussed: the study considered both *only-timber* truss wall and timber-mortar walls. Monotonic and cyclic test were performed. Strength and stiffness showed by the complete timber-mortar wall are comparable with the mechanical properties of a typical LFT; furthermore an higher ductility was shown by timber-mortar walls. Timber-mortar constructions guarantee high comfort and quality of indoor living given by the use of only natural raw material, such as wood, lime, perlite and hemp. The presented constructive system can be considered as valuable alternative to traditional structural timber shear-wall for low-rising buildings.

6 ACKNOWLEDGMENTS

The authors would like to acknowledge the CNR-IBE (San Michele all'Adige) mechanical test laboratory staff: Mario Pinna, Diego Magnago.

REFERENCES

[1] Langenbach R. (2006). From Opus Craticium "to the Chicago Frame": earthquake resistant traditional con-

https://doi.org/10.52202/069179-0456

struction. In Proceedings of Stuctural analysis of historical constructions, New Dehli.
[2] Tobriner S. (1997). La casa baraccata: un sistema antisismico nella Calabria del XVIII secolo. Costruire in laterizio, (56), 110-115.
[3] Ruggieri N., Tampone G., & Zinno R. (Eds.). (2015). Historical earthquake-resistant timber frames in the Mediterranean area. Springer.
[4] Makarios T., & Demosthenous M. (2006). Seismic response of traditional buildings of Lefkas Island, Greece. Engineering structures, 28(2), 264-278.
[5] Doğangün A., Tuluk Ö. İ., Livaoğlu R., & Acar R. (2006). Traditional wooden buildings and their damages during earthquakes in Turkey. Engineering Failure Analysis, 13(6), 981-996.
[6] Gülhan D., Güney İ. Ö. (2000). The behaviour of traditional building systems against earthquake and its comparison to reinforced concrete frame; experiences of Marmara earthquake damage assesment studies in Kocaeli and Sakarya. In Proceedings of International Conference on the Seismic Performance of Traditional Buildings, Istanbul, Turkey.
[7] Kaushik H. B., & Jain S. K. (2007). Impact of great December 26, 2004 Sumatra earthquake and tsunami on structures in Port Blair. Journal of performance of constructed facilities, 21(2), 128-142.
[8] Kaushik H. B., Dasgupta K., Sahoo D. R., & Kharel G. (2006). Performance of structures during the Sikkim earthquake of 14 February 2006. Current Science.
[9] Ferreira J. G., Teixeira M. J., Duţu A., Branco F. A., & Gonçalves A. M. (2014). Experimental evaluation and numerical modelling of timber-framed walls. Experimental techniques, 38, 45-53.
[10] Vasconcelos G., Poletti E., Salavessa E., Jesus A. M., Lourenço P. B., & Pilaon P. (2013). In-plane shear behaviour of traditional timber walls. Engineering Structures, 56, 1028-1048.
[11] Poletti E., Vasconcelos G., & Oliveira D. V. (2013). Influence of infill on the cyclic behaviour of traditional half-timbered walls.
[12] Dutu A., Sakata H., Yamazaki Y., & Shindo T. (2016). In-plane behavior of timber frames with masonry infills under static cyclic loading. Journal of Structural Engineering, 142(2), 04015140.
[13] Meireles H., Bento R., Cattari S., & Lagomarsino S. (2012). A hysteretic model for “frontal” walls in Pombalino buildings. Bulletin of Earthquake Engineering, 10, 1481-1502.
[14] Ruggieri N., Tampone G., & Zinno R. (2015). In-plane versus out-of-plane “Behavior” of an Italian timber framed system - The Borbone constructive system: Historical analysis and experimental evaluation. International Journal of Architectural Heritage.
[15] Sandak J., Ruggieri N., Riggio M., Fellin M, Sandak A., Polastri A., Ceccotti A., (2015), An Italian historic timber framed wall: damage progression through DIC analysis, 3rd International Conference on Structural Health Assessment of Timber Structures, Poland
[16] Ali Q., Schacher T., Ashraf M., Alam B., Naeem A., Ahmad N., & Umar M. (2012). In-plane behavior of the dhajji-dewari structural system (Wooden Braced Frame with Masonry Infill). Earthquake Spectra.
[17] Quinn N., & D’Ayala D. (2014). In-plane experimental testing on historic quincha walls. In 9th International Conference on Structural Analysis of Historical Constructions; F. Peña & M. Chávez (eds.), Mexico.
[18] Chand B., Kaushik H. B., & Das S. (2020). Lateral load behavior of connections in Assam-type wooden houses in the Himalayan region of India. Construction and Building Materials, 261, 119904.
[19] Liang W., Lan J., Zou Z., Zhu Z., Zhai S., Mo Y, Li X., Meng S. & Cai Y. (2022). Seismic behavior of Chuan-dou timber frames with different infilled walls. Construction and Building Materials.
[20] Vieux-Champagne F., Sieffert Y., Grange S., Polastri A., Ceccotti A., & Daudeville L. (2014). Experimental analysis of seismic resistance of timber-framed structures with stones and earth infill. Engineering Structures, 69, 102-115.
[21] Bettini N. (2010). Il ritorno della terra cruda per l'edilizia sostenibile: la duttilità dei tamponamenti negli edifici soggetti a sisma (Doctoral dissertation, University of Trento).
[22] Wadi H., Amziane S., Toussaint E., & Taazount M. (2019). Lateral load-carrying capacity of hemp concrete as a natural infill material in timber frame walls. Engineering Structures, 180, 264-273.
[23] Amziane S., Arnaud L., & Challamel, N. (2013). Bio-aggregate-based building materials. Application for hemp concrete, Ediia, 1, 1-11.
[24] Dartois S., Mom S., Dumontet H., & Hamida A. B. (2017). An iterative micromechanical modelling to estimate the thermal and mechanical properties of polydisperse composites with platy particles: Application to anisotropic hemp and lime concretes. Construction and Building Materials, 152, 661-671.
[25] Gross C., & Walker P. (2014). Racking performance of timber studwork and hemp-lime walling. Construction and building materials, 66, 429-435.
[26] Chabannes M., Becquart F., Garcia-Diaz E., Abriak N. E., & Clerc L. (2017). Experimental investigation of the shear behaviour of hemp and rice husk-based concretes using triaxial compression. Construction and Building Materials, 143, 621-632.
[27] EN 594:2011 (2011), Timber Structures - Test Methods - Racking Strength and Stiffness of Timber Frame Wall Panels, Brussels, Belgium: CEN, European Committee for Standardization.
[28] EN 12512:2001 (2005) Timber structures – Test methods –cyclic testing of joints made with mechanical fasteners. Brussels, Belgium: CEN
[29] Casagrande D., Grossi P., Tomasi R. (2016) Shake table tests on a full-scale timber-frame building with gypsum fibre boards, European Journal of Wood and Wood Products, 74 (3), pp. 425-442.
[30] Grossi P., Sartori T., Tomasi R. (2015) Tests on timber frame walls under in-plane forces: Part 2, Proceedings of the Institution of Civil Engineers: Structures and Buildings, 168 (11), pp. 840-852.
[31] EN 1995-1-1:2004/A2 (2014) Eurocode 5: Design of timber structures. Part 1-1: General. Common rules and rules for buildings.

World Conference on Timber Engineering Oslo 2023

SHEAR PERFORMANCE OF STRUCTURAL PARTICLEBOARD-SHEATHED LIGHT-FRAME WALL

Chul-Ki Kim[1], Min Lee[2], Kugbo Shim[3]

ABSTRACT: The National Institute of Forest Science developed structural particleboard (PB), which is made of domestic wood, to substitute for imported OSB (Oriented Strand Board) used as a structural sheathing panel in light-frame construction. To investigate whether structural PB could be used as sheathing panel of light-frame wall or not, shear resistance of light-frame wall sheathed with structural PB compared with that of light-frame wall sheathed with OSB. Shear resistance was evaluated using a hysteresis curve by applying a quasi-static load. Shear strengths of wall sheathed with OSB and PB were 7.9 and 8.7 kN/m, respectively. It was confirmed that secant shear modulus for OSB and PB walls at 40% of the maximum load was 2.4 and 3.7 kN/mm, respectively. In addition, ductility was shown as 8.3 and 10.0 in OSB and PB walls, respectively. It was confirmed that shear resistance of PB wall was higher than that of OSB wall. From the results in this study, it is considered that structural PB manufactured using domestic wood can be used for sheathing material of light-frame construction, and it is expected that it can contribute to the national carbon stocks.

KEYWORDS: Light-frame wall, Shear resistance, OSB, Structural PB

1 INTRODUCTION

Korean wood building market is a little bit small compared with North America, Japan and etc., but constant. Since 2009, about 10,000 houses per year have been commenced steadily. From the statics about total floor area commencement, small houses having a total floor area of about 100 m^2 dominate in Korean wood building market. Because of economical and easy-to-build construction, light-frame construction is normally used for small houses.

Problem is that imported wood or wood-based products are usually used for light-frame construction in Korea. So, that need to develop substitute for the imported products occurred in view of the carbon-neutral and increasing price of materials. Because of climate crisis, increase of construction material made by domestic wood is required. By using HWP (Harvested Wood Products), it can take advantage of compliance with UNFCCC (United Nations Framework Convention on Climate Change) through carbon fixation and GHG (Green House Gas) substitution effect. On the other hand, the price change of imported dimension lumber and OSB (Oriented Strand Board) increased rapidly after COVID-19. Compared with 2020, the price of dimension lumber and OSB after COVID-19 are 2.9 and 2.7 times higher in Korea.

The National Institute of Forest Science has developed structural particleboard (PB) to substitute for imported OSB since 2020. Considering the scale of PB industry in Korea, it was concluded that it was advantageous to make a structural PB first. In a previous study, it was confirmed plant production possibility for structural PB. In this study, therefore, the shear resistance of structural PB was investigated whether structural PB could be used as a sheathing panel in light-frame construction.

2 MATERIALS AND METHOD

2.1 WOOD FRAME MATERIALS

For wood frames, dimension lumber of 2 by 6 was used, and the species was SPF. the grade of dimension lumber was 2 and better. The Structural PB was manufactured to be suitable for domestic industry conditions. A MFU (melamine-urea-formaldehyde) resin adhesive and isocyanate were used to provide water resistance. The ratio of the surface layer to the middle layer of the structural PB was 40:60, and the target density was set to 700 kg/m^3. The hot press conditions were a temperature of 200 ℃ and a time of 7.3 s/mm, and the amount of pressure was 50 kgf/cm^2. OSB imported from North America for rate sheathing was also used to compared to structural PB. The span rating of OSB was 24 per 16 inches.

[1] Chul-Ki Kim, Forest Products and Industry Dept., National Institute of Forest Science, ckkim0407@korea.kr
[2] Min Lee, Forest Products and Industry Dept., National Institute of Forest Science, mlee81@korea.kr
[3] Kugbo Shim, Dept. Agriculture, Life & Environment Science, Chungbuk National University, kbshim@chungbuk.ac.kr

https://doi.org/10.52202/069179-0457

Figure 1: *Surface (top) and side(bottom) image of structural PB*

2.2 ASSEMBLY WOOD FRAME

To assemble wood frame, nailing such as nail size, number of nails, nailing spacing, etc. was done in accordance with ASTM E72. Sheathing panel was attached to the dimension lumbers by using 8d common nail at 150 mm one center at the center of a panel and at 300 mm one center at the edge of a panel, respectively. In case of nailing distance from the edge of panel, different nailing distances for each panel were used for preventing occurrence of failure in the edges. For OSB, nailing distance from the edge of panel was 10 mm, on the other hand, the nailing distance was 15 mm for structural PB. Total size of shear wall was 2,440×2,440 mm. The center distance between studs was 610 mm. Figure 2 shows shear wall configuration.

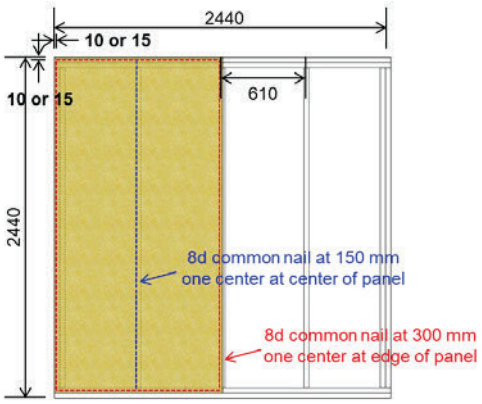

Figure 2: *Shear wall configuration (unit: mm)*

2.3 EVALUATION OF SHEAR RESISTANCE

Two hold-downs and anchor bolts were installed to fix test equipment (Dongyang, Korea). To prevent bulking during evaluation of shear resistance, four lateral supports were set up as shown in Figure 3. ISO 16670 protocol as quasi-static load in accordance with ASTM E2126 was applied to evaluate shear resistance. In the protocol, ultimate displacement was 83.3 mm, and it was determined from previous static shear wall test. The displacement pattern consists of phases, each containing three fully reversed cycles of equal amplitude, until 120 % of the ultimate displacement.

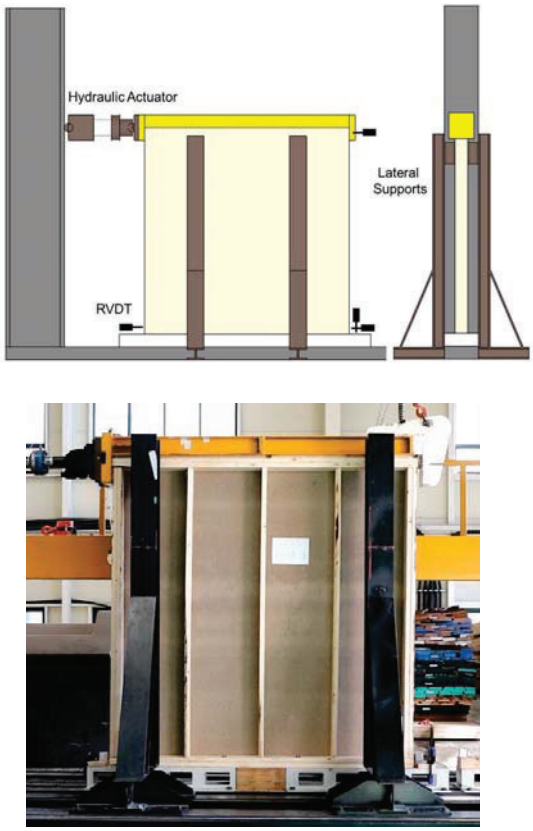

Figure 3: *Shear wall test setup (top) and picture (bottom)*

Envelop and EEEP (Equivalent Energy Elastic-Plastic) curve obtained hysteresis curve were used to calculated shear resistance such as shear strength, secant shear modulus at 0.4 of peak load and peak load, and ductility ratio. Each value for evaluating shear resistance was calculated as follows,

$$v_{peak} = \frac{P_{peak}}{L} \tag{1}$$

$$G' = \frac{P}{\Delta} \times \frac{H}{L} \tag{2}$$

$$D = \frac{\Delta_u}{\Delta_{yield}} \tag{3}$$

where, v_{peak} = shear strength (N/m), P_{peak} = maximum load resisted by the specimen in the given envelope (N), L = length of specimen (m), G' = shear modulus of the specimen obtained from test (N/mm), P = applied load, 0.4 of peak and peak load, measured at the top edge of the specimen (N), Δ = displacement of the top edge of the specimens as applied load based on test (mm), H = height of specimen (m), L = length of specimen (m), D =

https://doi.org/10.52202/069179-0457

ductility, Δ_u = ultimate displacement (mm), Δ_{yield} = yield displacement (mm). Detail calculation of shear resistance of wall can be confirmed in ASTM E2126.

3 RESULTS AND DISCUSSION

Figure 4 and 5 shows hysteresis, envelope, and EEEP curve for light frame shear wall sheathed with OSB and structural PB, respectively. As it was considered that the difference of positive and negative envelop curve was small for both shear wall sheathed with OSB and structural PB, average envelop curve was used to calculate shear resistance. The maximum difference of peak load was 8% for structural PB shear wall in the group of shear wall test.

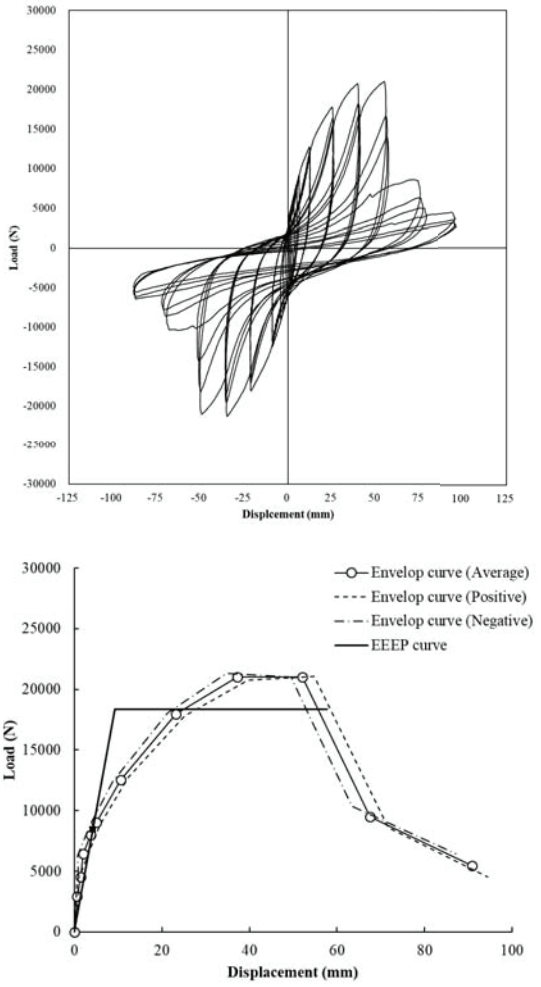

Figure 4: *Results of shear wall test of OSB sheathed light-frame wall*

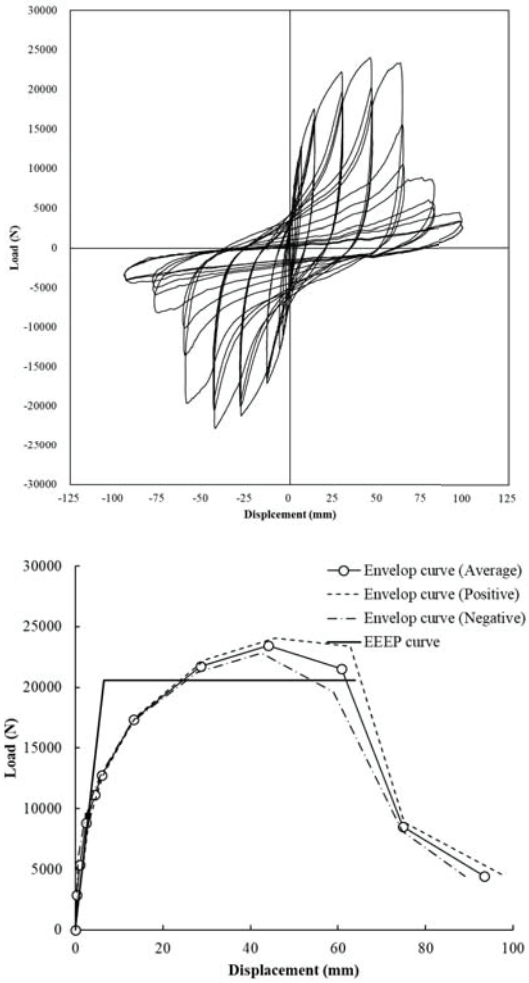

Figure 5: *Results of shear wall test of structural PB sheathed light-frame wall*

Table 1 presents the average shear resistance of wall according to the type of panel. Shear strength and secant shear modulus at 0.4 of a peak load for OSB wall were 7.9 kN/m and 2.3 kN/mm in the first order of cycles, respectively. The order of cycles means a sequence among three fully reversed cycles of equal amplitude in ISO 16670 protocol. As the order of cycles increased, shear strength decreased in case of OSB wall. But the result of ductility was inconsistent. As the order of cycles increased, ductility of OSB wall increased. The shear modulus at peak load was nearly constant regardless of the order of cycles. The shear strength and secant modulus at 0.4 of a peak load for structural PB wall were 9.0 kN/m and 3.0 kN/mm in the first order of cycles. Results of shear strength, shear modulus, and ductility according to the order of cycles is consistent in the case of that OSB wall.

https://doi.org/10.52202/069179-0457

Table 1: *Average shear resistance of wall*

Type		v_{peak} (kN/m)	G (kN/mm)		D
			$0.4P_{peak}$	P_{peak}	
OSB	Cycle 1	7.9	2.3	0.5	8.3
	Cycle 2	7.1	2.7	0.5	9.9
	Cycle 3	6.7	2.9	0.4	10.6
PB	Cycle 1	8.7	3.7	0.5	10.0
	Cycle 2	8.1	3.4	0.6	10.8
	Cycle 3	7.3	3.7	0.6	11.9

The difference of shear strength between the first order cycles and the third order of cycles was 1.28 kN/m for OSB shear wall, and 1.43 kN/m for structural PB shear wall. From the difference, it was concluded that structural PB shear wall had better toughness property than OSB shear wall. As Toothman (2003) reported toughness is positive relation with energy absorb, it was considered that structural PB shear wall had advantage considering the ground motions produced by earthquakes. It was confirmed that shear resistance of structural PB wall is better than that of OSB wall for all order of cycles. It meant that structural PB wall has higher load capacity with less displacement and higher energy absorption capability.

Figure 6, 7, and 8 show failure mode during shear wall test. Regardless of the type of panel, the same failure modes were detected. One was nail shear failure between wood frame and panel, the other was bending of wood frame members within an elastic region.

Figure 6: *Failure mode (Nail shear failure) during OSB shear wall test*

Figure 7: *Failure mode (Nail shear failure) during PB shear wall test*

Figure 8: *Failure mode (bending of stud in wall) during PB shear wall test*

In this study, the walls anchored fully by holddown were test. Because of that, uplift forces are transferred from the sheathing into the studs and then directly into the foundation (Seaders *et al.*, 2008). Therefore, it was concluded that the location of nail shear failure was sheathing-to-stud at edge of wall. Nail shear failure in structural PB shear wall occurred frequently compared with OSB shear wall. Moreover, Nails in the structural PB did not pull out as easily. So, it enabled the friction to continue to dissipate more energy in case of structural PB shear wall.

Because structural PB is more brittle than OSB, nailing distance from the edge of panel in structural PB is 5 mm more than that in OSB. The expected nail shear failure was achieved by increasing the nailing distance from the edge of panel in PB wall. From the results of failure modes, the theory for estimating shear resistance of OSB wall might be used to predict shear performance of structural PB wall.

4 CONCLUSION

Compared with OSB wall, shear resistance of structural PB wall was higher. In the first order of cycle, shear strength, shear modulus and ductility of structural PB wall were 1.1, 1.3 and 1.1 times higher than that of OSB

https://doi.org/10.52202/069179-0457

wall. It is expected that structural PB made by domestic wood can contribute to achieving carbon neutral in the building sector.

REFERENCE

[1] Bagheri, M. M., Doudak, G. Structural characteristics of light-frame wood shear walls with various construction detailing. Engineering Structures, 205, 110093, 2020.

[2] De Araujo, V. A., Cortez-Barbosa, J., Gava, M., Garcia, J. N., de Souza, A. J. D., Savi, A. F., ... Lahr, F. A. R. Classification of wooden housing building systems. BioResources, 11(3), 7889-7901, 2016.

[3] Di Gangi, G., Demartino, C., Quaranta, G., Monti, G. Dissipation in sheathing-to-framing connections of light-frame timber shear walls under seismic loads. Engineering Structures, 208, 110246, 2020.

[4] Gattesco, N., Boem, I. Stress distribution among sheathing-to-frame nails of timber shear walls related to different base connections: Experimental tests and numerical modelling. Construction and Building Materials, 122, 149-162, 2016.

[5] Germano, F., Metelli, G., Giuriani, E. Experimental results on the role of sheathing-to-frame and base connections of a European timber framed shear wall. Construction and Building Materials, 80, 315-328, 2015.

[6] Kirkham, W. J., Gupta, R., Miller, T. H. State of the art: Seismic behavior of wood-frame residential structures. Journal of Structural Engineering, 140(4), 04013097, 2014.

[7] Martin, K. G., Gupta, R., Prevatt, D. O., Datin, P. L., van de Lindt, J. W. Modeling system effects and structural load paths in a wood-framed structure. Journal of architectural engineering, 17(4), 134-143, 2011.

[8] Poletti, E. Characterization of the seismic behaviour of traditional timber frame walls. PhD Thesis. Universidade do Minho (Portugal), 2013.

[9] Seaders, P., Gupta, R., Miller, T. H. Monotonic and cyclic load testing of partially and fully anchored wood-frame shear walls. Wood and Fiber Science, 145-156, 2009.

[10] Sinha, A., Gupta, R. Strain distribution in OSB and GWB in wood-frame shear walls. Journal of Structural Engineering, 135(6), 666-675, 2009.

[11] Toothman, A. J. Monotonic and cyclic performance of light-frame shear walls with various sheathing materials. PhD Thesis. Virginia Tech, 2003.

[12] White, K. B., Miller, T. H., Gupta, R. Seismic performance testing of partially and fully anchored wood-frame shear walls. Wood and fiber science, 396-413, 2009.

https://doi.org/10.52202/069179-0457

World Conference on Timber Engineering Oslo 2023

Deployable Wood Structures for Disaster Relief and Military Use

Jayson Leonard[1], Weichiang Pang[2], Michael Stoner[3], Dustin Albright [4]

ABSTRACT: Rapidly deployable structures may be used to speed up the recovery after natural disasters and to provide shelters for military personnel in hostile zones. The recent unforeseen disruptions caused by the COVID pandemic highlighted the needs for temporary testing centers or backyard pop-up offices. This paper investigates the development of deployable wood structures via four key factors, namely (1) deployability, (2) transportability, (3) functionality, and (4) cost. Currently, the military does not have an optimum design that excels in all the previously mentioned criteria. This study aims to design a rapidly deployable structure for emergency response such as disaster relief with the potential for military applications. This research begins by covering existing deployable shelters used for disaster relief and military applications. Next, it presents several alternative designs using different materials and different functionality. Then, it addresses how these new designs compare to the existing shelters in each category. Finally, it discusses tests performed on the folding mechanism being used throughout the design of a deployable wood structure. As a result of the study, new designs are shown to be competitive with the existing ones. The results of an experimental study of how hinges perform as structural elements will be discussed.

KEYWORDS: Cross-Laminated Timber, Deployable Structure, Disaster Relief, Military Shelters, Hinge

1 INTRODUCTION

As a society, we have all come to realize it is not always possible to know when disaster will strike. Disaster can take the shape of many forms including but not limited to, natural disasters, man-made disasters, war, and more recently, pandemics. When these events happen there is potential for people to be displaced from their homes and resources to be overwhelmed. This immediately calls to action the need for new structures, such as temporarily shelters and medical facilities. To build one of these from the ground up can be time-consuming and demanding for labor and materials. Therefore, the use of prefabricated or deployable structures could be put into place instead. The two primary uses for these structures investigated in this study are post-disaster and military applications.

The U.S. military currently has both expandable and non-expandable rigid wall tactical shelters. For easier reference, National Stock Number, which is an identifying number assigned to materials and items, is used by the U.S. military to identify a shelter. One example of an expandable unit is shelter designated NSN 5411-01-136-9838, an expandable unit with interior dimensions (expanded) of 18’ 4” L x 21’ 6” W x 7’ 1” H (Figure 1). The nonexpanded exterior dimensions are 19’ 11” L x 8’ W x 8’ H. This unit has a weight of 6900lbs and an assembly time of only 30 minutes with four soldiers. These units are designed to have dimensions consistent with a standard ISO shipping container of 20’ L x 8’ W x8’ H. This allows for easy and consistent transportation methods. These units are also made from steel which gives the units a rugged and durable finish. Along with traditional transportation methods, the military may also drop these units from aircraft with parachutes.

Figure 1: *An Example of Expandable Rigid Wall Shelter (NSN 5411-01-136-9838)*

The U.S. military also utilizes soft wall shelters as a means of less permanent shelter. The soft wall shelters are typically a stretched fabric supported by either a frame or pressurized air. An example of a frame-supported soft wall shelter is NSN 5419-01-465-3025EJ. The dimensions for this unit assembled are 20’ x 32.5’. The weight of this unit is 1250 lbs., and the erection time is less than an hour with four soldiers. An example of an air-supported soft wall shelter is the Airbeam tent NSN 8340-01-558-8707 (Figure 2). This structure is supported by a series of Airbeams that are inflated onsite. The weight of this structure is around 1000 lbs. With the supplied compressor, the erection time is only 15 minutes with four

[1] Jayson Leonard, Graduate Research Assistant, Clemson University, USA, jbleona@g.clemson.edu
[2] Weichiang Pang, Professor, Clemson University, USA, wpang@clemson.edu
[3] Michael Stoner, Lecturer, Clemson University, USA, mwstone@clemson.edu
[4] Dustin Albright, Associate Professor, Clemson University, USA, dalbrig@clemson.edu

https://doi.org/10.52202/069179-0458

soldiers. The deployment of this structure requires electricity.

Figure 2: *An Example of Air Supported Soft Wall Shelter (NSN 8340-01-558-8707)*

2 DESIGN OF STRUCTURES

The goal of this research is to design prefabricated and rapidly deployable structures using wood, a sustainable and renewable material. There will be four distinct shelter designs that fall under two separate categories. The two categories are construction material and deployment strategy. The material choices are light-frame wood construction or cross-laminated timber (CLT). The deployment strategies include non-foldable (static) and foldable (dynamic).

The need for rapidly deployable structures can be seen in many different environments and cases. This played a large role in the design of the structures and was one of the first areas of concentration. On the civilian side of this research, the expected mode of shipment is by land through the use of semi-trucks. In order to make shipment of these units as easy and seamless as possible, ISO standard shipping sizes played a large role in the design footprint (ISO, 2020). A twenty-foot-long unit became the basis of design due to standardization and practicality. The most typical 20 ft long shipping container is 8 ft wide x 8.5 ft tall. Another standard-size shipping container is known as the “high cube” container. These containers are 20 ft long x 8 ft wide x 9.5 ft tall. By moving up to the high cube size, the structures become more liveable and comfortable with more headroom. Table 1 shows the key dimensions of the static and dynamic structure types. The static unit does not fold; therefore, the folded dimensions are not applicable for this unit type.

Table 1: Dimensions of the Static and Dynamic Structures

Unit Type	Deployed			Folded		
	Length	Width	Height	Length	Width	Height
Dynamic	20'	19' 5"	8' 3"	20'	6' 8"	8' 3"
Static	20'	8'	9' 6"	NA	NA	NA

2.1 Static Unit

The static unit follows a shipping container-like design that conforms to ISO high cube dimensions. The unit is 20’ long x 9.5’ tall x 8’ wide. These units can be fitted out to take a role such as a housing or medical unit. Figure 1 shows a static unit being used as a temporary housing structure. With around 160 sq. ft. of living space, the unit is not abundantly spacious, however, the space that is provided is highly functional.

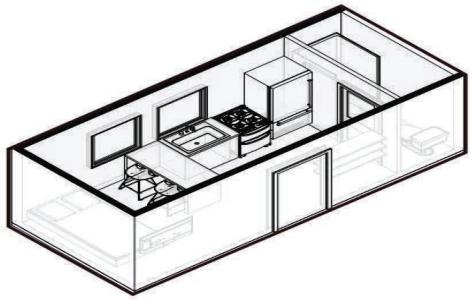

Figure 3: *A Floorplan for a Static Unit.*

2.2 Dynamic Unit

The dynamic unit is 20’ long x 8’-8” tall x 7’-3” wide when folded. When the unit is unfolded, it is 20’ long x 8’-8” tall x 21’-8” wide. Figure 2 shows one of many possible finished floorplans for a dynamic unit. The structure is supported only by the exterior walls allowing for the interior to be fully customized by the end-user. The top series of images shows the folding process. The bottom left image shows an exploded view of the entire unit, while the bottom right image shows the plan view of the floorplan.

By having both a static and a dynamic unit, users can choose based on their needs. For example, the end-user may prefer to have a static unit because it can be completely finished before shipment. Since the unit does not fold, all furnishings and finishes can be done before the end-user receives the unit. Also, there is no additional work once the unit is set on a foundation because the unit does not need to be unfolded. A dynamic unit may be chosen because they provide a larger liveable space that requires less room for storage and transportation.

When designing the dynamic unit, one of the first parts that needed to be figured out was how these units would expand and contract. There are many different strategies and designs that have been used in the past to achieve this task. For this research, continuous hinges were used as the folding mechanism. In addition, the hinges are designed to carry structural loads, namely, shear and uplift forces. By choosing hinges, the method of deployment would be through foldability of panels about the axis the hinge lies. This deployment method had many impacts on the design of the structure. One of which is the dimensions of each panel. Getting the structure within the ISO shipping standard sizes while also maximizing useable space took careful planning. Figure 3 shows the foldable unit in its final deployed state and locations of hinges needed for folding mechanism and for shear strength.

https://doi.org/10.52202/069179-0458

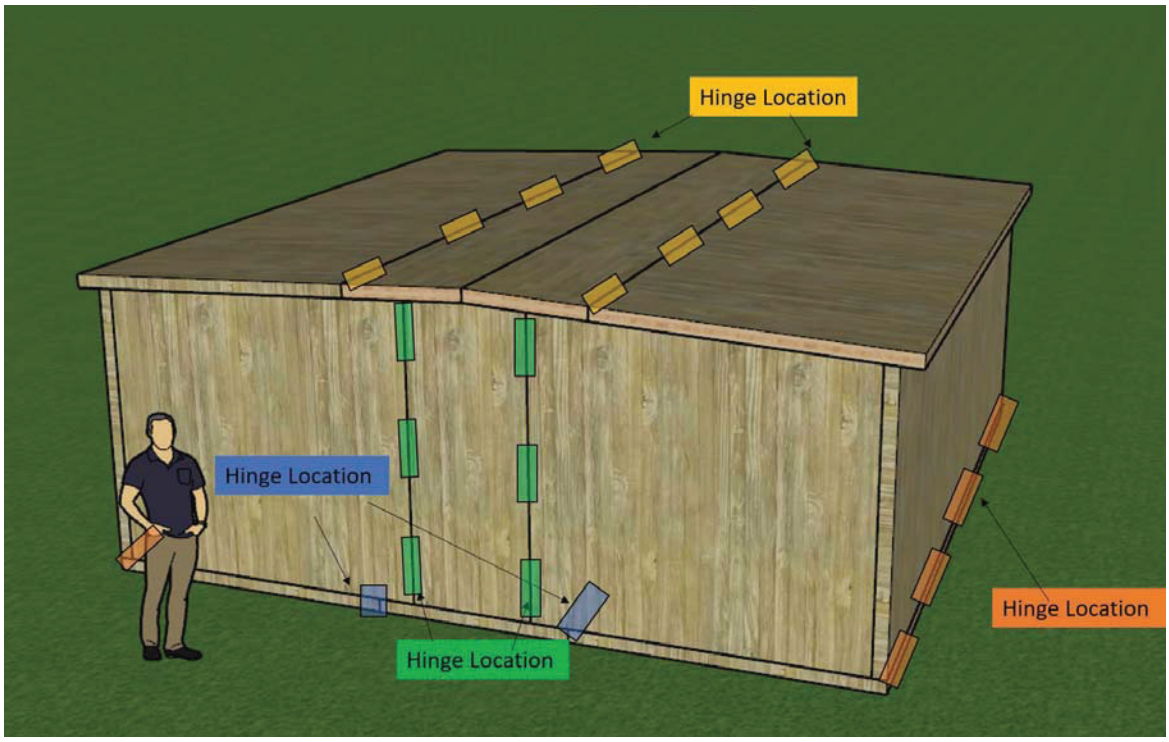

Figure 3: *Foldable Unit in Final Deployed State and Locations of Hinges Required for Foldability and Shear*

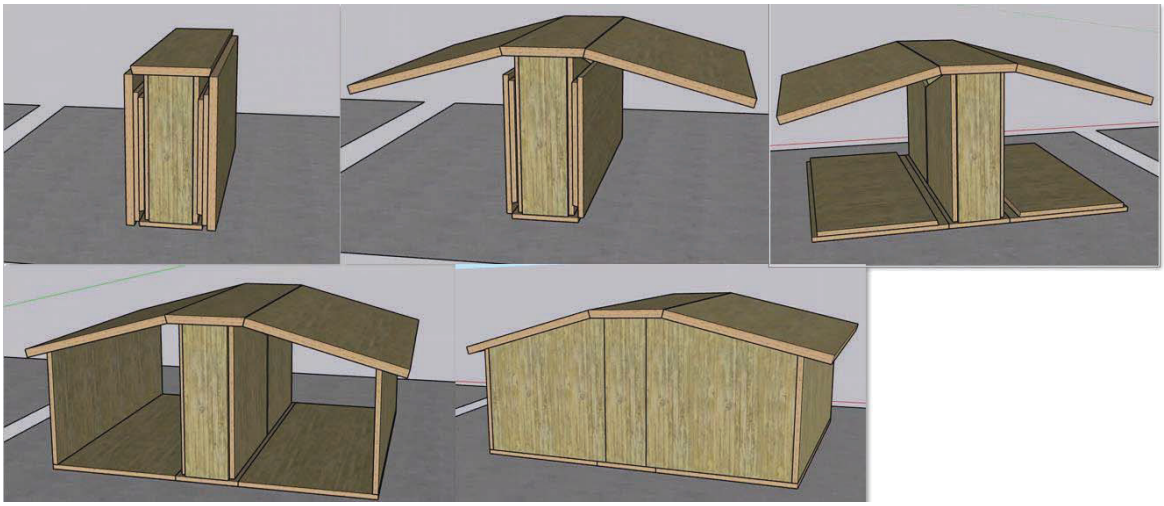

Figure 4: *Process of unfolding the dynamic unit.*

2.3 Light-Frame and Cross-Laminated Timber

Two materials are considered for both the static and dynamic units, namely light-frame wood and cross-laminated timber (CLT) panels. Light-Frame units are designed with traditional 2x dimension lumber or sawn lumber. The CLT units are designed using 3- and 5-ply Southern Yellow Pine CLT panels.

The static and dynamic units, each has its advantages and disadvantages. The light-frame units will be lighter than the CLT units allowing them to be transported and deployed more easily. Also, the light-frame units will have wall cavity space than can be filled with insulation which can provide a more comfortable and energy-efficient shelter. Light-frame units are also easier to hide electrical and plumbing within the walls. Also, since light-frame uses less wood than CLT, the final costs of these units are expected to be less than their CLT counterparts. The CLT models are much stronger and can be used in more extreme conditions. For example, CLT units should be able to provide greater resistance to threats such as blasts and ballistics.

https://doi.org/10.52202/069179-0458

3 EXPEIRIMENTAL TESTING

3.1 Hinge Testing

This research also contains load testing on hinges that will be used within the dynamic structures. The hinges' main role is to provide a means of rotation for individual panel elements. Typically, the hinges would be ignored as structural elements, however, there is potential to expand the use of the hinges to act as shear and hold-down connections for the wall panels. The hinges would also need to be able to take the moment and shear applied by the wall members during deployment. Therefore, by gathering data on the strength of the hinges, one will be able to identify the capacity of the hinge connections.

A series of tests were performed on hinges to determine the structural load carrying capacities. There were two hinge types that were used for the testing in this research, continuous style hinges, also known as piano hinges, and residential butt hinges. Table 2 shows the hinge types and properties. For simplicity of naming and referencing, each hinge type may either be referred to as hinge A or hinge B throughout this research. Figure 5 shows some key dimensions of each hinge type.

Table 2: *Hinge Properties.*

	Hinge	
Property	A	B
Hinge Type	Continuous	Butt
Leaf Thickness	0.12"	0.0855"
Pin Diameter	3/8"	15/64"
Length	12"	4"
Width	5"	4"
Screw Diameter	0.25"	0.137"
Screw Length	3.5"	1"

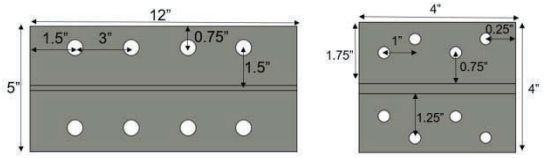

Figure 5: *Key Dimensions of the continuous hinge (left) and the butt hinge (right).*

Each hinge type was tested in two directions, loading parallel and perpendicular to the pin. Parallel to the pin tests will be referred to as shear tests, and perpendicular to the pin test will be called tension tests. Figure 6 shows a conceptual drawing of the directions each hinge was tested in. Multi-directional strength properties are important because the deployment stage will induce forces on the hinges. By completing these tests, the hinges could be incorporated into the structure's strength rather than ignored when in the deployed state. Along with the load tests performed on the hinges, there was also a material test performed on the leaf of each hinge. The material test provided key materialistic properties such as ultimate stress, yield stress, and modulus of elasticity of the steel used in the hinges. All these properties are important metrics when describing how a structural element performs. A summary of the load tests performed on the hinges can be found in Table 3.

Table 3: *Summary of Tests Performed on Hinges*

Test No.	Loading	Hinge Type
1A	Shear	A
1B	Shear	B
2A	Tension	A
2B	Tension	B

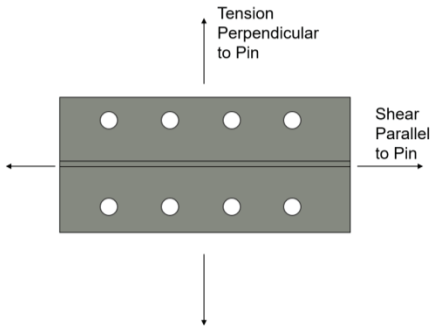

Figure 6: *Testing Directions on Hinges.*

3.2 Shear (Parallel to Pin) Test

Shear tests were performed on the continuous and butt hinge and are referred to as Test 1A and 1B, respectively. The shear tests were done to gather data on how these hinges would perform when loaded in the direction parallel to the pin. One way this type of loading could be observed in a structure is when shear is transferred from wall to floor panels. Both tests, 1A and 1B, were performed with cyclic loading. Cyclic loading is when a load is applied in one direction, then removed and applied in the opposite direction. The loading setup in both shear tests was set to follow CUREE standard loading protocol. Cyclic loading is often chosen over monotonic loading, single-direction loading without load removal, because it may represent loading caused by wind gusts or earthquake accelerations better. Figure 7 shows a conceptual drawing of the test setup for Test 1A (Shear of Continuous Hinge). Figure 8 shows the picture of Test 1A. 3-ply southern yellow pine CLT panels were used as the main member throughout these tests.

The string potentiometers were used to measure localized displacement, and the actuator was used to measure forces and displacements of the entire system. A displacement-controlled reversed cyclic loading protocol was utilized to perform the shear test. Figure 9 shows the force vs. actuator displacement of Test 1A. The figure also shows the expected design strength as well as measured stiffness. For the continuous hinge, Simpson Strong-Tie SDS screws were used to fasten the hinges to the CLT panels. The manufacturer provided the design ASD values, which are displayed in blue. The ASD value was then multiplied by the format conversion factor (K_F of NDS) to show a

https://doi.org/10.52202/069179-0458

non-factored LRFD value (green line). A strength reduction factor was not used because the goal was to try to estimate the test peak value rather than a design value. Figure 10 shows the failure mechanism of Test 1A.

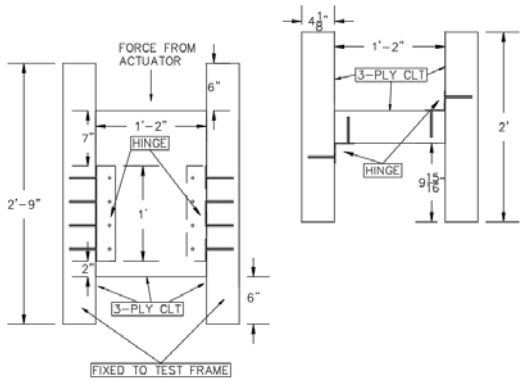

Figure 7: *Setup for Shear Test of Hinge Connection.*

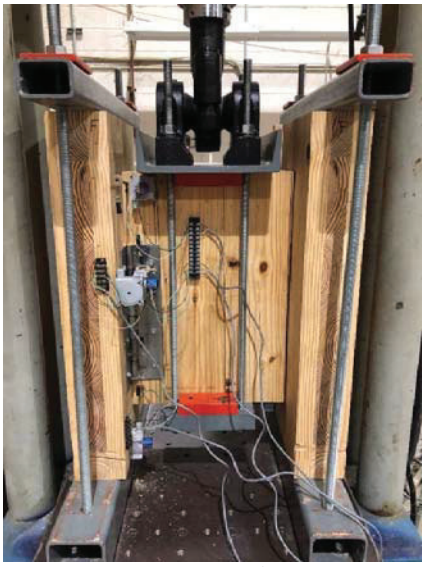

Figure 8: *Test 1A Setup and Instrumentation.*

The ultimate strength, yield strength, and initial stiffness of each hinge connection were determined from the test (Table 3). The ultimate strength was determined by identifying the peak force for the push and pull cycles. The yield strength was determined by offsetting the initial stiffness by 5% of the screw diameter (ASTM, 2018). The initial stiffness was determined by taking the slope of the initial part of the curve.

Table 3: *Summary Results of Shear Test 1A*

	Hinge A		
	Push	Pull	Average
Ultimate Strength (kip)	9.06	6.72	7.89
Yield Strength (kip)	5.08	3.12	4.1
Initial Stiffness (kip/in)	35.62	35.68	35.57
Initial Stiffness (kip/in)	18.1	21.9	20.0

Figure 10: *Failure in Test 1A*

3.3 Tension (Perpendicular to Pin) Test

Tension tests were performed on the continuous and butt hinge and are referred to as Test 2A and 2B, respectively. The tension tests were performed to gather data on how these hinges would perform when loaded in the direction perpendicular to the pin. Loading conditions that could cause these forces on the structure could be through deployment, raising panels into place, and forces that act normal to the panels, such as suction caused by wind. Both tests, 2A and 2B, were performed with monotonic loading, which is when a load is applied in one direction at a constant rate until failure. Monotonic loading was chosen for this direction because compression toward the pin would not provide useful or practical data. Figure 11 shows the test setup for Test 2A.

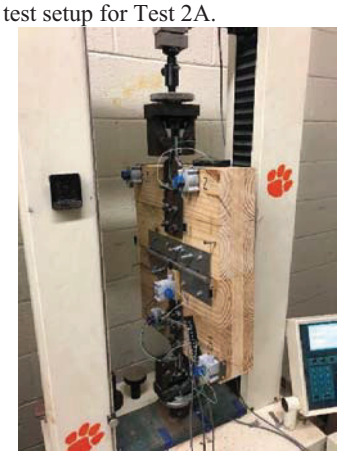

Figure 11: *Test 2A (Tension of Continuous Hinge)*

Table 4: *Characteristic Properties Concluded from Test 2A.*

Ultimate Strength (kip)	8.4
Yield Strength (kip)	3.6
Initial Stiffness (kip/in)	42.2

https://doi.org/10.52202/069179-0458

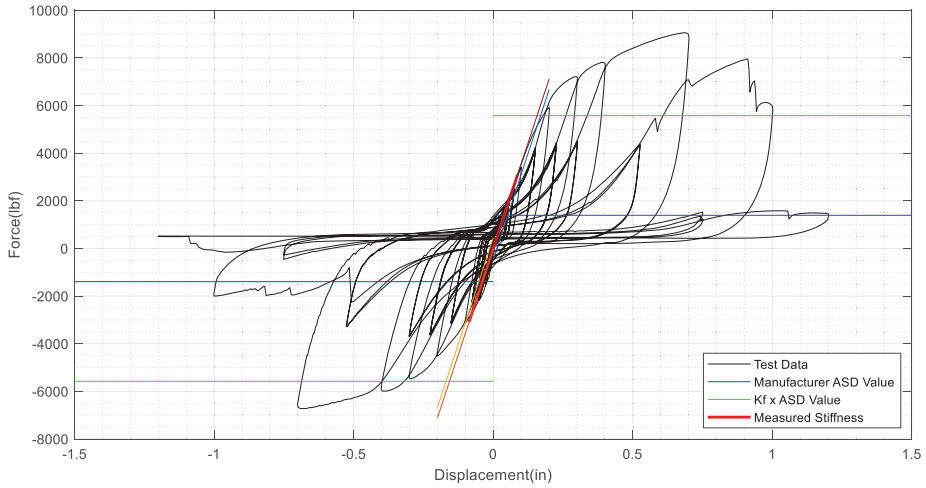

Figure 9: *Force versus Displacement of Continuous Hinge (Test 1A).*

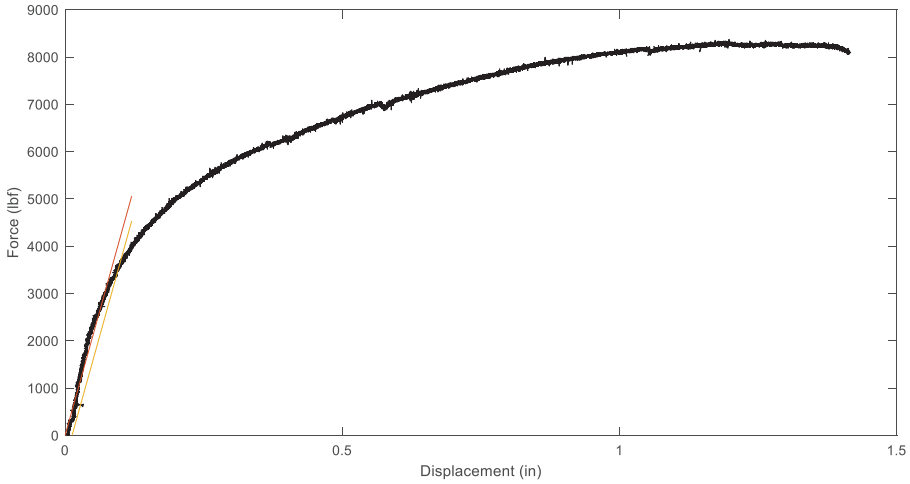

Figure 12: *Force versus Averaged Displacement of SP1 and SP5 for Test 2A*

4 PERFORMANCE MEASURES

Both the static and dynamic units were designed for gravity loads (live and dead loads), wind and seismic loadings. The results from the hinge tests were used to design the dynamic units. Four designs were produced from this study: (1) Static Light-frame Unit, (2) Static CLT Unit, (3), Dynamic Light-frame Unit, and (4) Dynamic CLT Unit. Four metrics were used to measure the performance of each of the four designs. These metrics are (1) Deployability, (2) Transportability, (3) Cost, and (4) Building Envelope Resistance. By providing each structure design with a score in each category, the end user can quickly determine which structure will best suit their needs. Some of these categories could be subjective; however, the goal of the scores is to relate the structures relative to each other. Scoring in each category ranges from 1 to 4. A score of 1 means the structure did not perform relatively well in that category. A score of 2 or 3 means that the structure performed about on average in that category. A score of 4 means that the structure performed the best.

4.1 Deployability

Deployability is a measure of how easy it is for the structure to be deployed. Factors that affect deployability include weight, time to assemble/erect, and required tools. Deployability is an important metric as it relates to ease of use. The concept of disaster relief is to be able to provide assistance in a quick and easy manner. If a structure requires specialty tools or labor to be usable, it would not be considered especially deployable. Another reason deployability is important is that in remote areas, there may not be access to large machinery to lift the panels to unfold the unit. As a full-scale model was not in the scope of this research, assembly time could not be measured. However, estimation could be made from similar-sized structures used in the military. Also, an exact time deployment is not as important as the general time between each structure as this scoring system is only meant to compare relatively between each four structure designs. A score of 1 in deployability would be because a structure is lightweight, requires very little if any work upon arrival, and does not require special tools or machines.

https://doi.org/10.52202/069179-0458

4.2 Transportability

The transportability category is a measure of how easy it is to transport these structures. Another consideration is how many structures can be shipped on one truck. Transportability is a function of the weight and size of the unit. All these units were designed to be within ISO standard shipping sizes. The maximum weight of a step deck trailer is 45 kips, and the maximum dimensions are about 50 ft long x 8.5 ft wide x 10.5 ft tall. This limits both the static and dynamic units to two units per shipment. However, when looking at shipment in terms of square feet per shipment, the dynamic units has clear advantage. The light-frame dynamic unit scored the best because it is relatively lightweight and can deliver more usable square footage than its static unit counterpart. The CLT dynamic unit scored the worst because it weighs the most.

4.3 Cost

Cost is important because it shows the feasibility of implementing these structures on a wide scale use. As with any product, the price can fluctuate depending on the materials used in production. Also, the price can be reduced when built in large quantities. However, for this research price of a single unit will be estimated at the current prices. The current price for 3-ply southern yellow pine CLT is around $39 to $44 per sq. ft. (J. Gouge, personal communication, January 19, 2022). For the CLT structures, a cost of $40 per sq. ft. was used as this is within the expected price range. These prices do not include the assembly of the units.

4.4 Building Envelope Resistance

Building envelope resistance is an important category for consideration in both civilian and military sectors. Some factors that could be used in this category include debris impact resistance, insect resistance, and fire resistance. Some factors that may play a larger role in military use are ballistic and blast resistance. The latter two factors will be used to create a score for each structure in this category.

The ballistic performance of the CLT panels was estimated using the THOR CLT model introduced earlier and shown in equation 2.5.2-1. The calculation was performed for a half-inch diameter steel ball projectile. The estimated striking velocity that can be resisted by a 3-ply southern yellow pine CLT panel is 1650 fps. Modern firearms do not use spherical steel balls as projectiles, and therefore these results are difficult to compare to real-world ammunition types. However, comparing the striking velocity to the velocities shown in Figure 2.8, it can be estimated that the CLT structures may show ballistic performance around the III-A NIJ rating. This roughly means that the CLT structures could be able to all common handgun bullets. Level III-A exceeds or meets most law enforcement agencies' requirements in the U.S. (T. Muszynski, personal communication, June 27, 2022). The light-frame walls are built up from ½ in. dry wall and 7/16 in. OSB sheathing with studs spaced at 24 in. O.C. The light-frame walls will provide practically zero ballistic resistance. These walls will not even meet the lowest NIJ rating of level I.

4.5 Performance Measure Summary

Each structure was assigned scores in the categories of deployability, transportability, cost, and building envelope resistance. A radar chart shown in Figure 13 was made to show each performance category for all structure types together. This chart makes it easy to see which units perform best in each category and helps the end user determine which unit is right for their purposes. If a structure type has a higher score, it means that it performs comparatively well in that category.

5 CONCLUDING REMARKS

This research has contained the design of four types of rapidly deployable structures using different materials and deployment strategies. These units could be used in many different environments for multiple purposes; therefore, variety is important. There have also been tests performed on multiple hinges that will be used to gather important parameters. Moving forward experimental testing on the hinges will be completed and a better understanding of their behavior will be discussed.

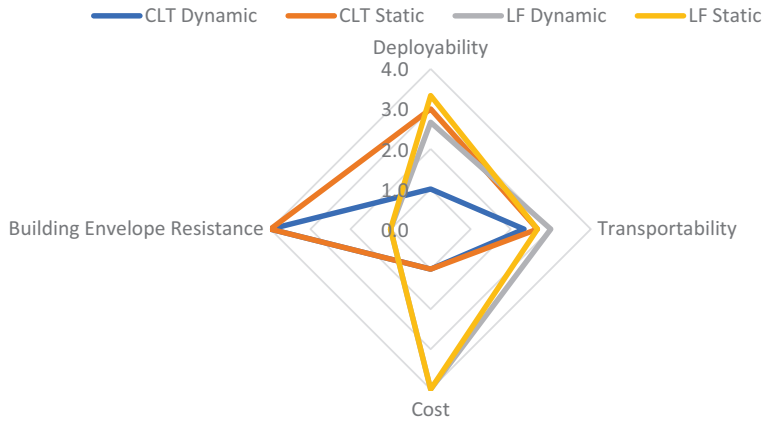

Figure 13: *Radar Chart Showing the Results of the Performance Measures*

https://doi.org/10.52202/069179-0458

ACKNOWLEDGEMENT

The materials presented in this paper is supported in part by the Clemson University Glenn Department of Civil Engineering and the U.S. Department of Agriculture (USDA) Forest Service.

REFERENCES

[1] D'Arenzo, G., Casagrande, D., Reynolds, T., & Fossetti, M. (2019). In-plane elastic flexibility of cross laminated timber floor diaphragms. Construction and Building Materials, 209, 709-724. doi: 10.1016/j.conbuildmat.2019.03.060.

[2] Structural Engineering Institute: Minimum design loads for buildings and other structures. ASCE 7, Reston, VA. 2022

[3] American Wood Council: Special Design Provisions for Wind and Seismic, 2021.

[4] American Wood Council: National Design Specification for Wood construction. 2018

[5] Spickler, K., Closen, M., Line, P., and Pohll, M. (2015),. Cross Laminated Timber Horizontal Diaphragm Design Example. Structurlam-CrossLam.

[6] Lawson, J., Breneman, S., & Lo Ricco, M. (2023): Wood Diaphragm Deflections. Part I: Generalizing Standard Equations Using Mechanics-Based Derivations for Panel Construction. ASCE Journal of Architectural Engineering

[7] Krawinkler, H., Parisi, F., Ibarra, L., Ayoub, A., & Medina, R. (2001): Development of a Testing Protocol for Woodframe Structures. Department of Civil and Environmental Engineering, Stanford University.

[8] Bhardwaj, B., Pang, W., & Stoner, M. (under review). Experimental Characterization of Cantilever Cross-Laminated Timber Diaphragms under In-plane Shear Load. Journal of Structural Engineering.

https://doi.org/10.52202/069179-0458

World Conference on Timber Engineering Oslo 2023

GLUED TIMBER TRUSSES

Tuomo Poutanen[1], Markku Karjalainen[2], Valtteri Paananen[3], Jouko Tanskanen[4]

ABSTRACT: Current timber trusses are mainly made using steel fasteners, nail plates, or dowels with slotted plates. Glued timber trusses are applied commercially by two companies: German PERI produces trussed joists for concrete casting and Canadian Barret Structural makes trussed joists for residential floors. These trusses are based on finger joints made using a cursor. Recently, a Finnish company Teeri-Kolmio Oy started manufacturing glued trusses for residential floors with the joint processed using a saw blade. The such joint enables deep chord routings up to through the chord, long fingers, large web-chord glue areas, minimal timber splitting, and high resistance and reliability. There are further special characteristics. Top chord support is possible without hangers. The truss can be manufactured as a long billet, stored at lumberyards, and cut for actual needs. The truss can be manufactured without open routings and water pockets. The truss is strong and reliable and can be applied for the roofs of commercial buildings up to about 30 m spans. Our study shows that the trussed roof is more cost-effective than the glulam roof which opens a promising new business possibility.

KEYWORDS: Glue, Truss, Joist, Billet, Trimming, Visual joint

1 INTRODUCTION

The glue is the cheapest, stiffest, and often the strongest timber fastener. The truss is the most effective structural model in horizontal structures with the least material and the best flexibility. Timber is a renewable structural material.

Prefabrication and automation are demands for effective construction. It means that the horizontal structures are made of joists with uniform height. The glued timber truss is the most cost-effective and ecological horizontal joist with uniform height.

Timber trusses are mainly applied for floors and roofs. The floor trusses are always parallel chord trusses with uniform height. Roof trusses are normally pitched. The authors believe that the parallel chord trusses gain market in the roofs, too, as such trusses are well suited to off-site construction and prefabrication and further suit well for attic roofs.

Currently, timber trusses are not applied to roofs. In this article, calculations are presented which show that glued timber trusses have potential in roofs, especially in long-span commercial roofs, with spans normally 15-25 m but up to about 30 m. Our study shows that the trussed roof is more cost-effective than the glulam roof which opens a promising new business possibility.

Consequently, the glued timber truss has potential.

This article focuses on timber trusses with uniform height made of timber and glue only. Timber trusses with steel connectors are touched as a comparison only [1-5].

1.1 LIGHT TIMBER TRUSSES

Light trusses are made of small timber members like sawn wood. Current light timber trusses are mainly made of nail plates. The global market exceeds €10 bill. The glued trusses play a minor role, apparently less than €0.2 bill.

The glued joint has some advantages over the nail plate joint:

- In a glued joint the web chord load path has only one shear joint, but two shear joints are needed in the nail plate joint. Thus, the glued joint is more cost-effective in this regard.
- The glued joint has a lower slip due to a more rigid joint and a lower number of shear joints.
- The glue cost per share area is only about 5 % of the nail plate but the effective shear resistance of the glued joint is about 50 % less. Further, excess timber is needed in the glued joint due to web fingers. The overall glued joint cost is less than the nail plate joint cost.
- In a nail plate joint the web width must be the same as the chord width, which normally is not optimum regarding the web resistance. Especially, in the parallel chord nail plate trusses, the web width, about 100 mm, is defined due to the joint resulting in about a twice bigger web volume and cost than needed for the web resistance. The glued truss lacks this deficiency.
- Glued trusses are mainly used concealed. The glued joint does not require the precise timber cross-section and the planing is not needed,

[1] Tuomo Poutanen, Tampere University, Finland, tuomo.poutanen@tuni.fi
[2] Markku Karjalainen, Tampere University, Finland, markku.karjalainen@tuni.fi
[3] Valtteri Paananen, City of Ylöjärvi, Finland, valtteri.paananen@ylojarvi.fi
[4] Jouko Tanskanen, Kerimäki, Finland, jouko.tanskanen@ideastructura.com

https://doi.org/10.52202/069179-0459

while needed in the nail plate trusses. For this reason, the glued timber truss has a 5…10 % timber cost advantage.
- The fire resistance of the nail plate truss is defined by the negligible fire resistance of the nail plate. The fire resistance of the glued truss is defined by the wood charring.
- The nail plate truss has poor resistance in the open air. The glued truss can be used in the open air, the resistance is normally defined by the wood, not the joint.

On the other hand, the nail plate joint has advantages over the glued joint:
- The glued joint needs finger routing in the web and in the chord with excess cost. However, this cost is negligible in automatic manufacturing.
- The finger routings in chords weaken a little the chord resistance. This issue is negligible as the chord routings make only local defects in timber analogous to knots. The primary design criteria in trusses with uniform height are deflection and joint resistance, and the chord resistance is secondary.
- It is difficult to implement the glued joint in complicated cases like pitched trusses. On the other hand, the nail plate joint is flexible and can easily be implemented in complicated pitched trusses and frames.

The glued joint is most suitable for standardized applications like parallel chord trusses with uniform height. Implementing a glued joint to pitched trusses is challenging.

1.2 ROBUST TIMBER TRUSSES

Robust timber trusses are made of robust timber members like glulam. The authors made a study to obtain a robust timber truss using only glue in the joint, patent US2008092988. The joint needed sophisticated CNC processing and did not reach the commercial market.
There are research studies for robust timber truss joints made of glue and steel rods or plates. However, such trusses have not gained a significant commercial market.
The current robust timber trusses are made of dowels with slotted steel plates. Such joint has high material and labor costs and therefore the commercial competitiveness is not good regarding other alternatives like steel trusses.
Current primary girders are placed normally 4…6 m apart from each other where a secondary structure is needed. An alternative concept is explained here: the trusses are about 0.5 m apart from each other. A secondary structure is not needed. This article explains that this glued timber truss roof concept offers a profitable business potential as it seems to be more cost-effective than the glulam roof.

1.3 RISK REVIEW

Glued timber trusses are applied commercially little though the high potential. This is apparently due to the perception of the unreliability of the glued joint. The resistance of the glued joint is prone to timber defects like knots and inclined fiber and the resistance of the glued shear joint. The glue must be spread reliably, and the glue must not be decayed. One inproper joint may be fatal for the overall resistance of the truss. Thus, the glued joint must be subjected to strict quality routines analogously to welded joints in steel trusses.
The current manufacturers of glued trusses for the structural market have secured quality issues by proof-loading each commercial glued truss to 1.5…1.8 times the allowable i.e., characteristic load. This quality routine makes a more reliable outcome with a proper proof load than in the code-based design, but it makes considerable excess cost and is difficult in trusses made as a billet and in long-span roof trusses.
The authors believe that proof-loading is not necessary when careful quality measures are taken:
- The basic principle of a glued timber joint is that the failure should not occur in the glue line. It is possible to fulfill this requirement in the glued truss joint.
- The timber quality on webs and especially on the web fingers is critical. Therefore, the webs should be appropriately graded to avoid critical defects, especially big knots.
- The chords should be graded too analogously to the grading of the flanges of I-joists.
- In the glued joint the glue must be spread all over the joint and the glue must not be decayed. The glue cost in the truss is negligible and therefore it is feasible to overdesign the glue joint in critical cases for example by limiting allowable mean glue shear stress to a low value, e.g., about 0.3 N/mm^2 for the characteristic load. The glue cost in the glued truss is little and the overall effect is negligible.
- It is beneficial to make the joint and the fingers big when small knots in the timber are allowed as they play a negligible role.
- The glue should be spread using a robot to exclude human errors and further, an automatic camera checking should be applied to secure the outcome.
- In critical points like truss ends, multiple adjacent webs may be applied to reduce stresses and increase reliability. The web cost in a glued truss is negligible and therefore multiple webs make only a minor excess cost.

1.4 WOOD MATERIAL

Any sawn wood with minor defects especially minor knots like spruce is suitable for glued trusses. Glulam, LVL, and other glued products are feasible, too.

2 EARLIER GLUED TIMBER TRUSSES

There were three glued truss concepts on the market, one based on finger joints and two based on lap joints.

2.1 DSB

DSB, patent US2780842, is the first commercial glued timber truss manufactured in Germany for floors and roofs in multiple plants from about 1950’ through 1970’.

https://doi.org/10.52202/069179-0459

The production was terminated apparently due to quality assurance issues.

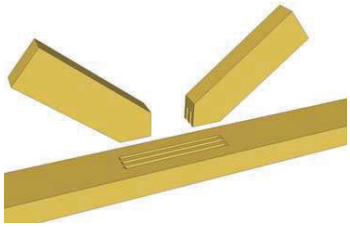

Figure 1: *DSB joint, the fingers are not tapering and the webs are not connected to each other.*

2.2 IU-TRUSS

Finnish inventor Pertti Purontakanen filed a patent FI54008 in 1979, for a glued timber truss where the chords are double planks, webs are planks and are inserted between the chord planks, and 3 mm plywood is between the chord plank and the web plank. The purpose of the plywood is to avoid stress peaks in the glue joist and to simplify the glue application as the glue is spread on the plywood. A batch of trusses was stacked on top of each other and pressed together using a hose and air pressure.
IU-truss was on the Finnish market for about a decade. The production terminated due to stability issues of the upper chords and webs causing a roof collapse at least in one case. In the IU-truss, both upper chord planks must be nailed to the battens to avoid lateral buckling.

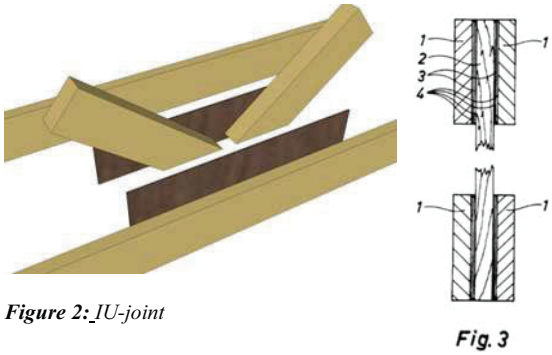

Figure 2: *IU-joint*

Fig. 3

2.3 A-TRUSS

Finnish inventor Arvo Hyvärinen developed A-truss which is like a nail plate truss, but the nail plates are replaced with birch plywood glued to chords and webs. The assembly of the A-truss is the same as in the IU-truss. Although the A-truss is more expensive than the nail plate truss, the A-truss was on the market for two decades. The A-truss fabricator specialized in complicated cases which the connector truss fabricators opted not to do. One may think that the resistance of the A-truss is doubtful, but the authors do not know of one failure with these trusses.

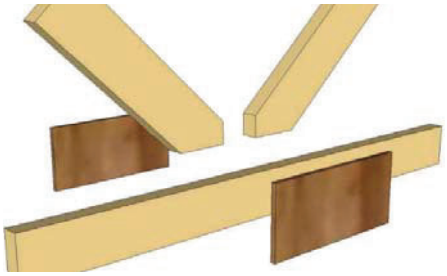

Figure 3: *A-joint*

3 CURRENT TIMBER TRUSSES

Nakashima et al [4], patent JP2014055406A, developed an interesting joist which is a combination of truss and I-joist.

Figure 4: *Nagashima's joist*

There are three glued timber trusses on the market, all based on finger joints.

3.1 PERI

The PERI truss, patent CH306573, is like the DSB-truss, but the webs in the joint are connected to each other by a finger joint with tapering fingers. The PERI-joint has high resistance which is due to deep chord routing and high chord thickness, about 60 mm. The PERI-truss is used as a joist for concrete casting. The PERI-truss is currently exploited extensively on the market.

https://doi.org/10.52202/069179-0459

Figure 5: *PERI-truss and joint*

3.2 TRIFORCE

A more improved product with a tapering finger joint in the web-chord joint and in the web-web joint was developed in Canada some 30 years ago, patent CA2335684, https://www.openjoisttriforce.com/. The web cross-section is rectangular 38*38 mm^2, and the chord routing is shallow, 16 mm. This joist has established a solid position in the residential floor market in the US and Canada. It is produced in standard lengths with an option for 600 mm trimming on one end.

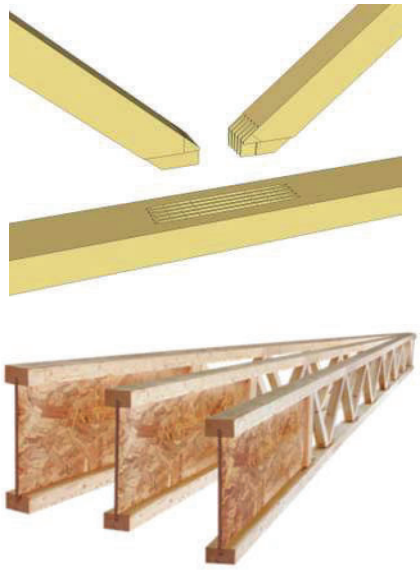

Figure 6: *Triforce joint and truss*

3.3 G-TRUSS

G-truss is the latest glued timber truss on the market explained in more detail in the next paragraph, www.gjoist.com, www.tk-palkki.fi

4 G-TRUSS

The authors started the glued truss development more than 20 years ago. In the beginning, the focus was to develop a joint suitable for light and robust trusses without open routings [1, 2]. A patent US7975736 was granted to a joint where routings were processed using a cursor moving in the axial direction. This embodiment did not reach the commercial market.

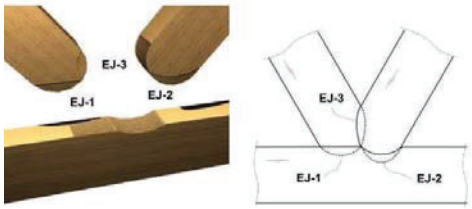

Figure 7: *Glued truss joint, US7975736, suitable for light and robust trusses.*

In 2014-2017 the authors realized a development project where more than 10 joint models and more than 300 full-scale trusses were tested [3]. Innovations were made and three patents were granted EP3620588, US11162262, and US11220821. The new truss was named “G” glued truss and glued joist.
The G-truss consists of some new features:

4.1 Simplicity

All webs in the G-truss are similar and there are no verticals. There are only three different timber member types in each truss. Upper chord, lower chord, and web. All mortise routings in the chords are similar and all tenon fingers on the web ends are similar, too. Thus, the timber members are easy to make and assemble.
The simplicity applies to the structural design, too. As the web pattern is the same along the truss, the resistance also is the same along the truss. The G-truss can be turned upside down. These features are significant in a truss manufactured as a billet.

4.2 Saw blade routing

The fingers in the joint, the tenon web fingers, and the mortise chord fingers are processed using a saw blade. The fingers are tapering and therefore the processing is made in two steps in two saw inclinations, as shown in Figure 8. The saw blade makes a good surface for gluing and a small knot in the finger does not make any timber splitting.

https://doi.org/10.52202/069179-0459

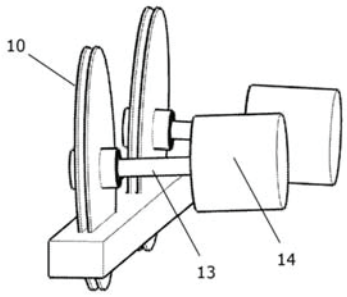

Figure 8: *The saw blade routing is processed in two steps to obtain the tapering fingers.*

4.3 Trough routing

The web finger punches the chord, which results in a big joint. The joint size is the maximum possible i.e., the whole overlapping area of the web and the chord. In such a joint, a small knot is not critical. The web-chord glue area is large meaning small shear stress in the glued shear joint. The mean glue shear stress for the characteristic load is about 0.3…0.5 N/mm^2

4.4 Only one or two fingers per web

In the glued timber truss joint the resistance of one web finger decreases when the number of fingers per web increases on the web. The G-web has only one or two fingers per web and therefore the web finger is effective.

4.5 Upper chord support

The upper chord support is possible without a hanger as the web finger is long and reaches above the support. This feature makes about a 20 % cost advantage in cases when the hanger can be avoided.

Figure 9: *The G-web finger punches the chord.*

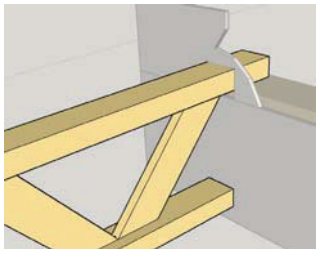

Figure 10: *The upper support is possible without a hanger.*

4.6 Free web layout

The webs in the G-truss may be connected to each other as is normal in a truss, but the webs may be apart from each other. This enables two features missing in a normal truss where the web pattern and the node points normally are fixed:

- The node points within the truss can be fixed to match the extra support along the truss and thus the reinforcement of the truss is not needed in the support. The extra support may be on the bottom chord or on the top chord.
- The crosswise opening which may be excessively big can be fixed arbitrarily. It is possible to fix a continuous crosswise opening along adjacent trusses for MEP or to assemble a crosswise girder inside the adjacent trusses.

The web layout normally means that the webs make an X-pattern. In this embodiment, the supports and the openings in a truss may be fixed to fully match the actual situation in the building. Figure 11 shows a truss with a special web layout.

In a normal truss, the webs and the chords have no or negligible moment stresses. When the webs are fixed apart from each other in the chord joint, excess and harmful moment stresses are induced, in the joints, webs, and chords. These excess stresses set some demands on the joint and the truss.

- The joint must be reliable and strong.
- Normally at least one extra web is needed in critical cases to shear the excess stresses to multiple webs and joints.

In the G-truss, the webs may be fixed apart from each other as the joint is strong and an extra web may be fixed anywhere along the truss.

Figure 11: *A truss with a special web layout.*

4.7 Billet manufacturing

Current trusses are manufactured for fixed length (with eventual trimming option at ends) with supports at bottom chord ends. G-truss can be manufactured as a long billet like I-joist and solid joist and cut arbitrarily to make multiple working trusses. Each joist can be supported at

https://doi.org/10.52202/069179-0459

the bottom chord, top chord, between chords, or along the truss.

Figure 12: *A billet truss that can be cut for multiple working trusses.*

If the support does not match a node point reinforcement is needed at the support. Figure 13 shows a reinforcement when the support is in the upper chord at the joist end. OSB panels and steel U-rail are nailed on the chord edges.

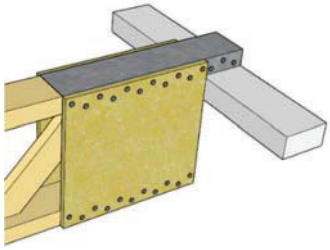

Figure 13: *The billet truss can be cut arbitrarily, if the cutting point does not match a node point a reinforcement is needed. The upper support reinforcement is realized by fixing OSB-paned and steel U-rail.*

5 FLOOR TRUSSES AND JOISTS

The global timber floor joist market is about €5 bill. The I-joist is the market leader with a 50 % market share due to low material cost, simple manufacture, and the option for billet manufacturing.
The floor sets many special demands for the joists. The current joists match differently these demands.

5.1 Horizontal openings

The residential floor often includes MEP installation. The space between the joists can be utilized for MEP. Often the installation across the joists is needed, too when crosswise openings are useful. A truss has crosswise openings without extra cost. Such openings are not possible in the solid joist and I-joist perforation is limited and causing extra cost.

5.2 Support

Floor joists are mostly supported at the lower edge. However, the hanging support suits better, especially for the supporting beam and normally for the wall structure, too. The truss can be supported at the upper chord which allows the advantages of the hanging support. A hanger corresponding to about 20 % excess cost is needed in the I-joist and in the solid joist.
Hanging support is an increased trend in construction. It is especially useful in off-site construction and in prefabrication.
G-truss can be supported at the top chords without a hanger.

5.3 Cross bracing

Walking on the floor makes impact loads which should be distributed to multiple joists to avoid harmful local deflection and vibration. Therefore, there should be a cross-bracing "strong back" like a 50*150 mm^2 board across the joist which shares the impact load with multiple joists. Such cross bracing is impossible in the I-joist and in the solid joist and therefore these joists need some greater height to compensate for the missing cross bracing inducing excess cost.

5.4 Billet manufacturing

I-joist and solid joist are manufactured as a billet, kept in stock, and cut to actual need which is effective regarding logistics and the overall economy. G-truss is the only truss that can be manufactured as a billet which is due to the high joint resistance.

5.5 Vertical openings

The residential floor virtually always has a vertical opening like a staircase or chimney where joists hitting the opening are cut and excess joists are fixed by side of the opening. Cross beams are needed to support the cut joists. Currently, the cross beams are fixed at the perimeter of the opening and fixed by the faces of the excess joists. G-truss has three characteristics that enable a simple and flexible structure:

- The cross beams can be fixed inside the G-trusses i.e. they need not be by side of the opening. For this reason, the cut beams may run beyond the cross beams to make overhangs. Cutting of the overhangs is arbitrary and therefore the form of the opening is arbitrary, for example, a circle. Currently, the form of the opening can be rectangular only.
- The cross beams are not supported at the faces of the excess joists, but inside them, which denote simple joints e.g. hangers are not normally needed.
- The crossbeam may be excessively long to be supported by multiple joists and thus sometimes extra joists are not needed.

Figure 14 shows the principle of the new structure.

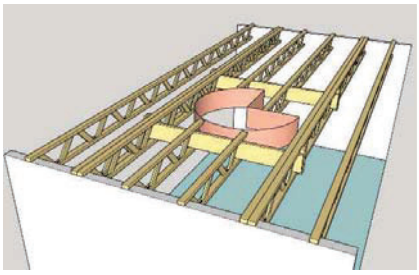

Figure 14: *the principle of the new opening structure.*

https://doi.org/10.52202/069179-0459

5.6 Costs

The special features explained above have cost effects different for each joist.
Figure 15 shows approximate costs for a typical 6 m residential floor.
G-truss has the least material cost and has no excess costs regarding the special features.
In this Figure, the factory price of the G-truss is €7/m. The high price is due to patent royalties and good profit for the licensee manufacturer.
In the long run, the factory price of the G-truss and the I-joist should be about the same.
Approximate CO2 emissions are given, too, the G-truss is the most effective in this regard.

	G-joist	I-joist	Metal web joist	Plated joist	Wood joist
Material	3.2	3.5	5.0	5.5	9.0
Manufacturing	2.3[1]	1.0	2.0	2.5	-
Overhead costs	1.5	1.5	1.5	1.5	-
Factory price	**7.0**	**6.0**	**8.5**	**9.5**	**9.0**
1.Perforation	-	0.5	-	-	0.5
2.Support	-	1.0	≈0.5	≈0.5	1.0
3.Cross bracing	-	0.5	-	-	0.5
4.Billet opt	-	-	1.0	1.0	-
5.Openings	-	0.5	0.5	0.5	0.5
Reference price	**7.0**	**≈8.0**	**≈9.5**	**≈10.5**	**≈11.0**
CO2ekg/m	**0.3**	**0.6**	**2**	**2**	**3**
Current market		**2 500 MC**	**2 500 MC**		

Figure 15: *Approximate floor joist costs, €/m at 6 m span.*

6 ROOF TRUSSES

The global roof demand is huge. Currently, timber is competitive in residential roofs mainly via the nail plate truss. Steel and concrete dominate the commercial roof market.

6.1 RESIDENTIAL ROOFS

The nail plate timber truss dominates the residential roof market due to its low cost and flexibility to accommodate multiple geometric and structural forms. However, the nail plate truss has some deficiencies:

- The nail plate truss needs height which means that the prefabrication of the roof is not feasible. The roof must be constructed on-site from prefabricated trusses.
- The nail plate truss is not effective for a house with an attic, either the truss will be very expensive, or the attic space is limited.
- A roof opening in a nail plate truss roof is complicated and expensive.

Glued timber trusses are not currently applied in residential roofs. Joists with uniform height, I-joists, solid joists, or nail plate trusses are sometimes applied for residential roofs. The glued joist would be more cost-effective.
Off-site construction and prefabrication are strong drivers and trends in construction. Therefore, the authors believe that the joisted roofs gain market.
The mono-pitch residential roof is the most cost-effective for the glued truss as it suits the offsite manufacturing of panel components. A double-pitched roof can be prefabricated effectively too if the joists can be fixed parallel to the ridge. Ridge beam plus joists along pitches are feasible, too.

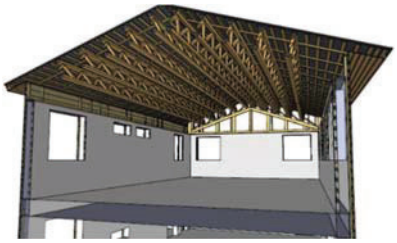

Figure 17: *Pitched roof can be constructed effectively using joists by fixing the joist parallel to the ridge.*

6.2 COMMERCIAL ROOFS

The nail plate truss can be applied for commercial roofs up to about 30 m spans. The truss cost is low, but the roof can't be prefabricated. The expensive on-site construction work deteriorates the overall economy.
The glued truss enables roof prefabrication and automation and is feasible in long-span commercial roofs where strict deflection and dynamics demands are missing. The feasible height of the glued truss is about span over 25. The reliability without proof loading is obtained using the measures explained above. The overall economy is good and there is commercial competitiveness even with proof loading.
Next, two commercial buildings are compared regarding roofs, one building has a G-roof, and the other has a consistent glulam roof [5]. The walls and roof of both buildings are rigid diaphragms to resist horizontal forces. The columns in the glulam building resist the vertical forces only.
The snow load is 2.2 kN/m^2. The net inner height is 5.2 m, and the width is 18 m. In both cases, the roof consists of 2.4 wide and 18 m long prefabricated elements. The measures of the glulam girder is 1164 mm…1440 mm*190 mm, GL30c, c/c 6 m.
The 18 m long G-truss has a height 780 mm, chords are 60*195, and webs are 45*73 doubled at the ends.

Figure 18: *The 18 m long G-truss*

Figure 19 shows the cross-section of the G-roof element. Soft mineral wool insulation or loose insulation is applied to enable simple application in spite of the inclined webs. Semi-hard insulation panels are at the sides to make a good seam between the elements.
We see that the basic structure is flexible:

- Additional trusses can be fixed in cases when extra resistance is needed e.g., in point loads or in roof openings.

https://doi.org/10.52202/069179-0459

- A crosswise girder for extra support, crosswise overhang, or point load may be added.
- The G-truss can be supported at the top chord which is beneficial in the beam support.
- The G-roof element can be fixed to the wall or a beam by processing above the element, with no fixing nor sealing below the element needed.
- The sealing between the elements is simple, only the upper membrane must be fixed onsite.
- The seam includes a big assembly tolerance, though it is air and moisture tight.

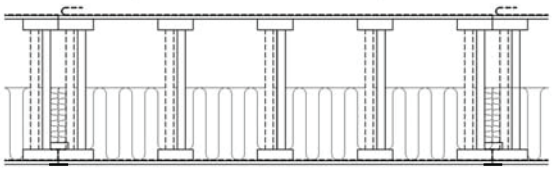

Figure 19: *Cross section of 2.4 m wide roof element of G-roof. The element includes five G-trusses.*

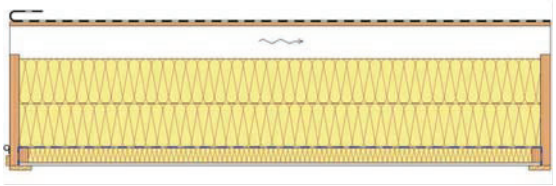

Figure 20: *Cross section of roof element supported on glulam beams, such element is dominantly used in Finland, disclosed in LVL Handbook, Figure 2.39 https://proofer.faktor.fi/epaper/LVLHandbook_2020/#76.*

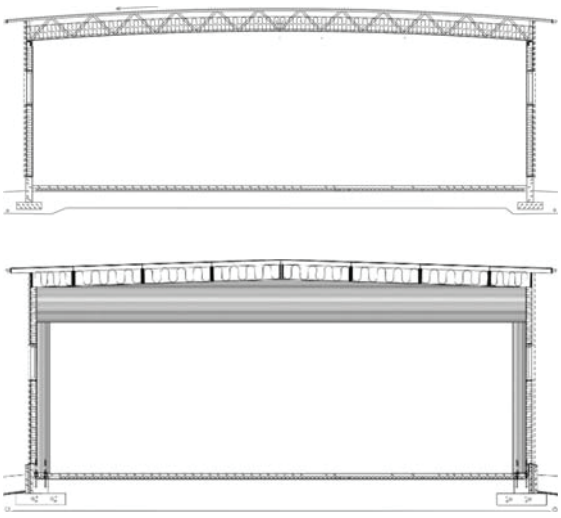

Figure 21: *Cross section of the G-building above and the glulam building below, the net inner height is 5.2 m and the width is 18 m. The wall height of the glulam building is 6864 mm, and 5920 mm in the G-building. The overall roof height in the G-building is about 50 % less. The glulam building has a secondary and normally harmful building volume between the beams, 25 % of the net volume.*

Table 1 includes wood volume, approximate wood cost, and approximate CO2 emission for the G-roof and for the consistent glulam roof in 18, 24, and 32 m spans. The calculation is based on the sawn timber cost €300/m^3, and glulam and LVL cost €600/m^3. The assembly cost of the G-truss is €3/m [5]. The table includes the wood cost only, the lower and the upper cladding and the insulation are the same in both structures and these costs are excluded.

We see that in all cases the overall wood volume is about the same in all alternatives, but the G-roof is about €20/m^2 cheaper as the G-roof consists of low-cost sawn timber only. The G-roof has lower CO2 emissions.

In the G-buildings, there are further advantages resulting in lowers costs not considered in the figures of Table 1:

- The wall area is less.
- The volume of the building is less requiring lower heating/cooling costs.
- Columns and column foundations are not needed when the roof is supported on walls.
- The secondary structure of the roof costs less. In both cases the assembly of the 2.4 m*18 m roof element is manual. The assembly of the G-element costs less as it has only 8 wood components per element whereas the glulam roof element, FigSure 20, has 75 wood components.
- The construction work is simple including the walls, and the roof only, the building skeleton, columns and girders, and the column foundations are not needed.

The factors listed above make further benefits for the G-building and the overall advantage is about 10 % of the overall cost of a commercial building.

Table 1: *Comparison, G-roof vs glulam roof [5]*

	Span (m)	18	24	32
G-roof	Wood (m^3/m^2)	0.061	0.106	0.195
	Wood (€/m^2)	25.6	37.9	64.8
	CO2 (kg/m^2)	4	5	8
Glu-lam	Wood (m^3/m^2)	0.078	0.104	0.179
	Wood (€/m^2)	43.2	58.0	103.2
	CO2 (kg/m^2)	8	9	14

7 DISCUSSION

The G-trussed joist used in residential floors seems to be more cost-effective than other timber joists. The cost advantage is €1-3/m i.e., €2-6/m^2. The high floor cost is an Achilles heel in timber engineering, especially in long spans. In this regard, the G-truss increases the competitiveness of timber engineering.

The authors believe that the joisted roofs gain market due to prefabrication and automation. The G-truss apparently is the most cost-effective joisted roof structure.

G-truss economically reaches long spans up to about 30 m. There are two prefabricated wood elements that reach long spans, too: LVL box slab https://proofer.faktor.fi/epaper/LVLHandbook_2020/#76 and modified I-joist-box-slab https://www.kielsteg.com/. Both are more expensive than the G-truss, as in these elements the wood plus glue cost is about 100 % higher, and the CO2 emissions are manifold. Further, these slabs have difficulties in thermal insulation, assembly at the

https://doi.org/10.52202/069179-0459

site, vertical and horizontal openings, supports, crosswise connections, air circulation, crosswise girder, and crosswise overhangs.

The G-truss seems to be sufficiently economical to undercut the costs of the current dominant structural model of commercial buildings: a skeleton arrangement plus a secondary structure. Thus, the G-truss has the potential to change the construction paradigm.

G-truss roof is competitive against steel and concrete roofs, too. Thus, the G-truss increases the competitiveness of timber in construction.

Only floor and roof glued trusses are addressed here. However, glued trusses are feasible in other applications, too like bridges, scaffoldings, railings, joists for concrete casting, and studs.

The truss is a complicated structure; however, the G-truss is simple, and it goes in for prefabrication and onsite automatic construction:

- The G-truss is flexible, therefore residential floors can be built with no excess labor regarding special issues like support, openings, and cross-bridging.
- Residential roofs can be built offsite using automation with negligible onsite labor and enabling effective use of attic space.
- Commercial buildings can be constructed without a skeleton.

Timber structures are more design intensive than concrete and steel. The authors have worked with codes and suggested modified allowable stress design. It simplifies the timber codes and makes considerable material savings when the excess reliability for the loads with low variability is removed [7].

8 CONCLUSIONS

Glued trussed joist is feasible for residential floors due to its low cost and flexibility and seems to be more cost-effective than other timber joists.

The nail plate timber truss dominates the residential roof market mainly due to its flexibility for multiple geometric forms. However, the nail plate truss poorly suits prefabrication and construction automation. If the roof can be constructed using joists with uniform height the glued truss is a feasible option.

Our study shows that the glued truss roof in commercial buildings up to about 30 m spans is more cost-effective with lower CO2 emission than a consistent glulam commercial building. In this regard, the glued truss may change the current construction paradigm.

The glued timber truss simplifies timber engineering.

REFERENCES

[1] Poutanen T. Ovazza C.: Glued timber trusses, WCTE2010, Trentino, Italy, 2010.

[2] Paananen V.: Glued timber trusses, Bachelor's Thesis, Tampere University of Applied Sciences, Tampere, Finland, 2016.

[3] Pasanen S., Vierisalo J.: Manufacturing and testing of glued timber trusses, Bachelor's Thesis, Lahti University of Applied Sciences, https://urn.fi/URN:NBN:fi:amk-2017052410105, Lahti, Finland, 2017.

[4] Nagashima T., Hisoyoshi S, Yasuhiro I., Yoshimitsu O.: Development of I-beam using kizure panel and LVL, WCTE2016, Vienna, Austria, 2016.

[5] Tanskanen J.: Glued timber truss, Master's thesis, Tampere University, Tampere, Finland, 2023.

[6] Trummer A., Eicher S., Krestel S.: Kielsteg – Defining the Design Parameters for a Lightweight Wooden Product. WCTE2016, Vienna, Austria, 2016.

[7] Poutanen T., Code Calibration of the Eurocodes. *Appl. Sci.* **2021**, *11*, 5474. https://doi.org/10.3390/app11125474

World Conference on Timber Engineering Oslo 2023

3DP BIOWALL – CIRCULAR ECONOMY IN WOOD CONSTRUCTION THROUGH ADDITIVE MANUFACTURING OF FULLY RECYCABLE WALLS

Benjamin Kromoser[1], Sara Reichenbach[2], Roman Myna[3], Raphaela Hellmayr[4], Bernhard Reinholz[5], Rupert Wimmer[6]

ABSTRACT: To further increase the environmental potential of renewable raw materials, a new construction concept for fully recyclable bio-based wall elements assembled by additive manufacturing, called 3DP Biowall, is presented. The proposed concept considers the entire life cycle from material converting, to manufacturing and application, over to recycling and restarting a new construction phase. With the help of this method the materials are kept significantly longer in a closed material cycle, with conceptually no waste production. A fully biobased material mixture of wood particles and Biomix (sodium lignosulfonate and starch) is used. The present paper describes the basic approach, first production experiments as well as the achieved mechanical performance within compression and flexural tests performed with first test specimens. Furthermore, the potential of the closed material loop approach is assessed through an LCA and by comparing the 3DP Biowall to other well-known exterior wall systems. All production life cycle phases were regarded and experimentally investigated. The successful production tests and the achieved mechanical characteristics prove the feasibility and potential of the new approach. The performed LCA points out further optimisation potential regarding the mixture with the starch component having a comparatively high impact at the environmental footprint of the material mixture.

KEYWORDS: 3D Printing, Additive Manufacturing, Cradle-to-Cradle, Biobased Building Construction, Life Cycle Assessment (LCA), Renewable Materials, Recycling

1 INTRODUCTION

There are different approaches to obtain resource-efficient constructions, for one by choosing an appropriate material, for the other by optimizing the structure and furthermore by optimizing the production processes [1]. New methods and processes can be found throughout the industry and in literature, with renewable materials and additive manufacturing showing great potential (e.g. [2]). Unfortunately, most additive manufacturing concepts for production of whole building components or buildings rely on the use of mineral-bound materials such as mortar or concrete which have a very high environmental footprint. To push forward a more sustainable building mentality other materials have to be brought into the equations, with wood constructions showing great potential as wood is able to partly store CO_2 during the tree's growth phase.

However, wood is also a limited resource and currently a considerable amount of the processed raw material ends up in a secondary stream and directly used as an energy source. In 2019, approximately 40% of harvested trees was not used for sawn timber products [3].

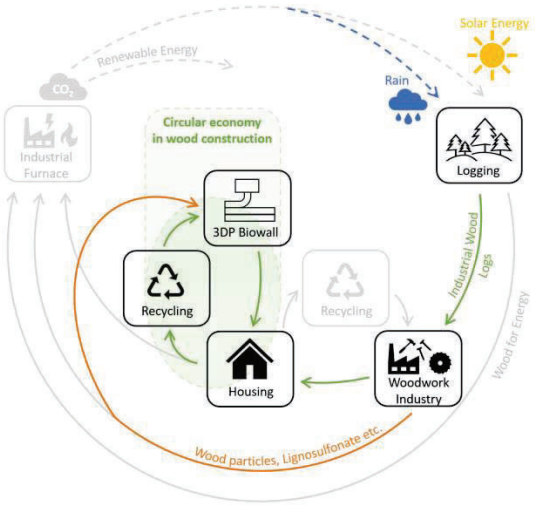

Figure 1: *Circular economy in wood construction based on* ***[4]****, including the future 3DP Biowall concept.* ***[5]***

[1] Institute of Green Civil Engineering, University of Natural Resources and Life Sciences, Vienna (BOKU), Austria, benjamin.kromoser@boku.ac.at
[2] Institute of Green Civil Engineering, BOKU, Austria, sara.reichenbach@boku.ac.at
[3] Institute of Green Civil Engineering, BOKU, Austria, roman.myna@boku.ac.at
[4] Institute of Wood Technology and Renewable Materials BOKU, Austria, raphaela.hellmayr@boku.ac.at
[5] Institute of Green Civil Engineering, BOKU, Austria, bernhard.reinholz@boku.ac.at
[6] Institute of Wood Technology and Renewable Materials BOKU, Austria, rupert.wimmer@boku.ac.at

https://doi.org/10.52202/069179-0460

This together with material consumption surpassing the growth of population significantly [6], reveals that a circular approach, structure optimised design and use of secondary streams for manufacturing construction components is indispensable. The newly presented 3DP Biowall construction concept combines the high environmental friendly potential of grown renewable raw material mainly coming from secondary streams (e.g. wood particles, lignosulfonate) including a completely new binding concept [5,7], which allows for a closed-loop process (Figure 1), with a new production strategy resulting in new truly resource-efficient construction method.

2 MATERIAL CONCEPT

Various boundary conditions were set for the printing material to be used within 3DP Biowall: (1) A pure mixture of grown renewable materials, (2) Preferably side stream resources; (3) Recyclability of the end product, as well as (4) Ability to be extruded and develop a sufficient bond to the previously deposited layer. The resulting material mix consists of diverse wood particles (Figure 2c) and a bio-based binder (consisting of industrial starch and lignosulfonate, Figure 2 a) and b), respectively) which can be mixed in a dry state before water is added within the printing process.

The use of lignosulfonate adhesives has a long tradition in commercial use for paper glues. As technical lignins are not able to act as a binder without crosslinking agents or other additives [8], the material is currently mainly burnt for energy production processes [9]. The hydrophobic behaviour it shows due to its aromatic moieties, together with the presence of the hydroxyl groups suggests its compatibility with starch, a renewable resource that is also often used within adhesives production, especially for the paper industry. When applying starch as wood adhesive, the biggest challenge is its water resistance.

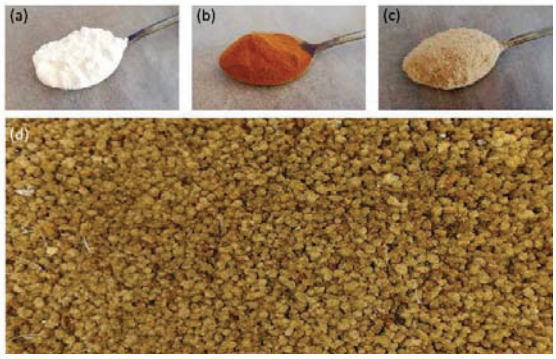

Figure 2: *Components for biobased wall systems* ***[5]***

The results of blending starch and lignin show very good mechanical behaviour for wood bonding as well as full recyclability [7], while the hydrophilicity can be adjusted using different measures. Within in the bio-based binder lignosulfonate acts as a dispersant, whereas the use of starch ensures the strength development of the bond line.

For good adhesion a homogenous distribution of the particulate mixture is critical. This can be supported by using triboelectric charging, where different components receive opposite charges. The created electrostatic potential attracts the individual Biomix and wood particles to each other. Unlike commonly used 3D-printing techniques, which are either based on thermoplastic melting and solidification or chemical reacting of fluid material, the proposed production method is based on dry extraction with minimal water dispersion afterwards.

3 PRODUCTION CONCEPT

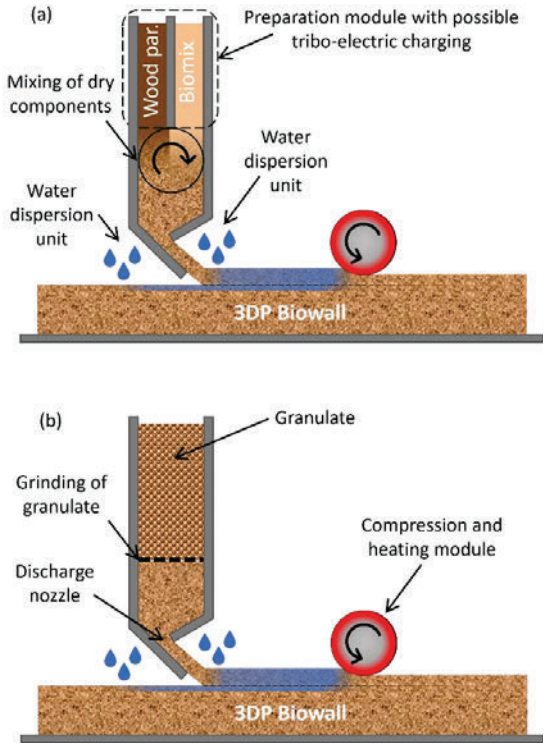

Figure 3: *Printing head concept for a (a) fully-integrated production (b) granulate-based production* ***[5]***

Two concepts (Figure 3) for the material preparation and the printing head are being developed to provide a continuous printing process of the 3DP Biowall. The first approach is a fully integrated production (a), where mixing of all components is implemented in the printing head for immediate application. The second approach is a granulate-based production (b), with the granulate (Figure 2(d)) produced beforehand. Advantages and disadvantages of both production processes are listed in Table 1.

Within option (a) the dry materials (wood particles with Biomix) must be mixed properly in dry state before the extrusion (Figure 3 (a)). Integrating a triboelectric mixing device into the printing head could be a promising supplement resulting in a more homogeneous distribution.

https://doi.org/10.52202/069179-0460

To ensure proper bonding, the bottom layer and the extruded mixture need to be moistened e.g., using water vapor prior to compressing and heating.

Table 1: *Assets and drawbacks of a (a) fully integrated production (b) granulate-based production* ***[5]***

	Fully integrated	Granulate based
Advantages	• Well suited for dry recycled wood components • Easy (automated) adaption of process parameters (mixture ratio) • Higher degree of compression possible, therefore ideal for hollow wall elements • Very homogeneous distribution of the different materials resulting in higher compression strength • All work steps are integrated in one tool • Shorter time frame from shredding to printing	• Fresh wood particles (high moisture content) can be directly used in granulate production without drying • Easy storage and transport, simplifying the printing on site • Can be used for other applications, e.g. ceiling filling • The high moisture content of the wood particles results in significantly less water consumption • Printing head has a simple design, therefore robust and reliable • Production of granulate can take place e.g. at sawmills, creating further added value
Disadvantages	• Materials have to be dried for transport otherwise they can be affected by rot • Higher complexity of the printing head • High water consumption	• Mixing ratio of individual components cannot be adapted in the printing head • Additional crushing unit needed in the printing head • Lower degree of compression possible

For the granulate-based production (Fig. 3 (b)), the granulate is produced directly after gathering of the wood particles, e.g. in the saw mill. By mixing the fresh wood particles with the Biomix-blend, a process of self-agglutination of the components is initiated. The adjustment of size and properties of the granulate is done either via variation of raw materials and mixing proportions or by choosing different process parameters.
The 3D-printing process allows Biowalls to be designed and produced with variable thicknesses and densities. Either a solid or hollow wall structure is conceivable, while the latter allows for an addition of further materials to match desired criteria like thermal insulation, fire resistance or sound insulation. Even complex and structural optimised patterns are achievable by applying selective material distribution/moistening/curing.
For that, the following aspects need to be considered and optimised in the printing process: (1) used material composition (Biomix – wood particles mixing ratio), (2) layer thickness, compression force and temperature as well as their interaction to obtain a homogeneous structure, (3) amount and time at which water is added for optimal wetting of the Biomix– wood particles mixture without clogging the printing nozzle, as well as the (4) production speed.
The independent development of the printing head and carrier system allows for an application und various conditions, e.g. on-site construction with a robot or portal system or off-site using an indoor robot system, as shown in Figure 4.

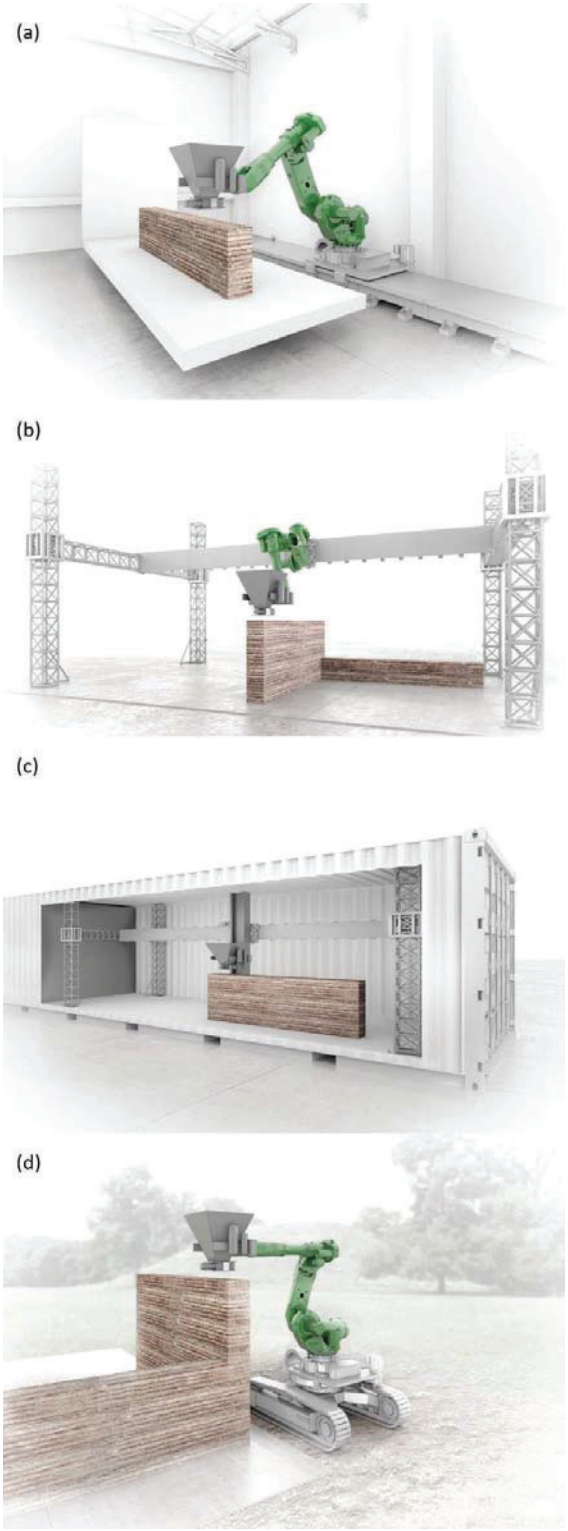

Figure 4: *Illustration of possible carrier systems for the printing head and construction strategy* ***[5]***

https://doi.org/10.52202/069179-0460

The successful implementation on the indoor robot-system of the institute is shown in Figure 5(a). This setup allows to study the fully automated production in future under constant laboratory conditions.

4 RECYCLING CONCEPT

As the 3DP Biowall is completely bio-based, reusing the material offers great potential. In comparison with well-established wood products, the material of the 3DP Biowall is designed for direct and true recycling (without downcycling or the addition of supplemental material) and therefor is in line with the shown principle of a circular economy (Figure 1). To reopen the created glue lines, an optimised disaggregation process needs to be defined, in which moisture treatment together with mechanical disintegration take place without changing the size or form of the wood particles. An essential step towards a fully reuse of the recycled material is a proper separation of the wood particles from each other. This leads to a conceptionally endless process, where multiple printing of 3DP Biowalls without the addition of adhesives is conceivable. As the used material is neither harmful to humans nor the environment, pyrolysis or composting could be a possible end-of-life scenario.
3DP Biowalls are not foreseen to replace the current solid wood applications, but rather to give the opportunity to increase the yield rate by means of using secondary material streams.

5 PRELIMINARY DATA AND ENVIRONMENTAL IMPACT

The data derived from first preliminary experiments on 3DP Biowall specimens consisting of a 1:1 mixture of dry wood particles and Biomix (50% sodium lignosulfonate and 50% corn starch). In addition to this blend, further Biomix variations were prepared adding sodium chloride and ash.
The production of small-scale specimens (Figure 5(c)) followed the four specific steps for each layer:

I) Application of water onto the bottom layer using high-pressure spray guns
II) Distribution of the dry mixture with constant layer thickness as shown in Figure 5(b)
III) Application of water onto the new layer with low pressure to not disrupt the particles
IV) Compression of the new layer using a hydraulic press at temperatures higher than 150°C

The process was repeated until the specimen height reached 40mm. After production it was stored at standard conditions (20°C and 65% rel. hum.) for one week before being cut [5].
The developed prototype of the printing head allowed a semi-automatically production of the specimens, with only step (IV) needed to be done manually. Currently the integration of automated compression and heating in

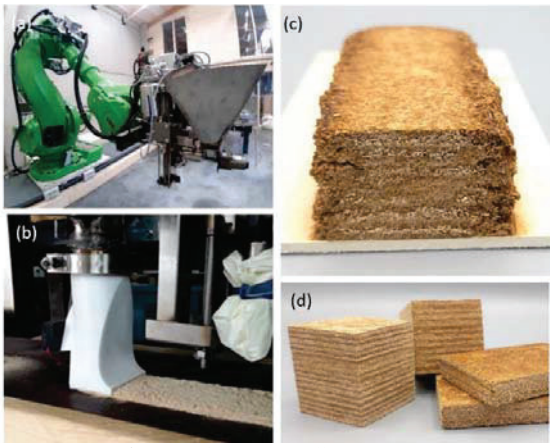

Figure 5: *Production of 3DP Biowall specimens* ***[5]***

order to automate the entire process are being developed and tested. A variety of small-scale specimens with different compression, amount of water to dry material ratios and various additives (NaCl and Ash) were produced and tested against their fire resistance, their water sorption behaviour and mechanical behaviour, including flexural and compressive strength. For the flexural strength measurement prisms with the dimensions of 160mm by 40mm by 40mm were tested, before being cut to 40mm cubes for the subsequent compression tests. The cubes can be seen in Figure 5(d). The alternating shade of color is a consequence of boundary layer development between the printed layers during the process.
The results, including the Young's modulus, are shown in Figure 6 with the Biowall specimens named Biowall or Regular, NaCl or Ash.

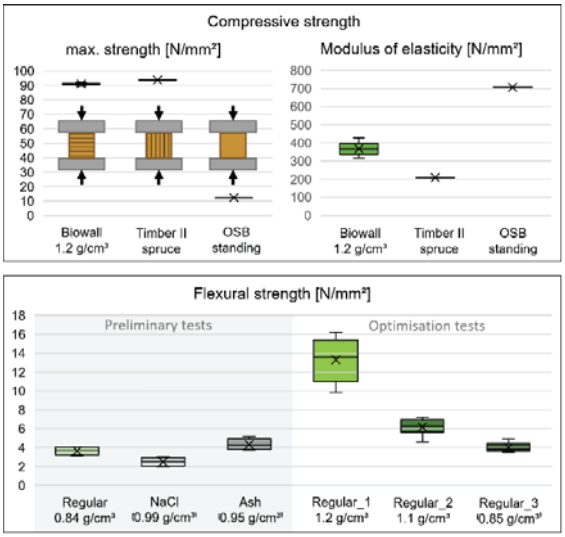

Figure 6: *Mechanical properties* ***[5]***

Within the DVS measurement different relative humidity levels (from 0 % to 95 %) were set until equilibrium and the mass of the sample (10mm x 10mm x 1.5mm) was continuously recorded by a microbalance in the device. The results of the DVS measurement are presented in Figure 7 and show a wood like behaviour. The Biowall samples reached a 15% higher fibre saturation point compared to solid wood; a characteristic that is linked to lignosulfonate and its hydrophilic behaviour.

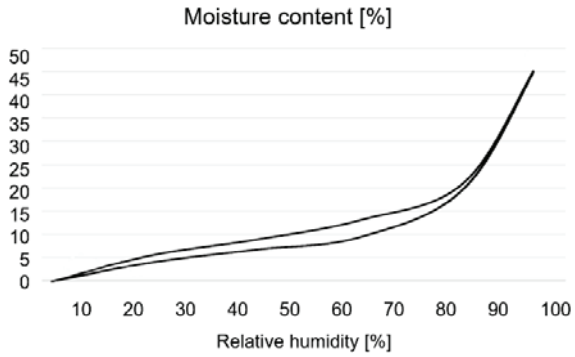

Figure 7:*DVS measurement* ***[5]***

The single flame source test results according to EN ISO 11925-2 were very promising. As a reference solid spruce was chosen. The 40mm by 40mm by 150mm samples were placed directly to the flame source having a 45° tilted orientation plane, with an exposure time of 30s. No ignition occurred for the Biowall specimens. The average flame size was 18mm x 40mm, showing anisotropic behaviour. Additionally, the time required resulting in a flame front height of 150mm was evaluated. After 30 min exposure the flame front had a height of 80mm without ignition, so the test was stopped. The reference sample showed a flame front of 2.5mm by 8.1mm after only 30 seconds with the height of the flame front exceeding 150mm after 3 min.

In addition to these tests the material was subjected to microscopic analysis. The images show the interaction between the two ingredients of the Biomix (Figure 8 (a)) and the dispersion of the binder within the saw dust when dry-blended (Figure 8 (b)). The tensile shear stress of Biomix was investigated in [7], and showed promising properties compared to urea formaldehyde, a conventional adhesive in wood industry.

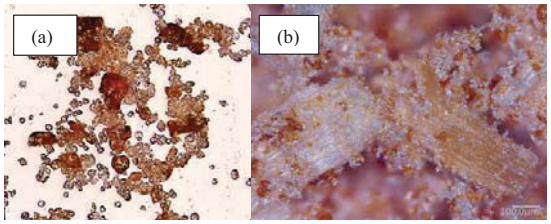

Figure 8: *Microscopic images* ***[5]***

In order to make a statement on the resource-efficiency and the ecologic aspect of the newly developed material an LCA focussing solely on the material production (Figure 9) was conducted. In a second step the material was considered within the boundaries of a constructed exterior wall system including insulation. In comparison with other well-known exterior wall systems (Figure 10) with similar U-values the environmental indicators consistently decrease with every further recycle cycle and therefor proof the closed material loop approach.

Within this paper only the Global Warming Potential (GWP) in kgCO2-equivalent and Primary Energy Non-Renewable - Total (PENRT) in MJ are presented with further environmental impact indicators discussed in [5]**.** Evaluating the material itself a distinction is made between primary and secondary resources, where secondary resources are by-products or even waste and primary resources products produced specifically to obtain that specific resource. The analysis shows the high impact of starch on each indicator. Therefore, to reduce the environmental footprint alternatives need to be considered, to either substitute the starch completely or partly.

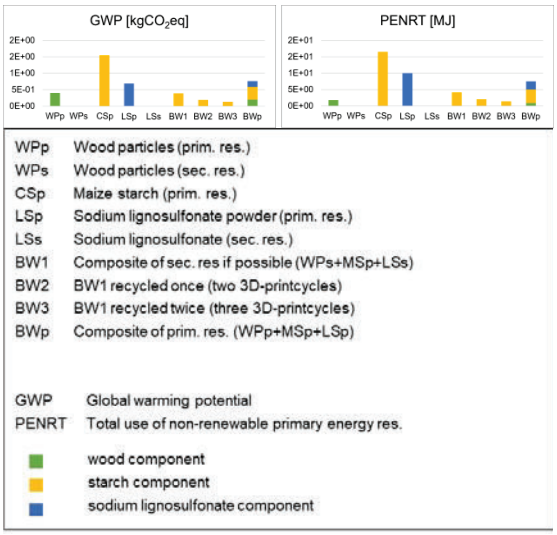

Figure 9: *LCA of the material (wood+Biomix)* ***[5]***

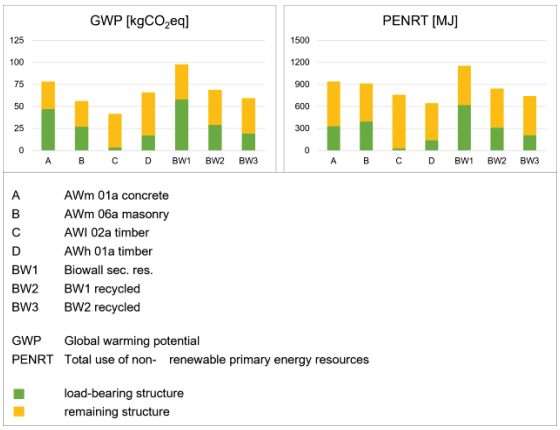

Figure 10: *LCA of complete wall systems* ***[5]***

https://doi.org/10.52202/069179-0460

Compared to wall systems that are currently in service, see Figure 11, the environmental evaluation for the production phase per functional unit of 1m^2 wall the 3DP Biowall showed elevated values of both GWP and PENRT, when not considering recycle cycles. Recycling the Biowall composite drives these values down on every cycle.

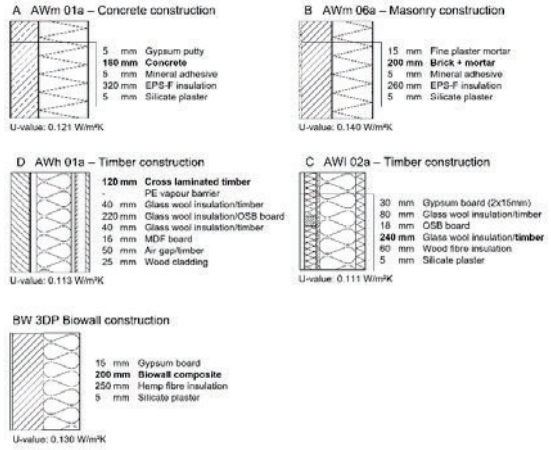

Figure 11: *Cross sections of considered wall systems* ***[5]***

6 THEORETICALLY FEASIBLE PROJECTS

According to Austrian standards no differentiation between one and four storey building is made in terms of the fire resistance requirements of load-bearing structures. Therefor and in order to show economically and environmental feasibility the mechanical properties of the introduced 3DP Biowall should developed in such a manner so that the wall system can be used for these types of buildings.

Examples for such state-of-the-art buildings, made of timber, are "Kleiner Prinz" in Munich (GE) and "Max-Mell-Allee" in Graz (AT), with both having four floors and built using timber frame construction technique with outer walls similar to the wall type awrhhi01a-03 [10]. Based on these designs a maximum design compressive load under normal conditions of around 60 kN/m arises. For this load case the resulting compression stresses and height decreases of the 3DP Biowalls with different wall thickness are summarised in Table 2 based on the model as shown in Figure 12, where the height H is 3 meters.

The stresses for the assumed load are lower than 1N/mm^2 while the mean maximum strength of Biowall under compression is around 90N/mm^2 according to Figure 6. This gap of order two suggests that not only four storey buildings but buildings with even more than four floors can be designed with the 3DP Biowall.

The modulus of elasticity for calculating the compression strain and therefor the compressions is also taken from Figure 6 and approximated with 350N/mm^2. Here again the authors are aware of the 350N/mm^2 not being the characteristic value typically used in a proper dimensioning tasks. The maximum compression is about 5mm for a 100mm thick Biowall and therefore of one magnitude smaller than the expected reduction in height as a consequence of drying shrinkage and creep for a two storey log cabin with a 94mm thick wall made of softwood [11].

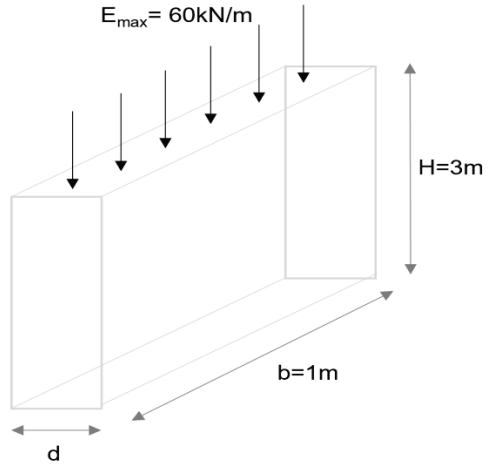

Figure 12: Wall model used for calculation

Taking into account the thermal resistance of the complete wall system, Figure 11 suggests to combine a 200mm thick Biowall with a 250mm hemp fibre insulation. For this Biowall thickness stress and strain are halved.

Table 2: *Stress and Compression for Biowall*

Thickness d [mm]	100	200	300	400
Stress [N/mm2]	0.60	0.30	0.20	0.15
Strain [mm/m]	1.71	0.86	0.57	0.43

The Biowall section can also be split into two pieces sitting on both sides of the insulation layer with each part having a thickness of for example 100mm. This would also increase the flexural stiffness by a factor of approximately seven as well as the sound insulation.

Additionally it is conceivable to replace the hemp fibre by Biowall material with less density as outboard sections of the wall. The material characterisation regarding is thermal insulation potential is part of the project too and will be done in future work.

7 CONCLUSIONS

The positive results of the first preliminary tests and the LCA show that, although challenging obstacles like the further development of the material mix, the production process and the optimisation of their interaction must be overcome to be truly competitive in terms of both environmentalc and economic reasons, 3DP Biowall has the potential to establish closed material loops and implement automation within the construction process, resulting in wood being used in a completely new form full of possibilities.

https://doi.org/10.52202/069179-0460

ACKNOWLEDGEMENT

This research is funded by FFG under the THINK.WOOD initiative. The authors like to thank FFG for that. In addition we like to thank our company partners Rubner Holzindustrie Gesmb, CRS Control & Robot Service GmbH and AustroCel Hallein GmbH as well as the Department of Forest Biomaterials and Technology from Swedish University of Agricultural Sciences for their support.

REFERENCES

[1] Kromoser B. Betonkalender 2021: Fertigteile; Integrale Bauwerke - III Ressourceneffizientes Bauen mit Betonfertigteilen. Wien: Ernst & Sohn GmbH; 2021.

[2] Home | ICON 2021. https://www.iconbuild.com/ (accessed June 1, 2021).

[3] Branchenbericht 2019/2020: Ein Rohstoff voller Leben. Holz. Fachverband der Holzindustrie Österreichs; 2020.

[4] TripleWood 2021. https://www.triplewood.eu/de/bauen-mit-holz/kreislaufwirtschaft_de (accessed September 15, 2021).

[5] Kromoser B, Reichenbach S, Hellmayr R, Myna R, Wimmer R. Circular Economy in Wood Construction – Additive Manufacturing of Fully Recyclable Walls Made from Renewables: Proof of Concept and preliminary Data n.d.;Construction and Building Materials.

[6] OECD. Global Material Resources Outlook to 2060: Economic Drivers and Environmental Consequences. OECD; 2019. https://doi.org/10.1787/9789264307452-en.

[7] Hellmayr R, Myna R, Reichenbach S, Kromoser B, Wimmer R, Šernek M, et al. Heat bonding of wood with starch-lignin mixtures creates new recycling opportunities. Materials Today Sustainability 2022.

[8] Dunky M. Wood Adhesives Based on Natural Resources: A Critical Review Part II. Carbohydrate-Based Adhesives. Reviews of Adhesion and Adhesives 2020;8:333–78. https://doi.org/10.7569/RAA.2020.097310.

[9] Mäki E, Saastamoinen H, Melin K, Matschegg D, Pihkola H. Drivers and barriers in retrofitting pulp and paper industry with bioenergy for more efficient production of liquid, solid and gaseous biofuels: A review. Biomass and Bioenergy 2021;148:106036. https://doi.org/10.1016/j.biombioe.2021.106036.

[10] Dataholz. Wohnunsbau Kleiner Prinz 2023. https://www.dataholz.eu/anwendungen/holzbauprojekte/wohnungsbau-kleiner-prinz-prinz-eugen-park-muenchen-de.htm.

[11] Ein Holzhaus! Aber für welche Bauweise entscheide ich mich? 2023.

https://doi.org/10.52202/069179-0460

World Conference on Timber Engineering Oslo 2023

SEISMIC ANALYSIS OF A MULTI-STORY TIMBER-CONCRETE BUILDING AND DESIGNING FOR REUSE

Sivert Lie[1], Themistoklis Tsalkatidis[2]

ABSTRACT: This research paper seeks to investigate the seismic performance of a hybrid timber-concrete building with multiple stories and explore the possibility of designing for reuse in low-seismicity regions. The building design incorporates hollow-core slabs (HCS) as flooring, a cross-laminated timber (CLT) panel core, and moment-resisting timber frames (MRTF). Various types of beam-to-column connections (BCC) from prior research are adopted in the MRTF. Modal response spectrum analysis of the building is conducted using the Eurocode 8 method, which takes into account the effect of connection ductility. The connections are assessed based on several factors, including story drift, on-site construction ease, disassembly ease, and the reuse potential for beams, columns, and connecting element. The advantages and disadvantages of the concept are discussed. The results show that a higher rotational stiffness in beam-to-column connections shifts the buildings first torsional mode to a higher mode and lower frequency, but generally lowers the reusability of the structural components.

KEYWORDS: Design for reuse, seismic design, disassemble, connections, sustainability, hollow-core slab

1 INTRODUCTION

The construction industry and the production of structural elements contributes to significant parts of the global carbon dioxide production [1]. The need for sustainable buildings that meet the demands from increasing population worldwide and limiting the increasing global temperature due to greenhouse gasses, requires structural engineers to adapt traditional methods of design into more environmentally friendly solutions. While being a large part of a building's mass [2], the use of innovative and emerging materials is generally considered harder for structural elements than for other parts of the building [3]. Recently, the concept of designing for reuse has been implemented in several projects with promising results.

Designing for future reuse increases the possibility of reusing structural elements in order to reduce the carbon footprint of a new building and the waste production from a demolished building. Combining sustainable materials like timber with reused concrete elements can be an important part of reducing the global climate emission from the construction industry, where the production of structural elements is responsible for a share of 15% [4]. The concrete production is a large part of this share due to the high number of concrete projects [5].

The yearly production of Hollow-core slabs (HCS) has been reported to reach 150 million cubic meters per year [6]. The concept of reusing HCS has only been implemented in niche projects until now, but a newly published standard NS 3682:2022 describes the process of demounting, documenting, and evaluation of the element quality [7]. Traditionally, HCS has been regarded as a diaphragm [8]. However, designing HCS with the goal of facilitating disassembly and reuse may necessitate the development of novel methods for interconnecting elements and for connecting to the supporting structure.

The concept of reusing timber elements has not been implemented in a large scale and it is relatively new. This is reported to be due to several factors, including the aging of timber, duration of load and load intensity. The general view, however, is that the bending strength and stiffness are not, or only marginally, affected by this, but investigation is difficult due to large natural variability of timber [9].

Timber-concrete buildings have been extensively investigated, and light-frame wood buildings have shown great resistance against earthquake, due to low mass [10] and ductility of nails [11]. When using engineering wood products in construction, such as glulam or Cross-laminated timber (CLT), the mechanisms for seismic energy dissipation are different than for steel or concrete buildings [12]. Seismic design of moment-resisting timber frames (MRTF) necessitates the incorporation of ductile failure in connections to enable energy dissipation, as timber exhibits brittle material characteristics. For structures located in low-seismicity regions, this approach can be combined with design for future reuse of structural components.

2 METHOD

The suggested method is based on a reference building, preliminary designed according to Eurocode 5 [13], using an ULS utilization ratio of approximately 70% for critical elements.

[1] Sivert Lie, Norwegian University of Life Sciences (NMBU), Norway, sivert.lie@nmbu.no
[2] Themistoklis Tsalkatidis, NMBU, themistoklis.tsalkatidis@nmbu.no

https://doi.org/10.52202/069179-0461

A numerical model of the building is modelled using SAP2000 [14], where beams and columns are modelled as frames with orthotropic material parameters. CLT is modelled as orthotropic thin shell with material property calculation according to [15]. HCS are modelled as thin shell with membrane thickness corresponding to the element height and bending thickness as 92% of the membrane thickness. To ignore the transverse bending stiffness, a modification factor is applied to reduce the transverse bending stiffness contribution to 1% of the longitudinal stiffness, creating a one-way slab. Table 1 shows the materials, the mass density of structural elements, and loads applied to the structure.

Table 1: *Weight and density of elements and applied loads.*

Element	Weight/Density
HCS 200 mm	271 kg/m^2
HCS 320 mm	425 kg/m^2
Glulam beam and columns	460 kg/m^3
CLT wall-panels (5-L, 200 mm)	440 kg/m^3
Additional dead load	1 kN/m^2
Snow load	2.8 kN/m^2
Live load	3.0 kN/m^2

2.1 REFERENCE BUILDING

The 8-floor reference building is shown in Figure 1. The central core consists of CLT-panels and the remaining bearing structure is glulam beams and columns, working as MRTF, with beam dimension of 480x765 mm^2. Column dimensions vary from 480x900 mm^2 for columns in grid A/F and E/F, and 480x720 mm^2 in grid B/C and D/C. HCS works as the separating floor. The top floor is +34 295 mm, and the general story height is 2.8 m. The first floor differs with a story height of 7 695 mm in grid A/F and E/F, and story height of 4980 mm in grid B/C and C/D. The global X- and Y-axis is parallel with gridline F4 and A1, respectively.

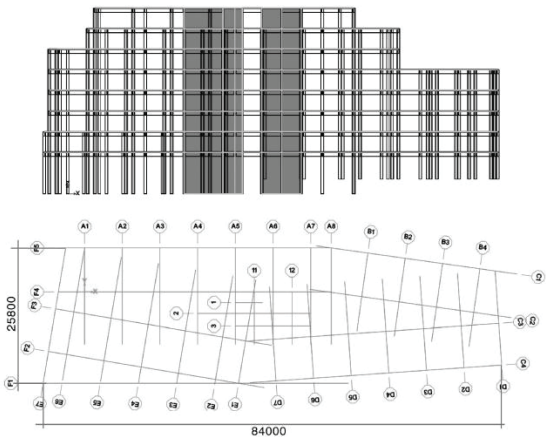

Figure 1: *Outline of reference building and grid.*

2.2 BEAM-TO-COLUMN CONNECTIONS

Several types of beam-to-column connections (BCC) from available research are implemented in the model. The connections are adjusted to fit the dimensions of the structural elements in the reference model, and all connections are based on continuous columns and intermediate beams. All connections are implemented in the analytical model as rotational springs at the beam ends. Two reference connections are made in order to investigate the effect of stiffness of the connections and get comparable extreme values. Pinned connection has springs with zero rotational stiffness, while the rigid connections are implemented with infinite rotational spring stiffness. The rotational stiffness K_R for each connection is based on the analytical formulation found in the respective research.

Following the results from experimental testing where the inclusion of lateral springs did not affect the results relatively much [16], lateral springs are set as rigid in all connections to get comparable results. Rotation of the connection about the column longitudinal axis is neglected as the HCS are assumed to prevent this motion.

Each connection is classified as either pinned, semi-rigid, or rigid according to EC3-1-8 [17], where the stiffness of a typical beam element is used. As the column distances are different in the two global directions, two classification values are used for X and Y, with beam length $L_{b,x}$ = 7200 mm and $L_{b,y}$ = 8400 mm, respectively.

2.2.1 Bolted connection

The determination of K_R for the bolted connection (BC) is based on traditional calculation methods described by EC5 with bolts and slotted steel plates [13]. Using the slip modulus of a single fastener K_{ser} and the corresponding radius from center of rotation r_i, the rotational stiffness in ULS is found using Equation (1):

$$K_R = \sum_{i=1}^{n} \left(2 \cdot \frac{2}{3} \cdot \frac{\rho_m^{1.5} \cdot d}{23} \right) \cdot r_i^2 \tag{1}$$

where ρ_m is the mean density of the connected element and d is the diameter of the bolt. The rotation point is assumed in the center of gravity of the bolts in the beam.

2.2.2 Top-and-seat steel angles connection

The top-and-seat steel angles connection (TS) is evolved from [18], using steel angles on both sides of the column for intermediate BCC connections. The calculation of the rotational stiffness K_R is based on formulation from [19, 20], and is seen in Equation (2):

$$K_R = \frac{h_b^2}{\frac{1}{K_{top}} + \frac{1}{K_{bot}}} \tag{2}$$

https://doi.org/10.52202/069179-0461

where h_b is the height of the beam. K_{top} depends on the bearing stiffness of the column face K_{cc}, axial stiffness of the bolt K_B and the tensile stiffness of the angle horizontal leg K_t. K_{bot} does not include the axial stiffness of the bolt as it is assumed that the bolt has no withdrawal stiffness. The springs are added as a series of springs. K_{CC} is expressed in Equation (3):

$$K_{CC} = \frac{E_{90}\, b_c\, l_{eff,cc}}{h_c} \tag{3}$$

where E_{90} is the modulus of elasticity perpendicular to grain, b_c is the width of the column, $l_{eff,cc}$ is the effective length of the area in compression and h_c is the depth of the column [21]. K_B is expressed in Equation (4) according to [22], using the modulus of elasticity for steel E_s, the cross-sectional area of the bolt A_b and the effective length of the bolt L_b. n is the number of bolts considered to contribute to K_R.

$$K_B = \frac{A_b\, E_s}{L_b} \cdot n \tag{4}$$

K_t is found using the steel angle dimensions and the distance from the critical yielding point to the vertical bolt [22], as seen in Equation (5):

$$K_t = \frac{E \cdot p \cdot t}{a'} \tag{5}$$

2.2.3 Glued-in steel rods connection

The calculation of K_R for the glued-in steel rods connection (GIR) is found using the tensile stiffness of glued-in rods for the tensile stiffness K_{tens} of the connection. The compressive stiffness K_{comp} of the connection is found adding a series of springs where the shear stiffness of the column K_{CS} is expressed by [21], the transverse stiffness of the column K_{CC} as in Equation (3) and the stiffness of the glulam beam in compression K_{BC} defined by [23]. Based on an adapted version from [21], an equation for the rotational stiffness is shown in Equation (6):

$$K_R = \frac{z_{eq}^2}{\frac{1}{K_{tens}} + \frac{1}{K_{comp}}} \tag{6}$$

Where z_{eq} is the equivalent lever arm between the tensile and compressive resultant. K_{tens} is found using the effective stiffness of a rod row and the distance from the bolt row to the center of compression [21]. The design of this connection leads to the connections showing great ductility in experimental testing [24].

2.2.4 Inclined threaded rods connection

The inclined threaded rods connection (ITR) is adopted from [25] and consist of screwed in rods in both the column and beam. The rods are fastened with steel rings, and the rings work as load transferring between the beam and column.

The calculation of K_R is based on component-method, where the stiffness contribution at the column side $K_{ax.c}$ is found using the axial stiffness $K_{ax,l0}$ and the withdrawal stiffness $K_{ser,ax}$ of the rods. Compliance terms S_{xx} and S_{xy} are used to consider the angle of rods. By converting from at point load to a uniformly distributed load acting on a clamped beam, the expression for the stiffness contribution at the column side $K_{R,C}$ is expressed in Equation (7):

$$K_{R,C} = \frac{h_b^2}{\left(S_{xx,c}^{c_1-c_2} + S_{xx,c}^{c_3-c_4}\right) + \left(S_{xy,c}^{c_3-c_4} - S_{xy,c}^{c_1-c_2}\right) \cdot \frac{3h_b}{L_b}} \tag{7}$$

For the stiffness at the beam side $K_{R.B}$, the lateral stiffness K_v of the rod is included in the compliance terms to consider the global direction of the rods:

$$K_{R,B} = \frac{h_b^2}{\left(S_{xx,b1} + S_{xx,b2}\right) + \left(S_{xy,b2} - S_{xy,b1}\right) \cdot \frac{3h_b}{L_b}} \tag{8}$$

The stiffness contribution from the steel rings $K_{R,con}$ is found through numerical analysis and provides 484 kN/mm and 600 kN/mm in compression and tension, respectively [25]. This leads to the equation for K_R seen in Equation (9):

$$K_R = \left(\frac{1}{K_{R,C}} + \frac{1}{K_{R,B}} + \frac{1}{K_{R,con}}\right)^{-1} \tag{9}$$

2.2.5 Overview of rotational stiffness

By applying the dimensions of the structural elements described in 2.1, where some of the connections depend more on the orientation and dimensions of the column, the rotational stiffness for each connection is presented in Table 2. Notation 1 indicates connections located at grid A/F or E/F, while notation 2 refers to grid B/C and C/D, see Figure 1. For the TS, GIR and ITR, four planes of rods are used, and for the bolted connection 16 M16 bolts are placed in a rectangular formation.

Table 2: *Calculated rotational stiffness of investigated connections.*

Connection	Global direction	K_R [kNm/rad]	Rigidity-class
Pinned		0	Pinned
Rigid		∞	Rigid
Bolted		5 629	Pinned
Top-and-seat steel angles	X Y_1 Y_2	49 961 26 684 30 191	Semi-rigid
Glued-in steel rods	X_1 X_2 Y_1 Y_2	53 481 33 938 50 741 38 669	Semi-rigid
Inclined threaded rods	X Y_1 Y_2	51 606 58 705 54 970	Semi-rigid

2.3 CONNECTION HOLLOW-CORE SLABS

The slab consisting of HCS is assumed as a diaphragm with rigid interconnections in the numerical analysis. The connection between HCS to timber beams is based on the connection of a timber-concrete-composite from [26], using vertical glued-in rods glued in the glulam beam and casted together with the HCS. This connection is implemented as a hinged connection in the numerical analysis.

2.4 MODAL RESPONSE SPECTRUM ANALYSIS

Modal response spectrum analysis (MRSA) is done according to EC8 [27] for each connection case, where the value for peak ground acceleration (PGA) is assumed for a building located in Oslo, Norway. This leads to a ground acceleration of reference ground acceleration of 0.3 m/s^2.

As the building is vulnerable for torsional effects, the Complete Quadratic Combination (CQC)-method proposed by EC8 is used for combination of modes. The seismic effect in the global directions X and Y is combined by adding 30% of the seismic effect from one direction to the other.

For a building in seismic class IIIa and ground type D, the parameters Type 2 design response spectrum is shown in Table 3. The average joint absolute drift for each connection case is found. A behavior factor of q = 1.5 is used for the design spectrum for all connection cases except GIR, where q = 2.5.

Table 3: *Parameters for creating Type 2 elastic spectrum.*

Ground type	S	T_B [s]	T_C [s]	T_D [s]
D	1.8	0.1	0.3	1.2

3 CONNECTION EVALUATION

The results from the analysis show that less rigid connections lead to a torsional mode being present at a lower frequency. Increasing the rigidity of the BCC leads to torsional modes being present at higher frequency and less participating modes. The comparison of results from the MRSA for each BCC indicates that increasing the rotational stiffness increases the absolute- and interstory drift.

3.1 PINNED CONNECTION

For the pinned connection, the modes and corresponding contributing mass are listed in Table 4. The first mode is a torsional mode, and the cumulative mass participation ratio exceed 90% in mode 6.

Table 4: *Modes and participation ratio for pinned connection.*

Mode	Period [s]	m_X [%]	m_Y [%]	m_{RZ} [%]
1	2.81	0.1	0.0	70.4
2	1.442	1.1	76.4	0.0
3	1.286	78.2	1,1	0.1
4	0.794	0.1	0.0	17.5
5	0.415	12.1	1.4	0.0
6	0.403	1.5	12.5	0.1
	∑	**93.5**	**91.4**	**88.3**

For the MRSA of the pinned connection, the average story displacement is shown in Figure 2, with a maximum drift of 30.7 mm at the top story. The maximum interstory drift of 5.5 mm is found in story 1 with seismic loading in global Y as the dominant load.

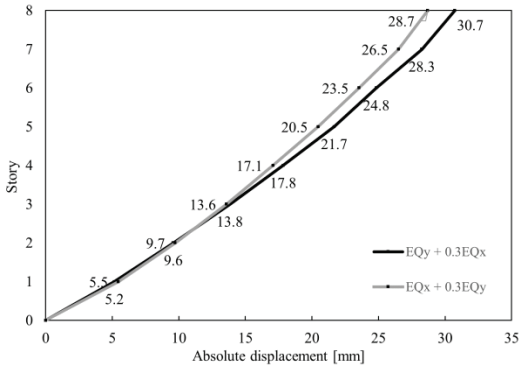

Figure 2: *Average story displacement for pinned connection.*

3.2 RIGID CONNECTION

For the rigid connection, the modes and corresponding mass participation ratios are listed in Table 5. The first torsional mode occurs at mode 3 and the cumulative mass participation ratio exceeds 90% in mode 5.

https://doi.org/10.52202/069179-0461

Table 5: *Modes and participation ratio for rigid connection.*

Mode	Period [s]	m_X [%]	m_Y [%]	m_{RZ} [%]
1	1.184	21.2	64.4	1.3
2	1.065	59.1	23.1	4.3
3	1.003	4.7	0.0	81.7
4	0.349	2.3	6.2	0.0
5	0.318	7.0	2.0	0.0
	∑	**94.3**	**95.7**	**87.3**

For the MRSA of the rigid connection, the average joint absolute drift is shown in Figure 3, with maximum drift of 46.7 mm at the top story. The maximum interstory drift of 14.4 mm is found in story one with the seismic loading in global X as the dominant load.

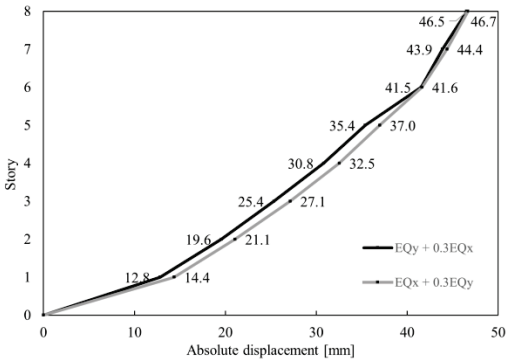

Figure 3: *Average story displacement for rigid connection.*

3.3 BOLTED CONNECTION

For BC, the modes and corresponding contributing mass are listed in Table 6. The first mode is a torsional mode, and the cumulative mass participation ratio exceed 90% in mode 6.

Table 6: *Modes and participation ratio for BC.*

Mode	Period [s]	m_X [%]	m_Y [%]	m_{RZ} [%]
1	2.407	0.1	3.0	72.1
2	1.401	0.0	75.5	2.3
3	1.245	80.6	0.0	0.1
4	0.734	0.1	0.0	14.6
5	0.409	2.9	10.1	0.0
6	0.387	9.6	3.1	0.1
	∑	**93.3**	**91.7**	**89.2**

For the MRSA of BC, the average story displacement is shown in Figure 4, with a maximum drift of 25.9 mm at the top story. The maximum interstory drift of 5.4 mm is found in story 1 with seismic loading in global X as the dominant load.

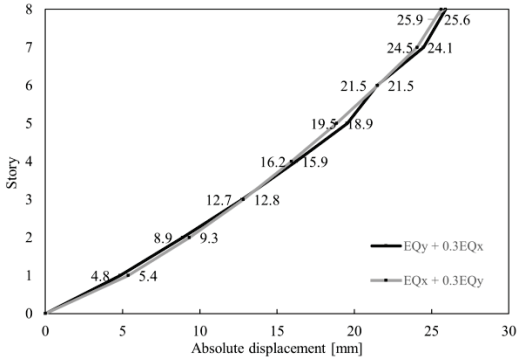

Figure 4: *Average story displacement for BC.*

3.4 TOP-AND-SEAT STEEL ANGLE CONNECTION

For TS the modes and corresponding contributing mass are listed in Table 7. The first torsional mode occurs at mode 3, and the cumulative mass participation ratio exceed 90% in mode 6.

Table 7: *Modes and participation ratio for TS.*

Mode	Period [s]	m_X [%]	m_Y [%]	m_{RZ} [%]
1	1.303	0.0	68.2	13.2
2	1.126	81.8	0.2	2.2
3	1.121	2.3	12.2	65.2
4	0.394	0.1	10.5	1.4
5	0.344	0.1	1.2	9.4
6	0.340	10.2	0.1	0.1
	∑	**94.5**	**92.4**	**91.5**

For the MRSA of TS, the average story displacement is shown in Figure 5, with a maximum drift of 23.6 mm at the top story. The maximum interstory drift of 6.1 mm is found in story 1 with seismic loading in global X as the dominant load.

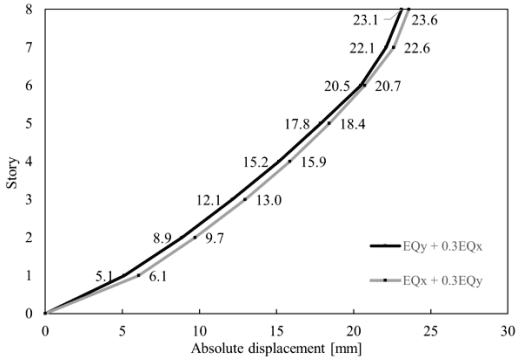

Figure 5: *Average story displacement for TS.*

https://doi.org/10.52202/069179-0461

3.5 GLUED-IN STEEL RODS CONNECTION

For GIR, the modes and corresponding contributing mass are listed in Table 8. The first torsional mode occurs at mode 3, and the cumulative mass participation ratio exceed 90% in mode 6.

Table 8: *Modes and participation ratio for GIR.*

Mode	Period [s]	m_X [%]	m_Y [%]	m_{RZ} [%]
1	1.283	0.2	69.8	11.9
2	1.122	83.8	0.0	0.6
3	1.110	0.4	11.2	68.8
4	0.391	0.2	10.8	0.8
5	0.340	0.4	0.7	0.8
6	0.332	9.7	0.1	9.3
	∑	**94.6**	**92.6**	**91.7**

For the MRSA of GIR, the average story displacement is shown in Figure 6, with a maximum drift of 16.7 mm at the top story. The maximum interstory drift of 3.9 mm is found in story 1 with seismic loading in global X as the dominant load.

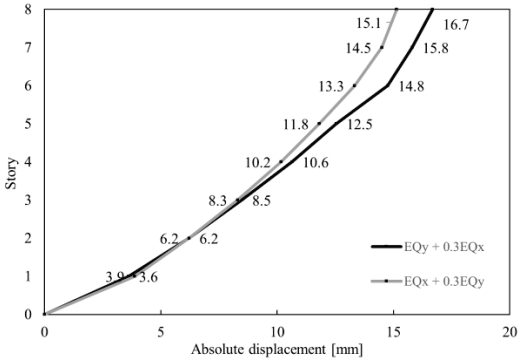

Figure 6: *Average story displacement for GIR.*

3.6 INCLINED THREADED RODS CONNECTION

For ITR the modes and corresponding contributing mass are listed in Table 9. The first torsional mode occurs at mode 3, and the cumulative mass participation ratio exceed 90% in mode 5.

Table 9: *Modes and participation ratio for ITR.*

Mode	Period [s]	m_X [%]	m_Y [%]	m_{RZ} [%]
1	1.246	3.6	71.4	7.6
2	1.120	80.7	3.0	0.7
3	1.092	0.0	7.4	74.1
4	0.384	2.3	8.6	0.1
5	0.339	7.6	2.5	0.4
	∑	**94.2**	**92.9**	**82.9**

For the MRSA of the inclined threaded rods connection, the average story displacement is shown in Figure 7, with a maximum drift of 24.6 mm at the top story. The maximum interstory drift of 6.3 mm is found in story 1 with seismic loading in global X as the dominant load.

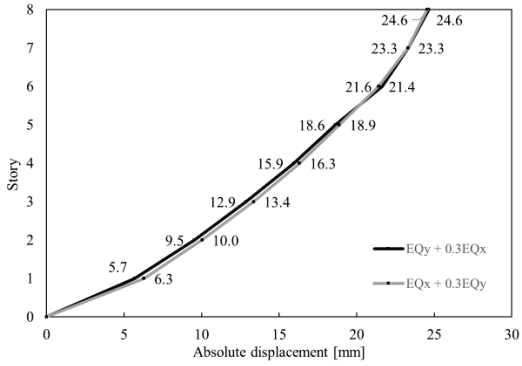

Figure 7: *Average story displacement for ITR.*

4 DISCUSSION

In addition to the numerical results presented, each BCC is discussed based on several parameters: ease of construction on-site, ease of disassembly, reuse potential of beams, columns and connecting elements and aesthetics of connection.

4.1 STRUCTURAL BEHAVIOR

The absolute displacements from the MRSA are calculated using the average joint displacements in each floor. For connection cases where two torsional modes are present before the cumulative mass participation ratio exceeds 90%, the internal variation in joint displacement is higher than connections with only one torsional mode.

By comparing the result from the MRSA with E_Y as the dominant seismic load, Table 10 shows that the tendency is that connections that offer lower rotational stiffness has the first torsional mode outside of the spectrum where the pseudo-acceleration is significant.

For a building in an area with low value for ground acceleration, this means that a connection with low rotational stiffness can be a better option with regards to seismic performance.

Table 10: *Comparison of first torsional mode, torsional mass participation ratio, and the corresponding pseudo-acceleration.*

Connection	T [s]	m_{Rz} [%]	a_g [g]
Pinned	2.810	70.4	0.008
Rigid	1.003	81.7	0.034
BC	2.407	72.1	0.008
TS	1.121	65.2	0.031
GIR	1.110	81.2	0.019
ITR	1.092	74.1	0.032

https://doi.org/10.52202/069179-0461

4.2 EASE OF CONSTRUCTION ON-SITE

The ease of construction on-site is critical for efficient construction process of a building. BCC with an extensive process with necessary high precision is time consuming and harder to construct on-site.

ITR is rather comprehensive to construct and require high precision to acquire the rotational stiffness from the numerical formulation. The effect of different rod-to-grain angle than used to calculate the rotational stiffness affects the rotational stiffness significantly [25]. Following this, the insertion of rods in both the beam and the column should be done in a controlled environment (typically off-site) and leads to low on-site flexibility.

The same applies to GIR because contact between the beam and column faces is critical. This is due to the spring stiffness of the column face, K_{cc}, which is one of the decisive parameters for the rotational stiffness. As a result, the mounting process is time-consuming and has minimal tolerance for errors both in production and during assembly. However, if the on-site margin of error is within the tolerance limits and the necessary off-site preparations are completed, the assembly process may be time-effective.

4.3 EASE OF DISASSEMBLY

The ease of disassembly is critical for efficient tear-down of buildings and possibility for reusing structural elements. Connections with more permanent connecting elements, typically glue or welds, are considered having lower reuse potential [28] and a relatively low reversibility [29].

This leads to GIR being a less suitable alternative when considering possibilities for future reuse of beams and columns. The structural performance of this connection depends on the withdrawal capacity of glued-in rods, making the reversibility of the connection, without causing damage to the column, beam, or rods, low.

Conversely, connections that utilize bolts and screws as connecting elements require less time for disassembly [29]. This implies that the traditional bolted connection, the steel angle connection, and the inclined threaded rods connection may all be relatively easy to disassemble.

4.4 REUSE POTENTIAL OF BEAMS, COLUMNS AND CONNECTING ELEMENTS

The reuse potential for the components in each BCC is discussed, where the potential is based on the possible failure mode of the BCC, and the affected area of the beam and column. The reuse of connected and connecting elements is based on the possibility of reusing components of the connection. Connections with more permanent connecting elements, typically glue or welds, are considered having lower reuse potential [28].

One issue with the traditional type of timber connections, like BC, can be residual displacement caused by non-linear behavior of the timber under initial load. This happens due to imperfections in the timber surface facing the connector and occurs even if the dowels are tightly fitted [30]. This means elements involving bolts should be checked for damages, and most probably the portion of the elements with bolt holes should be deposited. Bolted connections should also generally be designed for ductile failure of the connector [13] and due to this requirement, the bolts should not be reused for structural purpose. The possibility of removing the affected portion of the beam and column is incidentally the cased for all connections discussed, but especially relevant for GIR, as the rods are time-consuming to remove.

ITR can have the highest potential for reuse, but this requires designing the next project based on the available beams and columns. This concept is referred to as stock-constrained design [31].

4.5 REUSE OF HOLLOW-CORE SLABS

To include HCS in the design of a sustainable building, the design process should evaluate if the building is going to be designed using an existing stock of materials, designed for future reuse. The optimal solution would be to combine these two concepts, but as for HCS, the concept of including already existing elements seems to be the better option. The reasoning behind this is the large amount of already produced HCS.

The HCS should be connected to the timber beams using the same concept as for glued in shear studs, creating a timber-concrete composite. This is shown to reach good shear capacity [26] and can also be utilized to reduce the necessary cross-sectional area of the timber beams due to timber-concrete-composite effect.

4.6 EVALUATION OF THE CONCEPT

The advantages with the concept of reusing and designing for future reuse is described to be of significant value. Utilization of already produced structural elements introduce a potential of reducing significant amounts of global greenhouse gas emissions. The disadvantages are, on the other hand, what significantly raises the threshold to fully utilize the potential reduction of environmental burden the construction of a new building.

For structural elements, the process of tearing down a building often implies rough treatment for vulnerable elements like timber. To facilitate future reuse of these elements, the process needs to be changed from demolition to disassembling. The integration of disassembling will increase the time consumption of tearing down a building significantly and consequently increasing the cost.

To implement connections with higher rotational stiffness more suitable for modular buildings, the concept of stock-

constrained design may be an effective method to utilize already produced elements. However, when using this method, the design of the new building is restricted by available materials. This could lead to a lower utilization of available land area, and implicit meaning a higher cost per area.

5 CONCLUSION

In this paper a modal response spectrum analysis according to EC8 is done for a reference building consisting of a variety of beam-to-column connection from available research, hollow-core slabs as separating floor and a CLT-core.

The results of the presented study show that a higher rotational stiffness in beam-to-column connections shifts the buildings first torsional mode to a higher mode and lower frequency, but generally lowers the reusability of the structural components. Therefore, in the cases where the reusability is prioritized, the evaluated connections with higher rotational stiffness beam-to-column connections may not be the best alternative. However, according to the findings of the numerical investigation, it is possible to combine design for seismic loadings in low-seismicity regions with designing for future reuse by selecting beam-to-column connections with appropriate characteristics. Overall, this is a promising option for the design of future projects.

REFERENCES

[1] Ghayeb H. H., Razak H. A., Sulong N. H. R.: Evaluation of the CO2 emissions of an innovative composite precast concrete structure building frame. *J Clean Prod*, 242:118567, 2020.

[2] Eberhardt C. L. M., Birgisdóttir H., Birkved M.: Life cycle assessment of a Danish office building designed for disassembly, 2018.

[3] Peretti G., Druhmann C. K., Bleiziffer S., Brown J., Campama Pizarro M., del Río Merino R., *et al.*: Working Group Three Report: Regenerative Construction and Operation. *RESTORE - REthinking Sustainability TOwards Regenerative Economy*, 2019.

[4] Joensuu T., Leino R., Heinonen J., Saari A.: Developing Buildings' Life Cycle Assessment in Circular Economy-Comparing methods for assessing carbon footprint of reusable components. *Sustain Cities Soc*, 77:103499, 2022.

[5] Adesina A.: Recent advances in the concrete industry to reduce its carbon dioxide emissions. *Environmental Challenges*, 1, 2020.

[6] de Castilho V. C., Nicoletti M. do C., el Debs M. K.: An investigation of the use of three selection-based genetic algorithm families when minimizing the production cost of hollow core slabs. *Comput Methods Appl Mech Eng*, 194(45–47):4651–4667, 2005.

[7] Standard Norge: NS 3682:2022 Hulldekker av betong til ombruk, 2022.

[8] Memari A., Ramaji I. J.: Identification of structural issues in design and construction of multi-story modular buildings, 2013.

[9] Niu Y., Rasi K., Hughes M., Halme M., Fink G.: Prolonging life cycles of construction materials and combating climate change by cascading: The case of reusing timber in Finland. *Resour Conserv Recycl*, 170, 2021.

[10] Bağbanci M. B., Bağbanci Ö. K.: The Dynamic Properties of Historic Timber-Framed Masonry Structures in Bursa, Turkey. *Shock and Vibration*, 2018.

[11] Pan Y., Tannert T., Kaushik K., Xiong H., Ventura C. E.: Seismic performance of a proposed wood-concrete hybrid system for high-rise buildings. *Eng Struct*, 238:112194, 2021.

[12] Gallo P. Q., Carradine D. M., Ramiro Bazaez ·.: State of the art and practice of seismic-resistant hybrid timber structures. *European Journal of Wood and Wood Products*, 79:5–28, 2021.

[13] EN 1995-1-1: Eurocode 5: Design of timber structures - Part 1-1: General - Common rules and rules for buildings. Standard Norge, NS-EN 1995-1-1:2004+A1:2008+NA:2010 2004.

[14] CSI America.: SAP2000, 2021.

[15] Follesa M., Christovasilis I. P., Vassallo D., Fragiacomo M., Ceccotti A.: Seismic design of multi-storey cross laminated timber buildings according to Eurocode 8. *Ingegneria Sismica*, 4, 2013.

[16] Vilguts A., Stamatopoulos H., Malo K. A.: Parametric analyses and feasibility study of moment-resisting timber frames under service load. *Eng Struct*, 228:111583, 2021.

[17] EN 1993-1-8: Eurocode 3: Design of steel structures - Part 1-8: Design of joints. NS-EN 1993-1-8:2005+NA:2009, 2005.

[18] Zhou S. R., Li Z. Y., Feng S. Y., Zhu H., Kang S. B.: Effects of bolted connections on behaviour of timber frames under combined vertical and lateral loads. *Constr Build Mater*, 293:123542, 2021.

[19] Tsalkatidis T., Amara Y., Embaye S., Nathan E.: Numerical investigation of bolted hybrid steel-timber connections. *Front Built Environ*, 4, 2018.

[20] Karagiannis V., Málaga-Chuquitaype C., Elghazouli A. Y.: Behaviour of hybrid timber beam-to-tubular steel column moment connections. *Eng Struct*, 131:243–263, 2017.

[21] Yang H., Liu W., Ren X.: A component method for moment-resistant glulam beam–column connections with glued-in steel rods. *Eng Struct*, 115:42–54, 2016.

[22] Málaga-Chuquitaype C., Elghazouli A. Y.: Component-based mechanical models for blind-bolted angle connections. *Eng Struct*, 32(10):3048–3067, 2010.

https://doi.org/10.52202/069179-0461

[23] Tomasi R., Zandonini R., Piazza M., Andreolli M.: Ductile End Connections for Glulam Beams. *Structural Engineering International*, 18:290–296, 2008.
[24] Fairweather R. H.: Beam Column Connections for Multi-storey Timber Buildings A Report, 1992.
[25] Stamatopoulos H., Malo K. A., Vilguts A.: Moment-resisting beam-to-column timber connections with inclined threaded rods: Structural concept and analysis by use of the component method. *Constr Build Mater*, 322:126481, 2022.
[26] Ling Z., Zhang H., Mu Q., Xiang Z., Zhang L., Zheng W.: Shear performance of assembled shear connectors for timber–concrete composite beams. *Constr Build Mater*, 329:127158, 2022.
[27] EN 1998-1: Eurocode 8: Design of structures for earthquake resistance - Part 1: General rules, seismic actions and rules for buildings. NS-EN 1998-1:2004+A1:2013+NA:2021, 2004.
[28] Hradil P.: Barriers and opportunities of structural elements re-use, 2014.
[29] Kondo Y., Deguchi K., Hayashi Y. I., Obata F.: Reversibility and disassembly time of part connection. *Resour Conserv Recycl*, 38(3):175–184, 2003.
[30] Reynolds T., Harris R., Chang W.-S.: In-service dynamic stiffness of dowel-type connections, 2013.
[31] Warmuth J., Brütting J., Fivet C.: Computational Tool for Stock-Constrained Design of Structures, 2021.

World Conference on Timber Engineering Oslo 2023

DEVELOPMENT OF TEMPORARY STRUCTURE USING CLT PANEL: INVENTION OF CONSTRUCTION AND VERIFICATION BY CONSTRUCTION EXPERIMENT

Hiroaki Kubotera[1], Toshiaki Sato[2], Yohei Aioi[3] and Kazuo Niikuma[4]

ABSTRACT: Temporary buildings have the advantage of being able to meet sudden demand. In recent years, the demand has been affected not only in the event of a disaster but also due to COVID-19 infection. This paper shows a temporary structure that can be used repeatedly for the purpose of constructing a temporary building using Cross Laminated Timber (CLT), and confirmed its practicality through construction experiments.

KEYWORDS: CLT, Temporary Construction, Experimental Study

1 INTRODUCTION

Buildings are divided into temporary buildings and permanent buildings according to the period of use, and in particular, temporary buildings have the advantage of being able to meet sudden demand. In recent years, the demand has been affected not only in the event of a disaster but also due to COVID-19 infection, and the Japanese government has approved the use on the street for the purpose of taking out and installing terrace seats, so temporary buildings are also used in restaurants. Under these circumstances, wood is lightweight and easy to process, and deterioration does not pose a major problem on the premise of dismantling and repairing, so it has the potential as a material for temporary buildings. From the perspective of creating demand for timber in Japan, it is meaningful to aim for the general spread of wood-based materials in the field of temporary construction, where a large amount of demand can be expected from local governments and private companies.

Against this background, we designed a temporary structure that can be used repeatedly for the purpose of constructing a temporary building using Cross Laminated Timber (CLT), and confirmed its practicality through construction experiments. The developed temporary structure is composed of CLT panels with four corners machined and steel joints, which facilitates on-site assembly.

2 DESIGN OF TEMPORARY STRUCTURE USING CLT PANELS

2.1 OUTLINE OF STRUCTURAL SYSTEMS

The temporary structure developed in this paper is composed of four CLT (3-layer, 3-ply, Japanese cider) panels with the same cutting at the four corners and a steel joint with a truss mechanism. Fig. 1 shows the elevation of the temporary structural system on each side, and Fig.2 shows an image of using as restaurant on the street.

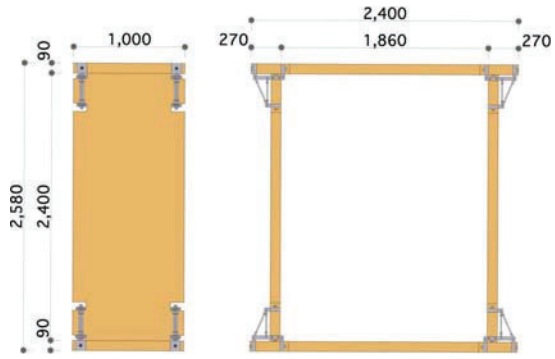

***Figure 1**: Elevation of temporary structural system*

***Figure 2**: Image of terrace seats with the developed unit as the core*

[1] Hiroaki Kubotera, Senior Technician, Kyushu University, Japan, kubotera@arch.kyushu-u.ac.jp
[2] Toshiaki Sato, Dr. Eng., Assoc. Prof., Kyushu University, Japan, sato@arch.kyushu-u.ac.jp
[3] Yohei Aioi, Former Bachelor Student, Dept. of Arch., Kyushu University, ya616cronaldo7@gmail.com
[4] Kazuo Niikuma, President, MASA LABO Co. Ltd., niikuma@masalabo.co.jp

https://doi.org/10.52202/069179-0462

In Fig. 1, The truss mechanism resists the horizontal force in the frontage direction, and the wall itself resists in the direction of the wall orthogonal to it.

Temporary buildings, which are supposed to be demolished in a certain period of time, consume resources faster, so consideration must be given to material reuse and material recycling, and this project also emphasized this. In particular, the dimensions and fabrication of the four CLT plates were standardized for convenience in repeated assembly and disassembly as a temporary unit, and the shapes of the eight steel joints were also standardized for easily removal.

2.2 COMPONENT DESIGN

All CLT panels are processed in the same way to ensure reusability. At the prototype stage, as shown in Fig. 3, we considered a plan to provide tenons with notches at the four corners of the CLT, and a plan to replace the tenons with steel materials. In consideration of restraint, we adopted a plan to make a through hole at the position where the tenon was supposed and pass a bolt (diameter = 16 mm) through it. As a result, the rattling caused by the error of wood processing can be corrected by tightening the nut. The outline of the processing of the entire CLT panel is as shown in Fig. 4.

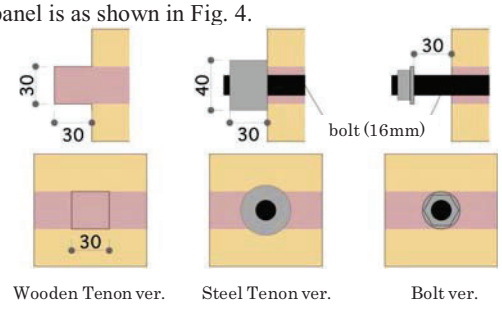

***Figure 3**: Wood processing and trial production of joints*

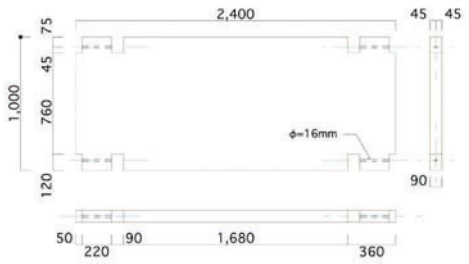

***Figure 4**: Outline of CLT panel processing*

Fig. 5 shows an outline of the steel joint and the parts of each part constituting the joint. All parts are made of steel (ss400) and are integrated into one joint with four pins, which can be easily assembled and disassembled by attaching and detaching them. In order to reduce the cost of electric discharge machining, the member B was divided into three parts and fixed with M8 countersunk screws. For member C, since it is a truss mechanism that applies only axial force to the member, it is necessary to use a pin joint, and rod end bearings are used at both ends of the M10 bolt.

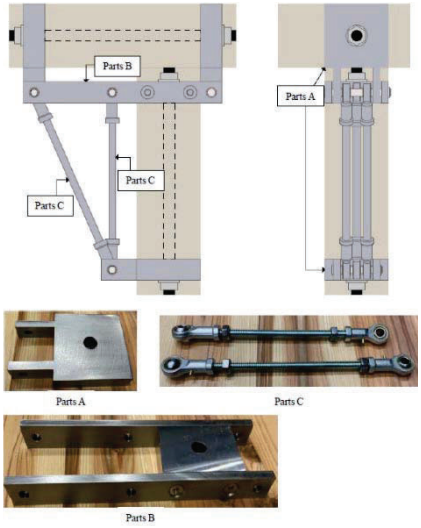

***Figure 5**: Steel joint configurations and parts*

In the design of this joint, the dimensional error of each member was also examined in consideration of on-site work. Compared to wood processing, steel processing causes almost no dimensional error, so for the hinge part that is completed only with steel, the hole diameter and hinge pin diameter are both 10 mm, and a hinge pin with a negative tolerance was selected. The through hole of the bolt, which is expected to be affected by the processing error of the wood, was 0.5 mm larger and the wood was processed. In addition, in order to absorb dimensional errors in the CLT cutting process, the bolts of part C are designed to have a margin of 5 mm between the rod end bearings, and the length of the entire member C can be adjusted by fastening the bolts during construction.

3 INVESTIGATION OF STRUCTURAL PERFORMANCE

3.1 OVERVIEW OF INVESTIGATION

The temporary units proposed in this research do not examine the basic conditions that the building must satisfy, such as ensuring fire resistance and fixing methods to the ground. Safety based on allowable stress calculations against long-term loads and rarely occurring loads and external forces, with the goal of ensuring performance equivalent to temporary structures according to the Japanese Building Standards Law, considering the assumed usage. We decided to verify the Tables 1 & 2 list the mechanical properties of the steel and wood used in the study.

***Table 1:** Mechanical property of steel*

Steel type	Reference strength [MPa]	Long-term allowable stress		Short-term allowable stress
		σ	τ	
SS400	$F = 235$	$F/1.5$	$F/1.5\sqrt{3}$	F

https://doi.org/10.52202/069179-0462

Table 2: *Mechanical property of Wood*

Species	Design strength [MPa]			
	Comp-ression	Tensile	Bending	Shear
Japanese cidar	17.7	13.5	22.2	1.8

Structural performance was confirmed by the following procedure. Since this temporary structure is a composite structure of wood and steel, we first verified the safety of the steel joints against the assumed external force, and then modelling the joints on the upper part of the unit as a static rigid frame assuming rigid joints. Considered the safety of wood. According to the design guidelines for temporary structures, when the scale is small, the external force assumed in the design against snow load and wind load is often reduced, but with reuse in mind, each member should have a certain amount of surplus performance. Therefore, we decided not to conduct this study.

3.2 EVALUATION OF STRUCTURAL PERFORMANCE

Fig. 5 shows the mechanical model of the steel joint. In the actual design, bolt fastening force is generated against the steel plate sandwiched between the stud bolts (φ = 16 mm) passed through the CLT, but this model ignores that effect as an evaluation on the safe side. Then, consider only the effect of preventing the bolt from coming off.

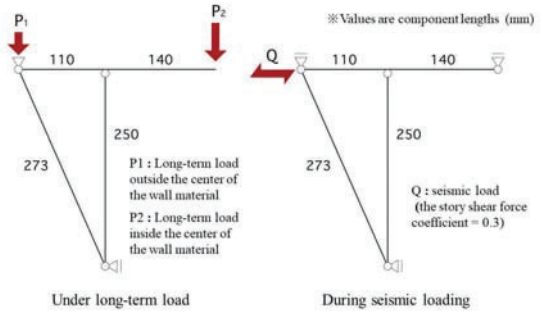

Figure 6*: Mechanical model of steel joints*

Regarding the long-term load P shown in Fig. 6, the dead load is generally calculated as a uniformly distributed load. The conditions were set such that the portions inside the wall material act on both ends of the joint as concentrated loads P_1 and P_2, respectively. Assuming a cedar density of 0.38 and a gravitational acceleration of 9.8 [m/s^2]

$$P_1 = 0.38\times10^{-6}\times500\times225\times90\times9.8 = 37.8\ [\mathrm{N}]$$

$$P_2 = 0.38\times10^{-6}\times500\times975\times90\times9.8 = 163.4\ [\mathrm{N}].$$

Similarly, regarding the seismic load Q in Fig. 5, the dead weight of the ceiling material, two wall materials, and steel joints (approximately 9.0 kgf) is assumed to be the fixed load used to calculate the story shear force, and the story shear force coefficient was set to 0.3 as a safe side evaluation. From the above conditions

$$Q = 0.3\times W/2 = 415\ [\mathrm{N}].$$

The reason for dividing by two in the above formula is that when the unit is viewed from the frontage direction, it is assumed that the two steel joints at the front and back will simultaneously resist the seismic load.

Table 3 shows the maximum stress in each member of the steel joint as a result of the investigation based on the above. From the results shown in Table 3, all values are well within the allowable stress shown in Table 1, confirming its safety.

Table 3: *Maximum stress of steel joints members*

Load	Member	σ_{max} (axial) [MPa]	σ_{max} (bending) [MPa]	τ_{max} [MPa]
Only dead load	Diagonal	5.2	–	–
	Vertical	4.8	–	–
	Horizontal	–	0.52	7.7
Seis mic force	Diagonal	13.2	–	–
	Vertical	12	–	–
	Horizontal	–	1.4	19

Following the investigation of the steel joints, Fig. 7 shows the mechanical model used for investigation of CLT panel.

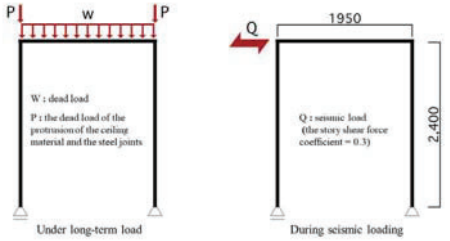

Figure 7*: Mechanical model for investigating CLT panel*

Regarding the long-term load shown in Fig. 7, the uniformly distributed load w in the figure represents the dead load of the ceiling material, and the vertical load P represents the dead load of the protrusion of the ceiling material and the steel joints. Each value is

$$w = \frac{0.38\times10^{-6}\times1000\times1950\times90\times9.8}{1950} = 0.34\ [\mathrm{N/mm}]$$

$$P = \left(0.38\times10^{-6}\times1000\times225\times90 + 9.0\times2\right)\times9.8 = 252\ [\mathrm{N}]$$

https://doi.org/10.52202/069179-0462

The seismic load Q shown in Fig. 7 is the same as in the investigation of steel joints, but since it is a model of the entire unit here, it is set to 830 N before dividing by two. Table 4 summarizes the maximum stress generated in the CLT based on the calculation results of the stress in each part based on the above discussion. As with steel joints, all values in Table 4 are within the allowable stress shown in Table 2, confirming its safety.

Table 4: *Maximum stress of CLT panel*

Load	Member	σ_{max} (axial) [MPa]	σ_{max} (bending) [MPa]	τ_{max} [MPa]
Only dead load	Wall	6.5×10^{-3}	–	–
	Ceiling	–	5.6×10^{-3}	0.12
Seismic force	Wall	1.2×10^{-2}	1.4×10^{-2}	1.5
	Ceiling	9.2×10^{-3}	1.7×10^{-2}	1.5

As the final part of the member study, the results of other parts such as bearings and pins, as well as the buckling of bolts, are summarized below. The bearing used this time has a radial static load rating of 13.2 kN. It can be seen that there is sufficient margin even when compared with the axial force of 1445 N, which is the largest stress shown in Table 3, 18.4 (N/mm2), multiplied by the cross-sectional area of 78.5 mm2 of member C (Fig. 5).

According to the results in Table 3, the largest force acting on the pin is the axial force acting on the diagonal member, which is 13.2 [MPa] x 78.5 [mm^2] = 1036 N. These are divided into two components, vertical and horizontal. We evaluated the stress generated in the hinge pin using two simple beam models. Fig. 8 shows the dynamic model used in the study of the pin, and Table 5 shows the calculation results using it.

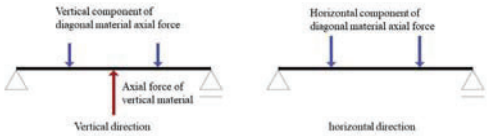

Figure 8*: Mechanical model for evaluating hinge pin stress*

Table 5: *Maximum stress of hinge pin*

Direction	σ_{max} (bending) [MPa]	τ_{max} [MPa]
Horizontal	41.2	4.29
Vertical	78.5	9.71

The hinge pin adopted in this research is carbon steel S35C for machine structural use. Although this is stronger than SS400 material, the maximum stress of the hinge pin is within the allowable stress of SS400 shown in Table 1, so the safety can be confirmed.

The double-ended bearing material (member C) does not become plastic within the design load range, but confirms that buckling does not occur within the elastic range. The buckling stress σ_{cr} is generally obtained from the following equation.

$$\sigma_{cr} = \frac{\pi^2 E}{\lambda^2} \text{ where } \lambda = \frac{L_k}{i} \qquad (1\text{-}1, 2)$$

In the above equations, E : Young's modulus, λ : slenderness ratio, L_k : buckling length, i : cross-sectional secondary radius. The buckling length L_k is the same as the length of the member because the double-end bearing material can be regarded as a double-end pin. As the Young's modulus of SS400 is 205 [GPa] and member cross section is circular with a diameter of 10 mm,

$$\text{Diagonal}: \sigma_{cr} = \frac{\pi^2 \times 2.05\times10^5}{(273/2.5)^2} = 169\ [\text{MPa}]$$

$$\text{Vertical}: \sigma_{cr} = \frac{\pi^2 \times 2.05\times10^5}{(250/2.5)^2} = 202\ [\text{MPa}]$$

is calculated. Comparing this with the stress shown in Table 3, it is considered that buckling does not occur within the range of the design load this time.

4 VERIFICATION OF EFFECTIVNESS BY CONSTRUCTION EXPERIMENT

4.1 OUTLINE OF CONSTRUCTION TEST

A construction experiment was conducted to verify the effectiveness of the temporary unit. At the design stage, we were thinking of a procedure to assemble the unit with the unit laid on its side, and then pull the roof panel to raise it. However, in this experiment, from the viewpoint of ensuring construction space and safety, we adopted the method of attaching the wall panel first and joining it with the roof panel with a crane as shown in Fig. 9.

In this construction experiment, it took about 2 hours to rework the wood part due to the small error of the hinge part. The actual assembly time was about 30 minutes, and After the completion of the construction experiment, no distortion or twisting was observed in the entire unit within the range of visual observation. It was confirmed that it was very stable under the load of its own weight, which is enough to lift the whole with a crane, and no large gaps were found in the joints.

4.2 EXAMINATION OF PROBLEMS SEEN DURING CONSTRUCATION

(a) Hinge part

First of all, the poor workability of the hinge part was a problem. At the design stage, there was no dimensional leeway in the hinge part, but with only the negative tolerance of the hinge pin, the workability was poor, and there were some cases where the pin did not pass through.

https://doi.org/10.52202/069179-0462

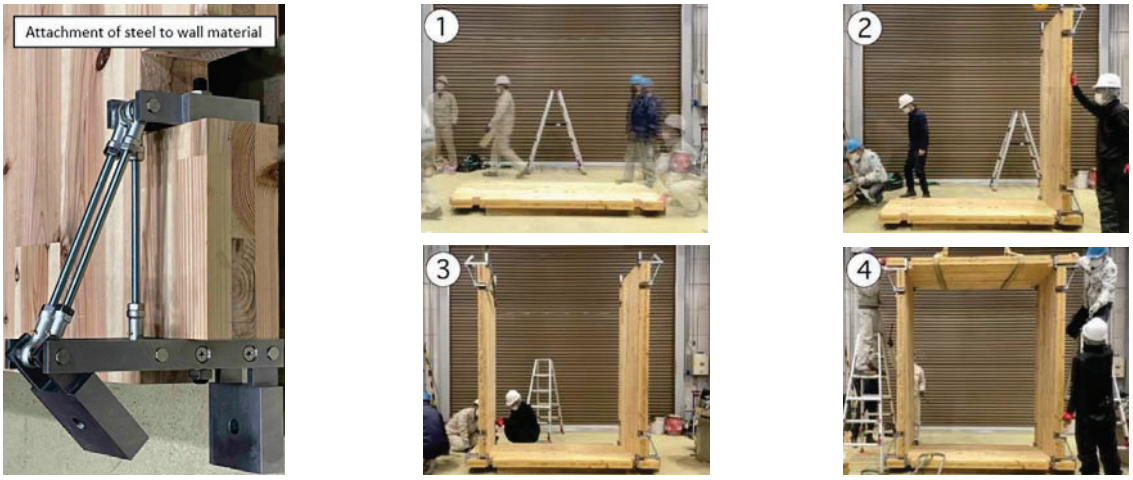

***Figure 9**: Procedure of construction experiment*

We think that the diameter of the through holes at both ends of the member B should have been designed to be 0.5 to 1 mm larger.

(b) Weight

The second point is the problem of weight. In this construction experiment, a overhead crane was used, so there were no particular weight problems, but considering the actual operation as a small-scale temporary unit, it is necessary to consider the possibility of assembling and dismantling only by human power. Especially, the weight of CLT is a problem, and at present it is about 85 [kgf] per piece even after processing, which is likely to adversely affect workability. In order to be able to flexibly respond to changes in shape and processing during the design process, including the steel joints, there was an aspect of giving a margin to the cross section of each member at the initial stage of selecting members. Considering the surplus performance, it may be necessary to reconsider the thickness of the laminated board and the cross-sectional area of each steel material to optimize the weight.

(c) Machining accuracy

The CLT prepared in this study was not pre-cut at the factory, but was hand-processed at the site. A particular problem was the machining error in machining the 16mm through-hole for the stud bolt to pass through, which exceeded the expected error in the design stage. The cause was thought to be the storage method of the CLT before processing, and about 2 mm of warpage occurred in the long axis direction during processing. In manual drilling, it is difficult to keep vertical and horizontal, but warping made this process even more difficult. As a result, in this construction experiment, as shown in Fig. 10, the hole drilled during processing was expanded to a maximum of 21 mm and assembled. If the steel joints are assembled first, as in this case, the error absorption performance of the steel cannot be fully demonstrated, so it can be said that it is necessary to improve it to absorb the deformation of the wood after processing, assuming reuse.

***Figure 10:** Through hole in CLT before and after modification*

(d) Truss members

When I checked the condition of each part after the unit was assembled, it was found that among the members (member C) with bearings attached to both ends in the steel joint, six at the bottom of the unit were clearly in a state where no axial force was generated. The reason is that the initial deformation of the wall material during assembly is within the error absorption range assumed at the design stage, and no force is generated in the member in the first place, or the stud bolt passed through the CLT is tightened with nuts from both sides. Therefore, it is conceivable that the force is concentrated on the bolt and the horizontal member (member B). Since the load is only due to its own weight, it is a matter of speculation. It is considered desirable to have a design that can adjust the axial force before and after assembly by applying two chamfers between materials for right-hand and left-hand threads.

https://doi.org/10.52202/069179-0462

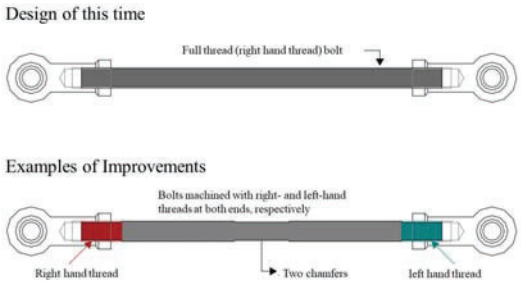

***Figure 11**: Example of improved ended bearing members*

5 CONCLUSIONS

In this study, we designed a temporary unit using a CLT panel and confirmed its effectiveness from construction experiments. The findings obtained are as follows.

1) Even with CLT panels, it is more difficult to secure machining accuracy than steel materials, and appropriate error management is required.
2) It was a rather heavy unit to assemble manually after undergoing construction experiments. It is necessary to consider whether to assemble with heavy machinery and to optimize the dimensions and weight in consideration of the balance with the structural performance.

ACKNOWLEDGEMENT

We would like to our sincere gratitude toward the technical staffs of faculty of engineering in Kyushu University for their assistance in fabricating the components of this temporary unit, and also the staff of PLAM Co. Ltd. help our works with the wood processing and unit assembly work in construction experiment.

APPENDIX

(A) Processing CLT Panel

Figure A shows how the notch was processed manually by a skilled carpenter. The notch portion was processed by first making cuts from both sides of the laminated board using a circular saw, and then using a multi-tool to cut the portion that could not be completely cut due to the circular saw.

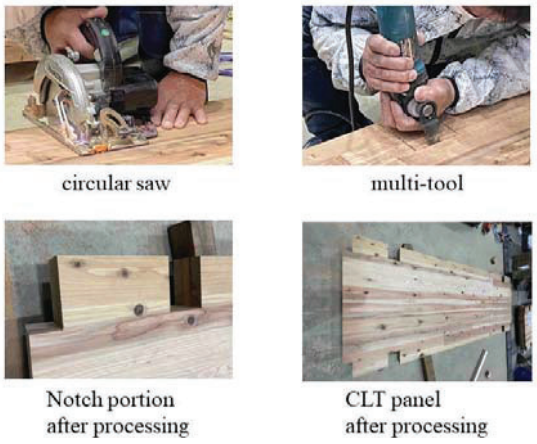

***Figure A**: Photos of the notch being processed*

(B) Records of construction experiments

On January 18, 2022, we conducted a construction experiment of a temporary unit using CLT panels, which is the subject of this research. The experiment was conducted in a large-scale experimental facility at a university. The experiment is roughly divided into the steps shown in Fig. B, and the records of each step are summarized as supplements.

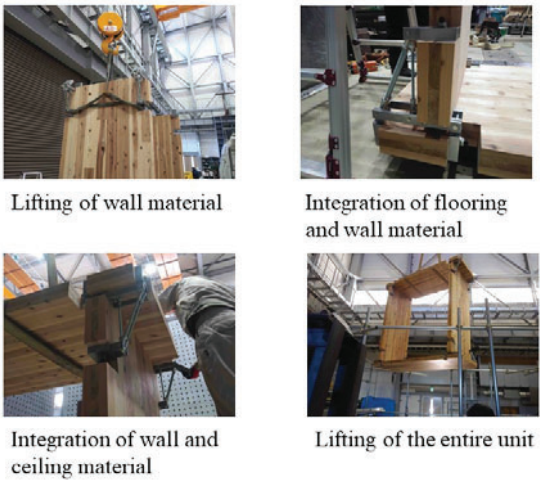

***Figure B**: Experiment process and photos*

(1) Lifting wall panels

The wall panels were lifted by an overhead crane by attaching a belt to the notch of the CLT panel. The ceiling material was lifted by passing two belts through the middle of the material. The overhead crane used here has a capacity of 4.8 tonf.

(2) Integration of floor and wall materials

Regarding the unification of the flooring and wall panels, in this construction flow, the wall panels were constructed while they were being lifted by an overhead crane. We were able to put it in place. However, since it

is difficult to secure means to replace cranes at actual sites, this point needs to be examined in the future.

(3) Integration of ceiling and wall materials

Regarding the integration of the wall material and the ceiling panels, in the previous procedure, there were two steel joints. As a result, it was confirmed that the error was concentrated in the final joint and the stud bolt could not pass through. As mentioned above contents, the expansion of the through hole of the CLT panel was made the largest in this part, and it is necessary to review the assembly error.

(4) Movement of the whole unit

After completing the construction experiment, the entire unit was moved by an overhead crane. In the study of structural performance shown in this paper, such a situation is not assumed, but for example, when a temporary unit is assembled at a factory and then transported to the place of use, there is no situation in which the entire unit is lifted and moved. Easy to imagine. This time, as shown earlier, there was a considerable amount of leeway in the stress generated in the members, so there was no deformation of the unit within the scope of visual confirmation even after the move, but in the future, we will be able to operate under such special conditions. It is considered necessary to conduct a safety evaluation as well.

https://doi.org/10.52202/069179-0462

World Conference on Timber Engineering Oslo 2023

HOW TIMBER BUILDINGS CAN BE DESIGNED FOR DECONSTRUCTION AND REUSE IN ACCORDANCE WITH ISO 20887

Ylva Sandin[1], Marlene Cramer[2], Karin Sandberg[3]

ABSTRACT: There is a need for a shift towards circular economy in the building and construction sector. Design for deconstruction and reuse (DfDR) and design for adaptability (DfA) have been suggested as means to facilitate reuse of buildings and diminish waste and material consumption. A standard, ISO 20887:2020, has appeared to support the implementation of DfDR/A. One objective of this study is to demonstrate timber building design examples that can be considered consistent with the standard and designs that should be avoided. Another objective is to examine if there are important aspects of DfDR/A for timber buildings that are insufficiently covered by ISO 20887:2020. The broader, long-term aim of the work is to remove thresholds to DfDR/A by providing support for designers and industry in applying the standard. The principles and strategies in ISO 20887:2020 are illustrated with practical examples from case studies, organised in a searchable database.

KEYWORDS: Disassembly, adaptability, circular economy, timber building, ISO 20887

1 INTRODUCTION

1.1 BACKGROUND

Greenhouse gas emission, raw material consumption and waste production from the building sector is huge [1]. If buildings (or their parts) were reused to a higher degree, material consumption and waste production could be minimised. For timber buildings, it is currently not viable and economic to extract timber for reuse [2]. The design philosophies *design for deconstruction and reuse* (DfDR) and *design for adaptability* (DfA) have been suggested to facilitate reuse of buildings, and a standard, ISO 20887:2020 (hereafter referred to as ISO 20887), has been published to support the implementation of these philosophies [3]. As this publication is recent, using it in timber building design is not yet standard practice. Also, the standard is comprehensive and general, and it needs to be interpreted. There is a need for showing timber building solutions that are in line with the standard and solutions that should be avoided.

1.2 AIM AND OBJECTIVES

The broader aim of the study is to support circular economy by removing thresholds to DfDR/A.
The objectives are:

- To show how the principles and strategies of ISO 20887 can be interpreted and fulfilled in practical timber building design.
- To examine if there are important aspects of DfDR/A for timber buildings that are insufficiently covered by ISO 20887.

2 METHOD

2.1 GENERAL METHODOLOGY

Case studies were carried out, where timber building designs were examined with respect to DfDR/A. The resulting advantages and disadvantages were then used to illustrate the ISO 20887 design principles. The study included three steps:

1. *Data collection in case studies*. Interviews were carried out to identify what manufacturers, builders and designers consider as advantages and disadvantages to DfDR/A in the design of timber buildings [4-6]. Drawings and documents were studied. Field studies were carried out. The result is a list of advantages and disadvantages, illustrated by pictures and design drawings.
2. *Interpretation of ISO and re-evaluation.* First, the structure of the standard was analysed. Thereafter, the advantages and disadvantages identified in step 1 were re-evaluated to identify

[1] Ylva Sandin, RISE Research Institutes of Sweden, Sweden, ylva.sandin@ri.se
[2] Marlene Cramer, Edinburgh Napier University, UK, m.cramer@napier.ac.uk
[3] Karin Sandberg, RISE Research Institutes of Sweden, Sweden, karin.sandberg@ri.se

https://doi.org/10.52202/069179-0463

which principle(s) in ISO 20887 they illustrate, if any. The result is a set of documented experiences from using the standard.

3. *Establishing a database of design examples*. Design examples were organized to illustrate the ISO design principles specifically for timber buildings.

2.2 COMMENT ON CASE STUDIES AND THEIR METHOD

Six practical deconstructions and eight simulated deconstructions of timber buildings in different European countries were analysed. All case studies represent modern timber buildings with different building systems (post and beam, volumetric or planar modules and either mass timber or light timber frame). The practical deconstruction and reconstruction cases (all in Sweden) include a hall (post and beam, mass timber), an office building (volumetric, light timber), a residential building (volumetric, mass timber), two pavilions (one with planar elements, mass timber and one with post and beam structure, mass timber). Four of them are illustrated in Figure 1, the fifth is shown in Figure 2.

Figure 1: *Four of the studied practical deconstructions. Photos: Masonite Beams (above left), Olof Mundt-Petersen and Oskar Linderoth (above right), IsoTimber (below left), Folkhem (below right).*

The simulated cases all regarded industrially produced systems and residential buildings in two stories: three light timber systems, one mass timber system in planar elements and one a combined post and beam/light timber system.

As the different designs were evaluated in interviews, the identified advantages and disadvantages are somewhat subjective and do not necessarily represent a comprehensive list of strengths and weaknesses in each case study. Especially in the simulated case studies, only information that was volunteered by third parties and interpreted based on informed assumptions could be included in the analysis, without the option to verify it in full scale deconstructions or in laboratory. Nonetheless, it is expected that each case study captures the most important aspects of DfDR/A. All interviews involved knowledgeable people. On average, there were 3-4 people per case study who participated with different competences and experiences in construction and deconstruction. One of the simulated deconstructions involved a person who had disassembled and reassembled a similar building and now lives in it.

Figure 2: *A hall with post and beam structure, that first served as a temporary market hall and later became a sports hall. The photo shows the hall in its first use. Photo: Ylva Sandin*

2.1 LIMITATIONS

The study concerns *loadbearing structures* of timber buildings. The focus of the case studies was on DfDR, and although some of them gave considerations also to DfA, the gathered examples do not capture a comprehensive overview of DfA designs.

3 RESULTS AND DISCUSSION

3.1 DATA PRESENTED

In this section, one of the case studies, concerning the deconstruction and reconstruction of a hall, is first presented as an example of the case study method (section 3.2). Then, advantages and disadvantages to DfDR that were identified for that case are given (section 3.3). Thereafter, the ISO 20887 is presented, and examples are given of how data from the hall case can be re-evaluated with respect to the standard (section 3.4). It is then shown how the standard could be enhanced with a database of design examples (section 3.5). Finally, some reflections on the ISO 20887 following from the evaluation of all case studies are given (section 3.6).

https://doi.org/10.52202/069179-0463

3.2 CASE STUDY EXAMPLE: TEMPORARY MARKET HALL

A temporary hall was erected at Östermalmstorg in Stockholm, Sweden, to enable the traders in the market hall "Östermalmshallen" to continue their businesses while the hall was renovated. The temporary hall was designed by Tengbom architects and was in use as market hall 2016-2020 (Figure 2). It has a post and beam structure of glulam and LVL (Laminated Veneer Lumber). The building was disassembled in spring 2021 (Figure 3) and reassembled in spring 2022 as a sports hall in Mölnlycke, Sweden (Figure 4). The entire frame was reused, as were all the façades. Much of the installations and other layers were also reused (see also [5] and [7].)

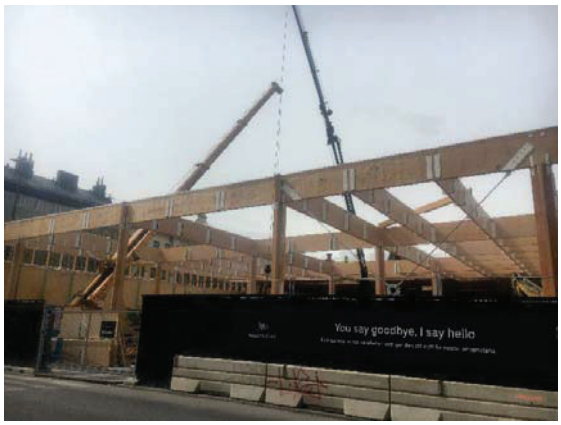

Figure 3: *The hall is disassembled, April 2021. Photo: Andres Zabala Mejia.*

Figure 4: *The hall during reconstruction. Photo Ylva Sandin.*

For this case, data was collected on four occasions. First, one of the architects that had worked with the design was interviewed. Then, the deconstruction site was visited during disassembly and the project manager was interviewed. On a third occasion, the project manager was interviewed on video during reassembly and finally the reconstruction site was visited during reassembly and both the project manager and people from the construction firm were interviewed. The deconstruction and reconstruction sites were documented in photos.

3.3 IDENTIFIED ADVANTAGES AND DISADVANTAGES TO DFDR

When asked about advantages of the design, based on their experiences from deconstruction and reassembly, the project manager and construction firm mentioned the following.

3.3.1 Advantages

Adaptable to new use: The transformation from market hall to sports hall was successful. The post and beam system was flexible and adaptable to the new use. Posts could be moved without changing their dimensions. Roof beams affected by larger stresses, following the change of post position, were reinforced with steel fittings (Figure 5). Lengths of posts were adjusted with steel details. Steel details were considered as positive aesthetic expressions, showing that the hall is reused.

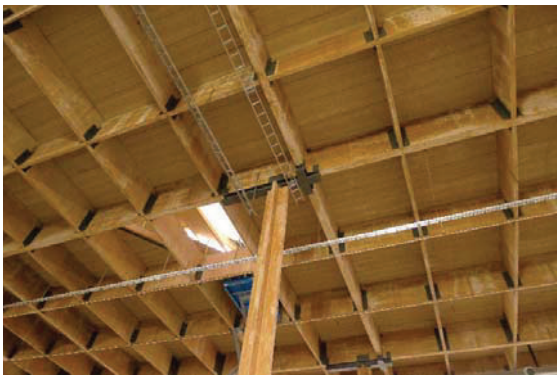

Figure 5: *A roof beam adapted with steel as bending moment changed when a post got a new position. Photo: Ylva Sandin.*

No waste: All parts of the loadbearing structure were reused – there was no waste (ignoring waste that did not concern the structure, particularly roof insulation.) Posts and beams were robust and durable. There were only minor marks on them from disassembly and transport, nothing major.

Prefabricated frame: The frame was prefabricated, and the disassembly process could be done as the assembly in reverse order. The roof was originally designed to be lifted into place quickly, in a narrow and busy urban environment.

Easily accessible and readable frame: The loadbearing and sound absorbing wood wool roof elements were attached one at a time and lifted. After this, the beams and posts were easily accessible, visible, and understandable. It was largely obvious how it would be dismantled.

Bolted connections: Beam-to-beam connections and beam-to-post connections were bolted, and the bolts were removable (Figure 6). There were no unforeseen connectors in the post and beam system.

https://doi.org/10.52202/069179-0463

Figure 6: *Bolted connections could be undone. Photo Andres Zabala Mejia.*

Separable services: Mechanical and electrical services were independent of the frame and could be easily separated.
Documentation available: Original documentation and drawings were available, and the design was consistent with the drawings. Half of the original drawings could be reused; the new parts were just added.
Transportability: It was easy to transport the parts. An advantage of the LVL beams was that they provided smaller dimensions than glulam would have done.

3.3.2 Disadvantages

Extensive planning needed: It was time consuming and difficult to make plans for numbering, labelling and logistics. A logic way to number and label the parts of the structure (having for example more than one thousand roof elements) had to be found, considering how and in what order parts were to be dismantled, transported, and stored. This was pointed out as something that could have been thought of and documented already in the original drawings.
Invisible screw heads: The loadbearing wood wool roof elements were connected to roof beams with countersunk screws. The exact position of screws was not known but had been decided on site during original assembly and carpenters had made slightly different choices. At deconstruction, screw heads were therefore not easily visible and had to be searched for, which was time consuming.
Stabilising members optimised for original location: Some elements in the outer walls were included in the stabilization for wind load, but were not dimensioned for the new, higher wind load at the new location. They could easily have been oversized at low cost to take larger wind loads.
Walls dismantled with difficulties: Connections in the façade walls were hidden and difficult to dismantle. They had to be sawn apart.
Fire protective layer sensitive to moisture: The fire protection treatment for indoor use on the LVL beams was sensitive to moisture. It became sticky when wet and cracked when it dried.
Physical labelling: Once labelling of all the roof beams was done, it turned out to be hard to see the labels when beams were unloaded and stacked on the re-assembly site.
Weather protection of sensitive beams: It was difficult to plan how the LVL beams should be covered from rain during dismantling.
Adaptation for reuse with high aesthetic requirements: High ambitions for the aesthetics with the ambition that the reconstructed building should still be a beautiful, was a challenge. New steel reinforcements had to look good while at the same time signalling reuse. The property owner and architect did not want to change dimensions and they wanted to preserve the symmetry and other architectural qualities. All additions had to fit and could not be too much or too visible.

3.4 INTERPRETATION OF ISO 20887 AND RE-EVALUATION OF PROPERTIES

3.4.1 Presenting the ISO 20887

The standard presents three *principles for DfA* (Versatility, Convertibility and Expandability) and seven *principles for DfDR* (Ease of access to components and services, Independence, Avoidance of unnecessary treatments and finishes, Supporting re-use (circular economy) business models, Simplicity, Standardization and Safety of disassembly). Important advice is also given under the headings *General disassembly principles* and *Documentation and information*. The standard states that each of the principles should be examined on five *levels of analysis* (Systems, Elements, Components, Sub-components, and Materials). In this study, only one level per case is considered for analysis, based on relevance with respect to reuse scenarios. For example, the temporary market hall was analysed on the elements level as it was deconstructed into assemblies and components for reuse in a similar building. Apart from principles, the standard presents *strategies* and *guidance*.

3.4.2 Re-evaluation of advantages and disadvantages

The recorded advantages and disadvantages discovered in the interviews were compared to the principles and guidelines of ISO 20887. An interpretation was made of how each aspect corresponds to the ISO. This was done for all cases. Examples are shown here from the analysis of the temporary market hall.
Table 1 shows aspects of the design that can be interpreted as compliant with the standard, and Table 2 shows aspects that can be interpreted as inconsistent with the standard. Data from all cases was re-evaluated in a similar way.

https://doi.org/10.52202/069179-0463

Table 1: *Advantages to DfDR and connection to ISO 20887. Examples from case study on temporary market hall.*

Advantage	Compliant with principle/guideline
Adaptable to new use	• Versatility, convertibility and expandability
No waste	• Supporting re-use (circular economy) business models: Reusability
Prefabricated frame	• Supporting re-use (circular economy) business models • Simplicity • Standardization
Easily accessible and readable frame	• Ease of access to components and services • Simplicity • Safety of disassembly
Bolted connections	• Independence: Reversible connections
Separable services	• Independence: General
Documentation available	• Documentation and information
Transportability	• General disassembly principles

Table 2: *Disadvantages to DfDR and connection to ISO 20887. Examples from case study on temporary market hall.*

Disadvantage	Inconsistent with principle/guideline
Extensive planning needed	• Documentation and information
Invisible screw heads	• Independence: Reversible connections • Ease of access to components and services • Safety of disassembly
Stabilising members optimised for original construction	• Convertibility and expandability
Walls dismantled with difficulties	• Independence: Reversible connections • Ease of access to components and services • Safety of disassembly
Physical labelling	• Documentation and information
Weather protection of sensitive beams	• Supporting re-use (circular economy) business models: Reusability • General disassembly principles
Adaptation for reuse with high aesthetic requirements	• Versatility and convertibility

The analysis of advantages and disadvantages and their comparison to principles and strategies in ISO 20887 is somewhat ambiguous - some properties could be associated with many principles and for others it was less obvious (but not impossible) to find any match in the standard. For example, solutions and problems around intermediate storage of recovered parts were usually interpreted to fit under *General disassembly principles*, though the ISO does not make explicit mention of storage requirements.

3.5 ILUSTRATING THE ISO 20887 PRINCIPLES AND STRATEGIES

Having re-evaluated the results according to the ISO 20887 design principles, a catalogue illustrating principles and strategies with practical examples from the studied cases was attempted using the general structure in Figure 7. This catalogue is a text document, aiming to fulfil the first objective of this study.

General disassembly principles
- Example 1
- Example 2
- ---

Ease of access to components and services
- Example 1 etc.

Independence
- Example 1 etc.

Avoidance of unnecessary treatments and finishes
- Example 1 etc.

Supporting re-use (circular economy) business models
- Example 1 etc.

Simplicity
- Example 1 etc.

Safety of disassembly
- Example 1 etc.

Standardization
- Example 1 etc.

Figure 7: *Principles and strategies in ISO 20887 can be illustrated with practical examples from the studied cases to form a catalogue, showing how the abstract principles can be treated in practice.*

Some of the designs in line with *General disassembly principles* found in case studies and stored in the catalogue are:

- *Example 1: Lifting points are marked out physically on the structure for future disassembly.*
  This can be done with paint or, in some cases, by leaving lifting loops in the structure during assembly, which will efficiently show where elements are supposed to be lifted, Figure 8.

***Figure 8**: Lifting loops in an element. Photo: Ylva Sandin.*

- *Example 3: Members are designed for easy transport*
  Members can be designed to have dimensions that are practical to handle. In the temporary market hall case, it was pointed out that choosing LVL instead of glulam for some members led to less heavy members, Figure 9.

***Figure 9:** Laminated veneer lumber beams (right). Photo Andres Zabala Mejia.*

- *Example 2: Modules are designed for easy transport.*
  The structure can be modular, with dimensions optimised for transport and handling, Figure 10 and Figure 11.

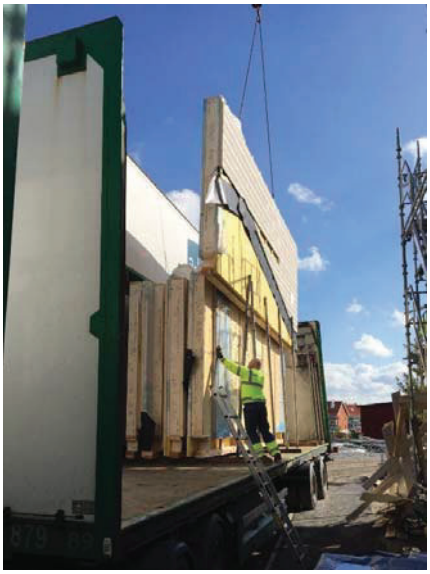

***Figure 10:** Modules designed for efficient transport: planar wall elements. Photo: Derome.*

***Figure 11:** Modules designed for efficient transport: volumetric modules. Two modules can be transported with one vehicle. Photo: Masonite Beams.*

However, the amount of data in the catalogue became unpractical to handle as a text document. Many design examples were obtained from the case studies, showing both designs in compliance with the standard and designs that are inconsistent with the standard.
To store and arrange the large amount of data, the study uses a web application for data management (Notion). Data can thereby be sorted and filtered, for example by case or by ISO principle, Figure 12-Figure 14.

https://doi.org/10.52202/069179-0463

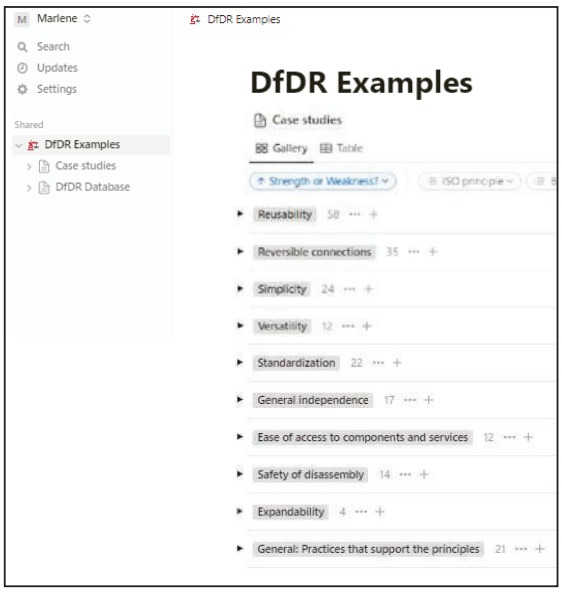

Figure 12: *Data is stored case by case and tagged to be sortable and filterable by ISO principle. A data management tool (Notion) is used.*

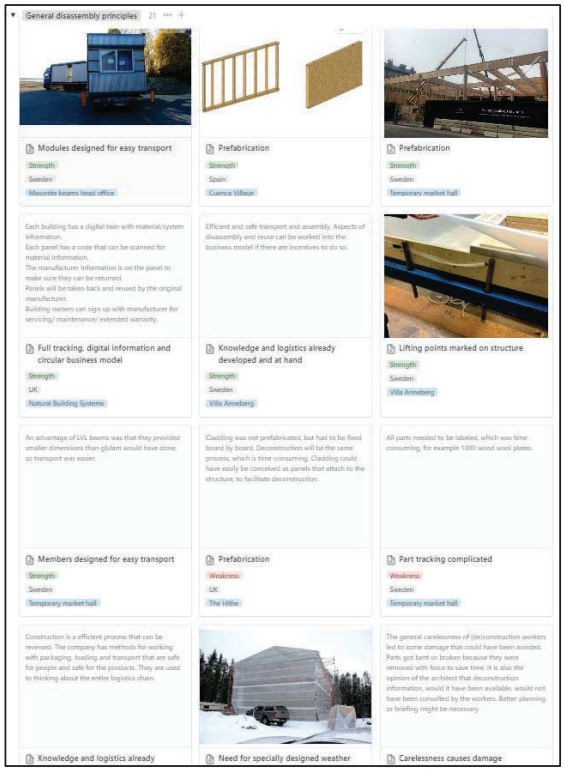

Figure 13: *Filtering data by choosing "General disassembly principles" will show case study data associated with this aspect. The picture shows a small sample of the data associated with this aspect.*

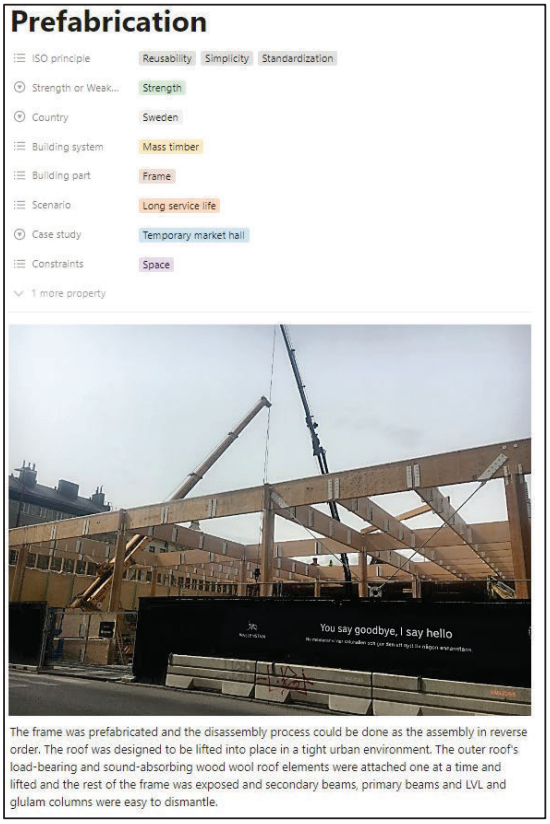

Figure 14: *Each design example is tagged under different headlines, e.g. country or building system, to allow users to filter for relevant context*

Storing the data this way makes it possible to get an overview of cases, see patterns and find inconsistencies. As an example of an inconsistency found, I-beams were judged reusable (compliant with the ISO) in two cases, and not reusable (inconsistent with the ISO) in another case. For one of the cases, the property owner pointed out that knowing the brand of the beams was an important basis for judgement and that having a personal knowledge of the product made it possible to rely on its reusability. This indicates that further investigations might be needed to find out if there are differences in quality of beams or differences in viewpoints between persons. It would be valuable to further study the effect of age on different timber materials.

The database is a prototype and a suggested methodology for collecting more data. Data from nine out of the fourteen case studies has been added to date (February 2023) and the work is ongoing.

More case studies should be carried out and data be added to the database, so that several examples of each type of timber structure is included.

The database is specific to timber construction. The intention is to show a multitude of examples, some describing practical experience, and show that contrasting views and evidence might exist. Contrasting views also

https://doi.org/10.52202/069179-0463

suggest that lessons from the case studies might only apply to a certain building system, deconstruction scenario or regional context, and the database should allow to filter examples according to these criteria.
As researchers, property managers and manufacturers might seek different types of information and sort data in different ways, it is important at this stage to involve different stakeholders in a dialogue on the kind of data and sorting possibilities, as the work with collecting more data goes on.

3.6 REFLECTIONS ON THE ISO 20887

3.6.1 Examining if important aspects are insufficiently covered

Our second objective of the study was to examine if there are important aspects of DfDR/A for timber buildings that are insufficiently covered by ISO 20887. The result is ambiguous.
On the one hand, the standard *can in fact be said to cover the important aspects* identified in case studies. None of the stakeholders in any of the case studies set out to incorporate the ISO principles in their design, yet all design examples (advantages/disadvantages to DfDR) could be assigned to one or more of the ISO principles.
On the other hand, important aspects *are not explicitly treated*. The standard is generic and independent of structural material and cannot list design examples for every building type or civil engineering works. The specific and tangible aspects of DfD/A that emerge from case studies will not be found in the standard. It remains abstract and needs to be interpreted.
Some timber specific advantages/disadvantage not explicit in the ISO are given below.
Transportability. In several case studies, interviewed persons stressed as a significant advantage, that the structure (or rather its deconstructed parts) was well adapted for transport. As timber is a light material, this property might be characteristic to timber structures and should be recognised as a large benefit when choosing structural system for a building.
Designing for transportability is included in the standard, but the aspect is rather hidden. It is not a principle but mentioned among several practices that can support general disassembly principles: "When possible, materials and components, which can be easily, safely, and more cost-effectively replaced or removed and transported, should be used. […] Components that are sized to suit the intended means of handling should be used. Various possible handling options at all phases of assembly, disassembly, transport, reprocessing, and reassembly should be considered." (ISO 20887, section 5.3.1.)
Reversible connections. One of the principles in the ISO is Independence and a sub-category of this is Reversible connections. While it is easy to intuitively understand that this is important, it is not very clear how the principle shall be interpreted in practical timber construction. The standard (section 5.3.3.2) states that "Reversible connections can be disconnected and/or disassembled for easy alterations and additions to structures.". The interpretation of the principle was repeatedly discussed in case studies. The cases showed that bolted joints, screwed joints and nailed joints might all be considered reversible as bolts can be removed and the others can normally be sawn apart without causing damage to the connected members, although fasteners themselves will not be reusable. For timber structures, we suggest that "reversible connections" might be defined as connections that can be separated without damaging the connected members (at least not to a degree that generates waste or makes substantial refurbishment necessary). Thus, the choice of connector does not necessarily define the reversibility.
Handling moisture. It is crucial to protect a timber structure from moisture during disassembly, temporary storage, and reassembly. The ISO does not give explicit advice on weather protection and storage but whether timber parts are protected or not might strongly influence their reusability.

3.6.2 Some comments on the reinterpretation of the case study examples

The DfDR strategies are interconnected. Each design example found in case studies was assigned to 2.6 ISO principles on average. The reinterpretation of the case study examples gave insight in the relative importance of each design principle for the sample, Figure 15. *Reusability*, a sub-category to Supporting re-use (circular economy) business models, was by far the principle most design examples were assigned to, followed by *Reversible connections*, a sub-category to Independence.
Some principles were well matched in design examples, others were more problematic. Some examples are shown below.

Good match: *Reusability*
Case study examples that were assigned to this principle mostly covered one of four aspects:

- The condition of recovered parts, i.e. damage and remaining service life
- The generality of recovered parts and the resulting freedom in reuse options, e.g. the size and shape of recovered panels
- Barriers to reuse, e.g. timely and costly reconditioning, storage, adaptation
- Verification or available information for materials

All four aspects are mentioned in the ISO, although they could be more clearly separated and linked to examples.

Slight mismatch: *General Independence*
Under this principle, the standard mostly highlights the merits of independent layers, i.e. separating layers with different expected service lives. Although the case studies did not explicitly work with the concept of layers, design examples fit the principle well and mostly concerned:

- Independent installations

https://doi.org/10.52202/069179-0463

- Separating the vapour control layer
- Independent façade

One difference between the description in the ISO and the case study observations was noted: While the ISO described the most important layers to be separable should be the most reusable ones, the case study examples showed problems were related the accessibility of the least reusable layer. This was because most cases targeted assembly reuse, and the least reusable layers often need to be accessed for replacement.

An aspect that is not explicit in the standard is the advantage of self-contained assemblies. It became clear that independence is as much about keeping similar parts together as it is about keeping different parts apart. Self-contained functional units are more easily separated and independently reusable, e.g., self-contained pods are more independent upon recovery than open panels that need to be finished with additional materials.

Stark mismatch: *Avoidance of unnecessary treatments and finishes*

The ISO states that treatments which would limit reuse should be avoided. Timber preservative and fire-retardant treatments generally do not limit its reuse options, but they should still be avoided where unnecessary to limit environmental impact (which is out of scope of this study). Finishes that hide the wood surface might limit visual inspection methods for verification, so these should be avoided as well. The ISO might need to clarify the motivations for avoiding different finishes and give specific examples relevant to different materials.

The principle was also interpreted more widely as avoidance of unnecessary components and finishes, so that recurring examples could be assigned:

- Avoidance of sensitive materials, e.g., the vapour control layer, though by no means unnecessary in all types of timber construction, can be eliminated in vapour-open systems, avoiding the use of damage-prone materials.
- Avoidance of wet construction methods, e.g., foundations can be minimised when designing lightweight structures.
- Avoidance of excess connectors, e.g., avoiding the need for unplanned connectors by providing temporary bracing during construction

Although most design examples could be matched to the ISO principles reasonably well, there is quite an amount of work left to do to adapt the standard to reflect the real world rather than the real world to illustrate the standard. Future guidelines to the standard could aim to include a wider range of strategies, so that common design considerations are made obvious to designers. It would be necessary to analyse a wide range of buildings and civil engineering works, in a similar way as in this study, to get a better understanding of the most important strategies, without it becoming too comprehensive.

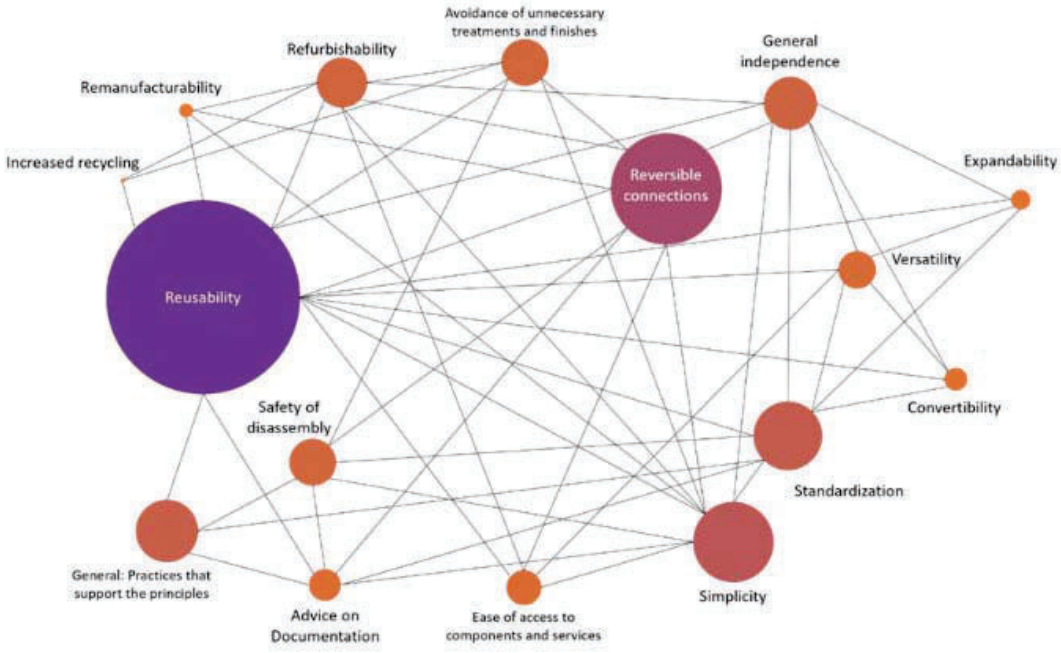

Figure 15: *ISO 20887 principles and their connection as given by data from nine case studies on timber structures of different sizes and types. The size and colour of the circles indicates how many examples were assigned to each principle and a connection was added between circles when at least one example illustrates both principles.*

4 CONCLUSIONS

The case study approach [4] resembles a top-down approach: An existing design is evaluated for its advantages and disadvantages to DfDR/A. This involved gathering the right expertise and discussing the design, its future deconstruction and reuse, recording advantages and disadvantages. This method was used in case studies simulating deconstruction and was found to be an easy, pragmatic, and inspiring process that provoked ideas for modified designs. The case study method results in specific design examples, but also reveals general DfDR/A barriers and solutions in the given context.

A bottom-up approach for developing new designs adapted to DfDR/A is described in ISO 20887. The standard follows a broad and holistic approach, including decision-making, design principles, documentation, and implementation of DfDR/A. It is, however, not easy to apply in practice.

When the DfD/A design examples gathered with the case study method were re-evaluated to fit under the ISO 20887 principles, it became clear that the standard reflects the overarching principles of DfD/A design well. Keeping the aim of the ISO, to give an overview of DfD/A principles for all buildings and civil engineering works, in mind, it is still not feasible to fully represent all these different structures with examples, and the standard will likely remain somewhat general and abstract.

Both approaches combined can provide valuable support for designers in creating and evaluating deconstructable designs. The result of this work is a non-exhaustive database of specific examples illustrating ISO 20887 design principles. A database that focuses on timber buildings, to narrow down the scope and become more accessible, can complement the ISO and provide the link between DfD/A principles and the real world. The database draws from reality rather than from abstract principles, and it does not only show the many good solutions that have been developed already but also mistakes from the past, to help avoid pitfalls even with best intentions. This study is only the beginning, providing design examples for the loadbearing structure of nine timber buildings. Further examples are needed, covering all chapters of the standard and more building types, layers, and levels. As the continued collection of case studies progresses, the experiences will form a base for guidelines showing how the ISO can be interpreted for timber buildings.

ACKNOWLEDGEMENT

We wish to express our thanks to RISE Research Institutes of Sweden and to ForestValue ERA-Net Cofund (with funding from the European Union's Horizon 2020 research and innovation programme under grant agreement N° 773324) for supporting the work, partly mase possible through the InFutUReWood project.

REFERENCES

[1] European Commission*: Circular Economy Action Plan: The European Green Deal*., 2020.

[2] Nasiri, B., Piccardo, C. and Hughes, M., Estimating the material stock in wooden residential houses in Finland. *Waste Management*, 135: 318-326, 2021.

[3] ISO 20887:2020 *Sustainability in buildings and civil engineering works -Design for disassembly and adaptability - Principles, requirements, and guidance.*

[4] Sandin, Y., Shotton, E., Cramer, M., Sandberg, K., Walsh, S. J., Östling, J., … Zabala Mejia, A.: *Design of Timber Buildings for Deconstruction and Reuse — Three methods and five case studies.* RISE Report 2022:52, 2022.

[5] Sandin, Y.: *Att mäta demonterbarhet och återbrukbarhet hos träbyggnader baserat på fallstudier och ISO 20887:2020*. RISE rapport 2022:142 (In Swedish). 2022.

[6] Sandin, Y., Mundt-Petersen, O., Linderoth, O., & Sandberg, K.: *Experiences from the Deconstruction of a Timber Building.* RISE Report 2022:09. 2022.

[7] Sandin, Y., & Sandberg, K.: *Design for deconstruction and reuse of timber buildings - testing an assessment tool in a workshop.* RISE Report 2021:50. 2021.

https://doi.org/10.52202/069179-0463

World Conference on Timber Engineering Oslo 2023

PUSH-OUT TESTS ON CONNECTIONS FOR DEMOUNTABLE AND REUSABLE STEEL-TIMBER COMPOSITE BEAM AND FLOORING SYSTEMS

Alfredo Romero[1], Jie Yang[2], François Hanus[3], Hervé Degée[4], Christoph Odenbreit[5]

ABSTRACT: Engineered timber panels made of laminated veneer lumber (LVL) can represent an alternative to concrete in a typical steel-concrete composite beam and the entire flooring system. The performance of LVL in strength reaches values, which are comparable to concrete. In addition, and according to policies to reduce greenhouse gas emissions and resources depletion (e.g. the European Commission´s Green Deal) the construction sector demands more and more circularity in construction. On that basis, the research project "Prefa-SeTi" (FNR Grant 15695062) investigates the load bearing- and displacement behaviour of steel-timber composite beams and especially the shear connection between the steel and timber. The work pursues a development, which was started within the European REDUCE project (RFCS GA 710040), which investigated solutions for composite structures in steel and concrete, and the demo project "Petite Maison" of Esch2022 the European Capital of Culture. In "Prefa-SeTi", nine push-out specimens were tested to investigate three newly developed shear connections. To comply with circularity, the connections are dismountable and robust enough to protect the structural elements from damage at serviceability limit state. This paper presents the demountable timber connectors and results of the push-out tests. Along with the results and the respective discussions, the paper outlines the tested mechanical properties of the LVL, the push-out test setup, and the testing procedure.

KEYWORDS: Shear connection, push-out test, steel-timber composite, demountable, reuse, circular economy, LVL

1 INTRODUCTION

Timber is a renewable material with strength properties which are comparable to concrete. Therefore, engineered timber products such as LVL can represent an alternative to concrete in steel-concrete composite beam and flooring systems. In addition, timber is ideal for prefabrication, fast erection, and deconstruction.

The policies targeting carbon neutrality and minimization of resources depletion such as the European Commission's Green Deal and the United Nation's Sustainable Development Goals are pursuing a transition towards a circular economy. The construction sector is not an exception to this; consequently, the sector demands more circular solutions.

Currently, most design and construction procedures are not well suited for deconstruction and reuse of the structural components. To cope with this issue, recent studies, such as the REDUCE project [1] have developed demountable and reusable solutions for steel-composite structures [2]. The research project "Prefa-SeTi" (FNR Grant 15695062) pursues a development, which started within the European REDUCE project (RFCS GA 710040) [1]. This project investigates the load bearing- and displacement behaviour of steel-timber composite beams and especially the shear connection between the steel and timber.

In composite structures, the shear connection is a key element which transfers shear forces between the components to achieve effective composite action. The existing steel-to-timber connections (e.g. screws, bolts, C-type connectors, adhesives, and their combination) have setbacks when the target is deconstruction and reuse of the components of steel-timber composite flooring systems. Therefore, within the framework of "Prefa-SeTi" three demountable shear connectors were developed and their load-slip response were investigated through push-out tests. Along with the results and the respective discussions of the tests, this paper outlines the tested mechanical properties of the LVL, the components of the demountable shear connections, the push-out test setup, and the testing procedure.

2 LAMINATED VENEER LUMBER (LVL)

LVL is made of veneers with a thickness of 3mm, bonded together with weather-resistant phenolic adhesive (see

[1] Alfredo Romero, ArcelorMittal Chair of Steel Construction at the University of Luxembourg, Luxembourg, alfredo.romero@uni.lu
[2] Jie Yang, ArcelorMittal Chair of Steel Construction at the University of Luxembourg, Luxembourg, jie.yang@uni.lu
[3] François Hanus, ArcelorMittal Steligence®, Luxembourg, francois.hanus@arcelormittal.com
[4] Hervé Degée, Hasselt University, Belgium, herve.degee@uhasselt.be
[5] Christoph Odenbreit, ArcelorMittal Chair of Steel Construction at the University of Luxembourg, Luxembourg, christoph.odenbreit@uni.lu

https://doi.org/10.52202/069179-0464

Figure 1). The dimensions of the final LVL product are not limited by the dimensions of the raw material, and small-diameter logs can be used to produce large LVL members. When veneer logs are peeled to produce veneer, any natural defects in the wood, such as knots, are dispersed. This together with the lamination effect, significantly reduces the impact of defects and results in homogeneous properties. Thus, the variance on the properties is smaller, this translates in a smaller partial safety factor for design calculations, and therefore, higher design strength values compared to other timber products such as cross laminated veneer lumber (CLT).

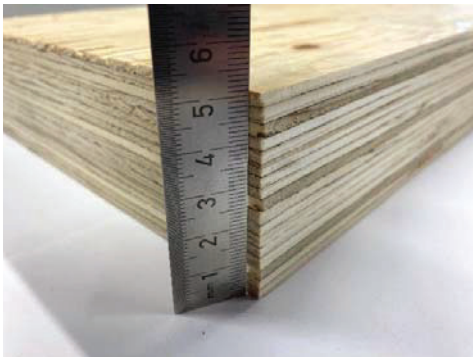

Figure 1: *Laminated veneer lumber (LVL).*

There are two main types of LVL products depending on the veneer layup: LVL with all veneers oriented in the same direction (e.g. LVL-P) and LVL with approximately 20% of veneers oriented crosswise at 90° with respect to the grain direction (e.g. LVL-C).

The mean and characteristic values of some mechanical properties of the LVL products commonly used for structural design are given by the LVL manufacturers. However, the reports of the tested mechanical properties and the respective stress-strain and load-deformation curves are hardly available. Berschoten [3] reported mechanical properties of LVL made of New Zeeland's Radiata pine and Chybinski et al. [4] reported some mechanical properties of European LVL-P panels.

To the knowledge of the authors there are no references dealing with the mechanical characterisation of LVL panels made of Scandinavian spruce wood with crossbanded veneers. Therefore, in this contribution we present mechanical properties obtained in tests of Kerto-Q panels (i.e. crossbanded LVL-C). The tests were done according to the European standards EN 408 [5] and EN 789 [6].

Wood is an anisotropic material but for engineering purposes it is considered as orthotropic. Hence, in the material testing campaign conducted within the framework of this research project, the orthogonal directions were defined as shown in Figure 2.

The mean strength values as well as elasticity modulus in the three orthogonal directions are presented in Table 1 for compression and tension. The mean stress-strain curves are shown in Figure 3 for compression and tension.

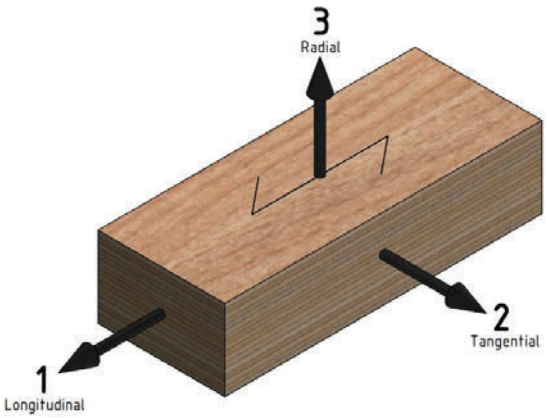

Figure 2: *Orthogonal directions of the LVL.*

Table 1: *Mean strength values and elasticity modulus of LVL made of spruce wood (Kerto-Q)*

Strength		Modulus of elasticity	
Symbol	Value [MPa]	Symbol	Value [MPa]
$f_{c,1}$	40.41	$E_{c,1}$	7 917.08
$f_{c,2}$	11.14	$E_{c,2}$	1 764.47
$f_{c,3}$	3.99	$E_{c,3}$	95.49
$f_{t,1}$	37.76	$E_{t,1}$	10 680.01
$f_{t,2}$	8.33	$E_{t,2}$	2 199.90
$f_{t,3}$	0.56	$E_{t,3}$	92.05

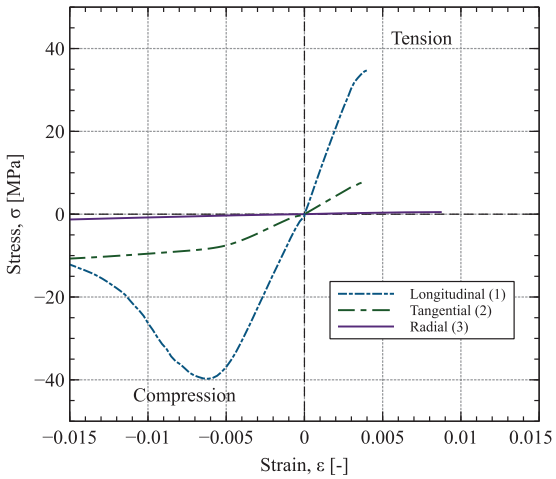

Figure 3: *Mean stress-strain curves of LVL for uniaxial tension and compression in the three orthogonal directions.*

These tests show that the strength of LVL in compression in the direction of the grain (i.e. $f_{c,1} = 41.03\ MPa$) reaches values which are comparable to concrete. Therefore, this material could represent an alternative to concrete in steel-composite beams and flooring systems.

https://doi.org/10.52202/069179-0464

3 THE DEVELOPED DEMOUNTABLE SHEAR CONNECTORS

Steel-to-timber connections with screws and bolts alone or in combination with C-type connectors and/or glue allow for deconstruction of STC structures. However, the drilling effect of screws and the preloading of high-strength bolts lead to damages in the timber elements which hinders the reusability of the structural components. Hence, alternative shear connectors are needed to develop structural solutions complying the principles of circular economy.

The three connections presented in this paper were developed to comply circularity and are robust enough, to protect the structural elements from damage at serviceability limit state (SLS).

The three demountable connections were denominated as follows: Shear Connection -Type 1 (SCT-1), -Type 2 (SCT-2), and -Type 3 (SCT-3).

These connections consist of a part embedded in the timber, the "shear connection device" (see Figure 4), and removable parts (i.e. bolt, washers, nut). The shear connection device consists of a steel-tube (S460) fitting the drilled hole in timber, at the steel-timber interface the connection is reinforced by steel elements welded to the tube: (i) a round steel plate (S460), (ii) a geka connector or (iii) a rectangular steel plate (S460) with four inclined screws, respectively for each connection type (see Figure 4). The details of the connections are shown in Figure 5 to Figure 8.

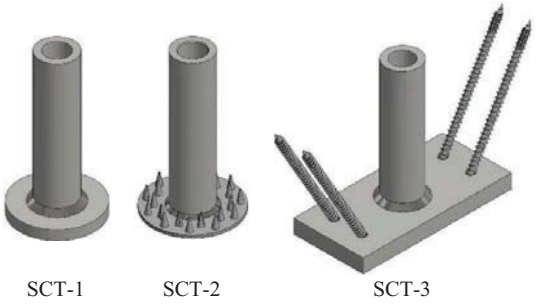

Figure 4: *Shear connection devices developed in Prefa-SeTi project.*

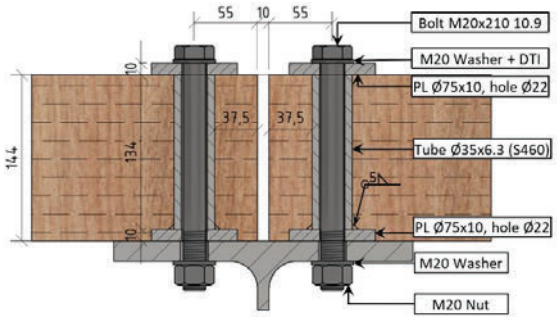

Figure 5: *Details of shear connection type 1 (SCT-1).*

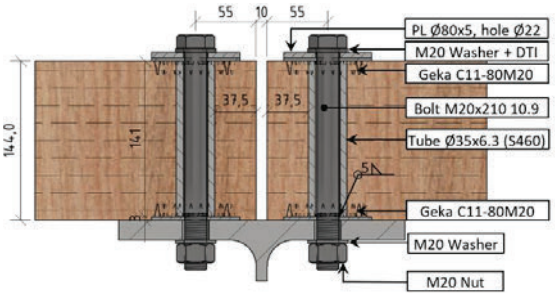

Figure 6: *Details of shear connection type 2 (SCT-2).*

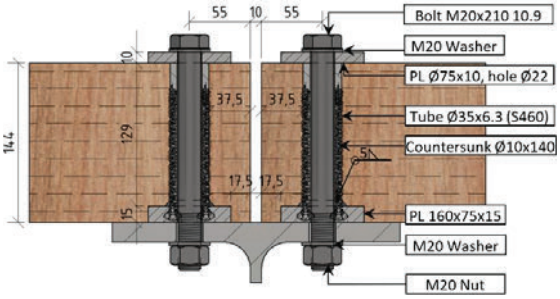

Figure 7: *Details of shear connection type 3 (SCT-3), transversal cut.*

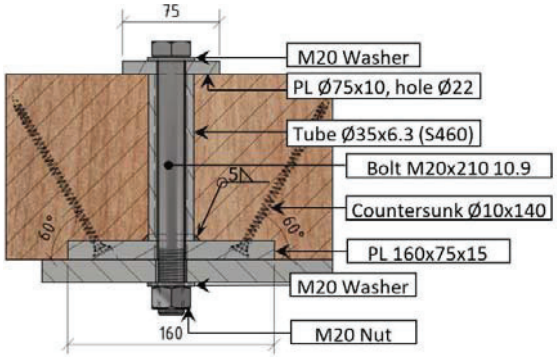

Figure 8: *Details of shear connection type 3 (SCT-3), longitudinal cut.*

The steel tube reinforces the hole, increases the surface in which the forces are transferred to the timber, and allows to achieve the preload of the high-strength bolts while preventing crushing of the timber.

4 EXPERIMENTAL PUSH-OUT TESTS

4.1 TEST SERIES

The load-slip behaviour of the connections was investigated through a series of push-out tests. Three identical specimens of each connection were tested. Therefore, in total 9 push-out tests were performed in this testing campaign. A summary of the test series is presented in Table 2.

https://doi.org/10.52202/069179-0464

Table 2: *Mean strength values and elasticity modulus of LVL made of spruce wood (Kerto-Q)*

Test series	Connection	Test IDs	Specimen IDs
Push-out test series 1	Type 1 (SCT-1)	POT1	POT1-1 POT1-2 POT1-3
Push-out test series 2	Type 2 (SCT-2)	POT2	POT2-1 POT2-2 POT2-3
Push-out test series 3	Type 3 (SCT-3)	POT3	POT3-1 POT3-2 POT3-3

4.2 SPECIMEN DETAILS

The connections were installed and tested in Kerto-Q LVL (LVL-C) plates made of spruce wood with dimensions of 650x300x144mm. The grain direction of the plates was aligned with the load direction.

The steel profile used in the setup was a standard European section HEB 260 (S355) with a length of 700mm.

The connections were installed symmetrically in both flanges of the beam. In total, 8 shear connectors were installed in each specimen, 4 connectors in each flange of the steel beam arranged in two rows. The spacing between the two rows of connectors was 250mm.

Partially threaded bolts M20x210 grade 10.9 were implemented in the connections. These bolts were preloaded at 70% of their ultimate tensile strength. This preload was achieved using a calibrated torque wrench plus a certain nut rotation. In addition, direct tension indicators (DTI) were used to ensure the minimum preload was reached.

The specimen details and dimensions are shown in Figure 9 and Figure 10.

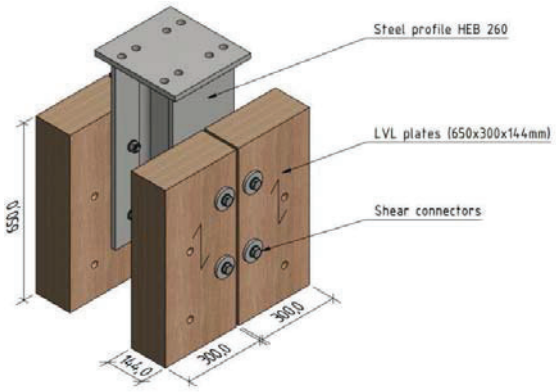

Figure 9: *Main components and dimensions of the push-out test specimens.*

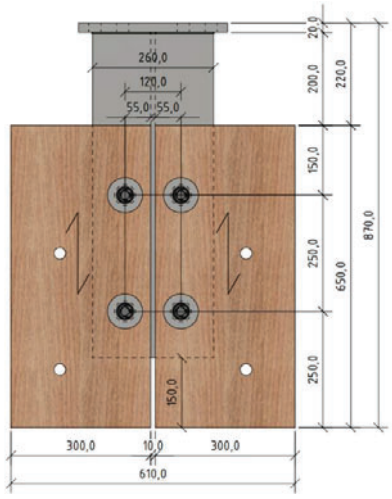

Figure 10: *Dimensions of the push-out test specimens.*

4.3 TEST SETUP

The specimen was placed on a thick steel block covered by neoprene strips (see Figure 11 and Figure 12). Steel L-profiles fixed with threaded rods were used to prevent the opening of the gap between the timber plates in the bottom of the specimen and a steel plate was used on the top to prevent the closing of the gap. Similar L-profiles were placed in the parallel faces of the timber plates to prevent the parts from falling apart once the connection was lost. In this case, a gap of 3 mm between the timber plates and the L-profiles was left to allow detaching of the timber from the steel beam.

Linear Variable Differential Transformer (LVDT) sensors were installed to measure the relative displacements between the steel beam and the timber plates in the direction of the load (measuring the slip) and perpendicular to the load (measuring the timber plates detachment from the beam flanges). Figure 11 and Figure 12 show the push-out test setup.

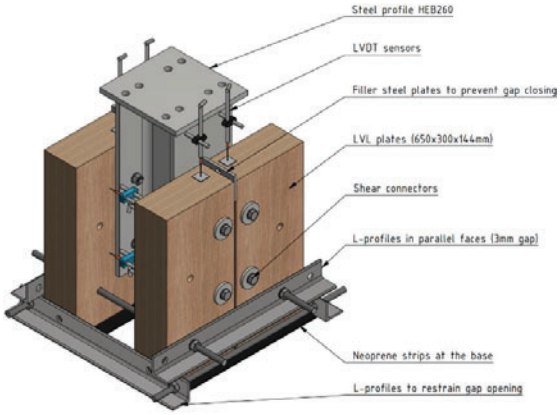

Figure 11: *Components of the test setup.*

https://doi.org/10.52202/069179-0464

Figure 12: *Push-out test setup.*

4.4 LOADING PROCEDURE

To define the loading procedure a maximum load of 1200kN was considered. This loading procedure consists of an initial load to reach 40% of the maximum estimated load (480 kN) and then 25 cycles between 5% (60 kN) and 40% (480 kN) of the expected maximum load (1200 kN) at a frequency of 1 cycle per minute. Subsequent loading and unloading steps were carried out. For two of the specimens of each series the load was stopped when the failure of the connection or the maximum displacement was reached, for the remaining specimen the load was stopped at a displacement of about 40mm.

The initial loading/unloading steps along with the 25 cycles were performed in force control mode, the subsequent loading/unloading steps were carried out in displacement control mode. Figure 13 shows the time history of the loading procedure.

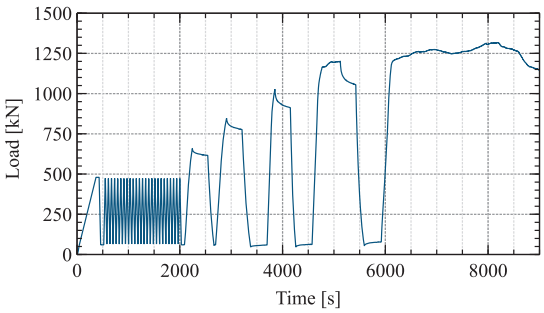

Figure 13: *Time history of the loading sequence.*

5 RESULTS AND COMPARISSON

5.1 RESULTS

The load slip curves of the three push-out test series are shown in Figure 14 to Figure 19.

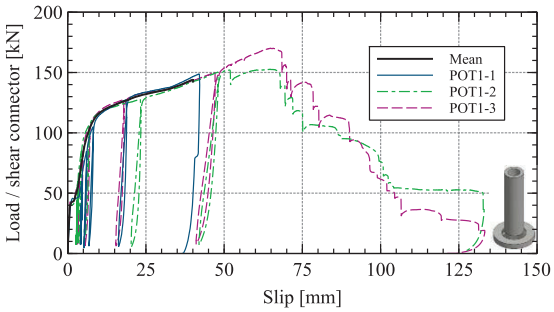

Figure 14: *Load-slip curves up to 150mm slip of push-out tests series 1 (POT1) of shear connection type 1 (SCT-1).*

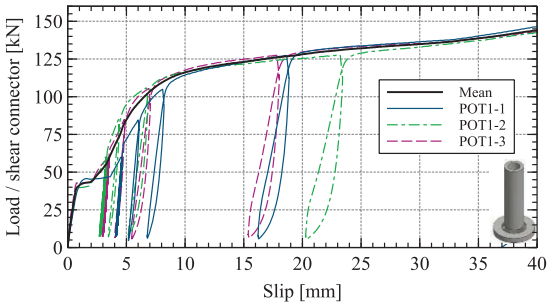

Figure 15: *Load-slip curves up to 40mm slip of push-out tests series 1 (POT1) of shear connection type 1 (SCT-1).*

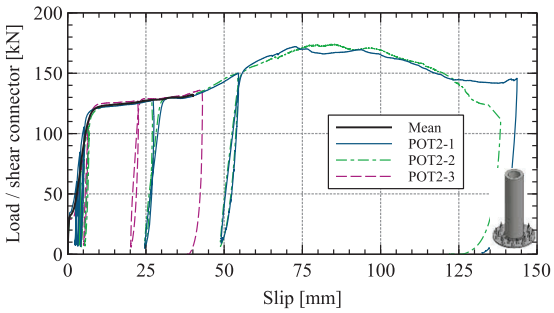

Figure 16: *Load-slip curves up to 150mm slip of push-out tests series 2 (POT2) of shear connection type 2 (SCT-2).*

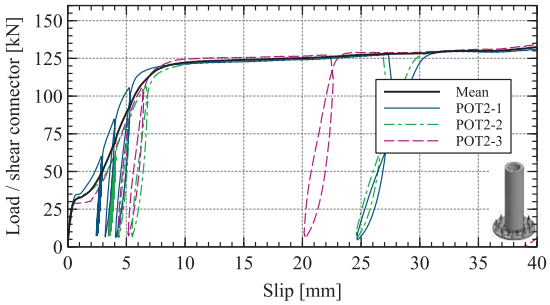

Figure 17: *Load-slip curves up to 40mm slip of push-out tests series 2 (POT2) of shear connection type 2 (SCT-2).*

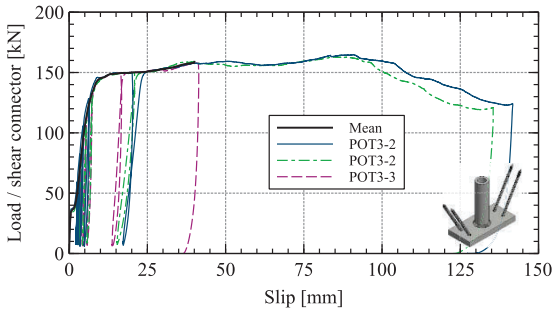

Figure 18: *Load-slip curves up to 150mm slip of push-out tests series 3 (POT3) of shear connection type 3 (SCT-3).*

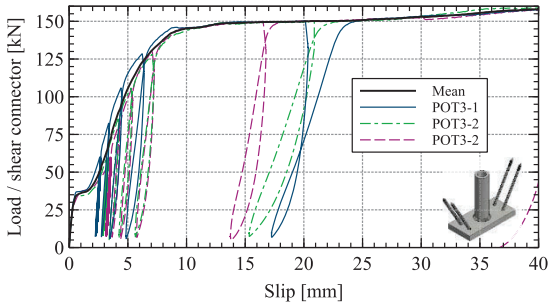

Figure 19: *Load-slip curves up to 40mm slip of push-out tests series 3 (POT3) of shear connection type 3 (SCT-3).*

The three connections showed large deformation capacity. The load-slip behaviour and the stiffness of the connections is different in terms of magnitude for each connection type. However, the three connections follow a similar pattern in their load slip behaviour.

Due to the preload of the bolts, the three connections have an initial slip capacity, when this slip capacity is reached, there is a slip of about 2-4mm with no increase in load because the bolt moves within the hole until there is contact between the bolt and both the flange of the beam and the inner surface of the connection device. After contact, there is bearing and shear in the bolt and then, there is embedment of the connection device in the timber plate.

Figure 20 is a longitudinal cutting of SCT-1, this figure illustrates the typical deformed shape observed in the three shear connection types. The veneers closer to the steel-timber interface crushed and one plastic hinge appeared in the connectors.

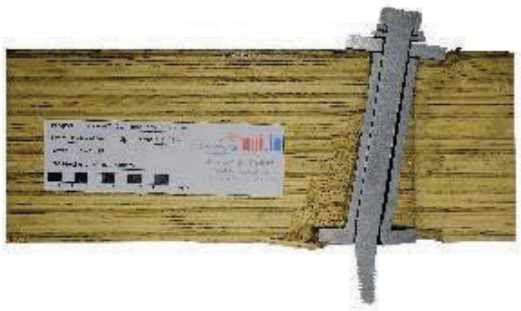

Figure 20: *Longitudinal cutting of SCT-1 showing the deformed shape after the test.*

5.2 COMPARISSON

SCT-1 and SCT-2 exhibited similar behaviour in the initial loading stages, whereas the SCT-3 showed higher stiffness. However, higher peak loads were reached with SCT-2. In addition, only in some specimens of SCT-1 the bolts failed, in SCT-2 and SCT-3 the tests were stopped because the maximum possible deformation (about 140mm) of the test setup was reached.

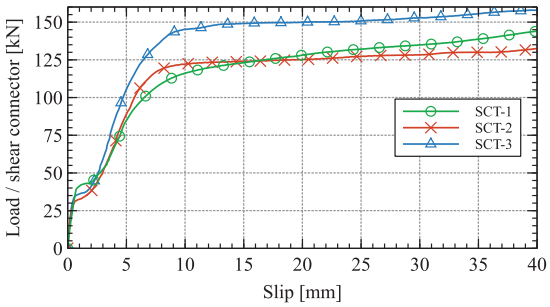

Figure 21: *Comparison of the mean load-slip curves of the three shear connections.*

6 CONCLUSIONS

The main conclusions of this contribution are the following:

- The three newly developed connections are capable of withstanding significant deformations and can bear loads of comparable magnitude. To illustrate, at a 6mm slip, SCT-1, SCT-2, and SCT-3 had average loads of 96kN, 104kN, and 120kN, respectively.
- The connections presented in this paper comply with the principles of circular economy.
- The novel connections, unlike existing steel-to-timber connections allow to reach the required preload for high strength bolts while preventing premature damages in timber due to crushing of the timber in the radial direction. Meaning the slip resistance can be activated.
- The use of crossbanded LVL prevented the occurrence of splitting failure. This demonstrates one of the benefits of using this type of LVL compared to non-crossbanded LVL and other timber materials which are known to be susceptible to this type of failure, as shown by other researchers in similar tests [7,8].
- The behaviour of the connections is non-linear, it is characterized by (i) an initial stiff response until the slip resistance given by the bolt preload is overcome, (ii) when the slip resistance is overcome, there is sliding friction, which results in a small displacement of about 2-4mm with no increase in the load until contact bearing between the bolt and both the steel flange and the connection device starts, (iii) then there is bearing and shear in the bolt and embedment of the connection device in the timber, which produce a monotonic increasing branch in the load-slip curve.
- Further studies will be useful to determine the influence of certain parameters such as the thickness of the timber plates, bolt size and grade, size of bottom steel plate, connectors arrangement, etc.

https://doi.org/10.52202/069179-0464

ACKNOWLEDGEMENT

The authors gratefully acknowledge Prefalux, ArcelorMittal and MetsäWood for their support in this research project; and the Luxembourg's National Research Fund (FNR) for its support through the PhD Industrial Fellowship Grant No. 15695062. The authors wish to thank also the laboratory team (Gilbert Klein, Marc Seil and Ed Weyer) and the former student Melis Pelivani for their support in this testing campaign.

REFERENCES

[1] M. Sansom, A. Girao Coelho, R. Lawson, and et. al.: Reuse and demountability using steel structures and the circular economy (REDUCE). Final Report, Project No. 710040, European Commission, Directorate-General for Research and Innovation, Brussels, Belgium, 2020.

[2] I. Jakovljević, M. Spremić, and Z. Marković: Demountable composite steel-concrete floors: A state-of-the-art review. Gradjevinar, vol. 73, no. 3. 2021, doi: 10.14256/JCE.2932.2020.

[3] W.A. Beerschoten: Structural Performance of Post-tensioned Timber Frames under Gravity Loading. PhD Thesis, University of Canterbury, 2013.

[4] M. Chybinski: Experimental and numerical investigations of laminated veneer lumber panels. Archives of Civil Engineering, Vol. 67, pages 351-372, 2021, doi: 10.24425/ace.2021.138060

[5] CEN, EN 408:2010+A1:2012: Timber structures - Structural timber and glued laminated timber - Determination of some physical and mechanical properties, European Committee for Standardization (CEN), 2012.

[6] CEN, EN 789:2004: Timber structures - Test methods - Determination of mechanical properties of wood based panels, European Committee for Standardization (CEN), 2004.

[7] M. Chybinski and L. Polus: Experimental study of Aluminium-Timber Composite Bolted Connections Strengthened with Toothed Plates. Materials 2022, Vol. 15, Page 5271, vol. 15, p. 5271, Jul. 2022, doi: 10.3390/MA15155271.

[8] Y. Zhao et al.: Experimental study on shear performance of steel-timber screw connectors with grout pockets, Engineering Structures, vol. 266, p. 114535, Sep. 2022, doi: 10.1016/J.ENGSTRUCT.2022.114535.

World Conference on Timber Engineering Oslo 2023

STRUCTURAL PERFORMANCE OF TIMBER-CONCRETE COMPOSITE FLOOR ELEMENTS WITH DECONSTRUCTABLE CONNECTORS AND ITS POTENTIAL FOR REUSE

Mohammad Derikvand[1], Gerhard Fink[2]

ABSTRACT: By incorporating design methods that allow for disassembly, buildings can be deconstructed at the end of their service life, thereby supporting the principles of circular economy and reducing waste. This paper provides a summary of the latest research advances by the research group for Wooden Structures (Aalto University) on the development and mechanical characteristics of a deconstructable connection system for timber-concrete composite (TCC) floors. This includes an overview of the experimental investigations conducted to date, focusing on the performance of the proposed system both at the connection level and at the floor level. At the connection level, the paper highlights the experimental investigations on the static and cyclic shear properties, as well as the ease of deconstruction after being exposed to substantial loads. Additionally, the floor level examination includes an overview of the bending properties, vibration characteristics, and deconstructability after reaching the failure point. A subsequent experiment is also reported here on the flexibility of the deconstructable connector for reuse and the influence of pre-existing concrete cracks on the performance of prefabricated TCC floors. The paper concludes with an outlook on the future of designing for deconstruction of TCC structures, as it not only reduces the environmental impact of construction but also allows for the efficient reuse of valuable resources.

KEYWORDS: Timber-concrete composite, cross-laminated timber, design for disassembly, vibration, four-point bending, cyclic shear test, self-tapping screws

1 INTRODUCTION

Deconstructable timber-concrete composite (TCC) structures combine the advantages of both timber and concrete in such a way that would allow for the structure to be disassembled at the end of its service life. This eases the process of recycling or reuse of the materials, which makes it a more environmental-friendly option compared to conventional forms of TCC structures. Therefore, deconstructable TCC structures are gaining more attention because of their potential to reduce waste and the environmental impact of buildings [1-5]. However, they are relatively new in the field of construction and the connector options for such structures are limited on the market, especially for the cast-in-situ construction method (i.e., the wet-dry system). Accordingly, the current knowledge on certain attributes of deconstructable TCC connectors is quite limited, specifically regarding their mechanical performance such as long-term static or dynamic properties or even their ability to be disassembled and taken apart at the end of their service life.

A number of factors play a major role in determining the efficiency and success of a deconstructable TCC connector. This includes technical requirements, such as the resistant of the connector against loads and environmental exposures factors such as humidity and temperature fluctuations without a considerable decrease in its performance; practicality factors, such as simplicity and easy installation effort, if possible, without additional training for the construction worker and without requiring specialized tools; versatility factors, such as suitability for various construction methods; market success factors, such as cost-effectiveness and viability for the target market in comparison to the regular connectors.

Considering the above factors, a deconstructable TCC system has been recently developed at the research group for Wooden Structures (Aalto University, Finland) using self-tapping screws. In this paper, the research activities related to the development and experimental investigations of the deconstructable TCC system are shortly summarized and discussed. Furthermore, a test report is provided which highlights both the potential of the deconstructable connector for reuse and the importance of preventing concrete cracks in prefabricated deconstructable TCC floors. The paper also highlights the outlook of the topic of design for deconstruction of TCC structures, with emphasis on raising awareness about the benefits of deconstructable connection systems to promote their use in sustainable construction projects.

[1] Mohammad Derikvand, Department of Civil Engineering, Aalto University, Finland, mohammad.derikvand@aalto.fi
[2] Gerhard Fink, Department of Civil Engineering, Aalto University, Finland, gerhard.fink@aalto.fi

https://doi.org/10.52202/069179-0465

2 DECONSTRUCTABLE TCC CONNECTOR

The existing deconstructable TCC connectors in the literature have been made using either screws or bolts [e.g., 3,4,6,7]. In most cases, the mechanical performance of the proposed connectors has been investigated only either for a certain type of construction or for a certain floor type. Therefore, the versatility aspects remain to be demonstrated.

Our project at Aalto University was initiated by evaluating various deconstructable connector prototypes. To be able to disassemble a TCC connection in general, the following two conditions were found to be vital:

1. The connector inside the concrete must be accessible. The connectors in a regular TCC system are normally covered by concrete and cannot be reached.

2. The connector must be removable. Some connectors are not removable even if they can be accessed inside the concrete, e.g., glued-in plates or glued-in steel rods.

Considering these conditions, self-tapping screws were selected as the target connector, as they can be removed if they can be accessed. To enable the accessibility, the upper parts of the screw must be protected from being covered by the concrete. The design and the material type of the protection layer were investigated during the prototyping. One of the early prototypes consisted of a protective layer (or plug) made with polyvinyl chloride (PVC) and a lid and a level adjuster made of silicon rubber. Several versions of this prototype were tested during the preliminary investigations, see the results here [8]. Overall, the connector was easy to use; however, it did not provide sufficient shear properties compared to a regular screw, which was attributed to the design and the material type of the protective layer.

After the pre-investigation, it was decided to use a thin protective layer that mimics the shape of the screw threads. To accomplish this, heat-shrink tubing (HST) was chosen as it is cost-effective and can create a thin layer around the screw threads by shrinking around them when heated. The configuration of the connector is shown in Figure 1.

For cast-in-situ fabrication of TCC floors and prefabrication in the wet-dry system, the connector can be used in the same way as a regular screw, in which the connector is first driven into the timber component, then concrete is poured on top.

For prefabrication in the dry-dry system, the connector is inserted into the base of a formwork before pouring concrete to create the slab. Once the slab has dried, the screw is detached, the slab is then laid on top of the timber member and the screw is reinserted through the connector hole in the slab into the timber.

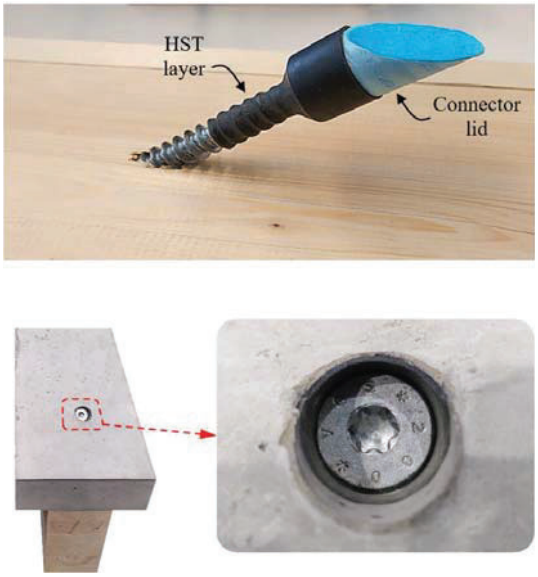

Figure 1: *The deconstructable connector components (top); a glulam-concrete composite connection made with the connector (bottom).*

In both wet-dry and dry-dry construction methods, the TCC system can be deconstructed by removing the screw from the connector hole in the concrete section. Once the screw is removed, the timber component and the concrete slab can then be separated.

3 EXPERIMENTAL INVESTIGATIONS OF THE TCC CONNECTOR

In the following sections a summary of the experimental investigations on the deconstructable TCC connector is presented.

3.1 SHEAR TESTS OF THE CONNECTOR UNDER STATIC LOADS

In an early study [1], the static shear strength and stiffness of the deconstructable connector concept were evaluated on several glulam-concrete composite connections. The focus of the study was on the wet-dry construction system, however, the application in the dry-dry system was also investigated to confirm the versatility of the connector and its potential for use in different types of construction. Other test variables included insertion angle, screw type and diameter, and screw arrangement.

A push-out shear test set-up was used to load the connection specimens (Figure 2). At the end of the tests, some of the tested connections were evaluated for deconstructability by removing the screw from the assembly.

https://doi.org/10.52202/069179-0465

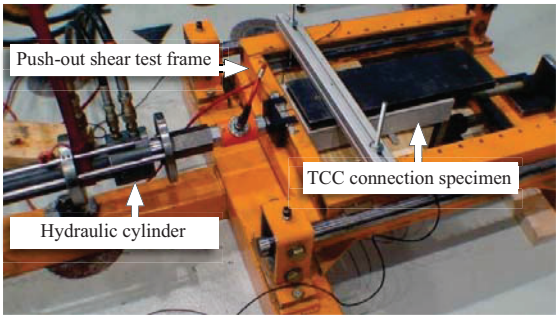

Figure 2: *Example cyclic load-slip curve of a deconstructable connector.*

The strength and stiffness of the deconstructable connections were relatively similar to those of identical connections made with regular self-tapping screws. The difference between the shear properties of the two connector types was the lowest when the connectors were inserted at 30˚ angle. Furthermore, it was demonstrated that the deconstructable connectors with 30˚ insertion angle can still be disassembled even if 15 mm slip is reached at the timber-concrete interface under loading. However, this level of slip prevents the disassembly of the connectors with a larger angle of insertion.

3.2 SHEAR TESTS OF THE CONNECTOR UNDER CYCLIC LOADS

In an ongoing study, the shear properties of the deconstructable connector were evaluated in a CLT-concrete composite system under cyclic loading. One objective was to determine how much the cyclic shear properties of the deconstructable connector might differ from those of a regular screw. Another objective was to evaluate the deconstructability of the connector at the end of cyclic loading.

For the shear tests, the push-out load set-up shown in Figure 2 was used. Several load levels within the serviceability range were applied, where the lower load level represented the dead load on the structure in an office floor and the upper load level represented the combination of the dead load and possible live loads. Each specimen was loaded up to about 130 k load cycles. They were then disassembled, reassembled, and then loaded to failure.

The results of the study showed that the trends in the load-slip behaviour of both types of connections were similar. An example load-slip curve during the cyclic loading of a deconstructable connection can be seen in Figure 3. The deconstructable connections were able to reach the same initial level of shear stiffness as the regular connections, which was likely due to the same CLT-concrete interface characteristics.

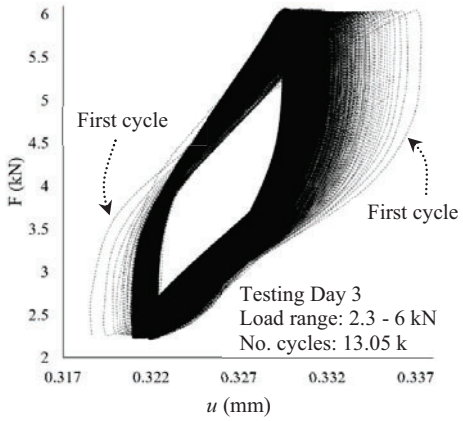

Figure 3: *Example cyclic load-slip curve of a deconstructable connector.*

As the cyclic test progressed, the shear stiffness increased as a result of the wood fibers hardening at the screw contact points but this also led to an increase in accumulated slip. Interestingly, the accumulated slip for the deconstructable connections was found to be lower than that of the regular connections during the cyclic loading.

The disassembly and reassembly processes of the connections were straightforward because no detectible plastic hinge had been formed in the connectors. After the reassembly process, the deconstructable connections retained 70% of their initial shear stiffness and their load-bearing capacity remained comparable to that of the regular connections.

3.3 BENDING TESTS OF A CLT-CONCRETE FLOOR ELEMENT

Following the completion of the test at the connection level, the effectiveness of the deconstructable connector was further evaluated in a CLT-concrete composite floor system, see [2]. To do this, a number of composite CLT-concrete beams, representing a strip of a full-scale floor, were constructed using the new connector. The properties of the beams were experimentally evaluated, including vibration performance, bending properties, interface slip, failure modes, and ease of disassembly. A control group of composite beams made with regular self-tapping screws was also fabricated and tested to provide a point of comparison. During the fabrication of the specimens, concrete was poured in such a way that a 3-mm concrete layer would form above the connector's lid. As a result, the composite beams made with both deconstructable and regular connectors were visually identical (Figure 4).

https://doi.org/10.52202/069179-0465

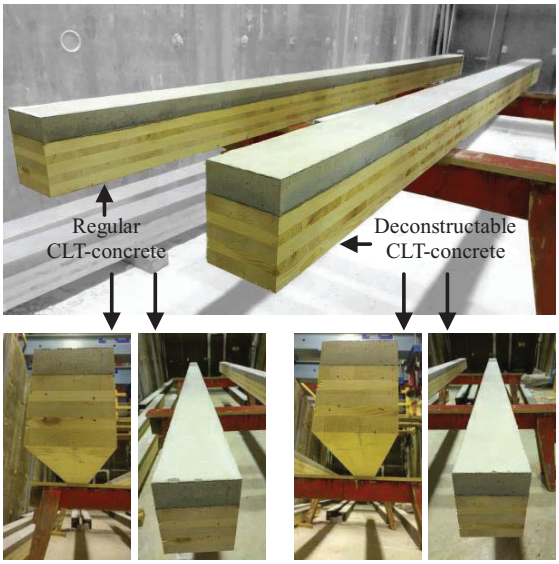

Figure 4: *The visual characteristics of a deconstructable and a regular CLT-concrete composite beam tested in: [2].*

Overall, the study found that the natural frequency, bending strength, and bending stiffness of the deconstructable composite beams were similar to those of the beams made with regular screws. Furthermore, the connectors inserted at a 30˚ angle did not show any detectable signs of plastic deformation, even after undergoing significant deformation under bending load. This indicates that the new connector system is able to maintain its deconstructability even under large loads.

4 DECONSTRUCTABLE CLT-CONCRETE FLOOR MADE WITH REUSED ELEMENTS

After the completion of the tests in the previous study [2], the deconstructable CLT-concrete composite beams were disassembled; one example is shown in Figure 5. A subsequent experiment was then undertaken aiming to connect one of the disassembled concrete slabs, with pre-existing cracks, to a fresh CLT beam using the self-tapping screws that were also disassembled in the previous study. The objectives were to a) evaluate the effect of concrete cracks on the performance of the system and b) demonstrate the ability of the connector for reuse in a disassembly-reassembly process. The composite beam was fabricated using 5-layer CLT with the dimensions of $b \times h \times l = 145 \times 130 \times 4000$ mm^3. The dimensions of the concrete slab were $b \times h \times l = 145 \times 55 \times 4000$ mm^3. The concrete slab contained multiple cracks along the span due to the previous bending tests (as shown in Figure 6).

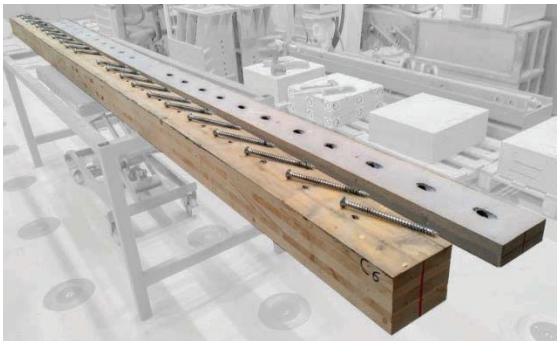

Figure 5: *A CLT-concrete composite beam deconstructed after destructive bending test.*

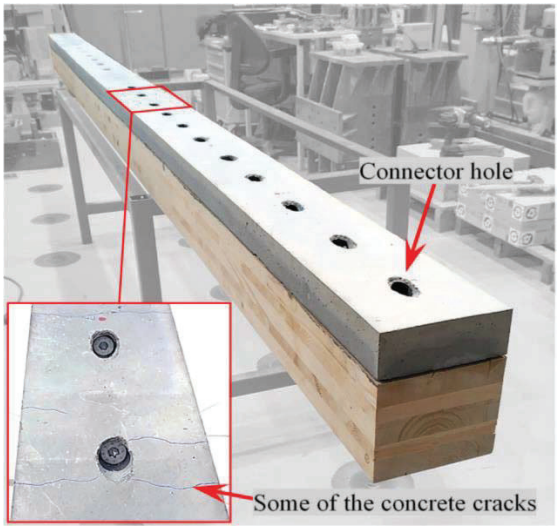

Figure 6: *The composite beam with concrete cracks.*

The first eigenfrequency (f) and the damping ratio (ζ) of the CLT beam prior to the assembly process and those of the composite beam with cracks were measured from several points along the beams using a hammer, an accelerometer, a charge amplifier, and a dynamic signal analyzer. The effective bending stiffness (EI_{eff}) of the CLT beam was measured in the elastic region prior to the assembly process using a four-point bending test set-up in accordance with EN 408 [9]. The bending properties of the composite beam with cracks were also measured using the same test set-up; however, the loading continued until after the failure point was reached.

The vibration characteristics of the pure CLT and the composite beam with cracks are given in Table 1. The results of the vibration test on the composite beam without cracks from the previous study [2] are also presented as a reference. The composite beam without cracks is the same one from which the concrete slab and the screws reused in the new beam were obtained.

https://doi.org/10.52202/069179-0465

Table 1: *The vibration characteristics and bending performance of the beams.*

Characteristics	CLT	CLT-concrete	
		With cracks	Without cracks
f (Hz)	18.3	18.8	19.8
ζ (%)	2.9	5.6	3.1
EI_{eff} (kN.m^2)	227.6	677.9	898.7
F_{max} (kN)	-	27.6	28.9

The first eigenfrequency (f) of the composite beam with cracks was only 2.7% higher than that of the pure CLT beam and about 5.3% lower than that of the composite beam without cracks (Table 1). Nevertheless, the damping ratio (ζ) was considerably higher for the composite beam with pre-existing cracks. The higher damping ratio is a result of cracks and related gaps in the concrete which can further dissipate the vibration energy.

The load-deflection curves of the composite beams with and without concrete cracks as well as that of the pure CLT beam are illustrated in Figure 7. The maximum load carrying capacity (F_{max}) of the composite beams were relatively similar. However, F_{max} was governed by the finger joint failure in the bottom lamella and, therefore, is not discussed further. The most apparent difference in the load-deflection curves of the two composite beams appeared at the initial stages of the loading. The composite beam without cracks exhibited a nearly linear trend up to F_{max}. The composite beam with cracks, however, initially exhibited a larger deflection up to approximately 15 kN load level. Afterwards, the slope of the load-deflection curves of the composite beams was relatively similar up to the failure point. The composite beam with cracks exhibited a significantly higher bending stiffness than the pure CLT beam. Nevertheless, the bending stiffness was lower than that of the composite beams without cracks.

Overall, this preliminary experiment provided a quantitative comparison between the performance of TCC floor elements with cracked and uncracked concrete slabs. The results tend to indicate that the benefits of the composite system are considerably minimal when cracks exist in the concrete slab. Therefore, it is important to reduce the likelihood of crack development during transportation and assembly of TCC structures, especially when the dry-dry system is used and the concrete slab is prefabricated and transported separately.

Furthermore, this experiment demonstrated the flexibility of the deconstructable connector for disassembly-reassembly process. This can offer some advantages in TCC structures such as e.g., flexibility for repairs or design changes in buildings, in addition to its potential for easing the reuse process of the materials at the end of service life.

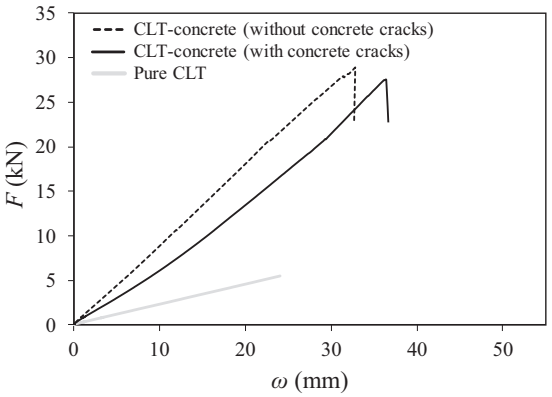

Figure 7: *Load-deflection curves of the beams.*

5 CONCLUSIONS AND OUTLOOK

Overall, the research works summarized in this paper have demonstrated the performance of the deconstructable TCC connection system, making it a viable alternative for applications where easy disassembly is of interest. This can be important not only for improving the circularity aspects of regular buildings, but also for other applications such as for temporary structures or for future design changes or repairs in buildings.

Although it was demonstrated that deconstructable solutions can be highly effective, to realize their true potential and promote their use, more needs to be done to educate and raise awareness in the field of design for deconstruction. For this, various strategies such as establishing design for deconstruction guidelines as well as providing training programs and other educational resources for designers and builders could be considered. Furthermore, showcasing and providing examples of successful deconstruction projects can help to educate and inspire designers and builders to create sustainable buildings that can be easily taken apart and recycled or repurposed.

REFERENCES

[1] Derikvand M., and Fink G.: Deconstructable connector for TCC floors using self-tapping screws. Journal of Building Engineering, 42, 102495, 2021. https://doi.org/10.1016/j.jobe.2021.102495.

[2] Derikvand M., and Fink G.: Bending properties of deconstructable CLT-concrete composite floor elements. Wood Material Science & Engineering, 17(4), 253-260, 2022. https://doi.org/10.1080/17480272.2022.2077658.

[3] Khorsandnia N., Valipour H., Schänzlin J., and Crews K.: Experimental investigations of deconstructable timber–concrete composite beams. Journal of Structural Engineering, 142(12), 04016130, 2016.

[4] Khorsandnia N., Valipour H., and Bradford M.: Deconstructable timber-concrete composite beams with panelised slabs: Finite element analysis.

https://doi.org/10.52202/069179-0465

Construction and Building Materials, 163, 798-811, 2018. https://doi.org/10.1016/j.conbuildmat.2017.12.169.
[5] Pang S. J., Ahn K. S., Jeong S. M., Lee G. C., Kim H. S., and Oh J. K.: Prediction of bending performance for a separable CLT-concrete composite slab connected by notch connectors. Journal of Building Engineering, 49, 103900, 2022.
[6] Lukaszewska, E.: Development of prefabricated timber-concrete composite floors. Doctoral dissertation, Luleå tekniska universitet, 2009.
[7] Thai M. V., Ménard S., Elachachi S. M., and Galimard P.: Performance of notched connectors for CLT-concrete composite floors. Buildings, 10(7), 122, 2020. https://doi.org/10.3390/buildings10070122
[8] Derikvand M., and Fink G.: Deconstructable timber-concrete composite connectors. In *the 63rd Society of Wood Science and Technology International Convention*, online, 98-105, 2020.
[9] EN 408: 2010. Timber structures – Structural timber and glued laminated timber – Determination of some physical and mechanical properties, 2010.

World Conference on Timber Engineering Oslo 2023

ENVISIONING MASS TIMBER BUILDINGS FOR CIRCULARITY: LIFE CYCLE ASSESSMENT OF A MASS TIMBER BUILDING WITH DIFFERENT END-OF-LIFE (EOL) AND POST-EOL OPTIONS

Namhyuck Ahn[1], Christina Bjarvin[2], Mariapaola Riggio[1], Lech Muszynski[1], Laurence Schimleck[1], Catarina Pestana[2], Ambrose Dodoo[3], Maureen Puettmann[4]

ABSTRACT: The foundation of the circular economy in the construction sector is based on implementing the deconstruction and reuse of buildings, providing the potential for a closed loop of building materials within the supply chain. Mass timber buildings using large, prefabricated elements and certain types of reversible mechanical connections are deemed to have great potential for post end-of-life (EoL) options, including recycling and reuse. To fully characterize the benefits of reusing post-use mass timber in new construction projects, it is crucial to conceptualize a 'grave-to-gate' approach, including the complete analysis of post-EoL activities and impacts on the material's second life. In this study, a comparative life cycle assessment (LCA) including different EoL and post-EoL options for a virtual reference mid-rise mass timber building in the Pacific Northwest (PNW) of the United States was conducted. Among four different deconstruction and reuse scenarios examined in this study, a case of nearly complete reconstruction of a mass timber building for the second service life used as an idealized reference established an optimistic limit for reduction of global warming potential (GWP) by 13-41% compared to the 'demolish and landfill' decision, depending on the scenario. The demolition and landfill scenario had the lowest net impact since the GWMP calculations accounted for the carbon storage benefits in the landfill in addition to the carbon stored in the building.

KEYWORDS: Mass Timber, Circular Economy, Deconstruction and Reuse, End-of-Life, Life Cycle Assessment

1 INTRODUCTION

Opposed to the "use and dispose" linear economic model, implementing the circularity of materials in the construction industry (recycling/reuse) is a critical issue in carbon footprint discussions. In Europe, the Climate Regulation of 2021 [1] aims to reduce greenhouse gas (GHGs) emissions by at least 55% below 1990 levels by 2030 as an intermediate goal. In the same year, along with this ambitious goal of the EU, the United States also introduced the Climate Leadership and Environmental Action for our Nation's (CLEAN) Future Act to drastically reduce GHGs emissions to at least 50% below 2005 levels by 2030. Under the Buy Clean Actions [2], the U.S. government also plans to expand the development of life cycle assessment (LCA) data for building materials purchased for any federal-funded projects. There is a need for lower carbon footprint buildings, and mass timber has gained popularity as a sustainable alternative to traditional construction materials and has led to revolutionary developments in timber construction [3, 4].

1.1 MASS TIMBER BUILDING FOR CIRCULARITY

Mass timber buildings typically utilize large engineered wood panels custom-ordered and manufactured for load-bearing structures such as floors and walls [5]. Because of the lightweight nature of the material [6], mass timber construction requires smaller cranes than other construction types, such as precast concrete, while maintaining the required structural performance. Connection hardware is one of the important parts of mass timber buildings, and they heavily influence the structural performance of such buildings [7]. Panel assemblies usually have screws instead of nails and use bolts and plates for some connection systems. Depending on the type and number of connections, mass timber assemblies may be disassembled at the end of building's life and re-assembled in new construction. The presence of fewer, localized connections, in some mass timber designs may minimize damage to panels, thus facilitating reuse. Compared to the deconstruction of conventional wood light-frame buildings, which requires extra effort and time during the de-nailing process, deconstruction of mass timber buildings and recovering mass timber panels for

[1] Namhyuck Ahn, Oregon State University, Wood Science and Engineering, USA, namhyuck.ahn@oregonstate.edu
Mariapaola Riggio, Oregon State University, Wood Science and Engineering, USA, mariapaola.riggio@oregonstate.edu
Lech Muszynski, Oregon State University, Wood Science and Engineering, USA, lech.muszynski@oregonstate.edu
Laurence Schimleck, Oregon State University, Wood Science and Engineering, USA, laurence.schimleck@oregonstate.edu
[2] Christina Bjarvin, University of Washington, School of Environmental and Forest Sciences, USA, bjarvin@uw.edu
[3] Catarina Pestana, Oregon State University, Civil and Construction Engineering, USA, catarina.pestana@oregonstate.edu
[4] Ambrose Dodoo, Linnaeus University, Department of Building Technology, Sweden, ambrose.dodoo@lnu.se
[5] Maureen Puettmann, WoodLife Environmental Consultants, USA, maureen.puettmann@woodlifeconsulting.com

https://doi.org/10.52202/069179-0466

reuse rather than disposal at the end of the building's service life seems an attainable EoL scenario (Figure 1).

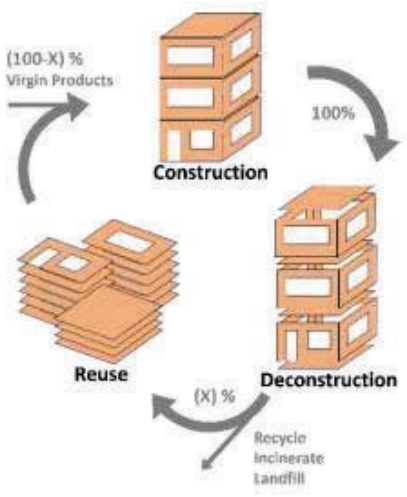

Figure 1: *Deconstruction and reuse of mass timber buildings.*

This is also well-aligned with circular economy principles that aim to maximize resource value and reduce environmental impacts. Moreover, the advantage of the reuse scheme is realized when the benefits of reusing mass timber panels are fully accounted for throughout their expected life.

1.2 LIFE BEYOND BUILDING END-OF-LIFE: EXTENDED LIFE CYCLE ASSESSMENT OF MASS TIMBER BUILDINGS

Conventional life cycle assessment (LCA) methodology is insufficient to assess the environmental impacts of mass timber building deconstruction and material reuse due to its focus on the first life cycle. Although the International Organization for Standardization (ISO) 14040 [8] defines module D to account for potential net benefits from reuse in ISO 14044 [9], it is still outside the system boundary. ISO 14044 instructs avoiding miscounting benefits from reusing by expanding the product system to the second product use [10]. Yet, it does not specify how these scenarios can be implemented, with or without a remanufacturing phase.

By extending part of the building material's lifespan at the end-of-life stage to the second lifecycle (Figure 2), there can be a proper evaluation of the circularity value of buildings that otherwise might have been overlooked [11]. For instance, if mass timber panels can be reused in another construction project after building deconstruction, the burden of producing panels from virgin timber can be avoided. Reusing panels instead of landfilling them also avoids the burden of panel waste processing. Moreover, reusing or landfilling panels can reduce the cumulative cradle-to-grave global warming potential (GWP) associated with the first building due to the carbon storage benefits of wood [12,13]. These benefits and avoided burdens can lower the environmental impacts of buildings, thus improving the potential of circularity as a viable option for sustainable construction. However, to fully account for the benefit of deconstruction and reuse, the first step is to incorporate this gate-to-gate impact into the system boundary.

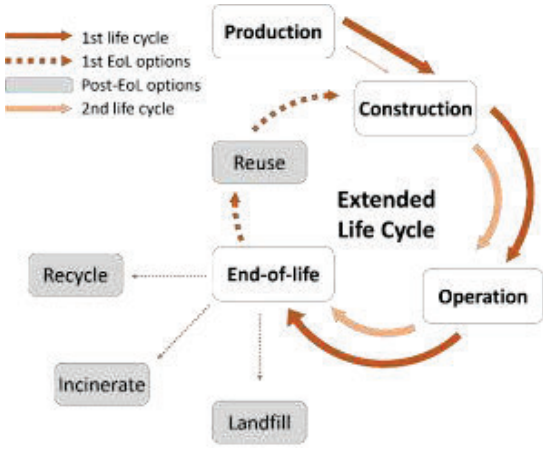

Figure 2: *Extended life cycle of buildings.*

While there have been attempts to address the benefit of reusing building materials at large using LCA [14-16], several studies have focused on timber-based buildings. LCA research investigating wood-cascading scenarios for glue-laminated timber beams in a virtual building indicated that reusing timber is beneficial as it provides the substitution effect for structural building materials [17]. However, the environmental impact assessment excluded construction, operation, and transportation stages for simplicity, and there was no comparison among different post-EoL options. Comparative LCA of CLT reuse, focusing on the second life [18], has also been conducted. Different CLT reuse rate scenarios were used to compare the avoided environmental impact of A1-A3 and C2-C4 modules on the overall carbon footprint. Again, this research also focused exclusively on the second life of mass timber panels, while there were no variations in post-EoL options. Recent work focuses on the first life of mass timber and EoL impacts after deconstruction [19]. In the research, various post-EoL options were implemented, including reuse, recycling, landfill, and incineration, using a dynamic LCA approach for comparison over two life cycles. Yet, the research focused more on the first life, leaving research needs for more in-depth analysis focusing on the second life with EoL alternatives to draw a comprehensive overview of circularity potential and its benefits for mass timber buildings.

1.3 OBJECTIVE AND SCOPE

The main objective of this study is to explore the circularity potential of mass timber buildings in their theoretical and practical reuse scenarios to help decision-

https://doi.org/10.52202/069179-0466

makers fully consider mass timber's carbon storage potential with its second life. Comparative LCA of a reference mass timber panel (MTP) building with various EoL and post-EoL options, including deconstruction, reuse, recycling, energy recovery, and landfill, are considered in this study.

2 MATERIALS AND METHODS

To analyze the environmental impacts of EoL and post-EoL options, we designed a comparative whole-building LCA of a reference MTP building, starting with the deconstruction and EoL processing of the first building and ending with the construction of a second identical building. In this manner, any recovered MTPs from the first building were assumed to be reused for the second building without changes in design.

2.1 REFERENCE BUILDING MODEL

The reference building for this study was based on mass timber building Type IV-C construction guidelines established in the 2021 International Building Code revision. The building was designed as an eight-story residential mixed-use building with a simple rectangular shape, a core elevator shaft, and stairs in the central space [20]. The building was designed to be located in the Pacific Northwest (PNW) region of the United States, and as such, it meets the building code requirements of that region. It was assumed that the first and second buildings were in the same Portland metropolitan area in Oregon. The study also included an ideal scenario, which reuses the foundation of the first building. This will be explained in detail in section 2.3..

With the specific region in consideration, seismic requirements were applied to the building design (e.g., a lateral force resistance system). For walls and floors, cross-laminated timber (CLT) was used, while glue-laminated timber (GLT) was used for the columns and beams. While mass timber products are mostly selected for building design, steel and concrete are also used in foundations and some structural elements. A conventional reinforced concrete structure with identical function and shape was designed for comparison with the reference mass timber building. Detailed building information is summarized in Table 1.

Table 1: *Description of the mass timber building used for LCA in this study.*

Type	Description
Building Use	Mixed-use
Construction Type	Type IV-C
Mass Timber Product Type	CLT (walls and floors), GLT (columns and beams)
Stories	8 (residential 6 + commercial 2)
Height	26 m
Total Floor Area	9,476 m^2

2.2 EOL AND POST-EOL OPTIONS FOR THE SYSTEM BOUNDARY

In this LCA, we set the system boundary to encompass EoL processing (module C) for the first building and production-and-construction (module A) for the second building. Either deconstruction or demolition was considered for the EOL option, depending on if panels were going to be reused or not. For post-EoL options, it was assumed that mass timber products (both CLT panels and GLT columns/beams) were reused (RU), recycled (RE), incinerated (IC), or landfilled (LF) in different proportions, depending on the case (Table 2). The whole system boundary information is summarized in Figure 3.

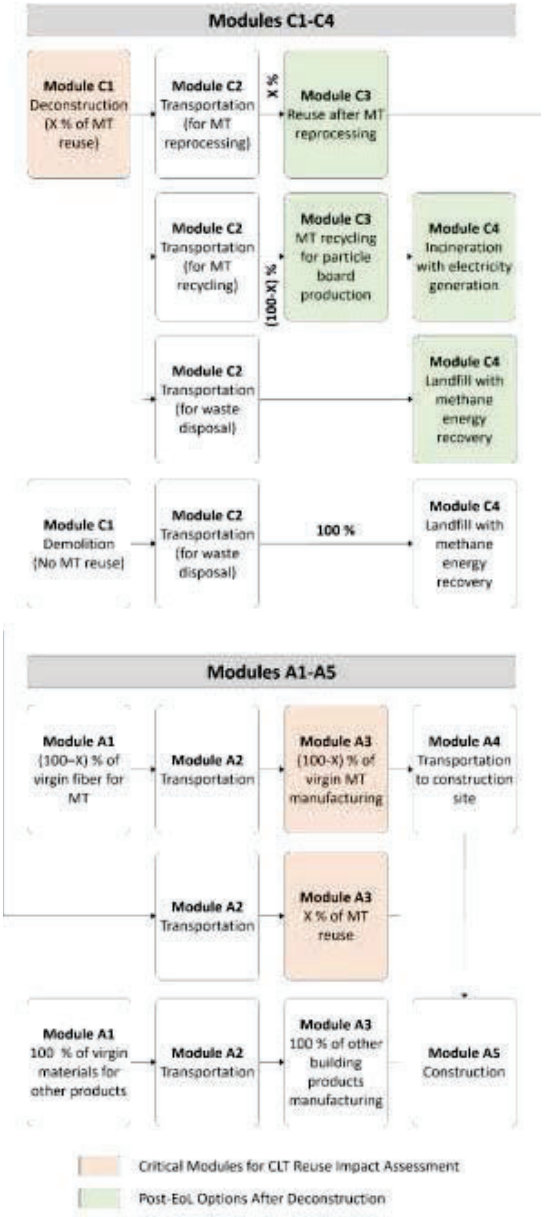

Figure 3: *System boundary applied to EoL and post-EOL of CLT in the study.*

https://doi.org/10.52202/069179-0466

In RU, mass timber products are reprocessed in the manufacturing facility located in Oregon and then transported to the new mass timber building construction site for a second life. Reprocessing for reuse included minimal treatment, such as cleaning, connection removal, and repackaging. The volume of panels required for the second building that was not satisfied by reused panels was made from virgin materials. In RE, mass timber products are recycled in the manufacturing facility in Oregon to produce particleboard for the general market. In IC, mass timber products are incinerated in the plant facility for electricity generation, while in LF, products are landfilled in the same facility with methane energy recovery.

2.3 DECONSTRUCTION AND REUSE SCENARIOS

Mass timber buildings are still relatively young compared to other building types, and almost none of the existing cases worldwide have reached the end of their service life. Consequently, few studies have investigated the potential reuse of mass timber panels for a new building design [18,19,21]. Based on this fact, the rate of use of recovered panels for the second building after the deconstruction of the first building was determined by hypothetical assumptions (Table 2).

Table 1: *LCA cases used in this study.*

Case		MT Deconstruction and Reuse	
		CLT	GLT
Ideal	1	90% RU 10% RE	
Optimistic	2	70% RU 30% RE	90% RU 10% RE
	3	70% RU 30% IC	90% RU 10% RE
	4	70% RU 30% LF	90% RU 10% RE
Conservative	5	50% RU 50% RE	90% RU 10% RE
	6	50% RU 50% IC	90% RU 10% RE
	7	50% RU 50% LF	90% RU 10% RE
No reuse	8	100% LF (construct a new mass timber building)	
	9	100% LF (construct a new reinforced concrete building)	

In 'conservative' scenarios, 50% of CLT panels used in the first building are assumed to be reused for the second building. 70% reuse is assumed in 'optimistic' scenarios because the reuse of CLT in the future may be easier than it is today because of continuous technological advancement (for instance, technology capable of separating CLT and concrete from a composite floor system without damaging CLT panels). In addition, a case of nearly complete reconstruction of a mass timber building for the second service life was used as an idealized reference to establish an optimistic limit for the reduction of global warming potential (GWP). In this scenario, it is assumed that 90% of the panels are recovered in an intact condition, which requires minimal on-site reprocessing (e.g., removing connectors and cleaning).

Notably, 90% of GLT beams and columns are reused in all cases except the demolition with 100% landfilling options (Cases 8 and 9). For all scenarios, connectors for mass timber products are assumed not to be reused for safety reasons.

In the ideal scenario, the building's foundation is also assumed to be reused. This is unrealistic in the legal and planning aspects of the project, but from the engineering perspective, it is a sufficiently possible scenario considering the durability of the concrete foundation. It is also a recommended practice, if possible, from the circular economy point of view. In this scenario, the distance between the reprocessing facility and the mass timber building was assumed to be the same as in other cases to avoid changes in impacts in module A4.

Two additional cases in which mass timber products were not reused, which were described as 'no reuse' scenarios in this study, were further analyzed for comparison. One is to construct a new identical mass timber building after the demolition of the first mass timber building, and the other is to construct a functionally equivalent building with a reinforced concrete structure. In both cases, all mass timber panels from the first building would be landfilled.

2.4 LCA METHODOLOGY

In addition to the GWP values associated with modules C and A, the module D benefits associated with storing carbon in mass timber for all cases were calculated using the Lashof accounting method [22]. For cases involving incineration or landfill EoL options, the benefit of replacing fossil fuels with biofuel generated during energy recovery was calculated.

LCA in this study was extended beyond the scope of conventional static LCA by adopting a dynamic approach, which accounts for the timing of different emissions generated in modules C and A over a period of 100 years. A previously created novel dynamic LCA model was used in this study to account for the radiative forcing caused by GHG emissions. The model emulates the atmospheric decay of the emissions over time, producing a dynamic LCA result [19,23].

3 RESULTS

We calculated the 100-year cumulative fossil GWP values, global warming mitigation potential (GWMP) values, and net climate impacts (the sum of the GWP and GWMP) in Modules C1 – A5 for each of the eight scenarios from Table 1 (Figures 4 - 7). The GWMP

includes benefits from carbon storage in wood products but not the benefits from energy recovery.

Comparing the two extreme scenarios (Case 1, "Ideal," and Case 8, "No Reuse") demonstrates the stark difference in GWP values when MTP materials are reused instead of landfilled (Figure 4). However, the "No Reuse" case had more carbon storage benefits because in this scenario, we accounted for the carbon stored in the landfill [13] *and* the carbon stored in the building, while in the Ideal case, we only accounted for the carbon stored in the building and in the recycled timber products. Bringing in virgin timber increases the GWP of the building, but it also increases the opportunity for carbon storage benefits. However, in both cases, the carbon storage benefits outweigh the GWPs, making the building a net sink for carbon due to the use of mass timber.

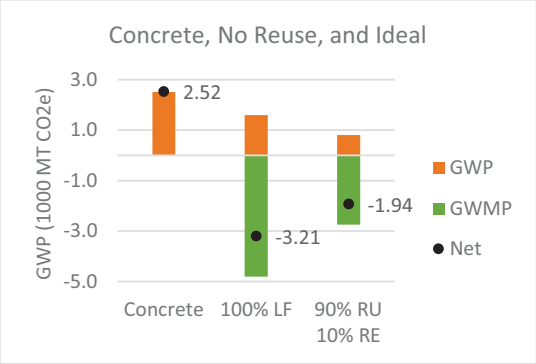

Figure 4: *Global warming potential (GWP), carbon storage benefits (GWMP), and net GWP values in Cases 8 (left) and 1 (right).*

Comparing the optimistic (70% reuse) and conservative (50% reuse) cases for each EOL option demonstrated similar differences. The optimistic cases had lower GWP values than the conservative cases, but conservative cases had more carbon storage benefits. These differences are shown in Figures 5-7. Comparatively, the GWP values associated with recycling are lower than those associated with incineration and landfilling.

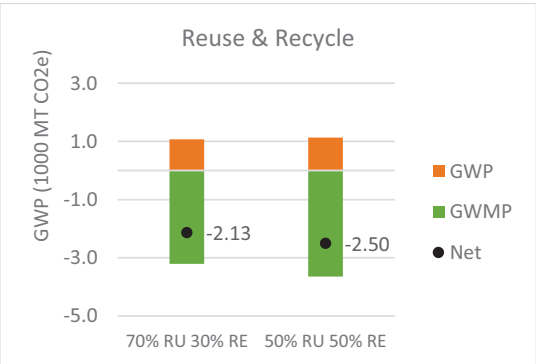

Figure 5: *Global warming potential (GWP), carbon storage benefits (GWMP), and net GWP values in Cases 2 (left) and 4 (right).*

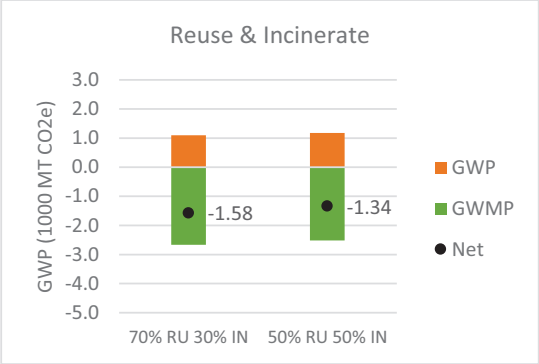

Figure 6: *Global warming potential (GWP), carbon storage benefits (GWMP), and net GWP values in Cases 3 (left) and 6 (right).*

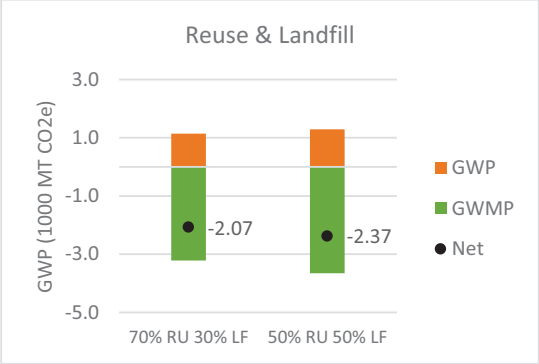

Figure 7: *Global warming potential (GWP), carbon storage benefit (GWMP), and net GWP values in Cases 4 (left) and 7 (right).*

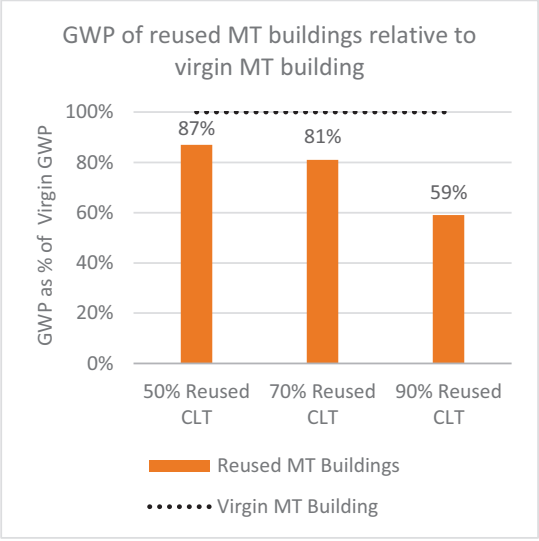

Figure 8: Fossil GWP of the 8-story mass timber (MT) building constructed from 50%, 70%, ***or 90%*** reused CLT as a percentage of the virgin mass timber building GWP.

https://doi.org/10.52202/069179-0466

Finally, the GWP values of the buildings constructed from reused timber in the Optimistic and Conservative cases are compared relative to the GWP of the virgin timber building (Figure 8). These GWP values are shown as a percent of the virgin MT building GWP, with the virgin MT GWP equaling 100%).

4 CONCLUSIONS AND FUTURE RESEARCH

This research analyzed the climate impacts of four different post-EoL options (reuse, recycling, landfill, and incineration) on the second life of a virtual mid-rise mass timber building in the PNW of the United States after four different post-deconstruction scenarios for the first life of the building (no reuse, conservative, optimistic, and ideal used to establish an optimistic limit for potential benefits). Although the presented analysis uses some oversimplified assumptions (e.g., reuse of the same foundations, reuse for the same design) and has demonstrable bottlenecks, this research indicates the aim for the mass timber industry on the path to the circular economy age and a vision of its potential impact on the environment. The study also demonstrates that reusing mass timber products may contribute to sustainable forest practices by reducing the pressure on harvesting, a value that cannot be fully expressed in conventional LCA approaches.

Compared to a conventional static LCA, using a dynamic LCA approach achieved by incorporating the temporal variations of GHG emissions and their atmospheric decay rates into LCA allows for a more realistic representation and a more comprehensive understanding of global warming impacts. This is particularly applicable to the *recycle* and *incinerate* EoL options predicted to generate emissions at different times throughout the time horizon instead of all at once.

Future research includes another round of analysis with a systematic approach to refined mass timber cascading scenarios and practical second-building design interventions with a different configuration than used in this presented study. In addition, observational research to gather information, such as the actual attrition rate of recovered panels from multi-story mass timber test structures, is also planned.

ACKNOWLEDGEMENT

This work is partially supported by the U.S. Department of Agriculture's Agricultural Research Service (USDA ARS Agreement No. 58-0204-0-099). The lead author is a recipient of 2021 OSU Provost's Distinguished Graduate Fellowship and 2022 College of Forestry Dean's Distinguished Graduate Fellowship.

The dynamic LCA model was created by researchers Christina Bjarvin, Dr. Francesca Pierobon, and Dr. Indroneil Ganguly at the University of Washington's Center for International Trade in Forest Products lab (CINTRAFOR).

REFERENCES

[1] European Climate Law: Regulation (EU) 2021/1119 of the European Parliament and of the Council of 30 June 2021 establishing the framework for achieving climate neutrality and amending Regulations (EC) No 401/2009 and (EU) 2018/1999. Official Journal of the European Union, 64: 1-18, 2021.

[2] FACT SHEET: Biden-Harris Administration Announces New Buy Clean Actions to Ensure American Manufacturing Leads in the 21st Century, https://www.whitehouse.gov/briefing-room/statements-releases/2022/09/15/fact-sheet-biden-harris-administration-announces-new-buy-clean-actions-to-ensure-american-manufacturing-leads-in-the-21st-century/, 2022.

[3] D'Amico, B., Pomponi, F., & Hart, J.: Global potential for material substitution in building construction: The case of cross laminated timber. Journal of Cleaner Production, 279, 123487, 2021.

[4] Felmer, G., Morales-Vera, R., Astroza, R., González, I., Puettmann, M., & Wishnie, M.: A lifecycle assessment of a low-energy mass-timber building and mainstream concrete alternative in central Chile. Sustainability, 14(3), 1249, 2022.

[5] Ahn, N., Dodoo, A., Riggio, M., Muszynski, L., Schimleck, L., & Puettmann, M.: Circular economy in mass timber construction: State-of-the-art, gaps and pressing research needs. Journal of Building Engineering, 53, 104562, 2022.

[6] Izzi, M., Casagrande, D., Bezzi, S., Pasca, D., Follesa, M., & Tomasi, R.: Seismic behaviour of Cross-Laminated Timber structures: A state-of-the-art review. Engineering Structures, 170, 42–52, 2018.

[7] Bhandari, S., Riggio, M., Jahedi, S., Fischer, E. C., Muszynski, L., & Luo, Z.: A review of modular cross laminated timber construction: Implications for temporary housing in seismic areas. Journal of Building Engineering, 105485, 2022.

[8] ISO 14040: Environmental Management - Life Cycle Assessment - Principle and Framework. 2006.

[9] ISO 14040: Environmental Management - Life Cycle Assessment - Requirements and Guidelines. 2006

[10] Joensuu, T., Leino, R., Heinonen, J., Saari, A.: Developing Buildings' Life Cycle Assessment in Circular Economy-Comparing Methods for Assessing Carbon Footprint of Reusable Components, Sustainable Cities and Society, 77: 103499, 2022.

[11] Suhariyanto T. T., Wahab D. A., and Rahman M. N. Ab.: Multi-Life Cycle Assessment for sustainable products: A systematic review. Journal of Cleaner Production, 165:677-696, 2017.

[12] Liang, S., Gu, H., and Bergman, R.: Environmental Life-Cycle Assessment and Life-Cycle Cost Analysis of a High-Rise Mass Timber Building: A Case Study in Pacific Northwestern United States. Sustainability, 13:7831, 2021.

[13] U.S. EPA, Documentation for Greenhouse Gas Emission and Energy Factors Used in the Waste Reduction Model (WARM). 2020.

[14] Van Stijn, A., Malabi Eberhardt, L. C., Wouterszoon Jansen, B., & Meijer, A.: A Circular Economy Life Cycle Assessment (CE-LCA) model for building components. Resources, Conservation and Recycling, 174, 105683, 2021.
[15] Minunno, R., O'Grady, T., Morrison, G. M., & Gruner, R. L.: Exploring environmental benefits of reuse and recycle practices: A circular economy case study of a modular building. Resources, Conservation and Recycling, 160, 104855, 2020.
[16] Anastasiades, K., Blom, J., Buyle, M. & Audenaert, A.: Translating the circular economy to bridge construction: Lessons learnt from a critical literature review. Renewable and Sustainable Energy Reviews, 117, 109522, 2020.
[17] Niu, Y., Rasi, K., Hughes, M., Halme, M., & Fink, G.: Prolonging life cycles of construction materials and combating climate change by cascading: The case of reusing timber in Finland. Resources, Conservation and Recycling, 170, 105555, 2021.
[18] Passarelli R. N.: Environmental Benefits of Reusable Modular Mass Timber Construction for Residential use in Japan: an LCA Approach. Proceedings of the Modular and Offsite Construction. Banff, AB, Canada, 2019.
[19] Bjarvin, C.: Assessing the Carbon Balance for Mass Timbers Beyond the First Life. 2022. M.S. Thesis. University of Washington.
[20] Puettmann, M., Pierobon, F., Ganguly, I., Gu, H., Chen, C., Liang, S., Jones, S., Maples, I., & Wishnie, M.: Comparative LCAs of Conventional and Mass Timber Buildings in Regions with Potential for Mass Timber Penetration. Sustainability, 13(24), 13987, 2021.
[21] Passarelli R. N.: The Environmental Impact of Reused CLT Panels: Study of a Single-Storey Commercial Building in Japan. Proceedings of the 2018 World Conference on Timber Engineering. Republic of Korea, 2018.
[22] Fearnside, P. M., Lashof, D. A., & Moura-Costa, P.: Accounting for time in Mitigating Global Warming through land-use change and forestry. Mitigation and Adaptation Strategies for Global Change, 5(3), 239–270, 2000.
[23] Ganguly, I., Pierobon, F., & Sonne Hall, E.: Global Warming Mitigating Role of Wood Products from Washington State's Private Forests. Forests, 11(2), Article 2, 2020.

https://doi.org/10.52202/069179-0466

World Conference on Timber Engineering Oslo 2023

A REUSE-READY TIMBER SLAB-AND-COLUMN SYSTEM FOR MODULAR BUILDING STRUCTURES

Xavier Estrella[1], Alex Muresan[2], Dario Redaelli[3], Jan Brütting[4], Jonas Warmuth[5], Corentin Fivet[6]

ABSTRACT: The construction industry is a significant contributor to resource consumption and waste generation. To address this issue, component reuse has been proposed as a way to prevent valuable building elements from being discarded and avoid producing new ones. However, the lack of circular economy principles in existing structures makes it difficult to extract and exploit reusable components fully. This paper presents a new load-bearing timber system (Pixel Slab) designed for disassembling and reassembling multiple times over the building's lifespan. The system goes beyond the traditional concepts of modularity and reversibility, providing designers with a minimum kit of parts that can be used to make localized adjustments and accommodate a wide range of building designs – such as floor geometry, load conditions, and supports distribution – with little to no new material input. This allows for functional design requirements that are difficult to predict over the long term. The system also focuses on low-tech assembly and disassembly processes, embodied environmental impacts, and manufacturing costs, all of which aim to increase the potential for component reuse. The proposed timber solution proved to be particularly suited to increase the sustainability of short-lived buildings.

KEYWORDS: Component reuse, design for deconstruction, timber structures, circular economy, sustainable buildings, construction and demolition waste, material recovery.

1 INTRODUCTION

Over the last few decades, the construction industry has been at the center of ample criticism because of its role in the climate change emergency that societies face nowadays. Due to the high growth rates of newly built infrastructure and the widespread use of highly pollutant construction materials, the industry has been identified as responsible for 15% of the world's CO2 emissions [1] and one-third of the waste production [2]. Besides, recent research associates it with 50% of the exploitation of natural resources [3,4] and 36% of global energy consumption [5]. As the demand for new housing and civil infrastructure is expected to grow in the upcoming decades, measures are urged by private and public organizations to deal with such a multiscale challenge.

In this context, timber structures arise as an environmentally friendly strategy to tackle the aforementioned issues, providing the means to reduce the carbon footprint of the construction industry. For instance, previous studies have shown that the energy consumption of concrete houses is 60-80% higher compared to timber houses [6], and that the CO_2 production during the life span of a concrete building is 30-130 kg/m^2 greater [7]. In seasonal countries with cold winters and hot summers, it has been calculated that a timber house consumes around 15% less energy for heating/cooling when compared to a concrete or steel house, and over a period of 100 years, it is estimated that a timber house could reduce the net emissions of greenhouse gases by between 20% and 50% when compared to traditional systems [8].

On the other hand, the inclusion of Circular Economy principles into construction practices has also proved to be an effective approach to alleviate the environmental impact of new infrastructure. In particular, the reuse of construction components has been gaining traction lately [9], with the aim of keeping construction components in a closed loop at their highest value and extending their lifespan over several building cycles. This way, components are brought back into the construction supply chain with little/no maintenance after the initial structure reached obsolescence, minimizing new production and diverting valuable resources from landfilling.

The current practice of timber construction does not allow a straightforward inclusion of reuse techniques at the end-of-life phase of existing buildings. Therefore, once timber structures have reached obsolescence, their components are discarded or must undergo time/energy-consuming procedures to be reused in different building applications. And even though mass-timber structures generally employ reversible and standard connections that facilitate assembly/disassembly procedures, their future reuse potential cannot be guaranteed beforehand. This is mainly due to the lack of open-ended reuse principles in current timber construction practices, such as adaptivity to different architectural requirements and load conditions, use of standard and interchangeable components and connectors, embracing long-term purpose uncertainty, and easy repairability, replaceability, and transportability.

[1] Xavier Estrella, EPFL Structural Xploration Lab, Switzerland, edisson.estrellaarcos@epfl.ch
[2] Alex Muresan, Aeternum Technologies, Switzerland, alex.muresan@aeternum-tech.com
[3] Dario Redaelli, University of Applied Sciences Western Switzerland, Switzerland, dario.redaelli@hefr.ch
[4] Jan Brütting, EPFL Structural Xploration Lab, Switzerland, dis_jan.bruetting@epfl.ch
[5] Jonas Warmuth, EPFL Structural Xploration Lab, Switzerland, jonas.warmuth@epfl.ch
[6] Corentin Fivet, EPFL Structural Xploration Lab, Switzerland, corentin.fivet@epfl.ch

https://doi.org/10.52202/069179-0467

Therefore, this paper presents a novel timber slab-and-column system "Pixel Slab" designed for open-ended reuse over multiple life cycles. The system goes beyond the traditional wooden concepts of modularity and reversibility, providing designers with a minimum kit of parts that can be used to make localized adjustments and accommodate a wide range of building designs – such as floor geometry, load conditions, and supports distribution – with little to no new material input. This allows for functional design requirements that are difficult to predict over the long term. The system also focuses on low-tech assembly and disassembly processes, embodied environmental impacts, and manufacturing costs, all of which aim to increase the potential for component reuse of current timber construction practices.

2 MATERIALS AND METHODOLOGY

This study follows a Research-through-Design (RtD) approach in the development of the Pixel Slab system. The RtD methodology generates new knowledge through a systematic and iterative process of evaluating design results and feedback [10]. This approach combines theoretical concepts with design and development, allowing for exploratory ideas and a disruption of the status quo in a scientifically controlled environment. The RtD framework for this investigation, as shown in Figure 1, consisted of six main stages: (1) goals and functional requirements definition, (2) iterative design sessions, (3) conceptual design, (4) structural implementation, (5) feasibility analysis, and (6) full-scale validation.

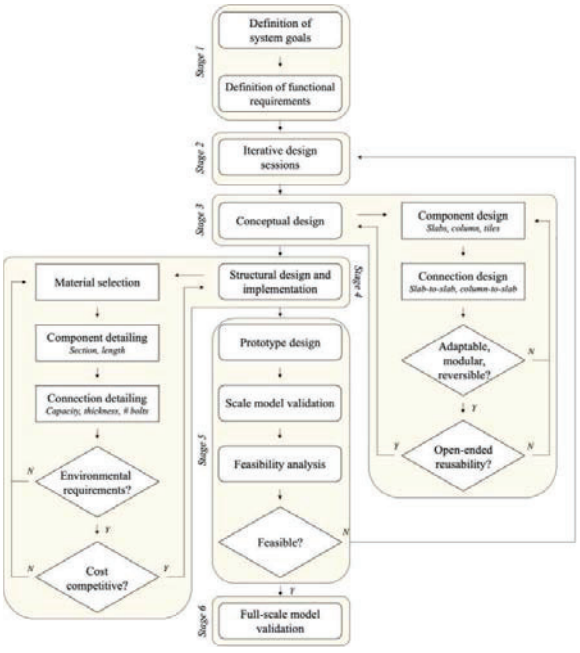

Figure 1. *Methodological workflow for the development of the Pixel Slab system.*

A set of system goals was defined early in the development of the Pixel Slab system aiming at guiding its design principles and requirements. Adhering to a downstream component reuse philosophy [9], the system aims to bridge the gap between reusability and its practical application in timber construction. At the same time, it incorporates Circular Economy principles into the design phase to account for future uncertainty and maximize the potential for open-ended reuse. The goal is to design timber structures that are easily repairable, replaceable, demountable, and transportable. Accordingly, the system goals are stated as follows, in descending order of hierarchy:

- To maximize the open-ended reuse potential of timber structures by implementing design-for-reassembly principles in such a way that it can meet unpredictable scenarios and boundary conditions.
- To minimize the detrimental environmental impacts related to manufacturing, handling, maintenance, and end-of-life.
- To reach manufacturing and operation costs that are competitive to conventional products in the long term and over several life cycles.

A comprehensive set of functional requirements was established to provide a clear research framework by considering past, present, and future reuse practices, and to establish the boundaries and conditions for the new timber solution. The requirements aim to ensure the structure's technical and economic appeal under various future scenarios and promote the open-ended reuse of the structural system and its components. To facilitate the implementation during the conceptual design phase, the functional requirements were grouped into three categories: (1) structural, (2) assembly and disassembly, and (3) versatility and modularity.

The structural requirements establish the scope and niche of the proposed timber system in terms of its intended applications and performance:

- To provide a load-bearing structural system for low- to mid-rise office or residential timber buildings.
- To create a continuous load path and carry vertical loads down to the foundation system. The system is not intended to carry horizontal loads and should be designed along with a lateral resistant system (e.g., core walls, bracing system, among others).
- To allow versatility of vertical load levels and spans between vertical supporting elements.
- To provide an effortless installation of vertical shafts, pipes, and non-structural elements.

Assembly and disassembly requirements define the design boundaries with the aim of maximizing the structure's reuse potential in unspecified future scenarios:

- To employ dry, readily accessible, reversible mechanical connections for assembling elements and components.
- To minimize the number of connections between elements, assemblies, non-structural components, and the main structural system.
- To maximize the use of standard connections across the different system levels (substructure, superstructure, flooring, and non-structural components).
- To employ only low-tech tools and procedures for assembling and disassembling. Likewise, to provide means for easy handling and transportation of components.

https://doi.org/10.52202/069179-0467

Versatility and adaptability requirements aim to ensure that the Pixel Slab system can be adjusted and reconfigured for future reuse scenarios, making it flexible and capable of being used in a wide range of applications:

- To allow open-ended re-arrangements of structural and non-structural components in the system.
- To employ interchangeable modular elements and connections, facilitating reorganization and replacement of system components.
- To allow unplanned inclusion or removal of openings across the floor layout, e.g., for staircases, elevators, shafts, technical installations, or building extensions.
- Not to restrict the inner partitioning layout and to ease parallel disassembly if modifications are required.

3 RESULTS: PIXEL SLAB

Figure 2 shows the resulting timber Pixel Slab system. It comprises slab elements set horizontally to create a lateral surface and column elements to transfer vertical forces to the foundations. Slab elements are made up of glue-laminated timber beams connected orthogonally to form a uniform flat grid. Individual beams are 80×240 mm spaced at 400 mm from their longitudinal axis. Beams are manufactured by gluing eight timber laths (80×30 mm each) with alternating discontinuities, as observed in Figure 3. This allows a grid-like slab with uniform properties in both directions. This configuration achieves spans of up to 6 meters based on the loading requirements specified in the Swiss SIA 261 standard [11] for office and residential buildings. Slabs are 2.4×2.4 m to facilitate handling, transportation, and storage. Besides, the beams' discrete placement results in a uniform distribution of slab openings that makes room for columns, vertical shafts, or non-structural elements, resulting in a low-weight solution compared to traditional flooring systems.

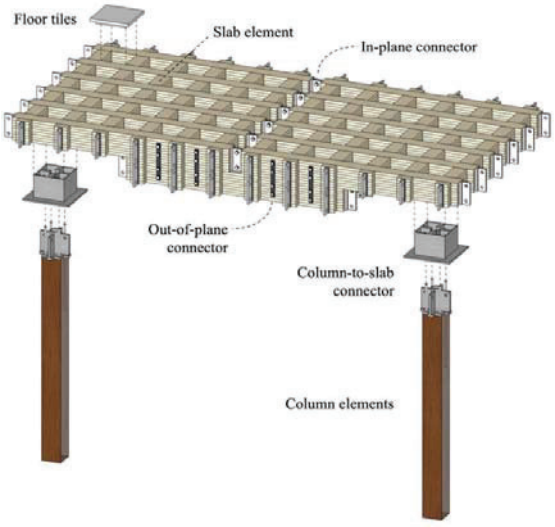

Figure 2. *Overview of the Pixel Slab system and its components.*

Flexible floor configurations can be designed by attaching slab elements with in-plane connectors, which transfer axial, bending, and shear loads between two adjacent slabs. In-plane connections were designed employing 240×83×15 mm steel plates grade S355, 660 mm long threaded steel rods grade 8.8, and two M27 steel bolts class 10.9, as per Figure 3. Threaded rods are embedded into timber into pre-drilled holes and glued-in employing epoxy resin, and subsequently welded to the steel plates. This way, in-plane connections are reversible and allow effortless construction, deconstruction, and reuse.

The structural capacity (strength and stiffness) of slab elements can be increased by stacking them vertically with out-of-plane connections, which are designed to bear the shear and axial loads that arise at the interface between slabs while not blocking the installation of vertical pipes or shafts through the openings. Out-of-plane connectors employ 380×60×5 mm steel plates grade S235 and four M16 steel bolts class 8.8, as Figure 3 shows. With this design, out-of-plane connectors provide a convenient and reversible method to reinforce areas that experience high demands or to accommodate longer spans.

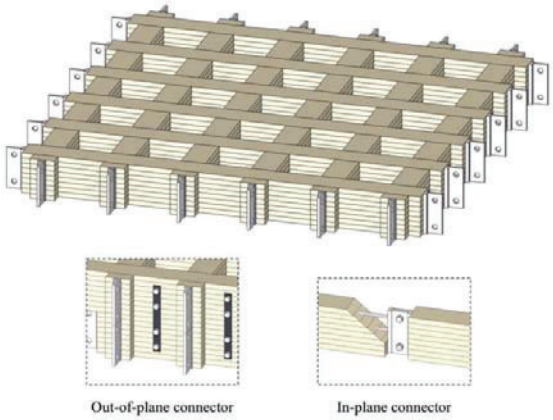

Figure 3. *Slab element with in-plane and out-of-plane connectors.*

Vertical loads are transferred across stories down to the foundation through conventional mass-timber columns. Forces between slabs and columns are taken by column-to-slab connectors that fit into the slab openings and nest the upper and lower columns, as Figure 2 depicts. Column-to-slab connectors employ high-strength steel and bolts, and their dimensions might vary based on the column sizing. Thanks to this versatile design, columns can be placed at any slab opening across the floor plan to accommodate different engineering or architectural requirements. It should be noted that the system described here is not intended to bear lateral loads, such as wind or earthquake, and should be designed as a gravity frame system without ductile capacity. Yet, the slab components must have adequate in-plane stiffness to effectively transfer lateral loads to the stiff core or bracing system.

Finally, floor tiles are installed on top of the slab elements to create a continuous surface for other finishing layers to be added, as illustrated in Figure 2. The dimensions of the floor tiles are designed to fit into one or multiple slab openings at once, with joint lines of minimum thickness to ensure proper sealing between components. This allows the tiles to meet technical requirements and fulfill non-structural functions such as smoke barriers or sound insulation. Tiles are attached to the slab components through reversible connections (i.e., bolts and nuts), allowing for future replacement of units and simple construction/deconstruction processes.

https://doi.org/10.52202/069179-0467

4 EXPERIMENTAL TESTING

A full-scale experimental campaign was carried out to evaluate the structural performance of the Pixel Slab system, and 19 different specimens were tested under bending load. Each specimen consisted of single-span components designed to be representative of the GLT beams used for the Pixel Slab system shown in Figure 2.

Beams were manufactured using mechanically graded GL32h timber with an elasticity module E = 13000 MPa and characteristic bending strength $f_{m,k}$ = 32 MPa. Single beams were 80×240 mm made up of 8 timber laths glued with polyurethane adhesive. The beams' span was 4800 mm, equal to the length of two Pixel Slab modules together. For double beams (laterally adjacent), the distance between their longitudinal axis was 400 mm. Besides, specimens had alternating discontinuous laths to simulate the discontinuity of orthogonally intersecting slabs. Finally, in-plane and out-of-plane connections were manufactured as per the specifications listed in Section 3.

Single-layer specimens ("S", "D", and "IP") were tested with a 4-point setup, while double-layer specimens ("OP" and "IPOP") with a 3-point setup. This was done to guarantee a bending failure in double-layer beams and not to reach the max shear strength. All tests used a 200 kN hydraulic jack fixed to a steel reaction frame and a loading beam was used to transfer the load from the jack to the specimens at the application points. For the 4-point setup, point loads were applied at 1800 mm from the beam ends.

Table 1. *Labelling and description of tested specimens.*

Test ID	Configuration	Description
S		Traditional GLT beam (×3).
D		Double beam with discontinuities (×4).
IP		Two discontinuous double-beams with in-plane connectors (×3).
OP(a)		Two stacked discontinuous double-beams with 11 out-of-plane connectors (×2).
OP(b)		Two stacked discontinuous double-beams with 6 out-of-plane connectors (×1).
OP(c)		Two stacked discontinuous double-beams with 90º and 45º screws (×1).
IPOP(a)		Two stacked discontinuous double-beams with in-plane and out-of-plane connectors (×4).
IPOP(b)		Two stacked discontinuous double beams only with in-plane connectors (×1).

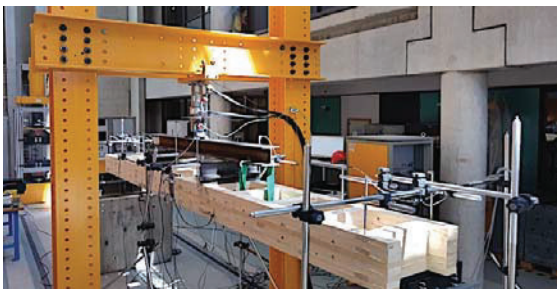

Figure 4. *Testing setup for "D" specimens.*

Specimens were installed on top of steel bearings and support beams placed 200 mm from the ends to allow free rotation under bending deformation. Displacement transducers (LVDTs) were installed to measure mid-span displacements, settlements at supports, slip between steel plates, and relative displacements between two stacked beams. Tests were conducted by applying load until the specimen's failure, defined as a 20% drop from the maximum recorded load. Figure 5 shows the force-displacement results for all "D" beams.

Test results showed that, when compared to traditional GLT specimens, beams with discontinuities had a reduction in the maximum moment M_{max} and elastic stiffness EI of 58.9% and 40%, respectively. This is mainly due to the presence of discontinuities along the longitudinal direction of the beam, which does not allow exploitation of the full cross-section and forces the continuous laths to take most of the tensile and compression stresses. Besides, the use of in-plane connections proved to be an efficient solution to join two GLT beams along their longitudinal axis, properly transferring axial, shear, and bending loads between the members. In this sense, employing glued-in rods showed to have a reinforcement effect on the capacity of the specimens, increasing the maximum moment M_{max} and elastic stiffness EI by 13.67% and 10.56%, respectively.

Finally, it was found that conventional beam design equations can be used to estimate the strength and stiffness of discontinuous GLT beams. To do so, the negative effects of the discontinuities can be considered as a reduction of the beam height, since fewer laths contribute to its capacity. To compute the maximum moment M_{max}, a reduced height h_{red} = 0.6×h was found to be consistent with the lab results. To estimate the stiffness EI, a reduced height h_{red} = 0.75×h is recommended.

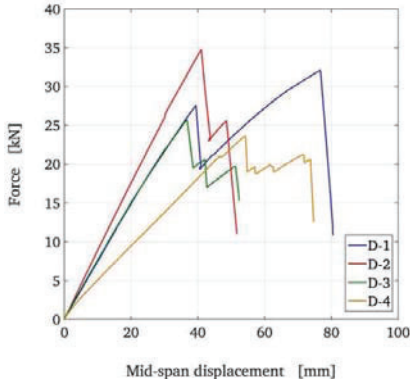

Figure 5. *Force-displacements data for "D" specimens.*

https://doi.org/10.52202/069179-0467

5 CHALLENGES AND FUTURE WORK

As part of the development of the Pixel Slab system, a full-scale prototype was manufactured following the specifications outlined in previous sections, as show in Figure 6. After conducting a set of detailed evaluations, results showed that the manufacturing processes do not require specialized knowledge and can be performed by traditional companies and assembly lines. However, more development is needed to further reduce the manufacturing costs of the connections and/or their quantity per linear meter of interface.

Additionally, the results confirmed that the construction and deconstruction process is straightforward and does not require particularly trained workers or special tools, making it well-suited for prefabrication and dry procedures. Yet, it highlighted the relevance of paying close attention to dimensional tolerances to prevent deformation of components due to manufacturing imperfections, thermal effects, and creep or shrinkage.

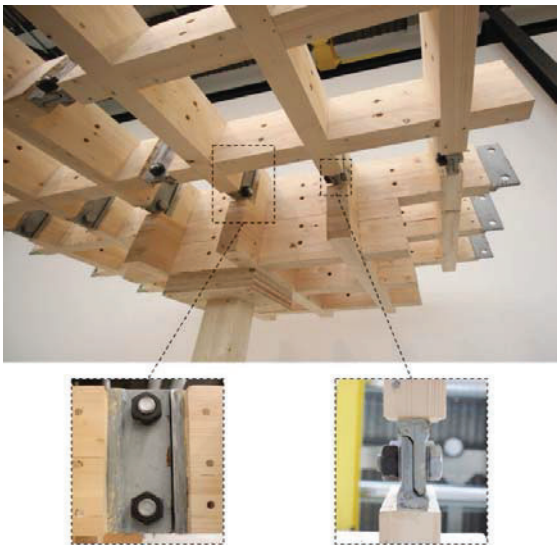

Figure 6. *Full-scale prototype of the Pixel Slab solution and connection details between beams.*

On the other hand, it is important to note that the full environmental benefits of the Pixel Slab system may only be realized over the long term. As part of the present research project, a preliminary life cycle analysis (LCA) was performed to compare the Pixel Slab system with a typical reinforced concrete system. The outcome of the analysis revealed that if only a single building lifespan is taken into account, the Pixel Slab system generates higher levels of emissions compared to the concrete solution. The primary reason for the higher emissions in the Pixel Slab system is the considerable amount of steel connections involved in the reusable solution. The production of steel accounts for a substantial portion of the total CO2 emissions. Nevertheless, when multiple lifespans are considered, the environmental impact per cycle of the Pixel Slab system decreases, and it becomes significantly lower than that of conventional systems. For instance, in a scenario with four lifespans, the emissions from the concrete system were ~80% higher compared to those generated by the Pixel Slab system. These results suggests that a potential entry market for the Pixel Slab are short lifespan buildings such as temporary classrooms or offices for ephemeral cultural or sport events.

These findings emphasize the potential of the Pixel Slab to decrease the carbon footprint in the construction sector. However, prior studies have highlighted that the emissions resulting from the disassembly and transportation of recovered components might have negative impacts on the environmental footprint [12–14]. This latter is largely due to the prominent levels of greenhouse gases associated with longer demolition periods, the use of heavy machinery, and the long-distance transportation of components (>1000 km) [12]. Further research is necessary to examine the relationship between these implications and the emission savings achieved through reuse, reduced landfilling and recycling, and lower production of new components.

6 CONCLUSIONS

This paper presents a new load-bearing timber system (Pixel Slab) designed for deconstruction and reuse over multiple building lifespans. The Pixel Slab system offers an alternative timber structural system for buildings designed for assembly and deconstruction by employing reversible connections and standardized components, with the main goal of increasing the open-ended reuse potential of building elements. In this sense, the proposed system incorporates a modular nature that provides constructors with an adaptable design framework with respect to floor geometries, spans, load conditions, and component distribution, making room for a diverse range of realistic solutions regarding architecture and engineering. Widespread implementation of the proposed solution is expected to support reducing global warming levels, resource depletion, and waste generation caused by the construction industry. The main features of the proposed system can be summarized as follows:

- The system is reversible and can be easily disassembled without damage to its components.
- The system is transformable into diverse floor plans and layouts since the columns' placement is highly flexible and slabs' thickness is reconfigurable.
- The system is adaptable and allows parallel assembly and disassembly, i.e., slab modules and tiles can be installed, removed, or replaced without disturbing adjacent components.
- The system allows full integration with non-structural components and sub-systems.
- No high-tech procedures and tools are required for the assembly and disassembly of the system and common equipment can be employed.
- Handling, storage, and transportation of components are facilitated due to compact dimensions.
- The construction process is dry and produces no waste on-site.

Future research is needed to propose standard procedures to estimate the residual properties of demountable elements and the environmental impacts of deconstruction and transportation related to disassembly and reuse. Likewise, further policy work that encourages reuse is still deemed necessary to boost reuse in the upcoming years.

https://doi.org/10.52202/069179-0467

REFERENCES

[1] United Nations Environment Programme. 2022 Global Status Report for Buildings and Construction. Nairobi: 2022.

[2] European Commission. Development and implementation of initiatives fostering investment and innovation in construction and demolition waste recycling infrastructure. European Commission, Brussels, Belgium: 2018.

[3] WST. Sustainable Steel: At the Core of a Green Economy. World Steel Association, Brussels, Belgium: 2012.

[4] Herczeg M, McKinnon D, Milios L, Bakas I, Klaassens E, Svatikova K, et al. Resource efficiency in the building sector. ECORYS Nederland BV, Rotterdam The Netherlands: 2014.

[5] UN. Towards a zero-emission, efficient, and resilient buildings and construction sector. Global Status Report 2017. UN Environment and International Energy Agency: 2017.

[6] Börjesson P, Gustavsson L. Greenhouse gas balances in building construction: wood versus concrete from life-cycle and forest land-use perspectives. Energy Policy 2000;28:575–88.

[7] Gustavsson L, Pingoud K, Sathre R. Carbon dioxide balance of wood substitution: comparing concrete- and wood-framed buildings. Mitig Adapt Strateg Glob Chang 2006;11:667–91. https://doi.org/10.1007/s11027-006-7207-1.

[8] Upton B, Miner R, Spinney M, Heath L. The greenhouse gas and energy impacts of using wood instead of alternatives in residential construction in the United States. Biomass Bioenergy 2008;32:1–10. https://doi.org/10.1016/j.biombioe.2007.07.001.

[9] Fivet C, Brütting J. Nothing is lost, nothing is created, everything is reused: structural design for a circular economy. The Structural Engineer 2020;98:74–81.

[10] Zimmerman J, Forlizzi J. Research through design in HCI. Ways of Knowing in HCI, Springer; 2014, p. 167–89.

[11] Swiss Society of Engineers and Architects. SIA 261: Actions on structures. Zürich, Switzerland: 2003.

[12] Brambilla G, Lavagna M, Vasdravellis G, Castiglioni CA. Environmental benefits arising from demountable steel-concrete composite floor systems in buildings. Resour Conserv Recycl 2019;141:133–42. https://doi.org/https://doi.org/10.1016/j.resconrec.2018.10.014.

[13] Huuhka S, Hakanen J. Potential and Barriers for Reusing Load-Bearing Building Components in Finland. International Journal for Housing Science and Its Applications 2015;39:215–24.

[14] Nußholz JLK, Nygaard Rasmussen F, Milios L. Circular building materials: Carbon saving potential and the role of business model innovation and public policy. Resour Conserv Recycl 2019;141:308–16. https://doi.org/https://doi.org/10.1016/j.resconrec.2018.10.036.

https://doi.org/10.52202/069179-0467

World Conference on Timber Engineering Oslo 2023

ENGINEERED WOOD PRODUCTS MANUFACTURED FROM RECLAIMED HARDWOOD TIMBER

Daniel F. Llana[1], Violeta González-Alegre[2], María Portela[3], Justo García-Navarro[4], Guillermo Íñiguez-González[5]

ABSTRACT: The circular economy is commonly applied in recent years in order to reduce the amount of wood waste with many environmental benefits. The construction and demolition sector generates a large amount of wood waste that can be potentially reused or recycled into different wood-added-value products. The InFutUReWood and the RECOWERS European projects deal with reusing and recycling recovered timber as a structural material. One of the potential applications of recovered wood from construction and demolition sources is in manufacturing Engineered Wood Products (EWP). Twelve Cross Laminated Timber (CLT) panels and twelve glued-laminated timber (glulam) pieces from European oak were manufactured and tested in the present work. Four different 3-layer CLT panel configurations and two different 5-lamella glulam pieces configurations were manufactured using recovered and new European oak timber. The results show that there is significant potential in using recovered timber for manufacturing EWP. The modulus of elasticity of CLT panels and glulam pieces from recovered and new timber is similar while bending strength is lower in the case of EWP from recovered timber than from new timber, but still enough high for structural applications. The timber yield producing EWP from recovered timber is really low due to the great amount of wood waste generated during manufacturing.

KEYWORDS: cascading, circular economy, mass timber products, recovered, recycling, salvaged, secondary timber

1 INTRODUCTION

The circular economy is a new production model to reduce the amount of waste by reusing it or recycling it as added-value products, reducing the consumption of raw materials. The long-term carbon sequestration stored in timber constructions and the reuse of building materials contributes to the mitigation of climate change. Furthermore, the increase in timber demand for construction purposes in Europe will lead to a lack of enough new timber resources. Therefore, improvement of the circular economy model in the timber sector is absolutely recommended.

Several European projects dealt with this topic in recent years. The CaReWood project (2014-2017) [1] focused on the potential recycling of recovered timber in glued laminated products in order to replace sawn timber for different applications (furniture, window frames, mouldings and fittings). However, no promising results were found for structural applications in load-bearing construction elements, due to wood waste usually comes from different mix species, which it would be difficult and expensive to identify and classify [2].

InFutUReWood was a 3-year European project (2019-2022) that focused on design for deconstruction of timber structures; enhance the current demolition techniques to maximize the amount of recovered timber and recycling of current recovered wood as structural material in different mass timber products [3].

RECOWERS is a 2-year Marie Skłodowska-Curie Actions (MSCA) European project (2022-2023) that focuses on grading recovered timber from demolition for structural purposes [4]. There is a lack of a reliable classification or grading system that estimates the properties of recovered timber in order to reuse it for structural applications.

[1] Daniel F. Llana, Timber Construction Research Group GICM-UPM and Department of Forestry and Environmental Engineering and Management, MONTES (School of Forest Engineering and Natural Resources), Universidad Politécnica de Madrid, Madrid, Spain, d.f.llana@upm.es
[2] Violeta González-Alegre, Orgánica Ingeniería en Madera, Valladolid, Spain, violetagonzalezalegre@gmail.com
[3] María Portela, PEMADE - Research Platform on Structural Wood Engineering, Agroforestry Engineering Department, Higher Polytechnic School, Universidad de Santiago de Compostela, Lugo, Spain, maria.portela.barral@usc.es
[4] Justo García-Navarro, Research Group on Sustainability in Construction and Industry giSCI-UPM, E.T.S.I.A.A.B. (School of Agricultural, Food and Biosystems Engineering), Universidad Politécnica de Madrid, Madrid, Spain, justo.gnavarro@upm.es
[5] Guillermo Íñiguez-González, Timber Construction Research Group GICM-UPM and Department of Forestry and Environmental Engineering and Management, MONTES (School of Forest Engineering and Natural Resources), Universidad Politécnica de Madrid, Madrid, Spain, guillermo.iniguez@upm.es

https://doi.org/10.52202/069179-0468

The construction and demolition sector creates a large amount of wood waste, much of which is nowadays used for energy recovery and panel manufacture [5, 6]. In the case of Spain, recovered wood is usually used in the form of chips for energy production and manufacturing particleboards [7]. Much of that wood waste has the quality to reuse or recycle in added-value structural products. Potential end-use structural possibilities include high-quality Engineered Wood Products (EWP) such as glued-laminated timber (glulam), solid wood panels, and Cross Laminated Timber (CLT) [8]. Previous tests on CLT from recovered mixed softwood timbers showed higher stiffness capacity and lower strength than CLT from new sawn softwood timber [9]. However, this was based on a limited number of tests.

The main objective of this paper is to compare the mechanical properties of CLT panels and glulam pieces manufactured from recovered European oak timber with CLT panels and glulam pieces manufactured from new sawn European oak timber.

2 MATERIALS AND METHODS

2.1 MATERIALS

From large cross-section (145 by 165 mm^2) European oak (*Quercus robur* L.) pieces recovered from a demolition of a 150-year-old house (Figure 1), recovered timber boards were sawn to a cross-section of 25 by 108 mm^2 (Figure 2).

***Figure 1**: Recovered timber pieces*

***Figure 2**: Recovered sawn timber boards*

Planed boards of final cross-section 20 by 100 mm^2 and variable-length from recovered and new European oak timber were used to manufacture CLT panels and glulam pieces. A total of twelve 3-layer (two external longitudinal layers and one internal cross-layer) CLT panels were manufactured. Three CLT panels were manufactured from recovered sawn timber, other three using recovered timber only in the longitudinal layers and new timber in the cross-layer, other three using recovered timber only in the cross-layer and new timber in the longitudinal layers and finally three more panels from new timber. Twelve 5-lamella glulam pieces were manufactured; six using recovered timber and six more using new timber. The number of CLT panels and glulam pieces, kind of timber and dimensions are shown in Table 1.

***Table 1:** CLT 3-layer panels and 5-lamella glulam pieces characteristics*

CLT panels					
No.	Kind of timber		Dimensions (mm)		
	Long. layers	Cross layer	Length	Width	Thickness *layer
3	R	R	1800	300	20*3
3	R	N	1800	300	20*3
3	N	R	1800	300	20*3
3	N	N	1800	300	20*3

Glulam pieces				
No.	Kind of timber	Dimensions (mm)		
	Lamellae	Length	Width	Thickness *layer
6	R	1900	100	20*5
6	N	1900	100	20*5

R: recovered timber
N: new timber
Moisture content: circa 15%

2.2 METHODS

Recovered and new timber European oak boards were planed until a final cross-section 20 by 100 mm^2 giving an aspect of ratio of 5. According to European standard EN16351 [10] when the board-dimension ratio is higher than 4, the bending test on CLT panels can be carried out over a span of 18 times the panel thickness. However, in order to avoid rolling shear, four-point bending test over a span of 24 times the thickness was conducted. In case of glulam pieces four-point bending test over a span of 18 times was carried out according to EN408 [11]. The test arrangement for CLT panels is shown in Figure 3 and for glulam pieces in Figure 4.

https://doi.org/10.52202/069179-0468

***Figure 3**: Four-point bending test set-up on a 3-layer CLT panel according to the standard EN16351.*

***Figure 4**: Four-point bending test set-up on a 5-lamella glulam beam according to the standard EN408.*

Density and Moisture Content (MC) were determined after mechanical testing from a slice. Density as mass by volume and MC according to EN13183-1 [12]

3 RESULTS

***Table 2:** Mechanical properties of CLT 3-layer panels and 5-lamella glulam pieces*

CLT panels						
Kind	MOEglo12		MOR		DEN12	
	Mean N/mm^2	CoV %	Mean N/mm^2	CoV %	Mean kg/m^3	CoV %
RRR	12106	4.95	44.74	20.02	769	3.06
RNR	11989	1.54	46.49	7.23	768	2.09
NRN	11180	6.72	72.80	2.60	761	2.48
NNN	11707	3.18	74.01	3.11	730	2.58

Glulam pieces						
Kind	MOEglo12		MOR		DEN12	
	Mean N/mm^2	CoV %	Mean N/mm^2	CoV %	Mean kg/m^3	CoV %
R	11175	7.00	38.11	15.76	770	4.59
N	11777	8.36	73.51	17.61	713	3.40

R: recovered timber
N: new timber
MC: circa 15%

Table 2 shows the results of static modulus of elasticity (MOEglo12), bending strength (MOR) and density (DEN12) obtained by mechanical testing adjusted to 12% MC according to EN 384 [13] of CLT panels and glulam pieces by the kind of timber (recovered and new) used for manufacturing.

Due to the small number of specimens, it was not possible to determine the 5º percentile of MOR and density. The lowest value of MOR was 35.81 N/mm^2 in the case of CLT panels and 31.87 N/mm^2 in the case of glulam pieces. The lowest value of density was 709 kg/m^3 in the case of CLT panels and 677 kg/m^3 in the case of glulam pieces.

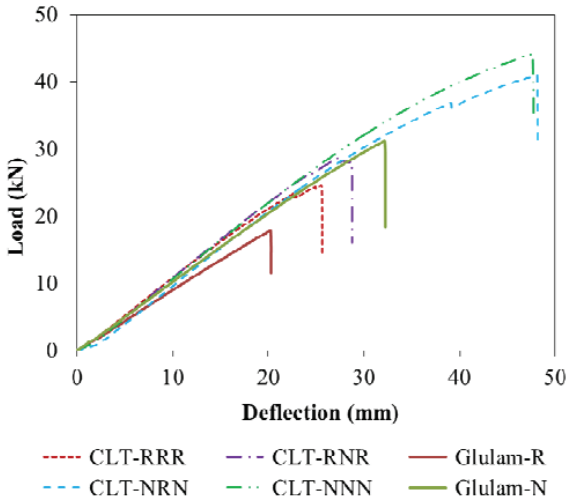

***Figure 5**: Load-deformation response in CLT panels and glulam pieces according their timber configuration (R recovered, N new timber).*

Fig. 5 shows load-deformation graphics for the four configurations of CLT panels and the two configurations of glulam pieces tested. The elastic behaviour was similar in all kind of configurations with recovered or new timber. However, the final load is higher by far in the case of CLT manufactured using new timber in the longitudinal layers (NRN and NNN) than those using recovered timber in the longitudinal layers (RRR and RNR) and also in the case of glulam pieces manufactured with new timber (N) is higher than those manufactured with recovered timber (R). In the case of CLT panels, it looks like that the material used in the cross-layer is not affecting the MOR values as was also reported by another author testing CLT from recovered timber [14].

https://doi.org/10.52202/069179-0468

***Figure 6**: CLT panel failure in tension*

Qualitative analysis of rupture sections was carried out after mechanical tests. All of the CLT panels and glulam pieces tested broke by wood failure in the tension face and the central third (between the two point loads), as shown in Figures 4 and 6. No failure differences were visually detected among CLT panels and glulam pieces manufactured with recovered and new timber. Other failures for example by rolling shear or glue-line were not reported.

In order to determine if there are statistically significant differences among the values of MOE and MOR obtained in the mechanical testing of different configurations of CLT panels and glulam pieces, ANOVA tests were carried out at a 95% of confidence interval (Figures 7 and 8).

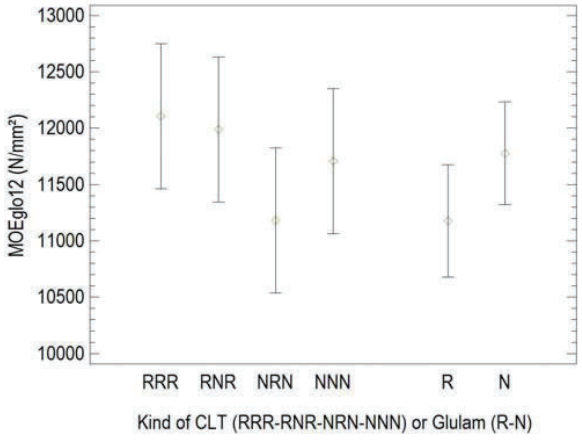

***Figure 7**: MOEglo12 ANOVA mean test for CLT panels and glulam pieces*

In the case of MOE (Figure 7), statistically non-significant differences were found at a 95% confidence interval among different kinds of CLT panels and glulam pieces timber configurations. The MOE of EWP manufactured with recovered European oak timber is not higher or lower than the MOE of EWP manufactured with new European oak timber.

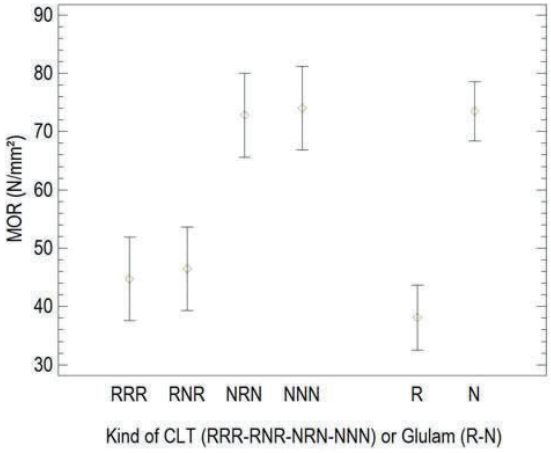

***Figure 8**: MOR ANOVA mean test for CLT panels and glulam pieces*

In the case of MOR (Figure 8), statistically significant differences were found at a 95% confidence interval between CLT panels manufactured using recovered timber in the longitudinal layers (RRR, RNR) and using new timber in the longitudinal layers (NRN, NNN), and also between glulam pieces manufactured from recovered timber (R) and from new timber (N). The MOR of EWP manufactured with recovered European oak timber is further lower than the MOR of EWP manufactured with new European oak timber.

In previous studies testing recovered solid-sawn timber was reported that MOE is not changing over time, while MOR is lower over time in softwoods and hardwoods species [15-17]. Some authors explained this MOR reduction due to the load history [18], others by the nails and holes present in old timber [16], others by the increase of brittleness in old wood [19] and others by the quality of the original timber [17]. Probably the reason will be a mix of all these explanations.

Regarding other authors testing EWP manufactured from recovered timber, Rose et al. [9] reported higher MOE and lower MOR in the case of CLT panels manufactured from a mix of recovered softwood timber species, while Arbelaez et al. [20] reported the same MOE but lower MOR testing CLT panels manufactured with recovered Douglas-fir timber.

Considering the reduction of the MOR in the case of recovered timber and checking the values obtained in the present study, the minimum values of MOR achieved, 35.81 N/mm^2 in the case of CLT panels and 31.87 N/mm^2 in the case of glulam pieces, are still enough for manufacturing EWP from recovered timber for structural purposes.

Regarding the timber yield of manufacturing EWP with recovered timber, the yield was really low. When boards were sawn from original recovered pieces, a great amount of sawdust is produced and most of the external parts of the pieces are not suitable for EWP because are

https://doi.org/10.52202/069179-0468

twisted or containing nails. Furthermore, some parts like holes or big cracks should be removed from the boards after sawing. Finally, boards should be planed to the final dimension not more than 24 hours before bonding. In the present study the final yield was around 13% because the original recovered timber was large cross-section. Other authors using as recovered timber medium size cross-sections obtained better yields. In the case of Irle et al. [2] manufacturing glue laminated products the yield obtained was around 30%. In the case of the InFutUReWood project manufacturing CLT panels in Ireland was around 28% [21]. In both cases the yield was approximately double than in the present study. That means that in the timber yield there is a great influence of the dimensions and condition of the recovered timber using for manufacturing EWP.

4 CONCLUSIONS

The results from the testing indicate the capability of the recovered timber from demolition sources to be used for the manufacturing Engineering Wood Products (EWP) in the present study Cross-Laminated Timber (CLT) panels and glued-laminated timber (glulam) pieces.

Four-point bending tests showed no significant differences between modulus of elasticity obtained in CLT panels and glulam pieces manufactured from recovered and new timber. While, bending strength was far higher in new than in recovered timber in CLT panels and glulam pieces. In the case of CLT panels only the kind of timber (recovered or new) used in the longitudinal layers is determining the differences in bending strength values.

In spite of bending strength values in CLT panels and glulam pieces manufactured from recovered timber are lower than in the case of new timber, these values are still high enough for structural applications of the manufactured EWP.

Recycling recovered timber in EWP produce a low timber yield (around 13% in the present study), with a great amount of wood waste generate during the manufacturing.

ACKNOWLEDGEMENT

The RECOWERS project has received funding from the European Union's Horizon 2020 research and innovation programme under the Marie Skłodowska-Curie grant agreement No. 101025786.
The InFutUReWood project was supported under the umbrella of ERA-NET Cofund ForestValue and has received funding from MICIU-Spain [PCI2019-103544].
The authors would like to thank Mr. Alfonso Cía-Armendáriz from Cía Mobiliario Macizo (Estella, Navarra, Spain) and Mr. Óscar Fernández, Mr. Raúl Fernández and Mr. Andrés from AsturAraba (Vitoria, Álava, Spain) for freely supplying the timber pieces and manufacturing the CLT panels. The authors would also like to thank Mr. César Nicolás and Mr. Diego Mendaza of Manufacturas Nicolás NISA (Viana, Navarra, Spain) for freely preparing timber boards in their facilities for CLT manufacturing. The authors would also like to thank Prof. Dr. Manuel Guaita from PEMADE USC (Lugo, Galicia, Spain), for freely providing their testing facilities.

REFERENCES

[1] CaReWood European project website. https://carewood.iam.upr.si/ Accessed 06.01.2023.
[2] Irle, M., Privat, F., Couret, L., Belloncle, C., D´eroubaix, G., Bonnin, E., Cathala, B. Advanced recycling of post-consumer solid wood and MDF, Wood Mater. Sci. Eng. 14(1):19–23, 2019. https://doi.org/10.1080/17480272.2018.1427144.
[3] InFutUReWood European Project website. https://www.infuturewood.info/ Accessed 06.01.2023.
[4] RECOWERS European Project website. https://recowers.wordpress.com/ Accessed 06.01.2023.
[5] Irle M., Privat F., Deroubaix G., Belloncle C. Intelligent recycling of solid wood. Pro Ligno. 11(4):14-20, 2015.
[6] Azambuja, R.R., Gomes-de-Castro, V., Trianoski, R., Iwakiri, S. Recycling wood waste from construction and demolition to produce particleboards, Maderas-Cienc. Tecnol. 20(4):681–690, 2018. https://doi.org/10.4067/S0718-221X2018005041401
[7] Llana D.F., Íñiguez-González G., Arana-Fernández M., Uí Chúláin C., Harte A.M. Recovered wood as raw material for structural timber products. Characteristics, situation and study cases: Ireland and Spain. In the proceedings of the 63rd International Society of Wood Science and Technology (SWST) convention, 117-123, 2020.
[8] Hafner A., Ott S., Winter S. Recycling and End-of-Life Scenarios for Timber Structures. In the book: Materials and Joints in Timber Structures, RILEM Bookseries 9, 89-98, 2014.
[9] Rose C.M., Bergsagel D., Dufresne T., Unubreme E., Lyu T., Duffour P., Stegemann J.A. Cross-Laminated Secondary Timber: Experimental testing and modelling the effect of defects and reduced feedstock properties. Suistanability, 10(11):4118, 2018. https://doi.org/10.3390/su10114118
[10] EN16351. Timber structures – Cross laminated timber – Requirements. European Committee of Standardization (CEN), Brussels, Belgium. 2015.
[11] EN408:2010+A1. Timber structures. Structural timber and glued laminated timber. Determination of some physical and mechanical properties. European Committee for Standardization (CEN), Brussels, Belgium. 2012.
[12] EN 13183-1. Moisture content of a piece of sawn timber. Part 1: Determination by oven dry method. European Committee of Standardization (CEN), Brussels, Belgium. 2002.
[13] EN384:2016+A1. Structural timber. Determination of characteristic values of mechanical properties and

density. European Committee of Standardization (CEN), Brussels, Belgium. 2018.
[14] Stenstad, A., Lønbro-Bertelsen, S., Modaresi, R. Comparison of strength tests for evaluating the secondary timber utilisation in Cross Laminated Timber (CLT). In the proceedings of the 16th World Conference on Timber Engineering (WCTE 2021). August 9-12, Santiago de Chile, Chile. 2201-2206, 2021.
[15] Rammer, D.R. Evaluation of recycled timber members. In the proceedings of the 5th ASCE Materials Engineering Congress. May 10–12, Cincinnati, Ohio USA. 46-51, 1999.
[16] Nakajima, S., Murakami, T. Comparison of two structural reuse options of two-by-four salvaged lumbers. In the book: Sustainable construction. Materials and practices. Portugal SB07. 561-568, 2007.
[17] Cavalli, A., Cibecchini, D., Togni, M., Sousa, H.S. A review on the mechanical properties of aged wood and salvaged timber. Constr. Build. Mater. 114:681–687, 2016. https://doi.org/10.1016/j.conbuildmat.2016.04.001
[18] Crews, K., MacKenzie, C. Development of grading rules for re-cycled timber used in structural applications. In the proceedings of the 10th World Conference on Timber Engineering (WCTE 2008). June 2-5, Miyazaki, Japan. 8 pages, 2008.
[19] Kránitz, K., Sonderegger, W., Bues, C.T., Niemz, P. Effects of aging on wood: a literature review, Wood Sci. Technol. 50:7–22, 2016. https://doi.org/10.1007/ s00226-015-0766-0
[20] Arbelaez, R., Schimleck, L., Sinha, A. Salvaged lumber for structural mass timber panels: manufacturing and testing, Wood Fiber Sci. 52(2):178–190, 2020. https://doi.org/10.22382/wfs-2020-016
[21] Sandberg, K., Sandin, Y., Harte, A.M., Shotton, E., Hughes, M., Ridley-Ellis, D., Turk, G.. Íñiguez-González, G., Risse, M., Cristescu, C. Summary Report InFutUReWood. 62 pages, 2022. https://doi.org/10.23699/p41e-ae46

 https://doi.org/10.52202/069179-0468

World Conference on Timber Engineering Oslo 2023

REUSE OF LOAD-BEARING TIMBER ELEMENTS – CASE STUDY OF A LOOKOUT TOWER IN LAUSANNE, SWITZERLAND

Jonas Warmuth[1], Xavier Estrella[2], Benoît Kälin[3], Johannes Natterer[4], Corentin Fivet[5]

ABSTRACT: The construction industry is jeopardizing Earth's environment; current mitigation efforts do not suffice; and additional sustainable strategies are required. One such strategy consists of reusing structural building elements over multiple service lives. In this context, this paper introduces a new framework for the design of timber structures made from reused structural elements. Beyond general approaches to reuse structural elements, the proposed framework provides a computational approach that supports architects and engineers in their design and decision making. In this course, optimization techniques such as Best-Fit heuristics are implemented to optimally utilize available stock elements in a new design. The introduced framework is applied to a real-world case study where a lookout tower is designed from timber elements salvaged from a soon-to-be-demolished lookout tower. Results show that a new design that makes optimal use of available stock elements and that meets architectural and statical requirements exists. In the long run, the introduced framework for the reuse of structural elements encourages the design of more sustainable structures with lower environmental impact.

KEYWORDS: Reuse, Structural Design, Computational Design, Life Cycle Assessment, Circular Economy

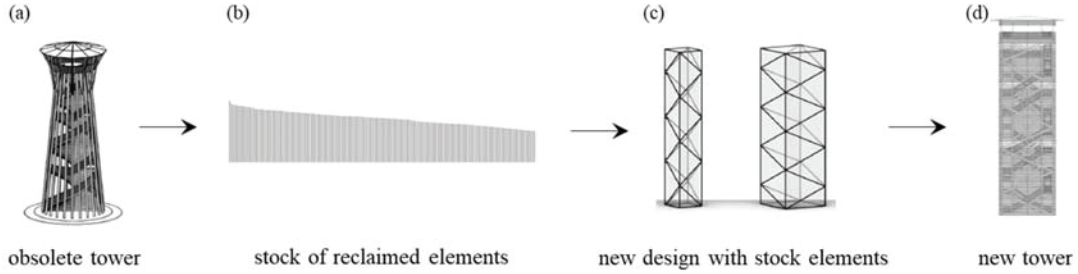

Figure 1. *Conceptual workflow for the design of a new lookout tower made from reused elements*

1 INTRODUCTION

The construction sector is responsible for a significant amount of global greenhouse gas emissions, resource exploitation and waste generation [1]. One way to remediate this detrimental condition and to reduce the environmental impact (EI) of built structures is the introduction of a circular economy and, associated with that, the reuse of structural elements in new structures. Apart from a few unique examples, however, this approach is rather the exception in today's building practice. The reason for this is that the conventional design approach is inverted in the case of reusing structural components, as the synthesis of a structural system (including topology and geometry) must comply with the geometric and static characteristics of the available elements. Consequently, this leads to challenges in everyday construction. One solution to this challenge is the use of computational tools, that make use of algorithmic formulations to assist the design with a fixed inventory of elements. An early computational approach was presented by Fujitani and Fujii [2] who optimized plane frames of fixed topology subject to given elements of known length and cross-section. Brütting et al. [3] presented structural optimization techniques to design truss structures from reused steel elements. Regarding timber, Bukauskas et al. [4] have developed a strategy based on heuristics to form-fit a stock of wood logs to statically-determinate trusses. Amtsberg et al. [5] presented a design-to-fabrication workflow using a geometric matching algorithm that makes best use of available tree forks. Huang et al. [6] employed the Hungarian Algorithm to design wooden geodesic domes from a stock of elements. Moreover, they provide a comparison of different algorithmic formulations for reuse-driven design in computational tools. In previous

[1] Jonas Warmuth, École Polytechnique Fédérale de Lausanne EPFL, Switzerland, jonas.warmuth@epfl.ch
[2] Xavier Estrella, École Polytechnique Fédérale de Lausanne EPFL, Switzerland, edisson.estrellaarcos@epfl.ch
[3] Benoît Kälin, École Polytechnique Fédérale de Lausanne EPFL, Switzerland, benoit.kaelin@hotmail.com
[4] Johannes Natterer, École Polytechnique Fédérale de Lausanne EPFL, johannes.natterer@epfl.ch
[5] Corentin Fivet, École Polytechnique Fédérale de Lausanne EPFL, Switzerland, corentin.fivet@epfl.ch

https://doi.org/10.52202/069179-0469

work, Warmuth et al. [7] introduced a computational tool subject to support architects and engineers in designing structures with reused elements. This tool was built upon a mixed-integer-linear-programming (MILP) formulation to optimally assign stock elements to a given structure and was later extended by a Best-Fit heuristic to accelerate result generation. Their studies centred around the evaluation of steel and concrete as reusable materials. In this paper, the range of applicability is extended to timber structures, and the computational techniques from [6, 7] are implemented into a novel framework that allows for the design of timber structures made of reused elements in a flexible, interactive, and designer-driven workflow. The extension is demonstrated via a real-world case study, the new design of a lookout tower in Lausanne, Switzerland, made from an already existing tower on-site that became obsolete. Figure 1 shows the conceptual workflow for this: first, structural elements from the obsolete tower (Fig. 1a) are assessed and inventoried into a stock of elements (Fig. 1b). Then, a new design is developed based on the characteristics of the obtained stock (Fig. 1c) that leads finally to a new tower making optimal use of the available elements (Fig.1d). As per previous research on the topic [9, 10], it is expected that this significantly lowers the EI of the tower, the demand for resource mining, and waste production, compared to one built of new elements.

2 REUSE OF TIMBER

The goal in a circular economy is to maintain material, product, and components at their highest value for as long as possible. In case of timber, the amount of CO_2 emitted during combustion is equal to the amount absorbed by the plant during its growth, making timber a useful carbon sink [11]. In addition, reusing timber prevents its decomposition under anaerobic conditions, which would lead to the release of methane and contribute to greenhouse gas emissions [12]. And thanks to dismountable connections, timber structures are generally presenting high potential to be reused. Despite all these valid reasons to reuse timber, component reuse, regardless the material, is not the norm in building practice. The reasons for that are manifold. Conventional demolition processes tend to yield very little reusable material due to the use of heavy machinery. Reclaiming such material implies to process a meticulous disassembling of the structure that, as expected, has an impact on costs. However, Schultmann et al. [13] illustrate that environment-friendly dismantling and reuse strategies can even be advantageous from an economic point of view. In response to demolition costs, reusing timber has very variable cost implications, from cost savings of up to 80% depending on application and quality [14]. To ensure a safe reuse of timber components, their mechanical properties need to be assessed. In addition to natural aging phenomena of wood and duration of load, the presence of mechanical damage and biological attack must be considered. Although researchers seem to agree that aging has no, or only marginally, effects on bending capacities, the duration and intensity of the applied load have a direct effect on the material properties [15] and are known to cause strength reductions on a logarithmic scale [16]. The direction of loading should also be considered when assessing the remaining mechanical properties of reclaimed timber. Nevertheless, laboratory tests by Brol et al. [17] on 130 year old timber elements indicate that elements which worked as beams for many years can still be integrated in new structures as elements with axial loading. Moreover, Davis [18] states that timber is resilient over time and maintains much of its original capacities despite the effect of moisture, loading, temperature, and weathering [18]. And still, despite all these promising indicators to reuse timber, this strategy is rarely pursued today, albeit this was not always the case in the past. Küpfer & Fivet [19] state that dismantling timber structures and reusing their components were common practice before the Industrial Revolution. But due to new means of production and transportation, the common reuse and valorisation techniques were progressively abandoned. An example on how timber was reused in the past is shown in Figure 2.

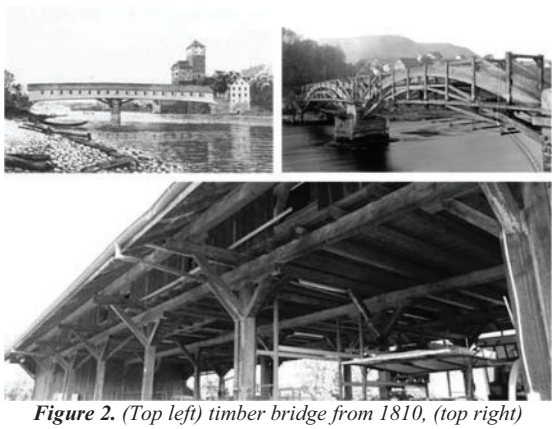

Figure 2. *(Top left) timber bridge from 1810, (top right) deconstruction in 1919, (bottom) new barn built in 1920 and still in use*

On the top left, a bridge can be observed that was built in 1810 in Eglisau at the German Swiss border to cross the river Rhine. After more than 100 years in service, it was decided to deconstruct it in 1919 due to a water level elevation of the river. Instead of landfilling its components after deconstruction, a new barn in Rheinhau, Switzerland, was built in 1920 from components of the deconstructed timber bridge. The barn is still in use and in good condition. The building is more than 100 years old but made from oak and spruce components that are over 200 years old. This simple illustration effectively demonstrates the mentality necessary for material-caring building practices.

3 DESIGN METHODOLOGY

The main objectives of this paper are (1) to introduce a new design framework and (2) to develop a case study i.e., the design of a load-bearing structure for a timber lookout

https://doi.org/10.52202/069179-0469

tower made of reclaimed elements. Again, it should be noted that the design of structures with reused elements from an available stock inverts the conventional design process. Typically, the structural layout determines the required elements to be manufactured. Instead, the design of structures through reuse describes the inverse: structure topology and geometry must be designed to make the best use of available stock elements. To achieve this goal, the workflow shown in Figure 3 is employed.

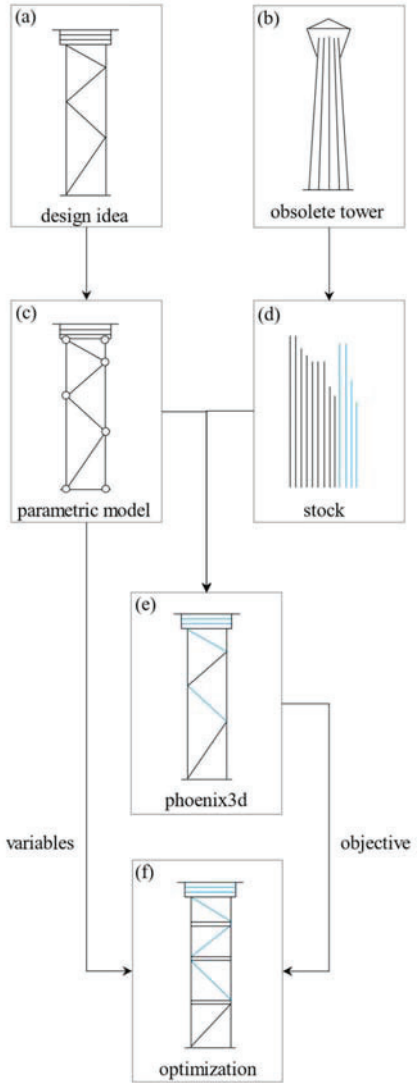

Figure 3. *Workflow of the introduced framework with new elements (blue) and reused elements (black)*

First, an initial design idea is conceptualised either by a hand sketch or a digital drawing (Fig. 3a). Based on this, a parametrized design model is created (Fig. 3c). In parallel, the source material from the obsolete tower (Fig. 3b) is identified and assessed. Once assessed, the stock of reused and new elements can be inventoried (Fig. 3d) where reused elements come from the obsolete tower and new elements are assumed to be available from new production. Assigning available stock elements to the parametric model such that the stock is utilized optimally is a time-consuming task when done by hand. Therefore, the computational tool Phoenix3D (P3D) [20] is assigned this process (Fig. 3e). P3D takes both the stock and parametric model as an input and returns the model with optimally assigned stock elements subject to minimize upfront global warming potential of the structure manufacturing. Finally, a global optimization process (Fig. 3f) modifies the set of variables of the parametric model such that the configuration with the least EI is found. More details of each step are given in the following sections.

3.1 PARAMETRIC MODEL AND STOCK IDENTIFICATION

The computer aided design software Rhino3D [21] is used to set up the parametric model. Included in Rhino3D is the visual programming plugin Grasshopper that takes care of the parametrization of the design idea. This allows a fast alteration of the design idea. Before setting up the parametric model, some constraints for the design have to be taken into account. For reasons of rationality, it was decided to allow only rectangular geometries. Moreover, the loadbearing structure is considered to be made of two sub-structures: an inner and outer truss. Furthermore, a tower height of at least 30 m is chosen to ensure a 360° panorama view, since the trees surrounding the tower have approximately this height. Within these constraints, the model can be created.

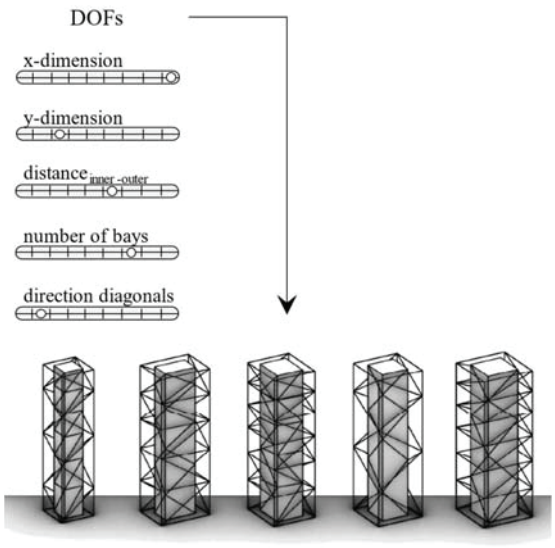

Figure 4. *Various tower configurations within the parametrization*

When setting up a parametric model, parameters, so called degrees of freedom (DOFs), have to be chosen. Ideally, the quantity of DOFs should be controlled in such a manner as to avoid losing control of the model, yet still allow for sufficient modification. The degrees of freedom

chosen in this case study are shown in Figure 4 and consist of the x- and y-dimension, the distance between inner and outer truss, the number of bays, and the direction of diagonals. In order to reuse structural elements and to employ P3D, a stock needs to be set up. This stock contains both reusable elements that were sourced from the obsolete tower (discussed specifically in Section 4.3) and elements that were newly produced. Reused elements have to be assessed for their mechanical and geometric properties. To retain the degree of complexity in this investigation, it is assumed that all available new elements are of same cross-section as available reused elements. Moreover, for new elements, only mechanical properties are taken into account because they can be provided in customized lengths.

3.2 STOCK ASSIGNMENT BY PHOENIX3D

The assignment of stock elements to the design model is here described as a discrete optimization problem and is carried out by P3D. P3D is an open-source tool to design optimum truss structures made from a stock of new and reused elements. It is implemented by the authors based on previous research in the field [8]. The core of P3D is moulded by two optimization algorithms: (1) a MILP formulation that delivers globally optimal results but is computationally expensive, and (2) a Best-Fit heuristic combined with a finite element analysis (FEA) of first order that delivers just close-to-optimal results but in real-time and with low computational costs. The objective function is to minimize EI which is computed by a Life-Cycle-Assessment (LCA). Details for the implementation of the optimization algorithms as well as the LCA can be found in [6, 19]. Figure 5 shows the workflow of the tool.

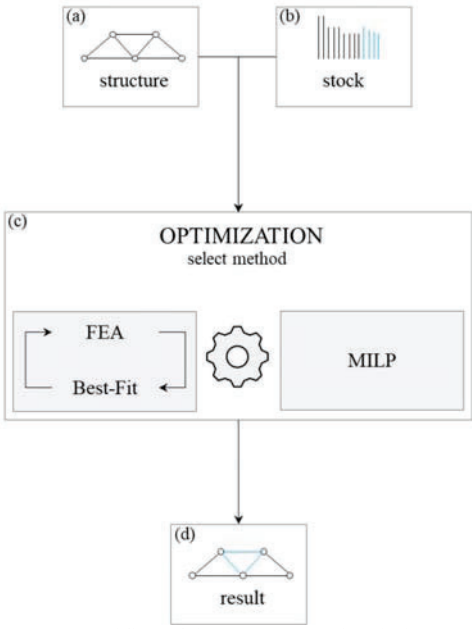

Figure 5. *Workflow of the computational tool Phoenix3D*

An initial intended structure serves as input (Fig. 5a) to which reusable stock elements are assigned as well as newly-manufactured elements (Fig. 5b). Subsequently, users can select which of the two optimization algorithms should be utilized to optimally assign the stock elements to the structure (Fig. 5c). As an output, the structure with the assigned stock elements is displayed (Fig. 5d) including statistics about the run optimization. Among these are the EI in [kgCO_2eq] and the percentage of reused and new elements in the structure, which will be used in Section 4 to assess the case study.

3.3 DESIGN OPTIMIZATION

Although P3D already optimally assigns stock elements to a given structure, the structure geometry itself can be modified as well to better fit to available stock elements. Thanks to the parametric implementation of the model, this can also be described as an optimization problem where the parameters of the model are serving as design variables and the computation of EI in P3D serves as an objective function (see Fig. 3). The tool used for this optimization is Wallacei [22], an evolutionary optimization and analytic engine for Grasshopper. Besides the objective of minimizing the EI, there are other factors that need to be taken into account. One is to utilize the available stock elements from the obsolete tower as much as possible because they would become waste otherwise. Another constraint considers aesthetic aspects of the design, which are evaluated by the designer. The compliance of these constraints is evaluated by the designer and therefore not subject of the optimization process. This means, however, that several iterations are necessary to end up at the final solution.

4 RESULTS: DESIGN OF THE SAUVABELIN TOWER IN LAUSANNE

In the following, results for a new design of the Sauvabelin lookout tower in Lausanne, Switzerland, are explained using the methods described in Section 3. Figure 6 shows the 20-year-old tower, now obsolete and in need of replacement.

Figure 6. *The Sauvabelin tower, October 2021*

For the case study, only the structural system is taken into account. However, it is aimed to apply common rules of

https://doi.org/10.52202/069179-0469

best practice for timber structures. This includes the protection of exposed elements from weather as well as homogeneous connection designs for constructive and economic reasons.

4.1 INTRODUCTION TO THE SAUVABELIN TOWER

In order to produce a viable project that addresses structural, architectural, societal, and environmental considerations, it is crucial to understand the importance of the existing tower. The Sauvabelin lookout tower was constructed in 2003 and since then has become a renowned landmark in the city of Lausanne located on the shores of Lake Geneva. Figure 7 depicts the tower during its construction phase. The overall concept encompasses a spiral staircase culminating in a viewing platform at its apex.

Figure 7. *Construction of the tower, 2003*

The Sauvabelin Tower, despite its popularity and emotional resonance among the residents of Lausanne, is slated for demolition due to considerations of safety and economy. The estimated service life was originally predicted to be 20 years. However, this projection of service life does not necessarily equates to the end of its structural components' service life. With proper maintenance and restoration, it is possible to extend the service life of the tower. Thus, between the years 2012 and 2017, the tower underwent maintenance work that involved the replacement of defective components. Figure 8 illustrates the replacement of the stair ends that were weathered.

Figure 8. *replacement of end parts of the stairs*

It is projected that the costs associated with maintaining the structure will continue to rise as the tower ages and reaches its revised estimated service life of 30 years in 2033. However, due to the design of the tower's structure, the maintenance costs would eventually surpass their limits, resulting in the tower's demolition. A potential solution to this scenario is to disassemble the tower now, salvaging its structural components that are still in good condition, and use them to construct a new tower that adheres to construction standards that prevent the elements from causing premature aging.

4.2 EXPLANATION OF AVAILABLE STOCK ELEMENTS

The stock of salvaged elements for this case study involves an evaluation of the current state of all structural components of the existing tower. The evaluation of the structural elements was conducted in September 2021 and was based on a visual inspection of the tower as well as information obtained from the original construction plans. As illustrated in Figure 9, the tower can be segmented into four categories of structural elements: the stairs, poles, stands, and roof. Each category is subjected to an individualized evaluation to determine its viability for reuse.

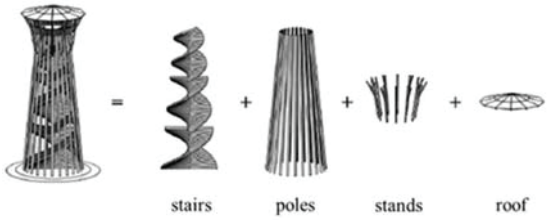

Figure 9. *Composition of the Sauvabelin tower*

The composition of the tower is comprised of 214 m^3 of timber, of which 141 m^3 are Douglas Fir and 73 m^3 are Spruce, sourced from nearby forests. The exact metrics can be viewed in Table 1.

Table 1. *tower composition*

	Stairs	Poles	Stands
Species	Douglas fir	spruce	Spruce
Amount	151	24	24
Cross-section	20/40cm	20/20cm	20/20cm
Length	6.0-12.0m	34.0m	8.0m

The tower's staircase comprises 151 steps, which range from 6.0 m to 12.0 m, with a linear distribution in between, and have been assigned a grade of C24 based on the Swiss construction code. It was found that, due to the maintenance work from 2012 – 2017, all steps can be reused, albeit in a different static configuration. As previously mentioned, research conducted by Brol et al. [17] has shown that reused timber elements can withstand a change in the direction of applied loading from bending to axial stress, which would apply to the proposed truss system in this case study. The tower features 24 poles forming its outer finish, however, due to their exposition and the presence of numerous metal connections that weaken their cross-section, these elements have been excluded from this study. The roof, which has a diameter

of 13.0 m and is comprised of elements with varying lengths and cross-sections, is in good condition and could be reused in its entirety. For the sake of simplicity and consistency, the decision was made to reuse only the staircase elements, which is the reason why the stands are also excluded, although they are in good condition and could potentially be reused.

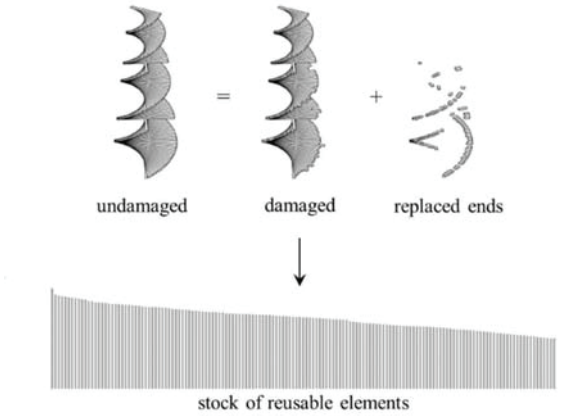

Figure 10. *Extraction of reusable elements from staircase of obsolete tower*

Figure 10 depicts the inventory of refurbished staircase elements that were installed during the previously mentioned maintenance work on the tower. The full stock comprises therefore 151 elements with a cross-section of 20/40 cm and varying lengths between 6.0 m to 12.0 m which results in a total stock mass of 54,319 kg considering a density of 530 kg/m^3.

4.3 DESIGN PROCESS AND FINAL RESULT

As outlined in Section 3, the goal of this case study is to reuse as many stock elements as possible to prevent them from being disposed in a landfill, while keeping the EI low.

Table 2. *results of iterations for tower design*

Iteration [-]	EI [kgCO_2eq]	Reused [kg]	Usage [%]
0	14,521	29,177	54
1	15,127	30,648	56
2	14,994	29,993	55
3	14,365	29,187	54
4	14,349	29,201	54
5	15,055	29,679	55
6	14,346	20,193	54
7	19,813	40,370	74
8	21,842	44,782	82
9	22,137	44,771	82
10	22,061	44,781	82
11	24,889	51,164	94
12	30,505	52,373	96
13	**24,564**	**49,504**	**91**
newly made	44,452	0	0

Although minimizing EI is a factor in the design process, it is not the only deciding one, i.e., designs with higher EI than other solutions may still be selected as the final design, as long as the EI is lower than a comparable tower made entirely of new components. Design decisions must balance construction and economic practicality with the aim of minimizing the EI of the structure, while considering personal design preferences. By employing the methods explained in Section 3, numerous suitable designs were found. The chosen designs were selected based on the designer's preferences and are listed in Table 2, including their EI in kgCO_2eq, weight of reused elements in kg, and the percentage of utilized stock elements. This usage is calculated by dividing the reused elements in kg by the total amount of reusable elements in kg, with the assumption that the difference is discarded and therefore waste. In Figure 11, the selected designs are represented on a graph, with the EI of the design shown on the vertical axis and the utilization of the stock on the horizontal axis. This visual representation shows that the optimal designs are located in the bottom right corner of the graph, where both a low EI and a high utilization of the stock elements are achieved.

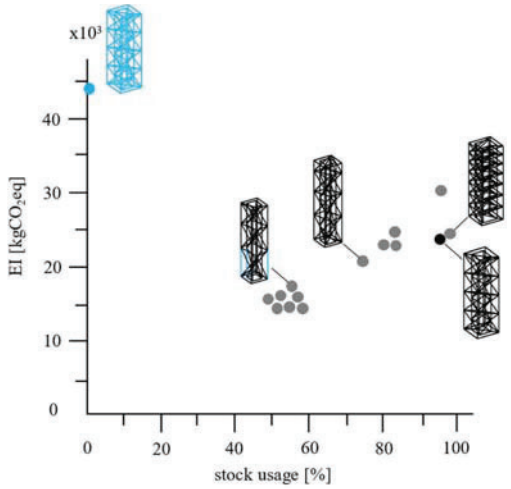

Figure 11. *Design iterations; black dot indicates final design, blue dot indicates final design made of entirely new elements*

After evaluating numerous designs through the optimization process described in Chapter 3, iteration 13 was determined to be the most suitable as the final design. This decision was made due to the high usage of old elements, corresponding to 91%. Furthermore, the design boasts a relatively low EI of 24,565 kgCO_2eq. Additionally, the design satisfied the aesthetic preferences of the designer. To validate this selection, in iteration 14, the EI of the final design was computed again, with the assumption that it was constructed solely using new elements. The results show an EI of 44,452 kgCO_2eq, indicating that the chosen design has a 45% lower EI compared to a comparable tower built entirely from new elements. The findings in Figure 11 also suggest a linear correlation between the EI and the stock elements used. This is likely due to the fact that only a few designs used

https://doi.org/10.52202/069179-0469

newly manufactured elements and were constructed almost exclusively with reused elements, resulting in a linear calculation of their EI through the corresponding LCA. Figure 12 presents renderings of the selected design to provide an understanding of how the new tower interacts with its environment. In addition to the outcome from iteration 13 shown in Table 2, a roof and cladding were added to protect the structural components from the weather.

Figure 12. *Renderings of the newly designed tower made of structural elements from the obsolete tower*

5 CONCLUSIONS

In conclusion, this study presents a novel framework for the design of timber structures from reused structural elements. The framework is validated through a case study of the Sauvabelin lookout tower in Lausanne, Switzerland. In this context, computational tools, such as Phoenix3D, can be employed to optimally utilize available stock elements. Results show that the introduced computational framework enables for the design of a new structures tailored to the available stock elements, i.e., making best use of available reused elements. Moreover, the proposed approach can significantly reduce the environmental impact of the new tower, with a reduction of 45% compared to a similar tower constructed entirely from new elements. The adoption of this framework has the potential to enhance sustainability in the construction sector and move towards a more circular economy.

REFERENCES

[1] J. M. Allwood and J. M. Cullen, "Sustainable materials: with both eyes open," in *UIT Cambridge*, Cambridge, UK, 2012

[2] Y. Fujitani and D. Fujii, "Optimum structural design of steel plane frame under the limited stocks of members," in *Proceedings of the RILEM/CIB/ISO International Symposium, Integrated Life-Cycle Design of Materials and Structures*, Helsinki, 2000, pp. 198–202

[3] J. Brütting, J. Desruelle, G. Senatore, and C. Fivet, "Design of Truss Structures Through Reuse," *Structures*, vol. 18, pp. 128–137, 2019, doi: 10.1016/j.istruc.2018.11.006

[4] A. Bukauskas, P. Shepherd, P. Walker, B. Sharma, and J. Bregulla, "Form-Fitting Strategies for Diversity-Tolerant Design," Sep. 2017

[5] F. Amtsberg, Y. Huang, D. J. Marshall, K. M. Gata, and C. Mueller, "Structural up-cycling: matching digital and natural geometry," *Advances in Architectural Geometry*, 2020

[6] Y. Huang, L. Alkhayat, C. De Wolf, and C. Mueller, "Algorithmic circular design with reused structural elements: method and tool," presented at the International fib Symposium - Conceptual Design of Structures 2021, Sep. 2021, pp. 457–468. doi: 10.35789/fib.PROC.0055.2021.CDSymp.P056

[7] J. Warmuth, J. Brütting, and C. Fivet, "Computational Tool for Stock-Constrained Design of Structures," in *Proceedings of the IASS Annual Symposium 2020/21 and the 7th International Conference on Spatial Structures*, Guilford, UK, 2021. https://infoscience.epfl.ch/record/287984

[8] J. F. G. Brütting, "Optimum design of low environmental impact structures through component reuse," PhD, EPFL, Lausanne, 2020. doi: 10.5075/epfl-thesis-8448

[9] J. Brütting, G. Senatore, M. Schevenels, and C. Fivet, "Optimum design of frame structures from a stock of reclaimed elements," *Frontiers in Built Environment*, vol. 6, no. 57, pp. 1–18, May 2020, doi: 10.3389/fbuil.2020.00057

[10] J. Brütting, C. Vandervaeren, G. Senatore, N. De Temmerman, and C. Fivet, "Environmental impact minimization of reticular structures made of reused and new elements through Life Cycle Assessment and Mixed-Integer Linear Programming," *Energy and Buildings*, vol. 215, 2020, doi: 10.1016/j.enbuild.2020.109827

[11] H. Schmid, *Arguments en faveur du bois [online]*. Zurich: Lignum, Economie suisse du bois, 2019. Accessed: Feb. 02, 2023

[12] J. Taylor and M. Warnken, *Wood recovery and recycling: a source book for Australia*. 2008

[13] F. Schultmann, A. Seemann, E. Garbe, and O. Rentz, "Methodologies and Guidelines for Deconstruction in Germany and France," 2001

[14] ARUP, *Evaluating re-use potential: Material profiles - Arup*

[15] Y. Niu, K. Rasi, M. Hughes, M. Halme, and G. Fink, "Prolonging life cycles of construction materials and combating climate change by cascading: The case of reusing timber in Finland," *Resources, Conservation and Recycling*, vol. 170, p. 105555, Jul. 2021, doi: 10.1016/j.resconrec.2021.105555.

[16] M. J. Smith, "An investigation into the strength properties of reclaimed timber joists," doctoral,

Northumbria University, 2012. Accessed: Apr. 28, 2022
[17] J. Brol, S. Dawczyński, A. Malczyk, and K. Adamczyk, “Testing timber beams after 130 years of utilization,” Oct. 2012
[18] J. B. Davis, “Suitability of salvaged timber in structural design,” Thesis, Massachusetts Institute of Technology, 2012. Accessed: Feb. 02, 2023
[19] C. Küpfer and C. Fivet, Eds., *Déconstruction sélective - Construction Réversible: recueil pour diminuer les déchets et favoriser le réemploi dans la construction*. Lausanne, Switzerland: EPFL, 2021. doi: 10.5281/zenodo.4314325
[20] J. Warmuth, J. Brütting, and C. Fivet, “Phoenix3D.” EPFL, 2021. Available: http://sxl.epfl.ch/Phoenix3D
[21] R. McNeel and Associates, “Rhino 3D.” Robert McNeel & Associates, 2021. Available: https://www.rhino3d.com/
[22] “Wallacei.” 2021. Available: https://www.wallacei.com/

https://doi.org/10.52202/069179-0469

World Conference on Timber Engineering Oslo 2023

VALUES OF RECLAIMED TIMBER

Maxence Lebossé[1], Franck Besançon[2], Gilles Halin[3], Alain Fuchs[4]

ABSTRACT: France's current 'wood wastes' management seems inefficient in settling on a durable reclaimed timber branch that would support reuse practices in architecture. We assume that there is a set of 'values' attached to timber members that should be revealed to estimate their market value better. Through the literature, we observe that the economy of a deconstruction project used to be considered significant, while embodied carbon is nowadays of major concern. Moreover, as Circular Economy and Cascading concept emerged, the meaning of durability has decreased in favour of reversibility that could guarantee a flow of material circulation. The problem is that these ideas involve probable rebound effects due to energy engaged in transportation and the transformation of reclaimed resources. Our reflection comes from a field study experience where we participated in the reuse process of timber members deconstructed from a textile mill. We observed that the lack of economy and the lack of 'values' identification resulted in depreciating the operation's efficiency, whose initial objective was to maximise the extraction and diffusion of reusable elements as much as feasible. Our research focuses on construction materials and massive structural timber members, which still seem challenging to reintegrate into new buildings.

KEYWORDS: Reclaimed Timber, Value, Reuse, Economy, Deconstruction.

1 INTRODUCTION

Since it appears as a solution to mitigate the environmental impacts of the construction sector, 'reuse' tends to become a current practice again [1]. Structural elements, such as timber joists, extracted from existing buildings must be able to respond to the direct competition of new timber products in terms of cost, availability, and traceability. Compared to past centuries, the reuse of reclaimed materials demands more information to fit contemporary norms and laws that rule the construction sector. Consequently, assessment, extraction, refurbishment and reintegration of reclaimed materials, which constitute the reuse process, should be considered interconnected, to ensure an optimised transmission of information and material in parallel between all stakeholders involved.

In France, less than 4% of what is qualified as 'wood wastes' produced by deconstruction and demolition worksites are reused or up-cycled. In contrast, it is estimated that 85% of that annual amount of 'wood wastes' comes from structural elements, including 46% with a section superior to 70x150 mm [2], and that a third are 'cut-to-length' [2]. Thus, let us think: is the supposed high potential of demountability of timber structures enough to make the use of reclaimed timber a current and effective architectural practice? It seems not. We wanted to gather assumptions about reclaimed timber members' values, to enlighten research on the subject. From a reduced perspective, the construction sector is about individuals producing materials that others will buy to construct buildings. Thus, we assume that the reuse process should aim to create 'values' attached to existing timber members, but, through a combination of architectural, technical, social and ecological aspects, not only from an economic perspective.

We observed that 'the economy' (also in the sense of minimising the use of material [3-4]) of deconstruction and reclamation was present in early studies from the 2000s [5-6]. An orientation of research that got sense since Architecture, Economy and Ecology are interdependent, deeply linked by their etymology, *'οἶκος'*, the ancient Greek term [7-8]. In France the construction sector weight (in added value) in 2021 is 5.7% of the Gross Domestic Product, even up to 30% if we enlarge to the industry sector and real estate branches which are also concerned by our habitat management [9]. This shows that the economy of the construction sector is deeply related to social and political aspects. Besides, family structure, population growth and ecological ambitions impact the development of the construction sector [10], and reuse has a role to play in it.

To build this paper we rely on readings based a wide span of texts related to reuse, timber, and sustainability. These different resources help us to analyse our case study, a textile mill deconstruction, in which we focus our attention on the reuse process of timber members.
To introduce our subject, part 2 emphasises that reuse is not an objective in itself but that it is more a solution to overcome a lack of durable uses. In a previous paper [11], we have exposed the fact that we should speak about 'resource' and 'deconstruction', instead of 'waste' and 'demolition'. Since architecture is about communication [12] we should be careful of the meaning of the terms we use. We will follow that idea by questioning concepts of circularity and cascading in part 3. Part 4 presents which 'values' are concerned, before concluding in part 5 in what way prices, market values, and deconstruction costs should be studied to support that subject.

[1] Maxence Lebossé, MAP-CRAI, École Nationale Supérieure d'Architecture de Nancy, France, maxence.lebosse@nancy.archi.fr
[2] Franck Besançon, MAP-CRAI, École Nationale Supérieure d'Architecture de Nancy, franck.besançon@nancy.archi.fr
[3] Gilles Halin, MAP-CRAI, Université de Lorraine, gilles.halin@univ-lorraine.fr
[4] Alain Fuchs, MAP-CRAI, École Nationale Supérieure d'Architecture de Strasbourg, alain.fuchs@strasbourg.archi.fr

https://doi.org/10.52202/069179-0470

2 SUSTAINABILITY AND DURABILITY

2.1 WHY RECLAIMING TIMBER

In France, two main reasons drive the development of strategies to reuse reclaimed timber. Both have got climate change for trigger. On the one hand, like other countries, France has introduced the obligation to assess the material composition of buildings that owners want to demolish or rehabilitate. Materials must be quantified, qualified and classified according to whether they should be reused, repurposed (up-cycled), recycled (down-cycled), or landfilled [13]. Thus, political decisions aimed to enhance better material sorting during deconstruction. This resulted in the potential availability of timber members that used to be discarded.

On the other hand, it is now commonly known that the construction sector can take advantage of timber construction to store carbon and allow us to build and renovate our dwelt environment in the future [14]. Additionally, climate change has already put and should increase, pressure on forests and thus can create tension around wood resources [15]. Thus, developing strategies to reuse timber could help in the future to be resilient to unexpected climatic events, therefore allowing us to pursue the development of the timber sector while limiting the pressure we put on forest regeneration [16-17]. Timber members susceptible to being deconstructed and stored in the building stock could be seen as a local source of timber, already extracted and manufactured.

2.2 HIERARCHY OF PRACTICES

Following the words of Fivet et al. [18], '*maintain in time an already manufactured capital*', in place, we could say, '*with effect to simultaneously contribute to the natural capital protection and the fulfilling of human capital*' there is a hierarchy, almost a moral one, in the way we now decide to manage our built environment. Preserve it, transform it, or expand it. Climate change effects challenge the construction sector to find ways to reduce its impact on our shared environment while guaranteeing access to comfort. Two interconnected parameters drive the evolution of practices, resource extractions and carbon emissions. The dilemma is that to reduce the energy consumption of already built square metres and future ones, we will need new resources, as the human population grows, and part of the building stock becomes technically obsolete. These resources will need to be as renewable and limited as possible, like the energy used for their extraction, transformation, and implementation. Consequently, following the 9 R's [19] principles, the reuse of construction material is not the priority. To sum up a transposition of that hierarchy of actions could be structured as follows:

- Stop building and preserve uses of existing ones.
- Rehabilitate and develop existing buildings.
- Redesign at different scales (from furniture to urban) with 'Design for…' principles [20-21].
- Use renewable materials that store carbon and emit few to be produced.
- Use fewer materials.
- If Adaptive Reuse is not feasible, reuse existing materials.
- If Reuse is not feasible, Up-cycle, Down-cycle, or Energy Recovery.

2.3 PRECARITY OF REUSE

All those perspectives of actions are part of a vast aim to turn our economic system toward a 'circular' dimension instead of a 'linear' one.

Stop building and preserving the existing as much as technically and economically feasible, by rehabilitation seems to be a robust solution. But adaptive reuse has three primary limits:

- The presence of polluted materials, asbestos, lead or hydrocarbons, can condemn building components to landfills.
- Deterioration of the building due to a lack of maintenance and abandonment can foster demolition or deconstruction instead of adaptive reuse.
- Inadequacy of uses between the existing and the future programme, at different scales, from room to the city block level, can tip the balance in favour of demolition or deconstruction at best.

If they credit the fact that demolition or deconstruction will happen, these three parameters should also warn us on the limits of the 'Urban Mining' concept; pollutions and deteriorations deeply influence sorting towards landfilling, energy recovery, or recycling in best cases.

2.4 REVERSIBILITY LIMITS, THE IKEA ANALOGY

Worldwide, craft timber structures, from Half-timbered houses [22-23] to Minka [24], including Maloca house [25] and their contemporary examples [26], follow a logic of prefabrication that include reuse aptitudes by default. They integrate a dimension of demountability deeply connected with the way wood is transformed into construction material, close to human scale, and assembled with reversible joints. But being made from wood is not a guarantee of reversibility for a building. Although the technicity of certain materials and of building composition has increased, it is not an indefectible sustainability label. The most famous and experienced example of the limits of reversibility is Ikea furniture items. These latter are not renowned for their ability to be disassembled multiple times without losing quality, degrading their structural abilities and their global durability. Even if they can easily be repurposed, transformed or adapted, a loss of pieces and integrity seems inevitable [27-28]. Following the Ikea case study, the material's quality and 'purity' are also part factors potentially condemning furniture pieces after dismantling. The closer a material is to its original form, the more it is reusable or repurposable, and the less it is losing quality or generates loss through time and use. For example, stone blocks, hewn wooden beams or earth are construction materials 'Close to Cradle' that might lose part of their unity but not their absolute integrity. During the documentation of our case study, we observed that the first-floor joists were not linked to the steel beams that support them (see Figure 1. a and 1. b). They were only placed and wedged by a notch cut at their ends. This design facilitates the deconstruction and allows to deconstruct by hand without involving machine assistance. Figure 1.a shows an operator lifting a joist with his right shoulder to 'denotch' it and sliding a wooden wedge between the joist and the steel beam. In Figure 1. b, we can see the second step of joist deconstruction, which consisted in using two ropes attached to

https://doi.org/10.52202/069179-0470

the joist extremity to take it down in two movements. Ikea's furniture reuse problem is not precisely proportional to building scale. Still, some reversible design strategies have weaknesses that we should consider, or at least assume as inevitable losses, such as screws and nails or wooden bars with sections inferior to 5 x 5 cm [29].

Figure 1.a et 1.b: *1.a shows joists 'denotching' from the I-steel beam. 1.b shows the descending of a joist with the rope system.*

3 SEMANTICS OF RECLAIMED TIMBER ECONOMY

3.1 CIRCULARITY AND CIRCULATION

3.1.1 Circularity. Feasible to what extent?

Since the reuse of reclaimed timber is inscribed in the scope of 'Circular Economy', we wanted to explore and precise some aspects of this concept regarding the 'values' we will develop in the following parts. 'Circular Economy' and 'Circularity' concentrate all the attention and seem to crystallise the economic frame of reuse practices [30]. Still, it must be used carefully because they are concepts with multiple interpretations [31-32]. It somehow glorifies an economic system we would like to see happen, but which demands massive socio-economic efforts, or can only stay abstract due to the limits of physics laws.

Even if wood, with other plant-sourced materials, seems to be the best example of an object that starts from a 'point' and could return to this same 'starting point', closing a perfect loop, it never strictly happens in practices. Even if the scenario of wood chips or ashes scattered on top of forest soil is not utopian, it depends on a rigorous protocol [33-34]. Bringing back, after centuries of use, the residues of a joist where the tree was first cut seem complex enough never to happen. Even more if it has been repurposed into furniture, then into particleboard, paper, to be finally burned. The closest architectural demonstration to the circularity concept is the Maloca house [25], which was built, reused, and burned in the same area.

3.1.2 Circulation. A concept that needs delimitation.

Another argument toward precautions with the use of the 'circularity' term is that the complete process briefly described earlier can make us drift from the first objective of sustainability of the circular economy, limiting resource extraction and carbon emission induced by increasing the time of first use. Circularity lets us think that, as we can 'close the loop', we can endlessly extract and operate natural resources. For reclaimed timber, a rebound effect of circularity is depicted by Ghyoot et al. [1] with the example of TerraMai, who collects reclaimed wood from Asia to South America to sell it in the USA. Similar globalised circularity was identified through interviews with carpenters or resellers who mainly bought reclaimed wood from Poland [35]. In addition to the impact of transport, this wood can also be crafted, implying energy consumption. Besides, as Ghyoot et al. exposed it, this migration of resources from developing to developed countries take part to destabilises the socio-economic systems of origins, mainly by depriving the local inhabitants of material resources that would still be useful to them. In those terms, we considered circularity and circular economy as a system in which materials can circulate or move or go through, in the sense of expressing a flow of products through time and space. But even there, the idea of movement keeps ambiguous statutes because movement and transportation imply energy whereas the immobility of things means 'continuity of use', which is less harmful to the environment.

3.2 THE STAIRCASE BEHIND THE CASCADE

3.2.1 Toward the 'tread' extension.

The cascading concept is much more honest on the downgrade aspect of material uses. As Niu et al. [36] propose, cascading is much more complex, suggesting that the materials can go up and down in terms of economic and 'use value'. But cascading keep the metaphor of water flow (waterfall), with water returning to this starting point, still support, like the loop of Circular Economy, an abstracted view of a much more complex system. Speaking of a 'staircase' seems clearer in depicting how we manage wood products through time and 'use value'. Step by step, a cubic metre of wood gets dispersed and disseminated in soil and air through different appropriation processes. At least, the representation of optimal sustainable use of a cubic metre of wood is not to go down the staircase, step after step but to extend as long as feasible the length of the 'tread', seen here as a platform, as figure 2 expresses it.

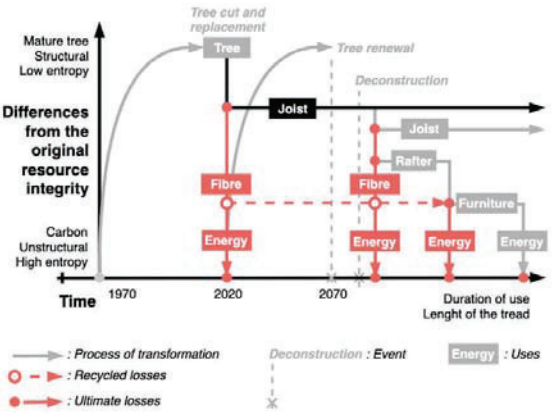

Figure 2: *Diagram of the 'staircase' of timber uses. It shows that the risers, as the steps, should be limited as much as possible, while the treads should be extended as much as possible. The joist black line illustrates the 'platform'.*

https://doi.org/10.52202/069179-0470

3.2.2 Designed to last and limit the entropy.

A sustainable conception of timber construction should find a way to combine all the 'Design for…' approaches [20].
Hazardous and composite materials have created disorders in reappropriating the building stock. Asbestos and lead are the more telling examples. Specifically for wood, treatment has brought more disorders; if we take into account that a better design should consider durability and design strategies not to put the wrong species in the wrong place, or at least to take on a limited lifespan. Glues or too-strong binders are the worst enemies of reuse. An example of this phenomenon is the up-cycling of brick panels in a housing project of 92 flats called Resources Rows, designed by the architecture firm Lendager Group and built in 2020 in Oerestad, Copenhagen [37].
A similar effect can be found in the car industry; where the increased complexity impacts building reliability through time and adaptability [38-39]. This points out the necessity to channel conception toward 'pure' and 'natural' material, closer to their original form when extracted. 'Closer to Cradle' may be better than Cradle to Cradle. Initiatives have taken a pathway in that sense [40-41]. The final challenge is not to see the log house as the best solution but to consider its parameters to integrate it into more creative solutions, such as the 'Breathing wall mass timber research project' supervised in the framework of the Rural Studio, in 2021 [42].

3.2.3 Definitions for wood that goes Up and Down.

A fascinating aspect of wood material is its transformability and appropriability faculties. That specificity opens a broad panel of potential futures for a single piece of timber.
To illustrate our thinking, we will use here the example of a floorboard piece. If reuse is not reached, it can be at best up-cycled or, in most cases, down-cycled. In France, it is estimated that on the annual average amount of wood waste of the construction sector, 48% is energy recovered, 42% is recycled, 7.5% is landfilled, and 2.5% is reused/up-cycled [2]. French legislation (Environment Code, Article L. 541-1-1) differentiates reuse (*réemploi* = re-employed) from up-cycling (*réutilisation* = re-utilisation) and down-cycling (*recyclage* = recycling). See Godina's lexicon [43], which depicts these terms toward 'universal' definitions. We see here how complicated it is to escape from terms that include '-cycling'.

- Reuse/*Réemploi* may not involve a radical transformation of the element, such as cuts. A floorboard must keep its original use, but it could be brushed, planed, varnished, etc.
- Up-cycling/Up-grade/*Réutilisation*, would mean here that our floorboard could becomes something between furniture and glue laminated beams.
- Downcycling/Down-grade/*Recylage* signifies that the floorboard will be crushed and, for example, used for particleboard production. Recycling, unlike Up-cycling, completely make the original timber piece disappear.

3.2.4 Where cascading gets blurred by prices.

Up- and Down-cycling blurs the cascading process. If we look for example at the market value of 1m3 floorboards and transform them into a chair with a similar design, niche products (Scrapwood Oak Chair) are seven times more expensive than mass products (Lisabo); see Figure 3. Mass products chairs keep the same value as a newly produced cubic metre of floorboards for the same volume of wood. On the contrary, based on volume unit, a cubic metre of glue laminated beam is worth less than one transformed into a chair or a cubic metre of reused floorboards.

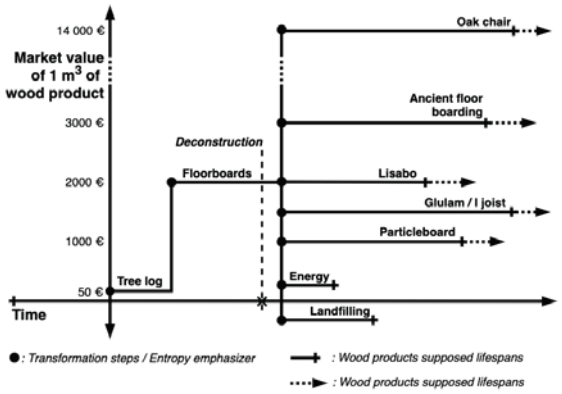

Figure 3: *Diagram of the market value of 1m3 of wood products market after their first use, here as floorboards, and from their original shape as a tree log.*

Consequently, we see that timber elements can go up and down through the 'cascade', see Figure 4, blurring the concept of cascading.

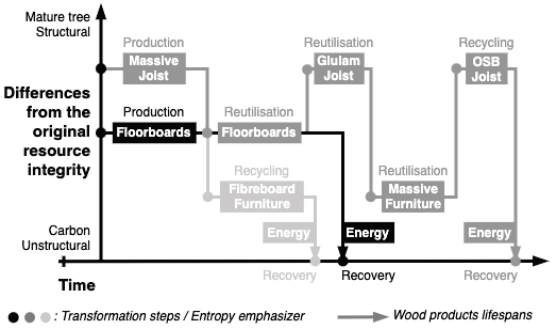

Figure 4: *Diagram of the three main scheme wood products lifespans, black: 'platform', dark grey 'crenel', light grey: 'staircase'.*

Up-cycling can contribute to down-grade the material (cuts, crushes, …) but can increase the value of the same cubic metre of wood. Oriented Strand Board or particleboard down-grade an original joist but can so up-grade if it is turned into an I-joist with panel web ('Steico Joist 45' professional price at a cubic metre, average web-based panel for glulam beam).
Up-cycle can save most wood resources, but not at no cost; material loss must be carefully considered in the transformation process. Student works involved in the research show that an average of 30% of the material will be lost in reappropriating the reclaimed timber. One group had to build furniture out of floorboards, and another a micro-house (4m2) based on a batch of cut-offs from our case study [35]. Other researchers identified a loss of up to 46% of the volume that will be recycled or recovered [44].

https://doi.org/10.52202/069179-0470

More recent work on the evaluation of timber purchase with the aim of up-cycling confirms these tendencies towards a range between 30 and 50% of loss in the reclamation of timber members produced before the 1950s, mostly not standardised. Consequently, as the original volume of wood is transformed, its virtual embodied carbon stock depreciates due to energy (and so related Green House Gas) involved in the transformation.

3.3 ON LIMITS OF BRAND-DUFFY SCHEMES

3.3.1 Layers that hide the need for durability.

Stewart Brand's scheme [45] (expansion of Frank Duffy's concept) conveys a misinterpreted general idea that the lifespan of materials (element, component) has definite lengths. Technical useful life is subject to multiple and variable factors influencing lifespan lengths. These include urban reconfiguration, frequency and degree of building occupancy, degree of climatic exposure, degree of rehabilitation, and natural wear of the material, all linked to 'uses' and, thereby, to the 'human factor'. Users also take part in determining the length of the lifespan with criteria of comfort, optimal use, norms, trends, and perception of wear.

All those criteria reveal that we must think about life expansion rather than life cycles that can legitimate a materials turnovers independently from useful life, a logic present in the office real estate industry.

3.3.2 Unusable or old-fashioned?

From Duffy and Brand's scheme perspective, what is not structural is not supposed to last more than decades [46]. But wood objects proved multiple times their ability to last after decades, if not centuries. Figure 5 shows examples of a dining room where most non-structural components are aged more than the supposed end of their lifecycle. The house containing these objects was built during the 1930s. The present owner, attached to the idea of limiting his environmental footprint, chose to perpetuate the use of objects that could be judged obsolete but still fit his needs.

Besides, this example introduces two values, sentimental and aesthetic. The first relates to our relationship with an object if it has an intimate story, as in our example case. The second one is related to artistic dimensions and subjectivity of taste, which is less present but not absent for structural elements. Thus, these two values are strong because they are the foundation of preservation and transmission, two parameters favouring continuity of use. Museums are the main manifestations of this statement, conserving objects defined as having high aesthetic value and being considered with a sentimental aspect by a population.

Let us again take the example of the 'Oak Chair in Scrapwood' design by Piet Hein Eek [46]. It supports the idea that if floorboards cannot be reused, they still have value after being up-cycled, with the assurance that a 500 € chair will probably last longer than or as long as the building that contains it or used to contain it.

Other concepts have tried to review the Brand-Duffy proposition from a more technical perspective [47] but keeping the structure of 'cycles', which conveys the idea of a substantial turnover of building components. Replacement should be possible essentially if it is technically necessary. Still, independently from a life cycle perspective, a wooden table can be used for decades, and tiles for plumbing are supposed to be reparable. Systems (HVAC) could be less machine aided by following passive principles [48-49], thus limiting maintenance and needs for components with rapid wear.

Figure 5: *M.dF's dining room. In the upper left is a classic example of 'Lundia' shelf in massive wood, dating from the late 1970s early 1980s; in the centre, the table is made with reclaimed planks and used as it has been since the 1930s; back in the centre, the double door in wood and glass (paint in white) is an original feature of the house since the 1930s; on the right, the sideboard is dated from the 1940/50s.*

4 VALUES OF A RECLAIMED TIMBER MEMBER

4.1 HISTORICAL VALUE

We start here with the most subjective value, as we introduced in part 3.3.2 and as know-how value expressing it in part 4.2, price and reclamation criteria depend not only on material aspects. Values attached to timber members also rely on their 'story'. Which building contains it? Has this building played a role in the site's historical background? A prominent example of that concept was brought to the public when Notre-Dame de Paris burned on April 19th 2019. More than losing a roof, a system dedicated to protecting the cathedral interior from climate contingencies, more than losing over 1500m^3 of wood, the cathedral loses her 'forest', the timber-frame nickname that emphasises roof personification and gives it a 'mystical value'. Moreover, the roof's members were precious archives of the medieval climate [50]. This gives more credit to the preservation of old pieces of wood present in buildings worldwide, or at least to the collection of data they contain. Historic value can be acquired after the first period of use, as an example of a barn built in 1920 in Rheinau (Swiss), reported by J.Brütting and C.Fivet [18-51]. The latter was constructed out of reclaimed timber members of a bridge built in 1810 in Eglisau. The historical value of the original bridge was transferred and developed by the fact that it became a barn, still in use a century after.

4.2 KNOW-HOW

Following the example of Bridges, the website 'Bridgehunter.com' [52] gathered at least 55 examples of bridges that were relocated, i.e. reused. More than a practical way of crossing a gap, these bridges stand for a legacy of timber engineering and are historical landmarks. With the idea that timber members have embodied immaterial values, we can assume that both crafted and industrial components and their elements can be characterised by their 'added values'. These added values stem from their design that 'contains' hours of conception to accomplish specific structural objectives (e.g. a span of a dozen meters) and hours of labour to transform wood to fit the design. Reclaimed timber members got added value for works already done and knowledge they can conserve and convey [53]. Since the medieval age, timber members have been included in chains of reclaimed materials [54]. At that time, timber reclamation might have been based on the aim of preserving a previous wood selection (related to strength grade), judged good for a structural purposed, still after reclamation. In addition, reuse interests must have been motivated by preserving the benefice of efforts made to extract and transform, by hand, a raw piece of wood into a usable member, indirectly including human energy and its apprenticeship [55]. Work, labour, as illustrated in Sebastião Salgado's book 'Workers' [56] or expressed in Graeber's theory of value [57], show how connected humans are or used to relate to what they produce, which is not only part of having an economic impact but also a cultural once.

4.3 EMBODIED CARBON

Notre-Dame de Paris fire can be supposed to have emitted over 1800 m ^{3} of C02. Following this example, embodied carbon in reclaimed timber can be seen as a value that must be part of its traceability when sold. Then, CO2 seems to be only the visible part of the iceberg of the environmental impact. It misses resources unextracted and unimpacted to produce new members (ozone, soils and water acidification, eutrophication, air and water pollution, abiotic resources depletion, fossil or not, unused energy, unproduced wastes, …). This lets us consider which values should be taken into account, whether there is a hierarchy, and how data can be collected, evaluated and transmitted concurrently to the element progression in the cascade/stairs, as represented by Figure 2. Recent advancements have been made toward assessing the environmental impact of reclaimed materials [58]. Nonetheless, the externalities of reuse still need to be investigated, by considering all the reuse process, which could entail, for example, deconstruction, milling, transportation, and implementation in the new project. All these activities also participate in increasing our entropy [59]. Furthermore, the environmental impact becomes even more complex if we include facts such as the renewal of biomass that occurred as long as a timber member remained in use and the induced avoided purchase of new products. Until now, the French Environmental Reglementation (RE 2020, see Decree n° 2021-1004) defines the framework for the Life Cycle Assessment (LCA) of new construction. In the LCA, reclaimed materials are currently worth 0 kg of CO2 by default. Thus, creating support to reuse initiatives might not remain a permanent rule. Here we saw that carbon value estimation and traceability would be necessary to reach an accurate LCA that integrates reclaimed timber members, to recognise the impact depicted above. Biogenic carbon could become part of a carbon market that would increase timber member market value.

4.4 MARKET VALUE AND USE VALUE

4.4.1 How much is it? About price estimation.

As we experienced through our field study, see part 5; price is a significant value parameter that could channel timber members toward reuse or not. In other words, value creates value. A low estimation and a lack of purchasers will limit the efforts of a preserved deconstruction, thus limiting in return the quality and the quantity of the timber members that could be sold. We hypothesise that the market value attributed to a timber member is also a label of its 'use value'. The higher the market value, the closer the timber member is to reuse. A lower price indicates a low aptitude to respond to the original use and to be competitive to new products and up- and down-cycling orientations [60].

As we will see in part 5.2.2, to evaluate the latent value of the timber stock of our case study, we align the latent market value of the building stock to the identified prices of the new and reclaimed products on the market by equivalence, as close as possible, by matching, length, section and species. We then adjust the latent value using coefficients: 1 (new, as new or with high historical value), 0.7 (reusable as it is), 0.5 (reusable with low processing) and 0.3 (reusable with high processing), 0.1 (up-cyclable).

4.4.2 Stock and logistics, blind spots of the reclaimed timber value.

The management of the reuse process takes part in adding or removing values, heightening the role and the aspects dual of stock and logistics. During their use, timber members are stored 'for free'. After deconstruction, the created supply of timber members must be protected from climate degradation (e.g. rain, UV, snow…) and eventual thefts (see part 5.2.1). When the protection used to be free, it can now cost to preserve the timber stock integrity. It could be said that value chains do not like storing 'useless' items, as demonstrated by numerous methods developed in the car industry and construction sectors, from Fordism to Lean construction [61]. If it is useless on the site, if it should be moved to find a use, or transformed to be used, it will cost, degrading profit margins, or at worse, diverting initiative in favour of reclamation towards recycling.

4.5 MECHANICAL PROPERTIES

The process of grade identification participates in attesting the value of timber members when facing insurance organisations who need proof of quality and durability/sustainability to ensure that the material will not be charged for the sinister in case of doubt. In that sense, if we look at the etymology of the term 'value', '*valere'* in Latin means to 'be strong' and to 'be valid for'. 'Strong for' (resistant enough), 'valid for' (mechanically adequate), structural purpose. What gives its value to a timber member is its faculty to bear loads. Values attached to mechanical properties are hard to evaluate in a context where we face 'unknown' pieces of wood, sometimes

https://doi.org/10.52202/069179-0470

without any load background and characterisation traceability. To complete the reuse of deconstructed timber elements, a grade datum is necessary for load simulation and structure design accomplishment. As we know, ageing has no significant incidence on bending strength and bending stiffness [62]. Nonetheless, this fact raises an important question concerning the sorting of timber elements to avoid reusing timber that does not enter the norms' criteria (NF EN 338, EC5). Variability of quality, from a mechanical perspective, engages us in developing strategies to avoid potential future disorders:

- Precise assessment methods to identify sources of 'de-grading', before and during the deconstruction.
- Evaluate timber mechanical properties of some pieces and extrapolate to sort them by similarities (dimensions, context of use, aspect, tree species, etc.) and create batches.
- Oversize structures made of reclaimed timber members.
- Consider a batch of timber members as part of one unique grade (C18, lower grade, for softwood and structural use, in our case).
- Evaluate timber mechanical properties of every piece to sort them individually.

Despite its seeming simplicity, this visual grading method is hard to apply on reclaimed timber following the norms ISO 9709:2018 and EN 14081-1+A1 due to aspects gaps with new timber products. A merging with approaches developed in EN 17121 should be interesting to elaborate a specific norm [63]. Another fact of poor adaptability of existing norms is the constraints induced by the reuse process. A strict application of the norms on reclaimed timber can take 5 to 10 minutes for two persons, without including handling time for and between each piece of wood. Therefore, visual grading of an entire timber stock from a building deconstruction can take days and cost enough to degrade the profit margin of the resale. Besides, the gap between norms conceived for brand-new timber products will reject reusable members. From our experiences, we see through visual grading a practice that could help to pre-classified batches of members before their machine grading based on significant characteristics. In our case study, we have experimented vibratory grading method based on MOE evaluation. Bending stiffness is determined by calculation after the caption of the frequencies with accelerometers. As the method is in the reliability assessment process, it is not relevant to give robust results. But trends are identified to avoid risks of keeping timber members inferior to the expected MOE, 7 kN/mm ^{2,} for structural members. Another trend identified is a division into 4 groups, see figure 6. One group is between 7 and 9 kN/mm ^{2}, a second between 9 and 11 kN/mm ^{2}, and a third from 11 kN/mm ^{2}. Each represents more or less a third of our sample batch, with the last of the 4 groups composed of timber members evaluated under 7 kN/mm ^{2}, representing less than 5% of the batch. The main problem is that MOR remains unknown, and mechanical evaluation must be completed to be reliable. But from our perspectives, MOR assessment is still constraining in determining grades, it demands heavy equipment and can generate losses. Therefore, we focus our research on non-destructive and reliable techniques. We try to maximise 'values' embodied in the timber members by preserving as many timber products as possible to sell them, so that they will be effectively reused and be able to transmit their 'values' once again.

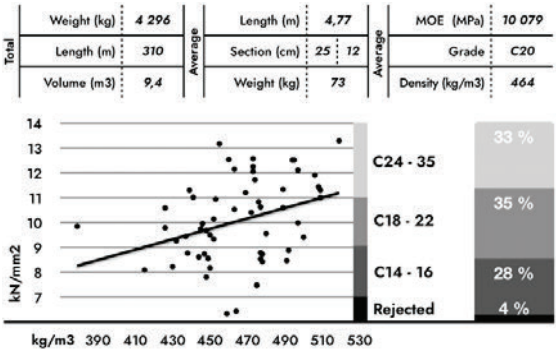

Figure 6: *In the upper part, the table gives general information on the joists batch studied. Lower part graphs depict the supposed strength grades and associate classes (EN 338), based on stiffness assessment with vibratory technique.*

5 AVOIDING FAILURES BY VALUATION

5.1 CASE STUDY CONTEXT

5.1.1 Description of the site.

Our case study is a textile mill, supposed to have been built around 1910 in Épinal, northeast of France. The specific part of the factory we studied was supposed to be designed for the offices of administrative activities. It then became a space for storing archives in the attic and first floor, and the last recent occupation of the ground floor was dedicated to a sewing workshop and a store. But still, we have not yet been able to track down the whole history of the building, which limits the structural analysis introduced in part 4.5.

The building was located in an urban renewal area; a part of the factory was kept, mainly shed volumes, to host economic activities. Our building was demolished to be replaced by a new collective housing project.

We estimate that over 80 m ^{3} were at least 'up-cycled'. The initial stock of wood was evaluated at 146 m^{3} in total, with 126 m ^{3} judged as healthy to be reclaimed for 'reuse', eliminating 17 m ^{3} damaged by fungi, insects, or polluted materials (tar mainly present on roof members) and 3 m ^{3} due to cut-offs.

5.1.2 Socio-economy of the project.

At the time of the field study, in spring 2021, timber product prices were rising unexpectedly. Meanwhile, reclaimed timber members extracted from our site were not affected by this phenomenon. Even the contrary happened while the reusability of the timber members was shared by all stakeholders taking part in the deconstruction.

In our case study, materials were proposed explicitly for sale to private individuals and not oriented towards private professional purchasers. However, in the early stage of the deconstruction, a sawmill offered to buy all the timber members' stock. That choice influenced the final rate of reuse and up-cycling.

We conclude from that experience that the more we divide the original stock by many uncertain buyers, the more we augment dispersion and loss of the resource. Besides, regarding the survey of the 'reuse practices', private individuals mainly up-cycled the timber stock, using joists as a post or cutting them in length for other structural purposes. Only floorboards were mostly strictly reused. This mismatch also provides evidence for the need for a method to define resource prices. On the one hand, sellers need to estimate the latent value of their timber stock to 'take the risk' of investing in deconstruction instead of demolition. On the other hand, buyers (companies) need timber members to be 'certified' to ensure their future clients that they are still safe to be reintroduced in new construction. Timber members are less susceptible to convince of their reusable faculties without 'values' attached and thus without investigation to create traceability.

5.2 LACK OF VALUE, LACK OF ECONOMY

5.2.1 If it is worth to be stolen, it is worth to be sold.

What could be seen as anecdotal looks relevant regarding the lack of values attached to reclaimed timber members. A batch of a hundred joists, part of timber members that were supposed to be reused, has 'disappeared', stolen, maybe reclaimed, by an anonymous person unmasked until now.

The main reason for this 'failures' was that the contractors did not achieve to include this batch in its new project, which was already drawn but still not under construction. Its original storage place, an empty yet still standing part of the textile mill owned by the town hall, needed to be evacuated, letting the joists batch outside, stored on the building site, with no protections, waiting to be reclaimed.

Disappearance, or thefts, advocate for the embodied value in what we could call a brownfield, industrial wasteland, or old building. Here, it points out that this joist batch has values, but these values were not taken into consideration enough to prioritise their final and effective reuse.

Another telling fact of the market value of elements waiting to be reclaimed is the need to close the access to the deconstruction site (also for security reasons) and the surveillance applied to avoid thefts. Recently we notably observed the change from human oversight toward camera-assisted monitoring to avoid guards' complicity with an organised group of thieves (EPFGE site visit).

5.2.2 What it costs and what it is worth.

For our case study, we compare the balance sheet of effective earnings, identified until now, with the potential earnings if prices have been better estimated and sales better organised to maximise profit, with no processing.

As Figure 7 shows it, after re-evaluation (with the method exposed in part 4.4.1), earnings from timber stock sales could have been able to finance its deconstruction and the connected practices linked to it, such as species analysis. Related to the cost of deconstruction, we observed that manual deconstruction is slower than mechanical deconstruction. The latter is ten times more expensive if we look at the cost per hour, circa 15 compared to 150€ from data we collected during the field study, with operators being paid following the French minimum wage at that time, 2021, taxes and fees included. Manual deconstruction involved punctual aids of equipment such as mobile scaffold towers, and portable power tools. Mechanical deconstruction involved equipment such as telescopic handlers or crane trucks.

As energy costs rise [64], we assumed mechanical practices would be less resilient than manual practices. Human portable size of construction materials could be allowed to keep a low cost of deconstruction in the future. Besides, if norms are respected, involving human work instead of machines participates in a more sustainable way of deconstructing also at a social level. At the same time, waste management and treatment costs are rising year after year [65]. Discarding a cubic metre of timber members costs 25€/m3 (0.5 wood density) in 2022; this does not include deconstruction costs and waste management up to the collection point. The global cost is estimated at 45€/m3 (0.5 wood density) [66]. As a comparison, we estimated that the average price for extracting a cubic metre of wood from our case study was around 322€ (including extraction of building layers to access timber members), while the estimated price of a reusable cubic metre of timber members was 465€.

Timber members types	Joists	Trusses	Purlins	Boards & Floorboards	Rafters	Total	Economic efficiency
Potential earnings at estimate prices	30 205 €	6 972 €	6 719 €	12 541 €	2 365 €	58 802 €	11 784 €
Potential earnings at effective prices	2 752 €	6 000 €	309 €	2 882 €	702 €	12 645 €	-34 373 €
Effective earnings at effective prices	1 397 €	0 €	197 €	1 180 €	480 €	3 254 €	-43 764 €
Deconstruction practices	Project manag.	Wood assess.	Manual decon.	Mechanical decon.	Waste manag.	Total	
Deconstruction costs for the timber stock	1 200 €	14 650 €	11 236 €	13 883 €	6 050 €	-47 018 €	

Figure 7: *This table present earnings differences and their impact on final economic efficiency of the deconstruction.*

6 CONCLUSIONS

Reuse of reclaimed timber is not guaranteed by the reversibility and appropriability of the wood material. The continuity of original use is in direct technical and economic competition with recycling and energy recovery. But reuse, compared to these, is still a relevant practice to limit our entropy. We introduced this paper with reflections on sustainability, durability, circular economy and cascading of wood products. These terms need to be more carefully used and reconsidered. We proposed that the lifespan of wood products and their representation should rely on the material integrity, rewarding the extension of the original use rather than steps of transformation. In response, we illustrated that idea with the concept of the 'staircase'. Based on observations we made during the deconstruction of a disaffected textile mill, we got interested in the role of values attached to timber members. After the deconstruction of our case study, we re-evaluated the estimated latent value of the timber stock and compared it with the effective cost of the work site. We also experienced grading practices that could give the right value to structural timber members. We found that taking care of the 'values' could optimise the reuse process and its effectiveness, by remunerating a preserving deconstruction with the earnings from reusable or up-cyclable timber members' sales. This paper only gives a glimpse of the subject of reclaimed timber 'values'.

https://doi.org/10.52202/069179-0470

These values need to be confronted with other field studies to get a comparison and collect price data that appear challenging due to the frequent approximation of stakeholders about the unit of time, volume, weight, costs, and prices. The full reuse of all the timber members extracted from our case study has not been completed until now. We will continue the restitution of research that is related to it by describing the final process of timber members' reintegration. We present here trends rather than final results, and future works will continue to investigate this theme through other deconstruction worksite visits, interviews and reviews. Assessment practices are at the heart of the creation of values. Wider research should be done to identify universal values and clarify the way they are assessed. A connection can be made with heritage approaches as they are similar in many ways.

ACKNOWLEDGEMENT

The French Agency for Environment and Energy Management (ADEME-CLIMAXION).
Mixed Research Unit N° 3495 Model and Simulations for Architecture and Heritage, Research Centre in Architecture and Engineering, Nancy National School of Architecture. (UMR N° 3495 MAP-CRAI, ENSA NANCY).
Épinal National School of Wood Technologies and Industry. (ENSTIB).
Public Establishment of Land of Great-East Region. (EPFGE).

REFERENCES

[1] M. Ghyoot, L. Devlieger, L. Billet et A. Warnier, Déconstruction et réemploi. Comment faire circuler les éléments de construction, Presses Polythecniques et Universitaire Romandes, Lausanne, 2018.

[2] FCBA, Xerfi Spécific, France Bois Forêt, CODIFAB, Gestion des déchets Bois du Bâtiment, Phase 1: Gisement et devenir des déchets bois issus de la construction neuve, de la demolition et de la renovation du bâtiment, April 2022. Online Report, Accessed 12/02/23.

[3] J. Jeanloz, Réemploi: des bonnes paroles à la réalité, Mode Réemploi, Espazium, Tracés n°3525, pages 24-27 2022.

[4] M. C. Moynihan and J. M. Allwood, Utilization of structural steel in buildings, *Proceedings of the Royal Society A: Mathematical, Physical and Engineering Sciences, 470(2168):20140170, 2014.*

[5] A. R. Chini, editor. Deconstruction and Materials Reuse: Technology, Economic, and Policy*, Proceedings of the CIB Task Group 39, CIB World Building Congress, CIB Publication 266*, Wellington, New Zealand, 2001.

[6] F. C. Rios, W. K. Chong, and D. Grau, Design for Disassembly and Deconstruction - Challenges and Opportunities, Procedia Engineering, 118:1296-1304, 2015.

[7] A.M. Friend, Economics, ecology and sustainable development : Are they compatible ?, Environmental Values, White Horse Press, 1(2):157-170, 1992.

[8] J. B. Foster, & M. Mellor, Economy and ecology: Introducing citation classics and foundational works. Organization & Environment, 10(1):12-15, 1997.

[9] INSEE, Valeur ajoutée par branche, Données annuelles de 1949 à 2021. Accessed 16/01/23.

[10] M. Agriantoni, Towards sufficiency in housing: Agent-based model and transition scenarios, PhD Thesis, Lausanne, EPFL, 2022.

[11] M. Lebossé et al. Incorporating BIM Practices into Reuse Process of Timber - Propositions of a digital workflow and tool for reclaiming structural pieces of wood, *Proceedings of the 40th eCAADe Conference, Co-creating the Future: Inclusion in and through Design*, 205-214, 2022.

[12] M.-L. Chiu, An organizational view of design communication in design collaboration, Design Studies, 23(2)187-210, 2002.

[13] Décret n° 2021-821 du 25 juin 2021. Accessed 16/02/23.

[14] A. Himes, G. Busby. Wood buildings as a climate solution. Developments in the Built Environment, 4:100030, 2020.

[15] A. Taccoen. Assessing the potential impact of recent climate change on the mortality of European tree species. Sylviculture, foresterie. PhD Thesis. AgroParisTech, 2019.

[16] J. Hart, F. Pomponi. More Timber in Construction: Unanswered Questions and Future Challenges. Sustainability, 12(8):3473, 2020.

[17] G. Mozgeris, V. Kazanavičiūtė, D. Juknelienė. Does Aiming for Long-term non-decreasing flow of timber secure carbon accumulation: A lithuanian forestry case. Sustainability, 13(5):2778, 2021.

[18] C. Fivet, C. Küpfer, M. Bastien-Masse, SXL Lab , EPFL, Matériaux rejetés et nouveaux défis, Mode Réemploi, Espazium, Tracés n°3525, pages 8-13, 2022.

[19] J. Potting et al., 2017. Circular Economy: Measuring Innovation in the Product Chain. English translation, PBL, Netherlands Environmental Assessment Agency. Accessed 17/01/23.

[20] K. Ostapska, K. Gradeci, & P. Ruther, Design for Disassembly (DfD) in construction industry: a literature mapping and analysis of the existing designs. Journal of Physics: Conference Series, 2042(1):012176, 2021.

[21] M. R. Munaro, S. F. Tavares, and L. Bragança, The ecodesign methodologies to achieve buildings deconstruction: A review and framework, Sustainable Production and Consumption, 30: 566-583, 2022.

[22] C. Cristescu et al. Design for deconstruction and reuse of timber structures. State of the art review. Innovative design for the future. Use and reuse of wood Building Components. Report 1, In FutURe Wood, ForestValue, 2020. Accessed 19/01/23.

[23] C. Griffin-Kremer. Back to the future. Squaring folk life and cultural diversity at the Alsace Ecomuseum. Folk Life, 58(1):57-66, 2020.

[24] A. Clark, E. Yokoyama, Recycling Our Cities, One Building at a Time, CityLab+GreenBy, Bloomberg.com, Updated on 24 November 2022 at 07:01 am. Accessed 12/12/2022.

[25] M.N. Rossana, La Maloca: Arquitectura vernacular amazónica sustentable, Universidad Femenina del Sagrado Corazón (UNIFÉ), Consensus, 17(1):129-142, 2012.

[26] R.M. De carvalho, B.T. De oliveira lobato, Arquitetura em Madeira: do vernacular ao erudito, concepções amazônicas. RCT-Revista de Ciência e Tecnologia, V.7, 2021.

[27] M.W. Harkness. Reforming IKEA: Do-it-Yourself Projects and Everyday Objects in Disposable Culture. MDes, Emily Carr University of Art + Design, BFA, The University of British, Columbia Okanagan, 2017.
[28] A. Jenkins. Assembling IKEA. Queen's Quarterly, 128(3), 372-377, 2021.
[29] T. Capelle, S. Brancart, A. Paduart, S. Elsen, W. Lanckriet, J. Poppe, S. Mantell, M. Steinlage, C. Henrotay, M. Farnetani, Lowres, F., K. Balson, E. Durmisevic, E-J Mul, L. Luscuere, C. Morizur, & M. Delatte, Testing BAMB results through prototyping and pilot projects: D14 - 4 pilots built + feedback report, 2019.
[30] K. Campbell-Johnston, W. J. V. Vermeulen, D. Reike, & S. Brullot, The Circular Economy and Cascading: Towards a Framework. Resources, Conservation & Recycling. 10(7):100038, 2020.
[31] M. Geissdoerfer et al. The Circular Economy – A new sustainability paradigm?, Journal of Cleaner Production, 143:757-768, 2017.
[32] J. Kirchherr, D. Reike, and M. Hekkert, Conceptualizing the circular economy: An analysis of 114 definitions, Resources, Conservation and Recycling, 127:221–232, 2017.
[33] UNECE and FAO, Circularity concepts in forest-based industries, Geneva timber and forest study paper 49, United Nations Publication, Forestry and Timber Section, Geneva, Switzerland, Report, May 2022.
[34] Dufossé, Marie-Charlotte, M., Augiseau, V., Henrion, T., & Djelal, H. Quantification and Environmental Assessment of Wood Ash from Biomass Power Plants: Case Study of Brittany Region in France. Sustainability, 14(1): 99, 2021.
[35] M. Lebossé et al., Reuse of timber in the Vosges and its surroundings. Investigations and experimentations. CRAI, ENSAN, ENSTIB, Unpublished, 2022-2023.
[36] Y. Niu et al., Prolonging life cycles of construction materials and combating climate change by cascading: The case of reusing timber in Finland, Resources, Conservation and Recycling, 170:105555, 2021.
[37] M. Braam, The re-use of brick from dutch post-war housing (1945-1970) in the circular built environment. Faculty of Architecture & the Built Environment, Delft University of Technology, Julianalaan, 2021.
[38] N. Krayner and R. Katz, Experimental method for measuring simplicity in mechanical design, Journal of Engineering Design, vol. 29(1-2): 1-19, 2018.
[39] R.U. Ayres. Complexity, reliability, and design: Manufacturing implications. International Institute for Applied Systems Analysis Laxenburg, Austria, August, 1989, Reprinted from Manufacturing Review, 1(1), March 1988.
[40] J. Geno et al. Parametric design and robotic fabrication of whole timber reciprocal structures, Automation in Construction, 138:104198, 2022.
[41] M. Islam, Z. Mollica, S. Shah, S. Vegesana, Y-C. Yang, (Stu) et al. Hooke Park, AA Wood Campus, MArch/MSc Design + Make, Wood Chip Barn. Dorset, 2016.
[42] Rural Studio, S. Craig, K. Moe, D. Kennedy, A. Freear, Breathing wall mass timber research project, 2019-2021. Accessed 23/01/23.
[43] M.Godina. Strategies for salvaging and repurposing timber elements from existing buildings, Elliott Wood Partnership LtdStrategies, CIOB, UCEM, February 2022.
[44] A. Klinge et al., Design concept for prefabricated elements from CDW timber for a circular building, IOP Conference Series: Earth and Environmental Science, 323(1): 012022, 2019.
[45] S. Brand, How Buildings Learn, Viking, New York, 1994.
[46] P. Hein Eek, Oak chair in scrapwood, designed in 2005, observed prices go from 485 to 576 € depending on chosen treatment, accessible at: https://pietheineek.nl/en/product/oak-chair-in-scrapwood. Accessed 12/02/23.
[47] C. Nijs, E. Durmisevic, and J. I. M. Halman, Interface Design For Open Systems Building. Open House International, 36(1):35-43, 2011.
[48] F. Manzano-Agugliaro, F. G. Montoya, A. Sabio-Ortega, & A. García-Cruz. Review of bioclimatic architecture strategies for achieving thermal comfort. In Renewable and Sustainable Energy Reviews, 49:736-755, 2015.
[49] Versus: heritage for tomorrow, Vernacular Knowledge for Sustainable Architecture / edited by Mariana Correia, Letizia Dipasquale, Saverio Mecca, Firenze University Press, 2014.
[50] Daux, Hatté, C., Boisgueheneuc, D. du, Beck, L., & Richardin, P. The 'forest' of Notre-Dame de Paris: A possible path into medieval climate and time. Journal of Cultural Heritage, In Press, Corrected Proof, 2022.
[51] C. Fivet and J. Brütting, Nothing is lost, nothing is created, everything is reused: structural design for a circular economy, The Structural Engineer, 98(1):74-81, 2020.
[52] Historic Bridges Foundation and these contributors, 2021. Accessible at: https://bridgehunter.com/ga/dekalb/stone-mountain/ (Example of a Lattice-Covered Bridges in Georgia).
[53] J. Bláha. Historic traceology as a complex tool for rediscovery of lost construction skills and techniques. WIT Transactions on The Built Environment. STREMAH 2013, 131:3-13, 2013.
[54] C. Sabathier. La récupération et le réemploi des matériaux dans les villes du sud-ouest de la France pendant la guerre de Cent Ans. In Mélanges de l'École française de Rome - Moyen Âge, 129-1, 2017.
[55] K-E. Larsen, N. Marstein. Conservation of Historic Timber Structures: An Ecological Approach. Butterworth-Heinemann Series, Conservation and Museology (2000), ICOMOS Open Archive, Oslo, 2016.
[56] S. Salgado, Workers, An archaeology of the industrial age, Aperture, New York, 1993.
[57] D. Graeber. Toward an anthropological theory of talue: The false coin of our own dreams. New York: Palgrave, 2001.
[58] M. Sié, N. Basch, Mobius Dall'R 30/38 mm Brut - Plancher technique surélevé non revêtu de réemploi monté sur vérins neufs (v.1.5), FDES, INIES, Accessed 12/02/23.
[59] N. Georgescu-Roegen, J. Grinevald & I. Rens. La décroissance. Entropie, Écologie, Économie, Sang de la Terre, 2020.
[60] F.Privat, Faisabilité du recyclage en boucle fermée des déches post-consommateurs en bois massif, PhD Thesis, Nantes, École Centrale, 2019.
[61] P. Dupin, Le Lean appliqué à la construction, Comment optimiser la gestion de projet et réduire coûts et délais dans le bâtiment, Eyrolles, 2014.
[62] Cavalli A. et al. A review on the mechanical properties of aged wood and salvaged timber. Construction and Building Materials 114:681-687, 2016.
[63] M.Bather, The assessment of the mechanical and physical properties of in situ timber, PhD Thesis, Edinburgh, Napier University, 2022.
[64] B. H. Kreps, The Rising Costs of Fossil-Fuel Extraction: An Energy Crisis That Will Not Go Away, American Journal of Economics and Sociology, 79(3):695-717, 2020.
[65] KPMG Audit for FEDEREC Index.
[66] FCBA, Plan Déchets du CSF Bois, Synthesis, CODIFAB, Version 1, May 2022.

https://doi.org/10.52202/069179-0470

World Conference on Timber Engineering Oslo 2023

CHALLENGES IN THE DESIGN OF A MODULAR MULTI-STOREY CLT BUILDING USING IRISH TIMBER

Hung Quang Phung[1], Conan O'Ceallaigh[2], Patrick J. McGetrick[3], Annette M. Harte[4], Rimjhim Kashyap[5]

ABSTRACT: Cross Laminated Timber (CLT) has been developed in recent years to the stage of automation in production, from timber classification, joining boards, applying adhesive, assembly pressing and CNC machining to form completed CLT panels. Volumetric buildings incorporating CLT are now being developed and completed, showing promising results as sustainable solutions for the construction industry. The majority of European CLT panel manufacturers use grade C24 timber, while countries such as Ireland also have an increasing supply of Sitka Spruce grade C16 timber which has been shown to be suitable for use in CLT. This paper presents elements of a larger research project and focuses on the preliminary design and development of a proposed modular seven-storey building in CLT manufactured from Irish timber, addressing the usage of CLT in volumetric modular construction. Challenges in delivering a building of this type are addressed in terms of building layout, loading arrangement, transportation, and structural design of panels. Design for deconstruction is also considered for the connections between the units to enable future reuse.

KEYWORDS: Modular construction, Circular economy, Cross-Laminated Timber (CLT), Irish timber

1 INTRODUCTION

The current level of housing demand and projected future population growth of 1.5 million people by 2051 in Ireland [1] places pressure on residential building construction – a requirement for an average rate of completion of 33,000 new homes per annum is projected within the next decade [2]. This figure has the potential to rise as high as 50,000 and is a significant challenge as current completion rates lie just under 30,000 per annum as of 2022 [3]. As the supply of raw material from Irish forests has been forecasted to double between 2017-2035 [4], there exist opportunities for the promotion and development of engineered wood product solutions for the sustainable construction of homes to both meet this housing demand and achieve lower building carbon footprints.

In parallel to this, the increase in the prominence of modern methods of construction over the past couple of decades, including automation and offsite manufacturing, has included the development of modular building systems. Modular building systems can generally be categorised into one of two types: 2D panellised, where components such as walls and floors are installed on site to form the building, or 3D volumetric, whereby whole finished modules are installed directly on site [5]. Where a project allows for repeatable building units (2D or 3D), these systems offer faster construction with reduced time on site, higher quality control and efficiency associated with factory assembly and prefabrication, and lower environmental impacts compared to traditional approaches. Developments in the automation of offsite manufacturing procedures have normalised low-rise modular construction, typically 4 storeys or less. However, Thai et al [5] note that modular construction for high-rise buildings is not yet as popular due to lack of design guidelines, inter-module connection techniques and sufficient understanding of structural behaviour, global stability and structural robustness of modular buildings. The majority of multi-storey modular buildings are constructed using reinforced concrete or steel (including cold-formed light gauge steel), or composite construction using both [5]; structural stability is typically provided by a steel bracing system, reinforced concrete cores or walls, or again, a hybrid of both.

Although concrete modular systems tend to have better fire resistance, water proofing and acoustic performance than steel systems, due to its heavier weight, modular concrete units incur higher costs for lifting requirements by crane, and can offer less flexibility in terms of design and connections. For these reasons, as modular buildings become taller, steel or hybrid systems can be preferred, particularly if 3D volumetric modules are being used to reduce internal finishing requirements on site. More

[1] Hung Quang Phung, Timber Engineering Research Group (TERG), University of Galway, H.Phung1@universityofgalway.ie
[2] Conan O'Ceallaigh, TERG, University of Galway, conan.oceallaigh@universityofgalway.ie
[3] Patrick J. McGetrick, TERG, University of Galway, patrick.mcgetrick@universityofgalway.ie
[4] Annette M. Harte, TERG, University of Galway, annette.harte@universityofgalway.ie
[5] Rimjhim Kashyap, TERG, University of Galway, r.kashyap1@universityofgalway.ie

https://doi.org/10.52202/069179-0471

recently, developments in timber offer alternative solutions with similar benefits.

Harte [6] outlines the introduction to the construction industry of mass-timber products, such as Cross Laminated Timber (CLT), with excellent load carrying characteristics that over the past two decades have enabled timber to be used in larger and more complex structures, including modular construction. CLT panels for use in structures can be fabricated at lengths up to 16 m, widths up to 3 m and thicknesses up to 500 mm. Currently, the tallest all timber building in the world is the mixed-use 18-storey Mjøstårnet building in Norway, completed in 2019 and standing at 85.4 m [7]. Examples of modular mass-timber buildings include the 14 storey, 49 m tall Treet Building in Bergen, Norway which was completed in 2015 and was constructed using volumetric CLT modules achieving Passive House standard [7]. However, the majority of existing modular CLT buildings tend to be 7 storeys or less in height [8].

The success of timber modular construction to date has been reported as being dependent on local or regional production capacity and regulations [8], and its development has been focused primarily in Europe, followed by North America. Bhandari et al. [8] acknowledge that there is a need for a systematic review of modular CLT connection systems in terms of constructability, reuse and potential for rapid building deployment, including further study of the impacts of the transportation distance on cost and efficiency. Furthermore, with increasing demand for sustainable building solutions, international best practice in modular timber construction is expected to become more widespread.

The increased use of timber in construction has tended to be perceived as having the potential to make a significant contribution to reducing greenhouse gas emissions from the construction sector, particularly when it is being used in place of reinforced concrete or steel. This is becoming of greater significance now as many countries are introducing policies and initiatives that target net-zero emissions, such as the European Green Deal [9], with associated regulation and carbon footprint limits for new buildings. There has been limited research published on the lifecycle impact of modular volumetric CLT construction but recent research [10] has highlighted the significance of the energy production profile for this type of construction. The product, construction and end-of-life stages hold the most significant share of the building's lifecycle impact, while optimising the modular CLT building configuration and use of efficient fasteners can reduce the overall impact by around 5% [10]. The authors are also carrying out ongoing research on the lifecycle assessment of timber buildings and modular CLT construction as part of the wider Modular Mass Timber Building for the Circular Economy (MODCONS) project. This paper presents aspects of the MODCONS project on the preliminary design and manufacturing of a seven-storey residential building in CLT based on material properties of Irish C16 timber, following the volumetric modular approach. While 2D panellised solutions can offer flexibility, a 3D volumetric modular approach also offers a number of advantages, including the quality control and efficiency associated with factory assembly and reduced sitework. The volumetric approach also has the advantage of producing whole modular units that can be reused or refurbished, supporting a circular economy in construction and offsetting the need for virgin materials. European CLT panel manufacturers primarily use grade C24 timber, which has slower growth rates but higher strength than fast-grown Irish Sitka Spruce (*Picea sitchensis*) grade C16 timber. It follows that the capacity and opportunity for the increased supply of Irish timber to be used in added-value products in construction must be illustrated, supporting a reduction in the carbon footprint of the built environment [6]. The following sections outline the preliminary building layout and design including reuse, loading arrangements, transportation requirements, and the associated challenges.

2 DESIGN CONCEPT AND DEVELOPMENT

Following the current Irish building regulations (and associated technical guidance documents on structure, fire safety, access) [11], planning guidance [12] and European standards for actions on structures and structural design [13-16], the design of the volumetric units was developed assuming mass production of prefabricated units under factory conditions. The milestones of the preliminary design workflow are highlighted in Figure 1 below, beginning with (i) the selection of the volumetric construction method, (ii) the design and layout of individual modular units and plan design, meeting transportation requirements and internal sizes in line with the minimum area required by the local regulations [12], and (iii) structural design of the CLT panels required to transfer loads from the floors and ceilings to walls and foundations. Lifting systems and connections are also key considerations in the design for deconstruction targeting future reuse, however, limited discussion is provided here on consideration of these.

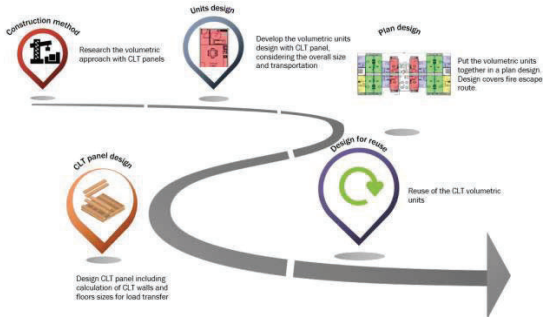

Figure 1: *Milestones of the design development*

2.1 SITE LOCATION

The site location for the seven-storey residential building was assumed in an urban location in Dublin, Ireland. The ground conditions and foundation design are not considered in this paper but based on existing

https://doi.org/10.52202/069179-0471

developments in this location, it is assumed that the geotechnical conditions will be suitable for the proposed building. The focus here is therefore on the building superstructure only.

2.2 ACCESS AND TRANSPORTATION

The design criteria for the CLT units are also informed by transportation within this urban location i.e. by access, size and weight limits. The modular unit height is limited at 4.65 m from ground to the top of the load being carried or top of the vehicle. This can be increased by a local authority permit [17]. The modular unit length is limited at 12 m + 3 m overhang for one piece [17,18]. This can be increased to 27.4 m with a permit from An Garda Síochana, and increased to more than 27.4 m with a local authority permit [17]. The modular unit width is limited at a maximum of 2.9 m (including a 300 mm overhang) [17,18]. This limit can be increased to 4.3 m with a permit from An Garda Síochana, and over 4.3 m with a local authority permit. Based on the above limitations and assuming the necessary permits are obtained, the size and dimensions of the modular CLT units were therefore limited to 4.3 m external width, 15 m external length, and 4 m in external height. Figure 2 provides an example illustration of the modular unit size for transportation, showing the unit overhang on the transporting vehicle. provides Supporting beams, not shown here, are also required to ensure the unit is supported by the walls during transportation.

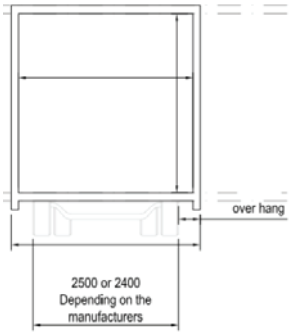

Figure 2: *Example illustration of modular unit transportation (not to scale, dimensions in mm)*

The maximum allowable modular unit weight is maintained below 24 tonnes to remain within transportation vehicle laden weight limits [19]. More detail on the weights of the designed modular units is provided in Section 2.3.

2.3 BUILDING LAYOUT AND MODULAR UNIT TYPES

The general arrangement of the building and plan layout design are dependent on the arrangement and combination of the volumetric unit types. Three apartment configurations were considered in the completed plan layout for the proposed seven-storey building, with a rectangular footprint on plan of 45 m × 25.32 m excluding balconies. The same floor plan (Figure 3) is repeated at all seven storeys, with reinforced concrete cores (3.48 m × 5.53 m on plan; 300 mm thick walls) located at each end of the building to provide access stairways, fire escape routes and lateral stability for the building structure. A central communal area is provided, meeting minimum area requirements [12]. Fire safety provisions and emergency access are based on Technical Guidance Documents B and K [11]. The stair cores are designed to be constructed on-site using reinforced concrete as a non-combustible material. The maximum distance from an apartment entrance door to the stairs is limited to 15 m. This plan is designed to ensure each bedroom receives natural light and it also allows for additional units and cores to be added.

To form the three apartment configurations, either single modular CLT units or a combination of units are employed. The four volumetric unit types designed are shown in Figure 4 – Types 1 (green) and 2 (yellow) are combined to form the two-bedroom apartments, Types 1 and 3 are combined to form the one-bedroom apartments, and Type 4 is a single studio unit (red). These exceed the minimum overall areas by at least 10% [12] while minimum widths of apartment rooms are also defined by [12]. A standardised width of 3.6 m is used for both one and two-bedroom apartments to reduce volumetric unit variation for manufacturing. However, for the studio apartment, a minimum internal width of 4.0 m is required. All modular units are l_e = 3.25 m in height, resulting in a total building structure height of 22.75 m.

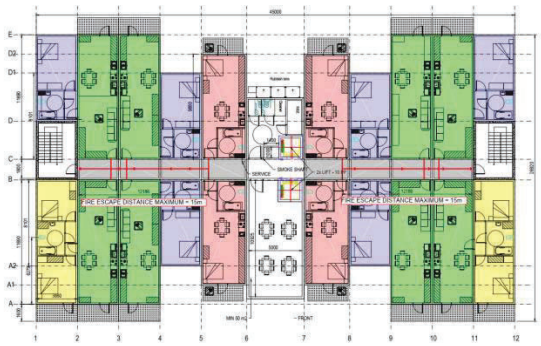

Figure 3: *Proposed building plan layout (not to scale, dimensions in mm)*

The units are designed to reduce the number of volumetric unit types required to form the building. This reduces structural variation, optimising unit standardisation to improve production efficiency. Furthermore, for the CLT panel supply chain, cost and time savings can be made when the same panel sizes can be ordered, manufactured and supplied in large quantities. The internal design of the apartments accommodates a standard plan layout. However, the skeleton frame of the volumetric units can be used with different interior designs of the apartments. This means the core CLT volumetric unit can be used in a different applications – allowing standardised mass production. Overall, the building consists of 12 apartments per floor, configured from 20 CLT modular units per floor, totalling 140 modular units.

https://doi.org/10.52202/069179-0471

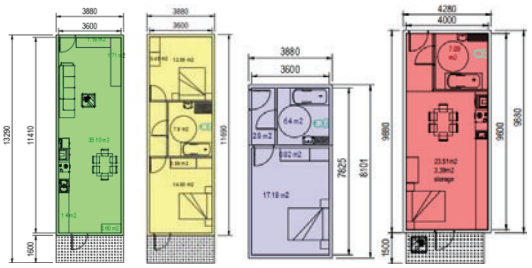

Figure 4: *Plan layouts of volumetric modular CLT units (a) Type 1 (b) Type 2 (c) Type 3 (d) Type 4 (not to scale, dimensions in mm)*

The estimated weights of the volumetric units are provided in Table 1; these values assume the prefabrication of the units including balconies for a conservative comparison with permitted transportation limits i.e. weight under 24 tonnes and length less than 12 m + 3 m overhang. All unit widths are under 4.3 m. Common practice would likely dictate site installation of balcony units post assembly of the building modules. Mobile cranes with suitable capacity are available for these modules and building dimensions, such as the Demag AC220-5.

Table 1: *Modular CLT unit dimensions and weights*

Type	External width (m)	External length including balcony (m)	Estimated weight (tonnes)
1	3.88	13.29	20.32
2	3.88	13.29	22.78
3	3.88	9.7	18.11
4	4.28	11.38	21.86

3 CLT PANEL DESIGN

3.1 LOADING

Figure 5 shows an indicative cross section for the modular CLT units, showing the proposed balloon arrangement of CLT panels for walls, floors and ceilings. This allows modules to be stacked on top of one another with gravity load transfer directly between walls, removing the risk of compression perpendicular to grain in floor panels in the more popular platform construction approach. For unit types 1-3, the clear span for floors and ceilings is the 3.6 m internal width, while for unit type 4, the clear span is 4 m. The floor and ceiling panel designs are based on the larger L = 4 m span.

The gravity loading acting on floors and ceilings is adopted based on [14], while wind loading is calculated based on the Irish National Annex to Eurocode 1 - Part 1-4 [14], giving a peak wind pressure of 1.27 kN/m^2. The characteristic variable action (unfactored imposed load) adopted for the unit floors is 2 kN/m^2 based on domestic loading, while the ceiling panels are designed for imposed loads of 0.6 kN/m^2 during the construction stage only. A flat roof is assumed with limited access for maintenance and repair only, with ceiling panels in units at roof level designed for an imposed load of 1.5 kN/m^2; this can be reduced to 1.0 kN/m^2 where permanent access to those panels is not provided. Including self-weight, the ultimate design loading for a 1 m strip of the floor is 4.47 kN/m. For the ceilings, the corresponding loading is 2.12 kN/m. All corridors and access areas are designed for an imposed load of 4.5 kN/m^2. Floors in corridors are to be supported by the CLT module walls and are included for loading calculation purposes only.

The preliminary wall design is based on the maximum gravity loading experienced by ground floor walls, allowing the resultant design to be used at any floor. It is assumed that the walls are encapsulated with plasterboard providing at least 60 minutes of fire resistance – this is expected to be a minimum requirement under current Irish practice. As the building is multi-storey, the total imposed loading on the walls has been reduced by a factor of 0.79 in accordance with Equation (6.2) of Eurocode 1: Part 1-1 [14]. These loads result in an ultimate axial design load on the wall of F_d = 112 kN/m. The ultimate transverse load acting on the wall due to wind, calculated using the peak wind pressure, is $q_d = 1.5 \times 1.27 = 1.91$ kN/m^2.

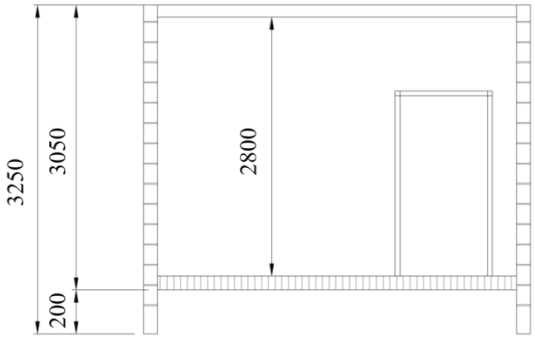

Figure 5: *Indicative cross section of volumetric modular CLT units (not to scale, dimensions in mm)*

3.2 MATERIAL PROPERTIES AND SOURCING

Irish Sitka Spruce (*Picea sitchensis*) grade C16 timber is assumed for the design of all CLT elements. While C24 grade timber is more commonly used for the manufacture of CLT in Europe, this study is intended to illustrate the feasibility of using locally sourced rather than imported timber, which at a minimum, can offer potential savings in transport emissions. This is also being investigated by the MODCONS team at University of Galway but is beyond the scope of this paper. The relevant adopted material properties for design in accordance with Eurocode 5 [15] are presented in Table 1 below, adopted from [20-22].

https://doi.org/10.52202/069179-0471

Table 2: *Material properties for C16 grade timber used for design*

Property	Value for C16	Unit
Characteristic bending strength, $f_{m,k}$	16	N/mm^2
Characteristic compressive strength along the grain, $f_{c,0,k}$	17	N/mm^2
Characteristic compressive strength perpendicular to the grain, $f_{c,90,k}$	2.2	N/mm^2
Characteristic shear strength, $f_{v,k}$	3.2	N/mm^2
Mean value of modulus of elasticity, along the grain, $E_{m,0,mean}$	8000	N/mm^2
Fifth percentile value of modulus of elasticity, along the grain, $E_{m,0,05}$	5400	N/mm^2
Shear modulus, $G_{0,90}$	500	N/mm^2
Rolling shear modulus, $G_{90,90}$	50	N/mm^2
Density, ρ	390	kg/m^3

3.3 PANEL DESIGN SUMMARY

Following the design approach based on beam theory [15,16] and outlined in [22], the assumed building layout shown in Figure 3, loading outlined in Section 3.1, and using C16 timber properties provided in Table 2, three common CLT panel build ups have been designed for the unit walls, ceilings and floors respectively for all unit types; these are summarised in Table 3. Service Class 1 is assumed. Values of k_{mod} = 0.8 for medium term actions [15, 22], k_{mod} = 0.6 for permanent actions [15, 22], γ_M = 1.25 [15] and k_{def} = 0.85 [22] are adopted for design calculations.

Table 3: *Summary of panel design*

Element	No. layers	Total thickness (mm)	Layer thickness (mm)	Layer orientation (degrees)
Walls	3	120	40	0
			40	90
			40	0
Ceilings	3	110	40	0
			30	90
			40	0
Floors	5	140	40	0
			20	90
			20	0
			20	90
			40	0

3.3.1 Floors and ceilings

The floor and ceiling panels both comfortably pass design checks for bending and shear, with low utilisation ratios. It is desirable at this preliminary stage to keep utilisation ratios below 75% for floors and ceilings. For example, for the CLT floor panel, the design bending strength, $f_{m,d}$ =10.24 N/mm^2 is considerably greater than the design bending stress σ_d = 2.96 N/mm^2. Similarly, the design shear strength, $f_{v,d}$ = 2.05 N/mm^2 is greater than the design shear stress, τ_d = 0.13 N/mm^2.

The critical design criteria for the floor and ceiling panels are deflections, which are limited to a maximum of L/250 = 16 mm here for the L = 4 m span [15]. The net final deflections are calculated here according to equation 7.2 of [15], reproduced as Equation (1) assuming zero pre-camber:

$$w_{\text{net,fin}} = w_{\text{inst}} + w_{\text{creep}} \quad (1)$$

where $w_{\text{net,fin}}$ is the net final deflection, w_{inst} is the total instantaneous deflection (variable + permanent) and w_{creep} is total deflection caused by creep (variable + permanent). For permanent actions, $w_{\text{creep,g}} = k_{\text{def}} w_{\text{inst,g}}$ and for variable actions, $w_{\text{creep,q}} = \psi_2 k_{\text{def}} w_{\text{inst,q}}$ where $\psi_2 = 0.3$.

For the floor panels, $w_{\text{inst}} = (w_{\text{inst,q}} + w_{\text{inst,g}}) = (4.24 + 1.16) = 5.40$ mm under variable and permanent actions, respectively, which is less than the corresponding limit of L/300 = 13.33 mm. The net final deflection $w_{\text{net,fin}}$ = (2.16 + 5.32) = 7.48 mm (< 16 mm). Reducing the outer layer thicknesses by a typical step size of 10 mm or greater would cause the section to exceed the 75% utilisation ratio in deflection thus no further changes are made to the section size and layers.

In terms of vibration serviceability requirements, the natural frequency of the floor is $f_{1,fl}$ = 12.93 Hz, and that for the ceiling is $f_{1,ceil}$ = 9.27 Hz, calculated using equation 7.5 of Eurocode 5 [15]. Both of these panels satisfy the simplified vibration serviceability calculation method in Eurocode 5 for residential floors however, it should be noted that the acoustic performance has not been assessed here - this is part of a larger task on the MODCONS project.

3.3.2 Walls

The wall design is more critical due to the loading accounting for vertical load from 7 storeys and wind loading. Following Clause 6.3.2 of [15] for combined compression (due to F_d) and bending (due to q_d), the 120 mm thick panel is checked for the 11.69 m long wall in unit Types 1 and 2. Due to openings for windows, the effective width, $b_{ef,}$ of the wall is taken as 6.5 m. Buckling is checked in the ultimate limit state according to Equation (2).

$$\frac{\sigma_{c,0,d}}{k_{c,y} f_{c,0,d}} + \frac{\sigma_{m,y,d}}{f_{m,y,d}} \leq 1 \quad (2)$$

where $\sigma_{c,0,d}$ is the design compressive stress along the grain, $f_{c,0,d}$ is the design compressive strength along the

https://doi.org/10.52202/069179-0471

grain, reduction factor $k_{c,y}$ can be obtained using equation 6.5 in [15], $\sigma_{m,y,d}$ is the design bending stress about the principal y-axis, $f_{m,y,d}$ is the design bending strength about the principal y-axis. $\sigma_{c,0,d}$ can be calculated based on a 1 m strip of wall (from the width b_{ef}) as $N_d/A_{x,net}$, as per [22]. Here, N_d = 201 kN is the vertical load and $A_{x,net}$ = 80,000 mm^2 is the cross sectional area of the two outer layers, giving $\sigma_{c,0,d}$ = 2.51 N/mm^2. $\sigma_{m,y,d}$ can be calculated as $M_{y,d}/W_{x,net}$, where $M_{y,d} = \frac{q_d l_e^2}{8}$ is the design moment due to wind loading and $W_{x,net}$ is the section's net moment of resistance. Here $\sigma_{m,y,d}$ = 1.95 N/mm^2. With $k_{c,y}$ = 0.43, $f_{c,0,d}$ = 8.16 N/mm^2 and $f_{m,y,d}$ = 7.68 N/mm^2, Equation 2 can be evaluated as 0.97 < 1, which passes but with a high utilisation ratio. Any further increase in thickness to reduce this utilisation ratio is not desirable as it would increase the weight of units beyond the 24 tonne transportation limit. However, further refinement of panel thicknesses is possible between unit types with consideration of the impact of increased variation in manufacturing.

3.4 CONNECTIONS AND DESIGN FOR REUSE OPPORTUNITIES

The common panel design for all units allows the modular units to be used in alternative arrangements i.e. the same unit can be used at any storey within this seven storey building. Furthermore, this also enables provision for reuse of the units at the end of, or during, the building's design life which supports the reduction of its environmental impact. While 2D panellised CLT systems may remain more popular and practical for construction, the whole unit reuse option remains an advantage for volumetric units. There are two options for reusing the units: (i) reuse the fully completed CLT units (with interior fit out) and (ii) reuse only the structural frame; the latter has been employed for volumetric construction in steel. However, associated challenges exist, for example, in the limited capacity to add new openings to walls, the detailing of demountable connections, maintaining overall building stability and modularisation of Mechanical and Electrical systems. Alternative solutions currently being assessed include straightforward options such as connections using screws instead of nails, no adhesive used to connect components to CLT, recessed lifting points located at the top of the unit wall panels etc. Connection groups currently being reviewed for this building system include:

- Alternative options for wall to floor and wall to ceiling connections, including standard angle brackets and timber rails above or below panels considering fire protection
- Inter-module connectors i.e. as part of the lateral stability system
- Connections for lifting and transportation
- Volumetric unit connection to substructures

4 CONCLUSIONS

This paper has demonstrated the feasibility and capacity of CLT panels manufactured using Irish C16 grade timber to be used in multi-storey volumetric modular residential construction. Due to a common CLT panel design between the four modular unit types proposed for use across all 7 storeys, wall panels at the ground floor level are the critical elements. However, the current design with 5-layer 120 mm thick wall panels provides flexibility to use the same volumetric modular unit at any of the seven floors. While 2D panellised systems grow in terms of popularity and standardisation, volumetric modular systems still hold the advantage of enabling reuse of a whole finished unit. The MODCONS project team's ongoing work involves the review the lifecycle impacts of this, considering the comparative ease of deconstruction of panellised systems for reuse. Furthermore, the proposed design, detailing, structural testing, and fire performance testing of connection systems for both volumetric and panellised systems using Irish C16 timber is ongoing.

ACKNOWLEDGEMENT

The authors wish to express their gratitude for the support and funding received from the Department of Agriculture, Food and the Marine's Competitive Research Funding Programmes, Project Ref: 2019R471 (MODCONS).

REFERENCES

[1] Central Statistics Office Ireland, Population and Labour Force Projections 2017 – 2051, https://data.cso.ie/, 2018, Accessed 18 January 2021.

[2] Government of Ireland. *Housing for All – A new Housing Plan for Ireland*, Department of Housing, Local Government and Heritage, 2021.

[3] Central Statistics Office Ireland, New Dwelling Completions Q4 2022, https://www.cso.ie/en/releasesandpublications/ep/p-ndc/newdwellingcompletionsq42022/, 2023, Accessed March 2023.

[4] Phillips, H., Corrigan, E., McDonagh, M., Fairgrieve, M., Farrelly, N., Redmond, J., Barrett, F. and Twomey, M. *All Ireland Roundwood Production Forecast 2016-2035*. COFORD, Department of Agriculture, Food and the Marine, Dublin, Ireland 2016.

[5] Thai, H.T., Ngo, T. and Uy, B. A review on modular construction for high-rise buildings. Structures, 28: 1265-1290, 2020.

[6] A.M. Harte. Mass timber – the emergence of a modern construction material, J. Struct. Integr. Maint. 2 (2017) 121–132. doi:10.1080/24705314.2017.1354156

[7] Council on Tall Buildings and Urban Habitat. Tallest Mass Timber Buildings: https://www.ctbuh.org/mass-timber-buildings. Accessed 27th February 2023.

[8] S. Bhandari, M. Riggio, S. Jahidi, E. C. Fischer, L. Muszynski, Z. Luo. A review of modular cross

https://doi.org/10.52202/069179-0471

laminated timber construction: Implications for temporary housing in seismic areas. Journal of Building Engineering, Volume 63, Part A, 2023, https://doi.org/10.1016/j.jobe.2022.105485.
[9] European Commission, Directorate-General for Communication, (2021) *European green deal: delivering on our targets*. Publications Office of the European Union, https://data.europa.eu/doi/10.2775/373022.
[10] A. Al-Najjar and A. Dodoo. Modular multi-storey construction with cross-laminated timber: Life cycle environmental implications, Wood Material Science & Engineering, 2022, DOI: 10.1080/17480272.2022.2053204
[11] Technical Guidance Documents (2020). Available at: https://www.gov.ie/en/collection/d9729-technical-guidance-documents/?referrer=http://www.housing.gov.ie/housing/building-standards/tgd-part-d-materials-and-workmanship/technical-guidance-documents#technical-guidance-document-a-structure; Accessed: 11 March 2021.
[12] Government of Ireland. *Sustainable Urban Housing : Design Standards for New Apartments*, Department of Housing Local Government and Heritage, 2020.
[13] National Standards Authority of Ireland (NSAI), I.S. EN 1990, Eurocode 0: Basis of structural design, 2002.
[14] National Standards Authority of Ireland (NSAI), I.S. EN 1991, Eurocode 1: Actions on structures, 2002, including Irish National Annex (2013).
[15] National Standards Authority of Ireland (NSAI), I.S. EN 1995, Eurocode 5: Design of timber structures, 2004.
[16] National Standards Authority of Ireland (NSAI), I.S. EN 16351, Timber structures - Cross-laminated timber Requirements, 2015.
[17] Government of Ireland, Road Traffic (Construction and Use of Vehicles) Regulations 2003
[18] Road Safety Authority of Ireland. *Weights & Dimensions.* Available at: https://www.rsa.ie/en/RSA/Your-Vehicle/About-your-Vehicle/Weights--Dimensions-/ (Accessed: 24 April 2020).
[19] Road Safety Authority of Ireland. *Guidelines on Maximum Weights and Dimensions of Mechanically Propelled Vehicles and Trailers, Including Manoeuvrability Criteria*. March 2023.
[20] CEN, EN 338 Structural timber - Strength classes, Comité Européen de Normalisation, Brussels, Belgium 2016.
[21] C. O'Ceallaigh, K. Sikora, D. McPolin, A.M. Harte, Modelling the hygro-mechanical creep behaviour of FRP reinforced timber elements, Constr. Build. Mater. 259 (2020). doi:10.1016/j.conbuildmat.2020.119899.
[22] Swedish Wood: The CLT handbook: CLT structures - Facts and Planning. Swedish Wood, Stockholm, Sweden, 2019.

World Conference on Timber Engineering Oslo 2023

RE:SOURCE PAVILION – EXPLORING THE CIRCULAR USE OF WOODEN BUILDING MATERIALS

Ute Groba [1], Samuel Blumer[2]

ABSTRACT: The pavilion as a building task is a contested typology as both its functional life span and constructive durability tend to be limited. However, this ephemerality makes the questions of the materials' origin and the construction elements' later reuse a pressing issue which is of great importance for rethinking architecture of greater scale as well and render the pavilion a suitable format for study and exploration. This paper describes the conception, design and planned mounting of a timber pavilion as part of a master studio taught at The Oslo School of Architecture and Design. The pavilion is planned to be built and exhibited parallel to the World Conference on Timber Architecture 2023 in Oslo. Special focus is directed towards the implication of "disregarded" wooden materials for architectural design and constructive solutions. "Disregarded" wooden materials include cut-offs and cut-outs, materials found on waste sorting plants, pre-used materials from buildings soon-to-be demolished or erroneous deliveries. Specifically, the focus is on joining smaller members or members of varying sizes to larger load-bearing elements or to indoor and outdoor planes and surfaces. The paper discusses the insights this design task provided, highlights new questions that arose during the process, and suggests how these may inform timber architecture in general.

KEYWORDS: Timber construction, reclaimed wood, engineered wood, circular architecture, design for disassembly

1 INTRODUCTION

1.1 THE PAVILION AS A CONTROVERSIAL DESIGN TASK

The dichotomous demands towards sustainable building materials to be both permanent and ephemeral become overly apparent in pavilions as a building typology – permanent as materials are supposed to last long, and ephemeral as materials are supposed to be compostable (or combustible for energy production) instead of ending in landfills [1].

For many, the pavilion is a contested building task. As its function tends to be limited and its construction less durable, the pavilion may be criticised for its use of resources. However, the pavilion may also serve as a test bed for new architectural and constructive ideas and exhibit these to the public [2]. Bringing together the necessary expertise for non-standard design and construction endeavours may even initiate future collaboration.

When its materials have been pre-used or would have been discarded otherwise, and when the pavilion's functional and constructive conception allows for a relocation after its primary exhibition phase – in parts or as a whole, the critique of wasting resources is less apposite. Both using pre-used materials and designing the pavilion for later disassembly and reassembly may on the contrary provide an important opportunity to explore circular construction concepts that are not possible, feasible or common in full-scale buildings at present – either for logistic challenges, due to clients' short-time perspective and corresponding budget, or owing to expectations for the materials' visual and performative properties. The pavilion's focus on circular materiality also brings these issues to a broader public awareness, and if designed in an education context, equips future architects with a corresponding mindset and skills that they can bring to future projects.

1.2 FOUR CIRCULARITY FOCUS AREAS

Even when employing renewable resources that in addition store carbon, such as timber, the environmental benefits are maximized when the materials are in use as long as possible and when their use is planned in a cascading circle – not ending in a landfill[3] but feeding into energy or soil production [3]. This cascading circle may be understood as a perpetual succession of four use stages, or focus areas, that each tries to minimize material or energy losses along the way.

- *"Plan A":* The first focus should always be on extending a building's life span. This is supported by the construction's durability, the building's maintenance, the layout's and surfaces' adaptability and the building's overall lovability and acceptance [4].

[1] Ute Christina Groba, AHO The Oslo School of Architecture and Design, Norway, ute.christina.groba@aho.no
[2] Samuel Blumer, sblumer ZT GmbH, Austria, samuel.blumer@sblumer.com

[3] Since 2009, landfills with biologically degradable materials such as wood are not allowed in Norway.

https://doi.org/10.52202/069179-0472

- *"Plan B":* If at some point, the building needs to be taken down, it should be possible to reuse it as a whole, or its components with the least modification and the least loss of material possible (design for disassembly) [5]. The re-use of building components is eased by access to their documentation or information about previous approval details (e.g. catalogued in a database). It furthermore requires the space and the logistics of storing and marketing them.

- *"Plan C":* When building components do not allow any further reuse, their materials' recycling will give them another life. Even when flagged as "upcycling" however, this new life is sometimes a dead end, for example when the materials' treatment only allows for later disposal in a landfill. The recycling of materials is supported by their non-toxicity and their separability into components.

- *"Plan D":* Materials should always be treated in a way that does not impede their later composting for soil amendment or their combustion for energy production. However, some paints or impregnations turn wooden materials into hazardous waste, and composites are often impossible to separate into their organic and inorganic constituents.

While previous "Timber Studio" courses at The Oslo School of Architecture and Design (AHO) have mainly dealt with "Plan A", this course's task has been designed to predominantly address "Plan B" and "Plan C". Focussing on wooden construction materials, the course paid special attention to their provenience (e.g. pre-used, cut-offs, waste, left-overs) and to their afterlife (not impeding composting or combustion). It furthermore engaged in design for disassembly and scenarios for subsequent uses.

2 METHODS

2.1 A DESIGN-BUILD MASTER STUDIO

The master's studio course *Re:Source Pavilion* was taught during the fall semester 2022 at AHO. It has developed the concept, program, design, construction, details, production and assembly plans of a wooden pavilion that is planned to be exhibited on a city-centre site during the World Conference on Timber Engineering 2023 in Oslo. Its 21 students from Norway and from abroad were at different stages of their master studies. The teacher team had special expertise in architectural design and theory, timber construction, parametric design, and static engineering. Both at a midterm review and at the final review, invited guest critics provided critical feedback.
The students worked with a variety of individual and group tasks, and in changing group constellations. Each student wrote one lecture report, presented one precedent analysis, and shared photographs of their favourite details from a study trip to Switzerland.
The students' playful first design task was individual as well. Each student got 1m of AHO terrace boards that had been retained when the school's deck got shifted during summer vacation. Only by subtracting material (grinding, sawing, cutting, sanding etc.), the students transformed their boards into something new, and formulated their thoughts in a short poem. The ensuing discussions among the entire group introduced a wide range of topics with relevance to the course's focus on wooden materials and their repeated use.
The students then suggested pavilion concepts in groups of 2, voted for which ones to refine, worked on pavilion designs in groups of 4, voted for which ones to continue with, and in groups of 7 contributed to develop the 3 final conceptual, spatial, and constructive pavilion designs that will be described more in detail in this paper. The diagram in
Figure 1 illustrates each student's path through the semester's group constellations.
Several efforts were made to foster the sense of contributing to the entire group's knowledge gains instead of individual achievements. As an example for the sharing of ideas across projects, when voting for the projects to continue with, the students would also point out ideas or aspects they would like to see followed up in later designs, without the project the ideas originated from claiming exclusive ownership to these. In the large final groups, each student developed an individual field of "nerd expertise", diving deeper into the different aspects of the project (e.g. parametric modelling; detail drawing; the logics of prefabrication, transportation, assembly and disassembly; or building and mounting 1:1 mock-ups).

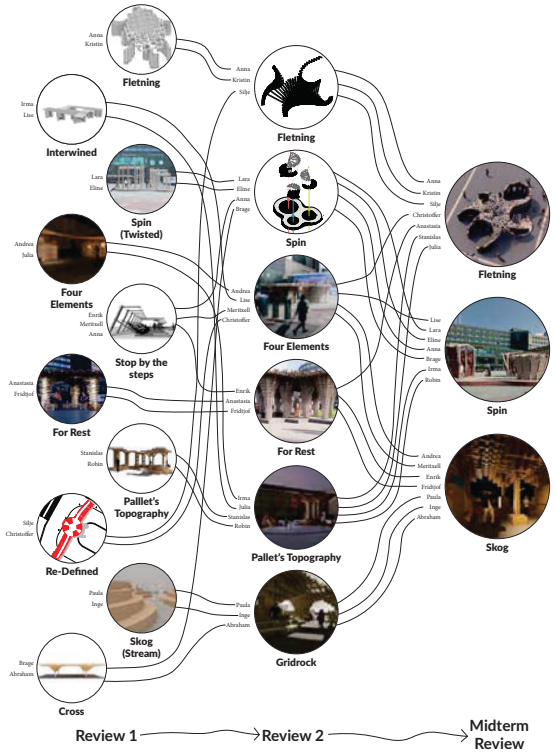

Figure 1: *21 students contributed to the projects in varying group constellations (Illustration: S. Corbevin).*

https://doi.org/10.52202/069179-0472

2.2 WORKSHOP EXPERIMENTS

A series of experiments in 1:1 scale was conducted at the school's workshop hall. In a first session, "disregarded" wooden materials reclaimed from waste facilities, a CLT producer and a disassembled, obsolete barn were joined into larger construction members.

The students' suggestion *Leftover Ceiling* created dowel-laminated slabs consisting of leftover boards with different formats and surface qualities, their edges aligned to a flush surface on one side and with a varied relief on the other side, imagining that the irregular side could remain visible in the room underneath (Figure 2).

To Glue or Not to Glue tested glue and wooden dowels as alternatives for joining pallet boards into thicker and longer elements that were used in a block construction and a cross-laminated floor slab (Figure 3).

Pillar and Beam made use of rescued plywood pieces to vertically join old components to longer columns. The plywood pieces were joint horizontally by adding simple top- and bottom flanges that only needed few screws to be held in place, resulting in wooden I-beams (Figure 4). This was also imagined to be a way to vertically join the ancient columns from pre-industrial barns that had been retrieved for this workshop.

Gradient Wall explored varying degrees of transparency by inserting plywood pieces in gradient angles between a top and a bottom beam made from CLT parts that had been cut out of CLT walls to create openings (Figure 5).

Stacked Triangles explored ways of joining boards into triangular segments and stacking these or connecting them in one plane (Figure 6).

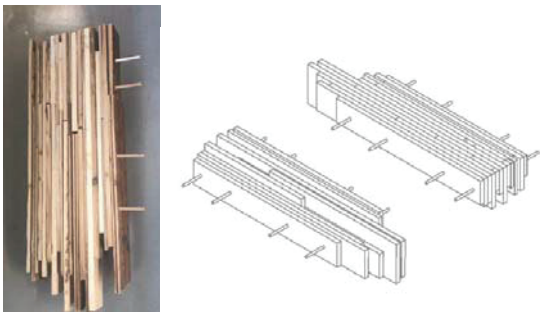

Figure 2: *Leftover Ceiling*

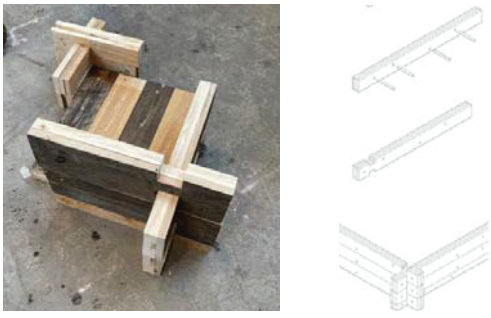

Figure 3: *To Glue or Not to Glue*

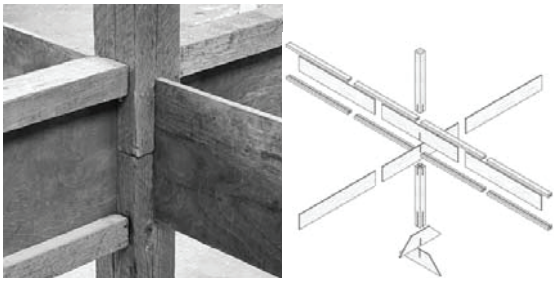

Figure 4: *Pillar and Beam*

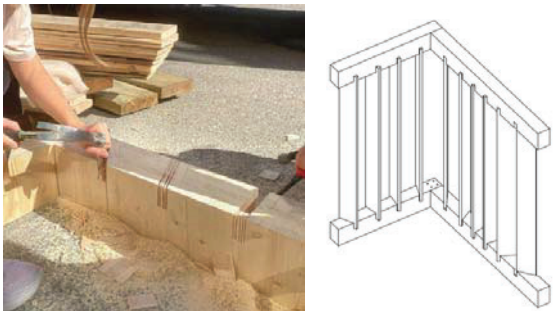

Figure 5: *Gradient Wall*

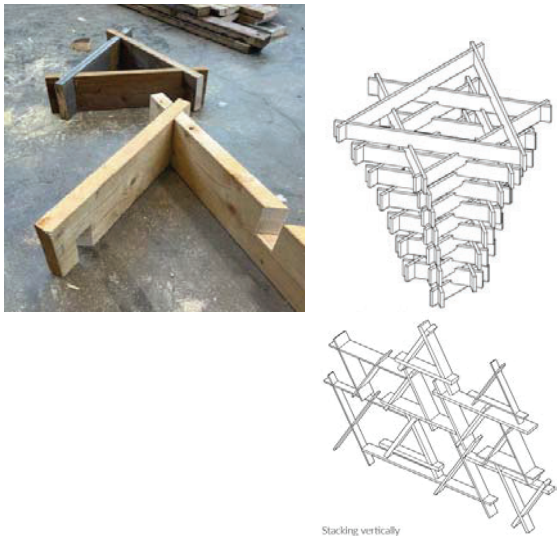

Figure 6: *Stacked Triangles*

As part of a later task, the students' pavilion designs were tested in 1:1 detail models, and a section of each of the three final pavilion designs was built as a full scale mock-up for the final review and exhibition at the AHO gallery (Figure 10, Figure 14, Figure 18).

https://doi.org/10.52202/069179-0472

3 RESULTS

3.1 FINAL PAVILION PROJECT 1: SKOG

"Skog" means forest in Norwegian, and the project departed from the wish to recreate the experience of being under a forest's treetop canopy, with the light filtered through different layers of leaves and branches, and an undulating forest floor beneath (Figure 7). From the outset, this intention was formulated and explored through hand drawings, a poem, various model iterations and digital visualizations.

The final project consists of 13 trees with a wooden gridwork symbolizing the tree crowns. The trunks consist of four square parts that are anchored in a base plate which is hidden in a modular stepped landscape. The landscape can be used as an informal sitting amphitheatre or during presentations and other events, and indicates areas for the exhibition of objects or prints (Figure 8). Due to the limited possibility of clamping the trees at the base, they were also connected to each other at the top. This creates a so-called social static system with a frame effect. In the case of local overload, the stress peaks are taken over by the neighbours.

The physical mock-up was made from left-over materials (2'x2' battens) after another course's concrete workshop at AHO (Figure 10). While the physical and digital models suggest standard 2'x2' formats in defined lengths, one can also imagine members with varying cross sections and/or lengths as well as surface qualities, especially in the places where these are only attached to the gridwork on two sides.

The students considered options to protect the gridwork's end-grain parts, either with a translucent roof plate or with small caps covering the horizontal cut faces. They finally decided to leave the wood unprotected and to embrace and exhibit its degrading process – possibly even at a secondary site in the forest where the construction materials originally came from (Figure 9).

Figure 7: *Light filtered through the trees' canopy (rendering).*

Figure 8: *The existing stairs at Oslo S may extend the pavilion's sitting landscape (rendering).*

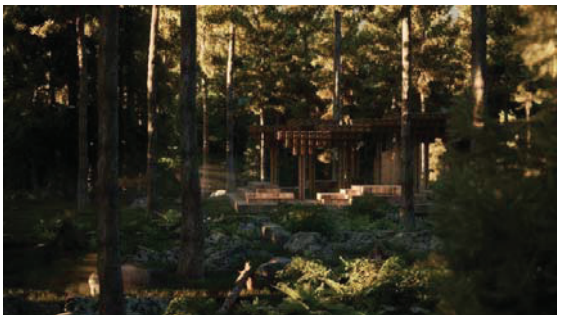

Figure 9*: Imagining the pavilion returning to its materials' place of origin, re-entering the biological cycle and decomposing in the forest.*

Figure 10: *The students built a quarter of one tree as a 1:1 mock-up.*

https://doi.org/10.52202/069179-0472

3.2 FINAL PAVILION PROJECT 2: SPIN

Spin consists of three pavilion segments that can be rotated in order to create a wide range of spatial constellations that facilitate different activities, such as lectures, presentations and concerts, a pathway along the pavilion's differently treated panels or other smaller exhibitions, large audiences, smaller groups and coincidentally attracted passers-by. The rotation is made possible by mounting the pavilion segments onto the slewing rings from disused excavators. These are hidden in a stepped base plate construction (Figure 13).

With the wood stemming from an obsolete barn close to Oslo, the pavilion's dimensions are conditioned by the materials available. The students were able to make use of pre-existing 3D data of the barn's elements in order to maximize material efficiency. Former beams and columns make up the pavilion's load bearing frames (Figure 11). Wooden dowels are used for the pavilion's permanent connections, with rescued plywood parts reinforcing the joints (Figure 14). Demountable parts are joined by steel dowels. The old cladding makes a reappearance in the pavilion's vertical spaces between the frames. They are treated (sanded, oiled, painted, engraved, etc.) in various ways in order to show the wealth of options for processing or upgrading pre-used materials. Disused surfing sails are used to protect the wood from rain and to add colour to the design (Figure 12).

Figure 11: *An obsolete barn's construction members constitute Spin's main materials (rendering).*

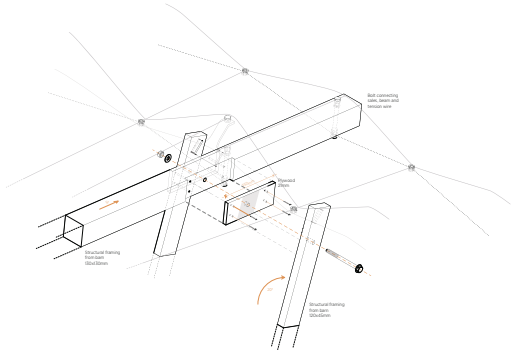

Figure 12: *Old surfing sails protect the wood.*

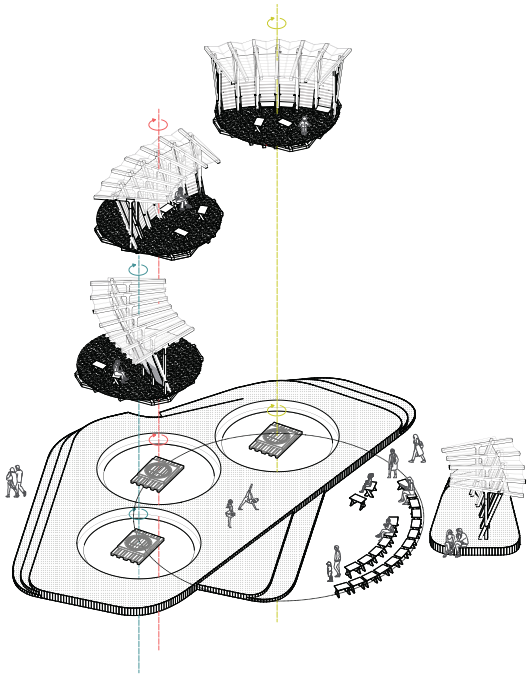

Figure 13: *Mounted on disused slewing rings, the pavilion's segments can be turned to create a variety of spatial constellations on and around the "connective tissue" base.*

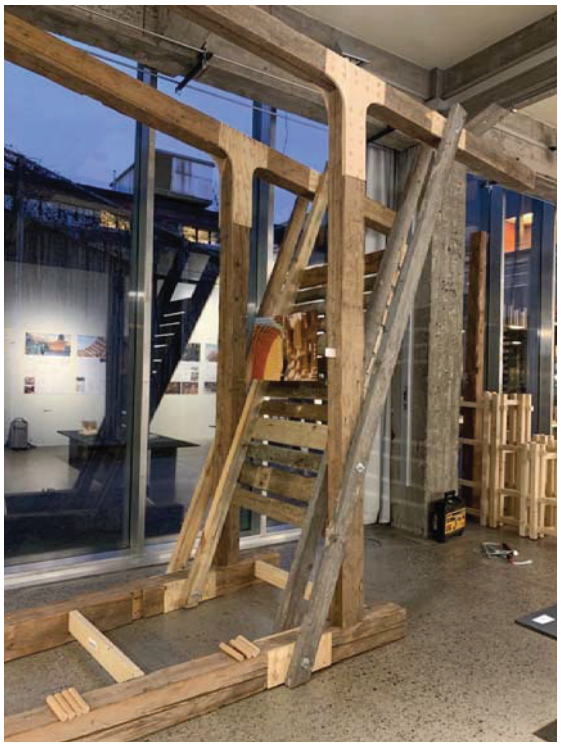

Figure 14: *Plywood parts reinforce the wood dowel connections (1:1 mock-up).*

https://doi.org/10.52202/069179-0472

3.3 FINAL PAVILION PROJECT 3: FLETNING

During the processing of wood into standardized industrial building materials, wood loses one of its original qualities, namely the organic shapes of the tree and its parts. This pavilion project's ambition was twofold: to create organic shapes with highly standardized industrialized wooden materials, and to mainly use short dimensions as more readily available from wood waste and cut-offs.

"Fletning" means weaving in Norwegian. By stacking rows of short, offset 2'x4' pieces ("wood bricks") with altering angles, the resulting semi-transparent walls allow glimpses through the construction that vary with every step when passing by (Figure 15). Towards the wall's top, the pieces gradually increase in length and create a cantilevering canopy (Figure 18). In some places, other walls' tops complete the geometry of an archway. Three such walls are arranged in a curved geometry that both ensures stability and creates subspaces for smaller exhibition sections, sitting areas or a podium. The structure's geometry has been parametrized in a digital model for full flexibility in the form-finding process. In order to compensate for the laterally projecting walls' lack of weight, the students suggest a disk-shaped roof element that is filled with earth for weighing down the pavilion against wind forces. It is clad with disused offprint metal sheets that mirror the construction and visually continue the pavilion's central space (Figure 16). Another option could be to omit the roof plate and to hide sandbags in the two podiums instead. The wall itself is made up of smaller ca.1m wide blocks that consist of 11 wood brick layers and weigh about 38kg each. They are joint by long wooden dowels that create a loose fit with the middle layers' holes and a tight and permanent connection with the outer layers. Stacks of these blocks are held together with steel rods, and these segments are joined with other stack segments (Figure 17).

Depending on the "re:source's" provenience – either from a waste facility or collected at a production facility – the materials' surface will either be weathered or more or less pristine. In contrast to most conventional products with the exposed surfaces aligned with the wood fibres' direction, here the end-grain's cut fibres face the visitor. If most pieces are cut to length, only a few weathered pieces will mix up the frontal view's colouring, but due to their angled placement, also the lengths' surfaces will be discernible. As only parts of the pavilion are protected by a roof, its walls will weather differently and increase the walls' visual homogeneity.

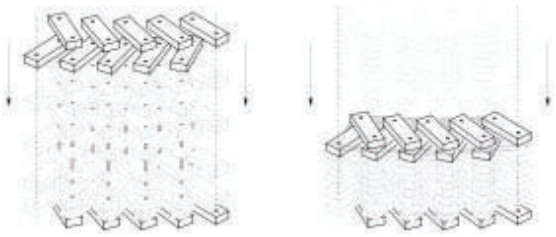

***Figure 15**: "Wood brick" layers are joined into a block and then stacked. Altering in orientation, they create varied transparency.*

***Figure 16:** Fletning's organic curves visually continue as a reflection in the roof disk (rendering).*

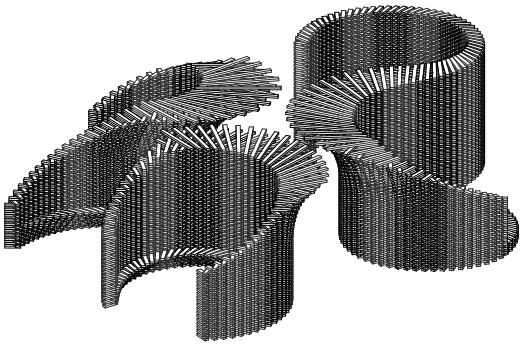

***Figure 17:** Wall segments are assembled into curving walls for stability and spatial differentiation.*

***Figure 18:** The "wood bricks" increase in length to create a sitting bench and to extend into a partial roof (1:1 mock-up).*

https://doi.org/10.52202/069179-0472

4 DISCUSSION AND CONCLUDING COMMENT

The work on the pavilion projects and the course's accompanying tasks addressed a number of issues that are specific for the design with "disregarded" wooden materials.

4.1 STRATEGIES TO JOIN SMALL PARTS INTO LARGER CONSTRUCTION MEMBERS

There is an element of unpredictability of the available sizes and qualities when harvesting disregarded materials. The students realized that shorter pieces were more common to find than long boards, panels, beams or large plates.
Different products were aimed at when joining small parts into larger construction members and thereby creating larger surfaces or increasing lengths and spans: planes (slabs), linear members (columns and beams), gridworks and bent surfaces with varying degrees of transparency.
Availability, fabrication, logistics and assembly on site were discussed and are mirrored in the resulting connections.

4.1.1 Permanent and disassemblable joints

The projects made a differentiation between permanently assembled construction members and joints between such members that need to allow for repeated assembly and disassembly.
Permanent connections typically involved glue or wooden dowels in places where a later dismantling was not considered relevant. For the wooden dowel connections, dried wooden poles were inserted into slightly more narrow pre-drilled holes. When the wooden poles adapt to the ambient moisture and expand, they permanently lock the parts together. It is difficult to dismantle connections with wooden dowels without destroying them. For example, the wooden dowel connections in *Spin* can only be removed by sawing them or by drilling them out. The wooden dowels permanently join beams and pillars into parts that still fit into a container and that can be raised by manpower.
Steel bolts in the connection details between these segments can be attached and detached repeatedly.
In *Fletning*, wooden dowels connect 11 layers of "wood bricks" into permanently joint blocks. Weighing about 38kg each, these can be handled by manpower. The stacked blocks are joined with removable steel rods and attached to other stacks.

4.1.2 Including diverging dimensions while minimizing cuts

Some of the workshop studies addressed the issue of minimizing adjustments to obtain equal formats when found materials differed in cross-section and/or length. Among the preliminary workshop experiments, *To Glue or Not to Glue* avoided the problem by basing their proposal on the components of standardized pallets. *Leftover Ceiling* aimed to expose the differing heights and lengths of the included reclaimed boards on one side, aiming to activate the visual and narrative potential of their product. *Stacked Triangles* also suggested versions where the boards circumscribed equal triangles while continuing outwards according to the found lengths.

Many of the pavilion projects were initially imagined with freely defined formats as usual in conventional projects where one can choose from a range of available formats and looks, and only later turned to embracing the unique and unpredictable qualities and dimensions of reclaimed wooden materials. However, also the final projects all have some potential to integrate found formats to a greater degree.

Skog: While the students aimed for a clear overall geometric shape and envisioned the pavilion with identical 2'x2' profiles, the canopy's construction system would also allow for integrating different lengths, resulting in a geometrically less controlled underside or top (or both). In contrast to other parts in the crowns' gridwork, its (at present) shortest pieces are only attached on two sides, which would allow for attaching other formats than 2'x2' cross sections as well. Visual consequences could be studied in the pavilion's digital model that served for visualizations and for a VR tour of the project.

Spin: The dimensions of an actual obsolete barn considered suitable as re:source co-defined the size and shape of the pavilion. As described above, the use of pre-existing 3D data of the barn's elements allowed the students to maximize material efficiency. With longer or shorter members available, for example from another obsolete barn, the pavilion's parametric model can be adjusted accordingly.

Fletning: Confronted with the complexity and laborious production of their pavilion, the students highlighted that 70% of their "wood bricks" were identical, while the rest differed in length. However, the key invention in mastering the complexity may lie in using the same drilling stencil with a defined distance between the holes for the dowel connections in all wood pieces, no matter their length (or even height if it is the same for an entire layer). Precision in the distance between these holes is of key importance for the pavilion's assembly, while – as is the case in *Skog* as well - precision in the components' length only matters visually.
The flexibility to include different formats (as long as they have the same height per layer) might alleviate one fallacy: the pavilion's design is based on cut-offs in the most common dimension, as these are most likely to find at waste facilities. However, this universally applicable format also makes these the most sought-after pieces. The further refinement of the design could integrate pieces that are less attractive for subsequent users.
Catering for a greater variety of lengths when minimizing cuts, one could align the pieces in a different way than in the students' project, for example creating several partial covers over each curve instead of the central area between the three curves, or creating random reliefs on one or both sides of the walls. Using the same basic design as the student's proposition but with random (found) lengths, the increasingly cantilevering walls would create vaults and

https://doi.org/10.52202/069179-0472

archways of a less regular geometry. These geometrical options may be explored in the pavilion's parametric model.

4.2 WEATHER PROTECTION

The pavilions feature different ways of handling the protection against weathering and decay. *Skog's* student team explored several options, but favours to expose the pavilion fully to the elements. *Fletning* suggests partial coverage, and *Spin* provides protection of all upright elements except for the base.
If the pavilions are no longer used as a temporary structure, adequate structural wood protection must be provided. The roofs should be constructed in such a way that the joints are not directly exposed to the rain.

4.3 ADDED WEIGHT

On an exposed site, high wind-induced uplifting forces occur. In order to compensate for wood's light weight and the lack of foundations in the temporary constructions, weight is added to the pavilions' roof or floor construction: the designs allow for adding sandbags, earth or other heavy materials in *Skog's* landscape, in *Spin's* base or in *Fletning's* roof plate or podiums. The added weight helps to fix the temporary pavilions in place against strong winds without the need of fastening them to a foundation on site.
Connecting several elements like in *Skog* or arranging connected frames in a half circle like in *Spin* additionally stabilizes the construction.

4.4 PROVENIENCE AND PROVENANCE

The re:sources' provenience as their place of extraction, or more precisely, retrieval, has been important – both as a justification for the pavilion as a building task, and as a specific area of investigation, as the materials' previous function, use, treatments, removal (cautious or careless) and storage all condition their visual and performative qualities as well as choices for their later processing and according use of tools in a technical perspective.
The material's previous life entails yet another dimension than just the performative one, which has been embraced in different ways in the student projects. In contrast to provenience as the exact location of retrieval, the term provenance is used to address the detailed history of an object, for example the different owners and exhibition or storage circumstances of an artwork. The materials used by the students all witness of their history, for example with traces of axe cuts from times before other tools were invented, with different layers of paint, with insect holes, with the overall roughening effect of weather exposure or the locally smoothing effect of repeated touch.
How these signs of previous life were valued differed – in some cases, they were consciously preserved and exhibited (e.g. in *Spin's* frames and parts of its cladding, or in *Fletning's* wood bricks), in other cases, they were ignored, evened-out or removed (e.g. in *Skog's* gridwork or in other parts of *Spin's* cladding).
The materials' provenience and provenance were of particular interest when discussing the use of obsolete barn materials, some of them from preindustrial times. The abundance of disused barns all over rural Norway most often leads to their demolition – in some cases, they at least serve for fire brigade exercises before turning to waste.
If the oftentimes quite solid materials can be used in constructions instead, even when just hidden between gypsum boards, they can still play an important load-bearing role and replace more harmful materials or ease the pressure on fresh wood. The same is true when cutting or planing the material to obtain parts that are straight or equal. Then, the old traces may still be discernible in part, while including the retrieved components mostly untreated will expose these qualities more fully.
In order to access a greater part of these narratives than only the visually accessible ones, some circular building projects label the materials with QR-codes for the visitor's information. This additional information beyond the architecture's mere atmospheric experience may even change the appreciation of the architecture's visual, experiential and functional qualities. What may be criticized in other cases is potentially valued when associated with the materials' previous life and the intentions behind their reuse.

4.5 PROJECT STATUS

The three final projects, together with the terrace board exercise and the workshop experiments, have been exhibited at the AHO gallery in December 2022 and are planned to be shown again during the conference.

It had been the wish of the WCTE arrangers to erect one pavilion at Oslo's Central Station during the World Conference on Timber Engineering in the summer of 2023. Out of the three final projects, a jury recommended *Fletning* to be built in full size for this purpose. The jury consisted of the course's external censor (Siv H. Stangeland from Helen&Hard), the course's teachers (3 architects and one engineer), a representative of WCTE and a representative of the engineering firm that was going to act as the responsible applicant (Sweco). The assessment criteria collectively agreed upon were the projects' poetic and conceptual approach, experiential qualities, functionality, resource use, originality and innovation, feasibility, disassembly and reuse options, and transferability of research insights.

At the point of this paper's submission deadline, the process of realizing the winning proposal has not started yet; an update will be included in the conference presentation.

4.6 EXPECTED CHALLENGES

A number of challenges are expected when realizing the winning proposal. *Fletning* is considered to be buildable, but intermediate storage and timing are expected to be the main challenges.
The manual assembly of *Fletning* has been tested by students in 1:1 mock-ups; it is relatively simple and can be done by untrained workers, but time-consuming and difficult to estimate for the pavilion's entirety. All larger pieces must be prepared in advance and their assembly

well-planned and tested, as the time window for mounting the pavilion on site is short. Possible unevenness of the site may complicate the pavilion's assembly somewhat. The storing of gathered materials and assembled parts will require adequate storage space over longer time. Security issues and possible vandalism need to be addressed carefully. The pavilion's after-life is not decided at the point of the paper's submission.

4.7 CONCLUDING COMMENT

The results of AHO's master's course *Re:Source Pavilion* showcase that vast architectural variety is possible when basing the design on readily available, disregarded wooden materials. Joining smaller and irregular pieces into larger construction members will be relevant for larger building projects as well. In the load-bearing parts of conventional projects, the formal and atmospheric potential of disregarded materials such as waste wood, cut-offs, cut-outs from CLT production and materials directly retrieved from obsolete buildings may not be fully taken advantage of.

The narrative and associative potential of discernibly reused materials may elevate their value for some, especially when their visually accessible qualities are complemented by information on their previous location(s), function(s) and modification(s).

In more rational (purely functional) assemblies, disregarded wooden materials may still play an important role in replacing more harmful materials and reducing the need for fresh wood, while at the same time maximising the life cycle and thus carbon storing benefits of wooden construction materials.

The necessary labour and related need for storage and transportation need to be carefully assessed in order to avoid the latent risk of promoting circularity for its own sake [6]. However, what is not established and competitive today (both budget-wise and in a LCA perspective) may become easier to achieve and more feasible in the future – both due to more established routines and systems, and potential legal changes.

ACKNOWLEDGEMENTS

The timber studio *Re:Source Pavilion* reflects the engagement and collaboration of a number of teachers without whom neither the pavilion as a built project nor as a contribution to architectural discourse would have been possible. Besides the paper's main author and course responsible Ute Groba, Samuel Blumer, Rune Veslegard and Moritz Groba have been part of the course's set-up and content and have contributed to this paper.

Likewise, the course students' ideas, explorations and work efforts are essential part of this endeavor. Thank you to A.B. Visiedo, J. Böttcher, S. Cornevin, F. S. W. Fønstelien, K. Guðmundsdóttir, R. Haugaas, L. B. Heidenreich, I. Jorganovic, C. I. Kirsby, L. B. Kjeldseth, N. A. G. Lerkerød, B. B. Lervåg, M. M. Barril, E. R. Martínez, P. R. García, A. M. Skelton, E. Svelle, A. Uusihärkälä, S. M. H. Vikene, A. Volkova and I. Wiig.

Furthermore, the course has been sponsored with materials for the workshop experiments and final mock-ups. Our deep gratitude goes to Omtre and Kristine Nore. We are also grateful for extra support during the pavilion's realization by sblumer GmbH.

REFERENCES

[1] Junyk, Ihor. '"Not Months but Moments": Ephemerality, Monumentality, and the Pavilion in Ruins'. *Open Arts Journal*, no. 2 (December 2013).

[2] Bevan, Robert. 'In the Pursuit of Pleasure: The Not so Fleeting Life of the Pavilion and Its Ilk'. *Architectural Design* 85, no. 3 (May 2015): 16–25.

[3] McDonough, William, and Michael Braungart. *Cradle to Cradle: Remaking the Way We Make Things*. 1st ed. New York: North Point Press, 2002.

[4] "Only things people like get a long life" states architect Dietmar Eberle. Sattrup, Peter Andreas. 'Arkitekter, arkitektur og ressourcer: Interview med Dietmar Eberle'. *Arkitekten* 11 (2008): 42–43. Translation by the author.

[5] Huuhka, Satu, and Inge Vestergaard. 'Building Conservation and the Circular Economy: A Theoretical Consideration'. *Journal of Cultural Heritage Management and Sustainable Development* 10, no. 1 (28 November 2019): 29–40.

[6] Harris, Steve, Michael Martin, and Derek Diener. 'Circularity for Circularity's Sake? Scoping Review of Assessment Methods for Environmental Performance in the Circular Economy.' *Sustainable Production and Consumption* 26 (April 2021): 172–86.

https://doi.org/10.52202/069179-0472

World Conference on Timber Engineering Oslo 2023

ADAPTABILITY IN MULTI-STOREY TIMBER BUILDINGS – TOWARDS DIFFERENTIATED DURABILITY LAYERS IN ARCHITECTURE

Esther Vandamme[1], Mario Rinke[2]

ABSTRACT: The rise of multi-storey timber architecture has been recognized by multiple actors in the field. Most contributors discuss new timber buildings made with engineered wood products (EWP) almost entirely technologically, neglecting both spatial-architectural and organisational-functional aspects within buildings. Furthermore, even though today's timber structures are designed for longevity, studies show that more than half of all buildings are demolished not because of technical deficiencies but because of vacancy. This suggests that most buildings have an insufficient potential for adaptation.

This paper critically discusses current approaches of adaptability in timber construction and examine their relevance and effectivity within the larger theoretical framework of architectural adaptability. For this purpose, both areas are discussed based on existing literature and compared in their central aspects. Based upon three case studies in Europe, the principles of adaptability for timber buildings are visually traced and analysed.

In conclusion, precise demands for zones of changeability and permanence within the building can be predicted and timber components can be applied accordingly in a targeted manner. The paper proposes strategies for designing a timber construction that is differentiated according to the functional layers and designed to be able to adapt over time.

KEYWORDS: Circularity, Adaptability, Flexibility, Timber Engineering, Structural Design

1 INTRODUCTION

Thanks to new technology and advances in material research, wood is experiencing a renaissance as a modern building material. The ground-breaking improvements in engineered wood products (EWP) in the last decades have fundamentally changed timber architecture. Moreover, the rise of multi-storey timber architecture has been recognised by multiple actors in the field, i.e., architects, engineers, manufacturers and academics alike. However, most contributors discuss new timber buildings with four storeys or more almost entirely technologically, neglecting both spatial-architectural and organisational-functional aspects within buildings. [1] In general, studies show that more than half of all buildings are demolished not because of technical deficiencies but because of lying empty. [2, p. 421] Therefore, even though today timber structures made with EWP are designed for longevity, most buildings most have an insufficient potential for adaptation. As Geldermans (2016) notes, adaptability is a prerequisite for circularity, as it generates quality and added value.[3] This raises questions about the current discourse of adaptability in timber architecture regarding the actual circularity of a modern timber construction beyond the promising role of the biomaterial.

In recent years, a certain amount of important work have addressed the circularity of timber buildings. In general, Ellen MacArthur Foundation's definition of the circular economy as an 'economy that is restorative and regenerative by design, and which aims to keep products, components and materials at their highest utility and value at all times, distinguishing between technical and biological cycles' is accepted in architectural and timber engineering literature. [4, p. 5] In this respect, the six ReSOLVE Framework actions for the implementation of circular economy (Regenerate, Share, Optimise, Loop,

[1] Esther Vandamme, University of Antwerp, Belgium, esther.vandamme@uantwerpen.be
[2] Mario Rinke, University of Antwerp, Belgium, mario.rinke@uantwerpen.be

https://doi.org/10.52202/069179-0473

Virtualise, Exchange) are too broad to be directly applied as guidelines for the design of circular buildings. [5] Instead,, Cheshire outlines five design principles for applying circular economics: building in layers, designing out waste, design for adaptability, design for disassembly and selecting materials. [6] Similarly, in structural engineering, design for robustness, design for durability and design for repairability can be added as circularity strategies. [7] In this paper, we focus on adaptability following the findings of previous studies that 14% of the embodied greenhouse gas emissions can be prevented if a structure is reused instead of recycling its materials. [8, p. 9] Although referred to as 'flexibility' in several publications, [9], [10] we accept Schmidt and Austin's definition of adaptability as a capacity of a building to accommodate the evolving demands of its users and environment effectively, thus maximising value through life. [11]

While research on adaptability in architecture has developed a nuanced understanding of the gradual permanence of building layers throughout the lifespan of a building, the discussion on adaptable timber buildings mainly considers general technical aspects such as those of the building elements and connections. Besides these aspects, most literature neglects social and economic indicators. [12, p. 18] Hence, the architectural discourse can expand the technical discourse of adaptability of multi-storey timber architecture by taking into account social, cultural and economic indicators. In so doing, it can reveal strategies for designing a timber construction that is differentiated according to the functional layers and designed to evolve over time. In this way, building adaptability brings an overarching coordination layer to the design process, in which material and constructability decisions can then be coordinated explicitly concerning overall long-term goals. As consumer expectations, technological progress and competitiveness are increasing, the need for adaptability is likely to increase as well. [13]

The aim of this paper is to critically discuss the current approaches of adaptability in timber construction and examine their relevance and effectivity within the larger theoretical framework of adaptability in architecture. For this purpose, adaptability in timber engineering and architecture are discussed based on existing literature and compared in their central aspects. Subsequently, they are brought together in spatial diagrams in which the potentials and conflicting goals are described.

2 METHODOLOGY

For the purposes of this paper, the particular features of 'circularity' and 'adaptability' in timber engineering are analysed through a comprehensive literature review. Previous research on the topic of adaptability and circularity in timber engineering is searched for in the online databases Scopus, Jstor and Web of Science. The searches conducted in April 2022 requested the key words: timber AND engineering AND circular OR circularity OR adaptable OR adaptability, and was repeated in November 2023. Based upon these findings, the list of circularity facilitators in section 3 is distilled. These themes are examined with a focus on their inherent environmental goals and circular strategies.
Similarly, in section 4 the most significant approaches to adaptability in architecture are discussed. The canonical work of Schmidt and Austin, and Leupen and their references are taken as a starting point for the definition of adaptability. Additionally, the data-driven study of Ross (2016) and its preliminary results are a basis for a theoretical framework of adaptability enablers, complemented with the references of the theory of adaptability. This is followed by a critical positioning of the technical engineering approaches therein.
In section 5, the insights from key papers and books discussed here are supplemented by applications in practice that have been discussed and referred to by scholars. The most recent literature on the rise of timber architecture (from 2020 onwards) is taken as a base for the analysis of the trends and the identified indicators. These indicators are evaluated against three cases, chosen for their variety and exemplarity of the current trends. The case studies in Europe are multi-storey buildings of various sizes and functions which are illustrative of the circularity and adaptability approaches found in the literature. The analysis of the cases is based upon the published plans and sources cited. As visual feedback is important for experts in the field [14, p. 10], the principles of adaptability are visually traced, modelled and analysed. This diagrammatic approach is based on Leupen's visual studies and Rinke and Pacquée's concept of structural porosity. [15] The method proposed here illustrates the sustainability potential of EWP and their contributions to adaptability discussed from the literature and relates them to the permanence layers of adaptability in architecture.

3 TIMBER ENGINEERING ON CIRCULARITY

Since wood is part of the biological cycle of the circular economy, structural timber has a high inherent circularity potential. Other inherent environmental benefits associated with structural timber are carbon storage, renewability, lower energy demand, malleability, durability, visual quality, thermal conductivity, lightness and recyclability. [16, p. 141], [17, p. 3] This is proven by multiple life cycle assessments comparing mass timber structures with similar variants in other materials. Even though carbon sequestration could suggest that maximising the use of timber is the most sustainable, this renewable natural resource should be applied efficiently: reduce, reuse, recycle. [18, p. 25]

Nowadays, sustainability objectives generate many incentives for larger timber construction, supported by subsidies and a growing expertise. However, circularity in

 https://doi.org/10.52202/069179-0473

timber buildings is faced with several threats, organisable in three categories: market forces, regulations, and physical conditions. First, due to resources running out, the competitiveness for forest products plead for intelligent use of timber. [16, p. 145], [19, p. 8] Also, the low material cost gives little incentive for recycling [16, p. 149], [19, p. 7]. Studies focus on the environmental impact of reusing or reprocessing salvaged timber in mass timber products or (non-)structural applications. [12, p. 18], [20, p. 9] However, there are very few examples in practice where structural timber has actually been recovered and reused, and just like other materials, timber has been downcycled or recuperated for bioenergy in Europe. [21]

Second, national regulations are inconsistent relative to timber building construction. The absence of adequate guidelines in the current edition of The European Standard Eurocode 5: Design of timber structures is particularly pointed out, although a new version is in the making. [17, p. 7], [22]

Third, some technological risks are also to be considered. The assessment of the structural performance of elements for reuse is difficult. [19, p. 7] Seismic resistance, acoustics, moisture performance and fire resistance are yet to have universal solutions with predictable behaviour and efficiency. [1, p. 103] The overall costs and risks of this relatively new mode of construction can be higher than standard structure, leaving little room for circularity. [1, p. 134].

This newness also provides an opportunity for establishing the regulations and expertise with a circular viewpoint from the start.

To design for circularity, the benefits and risks need to be clearly identified. In current timber engineering research, the main facilitators or strategies for circularity are:

1. Disassembly potential connections [1], [7], [16], [18]–[20], [23]–[25]
2. Avoiding glues, non-compostable coatings or elements [16], [18]
3. Keeping timber inside the thermal and waterproofing system and eliminating risks from internal water damages [16], [23]–[25]
4. Standardising components or modularity [1], [20], [23], [25]
5. Certification of circularity and reuse [16], [19]
6. An independent building envelope [1], [18], [23], [25]–[27]
7. Durability and possibility to repair or replace the damaged parts [19], [20], [26]
8. Facilitating the adaption to increased loads [19], [26]

The abovementioned strategies for wood as a circular structural material can be seen as design for disassembly (1, 2, 4, 5, 6), design for robustness (8), design for durability (3, 5, 7), or design for repairability (3, 7). Although design experts rate design for deconstruction/disassembly as one of the least effective enablers for adaptability [2, p. 426] [24, p. 25], it is mentioned most in timber literature. These strategies primarily focus on the material and components level of circularity. Very few studies focus on the scale of a building for circularity and on design for adaptability although this leaves the most of the embodied carbon in place. [28]

As Campbell argues [16, p. 150], there is a need for mass timber construction research concentrating on durability and adaptability for buildings as a whole. Also, Ahn argues that there is a lack of expertise and knowledge on circular mass timber construction and stresses the lack of research attention in the timber construction sector directed towards public and stakeholder awareness for the circular economy. [20, p. 12]

In summary, it can be stated that the technical conceptualisation for adaptability is limited to the element and material level and that the elements are discussed here largely independently of their local and functional use in the building.

4 ADAPTABILITY IN ARCHITECTURE

The disposable building culture has been called upon by multiple authors in the twentieth century. Nowadays, many features of the built environment are purpose-built. Before adaptability became a research subject, many vernacular buildings were already genuinely adaptable to functional problems and responded to changes. [29] The foundations of adaptable architecture are is found in the early Modernist movement and applied in Europe in the housing crises following the first and second world war. [9], [30], [31, p. 158] In the early sixties, the Dutch architect Habraken proposed a participative concept for public housing and thereby introduced the terms ‘base building’ and an adaptable ‘infill’. [32] The Open Building design movement was based on this first work. [33]

The definition of adaptability from Schmidt and Austin as given above can be understood both as a characteristic to accommodate the demands without changes to a space - also known as polyvalence [31, p. 26]- or by altering the physical form of a space. Therefore, they introduce six types of change: adjustable as a change of task, versatile as a change of space, refitable as a change of performance, convertible as a change of use, scalable as a change of size, movable as a change of location. According to Schmidt and Austin, the structure of a building interacts with versatility, convertibility, and movability, but scalability could be added. Circularity is not mentioned in the book, however the concept of adaptability clearly is linked to the circular economy.[11]

Even though all types of adaptability are to a certain extent realisable for any building, universal adaptability is not realistic nor advantageous. [11, p. 274] Many design practices are wasteful and over specify for instance electrical services or one-system connections which could be outdated or unavailable promptly. [11, p. 7] Modelling

https://doi.org/10.52202/069179-0473

building adaptation is in a nascent stage. [34, p. 284] Data-driven models are rare, but Ross (2016) cites four enablers for adaptability based upon expert reviews: separation of building systems, whether interiors are free of structural elements, reserve capacity and as-built documents. [2] These four enablers are discussed in following points in detail.

4.1 Distinct Layers

One could go back to Laugier's primitive hut [35] and discern a structure and a protective layer as two separate building systems. Also, Semper's [36] four elements - hearth, earthwork, roofwork and enclosure – can be understood as the origins of the layer's theory. In a modern context, Duffy (1992) recognizes distinct elements of (office) buildings in a modern context: shell, services, and scenery. The literature on circularity mostly cites Brand (1995), who proposes buildings consisting of shearing layers. [31, p. 31] Schmidt and Austin later defined building layers as nominal categorisations that describe a building at a given scale that allow for the stratification (decomposition) of a building as a way of gaining further insight into how it will change over time. [11] The separation of building systems facilitates change, as adjusting one layer does not imply other layers have to be adjusted. The differentiated rate of change of the structure versus - for example - the scenery creates a hierarchy between the layers. To the layer model, ARUP (2016) adds a system level to cover more of the built environment than just buildings. The report crosschecks the ReSOLVE framework with the layers of Brand.[37] Leupen, in 2006, spatially related the layers in axonometric schemes and theorized the frame and the generic space as a less hierarchical model. [31] His layers: 'structure', 'skin' (building envelope), 'access' (circulation), 'service', 'scenery' (interior) are accepted in this paper. The distinction of these layers is seen as the first enabler for adaptability.

4.2 Spatial overcapacity

The literature is unanimous about adaptability due to spatial overcapacity. 'Loose fit' promotes a larger floor area than is strictly necessary for the first use.[38], [39] An open plan free of permanent objects in space allows for easy conversion, stated as the second enabler. Loadbearing walls should be minimized. [11, p. 21] [24, p. 25] Likewise, heigh ceilings allow for maximum daylight, other uses and intermediate floors. Structural typologies such as a short or a wide span, skeletal or massive structures are likely to persist, since they are the backbone of a building. [11, p. 73] Overcapacity could also mean extra storage space, a bigger window size or a predesigned fire safety division. [11, p. 4] For example, constructions built before 1970 often have this extra load-bearing capacity or large dimensions and are therefore favoured by developers for reconversion. [40, p. 4]
To conclude, spatial overcapacity is incorporating the third enabler 'reserve capacity' for facilitating changes. [13, p. 213] A wall-based or column-based structural system and its floor height are seen as key parts in adaptability. Therefore, the choice of a structural system has a significant impact on its adaptability. The equilibrium between over-dimensioning and reducing material use generates a potential conflict which has to be assessed case by case. [17]

4.3 Readability

Readability is about conveying a message to be adaptable. Hence, as-built documents – the fourth enabler - are vital deconstruction information in order to disassemble parts but also to assess load capacity, demolition or repair diagnostics. [20, p. 7] [24, p. 23] Sometimes, however, readability is understood as simplicity. Schmidt and Austin expanded the concept of legibility as a straightforwardness and implicitly clean and exposed joints. [11, p. 96] Others go further and focus on easily understood load paths and repeating thus predictable layouts and grids. [2, p. 422] [13, p. 215] However, when Hertzberger accepts the rigidity of a structure on which an identity can be based, he accepts a structure which suggest spatial possibilities. [32, p. 24]
Simplicity could bring in functional neutrality. For example, 'Solids' are designed as urban buildings with different functions in mind. [40, p. 7] This neutrality is seen as a means of adaptability. Nevertheless, Leupen mentions 'articulating the frame' as a way to give it cultural significance. By adding architectural expression instead of neutrality, the permanent gains meaning and therefore endurance, it becomes an intelligent ruin. [31, p. 33] Or as architect Mies Van de Rohe states: 'Only a clear expression of the structure could give us an architectural solution which would last.' [31, p. 63]

Even though many strategies like these four enablers can be applied at little or no raise of the construction cost – with standard construction methods and decrease in construction time [13, p. 216] - universal adaptability of an entire building is not reasonable nor useful. [11, p. 274] Adaptability has mostly been researched at a building level. [41, p. 118] Aside of these most effective enablers, we propose to add zones of changeability where adaptability in a building is most expected depending on changing demands.

4.4 Degrees of permanence

The theory of shearing layers can provide the framework for applicable design principles, but they mostly refer to a building as a whole. Therefore, the hierarchy of the circularity layers and their durability should be adjusted to their degrees of permanence diversified in a building. While the structure could be designed to last one hundred years, the services and scenery will most likely be adapted in about 15 years. [42] As argued by Rinke and Pacquée in [15], access routes in buildings are less likely to be adapted because of their essentiality. A differentiated look at the structure has to be adopted. The function of a space

 https://doi.org/10.52202/069179-0473

as an access route demands a more permanent structure than the division between two programs. The shearing layers that were previously conceived for the entire building would therefore have to be related to the specific functional zones of the building.
Rinke and Pacquée define the porosity of structural surfaces, related to the higher-level porosity of the building, as the capacity to open walls or slabs. They suggest specific zones of a building which could be designed for disassembly, as a hierarchy of substructures and demountable components. Therefore, they refer to the first half of the twentieth century, where material economy and post-war reconstruction demanded faster and cheaper modes of construction. Their critique on the layer model challenges the unitary view of an entire building without differences in zones of permanence. The load-bearing structure, the functional areas, the access routes and the horizontal and vertical circulation of supply and people are seen as more permanent. [15, p. 4]
As the circulation system and access are critically necessary, they rarely are subject to changes. Other authors also consider vertical circulation as necessarily permanent. For example, Habraken mentions the staircase as a lasting feature. [32, p. 184] To improve the flow of people and things, the location and the number of cores (service risers) are critical adaptability parameters because of their difficulty to change. [11, p. 73] [13, p. 215] According to Leupen, access has significance and permanence if it takes up an extra function, for example a gallery being more than a corridor. [31, p. 114] Access could thus be a permanent layer.
In contrast, Remøy and Van der Voordt see the plinth of a building as more subjected to change. Consequently the ground floor could be the ultimate place for adaptability investments such as ceiling height and open plan. [43, p. 4] Also, in the centre of a building, Leupen intends an adaptable structure with an open zone which could be filled in with a wooden floor or accommodate service risers. [31, p. 166] These two examples demonstrate strategies for more volatile zones of permanence.
A structure's adaptability characteristics should be adjusted to the degrees of permanence of the structural members in the building.

4.5 Non-physical aspects

Other aspects of adaptability which are rarely included in timber literature, but which are very influential, are location (such as social image, amenities, public transport) and non-physical values such as acquisition and operation costs. [11, p. 152] A building always has a social function and has the ability for social change. [11, p. 20] Many of the experts involved in multi-storey timber projects are motivated by social, economic, and environmental aspects of working with the built environment and its stakeholders. Process adaptability should not be minimised but falls out of the scope of this paper. [34, p. 275]

4.6 Adaptability in timber literature

The abovementioned enablers and the nuanced zones of permanence can be compared with the strategies for circularity in timber engineering literature identified in section three.
Firstly, in the list of facilitators for circularity the concept of layering is presented as the building envelope 'skin' independent of the 'structure.' However, the detachment of other functional building parts, such as Leupen's other layers: 'access,' 'service,' 'scenery,' regarding timber architecture are not discussed. Nevertheless, Kaufmann mentions layers of timber structures for maintenance, disassembly and recycling. [18, p. 27]
Secondly, overcapacity is revealed as a technical option to facilitate higher loads, but spatially only Jockwer points out the possibility to adapt according to the comfort demands regarding room size and structure, acoustic and interior performance. [19, p. 9], [26, p. 2] The open plan, in this paper identified as part of spatial overcapacity, is not to be found as a strategy in the timber literature on circularity.
Thirdly, readability of a structure or the exposure of structural members is not detected in studied literature. The cited certification of circularity fixates on labelling components, while a full as-built dossier or a straightforward structure which could make the whole timber building readable.
Lastly, the focus on components and design for disassembly in timber literature demonstrates the conceptual design mode, where the building exists as a whole and can be disassembled. It overlooks the possibility for gradual changes through zoning and corresponding degrees of permanence. The closest to this strategy is repairability, which seeks the replaceability of damaged parts in an intermediate scale between component and building.

As Brand mentions, the buildings which proved to be the most adaptable (like Amsterdam canal houses) are built upon knowledge acquired by centuries of trial and error. [11, p. 14] Therefore, the abovementioned existing research on adaptability could be a basis for analysing and frame the current trends of multi-storey timber construction.

5 CASE ANALYSIS

5.1 Adaptability in practice

The current trends in multi-storey timber buildings are studied in [1], [17], [44], [45]. Recent developments in practice like prefabrication, system construction and rigid structural grids are critically discussed against the background of the presented adaptability research. In the following, these trends are assessed against the enablers for adaptability and the degrees of permanence.

For risk mitigation and time saving, onsite works are increasingly minimized and prefabrication is introduced. Since most prefabricated projects are focussed on simple

https://doi.org/10.52202/069179-0473

assembly on site, disassembly can be designed in a similar fashion. In contrast, old-school timber framed buildings are not designed for disassembly because of the extensive fixing of materials to the frame. However, the adaptability of contemporary timber structures might depend on the size and development of the prefabricated units. The deconstruction effort and cost depend on the size and weight of elements, the number and type of connections, and their location in the building. Disassembly might require heavy construction equipment like cranes and temporary scaffolding, just like during the construction phase. [20, p. 2] The larger (façade) units can complicate disassembly since they often arrive fully equipped and watertight on the construction site. [1, p. 134] This might also complicate the readability of a timber structure. Furthermore, when services are hidden behind a structural lining, the adaptability or refitability will be restricted. Above all prefabrication targets, services as well as all layers should remain separable.

System construction is an important trend in timber construction. As Kolb described the size of the prefabricated units as room modules, wall or plan units, or small modules, one can discern volumetric, planar or linear (post and beam or frame) systems. [46, p. 44] The earlier multi-storey timber buildings are mostly constructed in a cross-laminated structural system. Volumetric and planar elements were the two most common structural systems. [17, p. 3], [44], [45, p. 22]
The first structural system, volumetric modules, is programmatically very specific, as it is limited to room spaces. Hotels, (affordable) collective housing projects, retirement homes and schools are the most frequent programs in volumetric modules. These specific programs do not imply a high possibility of convertibility. [45] The entire volumetric modules can be removed but these blocks are often too large for changes in individual demands. [19, p. 8] In a repetitive and enclosed structure made of volumetric modules, there is no possible diversification based upon degrees of permanence. At the moment, volumetric modules incorporate few architectural versatility and there is no market push towards the functional versatility of volumetric modules. [24, p. 21]
The second structural system of the early multi-storey timber buildings comprises planar structures. Mostly up to 10 stories, the CLT structures allow only limited spans and require many wood resources. [47, p. 27] The massive use of CLT between functional spaces or room modules with two load-bearing walls contradicts the spatial overcapacity, open plan and the degrees of permanence of architectural adaptability. Out of 350 studied projects in [45], 79% of the buildings with planar systems have residential programs. This suggests a limited convertibility.
From 2011 onwards, hybrid and frame structures are rising, especially in the tallest timber towers. [17, p. 3], [44], [45, p. 22] The open plan makes space for spatial overcapacity. Unsurprisingly, linear systems have more evenly distributed programs with a focus on commercial, which implies high convertibility. [45, p. 22] There is a shift from residential planar structures to commercial linear structures. This suggests that timber buildings are evolving towards more open plans and thus provide more adaptable structures.

However, the linear systems are very dependent on the spans for their plan layout. In multi-storey residential buildings, smaller spans are usually used in timber construction compared to conventional solid construction with reinforced concrete ceilings, resulting in rigid structural grids. [1, p. 25] Based upon the principle of spatial overcapacity, a large span is desirable for adaptability. One can argue that this would use more timber resources than a smaller grid. However, the total cost of a timber frame structure with a larger grid is lower, as there are fewer joints, and those are the most cost-intensive factor. [46, p. 90] Also, the optimal column spacing is material specific. Still, many grid layouts are based the historically used materials like concrete and steel and are therefore not efficient. [48, p. 1]
Nowadays, the grid layout of rectilinear volumes with regular flat extrusion is dominant in multi-storey timber structures. Probably because of the industrial (pre)fabrication processes and the resulting linear or rectangular geometries, any deviation turns out more costly. [47, p. 30] Often, when greater design freedom is needed, other structural materials are used. Svatoš-Ražnjević challenges how these rigid timber structures will adjust to complex urban contexts. [45, p. 29] The repetition of the grid might suggest a readability and an open plan. Indeed, the rigidity of the element geometry could accommodate adaptability and the high degree of modularity required. However, more combination systems and hybrid structures can multiply the possibilities for a structure based upon the degrees of permanence. The specification of the structural grid is crucial for adaptability and a weighted effort of the expectations of the owner, architect, engineer and contractor. [48, p. 8]

To conclude, in multi-storey timber structures, the practice focuses on efficiency and technological developments. Yet, currently in conventional high-end taller building typologies spatial design is part of the development and engineering focus. [49, p. 8] Moreover, the architectural expression is purely the exposure of timber as a material. [45, p. 4] The discussion of the current trends shows that developments in modern timber construction are very dynamic. Their limited reflection together with increasing longevity demands suggest that more complex design strategies need to be discussed and applied.

In the following section, three cases are analysed against the adaptability types of Schmidt and Austin and the identified adaptability enablers.

https://doi.org/10.52202/069179-0473

5.2 Adaptability Case Vodafone Headquarters

The Vodafone Headquarters in Newbury, United Kingdom, is an example given by Schmidt and Austin (2016) for all adaptability types except movability. It is a part of the campus designed by Fletcher Priest Architects. Since 2003 the headquarters have been made up of seven non-timber buildings linked by demountable footbridges. The building's layers are distinct, as the separation walls are movable, the cladding part of the skin is replaceable while it contains loadbearing elements, and there are several free-standing cores for circulation and services (fig. 1).

It offers great convertibility due to the generous provision of good daylight through a central atrium in a doughnut plan. This is part of the spatial overcapacity with an open plan, polyvalent spaces, and a column-based structure. The typical floor plan reads easily and consists of two connected rectangles. The campus buildings are standardised, although of different lengths. The scalability is demonstrated by its possibility to split a building up into two bays or per floor thanks to multiple access points. However, there is no compliance with the degrees of permanence as the structure is uniform throughout a building. The architectural expression of the structure has not been discussed in the literature. This case is featured as an exemplary project for the current understanding of adaptability in the architecture literature. [11, pp. 215–217]

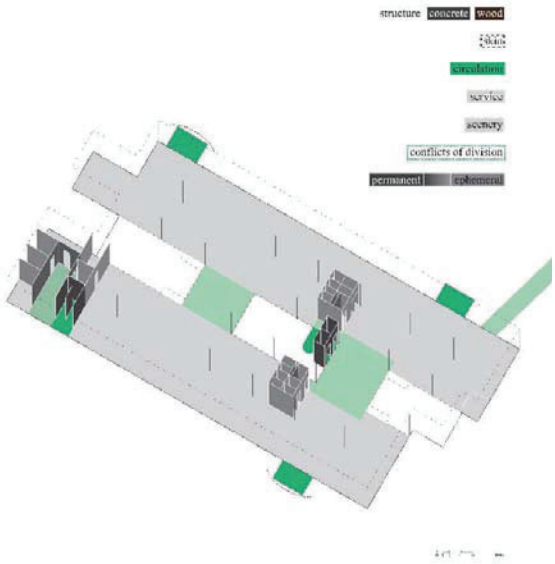

Figure 1: *Leupen 's layers and degrees of permanence on a typical floor of Vodafone Headquarters Newbury*

5.3 Timber Case Kajstaden, Västerås

In Västerås, Sweden C.F. Møller Architects and Bjerking designed a 2,400 m² tall building with a cross-laminated timber (CLT) structure. The CLT core provides structural stability to this nine-storey high housing block which opened in 2019. Thanks to the mechanical joints, the building is designed for disassembly. However, this building has little adaptability characteristics. The basic ceiling height of 2.5 m is generally limited with only an elevated ground floor and higher ceilings on the top floors featuring a spatial overcapacity. The façade 'skin' is loadbearing, and the structure is also the 'scenery' (fig. 2), which means that most conceptualised wall parts are directly translated into CLT panels. The division of the typical floor plan by load-bearing walls, however, might conflict with its versatility, as the load-bearing flat partition walls do not allow the floor plan to be rearranged at a later stage to accommodate larger units of use. Thus, there is no zoning according to the degrees of permanence, as the whole typical floorplan has a regular, non-hierarchical structural logic. The current size of the units, together with the given floor height, practically limits their use to residential. In the interior, there are no visible wooden surfaces, but the structure certainly has architectural expression in the façade.

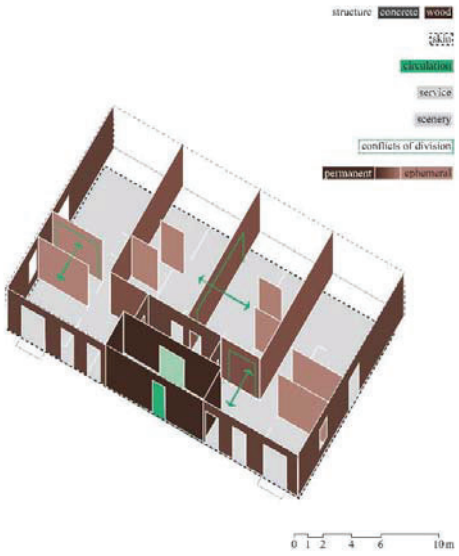

Figure 2: *Leupen 's layers, adaptability conflicts and degrees of permanence on a typical floor of Kajstaden, Västerås*

5.4 Timber Case Haut, Amsterdam

Team V and ARUP designed Haut as a housing timber-concrete structure in the Netherlands in 2022. The 21-storey building has a central concrete core and CLT load-bearing walls (fig. 3). The ceiling is left bare for appreciation of the hybrid wood-concrete slabs. The non-loadbearing façade is a detachable skin. The CLT walls divide the gross floor area of about 550 m² into eight spaces between 38 and 100 m². As Svatoš-Ražnjević writes, this post-and-beam construction at the perimeter with inner load-bearing walls might suggest "a link between heterogeneous structures and architectural

https://doi.org/10.52202/069179-0473

variety, or a compromise to achieve more flexible open spaces." [45, p. 16] Indifferent of the circulation, the same structural logic is applied to the whole semi-orthogonal floor. The combination of load-bearing walls and an undiversified structural logic with dispersed technical shafts might hinder its adaptability in the future. Even though the internal walls provide necessary stiffness against wind loads and torsion on the tower on serviceability limits, they are not necessarily always needed where rooms are divided. To detach the structure from the scenery and possible later circulation, some of the walls can be identified as conflicting with adaptability layers which should be reconsidered in an early design stage. This means that such walls, which delimit the corridor next to the lift or whole organisational segments of the building, are likely more permanent and thus well made of load-bearing panels. Other space-dividing walls between single room units, on the other hand, which could be removed to couple rooms later, should rather consist of frames that are then optionally filled.

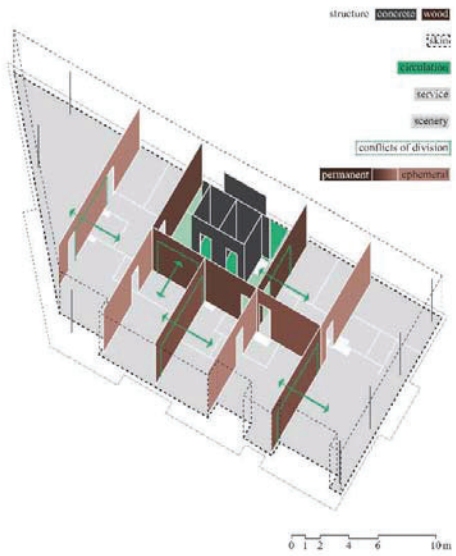

Figure 3: *Leupen 's layers, adaptability conflicts and degrees of permanence on a typical floor of Haut Amsterdam*

6 CONCLUSION

The premise of the paper has been that the design of multi-storey timber buildings has been discussed solely technologically. Even though timber is part of the biological cycle, experts need to work with the market forces, the regulations, and the physical conditions of wood to design for circularity. Circularity, as demonstrated in this paper, is considered very differently in engineering and architecture as both often refer to distinct levels of change. In timber engineering literature, circularity is focussing on design for disassembly and looking at components or materials regardless of their position in the building. In architecture, design for adaptability is based on several concepts, such as the separation of functional layers, providing spatial overcapacity and a readable plan layout. These strategies are not to be found in the timber literature. Also, mostly buildings are looked at here as a whole but omit the desirable diversification of adaptability according to the degrees of permanence.

The trends in timber buildings towards more prefabrication and volumetric modules are challenging the very concept of adaptability. However, there is a shift from planar residential structures to commercial linear structures, which suggests timber buildings are evolving towards more open plans and adaptable structures. The rectangular grid plan layout provides readability but might overlook architectural expression through its structure. The three cases exemplify the potential of adaptability concepts and demonstrate that more complex design strategies could be beneficially applied to timber architecture.

It is important to emphasize that the accessibility of the literature and availability of structural information on the case studies limit our findings.

The focus on material and components in the literature on circularity of timber architecture can be related to the massive influence and the relative newness of engineered wood products. Framing their potential for sustainable timber buildings within the conceptual architectural framework of adaptability, precise demands for zones of changeability and permanence within the building can be predicted and timber components can be applied accordingly in a targeted manner.

It would be insightful to apply the demonstrated methodology to contemporary multi-storey timber buildings which have been converted, but so far none are known. A post-completion analysis of timber buildings could significantly enhance circularity strategies in the field. Also, the stakeholders of these cases could be involved in further research on adaptability in timber buildings to better understand design conflicts.

REFERENCES

[1] M. Rinke *et al.,* editors.: Architektur fertigen: Konstruktiver Holzelementbau. Triest Verlag, 2020.

[2] B. E. Ross, D. A. Chen, S. Conejos, and A. Khademi. Enabling Adaptable Buildings: Results of a Preliminary Expert Survey, *Procedia Eng.*, 145:420–427, 2016, doi: 10.1016/j.proeng.2016.04.009.

[3] R. J. Geldermans. Design for Change and Circularity – Accommodating Circular Material & Product Flows in Construction. *Energy Procedia*, 96:301–311, Sep. 2016, doi: 10.1016/j.egypro.2016.09.153.

[4] 'Towards a circular economy - Business rationale for an accelerated transition', Ellen MacArthur Foundation, 2015.

[5] 'Growth within: a circular economy vision for a competitive Europe', Ellen MacArthur Foundation, 2015.

https://doi.org/10.52202/069179-0473

[6] D. Cheshire. Building Revolutions: Applying the Circular Economy to the Built Environment. Routledge, 2019.
[7] P. Palma, editor. State of the Art Report COST Action CA 20139 Holistic design of taller timber buildings (HELEN), Dec. 2022.
[8] H. Kröhnert, R. Itten, and M. Stucki. Comparing flexible and conventional monolithic building design: Life cycle environmental impact and potential for material circulation. *Build. Environ.*, 222:109409, Aug. 2022, doi: 10.1016/j.buildenv.2022.109409.
[9] H. Estaji. A Review of Flexibility and Adaptability in Housing Design. *Int. J. Contemp. Archit. New ARCH*, 4(2): 37–49, Aug. 2017, doi: 10.14621/tna.20170204.
[10] R. Askar, L. Bragança, and H. Gervásio. Adaptability of Buildings: A Critical Review on the Concept Evolution. *Appl. Sci.*, 11(10):10, Jan. 2021, doi: 10.3390/app11104483.
[11] R. Schmidt III and S. Austin: Adaptable Architecture, 0 ed. Routledge, 2016. doi: 10.4324/9781315722931.
[12] L. Tupenaite, V. Zilenaite, L. Kanapeckiene, T. Gecys, and I. Geipele. Sustainability Assessment of Modern High-Rise Timber Buildings. *Sustainability*, 13(16):8719, Aug. 2021, doi: 10.3390/su13168719.
[13] E. S. Slaughter. Design strategies to increase building flexibility. *Build. Res. Inf.*, 29(3)208–217, May 2001, doi: 10.1080/09613210010027693.
[14] G. Kelly, R. Schmidt, A. Dainty, and V. Story, Improving the design process for adaptability: linking feedback and architectural values. Loughborough University, 2011.
[15] M. Rinke and R. Pacquée. Structures and change – Tracing adaptability based on structural porosity in converted buildings. *Archit. Struct. Constr.*, 2(4):699–710, Dec. 2022, doi: 10.1007/s44150-022-00054-9.
[16] A. Campbell. Mass timber in the circular economy: paradigm in practice?, *Proc. Inst. Civ. Eng. - Eng. Sustain.*, 172(3):141–152, 2019, doi: 10.1680/jensu.17.00069.
[17] V. Žegarac Leskovar and M. Premrov. A Review of Architectural and Structural Design Typologies of Multi-Storey Timber Buildings in Europe, *Forests*, 12(6):757, 2021, doi: 10.3390/f12060757.
[18] H. Kaufmann, S. Krötsch, and S. Winter, Manual of multi-storey timber construction. Munich: Edition Detail, 2018.
[19] R. Jockwer and Y. Goto. Design for adaption - making timber buildings ready for circular use and extended service life. In: Proceedings of the World Conference on Timber Engineering (WCTE 2021), 7–13, 2021.
[20] N. Ahn, A. Dodoo, M. Riggio, L. Muszynski, L. Schimleck, and M. Puettmann. Circular economy in mass timber construction: State-of-the-art, gaps and pressing research needs. *J. Build. Eng.*, 53:104562, Aug. 2022, doi: 10.1016/j.jobe.2022.104562.
[21] A. L. Bais-Moleman, R. Sikkema, M. Vis, P. Reumerman, M. C. Theurl, and K.-H. Erb. Assessing wood use efficiency and greenhouse gas emissions of wood product cascading in the European Union. *J. Clean. Prod.*, 172:3942–3954, Jan. 2018, doi: 10.1016/j.jclepro.2017.04.153.
[22] *EN 1995-1-1:2004 - Eurocode 5: Design of timber structures - Part 1-1: General - Common rules and rules for buildings*. 2004.
[23] G. Finch. Applications and Opportunities for Timber Space Frames in the Circular Economy, In: CIB World Building Congress, 161-170, 2019.
[24] K. Rodionova. Adapting our Buildings for Circular Economy: Harnessing Risks and Opportunities of Structural Timber. Master dissertation, University of Cambridge, Wolfson College, 2021.
[25] Y. Sandin et al. Design of Timber Buildings for Deconstruction and Reuse —Three methods and five case studies. Apr. 2022.
[26] R. Jockwer and Y. Goto. Design for adaption - making timber buildings ready for circular use and extended service life. In: World Conference on Timber Engineering (WCTE 2021), 7-13, 2021.
[27] F. Nakib. Toward an Adaptable Architecture Guidelines to integrate Adaptability in the Building. In: CIB 2010 World Congress: Building a Better World, 276–286, 2010.
[28] F. Pomponi and A. Moncaster, Circular economy for the built environment: A research framework. *J. Clean. Prod.*, 143: 710–718, Feb. 2017, doi: 10.1016/j.jclepro.2016.12.055.
[29] R. Kronenburg.: Flexible : architecture that responds to change. London: Laurence King, 2007.
[30] J. Till and T. Schneider: Flexible Housing. Routledge, 2016. doi: 10.4324/9781315393582.
[31] B. Leupen: Frame and Generic Space. 010 Publishers, 2006.
[32] N. J. Habraken: Supports : an alternative to mass housing. London: The Architectural Press, 1972.
[33] E. Durmisevic: Transformable building structures: Design for dissassembly as a way to introduce sustainable engineering to building design & construction. 2006.
[34] Z. R. Rockow, B. Ross, and A. K. Black. Review of methods for evaluating adaptability of buildings. *Int. J. Build. Pathol. Adapt.*, 37(3):273–287, Jun. 2019, doi: 10.1108/IJBPA-01-2018-0013.
[35] M.-A. Laugier: Essai sur l'architecture. A Paris : Chez Duchesne, Libraire, rue S. Jacques, au-dessous de la Fontaine S. Benoît, au Temple du Goût, 1755.
[36] G. Semper: The Four Elements of Architecture and Other Writings. Cambridge University Press, 1989.
[37] R. Zimmann, H. O'Brien, J. Hagrave, and M. Morrell, The Circular economy in the Built Environment, Arup, 2016.
[38] H. Hertzberger: Lessons for students in architecture, 4 ed. Rotterdam: 010 Publishers, 2001

https://doi.org/10.52202/069179-0473

[39] A. Lifschutz. Long Life, Loose Fit, Low Energy. *Archit. Des.*, 87(5)6–17, Sep. 2017, doi: 10.1002/ad.2210.
[40] H. Remøy and T. Van der Voordt. Sustainability by adaptable and functionally neutral buildings. In: 3rd CIB International Conference on Smart and Sustainable Built Environments, 2009.
[41] J. Gosling, M. Naim, P. Sassi, L. Iosif, and R. Lark. Flexible buildings for an adaptable and sustainable future. In: Procs 24th Annual ARCOM Conference, 115-124, Sept. 2008.
[42] S. Brand, *How Buildings Learn: What Happens After They're Built*. Penguin, 1995.
[43] H. Remøy, 'Sustainability by adaptable and functionally neutral buildings', p. 8, 2009.
[44] V. Salvadori. Multi-Storey Timber-Based Buildings: An International Survey of Case-Studies with Five or More Storeys Over the Last Twenty Years, 2021. doi: 10.13140/RG.2.2.14822.55360.
[45] H. Svatoš-Ražnjević, L. Orozco, and A. Menges. Advanced Timber Construction Industry: A Review of 350 Multi-Storey Timber Projects from 2000–2021. *Buildings*, 12(4)404, Mar. 2022, doi: 10.3390/buildings12040404.
[46] J. Kolb. Systems in timber engineering : loadbearing structures and component layers. Basel: Birkhäuser, 2008.
[47] S. Ø. Nesheim, Competitive timber floors: Optimisation of hollow section timber floor elements for adaptable buildings. Norwegian University of Science and Technology, 2021.
[48] R. McLain and G. Kingsley, Efficient Structural Grid Designs for Mass Timber Buildings The engineer's role in optimization, In: World Conference on Timber Engineering 2020, 2020.
[49] I. Kuzmanovska, E. Gasparri, D. T. Monne, and M. Aitchison. Tall Timber Buildings: Emerging Trends and Typologies. In: World Conference on Timber Engineering 2018, 2018.

 https://doi.org/10.52202/069179-0473

World Conference on Timber Engineering Oslo 2023

PROPOSAL OF INTERACTIVE WORKFLOW FOR CIRCULAR TIMBER STRUCTURE DESIGN

Marcin Luczkowski[1], Sverre M. Haakonsen[2], Artur Tomczak[3], Bunji Izumi[4]

ABSTRACT: The methodology and design methods are often neglected and not discussed as indicators for the popularization of circular design. In this paper, which is part of ongoing research, we propose a design strategy and method for designing a building from reclaimed wooden elements, based on the actual building project case study in Oslo. The design method is a plugin for the Algorithms-Aided Design environment integrated with the database of available reclaimed elements. The plugin is based on algorithms suggesting suitable elements from the database in real-time. This helps the designer in tedious selection processes. Used in the concept and engineering phase of the building process, it can save time and rationalize design choices. The optimization objective is the structural performance and environmental impact of the final structure.

KEYWORDS: knowledge-based design, circular economy, timber structures, parametric modelling, algorithm aided design

1 INTRODUCTION

Timber products are light, relatively sustainable and have a good strength to density ratio. Increasing the usage of timber in construction is one of the priorities to decrease the environmental impact of the building sector[1]. The annual production of timber products is growing yearly worldwide, at the same time, timber production is limited by the sustainable forestry area in every country[2]. Some countries are already at the limit of their wood production capacity. Moreover, the use of timber is limited by the material price, which increased significantly in recent years [3].

Timber elements usually end their life being downgraded or burnt after the demolition of the building [4]. Downgraded timber elements sometimes come back to the building industry as plywood or other derivative products. Those products often require chemicals, such as glues, which make them structurally weaker, less sustainable, and sometimes more toxic. Every operation made to downgrade or even upgrade the timber product will lead to an increase in CO2 emission.

Today, the designed life span of the building is only 50 years [5]. The growing population of cities and changes in lifestyles require us to build higher and bigger buildings. In most of those buildings, the trouble with the structural system was not the leading cause of demolition[6]. Often the structural (load-bearing) elements are wasted, although they are in good technical condition and could be in use for the next decades. Timber elements are even great loss because the timber absorbs stresses with time, and it is rational to use it with a long lifetime.

To encourage engineers to involve circular economy aspects in the design, international standards have been created [7]. In those standards, it is highly recommended to pay attention to sustainability aspects of the structure already at the conceptual stage when it is still cost-effective. Our research group focuses mostly on conceptual timber design [8]. In this article, we want to show the study case in which the key concepts of the circular economy have been applied in digital design.

We observe a need for developing methods and methodologies to increase the usage of reclaimed timber elements in the building sector. The number of scientific articles, start-ups, and projects involving reclaimed timber is growing yearly. From a circular economy perspective, the ideal situation would be to extend the lifetime of buildings and not demolish but just renovate or repair them. Unfortunately, in many cases, the topology of the building must change. In this scenario, the reuse of deconstructed elements should be the priority.

The reusing of timber elements can be split in several steps. One of the most important is the timber classification. Many timber elements have been in use for decades. Timber properties can change due to rheology

[1] Marcin Luczkowski, NTNU Norwegian University of Science and Technology, Norway, marcin.luczkowski@ntnu.no
[2] Sverre Haakonsen, NTNU Norwegian University of Science and Technology, Norway, sverre.m.haakonsen@ntnu.no
[3] Artur Tomczak, NTNU Norwegian University of Science and Technology, Norway, artur.b.tomczak@ntnu.no
[4] Bunji Izumi, NTNU Norwegian University of Science and Technology, Norway, bunji.izumi@ntnu.no

https://doi.org/10.52202/069179-0474

and defects. Those information have to be set and preferably digitalized to be useful in common design process. After assessing all of the information, the database can be generated. The database should be usable in the design environment to provide an immediate feedback. It means that the access to the database should be provide directly from design software.

1.1 OBJECTIVES

The aim of this project is to show a possible change in the methodology of design by implementing a computational design method focused on using the available stock of reclaimed materials , also called Material Bank [9]). This project uses as a study case the design process for a small timber building in Oslo. The building called "Sletteløkka" is a timber extension of the existing building. It has its own supporting system built on the axial grid with a spacing of 2.5 meters. The length of the building is 10 meters, and the width is 5 meters. It has two stories with a floor height of 2.6 meters. The rooftop is placed 7.1 meters above the ground.

This project illustrates one possible computational method and methodology of conceptual design to reuse timber elements. Gathering the material stock (used elements), creating a digital material bank (a database with the digital representation of timber elements) and finally using a material bank in the conceptual and engineering design deliver several unknowns and important issues. How can we design from used elements? What is the best design strategy for the circular economy? How can the new technologies improve designing from material stock? How can we involve timber-specific mechanical properties and imperfections already in the concept design? How will reclaimed elements influence the structural and architectural performance of the building? Those are questions addressed in this work.

1.2 METHODOLOGY

This is a proof-of-concept paper describing an innovative strategy of supporting the design. In common design strategy, the decisions are in the linear form. Design steps must follow the decision made in the previous phase. Very often, choosing the cross-section of the elements is the last decision made by the architect or structural engineer. In design based on the circular economy, the geometry of the available reclaimed elements strongly impacts the design space. The designer has access to limited elements with limited shapes and sizes. Moreover, from an environmental perspective, the more reclaimed elements are used from material bank the more sustainable structure is. These facts demand implementing methodology with automated design methods. This design method should automatically map elements from the database with the building concept.
In a project like this, the methodology should use available design methods in the best way. This way, one of the challenges of designing with reused elements, namely the assignment of old elements to appropriate positions can be solved. The tool for matching old and new elements is a necessity in this project. Moreover, the whole concept design should be made in a more generative way. In this project, we used the Rhino/Grasshopper environment to apply a parametric workflow and to open the project for possible quick modification or optimization.

2 DESIGN AND WORKFLOW CREATION PROCESS

2.1 IDEA - BUILDING

The function of the building is a social, open-for-public space. With the help from the municipality of Oslo, volunteers and resident from Sletteløkka and Bydel Bjerke, together with the architects, initiated this project in 2019. Thereby providing a social space for all residents in the area. The architectural assumptions are to create an open and easy-access two-storey building. It should be accessible from both floors, and it should be easy to build. Since the neighbourhood society could be involved in erecting the building. One of the design limitations is that building from one side is touching the existing shop (see figure 1), but structurally it should be an independent structure. It means that the stiffness and structural performance of the structure does not depend on the surrounding structure.

Figure 1: *Front façade of the structure, on the right side of the structure, it is visible the existing shop building.*

However, the building is not as important as the materials which will be used to build it. The design team assumed to use as many reclaimed elements as possible. The reclaimed elements are used to create a primal structural system and also to use in not load-bearing elements. The façade system for the glass panels is produced from Japanese timber[7]. The elements used to create the structural system come from deconstructing an old barn in south Norway. In figures 2 and 3 the elements are marked with different colours and annotations, depending on their source. Norwegian timber has been reclassified as at least C30, and it can be used for structural elements. Timber from Japan is Japanese cedar (Cryptomeria japonica). It is a little bit weaker and elements from it has been dedicated only to transferring external forces to the main system.

https://doi.org/10.52202/069179-0474

Most of the elements have been 3D scanned from outside and physically tested on the macroscopic level.

2.2 IDEA - FRAMEWORK

The objective of this research is to find an appropriate design strategy to enable building it with reused elements. The design strategy, which follows and methods are algorithms, software, and tools which can lead to making this strategy as efficient as possible. Before it is explained how the framework has been applied, the assumptions are highlighted:

- In this project, the structural elements' database is known, but the design object can be adjusted. It is then needed to maximize the usage of those elements and, by this, increase the sustainability of the building
- The project is led by architects who would like not to change their habits to work in computational design. It is, therefore, necessary to implement a framework inside the design software, preferably with optimization working in the background.
- All the design decisions should be based on structural analysis. The algorithms should be using Finite Element Method (FEM) as the basic investigation tool.

Complying with these statements, the conceptual design is based on the parametric model made in Rhino and Grasshopper. Using this environment allows the inputs that define the geometry can be changed and adjusted. The axis spacing, floor height, roof angle or bracing position can be easily changed. The structural analysis of the structure is made in Karamba3D, which is merged with the parametric model. The outcome of Finite Element Analysis (FEA) is utilization and deformation. After creating an interesting topology of the structure and assigning sections, the matching algorithm is connected. After assigning the elements from the material bank one more time, the FEA proceeded. The last structural analysis is finally checking all the ULS and SLS criteria of the building (see the scheme of the framework in the figure 5).

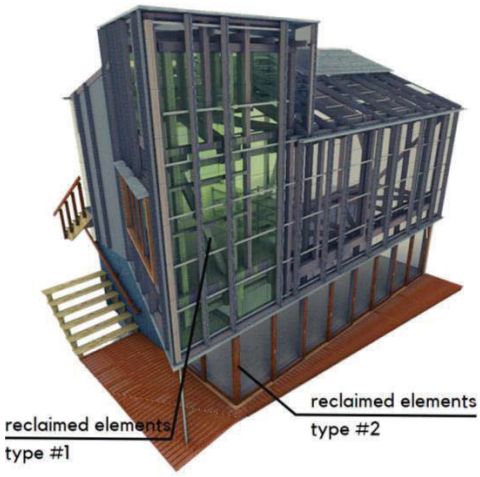

Figure 2: *General view of the structure with the facade, type #1 elements come from Norway, type #2 come from Japan.*

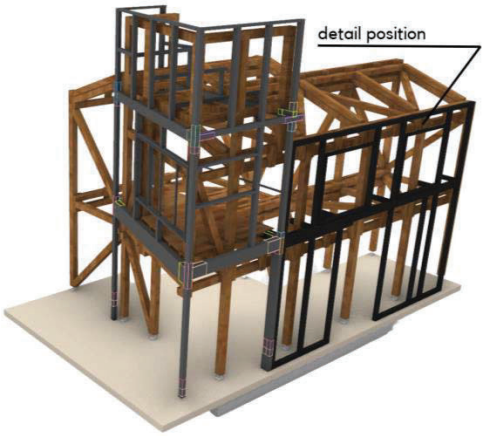

Figure 3: *General view of the structure without the facade, brown elements come from Norway, gray and black elements come from Japan.*

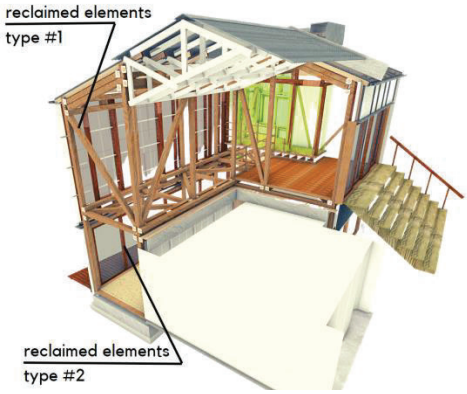

Figure 4: *General view of the structure from inside, type #1 elements come from Norway, type #2 come from Japan.*

https://doi.org/10.52202/069179-0474

The framework is oriented to maximize the usage of reclaimed timber elements in the structure from the available elements in the material bank. The algorithm to map the elements from the material bank has been created as a Python tool [Insert Artur et. al] with a wrapper for using it in Grasshopper. To create a material bank, we scanned (see figure 6) or measured available elements. The information about them are stored in a database which is available during the design and can be changed at any time. Since timber is an orthotropic material which has the best performance in the direction longitudinal to the grain, the decision was made to adjust optimization algorithms towards beam elements. It means that the axial direction of the elements is leading the matching algorithms. After scanning of reclaimed elements, the mesh is imported into Grasshopper where the length, and cross-sectional data needed for the material bank is extracted.

Figure 7 illustrates how different design options obtains different placement and amount of reclaimed elements in the database. This way, multiple options can quickly be evaluated and compared with regards to sustainability in addition to all other aspects. The idea of the framework is to deliver the designer a tool which, in real-time, will be reacting to topological changes in the building system. It means that if the designer changes the topology, the algorithm should automatically propose the best location of the available materials from the stock. The matching algorithm tries to assign the elements from the material bank to the design structure based on the specific features. The cross-section of the element from the material bank cannot be smaller than those from the structural analysis made before matching, and the length of the element cannot be shorter than the ones in the design model. Also, the algorithm to avoid locations of pockets (fabrication elements for detail generation) and imperfections cannot be in the sensitive places of beams and columns.

Figure 8 is a final presentation of the matching algorithm; each colour link is connecting elements from the databank to design model.

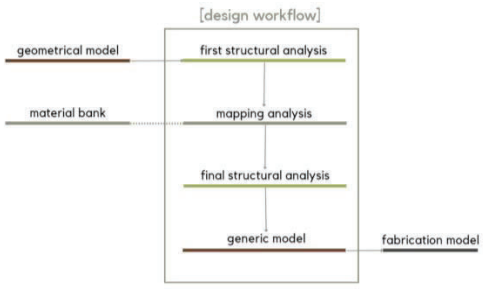

Figure 5: *Scheme of the framework.*

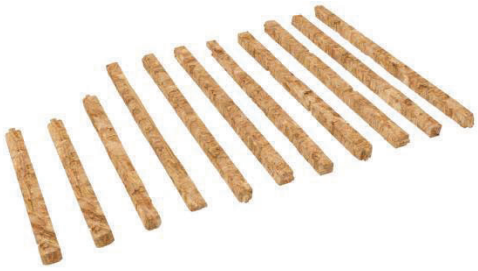

Figure 6: *Scans of reclaimed timber elements.*

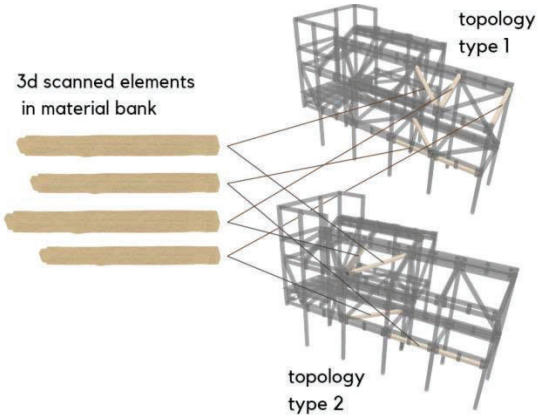

Figure 7: *The concept of the framework.*

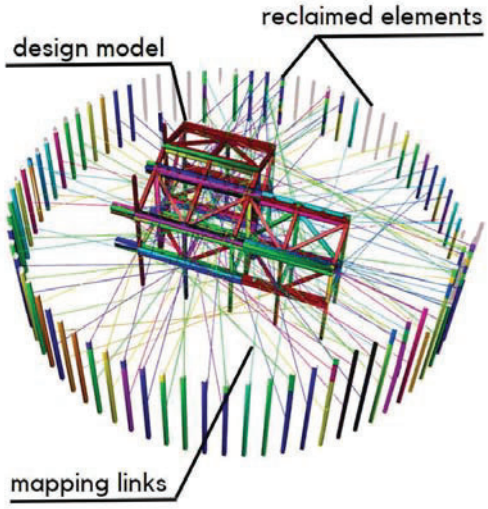

Figure 8: *The visualization of the matching produced by the algorithm.*

2.3 THE FINAL DESIGN

The timber building is designed to resist dead and live loads. The building is a public space category and has to resist 5kN/m2 on every floor. The snow load on the roof is estimated to be 3.8 kN/m2. The wind load of magnitude 0.3 kN/m2 is considered from three sides.

https://doi.org/10.52202/069179-0474

As mentioned before, the stock of timber elements origins from an old barn deconstruction. Figure 6 presents 3D-scans of some elements after deconstruction. The specialist categorized the timber quality as C30. A lot of elements have small imperfections, and the endings of the elements have the remains of the old joint systems. To see all those defects and judge if they comply with the architectural vision, we decided to include a 3Dscan of the material bank. Each element was scanned and represented with a 3D mesh with texture. What is also important, precise digital representation of the elements allow to involve the imperfections in the matching algorithm. matching

In this particular design, it occurred that the material bank was not covering all needed elements. The workflow allows for a combination of new and old elements. Importantly, the LCA calculations were made in real-time, giving the designer feedback about the current design's performance. Figure 4 presents the architect's desired structure together with the elements from the material bank (displayed in a circle around the model). The illustration depicts the final design which, at the moment the paper is written, waits for building acceptance by Oslo authorities.

3 CONCLUSION

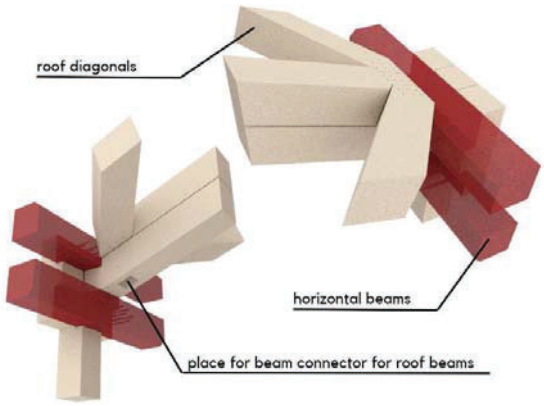

Figure 9: *Detail of the connection.*

The construction project is to be started before the summer of 2023. In this project, we do not only focus on the conceptual design and algorithms. The extra goal is also to measure the values of environmental and structural (displacement) performance.
The work made till now can be summarized in the following points:

• Creating an innovative design methodology, which quickly matches reclaimed elements from the material bank with the initial design model.

• Implementing several matching algorithms, in Python, and wrapped in a Grasshopper module to link it with parametric design.

• Visualizing the impact of using reclaimed elements by adding the 3D scanned meshes to the design model based on the results from the matching algorithms.

ACKNOWLEDGEMENT

The project is done thanks to great work made by architects and engineers: Ryoko Iwase, Toshikatsu Kiuchi, Sudarshan Khadka, Kozo Kadowaki and Alexander Eriksson Furunes, Makoto Isono, Lars Eivind Bjørnstad. The project is done in collaboration with OmTre company, who supply reclaimed timber elements and provide storage and testing facility. The Oslo Kommune was involved in finding the correct place for the project and support in financing the construction.

REFERENCES

1. Morris, F., S. Allen, and W. Hawkins, *On the embodied carbon of structural timber versus steel, and the influence of LCA methodology.* Building and Environment, 2021. **206**: p. 108285.
2. Rautio, P., et al., *Perspectives: Lean forestry – A paradigm shift from economies of scale to precise and sustainable use of ecosystem services in forests.* Forest Ecology and Management, 2023. **530**: p. 120766.
3. Górna, A., et al., *Biomass Price Prediction Based on the Example of Poland.* Forests, 2022. **13**(12).
4. Guldager Jensen , K.S., John *Building a Circular Future*. 3 ed. Vol. 248. 2016, Denmark: GXN.
5. construction, B. *Which Factors Determine the Lifespan of a Building?* 2021; Available from: https://bciconstruction.us/which-factors-determine-the-lifespan-of-a-building/#:~:text=In%20general%2C%20the%20lifespan%20of,concrete%2C%20steel%2C%20and%20iron.
6. Tomczak, K., *Blue Ocean Strategy for business case of building components designed for disassembly*, in *11th Nordic Conference on Construction Economics and Organisation*. 2022
7. 2020, I., *Sustainability in buildings and civil engineering works — Design for disassembly and adaptability— Principles, requirements and guidance*. ISO 20887:2020(E). p. 35.
8. Haddal Mork, J. and M. Luczkowski, *JointSearch: Efficient parametric detailing preparation through user-defined and property-based joint type filtering.* International Journal of Architectural Computing, 2020. **19**(3): p. 386-400.
9. BAMB. *Buildings as material banks*. 2023; Available from: https://www.bamb2020.eu/.

World Conference on Timber Engineering Oslo 2023

ENERGY DEMAND FOR THE DRIVING IN OF SELF-TAPPING TIMBER SCREWS AND ITS APPLICABILITY

David Glasner[1], Andreas Ringhofer[2], Gerhard Hubmann[3], Werner Braun[4]

ABSTRACT: The following paper proposes a test method to evaluate the insertion energy of self-tapping timber screws in order to gain data that can be used in life cycle assessments. The proposed test configuration is based on an established setup to test the torsional resistance for driving in screws. Experimental data show the usability of the test method to distinguish different screw types with regard to their energy consumption. It was found that the insertion energy is highly influenced by timber density, screw diameter and insertion length. This correlation was used to derive an empirical model to predict the insertion energy of Tenz® screws. Of course, the presented approach may also be adapted for other screw types and serve as a tool for screw comparison and optimisation. Furthermore, the insertion energy has the potential to serve as a key value in the quality control of screwed connections.

KEYWORDS: self-tapping timber screws, screw application, insertion moment, insertion energy, RILEM TC TPT

1 INTRODUCTION AND THEORETICAL BACKGROUND

The ongoing climate crisis has been a major topic in engineering and has also put a spotlight on energy consumption in construction. Although nowadays the energy demand for the production of construction materials and engineering products is relatively well known as it is vital for the life cycle assessment (LCA) of structures, lesser is known about the energy consumption during their application or usage. In timber engineering, one of these widely used products are self-tapping timber screws. The amount of energy needed to drive in a screw has not yet received much attention and as a result, the comparability of different products in regard to the demanded insertion energy is not given.

Furthermore, although some influencing factors on the insertion energy such as timber density and screw diameter have been hinted at in previous work (cf. [1]), their effect has not been quantified while other screw related characteristics such as screw type, head type and insertion length or timber related characteristics such as axis to grain angle and timber species did not receive any attention at all. Such information however may become very valuable in the future as the insertion energy has the potential to serve as a predictor for the withdrawal strength and the axial stiffness of a screwed connection (cf. [2]) and be therefore used in quality control.

In the following the insertion energy W is defined as the amount of work performed during the insertion of the screw, which is equivalent to the Integral of the power demand P during that process. In the scope of screw insertion, P can be determined in two ways:

- Measurement of voltage U and electric current I and calculation of the electric power demand of the electric drive with $P = U \cdot I$
- Measurement of insertion moment M and angular velocity ω and determination of the rotational power demand during the insertion process with $P = M \cdot \omega$

The determination of the electric power demand can be done relatively easy. However, the hereby calculated insertion energy also includes losses within the setup itself. As a result, the approach using M and ω is favourable for standardized testing as it only contains the energy demand of the screw-timber-interaction.

The synchronized measurement of the insertion moment M and the angle of rotation φ allows the calculation of the insertion energy according to Equation (1):

$$W_\omega = \int M \cdot \omega \, \partial t \tag{1}$$

where $\omega = \partial\varphi / \partial t$ = angular velocity. To be able to calculate the insertion energy without direct measurement of the angle of rotation, the following correlation between angular velocity ω, thread pitch p and insertion length l_i is utilised:

$$l_i = \frac{\varphi}{2\pi} \cdot p \rightarrow \frac{\partial l_i}{\partial t} = \frac{\partial \varphi}{\partial t} \cdot \frac{p}{2\pi} \rightarrow \partial t = \frac{\partial l_i}{\omega} \cdot \frac{2\pi}{p} \tag{2}$$

Inserting Eq. (2) in Eq. (1) yields:

[1] David Glasner, Institute of Timber Engineering and Wood Technology, University of Technology Graz, Austria, david.glasner@tugraz.at
[2] Andreas Ringhofer, Institute of Timber Engineering and Wood Technology, University of Technology Graz, Austria, andreas.ringhofer@tugraz.at
[3] Gerhard Hubmann, TENZ GmbH, Graz, Austria, gerhard.hubmann@tenz.at
[4] Werner Braun, AVVIO GmbH & Co KG, Graz, Austria, werner.braun@avvio.at

https://doi.org/10.52202/069179-0475

$$W_l = \frac{2\pi}{p} \int M \, \partial l_i \qquad (3)$$

2 MATERIAL AND METHODS

2.1 Test setup and evaluation

On basis of the established test configuration for testing the torsional resistance when driving in screws provided in EN 15737:2009 [3], an adapted test configuration was developed to determine the energy demand as an additional property, see Figure 1.

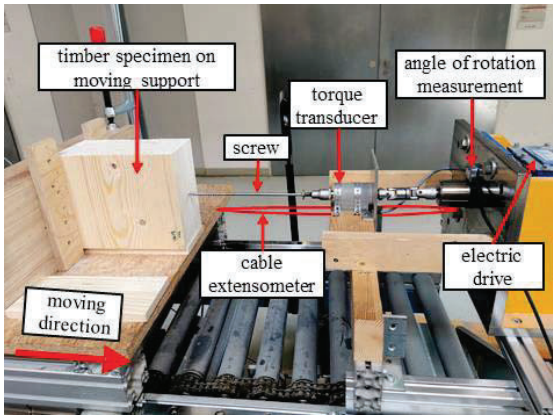

Figure 1: *Test configuration to determine the insertion energy*

The proposed configuration consists of a fixed electric drive and a moving support on which a timber block is placed. At the shaft of the electric drive a sensor to measure the angle of rotation as well as a torque transducer are installed. A pneumatic cylinder presses the moving support with the timber block against the screw, which is placed horizontally between timber and torque transducer. A cable extensometer, which is connected to both fixed and moving support, measures the insertion length.

During the tests in the scope of this paper, the pressure of the pneumatic cylinder and the renditions per minute of the electric drive were varied depending on the screw length but not recorded, as they show no influence on the insertion energy according to investigations in [2]. The dimensions of the timber specimens were chosen in agreement with the specifications given in EN 15737:2009 [3] meaning that the specimens were at least 20 d in length, 10 d in width and the screw length in height. Unless stated otherwise in one of the detailed descriptions of the test series in the following Sections 2.2 to 2.5, the timber specimens were made of spruce softwood (*picea abies*) with an almost equal mean density $\rho_{12,mean}$ of approx. 420 kg/m³ for all test series, which was done by matched sampling.

After the insertion test, the moisture content and density were determined according to EN 13183-1 [4] respectively ISO 13061-2 [5] on small scale specimens with a quadratic cross section and a length equal to the screw's insertion length. The small-scale specimens included the whole screw channel which was positioned in the centre of the specimen. For the evaluation, the density was corrected to a reference moisture content of 12 % according to ON EN 384 [5].

Figure 2 exemplarily shows the results of an insertion test carried out with a screw with a nominal diameter d_{nom} = 8.0 mm and a length l =240 mm in a piece of spruce softwood. The top graph shows the relationship M vs. t, which is used for the determination of the torsional resistance of driving in screws. The peak at the end of the driving in marks the insertion of the screw head in the timber. The middle graph shows power P vs. time t. The similar shape compared to the graph M vs. t is a result of the constant angular velocity for the majority of the test run. The bottom diagram shows the increase in insertion energy over time, which is equal to the area under the P vs. t relationship (marked in grey in the middle diagram). The insertion energy was then evaluated at two points: W_{shaft} including the insertion of screw tip, thread and shank but without the portion of the head insertion and W_{head}, including a flush head insertion to the timber surface.

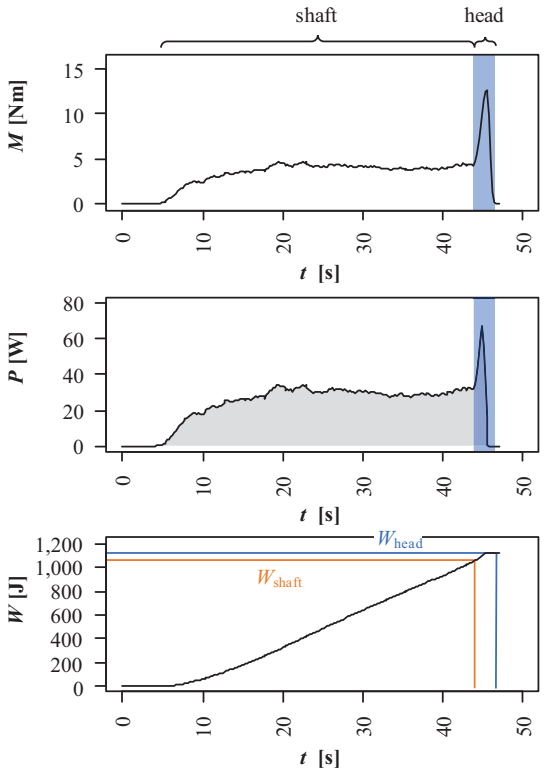

Figure 2: *M, P and W vs. t exemplarily for a TENZ® screw with d_{nom} = 8.0 mm and l = 240 mm*

2.2 Set 1: Comparison of different screw types from different manufacturers

The main aim of this set was to compare different screw types from different manufacturers with regard to the insertion energy. The tested screws are given in anonymized form in Table 1 and visualized in Figure 3. Groups one and two consist of partially threaded screws

with a nominal diameter of 6.0 mm respectively 8.0 mm;, the screw length was 160 mm respectively 240 mm. The test series were then compared to Tenz WBS screws of test series 29 respectively 30, see Section 2.3, Table 2. The Tenz screw of test series 23 with diameter 6.0 mm had a length of 240 mm; the insertion energy was therefore also evaluated at an insertion length of 160 mm. Group three included dry wall screws with diameters varying between 3.0 mm and 4.2 mm and lengths in the range of 35 mm to 70 mm. For a better comparison in-between this group, the insertion energy of the dry wall screws was evaluated at an insertion length of 30 mm.
All screws except for screw types one, nine and 18 had a countersunk head (CS) with or without additional features. Screw types one and nine had a staggered head with saw tooth, screw type 18 had a washer head (WH).

Table 1: *Summary of the tested screws for set 1*

	Screw Type [-]	*n* [-]	*l* [mm]	l_{thread} [mm]	p^* [mm]
d_{nom} = 6.00 mm	1	7	160	70	4.9
	2	7	160	75	4.6
	3	7	160	70	2.7
	4	7	160	65	5.0
	5	7	160	70	3.7
	6	7	160	70	3.7
	7	7	160	70	4.7
d_{nom} = 8.00 mm	8	7	240	80	5.3
	9	7	240	95	5.6
	10	6	240	95	5.6
	11	7	240	100	5.8
	12	7	240	100	6.7
	13	7	240	100	5.6
	14	7	240	100	6.5
	15	7	240	90	4.8
	16	7	240	100	5.6
	17	7	240	100	5.6
	Screw Type [-]	*n* [-]	d_{nom} [mm]	*l* [mm]	p^* [mm]
dry wall screws$^+$	TENZ DWS	7	4.20	50	2.8
	18	7	4.20	38	3.6
	19	7	4.20	70	3.6
	20	6	4.20	70	3.5
	21	7	4.20	70	3.3
	22	7	4.20	70	2.8
	23	7	3.90	45	2.8
	24	7	3.90	55	3.2
	25	7	3.90	35	2.9

*the mean thread pitch was measured on one screw per series along 10 turns

$^+$dry wall screws were evaluated at an insertion length of 30 mm

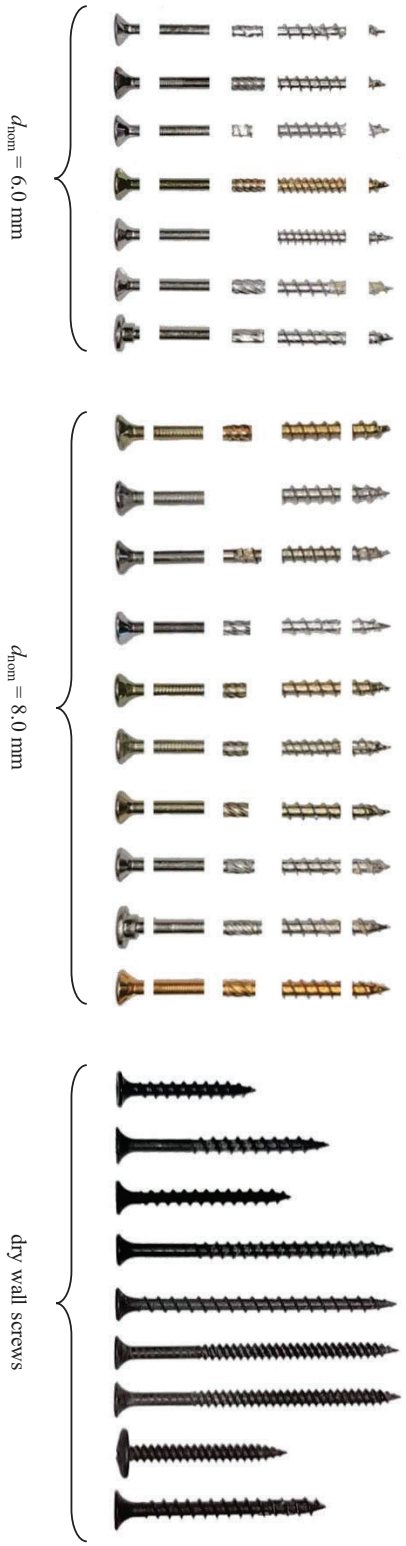

Figure 3: *Screws compared in set 1; also included are Tenz screws used in series 29 and 30 see section 2.3*

https://doi.org/10.52202/069179-0475

2.3 Set 2: Influence of density, length and diameter

The test series within this set were used to quantify the influence of timber density, screw length and screw diameter which have been identified to have a major impact on the insertion energy in [1]. For this purpose, three density classes were formed, which contained three test series each, one for each tested diameter. The test data of this set were also used to derive an empirical model to estimate the insertion energy for the whole Tenz screw portfolio. Consequently, additional test series were included on selected screws of type Tenz WS and Tenz DS. The test series of set 2 are given in Table 2 and depicted in Figure 4. The head types of all screws, except for Tenz WBS 8.0x600 mm which had a WH, were CS.

Table 2: *Test series of set 2*

	series	*n*	targeted ρ_{12}	d_{nom}	*l*	*p**
	[-]	[-]	[kg/m³]	[mm]	[mm]	[mm]
TENZ WBS	26	10	370	6.0	240	4.5
	27	10	370	8.0	240	5.2
	28	10	370	10.0	240	5.6
	29	10	420	6.0	240	4.5
	30	10	420	8.0	240	5.2
	31	10	420	10.0	240	5.6
	32	10	520	6.0	240	4.5
	33	10	520	8.0	240	5.2
	34	10	520	10.0	240	5.6
	35	10	420	6.0	30	4.5
	36	10	420	8.0	600	5.2
	37	10	420	10.0	100	5.6
	38	10	420	10.0	600	5.6
TENZ WS	39	10	420	4.0	25	2.8
	40	10	420	6.0	240	4.7
	41	10	420	8.0	240	5.2
	42	8	420	8.0	400	5.4
TENZ DS	43	10	420	6.0	150	3.6

*the mean thread pitch was measured on one screw per series along 10 turns

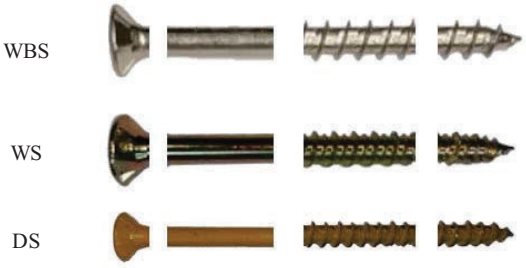

Figure 4: *Screws used in test set 2*

2.4 Set 3: Influence of axis-to-grain angle and head type

This test set served to investigate the influence of the axis-to-grain-angle α and the head type on the insertion energy. The tested screw type was Tenz WBS 8.0x240 mm with a pitch p =5.2 mm. A summary of the test series can be found in Table 3.

Table 3: *Test series of set 3*

	series	*n*	α	*head type*	*additional characteristic*
	[-]	[-]	[°]	[-]	[-]
TENZ WBS	44	10	45	CS	-
	45	10	0	CS	-
	46	10	90	WH	WH flush on timber surface
	47	5	90	CS	CS sunk approx. 1 cm in timber

2.5 Set 4: Influence of timber material

The investigation of different timber species and timber products was carried out in set 4. Within this set, Tenz WS 5.0x60 mm screws with p = 3.3 mm were used. The test series of this set are summarised in Table 4.

Table 4: *Test series of set 4*

	series	*n*	*timber species / timber product*
	[-]	[-]	[-]
TENZ WS	48	6	spruce (*picea abies*)
	49	6	MDF board
	50	6	beech (*fagus sylvatica*)
	51	6	beech LVL

3 RESULTS AND DISCUSSION

3.1 Comparison of different evaluation methods

Figure 5 shows the residuals of the insertion energy of the whole data set calculated by Eq. (1) versus Eq. (3) for the insertion energy including screw head insertion (Figure 5 left) and without screw head insertion (Figure 5 right).

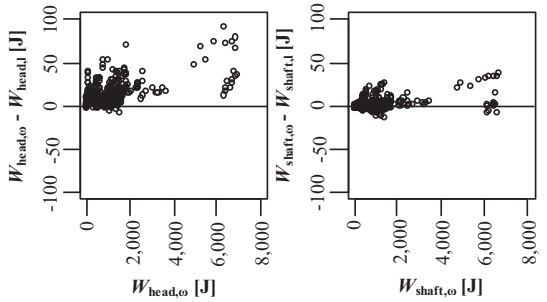

Figure 5: *Residuals for the insertion energy in dependence of the evaluation method. left: W_{head} including the head; right: W_{shaft} for the shaft only*

It can be seen that although the scatter does not show a trend along the tested spectrum, suggesting both calculation methods to be comparable, there is a shift to the positive side for the insertion energy including the head. This should be kept in mind when evaluating W_{head}. However, the knowledge of the thread pitch p is crucial for the applicability of Eq. (3) in both cases.
For the more detailed discussion in the remaining paper, the results of W_{ω} acc. to Eq. (1) will be discussed as it is seen as the more reliable method.

3.2 Set 1: Comparison of different screw types and manufacturers

The overall mean density $\rho_{12,mean}$ for test series of screws with d_{nom} = 6.0 mm of set 1 was 420 kg/m³. The minimum $\rho_{12,mean}$ of a single test series was 414 kg/m³and the maximum $\rho_{12,mean}$ was 424 kg/m³ indicating a successful matched sampling process. The average moisture content was u = 14.0 %. For more details regarding each test series, please refer to Table A-1 in the Annex.
Figure 6 compares the insertion energy of each test series of set 1 with diameter 6.0 mm with the corresponding Tenz screw (test series 29) which was for this purpose evaluated at an l_i of 160 mm. Except for series 1 and 5, statistically significant differences between Tenz and the other test series were found using unpaired two-sample t-tests assuming a significance threshold of $\alpha = 0.05$. Especially test series 3 differs from the other test series. Although not analysed in detail, this was the only series without any screw features (no compactor, cutter etc.) which could be the reason for the higher insertion energy.

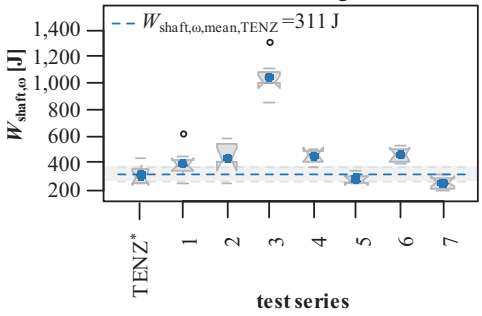

Figure 6: *Boxplots and mean values for $W_{shaft,\omega}$ of screws with d_{nom} = 6.00 mm and l =160 mm; 95%-CI for TENZ. *TENZ screw with l =240 mm was used and evaluated at an insertion length of =160 mm*

For the screws with diameter 8.0 mm, $\rho_{12,mean}$ of all series was 429 kg/m³. The minimum $\rho_{12,mean}$ of a single test series was 401 kg/m³ and the maximum $\rho_{12,mean}$ was 433 kg/m³. The average u was 14.2 %. A detailed summary can be found in Table A-2 in the annex.
The insertion energy results of each test series of this group can be seen in Figure 7. Again using unpaired two-sample t-tests statistically significant deviations can be found between Tenz (test series 30) and test series 8, 11, 12, 13 and 16.

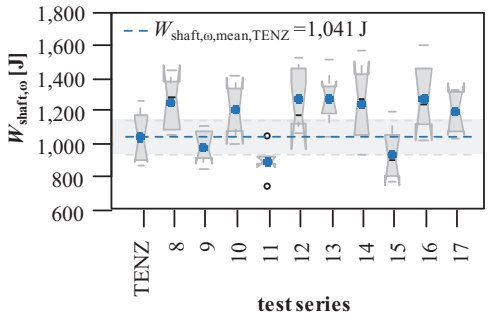

Figure 7: *Boxplots and mean values for $W_{shaft,\omega}$ of screws with d_{nom} = 8.00 mm and l =240 mm*

The timber specimens of the test series with the dry wall screws had an overall $\rho_{12,mean}$ of 414 kg/m³, the minimum density of a single series was 407 kg/m³, the maximum was 428 kg/m³ while the average u was 10.9 %. The main statistics of this set is summarized in Table A-3 in the Annex. Figure 8 shows the insertion energy of dry wall screws evaluated at a constant insertion length of 30 mm.

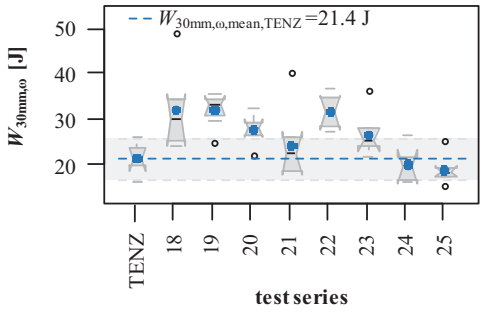

Figure 8: *Boxplots and mean values for $W_{30mm,\omega}$ evaluated at an insertion length of 30 mm for dry wall screws; 95%-CI for TENZ.*

Unpaired two-sample t-tests between Tenz and test series 18, 19, 20 and 22 showed a statistically significant difference while the difference to the remaining test series of this group were statistically insignificant.

3.3 Set 2: Influence of density, length and diameter

The main statistics of this set can be found in Table A-4 in the Annex.
During the execution of test series 36 with screws 8.0 x 600 mm, a bending of the screws was observed during insertion. As this was the only test series showing such behaviour, it is likely that the high slenderness of this specific screw is the reason for the bending. It is assumed that the bending causes the screw shank to press against the screw channel during insertion resulting in a higher insertion energy due to the increased friction.
As ρ, d and l were identified as the predominant factors regarding the insertion energy in a past investigation (see [1]), a nonlinear least squares regression analysis to describe $W_{shank,\omega}$ was made using the basic approach according to Eq. (4).

https://doi.org/10.52202/069179-0475

$$W_{TENZ} = W_0\left(\frac{\rho}{420}\right)^{k_\rho}\left(\frac{d_{nom}}{8.0}\right)^{k_d}\left(\frac{l}{100}\right)^{k_l} \quad (4)$$

Furthermore, it was assumed that the factors k_ρ, k_d and k_l are constant irrespective of the screw type (WBS, WS or DS). The initial regression was executed on the data of Tenz WBS screws though test data from test series 36 were excluded from this regression analysis due to the aforementioned bending effects. The resulting factors are $k_\rho = 1.713$, $k_d = 1.976$ and $k_l = 1.480$, which in the following were set to $k_\rho = 1.7$, $k_d = 2$ and $k_l = 1.5$. Based on these factors, screw specific nominal insertion energies W_0, definded as the insertion energy needed to drive in an 8.0x100 mm screw in spruce with density 420 kg/m³, were derived see Table 5.

Table 5: *nominal insertion energies W_0 for Tenz screw types*

screw type	W_0 [J]
Tenz WBS	267
Tenz WS	371
Tenz DS	496

The prediction of the empirical model is plotted against experimental data in Figure 9. An - especially in timber engineering - unusually high agreement between model prediction and experimental data is given ($R_{adj}^2 = 0.99$) when test series 36 is excluded. The correlation remains high even if series 36 is considered ($R_{adj}^2 = 0.95$).

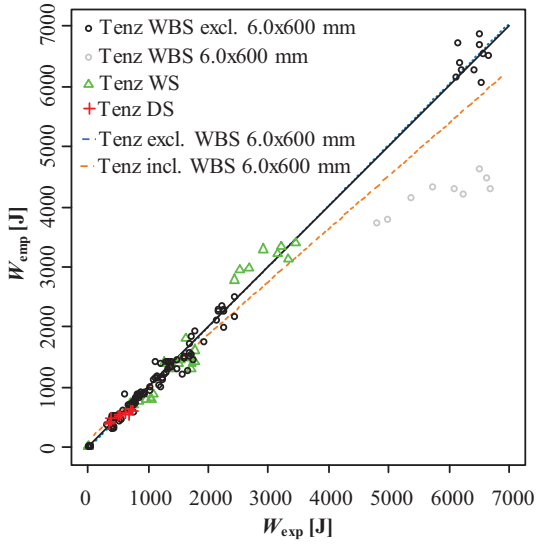

Figure 9: *Model prediction vs. experimental data for Tenz screws*

Figure 10 shows the accompanying residuals of the model. Overall, a uniform distribution of the residuals can be observed for the whole dataset (again excluding test series 36), confirming the general suitability of the model. Because the residuals for Tenz WS are also distributed without a recognizable trend along the tested spectrum even though the model's underlying factors (except for the nominal insertion energies W_0) were derived based on Tenz WBS screws it can be concluded that the assumption of the factors' independency of the screw type is valid. However, it remains uncertain whether this also applies for other screw manufacturers and especially for fully threaded screws.

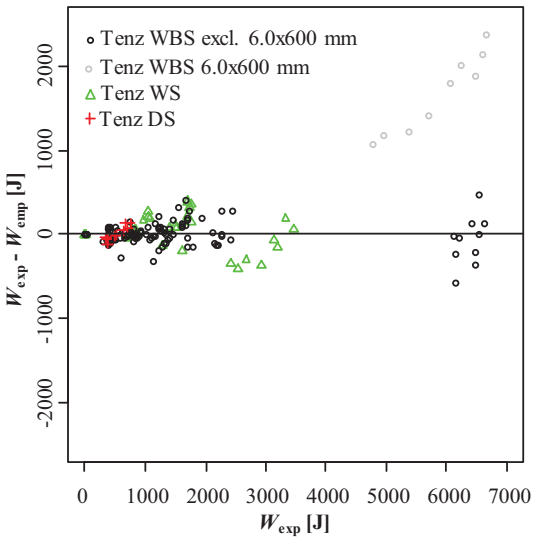

Figure 10: *Residual plot for data according to Eq. (4)*

3.4 Set 3: Influence of screw axis to grain angle and head type

A summary of the results of set 3 can be found in Table A-5 in the Annex. The mean densities of the respective test series range from $\rho_{12,mean} = 412 \div 423$ kg/m³ with a mean density of 418 kg/m³ of the total set 3. The average moisture content was 13.8 %.

Figure 11 shows the influence of the axis to grain angle α on the insertion energy. Between 90° (perpendicular to grain insertion) and 45°, a decrease of around 20 % of the insertion energy is observed. However, between 45° and 0° (parallel to grain insertion) no further reduction is given.

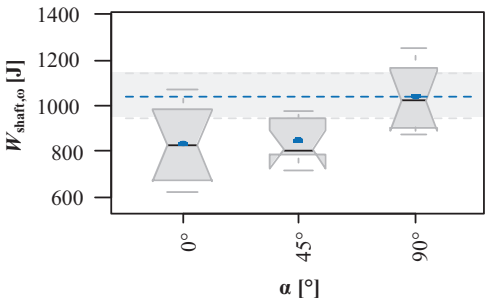

Figure 11: *Screw axis to grain angle α vs. insertion energy $W_{shaft,\omega}$*

The effect of different head types can be seen in Figure 12 with the head portion of the insertion energy calculated as $\Delta W_{head} = W_{head} - W_{shaft}$. In the presented case of an 8.0 x 240 mm screw, the CS placed level on the timber

surface results in an increase of the total insertion energy of approximately 10 % W_{shaft} ($W_{shaft,mean}$ = 1,041 J). However, if the CS is sunk 10 mm into the timber, the ratio ΔW_{head} / W_{shaft} is 25 %, which will increase even further for shorter screws. It is assumed that the higher ΔW_{head} of the WH compared to the CS mainly results from the larger diameter of the head though the shape of the head may also be of importance.

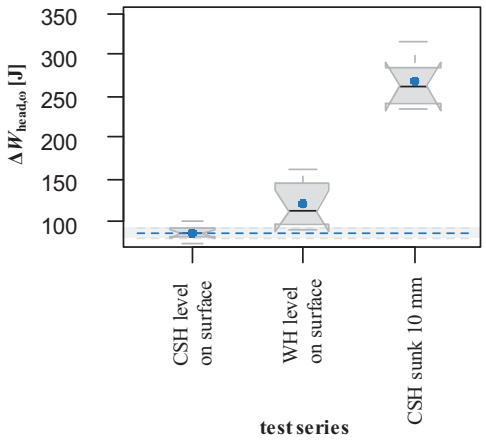

Figure 12: *Head portion of the insertion energy*

3.5 Set 4: Influence of timber material

In Figure 13 and Figure 14 the densities and insertion energies for set 4 are compared; a detailed summary of the test data can be found in Table A-6 in the annex. The low scatter of the densities of MDF board, beech and beech LVL results from the single specimens being manufactured from the same respective base material.

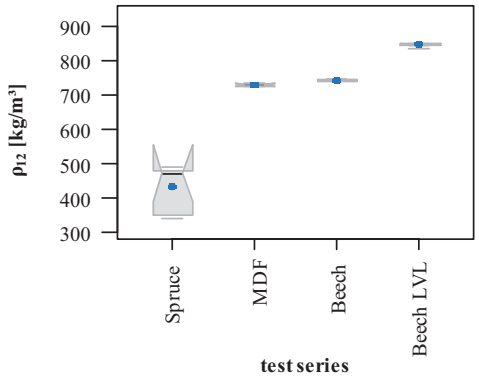

Figure 13: *densities of different timber materials of set 4*

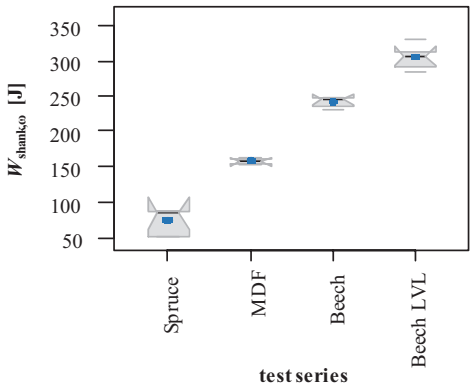

Figure 14: *insertion energy of different timber materials of set 4*

Based on the findings in 3.3, it comes to no surprise that the observation of an increased insertion energy with increasing density qualitatively is also true for different timber species and timber materials. However, when comparing the insertion energies in MDF and beech, they differ greatly even though the densities are very similar. This leads to the conclusion that the correlation between density and insertion energy is a material specific property.

4 SUMMARY AND CONCLUSION

This contribution deals with the insertion energy for screws, its influencing factors and possible applications. In the following, the main outcome of the paper at hand is summarized:

- The insertion energy of screws may become an important input factor for life cycle assessment of structures due to their widespread and still increasing use.
- A test configuration for the insertion energy is presented, which is based on the existing setup according to EN 15737:2009 for the torsional resistance of driving in screws by simply adding a measurement for the rotation angle.
- A simplified calculation method is derived that uses the correlation between insertion length, thread pitch and rotation angle that allows the evaluation of the insertion energy without direct rotation angle measurement. Both methods are equivalent if the head portion of the insertion energy is excluded and the exact thread pitch is known.
- Tests carried out with the mentioned configuration show a strong correlation between insertion energy and insertion length, screw diameter and timber density. The latter however can only be applied within a timber species/ timber product and the magnitude of the effect is currently only quantified for spruce.
- The insertion energy is highest when a screw is inserted perpendicular to the grain and is reduced

https://doi.org/10.52202/069179-0475

up to 20 % for axis to grain angles of 45° or lower.

- The correct placement of the screw has a great effect on the insertion energy, as the insertion of the head through inaccuracies during screw insertion significantly increases the energy needed.
- Regarding quality assessment of screw connections, the insertion energy may serve as an important benchmark due to its correlation with the density and subsequently with the withdrawal properties.

ACKNOWLEDGEMENT

This paper is based on the results of the FFG research program "Innovationsscheck-Plus", which received public funding from the Austrian Research Promotion Agency (FFG) and private funding from TENZ GmbH. Their support is thankfully acknowledged. It is linked to the work in RILEM TC TPT "Tests methods for a reliable characterization of resistance, stiffness and deformation properties of timber joints".

REFERENCES

[1] Ringhofer, A; Bretterklieber, T; Neumayer, M: eTENZ – Machbarkeitsstudie betreffend die Konzeption eines Energieverbrauchstest-Setups (in German). University of Technology Graz, 2020.

[2] Eckert, A; Brandner, R; Glasner, D: Experimental study on control parameters for automated application and in- situ performance assessment of joints with self-tapping timber screws. WCTE'23, Oslo, Norway.

[3] ÖNORM EN 15737:2009-09-15. Timber Structures - Test methods - Torsional resistance of driving in screws.

[4] EN 13183-1:2002 + AC:2003. Moisture content of a piece of sawn timber – Part 1: Determination by oven dry method.

[5] ISO 13061-2:2014/AMD 1:2017-07-12. Physical and mechanical properties of wood – Test methods for small clear wood specimens – Part 2: Determination of density for physical and mechanical tests – AMENDMENT 1.

[6] ON EN 384:2022-11-01. Structural timber – Determination of characteristic values of mechanical properties and density.

5 ANNEX

Table A-1: *Main statistics for screws from set 1 with d_{nom} = 6.00 mm and l = 160 mm; mean values and CoV*

Screw Type	n	ρ_{12}	CoV [ρ_{12}]	u	$W_{head,\omega}$	CoV [$W_{head,\omega}$]	$W_{head,s}$	CoV [$W_{head,s}$]	$W_{shaft,\omega}$	CoV [$W_{shaft,\omega}$]	$W_{shaft,s}$	CoV [$W_{shaft,s}$]
[-]	[-]	[kg/m³]	[%]	[%]	[J]	[%]	[J]	[%]	[J]	[%]	[J]	[%]
1	7	424	8.25	14.1	439	24.9	429	25.1	395	24.8	393	24.7
2	6	424	7.10	13.6	475	24.2	465	24.2	439	24.4	435	22.3
3	7	422	8.05	13.8	1,112	11.0	1,089	11.1	1,041	11.5	1,026	11.5
4	6	420	6.80	13.7	485	10.4	481	10.4	450	10.9	453	10.7
5	7	414	4.42	14.2	309	10.8	300	10.7	279	10.8	275	10.7
6	7	414	6.09	14.4	505	11.2	487	11.0	459	11.6	449	11.4
7	7	420	6.43	14.3	279	15.9	270	15.7	248	15.5	245	15.3

Table A-2: *Main statistics for screws from set 1 with d_{nom} = 8.00 mm and l = 240 mm; mean values and CoV*

Screw Type	n	ρ_{12}	CoV [ρ_{12}]	u	$W_{head,\omega}$	CoV [$W_{head,\omega}$]	$W_{head,s}$	CoV [$W_{head,s}$]	$W_{shaft,\omega}$	CoV [$W_{shaft,\omega}$]	$W_{shaft,s}$	CoV [$W_{shaft,s}$]
[-]	[-]	[kg/m³]	[%]	[%]	[J]	[%]	[J]	[%]	[J]	[%]	[J]	[%]
8	6	426	4.64	14.0	1,334	11.4	1,300	11.3	1,253	11.5	1,230	11.4
9	7	420	5.10	14.3	1,076	8.44	1,068	8.43	986	9.28	988	9.26
10	4	433	7.38	14.4	1,262	12.6	1,266	12.7	1,208	12.5	1,219	12.5
11	5	421	6.49	14.3	930	11.0	916	10.9	891	11.0	883	10.8
12	7	419	4.70	14.1	1,347	14.4	1,339	14.3	1,276	14.7	1,277	14.6
13	7	422	5.54	14.2	1,331	10.7	1,326	10.8	1,269	11.6	1,272	11.6
14	7	401	6.33	14.4	1,307	16.8	1,292	16.8	1,244	18.0	1,237	17.9
15	7	424	7.82	14.2	1,008	17.2	995	17.1	938	17.9	932	17.8
16	6	422	5.75	14.2	1,354	14.1	1,347	14.0	1,277	15.7	1,278	15.6
17	6	432	5.97	14.0	1,267	11.4	1,264	11.4	1,194	10.8	1,199	10.8

https://doi.org/10.52202/069179-0475

https://doi.org/10.52202/069179-0475

Table A-3: *Main statistics for dry wall screws; mean values and CoV*

Screw Type	*n*	ρ_{12}	CoV [ρ_{12}]	*u*	$W_{head,\omega}$	CoV [$W_{head,\omega}$]	$W_{head,s}$	*CoV* [$W_{head,s}$]	$W_{30mm,\omega}$	*CoV* [$W_{30mm,\omega}$]	W_{30mm3s}	*CoV* [$W_{30mm,s}$]
[-]	[-]	[kg/m³]	[%]	[%]	[J]	[%]	[J]	[%]	[J]	[%]	[J]	[%]
TENZ DWS	5	415	9.05	11.0	55.6	11.4	49.2	10.8	21.4	14.9	22.0	14.6
18	6	416	5.74	10.7	67.6	18.1	59.4	22.8	32.0	25.4	30.9	25.4
19	7	412	8.32	11.4	139	11.4	123	10.6	32.1	11.5	31.5	11.3
20	6	423	7.83	11.1	124	15.1	115	15.1	27.6	12.5	28.0	12.2
21	6	407	8.30	11.5	117	23.2	105	23.7	24.0	31.9	24.6	31.5
22	7	413	7.80	10.6	154	12.7	142	13.7	31.7	11.2	32.5	11.0
23	6	410	12.8	10.5	64.8	22.7	55.7	23.1	26.7	16.4	27.0	15.0
24	5	428	8.78	10.6	73.3	15.7	60.5	16.8	20.2	18.5	20.2	18.3
25	5	408	8.26	10.7	30.1	11.2	27.0	14.5	18.9	17.0	19.0	17.1

Table A-4: *Main statistics for test series of set 2; mean values and CoV*

	series	*n*	ρ_{12}	CoV [ρ_{12}]	*u*	$W_{head,\omega}$	CoV [$W_{head,\omega}$]	$W_{head,s}$	CoV [$W_{head,s}$]	$W_{shaft,\omega}$	CoV[$W_{shaft,\omega}$]	$W_{shaft,s}$	CoV[$W_{shaft,s}$]
	[-]	[-]	[kg/m³]	[%]	[%]	[J]	[%]	[J]	[%]	[J]	[%]	[J]	[%]
WBS	26	9	376	5.62	13.8	425	11.1	425	11.1	402	11.6	405	11.4
	27	9	382	8.63	14.0	879	21.1	872	21.2	813	21.1	814	21.1
	28	10	370	5.09	13.5	1,349	8.35	1,340	8.34	1,251	9.24	1,254	9.19
	29*	10	425	6.63	14.3	533	20.9	531	20.9	510 (311)	21.7 (20.2)	513 (314)	21.6 (20.1)
	30	10	422	6.24	14.5	1,126	12.7	1,116	12.6	1,041	13.0	1,041	12.9
	31	10	420	5.79	13.8	1,621	15.4	1,607	15.3	1,493	15.7	1,494	15.6
	32	9	520	5.26	14.3	823	7.12	819	7.06	784	6.56	786	6.55
	33	10	515	4.99	14.5	1,716	8.09	1,680	7.80	1,587	8.33	1,582	8.37
	34	10	517	4.26	14.7	2,374	7.19	2,349	7.05	2,209	7.92	2,204	7.78
	35	9	414	8.94	13.3	56.3	27.4	36.1	17.9	24.4	22.2	24.4	21.6
	36	9	437	3.88	15.0	6,082	11.0	6,011	11.0	5,886	11.4	5,856	11.4
	37	10	410	13.1	14.9	617	21.1	579	20.9	476	22.6	462	22.4
	38	10	432	2.30	15.4	6,618	3.23	6,592	3.13	6,380	2.94	6,379	2.92
WS	39	10	449	12.8	12.6	22.4	55.0	21.9	47.0	11.0	26.3	11.8	25.2
	40	10	424	4.22	13.8	931	15.1	931	15.2	878	15.9	883	15.9
	41	10	434	5.72	14.8	1,689	10.3	1,670	10.3	1,598	10.1	1,590	10.1
	42	10	434	3.88	15.3	3,086	12.2	3,070	12.2	2,960	12.1	2,956	12.1
DS	43	10	432	8.48	13.8	573	27.3	570	27.1	527	27.3	529	27.0

*the values in brackets were evaluated at an insertion length of 160 mm

Table A-5: *Main statistics for test series of set 3; mean values and CoV*

	series	*n*	ρ_{12}	CoV [ρ_{12}]	*u*	$W_{head,\omega}$	CoV [$W_{head,\omega}$]	$W_{head,s}$	CoV [$W_{head,s}$]	$W_{shaft,\omega}$	CoV[$W_{shaft,\omega}$]	$W_{shaft,s}$	CoV[$W_{shaft,s}$]
	[-]	[-]	[kg/m³]	[%]	[%]	[J]	[%]	[J]	[%]	[J]	[%]	[J]	[%]
WBS	44	9	412	6.83	13.9	923	10.5	917	10.5	851	11.0	854	10.9
	45	10	418	7.88	13.2	888	18.2	878	18.3	830	18.9	829	18.9
	46	10	423	7.25	14.1	1,260	17.5	1,233	17.5	1,140	17.4	1,139	17.4
	47	5	422	7.64	14.1	1,325	12.1	1,309	12.0	1,057	13.2	1,057	13.1

Table A-6: *Main statistics for test series of set 4; mean values and CoV*

	series	*n*	ρ_{12}	CoV [ρ_{12}]	*u*	$W_{head,\omega}$	CoV [$W_{head,\omega}$]	$W_{head,s}$	CoV [$W_{head,s}$]	$W_{shaft,\omega}$	CoV[$W_{shaft,\omega}$]	$W_{shaft,s}$	CoV[$W_{shaft,s}$]
	[-]	[-]	[kg/m³]	[%]	[%]	[J]	[%]	[J]	[%]	[J]	[%]	[J]	[%]
WBS	48	6	436	14.3	13.9	103	15.8	93.4	22.7	74.7	22.3	76.0	22.4
	49	6	731	0.64	5.77	233	5.65	222	4.65	158	2.48	155	2.65
	50	6	746	0.31	9.70	311	4.44	298	4.19	242	2.47	240	2.50
	51	6	847	0.62	7.42	394	6.71	370	5.60	305	5.08	301	4.90

https://doi.org/10.52202/069179-0475

World Conference on Timber Engineering Oslo 2023

INFLUENCE OF THE SPECIMEN PREPARATION ON THE EMBEDMENT STRENGTH OF SELF-TAPPING SCREWS

Michael Gstettner[1], Andreas Ringhofer[2]

ABSTRACT: Due to their simple application and their wide-ranging applicability, self-tapping timber screws are either used for various types of connections or reinforcements in timber constructions. Apart from axial loading, self-tapping timber screws can be also loaded lateral, whereas the embedment strength f_h is one of the major parameters in the design process. The experimental determination of the embedment strength f_h, following EN 383, demands test procedures with thin timber specimen, whereas during the screw-application initial crack forming under specific conditions occur. As this has an unwanted and negative influence on f_h, a new way of specimen preparation was developed, with which initial crack formation can be excluded. Besides the presentation of this new method, the contribution also contains an experimental verification, which may lead to a significant modification of the current design model of f_h of self-tapping screws.

KEYWORDS: embedment strength, self-tapping screws, initial checks, novel preparation method, RILEM TC TPT

1 INTRODUCTION

Due to their versatile applicability and their simple installation without pre-drilling, self-tapping timber screws are frequently applied in contemporary timber constructions. Thereby, they are either loaded in axial or in lateral direction or in a combination of both. In the latter cases, their design according to Eurocode 5 [1] bases on the European Yield Model (EYM), where their yield moment M_y and the timber member's embedment strength f_h serve as main material properties. With regard to the embedment strength, there are two alternatives for a related calculation; one given in the present version of Eurocode 5 (where rules for nails and dowels are adopted for self-tapping screws in dependence of the size of their thread diameter) and one, which was specifically developed for self-tapping screws (c. f. Blaß et al. [2]) and is anchored in the majority of European Technical Assessments (ETAs) of self-tapping timber screws.
Comparing both approaches, especially the way how they consider the load-to-grain angle α, which is exclusively done by the Eurocode 5 approach, leads to a significant overestimation of experimentally determined f_h while for the ETA-approach (basing on Blaß et al. [2]) a high agreement between test results and model prediction was found, c. f. Gstettner [3]. In fact, this is surprisingly since the impact of the load-to-grain-angle α represents timber's well-known orthotropic material behaviour, established and successfully verified for f_h of other dowel-type fasteners such as dowels or bolts. The reason for the deviating behaviour, found for self-tapping screws, is discussed in Section 2.

2 RESEARCH ISSUE

Following the regulations according to EN 383 [4], aiming to avoid fastener's bending and to test a realistic application scenario, Gstettner [3] conducted screw embedment tests with a specimen-thickness $t = 2\,d$ without pre-drilling in advance. Thereby, the embedment strength f_h of several different screw types with their individual tip-characteristics applied in solid timber specimen with varying load-to-grain-angle (α), as well as the fastener axis-to-grain angle (ε), see Figure 1, was determined.

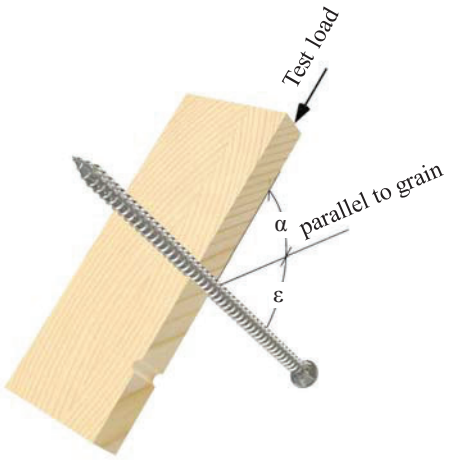

Figure 1: *Definition of the load-to-grain (α) and axis-to-grain angle (ε)*

[1] Michael Gstettner, m.gstettner@tugraz.at
[2] Andreas Ringhofer, andreas.ringhofer@tugraz.at
both Graz University of Technology, Austria

https://doi.org/10.52202/069179-0476

In addition, to investigate an impact of the timber density on f_h, tests with three different timber-density classes of softwood were executed. In the frame of this campaign and especially for specific variations {α =var. | ε = 90°}, initial crack forming due the material displacement in the frame of screw insertion was observed. Thereby, the crack size and length were found to depend on the tip features of the screw. Results of some preliminary insertion tests indicate that RAPID® screws (8.0 x 220 mm, d_i = 5,2 mm), equipped with a tip-compressor and a half cut in combination with a low insertion speed, lead to crack formation in a tolerable amount. A related example is shown in Figure 2 (top). Even though this specific form of application was chosen, the crack formation due to the small specimen thickness according to EN 383 [4] still had a negative impact on screws loaded parallel to grain (α = 0° | ε = 90°). One consequence was that α did not influence the size of f_h at all. This observation is equal to the one made by Blaß et al. [2], with significant consequences for the regulation in currently valid ETAs of self-tapping screws, but stands in clear contrast to timber's orthotropic characteristics, as e.g. expressed by the Hankinson-formula, which rules the increase of f_h with decreasing α for laterally loaded dowels in EN 1995-1-1 [1].

To conclude: the challenge of the current determination of f_h for self-tapping screws is, that its empirical background bases on tests with comparatively thin specimens (aim: avoid fastener's bending during testing), which do not fulfil the minimum thickness requirements according to ETA and thus have a significantly negative impact on the initial crack formation. As pre-drilling turned out to be not a suitable alternative (note: pre-drilling leads to a differently pronounced densification of the timber surrounding the screw), the aim of the present investigation was to find a way of test specimen preparation, leading to a required specimen thickness according to EN 383 [4] on the one hand and avoiding initial crack formation as a consequence of a too thin specimen thickness on the other. The successful result of this finding process in form of a new specimen preparation method is shown in Figure 2 (bottom).

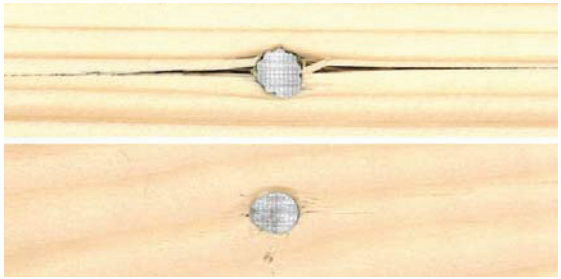

Figure 2: *Influence of the timber-specimen preparation on the embedment strength (f_h); (top) without- (bottom) with special specimen preparation*

The following sections comprise an explanation of this new method, the experimental programme to verify its impact on f_h as well as the gained test results and the proposals to modify the present approaches for determining f_h.

3 MATERIALS AND METHODS

3.1 OVERVIEW OF THE TEST PROGRAM

Inspired by the test program of Gstettner [3] an additional program in order to determine the influence of the specimen preparation process on the embedment strength (f_h), especially for α = 0°and ε = 90° was carried out. Next to a variation of the inner thread diameter (d_i) and the tip features, also the influence on the embedment strength (f_h) of three different application cases AC = {h | m | t} was investigated. Within each single test series, a minimum number of n = 18 tests was planned. The test program is shown in Table 1.

Table 1: *Overview of the test program, including the planned number of tests (n) within the test series*

⇩ Screw Type	AC ⇨	(h)	(m)	(t)
StarDrive	6.0 x 160	n = 18	18	18
RAPID®	8.0 x 220	18	18	18
RAPID®	8.0 x 240	18	18	18
RAPID®hardwood	8.0 x 320	18	18	18

3.2 MATERIALS

3.2.1 Timber Specimen

Due to its widely use in timber engineering and its status as a reference material in fastener testing, see EAD 130118-01-0603 2019 [5], pre-graded and kiln-dried structural timber lamellas with strength grade C24 acc. EN 338 [6] were used as a test material. They comprised a mix of Norway Spruce (*Picea Abies, Pinaceae*) and European Fir (*Abies Alba, Pinaceae*). Due to their similar mechanical properties, both wood species are treated as one assortment in practise. Within those lamellas, sections, free from any local growth characteristics (knots, pitch pockets, etc.) were used to gain high-quality preliminary timber specimen (t_{pre} = 40 mm), which were thereafter conditioned at 20 °C and 65 % relative humidity in order to reach an equilibrium moisture content u = 12 % according to SC 1 [1].

The dimensions $\{l_{(\alpha,\varepsilon,d)} \mid w_{(\alpha,\varepsilon,d)} \mid t_{(\lambda,d)}\}$ of the finished solid timber specimen are based on the regulations of EN 383 [4] for bolts and dowels, applicated in solid timber or wood-based panels, depending on the axis-to-grain angle α = {0° | 90°}, the nominal fastener diameter (d), as well as the slenderness (λ) as an ratio between the specimen-thickness (t) and the nominal fastener diameter (d). For specimen with {α = 0° | ε = 90°}, i. e. the load is applicated parallel to grain, while screw insertion is perpendicular to grain, EN 383 [4] proposes a specimen width $w_{(\alpha=0,d)} = 2\,a_1$, a length $l_{(\alpha=0,d)} = l_1 + l_2$ and a corresponding thickness $t = \lambda \cdot d$. To avoid fastener bending and to ensure embedding as a failure mode solely, λ was defined with 2. To prevent the specimen from further in-grain splitting during test execution, initiated throughout the screw application, additional 2 d were added to the distance to the loaded end (l_1). It is worth mentioning, that this setting was equal to the one by

https://doi.org/10.52202/069179-0476

Gstettner [3], enabling comparability to his investigations without this special form of specimen preparation. The final dimensions of the specimen are given in Table 2.

Table 2: *Dimensions of the finalised timber specimens*

		EN 383 [4]	Gstettner [3]
a_1	(unloaded edge)	$\geq 3\,d$	$7\,d$
l_1	(loaded end)	$\geq 10\,d$	$(10+2)\,d$
l_2	(unloaded end)	$\geq 10\,d$	$10\,d$
t	(thickness)	$(1.5 \div 4)\,d$	$2\,d$

In general, the new and improved specimen preparation process is based on the assumption, that the initial cracking mainly depends on the specimen thickness, see section 2. In order to enable screw insertion in a timber specimen with sufficient (practical) thickness to prevent initial cracking ($t_{pre} = 40$ mm) and to enable screw testing with the desired thickness according to EN 383 [4] ($t = \lambda \cdot d$), four major steps (A ÷ D), independent of the screw insertion {h | m | t}, were executed. Apart from a pre-drilling with a drill bit ($d_d = d + 2$ mm), which simplifies the removing of the slab (A) and the application of the self-tapping screw without predrilling thereafter (B), several circular saw cuts were carried out (C). For a perfect alignment of the self-tapping screw a specific template was used. To prevent the saw blade hitting the fastener, a safety distance was essential; the remaining wood material was removed with a chisel to complete the specimen preparation procedure (D), see Figure 3.

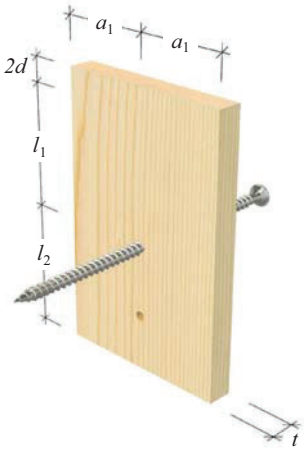

Figure 3: *Specimen dimensions, inspired by EN 383 [4]*

In order to cover the determination of the embedment strength f_h and to test a realistic application scenario of self-tapping screws without predrilling for three different cases {h | m | t}, different specimen application cases were carried out, see Figure 4. Whereas within case (h) the initial crack appears head-sided, i. e. the slab is removed on the side of the tip (see Figure 4, step A, highlighted **in blue**), both slabs are cut off for case (m), i. e. no initial crack occurs on both sides and for case (t) the initial crack occurs tip-sided, therefore the slab is head-sided removed (see Figure 4, step A, highlighted **in green**).

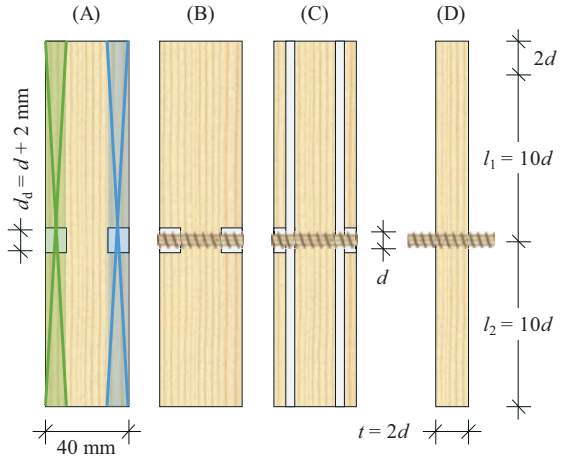

Figure 4: *Manufacturing process of the specimen*

3.2.2 Self-tapping screws

A self-tapping screw can be characterized as a hardened and coated carbon-steel rod, which consists of a head-part (h) including the drive, a middle member (m) with its thread and/or shank, as well as the tip (t), which are mostly equipped with varying features (*tf*). In the frame of the present investigation, four different screw types (ST1 ÷ ST4) according to ETA-12/0373 [7] were investigated, see Table 3 and Figure 5.

Table 3: *Thread specifications acc. to ETA-12/0373*

	d	d_i	P	l_t	*tf*
ST1	6.0 ±0.30	3.8 ±0.19	2.6 ±0.26	7.3 ±1.9	–
ST2	8.0 ±0.40	5.2 ±0.26	3.8 ±0.38	8.2 ±2.1	✓
ST3	8.0 ±0.40	5.2 ±0.26	3.8 ±0.38	8.2 ±2.1	✓
ST4	8.0 ±0.40	6.1 ±0.31	4.0 ±0.40	11.6 ±2.6	✓

Those differ once in their (nominal) outer thread diameter (d), inner thread diameter (d_i), thread pitch (p), tip-characteristics, including special tip-features (*tf*) and the coating; the latter responsible for corrosion-protection and added for easy application.

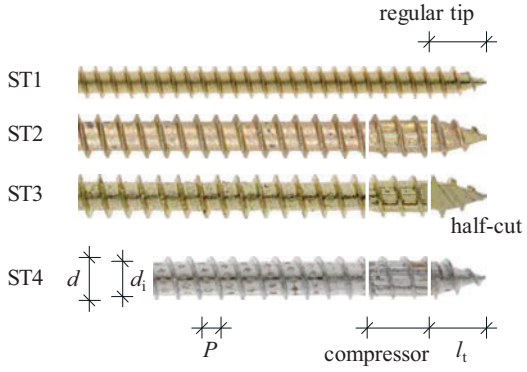

Figure 5: *Classification of self-tapping screws with their individual tip-characteristics (top to bottom: ST1 to ST4)*

Whereas the screw types ST1 (“StarDrive”, $d_i = 3.8$ mm) and ST2 ÷ ST3 (“RAPID®”, $d_i = 5.2$ mm) are designed for application in softwood, ST4 (“RAPID®hardwood”) with $d_i = 6.1$ mm is especially, but non-exclusively seen for application in hardwood. ST2 to ST4 are equipped with a tip-compressor, which shall decrease the insertion moment. While the tip characteristic of ST3 provides a half-cut, all other screw types are designed with a regular tip (see Figure 5).

3.3 TEST–SETUP AND EXECUTION

In order to determine the embedment strength f_h of laterally loaded self-tapping screws, full-hole embedment tests following EN 383 [4] were carried out. The test setup consisted of two load-bearing steel brackets ①, which were connected rigidly with the universal test rig lignum_uni_275 ② (ZwickRoell GmbH & Co. KG), see Figure 6. The timber specimen with its already applicated screw was thereby embedded in steel clamps ③, in which the shape of the screw-thread had been removed by milling in order to guarantee a perfect bearing during testing. To minimize fastener bending, the distance between the steel brackets and the specimen was kept as low as possible; only to allow a free side-deformation of the timber specimen. While testing, the force transmission between the test rig and the timber specimen was realized throughout a custom-made adapter ④, which was made of beech plywood. The local displacement measurement was realised by two displacement transducers ⑤ (type WA-L), which were aligned symmetrically to the test axis. Thereby the interaction between the test specimen and the transducers was achieved by a dowel ⑥.

Figure 6: *Image of the test-setup ST1 with its single steel-components; configuration {α = 0° | ε = 90°}*

With regard to the test execution, all tests were performed acc. to EN 383 [4], but without the recommended hysteresis loop. The max. test load should be reached within 300 ±120 s and is defined as $F_{max,i} = \max\{F_{w=5,i} \mid F_{max,w<5,i}\}$.

3.4 POST-PROCESSING

The embedment strength $f_{h,i}$ was calculated acc. to EN 383 [4] by the following Equation (1).

$$f_{h,i} = \frac{F_{max,i}}{d \cdot t_{i,sp}} \quad \left[\frac{N}{mm^2}\right] \tag{1}$$

Thereby, the specimen thickness $t_{i,sp}$ was determined after the test execution of every single specimen.

As main indicators of strength and stiffness properties, the timber density $\rho_u = m_u / V_u$ acc. to ISO 3131 [8] and the moisture content $u = (m_u - m_0) / m_0$ acc. to EN 13183-1 [9] of each specimen were determined using a small piece of the test specimens, taken next to the applied screw (see Figure 3). Minor deviations of the moisture content, influencing the wood density were adjusted by using Equation (2) acc. to EN 384 [10].

$$\rho_{12} = \rho_u \cdot (1 - 0.005 \cdot (u - u_{12})) \quad \left[\frac{kg}{m^3}\right] \tag{2}$$

whereas ρ_{12} is the moisture adopted timber density, ρ_u the timber density, determined immediately after testing, u the corresponding moisture content and $u_{12} = 12$ % the reference moisture content.
The embedment strength of every test series including a certain number of specimen n was subjected to an outlier adjustment ($\tilde{n}$), see Gstettner [3].

https://doi.org/10.52202/069179-0476

4 RESULTS AND DISCUSSION

4.1 TIMBER DENSITY | MOISTURE CONTENT

An overview of the main statistics for physical timber properties, such as the moisture content (u) and the wood density (ρ_{12}) is given in Table 4.

Table 4: *Main Statistics of physical timber properties*

	AC	$n = \bar{n}$	u_{mean}	$\rho_{12,mean}$	CoV[ρ]
		[-]	[%]	[kg/m³]	[%]
ST1	(h)	18	10.7	412	6.6
ST1	(m)	18	11.4	406	4.1
ST1	(t)	19	11.0	414	5.2
ST1	**–**	**18**	**13.3**	**406**	**4.03**
ST2	(h)	18	12.1	414	7.6
ST2	(m)	17	12.0	408	5.6
ST2	(t)	18	12.0	413	6.3
ST3	(h)	18	12.0	416	5.9
ST3	(m)	18	12.2	411	4.7
ST3	(t)	20	11.9	413	5.4
ST3	**–**	**19**	**12.7**	**417**	**5.61**
ST4	(h)	18	11.9	409	7.3
ST4	(m)	16	12.0	420	7.0
ST4	(t)	17	12.3	409	5.8
ST4	**–**	**19**	**13.3**	**412**	**4.58**

☐ research results of Gstettner [3]

For all test series, an average moisture content of $u = 12$ % (SC 1 acc. to EN 1995-1-1 [1]) was tried to reach. As a result, there are comparable moisture contents u_{mean} within the new series, while for the ones of Gstettner [3], higher moisture contents were observed. A longer storage of the new specimens under standard climate conditions (app. 2.2 years), led to a better converge to $u_{SC1} = 12$ %, as assumed. Regarding the timber density $\rho_{12,mean}$ a good match to $\rho_{mean,C24} = 420$ kg/m³ acc. to EN 338 [6] can be observed for all considered test series.

4.2 EMBEDMENT STRENGTH

In Table 5, the main statistics of f_h of the new test series are given in dependence of the screw type (ST1 to ST4) and compared with the reference ones of Gstettner [3]. Therefore, the ratio η according to Equation (3) is used to draw precise conclusions; here $f_{h,mean}$ is the average embedment strength of the test series with varying application cases {h | m | t} and screw types (ST1 ÷ ST4) while $f_{h,ref,mean}$ acts as a reference strength, taken from Gstettner [3].

$$\eta = \frac{f_{h,mean}}{f_{h,ref,mean}} \quad [-] \qquad (3)$$

Table 5: *Main statistics of the embedment strength (all test series), including the research results of Gstettner [3]*

	AC	*d*	d_i	*tf*	$\bar{n}$	$f_{h,mean}$	CoV[f_h]	η
		[mm]	[mm]		[-]	[N/mm²]	[%]	[-]
ST1	(h)	6	3.8	–	16	19.89	10.8	1.26
ST1	(m)	6	3.8	–	16	17.94	13.0	1.16
ST1	(t)	6	3.8	–	17	17.36	15.0	1.12
ST1	**–**	**6**	**3.8**	**–**	**19**	**15.61**	**12.0**	**1.00**
ST2	(h)	8	5.2	✓	18	18.95	8.7	–
ST2	(m)	8	5.2	✓	15	19.77	7.5	–
ST2	(t)	8	5.2	✓	20	18.03	9.9	–
ST3	(h)	8	5.2	✓	19	22.53	12.0	1.11
ST3	(m)	8	5.2	✓	18	22.40	11.2	1.10
ST3	(t)	8	5.2	✓	17	21.47	11.6	1.05
ST3	**–**	**8**	**5.2**	**✓**	**19**	**20.44**	**10.51**	**1.00**
ST4	(h)	8	6.1	✓	17	16.37	14.1	1.17
ST4	(m)	8	6.1	✓	16	16.59	13.2	1.19
ST4	(t)	8	6.1	✓	17	15.27	16.4	1.09
ST4	**–**	**8**	**6.1**	**✓**	**17**	**13.67**	**7.17**	**1.00**

☐ results of Gstettner [3]

First of all, the reference results of Gstettner [3] shall be discussed. In general, Gstettner [3] observed a regressive behaviour of the embedment strength f_h with an increasing screw diameter d. In addition, a significant reduction of the embedment strength was detected once for ST1 and also ST4, which was in fact not expected. It is assumed, that the initial crack forming during the screw application leads to this specific behaviour. ST4 is not equipped with a half-cut and has a higher inner thread diameter $d_i = 6.1$ mm, compared to ST3 ($d_i = 5.2$ mm). In case of ST1, there are no tip-features at all (see Figure 5).

Second and concentrating on the embedment strength as a consequence of the application cases {h | m | t} for all ST, significantly higher values of the embedment strength f_h compared to Gstettner [3] are given. The assumption of a positive effect on the embedment strength f_h by the new specimen preparation process is verified. This positive effect of the specimen preparation process on the embedment strength f_h is shown in Figure 7, exemplarily for ST1.

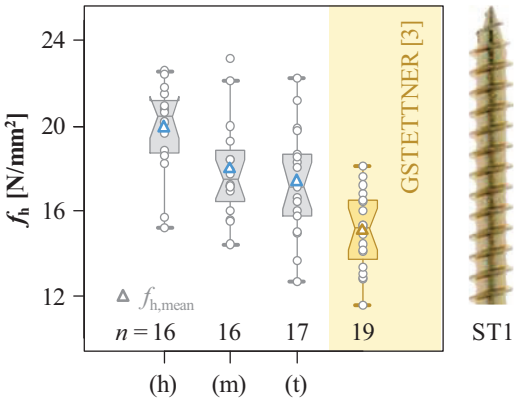

Figure 7: *Boxplot of f_h vs. application case for ST1, {d = 6 mm | d_i = 3.8 mm}*

Whereas the relative size of f_h for the application cases {h | m} of ST2 ÷ ST4 is almost equal, those of ST1 show a notable positive gap. With regard to the difference to the reference results and irrespective of the screw type, the application case (t) has the smallest increase of f_h compared to the results of Gstettner [3].

5 SUMMARY AND CONCLUSION

With focus on the lateral loading of self-tapping timber screws, an experimental research program was carried out to determine their embedment strength f_h. Thus, Gstettner [3] executed embedment tests using thin softwood specimen (t = 2d), following EN 383 [4]. Among others, a possible influence of the load-to-grain angle (α), screw axis-to-grain angle (ε), timber density (ρ) and several screw diameter (d) have been investigated. The outcomes of determining the embedment strength f_h for ST3, varying α are exemplarily shown in Figure 8.

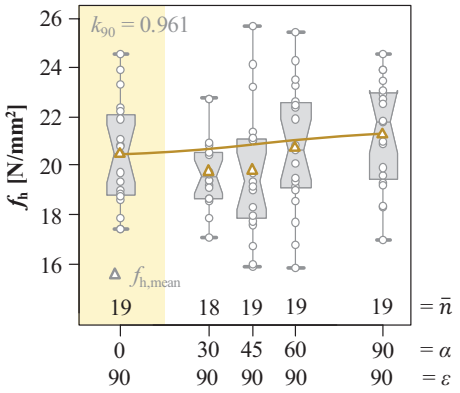

Figure 8: *Boxplot f_h vs. α for ST3, {d = 8 mm | d_i = 5.1 mm}*

Thereby, similar embedment strength (f_h) at a load-to grain angle α = 0°, compared to α = 90° was observed; which stands in a clear contrast to the general assumption of timber as orthotropic material. A negative impact of the specimen preparation and the application of the self-tapping screw without pre-drilling, especially for α = 0°, on the embedment strength (f_h) is assumed as a reason, see Gstettner [3]. Therefore, a new specimen-preparation process was developed, in order to disable an unwanted and negative influence of initial crack forming on the embedment strength. f_h, see section 3.2.1.

Within this experimental research, executed after the one of Gstettner [3], three different application cases, using various self-tapping timber screw types have been investigated. Whereas in application case (h) the initial crack appears head-sided and within (t) tip-sided, no initial cracks occur within the application case (m). In fact, a remarkable impact of the new and improved specimen preparation process on the embedment strength f_h, i. e. independent of all application cases {h | m | t} and the screw types {ST1 ÷ ST4} was observed, see Table 5. With focus on the application cases (h) and (m), barley no difference of the embedment strength f_h was observed, whereas in the case (t), where the initial crack occurs tip-sided, f_h converges to the test results of Gstettner [3]. Furthermore, with focus on the different screw types with their individual tip-features and different inner thread diameters (d_i), a significant influence on the embedment strength f_h was observed.

On this basis the following proposals can be made: Since the new and approved specimen preparation process led to significant increased embedment strengths f_h, an implementation of the specimen preparation procedure in the current standards EAD 130118-01-0603 2019 [5] and EN 14592 [11] is recommended. Whereas Gstettner [3] proposes a $k_{90} \approx 1.0$, for self-tapping screws with their individual tip characteristics and inner thread diameters (d_i), following ETA-12/0373 [7] for practical purpose, a factor k_{90}, see equation (4) and (5), considering the increase of the embedment strength f_h due to this new and improved specimen preparation is recommended.

$$f_{h,\alpha} = (k_{90} \cdot \cos(\alpha)^2 + \sin(\alpha)^2) \cdot f_{h,90} \quad (4)$$

$$k_{90} = \begin{cases} 1.10 & \text{for timber member head-sided} \\ 1.20 & \text{for timber-member tip-sided} \end{cases} \quad (5)$$

Thereby, k_{90} for head-sided timber members is determined throughout a minimum (see Figure 9), comprising the application cases (h) and (t).

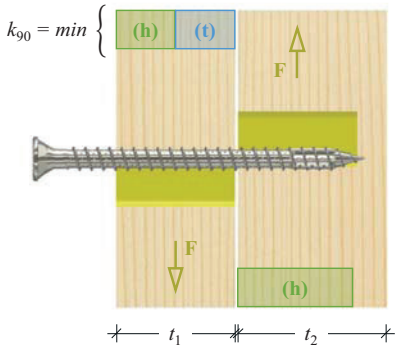

Figure 9: *Exemplary sketch of a timber-to-timber connection, executed with self-tapping screws*

It is worth mentioning, that the size of the embedment strength f_h was found to highly depend on the individual screw type, equipped with several tip-features and varying thread designs. Thus, a general applicability of k_{90}, shown in this contribution, can not be guaranteed. Therefore, further research work, also including a verification of α ≠ 0° is recommended, since it is assumed, that the initial crack forming does not influence at least specimen with α = 90°.

ACKNOWLEDGEMENT

The authors gratefully acknowledge the financial and industrial support of Schmid Schrauben Hainfeld GmbH and WIEHAG GmbH, as well as the project "SCREW_STIFFNESS" (No. 861554), which received public funding by FFG.

https://doi.org/10.52202/069179-0476

REFERENCES

[1] EN 1995-1-1 +AC, A1, A2: Eurocode 5: Design of timber structures – Part 1-1: General – Common rules and rules for buildings. ASI, 2015-06.

[2] Blaß H.J, Bejtka I, Uibel T: Tragfähigkeit von Verbindungen mit selbstbohrenden Holzbauschrauben mit Vollgewinde. In: Karlsruher Bericht zum Ingenieurholzbau, 2006. (in German).

[3] Gstettner M: Experimentelle Untersuchung des Tragverhaltens lateral beanspruchter, selbstbohrender Holzbauschrauben, Master thesis, Instiute of Timber Engineering and Wood Technology, Graz University of Technology, 2019. (in German).

[4] EN 383: Timber structures – Test methods – Determination of embedment strength and foundation values for dowel type fasteners, 2007-01.

[5] EAD 130118-00-0603: European Assessment Document – Screws for use in timber constructions. 2016-10.

[6] EN 338: Structural timber – Strength classes, 2016-06. ETA-12/0373: Screws for use in timber constructions. Vienna: OIB, 2016-04.

[7] ETA-12/0373: Screws for use in timber constructions. Vienna: OIB, 2022-03.

[8] ISO 3131: Wood – Determination of density for physical and mechanical tests, 1995-01.

[9] EN 13183-1: Moisture content of a piece of sawn timber – Part 1: Determination by oven dry method, 2002-02.

[10] EN 384: Structural Timber – Determination of characteristic values of mechanical properties and density, 2016-08.

[11] EN 14592: Timber structures – Dowel-type fasteners – Requirements, 2017-06.

World Conference on Timber Engineering Oslo 2023

INFLUENCE OF TEST METHODS ON THE PARALLEL TO GRAIN EMBEDMENT STRENGTH AND FOUNDATION MODULUS CHARACTERIZATION

Caroline D. Aquino[1], Leonardo G. Rodrigues[2], Meta Kržan[3], Michael Schweigler[4], Zheng Li[5], Jorge M. Branco[6]

ABSTRACT: Different test setups have been reported in the literature for the determination of the embedment strength in timber elements. These variances hinder a straightforward comparison between available test data. It is difficult to determine if the source of variability lies in intrinsic timber properties or is related to the test protocol used. This paper aims to provide a better insight into the influence of embedment strength test methods, comparing experimental results from different test setups within the guidelines of EN 383 and ASTM D 5764-97a for Scots pine wood (*Pinus sylvestris*) and Spruce (*Picea Abies*). A robust statistical analysis was performed to identify statistically significant differences between the groups evaluated. The analysis of the parallel to grain embedment strength showed that the results differed between standards, pointing out the potential bias inserted in the embedment properties given their evaluation method. Moreover, the thickness of the specimen tests also proved to influence the yield and ultimate embedment strength for the wood species tested.

KEYWORDS: Embedment Strength, Test methods, Dowel-type Connections, RILEM TC TPT

1 INTRODUCTION

The embedment strength, which is a property of utmost importance in dowel-type timber connections, is often determined through empirical expressions proposed in the literature. For instance, the European standard (Eurocode 5) [1] proposes an expression relating the dowel diameter and the wood density to the embedment strength, while the American Wood Council NDS [2] proposes an expression only based on the wood density. Nonetheless, because these empirical expressions are generalized, they fail to reliably predict the embedment strength for some wood species.

In that sense, alternative expressions have been studied based on experimental analysis of varying wood species [3,4]. The American standard, ASTM D 5764-97a [5], and the European standard, EN 383 [6], are the two most often used test standards for this purpose. The main difference between these standards is that ASTM D 5764-97a [5] allows for both half-hole and full-hole test specimens and bases the embedment strength on the yield load. On the other hand, EN 383 only allows for a full-hole test specimen and bases the embedment strength on the ultimate load capacity within 5 mm deformation. The two standards also reflect different dowel load conditions. Whereas the EN 383 standard loads the dowel on its ends, the ASTM D5764-97a [5] standard loads the dowel uniformly along its length. As a result, the EN 383 [6] test method is more likely to produce a bending effect than the ASTM D5764-97a [5], as reported in [7]. In terms of displacement measurement, EN 383 [6] recommends a local measure between the fastener and timber specimen, while ASTM D5764-97a [5] proposes a global measure between upper and lower support.

The standards also differ concerning the loading protocol. While ASTM 5764-97a [5] predicts a single loading cycle in displacement control, EN 383 [6] includes an additional cycle in load control of 40% of the estimated load-carrying capacity. This cycle was included to obtain the foundation modulus but at the expense of slightly conservative embedment values [8,9].

Moreover, when it comes to the thickness of the specimens, the protocols also differ. While EN 383 [6] proposes a range for the specimen thickness varying from

[1] Caroline D. Aquino, Department of Civil Engineering, University of Minho, ISISE, Guimarães, Portugal, carolinedapieve@gmail.com
[2] Leonardo G. Rodrigues, University of Nottingham, Faculty of Engineering, Nottingham, United Kingdom, leonardo.rodrigues@nottingham.ac.uk
[3] Meta Kržan, Slovenian National Building and Civil Engineering Institute, Ljubljana, Slovenia, meta.krzan@zag.si
[4] Michael Schweigler, Linnaeus University, Växjö, Sweden, michael.schweigler@lnu.se
[5] Zheng Li, Tongji University, Shanghai, China, zhengli@tongji.edu.cn
[6] Jorge M. Branco, Department of Civil Engineering, University of Minho, ISISE, Guimarães, Portugal, jbranco@civil.uminho.pt

https://doi.org/10.52202/069179-0477

1.5 up to 4 times the dowel diameter, ASTM D 5764-97a [5] only defines a minimum value (the smaller between 38 mm and two times the diameter). The European standard defines a maximum value for the thickness mainly to avoid the bending of the dowel.

The variances between test protocols and specimen dimensions described hinder a straightforward comparison between available test data. It is difficult to determine if the source of variability lies in intrinsic timber properties or is related to the test protocol used. This paper aims to provide a better insight into the influence of embedment strength test methods, comparing experimental results from different test setups within the guidelines of ASTM D 5764-97a [5] and EN 383 [6].

2 MATERIALS AND METHODS

2.1 EMBEDMENT TESTS

This study investigates the effect of different test setups and protocols on the embedment properties of Scots pine timber. The influence of the thickness of the specimens, as well as the test configuration (load application) are investigated within the guidelines of ASTM D 5764-97a [5] and EN 383 [6]. A total of 264 specimens of Scots pine *(Pinus sylvestris*) were tested according to both standards for a dowel diameter (d) of 8 mm. Their minimum dimensions are shown in Figure 1 and Figure 2, respectively.

Within the scope of ASTM D 5764-97a [5], the height (h) and width (w) of the specimens were defined as h = 80 mm and w = 95 mm. Regarding the thickness (t), four different groups were tested: 20 mm, 25 mm, 30 mm, and 35 mm, whereas only one group with t = 20 mm was considered for EN 383 [6]. The height and width for the specimens tested according to the European standard were h = 160 mm and w = 65 mm. Mean and standard deviation values of oven-dry density (ρ) and moisture content (MC), calculated from mass and volume, are presented in Table 1.

Table 1. *Basic properties of Scots pine specimens tested according to ASTM D 5764-97a [5] and EN 383 [6] for a dowel diameter of 8 mm*

Thickness [mm]	N [no.]	ρ [kg/m^3]	MC [%]
ASTM D 5764-97a [5]			
20	53	500±48	11.5±1.0
25	52	495±58	12.1±0.4
30	45	511±49	11.7±0.8
35	60	497±51	12.0±0.6
EN 383 [6]			
20	54	522±69	11.2±1.3

An additional investigation was conducted regarding the method of load application within the scope of EN 383 [6]. Two test configurations - Setup 1 and Setup 2 - were evaluated (see Figure 2) since both were founded in the literature [10,11]. The main difference between setups lies in the load application. For Setup 1 the load is applied to the timber specimen while the dowel is kept fixed. For Setup 2, the load is applied on the steel dowel while keeping the specimen fixed. Scots pine (*Pinus sylvestris*) and Spruce (*Picea abies*) were tested for dowels of diameter 12 mm for both setups. Similar, mean and standard deviation values of ρ and MC are presented in Table 2.

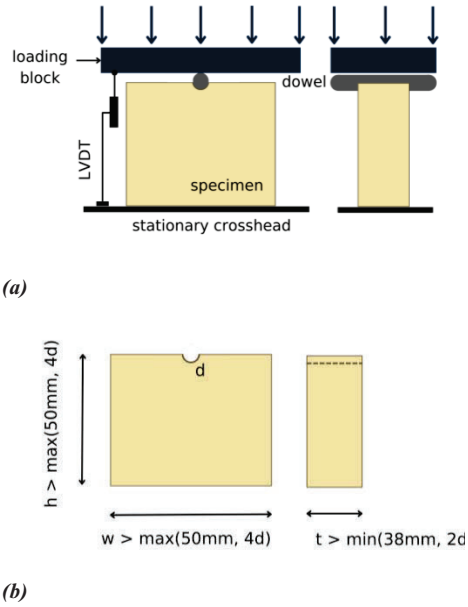

Figure 1: *(a) Test setup for ASTM D 5764-97a [5] and (b) corresponding specimen*

Table 2. *Basic properties of Scots pine and Spruce specimens tested according to EN 383 [6] for dowel diameter of 12 mm*

Setup [-]	Thickness [mm]	N [no.]	ρ [kg/m^3]	MC [%]
Scots pine (*Pinus sylvestris*)				
Setup 1	30	21	445±62	11.1±0.4
Setup 2	30	21	424±58	11.1±0.5
Spruce (*Picea abies*)				
Setup 1	25	23	357±45	11.5±0.7
Setup 2	25	23	365±44	11.4±0.5

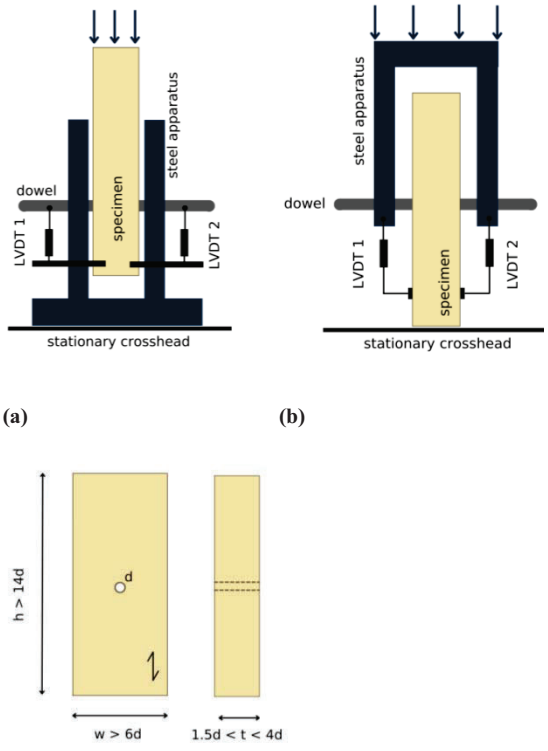

Figure 2: *Test setup for EN 383 [6] (a) Setup 1, (b) Setup 2, and (c) corresponding specimen*

The half-hole specimens tested according to ASTM D5764-97a [5] were loaded at displacement control at a constant rate of 0.02 mm/s. The test setup, presented in Figure 3, has a hydraulic actuator, equipped with a load cell of 25 kN, and a displacement range of 200 mm. To measure the joint slip, one linear variable differential transformer (LVDT) was fixed at the steel loading block. The tests were terminated at an embedment of one-half the fastener diameter or after the maximum load was reached.

The full-hole specimens tested according to EN 383 [6] were loaded into five different branches. The first part consisted of a loading branch, followed by a plateau where the load was kept constant and equal to 40% of the estimated capacity for 30 seconds. After, the load was diminished until it reached 10% of the estimated capacity and then kept constant for another 30 seconds. Thereafter, the test was performed under displacement control with a constant rate of 0.02 mm/s for specimens with dowels of 8 mm and 0.025 mm/s for dowels of 12 mm in diameter. Both loading and unloading branches were force controlled with a constant rate of 0.025 kN/s and 0.013 kN/s for dowels of 8 mm and 12 mm in diameter, respectively. The test setup, presented in Figure 4, has a hydraulic actuator, equipped with a load cell of 25 kN, and a displacement range of 200 mm. To measure the joint slip, two LVDTs were fixed on both sides of the connection. These two LVDTs were placed diagonally opposite the central timber member. The tests were terminated after the maximum load was reached or when the actuator displacement reached the threshold of 5 mm.

Figure 3: *Test setup within ASTM D 5764-97a [5]*

(a) **(b)**

Figure 4: *Test setups within EN 383 [6] (a) setup 1, and (b) setup 2*

2.2 QUANTIFICATION OF PROPERTIES

The embedment properties retrieved from the recorded load-displacement curves for ASTM D5764-97a [5] and EN 383 [6] protocols, are shown in Figures 5a and 5b, respectively. A significant difference between these standards lies in the definition itself of embedment strength. While the EN 383 [6] definition is based on the ultimate load capacity, the ASTM D5764-97a [5] standard defines the embedment strength based on the yield load. The yield load is obtained by the intersection between the offset line of the initial linear portion of the load-deformation curve by a deformation equal to 5% of the fastener diameter. Nonetheless, if the offset line and the load-deformation curve do not intersect, the yield load can be regarded as the ultimate one. The ultimate embedment strength ($f_{h,u}$) and the yield embedment strength ($f_{h,y}$) were calculated according to Equation (1) and Equation (2), respectively.

https://doi.org/10.52202/069179-0477

$$f_{h,u} = \frac{F_{max}}{dt} \quad (1)$$

$$f_{h,y} = \frac{F_{yield}}{dt} \quad (2)$$

Although ASTM D5764-97a [5] does not make a reference to the initial or elastic foundation modulus (K_s), it can be interpreted as the slope of the initial linear portion of the load-displacement curve divided by the product of d and t. Nguyen et al. [12] computed K_s through a linear regression between 15% and 40% of the ultimate load. Xu et al. [13] considered the portion between 10% and 40% of the ultimate load, as recommended by EN 383 [6]. Santos et al. [7] only refer to the slope of the linear portion, not defining the4 range of load from which it was obtained. In this study, the portion between 20% and 30% of the ultimate load was chosen to be consistent with the approach adopted for the EN 383 [6] protocol based on the discussion of Van Blokland *et al.* [9]. The load at which the load-deformation curve deviates from a straight line fitted to its initial linear portion is known as the proportional limit load.

From the EN 383 [6] protocol, three foundation moduli were determined: the initial foundation modulus (K_s), related to the initial loading branch, and the elastic foundation modulus (K_e) related to the slopes of the unloading (K_{e-}) and reloading cycles (K_{e+}). According to Van Blokland et al. [9], non-linearity can be observed in the last part of unloading, which is between 10% and 20% of the maximum estimated force ($F_{max,est}$) in their tests. Therefore, to avoid this, the load levels between 20–30% of $F_{max,est}$ were used to obtain K_{e-}. Consistently, the same range was adopted for K_s and K_{e+}.

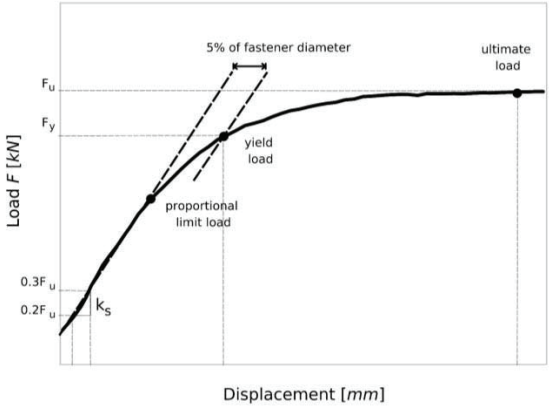

(a)

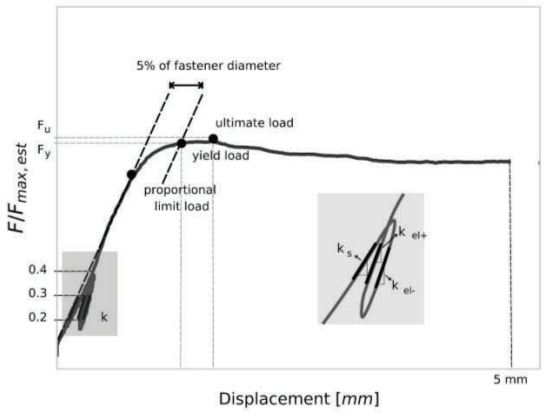

(b)

Figure 5: *Embedment parameters determined from the load-displacement curves for (a) ASTM D 5764-97a [5], and (b) EN 383 [6] (based on Van Blokland et al. [9])*

2.3 STATISTICAL ANALYSIS

A statistical software program (IBM SPSS Software, IBM, Armonk, United States) was used to perform the analysis with a significance level of 0.05. The normality of the data was diagnosed by the Shapiro-Wilk test and homoscedastic by the Levene test. A one-way Bonferroni analysis of variance (ANOVA) was performed to compare the embedment properties within different thicknesses tested according to ASTM D5764-97a [5]. Due to the non-normality of the data, bootstrapping procedures (1000 resamplings; 95 % CI, bias-corrected and accelerated - BCa) were implemented to obtain greater reliability of the results to correct deviations from the normality of the sample distribution and to present a 95 % CI for differences among means [14].

The statistical significance regarding the test protocol (ASTM D5764-97a [5] vs. EN 383 [6]) and setup (Setup 1 vs. Setup 2 from EN 383 [6]) was assessed via an independent t-test since data was diagnosed as normally distributed through the Shapiro-Wilk test and their variances was verified to be homogeneous by the Levene test.

3 RESULTS AND DISCUSSION

3.1 INFLUENCE OF THICKNESS WITHIN ASTM D5764-97a [5] PROTOCOL

The largest differences were found for the embedment strength, as a result of thickness. A p-value<0.001 was achieved in the analysis of variance for both $f_{h,y}$ and $f_{h,u}$. A post-hoc Bonferroni analysis indicated that the source of difference relies on the group with a thickness of 35 mm, which can also be noted by visually comparing the mean load-displacement curves shown in Figure 6 and the distribution of $f_{h,u}$ showed in Figure 7.

To ensure the representativeness of the data, a power (by mean of averages, OpenEpi) [15] was calculated for the ultimate embedment strength, comparing the high (mean

https://doi.org/10.52202/069179-0477

= 42.29 MPa, standard deviation = 4.9, sample size = 53, thickness = 20 mm) and low group (mean = 33.61 MPa, standard deviation = 5.4, sample size = 60, thickness = 35 mm) and power of 100 % was achieved.

It is important to highlight here that the Bonferroni analysis pointed out a significant difference (p-value = 0.009) in density for the group of thickness = 30 mm compared to the others (see also Table 1). Therefore, the group shall not be considered for the analysis regarding the thickness influence since it is not representative.

No significant difference was found for the initial foundation modulus, which can also be noted by its distribution presented in Figure 8.

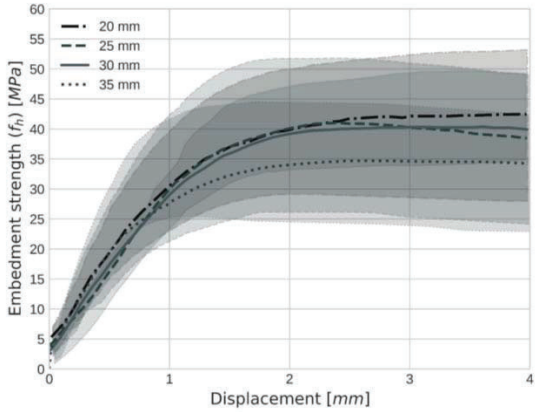

Figure 6: *Mean load-displacement curves for specimens tested according to ASTM D 5764-97a [5] for a dowel of 8 mm*

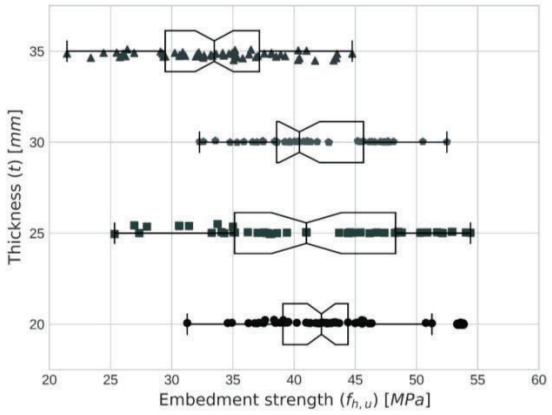

Figure 7: *Embedment strength for different member thicknesses according to ASTM D 5764-97a [5] for a dowel of 8 mm*

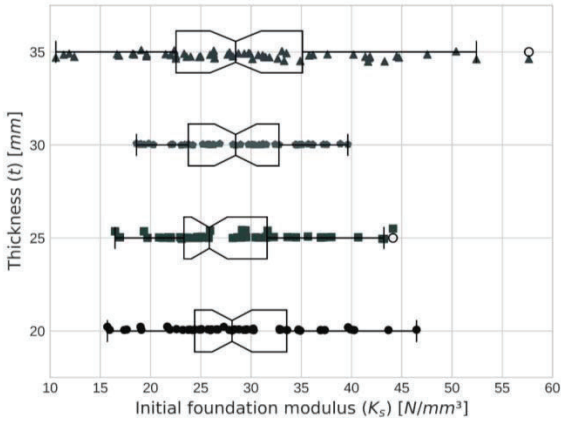

Figure 8: *Initial foundation modulus for different member thickness according to ASTM D 5764-97a [5] for a dowel of 8 mm*

The relationships between density and embedment strength ($f_{h,u}$) is presented in Figure 9.

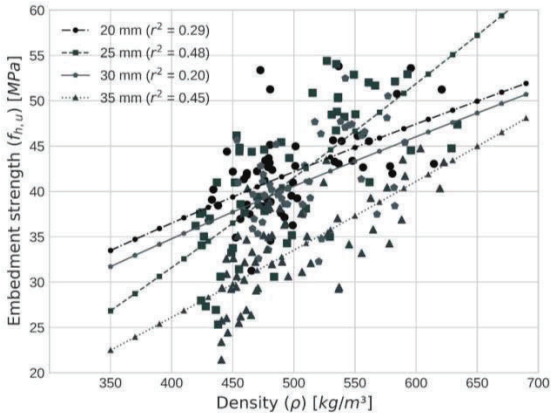

Figure 9: *Scatter plot of density versus embedment strength for specimens tested according to ASTM D 5764-97a [5] for a dowel of 8 mm*

3.2 ASTM D5764-97a vs. EN 383

A significant difference (p-value<0.001) was found, according to the independent t-test, for all the embedment properties retrieved from the load-displacement curves obtained according to ASTM D5764-97a [5] and EN 383 [6] protocols. The statistical test was also conducted to guarantee that there was no statistically significant difference in the densities of each group to avoid bias in the results.

Figure 10 shows the mean-load displacement curves according to both standards. The distribution of the ultimate embedment strength ($f_{h,u}$) and the initial foundation modulus (K_s) is presented in Figures 11 and 12, respectively. The relationships between density and embedment strength ($f_{h,u}$) is presented in Figure 13.

The analysis showed that the $f_{h,u}$ obtained from the ASTM D5764-97a [5] curve is 18.7% bigger than the one obtained from EN 383 [6]. The difference decreases to 9.9% when comparing $f_{h,y}$ from ASTM D5764-97a [5]

https://doi.org/10.52202/069179-0477

with $f_{h,u}$ from EN 383 [6]. In terms of the initial foundation modulus (Ks), the EN 383 protocol yielded a value 39.7% bigger than the one obtained from ASTM D5764-97a [5].

Frankel and Magnière [11] and Van Blokland *et al.* [9] compared the test setup between the investigated standards for Spruce (*Picea abies*) with dowel diameters of 12 mm and 10 mm, respectively, and conclude that the test specimen configuration (half-hole or full-hole), has a relatively small and not statistically significant effect on the embedment strength. Both test configurations followed the loading protocol of EN 383. Nonetheless, Van Blokland *et al.* [9] argue that despite no significant difference being found, embedment strength was around 7% higher for half-hole specimens. The study also found that K_s was 80–180% higher when determined in the half-hole compared to the full-hole test setup, differing from the results found in this study. Santos et al. [7] performed a comparison for Maritime Pine (*Pinus pinaster*) with a dowel diameter of 14 mm by changing both the specimen configuration and the loading protocol. The results showed no significant difference in terms of K_s and $f_{h,u}$. This could indicate the variability of test methods is also dependent on the wood species evaluated and the dowel diameter. An additional comparison was made to infer the influence of the diameter of Scots pine (*Pinus sylvestris*) (see Figure 14) within the scope of EN 383 [6]. Specimens with the same slenderness ratio were considered for the comparison (t/d = 2.5). The largest difference was found for K_s. The specimens with a dowel diameter of 8 mm had a mean initial foundation modulus 42.3% higher than the ones with 12 mm. With respect to the embedment strength, a difference of 17.4% was found.

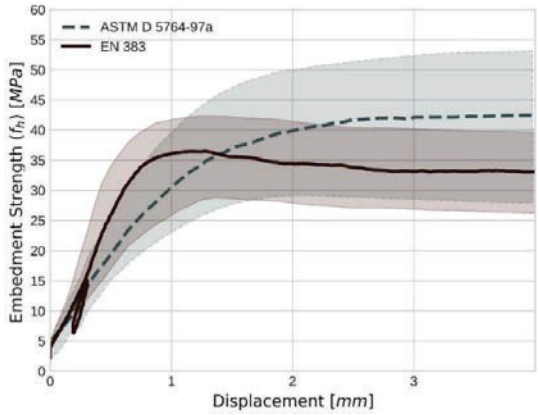

Figure 10: *Mean load-displacement curves according to ASTM D 5764-97a [5] and EN 383 [6] for a dowel of 8 mm and timber specimen 20 mm thick*

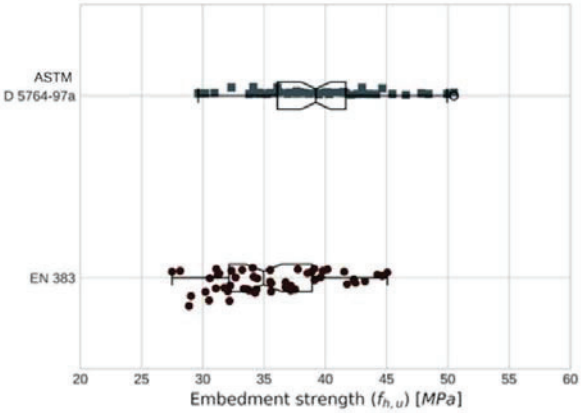

Figure 11: *Embedment strength according to ASTM D 5764-97a [5] and EN 383 [6] for a dowel of 8 mm and timber specimen 20 mm thick*

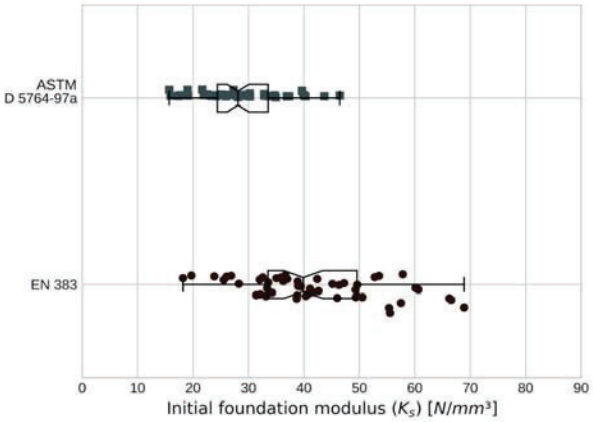

Figure 12: *Initial foundation modulus according to ASTM D 5764-97a [5] and EN 383 [6] for a dowel of 8 mm and timber specimen 20 mm thick*

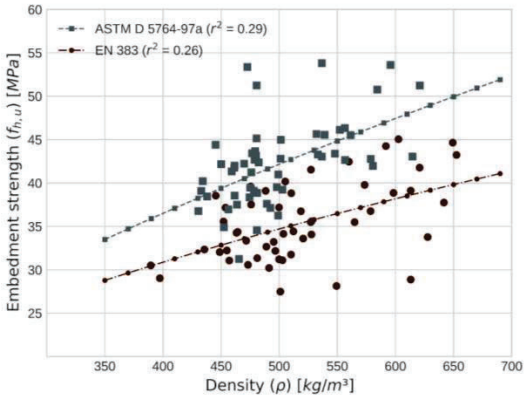

Figure 13: *Scatter plot of density versus embedment strength for specimens tested according to ASTM D [5] 5764-97a and EN 383 [6] for a dowel of 8 mm and timber specimen 20 mm thick*

https://doi.org/10.52202/069179-0477

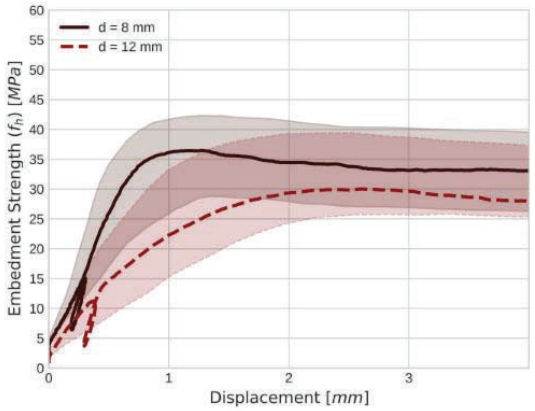

Figure 14: *Mean load-displacement curves for Scots pine (Pinus sylvestris) according to EN 383 for a dowel of 8 mm (t/d = 2.5) and 12 mm (t/d = 2.5) in diameter*

3.3 INFLUENCE OF TEST SETUP WITHIN EN 383

For the test setup within the scope of EN 383 [6] investigated in this study, no statistically significant difference was found for the embedding properties. The mean displacement curves for both wood species investigated are shown in Figures 15 and 16. This led to the conclusion that once the embedment failure is guaranteed within the experiment, that is, there was no premature splitting or bending of the dowel, the impact of the test setups evaluated is not significant to the results. This was guaranteed by following the recommendations of specimen dimensions of EN 383. A slenderness ratio (t/d) between 2 and 2.5 was adopted for the tests presented.

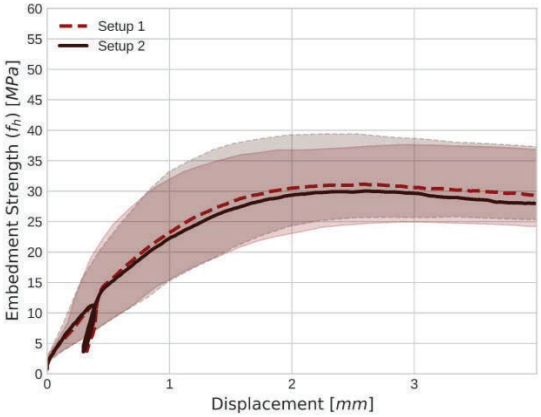

Figure 15: *Mean load-displacement curves for Scots pine (Pinus sylvestris) according to EN 383 for a dowel of 12 mm in diameter and specimens' thickness of 30 mm*

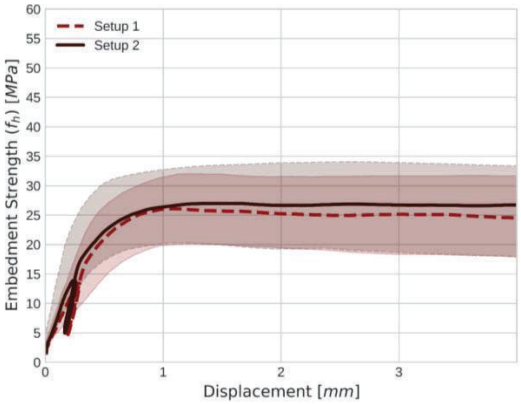

Figure 16: *Mean load-displacement curves for Spruce (Picea abies) according to EN 383 for a dowel of 12 mm in diameter and specimens' thicknesses of 30 mm*

4 CONCLUSIONS

This paper presents an experimental investigation related to testing methods and setup for the timber embedment strength and foundation modulus, two important properties for the connection behaviour. The investigation mainly covered the influence of specimen thickness within the scope of ASTM D5764-97a [5] and the influence of the test protocol in the quantification of the timber embedment according to the grain direction. The latter investigation was conducted by evaluating the embedment strength following both ASTM D5764-97a [5] and EN 383 [6] standards. An additional investigation was also conducted regarding the test setup (load application) of EN 383.

The results showed that the thickness had a significant impact on specimens with 35 mm (4.4d) compared to the ones with 20 mm (2.5d) and 25 mm (3.1d). No difference was found in the initial foundation modulus (K_s). This result points to the need for a deeper investigation regarding the influence of the member thickness on the embedment strength, especially since reference cross-sections of timber elements, commonly used in timber connections, have thicknesses greater than 40 mm. A broader experimental campaign involving other wood species, as well as a robust numerical analysis shall be conducted to confirm the trend found. For this, the half-hole specimen should be used to avoid dowel bending.

The investigation between test protocols resulted in a significant difference for both the embedment strength (yield – $f_{h,y}$ and ultimate – $f_{h,u}$) and the initial foundation modulus (K_s). The results differed from similar investigations found in the literature on different wood species. This could indicate the variability of test methods is also dependent on the wood species evaluated and the dowel diameter.

No significant difference was found in terms of the load application according to the EN 383 [6] standard.

https://doi.org/10.52202/069179-0477

ACKNOWLEDGEMENT

This work was financed by FCT – Foundation for Science and Technology within the scope of the Timquake project POCI-01-0145-FEDER-032031 and through a PhD grant 2021.07308.BD conceded to the first author. This work is also linked to the work in RILEM TC TPT "Tests methods for a reliable characterization of resistance, stiffness and deformation properties of timber joints".

REFERENCES

[1] EN-1995-1-1. Eurocode 5: Design of Timber Structures - Part 1-1: General - Common Rules and Rules for Buildings. Brussels, CEN, 2005.

[2] NDS: National Design Specification for Wood Construction, American National Standards Institute and American Forest & Paper Association, 2015

[3] A. Leijten, J. Köhler, A. Jorissen. Review of probability data for timber connections with dowel-type fasteners. Proceedings of CIB-W18/paper, 37–7, 2004.

[4] S. Franke, P. Quenneville. Investigation of the embedding strength of New Zealand timber and view for the NZ standard. Incorporating Sustainable Practice in Mechanics and Structures of Materials, 897–902, 2010.

[5] ASTM D5764-9a. Evaluating dowel-bearing strength of wood and wood-based products. West Conshohocken, United States, ASTM, 2007.

[6] EN 383. Timber structures - Test methods - determination of embedding strength and foundation values for dowel-type fasteners. Brussels, CEN, 2007.

[7] C. L. Santos, A. M. P. De Jesus, J. J. L. Morais, J. L. P. C. Lousada, A comparison between the EN 383 and ASTM D5764 test methods for dowel-bearing strength assessment of wood: experimental and numerical investigations. Strain, 46(2), 159-174, 2010.

[8] L. R. J. Whale, I. Smith. A method for measuring the embedding characteristics of wood and wood-based materials. Materials and Structures, 22, 403-410, 1989.

[9] J. Van Blokland, S. Florisson, M. Schweigler, T. Ekevid, T. K. Bader, S. Adamopoulos. Embedment properties of thermally modified spruce timber with dowel-type fasteners. Construction and Building Materials, 313, 125517, 2021.

[10] C. Sandhaas, G.J.P. Ravenshorst, H.J. Blass, J.W.G. Van de Kuilen. Embedment tests parallel-to-grain and ductility aspects using various wood species. European Journal of Wood and Wood Products, 71(5), 2013.

[11] S. Frankel, N. Magnière. Discussion of testing and evaluation methods for the embedment behaviour of connections. Proceedings of the International Network on Timber Engineering Research. INTER/47-7-1, Bath, United Kingdom, 2014.

[12] H. H. Nguyen, B. P. Gilbert, R. L. McGavin, H. Bailleres, H. Karampour. Embedment strength of mixed-species laminated veneer lumbers and cross-banded laminated veneer lumbers. *European journal of wood and wood products*, *78*, 365-386, 2020.

[13] B. H. Xu, J. B. Lin, Y. H. Zhao, A. Bouchaïr. Embedment behaviour of fully threaded bolts in glued laminated timber. European Journal of Wood and Wood Products, 1-18, 2022.

[14] J. S. Haukoos, R. J. Lewis. Advanced statistics: bootstrapping confidence intervals for statistics with "difficult" distributions. Acad Emerg Med, 12(4), 360–5, 2005.

[15] A.G. Dean, K. M. Sullivan, M. M. Soe. OpenEpi: Open Source Epidemiologic Statistics for Public Health, Version. www.OpenEpi.com, updated 2013/04/06.

World Conference on Timber Engineering Oslo 2023

DEVELOPMENT OF COMPREHENSIVE TESTING PROCEDURES FOR HIGH-PERFORMANCE BONDED-IN RODS

Robert Jockwer [1], Pedro Palma [2], Arthur S. Rebouças [3], Alexander Salenikovich [4]

ABSTRACT: Bonded- or glued-in rods are a highly efficient fastening technology. The complexity of the interaction of different materials in the joint (adhesive, rod, and wood) and non-linear stress distribution along the bondline present special challenges for the precise characterisation of the strength and stiffness properties relevant for the design. The existing test standards and protocols specify only the bare minimum for the utilisation of these connections. The following aspects need a more detailed consideration in test specifications: rods in different wood-based products; impact of spacing and end/edge distances; group effects; quality assurance; fatigue; impact of environmental conditions, fire resistance, etc. In the paper, a detailed state-of-the-art regarding testing of bonded-in rods is given and the different aspects with need for further test development are discussed. Proposals are also made on how to better characterize experimentally the properties and behaviour bonded-in rods and on how to fully utilize their potential in design.

KEYWORDS: glued-in rods, bonded-in rods, combined loading, fatigue, group effects, spacing, end/edge distances, RILEM TC TPT

1 INTRODUCTION

Bonded-in or glued-in rods are highly performant fastening technologies, especially when used to transfer axial forces or moments by means of metal or FRP rods into wood members. If properly designed and produced, they can achieve a very high stiffness, load-carrying capacity, fire resistance and be aesthetically pleasing and cost effective. However, due to the complex interaction of the rod, adhesive, and wood, a reliable characterisation of the properties of the bonded-in rods is particularly challenging and consequently, so is the design.

2 STATE OF THE ART

2.1 Development

The development and utilization of bonded-in rods started in the 1970s. Early developments of bonded-in rods can be traced back to the need to introduce high forces into wood members, especially in the direction parallel to the grain [1]-[3], as well as for reinforcements of existing structures, restoration and renovation [4]&[5]. Through the pioneering work of Turkovsky [6]&[7], joints with inclined bonded-in rods have been successfully used in large-span and outdoor timber structures in the USSR and then in Russia since the 1980s [8] (Figure 1). Major advancements in testing and design of bonded-in rods were achieved in the GIROD project [9]&[10]. In recent years, special systems of bonded-in rods have been developed, favouring a ductile failure in the rod to protect the joints form brittle failures [11]&[12]. Otero-Chans et al. [14] divided potential improvements of bonded-in rod systems into four groups: (1) hooped systems, (2) hybrid joints, (3) modified rod shapes and (4) modifications in the shape of the drilled hole (Figure 2).

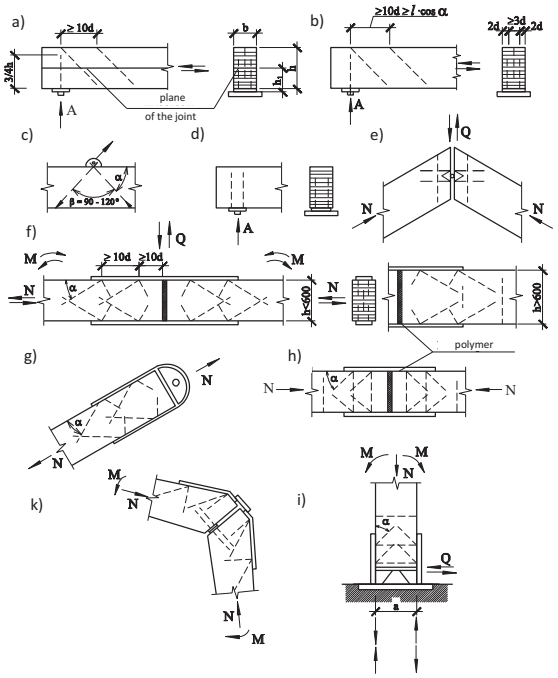

Figure 1: *Applications of inclined glued-in rods.[13]*

[1] Robert Jockwer, Chalmers University of Technology, Gothenburg, Sweden, robert.jockwer@chalmers.se
[2] Pedro Palma, Empa, Structural Engineering Research Lab, Switzerland, pedro.palma@empa.ch
[3] Arthur S. Rebouças, Federal Institute of Education, Science and Technology of Rio Grande do Norte (IFRN), Brazil arthur.reboucas@ifrn.edu.br
[4] Alexander Salenikovich, Laval University, Québec, Canada, alsal10@ulaval.ca

https://doi.org/10.52202/069179-0478

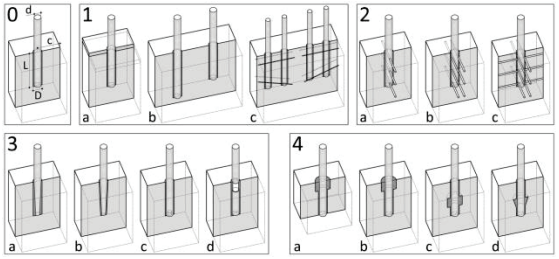

Figure 2: *Potential improvements of bonded-in systems. [14]*

2.2 Structural behaviour of bonded-in rods

Joints with bonded-in rods rely on the interaction between three components – the wood, the rod, and the adhesive – and the performance of the connection depends first and foremost on the adhesive bond between the wood and the rod (Figure 3). Careful planning, design, preparation, execution, and quality control are required to ensure the integrity, resistance, and durability of the bonded-in rod connection during the design working life of the structure.

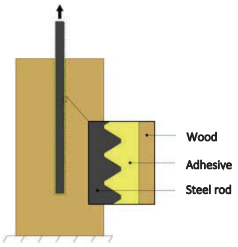

Figure 3: *Glued-in rod composite system.[15]*

The failure of joints with bonded-in rods can occur in the wood substrate, in the rod, in the adhesive, or at the wood-adhesive or rod-adhesive interfaces. For axially loaded bonded-in rods parallel to the grain, the following failure modes [12]-[16] are considered in the most recent draft of prEN 1995-1-1 *Eurocode 5* [17] (Figure 4):

a) tensile failure of the rod
b) compression (buckling) failure of the rod
c) failure of the adhesive within the glue line or in the bondline with the rod and/or timber
d) shear failure of the wood adjacent to the bondline
e) splitting of the wood starting from the bonded-in rods
f) plug shear failure of the wood in a joint with several bonded-in rods
g) net tension failure of the wood et the end of the rod.

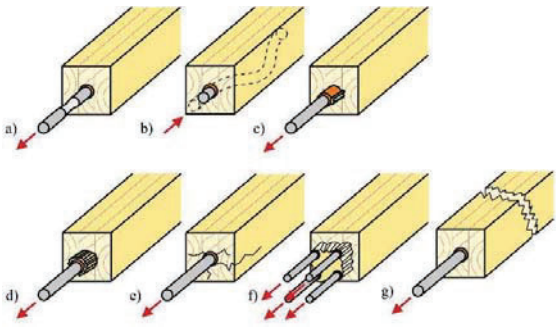

Figure 4: *Failure modes of axially loaded bonded-in rods (based on [16]).*

For the assessment of the load-carrying capacity and the governing failure modes, the different behavior of the joint components at the various locations must be considered. For example, the wood, the adhesive, and the bondline are characterized by large variability in load-carrying capacity and propensity to brittle failure modes. In contrast, mild-steel rods fail through yielding in a ductile manner and their load-carrying capacity is more predictable, especially if the quality of steel is controlled. Therefore, different partial safety factors are considered for the different failure modes in the design. When the yield failure mode governs the design, the bond strength is underutilized, but it is capacity protected (Figure 5).

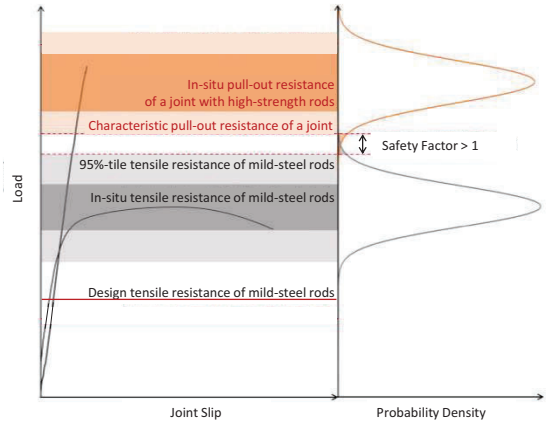

Figure 5: *Graphic illustration of the design philosophy of joints with bonded-in rods.[18]*

2.3 Standards for testing and design

The complex interaction of the different materials in the joint and the non-linear stress distribution along the bondline present special challenges for the precise characterisation of the strength and stiffness properties relevant for the design.

The testing requirements for bond shear strength of bonded-in rods in glued structural timber products are specified in EN 17334 [19]. Except for the Russian design standard [20], it is the first European test standard for bonded-in rods which sets the basis for the declaration of performance and design. In 2022, ICC-ES published Acceptance Criteria for bonded-in rods used as connections in tension and compression [42].

Several national timber design standards and design guides provide guidance for connections with bonded-in rods [21]-[27] with various degrees of detail. The next generation of prEN 1995-1-1 *Eurocode 5* [17], to be published in 2025, will include a chapter on bonded-in rods and will provide general design rules based, amongst other parameters, on the bond strength determined in accordance with EN 17334 [19].

Despite the lack of uniform European or international design guidelines, bonded-in-rods have been successfully applied in a variety of projects across the world. This has allowed further experience to be gained in their use. As a result, various approval documents have been issued for the use of bonded-in rods in timber structures, such as:

https://doi.org/10.52202/069179-0478

- Z-9 1-705 2K-EP-Klebstoff WEVO-Spezialharz [26]
- Z-9.1-896 2K-PUR Klebstoff LOCTITE CR 821 PURBOND [29]
- Z-9 1-778 2K-EP-Klebstoff GSA-Harz [30]
- Z-9.1-791 Studiengemeinschaft Holzleimbau [31]
- Technical Assessment 3/12-716 Societé SIMONIN SAS [32]

Recently, European Technical Assessments (ETA) have also been issued for products from various manufacturers [33]&[34] based on EAD 130006-00-0304 [35].

Based on these approvals, available bonded-in rod solutions can be categorized in two main approaches:

- adhesive-based solutions [29]: adhesive manufacturers have developed and certified special adhesives to produce bonded-in rods for specific customers. In the certification documents, the bond strength is specified without specific consideration of the joint configuration.
- system-based solutions [30]&[32]: other manufacturers have achieved approval and certification of proprietary systems of bonded-in rods, considering joints with particular combinations of rods, wood members, and adhesives.

These two approaches allow enough flexibility and specialisation to address the needs of different customers. Adhesive-based solutions require a higher level of detail in the generalized testing and in the description of design procedures to achieve the same desired level of performance in the application, whereas system-based solutions provide exclusive but potentially optimized configurations and range of applications.

In the specifications of the test procedure, EN 17334 [19] focuses primarily on the determination of the bondline shear strength as part of the description of failure mode c) according to the list in Section 2.2. The selection of the dimensions of the timber specimens and steel rods aims at avoiding failure modes comprising yielding of the steel or splitting of the timber members. This means that only some aspects of the bonded-in rod system are considered.

3 SELECTED CHALLENGES IN BONDED-IN ROD TESTING

The main challenges in testing and evaluation of bonded-in rod connections are related to the impact of the material characteristics, connection geometry, load direction and ambient conditions on the load-deformation behaviour, durability, and failure modes. The following selected challenges will be addressed in this paper:

- impact of the adhesive, wood product and grain orientation,
- quality assurance of the bond,
- behaviour in fire,
- stiffness and deformation capacity, and
- multiple rods

3.1 Impact of the adhesive, wood product and grain orientation

The strength of the adhesive bond is limited by the shear strength of the wood, the shear strength of the adhesive, and the bond between them. The shear strength of epoxy adhesives is in the range of 16 to 20 N/mm^2 [36]. PUR adhesives possess similar strength but are softer and have a lower glass transition temperature [37]. The high strength can only be exploited when rods are used in hardwoods [38]. In softwoods, the adhesive bond strength is generally limited by the shear strength of the wood [39] and the adhesive joint can only be utilized up to a shear strength of about 6 to 8 N/mm^2.

The bond strength depends on the bondline thickness. It is recognized in EN 17334 [19], which calls for evaluation of bondline thickness from 2 to 6 mm. Furthermore, researchers use larger and/or variable glue line thickness in search of improving the overall performance of the joints [14],[40].

In the case of rods bonded-in parallel to the grain and loaded in axial tension, failure occurs due to an irregular breakout cylinder depending on the local strength of the wood. Therefore, an effective bond strength is used in the design, which must be determined for the individual combination of adhesive, wood and size of the rod or reinforcement type according to EN 17334 [19].

The dependence of the bond strength on the bonded length described in EN 17334 [19] was chosen according to DIN EN 1995-1-1/NA:2013 [21]. Aicher and Stapf [39] discuss various other functions for the reduction of the adhesive bond strength as a function of the bonded length and compare them with test results. In a preliminary draft of EN1995-1-1:2004 *Eurocode 5*, a 10% reduction was proposed for rods bonded-in perpendicular to the grain.

The dependency of the bond strength on the bonded length is based primarily on the studies of bonded-in rods parallel to the grain in softwood glulam. It was observed that in joints with rods bonded-in perpendicular to the grain, the bond strength shows a lower dependency on the bonded length, because wood is much softer in this direction. Therefore, the shear stress distribution is assumed to be constant along the bondline, which cannot be said about the stress distribution along the rods bonded-in and loaded parallel to the grain (Figure 6). For this reason, a constant value can be assumed in design of rods bonded-in perpendicular to the grain within certain limits [40]. In addition, since the bondline failure of rods parallel to the grain can be initiated by the exceedance of failure strain of the wood, the bond strength definition in different wood products and wood species should be determined individually as a function of the angle to the grain. Therefore, the ICC-ES AC526 [42] requires tests of bonded-in rods at various angles to the grain.

https://doi.org/10.52202/069179-0478

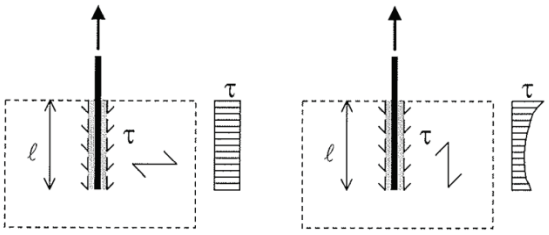

Figure 6: *Approximation of the stress distribution by gluing perpendicular and parallel to the grain direction. [40]*

To determine the bond strength in accordance with EN 17334 [19], the strength class or yield strength of the steel rod is chosen, depending on the rod diameter and the bond length, to achieve the bond or wood failure without rod yielding. Likewise, AC526 [42] requires that every rod diameter is tested at the maximum, minimum and at least one intermediate bond length using high-strength steel rods that have sufficient strength to develop the bond strength. To determine performance parameters of the joints other than the bond strength, the rods used in the tests should be representative of the class of steel intended for the application.

Bonded-in rods in cross-laminated timber (CLT) are permitted according to the next generation of prEN 1995-1-1 *Eurocode 5* [17]. However, Vallée et al. [43] state that the prediction of the load-carrying capacity of bonded-in rods in CLT is more challenging than in glued-laminated timber due to the increased anisotropy arising from the orthogonal arrangement of the layers. Brittle failure modes of the rods with tear-out of wood blocks from the different layers of the CLT were observed in tests in [44]&[45]. The complex brittle failure modes are influenced amongst others by the rod-to-grain angle, the distances to the cross-layers, spacing between the rods, and also include the rolling shear failure in the interface between the layers.

3.2 Quality assurance of the bond

Bonded-in rods are very demanding in terms of execution, as even minor defects and flaws in production can have a decisive impact on the bond performance. Care must therefore be taken to ensure careful and accurate production and quality assurance.

The effects of various production defects on the load-carrying capacity have been studied in detail [46]. It was found that insufficient grouting and voids along the bondline have the greatest influence on reducing the load-carrying capacity of the joint. Other defects include remaining wood chips in the drilled hole or insufficiently degreased threaded rods.

Gonzalez et al. [47] studied the impact of placing 12.7 mm rods of various lengths off-center during fabrication and did not observe any influence on the resistance nor failure modes. While this may be true for the smaller rods and generous edge distance, for rods of larger diameter and bond length and smaller spacing, the deviation of rod axis off-center may become a reason for splitting of the wood around the rod, which was observed by Salenikovich et al. [48] who tested 16 mm rods in glulam and MPP.

Another serious challenge in bonding of joints is the presence of cavities and gaps between laminations in CLT, where the glue may leak and result in starving joints. The gaps not only increase the consumption of the adhesive dramatically, but the starving joints may also not guarantee the full coverage of the adherends and result in defective bondlines.

One challenge relates to the assurance of the correct curing of the adhesives in the connections. Parameters that can have an impact on the curing of the adhesive are, e.g., the ambient and material temperatures during bonding and curing, the correct mixing ratio, and the moisture content of wood. Errors in the estimates of the wood temperature in cold climates may lead to the reduced pot life of the glue and defective bond.

Compliance withdrawal tests that can be used as an indicator for the correct curing of the adhesive in the bondline of bonded-in rods were developed together with the design and execution guidelines for the next generation of prEN 1995-1-1 *Eurocode 5* [17] and should be included in the next revision of EN1382 [49].

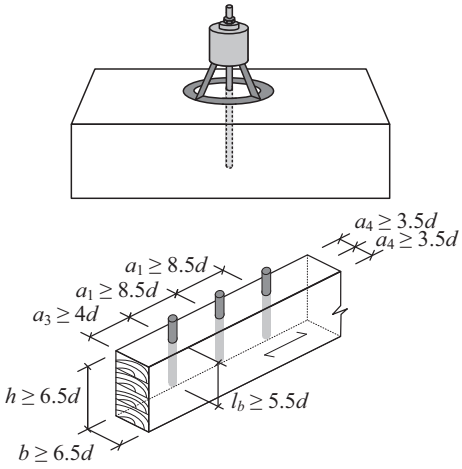

Figure 7: *Example of the compliance withdrawal test arrangement and the specimen geometry*

Such compliance withdrawal test may be carried out in *pull-beam*, *pull-compression,* or *pull-pile foundation* configurations as illustrated in Figure 7. The rods should be bonded in the direction perpendicular to the grain, to avoid splitting of the timber in the vicinity of the bondline. To avoid premature splitting of the wood member, the spacing and end and edge distances should be sufficiently large and exceed the minimum required values in the design regulations. Since the bond shear test is aimed at the bondline failure, the bonded length may be shorter than the minimum values given in the design standards, and a length of $5.5 \cdot d$ can be proposed for softwood. This test procedure is very similar to the quality assurance tests conducted in accordance with GOST R 56710 [20] except that the rods are pushed through (Figure 8).

https://doi.org/10.52202/069179-0478

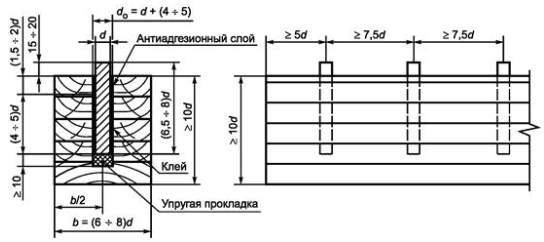

Figure 8: *Control specimens for bonded-in rods. [20]*

The wood material for the test specimens should be representative of the wood product intended for the application. Test pieces made from hardwood species (e.g., beech LVL) are also suitable for the checking of the curing of the adhesive of bonded-in-rods.

To achieve a representative comparison of the adhesive properties and curing in the compliance tests and the actual connections, the fabrication of the test joints shall be performed following the same procedures as for the bonded-in rods in the application. The test pieces should be stored under equal conditions as the bonded-in rods in the application until the full curing before testing.

The testing of the specimens is done as a reference testing, which means that the tested bond strength is benchmarked against a previously determined reference value.

The sampling procedures for compliance and acceptance testing should be in accordance with ISO 2859-1 [50]. A reference value of bond strength should be determined for the specimens stored at least until full curing of the adhesive under reference conditions at 20±2 °C and 65±5% relative humidity.

The bondline strength, corrected for the density, determined during the compliance tests shall be greater than or equal to the corresponding declared value of characteristic bond strength of the adhesive.

3.3 Behaviour in fire

Timber connections with exposed metal fasteners and steel plates are known to conduct heat into the core of the timber cross-section, which leads to increased charring and reduced load-carrying capacity in the connection area [51]-[53]. For connections with dowel-type fasteners, additional protection using panels or wooden plugs can be used to provide some cover to the otherwise exposed ends of the fasteners [54], contributing to increased fire resistance.

Bonded-in rods are inherently embedded in the wood cross-section, which can provide a significant advantage regarding fire resistance. Fire resistance tests on bonded-in rods have been performed with thermal insulation protecting the protruding end of the steel rod [55]-[57] or the other steel parts of the connection [58]. This prevents heat from being conducted from the steel parts into the adhesive, which would severely reduce the fire resistance. The fire resistance of connections with bonded-in rods cannot, therefore, be assessed solely based on the fire resistance of a fully embedded rod. The protection and detailing of the hub or plate connecting the rods to the next member is also a crucial aspect of the fire resistance of these connections [55]. Gaps between the surfaces of connected timber members can have a significant influence in the fire resistance and even small gaps can increase during fire exposure and lead to initially protected steel surfaces becoming exposed [53]. Therefore, an accurate evaluation of the fire resistance of a connection with bonded-in rods can only be made considering the configuration of the entire connection.

Performance criteria for fire resistance testing (maximum deformation or deformation rate) are also not specifically prescribed in EN 1363-1 [59] for structural timber connections, which often leads to different failure criteria being adopted in different studies.

3.4 Stiffness and deformation capacity

Axially loaded bonded-in rods exhibit very high stiffness and slip modulus due to nearly “slip-free” bonding in the joint. Various approvals therefore generally describe connections with bonded-in rods as “rigid”. A high stiffness is often desirable to achieve high efficiency in a moment-resisting connection and to reduce its rotation. However, this assumption might overestimate the stiffness of the joint, especially in the transition between the timber member and connected steel parts. Not only the stiffness of the bonded length of the rod but also the unbonded rod length and the flexibility of connected steel parts need to be considered in the design.

One challenge in determining the slip modulus in tests is the proper arrangement of the measuring equipment to correctly measure the decisive deformation. For example, the free, unbonded length of the rod has a significant share in the total deformation, and the distance between the reference points must be considered in test results.

Stiffness values reported in the literature vary a lot because they are measured differently and on different size, length and number of rods [47],[48]&[60]-[65]. For the rods of 16 mm in diameter, Bouchard et al. [65] and Salenikovich et al. [48] reported the slip moduli between 115 kN/mm and 212 kN/mm per rod. Gonzales et al. [47] and Verdet et al. [64] measured the slip modulus between 60 kN/mm and 110 kN/mm for rods of 12.7 mm and 8 mm in diameter. The latter values are comparable value to that given in the Simonin/Ducret approval [32] of 71 kN/mm. These values are somewhat higher than the slip moduli determined by Blaß and Steige [66] for screwed-in threaded rods, which are the basis for the approach in the most recent draft of prEN 1995-1-1 *Eurocode 5* [17]. To allow for a more effective and competitive use of bonded-in rods, the actual stiffness values of the system need to be determined during the bond strength tests. The placement of slip measuring devices should follow requirements of EN 17334 [19] or AC526 [42]. Characteristics of the bonded-in rod system such as an unbonded length, constriction, or the connection details should be considered in the determination of the real connection stiffness.

https://doi.org/10.52202/069179-0478

3.5 Multiple rods

3.5.1 Situation

During the last 30 years, several studies have been carried out on bonded-in rod connections, mainly focused on the pull-out resistance and on the bond behaviour between the rod and the wood. Most of the literature on the subject was initially focused on investigating the load-slip relationship and defining the failure mechanisms for a single-rod connection.

The few existing design codes with specific guidance for bonded-in rods, such as DIN EN 1995-1-1/NA [21], deal with the definition of the load-carrying capacity of a single rod or provide a simple adjustment to account for the uneven load distribution between the rods [13]. In the most recent draft of prEN 1995-1-1 *Eurocode 5* [17], the chapter on bonded-in rods addresses primarily joints with single rods and is based on bond strength determined in accordance with EN 17334 [19], which is also determined on single rod test specimens.

In practice, bonded-in rods are used in groups and a more detailed knowledge of their structural behaviour is relevant for the research community and designers [67]. That is why AC526 [42] requires testing groups of four rods placed at distances representative of the minimum allowed spacing for the system.

Due to a very high stiffness, bonded-in threaded rods cannot easily ensure redistribution of loads unless the rods start yielding. However, if the yield strength of the rods is higher than the bond strength, then the redistribution may not be possible and an uneven loading in a group of fasteners will lead to a brittle failure of the overloaded rod [65]. That is why the current design philosophy favours the design of joints with bonded-in rods where the yielding of the rods governs.

Unlike single joints, few data are available in the literature for multiple bonded-in rod connections. In general, available studies can be divided into pull-out tests (almost equally loaded tension joint) and moment-resisting connections (unequally loaded joints).

A reduction for the load-carrying capacity due to uneven force distribution is given by Turkovsky [4], based on the USSR standard of 1982. There, the reduction in load-carrying capacity due to uneven load distribution between rods is applied by reducing the load-carrying capacity 10% for two rods and 20% for three rods in a row parallel to the grain. The resistance is further reduced 10% if the bars are arranged in two rows perpendicular to the grain. Buchanan [24] proposed the following reduction of the load-carrying capacity for "closely spaced" rods: the full load-carrying capacity can be used for one or two rods, it must be reduced 10% for three or four rods, and reduced 20% for five or six rods. Based on the above recommendations, in the most recent draft of prEN 1995-1-1 *Eurocode 5* [17], a reduction of 10% is suggested for three to four rods and 20% for five or more rods, unless a uniform load distribution can be assumed. Connections with more than six rods are not recommended without a uniform load distribution.

In moment resisting connections, such as knee joints, with several layers of rods bonded-in parallel to the grain, Buchanan [24] recommended to have staggered bonded lengths by offsetting the rod ends by at least 75 mm to minimize the risk of splitting along the rods and to reduce the stress concentrations at the rod ends (Figure 9). In addition, it is recommended to check the wood fracture at tips of steel rods for the tensile force acting in each layer in such connections [26] (Figure 10).

3.5.2 Multiple rods pull-out tests

Several studies have focused on observing the failure modes, verifying the possibility of achieving ductile failure and evaluating the influence of the main geometric parameters (rod diameter, distance between rods, distance to edges, bonded length) and mechanical properties (yield and ultimate strength of rods) on the structural behaviour of the joints [47]&[68]-[71].

The test setups and procedures used are very similar to that for single rod joints and the loading protocol follows the recommendations given by ISO 6891 [72]. The maximum load, failure mode and displacement at failure are measured. From these tests, the load-carrying capacity of the joint is compared with the pull-out capacity of a single rod and the tensile resistance of the rod, which are usually predicted from analytical formulations. A group reduction factor for connections with multiple rods can be derived from this comparison.

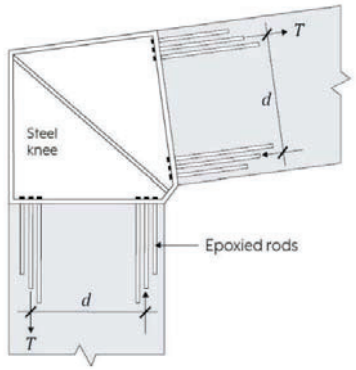

Figure 9: *Staggered rod ends in a knee joint. [26]*

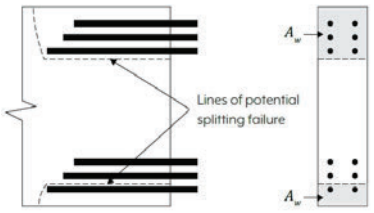

Figure 10: *Wood area for checking wood fracture capacity in a knee joint. [26]*

In many cases, failures occur due to splitting that starts at the end of the wood member and extends along the length of the rod before the onset of yielding. This could be in part due to the difficulty of fabricating connections with multiple rods that are perfectly aligned. Sometimes, there are defects in the bondline along the length of the rods. To mitigate the splitting failures, it is possible to reinforce the

https://doi.org/10.52202/069179-0478

wood member using perpendicular fasteners such as screws or smaller bonded-in rods. In fact, in Russia, the use of bonded-in rods parallel to the grain is not recommended, and transverse reinforcement is required in all connections [13].

In connections with multiple bonded-in rods, it is often aimed at small edge distances to increase the overall efficiency of the connection (i.e., less than $2.5 \cdot d$, which is the minimum distance recommended by most current standards to avoid splitting). When testing the bondline strength according to EN 17334 [19] larger edge and end distances of single rods are used. Gonzalez et al. [47] suggested a minimum edge distance of $3 \cdot d$ to avoid splitting and a minimum spacing of $5 \cdot d$ between rods to prevent splitting. When smaller spacings are used, special measures can be taken to minimize the risk of splitting, such as the use of a not-bonded length towards the end of the timber member. In the current test standard EN 17334 [19], such special measures are not specifically addressed. However, to evaluate the full performance of bonded-in rod system, the bond strength must be tested in combination with the specific measures to reduce the risk of splitting. That is why the not-bonded length and other features may be tested under AC526 [42].

The impact of the rod ductility and redistribution of load was evaluated by Gehri [73] and by Bouchard et al. [65] for connections loaded in axial tension. Larger test series on connections with multiple rods were described by Parida et al. [68], where the influence of low and high steel quality on the failure mode, capacity and ductility were investigated. Steiger et al. [74] stated that the use of "mild steel as well as more bars of smaller diameter are effective measures to increase the ductility of the connection." Especially for connections with several rods where unequal loading in the rods is expected, a high ductility of the joint is required to allow balancing and redistribution of the load.

It can be concluded that not only a single bonded-in rod joint, but the entire connection should be tested and that the system behaviour of the bonded-in rods should be considered. For pull-out tests, it is important to keep an even distribution of stresses across the section so that all rods are equally loaded. This can be achieved using a rigid plate at the end of the rods, fixing them with an extra length so that the rods could deform. However, it is not necessarily representative of the real joint configuration. In general, mild-steel rods are recommended for testing connections with multiple bonded-in rods, as well as in design, to facilitate the yielding and redistribution of loads between rods before other failure modes occur or any imperfections during production of the connection may result in much lower capacity than expected (see Fig.4).

4 PROPOSALS

The complexity of bonded-in rod connections as a system requires further development of tests methods, procedures, and protocols. Some of the most relevant aspects are:

- Rods in different wood-based products. The current European standard test procedures are based on rods bonded parallel to the grain in glued laminated timber or in CLT. The bond strength of rods bonded perpendicular to the grain is assumed to be equivalent. The impact of cross-layers in CLT and veneers in LVL and other wood-based products should be evaluated, especially regarding layer thickness and distribution, edge distances and potential edge intersection with the rod. The literature review revealed the occurrence of undesirable failure modes, including rolling shear of the cross-layers, depending on the specimen configuration.
- Quality assurance of the bond. The quality of the bondline must be verified to ensure the intended performance of the bonded-in rods. Quality assurance testing on representative specimens prepared in parallel to the production of the actual bonded-in rod joints, like it is done in Russia [20], can be a way to verify the correct curing of the adhesive in the bondline under the same environmental conditions and materials. In addition, it would be desirable to perform non-destructive tests to assess the integrity of the bondline after curing (e.g., proof-loading, X-ray scanning).
- Behaviour in fire. The bonded length of the rods is protected by the wood, but different adhesive systems show different sensitivity to high temperatures. The rod end is often exposed and connected to other metallic components that can act as a heat bridge into the connection and bondline. Gaps between connected members also influence the fire performance. The exact configuration of the system and not fully protected rods should be experimentally evaluated.
- Testing groups of rods. Bonded-in rods are most often used in groups, either acting all together with almost equal loading (such as in a tension joint) or with unequal loading (such as in a moment-resisting joint). In both cases, group effects, i.e., reduced load-carrying capacity of the group of rods compared to the sum of the individual rod capacities, may be observed. This aspect should be considered in the testing of the bonded-in rods in a system. Procedures developed in AC526 [42] can be taken as a starting point.
- Rod spacing and improved systems. So far, only tests on single rods with relatively large edge distances have been standardized in Europe for the determination of the bond strength. According to the proposal in the most recent draft of prEN 1995-1-1 *Eurocode 5* [17], the minimum spacing and edge distances must be chosen depending on the bond strength assumed in the design. Hence, to account for a higher bond strength, a larger spacing, a recess (not-bonded length), or any other potential improvements can be required for qualification testing. However, specific spacing requirements for different wood-based products, particularly for hardwoods and LVL, are missing. Procedures developed in AC526 [42] can be taken as a starting point.

https://doi.org/10.52202/069179-0478

- Fatigue behaviour. Bonded-in rods are often applied in conditions prone to fatigue loading. Depending on the configuration, the fatigue strength is typically governed by properties of the rods. However, the fatigue strength of the adhesive bond or wood may also govern. To reliably predict the performance of the connection, the exact configuration of the system should be evaluated.
- Impact of temperature and moisture conditions. The environmental conditions during curing of the adhesive and in the final application have an impact on the performance of the connection. More practical test procedures must be developed to quantify these effects. AC526 [42] may be used as an example.

5 CONCLUSIONS

A review of the state-of-the-art regarding testing of bonded-in rods is given and the different aspects that need for further development of test specifications are discussed.

Proposals are made on how to better characterize the properties and behaviour of groups of bonded-in rods in tests and how to fully utilize their potential in design.

ACKNOWLEDGEMENT

The paper is based on the work of the working group on bonded-in rods in RILEM TC TPT "Tests methods for a reliable characterization of resistance, stiffness and deformation properties of timber joints".

REFERENCES

[1] A. Baumeister, H. Blumer, H. Brüninghoff, J. Ehlbeck, B. Koehlen, P. Köster, G. Maier, K.-H. Meyer, D. Steinmetz, and J. Wenz. 1972. Neuere Karlsruher Forschungsarbeiten und Versuche im Ingenieurholzbau. Bauen mit Holz 74, 6 (1972), 298–317.

[2] G. Edlund. 1975. In Brettschichtholz eingeleimte Gewindestangen. Svenska Träforskningsinstitutet, Med. Serie B 33 (1975).

[3] H. Riberholt. 1979. Eingeleimte Gewindestangen. Danmarks Tekniske Højskole, Afdelingen for Baerende Konstruktioner, Lyngby, Denmark.

[4] Klapwijk, D. 1878. Restoration and preservation of decayed timber structures and constructions with epoxies. Preprints of the contribution to the Oxford Congress, London, UK, pp.75-76.

[5] Taupon, J. 1980. Restauration à la résine époxyde de planchers et charpentes au Monastère de la Grande Chartereuse. *Bulletin d'Informations Techniques 92*, 34-43.

[6] S. Turkovsky. 1989. Designing of glued wood structures joints on glued-in bars. Paper 22-7-13, In Proc. of the CIB-W18 Meeting 22, Berlin, Germany.

[7] Turkowskij, S. 1991. "Prefabricated Joints of Timber Structures on Inclined Glued-in Bars." In Proceedings of the 1991 International Timber Engineering Conference, TRADA, London, UK.

[8] С. Б. Турковский, А. А. Погорельцев, И. П. Преображенская. Клееные деревянные конструкции с узлами на вклеенных стержнях в современном строительстве (система ЦНИИСК). Москва, РИФ «Стройматериалы». 2013. (in Russian)

[9] TRADA. (2001). "GIROD -Glued-in Rods for Timber Structures WP 8 -Draft Design Rules for Eurocode 5 - 36th Month Progress Report." UK.

[10] Bengtsson, C., and C.-J. Johansson. (2002). GIROD-Glued in Rods for Timber Structures. SMT4-CT97-2199.

[11] Steiger, R., E. Gehri, and R. Widmann. (2007). "Pull-out Strength of Axially Loaded Steel Rods Bonded in Glulam Parallel to the Grain." Materials and Structures/Materiaux et Constructions 40 (1): 69–78.

[12] R. Steiger. 2012. In Brettschichtholz eingeklebte Gewindestangen – Stand des Wissens zu einer leistungsfähigen Verbindungstechnik. In Proc. of the Internationales Holzbau-Forum, Garmisch-Partenkirchen, Germany.

[13] CP382. Glued laminated timber structures with glued-in rods. Design methods. Moscow, RF, 2018.

[14] D. Otero-Chans, J. Estévez-Cimadevila, E. Martín-Gutiérrez, F. Suárez-Riestra. 2019. Systems that improve the behaviour of joints made using glued-in rods. European Journal of Wood and Wood Products. 77:1079–1093 https://doi.org/10.1007/s00107-019-01461-4

[15] R. Bouchard. 2021. Comportement en traction longitudinale d'assemblages multi-tiges encollées dans le bois lamellé-collé. Mémoire M. Sc. Université Laval. http://hdl.handle.net/20.500.11794/69035

[16] G. Tlustochowicz, E. Serrano, and R. Steiger. 2011. State-of-the-art review on timber connections with glued-in steel rods. Materials and Structures/Materiaux et Constructions 44, 5 (2011), 997–1020.

[17] prEN 1995-1-1: Eurocode 5 Design of timber structures — Part 1-1: General rules and rules for buildings. CEN/TC 250/SC 5 N 1650, CEN European committee for standardization, Brussels, Belgium, 12-2022.

[18] A. Salenikovich, R. Bouchard, C. Frenette, G. Bédard-Blanchet. A study of the tensile behaviour of joints with multiple glued-in steel rods in glued-laminated timber. In: *Proceedings of WCTE 2021*, Santiago, Chile. 2021.

[19] EN 17334 - Glued-in-Rods in Glued Structural Timber Products — Testing, Requirements and Bond Shear Strength Classification. European Committee for Standardization CEN, Brussels, Belgium, 2021.

[20] ГОСТ Р 56710-2015. Соединения на вклеенных стержнях для деревянных конструкций. Технические условия. Москва. Стандартинформ. 2016. (in Russian)

[21] DIN EN 1995-1-1/NA: National Annex - Nationally Determined Parameters - Eurocode 5: Design of Timber Structures - Part 1-1: General - Common Rules and Rules for Buildings. Berlin, Germany: DIN Deutsche Institut für Normung e.V., 2013.

[22] SIA. 2021. Norm SIA 265:2021 - Holzbau. SIA - Schweizerischer Ingenieur- und Architektenverein: Zürich, Switzerland.
[23] CNR. 2007. CNR-DT 206-2007, Istruzioni per la Progettazione, l'Esecuzione ed il Controllo delle Strutture di Legno. Consiglio Nazionale delle Richerch, CNR, Commissione di studio per la predisposizione e l'analisi di norme tecniche relative alle costruzioni.
[24] A. Buchanan. 2007. NZW 14085 SC, New Zealand Timber Design Guide. Timber Industry Federation Inc., Wellington, New Zealand.
[25] Svenskt Trä. 2016. Limträhandbok, Projektering av limträkonstruktioner, Del 2. Svenskt Trä, Föreningen Sveriges Skogsindustrier, Stockholm, Sweden.
[26] WMPA. Portal knee connections. NZ Wood Design Guide. Chapter 12.5. April 2020.
[27] D. Moroder. Design of glued-in rods or bars. 2020. New Zealand Timber Design Journal. Vol. 28, issue 3:26-31.
[28] DiBt.Z-9.1-705 2K-EP-Klebstoff WEVO-Spezialharz EP 32 S mit WEVO-Härter B 22 TS zum Einkleben von Stahlstäben in Holzbaustoffe, WEVO-CHEMIE GmbH. Deutsches Institut für Bautechnik, Berlin, Germany, 2021.
[29] DiBt. "Z-9.1-896 2K-PUR Klebstoff LOCTITE CR 821 PURBOND Zum Einkleben von Stahlstäben in Tragende Holzbauteile, Henkel & Cie. AG." Berlin, Germany: Deutsches Institut für Bautechnik, Berlin, Germany, 2020.
[30] DiBt. "Z-9.1-778 2K-EP-Klebstoff GSA-Harz Und GSA-Härter Für Das Einkleben von Stahlstäben in Holzbaustoffe, Neue Holzbau AG." Berlin, Germany: Deutsches Institut für Bautechnik, Berlin, Germany, 2017.
[31] DiBt. Z-9.1-791 Verbindungen mit faserparallel in Brettschichtholz eingeklebten Gewindestangen für den Holzbau, Studiengemeinschaft Holzleimbau e. V. Deutsches Institut für Bautechnik, Berlin, Germany, 2021.
[32] CSTB. Avis Technique 3.3/19-986. Assemblage pour structure bois. Goujons collés RBF. Titulaires: Societé SIMONIN SAS, Societé JPF-DUCRET SA. Champs-sur-Marne, France, 2019.
[33] OIB. "ETAssessment 19/0752 - GSA® - Technologie, Glued-in Rods for Timber Connections." EAD 130006-00-0304. Vienna, Austria: OIB Austrian Institute of Construction Engineering, 2020.
[34] OIB. "ETAssessment 20/0834 - Hilti HIT-RE 500 V4, Timber Structures - Glued-in Rods for Timber Connexions." EAD 130006-00-0304. Vienna, Austria: OIB Austrian Institute of Construction Engineering, 2020.
[35] EOTA. "EAD 130006-00-0304 - Glued-in Rods for Timber Connections." Pending for Citation in OJEU. Brussels, Belgium: EOTA - European Organisation for Technical Assessment.
[36] E. Gehri. 1995. Krafteinleitungen mittels Stahlanker. In Brettschichtholz - Material, Bemessung, Ausführung, Qualitätssicherung, Weinfelden, Switzerland.
[37] M. Verdet. 2017. Étude du comportement à long terme de systèmes d'assemblages par goujons collés en conditions climatiques variables. Thèse PhD. Université Laval. http://hdl.handle.net/20.500.11794/27530
[38] O. Bletz-Mühldorfer, L. Bathon, D Grundwald, T. Vallee, S. Myslicki, and F. Walther. 2017. Eingeklebte Stäbe in Laubholzkonstruktionen. Bauen mit Holz 4 (2017), 34–39.
[39] S. Aicher and G. Stapf. 2017. Eingeklebte Stahlstäbe - state-of-the-art - Einflussparameter, Versuchs-ergebnisse, Zulassungen, Klebstoffnormung, Bemessungs- und Ausführungsregeln. In Internationales Holzbau-Forum (IHF 2017), Garmisch-Partenkirchen, Germany.
[40] Schober, K., and T. Tannert. 2016. "Hybrid Connections for Timber Structures." European Journal of Wood and Wood Products 74, no. 3: 369–77. https://doi.org/10.1007/s00107-016-1024-3.
[41] A. Bernasconi. 2001. Behaviour of axially loaded glued-in rods – requirements and resistance, especially for spruce timber perpendicular to the grain direction. Paper 34-7-6. CIB-W18 Meeting 34, Venice, Italy.
[42] ICC-ES AC526. Acceptance criteria for factory installed glued-in rods in wood structural elements. 2022.
[43] Vallée, Till, Hossahalli Ramesh Rakesh, and Thomas Tannert. "Load-Carrying Capacity Prediction of Single Rods Glued into Cross-Laminated Timber." European Journal of Wood and Wood Products 80, no. 5 (October 1, 2022): 1041–55. https://doi.org/10.1007/s00107-022-01835-1.
[44] Azinović, Boris, Erik Serrano, Miha Kramar, and Tomaž Pazlar. "Experimental Investigation of the Axial Strength of Glued-in Rods in Cross Laminated Timber." Materials and Structures 51, no. 6 (October 18, 2018): 143. https://doi.org/10.1617/s11527-018-1268-y.
[45] Ayansola, G.S., T. Tannert, and T. Vallee. "Glued-in Multiple Steel Rod Connections in Cross-Laminated Timber." Journal of Adhesion 98, no. 6 (2022): 810–26. https://doi.org/10.1080/00218464.2021.1962715.
[46] N. Ratsch, S. Böhm, M. Voß, M. Kaufmann, and T. Vallée. 2019. Influence of imperfections on the load capacity and stiffness of glued-in rod connections. Construction and Building Materials 226, (November 2019), 200–211. DOI: https://doi.org/10.1016/j.conbuildmat.2019.07.278
[47] E. Gonzales, T. Tannert, T. Vallee, The impact of defects on the capacity of timber joints with glued-in rods, Int. J. Adhesion & Adhesives 65 (2016) 33–40 DOI: https://doi.org/10.1016/j.ijadhadh.2015.11.002
[48] A. Salenikovich, É. Lapointe, B. Zumbrunn-Maurer, T. Brotschi, A. Kramer. Performance of glued-in rods in glulam and MPP in tension and compression. In: *Proceedings of WCTE 2023*, Oslo, Norway. 2023.
[49] EN 1382: 2016. Timber structures - Test methods - Withdrawal capacity of timber fasteners. CEN European committee for standardization, Brussels, Belgium, 2016.

https://doi.org/10.52202/069179-0478

[50] ISO 2859-1:1999/Cor 1:2001. Sampling procedures for inspection by attributes — Part 1: Sampling schemes indexed by acceptance quality limit (AQL) for lot-by-lot inspection.
[51] P. Palma, A. Frangi, E. Hugi, P. Cachim, H. Cruz, Fire resistance tests on steel-to-timber dowelled connections reinforced with self-drilling screws, in: Proc. 2nd Ibero-Lat.-Am. Congr. Fire Saf. – 2nd CILASCI, Coimbra, Portugal, 2013: p. 11.
[52] P. Palma, A. Frangi, E. Hugi, P. Cachim, H. Cruz, Fire resistance tests on timber beam-to-column shear connections, J. Struct. Fire Eng. 7 (2016) 41–57. https://doi.org/10.1108/JSFE-03-2016-004.
[53] P. Palma, Fire behaviour of timber connections, Doctoral thesis, ETH Zürich, 2016.
[54] EN 1995-1-2:2004. Eurocode 5: Design of timber structures – Part 1-1: General – Structural fire design, European Committee for Standardization (CEN), Brussels, 2004.
[55] S. Harris, Fire resistance of epoxy-grouted steel rod connections in laminated veneer lumber (LVL), MS, University of Canterbury, 2004. http://www.civil.canterbury.ac.nz/fire/pdfreports/S_Harris04.pdf.
[56] S. Harris, W. Lane, A. Buchanan, P. Moss, Fire performance of laminated veneer lumber (LVL) with glued-in steel rod connections, in: Struct. Fire - Proc. Third Int. Workshop, Ottawa, Canada, 2004: pp. 411–424. http://www.structuresinfire.com/corpo/conferences/sif04.pdf.
[57] L. Luo, B. Shi, W. Liu, H. Yang, Z. Ling, Experimental investigation on the fire resistance of glued-in rod timber joints with heat resistant modified epoxy resin, Materials. 13 (2020) 2731. https://doi.org/10.3390/ma13122731.
[58] T. Oksanen, J. Kangas, Strength and fire resistance of connections based on glued-in rods, VTT Technical Research Centre of Finland, Espoo, 1999.
[59] EN-1363-1:2020. Fire resistance tests – Part 1: General requirements. CEN European committee for standardization, Brussels, Belgium, 2020.
[60] E. Gonzalez, C. Avez, and T. Tannert. 2016. Timber joints with multiple glued-in steel rods. The Journal of Adhesion, 92, 7–9 (2016), 635–651.
[61] F. Hunger, M. Stepinac, V. Rajčić, and J.-W. van de Kuilen. 2016. Pull-compression tests on glued-in metric thread rods parallel to grain in glulam and laminated veneer lumber of different timber species. European Journal of Wood and Wood Products 74, 3 (2016), 379–391.
[62] J. Ogrizovic, R. Jockwer, and A. Frangi. 2018. Seismic Response of Connections with Glued-in Steel Rods. In Proc. of the INTER Meeting 5/Paper 51-7-5, Tallinn, Estonia.
[63] M. del Senno, M. Piazza, and R. Tomasi. 2004. Axial glued-in steel timber joints—experimental and numerical analysis. Holz Roh Werkst 62, 2 (April 2004), 137–146. DOI: https://doi.org/10.1007/s00107-003-0450-1
[64] M. Verdet, A. Salenikovich, A. Cointe, J.-L. Coureau, P. Galimard, W. Munoz Toro, P. Blanchet, and C. Delisée. 2016. Mechanical Performance of Polyurethane and Epoxy Adhesives in Connections with Glued-in Rods at Elevated Temperatures. BioResources 11, 4 (August 2016), 8200–8214
[65] R. Bouchard, A. Salenikovich, C. Frenette, and G. Bedard-Blanchet. 2021. Experimental investigation of joints with multiple glued-in rods in glued-laminated timber under axial tensile loading. Construction and Building Materials 293, (July 2021), 122614. DOI: https://doi.org/10.1016/j.conbuildmat.2021.122614
[66] H.J. Blaß and Y. Steige. 2018. Steifigkeit axial beanspruchter Vollgewindeschrauben. DOI: https://doi.org/10.5445/KSP/1000085040
[67] Stepinac M, Hunger F, Tomasi R, Serrano E, Rajcic V, van de Kuilen JW. Comparison of design rules for glued-in rods and design rule proposal for implementation in European standards. In: Rainer Görlacher, editor. Proceedings of CIB-W18 Meeting 46, Vancouver, Canada; 26–29 August 2013.
[68] G. Parida, H. Johnsson, and M. Fragiacomo. 2013. Provisions for Ductile Behavior of Timber-to-Steel Connections with Multiple Glued-In Rods. J. Struct. Eng. 139, 9 (2013), 1468–1477. DOI: https://doi.org/10.1061/(ASCE)ST.1943-541X.0000735
[69] Gehri E. Ductile behaviour and group effect of glued-in steel rods. Joints in Timber Structures. In: International RILEM symposium, Stuttgart, Germany; 2001. p. 333–42.
[70] Broughton JG, Hutchinson AR. Pull out behaviour of steel rods bonded into timber. Mater Struct 2001;34–2:100–9.
[71] Gattesco N, Gubana A, Buttazzi M. Pull out strength of bar glued-in-joints. In: Proc. of the 11th world conference on timber engineering, Riva del Garda, Italy; 2010.
[72] ISO 6891:1983. Timber structures — Joints made with mechanical fasteners — General principles for the determination of strength and deformation characteristics. Reapproved in 2021.
[73] E. Gehri. 2016. Performant connections - A must for veneer-based products. In Proc. of the World conference on timber engineering WCTE, Vienna, Austria.
[74] R. Steiger, E. Serrano, M. Stepinac, V. Rajčić, C. O'Neill, D. McPolin, and R. Widmann. 2015. Strengthen-ing of timber structures with glued-in rods. Construction and Building Materials 97, (October 2015), 90–105. DOI: https://doi.org/10.1016/j.conbuildmat.2015.03.097

World Conference on Timber Engineering Oslo 2023

PROTOCOLS AND RESULTS ANALYSIS METHODS FOR CYCLIC TESTS OF TIMBER JOINTS. A DISCUSSION

Meta Kržan[1], Caroline D. Aquino[2], Michael Schweigler[4], Zheng Li[5], Jorge M. Branco[6]

ABSTRACT: Current testing procedures for cyclic loading are quite flexible and the influence of fundamental testing parameters on the obtained load-deformation behaviour is often questioned (number and amplitude of the loading cycles, loading rate, number of specimens, etc.). On the other hand, different methods for data assessment have been used for the definition of stiffness, ductility, strength and stiffness degradation, as well as parameters for analytical and numerical models. However, reliable and well-established assessment methods are required, to support the safe and economic design of timber joints. Fundamental parameters for seismic design, such as ductility or strength degradation, cannot depend on the testing protocol and method for assessment of the data results. In this context, it is important to compare the most representative loading protocols, and assessment methods of the test results, through detailed analysis and discussion. Different types of timber connections, made of distinct materials and tested in different laboratories, must be evaluated. This work will be developed within the RILEM TC TPT, and this paper represents a first contribution to a needed discussion about the testing protocols to evaluate timber connections. In the end, it is expected to present proposals on how to characterize better the properties and behaviour of timber connections under cyclic loading and how to fully utilize their potential in design.

KEYWORDS: Testing protocols, Cyclic loading, Data assessment, Timber connections, RILEM TC TPT

1 INTRODUCTION

The behaviour of timber joints is one of the most important topics in the field of timber structures, and one of the most studied, given their critical role and importance in the local and overall behaviour of timber structures. Due to the brittle nature of wood material, timber elements must be considered elastic, while the nonlinear responses must be concentrated on the joints. The yielding of the metallic dowel-type fasteners can ensure the dissipation of seismic energy together with deformation capacity [1]. As a result, mechanical connections have to be properly designed in order to show adequate low-cyclic fatigue strength, developing plastic deformations with medium-to-high amplitude when subjected to cyclic loads [2]. Given the complexity of their behaviour (anisotropic behaviour of wood, stress concentration around fasteners, variability of mechanical properties, moisture-dependency, size effects), in particular under cyclic loading, research is often based on the experimental evaluation of joints.

Current testing procedures for cyclic loading are quite flexible and the influence of fundamental testing parameters on the obtained load-deformation behaviour is often questioned (number and amplitude of the loading cycles, loading rate, number of specimens, etc.). On the other hand, different methods for data assessment have been used for the definition of stiffness, ductility, strength and stiffness degradation, as well as parameters for analytical and numerical models [3]. Several studies have highlighted the importance of achieving a general consensus within the research community to define a unique cyclic-test procedure and the appropriate definition of yield and ultimate slips to avoid inconsistencies due to high variability in the definition of ductility [3, 4]. Following the initiatives of research and professional community, a technical report ISO/TR 21141 entitled "Timber structures – Timber connections and assemblies – Determination of yield and ultimate characteristics and ductility from test data" was published in 2022 [5] as a result of work and discussions of the ISO/TC 165 technical committee for timber structures. In the document, different methods for determining the yield and ultimate characteristics and ductility of joints and assemblies from test data used in existing standards in Europe, North America and Far East Asia are described and the basic data for unifying the evaluation methods of

[1] Meta Kržan, Slovenian National Building and Civil Engineering Institute, Ljubljana, Slovenia, meta.krzan@zag.si
[2] Caroline D. Aquino, DECivil, University of Minho, ISISE, Guimarães, Portugal, carolinedapieve@gmail.com
[3] Michael Schweigler, Linnaeus University, Växjö, Sweden, michael.schweigler@lnu.se
[4] Zheng Li, Tongji University, Shanghai, China, zhengli@tongji.edu.cn
[5] Jorge M. Branco, DECivil Engineering, University of Minho, ISISE, Guimarães, Portugal, jbranco@civil.uminho.pt

https://doi.org/10.52202/069179-0479

parameters by clarifying their similarities and differences is provided.
Meanwhile, a guideline to determine ultimate slip and consequently ductility of timber joints from cyclic tests by considering also strength degradation and impairment is included within an annex to the new Eurocode 8 proposal, namely prEN 1998-1-2:2022, Annex N [6]. However, the relationship between strength degradation and ductility has not been discussed in detail.

2 CYCLIC TEST LOADING PROTOCOLS AND RESULTS ANALYSIS METHODS

The most representative load protocols for cyclic tests are the EN 12512 [7] and ISO 16670 [8]. Equally important, the method used to analyse the test data can differ. Widely used are the analysis methods according to EN 12512, Yasumura and Kawai [9], Kobayashi and Yasumura [10] and the ASTM E2126 [11].

2.1 Cyclic loading protocols

For both EN 12512 and ISO 16670, the loading protocols are defined in dependence on the non-linear response of the connection obtained under monotonic loading, conducted according to EN 26891 [12] and ISO 6891 [13], respectively.
However, according to EN 12512 (and the prEN1998 as well), the imposed cyclic loading in terms of the cyclic displacement schedule (Figure 1) is set based on yield displacement, obtained in monotonic test ($v_{y,M}$), while in ISO 16670, the loading time history is defined based on ultimate displacement ($v_{u,M}$).

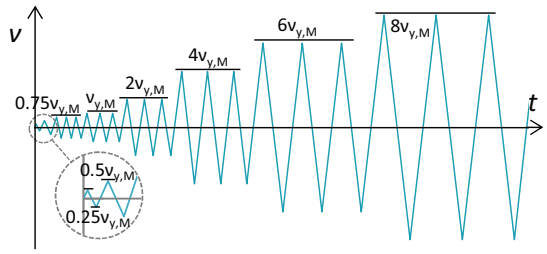

Figure 1: *Loading protocol defined in dependence of yield displacement according to EN 12512 [7].*

The loading protocol in EN 12512 is definite; the first two loading steps applied in one loading cycles (amplitudes 25% and 50% of v_y), are followed by subsequently increased amplitude displacements each with three loading cycles (75%, 100%, 200%, 400%, 600%,… of v_y).
On the other hand, initial loading amplitudes in ISO 16670 up to 10%v_u. (1.25%, 2.5%, 5% and 10% of v_u), are conducted with one loading cycle, but may be omitted or repeated depending on the joint stiffness and testing/measuring equipment. All the subsequent amplitude displacements are loaded in three loading cycles (20%, 40%, 60%,… of v_u).
The ASTM E2126 is more flexible with loading protocols allowing the displacement-controlled loading to be conducted according to: a) Sequential Phased Displacement (SPD) Loading Protocol, which involves displacement cycles grouped in phases at incrementally increasing displacement levels (either sinusoidal or triangular); b) ISO 16670 loading protocol or c) CUREE Basic Loading Protocol, with displacement cycles grouped in phases at incrementally increasing displacement levels and the loading history starting with a series of (six) initiation cycles at small amplitudes (of equal amplitude). Further, each phase of the loading history consists of a primary cycle with amplitude expressed as a fraction (percent) of the reference cycle deformation and subsequent trailing cycles with an amplitude of 75 % of the primary one.
The loading rates also differ according to the standards; the slip rate should according to EN 12512 be constant and may range between 0.02 and 0.2 mm/s, while according to ISO 16670 alternative cyclic displacement schedules – either velocity or frequency based - are allowed with the slip rates between 0.1 and 10 mm/s. Similar is according to ASTM E2126, where the displacement loading rate should be between 1.0 and 63.5 mm/s (standard intended for both lateral resisting systems and shear and hold-down connections) and the cyclic frequency range from 0.2 to 0.5 Hz.
Regarding the loading protocols, Casagrande *et al.* [2] concluded that an increase in the number of cycles leads to greater precision of the results and propose an amendment to the cyclic test protocol given by EN 12512.

2.2 Analysis of the test results

From the lateral force-deformation hysteresis curves various characteristics can be evaluated; besides the performance of the connection in terms of strength and deformation, hysteresis with repeated cycles enables the analysis of strength and stiffness degradation and energy dissipation.
To compare different responses, hysteresis envelope curves are often used. Important parameters, such as elastic and plastic stiffness, yield and ultimate displacement (slip), and ductility are evaluated from hysteresis envelopes by considering agreed criteria for idealisation.

Ductility is defined as the ultimate to yield slip ratio and it therefore highly depends on both yield and ultimate slip definitions.
Ultimate slip v_u is commonly defined as the smallest of failure slip, slip at 20% of strength drop considering 1st Load-Slip Envelope Curve (1st LEC) or absolute slip limit (30 mm in EN 12512).

Yield slip v_y can according to EN 12512 be calculated considering two different procedures. When the 1st LEC presents two well-defined linear parts, the yield slip v_y is determined by the intersection between the two lines

https://doi.org/10.52202/069179-0479

(Method A). When two well-defined linear parts are not observed, ν_y is determined by the intersection of two additional lines (Method B): the first line (denoted as the elastic line), with slope K_α (stiffness), is determined as that drawn through the point on the curve corresponding to 10% of the maximum load F_{max} and the point on the curve corresponding to 40% of F_{max}. This stiffness is in the paper labelled $K_{10\text{-}40}$, in the prEN 1998-1-2 proposal $K_{SLS,v,c}$, but it is also commonly referred to as elastic stiffness and labelled K_e. The second line (denoted as plastic line) is the tangent to the backbone curve having an inclination K_β equal 1/6 inclination of the first line (K_α).

ASTM E2126 [11] and Kobayashi and Yasumura [10] apply the Equivalent Energy Elastic-Plastic (EEEP) method to determine the yield slip ν_y and the ductility (D), through the definition of equivalent bi-linear ideally elastic, ideally plastic curve. In general, to determine such a curve considering the EEEP criterion, two more criteria besides EEEP are needed. While there are not many differences in the definition of ultimate displacement (one criterion), the other criterion may either be assumed/defined effective stiffness and less commonly assumed/defined idealised strength capacity. The first is adopted by Kobayashi and Yasumura, who determine yield slip ν_y through EEEP by assuming K_{ef} and calculating idealised force. The K_{ef} is in their case defined according to Yasumura and Kawai [9] as the point in the curve at the same force, at which the secant line through 10 and 40% F_{max} intersects a tangent line to the curve with an inclination of a secant line through 40 and 90% F_{max}. Similar is proposed in ASTM E2126, where the assumed effective stiffness K_{ef} is defined as stiffness at 40% F_{max}. Some authors use in a similar way the EEEP criterion to define the bi-linear curve considering the effective stiffness determined from EN 12512 (stiffness corresponding to ν_y) and to evaluate ductility more conservatively in comparison to EN 12512 by defining the yield slip as the elastic displacement of the idealised bi-linear curve. The use and comparison of such idealisation are presented in the paper for the second case study.

Within the revision process of Eurocode 8, Casagrande *et al.* [1] proposed a novel methodology, which defines an interaction between the strength degradation and the ductility capacity, offering two major contributions to the field: i) it defines a relationship between the slip amplitude and the impairment of strength from the 1st to 3rd cycle and provides an additional condition for determination of ultimate slip in dependence of strength impairment limit; and, ii) it considers the strength degradation as an additional condition for the determination of ultimate slip of dissipative connections subjected to low-cyclic load testing.

The strength impairment factor φ_{imp} is determined as the ratio of reduction of resistance between the 1st (F_1) and the 3rd (F_3) loading cycle to the resistance obtained at the 1st loading cycle (F_1) for the evaluated amplitude displacement ν_i (Equation (1)).

$$\varphi_{imp}(\nu_i) = \frac{F_1(\nu_i) - F_3(\nu_i)}{F_1(\nu_i)} \quad (1)$$

According to the prEN 1998-1-2, Annex N, the φ_{imp} should be lower than 0.3 and if reached or exceeded, the corresponding deformation should be considered as ultimate deformation.

The strength degradation factor k_{deg} is calculated as the ratio of the resistance obtained in 1st loading cycles (in cyclic tests) to the mean resistance obtained in monotonic tests $F_{max,M}$ (Equation (2)).

$$k_{deg} = \frac{F_1}{F_{max,M}} \quad (2)$$

According to the proposal, the value of k_{deg} should not be smaller than 0.8; if this value is not reached at all, the joint should be considered as non-dissipative, whereas otherwise the deformation at which the defined k_{deg} limit is reached is set as ultimate displacement.
At this point, it can be mentioned that to the authors' knowledge, the reductions of ultimate lateral displacements, apart from those specified also in the current EN 12512 (failure slip, 1st LEC post-peak strength reduction or/and absolute displacement limit) are very rare in the literature for both connections and structural elements. One example is the limitation of ultimate displacement to the intersection of the 1st LEC and the idealised bi-linear curve, obtained with EEEP, in the idealisation of non-linear response of structural masonry walls [14], which is however not used in current practice.

Energy dissipation is another important parameter of non-linear behaviour that is according to EN 12512 evaluated from the tests results in terms of equivalent viscous damping coefficient, ν_{eq}. As opposed to the original definition for its calculation by Jacobsen [15], (Equation (3)), which considers dissipated and input/potential energy (E_D and E_P, respectively) of the whole loading cycle as defined in Figure 2a, EN 12512 considers only half loading cycle (Equation (4)) with E_D and E_P as defined in Figure 2b.

$$\nu_{eq} = \frac{E_D}{4\pi E_P} \quad (3)$$

$$\nu_{eq} = \frac{E_D}{2\pi E_P} \quad (4)$$

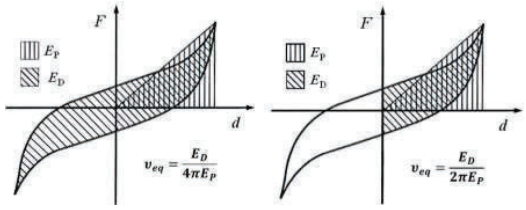

Figure 2: *Equivalent viscous damping according to a. Jacobsen [15], and b. EN 12512 [7].*

https://doi.org/10.52202/069179-0479

3 COMPARISON BETWEEN THE EN 12512 AND ITS PROPOSAL UPDATED FOR ANALYSIS OF RESULTS IN 2019

A first comparison of different methods for the analysis of cyclic test results is presented. In an experimental campaign conducted at the University of Minho (UMinho), a series of angle brackets (AE116) and hold-down (HTT22) connections have been tested under monotonic and cyclic loading. Tension and shear loads were considered while varying the support element (steel and CLT). The loading protocol adopted for the cyclic tests was the one proposed by Casagrande *et al.* [2]. However, two different approaches have been used to analyse the results of the tests. The current version of EN 12512 [7] and a new proposal for this standard presented within the CEN/TC250/SC8/WG3 in 2019 [16], have been used. It is worth mentioning that the definition of the cyclic test protocol was based on yielding displacement quantified based on the method suggested in [16], which is in accordance with ASTM E2126 [11], see Figure 3.

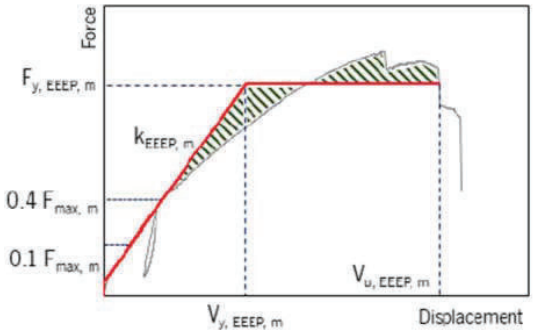

Figure 3: *Analysis of the data from a monotonic test made following EN 26891, as defined by [6] and [14].*

Regarding the degradation factor, which represents a load reduction factor between the 1st Load-Slip Envelope Curve (1st LEC) and 3rd Load-Slip Envelope Curve (3rd LEC), the new proposal [16] does not recommend values less than 0.6, while the current version [7] says nothing about it. The quantification of the different parameters and definition of the bilinear curve is analogous to the monotonic tests, it is being quantified through the 1st Load-Slip Envelope Curve (1st LEC), as can be seen in Figure 4. To define the ultimate displacement, besides those reported for monotonic tests, it can be given by the minimum value of degradation factor (0.6). However, it is important to note that the 3rd Load-Slip Envelope Curve (3rd LEC) can be crucial for the quantification of the ultimate displacement. On the other hand, the strength degradation and the 1st LEC can only be quantified if the total number of cycles is applied to the step.

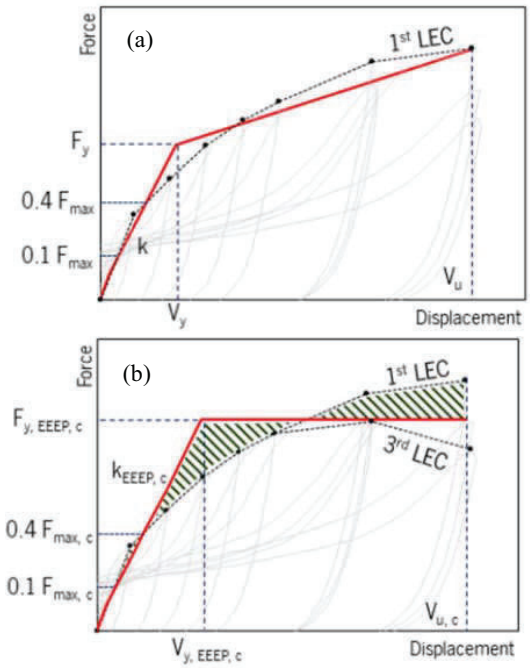

Figure 4: *Brief comparison of the analysis of cyclic tests data between current EN 12515 [7] (a) and the new proposal [14] (b).*

Table 1 summarizes the main results as the average of the three cyclic tests performed for each case studied considering both directions of loading as suggested by [16].

Table 1: *Results of the cyclic tests applying the EN 12512 [7] and the new proposal [16].*

Sample	Method	$K_{10\text{-}40}$ (N/mm)	v_y (mm)	v_{eq} (%)	D
AE116	[7]	6141	3.3	15,6	5,4
Shear	[16]	5392	5.7	3.9	3.3
Steel base	Δ (%)	12.2	70,9	74,8	39,4
AE116	[7]	2749	4.4	20.6	4,9
Shear	[16]	2282	7.7	5.0	2.6
CLT base	Δ (%)	17.0	75.5	75.8	48.2
AE116	[7]	7263	2.6	17.2	8.4
Tension	[16]	5626	6.5	8.7	3,6
Steel base	Δ (%)	22.5	152	49.5	56.7
AE116	[7]	12337	0.6	47.8	7.8
Tension	[16]	6535	2.0	22.5	3.2
CLT base	Δ (%)	47	235	52.8	58.4
HTT22	[7]	8624	2.9	36.5	6.5
Tension	[16]	6456	6.6	19.8	2.9
	Δ (%)	25.1	125	45.8	55.2

The comparison between the methods of analysis come out a difference for all mechanical parameters, where the smallest differences are relative to the elastic stiffness ($K_{10\text{-}40}$). It is possible to see higher values of yielding

https://doi.org/10.52202/069179-0479

displacement (v_y), and, on the other hand, lower values of equivalent viscous damping (v_{eq}), and ductility (D), applying the new proposal discussed within CEN/TC250/SC8/WG3 [16] in comparison to the current EN 12512 [7].

4 COMPARISON BETWEEN THE EN 12512 AND THE prEN 1998-1-2, ANNEX N PROPOSAL

In the second case study, the impact of the analysis method is evaluated for experimental tests conducted according to EN 12512 [7]. The results are analysed according to the referred standard and according to the new proposed prEN 1998-1-2, Annex N[6]. For the comparison, the results of an extensive testing campaign studying the shear behaviour of cement-particle board-to-timber connections by metal staples, conducted at the Slovenian National Building and Civil Engineering Institute (ZAG), have been re-evaluated according to the proposed guideline. The chosen experimental tests are interesting for comparison, because in cyclic tests, large strength degradation was obtained for the connections already before achieving maximum load-bearing capacity (evident from typical backbone envelope hysteresis curves presented in Figure 5, lower). Furthermore, the performance of the studied sheathing-to-timber connections were tested also on the level of structural elements. The connections were used in the construction of light-frame timber shear wall panels (LFTP) whose behaviour under in-plane monotonic and cyclic loading has been experimentally tested as well.

Monotonic and cyclic shear tests were conducted for two variations of boards-to-timber connections with different staple geometry and cement-particle board thickness. They were labelled in dependence of the boards' thickness; B12 for 12-mm and B16 for 16-mm board, respectively, with corresponding staple geometry 1.53 × 11.25 × 45 mm and 2.0 × 11.76 × 50 mm. More specific details on the materials, test specimens and on the test setup of the experimental monotonic and cyclic shear tests of two variations of connections can be found in [17] where the experimental results of cyclic shear tests on LFTP constructed using the tested connections are presented as well.

The test results of connections analysed according to current EN 12512 [7] proved that the connections exhibit large ductility both under monotonic (Figure 5, upper) as well as under cyclic loading (Figure 5, lower). Calculated average ductilities, D, the corresponding yield slip, v_y, the load-bearing capacity, F_{max}, and elastic stiffness, $K_{10\text{-}40}$, are for the conducted tests of connections with monotonic (M) and cyclic (C) loading protocols summarised in Table 2. Furthermore, the table presents ductility calculated by considering EN 12512 and additional EEEP criterion (definition of yield point is equal to elastic displacement v_e of the bilinearly idealised hysteresis curve defined considering equal input energy, see Figure 6), and by considering Kobayashi and Yasumura idealisation criteria [10]. For both tested connections at least three tests were conducted and are considered in statistics for both loading protocols (monotonic and cyclic).

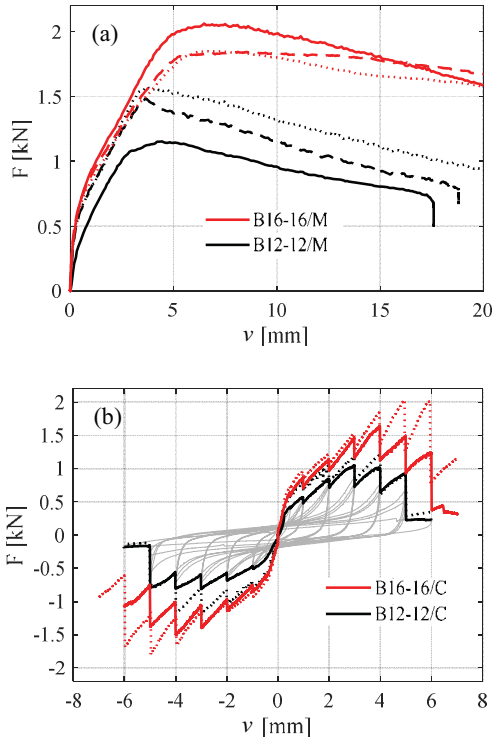

Figure 5: *Lateral load-lateral displacement curves obtained for the two studied sheathing-to-timber connections with staples in monotonic (a) and cyclic ((b), hysteresis backbone envelopes and one full hysteresis curve presented) shear tests.*

Results show that significant differences in ductility are obtained if different yield point definitions are assumed for its calculation. More conservative ductility compared to EN 12512 was obtained considering EN 12512 and additional EEEP criterion. The obtained ductilities in cyclic tests are then lower by 28 and 27% for B12 and B16 connections, respectively. Idealisation by Kobayashi and Yasumura produced even more conservative ductility results, i.e. ductility is in average for 42% and 39% lower than according to EN 12512 for B12 and B16 connections, respectively. Both criteria which consider EEEP are more conservative, since the yielding point for ductility calculation is considered as the yielding point of the idealised bi-linear curve, which is larger than then the yielding point according to EN 12512.

https://doi.org/10.52202/069179-0479

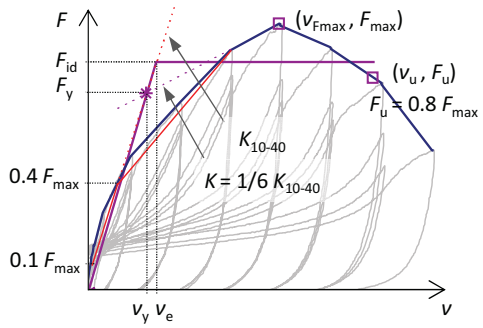

Figure 6: *Idealisation according to EN 12512 and idealisation to bi-linear curve with additional EEEP criterion.*

Furthermore, large differences in average lateral strength were obtained between monotonic and cyclic tests. As evident from the table, the average lateral strengths obtained in the first loading direction of cyclic tests are 14.2 and 17.0% lower than those obtained in monotonic tests for the B12 and B16 connections, respectively. Moreover, the difference in the lateral strength capacities obtained in the two testing directions was not negligible. The strength results are for both connections in the second loading directions lower on average by 12%. The average values of both loading directions are for all the characteristic results too presented in Table 2 (in brackets next to the first loading direction results). For the B16 connection, the average lateral cyclic strength capacity in both directions ($C^{+,-}$) is on average 20% lower than monotonic (M) lateral strength.

While the lateral strength capacity was in the second loading direction evidently smaller, there was however no significant change in ultimate displacements achieved in the two loading directions (that is in case only EN 12512 limit for ultimate displacements, i.e. 20% post-peak maximum lateral strength drop in hysteresis envelope, is considered).

Table 2: *Average results of the monotonic (M) and cyclic tests in first (C) and both loading directions ($C^{+,-}$, in brackets) with evaluated idealised parameters according to EN 12512 [7], EN 12512 with additional EEEP criterion and Kobayashi and Yasumura criteria [10].*

Connection	Loading protocol	No. of tests	$F_{max/staple}$ [kN]	K_{10-40} [kN/mm]	v_y [mm]	v_e [mm]	D	D	D
				EN 12512 [7]	EN 12512 [7]	EN 12512 +EEEP	EN 12512 [7]	EN 12512 +EEEP	Kobayashi and Yasumura [10]
B12	M	3	1.41	1.00	1.09	1.29	9.9	8.2	7.7
	C ($C^{+,-}$)	10	1.21 (1.14)	1.15 (1.10)	0.71 (0.69)	0.94 (0.92)	7.8 (7.8)	5.6 (5.6)	4.54 (4.55)
	Δ (%)		14.2 (19.1)	-15.0 (-10.0)	34.9 (36.7)	27.1 (28.7)	21.2 (21.2)	31.7 (31.7)	69.5 (69.1)
B16	M	3	2.00	0.96	1.25	1.68	18.3	13.2	11.6
	C ($C^{+,-}$)	8	1.66 (1.56)	1.21 (1.20)	0.93 (0.83)	1.21 (1.07)	8.5 (9.7)	6.2 (6.5)	5.20 (5.45)
	Δ (%)		17.0 (20.0)	-26.0 (-25.0)	25.6 (33.6)	28.0 (36.3)	44.1 (36.2)	45.1 (42.5)	123 (113)

The minimum, maximum and average values of ultimate cyclic displacements obtained considering strength impairment limitation equal 0.3, $v_{u,\varphi 30}$, relative to ultimate cyclic displacements, $v_{u,c}$, are presented in Table 3. Similarly, relative comparison of obtained ultimate displacements calculated considering the strength degradation limit equal 20% (k_{deg} = 0.8), $v_{u,kdeg0.8}$, compared to ultimate displacement is presented in Table 4. Since the yield slip v_y is according to prEN 1998-1-2, Annex N the same as according to EN 12512, the presented reductions of ultimate displacements apply for the ductility as well. Nevertheless, the obtained values of ductility corresponding to these reductions are for clarity stated in the tables; ductility calculated according to prEN 1998-1-2 considering both strength impairment and degradation criteria is presented in Table 4 ($^*D$).

With strength impairment limitation equal to 0.3, a significant reduction in ultimate displacements is obtained; $v_{u,\varphi 30}$ range from 0.558 to 0.745 $v_{u,c}$ for B12 and from 0.712 to 0.962 $v_{u,c}$ for B16 connections with average 0.679 and 0.822 $v_{u,c}$, respectively. It should be noted that for B12 connections the strength impairment equal to or higher than 0.3 was achieved prior to maximum strength in 60% of tests, while for B16 connections in 25% of tests. The minimum, maximum and mean strength impairment values obtained at maximum strength displacements in the first loading cycle direction $\varphi_{imp}(v_{Fmax})$, are presented in Table 3.

Table 3: *Minimum, maximum and mean values of strength impairment for maximum strength displacements φ_{imp} (v_{Fmax}), relative values of reduced ultimate displacements $v_{u,\varphi 30}$ and ductility D obtained considering strength impairment.*

Connection		φ_{imp} (d_{Fmax})	$v_{u,\varphi 30}$ / $v_{u,c}$	D = $v_{u,\varphi 30}$ / v_y
B12	Min	0.251	0.558	2.96
	Max	0.419	0.745	8.10
	Mean	0.330	0.679	5.27
	(CV)	(7.9%)	(7.9%)	(26.3%)
B16	Min	0.339	0.712	4.00
	Max	0.233	0.962	16.69
	Mean	0.268	0.822	7.17
	(CV)	(12.9%)	(8.8%)	(55.2%)

https://doi.org/10.52202/069179-0479

The average strength degradations obtained at maximum strength in the first loading directions of cyclic tests were 0.853 and 0.828 for the B12 and B16 connections, respectively, with minimum values 0.680 and 0.653 for the two connections, respectively.

For the particular tests, in 40% of B12 and in 38% of B16 cyclic tests the strength achieved in the first loading direction did not reach 80% of the average connection strength achieved in monotonic tests, $F_{max,M,mean}$, and the connections should according to prEN 1998-1-2 be classified as non-dissipative ("N.D." in Table 4). If the second (negative) loading direction is considered, 60% and 75% of the tested B12 and B16 connections, respectively, do not meet this criterion. It can also be noted that strength degradation at maximum resistance was in most cases higher in the second (negative) loading direction. The average k_{deg} at maximum resistance in negative loading direction were 0.766 and 0.721 for the B12 and B16 connections, respectively, with minimum values as low as 0.577 and 0.634.

The strength degradation criterion is, however, for the tested connections in all cases except for one B16 test, not critical in comparison to the strength impairment criterion in case the strength in cyclic tests indeed reached 80% $F_{max,M,mean}$. For these tests the mean reduced ultimate deformations due to set strength degradation limit, $v_{u,kdeg0.8}$, are 0.965 and 0.920 $v_{u,c}$ for B12 and B16, respectively.

Table 4: *Minimum, maximum and mean relative reductions of ultimate displacements $d_{u,kdeg0.8}$ and resulting ductility D due to strength degradation and final ductility $^{*}D$ according to prEN 1998-1-2, Annex N, obtained from cyclic tests.*

Conn-ection		$v_{u,kdeg0.8}$ / $v_{u,c}$	D = $v_{u,kdeg0.8}/v_y$	$^{*}D$ acc. to prEN8-1-2, Annex N
B12	Min	**0.887	**4.23	**2.96 (N.D.)
	Max	1.00	10.7	6.60
	Mean	**0.965	**7.39	**5.17 (N.D.)
	(CV)	(4.5%)	(27%)	(23.7%)
B16	Min	**0.738	**4.66	**3.99 (N.D.)
	Max	1.00	6.48	5.45
	Mean	**0.935	**5.75	**4.72 (N.D.)
	(CV)	(10.6%)	(11.4%)	(10.2%)

Note: * both $v_{u,\varphi30}$ and $v_{u,kdeg0.8}$ considered
** 6/10 specimens considered (4/10 specimens did not achieve 0.80 $F_{max,M,mean}$)
** 5/8 specimens considered (3/8 specimens did not achieve 0.80 $F_{max,M,mean}$)
Connections should be declared as non-dissipative (N.D.) according to prEN 1998-1-2

Whether it is reasonable to declare the tested connections as non-dissipative, could somewhat be opposed with the results of cyclic tests of LFTPs constructed with the tested connections. For all the tested panels with symmetric board and fastening disposition, ductility higher than 4 was obtained, if more conservative EN 12512 idealisation with additional EEEP criterion was considered (4.82 for panels with B16 connections and 4.14 for panels with B12 connections) and higher than 5 if no EEEP was considered (6.93 and 5.76 for B16 and B12 panels, respectively).

5 SHORT SUMMARY OF MAIN RESULTS AND POINTS FOR DISSCUSSION

The following can be concluded from the conducted and re-evaluated test results:

- The proposed new idealisation considering strength impairment and strength degradation may in some cases significantly reduce the ultimate deformation capacity, and consequently also the ductility.
- For the presented re-evaluated test results of stapled connections, the ultimate slip limitation by strength impairment is more critical than by strength degradation, in case 80% of monotonic strength capacity was at all obtained in cyclic tests; approximately 40% of cyclic tests did for not achieve strength degradation factor equal 0.8.
- The strength degradation limit defined in prEN 1998-1-2 may result in declaring as non-dissipative connections, which exhibit ductile behaviour and enable ductile failure of structural elements.

While the new proposal upgrades the analysis of test results by considering strength impairment and strength degradation criteria, its positive and negative effects should be discussed together with other open questions/issues regarding analysis, some of them being:

- Is considering the results of the second loading direction in case of cyclic shear tests of symmetrical connections relevant; is neglecting them safe? As evident also from the second presented case study, most commonly the strength in the second loading direction is lower than in the first loading direction.
- Should lateral strength obtained in monotonic tests be considered as nominal strength and the characteristic value for design be evaluated from it? It can be seen from the test results that the differences between monotonic and cyclic tests may be quite high. If so, this should be considered in defining the safety factors in the design guidelines.
- What are the results of cyclic (and monotonic) tests intended to be used for? Besides determining resistance, stiffness, and ductility for the design perhaps also for comparisons, modelling, and other applications? If so, should the behaviour be idealised and how and which results should be reported? According to ISO 16670, the testing report should among other present also the tabulated envelope curves

https://doi.org/10.52202/069179-0479

for both loading directions, enabling further test analysis to other parties if needed. In comparison to EN 12512 it is according to ISO 16670 not necessary to report the strength impairment and damping ratios for each loading steps (time consuming and expensive analysis if not automated). On the other hand, it is according to EN 12512 not necessary to report stiffness, e.g. $K_{10\text{-}40}$, though it is necessary to calculate it to obtain the yield slip modulus.

- How should the initial slip, often evident in the curves as part with significantly smaller stiffness, be considered in determining the yield and ultimate slip? Specially in test results, where the loading protocol is not controlled through the deformation measured directly in the joint, but for instance through the actuator, this slip may be quite big. While not eliminating it results in conservative estimations of ductility, it increases absolute values of yield and ultimate displacements potentially limiting also ultimate displacements (if higher than absolute limits, such as 30 mm in the current code).
- Does considering the strength impairment and degradation for determining ultimate displacements indeed produce "better" or more safe results? What are their advantages in comparison to considering other criteria which yield lower ductility, such as the EEEP criterion in Kobayashi and Yasumura or EN 12512, but do not reduce ultimate displacements? Are the over-conservative assumptions on ultimate deformation capacity (and ductility) beneficial for performance-based assessment of structures, which is displacement-based?
- Should the new prEN 1998-1-2, Annex N proposal specify also the minimum number/percent of the tested specimens in group, which can exhibit non-dissipative behaviour in terms of strength degradation, that the connection would/could in general still be considered as ductile (as in the presented second case study)?
- Are the definitions of input and potential energy in dependence of "half cycles" for calculation of equivalent viscous damping optimal? They are in comparison to original definition (set in dependence of the "entire loading cycle") beneficial for shear testing of non-symmetrical connections or testing of the connections in tension and compression. It may however be less convenient for non-symmetrical connections or connections loaded in tension and compression that the "halves" are determined in dependence of deformation (positive and negative slip) and not loading (positive, negative); the ratio of input to dissipated energy can vary significantly in dependence of loading direction and corresponding damage/failure mechanism.

The differences in the loading protocols between different standards, which may influence the behaviour, need to be discussed as well but with considering also other criteria related to tests executions and objectives. Some of these considerations are:

- Regarding the loading rates; the allowed ranges provided in the codes are not the same but are quite large, which is beneficial due to enabling tests execution with various testing and measuring equipment and in acceptable time, but negative in terms of results comparison. The use of EEEP criterion in idealisation of results may be beneficial to reduce the effect of the loading rate, since the influence of loading rate is smaller on the input energy than on the resistance and deformation behaviour (commonly with higher loading rate higher resistances and lower deformation capacities are obtained).
- Regarding the changes of the loading rate within the tests; the possible changes allowed in ISO 16670 enable faster test execution, because for loading cycles with higher displacement amplitudes, higher loading rates can be assigned.
- Regarding the execution of initial slip loading cycles; ISO 16670 is again more flexible by allowing the initial cycles to be omitted and this way enabling the use of wider range of equipment, since inducing loading through very small controlled initial slips according to EN 12512 results in demand for high accuracy controlling and measuring equipment.
- Regarding the definition of amplitude displacements and number of cycle repetitions; issue on how to obtain the proper failure modes of connections under cyclic loading, related to the objectives of the tests, should be addressed; which loading protocol should be used for instance in case of studying the low-cycle fatigue behaviour of the connection or which in case of studying the behaviour under seismic loading.

6 CONCLUSIONS AND OUTLOOK

In the paper, a more detailed state-of-the-art regarding cyclic testing of timber connections is given and the different aspects with need for further test development are discussed. A first comparison of different testing protocols and methods for data assessment is applied for a variety of timber joints. In the case of the experimental campaign performed at UMinho, it was possible to verify large differences between the obtained values by applying two methods for data analysis, namely the current EN 12512 [3] and a proposal discussed within CEN/TC250/SC8/WG3 [14] that has been used as base for Casagrande *et al.* [1]. In this comparison, the smallest difference is relative to the elastic stiffness. Large differences in final results were found also for the second presented case study conducted at ZAG that compares the results of experimental tests analysed according to EN 12512 and the prEN 1998-1-2, Annex N [6]. While

already the strength impairment limitation significantly reduces the ultimate displacements (and consequently ductility), the strength degradation limit set in prEN 1998-1-2 is for the presented experimental campaign in most tests not reached. The connections are therefore according to the new proposal classified as non-dissipative, even though they exhibit significant ductility in cyclic tests of connections as well as in the cyclic test of structural elements.

The need for a unified testing standard for cyclic testing of timber connections and analysis of results is often emphasised within the research community and would be beneficial for the industry as well to enable easier sales and use of products in various markets. Nevertheless, aspiration toward such standards should be accompanied by awareness of all the different purposes such tests are carried out for, the implications of the proposed specific guidelines, as well as of the limitations that laboratories/institutes might have in their implementation.

ACKNOWLEDGEMENT

The paper gives an insight into the ongoing work of the RILEM TC TPT "Tests methods for a reliable characterization of resistance, stiffness and deformation properties of timber joints". The Slovenian Research Agency is acknowledged for financing the second research case study through Research Core Funding No. P2-0273.

REFERENCES

[1] A. Jorissen and M. Fragiacomo, 'General notes on ductility in timber structures', *Engineering Structures*, vol. 33, no. 11, pp. 2987–2997, 2011, doi: https://doi.org/10.1016/j.engstruct.2011.07.024.

[2] D. Casagrande *et al.*, 'A methodology to determine the seismic low-cycle fatigue strength of timber connections', *Construction and Building Materials*, vol. 231, p. 117026, 2020, doi: https://doi.org/10.1016/j.conbuildmat.2019.117026.

[3] W. Muñoz, M. Mohammad, A. Salenikovich, and P. Quenneville, 'Need for a harmonized approach for calculations of ductility of timber assemblies', in *Proceedings of the Meeting*, 2008, vol. 41.

[4] M. Piazza, A. Polastri, and R. Tomasi, 'Ductility of timber joints under static and cyclic loads', *Proceedings of the Institution of Civil Engineers - Structures and Buildings*, vol. 164, no. 2, pp. 79–90, 2011, doi: 10.1680/stbu.10.00017.

[5] ISO, 'ISO/TR 21141 Timber structures – Timber connections and assemblies – Determination of yield and ultimate characteristics and ductility from test data'. ISO, 2022.

[6] CEN/TC 250/SC 8/WG3 N156, 'prEN 1998-1-2:2022 (E), Annex N - v.2022.05.12 (informative) Determination of mechanical properties of dissipative components in timber buildings from experimental cyclic test data', May 2022.

[7] EN 12512:2005, 'Timber structures - Test methods - Cyclic testing of joints made with mechanical fasteners'.

[8] 'ISO16670:2003 Timber structures - Joints made with mechanical fasteners - Quasi-static reversed-cyclic test method'.

[9] M. Yasumura and N. Kawai, 'Estimating seismic performance of wood-framed structures', in *Proceedings of 5th WCTE*, 1998, vol. 2, pp. 564–571.

[10] K. Kobayashi and M. Yasumura, 'Evaluation of plywood sheathed shear walls with screwed joints tested according to ISO 21581', in *Proceedings of CIB-W18 meeting. KIT, Alghero, Italy*, 2011, vol. 10.

[11] ASTM, 'ASTM E2126-11 - Standard Test Methods for Cyclic (Reversed) Load Test for Shear Resistance of Vertical Elements of the Lateral Force Resisting Systems for Buildings'. ASTM, 2018.

[12] CEN, 'EN 26891:1991 Timber structures - Joints made with mechanical fasteners - General principles for the determination of strength and deformation characteristics (ISO 6891:1983)', 1991.

[13] ISO, 'ISO 6891:1983 Timber structures — Joints made with mechanical fasteners — General principles for the determination of strength and deformation characteristics', May 1983.

[14] M. Tomaževič, *Zidane zgradbe na potresnih območjih*. Fakulteta za arhitekturo, gradbeništvo in geodezijo, VTOZD Gradbeništvo in …, 1987.

[15] L. S. Jacobsen, 'Steady forced vibration as influenced by damping', *Transactions of ASME*, vol. 52, p. 13, 1930.

[16] CEN/TC 250/SC8/WG3A, 'A proposal for the revision of the European Standard EN 12512, Timber structures - Test methods - Cycling testing of timber connections and assemblages for seismic design, Version n. 20190312'. 2019.

[17] M. Kržan, T. Pazlar, and B. Ber, 'Improved seismic response of light-frame-timber panels with cement-particle-board sheathing of various thicknesses and different configurations of fasteners', *Engineering Structures*, vol. 253, p. 113757, 2022, doi: https://doi.org/10.1016/j.engstruct.2021.113757.

 https://doi.org/10.52202/069179-0479

World Conference on Timber Engineering Oslo 2023

USAGE OF A BAMBOO HONEYCOMB STRUCTURE (COMBOO) IN TIMBER ARCHITECTURE

Andreas Loth[1], Ralf Förster[2]

ABSTRACT: This paper gives an overview of recent developments of the ecological bamboo based honeycomb like sandwich core material COMBOO and its usage in civil engineering and timber architecture. A brief introduction gives insight into to material bamboo itself and its excellent mechanical properties. The manufacturing process of the COMBOO structure will be described in detail. Previous results from mechanical validation, e.g. 3- and 4 point bending test as well as compression tests will be presented. Main focus of this paper is put on the interesting properties of the bamboo sandwich in acoustics and thermal insulation. The hollow structure with "entrapped" air provides here interesting properties. A good acoustical damping in a frequency range was observed with an artificial and a real COMBOO structure. The results were compared to common acoustic panels. The heat transfer comparison with conventional materials like concrete, double-glazed glass structures (windows) and aerated concrete reveals comparable or better insulation values. This makes the structure suitable for wall and floor elements, acoustic panels, transport boxes and structures in modern transport. Further improvements will be discussed.

KEYWORDS: COMBOO, core material, sandwich construction, insulation, acoustic panels, honeycomb

1 INTRODUCTION

Conventional core materials of sandwich structures mainly consist of polymer foams, metallic foams, aramid honeycomb or balsa wood. The materials are somehow environmental problematic as they consume large amounts of energy during production, were based on mineral oil or grow in monocultures.

A new approach called COMBOO uses honeyCOMB arrangement of bamBOO rings, where the face sheets were covered with glass or natural fibres and a resin. Another type of new material consists of top layers of wood or plywood and a core of bamboo rings, forming a sandwich.

Bamboo itself is a grass with a hollow stem divided by nodes and a hard outer rim. Big advantages lay in the CO_2 storage capabilities of the raw bamboo, the growth rate of up to one meter per day, the height of up to 40 m and its mechanical properties. A tensile strength of up to 370 N / mm^2 and a density between 0.6 and 0.75 g / cm^3 (for comparison: pine 0.45 g / cm^3) were reported. Density distribution across the stem is different to timber. The inner part has a lower density, increasing to the outer area. I can be harvested after just seven years and a reforestation is not necessary. [1]

Bamboo is known in Asia as building material for centuries, while it's nowadays often used for scaffolds, furniture, reinforcements for concrete walls, laminates, laminated beams or chopping boards, where the material is more or less processed.

Bamboo for beams, boards or laminate floor is usually cut in length into smaller stripes, than grinded or milled to receive a rectangular shape, arranged and finally glued together. The price for this procedure is losing the outer regions of the bamboo column with the highest density.

Machining of bamboo requires sharp tools, a coating on hard metals is recommended for milling and sawing. Holes perpendicular to length axis or screws / nails were problematic as the materials tends to split. Splitting of bamboo occurs often during drying. Penetrating the nodes might help. [1]

1.1 PROPERTIES OF COMBOO

Following the COMBOO approach and forming a sandwich structure, excessive machining or processing is not necessary. This saves lots of the overwhelming properties of the natural bamboo. Excellent bending properties, a good compressive strength and a delivery of light through the COMBOO structure if covered with transparent GFRP were interesting features of the new approach (e.g. lower right part of Figure 1).

In addition to the aforementioned properties, density of COMBOO structure through the arrangement of several rings is another main advantage. It is much lower than density of bamboo (wood) itself due to the proportion of wood and air. Density values of 0.2 and 0.25 g / cm^3 were measured.

Mechanical and geometrical properties depends on the chosen bamboo species and the diameter of bamboo, because this determines the ratio between air and material in the core layer. For example Tonkin-bamboo itself reached compression test values of 109 N/mm^2, while other species reach lower values e.g. Moso-bamboo 74 N/mm^2 (when using ring area for calculation). [2], [3], [4]

[1] Andreas Loth , Berliner Hochschule für Technik, Berlin, Germany, aloth@bht-berlin.de

[2] Ralf Förster, Berliner Hochschule für Technik, Berlin, Germany, rfoerster@bht-berlin.de

https://doi.org/10.52202/069179-0480

1.2 IDEA OR APPROACH

The hollow chambers, filled with air, of the COMBOO structure can be used for another topic especially interesting for applications inside a house or factory, the soundproofing of walls.
Acoustic noise in our environment like household, office or at work affect human body. High energetic levels of noise of around 120 dB provide sudden pain and can cause Tinnitus, deafness or sudden hearing loss. But also much lower levels influence wellbeing or concentration especially in resting phase. Sleep disturbances, cardiovascular effects lower productivity at work or school and hearing impairment can occur as long- or short-term effects. [5], [6]
Energy and resource efficiency is a major aim of our time. A closed hollow structure from a natural and renewable source like bamboo could provide a good thermal insulation by the enclosed air. Nearly all bamboo species offer this hollow structure, which might also be also an interesting field of COMBOO usage.
Transferring and extending application opportunities of the new COMBOO structure from mainly mechanical engineering or transportation to civil engineering and architecture is scope of this paper.

2 MATERIALS AND METHODS

The manufacturing of the COMBOO structure itself consists of a few simple steps that can be done without a high level of machinery. For mass production or larger projects, another solution is required.
First, the outer surface of bamboo columns has to be roughened by using sandblasting or grinding. The second step is a cutting process of bamboo rings of equal height. The third step is the arranging of the bamboo rings in a honeycomb pattern in combination with a gluing (wood, plywood or sheet materials) or lamination step (natural or artificial fibres) on both sides, to form a sandwich material.
Surface preparations were found to be a good strategy to improve shear and bending strength of the sandwich, as raw bamboo has an adhesive or coating repellent surface. [2]
In Figure 1, the manufacturing process of COMBOO structure is shown.

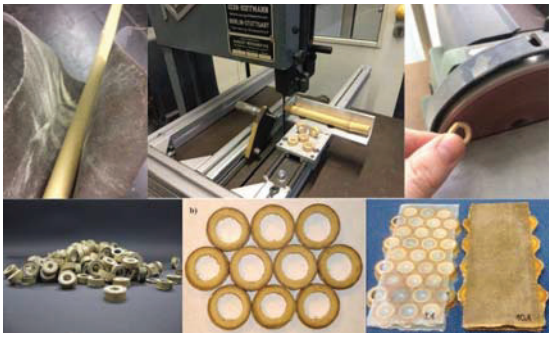

Figure 1: *Manufacturing of COMBOO material (grinding. cutting, deburring, arranging, laminating)*

Besides the flat board like structures, curved COMBOO components were possible too. The type of cover material artificial like fibres or renewable like wood depends on application. Therefore different strategies for connection have to be evaluated.

2.1 INVESTIGATION OF SOUND AND ACOUSTIC BEHAVIOUR

Sound is mainly understood as the spreading of pressure or density fluctuations in “elastic” materials like structures liquids and gases. It can be differed for our application into air-borne and structure-borne noise.
The Sound pressure level is the local pressure deviation from the surrounding or average pressure level. A higher sound pressure refers to a louder incident.
The frequency represents the number of pulsations of the sound per second. The sensitivity of human hearing is adopted to the frequency range of human voice of (250 - 2.000 Hz), but a range between 16 - 16.000 Hz or even higher can be recognized. [9] The range of frequencies interesting for room acoustics is between 100 Hz and 5.000 Hz.
Reverberation time is the period needed for fading of a sound incident to a specified grade. Allowable values depend on application (e.g. office, school or concert hall). It is influenced by sound absorption coefficient α, a value ranging from 0 (total reflection) to 1 (total absorption). Sound absorption coefficient α depends strongly on frequency. Measurement of the coefficient can be done by using an acoustic / reverberation chamber or an impedance / Kundt's tube. [10], [11], [12]
The impedance tube is often used for research and development due to its requirement of much smaller material specimen. It is limited to a sound incident perpendicular to the specimen, whereas a reverberation chamber can be used for a diffuse sound signal direction. In this work a Kundt's tube in single microphone arrangement was used, due to availability at university.

2.2 APPLICATION ACOUSTIC PANELS

The first approach presented here is the usage of the COMBOO structure as an acoustic panel used as absorber. Acoustic panels mounted to walls or ceilings were often used to improve the sound climate in offices, schools, concert halls or factories. A damping of the total amplitude or of certain frequencies or a reduction of the reverberation time can be the aim. Mainly used technical principles to achieve these targets were absorbers, plate transducers or resonators. They often work in a specific frequency range. [7]
Absorbers, often porous, transform the sonic energy into other energy forms mainly heat. Dissipation of energy is a result of friction or contact between air molecules with other air molecules and surrounding structures. Therefore, longer open and narrow pores are required. They often contain either mineral or organic materials. [8]. Porous absorbers can effectively be used for damping in the middle or higher frequency range

https://doi.org/10.52202/069179-0480

Examples for “soft” porous absorbers were typical polymer materials in industry like rebounded foams mainly consisting of PU (polyurethane) and soft foam chopped recombined with a good sound absorption also due to its mass, melamine resin foam wits a low density but many pores, PU or viscoelastic foams. [13], [14]
Wood wool, textile fibre compounds, hemp fibres or moss were porous fibre based sound absorber. They were manufactured by adding cement and water, pressure and heat or a special conservation treatment to be formed. The often provide a wide frequency range for damping. [15], [16], [17]
Sandwich materials i.e. a combination of plates with mainly small holes, a carrier plate and often an acoustic fleece can be found in literature. [18]
Resonator systems were Helmholtz resonators, plate transducers or perforated plate transducers. The working principle is a spring mass design with an optimum working point at their resonance frequency. The mass is often timber, plasterboard or plywood or even air while the spring is an entrapped volume of air. Perforated plate transducers have a regular distributed pattern of holes or slots often combined with porous absorbers for a better absorption range. Common resonator systems can be mainly used at lower frequencies.

2.2.1 Manufacturing and preparation

One suitable way for acoustic measurement is using a Kundt's tube to measure the sound absorption and sound transmission coefficient of small samples with perpendicular sound incidence, as described above. Therefore several conventional materials for acoustic absorption or damping were prepared to compare with the COMBOO structure (ref. Figure 2).

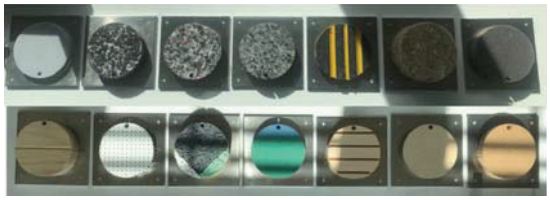

Figure 2: *Materials for acoustic comparison*

They were mainly cut out using a band saw, as can be seen in Figure 3, left side.

Figure 2*: Material preparation (cutting und gluing)*

Bamboo as a natural product is inhomogeneous. For homogeneity and better understanding of the effects, MDF (medium density fibre board) and wood boards with CNC milled holes (15 - 20 mm) were mainly used instead of the more irregular bamboo pattern. Bamboo rings were used for comparison.
The surface of the COMBOO specimen was covered with a 4 mm MDF layer with laser cut holes from 3 - 10 mm (ref. Figure 4). The hollow chamber under the top sheet can be seen as well.

Figure 3: *COMBOO acoustic panel [19] a) top layer b) core material c) bottom layer – left bamboo, right MDF based*

Plain or unmodified materials (aluminium, plywood, MDF, pine (slotted), pine) have been prepared for measurements in Kundt’s tube too, to acquire comparable data of the unmodified surface.
Figure 5 shows prepared COMBOO style structures made of MDF, timber and bamboo.

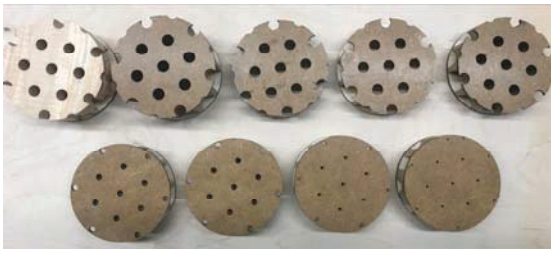

Figure 4*: COMBOO style MDF acoustic panels*

A MDF COMBOO specimen with a hole diameter of 20 mm (inner core region) and 10 mm hole (face sheet) was filled with polymer foam, to combine two absorber principles.
All specimens were mounted to an aluminium sheet, to be fixed at one end of the Kundt's tube. A speaker on the other side generates a signal at different frequencies, here in a range up to 1800 Hz, due to the tubes diameter. A microphone probe, guided through the test specimen acquired the signal, analyzed by an oscilloscope. The test setup is shown in Figure 6 and each test was performed three times.

https://doi.org/10.52202/069179-0480

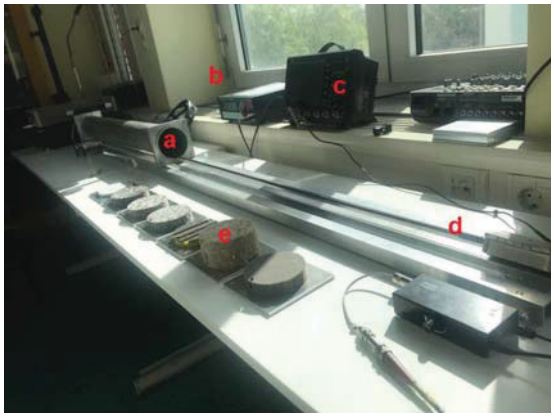

***Figure 5**: Kundt's tube (a) and measurement setup (multimeter (b), oscilloscope (c), microphone probe (d), test specimen (e)*

2.3 INVESTIGATION OF THERMAL INSULATION / THERMAL TRANSFER BEHAVIOUR

Second approach is a comparison of heat transfer through different materials. Therefore five typical materials of civil engineering were chosen, set to identical geometric parameters including thickness. The specimen were the COMBOO structure with a 0.3 mm GFRP layer on both sides, concrete, aerated concrete, styrofoam and a double-glazed window with two 6 mm glass sheets (ref. Figure 7). The dimensions were set to 150 mm x 150 mm x 20 mm. A test chamber (1) according to Figure 7 was created, using a hot air gun (2) to deliver warm air at a temperature of 55 °C. Warm air goes in from left side (in) and leaves the heating area through a smaller hole on the right side (out) to prevent overpressure. Five thermocouples connected to a pc via a precision measurement device (4) (ALMEMO 2890-9- Ahlborn Inc. Germany) were integrated into the chamber to measure the temperature at different positions. The first thermocouple was placed in the heating zone, aside of the direct blast of the hot air pistol. Two thermocouples were located directly above a hole in a bamboo ring and over the covering ring surface (Figure 7, right) of the COMBOO specimen (3). Two thermocouples (T_1, T_2) are behind the rear wall of the test specimen. Additional thermocouples were placed outside for reference. A thermo camera (5) (Optris, Germany) in the front end of the chamber was used to acquire the temperature distribution over the whole surface of the specimen.
Figure 8 shows three different test materials in the heat box. Thermocouples can be seen on specimen surface

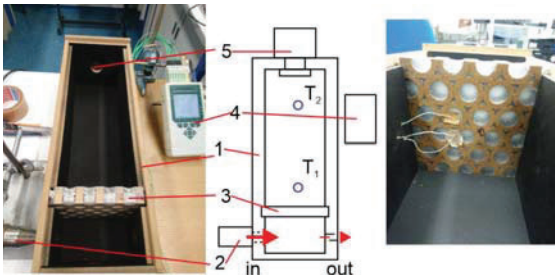

***Figure 6:** Measurement setup and heat box (left / middle), thermocouples on "COMBOO" surface (right)*

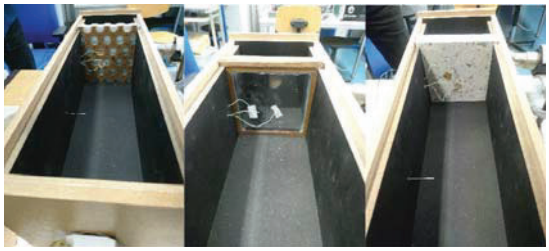

***Figure 7:** Sample structures for thermal measurements*

The hot air gun was activated for at least 60 minutes after the initialization of the measurement devices. According measurement data have been logged. Between the investigations, the whole heat box was cooled down to ambient temperature.

3 RESULTS AND DISCUSSION

3.1 PROPERTIES FOR COMBOO AS MATERIAL FOR ACOUSTIC PANELS

First of all, the sound absorption coefficient was determined for plain or unmodified timber and metal materials. It can be seen (Figure 9) that all materials provide a damping of more than 40 % in the very low (f < 125 Hz) and respectively high frequency (f > 1250 / 1600 Hz) range. Even the aluminium sheet metal shows a damping of more than 20 percent starting at 1250 Hz.

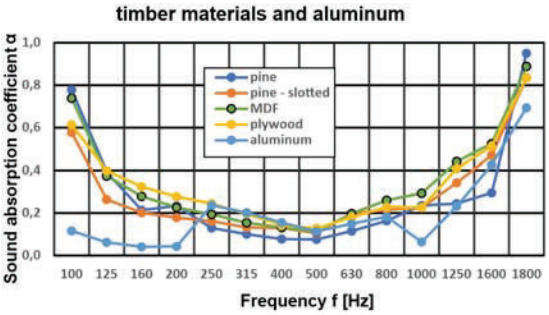

***Figure 8:** Sound absorption coefficient α - unmodified materials*

Further experiments with soft wood like for example Balsa, Paulownia or the inner region of palm wood can be interesting here.
Absorber materials as presented in Figure 10 provide a better damping and hence a higher absorption coefficient.

https://doi.org/10.52202/069179-0480

Especially hemp fibres reach values over 50 %, while wood fibres or wood sandwich material show values comparable to unmodified material. PU is also suitable for damping with a drop in the 500 Hz region.

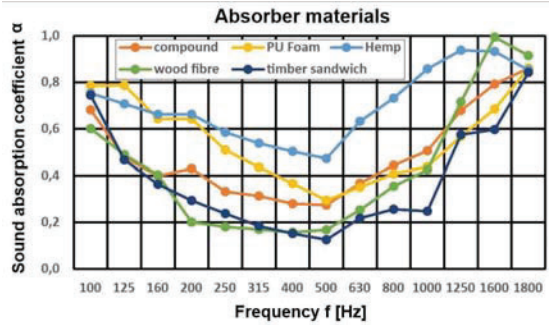

***Figure 9**: Sound absorption coefficient α of absorber materials*

The acoustic composite foams reached these values in the range between 200 Hz and 500 Hz, while the absorption of the fibre materials depends on type of fibre. Special acoustic absorption sandwich materials show similar or slightly different values in a wider range, depending on structure and materials.

The sound absorption coefficient of the COMBOO structures reached α values between 0.2 and 0.56 in a frequency range between 315 Hz – 800 / 1250 Hz, as can be seen in Figure 11. It depends only slightly on inner diameter of the chamber (15 mm – not shown vs. 20 mm) but on the hole diameter of the cover plate. Best damping results have been reached with smallest borehole in the top sheet of 3 mm. Here is a peak at around 500 Hz, providing an extra damping effect. This can be found also at the lower hole diameter of 15 mm, but with slightly lower values.

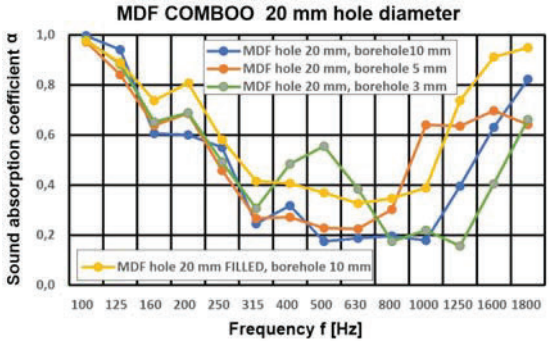

***Figure 10:** Sound absorption coefficient α - MDF COMBOO – hole diameter 20 mm different borehole diameter in top sheet*

Very interesting are the results from combination of COMBOO structure with PU foam (yellow line in Figure 11), where a hole or chamber diameter of 20 mm with a borehole diameter of 10 mm was used. The curve is comparable to the unfilled structure but just shifted upwards by a factor to better absorption.

Hence a combination might be an alternative or an improvement to reach a wider absorption frequency range.

A difference between the artificial COMBOO structures (MDF) and real bamboo could not be found, so the MDF is a suitable substitute for experiments with directly comparable structures.

1.2 INSULATION / THERMAL TRANSFER PROPERTIES OF COMBOO

Several tests have been performed to identify material properties. The logged data were plotted over time and analysed.

A typical set of acquired data is plotted in the next Figure 12, here at the COMBOO structure with GFRP sheets. Immediately after starting the hot air pistol, the temperature increases in the heating zone. After approximately 2 minutes a temperature of above 50 °C is reached, after about 10 minutes the final temperature of 55 °C with light fluctuations.

The temperature directly on the surface of the test specimen is slightly different. Directly on a hole, temperature is 1 K higher then on massive COMBOO structure. The temperature increases from 26 °C to 36 °C and 35 °C respectively. Ambient temperature remains mainly constant at 31 °C but shows fluctuations probably from air movement in the laboratory. The temperature behind the test specimen remains quite constant. Both thermocouple positions (near specimen and in the rear part of the heat box) show finally a nearly similar temperature of 29 °C.

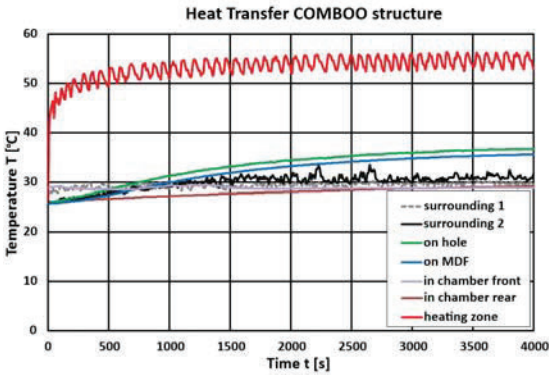

***Figure 11**: Temperature data over time at different locations for testing COMBOO structure in heat box*

Next Figure 13 represents the measured data for all five test specimen. Two temperature values are given for each material. The blue column represents the difference in temperature between the heating zone of the test box at always 55 °C and the average temperature directly on the rear side of the test specimen. Green columns show the temperature difference between the average temperatures (T_1 and T_2) behind the test specimen.

Both columns of the Styrofoam represent the best results, as expected. The difference between heating zone and rear side of the specimen was calculated to 21.05 °C, while

https://doi.org/10.52202/069179-0480

difference between inside and outside of the test box is 2.55 °C.
COMBOO structure showed a lower surface temperature difference (18.85 °C) than the double glazed window (18.4 °C) and much lower value than conventional concrete (13.85 °C). The surface temperature difference of the aerated concrete was 20.5 °C and hence 10 percent better than the COMBOO structures value, which is attributed to the higher mass and the low conduction value, due to encapsulated air at small scale.

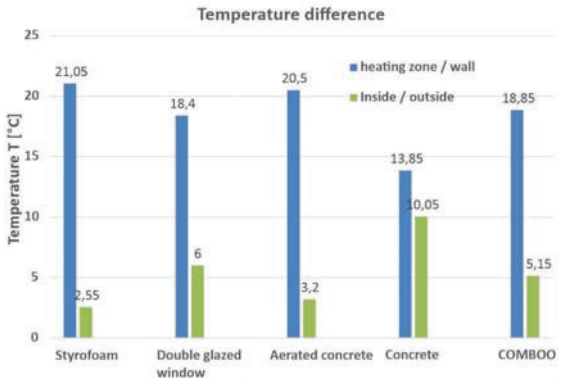

Figure 12: *Temperature difference between: heating zone and rear part of specimen (blue), inside / outside of test box (green)*

A multilayer or multi chamber approach within the COMBOO structure is currently under investigation, also in combination with plywood sheets as top and bottom material. It is assumed that relatively large volume leads to convection inside the chambers and hence a higher temperature exchange. Same problem would occur at the double glazed window with even higher total volume.
Especially the approach with plywood top and bottom sheet and a double layer COMBOO structure would provide a good insulation, a high mechanical stability and a conventional machining / manufacturing of floors and transport boxes.
The infrared camera was used to visualize temperature distribution over the surface area, as thermocouple represent only point measurements. The result is shown in Figure 14, where picture of the COMBOO structure are shown. Time steps are integrated into each single picture. It can be seen, that infrared radiation was detected by thermal camera. First of all temperature distribution is homogeneous in colour over the whole area, while with increasing time, colour of the holes turns to yellow. It can be seen, that temperature rises at the holes. Due to the camera itself, a temperature adaption takes place shifting the colour scale between hottest and coolest points.
In the upper left part of nearly all pictures, a small temperature leak can be seen, as insulation of the rim was disturbed. Camera measurements of the COMBOO structure couldn't be repeated, as a software problem of the old operating system occurred.
Temperature distribution for the other specimen was homogeneous over the whole area during each experiment. The glass surface had to be coated with black dye as reflection disturbed the measurements.

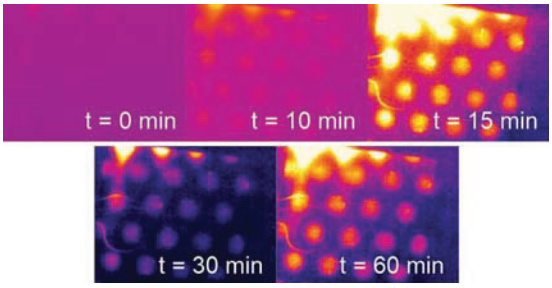

Figure 13: *Pictures of thermos camera at different time steps*

4 SUMMARY AND CONCLUSIONS

This paper described extended research for an alternative sandwich core material made of bamboo. The new material is called COMBOO and it provides not only superior mechanical properties like high compressive and bending strength but also good results in thermal insulation and acoustic damping.
The comparison of sound absorption coefficient in a Kundt's tube of composite foams, fibre materials and COMBOO structures revealed good damping or absorption results in a broad frequency range of the new structure. Different geometrical dependencies have been successfully identified, as the chamber diameter has much lower influence on damping value than the hole diameter in the top sheet. An enhancement of total absorption over the whole frequency range was received when filling the chambers with polymer foam.
Next steps will be an investigation of the effects of chambers depth, a combination of several different hole diameters at one top sheet material and different fillings of the chambers. This might improve damping, also over a wider frequency range.
A visible COMBOO structure (GFRP or polymer sheets) could be very interesting in acoustics if a sound absorption has to be combined with certain requirements of surface stability or stiffness. The specific honeycomb appearance could also be interesting. A fibre filling could provide interesting optical effects.
The other investigation in this paper concerned heat transfer or insulation characteristics of five typical materials for civil engineering. It was found that the heat transfer through a GFRP covered COMBOO board, acquired by the measurement of the surface temperature is lower than through double glazed windows or concrete panels of same thickness and slightly higher than through aerated concrete boards. Best insulation was reached by a styrofoam block.
Next research steps will be the estimation of heat transfer coefficients and improvements of the COMBOO structure. Therefore the thermal analysis of single GFRP sheets might help. The aforesaid multi-layer attempt could reduce possible convection and improve insulation.
In combination with the high compressive strength of the COMBOO structure, utilization as transport container conditioned box or floor material is possible especially if plywood is used as top and bottom sheet.

https://doi.org/10.52202/069179-0480

5 OUTLOOK

In addition to the classic applications of the newly developed COMBOO sandwich material in the area of apartment, house and modular construction, its very interesting properties can also be used for technical applications such as acoustic insulation boards and thermal insulators. This also opens up applications in refrigerated box construction for trucks. A special advantage here is the recyclability of the material, which consists of renewable materials.

REFERENCES

[1] Dunkelberg, K., ”Bambus - Bauen mit pflanzlichen Stäben IL 31“, Karl Krämer Stuttgart, 2005.

[2] Loth, A. et al, “Evaluation and comparison of a lightweight bamboo composite”, AIP Conference Proceedings, 1769, 170010, 2016.

[3] Loth, A., Förster, R., “COMBOO - A novel core material for composite sandwich structures from renewable sources”, Proceedings ECCM 2018, Athens, pp 6, 2018.

[4] Loth, A., Förster, R., “First advances of COMBOO, a novel lightweight bamboo based composite material for structural and environmental applications”, Proceedings WCTE 2018, Seoul, pp 6, 2018.

[5] https://www.bafu.admin.ch/bafu/de/home/themen / laerm/fachinformationen/auswirkungen-des-laerms /gesundheitliche-auswirkungen-von-laerm.html, acquired 10.1.2023.

[6] https://www.who.int/europe/news-room/fact-sheets/item/noise, acquired 10.1.2023

[7] https://www.baunetzwissen.de/akustik/fachwissen/ schallabsorption/absorberarten-147703, acquired 10.2.2023

[8] https://www.baunetzwissen.de/akustik/fachwissen/ schallabsorption/poroese-schallabsorber-147715, acquired 10.2.2023.

[9] Möser, M., „Technische Akustik“, Springer Berlin, VDI Book, Ed. 6, 2005.

[10] Fuchs, H., „Schallabsorption und Schalldämpfung“, VDI Book, Springer Berlin, 2004.

[11] DIN EN ISO 10534-1:2001-10. Akustik – Bestimmung des Schallabsorptionsgrades und der Impedanz in Impedanzrohren – Teil 1: Verfahren mit Stehwellenverhältnis

[12] DIN EN ISO 10534-2:2001-10. Akustik – Bestimmung des Schallabsorptionsgrades und der Impedanz in Impedanzrohren – Teil 2: Verfahren mit Übertragungsfunktion.

[13] http://www.hsschaumstoff.com/produktion/schaumstoffprodukte/verbundschaeume.html, acquired 14.2.2023.

[14] https://www.melaminharzschaum.de/materialeigenschaften-von-melaminharzschaum/, acquired 14.2.2023.

[15] https://www.baux.com/acoustic-products/, acquired 20.2.2023.

[16] https://solidbau.at/artikel/wellness-fuer-die-ohren-bessere-akustik-mit-natuerlichen-schall-absorber platten-aus-hanffaser/, acquired 20.2.2023.

[17] https://freundgmbh.com/produkte/green/evergreen-moos-premium, acquired 20.2.2023.

[18] https://tandem-acoustics.com/#technik, acquired 20.2.2023.

[19] Jomeah, Y., “Akustische und photometrische Untersuchung von bambusbasierten Leichtbau-strukturen“, Masterthesis, Beuth University of Applied Science, 2020.

World Conference on Timber Engineering Oslo 2023

BENDING OF CLT BY THE LATTICE HINGE METHOD

Laurane Néron[1]

ABSTRACT: This study provides an overview of ongoing research on cross-laminated timber (CLT) panels bent with the lattice hinge method: a system that has been explored by ArtBuild and Ney & Partners WOW for two temporary structures. First, the parameters that define the lattice hinge cutting process are described and exposed at the scale of CLT panels. Second, the results of a series of experimental tests will be investigated to define the structural behaviour and properties of slotted CLT panels. Finally, the two projects that were built will be presented in terms of architecture and structural details. The first one is a pavilion built for the Libramont Fair in 2019, and the second one, is an ephemeral auditorium that has been set up in the ephemeral Grand Palais in Paris for the International Wooden Construction Forum (Forum Bois Construction) in 2021.

KEYWORDS: CLT, lattice hinge, bending method, CNC manufacturing

1 INTRODUCTION

Traditional methods for wood bending can be classified into four categories:

(1) In-plane cutting of curved piece

The easiest way to obtain a curved piece of wood is to cut it out of a larger raw element. The advantage of this technique is that it is very simple and does not generate internal stresses in the piece of wood. However, it generates large losses of material and is not feasible for large elements and thicknesses. In addition, the wood grain of the curved element is interrupted by the cut-outs and reduces its bearing capacity.

(2) Hot bending

When the moisture content of wood increased it becomes softer and easier to bend. The hot bending process consists of immersing wood in hot water or subjecting it to steam (usually under pressure). Then, it is placed in a bending mould while it dries. Once dry, the wood will keep the curvature that was imposed by the mould. This method requires a lot of time and specific equipment.

(3) Gluing of lamellas

The technique commonly used for glued laminated timber offers the ability to easily create curved beams. The standard lamellas of 40 mm thick have a low rigidity and are easy to bend. The successive gluing of lamellas can be done by a hydraulic press or mould in order to shape the beam with the required curvature.

(4) Notching of wood

The purpose of the notches is to reduce the stiffness of the wooden piece by removing some parts of the material. The advantage of this method is to be reversible because the curvature can be maintained by mechanical fasteners instead of glue. It is commonly used for the realization of musical instruments such as violin and sees its success growing the last few years with the arrival of laser cutters which allow to multiply the number of possible cutting patterns. The lattice hinge method enters in this category.

All these techniques can be applied to solid wood and glulam beams, but it is more complicated for large timber panels such as CLT. Therefore, this study aims to provide a bending technique for CLT panels in order to explore a new architectural typology.

2 LATTICE HINGE : DEFINITION AND PARAMETERS

2.1 DEFINITION

The ‘lattice hinge’ is formed by an array of parallel overlapping cuts in a flat wooden panel. By dividing the panel into a set of thin columns, each column can twist on its own axis and rotate. The length of these so called “torsion legs” drives the overall curvature radius of the panel. The longer the leg, the more flexible the panel. The piece of CLT that links two torsion legs are considered as planar surfaces and have no influence on the overall curvature of the panel.

2.2 GEOMETRICAL PARAMETERS

2.2.1 Panel dimensions

The external dimensions of the CLT panel are determined by its length L, width W and thickness h.

[1] Laurane Néron, Ney and Partners WOW, Belgium, LANE@ney.partners

https://doi.org/10.52202/069179-0481

2.2.2 Lattice hinge pattern dimensions

The cutting pattern of the lattice hinge is defined by the number of torsion legs required across the width n and height N_{div} of the panel, as well as the width b of the legs.

2.2.3 Panel curvature

The bending curvature of the panel is defined by the radius of curvature R. It is also possible to calculate the sag f of the panel once bent, the final reduced width (or chord of the arc C) and the global angle of rotation of the panel φ with the following equations:

$$f = R \cdot \left(1 - \cos\left(\frac{\varphi}{2}\right)\right) \quad (1)$$

$$C = 2 \cdot R \cdot \sin\left(\frac{\varphi}{2}\right) \quad (2)$$

$$\varphi = \frac{W}{R} \quad (3)$$

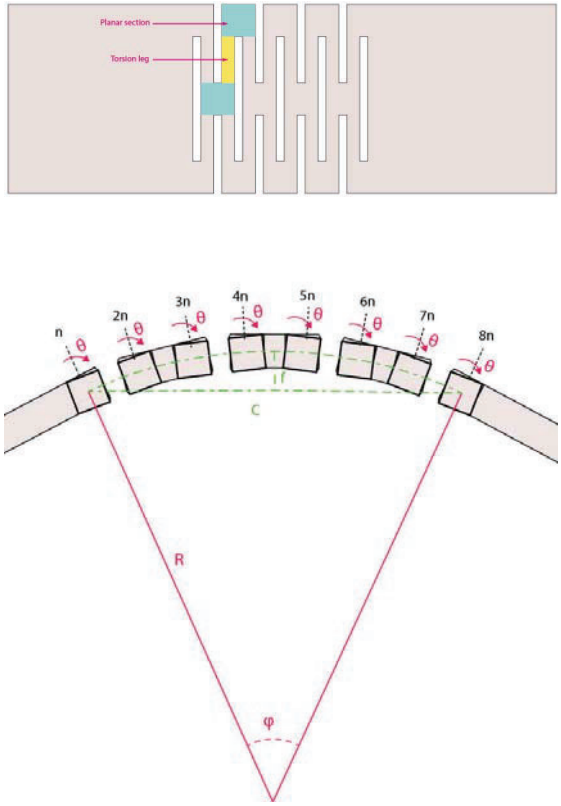

Figure 1: *Geometric parameters of lattice hinge [3] [6]*

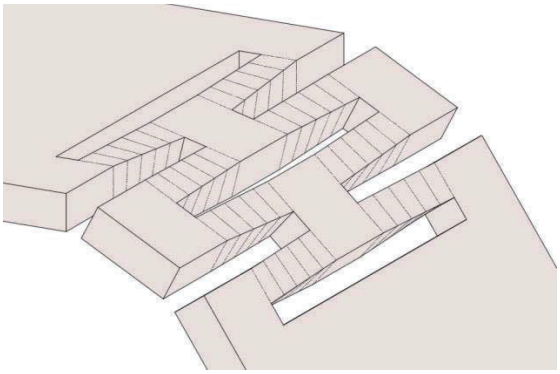

Figure 2: *3D view of twisting mechanism by lattice hinge [3][6]*

2.3 DESIGN OF TORSION LEGS

To bend a CLT panel, each torsion leg rotates around its own axis, with an angle:

$$\theta = \frac{\varphi}{n} \quad (4)$$

The torsion legs are submitted to shear stresses due to a torsion moment. The torsion moment in a square wooden element can be expressed by two formulas [10] - depending on the angle of rotation of the torsion leg (5) or depending on the shear stress (6):

$$T = \frac{G_{eq} \cdot \theta \cdot J}{l} \quad (5)$$

$$T = \tau \cdot \alpha \cdot h \cdot b^2 \quad (6)$$

By combining the two formulas, we can define the expression of the minimal required length for torsion legs in function of the desired curvature and the maximum shear stress allowed $\tau = \tau_{max} = f_{v,d}$:

$$l_{min} = \frac{G_{eq} \cdot \theta \cdot J}{f_{v,d} \cdot \alpha \cdot h \cdot b^2} \quad (7)$$

where:

- G_{eq} is the equivalent shear modulus of a torsion leg that has been defined by a series of tests. The resulting value is given in the table below as well as the standard values for shear modulus of CLT for comparison.

Table 1: *Standard shear modulus value for CLT*

		Design values	
Shear modulus CLT	$G_{0,mean}$	690	N/mm²
Rolling shear modulus CLT	G_R	50	N/mm²
Equivalent shear modulus	G_{eq}	210	N/mm²

- $f_{v,d}$ is the shear resistance capacity of CLT. Bending is applied as a permanent loading, therefore we assume $k_{mod} = 0.6$ and $\gamma_M = 1.25$ for CLT.

$$f_{v,d} = f_{v,k} \times \frac{k_{mod}}{\gamma_M} \quad (8)$$

https://doi.org/10.52202/069179-0481

$$f_{v,d} = 1.68\ N/mm^2$$

- J is the torsional inertia of a rectangular cross-section. As CLT is made of several cross layers of wood, rolling shear probably has an influence on the J value. This interaction will be studied by a series of experimental torsion tests on CLT.

$$J = \beta \cdot h \cdot b^3 \quad (9)$$

– α and β are form coefficients defined with empirical values from the table below.

Table 2: *Form coefficients for torsional inertia [12]*

h/b	1	1,5	2	3	6	10
$\boldsymbol{\alpha}$	0,208	0,231	0,246	0,267	0,299	0,313
$\boldsymbol{\beta}$	0,141	0,196	0,229	0,263	0,299	0,313

2.4 PARAMETRIC MODELLING

All parameters and formulas listed in the previous section have been implemented in a parametric model with Grasshopper/Rhino. The input data are the panel dimensions and the required radius of curvature. The lattice hinge pattern dimensions are given as output and drawn on any given developable surface.

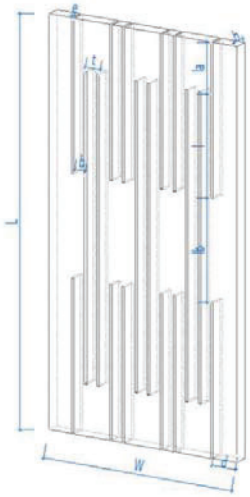

Figure 3: *Axonometric view of slotted CLT panel and dimension parameters*

3 EXPERIMENTAL TESTS

The aim is to define the structural behaviour of a slotted CLT panel for each loading types and directions. A total of 5 different load tests have been realised :

- Torsion test
- Transversal bending test
- Longitudinal bending test
- Axial tension test
- Axial compression test

[5] Ecole Centrale des Arts et Métiers, Brussels, Belgium

The results of those tests helped to quantify the loss of stiffness due to the slots in the CLT panels.
First, the torsion test will be described in order to find the equivalent shear modulus value that is needed to define the length of the torsion legs for the cutting pattern. Then, only transversal bending test is described in this paper as it has the biggest impact on the loss of stiffness for the CLT panel. All test results can be found in [7].

3.1 TORSION TEST

Since torsion tests are rarely performed on wood and the partner laboratory (ECAM[5]) does not have a machine specifically dedicated to torsion tests, an experimental system was designed and implemented on a test bench to allow testing of CLT samples.
A total of 8 samples have been tested in CLT 60 3s:

- 4 samples of 20 mm wide and 800 mm long
- 4 samples of 30 mm wide and 800 mm long

The loading system is composed of a lever arm fixed to the sample by a bolted connection and a rod allowing the placement of weights at the other end. Measures of deflections are taken in the centre and at both supports in order to retrieve the relative rotation angle of the sample. The torsional moment is determined by multiplying the load applied at the end of the lever arm by the distance to the sample.

Figure 4: *Torsion test system*

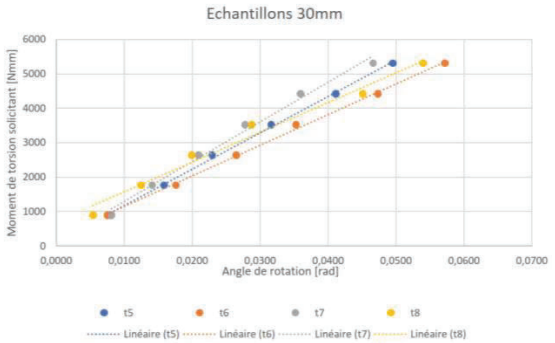

Figure 5: *Rotations* $\boldsymbol{\theta}$ *of the sample in function of the torsional moment* $\boldsymbol{T}$ *applied*

https://doi.org/10.52202/069179-0481

The value of the equivalent shear modulus can be deducted from equation (5), considering that the values J and l are constant for a given cross section. The mean result for all samples is: $G_{eq} = 210\ N/mm^2$.

3.2 TRANSVERSAL BENDING TEST

A 3-point bending test was performed on slotted CLT panel. The loading was done by sand bags.3 samples have been tested in CLT 60 3s with a span of 715 mm.

Figure 6: *Transversal bending test system*

The parameter EI governing the transverse bending stiffness of the panel can be expressed using the deflection formula for a bi-supported beam subjected to point loading as follows:

$$u = \frac{q \cdot L^3}{48 \cdot E \cdot I} \quad \rightarrow \quad EI_{eq} = \frac{q \cdot L^3}{48 \cdot u} \qquad (10)$$

where u = deflection at the centre of the panel, E = modulus of elasticity, I = inertia, q = load and L = span.

Table 3: *Values of deflections for maximum load of 3,125 kNm/m*

Samples	1	2	3	Mean value	CLT (no slot)
u [mm]	33	28	39	33.50	0.32

For CLT, the transversal stiffness is given by the coefficient D_{22} in the stiffness matrix. For a 3-layer CLT panel of 60 mm: $D_{22} = 7{,}733\ kNm^2$. The tests gives a value of $D_{22,eq} = EI_{eq} = 0.071\ kNm^2$. Therefore, the loss of stiffness of a slotted CLT panel compared to a full CLT in transverse direction is about 99%. The panel loses most of its bending capacity, so an external system must be put in place to maintain it in the transverse direction. This was achieved in two different ways for the two projects where curved CLT was used (see section 5).

4 CLT PANEL PROPERTIES FOR NUMERICAL ANALYSIS

Thanks to the test results, we were able to define an equivalent stiffness matrix for a slotted CLT panel. This stiffness matrix is then used in a Finite Element software (SCIA) in order to define a simplified calculation model that is used to check the global behaviour of a structure with slotted CLT panels.

Table 4: *Stiffness matrix for slotted CLT panel*

CLT	60-3s
D11 [MNm]	$2{,}088 \cdot 10^{-1}$
D22 [MNm]	$7{,}100 \cdot 10^{-5}$
D12 [MNm]	0
D33 [MNm]	$6{,}732 \cdot 10^{-3}$
D44 [MN/m]	4,423
D55 [MN/m]	13,800
D66 [MN/m]	480,000
D77 [MN/m]	240,000
D67 [MN/m]	0
D88 [MN/m]	25,969

5 CASE STUDY

5.1 NAUTILE SYLVESTRE

5.1.1 Project background

Commissioned for the 85th edition on the occasion of Demo Forest, an event that follows the Libramont Fair, the wooden pavilion named “Nautile Sylvestre” was conceived by ArtBuild Architects, Saïse Design and Ney & Partners WOW as a totem for forestry and timber trades. It is the first structural use of bent CLT panels.

Figure 7: *General view of the pavilion*

5.1.2 Architectural design

Inspired from the bio-structure of the banana stem, a double revolution staircase gives access to a central elevated platform at 4.5 m above ground level. The upper and lower side of the staircase offer respectively, a point of view and an exhibition gallery. Visitors can wander easily by following the curvature of the walls and crossing the pavilion from one side to the other.

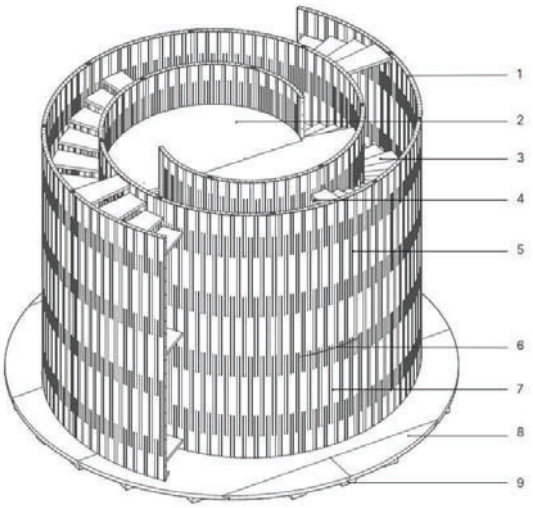

Figure 8: *Axonometric view of the Nautile Sylvestre pavilion – 1. Metal plate at the head of CLT walls assembled with splice joints / 2. Slab with CLT 60 mm assembled by lap joints / 3.Stair steps with CLT 60 mm / 4.Supporting joist for steps / 5.Bent walls with CLT 60 mm / 6. Curved door in metal frame / 7. Invisible locksmithing elements / 8. Base plate with CLT 90 mm / 9. Support wedges 300 x 300 mm*

5.1.3 Connection system of multiple slotted CLT panels

We studied several options to maintain the panels curvature and we retained a combination of three options adapted to each part of the panels. At the base, the panels are inserted into a notch that has been milled in the platform following the spiral geometry. At the top edge, an 8 mm steel plate has been added in order to not only maintain the curvature but also act as protection against rain water. Since the panels are 5.50 m high, we also defined a minimum of two intermediate lateral supports to ensure a constant curvature over the height and serving as supports preventing buckling of the panels. The staircase steps, that are laterally screwed to the CLT walls, are fulfilling this role. The whole structure gains in structural efficiency thanks to the multi-layered shell created by the successive walls of bent CLT-panels connected together : a static diagram that accurately reproduces the functioning of the banana stem.

Figure 9: *Interior view of the staircase*

5.1.4 Mounting process & reuse

For the milling process, a CNC machine was used to make the cuts in the panels. A 10 mm wide saw was chosen over milling to save production time.

Once milled with lattice hinge pattern, the prefabricated panels can be transported flat to the site. This suggests a significant economy in terms of transport costs.

On-site, the panels were curved, erected and assembled by carpentry students in a few days. First, the steel plates were screwed to the top flange and wooden pieces screwed to the bottom flange of the CLT panel to give it the right curvature. Then, the panels were lifted with a mobile crane to move them to their final position. The construction started from the centre and extended symmetrically to the outer edges of the pavilion.

After the fair, the structure was dismantled and the panels returned to their original flat condition. They were stored in a workshop waiting to be reused for the next fair.

https://doi.org/10.52202/069179-0481

Figure 10: *Lifting of curved CLT panel*

5.2 EPHEMERAL AUDITORIUM

5.2.1 Project background

On the occasion of the 10th edition of the “Forum International Bois Construction" in Paris, the ephemeral auditorium stands in the centre of the ephemeral Grand Palais. A total amount of 64 CLT panels are bended and assembled together to create the plenary room for conferences. This temporary structure is easily dismantled and is intended to be reused for other events.

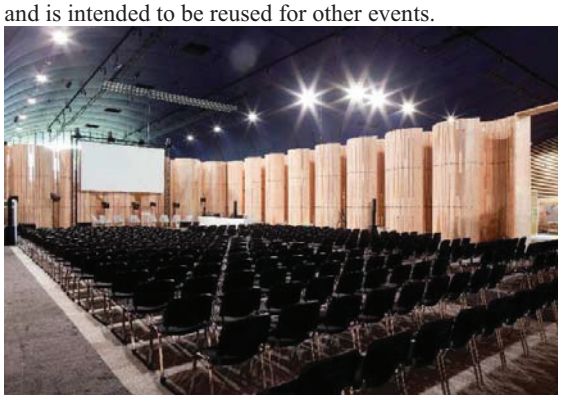

Figure 11: *Interior view of the auditorium*

5.2.2 Architectural design

The auditorium is a rectangular room with seating for 350 people. The perimeter walls cover an area of 29 m x 19 m with a modular construction made of bent CLT panels connected by steel bracings. This wooden curtain provides privacy but it also allows for some subtle transparency. The notches in the wood act as a sound trap and provide an acoustic barrier for the auditorium.

A single panel has a dimension of 2,40 m x 5,25 m and weigh about 300 kg. In order to stand as a stable structure, a minimum of three panels must be connected to each other. This project is made of three different constructive modules : linear walls, doors and angles. They can be inter-connected in many configurations to be able to adapt to the future needs.

The CLT panels are made of Douglas fir wood, a natural durable species. This maximizes the potential for reuse of the structure as it enables it to be used as an outdoor structure (if covered and protected from rain).

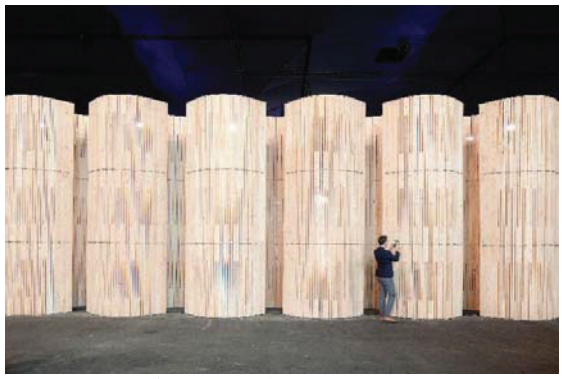

Figure 12: *Wooden curtain of CLT*

5.2.3 Connection system of multiple slotted CLT panels

The curvature of the panels is maintained by a post-tensioning system developed specifically for the project. Custom-made cast iron pieces are inserted into the slots and tensioned by a steel rod at each end. The geometry has been defined according to the curvature of the panel. Holes are integrated on both sides to integrate a steel rod that acts as post-tension to maintain the panel in its curved position.

All these parts can be disassembled to put the panels back flat and facilitate transport.

Figure 13: *Connection detail between curved CLT panels*

6 CONCLUSIONS

Interest in lattice hinge has been revived thanks to the growth of digital tools. This study shows how it has been implemented in CLT panels at a structural scale.

Bending by the lattice hinge method implies that wood is submitted to local torsion. As a multi-layered material, CLT does not behave like solid wood in torsion and the formulas found in the literature to calculate shear stresses due to torsion turned out to be invalid. Therefore, the torsion of CLT has been studied through a series of test to define an equivalent shear modulus that can be used for torsion calculations. Moreover, the global analysis of the projects was performed by using an equivalent stiffness matrix for CLT based on the tests results.

https://doi.org/10.52202/069179-0481

The first application was to create curved bearing walls for a temporary pavilion. In the future, bent CLT panels could be used in buildings for walls or facades. Studies are still on-going to define new developments and potentials for curved CLT panels.

REFERENCES

[1] Artbuild, Nautile Sylvestre - Welcome Pavilion, 2019, [online], accessed on February 7, 2022, https://www.artbuild.com/lab/nautilus-tlc-exploration

[2] Artbuild, OSA - The ephemeral auditorium, Paris - France, 2021, [online], accessed on February 7, 2022, https://www.artbuild.com/lab/osa-the-ephemeral-auditorium-paris-france

[3] Bitoun S., Le potentiel architectural du bois plié, ENSAPM - Département transitions, 2016, [mémoire], 30 p.

[4] Deferred Procrastination, Latice Hinges Design - choosing torsional stress, [online], accessed on February 8, 2022, https://www.defproc.co.uk/analysis/lattice-hinge-design-choosing-torsional-stress/

[5] Deferred Procrastination, Latice Hinges Design - minimum bend radius, [online], accessed on February 8,2022, https://www.defproc.co.uk/analysis/lattice-hinge-design-minimum-bend-radius/

[6] Deguine L., Lattice Hinge, développement d'une méthode générique, ENSAPM, 2016, [mémoire], 82p.

[7] Malache Y., CLT cintré par la méthode du Lattice Hinge : les prémisses d'une utilisation structurelle, ECAM, Brussels, 2022, [mémoire], 110p.

[8] Ney and Partners WOW, Nautile Sylvestre pavilion, 2019, [online], accessed on March 1, 2023, https://wow.timber-engineering.partners/projects/totem-foire-de-libramont/

[9] Ney and Partners WOW, Nautile Sylvestre pavilion, 2019, [online], accessed on March 1, 2023, https://wow.timber-engineering.partners/projects/ephemeral-auditorium/

[10] PUECH V., CLT, du panneau plan au mur courbe, Ecole Nationale des Ponts et Chaussées, Paris, 2017, [mémoire], 120 p.

[11] Pro Holz, Cross Laminated Timber structural design, Basic design and engineering principles according to Eurocode, 2014, 191 p.

[12] SCIA Engineer, Calcul des caractéristiques de base du profil, [online], accessed on November 26, 2022, https://help.scia.net/17.0/fr/rb/crosssections/calculation_of_sectional_characteristics.htm

https://doi.org/10.52202/069179-0481

World Conference on Timber Engineering Oslo 2023

STRATOCONCEPTION®, AN ADDITIVE MANUFACTURING PROCESS FOR TIMBER ARCHITECTURE: CHALLENGES AND OPPORTUNITIES

Victor Fréchard[1], Laurent Bléron[2], Julien Meyer[3], Franck Besançon[4], Gilles Duchanois[5]

ABSTRACT: The additive manufacturing has been recently adopted by the construction industry to overcome the existing design limitations and to build large-scale structures. The timber architecture and construction have not yet adopted the additive manufacturing technologies. This paper focuses on the understanding of the use of the Stratoconception® additive manufacturing process for timber architecture and construction by identifying the opportunities it offers and the challenges it presents. First, we outline the Stratoconception® process. Furthermore, we highlight and assess by experiment the opportunities and the challenges of the implementation of this process. We target the complex shape design and the multi-functionalization of the components as important opportunities that can lead the design of new high-value building components for timber architecture. Next, we introduce the potential use cases for the process and emphasize the capacity of the technology to be implemented in the common timber construction practices. The lack for Stratoconception® use in the context and in the dimensions of architecture brings the challenges of scaling-up the process and integrating it into the multicriteria architectural design process which exceed the existing methods and tools. We describe the overriding issue of managing the waste of material caused by the micro-milling phase of the process. The building of a knowledge base of relation between Stratoconception® and timber architecture reveals the need for an adapted and efficient design framework for the process use for timber architecture projects. Thus, we propose and describe a theoretical design framework achieving the integration of the AEC issues into a design process and fostering the development of new efficient building components by guiding the designer towards rational decision making.

KEYWORDS: Timber Architecture, Additive Manufacturing, Stratoconception®, Design for Additive Manufacturing, Computational design

1 INTRODUCTION

1.1 CONTEXT

The adoption of computational design and digital fabrication in architecture, based on Computer Numerical Control (CNC) machining and robotics, fosters a development of an innovative, efficient, and expressive contemporary timber architecture [1]. The formal and structural advances from the digital tools adoption encompass an emergence of new architectural tectonics [2-4], which in the current environmental context are fostering the use of timber [5].

The Additive Manufacturing (AM), comprising a range of processes [6,7], shares the common origin with CNC machining but differs in the ability to produce directly the high level of complexity parts that cannot be achieved by subtractive or formative methodologies. In recent years, we have observed a substantial increase in research topics studying the use of AM methods and their first implementations in the construction industry [8-11] for the large-scale building components and structures by applying the processes based on cementitious materials [12-15], alongside with earth-based [16,17], sand-based [18], polymeric [19], or metal materials [20].

The motivations for the adoption of AM by the construction industry mainly focus on the productivity gains, the reduction of materials waste, the worker availability and safety, or the reduction of the production cost of the complex parts. Also, these motivations correspond to the core challenges of the automation in construction and of digital fabrication adoption. The AM use today is often limited to these core challenges but does not *"reshape the way we think about architectural components"*[21]. According to Labonnote et al. [8], an architectural paradigm shift exploring the inherent potentials of AM is required to improve current construction design approaches. To foster this paradigm shift, the AM constraints must be considered on the early stage of the design, to allow rational decision-making.

Furthermore, the environmental issues require for the use of more sustainable, renewable, and non-petroleum-based materials. Wood could be used in several AM processes [22-24], however the research and technology advances are still needed to meet the requirements of large-scale construction.

[1] Victor Fréchard, LERMAB, Nancy National School of Architecture, France, victor.frechard@nancy.archi.fr
[2] Laurent Bléron, LERMAB, University of Lorraine, France, laurent.bleron@univ-lorraine.fr
[3] Julien Meyer, MAP-CRAI, Nancy National School of Architecture, France, j.meyer@nancy.archi.fr
[4] Frank Besançon, MAP-CRAI, Nancy National School of Architecture, France, franck.besancon@nancy.archi.fr
[5] Gilles Duchanois, MAP-CRAI, Nancy National School of Architecture, France, gilles.duchanois@nancy.archi.fr

https://doi.org/10.52202/069179-0482

This paper reviews the use of Stratoconception® for timber architecture and its integration into the design-to-manufacturing process. First, we define the Stratoconception® process (Section 1.2) and research scope (Section 1.3). Second, we define the experiment context (Section 2). Third, the paper discusses the opportunities of the implementation of this AM process in Architecture, Engineering and Construction (AEC) (Section 3) and summarizes the challenges of its implementation (Section 4) identified during our experiments. The last section outlines the proposal of a framework of architectural design for additive manufacturing (DfAM) by Stratoconception® (Section 5).

1.2 STRATOCONCEPTION®

Stratoconception® belongs to the sheet lamination family of AM processes [6], [25]. It consists in slicing the 3D model of the part by computing into a set of layers called *strata* (Figure 1). Each *stratum* is laid out on a sheet material and is machined on both sides with 2.5 axis rapid micro-milling. Next, the strata are assembled with the relevant techniques. In the production of parts whose dimensions are larger than those of the machines or those of the raw material, the strata decomposition step is added to the process. This process refers to the initial patents [26-27] based on cutting and joining the multiple sheets of material to form the part. The use of multi-axis CNC machining to mill in 2.5 axis the edges of each stratum offers the elimination of the stair-step effect issue due to the sheet lamination process and thus allows to better match the 3D model's shape [28].

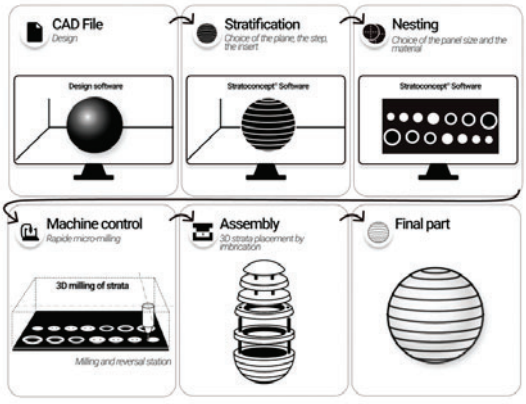

Figure 1: *Scheme of the Stratoconception® process.*

1.3 RESEARCH SCOPE AND ADDED VALUE

The Stratoconception® process application to architecture are currently limited to the scale models and the prototypes, to the formworks for concrete construction, and it is not yet applied to building components. However, the basic technical and material means such as three-axis CNC machining and timber panel materials are commonly used today in timber architecture and construction, thus they create potential opportunities for Stratoconception® process implementation. Despite the lack of the implementation in AEC, we hypothesize that the Stratoconception® process could be beneficial for the construction of complex and expressive large-scale structures or for the production of high-value-adding multifunctional building components.

An identification of the opportunities, of the limitations and the challenges of its implementation in timber architecture and construction is necessary to establish the knowledge base and the design-to-manufacturing framework. This will guide the architects, the engineers and the builders in their work in ways to benefit from the Stratoconception® process. Moreover, this will guide their digital collaboration and the workflow of the design and production of novel timber architecture products and projects.

2 EXPERIMENT DESCRIPTION

Our research is a practice-led research project identifying, emphasizing and analyzing the mechanisms of the use of Stratoconception® design-to-manufacturing process for AEC projects. Thus, our research aims to conduct experiments of Stratoconception® design and manufacturing and to build a knowledge base for the future proposal of a framework of design to additive manufacturing by Stratoconception®.

The experiment had three phases (Figure 2) studying the project *design*, the scale model *prototyping* and the project components *manufacturing*. The phase 1 studies the influence of Stratoconception® use at the early design stage on the final design of the project, by identifying the technical and architectural impact of the design choices, and by collecting the used and exchanged project data. In the phase 1.1, we ran a design experiment with the master program students at the National School of Architecture of Nancy (France). First, the main features of the AM process were introduced. Next, the students worked in teams on freeform architectural projects corresponding to a given program. Stratoconception® was imposed as a constructive system, influencing their design choices. In the phase 1.2, we study the issues of the strata use and influence on the architecture and design with renderings and scale models.

In the phase 2, scale models are used as prototypes to assess the existing digital workflow from design to manufacturing. This highlights the interoperability issues between the architectural CAD software and the Stratoconception® software.

In the phase 3, we design and manufacture the *functional prototypes* to identify the process scale up issues and to analyze the specifics of a building component design (phase 3.1) as well as an entire architecture (phase 3.2). In phase 2 and 3, we updated the inventory of the data exchanged between design and manufacturing.

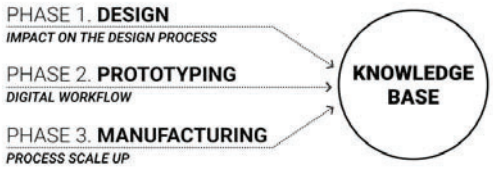

Figure 2: *Scheme of the aim of the experiment phases.*

https://doi.org/10.52202/069179-0482

The results of this experiment are summarized and discussed in Section 3 (opportunities) and Section 4 (challenges).

3 STRATUM AS AN OPPORTUNITY

The architecture development follows an iterative cycle, where the new technologies are developed in response to overcome the existing limits establishing new design paradigms with their own limits [29]. In this context and with its ability to design any shape mathematically [30], AM is a promising new technology to overcome the current limits of timber architecture with the new applications of freeform shapes or multifunctional building components which are today expensive or impossible to produce using the standard fabrication methods. This section overviews the new timber architectural opportunities of the Stratoconception® use.

3.1 NEW DESIGN OPPORTUNITIES

3.1.1 Timber construction existing limitations

The history demonstrates the ability of timber architecture to reinvent itself to develop the optimized building systems allowing to design the freeform shapes. Yet, the limitations still exist in the production of double-curved parts, the management of the envelope-structure relationship in complex shapes, the access to internal geometries or the challenge of achieving three-dimensional timber joints. These limitations are due to the high costs of production of the complex parts, requiring specific and unique approaches; or due to the technical inability to manufacture the three-dimensional parts with exterior and interior geometries on an industrial scale with the current means of timber construction.

3.1.2 Complex shapes: expression and optimization

As AM can mathematically produce any shape [30], it is a relevant solution to fabricate the double-curved geometries of parts. By overcoming the limitations of the standard manufacturing methods, architects can design new shapes for timber architecture and can *"encourage the appearance of new constructive and architectural vocabularies"* [4]. This exploration of new designs encompasses both the purely formal expression and the topology optimization to satisfy technical criteria. Thus, Labonnote et al. describes AM as *"an opportunity for making the link between well-developed, computational-based, optimization and the previously missing physical processes required to reproduce optimized structures"* [8,31]. The optimization usually aims to reduce the material consumption, and it is performed within the functional limits of the part, the material properties, and the constraints of the manufacturing processes. This optimization can also be applied to the thermal, acoustic, or other fluids properties. The recent research on the use of topology optimization in architecture illustrates how AM can enable the production of new complex shapes for the architecture within the limits of its processes [32].

3.1.3 Lightweight and multi-functional parts

The ability to easily access the inside of a part by the designers is, perhaps, AM's most disruptive and relevant contribution to timber construction. Thus, the hollowing out of the parts becomes possible, and it optimizes the amount of material used in the final part. Unlike the other AM processes, Stratoconception® can reduce the weight of the part by designing voids, but it does not allow to optimize the amount of consumed material by the hollowing out material, because the creation of voids during the micro-milling phase generates of as much material waste (see 4.1.2).

Today, timber buildings are composed of the materials layers with different functions such as structural, thermal, acoustic, waterproofing or building systems. The design of the voids allow to integrate a range of such various functions into a single part [7,13]. This can reduce the use of different materials, including the materials with a high environmental impact as well as the amount of assembly operations and it can provide new technical solutions for timber architecture. This may also improve the management and the properties of the envelope-structure relationship for complex structures and produce high-value-adding multifunctional building components.

The section 3.2 emphasizes how these opportunities of AM can be applied to timber construction, using Stratoconception®, by strengthening the envelope-structure relationship of the complex walls or by designing new technical parts.

3.2 APPLICATION EXAMPLES

The phase 1 design experiment proposes a non-exhaustive outline of the fields of structural and non-structural Stratoconception® uses for timber architecture. We present a shell wall project and a three-dimensional mesh joint as two use-cases of Stratoconception® application opportunities.

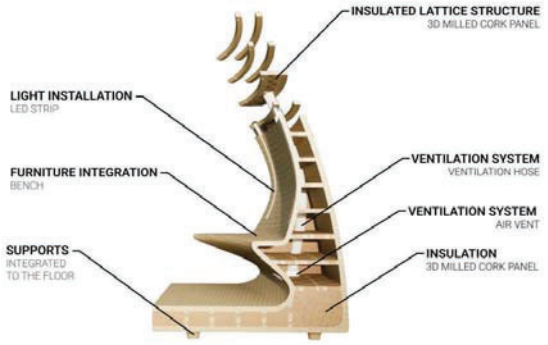

Figure 3: *Proof of concept of a complex multifunctional wall.*

Figure 3 presents a *stratoconceived* shell wall integrating various functions such as structural, thermal, and acoustic insulation, ventilation, electrical systems, and even as the element of furniture (a bench). In the conventional designs of three-dimensional structures these functions are held by different components, systems and materials, which are often assembled with the complex junctions. However, with Stratoconception® these functions may be united in a single component. In such complex double-curved shell wall, the envelope-structure relationship is enhanced. Thus, with the strata, we minimize the amount of the high environmental impact materials and of the

joining operations between the building wall layers. However, we hypothesize that the use of the Stratoconception® process for large-scale structures could have a high impact on the consumption and the wastes of material (see 4.1.2) and thus on the efficiency of the constructive system facing environmental and economic issues. The assessment of the performance of large-scale *stratoconceived* structures is required to validate, or not, the relevance of this particular use of Stratoconception® in AEC projects.

A three-dimensional timber mesh structure type is an elegant and efficient building system. However, it is often built with the metal joints, altering the environmental impact of such type of structure. The Figure 4 presents a timber joint of a three-dimensional timber mesh as an alternative to the metal joints. With Stratoconception®, the timber joint is lightened by hollowing out and it functions as structural element and as lights installation slot. Its use reduces the environmental impact of the project by avoiding the use of metal.

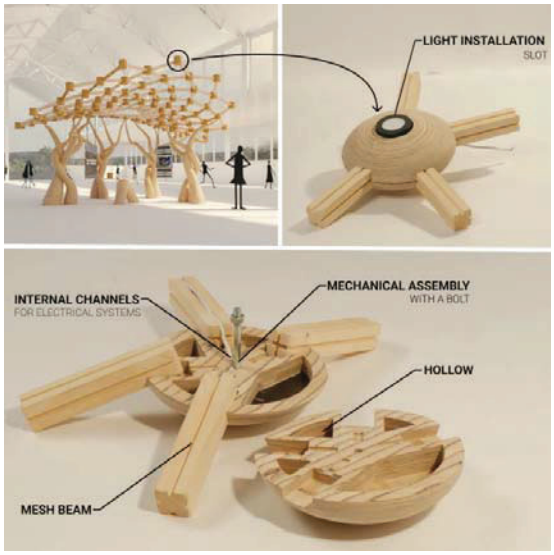

Figure 4: *Prototype of a multifunctional timber mesh node.*

The experiment results indicate other Stratoconception® relevant applications like the technical building parts production and maintenance, the windows and stairs manufacturing, the architectural heritage restoration, the furniture design, the bending mold or even the ornamentation. The further works will portray these identified relevant applications.

3.3 CAPACITY OF IMPLEMENTATION

The attempts of implementation of the automation principles of the manufacturing industry into the construction industry have not yet succeeded, nor have been transferred as a common practice to make a more sustainable impact. According to Wagner et al., *"there is a little doubt that methods of digital automation that aim for a broad impact on the industry will be ultimately judged based on their level of achieved organizational flexibility"* [33] depending on machinery and digital workflows. They identify two relevant success factors of such implementation, which are the economic viability and the architectural discourse which emphasize the opportunities to "*enrich the spatial and cultural qualities of the built environment*" [Ibidem]. We highlighted in the previous sections how the Stratoconception® process provides new opportunities for the timber architecture design.

Stratoconception® uses the basic technical and material means of the timber construction industry such as three-axis CNC machining and timber panel materials. The implementation of the adaptive slicing strategies for the fabrication in the computational design with Stratoconception® allow to machine the strata with the three-axis micro-milling following a digitally generated customizable toolpath.

This means that complex and *stratoconceived* parts can be machined in the same way as the standard parts, thus achieving a high degree of flexibility without additional fabrication costs.

Furthermore, the use of the similar machines in the timber construction companies facilitates the transfer of this new technology to the local construction context and to be used for specific contextualized projects.

However, in order to provide a full flexibility to the Stratoconception® process, the use of the standard technical means must be supported by a relevant digital and physical workflow linking computational design, the CNC milling and the manual construction operations.

3.4 ARCHITECTURAL VALUE

Most architectural projects use the timber panel as the topographic stratum, like in the case of the office and cafe building in Osaka where Kengo Kuma stacks the timber layers (Figure 5). In addition to directing the space and the circulation, the designed shape makes it possible to create a space with the floor, ceiling or walls function also as furniture. This example of the open flight strata emphasizes the layering and confers the apparent lightness of the space. It contrasts with the dense, monolithic strata as if the space was carved out of in a single piece of timber like the National Museum of Qatar Gift Shops where the architect Koichi Takada was inspired by the Dahl Al Misfir, also known as the "Cave of Light" (Figure 5).

Figure 5: *Open layered panels by Kengo Kuma (left) and carved cave by Koichi Takada (right).*

https://doi.org/10.52202/069179-0482

In most cases, timber strata are not used as structure but only as cladding or decoration. In architecture, a "stratum" may offer a design order or a superposition of various layers comprising structural (walls, floors, roofs, floor joists, beams, columns) and finishes (wooden cladding, siding, decorative elements) parts of a building. The stratum is important in the design and construction of a building because it helps to define the overall aesthetic and structural integrity of the building. In timber architecture, multiple strata can create a light and shadow play effect, generate natural textures and patterns, and provide a sense of warmth to the building.

The layering technique, in the case where the stratum remains visible, may prove aesthetic benefits to the design. For example, the lines created by the strata orient and structure the architectural space: high vertical strata generate a perception of monumentality while long horizontal strata give an impression of stability.

Actually, the architecture of strata overcomes the necessity to be thought through such separate elements as walls, floor or roof as is rather a continuous structure that encompasses the space because it creates a seamless integration of the different layers of the building [4]. Each stratum may have different functions and features. From the technical point of view, each stratum can carry different functions, such as structural support, insulation, weather resistance, or aesthetic appeal. The strata are also connected and integrated together in a cohesive system. From the architectural space point of view, the concept of the encompassing space is often used to create an impression of privacy, security, intimacy of the space, and can serve distinct functions for comfort, aesthetic and sustainability of a building.

4 RELEVANT CHALLENGES

In this section, we present the observed from the experiment challenges of the implementation of this process in AEC such as the design and the manufacturing of large-scale structures *stratoconceived*, the material waste management and the lack of the relevant and efficient design framework and methods.

4.1 PROCESS CHALLENGES

4.1.1 The scale-up is not a homothety

The manufacturing of large-scale structures challenges the ability of Stratoconception® process to scale up. The machines and the materials are limited by their dimensions, and the builders are limited by the human physical abilities. These limitations do not allow the scaling-up by a simple homothety applied to the slicing strategies, the fabrication, the assembly and the finishing operations. The phase 3 of the project components manufacturing experiment highlighted that the small building components and the large-scale structures differ significantly in their design-to-manufacturing process because of their size and of their functions.

The production of large-scale structures requires the use of strata decomposition strategies to overcome the limitations of the machines and material size by decomposing each stratum in smaller parts, consequently increasing the number of required assembly operations. The operations of clamping, flipping the panels for machining, assembling the strata and finishing are altered by the large-scale of the project and cannot perform as the small parts manufacturing. Thus, the Stratoconception® use for large-scale projects requires for the specific methods. There is a lack of knowledge about the effects of the project scale on the fabrication and the construction phases of Stratoconception® in AEC industry context, thus further research is required to confirm and precise our observations about these limitations.

4.1.2 Material waste management

Although Stratoconception® is an AM process, it includes a micro-milling phase of removing material to manufacture the designed strata. Therefore, the material waste needs to be analyzed and managed at the design phase to use this process and to satisfy both the economic and environmental performance criteria. For the analysis and the management of the material waste, we outlined the use of the raw material against its products, the strata and the reusable panel offcuts, and its wastes, the wood sawdust and the non-reusable panel offcuts (Figure 5). The material waste is caused by the nesting strategies, to the 3D milling of the strata edges, and to the light-weighting of the part (see 3.1.3).

The scale model prototyping and the project components manufacturing experiment allowed us to measure the material waste (Table 1) from the fabrication of the prototypes and to identify the relevant factors impacting the amount of these wastes in this specific use-case.

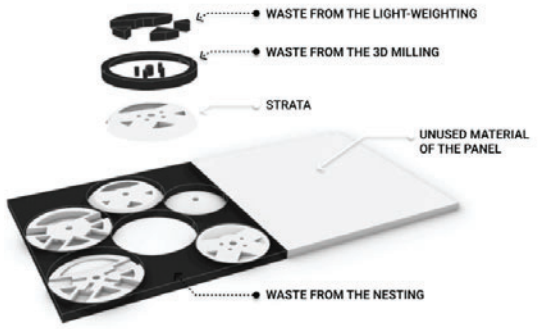

Figure 6: *Material use in the Stratoconception® process. Example of the multifunctional timber mesh joint fabrication (see 3.2).*

Table 1: *Material yield of the multifunctional timber mesh joint fabrication. The results are obtained by the geometric analysis of the nesting presented in figure 5.*

Waste type	Proportion of the material used (%)
Strata	26.13
Total material waste	73.87
Waste from the 3D milling	*31.32*
Waste from the nesting	*34.22*
Waste from the light-weighting	*8.33*

The results highlight that the waste from the 3D milling of the strata is significant when the thickness of the strata is thin in comparison to the thickness of the panel,

requiring for the large facing operations. The thin strata are the result of the implementation of the slicing planes required to guarantee the feasibility of the part and of the use of panels whose thickness does not perfectly fit the size of the part (Figure 6A). In addition, the higher tilt of the strata profile results in higher material waste. Yet, in the fabrication of the large-scale strata, the thickness of the timber panels is limited to their relatively small dimensions in comparison to the final structures. Thus, the profile of the part is highly discretized in strata and reduces the material waste in proportional comparison to the small part composed of strata which share the same order of magnitude with the final part (Figure 6B).

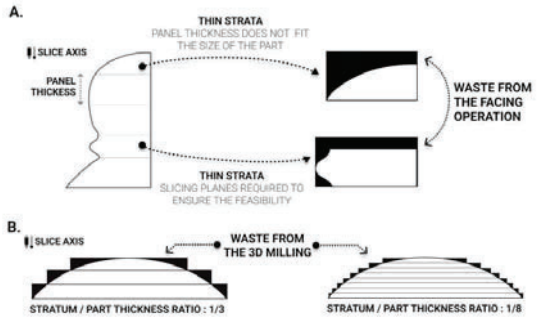

Figure 7: *Factors influencing the wastes from the 3D milling: the facing operations caused by the thin strata (A) and the ratio between the strata thickness and the size of the part (B).*

The waste caused by the nesting of the strata on the panel depends on the nesting algorithm implemented, as well as on the ability of the strata to nest in each other through their geometry (Figure 6). Thus, the minimization of nesting wastes requires for development of specific decomposition and slicing strategies considering the size and the shape of the strata, to enable optimized nesting.
At the present time, there is the lack of analysis tools to measure the material use balance, of evaluation tools to optimize the design choices and, of design strategies and methods based on the material waste management since such management is crucial to provide the economic and ecological efficiency of the use of the Stratoconception® in timber architecture and construction. We identified that a novel design approach is required for the use of Stratoconception® for AEC to manage the material waste. Further work will quantify the material waste balance depending on the size of the parts, for the small building components and the large-scale structures prototypes. The influence of the size of the part on the preponderance of a material waste type will be analyzed in further works.

4.1.3 Timber for Stratoconception® use

The Stratoconception® process uses all available material types in the panel format. The process use for timber construction requires for the structural engineered timber products in panel format such as Cross-Laminated Timber (CLT), Laminated Veneer Lumber (LVL) or Plywood. These are preferred due to the standardized format, the improved dimensional stability and to more homogeneous mechanical and machining properties which facilitate their processing by the CNC machines. However, we must consider that the use of these families of engineered timber products limits the thickness of the strata because of the available timber panel thicknesses, which are small in comparison to the large-scale structures. Thus, the timber panel thickness is a relevant parameter in the manufacturing process for large-scale structures project. This requires for decomposition strategies, the fabrication and the assembly of the large number of elements due to the size limitations. For the small parts, reducing the thickness could minimize the wastes from the 3D milling (see 4.1.2), but also it could complicate the machining and the assembly because of the possible need for thin strata. The use of panels also encompasses the waste materials issues caused by the nesting of the strata on the panels, a lack of diversification of the species used and an environmental impact due to the wood transformation process and the transport, as the transformation plants are rarely local to the projects and the construction firms.
However, timber is not only available as the panel products, thus our research must consider all the products as alternatives that can bring added value to the process. Thus, we hypothesize that the use of Glue Laminated Timber (GLT) can provide an alternative for the fabrication of large-scale strata by avoiding the nesting operation, each stratum corresponding to a single glulam element, and overcoming the dimension limitations of the panels thickness since the GLT products can be thicker. We also hypothesize that the use of the plank timber as an economic and ecological alternative for the manufacturing of small parts although it increases the complexity of the mechanical simulation and of the 3D milling surface quality control for example. Further research is required to explore the use of these alternatives in *stratoconceived* AEC projects.

4.2 DESIGN CHALLENGES

4.2.1 The need of new design approach

The Stratoconception® process follows the design of the part phase, and it begins with a manufacturing preparation phase in which the designer's choices are evaluated from the one prospect of the feasibility. The first experiment phase emphasizes that an AEC project design should be guided by the potentials and by the limitations of the manufacturing process from its early stages. We observe that there is an interdependence between the design and the manufacturing, the design is driven by the manufacturing process and the success of manufacturing depends on the design choices.
Furthermore, the design choices of an AEC project using Stratoconception® also must be assessed and optimized for the architectural, the engineering and the construction requirements for the project success. The slicing design strategies are typical of this phenomenon. They influence the design of all aspects of the project and highlight that the multi-criteria decision-making is required for the design based on the feasibility and performance evaluation. The slicing and the decomposition of the large-scale strata choices influence and are influenced by the visual aspect of the project, the material size and properties, the structural performance, the material yield,

https://doi.org/10.52202/069179-0482

the complexity of the construction and are limited by the fabrication feasibility (Figure 7).
These design criteria are interdependent and may have contradictory purposes. For example, the most efficient slicing direction choices may be contradictory to the intended aesthetic of the project. Similarly, maximizing the structural properties of the part in one direction involves orienting all the strata on the panel in the same direction to respect the wood's grain direction, hence altering the management of the wastes caused by the nesting.

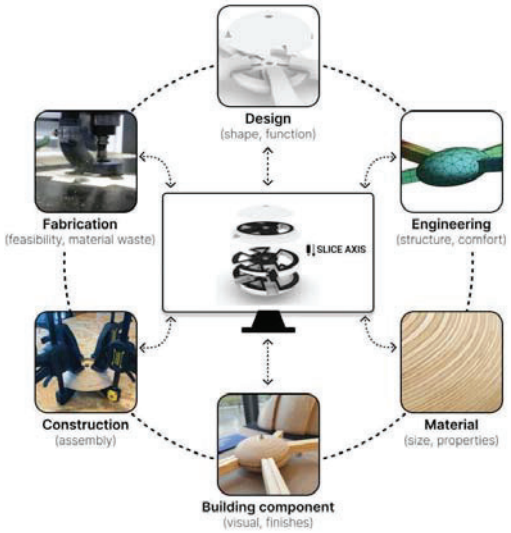

Figure 8: *Scheme of the interdependence of the slice strategies and the AEC project multi-criteria.*

The design experiment with the students has illustrated that the AEC multi-criteria approach of the project, the shape complexity and the functional complexity make the design process unintuitive, and they do not lead to efficient and rational decision-making; nor it is efficient without the implementation of an adapted design environment at the early design stages. The design to manufacturing process becomes a non-linear, dynamic and iterative process with the use of the Stratoconception® process. The level of integration of the AEC issues and the interdependence of design and manufacturing goes beyond the existing construction and Stratoconception® frameworks and design tools then requires for a new customized approach. The increase of a more detailed knowledge of the use of Stratoconception® in AEC projects and the interdependence of the design criteria will help the architects to seize this new manufacturing process and to explore new ways to design and build.

4.2.2 The lack of relevant digital workflow

The customized design to manufacturing approach with Stratoconception® requires for collaboration of the architects, the engineers and the builders. Such collaboration is based on data exchange efficiency which is correlated with the ability to connect different software of each project stakeholder. We have emphasized the lack of relevant design tools for architects and engineers (see 4.2.1). The second experiment phase identifies the lack of interoperability between the design software and the Stratoconception® CAM software.
Two CAM Stratoconception® software tools exist. The first one is StratoPro® CAM software which lacks the tools for evaluation of design choices and has limited exchange from CAD software to the 3D model through an import of the part as the STL file which structures the design-to-manufacturing process as linear with no feedback of the manufacturing preparation to the design (Figure 8). The second software is TopSolid'Strato, an add-in, with the same functionality as StratoPro®, integrated to TopSolid which is a CAD-CAM software used for mechanical engineering. With the development of the add-in of TopSolid the digital information continuum from design to manufacturing with Stratoconception® is supported by the same and only one software. However, this software is not a tool adapted to architectural design. The use of design software adapted to architecture breaks the digital information continuum of the TopSolid'Strato software by the import of the 3D model of the part which, again, prevents the feedback of the manufacturing issues at the design phase whereas we highlight the interdependence between the design and the manufacturing (see 4.2.1). This lack of feedback is not inevitable and the development of the interoperability between TopSolid' and the AEC design software provides an alternative to the existing workflow [34].

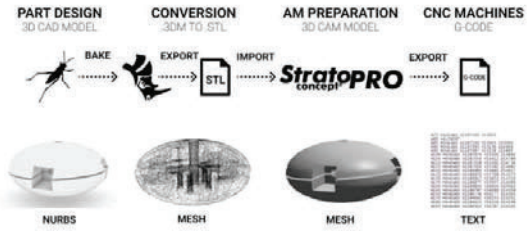

Figure 9: *Linear and non-retroactive digital workflow of the multifunctional timber mesh joint design to manufacturing experiment.*

The experiment confirms that the existing workflow is not continuous (digital data continuity is hindered), inefficient (need for various software tools without clear interoperability) and uninstructive (does not illustrate all the project information and design possibilities, thus hindering the design choices). Despite the interdependence between the design and the manufacturing choices of the Stratoconception® process, the software solutions do not offer an efficient collaboration due to their linear workflow structure, with no feedback on the design, and the lack of multi-criteria evaluation and optimization tools. A new digital workflow must be implemented with the relevant tools for the design and the manufacturing process and with interoperability between all the software for efficient collaboration.

5 PROPOSED DESIGN FRAMEWORK

In section 4, we emphasized the lack of methods and tools integrating the AEC issues, for example the structure or the visual aspect, in the design to manufacturing process

by Stratoconception®. We present in Figure 9 the proposed design framework for the integration of AEC issues into the multicriteria design process. The design framework comprises three phases consistent with the three categories of the Design for Additive Manufacturing research identified by Wiberg et al. [35], thus the "*system*, *part* and *process design"*. It is intended to be flexible to the scale of the designed building component and to the muti-objectives of the project. Three further phases follow the design and include the fabrication of the strata, the construction by assembling the strata and the delivery of the building components. The framework has not yet been fully implemented. It is developed to be independent from a specific software, with a parametric environment which is better adapted to optimize the design choices.

5.1 SYSTEM DESIGN

The *system design* phase aims to identify which project components may be designed and manufactured with Stratoconception® and to define the geometrical and functional boundaries of the design. This phase is led by the opportunities of the Stratoconception® use in timber architecture and construction (see Section 3). The designer relies on the knowledge base of these opportunities to assess whether the use of the AM process adds value to the design or the manufacturing of the component. Next, we establish the specifications of the component which include the geometrical boundaries of the component, its interconnection with the other components of the system and the functionalities that the component must integrate. The multi-functionalization and the shape complexity opportunities provided by the AM use could improve creativity and foster novel designs.

5.2 PART DESIGN

Following the *system design phase*, the *part design phase* leads the designer towards the best design of the previously selected component. The result of this phase is the precise definition of the strata geometry approved for manufacturing.

The phase has three steps: the initial design, the slicing and decomposition of the 3D model, and the assembly of the strata. The initial design is achieved with one of two approaches, either the architect creates the geometry of the component or the architect creates the process generating this geometry in the definition domain stated in the system design using, for example, topological optimization algorithms.

Then, we integrate the slicing and the decomposition of the 3D model at the part design phase before the preparation for manufacturing where it occurs in the existing process. Yet, we have identified that the strata impact the visual aspect of the architecture, if they are visible, and can therefore influence the slicing direction choices. Moreover, the optimal slicing strategies are not always the most intuitive and they depend on the goals defined by designer. Finally, the assembly step creates the final geometry of the strata.

The main contribution of the proposed framework is the coupling of each step of the part design to simulation engines. It satisfies the identified need for assessment of the design choices to lead to efficient and rational decision-making in a flexible and dynamic process. The assessments can be launched at every step of the part design and they adapt to the increase of the level of detail of these steps and to the expectations of the designer. We use four main simulation engines: the fabrication, the construction (the assembly of the strata), the structure and

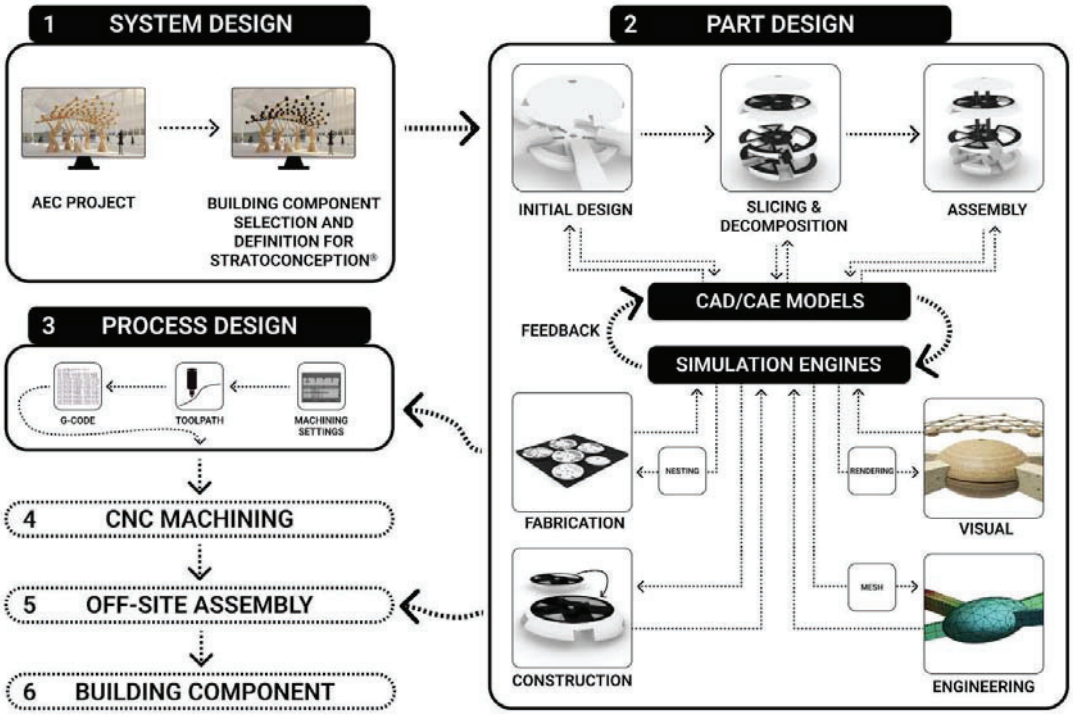

Figure 10: *Proposed design framework comprising the three phases of the system, part and process design.*

https://doi.org/10.52202/069179-0482

the visual aspect of the project if the strata are visible. The fabrication assessment addresses the feasibility and the material yield of the part design. Therefore, the nesting of the strata is integrated into the core design process. Thus, it is a support for optimizing the design choices and it is not confined to a step in the manufacturing preparation process as it is now. Other simulation engines can be developed such as life cycle analysis or time and cost assessment. The simulation engine supports the optimization of the design choices. The optimization objectives may be the minimization of weight of the component, the material waste, the cost, the environmental impact, the structural or the thermal performance. The optimization objective may be one or various.

The integration of the simulation engines into the part design process fosters an integrative approach, involving the strengthening of the relationship of the architect, the engineer and the builder, and goes beyond a design focused solely on architectural concerns or construction feasibility.

5.3 PROCESS DESIGN

Next, the *process design phase* prepares the fabrication of the component and results in the generation of the G-Code that will control the CNC machine. The phase is based on the nesting of the strata approved at the *part design phase*. The steps of this phase are those of the existing process such as the definition of the machining settings and the generation of the toolpath. A contribution to the existing methods and tools of this phase would be to consider the wood anatomy, the species and the wood grain orientation in the definition of the machining settings to improve the surface quality by using adaptative milling.

The design process is followed by the fabrication of the strata, the construction by assembling the strata in the workshop and the delivery of the building components. The assembly of the strata is guided by the assembly documents from the construction simulation engine.

5.4 FURTHER WORK

The implementation of the proposed design framework requires for further work on:

- The summary of the knowledge base of the opportunities and the limitations of the Stratoconception® use in timber AEC, with a detailed study of use-cases, so that architects, engineers and builders can adopt this new technology and identify the building components they can thus design.
- The automation of the non-creative activities of the process and the development of new strategies adapted to the building components, for example, decomposition strategies of the strata minimizing the material wastes.
- The interoperability between different software of the fragmented AEC industry in order to minimize the data waste and the errors caused by the file exchange and to gain efficiency and design integration.
- The development of reliable mechanical, thermal or Life Cycle Assessment (LCA) simulation engines for each step of the part design and go beyond the limits of the conventional tools that lack flexibility for use on non-standard building components.
- The introduction of new materials, such as glue laminated timber, and the adaptation of the operations and practices thus induced in the process to offer an alternative to the use of the timber panel.

Further steps of the research and developments should be conducted to improve step by step the proposed framework.

6 CONCLUSION

As additive manufacturing becomes increasingly implemented in the construction industry, it is important to understand how these new technologies affect the way we design and build timber architecture. By assessing the use of the Stratoconception® process with several experiments, this study established that additive manufacturing could overcome the existing limits of timber architecture to produce new high-value-adding building components. We have addressed a number of key issues and identified the relevant challenges of scaling-up the process and managing the material wastes. We also outlined that *there is a lack of design framework adapted to the multi-criteria decision making required using Stratoconception® in timber architecture and construction*. This paper contributes to the proposal of a framework of timber architectural design for additive manufacturing using the Stratoconception® process in a design-to-manufacturing process. Further research will focus on the implementation and the assessment of the proposed framework.

ACKNOWLEDGEMENT

This research was financially supported by the partnership chair *"Timber architecture and construction: from heritage to digital"* and by the French Ministry of Culture. The authors also acknowledge the students at the National School of Architecture of Nancy for their participation in the pedagogical exercises related to this work.

REFERENCES

[1] A. Menges, T. Schwinn, and O. D. Krieg: Advancing wood architecture: a computational approach. Routledge - Taylor & Francis Group, 2016.

[2] K. Frampton: Studies in tectonic culture: the poetics of construction in nineteenth and twentieth century architecture. MIT press, 1995.

[3] H. U. Buri and Y. Weinand: The tectonics of timber architecture in the digital age. Prestel Verlag, 2011.

[4] J.-C. Bignon, O. Gamez, J. Meyer, and F. Besançon. Poetic structuralism, new figures in wood architecture. In: World Conference on Timber Engineering 2021, 819-826, 2021.

[5] M. H. Ramage et al., The wood from the trees: the use of timber in construction. Renewable and sustainable energy reviews, 68:333-359, 2017.
[6] ISO/ASTM 52900: 2021 Additive Manufacturing-General Principles-Terminology. 2021.
[7] I. Gibson, D. Rosen, B. Stucker, and M. Khorasani, Additive Manufacturing Technologies. Springer International Publishing, 2021.
[8] N. Labonnote, A. Rønnquist, B. Manum, and P. Rüther. Additive construction: State-of-the-art, challenges and opportunities. Automation in Construction, 72:347-366, 2016.
[9] A. Paolini, S. Kollmannsberger, and E. Rank. Additive manufacturing in construction: A review on processes, applications, and digital planning methods. Additive Manufacturing, 30:100894, 2019.
[10] D. Delgado Camacho et al. Applications of additive manufacturing in the construction industry - A forward-looking review. Automation in Construction, 89:110-119, 2018.
[11] F. Craveiroa, J. P. Duartec, H. Bartoloa, and P. J. Bartolod. Additive manufacturing as an enabling technology for digital construction: A perspective on Construction 4.0. Automation in Construction, 103:251-267, 2019.
[12] J. Pegna. Exploratory investigation of solid freeform construction. Automation in Construction, 5:427-437, 1997.
[13] B. Khoshnevis. Automated construction by contour crafting - related robotics and information technologies. Automation in Construction, 13(1):5-19, 2004.
[14] R. A. Buswell, R. C. Soar, A. G. Gibb, and A. Thorpe. Freeform construction: mega-scale rapid manufacturing for construction. Automation in Construction, 16:224-231, 2007.
[15] F. Bos, R. Wolfs, Z. Ahmed, and T. Salet. Additive manufacturing of concrete in construction: potentials and challenges of 3D concrete printing. Virtual and Physical Prototyping, 11(3):209-225, 2016.
[16] A. Veliz Reyes, M. Gomaa, A. Chatzivasileiadi, W. Jabi, and N. M. Wardhana. Computing craft: early stage development of a robotically supported 3D printing system for cob structures. In: eCAADe 2018, 791-800, 2018.
[17] A. Dubor, E. Cabay, and A. Chronis. Energy efficient design for 3D printed earth architecture. In: Humanizing Digital Reality, 383-393, 2018.
[18] M. A. Meibodi et al. Smart Slab. Computational design and digital fabrication of a lightweight concrete slab. In: ACADIA 2018, 434-443, 2018.
[19] R. Rael and V. San Fratello: Printing architecture: Innovative recipes for 3D printing. Chronicle Books, 2018.
[20] L. Gardner, P. Kyvelou, G. Herbert, and C. Buchanan. Testing and initial verification of the world's first metal 3D printed bridge. Journal of constructional steel research, 172:106233, 2020.
[21] R. Rael and V. San Fratello. Developing concrete polymer building components for 3D Printing. In: ACADIA 2011, 152-157, 2011.
[22] D. Krapež Tomec and M. Kariž. Use of wood in Additive Manufacturing: Review and future prospects. Polymers, 14(6):1174, 2022.
[23] B. Kromoser, S. Reichenbach, R. Hellmayr, R. Myna, and R. Wimmer. Circular economy in wood construction - Additive manufacturing of fully recyclable walls made from renewables: Proof of concept and preliminary data. Construction and Building Materials, 344:128219, 2022.
[24] B. Buschmann, K. Henke, D. Talke, B. Saile, C. Asshoff, and F. Bunzel. Additive manufacturing of wood composite panels for individual layer fabrication (ILF). Polymers, 13(19):3423, 2021.
[25] C. Barlier, inventor. Procédé pour la création et la réalisation de pièces de C.A.O et pièces ainsi obtenues. French Patent, 91-02437, 1991, European Patent, 0.585.502, 1992.
[26] J. E. Blanther, inventor. Manufacture of contour relief maps. US Patent, 473.901, 1892.
[27] G. J. Peacock, inventor. Method of making composition horseshoes. US Patent, 746.143 1902.
[28] I. Gibson, D. W. Rosen, and B. Stucker. Sheet Lamination Processes. In: Additive Manufacturing Technologies, pages 223-252, Springer US, 2010.
[29] I. Caetano and A. Leitão. Architecture meets computation: an overview of the evolution of computational design approaches in architecture. Architectural Science Review, 63(2):165-174, 2020.
[30] A. Anastasiou, C. Tsirmpas, A. Rompas, K. Giokas, and D. Koutsouris. 3D printing: Basic concepts mathematics and technologies. In: 13th IEEE International Conference on BioInformatics and BioEngineering, 1-4, 2013.
[31] R. Soar. Additive manufacturing technologies for the construction industry. Rapid manufacturing: an industrial revolution for the digital age, Wiley Online Library, 249-273, 2006.
[32] T. P. Ribeiro, L. F. Bernardo, and J. M. Andrade. Topology optimisation in structural steel design for additive manufacturing. Applied Sciences, 11(5):2112, 2021.
[33] H. J. Wagner, M. Alvarez, A. Groenewolt, and A. Menges. Towards digital automation flexibility in large-scale timber construction: integrative robotic prefabrication and co-design of the BUGA Wood Pavilion. Construction Robotics, 4(3):187-204, 2020.
[34] A. W. Ismail and P. Marin. Direct interoperability between industrial engineering and AEC: Technical and geometric challenges. In: eCAADe 2022, 537-546, 2022.
[35] A. Wiberg, J. Persson, and J. Ölvander. Design for additive manufacturing: a review of available design methods and software. Rapid Prototyping Journal, 25(6):1080–1094, 2019.

https://doi.org/10.52202/069179-0482

World Conference on Timber Engineering Oslo 2023

HYPERBOLIC PARABOLOID SHELLS MADE OF DIAGONAL LAMINATED TIMBER ELEMENTS

Matthias Arnold[1], Philipp Dietsch[2], Stefan Winter[3]

ABSTRACT: This paper deals with the design, calculation, and construction of hyperbolic paraboloid shells made from mass timber elements. Considering the geometrical definition, hyperbolic paraboloid shells can be described as doubly ruled surfaces and can therefore be assembled from twisted rectangular plates.

The membrane theory of the hyperbolic paraboloid shell is derived and compared to previous analytical approaches. A challenge is the realization of the shell using the orthotropic material timber. Therefore, the torsional stiffness of multi-layered mass timber elements is determined by means of analytical and experimental investigations. Taking into account the semi-rigid connection between the layers, resulting in additional shear deformations, nailed and diagonal laminated timber elements are investigated towards the construction of HP-shells.

KEYWORDS: hyperbolic paraboloid shell (HP-shell; hypar), membrane theory, diagonal laminated timber (DLT), nailed laminated timber (NLT), semi-rigid connections, laminate theory, torsional stiffness

1 INTRODUCTION

1.1 BACKGROUND

The application of HP-shells made of timber found its temporary peak around 1970, for example at the exhibition pavilion for the Federal Garden Show in Dortmund, Germany, 1969. For the assembly of the shell, five layers of single laminations were laid on top of each other and fixed by mechanical fasteners, e.g. nails. Timber shells offer many advantages, for example the fast erection, the low weight, and the high quality of the surface. Experiments with timber HP-shells were first carried out at University of Kansas in 1956 [1]. A similar project was realized in Stuttgart in 1963 [2] (Fig. 1).

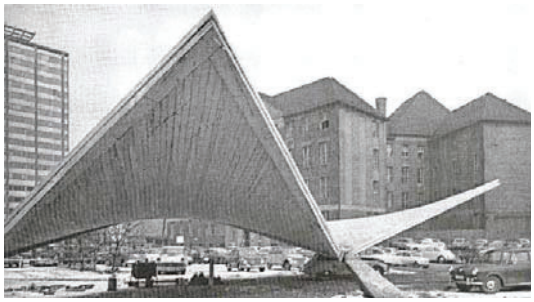

Figure 1: *Experimental timber HP-shell (span l´= 15.0 m) in front of Stuttgart University, 1963* [2]

In general, a hypar can be described mathematically as a translational surface (fictive parabolas in x´ and y´ direction, acting in tension and compression only, Fig. 2) and as doubly ruled surface (straight lines in x or y direction forming rectangular plate elements, acting in in-plane shear only, Fig. 3).

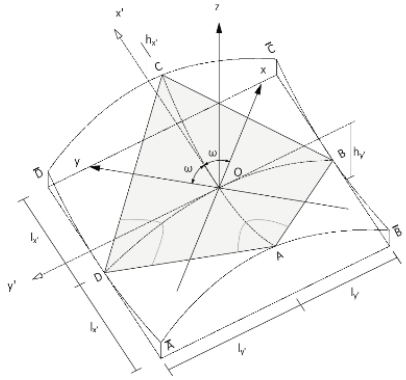

Figure 2: *Hypar described by a translational surface* [3]

The translational surface is given by Eq. (1). By rotating the x' and y' axis by the angle ω, to correspond with the asymptotes of the hyperbola, a new description based on the global x and y axis is introduced—see Eq. (2) [4].

$$z = \frac{h_{x'}}{(l_{x'})} \cdot x'^2 - \frac{h_{y'}}{(l_{y'})} \cdot y'^2 \tag{1}$$

$$z = \frac{4 \cdot sin^2\omega \cdot h_{y'}}{(l_{y'})^2} \cdot x \cdot y \tag{2}$$

$$z = \frac{h_{y'}}{(l_{y'})^2} \cdot 2 \cdot x \cdot y = \frac{h}{ab} \cdot x \cdot y = k \cdot x \cdot y \tag{3}$$

A symmetrical hypar ($h_{y'} = h_{x'}$) over a square plane projection ($2\omega = 90°$) can therefore be described by Eq. (3) using the global x and y axis [5]. Fig. 3 show that

[1]Matthias Arnold, Technical University of Munich, Germany, matthias.arnold@tum.de
[2]Philipp Dietsch, Karlsruhe Institute of Technology, Germany, dietsch@kit.edu
[3]Stefan Winter, Technical University of Munich, Germany, winter@tum.de

https://doi.org/10.52202/069179-0483

the ruled surface can be assembled from single, twisted rectangular elements.

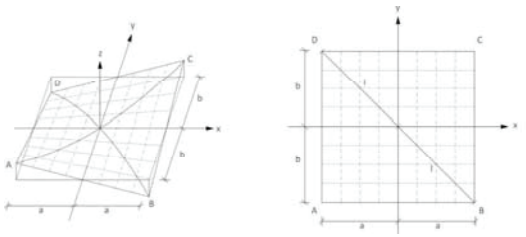

Figure 3: *Hypar described by a ruled surface* [3]

1.2 OBJECTIVE

The objective of the research presented is to create a HP-shell from prefabricated, large-scale NLT or DLT plates and thus to create HP-shells with a high degree of prefabrication. Thereby the elements remain plane during production and get twisted on the construction site, by connecting them to edge beams. In a second construction step, the elements are connected to the adjacent elements, taking the in-plane shear forces n_{xy}.

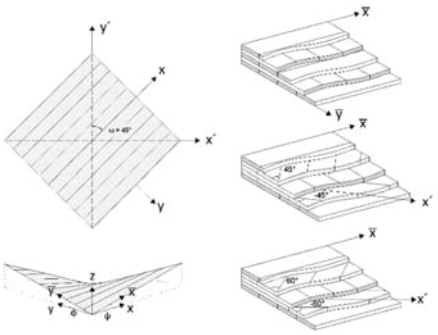

Figure 4: *Exemplary layups of DLT elements according to the geometry of the shell in the plane projection*

Depending on the fictive compression and tension parabolas, the layup of the mass timber elements can be adapted to the principle membrane forces ($n_{x'}$ and $n_{y'}$) by rotating individual layers during production. The resulting multi-layered element is a balanced and symmetric laminate (Fig. 4, right). This means, for each $+\theta$ ply in the laminate there is an equally thick $-\theta$ ply (referred to the symmetry axis). The layers of the laminate are a mirror image about the geometrical midplane.

Within previous research [6; 7] mass timber elements featuring diagonally arranged layers had been defined as DLT. In general, the diagonal layer arrangements of DLT elements lead to an increase of the torsional stiffness compared to conventional CLT elements. This is also due to the high out-of-plane shear stiffnesses S_{xz} and S_{yz} of DLT [8]. In case of the application on HP-shells, the DLT elements should provide a small torsional stiffness in order to not disturb the membrane stress state due to the additional load case of torsion caused by the twisting of the elements. Therefore, a semi-rigid connection of the layers by mechanical fasteners (nails) is introduced.

2 SERIES INVESTIGATED

2.1 LAYUPS

Tab. 1 gives the layup and stacking sequence of the specimens investigated. DLT_n is the designation for nailed DLT. All specimens are made of spruce (see Chapter 2.2). In addition, the number n of specimens investigated is given.

Table 1: *Specimens per Series for the mechanical testing*

series		n	[1)]orientation θ [°]	t [mm]
O1	CLT	4	0°, 90°, 0°, 90°, 0°	100
O2	NLT	4	0°, 90°, 0°, 90°, 0°	105
O3	CLT	2	0°, 90°, 0°	60
O4	NLT	3	0°, 90°, 0°	63
D1	[2)]DLT±45°_n	3	0°, 45°, 90°, -45°, 0°	105
D2	[2)]DLT±30°_n	3	0°, 30°, 90°, -30°, 0°	105
D3	DLT±45°	3	0°, 45°, 90°, -45°, 0°	100
D4	DLT±30°	3	0°, 30°, 90°, -30°, 0°	100

[1)]layer orientation referred to the local $\bar{x}$ axis of the specimens
[2)]DLT specimens with semi-rigidly connected layers using nails

2.2 MATERIAL PROPERTIES

The CLT elements were produced using material properties according to ETA 20/0023 [9]. The DLT elements were produced using according to ETA 16/0055 [10]. Each layer of the CLT has a thickness of $d = 20\ mm$. The laminations are not edge-glued and the board width is $b = 180\ mm$. The modulus of elasticity (MoE) was cross-checked by compression tests according to EN 408 [11] and was $E_{c,0,mean}$ = 10282 MPa (COV 0.56 %). The NLT and DLT_n elements were produced according to ETA 15/0760 [12]. Each layer has a thickness of $d = 21\ mm$. The MoE was determined by four-point bending tests according to EN 408 [11] and was $E_{m,0,mean}$ = 11044 MPa (COV 1.21 %).

At the beginning of the mechanical testing the moisture of each specimen was determined by means of ram in electrodes at a depth of approximate 15 mm. On each specimen 5 measurements were taken. The mean value $u_{mean,15mm}$ of the initial moisture content was 11.2 % (COV 7.6 %). The moisture content u of all specimen was in the range of $12 \pm 2\%$. The mean value of the density at $u = 12\%$ was exemplary determined for series O1 according to EN 384 [13]. The mean value ρ_{mean} was 458 kg/m³ (COV 4.3 %).

2.3 CONSIDERATION OF THE NAILING

The layers of the NLT and DLT_n are connected to the underlying layers with aluminium grooved nails ($t = 2.5\ mm$) [12]. During production, the nailing unit moves over the layers at the same predefined spaces and shoots the single nails into the laminations. Using a Monte-Carlo-Simulation (MC-simulation), the probability of inserting a number m of nails per crossing point of the single laminations is calculated statistically. Nails between the edges of the boards or outside the required minimum edge distance must not be used for the calculation of the stiffness properties of the composites (circled nails in Fig. 5).

https://doi.org/10.52202/069179-0483

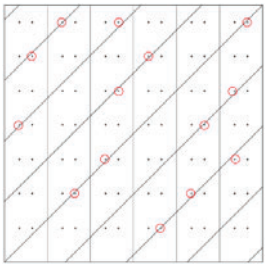

MC-simulation:

nails per element: 84
runs: 1000
nails in total: 84000
crossing-points with m nails:
0: 2000 (7.1 %)
1: 2000 (7.1 %)
2: 8000 (28.6 %)
3: 12000 (42.9 %)
4: 4000 (14.7 %)

Figure 5: *Exemplary distribution of nails for joining two layers (crossing angle at 45°) using statistical evaluation*

Determining the statistical distribution of nails per crossing-point, an average effective number of nails per crossing of two layers (1.20 m / 1.20 m) can be calculated (mean value). The result of the simulation is verified by counting the actual nails per layer and crossing-point on the specimens (Fig. 6).

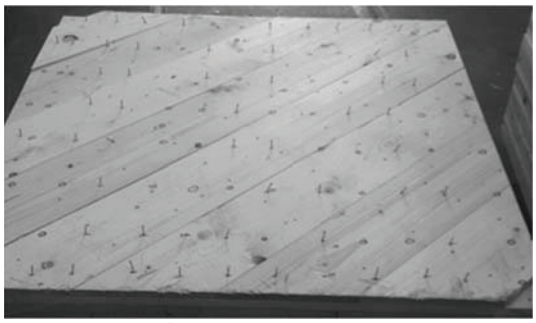

Figure 6: *Exposed nail pattern between two layers, crossing under 45°*

Tab. 2 compares the results of the MC-simulation to the nails counted for two layers crossing under 45°, 60° (30°), and 90°. The number of nails that can be effectively applied per crossing-point are used for the calculation of the stiffness values.

Table 2: *Effective number of nails per crossing of two layers of the NLT and DLT_n specimens*

crossing angle	crossing points with n nails (MC-Simulation) [%]					calculated effective nails (1.20/1.20)	[1]counted effective nails (1.20/1.20)
	m= 0	m= 1	m= 2	m= 3	m= 4		
45°	7,1	7,1	28,6	42,9	14,7	78	80
60°	5,3	0,0	15,8	52,6	26,3	80	80
90°	14,3	9,5	52,4	23,8	23,8	111	114

[1]mean value of the counted nails at the crossing of two layers (1.20/1.20)

3 ANALYTICAL INVESTIAGIONS

3.1 STIFFNESS PROPERTIES OF DLT AND NLT

The stiffness properties of multi-layered timber elements can be determined by the stiffness properties of the individual layers i and their interaction as a composite. The laminate theory of orthogonally glued CLT can be taken from several previous publications [14; 15]. Laminates are characterized by their response to mechanical loading, which is associated with a description of the coupling behavior. The matrix notation of the law of elasticity on the plate element consists of submatrices. These refer to the extensional stiffness A, the bending-extension coupling stiffness B, and the bend-twist coupling stiffness D (ABD-relation). Taking into account the transverse shear deformations, which are decoupled from the ABD-relation, a fourth submatrix E has to be introduced [15]. The stiffness parameters can be taken from the ABD-E stiffness matrix. For antisymmetric, balanced laminates, simplifications within the stiffness matrix can be made ($A_{16} = A_{26} = D_{16} = D_{26} = B_{11} = B_{12} = B_{22} = B_{66} = E_{54} = 0$) which leads to the stiffness matrix given by Eq. (4).

$$[Q] = \begin{bmatrix} A_{11} & A_{12} & 0 & 0 & 0 & B_{16} & 0 & 0 \\ A_{21} & A_{22} & 0 & 0 & 0 & B_{26} & 0 & 0 \\ 0 & 0 & A_{66} & B_{61} & B_{62} & 0 & 0 & 0 \\ 0 & 0 & B_{16} & D_{11} & D_{12} & 0 & 0 & 0 \\ 0 & 0 & B_{26} & D_{21} & D_{22} & 0 & 0 & 0 \\ B_{14} & B_{24} & 0 & 0 & 0 & D_{66} & 0 & 0 \\ 0 & 0 & 0 & 0 & 0 & 0 & E_{55} & 0 \\ 0 & 0 & 0 & 0 & 0 & 0 & 0 & E_{44} \end{bmatrix} \quad (4)$$

For CLT and DLT elements, the entries for S_{xz} (E_{44}) and S_{yz} (E_{55}) have to be multiplied by shear-correction factors k_z. A possible calculation of the shear-correction factors in the global x and y direction is based on the Timoshenko Beam Theory [16] according to Eq. (5). The derivation of Eq. (5) is based on the principle of virtual displacements (method of consistent deformations; force method) and the equilibrium between shear and bending stiffnesses over the cross-section [17].

$$\frac{1}{k_z} = \frac{\sum G_{iz} A_i}{\left(\int_{-\frac{t}{2}}^{\frac{t}{2}} E_i(z) z^2 \, dz\right)^2} \cdot \int_{-\frac{t}{2}}^{\frac{t}{2}} \frac{\left(\int_z^{\frac{t}{2}} E_i(z) z \, dz\right)^2}{G_{iz}(z)} dz \quad (5)$$

For NLT and DLT_n on the other hand, the semi-rigid connection of the layers has to be taken into account; the contribution of the layers—especially the transverse layers—on the shear deformations become marginal. Therefore, the laminate theory and shear-strain relation stays no longer valid. DIN EN 1995-1-1/NA [18] provides an analytical method for the calculation of out-of-plane shear stiffness values of semi-rigid connected mass timber elements by Equations (NA.40) and (NA.42). The calculation is based on the *Shear Analogy Method* [19] and considers a constant shear flow over the effective heights (shear area) a (Eq. (6)).

$$\frac{1}{S_{xz/yz}} = \frac{1}{a_{x/y}} \cdot \left[\sum_{i=1}^{n-1} \frac{1}{k_{x,i/y,i}} + \frac{d_1}{2G_{xz/yz}} + \sum_{i=1}^{n-1} \frac{d_i}{G_{xz,i/yz,i}} + \frac{d_n}{2G_{xz/yz}} \right] \quad (6)$$

with
$n = \ number\ of\ layer$ [/]
$a = \ effective\ heigths$ [19]
$G_{xz,\frac{i}{yz},i} = shear\ modulus\ of\ the\ respective\ layer,$
(for layer arranged under 45°, $G_{45} = 370\ MN/m^2$)
$d_i = \ layer\ thickness\ [mm]$]
$k_i = slip\ modulus\ between\ the\ layers\ [N/mm]$

https://doi.org/10.52202/069179-0483

ETA 15/0760 [12] gives an approximate analytical method for the calculation of the out-of-plane shear stiffness values of NLT and DLT_n, taking into account the number of layers n, the effective number of nails per crossing-point m (see Tab. 2) and the initial slip modulus K of the nails. Therefore, the slip modulus k between the layers—see Eq. (6)—is substituted, using Eq. (7).

$$\sum_{i=1}^{n-1} \frac{1}{k_{x,i/y,i}} = \sum_{i=1}^{n-1} \left(\frac{1}{f} \cdot \frac{1}{m \cdot \left(\frac{K}{b_x \cdot b_y} \right)} \right) \tag{7}$$

with
m = *number of nails per crossing point* [/]
K = *initial slip modulus of a single nail* [N/mm]
$b_x = b_y$ = *board width* [mm]
$f = 1{,}25\ for\ m = 4, and\ f = 1{,}5\ for\ m = 2$

3.2 MEMBRANE FORCES OF THE HP-SHELL

3.2.1 Equilibrium conditions and differential equation

Pucher [20] established a method for the calculation of membrane forces in arbitrary shell structures by transferring stress resultants on infinitesimal elements, to their plane projection (Fig. 7). The plane projection is in the state of equilibrium in x and y direction. Fig. 7 shows the geometric relationships $tan\varphi = \partial z/\partial x$ and $tan\psi = \partial z/\partial y$ introducing a third equilibrium in z-direction.

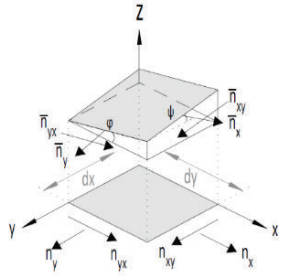

Figure 7: *Transfer of stress resultants to the plane element*

Eq. (8) gives the equilibrium conditions on the plane element.

$$\bar{n}_x = n_x \cdot \frac{cos\varphi}{cos\psi} \;\; ; \;\; \bar{n}_y = n_y \cdot \frac{cos\psi}{cos\varphi} \; ; \quad n_{xy} = \bar{n}_{xy} \;\; ; \;\; n_{yx} = \bar{n}_{yx} \tag{8}$$

The calculation of stress resultants on the infinitesimal shell elements is based on the assumption of the membrane theory for thin shells (transverse shear forces, bending moments, and torsional moments are neglected [21]). This means that the shell is statically determined; Three unknown stress resultants face three equilibrium conditions ($\sum F_x = 0, \sum F_y = 0, \sum F_z = 0$). Hereby, the stress resultants can be calculated without material or kinematic conditions. The derivatives of the equilibrium relations (Eq. (9)) are inserted into the *Airy Stress Function F* (Eq. (10)) to achieve the ordinary differential equation (Eq. (11)) [20].

$$n_x = \frac{\partial^2 F}{\partial y^2} - \int p_x d_x \; ; \quad n_y = \frac{\partial^2 F}{\partial x^2} - \int p_y d_y \; ; \quad n_{xy} = n_{yx} = -\frac{\partial^2 F}{\partial x \partial y} \tag{9}$$

$$F = \frac{\partial^2 F}{\partial y^2}\frac{\partial^2 z}{\partial x^2} - 2\frac{\partial^2 F}{\partial x \partial y}\frac{\partial^2 z}{\partial x dy} + \frac{\partial^2 F}{\partial x^2}\frac{\partial^2 z}{\partial y^2} \tag{10}$$

$$F = -p_z + p_x \frac{\partial z}{\partial x} + p_y \frac{\partial z}{\partial y} + \int p_x d_x \frac{\partial^2 z}{\partial x^2} + \int p_y d_y \frac{\partial^2 z}{\partial y^2} \tag{11}$$

The surface equation $z = k \cdot xy$ (Eq. (3)) is derived according to Eq. (11) to receive the ordinary differential equation of a hyperbolic paraboloid (Eq. (12)) [22]:

$$-2k \cdot \frac{\partial^2 F}{\partial x \partial y} = -p_z + p_x \cdot y \cdot k + p_y \cdot x \cdot k \tag{12}$$

To derive the membrane forces n_x and n_y as well as the in-plane shear forces n_{xy} the equilibrium conditions (Eq. (8)) are solved. A uniform loading p_z leads to in-plane membrane forces n_{xy} only, within the global x-y coordinate system (Eq. (13)).

$$n_{xy} = \frac{-p_z + p_x \cdot y \cdot k + p_y \cdot x \cdot k}{2k} \tag{13}$$

The membrane forces n_{xy} are equivalent to normal forces in the x´-y´ coordinate system. This means that the in-plane shear force n_{xy} can be split into normal forces $n_{x'}$ and $n_{y'}$ (normal forces acting along the fictive compression and tension parabolas of the HP-shell). Therefore, the membrane forces can be calculated on the plane projection of an infinitesimal shell element, taking into account the boundary conditions of the edges. The main boundary conditions are classified into free edges ($n_x = n_{xy} = 0$), linear supported edges (edge beams; $n_x = n_y = 0$ and $n_{xy} \neq 0$) and clamped/ edges ($n_x = n_{xy} \neq 0$) [23].

3.2.2 Simplified calculation method

The basic idea of Parme in 1960 [24] was to describe the load transfer in HP-shells by fictive compression and tension parabolas (Fig. 8). This idea was further developed by Hempel in 1967 [25] and Krauss in 1969 [26].

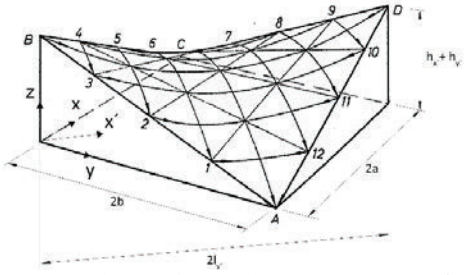

Figure 8: *Distribution of the shell into compression and tension parabolas* [26]

https://doi.org/10.52202/069179-0483

Since the solution of the membrane forces are a function the loading, Parme [24] assumed that a uniform load q_z [kN/m²] on a double symmetric HP-shell over a square projection gets equally distributed between two perpendicular parabolas.

For the boundary condition of linear supported edges ($n_x = n_y = 0 \; and \; n_{xy} \neq 0$) the normal force N—acting along the edge beams—result from the calculation of the horizontal and vertical reactions of the compression and tension parabolas, taking into account load-distribution factors $\chi_{x'/y'}$ (Eq. (14) and (15)) [26].

$$H_{x'/y',\,n} = \chi_{x'/y'} \cdot q_z \cdot \frac{\left(2 \cdot l_{x'/y',n}\right)^2}{8 \cdot h} \tag{14}$$

$$V_{x'/y',\,n} = \chi_{x'/y'} \cdot q_z \cdot \frac{2 \cdot l_{x'/y',n}}{2} \tag{15}$$

$with$

$$\chi_{x'} = \frac{1}{1 + \frac{\sum EA_{y',i}}{\sum EA_{x',i}} \cdot \frac{l_{x'}^4}{l_{y'}^4}} \quad ; \quad \chi_{y'} = 1 - \chi_{x'}$$

If the distribution of the axial rigidity is the same in x´ and y´ directions ($\chi_{x'} = \chi_{y'} = ½$)—which is the case for the chosen series (Tab.1)—the shear force n_{xy} equals the resultant R of the horizontal reactions of the fictive compression and tension parabolas (Fig. 9).

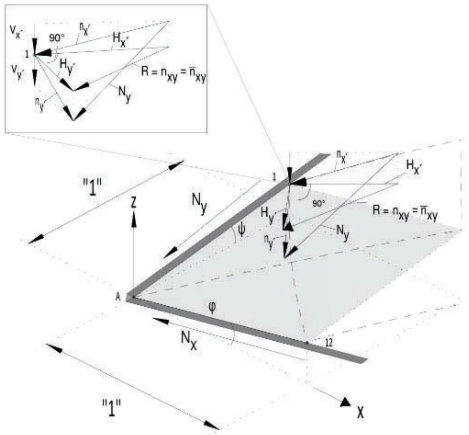

Figure 9: *Resulting forces in the HP-shell and in the edge beams under a uniformly distributed load p*

The geometric relationship of Fig. 9 can also be proven mathematically by comparing n_{xy}—calculated from $n_{x'}$ and $n_{y'}$ according to Pythagoras' Theorem—with n_{xy} according to the membrane theory under a uniform surface load q_z.

4 EXPERIMENTAL INVESTIGATIONS

4.1 TEST SETUP

After analytical investigations of the torsional stiffness properties, NLT, CLT, and DLT specimens featuring layups according to Tab. 1 with a side length $a = 1200\ mm$ are twisted in biaxial bending tests. The aim is to determine the torsional stiffness properties of the various specimens from the deformation of the elements under an external point-load, in order to make statements on the additional out-of-plane load case of torsion at the assembly of HP-shells. Parts of the results of the mechanical testing on CLT and DLT were already published within [7] and [8]. Fig. 10 shows the test setup of the biaxial bending test.

The point-load, directed vertically downwards, is applied to the free corner of the specimens by a hydraulic cylinder. The load-application point as well as the supports are realized by steel plates ($120/120/12\ mm$). They each are articulated and offset inwards by 100 mm from the free edges of the specimens. No reinforcement for compression perpendicular to the grain stresses in form of self-tapping screws is applied.

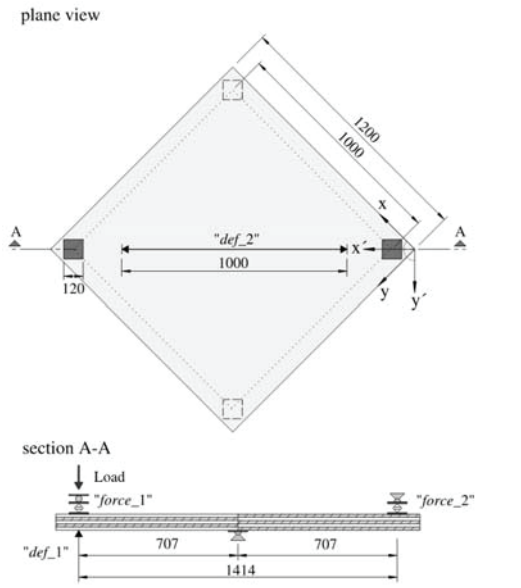

Figure 104: *Biaxial bending tests to determine the torsional stiffness of CLT, DLT, and NLT specimens*

The applied loading "$force\_1$" (point-load F) as well as at the reaction force on the opposite support "$force\_2$" are measured by force transducers. Deflection "def_1" (deflection w in z direction) is measured using a rope extensometer which is attached at the opposite side of the load-introduction point at the bottom of the test specimens. In addition, the change in the curvature κ_{xy} is measured determining the arc length "def_2" over 1000

mm by means of a second rope extensometer on the upper side of the specimens. The mechanical testing is carried out deformation-controlled. This means that each test specimen is loaded until a unit-deflection w (def_1) of $100\ mm$ (geometrical limit imposed by geometry of load-introduction) or failure. All specimens are loaded with a constant feed rate of about $0.30\ mm/s$. The corresponding forces F ("$force\_1$" = "$force\_2$") are measured as a function of the time.

4.2 TEST RESULTS AND COMPARISON TO AN ANALYTICAL APPROACH

Fig. 11 exemplary gives the load-deflection diagrams for the NLT and DLT_n series. Load-deflection diagrams for the CLT and DLT series can be taken from [7].

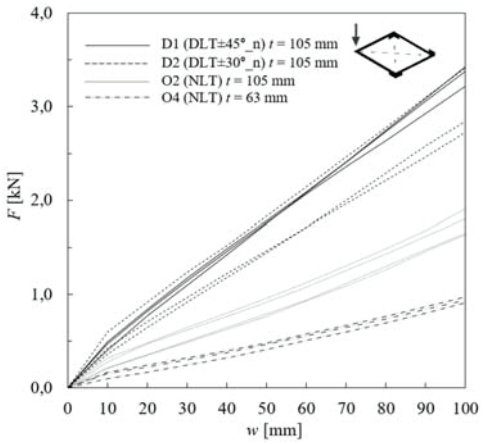

Figure 11: *Load-deflection diagrams of the NLT and DLT_n specimens under biaxial bending*

The load-deformation curves show a kink when overcoming the static friction force in the joint between the board layers ($F_{st,fr} < 0.2F_{w_{100}}$). The torsional stiffness for each specimen is calculated within the linear elastic range $0.2F_{max}$ $(0.2F_{w_{100}})$ and $0.4F_{max}$ $\left(0.4F_{w_{100}}\right)$ using linear regression. The torsional stiffness values determined experimentally are effective torsional stiffness values $B_{xy,eff,exp.}$ since the transversal shear deformations are included in the total deformation w measured by the rope extensometer [7]. For all specimens that did not reach a failure load, the corresponding load F_{w100} to reach the unit deformation of $100\ mm$ is used instead of F_{max} to determine the effective torsional stiffness. The evaluation is based on the force method (Eq. (16)) and carried out using Eq. (17) [7, 27].

$$w = \int \frac{m_{xy} \cdot \widetilde{m_{xy}}}{2 \cdot B_{xy}} \cdot dx = \int \frac{F \cdot a \cdot \bar{1} \cdot a}{2 \cdot B_{xy}} \cdot dx \tag{16}$$

$$B_{xy,eff,exp} = \frac{F \cdot a^2}{2w} = \frac{(0.4F_{max} - 0.2F_{max}) \cdot a^2}{2\left(w_{0.4F_{max}} - w_{0.2F_{max}}\right)} = \frac{1}{2} \cdot m \cdot a^2 \tag{17}$$

In order to compare the results of the numerical models with analytical solutions, out-of-plane shear deformations have to be taken into account within the analytical derivation of stiffness values. These values are referred being "effective" stiffness values and depend on the loading and equivalent static system. For thick plates and shells, taking into account out-of-plane shear deformations is mandatory (Reissner-Mindlin plate theory). Within this investigations, no comparable thick series ($t \geq 200\ mm$) was investigated. Nevertheless, the analytical approach shall be described in the following, because for NLT the semi-rigid connection—and therefore the low out-of-plane shear stiffness—has to be taken into account also for comparable thin layups:

Analytically, effective torsional stiffnesses ($B_{xy,eff}$) can be determined using the method of consistent deformations (force method) on equivalent static systems. Fig. 12 shows the extended girder grid model. Here, in addition to torsional stiffness, shear and bending stiffnesses are assigned to the girders (dx/dy).

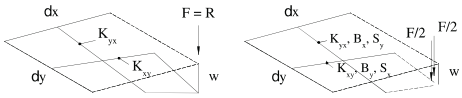

Figure 12: *Girder grid model of an infinitesimal element taking into account bending and shear deformations* [7]

Following the girder grid model in Fig. 12, the following energy theorem results (Eq. 11):

$$w\delta_{ij} = \int_0^1 \frac{\delta m_{xy} \cdot m_{xy}}{2K_{xy}} dx + \int_0^1 \frac{\delta m_x \cdot m_x}{B_y} dx + \int_0^1 \frac{\delta m_y \cdot m_y}{B_x} dy + \int_0^1 \frac{\delta V_x \cdot V_x}{S_{xz}} dx + \int_0^1 \frac{\delta V_y \cdot V_y}{S_{yz}} dy \tag{11}$$

The bending and torsional stiffnesses $B_x, B_y,$ and B_{xy} refer to the entries ($D_{11}, D_{22}, and\ D_{66}$) of the ABD-E Matrix (Eq. (4)). For CLT and DLT, the shear stiffnesses S_{xz} and S_{yz} can be taken from the entries E_{55} and E_{44}, multiplied by k_z (Eq. (5)). For NLT and DLT_n, S_{xz} and S_{yz} should be determined according to Eq. (6). Based on Eq. (11) the equilibrium of Eq. (12) applies to the total deformation w of the element, taking into account the transverse shear deformations.

$$\frac{F \cdot dx \cdot dy}{B_{xy,eff}} = \frac{F \cdot dx \cdot \bar{1} \cdot dy}{2D_{66}} + \frac{1}{3}\frac{\frac{F}{2} \cdot dx \cdot \bar{1} \cdot dx}{D_{22}} + \frac{1}{3}\frac{1 \cdot F/2 \cdot dy \cdot \bar{1} \cdot dy}{D_{11}} + \frac{F/2 \cdot \bar{1}}{E_{55}} + \frac{F/2 \cdot \bar{1}}{E_{44}} \tag{12}$$

From this, effective torsional stiffness values are analytically calculated according to Eq. (13).

$$\frac{1}{|B_{xy,eff}|} = \frac{1}{|B_{xy}|} + \frac{1}{6 \cdot |B_x|} + \frac{1}{6 \cdot |B_y|} + \frac{1}{2 \cdot |S_{xz}| \cdot dx} + \frac{1}{2 \cdot |S_{yz}| \cdot dx} \tag{13}$$

https://doi.org/10.52202/069179-0483

Tab. 3 gives the results of the evaluation of the effective torsional stiffnesses from the experimental investigations ($B_{xy,eff,exp.}$) compared to the analytical approaches ($B_{xy,eff}$ and B_{xy}) for each series investigated. For the determination of the analytical solutions, material parameters according to [9; 10; 12] and the effective number of nails according to Tab. 2 are used (see Chapter 2). In this paper the Poisson's ratios according to Halász and Scheer [28] ($\nu_{xy} = 0.380$; $\nu_{zx} = 0.018$) have been chosen for the calculation of the stiffness matrix. However, when calculating the stiffness properties of CLT and DLT, the chosen values for the Poisson's ratio have no decisive influence.

Table 3: *Torsional stiffness of the series following the experimental (mean values in bold) and analytical approach*

		experimental		analytical	
		$B_{xy,eff,exp.}$		$B_{xy,eff}$	[1)]B_{xy}
specimens	series	[MNm²/m]		[MNm²/m]	[MNm²/m]
O1-1	CLT 0°, 90°, 0°, 90°, 0° t = 100 mm	0.159	**0.155** COV 2.0	0.102	0.115
O1-2		0.154			
O1-3		0.153			
O1-4		0.153			
O2-1	NLT 0°, 90°, 0°, 90°, 0° t = 105 mm	0.013	**0.014** COV 2.3	0,027	[2)]~~0.133~~
O2-2		0.014			
O2-3		0.015			
O2-4		0.015			
O3-1	CLT 0°, 90°, 0° t = 60 mm	0.030	**0.031** COV 3.5	0.025	0.029
O3-2		0.032			
O4-1	NLT 0°, 90°, 0° t = 63 mm	0.007	**0.008** COV 3.2	0.013	[2)]~~0.031~~
O4-2		0.008			
O4-3		0.008			
D1-1	DLT_n 0°,45°, 90°, −45°,0° t = 105 mm	0.023	**0.023** COV 3.5	0.037	[2)]~~0.220~~
D1-2		0.023			
D1-3		0.022			
D2-1	DLT_n 0°, 30°, 90°, −30°, 0° t = 105 mm	0.019	**0.020** COV 6.3	0.036	[2)]~~0.199~~
D2-2		0.021			
D2-3		0.018			
D3-1	DLT 0°,45°,90°, −45°,0° t = 100 mm	0.201	**0.199** COV 1.6	0.134	0.188
D3-2		0.196			
D3-3		0.202			
D4-1	DLT 0°, 30°,90°,−30°,0° t = 100 mm	0.200	**0.189** COV 5.6	0.122	0.170
D4-2		0.178			
D4-3		0.189			

[1)] values without consideration of transverse shear deformations of the layers
[2)]values without consideration of the semi-rigid connection between the layers and without consideration of transverse shear deformations

Compared to the five-layered CLT series O1 with an overall thickness of $t = 100\ mm$, the effective torsional stiffness $B_{xy,eff,exp}$ of DLT±45 series D3 is increased by 28.4 %, for DLT±30 series D4 by 21.9 % (mean values). Following the results of the mechanical testing, a considerable ratio of stiffness increase can be determined for DLT_n series with a layer thickness of $21\ mm$ and semi-rigid connected layers, compared to the orthogonal layered NLT series. Compared to the NLT series O2, the effective torsional stiffness of DLT±45_n series D1 can be increased by 76,9 %, for DLT±30_n series D2 by 69.2 % (mean values). The torsional stiffness of the 3-layered orthogonal CLT series O3 is smaller by a factor of 4.94 compared to the 5-layered orthogonal series O1. The DLT_n (series D1 and D2) consisting of five layers can be compared to the NLT consisting of five layers under 0° and 90° respectively (O2). By rotating the laminations of the 2nd and the 4th layer by ±45 (D1), an increase in torsional stiffness of 90.5 % can be achieved compared to the NLT with five laminations under orthogonal orientation (series O2). By rotating the laminations of the 2nd and the 4th layer by ±60° (series D2), an increase in torsional stiffness of 70.6 % can be achieved compared to series O2 (see Fig. 13).

For the glued CLT and DLT series, the pure torsional stiffness values of (B_{xy}) represent the experimental results better than the analytical values of $B_{xy,eff}$—albeit not significant. This is not surprising, since the application limits/criteria of the calculation theories according to *Kirchhoff-Love* (B_{xy}) and *Reissner-Mindlin* ($B_{xy,eff}$) retain their validity for the rigid DLT and CLT series. To further underline this, additional test results on the torsional stiffness of CLT and DLT from previous studies on DLT [7] are given in Tab. 4. The O5 and D5 series have the same stacking sequence as the O1 and D3 series, but this time with a layer thickness of 40 mm and thus a total thickness of 200 mm, instead of 100 mm.

Table 4: *Exemplary additional investigations on the torsional stiffness of the series with t = 200 mm* [7]

		experimental		analytical	
		$B_{xy,eff,exp.}$		$B_{xy,eff}$	[1)]B_{xy}
specimens	series	[MNm²/m]		[MNm²/m]	[MNm²/m]
O5-1	CLT 0°, 90°, 0°, 90°, 0° t = 200 mm	0.898	**0.791** COV 9.1	0.774	~~0.920~~
O5-2		0.757			
O5-3		0.745			
O5-4		0.764			
D5-1	DLT 0°,45°,90°, −45°,0° 0° t = 200 mm	0.973	**1.006** COV 5.5	1.007	~~1.502~~
D5-2		0.982			
D5-3		0.980			
D5-4		1.089			

[1)]values without consideration of transverse shear deformations of the layers

Without taking the transverse shear deformations into account, the torsional stiffness values B_{xy} fail to represent the experimental values on the thick plate elements. The influence of the out-of-plane shear stiffness and therefore the transversal shear deformation of the 40 mm thick layers are much more pronounced, compared to the series with 20 mm layers. The effective torsional stiffness values $B_{xy,eff}$ on the other hand nearly hit the experimental investigations and confirm the analytical solutions.

When comparing the experimentally determined effective torsional stiffnesses $B_{xy,eff,exp}$ of NLT and DLT_n with the torsional stiffnesses previously derived analytically, it becomes clear that the derived approach for considering transversal shear deformations (Eq. (13)) in combination with Eq. (6) and Eq. (7) leads to satisfactory values for the effective torsional stiffness properties $B_{xy,eff}$. As previously described, values B_{xy}—neglecting both, the out-of-plane shear deformations of the layers and the semi-rigid connection between the layers—are inappropriate to represent the actual/effective torsional stiffness of NLT and DLT_n. The analytical values for $B_{xy,eff}$, on the other hand, can represent the relatively negligible torsional stiffness of the nailed specimens.

5 EXAMPLE OF APPLICATION— DOUBLE SYMMETRIC HP-SHELL

In the following a reference HP-shell from twisted DLT elements is exemplary constructed and calculated. The double symmetric hyperbolic paraboloid to be planned over a square projection has the dimensions $l_x = l_y = 5.30\,m$ and $h_{x'} = h_{y'} = 2.00\,m$; $h = 4.0\,m$. In the context of application-optimized mass timber elements DLT±45°_n elements are used for the construction of the load-bearing structure (ref. to D1 series). The elements remain plane during production and get twisted on site by connecting them to edge beams. Each DLT_n element has a length of about 10.60 m and therefore a width of 1.0 m (without consideration of distortions acc. to Eq. (8)). The plate is loaded with a constant surface load of p = 3.6 kN/m² composed by the self weight (lower right, Fig. 13) and snow (upper right side, Fig. 13).

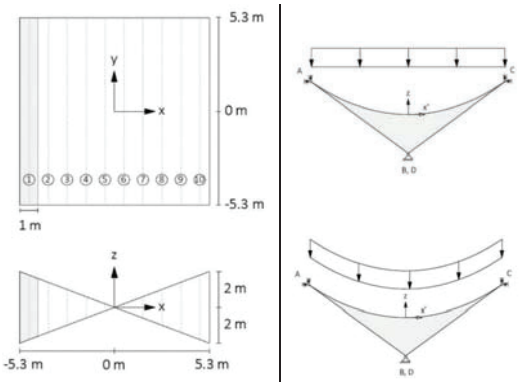

Figure 13: *Ground plan and side view of the HP-shell, divided in sections, representing the DLT elements* [3]

The uniform surface load p_z= 3.6 kN/m² leads to in-plane membrane forces n_{xy} in the shell. Therefore, the connections between the elements have to be dimensioned mainly for in-plane shear forces. The connections are fitted on site after twisting the elements by screwing, or dowelling the longitudinal element edges.

The analytical solutions (membrane theory and simplified approaches) according to Chapter 3.2 show in-plane shear forces only (n_{xy} = 25.28 kN/m). In order to evaluate the calculation methods, girder grid models are chosen as well as finite element method (FEM) models using the software Dlubal RFEM 5.23 (Quadrangle tool or RF Laminate tool) by inserting the previously calculated *ABD-E* stiffness matrix (Fig. 14).

Figure 14: *FEM shell model created with Dlubal RFEM* [3]

Fig. 15 shows the distribution of shear forces n_{xy} .

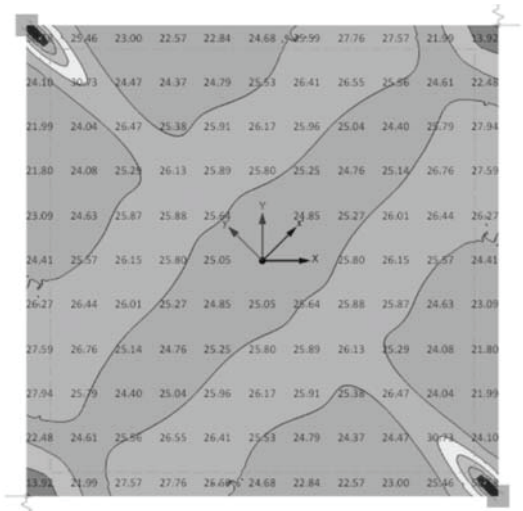

Figure 15: *Shear forces n_{xy} acting in the calculated with Dlubal RFEM* [3]

The shear forces converge to the solution of the membrane theory (n_{xy} = 25.28 kN/m). Bending moments m_x and m_y vanish (extreme values according to the FEM model: $m_x = 0.30\ kNm/m$). With respect to the segmentation and assembly of the shell small torsional moments will occur due to the twisting of the elements on site. These moments should be considered by an additional load case within the model. The torsional stiffness of the elements of D1 series is 0.023 MNm²/m (see Tab. 3). The torsional moment M_T acting within the elements due to the selected element geometry ($w/l = 1.06m/10.6m$) and hights h of the shell is 0.78 kNm—calcualted by Eq. (16). For glued DLT series D3, M_T would appear to be 7.08 kNm. The moment M_T is easily taken by the edge beams (exemplary $w/l = 2 \cdot 0.26m/0.20m$) connected (bolted) to the shell, beyond and above of the edges (Fig. 16).

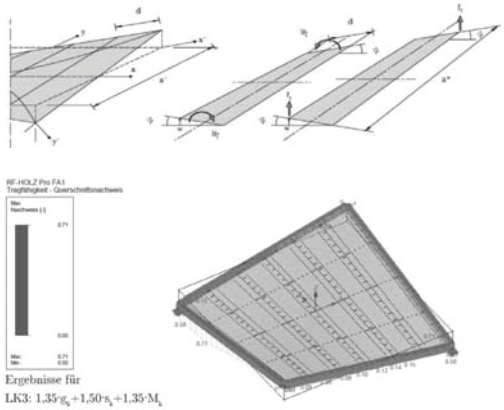

Figure 16: *Torsional moments by twisting the elements (upper sketch) and verification of the load bearing capacity of the beams in the ULS* [30]

https://doi.org/10.52202/069179-0483

As described previously in Chapter 3.2.2, the normal forces acting along the fictive compression and tension parabolas can be calculated by varius simplified methods. For the given example the 4th or 2nd layer of the chosen DLT follows these parabolas providing a high axial rigidity (extensional stiffness) in x´and y´direction. By using these simplified methods, the normal forces within the edge-beams can be estimated without FEM models (Fig. 17).

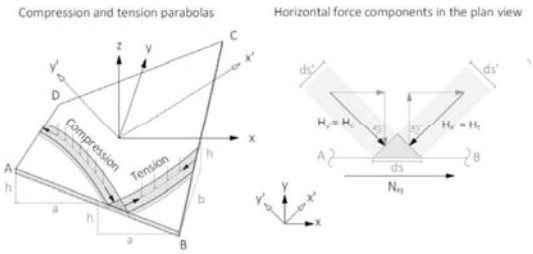

Figure 17: *Disassembling of the stress resultants acting on the edge beam according to Parme* [3; 24]

As in the entire shell, no bending moments act on the edge beams under the given load—besides the small torsional moments from the twisting of the elements. The surface load results in normal forces N, which are the product of the shear force n_{xy}, multiplied by the length of the edge beams. For the chosen example the normal foces N_x and N_y at the support apper to be 286,4 kN each and are taken by steel connectors and concrete supports.

6 CONCLUSIONS

This paper deals with both, results from the fild of structural analysis and timber engineering, leading to the HP-shell. The HP shell is an architecturally sophisticated, wide-span timber structure that can also be used to roof industrial buildings (Fig. 18). With its structural and architectural relevance, the HP-shell may be brought back into the focus of planners.

Figure 18*: Roof structure of the "Silhouette Corset Factory, Market Drayton" made form symmetric timber HP-shells* [31]

In addition, the basics of the plate theories according to Kirchhoff-Love and Reissner-Mindlin multi-layered mass timber elements under biaxial bending are applied. This leads to an analytical approach for the determination of the stiffness properties of DLT—with and without consideration of the transverse shear deformations. In addition an analytical approach for the consideration of semi-rigid connected layers of NLT and DLT_n is derived. Extensive series of mechanical experiments are carried out and serve to verify the analytical solutions. At the same time, the test data forms the basis for the calculation and construction of HP-shells using FEM and girder grid models.

Regardless the findings on the sophisticated HP shell structure, the enormous potential of diagonal layer arrangements within mass timber elements becomes obvious. DLT achieves significantly improved torsional properties with the same amount of material. The main outcomes achieved of the experimental investigations are as follows:

- The increase in the effective torsional stiffness of DLT_n elements compared to the NLT elements is undeniable. Compared to the five-layered NLT series with an overall thickness of 105 mm, the effective torsional stiffness $B_{xy,eff}$ of DLT±45_n elements is increased 76.9 % on average. For DLT±30° with t = 100 mm the increase is 69.2 % on average.
- The increase in the effective torsional stiffness of five-layered DLT elements compared to CLT elements with a thickness of 100 mm is 33 % on average for DLT±45°. For DLT±30° with t = 100 mm the increase is 24 % on average.

The investigations show that the torsional stiffness of DLT elements is significantly higher compared to CLT elements. The outcomes of this research render DTL ideal for plates under biaxial bending and concentrated loading, as required for point-supports [32] and promotes a more efficient use of mass timber elements.

ACKNOWLEDGEMENT

The NLT and DLT_n specimens were provided free of charge by Massiv-Holz-Mauer Entwicklungs GmbH. Thank you, Mr. Rainer König. The CLT specimens were produced by Pfeifer Timber GmbH. Thank you Mr. Bernd Gusinde. The DLT specimens were produced by Holzbau Unterrainer GmbH. Thank you, Mr. Leonhard Unterrainer and Dr. Roland Maderebner. The research was carried out within the research project InnoCrossLam and has received support within ERA-NET Cofund ForestValue by FNR (Federal Ministry of Food and Agriculture, Germany) and funding from the European Union's Horizon 2020 research and innovation programme under grant agreement N° 773324.

REFERENCES

[1] Sprague, T. S.: *Beauty, Versatility, Practicality: the Rise of Hyperbolic Paraboloids in post-war America (1950-1962)*. Construction History, 28 (1), pp. 165–184, 2013.

[2] *Hyperbolisch-parabolische Schale aus Holz*. Bauen + Wohnen, 17 (10), pp. 12–14., 1963.

[3] Fuchs, M.: *Hyperboloidal Roof Structures made of Timber*. Master´s Thesis, Technical University of Munich, 2020.

[4] Farshad, M.: *Design and analysis of shell structures*. Springer Science & Business Media, Luxemburg, 2013.

[5] Candela, F.: S*tructural Applications of Hyperbolic Paraboloidical Shells*. American Concrete Institute, 26, pp. 397–415, 1954.

[6] Bejtka, I.: *Cross (CLT) and diagonal (DLT) laminated timber as innovative material for beam elements*. Karlsruher Berichte zum Ingenieurholzbau, Band 17, KIT Scientific Publishing, Karlsruhe, 2011.

[7] Arnold, M.; Dietsch, P.; Maderebner, R.; Winter, S.: *Diagonal Laminated Timber—Experimental, Analytical, and Numerical Studies on the Torsional Stiffness*. Construction and Building Materials 322, 126455, 2022.

[8] Arnold, M.; Maderebner, R.; Dietsch, P.; Winter, S.: *Diagonallagenholz (DLH): Ressourceneffizienz durch diagonale Orientierungen einzelner Lagen. Teil 1: Bestimmung der Steifigkeitsparameter und Verformungsanalysen*. Under review for Bautechnik, Sonderheft Holzbau,2023.

[9] *ETA-20/0023*, European Technical Assessment. Pfeifer CLT Brettsperrholz. Österreichisches Institut für Bautechnik (OIB), Vienna, 2020.

[10] *ETA-16/0055*, European Technical Assessment. Radiusholz. Österreichisches Institut für Bautechnik (OIB), Vienna, 2020.

[11] *EN 408:2012*: Timber structures – Structural timber and glued laminated timber – Determination of some physical and mechanical properties. CEN – Comité Européen de Normalisation, Brussels, 2012.

[12] *ETA-15/0760*, European Technical Assessment. MHM – Wandelement. Österreichisches Institut für Bautechnik (OIB), Vienna, 2019.

[13] *EN 384:2016*: Structural timber - Determination of characteristic values of mechanical properties and density. CEN – Comité Européen de Normalisation, Brussels, 2016.

[14] Nettles, A.T.: *Basic Mechanics of Laminated Composite Plates*. NASA-RP-1351, NASA Marshall Space Flight Center, 1994.

[15] Schickhofer, G.: *Starrer und nachgiebiger Verbund bei geschichteten, flächenhaften Holzstrukturen. Dissertation*, Verlag der Technischen Universität Graz, 1994.

[16] Timoshenko, S. P.: *On the correction for shear of the differential equation for transverse vibrations of prismatic bars*. The London, Edinburgh and Dublin Philosophical Magazine and Journal of Science, 41:245, 744-746, 1921.

[17] Bogensperger, T.; Silly, G.: *Zweiachsige Lastabtragung von Brettsperrholzplatten*. Bautechnik 91, No. 10, 742-752, 2014.

[18] *DIN EN 1995-1-1/NA:2013-08*, Eurocode 5: Nationaler Anhang - National festgelegte Parameter - Eurocode 5: Bemessung und Konstruktion von Holzbauten - Teil 1-1: Allgemeines - Allgemeine Regeln und Regeln für den Hochbau. Deutsches Institut für Normung (DIN), Berlin, 2013.

[19] Kreuzinger, H.; Scholz A.: *Wirtschaftliche Ausführungs- und Bemessungsmethode von ebenen Holzelementen (Brücken, Decken, Wände)*. Schlussbericht. Institut für Tragwerksbau, Technische Universität München, 1999.

[20] Pucher, A.: *Über den Spannungszustand in gekrümmten Flächen*. Beton und Eisen, 33 (19), pp. 298–304, 1934.

[21] Zingoni, A.: *Shell structures in civil and mechanical engineering. Theory and closed-form analytical solutions*. Thomas Telford Publishing, London, 1997.

[22] Flügge, W.: *Statik und Dynamik der Schalen*. Berlin, Springer-Verlag, 1962.

[23] Flügge, W.; Geyling, F.T.: *A general theory of deformations of membrane shells*. IABSE publications, 17, pp. 24–46, 1957.

[24] Parme, A. L.: *An Elementary Analysis of Hyperbolic Paraboloid Shells-1. Geometrics and Basic Theory*. Indian Concrete Journal, 34 (12), pp. 464–470, 1960.

[25] Hempel, G.: *Hyperbolische Paraboloid-Dächer*. Bauen mit Holz, (10), 479–486. Bruder-Verlag, Karlsruhe, 1967.

[26] Krauss, F.: *Hyperbolisch paraboloide Schalen aus Holz*. Stuttgart, Karl Krämer Verlag, 1969.

[27] Mestek, P.; Winter, S.; Kreuzinger, H.: *Brettstapeln, Brettsperrholz und Verbundkonstruktionen.* Teilprojekt 15 des HTO-Verbundforschungsvorhabens "Holzbau der Zukunft". Technische Universität München, 2008.

[28] Glaser P., Ihler T., Aondio P.: *Untersuchungen zu Segmentschalen aus ebenen Brettsperrholzplatten unter Berücksichtigung nichtlinearer Verbindungseigenschaften*. Der Bauingenieur, VDI Verlag, Düsseldorf, 2020.

[29] Halász, R. von; Scheer, C.: *Grundlagen, Entwurf, Bemessung und Konstruktionen.* Holzbau-Taschenbuch, 9. Auflage. Ernst&Sohn, Berlin, 1996.

[30] Arnold, M.: *Hyperbolische Paraboloid-Schalen aus Brettsperrholz-Theorie, Formfindung & Konstruktion*. Master´s Thesis. Technical University of Munich, 2018.

[31] McCaig, I.; Ridout, B.: *Practical Building Conservation – Timber*. English Heritage, London, 2012.

[32] Arnold, M.: *Mechanical Properties of Diagonal Laminated Timber (DLT) with Respect to Point-Supported Mass Timber Slabs*. Dissertation in progress. Technical University of Munich, expected 2023.

https://doi.org/10.52202/069179-0483

World Conference on Timber Engineering Oslo 2023

MASS TIMBER PANELIZED WORKFORCE HOUSING IN OREGON, U.S.

Judith Sheine[1], Mark Fretz[2], Simone O'Halloran[3], Mikhail Gershfeld[4], Jason Stenson[5]

ABSTRACT: Mass timber panel production came to the United States after developments in Europe and Canada; the first domestic structural cross-laminated timber (CLT) panels were manufactured by DR Johnson Wood Innovations in Riddle, Oregon in 2015. With its history of timber product manufacture, the state has embraced this new material for its potential for economic development and environmental stewardship and Oregon has become the epicentre of mass timber development in the U.S. As in many places in the U.S., Oregon has a critical shortage of affordable housing and it has been challenging to find paths for mass timber to enter this market where light-wood-frame construction is dominant. In 2018, Freres Engineered Wood, working with the TallWood Design Institute, a collaboration between the University of Oregon and Oregon State University, developed a new product: mass plywood panels (MPP). This product provides a possibility for constructing single-family houses economically with mass timber using thin panels derived from small diameter logs. This paper describes the research leading to a pilot project utilizing MPP for workforce housing in Milwaukie, Oregon.

KEY WORDS: Mass Timber, Affordable Housing, Oregon

1 INTRODUCTION

Mass timber panel production came to the United States, after developments in Europe and Canada; the first domestic structural cross-laminated timber (CLT) panels were manufactured by DR Johnson Wood Innovations in Riddle, Oregon in 2015. With its history of timber product manufacture, the state has embraced this new material for its potential for economic development and environmental stewardship and Oregon has become the epicentre of mass timber manufacture, design, research, testing and construction in the U.S.

While timber production has been central to Oregon's economy since its founding, timber production has fallen significantly over the past 50 years, due to environmental regulations restricting timber harvest, and job losses have been severe due to the reduced production and to automation in the industry [1]. Combined with changes in tax laws that have led to further losses of income, rural counties in Oregon have suffered significant economic declines which have exacerbated tensions between environmentalists and those in the timber industries and communities [2]. However, with climate change leading to worsening drought conditions in the American West and years of forest management policies restricting harvest, coupled with the promotion of fire suppression, devasting wildfires have served as an impetus for change [3]. Because mass timber utilizes small diameter logs that can be harvested from forest restoration projects that reduce wildfire risks, environmental groups and the timber industries have been able to find common ground in advocating for changes in forest management policies that allow for additional selective harvesting. Mass timber manufacture provides economic benefits by creating well-paid high tech jobs manufacturing mass timber panels and environmental benefits by utilizing forest restoration products and by substituting a bio-based carbon sequestering material for steel and concrete [4].

Because the state recognizes these benefits, the Oregon Legislature provides funding for the TallWood Design Institute, (TDI) a collaboration of the University of Oregon's (UO) College of Design and Oregon State University's (OSU) Colleges of Forestry and Engineering. TDI's mission is to promote economic development and environmental stewardship by advancing engineered timber products through research, testing, outreach and education. TDI has been critical in providing research and testing for DR Johnson Wood Innovations to produce their CLT panels and worked closely with Freres Engineered Wood in Lyons, Oregon, to develop a new mass timber product, mass plywood panels (MPP).

At the University of Oregon, we have engaged in design research projects demonstrating the feasibility of using mass timber products in a variety of building applications.

[1] Judith Sheine, University of Oregon (UO), United States, jesheine@uoregon.edu
[2] Mark Fretz, University of Oregon (UO), United States, mfretz@uoregon.edu
[3] Simone O'Halloran, University of Oregon (UO), United States, simoneo@uoregon.edu
[4] Mikhail Gershfeld, California State Polytechnic University, Pomona (CPP), United States, mgershfeld@cpp.edu
[5] Jason Stenson, University of Oregon (UO), United States, jstenson@uoregon.edu

https://doi.org/10.52202/069179-0484

However, demonstrating that mass timber can provide affordable and energy efficient housing at single-family scale has been an elusive goal. With the development of MPP, we saw an opportunity to use thin, very strong panels that could be fabricated with digital workflows to make affordable single-family houses, adding social equity to mass timber as an additional benefit for Oregon.

2 BACKGROUND

As in much of the U.S., Oregon has a critical shortage of housing that is affordable. Lack of housing inventory and spiraling home prices have reached a crisis point in both rural and urban communities; over the next 20 years, Oregon will need about 584,000 new homes [5]. It has been challenging to find paths for mass timber to enter this market where the dominant construction method for up to five stories of a structure is light-wood-frame; since CLT uses comparably more wood fibre it can be more costly. However, MPP is 20% stronger than CLT and allows the use of thin panels (51-76 mm) derived from small diameter logs (as small as 127 mm) [6], providing a new possible path for a sustainable mass timber product to be used in residential construction [7].

To address the housing shortage, the Oregon Legislature passed House Bill 2001 in June 2019; it requires cities with a population over 10,000 to eliminate single-family zoning and allow two or more units on sites that were previously zoned for only single-family houses. In the metropolitan area around Portland, the largest population centre in the state, the law has allowed cities and counties to permit quadplexes and groups of small units ("cottage clusters") in areas previously zoned for single-family housing. This law was meant to promote the creation of more housing units and to reduce their cost by increasing land use intensity on sites formerly zoned for only a single house.

The City of Milwaukie, just outside Portland, took a proactive approach to respond to these new requirements and commissioned a planning study of the impacts of this required land use change with recommendations for the new standards [8]. These included updating their existing "cottage cluster" code to stimulate development of these groups of small freestanding houses arranged around a communal open space, and also allowing for groups of attached houses, known as "middle housing," all on single-family lots with bicycle storage, open space and tree canopy standards, and associated reduced parking requirements.

3 UNIVERSITY OF OREGON DESIGN RESEARCH STUDIO

At the University of Oregon, Professor Judith Sheine taught a design studio in winter 2020 focused on creating modular mass timber housing for a single-family double lot in Milwaukie that was part of the cottage cluster feasibility study. The studio followed the land use and massing guidelines recommended in that study and focused on using volumetric modules of MPP, producing some compelling designs that were presented to the Milwaukie planning staff, who found the visualizations of these zoning proposals useful for their development of their new land use regulations. These regulations evolved over the next two years, and were finally adopted by the City of Milwaukie in June, 2022, allowing for cottage clusters and middle housing on a single lot.

Figure 1: *MPP Modular Housing, Milwaukie, Oregon; University of Oregon Student project by Flynn Casey*

4 PROJECT

Following the studio project, UO faculty Sheine and Mark Fretz and structural consultant Mikhail Gershfeld, started a collaboration to design a small, energy efficient house constructed with MPP panels that would result in publicly available documents for application in cottage clusters, or stand-alone units, affordable to households with 80-100% of the area median income, which includes middle class households for whom housing in Oregon has become unaffordable. Swinerton Builders, a construction firm with significant expertise in mass timber, joined the team and provided critical practical advice on cost and construction efficiency. At their urging, the design team decided to embrace panelised prefabrication of the modular units, to avoid the transportation challenges of the volumetric modular model and to produce a design that could be built by small construction firms on a variety of sites with panels that could be prefabricated in a small warehouse facility or in a large factory.

The design team partnered with an affordable housing developer, HomeWork Development, that was interested in using these units for a pilot project in Milwaukie, on the lot that was the site for the 2020 design studio and some nearby lots. A large healthcare provider, Providence Health, which was eager to provide affordable, healthy housing for their workforce in Milwaukie, decided to invest in the project and contribute two small conjoining lots; however, due to the economic conditions following the Covid-19 pandemic, Providence was unable to follow through on this commitment and the pilot project was scaled down to two lots. The design team explored a variety of site configurations over the two-year period that the new Milwaukie zoning ordinance was being

https://doi.org/10.52202/069179-0484

developed and, once the ordinance was adopted, found that the most efficient site utilization resulted in cottage clusters of free-standing units, with 11 units on one site (Figures 2, 3) and 15 units on the second one, for a total of 26 units. While originally the designers had planned for both two-and three-bedroom prototypes, the developer advocated for one repeatable two-bedroom unit for maximum site utilization and potential cost efficiencies.

Figure 2: *MPP Panelized Housing, Milwaukie, Oregon; rendering by Simone O'Halloran*

4.1 THE OREGON MASS TIMBER COALITION

Following devasting wildfires in September 2020 in Oregon, which burned 4,452 square kilometres and destroyed over 4,000 houses, many of them manufactured houses occupied by low-income households, several Oregon state agencies started holding (virtual) discussions about how to address reduction of wildfire danger and the creation of affordable and more resilient housing. Business Oregon (BO), the state's economic development agency, the Department of Land Conservation and Development (DLCD), the Oregon Department of Forestry (ODF) and the Port of Portland (Port) joined with TDI, which included UO and OSU, to strategize about creating mass timber housing at a large scale, housing that would be far more resilient than the manufactured houses built with light-wood-frame to minimal standards that had burned in the wildfires and that would provide economic and environmental co-benefits by expanding the mass timber market.

These discussions evolved into the Oregon Mass Timber Coalition (OMTC) that applied in October 2021 to the U.S. Economic Development Administration's (EDA) Build Back Better Regional Challenge (BBBRC) to address economic development, environmental sustainability and social equity with investments in research and development and infrastructure that would drive a new industry. The OMTC proposed a group of projects that spanned the mass timber housing supply chain, from forest restoration and mass timber manufacturing (ODF and OSU) to updated land use legislation (DLCD) to MPP panelised prefabricated housing development (UO) to infrastructure for a mass timber housing factory at an industrial site in Portland (Port), along with new research facilities for testing mass timber assemblies for acoustic and fire resistance ratings at UO and OSU, respectively, and workforce development in forest restoration, mass timber manufacture, and housing construction (Port, ODF, OSU, DLCD). The OMTC was one of 60 regional coalitons (out of 529 applicants) to receive Phase 1 funding ($500,000) and one of 21 coalitions to receive finalist funding: $41.4 million; Business Oregon supplied an additional almost $6 million in required matching funds for UO and OSU. Out of this funding, $2 million was awarded to UO for developing and building prototypes of the MPP panelised housing, to determine the most efficient construction methods and the labour and material costs. This work will be undertaken over the next several years, 2023-2025.

In order to continue to develop the design of the MPP housing unit for prototype construction, funding was supplied by TDI and by the developer, HomeWork, with funding from two U.S. Forest Service Wood Innovation Grants for design development and an Energy Trust of Oregon Fellowship for energy efficiency analysis, and funding from the EDA BBBRC Phase 1 award.

4.2 UNIT DESIGN

Mass timber panels are a prefabricated building material as either small lumber or veneer elements are glued together and pressed into large panels, beams and columns in a factory, as opposed to framing a wall on site as is done with light-wood-frame construction. These panels can be manufactured to order and can be digitally pre-cut and routed to achieve panels with door and window cut outs to be quickly assembled on site. Additionally, vapor barriers, insulation and cladding can be pre-applied off-site, to simplify construction in the field. While even more efficiencies can be achieved with assembling a volumetric module in a factory [9], it is more efficient to ship flat panels which may not require special permits (and costs) for oversized truck loads. In the case of our pilot project, while the panels can be prefabricated in a factory, the mass timber housing factory is still at least several years from existence in Oregon, and the panels can also be fabricated in a smaller warehouse setting with existing facilities.

In order to allow the MPP construction to compete in cost with light-wood-frame, it was necessary to work with the panel sizes that Freres Engineered Wood manufactures and to minimize waste. The length of the basic unit footprint was established as half of the maximum panel length Freres produces, or 7.3 m (total maximum panel length of 14.6 m), and the width was based on a combination of the panel widths in the Freres catalogue, or about 4.9 m. As noted above, the units are identical two-bedroom units; in order to fit a maximum number of units on each site, the units are two-stories (about 6.5 m at the top of the gable roof).

For this project, only stand alone and duplex units were considered, due to higher fire ratings required by triplex and quadplex units, which would have added additional wood fibre or the inclusion of gypsum board to achieve

the required fire resistance. The design team wanted to avoid the use of gypsum board, with its high carbon footprint. And, in order to maximize the number of units allowed within the new Milwaukie zoning code, the units are stand alone in cottage clusters, which did not require any on-site parking (Figures 2, 3).

The units have living spaces on the ground floor and two bedrooms on the upper floor. The upper floor bathroom is stacked over the half bath and kitchen, with one plumbing wall applied as a chase over the MPP panel, in order to separate it from the exterior solid wall panel. Apart from the plumbing walls, all interior surfaces are MPP, eliminating the need for finishes (Figure 4).

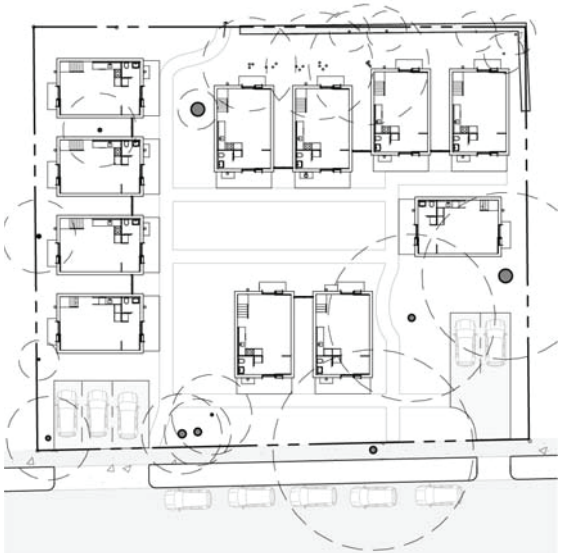

Figure 3: *MPP Panelised Housing, Cottage Cluster, Site 1, Milwaukie, Oregon*

Within the cottage clusters, units are set 1.8 meters apart (a code requirement), leaving the front and back elevations as the best locations for windows. These were aligned on the upper and lower floors to allow sufficient solid panels to support the roof. To allow more light into the units, skylights were added, and a space was opened to below adjacent to the stairs, allowing light to penetrate to the lower floor. A translucent polycarbonate material is used in strategic locations to allow more light to penetrate the unit. (Figures 4, 5, 6).

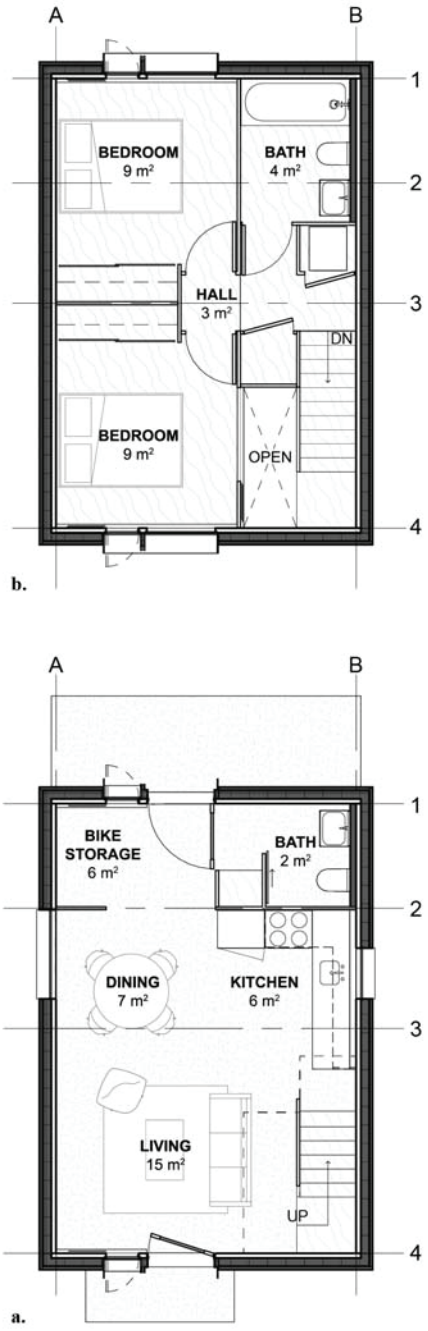

Figure 4*: MPP Panelised Housing, Floor Plans. a. Ground Floor Plan, b. Upper Floor Plan*

https://doi.org/10.52202/069179-0484

Figure 5: *MPP Panelised Housing, Elevations: a. Side elevation; b. Front Elevation*

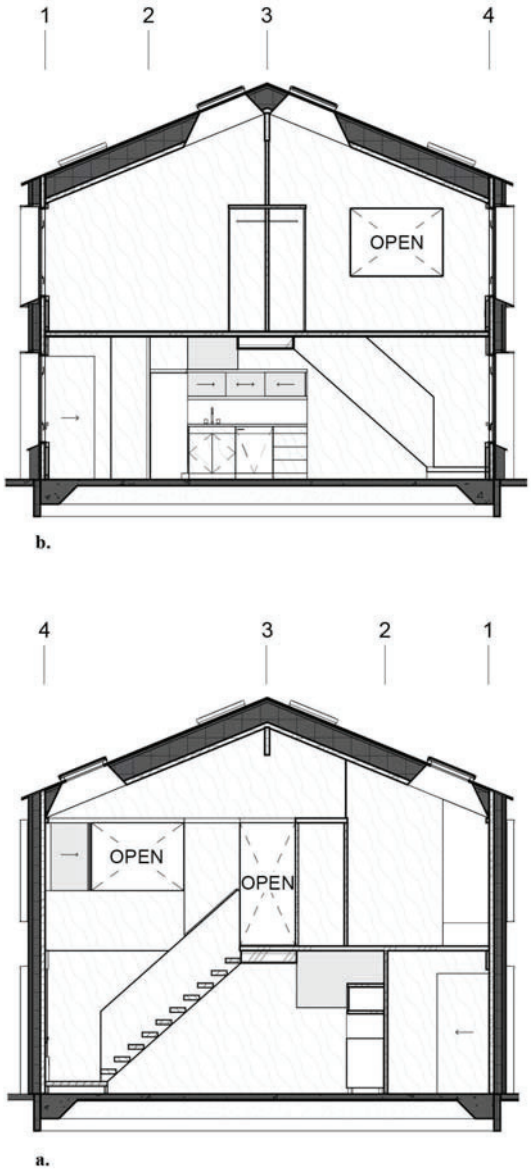

Figure 6: *MPP Panelised Housing, Sections. a. Section through Stair b. Section Through Living Space*

4.3 STRUCTURAL DESIGN

The use of MPP panels, 51 and 76 mm, would reduce the use of wood fibre but does not currently meet the code requirements of SDPWS 2021 [10]. Comprehensive testing of MPP to assess the global and local stability performance of thinner shear walls resisting both gravity and lateral loads is not currently available.

Based on Frerres MPP design guidelines, it was determined that a minimum of 76 mm panels would be required for the roof, floor and exterior wall construction assemblies. The use of 51 mm panels placed horizontally for the exterior walls that are not supporting roof or floor loads, and thus non-bearing, was explored. This design would require the addition of posts, would complicate the construction process and could be significantly below approved lateral system requirements. Thus, 76 mm panels were considered a more effective solution for all exterior walls. All non-bearing interior walls remained at 51 mm (Figures 7, 8).

Also, hybrid construction (MPP + light-wood-frame) vs. an entirely panelized system was considered. While hybrid construction would reduce wood fibre use, it would impact prefabrication potential and efficient constructability and thus overall cost.

The panelised system selected requires beams at two locations; a ridge beam, 76 mm MPP, at the intersection

of the roof panels and a wide MPP floor beam, to break the floor span sufficiently to allow the use of a 76 mm floor panel. The wide beam (flat use) was chosen to minimize its intrusion into the ground floor space, keeping it as open as possible (Figures 7, 8). MPP ledgers are used to support the floor and roof MPP panels and also help to create spaces for electrical routing, lighting and window shading.

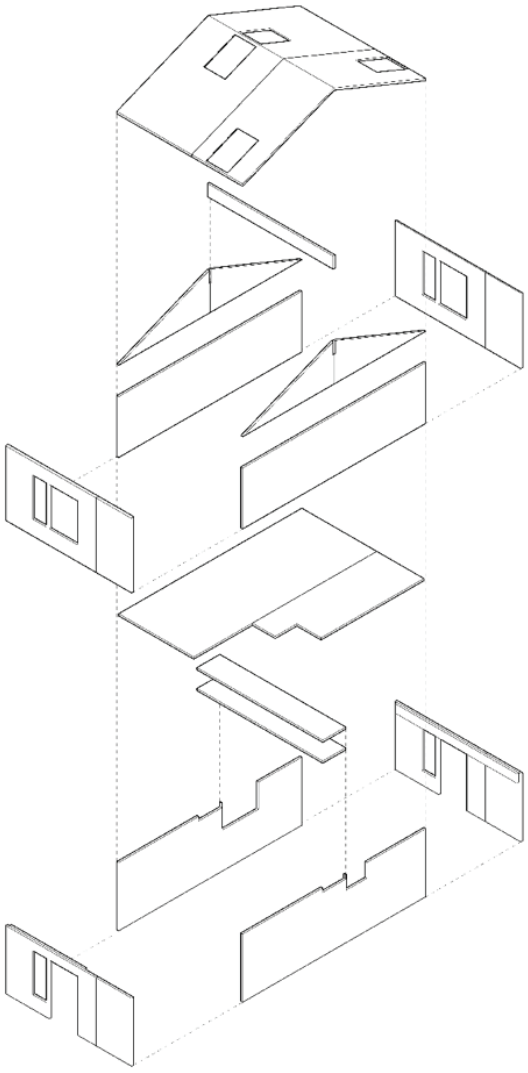

Figure 7: *MPP Panelised Housing, Assembly*

4.4 MATERIAL EFFICIENCY

An additional consideration was minimizing waste in the usage of the panels. Trials with panel layouts eventually allowed a realization of around 95% utilization for 51 mm material (Figure 9) and around 90% utilization for 76 mm material (Figure 10). The overall wood fibre volume for the house, which includes structure, partitions, doors and casework, is approximately 19.9 m^3. To eliminate the

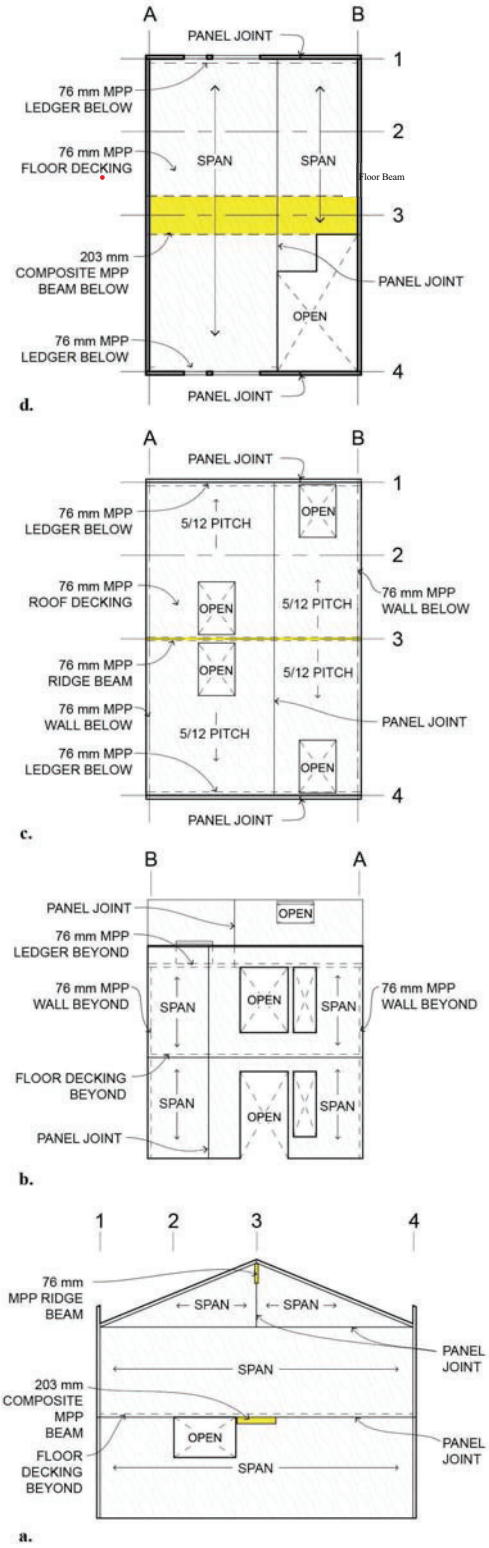

Figure 8: *MPP Panelised Housing, Framing. a. Side Wall Framing Elevation; b. Front Wall Framing Elevation; c. Upper Floor Framing Plan; d. Roof Framing Plan*

https://doi.org/10.52202/069179-0484

expense of transporting oversized loads, panels that are no more than about 2.4 meters wide were used.

One issue to be resolved in the first, iterative prototype is whether window and door openings for the front and back walls of the unit will be cut out of the panels, or assembled through a series of straight cuts that are infilled with rectangular panels above and beneath those openings. The latter method would result in an approximate 5% increase in material use efficiency due to not having the leftover fibre from the cut-outs, but would also increase the number of parts to handle from 25 to 41. Therefore, a higher fibre utilization could be offset by higher labour. Also the cost of routing the openings using a CNC versus cutting them with a handheld electric panel saw using a prefabricated jig will be compared.

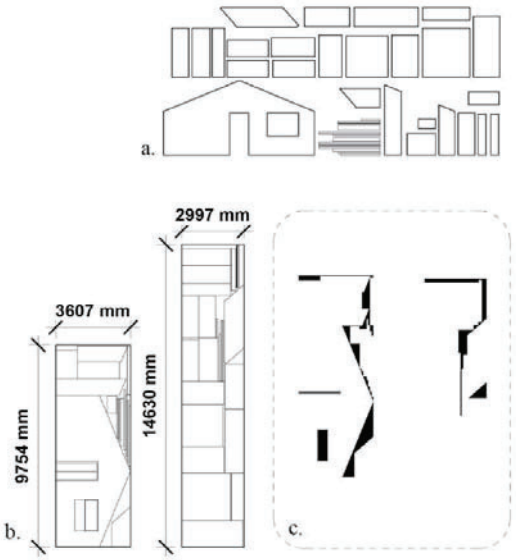

Figure 9: *MPP Panelised Housing, 51 mm Material Efficiency. a. Panels for Project; b. Panels Arrainged on Standard-Size Billets for Material Efficiency; c. Unused MPP Material.*

4.5 ENERGY EFFICIENCY

The goal of the study funded by Energy Trust of Oregon was to meet net zero energy goals while reducing the cost of these standards in construction in the residential sector, a primary barrier to deploying net zero ready construction at scale without substantial subsidy. The use of MPP to create a higher performing thermal envelope was explored by the design team. With MPP, the envelope is more monolithic than light-wood-frame construction, with fewer joints for air infiltration, and outboard insulation that wraps the entire structure with fewer thermal bridges. Furthermore, the MPP itself has insulative properties. The panelized wall assemblies facilitate a novel window integration (Figure 11) that seeks to increase the energy performance and esthetics of low cost off-the-shelf windows, employing a twin-wall polycarbonate shade and

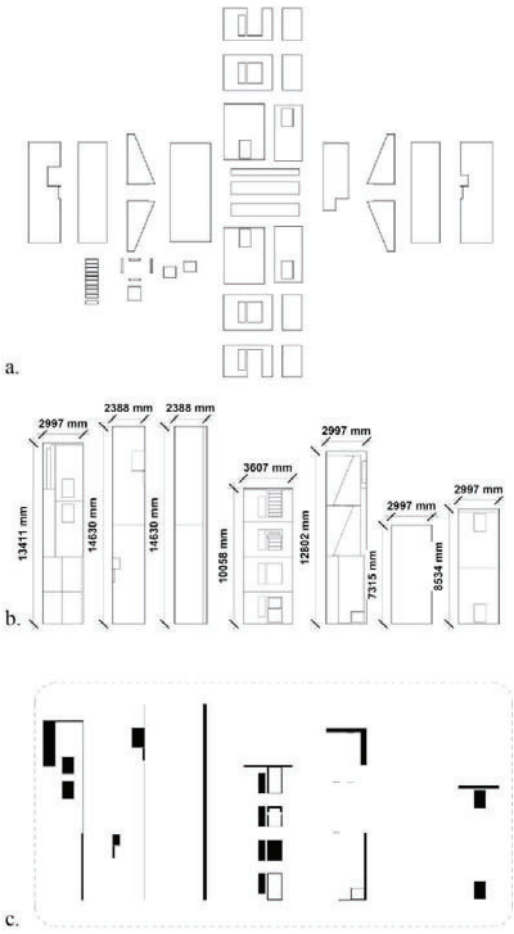

Figure 10: *MPP Panelised Housing, 76 mm Material Efficiency. a. Panels for Project; b. Panels Arrainged on Standard-Size Billets for Material Efficiency; c. Unused MPP Material.*

deep inset for solar shading while maintaining simplicity to reduce construction costs. Moreover, as the new MPP units can be arranged in dense courtyard clusters they create opportunities where the units could share thermal energy through district heating/cooling strategies and charging of a high-mass ground floor slab and shared peer-to-peer solar photovoltaic energy, thus simultaneously preserving existing tree canopy while balancing loads across the site and larger energy grid. The buildings themselves will serve as thermal storage, with the concrete slab and the high-performing thermal envelope facilitating proactive strategies for optimizing when and how energy is consumed on site.

This study included:

1. An energy model of a prototypical MPP panelized single-family house with concrete slab-on-grade, and an all-electric monobloc heat pump system configured either individually for each unit or as a district strategy.

https://doi.org/10.52202/069179-0484

2. A physical mockup of a higher-performance low cost window that includes infiltration testing (Figure 12) and thermal imaging (Figure 13).

4.5.1 Energy Model

The energy analysis was based on a combination of Honeybee 1.4.0 (via Grasshopper and Rhinoceros 7) and OpenStudio 3.3.0, both of which rely on EnergyPlus 9.6.0 for the annual energy calculations. The MPP model geometry was based on the most recent design documents, while the model performance is reflective of the U.S. Department of Energy (DOE) Zero Energy Ready Homes (ZERH) standard. The model is currently set with a packaged air-to-air heat pump system as baseline. The team is exploring system options, including an air-to-water district heat pump and hot water strategy to serve multiple units. Targeting the ZERH standard for the basis of design, the simulated preliminary results show an EUI of 52.7 kWh/ m^2 with the majority of energy consumption attributed to heating and interior equipment. Additional selection and testing of low cost windows will be performed in future prototyping, in order to meet the prescriptive requirements of the ZERH standard

The design of each housing unit is configured for hydronic heating, cooling and coupled domestic hot water. Units can be coupled with a district heating loop that supplies domestic hot water all year using a dedicated heat exchanger and additional space heat to the floor slab during heating and shoulder seasons. During the cooling season, natural ventilation will provide the primary cooling with supplemental cooling provided by centralized heat pumps that are staged to deliver chilled water via a cooling loop and floor slab hydronics valved to switch from heating to cooling. For both space heating and cooling seasons, the slab and centralized thermal storage tanks can be either heated or chilled at night to take advantage of off-peak electrical rates from the grid. This design is intended to not only reduce unit energy use but provide overall operational affordability, load sharing and resilience since the centralized heat pumps can be operated by site microgrid photovoltaics during a grid outage.

In the case of a single unit configuration, the district heating and cooling loops can be substituted by an air-to-water heat pump and a small heat exchanger for domestic hot water.

Primary cooling will be provided by cross-ventilation and stack ventilation using operable skylights. Supplemental cooling will be provided by a chilled slab using an air-to-water heat pump coupled to a hydronic cooling loop.

4.5.2 Physical Mockup

While the MPP can create a tight thermal envelope, the performance of the windows is critical to overall energy efficiency. The team explored an alternate to costly triple-pane windows by employing a double-pane window coupled with a sliding shutter of twinwall polycarbonate, which would provide additional thermal insulation while allowing some light into the interior (versus a solid panel). The upper track for the shutter additionally conceals LED strip uplighting. The space between the lower track and the floor allows for a service chase running the width of the window wall to be used for electrical and other services without any penetrations or chases occurring through the MPP exterior wall panel.

An assembly detail prototyped with the mock-up had the window frame sit within the thickness of the MPP panel, including 51mm of MPP (R-value of 2.50) covering the window frame when viewed from the interior. The intent was to have the MPP serve as structure, finish material and frame insulation; thus, requiring no additional trim work or finish treatment (Figures 11, 12, 13).

The relatively thick outboard insulation with rainscreen and cladding at the exterior allows the window plane to be recessed providing some inherent exterior shading. A sheet metal window surround including a vertical mullion between the two windows adds some depth and improves shading performance while acting as window trim. The sheet metal work proved a complex process between model, fabrication, and installation. A number of interface issues will be able to be refined and improved based on mocking up this façade integrated element. Alternate materials (e.g., fiberglass, plate steel, wood) may also be pursued for constructability, cost, thermal and durability considerations.

The tolerance for a CNC-cut window opening was much tighter than that of a conventional light-wood-framed rough opening, where a process of shimming and squaring a window during installation requires extra space in the site-built structure. The precision fabrication possible on the CNC allowed for the rough opening in the MPP to be less than 2 mm larger than the window itself on each side, whereas window manufacturers require rough openings for conventional construction to be anywhere from 13 mm to 25 mm larger on each side. The tighter tolerance meant that the window was square as soon as it was placed in the opening and air sealing was more precise.

One benefit to panelized wall construction using MPP is a significant reduction in the possible locations for air infiltration to occur. With fasteners not penetrating the surface, potential infiltration locations are limited to panel-to-panel joints and panel penetrations like window openings. Furthermore, electrical outlets located on exterior walls are all surface mounted on the interior, thereby reducing the need to pay particular attention to outlet air sealing.

For performance testing, an enclosure was constructed and air sealed to the interior side of the mock-up for use of a blower door fan and instrumentation to positively pressurize the interior of the wall assembly. Smoke was introduced to the pressurized interior side of the mock-up at 30 Pascals and ramped to 62 Pascals while the exterior

https://doi.org/10.52202/069179-0484

was visually inspected for smoke leakage. Window penetrations were sealed with a liquid applied membrane (Soprema Sopraseal Liquid Flashing, SKU: A508). Minimal smoke leakage was observed around the window; the team plans to explore further sealing steps in the larger prototypes.

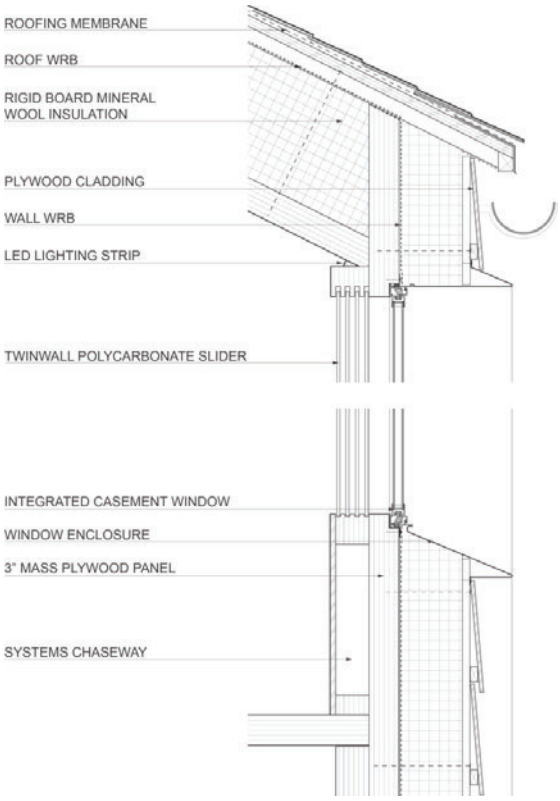

Figure 11: *Detail of window mockup showing wall and roof assemblies*

4.6 PROTOTYPES

The EDA BBRC award with BO match will allow the team to test and refine the design and construction methods of the MPP unit. The first prototype will be constructed in TDI's A. A. "Red" Emmerson Advanced Wood Prodcuts Lab, using the strong floor and wall to conduct structural tests of the MPP building envelope, which will be required by building departments in local jurisdictions in order for permits to be issued. This prototype will also entail fabrication of the MPP panels with insulation and cladding, iterative assembly and evaluation of details, including window assembly, panel connections, and electrical, mechanical, and plumbing systems integration. Following the documentation and disassembly of the first prototype, a contractor will be employed to fabricate and construct a second prototype in the Emmerson Lab's exterior yard. This will test construction means and methods, including evaluation of shipping efficiency and field assembly, and include documentation of costing of materials and labor. The team will test the performance of the design, including

Figure 12: *Window mockup*

Figure 13: *Window Mockup Thermal Performancem, False Color Infrared Image*

confirmation of energy modeling by measuring envelope infiltration, and acoustic testing, followed by documentation and disassembly. Documentation will include data collection and fabrication- and construction-

https://doi.org/10.52202/069179-0484

ready documents, including digital files. Prototyping is scheduled to begin in June 2023.

5 CONCLUSIONS

The success of this project depends on the efficient utilization of the MPP panels, including digital fabrication workflows, reduction in finish materials, the capacity to offset small cost increases above light-wood-frame with more efficient energy performance, and their affordability to the workforce market (those earning 80-100% of the area median income). The preliminary costing model indicates that this is achievable, but the prototyping of the project will be able to provide proof of concept for the open-source documents that will be available for construction on multiple sites in Oregon.

ACKNOWLEDGEMENT

The authors wish to acknowledge the contributions of Swinerton Builders and the support of the TallWood Design Institute for this work. Funding was also provided by HomeWork Development and Shortstack LLC via subaward from two U.S. Forest Service Wood Innovation Grants, "Milwaukie Courtyard Housing Project," Grant # 22DG11062765744, and "Shortstack Housing Mass Timber Platform to Develop Prototype Replicable Affordable Housing," Grant #21DG11062765738, and a fellowship from the Energy Trust of Oregon, Contract #3431. Additional funding was provided by a subaward from the Port from the EDA BBBRC Phase 1, "Build Back Better with Mass Timber," Grant #ED22HDQ3070069. The prototyping is funded by the EDA BBBRC "Mass Timber Prefabricated Panels for Affordable Housing Prototypes," Grant # 07-79-07906, and by Business Oregon's University Innovation Research Fund, Contract # C2022840.

REFERENCES

[1] Daniels J. M., Wendel K.: Production, Prices, Employment, and Trade in Northwest Forest Industries: 1958-2019. Portland, OR: U.S. Department of Agriculture, Forest Service, Pacific Northwest Research Station, 2020.

[2] Bosworth D., and Brown H.: After the timber wars: community-based stewardship. *Journal of Forestry*, v.105 no. 5 271-273, 2007.

[3] Stephens S. C., Battaglia M. A., Churchill D. J., Collins B. M., Coppoletta M., Hoffman C. M., Lydersen J. M., North M. P., Parsons R. A., Ritter S. M., and Stevens J. T., Forest Restoration and Fuels Reduction: Convergent or Divergent?, *BioScience,* Volume 71, Issue 1, 85–101, January 2021.

[4] Mishra, A., Humpenöder, F., Churkina, G. Reyer C. P. O., Beier F., Bodirsky B. L., Schellnhuber H. J., Lotze-Campe H., and Popp A.: Land use change and carbon emissions of a transformation to timber cities. *Nat Commun* **13**, 4889, 2022.

[5] Oregon Housing and Community Services: Building on New Ground: Meeting Oregon's Housing Need, February 2021.

[6] Freres Engineered Wood: MPP Mass Plywood Panels by Freres Lumber Co., Design and Construction Guide. Lyons, Oregon, 2021.

[7] Puettman, M., Sinha, A.: Life Cycle Assessment of Mass Ply Panels Produced in Oregon, November 2020.

[8] City of Milwaukie: Milwaukie Cottage Cluster Analysis, June 2019.

[9] McKinsey Global Institute: Reinventing Construction: A Route To Higher Productivity, 2017.

[10] ANSI/AWC 2021 *Special Design Provisions for Wind and Seismic (SDPWS)* Appendix B3.1

https://doi.org/10.52202/069179-0484

World Conference on Timber Engineering Oslo 2023

UTILIZING LOW-VALUE WOOD SPECIES FROM FOREST RESTORATION PROJECTS IN LOCAL CLT MANUFACTURE AND DESIGN

Payton Narancic[1]

ABSTRACT: Years of wildfire suppression and ever-extending periods of drought are fanning the flames of catastrophic wildfires at an unnatural scale. The west coast of the United States has suffered the brunt of these negative impacts as wildfire seasons are becoming increasingly worse every year. The abundance of small-diameter trees and dry fuel accumulating in forests is reinforcing the need for better forest management practices as human activity in the last century has proven to be detrimental to the global climate. The goal of this research is to examine the relationship between collaborative forest restoration and local mass timber production to showcase the use of mass timber as a means to improve wildfire resilience and push the United States toward developing its mass timber industry at a local scale. The use of low-value species, harvested from forest restoration projects, in mass timber panels can create a symbiotic relationship between forestry, architecture, and the respective local economy. This project addresses the utilization of low-value species (Ponderosa pine) from forest restoration projects in the Sierra Nevada forests of California to manufacture mass timber locally that, in return, can provide the material for public lands facilities as demonstration projects in parks affected by wildfires.

KEYWORDS: CLT, Ponderosa pine, wildfire management, forest restoration, public lands facilities

1 INTRODUCTION

Forest management policies in the western United States are worsening the effects of climate change and, thus, causing forests to suffer. Years of wildfire suppression due to human intervention has caused forests to become increasingly vulnerable to unnatural fire behaviour [1, 2] Although forest restoration projects, including thinning efforts, are effective at creating forest resiliency, these efforts are often expensive ventures and harvest low-value wood species that are used for low-yield profit products such as biofuel and paper pulp; this results in immense expenditure losses that government agencies are typically burdened with. Mass timber products offer an alternative for lower-grade species as they can be engineered to enhance the wood's structural capabilities. Unfortunately, the production of mass timber, such as CLT (cross laminated timber) panels, can require significant investment in expensive equipment in an industry that is still developing in the United States. For this reason, mass timber production has been largely unattainable for small-scale production. All of these intersecting issues lead to the primary research question: how can forest restoration and thinning, used to reinforce wildfire resilience in forests, create local benefits by using mass timber production generated from associated local forest restoration endeavours? Addressing this question can expand the narrative of the possibilities of mass timber production in the United States while also tackling the issue of wildfire vulnerability in forests.

1.1 WILDFIRE THREATS TO PUBLIC LANDS

Public lands, such as national and state parks, in the western U.S. are facing increased wildfire activity driven by severe drought and an abundance of small diameter trees and dry fuel. The KNP complex fire in Sequoia National Park decimated an estimated 3-5% of California's giant sequoias and, in the past two years, 20% of all sequoias have been lost due to fire activity [3]. In addition to ecosystem devastation, the built environment is also severely affected. In August of 2020, Big Basin Redwoods State Park, the oldest state park in California, suffered catastrophic losses as a result of the CZU complex fire; nearly all of the park's facilities were destroyed leaving only charred remains of the park's historic structures. Lassen Volcanic National Park fell victim to the 2021 Dixie Fire, the second largest wildfire in California history, which not only devastated significant acreage in the park, but also laid ruins to the nearby communities of Greenville, Warner Valley, Canyon Dam, and Indian Falls, amongst others; wildfire threats are not isolated on public forest lands, but also the communities that surround and exist within them. As climate change continues to worsen wildfire seasons, we can expect to witness more and more environmental destruction, both natural and built. For these reasons, this

[1] Payton Narancic, University of Oregon, School of Architecture and Environment, USA, pcn@uoregon.edu

https://doi.org/10.52202/069179-0485

project explores the designs of typical public forest lands facilities to address the replacement of these structures that are in the most vulnerable wildfire regions.

1.2 FOREST RESTORATION AND MASS TIMBER

Wildfire and forest management are complex issues that are becoming increasingly urgent to address due to catastrophic fire behaviour. With each fire season becoming increasingly worse on the U.S. west coast, creative solutions involving collaborative measures are beginning to unfold [4]. Forest restoration collaboration projects are currently underway such as the A to Z Forest Restoration Project in Colville, Washington. This project is a collaboration between Vaagen Timbers and the US Forest Service that focuses on allocating harvesting from restorative operations to Vaagen Timbers in order to offset the costs that the US Forest Service would typically be responsible for funding [5]. In return, Vaagen is able to utilize the harvested timber to create mass timber products and sell them for a profit. However, not many projects like this exist. Additionally, a small number of companies are beginning to venture into small-scale mass timber production such as Stoltze Timber in Montana and Timber Age Systems in Colorado. Timber Age Systems (TAS) is producing CLT made of Ponderosa pine, a species that has generally been deemed as low value for construction uses. The company is the first CLT producer in the U.S. Southwest and is capitalizing on the need for healthier forests and more sustainable construction materials [6]. The Sierra Institute for Community and Environment in Taylorsville, California is also developing small-scale, local mass timber production in tandem with their forest restoration projects which often result in harvesting lower-value species of timber [7]. The intersection between forest management and mass timber production has the potential to create a synergetic relationship that addresses multiple issues at once: the need for forest thinning and a sustainable mass timber market in the United States.

2 APPROACH

This project is a demonstration of the use of small-scale, Ponderosa pine CLT that can be harvested from forest restoration projects in the Sierra Nevada mountains of California and used to replace public forest lands structures that were destroyed in wildfires. The intent of this design demonstration is to show a variety of typical park buildings that cover a range of spans, sizes, and levels of complexity as well as to exhibit the unique relationship between forestry and architecture. The designs of these buildings reflect the redefining of park architecture in the U.S. to demonstrate a more contemporary approach, versus a more conventional rustic one, that celebrates the use of modern technologies and natural materials. The use of timber from forest restoration-harvests also provides the opportunity for local mass timber production. The basis of this design project makes use of TAS's production processes, structural data, and 152cm x 305cm Ponderosa pine CLT panels.

2.1 TIMBER AGE SYSTEMS PONDEROSA PINE CLT

TAS utilizes Ponderosa pine harvested from forest restoration projects to produce vacuum-pressed CLT panels that are 152cm x 305cm and 76mm or 127 mm thick for 3-ply and 5-ply panels respectively; the company has invested approximately 1.2 million USD total into their operations and functions under a vertically integrated system from log hauling and milling to kiln drying and pressing. The panels they are currently producing have been accepted for local building department permitted use and have undergone evaluation from a local university engineering department, with validation by an external engineering peer review, to demonstrate that they meet the requirements of IBC 2018; TAS is currently seeking ANSI PRG 320 certification for their CLT panels. This project demonstrates the design opportunities for the use of forest-restoration-harvested Ponderosa pine CLT panels manufactured using this vacuum press process by showing their design application in a series of typical public lands' facilities, which are more typically constructed of light wood frame and/or heavy (sawn) timber. The central question regarding the application of these CLT panels is the following: What are the implications of the Ponderosa pine CLT panel sizes and structural characteristics (e.g., what is the best way to address connections and openings for windows and doors, and long span conditions)?

2.2 PUBLIC LANDS BUILDINGS

Public lands are home to various types of buildings that serve a multitude of purposes. After an in-depth evaluation of the types of buildings found in public lands, the following building types were chosen as a representative sample of typical scales, spans, and details that could be applied to not only the building types they represent, but also other park facilities of a similar nature: a visitor center, information center, restrooms, cabin, and entrance fee station.

3 DESIGN DEMONSTRATION

In the proposed designs, both dimensional lumber and heavy timber sourced from Ponderosa pine are used in tandem with the Ponderosa pine CLT to achieve larger roof spans; the intention is to maximize the use of forest restoration-harvested Ponderosa pine and maintain its connection to the local communities that will manufacture these products. However, the dimensional lumber and heavy timber are not limited to strictly Ponderosa pine; other species harvested from forest restoration projects that are structurally appropriate can also be used. Glulams were intentionally not chosen for additional structural members to avoid sourcing that may not be local and employs a different technology. Strategies for windows, doors, and other details were also developed. With structural engineering guidance from Professor of Civil Engineering Mikhail Gershfeld of California State Polytechnic University, Pomona, it was determined that no more than two panels should be stacked vertically

https://doi.org/10.52202/069179-0485

without additional structural support to avoid buckling at the horizontal splines.

3.1 DETAILS FOR PANEL APPLICATION AND WILDFIRE RESILIENCE

Systems for typical details were developed as standards for the application of Ponderosa pine CLT panels and wildfire resilience strategies. The wall assembly in Figure 1 maximizes the use of bio-based materials such as CLT, wood fibre insulation, wood furring, and wood siding. Ideally, all of the wood-based products can be sourced from forest restoration-harvested timber including species that are not Ponderosa pine. This idea reinforces local sourcing, manufacturing, and maximum wood utilization. Fire resilience is also a critical aspect of these structures. Although the intent is to maximize the use of low-value wood from forest restoration projects, metal siding can also be used in place of wood siding to increase fire resilience. Other fire resilience strategies include minimal roof overhangs, metal roofing, mass panel wall construction, and fire-resistant insulation. Eaveless roofs prevent flames and embers from catching underneath overhangs, which can cause the entire building to combust. The CLT wall and roof panels also create a continuous envelope that are intended to improve thermal performance and mitigate fire spread. Similar to CLT panels, wood fibre insulation carbonizes when exposed to fire which helps to insulate the rest of the assembly from fire spread [8]. Wood fibre insulation treated with borate provides fire protection [8]; however, mineral wool insulation can also be used for increased fire resistance.

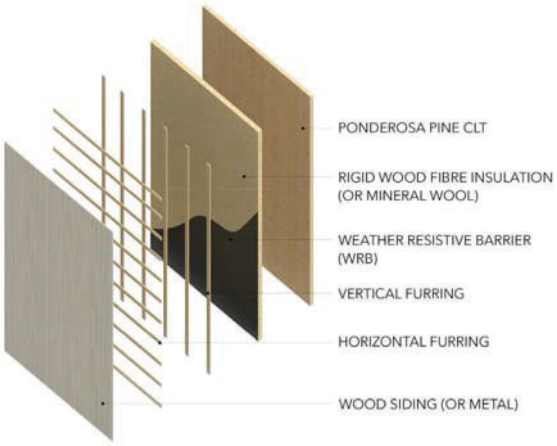

Figure 1: *Typical wall assembly*

Strategies for window and door openings were also developed. Although openings can be cut directly out of a panel, best practice is to avoid cut out openings due to the panels' small size and to minimize waste. Where appropriate, windows should fit between panels as illustrated in Figure 2. Additionally, windows that are carried to the underside of a CLT roof can use the roof panel itself as a header. This approach also prevents waste from panel off-cuts. Small skylight openings should not be cut from the centre of the panel, but rather at the ends of a panel to maintain structural properties. It is important to note, however, that these strategies may not be appropriate for every building. Openings are dependent on a building's program and may require other configurations.

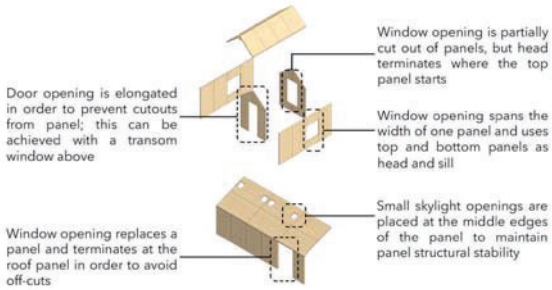

Figure 2: *Strategies for panel openings*

Because these structures could be located in a variety of landscapes, two different foundation systems were developed to accommodate possible site constraints. A concrete foundation with a concrete floor, as shown in Figure 3, would be an appropriate application in larger scale buildings, restrooms, and any building requiring a permanent foundation with few site challenges.

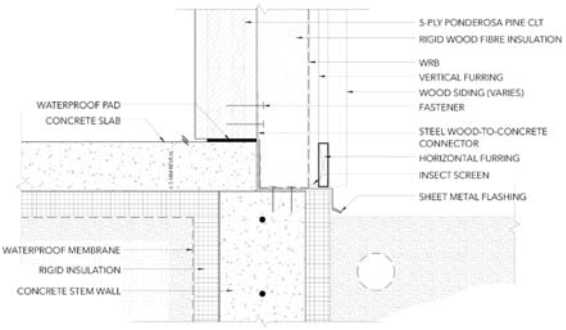

Figure 3: *Concrete foundation with concrete floor detail*

A pier foundation, as seen in Figure 4, would be appropriate for buildings in difficult terrain; the pier system enables the building to be lifted above grade and placed where necessary on its respective topography, which may be appropriate for cabins.

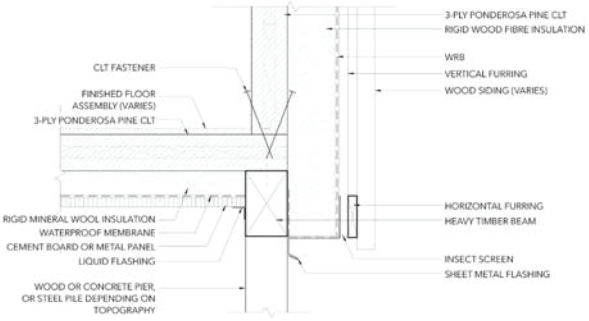

Figure 4: *Pier foundation with CLT floor detail*

https://doi.org/10.52202/069179-0485

3.2 VISITOR CENTER

Figure 5: *Visitor centre rendering*

The visitor centre is intended to accommodate different site variations by dividing the program into three separate buildings: an exhibit area, gift shop, and cafe. Restroom facilities for guests are a separate building type that can be placed near the visitor centre. Each building is connected to the others through a breezeway that can either be open air or enclosed depending on the climate.

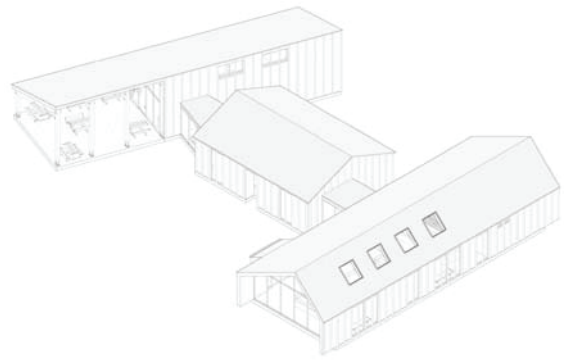

Figure 6: *Axonometric of visitor centre*

Figure 7: *Floor plan of visitor centre*

Due to roof span structural demands, the buildings have Ponderosa pine beams. The gable roofs of the exhibit area and gift shop require beams and steel collar ties, while the shed roof of the cafe requires beams with knee braces. These building types can also host different programmatic functions depending on the needs of the park; for example, the cafe can also be used as park ranger headquarters. In brief, the intent of this programmatic composition is to allow for the most amount of flexibility with straightforward construction solutions. Five-ply CLT is used for the walls and roofs of these structures and light-wood-frame is used for walls that require plumbing for toilets and sinks.

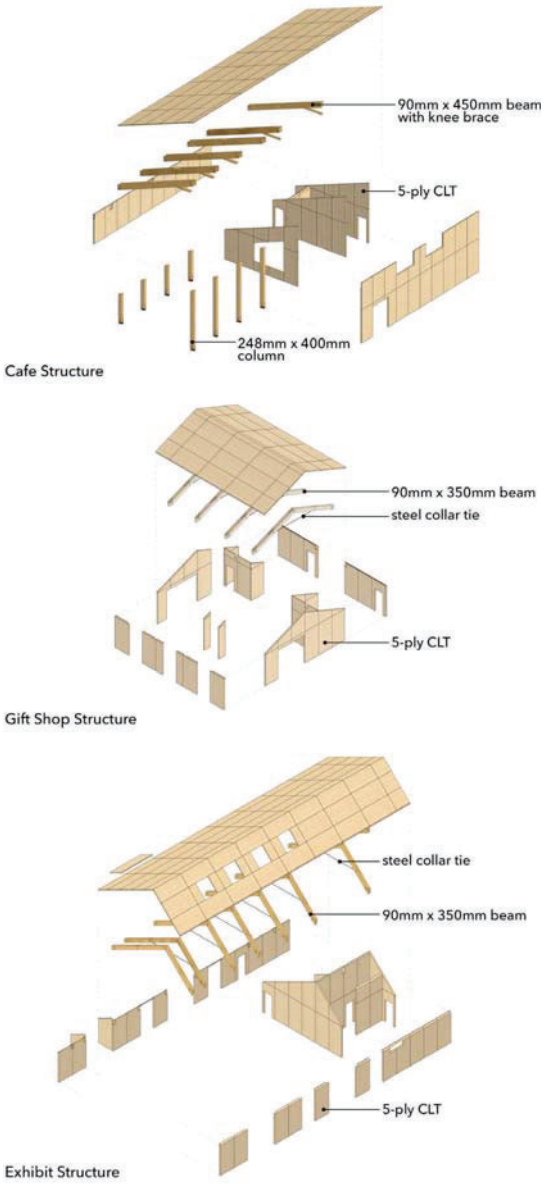

Figure 8: *Visitor centre structure*

https://doi.org/10.52202/069179-0485

3.3 INFORMATION CENTER

Figure 9: *Information centre rendering*

The information centre is intended to be used near park entrances and/or operate as a ranger station. The program features an information desk for guests, restrooms, and an office for park staff.

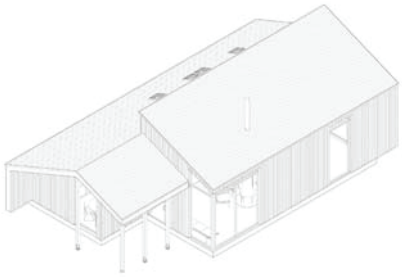

Figure 10: *Axonometric of information centre*

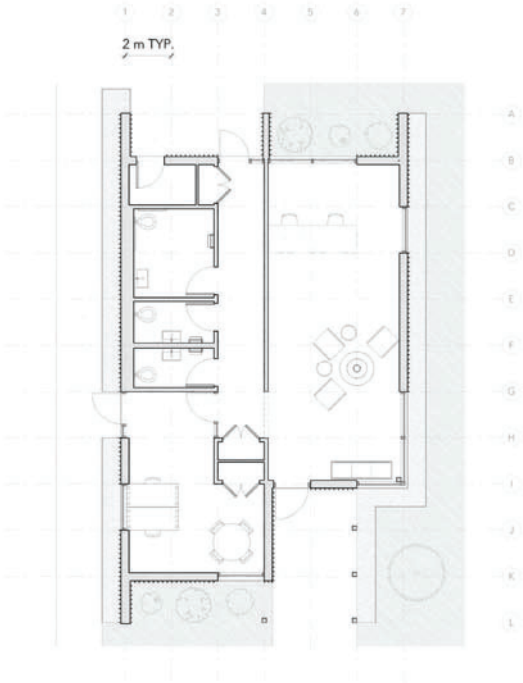

Figure 11: *Floor plan of information centre*

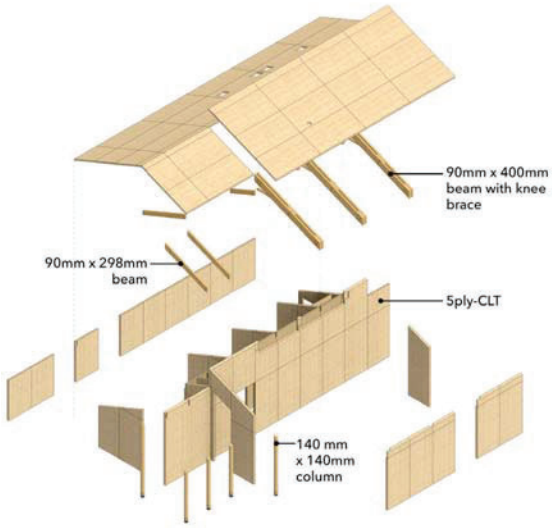

Figure 12: *Information centre structure*

Due to the building's small footprint, simple beam systems are used to span the roof with knee braces where necessary. Five-ply CLT is used for the walls and roof of this building and light-wood-frame is employed for walls that require plumbing for toilets and sinks.

3.4 RESTROOM FACILITIES

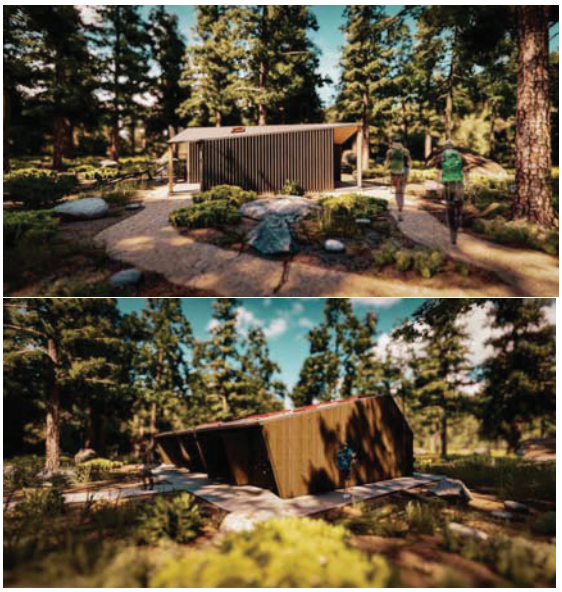

Figure 13: *Restroom renderings*

This building type consists of two different designs: small restroom structures intended to be scattered throughout a park and larger restroom facilities for busier parts of a park and its campgrounds. The small restroom facility is constructed with 3-ply CLT and utilizes a Ponderosa pine column where the roof cantilevers. The program consists of two private accessible stalls and a small utility closet. The larger restrooms are comprised of a flexible program

https://doi.org/10.52202/069179-0485

that allow it to be adapted to different needs of a park. For example, showers can be added to the building to accommodate a campground and stalls can be added to the floor plan as needed. This facility is also constructed of 3-ply CLT and does not require additional structural members to support its roof. Light-wood-frame is used for walls that require plumbing for toilets and sinks. Due to the nature of this building type, the roof and wall assemblies do not need to be insulated and the building does not need to be conditioned which significantly simplifies construction.

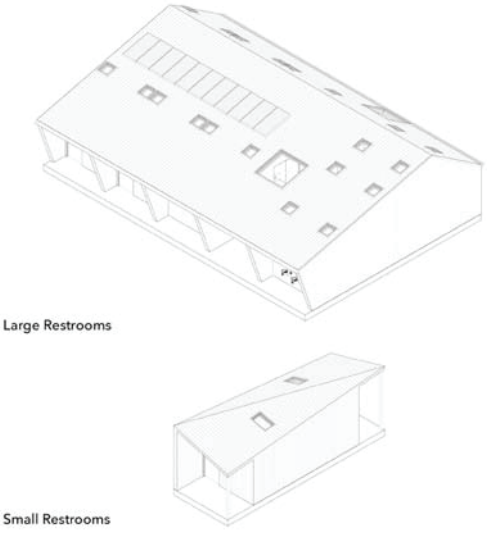

Figure 14: *Axonometric of restrooms*

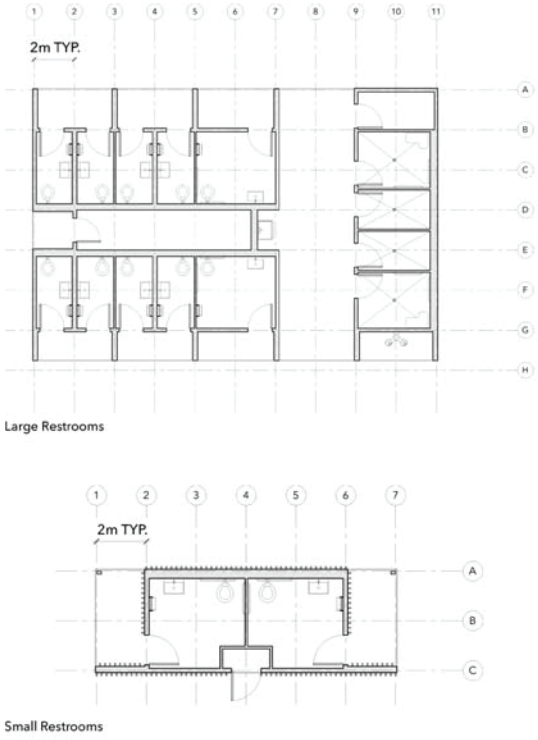

Figure 15: *Floor plan of restrooms*

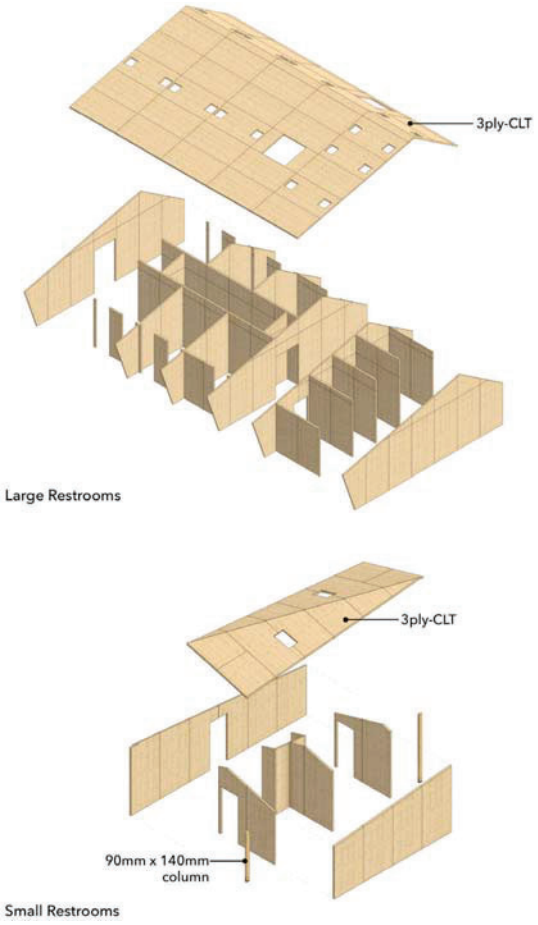

Figure 16: *Restrooms structure*

3.5 CABIN

Figure 17: *Cabin rendering*

The program for this building type is a one-bedroom space with designated sleeping, lounging, and eating areas. This structure requires 3-ply CLT, a ridge beam, steel collar ties, and a column to support the roof cantilever. The cabin is intended to be placed in nearly any condition and can be supported on a simple pier or pile system.

https://doi.org/10.52202/069179-0485

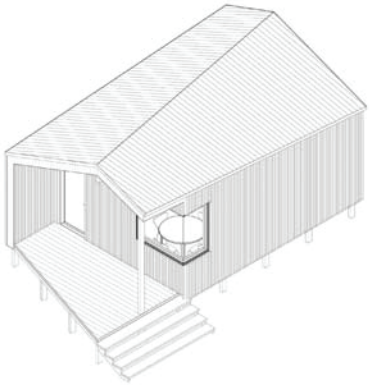

Figure 18: *Axonometric of cabin*

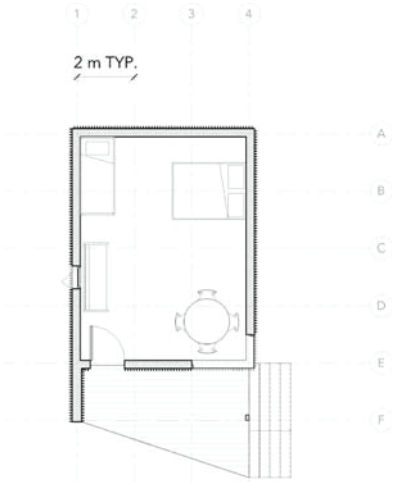

Figure 19: *Floor plan of cabin*

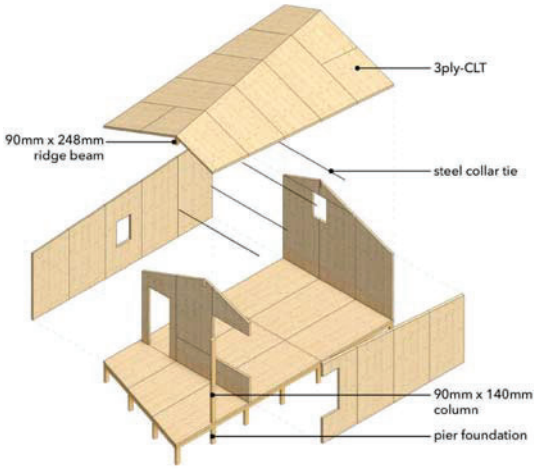

Figure 20: *Cabin structure*

3.6 ENTRANCE FEE STATION

Figure 21: *Entrance fee station rendering*

This small-scale building has a simple structure. Due to its small loads, the roof can be spanned using only 3-ply CLT and a ridge beam at the roof. This program features adequate space for 2-3 park employees and drive-up windows for incoming guests.

Figure 22: *Axonometric of entrance fee station*

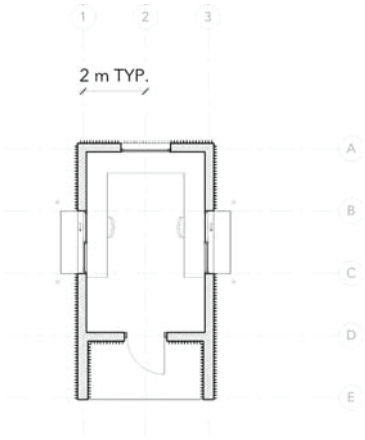

Figure 23: *Floor plan of entrance fee station*

https://doi.org/10.52202/069179-0485

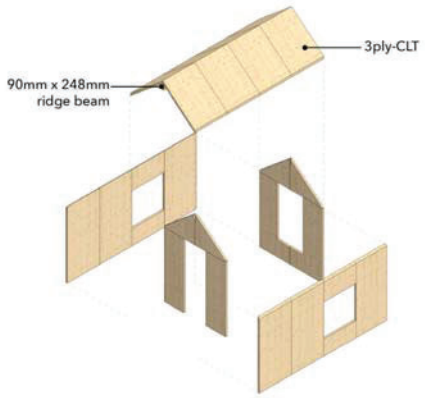

Figure 24: *Entrance fee station structure*

4 CONCLUSIONS

Although the structural properties of Ponderosa pine are less robust than some other wood species such as Douglas fir, Ponderosa pine CLT panels can be an effective structural system with proper detailing and an understanding of small mass timber panels. Unlike most CLT panels on the market, 152cm x 305cm Ponderosa pine panels require integrating other structural systems to carry longer roof spans. These secondary structural systems can also be sourced from Ponderosa pine, but may not necessarily be Ponderosa pine or from forest restoration projects; heavy timber and dimensional lumber can either be sourced from a productive site, other low-value species, or can be recovered from past burn sites; it is important to note that Ponderosa pine can reach a diameter of 66cm in 30 years and diameters of 76cm to 127cm are not uncommon for the species [9]. These CLT panels also have significant height restrictions; because they are only 3 meters tall, panels need to be stacked vertically to achiever taller wall heights. However, it is advisable not to stack more than two panels to maintain structural wall stability. Furthermore, compared to conventional light-wood-frame and heavy timber buildings typically found in public lands, the Ponderosa pine CLT allowed for greater design flexibility in terms of architectural expression. Because the structures do not require conventional wood framing, the panels can be prefabricated to create expressive forms that can be rapidly assembled. CLT also provides opportunities for faster construction time, less construction waste, off-site pre-assembly, and less on-site labour when compared to other construction types. In conclusion, the exercise of designing public lands facilities from small-scale, low-value species mass timber panels sourced from forest restoration proved to be a viable construction type for replacing buildings in wildfire vulnerable areas.

In addition, this project addresses only one timber species and one CLT manufacturing process. There is much more research that can be done on alternative low-value species mass timber products from varying regions across the U.S. and Canada as well as on a variety of manufacturing processes (dowel-laminated timber, interlocking timber, etc.) that can make up an array of different mass timber products for local applications in the future. White fir, for example, is a low-value species that only has preliminary structural data, but could potentially be used in a similar application to Ponderosa pine in CLT. There are several recently completed and planned low-value species testing projects undertaken at the TallWood Design Institute and Oregon State University on Oregon-harvested Ponderosa pine in collaboration with Vaagen Timbers, and, additionally, California white fir and Alaskan spruce using a more capital-intensive process with a large timber press; there is growing interest in the structural and commercial possibilities for these materials, along with the increasing local, less-capital intensive efforts as noted above [10–12]. Furthermore, continued development of construction details and the application of these panels to other building types, such as housing and multi-story structures, is a potential area of study. Much more work in this area should be coming in the near future and this project should become part of the growing efforts to create a sustainable mass timber industry in the U.S. supporting forest restoration efforts.

ACKNOWLEDGMENTS

This research is supported by the University of Oregon as part of the Master of Science degree, Mass Timber Design focus area. Thank you to my graduate committee members Mark Fretz, Mariapaola Riggio, and Judith Sheine, among others from the School of Architecture & Environment at the University of Oregon and the College of Forestry at Oregon State University, for your guidance and support. Thank you to Professor Mikhail Gershfeld from California State Polytechnic University, Pomona for offering structural engineering expertise and advice for this project. And lastly, thank you to Timber Age Systems for supporting my work and providing me with the necessary data to make this project possible.

REFERENCES

[1] S. Liang, M. D. Hurteau, and A. L. Westerling, "Large-scale restoration increases carbon stability under projected climate and wildfire regimes," *Front Ecol Environ*, vol. 16, no. 4, pp. 207–212, May 2018, doi: 10.1002/fee.1791.

[2] A. P. Williams *et al.*, "Observed Impacts of Anthropogenic Climate Change on Wildfire in California," *Earths Future*, vol. 7, no. 8, pp. 892–910, Aug. 2019, doi: 10.1029/2019EF001210.

[3] L. Sediman, "How the KNP Complex fire devastated one giant sequoia grove - Los Angeles Times," *LA Times*, Nov. 26, 2021.

[4] A. A. Ager, K. C. Vogler, M. A. Day, and J. D. Bailey, "Economic Opportunities and Trade-Offs in Collaborative Forest Landscape Restoration," *Ecological Economics*, vol. 136, pp. 226–239, Jun. 2017, doi: 10.1016/j.ecolecon.2017.01.001.

[5] R. Vaagen, "A to Z Forest Restoration Project."

[6] "Timber Age Systems, Inc." www.timberage.com

[7] L. Redmore *et al.*, "Mass Timber and Other Innovative Wood Products in California: A Study

https://doi.org/10.52202/069179-0485

of Barriers and Potential Solutions to Grow the State's Sustainable Wood Products Sector," 2021.
[8] "FAQ - TimberHP by GO Lab." https://timberhp.com/faq/
[9] "Ponderosa Pine (Pinus ponderosa)," *University of California Agriculture and Natural Resources*.
[10] S. Jahedi, S. Bhandari, L. Muszynski, and M. Riggio, "Investigating a potential for utilization of low value Ponderosa Pine lumber in CLT modular structures," 2021.
[11] S. Bhandari, S. Jahedi, M. Riggio, L. Muszynski, Z. Luo, and A. Polastri, "CLT modular low-rise buildings: a DfMA approach for deployable structures using low-grade timber," 2021.
[12] I. Macdonald, J. Dettmer, B. Miyamoto, C. Barkley, P. Mann, and T. Deboodt, "Cross-Laminated Timber Layup Tests Using Western Wood Products Association (WWPA) White fir Species Group," 2021.

World Conference on Timber Engineering Oslo 2023

AMAZONIAN MASS TIMBER IN THE NEW CIPEM'S HEADQUARTERS – MATO GROSSO, BRAZIL

Roberto Lecomte[1], Sheila Beatriz[2]

ABSTRACT: The Mato Grosso Timber Production and Export Industries Center (CIPEM) is the union of eight forest-based employers' unions, whose purpose is to organize and strengthen the sector. It encourages the productivity and conscious consumption of wood and its forest-based products regarding the current legislation and in a sustainable basis. Cipem is at vanguard of sustainable forest management in Brazil and there is a huge potential of exploiting medium and low density amazonian species that are ignored by the market. Its new headquarters was designed by using mass timber made of Amazonian wood. The partnership between Cipem and mass timber brazilian manufactors will allow all the required certification for those species' behavior aiming to produce CLT and glulam components. The design of the building had as premisses the fast assembling of the timber structures based on its constructive rationalization, the maximum exposure of the variability of the amazonian species managed by Cipem and the search for an architectural language and contemporary design. Huge poles with 10m heigh and coming from the Amazonian forest will be highlighted in the building, aiming to show the amazing transformation from this raw material into a contemporary constructive material.

KEYWORDS: Wood, Amazonian Wood, Mass Timber, Timber Structures, Contemporary Design

1 INTRODUCTION

CIPEM is the entity that represents the forestry sector in the state of Mato Grosso and its objective is to organize and strengthen this sector. The entity promotes the productivity and conscious consumption of wood and forest based products in a sustainable way, in accordance with current legislation and in harmony with the environment. Within this philosophy and with the aim of promoting the use of Amazonian wood in the construction sector, the design of its new headqurters was developed with mass timber solutions that highlight the material. This article presents the design of this building.

2 METHODOLOGY

The project of the Cipem's new headquarters was developed from the following premises:

- use of lesser-known species added to efficient timber structures to promote the quality of native essences;
- definition of constructive solutions based on mass timber components made of Amazonian woods;
- use of several Amazonian wood species managed by CIPEM in different uses in the building;
- highlight colour, texture, and workability of this raw material.

3 DESCRIPTION OF THE PROJECT

The design of the building was conceived with two main areas of interest, a 3 stories central area were administrative and technical staff will be installed, and an auditorium linked to a central hall that connects all areas of the building. Figure 1 shows its ground floor plan, and a section of the building can be viewed in Figure 2.

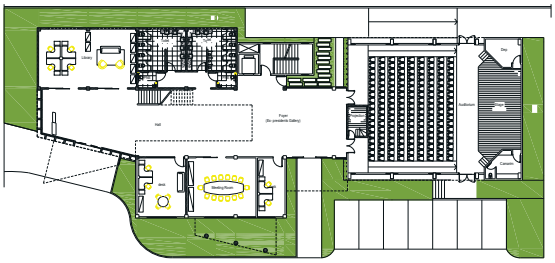

Figure 1: Ground floor plan

Figure 2: Section

[1] Roberto Lecomte, Casacerta Architecture Design & Building, Brasília, Brasil, roberto.lecomte@gmail.com

[2] Sheila Beatriz, Casacerta Architecture Design & Building, Brasília, Brasil, sheilatriz@hotmail.com

https://doi.org/10.52202/069179-0486

The fist and second pavement of the building are illustrated in Figures 3 and 4 highlighting several levels of the timber structures. Figure 5 shows a cross section of the building.

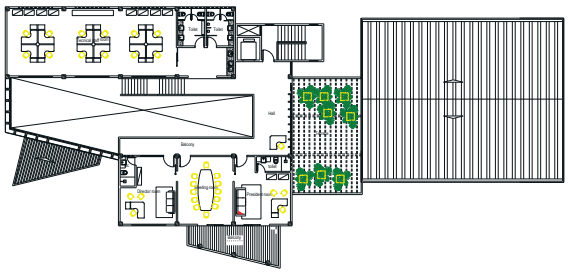

Figure 3: *First pavement*

Figure 4: *Second pavement*

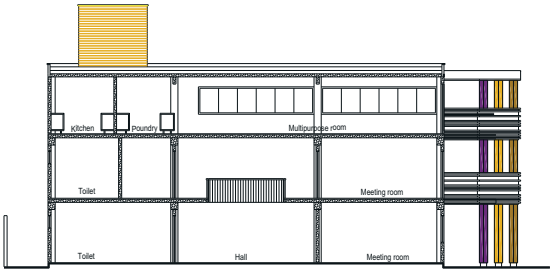

Figure 5: *Cross section of the building*

Wood species were selected according to CIPEM's priorities related to market strategies and aiming to promote lesser-known essences. Also, their physical and mechanical properties were considered taking in account their specific use in the proposed timber structures.

Low density species like Cedrinho (*Erisma uncinatum*), Amescla (*Trattinnickia burseraefolia*) and Marupá (*Simarouba amara*) were selected for glulam and CLT. Secondary structures, flooring and finishings will be made with Tauari (*Couratari sp.*), Roxinho (*Peltogyne sp.*), Cumaru (*Dipterix sp.*), Muiracatiara (*Astronium lecointei*) and Orelha de Macaco (*Enterolobium contortisiliquum*). Figure 5 illustrates those selected Amazonian woods.

Wood came from different exploitation regions and this diversity represents the eight forest-based employers' unions that are organized by CIPEM.

Figure 5: *Selected Amazonian woods*

4 BUILDING PROCESS

The use of amazonian wood in the buildings starts with applied research related to the physical and mechanical behavior of these species. For example, glulam can be manufactured using both softwood and hardwood and can use a variety of different types of timber.

https://doi.org/10.52202/069179-0486

CLT has many applications in the building as it is used for walls, floors, and roofs. CLT and glulam products are significantly lighter the traditional building materials, so foundations were designed to support smaller load and therefore use less material.

The building structural system was based on a glulam post and beam structure with CLT slabs, walls, and ceiling. Post and beam construction utilizes large, widely spaced wood to provide structural support to the building, allowing the desirable freedom in developing both interior and exterior space of the building, as showed in Figures 6 and 7.

Figure 6: *Post and beam MLC consumption is about 80 m3*

Figure 7: *CLT slabs and walls' consumption is 330 m3*

CLT and glulam will be fully fabricated before transportation to site. It will enable quicker construction times compared to other materials, and cost savings.

The construction will start with the execution of foundations and concrete core. Concrete core aids the building's structural stability and provides access and escape via lifts and stairs, regarding fire code requirements. Figure 8 shows an image of the building highlighting mass timber and concrete core.

Figure 8: *Aerial 3D image of the CIPEM's new headquarters*

Amazonian wood will be used to create delicate and warm spaces inside the building. Research has demonstrated that like the way indoor plants can help ease stress, using indoor natural wood surfaces can also improve physiological health.

Figures 9 and 10 illustrates the central area of the building where mass timber solutions made of Amazonian wood are exposed.

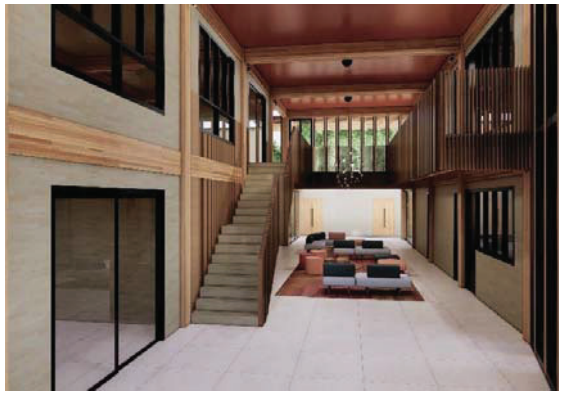

Figure 9: *Internal view of the central hall of the building*

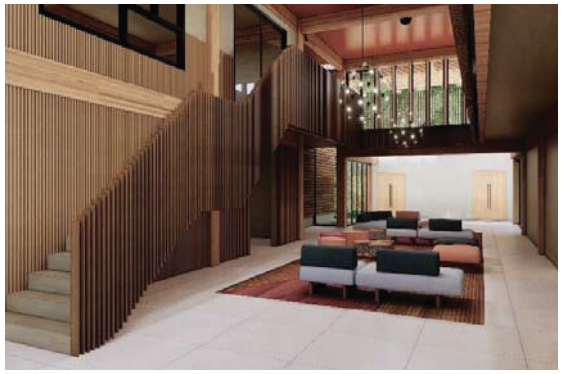

Figure 10: *Internal view*

https://doi.org/10.52202/069179-0486

Aesthetics reasons and the warmth given using wood are key elements of the auditorium, and room acoustics are improved. As showed in Figures 11 and 12, the presence of wood gives a contemporary design and instantly adds a natural light to the interior.

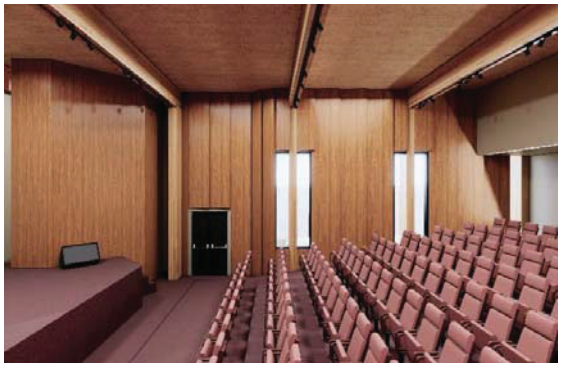

Figure 11: *Internal view of the auditorium*

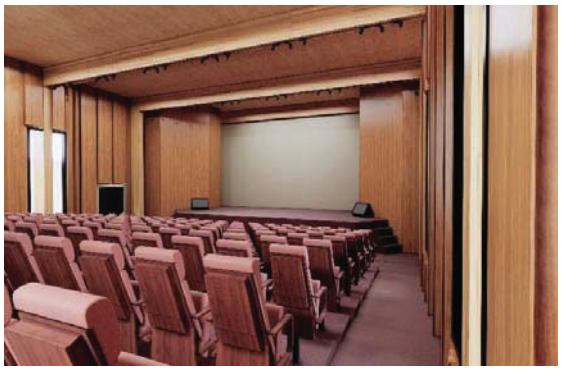

Figure 12: *Internal view*

Wooden cladding made of Amazonian species will give durability, colour options and easy-maintenance to the facades of CIPEM"s new headquarters. They are not structural elements and form a protective layer on the building.

They are more than just decorative elements and help in aiding sound insulation. Wooden cladding can be easily recycled, renewed, or painted over to provide a whole new look. Figures 13, 14 and 15 illustrates the use of Amazonian wood cladding in the facades of the building.

Figure 13: *Wood cladding in the main entrance of the building*

Figure 14: *Main entrance*

Figure 15: *External wood cladding in the auditorium*

Huge poles with 10m heigh and coming from the Amazonian Forest will be highlighted in the building, aiming to show the amazing transformation from this raw material into a contemporary building material.

High density species like Roxinho (*Peltogyne sp.*), Cumaru (*Dipterix sp.*) and Orelha de Macaco (*Enterolobium contortisiliquum*) will be placed in the facade. Figure 16 shows the presence of Amazonian timber poles in the building.

https://doi.org/10.52202/069179-0486

Figure 16: *Amazonian timber poles in the façade*

Thermoacoustic roof will be installed in the building and external pergolas will act as green roofs with many benefits in terms of sustainability because the vegetation will convert CO2 into oxygen and filters particulate matter from the air.

The pergolas will provide shade, remove heat from the air and reduce temperatures of the roof surface and surrounding air. They can also contribute to moderate the heat island effect specially in a city with hot climate. The building is in Cuiabá, the capital of Mato Grosso State. Figure 17 shows an aerial view of the building highlighting the presence of the pergolas.

Figure 17: *Aerial view showing the pergolas*

5 CONCLUSIONS

The experience of designing CIPEM's new headquarters with mass timber made of Amazonian wood confirms the several possibilities of building with this raw material, aiming to create an unique Mato Grosso's native wood showcase.

The use of mass timber in our country is increasing in a remarkable rate, and due to its huge market Amazonian timber has strategic role in this field. The reduction in the assembling time that is typical of the prefabricated structures is added to the aesthetics given by the presence of wood, making it very competitive against other building materials.

Some advantages of using glulam and CLT structures like prefabrication of large components at the factory and short assembly times at the construction site will be highlighted to improve timber construction techniques in Brazil's central region.

The use of Amazonian timber structures is evidence of the flexibility of this sustainable and locally sourced material. It should be pointed out the importance of demystifying the use of timber structures as "non-ecological" in our country, because wood is the only choice for a renewable and sustainable building material and wood materials are desirable for their strength, durability, beauty, and cost-effective construction.

ACKNOWLEDGEMENT

The authors thank CIPEM for the support in all stages of the conception of the building, as well as in the presentation of this article.

REFERENCES

[1] IBDF. Amazonian Timbers: Characteristics and Utilization. CNPq, Brasília. 1981.

[2] IBDF/DPq/LPF. Amazonian Timbers: characteristics and utilization. Curuá-Una Experimental Forest Station. Brasília. 1981.

[3] Camargos, J.A.A., Coradin, V.T.R., Czarneski, C.M., Oliveira, D. and Meguerditchian. Brazilian Trees Catalog. IBAMA. Brasilia. 2001.

[4] Melo, J.E. and Camargos, J.A.A. Wood and its uses. SFB/LPF/MMA. Brasilia. 2016.

[5] Mello, R.L. Designing with wood: a new approach. *Master Thesis.* UNB. Brasilia. 2007.

[6] Mello, R. L., Melo, J.E., Wood Pavilion. *Proceedings of Eighth World Conference On Timber Engineering: WCTE 2004,* 2004. Lahti, Finland.

[7] Mello, R. L., Melo, J.E., Wood structures in the new building of CENAFLOR in Brasilia – Brazil. *Proceedings of Nineth World Conference On Timber Engineering: WCTE 2006,* 2006. Portland, USA.

[8] Mello, R. L., Melo, J.E., Glulam structures in the new IBAMA's Laboratory of Biomass Energy. *Proceedings of Tenth World Conference On Timber Engineering: WCTE 2008,* 2008. Miyazaki, Japan.

[9] Mello, R. L., Sette, R., Glulam structures in the new LPF's Wood Drying and Wood Treatment Laboratories – Brazil. *Proceedings of Eleventh World Conference On Timber EngineerinG: WCTE 2012,* 2012. Auckland, New Zealand.

https://doi.org/10.52202/069179-0486

[10] Melo, J.E., Valle, I.R.M., Mello, R.L., Souza, M.R., Popular wooden house. IBAMA. Brasília. 2002.

[11] CIPEM. (2017). Sales Magazine. Cuiabá.

World Conference on Timber Engineering Oslo 2023

INTEGRATING TIMBER PANEL ELEMENTS INTO HISTORIC CHINESE TIMBER-FRAMED HOUSES TO ENHANCE MULTIPLE BUILDING PERFORMANCES

Harrison Huang[1], Kapulanbayi Ailaitijiang[2], Hui Zhan[3]

ABSTRACT: The traditional timber-framed house has a several thousand-year-long history in China, and it is an important part of Chinese architectural culture. Despite their high historic value, these buildings have limitations in comparison with today's standards, especially in terms of indoor comfort. This study explores the potential of integrating modular timber panel elements (TPE) into historic Chinese timber-framed houses to enhance multiple building performance, i.e., thermal-acoustic insulation for a comfortable indoor environment and better noise reduction. Comprehensive analyses are carried out on the application of TPEs for the building envelope, including exterior walls, roofs, floors, doors, and windows, to demonstrate the feasibility of using these techniques and to quantify the improvement of building performance. This study innovatively contributes to healthy and energy-efficient living conditions by revitalizing historic Chinese timber-framed houses.

KEYWORDS: Timber panel element, Historic Chinese timber-framed house, Building performance enhancement, Prefabrication potential, Thermal-acoustic insulation

1. INTRODUCTION

Timber framing has been a traditional building method for constructing framed structures in many regions of the world for millennia [1]. China is one of the earliest countries to adopt wooden structures. Timber buildings are the protagonist of ancient Chinese architecture, representing an important part of Chinese traditional culture [2]. A fundamental achievement of Chinese timber architecture is the load-bearing timber frame, a network of interlocking wooden supports forming the skeleton of a building. This is considered China's major contribution to architectural technology worldwide [3]. Although these historic timber-framed houses have such a high historic value, these buildings have largely failed to meet people's modern living standards due to the increase in living requirements [4]. This is because some functions of the building envelope are inadequate, such as thermal and sound insulation and fire prevention. Therefore, these historic buildings need to be transformed for modern use. According to international experience in renovating traditional timber-framed buildings, many methods have been used to improve indoor comfort, structural stability, fire protection, and other building performance [5]. Among them, the use of timber panel elements (TPEs) can not only improve building performance but also help reduce costs. Therefore, TPEs have become increasingly popular in the European building industry in recent years [6]. It is worth mentioning that no scientific research results related to using TPEs in Chinese timber-famed houses have been found after a literature review. There is no concrete evidence to verify whether TPEs suit these specific building types. Therefore, this paper explores the integration of TPEs into Chinese historic timber buildings and simulates and analyses to what extent TPEs enhance building performance.

2. ANALYSIS AND METHODS

2.1 BACKGROUND ANALYSIS

Chinese timber buildings can be categorized into three types in terms of structural forms, namely, *Chuandou* (column and tie construction), *Tailiang* (post and lintel construction), and *Jinggan* (log cabin construction). Although the two former types are both timber-framed structures, *Chuandou* consumes less timber and is more structurally stable than *Tailiang*. Therefore, the vast majority of traditional ordinary residential buildings were built as *Chuandou*. Their exterior walls define the building enclosure but may not be load-bearing elements [3]. The enclosure system is relatively independent of the main structure.

According to the "shearing layers" concept, first conceived by architect Frank Duffy and later developed by Steward Brand in his book *How Buildings Learn: What Happens After They're Built* [7], there are 6 layers of a building: site, structure, skin, service, space plan, and stuff. Based on this 6S theory, TPEs can be applied to structure, skin, and service. However, a TPE has the most potential as a skin layer in relation to improving the performance of Chinese historic timber-framed buildings.

[1] Harrison Huang, College of Civil Engineering and Architecture & Balance Architecture Research Center, Zhejiang University, Hangzhou, China, harrison@zju.edu.cn
[2] Kapulanbayi Ailaitijiang, College of Civil Engineering and Architecture & Architectural Design and Research Institute, Zhejiang University, Hangzhou, China, Qaplanbay@zju.edu.cn
[3] Hui Zhan, Design & Research Institute of Shanghai Jiaotong University, Shanghai, China, 1796427208@qq.com

https://doi.org/10.52202/069179-0487

As mentioned above, the enclosure system is often independent of the load-bearing structure system, so the skin can be renewed and replaced during the entire life cycle of a building. For the application of TPEs, the envelope elements in *Chuandou* houses, including exterior walls, roofs, foundations, floors, windows, and doors, need to be first analyzed (Figure 1).

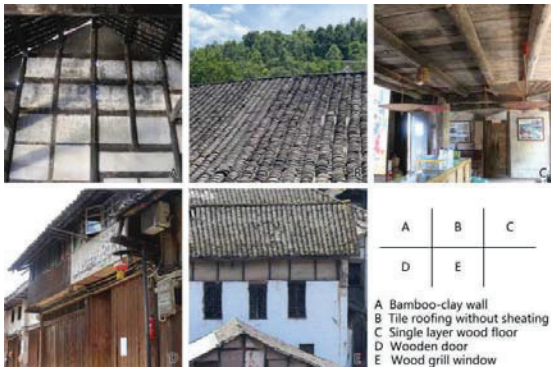

Figure 1: *Envelope system of a historic Chuandou house*

2.1.1 Exterior walls

The exterior walls take up the largest proportion of the envelope system, and their thermal performance also directly affects the building's indoor comfort. Wall infill materials are mainly clay, stone, and brick, among which clay has the longest history and widest prevalence [8]. Compared with walls made of other materials, clay walls are more economical and durable and have better performance in terms of fire prevention, sound insulation, and heat preservation. Despite the advantages of clay walls, there are also many difficulties in evaluating wall performance. The wall thickness and composition vary greatly in different places according to the local climate and natural environment. The wall is usually made of a mixture of several local materials, such as clay, straw, and bamboo, and it is difficult to check the thermal or acoustic standard values, and it is necessary to measure the relevant indicators for every single case.

2.1.2 Roofs

The roofs in a building envelope should not only prevent the intrusion of rain and snow but also offer good insulation. For the vast majority of *Chuandou* buildings, the double-pitch roof is the most common form. Taking houses in southern China, for example, tile roofing without sheathing is very common because of its simple structure, convenient construction, and economical applicability [9]. However, the thermal and sound insulation performances of the roofing are abnormally poor and do not meet the thermal and sound insulation requirements of today's building codes.

2.1.3 Foundations and floors

The foundation not only bears all the loads transmitted from the superstructure but also prevents moisture from penetrating. There are many types of foundations for historic *Chuandou* buildings, such as raw soil, composite soil, slate, and mortar [10]. Among them, composite ground has a wider range of applications because of its better thermal properties and stability. For floors, wooden planks are often laid directly on top of beams. This is a simple and common method, but the sound insulation performance is seriously poor.

2.1.4 Door and windows

Regardless of the types of exterior walls, the typical doors of traditional houses are made of single-layer wooden boards. As far as the material is concerned, wooden doors have good thermal performance, but the boards are vulnerable to deformation, and gaps can appear between the boards. If not properly maintained, the airtightness will be extremely poor, especially between the door leaves, threshold, and walls, where large gaps are located. Similar problems occur in windows, as the materials used are the same as in doors. Since most windows are used solely for lighting and ventilation, there is no consideration for airtightness or sound insulation at all [10].

2.2 DATA MODELING

Integrating TPEs into a *Chuandou* building has the potential to improve building performance. To determine the thermal and sound insulation performance enhancement, this study proposed possible TPE applications and compared the performance of building envelope elements with the original state. The size and number of panel elements are directly related to the size and spacing of the columns and ties in the building.

In this study, typical *Chuandou* houses in the Sichuan Basin in south-western China are used as modelling prototypes. The experimental design was carried out based on the research results of Huang's study [11] and the personal survey of the authors in the ancient village of Fubao in Sichuan Province. The foundation of the building model is set as 5×8 m, and the height is 7.5 metres. The first floor is 3.5 metres high, and the attic floor is 2–4 metres (Figure 2) [11]. According to local construction methods, the double-pitch roof is covered by the most common tile roofs 25 mm thick. The exterior wall is set to 50 mm thick with bamboo-clay infills, and the foundation material is set as 150 mm thick and mixed with lime, sand, and clay. Because the historic wooden doors and windows are made of a single-layer wooden board, they are uniformly set as 20 mm thick pine boards in the model. Based on the research and calculation of local buildings and the references of papers in related fields [10] and the comparison with the building code *Design Standard for Energy Efficiency of Rural Residential Buildings (GB/T 50824-2013)* [12], the following data have been obtained (Table 1).

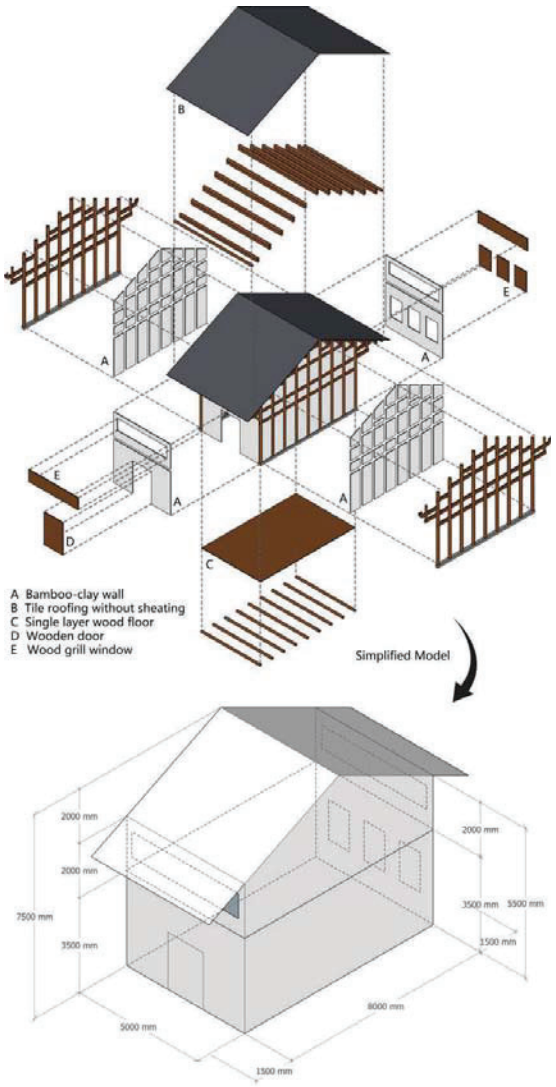

Figure 2: *Simplified model from a historic Chuandou house*

Table 1: *Thermal performance of the building envelope*

Envelope elements	Thermal Resistance/R (m²·K/W)	Standard Requirement/R (m²·K/W)	Comment
Walls	0.29	0.52	○
Roof	0.18	1.10	○
Ground	0.22	-	-
Floors	0.216	-	-
Doors	0.14	0.18	○
Windows	0.14	0.16	○

○Unqualified - Inapplicable

In addition, the computational model in this study is set to a location in Fubao in south-eastern Sichuan Province. Based on the thermal analysis of this building model by Ecotect Software, the following results can be drawn. It illustrates the energy gain/loss for a year from 1 January to 31 December (Table 2, Figure 3). The process of conduction through the building envelope loses the maximal heat by approximately 91.6%. Heat gains that disrupt comfort in summer months are approximately 26.2% because of conduction. Passive solar radiation gains that affect the architecture of the building are approximately 48.9% over a year. According to the data, the heat lost in the form of conduction through the building envelope accounts for the vast majority.

Table 2: *Heat gains for the original model*

Category	Losses		Gains	
	Heat (Wh)	Proportion (%)	Heat (Wh)	Proportion (%)
Fabric (Conduction)	727,886	91.6	359,426	26.2
Sol-Air	0	0	670,837	48.9
Solar	0	0	45,271	3.3
Ventilation	58,008	7.3	42,528	3.1
Internal	0	0	237,331	17.3
Inter-Zonal	8,741	1.1	17,834	1.2
Total	794,635	100	1,373,227	100

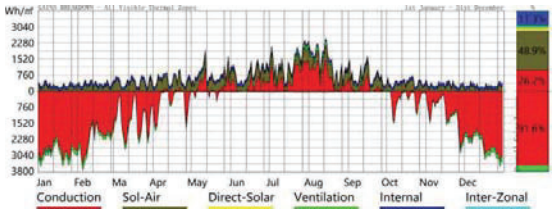

Figure 3: *Thermal performance of the original model*

A temperature analysis of the hottest and coldest days in the year was conducted, from which the related analysis results can be observed in Figure 4. The green and orange lines indicate the hourly internal temperature change of the ground and attic floors of the original model, respectively. The blue line indicates the outdoor temperature change. The differences between indoor and outdoor temperatures are very small, which indicates that the thermal insulation performance of the building envelope is weak.

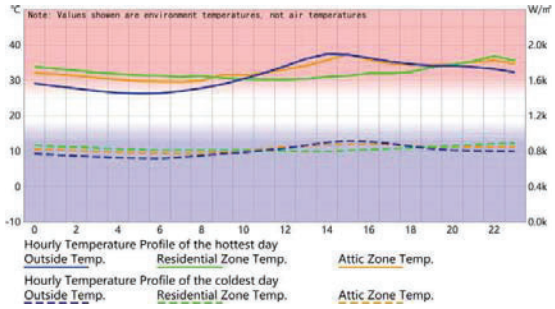

Figure 4: *Hourly temperature change on the hottest and coldest day in a year*

Figure 5 indicates that much more heat is lost or gained through the building envelope than through ventilation. On the hottest day, the conducting heat gain of the building envelope can reach 9,000 W or more. The situation in winter is even worse, and the conducting heat loss can reach 12,000 W.

https://doi.org/10.52202/069179-0487

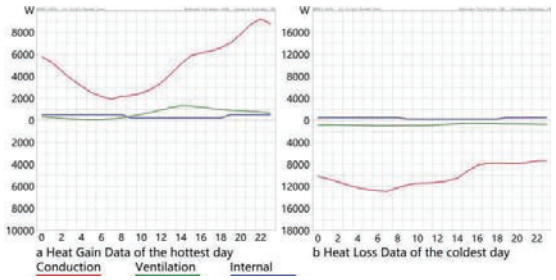

Figure 5: *Heat gain and loss on the hottest and coldest days in a year*

According to the thermal analysis above, the building envelope is the key factor in improving the building's thermal performance.

In addition to the bad thermal performance, the sound insulation is also poor. This problem is closely related to the structure, materials, and constructional characteristics. The roof has no sound insulation measures because of the clay tiles directly on the rafters, so the falling sound of rainwater can be noisily heard inside, especially on the attic floor. The low density and poor airtightness of bamboo–clay walls and wooden board walls are the main causes of poor sound insulation performance. The plank floor laid directly on the wooden beams has poor resistance against walking noises concentrated at 20–200 Hz. When walking, there is also noise from the mutual squeezing of the wooden boards caused by slight deformation. Doors and windows are also problematic for sound insulation. According to field research and a literature analysis, the standardized sound pressure level differences of enclosure structural components such as walls and floors are all no more than 30 dB. According to the requirements in the relevant specifications (*Technical Standard for Infills or Partitions with Timber Framework GB/T 50361-2018*[13] and *Code for Design of Sound Insulation of Civil Buildings GB 50118-2010*[14]), the acoustic environment is not qualified.

3. INTEGRATING A TPE INTO A BUILDING ENVELOPE

3.1 DESIGN OF TPE COMPONENTS

Prefabricated timber panels are elements that are produced in a factory and can be well-insulated, fireproof, waterproof, or soundproof. Their dimensions can vary according to the structural system and the material used. Various performances that provide energy conservation or efficiency can be realized in a prefabricated TPE that improves the living quality of the indoor environment by providing visual, thermal, and acoustic comfort [15]. The thermal and sound insulation performance are examined using Ecotect and INSUL after construction designs are implemented to integrate the TPE into the building envelope parts of the *Chuandou* house.

3.1.1 Exterior walls

TPEs have the potential to be applied in infill compartments in the exterior walls of the *Chuandou* house (Figure 6). The TPE infill wall is composed of a 10 mm plaster board, 15 mm gypsum fibre board, 90×45 mm timber studs, mineral wool, vapour barrier, and 15 mm gypsum fibre board from outside to inside. This allows for calculating the heat transfer coefficient and thermal resistance of this wall scheme according to the thermal parameter table of building materials in *Thermal design code for civil buildings (GB/T 50176-2016)* [17]. The calculation indicates that the U value (thermal transmittance) of the wall is 0.42 W/(m²·K), and the R-value (thermal resistance) is 2.35 m²·K/W, meeting the related requirements in the same design standard [12]. The sound insulation performance of the wall was simulated in INSUL, and the following data were obtained (Figure 7). The air-weighted sound insulation R_w of the wall is 53 dB, the traffic noise spectrum correction C_{tr} is -6 dB, and the R_w+C_{tr} value is 47 dB, which meet the relevant requirements in the *Code for Design of Sound Insulation of Civil Buildings (GB 50118-2010)* [14].

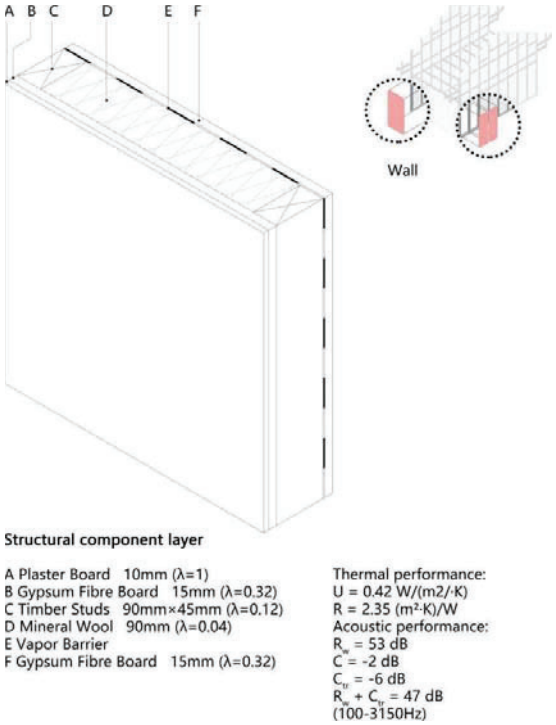

Figure 6: *Construction of the TPE infill wall*

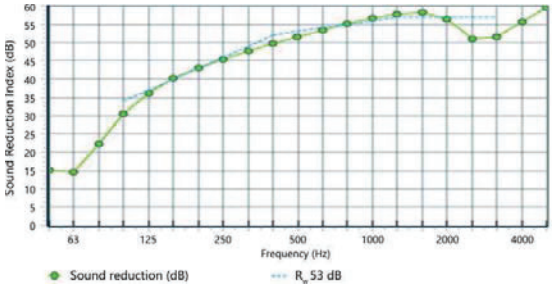

Figure 7: *Sound insulation simulation of the TPE infill wall*

3.1.2 Roof

There is the possibility of introducing a TPE into a traditional double-sloping roof as an intermediate layer

between purlins and tiles. Figure 8 shows the construction design of the TPE roof layers, which consist of 80 mm thick wood battens, a waterproof membrane, 12 mm OSB, 90×45 mm timber studs, mineral wool, a vapour barrier, 15 mm OSB and 15 mm gypsum fibreboard from outside to inside. It is calculated that the U value of the roof is 0.41 W/(m²·K), and the R-value is 2.46 m²·K/W, meeting the relevant requirements in *GB/T 50824-2013*[12]. The sound insulation performance of the roof was also simulated in INSUL, and the following data were obtained (Figure 9). The L_{iA} value (floor impact sound level) of the roof is 45 dB, which meets the relevant requirements in *GB 50118-2010* [14].

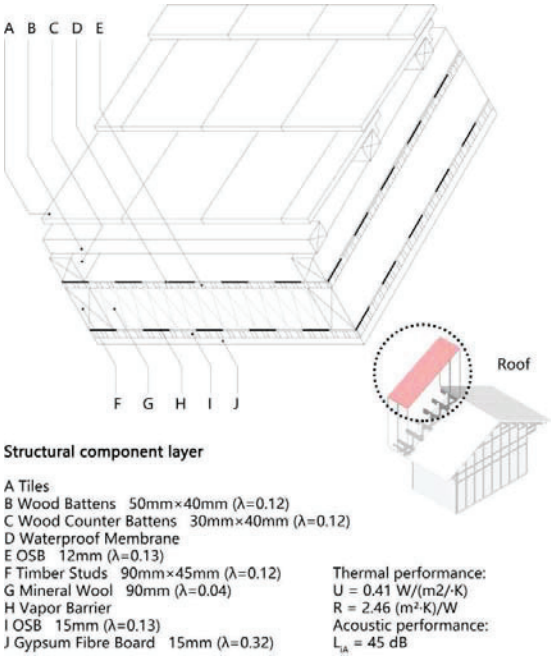

Figure 8: *Construction of the TPE roof*

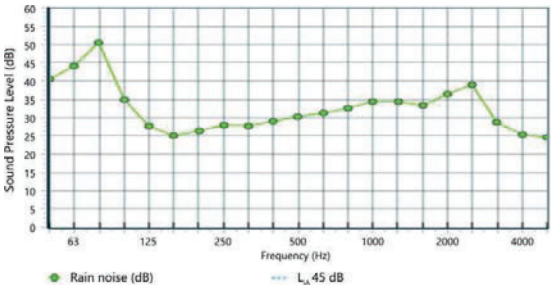

Figure 9: *Sound insulation simulation of the TPE roof*

3.1.3 Floors

It is possible to apply the TPE on top of the floor beams. Figure 10 shows the construction design of the TPE floor layers, which is composed of 12 mm OSB, 90×45 mm timber studs, mineral wool, 15 mm OSB, and 12 mm gypsum fibreboard from upside to downside. It is calculated that the U value of the floor is 0.40 W/(m²·K), and the R-value is 2.50 m²·K/W. The sound insulation performance of the floor was simulated in INSUL, and the following data were obtained (Figure 11). The $L_{n,w}$ value (weighted normalized impact sound pressure level) of the roof is 68 dB, which meets the relevant requirements in *GB 50118-2010* [14].

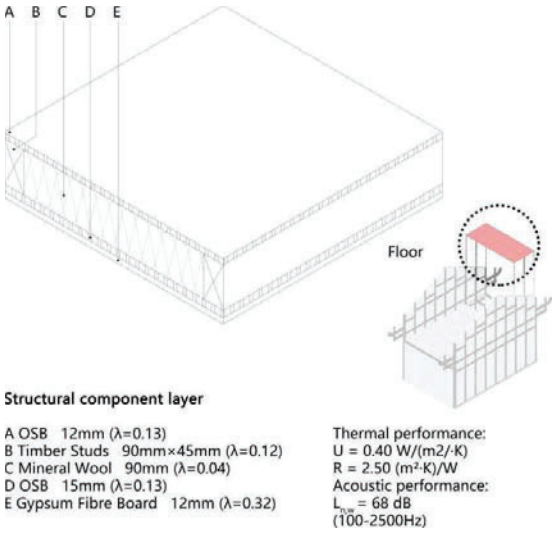

Figure 10: *Construction of the TPE floor*

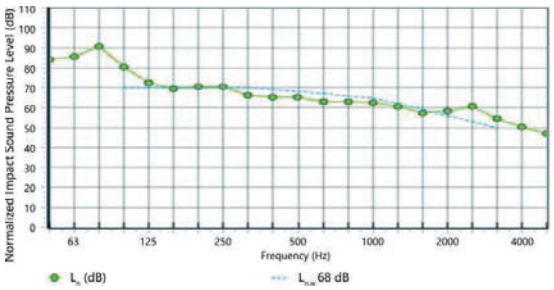

Figure 11: *Sound insulation simulation of the TPE floor*

3.1.4 Door and windows

Traditional doors and windows can also be transformed into TPEs, optimizing the physical properties. The doors are constructed of double wooden panels sandwiching a 20 mm particle board, while the windows are constructed of double glazing sandwiching a 15 mm air layer (Figure 12). It is calculated that the U values of the doors and windows are 0.95 W/(m²·K) and 1.5 W/(m²·K), and the R values are 1.06 m²·K/W and 0.67 m²·K/W, respectively, meeting the relevant requirements in *GB/T 50824-2013*[12]. The sound insulation performance of the doors and windows are simulated in INSUL, and the following data were obtained (Figure 13). The R_w-value of the doors is 36 dB, the pink spectrum correction C is -2 dB, and the R_w+C value is 34 dB. The R_w-value of the windows is 36 dB, the traffic noise spectrum correction C_{tr} is -5 dB, and the R_w+C_{tr} value is 31 dB. Both meet the relevant requirements in *GB 50118-2010* [14].

https://doi.org/10.52202/069179-0487

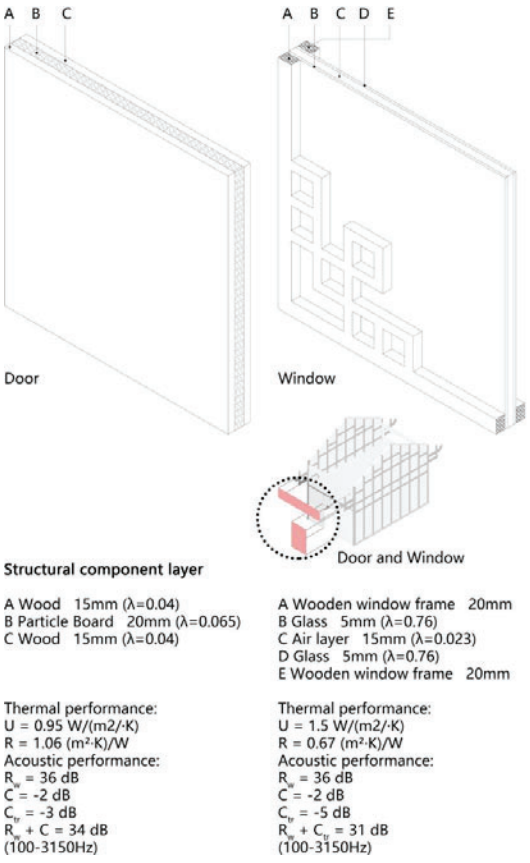

Figure 12: *Construction of the TPE door and window*

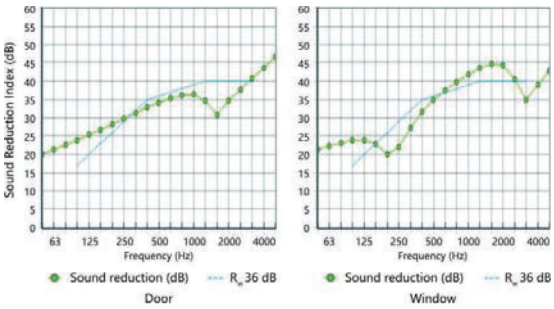

Figure 13: *Sound insulation simulation of the TPE door and window*

3.2 BUILDING PERFORMANCE ENHANCEMENT

Table 3 and Table 4 show the thermal and sound insulation performances of each envelope component. It can be seen from the data that the thermal and sound insulation performance of the building enclosure layer has been significantly improved after using TPEs, all of which have filled the relevant national specifications and standards *(GB/T 50824-2013* [12]*, GB/T 50361-2018* [13]*, GB 50118-2010* [1]*)*.

Table 3: *Thermal performance of TPEs*

Envelope structure parts	Original Thermal Resistance/ R (m²·K/W)	TPE Thermal Resistance/ R (m²·K/W)	Increased ratio	Comment
Walls	0.29	2.35	810.34%	●
Roof	0.37	2.46	664.86%	●
Floor	0.216	2.50	1157.41 %	-
Door	0.14	1.06	757.14%	●
Windows	0.14	0.67	478.57%	●

● Requirement filled - Inapplicable

Table 4: *Acoustic performance of TPEs*

Envelope structure parts	Original Sound Insulation	TPE Sound Insulation (dB)	Standard Requirement (dB)	Comment
Walls		R_w+C_{tr}=47	$R_w+C_{tr}\geq45$	●
Roof		L_{iA}=45	$L_{iA}\geq40$	●
Floor	＜30 dB	$L_{n,w}$=68	$L_{n,w}$＜70	●
Door		R_w+C=34	R_w+C≥30	●
Windows		R_w+C_{tr}=31	$R_w+C_{tr}\geq30$	●

● Requirement filled

On the basis of the original architectural model, the wall was designed as a 130 mm thick TPE wall, the roof part was replaced with a 212 mm TPE roof, a 129 mm TPE floor was added, and a 50 mm thick soundproof door and 65 mm thick windows were added. In this study, the above structures were brought into the original model, thermal analysis was carried out in Ecotect to obtain new simulation data, a comparison between the original data and the optimized data was carried out, and finally, a conclusion was drawn.

By applying all the designed TPE envelope components in the presented building model, it can be seen that the amount and ratio of heat loss or gain through the building envelope in the whole year are significantly reduced after using TPEs. Especially in summer, heat conduction through the building envelope is nearly ten times lower than before, with original values of 359,426 Wh to 37,593 Wh (Table 2, Table 5, Figure 14). The fabric heat loss is reduced to 93,597 Wh from 727,886 Wh. Passive solar radiation gains that affect the architecture of the building are also reduced to 52,092 Wh from 670,837 Wh. This is a reduction of almost 13 times. In addition, the total heat loss and gain of the building throughout the year have been significantly reduced, and the proportion of the building envelope in heat transfer has also been decreased. This shows that the thermal insulation performance of the TPE is very superior.

Table 5: *Heat loss and gains after installing TPEs*

Category	Losses		Gains	
	Heat (Wh)	Proportion (%)	Heat (Wh)	Proportion (%)
Fabric (Conduction)	93,597	56.1	37,593	10.2
Sol-Air	0	0	52,092	14
Solar	0	0	32,433	8.8
Ventilation	59,729	35.8	36,119	9.8
Internal	0	0	198,653	53.9
Inter-Zonal	13,347	8.1	12,162	3.3
Total	166,673	100	369,052	100

https://doi.org/10.52202/069179-0487

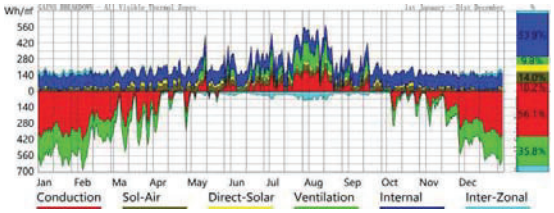

Figure 14: *Thermal performance for the model using TPE*

Figure 15 shows that the temperature difference between the outside and the inside of the building has widened by using TPEs. Especially on the coldest day of the year, the indoors are always warmer than the outside the whole day long, and the temperature difference is more than 5 ℃. However, the indoor temperature on the hottest day of the year is kept at approximately 35 ℃, which is 2 to 3 ℃ warmer than before. This may have something to do with the abated natural ventilation in the building due to the improved airtightness.

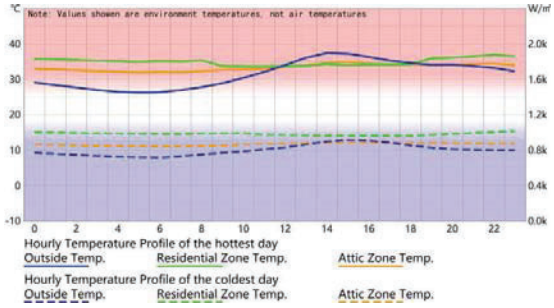

Figure 15: *Hourly temperature change of the hottest and coldest day in the year after using TPEs*

Figure 5 and Figure 16 show that the maximum heat gain on the hottest day is reduced from 9,000 W to 1,200 W, and the maximum heat loss on the coldest day is also reduced from 13,000 W to 1,600 W after using TPEs. The heat lost or gained by the building through heat conduction is approximately 7-8 times less than the original value.

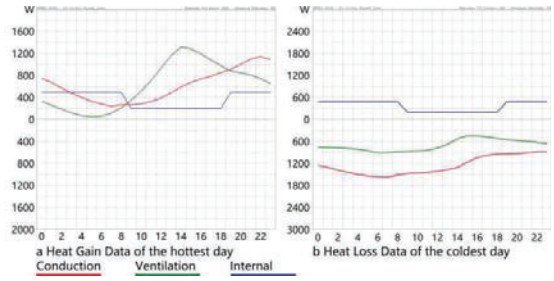

Figure 16: *Heat loss and gain on the hottest and coldest days in the year after using TPEs*

Figure 17 shows the yearly total hours by temperature in the simulation. The time for indoor temperature within the comfort band between 18 ℃ and 26 ℃ lasts 3,968 hours and takes up 45.3% of a year without using TPEs. After using TPEs, the comfort time increased to 4,573 hours and accounted for 52.2% of the total hours for the year, with a 6.9% increase. From this comparison, it can be concluded that the thermal comfort of the historic *Chuandou* house has been improved in general through the application of TPEs.

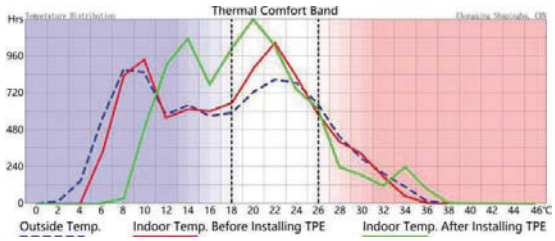

Figure 17: *Comparison of total hours by temperature*

4. DISCUSSION

Through this study, it can be seen that the use of TPEs plays a significant role in improving the performance of historic Chinese timber-framed buildings. TPEs, which integrate the functions of enclosure, heat preservation, and sound insulation, can effectively improve living comfort. The proposed solutions consist of cladding the building envelope with a new skin based on prefabricated timber panels, improving the thermal and acoustic performance and architectural quality. The use of preassembled timber-based components and external installation reduces construction costs and time and embodied energy, which is a sustainable approach from social, economic, and environmental viewpoints.

However, this approach of this study also shows limitations. Only two performance, thermal and acoustic insulation, have been simulated and compared. Other performance, such as fire resistance and moisture-proofing, are ignored in the analysis.

In the simulation, the thermal insulation of the building in winter has been significantly improved, but the indoor temperature in summer is surprisingly higher than without TPEs. The factor leading to this result may be that the airtightness of the building has improved, so the natural ventilation for heat dissipation is also reduced. In fact, for houses in southwestern China, which are very warm in summer, the natural ventilation of the building should also be considered.

This study only designed the details of the TPE components themselves, but the details for the interface and connection between TPEs and the main building structure are not considered. Therefore, cold bridges may occur in practice and differ greatly from the experimental results. In addition, the weight of the TPE components was not taken into account, which in fact has something to do with structural safety.

5. CONCLUSION

China's historic timber construction technology used to be extensively spread and advanced, but new developments in modern timber construction in Europe and North America has progressed forwards in many aspects. With the promulgation and implementation of China's national standard *Technical Standards for Prefabricated Wooden Structures* and the new version of *Standard for Design of Timber Structures (GB 50005-2017)* [17] and the

https://doi.org/10.52202/069179-0487

promotion of national policies to encourage the development of prefabricated buildings, China's timber construction industry is experiencing steady growth.

This paper has gone through the design of building envelope components, integrating TPE prefabricated components into historic Chinese buildings, and obtained experimental results by software simulations. The results show the potential effectiveness of TPEs in improving building performance and demonstrate their application feasibility. However, these simulations still need practical verification, which will be a further research direction in the future. Moreover, this paper can provide a reference for the research and development of the modern adaptability of historic Chinese timber architecture.

ACKNOWLEDGEMENT

This research was funded by the Start-up Foundation for the Hundred-Talent Program, Zhejiang University, and a project grant from the Centre for Balance Architecture of Zhejiang University.

REFERENCES

[1] I. Smith, M. A. Snow. Timber: An ancient construction material with a bright future. The *Forestry Chronicle*, 84(4), 504-510, 2008.

[2] Z. Que, Z. Li, X. Zhang, Z. Yuan, and B. Pan. Traditional wooden buildings in China. Rijeka: *InTech*, pages 197-221, 2017.

[3] Ancient Chinese wooden architecture. (March 25, 2023). Retrieved April 16, 2023, from Wikipedia: https://en.wikipedia.org/wiki/Ancient_Chinese_wooden_architecture.

[4] X. Gao, R. Hu, and F. Wang. Transformation of China’s urban housing system. In *The geographical transformation of China*. Routledge. Pages 236-261, 2014.

[5] M. Dong, G. Jin. Analysis on the protection and reuse of urban industrial architecture heritage. In *IOP Conference Series: Earth and Environmental Science* (Vol. 787, No. 1, p. 012175). IOP Publishing.

[6] M. Dickson, D. Parker. *Sustainable timber design*. Routledge, 2014.

[7] S. Brand. *How buildings learn: What happens after they're built*. Penguin, 1995.

[8] YJ. Kim, S. Park. Tectonic traditions in ancient Chinese architecture, and their development. *Journal of Asian Architecture and Building Engineering*, 16(1), 31-38.

[9] D. Zhang. Classical courtyard houses of Beijing: architecture as cultural artifact. *Space and Communication*, 1(1), 47-68, 2015.

[10] Y. Xu, Z. Yang. Research on indoor thermal environment and enclosure’s thermal characteristics of dwelling with muddy wall circled by bamboos. *Journal of Chongqing University*, 44(03):22-30, 2021.

[11] H Huang. *Holzarchitektur in Fubao*. Diss. Technische Universität München, 2020.

[12] Standardization Administration of the People's Republic of China. *Design standard for energy efficiency of rural residential buildings (GB/T 50824-2013)*, 2013. Beijing, China.

[13] Standardization Administration of the People's Republic of China. *Technical standard for infills or partitions with timber framework. (GB/T 50361-2018)*, 2018. Beijing, China.

[14] Standardization Administration of the People's Republic of China. *Code for design of sound insulation of civil buildings. (GB 50118-2010)*, 2010. Beijing, China.

[15] S. Roberts, N. Guariento. *Building integrated photovoltaics: a handbook.* Walter de Gruyter, 2009.

[16] Standardization Administration of the People's Republic of China. *Thermal design code for civil building. (GB/T 50176-2016)*, 2016. Beijing, China.

[17] Standardization Administration of the People's Republic of China. *Standard for Design of Timber Structures. (GB 50005-2017)*, 2017.

World Conference on Timber Engineering Oslo 2023

ARCHITECTURAL POTENTIAL OF NEW WOODEN MATERIALS & TECHNOLOGIES

Ramona Schwertfeger[1], Markus Lager[2], Studio LAGERSCHWERTFEGER

oo

ABSTRACT: In this text, we like to showcase some of our more ambitious projects: The first high-rise in timber construction in Germany, our project SKAIO received the so-called DGBN certificate in gold, a proof of air quality, and a DGBN-Diamond award. In addition, it exemplifies our approach to design for disassembly—all materials can be clearly separated. SHAA, a university and office building we currently design in timber construction, advances some of the findings we gained in a recently finished university building: here, we develop a building frame at once simple and able to accommodate pipes and cables. In office areas, glued laminated timber slabs [Brettstapeldecken] span the timber frame, in corridor areas cross laminated timber elements span in two directions, so that we can dispense with bearers to incorporate wiring and plumbing. Another project of ours, NXT, is an attempt to design quite an ordinary office building. By that we mean a focus on comfort and flexibility for third party users. We devise a flat slab with integrated bearers. The timber–concrete composite slab spans from beam to the façade.

KEYWORDS: LAGERSCHWERTFEGER, Berlin, Germany, Timber architecture, housing, education

1 Introduction

Between 2012 and 2021, the architecture practice Kaden+Lager, the former office of Markus Lager, realized a large number of hybrid-timber construction projects in the so-called building classifications four and five, comprising all buildings higher than seven meters. Berlin's building code allows for such constructions since 22 March, 2018. Previously, architects had to have such constructions approved as departures from the norm and through individual exceptions, which required huge efforts both in terms of time and money. Meanwhile, four of sixteen state building codes in Germany allow for the use of timber constructions in said building classifications. In addition, since mid-2021, the federal states integrated what is called Musterholzbaurichtlinie MHolzBauRL (Construction Guideline for Timber Construction) into their administrative regulations on technical building codes. This regulation basically controls the use of timber in building classifications four and five, respectively, and it allows for superstructures already used in buildings between 2012 to 2021.

While this new guideline for timber constructions has been developed and introduced, an increasing number and size of realized structures helps to technically advance applied timber constructions: referring back to already existing structures makes the design and construction of new ones much easier. We can now simplify superstructures, for instance, by reducing individual layers in their buildup. And not least do we have to use materials according to their nature. Between 2012 and 2021, errors occurred during the planning and execution phases, both in our own practice and more generally. Statistically, an increasing number of timber-constructions will inevitably lead to an increase in water and fire damage. As a consequence, we need to take stock of our projects to date and the concomitant regulations they entailed. It is not a question of lowering our protection goals or of unconditionally reducing complexity; rather, timber constructions must become more robust. There is, for instance, still a lack of solutions for both temporary and permanent waterproofing of construction sites and bathrooms. Another example is the integration of building technology mainly in prefabricated wall and ceiling elements. This article aims to trace the above-mentioned developments through the lens of our own projects. In addition, this article offers an outlook on current tasks that are constantly changing.

2 SKAIO

SKAIO is Germany's first wooden high-rise and—at the time of its opening—the country's tallest wooden building. Measuring 34m in height, its timber-frame construction is to large extents prefabricated, comprised of supporting structures made of laminated timber, and wooden slabs which rest on steel ring beams that resonate to the slim design of the construction. The project is part of the recently developed residential quarter Neckarbogen, an urban district in Heilbronn. The residential block features ten storeys and offers 60 apartments, 40% of which are subsidized by the state.

The internal layout has been adapted to reflect the new urban realities, in which the nuclear family no longer represents the sole point of reference. SKAIO instead offers apartment types which are usually hard to come by in a contemporary city: 56 smaller studios and one-bedroom apartments. These individual units, however,

[1] Dipl. Ing. Architektin AK Berlin Ramona Schwertfeger, head and owner of LAGERSCHWERTFEGER
[2] Dipl. Ing. Architekt AK Berlin Markus Lager, head and owner of LAGERSCHWERTFEGER

https://doi.org/10.52202/069179-0488

can be easily combined to accommodate future changes in use. In addition, four shared apartments are dedicated to socially disadvantaged members of society, run by two of Heilbronn's social welfare organizations.

Above an underground car park, the ground floor features commercial spaces, common spaces—laundry room, communal kitchen—and ample bicycle parking. Common laundry rooms in Germany tend to be rare and save valuable surface area in each apartment. A central core made of reinforced concrete contains the safety-stairwell and an elevator, which allows for barrier-free access to all apartments. While the primary structure in the basement, ground floor, and first floor are made of reinforced concrete, all other load-bearing components are made of timber or wood-steel hybrids.

The studios start, in floor space, at 40 square meters; the largest flats offer 90 square meters. Every apartment has its own loggia, floor to ceiling windows to provide for a maximum amount of daylight, and energy-efficient underfloor heating. The roof has a common garden terrace, partly furnished, partly green, with produce gardens and stunning views across the city.

During the so-called Bundesgartenschau 2019, a biennial federal horticulture show held in Germany, SKAIO marked the entrance to the show, constituting one of three landmarks in the vicinity.

2.1 Structural Contribution

SKAIO's ceiling and wall structure can be dismantled into its individual parts, that is, all materials can be separated by type. What is more, all superstructures are dry to guarantee a fast and clean construction process. Floor slabs are smoke-proof, a property we achieved by using so-called panel bundles in conjunction with a continuous layer of Fermacell above the impact sound insulation. That part of the primary timber construction facing the apartments we did not cover with plasterboard, something the MHolzBauRL (the guideline for timber construction) commonly asks for. The underside of the 26cm thick cross-laminated timber ceiling remains visible. On top of this ceiling panel, we installed lighting and sprinklers which are then brought down through drill holes. A wall of 12cm thick cross-laminated timber panels on the inside closes of the living space. The degree of prefabrication of walls is quite common in many other timber constructions. Prefabrication of the ceilings, however, is limited to the joinery of the cross-laminated timber elements.
The dry floor construction can only be made in situ, as the high-pressure water mist firefighting system has to be installed first throughout all apartments and in the safety stairwell. Even though it is possible to use a dry construction method that does not impede construction progress with drying time or require the use of chemicals to accelerate any drying, the complexity of this method is rather high. SKAIO's shell received a total of around 26,400m2 of panel materials, which is equivalent to the size of almost four soccer fields, an amount that adds to the complexity of the construction site. In comparison, prefabricating the ceiling panels with dry construction in the workshop might have been significantly less complex. However, the installation of the sprinkler system in particular would not have been possible with prefabrication.

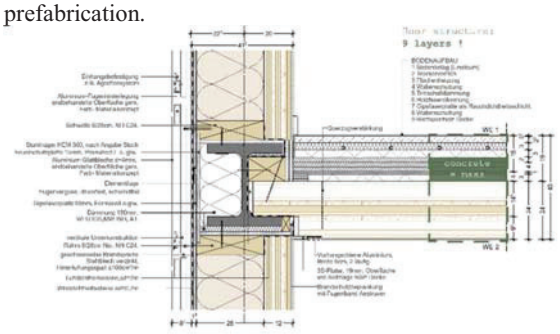

Figure 1 – *ceiling SKAIO, dry flooring, heating, beams*

Figure 2 - *SKAIO MockUp of ceiling construction connecting walls*

2.2 Facts

SKAIO	
Planning	2016 – 2018
Realisation	2018 – 2019
BGF	5.685 m²
Amount of flats	60
SQM	3.300 m²
Costs KG 300/400	12.6 Mio €
Gebäudeklasse	5

https://doi.org/10.52202/069179-0488

Figure 3: *view SKAIO: aluminiumfacade, skeleton construction, columns on public ground*

3 TzW, Hamburg

In 2015, Kaden+Lager won a competition for "Baakenhafen, Baufeld 89," with the design of a residential building in hybrid-timber construction eight stories high. The building group inhabiting this structure consists of 29 parties and is made up of families, couples, singles—younger as well as older residents. Our aim was to build privately-owned, affordable housing with a high standard of living in Hamburg's HafenCity, by virtue of sustainable, ecological, climate-friendly construction methods. Completed in 2022, the apartment building is located alongside the Elbe River on the west side of a new urban block offering direct vistas onto the famous philharmonic. Towards the river, the block is open, providing light and air to its courtyard. All apartments face westward towards the city, and east towards the courtyard, providing excellent conditions for light and ventilation. Through participatory workshops we developed individual apartments according to the specific needs of each user.

Thanks to the building's robust primary structure, we could ensure cost security in construction, as well as a high degree of flexibility for potential conversions in the future over the entire life cycle of the building, while also providing a great variety of individual floor plans. Two staircases—each one of them leading to two apartments on every floor—provide access to the building. Three cross walls run unbroken through the entire building, dividing it longitudinally into four units which then get stacked on top of each other, and which contain the individual apartments. Easily adaptable, lightweight walls respond to the specific needs of each party. The curtain wall features rear ventilation and consists of light, large-format ceramic elements. Two different window formats as well as balconies and loggias, offset floor by floor, subdivide the facade and give rhythm to it. The floor-to-ceiling windows and French doors provide very good natural lighting for the apartments while at the same time offering views onto Hamburg's harbor. The inhabitants can use the roof terrace collectively as a communal area and playground. The rest of the roof area is green and serves for rain retention, cooling, and to increase biodiversity. The building received the HafenCity Gold eco-label.

3.1 Structural Contribution

The building is constructed as a solid timber structure. For reasons of flood protection, we devised the two-story dwelling mound as well as the stairwells and fire walls as a solid construction in reinforced concrete to ensure both bracing and emergency exits with economic means. All other structural elements, ceilings, cross walls, exterior walls and balconies are made of cross laminated timber. Here, too, we exclusively employed certified timber and took into account that this building might have to be dismantled at one point, which is also why it contains no harmful substances. The interior atmosphere is characterized by an interplay of natural wood surfaces, reinforced concrete, and neutral wall surfaces. During the construction phase, the TzW suffered from significant water damage due to water entering through leaking, temporary balcony sealing. Defective or incorrectly installed sanitary objects bring about further water ingress. The resulting damage prompted us to scrutinize the so-called DIN 18534-2 (a building norm addressing construction waterproofing), and to publish a solution better suited than the existing two-layer sealing.

3.2 Facts

TZW	
Planning	2016 – 2019
Realisation	2018 – 2022
BGF	4.614 m²
Amount of flats	29
SQM	3.300 m²
Costs KG 300/400	7.2 Mio €
Gebäudeklasse	5

https://doi.org/10.52202/069179-0488

***Figure 4** – Tor zur Welt, Hamburg, west facade, grid of balconies*

4 UWH

The private university Witten/Herdecke in the southern Ruhr area is committed to teaching its students issues of culture and morality, as well as exposure to nature and production processes. Such concerns are fundamental to the relationship between people. Perhaps as a reaction to this, many students wanted to get involved in the design of a new central building, and in developing ideas about the arrangement of rooms and the materials used. The university opted for a timber construction able to bind carbon dioxide, thus contributing to the decarbonization of our planet.

The structure has many diverging tasks to fulfil at the same time: as a link between already existing, different buildings on campus, it also acts as an independent center that contains the library which spreads out across two floors. It also houses seminar rooms and work spaces. Rooms are used simultaneously or consecutively for different purposes. One can find silence and concentration side by side with lively discussions and teamwork. Many different parties require short paths out of different areas while in other parts of the building ask for much less circulation.

To make all this possible, we as architects subdivided the building into a square grid to keep the volume compact on one hand, while on the other to allow for individual rooms to contract or expand. Whether different functions remain separate or conjoin, things remain straight and simple.

Whereas to the south the building folds into the slope and adjacent park, towards the north it creates a new public square. The new building frames one side of a wide rectangle, while the large lecture and conference hall as well as a café open up towards the square. From here we catch a glimpse of the wide spiral staircase behind the main entrance, leading students and teachers into the first floor. This staircase is part of what we call ”aorta,” a central circulation area which not only opens up parts of the building, but which also offers niches to study and suites for discussion.

Materials can be experienced on the facade as well as inside: The open structure, walls and ceilings are made of wood, and large windows let in plenty of daylight. Towards the park, parts of the volume recede and thus create roof terraces. Of course, there is a bus stop directly in front of the campus, and those who come by bike can store it in the covered bicycle garage. Clear components for a climate-friendly future.

***Figure 5** – campus at UWH*

4.1.1 Structural Contribution

We applied the above-mentioned grid throughout the entire building. This allows for an efficient use of cross-laminated timber: within the grid, three fields in a row exactly match the length that can be easily manufactured and delivered to the construction site. From the onset, the manufacturer is involved in the process, which simplifies the planning in terms of optimisation and efficiency. Ecological balance sheets reflect both transportation and the CO2 emissions associated with it, which in turn drive of the cost of construction.

In a university building the units are larger than in a residential building. In the case of the University of Witten/Herdecke with a gross floor area of 6,880m2 there are a total of 14 units each up to 550m2 in size (compared to SKAIO with a GFA of 5,685m2 and 63 units). In general, the number of users per unit and in absolute terms is significantly higher in university or commercial buildings than in residential buildings of the classifications four and five. The large number of users is usually met with more powerful building technology. While the university’s own residential projects mostly manage without mechanical ventilation, this is impossible to maintain in lecture and seminar spaces as they are commonly used today. Here, the air is conditioned accordingly. However, the new UWH building features mechanical ventilation only in those rooms whose number of users does not allow for natural ventilation by means of simply opening windows. In office spaces without mechanical ventilation, we installed simple ceiling fans to lower the inhabitant’s sensitivity to temperature by around 2 degrees Celsius. In doing so, there is no need to further cool the building, a condition which helps significantly reduce the use of energy-intensive technologies.

https://doi.org/10.52202/069179-0488

We designed the building as a simple timber frame structure. The posts connect with double tie joints to the beams of the ceiling, which is made of cross-laminated timber, spanning across three fields of the grid (which equals 13.95m/3 x 4.65m). The exterior walls are made of timber panels, in part of solid timber construction, and clad with an untreated larch wood facade, which features rear ventilation.

A column-free structure for the lecture hall spans across 15m, on top of which there are two floors with office space. Here, one can detect the truss system directing the loads of the office spaces on the ground floor to the outside, thus making posts unnecessary. UWH's design has been subject to repeated changes. To be sure, both the organizing grid and our construction method demonstrate a sufficient degree of flexibility to respond to changing requirements. It became apparent, however, that we could not consider the construction alone, without creating enough space for the HVAC and electrical installations.

***Figure 6** – Sprengwerk as classic carpentry*

4.2 Facts

UWH	
Planning	2018 – 2019
Realisation	2020 – 2021
BGF	6.880 m²
Timber volume	1.200 m³
Gebäudeklasse	5 / Sonderb.
Special rooms	
9 seminarrooms, 7 flex.	
3 storey library	
café and lounge	
room of silence	
winter garden	
3 rooftop terraces	
flexible eventspace	
100 office workplaces	
26 student workspaces	

5 SHAA

The university campus of Aalen, a city located in the eastern part of the German state Baden-Württemberg, is continuously expanding, and in the course of this expansion the Steinbeis Stiftung für Wirtschaftsförderung (foundation for economic development) wants to create an office building, the so-called SHAA, on the campus Burren. Exposed to an adjacent state road, the so-called Bundesstraße 29, the building serves as a landmark, thus completing the height development sloping down from the east Unclear to me and offering its future users distant views over the Ostalb. The office building, consisting of a three-story wing and a seven-story tower, is built in wood; only the two cores and the basement are made of reinforced concrete. Due to its construction method and delicate wooden facade design, the building blends into its vernacular neighborhood as much as into the overall layout of the campus Burren. While the lower floors will be open to the public—here the university will primarily accommodate lecture halls and spaces for leaning—the upper floors will house exclusive office spaces.

***Figure** 7 – view from campus on 7-storey timber construction and larch-façade with changing fins*

5.1 Structural Contribution

The SHAA project, too, is designed as a timber-frame construction. Based on the experience we gained from realizing the UWH project, this structure required that all HLS/E (in principal HVAC and electricity) ducts can be installed everywhere without having to cross or go below beams. Thus, we created a post and lintel structure with double tie joints Correct? based on a grid of 5,20 m. In office areas, glued laminated timber slabs span the timber frame across one unit of the grid. In corridor areas cross laminated timber elements span in two directions so that we can dispense with bearers to incorporate wiring and plumbing. As these elements structurally engage in two axes, here we can avoid the use of double tie joints and building technology can run through the entire structure without crossing any beams. One layer of beams spans two lecture halls, located on the first and second floors,

https://doi.org/10.52202/069179-0488

the gaps of which we used to accommodate building technology which runs between individual beams.

***Figure 8** – HLS / E + pipes integrated in construction*

For the facade, we used prefabricated elements made of preaged larch that is treated with grey pigment. Below ground, geothermal probes extract soil heat for heating and cooling the building.

5.2 Facts

SHAA	
Planning	2020 – 2023
Realisation	in planning
BGF	6.345 m²
Gebäudeklasse	5 / Sonderb.

6 NXT

The first out of nine buildings of the NXT Airport Collaboration Village grouped around the village green is an office building we havedevised since 2021. Its presence and appearance point the way towards the future, as a harbinger for the village still under construction near Berlin's airport BER. Welcoming first users, this structure is a place for physical and virtual networking as it creates a vital environment to foster cooperation, creativity and growth.
A wooden frame used as a balcony and placed in front of the main facade Correct? welcomes the arriving users. Inside, the scheme offers contemporary office spaces, highly flexible and geared towards co-working. Public areas include a café and a multifunctional space connected to the central foyer located on the first floor, as well as outdoor spaces.

6.1 Structural Contribution

The design of NXT aims at commercial clients. Here our goal was to achieve the same level of comfort in the planning and operating phases one is used to from conventional construction. Due to high levels of vibration in the ground, we used timber-concrete composite slabs that are supported by glued-laminated timber posts and so-called delta beams, that is, composite beams of steel and concrete. This construction is akin to a flat ceiling and offers maximum flexibility with regard to the installation of building technology and potential changes to all non-load-bearing interior walls during the building's future use.

6.2 Facts

NXT	
Planning	2021 – 2023
Realisation	in planning
BGF	8.200 m²
Gebäudeklasse	4 / Sonderb.

***Figure 9** – Kopfbau and facade NXT Berlin*

7 Silos - An Outlook

We currently develop a project on our own initiative. Instead of demolishing existing silos—as is proposed in the correlating master plan—we seek to preserve and repurpose this structure. Thus, we create residential and commercial spaces as we use the remaining volume of industrial buildings to store energy and potentially implement an indoor farm.
So far, we can share the following observations: The existing structures already cover the spatial requirements as laid out in the master plan. Furthermore, additional floor space can and should be created. By not demolishing the existing silos and doing without new structures we can save almost 70% of gray energy, evidence of which we provide by virtue of CO2 and life cycle assessment. Those building parts not dedicated to living and working can store electricity from renewable sources, which in turn can supply 18,000 households per day with power. We propose different options for energy storage and exchange these ideas with Flensburg's municipal utilities.

https://doi.org/10.52202/069179-0488

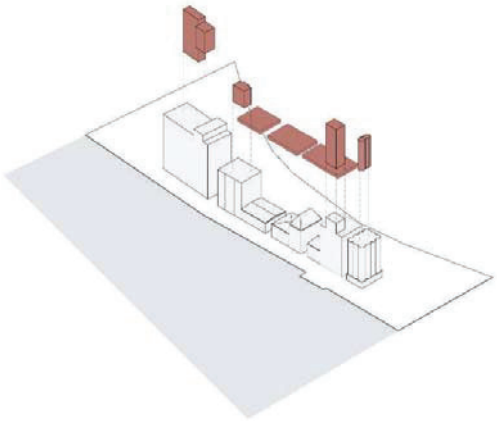

Figure 10 *– potenzial battery volume in Silos*

7.1 Structural Contribution

Here, the aim is to convert existing structures with as little effort as possible. To this end, we provide prefabricated wooden panels and solid wood elements that can be easily attached to the existing buildings and that already contain all necessary installations, so as to simplify the production processes on site.

8 Conclusion

During the time of this work, the design of timber constructions in particular has continued to develop gradually towards greater comfort and more simplicity. Above all, interdisciplinary planning processes from the beginning turn out to be essential and veryproductive. In order to keep the currently rising numbers of projects in timber constructions free of damage, we require proper planning solutions as much as manual dexterity in prefabrication and on the construction site.

https://doi.org/10.52202/069179-0488

REFERENCES, FIGURES

[1] Detail-drawing, Kaden + Lager
[2] Photograph, Markus Lager
[3] Photograph, Bernd Borchardt
[4] Photograph, Bernd Borchardt
[5] Photograph, Hiepler Brunier
[6] Photograph, Markus Willeke
[7] Visualisation, Atelier Noise
[8] Structure rendering, Markus Lager
[9] Visualisation, Atelier Noise
[10] Isometries, LAGERSCHWERTFEGER

https://doi.org/10.52202/069179-0488

World Conference on Timber Engineering Oslo 2023

SPECIAL SIZED TIMBER POLES AS MAIN STRUCTURAL MATERIAL IN TWO SPORTS GYMS AND A WINERY – BRAZIL

Roberto Lecomte[1], Sheila Beatriz[2]

ABSTRACT: Brazil has a long tradition of building with concrete. Although our country possesses the largest tropical forest of the planet, timber structures aren't the first choice for designers and builders. The urgency of develop low-carbon solutions to built environment is the key element of promoting the only construction system sequestering carbon and engineered to be “energy positive”, and this raw material is wood. In central Brazil, due to its geographic location, there are suppliers for both hardwood from the Amazon region and softwood from the southern. Starting from the experience of several timber structures executed in this region, it was proposed the use of pressure treated eucalyptus poles as the main structural material in two sports gyms and a winery, also using sawed hardwood as secondary structure. The structural system of the gyms is composed of porticos and the size of the rounded pieces reaches 24m long. A spatial structure was proposed to the winery according to contemporary design. The remarkable aesthetics given by the natural appeal of timber along with its sustainable aspects became powerful marketing tools to the enterprises.

KEYWORDS: Timber Structures, Low-carbon Solutions, Eucalyptus Poles, Structural System.

1 INTRODUCTION

Although timber structures are yet undervalued as building solutions in Brazil, new demands coming from the urgency of develop low-carbon solutions are indicating that wood products are strategic to the planet.
Starting from the experience of several timber structures executed in central Brazil, it was proposed the use of pressure treated eucalyptus poles as the main structural material in two sports gyms and a winery. This article shows the design and construction of these buildings.

2 METHODOLOGY

The projects of the buildings were developed from the following premises:
• structural modulation that optimizes the dimensions of the porticos and the size of the eucalyptus poles;
• intensive use of continuous members to the whole structures looking for simplify construction;
• standardization of bolted joints and carvings aiming to rationalize its assembling system;
• timber structures designed with base fixity and a consequent reduction in bracing elements;
• use of Amazonian sawed wood as secondary structure.

3 DESCRIPTION OF THE PROJECTS

As the main structural material of the related buildings, wooden poles are ecological materials that comes from reforestation and need much less energy for their production, and that production does not involve non-renewable components.
The wooden posts are much lighter than the concrete posts, reducing the cost of transportation. In addition, the handling of these poles is very simple, as it does not require the use of special equipment. It is also important at the time of installation, which is much easier to do.

3.1 UNIQUE GYM EXPANSION

Unique Gym is a remarkable building made of eucalyptus timber poles and since 2005 stands out as one of the most original gyms in our city as showed in Figures 1 and 2.

Figure 1: *External image of the Unique Gym*

[1] Roberto Lecomte, Casacerta Architecture Design & Building, Brasília, Brasil, roberto.lecomte@gmail.com

[2] Sheila Beatriz, Casacerta Architecture Design & Building, Brasília, Brasil, sheilatriz@hotmail.com

https://doi.org/10.52202/069179-0489

Figure 2: *Internal view of the wooden building*

The covering of the building's expansion is a mix between ceramic tiles and thermoacoustic covering according to the plan is showed in Figure 3.

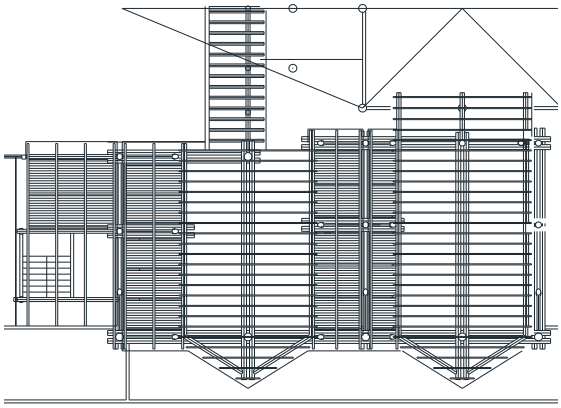

Figure 3: *Plan of the covering showing timber pieces*

The design of the expansion of the original Unique Gym was conceived considering its location over an existing concrete slab area. Due to this special location its structural system was designed by using 12m long beams, aiming to reach special sized pillars installed outside the slab area as illustrated in Figures 4, 5, 6, 7 and 8.

Figure 4: *Assembling of the timber structure over the existing concrete slab*

Figure 5: *Assembling of the timber structure*

Figure 6: *Assembling of the covering timber structure highlighting the 12m long beams*

Figure 7*: Execution of the covering*

Figure 8: *Internal view showing the original building and the expansion of the gym*

Besides providing both vertical and horizontal structural support to the gym's expansion, the presence of timber pole's structural system reveals its outstanding aesthetics that links the to the original building and highlight wood as the main building element of the sports complex. Figures 9, 10 and 11 shows images of the buildings.

Figure 9: *External view of the buildings*

Figure 10: *External view of the buildings*

Figure 11: *External view of the finished wooden pole structure*

3.2 NEW UNIQUE GYM

The design of the new Unique Gym was defined according to timber structural solutions experienced in the original building. Eucalyptus timber poles of special sizes allows larger spans and heights resulting in a 3 times bigger building then the original. Figures 12, 13, 14, 15 and 16 shows the plan and a scale model of this building.

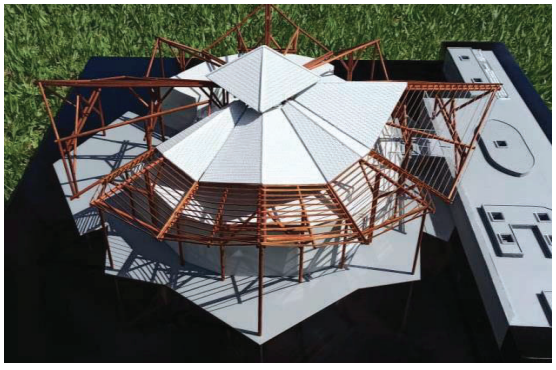

Figure 12: *Scale model of Unique new building*

Figure 13: *External view of the model*

Figure 14: *Internal view of the model*

Figure 15: *Internal view of the model*

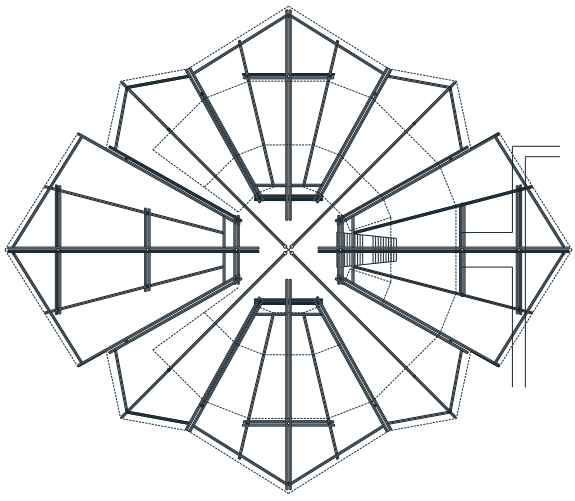

Figure 16: *Plan of the new Unique Gym*

https://doi.org/10.52202/069179-0489

3.3 WINERY

The building consists in a massive reinforced concrete block where's the winery central core, sheltered by a wood cantilever umbrella cover that defines a terrace with panoramic view of the vineyards. Figures 17 and 18 shows a covering plan and a section of the building.

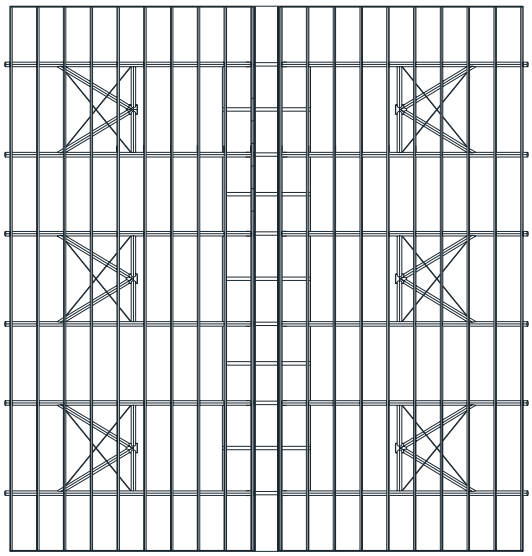

Figure 17: *Plan of the covering of the winery*

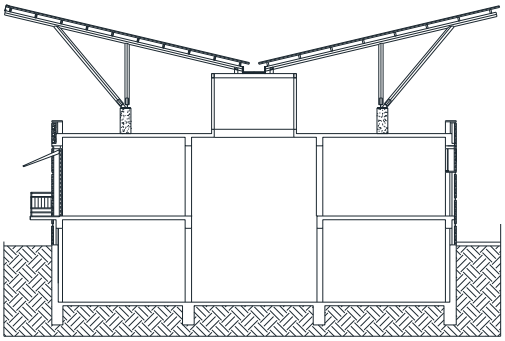

Figure 18: *Cross section of the building*

In this building timber poles are typically utilised to provide support for gravity loads and resistance against lateral forces. But the natural appeal of timber ensures that its role is not purely structural however, and it enables the design conception to take full advantages of beautiful outlooks as it can be viewed in this winery.
Due to its larger sizes such as 12m long beams, poles where spaced further apart than is usual, creating a more spacious building interior, that allowed greater interior design flexibility to the terrace.

Figures 19, 20, 21 and 22 illustrates the designed pole frame and its base plated connections and steel bracing sets. Columns were designed from the outset as columns with pinned bases. A grid of sawed hardwood was used to install the thermos acoustic metallic covering.

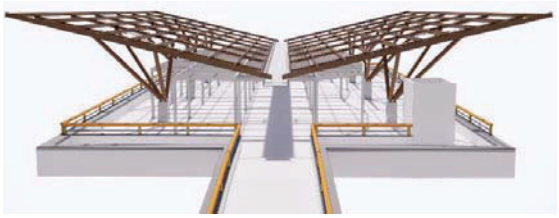

Figure 19: *3D image of the timber structure of the winery*

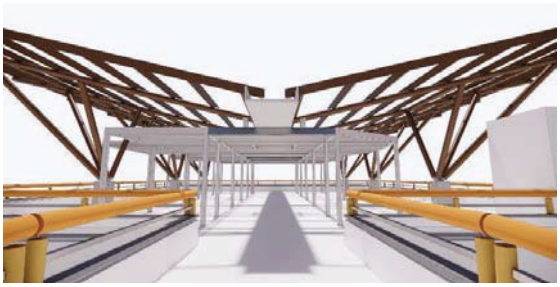

Figure 20: *External 3D image of the terrace*

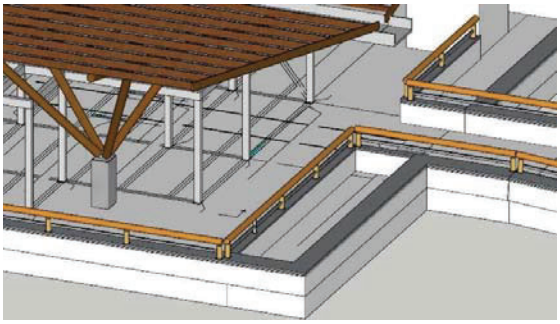

Figure 21: *3D image of the terrace*

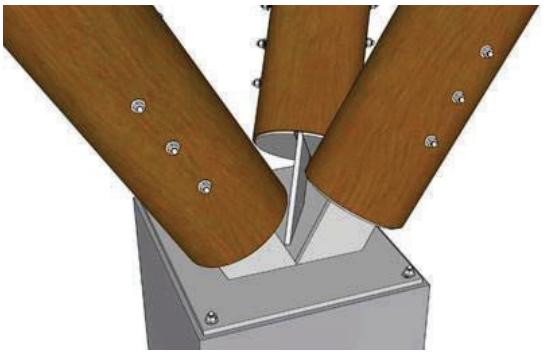

Figure 22: *Base plated connections detail*

Pole frame construction was extremely adaptable to architectural expression as showed in Figures 23,24, 25, 26, 27, 28 and 29.

Figure 23: *External view of the spatial structure of the winery*

Figure 24: *External view of the pole frame*

Figure 25: *Internal view of the pole frame*

Figure 26: *External view*

Figure 27: *Panoramic view of the terrace*

Figure 28: *External view of the winery*

Figure 29: *External view*

4 CONCLUSIONS

The experience of designing timber structures with special sized eucalyptus poles confirms the several possibilities of building with this raw material.

https://doi.org/10.52202/069179-0489

The excellent balance between its weight and resistance results in lighter components that can be more easily transported and assembled.

Finally, it should be pointed out the aesthetics benefits that come from the presence of the timber structures in the buildings, once complementing architectural designs and promoting low-carbon solutions.

REFERENCES

[1] IBDF. Amazonian Timbers: Characteristics and Utilization. CNPq, Brasília. 1981.

[2] IBDF/DPq/LPF. Amazonian Timbers: characteristics and utilization. Curuá-Una Experimental Forest Station. Brasília. 1981.

[3] Melo, J.E. and Camargos, J.A.A. Wood and its uses. SFB/LPF/MMA. Brasilia. 2016.

[4] Mello, R.L. Designing with wood: a new approach. *Master Thesis.* UNB. Brasilia. 2007.

[5] Mello, R. L., Melo, J.E., Wood Pavilion. *Proceedings of Eighth World Conference On Timber Engineering: WCTE 2004,* 2004. Lahti, Finland.

[6] Mello, R. L., Melo, J.E., Wood structures in the new building of CENAFLOR in Brasilia – Brazil. *Proceedings of Nineth World Conference On Timber Engineering: WCTE 2006,* 2006. Portland, USA.

[7] R. L. Mello, J. E. Melo. Use of wood structures in the new headquarters of the National Centre of Research for the Conservation of Natural Predators – CENAP/IBAMA – Brazil. *Proceedings of the 10th World Conference on Timber Engineering*, 2008. Miyazaki, Japan.

[8] R. L. Mello, S. B. Oliveira. Amazonian timber structures at Cipem's stand. *Proceedings of the 16th World Conference on Timber Engineering*, 2021. Santiago, Chile.

World Conference on Timber Engineering Oslo 2023

MODULAR CONSTRUCTION WITH LOW-GRADE HARDWOOD CROSS-LAMINATED TIMBER

Edward Becker [1]

ABSTRACT: In this paper the author evaluates the results of a design-build project that employed the use of prefabricated, modular construction with cross-laminated timber (CLT) panels custom-developed from local, low-grade hardwood (Yellow Poplar, Liriodendron tulipifera). The American Institute of Architects award-winning project is the first permanent building in the United States to be granted a building permit for, and complete construction with, hardwood CLT. The paper presents and evaluates the attainment of each of the following research objectives in the design-build process and includes a review of the mechanical and structural testing underpinning panel performance. The project's research objectives included: (1) the development of locally-sourced, pressed, and utilized hardwood CLT that mechanically outperforms commercially available softwood CLT; (2) the development of low-carbon project logistics that allowed for all design and construction steps – from wood harvesting to CLT layup and utilization – to occur within a 3-hour driving radius of the project site; and (3) the development of prefabricated, modular construction workflows for the project's structural, exterior-exposed hardwood CLT. The 10-meter-tall hardwood CLT project was completed, passed all inspections, and opened to the public in 2021.

KEYWORDS: Hardwood cross-laminated timber, Modular timber construction, Local-species CLT development

1 INTRODUCTION

1.1 PROJECT BACKGROUND

The following paper presents the material development process of Yellow Poplar (Liriodendron tulipifera) hardwood cross-laminated timber (HCLT) and a built structure resulting from the HCLT's application in the public realm. The author focuses specifically on the development and testing of the HCLT product as it relates to the modular construction methods employed for the construction of the built structure, the New River Train Observation Tower in Radford, Virginia. The handicap-accessible train viewing tower is the first permanent building in the United States to be granted a building permit for, and complete construction with, hardwood CLT.

The author of this paper was approached in Fall 2017 by a colleague at Virginia Tech to help co-lead a new design-build project funded by the nearby City of Radford, Virginia. The city sought to build a train observation tower to provide public, handicap access to views over the New River and a historic railway line adjacent to the city's history museum. Over the following two-and-a-half-year period, the author and Professor Kay Edge led the development of full-size, 5 foot by 10 foot, structural, exterior exposed HCLT panels created from locally-sourced, low-grade Yellow Poplar. The panels were subsequently assembled off-site into two prefabricated modules joined by a heavy timber base frame, transported to the site, and attached by crane to a steel and helical pile substructure. The project was completed in 2021. The project has won local, state, national, and international design awards.

1.2 COURSE ORGANIZATION

1.2.1 Course Types

Upon the launch of the design project for the New River Train Observation Tower in Spring 2018, the two faculty leaders co-taught a graduate-level design studio, as well as co-taught a seminar course that paired students from the Department of Sustainable Biomaterials at Virginia Tech with graduate architecture students.

Figure 1: *View from railroad of completed tower*

Faculty from Wood Science, Timber Engineering, and Forestry were also involved in joint teaching sessions. The multi-disciplinary teams presented numerous design schemes to the City of Radford and received feedback. Over the forthcoming semesters, students across the

[1]Edward Becker, Virginia Tech, United States, egb@vt.edu

https://doi.org/10.52202/069179-0490

undergraduate and graduate curriculum were engaged in various aspects of the project. Third-year undergraduate students developed façade studies while graduate design-build students designed technical details for construction, for example. The faculty led the design development project phase and a graduate student assumed project and construction management responsibilities, as well as late-stage project design work for his M.Arch thesis project.

1.2.2 Concept and Schematic Design

The project site is located adjacent to Norfolk Southern rail lines, an industrial tar storage site, and an industrial access road. The site descends from the road level approximately 16 feet to the base of the structure, and subsequently another 20-25 feet to the rail lines. The students began conceptual design with the idea that the building should showcase the structural potential of softwood cross-laminated timber (CLT), as well as its warm aesthetic, by exposing the material on the interior and exterior of the structure. Following numerous design iterations over a multi-month period, the students created a design whereby the difficult site conditions could be managed through off-site prefabrication of timber modules. Two modules were to be constructed with CLT and were each approximately ten by fifteen by ten feet. The modules were to be placed atop both a steel (Module A) and concrete (Module B) substructure per site conditions. The modules were then designed to be bisected by a pedestrian bridge such that the bridge would serve as a structural datum tying the entire building together while also helping to minimize pendulum vibrations from foot traffic. Module A was designed to be 18 feet above grade and closest to the railroad tracks while Module B was designed to be two feet above grade and closest to the access road (see Figure 2). Both modules were to be built entirely of CLT. To reduce the potential for structural degradation over time, Module A was adapted such that it would be primarily supported by a heavy timber frame atop a steel, hollow tube substructure. If damage were to occur over time to the CLT, a new module could easily be installed to replace it.

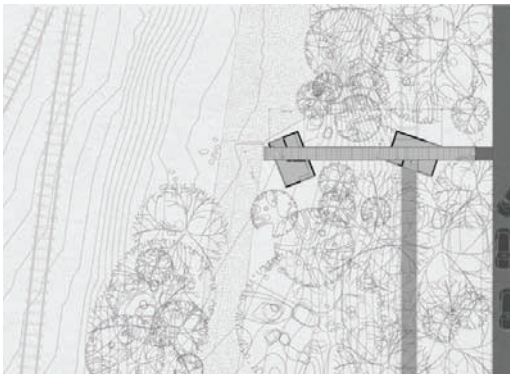

Figure 2: *Site Plan*

As the team moved closer to construction, it became apparent that softwood CLT would not be available regionally as wait times for production and delivery were significant. Additionally, CLT sourced from Canada, Europe, or the Pacific Northwest of the Unites States had such a high carbon cost for transport that it did not meet the sustainability goals of the design.

1.3 YELLOW POPLAR CLT DEVELOPMENT

1.3.1 Lab Testing Background

Due to the lack of softwood CLT availability, the project team consulted with faculty from the Department of Sustainable Biomaterials at Virginia Tech who had been intimately engaged with hardwood CLT research during prior years using locally-sourced Yellow or Tulip Poplar. Sustainable Biomaterial faculty had worked with the product at a lab-sample size and had not yet produced full size panels. A decision was made by the project team to develop full-size panels and apply them to the project based upon the lab-scale testing that the Sustainable Biomaterial faculty had undertaken. Their knowledge of the product was well developed. By 2018, Virginia Tech timber researchers in coordination with West Virginia University had published more articles on hardwood CLT than any other university unit globally for both Beech and Yellow Poplar based products. Their work focused specifically on the mechanical properties and yield analysis of Yellow Poplar CLT [1]. Even with that research background, when the author first began working on hardwood CLT with the Sustainable Biomaterial faculty, including Dr. Daniel Hindman and Dr. Henry Quesada, testing had only recently been completed at West Virginia University regarding Yellow Poplar CLT delamination and other key mechanical properties.

1.3.2 Mechanical and Structural Literature

Dr. Omar Espinoza and Dr. Urs Buehlmann have written about the "technical and economic feasibility" of hardwood CLT in the United States. They provide an overview of current applications of HCLT, including projects by Hasslacher Norica, Waugh Thistleton, and IDK [2]. Additional projects by Alison Brooks Architects and DRMM in the UK, in association with the American Hardwood Export Council (AHEC), have increased public attention on hardwood cross-laminated timber (HCLT) products. The Journal of Contemporary Wood Engineering article "The Quality Assurance of Tulipwood Cross Laminated Timber (CLT) for Multi-Ply" directly addresses AHEC's work with American hardwood in a British context [3]. Other recent research had been completed on the mechanical and structural performance of Yellow Poplar CLTs before the Virginia Tech project team attempted the production of a full-scale panel [4, 5].

Mechanical and structural testing by Dr. Daniel Hindman was key to the project team's product development work. The report "Mechanical Performance of Yellow-Poplar Cross Laminated Timber" (2015) by Milad Mohamadzadeh and Dr. Hindman was particularly useful as the purpose of the research was to "evaluate mechanical performance of yellow-poplar CLT as an alternative for standard CLT made of softwood species" [6].

https://doi.org/10.52202/069179-0490

Mohamadzadeh and Hindman tested "mechanical properties such as bending strength and stiffness as well as bond line shear strength and face delamination of three layered yellow-poplar CLT" to determine the product's feasibility for structural engineering applications [7]. They concluded that the "bending stiffness, bending strength and interlaminar shear capacity were significantly greater than specified values for Grades V1 and V2 in PRG 320" per ANSI/APA guidelines in 2012 [8]. Bending strength, bondline shear strength, face delamination, wood failure, and interlaminar shear capacity were deemed appropriate for HCLT structural applications, while the authors recommended further long-span testing and noted that relatively high glue failure was likely the result of the HCLT's uniquely high shear strength per the wood type, Yellow Poplar [9].

Notably, AHEC's "Tulipwood CLT Properties and Manufacturing Requirements" document, published September 2019, was created after the Virginia Tech project team had already settled on a product development path using Dr. Hindman's aforementioned research. AHEC's document, produced in coordination with the Centre for Offsite Construction + Innovative Structures at Edinburgh Napier University, the Construction Scotland Innovation Centre, and others, provides a thorough overview of the key considerations of Yellow Poplar CLT including sourcing, fabrication, and application. From procurement, pre-processing of lamellae, assembly, and post-processing, AHEC's document focuses on the production process in the UK in coordination with European Standard (EN) regulations. For the Radford project, many of the same production steps were followed. The manual would have been used by the project team if it would have been available at the appropriate time.

2 RESEARCH OBJECTIVES

2.1 DEVELOPMENT OF LOCALLY-SOURCED HCLT

Due to the availability of Yellow Poplar CLT manufacturing knowledge and the logistical difficulty to access softwood CLT, the project team chose to develop our own HCLT product using locally-sourced, low-grade wood. The project was an attempt to illustrate the economic potential for an overlooked and underutilized forest resource, low-grade Yellow Poplar, and also an opportunity to showcase the upcycling potential of under-valued local resources. The Virginia Tech team partnered with the Southern Virginia Higher Education Center (SVHEC) to produce the panels on the same equipment where the lab-sample panels had earlier been produced for structural testing. SVHEC's manufacturing facility was the only facility within a 300-mile radius of Virginia Tech's campus capable of pressing full-size HCLT panels. The facility had modified an industrial plywood press such that it was capable of achieving the required pressure to press the HCLT. Wood was sourced from multiple regional sawmills and refined on site at SVHEC. The boards were planed and aligned before gluing and pressing. After pressing, the rough-edge panels were cut on an industrial CNC. Unlike the Scottish production process for Multi-Ply's HCLT panels as outlined in the AHEC manufacturing document, SVHEC used a hydraulic press rather than a vacuum press.

Figure 3: *Advantage EP-950A glue application by student during assembly.*

While the panels looked factory finished after manufacture, the project team noticed 1/16" or less hairline gaps at the panel edges between lamellae. At the time, the project team assumed that there may have been a glue distribution error or a lack of hydraulic press pressure within two-inches of the panel edge. The latter was determined to be the issue and this gap later led to minor delamination of the product in south-facing, vertical applications. The HCLT panels were noticeably heavier and denser in comparison to a softwood CLT panel made of Southern Yellow Pine or Spruce-Pine-Fir. As such, project team needed to develop our own internal workflows to handle the panel finishing and assembly for panels with such unique properties, as well as work with our project engineer to make sure that the heavy panels were suitable for the modular construction methods that we planned to use per the difficult project site.

2.2 LOW-CARBON PROJECT LOGISTICS

Through the project partnership with the SVHEC, the project team was able to source local materials, use a locally-upcycled press, assemble panels within a 15-mile radius of the project site, and efficiently deliver and construct the tower. This highly-localized process can be compared to the primary alternative which would have entailed shipping panels hundreds or even thousands of miles to the project site while local, low-grade Yellow Poplar resources remained unused. The SVHEC manufacturing facility is housed in a former tobacco warehouse that was adaptively reused, thereby also lowering tangential carbon emissions compared to a workflow that used facilities with high-embodied carbon. In fact, the SVHEC facility will be prioritized for future projects simply because it aligns with the low-carbon, circular economy mission of the project and supports the

https://doi.org/10.52202/069179-0490

overarching goal of lowering carbon emissions holistically across the entire project ecosystem. The bullet points below list the 'project strategies' (PS) that saved operational and embodied carbon versus the 'typical alternative' (TA) to the relevant issue as shown below:

Radford Train Tower Carbon-Smart Strategies
PS1: Upcycling of tracked, local, low-grade timber
TA: Variable; Non-specific material approach
PS2: Layup conducted in low-embodied carbon facility
TA: Support of high embodied carbon facilities via use
PS3: High-efficiency, low waste, offsite assembly
TA: Low-efficiency, high waste, on site assembly
PS4: Design for replacement and disassembly
TA: Disassembled and discarded after useful life

Despite the successes of a highly localized material sourcing, upcycling, shipping, assembly, and delivery process, the project's carbon ecosystem could have been improved via the following 'strategies' (S):

S1: All-wood structure with replaceable foundations
S2: Use of hardwood-nail or dowel-laminated timber
S3: Use of a carbon-tracking digital management system
S4: Holistic use of renewable energy (saws, delivery vehicles, computers, etc.)

Underpinning all of the carbon strategies in the project is the modular approach to construction. If the project were site built, the project team estimates that even with all the realized and unrealized carbon-saving strategies aforementioned effectively implemented, the project would still be carbon positive simply due to the inefficiency of on-site construction. Tangential carbon emitting sources such as finishing materials (e.g., EDPM, adhesives, waxes, etc.) plus the inefficiency of labor (e.g., additional food costs, wear on vehicles from excessive trips to the site, etc) would offset the carbon saved for a project of this scale.

The project effectively accomplished multiple key carbon-reducing strategies, but there are also improvements that can be made. Through offsite manufacturing and descriptive material-IDs affiliated with each building product used, the entire construction process could be tracked and carbon inefficiencies reduced – see restado.de and Concular, as well as Madaster digital carbon management systems [10,11].

2.3 MODULAR CONSTRUCTION WORKFLOWS

2.3.1 Panel Preparation

Following the arrival of the HCLT panels at Virginia Tech's Research and Demonstration Facilty (RDF), each panel underwent a three-step process: (1) hard wax was applied to lamellae end grain; (2) pilot holes were drilled for the forthcoming 12" timber screws; and (3) certain panel faces were treated with a base coat of linseed-oil-pine-tar mix. As some panel end grain would be concealed by other panel faces after assembly, the end grain of exposed lamellae was treated in advance. The project team was concerned about water absorption through the end grain if the panel was immersed in standing water after construction on site. Pilot holes were drilled into each panel in a staggered manner so as to avoid the timber screws splitting the wood when installed. The pilot holes were drilled multiple inches away from the panel's edge and in a manner that would allow them to align with the adjacent lamella, as opposed to a glue joint.

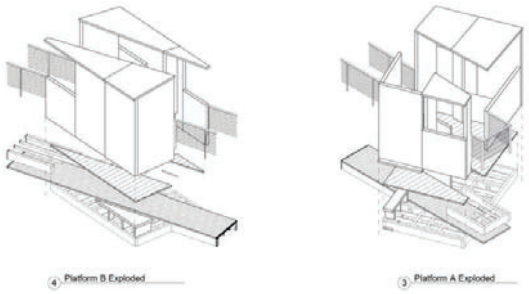

Figure 4: *Structural drawing of Module A*

Drawing upon the history of Virginia as a tar-producing state and the aesthetic and smell of the adjacent railroad tracks, the project team chose pine tar as the protective coating for the exterior of the HCLT. A 50% pine tar and 50% linseed oil mix was used to maximize the tar's penetration into the wood grain for maximum protection. Both the linseed oil and pine tar are natural products. The linseed oil significantly slowed the drying time of the pine tar application, but allowed for a deep grain penetration. The pine-tar-linseed-oil mix took approximately one week to dry per coat. The base coat was applied at the RDF facility and quickly soaked into the HCLT, forming a dark low-mess coating. Subsequent onsite applications were significantly slower to dry and were generally more messy to apply.

Figure 5: *Module A and B bisected by bridge*

2.3.2 Modular Construction

The modular assembly of HCLT panels occurred at RDF following panel preparation. The base of Module A was designed as a heavy timber structure for the following reasons: (1) a concern that the HCLT should not be the

primary substructure due to its exposure to the elements and potential to delaminate over time; (2) the structural need to support cantilevering elements of the module off the hollow-core steel substructure; and (3) the ease of structural attachment that heavy timber provided over a more thin, panelized timber product. The module assembly team was primarily composed of two people, a forklift operator and a labourer whose primary role was to stabilize the panel in place, fine tune its location with a rubber hammer, and screw the HCLT panel in place via the pilot holes. The HCLT was exceptionally heavy due to its density and therefore special consideration in regard to the forklift movement and driving surface needed to be considered. Due to the HCLT's eventual exposure to the elements, all timber screws were coated with liquid wax before being driven into the pilot holes. The project team took this unusual step to avoid water being sucked into each screw hole due to capillary action, thus leading to wood rot. By impregnating each hole with liquid wax, the project team sought to keep the screw holes free of water. A staggered screw placement allowed the HCLT panels to have an enhanced moment resistance when attached to the thick heavy timber beams. Each screw was determined by the engineer to carry 200 pounds of load and the screws were spaced approximately every twelve inches across the HCLT-to-HCLT and HCLT-to-timber joints.

Figure 6: *Wax application by student during assembly*

2.4 TRANSPORTATION AND ON-SITE LOGISTICS

Each timber module weighed in excess of 2,000 pounds. Module A was assembled offsite at RDF and transported via an industrial forklift and low-boy trailer to the construction site. Module B was partially assembled offsite before being transported to the site flat packed and assembled on site. It was determined that Module A was structurally robust enough for full prefabrication, transport, and crane assembly due to its 90-degree corner joints and HCLT interior columns. Module B was less rigid and prefabrication was determined to be detrimental to the assembly process.

Figure 5: *Industrial forklift transporting Module A*

3 POST-CONSTRUCTION VISUAL INSPECTION

3.1 OVERVIEW

The New River Train Observation Tower opened to the public in 2021. The author conducted a limited visual inspection in February 2023 to assess potential deterioration of exterior exposed HCLT, as well as any general aesthetic changes due to sunlight, freeze-thaw cycles, and insects. The project's modular design allows for the replacement of HCLT components. As such, regular visual inspections should be conducted to determine if any exterior-exposed HCLT elements need to be repaired or replaced. This visual inspection did not address the current structural condition of the tower as its primary objective was to denote the aesthetic changes that have taken place since construction completion.

3.2 DISCOLORATION

Despite the HCLT modules being protected with a pine-tar-linseed-oil finish on one face and a clear ASTM-D4446-rated sealant on the other, some discoloration of the wood product and finishes has occurred. The discoloration that has occurred is not unexpected for UV-exposed surfaces. The sharp black pine-tar-linseed-oil treatment has dulled to a dark gray or soft matte black finish. Multiple coats of the mixture were originally applied to exterior-facing elevations of the HCLT product and the treated surfaces held their color for the first year. It is recommended that the wood surfaces be re-coated every two years in the project's maintenance manual and it seems unlikely that such a re-coat has occurred. The faces coated with a clear wood sealer have maintained their warm, natural wood color, minus a slight dulling of the color from a soft brown to a warm gray or tan.

3.3 DELAMINATION

Perhaps the most serious visual change in the project observed during the visual inspection was the partial delamination of the outermost lamellae on south-facing HCLT panels wherein the outmost layer of lamellae is oriented vertically. Per prior text, the project team was concerned during the manufacturing process that the

https://doi.org/10.52202/069179-0490

custom-engineered press was not able to achieve the proper pressure on the outer two inches of each 5 foot by 10-foot panel. The project team hypothesizes that south facing HCLT panels receive a greater thermal load than other panels in the module and therefor the improper pressing process has led to micro delamination or cracking. The cracking has then allowed water to infiltrate and through freeze thaw cycles and has exacerbated the delamination. An alternate hypothesis is that the panels were already deaminating in a minor way when installed. Freeze-thaw cycles have therfore simply exacerbated cracks that were already present during manufacture. While the delaminating lamellae only have a maximum separation of .25 inches or less, maintenance will need to be performed before any additional separation occurs. The HCLT modules were prefabricated such that panels were oriented vertically as a means to align the strongest axis of the product with the highest tensile forces resulting from module transportation, each panel needing to be strong enough to support its own self-weight. Thus, the vertical panel orientation is better than a horizontal panel orientation at channelling rainwater away from the exterior seams of the lamellae, but there is still significant water exposure for the panel.

3.4 INSECTS

The author did not observe any modifications to the panels' physical integrity due to insect activity. The author was concerned about termite damage to the exterior exposed HCLT panels, but no evidence was present of any insect activity.

4 CONCLUSIONS

Through the achievement of the project's research objectives, the author and project partners were able to establish workflows for future projects that seek to utilize Yellow Poplar cross-laminated timber for modular, offsite construction. The built project illustrates the architectural and structural potentials for HCLT use in modular assembly workflows and confirms certain architectural and spatial potentials for the product, notably its free-span potential at a relatively thin cross-sectional thickness. Certain project decisions, including the use of a laminated product for an exterior application were justified due to the experimental nature of the structure and use of the structure as a prototype. However, the application of the HCLT product in a long-term or permanent use case wherein it is exposed to water, and thus freeze-thaw cycles, is not recommended, even with high-performance surface treatments. This follows common guidance on the use of structural, engineered wood products in exposed settings. The procedural decision to pre-drill pilot holes in the HCLT for wood screws to prevent cracking, as well as to impregnate the holes with a liquid wax, has proven to be a workable approach as confirmed by the two-year visual inspection. Lastly, but perhaps most importantly, the author recommends a highly-controlled fabrication/pressing process for any HCLT product that is produced in smaller factory setting less accustomed to industrial CLT standards and workflows. The production process can use AHEC's manufacturing requirements document as a guide. Quality control during a distributed manufacturing process is difficult to achieve, but necessary to ensure product quality and safety.

Figure 7: *Yellow Poplar CLT panels before surface treatment*

ACKNOWLEDGEMENT

The author wishes to acknowledge the seminal Yellow Poplar research by Dr. Daniel Hindman and Dr. Henry Quesada that underpinned the Radford design-build project, as well as the USDA's Wood Innovations program for early-stage research funding for HCLT development and testing. Additionally, key project partners including Walder Foundation Products, Henard Metal and Fabrication, the City of Radford, and Virginia Tech donors were key to the project's completion. The author would like to thank Professor Kay Edge, Robert Riggs, and Kirt Hilker for their project efforts.

REFERENCES

[1] Espinoza O., Buehlmann U.: Cross-Laminated Timber in the USA: Oppurtunity for Hardwoods? Current Forestry Reports, 4:4, 2018.

[2] Espinoza O., Buehlmann U.: Cross-Laminated Timber in the USA: Oppurtunity for Hardwoods? Current Forestry Reports, 4:1-12, 2018.

[3] Hairstans R., Plowas W., Calcagno C., Milne M.: "The Quality Assurance of Tulipwood Cross Laminated Timber (CLT) for "Multi-Ply." Wood Design Focus, 29(2):20-26.

[4] Hovanec, D.: Effect of Wood Characteristics on Adhesive Bond Quality of Yellow-Poplar for Use in Cross-Laminated Timbers. Graduate Theses, Dissertations, and Problem Reports. 5826. https://researchrepository.wvu.edu/etd/5826 , 2015.

[5] Thomas R., Buehlmann U.: Using Low-Grade Hardwoods for CLT Production: A Yield Analysis. In *International Scientific Conference on Hardwood Processing,* pages 199-206, 2017.

[6] Mohamadzadeh M., Hindman D.: Mechanical Performance of Yellow-Poplar Cross Laminated

Timber. Virginia Tech Report No. CE/VPI-ST-15-13, page 4, 2015
[7] Mohamadzadeh M., Hindman D.: Mechanical Performance of Yellow-Poplar Cross Laminated Timber. Virginia Tech Report No. CE/VPI-ST-15-13, page 4, 2015
[8] Mohamadzadeh M., Hindman D.: Mechanical Performance of Yellow-Poplar Cross Laminated Timber. Virginia Tech Report No. CE/VPI-ST-15-13, page 17, 2015
[9] Mohamadzadeh M., Hindman D.: Mechanical Performance of Yellow-Poplar Cross Laminated Timber. Virginia Tech Report No. CE/VPI-ST-15-13, page 17, 2015
[10] Companella D, Concular: The Digitisation of Materials in Buildings. In Heisel F., Hebel D., Webster K., editors, Circular Construction and Circular Economy, pages 114-117. Birkhauser, Basel, Switzerland, 2022.
[11] Rau-Oberhuber S, Material Passports: Enabling Closed Material Loops. In Heisel F., Hebel D., Webster K., editors, Circular Construction and Circular Economy, pages 118-121. Birkhauser, Basel, Switzerland, 2022.

https://doi.org/10.52202/069179-0490

World Conference on Timber Engineering Oslo 2023

MASS TIMBER, SMALL FORMAT: OPEN SOURCE FURNITURE PROTOTYPING FROM MASS TIMBER SCRAPS

Cory Olsen[1], Linda Zimmer[2]

ABSTRACT: In assessing current mass timber manufacturing practices, the project team has identified an opportunity to generate well-designed human-scale furniture pieces from commonly occurring small sized offcuts in the factory setting. Typically destined for biomass/cogen or even the landfill relative to local environmental legislation, the possibility of upcycling these scraps by creating furniture instead preserves more embodied energy and sequestered carbon, and may generate additional profit as a value-add offering for mass timber manufacturers.

Through partnerships with the Tallwood Design Institute/Emmerson Lab of Oregon State University as well as DR Johnson Wood Innovations in Riddle, Oregon, the research team has produced both digital as well as built prototypes to test production viability and market interest. With an eye towards open source file sharing, the long term goal is to provide designs to interested mass timber manufacturers in order to reduce unnecessary material inefficiencies in the mass timber production cycle. One of the built prototypes has already gained considerable traction and was showcased at WantedDesign's LaunchPad as part of ICFF (International Contemporary Furniture Fair) NYC in May 2022.

KEYWORDS: Upcycling, Furniture, Offcuts, Value-Add, Open Source

1 INTRODUCTION

By way of a hypothesis from individuals not intricately involved in the mass timber industry, the research team speculates that mass timber manufacturers must inevitably generate an assortment of scraps as panels are sized and architectural fenestration is accommodated [1]. In speaking with industry experts we discovered this to hold true and found that from lack of alternative, current practices relegate this material to indeterminate long term storage, chipping, incineration, or landfill. We propose that an opportunity exists to translate some portion of this remaindered material into useful, well designed furniture pieces and preserve the embodied energy contained in the mass timber product.

2 INDUSTRY INTERVIEWS

To date the research team has interfaced primarily with three entities for interviews on material, production, and life cycle: the Tallwood Design Institute of Oregon State University, Freres Lumber in Lyons, Oregon and DR Johnson Wood Innovations in Riddle, Oregon. These represent two key profiles in the mass timber ecosystem: a research lab and two manufacturers- one of mass plywood and the other of CLT.

2.1 TALLWOOD DESIGN INSTITUTE

TDI hosts a variety of mass timber research projects across various scales in its Emmerson Lab, from small CLT sample chunks for mold and mildew testing to multi-story structural assemblies on a seismic table. The materials used in these mockups and tests have little to no application after they have served their initial research intent. In speaking with then-Technical Manager Jörn Dettmer we found that most material would be relegated to the landfill as local environmental codes limited opportunities for incineration due to the adhesives present across the various materials in the lab (CLT, MPP) [2]. As part of the lab's research posture, they have a suite of fabrication tools available including a small format CLT press, an Italian Biesse CNC panel cutting machine, and a track mounted KUKA industrial robotic arm with a positioning table.

2.2 FRERES ENGINEERED WOOD

Freres is a central Oregon plywood producer that expanded their facilities to become a domestic producer of mass plywood panels in 2017. Speaking with their design and engineering team gave the research team key insights into their (proprietary) target efficiency goals for each architectural project regarding percentages in panel efficiency. Additionally, we were provided an informative disclosure of how they currently address

[1] Cory Olsen, Department of Interior Architecture, University of Oregon, United States, coryo@uoregon.edu
[2] Linda Zimmer, Department of Interior Architecture, University of Oregon, United States, lzimmer@uoregon.edu

https://doi.org/10.52202/069179-0491

scraps- thin panel clean-ups are collected and periodically taken to their offsite facility for cogen electricity production, while larger scraps are piled and covered in their yard for long term storage, Figures 1,2. The larger pieces are occasionally informally sold to local DIY-minded fabricators but there are no recurring outlets for the large scraps to be repurposed at the moment.

***Figure 1**: Thinner and small scale scraps of MPP suitable for chipping and cogen collected at Freres' Cedar Mill facility.*

***Figure 2**: MPP saved scraps, of a scale and dimension suitable to furniture reuse but irregular and impractical for building applications.*

Freres utilizes a German made Weinnman 5-axis CNC to size and cut their panels.

2.3 DR JOHNSON WOOD INNOVATIONS

Following an industry presentation of our research hypothesis, Levi Huffman of DR Johnson Wood Innovations reached out to the research team. He confirms that DRJ has been looking for ways to utilize scraps generated in their CLT production line [3]. Equally interesting, we were informed that some panel waste is necessary in their production to maximize press efficiency when transitioning between orders by gluing multiple 3 or 5-ply panels simultaneously even if the additional panel width exceeds project spec. In our eyes, this material is prime grounds for furniture forms that can take advantage of CLT spanning abilities, such as elongated benches for public lobbies and school projects.

DR Johnson utilizes a German Hundegger CNC panel cutter.

3 DESIGN THINKING

3.1 MATERIAL PROPERTIES

To design viable furniture proposals, the research team first assessed the material properties of CLT and MPP. Key considerations throughout the design process have been material visual scale, volumetric weight, standard thicknesses, and sound joinery detailing. Material consistency, particularly in CLT, is understandably variable and designs have sought flexibility in accommodating surface gaps, voids from wanes, and a minimization of slivered remnants from certain cut angles and depths. As CLT is not edge glued there is a certain risk that some acute cuts may result in unadhered geometries. Mass plywood is available in an array of thicknesses beginning at 2" up to 24" in one inch increments, while CLT is assembled in odd number plys, most commonly in 3-ply which is approximately 4" or 105mm. While mass ply can be considered more-or-less uniform for designing joinery, the scale of the alternating laminations in CLT requires that grain direction and board orientation be thoughtfully considered.

3.2 MANUFACTURERS TOOLING

Our designs operate under a basic assumption that mass timber manufacturers will have tooling on hand to create cuts in panels for overall sizing, craft bevels/miters, and cut out openings (either via plunge saw or router milling heads). The OSU Emmerson lab additionally has a KUKA robotic arm which has been utilized for prototyping but may exceed a baseline manufacturing ability expectation.

Our interviews with mass timber manufacturers regarding their tooling abilities and strategies was very illuminating. While our proposal for utilizing scraps was widely well met, a variety of potential obstacles presented including:

- A CNC bottleneck in current existing production slows jobs and additional machine time for

https://doi.org/10.52202/069179-0491

furniture components would have to be well justified. Minimizing tool changes and optimizing for fast cutting operations would alleviate- routing a profile takes considerably longer than rip cuts with a circular blade, for example.

- Small scale objects present an operational challenge relative to the CNC panel cutter setups. Panels are supported by spaced bucks with sacrificial cutting layers, but small components could potentially occur between supports. An object cut free could pose an operational risk if it were to bind with a cutter head if unsupported. As a result, machine operators will sometimes prefer to "dust" smaller areas to avoid captured objects and tabbed elements that could bind in the CNC
- For torsional integrity during installation, some panels will ship with openings still tabbed in place, effectively removing the scrap from the factory and placing it at the jobsite where it may be more challenging to recapture.

3.3 PRECEDENT

As mass timber panels are a relatively new building material, there are understandably few direct precedents for mass timber furniture. One notable collection is the Pipedreams set of residential scale pieces by Douglas & Company based in Cape Town [4]. Their pieces utilize reclaim material from an architectural project and manifest as a daybed, bench, and stool.

The mass of our potential pieces led us also to various precedents of other wooden construction, with significant relevance towards laminated plywood constructions and milled solid timber pieces. Similar in form to the Squall is Nadaaa's Bob Sidetable, constructed from a billet of laminated plywood pieces and milled [5]. Bernard Cache and Patrick Beauce's Objectile outputs are another CNC produced form of laminated and formed plywood construction [6]. The studio furniture of the late Wendell Castle reveals a more intuitive approach to a stereotomic carving of wooden mass [7]. And recently the works of Gareth Neal such as his Hack Chair and Of Cuts series emerge from a starting point of mass [8].

4 PROTOTYPING

4.1 DIGITAL MODELS

The research team initially develops digital proposals to explore aesthetic quality, scale, material relationships, and joinery. These models are created as 3D digital forms in Rhino, which allows for volumetric file sharing through a variety of file extension types (OBJ, STL, DXF, SAT, etc). This flexibility allows reasonably easy interface with a variety of CAM software that may be used across the mass timber manufacturing spectrum. Beyond a proof of concept in generating prototypes, our goal is that panel manufacturers can incorporate these component cuts into their active production lines as an open-source design sharing model and fabrication opportunity.

Through the use of rendering software such as VRay, materials are accurately mapped to test the visual character of each piece, Figures 3,4. Renderings also enable a discussion with manufacturers in regards to parts orientation and grain direction, again particularly relevant when considering CLT and joinery, Figure 4,5.

***Figure 3**: Mesa Bench visualization*

***Figure 4**: Facet Table visualization*

***Figure 5**: Facet Parts illustration for visual communication to saw operators*

4.2 TDI EMMERSON LAB : SQUALL STOOL

Capitalizing on the availability of the Emmerson lab KUKA robotic arm, an initial prototype was produced that leveraged the tools spatial flexibility to create a complex undulating surface, Figure 6. Named the Squall Stool, see: Figure 7, the piece consists of a stack lamination of four pieces of 3-ply CLT milled to a compound flowing

surface. The design is parametric in nature, such that every stool produced can easily incorporate formal variations for each to be unique within a family of serial difference. The Squall was recently shared with an international audience at the 2022 ICFF as part of WantedDesign's LaunchPad prototypes feature.

***Figure 6**: KUKA robotic arm milling Squall prototype*

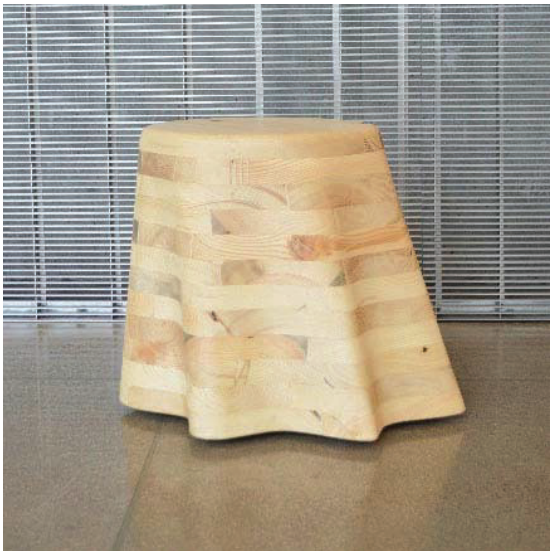

***Figure 7**: Squall Stool*

The Squall took approximately 7 hours to mill on the KUKA as an initial prototype run. While a considerable amount of time, in the lab setting the machine is rarely occupied and this form is a capitalization of its abilities and components, including the positioning table for milling pieces in the round. With further experience, refinement and optimization the milling time could be reasonably expected to reduce.

The stool sits on 5 rotational casters for ease of movement. The recesses for the casters were machined by hand while the team was iterating through options, though these also offer an opportunity to leverage the KUKA while the piece is being fabricated.

As a furniture piece the Squall provides an ergonomic seating height at 16.5" suitable for table height work and casual use, figure 8. It can easily serve a secondary role as a side table as well. Aesthetically the smooth surface provides a novel visual to the CLT where the 90 degree alternating laminations blend smoothly from edge grain to end grain. Each milled blank will reveal a different grain pattern and coloration adding to the uniqueness of the serial family.

***Figure 8**: Squall in use*

https://doi.org/10.52202/069179-0491

4.3 TDI EMMERSON LAB : THE "SUITCASE"

Following the success of the Squall, an additional prototype the "Suitcase" has been produced with the assistance of the TDI labs, Figures 9, 10, 11. Recognizing that the utilization of the KUKA may exceed industry capabilities, the design team shifted our focus to the panel CNC. The "Suitcase" as it is currently codenamed represents a culmination of our learning since embarking on our mass timber furniture research. The design consists of four bevelled CLT strips that are assembled together into a single mass. The component widths are sized to take advantage of linear narrow scraps, such as those common in the DRJ production when they are pressing multiple panel specs in job transitions. The components are cut with a vertical or bevel rip cut, utilizing the circular blade of TDI's Biesse CNC machine. The length of the suitcase can be anything from a single seat to the full length of a mass timber panel. From an efficiency standpoint, longer lengths negate concerns about pieces being unsupported by the saw bucks. Each rip cut takes from seconds to minutes, adding a minimal amount of machining time to any job. The small single seat Suitcase was assembled using Domino XL joinery and adhesive, while a larger prototype has been assembled using CLT wood screws. On reflection, using wood screws has benefits of allowing lighter individual parts to be transported and assembled on site quickly with tools that will already be in use. Parts could be delivered pre-sanded and prefinished or completed on location.

After lamination, a simple bent steel backrest is bolted on along with a linear dimensional lumber lumbar support, maintaining the SPF materiality of the CLT itself. Similar to the Squall, the individual Suitcase rests on four recessed casters to allow an ease of movement despite the overall weight of the piece. For longer runs of the Suitcase a fixed foot strategy would be utilized to make it into a stationary monumental installation.

***Figure 9**: Suitcase parts at TDI fresh from the Biesse Saw*

***Figure 10**: Suitcase Seating prototype in a single width*

***Figure 11**: Suitcase in use. Bevel angle allows for natural footrest and backrest placement.*

https://doi.org/10.52202/069179-0491

4.4 DR JOHNSON

In partnership with DRJ, files have been shared so that they may pursue factory produced prototypes. These are generated in between panel production runs at the discretion and availability of the saw operators. One design has been produced in multiple, the Torii Bench as shown in Figure 12. Additional pieces are available in their queue and will be produced as their fabrication schedules allow. This includes designs from a family of related forms named the Capsule Collection, see Figure 13.

Figure 12: *Torii Bench cut and assembled by employees at DR Johnson's Riddle, OR location.*

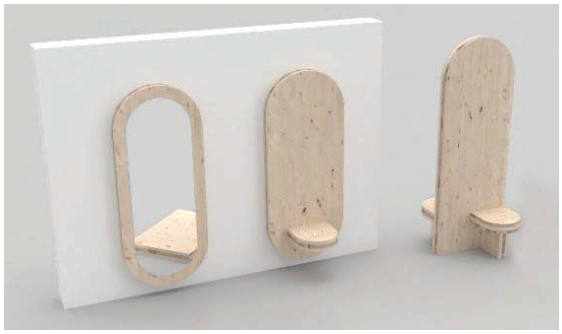

Figure 13: *Capsule Collection showing wall mounted mirror, seat, and freestanding 'Tete a Tete' chair sharing a common pill shape feature geometry.*

5 FUTURE-CASTING

5.1 DESIGN FOR DECONSTRUCTION/DISASSEMBLY

One of the leading arguments for the environmental benefit and sustainability of mass timber architecture is its ability to sequester carbon [9]. While most mass timber structures are too recent to be facing replacement those days will inevitably come. The tectonic nature of mass timber assembly can lend to an organized disassembly enabling building elements to be recaptured and reused [10]. Ideally architectural panels could be recycled into new architecture but this would require a considerable amount of planning, anticipation and execution. The research team proposes that a highly flexible secondary application for recaptured mass timber would be furniture scale objects. Oddly shaped, unique, or damaged panels could be reasonably easy to optimize through parts nesting, with the majority of the sequestration volume left intact.

6 CONCLUSIONS

Scraps and offcuts are known to occur in mass timber production though current means of utilizing these are limited. Furniture design prototypes have been produced as a means to upcycle and preserve the embodied energy of these materials, and the research team hopes to involve more interested manufacturers to reduce waste stream volumes while providing functional, aesthetically pleasing furnishings to projects. Further, as mass timber constructions reach their end of life, the potential for reuse increases with avenues such as furniture and products.

ACKNOWLEDGEMENT

This research has been supported by a grant from the Oregon State University Tallwood Design Institute and the United States Department of Agriculture's (USDA) Agricultural Research Service.

REFERENCES

[1] Waugh Thistleton Architects. Cutting and Routing. *100 Projects UK CLT*, page 47. Waugh Thistleton Architects, Canada, 2018.

[2] Interview with Emmerson Lab Technical Director Jörn Dettmer, February 2, 2021.

[3] Correspondence with DR Johnson, Levi Huffman, August 19, 2021.

[4] "Pipe Dreams." Douglas & Company. Accessed January 10, 2023. https://www.douglasandco.co.za/pipedreams.

[5] "Bob Sidetable." NADAAA, March 28, 2019. https://www.nadaaa.com/portfolio/bob-sidetable/?id=3786.

[6] "Objectile." Archilab 1999 English -. Accessed January 10, 2023. http://www.archilab.org/public/1999/artistes/obje01en.htm#exposition.

[7] "Wendell Castle- Contemporary." Wendell Castle, October 6, 2017. http://www.wendellcastle.com/avada_portfolio/contemporary/.

[8] Gareth Neal. "Collect Art." Gareth Neal, May 10, 2021. https://www.garethneal.co.uk/art.

[9] Souza, Eduardo. "There is Life After Demolition: Mass Timber, Circularity and Designing for Deconstruction" July 27, 2021. ArchDaily. Accessed January 14, 2023. https://www.archdaily.com/963070/we-must-think-about-the-future-of-buildings-after-demolition-mass-timber-circularity-and-designing-for-deconstruction

[10] "Full Circle: Designing and Specifying for End-of-Life." Think Wood, September 27, 2022. https://www.thinkwood.com/blog/coming-full-circle-designing-for-end-of-life.

https://doi.org/10.52202/069179-0491

World Conference on Timber Engineering Oslo 2023

CARPENTER AND ROBOT: HOW TO BENEFIT FROM THE KNOWLEDGE OF CRAFTSMEN AND THE STRENGTH OF ROBOTS

Wolfgang Schwarzmann[1]

ABSTRACT: In this research project, the working process of carpenters using a CNC joinery robot was observed, documented and evaluated on the basis of a small building, the *'Werkraum Häuschen'*. Designed as a building made of traditional timber joints, the entire construction was produced on a modern CNC joinery system. Under aspects such as the utilization of mono materials, simplified disassembly and reuse, as well as the need for later deconstructability, the wooden knots proved to be functional and resilient. According to interviews with the craftsmen, not only the skills of experienced carpenters but also the advantages of a modern CNC-joinery machine contributed significantly to the success of the project.

KEYWORDS: CNC robot, craft, carpenter, tradition, human-machine interaction,

1 INTRODUCTION

The profession of carpenters has always been in a constant process of change parallel to our society [1,2]. While in former times purely manual work was significantly changed by the emergence of metal tools, steam power and later on electricity, today, a major driver in this process of change is computer-controlled joinery robots [3]. By opening up new applications, these machines offer additional possibilities from the construction and design perspective. While a lot of research projects start from a process optimisation perspective when considering new digital tools [4,5,9], the focus of this paper is on the merged potential of the craftsmen's knowledge and the opportunities offered by joinery machines. As described by Nonaka and Takeuchi, craft professions involve profound tacit knowledge [6], and therefore it is highly relevant to not only conduct research on new applications but also on the context of knowledge generation and manufacturing processes from a craftsman's perspective. In the context of this research, tacit knowledge and the associated perception of the craftsman is explored and discussed in relation to the contemporary technological developments of a cnc-joinery robot.

1.1 NEW SKILLS UNDER AN OLD LABEL:

With a history of more than 7,000 years, the craft of carpentry can look back on a long and dynamic history [1]. Besides the historical evolutionary stages related to steam engines and the introduction of electricity, digitalisation in the craft of carpenters can be considered as a further, fundamental moment of transformation [3]. While craftsmen once had to prepare raw tree trunks themselves, nowadays they can access an almost infinite range of electrically powered and digitally controlled tools. Today, modern joinery robots and corresponding CAD systems mean that much of the work that once had to be done by hand is now done by digitally controlled machines. Apart from these technological changes, wood has remained central as a building material over all that time. A rather similar situation can also be observed in the job description. Although the work of the craftsmen has changed fundamentally, we still refer to them as carpenters today.

This changing field of work for carpenters was already examined in connection with their working process [7], their tradition, and the role of the technologies involved [8]. In this paper, we examine the task of the craftsmen and how they experience their work alongside the joinery robot.

1.2 A MOBILE STRUCTURE MADE OF WOOD

As part of the exhibition Constructive Alps 2021, the *'Werkraum Häuschen'* was built at the *Werkraum Bregenzerwald* in Andelsbuch in autumn/winter 2021. The region of the Bregenzerwald in Vorarlberg, Austria, is known for its timber construction culture and its high regard for craftsmanship. A debate concerning modern manufacturing methods and traditional craft culture is particularly exciting in this region.

The *'Werkraum Häuschen'* (Figure 1) is a small, mobile building, constructed from solid wood. The intersections and corner joints were resolved as pure wood-wood joints. Fully erected, it measures 5.50m x 2.80m x 4.36m (l/d/h). The locally harvested, sawn and dried wood (within a radius of 18km) was processed on a joinery robot. The connections were designed and manufactured as dovetail joints, mortise-and-tenon joints or similar. In the manufacturing process, great care was taken to use traditional, i.e., once commonly used, timber connections, whereby these connections were now fabricated by a joinery robot. All parts were manufactured on a state-of-the-art joinery machine, a Hundegger 'Robot-Drive'

[1] Wolfgang Schwarzmann, Architecture University Liechtenstein, Vaduz, Liechtenstein, Institute of architecture and planning , wolfgang.schwarzmann@uni.li

https://doi.org/10.52202/069179-0492

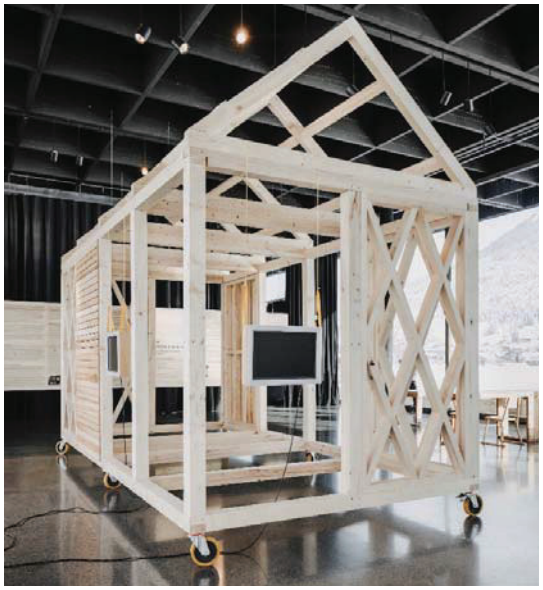

Figure 1: *The 'Werkraum Häuschen' a modular wooden construction kit, after completion, ready for the upcoming contributions of the craftsmen*

1.3 THE WORKING PROCESS AS FIELD OF RESEARCH

As an essential part of the qualitative research work, the construction process was documented with photos, video and audio, and then transcribed. In just one day, the structure was assembled and erected by 3 craftsmen (1 craftsman and 2 trainees) as well as the author himself (Figure 2).

Figure 2: *A carpenter assembling the wooden frame. The complicated connections in the frame are still visible.*

After approximately 3-4 weeks, all the craftsmen that had worked on the project were invited to participate in interviews. They were asked about the manufacturing process, sharing their insights concerning the challenges but also the positive qualities related to the robotically manufactured construction components. The interviews were supported by drawings of the construction as well as a time-lapse video of the construction process and photos of the assembly. It was intended to spotlight the assembly process once again. In addition to the 3 assembling craftsmen, the two CAD draftsmen responsible for the working plans but also for programming the joinery robot were interviewed. This wide range of audio and video material formed the basis of this research work.

1.4 A JOINT DESIGN AND PLANNING PROCESS:

Based on an initial meeting with a team of curators and carpenters, a simple CAD sketch was developed. This sketch already illustrated the requirements for the finished project without detailing the timber construction.

The basic principles of the concept sketch were:

- **Simple load-bearing structure:** the geometry of the building is formed by a simple load-bearing system made of wood. Similar to a shelf, the supporting structure is intended to form the framework for the contents.
- **Modularity:** Modules will be inserted into this supporting structure by the craftsmen. The individual wall, floor and ceiling modules should be insertable at any desired position.
- **Mobility:** The finished building should be just large enough to be transportable by truck. This building should be able to function in a variety of places. Wheels on the underside allow an uncomplicated positioning of the building.
- **Circularity and deconstructability:** All solutions for the project should be developed under the aspects of circularity and deconstructability. If possible, hybrid materials like glued beams or plywood should be avoided. The individual modules should be reusable for other purposes later.

2 METHODS

Based on these principles, several workshops and discussions were organised with the carpenters. Step by step, the craftsmen worked out the individual details. In the process, attention was paid to ensuring that the experience, the expert knowledge, and ideas of the carpenters could be implemented as effectively as possible while relying on the 4 basic principles.
The resulting sketches and CAD drawings, as well as notes from discussions were recorded and integrated as data for the project. Over the duration of approx. 8 weeks, a design was developed that could then be manufactured on a CNC joinery system (Figure 3).

https://doi.org/10.52202/069179-0492

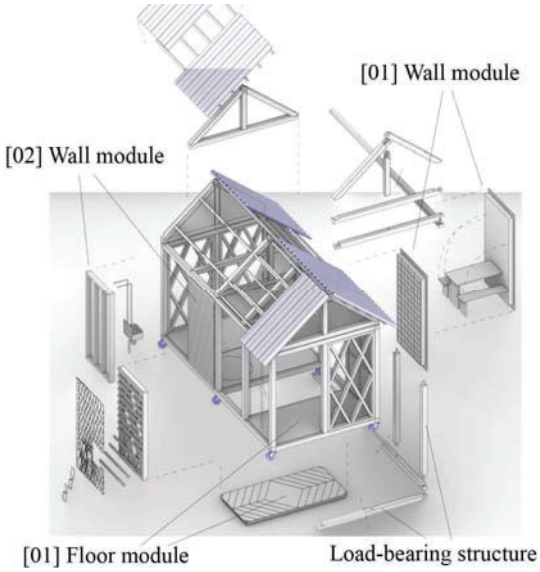

Figure 3: *Modular, dismountable and transportable; the small house was designed to work in different application scenarios.*

2.1 MANUFACTURING OF COMPONENTS AND CONSTRUCTION:

All parts of the supporting structure (columns, bottom plate, roof structure etc.) were manufactured on a 'Hundegger' joinery machine. The previously discussed construction details like dovetail, tenon, groove etc. were adapted and translated by an experienced carpenter to the technical possibilities of the machine. In order to be able to use mono materials and deconstructable connections, all the corner joints were designed as pure wood-wood connections. As a result, it was possible to omit further steel parts from the load-bearing structure. The stability of the construction was made possible by interlocking rhombic lattices that were installed as frames at each corner. At some points, the construction was stabilised with screws for safety and transportation reasons. The 6 wheels were also fixed with 4 screws each. The spruce wood was harvested in the region (12km distance) and stored and dried directly in the carpentry workshop (0km). A young carpenter operated the joinery robot and selected the raw wooden beams for their quality, as not all wooden logs offered the same properties in terms of straightness and stability. The finished beams were then delivered to the *Werkraum Bregenzerwald* (6km distance).
In a joint work process (1 carpenter, 2 trainees and the author) it was possible to erect the construction within one day. None of the carpenters who erected the structure at the *Werkraum Bregenzerwald* had been involved in the planning process before. This decision was intentional, as it meant that it was the first time for them that they came into contact with the project. This division between the planning and the construction process was made intentionally. Due to this separation, the craftsmen's comments during the construction were particularly interesting. They had to rethink the construction plans, the building parts and the construction process and develop their own approach to the project.

Figure 4: *The assembly of the wooden construction was completed within one day by 4 people.*

2.2 DEBRIEFING WITH CRAFTSMEN:

About 3 weeks after the completion of the construction, the craftsmen were interviewed in a semi-open interview to discuss and share their perspectives on the project. The interviews were supported by a video (duration 2:25 min.) showing the construction process of the building and by a selection of pictures illustrating the fabrication process (approx. 20 photos). The persons were interviewed in small groups and divided into 3 main work themes: (1) CAD and workshop drawing; (2) programming and application of the joinery robot ; (3) assembly and erection of the construction. The individual craftsmen were asked about their role as craftsmen in the process, how they used their expertise, and what the work process with a joinery robot meant to them.

Referring to the following research question, the collected data were transcribed, coded and analysed accordingly:

What are the perceptions of timber construction experts in the work process with a joinery robot in the development of alternative timber joint details.

3 RESULTS

Considering the collected data and the question defined above, 3 main phenomena could be observed:

3.1 THE RIGHT TOOL, AT THE RIGHT TIME:

One main observation was that the craftspeople always had to decide which tool would provide a good and correct solution at the right time. This situational problem-solving competence can be seen as a key component in the success of the project and ultimately as a crucial skill of their

https://doi.org/10.52202/069179-0492

profession. Whether the tool selected was an electrically powered circular saw, a manually guided plane or a digitally controlled joinery robot was of secondary importance to the craftsmen. For example, it could be observed that although the joinery robot is capable of producing complex solutions quickly and efficiently, the interviews revealed that the correct positioning of an appropriate timber joint was based on the expertise and experience of the CAD draftsman.

Figure 5: *Angled and sloping tenons are not a time-consuming challenge for the machine. However, most tenons still had to be cleaned by hand to ensure smooth assembly later.*

With his knowledge as a carpenter and a CAD draughtsman, this expert had previously designed the building in his head and simultaneously step by step on the computer. Thanks to his experience as a craftsman, he was able to imagine the subsequent assembly process in working-stages and thus could optimise it correspondingly. The joinery robot was then able to perform the job in a comparably short time. For the craftsmen, this computer-controlled production of the components was a significant reduction in their workload. However, as they explained in the interviews, the robot did not do anything that they could not have done themselves in a more manual process.

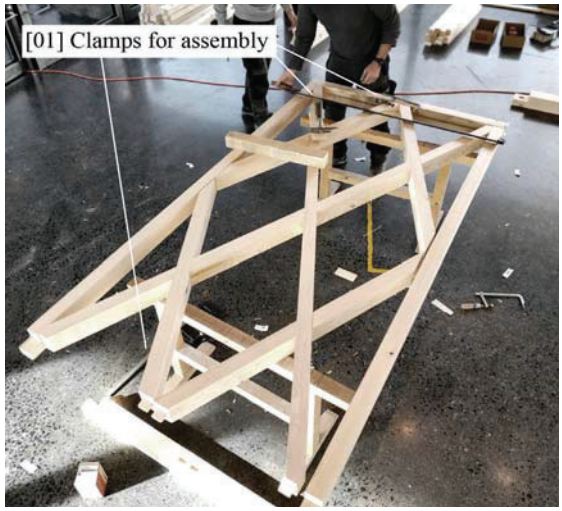

Figure 6: *At the right time, in the right place; the skilled application of screw clamps is crucial when it comes to precise assembly. The CNC robot is quick and accurate, but the assembly of the parts is still demanding.*

3.2 EARLY COMMUNICATION IN THE PROJECT PLANNING

Several rounds of talks were held with the project participants before the first CAD drawings for the joinery robot were produced. These preliminary discussions about statics, structure, construction, and design clarified and fixed fundamental details at an early stage. This preliminary coordination between the project participants demanded knowledge and experience from everyone involved. Problems that occurred later during assembly can be related to late involvement in the project or an inadequate flow of information. For example, a timber beam was installed in the wrong place during assembly. Except for 3 small boreholes, the column also fitted in the other place. Interestingly, the craftsmen already realised this irregularity during assembly and mentioned that the joinery robot must have made a mistake. Afterwards, they simply drilled some additional holes by hand. It was only at the end of the project that it turned out that two columns had been mixed up. This situation might have been avoidable with more accurate coordination, simpler drawings and a correspondingly more intuitive labelling. However, it was also impressive to see how the craftsmen solved the apparent machine error in just a few moments and then continued with the process.

https://doi.org/10.52202/069179-0492

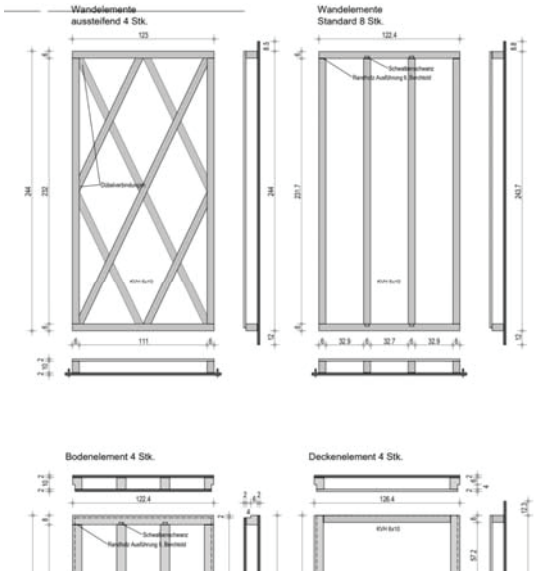

Figure 7: *Sketches, construction drawings, 3D plans; and in-between, there were meetings and discussions. The early and intensive exchange between all the project participants contributed significantly to the success of the project.*

3.3 MAN AND MACHINE COMPLEMENT EACH OTHER

As all the project participants mentioned, the craftsmen would have been able to produce the *'Werkraum Häuschen'* even without a joinery robot. The complexity of the project and the wooden details in the process are time-consuming in most cases, but in terms of production geometry they are not exceptionally complex. The project has shown the importance of the carpenter's expertise, both on the computer and in assembly. In addition to these cognitive skills, it was also the strength, speed and precision of the joinery robot that provided space for the valuable human resources. Because of the mechanical manufacturing, tenons traditionally designed as angular were realised in a round shape. Therefore, there was an adjustment of the timber construction geometry in favour of the machine production. Unfortunately, this geometrical solution could not be applied to all details. Since a joinery robot is not able to produce sharp-edged inner corners (Figure 8; '*[01] Remaining piece'*), the craftsmen had to rework them with a chisel and hammer and with an oscillation tool (Figure 9).

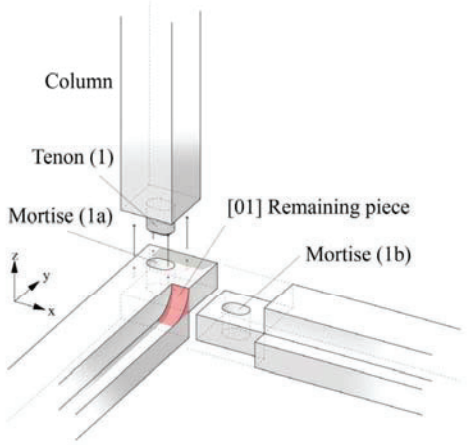

Figure 8: *Due to the technical limitations of the CNC joinery machine, the red corner had to be reworked by hand.*

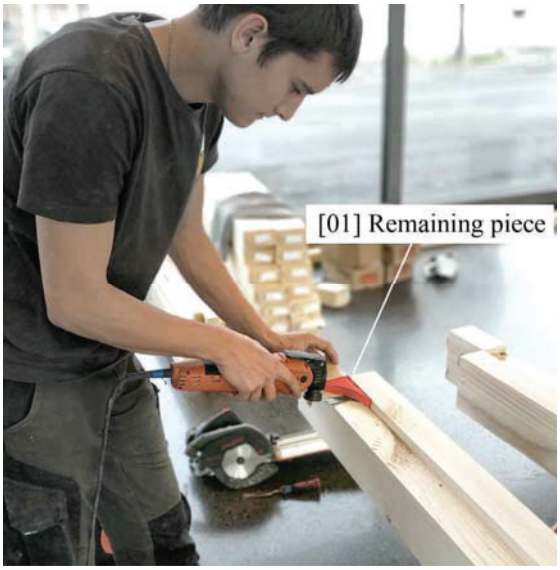

Figure 9: *During assembly, the remaining piece was removed by hand with an oscillating tool.*

In this case, it would not have been possible to simply modify the geometry, as in the case of the tenons. The joint work process, i.e., rapid production on a joinery robot and completion by experienced craftsmen, proved to be an effective and favourable solution in this case.

4 DISCUSSION AND CONCLUSION

In this paper, the question was asked how carpenters perceive their work in relation to a joinery robot in an exploratory construction process, the *"Werkraum Häuschen"*.

Where do the carpenters see their human skills as a key strength, and what kind of work can be performed efficiently and effectively by a joinery robot? As the results illustrate, the carpenters' expertise in the areas of assembly and construction is essential, regardless of

https://doi.org/10.52202/069179-0492

whether they are working with a hand-held circular saw or a joinery robot. This knowledge is central in the project discussion, the creation of the CAD plans, and the production on the joinery robot as well as the subsequent assembly.

While in this case a purely manual production of the construction would have been too time-consuming and therefore too expensive, the joinery robot was able to produce the laborious timber joint details quickly and efficiently. Furthermore, the joinery machine can be seen as a physical extension of human capabilities. Traditional timber joints could be interpreted and translated in a new context, where the strengths and expertise of the craftsmen were shown to be a key competence. The joinery robot and the corresponding software package can simplify and speed up work processes, but the underlying skills of the people operating the machine remain a key resource in this process.

With regard to future developments in timber construction, the question can be asked how the profession of carpenters will continue to change, what role their knowledge and experience will have in the process, and where new necessities will arise.

5 OUTLOOK AND LIMITATIONS:

As the project review has shown, there are certainly further, more detailed options to be explored in the project. Due to the very tight schedule of the project, new wooden beams were used. Retrospectively, the use of already used wooden beams from, for example, a demolished building would have been a significant enrichment to the findings. Furthermore, a consequent expansion of the wooden joints would be conceivable. In a next step, it would be conceivable to replace the screws used with wooden solutions such as wooden nails or similar. Another point worth exploring would be to optimise the geometry in order to further benefit from the potential of the joinery machine. Due to the limited time available, the focus was placed on the joint working process of developing and implementing pure timber joints and the subsequent assembly process.

ACKNOWLEDGEMENT

This research project was funded by the Research Promotion Fund of the University of Liechtenstein (FFF). New insights were gained as part of the project *'Digitale Meister'* (Digital Masters). Furthermore, we would like to thank the craftspeople and the *Werkraum Bregenzerwald* for supporting this project.

REFERENCES

[1] Zwerger K., and Valerio O., Das Holz und seine Verbindungen: Traditionelle Bautechniken in Europa, Japan und China. 2nd rev. and exp. ed. Birkhäuser, 2012.

[2] Gerner M., Die Kunst der Zimmerer: Meisterwerke aus Europa, Amerika und Asien. DVA, 2002.

[3] Schindler C., Ein Architektonisches Periodisierungsmodell Anhand Fertigungstechnischer Kriterien, Dargestellt Am Beispiel Des Holzbaus. ETH, 2009, doi.org/10.3929/ethz-a-005956976.

[4] Robeller C., Weinand Y., "Integrale Verbindungen Für Faltwerke Aus Holzwerkstoffplatten." In *Detail, 1/2,* pp. 68–74. infoscience.epfl.ch/record/217951/files/DETAIL_2016_1_Technik_Robeller.pdf?version=1.

[5] Willmann, J. et al., "Robotic Timber Construction — Expanding Additive Fabrication to New Dimensions." *Automation in Construction,* vol. 61, 2016, pp. 16–23. doi:10.1016/j.autcon.2015.09.011.

[6] Ikujiro N., and Takeuchi H., The Knowledge Creating Company: How Japanese Companies Create the Dynamics of Innovation. Oxford University Press, 1995.

[7] Schwarzmann, W., "How New Technologies Can Promote the Reintroduction of Traditional Knowledge in the Profession of a Carpenter." *Space and Digital Reality: Ideas, Representations / Applications and Fabrication,* edited by Jüri Soolep et al., 2019, pp. 62–68. issuu.com/artun/docs/space_and_digital_reality_web.

[8] Schwarzmann, W., "Traditional Knowledge on Modern Milling Robots: How CNC-Joinery Machines Promote a Renaissance to Lost Techniques in the Profession of a Carpenter." *Anthropologic: Architecture and Fabrication in the Cognitive Age* - Proceedings of the 38th ECAADe Conference, Berlin, eCAADe. 2 vols. edited by L. Werner and D. Koering, 2020, pp. 579–604. papers.cumincad.org/cgi-bin/works/paper/ecaade2020_297.

[9] Robeller, C., and Weinand, Y., "A 3D Cutting Method for Integral 1DOF Multiple-Tab-and-Slot Joints for Timber Plates, Using 5-Axis CNC Cutting Technology." *World Conference of Timber Engineering WCTE 2016*, Vienna, Austria, August 22-25, 2016, pp. 2576–84. infoscience.epfl.ch/record/222484.

https://doi.org/10.52202/069179-0492

World Conference on Timber Engineering Oslo 2023

A BIM-BASED MODULE DESIGN METHODOLOGY FOR THE ROOF PLANNING OF MODERNIZED KOREAN TRADITIONAL WOODEN BUILDINGS

Dongwook Kim[1], BongHee Jeon[2*], Gee Heon Kim[3]

ABSTRACT: This study proposes a design methodology for modernized Korean traditional wooden buildings, *modernized-Hanok*, with a roof-*Kan* module based on parametric design. In the *modernized-Hanok*, the subordinate relationship between the body and roof structures has been diminished. Therefore, the purpose of the design methodology is to provide a tool that allows designers to plan the roof-frame structures unconstrained by plane shapes using Autodesk's Revit. Once the user determines the desired roof type, purlin number, module size, and reference dimensions, the parameters of families in the module interact with each other with functional formulas. As a result, the roof-frame module is automatically placed at the designated position with the appropriate roof shape. This module-based methodology provides users with a high degree of freedom in design.

KEYWORDS: Korean traditional wooden buildings, Roof-frame, Module design, *Modernized-Hanok,* BIM

1 INTRODUCTION

The *Hanok,* a Korean traditional timber-frame structure created by assembling elements, is one of the most challenging architectural types in terms of design, modeling and construction due to its atypical morphological characteristics. Recently, to overcome the difficulties of planning and constructing *Hanok* and to promote its market expansion, R&D projects for modernizing *Hanok* have been actively pursued, with efforts to create an environment that allows for more convenient design and modeling while securing structural and construction performance [1, 2].

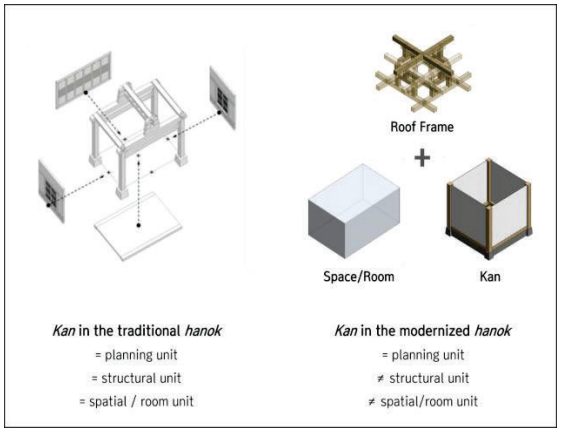

Figure 1: *Concept diagram of Traditional Korean House(Left) & Modernized-Hanok(Right)*

The research of design and modeling methodologies laid the groundwork for the *modernized-Hanok* and securing the structure and construction performance. The precedent *Hanok* BIM design methodologies are as follows. First is the member-unit design methodology, in which the modeling data is completed by stacking members [3]. Second is the joint-unit design methodology, in which the joinery is constructed by assembling members and placing the modeling data [4, 5]. The third is the integrated *Kan* unit design methodology, in which a *Kan* is an integrated unit of the shape of each member and joinery and surface elements such as floors and wall libraries [6]. The limitation of these methodologies is that they focus on the modeling process rather than the design process; therefore, they deteriorate the ability to respond to design change with a low degree of freedom.

In contrast to the precedent methodologies, the research team proposed a 'module-based design methodology' as a solution to the fragmented modeling-based design process. With the 'module-based design methodology' presented, the research team recently developed a '*Hanok* BIM Design Support Program' that allows the users, including both experts and non-experts to approach the *Hanok* design process in a more user-friendly way and contribute to the revitalization of the *Hanok* industry with the support of the Ministry of Land, Transport, and Maritime Affairs of the Korean Government.

The overall design process of the '*Hanok* BIM Design Support Program' is carried out through the arrangement of the modules. Meanwhile, the simple repetitive arrangement tasks, which do not correspond to the

[1] Dongwook Kim, Seoul National University, Republic of Korea, kdwooks@gmail.com
[2*] Contact Author: BongHee Jeon, Dept. of Architecture and Architectural Engineering · Institute of Construction and Environmental Engineering · Institute of Engineering Research, Seoul National University, Republic of Korea, jeonpark@snu.ac.kr
[3] Gee Heon Kim, Seoul National University, Republic of Korea, aiden.gkim92@gmail.com

https://doi.org/10.52202/069179-0493

designer's substantive design tasks, fall within the scope of automation. For example, the beginning of the design process provides an environment in which modules could be used to derive various plans using the spatial module. Then, the roof frame module is placed on the rectangular grid system of the building, completed with the spatial module, and an independent roof structure is created with members such as purlins and beams. Finally, in the latter part of the design, the details could be designed reasonably by replacing the already determined modules with members, and roof tiles are placed on each reference point of the planned roof frame.

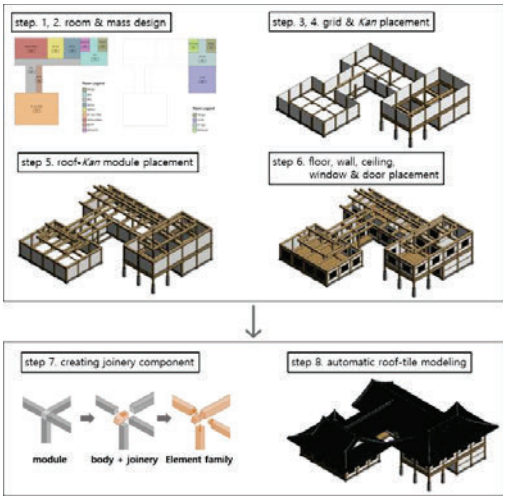

Figure 2: *Design process of the 'Hanok BIM Design Support Program'*

This paper specifically concerns the methodology of the roof frame design step of the '*Hanok* BIM Design Program' that the research team developed and proposed. One of the limitations of planning traditional *Hanok* is that the *Kan,* a bay unit, contains all of the body and roof structures and space in one unit. However, in the *modernized-Hanok*, the subordinate relationship between the body and roof structures has been diminished due to improved structural performance, such as horizontal expansion in the direction of the beam without columns. As a result, the modern *Kan* is no longer a composite unit of the body and roof structures. Therefore, isolating the roof structure from the body structure in the design process on the premises became crucial.

Hence, the research team approached the roof as an independent structure and proposed a module-based methodology to devise a roof-*Kan* module that allows designers to plan the most complicated 3D atypical curved roof-frame structure unconstrained by the body structure. This roof-*Kan* module was developed by extracting data from traditional *Hanok* and implemented using Autodesk Revit, a widely used BIM tool, to approach the design process in a more user-friendly way and contributes to the revitalization of the *Hanok* industry. The '*Hanok* BIM Design Support Program' was completed as a Revit's Plug-in, and released to the public through 'Autodesk's BIM guidebook' and the department of Architecture and Architectural Engineering, Seoul National University.

2 MODERNIZED-HANOK DESIGN, MODELING AND ROOF-KAN MODULE

2.1 HANOK MODELING METHODOLOGY AND ROOF-FRAME PLAN

The design methodology of what the library unit is composed of in precedent research can be classified into individual component units (M1), joint units combined by Skeleton-Assembly (M2), and integrated modules that are unitized by both the body and the roof (M3), depending on the unit type and level of detail (LOD) in *Hanok* design, modeling methodology, and planning [8]. As mentioned above, the roof and body are unbinding independent structures in *modernized-Hanok* and can be planned separately.

The roof planning methodology's strength comes from the ability of establishing various planning unit libraries. Additionally, the amount of libraries necessary is inversely proportional to the level of detail (LOD). Therefore, many libraries are required in cases where the *Family in Family* concept is weakly applied, such as in M1 and M2, while M3 requires a smaller number of libraries. On the other hand, the relationship equation within the unit is proportional to the number of families within the planning unit. In other words, while the relationship equation is defined at the level of component size for M1, it extends to the scope of detail design, such as connections for M2, and M3 has the possibility of parametric design based on the relationship between components.

Therefore, regarding roof planning, M1 effectively represents the details of the roof's shape as various components are differentiated and detailed. On the other hand, the unit planning elements of M3 are advantageous for organizing each part's shape, size, and composition, as multiple components are interconnected.

Table 1: *Classification of precedent Roof frame structure Design Methodology*

Metho-dology	M1	M2	M3
Library Unit	Member	Skeleton-Assembly Joinery	Kan
LOD	5	2 → 5	5
Relation with Design Process	Low	High	Low
Relation with Body part	Low	Medium	Equal

https://doi.org/10.52202/069179-0493

Possibility of Parametric Design in Unit	Low	Medium	High
Link with Other Units	Very High	Medium	Low
Difficulty	Difficult	Medium	Easy

The *modernized-Hanok*'s roof structure is mediated by the body structure but can create an independent shape. In particular, since the structure of the *Jungdori* (middle purlin) and the *Jongdori* (top purlin) is separate from the body structure, related lower components can be planned independently. In other words, since the pre-defined information is associated with the *Jusimdori* (column-raw purlin), the *Daedulbo* (main beam*)* connected to the body, the horizontal range of the roof part can be adjusted through these components, and the lower pieces are linked as independent relational functions. Therefore, the information that needs to be input to create the shape, height, and curve of the roof is the roof type, the position of a *Jungdori* and a *Jongdori*, and the relational function information that can adjust the lower components. Once the input of information about the wooden structure is completed, the roof tiles can be generated, and the position of the tiles can be determined with the *Seokkarae* (rafters) and the *Gaepan* (shingle) based on the reference points of the purlins. However, information related to the definition of the outermost coordinates of the roof, eaves extension, *Buyeon* (double rafters*)*, the curves of the rafters (hipped and hipped-gabled roof), location of the gable (hipped-gabled roof), length of purlin extension (gabled roof) must be defined independently.

Table 2: *Classification of Roof-element's Information by Process*

Type of Information	Subject	By Para-meter	By User
Pre-defined Information	Geometry of Jusimdori & Daedulbo	-	
Information to define	Roof type		●
	Geometry of Jongdori		●
	Geometry of Jungdori & Jongbo		●
	Geometry of Seokkarae	●	
	Geometry of Gaepan	●	
Information to be defined	Extruding of Eaves		●
	Installation of Buyeon		●
	Ang-gok & Anheorigok (Paljak or Woojingak)		●
	Location of Hapgak (Paljak)		●
	Length of Bbaelmok (Matbae)		●
	Composition of Hoecheom		●

2.2 DEFINING THE ROOF-KAN COMBINED MODULE

The design and modeling of *Modernized-Hanok* differ from traditional *Hanok* in that it can plan the body and roof in a loose relationship. Therefore, the planning stages of the body and roof can be done independently, and using modules that meet the objectives of each step is highly effective in the early stages of design. In other words, the main focus of roof planning is to define the shape and scale of the roof. The conditions that modules should have are as follows.

2.2.1 COMPONENTS OF INDIVIDUAL MODULE

To plan the roof part of *Modernized-Hanok*, the roof-*Kan* combined module should be considered from two significant aspects. First, it should follow the principles of traditional wooden architecture for roof construction while simultaneously accommodating the wide spans in the beam direction. In other words, it should reflect the planning logic of the body part but should not be entirely dependent on the structural logic of the body by forming an independent roof structure. Therefore, it should be possible to independently implement the morphological characteristics of the roof, such as *Matbae* (gabled), *Paljak* (hipped-and-gabled), *Woojingak* (hipped), and linked to the planar system.

Firstly, it is necessary to define the scope of the components included in the roof-*Kan* module. In *Modernized-Hanok*, the roof is composed of four main layers, including the roof tile surface, the *Boto* (roof-filling soil) and the *Jeoksim* (roof-filling wood) layer, the *Seokkarae* and *Gaepan* layer and the purlin and related substructures, which are components of the roof-*Kan* combined module. However, since the *Jusimdori* and the *Daedulbo* located at the boundary of the building must be modified according to the orientation of the building's facade, it is reasonable to include them in the roof plan to minimize errors. On this premise, the components in the vertical range of the roof-*Kan* module consist of the *Jusimdori*, *Daedulbo, Jungdori*, *Jongbo*, D*ongjaju* (short-column on beam*)* and *Daegong* (truss post). The horizontal range is one *Kan* unit of the body in the purlin direction and the entire *Kan* unit in the beam direction, and this is repeated within each *Chae,* a building unit, to implement the roof for each house.

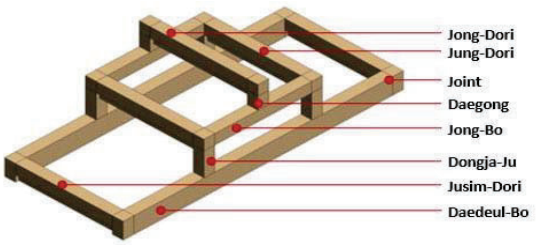

Figure 3: *Roof-Kan Assembly Module Basic Type*

https://doi.org/10.52202/069179-0493

2.2.2 TYPES OF THE ROOF-KAN COMBINED MODULE

The *Modernized-Hanok*'s roof frame is consisting the edge-*Kan*, which defines the shape and scale of the roof, and the middle-*Kan*, which defines only the scale. This research suggests that the proposed roof-*Kan* module should also reflect this characteristic of *Modernized-Hanok* and be operated in a dualized module.

The vertical position of the roof parts can be divided into three levels based on the purlin members to determine the roof scale. First, the *Jusimdori* and the *Daedulbo* are placed at the lower level of *Jusimdori*. The *Jungdori* and the *Jongbo* should be placed at the *Jungdori level* and the *Jongdori* at the *Jongdori* level. Additionally, the *Dongjaju* and *Daegong* are placed at each level, and a purlin connecting member is created in the outer direction of the beam to correspond to the cornered houses.

The middle-*Kan* is composed of only the substructures mentioned above, but the edge-*Kan* requires additional substructures that can determine the shape of the roof. The starting position of *Jongdori* and *Jungdori* determines the shape of the edge-*Kan*. And the *Jongdori, Jungdori*, and *Jusimdori* touch the surface parallel to the outer edge of the edge-*Kan* in the *Matbae* roof. At the same time, the *Jungdori* is on the linear of 45 degrees to the direction of the *Jusimdori*, and the *Jongdori* is on the vertical plane in *Paljak* roof. In the case of the *Woojingak* roof, it creates the roof surface by allowing the starting points of the *Jungdori* and *Jongdori* to touch the linear that is 45 degrees to the direction of the *Jusimdori*. Therefore, the edge-*Kan*, the types of roof are determined by the existence of the *Chunyeo* (angle rafters) located on a straight line in the 45-degree direction, and the starting coordinate of the *Jongdori* again defines the *Paljak* and *Woojingak*. In addition, each roof requires different substructures to form its shape, with *Matbae* requiring extended purlins, while *Paljak* and *Woojingak* need *Chunyeo, Waegidori (*outer purlin*)*, and *Chungryang (additional beam on purlin direction)*. Therefore, the module must secure the required substructures to create desired roof shape [9].

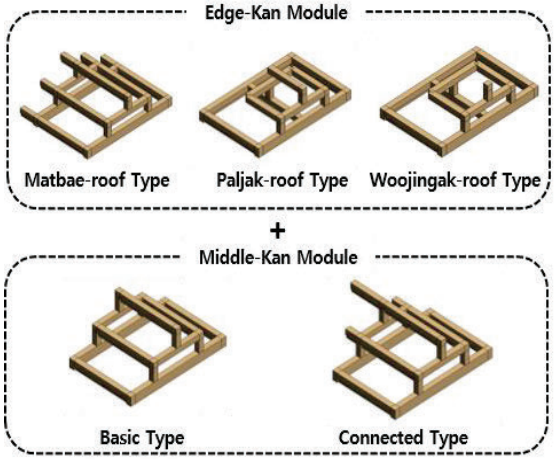

Figure 4: *Type of Roof-Kan Assembly Module*

3 IMPLEMENTAION OF ROOF-KAN COMBINED MODULE

3.1 ROOF SHAPE DETERMINATION FORMULA

A correlated function is a logic that can implement changes in each target by controlling the common factors among multiple targets. Revit's parameters consist of the parameter's name, the parameter's value, and the formula between parameters, and they work by connection with the target element.

The parameters work in two ways. The first is to link the parameter's value to the target element. For example, when modeling a rectangular shape, values for length, width, and height are defined simultaneously during the modeling process. By creating a parameter and linking it to the length, width, and height of the target element, the length value of the parameter can be linked to the length value of the target absence, allowing for changes in the shape of the target element through the parameter.

The second method involves linking each parameter through a formula. For example, "Height = Length/12" is a simple function that defines the dependent parameter "Height" as the value of the independent parameter "Length" divided by 12. If the parameters "Height" and "Length" are linked to the height and length of the target element, adjusting the parameter value for "Length" can adapt not only the length but also the height. The defined formula expression serves as the algorithmic basis for enabling continuous changes to the target element and reflecting the actual construction or modeling principle. In addition to arithmetic operations, conditional statements such as "if" can also be used to define the value through the formula for when conditions are met. For example, Users can reconfigure most simple functions, such as the visibility of the target element or specifying its material. Therefore, complex shapes can be easily created by adjusting a few independent parameters by defining dependent parameters with various formula expressions.

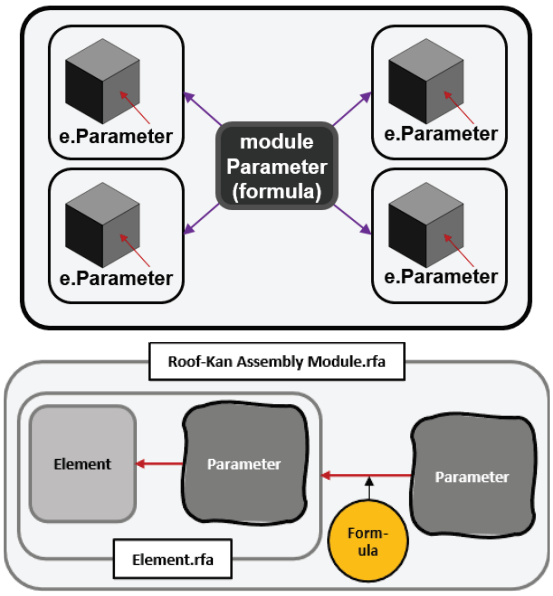

Figure 5: *Concept diagram of Parameter and Formula*

https://doi.org/10.52202/069179-0493

The roof-*Kan* combined module proposed in this study comprises multiple parameters and families within a single family, and their correlation allows the creation of each roof shape.
The edge and middle *Kan* modules can implement five and three-purlin structures and connect the roof type and the *Kan*. The operation of parameters is defined as an essential element of each direction's length, material, and component name within the module family, while the parameters specified within the module family are again defined as a formula of the parameters defined in the module.
For example, creating a *Matbae* roof with a three-purlin structure can be replaced with the logic of defining two independent parameters, one with the roof shape (Name) as *Matbae* (Value) and the other with the number of purlins (Name) as three (Value) in the edge-*Kan* module. Once the value of "*Matbae* roof with a three-purlin structure" is created, the value shapes the defined roof through the formulas previously specified for each component. Also, each roof shape is differentiated by the presence and position of each component; therefore, the roof-*Kan* combined module is created with type parameters [10].

3.2 LAYOUT LOGIC FOR ROOF-KAN COMBINED MODULE

The initial layout of the module begins by defining the main facade of the building based on the number of the body module in perpendicular and horizontal directions, which is already placed in the previous steps. For the roof-*Kan* module to be placed on the top of the body module, the building must be hypothetically divided into an independent l-shaped building, *Chae*. A main and subordinate *Chae* is distinct by a change in the number of *Kan* in the vertical direction of the main facade.

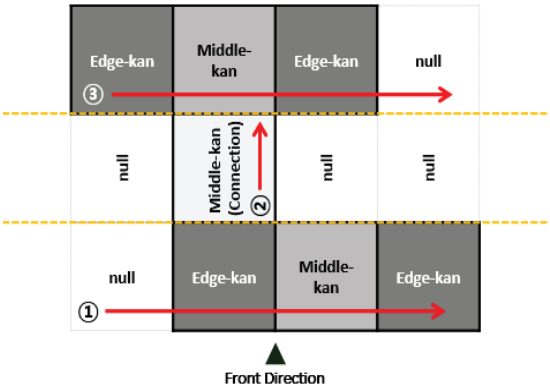

Figure 6: *Arrangement process of Roof-Kan Assembly module*

Once the buildings are separate, the roof frame module is placed from the lower-left *Kan* of each *Chae,* where the coordinate is set to 0, 0. The module first decides whether it is an edge-*Kan* module or a middle-*Kan* module based on the existence of the adjacent module, then it is placed from left to right accordingly in the independent *Chae*. The rest of the independent *Chae* repeats the same process to complete the placement of all roof frame modules.

The rules for placing the roof-module combinations in each *Chae* are further divided based on the number of *Kan* in the front facade. If the building has three or more *Kan*, the initial module will be an edge-*Kan* with a defined roof shape while hiding the *Daedulbo* and *Jongbo*. And the module type of the second *Kan* is determined according to the existence of a *Kan* to the right.
For the first middle-*Kan* module of the second *Kan*, all the parts of the *Jusimdori* level are generated, while the *Dadulbo* and *Jongbo* on the left are hidden for the rest of the middle-*Kan* module. Finally, the right edge-*Kan* of the *Chae* is placed while hiding the *Dadulbo* and *Jongbo* on the left to complete the placement of the module. This process minimizes the error in the quantity data and ensures there are no overlapping elements once the entire roof-*Kan* module is placed.
Only the edge-*Kan* module is placed in the building with two *Kan* in the front facade. The first module generates all the *Daedulbo* at the *Jusimdori* level, while the second module hides the left *Daedulbo* and *Jongbo*. In the case of a building with only one *Kan in the* front facade, only one module is placed.

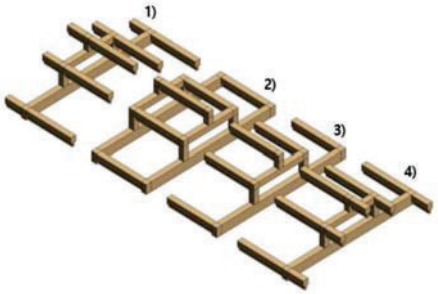

Figure 7: *Arrangement Process of Edge-Kan and Middle-Kan Module*

A middle-*Kan* module is generated to create the connecting edge in the corner of the house where two or more *Chaes* meet vertically. The additional elements must be created outside of the module range in this process.
The current module placement has each *Chae* as an independent state; therefore, the *Chaes* must be connected with purlins. The connection process of *Chaes* is followed. First, a main *Chae* and a subordinate *Chae* are determined, then the subordinate *Chae*'s middle-*Kan* module generates the connecting purlins. Once the connecting purlins are created, the cornered house is completed, adjusting the height of purlins according to the hierarchy of the *Chae*. The *Matbae* roof requires the purlin extension that goes beyond the boundary of the roof-*Kan* module. However, the edge-*Kan* module that determines the roof's shape is always placed at the beginning and end of the *Chae*, and the purlin extension is created outside the *Chae*, so it does not affect the adjacent *Kan*. Therefore, the purlin extension for the *Matbae* roof is made outside the boundary of the roof-*Kan* module using the same logic as the middle-*Kan*'s connecting purlin creation.
On the other hand, for the *Woojingak* roof, the *Chunyeo* extends to the *Jongdori*, which means the *Jongdori*, *Daegong*, and *Jongbo* need to move inside the *Chae*. This means it can affect the adjacent *Kan*, but this is

https://doi.org/10.52202/069179-0493

resolved by separating the constraints of the *Daedul-bo* and *Jongbo*.

3.3 COMPLETION OF ROOF PLANNING AND MODELING

The roof planning process takes place after the completion of the body plane planning, with the lower *Jusimdori* level fixed, where the body and roof intersect. Therefore, the user can independently define the roof type, scale, purlin structure, and the rafters' curve. During the roof-*Kan* module placement, the program automatically identifies the designated plan below and creates the user-interface presenting the pre-view of the floor plan and the section for the user to decide which floor or *Chae* to work on.

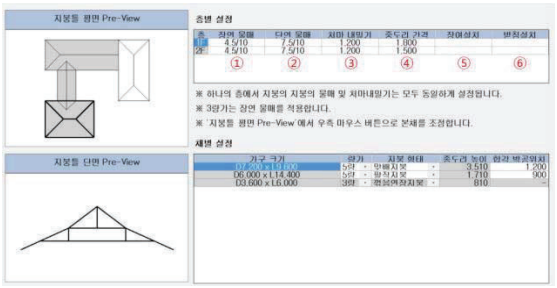

Figure 8: *Pre-view of roof planning UI*

On the 'floor' part of the UI, the users can type-in the desired values of the angle of rafters, overhang depth, and purlin spacing and etc. However, the range of these values is pre-set based on the analysis of existing *Hanok* to prevent users from creating an impractical roof. On the other hand, users can determine the roof type, the purlin structure, and the location of the bargeboard on the '*Chae*' part of the UI. This process allows users to determine the roof type of each *Chae* independently while suggesting the appropriate purlin structure according to the scale of the body structure. The purpose of this program is to reflect the principles of the *Hanok* construction while promoting efficient modeling.

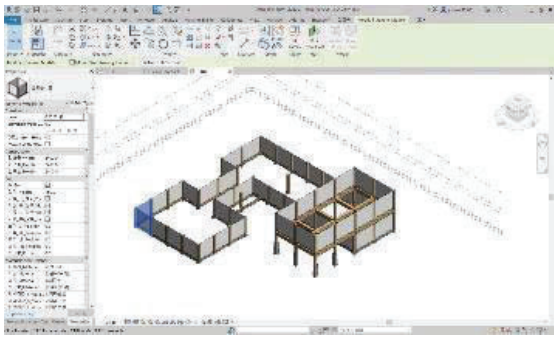

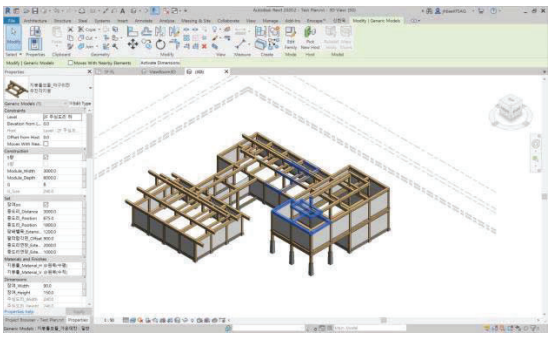

Figure 9: *Before and after the roof-Kan module placement*

4 CONCLUSIONS

It is crucial to solve the difficulties of *Hanok* design for the growth of the Modern *Hanok* industry. The roof of *Hanok*, in particular, requires a curved roof with a combination of various wooden structures, which is the biggest obstacle in the design process of *Hanok*. Therefore, this study regarded the roof frame as an independent structure, breaking out of a general notion that the roof frame is a subordinate structure of the body, and proposed a roof-*Kan* combined module.

The significances of this research are as follows. First, it defines criteria for separating the body and roof parts by focusing on the module-based design methodology. In addition, it distinguishes information that has already been determined in the preceding stage, information that is automatically generated through it, and information that needs to be redefined by the user and aims to improve design efficiency by accumulating data.

Secondly, it provides a basis for constructing a cornered roof efficiently. Considering the timing of placing the roof-module combinations, the modules were divided into middle-*Kan* and edge-*Kan*, and an effective methodology for placing the modules between *Chae* and between adjacent *Chae* was proposed.

This study is part of developing a Modernized *Hanok* design tool that can be easily used by non-experts who are not familiar with *Hanok* architecture. This tool is expected to provide a better *Hanok* design environment by accumulating information from the plane, elevation, and cross-section plane of the building to the details of each member.

ACKNOWLEDGEMENT

This study was supported by the Ministry of Land, Transport, and Maritime Affairs of Korean Government Under Grant No. 20AUDP-B128638-04
(Development of Modernized *Hanok* Technology), and Institute of Engineering Research at Seoul National University.
This research was supported by the BK21 FOUR (Fostering Outstanding Universities for Research) funded by the Ministry of Education(MOE, Korea) and National Research Foundation of Korea(NRF)

https://doi.org/10.52202/069179-0493

REFERENCES

[1] Kim, S. (2019). A Study on Architectural Characteristics of Hanok for Housing Newly Built in Seoul since 2000, Thesis, Seoul National University, 80.

[2] Kim, Y. (2020). Preliminary Study on the Structural Characteristics of Empirical Construction of Long-span Hanok, Proceedings of Annual Spring Conference of the Architectural Institute of Korea, 2020.4, 344-345

[3] Cho, Y. & Jo, G. (2008). A Study on the Development of an Intelligent Modeler for Modernized Korean Traditional Buildings using BIM Systems, Journal of the Korean Housing Association, 19(6), 55-62.

[4] Choi, B. & Cho, J. (2012). A Basic Study on Hanok Wooden Structure Modeling Process based on BIM - Focused on Skeleton-Assembly Process by Wizard, Journal of the Architectural Institute of Korea, Planning and Design Section, 28(2), 121-130.

[5] Park, S. & Choi, J. (2012). A Study on the Development of open BIM-based Design Supporting System for Han-ok, Design Convergence Study, 11(5), 148-160.

[6] Kim, J. & Jeon, B. (2010). A Basic Study on the Parametric Modeling System and Methods for Hanok, Proceedings of Annual Spring Conference of the Korean Association for Architectural History, 2010.5, 307-314.

[7] Kim, J., Kim, D. & Jeon, B. (2020). A Study on the BIM-based Design Methodology for New-Hanok with Planning-Kan Module, Journal of the Architectural Institute of Korea, Planning and Design Section, 36(12)

[8] Hanok Technical Development Research Institute (2013). LOD(Level of Detail) Manual. Retrieved November 30, 2020 from http://hanokkorea.auric.kr:8088/main/rnd/result/view.do?mid=1000&category=040101

[9] Kim, J., Kim, H. & Jeon, B. (2009). A Study on the Type of Corner-connections in the Korean Traditional House, Journal of the Architectural Institute of Korea, Planning and Design Section, 25(6), 177-186.

[10] Yu, J., Chin, D., & Kang, B. (2011). Proposal for Standard Parameter System of Architecture Object on Revit, Proceedings of Winter Conference Society for Computational Design and Engineering, 2011.1, 245-252.

World Conference on Timber Engineering Oslo 2023

STEPS TOWARDS A UNIVERSAL SCHEME FOR PARAMETRIC DETAILING OF COMPOUND TIMBER STRUCTURES

John Haddal Mork[1], Sveinung Ørjan Nesheim[2]

ABSTRACT: The paper presents potential steps towards a universal scheme for parametrically detailing compound timber structures. Two fundamental concepts are presented: Firstly, a method of combining manual 2D-detailing with parametric modelling, and a secondly concept of simplifying parametric detailing by splitting the detailing process into two. Achievable implications of the scheme are illustrated through a surface-based FEA model of a timber-building. The paper ends by discussing further development steps toward a universal parametric detailing scheme.

KEYWORDS: Parametric detailing, Information models, parametric method development, FEA

1 INTRODUCTION

1.1 BACKGROUND

The Norwegian timber sector is immature, and the industrial potential is underexploited. The market impact associated with an increased degree of completion for timber-based building elements is considerable[1], but the digital infrastructure required for cost- and resource efficient processes are currently fragmented. The digital transformation is suffering from lack of standards for interoperability and from various levels of maturity at the various stakeholders in the value chain. Increased digitalisation has the potential to manufacture cost- and resource effective products faster and with a higher degree of completion. For the timber industry increased digitization has the potential for unlocking a significant production volume of prefabricated elements with a high degree of completion, and therefore to act as an important contribution for the industry to meet climate goals. Parametric modelling has become an increasingly important method in this context and can increase efficiency in both planning, manufacturing, and construction phase. However, the tool is often limited to be applied by specialists, and building a parametric model is a time-consuming process. At worst the expense of developing a parametric model absorbs the profit of increased efficiency in other parts of the process.

Reindeer [2]is a tool that aims to reduce time demanded to prepare a parametric model and to simplify the process of detailing timber structures. However, the tool is limited to 1D-elements, and is not applicable for compound structures such as complete walls and slabs. A main challenge is the number of joint types that occurs in compound structures. Between modules, and between individual components. Hereby, the authors have identified a demand of a further improved scheme for parametric detailing.

1.2 OBJECTIVES

The paper presents potential steps towards a universal scheme for parametrically detailing compound timber structures. The scheme is built around a generic data model, and the output is hence applicable for both architects, engineers, manufacturers, and other stakeholders. Both 1D-elements (beams, columns, etc.) and 2D-elements (CLT, plywood etc.) are included.

In the present study the methodology is implemented in a framework to increase material efficiency, where the structural analysis is used as a vehicle for demonstrating the flexibility and applicability of the method. The case structure is a modular load-bearing building system purposed for multi-storied wooden buildings. The modules are principally standardized, but not fixed in size. Although the case is a building system for tall structures, the methodology has a high re-use value and is working across building systems and makes parametric design available to stakeholders who are not parametric experts.

2 FLIPPING THE MATRIX

The more logically consistent a building system is, the more reasonable the use of a parametric model. A geometric output can largely vary in shape if it is within the same logic. Simplified, one can say that the modular building system consists of four building elements: exterior walls, interior walls, slabs, and roofs. Thus, an intuitive approach is to develop four corresponding parametric modules. However, when taking into account the various the connections between the building elements, the complexity drastically increases while an intuitively clear logic is heavily disrupted by deviations.

The phenomenon is illustrated in Figure 1. Elements that are topologically similar, are coloured similarly. While one wall element is only connected to its parallel vertical and horizontal wall neighbours (grey-green), other walls are corners, connected to the roof, the ground, a slab or

[1] John Haddal Mork, Rallar AS, Norway, john@rallararkitekter.com
[2] Sveinung Ørjan Nesheim, SINTEF Community, Norway, Sveinung.nesheim@sintef.no

https://doi.org/10.52202/069179-0494

other combinations. In conclusion: If basing parametric modules on its building element type, the result is a dirty logic scattered by challenging topological variations. This challenge makes the foundation for the flipped matrix and the proposed scheme.

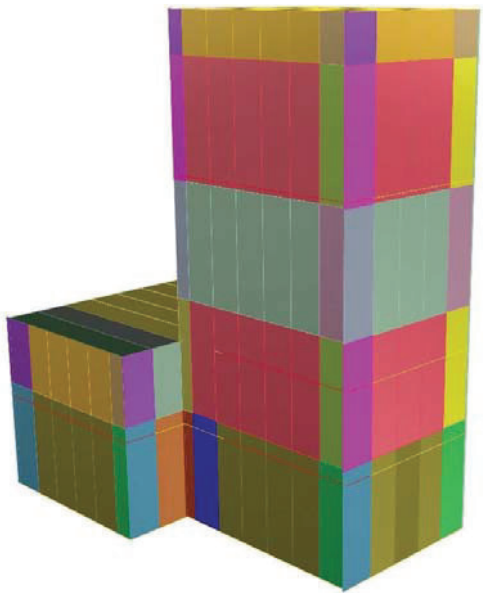

Figure 1: *Each color reprents topologically similar elements. Since the elements are connected in various ways, the amount of element types*

3 THE PROPOSED CONSEPT

The proposed concept has two main features. Firstly, the concept proposes a two-step detailing method that drastically reduces the complexity and deviations as described above. Secondly, a method of combining parametric modelling and manual detailing is introduced.

3.1 Two step detailing process

The proposed detailing concept flips the matrix. Instead of developing parametric modules based on its main building components, the proposal is to develop a two-step detailing system that firstly takes care of the individual joints between the building elements and secondly detailing the module itself.

This concept allows the single-responsibility principle(SRP) known from programming. A parametric module is now either a vertical connection between main building components or geometric population and detailing internally in a module.

The first detailing step determines the axis, orientations and boundary of the components directly related to the module joints. Knowing the boundary of the module, the internal components can be generated. The second detailing step determines how components within the module interacts, and hereby also determines the length of the components preliminary generated in step one.

The output of the scheme is a light, yet detailed representation of a structure, applicable for multi-scalar modelling[3]. This concept makes it very suitable as a feature in a building design and engineering framework, and the output of the parametric model may easily be adapted to support various design and analysis strategies.

3.2 MANUAL DETAILING

The Single-responsibility detailing principle not only simplifies the parametric model, but also enables the potential of combining parametric modelling and manual detailing. If a joint type in a structure has multiple variations within the same logic, e.g. wall corners with varying angle, a parametric joint can be powerful. However, in many cases, a detail is fixed and scattered in a structure. For such cases, developing a parametric detail is excessive – a manually drawn, fixed 2D-detail is less time-demanding.

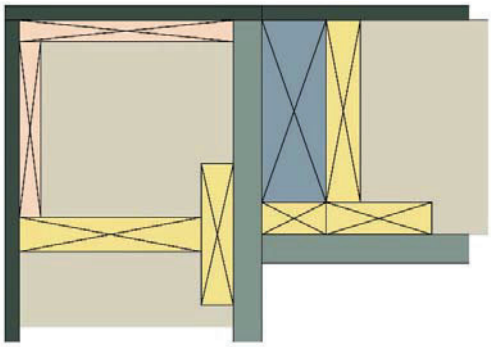

Figure 2: Manually drawn detail

However, an arbitrary 2D-detail is not directly readable by an algorithm. Figure 2 displays a manually modelled corner detail. Further, modern digital fabrication requires fully detailed 3D-models. Hence, it has been developed a rule-set for drawing 2D-details manually and a method for turning the detail into a parametric detail stored in the algorithm. The rules are as following:

1) Any component in the detail requires a parent. The parent is the element the component belongs to in the prefab-phase. In additions, some components might belong to the joint itself. Hence, in a joint where two elements connects, a component is connected to elem0, elem1 or joint. Further, any component requires designated material properties/functional names/purposes. See Figure 3

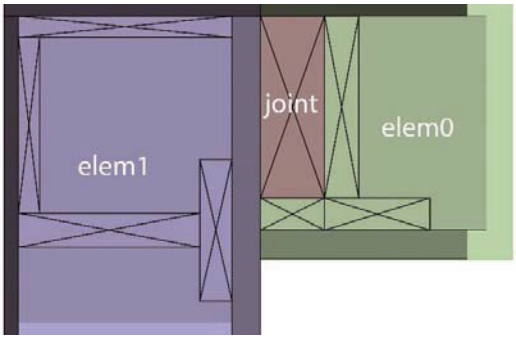

Figure 3: Parent elements

2) The joint requires a local plane. As seen later in the article, the origin of the local plane corresponds to the axis of the joint created from the element's reference surfaces. The X-axis is of the plane is parallel to elem0. See Figure 4

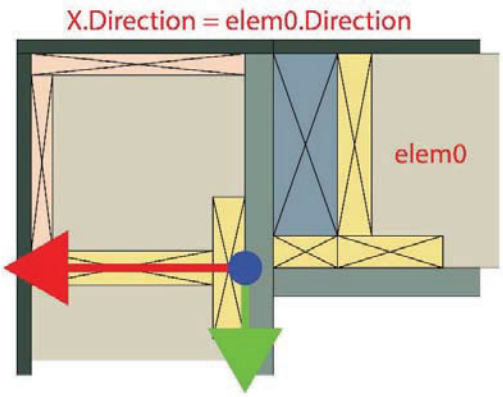

Figure 4: Local Plane

3) A component in the joint has either a defined cross-section within the boundary of the joint, or the cross-section is extend to another joint in the assembly. This is solved by two types of shapes: Closed cross sections are drawn as closed polygons, extended cross-sections are drawn as open U-shapes. See Figure 5

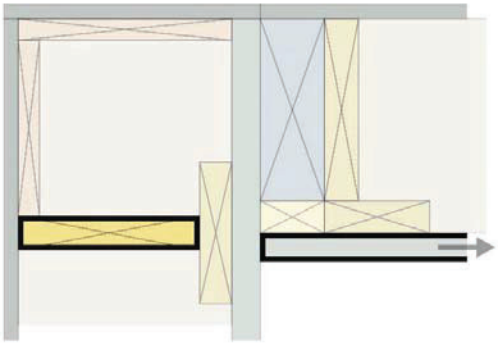

Figure 5: Closed and open cross-sections

Applying the three previous rules, an algorithm can turn the manually drawn joint into a lightweight information model. The joint is wrapped in a block anchored by the local plane. On a superior level, metadata can be connected to the joint it-self. Further, components are described as alpha-numerical enhanced local planes [4],positioned relatively to the main local plane. See Figure 6. Further, Figure 7 renders the data stored in the component's local plane. This is data extracted from the manual drawing, and is the data required to regenerate a physical component.

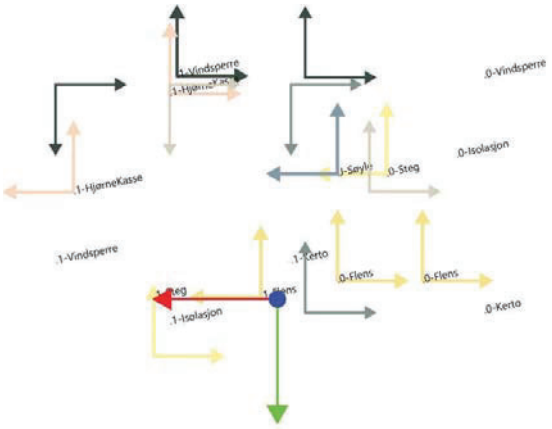

Figure 6: Lightweight joint description

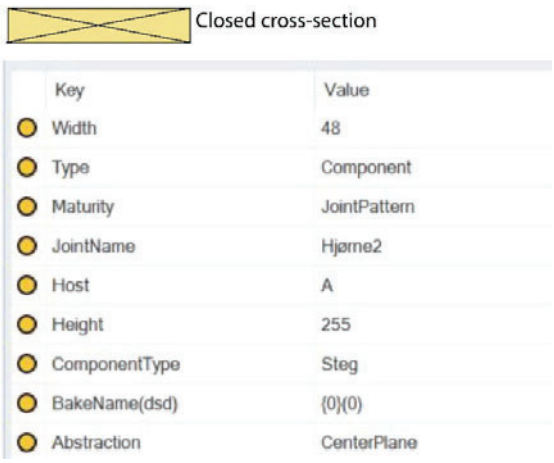

Figure 7: Component enhanced with alphanumerical data

The collection of planes is a simple representation of components in a detail, and contains information about cross-section width, length, element host and detail ID. These 2D-details are oriented to its linear joints, and the detail's components are generated in the assembly.

4 THE SCHEME STEP BY STEP

The proposed scheme consists of individual algorithms that step by step matures a geometric information model from a simplified reference model represented by surfaces and curves to a fully detailed structure. The steps relates

https://doi.org/10.52202/069179-0494

to a conventional parametric process and allows manual interactions between each step.

4.1 Normalizing input geometry and register basic geometric properties

For such workflow, the geometric input can vary. In some cases, a manually modelled geometry can be suitable, for other cases the geometry can be parametrically generated. Regardless, the geometry needs to be scheme-based, applicable for extracting precise geometry. The first step consists of cleaning the geometry, normalizing surface-vectors, and not least analysing the geometry and register its basic geometric properties. With help of a defined assembly vector, and the geometry itself, properties such as orientation, determination if the wall is exterior or interior, levels and an initial ID is set.

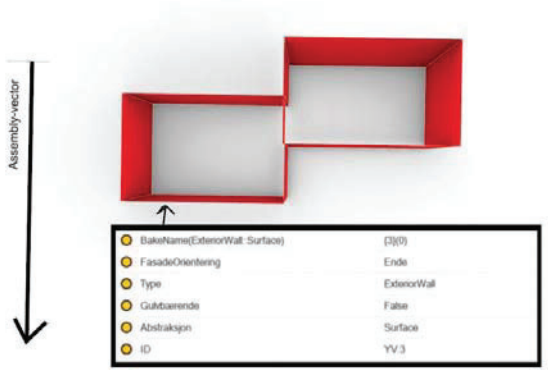

Figure 8 The geometry itself and the assembly-vector are the basis for basic for registering basic geometry properties

4.2 Dividing geometry into building elements

Most building systems divides its structure into elements. The case structure's logic divides the floors and walls into transportable widths and manufacturable heights. Hence the walls and floors are divided into sub-surfaces, inheriting its properties from its parent wall/floor, but adding information about its related axises and its levels.

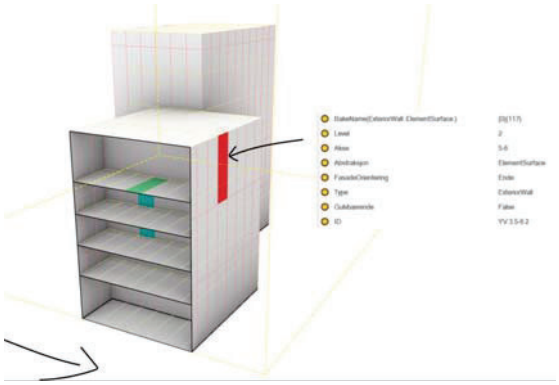

Figure 9. The element is part of its parent wall named YV3, is between axis 5 and 6 and is the third element vertically (2). Hence its ID becomes YV.3.5-6.2

4.3 Register all joints (linear joints) and store geometric properties

Now having all elements generated, the algorithm identifies all joints in the assembly. In this case, linear joints between the elements are the most relevant joints. The algorithm individually searches for joints between exterior or interior walls, between exterior and interior walls, and not least intersection internally between floors and in relation to its walls. The joint itself, is initially just a line and its local plane, but the registered properties and geometric orientation of the joint's walls/floors, and its internal relation, determines what type of joint it is. Following are a few examples:

- A joint between two north-facing walls at the same level, determines that the joint is a horizontal connection between parallel walls.
- A joint between two nort-facing walls, at different levels, becomes a vertical connection of parallel walls.
- A north facing wall and an east facing wall becomes a specific type of corner, and with help of the assembly axis, the joint also consist information about the assembly order of its elements.

Figure 10 A joint and its properties

4.4 Categorize joint type instances in the building and map matched joint types

Various joints are modelled according to the description in chapter 2. See Figure 12. Each joint type has multiple geometric requirements for a joint type instance to be applicable. This step analyse all joint instances in the structure and map its suitable joint type. This by orienting the described joint type local plane, to its joint instance local plane.

When the algorithm has finished this stage, all joints are populated with a joint detail represented as a series of property enhanced planes. Further, components in the joints can be extruded according to the length of its joint. Figure 13 displays a corner joint being extruded, while Figure 14 shows the structure being fully populated by the first detailing stage.

https://doi.org/10.52202/069179-0494

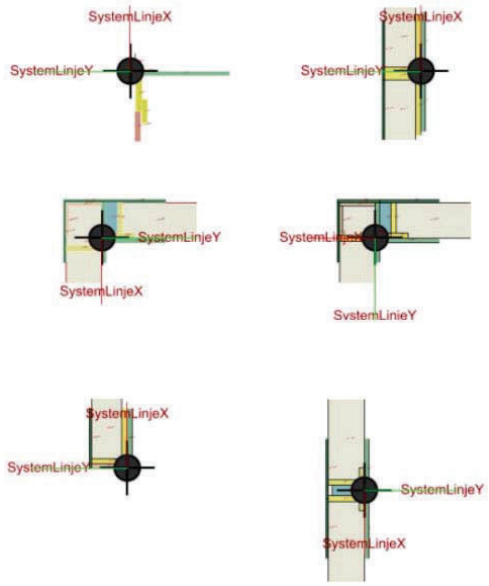

Figure 11 Joint types

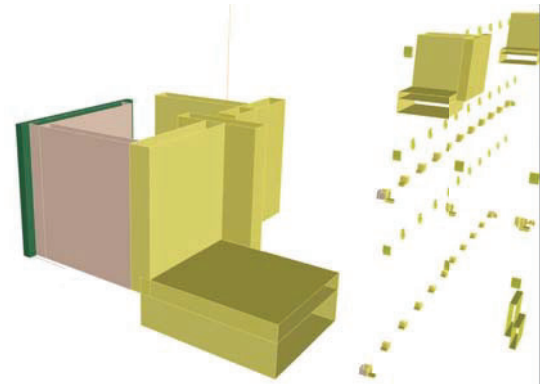

Figure 12 A corner joint being extruded

Figure 13: The structure partially populated

4.5 The second detailing stage

Now, the first detailing stage has determined the relationship between the main elements, and the next stage of populating the element itself, is simplified. This due to not needing to take neighbouring elements into account. Figure 15 shows a fully populated model

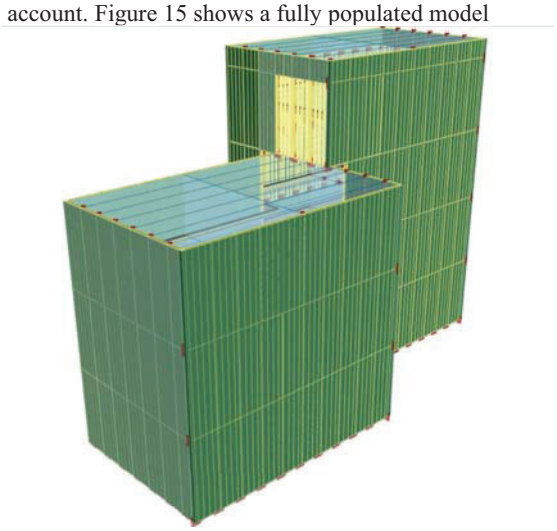

Figure 14 Fully populated model

4.6 Detail component connectons

By the last stage the model is fully populated, but not fully detailed. The last stage, not yet developed in this project, is to detail the connection between the components: the components in the described joints, and the joints made by the components internally in the elements. This procedure can be similar to the steps described in in chapter 4.3-4.4, but in this case, the joint is not a line, but a point in the intersection between two or more components..

https://doi.org/10.52202/069179-0494

4.7 Geometric representation

The above steps displays the components as boxes, but the geometry is still multi-scalar and can be rendered in different ways. By representing the parametric description of the compound timber structure as a surface with associated data, the benefit of object-oriented programming may readily be exploited. In the present project this yielded an efficient method of geometrical representation of the structure. Here additional information such as material model, cost, and embedded carbon emissions may be organized around the surfaces, rather than as a conventional method where this data is organized in logical functions.

The method of parametric description of compound timber structures was advancing in joint development of an element-based building system suitable for high-rise timber buildings. This building system is inherently parametric and modular and comprises solutions for loadbearing exterior and partition walls, flooring system and roof. The building system is based on continuous system planes and system axes from where the parametric rules defining the geometry is referenced, and where loads and linear connections are introduced. This design philosophy allows for a flexible positioning and distribution of both shear connectors and joints between modules. The principle of continuous system planes and system axes is beneficial for a parametric geometric representation, though not required for the scheme for parametric detailing as presented herein.

5 USE CASE

5.1 Methodology to minimise material use

One apparent outcome of the geometric representation is the establishment of an efficient computational finite-element representation of the structure. As a vehicle to demonstrate the potential outcome, a structure generated using this scheme was transformed into a surface-based finite-element model. Due to the object-oriented architecture of the parametric scheme, the base feature of the members associated with a given surface could be defined as beam, shell or solid. For the building system used in the present work, the members have a thickness to length ratio typically less than 0.25 and with transverse shear less important, shell elements are suitable for the numerical model. In Figure 16 a detail of the numerical representation is shown.

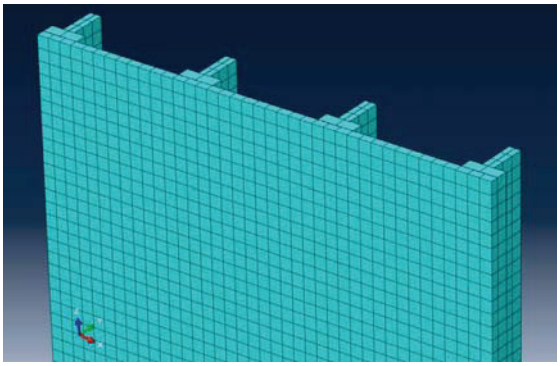

Figure 15: Shell elements with rendered thickness

The methodology permits any information associated with the surfaces to be accessed for a member. In this way the material properties, the associated connection lines of a surface, thickness, and orientation to mention some, are all accessible. Similarly, the properties of the associated connection lines are returned to obtain information about boundary conditions. Principally this enable any property that is stored and associated with a surface to be accessed, making the methodology very powerful and flexible.

This setup allows for easy automation of various tasks. The establishment of a live link between the parametric model and the FEA may be used in an optimization workflow to increase the material efficiency. Here the optimization of the structure may be done with respect to material volume, material cost or embedded CO2 to mention some. The constraints of the optimization is governed by the design code.

The advantages with letting the associated thickness of the shell be a variable parameter in an optimization algorithm may easily be exploited and may offer an efficient computational methodology to minimize material use. Results from finite-element analysis and material minimization of the complete building system referenced in the present work will be published in due time.

5.2 A Twin-transition Tool

The achievable implications of the scheme were assessed during the work of modelling and assessing the structural response of a high-rise timber building employing the building system briefly explained above. In industry 4.0, efficient and practical solutions for digitalisation is crucial. The present work has identified several achievable implications related to digitalisation, and that the methodology may offer an efficient expansion of the toolbox for digital transition of the construction sector.

As described in section 3.1 the scheme is a two-step detailing process, starting with the manual two-dimensional details of the joints of the building system. Due to this the possible implications of the method may be much larger than originally envisioned. Because of the two-dimensional details, the scheme may be used in the mapping of existing built works where only two-dimensional drawings exist. This may aid to digitalize

existing built works subject to renovation or extension, and therefore also an expansion of the toolbox for twin-transition.

The methodology is suitable for scalability and may be an additional and valuable tool in the work to build digital twins both for new and existing built works as well as for documentation.

6 DISCUSSION

The paper discusses potential steps towards a universal scheme applied when detailing parametrically. Creating an possibility for inputting manually drawn details into a complex algorithm is seen as promising concept. A key benefit is that the concept democratizes the use of a parametric model – further, time is saved if joint type variations are limited.
The two-step detailing process is seen as promising candidate to ensure single responsibility details, reducing the amount of joint types required. However, more investigation is required. Finally, a potential further development, is to turn the two-step detailing process into a generic, nested parametric detailing process, allowing infinite levels of parametric details within a parametric details.

ACKNOWLEDGEMENT

This project is funded by the Research Council of Norway, Project No. 309363, and Støren Treindustri AS.

REFERENCES

[1] E. G. Hertwich *et al.*, "Material efficiency strategies to reducing greenhouse gas emissions associated with buildings, vehicles, and electronics—a review," *Environ. Res. Lett.*, vol. 14, no. 4, p. 043004, 2019.
[2] J. H. Mork, "Parametric Timber Detailing A parametric toolkit customized for detailing fabrication-ready timber structures," 2020.
[3] P. Poinet, "Enhancing Collaborative Practices in Architecture, Engineering and Construction through Multi-Scalar Modelling Methodologies," 2020.
[4] R. van der Heijden, "Parametric Building Information Generation for Design and Construction," 2015.

https://doi.org/10.52202/069179-0494

World Conference on Timber Engineering Oslo 2023

MOISTURE PREDICTION OF TIMBER FOR DURABILITY APPLICATIONS USING DATA-DRIVEN MODELLING

Seyyed Hasan Hosseini[1], Jonas Niklewski[2], Philip Bester van Niekerk[3]

ABSTRACT: Durability and service life assessment is a major challenge for the design and use of timber in outdoor weather exposed environments. Rate of deterioration by fungal decay is closely linked to variations in wood moisture content. The objective of the present paper is to test and evaluate different data-driven models based on the multilinear regression (MLR) and artificial neural network (ANN) approach. Moisture content was predicted at the surface and core of a rain-exposed wooden element in the context of durability and service life assessment. Synthetic data stemming from a numerical model were used to fit time-series weather variables, including different combinations of time-lagged daily precipitation, relative humidity, and temperature, to temporal variations of daily average wood moisture content. Based on a set of statistical and qualitative analyses, using the weather variables lagged by 0 – 11 days as input variables for 11 mm depth moisture prediction, ANN showed the highest accuracy and least sensitivity to its initial setups, and could significantly outperform the MLR with the same input variables. The resulting models for surface and core moisture prediction were then tested against two different datasets consisting of measured data from wood specimens subjected to outdoor exposure.

KEYWORDS: Moisture content, Durability, Model, Artificial Neural Network (ANN), Regression

1 INTRODUCTION

Service life assessment is a major concern for timber in weather exposed environments. The problem largely stems from the natural deterioration caused by fungal decay, a mechanism that is exacerbated by poor moisture management and suboptimal use of materials. Recent efforts to systemise service life assessment of timber have resulted in various performance-based design guidelines for European conditions. The guideline in [1] is based on a dose-response relationship where the rate of fungal decay is expressed as a function of wood moisture content and temperature. Therefore, dose-response models enable service life assessment based on wood moisture content and temperature [2].

Wood moisture content is a measure of the material microclimate and one of the main vectors for biotic deterioration by fungal decay. In general, the moisture variation of wood depends on various factors such as local weather, the wooden element's distance to ground, and detailing. Brischke et al. [3] categorize these influences as 'indirect', since they are primarily linked to service life via their effect on moisture content. For modelling purposes, moisture content can either be obtained by measurement [4] or modelling [5,6].

Using a modelling approach, the wood moisture content is estimated based on these indirect factors and in a subsequent step, used with dose-response models to predict service life. Figure 1 shows how indirect variables (weather) can be used via numerical modelling to estimate direct variables (moisture content), which can then be used via empirical damage functions to model wood decay. The limit state defines the acceptable response in terms of material deterioration and the service life is defined as the period until the limit state is reached.

Numerical modelling of moisture transport in wood is an integral part of several branches of wood technology. Common applications include the migration of free water from green lumber during drying [7] and moisture gradients of sheltered structural timber during service [8]. These models transfer poorly to predictions of service life where the wood surface is subject to cycles of wetting and drying and the main region of interest lies above cell wall saturation. The simple numerical model developed in [6] was made specifically for use with dose-response models and integration with performance-based service life design.

The integration of numerical moisture modelling in service life prediction led to improved accuracy, but simultaneously introduced a dependency on commercial software and increased the computational time. These

[1] Seyyed Hasan Hosseini, Lund University, Department of Building and Environmental Technology, Sweden, hasan.hosseini@tvrl.lth.se
[2] Jonas Niklewski, Lund University, Department of Building and Environmental Technology, Sweden, jonas.niklewski@kstr.lth.se
[3] Philip Bester van Niekerk, University of Goettingen, Wood Biology and Wood Products, Germany, philipbester.niekerk@uni-goettingen.de

https://doi.org/10.52202/069179-0495

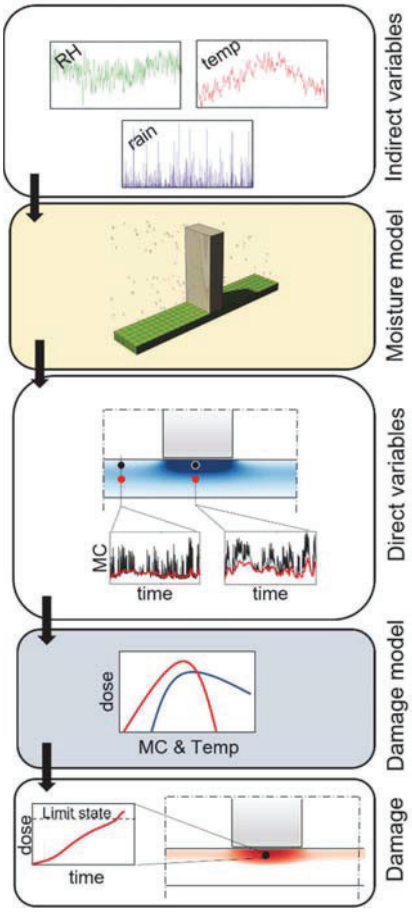

Figure 1: *Framework to predict moisture content and damage from environmental variables.*

downsides limit the practicality of numerical modelling. Alternatively, data-driven (DD) models that are considerably less computationally expensive than numerical models can easily be integrated into digital design tools for applications of service life prediction.

This paper explores new DD approaches for moisture content prediction of rain-exposed wood. The aim is to develop an efficient alternative to existing numerical models for moisture content prediction, with minimal loss in accuracy. For this purpose, synthetic data obtained from the numerical model in [9] were used for model development. A set of DD models based on the multiple linear regression (MLR) and artificial neural network (ANN) approaches, under various settings and input variable assumptions, were developed and evaluated via statistical and qualitative methods. The models are then tested against two different data sets based on real measurements.

2 METHOD

2.1 Data

2.1.1 Synthetic data for model development

Each data set (synthetic or measured) includes time-series of the moisture content at a specific depth from the wood surface (response/output variable) and relative humidity, precipitation, and temperature (predictor/input variables). A model was first fitted and verified against a set of synthetic data obtained from a one-dimensional numerical model for moisture transport in Norway spruce (*Picea abies*) wood [3]. The model geometry was modelled as 22 mm, reflecting the thickness, and transport properties reflecting moisture flux perpendicular to the grain direction. More details regarding the dataset can be found in [10], where the same data was used to map the decay hazard in a variety of different climates.

2.1.2 Measured data for testing

Two different datasets were used for testing the model against real measurements of varying moisture content. Both datasets consisted of measurements of moisture content obtained for Norway spruce boards in outdoor conditions, with weather data recorded in parallel. Moisture content was measured by resistance-type moisture sensors using insulated electrodes in both cases. Important to note is that the valid range of resistance-type measurements is (generally) below the point of cell wall saturation.

The first data set came from [11] and spanned a period of about 2.5 years. Measurements of moisture content were obtained from horizontal boards with a thickness of 22 mm. The top face was exposed to precipitation while the bottom face was considered sheltered and end-grain surfaces were sealed by silicone-based adhesive. Measurements were obtained at a depth of 11 mm from the top face, i.e., at half of the board's thickness. The geometry and exposure setup of the dataset were consistent with the numerical simulations used for DD modelling.

The second dataset came from [12] and spanned a period of about two years. Measurements of moisture content were obtained from inclined (45º) boards with a thickness of 20 mm. The test included specimens with both planed and pre-weathered top faces. Here, only the measurements obtained from pre-weathered samples were used. All short sides as well as the back face of the boards were sealed by silicone-adhesive, leaving only the top face exposed to the ambient weather. Surface moisture content was monitored every 5 minutes. After 18 months of exposure, the test setup was sheltered from precipitation, but remained outdoors for an additional 6 months. The specimens were similar to the geometry used for producing the synthetic data, but it should be noted that the specimen thickness was 2 mm less, the backside was sealed, and the boards were inclined. However, the small discrepancy in thickness nor the sealed bottom face were expected to have a significant influence on the surface moisture content of the exposed face.

https://doi.org/10.52202/069179-0495

2.2 MODELLING

The study includes several approaches for DD moisture prediction of rain-exposed wood, preliminary based on MLR and ANN approaches with various assumptions of input variables. The simplest MLR model can be defined as:

$$u_t = \beta_0 + \beta_1 \times RH_t + \beta_2 \times T_t + \beta_3 \times p_t \qquad (1)$$

where t is the index of time, and β_0, β_1, β_2, and β_3 are constants relating the relative humidity RH, temperature T, and precipitation p to the moisture content u at a given depth of a horizontal wood specimen (e.g., 11 mm). The reference values for u were outputs of a numerical model developed based on an average year of exposure for different climate data of about 550 sites across Europe [10]. More complex MLR could be achieved by relating u_t to RH, T, and p from t, t-1, t-2, …, t-L where L is a maximum time lag to consider potential contributions from previous time steps. The constants, as expected from eq. 1 (β_0, …, $\beta_{(L+1)\times 3}$), were obtained using the conventional least square method for a set of known u (synthetic data by numerical model). A suitable range of L was primarily estimated by cross-correlation analysis, which evaluates linear relationship between u and time-lagged versions of p, T, and RH. Then, L was fixed after evaluating the performance of ANN with multiple options from the estimated range, to take the non-linear relationships into account. These analyses were done for the 11 mm depth moisture content, but the resultant L was assumed valid for shallower depths too.

While the input variables used for MLR and ANN could be the same, the way they were related to moisture content was different. The equations used for ANN, are usually better described using an architecture resembling the neural network of a human brain, as exemplified in Figure 2.

For the example of Figure 2, each black node on the input layer includes a data vector corresponding to an average daily value of an input variable (e.g., RH). Then, each red neuron on the first hidden layer (HL) multiplied the input variables by a corresponding scalar weight w and added a scalar bias b to the sum of all weighted input variables. Finally, a transfer function (f) was applied to give a value n to the neuron. Thus, the mathematical expression for a neuron on the first HL (h=1) can be written as:

$$n_{j,h=1} = f\left(\sum_{i=1}^{4}(X_i \times w_{i,j,h=1}) + b_{j,h=1}\right) \qquad (2)$$

where j is the index of neuron (j=1, ..., 5 for h=1). Generally, a neuron on the second HL considers the results of the neurons on the first HL as input variables, and so forth for the next HL and output layer. To calibrate the parameters of ANN (w and b), an iterative optimization problem was solved to minimize the mean squared error (MSE) between the estimated and reference moisture u. The process starts with random initial parameters (variable between -1 and 1, similar range as the normalized input variables), which were changed at multiple iterations until a minimum MSE was achieved.

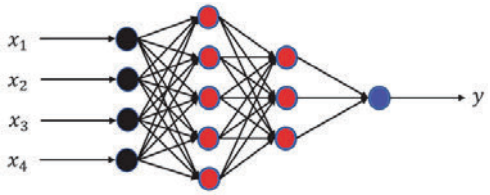

Figure 2: *A feedforward ANN architecture, connecting input variables X1-X4 to output variable y through two hidden layers (HLs) with five and three neurons (red) between input layer (black) and output layer (blue).*

Then, f had a mathematical form, making MSE differentiable with respect to the parameters w and b. In this study, $f(n)=n$ for the output layer, and $f(n)=(\exp(2\times n)-1) / (\exp(2\times n)+1)$ for the HLs as a conventional method. The suitable ANN architecture is usually a trial-and-error problem, and this study used up to two HLs and 4–20 neurons per HL.

Conventional ANNs are usually prone to overfitting due to the use of many parameters (i.e., perfect fit to the calibration data, but noisy for new data). To prevent this, a stopping rule was defined based on a part of the data (validation portion) separate to the data used for direct calibration of the ANN (training portion). This study used a so-called, "maximum validation fail (MVF)" criterion, which monitors validation MSE at the iterations. This criterion stops modelling when the MSE in the validation dataset increases for 10 consecutive iterations regardless of possible improvement in training for additional iterations. As a result, the parameterization is fixed based on the iteration that resulted in minimum validation dataset MSE (rather than training dataset MSE). The length of the study's dataset was near two hundred thousand, i.e., number of sites × (365 – L) days, due to the use of time-lagged inputs, which was quite long compared to the number of ANN parameters. So, overfitting could be less problematic. However, the MVF criterion was still useful to address the possible issue of ANN converging at a local minimum. To clarify, it is favourable to stop an ANN parameterization based on the MVF criterion and repeat it with new random initial parameters that are likely to end at a new final parameterization and exit the local minima. Finally, the ANN with minimum validation MSE among all repeats was selected. Alternatively, a hybrid of outputs from a few top ranked ANNs by validation MSE could be used, which was shown useful for generalization of the ANN outputs for other DD problems (see e.g. [13]).

As said at the beginning of this section, different models were developed based on various assumptions of input variables. These assumptions were different in, firstly, the number of lags used to consider effects of previous weather conditions, and secondly, the definition and number of principle components of the time-lagged input variables used based on the PCA method [14]. Thus, while L increased the number of input variables, PCA was a method to combine and reduce them. Thus, 12 different input variable combinations were defined as follows.

- **Direct_inputs**, where all the time-lagged versions of the three weather variables (lags 0, 1, …, *L* days) were directly used (without any reduction via PCA). So, in total, there were 3×(*L*+1) input variables.
- **All_PCA5**, **All_PCA6**, **All_PCA7**, **All_PCA8**, and **All_PCA9**, where all variables in **Direct_inputs** were reduced, in total, to 5, 6, 7, 8, and 9 variables, respectively, via PCA.
- **Lags_PCA3**, **Lags_PCA4**, **Lags_PCA5**, and **Lags_PCA6**, where, for each of the three weather variables, the *L*+1 time lagged versions were reduced to 3, 4, 5, and 6 variables; so, in total, there were 9 (=3×3), 12 (=3×4), 15 (=3×5), and 18 (=3×6) input variables, respectively.
- **Variables_PCA1**, and **Variables_PCA2**, where, for each of 0, 1, …, *L* lags, the three weather variables were reduced to 1, and 2 variables; so, in total, there were (*L*+1), and (*L*+1)×2 input variables, respectively.

The developed ANNs based on the above combinations of input variables were evaluated for a verification portion (Figure 3), separated entirely from the training and validation portions, using the modelling performance criteria Nash-Sutcliffe Efficiency (NSE) that is:

$$NSE = 1 - \sum \frac{(\hat{u}_i - u_i)^2}{(u_i - \mu)^2} \qquad (3)$$

where, $\hat{u}$ and u stand for estimated and reference moisture content, μ is average of u, and i denotes the index of the verification data. NSE can be reformulated as NSE=A–B–C; where $A=2\times\frac{\hat{\sigma}}{\sigma}\times\rho$, $B=(\frac{\hat{\sigma}}{\sigma})^2$, $C=(\frac{\hat{\mu}-\mu}{\sigma})^2$, $\hat{\mu}$ and $\hat{\sigma}$ are mean and standard deviation of $\hat{u}$, ρ is correlation coefficient (perfect linear relationship between $\hat{u}$ and u is ρ=1, while the lack of linear correlation is ρ=0), and σ is standard deviation of u. Hence, NSE is different from the coefficient of determination ($R^2=\rho^2$), in that it includes additional elements considering the biases in estimates of variance (in B) and mean (in C), along with ρ (in A) to describe the modelling performance. The perfect accuracy is NSE=1 while NSE<0 is a condition worse than the use of μ as a simple estimator. NSE is widely used as an independently interpretable performance index of DD predictive modelling relying on weather data in various fields (e.g., [15,16]).

It is noted that, for a fair distribution of variable moisture data, in all portions in Figure 3, the Scheffer climate index, SCI, as described in [17], was calculated for the studied sites to classify them into 40 classes, with a frequency of 13 to 14 sites per SCI class, equivalent to 0–2.5, 2.5–5, …, 95–97.5, 97.5–100 percentiles of SCI as shown in Figure 4. Then, from each class, one site was randomly selected for "verification", another for "validation", and the remaining 11-12 for "train".

Figure 3: *Splitting of the data length into portions.*

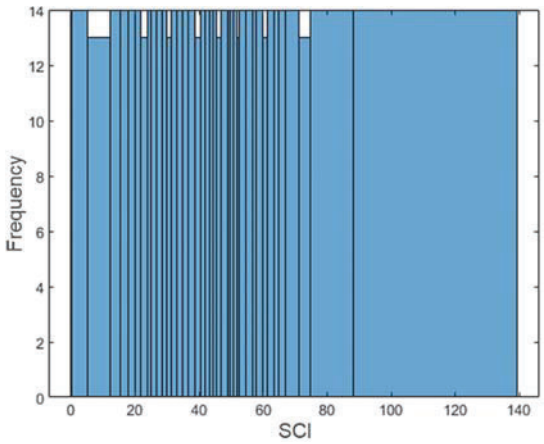

Figure 4: *Classification of the sites into 40 classes of SCI.*

3 RESULTS AND DISCUSSION

3.1 Model performance against synthetic data

To predict daily wood moisture content via ANN and MLR, *L* was defined first. Based on the cross-correlation analysis in Figure 5, among all weather variables, the highest correlation (ρ~0.55) was observed for *RH* at *L*=2; meaning that u had the highest linear relationship to relative humidity of two days earlier. For *RH*, ρ remains above 0.4 for up to *L*=10 and gradually decreases with further increases of *L*. Negative ρ for *T* indicates reverse changes of u and temperature. Among the variables, the absolute value of ρ dropped the fastest (slowest) for precipitation (temperature) from the max ρ at *L*=2 to the more stabilized ρ at higher *L*. Generally, a suitable range of options for *L* was estimated not to exceed 6 – 13 days, when ρ stabilized for different variables. Therefore, the development of ANNs using the 12 input variable combinations (as defined in section 2.2) was repeated for each choice of *L* between 6 – 13. The NSE of the ANNs are summarized in Figure 6a (for *L*=6–9) and Figure 6b (for *L*=10–13).

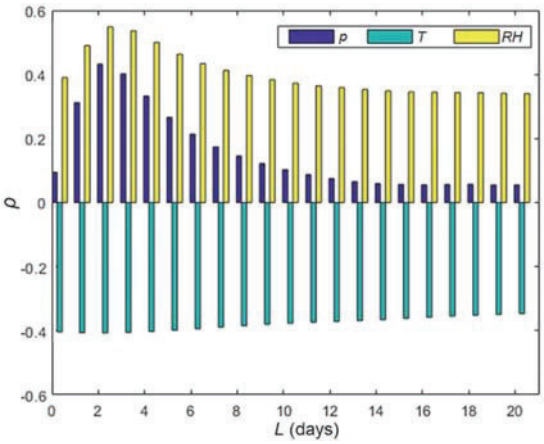

Figure 5: *Cross-correlation between 11 mm depth synthetic moisture content and three weather variables lagged by 0 – 20 days.*

https://doi.org/10.52202/069179-0495

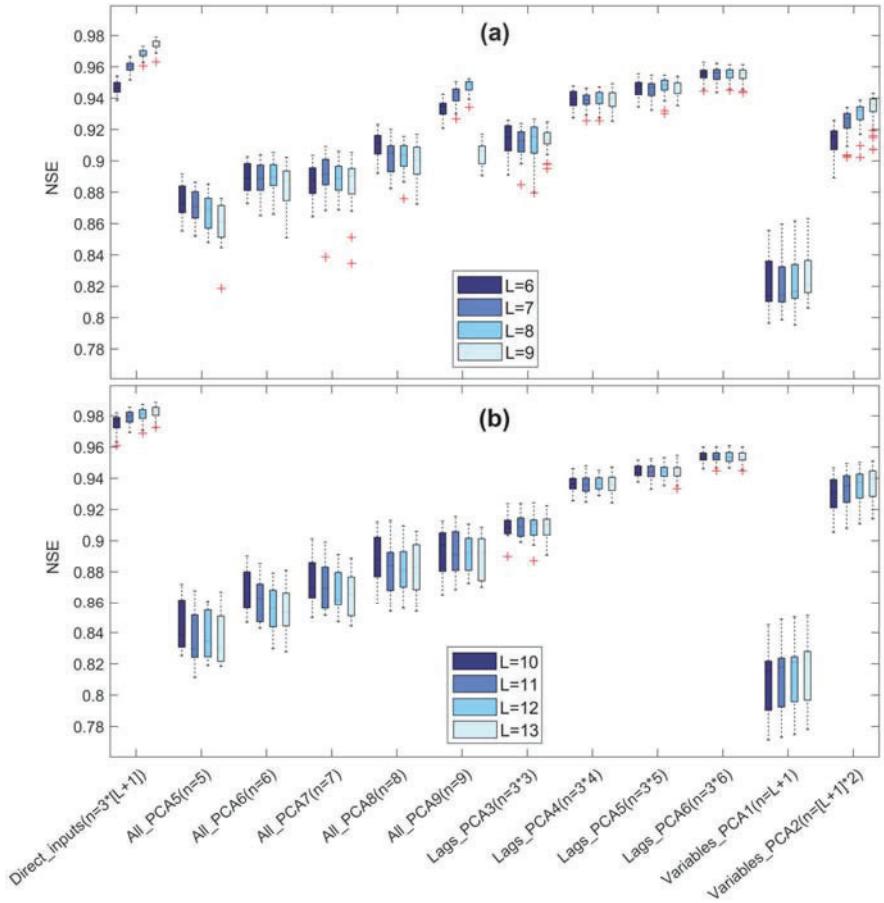

Figure 6: *Boxplots representing the range of NSE obtained from up to 25 repeats of ANNs developed for 11-mm depth moisture content modelling using time-lagged input variable combinations. On the horizontal axis,* n *gives the total number of input variables based on (a) L=6–9 days and (b) L=10–13 days. Red plus markers show outliers.*

The type of delayed response seen in Figure 5 and discussed in the previous paragraph is typical for moisture transport phenomenon. The delay primarily depends on the transport properties and depth. The increase in moisture content stemming specifically from lagged precipitation tends to decrease with decreasing distance to the rain-exposed surface. Therefore, less lags could be used for predicting the response at 1 mm (e.g., compared to 11 mm) depth. As mentioned earlier, the lags were, however, not varied between the two depths.

In Figure 6, for every input variable combination (e.g., Direct_inputs), eight boxplots are presented, corresponding to different choices of *L*. Each boxplot shows the range of obtained NSE for the repeats, where the bottom and top of each box corresponds to the first and third quartiles (q_1 and q_3, respectively), and the line within the box depicts the median NSE. The whiskers extend to the most extreme NSE, with outliers shown by the '+' marker. Outliers were greater than $q_3+w\times(q_3-q_1)$ or less than $q_1-w\times(q_3-q_1)$, where w was 2.7×(standard deviation of NSE). All the outliers in Figure 6 are located below the boxes (least NSE), which could mean that the outliers belonged to the repeats where ANN was trapped within the local minima of MSE.

As a result, while higher NSE is favourable, smaller intervals between the q_3 and q_1 (i.e., shorter boxes), show less sensitivity of modelling to the employed ANN architecture and initial random parameters in repeats. The shortest boxes were primarily observed for the ANN models using Direct_inputs, and Lags_PCAx (when x=6, 5, or 4). However, Direct_inputs resulted in the highest NSE that increased with increases of *L*, e.g., from 6 to 9 days (Figure 6a). Further increases of *L*, e.g., from 10 or 11 to 13 days (Figure 6b), did not result in a significant NSE increase for Direct_inputs. Lags_PCAx generally showed sensitivity to x rather than *L*.

Thus, the accuracy of predictions using input variable combinations of the form Lags_PCAx was mainly controlled by the adopted number of principal components, e.g., see the jumps in NSE values from Lags_PCA3 to Lags_PCA4 (Figure 6).

In view of the above, Direct_inputs and *L*=10 or 11 days seem to be enough for accurate prediction of the synthetic wood moisture content with a minimum sensitivity to ANN architecture and initial random parameters. Using such a combination for input variables, ANN could significantly outperform MLR. For example, by *L*=10, the

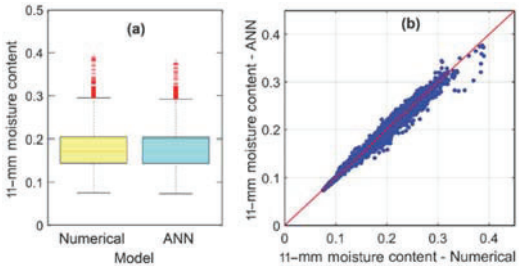

Figure 7: *Comparison of synthetic vs modelled (ANN) 11-mm moisture data in box plot (a) and scatter plot (b)*

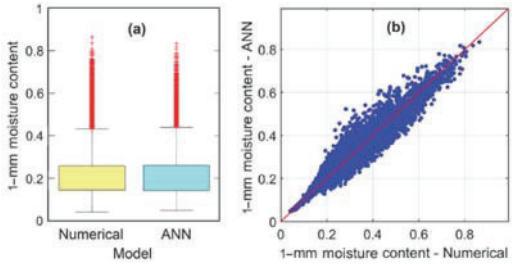

Figure 8*: Comparison of synthetic vs modelled (ANN) 1-mm moisture data in box plot (a) and scatter plot (b).*

corresponding NSE for MLR was 0.86, so 10% smaller than the least (outlier) NSE shown in Figure 6b for ANN under Direct_inputs and L=10 (0.96). Also, for an arbitrary ANN (not the best) with the same inputs, mean absolute error in verification of ANN was three times smaller than that of MLR (0.004 vs 0.013).

So far, the evaluations are based on the statistical performance criteria of the DD moisture content prediction at 11-mm depth. Figures 7 and 8 help to visually examine the predicted moisture content by ANN versus the synthetic moisture content by numerical model (as reference) at 11- and 1-mm depth, respectively. The box plots (Figures 7a and 8a) compare the synthetic and modelled data variability while the scatter plots (Figures 7b and 8b) compare the exact data points with the 45-degree line equivalent to the best fit for verification. Based on Figure 7a, except for a few top outliers ("+" markers), the elements of the boxplots for ANN and synthetic data match together, which is supported by the scatter plot (Figure 7b) showing a generally good agreement between ANN and synthetic data except for a few data points of synthetic values above 0.3 that are underestimated by ANN. Similarly favourable results can be observed for 1-mm moisture prediction in Figure 8. However, as seen in Figure 8b, the extreme data points (e.g., synthetic data below 0.2 and above 0.6) do not show significant over- or underestimations by ANN, and the highest discrepancies were observed for data points between 0.2 and 0.4.

Further evaluations of the moisture content predictions by the selected ANNs are described below by comparing the modelling outputs with the experimental measurements.

3.2 Model performance against measured data

Figure 9 shows the predicted daily average moisture content with measured data. Qualitatively, the model captures the seasonal variation, the timing of the peaks and the width of the peaks at the surface with reasonable accuracy. It should be emphasized that, due to measurement limitations, the amplitude of the rain-induced peaks cannot be compared. The final months of the measurement confirm that the model performs well in the absence of precipitation.

The comparison at a depth of 11 mm indicates that the model, at least initially, overestimates the rain-induced peaks, but is able to reproduce the seasonal variation quite well. The limitation regarding the valid moisture range is less problematic in the core of the sample, since the moisture content generally remains within the valid measurement range.

The vertical shaded lines indicate periods of time when one or several weather variables were missing. It can be noted that every instance of missing inputs results in a gap in the output equal to the window of missing data plus an additional 11 days (considering the required lagged inputs for DD modelling). So, the size of these gaps is consistent with L. To reduce the impact of missing data, smaller gaps

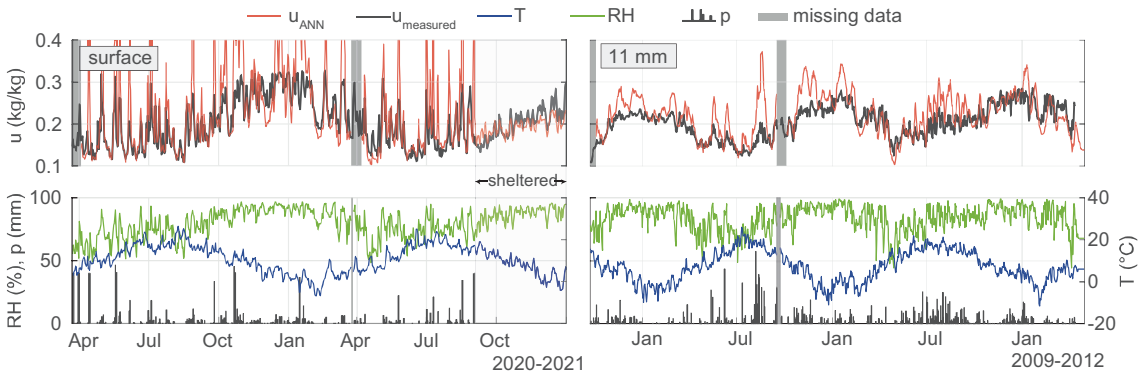

Figure 9: *ANN model compared against measured data (top row) from two different experiments where the moisture content was measured at different depths (surface and 11 mm) together with weather data over the respective periods (bottom row). Shaded vertical lines indicate periods when at least one weather variable is missing.*

https://doi.org/10.52202/069179-0495

can be filled by interpolation of weather prior to the estimations by modelling. Relative humidity and temperature can be interpolated linearly with reasonably low errors since the variation between adjacent days is usually small. Instances of missing precipitation can be substituted by zeros or data from near locations. A single missing rain event will then introduce an unknown degree of uncertainty in the following 11 days of predicted moisture content (if L=11 days) due to the usually high variability of spacetime precipitation. The related error will generally be significant a few days after the missing rain event, and will decrease as the weight of the lagged inputs decrease.

Figure 10 shows the relative time spent above a certain moisture content near the surface. Accordingly, the minimum and maximum measured daily average moisture content are approximately 10% and 32%, respectively, whereas the corresponding modelled values are 10% and >35%. The modelled time spent above a certain threshold remains accurate up until a threshold of u=23%, after which the modelled values increasingly exceed the measurements. As noted in section 2.1.2, this discrepancy can be mainly explained by the nature of the resistance-type measurements. Unless carefully calibrated (see e.g. [18]), measurements based on this technique tend to underestimate the moisture content in the over-hygroscopic moisture range. Consequently, model accuracy cannot be evaluated in the over-hygroscopic region and predicted values should be interpreted and used with caution. The discrepancy already at 23% moisture content is likely related to aggregation of the measurements to daily averages. To clarify, while measurements are relatively accurate up to around 25% moisture content, a daily average of 23% can include sub-daily measurements exceeding 25%. This limitation can be dealt with in durability applications by interpreting any values exceeding 25% as being favourable for fungal decay, and/or by adapting the decay model by reducing the critical moisture-threshold [2].

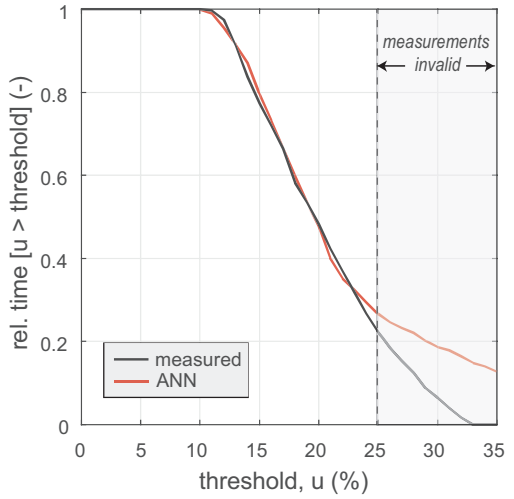

Figure 10: *Measured and modelled relative time spent above a certain moisture content-threshold near the surface.*

4 CONCLUSIONS

Data-driven models can be used to predict moisture content of rain-exposed wood. Contrary to numerical models, data-driven models are efficient and deployable and can thus be integrated into existing digital performance-based service life design frameworks for wood. This will potentially lead to improved and accessible service life prediction of wood.

Using simulated data for model fitting is not ideal, as any errors stemming from the numerical model are transferred to the DD model. In addition, the range of wood species for which the numerical model is valid is limited. On the other hand, when fitting a model to measured data, any uncertainties and limitations (such as the valid measurement range) of the system are instead transferred to the model.

In future work, the model will be used to map decay risk based on data sets with high spatial resolution (on different scales) and longer timespans (multiple years), where numerical models are too computationally expensive.

ACKNOWLEDGEMENT

The second author was funded by Formas (Swedish research council for sustainable development) [2021-02053]. The first and third authors were funded by the ForestValue project WoodLCC which is supported under the umbrella of ERA-NET Cofund ForestValue by the Ministry of Education, Science and Sport (MIZS) - Slovenia; The Ministry of the Environment (YM) - Finland; Research Council of Norway (RCN) - Norway; The Swedish Research Council for Environment, Agricultural Sciences and Spatial Planning (FORMAS), Swedish Energy Agency (SWEA), Swedish Governmental Agency for Innovation Systems (Vinnova) - Sweden; Estonian Ministry of the Environment; Estonian Research Council; Federal Ministry of Food and Agriculture (BMEL) and Agency for Renewable Resources (FNR) - Germany. ForestValue has received funding from the European Union's Horizon 2020 research and innovation programme under grant agreement N° 773324. Thanks to Brendan Nicholas Marais for proofreading the article.

REFERENCES

[1] Thelandersson S., Isaksson T., Suttie E., Frühwald E., Toratti T., Grüll G.: Service life of wood in outdoor above ground applications: Engineering design guideline - Background document. Technical report: TVBK-3061. Lund, Sweden, 2011.

[2] Isaksson T., Brischke C., Thelandersson S.: Development of decay performance models for outdoor timber structures. Materials and Structures, 46:1209–1225, 2013.

[3] Brischke C., Bayerbach R., Rapp A.O.: Decay-influencing factors: A basis for service life prediction of wood and wood-based products. Wood Material Science and Engineering, 1:91–107, 2006.

[4] Brischke C., Meyer L., Bornemann T., Bilstein M., Lauenstein B., Lück J.-M., Wulf C.: Service life of timber components: prognosis based on 3 years high-frequency monitoring. Eurean Journal of Wood and Wood Products, 71(1):79–90, 2013.
[5] Frühwald Hansson E., Brischke C., Meyer L., Isaksson T., Thelandersson S., Kavurmaci D.: Durability of timber outdoor structures: modelling performance and climate impacts. In: World Conference of Timber Engineering, 16-19, 2012.
[6] Niklewski J., Fredriksson M., Isaksson T.: Moisture content prediction of rain-exposed wood: Test and evaluation of a simple numerical model for durability applications. Building and Environment, 97:126–136, 2016.
[7] Awadalla H., El-Dib A., Mohamad M., Reuss M., Hussein H.: Mathematical modelling and experimental verification of wood drying process. Energy Conversion and Management, 45(2):197–207, 2004.
[8] Fortino S., Mirianon F., Toratti T.: A 3D moisture-stress FEM analysis for time dependent problems in timber structures. Mechanics of Time-Dependent Materials, 13:333–356, 2009.
[9] Niklewski J., Van Niekerk P.B., Brischke C., Frühwald Hansson E.: Evaluation of moisture and decay models for a new design framework for decay prediction of wood. Forests, 12(6):721, 2021.
[10] Van Niekerk P.B., Marais B.N., Brischke C., Borges L.M., Kutnik M., Niklewski J., Ansard D., Humar M., Cragg S.M., Militz H.: Mapping the biotic degradation hazard of wood in Europe–biophysical background, engineering applications, and climate change-induced prospects. Holzforschung, 76(2): 188–210, 2022.
[11] Isaksson T., Thelandersson S.: Experimental investigation on the effect of detail design on wood moisture content in outdoor above ground applications. Building and Environment, 59:239–249, 2013.
[12] Niklewski J., van Niekerk P.B., Marais B.N.: The effect of weathering on the surface moisture conditions of Norway spruce under outdoor exposure. Wood Material Science and Engineering, 1–11, 2022.
[13] Hosseini S.H., Hashemi H., Fakheri Fard A., Berndtsson R.: Areal Precipitation Coverage Ratio for Enhanced AI Modelling of Monthly Runoff: A New Satellite Data-Driven Scheme for Semi-Arid Mountainous Climate. Remote Sensing, 14(2): 270, 2022.
[14] Jolliffe I.T.: Principal component analysis for special types of data, Springer, 2002.
[15] Wong S.L., Wan K.K., Lam T.N.: Artificial neural networks for energy analysis of office buildings with daylighting. Applied Energy, 87(2): 551–557, 2010.
[16] Hosseini S.H., Hashemi H., Larsson R., Berndtsson R.: Merging dual-polarization X-band radar network intelligence for improved microscale observation of summer rainfall in south Sweden. Journal of Hydrology, 129090, 2023.
[17] Scheffer T.C.: A climate index for estimating potential for decay in wood structures above ground. Forest Products Journal, 21(10): 25–31, 1971.
[18] Otten K.A., Brischke C., Meyer C.: Material moisture content of wood and cement mortars–Electrical resistance-based measurements in the high ohmic range. Construction and Building Materials, 153: 640–646, 2017.

https://doi.org/10.52202/069179-0495

World Conference on Timber Engineering Oslo 2023

HYGRO-THERMAL EXPERIMENTAL ANALYSIS OF A FLAT ROOF STRUCTURE INTEGRATING A VARIABLE VAPOR-DIFFUSIVITY MEMBRANE

Riccardo Pinotti[1], Paola Brugnara[2], Stefano Avesani[3]

ABSTRACT: The work presented hereby aims at verifying the hygro-thermal performances of a non-ventilated timber frame flat roof structure integrating a variable vapor-diffusivity membrane. In particular, the objective is to verify the drying up process of the specimen after a humidity storage phase. These two phases have been determined referring to the typical conditions occurring in a European continental winter period (when, usually, humidity coming from indoor environments is stored by the structure) and a summer period (when, typically, the structure has should dry up). Hence, considering the specific use of variable vapor-diffusivity membrane, the main objective is to verify whether a drying process is allowed towards the indoor environment. An experimental test on a specimen has been performed in a double climatic chamber and the results have been used in order to validate an hygrothermal model. The model allowed then to study the structure's hygrothermal behaviour in different climatic conditions, showing promising outcomes related to the use of a variable vapor-diffusivity membrane in such envelope component.

KEYWORDS: Dynamic hygro-thermal behaviour, Modelling and simulation, Membrane and timber-based construction

1 INTRODUCTION

Vapor membranes are used to manage vapor transfer through the building structures.

It is well-known that excessive humidity levels within the building envelope may cause relevant damages to structures and materials, affecting both structural and physical performances (e.g., decreasing thermal conductivity) [1] [2] [3]

Typically, in continental climates, vapor-retarder or barriers membranes are used to prevent high level of moisture to reach the outer layers of the envelope in order to avoid condensation issues during the cold season.

Nowadays, the use of variable vapor-diffusivity membrane in the building sector is growing [4]. These membranes can vary their vapor permeability properties depending on the humidity of the environment in which they are embedded. In particular, they reach high vapor permeability when surrounded by high humidity levels and vice versa.

However, it is not a common approach to use this kind of membranes in roof structures since, in order to avoid condensation issues in the outer layer of the structure during cold season, vapor barriers or retarders are usually installed on the inner side of the structure. Actually, this approach does not consider eventual criticalities occurring on the building site while installing these membranes, since the posing procedure may cause dangerous leakages for vapor within the structure. Small damages, scratches and imperfections during the laying of those membranes may be the cause of potentially critical one-way vapor leakages through the envelope, in particular if timber based. The variable vapor-diffusivity membrane can potentially solve this issue, behaving as a vapor retarder within typical indoor relative humidity ranges, while becoming more vapor-open when surrounded by higher humidity values.

Hence, in this study, an alternative solution to the application of vapor retarders or barriers has been investigated, namely adopting an innovative variable vapor-diffusivity membrane. Such membrane has the capability of varying its permeability to vapor, behaving as a vapor open layer when embedded in high moisture conditions hence, allowing a higher flexibility in the application procedure, ensuring a drying potential to the structure containing high humidity levels. A detailed dynamic model of the construction has been setup, supported by experimental tests and a set of simulations has been run to calculate the whole construction hygro-thermal performance under different climates, aiming at validating the use of such innovative layer.

2 METHODOLOGY

To access the performances of the proposed solution, a typical timber frame roof structure integrating a variable vapor-diffusivity membrane has been tested in a controlled environment and a numerical model performed in Delphin 6 has been calibrated with test results. The

[1] Riccardo Pinotti, Eurac Research Institute for Renewable Energy, Italy, riccardo.pinotti@eurac.edu
[2] Paola Brugnara, Rothoblaas srl, Italy, paola.brugnara@rothoblaas.com
[3] Stefano Avesani, Eurac Research Institute for Renewable Energy, Italy, stefano.avesani@eurac.edu

https://doi.org/10.52202/069179-0496

model has been run for 10-years-long hygro-thermal simulations in different climatic conditions.
The following steps have been followed in order to set up the analyses:

1. Assembling of the prototype – the prototype has been assembled at EURAC Research laboratories, in order to allow an easy installation of the hygrothermal sensors within the material layers.
2. Pre-conditioning – the different layers, still not completely assembled, have been kept in a climatic chamber at high relative humidity level (~80%) and constant temperature for 3 days. This procedure ensured that the humidity content of the specimen would have been high enough at the beginning of the dynamic test, having reached an hygrothermal balance with the surrounding environment, and could have highlighted the drying process during in the following testing phases.
3. Dynamic test – after the pre-conditioning, the prototype has been completely assembled and installed within the testing facility (i.e., the Multifunctional Façade Lab, namely a double climatic chamber at EURAC Research laboratories). Here, dynamic test has lasted 15 days. Temperature and relative humidity of a continental summer weather condition have been replicated on the outer side of the specimen (one of the two chambers of the Multifunctional Façade Lab) in order to verify the drying potential towards a constant-condition inner side of the prototype (facing the other chamber of the testing facility).
4. Model calibration and extended simulations – measuring realistic dynamic hygrometric behaviours within building materials would require very long timespans, in the range of seasonal climatic variations, and this is of course not feasible to be performed in a laboratory on large scale specimens. Therefore, it has been decided to use the results from the tests to calibrate and validate a numerical model using Delphin 6. The model allowed to evaluate the hygrothermal behaviour of the structure in an extended timespan and in different climate conditions.

2.1 EXPERIMENTAL SET-UP

The tested prototype has an area of 1.44 m² (1.2m x 1.2m). The layer and material properties within the structure are described in Table 1.

Table 1: *Structure layers and material properties*

Layer (inside to outside)	Thickness	Density	Heat Capacity	Conductivity	Vapor Permeability
	[mm]	[kg/m³]	[J/kgK]	[W/mK]	Sd[m]; μ[-]
Gypsum fibre Board	12.5	744	1384	0.21	μ =4
Variable Vapour Diffusivity Membrane	*	*	*	*	Sd_variable = 0.15 ÷ 5
Mineral Wool Insulation	240	110	1030	0.036	μ = 3.5
OSB Panel	20	530	1880	0.1	μ = 280
Self-Adhesive Bituminous Membrane	*	*	*	*	Sd= 200
Self-adhesive Slate Bituminous Membrane	*	*	*	*	Sd= 280

** Delphin is not requiring this parameter for simulations*

The above-mentioned values have also been used in the simulation model. Anyway, for some of the materials, detailed data sheets were not available. For these specific cases, assumptions have been made using typical values for similar products. These values have been considered as main parameters to be calibrated in order to match model and test results.
The test has been performed in double climatic chamber and in order to monitor the hygrothermal conditions within the specimen, it has been equipped with 8 Amphenol T9602 sensors, measuring temperature (-20÷70°C ± 0.3°C) and relative humidity (0÷100% ± 2%). In Figure 1, Figure 2 and Figure 3, sensors' position within the prototype is represented.
Sensors 1,2 and 3 are placed between the OSB partner and insulation layer, being embedded in this last.
Sensors 4,5 and 6 are placed between the vapor variable diffusivity membrane and the insulation; hence, they are not in contact with the gypsum-fibre board.
Sensors 7 and 8 are positioned between two insulation layers, approximately in middle of the specimen thickness.

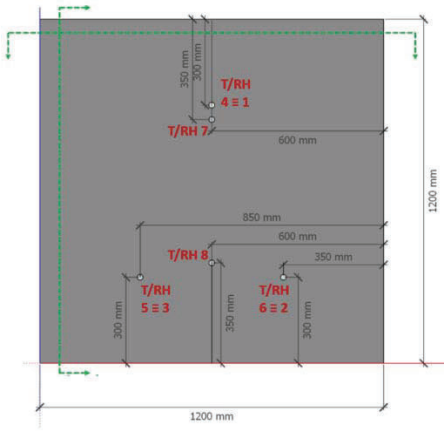

Figure 1: *Sensor positioning scheme, specimen front view*

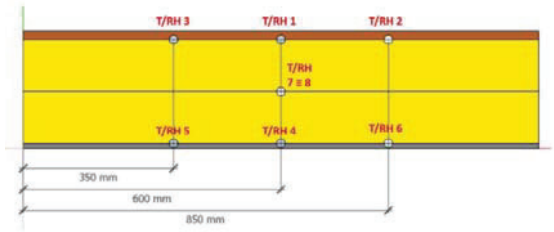

Figure 2: *Sensor positioning scheme, horizontal section*

https://doi.org/10.52202/069179-0496

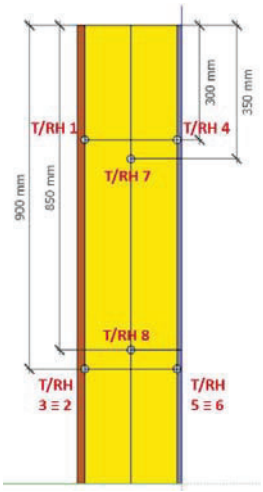

Figure 3: *Sensor positioning scheme, vertical section*

2.2 DYNAMIC TEST

Once the pre-conditioning phase, used to load the specimen of vapor, has been concluded (3 days at 80% relative humidity), the dynamic test started. Hence, operative conditions typical of a summer continental European climate have been reproduced within the facility.

In particular, in order to determine the external temperature and relative humidity conditions to be applied during the test, a typical climatic year related to Munich (Germany) has been used the weather file has been made available by the World Meteorological Organization (https://public.wmo.int/en) and downloaded by the Energy Plus website (https://energyplus.net/weather). From this reference hourly data, 4 summer days (middle of June) have been extrapolated and used to build the temperature and relative humidity curves to be reproduced by the testing facility's chamber representing the outdoor environment.

Concerning the conditions set on the indoor side, where humidity is free floating between 30% and 60%, temperature has been set to 20°C. A scheme of the test setting in shown in Figure 4, while a picture of the specimen installed in the Multifunctional Façade Lab is in Figure 5.

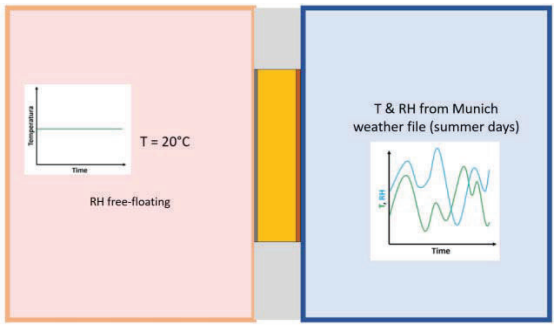

Figure 4: *Schematic view of the test setting within Multifunctional Facade Lab; the specimen is between indoor and outdoor conditions created in the chambers*

Figure 5: *Prototype installed in the testing facility*

Dynamic tests took about 17 days. In Figure 6 and Figure 7, the graphs are showing the monitored boundary conditions in the chambers during the test.

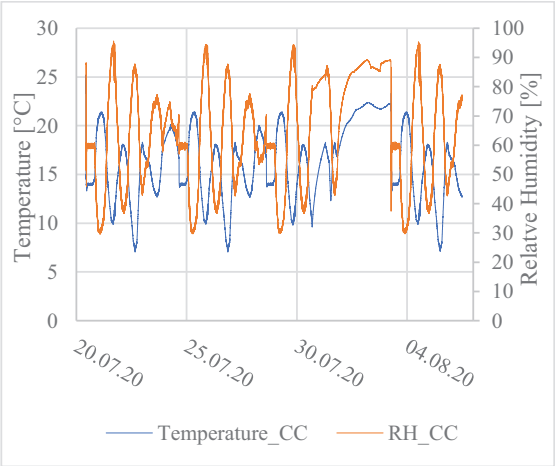

Figure 6: *Temperature and Relative Humidity conditions on the Outdoor side of the specimen during the test. "_CC" stand for "Cold Chamber", referring to the facility chamber reproducing the outdoor environment*

https://doi.org/10.52202/069179-0496

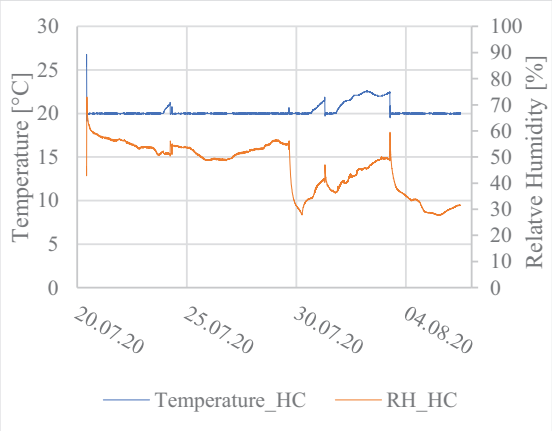

Figure 7: *Temperature and Relative Humidity conditions on the Outdoor side of the specimen during the test. "_HC" stand for "Hot Chamber", referring to the facility chamber reproducing the indoor environment*

2.3 MODEL CALIBRATION

After about two weeks of dynamic test, the data acquired by the sensors within the specimen have been used to calibrate a bi-dimensional hygro-thermal model, developed with the software Delphin 6. Hence, the model aimed at reproducing faithfully the testing conditions, also taking into account the gravity effect on vapor transfer dynamics, due to the vertical position of the prototype.

In Figure 8, a schematic representation of the bi-dimensional prototype geometry modelled is shown. The initial values for material properties used by the model are reported in Table 1.

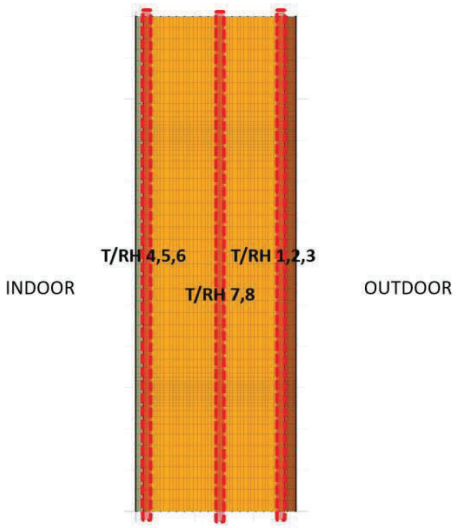

Figure 8: *Geometrical model used in Delphin 6; it is possible to notice the calculation mesh and the layers (marked in red) where the model outputs have been evaluated*

Figure 8 is also showing (in red) the layers in which temperature and relative humidity outputs from the model has been taken, as averaged value of the selected nodes within the mesh.

As a consequence of this, temperature (T) and relative humidity (RH) measured by sensors T/RH 1, 2 and 3 will be compared respectively with model outputs called T123 and RH123; values from sensors T/RH 4,5 and 6 will be compared with output T456 and RH456; values from sensors T/RH 7 and 8 will be compared with output T78 and RH78.

In the following graphs (from Figure 9 to Figure 14), calibration process' results are shown. In these graphs, it is possible to notice the comparison between monitored data and results from the model in the specific layer.

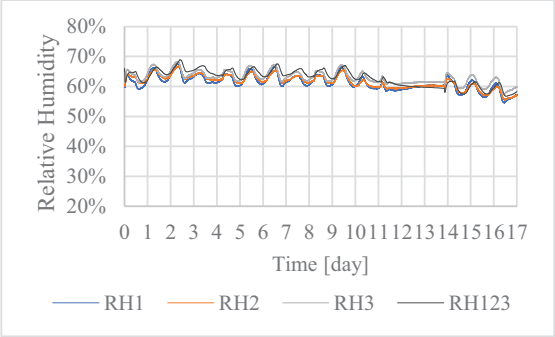

Figure 9: *Comparison between RH 1, 2 and 3 from tests with model results RH123*

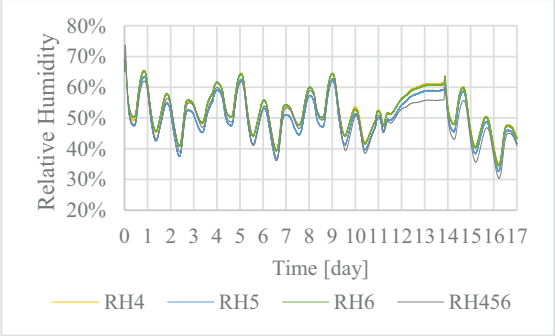

Figure 10: *Comparison between RH 4, 5 and 6 from tests with model results RH456*

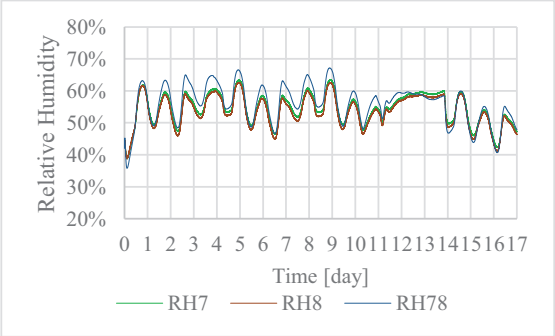

https://doi.org/10.52202/069179-0496

Figure 11: *Comparison between RH 7 and 8 from tests with model results RH78*

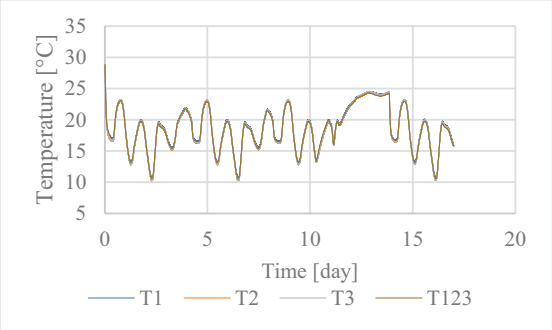

Figure 12: *Comparison between T 1, 2 and 3 from tests with model results T123*

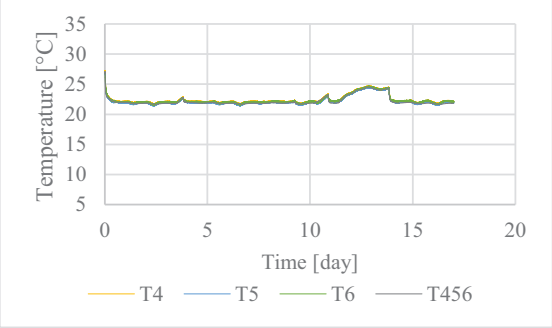

Figure 13: *Comparison between T 4, 5 and 6 from tests with model results T456*

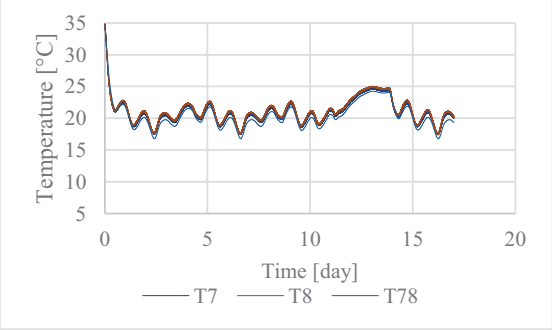

Figure 14: *Comparison between T 7 and 8 from tests with model results T78*

In the following Table 2 and Table 3, the Mean Absolute Error (MAE) and the Root Mean Square Error (RMSE) between model output and the average value of the sensors within the same layer are reported.

Table 2: *MAE and RMSE for relative humidity values*

	RH 123	RH 456	RH 78
MAE	0.014	0.019	0.023
RMSE	0.017	0.024	0.027

Table 3: *MAE and RMSE for temperature values*

	T 123	T 456	T 78
MAE	0.14	0.15	0.56
RMSE	0.17	0.18	0.60

To calibrate the model which brought to the above-mentioned results, it has been necessary to slightly modify the materials' properties within the software, applying some small variations on the values taken from the datasheets. Calibrated material properties used in the model are shown in Table 4. In particular, some change in the vapor permeability of the insulation layer has been applied. Nevertheless, this variation is acceptable, especially considering the high-compression and high-humidity levels of the material within the specimen. Some other variations of the vapor permeability of material have been adopted, but always within ranges reported on their technical sheets. Table 4 shows the material properties used in the calibrated model.

Table 4: *Material properties used after calibration process; for those values which have been modified respect to the initial one, this last is shown between brackets.*

Layer	Thickness	Density	Heat capacity	Conductivity	Vapor permeability
	[mm]	[kg/m³]	[J/kgK]	[W/mK]	Sd: [m]; μ:[ ]
Gypsum fibre Board	12.5	744	1384 (n.d.)	0.21	μ =4
Variable Vapour Diffusivity Membrane	*	*	*	*	Sd_variabile = 0.15 - 6
Mineral Wool Insulation	240	110	1030	0.036	μ = 3.5 (1)
OSB Panel	20	530	1880 (n.d.)	0.1	μ = 280 (90 – 150)
Self-Adhesive Bituminous Membrane	*	*	*	*	Sd=200
Self-adhesive Slate Bituminous Membrane	*	*	*	*	Sd=280

** Delphin is not requiring this parameter for simulations*

3 EXTENDED ANALYSIS IN DIFFERENT CLIMATES

Once performed the model calibration, it has been used to extend the hygrothermal study in different climatic conditions for 10-years-long simulations. The objective is to verify the effective drying potential of the structure in the summer period after and eventual humidity storage during the coldest season. Furthermore, a simulation set up (namely "Condition 2") verified a slightly different stratigraphy, also considering an additional insulation layer and a gypsum fibre board in the inner layers.

Being the simulation referred to a roof structure, the model has been set in horizontal direction, taking into account the gravity effect on moisture transport. This allowed to verify the real hygrothermal behaviour of the roof structure.
Table 5 is reporting the configurations used for extended hygrothermal analyses.

Table 5: *Boundary conditions for extended analyses*

Condition	Model stratigraphy	Internal condition T and RH	External condition T and RH
Condition 1	Stratigraphy calibrated with test results (**Errore. L'origine riferimento non è stata trovata.**)	WTA adaptive indoor climate model[1] implemented in software Delphin6.0	Yearly weather file Central Europe[2] Munich
Condition 2	Stratigraphy calibrated with test results (**Errore. L'origine riferimento non è stata trovata.**) + 5 cm insulation + gypsum fibre board	WTA adaptive indoor climate model[1] implemented in software Delphin6.0	Yearly weather file Central Europe[2] Munich
Condition 3	Stratigraphy calibrated with test results (**Errore. L'origine riferimento non è stata trovata.**)	WTA adaptive indoor climate model[1] implemented in software Delphin6.0	Yearly weather file hot and humid conditions[2] Brisbane
Condition 4	Stratigraphy calibrated with test results (**Errore. L'origine riferimento non è stata trovata.**)	WTA adaptive indoor climate model[1] implemented in software Delphin6.0	Yearly weather file hot and humid conditions[2] Abu Dhabi

[1] *WTA Adaptive Indoor Climate Model provided from DIN EN 15026; it allows to determine indoor temperature and relative humidity conditions in relation to the outdoor ones*
[2] *Outdoor climatic data to run the simulations have been provided by the World Meteorological Organization and taken on the Energy Plus website (https://energyplus.net/weather)*

Here below, for the modelled configurations, the trends for integral humidity content within the stratigraphy and the relative humidity value in the layer between insulation and OSB board (RH123) are reported. It may be noticed from Figure 15, Figure 16, Figure 17 and Figure 18 related to Condition 1, 2, 3 and 4 that the humidity content during the 10-years-long simulation is periodically increasing in winter seasons while dries during summer periods. It is important to highlight that humidity content peaks are growing in the first simulated years (around 3) and then they are constant for the rest of the simulation. Furthermore, these peaks are not even reaching critical relative humidity leading to over-hygroscopic content (95%). Indeed, higher relative humidity values within the structure, reached in Condition 1 simulation, are around 87%.

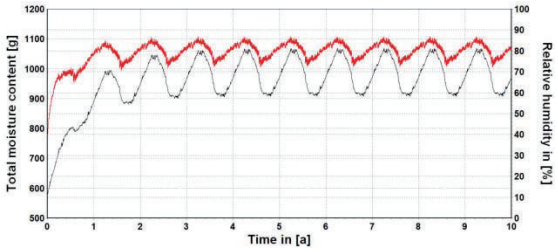

Figure 15: *Condition 1 Munich (Germany) - humidity content trend (black curve) and relative humidity at interface insulation-OSB (red curve)*

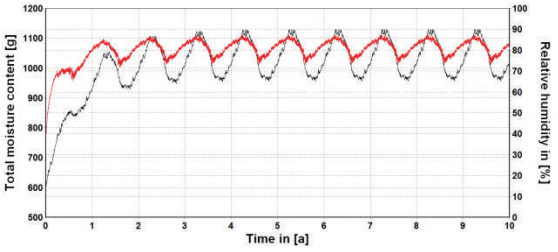

Figure 16: *Condition 2 Munich (Germany) - humidity content trend (black curve) and relative humidity at interface insulation-OSB (red curve)*

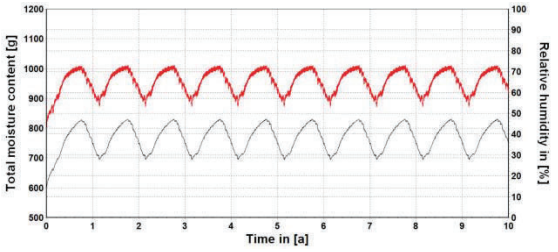

Figure 17: *Condition 3 Brisbane (Australia) - humidity content trend (black curve) and relative humidity at interface insulation-OSB (red curve)*

https://doi.org/10.52202/069179-0496

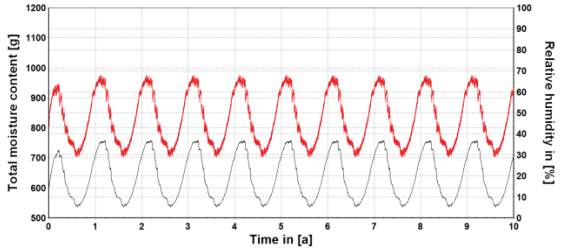

Figure 18: *Condition 3 Abu Dhabi (United Arab Emirates) - humidity content trend (black curve) and relative humidity at interface insulation-OSB (red curve)*

In Figure 19, the comparison of internal moisture content in Condition 1 (Munich climatic condition) with and without variable vapor diffusivity membrane is shown. It can be noticed that the moisture content is clearly higher in the condition without the membrane and, furthermore, this configuration is leading to cyclical creation (up to ~150 g) of over-hygroscopic content (Figure 20).
Despite the condensate dries every year, this condition is potentially dangerous for the envelope due to a possible mould-growth phenomenon or deterioration of materials.

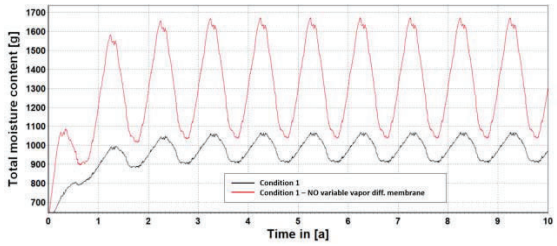

Figure 19: *Condition 1 - moisture content with (black curve) and without (red curve) variable vapor diffusivity membrane*

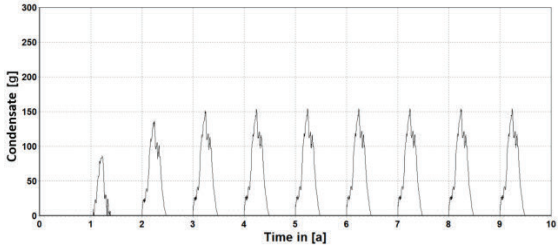

Figure 20: *Condensate in Condition 1 without variable vapor diffusivity membrane*

4 CONCLUSION

The methodology described allowed to successfully verify the hygro-thermal behaviour of a flat roof structure integrating a variable vapor diffusivity membrane.
After having performed 15-days-long experimental tests with dynamic boundary conditions across the specimen, temperature and relative humidity monitored values have been used to calibrate a numerical model developed with the software Delphin 6.
Once a detailed level of precision of the model was reached, it has been used to extend the analyses to 10-years-long period, evaluating the behaviour of the flat roof stratigraphy in different climatic conditions.
In all the simulated cases, the stratigraphy has not presented critical issues related to condensate formation, suggesting that the use of the variable vapor diffusivity membrane is effective to prevent from excessive moisture storage within the structure, allowing its drying during the warmer season.
As demonstrated by the simulation in Central European weather condition, without using the variable vapor diffusivity membrane, its presence is crucial to avoid periodical condensation events in the outer layers of the envelope during winter conditions.
The methodology applied to the specific stratigraphy analysed in this paper may be successfully replicated for developing further analyses, varying the application context and, hence, boundary conditions of the evaluated envelope structure.

REFERENCES

[1] N. May, «Breathability: the key to building performance» pp. 1-30, 2005.

[2] A. Karaglozls, M. Salonvaara, K. Kumaran, «The effect of waterproof coating on hygrothermal performance of a high-rise wall structure» *Thermal performance of the exterior envelopes of buildings,* n. 391-398, 1995.

[3] G. Coelho, F. Henriques, «Influence of driving rain on the hygrothermal behavior of solid brick walls» *Journal of Building Engineering,* pp. 121-132, 2016.

[4] H. Kunzel, «Adapted vapour control for durable building enclosures» *10th DBMC international conference on durability of building materials and components,* p. 8, 2005.

World Conference on
Timber Engineering
Oslo 2023

DEVELOPING SLIMMER TIMBER WINDOW FRAME.

Katarzyna Ostapska[1], Tore Myrland Jensen[2], Lars Gullbreken[3], Petra Ruther[4],

ABSTRACT: Demand for the ever-increasing performance of windows when it comes to the thermal insulation properties requires, among other things, designing thinner timber frames. Structural strength and dimensional stability of wood under changing climate condition is of the key importance. In this paper the experimental and numerical investigation of the mechanical behaviour of the typical wooden window frame is presented. Based on the results, a new, slimmer timber window frame is designed and evaluated numerically. Large material savings and thermal insulation gains can be achieved with retaining required structural strength by use of optimized frames. The new frame design requires however proper design of hinge connection, protection against moisture accumulation and sufficient wood laminating for dimensional stability when exposed to varying climate conditions.

KEYWORDS: slim window timber frames, DIC, FEA, timber-to-steel screw connection

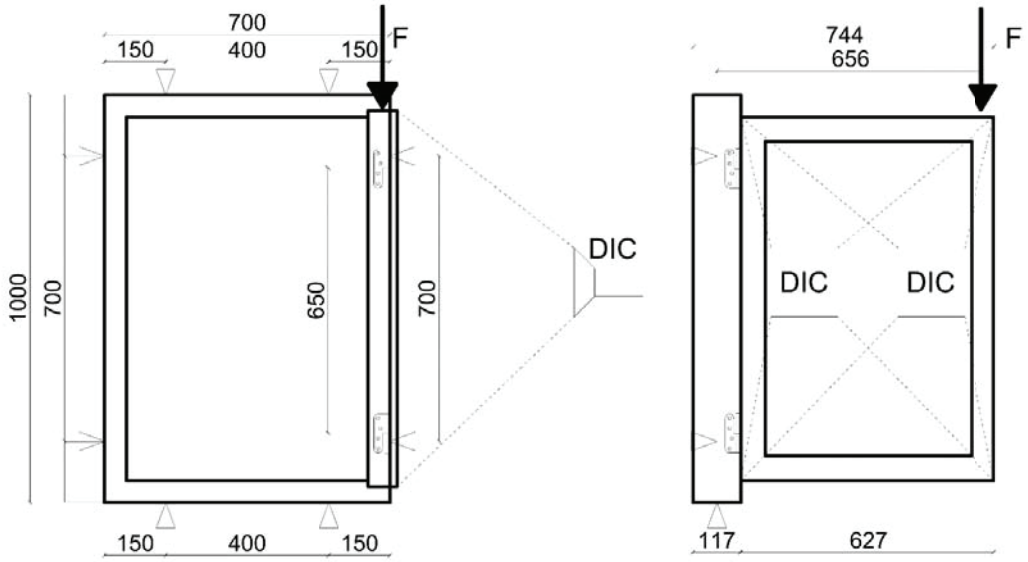

Figure 2.1: *Graphical scheme of the test set-up with optical measurement location.*

1 INTRODUCTION

Timber is the most popular material used for window framing. Its combination of high structural strength, good thermal isolation properties, and low carbon footprint makes it a natural choice for frame structures with crucial insulation functions. The further advantage of wood over plastic, aluminum and steel frames is its low energy demanding production and processing, renewability, and carbon storage qualities. To verify the design of the window, the thermal transmittance is commonly evaluated, e.g., with the formula shown in Equation (1) below:

$$U_w = \frac{U_{cg}A_g + \sum U_f A_f + \sum U_{eg}A_e}{A_t} \quad (1)$$

[1] Katarzyna Ostapska, SINTEF Community, Norway, Katarzyna.ostapska@sintef.no
[2] Tore Myrland Jensen, SINTEF Community, Norway, tor.m.jensen@sintef.no
[3] Lars Gullbreken, SINTEF Community, Norway, lars.gullbreken@sintef.no
[4] Petra Ruther, SINTEF Community, Norway, petra.ruther@sintef.no

https://doi.org/10.52202/069179-0497

where U- thermal transmittance, *A*- area measured in window plane, indexes: c-central, e-edge, f-frame, g-glass, t-total. The total thermal transmittance is thus dependent, among others, on the area of the frame in relation to the total area of the window in its plane. Reducing the area of the frame, not only decreases thermal transmittance but also increases glazing area that allows for energy gains due to irradiance [2], [3].

2 METHODS

2.1 EXPERIMENT DESIGN AND PROCEDURE

To establish current window frame capacity, the static loading test was performed on the 90-degree opened window frame with point force located at the top frame corner as shown in Figure 2.1. Such load case is important in case of exceptional load during fire emergency and evacuation. The estimated ultimate failure capacity based on the preliminary numerical simulation and analytical estimation was 1.5-2 kN and the load was applied discretely with 0.2 kN intervals by adding weight.

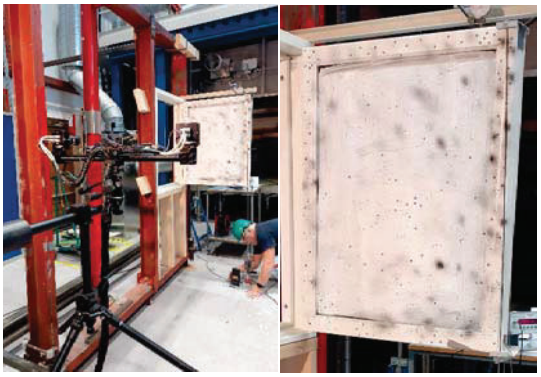

Figure 2.2: *Window frame and glazing painted for optical deformation tracking (left), image from the laboratory set-up.*

Deformations were measured optically on the whole window frame plane using commercial system of digital image correlation (DIC), ARAMIS, see Figure 2.2. Two cameras were used at a fixed distance and angle to produce the 3D displacement field that was required due to substantial out-of-plane deformation of the window during loading procedure.

2.2 NUMERICAL MODEL

The numerical mechanical model was built in the commercial software ABAQUS, where the internal stresses in wood were simulated with the use of finite element method (FEM) [1]. The geometry was based on the cross- section drawings of the original window design obtained from the producer (Røros Dører og Vinduer AS) and are shown together with subsequently modified frame sections in the Figure 2.3. The thinner frames dimensions are reduced across the thickness as the depth remains 117 mm. The thinnest frame design has wood volume reduced by 36%. This leads to the glass area increase by around 22% with the same external typical window dimensions of 1000x700mm.

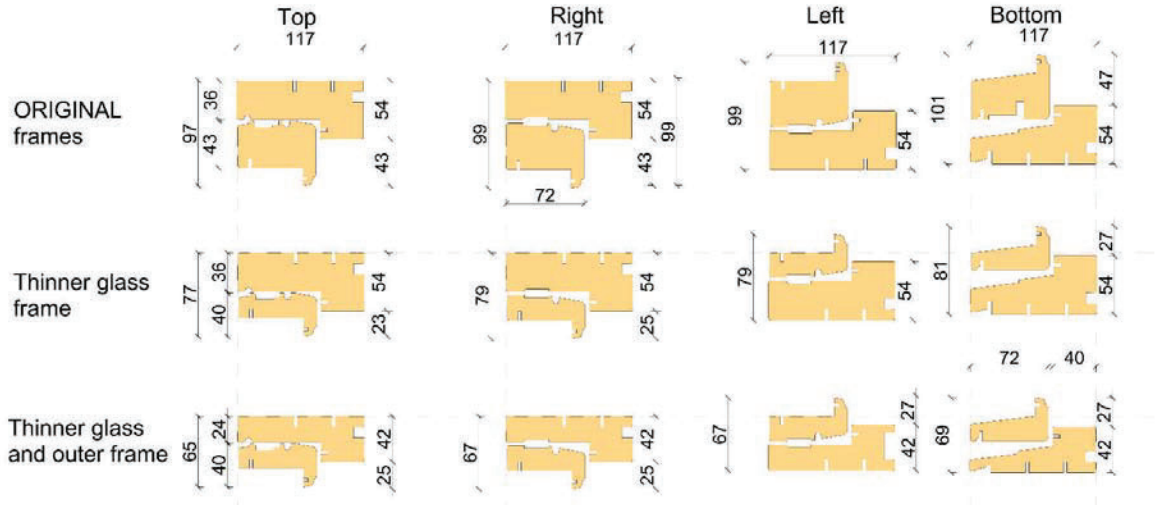

Figure 2.3. Cross section of the four frame parts for original (first row of drawings) and slim geometry after redesign (second and third raw).

Orthotropic elasticity was applied for wood material model, see Table 2.1, ideal elastic-plastic behaviour was assumed for steel hinged connection and elastic isotropic material model was used for glass (E = 50 GPa, ν=0.18).

Table 2.1*. Engineering constants for wood lamellas.*

Wood material properties [GPa]								
E_L	E_T	E_R	ν_{LR}	ν_{LT}	ν_{RT}	G_{LR}	G_{LT}	G_{RT}
10	0.6	0.6	0.5	0.5	0.8	0.6	0.6	0.06

The fixed steel-wood connection was used instead of screws for simplification in the preliminary model (model A). Screws were added to the model (model B) to

https://doi.org/10.52202/069179-0497

investigate the influence of their location and spacing on the force distribution in the hinge plate and timber. Screws were modelled with smooth shanks an assumed tied to the surrounding wood on the shank perimeter, see screw and hinge CAD geometry in Fig. 2.4.

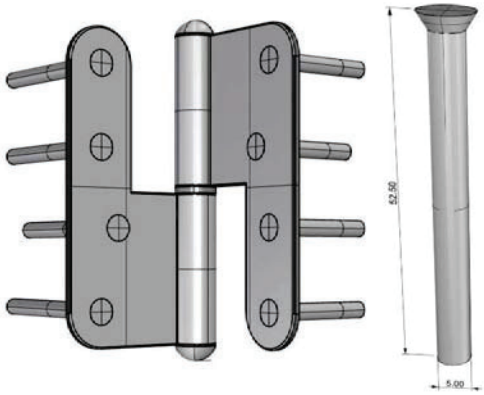

Figure 2.4: Hinge and screw model geometry.

Boundary conditions applied on the window encasing both in experiment and numerical analysis are depicted in Figure 2.5.

Finite element mesh was generated, see Figure 2.5 and 3.4, with continuous 3D solid elements. The two-layer glazing part was fixed to the timber frame part at the edges.

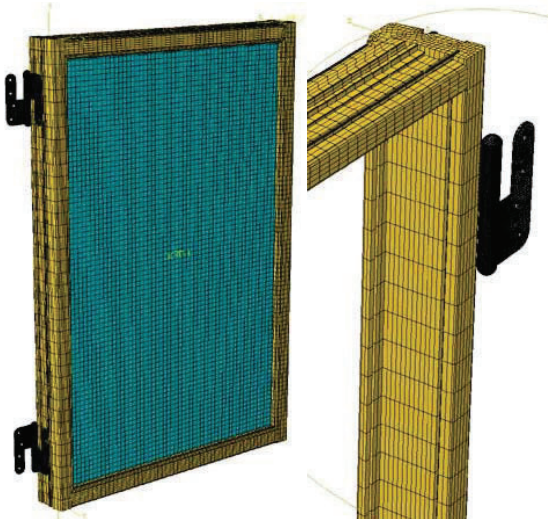

Figure 2.5: FE model geometry and mesh of the whole slim window with hinges (left) and timber frame corner detail (right).

3 RESULTS

3.1 DEFORMATIONS

The maximum measured total deformation corresponding to the maximum applied force of 1.6kN in the test was around 28 mm. The deformation is occurring in the hinge plates and the inner bolt undergoes localized bending and plastic hinge is formed.

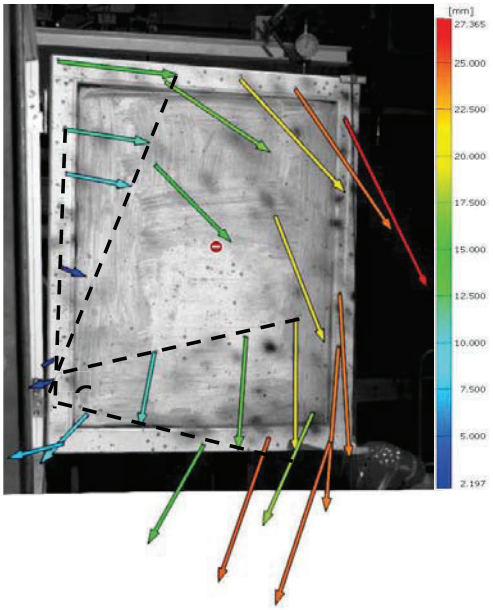

Figure 3.1: Deformations measured with DIC at 1.7kN load.

The window internal frame with glazing is rotating in plane initially as a whole, performing as a stiff shear plane component with slight in-plane shear deformations, see Figure 3.1. From the deformation field analysis, the centre of rotation is located in the vicinity of the bottom hinge. The frame is slender enough though and small out-of-plane force components caused by eccentricity of loading and boundary conditions (hinge fixings) lead to out-of-plane bending mode immediately. At this stage, large shear forces are transferred to the screw shank which leads to collapse of the frame element with glass.
Deformation modes obtained in the numerical analysis show similar behaviour and are depicted in the Figure 3.2.

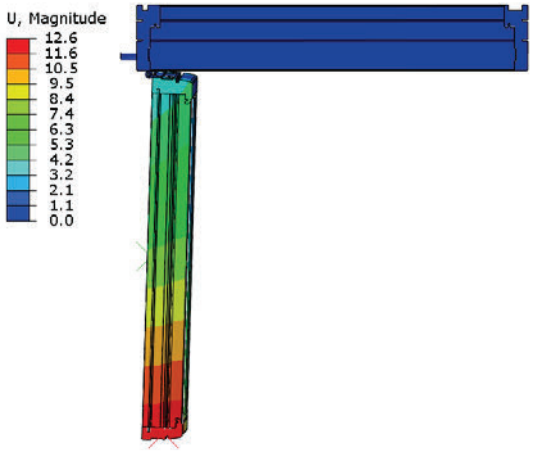

https://doi.org/10.52202/069179-0497

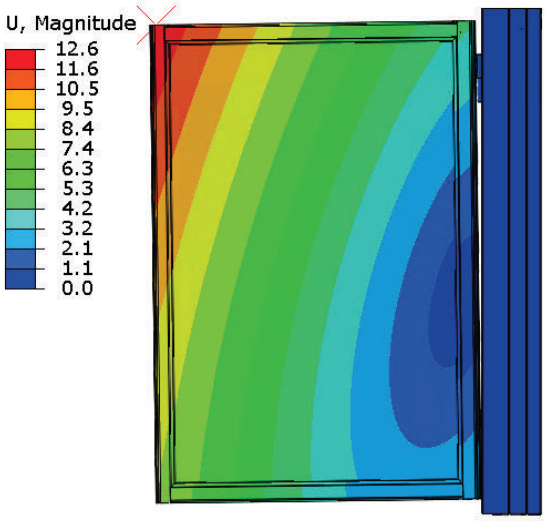

Figure 3.2: Deformation of the window in the numerical analysis from top and side view.

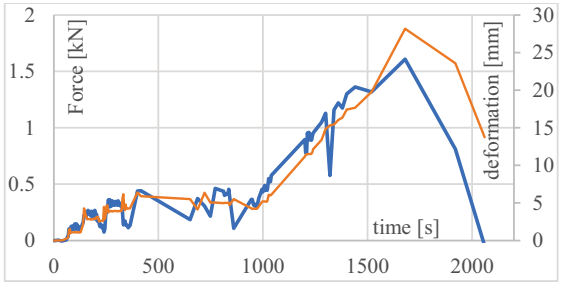

Figure 3.3: *Force (blue), load program (blue dashed) on the window frame and corresponding maximum deformation (red).*

3.2 STRESSES AND FAILURE MODE

3.2.1 STRESSES IN THE HINGE

Numerical simulation indicates the damage first occurs in the top plastic hinge, Figure 3.4, where the inner bolt starts to bend and steel plate bends because of resulting eccentricity. Based on that failure mechanism the window capacity was estimated at 1.5-2kN. Global stresses in timber frame sections are not exceeding the strength limits at the point of hinge connection failure.

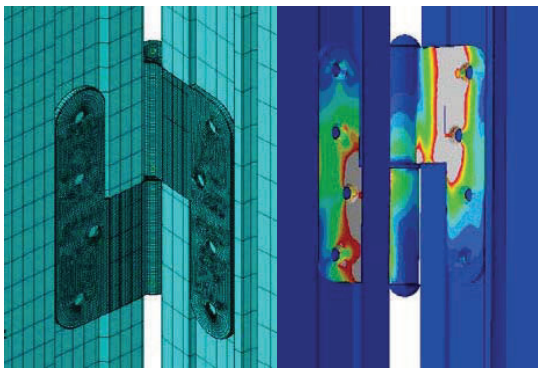

Figure 3.4: FE model of steel hinge connector (left) and stress distribution under 2kN Force (right). Gray colour areas indicate von Mises stress exceeding 250MPa.

3.2.2 STRESSES IN THE TIMBER FRAME

Timber frame is mostly not utilized in the performed test. Stresses in wood are exceeded only locally around the screw shanks, where critical concentrations start to occur as soon as 0.5kN load is reached.

Another stress concentration zone develops around the frame corners when the in-plane shear deformations and out-of-plane rotation starts. Rolling shear stresses and perpendicular to grain compression and tension in the corner of the bottom beam of the frame with glass are shown in figures 3.5 and 3.6. The presence of those stresses is a result of the twisting deformation in the glass-frame element occurring due to the eccentric and asymmetrical load.

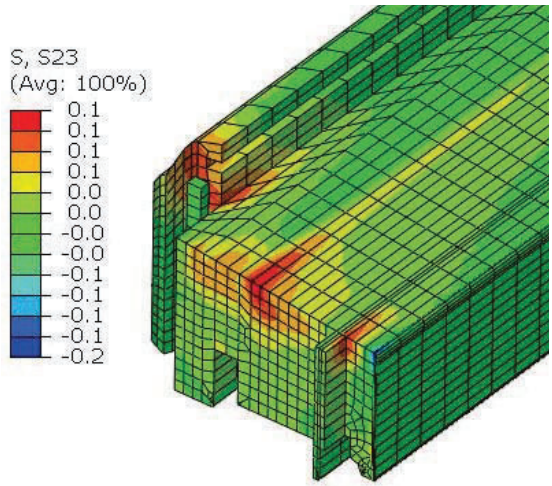

Figure 3.5: Rolling shear stresses in the end of the bottom beam of the window frame with glass at load of 1.6kN.

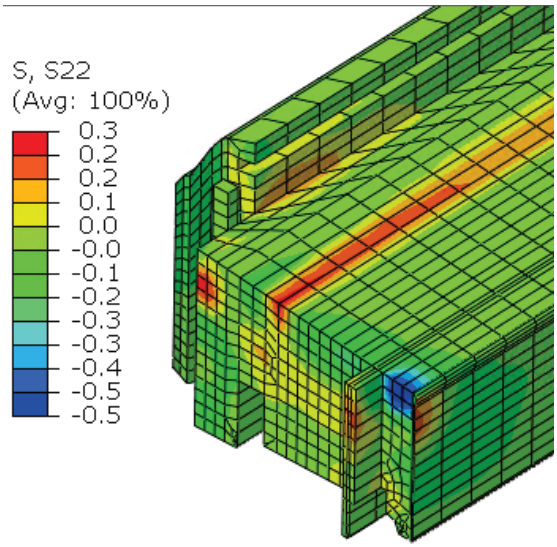

Figure 3.6: Perpendicular to grain stresses at the end of the bottom beam of the window glass frame at the load of 1.6kN.

https://doi.org/10.52202/069179-0497

3.2.3 STRESSES IN THE HINGE SCREWS AND IN WOOD AROUND THE SCREWS

Ultimate failure occurs in wood in shear around screws in the top hinge in the glass frame, see Figure 3.4.
The screws are not uniformly loaded since the plate of the connector is bended, and screw placement is not symmetrical. Forces in the screws from 1 to 4 were evaluated with the numerical model and their values are presented over the load history in Figures 3.8 and 3.9.
Screws are loaded both axially as intended and bended and pressed into the wood perpendicularly to the grain. This transverse force distribution is shown in the Figure 3.8. The top screw is subjected to the half of the total transverse force transferred from the glass frame through the hinge. The bottom screw shares only 8% of the transverse load. Axial forces in the screws are shown in the Figure 3.9. Screw number 3, the second from the top, is subject to the axial withdrawal, while remaining screws no 1, 2, and 4 (see Figure 3.7 left) are axially pressed into the timber.

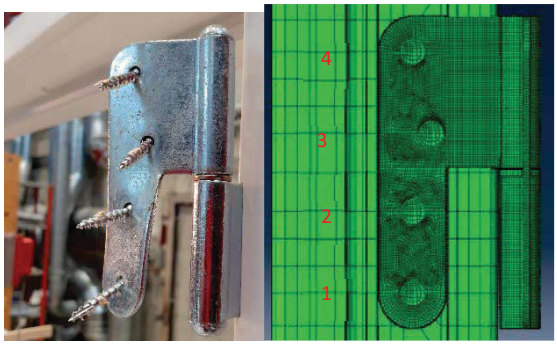

Figure 3.7: Screws in hinge after failure (left) and the numerical model with mesh and screw numbers (right).
The negative force (compression) transferred via screws 4,2, and 1 is in equilibrium with the positive (tension) force transferred by screw no 3. The screws do not cooperate in axial resistance to withdrawal, but are counteracting the hinge plate bending.

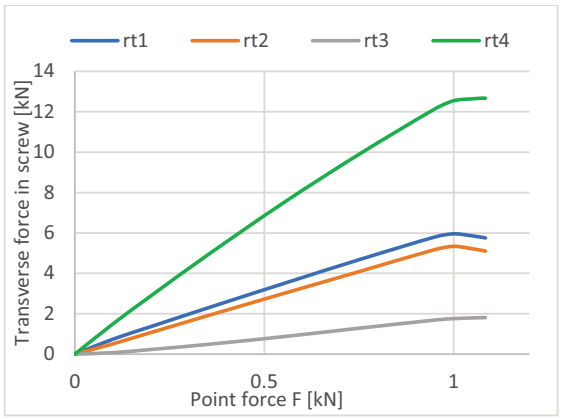

Figure 3.8: Distribution of transverse forces in the screws through loading history.

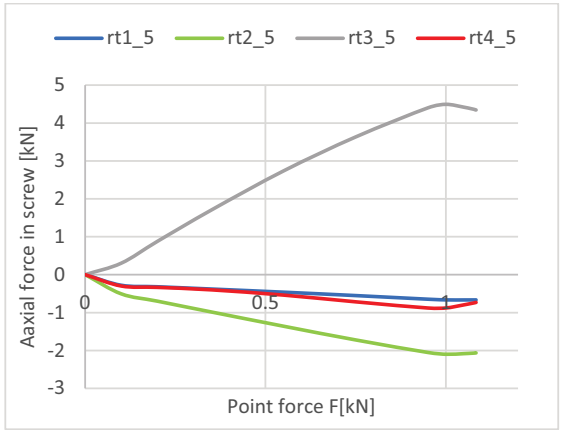

Figure 3.9: Deformation of the window in the numerical analysis from top and side view.

3.3 EXPERIMENTAL AND NUMERICAL RESULTS: COMPARISON

Window frame test shows plastic deformation in the top hinge and ultimate failure of wood around the screws in combined shear and perpendicular to grain tension at ca 1.6kN force, see Figure 3.7 to the left. The block shear failure in screws leads to sudden glass-frame collapse. The ductile deformation and onset of damage in wood-screw area can be visible much earlier, at around 0.6kN force (see both numerical and experimental force-displacement curves in Figure 3.10) and at around 1kN for the thinner frame according to the simulation.
The numerical analysis leads to good prediction of initial damage mechanism that can be set as the capacity limit for window frame in the considered load scenario.
The difference in the apparent stiffness can be mainly subjected to the different eccentricity of the initial set-up and force position in relation to the gravity centre of the glass-frame. The apparent stiffness is considerably higher for the thin frame that has 4 layer glass pack compared to the original 3-layer glass pack in the thick frame or the 3-layer glass pack thin frame model.

https://doi.org/10.52202/069179-0497

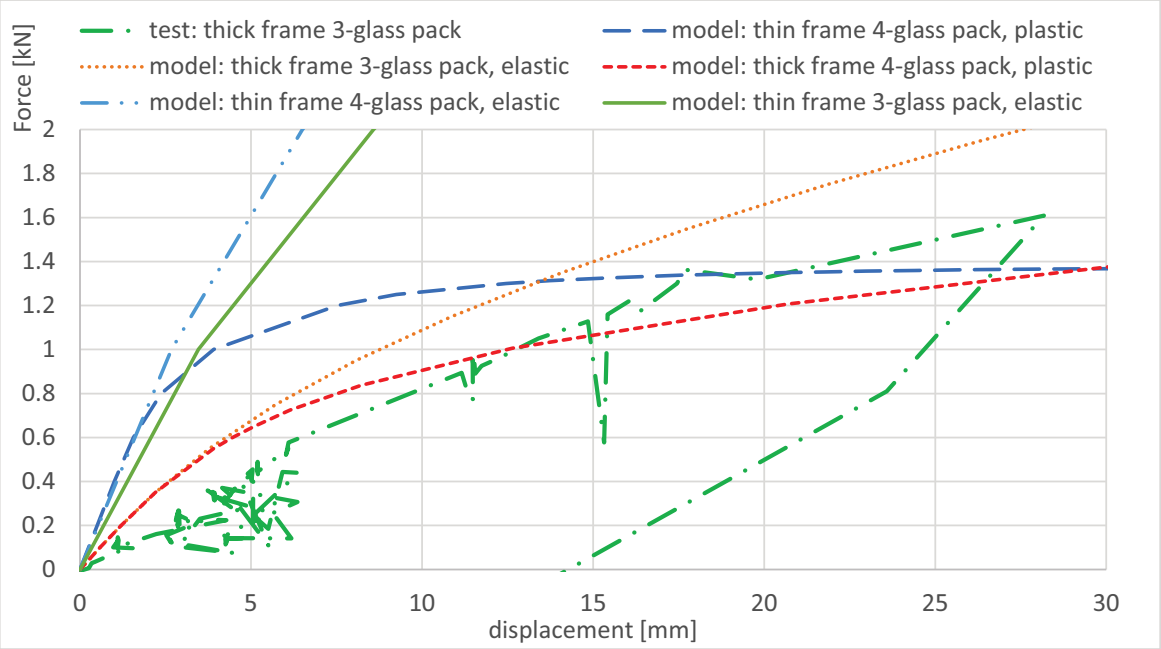

Figure 3.10: Force- displacement curves from the test and from the numerical model simulations for different settings.

4 DISCUSSION

Based on the validation via experiments, the numerical model of the thick frame with 3-layer glass pack was further developed into variants with the slim frame design and 3 and 4-glass packs. The new, slimmer design of the frame is subject to more impact from the localized failure around the screws due to the decreased dimensions so the detail study of the screw around the stresses was performed. The simulation shows that force distribution in screws is not as intended in the considered design case and leads to only one screw being effectively transferring withdrawal loads. The new shape of the hinge plate and optimized placement of the screws could improve the design. The analysis focuses on static strength and does not consider moisture variation that can introduce stresses and dimensional changes. Those dimensional changes due to moisture fluctuations would further increase the stresses localized in the frame corners that are more vulnerable due to the decreased area of the gluing.

During the development of the slimmer frame design, the need for rethinking the connection arose. The localized screwed in connection causes damage in slim frame to occur in wood shear failure (at 1-1.2kN according to the simulation) before hinge plasticisation. Better distribution of the stresses via use of linear hinge or a clamp should be considered in future investigations.

5 CONCLUSIONS

Current wood window frame thickness can be decreased from the structural point of view to improve thermal properties, increase glazing area, and save raw wood material and costs. The dimensional stability of the window over cycling moisture load is more critical than the static strength. The glass pack is found to be the main stiffness source for the frame. Screw configuration in the commonly used hinge is not transferring forces optimally and uniformly and can be optimized or redesigned.

ACKNOWLEDGEMENT

Authors acknowledge the Norwegian Research Council funding the HVIT project (Highly Insulating Windows and Doors with integrated Technology) and the project partner *Røros Vinduer og Dører AS* company.

REFERENCES

[1] Bathe K.-J.: Finite-Elemente-Methoden. Springer-Verlag Berlin Heidelberg New York, 2002.

[2] A. Gustavsen, B. P. Jelle, D. Arasteh, C. Kohler, State-of-the-Art Highly Insulating Window Frames – Research and Market Review, Project report, *SINTEF Building and Infrastructure* 2007.

[3] N. Van Den Bossche, L. Buffel, A. Janssens, Thermal Optimization of Window Frames. In: *Energy Procedia*, 78, pages 2500-2505, 2015.

World Conference on Timber Engineering Oslo 2023

OUTDOOR PANELS FROM NORWAY SPRUCE – THE EFFECT OF COATING COLOUR ON THE TEMPERATURE

Sebastian Svensson Meulmann[1], Åsa Rydell Blom[2], Michael Dorn[3]

ABSTRACT: Wood used outdoors is often surface treated with a paint to protect the wood from moisture and deterioration. If coated with a dark colour, the albedo value is lowered. A lower surface albedo generates greater amounts of energy absorption and makes the surface, and subsequently the wood, warmer and dryer. This study was carried out to increase knowledge of how different coating colours impact the temperature of the underlaying wood, and the effect this has on the moisture content (MC). The study was performed by exposing panels of Norway spruce [*Picea abies* (L.) H. Karst.] painted with three different colours (white, red, and black) to natural sunlight over a month during summer. Each panel fitted with a dry-bulb humidity sensor inside. The results showed a greater variation in calculated equilibrium moisture content (EMC) in the darker panels, since the temperature reached higher levels than the white panels when exposed to sunlight. The maximum recorded temperature was around 50 °C for the dark panels while the maximum for white was around 40 °C. Furthermore, it was shown that the temperature inside the panel reaches its maximum around the same time as the outside air, while the maximum values for EMC were recorded approximately 8-9 hours apart between the panels and the outside air.

KEY WORDS: Coated wood, Coating colour, Moisture content, Natural exposure

1 INTRODUCTION

Wood is a bio-based material which decomposes under unfavourable conditions. When used as a façade material, the wood is exposed to water in the form of precipitation which increases the moisture content in the wood. After long exposure, in situations where the wood cannot dry out, it can lead to discolouration or rot by wood-decay fungi. Both cause a decrease of the service life of the façade. To be able to fully implement wood as a construction material, research within the field is necessary.

Wood used for facades is often surface treated with a coating to protect it from moisture. This coating can have different colours which are affected differently through their surface albedo. The surface albedo causes dark surfaces to reflect less solar radiation than light surfaces, in turn making them warmer than a light surface subjected to the same amount of solar radiation [1]. This means that a façade panel coated with light paint should also be less warm than one painted with a darker paint.

All NCS-colours provide a number regarding the blackness, chromaticness, and hue. Since the blackness and chromaticness of the colour should be the factors theoretically most important regarding the effect of albedo, these will be studied closer in this study. The risk for fungal development and decay is closely related to the temperature [2-4]. A greater variation in temperature also leads to a greater variation of the equilibrium moisture content (EMC) in the wood [5]. Relative humidity is the factor that affects EMC the most [6]. The EMC is the point where the moisture content in a material is constant, and will not change as long as the RH and the temperature around is also constant [7]. A façade panel with different colours should in theory reach the same temperature during night-time without sunlight, causing darker panels to be subjected to a greater variation in temperature during a 24-hour span.

The increase in temperature of darker coloured paints has also been shown to create a more rapid moisture diffusion [8]. A greater variation in moisture content causes cracks in the wood as well as the paint layer at an earlier stage than for a constant MC [9,10]. Sources suggest that the risk for cracks in the wood occurs already when the EMC of the surrounding environment and the MC of the wood deviate with 2%, the risk increases the higher the difference [11].

Only few studies that investigate the effect of a specific coating colour on the moisture content and the temperature in a material have been carried out. Furthermore, most of the studies carried out measure the moisture content in the material either by weighing the entire test piece [8,12-15] or with electrical resistance [13,16].

This work aims to study the temperature and calculated EMC just below the coating. By collecting the data for the given exposure, it will increase the understanding of how

[1] Sebastian Svensson Meulmann, Department of Forestry and Wood Technology, Linnaeus University, Sweden, sebastian.svenssonmeulmann@lnu.se

[2] Åsa Rydell Blom, Department of Forestry and Wood Technology, Linnaeus University, Sweden, asa.blom@lnu.se

[3] Michael Dorn, Department of Building Technology, Linnaeus University, Sweden, michael.dorn@lnu.se

https://doi.org/10.52202/069179-0498

moisture and temperature in the wood fluxes under similar conditions. As this in turn is related to both microbial activity and crack formation, this will increase the understanding of the most suitable coating colour for a given situation, with regards to moisture and temperature related issues.

2 MATERIALS AND METHOD

A total of nine test pieces (panels) were made of Norway spruce [*P. Abies* (L.) H. Karst.], with dimensions 300x105x45 mm. The panels consisted of two boards of 22 mm thickness glued together with a silicone adhesive, creating a single panel with a thickness of 45 mm (Figure 1). The panel behind was added to prevent moisture from entering from the backside of the panel as the adhesive film between the two parts creates a vapor barrier (Figure 1).

A waterborne alkyd primer was used before applying the top coating according to the instructions from the manufacturer (Becker). All panels were top coated with waterborne acrylic paint in the three different colours: white (NCS S 0502-Y50R), red (NCS S 5040-Y80R) and black (NCS S 9000-N). Three panels were coated with each colour. By using the NCS atlas [17], the luminous reflectance factor (LRF) can be found. This value is based on both the blackness and chromaticness of the colour to represent the percentage of reflection of the colour when shone with a light. The values for white (NCS S 0502-Y50R) and black (NCS S 9000-N) were given as 87% and 4.0% respectively. The value for red (NCS S 5040-Y80R) was interpolated to be approximately 8.5%. These values were then used when studying the temperature increase found in the samples during sunlight.

Each of the nine panels were equipped with a dry-bulb relative humidity sensor (Sensirion SHT35-DIS-F), which also measured temperature. The sensors were placed within a pre-drilled hole and fixed 8 mm from the coated surface (Figure 1). The holes were then sealed with silicone to prevent moisture from entering from the back of the panel. The sensors were connected to a data acquisition system that logs the parameters in 5 min intervals and their respective time stamps to a .txt-file, see [18] for a general description of the system.

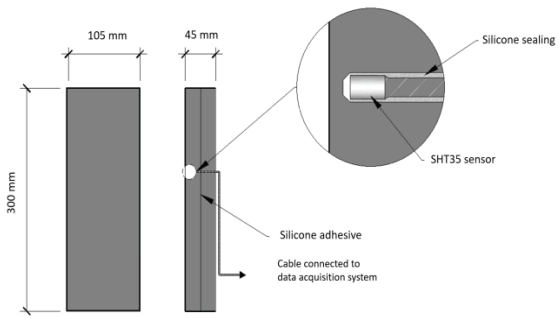

Figure 1: *Dimensions of the panels and placement of sensor*

The panels were placed outdoors in Växjö, Sweden, on a rack facing south, with an angle of 45° to the ground. Apart from the sensors in the boards, a separate sensor was placed freely without direct sunlight, which measured temperature and RH in the surrounding air.

The measured values for temperature and relative humidity were used to calculate the EMC using Equation 1 by Simpson [19]. The EMC indicates the MC once it has been stabilized and not the actual MC at a given time.

$$EMC(\%) = \frac{1800}{W}\left(\frac{K\,h}{1-K\,h} + \frac{(K_1\,K\,h + 2\,K_1\,K_2\,K^2\,h^2)}{(1+K_1\,K\,h + K_1\,K_2\,K^2h^2)}\right) \quad (1)$$

Where:

h = relative humidity in decimal form

$W = 349 + 1.29\,T + 0.0135\,T^2$

$K = 0.805 + 0.000736T - 0.00000273\,T^2$

$K_1 = 6.27 + 0.00938\,T - 0.000303\,T^2$

$K_2 = 1.91 + 0.0407\,T - 0.000293\,T^2$

T = temperature in °Celsius

The density of the panels was measured after the exposure by the simple displacement method. The mean value of the oven-dry density was 495.6 kg/m^3 (Table 1).

Table 1: *Saturated density and oven-dry density in the samples*

Sample	Saturated density (kg/m^3)		Oven-dry density (kg/m^3)	
	Mean	Std. deviation	Mean	Std. deviation
White	716.3	35.1	501.5	31.1
Red	743.4	11.8	505.5	15.3
Black	721.9	17.8	479.7	5.2
Overall	727.2	29.0	495.6	21.2

3 RESULTS AND ANALYSIS

The following weather data is collected from observations in Växjö, Sweden, by the Swedish Meteorology and Hydrological Institute (SMHI) during the month of July 2021 [20]. The total precipitation was 98 mm distributed over 16 days, where each day must have at least 0.1 mm of precipitation to be included. A total of 243 hours of sunlight was recorded, which is slightly higher than the average of 234 hours. The total global radiation during the month was 162.6 kWh/m^2.

All data presented is calculated as a mean value between all three panels of the same colour, the maximum and minimum values are therefore not extreme values for the individual panels but a calculated mean of all panels of the same colour at a given time. The only exceptions to this are found in Figure 6, where the values are instead shown individually for all samples.

3.1 TEMPERATURE ANALYSIS

The measured temperature for all values recorded during the month of July can be seen in Table 2.

https://doi.org/10.52202/069179-0498

Table 2: *Internal temperature for the different coating colours and the outside air during the entire month of July*

Sample	Temperature (°C)			
	Mean	Max	Min	Std. deviation
White	21.3	41.0	11.0	6.3
Red	23.3	49.7	11.0	8.5
Black	23.6	51.3	11.0	8.9
Outdoor	21.0	37.8	11.5	5.2

The results in Table 3 are based on measured values between 6:00 AM-6:00 PM from the whole measurement period. This interval lies safely between the average times of sunrise-sundown during July in Sweden. The table contains the mean, maximum, minimum, and standard deviation of temperature during all days of the month.

Table 3: *Internal temperature for the different coating colours and the outside air during the entire month of July between 6:00 AM-6:00 PM*

Sample	Temperature (°C)			
	Mean	Max	Min	Std. deviation
White	24.9	41.0	12.5	6.2
Red	28.7	49.7	12.9	8.4
Black	29.3	51.3	12.9	8.7
Outdoor	23.9	37.8	13.2	5.0

The table clearly shows the influence of the coating colour on the mean temperature during the month. The differences become even more pronounced when only studying values during a single day (Table 4).

Table 4: *Internal temperature for the different coating colours and the outside air during a single day between 6:00 AM – 6:00 PM*

Sample	Temperature (°C)			
	Mean	Max	Min	Std. deviation
White	25.2	32.8	15.9	5.2
Red	29.8	41.2	16.3	8.0
Black	30.5	42.4	16.3	8.4
Outdoor	23.8	29.9	17.1	4.0

3.2 EMC ANALYSIS

The calculated values of EMC considering all values of RH and temperature recorded during the month of July can be seen in Table 5. The calculated EMC of the surrounding air is included as a reference.

Table 5: *Calculated values of EMC presented for the different colours and the outside air during the entire month*

Sample	EMC (%)			
	Mean	Max	Min	Std. deviation
White	13.9	20.3	11.6	1.5
Red	11.8	26.5	8.4	3.4
Black	11.4	24.5	8.2	3.0
Outdoor	15.9	29.0	5.5	6.6

The results presented in Table 6 contain calculated values of EMC based on values measured between 6:00 AM-6:00 PM from the whole measurement period of July 1 until July 31.

Table 6: *Calculated values of EMC presented for the different colours and the outside air*

Sample	EMC (%)			
	Mean	Max	Min	Std. deviation
White	14.8	20.3	11.8	1.6
Red	13.7	26.5	8.6	3.9
Black	13.2	24.5	8.4	3.4
Outdoor	13.0	29.0	5.5	5.9

The standard deviation is much lower for the white panels than the red and black. Just like for the temperature, the differences are even more apparent when only studying the variation during a single day (Table 7).

Table 7: *Calculated values of EMC for the different coating colours day-time hours of a single day*

Sample	EMC (%)			
	Mean	Max	Min	Std. deviation
White	15.5	18.4	13.0	1.8
Red	16.4	24.6	10.4	5.1
Black	16.2	23.4	10.3	4.5
Outdoor	15.6	29.0	7.6	7.7

The variation in calculated EMC during every single day can be seen in Figure 2, where the y-axis values are the differences in maximum- and minimum EMC calculated from the values extracted during 24-hours for all days of the month.

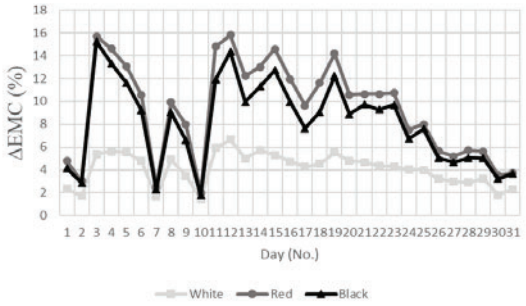

Figure 2: *Maximum daily absolute difference in EMC within the panels for all days of the month of July*

3.3 TEMPERATURE AND EMC IN THE PANELS COMPARED TO OUTSIDE AIR

The temperature in the panels fluctuates in phase with the outside air (Figure 3) while the EMC fluctuates counter-phase (Figure 4). The figures display a typical distribution during a single day with a clear influence of solar radiation.

https://doi.org/10.52202/069179-0498

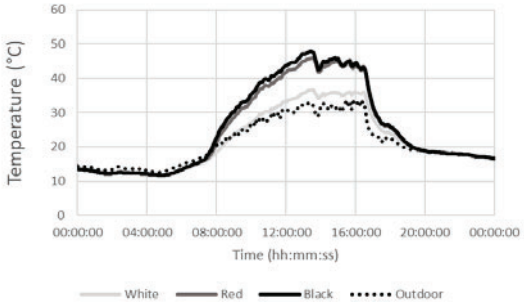

Figure 3: *Temperature distribution in the panels and outside air during 24 hours*

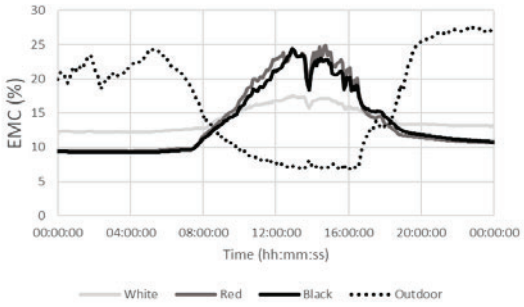

Figure 4: *Distribution of EMC in the panels and outside air during 24 hours*

The difference in time for the panels and outside air to reach its daily peak during the day is presented in Table 8. The results are presented as the average absolute difference between the time stamps at which the daily maximum was recorded for the outside air and within the panels, respectively. The darker panels reach their peak temperatures earlier than the white panels, while the peak temperatures in the outside air were generally recorded later in the day. The EMC shows barely any difference between the different coating colours.

Table 8: *Absolute difference in time of peak values between samples and outside air*

Sample	Difference to outside air (hours)	
	Temperature	EMC
White	0.52	8.60
Red	0.80	8.65
Black	0.90	8.62

The peaks in EMC in the ambient air predominately appeared close to midnight (the coldest period of the day), while the EMC peaks in the panels appeared during the early afternoon (the warmest period of the day). All peak values in temperature within the panels and in the outside air are shown in Figure 5.

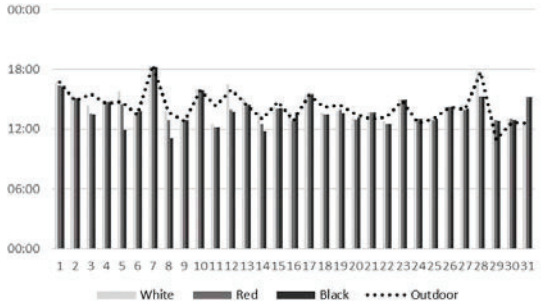

Figure 5: *The time of day when the maximum temperature was recorded in the panels and in the outside air*

3.4 THE INFLUENCE OF COATING LRF ON THE MAXIMUM TEMPERATURE

To isolate the albedo effect, the temperature differences in the panels compared to the outside air temperature at the same time were studied (Figure 6). The figure shows temperature difference when the difference between the outside air temperature and panel temperature was the greatest.

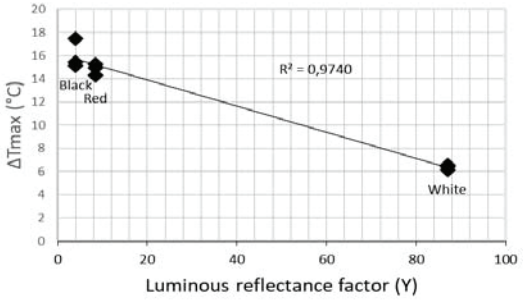

Figure 6: *Maximum temperature difference between the panels and outside air recorded during the month in dependence of the LRF*

The results show a greater variation in maximum temperature in the red and black samples than in the white samples. The LRF naturally has a negative correlation with the temperature increase in the panel compared to the ambient temperature during sunlight.

3.5 THE INFLUENCE OF TEMPERATURE ON THE EMC

Temperature is used to calculate the EMC, albeit weighed less than the RH.

The correlation was best explained with an exponential function for all samples, where T is defined between the minimum and maximum temperature recorded. See Table 9 for the equations used and the R^2-value related to the equations.

https://doi.org/10.52202/069179-0498

Table 9: *Data fit equation for the EMC depending on the temperature and their R^2-values*

Sample	Equation	R^2
White	$EMC(\%) = 10.483e^{0.0130T}$	0.60
Red	$EMC(\%) = 6.2917e^{0.0256T}$	0.80
Black	$EMC(\%) = 6.4383e^{0.0231T}$	0.81

Where:
EMC = The equilibrium moisture content (%)
T = temperature in °Celsius

The equation for the white samples is close to being linear within the defined range. The maximum value for EMC and temperature within the samples were predominantly recorded less than an hour apart.
The average time between reading of the maximum temperature and maximum EMC for the respective coating colours were, 57 minutes for white, 35 minutes for red, and 29 minutes for black.

4 DISCUSSION

With the temperature being measured within the board, it is likely that the difference in temperature at the surface could be even more pronounced. The temperature measured 8 mm behind the coating could vary between 16.3-42.4 °C in just 12 hours, as seen in the black panels (Table 4). The temperature at the surface is likely even higher than the recorded values.
Despite having a much lower blackness value than the black samples, the red samples reached temperatures very close to the black ones. This is likely due to the two colours having similar luminous reflectance factors (LRF), and therefore absorbing similar levels of sun light. This indicates that the chromaticness is also an important aspect regarding the increase in temperature of the panel. The black panels could reach temperatures which were more than 17 °C higher than the outside air at the same time, while the red samples were around 15 °C warmer than the outside air at most. Assuming that the back of the panel was closer to the temperature of the ambient air, this could generate significant temperature and hence moisture gradients within the panel. This could generate strains and, subsequently, cracking in the panels.
The results also showed a clear difference in calculated EMC between the samples of different coating colours. However, the EMC is not sufficient in determining the actual moisture content at a given moment in time. It is however useful when analysing the mean values over an entire month, as this is likely close to the actual mean moisture content. Therefore, the variations in EMC over a single day should be treated as indicators of possible variations, rather than actual variation. The variations in EMC in the darker panels could be close to the fibre saturation point and below levels of industrial drying during the same day, which is likely not possible for the actual moisture content. However, the increase in temperature is likely enough to create greater variations in MC in panels of darker colours than light colours, although to an unknown degree. A greater variation in EMC for the darker panels was calculated for all days during the month, not only those with high solar radiation. Surprisingly, the red panels achieved a greater average EMC than the dark panels, even though the LRF was lower, and lower average temperatures were recorded inside the panel.
It is also possible that the high temperatures achieved on the surface of the darker panels are enough to temporarily stop the mould growth, as temperatures around 40 °C can have a negative effect on growth [21].
The correlation between temperature and EMC within the panel is not surprising as an increase in temperature leads to an increase in vapor pressure.
The temperature within the panels and in the outside air fluctuated closely in-phase, while the EMC was affected by the slow water transition between the surrounding and inner relative humidity. The different correlations between EMC and temperature in the different coating colours could be explained by a faster spike in RH due to higher temperatures. The variations in relative humidity were greater in the outside air than in all the panels, while the variation in temperature was greater in the panels than in the outside air.
The white panels never reached the same maximum EMC as the red and black panels. This could have been caused by an increase in water evaporation due to higher temperatures within the darker panels and similar levels of water content. The water would then be concentrated around the area where the relative humidity was measured. However, this is only a hypothesis and should be studied further to increase understanding.
Analysing the minimum values of temperature showed that the minimum daily temperature in the panels never deviated with more than 0.2 °C between the different coating colours. This indicates that high solar absorption in non-reflective colours during the day does not affect the minimum temperature during the full 24 hours of a day. The minimum daily temperature in the panels were on average approximately 0.6 °C colder than the minimum in the outside air.
A similar study [13] also tested moisture conditions and temperature within samples of different colours. It was concluded that the lighter samples kept higher and more constant levels of moisture content than those of darker colour due to a lower absorption of sunlight. This corresponds well with the results acquired in this study. It should however be noted that the authors in [15] measured the MC by use of mass variation and electrical resistance, compared to the use of sensors in this study.

5 CONCLUSIONS

Using darker colours of paint increases both the fluctuation in temperature and moisture content within the panel over the course of a day. The temperature 8 mm below the surface decreased along with the reflectance factor of the colour. This suggests that both the blackness and the chromaticness of the colour are important regarding the solar absorption of a panel, and that the solar absorption of low-reflectance coatings can generate much higher temperatures inside the wood than the ambient temperature.

https://doi.org/10.52202/069179-0498

The temperature within panels of white coating is close to the outside temperature and barely deviates from the outdoor temperature when considering the monthly average. The calculated mean EMC in the red and black samples were similar, even though the mean temperature was slightly higher in the black samples. To further validate the results, the authors recommend testing common coating colours which have an LRF between the white and red colours used in this test. Furthermore, these values of both temperature and EMC are only applicable for the given geographical location and time of year. Also, the differences between the panels could be different at a different location of exposure. Comparing the results found in this study to a different location and/or time of year would aid in increasing the knowledge of how coating colours affect the wood.

Although this study shows some clear results and trends, the low number of samples decreases validity and further studies should be carried out with a greater sample size. Furthermore, weighing the samples during the exposure to measure the actual moisture content within the panels at a given time could enhance the value of the measurements. Efforts to further understand the temperature and moisture gradients, e.g., by using multiple sensors at different depths, could be helpful when assessing the risk for crack formation within panels of different coating colours.

ACKNOWLEDGEMENT

The authors acknowledge financial support from CBBT, the Centre for Building and Living with Wood Foundation as well as Södra's Foundation for Research, Development and Education.

REFERENCES

[1] Mulvaney, D.: *Green energy: an A-to-Z guide*. Vol. 1. Sage. 2011.

[2] Viitanen, H.A., *Modelling the Time Factor in the Development of Brown Rot Decay in Pine and Spruce Sapwood - The Effect of Critical Humidity and Temperature Conditions* Holzforschung: p. 99-106, 1997.

[3] Nielsen, K.F., G. Holm, L. Uttrup, and P. Nielsen, *Mould growth on building materials under low water activities. Influence of humidity and temperature on fungal growth and secondary metabolism.* International Biodeterioration & Biodegradation. 54(4): p. 325-336, 2004.

[4] Thelandersson, S. and T. Isaksson, *Mould resistance design (MRD) model for evaluation of risk for microbial growth under varying climate conditions.* Building and Environment. 65: p. 18-25, 2013.

[5] Esping, B., J.-G. Salin, and P. Brander: *Fukt i trä för byggindustrin*. Stockholm. SP Sveriges Provnings- och Forskningsinstitut. 2005.

[6] Siau, J.F.: *Transport processes in wood*. Vol. 2. Springer Science & Business Media. 2012.

[7] Gjullin, C.M., E.F. Rasmussen, G.A. Gronbech, G.B. Ramsey, J. Putnam, J.J. Byrne, J.L. Arend, J.M. Harvey, R. Royston, and J.S. McKnight: *Dry Kiln: Operator's Manual*. US Department of Agriculture, Forest Service. 1960.

[8] De Meijer, M. and H. Militz, *Moisture transport in coated wood. Part 2: Influence of coating type, film thickness, wood species, temperature and moisture gradient on kinetics of sorption and dimensional change.* Holz als Roh-und Werkstoff. 58(6): p. 467-475, 2001.

[9] Wood, J.D., C. Gauvin, C.R.T. Young, A.C. Taylor, D.S. Balint, and M.N. Charalambides, *Cracking in paintings due to relative humidity cycles.* Procedia Structural Integrity: p. 379-384, 2018.

[10] De Windt, I., J. Van den Bulcke, and J. Van Acker. *Continuous moisture measurement (CMM) to detect failure of moisture resistance*. in *40th Annual meeting of the International Research Group on Wood Protection (IRG/WP)*. 2009.

[11] Lamb, F.M. and W.D.K. Association, *Splits and cracks in wood.* 1992.

[12] Ekstedt, J.: *Studies on the barrier properties of exterior wood coatings*. 2002, Byggvetenskap.

[13] Grüll, G., M. Truskaller, L. Podgorski, S. Bollmus, I. De Windt, and E. Suttie, *Moisture conditions in coated wood panels during 24 months natural weathering at five sites in Europe.* Wood Material Science & Engineering. 8(2): p. 95-110, 2013.

[14] Sjökvist, T. and Å. Blom, *The influence of coating color, heartwood and sapwood, on moisture content and growth of microorganisms on the surface during outdoor exposure of Norway spruce boards.* Journal of Coatings Technology and Research. 16(3): p. 819-826, 2019.

[15] Ahola, P., H. Derbyshire, G. Hora, and M. De Meijer, *Water protection of wooden window joinery painted with low organic solvent content paints with known composition. Part 1. Results of inter-laboratory tests.* Holz als Roh-und Werkstoff. 57(1): p. 45-50, 1999.

[16] Engelund, E.T., B. Lindegaard, and N. Morsing. *Service life prediction of wood claddings by in-situ measurement of wood moisture content: Status after 5 years of outdoor exposure*. in *IRG 40 Annual Meeting*. International Research Group. 2009.

[17] Färginstitutet: *NCS Digital Atlas*. 1 ed., Stockholm. Scandinavian Colour Institute AB. 2007.

[18] Dorn, M., O. Abdeljaber, and J. Klaeson: *Structural Health Monitoring of House Charlie*. 2019, Linnaeus University, Faculty of Technology Department of Building and Technology.

[19] Simpson, W.T.: *Equilibrium moisture content of wood in outdoor locations in the United States and worldwide*. Vol. 268. US Department of Agriculture, Forest Service, Forest Products Laboratory. 1998.

[20] SMHI: *Juli 2021 - Nederbörd, solsken och strålning*. 2021, Swedish Meteorology and Hydrological Institute

[21] Gradeci, K., N. Labonnote, B. Time, and J. Köhler, *Mould growth criteria and design avoidance approaches in wood-based materials–A systematic review.* Construction and building materials. 150: p. 77-88, 2017.

World Conference on Timber Engineering Oslo 2023

HYGROTHERMAL PERFORMANCE OF NATURE-BASED INSULATION MATERIALS INTEGRATED IN TIMBER-BASED WALL-SYSTEMS

Dimitrios Kraniotis [1], Samee Ullah[2], Stine Lønbro Bertelsen[3]

ABSTRACT:

This study is part of the European research and innovation project Build in Wood and has investigated the hygrothermal performance of nature-based insulation materials in two timber-based wall systems: i) stud wall and ii) externally insulated cross-laminated timber (CLT). Six nature-based insulation materials were selected for the analyses. The analyses conducted have focused on optimization of exterior wall configurations to avoid moisture-related problems, i.e. interstitial condensation and mould growth, in the wall constructions under various climates in Europe. For this purpose, three European locations representing respective geographical parts of Europe and corresponding climate zones, were selected as input for the simulations: Oslo (Northern Europe), Paris (Central Europe), and Barcelona (South Europe), while different exterior and interior claddings were considered. A commercial 1D hygrothermal software, i.e. WUFI Pro 1D, was used for the computation of the hygrothermal performance of the wall systems, while the add-on software WUFI Bio has been further employed for the detailed evaluation of the risk for biodegradation. In total 684 numerical simulations were conducted. The results show the various insulating materials behave differently when integrated in timber-based system. Generally speaking, both wall systems, i.e. stud wall and CLT, function similarly in Oslo, while in Barcelona the CLT was systems show better performance. The climate of Paris is critical for most of the wall configurations. Furthermore, the existence of ventilated air cavity back from the exterior cladding has a positive effect on all assembly configurations, while the high water vapour diffusion resistance of the exterior cladding might be determinant, in a negative way, for the moisture problems in nature-based insulating materials.

KEYWORDS: CLT, Stud wall, Nature-based insulation materials, Hygrothermal performance, Moisture, Mould growth, Interstitial condensation.

1 INTRODUCTION

The European Commission aims at the decarbonization of building sector by 2050, starting the drastic reduction of greenhouse gas emissions (GHG) in the coming years; as of 2030, all new buildings must be zero-emission, while all new public buildings must be zero-emission already as of 2027 [1]. Given that energy efficiency in buildings has been on focus the last decades, the interest has been switched to life-cycle stages before as well as after operation. In particular, the extraction, production and manufacturing of building materials are stages with remarkably high embodied GHG emissions, therefore there is an increasing demand for building materials with low carbon footprint, such as structural timber and nature-based insulating materials, e.g. [2]. Wood-based wall systems have several advantages, such as low carbon footprint, moisture buffering effect etc., while they show durability against mould growth upon proper design [3]. Commercial wood-based insulation materials, e.g. wood fibreboard and wood woolboard, have also gained ground in building applications. In addition, other nature-based building materials such as hemp, cellulose, flax etc. have started getting integrated in building systems, usually as insulation materials. Generally speaking, material selection is a complex equation that considers various parameters, material properties, GHG emissions, availability, cost etc. In particular for insulation materials, durability is an important aspect, so that they can function adequately during operation stage, without increasing the need for replacement, which would have negative consequences for the total GHG emissions. In this study, the hygrothermal performance of innovative nature-based insulation materials integrated in timber-based wall systems is investigated and the risk for moisture damages and degradation is identified.

[1] Dimitrios Kraniotis, Norwegian Institute of Wood Technology, Oslo Norway, Oslo Metropolitan University – OsloMet, dkr@treteknisk.no, dimkra@oslomet.no +47 451 00 650
[2] Samee Ullah, Norwegian Institute of Wood Technology, Oslo Norway sul@treteknisk.no, +47 464 15 303
[3] Stine Lønbro Bertelsen Norwegian Institute of Wood Technology, Oslo Norway slb@treteknisk.no, +47 468 16 243

2 MATERIAL AND METHODS

2.1 Wall systems and assemblies

Two different exterior wall systems have been employed for the analyses: 1) stud wall and 2) externally insulated cross-laminated timber (CLT) (Fig.1). A short literature review of nature-based insulation materials gave an indication on various insulation types used in the

https://doi.org/10.52202/069179-0499

European market. According to [4], there are six different types of nature-based insulation materials: sheep's wool, hemp fibre, flax fibre, wood fibreboard, cellulose, and wood woolboard. In total 22 different products of the six different types of nature-based insulation were identified. One product of each of the six types has been selected for the analyses in this study. The six chosen insulation products are hemp fibre, sheep's wool, flax fibre, wood fibreboard, cellulose and wood woolboard.

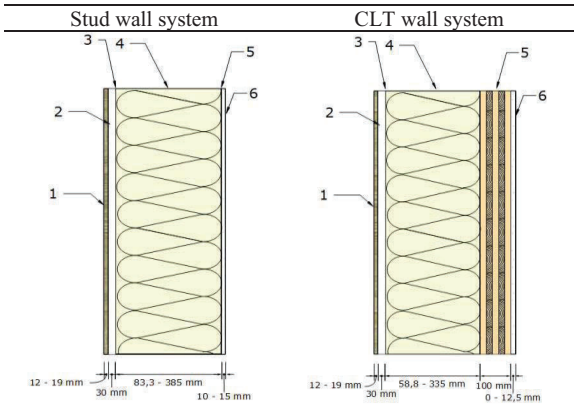

Stud wall system	CLT wall system
1. Exterior cladding	1. Exterior cladding
2. Air gap	2. Air gap
3. Wind barrier	3. Wind barrier
4. Nature based insulation	4. Nature based insulation
5. Vapor barrier	5. CLT element
6. Interior cladding	6. Interior cladding

Figure 1: *Overview of the two wall systems and the corresponding assemblies.*

2.2 Coupled heat and moisture transport (HAM)

A major challenge for all nature-based building materials is their potential vulnerability to moisture. A commercial 1D hygrothermal software i.e., WUFI® Pro 1D [5], has been used for the computation of the hygrothermal performance of the wall systems, with focus on the risk for interstitial condensation. WUFI® Pro is a dynamic simulation tool that accounts for the coupled heat and moisture transport across building components, including latent heat of sorption and heat and moisture storage in building materials, as mentioned by Karagiozis *et al.* [6]. In particular, WUFI® Pro 1D computes the variation of moisture content in each material/layer of building component, while it can provide additionally detailed information about temperature and relative humidity in numerous cross sections of the component and consequently provide the risk of condensation.

By integrating the results of WUFI Pro into an another (add-on) software of WUFI® family, called WUFI® Bio [7], the risk of mould growth and biodegradation can be classified. The latter is the most crucial parameter for the evaluation of nature-based insulation materials. WUFI Bio provides the mould growth coverage in building materials, expressed in mm. In addition, it includes an empirical model which has been developed by Viitanen [8] and computes the so-called mould index (MI). This index takes values from 0 to 6 and reflects the risk of biodegradation of building materials (Table 1).

Table 1. *Description of mould index (MI) according to Viitanen model [7, 8].*

Mould index	
0:	No growth
1:	Some growth visible under microscope
2:	Moderate growth visible under microscope, coverage more than 10%
3:	Some growth detected visually, thin hyphae found under microscope
4:	Visual coverage more than 10%
5:	Coverage more than 50%
6:	Tight coverage, 100%

For the classification, the 'signal light' is employed by the software (Table 2); the green light shows low or no risk for biodegradation, the yellow light reflects moderate risk and additional control may be needed and the red light reveals high risk for biodegradation and therefore the construction is considered as not acceptable. In this study, three different cross sections of the insulation layer have been checked; exterior, middle, and interior cross section. For each of these cross sections, the bio-hygrothermal analysis has been conducted and the respective results, in terms of 'signal light' are provided, in three positions: i) outer part of insulation, ii) middle part of insulation and iii) inner part of insulation.

Table 2.1. *'Signal-light' classification in WUFI Bio, reflecting the three different evaluations, i.e. green: acceptable, yellow: acceptable under conditions, red: not acceptable [7].*

		Surfaces inside constructions without direct contact to indoor air
	Mould growth (g_m): Mould-Index (MI): Assessment:	< 176 mm/year ≤ 2 Usually acceptable.
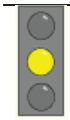	Mould growth (g_m): Mould-Index (MI): Assessment:	176 < g_m ≤ 239 mm/year 2 < MI ≤ 3 Additional criteria or investigations are needed for assessing acceptability.
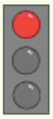	Mould growth (g_m): Mould-Index (MI): Assessment:	> 239 mm/year > 3 Usually not acceptable.

2.3 Exterior and interior climate

To investigate the impact of the exterior climate three European locations representing respective geographical parts of Europe and corresponding climate zones, were selected as input for the simulations: Oslo (Northern Europe), Paris (Central Europe), and Barcelona

(Southern Europe). The climate characteristics for each location are shown in Table 3.

Table 3. *Climate characteristics of the chosen locations for the numerical simulations – Oslo, Paris and Barcelona [5].*

	Oslo	Paris	Barcelona
Mean air temperature [°C]	6.8	10.9	16.3
Max. air temperature [°C]	29.3	36.3	34.3
Min. air temperature [°C]	-14.8	-8.9	-1.0
Mean air relative humidity [%]	73.1	80.6	66.8
Max. air relative humidity [%]	100.0	100.0	99.0
Min. air relative humidity [%]	15.0	19.0	13.0
Mean wind speed [m/s]	2.7	2.6	4.1
Normal rain [mm/year]	604.7	817.4	513.3
Counter radiation [kW/m^2*year]	2 641.4	2 851.5	not available
Mean cloud index [-]	0.67	0.67	not available

For the interior climate, the European standard EN ISO 13788 was used [9]. In particular, the indoor air temperature was assumed constant at 20°C, a humidity class of 3 has been considered. This class, among the five available (1-5), reflects better the moisture production in residential buildings, which is the majority of existing building stock in Europe. while the initial relative humidity across the wall systems have been set at 50%, which reflects dry state of the building materials. All the cases have been solved for 10 years period.

2.4 Thermal transmittance (U-value) of assemblies

The national building regulations in the three selected countries Norway, France and Spain, have set different requirements regarding the thermal transmittance in exterior walls. The chosen U-values for the wall systems in the three locations are: Oslo, 0.18 W/m^{2}K; Paris, 0.23 W/m^{2}K; Barcelona, 0.35 W/m^{2}K.

2.5 Categorization of hygrothermal numerical simulations

The hygrothermal numerical simulations were organised in 'Groups' for better overview:

- Group A – Wall systems with wooden panel (picea abies) as exterior cladding and gypsum board (standard density, ρ = 720 kg/m^3) as interior cladding. The CLT case has been additionally studied exposed, without the gypsum board as interior cladding.
- Group B – Wall systems with wooden panel as exterior cladding and two different interior panels: a) gypsum board of high density (ρ = 1 153 kg/m^3) and b) a plywood panel. The latter has been used only in the stud-wall system but not in combination with the CLT cases.
- Group C – Wall systems with various panels (two different types of cement-based board and wooden panel with fire retardant) as exterior cladding and gypsum board (standard density) as interior cladding. In particular, three boards were employed: a) a cement-based board with low density, ρ = 1 150 kg/m^3 b) a cement-based board with high density, ρ = 1 650 kg/m^3, and c) a solid wooden panel with fire retardant.

All the abovementioned cases have been computed having considered both limited-ventilated air cavity back from the exterior cladding and fully ventilated air cavity. In total, around 600 simulations have been performed.

3 RESULTS

3.1 Group A – Wall systems with wooden panel as exterior cladding and gypsum board (standard density) as interior cladding

3.1.1 Oslo

In stud wall systems (Fig. 2), all insulation materials have shown no remarkable moisture problems when used in a stud wall system with a wooden panel as exterior cladding and a gypsum board of standard density, i.e. ρ = 720 kg/m3. The materials that have showed the best performance, regardless the orientation nor the natural convection in air cavity, has been the wood woolboard followed by the flax fibre and cellulose (the last two have shown some minor issues at the edges of the insulation layer).

In contrast, the materials that have shown some issues, but only in the worst orientation and when assuming limited natural convection (ACH = 1h-1) are:

i) the sheep's wool and hemp fibre, which have shown risk for mould growth during a few weeks in summer, when the reverse of moisture transport occurs due to increase of partial air pres-sure outdoors. This is a common problem in Scandinavian exterior wall systems due to the presence of vapor retarder on the inner side of insulation layer, which causes temporal (sea-sonal) blockage of water vapor when the moisture transport is reversed.
ii) the wood fibreboard that shows risk of condensation on the cold side of insulation layer when the wall is exposed to the orientation with most wind and driving rain.

These materials have shown no moisture problems in all other wall orientations. Furthermore, when the air cavity back from the exterior cladding is fully ventilated by natural convection, no moisture problem has been identified (Fig. 3).

In CLT wall systems (Fig. 2 and 3), similarly to the stud wall, the wood woolboard and the flax fibre has shown the best performance, i.e. no moisture problems regardless the level of ventilation in the air cavity and the use (or not) of gypsum board on the interior side of the CLT. All the other four insulation products, i.e. sheep's wool, hemp fibre, wood fibreboard and

https://doi.org/10.52202/069179-0499

cellulose, require that the air cavity is ventilated by natural convection to avoid showing condensation problems and mould growth in a few years after the use of the building.

Figure 2: *Risk of mould growth in the insulation layer in Group A wall systems in Oslo, when the air cavity is limited ventilated.*

Figure 3: *Risk of mould growth in the insulation layer in Group A wall systems in Oslo, when the air cavity is well ventilated.*

3.1.2 Paris

In case of Paris (Fig. 4 and 5), natural convection back from the exterior cladding is essential in order to avoid moisture damages in the insulation layer. This has been observed both in stud wall systems as well as in the CLT walls without gypsum board on the interior side. When the CLT is covered by gypsum board, the results are considered generally as not acceptable for all the six materials, regardless the level of natural convection in the air cavity.

The only insulation material that has shown a moderate hygrothermal performance in stud wall system when there is limited natural convection in the air cavity, it's the wood woolboard. However, even this material has shown moisture problems in the worst orientation (West for Paris) when integrated in a stud wall system, while when used in CLT wall systems, the moisture diffusion resistance of interior cladding contributes positively.

For all other insulation products, ventilation in air cavity by natural convection contributes drastically to avoid biodegradation in stud wall systems, while in CLT walls there is the additional prerequisite of low water vapor diffusion resistance on the interior surface (no gypsum board).

Figure 4: *Risk of mould growth in the insulation layer in Group A wall systems in Paris, when the air cavity is limited ventilated.*

Figure 5: *Risk of mould growth in the insulation layer in Group A wall systems in Paris, when the air cavity is well ventilated.*

3.1.3 Barcelona

The wood woolboard has been the only insulation material showing no moisture problems regardless the type of wall system and the level of natural convection in the air cavity (Fig. 6). The source of problems for the other five insulation materials when used in the stud wall system is the presence of water vapor tight layer at the interior side of insulation, e.g. vapor retarder, vapor-tight

https://doi.org/10.52202/069179-0499

interior cladding. This because in hot and humid climates, such as Barcelona's, the moisture flow is expected to take place from outdoors to indoors for the longest part of the year (in contrast to colder climates like Oslo). A solution is to use a vapor retarder at the exterior side of the insulation layer in order to block the moisture transport from outdoors. It should be mentioned that this issue remains in the stud wall systems even when the air cavity is considered as fully ventilated (Fig. 7).

Figure 6: *Risk of mould growth in the insulation layer in Group A wall systems in Barcelona, when the air cavity is limited ventilated.*

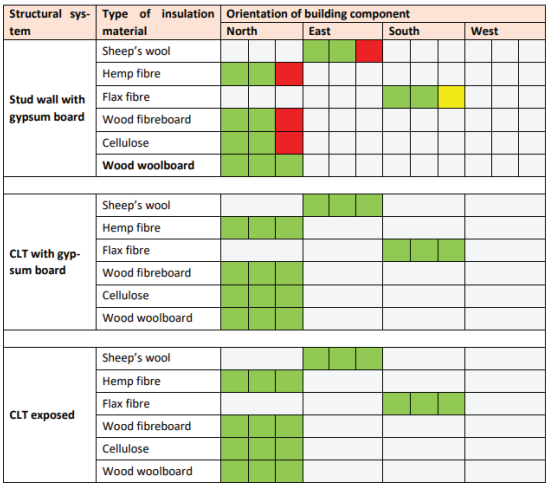

Figure 7: *Risk of mould growth in the insulation layer in Group A wall systems in Paris, when the air cavity is well ventilated.*

However, when the insulation materials are used in CLT walls, the hygrothermal performance becomes better. In particular, sheep's wool, flax fibre and wood woolboard show no moisture damages regard-less any other requirement. The other three materials, i.e. hemp fibre, wood fibreboard and cellulose, have shown biodegradation on their exterior parts when the air cavity is limited ventilated. By ensuring natural convection in the air cavity the risk of interstitial condensation will be drastically decreased both in stud wall and in particular in CLT wall systems, where no insulation material would show moisture problem.

3.2 Group B – Wall systems with wooden panel as exterior cladding and various panels (gypsum board of high density and 3-ply cross-laminated timber panel) as interior cladding

3.2.1 Oslo

The change of type of gypsum board, i.e. higher density, in the stud wall systems in Oslo (Fig. 8 and 9) hasn't showed any impact on the hygrothermal performance of the insulation materials. The findings are identical with the ones in the Group A, where the wood woolboard, the flax fibre and cellulose have showed the best performance. In contrast, the other three materials, i.e. sheep's wool, hemp fibre and wood fibreboard have shown moisture problems, either on the interior part of insulation layer (sheep's wool and hemp fibre) or at the exterior part of insulation layer (wood fibreboard). These problems disappear when the air cavity back from the exterior cladding is fully ventilated by natural convection (Fig. 9).

However, in particular for hemp fibre and wood fibreboard the already problematic hygrothermal performance in the stud wall systems becomes slightly worse when the plywood has been used as interior cladding. The change of interior cladding hasn't affected the other four materials. It is worth to mention that even in this case, i.e. 3-ply cross-laminated as interior cladding, all insulation materials have shown no moisture problems when the air cavity back from the exterior cladding is fully ventilated.

Figure 8: *Risk of mould growth in the insulation layer in Group B wall systems in Oslo, when the air cavity is limited ventilated.*

In the CLT wall systems (only the gypsum board has been considered as alternative here), only the wood woolboard has shown no biodegradation. The flax fibre has also shown good performance but there are some moisture problems on the outer part of the insulation

https://doi.org/10.52202/069179-0499

layer. All the other four materials have shown unacceptable hygrothermal performance. The natural convection in the air cavity would reduce drastically the risk for biodegradation and make all CLT wall systems acceptable.

Figure 9: *Risk of mould growth in the insulation layer in Group B wall systems in Oslo, when the air cavity is well ventilated.*

3.2.2 Paris

The change of type of gypsum board, i.e. higher density, in the stud wall systems in Paris (Fig. 10 and 11) hasn't showed any remarkable impact on the hygrothermal performance of the insulation materials. The wood woolboard is the only insulation material with acceptable performance, while all other materials have shown high risk of biodegradation. The use of the plywood as interior panel has made the performance even worse, even for the wood woolboard which in this case cannot be considered as acceptable. Similar situation in the CLT wall systems where all insulation materials have shown high risk for biodegradation.

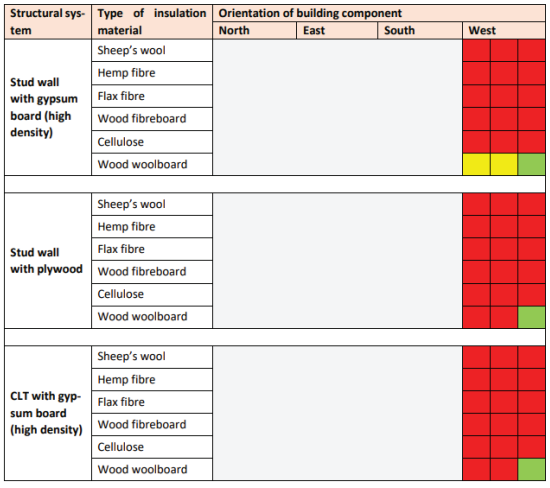

Figure 10: *Risk of mould growth in the insulation layer in Group B wall systems in Paris, when the air cavity is limited ventilated.*

All these results refer to the case of limited natural convection in the air cavity back from the exterior cladding (Fig. 10). The increase of air exchanges in the cavity will affect positively all the insulation materials, both in the stud wall and CLT systems resulting in acceptable hygrothermal performance (no risk for biodegradation) for all of them (Fig. 11).

Figure 11: *Risk of mould growth in the insulation layer in Group B wall systems in Paris, when the air cavity is well ventilated.*

3.2.3 Barcelona

In the stud wall systems in Barcelona (Fig. 12 and 13), the use of higher density gypsum board (with additional higher water vapor diffusion resistance) have shown higher risk for biodegradation compared to the respective Group A cases (gypsum board of standard density). This is rather expected because, as analysed in Group A above, the moisture transport by diffusion takes place towards indoors for the largest part of the year and therefore an increase in water vapor diffusion resistance at the inner part of the insulation layer would result in higher degree of vapor blockage and consequently higher mould growth. The only insulation material that has not been affected by the change of the type of the gypsum board and has shown as good hygrothermal performance as with the gypsum board of standard density (Group A) is the wood woolboard.

The use of plywood as interior cladding in the stud wall systems hasn't changed the overall picture; the wood woolboard has shown acceptable hygrothermal performance, while all other five materials have shown risk for biodegradation, either in parts of the insulation layer, i.e. in sheep's wool, wood fibreboard and cellulose, or throughout the entire layer, i.e. in hemp and flax fibre.

Remarkable but expected, the consideration of fully ventilated by natural convection air cavity back from the exterior cladding (Fig. 13) has only partly contributed positively in the cases of stud walls in Barcelona, in contrast for example to Paris. In particular, the inner parts of the insulation layers have still shown moisture problems due to the predominant water vapor flow to indoors.

https://doi.org/10.52202/069179-0499

Figure 12: *Risk of mould growth in the insulation layer in Group B wall systems in Barcelona, when the air cavity is limited ventilated.*

Figure 13: *Risk of mould growth in the insulation layer in Group B wall systems in Barcelona, when the air cavity is well ventilated.*

In Barcelona, the CLT wall systems have generally shown better hygrothermal performance than the stud walls. Even when the ventilation in the air cavity is limited, only three insulation materials have shown moisture problems: hemp fibre, wood fibreboard and cellulose. These problems appear only at the outer part of the insulation layer. The other three materials, i.e. sheep's wool, flax fibre and wood woolboard, have shown no risk for biodegradation when integrated in CLT wall systems. Last but not least, by ensuring fully ventilated air cavity the risk for biodegradation vanishes even for the hemp fibre, wood fibreboard and cellulose and all insulation materials can be considered as acceptable.

3.3 Group C – Wall systems with various panels (two different types of cement-based board and wooden panel with fire retardant) as exterior cladding and gypsum board (standard density) as interior cladding

3.3.1. Oslo

All insulation materials have shown poor overall hygrothermal performance when integrated into stud wall systems, regardless the type of exterior cladding. However, when the air cavity is fully ventilated by natural convection, flax fibre primarily followed by sheep's wool and hemp fibre have shown acceptable performance, when the exterior cladding is the wooden panel with the fire retardant. No wall configuration with cement board as exterior cladding can be considered as acceptable.

The CLT wall systems have shown similar moisture problems as the stud walls. When the cement board (either type, i.e. density) is used as exterior cladding, all insulation materials have shown high risk for biodegradation. When the air cavity is fully ventilated and the wooden panel with fire retardant is used as exterior cladding, the sheep's wool, the hemp fibre and the flax fibre have shown good hygrothermal performance, with minor moisture issues on the cold side of insulation. No wall configuration with cement board as exterior cladding can be considered as acceptable.

Figure 14: *Risk of mould growth in the insulation layer in Group C wall systems in Oslo, when the air cavity is limited ventilated.*

https://doi.org/10.52202/069179-0499

Figure 15: *Risk of mould growth in the insulation layer in Group C wall systems in Oslo, when the air cavity is well ventilated.*

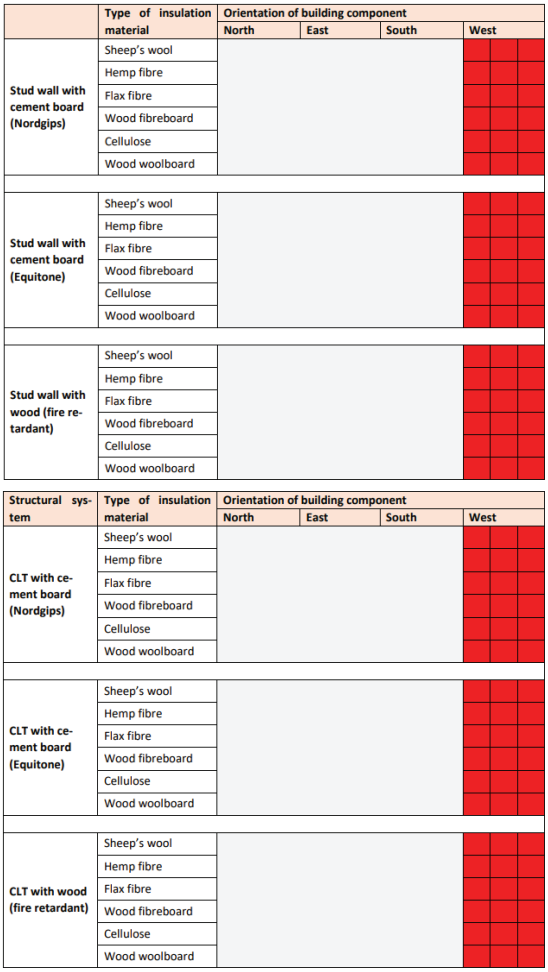

Figure 16: *Risk of mould growth in the insulation layer in Group C wall systems in Paris, when the air cavity is limited ventilated.*

3.3.2 Paris

In Paris, none of the wall configurations can be considered as acceptable, neither stud walls nor CLT walls. All the insulation materials have shown high risk of biodegradation, which can lead to the conclusion the cement board and the wooden panel with fire retardant (with a very high water vapor resistance) are not optimal choices foe getting combined with the specific nature-based insulation materials. The degree of natural convection in these case hasn't had any (positive) impact on the results.

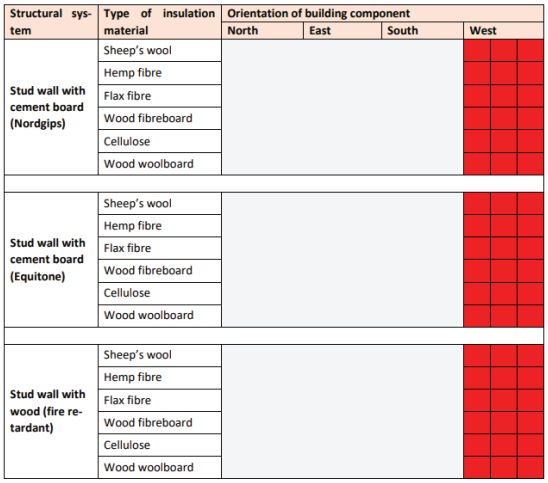

Figure 17: *Risk of mould growth in the insulation layer in Group C wall systems in Paris, when the air cavity is well ventilated.*

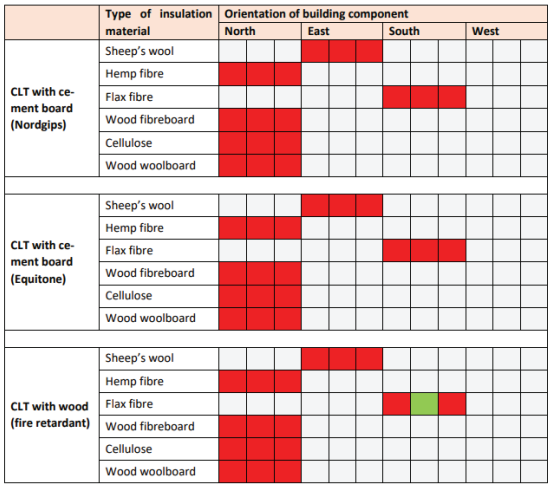

Figure 18: *Risk of mould growth in the insulation layer in Group C wall systems in Barcelona, when the air cavity is limited ventilated.*

3.3.3 Barcelona

In Barcelona, none of the insulation material have shown acceptable hygrothermal performance when integrated into stud wall systems, regardless the type of exterior cladding, i.e. cement board or wooden panel with fire retardant. The impact of natural convection in the air cavity is negligible.The CLT wall systems have shown better hygrothermal performance, but only when the wooden panel has been used as exterior cladding and the air cavity is considered as fully ventilated. In this case, the flax fibre and the wood woolboard have shown no risk for biodegradation, while the sheep's wool have shown some local moisture problems at the inner side of the insulation layer. All cases with cement board as exterior cladding cannot be considered as acceptable.

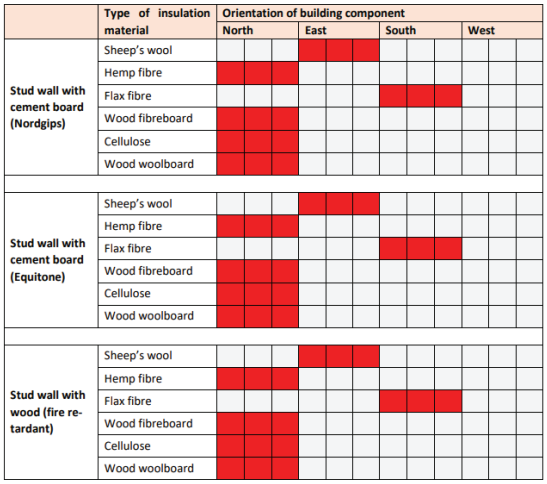

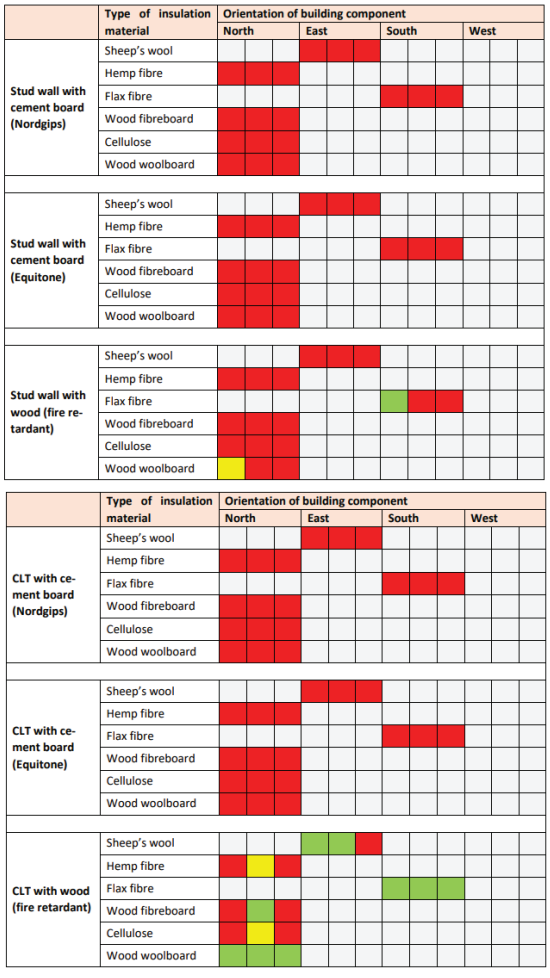

Figure 19: *Risk of mould growth in the insulation layer in Group C wall systems in Barcelona, when the air cavity is well ventilated.*

https://doi.org/10.52202/069179-0499

4 CONCLUSIONS

The following points summarize the most important findings from the hygrothermal analyses:

- Wood woolboard has shown good hygrothermal performance when integrated in different timber-based wall systems in different climates.
- Flax fibre, followed by sheep's wool and hemp fibre can also be considered as acceptable in some cases.
- Natural convection in the air cavity back from the exterior cladding contributes to drastic reduction of the moisture problems in most of the cases.
- Cement-based board should be avoided in wall systems with nature-based materials.
- Paris has a challenging climate for nature-based insulation materials.
- In Barcelona, CLT wall systems have shown less moisture problems than stud walls.

5 AKNOWLEGDEMENTS

This study has received funding from the European Union's Horizon 2020 research and innovation programme under grant agreement No 862820.

6 REFERENCES

[1] European Commission: Press Release - European Green Deal - Commission proposes to boost renovation and decarbonisation of buildings. Available at Renovation and decarbonisation of buildings (europa.eu), 2021.

[2] Korjenic A., Petránek V., Zach J., Hroudová J.: Development and performance evaluation of natural thermal-insulation materials composed of renewable resources. Energy and Buildings, 43(9):2518-2523, 2011.

[3] Kraniotis D., Langouet N., Orskaug T., Nore K., Glasø G: Moisture buffering and latent heat sorption phenomena of a wood-based insulating sandwich panel. World Conference on Timber Engineering WCTE 2016, Vienna, Austria, 22-26, 2016.

[4] Florea I., Manea D.L.: Analysis of Thermal Insulation Building Materials Based on Natural Fibers. Procedia Manufacturing, 32:230-235, 2019.

[5] WUFI® Pro 1D. Heat, air and moisture transport. Available from: https://wufi.de/en/software/wufi-pro/

[6] Karagiozis A., Künzel H., Holm A.: WUFI-ORNL/IBP—a North American hygrothermal model. In: Performance of Exterior Envelopes of Whole Buildings VIII, 2-7, 2001.

[7] WUFI® Bio, Webpage of the bio-hygrothermal add-on software WUFI Bio.

[8] Viitanen H., Ritschkoff, A-C.: Mould growth in pine and spruce sapwood in relation to air humidity and temperature. Sveriges lantbruksuniversitet: Institutionen för virkeslära. Rapport Vol. 221, 1991.

[9] ISO 13788:2012. Hygrothermal performance of building components and building elements — Internal surface temperature to avoid critical surface humidity and interstitial condensation — Calculation methods.

This page intentionally left blank due to withdrawn paper.

This page intentionally left blank due to withdrawn paper.

This page intentionally left blank due to withdrawn paper.

This page intentionally left blank due to withdrawn paper.

This page intentionally left blank due to withdrawn paper.

This page intentionally left blank due to withdrawn paper.

World Conference on Timber Engineering Oslo 2023

TIMBER CLADDING DISCOLOURATION IN TROPICAL MONSOON CLIMATES

Shinya Okuda[1], Laurent Corpataux[2], Kua Harn Wei[3]

ABSTRACT: This paper addresses the factors affecting timber facade discolouration in tropical monsoon climates. We measure the colour change of timber cladding in the northern (N), eastern (E), southern (S) and western (W) orientations in relation to the prevailing wind directions through a year-long field test. The objective is to find a way to guide the timber cladding discolouration in a more controlled manner. The background aim of this research is to reduce the existing negative preconception of timber resulting from the visual discomfort of uneven timber colour change, which contrasts with the established industrial aesthetic norms. The following tectonic configurations were tested: i. Red balau (*Shorea collina*) timber cladding in horizontal and vertical orientations and ii. Norway spruce (*Picea abies*) and red jabon (*Anthocephalus macrophyllus*) cross-laminated timber walls overlayed with ultraviolet-filtered glazing. The discolouration was measured using a Konica Minolta handheld spectrophotometer CM-2600d, and the results were assessed in the colour space of CIE *L* a* b**. The average discolouration (ΔE*) was the largest in the S- and W-side vertically oriented boards (ΔE* = 17.0-18.4) and the smallest in the N-side horizontally orientated boards (ΔE* = 10.2). The horizontally oriented boards exhibited lower and more uneven discolouration than the vertically oriented boards. The prevailing S and SSW wind direction on-site may have concentrated the driving rainwater on the S and W facades, resulting in faster and more even colour changes on the vertical boards.

KEYWORDS: Timber cladding; colour change; monsoon wind; weathering; tropics

1 INTRODUCTION

1.1 TIMBER AS INDUSTRIAL MATERIAL

While wood was the most prevalent building material before the nineteenth century, since the Industrial Revolution, we have relied on steel and concrete as the major building materials for the construction of our cities [1]. Wood's decline was furthered by the emergence of modern architectural styles that promoted the use of mass-produced industrialised components, often to achieve a universal aesthetic. Wood, with its ever-changing appearance resulting from chemical and physical degradation, was deemed unsuitable in the era of industrialisation.

The recent development of new composite wood products and timber construction technologies, along with amendments to building codes, has allowed timber construction to finally resurge in the late twentieth century [1].

Most buildings today are erected using hybrid construction techniques that utilise a combination of different materials for technical, functional or aesthetic reasons. When building with wood, non-combustible elements made of steel or concrete are frequently incorporated to enhance characteristics such as structural capacity, fire resistance and acoustic performance.

As a natural material, various properties of wood continue to change even after it has been harvested, sawn, dried, converted into building products and incorporated into structures. UV radiation gradually affect exposed wood, and the associated visible degradation of surfaces can be polemic topic. While some cultures may accept and appreciate the look of weathered and worn wood, it is not always the case when more permanent industrial aesthetics is preferred. The use of timber as a building material is increasing in urban environments, where the majority is made of industrial materials, such as concrete and steel, finding ways to incorporate ephemeral timber aesthetics with the established norm of industrial aesthetics is important and influence to the popularity of timber construction in the future [1].

1.2 PUBLIC PERCEPTION OF MASS-ENGINEERED TIMBER IN SINGAPORE

In Singapore, the Building & Construction Authority (BCA) is pushing the use of mass-engineered timber (MET) due to the increasing need for smarter, greener and higher-quality building structures. This positions MET as a valuable solution for heightened productivity and sustainability in construction. According to a survey by Low et al. [2], professionals in the Singapore construction industry recognise MET's normative and rational merits, including the enhancement of biophilic aesthetics, a decreased carbon footprint, shorter construction time and the reduction of on-site waste. However, cultural and cognitive barriers have been identified as the key factors preventing the adoption of MET in Singapore, including a lack of knowledge and expertise in MET, a shortage of commercial opportunity and challenging raw material acquisitions from overseas, in addition to the higher costs associated with importing MET. These challenges have resulted in the limited adoption of this technology, and few projects in Singapore using MET have been constructed to date. Interestingly, the 'enhanced beauty of buildings' is listed

[1] Shinya Okuda, National University of Singapore, Singapore, akiso@nus.edu.sg
[2] Laurent Corpataux, laurent1corpataux@gmail.com
[3] Kua Harn Wei, National University of Singapore, Singapore, bdgkuahw@nus.edu.sg

https://doi.org/10.52202/069179-0501

among the top drivers of MET adoption, which implies greater concern for the visual quality of MET projects. Therefore, understanding the key factors that cause changes in the colour of timber in tropical monsoon climates and ways to predict it in a controlled manner may help to promote the long-term adaptation of MET buildings in Singapore.

2 LITERATURE REVIEW

2.1 TIMBER DISCOLOURATION

Biodegradation, weathering and ageing can deteriorate wood as a natural material [3]. Wood discolouration is a complex phenomenon, mainly affected by heat, light, physiological and biochemical reactions and microorganism attacks [4].

The colour change manifests in a range from a reddish yellow to a dark brown tone depending on the intensity and duration of the radiation. The red tones in wood are often attributed to extractives within the wood, while the yellow tones are mainly dictated by the photochemistry of the wood, especially in relation to lignin [4].

2.1.1 Weathering

Hill et al. [5] explain that weathering is a combination of biotic and abiotic degradation mechanisms acting on the wood's surface. Prolonged exposure to ultraviolet (UV) light degrades the lignin in wood, which is an organic polymer responsible for binding the cellulose fibres together. The decomposed lignin is soluble in water and may therefore be dissolved and washed out by driving rain, leaving behind the white cellulose fibres [1].

The degradation of lignin produces fragments that act as nutrients for mould and fungi, leading to increased crack formations in the exposed wood. As weathering progresses, the bleached surface region of the wood develops a grey colour as the wood is colonised by mould and staining fungi (e.g., *Aureobasidium pullulans* and *Sclerophoma pithyophila*).

The length of time that the wood is wet is a significant factor in determining the likelihood that mould or stains will develop, and surfaces that dry rapidly because of prevailing winds are much less likely to show mould growth [5]. The completely weathered grey layer is only a few tenths of a millimetre thick, and, within two millimetres from the surface, the wood itself is not affected any further. The effect of weathering on strength properties is very limited [6].

2.1.2 Ageing

Matsuo et al. [3] explain that ageing proceeds slowly in wood through a combination of omnipresent oxygen and water. The ageing and subsequent change in wood colour begin at the time of tree harvesting. Colour properties are in direct relation to ageing (the lightness of the wood decreases, and the hue becomes slightly redder). The colour change during natural ageing could be explained as a mild thermal oxidation process. In other words, heat treatment could accelerate the wood's change in colour that occurs during ageing.

It is generally accepted that colour changes increase as the temperature increases. Heat can directly alter the colour by causing hydrolysis and the oxidation of the wood's components. As timber dries, extractives accumulate on the surface and oxidise, manifesting as a brown colour. According to White and Dietenberger [4], the darkening of wood due to heat is caused by the thermal degradation of hemicelluloses and lignin. Tolvaj et al. [7] studied the effects of steam on softwood's change in colour, which showed a slow but continuous increase in redness at 70°C and a linear correlation between lightness and colour hue at all steaming times and temperatures.

3 RESEARCH METHODOLOGY

The National University of Singapore (NUS) and City Developments Limited's (CDL) Tropical Technology (T^2) lab (Figure 1) was set up at the end of 2018 at NUS in Singapore to investigate the influence of aspects of tropical climates, such as sun, wind and humidity, on photovoltaic panels, green façades and natural ventilation and the behaviour of MET under tropical climate conditions. The MET façade field test was conducted for one year, from January to December 2019, at the T^2 lab, which was naturally ventilated with no casting shadows from the surroundings throughout the testing period.

Figure 1: *Tropical MET architectonics study set up at NUS-CDL T^2 Lab (Nov. 2018)*

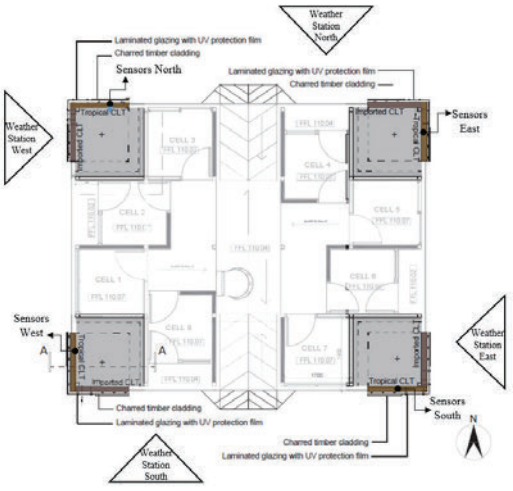

Figure 2: *The locations of the sensors and weather stations*

3.1 FIELD TEST

The four facades of the NUS-CDL T^2 lab are perfectly aligned to the north, east, south and west (N, E, S and W) orientations (Figure 2). The four test corners consisted of

NUS custom-made tropical cross-laminated timber (CLT) walls made of red jabon (*Anthocephalus macrophyllus*), a fast-growing tropical plant [8], in a side-by-side comparison with Norway spruce *(Picea abies)* CLT imported from Europe, which has been the local standard since 2012 due to Singapore's Eurocode compliance. Each CLT panel was 2.4 m in height and 1.4 m in width with 150 mm thickness and was clad with three façade configurations: horizontally (H) and vertically (V) oriented red balau (*Shorea collina*) timber cladding and UV-filtered grazing (Figure 3).

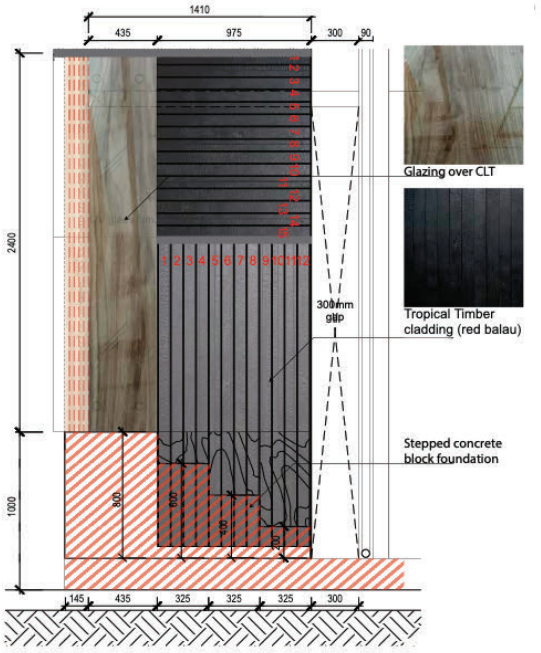

Figure 3: *An illustration of the typical CLT wall configuration at the T² lab.*

3.2 THE SELECTION OF TIMBER SPECIES FOR CLADDING

Untreated red balau (*Shorea collina*) was selected for timber cladding tests, which is classified as moderately durable for fungal and termite attacks according to BS EN350:2016. Red balau is also commonly used for outdoor decking and cladding in Singapore.

3.3 CIE-L*a*b* ANALYSES

In accordance with BS EN ISO 11664-4:2011, the change of colour coordinates (ΔL*, Δa* and Δb*) were calculated as the difference between the value of the control samples and the value of the tested specimen. We measured the average of two control samples for 200 timber boards across the four orientations.

The measurements were recorded using a Spectrophotometer CM-2600d (Konica Minolta), which was set to measure the samples' L*, a* and b*colour coordinates, where L* is lightness from 0 (black) to 100 (white), a* is chromaticity coordinate + (red) or − (green), and b* is chromaticity coordinate + (yellow) or − (blue). From the relative colour changes, ΔL*, Δa* and Δb* (i.e. changes between the weathered and control samples), the total colour difference, ΔE*, was calculated by equation (1) [9] to compare the individual colour shades.

$$\Delta E* = \sqrt{\Delta L*2 + \Delta a*2 + \Delta b*2} \quad (1)$$

There were noticeable natural colour differences among the timber specimens at the beginning of the tests (Figure 4, left). To minimise the influence of the natural colour variations, each board was measured at three points (left, middle and right for the H-oriented boards and top, middle and bottom for the V-oriented boards) to determine the average ΔE* for each timber board (Figure 4 Right).

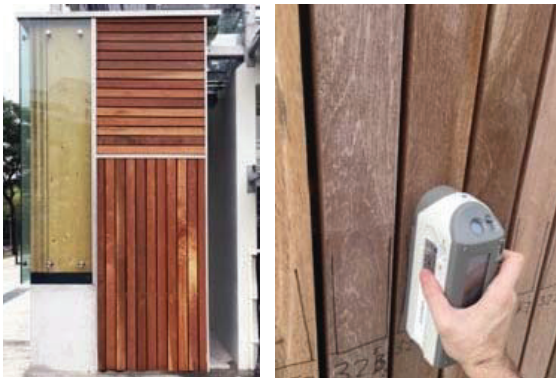

Figure 4 Left: *Newly installed tropical timber cladding (red balau). There were noticeable natural colour differences among the timber boards. (W side, Oct. 2018)* ***Right:*** *Colour measurement with handheld spectrophotometer (Konica Minolta CM-2600d). Each board was measured at three points to determine the average ΔE* for each timber board.*

3.4 UV-FILTERED GLAZING

Cross-laminated timber is only to be used for service classes 1 and 2 (BS EN 1995-1-1:2004+A2:2014), which means it is not possible to use it for service class 3: direct exposure to the weather (NA to SS EN 1995-1-1:2018). The UV-filtered glazing overlaying CLT walls could be considered as service class 2, which makes untreated timber visible through the glazing (Figure 4, left).

To effectively cut the UV exposure, 3M Prestige Window Film PR70 (Visible light transmitted: 69%/UV rejected: 99.9%/Infrared rejected: 97%/Total solar energy rejected: 50%) was applied inside the glazing. A point-fixing method was used to fix the glazing on both the NUS custom-made tropical CLT and the spruce CLT.

Wong et al. [10] simulated the surface temperature profile of a double-glazed wall in the context of Singapore. The external surface temperature of a double-glazed facade could become very high if heat absorption glass is used. But the mechanism of heat extraction, either by stack effect or mechanical fans, in the double-glazed cavity can maintain a lower internal surface temperature, thus minimising solar heat transfer to the internal spaces. As in the case of the fourth-floor east orientation, with the external surface of the inner layer glazed wall with no ventilation as the worst scenario, the most probable temperature is around 37–38°C. To

https://doi.org/10.52202/069179-0501

generate sufficient natural ventilation by stack effect in the façade cavity, we kept the bottom part and the vertical gaps between the two glazing panels open.

4 RESULT AND DISCUSSION

4.1 LEACHING EXTRACTIVES

Figure 5: *Brown stains on the concrete foundation were observed during the first few months after the installation. They were likely deposited by leached extractives from the red balau timber (red dotted circle, October 2018)*

The installation of timber cladding specimens was completed in October 2018. Temporary brown stains on the concrete foundation were observed for the first few months, which were likely deposited by leached extractives from the red balau façade. Those stains were later washed away by natural rainfall.

For the first two months between October and December 2018, the rapid discolouration (ΔE*) between the averages of the two control samples and the 200 specimens was recorded (ΔE* = 6.5–8.7, Figure 5, 7). There were noticeable natural colour differences among the 200 specimens initially (Figure 4, left), which might make the difference in the colour change (ΔE*) in the orientations less clear. After two months' exposure, the natural variations in colour among the specimens seemed to be relatively moderate. Therefore, we excluded those first two months (ΔE*) in the colour change analysis (Figure 7).

4.2 COLOUR DIFFERENCES IN ORIENTATION

The average colour coordinate of the two controlled samples was recorded as (L*: 48.24, a*:11.58, b*: 19.50) prior to the testing. The colour measurement of the 200 specimens in the NWSE orientations was recorded at two-month intervals between December 2018 and December 2019 for one year. The colour change field test result is shown in Figure 7.

The decrease in the lightness of the specimens was recorded for all samples. After the testing period, the overall colour change, ΔE^*, was the largest in the S- and W-side V-aligned cladding (ΔE^* = 17.0–18.4), which was classified as a different colour according to the colour change assessment guidelines (Figure 6). The smallest ΔE^* was the N-side H-aligned cladding (ΔE^* = 10.2), which was classified as a distinct colour change according to the same assessment guidelines.

ΔE^*	Description
$\Delta E^* < 0.2$	Invisible changes
$0.2 < \Delta E^* < 2$	Small changes
$2 < \Delta E^* < 3$	Colour changes visible by high quality filter
$3 < \Delta E^* < 6$	Colour changes visible by medium quality filter
$6 < \Delta E^* < 12$	Distinct colour changes
$\Delta E^* > 12$	A different colour

Figure 6: *Assessment guidelines for colour change* [11]

It is generally observed that the overall colour change (ΔE*) on the S and W sides increased faster than on the E and N sides, except for the E-side V-aligned boards, where the ΔE* increased as fast as the S and W sides. The colour change (ΔE*) differences in orientations generally grew wider over the testing period (Figure 7).

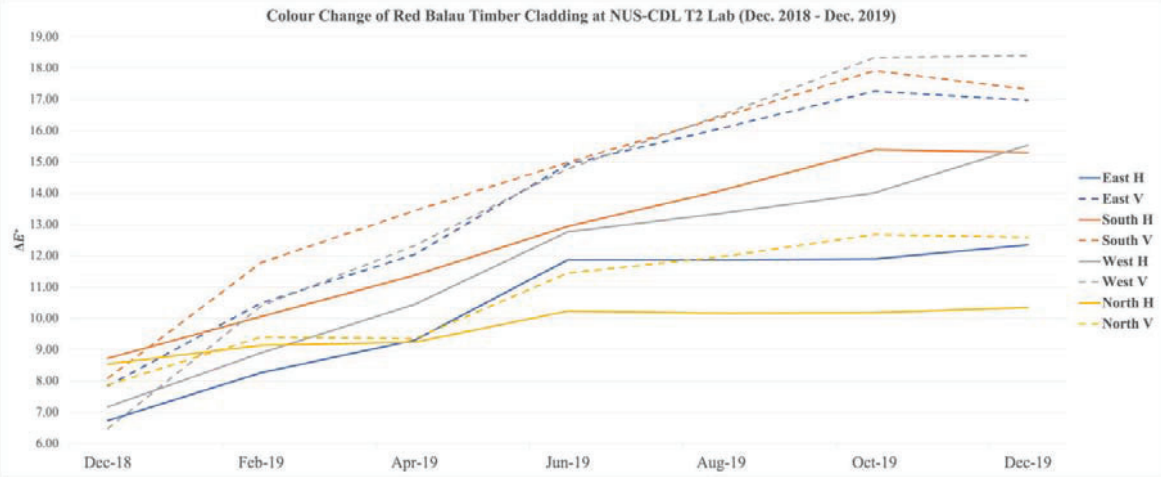

Figure 7: *Discolouration of the red balau V- and H-aligned cladding in NWSE orientations.*

https://doi.org/10.52202/069179-0501

4.3 HORIZONTAL/VERTICAL CLADDING

It was observed that the H-aligned boards exhibited lower overall discolouration (ΔE*) values than the V-aligned boards. Except for the first measurement in December 2018, when the initial natural colour variations among the specimens were still prevalent, all the other measurements exhibited lower ΔE* in the H-aligned boards than the V-aligned boards. Generally, the gaps in ΔE* between the H- and V-aligned boards continuously increased, except for the last measurement in December 2019 (Table 1).

Table 1: *The discolouration (ΔE*) comparison between H and V-aligned red balau timber cladding in the NWSE orientations. Except for the first measurement in December 2018, all other measurements exhibited higher ΔE* for the V-aligned boards than the H-aligned boards (Ref. red underlined figures).*

	Control Samples	ΔE*						
	(Oct-18)	Dec-18	Feb-19	Apr-19	Jun-19	Aug-19	Oct-19	Dec-19
East Horizontal (H)	0.00	6.73	8.26	9.30	11.87	11.86	11.90	12.34
East Vertical (V)	0.00	7.84	10.49	12.04	14.92	16.07	17.26	16.97
East V-H	0.00	1.11	2.23	2.74	3.05	4.21	5.36	4.62
South H	0.00	8.72	10.06	11.38	12.94	14.08	15.39	15.30
South V	0.00	8.08	11.78	13.44	14.99	16.43	17.91	17.32
South V-H	0.00	-0.64	1.72	2.06	2.04	2.35	2.52	2.02
West H	0.00	7.17	8.89	10.45	12.77	13.35	14.01	15.53
West V	0.00	6.48	10.40	12.32	14.79	16.49	18.33	18.40
West V-H	0.00	-0.70	1.50	1.87	2.02	3.14	4.32	2.87
North H	0.00	8.54	9.14	9.24	10.23	10.16	10.18	10.35
North V	0.00	7.87	9.40	9.35	11.45	11.97	12.68	12.59
North V-H	0.00	-0.67	0.27	0.12	1.22	1.80	2.50	2.24

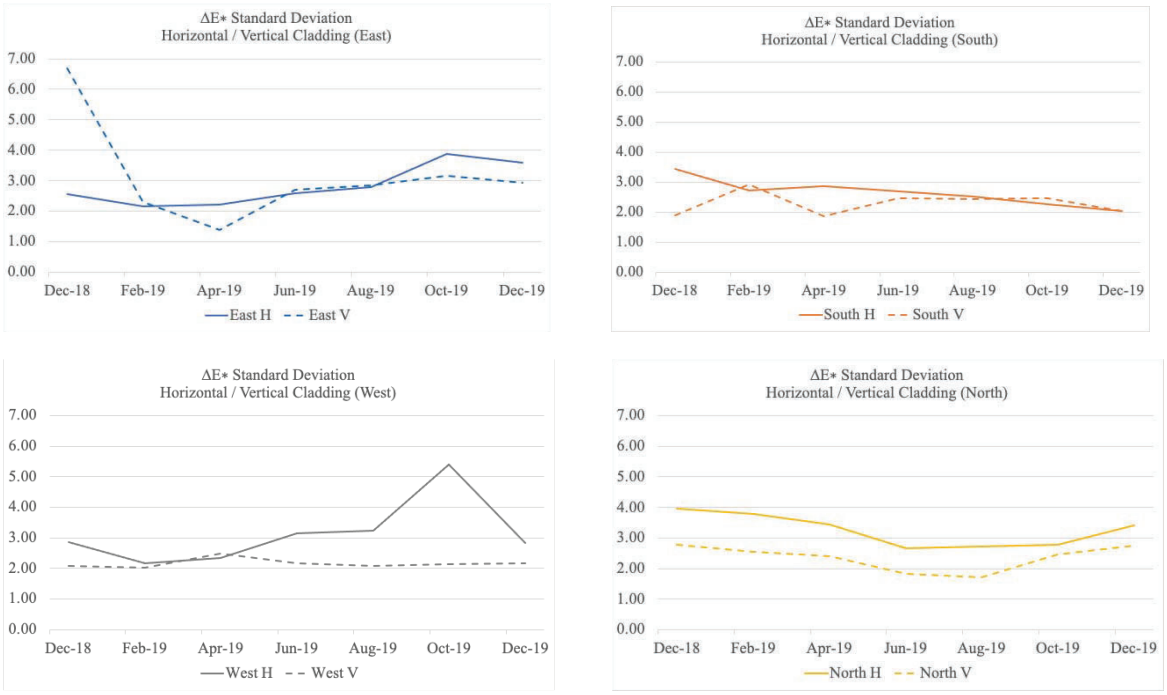

Figure 8: *ΔE* standard deviation among all H-aligned and V-aligned boards in each orientation (**Upper Left:** E, **Upper Right:** S, **Lower Left:** W, **Lower Right:** N.)*

https://doi.org/10.52202/069179-0501

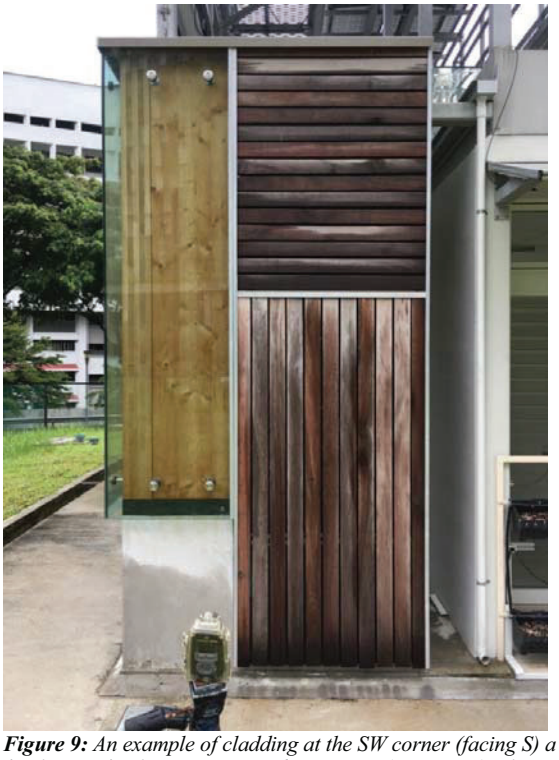

Figure 9: *An example of cladding at the SW corner (facing S) a few hours after heavy monsoon driving rain (Nov. 2019). The H-aligned cladding was mostly still wet, while the V-aligned cladding dehydrated relatively quickly.*

The ΔE* standard deviation among all H- and V-aligned boards in each orientation was computed to understand the degree of even discolouration. While it was generally observed that the discolouration (ΔE*) standard deviation became smaller in the S orientation, there were two exceptions: the E-side V-aligned boards at the beginning of the testing period and the W-side H-aligned boards in October 2019.

The former was due to the initial natural colour variations among the specimens, as the ΔE* standard deviation for the V-aligned boards in all orientations stabilised after six months.

The latter helps us to understand the cause of the late ΔE* standard deviation spike in the H-aligned boards, which fluctuated more than the V-aligned boards throughout the testing period. As UV-degraded lignin is washed away by rainwater, the fluctuated discolouration (ΔE*) standard deviation might be caused by water-flow patterns over the H- and V-aligned boards.

Figure 9 illustrates an example of the S facade a few hours after the heavy monsoon driving rain. While the H-aligned boards retained their wet surfaces for a longer period, the V-aligned boards exhibited a relatively quicker drying process, which implies that the driving rain ran smoothly along the direction of the wood grains. In contrast, the water flow direction was not aligned with the direction of the wood grains in the H-aligned boards, resulting in wet surfaces for relatively prolonged periods.

4.4 MONSOON WIND AND RAIN SHOWERS IN THE TROPICS

In the tropical monsoon climate, much of the rain is heavy and accompanied by monsoon wind. Timber weathering is caused by UV decomposing the lignin, which is soluble in water and may therefore be dissolved and washed out by driving rain [1]. Therefore, the prevailing wind direction is an important factor influencing timber weathering in the tropical monsoon climate.

Two monsoon seasons and two inter-monsoon periods define Singapore's local climate. The two monsoon seasons are the southwest monsoon season (June to September, south-easterly to southerly winds) and the northeast monsoon season (December to early March, northerly to north-easterly winds), while the two inter-monsoon periods take place from late March to May and from October to November with light breezes. Rainfall is plentiful in Singapore, with an average of 167 rainy days per year. The long-term mean annual rainfall from 1981 to 2010 was 2165.9 mm [12], which is approximately three times higher than the mean annual precipitation in Germany from 1991 to 2020 (728.9 mm) [13], for example.

According to the annual wind rose for 1981–2010 in Singapore [12], the two prevailing wind directions are NNE and S. However, the Figure 7 discolouration analysis indicated that the highest discolouration occurred in the S and W orientations, while the N orientation recorded the lowest level of discolouration.

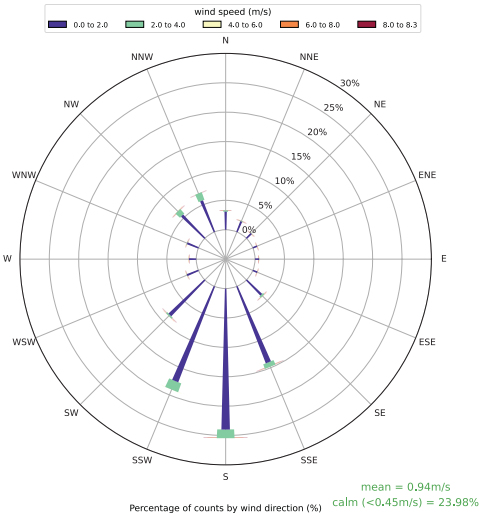

Figure 10: *Annual wind rose based on the measurement at the NUS-CDL T2 lab, January to December 2019*

We further analysed the wind data recorded at the rooftop level of the NUS-CDL T^2 lab. The 2019 annual wind rose at the T^2 lab (Figure 10) indicates the clear S and SSW dominant wind directions, which deviate from the prevailing monsoon wind direction. Therefore, the higher and faster discolouration in the S and W orientations might be a result of heavy monsoon driving rain by the locally dominant S and SSW wind at the T^2 lab site.

However, we are not certain of the cause of the deviated dominant wind direction at the T^2 lab site. The T^2 lab site was surrounded by high-rise residential buildings, which are typical in Singapore's high-density urban environment. This might be the cause of the varied wind directions at the rooftop level of the low-rise T^2 lab. This may indicate that local wind measurements are important for estimating the weathering effects in Singapore's high-density urban environment.

4.5 RAIN SPLASH WATER

The growth of decay-producing fungi only occurs if wood is continuously saturated with water in the presence of oxygen and its moisture content remains above 20% over prolonged periods. Construction details that either keep building components dry or help them to dry quickly will reduce the likelihood of infestation by wood-destroying fungi and insects. Best practices include raising wooden facades high enough above adjacent horizontal surfaces to prevent damage caused by splashing water [1].

According to the DIN 68800, the distance between the underside of exposed timber members or construction elements and the ground (or surrounding surface) must be at least 30 cm to prevent exposure to splash water. This distance can be reduced to 15 cm if additional technical measures, such as a gravel bed in front of the timber cladding, are taken to reduce the impact of splashing [14].

The greying of damp wood is generally due to the presence of stain fungi (*Aureobasidium pullulans*). The hyphae of these fungi are pigmented, and they tend to refract visible light; accordingly, the timber surface appears grey. Refraction varies depending on the surface moisture content, and weathered timber is always darkest when wet [15].

At the NUS-CDL T^2 lab, where there is no shade from the surroundings, generally strong splashes at the ground level were observed when tropical monsoon driving rain directly hit the concrete ground surface. We intentionally narrowed the gaps between the bottom end of the timber cladding to the ground level to 20 cm to observe how high the splash water could wet the timber façade with the tropical monsoon driving rain.

Figure 11 illustrates an example of timber cladding on the S side several hours after heavy monsoon driving rainfall. Generally, we observed that the wall base became wet and darker up to 40 cm in height in the S and W orientations. The tendency was less obvious in the N and E façades. If we were not mitigating the splash water through additional technical measures, it would probably have been better to raise the bottom end of the timber cladding at least 40 cm from the ground level to protect the timber façade from constant wetting, especially for the façade facing prevailing wind directions in the tropical monsoon climate.

Further investigation is needed to develop guidelines; however, the 30 cm guideline in the temperate climate is not sufficient in the tropical monsoon climate.

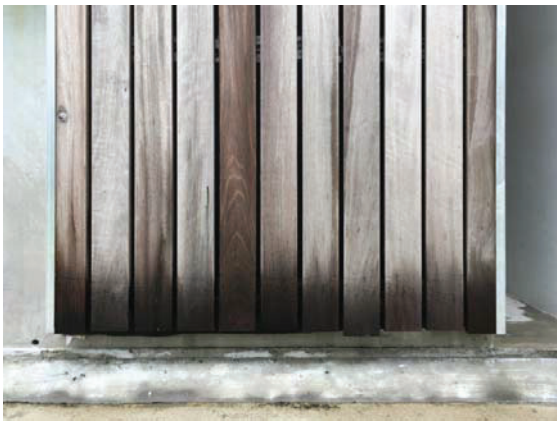

Figure 11: *An example of a wet timber cladding base several hours after heavy monsoon driving rainfall (November 2019) – generally, the bottom of the S and W façades became wet and grew darker because of the splash water up to 400 mm above ground level.*

4.6 UV-FILTERED GLAZING

The UV-filtered glazing overlayed CLT walls made of Norway spruce (*Picea abies*) and red jabon (*Anthocephalus macrophyllus*) to protect them from weathering and make them visible from the outside. As the UV-filtered glazing was point-fixed over the CLT walls, the colour change measurement via handheld spectrometer was restricted. Instead, the general discolouration observation was made visually after 28 months of exposure as a reference.

Figure 12: *Examples of colour changes after 28 months exposure behind UV-filtered glazing (April 2021).* ***Left:*** *Norway spruce (Picea abies),* ***Right:*** *Red jabon (Anthocephalus macrophyllus).*

As the UV-filtered glazing effectively protected the CLT walls from monsoon driving rain, there were no signs of grey colour weathering observed for both the Norway spruce and red jabon. However, noticeable colour changes were still observed, especially for the Norway spruce, which changed to a darker reddish colour over time, while the red jabon's change in colour was less obvious. There were also noticeable cracks on both the Norway spruce and red jabon CLT walls (Figure 12). The visually noticeable dark reddish colour changes of the Norway spruce and the moderate reddish colour of

https://doi.org/10.52202/069179-0501

the red jabon seemed to be a part of the ageing process, which is considered as a slow thermal oxidation [3]. It is generally observed that heat can directly alter the colour by causing hydrolysis and the oxidation of wood components. As timber dries, extractives accumulate on the surface, where they oxidise to a brown colour. The effect is usually short-lived, as rainwater will remove the extractives, although it can persist where the timber is protected [15]. It is also generally accepted that colour changes increase as the temperature increases. Long-term exposure to heated double facade cavities in hot and humid climates probably accelerates the ageing process. This phenomenon requires further investigation.

Figure 13 *Examples of overall timber cladding discolouration after 28 months exposure (April 2021).* ***Left:*** *N side,* ***Right:*** *S side. The S-side facade exhibits mostly darker colours, while the N-side facade exhibits more moderate and uneven colour changes.*

5 CONCLUSIONS

Timber weathering is caused by UV decomposing the lignin, which is washed out by the driving rain. In tropical monsoon climates, much of the rainfall is heavy and accompanied by monsoon wind. The mean annual rainfall in Singapore is approximately three times higher than in Germany. Therefore, the prevailing wind direction is one of the important factors influencing timber weathering and discolouration in tropical monsoon climates.

The overall colour change (ΔE^*) was the largest in the S- and W-side V-aligned cladding ($\Delta E^* = 17.0–18.4$), and the smallest ΔE^* was the N-side H-aligned cladding ($\Delta E^* = 10.2$). The dominant wind directions at the T^2 lab were S and SSW; therefore, monsoon driving rain seems to be the main cause. However, in Singapore's high-density urban environment, the prevailing wind direction in microclimates may differ from the prevailing monsoon wind direction. Therefore, on-site wind measurement is essential to estimating future weathering.

The general observation was made that the H-aligned boards exhibited lower overall discolouration (ΔE^*) than the V-aligned boards. The ΔE^* standard deviation for the H-aligned boards was generally higher than the V-aligned boards throughout the testing period. After a 28-month period, the V-aligned boards exhibited a relatively homogeneous facade outlook, while the H-aligned boards still exhibited uneven weathering (Figure 13).

Despite the UV-filtered glazing, the natural colour changes still occurred for the CLT walls, which seemed to be caused by a mild thermal oxidation process. The effect of prolonged exposure to the heated double-grazing cavity requires further investigation.

The discolouration of timber elements is unavoidable; however, if the discolouration could manifest more evenly, it could still resonate with the dominating industrial aesthetics. The field test demonstrated that vertical cladding constantly exhibited a lower ΔE^* standard deviation than horizontal cladding, which means that relatively even weathering can be expected. Overall, this is still an initial attempt to control the discolouration of timber facades in tropical monsoon climates. We must investigate with further variations in tectonics and more tactile strategies to control and blend in ephemeral timber aesthetics with the industrial aesthetic norms. We hope this may eventually ease the negative public preconception of timber and contribute to the adaptation of MET buildings in tropical monsoon climates.

ACKNOWLEDGEMENT

The NUS-CDL T^2 lab, Department of Architecture, College of Design and Engineering, National University of Singapore is financially supported by City Developments Limited, which aims to test various advanced building technologies related to the tropics, such as Building-integrated photovoltaics, green façades, natural ventilation and climate-responsive building design strategies. The CLT-filed test was funded by the MNDRF Innovative Mass Timber Construction Systems for High-density Urban Environment in the Tropics project (BCA RID 94.18.2.1).

REFERENCES

[1] U. Dangel, Turning Point in Timber Construction: A New Economy. 2016, pp. 1-192.

[2] S. P. Low, S. Gao, and S. K. Ng, "The adoption of mass-engineered timber (MET) in the Singapore construction industry: Barriers and drivers," *Journal of Cleaner Production,* Article vol. 327, 2021, Art no. 129430, doi: 10.1016/j.jclepro.2021.129430.

[3] M. Matsuo *et al.*, "Aging of wood: Analysis of color changes during natural aging and heat treatment," 2011.

[4] S. Sandoval-Torres, W. Jomaa, F. Marc, and J. R. Puiggali, "Causes of color changes in wood during drying," *Forestry Studies in China,* vol. 12, no. 4, pp. 167-175, 2010, doi: 10.1007/s11632-010-0404-8.

[5] C. Hill, M. Kymäläinen, and L. Rautkari, "Review of the use of solid wood as an external cladding material in the built environment," *Journal of Materials Science,* vol. 57, no. 20, pp. 9031-9076, 2022/05/01 2022, doi: 10.1007/s10853-022-07211-x.

[6] J. Bijen, "4 - Wood," in *Durability of Engineering Structures*, J. Bijen Ed.: Woodhead Publishing, 2003, pp. 139-157.

[7] L. Tolvaj, G. Papp, D. Varga, and E. M. Láng, "Effect of Steaming on the Colour Change of

Softwoods," *Bioresources,* vol. 7, pp. 2799-2808, 2012.
[8] L. Corpataux, S. Okuda, and H. W. Kua, "Panel and plate properties of Cross-laminated timber (CLT) with tropical fast-growing timber species in compliance with Eurocode 5," *Construction and Building Materials,* Article vol. 261, 2020, Art no. 119672, doi: 10.1016/j.conbuildmat.2020.119672.
[9] L. Reinprecht, M. Mamoňová, M. Panek, and F. Kačík, "The impact of natural and artificial weathering on the visual, colour and structural changes of seven tropical woods," *European Journal of Wood and Wood Products,* vol. 76, 01/01 2018, doi: 10.1007/s00107-017-1228-1.
[10] N. H. Wong, W. Liping, A. Chandra, A. Pandey, and W. Xiaolin, "Effects of double glazed facade on energy consumption, thermal comfort and condensation for a typical office building in Singapore,"*Energy and Buildings,* vol. 37, pp. 563-572, 06/01 2005, doi: 10.1016/j.enbuild.2004.08.004.
[11] M. Hrčková, P. Koleda, P. Koleda, Š. Barcík, and J. Štefková, "Color Change of Selected Wood Species Affected by Thermal Treatment and Sanding," *BioResources,* vol. 13, no. 4, 2018, doi: 10.15376/biores.13.4.8956-8975.
[12] Meteorological Service Singapore (MSS), Climate of Singapore [Online] Available: http://www.weather.gov.sg/climate-climate-of-singapore/
[13] Germany - Climatology [Online] Available: https://climateknowledgeportal.worldbank.org/country/germany/climate-data-historical
[14] W. e. a. Huss, "Timber Architecture Design and Construction," Technical University of Munich, Munich, 2015.
[15] I. P. Davies, "Moisture conditions in external timber cladding: field trials and their design implications," Doctor of Philosophy, School of Engineering and the Built Environment, Edinburgh Napier University, Edinburgh, U.K., 2011.

https://doi.org/10.52202/069179-0501

World Conference on Timber Engineering Oslo 2023

CREEP TESTING OF A TIMBER LATTICE FRAME USING IMAGE RECOGNITION

Nicolas Giron[1], Hideyuki Nasu[2]

ABSTRACT: A one year creep testing for an architectural project was conducted for a 8650mm span timber lattice frame. In parallel of the standard measurement with dial gauges, three cameras were set and 400 pictures were taken on a regular base for the full year. To process the picture data, an image recognition program was used. The displacement of each node of the lattice frame was extracted and the central deflection of the frame was evaluated. The deflection measured by dial gauge and the one estimated by image recognition were compared and a very good accordance was observed. In addition to the central deflection, deformation and stress of each member of the lattice frame can be estimated, allowing to understand the global and the detailed behaviour of the frame. Applications of the proposed method are presented.

KEYWORDS: Creep testing, Image recognition, Structural analysis

1 INTRODUCTION

As timber is a viscoelastic material, creep amplification, which refers to amplification of elastic deflection over time, is an important factor to consider when designing a timber structure. For a single structural element, the range of the amplification is well documented for various periods of time and types of loading [1]. However, for a composite structure like the lattice frame presented below, accurately evaluating the expected amplification is difficult due to factors such as connections and the mix of loading types. For non-conventional types of structure with long-term deflection that may be critical, creep testing is frequently undertaken.

While creep testing a large structure is costly and time-consuming, generally only a few measurement devices are used, mainly to estimate the central deflection, leading to an understanding of the global behaviour of the structure but not the behaviour of each element.

In 2018, a creep testing using standard measurement devices was conducted for a full year. At that time, it was expected that in image recognition algorithms would be improved and become a powerful tool to enhance the results of such a testing. Therefore, distinctive marks, hereafter templates, were placed on the node of the lattice frame in anticipation of future research.

This article proposes a method using image recognition to estimate the creep amplification factor, along with other meaningful structural characteristics. Without installing any recording devices like dial gauges or strain gauges, the complete behaviour of a structure can be recorded using pictures taken by a standard camera (in this study, NIKON COOLPIX W300 with 16.05 million effective pixels and a 1/2.3" CMOS image sensor)) and then analysed using an image recognition program.

The central deflection estimated through this proposed method shows good agreement with the measurement of the dial gauge. Additionally, the displacement and rotation of all the nodes, and the evolution of the length of each element of the lattice frame were estimated. While there are issues with accuracy and points to be improved, the authors believe that promising results were obtained, even if the testing that was planned for standard measurement method with no particular attention given to the proposed method.

A roof composed of frames similar to the tested lattice frame has been in service since four years in an elementary school in Japan (Figure 1), and to this day, the structural behaviour of the frames is within the design range.

Figure 1: Classroom of the Seijogakuen Elementary school with lattice framed roof form of superimposed lumber and joined by wood screws and LVL gussets

[1] Nicolas Giron, NIKKEN SEKKEI LTD, (Engineering Department, Structural Design Section, 2-18-3 Iidabashi, Chiyoda-ku, Tokyo) Japan, giron.nicolas@nikken.jp

[2] Hideyuki Nasu, Nippon Institute of Technology, (4-1 Gakuendai, Miyashiro, Minamisaitama-gun, Saitama) Japan, hideyuki.nasu@nit.ac.jp

https://doi.org/10.52202/069179-0502

2 CREEP TESTING SETUP AND RESULTS

2.1 TESTED FRAME OUTLINE

A lattice frame system composed of superimposed dimension lumber (38x140 SPF) and laminated veneer lumber (LVL) gussets was tested. Lumbers are arranged on a grid with horizontal spans of 910mm and vertical spans of 400mm. The frame includes horizontal, vertical and diagonal elements. The frame consists of three layers with one vertical lumber in the centre between two horizontal or diagonal lumbers, giving the frame a total thickness of 114mm. When lumbers from more than two directions meet at one point, 38mm thick LVL gussets are inserted, as shown in Figure 2. The lumbers are connected using wood screws as a double shear connection. The screw length is 110mm with a thread length of 40mm, and the screw material is carbon steel wire for cold heading and cold forging (SWCH) respecting JIS G3507-2 regulation. Ruspert anti-corrosion treatment is applied.
The lattice frame spans over 8.645m with a rise of 2m and a minimal depth of 400mm. Further details can be found in [2].

2.2 TESTING SETUP

Two frames were placed side by side in a hangar and connected at roof level by plywood. They were loaded with steel rebar for an entire year. Each frame was equipped with 3 dial gauges, as in Figure 3. In addition to the dial gauges, four cameras were placed (Cameras 1, 2, 3: NIKON COOLPIX W300, Camera 4: NIKON Keymission 170 (wide angle)). At each node of the frame, a template was placed (Figure 6) to facilitate the image recognition process. The frames were loaded using a total of 900 pieces of steel rebar, resulting in a total load of total load of 53kN, including the self-weight of the frames and the additional elements used to connect them. The total load corresponds to twice the expected long-term dead load considered in the design.
The testing began on August 27th, 2018, and ended one year later. The dial gauge data were collected every 10 minutes. During the first hour, pictures were taken every 10 minutes. Afterwards, picture were taken every hour until the next day, every 3 hours until the third day, every 6 hours until the fourth day, every 12 hours until the fifth day. Then, pictures were taken once a day during the first month and twice a week until the end of the testing for Cameras 1 to 3. For Camera 4, pictures were taken twice a week for 3 months.

2.3 RESULTS

The initial elastic deflection is approximately 17.82mm. The maximum deflections recorded after 1, 6 and 12 months are respectively 22.81mm (1.28 times), 27.29mm (1.53 times) and 33.08mm (1.86 times), respectively. The power law creep equation is used to evaluate the creep amplification coefficient at 50 years. The approximation of the power law equation parameters with the data recorded during one year yielded a 50-years deflection about 49mm and a creep amplification factor of 2.8. The results are presented in Figure 5.

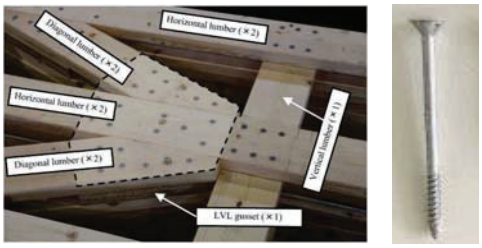

Figure 2: Left: LVL gusset connection, Right: wood screw

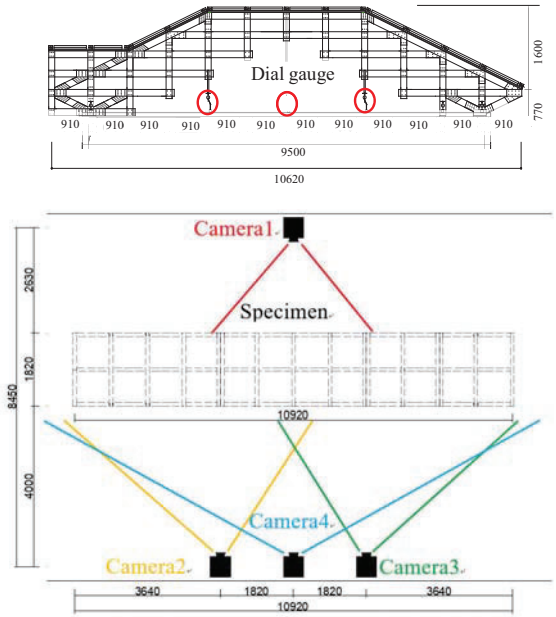

Figure 3: Top: Frame elevation, Bottom: Camera range

Figure 4: View from each Camera from 1 to 4

https://doi.org/10.52202/069179-0502

3 IMAGE RECOGNITION PROCEDURE

3.1 METHODOLOGY

The proposed method has been applied to the pictures from Camera 2 and Camera 3. The pictures from Camera 4 have large distortions due to the wide-angle lens and were not analysed this time. However, with an appropriate algorithm and some calibrations, it is possible to restore the true angles and geometry, allowing for the processing of the pictures in the same way.

The data are processed with a Python program using the OpenCV library for image recognition. The "matchTemplate" function is used, and results are calculated based on the normalized correlation coefficient. This function assigns a score between 0 and 1 to each pixel of the picture based on the resemblance between a given template and the corresponding picture area. For a single node, many matches are returned, and therefore, a filtering procedure is required to assign a unique coordinate to a node, as shown in Figure 7. The procedure is as follows:

In the first step, the images from Camera 2 and Camera 3 are combined to form a picture of the whole frame. The four marks of the overlapping area are used to determine the differences in scale and angular rotation of the two pictures, along with the coordinates where the images can be stitched. The two pictures are accordingly rotated, scaled and stitched, as shown in Figure 8.

In the second step, two areas of the pictures that are likely to be unchanged during the test process are chosen. Using the image recognition of the first step, all the pictures are scaled, rotated, resized and aligned to a common base with the same origin and axis from a reference picture, as shown in Figure 9. This allows the location of the marks in each picture to be compared, and the location variations correspond to the displacement of the frame.

In the third step, each node of the first picture is copied and rotated from -2.00 to 2.00 degrees with 0.01 degree intervals. The resulting images are saved as new templates for the next step, as shown in Figure 10.

In the fourth and last step, the original template is used to locate all the nodes. Then each node is compared with its dedicated template from -2.00~2.00 degrees from the first picture, and the template with the best matching is assumed to be the variation of the angle since the beginning of the testing. This process is detailed in the next section. In addition to the node marks, the three anchors of the frame to the ground are also located. Data is stored in an Excel sheet with coordinates and rotation angle of each node and the date of the picture. Also, the original pictures are edited with the located nodes, their number, and rotation angle, as shown in Figure 11.

The data is then available to be processed for structural analysis. The length of a known element is used to calibrate the pixel size, allowing the coordinates of each node to be calculated in millimetres.

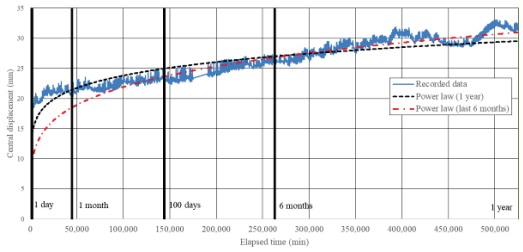

Figure 5: Creep testing records and power law approximations

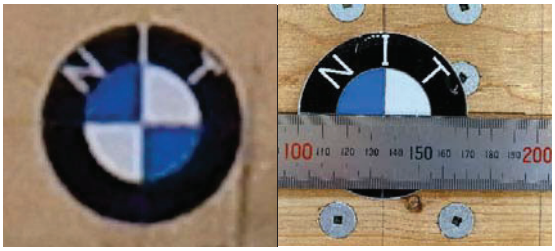

Figure 6: Left: Mark placed at each node with real picture resolution, Right: Size of the mark

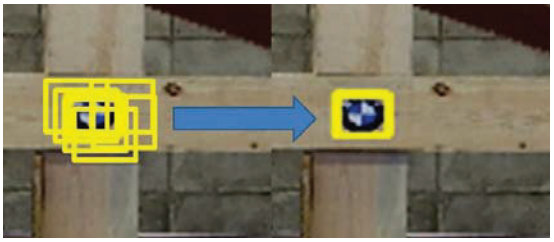

Figure 7: Results from the matching procedure before (left) and after filtering (right)

Figure 8: Step 1, pictures from Camera 2 and Camera 3 are rotated, scaled and stitched using the four centre marks

Figure 9: Step 2, reference picture on the left is used as a base to rotate, scale and align other pictures

Figure 10: Step 3, for each node templates are created (left) with rotation from -2.00 to 2.00 degrees (right)

https://doi.org/10.52202/069179-0502

3.2 ROTATION ANGLE

To identify the variations in the rotation angle of a mark, the mark is compared to templates of various angles and the best match is chosen. Initially, a common template was planned for all the nodes, but during the evaluation process, issues arose.

Testing was conducted with digital data and real pictures with various backgrounds using the layout and rotation angles in Figure 12. Accurate results were obtained for digital data, but for real pictures, noise from the background and picture distortion had a significant impact, as seen in Figure 13. To reduce the noise, two options were considered: making the template as small as possible to remove the background and keep only the mark, or using a different template for each node to include the background into the identification process. The latter option was chosen because reducing the mark of the creep testing which is already small (55x55 pixels), would also reduce the minimum resolution available, while using a local template would allow for a larger template size 135x135 pixels that includes the background, improving resolution. Additionally, when limited to a located area, the impact of image distortion in the templates and pictures is approximately the same, mitigating its impact on the identification process.

For the digital testing, the results showed a continuous distribution with an error of +/- 0.02 degree for a 150x150 template, as shown in Figure 14. For the full scale creep testing, a resolution of around 2x0.02x150/55 = 0.11 degrees is expected. However, with real pictures, the results included some noise, making it difficult to determine whether the best result is due to noise or is the true maximum. Results are expected to have a continuous bell shape distribution, and therefore, are approximated with a curve obtained with Savitzky-Golay filter, as in shown Figure 15.

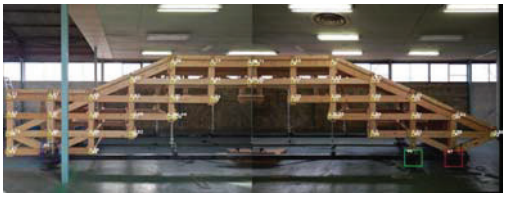

Figure 11: Step 4, each node is assigned a unique number and rotation angle. Coordinates are saved in an Excel file

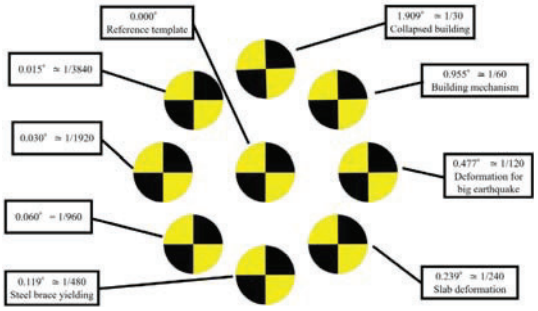

Figure 12: Rotation angle confirmation testing layout and angle

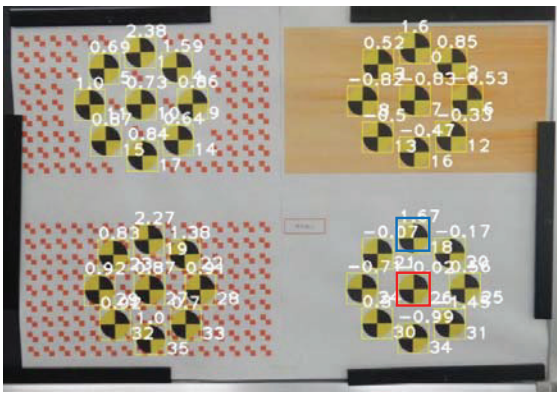

Figure 13: Results for different background with real picture (template in red)

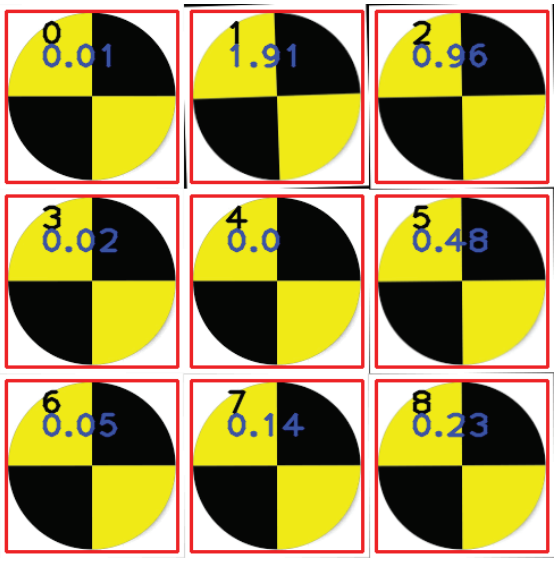

Figure 14: Red template from Figure 13 is rotated and placed as in Figure 12.

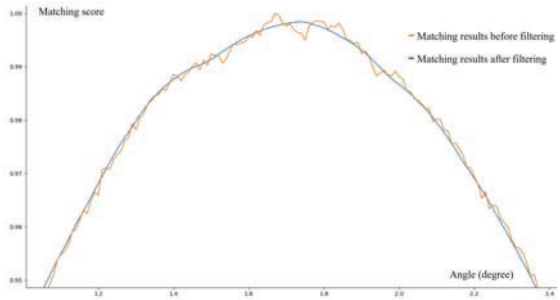

Figure 15: Scoring for each angle for the blue template of Figure 13

https://doi.org/10.52202/069179-0502

4 STRUCTURAL ANALYSIS

4.1 FRAME DISPLACEMENT

By estimating the location of each node, it is possible to create a digital twin of the frame, as shown in Figure 16. This enables measurements of the displacement in both vertical and horizontal directions of each node of the frame at a given time, in comparison of the vertical displacement of the three dial gauges.

The central deflection is plotted in Figure 17, which shows good agreement between the measured data and the estimated data obtained using image recognition.

During the creep testing, the hangar experienced large variations in temperature, causing the steel beam connecting the two extremities to dilate and inducing undesirable vertical displacement in the gauge measurement. Fortunately, the temperature of the room was also recorded along with the gauge displacement, and the results were adjusted accordingly. However, the proposed method eliminates the dependence to temperature, making the measurement more stable.

4.2 MEMBER STRESS

By knowing the horizontal and vertical coordinates and the angle of rotation of each node at each step, it is possible to calculate the displacement and the rotation of each extremity of the member composing the lattice frame. Assuming that all the displacements occur in the 2D plane and using an initial Young's modulus, it is possible to apply the stiffness matrix and to calculate the axial force, shear force and bending moment of all the members. However, the current testing setup does not account for the displacement at the connection, and the results for vertical and diagonal members may differ significantly from reality. Additionally, the accuracy of angle measurement is questionable at this stage of research, so only the axial stress is calculated. Nevertheless, theoretically, it is possible to obtain all stresses of a member with this method with Equation (1) below:

$$\begin{bmatrix} a_N & 0 & 0 & -a_N & 0 & 0 \\ 0 & 12a_M & 6La_M & 0 & -12a_M & 6La_M \\ 0 & 6La_M & 4L^2a_M & 0 & -6La_M & 2L^2a_M \\ -a_N & 0 & 0 & a_N & 0 & 0 \\ 0 & -12a_M & -6La_M & 0 & 12a_M & -6La_M \\ 0 & 6La_M & 2L^2a_M & 0 & -6La_M & 4L^2a_M \end{bmatrix} \begin{Bmatrix} u_1 \\ v_1 \\ \theta_1 \\ u_2 \\ v_2 \\ \theta_2 \end{Bmatrix} = \begin{Bmatrix} N_1 \\ Q_1 \\ M_1 \\ N_2 \\ Q_2 \\ M_2 \end{Bmatrix}, \quad a_N = \frac{EA}{L}, \quad a_M = \frac{EI}{L^3} \tag{1}$$

where L = member length, A = cross-sectional area, I = cross-sectional second moment of inertia, E = Young's modulus, u = axial displacement, v = transversal displacement, θ = the rotation angle, N = axial force, Q = shear force and M = bending moment for both extremities.

An example of results is shown in Figure 18 with a comparison to the computational model. The stress direction, i.e., tension or compression, shows rather good agreement. As for the intensity, good results are obtained for the centre and top part; however, close to the connection to the ground, result improvements are required. The main cause seems to be the picture distortion.

4.3 MEMBER CREEP

The overall creep of the frame is estimated with the central deflection. But not all the members of the frame participate equally to the creep amplification, and in the case of countermeasures to reduce the creep are required, knowing the members that suffer the most from creep can be very efficient. Indeed, by increasing the cross-section of such a member, it is possible to reduce the stress intensity and therefore to creep impact on the structure, allowing a cost-efficient design.

In Figure 19, the evolution of the length of several members from 30 minutes after the beginning of the testing to its end is shown. As an example, according to the recorded data, reinforcement of the member section between nodes 0-1 seems to be the best option to reduce the overall displacement, as this member has the largest change in length during the testing span.

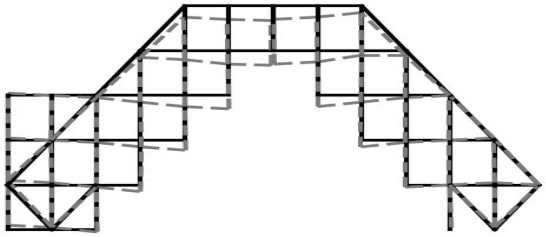

Figure 16: Original frame in black and estimated deformed frame in grey

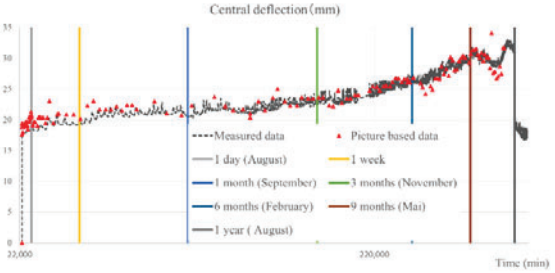

Figure 17: Comparison of the measured data and image recognition based estimations of the central deflection

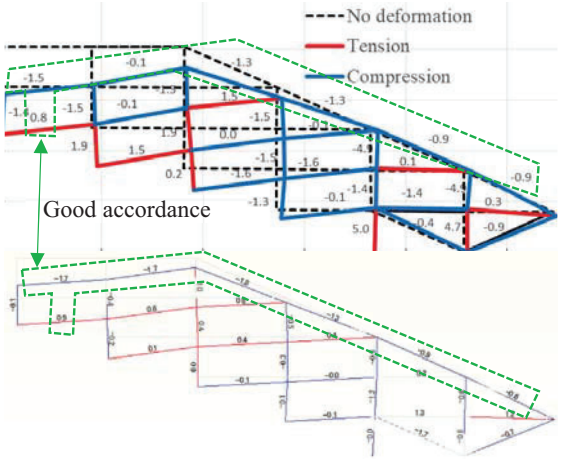

Figure 18: Stress intensity (in N/mm^2) comparison between the estimated model (top) and the computational model (bottom)

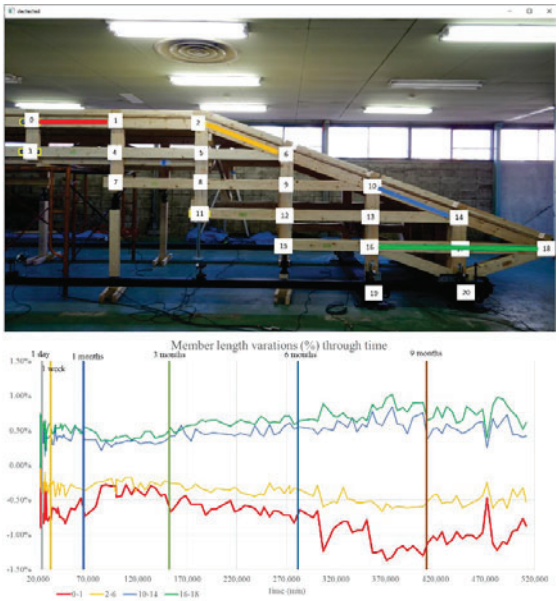

Figure 19: Top: Members layout, Bottom: Member length variations

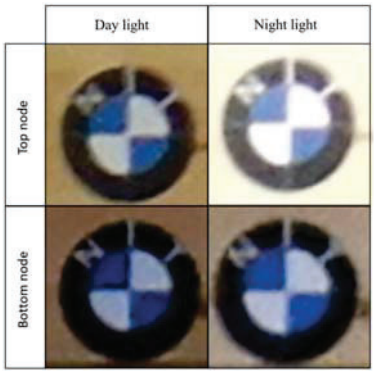

Figure 20: Comparison of 2 nodes during day and night time

5 LIMITATIONS AND IMPROVEMENT POINTS

5.1 TESTING SETUP

The testing setup was designed for standard creep testing and therefore was not optimized for the proposed method. For future developments, the following points should be revised.

5.1.1 Camera

The camera should be fixed on a weighted tripod to improve its stability. The camera should be actioned remotely to avoid any changes in distance or orientation relative to the frame and to avoid any blurring.

5.1.2 Environment

The lighting environment should be controlled to improve the continuity within a picture (space) and between the pictures (time), to reduce the disparities, as shown in Figure 20. Also, the camera should be set to manual to maintain the same aperture for all the pictures. The aperture should be around 8-12 to control lens aberration. A fixed low ISO is recommended to reduce the sensor noise.

5.1.3 Layout

The overlapping area of the cameras should be extended to improve the quality of the picture stitching. When better accuracy is required, the resolution and/or the number of cameras should be increased. In this testing, the resolution was about 70mm/55pixel or 1.3mm/pixel.

5.1.4 Additional marking

Distinctive marks should be added at anchor points and close to them on the ground to create fix points. In this setup, the anchor points were connected by a steel beam, so the effect of the horizontal thrust and corresponding horizontal displacement was neglected. For structure with significant horizontal sliding, independent fix points are required.

5.1.5 References

To obtain precise results, a reference, such as a lead wire, should be added to set the vertical axis. Also a reference should be added to calculate the pixel/millimetre ratio to calibrate the lengths.

5.1.6 Template

A larger template should be used to calculate the rotation angle. With a 55x55 template, only rotation about 1 (= arctan (1/55)) degree should be measurable. However, with the proposed image recognition procedure, subtle colour variations of the pixels are included, and a better resolution around 0.1 degree is obtained. The colours of the template should be selected to offer good contrast with timber or other testing material, and surrounding environment.

https://doi.org/10.52202/069179-0502

5.2 MULTILAYER STRUCTURE

The considered frame was composed of three layers. The marks were set only on the exterior layer, and therefore the displacement at the connection level due to the deformation of wood screws was not measurable. By adding additional marks close to the connection on the vertical member, as shown in Figure 21, the relative displacement between horizontal and vertical member at the connection can be estimated.

5.3 PROGRAMM

5.3.1 Step one and two: stitching and aligning

For the first step of the procedure, the picture stitching can be improved with the "SIFT" (Scale-Invariant Feature Transform) function from the OpenCV library. It locates key points on the both pictures and then compare them looking for similarities. It was tested for the available pictures of this test. However, the overlapping area was too small, with too large distortion and change in perspective, as shown in Figure 22. As a result, it was not possible to successfully apply it.

If enough trustable key points could be identified, the RANSAC (RANdom SAmple Consensus) algorithm could be applied to find a transformation (homography) that deforms continuously the first picture so that all its key points match those of the second picture.

This transformation process can also be applied to the second step to align and scale the pictures. However, only key points independent of the frame, i.e. which coordinates does not change over time, should be selected.

5.3.2 Step four: location and rotation

In the current procedure, the coordinates of the template mark are given in pixel, limiting the available precision. To improve this step, after the mark is located, a colour decomposition could be done to isolate the mark and identify its centre.

In this particular case of the presented testing, the mark is composed of blue, white and black. But, due to the lighting environment, white is sometimes considered as grey, and the blue/black mix is assimilated to violet in certain cases. Therefore, those two colours are also included in the allowed colour set for the mark isolation process. On the contrary, the wood colour is close to the yellow and red, and therefore, those two colours should be removed. The mark is obtained by adding the elements from the allowed colour set and subtracting the yellow and the red. A thresholding process is used to obtain a binary representation of the picture with the pixels of the mark in white and the other pixels in black, as shown in Figure 23. Then the "findContours" function from the OpenCV library is applied to identify the mark outer shape and estimate its centre with better precision. The mark is approximated by an ellipse, so that the length difference of the major and minor axis and their rotation angle can also be used to reduce distortion.

In addition, this method can also be used to locate accurately the straight lines of the mark and identify directly its rotation angle. The procedure should be faster, but resolution is likely to be worsen. An appropriate choice is needed according to the application.

5.3.3 Distortion

In the end, the most important improvement should be to add an algorithm to reduce or cancel the distortion from the lens and perspective, so that the proportions, parallel lines, and perpendicular lines are preserved.

Calibration of the camera using chessboard could be done along with other calibration depending on the layout of the testing setup.

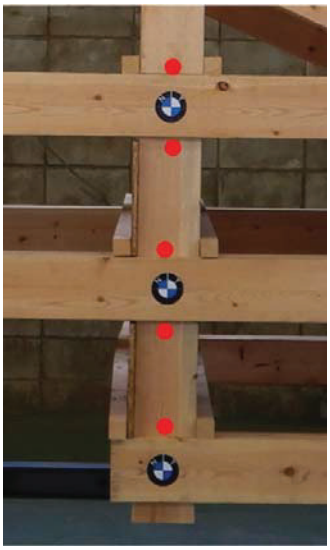

Figure 21: Example of additional marks to estimate inner layer displacement. Rotation is not required, therefore simple mark is enough.

Figure 22: Key points comparison for left and right picture

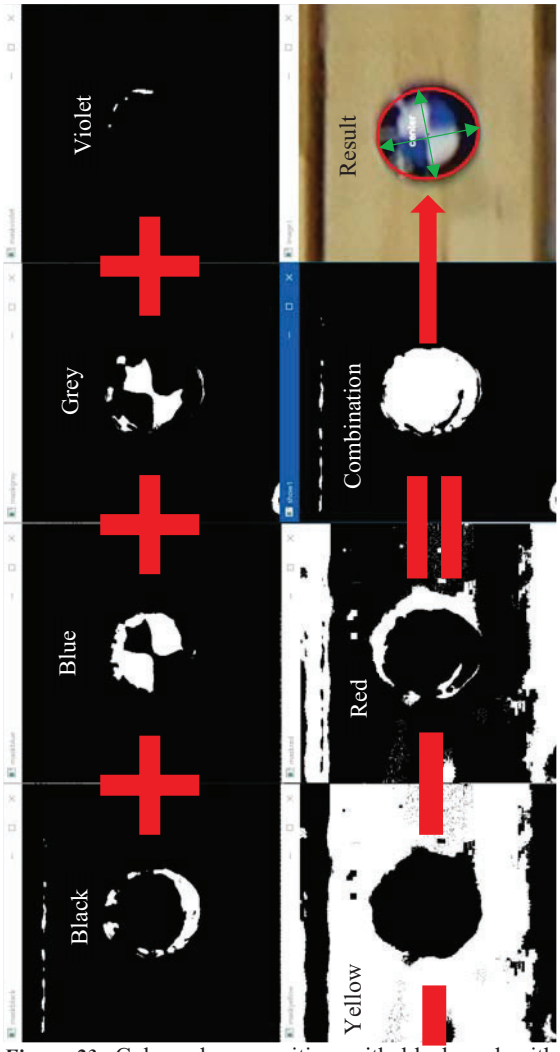

Figure 23: Colour decomposition with black and with thresholding followed by a combination to isolate the mark contour and identify its centre

6 CONCLUSIONS

In conclusion, the proposed method of using image processing and analysis techniques for measuring the deformation of timber structures has shown promising results.

However, there are limitations and improvement points that need to be addressed to increase the accuracy and reliability of the method. These include optimizing the testing setup, improving the stitching and aligning of the images, and reducing distortion from the lens and perspective. By addressing these issues, the proposed method has the potential to provide a cost-effective, non-destructive and precise means of measuring the deformation, stress of timber structures among other, which can have important applications in the field of civil engineering and architecture.

Further research and development in this area can lead to more accurate and efficient methods for monitoring the structural integrity of timber buildings and bridges, ultimately contributing to safer and more sustainable infrastructure.

REFERENCES

[1] S. M. Holzer, J. R. Loferski, and D. A. Dillard: A review of creep in wood: concepts relevant to develop long-term behavior predictions for wood structures. In:Wood and Fiber Science, 21(4), pp. 376-392, 1989.

[2] N. Giron, N. Nakanishi, K. Matsuo, R. Arai and H. Nasu: Lattice framed roof formed of superimposed lumber and joined by wood screws and LVL gussets. In: WCTE2021, 2027-2035, 2021.

https://doi.org/10.52202/069179-0502

World Conference on Timber Engineering Oslo 2023

A MOISTURE MANAGEMENT STRATEGY FOR CLT USING SENSOR TECHNOLOGY TO CREATE A ROBUST NORWEGIAN SCHOOL

Laura Vestergaard Kellgren[1], Astrid Charlotte Seeberg [2], David Hagle[3], John Øvregård[4], Jeppe Rasmussen [5]

ABSTRACT:

To monitor the use of cross-laminated timber (CLT) and how it is affected by moisture in the construction phase, Woodsense has incorporated sensor technology in the moisture management strategy and construction of the Sophie Radich school in Lillestrøm. The use of sensor technology supports several aims of the BREEAM-NOR manual, which seeks to increase the use of sustainable building materials and improve robustness to moisture damages. With a preventive approach in moisture management in the construction phase, it is possible to reduce resource waste, as damages can be found earlier in the process and before the building is put into use. After having used sensors on the Sophie Radich project, increased moisture levels were detected. The preventive approach made it possible to correct the cause of moisture increase, avoiding further damage to the construction while illustrating the advantages of sensor technology.

KEYWORDS: CLT, moisture management, sensor technology, sustainable building materials, BREEAM-NOR,

1 INTRODUCTION

More sustainable construction calls for solutions that reduce resource consumption and CO_2 emissions through an increased use of sustainable building materials such as timber. This is also emphasized in the new BREEAM-NOR manual V.60 [1] in issue MAT 01 – *sustainable material choices – LCA and climate gas calculation*s where points are given for using sustainable materials with low carbon emission. Although timber is a more climate friendly material than conventional structural materials such as concrete and steel, there are concerns with using it in construction due to challenges associated with moisture protection and management.

Some of the main barriers preventing the use of timber as a building material is the risk of moisture damage and as a result, a waste of resources. To document the moisture management of the Sophie Radich project - a Norwegian school constructed with cross laminated timber (CLT) - an intelligent sensor solution by Woodsense has been incorporated into the project. Through constant monitoring and automatic alarms, the sensors assist in carrying out an effective moisture content strategy with documentation of correct moisture management throughout the entire construction process.

The sensors are effectively used to, for example, document that there is no excessive moisture in the elements, and share said data between construction actors in the project. Additionally, the sensors contribute to the reduction of resource waste and a responsible use of building materials. This complies with the aim of issue MAT 05 *Robust and climate adapted buildings.* By preventively monitoring the growth of mold, the sensors also promote a healthy indoor climate to benefit the health and well-being of the building's users.

1.1 MOISTURE DAMAGES

Moisture is the leading cause of damage in construction, accounting for 71% of all damages from a study of 175 defect cases [2]. Of these damages, 69% occur within the first five years of a new construction project. In addition to causing damage, changes in wood moisture content can also impact the load bearing capacity and the tightening power of fastenings and screws, as studies show a reduction of WMC of 3-4% around threaded rods can lead to critical stresses leading to moisture induced cracks [3].

[1] Laura Kellgren, Woodsense DK, Denmark, laura@woodsense.dk
[2] Astrid Charlotte Seeberg, Arkitema AS, Norway, ascse@arkitema.com
[3] David Hagle, COWI AS, Norway, dahg@cowi.com
[4] John Øvregård, COWI AS, Norway, jnod@cowi.com
[5] Jeppe Rasmussen, Woodsense DK, Denmark, jeppe@woodsense.dk

https://doi.org/10.52202/069179-0503

The study between 2017-2020 shows that unventilated compact roofs and terraces (on concrete floors) are the most common building component exposed to damages mainly caused by precipitation. The study shows that around 80% of the defects on terraces are linked to penetration of precipitation, where leakages in the roof membrane and insufficient connections around terrace doors are recurring reasons for defects.
As climate changes cause more and more intense rainfall in short periods. Even with well designed building details and well done craftsmanship the risk of mistakes will always be applicable.
Measuring water content in building components before closing is well known. Disadvantage is that if small mistakes are done, the small mistakes can cause major damages. Sensor technology used during construction phase can discover the small mistakes before causing major damages.

1.2 MONITORING FOR CRUCIAL AREAS

Norwegian building regulations (Plan og bygningsloven and Byggteknisk forskrift) are familiar with timber constructions. Product and building components must be dry enough when installing and sealing that there is no risk of fungus, decomposition of organic materials or increased degassing.

Drying material takes time, especially components applied to one-sided drying, like sills in timber constructions. The moisture content must be measured in order to document that the required moisture content is met.

Pre-accepted moisture content to avoid fungal growth on timber is 20 weight percentage moisture. Building components with a low capacity for drying out the moisture content must be lower than 15 weight percentage moisture before closing the building component.

Risk strategies prepared according to MAT 05 *Robust and climate adapted buildings* should identify and propose risk reducing measures for parts of the building that are exposed for degradation as a result of the current and future climate. The risk strategy should also uncover risks of moisture damages caused by build in moisture during the construction phase.

The design phase should choose building materials and structural principles that are common. Roof constructions and access for maintenance are essential.
Norwegian Standard NS 3514:2020 *Moisture safe construction - Planning and execution* is meant to be a tool for the construction industry to prevent moisture-related incidents during the construction phase and create awareness about moisture-proof construction [4]. The standard shows guidelines and procedures related to moisture safe construction and reference to NS 3512 *Measurement of moisture in timber structures* [5].

1.3 DETAILS EXPOSED TO MOISTURE DAMAGES

Some construction principles can be risky to build. The figure below shows building details that above mentioned studies show that are exposed to moisture damages.

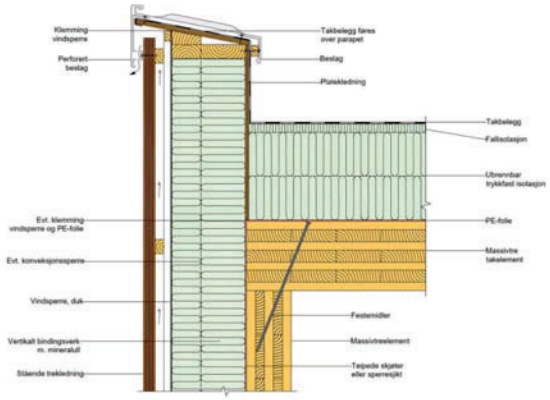

***Figure 1**: Principal detail parapet at unventilated compact roof and CLT-Element [6]*

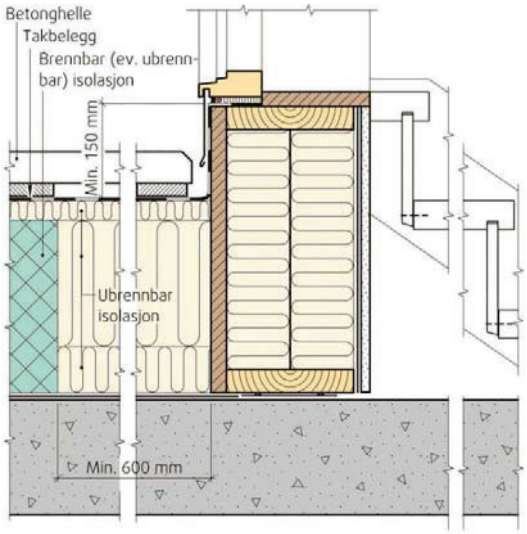

***Figure 2:** [7] Terrace door to unventilated compact roof.*

Overlight windows are often placed during the roofing. The construction on the inside is open and affected by large amounts of building moisture from for example concrete work and straightening of floors.

https://doi.org/10.52202/069179-0503

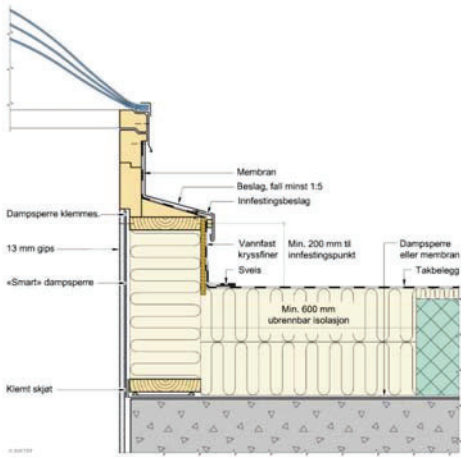

***Figure 3**: [8] Overlight in unventilated compact roof.*

These are examples of building components that are well known details and common to build and still risky for moisture damages.

2. SOPHIE RADICH PROJECT AND MOISTURE MANAGEMENT STRATEGY

Sophie Radich ungdomsskole in Lillestrøm is a Secondary school with a total area of approximately 130000 m2 and space for 720 students. The project has been developed in collaboration with contractor Kruse Smith and Lillestrøm municipality. Arkitema is involved as architect and landscape architect. The building is a CLT construction and has a very high environmental ambition with a blue-green focus. The school has a distinctive footprint shaped like a four-leaf clover. With a strong focus on the surrounding nature, students will experience an interaction between the indoor and outdoor environment.

Timber has been chosen as part of the main construction for the entire building, primarily from an environmental point of view. However, the choice is also based on the theory that the use of wood has a positive impact on physical and mental health [9]. Findings from another study regarding the use of wood in buildings show a significant decrease of systolic and diastolic blood pressure [10]. This is, in addition to an aesthetic consideration, the reason for choosing visible wood in the building's interior.

2.1 THE MOISTURE MANAGEMENT STRATEGY

The Norwegian climate posed a challenge during the construction process, as rain, moisture, ice formation and snow can cause major problems.
Using a tent during construction was considered, but this would mean additional costs which is a disadvantage compared to traditional construction methods. It was therefore decided not to cover the building during the construction period. It was expected that repair of any damage would be less than the cost of a tent / superstructure. Unfortunately, the autumn of 2021 was particularly rainy and windy, and there was some concern related to moisture, especially on the roof. An agreement was therefore made with Woodsense, to uncover any leaks and moisture problems.

3. USE OF SENSOR TECHNOLOGY TO AVOID DAMAGES CAUSED BY MOISTURE

When working with timber in construction, one of the main issues is related to moisture damage. The sensor solution by Woodsense seeks to address that issue by measuring wood moisture, temperature and humidity, and comparing the data with local weather data. By analysing the collected data, it is possible to detect leaks and conditions that can lead to mould and rotting of the wood. Through constant monitoring, moisture damage can be prevented, thus reducing resource waste. The embodied CO2 emissions associated with a moderate defect in terms of disposing of materials and replacing with new materials amounts to 572.32 Total GWP [kg CO2eq] equivalent to 2% of the entire buildings embodied carbon emissions [3].

***Figure 4**: Sensor that monitors wood moisture content, temperature and humidity from Woodsense.*

This strategy complies with the aim of issue MAT 05 *Robust and climate adapted buildings* which focuses on the reduction of the need to repair or replace damaged materials. It can also be part of the risk analysis which is needed to get the score in part 2 of MAT 05 – *Protect exposed parts of building against damage.*

https://doi.org/10.52202/069179-0503

Figure 5: *Blueprint from the 3rd floor. Sensor placement on this floor in wet rooms close to the concrete floor to detect leakages, on the balcony under a pavilion to ensure water doesn't get in and under a window to test window is tight during construction,*

Figure 6: *Sensor under window. © Kruse Smith*

The digital platform of the sensors has integrated the so-called mould curves, derived from mathematical models from research in the field. These are used, among other things, to visualise the environment of a given sensor and determine the risk of mould growth. By preventively monitoring the growth of mould, the sensors promote a healthy indoor climate to benefit the health and well-being of the building's users.

Sensors were placed on various locations in the main construction to monitor particularly exposed areas, detect critical moisture levels before damage could occur and document moisture management throughout the construction.

3.1 IMPORTANT DATA TO MEASURE CRITICAL FOR A HEALTHY BUILDING

According to *Sintef Byggforskserien 421.132 Fukt i bygninger. Teorigrunnlag.* To avoid moisture damage and other moisture-related problems during construction a critical moisture level is used as a limit to determine whether a material is dry enough to proceed in the construction process. Critical moisture level is usually given with the designation RH. Absolute moisture content is usually used for wood materials (Wood Moisture Content).
When RH in the surroundings is more than 80% and temperature above 0°C in some time, risk of mold growth can appear. Spruce and pine will have a WMC around 16-18%, when the RH in the surroundings are around 80%.
With well documented design phases and procedures to prevent moisture related damages there will always be some risks of moisture damages.
Due to tight schedules and time between planning and execution, drying of materials can be challenging.
Sintef byggforskserien 474.533 Uttørking og forebygging av byggfukt a sill as example for drying is made. For a sill 25 mm with natural one-sided drying from 28 to 18 weight percentage moisture in a building with 20°C and RH 60%. The drying time is estimated to be 21 days.

Developers have expressed their satisfaction when working with the sensors and digital platform, due to the ability to constantly monitor the moisture level. This leads to a higher sense of control with the moisture content of the construction materials.

4. CONTINUOUS ANALYSIS OF INCOMING DATA TO DETECT DAMAGES

4.1 WMC LEVELS IN DIFFERENT CONSTRUCTION PHASES

There are general thresholds of WMC values that are accepted in timber structures. These values vary based on whether the timber structures are exposed during construction or if they are enclosed and the building is in its maintenance period. Also, what measurements that are critical depends on the season and the local climate.

4.2 DURING CONSTRUCTION

The WMC can vary a lot during construction if the building is exposed to rain. Experts suggest that pools of water gets removed daily and that CLT shouldn't be above 20% for extended periods of time.
Many vendors of CLT put requirements for CLT to be enclosed at WMC levels below 12% to ensure no moisture is built in.

4.3 MAINTENANCE

In areas with high relative humidity, such as bathrooms and kitchens, the WMC of CLT elements should be kept below 20%. In other interior spaces with moderate humidity, such as living rooms and bedrooms, the WMC of CLT elements should be kept below 18%. In exterior wall and roof elements, the WMC should be kept below 16% to minimise the risk of decay due to exposure to the elements.

It is important to note that the WMC of timber can vary based on the ambient humidity and temperature conditions. In general, the WMC of timber will increase in humid environments and decrease in dry environments. This means that the WMC of timber may be higher in the summer months when relative humidity is typically higher, and lower in the winter months when relative humidity is typically lower.

Hence it is necessary to use an alarm system that takes into account all these parameters before it is possible to detect damages automatically without human supervision.

4.4 ANOMALY ALGORITHMS FOR DAMAGE DETECTION

Anomaly algorithms with multiple parameters have proven efficient to detect outliers in general data, but haven't been used before to detect damages in timber.

Anomaly algorithms work by forecasting a predicted value based on multiple parameters. On the Sophie Radich school Wood Moisture Content, Relative

https://doi.org/10.52202/069179-0503

Humidity, Temperature and local weather data were taken into account.

Table 1: *Ongoing measurements every 4 hours*

Measurement	**Location**
Wood Moisture Content (WMC)	In 20mm depth
Relative Humidity (RH)	From sensor at timber surface
Temperature	From sensor at timber surface
Precipitation, snow, outdoor humidity & outdoor temperature	From local weather station integrated into platform

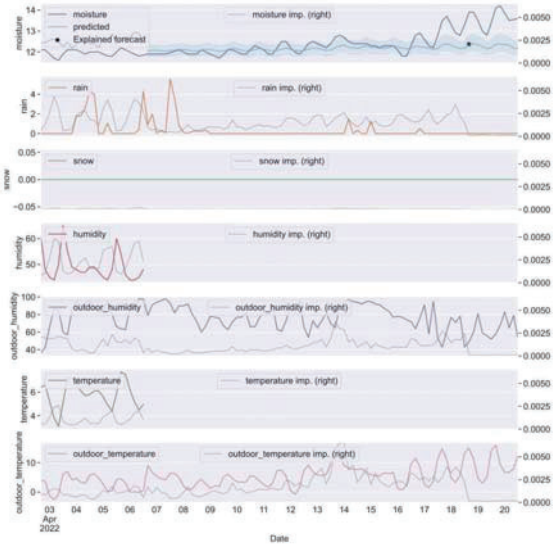

Figure 7: *Predicted value and the importance of supporting parameters in the prediction of that value.*

This result, when also taking into account the placement of the sensor, gives a strong indication when a sensor hits critical levels.

According to data from Woodsense, the WMC of CLT in roofs is the highest with a median value of 13.6 over an entire year, followed by slabs at 11.8 and external walls with 11.4.

4.5 TYPES OF ALARMS

In one of the selected areas, sensors were placed towards the edge of the roof, under rooflights, and on different facades to monitor the difference in north-, south-, east-, or west-facing facades. Additionally, a sensor was placed on a cornice to monitor the cover towards the edge. Here, the sensor found a mistake made by the roofer, as the covering had not been completed. This had resulted in water entering the construction and moisture levels rising to more than 30 %.

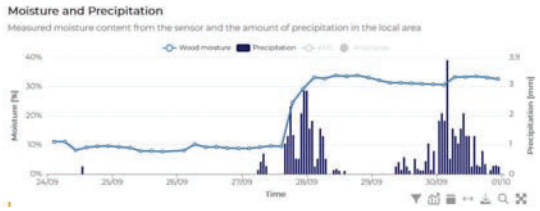

Figure 8*: Showing a rapid increase in WMC immediately after heavy precipitation.*

Had the sensor not detected the damage in the cornice, it could have led to a substantially more expensive repair, as the moisture could have been trapped in the construction for several months, potentially causing mould to establish. The same happened on a balcony where a temporary cover had been installed to protect the balcony from water damage. A sensor was installed beneath to monitor if the cover was efficient, but after just weeks of installation was the first water ingress found. This led to an immediate action to remove the water, dry the timber and improve the cover.
This exemplifies the advantages of sensor-based technology, as it is possible to capture situations such as these immediately.

Another sensor also detected a rise in wood moisture content, but a slower one over a 3 day period with ongoing rain. It is only normal to expect such an increase in WMC in the bottom of a facade element during construction when the building hasn't been enclosed, hence this did not trigger an alarm, but only led to a notification to the contractor.

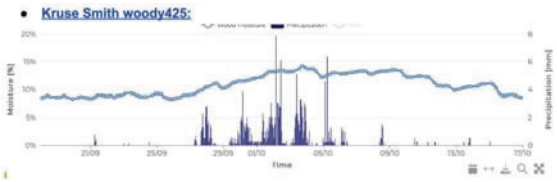

Figure 9**:** Showing the incremental moistening of a CLT slab due to continuous rain and increase in humidity, but not a leakage.

5. CONCLUSIONS

Using the sensor solution, several increases in moisture level were detected, which could have developed into more extensive moisture damage. The critical moisture levels found by the sensors exemplifies the advantages of sensor technology, as it is possible to immediately identify situations that can be damaging to the construction. Furthermore, developers and other participants of the project expressed their satisfaction with the product due to a higher sense of moisture control. Going forward, several sensors will remain on the roof to ensure that the green roof laid on top lasts as expected, and that the drains likewise work as intended.

https://doi.org/10.52202/069179-0503

Sensor technology can be used in most of the different building components. And the use of sensor technology should be more common in the future. To reduce the number of damages on terraces and similar components.

Further research can be done to investigate how different coating on the interior side of CLT, for example fire painting, affect the moisture storage in wood-based materials and the indoor climate. This can be done by using Woodsense sensor technology.

ACKNOWLEDGEMENT

The authors gratefully acknowledge the support of Kruse Smith and Lillestrøm municipality.

REFERENCES

[1] BREEAM-NOR v6.0.2016.
[2] Erlend Andenæs, Tore Kvande, Rolf André Bohne. 2020. “Footprints of failure: Quantifying carbon impacts of roof leakages in a single-family residential building Footprints of failure: Quantifying carbon impacts of roof leakages in a single-family residential building”
[3] N S Bunkholt, L Gullbrekken1, B Time, T Kvande. 2021. “Process induced building defects in Norway – development and climate risks”
[4] NS 3514 - Moisture safe construction - Planning and execution.
[5] NS 3512 - Measurement of moisture in timber structures.
[6] Norsk bygningsfysikkdag 2019, Wahlstrøm.
[7] Sintef Byggforsk 544.204 - Tekking med asfalt takbelegg eller takfolie. Detaljløsninger.
[8] Sintef Byggforsk 525.775 - Overlyselementer på kompakte tak.
[9] Tsunetsugu, Yuko, Yoshifumi Miyazaki, and Hiroshi Sato. 2007. “Physiological Effects in Humans Induced by the Visual Stimulation of Room Interiors with Different Wood Quantities.” Journal of Wood Science 53 (1): 11–16. https://doi.org/10.1007/s10086-006-0812-5.
[10] Rice, Jennifer, Robert Kozak, Michael Meitner, and David Cohen. 2007. “Appearance Wood Products and Psychological Well-Being.” Wood and Fiber Science 38 (January).

https://doi.org/10.52202/069179-0503

World Conference on Timber Engineering Oslo 2023

PRINTED SENSORS FOR MONITORING WOOD MOISTURE CONTENT INSIDE TIMBER BUILDING ELEMENTS

Boris Forsthuber[1], Michael Truskaller[2], Irene Spitaler[3], Pavel Kulha[4], Maximilian Scherf[5], Gabriel Partl[6], Albert Rössler[7], Gerhard Engelbrecht[8], Gerhard Grüll[9]

ABSTRACT: Moisture accumulation in wood constructions can lead to severe damage and premature construction failure. This is especially problematic for covered areas such as wet rooms (e.g. cross laminated timber (CLT) ceilings and covered dry walls), where moisture accumulation can occur without being noticed for a long time. The current paper describes the development and application of novel printed moisture sensors, that can be integrated directly into wooden construction elements, such as CLT or Glulam. This allows continuous *in-situ* monitoring of wood moisture content. A special wood primer was developed for the inkjet-printing process that is required to obtain high printing resolution and efficiency. The optimal sensor geometry on wood for highest measurement sensitivity was found by systematic variation of geometric details of the sensors and measuring conductance and impedance during a climate trial. The relative humidity was gradually increased while keeping the temperature constant within the chamber. After each step of moisture increase, impedance, phase angle and deduced variables at different voltages, currents and frequencies were measured. Furthermore, a proprietary measurement system was used. With the novel printed moisture sensors, it was possible to reliably monitor accumulation of moisture within CLT elements.

KEYWORDS: printed moisture sensor, moisture sensing, timber building, impedance measurements, capacitive moisture measurements

1 INTRODUCTION

Moisture accumulation can have severe consequences in wooden constructions. Short periods with higher moisture contents can be considered unproblematical, since wood destroying fungi need a wood moisture content at or above fiber saturation point (FSP) over longer time periods to grow. On the other hand, if the time of wetness is limited, the durability of the construction is usually not negatively affected [1]. It is therefore crucial to detect moisture entry into the construction as quickly as possible. According to Ott & Aondio [2], the design details of buildings play an important role here. For example, water penetration into a cross laminated timber ceiling is detected much later than on a beam ceiling. If drying of the wooden elements is restricted, moisture accumulation will enable fungal growth, leading to severe damage and premature construction failure. This is especially problematic for areas that are at least partially covered, such as CLT elements in wet rooms behind a dry wall.

Moisture accumulation can occur without detection for many years. When finally detected, costly renovation is inevitable. For that purpose, standards such as the ÖNORM B 2320 [3] require either at least two layers of bituminous sheeting with 8 mm thickness or an inspection port. Both can be avoided, if a moisture monitoring system is installed.

Several methods for measuring wood moisture content are available. While the gravimetric method gives by far the most accurate results, moisture monitoring on wood constructions is not possible as it is a destructive method. According to Dietsch et al. [4] requirements of a moisture monitoring system are as follows:

- The measurements must be taken without damaging the structure or taking samples
- The accuracy of the method should be consistent
- The system must be mountable on the structure itself
- Digital logging of the measurement results on different spots must be possible

[1] Boris Forsthuber, Holzforschung Austria, b.forsthuber@holzforschung.at
[2] Michael Truskaller, Holzforschung Austria, m.truskaller@holzforschung.at
[3] Irene Spitaler, Holzforschung Austria, i.spitaler@holzforschung.at
[4] Pavel Kulha, PROFACTOR GmbH, Austria, pavel.kulha@profactor.at
[5] Maximilian Scherf, PROFACTOR GmbH, Austria, maximilian.scherf@profactor.at
[6] Gabriel Partl, Adler-Werk Lackfabrik Johann Berghofer GmbH & Co KG, Austria, Gabriel.partl@adler-lacke.com
[7] Albert Rössler, Adler-Werk Lackfabrik Johann Berghofer GmbH & Co KG, Austria, albert.roessler@adler-lacke.com
[8] Gerhard Engelbrecht, tagtron GmbH, Austria, g.engelbrecht@tagtron.at
[9] Gerhard Grüll, Holzforschung Austria, g.gruell@holzforschung.at

https://doi.org/10.52202/069179-0504

- The timber moisture content should be measured and recorded in equal time intervals (e.g. one hour)

Generally, wood moisture content strongly affects the electrical properties of wood below the fibre saturation point [5]. Extractives which are not soluble in water are expected to decrease conductivity while the opposite is true for water soluble extractives [5,6].

The electrical resistance method fulfils all the requirements of a moisture monitoring system and is therefore available in many commercial systems [4]. However, electrodes must be placed inside the wood and is therefore destructive to a certain extent. Furthermore, the moisture measurements are locally restricted, as the moisture content is measured just between the two electrodes.

Aside from electrical resistance, capacitive moisture measurements of wood are also possible. Additionally, they do not need electrodes inside the wood and are therefore completely non-destructive. Measurements are taking place on the surface and an average wood moisture content near the surface (<35 mm) is measured [4]. Capacitive moisture measurements use the property that the dielectric constant of the wet wood increases with increasing moisture content, as the permittivity of water is higher than that of dry wood [7]. Since the relative permittivity of water ($\varepsilon_r \sim 80$) is many times higher than oven dry wood ($\varepsilon_r \sim 1.4$-4), capacitive techniques are well-suited for moisture measurements [7, 9]. Grain orientation is known to affect the dielectric properties of wood, where the complex dielectric constants are 20% to 50% higher in longitudinal direction compared to the direction perpendicular to the grain [7]. The dielectric constant of wood increases with increasing wood density [9]. Additionally, the dialectical properties of wood are affected by temperature and AC frequency [5, 10]. The higher the AC frequency of the measurement signal, the lower the dielectric constant [10]. However, it has to be noted, that the lower practical limit for most electrical meters is of the order of 6-8% and the highest limit is about 25% to 30% [11]. A low-cost capacitance sensor for wood moisture content was developed by Korkua and Sakphrom [12].

Another electrical method i.a. for wood moisture content is the measurement of the electrical impedance (Z). The impedance can be represented as a complex quantity with the resistance as real part and the (capacitive and inductive) reactance as imaginary part [6]. Since the impedance can be measured at several frequencies, this method is often described in the literature as electrical impedance spectroscopy (EIS) [6]. Impedance measurement was successfully used for evaluating the moisture content of sugi logs to monitor the drying process [13]. EIS was also used to determine wood decay [14].

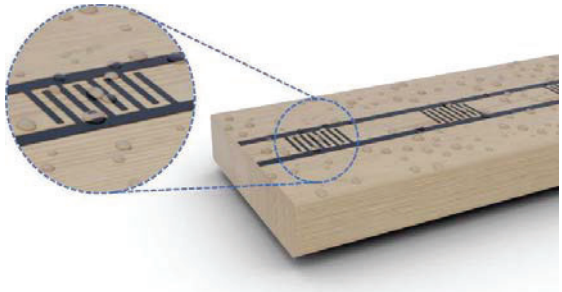

Figure 1: *Schematic of moisture sensors printed onto wood.*

The aim of the current study was the development of novel printed moisture sensors on wood. These sensors would allow *in-situ* monitoring of the moisture dynamics within construction elements such as CLT during use. In contrast to the resistance method, the printed sensors allow extensive area moisture monitoring, using an interdigitated electrode design (Figure 1). In terms of printing technology, digital inkjet printing offers many advantages over other printing techniques such as high throughput and flexibility of the printing pattern. Alternatively, screen printing was also investigated as a possible printing technique. In each case, carbon-based inks were used in order to not impose a problem for the recycling process after use of the construction elements.

2 MATERIAL AND METHODS

2.1 MATERIALS

For all printing trials, wood blocks measuring 150 mm x 75 x mm x 20 mm from Norway Spruce (*Picea abies, L.*), free from knots and with growth ring orientation of 5-45° (quarter-sawn) were used. All samples were planed and conditioned for at least one month in a climate room at 23°C and 50% RH to constant weight. Equilibrium wood moisture content was therefore at app. 9%.

For the inkjet printing process, a carbon-based Sicrys™ RI-6DM-3 ink with low viscosity (~3-5 cP) was used. For the dispensing and screen printing trials, a carbon-based Ink SE1502 from ACI materials with high viscosity was used. Screen printing was conducted using a commercial screen with mesh size 90T.

Two wood primers as pre-treatment for inkjet printing were investigated. The first primer was based on a highly viscous UV-curable putty "UV putty" for roller application. This variant was used with or without intermediate sanding. The second primer was based on a waterborne acrylic wood coating.

Wood primers were applied either by roller application (UV putty) or by spraying (water-borne coating). No primer was used for screen printing.

https://doi.org/10.52202/069179-0504

2.2 METHODS

For preliminary trials to obtain an optimal printing pattern, a dispensing printing process was used. The dispensing device was developed by Profactor GmbH and essentially consist of a motorized maneuverable platform with a controllable syringe head.
Inkjet printing was performed using a Süss LP50 printer with a KM512 print head from Konika Minolta. The cartridge temperature and the nozzle temperature were kept at room temperature.
Screen printing was performed manually without primer. Sintering for all samples was done at 120°C for 30 min in an oven.
Climate chamber tests were performed in a climate chamber SK40420 of Simtech (AT). The climates and corresponding equilibrium wood moisture contents are shown in Table 1. Each climate was kept constant, until the wood samples reached equilibrium. This was usually the case after 3 weeks. The samples were weighed at regular intervals, until the difference in mass was below a 0.3 g threshold, which was considered stable. After the end of the climate chamber tests, the samples were measured and weighted.

Table 1: *Climate settings and corresponding equilibrium wood moisture content (EMC) during the climate chamber test.*

Relative Humidity	Temperature	Corresponding EMC
50%	23°C	~9 %
71%	23°C	~13%
85%	23°C	~18%
93%	23°C	~22%
98%	23°C	~25%

Impedance and phase angle at different voltages, currents and frequencies were measured during the climate chamber test with an LCR measurement bridge, HM8118 from Rohde&Schwarz. For estimating the optimal printing pattern for maximizing sensitivity of the printed moisture sensors towards moisture uptake, a base pattern of interdigitated electrodes was varied systematically. The width, length and number of the strips were varied and regressed against the actual wood moisture content during the climate test. For the main tests, the optimized geometry was used and only the thickness of the ink-layer and the growth ring orientation were varied. Three samples for each variant were used.

3 RESULTS AND DISCUSSION

3.1 DEVELOPMENT OF INKJET-PRINTING PROCESS ON WOOD

For inkjet printing, inks with very low viscosity are required. Consequently, direct inkjet-printing on wood is not optimal, as a lot of ink is soaked into the wood. This significantly reduces efficiency, as the ink inside the wood hardly improves conductivity. Furthermore, the printing resolution is affected, as the ink gets transported, preferentially along the fibre direction, thus blurring the printing pattern. Therefore, several primers were investigated as suitable pre-treatment for the subsequent inkjet printing. Some of the pre-treatments were air drying while other systems were UV-curing.

Microscopic analysis revealed that the UV-primer with and without intermediate sanding led to interdiffusion of carbon ink particles into the coating which was reducing the conductivity (Figure 2). Better results were achieved with a water-borne primer where no visible interdiffusion occurred.

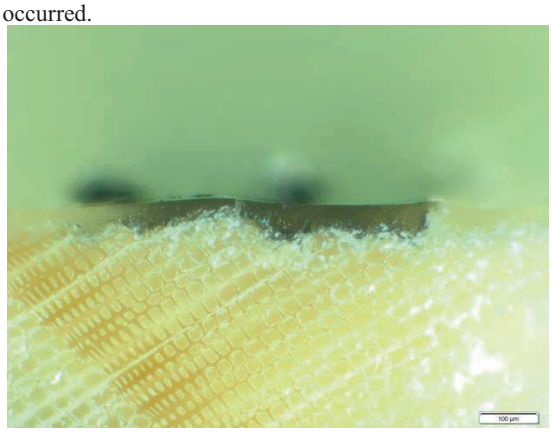

Figure 2: *Result of inkjet printing process on wood with UV-putty as primer; interdiffusion of ink into the coating. Cross section of spruce wood with clear primer and black printing under the microscope.*

The final results of the inkjet printing process, using the water-borne primer, revealed an interdigitated sensor pattern with very high resolution and sharp edges (Figure 3). The main advantage of the inkjet-printing process compared to other printing technologies is its high versatility and adaptivity. Hence, the printing pattern can be adjusted almost instantly and could be fine-tuned for optimal printing on the substrate almost in real-time. The downside of the inkjet process is the need for a primer, which inhibits direct contact between wood and printed sensors. This would be a major drawback for resistive sensors but not for capacitive sensors, as the primer can be seen as just another dielectric layer.

Figure 3: *Result of Inkjet printing process on wood with water-borne acrylic primer*

An alternative method used in this study is screen printing. Due to the higher viscosity of the screen printing ink, there is no need for a primer. This has the main advantage that the ink is in direct contact with the wood substrate, thus being able to measure the moisture directly without any layer in between. The printing quality of the printed electrodes is lower than those printed via inkjet (Figure 4), but still suitable for this purpose. The sharpness of the edges depends on the meshsize of the screen. Finer meshes (e.g. 90T or even 120T with 50µm/45µm mesh opening) allows printing of much finer details. However, the thickness of the ink-layers gets reduced, thus limiting the bulk conductivity. Nevertheless, the conductivity of the prints with meshsize 90T was still good enough for the intended purpose while the printing quality was high.

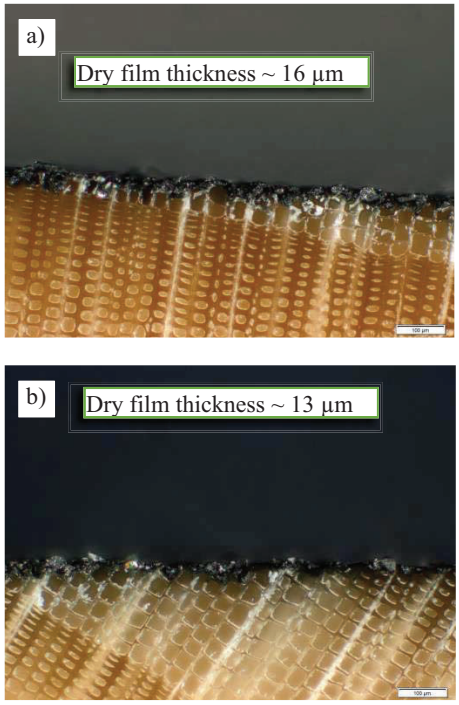

Figure 4: *Influence of screen printing meshsize on the dry film thickness of ink on wood; a) meshsize 43T; b) meshsize 90T.*

All inks needed sintering at elevated temperatures (120°C for 30 mins). Thus, wood moisture content had to be low (around 9%) before sintering to avoid cracking during the process. A systematic variation of the sintering times and temperatures revealed higher conductivity with higher sintering temperatures. Lower temperatures (100°C) for longer periods did not lead to the same conductivity.

3.2 OPTIMIZATION OF SENSOR GEOMETRY

The optimal sensor geometry for measuring the moisture content of wood was determined by a systematic variation of the sensor pattern from a base pattern of interdigitated electrodes. In this test, the number of electrode fingers, the distance between the fingers but also the thickness of the electrode fingers itself were varied systematically. During a test in the climate chamber, the response in terms of impedance and phase angle with increasing wood moisture content was measured.

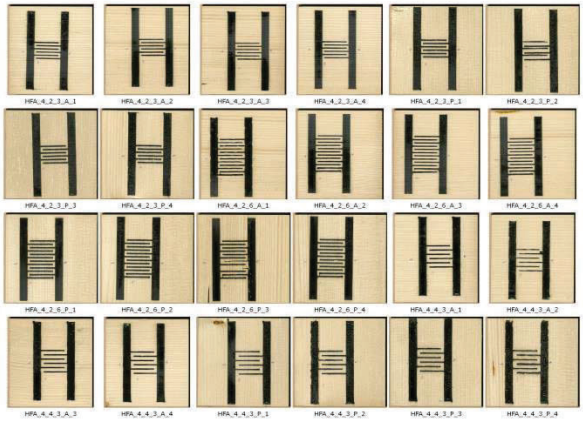

Figure 5: *Result of inkjet printing process on wood with UV-putty as primer; interdiffusion of ink into the coating. Cross section of spruce wood with clear primer and black printing under the microscope.*

The highest correlation of the measured impedance and phase angle to the actual wood moisture content was achieved with the pattern shown in Figure 6). The results revealed that the best correlation of the measured impedance with the increasing wood moisture content was with the highest sensor surface area and with the greatest number of interdigit probes.

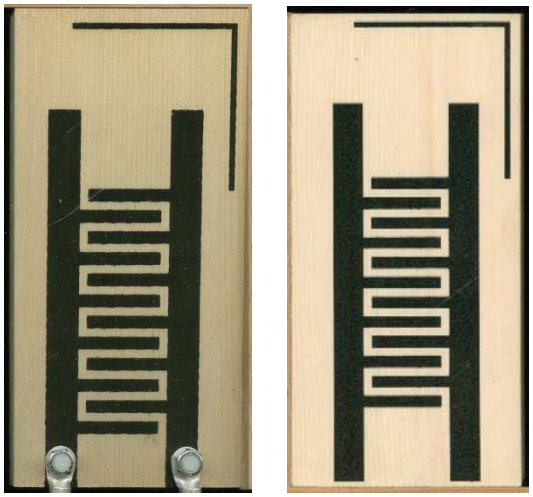

Figure 6: *Left: Screen printed moisture sensor: Right inkjet-printed moisture sensor. The optimal pattern was obtained from measurements during a climate test.*

https://doi.org/10.52202/069179-0504

3.3 CORRELATION BETWEEN ELECTRICAL SIGNALS AND WOOD MOISTURE CONTENT

For determining the relationship between the measured impedance and phase angle as well as derived values (e.g. capacity) with the wood moisture content, samples with the optimized sensor geometry were again subjected to tests in a climate chamber. Again, the moisture content within the chamber was increased gradually, until the equilibrium wood moisture content was reached. During this trial, the impedance and phase angle of the printed sensors were measured with different AC frequencies.

It was observed that the phase angle was frequency dependent and lower phase angles were seen with higher frequencies (Figure 7). This indicates lower capacitive reactance with lower frequencies compared to higher frequencies. This was expected, as the capacitive reactance decreases with increasing frequency and with increasing capacitance.

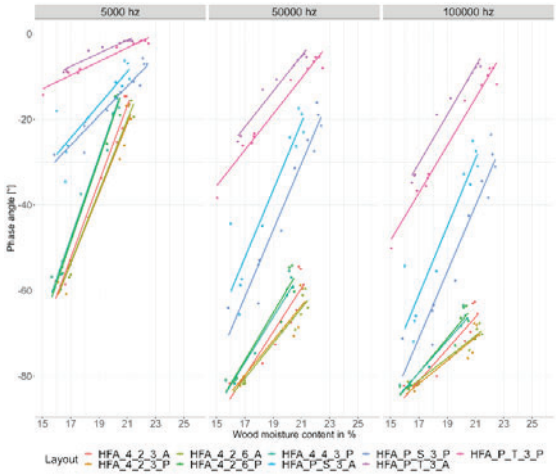

Figure 7: Phase angle vs. wood moisture content at different AC frequencies during a climate chamber test

In Figure 8, the impedance as function of the wood moisture content at different AC frequencies is shown. Generally, a strong correlation of the measured impedance with the wood moisture content was observed. Again, a clear influence of the measurement frequency was seen. The results revealed the highest regression coefficient/steepest slopes of the regression line with lower frequencies, e.g. 5000 Hz.

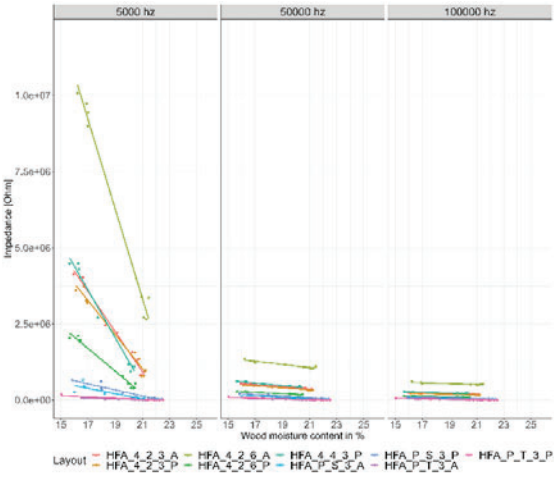

Figure 8: Impedance vs. wood moisture content at different frequencies during a climate chamber test

In figure 9, the influence of the voltage on the impedance for different wood moisture contents is shown. It is evident that the voltage does not seem to have a significant effect on the measurement result. Hence, the voltage was kept the same in later trials.

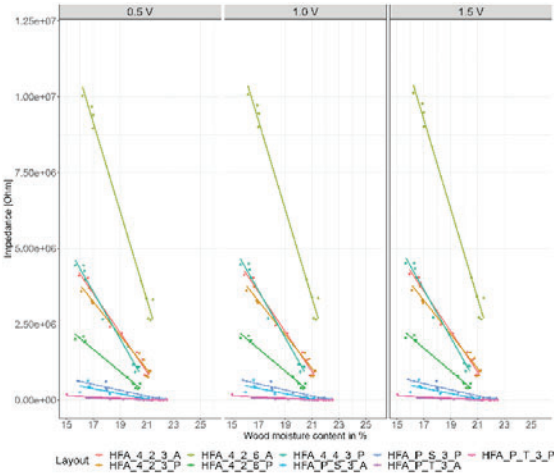

Figure 9 Impedance at different voltage levels vs. wood moisture content during a climate chamber test

The results reveal that the measured impedance at a frequency of 5000 Hz and a voltage of 1 V predicts the wood moisture content, with $R^2 = 0.94$, $F(1, 1155) = 2.03*10^4$, $p < 2.2*10^{-16}$.

It can be stated that the wood moisture can be monitored accurately with the printed moisture sensors. Since all the criteria mentioned by Dietsch et al. [4] for moisture monitoring systems are met, the developed method is highly suitable for monitoring the wood moisture content in timber constructions.

https://doi.org/10.52202/069179-0504

4 CONCLUSIONS

Two printing methods for conductive paths on wood were developed. Inkjet printing gave better printing quality but required a waterborne acrylic primer to achieve the desired printing quality. Screen printing was possible without primer and is therefore in direct contact with the wood surface.

The optimal printing pattern with highest sensitivity towards moisture accumulation during a climate chamber test was found. From the AC frequencies measured in these tests, a frequency of 5000 Hz showed the highest regression coefficients for predicting wood moisture content. As all requirements of a moisture monitoring systems are met, the developed method based on printed moisture sensors is highly suitable for monitoring the wood moisture content in timber constructions.

ACKNOWLEDGEMENT

The results presented in this paper are part of the research project ‘‘Mindwood’’. Financial support by the Austrian Research Promotion Agency (FFG) as well as companies and associations of the wood and coating industries is gratefully acknowledged.

REFERENCES

[1] Van Acker, J, et al.: Critical parameters on moisture dynamics in relation to time of wetness as factor in service life prediction. In: Proceedings of the IRG Annual Meeting, IRG/WP/14-20555, St. George, UT, USA. 2014. S. 11-15.

[2] Ott, S & Aondio, P.:Observations of Moisture Damages in Historic and Modern Wooden Constructions; XV DBMC; 15th International Conference on Durability of Building Materials and Components, 2020

[3] ÖNORM B 2330, 5 2022, Gebäude aus Holz - Technische Anforderungen. Austrian Standards

[4] Dietsch, P., Franke, S., Franke, B., Gamper, A., & Winter, S.: Methods to determine wood moisture content and their applicability in monitoring concepts. Journal of Civil Structural Health Monitoring, 5, 115-127, 2015

[5] Skaar C. (1988) Electrical Properties of Wood. In: Timell TE, Skaar C. (eds) Wood-Water Relations. Springer Berlin Heidelberg, Berlin, Heidelberg, pp 207–262, 1988

[6] Tiitta M, Kainulainen P, Harju AM, Venäläinen M, Manninen A-M, Vuorinen M, H.Viitanen H Comparing the Effect of Chemical and Physical Properties on Complex Electrical Impedance of Scots Pine Wood. Holzforschung 57(4):433–439. doi: 10.1515/HF.2003.064, 2003

[7] Oommen, B. A., & Philip, J.: Wood Moisture Content Measurement using planar Capacitive Sensors. In 2021 IEEE Second International Conference on Control, Measurement and Instrumentation (CMI), pp. 222-224, 2021

[8] Buschow K.H.J. Encyclopedia of materials. Science and technology / edited by K.H. Jürgen Buschow [et al.]. Elsevier, Amsterdam, London, 2002

[9] Fuchs A., Moser MJ, Zangl H, Bretterklieber T., 2001 Using Capacitive Sensing To Determine The Moisture Content Of Wood Pellets – Investigations And Application. Int. J. Smart Sens. Intell. Syst. 2(2):293–308. doi: 10.21307/ijssis-2017-352, 2017

[10] James, W. L.: Dielectric properties of wood and hardboard: variation with temperature, frequency, moisture content, and grain orientation (Vol. 245). Department of Agriculture, Forest Service, Forest Products Laboratory, 1975

[11] Tiitta M., Olkkonen H. Electrical impedance spectroscopy device for measurement of moisture gradients in wood. Review of Scientific Instruments 73(8):3093–3100. doi: 10.1063/1.1485783, 2002

[12] Korkua S.K., Sakphrom S. Low-cost capacitive sensor for detecting palm-wood moisture content in real-time. Heliyon 6(8):e04555. doi: 10.1016/j.heliyon.2020.e04555, 2020

[13] Suzuki Y, Ikeda K, Miyoshi Y, Fujimoto K, Sugiyama A Evaluation of Moisture Content of Sugi Logs Using Impedance Measurement. In: 2018 12th International Conference on Electromagnetic Wave Interaction with Water and Moist Substances (ISEMA). IEEE, pp 1–3, 2018

[14] Tiitta, M., Repo, T., & Viitanen, H. (2001). Effect of soft rot and bacteria on electrical impedance of wood at low moisture content. *Material und Organismen*, *33*(4), 271-287.

https://doi.org/10.52202/069179-0504

World Conference on Timber Engineering Oslo 2023

MOISTURE AND TIGHTNESS MONITORING WITH DIFFERENT MEASURING SYSTEMS AND METHODS - EXAMPLE APARTMENT BUILDING

Anton Kraler[1], Andreas Pomaroli[2]

ABSTRACT: Moisture monitoring is becoming an increasingly relevant technique to ensure that buildings remain in good quality. Building with wood, whether it is for family homes or mid-rise buildings, is more popular than ever. Rising prices, high-quality requirements and calls for swift construction completion are impacting contemporary modern architecture. These changes are far-reaching: after all, simple, straight structures offer enormous advantages in terms of systemisation, prefabrication and the mounting of buildings. Consequently, there has been a visible change from sloping roofs to flat roofs. In addition, even storey levels offer further advantages: compliance with distance regulations to neighbouring properties is facilitated. These areas can partly be used as terraces, gardens, and also for the installation of building service equipment (heat pumps, ventilation equipment, etc.). Concerning moisture issues, natural building materials must be handled with great care in order to ensure the durability of a building structure. Despite great craftsmanship in the construction of buildings, unforeseeable problems due to moisture penetration occur time and again. To counter such issues, a range of moisture and tightness monitoring systems have come onto the market in recent years. How do they work, which system is best suited for which monitoring purpose? Which dangers arise from installing additional structures? With the support of the Province of South Tyrol/Italy and the company Ligna Construct for this research project, it can be shown how important monitoring systems can be. The measurement results of the three installed monitoring systems show that already in the construction phase, but also in the later use phase, a high degree of safety is given with regard to moisture penetration and water ingress.

KEYWORDS: Moisture monitoring, area sensors, point sensors, wood moisture measurement, timber construction, flat roof, terraces

1 INTRODUCTION

Research institutions and companies have been working on the topic of moisture and tightness monitoring for years. The aim is to bring systems to the market for monitoring moisture and tightness in the sealing and insulation level, in addition to material moisture in order to increase moisture protection in wood buildings. In this research work, three quality-assuring active monitoring systems are presented, with which moisture-prone building components can be monitored. Components at risk of moisture penetration are e.g. roof and terrace sealings, insulation layers in warm roofs as well as the supporting wooden structures located under the sealing levels. Furthermore, measurement monitoring of water-bearing installations in floor and wall constructions is an important aspect. Active measurement monitoring involves monitoring with automated evaluation and alarming systems in case a defined threshold value is exceeded. Questions that arise in the context of leakage and material moisture monitoring are: How do active moisture monitoring systems work? Which systems are best suited for which monitoring tasks? Which risks arise from installing measuring systems? In order to provide answers to these and other questions, three active monitoring measurement systems were used in an apartment building. This research project, with a two-year time frame, was developed in cooperation with the timber construction company Ligna Construct from St. Pankraz in South Tyrol/Italy and with the financial support from the Province of Bolzano/Italy. The official research project ended in September 2022. The monitoring by means of the three measuring systems will be continued for the time being in order to obtain long-term data about the moisture behaviour in the specified areas.

2 PROJECT DESCRIPTION

The apartment building is a newly constructed three-storey building with five residential units, a garage in the basement and an adjacent existing single-storey building with a green roof. The two upper floors and parts of the floor slab on the ground floor were built in cross-laminated timber. Due to the multiple levels (flat roof, terraces, balcony, etc.) as well as changing materials (reinforced concrete, cross laminated timber, bitumen sheeting and plastic waterproofing) and the exposed location, this building is particularly well suited for

[1] Anton Kraler, University of Innsbruck – Unit for Timber Engineering, Austria, anton.kraler@uibk.ac.at
[2] Andreas Pomaroli, University of Innsbruck – Unit for Timber Engineering, Austria, andreas.pomaroli@uibk.ac.at

https://doi.org/10.52202/069179-0505

investigations of this kind. Planning and investigations began in September 2020.

Figure 1: *Investigated Apartment Building*

The first step is to determine which and how many measuring systems are to be used in and on the building. When determining the number of systems, special attention is paid to monitoring those areas of the building where there is a higher risk of moisture or water ingress. The number and types of measuring systems used are to be installed in such a way that leakage and moisture monitoring is provided for all flat or slightly sloping external surfaces such as roofs, terraces and greened areas. Furthermore, it is important that the measurement results of the installed monitoring systems can be compared with each other. The aim has been to obtain as many results and findings as possible for future timber buildings. In consultation with the timber construction company Ligna Construct, the following three moisture monitoring systems were used:

- Measurement of wood moisture content
- Measurement with area sensors
- Measurement with point sensors

Before installing the moisture and leakage monitoring systems, detailed installation plans are drawn up for all three measuring systems. They are discussed with the project partner on site and checked for completeness. All three measuring systems are equipped with a remote monitoring modem so that monitoring and reading data are accessible at any time.

2.1 MEASUREMENT OF WOOD MOISTURE CONTENT

The electrical resistance measuring method of the company Scanntronik Mugrauer GmbH is used to monitor wood moisture. Electrodes in the shape of stainless-steel screws of different lengths are mounted to measure the wood moisture distribution. The screw shaft is insulated with a shrink sleeve so that the moisture is only measured at the tip of the screw. This makes it possible to measure the wood moisture specifically at different depths of the wood. The distance between the electrodes is 30 mm. The measuring electrodes are connected to the material moisture meter with shielded coaxial cable, which may have a maximum length of 15 metres. Up to eight measuring points can be monitored with one device and, depending on the pre-setting, forwarded to a data logger and stored every second, minute or hour. Furthermore, it is possible to record the temperature (e.g. wood, air) and the relative humidity via a data logger in combination with a sensor unit. The measured values stored with the data logger can be received by e-mail. If there is a power connection to the measuring systems the data can be accessed via telephone. Otherwise a specified time interval is set and the data are sent via email. The output value of the wood moisture is provided in percent or in ohm. In addition, the temperature in the wood and the relative humidity in the interior of the building were recorded.

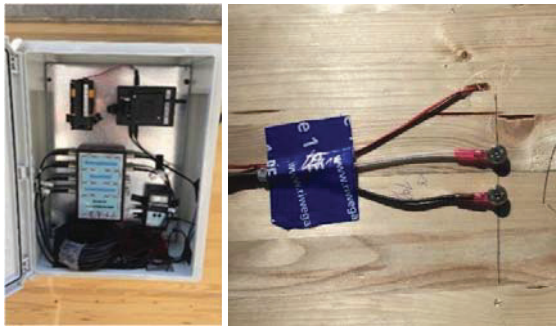

Figure 2: *The wood moisture measurement equipment, left data storage, transmission modem, right moisture sensors (below) and temperature sensor (above)*

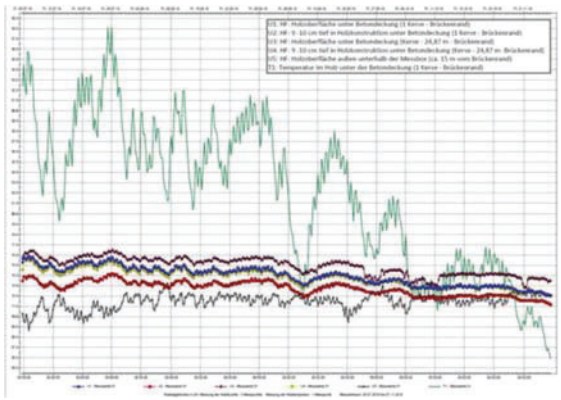

Figure 3: *Wood moisture data*

2.2 MEASUREMENT WITH AREA SENSORS

The Optidry® Monitoring System (OMS) is an active building monitoring and warning system for the early detection of hidden water damage. The area sensors are installed on the diffusion-inhibiting or vapour-blocking (warm roof) level as the flat roof covering is attached. Before installing the area sensors, the roof is divided into different zones (edges, main area, risky spots). Installation is straight forward and it depends on the waterproofing membrane used (bitumen, plastic, raw ceiling), whether the area sensors need to be glued or nailed. Up to eight

https://doi.org/10.52202/069179-0505

independent monitoring areas (area sensor units) can be connected via a bus system and the data saved in a control centre. If the specified upper humidity limit, gauged in digits, is exceeded, an alarm is triggered by the central unit and forwarded to the customer. The current moisture status at the sealing level can be accessed and evaluated directly on a smartphone, tablet or PC using the OMS Inspector app. Water ingress can thus be detected at an early stage and localised. In addition to flat roofs and terraces, the system is also used in wet rooms from service class W3. The Optidry Monitoring System can be integrated into smart-home systems or into the building technology equipment.

Figure 4: *Area sensor measurement*

The belt or area sensors are approx. 5 cm wide fabric strips containing two stainless steel wires. The moisture content in digits is determined via the resistance between the two wires.

Figure 5: *Area sensor measurement*

2.3 MEASUREMENT WITH POINT SENSORS

The system used, the RPM ROOF PROTECTOR, is a simple and efficient device to immediately detect moisture in roof structures and to take timely action. Indicators evenly laid out over the roof surface measure the moisture and temperature. This allows gaining insight into the moisture condition of a roof package (insulation package). The measuring system can be applied to all commercially available roof layers (waterproofing, insulation, etc.). The system also fulfils the additional measure required in ÖNORM B 3691 for the monitoring of flat roofs of use category 3. The recorded measurement data are stored on a central server of RPM Gebäude Monitoring GmbH and can be retrieved permanently and at any time via a web browser. The measuring sensor is located in the warm roof structure just above the sealing membrane (vapour barrier). In addition to measuring the humidity, which is indicated in digits, the temperature is also measured in the area of the vapour barrier and on the outside at the surface of the roof structure. The sensor is usually installed after the top waterproofing layer has been laid. The insulation material in the warm roof structure is drilled out with a so-called box drill, which has the same diameter as the point sensor, and the fully insulated point sensor is inserted there. The system used is battery-powered and is therefore self-sufficient and can be used wherever there is a radio contact for data transmission. The system measures the humidity and temperature in the insulation level and also on the sealing level of the raw ceiling.

Figure 6: *Point sensor measurement*

Figure 7: *Point sensor measurement*

3 INSTALLATION OF THE MEASURING SYSTEMS

The measuring systems are installed on three levels of the apartment building: on the flat roof (humidity measurement, area sensors, point sensor), on the first floor (area sensors) and on the ground floor (area sensors, point sensor). Area sensors are also installed in the six bathrooms. In this paper, however, only the measurement systems in the outdoor area are dealt with.

3.1 MEASURING SENSORS ON THE FLAT ROOF

Figures 8, 9 and 10 show the floor plan of the flat roof with the arrangement of the measuring circuits and measuring points. To provide a better overview, the related systems and measuring areas are shown individually in the floor plans.

https://doi.org/10.52202/069179-0505

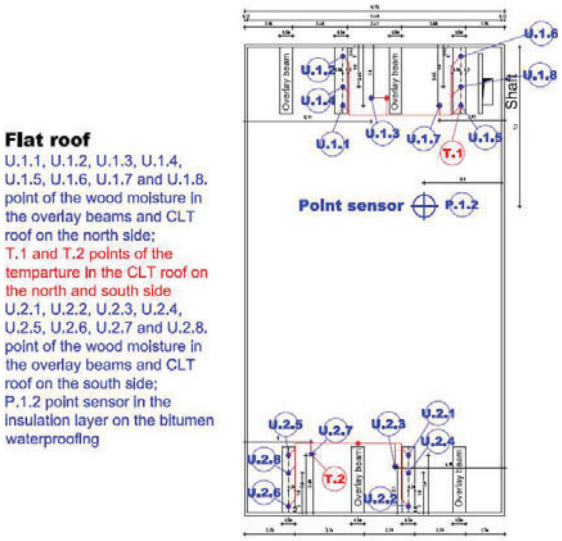

Figure 8: *One point sensor and 16 measuring points of the wood moisture and temperature measurement.*

The first flat roof plan shows the measuring points for the wood moisture measurement, of which eight measuring points each (label U) were installed on the south and north sides of the roof. The two temperature sensors used are marked T in red. The point sensor is also shown on this flat roof plan. The position was placed slightly outside the centre of the roof surface, in the north-east area. The reason is that the roof slopes to the east (water drainage) and an installation shaft penetrates the roof in the northeast. Thus, this area is considered to be the most vulnerable in terms of possible leaks.

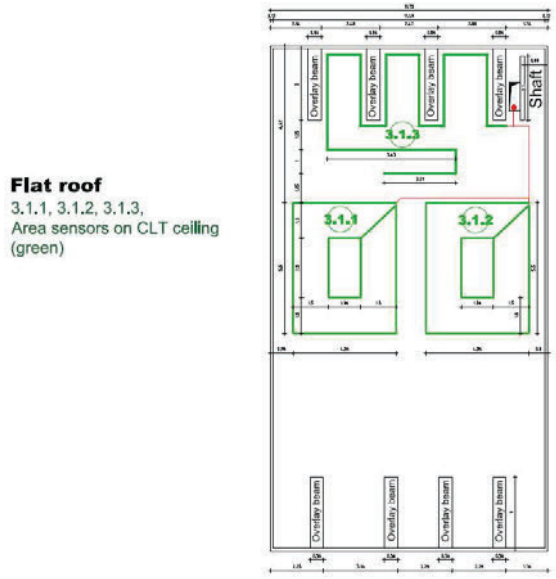

Figure 9: *Three area sensors on the solid wooden roof*

This flat roof plan shows three measuring circuits with area sensors mounted directly on the solid wooden roof. This arrangement was chosen because the deflection is greatest in the central area of the roof surface, i.e. in the event of water ingress, this area is likely to be the first to suffer moisture penetration. The measuring circuit on the north side was laid close to the statically required overlay beams. These beams have only a small amount of insulation on the above surface, i.e. the risk of condensation at low outside temperatures below the waterproofing layer is very high. Therefore, it should be monitored whether this minimal insulation also impacts the moisture situation on the surface of the supporting structure (cross-laminated timber) screwed to the overlays.

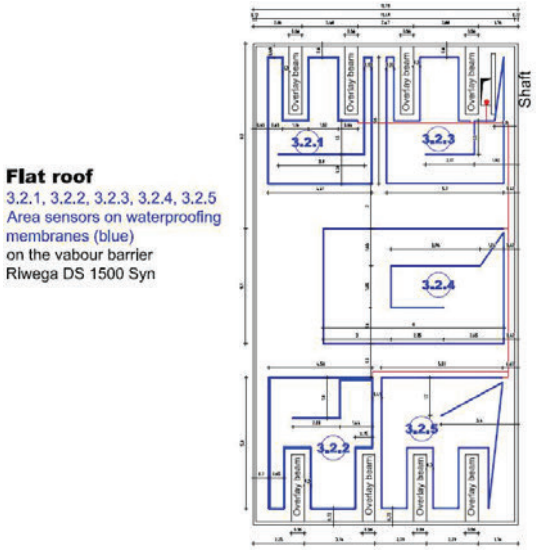

Figure 10: *Five area sensors on the waterproofing membranes*

This flat roof plan shows five measuring circuits with area sensors on the first sealing level (vapour barrier). The arrangement was chosen due to the roof pitch (towards the east) and to be able to monitor the entire roof surface for moisture.

3.2 MEASUREMENT SENSORS ON THE 1st FLOOR

On the 1st floor, area sensors were installed on the terraces and in the sanitation facilities. Three measuring circuits were attached to a bitumen seal on the terrace (west side) above the living space below. Further measuring circuits (shown in green) were installed in the three sanitation rooms directly on the raw ceiling made of cross-laminated timber. On the north side there is a roof-covered terrace with a passageway below. The measuring circuit was attached to the bitumen seal. This spot is interesting, because the temperature differences in this part of the building are significantly lower and due to the north-facing orientation little solar radiation can be expected in

https://doi.org/10.52202/069179-0505

the winter months. The investigation aim at this floor level is also to monitor the overall humidity and tightness. Furthermore, the monitoring should also provide information about the influence of the different thermal conditions.

Figure 11: *First floor - area sensors on bitumen (blue) - sanitation areas sensors on solid wood (green)*

3.3 MEASUREMENT SENSORS ON THE GROUND FLOOR

On the ground floor, the three sanitation rooms were also equipped with area sensors. The sensors were mounted on a reinforced concrete ceiling in the two bathrooms on the north side and on a cross-laminated timber ceiling in the bathroom on the south side. The area sensors in the outdoor area were arranged in such a way that they again enable extensive monitoring of the main building. The measuring circuits 1.2.2, 1.2.3 and 1.2.4 are mounted on the first bitumen sealing layer. Measuring circuits 1.2.2 and 1.2.4 are located above a roof-covered entrance and on a cantilevered balcony. In measuring circuit 1.2.3, the area sensors are partly installed above the living area and partly in the cantilevered area of the storey ceiling. The raw ceiling of these three measuring circuits is made of cross laminated timber. Measuring circuit 1.1.1 was laid directly on the reinforced concrete ceiling. The underground car park is located below this measuring circuit. Measuring circuit 1.2.1 was laid on a plastic membrane (vapour barrier) on the existing single-storey building. Originally, inside this building there was a swimming pool. At the time the measurement sensors were specified, it had not yet been decided whether the swimming pool would be put back into operation or whether it would be used as a fitness room. In addition to the flat roof sensor, another point sensor was installed on the west side of the newly built warm roof on the west side of the single-storey existing building. The position was chosen because this area of the green roof surface is usually without sun in winter due to the terrain formation.

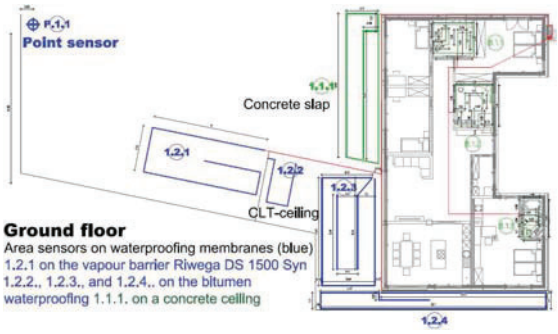

Figure 12: *Ground floor - area sensors on waterproofing membranes (blue) - on the raw ceilings (reinforced concrete; green), point sensor - single-storey existing building*

4 RESULTS FROM MOISTURE AND TIGHTNESS MONITORING

The diagrams and measurement results show an overview of the measurement process up until January 2023. It should be mentioned that due to the lockdowns that occurred during the investigation period, construction completion and therefore the commissioning of the measurement systems and the moving-in was delayed by approximately one year. From September 2021 to January 2022, there was partly no data transmission because the internet connection at the location of the building was inadequate and the installation of the fibre optic cables was delayed by several months. Therefore, there are no consistent area sensor measurement results for this period. The winter of 2022 to 2023 was the first season the premises were lived in. Thus, no meaningful results are yet available regarding the moisture behaviour in the sanitation rooms, on the roof and on the terraces. This means that it is not yet possible to answer the question whether in addition to the mere tightness monitoring of the waterproofing membranes, the habitation and use of the rooms, because of differing temperatures and relative humidity values, has an effect on the moisture conditions in the areas monitored.
The recordings to date show clear differences in humidity between summer and winter. The following diagrams give an overview of the measurement period and feature special conditions.

4.1 MATERIAL MOISTURE MEASUREMENT

The measurement diagram from the south side of the flat roof (Fig. 13) shows the wood moisture content of the eight measurement points (U 2.1 - U 2.8) as well as the temperature curve in the wood (T 2.1) and in the living room area of the first floor (T 2.3) where the data logger is located. The Y-axis of the diagram shows the temperature and wood moisture and the X-axis depicts the time progression. All other diagrams have the same

structure. The measuring system was put into operation on 08 April 2021. The measurement data in the diagram show the course of the wood moisture from the time of commissioning until 31January 2023. The course of the wood moisture lies in the normal range between approx. 8% and 15%. The differences in the wood moisture content can be explained by the different depths of the inserted measuring electrodes. At measuring point U 2.6, a steady increase in the wood moisture content of up to 15% can be seen from May 2021 to the beginning of October 2021, before it drops again in the winter months. At low temperatures, it is noticeable that the measuring system repeatedly experiences disturbances in data storage, as can be seen at measuring point U 2.7 from mid-December 2021 to mid-February 2022. The measured values have a high fluctuation range due to the temperature changes. It is also noticeable that in the winter months the temperature in the cross-laminated timber drops below 10°C, i.e. into the dew point range, despite the external insulation.

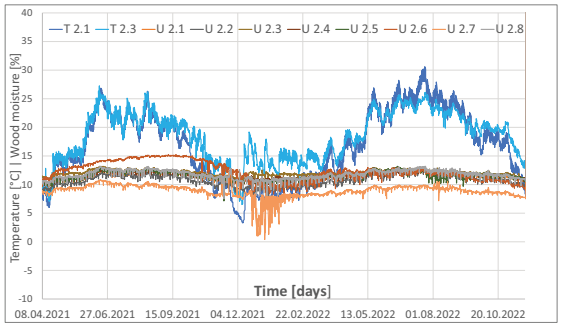

Figure 13: *Flat roof (south side) - wood moisture measurement U 2.1 - U 2.8; temperature in cross laminated timber - T 2.1; temperature interior 1st floor - T 2.3;*

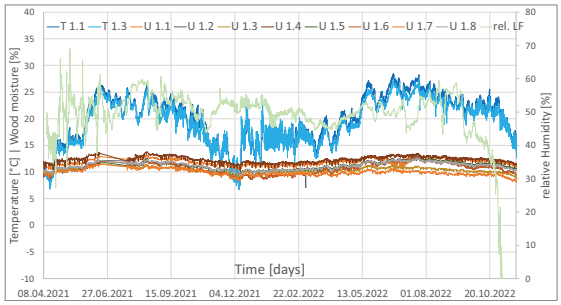

Figure 14: *Flat roof (north side) - wood moisture measurement U 1.1 - U 1.8; temperature in cross laminated timber - T 1.1; temperature and relative humidity in interior 1st floor - T 1.3 and relative humidity;*

The measurement period on the north side of the flat roof is the same as described for the south side (Fig.14). The wood moisture content is very even and inconspicuous over the entire measurement period. It can be seen, however, that the wood moisture content decreases somewhat over the course of time shown (April 2021 to November 2022). This also corresponds in principle to the behaviour of wood: The material becomes drier when professionally installed under the typical living room climate of 22°C and approx. 40 % relative humidity in the heated and occupied interior. In contrast to the south side, to check the indoor climate, the relative humidity in the interior of the 1st floor is also measured at this measuring station. In the period from 16-06-2021 to 15-08-2021, there was an interruption in the measurement recordings, because a cable was unintentionally detached from this measuring device during construction work.

4.2 AREA SENSORS

Not all area sensors on the flat roof, on the 1st floor and on the ground floor could be installed and commissioned at the same time due to the construction progress. This explains why for some measuring circuits the basic voltage is 120 digits. During commissioning, a steep increase in humidity can be seen in some cases, as in the case of measuring circuit 1.2.1 in Fig. 17. In each of the three diagrams (Fig. 15-17) it can be seen that there is one or more measuring circuits at each monitored floor level where there is already a high moisture content at the sealing level from the start. The reason for this is that water ingress occurred during the installation of the roof superstructures due to rain and snowfall and therefore the specified limit range of 11500 digits (laid on waterproofing membranes) was exceeded in some cases. Furthermore, it should be mentioned that there was no network connection from mid-September 2021 to the end of January 2022 and therefore no online access was available. However, it can be seen that the moisture content in the building components became significantly lower over the winter months. In spring, from around mid-March 2022, the moisture content on the waterproofing membranes (vapour barriers) begins to rise again. However, the increase is significantly lower than in the first year of monitoring in 2021. In the autumn months from September 2022 onwards, a clear reduction in moisture on the waterproofing layer is again evident. With the increase in outdoor temperatures, the moisture content on the sealing levels also increases in February 2023. In the coming months and years, monitoring will show which level the moisture content will adjust to over the course of the year (summer, winter). The measuring circuit 1.2.1 in Fig. 17 should be mentioned separately, as it shows a moisture behaviour that is not yet comprehensible. From about April 2022, there is a strong increase in humidity to about 10000 digits. This remains almost constant until the beginning of November 2022, after which the moisture content of this measuring circuit drops to approx. 1000 digits within 2.5 months. Measuring circuit 1.2.1 will therefore be monitored in particular over the next few months to find out whether the increase in humidity is possibly related to leaks in the upper sealing level. If the strong moisture fluctuations continue, the sealing level in the area of this measuring circuit will be opened, dried and resealed

https://doi.org/10.52202/069179-0505

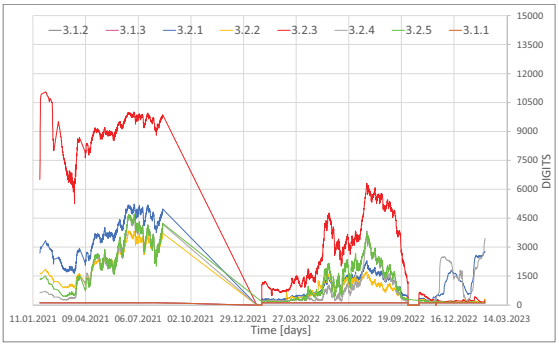

Figure 15: *Flat roof area sensors 3.1.1 - 3.1.3 on the cross laminated timber ceiling; area sensors 3.2.1 - 3.2.5 on the first sealing level (vapour barrier - plastic sheeting)*

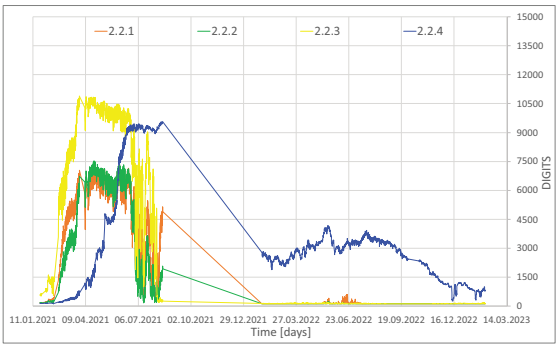

Figure 16: *First floor - area sensors 2.2.1 - 2.2.4 mounted on bitumen sheeting*

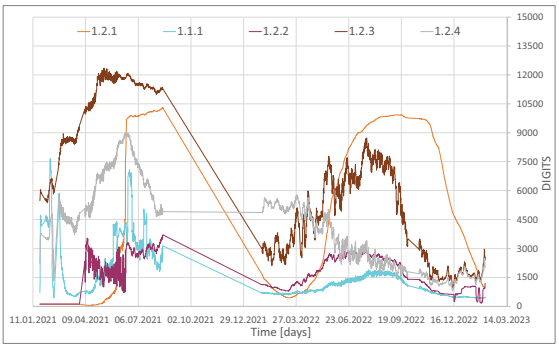

Figure 17: *Ground floor - area sensors 1.1.1 mounted on reinforced concrete ceiling; 1.2.1 - 1.2.3 mounted on bitumen sheeting; 1.2.4 mounted on plastic sheeting - vapour barrier*

4.3 POINT SENSORS

The point sensor on flat roof 1.2 (Fig. 18) is installed near measuring circuit 3.2.3 (area sensor). In the area of this measuring circuit, moisture penetration occurred when sealing the top sealing level. The increased moisture content is also indicated by the point sensor. At the end of January 2022, however, a very rapid drop in moisture occurred within a few days. This means that there must have been a strong drying process within this short time in the insulation level and on the sealing level. If we look at the moisture curve one year later, in February 2023, there is again a sudden sharp drop in moisture. This time, however, it is already in November. In December 2022, there is a brief intensive rise followed by a sharp drop in the measurement curve. The moisture behaviour in the insulation level is difficult to interpret using the point sensor as the measurement period is still relatively short. Questions as to how these very rapid increases in humidity and drying phases can occur still need to be investigated in detail. For point sensor 1.1 (on the green roof of the single-storey existing building), no changes in moisture or conspicuous moisture occurrences can be detected in the first year of monitoring. From June 2022 to mid-October 2022, there is a slight increase in moisture of up to 20 digits. Compared to the area sensors, the limit value for liquid water for the point sensors is 80 digits. Therefore, the value of 20 digits is considered a dry component. However, the reason for this slight increase in moisture has yet to be determined. One reason could be that the measuring device is subject to fluctuations. Otherwise, no other abnormalities can be detected in the insulation level of the green roof.

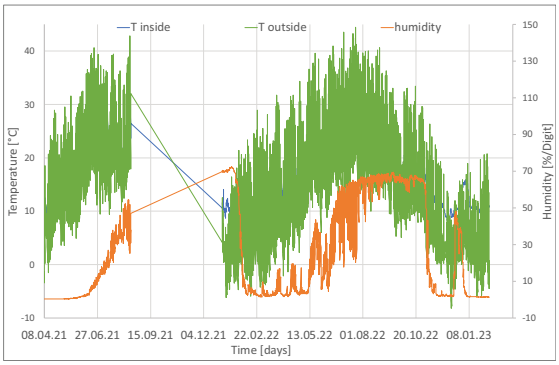

Figure 18: *Point sensor 1.2. on the flat roof*

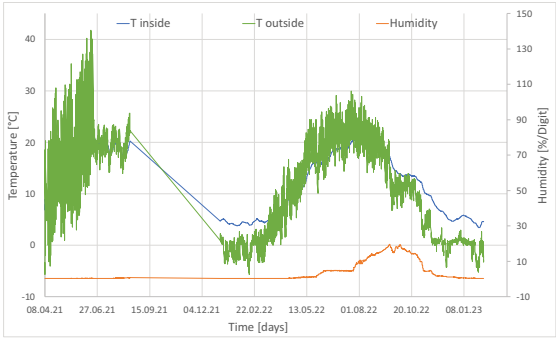

Figure 19: *Point sensor 1.1 on the green roof surface of the existing single-storey building*

5 CONCLUSIONS

The research results so far are as follows: The planning, installation and commissioning of the measuring systems

could be carried out without difficulties. Immediately after commissioning the measurement technology, leakages at the sealing levels could be detected and immediately repaired. Therefore, the positive effect of moisture and tightness monitoring systems was already evident during the construction phase. The interpretation and comparison of the measured values is still somewhat complex due to the different scaling units (percent, digits) of the measuring devices. Depending on the system or materials used (waterproofing, wood, concrete, etc.), the scaling of the measured values also changes.

The wood moisture is expressed in percentage points, the limit value, which must not be exceeded, is at a maximum of 20% wood moisture. Higher values lead to insect and fungal attack and thus to the destruction of the supporting wooden structure.

The moisture content of area and point sensors is displayed in digits. However, in different orders of magnitude. For the point sensors, the measuring range is between 0 and 150 digits. This measuring range is also known for determining the moisture on concrete surfaces. The limit value that should not be exceeded is approx. 80 digits. If the values are higher, there is increased moisture in the building material.

With the surface sensors, the measuring range is higher by a factor of 100. A distinction must be made here as to whether the sensors are installed on the raw material (wood, reinforced concrete) or on a sealing membrane (bitumen, plastic sealing). The measuring range starts at 120 digits and goes up to 15000 digits. The limit value with regard to increased moisture status is 11500 digits for waterproofing membranes and 3500 digits for installation on the raw material. The lower value for the raw material can be explained by the fact that the material can already absorb moisture and therefore a low moisture content, measured on the surface, is already sufficient to have increased building material moisture in the component. This is not the case with waterproofing membranes, as the material cannot absorb moisture.

Therefore, the use and installation of moisture and leakage monitoring systems requires precise documentation and recording of the measuring results and on which materials the measuring sensors are laid or installed in order to be able to carry out a professionally viable moisture assessment.

Of the five residential units in the apartment building, the first flat on the ground floor was occupied in autumn 2021. The remaining four flats were occupied in spring 2022. These four flats are rental flats or holiday homes. This means that they are not occupied throughout the entire year. At the time of the evaluation, the building has only been occupied for approximately one year. More precise interpretations and statements about the measurement results are usually only possible after three to five years of monitoring. Therefore, the monitoring will be continued in the coming years.

Based on the state of the investigation so far, the following can be stated:

- The planning, installation and commissioning of the measurement systems was simple and straight forward.
- Shortly after commissioning the area sensors, leakages in the sealing due to increased moisture could be detected. The quick repair of the defects in the sealing prevented future moisture damage.
- The interpretation of the measured values is still somewhat challenging due to the different scaling of the measuring devices and scarce empirical values. In addition, the limit values (area sensors) change when used on different materials. Therefore, accurate and complete documentation is essential during planning, installation and monitoring.
- At the beginning of the monitoring, the moisture values for some measuring circuits (area sensors) were in the limit range during the summer months resulting from increased component moisture. Therefore, it is not clear whether the moisture content is reduced or evened out over the year or whether the top sealing level should be opened in order to start drying measures.
- Due to the fact that the entire building has only been occupied for one year, results from the sanitary areas as well as the measuring circuits on the flat roof, which were laid on the cross laminated timber elements, are still missing as to what effects this has on the moisture content in the solid wood elements.
- The results so far show that, especially for the area and point sensors, several years of recordings and experience are needed in order to better assess the aforementioned challenges regarding to the evaluation of the results.

ACKNOWLEDGEMENT

This research project is financially supported by funds from the Province of South Tyrol for Consulting and Service Innovation and by the timber construction company Ligna Construct.

We would like to thank them for their willingness to support this project. For the timber construction sector, this is another important contribution to the quality and durability of timber buildings.

REFERENCES

[1] IFB; Richtlinie: Dichtheits- und Feuchtemonitoring; Ausgabe 1/2018].
[2] ÖNORM B 3691: Planung und Ausführung von Dachabdichtungen, Wien 2019
[3] ÖNORM B 3692: Planung und Ausführung von Bauwerksabdichtungen, Wien 2014
[4] https://www.optidry.at/de/; 25.03.2022
[5] https://www.scanntronik.de/; 25.03.2022
[6] https://www.gebaeudemonitoring.at/; 25.03.2022

https://doi.org/10.52202/069179-0505

World Conference on Timber Engineering Oslo 2023

A PROMISING APPROACH OF LINEAR TIMBER STRUCTURAL HEALTH MONITORING

Johannes Koch[1], Martin Ganß[2], Martin Kästner[3], Antje Simon[4]

ABSTRACT: Structural monitoring of timber bridges includes the moisture monitoring as well as strain and crack monitoring of critical parts, especially when considering new construction methods. Currently, single-point sensors are used for moisture monitoring on timber bridges. However, the parts of the structural components which are not being measured may be moist. The lack of monitoring can result in wet areas not being detected. This could result in major damage, e.g. due to fungal decay. A higher degree of protection can be achieved with linear or area sensors. The same applies for strain monitoring using electrical strain gauges. The possibility of monitoring larger areas using new measurement methods like distributed fibre-optical sensors and technologies may help to promote new construction methods and structural health monitoring (SHM) of timber bridges.
This paper presents a literature survey of moisture monitoring and fibre optical measurement techniques, own studies on moisture monitoring on timber bridges and the strain analysis in mechanical load tests on timber-concrete composite beams. Finally, an overview of the combination of moisture monitoring and fibre-optical measurement techniques is given.

KEYWORDS: structural health monitoring, fibre-optical sensors, FBG, distributed sensing, moisture monitoring

1 INTRODUCTION

A high timber moisture content is a problem for timber bridges as well as it is for any timber structure. This is associated with a high risk of insect infestation and infestation by wood-destroying fungi. Wood moisture contents of more than 20 mass-% over a longer period of time are considered as a potential problem.[1, 2].
Bridges must be regularly inspected in Germany [3]. However, this only offers a limited possibility to monitor the long-term development of the timber moisture content of a bridge. Therefore, monitoring concepts can help to ensure that the timber moisture content is kept within acceptable limits. If timber moisture levels higher than 20 mass-% are measured, it is possible to detect and remedy the problem before major economic damage occurs. For this purpose, new sensors, measurement methods and technologies are required that allow reliable monitoring of the structures.
High-performance fibre-optical measurement techniques allow accurate and distributed or closely spaced linear measurements of strain and temperature changes in large structures such as bridges. If it were possible to use distributed fibre-optical sensors to measure the timber moisture content in addition to strain and temperature changes, it would be a major step forward in structural health monitoring (SHM) of timber bridges.
On the one hand in this paper, the different measuring methods for determining the timber moisture content are presented. It is explained which measurement methods are used in practice and which current developments are known. On the other hand, fibre-optical measurement methods and the usage of these methods for strain and temperature measuring of structures are described. Finally, an outline of the combination of these two methods and new concepts is presented.

2 TIMBER MOISTURE MONITORING

2.1 OPPORTUNITIES OF TIMBER MOISTURE MEASUREMENT

Different methods are available to determine the timber moisture content. An overview is provided in Table 1, according to [4].
The direct measurement of the timber moisture content is possible in two ways. The first possibility is the measurement of the mass of water of a material sample by using the kiln-dry method or the distillation/extraction method. The kiln-dry method is standardised in Germany [5]. It is necessary to take a sample from the building

[1] Johannes Koch, University of Applied Sciences Erfurt, Germany, johannes.koch@fh-erfurt.de
[2] Martin Ganß, Materials Research and Testing Institute at the Bauhaus-University Weimar, Germany, martin.ganss@mfpa.de
[3] Martin Kästner, Bauhaus-University Weimar, Germany, martin.kaestner@uni-weimar.de
[4] Antje Simon, University of Applied Sciences Erfurt, Germany, antje.simon@fh-erfurt.de

https://doi.org/10.52202/069179-0506

components. Temperatures above the boiling point or solvents are used to extract the water from the sample. The moisture content is calculated by dividing the mass of the water by the mass of the dry sample. These methods are destructive but very accurate and therefore used as reference measurement methods.
The other possibility is the measurement of physical or chemical properties which correlate with the moisture content. Several methods are available, see Table 1. For these methods the dependency on moisture content of the electrical resistance (electrical resistance method), the dielectrical constant (dielectrical method), the energy absorption (microwave method), the braking process of neutrons (radiometrical method), the reflection of light waves (spectrometrical method) and the colour reaction of chemicals (chemical method) is used.

Table 1: *Timber moisture measurement methods*

Method	Measured parameters
Kiln-dry method	Direct measurement of the mass of water in the timber
Distillation/extraction method	
Electrical resistance method	Measurement of physical or chemical properties which correlate with the timber moisture content
Dielectrical method	
Microwave method	
Radiometrical method	
Spectrometrical method	
Chemical method	
Sorption method	Measurement of the relative humidity and air temperature close to a timber surface which correlate with the timber moisture content

An indirect way to determine the timber moisture content is the sorption method, which uses the hygroscopicity of the wood. For this method, a borehole is made in a structural timber component, into which a climate sensor is inserted and sealed off from the outside. The climate sensor is then positioned in an enclosed air volume that constantly changes its humidity due to the timber moisture of the walls of the borehole. The relative humidity and air temperature is measured and then converted into the material humidity.

2.2 MOISTURE MONITORING OF TIMBER BRIDGES IN PRACTICE

Not all of the methods described above are appropriate for monitoring timber structures. Only methods used for monitoring purposes are discussed below.
Timber moisture monitoring is often carried out using the electrical resistance measuring method. This method is standardised for sawn timber in DIN EN 13183-2 [6]. The measurement method is based on the correlation between electrical resistance and timber moisture content. The electrical resistance increases as the timber moisture content decreases. In particular, the type of wood has a considerable influence on the electrical resistance to be determined. Therefore, wood species-specific calibration curves must be used to determine the wood moisture content when using this method. Timber temperature has also a relevant influence on the electrical resistance. Therefore, a temperature compensation is necessary.

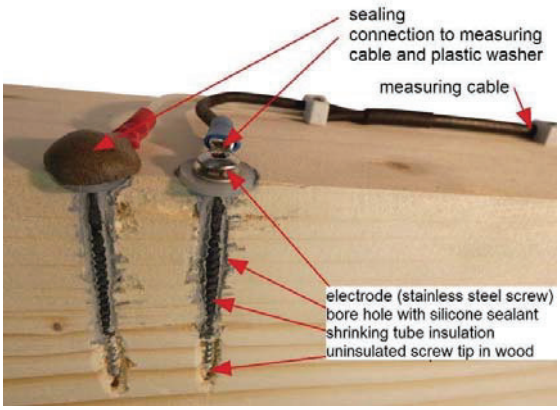

Figure 1: *Model of electrodes in a test specimen*

In a monitoring programme at the University of Applied Sciences Erfurt the following measurement setup was used [7], [8]: Stainless steel screws were used as electrodes, inserted into a pre-drilled hole and insulated with shrinking tube to the specified measurement depth. The exposed part of the thread was screwed into the wood without pre-drilling and the holes were sealed with silicone to prevent water and air ingress. Plastic washers and insulating putty were used to decouple the screw heads from the wood to prevent creepage currents on the wood surface (see Figure 1). The measuring equipment used was from the company Scanntronik Mugrauer GmbH. A similar measurement setup has been used in several other studies [9, 10, 11].
The sorption method has been used in a monitoring programme on several bridges in Norway [12]. Sensors were placed at different depths in the cross section of the main components of the bridges. The boreholes were sealed from the outside. The sensors measure air temperature and relative humidity in a small cavity. The moisture content was initially calculated using Simpson's equation for equilibrium moisture content [13]. However, a more accurate equation was found.

2.3 CURRENT DEVELOPMENTS

New sensors are currently being developed by several institutions. At the Bern University of Applied Sciences, a single-point sensor has been developed that also uses the sorption method. The advantages are the low costs and wireless data transmission of each sensor. This simplifies the application of this system. A gateway close to the sensors can transmit data to a server or send alerts to mobile phones [14].
Another approach is the usage of Radio Frequency Identification (RFID)-tags. An RFID-tag is a small device that uses radio waves to receive, store, and transmit data

https://doi.org/10.52202/069179-0506

to a reader. The capacitive measurement method is used. The water in the wood affects an RFID-tag antenna and causes its impedance to deviate from its intended design value. This effect becomes stronger as the moisture content of the surrounding medium increases. Therefore, it is possible to determine the moisture content. Tags are available which get their energy by electromagnetic transmission from the reader. Wires and an energy supply are not necessary, only a reader is required. The tags can be applied to the surface or inserted into the timber components. The disadvantages of this method are its low level of accuracy and the fact that it is a single-point sensor, as it is the case with many other techniques described before [14, 15, 16].

Single point sensor measurements only give information about the moisture content at the measurement points. It is not possible to detect potentially high moisture levels next to the measurement points. This disadvantage of single-point measurement is overcome by linear or area sensors. Such sensors are currently being developed as described in the following.

In [17] the development of a 'sensor lamella' is described, which can be used as a linear or area sensor. The measurement principle is based on the determination of the specific resistance of the wood volume between two plate electrodes. The system is suitable in the range of 10 mass-% to 20 mass-% but not for the detection of locally increased moisture content above the critical value of 20 mass-%.

Kühne et al. [18] describe linear sensors using dielectric measurement techniques such as Time Domain Reflectometry (TDR) and Damping and Phase Shift in the Alternating Voltage Field of Electrical Conductors (DPW). They allow local estimation of wood moisture, but require calibration for each application.

Research at the University of Applied Sciences Eberswalde is taking a different approach. In his dissertation [19], Winkler describes the use of piezoresistive wood adhesives. In [20] it was already shown that it is in principle possible to use such electrically conductive adhesives for timber moisture detection. In addition, strain can also be determined. It is therefore a technology that can be used in many ways to analyse timber structures. The measured resistance depends on the load, temperature change, moisture and the associated swelling and shrinking of the material. The task at hand is therefore to distinguish between the causes of this 'sum signal'.

Although commercially available linear and area moisture sensors are used to monitor bridges, they are used in particular for flat roofs. However, these sensors are not used to measure the timber moisture content, but only as a continuous check on the integrity of the waterproofing layer. These systems usually include a leak detection option. However, as the timber moisture content is not measured, these systems are not included in the following discussion.

3 THE USE OF A FIBRE-OPTICAL MEASUREMENT METHOD FOR THE ANALYSIS OF TIMBER STRUCTURES

3.1 FIBRE-OPTICAL MEASUREMENT METHODS

3.1.1 Principles

Fibre-optical sensors and measurement methods provide another approach for the analysis of timber structures. In principle, the sensor technology is based on passing a light wave through the core of an optical fibre and measuring the reflected and/or the transmitted light wave properties. External influences such as temperature changes and mechanical strains in the direction of the fibres cause them to stretch or compress and affect the light properties. This method may also be suitable for determining the timber moisture content i.e., by measurement of hygric strains of the timber or analysis of the relative humidity of the air close to wood using a fibre-optical sensor with humidity sensitive coating.

Fibre-optical sensors are divided into single-point, semi-distributed and distributed sensors. Single-point measurement systems and sensors are not part of the present discussion.

3.1.2 Fibre Bragg Grating (FBG) Sensors (semi-distributed measurement)

Very thin fibre-optical sensors, such as fibre Bragg grating sensors (FBGS), allow the measurement of changes caused by temperature and mechanical strain. Due to their insensitivity to electromagnetic interference, corrosion resistance and long-term stability, FBGS are widely used for structural monitoring in various applications [21], [22].

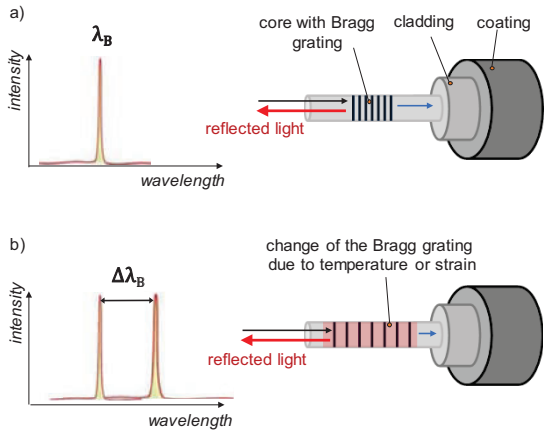

Figure 2: *Schematic representation of the principle of fibre Bragg grating sensors (a) FBGS with the reflected light spectra (wavelength at the maximum of the peak is the Bragg wavelength λ_B) and (b) shift of the Bragg wavelength ($\Delta\lambda_B$) due to changes in temperature and/or mechanical strain*

FBGS are light guiding optical fibres with zones where the refractive index in the fibre core is periodically modulated. The zones with modified optical properties are

called Bragg gratings [23]. When broadband light is passed through the fibre Bragg grating, a wavelength-selective reflection of the light occurs as schematically shown in Figure 2. The light is reflected at the Bragg wavelength λ_B [23].

If temperature or mechanical strain is applied to the fibre Bragg grating along the fibre axis, the Bragg wavelength is shifted to lower or higher wavelengths depending on the situation. The Bragg wavelength shift is given by Equation (1) below:

$$\frac{\Delta\lambda_B}{\lambda_B} = (\alpha + \xi) \cdot \Delta T + (1 - \rho e) \cdot \varepsilon \qquad (1)$$

with $\Delta\lambda_B$ = change in the Bragg wavelength, ρe = photoelastic constant, α = thermoelastic coefficient, ξ = thermo-optic coefficient, ΔT = change in temperature and ε = strain.

For more information on the relationship between the change in optical properties with temperature and strain see [23]. The Bragg wavelength shift depends on both temperature and mechanical strain. For strain measurements at constant temperature, the peak shift of the Bragg wavelength is typically converted into a measurement of strain along the axis of the optical fibre. If the temperature is not constant, temperature effects must be separated from mechanical strain effects using temperature compensation techniques. For strain measurements, the FBGS are normally attached to the surfaces of the structure of interest using structural adhesives. It has been shown that FBGS can also be used as embedded sensors in laminated composite structures [24] as well as in adhesive layers of structural joints [25]. Embedded FBGS can therefore provide detailed information on strain or temperature at different points in a structure [26].

3.1.3 Distributed Fibre Sensing

In recent years, distributed measuring fibre-optical systems have also become established. These measurement techniques use the light scattered back from 'defects' and inhomogeneities in the optical glass fibre itself. The optical fibres contain a characteristic reflection signal whose defined changes under the influence of temperature and mechanical force are analysed to determine temperature and strain. Special interferometer measurement techniques and defined tunable laser light sources are used to evaluate the light scattered back into the fibre.

Optical frequency domain reflectometry, which uses frequency analysis to evaluate the Rayleigh components in the backscattered light, is well established for applications requiring high spatial resolution in the millimetre range over the entire fibre. The measurement systems consist of a tunable narrow-band laser and a Mach-Zehnder interferometer, with one arm used as a sensor and the other as a reference. By using special analysis techniques and algorithms strains and/or temperatures can thus be continuously recorded over the entire optical fibre (over a length of up to 100 m) with high spatial resolution in the lower millimetre range. Usual optical fibres and optical fibre cables can be used for this measurement technique [27].

Other measurement techniques are used to analyse the Raman and Brillouin components in the backscattered light. These techniques can measure over distances of tens of kilometres, but their spatial resolution is limited [27].

A new technique of interest for spatially resolved strain monitoring is the combination of FBG technology and frequency domain reflectometry. By inscribing a large number of low reflective Bragg gratings of the same output wavelength into the fibre, a better backscatter signal is obtained. Strains of up to 30,000 µm/m can be measured with spatial resolution along a fibre length using frequency domain reflectometry [28].

3.2 EXPERIMENTAL STUDIES USING FIBRE-OPTICAL MEASUREMENT METHODS

3.2.1 Strain Measurement along the Joint of Adhesively Bonded Timber-Concrete Composite Beams for Bridge Construction

A research project [29] carried out at the Bauhaus-University Weimar included component tests on timber-concrete composite beams. The subject of the research project was the investigation of new types of composite joint configurations for timber-concrete composite road bridges with continuous bond between the concrete deck slab and the main timber girders. One of the composite variants investigated was the adhesive connection of the components using tolerance-compensating polymer mortar with mineral fillers. Together with the Materials Research and Testing Institute at the Bauhaus-University Weimar, a fibre-optical measurement system was used in two bending tests (beams HBV-11 and HBV-12), which allowed a nearly continuous measurement of the strains over the entire length of the adhesive joint. Detailed information on the investigated composite system and the results concerning deformation, load-bearing and failure behaviour of the components are documented in [29, 30, 31]. An overview of the fibre-optical measurements of the strains is given below. Further information can be found in [32].

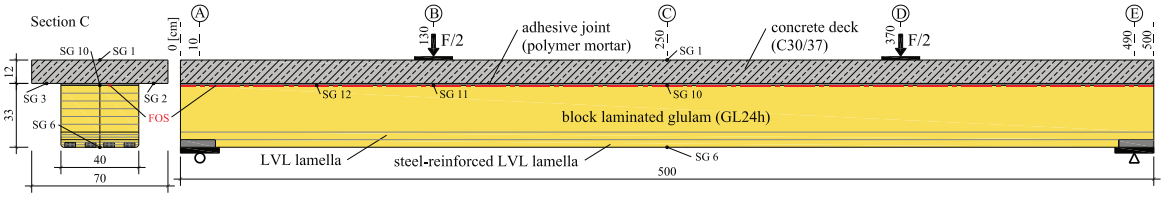

Figure 3: *Specimen dimensions of the four-point bending tests with fibre-optical strain measurement along the adhesive joint of the timber-concrete composite beams HBV-11 and HBV-12*

https://doi.org/10.52202/069179-0506

General information on the test specimens and boundary conditions are given in Figure 3. To prevent sudden failure of the wood, the glulam beams were reinforced with both tensile and shear reinforcements. Details can be found in [30]. The adhesive was applied to the full surface on top of the glulam beam over its whole length. The average thickness of the adhesive joint was approximately 13 mm (± 3 mm). The optical sensor fibre was previously applied over a length of 5 m in the area of the composite joint on the timber surface (see FOS in Figure 3) and, in the case of the HBV-12 beam, also in the bending tension zone. Strains along the sensor fibre were already measured using an optical frequency domain reflectometer during the production of the adhesive joint and during the short-term bending test. The global and local deflections were measured according to the relevant standard [33], as well as the relative displacement between timber and concrete components using inductive displacement transducers at different points on the composite beam. In addition, local measurement of longitudinal strains was carried out using electrical strain gauges in the following areas of the composite beam (see Figure 3):

- in the middle of the composite beam at the top and bottom surface of the concrete deck slab (SG 1, SG 2 and SG 3)
- in the middle of the composite beam at the top and bottom surface of the block laminated glulam (SG 10 and SG 6)
- in axis B at the top surface of the block laminated glulam (SG 11)
- in the middle between axis A and B at the top surface of the block laminated glulam (SG 12)

In the four-point bending tests the load was applied displacement controlled in four consecutive load cycles (see Figure 5) until failure at the end of the fourth cycle. Strain changes were detected along the whole length of the fibres during the production of the adhesive joint. Events such as loading due to the application of the concrete deck and strain reduction due to the hardening of the polymer mortar (reaction and cooling shrinkage) were identified.

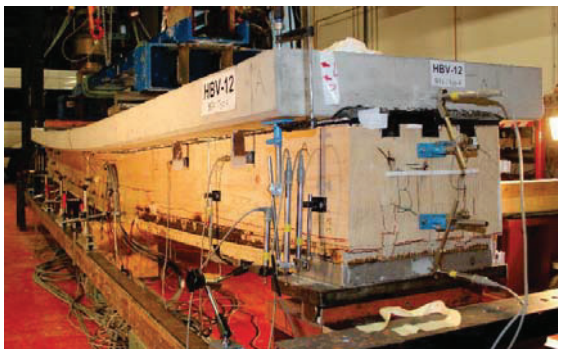

Figure 4: *Deformed timber-concrete composite beam HBV-12 at the end of the bending test; cracks in the LVL and in the glulam are marked in red*

Figure 4 shows the significantly deformed HBV-12 test specimen. Figure 5 shows the strain distribution determined by fibre-optical sensing in the adhesive layer along the whole specimen for five load levels. Using the optical frequency domain reflectometer, strains between -400 and +700 µm/m were determined up to final bending tensile failure at t = 2442 seconds. The maximum load was 1221 kN.

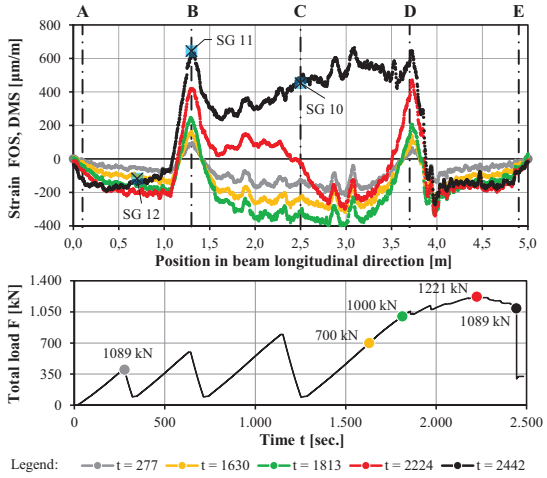

Figure 5: *Strain distribution along the fibre-optical sensor within the adhesive joint of the timber-concrete composite beam HBV-12 for five specific test times (above) and associated load levels (below)*

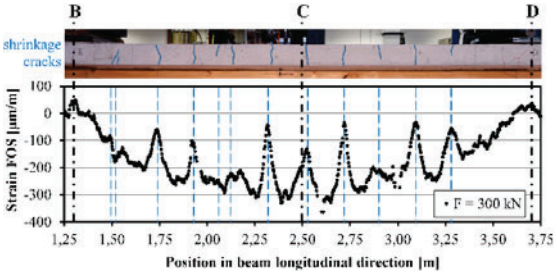

Figure 6: *Correlation between the location of shrinkage cracks within the concrete slab and local peaks in the strain distribution measured with the fibre-optical sensor along the adhesive joint of timber-concrete composite beam HBV-11*

The results of the strain measurements using strain gauges on the one hand and the fibre-optical measurement method on the other showed a high level of correlation (see Figure 5, for t = 2442 seconds). Due to the stiffness of the rigid-bonded timber-concrete composite beam, the sensor fibre is largely within the bending compression area of the undamaged test specimen (negative strains). Local influences, such as the concentrated load application in axes B and D, can be seen as peaks in the strain distribution. Below the load application points, local tensile strains of more than 600 µm/m were measured within the adhesive joint. The location of previously detected shrinkage cracks in the concrete slab correlates with the location of smaller strain peaks along the sensor fibre (see Figure 6). The theoretically

continuous force transmission is locally interrupted by the existing crack structure, which is clearly demonstrated by the measurement results.
The results of the studies presented here show that it is possible to measure strain values in the adhesive joint over the whole length with a high spatial resolution by using distributed fibre-optical sensors. If the data is correctly analysed and interpreted, it can be used to gain a lot of information. This allows the detection of local events as well as influencing factors from the production process and during the service life.

3.2.2 Optical Fibre Sensors for Strain Monitoring on Bridges

Fibre-optical sensor solutions have sporadically been used for the strain monitoring of bridges. In particular, fibre-optical displacement transducers and FBG sensors have successfully been used to monitor some bridges. In 2016, Roßteutscher et al. showed in the research project 'i.bridge' [34] that the deflection and vibration of a concrete bridge in need of repair can be measured using a fibre-optical measurement system based on optical frequency domain reflectometry and Rayleigh backscattering. Optical fibres were applied to the concrete surface, vehicle overpasses were analysed and correlated with sensor data [34]. Distribution measuring sensor systems based on Brillioun scattering have also been used [35, 36]. With this measurement technique, spatially resolved sensor data can be recorded at a distance of approximately 0.50 m. In the investigations by Wosniok et al. [37], the fibre-optical sensors were applied to the surface of the concrete structure of a bridge in Amsterdam. Static loads were induced by controlled truck overpasses, which were detected by the fibre-optical sensors with a spatial resolution of 0.20 m. The temperature compensation was done using unloaded areas of the sensor fibres [37].

3.3 CONCEPTS OF TIMBER MOISTURE MEASUREMENT USING FIBRE-OPTICAL SENSORS

3.3.1 Using the Sorption Method

As shown above, fibre-optical measurement methods are in principle very powerful technologies. They are particularly well-suited to monitoring long structures such as bridges. So far, the technology described has been used to measure strain and temperature in this field of application. It would be a major step forward in structural health monitoring if these methods could be used to measure the timber moisture content. There are different suitable possibilities.
One option is the combination of the sorption method and the fibre-optical measurement method. A humidity-sensitive fibre-optical sensor is required to calculate the timber moisture content from the relative humidity and temperature of a small cavity in the wood. The FBG technology is suitable to make this possible. The cavity could be a notch. The usage of a perforated stainless-steel capillary around the fibre might also be an option.
Normally FBGS are used to measure both temperature and longitudinal strain. To make the FBG sensitive to the relative humidity of the surrounding air a hygroscopic coating of this part of the fibre is necessary. Polyimide [38, 39] or ORMOCER® (organically modified ceramics) [40] are suitable coating materials. The coating induces strains in the FBG structure by hygroscopic expansion if the relative humidity is changing as given by Equation (2) below:

$$\varepsilon_{RH} = \beta \cdot \Delta\mathrm{RH} \tag{2}$$

with ε_{RH} = hygroscopic strain, β = humidity-induced expansion coefficient and ΔRH = change in relative humidity.
The strain ε in Equation (1) could be replaced with the hygroscopic strain ε_{RH}. The result is given in Equation (3) below:

$$\frac{\Delta\lambda_B}{\lambda_B} = (\alpha + \xi) \cdot \Delta T + (1 - \rho e) \cdot \beta \cdot \Delta\mathrm{RH} \tag{3}$$

This is only applicable if the fibre is not bonded to the wood and thus mechanical strain is excluded. To separate temperature and relative humidity temperature compensation techniques are necessary, e. g. an additionally temperature sensor close to the humidity sensor. Other techniques enable the separation within a single FBGS [40].
In [41] the development of a fibre-optical sensor is described that is suitable for measuring hygric induced strain, temperature and relative humidity. It is a combination of three FBGs. The humidity sensitive part is a commercially available polyimide coated FBG [42]. The timber moisture content was calculated according to [43]. The sensitivity of the sensor was customised and the temperature influence was compensated. Therefore, this measuring method seems to be a good alternative to established methods.

3.3.2 Using the Hygroscopic Strain of Wood

The other option is to use the hygric induced strain of the wood itself to determine the moisture content. The challenge in this case is to separate the measured signal into its component parts as there are:

- mechanical induced strains
- thermal induced strains
- hygric induced strains

The measured strain combines all of them in a 'sum signal'. This is described in Equation (4) below:

$$\frac{\Delta\lambda_B}{\lambda_B} = (\alpha + \xi) \cdot \Delta T + (1 - \rho e) \cdot (\beta \cdot \Delta\mathrm{RH} + \varepsilon) \tag{4}$$

Using an additional fibre that is unloaded or unloaded parts of the same fibre offer the separation of the thermal induced strain.
The separation between mechanical and hygric induced strain is more difficult. A concept must be developed for the separation taking into account the following aspects:

- strain direction and maximum strain value (swelling and shrinking is much different between grain direction and perpendicular to grain; and also different between radial and tangential wood anatomic direction),
- influence of wood defects like knots, cracks etc.,

https://doi.org/10.52202/069179-0506

- prevention of swelling and shrinking due to connected components like concrete slabs or perpendicular arranged timber layers.

One option is the definition of a 'sensor lamella'. As part of the research project 'HBVSens' concepts of the described measurement method will be tested in TCC structures.

4 CONCLUSIONS

Structural health monitoring can help to detect potential damage of timber bridges at an early stage and thus to prevent major economic damage. As presented, semi-distributed and distributed fibre-optical sensor methods are good solutions for strain sensing including temperature measurement. At present, the moisture monitoring is often carried out using single-point sensors. The disadvantages associated with this can be overcome by using fibre-optical sensing not only for strain and temperature, but also for moisture. On the one hand, this is possible by combining the sorption method with the use of FGBS. On the other hand, the hygric induced strain of the wood itself could be used to measure the moisture content. Both proposals require further investigations.

ACKNOWLEDGEMENT

Thanks go to the Fachagentur Nachwachsende Rohstoffe e.V. (FNR) and to the Federal Ministry of Food and Agriculture (BMEL) of Germany for funding the ongoing research project 'HBVSens' (FNR-project no.: 2221HV097) and the already completed FNR-project no. 22000612 [29] under the direction of Prof. Dr.-Ing. Karl Rautenstrauch. Thanks are also owed to the sponsors of the completed research project 'Protected Timber Bridges (ProTimB)': Federal Ministry of Education and Research of Germany, the companies of the Qualitätsgemeinschaft Holzbrückenbau e. V. (Schaffitzel Holzindustrie GmbH + Co. KG, Schmees & Lühn Holz- und Stahlingenieurbau GmbH, Grossmann Bau GmbH) and Setzpfandt Beratende Ingenieure GmbH & Co. KG.

REFERENCES

[1] DIN 68800-1: Holzschutz – Teil 1: Allgemeines. Berlin: Beuth, June 2019.

[2] Willeitner, H.: Kommentar zur DIN 68800-1:2011-10 – Holzschutz – Teil 1: Allgemeines. in: Marutzky R. [Hrsg.] Holzschutz – Praxiskommentar zu DIN 68800 Teile 1 bis 4. 2. completely revised edition. Berlin: Beuth, pp. 9–76, 2013.

[3] DIN 1076: Ingenieurbauwerke im Zuge von Straßen und Wegen – Überwachung und Prüfung. Berlin: Beuth, November 1999.

[4] Niemz, P; Sonderegger, W. U.: Holzphysik – Eigenschaften, Prüfung und Kennwerte. 2. updated edition, München: Carl Hanser Verlag, 2021.

[5] DIN EN 13183-1: Feuchtegehalt eines Stückes Schnittholz - Teil 1: Bestimmung durch Darrverfahren. Berlin: Beuth, July 2002.

[6] DIN EN 13183-2: Feuchtegehalt eines Stückes Schnittholz - Teil 2: Schätzung durch elektrisches Widerstands-Messverfahren. Berlin: Beuth, July 2002.

[7] Koch, J., Simon, A., Arndt, R.W. and Jahreis, M.G.: Diskussion zum Erfordernis der jährlichen Hauptprüfung geschützter Holzbrücken. Bautechnik, 99, pp. 23-31, 2022. https://doi.org/10.1002/bate.202100104

[8] Koch, J.; Simon, A.; Jahreis, M.G.: Effectiveness of structural protection measures for timber bridges – results of long-term moisture monitoring. in: Conference Proceedings of the 4th International Conference on Timber Bridges, CH-Biel/Bienne, 2022.

[9] Gamper, A.; Dietsch, P.; Merk, M.: Gebäudeklima - Langzeitmessung zur Bestimmung der Auswirkungen auf Feuchtegradienten in Holzbauteilen – Schlussbericht F 2962. Stuttgart: Fraunhofer-IRB-Verlag, 2015.

[10] Franke, B.; Müller, A.; Vogel, M.; Tannert, T.: Holzfeuchte-Langzeitmessung - Langzeitmessung der Holzfeuchte und Dimensionsänderung an Brücken aus blockverleimtem Brettschichtholz – Forschungsbericht 2775-SB-01. Biel: Fachhochschule Architektur, Holz und Bau, 2012.

[11] Brischke, C.: Untersuchung abbaubestimmender Faktoren zur Vorhersage der Gebrauchsdauer feuchtebeanspruchter Holzbauteile. Dissertation, University of Hamburg, 2007.

[12] Horn H.: Monitoring five timber bridges in Norway – result 2012. Oslo: Norsk Treteknisk Institutt, 2013.

[13] Simpson, W. T., Equilibrium Moisture Content of Wood in Outdoor Locations in the United States and Worldwide, Forest products Laboratory, Madison, WI, USA, 1998.

[14] Franke, S., Franke, B.; Schiere, M.; Bonifacio, S.; Müller, A.: Monitoring systems for quality assurance of timber bridges. in: Conference Proceedings of the 4th International Conference on Timber Bridges, CH-Biel/Bienne, 2022.

[15] Avery Dennison Corp.: Passive Sensors, A guide to the working principles and usage of our passive sensor products using Axzon Magnus® S2 and S3 ICs. 2021 (available under: https://rfid.averydennison.com/content/dam/rfid/en/products/rfid-products/product-guides/Passive-Sensors-Technical-Guide.pdf).

[16] Vogel, M.; Müller, A.; Andereggen, J.: Gebäudeerneuerung Oberwallis - Teil 3 Gebäudeanalyse und Dokumentation, 2022. https://doi.org/10.24451/t196-gb24

[17] Heite, D.; Englberger, A.; Osterloff, L.; Miebach, F.; Rödel, A.: H_2O-WoodController - Entwicklung eines sicherheitsrelevanten Überwachungssystems für feuchtetechnische Problemstellungen im Holzbau. Stuttgart: Fraunhofer IRB Verlag, 2018.

[18] Kühne, H.; Blüthgen, L.; Thiele, E.; Kuhne, M.; Döring, H.: Bautextilien für dauerhaftes Feuchtemonitoring. in: Holz- und Betonbauwerken, in: holztechnologie 55 (4), pp. 30–36, 2014.

[19] Winkler, C.: Process and material features influencing piezoresistive wood adhesives. Doctoral Dissertation, University of Natural Resources and Life Sciences, Vienna, Austria, October 2021.

[20] Winkler C.; Schwarz U.: Characterization of adhesively bonded wood structures by electrical modification of the bonding system. In: Eberhardsteiner J.; Winter W.; Fadai A. (eds) World Conference on Timber Engineering, Vienna, Austria, 2016.
[21] Schroeder, K.; Ecke, W.; Apitz, J.; Lembke, E.; Lenschow, G.: Fibre Bragg Grating Sensor System Monitors Operational Load in a Wind Turbine Rotor Blade. in: Measurement Science and Technology 17 (5), pp. 1167-1172, 2006.
[22] Zhou Z.; Graver, T. W.; Hsu L.; Ou J. P.: Techniques of advanced FBG sensors: Fabrication, demodulation, encapsulation and their application in the structural health monitoring of bridges. in: Pacific Science Review 5(1): pp. 116–121, 2003.
[23] Peters, K.: Fibre Bragg Gratings Sensors, Chapter 61, p. 1103: in Boller, C.; Chang, F.-K.; Fujino, Y.: Encyclopedia of Structural Health Monitoring, Vol. 2, Wiley & Sons, 2009.
[24] Hadzic, R.; John, S.; Herszberg, I.: Structural integrity analysis of embedded optical fibres. in: composite structures. Compos Struct47(1–4), pp. 759–765, 1999.
[25] Ganß, M.; Barnickel, J.; Kuhne, M.; Beinersdorf, H.; Hildebrand, J.; Bergmann, J. P.; Könke, C.: Zustandserfassung von strukturellen Klebverbindungen mittels faseroptischer Sensoren: Untersuchungen an geklebten Stahl-CFK-Verbindungen. in: Smarte Strukturen und Systeme, p. 51, Tagungsband des 4Smarts-Symposium, ISBN: 978-3-8440-5083-7, 2017.
[26] Peters, K.; Studer, M.; Botsis, J.; Iocco, A.; Limberger; H.; Salathe; R.: Embedded optical fiber Bragg grating sensor in a nonuniform strainfield: Measurements and simulations. Experimental Mechanics 41(1) pp. 19–28, 2001.
[27] Samiec, D.: Verteilte faseroptische Temperatur- und Dehnungsmessung mit sehr hoher Ortsauflösung. in: Photonik (6), pp. 34-37, 2011.
[28] Vlachopoulos, N.; Forbes, B.; Cruz, D.: The use of Distributed Optical Sensing Techniques for Ground Support; Not all Fiber Optic Methods are Similar, Proceedings of the 70th Annual Conference of the Canadian Geotechnical Society Geo Ottawa, Ontario, October 2017.
[29] Rautenstrauch, K.; Kästner, M.: Entwicklung einer ökologischen Straßenbrückenbauweise aus Holz und Beton mit kontinuierlichem Klebeverbund auf Basis (bio-)polymerer Reaktionsharzsysteme – Ein Beitrag zum Einsatz nachwachsender Rohstoffe für Verkehrsbauten. Schlussbericht FNR-Forschungsvorhaben 22000612, Bauhaus-Universität Weimar, 2017.
[30] Kästner, M.: Zum Tragverhalten von Polymermörtel-Klebverbindungen für die Anwendung bei Straßenbrücken in Holz-Beton-Verbundbauweise (Dissertation). Bauhaus-Universität Weimar, 2019.
[31] Kästner, M.; Rautenstrauch, K.: Polymermörtel-Klebverbindungen für Holz-Beton-Verbundbrücken Teil 1+2. in: Bautechnik 98, SH Holzbau, Ausgabe 1, pp. 23–39, 2021.
[32] Ganß, M.; Hildebrand, J.; Beinersdorf, H.; Kuhne, M.; Könke, C.: Monitoring von Klebverbindungen mittels faseroptischem Messsystem – MOFAS. Schlussbericht IGF Vorhaben 17777 BR, Bauhaus-Universität Weimar, 2015.
[33] DIN EN 408: Timber structures - Structural timber and glued laminated timber - Determination of some physical and mechanical properties; German version EN 408:2010+A1:2012, Berlin: Beuth, October 2012.
[34] Roßteutscher, I.; Wohlleben, P.; Waizenhöfer, U.: Intelligente Zustandsüberwachung von Brückenbauwerken mit Hilfe faseroptischer Sensoren basierend auf der Rayleigh-Rückstreuung, Fachbeitrag 18. GMA/ITG-Fachtagung Sensoren und Messsysteme 2016, Nürnberg, 10-11.05.2016.
[35] Grosso, A. D.; Inaudi, D.; Bergmeister, K.; Santa, U.: Monitoring of Bridges and Concrete Structures with Fibre Optic Sensors in Europe. in: IABSE Symposium Report, 2001.
[36] Inaudi, D.: Overview of Fiber Optic Sensing Technologies for Structural health Monitoring, Informacije MIDEM 40 4, pp. 265-274, Ljubljana, 2010.
[37] Wosniok, A.; Jansen, R.; Cheng, L.; Chruscicki, S.: Ortsaufgelöste Zustandsüberwachung von Brückenbauwerken mittels faseroptischer Sensoren. DGZfP-Jahrestagung, 2021.
[38] Wang L.; Fang, N.; Huang, Z.: Polyimide-coated fiber Bragg grating sensors for humidity measurements. in: High Performance Polymers—Polyimides Based—From Chemistry to Applications, Ch. 8, pp. 150-166, Ed.: M. J. M. Abadie, INTECH Open Access Publisher, Rijeka, Croatia, 2012.
[39] Makovec, A.; Berruti, G.; Consales, M.; Giordano, M.; Petagna, P.; Buontempo, S.; Breglio, G.; Szillasi, Z.; Benig, N.; Cusano, A.: Radiation hard polyimide-coated FBG optical sensors for relative humidity monitoring in the CMS experiment at CERN. in: Journal of Instrumentation, Vol. 9, p. C03040, 2014. http://iopscience.iop.org/1748-0221 /9/03/C03040
[40] Korenko, B.; Rothhardt, M.; Hartung, A.; Bartelt, H.: Novel Fiber-Optic Relative Humidity Sensor With Thermal Compensation. In: IEEE Sensors Journal 15(10), pp. 5450-5454, 2015. doi: 10.1109/JSEN.2015.2444100
[41] Franke S.; Magnière, N.; Schiere M.; Ferrazzini, T.; Meier, C.; Bossen A.: Einsatz von FBGS im Holzbau - Development and use of optimized Fibre Bragg Grating sensors for long term monitoring of timber components. Final Report No. 2838-PB-01. Bern University of Applied Sciences, Biel, 2016.
[42] Fiber Humidity Sensor. Ed.: O/E Land Inc., Canada, 2021. (available under: https://www.o-eland.com/SensorProducts/OEFHS-100-200%20Fiber%20Humidity%20Sensor.pdf)
[43] Dyken T.; Kepp, H.: Monitoring the Moisture Content of Timber Bridges. in: ICTB International Conference on Timber Bridges, Lillehammer, Norway, 2010.

https://doi.org/10.52202/069179-0506

World Conference on Timber Engineering Oslo 2023

FEDERATED USE OF HYGROTHERMAL MONITORING DATA IN MASS TIMBER BUILDINGS: OPPORTUNITIES AND CHALLENGES

Mariapaola Riggio[1], Jan Vcelak[2], Pekka Kaitaniemi[3], Andre R. Barbosa[4], Niki Hrovatin[5], Anna Sandak[6], Jakub Sandak[7], Michael Mrissa[8], Miklos Kresz[9], Anssi Yli-Jyrä[10], Ritva Toivonen[11], Laura Alakukku[10]

ABSTRACT: Several structural health monitoring projects have recently emerged to document the hygrothermal behaviour of mass timber buildings during both construction and service. Understanding moisture conditions on site can significantly impact the construction efficiency of mass timber structures. It is also essential to comprehend the effectiveness of moisture control strategies and construction practices in different climates to streamline project delivery and prevent long-term durability issues. This paper describes the first period of hygrothermal monitoring of three mass timber buildings in three different climate zones, outlining potential approaches for enhancing and integrating data, which can leverage the increasing availability of data from various monitoring projects.

KEYWORDS: moisture monitoring, mass timber, construction phase

1 INTRODUCTION

Faced with timber products and construction systems that are growing in scale and spreading to new climate zones, the mass timber building community increasingly needs information to understand the impacts of environmental exposure during a building's entire life cycle and the efficacy of existing moisture management practices. Several monitoring studies have provided insights on wetting, drying and durability performance of wall and floor assemblies in varying exposure conditions (for instance [1-7]), and have also highlighted the potential benefits of developing more unified monitoring methods and data-driven approaches to moisture management. Oregon State University, InnoRenew CoE, the University of Primorska and the University of Helsinki have established a research alliance to share information on mass timber buildings performance. The alliance will utilize monitoring data from three mass-timber projects, Peavy Forest Science Center (PFSC) in Oregon, USA, InnoRenew CoE in Slovenia, and the Hyytiälä Forestry Field Station in Finland. A federated use of data from the three monitoring projects presents an opportunity to provide valuable insights into the hygrothermal behaviour of mass timber buildings, enabling a comprehensive understanding of moisture levels in CLT panels during construction and in service, while taking into account specific building systems, construction processes, water management strategies and climate zones. However, data integration can be challenging due to differences in data collection methods, equipment, and techniques, as well as variations in the number and types of monitored locations and measurement periods. These differences can result in variations in accuracy, resolution, and quality of the data obtained. In addition, data ingestion and processing techniques can also significantly impact data integration, such as the way data is formatted, organized, and stored, affecting its usability and compatibility with other data sources. Variations in data processing techniques, including algorithms used for data cleaning, filtering, and normalization, can also impact data integration. This paper outlines the methodology used in the development of the three monitoring projects and provides examples of

[1] Wood Science and Engineering, Oregon State University, Corvallis, OR USA. Mariapaola.riggio@oregonstate.edu
[2] InnoRenew CoE, Izola, Slovenia. Czech Technical University in Prague - UCEEB, Czech Republic.jan.vcelak@innorenew.eu
[3] Hyytiälä Forestry Field Station, University of Helsinki, Korkeakoski. pekka.j.kaitaniemi@helsinki.fi
[4] Civil and Construction Engineering, Oregon State University, Corvallis, OR USA. andre.barbosa@oregonstate.edu
[5] InnoRenew CoE, Izola, Slovenia.niki.hrovatin@innorenew.eu
[6] InnoRenew CoE, Izola, Slovenia. anna.sandak@innorenew.eu
[7] InnoRenew CoE, Izola, Slovenia. jakub.sandak@innorenew.eu
[8] InnoRenew CoE, Izola, Slovenia. Faculty of Mathematics, Natural Sciences and Information Technologies, University of Primorska, Slovenia. michael.mrissa@innorenew.eu
[9] InnoRenew CoE, Izola, Slovenia. miklos.kresz@innorenew.eu
[10] Infra unit, Faculty of Agriculture and Forestry, University of Helsinki. Helsinki, Finland. laura.alakukku@helsinki.fi
[11] Department of Forest Sciences, University of Helsinki. Helsinki, Finland. ritva.toivonen@helsinki.fi

https://doi.org/10.52202/069179-0507

the challenges and opportunities that arise when using hygrothermal monitoring data from different mass timber buildings.

2 METHODOLOGY

2.1 SCOPING THE MONITORING PROGRAMS

The first crucial step in planning a monitoring program is to clearly define the project's objectives and the phenomena of interest. Next, the required measurands and data collection and management approach should be defined, taking into consideration factors such as budget and building constraints.

The PFSC is a three-story building completed in Corvallis, Oregon in 2019. The location has a Mediterranean/dry-summer subtropical climate with mean annual precipitation of 1295.4 mm and temperatures ranging from 2°C to 30°C over the course of the year. The building's gravity load-bearing system comprises glulam beams and columns, cross-laminated timber (CLT)-concrete composite floors, and a mass ply panel (MPP) roof. The lateral force resisting system features self-centering, post-tensioned CLT shear walls. The construction of the timber structure began in winter 2017 and was planned in three sequential spatial zones to minimize exposure to the weather. To protect against moisture during construction, a vapor permeable coating was applied in the shop to exposed end grains, such as panel edges, connections, and cut-outs, as well as to the faces of glulam members and visible CLT panels. Additionally, temporary tarps were placed on the upper edges of the CLT wall panels to prevent water from entering through any discontinuities (Figure 1).

Figure 1: *Zone 1 of the PFSC, Corvallis, Oregon, during construction (up), detail of temporary moisture protection during transportation and erection (bottom)*

The objectives of the hygrothermal monitoring plan during construction of the PFSC were manyfold: a) to provide benchmark data on the wetting/drying behaviour of domestically produced Douglas Fir CLT exposed to the rainy Pacific Northwest climate, b) to evaluate the effectiveness of localised moisture exclusion measures in reducing moisture uptake in CLT and glulam members and, consequently, mold risk; c) to provide indications on proper dry-out schedules to avoid build-in moisture that minimize checking and uncontrolled building movement. Additional MC, RH and T sensors were installed to evaluate conditions in service [8] and correlate hygrothermal behaviour and long-term performance of structural systems (such as, for instance, effects of mechano-sorptive creep and moisture induced movement on tension losses in post-tensioned shear walls [9]).

InnoRenew CoE's building is located in a Mediterranean seaside climate in Izola, Slovenia, with 1313 mm mean annual precipitation and temperatures ranging from 1.7°C to 28.9°C over the course of the year. It is a 4-story 8194m^2 building with a concrete podium and three timber stories featuring CLT panels and glulam. The building was completed in February 2022. No extraordinary measures against rainwater were taken during construction, and the building was exposed to outdoor conditions until the roof was installed. CLT panels were not equipped with protection membranes. However, in-plane panel-to-panel floor connections were sealed using surface-applied tapes to avoid water penetration between the panels (Figure 2).

The main objectives of the hygrothermal monitoring plan of the InnoRenew CoE building mostly target the service life of the building, after commissioning. Specifically, internal MC sensors were installed for early detection of leakages in wet room areas. MC, RH and T sensors in the envelope measure conditions in air-gaps or breathable materials.

Figure 2: *InnoRenew CoE's building, Izola, Slovenia, during construction (up), detail of the CLT floors (bottom*

https://doi.org/10.52202/069179-0507

Figure 3: *The main building of Hyytiälä Forestry Field Station after removal of construction shelter. Six groups of MC sensors are indicated with black text.*

The four new mass timber buildings at the Hyytiälä Forestry Field Station, Finland, are located in the boreal climate zone with 711.0 mm and mean monthly temperature extremes ranging from -10.3°C to 21.8°C. Construction started in spring 2021 and completion is scheduled in autumn 2023. The buildings have 1-2 stories with CLT walls and exterior wood cladding. Wooden pedestrian bridges and platforms connect the facilities. One week prior to the transportation of CLT elements to the construction site in early November 2021, a construction shelter was fully installed over the building. The top of the shelter was opened periodically until the roof construction was completed, at which point the tent was fully removed in late January 2022. To cover the window openings temporarily, plastic sheeting was used until the windows were installed in the first week of February (Figure 3). Measurements are taken from the interior CLT wall element located adjacent to the lower floor fenestration on the northwest side of the building.

Overall, the objective of wood moisture content measurements in the new Hyytiälä Forestry Field Station is to ensure the long-term health and safety of the building's structure by providing a reliable system for monitoring and maintaining the moisture levels of the CLT elements. In addition, data collected during the construction period enables monitoring the success of practices for protecting the elements from moisture during transportation, storage, and construction.

2.2 DATA COLLECTION

Sensor installation in the PFSC was conducted in two stages. During the initial construction phase, 19 permanent resistance-based MC sensors (SMT-PMM) were installed in the timber framing. These sensors were placed in the first erected CLT shear wall panels and a floor, which were deemed representative of areas in the building that could be affected by prolonged exposure to precipitation. Subsequently, 111 additional MC sensors were installed in locations where in-service wetting was a concern or where structural behaviour was being monitored. During the first monitoring period, in addition to continuous MC measurements, discontinuous MC readings were made using a resistance handheld meter (Delmhorst 18-ES), both in locations contiguous to those continuously monitored and in comparable locations but with different exposure conditions. Internal temperatures in the CLT wall panels were measured in specific locations to have accurate corrections of MC readings in internal CLT laminations. Air humidity (RH) and temperature (T) sensors were integrated in the local data acquisition systems. Weather data was collected by a nearby weather station [10]. Additional RH and T gauges were installed during the second phase.

One of the sampling criteria in the project was to include redundant sensors to account for potential malfunctions and data losses.

In the InnoRenew CoE's building, eleven (11) resistance-based MC sensors (MoistureGuard MHT sensors) were installed during construction, in 2020, but measurements started in April 2022 after the power and Ethernet networks were fully functional and the building was commissioned. One MC sensor was installed on each side of the building, on the external lower part of the exterior CLT walls. Seven additional MC sensors were placed in high-risk interior areas of the CLT structure to monitor water damage during normal building operations (toilets, bathrooms, and kitchens). Fifty-one (51) sensors for relative humidity (RH) and temperature (T) were installed in the building envelope to measure conditions within air gaps or breathable materials. (MoistureGuard HT sensors). During construction, measurements were taken manually on a weekly basis at 289 floor locations. Two types of moisture meters were used: a pin-type resistance meter (Humimeter WLW) to measure moisture content (MC) at a depth of 2.5cm, and a pinless capacitance moisture meter (Humimeter M20). Each location was labelled with a unique ID number, and manual measurements were continued until MC values reached 21% or lower, and there was no risk of additional wetting. Thermal imaging was used as a secondary, screening method [11] to identify possible wet spots in the interiors [12]. Data from two nearby weather stations were also used for data correction and post-processing.

In the Hyytiälä Forestry Field Station, continuous wood MC measurements were initiated already at the CLT plant, where 4 groups of 4 or 3 Wiiste WM1-WAN resistance-based wood moisture meter sensors (Wiiste Oy) with different measurement depths were pre-installed in CLT panels in November 2021. The panels were delivered on site in 5 days and erected in 9 days, hence the measurements also cover the short periods of storage and transportation. Additional 9 groups with 4 sensors were mounted in exterior CLT panels at the construction site in winter 2022 to cover a representative sample of microsites with potentially differing environmental conditions. Each group of four sensors in the 240 mm thick exterior CLT panels covers measurement depths from 13 mm to 218 mm at 5 to 50 mm intervals. The single group of three sensors in the 180 mm thick interior panel covers depths from 8 mm to 148 mm at 10 to 30 mm intervals. Weather data are constantly monitored near the building by both the Finnish Meteorological Institute and the University of Helsinki.

It is important to note that while some data collection occurred during transportation, the majority of the sensor installation was conducted after the wall elements were in place. This is because installing sensors during transportation or early construction phases requires an elevated level of coordination and significantly increases the risk of physical damage to the sensors.

2.3 DATA INGESTION

Table 1 shows measurement range, resolution and listed accuracy of the MC sensors used in the three buildings, as well as sample time intervals used in each monitoring project. Specifications of the hand-held meters used in the PFSC and InnoRenew buildings are also included in the table.

Table 1: *Sensor specifications in the three projects*

Project / sensor	measurement range	resolution	accuracy	sample interval
PFSC / PMM	8–30%	0.1%	+/-1%	1st phase: 1 minute - averaged hourly 2nd phase: 60 minutes
PFSC / Delmhorst 18-ES	5–60%	0.1%	Not available	1st phase: varying
InnoRenew / Humimeter WLW	7-150%	0.1%	+/-1%	1st phase: 1 week
InnoRenew / Humimeter M20	2-30 %	0.1%	Not available	1st phase: 1 week
InnoRenew / MHT	7–28%	0.1%	+/-1%	2nd phase: 15 minutes
Hyytiälä / WM1WAN	6–30%	0.1%	+/−1%	60 minutes

The data from the permanently installed MC sensors in PFSC is periodically transmitted to a local data acquisition unit, where it is stored and wirelessly transmitted to a dedicated computer equipped with a receiver. Finally, the data is synchronised with a cloud database for further analysis and storage.

In addition to the commercially available solution, the collected data is transmitted to a local, custom server, where data from other sensors/suppliers is also collected [13].

The MC sensors permanently installed in the InnoRenew CoE building are equipped with a digital RS485 wire interface and are powered by the same cable. The cable connects the sensors to EDGAR ethernet gateways, which are powered over ethernet and connected to the building's LAN. As a result, each sensor is accessible from any computer or system on the building's network. A dedicated PC runs a LabVIEW code developed by the research team which stores the data a local database for further analysis. To supplement the data collected from the sensors, precipitation data (daily sum in mm/day) is collected from the nearby official Slovenian Environmental Agency weather station in Strunjan (located 3km away). Additionally, temperature and relative humidity data are retrieved from the weather station in Portorož, which is situated 9 km away.

At Hyytiälä, the MC sensors are also equipped with sensors that measure ambient humidity and air temperature at the sensor positions on the faces of the CLT elements. The MC data collected from the construction site are transmitted periodically to a cloud database via a commercial LoRaWAN network, which is supported by a local repeater to improve the signal quality. To monitor the weather conditions at the site, open data collected by the Finnish Meteorological Institute is used, which is obtained from a weather station located 200 meters away from the building site.

2.4 DATA CONVERSION AND TEMPERATURE CORRECTION

Raw resistance ohmic values from MC sensors is converted to moisture content using equations designed for specific wooden species; published correction factors for Douglas Fir were used for the PFSC data, and for spruce and pine in the other two projects [14].

Temperature compensation is also applied to the data collected [14-16], using either temperature data from the closest thermistor depths (in some locations in PFSC [10]), air temperature measured in correspondence of each MC sensor (Hyytiälä), or air temperature values from nearby sensors (in some monitored locations in PFSC and in the InnoRenew's building).

The conversion of data and temperature correction are typically offered as post-processing features in dedicated hygrothermal monitoring platforms (e.g., SMT-Analytics). Alternatively, these functionalities can be implemented directly in sensors or developed through custom code.

2.5 DATA ENHANCEMENT

To facilitate automated data processing, unifying the data formats from various sources is the initial step. Moreover, it is essential to ensure the quality of the data is assessed and validated before integrating it into a larger dataset.

Hygrothermal data enhancement can be performed with several objectives in mind. These include: a) data cleaning by removing outliers, applying a moving average, performing wavelet packet analysis, and correcting for environmental effects; b) data enriching and correlation by calculating the equilibrium moisture content (EMC) from temperature and RH data using the Hailwood and Horrobin equation [14].

This section provides examples of data enhancement for the studied projects.

https://doi.org/10.52202/069179-0507

2.5.1 Reconstruction of missing data

Data monitoring infrastructures are not always fully dependable and data loss during communication is common. Wireless data transmission, such as the LoRaWAN network used in the Hyytiälä forest station monitoring project, is susceptible to various effects that can cause data loss, including signal attenuation in building structures, adaptive spreading factor and transmitting power, interference from other devices, changing transmission conditions, infrastructure outages, and cable interruptions.

To date, wired communication technologies are more reliable than wireless communication technologies. However, during construction works, cable connections and the entire power infrastructure may become less reliable, which can result in outages, and consequently data loss. Table 2 shows percentage of monitoring data loss for the three projects.

To obtain a complete time-series dataset that can be processed by advanced algorithms, such as mold growth models, missing data must be reconstructed using one of the standard methods, such as using the last previous valid data or using linear, cubic, or other interpolation techniques (see, for instance, [17]). Other methods for reconstructing structural health monitoring data, include machine learning and model-based estimation techniques [18-21].

Table 2: *Data loss observed in the three projects.*

Sensor ID & Type / Project	Communication type	Transmission period	Observed data loss
WM1 WAN 33874 / Hyytiälä	wireless LoRa	1 hour	11,2%
WM1 WAN 33875 / Hyytiälä	wireless LoRa	1 hour	8.9%
WM1 WAN 33876 / Hyytiälä	wireless LoRa	1 hour	16,4%
MHT03 + EDGAR converter / InnoRenew	wired RS485+Ethernet	15 min	17.7%
PMM562 / PFSC	Analogue (sensor->DAQ)+ wireless (DAQ -> cloud)	1hour	7.9%

Figure 4 shows an example of MC data reconstruction performed for the data in the Innorenew building using the last valid data in the set.

2.5.2 Data validity check

Temperature and RH measurements are typically assumed to be accurate within the specifications of the sensors used. As a standard practice, the average values of temperature and RH data from multiple sensors are compared to ensure the reliability of the measurements. However, obtaining accurate wood moisture measurements can be challenging due to numerous factors that can affect electric resistance measurements. These factors include the loss of contact between the electrode and the wood, which can lead to erroneous readings of very low moisture levels. Resistance-type meters are also commonly known to become less accurate beyond the fibre saturation point (FSP), as the presence of free water in the wood cell can affect resistance readings. Therefore, all out-of-range data should be filtered from the dataset. Loss of battery capacity can also be a phase during which the data can become corrupted. A simple moving average is often applied for cleaning MC data [6, 8]. When using moving averages in different projects, consistency in the used period is important. In some cases, statistical processing has been implemented to remove unreliable data. In [9-13], wavelet packet analysis was utilized to apply a standardized statistical filtering approach to data collected from various types of sensors. Figure 5 shows trimming of erroneous MC data measured by one of the WM1 WAN sensors in the Hyytiälä's building. Note that it was found that approximately 7% of the data were invalid because they fell outside of the sensor's measuring range. Removal of out-of-range data allowed to observe wood MC changes more accurately within the hygroscopic range.

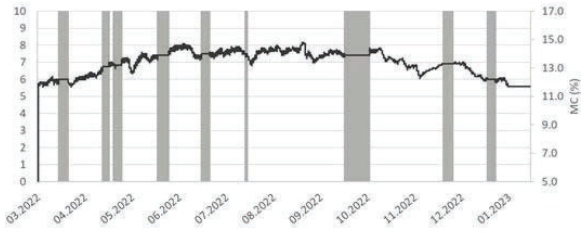

Figure 4. *MC data loss (grey bars) & reconstruction (MC measurement, InnoRenew).*

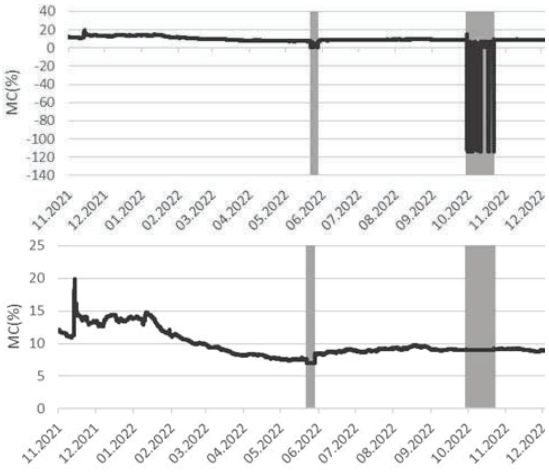

Figure 5. *Data validity check and trim (MC measurement, Hyytiälä) before correction (top), after correction (bottom).*

2.6 DATA ANALYSIS AND VISUALIZATION

This section presents examples of hygrothermal and climate data plotted against construction events, and predicted mold growth curves. The objective is to utilize visualization to facilitate a comprehensive understanding of the data and enable better-informed decision-making. The graphs in Figures 6 and 7 display moisture content (MC) data in CLT walls of the buildings in Corvallis and Hyytiälä, respectively, along with meso-climate data such as air relative humidity and temperature at the wall location, and macro-climate data (i.e., precipitation) recorded at the weather station locations. The unprocessed MC data can aid in identifying patterns in the behaviour of the material during construction, although it may exhibit unrealistic spikes during rainy periods and abrupt drops during lower humidity periods due to direct sensor exposure to precipitation. In addition to the measurements, the graphs in Figures 6 and 7 show the mold growth index calculated using meso-climate data. The Mould index (M-index) is computed utilizing the VTT model [22]. The model considers periods of mold decline, which are influenced by the duration of unfavourable environmental conditions, specifically when the RH falls below a certain threshold.

Vertical lines on the graphs depict certain construction key dates. Figure 6 refers to the first six months of construction of the PFSC in Corvallis. Throughout this period, the monitored location was continuously exposed to outdoor conditions. The plotted MC data correspond to measurements taken in the fourth ply of the CLT panel, from south to north, at the upper part of the tendon shaft of the shear wall. During the monitoring period, the location was subject to wetting, resulting in moisture content (MC) increases exceeding 24%. Subsequently, a slow drying process occurred, bringing the MC to around 18% after 5 months. The M-index, which was calculated using the air temperature and relative humidity (RH) data collected near the installed sensor, indicates a slight risk of mold growth.

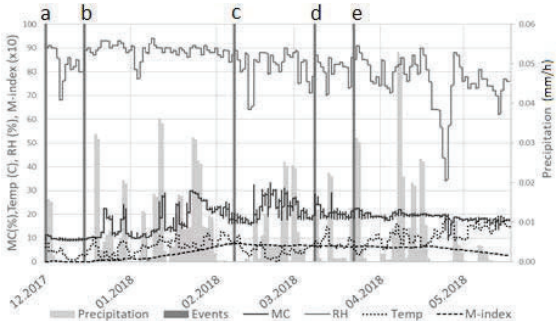

Figure 6. *Corvallis. MC, RH, Temperature, precipitation data, M-index. Vertical lines: (a) installation of sensors in the shear wall; (b) installation of the 1st floor, which partially sheltered the north side of the wall; (c) completion of the roof framing and (d) weather protection, with the exclusion of the stairwell where the monitored shear wall was located; and (e) temporary construction suspension.*

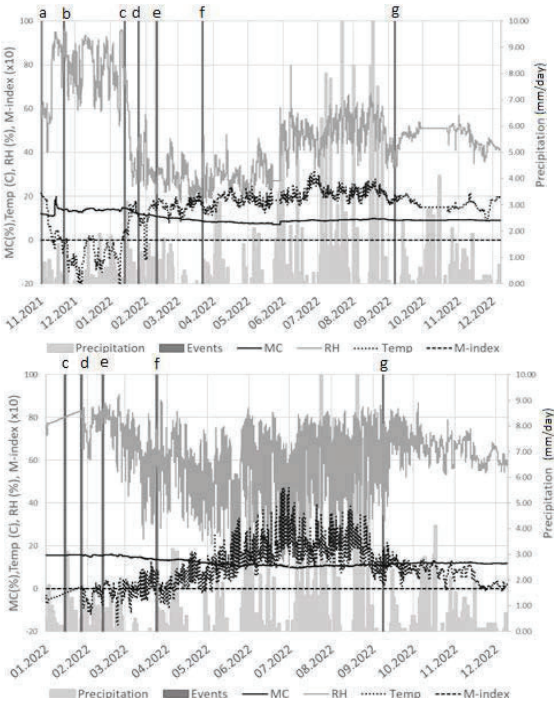

Figure 7. *Hyytiälä. MC, RH, Temperature, Precipitation data, M-index. Vertical lines: (a) installation of the sensors at the CLT facility, (b) wall erection complete, (c) removal of the temporary canopy, (d) installation of windows, (e) indoor heating started, (f) enclosure complete, (g) floor heating turned on.*

Figure 7 depicts the MC readings in two CLT wall locations in Hyytiälä covering a period from transportation to building decommissioning. In all the time the panels were protected from direct exposure to water. The data in Hyytiälä show that, despite some periods of heavier rain in summer, MC values in the panels remained stable and RH did not reach levels of concerns for the development of mold. This is supported

https://doi.org/10.52202/069179-0507

by the calculated M-index. The data also indicates that turning on the heating caused a rapid increase in temperature and a decrease in humidity, which led to a reduction in the wood MC and stabilization at 10%.
A third example, in Figure 8, shows discontinuous MC hand-held readings taken on a CLT floor panel in the building in Izola. The measurements were taken at different depths and positions close to an in-plane floor connection and the average of these readings is presented in the plot. The figure also includes climate data, key construction dates, and the calculated M-index.
As it can be observed, a spike in the MC corresponding to a period of heavy rainfall, which began in December 2020. During this time, the building's structure was complete, but the roofing assembly had not yet been finished, resulting in leaks and wetting of the floor connection details.
The plot also illustrates the increase in the M-index curve calculated from the RH values estimated using the inverse sorption equation based on the MC values [23], as no RH sensors were installed in that location at the time.

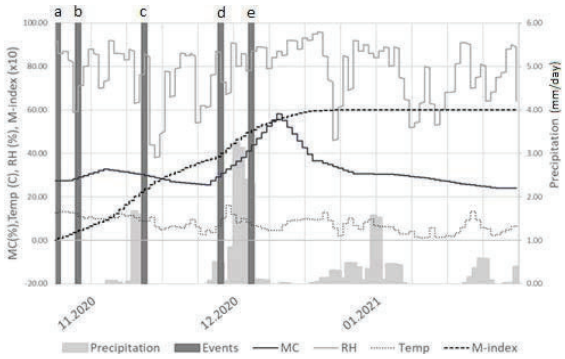

Figure 8. *Izola. MC, RH (estimated), Temperature, precipitation data, M-index. Vertical lines: (a) erection of the CLT floors (b) timber structure complete, (c) window installation complete, (d-e) period of heavy rainfalls and reported leaks.*

2.7 CONTINUING RESEARCH ON A UNIFIED FRAMEWORK FOR DATA EXCHANGE, INTEGRATION AND ANALYSIS

The examples presented in this paper underscore the significance of implementing a data integration framework that can effectively oversee the complexities of merging data from various monitoring projects, while also guaranteeing a smooth and precise integration process.
Such a framework can also provide tools for data analysis, knowledge extraction, and recommendation generation.
Our previous work [24] described a unified framework based on the concept of avatars [25], which are decentralized computing agents that use Web languages and protocols to create a virtual representation of entities such as buildings, building elements, and sensors. This avatar-based framework has been compared to state-of-the-art Structural Health Monitoring (SHM) solutions and offers a promising approach to data exchange, integration, and analysis.
In this approach, each entity in the framework is represented as an avatar, which is a software that operates on a device connected to a physical object. Avatars compute essential information about their corresponding physical objects locally and can share, integrate, and analyse data with nearby avatars. For example, an avatar installed on a building can combine its data with that from an avatar on a meteorological station for moisture monitoring. By elevating the avatar concept to represent individual buildings, the framework overcomes interoperability issues, enables the sharing of information and knowledge among buildings, and promotes the widespread adoption of SHM systems and data exchange.

3 DATA-CORROBORATED ON-SITE OBSERVATIONS

The areas of concern for moisture ingress were primarily observed at edges, gaps, and connection points. Despite the presence of local measures to protect against moisture, such as taping at the floor joints and using end grain sealant at panel cuts, extended exposure to precipitation and limited ventilation in these areas can result in water retention and create conditions that can lead to mold growth. Although using a temporary canopy was successful in preventing the structure Hyytiälä from becoming wet, this practice is not widely accepted in many countries. Therefore, it is important to consider alternative measures to prevent moisture accumulation in vulnerable areas. This can be achieved by locally deflecting water, implementing effective drainage systems, and promoting drying prior to enclosing the mass timber elements in less breathable assemblies.
The detection of checking in the CLT panels in Hyytiälä, developed during a period of significant temperature increase, indicates the need for not only monitoring excessive wetting during construction but also controlling the drying process once the building is enclosed and during its initial period of use. Hygrothermal monitoring data can aid in the creation of effective drying protocols on site to address these concerns.

4 CONCLUSIONS

This paper showcases three hygrothermal monitoring projects in mass timber buildings and emphasizes some factors in a project implementation that impact the quality of data and subsequent opportunities for data integration within a single project and among multiple projects. This paper also explores various methods for improving data quality and introduces a new integrated framework for data management and integration to facilitate the collective use of hygrothermal monitoring data across multiple mass timber projects. Certain data enhancement techniques were particularly applicable to utilizing data in predictive models, particularly for assessing the risk of mold growth.

https://doi.org/10.52202/069179-0507

The hygrothermal data was presented in a format that promotes more comprehensive comprehension of relevant phenomena and facilitates informed decision-making. Hygrothermal data was utilized in conjunction with visual inspection to identify areas of concern, highlighting the potential to improve wetting and drying control in mass timber panel construction through more effective use of data. Effective use of data across multiple projects requires intention and planning during the initial stages of a hygrothermal project. Nonetheless, it offers significant potential to advance our understanding of the behaviour of mass timber buildings over their lifespan, thereby supporting this growing industry.

5 ACKNOWLEDGEMENTS

The authors gratefully acknowledge the U.S. Department of Agriculture's Agricultural Research Service (USDA ARS) for funding the Oregon State University's projects (Agreements No. 58–0202-5–001 and No.58–0204-9–165); the European Commission for funding the InnoRenew CoE project (Grant Agreement #739574) under the Horizon2020 Widespread-Teaming program and the Republic of Slovenia (Investment funding of the Republic of Slovenia and the European Regional Development Fund). They also acknowledge the Slovenian Research Agency ARRS for funding the projects J2-2504 and BI-US/22-24-153. The Ministry of the Environment is also acknowledged for its funding of the University of Helsinki's project (grant VN/5671/2021) from the Aid Scheme for Growth and Development from Wood under the Wood Building Programme. Authors also acknowledge to project FW03010267, this project is financed from the state budget by the Technology Agency of the Czech Republic and the Ministry of Industry and Trade within the TREND Programme.

REFERENCES

[1] S. Kordziel, S. Pei, S. V. Glass, S. Zelinka, and P. C. Tabares-Velasco, "Structure Moisture Monitoring of an 8-Story Mass Timber Building in the Pacific Northwest," *J. Archit. Eng.*, vol. 25, no. 4, pp. 1–14, 2019.

[2] R. Lepage, J. Higgins, and G. Finch, "Moisture Uptake Testing for CLT Floor Panels in a Tall Wood Building in Vancouver," *15th Can. Conf. Build. Sci. Technol.*, no. Mc, pp. 1–17, 2017.

[3] R. McClung, H. Ge, J. Straube, and J. Wang, "Hygrothermal performance of cross-laminated timber wall assemblies with built-in moisture: Field measurements and simulations," *Build. Environ.*, vol. 71, pp. 95–110, 2014.

[4] J. Y. Wang *et al.*, "Durability of mass timber structures: A review of the biological risks," *Wood Fiber Sci.*, vol. 50, pp. 110–127, 2018.

[5] E. L. Schmidt, M. Riggio, A. R. Barbosa, and I. Mugabo, "Environmental response of a CLT floor panel: Lessons for moisture management and monitoring of mass timber buildings," *Build. Environ.*, vol. 148, 2019.

[6] E. Schmidt and M. Riggio, "Monitoring moisture performance of cross-laminated timber building elements during construction," *Buildings*, vol. 9, no. 6, 2019.

[7] E. Poblete, T. Messadi, C. Murray, and S. Zelinka, 2022. Moisture Monitoring of a CLT Structure in a Southern Climate. *Journal of Architectural Engineering*, 28(2), p.04022005.

[8] EJ. Baas, M. Riggio, and AR. Barbosa, 2021. "A methodological approach for structural health monitoring of mass-timber buildings under construction. *Construction and Building Materials*, 268, p.121153.

[9] E.J Baas, G. Granello, AR. Barbosa, M. Riggio, 2021. Post-tensioned timber wall buildings: design & construction practice in New Zealand & United States." In: *Proceedings of the World Conference on Timber Engineering*, WCTE 2021, Santiago, Chile, August 9-12

[10] M. Riggio, E. Schmidt, and G. Mustapha, 2019. "Moisture monitoring data of mass timber elements during prolonged construction exposure: The case of the Forest Science complex (Peavy Hall) at Oregon State University." *Frontiers in Built Environment*, p.98.

[11] M. Riggio, J., Sandak, and S. Franke, 2015. "Application of imaging techniques for detection of defects, damage and decay in timber structures on-site." *Construction and Building Materials*, 101, pp.1241-1252.

[12] E.Prelovšek, J. Niemelä, R. Acquah, U. Kavka, A.J. Niemelä , A. Kutnar, I. Šušteršič, M. Mikuljan, 2022. Weather Protection and Moisture Content of Large Mass Timber Buildings During Construction. In WoodRise Conference, 6-9 September 2022, Izola, Slovenia. pages 48-50 https://plus.cobiss.net/cobiss/si/sl/bib/135561475

[13] EJ. Baas, M. Riggio, and AR. Barbosa, 2021. "Structural health monitoring data collected during construction of a mass-timber building with a data platform for analysis." *Data in Brief*, 35, p.106845

[14] P. Garrahan, 1988. "Moisture meter correction factors," in *Proceeds of a Seminar on In-Grade Testing of Structural Lumber*. Madison, WI: Forest Products Laboratory; US Forest Service.

[15] S.V. Glass, S.L. Zelinka, "Moisture Relations and Physical Properties of Wood", Forest Products Laboratory, Madison, WI, 2010.

[16] F. Pfaff, and P. Garrahan 1986, "New temperature correction factors for the portable resistance-type moisture meter". *For. Prod. J*., 36, pp. 28-30.

[17] J. Song, C. Kim, and J. Park, "Structural health monitoring data reconstruction using interpolation techniques," *Journal of Civil Engineering and Management*, vol. 23, no. 6, 2017.

[18] H.P, Wan and Y.Q., Ni, 2019. Bayesian multi-task

 https://doi.org/10.52202/069179-0507

learning methodology for reconstruction of structural health monitoring data. *Structural Health Monitoring*, 18(4), pp.1282-1309.

[19] Bao, Y., Tang, Z. and Li, H., 2020. Compressive-sensing data reconstruction for structural health monitoring: a machine-learning approach. *Structural Health Monitoring*, 19(1), pp.293-304.

[20] Lei, X., Sun, L. and Xia, Y., 2021. Lost data reconstruction for structural health monitoring using deep convolutional generative adversarial networks. *Structural Health Monitoring*, 20(4), pp.2069-2087.

[21] Zhang, Y.M., Wang, H., Bai, Y., Mao, J.X. and Xu, Y.C., 2022. Bayesian dynamic regression for reconstructing missing data in structural health monitoring. *Structural Health Monitoring*, 21(5), pp.2097-2115.

[22] A. Hukka, and Viitanen, H.A. 1999. A mathematical model of mould growth on wooden material. *Wood Sci. Technol*. 33 (6): 475–485.

[23] P.H Mitchell, 2018. Calculating the equilibrium moisture content for wood based on humidity measurements. *BioResources*, 13(1), pp.171-175.

[24] M. Riggio, M. Mrissa, M. Krész, J. Včelák, J. Sandak, and A. Sandak. "Leveraging structural health monitoring data through avatars to extend the service life of mass timber buildings." *Frontiers in Built Environment*, *8*, 2022.

[25] M. Mrissa, L. Médini, J. Jamont, N. Le Sommer, and J. Laplace. "An avatar architecture for the web of things." *IEEE Internet Computing*, *19*(2), 30-38, 2015

World Conference on Timber Engineering Oslo 2023

TOWARDS DESIGN FLEXIBILITY AND FREEDOM IN MULTI-STOREY TIMBER CONSTRUCTION: ARCHITECTURAL APPLICATIONS OF A NOVEL, ADAPTIVE HOLLOW SLAB BUILDING SYSTEM

Hana Svatoš-Ražnjević[1], Anna Krtschil[2], Luis Orozco[3], Gregor Neubauer[4], Jan Knippers[5], Achim Menges[6]

ABSTRACT: This paper discusses the architectural design potentials of a novel hollow timber slab building system for flexible and adaptive multi-storey timber building typologies. Current timber building systems are defined by their standardized nature, which limits most structures to unidirectional, rigid grids and limits designs to rectilinear layouts. At the same time, recent developments in computational design and digital fabrication open new possibilities to overcome these limitations. In this paper we present four building design applications of a new multi-directional slab building system that allows for a greater level of spatial flexibility and adaptability with free column placement and a tuned network of internal shear webs. These examples expand on previous work through the co-development of building design, skin, building system, and building service integration strategies for a long lifespan and changeable building program. The design applications illustrate open, reprogrammable floor plates that can support three different program states: office, residential, and mixed-use. Furthermore, the novel conceptual approaches to building service integration and the resulting slabs are compared to approaches more common in mass timber construction. Finally, we contextualize the study with related developments and discuss how computational and integrated design thinking could lead to a greater level of design freedom in timber construction and an increased applicability to more complex site conditions than in conventional mass timber construction.

KEYWORDS: multi-storey timber buildings, flexibility, adaptability, multi-directional timber slab, digital design

1 INTRODUCTION

Since the early 2000's, there has been an increase in worldwide construction of multi-storey timber projects [1]–[3]. This is in part due to environmental issues [4], the urbanization and densification of cities [5], [6], and material and building system developments [7], as well as to policy changes that allow taller timber buildings [8]. Although current projections show is a global demand for more building area [9], there is ongoing stagnation in the building industry [10], [11]. Additionally, there is a contradictory situation in which usable buildings are being prematurely demolished when they are considered to no longer be valuable [12]. Adaptable buildings are increasingly important in the face of changing economic incentives, rising material costs that make reuse more economically viable, and climate change [13].

Housing in some Asian countries has always had a shorter life expectancy than in the West, with an average demolition age of about 30 years versus 50-70 [14]. However, studies have shown that in some European countries the average demolition age is between 30 and 60 regardless of the building's program [15]. Furthermore, future demolitions will include buildings constructed only fifty years ago due to current methods of renovation and changing energy performance requirements [16]. In addition, changes in building layers are not made due to elements being obsolete but mostly due to external factors, such as economic or business-models [17]. This may be not only due to buildings being difficult to adapt, but also not designed for longevity or to accommodate future needs.

Timber is suitable for tackling challenges related to stagnation in the building industry because it is a digital material that is easily machinable and highly suitable for prefabrication [8], [18]. It also has a good stiffness to weight ratio [19], making it relatively lightweight for

[1] Hana Svatoš-Ražnjević, Institute for Computational Design and Construction, University of Stuttgart, hana.svatos-raznjevic@icd.uni-stuttgart.de

[2] Anna Krtschil, Institute for Building Structures and Structural Design, University of Stuttgart, anna.krtschil@itke.uni-stuttgart.de

[3] Luis Orozco, Institute for Computational Design and Construction, University of Stuttgart, luis.orozco@icd.uni-stuttgart.de

[4] Gregor Neubauer, Institute for Building Structures and Structural Design, University of Stuttgart, gregor.neubauer@itke.uni-stuttgart.de

[5] Jan Knippers, Institute for Building Structures and Structural Design, University of Stuttgart, info@itke.uni-stuttgart.de

[6] Achim Menges, Institute for Computational Design and Construction, University of Stuttgart, achim.menges@icd.uni-stuttgart.de

https://doi.org/10.52202/069179-0508

transportation, and can address challenges related to decarbonization thanks to its great potential for carbon storage [20]–[23]. While timber construction allows for relatively easy building component and process modification compared to concrete and steel, its flexibility is limited by shorter spans and limited architectural typologies [3].

1.1 FLEXIBILITY IN ARCHITECTURE

In literature, the terms adaptability and flexibility have multiple definitions and characteristics attached to them, often with overlapping meanings, such as expandability, polyvalence, or partitionability [24]–[27]. Perhaps the most widely accepted concept is that of separating, or shearing, building layers by their rate of change [17], [28]–[30], because the "longevity of buildings is often determined by how well they can absorb new services technology" [31]. The authors distinguish between two terms: (i) design for flexibility, which refers to the manipulation of design factors that affect the building's adaptability to change [32], and (ii) process flexibility, or flexible planning, which can refer to the ability of a (design) process or a system to adjust to and accommodate change and disruption [33], [34]. Both of these are needed for adaptable buildings and building systems [13].

1.1.1 Approaches to flexible design

There have been many approaches to flexible design throughout history, including, recently, Open Building projects [35]. In general, flexibility has been achieved through the use of an open area as a universal floor plan that can be subdivided into spaces based on need [17]. Therefore, homogeneous spaces and a "generality" of space [36] define the modern concept of flexibility, as opposed to heterogeneous spaces, which exhibit a more diverse range of spatial qualities. Conversely, interchanging and removing components is important for building use conversion [29], [37] as can be seen in projects such as the Multifunk building, whose networks of services and shafts to handle transformation, or the CiWoCo building, which separates service layers and partition walls from the structure [38].

1.1.2 State of the Art flexible projects in timber

While there are many concrete projects with large open floorplates, there are still relatively few flexible projects in timber construction. One of the more flexible projects is Patch 22 in Netherlands, a mass-timber frame project with 9m spans. Its general layout is enabled by a Slimline floor, a concrete slab that rests on timber beams with integrated steel profiles that provide cavities for installations in the raised floor [39]. This floor enables the residents to swap technical systems themselves [40]. Together with hollow floors, no vertical structure in the apartment interiors, a central service core, a tall stories and a high floor load, this produces a flexible and durable design. Another proposal for flexibility in timber construction is the Kiubo construction system, where prefabricated timber modules can be inserted into a concrete skeleton structure [41]. They can be swapped or connected to extend or change the interior requirements. While modular construction is developed at an industrial level, research is also being conducted on future-oriented timber buildings. The project "Convertible wood hybrid for differentiated expansion stages" tested a seven-storey timber frame structure for the use of parking, living, and working [42]. The design aimed for a neutrality of use and utilized recyclable materials at the building, assembly, and material levels. This was achieved through load bearing and window elements that could be reused or had reversible connections, enabling the non-destructive dismantling of components. It had a grid of 5.4m x 7.9m in the beam direction.

1.2 FLEXIBLE TIMBER DESIGN CHALLENGES

Engineered wood products, such as CLT have enabled increased structural performance and new heights of construction. At the same time, studies show that multi-storey timber construction has so far been limited to grid-based and mostly orthogonal and rectangular designs [3], [43]. Although timber construction offers the advantages of automation and prefabrication in terms of speed and cost-effectiveness, current wood building systems are defined by their modular and standardized nature. Even though elements of almost unlimited size and shape can be fabricated out of engineered wood, transport and assembly requirements greatly limit the complexity and scale of these systems and the resulting buildings. This is also partly due to the lack of suitable load transferring connections in timber [44]. In contrast, conventional reinforced concrete or steel structures allow can have larger spans and be more adaptable to site constraints or design intent. Therefore, timber building systems with spans competitive to concrete construction are mostly post-and-beam structures with a comparatively greater structural depth. Beams and girders impact the placement of partition walls, reducing options for interior partitioning and compromising the building's adaptability for future changes of use and therefore its life span.

Timber construction faces additional challenges in terms of flammability and acoustics. Building service integration is therefore often problematic, as services and any openings must be pre-planned and prefabricated.

1.2.1 Building services in mass-timber construction

In mass-timber frame structures, services are most often hung below beneath slabs or integrated between beams to increase flexibility and because they are easier to place and access. Services can also be placed above the structure either as an accessible layer, such as in a raised access floor, or as a permanently embedded layer of the structure, in conduits that run through the concrete topping of the slab. In exposed timber post-and-beam structures, services can be even more integrated, and run through and between structural elements, either through cut outs in timber beams, by staggering the heights of the

beams, or by providing gaps in the structure, such as indents in the assembly of the structural elements. Table 1 shows how these service integration strategies, which can have different impacts on accessibility and freedom of placement of services, can be layered, embedded, or integrated into the building system.

Table 1: *Common horizontal building service integration strategies in post-and-beam mass-timber construction and type of integration based on accessibility.*

Service location	Integration type
Below structure	Layered
Above structure	Layered / Embedded
Through structure	Layered / Integrated

The structural system can inform or inhibit the way the building service systems appear and perform [45]. While the direction of beams can inform service paths, the structural grid can also intersect with MEP (mechanical, electrical, plumbing) paths, resulting in non-systematic overlaps. Additionally, current MEP systems, such as air ducting, are ill-suited to frequent changes of fit outs to adapt to new program or tenant requirements. Finally, the rectangular geometries and 90-degree corners of existing ductwork and mechanical systems are optimized for manufacturing and not for efficient air movement or distribution [46].
To allow timber construction to break free from current limitations and for its architectural possibilities to be competitive with concrete and steel construction, it is necessary to innovate on multiple levels, from design to fabrication processes, including service integration.

1.3 AIM AND SCOPE

This work investigates novel possibilities for multi-storey timber building designs. It showcases both a robust building design process and an adaptive building system capable of greater column spacing, lower structural ceiling depth, and an integrated approach to building services for greater adaptability in multi-storey timber construction. It will describe and compare four design applications of a novel building system as case studies to explore novel design possibilities and changes of building use. It will focus specifically on change in different operations cycles and building service requirements for different programs, and their impact on the design of the building system.
The authors define adaptability as the ability of the building to accommodate different programs throughout its lifetime with minimal costs or changes to the structure, as well as the ability of the building system to adapt to site and design intent. This paper asks the following questions. (I) How can digital fabrication and computational design methods enable novel multi-storey timber building typologies with innovative building service integration, and (II) what overarching, and timber specific design strategies are needed for a building that will change its program over a 100-year building life span.
The resulting case studies will address these questions as conceptual studies and integrative design proposals.

2 BACKGROUND

The research in this paper was conducted as an extension of that done on a resource efficient timber building system within the Cluster of Excellence on Integrative Computational Design and Construction for Architecture (IntCDC). This mono-material building system prioritizes timber over steel for its elements and joints, in contrast to the conventional mass-timber construction. The research included the development of new design, simulation, and fabrication workflows for this building system, as well as the Co-Design of a robotic prefabrication platform for its construction.
The development builds on top of the overarching methodology of Co-Design pursued within the IntCDC [47], and the integrative design workflows of the Institute of Computational Design and Construction (ICD) and Institute of Building Structures and Structural Design (ITKE) at the University of Stuttgart. These have previously been used in the design of resource-efficient high-performance fibre [48] and segmented timber shell structures [49], [50], and have now been extended to multi-storey timber construction. The design application case studies presented in the paper were developed within the "Integrative Technologies and Architectural Design Research" (ITECH) master's programme 20/21 design studio.

2.1 BUILDING SYSTEM DESCRIPTION

The building system is based on a hollow slab consisting of thin upper and lower cross-laminated timber plates connected by internal shear webs tuned to a column layout and allowing for greater flexibility through multi-directional spans (Figure 1).
This level of customization is possible due to direct feedback via an integrated computational design and engineering workflow, resulting in a differentiated web layout, slab segmentation and joint distribution. Several papers already present the following aspects of the system: conceptual development of two previous hollow and solid slab system iterations [51], structural development and integration of structural principles in a computational design methodology [44], different design and simulation methods for internal web reinforcement placement [52], and agent-based methods for column, plate, and web placement [53].
As described by Krtschil et al. [44], the system consists of a hollow slab, columns, and their connections. The slab itself consists of three layers: a top and bottom CLT plate with shear force transferring webs also made of CLT in the middle layer. The webs are oriented by the flow of forces in the slab. The slabs are connected with a glued, stepped edge connection [44]. The column-to-column and

https://doi.org/10.52202/069179-0508

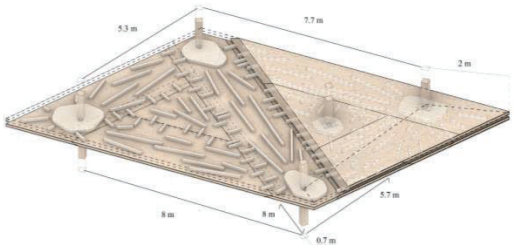

Figure 1: *Multi-directional hollow slab timber building system with internal shear webs.*

column-to-plate connections are reinforced with beech LVL. The columns are connected by a beech LVL pin that transfers the loads through the slab. The column-to-plate connections consist of a solid CLT column crown that brings the high moment and shear forces into the column. The columns can be placed freely inside the slab segments. The system is mono material as it requires no steel connectors.

2.2 STRUCTURAL CAPABILITIES

This first iteration of this building system enables spans up to 8 m and cantilevers up to 1.7 m with a 32 cm deep slab [44]. Further iterations may enable greater spans with only small adjustments in the overall slab depth.
The primary features of the novel system are: (i) large spans with a relatively shallow slab depth, (ii) cantilevers from 0.7 up to 2 m, (iii) corners that can meet at a variety of different angles, and (iv) irregular column placement with varying relations between them.

2.3 ARCHITECTURAL CAPABILITIES

Flat slabs are more flexible than those with beams because they allow greater freedom in partition wall placement. The building system enables design features currently not possible in flat slab timber construction. This includes aspects such as free slab edges, open corners, overhangs, greater freedom and variations in slab outline design and slab openings, non-orthogonal layouts, and large open floors (Figure 2). As such, in contrast to conventional mass timer construction, this building system can adapt to, rather than dictate, the design intent. The hollow cavity within the slab could also be enlarged, to either integrate services or be filled to improve the acoustic behaviour of the slab. The acoustic damping effect would be particularly notable for spans 12 m and above.

3 METHODS

The methods build on top of previous research and explore the application of the proto-architectural timber post and slab building system concept at an architectural scale. They are based on the integrated co-development of the overall building design, building system and building service integration strategies. This process considered robotic fabrication and assembly processes, alongside computational design and engineering methods for multi-storey timber construction.

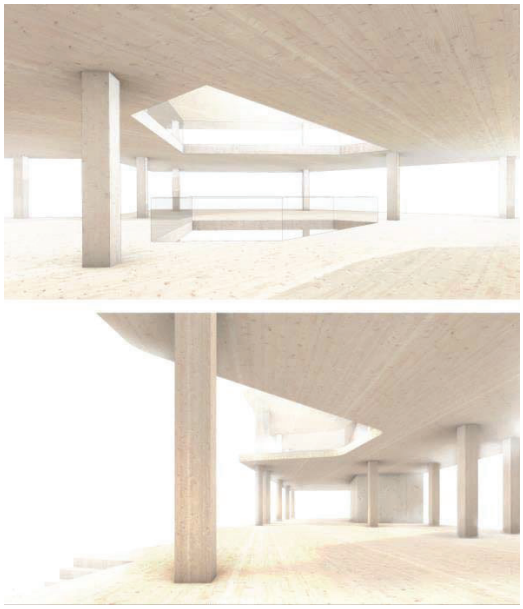

Figure 2: *Interior views of Case Studies 2 (above) and 3 (below).*

3.1 BUILDING DESIGN AND BRIEF

The design brief for the interdisciplinary design studio has been focusing on designing and developing a building system suitable for a long lifespan and change of building program; a “non-programmed” building with a minimum 100-year life span enabling a more flexible and multi-purpose use of space. Therefore, the main interest lies on the exploration of current technical possibilities in timber design and construction rather than on strict adherence to locally applied building codes and regulations.
The four Case Studies are two different architectural building designs on each of two different sites. As Figure 3 shows, the sites were selected due to constraints that typical mass-timber construction would have difficulty adapting to, such as a relatively irregular non-rectangular

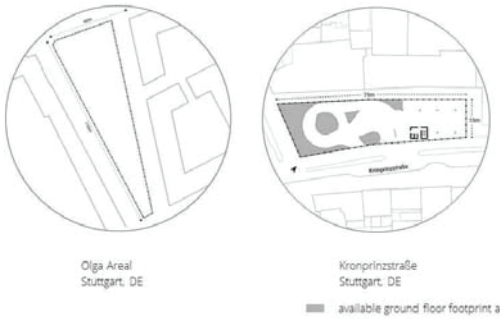

Figure 3: *Sites in Stuttgart, Germany: Olga Areal (left), and Kronprinzstraße (right).*

https://doi.org/10.52202/069179-0508

site form, proximity to neighbouring buildings, and limited footing for construction due to pre-existing construction on site (underground parking).

Within each Case Study the hollow slab building system was extended by considering lateral bracing strategies for the overall structure, building façade design, and an integrated building service distribution strategy.
Each Case Study was then tested in four use cases: (0) the "non-programmed" state, (1) office, (2) residential, and (3) mixed-use program combining commercial with residential, such as a hotel.

3.2 Building System Components and Lifespan

Within this research relative lifespans were established for different building layers or components: permanent structure, semi-permanent building skin and façade elements, and temporary building services frequently adjustable to program changes. Table 2 shows the conceptualized average life span in years.

Table 2: *Relative building elements rate of change*

Building layer	Lifespan (years)
Structure	100+
Building skin	25
Building services	5-15

3.2.1 Structure and Hollow Slab Building System

The focus of the structural system development was to increase lateral stability of the building. Each of the four building designs had their own concepts towards this aim. These included cores, an exoskeleton, shear walls, and timber bracing. Another focus of the building system development was the optimisation of structural timber use, rather than maximising its overall use, with the goal of replacing metal connections whenever possible. The slab system was also reconceptualised to integrate building services, which required new slab segmentation, web placement, and assembly strategy concepts.

3.2.2 Building Skin

The building skin was developed to a conceptual level only, as a semi-permanent substructure that would change minimally regardless of program and service requirements. As detail development was out of scope, this included only aspects such as materiality and modularity. Structural supports are aligned with the façade segmentation and further panel subdivisions are done with future program distribution in mind, as façade subdivision is closely related to internal layout.

3.2.3 Building Services

The following MEP services were considered in the development of the design application case studies: heating, cooling, ventilation, and air conditioning (HVAC), electrical wiring, and plumbing. The focus was on developing overall horizontal and vertical service distribution concepts that would work for all programs despite their different technical needs. Table 3 shows a short overview of these needs. As can be seen, the main challenges were the opposing requirements for quantity of wet spaces, and for centralised versus decentralized HVAC systems, between Office and Residential uses.

Table 3: *Overview of service needs for the programs*

Service type	Office	Residential	Hotel*
Mechanical	centralized	decentralized	both
Plumbing	low	high	high
Electric	exposed	concealed	both

*mixed-use commercial program

3.3 Case Study Comparison

Finally, the four resulting hollow slab building systems are compared from two perspectives: (i) structural, considering slab depth, maximum span, and span directionality, and (ii) building service integration strategy and accessibility concepts in relation to the hollow slab and horizontal distribution of services.

4 Results & Discussion

Figure 4 shows four building designs with different horizontal and vertical building service distribution strategies. Case Study 1 and 2 were designed for an empty wedge-shaped plot. Case Studies 3 and 4 were designed to be built on top of a pre-existing parking lot and to adapt to the car entry and the existing structural grid (Figure 3).

4.1 Case Studies Description

4.1.1 Case Study 1

Case Study 1 relies on its service distribution strategies to create flexibly programmable spaces. This includes cores and temporary shafts for vertical service distribution and a distributed network of services integrated into the hollow slab. The cores' hollow shear walls contain embedded service channels. The temporary vertical shaft locations provide a guideline for partition wall placement, but also act as access points for services in the slab when program change needs horizontal duct rerouting (Figure 4 -I). The partition walls can also provide additional horizontal service distribution. This has several implications on the slab system. One of the most relevant factors determining the possible service locations are the column locations as well as the slab segmentation, as openings for service accessibility need to be carefully considered for structural purposes. The service channels are placed inverse to the column location, which means that the slab openings are located mid span, away from areas with high shear forces, minimizing the structural impact (Figure 5).
The building façade was designed with a varying modular rhythm that matches possible future locations of partition walls. Movable shading modules allow for the enclosing and glazing aspects of the façade to be reconfigured,

https://doi.org/10.52202/069179-0508

reducing the need to disassemble façade panels during use changes. Figure 5 shows how each program can use a different combination of service distribution strategies based on its needs. In the open plan office state wet spaces can be organized around the core with minimal horizontal runs. Electricity can be hung from the ceiling, and HVAC systems can use the core for vertical distribution and the slab for horizontal distribution with ceiling vents at slab access panels. In the residential state, a combination of cores and temporary shafts for vertical distribution and partition walls for horizontal distribution would increase the number of possible wet spaces in the floorplan. HVAC systems would only need to vent kitchens and restrooms, which could be done through the façade by way of partition walls. Electricity could also be integrated in the partition walls. The mixed-use state, such as a hotel, would use the residential strategy for rooms and the office distribution strategy for communal spaces.

4.1.2 Case Study 2

The design of Case Study 2 consists of integrated service channels in the slab for horizontal distribution, and cores and temporary shafts for vertical distribution (Figure 4 - II). Temporary shafts can be deployed when necessary and placed where services from the cores' shear walls cannot reach. Horizontal service lines are branching pathways that run from the cores and cut across the main direction of the webs with access openings carefully positioned between columns. They are arranged based on the shortest path needed to optimize their distribution. The service pathways are envisioned as encased metal ducts ensuring fire and moisture protection. Therefore, in the office state (1), wet spaces are limited to the areas next to the core, while in the residential (2) and mixed-use (3) states the wet space locations can be extended by use of deployable shafts and horizontal plumbing limited to partition walls (Figure 5). HVAC ducts are planned within the slab with venting along the slab edge, while electrical lines are planned within walls and floors. The facade design concept uses a limited number of modular dimensions for easy replacement and maintenance. Only a few custom elements are used, for specific corner conditions, that are expected to have a longer life-span.

4.1.3 Case Study 3

Case Study 3 leverages its site constraints to provide maximum daylighting for both itself and its neighbouring buildings by using terraces and an atrium. The design of the massing, in particular the relatively shallow floorplate depth, enables a thin slab with no integrated services. Services are instead distributed through the cores, while a limited number of temporary shafts link not to the ground but to a service transfer level below the first floor (Figure 4 - III). Wet program placement is therefore limited to the areas within the maximum horizontal run within partition walls from the core and shafts. As such, in the open office scenario (1), plumbing is constrained to areas around the cores, while HVAC systems and electrics are suspended below the ceiling. In contrast, the residential scenario (2)

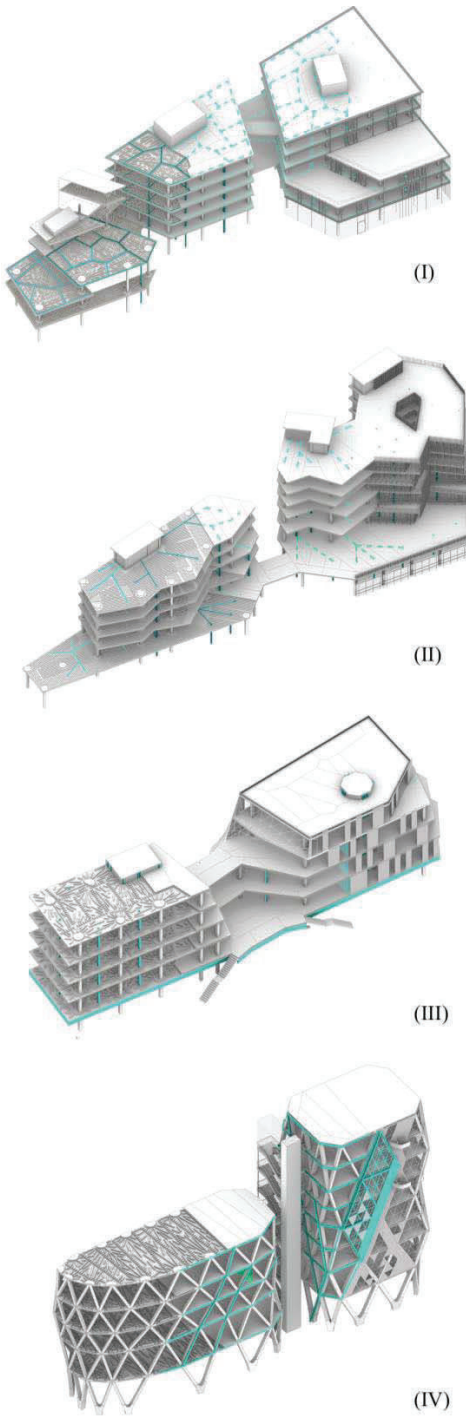

Figure 4: *Case Studies massings and exposed building system with highlighted service integration strategy and building skin design concept.*

Figure 5: *Case Studies plans by different program*

https://doi.org/10.52202/069179-0508

uses a decentralized ventilation strategy in partition walls with exchange vents integrated into the façade. Similarly, electricity and plumbing are mostly integrated into the partition walls. As in other case studies, a mixed-use scenario (3) uses a combination of the two approaches (Figure 5). The façade concept relies on modular segments that can be replaced and swapped over time. The facade provides transparent and opaque modules, and the same system could also integrate new technologies, such as solar panels, as façade elements.

4.1.4 Case Study 4

Case Study 4 is based on the idea of relieving interior space of structural supports for a maximum amount of flexibility and adaptation. Adaptability to the different technical requirements of various programs is achieved through an integrated exoskeleton: the façade, services, and structural supports are organized along the floorplate boundary. Figure 4 - IV show how the façade contains all vertical service distribution channels, while the edge of slab houses the horizontal service runs. From there, partition walls take and distribute the services within the floor plan. As this Case Study's structural core is not within the floor plate, all services are distributed either i) from the façade via partition walls, or ii) as exposed cabling or HVAC ductwork beneath the slab, as is commonly seen in open plan offices, regardless of program. Figure 5 provides an overview of the vertical shafts in the different program states.

The façade is designed to follow the supports, creating areas that are triangulated and subdivided into smaller panels which can be either transparent, for view, or opaque, to conceal services and provide enclosure. The façade frames are perforated to allow (future) services to run freely. The façade layer therefore dictates service placement, level of enclosure needed for the program (transparent or opaque panel), and the rhythm of the partition wall placement.

4.2 Case Study Comparison

4.2.1 Building structure and building system

The Case Studies utilize the circulation core and facades as their primary vertical load-bearing system, with the aim of minimizing the number of internal columns. In Case Study 1, there is only one column placed internally due to span limitations. In Case Studies 2 and 3, column spacing and placement adapt due to design of atriums, terraces, or openings in the slab for increased daylighting. These three studies all use the internal cores for lateral stability. Conversely, Case Study 4 only has structural supports along the façade with no internal columns due to its exoskeleton structure. This choice necessitated longer spans, up to 13.5 m, and therefore also a deeper slab. The case studies all maintained the 110mm dimensions of the top and bottom plates from the previously developed hollow slab system [44] but increased the height of the cavity and therefore the structural depth and the maximum spans (**Feil! Fant ikke referansekilden.**).

Internal web reinforcement and slab segmentation strategies were another factor that varied between Case Studies due to different horizontal service distribution strategies. As can be seen in Figure 5, Case Study 1 has three categories of internal webs based to their structural and service related functions: (i) webs forming closed internal channels to carry ducts for HVAC or electrical cables (plumbing was excluded due to the risk of water damage), (ii) longer span webs which act as internal beams, and (iii) shorter webs that connect different slab panels as well as fill the remaining slab space.

Case Study 2, meanwhile, aims to increase possible cantilevers by placing most webs orthogonal to the direction of the segmented slab. This orientation changes based on stiffness allocation in the slab but is limited to 90° or 45° rotations within the panel (Figure 5). In other Case Studies, slab segmentation and internal web placement are not constrained by service channels. The arrangement of webs is instead governed by the principal moment vectors at their position in the slab, and the slab segmentation is primarily governed by the spanning axis within the floorplate. In Case Study 3 this means a more irregular arrangement of panels, while in Case Study 4 this results in mostly rectangular panels with transitional trapezoidal panels due to the uneven distribution of vertical supports (Figure 5).

4.2.2 Service Integration Strategies

As mentioned in the comparison of internal web reinforcements, the Case Studies show several different approaches for horizontal service distribution within the slab (Figure 6). Case Studies 1-3 all utilize the core as the primary vertical distributor, along with temporary shafts that get utilized based on program needs (Figure 5). These slabs have openings that either are filled by the temporary shafts or act as access panels for maintenance. Whereas Case Studies 1 and 2 concepts embedded both their mechanical and electrical services within the slab, respectively, Case Study 3 relies completely on suspended

Table 4: *Structural depth and maximum span values of the Case Studies.*

Case Study	Structural depth (mm)	Internal cavity (mm)	Maximum span (m)	Service integration	mechanical	electric	plumbing
CS1	420	200	12	within	x	x	n/a
CS2	420	200	12	within	x	x	n/a
CS3	320	100	8	n/a	n/a	x	n/a
CS4	520	300	13.5	slab edge	x	x	x

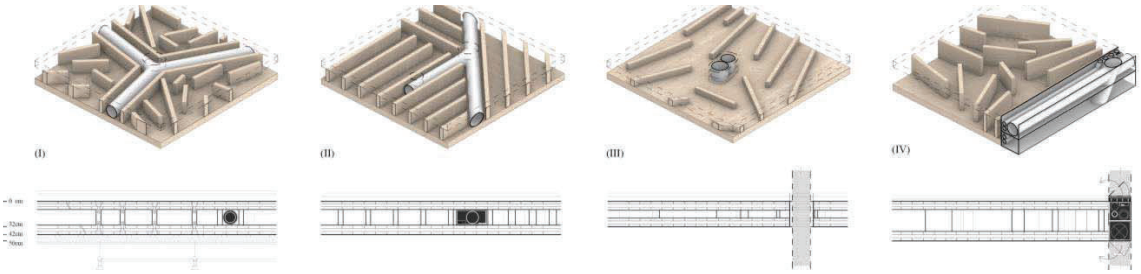

Figure 6: *Case Studies slab comparison with highlighted building service distribution strategies within the slab.*

suspended services or services integrated into partition walls for horizontal distribution. Although Case Study 3 does not integrate any services within the slab, the 100mm shallow cavity could theoretically allow electric cables to pass through. Similarly, Case Study 4 relies on services being integrated into partition walls or suspended below the ceiling. However, due to the façade based vertical distribution strategy, the slab still incorporates full MEP horizontal service distribution along its edge. While other concepts are more embedded or integrated into the slab, services are most separated from the slab in Case Study 4.

5 DISCUSSION

The developed multi-storey timber building system results in multi-directional spans with irregular point support layouts by creating a semi-monolithic slab out of segmented hollow slab plates. Embedding services inside the cavities of these plates results in a smaller overall floor depth, including services and floor and ceiling build-ups, when compared to typical mass-timber construction. This has two effects: the cavity could simultaneously contribute to better acoustic performance; and the system is more complex to fabricate than a solid CLT slab.

5.1 Comparison to common timber systems

As can be seen in Table 5, we compared the performance of some of the timber slab building system products on the market to the performance of the hollow slab system. Although there are products available that offer large spans, they either have greater structural depth, a composite or ribbed structure or offer only uni-directional spans. The most similar product in performance would be the TS3 flat timber slab system which offers bi-directional spanning up to 8x8m grid [54], but further research is being done on TS3 GridBox, a hollow box with a girder grid to reduce costs and save building material [55]. The building system showcased in this study may be more suitable for larger spans of up to 12 m due to increased fabrication complexity and lack of available solid flat slab systems with similar depth and spanning capabilities on the market.

Another aspect gleaned from the comparison is that most systems do not integrate building services in the building system development. This also shows that most building systems today are mainly developed without considering services. As a result, additional height and build-up are needed compared to the case studies of the hollow system where the increased structural height can save overall floor to ceiling height.

Table 5: *Structural depth and maximum spans designed for office use, spanning directionality values of common market slab system products, and potential for service integration (marked with "x" for possible integration within the element)*

Product	Depth (mm)	Max. span (m)	Span. directionality	Service integration	Slab system description
Research slab	310	8	Multi-	n/a	Hollow slab with internal webs [R]
Case Studies 1-2	410	12	Multi-	x	Hollow slab with internal webs
TS3*	400	8	Bi-	n/a	point supported solid CLT plate [57]
ThomaHolz100	212	5	Uni-	n/a	DLT slab [59]
StoraEnso rib panel	580	13	Uni-	n/a	CLT rib panel open R30 [60]
Kerto-Ripa	660	14.7	Uni-	x	LVL 5-rib floor [61]
Lignotrend	410	8	Uni-	x	Box slab [62]
Lignatur	440	10	Uni-	x	Hollow box-slab [63]
Kielsteg	380	13	Uni-	n/a	Flat hollow slab [64]
CREE	400	9	Uni-	x	Timber drop beams with concrete [65]

* Depth and max. span for a 5 kN/m² Live Load

https://doi.org/10.52202/069179-0508

5.2 Limitations of the work

The developed case studies are primarily of a conceptual character. They explore novel possibilities for design and construction while considering design, building service, structural, and fabrication limitations. However, they do not provide comprehensive or definitive solutions.

The case studies lack a specific consideration of fire code relating to building class, integration of services and exposure of timber elements. The integration of different elements, such as façade, its' substructure, even partition walls, and their interface with the building system, is also left open.

Our observation is that there are great potentials in integrating service within the structural layer of the slab. However, this development cannot be achieved only by automating service placement and installation in prefabrication. New innovative methods for service rerouting, replacement and maintenance or damage detection with new technologies are needed.

One future promising trajectory of research to address this would be mobile robot service installation or service extrusion. This could expand the possibilities of the timber slab design and make the suggested integration strategies more competitive with systems designed based on and operating on manual serviceability and accessibility. Additionally, it is important to acknowledge that it is very difficult to predict the dimensional, operational, and other requirements of future technologies. Questions about the minimum sizes for internal cavities and access panels for future requirements need to be balanced against structural considerations, particularly spanning performance.

Moreover, there is a trend away from use of suspended ceilings and towards exposed ductworks and services in office environments to gain room height. While in timber construction the use of beams and grid-based design can work in favour of typical ductwork, with a flat ceiling use of conventional service distribution strategies might lead to poor aesthetic quality. Already, enabled by computational design, novel airduct geometries are being developed that enhance air distribution and aesthetic quality [46].

This paper only presents a design proposal and a façade concept. Further analysis is needed on how to integrate lateral supporting structures — such as cores, walls, façade systems, or pre-existing structural elements in other materials — into the building system.

6 CONCLUSION

The presented research shows integrative development of four design applications, and therefore also timber building system variations, of a hollow multi-directional slab for multi-storey construction with structural and building service considerations. The studies showcase novel possibilities for design in timber construction, adapting to conventionally complex site conditions, creating interior spatial situations not currently possible in pure timber construction and change of use during the building life cycle, as well as initial conceptual strategies for building scale application. Compared to typical mass timber systems, the system allows for higher resource efficiency and decreased of wood use due to structurally informed placement of internal reinforcement within a cavity. One of the clear perspectives for new developments in terms of increasing flexibility relates to considering the full life cycle of the system past end of use. The current state of research focused on preventing the necessity of disassembly, however demountability of elements or their reusability were not considered.

The designs leverage complex timber elements that must be prefabricated with strict tolerances. The inherent advantages of integrated design have been used in the design of both the building and the building system. Integrating different phases of program use into the design planning enhances the outcomes of the project and is only possible through an adaptive building system and an adaptive planning process.

ACKNOWLEDGEMENT

The research has been supported by the Deutsche Forschungsgemeinschaft (DFG, German Research Foundation) under Germany's Excellence Strategy—EXC 2120/1—390831618.

The presented research was partially developed within the master's program "Integrative Technologies and Architectural Design Research" (ITECH) offered by ICD and ITKE at the University of Stuttgart by students of the ITECH 20/21 Design Studio: Pelin Asa, Erik Bauscher, Peng-An Chen, Ayşe Esin Durmaz, Peter Ehvert, Christelle El Feghali, Alan Eskildsen, Michał Gosk, Mengxi He, Harrison Hildebrandt, Matthew Johnson, Hyowook Kim, Philipp Kragl, Chien Chun Kuo, Carolina Leite Vieira, Yuxi Liu, Pinaki Mohanty, Alexandra Pittiglio, Maria Radulescu, Kevin Saslawsky, Ailey Simpson, Tina Soltani, Christian Steixner, Michael Tucker, Tzu-ching Wen, and Seyed Hossein Zargar. Following researchers were involved in the scientific development of the project: Anna Krtschil, Gregor Neubauer, Luis Orozco, and Hana Svatoš-Ražnjević. Special thanks to Visiting Prof. Markus Lager and Visiting Prof. Dr.-Ing. Jochen Stahl, for their timber construction expertise.

All images except for Figure 3 were produced by the authors or adapted and expanded by the authors based on Student Work.

The authors would like to acknowledge our colleagues Cristóbal Tapia and Dr. Simon Aicher (Materials Testing Institute), Theresa Müller and Prof. Philip Leistner (Institute for Acoustics and Building Physics), and Hans-Jakob Wagner (ICD), who developed the novel timber building system as part of IntCDC Research Project 3-1. Additionally, the authors would like to thank the entire class of ITECH 19/20 Studio and the remaining members of the tutor team who contributed to the system development: Simon Bechert and Daniel Sonntag (ITKE) and Dr. Felix Amtsberg (ICD).

REFERENCES

[1] I. Kuzmanovska, E. Gasparri, D. Tapias Monné, and M. Aitchison, 'Tall Timber Buildings: Emerging trends and typologies', *World Conference of Timber Engineering*, 2018.

[2] V. Salvadori, 'Multi-Storey Timber-Based Buildings: An International Survey of Case-Studies with Five or More Storeys Over the Last Twenty Years', 2021, doi: 10.13140/RG.2.2.14822.55360.

[3] H. Svatoš-Ražnjević, L. Orozco, and A. Menges, 'Advanced Timber Construction Industry: A Review of 350 Multi-Storey Timber Projects from 2000–2021', *Buildings*, vol. 12, no. 4, p. 404, Mar. 2022, doi: 10.3390/buildings12040404.

[4] United Nations, 'World Population Prospects–the 2017 Revision: Key Findings and Advance Tables', Department of economic and social affairs population division, New York, NY, USA, 2017.

[5] United Nations, *World urbanization prospects 2018: highlights*. NY, USA: United Nations, 2019.

[6] M. Kasanko *et al.*, 'Are European cities becoming dispersed?', *Landscape and Urban Planning*, vol. 77, no. 1–2, pp. 111–130, Jun. 2006, doi: 10.1016/j.landurbplan.2005.02.003.

[7] M. H. Ramage *et al.*, 'The wood from the trees: The use of timber in construction', *Renewable and Sustainable Energy Reviews*, vol. 68, pp. 333–359, 2017, doi: 10.1016/j.rser.2016.09.107.

[8] Mahapatra, Krushna and Gustavsson, Leif, *General conditions for construction of multi-storey wooden buildings in Western Europe*. Växjö, Sweden: School of Technology and Design, 2009.

[9] T. Abergel, B. Dean, and J. Dulac, 'Global Status Report 2017: Towards a zero-emission, efficient, and resilient buildings and construction sector', *United Nations Environment Programme*, vol. 48, 2017.

[10] McKinsey & Company, 'Reinventing Construction: A Route to Higher Productivity', Feb. 2017. [Online]. Available: www.revalue.dk

[11] S. Changali, A. Mohamman, and M. van Nieuwland, 'The construction productivity imperative'. McKinsey Quarterly, 2015.

[12] N. Kohler and W. Yang, 'Long-term management of building stocks', *Building Research & Information*, vol. 35, no. 4, pp. 351–362, Aug. 2007, doi: 10.1080/09613210701308962.

[13] J. Gosling, P. Sassi, M. Naim, and R. Lark, 'Adaptable buildings: A systems approach', *Sustainable Cities and Society*, vol. 7, pp. 44–51, Jul. 2013, doi: 10.1016/j.scs.2012.11.002.

[14] T. Eguchi, R. Schmidt, A. Dainty, S. Austin, and A. Gibb, 'The Cultivation of Adaptability in Japan', *OHI*, vol. 36, no. 1, pp. 73–85, Mar. 2011, doi: 10.1108/OHI-01-2011-B0009.

[15] S. Huuhka and J. Lahdensivu, 'Statistical and geographical study on demolished buildings', *Building Research & Information*, vol. 44, no. 1, pp. 73–96, Jan. 2016, doi: 10.1080/09613218.2014.980101.

[16] Metzger, Sebastian, Jahnke, Katy, Walikewitz, Nadine, Otto, Markus, Grondey, Andreas, and Fritz, Sara, 'Wohnen und Sanieren: Empirische Wohngebäudedaten seit 2002 Hintergrundbericht', Umweltbundesamt, ISSN 1862-4359, 2019. Accessed: Jan. 21, 2023. [Online]. Available: https://www.umweltbundesamt.de/sites/default/files/medien/1410/publikationen/2019-05-23_cc_22-2019_wohnenundsanieren_hintergrundbericht.pdf

[17] Schmidt, R., III, T. Eguchi, S. Austin, and Gibb, A., 'What is the meaning of adaptability in the building industry?', presented at the CIB 16th International Conference on Open and Sustainable Building, Bilbao, Spain, May 2010.

[18] A. Ruuska and T. Häkkinen, 'Efficiency in the Delivery of Multi-story Timber Buildings', *Energy Procedia*, vol. 96, pp. 190–201, Sep. 2016, doi: 10.1016/j.egypro.2016.09.120.

[19] 'Bauholz für tragende Zwecke - Festigkeitsklassen', no. DIN EN 338. Feb. 2010.

[20] G. Churkina *et al.*, 'Buildings as a global carbon sink', *Nature Sustainability*, vol. 3, no. 4, pp. 269–276, 2020, doi: 10.1038/s41893-019-0462-4.

[21] A. Mishra *et al.*, 'Land use change and carbon emissions of a transformation to timber cities', *Nat Commun*, vol. 13, no. 1, p. 4889, Aug. 2022, doi: 10.1038/s41467-022-32244-w.

[22] C. D. Oliver, N. T. Nassar, B. R. Lippke, and J. B. McCarter, 'Carbon, Fossil Fuel, and Biodiversity Mitigation With Wood and Forests', *Journal of Sustainable Forestry*, vol. 33, no. 3, pp. 248–275, Apr. 2014, doi: 10.1080/10549811.2013.839386.

[23] J. Hart, B. D'Amico, and F. Pomponi, 'Whole-life embodied carbon in multistory buildings: Steel, concrete and timber structures', *Journal of Industrial Ecology*, vol. 25, no. 2, pp. 403–418, Apr. 2021, doi: 10.1111/jiec.13139.

[24] B. Leupen, *Frame and generic space*. Rotterdam: 010 Publishers, 2006.

[25] Garaedts, Rob, 'Design for Change; Flexibility Key Performance Indicators', presented at the I3CON Conference, Loughborough, UK, May 2008.

[26] Kim, Young-Ju, 'On Flexibility in Architecture Focused on the Contradiction in Designing Flexible Space and Its Design Proposition', *Architectural research*, vol. 15, no. 4, pp. 191–200, Dec. 2013, doi: 10.5659/AIKAR.2013.15.4.191.

[27] O. Heidrich, J. Kamara, S. Maltese, F. Re Cecconi, and M. C. Dejaco, 'A critical review of the developments in building adaptability', *IJBPA*, vol. 35, no. 4, pp. 284–303, Aug. 2017, doi: 10.1108/IJBPA-03-2017-0018.

[28] F. Duffy, 'Measuring building performance', *Facilities*, vol. 8, no. 5, pp. 17–20, May 1990, doi: 10.1108/EUM0000000002112.

[29] E. S. Slaughter, 'Design strategies to increase building flexibility', *Building Research &*

https://doi.org/10.52202/069179-0508

Information, vol. 29, no. 3, pp. 208–217, May 2001, doi: 10.1080/09613210010027693.

[30] R. Schmidt and S. A. Austin, *Adaptable architecture: theory and practice*. London ; New York: Routledge, Taylor & Francis Group, 2016.

[31] S. Brand, *How buildings learn: what happens after they're built*. in A Pengiun book architecture. New York, NY Toronto London: Penguin Books, 1995.

[32] N. Slack, S. Chambers, and R. Johnston, *Operations management*, 5. ed., [Nachdr.]. Harlow: Prentice Hall/Financial Times, 2009.

[33] D. E. D'Souza and F. P. Williams, 'Toward a taxonomy of manufacturing flexibility dimensions', *Journal of Operations Management*, vol. 18, no. 5, pp. 577–593, Aug. 2000, doi: 10.1016/S0272-6963(00)00036-X.

[34] N. O. E. Olsson, 'Management of flexibility in projects', *International Journal of Project Management*, vol. 24, no. 1, pp. 66–74, Jan. 2006, doi: 10.1016/j.ijproman.2005.06.010.

[35] N. J. Habraken, 'Open Building as a Condition for Industrial Construction', presented at the 20th International Symposium on Automation and Robotics in Construction, Eindhoven, The Netherlands, Sep. 2003. doi: 10.22260/ISARC2003/0004.

[36] K. Arge and K. Landstad, 'Generalitet, fleksibilitet og elastisitet i bygninger', NTNU, 2002.

[37] R. S. Webb, J. R. Kelly, and D. S. Thomson, 'Building services component reuse: an FM response to the need for adaptability', *Facilities*, vol. 15, no. 12/13, pp. 316–322, Dec. 1997, doi: 10.1108/02632779710188306.

[38] Lammersen, Steven, 'How can we design for a remountable and flexible open building?', Delft University of Technology.

[39] Frantzen, Tom, 'PATCH22, highrise in wood', presented at the 8. Europäischer Kongress EBH 2015, Köln, Germany, Nov. 2015.

[40] Leijten, Pelle, 'Flexible housing for the amateur: Flexible building concepts explored in the age of the amateur', TU Delft.

[41] 'kiubo', *kiubo*. https://www.kiubo.eu/en/ (accessed Nov. 21, 2022).

[42] J. Graf *et al.*, 'Wandelbarer Holzhybrid für differenzierte Ausbaustufen', 2022, doi: 10.13140/RG.2.2.34197.81120.

[43] P. Steadman, 'Why are most buildings rectangular?', *Arq*, vol. 10, no. 2, pp. 119–130, Jun. 2006, doi: 10.1017/S1359135506000200.

[44] A. Krtschil *et al.*, 'Structural development of a novel punctually supported timber building system for multi-storey construction', *Journal of Building Engineering*, vol. 58, p. 104972, Oct. 2022, doi: 10.1016/j.jobe.2022.104972.

[45] Gray, Aaryn, 'Advantages and Implications of Utilitizing Mass Timber for Structural Efficiency and Service Integration in an Educational Building', Oregon State University, 2021. [Online]. Available: https://timbertectonics.com/2021/12/15/advantages-and-implications-of-utilizing-mass-timber-for-structural-efficiency-and-service-integration-in-an-educational-building-m-s-terminal-project-proposal-by-aaryn-gray/

[46] T. Schork *et al.*, 'The geometry of air: large-scale multi-colour robotic additive fabrication for air-diffusion systems', *Constr Robot*, vol. 5, no. 1, Mar. 2021, doi: 10.1007/s41693-021-00054-z.

[47] J. Knippers, C. Kropp, A. Menges, O. Sawodny, and D. Weiskopf, 'Integrative computational design and construction: Rethinking architecture digitally', *Civil Engineering Design*, vol. 3, no. 4, pp. 123–135, Sep. 2021, doi: 10.1002/cend.202100027.

[48] A. Menges, F. Kannenberg, and C. Zechmeister, 'Computational co-design of fibrous architecture', *ARIN*, vol. 1, no. 1, p. 6, Dec. 2022, doi: 10.1007/s44223-022-00004-x.

[49] M. Alvarez *et al.*, 'The Buga Wood Pavilion', presented at the ACADIA 2019: Ubiquity and Autonomy, Austin (Texas), USA, 2019, pp. 490–499. doi: 10.52842/conf.acadia.2019.490.

[50] H. J. Wagner, M. Alvarez, A. Groenewolt, and A. Menges, 'Towards digital automation flexibility in large-scale timber construction: integrative robotic prefabrication and co-design of the BUGA Wood Pavilion', *Constr Robot*, vol. 4, no. 3–4, pp. 187–204, Dec. 2020, doi: 10.1007/s41693-020-00038-5.

[51] A. Krtschil, L. Orozco, H. J. Wagner, A. Menges, and J. Knippers, 'Conceptual development and comparison of two punctually supported timber slab systems', presented at the 9. Doktorandenkolloquium Holzbau Forschung + Praxis 2022, Institut für Konstruktion und Entwurf Universität Stuttgart, Mar. 2022.

[52] L. Orozco, A. Krtschil, L. Skoury, J. Knippers, and A. Menges, 'Arrangement of reinforcement in variable density timber slab systems for multi-story construction', *International Journal of Architectural Computing*, vol. 20, no. 4, pp. 707–727, Dec. 2022, doi: 10.1177/14780771221135003.

[53] L. Orozco *et al.*, 'Design Methods for Variable Density, Multi-Directional Composite Timber Slab Systems for Multi-Storey Construction', presented at the eCAADe 2021: Towards a New, Configurable Architecture, Novi Sad, Serbia, 2021, pp. 303–312. doi: 10.52842/conf.ecaade.2021.1.303.

[54] S. Zöllig, 'TS3 – A New Technology for Efficient Timber Structures', *CTCSE*, vol. 4, no. 4, 2020, doi: 10.33552/CTCSE.2020.04.000592.

[55] D. Bissig and A. Frangi, 'Variantenstudium zur Entwicklung einer zweiachsig tragenden Hohlkastendecke aus Holz (german)', in *Doktorandenkolloquium Holzbau Forschung + Praxis*, 2022.

World Conference on Timber Engineering Oslo 2023

Reciprocal frames: an ancestral structural principle to use native wood species in Chile

Suzanne Segeur-Villanueva[1], Natalia Caicedo-Llano[2]

ABSTRACT: Using native wood species instead of introduced wood ones, like Radiata Pine (*Pinus radiata*), has lots of positive consequences from an environmental approach: 1) does not acidifies the soil, 2) makes possible to preserve native flora and fauna. Also, Roble (*Nothofagus obliqua*), Rauli (*Nothofagus alpine*) and Coïgue (*Nothofagus dombeyi*) are the most common native species and have very good structural properties compared to introduced ones. In Chile, regarding primary economic activities, forestry represents 19%. A percentage similar to the contribution to GDP of the agricultural market. However, even if today native species of wood represents 80% of surfaces of forest in the country, the exportation of native wood species represents only 2% of the total wood exportation. Also, in the local market nowadays, native species are used mainly as firewood. Could it be possible, thanks to the study of geometry, specifically an ancestral structural principle called reciprocal frames, to build big spans using only small battens? Is it possible to build structural components avoiding the use of glue or any other chemical products that have negative consequences on the environment? Platform-frame systems in Radiata Pine used for walls or for slabs could be replaced for this type of structural components?

KEYWORDS: nexorade, structural simulations, geometrical studies, revival of ancestral materials

1. INTRODUCTION

We chose wood as the primary material because of its environmental benefits. Wood is: 1) a material that is both renewable and recyclable, 2) one cubic metre of wood stores about one ton of CO_2, as in [1], 3) it has been demonstrated that increasing the use of wood in construction by 17% reduces carbon emissions to the atmosphere by 20%, as in [2], 4) the grey energy required for the transformation of one metre of wood corresponds to 80% of the consumption for concrete transformation and 2% of the consumption for steel transformation, as in [3].

We chose untreated wood, free of glue and free of any other chemical products. We excluded glue because most glues emit formaldehyde, a toxic component that has recently been shown to be carcinogenic, as in [4]. Even though using chemicals products may improve the characteristics of wood, they are also excluded from this research because they are inconsistent with their environmental goals.

We prefer native species of wood because of their natural durability. In other words, they are more resistant to biohazards (termites, bacteria, or fungi) or can withstand them equally to introduced species that have been impregnated. Nonetheless, the most part of impregnation treatments in Chile are with chemical products such as CCA (Chrome, Copper, and Arsenic), which is prohibited in countries such as France due to its toxicity, as in [5]. Some introduced species, such as the Radiata pine (Pinus radiata), present significant biological pollution risks, as in [6].

On top of this, the national native sawn wood production it's been progressively decreasing, preferring Pino Radiata (*Pinus radiata*) and other species. The 2020 formal production of native sawn wood were of 75.714 m3, 34,8% (26,363 m3) Lenga (*Nothofagus pumilio*), 22.6% (17.092 m3) Roble (*Nothofagus obliqua*), and 14.9% (11.282 m3) Coïgue (*Nothofagus dombeyi*), as in [7]. Approximately, 9 million cubic metres of firewood are used per year, as in [9], where 85,9% are native species, as in [8]. On top of this, firewood exploitation is done in an informal way, as in [9], without environmental management, and being the first cause of degradation of the native forest in Chile.

We select a reciprocal frame that is a structural principle made of battens that are supported one after the other. The point where battens meet is called a “nexor”. We divide this structural principle into two categories: one where elements of the structure have a different role, and the other where all elements have the same one, as shown in

[1] Suzanne Segeur-Villanueva, Universidad Politécnica de Valencia, España, susevil1@doctor.upv.es
[2] Natalia Caicedo-Llano, Universidad Tecnológica Metropolitana, Chile, ncaicedo@utem.cl

https://doi.org/10.52202/069179-0509

Figure 1, Figure 2, and Figure 3. We choose this principle instead of another one because it allows us to construct big spans only using short battens. Other structural principles with the same characteristics are tensegrity and interlaced carpentry. The first one is based on a system of isolated components under compression inside a network of continuous tension and arranged in such a way that the compressed members do not touch each other while the prestressed tensioned members delineate the system spatially, as in [10]. The second one is also called interlaced carpentry, in Spanish "*carpintería de lazo*" that means a carpentry made of bows, as in [11]. It is defined also as a combination of "wheels", in Spanish "*ruedas*", as an analogy between the wheel used in mechanics and the wheel drawing method based on the rotation of lines having a point as the centre. Nevertheless, the first one is a system with different materials and different thicknesses and in consequence it has a more complex constructive process. The second one, even choosing the simplest "*rueda*" requires cutting wood on many different angles. In consequence, both constructive systems require more time and are more expensive than the reciprocal frame one.

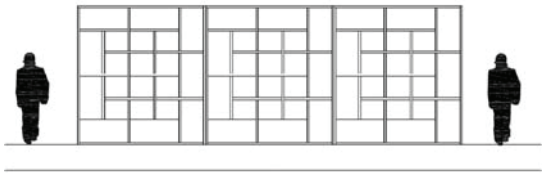

Figure 1. Type A: Reciprocal frame wall, with four jigs

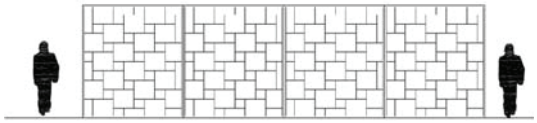

Figure 2. Type B: Reciprocal frame wall, with two jigs

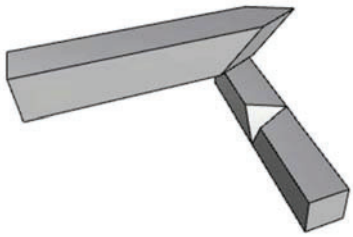

Figure 3. Construction detail of type B jigs

2. METHODOLOGY

We present the criteria considered for the purpose of this paper: a species selection, followed by a geometry selection and at the end a structural selection.

2.1 SPECIES SELECTION CRITERION

To select wood to be used, seven criteria were considered, using the database previously created (Caicedo y Segeur, 2021).

The following criteria, were selected:

C1 Origin of the wood, selecting native wood and excluding introduced species.

C2 Species conservation, excluding species at risk (NT), endangered (EN), or vulnerable (VU).

C3 Mechanical characteristics. The selection was done by their largest compressive parallel to grain stress.

C4 Mechanical characteristics. The selection was done by their largest compressive perpendicular to grain stress.

C5 Natural durability to bio- hazard, avoids the use of chemicals and others to protect the wood from the environmental conditions of the site.

C6 Capacity to dry naturally.

C7 Availability on the market.

Criteria C3, C4, C5, C6, is a numerical ordering value. Criterion C1, C2, C7 is an exclusion selection.

2.2 GEOMETRY SELECTION CRITERION

Several patterns of reciprocal structures were explored, using the geometry of the square as a basis, evaluating the ease of fabrication, assembly, and transport of each one of them. In figure 4 is shown reciprocal frame wall with four jigs. In the circles red and purple are shown the different types of joints. In yellow, pink, blue and green are shown the jigs. In figure 5 is shown a reciprocal frame wall with two jigs. On both examples the joint type is the one that determine the number of jigs. We exclude a different type of jig when the batten only needs to be cut when it is located on the periphery of the panel.

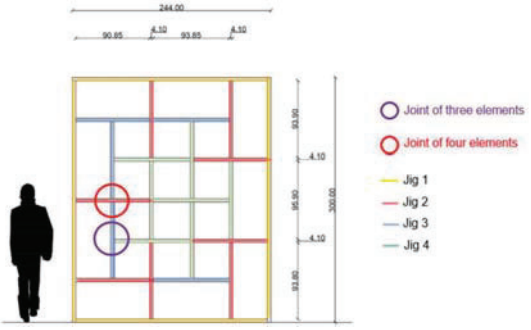

Figure 4. Reciprocal frame wall with four jigs.

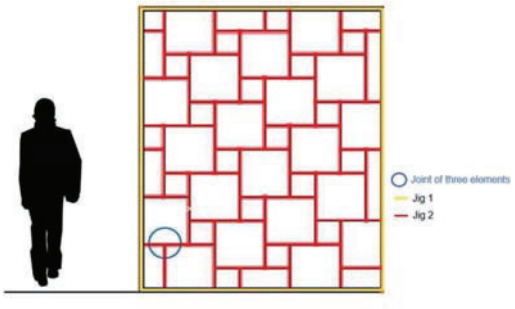

Figure 5. Reciprocal frame wall with two jigs.

To create models with different geometries we parameterized prototypes allowing us to make modifications with relative ease, developing adjustments to improve the performance of the whole system. We used the software Rhinoceros, more specifically a plug-in called Grasshopper as in Figure 6.

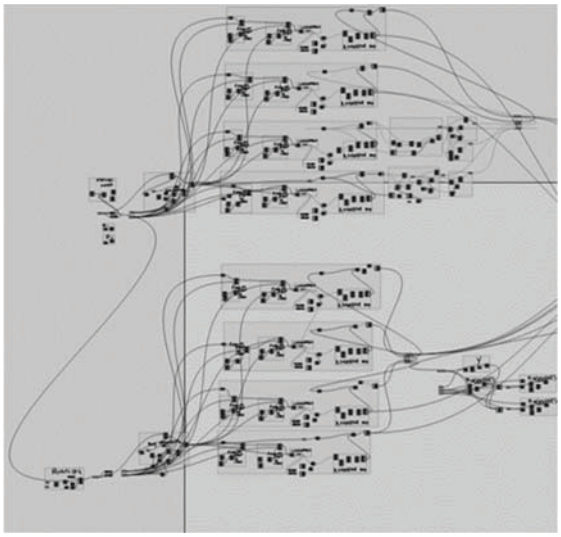

Figure 6. Algorithm wrote in Grasshopper to create different geometries.

Among the parameters used, the following two aspects were considered: batten morphology, and batten geometry. More specifically, the location of joints and the shim between them. In figure 7 is shown a jig modelled in Rhinoceros.

One of the aspects to consider is the size of joints. There is a 0,33 mm gap between the batten and the void where the batten will be placed in the 3D printing prototypes. This gap will have to be adjusted again when changing scale and materiality between models. Reaching a more accurate solution when working with native wood species.

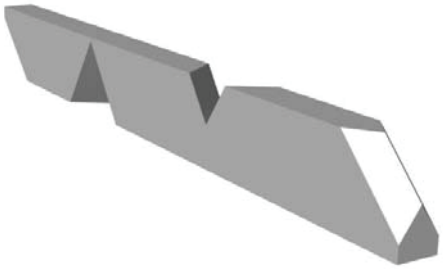

Figure 7. Jig modelled in Rhinoceros

2.3 STRUCTURAL SELECTION CRITERION

The third step was to compare structural simulations and budgets of a typical Radiata Pine (*Pinus radiata*) platform-frame module with a native wood species one based on a reciprocal frame. Because the mechanical properties of native species are better than the Radiata Pine (*Pinus radiata*) ones, the section of the first one is smaller.

For this purpose, preliminary evaluations of the prototype structure were carried out considering a 1.2 * 2.4 metres frame, since this module corresponds to the standardised wood measurements sold in Chile.

3. RESULTS

3.1 SPECIE SELECTION RESULTS

We gathered information from thirty-four wood species. From them, only thirteen can be considered because they fulfil criteria C1 and C2, origin and conservation respectively.

In figure 8 is shown a ranking of compressive parallel to grain stress of Chilean native wood species according to criteria C3.

https://doi.org/10.52202/069179-0509

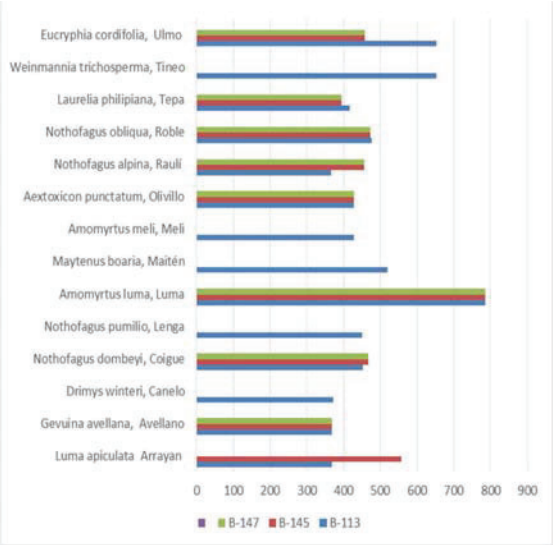

Figure 8 Ranking of compressive parallel to grain stress of Chilean native wood species

In figure 9 is shown a ranking of compressive perpendicular to grain stress of Chilean native wood species, according to criteria C4.

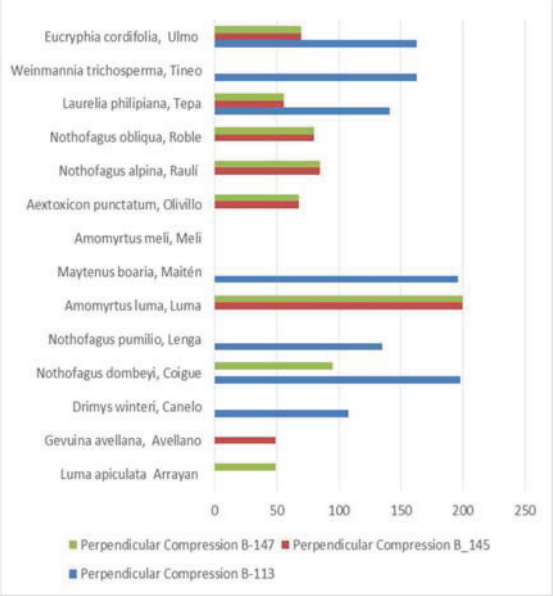

Figure 9 Ranking of compressive perpendicular to grain stress of Chilean native wood species

In figure 10 we present a ranking of natural durability to biohazards of Chilean native wood species

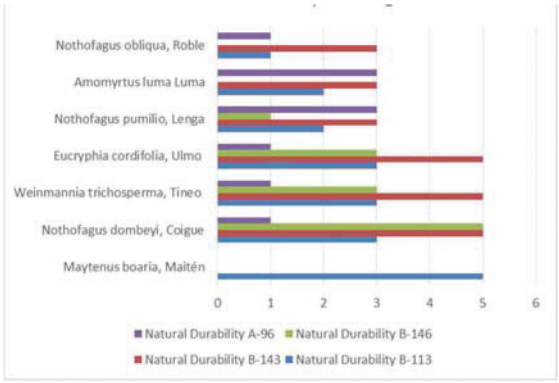

Figure 10 Ranking of natural durability to biohazards of Chilean native wood species

We select the top 7 species from the remaining thirteen species represented in Figures 8, 9 and 10. Based on rankings of compressive parallel to grain stress, compressive perpendicular to grain stress and natural durability. The new ranking is then generated based on a physical attribute of native species that is its capacity to dry easily. The final selection criteria considers seven species. Information is compiled from the following references: [12] corresponding to B-113, [13] corresponding to B-144, [14] corresponding to B-145, and [15]corresponding to B-147.

In figure 11 is shown a ranking of the capacity of drying of Chilean native wood species.

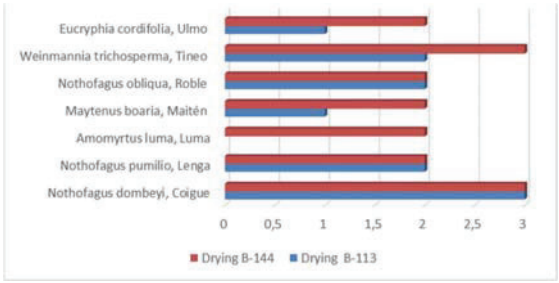

Figure 11 Ranking of the capacity of drying of Chilean native wood species.

The following four species with the best performance were chosen based on the final criterion C7.

Coigue (*Nothofagus dombeyi)*
Tineo (*Weinmannia trichosperma)*
Roble (*Nothofagus obliqua)*
Lenga (*Nothofagus pumilio)*

In table 1 is shown a comparison of Chilean native species filtered by price divided by cubic metre.

Table 1: *Comparison of Chilean native species filtered by price divided by cubic metre ($/m3), own elaboration, according to [7].*

Native species planed and nominal sizes	($/m^3)	Region
Coigue (*Nothofagus dombeyi)*	945	Malleco
Tineo (*Weinmannia trichosperma)*	561	Ranco
Roble (*Nothofagus obliqua)*	919	Llanquihue
Lenga (*Nothofagus pumilio)*	449	Ranco

3.2 GEOMETRY SELECTION RESULTS

Geometry studies were conducted to apply several structural systems to a particular geometry, as shown in the picture. The following literary works served as the foundation for the structure systems under study: reciprocal frame [16], "Armaduras de Lazo" as in [11], and as in Sebastiano Serlio's technique [17]. In Figure 12 is shown how a reciprocal frame based on a square with 2 jigs inscribed in a rectangle.

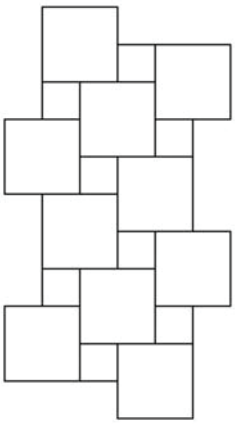

Figure 12 Reciprocal frame based on a square with 2 jigs.

The same wood section, a minimum number of jigs, and the simplest joints were the guiding principles for all geometrical analysis.

In Figure 13 is shown a plan of a standard panel prototype.

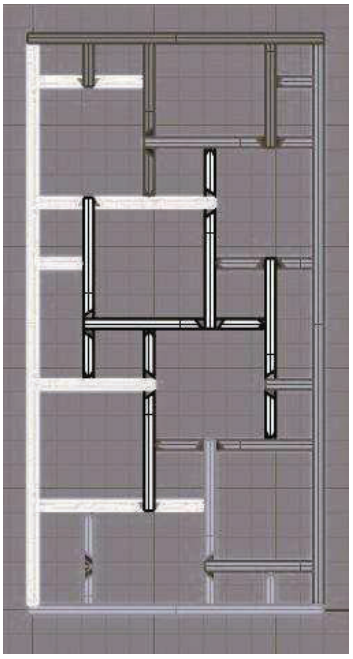

Figure 13 Plan of a panel prototype

When designing joints, we decided to optimise the production selecting 2 diagonal cuts instead of 2 verticals and 2 diagonals, as in Figure 14 and 15 respectively. Using this simplified type of batten fewer adjustments of the full-scale wood prototype are required.

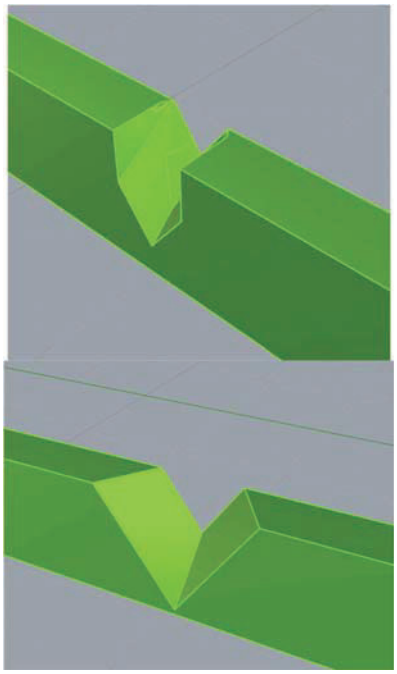

Figure 14 - 15 3D printed batten's prototype.

In Figure 16 is shown a 3D printed joint of two battens. In Figure 17 is shown a 3D printed portion of the prototype panel.

https://doi.org/10.52202/069179-0509

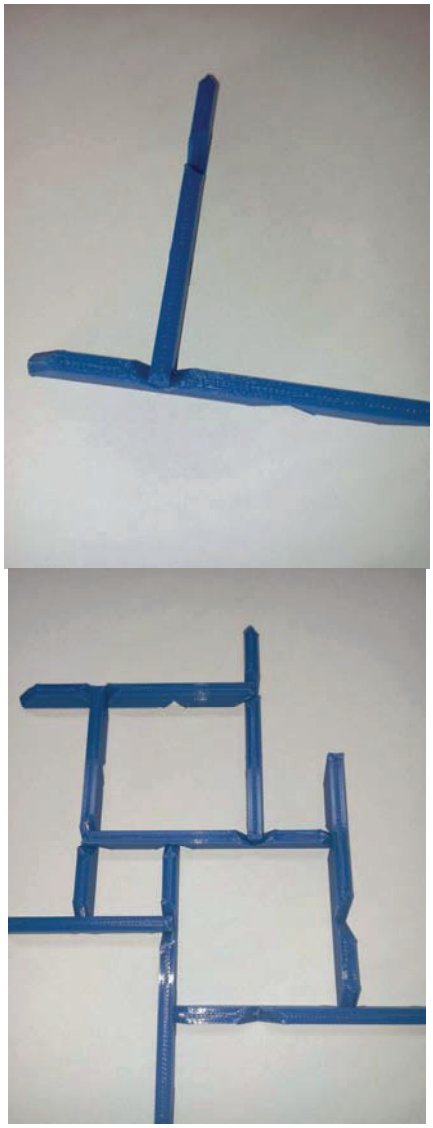

Figure 16 3D printed joint of two battens. **Figure 17** 3D printed portion of the prototype panel.

3.3 STRUCTURAL PRELIMINAR RESULTS

We calculated a traditional Radiata Pine (Pinus radiata) panel, and a Chilean native wood species based on a reciprocal frame geometry.

Seismic and wind loads were considered for the calculation of both panels. We considered a lateral load of 7 kN/m and a vertical load of 12,38 kN/m according to NCh 1537.

The results shown in the preliminary figures 18 and 19, demonstrate a smaller critical reaction in the first panel than in the second one, with 9,33 kN and 15,42 kN respectively. On the opposite, a smaller critical moment in the first panel than in the second one, with 2,03 kN/m and 0,32 kN/m respectively. Because critical reactions and critical moments are very close between both panels, we expect than the section required for the second panel is smaller because the mechanical properties of the Tineo (Weinmannia trichosperma) and the Roble (Nothofagus obliqua) are a lot better than the Radiata Pine (Pinus radiata) ones.

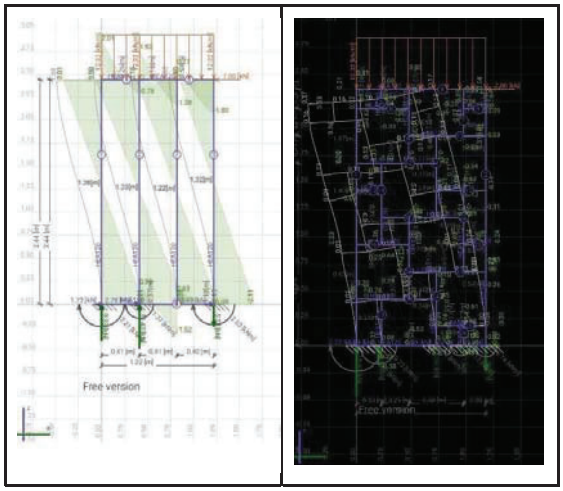

Figure 18-19 Preliminary traditional and reciprocal frame structural analysis

4. CONCLUSIONS

We conclude that it is conceivable to construct with small battens and large spans as a result of the study of geometry, notably the ancient structural principle known as reciprocal frames. Additionally, it is feasible to construct structural elements without using glue or any other chemical substances that have negative consequences for the environment. Radiata Pine (Pinus radiata) platform-frame systems used for walls or slabs can be swapped out for structural elements of a reciprocal frame.

Regarding the selection of native species, we decided to choose potential species that meet specific mechanical properties, a high natural durability, a high capacity to dry, and a low economic cost. We conclude that Tineo (*Weinmannia trichosperma*) is the species best suited for this purpose. His straight trunk can measure 40 m height and 2 m diameter. It would provide structural wood applications instead of current market use like finishes, veneer, or furniture. The second native species is Roble (*Nothofagus obliqua*). It was chosen to facilitate the prototype stage. Although this species has a less good drying capacity, it is easier to get due to its greater availability throughout Chile.

Regarding a geometric criterion, two sizes of square are the basis for the design of the chosen reciprocal frame. They are made from a single batten that is connected at two locations that are equally spaced from its edges. As a result, only two battens are needed, the bigger inner batten and the edge batten

https://doi.org/10.52202/069179-0509

that often makes up a fraction of the batten, need to be built for each panel. The structural frame serves as the foundation for fitting the final panel. The prefabrication of the parts is optimised by this design, resulting in higher quality, more control, and reduced costs.

In terms of joint design, changes must be made to ensure that the shim and pressure prevent slippage and the transfer of mechanical stresses between battens by simplifying the junction with a diagonal cut on both sides. To assess whether additional design modifications or the use of reinforcing dowels are necessary, these alterations should be compared on a full-scale.

One of the research's current constraints is the flexibility provided by the 3D printed members. It only permits a limited fit between parts and requires adjustments in wood size prototypes in order to change the design parameters and enhance the prototype outcomes. The usage of the selected species for the creation of the scaled prototypes and ultimately the full-scale prototypes for testing and assessment will constitute the second stage of the research.

REFERENCES

[1] Metzagroup, "Every wooden building is a carbon storage," 2020. https://www.metsagroup.com/en/Campaigns/IntelligentMetsa/urbancarbon/every-wooden-building-is-a-carbon-storage/Pages/default.aspx

[2] A. H. Buchanan and S. B. Levine, "Wood-based building materials and atmospheric carbon emissions," *ENVSCI</cja:jid> Environmental Science and Policy*, vol. 2, no. 6, pp. 427–437, 1999.

[3] G. Hammond and C. Jones, "Inventory of carbon & energy ICE." Sustainable Energy Research Team, Department of Mechanical Engineering, University of Bath, Bath Avon, U.K., p., 2008. [Online]. Available: http://perigordvacance.typepad.com/files/inventoryofcarbonandenergy.pdf

[4] Commission Européene, "2007/442/CE: Décision de la Commission du 21 juin 2007 concernant la non-inscription de certaines substances actives à l'annexe I de la directive 91/414/CEE du Conseil et le retrait des autorisations de produits phytopharmaceutiques contenant ce," *Journal Officiel de l'Union Européene*, vol. L 166, pp. 16–23, 2007.

[5] I. Subra, "Exposition professionnelle aux métaux lors de l'usinage des bois traites au cuivre, chrome, arsenic," *Cahiers de notes documentaires- Institut National de Recherche et de Sécurité*, no. 175, pp. 61–68, 1999.

[6] M. Garay, N. M. Amiotti, and P. Zalba, "Potencial riesgo de polución biológica asociado a la introducción de Pinus radiata en tierras de pastizales," *Phyton (B Aires)*, vol. 84, no. 2, pp. 280–287, 2015.

[7] Instituto Forestal, "Bosque Nativo. Boletin n° 22 Diciembre 2021 Área de información y economía forestal," 2021. [Online]. Available: https://bibliotecadigital.infor.cl/handle/20.500.12220/30463

[8] P. Emanuelli, "Perspectivas comerciales del manejo de bosque nativo de pequeños y medianos propietarios: una aproximación desde la experiencia del PCMSBN," *Bosques y comunidades del sur de Chile*, pp. 87–104, 2006.

[9] P. P. Olivares, C. Pavez, and J. L. Pérez, "Tipología de comerciantes de leña del sur de chile y principales instrumentos de apoyo. Neira FE y R. Reyes G.(Eds.). Proyecto 'Leña, energía renovable para la conservación de los bosques nativos del sur de Chile,'" *Boletín técnico*, no. 1, 2009.

[10] V. Gómez-Jáuregui, "Tensegrity structures and their application to architecture, Universidad de Cantabria," *Servicio de Publicaciones, Santander*, 2010.

[11] E. Nuere, *La carpintería de armar española*. Madrid, Spain: Ministerio de Cultura Instituto de Conservación y Restauración de Bienes Culturales, 1989.

[12] Instituto Forestal, *Compendio de Propiedades de las Maderas Nativas y Exóticas de Chile*. Instituto Forestal, 2009.

[13] J. Witte, *Maderas Del Sur de Chile*. Edit. Universitaria, 2004. [Online]. Available: https://books.google.cl/books?id=vQfeFA6kDVoC

[14] E. Torricelli Diaz, *Propiedades fisicas y mecanicas de las maderas chilenas*. 1941.

[15] Antonio. Fernandez Garcia and Eduardo. Torricelli Diaz, *La madera : su explotacion secamiento propiedades y utilizacion*. Santiago de Chile: Imprenta "La Sud-America," 1942.

[16] O. Popovic Larsen, *Reciprocal frame architecture*. Oxford: Architectural Press, 2008.

[17] S. Serlio and A. E. Santaniello, *The book of architecture*, First Edit. New York: B. Blom, 1970.

https://doi.org/10.52202/069179-0509

World Conference on
Timber Engineering
Oslo 2023

Development of a new type of building in tropical regions based on the energetic performance and recovery of recycled wood

Horly Luzolo Nsumbu[1, 2], Régis Pommier[1], Denis Bruneau [3], Alain Sempey[1]

ABSTRACT: The Congo Basin is the second world largest tropical forest. This world heritage plays a decisive role in the global warming and the services for the world populations. Its management and preservation is one of the success keys in the future. Despite a strong development of the wood industry in the region observed in recent years, almost no waste of products is sustainably recovered for a possible re use. Very few scientific works address the question of the valuation of related products from the wood transformation in Africa. In this present work, several ways of recovering this waste are studied. Based on a wooden made building case study, with local material in Gabon, we measure, simulate and optimize the hygrothermal comfort of the house from its components. The thermo-physical and mechanical characterization of some first materials consisting of Padouk sawdust plus a lime-based mortar are presented. The instrumentation work of the building made of these new materials completes the study in order to know the components best suited for a sustainable construction in tropical regions. Multi-physical measurements and modeling on the prototype building make it possible to propose new constructive solutions integrating the requirements and objectives of sustainable development.

KEYWORDS: re-use of wood waste, circular design for sustainability, building system, timber engineering, hygrothermal comfort, sustainable development, the Congo basin, tropical regions

[1] Institut de Mécanique et d'Ingénierie de Bordeaux, Université de Bordeaux I2M UMR 5295 CNRS, BP 33400 Talence, France
[2] Faculté Polytechnique, Université Kongo, BP 202 Mbanza-Ngungu, Kongo central, RD Congo
3 GRECCAU, Ecole Nationale Supérieure d'Architecture et de Paysage de Bordeaux, 33400 Talence, France

https://doi.org/10.52202/069179-0510

1 INTRODUCTION

The Congo Basin (CB), the second largest tropical forest massif in the world, just behind the Amazon, extends over 6 Central African countries including the DRC[3], Gabon, Congo, Cameroon, Equatorial Guinea and CAR[4] (fig. 1). Thanks to its area of approximately 6 million km² and its immense wealth of biodiversity (fauna and flora), this world heritage plays a crucial and determining role in climate regulation.

***Figure 1**: Cartography of rainforests of Congo Basin. (Source: G.A. Kombila & al., 2019).*

The importance of these Central African forests on the ecological, economic, social and cultural levels has placed them at the heart of international discussions aimed at preserving these unique ecosystems essential to the proper functioning of the planet (FRM, 2018). The timber industry in most of these CB countries is based mainly on the export of logs abroad. In Gabon, between 2004 and 2009, the annual volume of log exports averaged 1.7 million m3. And it is since 2010 that the export of logs is prohibited. This decision by the public authorities aims to encourage the private sector to carry out local wood processing, potentially generating more added value and better management of the resource (A.G. Kombila, 2019).

This obligation to process the wood locally has a direct impact on the production of logs on Gabonese soil. Indeed, the production of processed wood increased from a collection of 281,331 m3 in 2009 to 824,072 m3 in 2017, an increase of 192.9%. (A.G. Kombila, 2019). The local transformation of wood by total or partial cessation of log exports has become one of the major objectives of forestry development in most countries of the Congo Basin. These wood processing operations generate large quantities of waste (ranging from sawdust, shavings, to pieces of plank).

In Gabon, as in the other CB countries, waste from wood processing is very insufficiently valued. Almost all of it is used by local populations as a source of energy, as a sanitation component in the poultry sector, or else abandoned in wild dumps, thus contributing to environmental pollution. This waste is therefore not recovered under economically and ecologically satisfactory conditions, with a view to reuse by the wood industry or in another sector of crucial importance such as construction. The technologies for processing related products of the tropical timber industry within the reach of the populations of developing countries constitute a field that is very little addressed in the international scientific literature. At the same time, this BC sub-region, like most African countries where the majority of the population is rural, has a great deficit in decent housing. A study led by researchers from the London School of Hygiene & Tropical Medicine on the African continent between 2000 and 2015, estimates that 53 million urban Africans (in the countries analyzed) still lived in slum conditions in 2015 (UN-Habitat, 2016). A situation which should worsen with the strong demographic growth in forecast and which will have to be accompanied by a net increase in basic needs, including food and housing. According to the UN-Habitat report (2016), the African population will approach 2 billion by 2040. In addition, the concern to reduce energy consumption and the carbon footprint of the construction sector around the world and the preservation of exhaustible resources today make the use of bio-based on materials unavoidable. The aim is to integrate the tropical timber processing industry as best as possible into the process of sustainable development in the sub-region, so as not to suffer from waste, but to make it a lever for the development of the circular economy, guarantee of sustainable development.

In this work, we present a successful construction with only made of defects from the sawmill plus a raw red clay. The paper presents the material made and the first results

3 DRC: Democratic Republic of Congo

4 CAR: Central African Republic

https://doi.org/10.52202/069179-0510

on the building performance for which two types of wall are instrumented and the energy performance is analyzed.

2 MATERIALS AND METHODS

2.1 PRESENTATION OF THE STUDIED BUILDING

The building project is located in the special economic zone of Gabon, in Nkok, located 27 km from Libreville the capital (0° 23′ 24″ North, 9° 27′ 15″ East).

***Figure 2**: Prototype wood-frame building*

This wooden frame house, built from wood waste from the wood processing industry in Gabon. This building (R + 1) of approximately 85 m² of total living space, it is one of the first prototypes of an eco-responsible construction with a high rate of valorization of local resources in the special economic zone of Gabon (GSEZ). The species used mainly is Padouk, renowned for its good mechanical performance and its attractive natural durability, which make it the wood of choice for exterior landscaping. It is the wood used at more than 80%, mainly for load-bearing structures; This gives the building good durability in the face of Gabon's harsh climate. The building has two levels: ground floor and first floor. On the ground floor, the building serves as a staff house, consisting of a bedroom, a bathroom, a small living room, an external, independent kitchen, and a courtyard serving as a space of conviviality. Upstairs, there is a large room of around 50 m², which serves as a showroom and meeting room, and a small WC area of around 1 m².

2.2 MATERIAL PROCESSING TECHNOLOGY AND CHARACTERISATION

Large quantities of shavings and sawdust are produced in the sawmill but they are not still used in industry in Gabon. The question is highly critical when short solid woods are considered as a defect and burned in the best situation. Concerning solid wood, the technology used consist by the utilize of the French technology of green finger jointing i.e. wood undried in an undetermined moisture content (high to 15%) (R. Pommier & al) with a Polyurethane specially developed for hardwood from tropical region (R. Lissouck & al.). These solid woods are used in the building as the structural part and the cladding.

The other part of the by-products of the sawmill are used for filling and insulation. With a view to enhancing them effectively, a composite material made up of a mixture of sawdust and wood. An experimental design is made and followed in the next tables. Two categories of composite materials are designed. The first category consists of composite materials made by valuing shavings from Padouk and a hydraulic solution based on slaked lime from the local paint industry, used as a hydraulic binder (Table 1).

***Table 1**: Sample compositions of composite materials - category 1 and processing methods.*

	Wood chips [%.vol]	Sawdust [%.vol]	Aqueous solution of lime [%.vol]	How to implement
M1	50	25	25	Moulding without compaction
M2	50	25	25	Moulding with compaction

The second category (Table 2) includes composite materials made mainly from Padouk wood chips, local raw earth and slaked lime marketed in Gabon.

***Table 2**: Sample formulations of composite materials-category2*

C / F	Wood chips (%.mass)	Sawdust (%.mass)	Earth (%.mass)	Slaked lime (%.mass)
F1	30	0	40	30
F2	30	0	40	30
F3	40	0	40	20
F4	40	0	5	10
F5	0	50	20	30
F6	0	25	50	25
F7	25	0	60	15
F8	20	0	60	20

The goal is to find the right material, that is to say the best suited to the construction method of the chosen building and to the external climatic conditions that the building

https://doi.org/10.52202/069179-0510

must face. Thus, the material should represent a good compromise between thermal inertia and thermal insulation.

2.3 CONSTRUCTIVE MODE AND QUALITY OF THE BUILDING

2.3.1 Constructive mode

In order to reduce construction time and deal with logistical difficulties (for an average wood processing plant), the 1100 mm long panels are manufactured in the workshop and installed on site, thus requiring skilled labor. reduced work. About 12 m3 of wood is estimated for the entire construction, 100 % of which comes from offcuts and wood that cannot be marketed on the market. The wall consists only of an exterior facing (exterior cladding in Padouk), a polyethylene membrane and an interior facing (plywood of 15 mm), between which there is a void, representing an air gap of 80 mm (figure 3).

1: Plywood (15 mm); 2: Air (80 mm) ; 3: Polyethylene membrane (0.5 mm); 4: Exterior cladding in Padouk (10 mm)

***Figure 3**: Initial building wall composition*

2.3.2 Analysis of climate conditions and building quality

According to the Köppen classification, the Libreville region has a tropical savannah climate. Its average annual temperature is 26.3°C and its rainfall averages 1970.6 mm per year (DGMN, 2018). July is the driest month with 14 mm of precipitation, while October is the wettest month with 307 mm of rain. The building must then deal with these waves of heat and humidity, and guarantee to the occupants a good level of comfort. The building being light, the temperatures recorded inside the building are, for the most part, 30 – 33°C, temperatures above the recommended comfort limits (B. Givoni, 1978).

Wood material being a light and relatively rigid material, its acoustic insulation properties are not beyond reproach. In addition, the state of its surface which is compact and relatively smooth does not allow the wood to dampen noise, but it would tend to amplify it. The large hollow (void) in the walls also contributes to the propagation of noise. The integration of a material in the wooden frame structure is one of the possible solutions to optimize the performance of the building (hygrothermal and acoustic). In terms of energy, this material will have to provide, on the one hand, inertia and thermal insulation to limit heat exchange between the building and the outside environment through the walls, and on the other hand, sound insulation and thus improve the comfort of the occupants [17-18] and [21 - 25].

3 THERMAL ANALYSIS

3.1 THEMAL CHARACTERIZATION OF THE COMPOSITE MATERIAL

The guarded hot plate method (ISO 8302 standard) is used to determine the main thermal properties under steady state conditions. The principle of the experimental setup consists in maintaining a temperature difference ΔT between two flat parallel plates brought to constant temperatures T1 and T2. The sample of thickness e is positioned between the two plates (Ting-Ting Wu, 2011).

Several researchers worked on the thermal characterization of tropical wood. R. Mvondo & al. assessed the Influence of moisture content on the thermo-physical properties of tropical wood species; in (P.S. Ngohe-Ekam & al.) and (S.A. Smith & al.), thermal properties of some main tropical hardwood specie are studied and determined. In this current work, we then focus on the characterization of the designed composite material.

Using the thermal characterization bench of the I2M Bordeaux laboratory which is based on the “guarded hot plate” method, we determined the thermal conductivity (λ) and the specific heat capacity (Cp). Bulk density was also determined. Table 3 shows the main values of this characterization.

3.2 INSTRUMENTATION OF WALLS

The objective of the instrumentation is to ensure the measurement of the temperature and relative humidity gradients within the different walls and in the atmosphere, in order to evaluate the damping and the phase shifts in the different transient states studied (figures 5a, 5b and 5c). The selected temperature and humidity sensors are Sensirion SHT 85. These sensors have a standard tolerance announced by the manufacturer of 0.1°C between 20 and 60°C and 1.5% RH in humidity. They have the advantage of having a limited size (7 mm wide) but are sensitive in humid and alkaline environments [F. Collet & al, 2019]. We also use a mini Davis brand weather station which provides us with data on the site's microclimate. These data are temperature and relative humidity of the outside air, sunshine, precipitation, and wind speed and direction. The observation time is 3 days, from January 23 to 25, 2023.

https://doi.org/10.52202/069179-0510

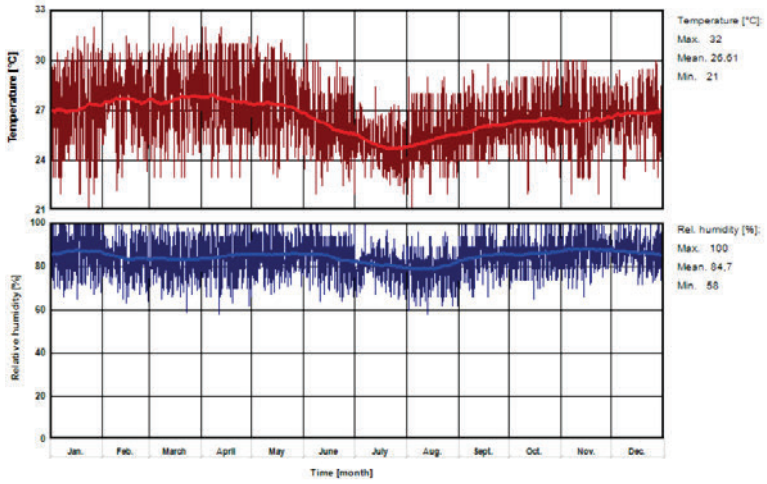

***Figure 4**: Climate conditions of Libreville: (a) Annual temperature; (b) annual relative humidity [ASHRAE].*

3.3.1 Integration of innovative composite material in the wall

***Figure 6**: Installation of materials based on wood chips in the wall and settle of temperature and humidity sensors.*

Blocks of dimensions 14 cm × 7 cm × 7 cm are used to fill one type of wall (wall 2).

For a first test, the installation of these insulating materials is done in a portion of the wall of the prototype building. The choice of the facade is meticulously analyzed by using SunEarthTools which is an open source tool specially designed for the sizing of solar plants. Libreville being at the level of the Equator, the sun passes through its highest trajectory. Consequently, the East and West facades will be the most exposed to sunshine for this geographical location, and therefore the most vulnerable to overheating in a construction in Libreville, while the North and South facades will be the least exposed to the sun. This analysis allows us to choose the west facade as an experimental wall for an analysis of the hygrothermal behavior of the building envelope because of its strong interactions with the outside, resulting from the activity of the sun on it.

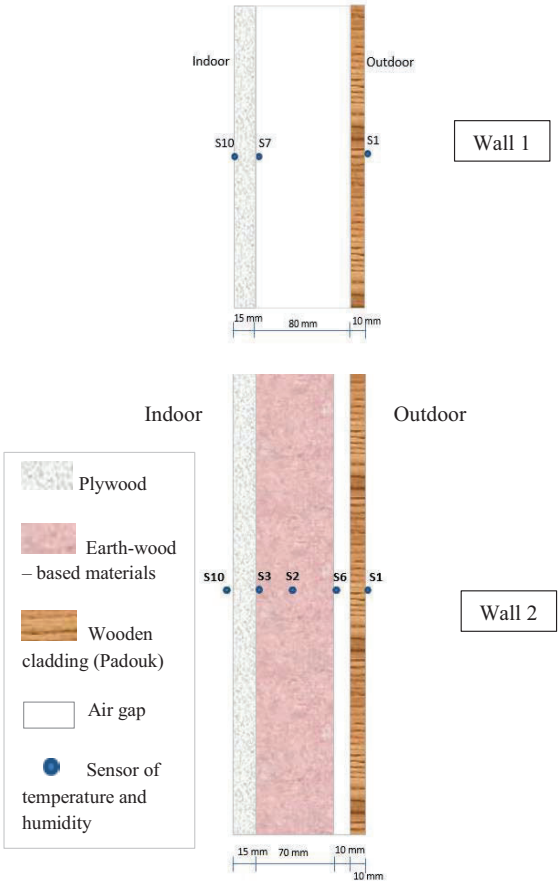

***Figure 5**: Two types of instrumented walls (Wall 1 and Wall 2)*

4 RESULTS AND DISCUSSIONS

4.1 RESULTS

https://doi.org/10.52202/069179-0510

The first results of the thermo-physical characterization of the samples are listed in Table 3.

At this stage, only samples of the first formulation (M1) are tested to determined thermal conductivity and thermal capacity. The analysis of the results from the thermal characterization of this composite material reminds us of chipboard wood panels,–due to the similarity of their thermo-physical properties (ρ, λ and Cp) [13-14].

The composite materials of category 2 (from F1 to F8) presented in the table 3, even without thermal test in the lab, are more cohesive and rigid.

***Tableau 3**: Characteristics of the samples of composite material*

	Apparent Density ρ [kg/m3]	Thermal conductivity λ [W/(m.K)]	Thermal capacity Cp [J/(kg.K)]	Drying time [days]
M1	735	0,1372 – 0.1530	1 500 - 1600	32
M2	850	-	-	32
F1	605	-	-	9
F2	630	-	-	10
F3	515	-	-	10
F4	450	-	-	12
F5	505	-	-	9
F6	520	-	-	9
F7	760	-	-	10
F8	850	-	-	12

These first results allow us to orient the use of the material in the wooden frame structure as filling material. Its low thermal conductivity value of around 0.15 (about ten times less than that of solid concrete) and its good thermal capacity (Cp > 1500 J/(kgK)) give it essential properties of an insulating material.

The figure 7 shows us the evolution of temperatures in the different layers of the wall of the wood frame building. Two cases are presented.

In the first type of wall (Fig. 7.a), the temperature at the surface of the interior facing **S7** varies in the same way as the temperature at the level of the wooden claddings, which constitute the exterior facing. We observe a slight phase shift of the order of 1 to 2 hours between **S1** and **S7** (37th hour and 39th hour of observation). The very low inertia of this wall (wall without heavy materials) promotes a fairly rapid increase in temperature under the influence of external conditions.

The large layer of air (80 mm) inside hardly behaves as an insulator because the inside air is not trapped and therefore subject to heat transfer by convection. This **S7** temperature climbs to reach 36°C on the second day of the observation while the outside air temperature is around 33°C.

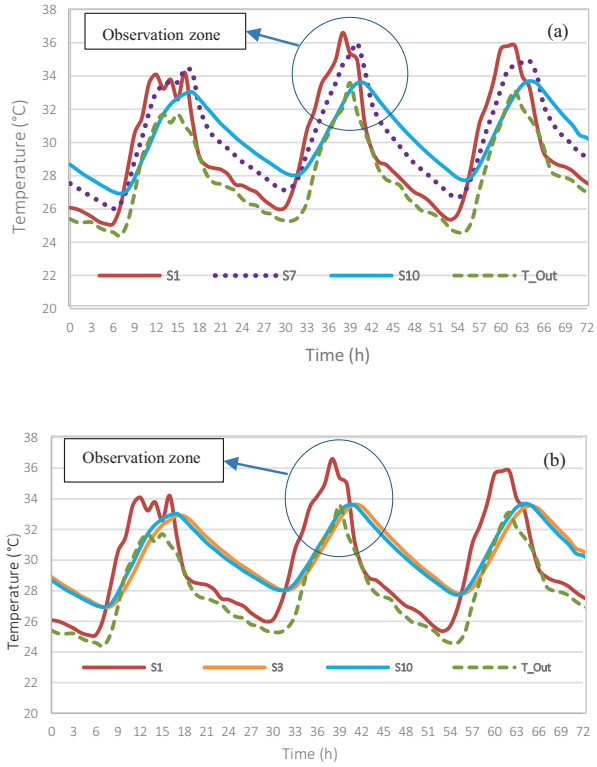

***Figure 7**: Temperatures in walls observed in 3 days: (a) wall 1 and (b) wall 2.*

In the second wall composition (figure 7.b), the integration of earth bricks and chips brings inertia to the wall. This results in a phase shift of 4h, observed between **S1** and **S3**.

5 CONCLUSION AND PERSPECTIVES

This work presented one of the ways of valorization of co-products of the wood processing industry in the construction sector. A prototype timber frame building made of reclaimed wood was presented and analyzed. Two types of vertical walls were considered in this study. The instrumentation of these walls made it possible to evaluate their thermal performance, according to the heat exchanges with the surrounding environment. From this analysis, the second type of wall show out interesting characteristics including thermal inertia, conferred on it by the integration of earth-wood chip bricks. This integration allows a significant phase shift and damping, compared to the first one (wall 1). In addition, these wood-

https://doi.org/10.52202/069179-0510

based on materials, installed in an optimal way, could have a positive effect and then contribute to improving the acoustic comfort of the occupants.

In this study, only heat exchanges were analyzed. The consideration of mass transfers in the evaluation of the comfort of the building could be the subject of a future study. Next research will be made, such as establishing the link between the composition of the earth, its microstructure and the mechanical behavior of these composite earth-wood chip materials. We will aim to extend the study period (over the two main seasons) to get the most exhaustive data possible from physical measurements in situ in order to analyze the hygrothermal behavior of the wall and to assess the impact of these wood-based materials. We will also think about determining the thermal, hydric and mechanical properties in the lab and using them in modeling and numerical simulation at the scale of the building.

ACKNOWLEDGEMENT

The authors would like to thank the E2WP Chair of the University of Bordeaux and the companies Cap Exo, Wood Tech Gabon for the material and financial support.

REFERENCES BIBLIOGRAPHIQUES

[1] FRM, 2018. Vision stratégique et industrialisation de la filière bois dans les 6 pays du bassin du Congo, horizon 2030. Rapport stratégique régional. Montpellier, France: FRM.

[2] A.G. Kombila-M., *L'arrêt de l'exportation des grumes au Gabon : enjeux et perspectives*, PhD Thesis, UPPA, 2019.

[3] UN-Habitat report (2016).

[4] ATIBT (Association Technique Internationale des Bois Tropicaux), 2017. Rapport d'activité 2017.

[5] CIFOR « Les forêts du bassin du Congo : État des Forêts 2021 », 2021.

[6] Reborredo F., 2013. *Socio-economic, environmental, and governance impacts of illegal logging. Environ. Syst. Decis*, 33(2), 295-304, doi.org/10.1007/s10669-013- 9444-7.

[7] R. Pommier, *Compréhension de l'aboutage du bois vert : détermination du procédé et principes physico mécaniques appliqués au Pin maritime*, 25èmes Rencontres Universitaires de Génie Civil 2007.

[8] R. Pommier and G. Elbèz*, Finger-jointing green softwood: Evaluation of the interaction between polyurethane adhesive and wood,* Wood Material Science & Engineering Vol 1, 2006

[9] R. Lissouck, R. Pommier, F. Taillandier and Lanvin Jd., *Ingénierie du bois comme outil de conservation de la diversité des essences ligneuses des forêts tropicales:cas du bassin du Congo*, Conference Paper · January 2012.

[10] Valentin Makomra, *Modelization of green-glued plywood behaviour in drying proces*s, PhD Thesis, UBx, 2020.

[11] R.R.N. Mvondo, JC. Damfeu, P. Meukam and Y. Jannot, *Influence of moisture content on the thermophysical properties of tropical wood species,* Heat and Mass Transfer vol 56, (2020).

[12] P.S. Ngohe-Ekam, P. Meukam, G. Menguy, P. Girard, *Thermophysical characterisation of tropical wood used as building materials: With respect to the basal density*, Construction and Building Materials Vol 20, Dec 2006.

[13] Smith S. A., Preko K., and Owusu F. W, *Study of Thermal Properties of Some Selected Tropical Hard Wood Species*, Forestry Research Institute of Ghana, 2016.

[14] FCBA, Fiches Produits Ouvrages Bois (POB): Panneaux de particules, 2015. http://www.catalogue-construction-bois.fr/

[15] P.S.Ngohe-Ekam, *Etude expérimentale des propriétés thermophysiques des bois tropicaux*, PhD Thesis, UCBL, 1992.

[16] Ł. Czajkowski, W. Olek, J. Weres and R. Guzenda*, Thermal properties of wood-based panels : specific heat determination,* Wood Sci Technol (2016) 50:537–545.

F. Collet, C. Lanos, T. Hautecoeur & F. Dubois, *Quelle métrologie thermo-hygrique implanter dans un démonstrateur en béton de chanvre ?* AJCE, vol 37, No 1 (2019).

[17] D. Sow, M. Ahmat, S. Gay, and I.K. Cissé, *Integration of Agricultural Waste in Local Building Materials for their Exploitation: Application with Rice Straw,* RJASET, 2014.

[18] T. Rakotoarivelo, F. Miranville, C. Gronfier and B. Malet-Damour*, Thermal comfort analysis: comparison between model and experimental data in tropical climate*, CISBAT 2021.

[19] Baruch GIVONI, L'homme*, le climat et l'Architecture*, traduction Jean-Louis IZARD, Editions du Moniteur, 1978.

[20] J-L IZARD and O. Kaçala, *Le diagramme bioclimatique du bâtiment*, Laboratoire ABC ENSA-Marseille.

[21] Ting-Ting Wu, *Formalisme des impedances thermiques généralisées. Application à la caractérisation thermique de parois de bâtiments*, PhD Thesis, University of Artrois, 2011.

[22] M. Donny Koerniawan and Weijun Gao*, Thermal Comfort Investigation in Three Hot-Humid Climate Theme Parks in Jakarta,* American Journal of Environmental Sciences, 2015.

[23] A. Sheriyev, Shazim Ali, Indira and Jong Kim, *Effect of Phase Change Materials on the Thermal Performance of Residential Building Located in Different Cities of a Tropical Rainforest Climate Zone, Revue Energies 2021.*

[24] A. Wali Bashir, B.C Coelho, *Performance of aerogel as a thermal insulation material towards a sustainable design of residential buildings for tropical climates in Nigeria,* Energy and Built Environment 3 (2022).

[25] Yingying Y., Zhoulin C.Tingting V.W, A. Sempey, J.C. Batsale, *In situ methodology for thermal performance evaluation of building wall: A review,* International Journal of Thermal Sciences, Volume 181, November 2022, 107687.

World Conference on Timber Engineering Oslo 2023

USING CO-DESIGN FOR DEVELOPING A NEW WOODEN FAÇADE SYSTEM

Camilla Schlyter[1], Karin Sandberg[2]

ABSTRACT: The objective is to demonstrate the co-operative design (co-design) and production development process of a new wooden façade system.

Today, architects and designers are seldom involved in the development process when designing new products within the wood building industry. The architect and the actors in the wood value chain are far from understanding their respective standpoints in new product development, thus creating a gap. This gap between actors hinders innovation and can mean that valuable design knowledge and methods are not used that can promote innovation in the wood building industry.

In this paper we demonstrate how the development process of the façade system is profoundly influenced and improved by incorporating knowledge of the design process.

Product development is becoming more and more complex and therefore more knowledge intense. This was addressed by working in parallel with partners coming from different areas of expertise, resulting in a co-design process considering aesthetic and functional requirements as well as the industrial manufacturing processes, interactively, throughout the entire development process.

Using co-design when designing an adaptable facade system has proven to enable assessment of complex requirements, resulting in a sustainable system that can ensure good quality on material, aesthetics, and functions.

KEYWORDS: Façade design, Cladding, Heartwood, Design process, Co-design, Adaptable design

1 INTRODUCTION

There are many divergent wishes on what a facade system should fulfil. From building regulations, government requirements to societal perspectives, as well as aesthetic and functional requirements such as adaptation to existing contexts.

Architects and builders are showing an increasing interest in using wood as façade material in urban contexts. A modern facade system must be attractive and easy to use for architects to design, easy to manufacture and easy to mount and maintain [1].

New product development in the wood building industry is complex and therefore knowledge intensive. Wood is a complex material that requires many skills in the value chain from the forest to the creation of new products.

Society demands that future building systems provide a well-designed environment, are sustainable, reusable and circular, adaptable design wise to different environments and manufactured in an environmentally sound and resource-efficient manner. This complexity leads to a need for an increased number of involved experts in new product development. According to Perks [2], these rapid changes mean that the demands on design knowledge increase dramatically. Researchers acknowledge that knowledge about design and design processes takes on an increasingly prominent role in product development [3], [4].

Actors in the wood value chain are often far from understanding each other's driving forces and needs, which creates problems concerning new product development. Architects, who are responsible for design, are used to collaborating in collective processes and "raising their gaze" in design processes and thereby contributing to a more holistic approach. The gap between actors hinders innovation in new product development and can mean that valuable design knowledge and methods are not used that can promote innovation in the timber construction industry.

In the project " Facade of the city Swift, Stylish, Smart" hereafter called the project, it was identified how the gap,

[1] Camilla Schlyter, RISE Research Institutes of Sweden, Sweden, camilla.schlyter@ri.se
[2] Karin Sandberg, RISE Research Institutes of Sweden, Sweden, karin.sandberg@ri.se

https://doi.org/10.52202/069179-0511

more specifically between architects' and industry's perspectives and goals could approach these challenges [5].

Faced with an abundance of classifications of collaborative activities within design, so called co-operative design (co-design), here the definition presented by Saunders and Stappers [6] is used.

Working systematically together using co-design methods has proven to be of vital importance resulting in product innovation and exchange of knowledge between partners. De Vere and Fennessy argues that "If … design has a role to play as an agent for change, an inclination to working in participatory ways with a co-design mindset seems sensible "[7]. The project shows that the architect can have a decisive role in the development of new products within the wood building industry by using knowledge of design and co-design methods.

Adaptable design is a design paradigm aiming at creating designs and products that can be adapted for different requirements and influenced by users. An existing design of a product can be adapted to create a new or modified design based on changed requirements. Adaptive design enables manufactures to produce standardized products that are possible for end users to customize [8].

The objective with this article is to demonstrate the co-design and production development process of a new wooden façade system [9,1]. A co-design process was developed considering design and functional requirements as well as industrial manufacturing processes throughout the value chain interactively and in parallel with partners coming from different areas of expertise. The purpose was creating an adaptable, changeable and flexible design easy to use for architects and still economically viable.

The result is increased knowledge about design processes using co-design methods in new product development within the wood building industry.

2 METHODS

A new wooden façade system must be fast and safe to assemble, there must be a variation in the aesthetical expression, and it must be sustainable, adapted to regulations and possible to manufacture industrially.

An industrially manufactured wooden facade system here refers to a facade solution for buildings consisting of a set of components that are fully or partially ready-made and dimensioned regarding adjustment for specific dimensions of buildings. The components of the facade system are joined industrially to facade elements, corners, footboards, cornices, and connections at openings. On the construction site, the facade system is assembled and mounted on a building. The result is that the construction site becomes more of an assembly site, where finished elements of the facade system are assembled. This differs from the methods that are common procedure today; were wooden facades are assembled with a nail gun board by board on the construction site or in a factory on a prefabricated wall structure.

2.1 PROJECT VALUE CHAIN

The participating partners covered the whole value chain, including researchers, engineers, architects, constructors, raw material suppliers, manufacturers, builders, and property owners.

The engineer and architect were responsible for the architectural and constructive design, the raw material supplier for the manufacture of the components, the manufacturer for assembly of the parts, the paint supplier and the chemical industry for surface treatments and paint, the contractor and building company for mounting and the manager for care and maintenance.

2.2 PROCESS

Customer requirements, building regulations and the market for facade systems were initially investigated, analysed, and compiled. The aesthetic design was developed with the purpose of making the facade attractive and easy for architects and builders to use. Wood properties and surface treatments were studied and verified in scientific tests to achieve fire safety and long service life. Heartwood of pine and spruce were chosen because of its suitable material properties for facades.

Wood properties and surface treatments were studied and verified in tests to achieve fire safety and long service life. The facade system's functions were verified in lab tests and by small scale design prototypes. Full scale tests of the mounting of the facade system were executed on two buildings in Luleå, where mounting time and functions were evaluated. A full-scale fire test of the facade system was carried out with Teknos´ fire protection paint, which passed the SP Fire 105 test. Overall, the façade system was developed to be market-competitive and contribute to a sustainable bio-based economy. To assure this, durability and circularity have been considered both in the design and the choice of materials.

2.3 CO-DESIGN

In the project the term co-design refers to a process where the participants collaborated in a design process, including all the participants' knowledge and reasons for participating and enabling them to together create knowledge development, ideas, and concept generation when developing the product. It also meant creating a foundation of trust and understanding enabling participants who were not trained in design to be co-designers. Co-design methods can be used in all stages of the design process, though they are mostly used in the idea or concept phase. In the project several co-design methods have been used to facilitate participation and cooperative design, such as workshops, making prototypes, mock-ups, discussions of drawings and scenarios. To verify the prototypes aesthetically, discussions with partners in the

value chain including a reference group of architects were engaged.

3 RESULTS

The development of the façade followed an interactive development process with interaction between design, function, and production, figure1.

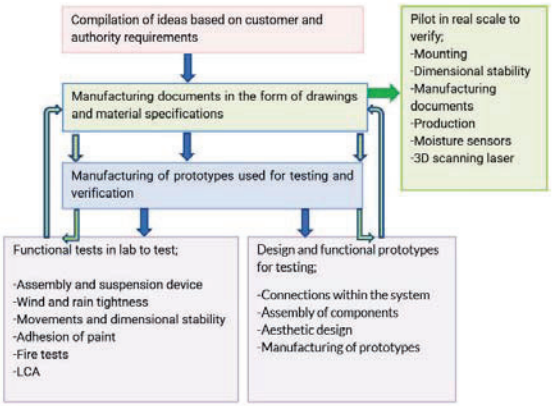

Figure 1: *Iterative development process in the project "Facade in the city Swift, Stylish, Smart", Development of the facades is based on requirements, laboratory tests and functional prototypes in an iterative process and thereafter verified as a pilot installation on two buildings [1]. (Image Karin Sandberg RISE).*

3.1 CO-DESIGN PROCESS IN THE FASADE PROJECT

The design was developed to make the facade attractive for architects and builders to use. The development process used in the project is described in full in a rapport [5].

3.1.1 Co-design in project managing, planning resources and anchoring decisions

Co-design enabled the partners to plan the project, asset manage, plan meetings and workshops alternating between including all participants and in smaller focus groups where specific tasks could be solved. The result of discussions, visualizations and prototypes were thoroughly documented in notes and the scientific tests, aesthetic tests, and functional verifications were described in rapports. The meetings with the partners were used to anchor decisions. The decisions were documented with meeting notes which were followed up by the project research leader who also distributed resources for implementation. Design choices and asset management were thus continuously updated leading to specification of the design criteria step by step.

3.1.2 Phases in the co-design process

The co-design process in the development of the facade system consisted of different phases,
-inventory phase
-analysis phase
-verification phase

The phases were developed in a semi parallel flow. The development took place iteratively where prototypes were tested and improved and adapted to production together with the partners in the project.

3.1.3 Inventory phase

Acknowledging the complexity and the nature of the scope at the very beginning of the project, the partners saw the benefit of establishing a common ground, thus creating engagement for the project. The common ground was the interest in the material, heartwood pine and spruce. The project established an interesting opportunity of understanding the material from different aspects, by reading it from the other partners perspectives, thus together creating more knowledge of its performance in a façade system including all aspects from design to manufacturing and mounting.

The design choices were based on an inventory that was carried out initially. It compiled customer requirements, building regulations and markets for facade systems and these were researched, analyzed, and compiled.
The engineers developed the scheme for verifying the performance through experimental design and appropriate test methods and technical equipment. The industrial partners gave input on production parameters important to consider.

Design criteria was summarized in a list of requirements on the product. The design criteria created a systematic and structured foundation for deciding on design, assessing criteria and discuss solutions. The design criteria enabled the partners to consider their own roles and connections with possible assets which was beneficial for the collective effort.

3.1.4 Analysis phase

In the analysis phase project drawings and visualizations were used, creating a foundation for testing the design decisions and further discussions. To verify the design decisions production feasibility and development of the manufacturing process design prototypes were built and tested. All prototypes were made of heartwood from Scots Pine (Pinus *Silvestris*) and Norway Spruce (*Picea abies* (L) Karts), figure 3.

Figure 3: *Prototype testing of different design of the façade boards. (photo Camilla Schlyter RISE).*

https://doi.org/10.52202/069179-0511

The cooperation in the value chain, from choice of material to production method resulted in, for example in a series of new expressions of the surface figure 4.

Figure 4. *Example of one of the protypes built in the façade project. The milling of the boards was tested together with assembly of the boards. (photo Camilla Schlyter RISE).*

3.1.5 Verification phase

In the production phase full scale prototypes were tested. A pilot test was executed on a building in Porsön, Luleå. Full scale tests of the mounting of the facade system were executed on two buildings in Luleå, where mounting time and functions were evaluated. A full-scale fire test of the facade system was carried out with Teknos´ fire protection paint and passed the SP Fire 105 test.
The raw material supplier manufactured the components and the components were thereafter assembled by the wood industry partner.

3.1.6 Co-design process

The requirement on the co-design methods was that communication should be enhanced and enable interactivity between the partners and thus promote innovation.

The co-design process was based on building trust and an understanding of the partners points of departure. It was from the start considered crucial to build a common ground, a common language and a willingness to share competence. The methods of arriving to a result at first differed amongst the partners for instance; concerning the design of the product, the engineer relied on scientific results and validation, the manufacturer on efficient production methods and the architect from synthesizing design decisions by developing aesthetic design solutions. The different points of departure sometimes resulted in conflict in the beginning of the project. Opinions, ideas and thoughts could be ventilated in the co-design process and knowledge was exchanged concerning how to pursue the project.

In figure 5 the co-design process in the façade project is shown.

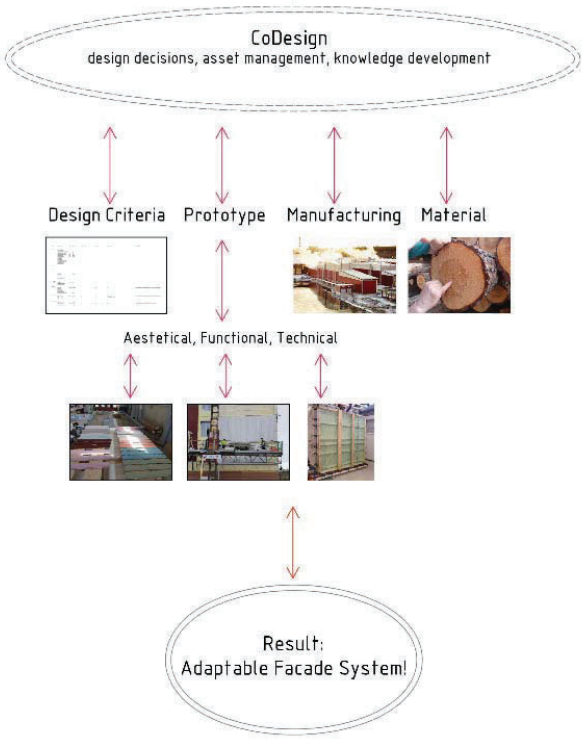

Figure 5: *Diagram over the co-design process. (Image Camilla Schlyter RISE).*

Attitudes, values, and expert knowledge was shared and communicated in the co-design process and conditions were created to enable tying together complex challenges in terms of design, materials, maintenance, and finances

https://doi.org/10.52202/069179-0511

and at the same time ensure that all voices were heard. By understanding the partners knowledge and starting points, consensus was created concerning the product idea and assessment of resources.

3.2 THE ARCHITECTS ROLE

The architect's role in the co-design process was to ensure that the products architectural values and design quality was upheld thru the process and result in an aesthetically pleasing and functional product. The architect used design knowledge to negotiate design criteria by translating and mediating diverging information and transform this knowledge into form by sketches, drawings, and visualizations and create drawings for the prototypes. The purpose was to ensure that all project partners were part of the design and that their knowledge, values and perspectives were lifted into the project and addressed. The role of the architect changed during the course of the project, from being considered the decision maker of aesthetic design to facilitating for others to participate in making the design decisions.

3.3 SUMMARY OF THE RESULTS

Alternatives in aesthetic design, manufacturing process and functional/technical design were formulated and tested in an iterative process between project partners, where everyone contributed with their knowledge and intent. A continuous dialogue and compilation of experiences from design choices took place against the background of design criteria. The design choices were verified through a series of aesthetic, functional and technical prototypes. The design was changed if it did not deliver the results the partners anticipated. New design and new prototypes were created until desired result was achieved.

The aim with the developed co-design process was to ensure that all the requirements were identified, met, and processed. A result with the process was that the participants became co-designers, and the architect acted as a facilitator concerning design methods leading, guiding, and listening to the participants aiding the process of creating knowledge and making design decisions. This resulted in that the partners gained knowledge concerning design and design methods.

The co-design method enabled a discussion in which the project partners could work with technical and aesthetic solutions in parallel. This was ensured by the architect and the research leader working closely together thus giving scientific methods and design methods equal value.

• Of importance was that the project management consisted of an engineer and an architect, which meant that functional and design aspects were discussed in parallel and guaranteed that they were of equal value. The architect and the research leader acted closely together and enabled conflicting issues to be resolved by facilitating and mediating the design process thru co-design methods. An interesting result of this collaboration was that parallels in working methods emerged scientifically on the part of the engineer and aesthetically on the part of the architect.

• Through frequent meetings with the partners, consensus and common starting points were created. Any conflicts, values and purpose of the project could be raised right from the start, which enabled creating a synthesized target goal with the project together, in collaboration. The initial discussions concerning the partners' driving forces and respective positions were crucial to create trust and commitment to the project. By understanding each other's knowledge and starting points, consensus was created around the product idea. Attitudes, values, and expert knowledge could be shared and communicated in the co-design process.

• Another important result of the project was allowing time in the initial phase to create understanding regarding function and design to be of equal value. Using design knowledge and methods from the start to the finished result was of importance for the result. The projects specific co-design process enabled complex criteria to be solved. This contributed to understanding the benefits of involving design knowledge. The architect became an "insider" engaged in the development of a new product.

• This method of collaborating throughout the project enabled criteria to be met, discussed, and communicated in a continuous dialogue between project partners. In the project several specialists' engineers but also industry partners were involved and they all co-operated leading to the common goal. Partners dared to be open to different hypothetical solutions and not decide on a solution too early. Although it took time to collaborate with many partners, the result generated that more aspects than expected were solved and discussed and more questions were raised. It also resulted in that important issues and ideas were not overlooked.

• Understanding of the value of creating knowledge together already in the formation of the consortium. This made it possible for criteria to be met, discussed, and communicated in a continuous dialogue between project parties. It resulted in a wooden façade system in which all parties in the consortium were involved.

The project has resulted in commercialization of one of the components in the façade system, the developed boards with different surfaces are now in production by one of the partners see figure 6. Discussions on commercializing the entire system are continuing.

https://doi.org/10.52202/069179-0511

Figure 6. *Image of one of the commercialized components in the façade system. (photo SCA).*

4 CONCLUSIONS

Demonstrated here are the possibilities of using co-design methods when developing a façade system. The aim with the prolonged design process developed in the project was making all parties involved in the design of the new product.

The project result shows that co-design methods profoundly influenced the product development and were valuable for promoting interdisciplinary communication and innovation concerning new product development.

The architect worked closely with the project research leader in mediating and facilitating the development process ensuring the quality of the design decisions. Coming from two different paradigms in research, essentially using scientific methods on the part of the research leader and design methods on the part of the architect the negotiations between them guaranteed that aesthetic and functional qualities were developed in parallel. The architect and research leader created a solid ground for design decisions by using co-design to create trust amongst the partners in the development process.

The identified gap between the actors in the value chain was considerably diminished by using co-design methods. This was verified in interviews with the partners in the project. As one of the partners commentated, he had never really understood how design knowledge could be used in new product development in the wood industry but after the project he understood the potential of co-design methods.

The co-design method used in the project can be applied to the development of other adaptive product families in the wood industry. The design method enables criteria to be met, discussed, and communicated in a continuous dialogue between project parties.

ACKNOWLEDGEMENT

Thanks to the strategic program Bioinnovation Construction & Design, IPOS – Innovations in wood-based building materials and products, subproject "The facade of the city Swift, Stylish, Smart". The project is founded equally by Vinnova Sweden's innovation agency, the Swedish Energy Agency, and Formas together with the industry partners. Thanks to E2B2 Swedish Energy Agency concerning the project Climate smart renovation with innovative façade system. A special thanks to SCA and Hedlunda for industrial input and KBAB.

REFERENCES

[1] Sandberg K., Serrano E., Sundqvist B., Henriksson F., (2021). IPOS – Innovations in wood-based building materials and products, RISE Report 2021:117, p44-79, http://urn.kb.se/resolve?urn=urn:nbn:se:ri:diva-63140.

[2] Perks H. et.al. Characterizing the Role of Design in New Product Development: An Empirically Derived Taxonomy, *J Prod Innov Manag* 2005;22:111–127, 2005.

[3] Turner, R. Design and Business, Who Calls the Shots? *Design and Management Journal*, 42–27 (Autumn), 2000.

[4]Von Stamm, B. Innovation. Creativity and Design Chichester 2003 /innovationleadershipforum.com, 2003.

[5] Sandberg K., Häggström U., Cristescu C., Schlyter C., Norén J., Pousette A., Tsantaridis L., Öhman M, Scharf A. Så tog vi fram fasadsystemet Fasaden i staden Snabb, Snygg, Smart, RISE Rapport 2021:116, ISBN 978-91-89561-07-6, 2021.

[6] Sanders E., Stappers P., Co-creation and the New Landscapes of Design, Article in Co-design. DOI: 10.1080/15710880701875068, 2008.

[7] Ian De Vere I. and Fennessy L. Refining industrial design: responding to emerging modes of practice. International conference on engineering and product design education. 12-13 sep. 2019.

[8] Zhanga J., Xueb D., Gua P., Adaptable design of open architecture products with robust performance, Journal of .Engineering Design, Vol. 26, Nos. 1–3,1–23, http://dx.doi.org/10.1080/09544828.2015.1012055, 2015.

[9] Sandberg K., Schlyter C., Arkitektonisk utformning och konstruktiva lösningar – Fasaden i staden Snabb, Snygg, Smart, RISE Rapport 2021:109, 2021.

World Conference on Timber Engineering Oslo 2023

MULTI-CRITERIA ASSESSMENT FOR FLEXIBILITY IN MODULAR TIMBER SCHOOL PROJECT BASED ON AHP-TOPSIS

Puxi Huang[1], Yiping Meng[2]

ABSTRACT: Sustainable development has been one important transition goal worldwide. The flexible design extends the frequency and lifespan of buildings by meeting the ever-changing needs of users to increase building sustainability. In this research, module coordination is selected to balance the modularity and flexibility of the modular timber school project. Functional flexibility is quantified by the AHP method based on a three-layer tree diagram assessment framework. The criteria and indicators are determined from the literature following the PRISMA systematic review process. According to the British Educational Building Design Code on area, the common module of school buildings is summarised by comparing the basic spatial dimensions of school buildings of different scales. Six modular grid sizes are selected as the scenarios for comparing the overall flexibility and flexibility in production, construction and service supported by the TOPSIS multi-criteria decision-making method. The ranking for the six sets of the modular grid for timber school classroom unit are summarized in different perspectives.

KEYWORDS: Flexibility, School project, Timber, Modular Construction, Quantification

1 INTRODUCTION

The UN document on sustainable development emphasizes the importance of building connections across economic, social, and environmental sustainability [1]. According to the report [2] and research studies [3], the construction industry consumes up to 35%-40% of the world's energy and generates 36% of greenhouse gas emissions [4], which can contribute to air pollution and material waste [5]. Decarbonization and achieving net-zero emissions have become new standards for the construction industry. The goals of sustainability and decarbonization are closely linked, both of which aim to reduce CO2 emissions for a sustainable future society and economic development.

To lower the impact of the construction industry on the environment, a variety of sustainable approaches have been proposed, e.g., industrial building system (IBS) andof industrialization and standardization in construction has proven to be an effective way of reducing time and waste [9]. Compared to traditional on-site construction methods, prefabrication and modular design/construction are more efficient in terms of time and materials [10,12].

To increase the sustainability of buildings and align with the UK's national strategies for Net Zero, Circular Economy, and Build Back Greener [13], one potential approach is to improve the flexibility of modular design to accommodate varying climates and conditions [14]. Architectural flexibility refers to a space's capacity to accommodate various customizations and layouts [15]. The degree of flexibility and adaptability in a building's design is crucial to meet its users' evolving social and environmental needs [16]. By repurposing existing structures, adaptive reuse can considerably minimize waste and help conserve the energy typically required for material manufacturing and construction [17].

The flexibility of the building can be achieved through design for adaptivity and modular construction [16,18].

The key challenge in designing a new construction project, particularly in the field of the school building, is to achieve flexibility at the design stage. This flexibility is essential in extending the lifespan of the building and meeting sustainability and Net Zero targets[19]. New design models and workflows must be developed to address the challenges posed by the new teaching, learning, and working patterns of a dynamic society in an ever-changing environment. In the post-pandemic era, it is crucial for new school buildings to be adaptable to their users' needs, with dynamic rather than static designs, taking into account the unique characteristics and requirements of the school community.

In the UK, the Department of Education (DfE) builds up to 200 new schools each year in order to fulfil the demand for student places and maintain its inventory. To optimize the learning and working environment, the DfE envisions better design methods, more efficient manufacturing

[1] Puxi Huang, School of Architecture and Arts, North China University of Technology, PRC, hpx@ncut.edu.cn
[2] Yiping Meng, School of Architecture, Building and Civil Engineering, Loughborough University, UK, y.meng@lboro.ac.uk

https://doi.org/10.52202/069179-0512

processes, increased productivity, and zero carbon emissions, enabling faster construction while promoting sustainability [20]. In the UK, the demands for mass construction and rebuilding of schools prioritize sustainability and addressing climate change [21]. Correspondingly, timber has been gradually applied in different types and different scale of projects worldwide because of its sustainable properties and reliable structural behaviours [22,24].

In modular construction of timber school buildings, the relationship between modularity and flexibility is a critical consideration. The principles of flexibility in construction, specifically the evolution for different users and usage rearrangement in the whole lifecycle [15, 25-26], provide a conceptual framework for understanding the meaning of "flexibility" in construction. his research aims to determine the quantified relationship between flexibility and the module of timber school buildings, enabling them to adapt to different functional requirements and meet sustainable construction needs. The study involves comparing module series of school-type buildings, beginning with the determination of an AHP tree to scope the criteria and impact factors of flexibility, followed by comparisons between different module sets using TOPSIS. Based on the simulated results, a numerical relationship between flexibility and module can be obtained, which can inform module coordination strategies.

2 METHODOLOGY

To quantify the flexibility, which is commonly defined qualitatively, the criteria and factors are retrieved from the literatures using PRISMA [27]. Based on the retrieved literatures, the assessment framework for flexibility of timber schools would be developed.

2.1 CRITERIAL AND INDICATORS RETRIEVAL

The identification for PRISMA is shown in Figure 1. Scopus and Web of Science (WoS) are selected as the database for searching. The Boolean syntax is applied for scoping the keywords, setting as follows: TITLE-ABS-KEY (‘Flexibility’ OR ‘ADAPTABILITY’ OR ‘REVERSABILITY’) AND TITLE-ABS-KEY (‘BUILIDNG’ AND ‘DESIGN’) AND TITLE-ABS-KEY (‘ASSESSMENT’). The range for the publication year is (2010,2022). The workflow for determining the final articles for reviewing is shown in Figure 2.

A total number of 617 literatures are selected after the first step of searching. 21 Literatures are selected for reviewing following main procedures of identification (536), screening (136), eligibility check (45) and final inclusion. The research area, title, keywords, and abstracts are checked throughout the whole workflow.

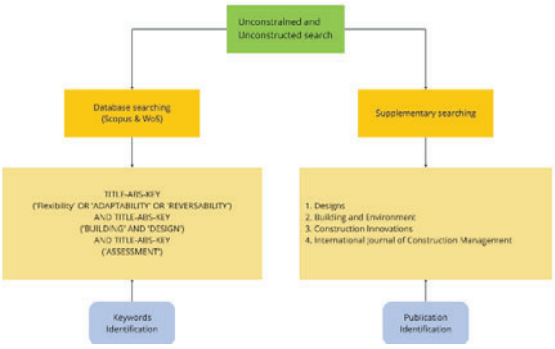

Figure 1: *Identification phase of PRISMA Method*

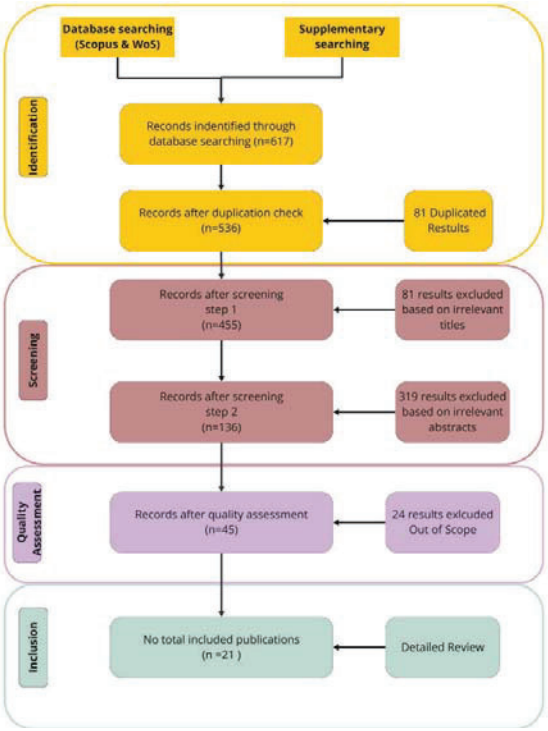

Figure 2: *Workflow for literatures retrieval*

2.2 FLEXIBILITY ASSESSMENT FRAMEWORK

The AHP-Tree Diagram assessment framework including the criteria and indicators are shown in Table 1. To cover the main stages of a cradle-to-cradle whole life cycle related to school building, three criteria have been established: Production, Construction, and Service [28]. The criteria and indicators identification follows the generic principles of flexibility [19, 29] the factors that influence the flexibility of school-type projects are selected from soft aspects [30]. For example, school buildings cater to a wide range of users with age-specific usage requirements, which is why multi-purpose spaces and components are highly demanded to meet their various needs. Under this consideration, the versatile

functionality and structural components are selected as the important indicators (Product types (C_2) and Potential for multifunctional use of space (C_{14})).

Following the AHP Tree Diagram, the weights are determined by collected 12 rating scale questionnaires. After the consistency check for the three factors in criterial level and the 16 factors in indicator level, the weights for the assessment framework ARE summarised in Figure 3.

Table 1: *Flexibility Assessment Framework for Timber School*

Target Level (A)	Criteria(B)	Indicators (C)	Reference
Flexibility	Production (B_1)	Pre-fabrication level (C_1)	[31]
		Product types (C_2)	[30]
		Specific connection (C_3)	[32]
		Structure layers (C_4)	[30]
		Geometry of plan (C_5)	[33]
	Construction (B_2)	Technological flexibility related to the easy installations (C_6)	[34]
		Installation Workflow (C_7)	[30]
		Modular Construction (C_8)	[35]
		System Interaction (C_9)	[36]
		System Zones(C_{10})	[37]
		Ease for deconstruction or disassembly (C_{11})	[38]
	Services(B_3)	Position of technical services (C_{12})	[33]
		Achieved degree of freedom of interior space(C_{13})	[33]
		Potential for multifunctional use of space (C_{14})	[33]
		Planning for future changes and service life (C_{15})	[30]
		Easy maintenance of installations (C_{16})	[34]

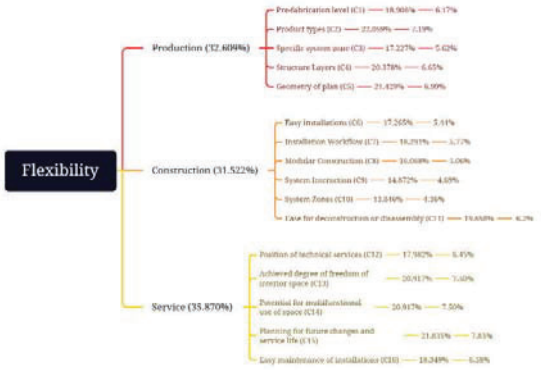

Figure 3: *Weights of the AHP Tree Diagram*

3 TOPSIS FLEXIBILITY ASSESSMENT

Based on the assessment framework, the multi-criteria assessment would be operated using TOPSIS based on the selected scenarios. The scenarios would follow the Net Capacity Guidance for the Mainstream School Design Guidelines from DfE [39]. In this research, the net area for teaching area is selected to determine the initial grid size scenarios. According to the net area guidance, the area for the same functions in primary school and secondary school are different, which are summarised in table 2 and table 3.

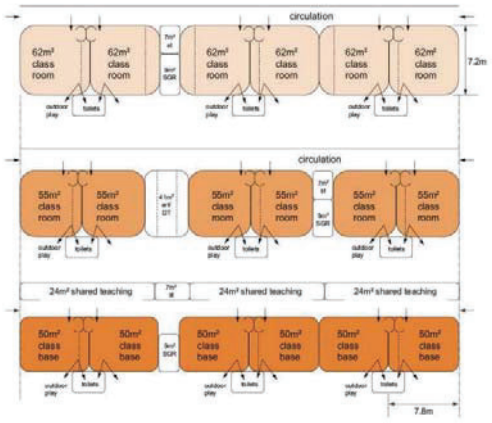

https://doi.org/10.52202/069179-0512

Figure 4: *Options for arranging basic teaching area, and associated storage, toilets and group rooms, in primary schools[39].*

The determination of grid size scenarios is based on the net area requirements for classrooms and group rooms in primary and secondary schools, listed in [39].

Table 2: *Teaching Space in Primary School*

Zone	Area Name	Size used in a SoA tool	Grid Size ($\boldsymbol{m} \times \boldsymbol{m}$)
B	Large group room	27m2 for 15	$\mathbf{7.2 \times 7.8}$
B	Classbase without/with sink	50 m2 for 30	$\mathbf{7.2 \times 7.2}$
C	Junior classroom	55m2 for 30	$\mathbf{7.2 \times 7.8}$
D	Reception classroom	62m2 for 30	$\mathbf{7.8 \times 7.8}$ $\mathbf{7.6 \times 8.4}$
D	ICT rich practical room	62m2 for 30	$\mathbf{7.8 \times 7.8}$ $\mathbf{7.6 \times 8.4}$
D	ICT-rich classroom	62m2 for 30	$\mathbf{7.8 \times 7.8}$ $\mathbf{7.6 \times 8.4}$
D	Music classroom	62m2 for 30	$\mathbf{7.8 \times 7.8}$ $\mathbf{7.6 \times 8.4}$
E	Science studio	69m2 for 30	$\mathbf{8.4 \times 8.4}$

The common grid size ranges from $\mathbf{7.2}\boldsymbol{m} \times \mathbf{7.2}\boldsymbol{m}$ to $\mathbf{8.4}\boldsymbol{m} \times \mathbf{8.4}\boldsymbol{m}$. According to normal module coordination set 300mm as the basic unit, then the modules for the timber floor could be $\mathbf{7.2}$, $\mathbf{7.2} + (\mathbf{2} \times \mathbf{0.3})$, $\mathbf{7.2} + (\mathbf{4} \times \mathbf{0.3})$. Timber manufacturing company would list the geometry size of their products. For example, the width of CLT floor panels from HESS timber is 2.2-3.2m with length up to 20m, which satisfies the module of gird size in this research. Based on the module range, six grid size scenarios for TOPSIS assessment are set. After the sum of squares normalization process, the TOPSIS assessment results for the six grid size scenarios are shown in Table 4-6. The positive ideal solution $\boldsymbol{A+}$ for construction criteria is: $[\mathbf{0.474}, \mathbf{0.557}, \mathbf{0.461}, \mathbf{0.522}, \mathbf{0.476}]$ and the negative ideal solution $\boldsymbol{A-}$ for construction criteria is $[\mathbf{0.355}, \mathbf{0.318}, \mathbf{0.329}, \mathbf{0.326}, \mathbf{0.317}]$. The positive ideal solutions $\boldsymbol{A+}$ for the other two criteria are $[\mathbf{0.522}, \mathbf{0.546}, \mathbf{0.551}, \mathbf{0.493}, \mathbf{0.486}, \mathbf{0.508}]$ and $[\mathbf{0.497}, \mathbf{0.497}, \mathbf{0.555}, \mathbf{0.547}, \mathbf{0.476}]$ respectively. The negative ideal solutions $\boldsymbol{A-}$ for construction and service criteria are $[\mathbf{0.326}, \mathbf{0.273}, \mathbf{0.344}, \mathbf{0.302}, \mathbf{0.324}, \mathbf{0.318}]$ and $[\mathbf{0.331}, \mathbf{0.311}, \mathbf{0.277}, \mathbf{0.328}, \mathbf{0.357}]$. The ranking for different grid size scenarios in different criteria are presented in Table 4-6.

4 MULTI-CRITERIA DECISION MAKING FOR FLEXIBILITY

Previous part operates the TOPSIS assessment for the six scenarios from production, construction and service criteria. When determining the module of grid size, for stakeholders from different fields, they would have different focuses on different criteria. Multi-criteria decision making (MCDM) could provide a comprehensive analysis for the flexibility of timber school.

Table 3: *Teaching Space in Primary School*

Zone	Area Name	Size used in a SoA tool	Grid Size ($\boldsymbol{m} \times \boldsymbol{m}$)
C	General classroom	55m2 for 30	$\mathbf{7.2 \times 7.8}$
D	Extensive classroom	62m2 for 30	$\mathbf{7.8 \times 7.8}$ $\mathbf{7.6 \times 8.4}$

Table 4: *TOPSIS Results for Production Criteria*

Module Scenario	Positive ideal distance $\boldsymbol{D+}$	Negative ideal distance $\boldsymbol{D-}$	Relative closeness $\boldsymbol{C}$	Ranking
$\mathbf{7.2 \times 7.2}$	0.284	0.266	0.484	2
$\mathbf{7.2 \times 7.6}$	0.272	0.180	0.398	4
$\mathbf{7.2 \times 7.8}$	0.252	0.162	0.391	5
$\mathbf{7.6 \times 7.8}$	0.277	0.216	0.438	3
$\mathbf{7.8 \times 8.4}$	0.287	0.180	0.386	6
$\mathbf{8.4 \times 8.4}$	0.246	0.290	0.541	1

Table 5: *TOPSIS Results for Construction Criteria*

Module Scenario	Positive ideal distance $\boldsymbol{D+}$	Negative ideal distance $\boldsymbol{D-}$	Relative closeness $\boldsymbol{C}$	Ranking
$\mathbf{7.2 \times 7.2}$	0.243	0.438	0.643	1
$\mathbf{7.2 \times 7.6}$	0.241	0.294	0.549	2
$\mathbf{7.2 \times 7.8}$	0.291	0.224	0.435	3
$\mathbf{7.6 \times 7.8}$	0.352	0.198	0.360	5
$\mathbf{7.8 \times 8.4}$	0.441	0.211	0.324	6
$\mathbf{8.4 \times 8.4}$	0.399	0.252	0.388	4

Table 6: *TOPSIS Results for Service Criteria*

Module Scenario	Positive ideal distance $\boldsymbol{D+}$	Negative ideal distance $\boldsymbol{D-}$	Relative closeness $\boldsymbol{C}$	Ranking
$\mathbf{7.2 \times 7.2}$	0.432	0.119	0.216	6
$\mathbf{7.2 \times 7.6}$	0.358	0.116	0.245	5
$\mathbf{7.2 \times 7.8}$	0.328	0.129	0.282	4
$\mathbf{7.6 \times 7.8}$	0.243	0.230	0.486	3
$\mathbf{7.8 \times 8.4}$	0.213	0.259	0.549	2

8.4 × 8.4	0.119	0.432	0.784	1

Table 7: *Weights of Entropy Method*

Indicator	Information entropy value e	Weights
C_1	0.9975	6.15%
C_2	0.9982	4.49%
C_3	0.9980	4.96%
C_4	0.9977	5.68%
C_5	0.9960	9.76%
C_6	0.9984	3.98%
C_7	0.9977	5.74%
C_8	0.9960	9.78%
C_9	0.9947	12.93%
C_{10}	0.9992	2.08%
C_{11}	0.9980	4.93%
C_{12}	0.9965	8.59%
C_{13}	0.9990	2.32%
C_{14}	0.9976	5.88%
C_{15}	0.9988	2.88%
C_{16}	0.9960	9.84%

For the comprehensive assessment framework, entropy method is selected to determine the weights for all the 16 indicators, shown in Table 7. After the sum of squares normalization process for the values of six scenarios, the comprehensive positive ideal solution $A+$ and negative ideal solution $A-$ are: $[0.474, 0.557, 0.461, 0.522, 0.486, 0.522, 0.546, 0.551, 0.483, 0.486, 0.508, 0.497, 0.497, 0.555, 0.547, 0.476]$ and $[0.355, 0.318, 0.329, 0.326, 0.324, 0.326, , 0.273, 0.344, 0.302, 0.324, 0.318, 0.331, 0.311, 0.277, 0.328, 0.357]$. Based on the ideal solutions, the results for TOPSIS assessment for flexibility are shown in Table 8.

Table 8: *TOPSIS Results for Flexibility Assessment*

Module Scenario	Positive ideal distance $D+$	Negative ideal distance $D-$	Relative closeness C	Ranking
7.2 × 7.2	0.573	0.526	0.479	2
7.2 × 7.6	0.511	0.364	0.416	4
7.2 × 7.8	0.514	0.291	0.361	6
7.6 × 7.8	0.510	0.373	0.423	3
7.8 × 8.4	0.568	0.381	0.401	5
8.4 × 8.4	0.483	0.580	0.545	1

The relative closeness and ranking of three main criteria and comprehensive flexibility for the six scenarios are summarised in Table 9, where S means the scenarios, the same as Table 8; C means relative closeness; R means ranking; B_1 to B_3 means criteria following Table 1.

Table 9: *TOPSIS Results for Whole Assessment Framework*

S	B_1		B_2		B_3		Flexibility	
	C	R	C	R	C	R	C	R
S1	0.484	2	0.643	1	0.216	6	0.479	2
S2	0.398	4	0.549	2	0.245	5	0.416	4
S3	0.391	5	0.435	3	0.282	4	0.361	6
S4	0.438	3	0.360	5	0.486	3	0.423	3
S5	0.386	6	0.324	6	0.549	2	0.401	5
S6	0.541	1	0.388	4	0.784	1	0.545	1

The rankings are demonstrated in Figure 5. For production, the 7.2×7.2 and 8.4×8.4 grid sizes rank top whereases 7.2×7.8 and 7.8×8.4 have less flexibility in production. For construction, the smallest modular grid size has the biggest flexibility in construction. With the increase of grid size, construction flexibility gradually decreases, but it shows an increasing trend when it reaches the maximum size. The scores for services increase as the grid size enlarges, showing a positive correlation. The highest level of flexibility for both the minimum and maximum grid sizes is observed. However, as the grid size increases, the construction flexibility gradually decreases until it reaches a minimum value, after which it begins to increase. The overall trend of flexibility is similar to that of production. Specifically, flexibility exhibits a pattern of decreasing, increasing, decreasing, and then increasing again.

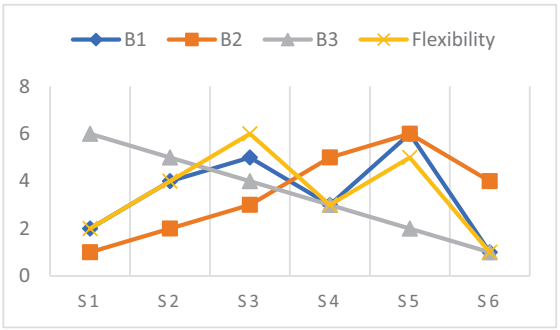

Figure 5: *Ranking for different Scenarios*

5 DISCUSSION AND CONCLUSIONS

This research develops a framework to quantify flexibility by identifying the criteria and indicators selected from the literatures aiming to cover cradle-to-cradle life cycle. Six modular grid sizes are set as the scenarios for comparisons following the net area design guidance of DfE of UK for primary and secondary schools. AHP is utilized to determine the weights of the tree diagram of the

https://doi.org/10.52202/069179-0512

assessment framework and TOPSIS is applied to finalise the value of different modular grid size scenarios. The MCDM results demonstrates that the biggest grid size 8.4×8.4 in this case has the biggest flexibly in production, services and comprehensive flexibility. The reason might be the bigger size provide more potential in layout changing for different functionalities. Modular grid size 7.2×7.2 ranks top in construction flexibility mainly because of the geometry size is easy to assemble. The comprehensive flexibility has the similar trend of production flexibility means the production pre-dominate the overall flexibility performance.

Based on the TOPSIS assessment results, for timber school projects, to achieve the maximum flexibility, module coordination [35] can be operated following the rules adjusted from the general rules :

- Delineation of hierarchy of the space;
- Define the zones for different functions;
- Select the area with demands/potential for flexibility as the reference system;
- Situated the components in different size according to the reference system;
- Choose one module series including the basic, multi- and sub module;
- Coordinate the module according to the function requirements.

Future work would be focusing on the specific workflow of module coordination for flexibility based on the TOPSIS assessment framework by setting 7.2-9m as a range to coordinate the module for maximum flexibility.

ACKNOWLEDGEMENT

The study is supported by the Ministry of Education of Humanities and Social Science Project of China, Grant No. 21YJCZH043.

REFERENCES

[1] O. Cf, 'Transforming our world: the 2030 Agenda for Sustainable Development', United Nations: New York, NY, USA, 2015.

[2] U. SBCI, 'Buildings and climate change: Summary for decision-makers. United nations environmental programme, sustainable buildings and climate initiative, paris, 2009'.

[3] R. E. López-Guerrero, S. Vera, and M. Carpio, 'A quantitative and qualitative evaluation of the sustainability of industrialised building systems: A bibliographic review and analysis of case studies', Renewable and Sustainable Energy Reviews, vol. 157, p. 112034, 2022.

[4] M. Yeheyis, K. Hewage, M. S. Alam, C. Eskicioglu, and R. Sadiq, 'An overview of construction and demolition waste management in Canada: a lifecycle analysis approach to sustainability', Clean technologies and environmental policy, vol. 15, pp. 81–91, 2013.

[5] Y. Han, T. He, R. Chang, and R. Xue, 'Development trend and segmentation of the US green building market: corporate perspective on green contractors and design firms', Journal of Construction Engineering and Management, vol. 146, no. 11, p. 05020014, 2020.

[6] L. Lima, E. Trindade, L. Alencar, M. Alencar, and L. Silva, 'Sustainability in the construction industry: A systematic review of the literature', Journal of Cleaner Production, vol. 289, p. 125730, Mar. 2021, doi: 10.1016/j.jclepro.2020.125730.

[7] G. Liu, R. Chen, P. Xu, Y. Fu, C. Mao, and J. Hong, 'Real-time carbon emission monitoring in prefabricated construction', Automation in Construction, vol. 110, p. 102945, 2020.

[8] S. O. Ajayi, L. O. Oyedele, M. Bilal, O. O. Akinade, H. A. Alaka, and H. A. Owolabi, 'Critical management practices influencing on-site waste minimization in construction projects', Waste management, vol. 59, pp. 330–339, 2017.

[9] S. Liu, Z. Li, Y. Teng, and L. Dai, 'A dynamic simulation study on the sustainability of prefabricated buildings', Sustainable Cities and Society, vol. 77, p. 103551, 2022.

[10] Z. Li, G. Q. Shen, and X. Xue, 'Critical review of the research on the management of prefabricated construction', Habitat international, vol. 43, pp. 240–249, 2014.

[11] A. A. Rahim and S. L. Qureshi, 'A review of IBS implementation in Malaysia and Singapore', Planning Malaysia, vol. 16, 2018.

[12] A. G. Gibb, Off-site fabrication: prefabrication, pre-assembly and modularisation. John Wiley & Sons, 1999.

[13] Net Zero Strategy: Build Back Greener. UK: HM Government, 2021.

[14] S. Masoud Sajjadian, 'A critique on the UK's net zero strategy', Sustainable Energy Technologies and Assessments, vol. 56, p. 103003, Mar. 2023, doi: 10.1016/j.seta.2022.103003.

[15] S. Groak, The idea of building: thought and action in the design and production of buildings. Taylor & Francis, 2002.

[16] J. Gosling, M. Naim, P. Sassi, L. Iosif, and R. Lark, 'Flexible buildings for an adaptable and sustainable future', in Proceedings of 24th annual ARCOM conference, 2008, pp. 1–3.

[17] P. O. Akadiri, E. A. Chinyio, and P. O. Olomolaiye, 'Design of A Sustainable Building: A Conceptual Framework for Implementing Sustainability in the Building Sector', Buildings, vol. 2, no. 2, Art. no. 2, Jun. 2012, doi: 10.3390/buildings2020126.

[18] G. Scuderi, 'Designing flexibility and adaptability: The answer to integrated residential building retrofit', Designs, vol. 3, no. 1, p. 3, 2019.

[19] J. Till and T. Schneider, 'Flexible housing: the means to the end', ARQ: architectural research quarterly, vol. 9, no. 3–4, pp. 287–296, 2005.

[20] 'School buildings: construction framework 2021', GOV.UK. https://www.gov.uk/government/publications/school-buildings-construction-framework-2021 (accessed Feb. 19, 2023).

[21] 'Sustainability and climate change: a strategy for the education and children's services systems', GOV.UK. https://www.gov.uk/government/publications/sustainability-and-climate-change-strategy/sustainability-and-climate-change-a-strategy-for-the-education-and-childrens-services-systems (accessed Feb. 19, 2023).
[22] A. B. Robertson, F. C. Lam, and R. J. Cole, 'A comparative cradle-to-gate life cycle assessment of mid-rise office building construction alternatives: Laminated timber or reinforced concrete', Buildings, vol. 2, no. 3, pp. 245–270, 2012.
[23] J. J. Morrell, 'Protection of wood: A global perspective on the future', in Wood is good: Current trends and future prospects in wood utilization, 2017, pp. 213–226.
[24] M. H. Ramage et al., 'The wood from the trees: The use of timber in construction', Renewable and Sustainable Energy Reviews, vol. 68, pp. 333–359, 2017.
[25] R. Kronenburg, Flexible: architecture that responds to change. Laurence King London, 2007.
[26] S. H. Kendall and J. Teicher, Residential open building. Spon Press, 2010.
[27] D. Moher, A. Liberati, J. Tetzlaff, D. G. Altman, and P. Group, 'Reprint—preferred reporting items for systematic reviews and meta-analyses: the PRISMA statement', Physical therapy, vol. 89, no. 9, pp. 873–880, 2009.
[28] M. Braungart and W. McDonough, Cradle to cradle. Random House, 2009.
[29] T. Schneider and J. Till, 'Flexible housing: opportunities and limits', Arq: Architectural Research Quarterly, vol. 9, no. 2, pp. 157–166, 2005.
[30] N. Israelsson and B. Hansson, 'Factors influencing flexibility in buildings', Structural Survey, vol. 27, no. 2, pp. 138–147, 2009.
[31] H. Kröhnert, R. Itten, and M. Stucki, 'Comparing flexible and conventional monolithic building design: Life cycle environmental impact and potential for material circulation', Building and Environment, vol. 222, p. 109409, Aug. 2022, doi: 10.1016/j.buildenv.2022.109409.
[32] H. Abuzied, H. Senbel, M. Awad, and A. Abbas, 'A review of advances in design for disassembly with active disassembly applications', Engineering Science and Technology, an International Journal, vol. 23, no. 3, pp. 618–624, 2020.
[33] M. Živković and G. Jovanović, 'A method for evaluating the degree of housing unit flexibility in multi-family housing', Facta universitatis-series: Architecture and Civil Engineering, vol. 10, no. 1, pp. 17–32, 2012.
[34] C. Cellucci and M. Di Sivo, 'The flexible housing: criteria and strategies for implementation of the flexibility', Journal of Civil Engineering and Architecture, vol. 9, no. 7, pp. 845–852, 2015.
[35] M. M. Singh, A. Sawhney, and A. Borrmann, 'Modular coordination and BIM: Development of rule based smart building components', Procedia Engineering, vol. 123, pp. 519–527, 2015.
[36] R. P. Geraedts, 'Open Building and Flexibility; an assessment method. Matching demand and supply for flexibility', in 1998 international symposium on open building, 1998.
[37] S. O'Connell, G. Reynders, F. Seri, and M. Keane, 'Validation of a flexibility assessment methodology for demand response in buildings', in IOP conference series: Earth and environmental science, 2019, vol. 352, p. 012014.
[38] C. Gillott, W. Mihkelson, M. Lanau, D. Cheshire, and D. Densley Tingley, 'Developing regenerate: A circular economy engagement tool for the assessment of new and existing buildings', Journal of Industrial Ecology, 2023.
[39] 'Area guidelines and net capacity', GOV.UK. https://www.gov.uk/government/publications/area-guidelines-and-net-capacity (accessed Feb. 27, 2023)
.

https://doi.org/10.52202/069179-0512

World Conference on Timber Engineering Oslo 2023

MONO-MATERIAL TIMBER CONSTRUCTION RE-INVENTION OF PRESS-FIT TIMBER CONSTRUCTIONS

Hans Drexler[1]

ABSTRACT: The paper presents the development of a building system made from solid timber that fulfils the requirements of modern buildings while expanding the design possibilities through re-inventing traditional timber techniques. Press-fit-timber connections, which were the basis of centuries-long building traditions all over the world, can be cost-efficiently used in contemporary buildings using modern manufacturing techniques.
The main goals of the research are:

- Develop a building system with mono-material timber structures (in contrast to hybridization with concrete and steel)
- Optimize the recyclability of building structures: Design to disassemble (on the level of the building and components)
- Improve cost-efficiency by industrial manufacturing methods for mono-material timber constructions.

KEYWORDS: Mono-material timber construction; building system; adaptability; recycling; design to dissemble;

1 INTRODUCTION

Before the advent of industrialization, timber was one of the essential construction materials due to its local availability, easy workability, good load bearing, and overall structural properties. For centuries, carpenters built impressive timber constructions without metal fasteners. Europe and Asia have a wealth of historical examples of timber joints for the widest variety of load cases and construction designs. Multi-story, large, and complex buildings were constructed with purely timber-based methods and only press-fit timber joints.

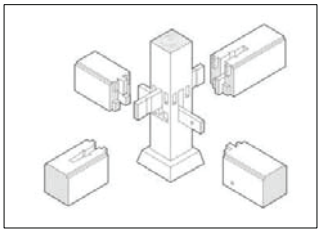

Figure 1: *Yatoi-Hozo-Sashi, three-dimensional joint of the Ashikatame post (main post), graphic: DGJ Architektur, based on Sato Hideo and colleagues [1].*

But this tradition fell into disuse in the wake of industrialization. Not only were such joints – made by highly skilled craftsmen in a time-consuming and thus wage-intensive manner – replaced by cheaper metal fasteners such as nails, screws, and bolts, but even timber itself was displaced as a primary construction material by new materials such as cast iron, steel, and concrete. To this day, these materials are sold at lower prices because they can be produced in higher volumes, and their external costs, especially environmental costs, are left out of the pricing equation. And even though solid timber has many advantages compared to other construction materials. Timber requires less energy than concrete or steel for its production. As a renewable resource, it stores atmospheric carbon during the lifespan of the building. Timber is central in the current discourse on carbon-neutral, energy- and resource-efficient construction [2]. The ecological and economic advantages make mono-material timber systems an interesting alternative for efficient and sustainable buildings.
In order to make the most efficient use of these opportunities, this research operates on two levels. On a first technological level, it offers transferable solutions for the local and the global structure of multistorey residential buildings, which are accompanied by an easy-to-use Excel tool for estimating the dimensions of the primary structural components. On a second architectural level, the research explores how the building system called '*Open Architecture'* [3] can be used to design a wide variety of flexible and adaptable residential buildings. It enables flexible, sustainable, and cost-effective construction with press-fit timber joints that can be easily recycled, and a design that adapts to the respective circumstances without sacrificing design quality and living comfort.

[1] Hans Drexler, Dr.- Ing. Dipl. Arch. ETH M. Arch (Dist.), DGJ Architektur GmbH, Walter-Kolb-Str. 22, D-60594 Frankfurt am Main / drexler@dgj.eu.

https://doi.org/10.52202/069179-0513

2 PRESS-FIT TIMBER CONSTRUCTION SYSTEM

Thanks to advancements in digital design and production technology, it is now possible with computer-controlled machines to produce perfectly fitting joints economically, regardless of the geometry's complexity.
New computational design and digital fabrication promise to enable different access to traditional construction materials. Digital timber fabrication (CNC-milling machines) allows for the precise and efficient milling of solid timber with very low tolerances. In addition, computational design strategies enable the development of adaptive and integrative design tools with a direct transfer of fabrication data, ultimately opening new potentials for design and production.

In two research projects, *DGJ Architektur* with *Pirmin Jung Ingenieure GmbH* has developed a timber construction system in which the entire load-bearing structure and all joints are press-fit without metal connectors [4]. Part of the research is a complete set of construction details so that the system fulfils today's regulatory requirements regarding fire protection, acoustic insulation, structural calculation, and industrial construction standards.

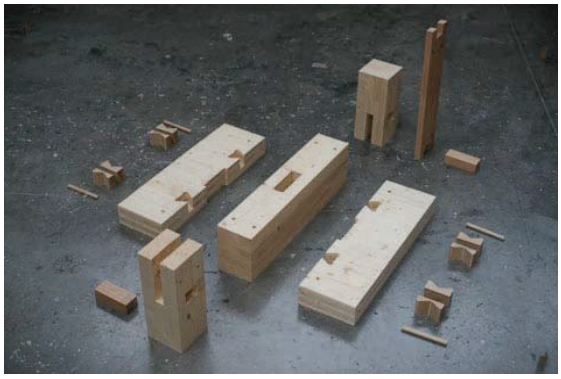

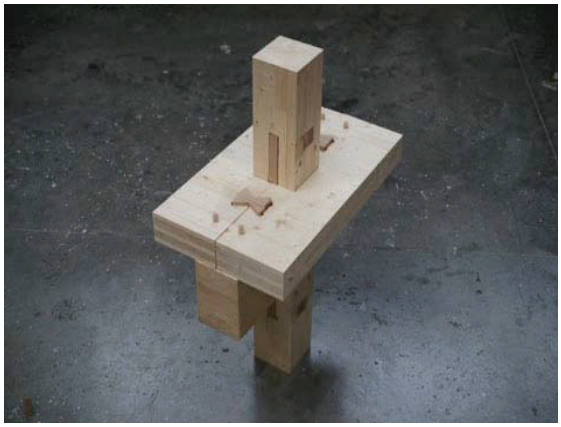

Figure 2 and 3: *Prototype of the construction detail: Intersection of column, beam, and ceiling, Photograph: Hans Drexler, DGJ Architektur, 2018.*

The construction system is based on readily available materials, technologies, and processes at all levels so that the system can be applied by all larger carpentry companies. Standardized materials, such as structural timber and CLT, can be used. The structural analysis of the load-bearing structure and the joints are based on the current Eurocode; in principle, any engineer can calculate and dimension them.
Thus, the innovative part is not newly developed materials or machines but the more intelligent and smart use of existing methods, technologies and materials and combining them into a system.
As part of our research project [4] an Excel-based design tool was developed that enables our system to be pre-dimensioned and costs and performance to be evaluated. It allows the designer to estimate the inputs (timber volume, costs) and performance (living space, efficiency (gross floor area/living space). The joints are designed using modern, three-dimensional CAD systems widely used by architects and engineers. Fabrication data can be generated in the design phase with little extra effort. The system, including press-fit joints, can be produced with widely available timber CNC milling machinery. In this way, traditional knowledge is translated into contemporary building technologies and materials.

3 STRUCTURAL SYSTEMS

Different structural systems for the building system were explored in developing the load-bearing structure: skeleton, hybrid, or solid timber. An essential part of the research is concerned with describing and evaluating the advantages and disadvantages of the various structural systems. A key parameter is the amount of timber required for the load-bearing systems. Other parameters that were examined included the usability and flexibility of the building, but also fire protection, acoustic insulation, and thermal construction physics as mentioned above.

3.1 SKELETON CONSTRUCTION

Timber – produced from tree trunks – is initially a linear, rod-shaped construction material, which lends itself to building skeletal constructions [5]. Given, for example, the high prices for timber and difficulties in the supply in 2022, the structure's efficiency is an important criterion, which was investigated by comparing different articulations of the building system. For non-load-bearing walls and facades, timber-panel and timber-frame constructions are used, which can be produced inexpensively, using less timber.

Another advantage of the skeleton system is flexibility. Taking Steven Groák's definition of flexible housing [6], i.e., a physically and structurally changeable structure, the skeleton construction offers the best opportunities to create flexible housing by separating space creation and load-bearing functions. As a result, the load-bearing skeleton allows both external and internal walls to be moved and altered. If one considers the rapid changes in lifestyles, resulting social structures and demographics (e.g., the declining number of families with the typical, traditional family structure and shrinking household

https://doi.org/10.52202/069179-0513

sizes), then inflexible housing layouts are not sustainable in the long term.

3.2 HYBRID SOLUTIONS: COMBINING SKELETON AND SOLID CONSTRUCTION

In the mid-1990s, a solid timber construction known as cross-laminated timber (CLT) came onto the market, which offered key advantages, especially for taller buildings, because solid wall panels perform better in terms of vertical load transfer and cross bracing of the global load-bearing structure. When developing this press-fit construction system, a combination of the advantages of the two construction methods was explored: parts of the skeleton structure are replaced by load bearing and bracing cross-laminated timber elements, which allow for an efficient transfer of the horizontal loads. Thus, a part of the walls enclosing the bathrooms, which are in the same vertical line on all floors, and a part of the party walls are designed to replace posts as load-bearing wall segments. The horizontal bracing is achieved by means of bracing walls of solid timber (cross-laminated timber) that are connected to the posts by means of tenons.

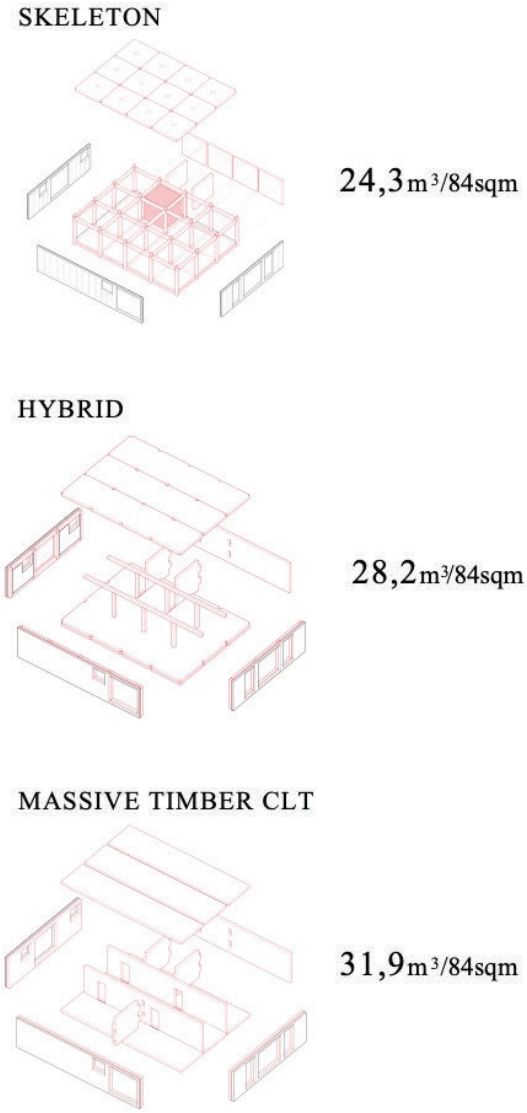

Figure 4: *Axonometric drawings of structure / Comparison of wood volume necessary in different construction methods for a typical apartment of 84 sqm. Designed by DGJ Architektur, Illustration: DGJ Architektur.*

Figure 4 shows a comparison of the consumption of wood in different construction methods. For the hybrid construction, consisting in part of solid walls, the amount of timber used in Case-Study 1 (*Collegium Academicum*), with a load-bearing timber skeleton, a bracing core, and ceilings of cross-laminated timber (CLT), totals 28,2 cubic-meter or 14% more timber than the skeleton construction.

3.3 SOLID TIMBER CONSTRUCTIONS

During the development of the system, it emerged that the introduction of cross-laminated timber resulted in a construction that combined aspects of a skeleton construction (i.e., only linear load-bearing elements) with aspects of a solid construction for ceilings and bracing walls. This led to redundancies at the intersections. The

https://doi.org/10.52202/069179-0513

bracing wall could take all loads vertically and thus replace not only the column but the beam as well. Thus, based on the grid, this system could be implemented as a solid timber construction. The disadvantage of solid interior walls is their low adjustability.
The solid construction for ceilings and bracing walls is more material-intensive, although the strength of the individual walls can be reduced by the uniform load transfer.

3.4 LOCAL STRUCTURES AND JOINTS

Given the wide variety of traditional timber joints such as tenon and mortise, lap joints, dovetails etc., the research examined which joints can easily be applied to modern production in real-life practice. Here two different approaches were examined and compared: integrated or differentiated joints.
The integrated joints are cut so that the elements fit into the geometric space of the adjacent elements and guarantee a press-fit joint via the interlocking of the elements' geometries. The initial idea of our construction approach was to produce geometrical locking and press-fit joints when cutting and sizing the elements, thus making fasteners unnecessary. Our reference point was a Japanese "Yatoi-Hozo-Sashi" joint, which fits two main beams into the geometric space of the post to form beam-to-post joints, but also forms a lapped end-to-end connection from beam to the beam by means of rod tenons, which are secured in place with wedges or cross tenons. The load of the beams is transferred not only via the rod tenons but, above all, via a parapet from beam to post, into which the beam is precisely fit. The principle of this joint is that the geometric spaces overlap, and the members are joined with comparably complex geometries.
Differentiated joints separate the geometric spaces of the components, which are then connected via secondary elements.

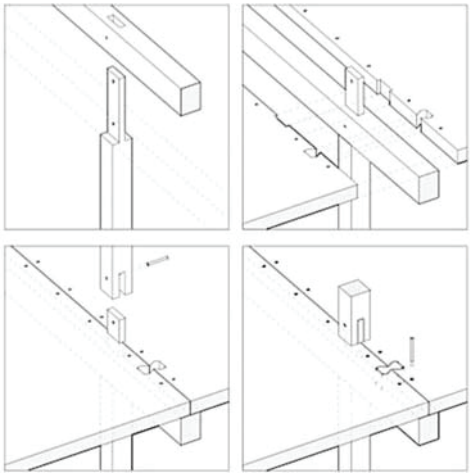

Figure 5: *DGJ Architektur, 3D model of the construction system's beam to post joints, DGJ, 2016.*

The combination of timber components is an advantage of the differentiated local system. The solid ceiling elements are joined to the post with dovetail joints made from hardwood. This type of joint is complicated to build on-site but allows for the transfer of shearing, compressive, and tensile forces. Beech dowels are used for the shearing forces between the ceilings and the beams. The final detail, the vertical connection between the two columns above and below the ceiling, is produced from hardwood (beech wood LVL), which allows for the transfer of the vertical forces through a smaller cross-section.
In this context, discussing the weakening of the supporting beams by such geometric joints is interesting. At first glance, the beams and columns sections increase the timber volume necessary for structural performance. But it became apparent during the development that there is a system synergy between fire protection and structural performance. When measuring the load-bearing capacity of the beams under fire conditions, the entire timber volume is not applied to the load transfer. Still, it is assumed in the case of fire that the outer layer of the beam burns away slowly, ensuring the remaining beam's stability for the required time. In the case of the press-fit joints, this layer is also part of the structural elements used for the joints, which serve as an integrated fire-resistant layer.
In the first case study (see Case Study 1: *Collegium Academicum*), the connections between posts and beams and beams and ceilings were increasingly simplified during the design process, i.e., separated into their own geometric spaces. Vertically, the forces are achieved by lapping the elements, which are secured in position with beech wood dowels. The stable plate effect of the ceiling elements is achieved by lap-joining ceiling elements with dovetail joints. This differentiated construction has two advantages: first, it makes the timber trimming process for the individual elements easier because the elements lie above and next to each other. The geometry of the components is more straightforward, and the production is cheaper. Second, the differentiated construction of the components allows the dimensional tolerance of the individual parts to be compensated across the load-bearing structure, as the horizontal accuracy of the fit is initially not decisive for the load transfer. The vertical inaccuracy can be compensated locally. The disadvantage of joining in this way is that the connections with beech wood dowels can only be released by drilling out the dowels, which makes dismantling more difficult.

3.5 DESIGN TO DISSASEMBLE

An essential aim of the research was to develop a mono-material construction system based on renewable materials. Since all parts of the structure are made from timber, the system is also easy to dismantle later. The disadvantage is that putting it together requires high precision and leaves little room for dimensional tolerance.

In the real-life buildings so far designed and studied, the idea of mono-material timber construction is only applied to the primary structure of the building. Therefore, secondary systems for facades and fit-outs would still use screws and other metal fasteners. Even though comparable automated methods for fixing panels using timber nails are readily available, the necessary

https://doi.org/10.52202/069179-0513

certificates are not. Also, timber nails do not offer the same performance as metal screws.

Figure 6: *Timber Prototype House, Photographs: Thomas Mueller, 2018.*

In a small-scale prototype building, the idea of mono-material timber construction was demonstrated comprehensively: The '*Timber Prototype House'*, which is part of the international building exhibition IBA Thüringen, is made from timber (and glass for the windows), joined by press-fit timber construction. The building still fulfils all technical requirements, including thermal insulation [5]. But the design and production processes are still too complicated and costly to allow for use in affordable buildings.

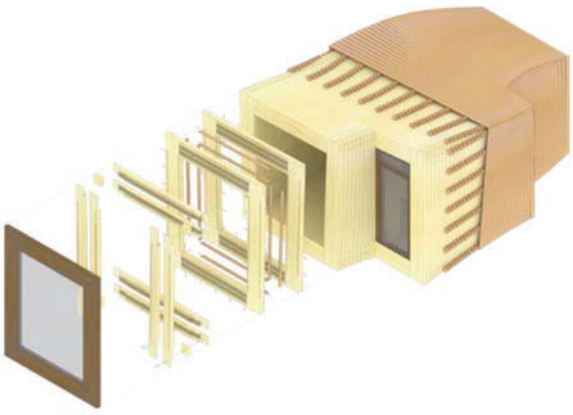

Figure 7: *Timber Prototype House, Graphics: ICD Stuttgart, 2018.*

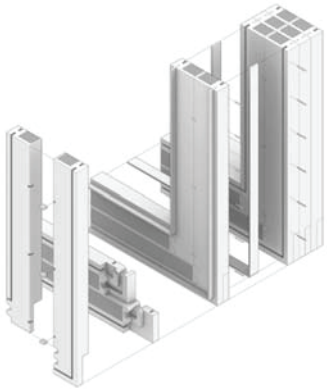

Figure 8: *Timber Prototype House, Graphics: ICD Stuttgart, 2018.*

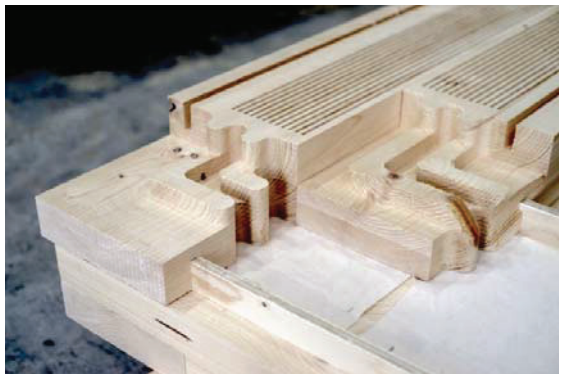

Figure 9: *Timber Prototype House construction detail, Photograph: Hans Drexler, 2018.*

4 RESEARCH BY DESIGN

The development of *'Open Architecture'* [3] as a building system was as much about exploring the architectural potential as the technical solutions. A series of case studies were used to incrementally improve the building system, using a set of criteria for sustainability, efficiency, and usability. The system was developed in 2015 through several 15 case studies [3]. During the research, the development of the system (planning and design methodology) was combined with analysis (evaluation and optimization). This has brought to light an essential aspect of explorative applied construction research: Design has both creative and analytical aspects, which interact with each other in iterations and recursions. In the day-to-day designing and planning process, iterations, parameters, criteria, and decision paths are seldom explicit, and as such, they are not transparent. They take place in numerous sketches, drawings, models, and discussions. In the research and development project, the analytical parts are made explicit and operative, thus complementing the design. From these analyses, tools were developed with which the construction system can be adapted to different locations and functions. In developing this system, the levels of research and parameters for a given object are evaluated and optimized.

https://doi.org/10.52202/069179-0513

The case studies are vehicles and research objects at the same time. The transferability and usability of the construction system are identified. Through the systematic research of the application parameters, load cases and characteristics, an estimate of the dimensions of the structure can be calculated for each application. To study the possibilities in terms of building typology, we first defined a series of design parameters, the permutations, which can be expressed as a matrix. The matrix is a parametric design tool for the performance and dimensions of the system, depending on the building-typological characteristics of the respective permutation. In the matrix, all three analysis levels – design, structure, and performance – are interlinked and influence each other.

4.1 CASE STUDY 1: *COLLEGIUM ACADEMICUM*

Animation: https://vimeo.com/459124025

Figure 10: *Case Study 1: Collegium Academicum in Heidelberg, Germany, designed by DGJ Architektur, Photographs: Copyright Thilo Ross Urh. Nr. 4026999.*

One of the first case studies was the *Collegium Academicum, a* project of the International Building Exhibition (IBA Heidelberg). It is a student residence with 176 units. A new housing typology was developed, which enables residents to change and adapt their apartments to various spatial configurations.

Figure 11: *Construction detail, Collegium Academicum. DGJ Architektur, and photograph: Hans Drexler, DGJ Architektur, 2018.*

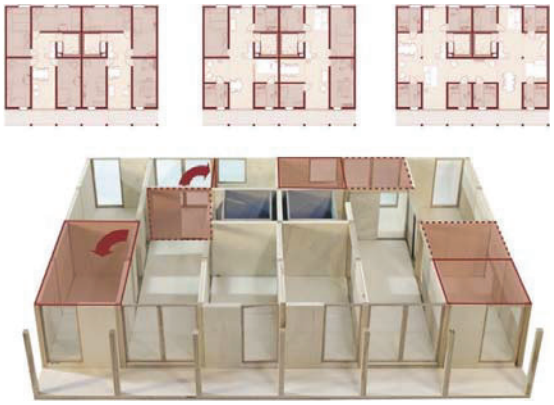

Figure 12: *Three possible floor plan configurations (top), physical model of the construction system, model scale 1:25, DGJ Architektur, and photograph: Hans Drexler, DGJ Architektur, 2018.*

The residents can quickly and easily reposition partition walls within the apartments, thereby changing the size of the rooms. The individual rooms consist of two sections: a core area of seven square meters and a flexible area of seven square meters, which can be used as personal space or be part of the apartment's shared space. Depending on individual preferences, the flexible area can remain completely open, partially separated by dividing elements (table, shelving), or partitioned off entirely by placing the wall between the core area and the flexible zone. Thus the building becomes an adaptable space where the individual inhabitants and housing communities can reconfigure and negotiate the space requirements.

The project is part of the program “Variowohnungen” of the German Federal Institute for Research on Building, Urban Affairs and Spatial Development (BBSR) in the Federal Office for Building and Regional Planning (BBR) and is additionally funded by the program “Holz Innovativ” of the state of Baden-Württemberg. “Holz Innovativ” is financed with the European Regional Development Fund (ERDF) funds.

Figure 13: *Model apartment, Collegium Academicum. DGJ Architektur, Photographs: Copyright Thilo Ross Urh. Nr. 4026999, Source: DGJ Architektur.*

https://doi.org/10.52202/069179-0513

4.2 CASE STUDY 2: *GEMEINSAM SUFFIZIENT LEBEN* (LIVING TOGETHER SUFFICIENTLY)

Figure 14: *'living together sufficiently', physical model of the construction system, model scale 1:50, DGJ Architektur, and photograph: Hans Drexler, DGJ Architektur, 2016.*

This building is designed for a small housing cooperative: a group of families and individuals who asked for a variety of apartment types and sizes within a comparatively small building. The design offers a wide range of different apartments that are suitable for families, senior citizens, couples, and individuals. However, due to the basic concept (*'living together sufficiently'*), the individual rooms are relatively small for the respective use and therefore offer little scope for other uses. The common areas and central facilities offer an advantage for long-term usability and the adaptability of the building. Different divisions and apartments on the floors can be realized, from a small two-room studio to a five-room family apartment. The building is planned as a skeleton structure with a stiffening core. The concentration of bracing around the access gives a high degree of freedom for the design of the floor plans. The flexible but clearly structured system has proven to be a suitable means of planning. The structure allows for individual requests and long-term customization without jeopardizing the integrity of the overall system.

Several types of apartments for different living needs were developed for dialogue with the living group. Ultimately, no variant is implemented similarly but redesigned in dialogue with future users. The large 4-room apartment was redesigned into a 5-room apartment, which was chosen together with the smaller 3-room apartment on almost all floors.

Figure 15: *Case Study 2: 'sufficiently living together', apartment layouts, graphics DGJ Architektur, 2016.*

The square grid permits different apartment layouts adapted to individual needs and wishes and flexibly combined. At the same time, the layouts of the apartments remain flexible/adjustable for future changes.

4.3 CASE STUDY 3: ARRIVAL CITY 4.0

Animation: https://vimeo.com/240369724/0d8d1520a6

Figure 16: *Case Study 3: Arrival City 4.0, model and photograph by DGJ Architektur, 2016.*

Arrival City 4.0 was designed to respond to the so-called refugee crisis at the end of 2015 in Europe. The project was intended to demonstrate how spatial and social structures can contribute to the creation of affordable housing and integration. The building system '*Open Architecture*' [3] was used to provide people not only a

place to live in the short term but also to give them a long-term perspective. *Arrival City 4.0* is an expandable design representing a general low-investment approach to housing shortages. The primary structure and a basic building envelope made from polycarbonate panels can be built with minimal investment in a short period of time. This basic shelter would gradually be transformed into a permanent building by the inhabitants by adding internal walls, technical systems, and more advanced façade panels.

Figure 17: *Case Study 1: Arrival City 4.0, model and photograph by DGJ Architektur, 2016.*

5 FINDINGS: CHALLENGES AND OPPORTUNITIES FOR PRESS-FIT TIMBER CONSTRUCTION

5.1 RE-USE AND RE-CYCLING

Due to the widespread use of non-renewable construction materials and given that most construction materials are rarely reused or recycled (only downcycled), the construction industry is responsible for a large share of waste that is generated today. This building practice also results in the high use of resources. Sustainable buildings must be built differently: The individual construction elements should be joined to be taken apart again. The shearing layers of construction should be joined to maintain, repair, or replace individually since they have different life spans.

For the primary structure, the developed mono-material timber constructions offer an alternative that can be reused and recycled into engineered wood products, such as OSB boards. The constructions' simplicity promotes sorting, an essential prerequisite for recycling materials.

The system is designed to allow components and materials to be dismantled and reused, but implementation is limited to the primary construction in the first use cases. Looking at the building, further potential for recycling needs to be raised. The ability to be dismantled, the reuse of components and the recycling of building materials are essential criteria for a holistically sustainable building design. Ideally, the buildings of the future will consist of components and materials that can either be reused as such elsewhere or that can be easily broken down into components suitable for reuse. The principles of circular construction should be applied systematically at all construction levels. Optimizing the construction system regarding a circular economy and closed material cycles is the most crucial technical optimization that must be addressed within the system. Even more, than in conventional construction, the system presented is suitable for meeting this requirement regarding flexibility and the construction hierarchy. These include in particular:

- Hierarchy of construction according to life expectancy and subsystems.
- Simple, removable, and self-explanatory constructions that favor dismantling.
- Use of renewable building materials.
- Use of materials that can be easily recycled.
- If possible, define parts and components that can be reused as a whole unit.

More precise planning and analysis of the assembly and disassembly processes and the subsequent recycling of the disassembled parts are required here. Analysis, evaluation, and optimization of all building materials installed in the system are necessary.

5.2 HIERARCHY OF CONSTRUCTION

The primary structure determines the basic structure of the building to a large extent. In today's construction, where a whole range of requirements and technology must be met, many other components and layers are added to this primary construction. The question of how these are structured and interconnected has received little attention from research. For example, no terms and definitions are introduced for the different hierarchies, which can be used to distinguish between different types of construction. In the following, such terms are developed to be able to categorize the other construction methods.

Within the construction, subsystems can be identified that are analogous to the 'Shearing Layers of Change' [7]:

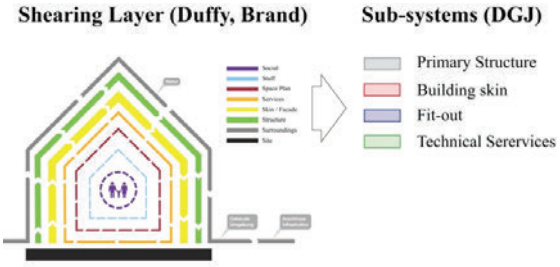

Figure 18: *Shearing Layers introduced by Frank Duffy, further elaborated by Stewart Brand [7], sub-systems for constructions graphics by DGJ Architektur, 2020.*

Structure: All primarily load-bearing and stiffening components of the skeleton structure fall into the subsystem of the supporting system.

Façade / building envelope: The subsystem of the building envelope includes all structural elements that form the primary external space closure. The corresponding components fulfil the basic functions of fire protection, heat, and weather protection.

https://doi.org/10.52202/069179-0513

Fit-out: Both fundamental components and individual component layers, which are necessary to meet the requirements for interior room closures, can be assigned to the subsystem of the interior design (e.g., for apartment partition walls and floor constructions).
Technical building equipment: Technical systems form a separate subsystem since interchangeability and flexibility should be guaranteed to an exceptionally high degree.

The definition of the subsystems was developed in the project to analyse buildings. The four subsystems can be viewed on three hierarchical levels because the interior and building services subsystems are arranged on the same hierarchical level [8]. Regarding the separability of materials, efficient assembly and the dismantling of components, a strategy for structuring the system should be selected that provides for a clear hierarchical structure in constructive-functional and temporal dimensions as well as the flexibility of the components. As part of the research, a series of constructions were developed and analysed, allowing the identification of categories of timber constructions. Depending on the degree of differentiation and/or overlap between the sub-systems, the constructions are more or less flexible and/or suitable for recycling.

The definition of the hierarchical levels is primarily linked to the expected life span of the individual materials and components. On the one hand, this should ensure flexibility in the assembly process since the components can be prefabricated together as larger modules or installed successively on-site. The system should, therefore, also be adaptable for project-specific circumstances and restrictions (transport, accessibility of the property, possibility of prefabrication, etc.). On the other hand, the service life is crucial, especially the ability to overhaul, exchange, convert, dismantle, and recycle the components. The clear separation of the hierarchical levels should, therefore, also be reflected physically, i.e., concretely in the components' constructive connection and geometric arrangement, to ensure that they can be separated according to type. For the assessment, the individual subsystems are assessed separately regarding accessibility and the possibility of adaptation.

5.3 SUSTAINABILITY

As a domestic, renewable resource, timber is the most sustainable construction material available since it is the only construction material that can be used for all construction tasks in large volumes and is not based on limited resources (fossil fuels, sand, iron ore …). Thanks to Germany's established, sustainable forestry industry, timber can serve indefinitely as a renewable raw material. Model computations indicate that the timber needed for the country's total construction activity can be covered by just one-third of its annual timber output [9]. Using timber as a renewable resource, our construction system has ecological advantages; improving the reusability of the construction elements can increase these advantages even further. The production and processing of timber require significantly less primary energy. Wood absorbs carbon dioxide from the atmosphere and thus stores it over the lifetime of the building. In the hybrid construction variant, the reduction of CO^2 emissions by wood is partially offset by high emissions related to secondary materials, like cement or steel.

5.4 COST EFFICIENCY

Regarding commercial viability, timber-only joints may have advantages over constructions using metal fasteners. The fasteners by themselves are high-quality and expensive construction elements, especially given the current high prices for metals and energy. Moreover, mounting the fasteners represents a considerable expenditure of time in the production and assembly at the construction site. When processing times are minimized, costs are also reduced. The high complexity of timber-trimming processes means longer processing times at the milling machine but reduced time for fasteners on site.
The building system's first real-life applications did not show a significantly lower price than conventional timber constructions. This could be because, in both buildings, the manufacturer used the press-fit structure for the first time and could not calculate prices more aggressively.

5.5 PRECISION

Press-fit joints require a high degree of precision in production and assembly. Especially in the case of larger buildings, where imprecision in construction elements and their fitting can add up, joining with press-fit elements is a challenge. In both real-life applications, the construction on site was faster than expected due to the higher precision achieved with the system. Within the press-fit construction, building components fit together as 3D puzzle, constantly eliminating impressions in the assembly process.

5.6 SOUND PROOFING

Timber constructions, in general, are comparatively lightweight and can, therefore, absorb sounds less efficiently than heavier materials such as concrete or bricks.
In press-fit timber constructions, an additional conflict of objectives is found: The press-fit connections should be as tight as possible for structural integrity. For soundproofing, decoupling of the elements would be preferable when building components continue through sound barriers, such as ceilings or walls between apartments. Two strategies can be used to minimize the problem: decoupling and stiffening. The sound transmission is minimal when the construction is decoupled using vibration isolation (high-density foam materials). For example, partition walls between apartments are designed as double walls and decoupled. The ceilings are equipped with sound insulation, which decouples them from the primary structure and the rooms below. Beams and load-bearing walls must be individually assessed as secondary noise transmission channels. Here the strategy was to stiffen the connection between the column and the beams, as well as between the walls and the ceilings, respectively, to a point where all components acted as a unified system. Due to the

increased mass, they absorb more sound energy, which will not be transmitted.

5.7 FIRE PROTECTION

Given the combustibility of the primary construction material, special care must be given to fire protection. In the simplest scenario, timber can protect itself from combustion. Timber forms a relatively stable charcoal coating in a fire, which in turn delays full destruction by fire. This effect is included in the dimensioning of the construction elements for fire conditions, in that the beams are sized larger than what they need to be to meet their load capacity requirements so that in case of fire, the remaining beams assure the stability of the building for the prescribed amount of time. Press-fit joints can, as a rule, be considered homogenous construction elements. In practice, however, care should be given that the joints are so tight that fire cannot penetrate them.

Supporting and bracing parts of the structure are generally not reached by a fire for five to ten minutes due to the low combustibility of a closed timber surface. In most cases, fires are fueled initially by furniture and fixtures so that houses have been evacuated by the time the fire reaches the supporting and bracing elements. This, in turn, means that the primary fire protection goal would be met. If added fire protection of the supporting and bracing elements is required, e.g. because it is prescribed by regulations and/or due to increased evacuation risks (higher buildings, more complex layout), the primary timber load-bearing structure can be additionally protected from fire by encasing it with cladding so that the combustible elements can be protected from the fire for a defined period of time (30 min., 60 min., 90 min.).

6 CONCLUSIONS AND OUTLOOK

6.1 CONCLUSIONS

The building system '*Open Architecture'* has so far been used for three residential buildings in Germany, which are constructed in Frankfurt, Heidelberg, and Mannheim. This indicates that the system fulfils all technical and legal requirements.

Given the technological advances in automated cutting and milling of timber, mono-material timber construction is a plausible solution for solving the problem of higher costs and carbon emissions caused by metal components and improving the recycling potential of timber buildings.

6.2 OUTLOOK: SIMPLICITY AS DESIGN PARAMETER

Mono-material timber construction's high ecological and economic potential needs a comprehensive approach. Most parts and all sub-systems of the building should be mono-material and/or designed to disassemble. Given the many requirements a contemporary building must fulfil, like structural performance, insulation against heat and cold, fire protection, soundproofing and many others, most building designs tend to translate each into discrete layers or components. This strategy adds to an enormous complexity in the construction, making the design and building process challenging and re-use or recycling almost impossible. To make extensive use of the simple and effective idea of press-fit timber construction, the complexity of the building construction must be dramatically reduced. At the same time, the hierarchy of the constructions, according to life span and functional sub-systems (or shearing layers), can be used as a design strategy.

REFERENCES

[1] Sato, H., Nakahara, Y.: *The Complete Japanese Joinery*. Hartley & Marks Vancouver: 2000.

[2] Churkina, G., Organschi, A., Reyer, C.P.O. et al. Buildings as a global carbon sink. *Nat Sustain* 3:269–276, 2020. https://doi.org/10.1038/s41893-019-0462-4.

[3] Drexler, H.: *Open Architecture: Nachhaltiger Holzbau mit System*. Jovis Verlag Berlin, 2021.

[4] Drexler, H. et al.: *Holz: Form- und kraftschlüssig – Entwicklung eines Vollholz-Bausystems mit Form- und kraftschlüssigen geometrischen Verbindungen*. 2020. https://www.baufachinformation.de/holz-form-und-kraftschluessig/fb/253213. Download link for the report and the Excel tool (German): https://www.dropbox.com/t/JwWuaVZzwGUHWcIh

[5] Menges, A., Bucklin, O., Krieg, O. D., Drexler, H.; Baukonstruktionen aus Massiv-Holz, welche durch Form und Fügung konstruktive und bauphysikalische Anforderungen des energie-effizienten und nachhaltigen Bauens erfüllen, Abschlussbericht. *Forschungsinitiative Zukunft Bau*, Band F 3122, 2019, Fraunhofer IRB Verlag.

[6] Groák, Steven. *The Idea of Building: Thought and Action in the Design and Production of Buildings*. London: E & FN Spon, 1992.

[7] Brand, Stewart, *How Buildings Learn: What Happens After They're Built*. London: Penguin Books, 1992.

[8] J. Albus, K. Doemer, and H. Drexler, "Prefabrication as Key-Technology for Sustainable and Affordable Housing," in *CESB 2016 - Central Europe Towards Sustainable Building 2016: Innovations for Sustainable Future*, 2016.

[9] Kaufmann, Hermann; Krötsch, Stefan; Winter, Stefan (et al.). *Atlas Mehrgeschossiger Holzbau: Grundlagen - Konstruktionen – Beispiele*. München: Edition Detail, 2022.

https://doi.org/10.52202/069179-0513

World Conference on Timber Engineering Oslo 2023

A DESIGN FRAMEWORK FOR TIMBER BUILDING SYSTEMS

Marius Nygaard[1], Kjetil Nordby[2]

ABSTRACT: The paper proposes a design framework as a means to invigorate considerations of ecological, social and economic sustainability in the development of industrialized timber building. The framework describes principles, participants, processes and tools. Central requirements are (1) open innovation, (2) user / inhabitant participation and influence, (3) simplified quality control and production of code compliant design documentation, (4) adaptability, (5) integration of self-build, (6) preparedness for material hybridity, and finally (7) circularity of materials, components and buildings. To test the relevance and design implications of these imperatives, a diagrammatic study of a four storey block of flats was carried out. The example shows that a high degree of adaptability can be achieved while maintaining openness for integration of a wide variety of light-weight timber structures. In turn, this provides options for the size and weight of elements and components. They can be adapted to different strategies for off-site production and on-site assembly. The design framework will impact the patterns of information and influence in design and construction processes. Sharing of solutions and experience will speed up the innovation needed to meet the sustainability goals of the building industry.

KEYWORDS: Timber, building systems, circular building, industrialized building

1 BACKGROUND

A holistic understanding of future building systems is vital to meet the UN sustainability goals. Unfortunately, architect-designed building systems tend to be beautiful but with limited spread. [1], [2]. One reason is that they focus on detailed design of key components instead of defining the boundaries and rules of the building system itself.

Modern building systems face a series of new challenges. For instance (A) the sorting, evaluation, and reuse of parts from used (demolished) structures must be facilitated in the system. (B) The components and subsystems or "layers" [3] of future buildings must be designed for variable cycles of construction, maintenance, exchange, disassembly and reassembly. And (C) user participation and self-build options should be integregrated, as they may affect the durability, costs and availability of housing.

N. John Habraken´s work on inhabitant participation in the early 1960s, and Norwegian examples of studies of building systems in the 1970s [4] have gained new relevance reflected in recent open building initiatives [5].

Against this backdrop we propose a design framework for timber building systems supporting open innovation. We define key requirements common to all building systems, and test their impact through a diagrammatic exploration of a system for lightweight, wooden buildings.

As example we have chosen a four storey timber block of flats. The advantages of low production emissions and sustained carbon storage in timber buildings are well documented [6]. Low-rise buildings in high-density urban patterns represent the biggest potential for increased use of timber. Lenient codes, especially up to 4 stories, make this building category a low-hanging fruit for innovators. Challenges regarding the future availability and cost of sustainably harvested timber also favour the efficient, light-frame structures suited for low-rise buildings.

2 A DESIGN FRAMEWORK FOR TIMBER BUILDING SYSTEMS

A design framework for building systems is the overarching structure that definine the key properties of the subsystems and components constituting a finished building. This comprise of the cyclic processes of design, production, use, disassembly, reuse, and the organizational structure of maintaining the system itself through open innovation. We propose the following key properties as useful for defining an effective design framework for building systems.

2.1 OPEN INNOVATION

To make the design framework expand and evolve according to the needs of users and industries we propose applying an open innovation process. Ollila & Yström (2016) [7] outline how a focus on engaging the participants of a community is central in open innovation projects. Because of this we suggest a focus on development of open-source design resources shared

[1] Marius Nygaard, The Oslo School of Architecture and Design (AHO), marius.nygaard@aho.no

[2] Kjetil Nordby, The Oslo School of Architecture and Design (AHO), kjetil.nordby@aho.no

https://doi.org/10.52202/069179-0514

under open licences such as creative commons [8] Open-source development is an ongoing process dependent on a system that is both used and expanded through the contributions of a community. In the case of a building design framework, we will emphasize the need to simplify use through making the design resources available as easy too use tools, such as integrations in common CAD applications or in emerging web based systems. The latter is crucial since online systems can better enable participants to access, discuss and add contributions to the system.

2.2 USER / INHABITANT CENTERED

Recent research (Groba 2021) [9] shows that user involvement may clarify architectural strategies that increase the understanding and appreciation and thus the durability of timber buildings. This also applies to the programming of private and common areas. The building design framework must define roles, interaction and output for the design process. It also needs to provide design resources such as tools and guidelines that are adapted to the requirements both of the future inhabitants and the participating architects, engineers and builders. All aspects can be supported by applying human centered desing processes such as ISO 9241-210:2019 [10]. The upper part of Figure 1, shows the outline of the design framework and its development through user-centered and interdisciplinary design processes.

2.3 SIMPLIFIED QUALITY CONTROL AND CLASSIFICATION

The design framework must give immediate access to qualified competence and certified products and solutions. Environmental, planning and building legislation, together with building codes, standards, and certifications constitute a regulatory control and information system for the building industry. It aims to secure democratic processes and reduce risk of damage to people, property or environment. However, its complexity has grown into an obstacle for overview and participation by users of buildings. In Figure 1, the control and information system is visualized as a table of information that has to be filled in to initiate and finalize each step in a building process. At the end of a building´s lifecycle, the system should enable tracing of all subsystem and component properties that are relevant for reuse. This is presently far from being implemented.

The design framework must contribute to information systems that support cicularity. It will harvest information from each production step for relevant materials, products and buildings, and integrate it in user / inhabitant - centered design processes. The overview in Figure 1 both of the regulatory system and the production of materials and construction of buildings must inform the processes and tools of the design framework.

In Norway, SINTEF / Byggforsk´s Building Research Design Guides [11] provide comprehensive and updated input to a design framwork for timber building systems. They are supplemented by SINTEF Technical Approval (TG) of building systems, modules and components, which is coordinated with European standards, marks and certification systems. Other product databases together with Environmental Product Declarations (EPDs) and building classification systems (e.g. BREEAM-NOR) offer important additional information. For Technical Approvals, not all data are open source, and several databases require subscription and payment for access. A systematic overview is required to optimize data access and exchange between the design framework and other sources. Sharing of information is essential. Open catalogues of design solutions may be an integrated part of the design framework, or maintained by the associated architects, consultants and builders. Combinations may also be developed.

Norwegian and EU codes and directives for qualification of architects and other design and construction professionals must be integrated in the recruitment of participants in the design framework.

2.4 ADAPTABILITY

The building system must be adaptable to local conditions. In Norway, this means a variety of climate zones and prospects of a warmer, wetter and wilder future. Topography and biodiversity, together with building heritage and urban patterns, also demand adaptabilty of building systems. A potential for density is necessary to limit land use and emissons related to transport. Many of these properties are embedded in timber building traditions, but they must be rediscovered and reinterpreted.

User needs will change according to the inhabitants´ life situation and with changes of residents. Adaptability of the dwellings is therefore essential. The spaces should be general, and the internal walls easily movable to facilitate refurbishment. During a buildings´s lifecycle, integration and separation of dwellings may vary, and this must be part of the system design. Expandability of dwellings is associated with detached, semidetached and terraced housing, but should also be considered in low-rise, multistory buildings.

Adaptability impacts the choice of structural systems, their span widths and the solutions for noise and fire protection. Moving or exchanging parts requires easy access to structurally and functionally independent subsystems and components. This affects the design of joints and details. In turn, these choices have implications for the readability of the building system and its architectural character and qualities. Clarification of these implications must be integrated in the design framework.

2.5 INTEGRATION OF SELF-BUILD

A user-centered design process based on open innovation will strengthen the inhabitants´ knowledge about the

https://doi.org/10.52202/069179-0514

buildings. It will prepare active participation in changes and maintenance. It will counteract the present loss of contact with construction, and also of mastering and appreciation of practical skills. Low-cost laser-based and magnetic instruments for measurement and detection improve precision in traditional do-it-yourself work. Better screws and multifunctional, loadable electric tools also push the limits for self-build. By integrating builders and craftsmen in the design processs, new divisions of labour and responsibility may be developed without sacrificing quality.

The adaption described above is not only dependent on access to and exchangeability of parts, but also on the size and weight of the components. When it comes to prefabrication of light-weight, multistory timber buildings in Norway, there is presently (spring 2023) a trend towards larger floor and façade elements (8 meters long and 3 storeys high), which means speedier montage [12]. At the same time, robots are being developed for operations within the heights and spatial constraints typical of multistory timber housing (Tekna 2018) [13]. This may represent an area of innovation where manual construction assisted by lifting tables and hoists gradually may include robots (Figure.1). It will also be a robust production environment which may backtrack to traditional methods if scarcity of money or high-tech components should occur. Small structural members and building elements expand the possibilities of self-build also of multistory buildings. They may be supplied by a large number of diverse producers. Small components reduce the dependency on transport by ship, train or heavy trucks, and montage by tower cranes. This also contributes to economic and logistic robustness. Division into small (demountable) components does not exclude larger assemblies to rationalize the initial on-site construction.

2.6 PREPARED FOR MATERIAL HYBRIDITY

We have recently experienced that pandemics, wars and blocking of shipping routes may disrupt supply chains. Wood-based building systems must therefore be prepared to include other materials. For timber, beetle attacks and climate-induced droughts, storms and wildfires may be more acute threats. They remind us that optimal use of timber in many buildings should be the aim, rather than maximized use of the same resources in fewer projects.

The distribution of emissions among the different building subsystems is important when combinations of materials are considered. Column and beam structures account for a small part of material-related emissions compared to floors and external walls. Thus converting to a steel skeleton will have minor effects. The slimmer steel columns and beams are easier to integrate in wall and floor constructions. Steel joints and details may be better suited for future disassembly and reuse than screws or wood-only connections (Vandkunsten Open source 2021) [14]. To limit the emissions from weight-increasing tiles in the large floor areas, using clay instead of concrete may be beneficial.

2.7 DESIGNED FOR CIRCULARITY

The adaption of dwellings to the inhabitants should be facilitated by reusable components and materials. Circularity starts inside a dwelling and continues at the end of the building´s service life. For each component, the size, geometry, robustness and integrity of form and function must be balanced against adaptability to new needs and preferences, both of the existing habitants and and future constructors and users of the next building. The next building should be designed to utilize a variety of materials inherited from donors in good shape.

In an environmental perspective, the slowing down of material cycles in buildings contribute to increased carbon storage. At the same time, climate change may impose threats to the long-term safety of building sites. Design for circularity also means preparedness for moving buildings instead of deserting or demolishing them.

3 EXPLORATION OF A SYSTEM EXAMPLE

To test the relevance and design implications of the design framework, we have applied it on a project example. A four storey block of flats was chosen as a case. As emphasized above, this is a large building category where timber is well suited. Low emissions related to production of sustainably harvested timber materials is a framework condition for the study. Figure 2 and 3 give an overview of the system example explored below.

3.1 PROCESS AND PARTICIPATION

The purpose of a diagrammatic study is to facilitate an immediate and active user or inhabitant participation in the design of buildings. In Figure 1 it would be carried out in the first phase of design within the design framework. It focuses on the main functional and architectural properties while maintaining openness for a variety of choices regarding materials, structures and details. Simplified quality control and classification should be embedded in the components that are introduced and then repositioned and transformed during this initial design phase. As emphasized above, qualified architectural and technical advice must be defined as a part of the design framework.

3.2 ADAPTABILITY TO CLIMATE, SITE AND URBAN PATTERNS

To ease the overview of the example, The authors have chosen to focus on a limited number of environmentally significant features that are shown in the upper diagrams in Figure 2.

https://doi.org/10.52202/069179-0514

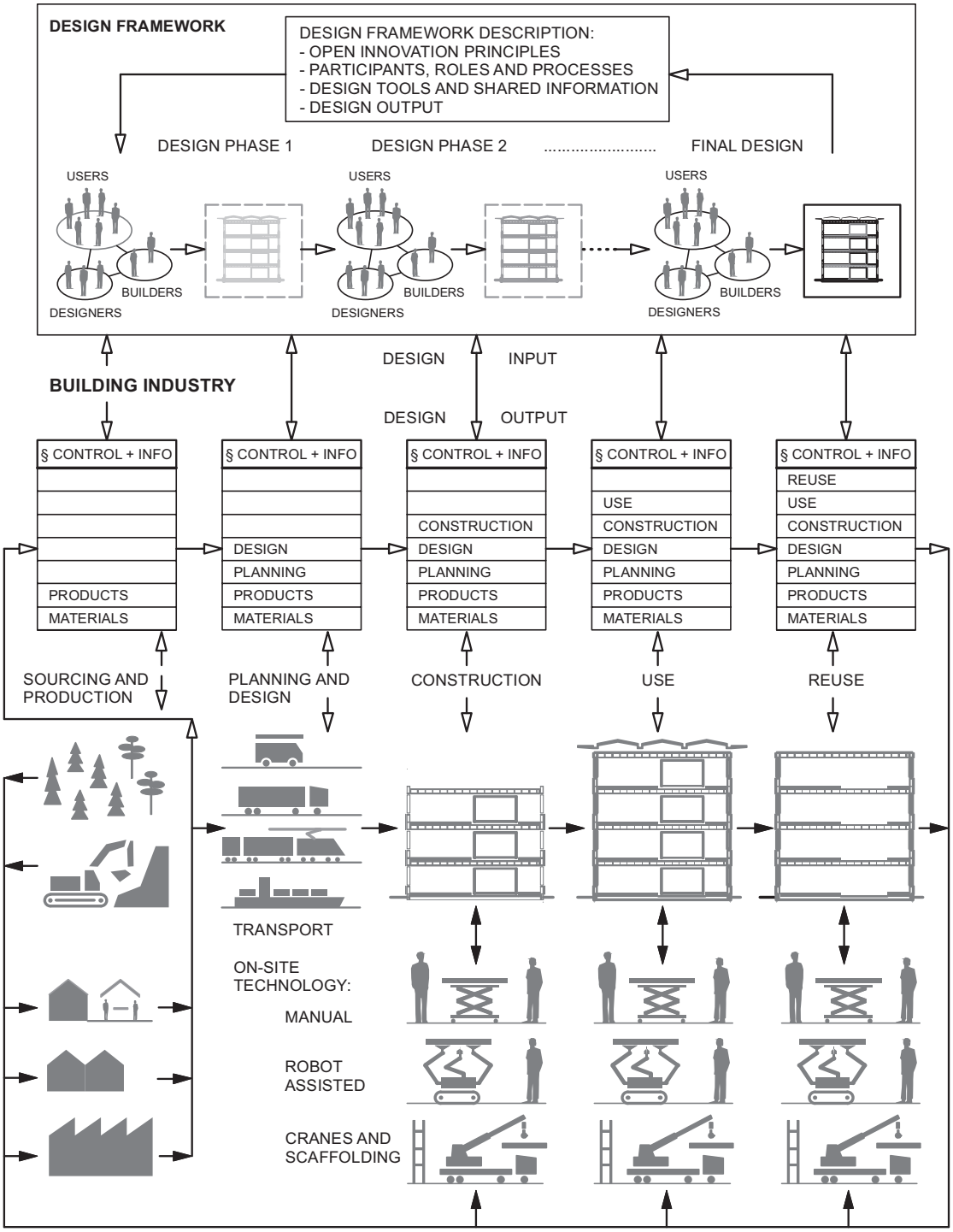

TOP: The design framework and the processes it defines
MIDDLE: The regulatory control and information system
BOTTOM: The cycles of materials and components, and the associated transport systems and construction technologies.
Black arrowheads mark material and mechanical flows, systems and interactions.
White arrows mark interaction and influence based on flows of information.

Figure 1: *Overview of design framework and building industry.*

https://doi.org/10.52202/069179-0514

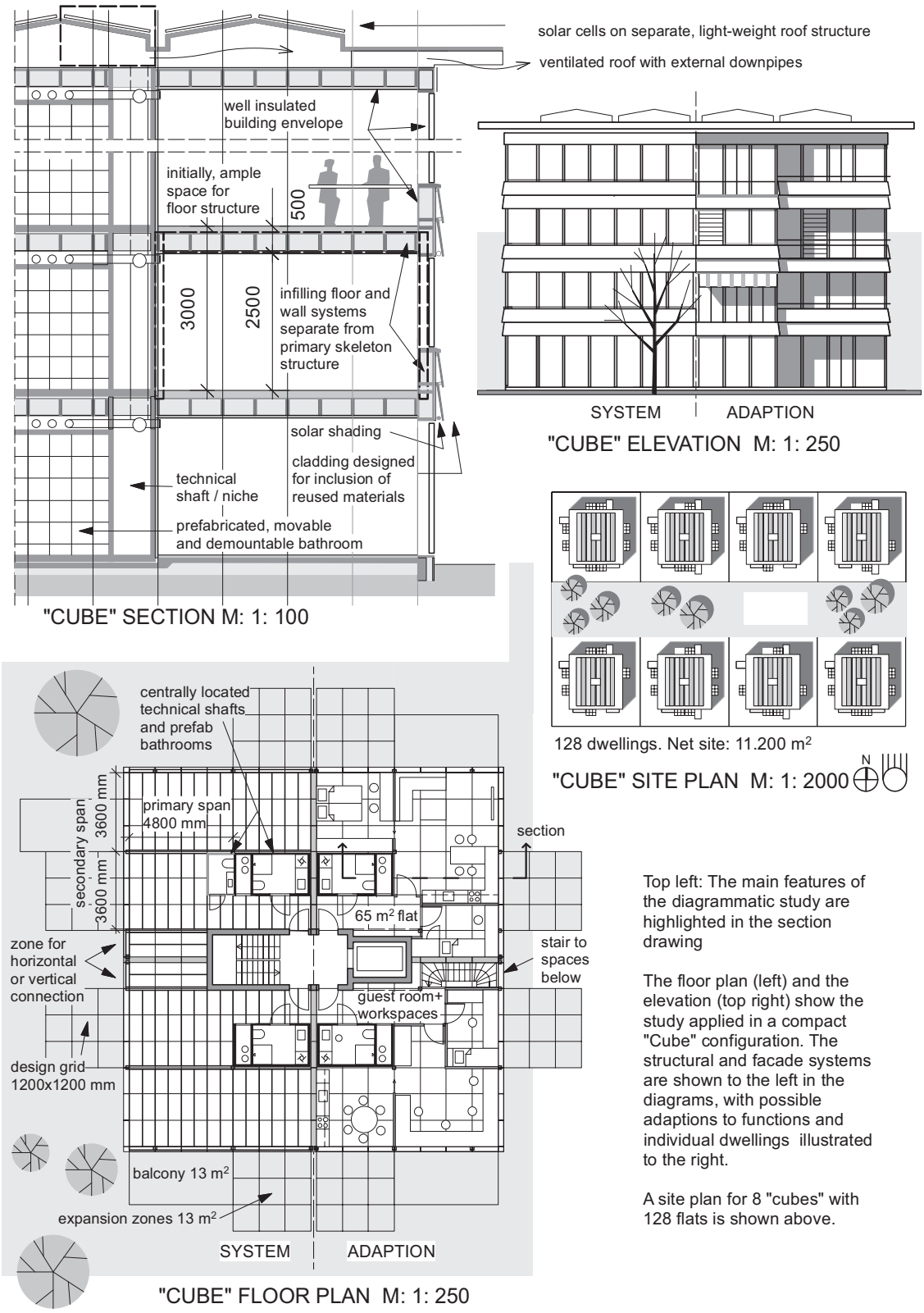

Top left: The main features of the diagrammatic study are highlighted in the section drawing

The floor plan (left) and the elevation (top right) show the study applied in a compact "Cube" configuration. The structural and facade systems are shown to the left in the diagrams, with possible adaptions to functions and individual dwellings illustrated to the right.

A site plan for 8 "cubes" with 128 flats is shown above.

***Figure 2**: Main features of the diagrammatic study, and their integration in the "Cube" example*

https://doi.org/10.52202/069179-0514

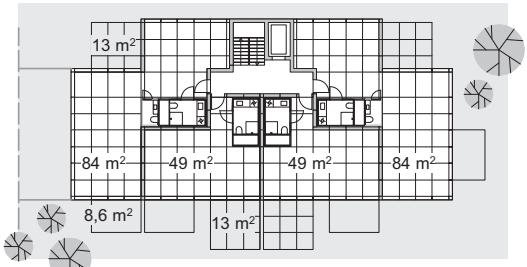

"BLOCK" FLOOR PLAN M: 1:500

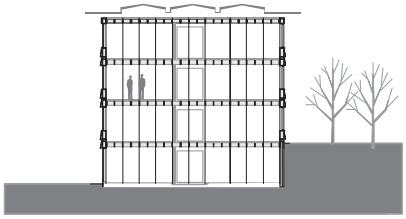

slope: ca.12°

"BLOCK" SECTION M: 1:500

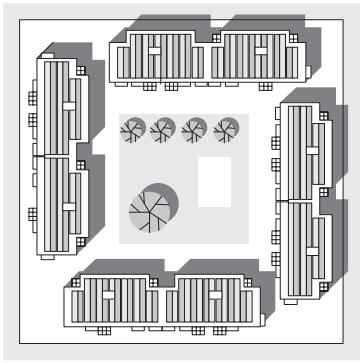

128 dwellings
Net site: 8.800 m²

"BLOCK" SITE PLAN M: 1.2000

"BLOCK" : ADAPTABILITY TO LANDSCAPE AND URBAN PATTERN

The solutions from the diagrammatic study applied in a slimmer volume (13.1 m), adaptable to moderate slopes and a typical urban block pattern.
The flexibility and expandability of the dwellings is maintained.

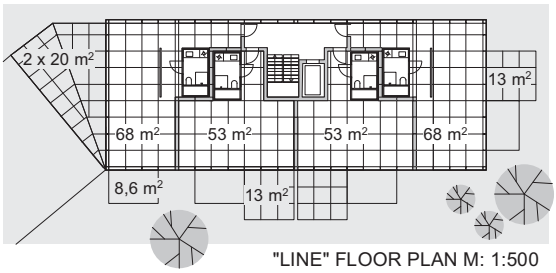

"LINE" FLOOR PLAN M: 1:500

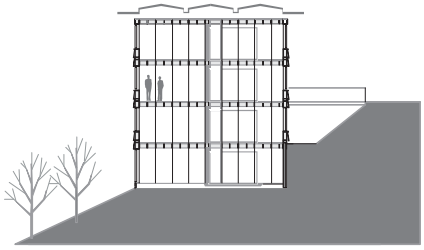

Slope: ca.20°

"LINE" SECTION M: 1:500

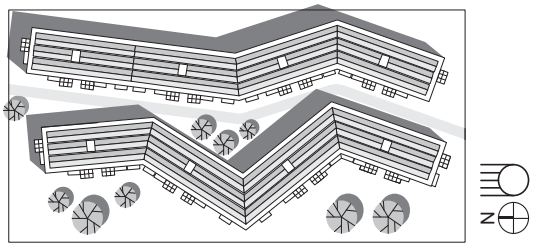

128 dwellings
Net site: 8.900 m²

"LINE" SITE PLAN M: 1.2000

"LINE" : ADAPTABILITY TO LANDSCAPE AND URBAN PATTERN

A still slimmer volume (11,0 m) for steeper sites and linear urban patterns.
Linking volumes with flexible geometries facilitate adaption to curved topographies.

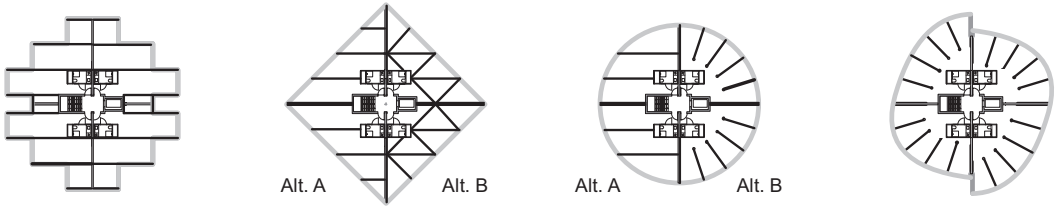

GEOMETRIC ADAPTABILITY OF MAIN STRUCTURAL GRID (SAME FOOTPRINT AREA)

Figure 3: *Solutions developed in the diagrammatic study applied in the "Block" and "Line" examples. Bottom: Geometric adaptions of the "Cube" example*

https://doi.org/10.52202/069179-0514

- A well insulated envelope that encloses a compact building volume. This limits heat loss to the exterior.

- A flat, ventilated (cold) roof with easily accessible gutters leading to external downpipes.

Ventilated roofs reduce melting and icing in near-zero temperatures, and also heating of the interior during summer. In a four storey building, a flat roof may serve as platform for solar cells with a signifcant area per apartment. It will be an important step towards lower energy demands. In Norway, 10 degree slope towards East and West is optimal on flat roofs. An elevated, lightweight roof structure will facilitate future maintenance or exchange of the photovoltaic panels. Significant roof overhangs will allow variation in the direction of the "solar waves" without affecting the overall character of the building. The overhangs will accentuate the separate roof. The folded geometry will improve ventilation and drainage. External downpipes eases local use of rainwater in landscaping, combined with measures for delayed stormwater runoff. There are also caveats linked to flat, ventilated roofs in arctic climate, but this is an opportunity for rethinking.

- The basic components can be applied in buildings with varying depth and orientation, adaptable to different topographies and urban patterns.

Figure 2 shows the starting point of the diagrammatic system study - called "Cube". As higher user involvement and lower costs are intended, the initial floor plan is dimensioned for four two-bedroom flats. They are adequate entry-level dwellings of 65 m2, served by a compact, central stair and elevator core. The total building however, is about 17,5 x 17,5 m, which demands a relatively level site. The four-sided orientation, which is optimal for views and daylight, puts limits to the arrangement of groups of such buildings. The "Cube" siteplan in Fig. 2 shows rows of separate, low-rise apartment buildings sharing a common, inner green belt.

In Figure 3, the upper diagrams show the "Block" alternative where the four combined apartments are rearranged within a slimmer (13,1 m) and two-sided building. This can be adapted to slightly steeper slopes (12%), and to a traditional urban block pattern, which is shown in the "Block" section and siteplan.

The middle diagrams of Fig.3 show the "Line" alternative, which is a still slimmer solution (11,0 m), adaptable to slopes of 20% or more. Such topographies demand a linear urban pattern, which should also be able to follow varying contours of hillsides. This is accommodated by introducing linking volumes with a flexible geometry.

A common requirement for all building types and urban patterns should be a capacity for high density. The site plans of "Cube", "Block and "Line" vary between 11,4 and 14,5 dwellings per 1000 m2 of the rectangular net sites shown in Figures 2 and 3. These are urban levels in a Norwegian context. The similarities in density indicate that the tree building alternatives can be combined in a diverse urban "vocabulary" without losing density.

3.3 ADAPTABILITY TO INHABITANTS´ FUTURE NEEDS

The primary structural system of the diagrammatic study is a regular and modular skeleton system, which allows for large spaces free of columns and loadbearing walls. The stair and elevator shafts, together with the floors provide lateral stiffness. The free spans are limited to 4,8 m, which is sufficient for housing (Drexler 2020) [15]. It opens for use of a variety of materials and timber technologies. The small and light structural members will be managable in manual building, and transportable by small vehicles. They may also be supplied by a large number of producers.

The sizes and weights of the infilling floor and external wall elements are also limited to be adaptable to different assembly procedures. As shown in Figure 2, the typical wall elements are 1.2 m wide, and typically ca. 2.5 m tall, which allows inclusion of doors and windows with free openings demanded for universal access and secure escape routes. The floor elements have a maximum free span of 3,6 m, A spatial zone of 50 cm height is assigned to the floor construction. This is a conservative starting point, may be controversially so. It allows for a variety of sound-insulating layers above and ceilings below beams, that also may vary in design, size and stiffness. (Required airborne sound insulation between dwellings in Norway is $R'_w \geq 55$ dB, and impact sound insulation $L'_{n,w} \leq 53$ dB.) The gross storey height is initially set to 3.0 m, which represents an incentive for slimmer floors that will increase spaciousness and daylight in the dwellings. The secondary, infilling systems are placed between, and not on top of, or overlapping the structural members of the primary, loadbearing skeleton. This limits construction heights and depths. The components are easily accessible and demountable to facilitate maintenance, modification and reuse. The section and façade diagram in Figure 2 show horizontal and overlapping bands of façade cladding which create depth and shadows, while opening for use and reuse of many types of materials. They also ease inclusion of different kinds of solar shading. The horizontal cladding and protruding eaves contrast the vertical modules of the external walls, forming a basis for further architectural development.

The possibility of expanding the size of spaces or dwellings is referred to as elasticity in buildings systems. In the plan drawing in Figure 2, bordering zones of adjacent flats are prepared for connections horisontally or vertically. The idea of allowing expansion, also outside the initial envelope of multistory buildings, is more radical. It is however, a natural next step in building adaptable, first dwellings. The plan diagram in Figure 1 shows a series of expansion zones of 3,6 x 3,6 m, offering substantial, functional additions to the dwellings. They

https://doi.org/10.52202/069179-0514

are based on the same structure and materials as the main volume, and will maintain views and daylight in the original spaces. Similar additions are prepared in the diagrams of "Block" and "Line" in Figure 3. Agreeing on the time and sequence of additions to different floors is a complex, but solvable issue. The initial building volumes of all alternatives are regular, which means that they will grow into complexity and hopefully, richness of expression. If such variety is carefully balanced in the intitial situation, expansions may be regarded as unwanted, or they may fill in gaps, resulting in bland regularity.

Rectangular structural grids are advantageous in accomodating varied floor plans and furnishing. They also ease alternative reuse of the infilling, secondary components. The design framework should however, not have inherent, geometric constraints, which have proven to be damaging to many building systems. Adaptability to different geometries is exemplified in the bottom diagram in Figure 3.

3.4 BATHROOM MODULES AS TECH CENTRALS IN APARTMENTS

The bathrooms contain the dwellings´most complex subsystems and components. Their design and production are subject to detailed, interdisciplinary coordination, regulation and control. Water damage is very expensive, and may induce health risks in the form of fungi. It is natural to expand the "technical core" to include ventilation and power supply. Service systems stand for a growing part of the emissions related to production of materials and components. Simplification and concentration may reduce emissions and at the same time free larger parts of the buildings of interference with the technical systems. Incorporating partially natural ventilation may play a role here.

The sound insulating layers that are required on top of timber floors (normally 100 mm or more) solve the problem of step-free access to bathrooms. The bathroom floors may substitute sound and fire insulation functions of the layers on top of timber floors. Bathrooms are typically produced as whole "plug-in" modules. This means that they are difficult to move, exchange or modify. An element-based design, both of bathrooms, technical niches and ventilation systems would ease the adaptability to changes in flat layout and available technology.

The bathroom unit shown in the "Cube" floor plan in Figure 2 is also used in the "Block" and "Line" alternatives. In the large, two-sided apartments in the "Block" solution, a separate toilet is added, linked to the technical core (also shown in Figure 2).

4 DISCUSSION AND CONCLUSION

Some architects regard building codes, standards, design guides and pre-accepted solutions as the place where innovative architecture goes to die. For the authors, this made it a good place to start. The search for a safe acoustic point of entry resulted in 50 cm thick floors, including a continous, double layered ceiling of gypsum boards. Fire concerns pointet towards columns and beams integrated in walls and floors, again hidden behind two layers of gypsum (fire resistance rating REI 60 in walls and floors between dwellings). Standard tables for structural capacity confirmed that with spans of 4,8 and 3,6 meters, timber could do the job alone, but slimmer steel profiles would ease the integration and protection of a skeleton structure in walls and floors.

Hiding the timber was not a wanted or final solution, but a choice of postponing its return to visibility until the implications for a detailed design (succeding the diagrammatic study) could be mapped. When structural timber enters interior spaces, it is usually upscaled to allow burning and charring while maintaining its loadbearing capacity until sprinkler systems or firefighters interfere. It may also need vibration damping in the form of elastomer pads or strips to prevent sound transfer between dwellings. Unlike concrete, appreciation of exposed timber does not get smaller when the the dimensions get bigger. Visible structures communicate how the building is constructed and how it can be used. They also frame the spaces and add interplay of materialities to the atmosphere of the interiors [9].

The principle of adding high quality timber to be sacrificed in the case of fire, could be substituted by a slimmer, hybrid solution that still conveyed the position and character of the structural system. For many inhabitants wood everywhere may be too much. Visibility is not the only way. A complete documentation will include 3D models of the different subsystems. They will enable Lidar-scanning smartphones to visualize the exact positions of columns and beams in a room.

With timber, sound and fire out of sight (until further notice), focus could be put on processes and principal solutions.

The systems overview (Figure.1) made clear some features and constraints that would support use of local resources and expertise and facilitate user involvement in adaption, and potentially in construction. Together with environmental parameters they were included in the design framework for the diagrammatic study.

The diagrammatic study was an exercise in modular stringency and extraction of a small number of standard parts. Having completed the initial "Cube" solution (Figure 1), developing the "Block" and "Line" variants proved to be surprisingly simple. Interestingly, the limited kit of parts forced compromises that (to the

https://doi.org/10.52202/069179-0514

authors) appreared new and appealing. The "too big" but multifunctional and generously daylit corridor in the flanking aparments in the "Line" alternative (Figure 3) may not have appeared in a more fine grained system.

The diagrammatic study may form the basis for a pilot system that can be easily visualized in open source and web-based 3D software. The digital model will then be integrated in quick cycles of user-centered design development. As a process example this may respond to the call for speeding up the adaption of the building industry to environmental demands. Cheaper and better housing is a central aspect of the UN goal for sustainable cities and communities. By maintaining compliance with industry standards, the process may also ease the production of documentation required for agreements and construction.

This combination of new design organization and new digital tools may affect several industrial patterns. First and foremost, the presence and influence of the user / inhabitant will be stronger. It will affect when and how the architect communicate with the users and other members of the design team. The dependency on dominating CAD systems may be reduced. Instead, they will be expected to communicate with high frequency output from open innovation processes. Open source publication of architectural details may demand more and speedier technical approvals, which will also be expected to be competitively priced and openly documented. Complete and tracable building data is vital for circular flows of materials and products. The vision of open and accellerated innovation challenges the knowledge gaps that are part of the economic foundation of many businesses within the building industry. Their skill and strength are vital to take on the inherent responsibilities and risks of large projects. On the other hand, tendencies of dominance by acquisitions rather than competitive innovation may postpone vital transitions beyond critical points. This paper argues that processes of real participation in designing buildings with real adaptability and real reuse, are necessary to limit the environmental risks embedded in present industrial trends.

ACKNOWLEDGEMENT

The authors thank the following colleagues and consultants for contributing to our understanding (with no responsibility for our suggestions and conclusions): Audun Fossum, Assistant professor at AHO (Structures), Christian Magnusson, consultant at COWI (Acoustics), Arnkell Petersen, Associate professor at NMBU (Energy and climatization), and Nils E. Forsén, dr.ing., consultant, previous adjunct professor at AHO (Codes and certifications).

.

REFERENCES

[1] Weston, R.: Utzon Inspiration-Vision-Architecture. Edition Blondal Hellerup Copenhagen 2007
[2] Byggeindustrien: https://www.bygg.no/snohetta-modular-konkurs/20004!/ Last accessed March 27 2022
[3] Brand S.: How Buildings Learn. Penguin Books 1995
[4] Apeland K, Larsen B and Prag M: Åpen systembygging. Project report The Oslo School of Architecture and Design 1975
[5] https://www.openbuilding.co/manifesto Last accessed 24 February 2023
[6] Nygaard M, Bashevkin IES, Groba U and Sunter C (2019) Increased Use of Timber in New Buildings in Oslo and Akershus: Potentials and GHG Emission Effects. Front. Built Environ. 5:131. doi: 10.3389/fbuil.2019.00131
[7] Ollila, S., Yström, A., 2016. Exploring design principles of organizing for collaborative innovation: The case of an open innovation initiative. Creativity and Innovation Management 25, 363-377
[8] Creative commons https://creativecommons.org/licenses/ Last accessed February 23, 2023
[9] Groba U.: Timber Tales – A Qualitative Study of Timber Materiality in Housing projects. PhD Thesis The Oslo School of Architecture and design 2021
[10] ISO 9241-210:2019. Ergonomics of human-system interaction — Part 210: Human-centred design for interactive systems
[11] Byggforsk:https://www.byggforsk.no/side/278/english_informasjon_paa_engelsk Last accessed 5 February 2023
[12] SINTEF article: https://www.sintef.no/siste-nytt/2022/skal-gjore-bindingsverkkonstruksjoner-med-opptil-atte-etasjer-konkurransedyktige/ Last accessed February 23, 2023
[13] Tekna seminar https://www.tekna.no/fag-og-nettverk/bygg-og-anlegg/byggbloggen/roboter-pa-byggeplass/ Last accessed February 23, 2023
[14] Vandkunsten Architects https://opensource.vandkunsten.com/07_FBABLisbjerg/ Last accessed 24 February 2023
[15] Drexler, H: Interaktion von Raum, Nutzung und Konstruktion: Explorative Entwcklung eines Holzbausystemes für den Wohnungsbau. PhD Thesis TU Berlin 2020

World Conference on Timber Engineering Oslo 2023

TAMANGO BUILDING: TYPOLOGICAL EXPLORATION FOR A 12-STOREY WOODEN APARTMENT BUILDING IN A SEISMIC AREA.

Gerardo Armanet[1] Juan José Ugarte G.[2], Sebastián Cárcamo[3], Andrés Sierra[4], Diego Valdivieso[5], Juan José Ugarte Á.[6]

ABSTRACT: In 2020, Tallwood was commissioned to build a 12-story building with a mixed commercial and residential program in Coyhaique, the gateway to Chilean Patagonia and one of the most virgin territories in the world, but also a city that has one of the worst pollution rates in Latin America and is part of one of the countries with the highest seismicity in the world.

This article explains the process and methodology behind the architectural and structural solution for the "Tamango" building, which today has a construction permit and is in the final phase of economic studies to start the construction of its 12-story tower and 21,112m2, which includes 2,806m2 for offices and commerce on a reinforced concrete plate and 9,528m2 for 68 apartments distributed in a hybrid structure of LVL columns and beams, CLT and reinforced concrete composite slabs, and vertical cores of reinforced concrete.

KEYWORDS: Wooden High-rise Buildings, Wooden Architecture, Hybrid Concrete and Wood Structures, Structures in Seismic Zones.

1 INTRODUCTION

1.1 THE PLACE

Coyhaique is one of the southernmost cities in the world. According to the 2017 census [1], it has approximately 57,818 inhabitants within the Aysén Region, where 103,158 people live in 109,024km2, resulting in a density of less than one inhabit/km2, being one of the least populated and most pristine areas on the planet.

However, Coyhaique is also among the most polluted cities in America [2]. In June 2018, the city reached an index of 166.8 PM2.5, considered a very unhealthy category, mainly due to the burning of wet firewood for heating.

Figure 1: *Aerial view of Coyhaique without air pollution. Source: Rakela.*

1.2 THE CLIENT

Considering the context described above, Tallwood was contacted by two families from the area interested in leaving a legacy in the area and doing it through a sustainable real estate project and efficient construction, also considering the problematic access to materials and skilled labor in the area.

Thus, the building takes the name of "Tamango," a traditional boot worn by Patagonian gauchos, as a symbol of the mixture between simplicity and comfort sought after the inclement Patagonian climate.

This is how it was decided to develop a structure in which the latest technologies for high-rise timber construction were put into practice, with mechanized elements of CLT, GLULAM or MLE, LVL engineered timber, and certified sawn timber with different structural grades. All of the construction systems, proven in other parts of the world, meet the requirements of the clients by coming from renewable sources and having, at the same time, advantages of prefabrication, such as shorter assembly times, dry and silent works, low emissions of particulate matter, and greater quality control in construction.

[1] Gerardo Armanet, Tallwood, garmanet@tallwood.cl
[2] Juan José Ugarte G., Tallwood, Pontifical Catholic University of Chile, jugarte@tallwood.cl
[3] Sebastián Cárcamo, Tallwood, Pontifical Catholic University of Chile, secarcamo@uc.cl
[4] Andres Sierra, Tallwood, Pontifical Catholic University of Chile, asierra@tallwood.cl
[5] Diego Valdivieso, Pontifical Catholic University of Chile, Chile, dnvaldivieso@uc.cl
[6] Juan José Ugarte Á., Tallwood, jugarte@tallwood.cl

https://doi.org/10.52202/069179-0515

The characteristics of these materials also greatly facilitate reaching efficient energy solutions for heating, and their hygroscopic quality of retaining and releasing moisture gives that feeling of comfort that has long been studied as beneficial for living.

Figure 2: *Landscape of "Cerro Castillo" in Aysen region, Chile and a original "Tamango" (traditional boot worn by Patagonian gauchos). Source: Corsilver and Guillermo Helo..*

1.3 THE LAND

The land where the project will be located is challenging since it is central -it is located three blocks from the main square of the city -will become an urban landmark- but it is also a boundary condition looking towards the nature of the "pampas" and the Coyhaique River.

Planning laws explain some architectural design decisions; local regulations require a continuous façade at least eight meters high. In addition, the height of the building is also obtained from the local rules, which indicates maximum constructability and height.

Figure 3: *In red, the future location of the building. Three blocks from the main square in a border condition facing the Coyhaique River. Source: Google Earth.*

1.4 THE LOCAL CONTEXT

Chile has a strong forestry vocation, 22.3% of the country's surface, equivalent to 16.9 million hectares, is covered by forests -14.6 million hectares are native forests, and 2.3 million hectares are forest plantations- [3]. However, the country is also part of the current challenges that the world of construction is experiencing, such as:

1. How to achieve, from the construction sector respond to the demanding environmental goals? Chile committed to being carbon neutral by 2050, but when this building was designed, it emitted 111 million TCO2, although it also captured 65 million tons through the forests. Thus, it is possible to contribute to the reduction of the so-called "30/30/30" of construction -36% of the final use of energy, 35% of solid waste, and 39% of emissions of CO2 [4]- through wooden structures.

2. How can we increase the productivity of the construction sector? For example, Chile is capable of building 0.24m2/person/day, in contrast with developed countries where are capable to build 0.37/m2/person/day are made, that is, ten floors versus fifteen in the same amount of time [5], which indicates the need for a profound change in the way of building.

However, currently it has been seen that between 2012 and 2020 progress was made from having 14% of homes with wood as the predominant material to 20% in 2020, having the realistic goal of reaching 30% by 2030.

Currently, proposing tall wooden buildings in Chile represents a great challenge and innovation, because in that country there are almost no buildings higher than four floors and all the buildings from 7 stories upwards are made in concrete and steel [6].

The phenomenon described above is aligned with the Chilean seismic code, which limits "inelastic drift" to 0.2%, one of the most restrictive seismic regulations worldwide.

1.5 THE MATERIAL

The idea of using engineered wood was, from the beginning, having to achieve competitive structural values but also using the advantages of wood in terms of: the use of a renewable resource and sustainability, its greater precision in manufacturing, its lower weight (470kg/m3 vs. 2500kg/m3) that would help to have fewer operations, faster assembly in a town located in the far south, and better-quality finishes.

For this, in parallel with the design of the building, a management process was carried out since in January 2020, when nine engineered wood suppliers from around the world were contacted, selecting the final supplier in March 2021, after an exhaustive evaluation that considered the following parameters: price; technical support during design; technical support during assembly; availability, type and quality of material; experience; and interest in the project.

https://doi.org/10.52202/069179-0515

Figure 4: *Wooden elements to be used in the project.*

1.6 THE ASSIGNMENT

The offer, with residential apartments with eight apartments per floor, is mainly addressed to two types of clients: families from Coyhaique who travel permanently and prefer to have an apartment in the city as their residence, and young families who are emigrating from the center to the south of Chile searching for new job opportunities, a better quality of life, or more significant contact with nature.

Thus, due to the conditions of the place, the client's interest, the land regulations, and the local context of the construction industry previously mentioned, the project also requested -among other parameters and requirements- that part of these structural elements of Engineered-Wood will be exposed, generating the following questions and challenges for the team of architects and structural engineers in charge of the design:

According to the order and the maximum height allowed on the land: How should a 12-story building in Coyhaique be designed with wooden structures?

According to the architectural program: Should the plinth or "podium" be designed in reinforced concrete or wood?

Considering the height and the architectural program: What structural typology is ideal for this type of building, which will have apartments between floors 3 and 12 and is located in a seismic country?

In the case of using composite or hybrid structures: How to solve the aerial floors making concrete and wood compatible, considering the seismic regulations of Chile?

One of the main conditions that were considered was the seismic recurrence of Coyhaique, with an average of 7 grade 7 earthquakes every 40 years, which is why the challenge of the Tamango building was unique in the combination of: Pre-existing real estate requirements of engineered-wood structures for tall buildings, and an area of high seismic risk.

2 METHODOLOGY

For the development of the architecture design, engineering, and management of the building, an interdisciplinary team of professionals with extensive experience in wooden projects -as well as in the development of public policies, academic activities, and industries- was formed, bringing together authors of pioneering works in wood in Chile -neighborhoods for 360 homes, 6-story light-framed towers and architecture with high-performance standards- and also, called the support of world-class international advisors from Finland, Slovakia, Poland, Germany, and Canada.

The initial design considered programmatic, regulatory, and economic requirements, coming from a previous study and pre-design developed by the real estate company -the client-, which was necessary to maintain:

Table 1: *Programmatic, regulatory, and economic requirements, from a previous study and pre-design developed by the real estate company -the client-which it was necessary to maintain.*

Nº	Requirement
1.	Three basements, with residential and rental parking capacity, warehouses, and technical rooms.
2.	Continuous façade of at least 8 meters high (by regulatory requirement) with approximately 2,000 m2 for commercial premises, equipment, and offices.
3.	Approximately 8,000m2 with apartments between 90 and 140 m2 in a maximum of 12 floors.
4.	Final sales values of approximately €3,200/m2, being competitive with the local market.
5..	Demonstrate compliance with all local structural engineering, fire resistance, and acoustic performance standards and regulations.
6.	Check the characteristics of sustainability and energy efficiency of the building.
7.	Leave some structural wood exposed.

Before the iteration with different models that would help to answer the questions posed by the project, basic design parameters were established, both from architecture and engineering, which served as a basis.

2.1 ARCHITECTURE PARAMETERS

After determining the theoretical volume using local regulations that establish plinth, constructability, and maximum height, initially, we had an elongated tower, with only four corners, on a 2-story shopping plaza.

2.1.1 Double deck plate

One of the first design decisions was to use a regulatory instance that allows 30% of the continuous façade to be transferred to the public space, creating a public access courtyard that connects with galleries and interior public terraces. One of the project's main goals was to make the

https://doi.org/10.52202/069179-0515

first-floor program responsive to the urgent needs of the city and open it to the public.

Figure 5: *Architectural design decisions for the two-story commercial plate.*

2.1.2 Six-cornered tower

A second significant move was to divide the building's block in two, in such a way as to make better use of the geometry of the terrain providing six corners with good views, ventilation, and sunlight instead of the initial four corners, which would eventually allow both towers to function, independently, when dilated.

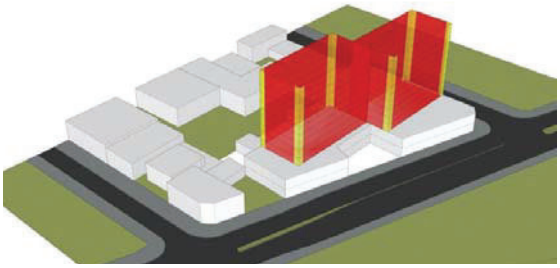

Figure 6: *Architectural design decisions for the six-cornered tower.*

2.1.3 Inclined upper faces

A third important design decision was to use the municipal requirement for roof slopes to generate "duplex" -two-story- and "triplex" -three-story- apartments on the upper level, with more commercial value, better views, and a more flexible architectural program.

Thus, due to the geometric characteristics of the site, the residential building was conceived as two independent volumes connected by circulations, making maximum use of views and sunlight.

From the beginning, all of these design decisions were accompanied with the engineering team, making models and testing different combinations and structural typologies until meeting the high standards required by both the team of professionals involved and international standards, as required by current seismic regulations.

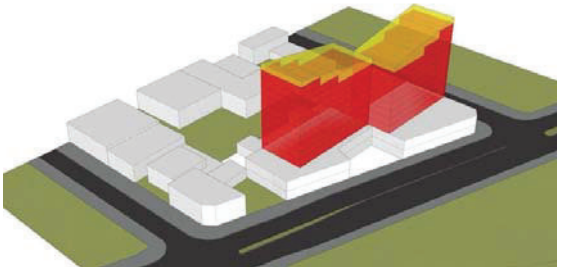

Figure 7: *Architectural design decisions for roof slope and top floors with two and three-story apartments on the upper level.*

2.2 ENGINEERING PARAMETERS

Considering the requirements indicated in the Chilean seismic standard, based on the different constructive and structural typologies [7] that have been part of the growth of this type of building globally [8], as well as consulting other design manuals, the following general criteria were adopted:

2.2.1 First two floors of reinforced concrete

The podium configuring the continuous façade and containing the commercial places and offices was designed from the beginning in concrete. Coyhaique is a city with a lot of precipitation and sporadic accumulation of snow, which is why, in any case, the design required protection for the wooden structures in contact with the natural terrain.

In addition, due to multiple environmental benefits, such as evapotranspiration for cooling, retention, and drainage of rainwater and a contribution to biodiversity through native flora, green roofs were included over the slabs, which added loads to the large slabs already projected.

2.2.2 Vertical cores of reinforced concrete

To provide stability for the seismic design, comply with the Chilean Standard, which allows a maximum relative displacement between two consecutive floors, measured at the center of mass in each of the directions of the analysis, which must not be greater than the height of mezzanine multiplied by 0.002 [9], makes it practically impossible for tall wooden buildings in Chile to comply with the deformations of the standard without having a reinforced concrete core that is capable of absorbing dynamic stresses.

Also, as well as based on similar experiences, such as the Brock Commons building, by Acton Ostry located in Vancouver [10], the project incorporated from the beginning the idea of using vertical cores of reinforced concrete, which were capable of stiffening the tower.

Preliminary analyzes suggested a maximum distance of approximately 12 meters from the edges of the wooden structure to the Reinforced Concrete cores. Therefore, in the first instance, it was decided to include two cores.

https://doi.org/10.52202/069179-0515

2.2.3 Aerial floors of wooden posts and beams and CLT composite slabs - reinforced concrete.

Also, was defined from the beginning to use a mixed slab. In this case, of 170mm CLT. and reinforced concrete of 100mm.

Thus, metal reinforcements would connect these slabs to the concrete cores, generating the necessary solidarity between both structural elements.

2.3 PARAMETERS OF OTHER SPECIALTIES

Among the more than 30 specialties involved, the following criteria were used for fire resistance, acoustic performance, and thermal performance, which directly affected the architecture and structure of the building:

2.3.1 Fire Resistance

According to the General Urban Planning and Construction Ordinance of Chile (OGUC), due to its size and use, the structure of the Tamango building must have a fire resistance of 120 minutes [11]. Bearing this in mind, engineers specialized in the field considered three main criteria:

Table 2: *Three main criteria for calculating fire resistance*.

Nº	Criteria
1.	Projected real fire (Burnout) using local regulations, Eurocode 5, and other technical texts.
2.	Carbonization and delamination analysis for exposed structural members.
3.	Carbonization and delamination analysis for protected structural elements.

The analysis with these criteria determined sections of structural elements and the necessary conditions to achieve "exposed wood" inside the apartments.

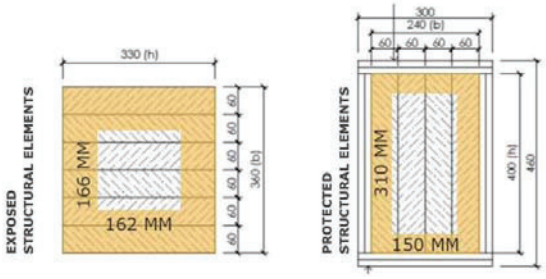

Figure 8: *Exposed and protected structural elements fire resistance analysis. The traditional carbonization factor of 0,7mm/min., modified according to delamination calculation.*

2.3.2 Acoustic performance

The acoustic performance of the dividing elements was analyzed to comply with the requirements for airborne noise and impact noise.

In Chile, for slabs, according to the General Urban Planning and Construction Ordinance of Chile (OGUC), a normalized impact sound pressure level (Ln,w) less than or equal to 75 dB is required. And for walls and floors, an acoustic reduction index (Rw+C) greater than or equal to 45 dB. Compliance with these requirements can be demonstrated by belonging to the List of Constructive Solutions for Acoustic Insulation of the Ministry of Housing and Urban Planning (MINVU) or by carrying out Test Reports or Inspection Reports issued by a laboratory with current registration.

Table 3: *According to the General Urban Planning and Construction Ordinance of Chile (OGUC), permissible decibels for airborne noise and impact noise*.

Noise Type	Requirement
Impact noise	Normalized impact sound pressure level (Ln,w) less than or equal to 75dB
Airborne noise	Acoustic reduction index (Rw+C) greater than or equal to 45dB.

This affected the sizes and stamps of the dividing elements. Not only local regulations considered but also international standards, assuming that the new inhabitant of the apartments, when faced with new materials and construction systems, can be more demanding than usual, even if it is comfortably complying with acoustic requirements established in the Chilean regulation.

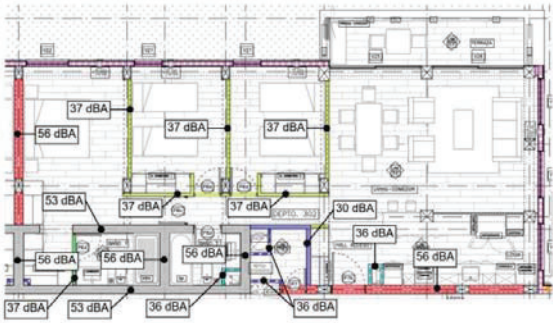

Figure 9: *Acoustic performance of elements in a typical department of the Tamango building.*

2.3.3 Sustainability and Energy Efficiency

Another fundamental specialty to integrate from the outset was Sustainability and Energy Efficiency, which had two fronts: the carbon footprint, which helps to explain, to a certain extent, the use of this amount of wood, and the performance during its use, that in addition to complying with the requirements of the "Coyhaique Atmospheric Decontamination Plan (PDA)" -a measure established to help reduce particulate material emissions that have Coyhaique as one of the most polluted cities of America- explains, to a certain extent, the design of the envelopes and the percentage of windows in the building.

Table 4: *Maximum allowable thermal transmittance [W/m2K]*

Thermal Zone	Roofs W/m2K	Walls W/m2K	Ventilated floors W/m2K	Doors W/m2K
Coyhaique	0,25	0,35	0,32	1,70

https://doi.org/10.52202/069179-0515

Regarding the carbon footprint, the building has 1,870m3 of wooden structure, which captures 1,230 tons of CO2 equivalent, discounting what is emitted in its manufacture and transport from Finland and Austria.

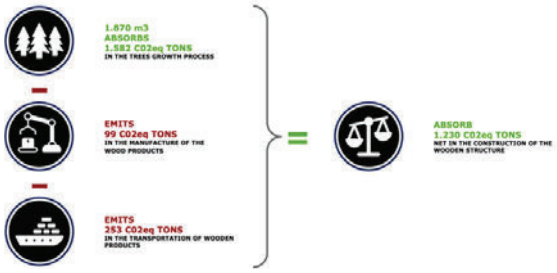

Figure 10: *Carbon footprint of the wooden structural elements of the building.*

Regarding the performance during use, five available heating systems were analyzed, resulting in the best evaluation of the "electric heat pumps" that heat the water for underfloor heating, reaching a 67% reduction in emissions according to a "base case" that It was used for the study and a 75% savings in monthly expenses by department.

This was also achieved thanks to an envelope designed with insulation, ventilated facades, and mechanical ventilation, which achieves a 60% saving in energy demand compared to a typical home with an equivalent classification from the Chilean Ministry of Housing and Urbanism (MINVU).

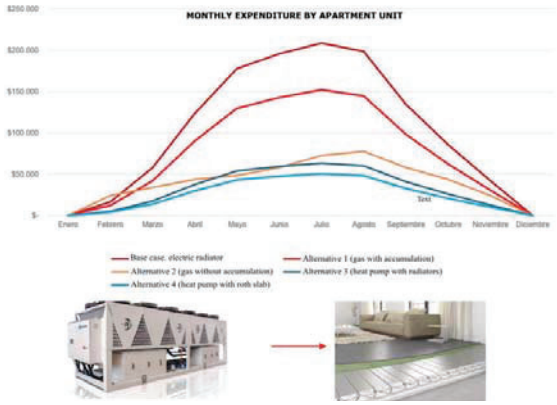

Figure 11: *Monthly expenditure by apartment unit, comparing five alternatives: Base case (electric radiator); Alternative 1 (gas with accumulation); Alternative 2 (gas without accumulation); Alternative 3 (heat pump with radiators); Alternative 4 (heat pump with roth slab).*

3 STAGES AND RESULTS

Once the essential criteria described above were agreed upon and having carried out a series of preliminary economic evaluations complying with precise real estate requirements, the design phase began, incorporating all the new needs.

Thus, different iterations of the architectural program and the structural elements were made during the project's development. In general, there were three main iterations:

3.1 CLT WALLS AND TWO REINFORCED CONCRETE CORES

The residential building, comprised of two independent volumes linked by circulations, was initially conceived with two reinforced concrete cores containing elevators and stairs. The preliminary analysis suggested a maximum distance of 12 meters from the edges of the wooden structure to these cores, so the architectural design was oriented under this premise at this stage.

The housing programs -unlike others, such as commercial premises and offices- are characterized by having a more significant number of enclosures and linear meters of wall. This, added to the client's requirement to leave the wood in sight, initially determined the decision to structure the apartments with CLT walls.

Following modeling and structural study, the projected CLT walls experienced significant stress, resulting in the modification factor being adjusted to reflect the system mentioned above accurately. This adjustment caused an increase in the base shear, causing a drift that more than doubled the permissible limit established in the Chilean code.

Figure 12: *Plan with CLT walls and two reinforced concrete cores.*

The CLT walls received a considerable amount of the total seismic cut, implying that the reduction factor used for the seismic analysis was associated with CLT. Although some studies suggest it may be higher, the consensus is to use R=2. This resulted in high seismic demand and a much higher than allowable drift.

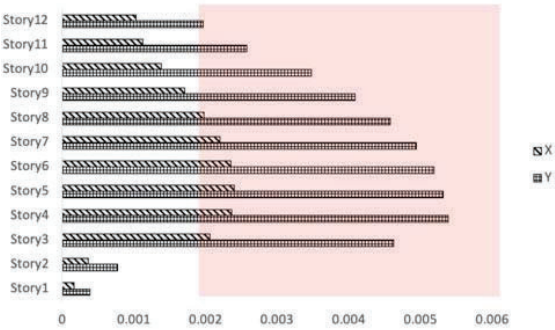

Figure 13: *Graph showing CLT walls received a considerable amount of the total seismic cut.*

https://doi.org/10.52202/069179-0515

Due to the lack of characterization of the CLT in the regulations, for the calculation of the structural model, a seismic reduction factor R=2 was used for the CLT compared to R=7 for reinforced concrete. The modeling results showed displacements greater than the 0.002*h allowed in the Chilean standard since it was considered during the calculation analysis that the CLT walls took the horizontal forces to a large extent, causing the earthquake to increase since most of the structures assumed R=2. Therefore, for the building to comply with the drift required by the standard, it would have been necessary to add a considerable amount of CLT walls, which was not viable from the habitability or commercial point of view.

Seeing the great distance that still existed for the viability of the proposed structure, it was decided to carry out a typological study of all the buildings with wooden structures of similar characteristics with the available information.

At the end of this stage, it was also decided to test a new model in which the concrete cores would mainly absorb the movements between floors. This test determined that the distance from the edges of the timber structure to the concrete cores needed to be reduced from 12 to 8 meters.

3.2 LVL COLUMNS AND BEAMS, FACADE WITH DIAGONALS AND TWO REINFORCED CONCRETE CORES

In this intermediate stage, the CLT walls were downsized to give the building rigidity and reduce previous deformations, and wooden bracing was installed on the facades. LVL columns and beams -material proposed because it achieves smaller sections than GLULAM to resist the same loads- replaced practically all of the CLT walls, leaving only a few, mainly in the living rooms, to expose the wood structure. These walls of the room continued towards the terrace - exterior balcony, which would later bring consequences after the criteria of wood protection from the design.

Programmatically, wet areas were left in the concrete cores to reduce eventual water infiltration problems in areas with wooden structures. In addition, during this stage, a third central core of CLT was configured, which contained the vertical circulations -elevator and stairs of the security area-.

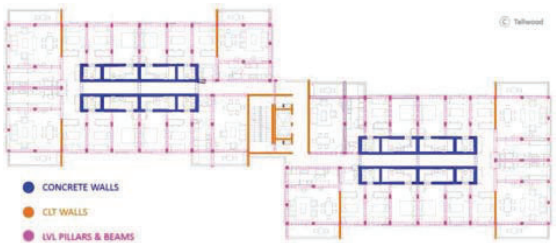

Figure 14: *Plan with LVL pillars and beams, facade with diagonals and two reinforced concrete cores.*

The models of the previous stage had presented more significant deformations at the ends of the tower, so at this stage, it was decided to incorporate diagonals in the short façades of the building. But, a milestone marked a change in this process: it was found that there is no consolidated criteria in Chilean regulations to determine what percentage of the shear, in the event of an earthquake, each element takes in hybrid structures.

Therefore, it was impossible to determine how much was assumed by a seismic reduction factor of R=2 for CLT walls or how much of R=7 for reinforced concrete core walls. Therefore, it was agreed, between the engineering team and the independent calculation reviewers, that only the R=7 of the reinforced concrete cores would be considered for calculating the cut. Therefore, it was necessary to eliminate all the wooden structural elements that would absorb lateral forces during earthquakes and eliminate from the design all the CLT walls and the LVL diagonals of the facades.

The bracing elements also experienced significant axial forces, resulting in the reduction factor being applied to the timber bracing system, the same as that used for the CLT walls in the previous iteration per Chilean code. This ultimately led to a similar level of deformation.

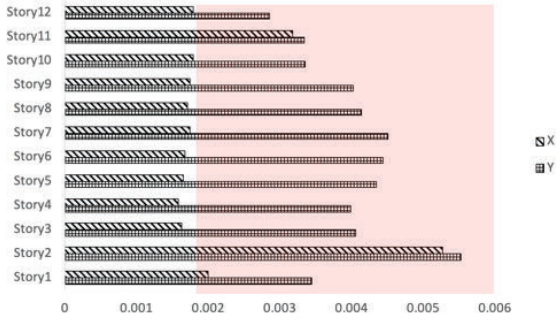

Figure 15: *Graph showing that the reduction factor being applied to the bracing timber system, which is the same as the one used for CLT walls, led to a similar level of deformation.*

3.3 LVL PILLARS AND BEAMS, THREE REINFORCED CONCRETE CORES AND EXPANSION JOINT

The third and final stage began with removing all CLT walls and LVL diagonals, which were replaced by a grid of LVL pillars at 3-4 meters connected by LVL beams.

One of the essential architectural requirements was to achieve large spaces without interference in the living areas, whose maximum spans of 5 meters dominated the design of the thicknesses of the CLT slabs.

https://doi.org/10.52202/069179-0515

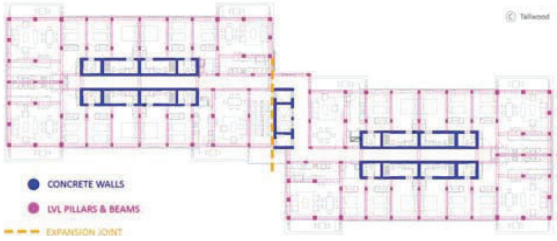

Figure 16: *Plan with LVL pillars and beams, three reinforced concrete cores and expansion joint.*

In this stage, a detailed analysis of the fire resistance for 120 minutes of the structural elements was carried out, as required by the Chilean standard for buildings with more than five floors for exposed and protected wooden structural components. Also, a detailed architectural evaluation accompanied this analysis to meet the requirements for element dimensions, concealed connector design, and the amount of exposed wood to meet the client's needs.

Various construction solutions certified and cataloged by the Ministry of Housing and Urbanism of Chile (MINVU) were used for the dividing walls. In the case of using unlisted construction solutions, they were tested and approved.

Another requirement -difficult for structural calculation and wood durability- was maintaining the usual Chilean standard for balconies or terraces. In this case, to avoid thermal and humidity conflicts caused by the continuity of the exterior-interior CLT slabs, it was decided to design the prefabricated metal balconies independently, with a fixing system using cranes to the load-bearing wooden structure. All the facades were designed to be prefabricated and assembled with cranes without scaffolding.

By not including additional lateral resistant elements to the concrete core, the modification factor was based solely on the reinforced concrete (RC) system. This resulted in the deformation of the building being within the permissible range established in the Chilean code.

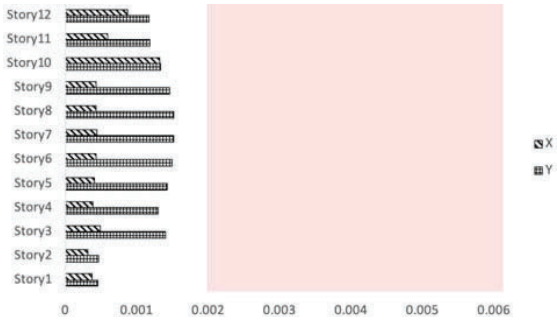

Figure 17: *Graph showing that not including additional lateral resistant elements other than the concrete core, resulted in the building's deformation within the permissible range stated in the Chilean code.*

Already having new structural models with positive results, complying with NCH 433, a consultancy was carried out to review the criteria with the Canadian structural engineering consultancy Timber Engineering Inc., which endorsed the results, suggesting adding a third central core of concrete for elevator. Subsequently, the independent calculation review, asked to include an expansion joint at the meeting of the two volumes of the residential tower.

4 CONCLUSIONS

The design of a hybrid high-rise structure of wood and reinforced concrete -in an area of high seismicity- was a complex process that forced innovation and required coordination and joint work, from its beginnings, between architecture, engineering and the more than 30 specialties that participated. Each of these stages required long study processes and iterations to arrive at these solutions, which are shown here in a simplified way.

The Tamango building now has a construction permit and a competitive budget. The main conclusion after this two-year work is that this experience shows that it is possible to build hybrid structures in wood and reinforced concrete in areas of high seismicity, complying with the highest standards. Also, the spatial conditions required for habitability, commercial requirements, and the requirements of Chilean law and international standards are met.

Figure 18: *Renderings with exterior views of the building.*

After this typological exploration process, a final design was reached with three vertically reinforced concrete cores, LVL beams and columns, and CLT - reinforced concrete composite slabs, where the maximum distance between the edges of the structure and the concrete

https://doi.org/10.52202/069179-0515

supports is 8 meters, requiring an expansion joint in the intermediate area.

For a 12-story building of these characteristics and in this location, a design of composite reinforced concrete structures is necessary to absorb shear forces and engineered-wood (LVL posts and beams + CLT slabs) for gravitational forces, being an viable option with the current technologies, economic conditions, and regulations.

The mixed slab of CLT + reinforced concrete, connected and solidary with concrete supports is a viable alternative to transfer the shear force to the reinforced concrete cores. A distance of 8 meters between the edge of the wooden structure and the concrete cores is feasible. Therefore, it is possible to comply with the Chilean regulation of fire resistance of 120 min with exposed and protected wooden structures. It is recommended that the balcony structures be independent of the main load-bearing wooden structure.

To arrive at the information required for the assembly of prefabricated structures, developing the so-called "Digital Twin" was critical, from which the data for manufacturing, machining, and all on-site assembly plans are obtained.

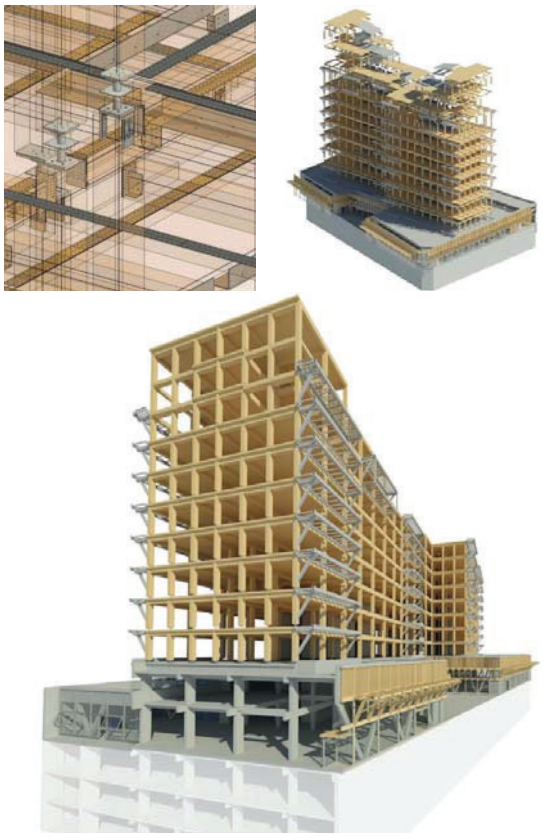

Figure 19: *Images of the BIM model with all the necessary information, so-called "Digital Twin".*

This digital model with the structure's detailing in BIM format allows the concept of "Build before Building," which produces the efficiency and quality of the on-site assembly, and also in this case, a “storyboard” or illustrative assembly sequence, which allows the constructor to be guided in the general evaluation of the project. Thus, an assembly speed of 200 m2/day is calculated, including facades. The wooden structure is assembled in 45 days, estimating a saving of 3 months of work.

According to the version delivered for bidding to construction companies, as well as for obtaining the Building Permit granted by the Coyhaique Municipal Works Directorate, Tamango building, has the following areas:

Table 5: *Architectural program and areas of the Tamango building*

Architectural program	Area
The total area of the project, with a mixed program and structure.	21.112 m2
Three underground floors, with 220 parking spaces, 95 warehouses, and the building's technical team.	8.778 m2
Two-story platform, with shops and offices.	2.806m2
Ten-story tower -between 3rd and 12th floor-, with 68 apartments, between 90 and 140m2 each.	9.528m2

Considered from the ground level, the wooden structure has also the following characteristics:

Table 6: *Characteristics of the building, related to the topic of this article*.

Structure Material	Area
The Total area of the project (100% from the ground level).	12.334m2
Wood Structure -CLT, LVL- (60%)	7.272m2
Reinforced Concrete Structure (35%)	4.370m2
Steel Structure -terraces- (5%)	692m2
Elements	**Quantity**
LVL elements -beams and columns-	2.446
CLT elements -slabs-	624
Metal connectors	6.141
Screws	339.417

https://doi.org/10.52202/069179-0515

Figure 20: *Rendering with interior view of the building.*

Finally, Tamango's experience also leaves many possibilities for improvement for new construction solutions and, at the same time, it can help to improve local regulations, incorporating new materials for Chile.

ACKNOWLEDGEMENTS

To Lago Azul Investments, the real-estate company that believes in this project; to the international experts from Storaenso and Timber Engineering, who contributed with their experience and work during the development of the design; and the professionals from the more than 30 specialties involved, including, especially, those in charge of reports on Fire Resistance -Contrafuegos Ingeniería-, Acoustic Performance -Laboratorio Centro Privado de Investigaciones Acústicas (CPIA)-, Sustainability and Energy Efficiency -Ernst Basler + Partner (EBP Chile)- and Landscaping and Irrigation Design -Paisaje Urbano (PAUR)-.

Figure 21: *Rendering with a view of the landscape project in the interior plaza of the building.*

REFERENCES

[1] National Statistics Institute (INE): Final results of Census, Santiago de Chile, 2017.IQ
[2] Air: New air quality data, 2019.
[3] Forestry Institute (INFOR): Forestry Yearbook 2021 Area of Forestry Information and Economics. Government of Chile, 2021.
[4] Global Alliance for Buildings and Construction: Global Status Report for Building and Construction Sector: Towards a zero-emissions, efficient and resilient buildings and construction sector. International Energy Agency, United Nations Environment Programme. 2019.
[5] de Solminihac, H., Dagá, J.: Labor Productivity in construction in Chile. Clapes UC, Santiago de Chile, 2018.
[6] Terraza, H., Donoso, R., Victorero, F., Ibáñez, D.: The construction of wooden houses in Chile: A pillar for sustainable development and the reactivation agenda. The World Bank, Washington DC, 2020.
[7] Foster, R., Reynolds, T., and Ramage, M: Proposal for Defining a Tall Timber Building. *Journal of Structural Engineering*, 2016.
[8] Wiegand, E., Ramage M.: The impact of policy instruments on the first generation of Tall Wood Buildings, *Building Research & Information*, 50:3, 255-275, 2022.
[9] National Institute of Statistics (INE): Chilean Standard NCh 433 Seismic Design of Buildings, Santiago de Chile, 2012.
[10] Fallahi, A.: Innovation in Hybrid Mass Timber High-rise Construction: A Case Study of UBC's Brock Commons Project. University of British Columbia, 2017.
[11] Ministry of Housing and Urban Planning (MINVU). General Urban Planning and Construction Ordinance. Government of Chile, Santiago de Chile, 2020.

World Conference on Timber Engineering Oslo 2023

MORPHOLOGIC STUDY OF HYBRID TALL BUILDING TOWARDS AN INTERDISCIPLINARY DESIGN

Sebastian Carcamo[1], Diego Valdivieso[2]

ABSTRACT: Interdisciplinary design for tall wood buildings (TWBs) is a challenging task mainly due to the ongoing research on the behaviour of TWBs and to achieve cost-effective designs that allow the construction industry to improve the sustainability of the building inventory. Although more than 40 TWBs projects have been built, the lack of a guide regarding the distribution of structural elements increases the time that preliminary design requires, which commonly implies several iterations of different proposals. Based on the morphologic study of six TWBs, this paper analyses qualitatively timber buildings with reinforced concrete cores and study different parameters that should be taken into consideration in the early stage of the project, in order to achieve a healthy structure in a reduced time period. A comparative table with a range of values for each proposed parameter is presented. A range of values for the different studied parameters are presented as a guideline for the RC core typology.

KEYWORDS: Tallwood Buildings, Interdisciplinary Design, Morphological Parameters, CLT, RC, RC Core

1 INTRODUCTION

In recent years, the construction of tall wood buildings (TWBs) has become increasingly popular due to its sustainability, energy efficiency, and aesthetic appeal. However, designing such buildings is still a challenge, as there are few precedents to follow. As a result, designing the static dimensions of such buildings can be difficult. Even more challenging is the design of lateral bracing elements for seismic events, as most timber buildings in the world have been constructed in non-seismic areas.

To address this challenge, interdisciplinary collaboration between architects and engineers is encouraged. In order to have a successful design process, the evaluation in early stages of the structural performance is crucial for an efficient design process. The definition of a representative floor plan defines, through the analysis of geometrical or morphological parameters, relevant decisions that impact its performance.

Therefore, the objective of this study is to provide guidelines for designers to develop tall timber buildings that are structurally healthy and safe, using a collaborative approach that combines the expertise of architects and engineers. By doing so, reducing the time and resources invested in the design process.

2 METHODOLOGY

The aim of this study is to investigate morphological parameters that help in early stages of TWBs design. To approach this challenge, only hybrid timber buildings with concrete cores as lateral system were studied. The decision is based on the potential use of the proposed morphological parameters in seismic zones. Taking in consideration the results of the Tamango project [1], the use of CLT shear walls on highly seismic prone areas, such as Chile, implies the definition of restrictive architectural programs due to the amount of shear walls needed versus a similar program with reinforced concrete (RC) shear walls. The reason is the modification factor associated with the ductility of each material, where the seismic coefficient of a building with CLT shear walls is more than three times higher than a building with RC shear walls in the Chilean code. Different studies have analyzed these values, but according to the studies presented by FPinnovations [2], the modification factor for CLT shear walls used on these calculations seems to be representative.

To select the correct buildings to study, only built projects with concrete cores were taken into account. A literature review of these buildings was performed, were several publications of TWBs inventories were presented, among them are the work done by Wiegand[3], Huseyin Emre[4], Fryer[5], Green[6] Ražnjevi´c[7] and Foster [8]. From these sources, only six tall timber buildings with the mentioned conditions and with available information were found: the WoodCube Building (2013) in Germany, LCT One (2012) in Austria, Brock Commons (2017) in Canada, Hault (2020) in the Netherlands, HoHo (2020) in Austria, and Ascent (2022) in the USA. Further details of these last two buildings, the most recent ones, were taken in consideration from the investigation of Fernandez[9] and Verhaegh[10].

[1] Sebastian Carcamo, Pontifical Catholic University of Chile, Chile, secarcamo@uc.cl
[2] Diego Valdivieso, Pontificia Universidad Católica de Chile, Centro Nacional de Excelencia para la Industria de la Madera (CENAMAD) & Centro de Innovación en Madera (CIM UC-CORMA, Chile, dnvaldivieso@uc.cl

https://doi.org/10.52202/069179-0516

For each building, a qualitative analysis of a representative structural floor plan was performed, which were redrawn approximately to study their morphological parameters. These parameters aim to quantify different structural properties regarding its performance. To define them a simplification of a typical floor plan is presented on Figure 1:

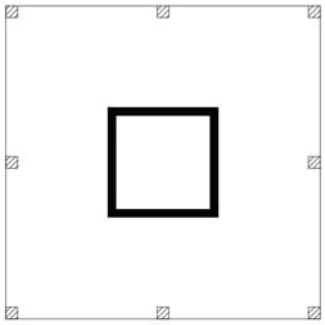

Figure 1: *Simplification of a TWB with concrete core*

Here, the RC core is painted in black, the vertical timber elements are painted with a light hatch and the perimeter of the slab y represented by a continuous line. From these idealization of a building plan, the morphological parameters studied are described:

- Eccentricities by direction (Ecc): The distance in both the X and Y directions between the center of rigidity (CR) and the center of mass (CM) of each floor. The center of mass was calculated as the approximate geometric centroid of the floor, ignoring any openings. The center of rigidity was calculated based only on the reinforced concrete shear walls. To represent them graphically on the studied buildings, they are drawn with a circle and a square, respectably, and their perpendicular distances are represented by a discontinued line rectangle. See Figure 2. This parameter is crucial to understanding the symmetry of the project and the possible torsion that it may experiment.

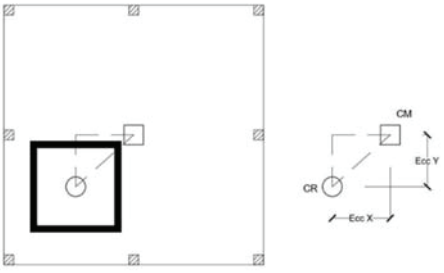

Figure 2: *•Eccentricities by direction (Ecc)*

- Density of shear walls by direction (ρ): The total area of reinforced concrete shear walls per floor in both the X and Y directions divided by the total floor area. Is possible to relate the overall stiffness per direction with the total area of the RC walls, which are graphically represented on Figure 3.

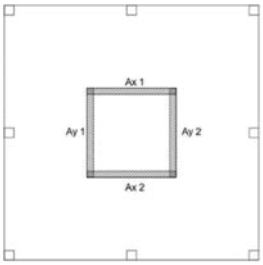

Figure 3: *• Density of shear walls by direction (ρ)*

- Slenderness ratio (S): This involved calculating the ratio of the longer length to the shorter length of each floor. This parameter is related to the deformation modes that the building may incur, and also quantifies symmetry. (Figure 4).

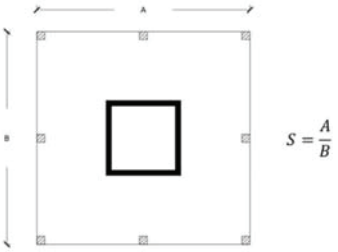

Figure 4: *• Slenderness ratio (S)*

- Maximum distance between the concrete core and the edge of the building (D): The distance between the concrete core and the farthest point of the slab. This parameter quantifies the amount of stresses on the slab, and in consequence, the level of deformation demand that the building may experience (Figure 5)

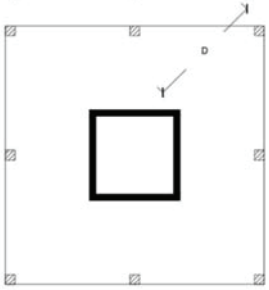

Figure 5: *• Maximum distance between the concrete core and the edge of the building (D)*

In Figure 06, all the representative floor plans of the studied buildings are presented in the same scale to demonstrate the proportion of each building relative to the others. The reinforced concrete shear walls are depicted in black, while the timber elements are shown with a light hatch. In addition, the maximum distance between the concrete core and the edge of the building is measured and annotated, and the center of mass (represented as a square) and the center of rigidity (represented as a circle) are graphically shown, both connected by a dashed rectangle to illustrate the eccentricity of each building. These visual representations provide a comprehensive understanding of the morphological parameters studied, and how each building's design differs.

3 RESULTS

The parameters studied for each building are summarized in Table 1. The country of origin is included to represent the seismic hazard that each building may face. Additionally, the material composition of the floor slab has been included as a relevant parameter, as it should directly relate to the capacity to increase the distance to the edge of the building from the RC core. These parameters provide insight into the morphological characteristics of each building, and how they are influenced by their respective loads' sources and location.

It is crucial to understand that the parameters presented in Table 1 should be considered only as rough approximations, and thus, they define a range of values rather than a statistically valid value. The purpose of the analysis was to identify morphological parameters that can provide guidance for designing TWBs with RC cores based on existing constructions, rather than conducting specific calculations for verifying the proposed design. Therefore, the parameters presented in Table 1 provides a general idea of the characteristics of the analysed buildings and should be used as reference values for similar design projects. It is important to keep in mind that specific designs may require further analysis and consideration of additional parameters to ensure the safety and stability of the building.

Table 1: Summary of Proposed Parameters

Case	Wood Cube	LCT One	BC	Hault	HoHo	Ascent
Stories	5	8	18	22	24	25
Height [m]	25	27	58	73	84	87
Year	2013	2012	2017	2020	2020	2022
Country	Germany	Austria	Canada	Netherlands	Austria	USA
Ecc $_x$ [m]	0,2	6,3	0,8	1,4	0,8	1,0
Ecc $_y$ [m]	0,2	6,7	4,6	0,2	2,0	2,3
ρ_x	1,4%	2,6%	1,8%	1,4%	1,7%	0,7%
ρ_y	0,8%	2,0%	0,6%	0,7%	4,0%	0,6%
S	0,89	0,54	0,27	0,42	0,87	0,52
D [m]	10	16	15	13	7	20
Slab	DLT	CLT-RC	CLT	CLT-RC	CLT RC	CLT

The eccentricities in both X and Y directions (see Figure 7) show that the center of rigidity and the center of mass do not necessarily coincide, which can affect the building's response to lateral loads. The shear wall density by direction (see Figure 8) indicates the amount of reinforced concrete shear walls needed to resist horizontal forces, which is influenced by the type of loads the building is subjected to. The slenderness ratio (see Figure 9) measures the elongation of the building in one direction and is an important factor in determining the building's lateral stability. The maximum distance between the concrete core and the edge of the building (see Figure 10) can give an indication of the distance lateral forces have to travel to be transferred to the core. Finally, the material of the slab is a relevant parameter to consider, as it affects the building's weight and stiffness.

https://doi.org/10.52202/069179-0516

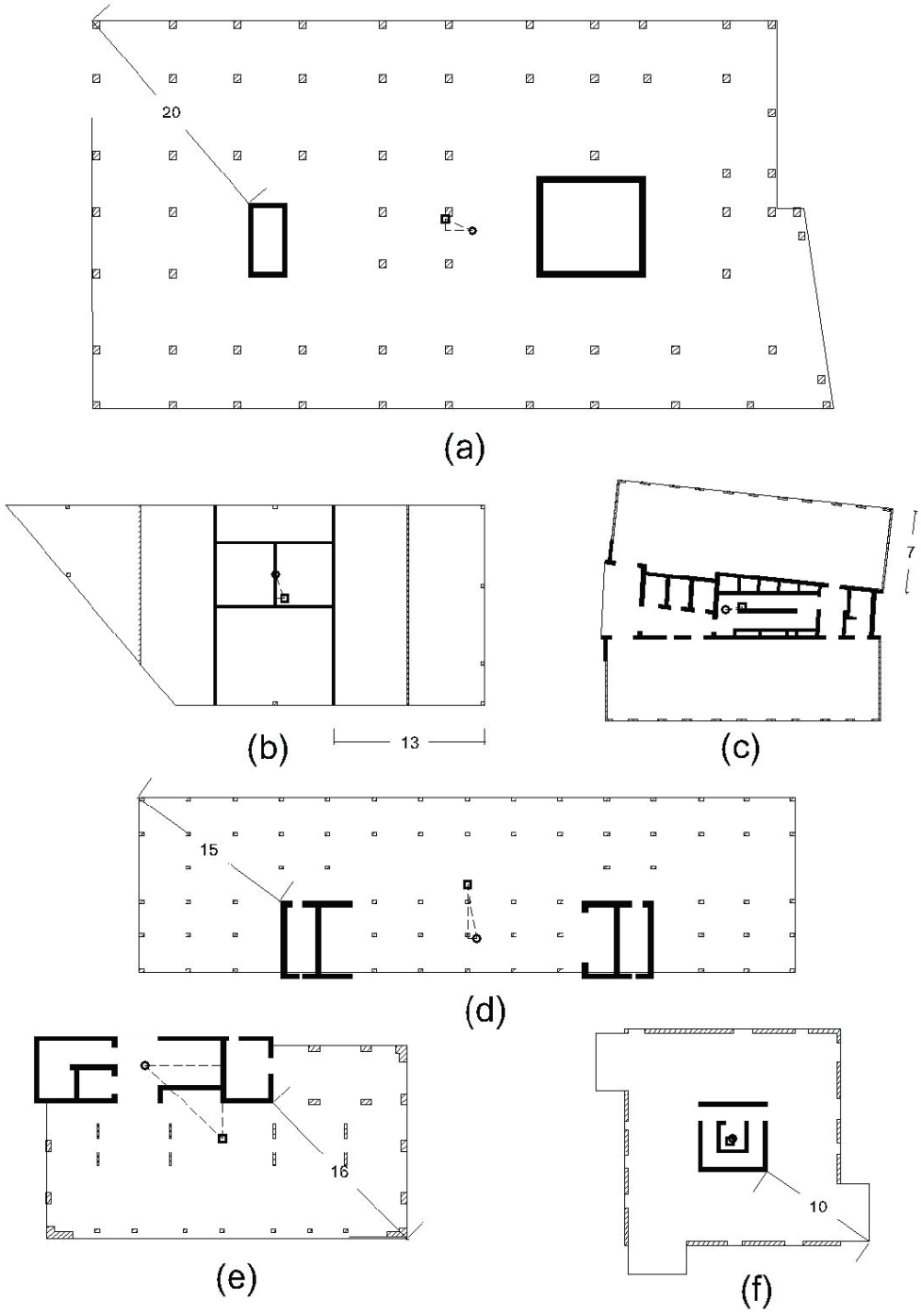

Figure 6: *Al six building plans with the distance Rigidity Center, Mass Center and D displayed. (a) Ascent, (b) Hault, (c) HoHo (d)Brock Commons, (e) LCT One, (f) WoodCube*

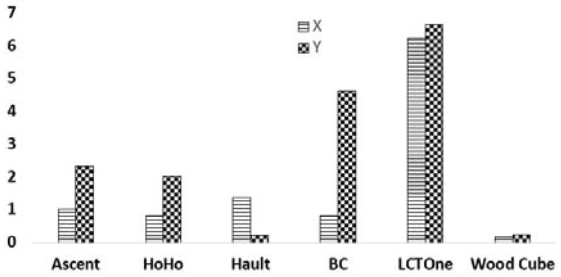

Figure 7: *Eccentricities for each building*

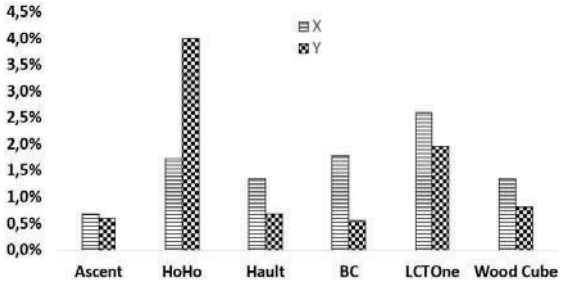

Figure 8: *Wall Densities for each building*

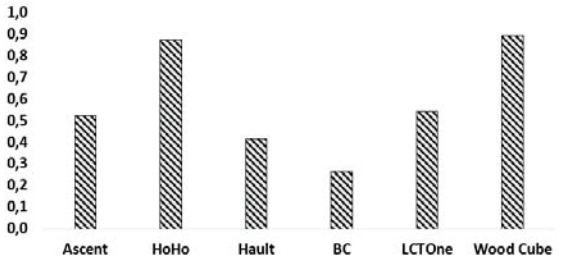

Figure 9: *Slenderness for each building*

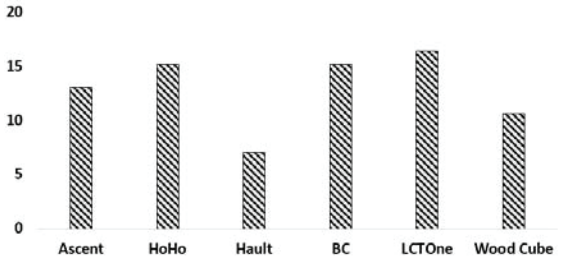

Figure 10: *Maximum distance between the concrete core and the edge of the building for each building*

4 DISCUSSION

The study of the six TWBs with RC cores provides information on the morphological parameters required to develop efficient designs for TWBs with RC cores. The qualitative analysis of each building's structural floor plans allows to identify and compare the eccentricities by direction, the density of shear walls by direction, the slenderness ratio, and the maximum distance between the concrete core and the edge of the building.

One of the most significant findings is that all six buildings had relatively low slenderness ratios, indicating that a squat and stable design is preferable for TWBs with RC cores, which is consistent with current design practices. Regarding the eccentricities, none of the studied buildings present perfect symmetry, and both BC and LC One have a considerable distance between their CM and CR. The density of shear walls varied significantly between the buildings, which indicates that there is no universal solution for designing TWBs with RC cores. However, there is some correlation between the slenderness of the building and the wall density indexes. The distance between the concrete core and the edge of the building also varied significantly between the analysed buildings, which may be related to different architectural requirements or loading conditions.

5 CONCLUSIONS

The analysis of the buildings reveals that the floor plans exhibit strong axes of symmetry and tend to be more square shaped in general. However, it is noteworthy that the buildings with lower slenderness ratios have the highest eccentricities. This can be attributed to the design approach of these buildings, which allows for larger open floor spaces compared to other buildings. There is a trade-off between maximizing floor space and minimizing eccentricities in the design of tall wood buildings. Designers should carefully balance these factors to ensure adequate structural performance and minimize the risk of structural failure.

In general, the studied parameters exhibit slight variations and fall within the following ranges: eccentricities ranging from 6 [m] to 0.2 [m], wall density ranging from 0.5% to 4%, slenderness ratios ranging from 0.3 to 0.6, and maximum distance from the core to the edge ranging from 7 [m] to 20 [m].

Although the study only considers six buildings, the number of wooden buildings with RC cores is not very high, and some of the buildings considered were identified as the tallest buildings with this typology according to Huseyin Emre [4]and Ražnjevi´c[7]. The building with the longest slab extension from the core is the most recent building, which is likely attributed to the development of the slabs used. It is noteworthy that this was achieved even with the use of cross-laminated timber (CLT) slabs instead of composite slabs (CLT RC). This suggests that advancements in timber technology are allowing for greater spans and more efficient use of materials in construction. Additionally, the use of timber slabs offers a more sustainable and environmentally friendly option compared to traditional concrete slabs.

It can be observed that there is no direct relationship between wall density and height or eccentricity. However,

https://doi.org/10.52202/069179-0516

some correlation between wall density and slenderness was founded. An example of this is the HoHo building, which has the highest wall density, but this is not necessarily due to lateral demands, but rather a design decision that allowed it to become the first 24-story wooden building. However, the variable of wall density appears to be particularly interesting in seismic territories when considering the study of damage in buildings after the Maule 2010 earthquake presented by Juneman[9], where it is defined that buildings with reinforced concrete walls that presented lower structural damage had a wall density greater than 2%. Given the great variability of wall densities in the studied buildings, and the lack of a clear trend on the seismicity of their zone, the study of wall density is proposed as an interesting topic by classifying their seismic zone. Nonetheless, the range defined can support the idea that timber buildings with RC cores should consider a wall density near a 2% on high seismic zones.

The performance of wooden buildings with RC cores has been studied due to the high applicability of this typology for buildings in seismic zones. The ductility of this material (i.e., using RC shear walls as lateral system) allows for much more favourable modification factors for seismic design, resulting in lower wall densities, if using CLT shear walls vs RC walls. However, the use of different lateral resistance systems implies uncertainty in the definition of the modification factor. It is recommended not to use CLT shear walls and RC shear walls together as lateral system in highly seismic zones. It is worth noting that two of the studied buildings, Hault and WoodCube, have CLT shear walls along concrete cores, but the studied parameters indicate that they could preliminarily do without them as stiffening elements, due to the amount of RC walls and the seismicity of their zones. This is particularly evident in the case of Hault, which has an RC core that varies along its height and replaces them with CLT walls, having more CLT walls and less RC walls in higher stories. This analysis is beyond the scope of this study and is proposed as a topic for further investigation.

The ranges for the morphological parameters studied in this article should be used only as references based on case studies, not as a design value, since no verification has been carried out and the dimensions used are approximate. Further research considering seismic zone and different typologies are being studied for future investigations.

6 REFERENCES

[1] Edificio Tamango. Un nuevo paso hacia la sustentabilidad. https://www.edificiotamango.cl/

[2] Karacabeyli, E., & Lum, C. (2022). *Technical Guide for the Design and Construction of Tall Wood Buildings in Canada Special Publication SP-543E*.

[3] E. Wiegand Cruz, “Towards a Tall Wooden Built Environment: The impact of policy instruments on the first generation of pioneer projects,” 2019.

[4] H. Emre Ilgın and M. Karjalainen, “Tallest Timber Buildings: Main Architectural and Structural Design Considerations,” in *Wood Industry - Past, Present and Future Outlook*, IntechOpen, 2023. doi: 10.5772/intechopen.105072.

[5] B. K. Fryer, “Wind Dynamics of the Next Generation of Tall Timber Buildings,” 2021.

[6] Michael Green and Jim Taggart, *TALL WOOD BUILDINGS DESIGN, CONSTRUCTION AND PERFORMANCE*. 2017.

[7] H. Svatoš-Ražnjević, L. Orozco, and A. Menges, “Advanced Timber Construction Industry: A Review of 350 Multi-Storey Timber Projects from 2000-2021,” *Buildings*, vol. 12, no. 4, Apr. 2022, doi: 10.3390/buildings12040404.

[8] R. M. Foster, T. P. S. Reynolds, and M. H. Ramage, “Proposal for Defining a Tall Timber Building,” *Journal of Structural Engineering*, vol. 142, no. 12, Dec. 2016, doi: 10.1061/(asce)st.1943-541x.0001615.

[9] A. Fernandez, J. Komp, and J. Peronto, “Ascent - Challenges and Advances of Tall Mass Timber Construction,” *International Journal of High-Rise Buildings*, vol. 9, no. 3, pp. 235–244, 2020, doi: 10.21022/IJHRB.2020.9.3.235

[10] R. Verhaegh, M. Vola, and J. de Jong, “Haut - A 21-storey Tall Timber Residential Building,” *International Journal of High-Rise Buildings*, vol. 9, no. 3, pp. 213–220, 2020, doi: 10.21022/IJHRB.2020.9.3.213.

[11] R. Jünemann, J. C. de la Llera, M. A. Hube, L. A. Cifuentes, and E. Kausel, “A statistical analysis of reinforced concrete wall buildings damaged during the 2010, Chile earthquake,” *Eng Struct*, vol. 82, pp. 168–185, 2015, doi: 10.1016/j.engstruct.2014.10.014.

World Conference on
Timber Engineering
Oslo 2023

AN INSIGHT INTO THE DEVELOPMENT OF TIMBER BRIDGES IN NORWAY AND SWEDEN

Martin Cepelka[1], Per-Anders Fjellström[2], Ashish Aeran[3]

ABSTRACT: Timber has historically played an important role as a building material for bridge construction both in Norway and Sweden. Although a decline was seen due to rise of other competing materials such as steel and concrete over the past century, it has regained popularity in recent decades due to pioneer developments in timber engineering including glued laminated timber and stress-laminated timber decks. There has been a specific focus on development of timber bridges in the Nordic countries after a Nordic Timber Bridge Project was started in 1994. Hundreds of bridges have been constructed throughout these countries including both pedestrian and heavy traffic bridges thereafter. Although the information about the number and type of these bridges can be found on several public administration sources, the information is very scattered and difficult to interpret. In the current study, several sources and databases were used to collect data on timber bridges in Norway and Sweden. Based on the collected data, a comparative view of the development of timber bridges in the two countries is presented with main focus on modern timber bridges built after year 2000. Detailed statistics are included in the study regarding year of construction, type of traffic, bridge types and bridge lengths. Discussions are presented in the end with focus on current trends and possible outlooks for use of timber bridges.

KEYWORDS: Timber, Bridges, Norway, Sweden, Statistics

1 INTRODUCTION

Timber bridges represent an environmentally friendly alternative to concrete bridges for medium-span bridges. As numerous LCA analyses have recently showed, by using timber instead of concrete, reduction of CO_2-equivalent can be achieved for bridge constructions [2]. Both in Norway and Sweden, number of modern timber bridges have been built since 1990's and good knowledge regarding the use of timber in modern bridge structures have been obtained [3]. An example of a modern timber bridge in Norway is shown in Figure 1. With today's focus on green transition, timber bridges can be utilized for lower environmental impact of infrastructure projects. Besides lower environmental impact, timber bridges feature low weight and rapid assembly on site due to large amount of prefabrication and manufacturing precision.

Lately, timber load-bearing structures have been facing tremendous growth in multi-story buildings in Norway and Sweden. According to Norwegian Byggfakta, timber was used in the load-bearing structure in about 40 % of all new school projects in Norway in 2021, while the share on the building market was about 10-20 % in past 10 years in average [1]. The reason behind the growth of share of timber buildings compared to other structural materials is believed to be facilitated mainly by use of a new technology by cross-laminated-timber (CLT), and increased focus on environmental impact of new projects. Given the large increase of use of timber in multi-story buildings, we were interested in investigating whether same trend can be observed for timber bridges. We found the available data being difficult to use directly and decided therefore to perform a statistical study based on own collected data for timber bridges in Norway and Sweden. The results of the investigation are presented in the current paper including details regarding bridge types and bridge lengths. The data are complemented with description of the current trends in timber bridge construction in order to provide an inspiration for bridge designers and bridge owners.

Figure 1: *Vinsnes Bridge over Rv. 22 near Lillestrøm in Norway from 2015. Design: COWI AS. Photo: Martin Cepelka.*

[1] Martin Cepelka, COWI AS, Norway, macp@cowi.com
[2] Per-Anders Fjellström, TBS Timber Bridge Specialists AB, Sweden, paf@timberbridgespecialists.se
[3] Ashish Aeran, University of Stavanger, Norway, ashish.aeran@uis.no

https://doi.org/10.52202/069179-0517

2 DATA COLLECTION

Neither in Sweden, nor in Norway, there exists an overall database governing all bridges within the countries. There are numerous bridge owners, each having their own databases with rather varying quality. In addition, the private owned bridges are not covered by any database. The collection of a total number of bridges is hence difficult. We have therefore chosen to collect data from the leading timber bridge contractors in Norway and Sweden: Moelven, Svenska Träbroar, Martinsons, and the central bridge databases Brutus (Norway) and BaTMan (Sweden), where most of road and pedestrian bridges over main roads are registered. In addition, some bridges were registered manually based on the authors' knowledge. All bridges were then checked across the different databases such that double-registration was avoided. For most bridges, GPS coordinates were available which gave possibility to plot the bridge locations for validation.
Besides data on timber bridges, we have also used Brutus and BaTMan to provide number of bridges built in concrete and steel for comparison and overall trend on the number of built bridges.

For most of the bridges, we have collected additional information in terms of bridge length, type of traffic on bridge (road, or pedestrian), and bridge type. This gave a possibility to look deeper into the development of timber bridges over time, as presented in Section 4.

We have chosen to focus on "larger" bridges built since year 2000. We were interested in bridges that either carry vehicle loads or pedestrian bridges that cross main roads or larger rivers. That means that smaller bridges, as for example park bridges, were disregarded. In some plots, we have also included data on bridges built before year 2000 to visualise a particular trend. However, it must be kept in mind that the data on older bridges bear higher uncertainty. All registered bridges are currently in operation, i.e. bridges that have been replaced or removed were disregarded (this is mainly relevant for older bridges).

The authors are of opinion that the vast majority of larger timber bridges in Norway and Sweden are covered in the study. However, it must be emphasized that the study does not cover all timber bridges due to the limitation of the data collection as it is very difficult, if not impossible, to obtain data on all bridges within the countries.

3 RESULTS ON NUMBER OF BRIDGES

This section presents an overview of the number of timber bridges built in Norway and Sweden. Additional statistics on bridge types is presented in Section 4. As the study does not cover all timber bridges, it must be kept in mind that trends, rather than absolute numbers, should be interpreted.

3.1 Timber bridges in Norway

The number of timber bridges in Norway since 2000 are presented in Figure 2. The number of bridges seems to be rather stable, and it fluctuates around a year-average of about 10 timber bridges per year. The bridge number is particularly high in 2019 due to contribution of 11 flyover arch road bridges on large motorway projects Rv. 3/Rv. 25 Løten–Elverum (8 bridges), and E6 Brumunddal-Moelv (3 bridges). Figure 3 presents the distribution of road and pedestrian bridges in Norway and it is fairly even in general. The total percentage of road bridges are 47 % compared to 53 % pedestrian bridges during the considered period. The total built lengths of these bridges are also presented in Figure 4. Although the total built length of road bridges is much higher in some years, the overall length is nearly the same during the considered period (4.47 km for road bridges and 4.03 km for pedestrian bridges). The historical development of road and pedestrian timber bridges over past decades is also presented and shown in Figure 5. Here, a clear trend in increase of number of road bridges can be observed after 1990s.

Figure 2: *Number of timber bridges built in Norway (both pedestrian and road bridges), based on selected database. The dotted line represents moving average with period of 2 years.*

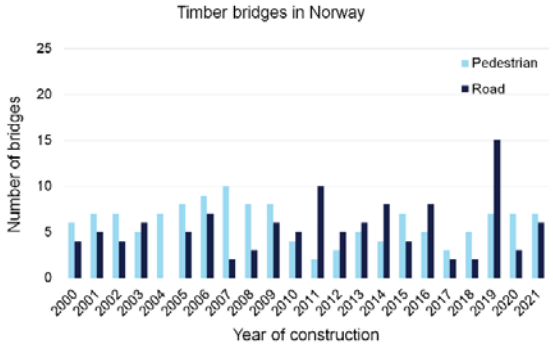

Figure 3: *Number of road and pedestrian timber bridges built in Norway, based on selected database*

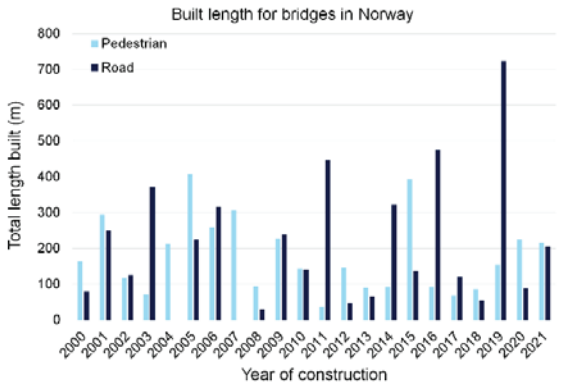

Figure 4: *Built length of road and pedestrian timber bridges built in Norway (2000-2021), based on selected database*

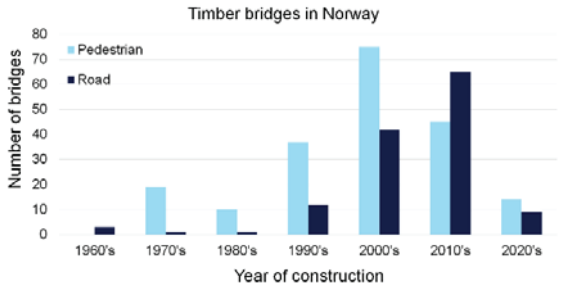

Figure 5: *Built length of road and pedestrian timber bridges built in Norway (1960-2021), based on selected database. Note that data on older bridges are less reliable.*

Figure 6 shows a comparison between share of timber, concrete, and steel bridges built in Norway. The share of timber bridges is relatively stable, and it fluctuates around 5 % every year for studied period.

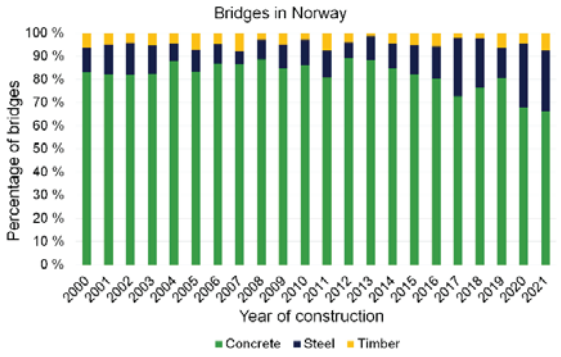

Figure 6: *Comparison of share between concrete, steel, and timber bridges built in Norway in period 2000-2021 as registered in Norwegian bridge database Brutus.*

3.2 Timber bridges in Sweden

The number of timber bridges in Sweden are presented in Figure 7. The number of bridges built in the early 2000's is around 50 bridges per year, and the trend seems to be decreasing in last 10 years.

Figure 7: *Number of timber bridges built in Sweden (both pedestrian and road bridges), based on the selected database. The dotted line represents moving average with period of 2 years.*

The distribution between road and pedestrian bridges is shown in Figure 8. Almost 70 % of the bridges are pedestrian during the considered period, although this gap seems to be decreasing in the recent years. The total built lengths of road and pedestrian bridges are shown in Figure 9 with pedestrian bridges around 15 km as compared to 4 km road bridges.

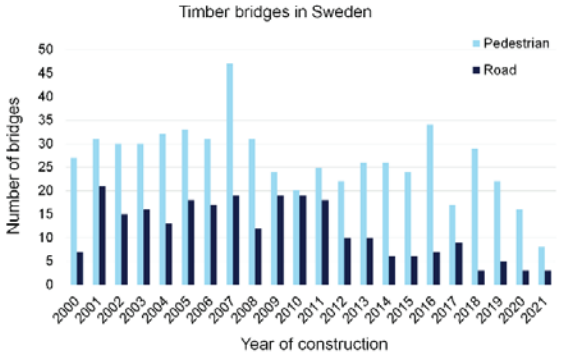

Figure 8: *Number of road and pedestrian timber bridges built in Sweden (2000-2021), based on selected database*

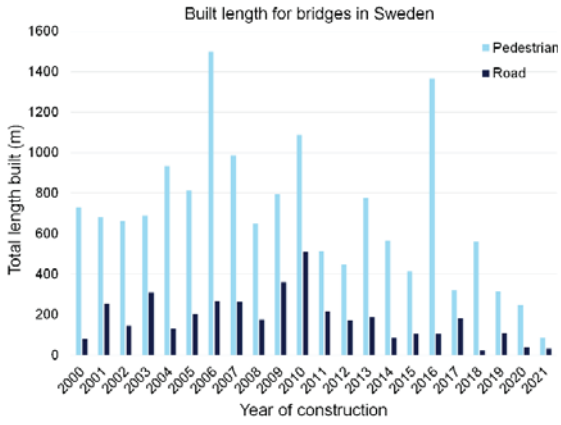

Figure 9: *Built length of road and pedestrian timber bridges built in Sweden (2000-2021), based on selected database*

https://doi.org/10.52202/069179-0517

Figure 10 shows a comparison between share of timber, concrete, and steel bridges built in Sweden based on the bridges registered in the national database BaTMan. The share of timber bridges is relatively stable, and it fluctuates between 3-7 % for studied period besides year 2021, for which no timber bridge has been registered in the database.

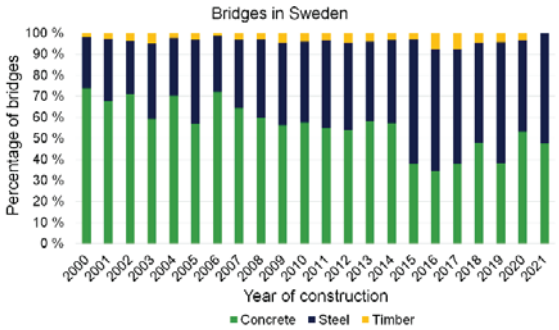

Figure 10: *Comparison of distribution between concrete, steel, and timber bridges built in Sweden in period 2000-2021. The data are only valid for state owned bridges registered in the Swedish Road Administrations bridge database BaTMan.*

3.3 Comparison of bridges in Norway and Sweden

A comparative study is done for timber bridges in Norway and Sweden as shown in Figure 11. The number of bridges is substantially higher in Sweden as compared to Norway. This is primarily due to a larger number of pedestrian bridges in Sweden as shown in Figure 12, annual built length, and Figure 13 the total built length. However, as also mentioned earlier, the gap between the number of road and pedestrian bridges is getting closer in the recent years, both in Norway and Sweden.

The number of road bridges is also much higher in Sweden, and this number is more than twice of that in Norway. However, interestingly, the total built length of road bridges is higher in Norway than Sweden, see Figure 14. Same trend can be observed for pedestrian bridges for which the factor of 6 in difference between Norway and Sweden in terms of number of bridges is reduced to 3 when comparing accumulated bridge length. This indicates that a typical timber bridge in Norway is longer compared to a typical timber bridge in Sweden.

Figure 11: *Total number of timber bridges built in Norway and Sweden (both pedestrian and road bridges), based on selected database*

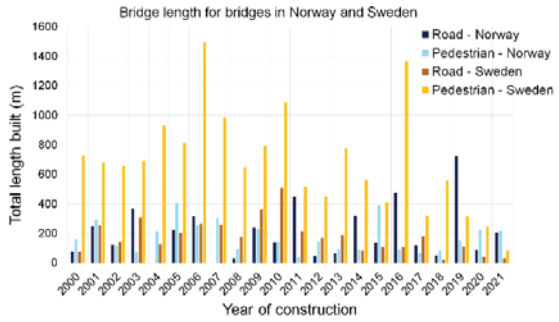

Figure 12: *Number of road and pedestrian timber bridges in Norway and Sweden, based on selected database*

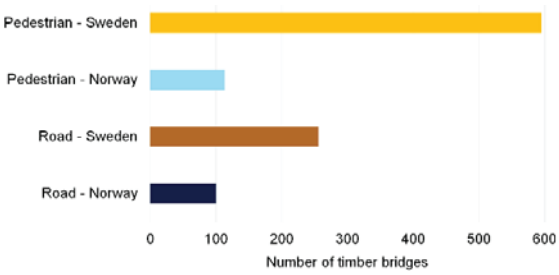

Figure 13: *Number of road and pedestrian timber bridges in Norway and Sweden (2000-2021), based on selected database*

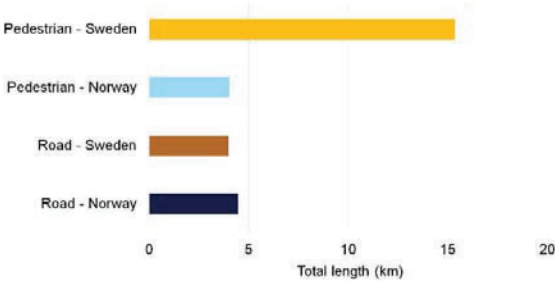

Figure 14: *Built length of road and pedestrian timber bridges built in Norway and Sweden (2000-2021), based on selected database.*

https://doi.org/10.52202/069179-0517

4 CURRENT TRENDS AND BRIDGE TYPES

4.1 From historical to modern timber bridges

Use of timber in bridges in the main load-bearing elemens has a long tradition both in Norway and Sweden. Up to the 20th century, timber was the main building material for both pedestrian and road bridges. Two examples of old timber bridges are Gamle bybro (1861) in Trondheim, Norway, and Lejonströmsbron (1737) in Skellefteå, Sweden shown in Figure 15. With the development of steel and concrete, timber bridges became less popular and up to 1990's, use of timber was limited to mainly smaller pedestrian bridges.

Figure 15: *The Lejonström bridge built in 1737 with a combined kingpost strut-frame design is still open for road traffic. Location Skellefteå, Sweden. Photo: Per-Anders Fjellström.*

Three Nordic Timber Bridge research projects were carried out from 1994 to 2001. The purpose of these projects was to increase knowledge and competitiveness for timber bridges in Norway, Sweden and Finland. Denmark and Estonia were also involved in some parts of the projects. In Norway, the focus was on developing the typical trusses and arches with dowel joints in combination with creosote treated glulam used today. In Sweden, focus was on the use of stress-laminated decks made of glulam of spruce, in combination with wood protection by design and structural health monitoring. In Finland, they focused on wood-concrete composite bridges and shear connections in treated glulam. The Nordic Timber Bridge projects represent a gamechanger in use of timber in bridges in Norway and Sweden. As can be seen in Figure 16 and Figure 17, both the number of bridges and bridge length accelerated noticeably in 1990s and 2000s, especially for road bridges.

4.2 Current trends in Norway

In addition to Nordic Timber Bridge project, important contribution to use of timber in load-bearing structures were Olympic games in Lillehammer in 1994. As there was a wish for more extensive use of timber in larger structures, a connection technique with slotted-in steel plates and dowels was developed allowing strong joints for large truss structures. In addition, production of glued laminated timber became more controlled and effective, which allowed for production of stronger and larger timber elements. For bridges, increased quality of pavement and need for improved durability of timber decks was required and later efficiently facilitated by using stress-laminated decks. This type of deck provides sufficient stiffness for asphalt pavements and can be protected by moisture membrane, similarly to concrete bridges [4]. In 1996, Evenstad bridge was erected, facilitating all afore mentioned techniques. This is widely considered as a new start, or renaissance, for timber bridge construction in Norway. The vast development in 1990s allowed for use of timber in road bridges that could compete with concrete bridges. These new types of bridges have normally stress-laminated plate decks that are either directly supported by substructure (plate bridges), or by transversal beams connected to arches (arch bridges) or trusses (truss bridges).

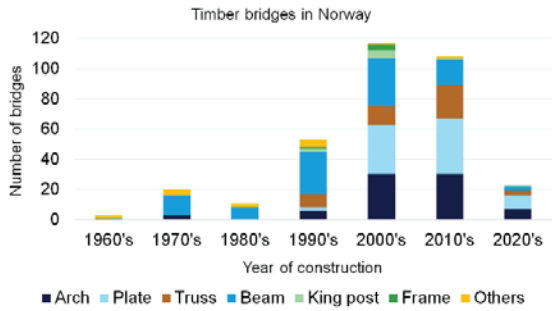

Figure 16: *Distribution of built timber bridges in Norway per bridge type and decade, based on selected database. Note that data are missing for some few bridges, and data on older bridges are less reliable.*

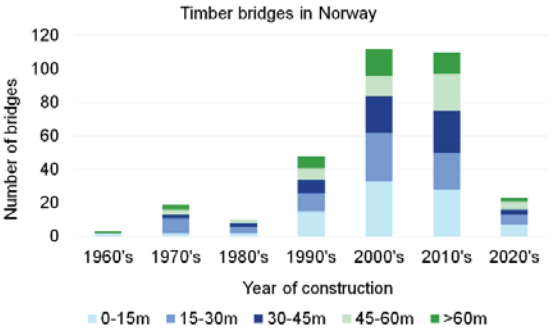

Figure 17: *Distribution of built timber bridges in Norway per built bridge length and decade, based on selected database. Note that data are missing for some few bridges, and data on older bridges are less reliable.*

https://doi.org/10.52202/069179-0517

As the statistics in Figure 16 shows, majority of timber bridges built in 1970s and up to approximately 1990s were beam bridges. These were typically pedestrian bridges with shorter spans and simple timber plank decks. As can be seen in Figure 18, the use of beam bridges has decreased over the past decades, and it is nowadays typically limited to shorter pedestrian bridges crossing streams or small rivers. These bridges are competitive due its simplicity and low weight allowing for fast and easy erection for cases where shorter service life than standard 100 years is acceptable. There were built few girder bridges where the beams were connected together with stress-laminated plate creating a T-beam. However, the low number of such bridges indicates that this structural system is probably not competitive to concrete bridges with prefabricated beams.

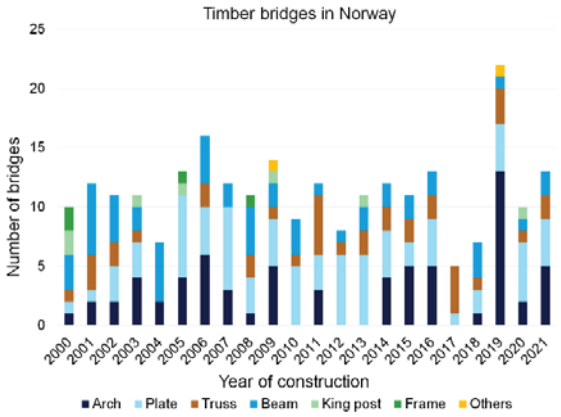

Figure 18: *Distribution of timber bridges per bridge type (2000-2021) in Norway, based on selected database.*

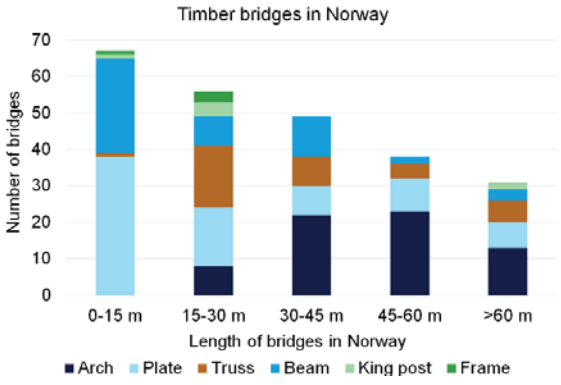

Figure 19: *Distribution of timber bridges per bridge type and built length (2000-2021) in Norway, based on selected database.*

Figure 18 shows a steadily increasing trend in use of plate bridges and arch bridges both for pedestrian and vehicle bridges. Plate bridges are used either as simply supported plates for shorter bridges over rivers or streams (often on secondary roads), or as continuous plates over several spans. The advantage of plate bridges is their low weight and low depth allowing for effective flyover bridges over existing roads and railways, see example in Figure 20. They facilitate normally very fast assembly, reducing considerably closure time of infrastructure beneath them. Typically, plate bridges are used for spans up to 15 m for road bridges, and up to 20 m for pedestrian bridges.

Figure 20: *Plate bridge with stress-laminated deck in Hell, Norway as flyover road bridge over railway from 2009. Photo: Martin Cepelka.*

Larger spans can be achieved by hanging the stress-laminated decks on arches or trusses. Arch bridges have lately been used as flyover bridges on numerous motorway projects. The arches can normally span 40-50 m which is sufficient to avoid any intermediate support in the road profile, as shown in example in Figure 21. This increases safety on motorways and provides high aesthetical value. For simple road geometry on the bridge (straight and narrow bridges), the arch bridges seem to give an effective and competitive solution.

Figure 21: *Arch bridge as flyover road bridge over E6 near Sorperoa, Norway from 2016. Photo: Google.*

Lately, several arch bridges with large spans over rivers have been obtained by combining timber arches and concrete decks together with network configuration of hangers. There is in total 6 such bridges built in period 2016-2022. Steibrua, shown in Figure 22, is the largest of those, and it is with its 88 m the longest spanning bridge with timber load-bearing structure in the world [5].

Figure 22: *Network arch bridge with concrete deck and timber arches. Steibrua in Alvdal, Norway from 2016. Photo: Martin Cepelka.*

Alternatively, truss structures have been used to obtain large spans. The longest spanning truss bridge is Flisa bru with 77 m span. Unfortunately, one of the largest timber truss bridges, Tretten bru, collapsed suddenly in August 2022. As the cause of the collapse could not easily be determined, Norwegian Public Road Administration decided to close several other truss bridges to allow for their thorough inspection. For the time being, the cause of Tretten bru collapse is still under investigation and the future use of truss bridges in Norway remains somewhat unclear.

An overall distribution of bridge types and built lengths for years 2000-2021 is shown in Figure 23 and Figure 24. Figure 23 shows that most timber bridges built in period 2000-2021 in Norway are plate bridges (32 %) and together with arch bridges, they represent around 60 % of all timber bridges. Figure 24 shows rather uniform distribution of bridge lengths sorted in groups per 15m for lengths 0-15 m, 15-20 m, and 30-45 m with approximately 25 % contribution each. Bridges with lengths 45-60 m, and more than 60 m represent 16 %, and 12 %, respectively. There are in total 14 bridges with lengths larger than 100 m. Flisa bru is the longest road bridge with 196 m length, and Midgardsormen bru is the longest pedestrian bridge with 230 m length.

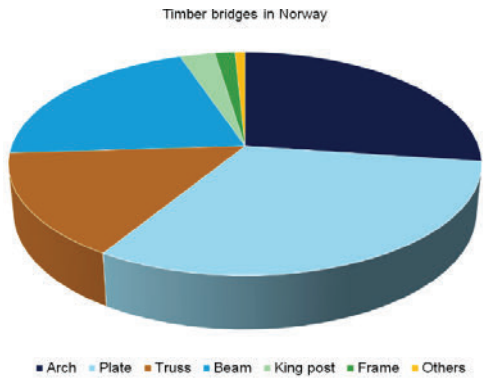

Figure 23: *Distribution of timber bridges per bridge type built in years 2000-2021 in Norway, based on selected database*

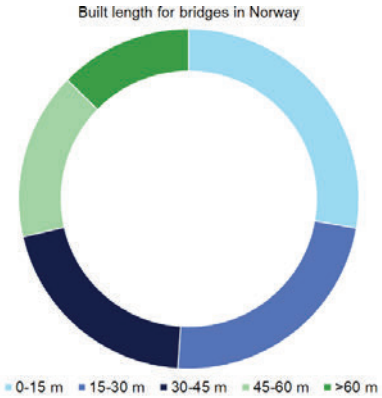

Figure 24: *Distribution of timber bridges per built length built in years 2000-2021 in Norway, based on selected database*

Since the new generation of timber bridges raised in 1990's, there is still increasing focus on durability. In Norway, required bridge service life is 100 years (independent of material). For timber bridges, this is believed to be achieved by use of both structural protection (load-bearing members are mechanically covered/protected by cladding or sheeting) and chemical treatment. In Norway, it is common to use double level of chemical treatment, typically salt treatment for single laminations and creosote treatment for the whole glued-laminated element. The creosote treatment provides very good protection against fungi and insects, in addition to reduction of moisture sorption. As a result, it is not necessary to cover timber elements entirely. This reduces maintenance need and gives more freedom to designers in choice of the structural scheme. In last 20 years, numerous spectacular truss bridges have been built. This is particular for Norway, as the use of creosote is not allowed in most other countries. It is expected that creosote will eventually be restricted in Norway as well, and the design of timber bridges will most likely turn towards trends in other countries where structural protection is the primer measure to obtain durability, as for example in Sweden as discussed further in Section 4.3. It can also be expected that new structural systems will appear in Norway. For example, in Germany and Switzerland, numerous modern bridges have lately been built with timber-concrete composite layout [6], [7]. Besides protection from weather, concrete deck in composite action with timber girders give effective structural system and allows for larger spans. Consequently, we might see a growth in use of beam bridges in Norway again.

4.3 Current trends in Sweden

As in Norway, the trend is to use more renewable materials as wood in larger constructions and buildings. However, the use of wood in bridges has been decreasing for the last decade. There are some obvious reasons for this:

https://doi.org/10.52202/069179-0517

One is that the market for building large timber structures is increasing rapidly and it is an easier and better market than in building timber bridges. The two dominating timber bridge producers are also two of the three largest glulam manufacturers in Sweden. A second reason or a factor is the Swedish road administrations moderate interest in developing and using timber bridges, opposite to the situation in Norway. Another minor reason is that the use of spruce in bridges have shown to be a little more complicated than first expected. Especially railings, cladding and the edges of stress-laminated decks were found to suffer from durability problems. This is a problem for the large forest companies, that owns a lot of small timber bridges, and they are now starting to replace damaged bridges with new steel bridges.

If we look back att the timber bridges built early last century, we will find that Sweden had a large number of strut frame bridges in one or several span often in combination with a kingpost on top of the strut frame, as the Lejonströms bridge. For larger spans, 50 – 125 m, it was common to build suspension bridges with timber towers. A couple of these bridges are still in use in Dalarna region. Another type of bridge that was used for crossing rivers, were floating bridges, two off that design remains over Dalälven, but not in their original design. Covered bridges were not so common in Sweden and only one remains, Vaholms Brohus built in the late 19th century.

For reasons there are very few remaining timber bridges built between 1940 - 1980. One obvious reason for this is that most of them have been replaced, and another is that most road bridges were built in concrete or steel. However, there is a large number of steel girder bridges built with timber deck in that period of time, many of them still in use.
The new era of timber bridges was started by the Nordic TB-project. It opened a new market for factory built modern timber bridges for both pedestrians and road traffic. In the early 1990's most bridges were built with chemically treated wood, NTR A. Now it's used only in pedestrian bridges with truss or beam design designed for 40 years' service life, and some smaller and temporary road bridges, mainly for the forest industry.
Most timber bridges are built of spruce, and they are designed for 80 years' service life.

Road bridges
The first road bridge with a stress laminated deck of spruce was built in 1994, followed by the first stress laminated bridge deck with a T-section of treated wood, one year after. The stress-laminated deck slab of spruce has become a very popular design with over 400 bridges built since 2000. For road bridges it's the most common design to use as a single- or multi span deck. The design is simple, robust and bridges are easy to produce and transport to the bridge site. One big difference between Norway and Sweden is the use of the stress-laminated design in combination with arches, kingpost or trusses. If we compare the number of arch bridges for road traffic, only one is built in Sweden, while in Norway, there is a quite large number of arch bridges.

Figure 25: *A typical stress-laminated timber bridge over railroad. Built 2017 in Hörle, Sweden, by Moelven Töreboda. Photo: Per-Anders Fjellström.*

Pedestrian bridges
The pedestrian bridges built from 2000 to today shows a great variation in both length and design. Some typical Swedish pedestrian timber bridges are the long span cable-stay-, medium span truss- and short span beam bridges and a number of stress laminated decks.

The most common designs are beam bridges and different combinations with a stress-laminated deck with more than 200 bridges built of each type.

Figure 26: *Pedestrian bridge to Strömsholmen in Eskilstuna, Sweden. The design is a 48 m 3-span beam bridge with a transverse plank deck. Built 2001 by Svenska Träbroar. Photo: Per-Anders Fjellström.*

The small Howe Truss bridge is another popular bridge design in spans up to 30 m with close to 100 bridges built the last 20 years.

https://doi.org/10.52202/069179-0517

Figure 27: *Pedestrian Howe Truss bridge to Kållandsö close to Lidköping, Sweden. The design is a 25m truss bridge with a transverse plank deck. Built 2017 by Martinsons. Photo: Per-Anders Fjellström.*

The modern version of the old suspension bridge in timber is the cable-stay design. It is a popular design and there is at least one ongoing project to build one next year in Ängelholm, Sweden. The Älvsbacka bridge in Skellefteå is the longest with a main span of 130 m. A total of 8 bridges have been built since 2000.

Figure 28: *Älvsbackabron is a cable-stay pedestrian bridge with a 129m span built 2012 over Skellefteälven, Sweden, by Martinsons. Photo: Per-Anders Fjellström.*

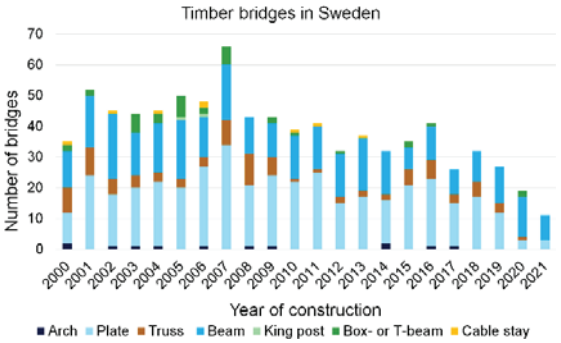

Figure 29: *Distribution of timber bridges per bridge type (2000-2021) in Sweden, based on selected database.*

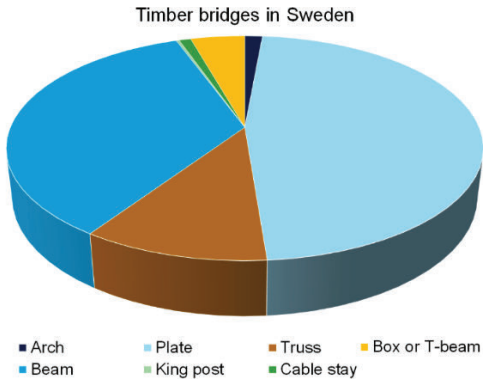

Figure 30: *Distribution of timber bridges per bridge type built in years 2000-2021 in Sweden, based on selected database*

A lot of work has been done to improve wood protection and durability over the years. Good wood protection by design in combination with factory installed sensors for moisture content measurements is the Swedish way to meet the demands for a long service life. It's an environmentally friendly and hopefully a cost-effective approach to durability. The use of spruce, a not durable species, in a bridge superstructure requires a different approach to inspections and there is still some work to do regarding reliable inspection methods. In the next years, we think that we will see new designs on the Swedish market such as timber-concrete composite, light weight long span designs as the InfraLIGHer winner BIFROST and, hopefully, new state of the art covered bridges.
The biggest question in Sweden is how the market and production of timber bridges will adapt to the fact that the two largest producers have closed down their timber bridge production from 2022.

Figure 31: *Factory installed M.C-sensors in a stress-laminated deck provide the owner with reliable data from inspections. Road bridge built 2022 by TBS, Junsele Sweden. Photo: Per-Anders Fjellström.*

https://doi.org/10.52202/069179-0517

5 CONCLUDING REMARKS

The current study reveals a great potential for use of timber in bridges as a possible measure for reducing environmental impact of infrastructure projects.

The results presented in Section 3 show an opposite trend in number of bridges compared to the recent growth of use of timber in buildings. In Norway, the number of timber bridges built every year is fairly constant, while in Sweden, a clear decreasing trend can be observed.

As demonstrated in Section 4, several modern timber bridge concepts have been developed since 1990s that can represent a competitive, and more environmentally friendly alternative to concrete bridges.

The choice is in the hands of bridge designers and bridge owners.

6 ACKNOWLEDGEMENTS

The authors would like to acknowledge Moelven and Martinsons for sharing their data. This was an important input into the study, and it is much appreciated.
We would also like to acknowledge Sara Holm for her contribution with data gathering in the beginning of the project.

REFERENCES

[1] Byggfakta, «Norsk byggebransje,» 09 11 2021. [Internett]. Available: https://norskbyggebransje.no/nyheter/trekonstruksjoner-i-sterk-vekst.

[2] A. Pousette,, K. A. Malo, S. Thelandersson, S. Fortino, L. Salokangas og J. Wacker, «Durable Timber Bridges: Final Report and Guidelines,» RISE, 2017.

[3] Statens Vegvesen, «Trebruer, Statens vegvesen Rapporter, Rapport Nr. 422,» Vegdirektoratet, 2017.

[4] O. Kleppe og T. Dyken, «The Nordic Timber Bridge Project and the Norwegian Approach to Modern Timber Bridge Design,» i *IABSE conference*, Lahti, Finland, 2001.

[5] J. Veie, T. Stensby, Y. Aartun og T. Dyken, «The development of timber as a construction material for bridges in Norway,» i *IABSE*, Vancouver, 2017.

[6] F. Miebach, «Robust Timber bridges without cladding,» i *4th International Conference on Timber Bridges*, Biel/Bienne, 2021.

[7] R. Widman og A. Müller, «History and development stages in timber bridge construction in Switzerland,» i *4th International Conference on Timber Bridges*, Biel/Bienne, 2021 .

World Conference on Timber Engineering Oslo 2023

NEBY BRU: ONE FOOTWAY, THREE WAYS OF SUSTAINABILITY

Manuel Sánchez-Solís[1], Gaute Mo[2], Fernando Ibáñez[3]

ABSTRACT: Degree of Freedom, in collaboration with the municipality of Tynset, has developed the detail design of a pedestrian bridge that will join the neighbourhood of Neby with the rest of the city, crossing the river Glåma. This project had a limited budget, so the design stage has been influenced by the materials optimization, the use of local resources and suppliers and the consideration of conventional constructive methodologies. The bridge was opened to pedestrian traffic in May 2020. This text describes the main characteristics of the structure and the methodology considered in the design.

KEYWORDS: Footway, cable, suspension, timber, steel, truss, sustainability, social, commitment

1 INTRODUCTION

Degree of Freedom has collaborated with the Municipality of Tynset (Norway) in the design of a pedestrian bridge crossing the river Glåma.

The original idea of the design was to create a light pedestrian timber bridge integrated in the natural environment and landscape where it is placed.

The new suspension footbridge will reconnect the neighbourhood of Neby with the rest of the city of Tynset, laying on the foundations of an old bridge destroyed during the World War II.

Given the social approach of the project, it has been decided to use local resources and suppliers, seeking their collaboration when providing their services: from the cables, which are provided by a Norwegian company, to the steel plates, which are delivered by a local workshop.

The bridge will also be constructed by local people and using technology available in the area, which has largely conditioned the conception of the construction process.

Since the design process, the economy of the project has been considered by optimizing the materials as much as possible.

Figure 1: *View of the Neby pedestrian bridge*

2 DESCRIPTION OF THE STRUCTURE

The Neby Bru is a suspension bridge, consisting in a continuous timber truss deck with steel diagonals, suspended from catenary cables by means of vertical hangers. There are towers at each riverbank, plus two intermediate towers supported over two existing isles. The bridge is then divided into three spans approximately 30m, 33m and 30m long, respectively.

The deck has a minimum horizontal clearance of 1.5m between handrails, which is extended up to 5m at the central towers to create a balcony. The balcony makes the top and bottom chord truss to be discontinuous at the central towers since top chord is stopped. An extra diagonal hanger connected to the central towers is then required in order not to overload the bottom chord adjacent to the balcony (refer to Figure 4).

The bridge main structural elements are described in the following sections.

2.1 MAIN CABLES

The bridge has two main cables 6x36 IWRC with 36mm nominal diameter, parallel in the longitudinal direction of the bridge, suspended from the towers and anchored to concrete anchorages blocks.

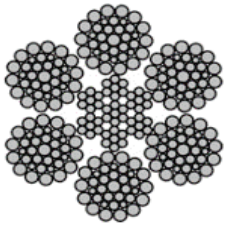

Figure 2: *Main cables section*

[1] Manuel Sánchez-Solís, Degree of Freedom SLU, Valencia, Spain, m.sanchez@dofengineers.com
[2] Gaute Mo, Degree of Freedom AS, Oslo, Norway, g.mo@dofengineers.com
[3] Fernando Ibáñez, Degree of Freedom SLU, Valencia, Spain, f.ibanez@dofengineers.com

https://doi.org/10.52202/069179-0518

Main cables rest over the four towers though steel saddles bolted at the top of the towers.

2.2 TOWERS

The towers on the river sides are composed by two timber columns and two lintels joining the top of them.

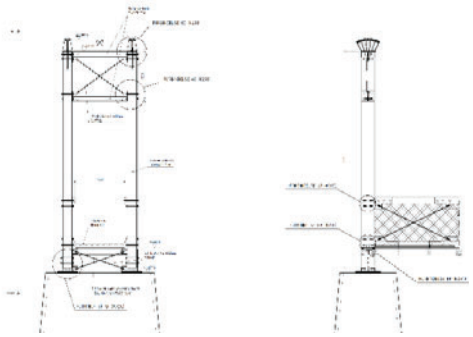

Figure 3: *Extreme towers*

For the towers in the central piles, in order to provide them with more stability they are designed with an A shape.

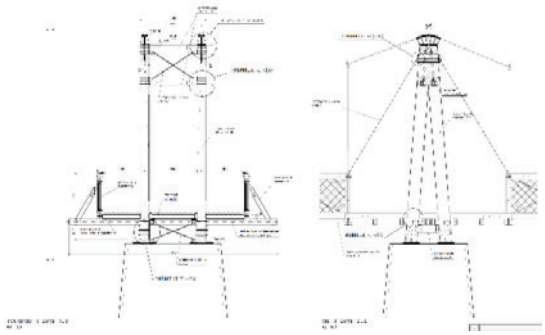

Figure 4: *Intermediate towers*

The height of the towers has been calculated assuming a ratio span/height = 5.25 which has been proved to work fine for this type of bridges. Then considering the central span we have:

H_{towers} = 33/5.25= 6.30 m

2.3 VERTICAL HANGERS

Vertical hangers are 16mm steel bars suspended from the main cables, supporting the bridge deck at a spacing of 33/12 = 2.75m.

Hangers are connected to the main cables though clamps and fork sockets.

The bottom meter portion of the hangers is threaded to be able to adjust the deck levels (adjusting nuts) at the required level in every construction stage.

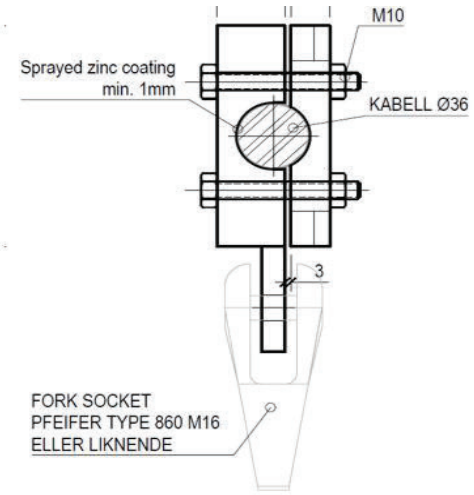

Figure 5: *Hangers clamp and fork socket*

2.4 TIMBER TRUSS DECK

The timber frames form two vertical trusses connected between them at the bottom by another horizontal truss that gives lateral stiffness to the bridge to resist loads in the gravity direction but also lateral forces from the wind. These three trusses form an open U-shaped section, so the top chord is also the handrail.

The following pictures show the preliminary design for a typical module of the bridge deck, which would be repeated every 2.75m.

The bridge deck will be ensembled in double and single 2.75m modules to facilitate the construction sequence.

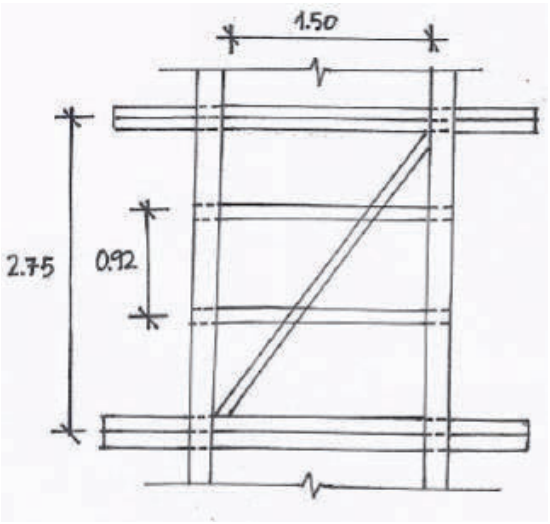

Figure 6: *Truss plan view*

https://doi.org/10.52202/069179-0518

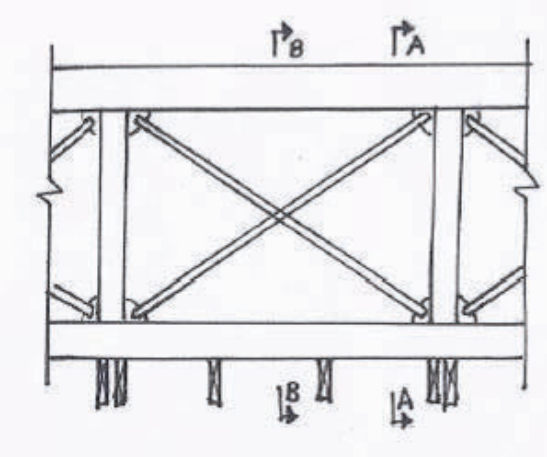

Figure 7: *Truss elevation*

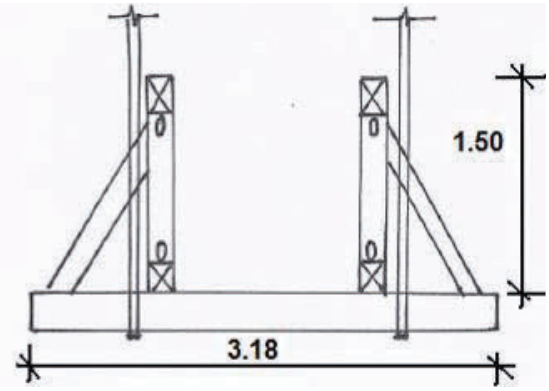

Figure 8: *Truss section A-A*

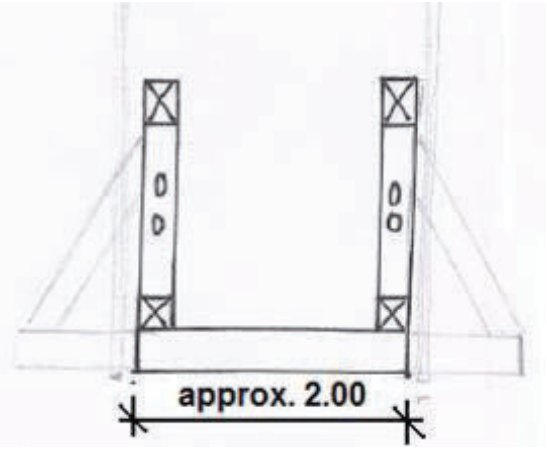

Figure 9: *Truss section B-B*

2.5 CONCRETE ANCHORAGE BLOCKS

Concrete anchorage blocks are located on both river sides, they are capable to resist the forces from the main cables.

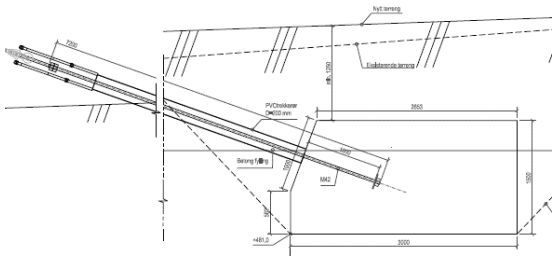

Figure 10: *Anchorage block*

3 BRIDGE ERECTION SEQUENCE

Bridge erection takes a leading role on the conception and design of the bridge as the construction sequence needs to use conventional methods able to be undertaken by the available local resources in Tynset.

It is assumed that the bridge will be erected following this simplified procedure:

1) Erect the supports (towers) over the concrete foundations (piers, abutments).
2) Hang the main cables from the supports and adjust it to have the required shape.
3) Hang the double modules from the hangers.
4) Erect the balconies modules, hanging them from the hangers and connecting them to the towers.

Figure 11: *Bridge erection (central span)*

5) Prestress the hangers (by adjusting nuts) to bring each module to the same vertical position (horizontal). Truss diagonals are not fixed during these phases (not taking loads).
6) Join the single modules by assembling on site the gaps between them.
7) Stretch all diagonals (by adjusting nuts), so they take just zero efforts.
8) Install horizontal bracing elements (steel L profiles).
9) Install deck floor except at modules adjacent to balconies.
10) Rise the deck (creating a parabolic shape) prestressing the hangers (by adjusting nuts)

https://doi.org/10.52202/069179-0518

11) Prestress end cables at the same time as previous phase (by adjusting anchorage element) to bring the extreme towers to the vertical position
11) Install remaining deck floor
12) Stretch non-tensioned diagonals, so they take just zero efforts
13) Install and adjust balcony ties, so they take just zero efforts.
The bridge construction sequence as detailed above has been included in the FEM model, so the accumulated loads and deformations of the bridge elements are considered.

Figure 12: *Bridge erection (lateral span)*

4 DESIGN CRITERIA

4.1 MATERIALS

4.1.1 TIMBER

The bridge main material is timber. Its strength, light weight, and energy-absorbing properties make it highly desirable for bridge construction. Main advantages of using timber as principal construction material are detailed below.
DURABILITY: Wood is inherently very durable when properly protected against rotting, shrinking, twisting, insect attack and everyday exposure to the elements. Properly treated timber will not crumble like concrete, will not rust like steel and can be used in any environment regardless of climate. Wood is not damaged by continuous freezing and thawing and resists harmful effects of de-icing agents, which cause deterioration in other bridge materials.
LOW MAINTENANCE: wood treated with preservatives requires little maintenance and no painting.
COST COMPETITIVE: From an economic point of view, wood is competitive with other materials on a first-cost basis and shows advantages when life cycle costs are compared.
QUICK CONSTRUCTION: Design constraints of using steel or concrete will slow down the installation process, whereas timber is a readily available resource and installation is quicker. Timber bridge construction can occur in any weather conditions, without detriment to the material.
Both solid timber and glulam are used in Neby pedestrian bridge. Glulam, an engineered timber product, provides greater strength than solid timber for longer span applications.
Glulam is manufactured by laminating individual pieces of sawn lumber together with waterproof structural adhesives.
GL 30c: Used in bridge towers and in bottom chord and transversal beam of balconies area.
$f_{m,g,k}$ = 30 N/mm² (bending strength)
$f_{t,0,g,k}$ = 19.5 N/mm² (tensile strength)
$f_{c,0,g,k}$ = 24.5 N/mm² (compression strength)
$\rho_{g,\,mean}$ = 430kg/m3
C24: Solid timber used in deck structural elements (transverse beams, vertical and diagonal posts, top and bottom chords)
$f_{m,k}$ = 24 N/mm² (bending strength)
$f_{t,0,k}$ = 14.5 N/mm² (tensile strength parallel)
$f_{c,0,k}$ = 21 N/mm² (compression strength parallel)
$\rho_{g,\,mean}$ = 420kg/m3

4.1.2 STEEL

S275J2: Used in connection plates and steel elements in the bridge deck (saddles and clamps)
f_y = 275 N/mm²
f_u = 390 N/mm²
S355J2: Used in steel rods (hangers and diagonals bars)
f_y = 355 N/mm²
f_u = 490 N/mm²

4.1.3 Concrete

B45: Used in the piers
f_{ck} = 45 N/mm²
B30: Used in concrete anchor block
f_{ck} = 30 N/mm²

4.2 LOADS

In addition to Self-weight, Superimposed dead load from the timber boards deck is set to 0.25kN/m^2. Parapet net attached to the handrail is treated separately as 0.05kN/m (each side). Permanent loads also include cable and hangers pre-stressing loads, modelled as temperature.
Uniformly distributed traffic load dependant on the loaded length has been considered, with a maximum UDL of 5kN/m^2 and a minimum of 2.5kN/m^2. With respect to horizontal loads, 10% of traffic vertical loads are considered longitudinally. When required, loads on pedestrian parapet were set to 1.5kN/m, vertical or horizontal.
Snow loads have been considered in combinations with just climatic actions as it cannot be combined with traffic loads.
Wind on deck is 0.6kN/m transversally, 0.3kN/m in the longitudinal direction and ±2.3kN/m in the vertical direction. Wind load in main cables has been set as 0.04KN/m and 0.02KN/m in hangers. Wind in towers is 0.57KN/m transversally and 0.19KN/m longitudinally.
Finally, thermal actions include ΔT expansion of 36ºC and contraction of 55ºC. For each situation, the unfavourable structural element (timber or steel) should have the extreme temperature, ΔT N,exp or ΔT N,con, and the other element should have a reduction ΔT=15ºC in relation to the extreme temperature.

https://doi.org/10.52202/069179-0518

4.3 FE MODEL

4.3.1 MODEL DESCRIPTION

A three-dimensional finite element model (FEM) was created to carry out the global analysis of the suspension bridge, consisting of frame elements modelling the main structural members and link elements modelling the connections between them, also considering the frame section offsets.

The global analysis allows the calculation of the whole bridge for determining the joint displacements and the internal forces at the different elements. This model was created and calculated considering the construction phases and two specific dates in the bridge life – at traffic opening (short term situation) and at infinite time (long term situation).

Deck truss chords, diagonals, transversal beams and bracings have been modelled using frame elements, placed at the centroid of the real element. These frame elements are interconnected at nodes by link elements, modelling frame section offsets and the stiffness of the connections between timber elements (Kser).

Piers have been modelled using frame elements and cables have been modelled using frame elements with no flexure stiffness.

Figure 13: *View of the FE model*

Two different groups of support restraints have been defined in the model:

1) End cables and timber towers rest onto concrete anchorage blocks and concrete piers, respectively, though simply supported joint restraints (rigid).

2) Timber deck rest vertically and transversally onto all the timber towers, while it is longitudinally supported just onto the central timber towers. All these supports are modelled considering the stiffness Kser of the connections (flexible).

4.3.2 ANALYSIS METHODOLOGY

An analysis which captures the cable behaviour is crucial when evaluating a suspension bridge.

P-Delta effect is a very important contributor to the stiffness of suspension bridges, as the lateral stiffness of cables is due almost entirely to tension since they are very flexible when unstressed.

A non-linear analysis which considers P-Delta effect plus large-displacements has been set.

In addition, the erection sequence is also fundamental in this kind of structures, as the operations carried out at each stage affect the shape of the cable, and therefore, the distribution of axial forces.

A stage construction analysis is carried out to evaluate the effects of the permanent loads by considering the erection sequence. The following analyses, which consider the effects of the different combination of variable loads, start from the results of this initial analysis.

Two different stage construction analysis are set, depending on the limit state which is evaluated (SLS/ULS).

In accordance with Premissedokument, as the distribution of member forces and moments is affected by the stiffness distribution in the structure, two different stiffness must be considered when modelling the timber elements. This leads to two design situation (short-term and long-term), where the elasticity modulus (E), the shear modulus (G) and the slip modulus (K_{ser}) are divided by a factor 3 when evaluating the long-term situation.

4.4 RESULTS

4.4.1 SLS VERIFICATIONS

In accordance with Eurocode 5, deflections should be limited under characteristic traffic loads to L/200 = 150mm. The maximum vertical sag occurs at midspan of every span for the different loading conditions considered. Maximum vertical deflection is 124mm, under the L/200 limit.

The main results of the modal analysis carried show that the 1st relevant lateral mode is 2.34 Hz and the 1st relevant vertical mode is 3.48 Hz. It is checked that, in accordance with the frequency range classification given by SETRA, the footbridge has a low risk of resonance for standard loading situations, both for vertical/longitudinal vibrations and for transverse horizontal vibrations.

Range 1: maximum risk of resonance.
Range 2: medium risk of resonance.
Range 3: low risk of resonance for standard loading situations.
Range 4: negligible risk of resonance.
Table 2.3 defines the frequency ranges for vertical vibrations and for longitudinal horizontal vibrations. Table 2.4 concerns transverse horizontal vibrations.

Table 2.3: Frequency ranges (Hz) of the vertical and longitudinal vibrations

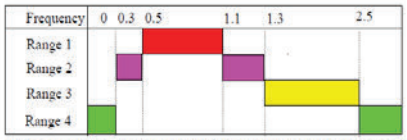

Table 2.4: Frequency ranges (Hz) of the transverse horizontal vibrations

Figure 14: *Frequency ranges given by SETRA*

4.4.2 ULS VERIFICATIONS

The tension in the cables varies during the life of the structure due to the long-term timber effect and to the temperature variation. The maximum values calculated are 270 kN for the main cables, 20 kN for the hangers and 100KN for the vertical truss bracing.

https://doi.org/10.52202/069179-0518

The timber sections of the bridge deck and towers and the connections between the different timber frames have been post-processed in order to check its capacity.
As expected, there is compression at top chord and tension at the bottom chord under vertical loads. In order to make the top and bottom chord profiles more effective and avoid increasing their size, the prestress of the hangers was used to create a precamber of the bridge that produces the opposite effect to the chords than the expected under normal loading condition (top chord is thus pre-tensioned and the bottom chord is pre-compressed). By this, they can resist a greater UDL, similarly to the prestress concrete theory.
All timber connections are designed with steel plates and bolts. They have been evaluated separately in order to optimize the number of bolts and the steel plates.

5 CONCLUSIONS

The design of Neby pedestrian bridge has been undertaken considering that it is a social project with a limited budget that is being built by local people. This makes material optimization more important than the duration of the construction period.
Timber quantities have been optimized by using the precamber of the truss to compress the bottom chord and tense the top chord, so they become more effective under normal loading condition.
An optimization of the connections has been considered by evaluating any connection separately, so the utilization is close to 1.
It has been decided to use local resources and suppliers, as well as local people to build the bridge with technology available in the area.
The use of wood as the main building material of the bridge, enhance the local industry and contributes to an environmental benefit.
Thus, it can be said that the Neby Bru project generates a clear social commitment, promoting sustainability from three different points of view: economic, environmental, and social.

ACKNOWLEDGEMENT

The authors would like to acknowledge the Municipality of Tynset and specially the contractor Ola Grønn-Hagen, chief engineer in Nordøstkonsult AS, for being collaborative and showing interest and skills during the detail design of the bridge.
Specialist advice on the tension elements design has been provided by Pfeifer Group.

REFERENCES

[1] Eurocodes and Norwegian National Annexes to EN 1990, EN 1991, EN 1992, EN 1993, EN 1995, EN 1997 and EN 1998.
[2] SÉTRA 2006. Technical guide Footbridges. Assessment of vibrational behaviour of footbridges under pedestrian loading. CEREMA, France 2006.
[3] HIVOSS – Human Induced Vibration of Steel Structures – Design of footbridges – Guideline.
[4] HIVOSS – Human Induced Vibration of Steel Structures – Design of footbridges – Background document.
[5] European Technical Approval ETA-12/0062: SFS self-tapping screws WR.
[6] European Technical Approval ETA-12/0114: SPAX self-tapping screw.

World Conference on Timber Engineering Oslo 2023

SKYTEBANEN BRIDGE – A TIMBER TRUSS BRIDGE WITH AN INTERMEDIATE SUSPENDED CONCRETE DECK

Alfred Skartveit[1], Kristian Mæland Rasmussen[2], Kristian B. Dahl[3]

ABSTRACT: Skytebanen bridge is a timber truss bridge built for the Norwegian Public Roads Administration in 2019. It has a single span length of 40.0 m and a width of 5.0 m with one notional traffic lane. It is constructed with two dual pitch timber frames, with a concrete deck between. The timber frames are mounted in an asymmetrical manner which gives an irregular aesthetical expression. The timber frames have a total height of 10.8 m. The bridge combines timber in its primary load carrying system with concrete deck and steel floor beams. In this paper some aspects of special interest from the design perspective are highlighted.

KEYWORDS: Timber truss bridge, Concrete deck, Stainless steel, Dowel type joints, Aesthetics, Norway

1 INTRODUCTION

This paper gives is a brief description of the Skytebanen bridge. Furthermore, it addresses some topics that can be of special interest for designers and architects working with timber bridges.

Figure 1: *Skytebanen bridge. Photo: Jan Inge Larsen*

2 STRUCTURAL CONCEPT

2.1 BEHIND THE DESIGN

The bridge is crossing highway E6 in Grane municipality, just south of the polar circle, in the northern part of Norway. Grane has a considerable wooden industry, and the nearest producer of wooden trusses is located just a few kilometres from the bridge site. The surroundings are scenic, located between two national parks. As a future portal to Grane it was a strong desire for a wooden bridge, and the choice of a truss bridge was partly because of the link to the local industry, and partly because it offered some interesting architectural opportunities.

Figure 2: *The bridge seen from the east side. Photo: Jan Inge Larsen*

2.2 ARCHITECTURAL EXPRESSION

The architectural design of the bridge was done by Karen Hatleskog Zeiner, Multiconsult, who described the idea behind as following:

"The design is a classic truss bridge with a twist. The trusses on each side of the bridge are mirrored, which creates a dynamic appearance, that changes depending on the point of view. The shape of the bridge reflects the surrounding mountains.

The lighting plays an important role, especially in the polar dark period, which lasts from November to February. The lighting emphasises the truss construction, and makes the bridge visible from afar, creating a landmark on the E6."

[1] Alfred Skartveit, Multiconsult Norge AS, Norway, alfred.skartveit@multiconsult.no
[2] Kristian Mæland Rasmussen, Multiconsult Norge AS, Norway, kristian.m.rasmussen@multiconsult.no
[3] Kristian B. Dahl, Multiconsult Norge AS, Norway, kristian.dahl@multiconsult.no

https://doi.org/10.52202/069179-0519

Figure 3: *Skytebanen bridge by night. Photo: Jan Inge Larsen*

To give the construction a simple aesthetical expression, it was emphasised that the underside of the bridge should look as smooth as possible, with no visible beams underneath.

2.3 TECHNICAL PREMISES

2.3.1 General regulations

All relevant Eurocodes as well as directions from the Norwegian Public Roads Administration (NPRA) valid in 2016 was applied in the bridge design.

2.3.2 General design - common solutions

The bridge is founded on drilled steel-pipe-piles supporting the concrete abutments. Horizontal forces are handled by friction-plates at the bottom of the abutments.

Figure 4: *Overview of the complete bridge*

The superstructure is a timber through truss with the deck located at the level of the bottom chord. The static system is based on a simple statically determinate system which is easy to check by simple means. However, some modifications are made to the system, like two pinned bearings, and a partly fixed bridge deck, resulting in a somewhat more complex system. Nevertheless, the horizontal stiffness of the abutments is very low, implying that the system is acting mainly as a simply supported truss.

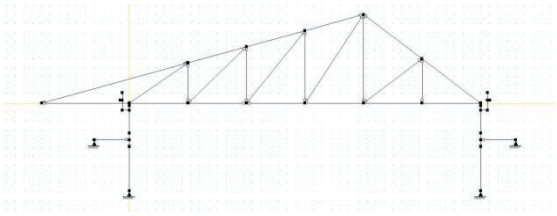

Figure 5: *Basic static system*

Stability of the upper chord against wind and buckling is mainly provided by a stiff connection between the floor beams and the vertical posts. The bridge is also provided with a top strut to transfer wind loads between the trusses, in addition to two upper lateral bracings with mainly aesthetical purposes. All truss members are made of homogenous glulam GL30h [1] to ensure that the dowel based connections have sufficient strength. The truss joints are mainly based on slotted in steel plates with dowels, a method frequently used for timber bridges in Norway, with detailed design rules given in [2]. All glulam parts are treated with copper preservatives in addition to creosote. All horizontal or sloped surfaces are protected against rain with zink fittings.

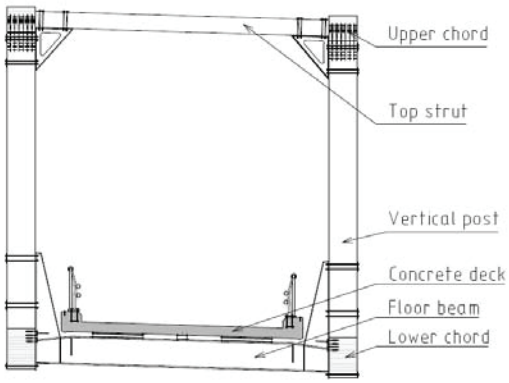

Figure 6: *Cross section of the bridge*

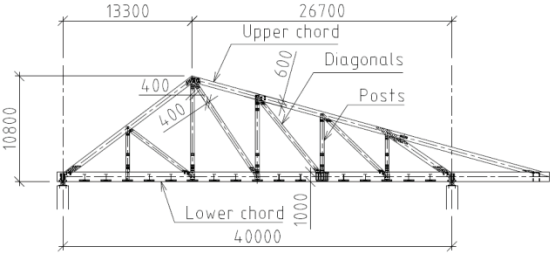

Figure 7: *Side elevation of bridge*

2.3.3 Bridge deck material

Most timber bridges in Norway are built with stress-laminated timber decks with waterproof membrane and asphalt. During preliminary design there was a general discussion regarding the durability of stress-laminated timber decks, and the client was concerned that a service

https://doi.org/10.52202/069179-0519

life of 100 years could not be achieved. Hence, it was decided that the bridge should be designed with a reinforced concrete deck.
A concrete deck is a robust solution, being durable and easy to maintain. However, a stress laminated timber deck may be a better solution for many timber truss bridges. In this particular case, the span width between floor beams could have been made larger due to lower self-weight. Hence, floor beams could have been supported at truss joints only, instead of also in-between. Moreover, a timber deck induces less constraining forces due to temperature and moisture fluctuations.
With the prohibition of creosote from 2023 it is expected that Skytebanen is not the last wooden bridge with a concrete deck in Norway.

2.3.4 Suspension of the bridge deck

The typical solution for timber truss bridges in Norway is to arrange the bridge-deck on transverse steel beams suspended below the truss joints in the lower chord, as shown in Figure 8.

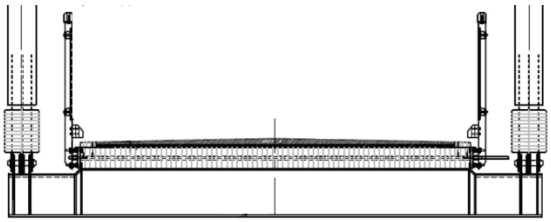

Figure 8: *Typical solution based on stress laminated deck and beams suspended under the lower chord*

For architectural reasons the distance between truss joints was chosen to be 6,67 m. In order to limit the required thickness and hence weight of the concrete deck, it was decided to use floor beams of steel every 2,22 m, i.e. with 2 supports between the truss joints, introduction bending moments in addition to truss forces in the lower chord. As outlined in Ch. 2.2 the floor beams were placed between the lower chords instead of underneath them, as illustrated in Figure 9.

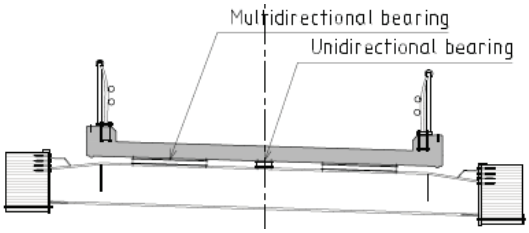

Figure 9: *Beams connected with lag screws to the lower chord*

In retrospect it is acknowledged that there are good reasons for suspending the floor beams underneath the lower chord, as shown on Figure 8, and that this design is easier to build and maintain. If there are architectural reasons to hide floor beams, this might be better solved by glulam panels mounted on the outside of the beam ends.

3 TECHNICAL CHALLENGES

Choosing a concrete deck combined with hidden floor beams led to some challenges that we had to overcome in the design. These challenges will be discussed in the following.

3.1 DIMENSIONAL CHANGES

Compared to concrete, timber has other properties for temperature, creep, shrinkage and moisture fluctuations. Thus, wood and concrete may be challenging materials to combine.
The effect of temperature on the strength and stiffness of wood is described, e.g. by [3] and [5], indicating a reduction of 2-5% for the maximum temperature. Temperatures above 20 °C for many hours will rarely occur at the bridge site. High temperatures will usually reduce the moisture content, and this will counteract the temperature effect. For temperatures below approximately 20 °C the strength and stiffness will be higher than the values used in design. Hence, the effects from temperature on stiffness and strength were ignored. Elastic deformations and creep were handled by the structural analysis and subsequent modifications.

3.1.1 Moisture content

In addition to dimensional changes, moisture fluctuations affect stiffness and strength of wood. The effect on strength and deformations was handled by estimating climate factors according to [2].
The moisture content of wood is highly dependent on the relative humidity in the environment, and not so much on the temperature [3], [4]. Based on conclusions in [6] an equilibrium moisture content of 12,5 % was assumed. To our knowledge there is no recognized method to determine the moisture fluctuations in massive wood constructions. Based on [6], [7] and [8] a maximum variation of ± 8 % was assumed, which resulted in a total free elongation of ± 16 mm for the lower chord in the length direction of the bridge.
Dimensional changes perpendicular to grain are much larger than in the longitudinal direction. Based on [7] and [8] the free dimensional change of the lower chord was calculated to ± 8 mm vertically. This affected design of the large joints in the lower chord, as further described in chapter 3.3.

3.1.2 Shrinkage in concrete

The total free shrinkage strain in the deck was, based on [9] and 80 % RH, calculated to be - 9 mm (i.e. contraction).

3.1.3 Temperature

Temperature expansion was estimated according to [8]. The free thermal expansion of the lower chord was calculated to be + 5 mm and - 8 mm in the length direction of the bridge. The thermal expansion of the concrete deck was calculated to be + 8 mm and -17 mm.

https://doi.org/10.52202/069179-0519

3.1.4 Combination of strains due to temperature and moisture

How effects from temperature and moisture expansion should be combined are not clearly described in the Eurocodes. It was assumed that the highest temperature will occur simultaneously with the lowest moisture content. This is conservative for the connection between deck and lower chord, because it gives the highest difference in movement between concrete deck and lower chord. For the design of the lower chord this will not be conservative, as the bridge is fixed at both bearings. However, temperature effects will give small constraint forces due to flexible abutments.

Table 1: *Comparison of different combinations of temperature and moisture content, and effect on chord elongation*

Load combination	Elongation (mm)
Lower chord: Lowest temperature occurring simultaneously with the highest moisture content.	8
Lower chord: Lowest temperature occurring simultaneously with the lowest moisture content.	-24
Bridge deck: Lowest temperature occurring simultaneously with maximum shrinkage.	-26

The assumption that high temperature/low moisture content and low temperature/high moisture content will occur simultaneously was questioned by the third party controller. Probably the most accurate assumption is somewhere in between. However, the conclusion is, regardless of how this is treated, that the structural integrity is sufficient.

3.2 CONNECTION DECK – FLOOR BEAMS

As described in chapter 3.1 the deformations in deck and lower chord are quite different. Without any measures introduced, this would have resulted in significant constraining forces. Based on discussions with NPRA it was concluded to install bearings between deck and floor beams, except for the seven beams at the centre of the main span, see Figure 9 and Figure 10. It is admitted that this solution is rather costly, and also introduces some challenges due to maintenance of the bridge.

Figure 10: *Bearings visible in the formwork shell. Photo: Viggo Jakobsen, Consto Nord AS*

3.3 CONNECTION FLOOR BEAMS - TRUSS

The connection between floor beams and the lower chord was designed with laterally loaded lag screws. Since the load is applied eccentrically it was also installed bolts in the bottom of the beam to reduce the action of torsional moments on the lower chord. Since the distance between the lag screw group and the lower bolts where quite big, the lower bolts were placed in vertically oversized holes to enable the wood to expand and contract due to moisture content, as outlined in Ch. 3.1.1.

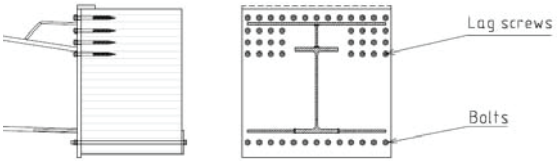

Figure 11: *Detail of connection floor beam to lower truss*

To ensure horizontal stability of the truss against wind and buckling a stiff bracket between each floor beam and vertical post was arranged. The bracket was designed to transfer bending moments only. Normal forces were handled by the dowel based connections in the truss, see Figure 6. Movements of the wood were enabled with oversized bolt holes also here.

3.4 CORROSION

It was decided to use acid proof stainless steel for all steel structures, instead of steel with a duplex coating consisting of hot-dip galvanizing and powder coating.

The background for the material choices is the required service life of 100 years, with low need for maintenance. Moreover, the design of the detail with the large steel-plate connected to the lower chord of the timber truss has some disadvantages regarding maintenance of a coating system:

- The plate has a large surface that is not available for inspection and maintenance
- Cracking of wood due to drying, in combination with rain and wind, may cause water to enter

https://doi.org/10.52202/069179-0519

behind the steel plate. The coated plate may then be exposed to moisture, which over time will increase the corrosivity and the risk of steel degradation

- The copper preservatives used to protect the wood are corrosive to steel if the coating is damaged or degraded over time

Figure 12: *Floor beams connected to lower chord. Photo: Viggo Jakobsen, Consto Nord AS*

4 CONSTRUCTION

The bridge was built for the NPRA, by Consto Nord AS. Glulam and steel constructions were delivered by Moelven Limtre AS. The bridge parts were produced in factory and the trusses assembled on site, before each truss and the transverse beams were erected by crane. The concrete deck was casted in-situ after erection of the trusses.

Figure 13: *Trusses after erection. Photo: Viggo Jakobsen, Consto Nord AS*

5 EXAMINATION AFTER TIMBER TRUSS BRIDGE COLLAPSES

Two major timber truss bridges in Norway have collapsed in recent years, Perkolo (2016) and Tretten (2022). The paper "Design flaws on Norwegian Timber Bridges" [15] summarizes some important findings and conclusions from the investigations after the collapse of Perkolo bridge. After the collapse of Tretten bridge, the NPRA have examined 14 timber truss bridges, among them Skytebanen. For Skytebanen bridge the examination concluded that there were some deviations/uncertainties in the design report, especially related to the handling of temperature and moisture variations. Moreover, it was pointed out some uncertainties regarding the rotational stiffness of the floor beams. The choices of climate class and strength modification factors were however deemed conservative. It was concluded that the bridge safety was satisfactory without any reinforcements or restrictions, and Skytebanen bridge is now, as one of the first of the investigated bridges, reopened for traffic [14].

6 CONCLUSIONS

It is concluded that using a concrete deck for timber truss bridges works well. It can also be noted that placing the floor beams between the lower chords, instead of underneath, is fully possible.

After the design of Skytebanen bridge was started, Norway has experienced two collapses of timber through truss bridges. Regardless of the reasons, both cases have reminded us that such bridges often are fracture-critical, and thus vulnerable to unforeseen actions, deficiencies and deviations during design and construction. On this background it is concluded that for these bridges a simple and clear static system which is easy to verify, build and maintain should be preferred.

Figure 14: *Skytebanen bridge at dawn. Photo: Jan Inge Larsen*

ACKNOWLEDGEMENT

The authors would like to thank colleagues in Multiconsult and all collaborating parties for their great efforts and contributions to Skytebanen bridge, a successful project and beautiful new landmark for the region. In particular thanks go to the NPRA for emphasizing architecture and aesthetics, and for the desire to try new design concepts and material combinations. Special thanks go to Moelven Limtre AS and Consto Nord AS for good collaboration during the execution phase.

REFERENCES

[1] Norwegian standard NS-EN 14080:2013 Timber structures. Glued laminated timber and glued solid timber, requirements

[2] Norwegian standard NS-EN 1995-1-1:2004+A1:2008+NA:2010 Eurocode 5: Design of timber structures - Part 1-1: General common rules and rules for buildings

[3] Ritter, Michael A.: Timber Bridges: Design, Construction, Inspection and Maintenance. U.S.

https://doi.org/10.52202/069179-0519

Department of Agriculture, Forest Service. Washington DC, USA 1990
[4] Norsk Treteknisk Institutt, Treteknisk Håndbok (ISBN 978-82-7120-201), 2009
[5] Aune, Petter: Trekonstruksjoner (ISBN 82-519-0950-3), pages 50-51, Tapir Forlag, 1992
[6] Dyken, Tormod.: Timber Bridges - Report no. 422 Norwegian Public Roads Administration, Department of Traffic Safety, Environment and Technology, 2017.
[7] Norske Limtreprodusenters Forening: Limtreboka (ISBN: 978-82-7129-324-6). 2015
[8] Statens Vegvesen, N400 Bruprosjektering, ISBN: 978-82-7207-680-0, 2015
[9] Norwegian standard NS-EN 1992-1-1:2004+A1:2014+NA2008 Eurocode 2 – Design of concrete structures – Part 1-1: General rules and rules for buildings
[10] Norwegian standard NS-EN_1990:2002+NA:2008 Eurocode – Basis of structural design
[11] Norwegian standard NS-EN 1991-2:2003+NA:2010 Eurocode 1: Actions on structures – Part 2: Traffic loads on bridges
[12] Norwegian standard NS-EN 1995-2:2004+NA:2010 Eurocode 5: Design of timber structures - Part 2: Bridges.
[13] Statens havarikommisjon: Informasjonsskriv nr. 2: Foreløpige undersøkelser av brukollapsen ved Tretten, 15.August 2022
[14] Dr. Ing A. Aas-Jacobsen: Fagverksbruer i tre 18-2924 – Skytebanen bru, Kontroll-/klassifiseringsrapport (2022)
[15] Hauke Burkart and Tormod Dyken. Design flaws on Norwegian Timber Bridges. *Proceedings ICTB 2017, 3rd International Conference on Timber Bridges*, pages 380-386, 2017

World Conference on Timber Engineering Oslo 2023

METHODOLOGY OF REHABILITATION OF TIMBER STRUCTURES IN HISTORIC BUILDINGS

Amorim Faria, José[1]

ABSTRACT: The objective of this paper is to present a methodology of the design process for the rehabilitation of Timber structures in Historic buildings. The methodology is based on the author's experience and on recognized standard knowledge, available on heritage documents and standards and expert's Principles of Intervention such as those defined in the 1964 Venice Charter. A real case study related with a roof Timber structure existing in the University of Coimbra, and originally built in the 16th century is used to illustrate the methodology. It is concluded that this type of interventions, on existing structures with a very high patrimonial interest, highly benefits from mixing full restoration principles with innovative tools and in situ modern construction processes and methodologies.

KEYWORDS: Design methodology; Rehabilitation of timber structures; Historic Constructions; Case study

1 INTRODUCTION

Rehabilitating heritage buildings for new uses, or modernizing an existing building with heritage value, introducing modern features, improving its habitability and healthiness and also functional performance in thermal and acoustic terms, is a very difficult task, in many cases, and requires a careful approach in the design phase in order to be able to meet the objectives of the program in terms of the quality of the intervention, respecting the historical memory of the buildings.

This article is mainly based on the experience of the author as a design engineer of wooden structures, and as Consultant of Site Supervision teams of rehabilitation works of ancient buildings with patrimonial value, developed on end-of-life buildings and/or with obsolete construction systems and/or very significant constructive anomalies.

It also benefits from the author's teaching experience in the rehabilitation of timber structures, exercised mainly in the last 20 years at the Faculty of Engineering but also in the Faculty of Architecture in Porto in several postgraduate courses attended by Architects and Engineers with experience in this activity.

In terms of bibliography, it is mainly based on books in which the author collaborated [6] and [7] and reference bibliography that the author regularly uses such as [1] and [2], as well as several articles previously published by the author on similar subjects, such us, [10].

Part of the inspiration of the methodology can also be attributed to Italian standard, UNI 11119, identified in bibliographic references as [3], and other more recent standards and recommendations such as [4] and [5], as well as in the fundamental updated documents of principles of restoration and rehabilitation published by ICOMOS, [8] and [9].

This paper aims to point out that historic buildings need to be used so that they last and are appreciated by the community and that this means that they should be updated technologically on a permanent basis.

Therefore, historic timber structures must be restored but, at the same time, the building needs to be updated and this implies a rehabilitation methodology done in parallel with the restoration process of the historic structures.

The proposed approach is multidisciplinary and integrated, although it gives special emphasis to architecture in all its components but especially in the 'construction' aspect and to foundations and structures, while still considering the issues associated with infrastructure (water supply, sanitation, rainwater, electrical installations, mechanical installations and Data networks), fire safety, thermal and acoustic comfort and general Health and Habitability, mainly measured by sustainability indicators of the projected intervention.

In the context of this Conference, the case presented concerns only the issues relating to wooden structures and refers to a case that is relatively unintrusive and almost totally 'non-destructive', on preexistence and considering the enormous size of the case used as an example, only addressing the rehabilitation of a small part of the current roof area and the existing space between the ceiling of the last floor and the roof in which the space is intended to be occupied with new uses.

[1] José Manuel Amorim Faria, Construct/Gequaltec, Faculty of Engineering of the University of Porto, Porto, Portugal, jmfaria@fe.up.pt

https://doi.org/10.52202/069179-0520

2 GENERAL DESIGN PROCESSES IN PATRIMONIAL BUILDINGS - MAIN PHASES

2.1 MAIN SPECIFICITIES OF A REHABILITATION PROJECT

The existing building (or built set) design processes are quite different from the processes adopted for new construction, since, in existing buildings and especially when the interventions to be carried out are not intrusive, the project is carried out on an existing object and at least this one must be previously well characterized and analyzed in all its components.

In this context, there are steps prior to the development of the project that must be carried out with great care and adequate development.

Thus, the main phases of a rehabilitation project are presented below, highlighting in parallel the specificities associated with the need to design on something existing, hereinafter referred to in this article as "pre-existence" as is usual in the specific language of restoration and rehabilitation of buildings.

2.2 MAIN PHASES OF THE REHABILITATION DESIGN PROCESS - A BRIEF DESCRIPTION

2.2.1 Preliminary survey

This initial phase includes:

- architectural, structural and geometric survey;

- survey of existing building systems (evaluation and complete characterization including foundations, structure, non-structural interior partitions, walls, roofing, facades, coatings and finishes, water, sanitation, electrical and other installations);

- survey of links to service providers in terms of water, sanitation, electricity, gas, rainwater and others, that may exist;

- geotechnical characterization of foundation and surrounding soils, including assessment of groundwater levels and their variation throughout the year.

2.2.2 Inspection and diagnosis

The inspection and diagnosis phase represents an essential preliminary work of the rehabilitation project process. It includes, inter alia, the performance of the following tasks:

- assessment of existing anomalies in existing construction and of their causes;

- characterization of the most relevant materials and components, namely the composition of masonry, physical and mechanical characteristics of stones and woods, characterization of the main coatings and finishes to be maintained, among others;

- definition of generic intervention suggestions to eliminate the causes of anomalies.

2.2.3 Propose an adequate program

This is one of the fundamental phases of the rehabilitation project process, since, often, it is incomplete or sometimes completely misadjusted to the pre-existence which may lead to completely failed rehabilitation works in terms of objectives.

In the restoration processes with maintenance of previous uses this is a less important problem, since it treats the existing building as a "museological object" of itself which facilitates the initial phase of project necessarily more creative and potentially intrusive compared to the existing one (this is the case of the example presented in this article).

In any case, it should be emphasized at the outset that doing a restoration with maintenance of previous use is often a strategic mistake, because it can miss "an opportunity" to rejuvenate and reorient the building to new uses compatible with pre-existence, more or less intrusive according to the needs and /or options of the designers in charge of the project and then with very positive implications in terms of cost-benefit of the future operation and maintenance of the building.

Generally speaking, this phase includes:

- the definition of a future use compatible with the existing object;

- the definition of a methodology of restoration or rehabilitation, more or less intrusive and appropriate to the future use, previously defined, and that allows to find a good cost-benefit ratio for the intervention.

2.2.4 Execution Design phase (D)

This article omits all project previous phases, prior to the “final execution design project” phase, for reasons of simplification of the approach.

Once the fundamental licensing issues associated with the need not to comply with the Regulations applicable for new works have been resolved, the design team starts the implementation project phase working on all documents and studies previously produced in the previous phases, as well as the knowledge of the pre-existence to be rehabilitated/restored, resulting from site visits and all preliminary studies.

This is the main specificity of any rehabilitation project. To detail, without respecting pre-existence, is to perform useless work. Designing new work on an existing building, without solving existing problems, leads to the new work being born with defects that will later be much more difficult to solve.

3 EXECUTION DESIGN PHASE – A METHODOLOGICAL PROPOSAL

3.1 INTRODUCTION

The methodology presented in this article is based mainly on this reality: to build a new work from scratch is mainly based on a well-thought-out and detailed project that can translate what the designer team

https://doi.org/10.52202/069179-0520

imagined and conceived; rehabilitating or restoring an existing building set presupposes "knowing" well the existing object and conceiving "on" something that already exists and that has already been designed and built by others and that has already been used, has undergone changes in construction systems and spaces, volumetric additions, changes in use, among others, i.e. a whole panoply of events that "strongly condition" the process of the restoration/rehabilitation project to prepare for the site.

Table 1 illustrates in a schematic way the methodological proposal presented in this article. In general terms, this proposal is based on the definition of ordered steps, defining the action of the Architects and Engineers and also on their interaction, aiming to produce the best job possible.

This methodology has a fundamental action at the beginning of the process (steps D1, D2, D3 and D4) and also it cannot fail to solve all the challenges in steps D5 and D6 with all the rigor, see Table 1.

Steps D5 to D8 are similar to common projects to be built on new “clean” plots, without pre-existences to be saved.

Table 1: *Design methodology*

Phase of design	Description
D1 (Arch., Fire Safety engineer)	Definition access building; Definition of vertical and horizontal communications
D2 (Architect ,Networks engineers)	Define complete paths of infrastructure networks
D3 (Architect)	Base design: Geometric tuning; Indoor/outdoor connection;
D4 (Structural engineer)	Resolve ventilation issues; Eliminate moisture problems ; Identify and solve existing problems 1 by 1;
D5 (Networks engineers)	Detailing; respect paths defined in phases D1, D2, D3
D6 (Structural engineer)	Detailing – Finish execution design; respect what has been previously established
D7 (Architect)	Detailing – Finish execution design; Finishes/Partitions
D8 (Other engineers)	Detailing – work close to architects to specify in complete match with them

3.2 VERTICAL AND HORIZONTAL ACCESS AND COMMUNICATIONS (D1)

In a process of rehabilitation of buildings with patrimonial value, with structure formed by exterior walls in stone or wood masonry and walls, floors, stairs and roofs in wooden structure, for new modern uses and fulfilling as much as possible current performance requirements, the first fundamental action of the project is associated with the complete and in-depth study of all the logic of access and movement of people in the areas of collective use, as well as in the areas of private use.

Nothing should advance in the execution project before solving the puzzle that often this issue represents, considering the need to be as intrusive as possible in pre-existence. Often this process is very conditioned and aggravated by the need to maintain larger value zones within the spaces, which can often greatly condition the new solutions to be designed, such as an existing chapel, although small, in the case study (problem not presented and discussed in detail in the article).

It will not often be possible to comply with the applicable regulations for new work and decisions will have to be made! Also often, with regard to the aspects of thermal and acoustic comfort and the general use of the building, difficult decisions should be made, especially with regard to the slope of stairs, the possibility or not of installing an elevator for vertical communications and the possible incompatibility between the maintenance of walls, doors and other building elements and the "will" to improve the thermal and acoustic performance of the building, among others.

In this first stage of the process, fire safety is of particular importance, since in general it is impossible to comply with regulatory requirements for new work and it will be necessary to agree with the licensing authorities the mitigating measures to be taken to improve existing behaviour, situations that often strongly condition the architectural options to be taken.

3.3 SCHEMATIC PATHS OF NETWORKS (D2)

Today, modern buildings include water supply infrastructure networks, other networks, such as sanitation, data, electricity and gas, mechanical and natural ventilation and air conditioning, that occupy large areas and volumes of the construction, and strongly condition the freedom of architectural design.
This problem is substantially aggravated in an existing building set, due to its complete absence in the original construction. It will therefore be necessary to integrate into existing buildings all the new networks needed for their operation in a modern context, using "paths" perhaps already existing or to be created, in a way compatible with the new use to be given to spaces and their own new configuration, trying to affect as little as possible the non-technical uses to be given to the sites and, at the same time, minimizing the occupation of areas and paths of technical infrastructure.
It is generally a very difficult exercise to solve, this should therefore be dealt with, as a priority, before moving forward with everything else.

https://doi.org/10.52202/069179-0520

3.4 GEOMETRICAL TUNING (D3)

The existing old buildings with heritage value, because of having been built using techniques and equipment less sophisticated than those currently available, have many "defects" of origin that translate into very inclined stairs, uncomfortable steps, narrow corridors, non-orthogonal walls to each other, walls "out of plumb", among others. It will therefore be necessary to consider all these problems in the Architecture design, thinking about "places of closing the spaces / volumes" and solutions of eventual disguise of existing defects such as false ceilings, steps, fillers or simply, assume these imperfections by conceiving spaces and solutions where they are properly "integrated" or assuming, quite simply, their geometric specificities i.e. their original geometric imperfections that occurred throughout the use of the building.

3.5 FUNDAMENTALS OF STRUCTURAL DESIGN (D4)

After stabilizing the geometry of the internal and external spaces, it is time for the structural engineer to assume the main role, evaluating and resolving all the situations resulting from the previous steps, namely:

- eliminating existing structural anomalies;
- introducing new structural systems compatible with the new uses, downgrading the service levels of existing structures, when they can not fulfill the new performances needed, always respecting the architectural design (done in cooperation);
- improving the "habitability" of environments with regard to the health of structures, in particular wooden ones (naturally ventilate spaces and eliminate all causes of moisture);
- solving problems caused by new infrastructure network paths;
- reinforcing/rehabilitating structures for possible new uses;
- solving problems of previous malfunction (vibrations, deformations, defects of original design, defects resulting from previous works poorly conceived or executed.).

The project design process should not move forward without, at least at design level, all structural problems being identified and generally addressed at the level of the principles and methodologies of resolution and the dimensions and location of existing and new structural elements.

3.6 CLOSURE OF THE DESIGN PROCESS (D5 TO D8)

Now, all designers can advance in parallel in the implementation project, respecting everything that was previously agreed.

In the border areas between engineering specialties and these with architecture everything should be properly detailed and compatible.

It should be noted that, at this stage of the process, the project methodology is totally analogous to the design of a new work done in a plot without pre-existence...

4 SPECIFIC RECOMMENDATIONS FOR TIMBER STRUCTURES

4.1 GENERAL RULES

Timber structures have their own specificities that justify the consideration of an autonomous subgroup in terms of rehabilitation. These specificities are essentially the result of the fact that the raw material of which they are made is of trees origin, which gives them a degradation process very different from that foreseen for structures executed based on materials of mineral origin. The main causes of wood degradation in structures are as follows:

- firstly, biological degradation by the effect of fungi, insects, mollusks and crustaceans (the latter in a marine environment);
- secondly, aging by effect of the hygrometric term action (wood is a material with anisotropic mechanical behavior and varies its dimensions and physical, chemical and mechanical properties depending on its water content, in turn variable with the absolute humidity of the environment that surrounds it);
- inadequate structural use due to inadequate design of the elements/components of each substructure, and also of their supports and connections.

It should be noted that humidity is not in itself a fact of degradation of wooden structures. The careless permanence of the structure in humid environments and in poor ventilation provides ideal living conditions to biological agents of wood degradation, which are a direct cause of wood degradation in these contexts. The following are a set of general concrete rules to be applied in the restoration of wooden structures:

- always check other structural systems (foundations, walls, bracings, ...) - stability and level of degradation;
- avoid disassembling the structural elements in wood: the future assembly will place these elements in different states of tension as a result of the new connections to be made;
- use strong solutions: use higher safety coefficients than in current “new” projects;
- make periodic inspections of structures (control the following factors: temperature, humidity, air renewal rate, wood water content, deformations and defects of structural elements, ...);
- improve the service conditions of wood parts: avoid connections with steel or glass if they do not allow the wood to be ventilated or to favor condensations;
- improve the general and localized ventilation of the spaces (air renewal is essential for wood);
- carry out periodic cleaning of the structure;

https://doi.org/10.52202/069179-0520

- eliminate all external causes of degradation (especially those arising from the surroundings of the building - walls and roofs);
- whenever possible, leave after the restoration intervention, the possibility of all structures being examined from the nearby physical and/or visual point of view;
- always place the wooden elements in the same class of service in environmental terms;
- ensure proper ventilation of the supports by avoiding direct contact of wood in these places, as far as possible, with other materials which may retain moisture or prevent wood from "breathing";
- avoid hiding the structural elements in wood with finishing materials mainly ceilings and false ceilings – the degradation will not be detectable;
- restore the building from the roof to the foundation, if it has not foundation problems– in this case, first solve the foundation problems;
- always ensure the stability and low deformability of the supporting elements before intervening in the wooden structures supported by them;
- always initially restore the most important elements – more robust and/or more degraded.

5 THE CASE OF TIMBER ROOFS

In a concrete case of rehabilitation of a wooden roof of a Historic Building four specific situations can occur:

- repair and point replacement of degraded elements using old techniques;
- repair and point replacement of degraded elements using old techniques and modern connecting solutions;
- integral replacement of the structure using old woods, modern materials and connecting techniques and architectural designs similar to the old ones;
- integral replacement of the structure by modern design solutions, wood elements, materials and connecting techniques to be used.

For historic buildings the ideal solution will be that which corresponds to situations a) or b). It is the author's opinion, however, that the ideal solution will preferably be a hybrid of approaches b) and d) as it ensures improved performance, higher economic value and a much higher durability of the rehabilitation intervention. Materials that ensure higher durability should be used as far as possible.

This can be justified by the following. In many cases, the existing timber structures cannot fulfill the “new design demands” without highly intrusive and expensive reinforcements, and it is very common to consider that it is not convenient to reinforce the existing systems and, therefore, solution b) coexists with “new structures” that occupy the same volumes and liberate architects for an eventually more intrusive program, which we may consider as a hybrid situation of approach b) and d). This is the situation presented in this case study, see section 6.

5.1 SUBSTITUTION AND PUNCTUAL REPAIRS USING TRADITIONAL CONNECTIONS

It's the most current situation in historic buildings in a restoration process, when the architectural program does not change significantly the performance demands of the structures. It assumes that the various elements in wood are generally in good condition, allowing the structure of the roof to remain in place with the existing form, before the intervention. The connections between partially replaced parts will be made using traditional solutions, similar to the original ones.

The most serious mistakes made in the past with wooden structures concern the poor ventilation of the structure, especially in the supports, which implies the biological degradation that is also transmitted rapidly to the support of the parts/connection with the masonry walls. In a specific intervention, adequate ventilation and protection against insects, namely termites, of the new elements/systems should be ensured.

5.2 SUBSTITUTION AND PUNCTUAL REPAIRS USING MODERN CONNECTIONS

It is a situation analogous to the one described above, but in which we seek to solve problems of connections using modern methods and techniques. The author thinks this is the most appropriate solution in general. It makes no sense to use nowadays handmade nails, with a relatively high corrosion speed, when it is possible to resort to stainless steel connecting systems, for example, that are much more durable and equally resistant and that also allow the reversibility of the assemblies by unscrewing.

With regard to support prostheses, the solution to be adopted will be influenced by the extension and strength of the eventually existing xylophagous attacks. If there are no major aesthetic limitations, the use of metal prostheses in situations of exclusive degradation of the elements near the supports will generally be more economical in the case of more extensive degradations. There are no universal rules indicating the best solution for each case. All operations involve the removal of roof tiles, and all other secondary elements of the roof, in order to access the structure both below and above, so that the reinforcements and substitutions may be done.

5.3 SUBSTITUTION OF TIMBER ELEMENTS AND SOLUTIONS USING “USED WOODS” AND MODERN CONNECTIONS

In some cases, for architectural or constructive reasons, it is not possible to carry out the restoration work

https://doi.org/10.52202/069179-0520

without dismantling the structure. In these cases, the pieces are carefully dismantled and put back on site following modern connecting techniques and using, when it is possible, used woods of equal or similar species, quality and eventually age.

Elements with degraded parts at the ends can be used to obtain smaller elements that can be used in other works or in other places in this same work. It should be noted that an old wood structural part of a durable species is a structural material of high value and should always be carefully assembled and stored for future use.

For example, a beam of 7 m long with 0.5 m of degraded parts on each side allows to realize a beam of 6m in length in optimal conditions, cutting the degraded tops from both sides. The geometry of the new structure is not necessarily coincident with the original structure and, as far as possible, follow the original design models so that one can maintain the memory of the building.

5.4 INTRODUCTION OF A NEW STRUCTURE MAINTAINING OR NOT THE EXISTING ONE

In many cases, the existing structures are not able to withstand the new performance demands. Still, they have historic value and in general should be kept in place as a memory, without structural function, or eventually fulfilling less demanding structural tasks such as supporting the ceilings of the last floor below (in many cases with very high patrimonial value, with “frescos” or decorated carved timber ceilings).

6 CASE STUDY

6.1 GENERAL DESCRIPTION OF THE BUILDING

The College of Arts is part of the University of Coimbra, founded in 1290. Currently, it is used as Faculty of Architecture. The construction of the College of Arts began in 1568, see Figure 1.

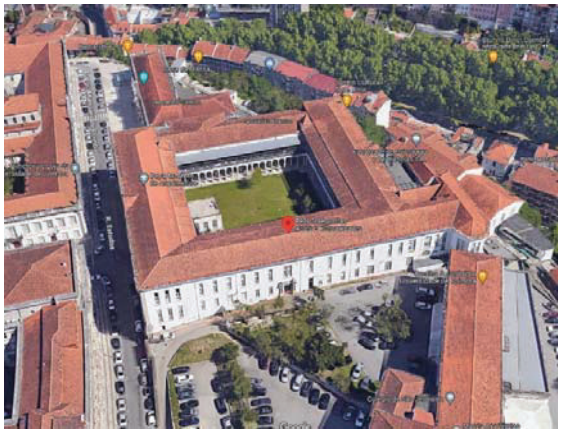

Figure 1: General view of the building

The building has undergone successive changes over time in terms of volumetry and use, highlighting a major reform on the early twentieth century, with the expansion of the construction in height and the use of new materials, such as cast iron columns on the raised floor, for the installation of the University Hospital of Coimbra, operating at this site until 1986.

The building belongs to the designated first University Pole of the University of Coimbra and currently presents a deployment area of about 6600m2.

The College of Arts belongs to the architectural ensemble of the University of Coimbra, which since 2013 has been classified as a World Heritage Site by UNESCO.

6.2 ARCHITECTURAL PROGRAM

The architectural program provides for the rehabilitation, restoration and refurbishment of the building of the College of Arts, of high heritage value and that today is naturally aged and weakened, with many conservation problems of various types.

In addition to the spatial and constructive aspects, the infrastructure sits outdated in view of the multipurpose functions it currently has, namely museum and higher education equipment (faculty of architecture).

In addition to the rehabilitation and conservation work of the existing construction systems to be maintained, the Architecture project provides for the demolition of some additions and annexes that were carried out on the northern outskirts of the building, during the operation as a university hospital.

Figure 2 shows a 3D image of the building after completion of the works that are today still in the design phase and beginning of the demolition works.

Figure 2: *3D view of the designed building at the end of the works*

6.3 FLOORS UNDER THE ROOF

The architectural design foresees that this space will become accessible, with offices, study and meeting

rooms, along the east, south and west parts of the building.

The floor under the roof on the north side is lower than the rest, so it will not be accessible. In this area, it is expected the complete demolition of the plastered ceilings of the floors below, so that the rooms and spaces of those lower floors obtain a double ceiling with the roof structure in sight. This part of the roof will essentially be restored, although improved in performance.

6.4 DESCRIPTION OF THE CURRENT CONSTRUCTIVE SITUATION

The roof analyzed in this article is of the traditional inclined type, with accessible floors under the roof, which are not used, today. The main current structure consists of wooden trusses that support girders and ceramic tiles. The trusses and the external walls support the floor structures that also support the stucco works of the ceiling of the floors below.

Figure 3 presents a roof plan, divided by zones with different constructive constitution.

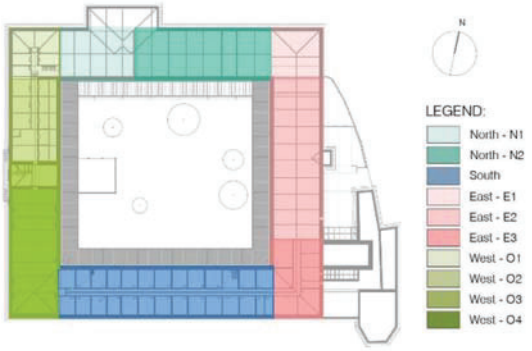

Figure 3: *Roof schematic plan*

This article refers only to the East, West, and South zones, that are all like each other.

6.5 EXISTING WOODEN STRUCTURES AND COATINGS

6.5.1 Exterior coatings

The coating of the roof in the different wings consist of ceramic tiles placed on wooden slats 45x30mm//0.35m and supported on wooden beams 70x110mm//0.50m.

6.5.2 Girders

The coatings of the roof are supported by wooden girders in solid wood, two by slope and one on the ridge, separated from each other around 1.9m to 2.3m approximately, see **Error! Reference source not found.**.

Figure 4: *General view of the roof*

On the top of the external walls in masonry, there are timber components of 100x100mm to 130x150mm in very bad condition, in many cases substituted by mortars or covered by mortars.

6.5.3 Trusses

The trusses are composed of elements in solid wood, overcome spans of approximately 11m and are separated from each other, about 3.5m and 4.3m.

The current truss presents a constitution as shown in figure 5 below. This design is not very common in Portugal and, also for this, has high patrimonial and historic values, although almost all the wooden elements are no longer original, having in general, the oldest, between 100 and 150 years.

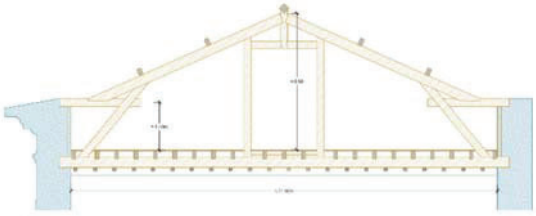

Figure 5: *Current truss*

Occasionally, some of these trusses received reinforcements, the most usual being the additional two timber elements that help to support the legs, see Figure 6.

https://doi.org/10.52202/069179-0520

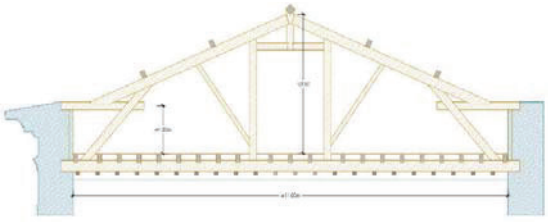

Figure 6: *Casual reinforcements on trusses*

6.5.4 Connections and supports

The connections between the different parts of the trusses are traditional, materialized by carpentry joints and with some metal connectors, see figures 4 and 7.

6.5.5 Floors under the roofs

The current floor is made of solid wood and has approximately 1560m2 along the east, south and west wings of the building, see Figures 4 and 7.

Figure 7: *Floor structure under the roof*

6.6 ANOMALIES IN EXISTING STRUCTURES

6.6.1 General anomalies

At the level of the roof, the coatings are partially fulfilling their function, but there are problems of water tightness, with traces of water and moisture entering the stone masonry walls, especially near the top of the roof.

The floors under the roof have no conditions to be used for any purpose, as they are today.

6.6.2 Structural anomalies

Regarding the trusses, despite the good general condition of most wooden parts, there are several indications of structural problems.

Some trusses have torsions, high deformations, excessive cracking, weakened and inadequate connections, and rot-damaged supports. There are also some reinforcements, carried out in previous apparently loose interventions, which aimed to correct some of those problems, but which were sometimes inadequate.

The girders and the wooden structures that support the floors are in a good state of conservation and have an adequate structural behavior, with malfunction problems in some places.

Most wooden parts do not appear to respect the levels of stress resistance and deformation in service, in accordance with the actual regulations, and it is also stressed that there are some critical situations, with a risk of local collapse, which must be corrected quickly, particularly in the trusses.

6.7 SOLUTION – APPLICATION OF THE INTEGRATED METHODOLOGY

The fundamental principle to follow is to restore the existing structure, applying the principles of restoration and start using it only as a support of ceilings on the lower floor.

Simultaneously, introduce a new wooden structure and coatings and finishes with current modern design fully suited to the new uses, involving the coatings of the roof and the new floors to be executed.

The architectural design is thus completely free to comply with the current, more demanding construction regulations, at the level of walls and infrastructure networks and above all to introduce solutions that allow to meet fire safety requirements and improve thermal and acoustic performance and water and air tightness and natural and artificial ventilation and lighting.

The solutions to be adopted include:

- Maintain the exterior image in ceramic tile and use a sub tile, lining in wood derivatives and waterproofing system with steam-permeable screens; Incorporate zenithal lighting, using skylights and windows in new mansards to be integrated following a geometrical pass compatible with the existing facades view;

-Integrate all new infrastructures (electricity, water, data, ventilation, air conditioning) in the new roof space. Ensure natural ventilation;

- Solve the problem of sanitation (the most difficult), using localized shafts and false ceilings to disguise the corresponding tubes networks.

On the floor below the roof, it is possible to take advantage of a large part of the existing floor structure, which is in good condition, and some current stuccoes (on the lower floor) should be repaired considering the cracking they present.

6.8 SOLUTION – STRUCTURAL INTERVENTION

The option of keeping the current trusses as the main structural element is not feasible because it involves very significant reinforcements that would completely change existing structures and make them loose their current historic authenticity.

The option to introduce new structures, more modern and efficient, keeping existing ones with lighter functions, allows greater protection of the heritage and allows to design a floor with the carrying capacity, comfort, vibration levels and deformation compatible with the new intended use, also avoiding at the same time to transmit the vibrations from the use of the floor to the current trusses, floors and stuccoes and thereby increasing the longevity of these existing structures and construction systems.

7 CONCLUSION

Historic buildings need to be used to increase their durability and economic interest.

The principles of the restoration of existing buildings with patrimonial value must be respected.

It is possible to respect "difficult" and demanding architectural programs following a methodology in which the introduction of modern construction systems and solutions walks in parallel with the restoration processes of the existing construction systems to preserve, occupying the same volumetric space without the two types of solutions imposing themselves on each other.

This is the solution that was chosen for the case presented in this paper in section 6, which means that the approach followed in the case study is a mix of systems b), restoration using modern connections and eventually materials, and system d), introducing completely new structures and materials, using a modern and highly performative design and approach, see section 5 for a more detailed explanation of the two design approaches.

The case under study represents an excellent example where this methodology is being successfully applied.

ACKNOWLEDGEMENT

This work was financially supported by: Base Funding - UIDB/04708/2020 of the CONSTRUCT - *Instituto de I&D em Estruturas e Construções*, funded by national funds through the FCT/MCTES (PIDDAC).

REFERENCES

[1] Arriga, F. ; Peraza, F. ; Esteban, M. ; Bobadilla, I. ; García, F.– Intervención en Estructuras de Madera – AITIM, Madrid, 2002 – ISBN: 84-87381-24-3

[2] Tampone, G. – Il restauro delle strutture di Legno – Hoepli Editore, Milano, 1996 – ISBN 88-203-2273-0

[3] UNI 11119:2004 – Beni Culturali – Manufatti lignei – Strutture portanti degli edifici. Ispezione in situ per la diagnose degli elementi in opera, UNI, Italia

[4] SIA 269-5: Bases pour la maintenance des structures porteuses. Société Suisse des Ingénieurs et des Architectes, Suisse, 2011

[5] EN 17121:2019: Conservation of Cultural Heritage – Historic Timber structures – Guidelines for the onsite assessment of load-bearing timber structures

[6] Peixoto de Freitas, V. et al – Manual de apoio ao Projecto de Edifícios Antigos – Ordem dos Engenheiros, Região Norte, Porto, Portugal, 2012– ISBN: 978-972-99918-7-5

[7] Negrão, J.; Amorim Faria, J.: Projecto de Estruturas de Madeira, Publindústria, Porto, Portugal, 2009 - ISBN: 978-972-8953-36-2

[8] ICOMOS: Principles for the Conservation of Wooden Built Heritage - Adopted by the 19th ICOMOS General Assembly, New Delhi, India, 15 December 2017

[9] ICOMOS: International Charter for the conservation and restoration of monuments and sites (The Venice Charter 1964) – Adopted by ICOMOS in 1965

[10] Amorim Faria, J. – Reabilitação de edifícios para Habitação e Comércio nos Centros Históricos de cidades portuguesas – Proposta metodológica – QIC 2016 – 2º Encontro Nacional sobre Qualidade e Inovação na Construção, 21-24 novembro 2016, LNEC, Lisboa, Portugal

https://doi.org/10.52202/069179-0520

World Conference on Timber Engineering Oslo 2023

WEB-GIS-TOOL: ESTIMATION OF GREENHOUSE GAS SAVINGS DUE TIMBER USE IN THE URBAN BUILT ENVIRONMENT

Caya Zernicke[1], Annette Hafner[1], Andreas Abecker [2], Harro Stolpe [3]

ABSTRACT: The development of German cities, municipalities and urban areas requires a high amount of material and energy. Responding to this requires a commitment to achieving national climate change targets, as they have different options for sustainable development. Especially urban planning can create linkages for climate protection measures through its interdisciplinary field of activity. Further, urban planning has an impact by directly affecting the construction and housing sector, one of the major emitters of greenhouse gas emissions. To support decision-making processes or measures for climate protection in urban areas, the web-GIS system Holzbau-GIS has been developed. This GIS-based web-tool calculates the GHG reduction potentials and temporal carbon storage for new construction and refurbishment with wood. This paper summarizes the method to calculate these potential GHG reductions due to timber use in the urban built environment. Through the intersection of spatial geodata and recent building-specific research data, various conclusions can be drawn within the web-GIS system regarding basic data, new construction, and refurbishment with wood. The paper also shows illustrative examples and their visualization in the web-GIS system. It became apparent that the Holzbau-GIS could serve as part of the digital transformation of municipalities and emphasize the contribution of timber buildings.

KEYWORDS: geographic information system GIS, timber construction, temporal carbon storage, climate protection

1 INTRODUCTION

1.1 GENERAL

Municipal self-governance is one of the essential principles of the political structure of the Federal Republic of Germany. In the increasing variety of multidisciplinary activities, municipal self-government plays a key role today more than ever before. Issues of municipal policy include, especially recently, the protection of the environment and natural resources, budgeting, and privatization. Here, the different spatial, socio-political, structural and geographical conditions will be considered specifically. [1] Consequently, cities, municipalities and urban areas must contribute to achieve the national climate protection targets, as they have various directing options toward a sustainable development. By acting responsibly, they can have a direct impact on regional urban development, especially with the focus on climate mitigation and climate adaptation. The building sector can be a key element of municipal climate protection since buildings usually have a central impact on urban development. They significantly shape the structure of the city by defining its use in terms of working, housing and infrastructure. [2-8]

In the past, the German construction industry has focused primarily on energy efficiency to meet climate protection targets. Now, the focus is shifting increasingly towards the material choice for new construction or refurbishment and, in terms of urban planning, wood as a building material is gaining in significance since. [4] In the future, the use of sustainable renewable materials will play a significant role in this context. [7, 9, 10] Therefore, the carbon footprint of building materials and the additional reduction potentials using life cycle assessments (LCA) move further into the spotlight. The emissions of building materials in production, processing and deconstruction must be considered in terms of their environmental impact, but also regarding the consumption of raw materials, flexibility, service life and recyclability, for instance. [2, 11]

1.2 MOTIVATION AND SIGNIFICANCE

Not just since Glasgow 2021, fundamental changes are needed to meet the 1.5°C target. In order to limit the temperature increase to this level, great efforts are required, especially at the regional level. Municipalities have to play a significant role in the implementation of these targets. Thus, the perspective must be directed towards the mechanisms and possibilities of urban planning. Especially urban planning can create possible

[1] Caya Zernicke, Ruhr-University Bochum (RUB), Germany, Resource efficient Building, caya.zernicke@rub.de;
[1] Annette Hafner, Ruhr-University Bochum (RUB), Germany, Resource efficient Building, annette.hafner@rub.de
[2] Andreas Abecker, Disy Informationssysteme GmbH (disy), Germany, andreas.abecker@disy.net
[3] Harro Stolpe, Ruhr-University Bochum (RUB), Germany, Environmental Engineering+Ecology, harro.stolpe@rub.de

https://doi.org/10.52202/069179-0521

linkages for climate protection measures through its interdisciplinary field of activity. [2-7]

Digital solutions are gaining importance and supporting innovative decision-making. For this purpose, digital solutions are increasingly being developed and offered to cities for sustainable development. Geographic information systems (GIS), for example, has been a common tool even in urban planning for many years. A GIS, in general, is a computer-based system, which processes geospatial data. This system consists of hardware, software, data, applications, and services (HSDA model). With these four components, geospatial data can be digitally captured, stored, managed, updated, analysed, and presented alphanumerically and graphically. Thus, complex issues can be presented in a structured way. Especially for urban development, GIS systems have become indispensable tools for planning and decision making. By linking spatial or locational data, solutions can be crystallized more quickly and effectively from GIS-based decision-making templates. [12-18]

In general, urban environmental protection including the construction of timber buildings is partially combined with the development of intelligent software solutions. The measures shown in the web-tool Holzbau-GIS certainly have the potential to contribute to environmental relief. However, the right parameters and framework conditions for realising these potentials must be established. [13]

2 PROJECT DESCRIPTION

The R&D project Holzbau-GIS (Timber Construction - GIS) provides information on potential greenhouse gas (GHG) reduction due to timber construction and contextualizes the results of the GHG calculation on a municipality-wide consideration. It is focusing on possible climate protection measures through buildings including potentials using renewable building materials. By intersecting spatial geodata and building-specific research data, various conclusions can be drawn within the web-tool regarding basic data, new construction, and refurbishment with wood. Different scenarios project feasible reduction potentials for new timber buildings or refurbishment measures on existing buildings.

2.1 SOFTWARE ARCHITECTURE

An interdisciplinary team (architects, software developers, environmental engineers) developed the web-GIS system Holzbau-GIS and piloted it in close collaboration with the sample municipality of Menden (Sauerland) in Germany. The project combined contributions from four operating areas:

- Geodata-Management (lead partner: eE+E)
- GHG-Calculation (lead partner: ReB)
- Scenario-Management (lead partner: ReB)
- Web-GIS system (lead partner: disy)

The Geodata-Management classifies the building level based on available geodata. Various available municipal geodata like building footprints, 3D building models, historical satellite images, etc. are utilised to set up basic data to provide a sound starting point for the GHG-Calculation by the research partner Environmental Engineering+Ecology (eE+E).

The GHG-Calculation defines the GHG reduction potential by replacing mineral constructions with timber constructions. In order to quantify this potential, established methods for the LCA of buildings according to DIN EN 15978 [19] and research data [9, 20-22] are utilised for new construction scenarios. For a more detailed description, see Chapter 3.1. For refurbishment, the calculation of potential reductions due to the material choice, it is necessary to introduce a new methodology for LCA of refurbishment measures, which can be found in [23, 24] and summarized in Chapter 3.2. Based on this, the research partner Resource efficient Buildings (ReB) calculates the GHG reduction potentials.

The Scenario-Management defines the total amount of GHG reductions, extrapolated to the study area of the test municipality of Menden (Sauerland). It is the first time of connecting geospatial data of a whole municipality with the results of recent developed methods of LCA for refurbishment and valid LCA data for new constructed buildings. Both, the geodata management and the development of the method for calculating the GHG reduction potentials enable the derivation of various scenarios for new constructions or refurbishment measurements.

Referring to the web-GIS system, the research partner Disy Informationssysteme GmbH provides the Holzbau-GIS tool, based on its business intelligence and geodata analytics platform disy Cadenza [25] Figure 1 shows main technical aspects of the client-server based web-GIS system. The data is stored in a PostgreSQL DBMS with the PostGIS extension for managing spatial data. The database is managed by the disy Cadenza platform, which provides services such as user, roles and rights management, logging functionalities, as well as interactive data access, visualizations, and analytics.

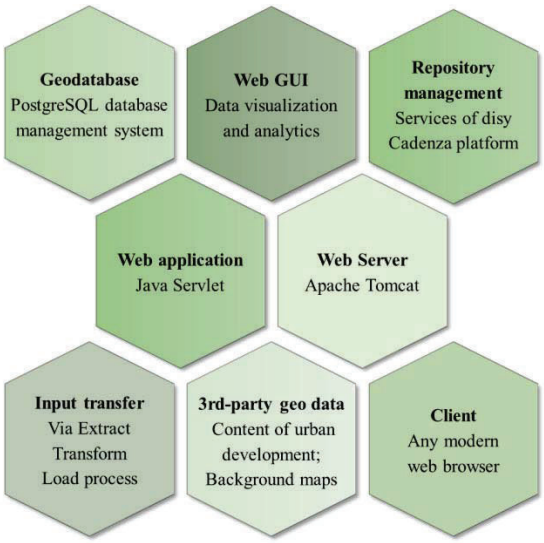

Figure 1. *The different components of the web-GIS system (random order)*

https://doi.org/10.52202/069179-0521

2.2 SOFTWARE FUNTIONALITY

Holzbau-GIS is an interactive web-based tool, which offers the option of selecting individual topics via the main menu. The display levels range from a very global overview down to the individual building. The data visualizations can be adapted or filtered according to the user's needs. The currently version provides basic functions, new construction scenario and refurbishment scenario. The data can be presented as interactive tables and charts or in a map view. Multidimensional data can also be aggregated on different spatial and temporal scales.

3 METHOD DESCRIPTION

In addition to the general data on the existing building stock, the web-GIS system contains further data on urban land use planning and environmental planning, among other things. This is followed by the results of the calculation scenarios.

This next section describes the procedures and methods utilised in these scenarios, while the main elements of the methodologies are presented in the following subsections 3.1 refers to the new construction scenario, while 3.2 describes the refurbishment scenario.

3.1 NEW CONSTRUCTION

Referring to Figure 2, the method of the new construction scenario starts with a compiled LCA data basis on new buildings. Therefore, data of former research projects "THG-Holzbau" [9, 21] for residential buildings and "HolzImBauDat" [20, 22] for non-residential buildings are operating as the general data basis for this scenario. In both projects, LCAs were conducted for the timber buildings and their functionally equivalent mineral buildings. By using this data, it is possible to obtain holistic statements on residential and non-residential buildings, shown here in Figure 2 in "building use". Further differentiations are also applied within the "building type", subdividing residential buildings into single-family and multi-family houses. For non-residential buildings, the new construction scenario provides conclusions for these different building types: agricultural or non-agricultural buildings, office and administrative buildings or other non-residential buildings.

These different "LCA results" were elaborated for each building type of new construction scenario: (1) GHG emissions of new buildings constructed with timber or as mineral buildings (2) GHG reduction potential by replacing mineral structures with wooden structures and (3) temporary carbon storage of the implemented renewable building materials. The outcomes of GHG emissions, GHG reduction potential, and temporary carbon storage refer to the gross external area (GEA) and thus the resulting units are given in kg CO2 Eq. /m² GEA.

The final phase of this methodology for new constructions includes the linkage of the LCA results (building-scale) to the "municipal level". Since new buildings are maximally planned without being built yet, those urban land use planning of the municipality can serve as the linking element, in detail, data of the urban land use planning is utilised to establish this connection.

Within the urban land use planning process, new construction areas are elaborated, ultimately permitted, and publicized in development plans. Using parameters which must be defined within this planning process and published as part of the development plans, we can calculate the maximum permitted GEA of the new construction areas. This output is given in m² GEA, which allows us to extrapolate the LCA results related to future construction activities of the municipality.

Summarized, this section described the methods of the new construction scenario including the differentiation of building types and LCA results. By combining given parameters of development plans and LCA results, quantitative data can be provided for GHG emissions, GHG reduction potential and temporary carbon storage for new construction.

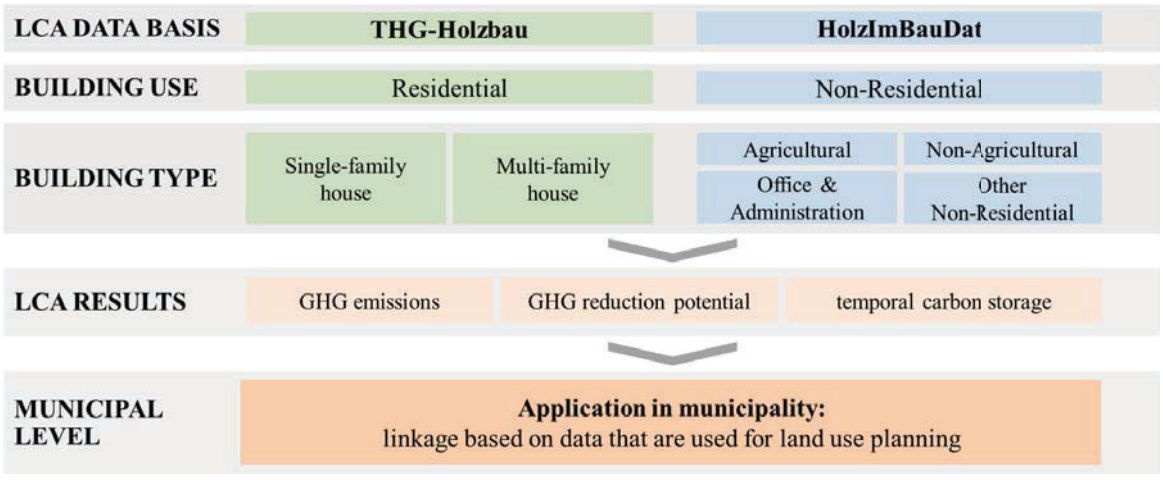

Figure 2. *Methodical structure, data basis and differentiations of the "new construction" scenario*

https://doi.org/10.52202/069179-0521

3.2 REFURBISHMENT

The following section will discuss the refurbishment of the municipal building stock. In detail, the scenario focuses on the energy-efficient refurbishment of the existing residential buildings. To provide a holistic and comprehensive tool for the municipality, it is essential to consider current issues such as the refurbishment of the building stock regarding climate protection measures related to the building sector. More precisely, refurbishment can be considered as a climate and environmentally friendly approach to reduce operating energy consumption at the municipal level. In addition, environmental aspects will become more prominent in public construction projects and their tendering. [26]

Figure 3 highlights the different elements and methods that characterize this refurbishment scenario. Starting with the left-hand element of Figure 3, various "geospatial data" were provided, already processed, and compiled by Geodata-Management, mentioned in Chapter 2.

One of the main features of a building is its geometric characteristic. Taking the outline of a building, the footprint of a building can be calculated. The representation in a three-dimensional format [27] allows the determination of further geometric data of the buildings, such as height, sloping roof surfaces or the building exterior surfaces. The building use is important for the differentiation between residential and non-residential buildings, which show differences in terms of structure and operating energy, among other things. Here, only the residential buildings are considered, since for these, the research results are more advanced and valid than for the heterogeneous non-residential building stock. The building type (single-family house, row house, multi-family house, etc.) is another aspect that is important for assessing the refurbishment potential. The building age is one more important feature for estimating the refurbishment potential. The GHG reduction potential increases with the age of the building because, in contrast, the materials and techniques applied in buildings have continuously gained in efficiency.

Since not every building is equally suitable for refurbishment, distinctions must be drawn between the type and age of residential buildings. Here, the differentiation bases on the German residential building typology of the Institute for Housing and Environment – Institut Wohnen und Umwelt GmbH (IWU) [28]. The term building typology contains several aspects, including the building's age, size, construction method and material, which can be identified for typical structures in certain architectural periods. The building typology represents a methodical classification of residential buildings into certain building age categories and building types based on technical, structural, and energy-relevant characteristics, which results in a national building type matrix. According to IWU, a building typology is a combination of defining these characteristics, groupings of individual buildings and the illustration of representative features with the help of exemplary buildings, which simplifies the energy evaluation of the buildings. [28] In order to provide decision guidance, the German residential building typology of IWU offers two refurbishment scenarios which are assigned to each of the exemplary buildings. These two standards correspond to the energy savings regulation EnEV 2014 [29] and the passive house standard [30]. Exemplary refurbishment measures are also indicated for the individual building elements, such as the external walls, roof, top floor ceiling, among others. In addition, the environmental impact of heating and hot water consumption is given for each exemplary building, for the current energy standard, but also for the refurbishment measures. [28]

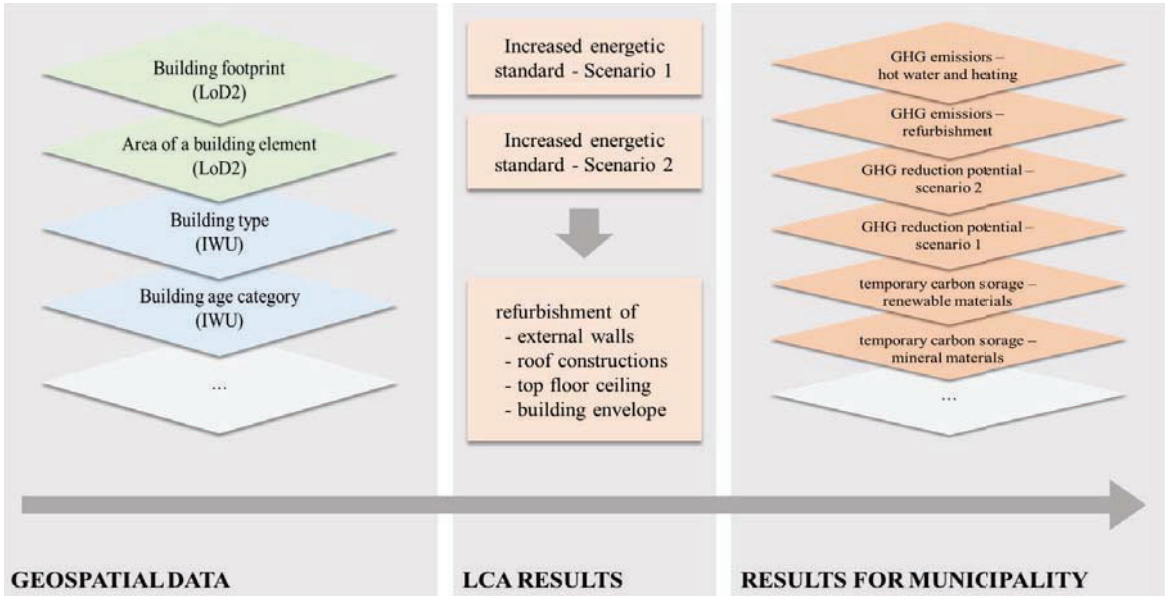

Figure 3. *Methodical structure, geospatial data and LCA procedures of the "refurbishment" scenario*

https://doi.org/10.52202/069179-0521

In case of Holzbau-GIS, an algorithm was developed, which automatically assigns the national building type matrix of the German residential building typology to the buildings in Menden using an iterative process and various geospatial data. Verification showed a high level of agreement, resulting in the continued implementation of this method. As a result, each residential building in Menden is assigned a building type, which is important as a main parameter for transferring the refurbishment potential to Menden. The building age was also identified with great effort for the entire building stock in Menden. More information on the procedure can be found in Menz et al. [31].

Continuing with the second element of the refurbishment scenario in Figure 3, the surface area of building elements, such as the external walls, roof, top floor ceiling or the exterior surface of the whole building envelope were calculated. Therewith, the geospatial data now provides enough information to apply "LCA results" of refurbishment measures to the building stock of Menden (Sauerland) utilizing the German residential building typology. The subsection 3.2.1 focuses on LCA methodology of refurbishment measures at the municipal level.

Analogous to the new construction scenario, various "results for the municipality" are provided: (1) GHG emissions for refurbishment measures constructed with timber or mineral materials (2) GHG reduction potential by replacing mineral structures with wooden structures and (3) temporary carbon storage of the implemented renewable building materials. Further results can be found in Figure 3 in the right-hand element.

3.2.1 LCA of refurbishment measures.

The following subsection focuses on LCA methodology of refurbishment measures at the municipal level. To explain the methodology further, it is necessary to give a more detailed account of LCA for refurbishments in the following section.

There is no common scientific consensus in the literature regarding the actual implementation of LCA for refurbishment measures. [32, 33] Consequently, a coherent LCA approach is needed for refurbishment measures as well as an extension of the framework to the municipal level.

Refurbishment measures are defined as changes to the structural substance of the exterior envelope of the building as well as to the technical installations of the building. [23]

For a municipal level of consideration, structural and material changes are primarily applied to the exterior walls, the roof, or the top ceiling of the building. The replacement of the building's cooling or heating system is also considered an energetic refurbishment but is usually covered at the municipal level by literature values and extrapolations.

Figure 4 displays the framework for LCA of refurbishment at municipal level. The scale of the municipality is not significant in the methodology, as the LCA of refurbishment measures is applied via extrapolations to the municipal level. The LCA is realized using a bottom-up approach for the building components, mainly the exterior building envelope, highlighted colourful in Figure 4. The buildings of the national building type matrix of IWU [28] have been included, whereas they differ in building type and age, indicated in Figure 4 with the colour subdivision of the building symbols.

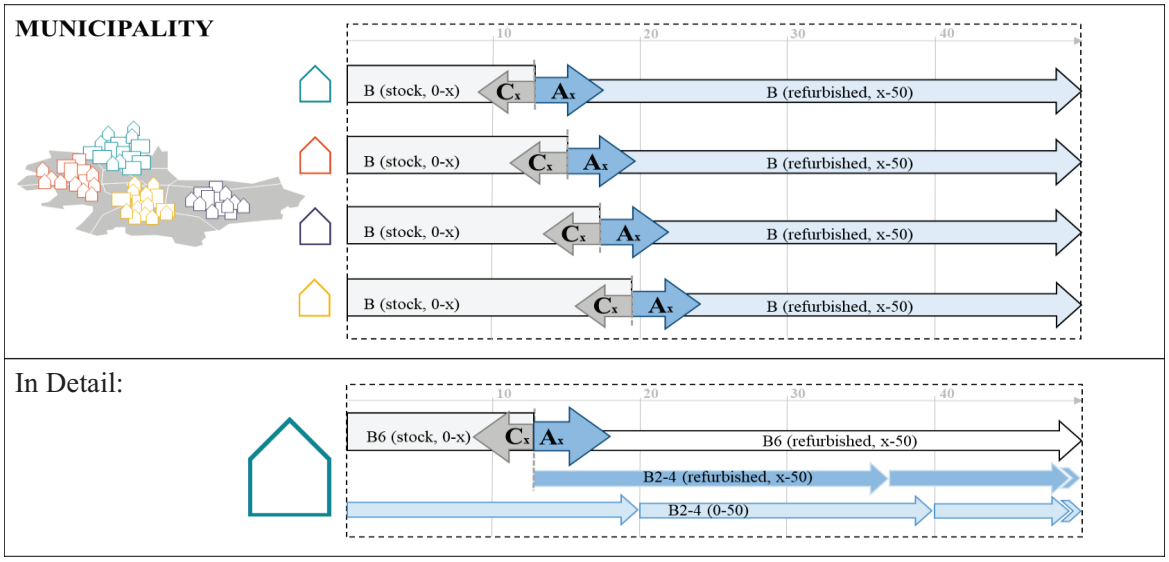

Figure 4. *Framework for LCA of refurbishment measures at municipal level – residential buildings categorized in building type and age (colour scheme) – module A includes production A1-A3 - module B includes maintenance B2, replacement B4 and operational energy consumption B6 – module C includes End-of-Life C1-C4*

The general framework for LCA of refurbishment at municipal level starts with these parameters:

- objects of assessment: building components
- system boundary: exterior envelope components
- Functional equivalent: 1 m² GEA
- reference study period: 50 years

Following DIN EN 15978:2011 [19] and DIN prEN 15978:2021 [34], the production and transport of all new building components and the disposal of removed components of any necessary construction measures are a part of this methodological approach, disregarding the actual time of refurbishment, see Figure 4.

Now, moving into the details of the LCA methodology for refurbishment, the starting point is year 0 of the reference study period. Here, the modules maintenance B2(0-x), replacement B4(x-0) and operational energy consumption B6(0-x) of the exterior building envelope are applied in the LCA approach. The moment within the reference study period where the refurbishment is executed, is symbolized with an x in Figure 4 of the LCA framework. Now, the life cycle phases for the refurbishment components will be supplemented. The modules End-of-Life C1-C4(x) will be added for the exterior envelope components that have to be demolished due to the refurbishment. Analogously, the modules production A1-A3(x) are included for the newly added building materials. At time x, the refurbishment is completed, the modules maintenance B2(x-50) and replacement B4(x-50) are additionally applied for the new exterior envelope components. In contrast, the modules maintenance B2(0-50) and replacement B4(0-50) of in-situ building components do not change during the refurbishment and therefore remain consistent since year 0. The operational energy consumption B6(x-50) continues as part of the LCA after the refurbishment but is reduced according to the now existing energetic standard to include the impacts of the refurbishment. By the end of the reference study period of 50 years, it is assumed that the municipality being studied will not be demolished leaving the existing buildings in place. As a result, the modules End-of-Life C1-C4(50) and Benefits and Loads D are not considered in the LCA framework.

Referring to Figure 4, the LCA approach is adapted to the spatial context of the municipality. Here, the German residential building typology of the IWU [28] provides the input for the LCA of the exterior envelope of municipal buildings. As mentioned before, the typology offers descriptions of the example buildings, including information on refurbishment options with data on the structure of the building envelope before and after refurbishment measures. With this information, the LCA of the exterior building envelope can proceed as described. Therefore, two linking parameters are used for extrapolation: the German residential building typology and the area of the building envelope components. Using the national building type matrix, a reference to the building stock in Menden can be established. Using the area of the building envelope components, the results of the LCA for refurbishment of the building envelope can be extrapolated. Then, the calculations can be performed for the entire municipality using the m² GEA for the residential buildings.

The material choice for the refurbishment can also be considered and compared within the LCA framework. In this way, the carbon storage can be accounted for each refurbishment approach. Additionally, by comparing different materials with the same measure, GHG reductions due to the material choice can be reported.

In this subsection, it was explained that the methodology requires a new approach for LCA of refurbishments. The following section deals with the demonstration of the results.

4 ILLUSTRATIVE EXAMPLES

In this section, some impressions and first results of the new construction scenario and refurbishment scenario within the web-GIS system Holzbau-GIS are presented.

After the initial log-in procedure, the user sees a short introduction page in the web interface and a view of a basic map of the research area of the sample municipality of Menden (Sauerland). Now, the user can select the topics of interest via a menu tree:

General data (Basisdaten): This category contains general building-specific information on the building stock, such as the building type or the building age, that was compiled by the project partners. [35]

Spatial overall planning (Räumliche Gesamtplanung): The spatial overall planning is subdivided into the categories of urban land use planning, specialized planning, and protected areas. Here, the forest inventory, nature reserves and biotopes are displayed. Among others, these issues are crucial for a comprehensive urban planning process.

Calculation scenarios (Berechnungsszenarien): There are two levels of consideration within the framework of Holzbau-GIS: new construction case studies of already passed development plans (what could have been...?) and GHG reduction potentials if the municipal residential building stock is energetically refurbished. The GHG emissions, GHG reduction potentials and temporary carbon storage are quantified and can be visualized in the web-GIS system.

In Figure 5, data of the the folder environmental planning (Fachplanungen) and subfolders forest (Wald) are shown. The map view of Figure 5 contains a range of different geodata like forest type (Waldart) and forest function (Waldfunktion). The forest type ist categorized in hardwood and softwood. Depending on the formation of the forest types, the category changes. The forest function gives information on recreation, emssion, climate or noise protection of the different forest areas.

https://doi.org/10.52202/069179-0521

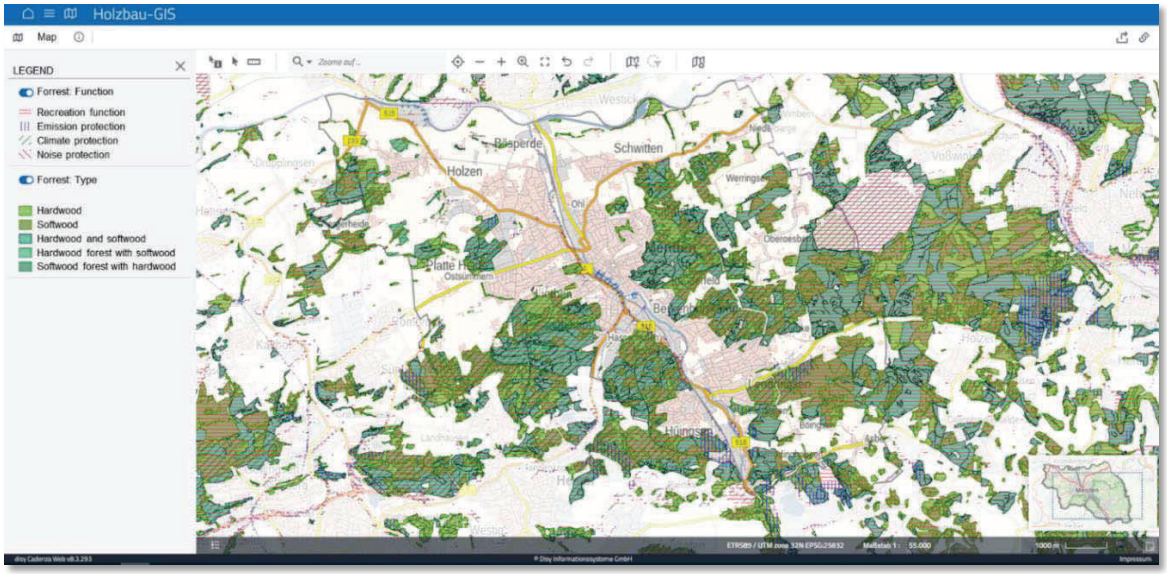

Figure 5: *Display of web-tool Holzbau-GIS: environmental planning*

4.1 NEW CONSTRUCTION

In Figure 6, the web interface shows a dashboard view, customised to the user's individual requirements as well as considering the presented data. Here, the dashbord includes a map view, two charts and a overall sum of one selected resulting parameter.

Figure 6 contains a component of the new construction scenario. A case study approach was chosen to gain a detailed understanding regarding the impact of material choices and to provide detailed illustrations of quantitative GHG reduction potentials and temporary carbon storage for new constructions mesures. This component of the new construction scenario gives an overview of five case studies, exemplifying new constructions in Menden (Sauerland). Development plans contain information on the permitted land uses and building types, as well as further information on permitted building characteristics. The development plans of the five case studies differ in terms of land uses and building types. [36, 37]

In Figure 6 the case study no. 221 as one of the five case studies is displayed. [38] The map view shows the location of the future construction areas according to the development plan no. 221. Within development plan no. 221 for eight construction areas, single-family houses (SFH) were permitted, visible via map view (white).

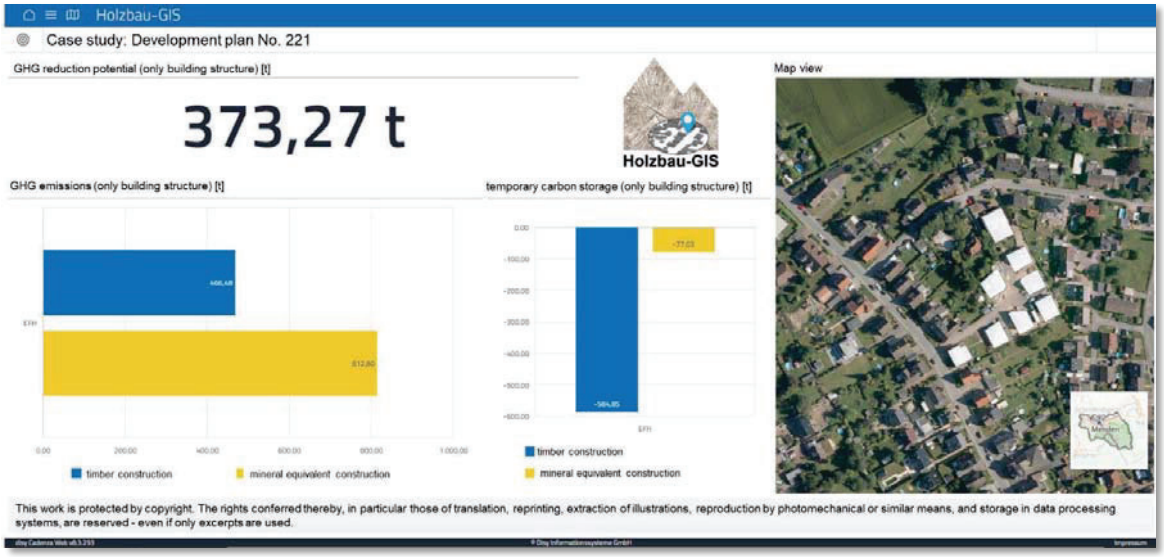

Figure 6: *Display of web-tool Holzbau-GIS: new construction*

The differences between the construction methods of the new building structure are highlighted in the left-hand chart in Figure 6. It shows the GHG emissions [t CO2-Eq.] for each construction method for the maximum permitted GEA, for the corresponding building type.

If the building structure of the SFHs will be a timber construction (blue), the GHG emissions will be at 466.48 t CO2-Eq. If the building structure of the SFHs will be built as a mineral construction (yellow), the GHG emissions will be about 812.80 t CO2-Eq.

The sum of total GHG reduction potential is additionally indicated as an absolute value in the dashboard. Overall, around 373 t CO2-Eq. GHG emissions could be saved for development plan 221.

The right-hand chart shows additional data about the temporary carbon storage for new constructions mesures. If the building structure of the SFHs will be a timber construction (blue), the temporary carbon storage will be at -584.85 t CO2-Eq. If the building structure of the SFHs will be built as a mineral construction (yellow), the temporary carbon storage will be about -77.03 t CO2-Eq.

4.2 REFURBISHMENT

For the refurbishment scenario, the GHG reduction potential is divided into two components: the GHG reduction potential from thermal refurbishment to passive house standard is given within this scenario. In this case, the GHG reduction potentials refer to the CO_2 emissions from heating and hot water. The second component includes the GHG reduction potentials by using timber for the refurbishment instead or mineral materials, that are illustrated in the web-tool Holzbau-GIS and shown in Figure 7. Here, the dashbord includes a map view and a chart. The dashboard displays the refurbishment potential of the municipality of Menden (Sauerland) subdivided into district specific data.

The map view contains the boundaries of the districts with additional data given as pie charts. These charts provide information on the GHG reduction potentials in percentage due to the refurbishment of the whole building envelopes, classified by the residential building type. The overall GHG reduction potential of the district is given within the pie chart, again in percentage. The pie charts display the GHG reduction potential for single-family houses (blue), row houses (yellow), multi-family houses (green), and large multi-family houses (not visible due to the small amount and consequently impact) for each district.

The right-hand chart of Figure 7 contains information as well on the GHG reduction potentials due to the refurbishment of the whole building envelopes, classified by the residential building type. Now the results are given as absolute values in t CO2-Eq. The GHG reduction potential are split by each district, giving summed-up results for single-family houses (blue), row houses (green), multi-family houses (yellow), and large multi-family houses (pink) for each district.

In Lendringsen, for example, a total GHG reduction potential of 6 660.71 t CO2-Eq. is given, if the whole building stock of this district is refurbished to passive house standard. Considering the SHFs, a GHG reduction potential of 4 146.01 t CO2-Eq. is provided for Lendringsen. Referring to the left-hand map view, these buildings generate 12.23 % less GHG emissions if the refurbishment measures are realized using renewable building materials.

In summary, these results show that the web-GIS system can provide different analysis capabilities and levels of analytical complexity for the presented data. By quantifying GHG emissions, GHG reduction potentials, and temporary carbon storage, differences resulting from building type, reference area, and material choice can be highlighted.

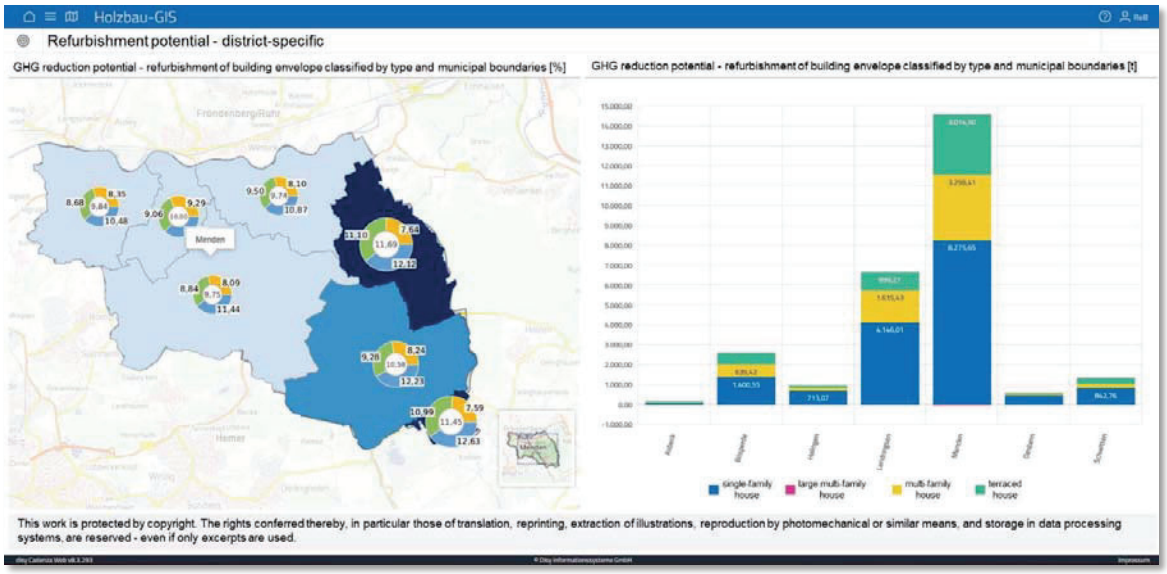

Figure 7: *Display of web-tool Holzbau-GIS: refurbishment*

https://doi.org/10.52202/069179-0521

5 IMPACT

In summary, there are two levels of consideration within the framework of Holzbau-GIS: new construction case studies of already passed development plans (what could have been...?) and GHG reduction potentials if the municipal residential building stock is energetically refurbished. The GHG emissions, GHG reduction potentials and temporary carbon storage are quantified and can be visualized in the web-GIS system. This creates an initial successful combination of geospatial data with LCA data for new construction and refurbishment. The LCAs of refurbishment measures represent a novelty in research which not only satisfies methodologically, but also generates significant LCA outcomes.

Starting with the new building scenario, this study establishes a quantitative framework for an extrapolation of valid building specific LCA data on a municipal scale, subdivided into different land uses and building types.

Referring to the refurbishment scenario, it was necessary to introduce a new methodology for LCA of refurbishment measures. For the implementation of the LCA the German residential building typology of the IWU [28] has been applied. In addition, for the first time, the data for the refurbishment measures of the residential building typology of the IWU were combined with practice-oriented building component structures and material quantities to perform the LCA.

Together, the current data highlights the importance of valid extrapolation to generate an initial estimation of potential GHG reductions at the municipal level. The focus in this context is on reducing environmental pollution and protecting resources, but also on utilizing the carbon storage capacity of renewable raw materials. Additionally, further provided data, e.g. the urban land use planning, support decision-making processes or planning measures for climate protection in urban areas.

6 CONCLUSIONS

The aim of the present study was to serve as a representative calculation to demonstrate the potential of timber construction to the decision makers of a municipality. The web-GIS system "Holzbau-GIS" enables a quantitative analysis of GHG reduction potentials for new buildings and refurbishment measures based on the city of Menden as a case model. The web-GIS system examines the impacts resulting from the use of renewable materials in the building sector at the municipal level. Consequently, we investigate the influence of various materials utilised during constructing new buildings or refurbishing existing ones.

However, these data should be interpreted with caution as certain assumptions must be applied. For an individual building, the calculated data is limited in its preciseness since various calculations were based on average values for standardized building types. A case-by-case assessment remains crucial in order obtain building-related information. To quantify the GHG reductions for a specific building, a comprehensive LCA should be considered in each case.

Regarding the significant role of refurbishment measures for the achievement of climate protection targets, it is necessary to use their potential as far as feasible. In other words, a high level of energy-efficient refurbishment is as essential as an increase of the refurbishment rate. [39]

Referring to the new construction scenario, with the assistance of an online application, users can determine data for future new construction projects. By entering the land use type, building use type, and proposed building type along with the corresponding GEA, the GHG emissions, GHG reduction potential, and temporary carbon storage can be projected. Further development should be pursued in the future to allow an open access tool available to the German municipalities to enable a large application.

The tool supports the sustainable and holistic transformation of the municipal building stock and offers different stakeholders and authorities the possibility to evaluate the environmental quality of refurbishment measures or new construction projects.

In future, we expect criteria such as GHG reduction potentials to play an increasing role when municipal projects will apply for funding.

Overall, constructing with timber, will take an important role regarding climate protection for the building sector, as suggested in the European Union Green Deal [40] and the European Bauhaus Initiative [41]. In this context, the "Holzbau-GIS" can support municipalities by integrating renewable materials as an additional option in their municipal climate protection concept.

Especially on a larger scale, carbon storage through technologies in and on buildings should be taken into consideration in the built environment. [39]

ACKNOWLEDGEMENT

This study was carried out based on the research project “Holzbau-GIS: Reduction of greenhouse gas emissions by building and renovating with wood” funded by the Federal Ministry of Food and Agriculture (BMEL) and the Federal Ministry for the Environment, Nature Conservation and Nuclear Safety (BMU), Waldklimafonds. The authors gratefully acknowledge the assistance of all concerned.

REFERENCES

[1] Büchner H.: Rechtliche Grundlagen kommunaler Selbstverwaltung. München. 2020

[2] Federal Ministry for the Environment, Nature Conservation, Nuclear Safety and Consumer Protection: Climate Action Plan 2050. Berlin. 2016

[3] Federal Ministry for Economic Affairs and Energy: Energy Efficiency Strategy for Buildings. Berlin. 2015

[4] Verbücheln M., Pichl J., Bunzel A., et al.: Stadtplanung und Stadtentwicklung als Hebel für den Ressourcen- und Klimaschutz. Dessau-Roßlau. 2021

[5] Paar A., Bergk F., Dingeldey M., et al.: Klimaschutzpotenziale in Kommunen. Dessau-Roßlau. 2022

[6] Hafner A., Slabik S., Storck M.: Urban Site Development as Temporal Carbon Storage—A Case Study in Germany. *Sustainability*, 12(14):5827. 2020

[7] Bürger V., Hesse T., Palzer A., et al.: Klimaneutraler Gebäudebestand 2050. Dessau-Roßlau. 2017
[8] Hecht R.: Automatische Klassifizierung von Gebäudegrundrissen. Rhombos-Verl., Berlin. 2014
[9] Hafner A., Schäfer S.: Comparative LCA study of different timber and mineral buildings and calculation method for substitution factors on building level. *Journal of Cleaner Production*, 167:630–642. 2017
[10] Hafner A., Rüter S.: Method for assessing the national implications of environmental impacts from timber buildings. *Wood and Fiber Science*, 50(Special):139–154. 2018
[11] Hafner A.: Klimaschutz und Holzbau. *AFZ-DerWald*, 21:33-35. 2017
[12] Turek T., Stępniak C.: Areas of Integration of GIS Technology and Smart City Tools. Research findings. *Procedia Computer Science*, 192(2):4681–4690. 2021
[13] Keppner B., Kahlenborn W., Libbe J., et al.: Direkte und indirekte Umwelteffekte von intelligenten, vernetzten urbanen Infrastrukturen. Dessau-Roßlau. 2022
[14] Bartelme N.: Geoinformatik. Springer Berlin, Heidelberg. 2005
[15] Bill R.: Grundlagen der Geo-Informationssysteme. Wichmann, Berlin. 2010
[16] Bill R.: Grundlagen der Geo-Informationssysteme. Wichmann, Berlin. 2016
[17] Harzer C.: GIS-Report 2018/19. Karlsruhe. 2018
[18] Stockwald M.: Geoinformationssysteme. Bayer. Staatsministerium der Finanzen, München. 2003
[19] EN 15978:2011, Sustainability of construction works – Assessment of environmental performance of buildings – Calculation method. Beuth Verlag GmbH, Berlin, 2012.
[20] Hafner A., Özdemir Ö.: Comparative LCA study of wood and mineral non-residential buildings in Germany and related substitution potential. *Eur. J. Wood Prod.*, 81(1):1–16. 2022
[21] Hafner A., Rüter S., Schäfer S., et al.: Treibhausgasbilanzierung von Holzgebäuden. Waldklimafonds, BMEL/BMUB. 2017
[22] Hafner A., Özdemir Ö.: HolzimBauDat: Datenbasis zur Bewertung einer Nachhaltigen und Effizienten Holzverwendung im deutschen Bausektor. FNR, BMEL. 2020
[23] Slabik S., Zernicke C., Storck M., et al.: A Methodological Approach for Life Cycle Assessment of Refurbishment Measures – From Building to Neighbourhood and Municipal Level. In: *Central Europe towards Sustainable Building 2022 (CESB22). (currently being published)*. 2022
[24] Slabik S., Storck M., Zernicke C., et al.: Proposing an LCA methodology for the assessment of neighbourhood refurbishment measures. *Environmental Research: Infrastructure and Sustainability*, 3(1). 2023
[25] Disy Informationssysteme GmbH: Treibhausgase einsparen durch Holzbauweise. Disy entwickelt mit der Ruhr- Universität Bochum ein „Holzbau-GIS“. Karlsruhe. 28.08.2020
[26] Federal Ministry of Food and Agriculture: Mitigating climate change. Creating value. Utilising resources efficiently. Bonn. 2021
[27] Bezirksregierung Köln (Ed.): 3D-Gebäudemodelle. www.bezreg-koeln.nrw.de/brk_internet/geobasis/3d_gebaeudemodelle/index.html, (accessed 2022-10-25).
[28] Loga T., Stein B., Diefenbach N., et al.: Deutsche Wohngebäudetypologie. Institut Wohnen und Umwelt GmbH, Darmstadt. 2015
[29] Institut für Energie-Effiziente Architektur mit Internet-Medien (Ed.): Energieeinsparverordnung - EnEV 2014. www.enev-online.com/enev_2014_volltext/, (accessed 2022-10-25).
[30] Heinze GmbH | NL Berlin | BauNetz (Ed.): Glossar - Passivhausstandard. www.baunetzwissen.de/glossar/p/passivhausstandard-3119421, (accessed 2022-10-25).
[31] Menz P., Jolk C., Zernicke C., et al.: Ermittlung und Überprüfung der Datengrundlage für das Modell zur Einsparung von Treibhausgasen durch stoffliche Holznutzung im Bauwesen im Holzbau-GIS für die Stadt Menden. In Fuchs-Kittowski F., Abecker A., Hosenfeld F., Ortleb H., Klafft M. (Eds.), *Umweltinformationssysteme – Vielfalt, Offenheit, Komplexität (currently being published).* Springer Vieweg. 2023
[32] Cabeza L.F., Rincón L., Vilariño V., et al.: Life cycle assessment (LCA) and life cycle energy analysis (LCEA) of buildings and the building sector: A review. *Renewable and Sustainable Energy Reviews*, 29:394–416. 2014
[33] Vilches A., Garcia-Martinez A., Sanchez-Montañes B.: Life cycle assessment (LCA) of building refurbishment: A literature review. *Energy and Buildings*, 135:286–301. 2017
[34] prEN 15978-1:2021, Sustainability of construction works - Methodology for the assessment of performance of buildings - Part 1: Environmental Performance; German and English version. Beuth Verlag GmbH, Berlin, 2021.
[35] Arbeitsgemeinschaft der Vermessungsverwaltungen der Länder der Bundesrepublik Deutschland (Ed.): Amtliches Liegenschaftskatasterinformationssystem. www.adv-online.de/AdV-Produkte/Liegenschaftskataster/ALKIS/, (accessed 2022-10-25).
[36] Abteilung für Planung und Bauordnung der Stadt Menden (Ed.): Bebauungspläne der Stadt Menden (Sauerland). www.menden.de/leben-in-menden/stadtplanung-bauen-verkehr/stadtplanung-1/bebauungsplaene-und-satzungen, (accessed 2022-10-25).
[37] Märkischer Kreis (Ed.): Open Data - Märkischer Kreis. gdi2.maerkischer-kreis.de/opendata.html, (accessed 2022-10-25).
[38] Zernicke C., Mattes C., Jolk C., et al.: Holzbau-GIS: Presenting first results of GIS-based modelling on reduction of greenhouse gas emissions, through construction and renovating with timber, on a municipal level. In: *Ecocity World Summit 2021-22 Conference Proceedings*. 2022
[39] Kuittinen M., Zernicke C., Slabik S., et al.: How can carbon be stored in the built environment? A review of potential options. *Architectural Science Review*, 65(1):1–17. 2021
[40] European Commision (Ed.): The European Green Deal. ec.europa.eu/info/strategy/priorities-2019-2024/european-green-deal_de, (accessed 2022-10-25).
[41] European Union (Ed.): New European Bauhaus. europa.eu/new-european-bauhaus/index_en, (accessed 2022-10-25).

https://doi.org/10.52202/069179-0521

World Conference on Timber Engineering Oslo 2023

In-plane Shear Test and Application Study of Seismic Retrofit Timber Frame with CFRTP Strands

Hina Takizawa[1],Nobuji Sakurai[2], Yuya Takaiwa[3]

ABSTRACT: In this study, we conducted a static in-plane shear test of a seismic retrofitted timber frame using CFRTP strands for the purpose of clarifying the usefulness of seismic retrofitting of timber buildings using CFRTP strands.The results were analysed to clarify the deformation mechanism. Based on the results, seismic retrofitting was carried out on the actual building, and the usefulness of seismic retrofitting and the area of application of the experimental results and design method were clarified.

KEYWORDS: Timber Frame, In-Plane Shear Test, Carbon Fiber, Thermoplastic, Seismic Retrofitting

1 Introduction

Carbon fiber-reinforced materials are advanced materials used in a wide range of fields in engineering, and are also attracting attention in the field of construction[1] Since carbon fiber composite materials have the characteristics of high strength, no rust, and no dew condensation, there are cases where they are suitable for seismic retrofitting of timber buildings instead of building steel materials [2]. In the previous study, the authors have developed an end fixing structure for CFRTP strands with toughness [3] [4] [5]. An in-plane shear test was conducted on a timber frame reinforced using CFRTP strands to clarify the in-plane shear performance. [6]. However, in the actual seismic retrofitting of timber buildings, there are cases where it is applied to a structure whose aspect ratio is different from that of the specimen, and it is not possible to adopt the same connection details as the specimen. At present, the design supervisors and contractors make decisions on a case-by-case basis at the construction site and many issues remain from the perspective of adapting to actual buildings. Therefore, we will conduct research aimed at clarifying the usefulness of seismic retrofitting of timber buildings using CFRTP strands. In order to achieve the purpose, in this report, the in-plane shear test was carried out and analyzed by adding a new specimen specification to the experimental result of the previous study [6].Then, the in-plane shear performance and deformation mechanism were clarified, and the usefulness was clarified by conducting a trial construction test by seismic retrofitting to the actual building. Therefore, it is possible to clarify the differences that may occur when applying the specimen specifications and the actual building, and to clarify the area of application and design method of the test results. Here, most of the previous study on the development of seismic retrofitting members for timber buildings is limited to understanding the in-plane shear performance when adapted to the specimens. On the other hand, in this study, the effectiveness is clarified not only by grasping the in-plane shear performance but also by performing adaptation verification by trial construction test s on actual buildings and hat is the feature of this research.

2 In-Plane Shear Test

An in-plane shear test was performed on a timber frame reinforced with CFRTP strands to examine the possibility of adapting the CFRTP strands to the vertical surface of a timber building.

2.1 The Outline of Specimen

2.1.1 Timber Frame

Assuming a general timber house, specimen were subjected to a static in-plane shear test using a timber frame with a wall height of 2910 mm, a wall width of 910 mm, and a wall width of 1820 mm. A total of 10 specimen were tested, 5 pieces each for a specimen with a wall width of 910 mm (910 specimens) and a specimen with a wall width of 1820 mm (1820 specimens). Figure 1 and Figure 2 show the specimens diagram, and Table 1 shows elements of specimen. The specifications of the specimen are shown in Table 2 and Table 3.and compared by 5 parameters. The first is the torque value of the stainless bolt at one end of the CFRTP strand, which was controlled by hand tightening at 2Nm and 10Nm. The second is whether or not the wood (a corbel) is fixed to attach the CFRTP strand to the column. Specimen 910-3,910-4,910-5,1820-1,1820-2,1820-3,1820-5 were fixed in 4 places with screws. The third is the difference in the shape of the holes made in the column to penetrate CFRTP strands.

[1] Hina Takizawa, Graduate School, Dept. of Architecture, Faculty of Science and Engineering, Toyo University,
[2] Nobuji Sakurai, Nose Structural Corporation Co., Ltd,
[3] Yuya Takaiwa, Associate Professor, Department of Architecture, Faculty of Science and Engineering, Toyo University, Dr. Eng. takaiwa@toyo.jp
2100 Kujirai, Kawagoe-shi, Saitama, Japan (350-8585)

https://doi.org/10.52202/069179-0522

The hole shape of specimen 910-1.910-2,910-3,1820-1,1820-2,1820-3 were circular, and the hole shape of specimens 910-4,910-5,1820-4,1820-5 are square. Figure 3 shows the fixing method of a corbel fixed with screws and the shape of the through hole of the CFRTP strand. The fourth is the presence or absence of side protrusions (protrusions of CFRTP socket) that are created when making a CFRTP socket. Specimens 910-1,910-2,910-3 and 1820 Specimen were designed to remove the protrusions of CFRTP socket, and Specimen 910-4 and 910-5 were specified to leave them. The fifth is the difference in the order when fixing the corbel of the CFRTP strand and the column. Specimen 910-1,910-2,910-3,1820-1,1820-2 and 1820-3 adjusted the torque value of the CFRTP strands after fixing the corbel to the column. Specimen 910-4,910-5,1820-4 and 1820-5 fixed the corbel to the column after tensioning the CFRTP strands.

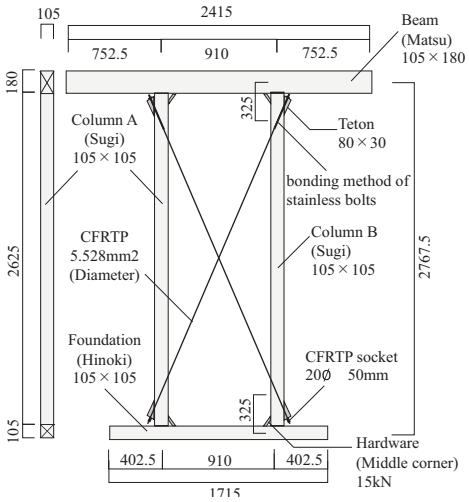

Figure 1: Specimen Diagram (910 specimen)

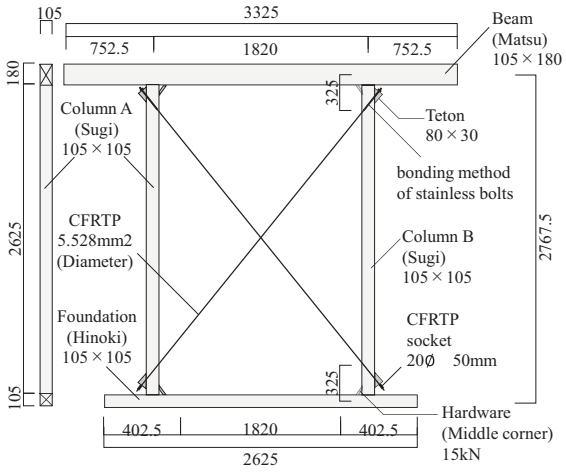

Figure 2: Specimen Diagram (1820 specimen)

Table 1: Elements of specimen

Element	Section size（mm)
Beam（Matsu)	105×180
Column（Sugi)	105×105
Foundation（Hinoki)	105×105
CFRTP	5.528(diameter)

Table 2: Details of specimen (910 specimen)

No.	The torque value	Fixing corbels	The shape of a hole of CFRTP	protrusions of CFRTP socket	Construction procedure	Diameter of CFRTP socket
910-1	10 Nm	noting	Round	Not Available	Fixing cobels ↓ tightening a bolt of CFRTP strand	20Ø
910-2	2Nm	noting	Round	Not Available	Fixing cobels ↓ tightening a bolt of CFRTP strand	20Ø
910-3	2Nm	screwed	Round	Not Available	Fixing cobels ↓ tightening a bolt of CFRTP strand	20Ø
910-4	2Nm	noting	Square	Available	tightening a bolt of CFRTP strand ↓ Fixing cobels	20Ø
910-5	2Nm	screwed	Square	Available	tightening a bolt of CFRTP strand ↓ Fixing cobels	20Ø

Table 3: Elements of specimen (1820 specimen)

No.	The torque value	Fixing corbels	The shape of a hole of CFRTP	Protuberance of CFRTP socket	Construction procedure	Diameter of CFRTP socke
1820-1	2Nm	screwed	Round	Not Available	Fixing cobels ↓ tightening a bolt of CFRTP strand	20Ø
1820-2	2Nm	screwed	Round	Not Available	Fixing cobels ↓ tightening a bolt of CFRTP strand	20Ø
1820-3	2Nm	screwed	Round	Not Available	Fixing cobels ↓ tightening a bolt of CFRTP strand	20Ø
1820-4	2Nm	noting	Square	Not Available	tightening a bolt of CFRTP strand ↓ Fixing cobels	30Ø
1820-5	2Nm	screwed	Square	Not Available	tightening a bolt of CFRTP strand ↓ Fixing cobels	30Ø

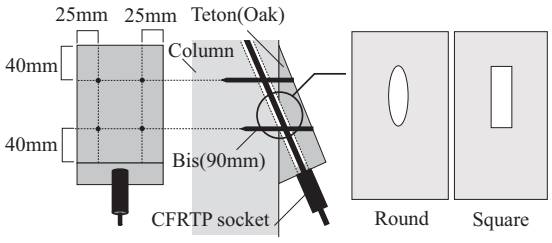

Figure 3: How to fix a corbel and The shape of hole of CFRTP

2.1.2 CFRTP strand

The CFRTP strand used in the test composed 7 twisted wires with a diameter of 2.1mm, and the cross-sectional area is 24 mm^2 and the tensile modulus of it is 110 kN/mm^2. The end fixing structure consists of two types. One side is a CFRTP socket, which is known to be ductile fracture at about 15 kN from experiments. The other side

https://doi.org/10.52202/069179-0522

is a bonding method of stainless bolt, which breaks brittlely with a load larger than 15 kN. Since the CFRTP socket yields before the stainless bolt, the CFRTP strand has toughness. Figure 4 shows the results of a pull-out test of a CFRTP strand suitable for this test. The test method was based on previous studies. As a result of the test, it was confirmed that the behavior of the CFRTP socket was that there was no brittle fracture even if a first yield point due to adhesive yielding, a second yielding point when the maximum yield strength was reached, and then a displacement of 40 mm occurred.

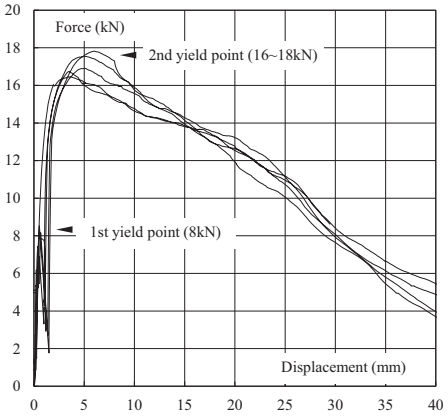

Figure 4: CFRTP socket Force-Displacement Relationship[6]

2.2 Method and measurement plan of the test

The loading device adopts a column base fixed type. It is fixed to the specimen with an in-plane restraint jig on the beam of the specimens, and the base is fixed to the specimen fixed beam. An oil jack is used to horizontally apply a positive and negative load to the specimen. In the loading cycle (repetition history), the apparent shear deformation angle of the specimen is ± 1/450, ± 1/300, ± 1/200, ± 1/150, ± 1/100, ± 1/75, ± 1/50 rad. Deformation control is performed three times, and a positive and negative load is performed once with a deformation angle of ± 1/30 rad. After that, the specimen is loaded until the maximum load is reached and the load drops (0.8Pmax) or a deformation angle reaches 1/10 rad or more. A total of 7 displacements are measured: horizontal displacement of the top of the specimen, horizontal displacement of the base of the specimen, vertical displacement of the column (2 points), horizontal displacement of the fixed beam, and vertical displacement of the jig (2 points). In addition, the strain is measured with a strain gauge at two points on the front and back of the CFRTP strands. Figure 6 and Figure 7 show respectively the displacement measurement points and strain gauge mounting positions. An in-plane shear test of a timber frame reinforced with CFRTP strands is performed to confirm the strength and fracture morphology. The shear deformation angle of the timber frame obtained by the displacement meter 1 and the displacement meter 2 was used for control.

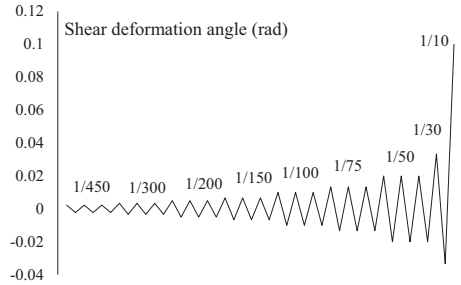

Figure 5: Repetition History

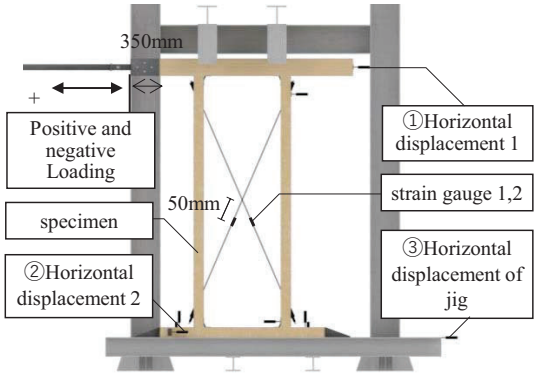

Figure 6: The Experimental Device and Specimen

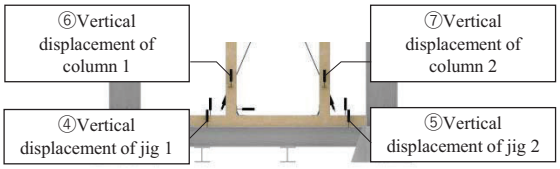

Figure 7: Points of Measurements on the Back

2.3 Result of the test

Figure 8 and Figure 9 show the relationship between the shear force (F) and the shear deformation angle (θ) of the 910 specimen and 1820 specimen, respectively. Tables 4 and 5 show the shear deformation angles of the 910 specimen and 1820 specimen at the first yield(θ_{yield}), the shear force of the timber frame at the first yield(P_{yield}), and the maximum shear force(P_{max}), respectively.

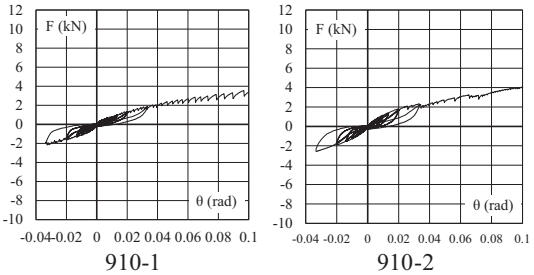

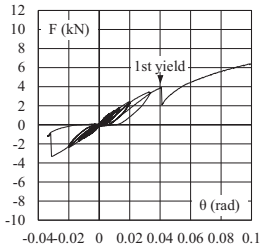

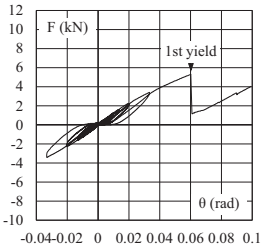

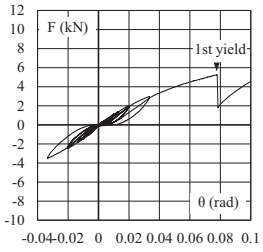

Table 4: Result of the test (910 specimen)

	θ_{yield} (rad)	P_{yield} (kN)	P_{max} (kN)
910-1	×	×	3.8
910-2	×	×	4.0
910-3	1/25	3.9	6.4
910-4	1/17	5.3	5.3
910-5	1/13	5.2	5.2

Figure 8: Shear Force-Shear Deformation Angle Relationship (910 specimen)

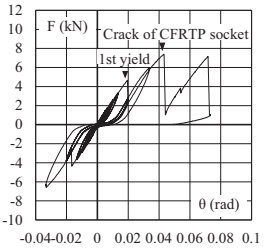

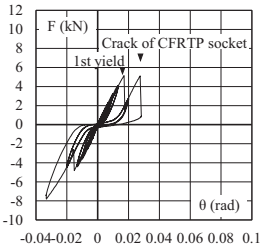

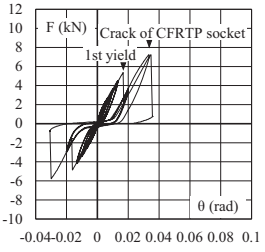

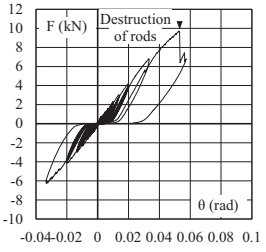

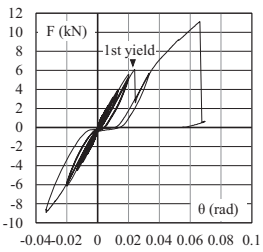

Table 5: Result of the test (1820 specimen)

	θ_{yield} (rad)	P_{yield} (kN)	P_{max} (kN)
1820-1	1/51	4.6	7.3
1820-2	1/58	5.1	5.1
1820-3	1/60	5.3	7.2
1820-4	×	×	9.6
1820-5	1/42	6.1	11.1

Figure 9: Shear Force-Shear Deformation Angle Relationship (1820 specimen)

2.4 Analysis

Analysis is performed based on the differences in the specifications of the specimens and the test results..

2.4.1 Torque value of stainless bolt

specimen 910-2 with a torque value of 2 Nm at one end of the CFRTP strand was compared with specimen 910-1 with a torque value of 10 Nm. Figure 10 shows the relationship between the shear deformation angle and the shear force of the specimen 910-1 and specimen 910-2. The specimen 910-1 with a large torque value had a maximum share force of 0.3 kN smaller than that of the specimen 910-2. It is considered that this is because the specimen bends inward when the torque value is large, and the force opposite to the shearing force of the timber frame is applied to it.

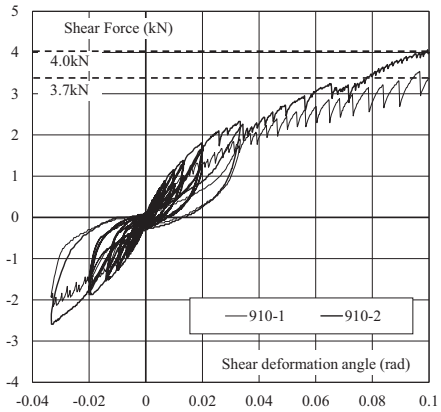

Figure 10: Shear Force-Shear Deformation Angle Relationship (910-1,910-2)

2.4.2 Fixing corbels

Specimen 910-2 and 1820-4, which allowed movement without fixing the corbels, and Specimen 910-3 and 1820-5, which had the corbels fixed with screws, were compared. Figure 11 and Figure 12 show the relationship between the shear deformation angle and the shear force of the specimen 910-2,910-3,1820-4 and 1820-5 respectively. specimen 910-2 and 1820-4 that did not fix the corbel allow the timber frame to be deformed by the corbel slipping on the column surface. Therefore, the CFRTP socket did not first yield. In the specimen 1820-4, the rod of the CFRTP strand broke. The CFRTP socket first yielded at 1/25 rad for the specimen 910-3 and 1/42 rad for the test body 1820-5 with the corbel fixed. When the corbel is not fixed, the deformation performance of the timber frame can be improved. It was confirmed that when the corbel is fixed, the maximum share force is 2.4kN for the 910 specimen 1.4kN for the 1820 specimen compared to the case where the corbel is not fixed.

https://doi.org/10.52202/069179-0522

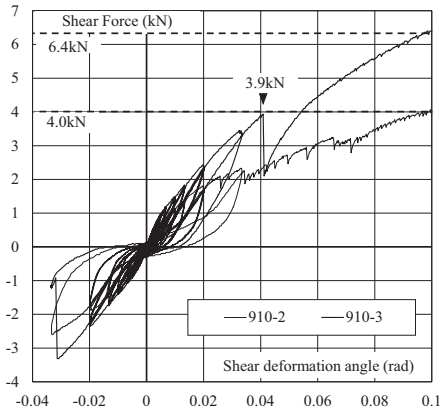

Figure 11: Shear Force-Shear Deformation Angle Relationship (910-2,910-3)

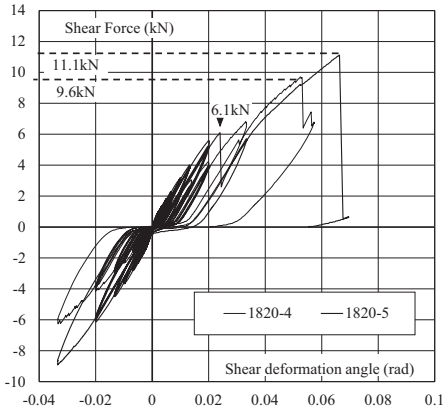

Figure 12: Shear Force-Shear Deformation Angle Relationship (1820-4,1820-5)

2.4.3 Protuberance of CFRTP socket

Specimen 910-3 without protuberance of CFRTP socket and specimens with it were compared with specimen 910-4 and 910-5. Figure 13 shows the relationship between the shear deformation angle and the shear force of the specimen 910-3, 910-4 and 910-5. Specimen 910-3 without protuberance of CFRTP socket occurred first yield at 1 / 25rad, and specimen 910-4 and 910-5 with it occurred first yield at 1/17 rad and at 1/13 rad, respectively. The maximum shear force was 6.4 kN at the shear deformation angle of 1/10 rad for the specimen 910-3, and 5.3 kN and 5.2 kN at the first yield for the specimen 910-4 and 910-5, respectively. If there is a protuberance of CFRTP socket, the timber frame is given nearly twice the deformation performance of 1/30 rad, which is the design criteria of a traditional timber building. n the other hand, when the CFRTP socket had no protuberance of CFRTP socket, the maximum yield strength was about 1 kN larger than that with it.

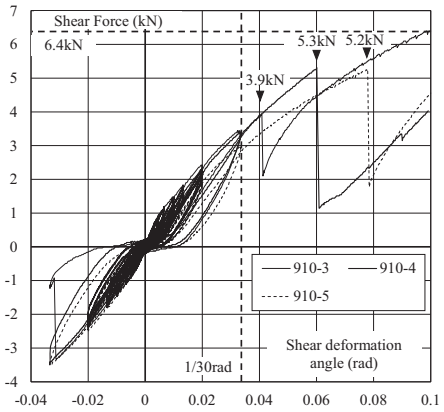

Figure 13: Shear Force-Shear Deformation Angle Relationship (910-3,910-4,910-5)

2.4.4 The shape of a hole of CFRTP strand

Specimen 910-3, which uses a circular hole to make a CFRTP strand through a column, and specimen 910-4 and 910-5 which have a square hole, are compared. Figure 14 shows the initial stiffness of a timber frame with a shear deformation angle of 0 rad to 1/450 rad, and Figure 15 shows difference of embedment due to the shape of a hole of CFRTP strand. Specimen 910-3 with circular holes for CFRTP strands have 1.3 to 1.8 times higher initial stiffness than specimen 910-4 and 910-5 with square holes. When the shape of the hole for the CFRTP strand is circular, it is considered that it is difficult to dig in because the contact area between the CFRTP strand and the wood is large.

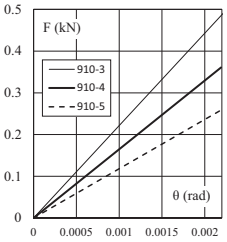

Figure 14: Initial stiffness (910-3,910-4,910-5)

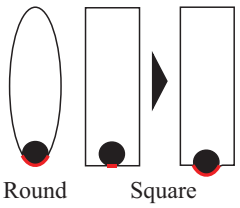

Figure 15: Difference of Embedment due to the shape of a hole of CFRTP strand

2.4.5 Construction procedure of CFRTP strands

The test results were compared due to the difference in the construction procedure when constructing the CFRTP strand. Figure 16 shows the difference in the construction procedure of the CFRTP strand. Specimen 910-3 tightened the bolt of the CFRTP strand after fixing the corbel. On the other hand, specimen 910-4 and 910-5 fixed the corbel after tightening the bolt of the CFRTP strand. When the receiving material of the CFRTP strand is fixed first, the hole for the CFRTP strand of the corbel and the column are fixed in the same position, so that the CFRTP strand easily sinks column inside the timber frame. On the other hand, if the bolt of the CFRTP strand is

https://doi.org/10.52202/069179-0522

tightened first, the position of the hole for the CFRTP strand of the corbel and the column is misaligned, so that it is easy to sink column the outside of the timber frame. The outer embedment of the timber frame has a greater contribution to the shear displacement of the timber frame than the inner.

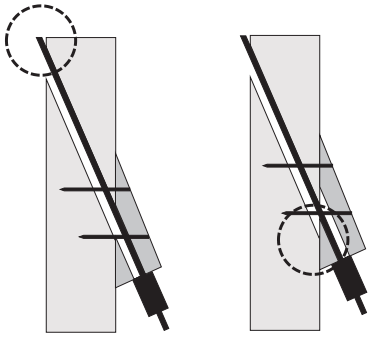

Figure 16: The Difference of Embedment of CFRTP Strand due to Construction Procedure

2.4.6 Diameter of CFRTP socket

A specimen 1820-1 using a CFRTP socket with a diameter of 20 mm and specimen 1820-5 using a CFRTP socket with a diameter of 30 mm were compared. Figure 17 shows the relationship between the shear deformation angle and the shear force of the specimen 1820-1 and 1820-5. When a CFRTP socket with a diameter of 20 mm was used, the shear force did not increase because the CFRTP socket cracked after the first yield, and the maximum shear force was 7.4 kN. On the other hand, the CFRTP socket with a diameter of 30 mm did not crack after the first yield, and the maximum shear force was 11.1 kN, which was the highest among all the specimens. By preventing the CFRTP socket from cracking, the shear force of the timber frame wall can be improved.

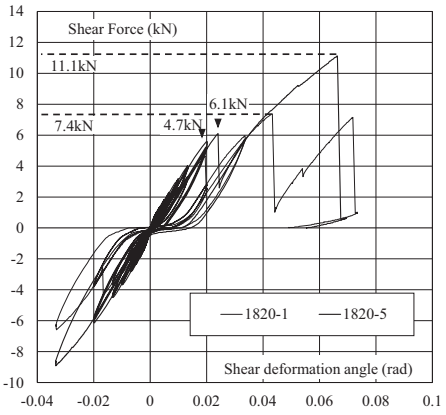

Figure 17: Shear Force-Shear Deformation Angle Relationship (1820-1,1820-5)

3 Analysis of Shear Deformation Mechanism of Specimen

3.1 The Outline of Analysis

It was analyzed how much the factors that cause shear displacement in the timber frame wall contribute to the actual shear displacement. Figure 18 shows each factor that causes shear displacement.

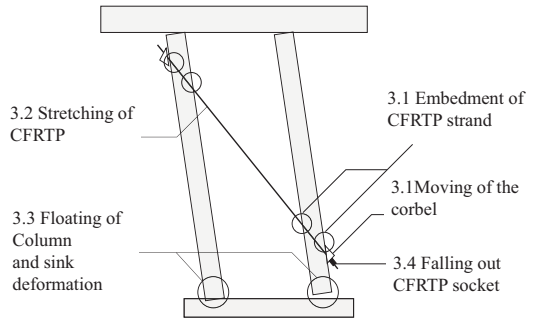

Figure 18: Factors Contributed to the Shear Deformation

3.2 How to Analyse

Using the analysis method of the factors that cause shear displacement of the timber frame proposed in the previous study [6], the contribution rate of each factor that causes shear displacement in the specimens is calculated.

3.3 The Results of Analysis

Tables 6 and Table 7 show the contribution rates of each factor that causes shear displacement of 910 specimen and 1820 specimen. In the tables, 3.1 shows Indentation deformation of CFRTP Strand and 3.2 shows axis deformation of CFRTP strand and 3.3 shows rotational deformation of the timber and 3.4 shows deformation of falling out CFRTP socket. In the 910 specimen, the shear displacements of the specimen 910-3, 910-4 and 910-5 with falling out the CFRTP socket account for about 30% of the total. In the 1820 specimen, when the CFRTP socket is fallen out, the effect on the shear displacement is larger than that in the 910 specimen. In specimen 1820-5, since all the sockets were fallen out, the shear displacement due to the sockets being fallen out was calculated to be larger than the actual one.

Table 6: Each Factor Causes the Shear Displacement (910 specimen)

	The Shear Displacement ration(%)				
	910-1	910-2	910-3	910-4	910-5
3.1	56.8	55.1	11.4	52.4	48.9
3.2	7.4	9.7	18.0	14.6	13.8
3.3	18.6	17.5	23.7	21.1	25.1
3.4	0	0	30.9	30	30.2
Total	82.8	82.4	84.2	118	118

https://doi.org/10.52202/069179-0522

Table 7: Each Factor Causes the Shear Displacement(1820 specimen)

	The Shear Displacement ration(%)				
	1820-1	1820-2	1820-3	1820-4	1820-5
3.1	-0.22	-5.1	-0.03	27.3	20
3.2	12.6	16	26.2	16.8	21.1
3.3	13.7	12.7	18.4	19.4	23.1
3.4	80.6	110	89.3	0	84.9
Total	106	133	134	63	149

4 Trial Construction Test by Applying to Actual Building

4.1 The Outline of the Building

The actual building, which has been seismically reinforced with CFRTP strands, is a timber building exhibited at National Museum of Ethnology. The actual building is shown in Photo 1 and Photo2, construction condition is shown in Photo 3, Adjustment of initial tension and the reinforcement drawing is shown in Figure 19.

Photo 1: View from outside of the building

Photo 2: View from inside of the building

Photo 3: Construction condition

Photo 4: Adjustment of initial tension

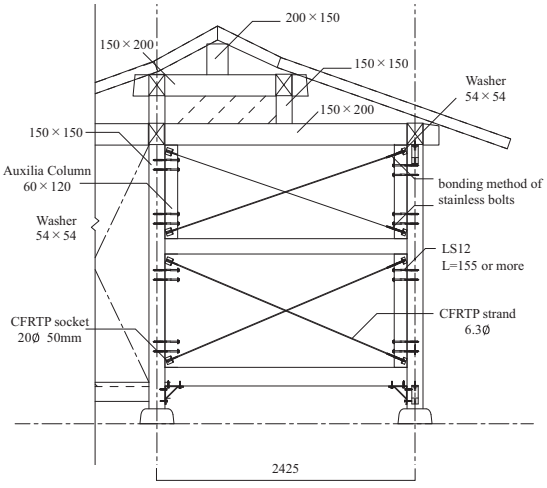

Figure 19: Drawing of Actual Building

4.2 Comparison of the Construction Status of the Specimen and the Actual Building

The construction status of the specimens and the actual building was compared. The difference between the specimens and the actual building will be described. There were the construction procedure when installing the CFRTP strand (4.3), the size of the washer installed between the CFRTP strand and the corbel (4.4), and the structural dimension of the wall reinforced by the CFRTP strand (4.5).

Table 8: The Difference specimens and actual building

		Specimens	Actual building
4.3	Construction procedure	(1) Fixing corbels ↓ Tightening a bolt of CFRTP strand (2) Tightening a bolt of CFRTP strand ↓ Fixing corbels	Fixing corbels ↓ tightening a bolt of CFRTP strand
4.4	The size of a washer (mm)	62×62	54×54
4.5	The size of a wall(mm)	(1)910×2767.5 (2)1820×2767.5	case-by-case

4.3 Impact of Construction Procedure

When constructing a real building, first tighten the bolts of the CFRTP strand and then fix the corbel. Therefore, it is considered that the CFRTP strands are easily sunk on the outside of the timber frame, and the deformation performance of timber frame is improved.

4.4 Impact of The Size of a Washer

A washer is installed between the CFRTP strand and the corbel. A washer of 62 mm x 62 mm was used in specimen, but a washer of 54 mm x 54 mm was used in the actual building. Using the formula (1), it was confirmed whether or not the washer would be dented due to the smaller washer. The allowable bearing stress is 23.3 kN. Since the axial force that can be borne by the CFRTP strand is 15 kN, it was confirmed that the washer does not sink into the corbel until the CFRTP strand breaks.

$$Fcv \times \frac{2}{3} \times \mathrm{A} \qquad (1)$$

F_{cv} : Basic strength of bearing (12N/mm) [7]
A:The area of a washer(2910mm^2)

4.5 Impact of Aspect Ratio of the Timber Frame

In order to obtain the change in the stiffness of the timber frame due to the change in the aspect ratio of the wall, it was verified using the formulas (2) to (5). The change in

https://doi.org/10.52202/069179-0522

the stiffness of 910 specimen to 1820 specimen is considered to be influenced by the change in the aspect ratio of the timber frame and the change in the stiffness of the CFRTP strand. First, the effect of the change in the stiffness of the CFRTP strand is removed from the change in the stiffness of the wall.

$$\frac{P_{1820}}{P_{910}} \div \frac{L_{b910}}{L_{b1820}} \tag{2}$$

P_{910}: Shear force at a shear deformation angle of 1/30 rad in 910 specimen (3.37kN)
P_{1820}: Shear force at a shear deformation angle of 1/30 rad in 1820 specimen (6.59kN)
L_{b910} : Length of CFRTP Strand of 910 Specimen (2304mm)
L_{b1820} : Length of CFRTP Strand of 1820 Specimen (2792mm)

The effect of wall stiffness due to changes in the aspect ratio of the wall of the actual building is shown in the formula (3).

$$K = k_{910} \times \frac{P_{1820}}{P_{910}} \div \frac{L_{b910}}{L_{b1820}} \div \frac{W_{1820}/H_{1820}}{W_{910}/H_{910}} \times \frac{W'/H'}{W_{910}/H_{910}} \tag{3}$$

K: Stiffness of actual building wall affected by changes in wall aspect ratio
W_{910}: Width of 910 specimen (910mm)
W_{1820}: Width of 1820 specimen (1820mm)
W': Width of the wall of actual building (2425mm)
H_{910}: Height of 910 specimen (2767.5mm)
H_{1820}: Height of 1820 specimen (2767.5mm)
H': Height of the wall of actual building (1224.9mm)

The effect of the change in the stiffness of the CFRTP strand on the stiffness of the wall is added to the formula (3).

$$k' = K \times \frac{L_{b910}}{L_b{}'} \tag{4}$$

k':Stiffness of the wall of actual building
$L_b{}'$: Length of CFRTP Strand of the wall of actual building (2530mm)

The axial force borne by the CFRTP strand is calculated using the wall stiffness calculated by the formula (4).

$$k' \times \frac{H'}{30} \times \frac{L_b{}'}{W'} \tag{5}$$

When an example of the wall of an actual building is calculated using the formulas (2) to (5), the stiffness of the wall is 0.23 kN / mm, and the axial force borne by the CFRTP strand is estimated to be 9.6 kN. This is less than the axial force (15 kN) that the CFRTP strand can bear and is designed within the area of application of the experimental results.

Table 9: Impact of Aspect Ratio of the Timber Frame

		910 Specimen	1820 Specimen	Actual Building
		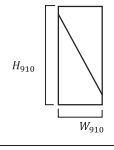	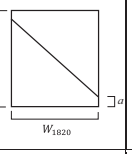	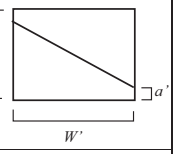
$\frac{W}{H}$	mm/mm	$\frac{W_{910}}{H_{910}}$	$\frac{W_{1820}}{H_{1820}}$	$\frac{W'}{H'}$
L_b	mm	$\sqrt{{W_{910}}^2 + (H_{910} - 2a)}$ $(=L_{b910})$	$\sqrt{{W_{1820}}^2 + (H_{1820} - 2a)^2}$ $(=L_{b1820})$	$\sqrt{(W')^2 + (H' - 2a)^2}$ $(=L_b{}')$
k_b	kN/mm	$\frac{E \cdot A}{L_{b910}}$	$\frac{E \cdot A}{L_{b1820}}$	$\frac{E \cdot A}{L_b{}'}$
P	kN	3.378 $(=P_{910})$	6.281 $(=P_{1820})$	$\frac{k_{1820} \times L_{1820} \times L_{b910} \times D' \times H_{1820}}{L_{910} \times L_b{}' \times H' \times D_{1820}} \times \frac{H'}{30}$
k	kN/mm	$P_{910} \cdot \frac{30}{H_{910}}$	$P_{1820} \cdot \frac{30}{H_{1820}}$	$\frac{k_{1820} \times L_{1820} \times L_{b910} \times D' \times H_{1820}}{L_{910} \times L_b{}' \times H' \times D_{1820}}$

W: Width of the wall
H: height of the wall
L_b: Length of CFRTP strand
k_b: Stiffness of CFRTP strand
P: Shear force at a shear deformation angle of 1/30 rad
k: Stiffness of the wall

5 Conclusion

A static in-plane shear test of a seismic retrofitted timber frame using CFRTP strands revealed the following.

(1) The initial tension of the CFRTP strand was examined using 910specimen. As a result, it was confirmed that when the torque value was changed from 2Nm to 10Nm, the shear force borne by the wall was reduced due to the initial deformation of the timber frame bending inward.
(2) It was confirmed that the stiffness of the timber frame in 910 specimen changes depending on whether or not the corbel of the CFRTP strand is fixed. It was clarified that when the corbel is not fixed, the corbel allows the sliding movement on the contact surface of the column and increases the shear deformation of timber frame.
(3) It was confirmed that the initial stiffness is affected when the shape of the hole for the CFRTP strand is different. It is presumed that this is because when the shape of the hole is circular, the contact area between the CFRTP strand and the timber is larger than when the shape of the hole is square, so it is less likely to be dented.
(4) It was confirmed that the deformation performance of the timber frame changes depending on the construction procedure of the CFRTP strand.It is clear that the procedure of tightening the bolts and then fixing the corbel has a larger shear displacement due to the digging of the columns of the CFRTP strand than the procedure of tightening the bolts of the CFRTP strand after fixing the corbel of the CFRTP strand.

Based on the findings mentioned above, we conducted an adaptation verification by construction experiments on

https://doi.org/10.52202/069179-0522

seismic retrofitting actual buildings using CFRTP strands. As a result, it was confirmed that seismic retrofitting is useful by considering the influence even if the specifications are different from the specimens. In this study, the effect of changing the aspect ratio of the wall was estimated using geometry, but experimental values that can verify the aspect ratio have not been obtained. In the future, in-plane shear test will need to be conducted to clarify the effects.

ACKNOWLEDGEMENT

This work was supported by JST COI Grant Number JPMJCE1315.

REFERENCES

[1] Kiyoshi Uzawa , Yoshihiro Saito , Atsushi Hokura ： APPLICATION OF COMPOSITE MATERIALS TO CIVIL ENGINEERING AND CONSTRUCTION FIELDS -NEW INITIATIVES THROUGH ADVANCED MATERIALS AND INNOVATIVE MANUFACTURING TECHNOLOGY-, Journal of Japan Society of Civil Engineers, Ser. A1 (Structural Engineering & Earthquake Engineering (SE/EE)) 73(5), II_1-II_9, 2017.5

[2] Yuya Takaiwa, Akina Furuie, Nobuji Sakurai, Koji Kubo, Kiyoshi Uzawa: STRUCTURAL PERFORMANCE EVALUATION OF TIMBER ARCHITECTURE WITH SEISMIC RETROFIT BY CFRTP, World Conference on Timber Engineering 2020 TA0706 2021.8

[3] Yuya Takaiwa, Katsuhiko Nunotani, Kiyoshi Uzawa：DEVELOPMENT AND RESEARCH OF END FIXING STRUCTURE FOR EXPANDING THE USE OF CFRP STRANDS，AIJ Journal of Technology and Design 28(68)，pp.36-41，2022.2

[4] Yuya Takaiwa, Katsuhiko Nunotani, Kiyoshi Uzawa：Development of tough CFRP strand end fixation，AIJ Journal of Technology and Design 27(65)，pp.108-113，2021.2

[5] Yuya Takaiwa, Katsuhiko Nunotani, Atsushi Hokura, Shiro Noguchi, Nobuaki Inui, Tadashi Sakuma, Kiyoshi Uzawa: INFLUENCE OF WELDING TEMPERATURE ON ADHESION PERFORMANCE OF CFRTP STRAND ROD-SOCKET, 16th Japan International SAMPE Symposium & Exhibition 3A-06 2019.9

[6] Hina Takizawa, Hiroki Matsumoto, Nobuji Sakurai, Kiyoshi Uzawa, Yuya Takaiwa: Structural Performance Evaluation of Timber Frame with CFRTP Reinforcement, 17th Japan International SAMPE Symposium & Exhibition S01 2021.12

[7] Architectural Institute of Japan: Fundamental Theory of Timber Engineering, Architectural Institute of Japan, 2010.10, p.98

World Conference on Timber Engineering Oslo 2023

POST-EARTHQUAKE ASSESSMENT AND DOCUMENTATION OF TIMBER ROOFS

Mislav Stepinac[1], David Anđić[2], Juraj Pojatina[3]

ABSTRACT: In 2020 Croatia was struck by two strong earthquakes. Croatian building stock is in big part made of masonry with timber floor and roof structures. Given that masonry structures are highly vulnerable to seismic actions, damage occurred to more than 70.000 buildings. Due to widespread damage, there is a great need for a detailed and more comprehensive post-earthquake damage assessment. This paper briefly presents the post-earthquake damage assessment in the historic parts of Zagreb and the surrounding area after the recent earthquakes in 2020. Special focus is set on traditional timber roofs – traditional roof systems in Croatia, damages to the load-bearing elements due to earthquake excitations, maintenance issues, wrong renovation of the attics, etc. Also, the role of UAVs, photogrammetry and laser scanners in the assessment and preservation of heritage buildings is shown.

KEYWORDS: Earthquake, Timber Roofs, Assessment, Laser Scanning, UAV

1 INTRODUCTION

The European building stock consists of a large number of masonry buildings with roofs and floors made of wood. This type of structures often gives ancient European cities a recognizable identity, but are vulnerable to seismic excitation. Therefore, knowledge of their current condition and possible structural upgrading is beneficial. In this context, the continuous assessment and monitoring of the seismic safety and vulnerability of buildings must be carried out at the highest level and according to the most modern principles [1–3].

In 2020, Croatia was hit by two strong earthquakes. After the earthquake in Zagreb in March 2020 (M_L =5.5), which damaged about 25,000 buildings, Croatia was again hit by a destructive earthquake of magnitude 6.2 in December 2020. Sisak-Moslavina County suffered the most severe consequences; many historical and cultural buildings were severely damaged. According to the Croatian Center for Earthquake Engineering (HCPI - in Croatian), more than 57,000 buildings were damaged [4,5]. World Bank estimates the total financial damage from the Zagreb earthquake as EUR 11.3 billion [6] and EUR 5.1–5.5 billion for the Petrinja earthquake [7].

Cities in continental Croatia were built on the legacy and principles of construction in Austro-Hungary at the beginning of the 20th century. Most of the historic city centres were built before the enactment of modern earthquake standards, and the buildings were not designed to be earthquake resistant. After the 1963 Skopje earthquake, the standards were developed and building styles changed, and different materials were used for the construction of new structures. Before the introduction of the earthquake standards, the most common building material used was a combination of masonry and wood. The walls were made of masonry and the mezzanines and roofs were made of wood. A large number of such buildings were not adequately maintained, resulting in significant damage to these facilities. Since the mezzanine structures are mostly made of wood, the structures lack the box effect - they are too weak to withstand horizontal actions [8–12]. While masonry buildings have been severely damaged, recent earthquakes have shown that no wood buildings were extensively damaged by the earthquake. However, parts of the structural systems were damaged, especially the timber roofs of typical masonry buildings.

This paper presents the typology of timber roofs in Croatia and the damage caused by the recent earthquakes. The presented results of the damages and the identification of typical damages after an earthquake should be useful for policy makers and for the future implementation of development strategies in the renovation of cities. Since the roof systems in Zagreb and other historic urban areas are similar, shown figures and photos can be of use in assessment of other damaged roof systems.

2 TYPICAL TIMBER ROOF SYSTEMS IN CONTINENTAL CROATIA

In this paper, the focus is placed on the distinct parts of Zagreb, where older buildings predominate, most of which are built with traditional timber roof systems. The roof structure is usually a king or queen post truss, but there are also many combined forms of timber roof structures. The basic types of traditional timber roof systems in Zagreb are shown in Figure 1. The purlins are almost always supported by brick or parapet walls. Spatial roof stabilization (bracing) is usually not executed. A

[1] Mislav Stepinac, Faculty of Civil Engineering, University of Zagreb, mislav.stepinac@grad.unizg.hr
[2] David Anđić, Studio Arhing ltd., david@studio-arhing.com
[3] Juraj Pojatina, Studio Arhing ltd., juraj@studio-arhing.com

https://doi.org/10.52202/069179-0523

small number of buildings have a concrete slab under the roof systems due to renovation works [13].

Figure 1: *Typical timber roof structures in Zagreb*

3 DAMAGES TO TIMBER STRUCTURES

The damage methodology for the roof elements and structure was divided into five damage levels: no damage, very minor damage, moderate damage, significant damage, severe damage. Figure 2 shows the extent of damage to roofing and wooden roof structures in the historic districts of Zagreb. In Donji Grad (Lower Town), the buildings are larger in plan than in Gornji Grad (Upper Town); therefore, the structural systems are also different. In the Upper Town, single-family houses and villas predominate, while in the Lower Town, multi-family houses with mostly 7 to 9 housing units are the most common buildings. According to the engineers' decision, the total number of severely damaged roofs was 274 in the Lower Town and 189 in the Upper Town. Damage to roofing was found on 598 buildings in the Lower Town and 516 buildings in the Upper Town [4,13].

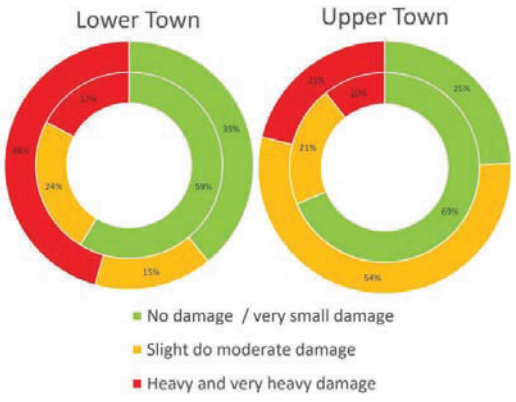

Figure 2: *Statistical data about damage to roofs (inner circle: damaged roof systems, outer circle: damaged roof coverings)*

In summary, the load-bearing parts of the roof structures remained mostly undamaged. The main damage observed at the roof level is damage to the roof coverings, i.e. tiles, decorative elements and non-structural elements.

The failure of non-structural elements such as chimneys and decorative elements on facades was observed on almost all buildings in the city center. Failure of gable walls, masonry columns, wall sections between or under windows, vaults, ceilings, staircases, etc. was common. Since the two materials (timber and masonry) have very different properties and masses, the post-earthquake damage was also very different. The two most typical masonry damages, due to the "pushing" of timber elements and the poor connection with masonry walls, are shown in Figures 3 & 4.

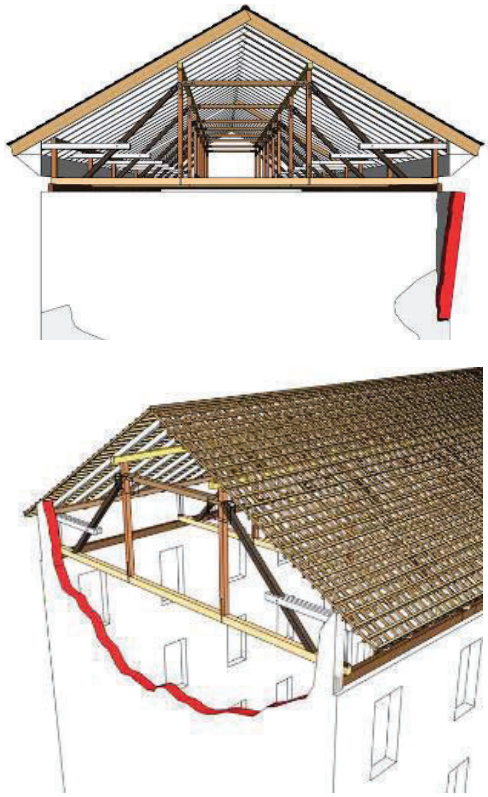

Figure 3: *Typical damages to masonry walls*

Figure 4: *Failure of gable walls (photo credit: M. Stepinac)*

https://doi.org/10.52202/069179-0523

Roof systems often become unstable due to the collapse of individual load-bearing walls beneath them or severe chimney failures (Figure 5 & 6). Post-earthquake inspections showed that many of the chimney failures resulted in direct damage to the roofs. In some locations, the chimneys damaged the supporting roof structure, but in most cases only the rafters broke and the integrity of the roof was maintained (Figures 7 and 8).

Figure 5: *Failure of timber elements due to chimney failure (photo credit: R. Gulić)*

Figure 6: *Timber roof collapse – Sisak cathedral (photo credit: Studio Arhing d.o.o.)*

Figure 7: *Failure of chimneys (from outside) (photo credit: M. Stepinac)*

Figure 8: *Failure of chimneys (from inside) (photo credit: M. Stepinac)*

Maintenance was identified as one of the most important aspects that contributed to the condition of buildings after the earthquake. Since a large number of buildings were poorly maintained or not maintained at all, the properties of the masonry deteriorated over the years, and the seismic performance of such buildings was worse [5]. In many cases, water penetration degraded the properties of both masonry and wood elements (Figure 9).

Figure 9: *Failure of timber elements due to water leakage and seismic excitations (photo credit: Studio Arhing d.o.o.)*

Timber beams on wall parapets along with attic ceiling wooden beams were severely deteriorated due to aforementioned lack of maintenance and due to original defects at the time of construction. The inadequate connections and bad detailing is common and one example is shown in Figure 10. As carpentry joint were used for connections, often, “secondary constructive” screws were missing. Although carpentry joints are considered good in terms of characteristic load combinations, when it comes to dynamic loading with cyclic nature, like earthquake, poor behavior was observed in several cases.

https://doi.org/10.52202/069179-0523

Figure 10: *Bad detailing (photo credit: Studio Arhing d.o.o.)*

Typical conversions of building spaces convert non-living spaces into living spaces (e.g., basements, attics, or utility rooms). This room conversion often involved demolition of partition walls, and undesirable intervention in the load-bearing walls is also common. The conversion of the attic for living purposes resulted in numerous changes to the roof structure. Often timber tie elements were cut to insert the door (Figure 11), which significantly changed the basic static system of the roof structure itself. Also, traditional timber structural systems were replaced by masonry or concrete elements as shown in Figure 12.

Figure 11: *Improper attic modifications (photo credit: HCPI* [4]*)*

Figure 12: *Improper attic modifications (photo credit: HCPI* [4]*)*

4 USING OF MODERN TECHNOLOGIES IN POST-EARTHQUAKE ASSESSMENTS

Regular post-earthquake assessments should be facilitated and improved by state-of-the-art technologies for preservation and digitization of cultural heritage buildings. The construction sector is the slowest to adopt new technologies and this should be changed [14,15]. This motivates the search for a technological solution for the safety assessment of existing structures and the digitization of cultural heritage buildings. The advantages and disadvantages of the new technologies, which are intended to complement the traditional methods, are discussed by [16–18].

Unmanned aerial vehicles (UAV) have proven very useful during the rapid assessment of roofs, as well as detecting defects/damage in hard- to-reach places. Figure 13 shows a post-earthquake assessment scenario using a UAV. An engineer cannot see what has happened on the higher floors or on the roof of a building during an on-site assessment from the street. With a UAV device the above information can be easily assessed.

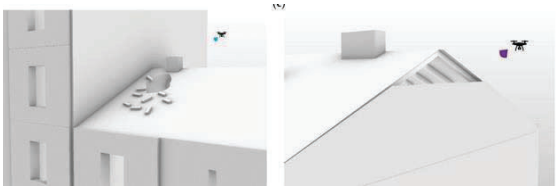

Figure 13: *Possible damage on the roof level of a building after an earthquake* [16]

While drones are very useful in rapid inspections of unreachable spots of buildings, detailed inspections, especially of heritage buildings, should be conducted in a more comprehensive manner. Since the entire city center of Zagreb is under heritage protection, special care was taken to document the building condition in terms of architectural style, details and design, but also in terms of structural impact and peculiarities.

In the following figures, an example of laser scanning is shown, which helped to better understand the structural system. Laser scanning was used to create a 3D point cloud of the interior and exterior of the building. The laser scanner used in the following case study is a Leica BLK360, a compact imaging laser scanner that uses a 360° laser distance meter and high-resolution panoramic images. The collected data is then processed using the Cyclone Register 360 software package. Using three spherical HDR panoramic cameras and a thermal imaging camera, 3D point clouds are delivered with millimetres accuracy. The point cloud can be further used to create an accurate 3D model, to create a precise 2D floor plan, or to convert it into a mesh for visualization. Since, in this particular buildings, it was not easy to see the force path, the point cloud of the laser scanner was very useful (Figures 14-16). Laser scanning has also proven to be a very useful tool for very complex geometries, both for heritage documentation and for easier navigation during post-processing to create 2D and 3D drawings. An added

value is also a 360° image for a specific location in the building. Figures 17 to 19 show the case study of the Zagreb Cathedral.

Figure 14: *Point cloud of a case study building*

Figure 15: *Point cloud of a case study building: cross section with "filming positions" (red dots)*

Figure 16: *Typical cross-section of the case study building*

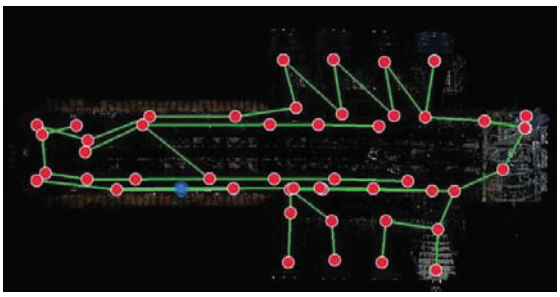

Figure 17: *Zagreb Cathedral with laser scanning "filming positions" (red dots)*

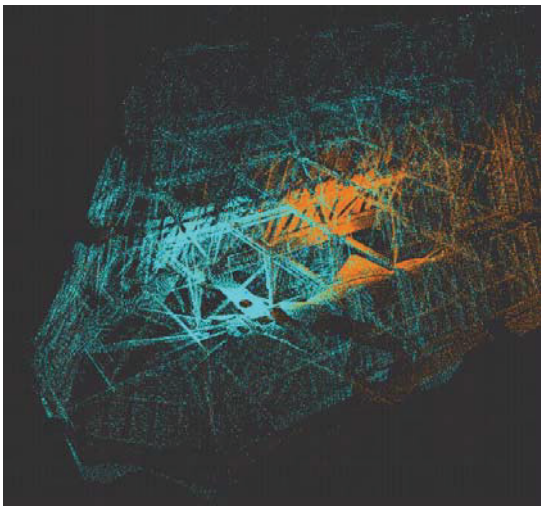

Figure 18: *Zagreb Cathedral – alignment of two scanning positions*

Figure 19: *Zagreb Cathedral – 360° image*

5 CONCLUSIONS

In this paper, a brief overview of damage to timber structural members after a moderate earthquake is presented. Basic statistical data on damage to roof structures after the Zagreb earthquake show the good behavior of timber roofs and give us an idea of why some of the roof structures collapsed.

When repairing roof structures, in most cases worn elements are replaced, elements with insufficient load-bearing capacity are strengthened and cracked elements are filled. During retrofitting, the influence of spatial stability of the roof structure is often forgotten, especially when spatial changes are made. The structural system

https://doi.org/10.52202/069179-0523

recognition and proper evaluation of former is also often miscarried. Unusual hybrid roof structures also add to the complexity of properly analysing and choosing the correct repair strategy. The influence of secondary elements such as chimneys and gables is also forgotten when the roof plays a stabilizing role in earthquake actions. In addition, the issue of details is questionable. The condition of the carpentry details is usually taken as given without considering the possibility that the distribution of forces in the system may change during lateral actions. In order to ensure the correct type of repair, it is important to have appropriate and high quality data on the condition of the structure and to use it for more detailed analysis so use of modern technologies is welcome. In this paper several benefits of laser scanners and UAVs is very briefly presented on two case studies.

ACKNOWLEDGEMENT

This research was partially funded by the Croatian Science Foundation, grant number UIP-2019-04-3749 (ARES project—assessment and rehabilitation of existing structures—development of contemporary methods for masonry and timber structures), project leader: Mislav Stepinac.

REFERENCES

[1] Dimovska S, Saloustros S, Pelà L, Roca P. Seismic Vulnerability Assessment of Representative Building Typologies from Barcelona‘s Eixample District 2021. doi:10.23967/sahc.2021.239.

[2] Funari MF, Silva LC, Mousavian E, Lourenço PB. Real-time Structural Stability of Domes through Limit Analysis: Application to St. Peter’s Dome. Int J Archit Herit 2021:1–23. doi:10.1080/15583058.2021.1992539.

[3] Stepinac M, Kisicek T, Renić T, Hafner I, Bedon C. Methods for the Assessment of Critical Properties in Existing Masonry Structures under Seismic Loads—The ARES Project. Appl Sci 2020, Vol 10, Page 1576 2020;10:1576. doi:10.3390/APP10051576.

[4] The Database of Usability Classification, Croatian Centre of Earthquake Engineering (HCPI - Hrvatski centar za potresno inženjerstvo), Faculty of Civil Engineering, University of Zagreb and The City of Zagreb, June 2020. n.d.

[5] Stepinac M, Lourenço PB, Atalić J, Kišiček T, Uroš M, Baniček M, et al. Damage classification of residential buildings in historical downtown after the ML5.5 earthquake in Zagreb, Croatia in 2020. Int J Disaster Risk Reduct 2021;56:102140. doi:https://doi.org/10.1016/j.ijdrr.2021.102140.

[6] Government of the Republic of Croatia and the World Bank. The Croatia Earthquake - Rapid Damage and Need Assessment 2020. 2020.

[7] World Bank Report: Croatia December 2020 Earthquake – Rapid Damage And Needs Assessment, 2020, March 2021, Government of Croatia. n.d.

[8] Ortega J, Vasconcelos G, Rodrigues H, Correia M. Assessment of the influence of horizontal diaphragms on the seismic performance of vernacular buildings. Bull Earthq Eng 2018. doi:10.1007/s10518-018-0318-8.

[9] Mirra M, Ravenshorst G, de Vries P, van de Kuilen JW. An analytical model describing the in-plane behaviour of timber diaphragms strengthened with plywood panels. Eng Struct 2021;235:112128. doi:10.1016/J.ENGSTRUCT.2021.112128.

[10] Stepinac M, Rajčić V, Barbalić J. Influence of long term load on timber-concrete composite systems. Gradjevinar 2015;67. doi:10.14256/JCE.1170.2014.

[11] Mirra M, Ravenshorst G, van de Kuilen J-W. Comparing In-Plane Equivalent Shear Stiffness of Timber Diaphragms Retrofitted with Light and Reversible Wood-Based Techniques. Pract Period Struct Des Constr 2021. doi:10.1061/(asce)sc.1943-5576.0000602.

[12] Moretić A, Stepinac M, Lourenço PB. Seismic upgrading of cultural heritage – A case study using an educational building in Croatia from the historicism style. Case Stud Constr Mater 2022;17. doi:10.1016/j.cscm.2022.e01183.

[13] Perković N, Stepinac M, Rajčić V, Barbalić J. Assessment of timber roof structures before and after earthquakes. Buildings 2021;11. doi:10.3390/buildings11110528.

[14] Bughin J, Manyika J, Woetzel J, Mattern FM, Chui S, Lund A, et al. A Future That Works: Automation, Employment, and Productivity. McKinsey Glob Inst 2017.

[15] McKinsey Global Institute. Global Media Report 2014. Glob Ind Overv 2014.

[16] Stepinac M, Gašparović M. A Review of Emerging Technologies for an Assessment of Safety and Seismic Vulnerability and Damage Detection of Existing Masonry Structures. Appl Sci 2020, Vol 10, Page 5060 2020;10:5060. doi:10.3390/APP10155060.

[17] Grazzini A, Chiabrando F, Foti S, Sammartano G, Spanò A. A Multidisciplinary Study on the Seismic Vulnerability of St. Agostino Church in Amatrice following the 2016 Seismic Sequence. Https://DoiOrg/101080/1558305820191575929 2019;14:885–902. doi:10.1080/15583058.2019.1575929.

[18] Baiocchi V, Dominici D, Mormile M. Uav Application in Post – Seismic Environment. Int Arch Photogramm Remote Sens Spat Inf Sci 2013;XL-1/W2:21–5. doi:10.5194/isprsarchives-xl-1-w2-21-2013.

World Conference on Timber Engineering Oslo 2023

EVALUATION OF VIBRATION CHARACTERISTICS OF EXISTING TIMBER ARCHITECTURE BY MICROTREMOR MEASUREMENT -EXAMINATION WHEN IT IS DIFFICULT TO INSTALL AN ACCELEROMETER IN THE ATTIC-

Hiroki Yoshinuma[1], Yuya Takaiwa[2]

ABSTRACT: In this paper, we investigate a method of understanding the natural frequency characteristics of existing two-story timber architecture by installing an accelerometer on the floor of the second floor and conducting microtremor measurement under the condition that an accelerometer cannot be installed in the attic. First, by surveying the trend of Registered Tangible Cultural Properties by the Agency for Cultural Affairs in Japan, we found that the architecture that needs seismic diagnosis in the future is two-story timber houses that are more than 50 years old. Next, we conducted a structural performance survey of existing timber architecture under the same conditions, using microtremor measurement and human excitation, and finite element analysis after the survey, and clarified the natural frequency characteristics of existing timber architecture by comprehensively judging the survey results.

KEYWORDS: Microtremor Measurement, Natural Frequency Characteristics, Seismic Diagnosis

1 INTRODUCTION

In Japan, the Law for the Protection of Cultural Properties was enacted in 1950 to protect and utilize architecture, paintings, sculptures, handicrafts, calligraphic works, classics, ancient documents, and other tangible cultural properties of high historical and artistic value, and to improve culture. In Japan, where earthquakes occur frequently, it is necessary to accurately understand the structural performance of old architecture and to reinforce it appropriately to utilize it. In 1996, the Agency for Cultural Affairs promulgated the "Guidelines for Ensuring Earthquake Safety of Cultural Property Buildings, etc." [1] to promote seismic retrofitting without compromising the cultural value of architectures. In this context, as a nondestructive seismic diagnosis method for architectures, microtremor measurement is utilized to grasp the structural characteristics of architecture on a global scale by installing highly sensitive accelerometers in the structure of the architecture to be investigated [2,3]. At present, earthquake-resistant diagnosis is steadily underway, and according to a survey on the current status of earthquake-resistant measures for national treasures and important cultural properties [4] conducted by the Agency for Cultural Affairs in 2019, 95% of national treasures and important cultural properties have been reinforced against earthquakes or measures have been taken to ensure the safety of users.

On the other hand, the Law for the Protection of Cultural Properties was revised in 1996 to introduce a system of registration of cultural properties to preserve more architectures with cultural value. Compared to national treasures and important cultural properties, the regulations of the cultural property protection system are less stringent, so registration is easier and the architectures are often small in scale. Nondestructive seismic diagnosis using microtremor measurement is desirable for such small architectures. However, most of the architectures, such as national treasures and important cultural properties, are relatively medium to large, and the accelerometers used for microtremor measurement were installed at any position by the investigator in the attic. However, in small architectures, it is difficult for the investigator to install the accelerometer at any position in the attic because the attic space is small and the cross-sectional dimensions of the components are small.

This study investigates a method to determine the natural frequency characteristics of an existing two-story timber architecture by installing an accelerometer on the floor of the second floor and conducting microtremor measurements under conditions where an accelerometer cannot be installed in the attic.

[1] Hiroki Yoshinuma, Graduate School, Department of Architecture, Faculty of Science and Engineering, Toyo University.

[2] Yuya Takaiwa, Associate Professor, Department of Architecture, Faculty of Science and Engineering, Toyo University, Dr. Eng. takaiwa@toyo.jp
2100 Kujirai, Kawagoe-shi, Saitama, Japan (350-8585)

https://doi.org/10.52202/069179-0524

2 Structural Performance Survey of Existing Architectures

Registered Tangible Cultural Properties provide a modest measure of protection against the loss of cultural heritage from the modern era due to rapid national and urban development in recent years. Compared to the recognition of National Treasures and Important Cultural Properties, the examination required for approval is less stringent, and the regulations for maintenance and management after recognition are also less stringent, making it easier to apply for protection.

2.1 Current Status of Registered Tangible Cultural Properties

Fig. 1 shows the changes in the number of registered tangible cultural properties during the period 1996 to 2021. In 1996, when the system of registered tangible cultural properties was established, 83 items were registered, and the number of registered items has been increasing every year since then, reaching 12,7740 items in 2021. From the change in the number of registered items shown in fig. 1, it can be seen that the trend of increase has been constant since the system was introduced, and is expected to continue to increase in the future.

In Fig. 2, we show a breakdown of the registered tangible cultural properties by year of completion as of 2022. From Fig. 2, it can be confirmed that the number of registered buildings is dominated by young architecture. The largest proportion of the registered architectures is from 1900 to 1950. The reason why the number of registered architectures between 1950 and 2000, which are the youngest in fig. 2, is small is that the number of architectures that meet the condition of "more than 50 years old" is generally small. More time is needed before the value of architectures from this period will be recognized as having cultural value worthy of preservation, and as time passes, the number of registrations will increase, as it has for architectures from other periods, and they will become the element that accounts for the largest percentage in the future.

Fig. 3 shows the registered uses of architecture for each age group, with the lowest percentage of "House" registered for architecture built before 1600 to 1750, and similar percentages for other uses. For architecture built between 1750 and 1800, "House" accounted for the largest percentage of registrations, followed by "Industries". For architecture built between 1950 and 2000, the percentage of "House" is smaller again. In the case of buildings built between 1950 and 2000, the share of "House" is again small. This is thought to be because the number of houses with cultural value is small in younger architecture. In other words, the ratio of the use of architecture in this age group is expected to change in the future.

Fig. 4 shows the number of floors of houses certified as registered tangible cultural properties. Fig. 4 shows that most of the houses of any age are "One story" or "Two-story". The ratio of "One story" houses is higher in older houses and the ratio of "Two-story" houses is higher as the age of the houses decreases. This trend is consistent with the history of multi-story houses in Japan due to modernization. However, we cannot discuss the trend of houses built between 1950 and 2000 because the number of registered houses is small at this stage.

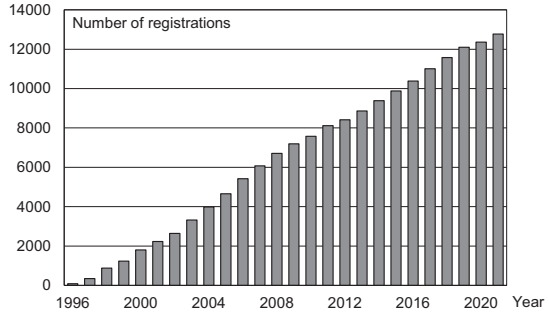

Fig. 1 *Number of registered tangible cultural properties*

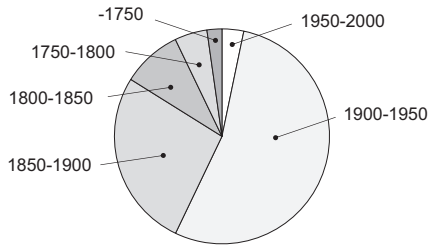

Fig. 2 *Breakdown of registered tangible cultural properties by year of completion*

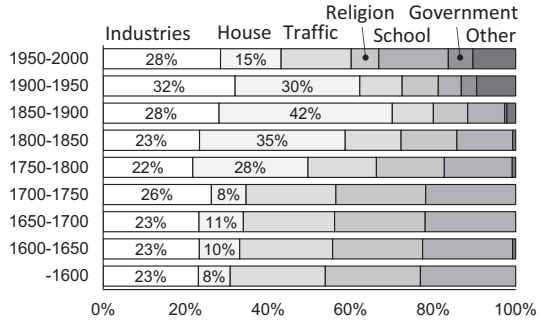

Fig. 3 *Architecture use*

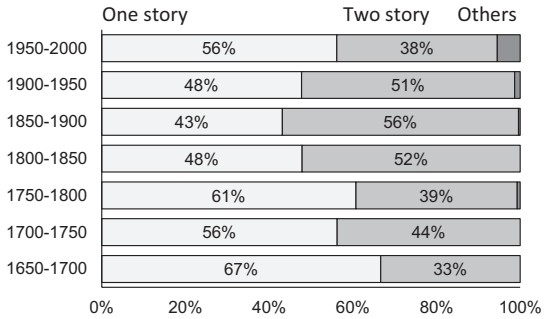

Fig. 4 *Number of Floors in Residential Architectures*

A survey of the trends in architectures recognized as registered tangible cultural properties revealed the following:

https://doi.org/10.52202/069179-0524

1. The number of registered architectures is increasing year by year.
2. The number of registered architectures that are young is high.
3. The number of registered architectures for housing use is high.
4. More two-story houses are registered.

Considering the above, a structural performance survey will be conducted for existing timber structures that are more than 50 years old and have a traditional building composition. In the survey, microtremor measurement will be carried out to understand the natural frequency characteristics of the housing scale structure.

2.2 Overview of the surveyed architectures

The architecture to be surveyed is an existing timber architecture in Taito-Ku, Tokyo. Built-in 1954, the architecture consists of four dwelling units surrounding a courtyard on the east side and another large dwelling unit on the west side. The architecture is located on the north side of the site, with a garden on the south side. Most of the architecture is one-story, and only the central part of the building is two-story. In the structural survey of the architecture, the area including the two-story part was chosen as the survey area.

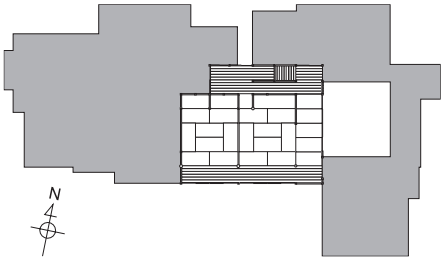

Fig. 5 *Scope of investigation*

Fig. 5 shows the survey area of the architecture. The horizontal force-resisting elements of the architecture are the full-wall and hanging walls, which consist of earthen walls, and the plank walls, which consist of three layers of small wide boards. The earthen walls have been in place since the construction of the architecture was completed, and the plank walls were replaced by earthen walls to improve the resistance of the architecture to seismic forces. The walls on the east and south sides of the survey area do not have any walls on all sides so that the view of the courtyard and garden can be seen from inside, and most of the bearing elements are hanging walls. On the other hand, the west and north sides of the architecture have many full-face walls as corridors and room boundaries.

In past earthquakes, one of the reasons for the collapse of timber architectures was the uneven distribution of load-bearing elements such as this architecture [5,6]. The uneven distribution of bearing elements has been observed in many existing architectures built before the establishment of seismic performance evaluation [7]. If the load-bearing elements are unevenly distributed, the architecture will exhibit twisting behavior during an earthquake, and the entire building will collapse in a twisting manner due to large deformation and destruction of the surface with few load-bearing elements (the surface facing the courtyard and garden in the present building).

2.2.1 Outline of the microtremor measurement

In the survey, multi-point simultaneous measurement using a total of six 3-axis wireless accelerometers is performed. Photo 1 shows the measurement system. Fig. 6, 7, and 8 show the installation locations of the accelerometers. The coordinate axes shown in the figures are the three-axis coordinates of the accelerometers, and the direction shown in the figures was chosen based on the installation conditions of the accelerometers. The measured acceleration waveforms were subjected to fast Fourier transform (FFT) to obtain the natural frequency from the transfer function. The input data of the transfer function is measured from one accelerometer installed in the garden, and the output data is measured from five accelerometers installed on the floor of the second floor.

Photo 1 *Measurement system*

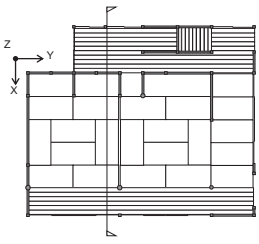

Fig. 6 *First floor plan*

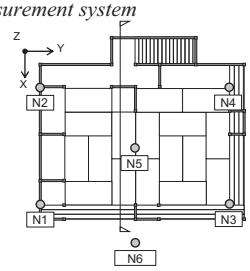

Fig. 7 *Second floor plan*

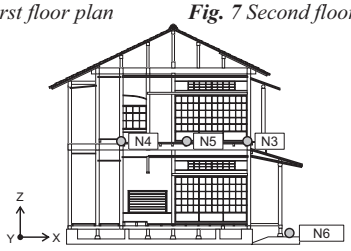

Fig. 8 *Cross-sectional view*

The sampling frequency of the measurement was set to 100 Hz so that the analysis frequency range would be 50 Hz, taking into consideration the fact that the main natural frequency of timber architectures is around 15 Hz at maximum and that the effect of aliasing caused by FFT should be eliminated. The measurement time is 360 seconds to accommodate a maximum FFT frame size of 32,768 points. When the FFT is performed on data with a sampling frequency of 100 Hz and a frame size of 32,768 points, the frequency resolution is approximately 0.00305 Hz, which enables analysis with fine precision. The FFT converts the sampled discontinuous microtremor waveform into a continuous waveform by using a window

https://doi.org/10.52202/069179-0524

function. The window function used is the Hanning window, considering that the microtremor is a continuous oscillation and that it can be analyzed with high-frequency resolution.

2.2.2 Human-powered excitation

An accelerometer was installed in the area to be investigated, and free vibration was induced by human force excitation. The natural frequencies are determined by the FFT of the acceleration data. Since the acceleration measurement is limited to the time when the vibration generated by human force excitation continues, the frame size for FFT is 1,024 points, which can be measured in about 10 seconds. As a result, the frequency resolution is inferior to that of FFT using a frame size of 32,768 points for constant microtremor measurement. Fig. 9 shows the direction of human-powered excitation, and Fig. 10 shows the locations of the accelerometers.

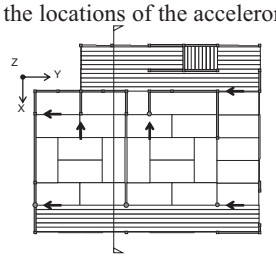

Fig. 9 *Direction of vibration*

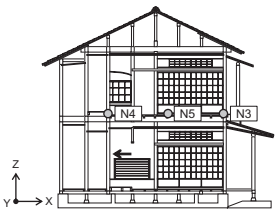

Fig. 10 *Installation location*

The locations of the accelerometers are the same as those used in the microtremor measurement, but accelerometer N6, which was installed in the garden in the microtremor measurement, is not used because the input vibration from the ground to the building does not need to be considered in the human force excitation measurement.

We decided to push the columns on the first floor so that the second mode, in which the horizontal movement of the second-floor floor dominates, would appear in the human power excitation. Some of the columns where the accelerometers were installed had walls attached to them, and such columns could not be physically pushed. Therefore, two pillars were pushed in the X-axis direction, and the pillars around N2 and the pillars directly below N1, N3 and N4 were pushed in the Y-axis direction. The pillars were chosen symmetrically in the direction of vibration to prevent artificial twisting due to excitation.

3 Results of various measurements

3.1 Results of normal microtremor measurement

The Fourier spectrum was obtained by FFT using the Hanning window as the window function for the acceleration data observed from the microtremor measurement. Next, the transfer function is obtained using the input waveform of accelerometer N6 installed in the garden and the output waveform of the other five accelerometers N1 to N5. The natural frequency of the architecture is determined to be the frequency at which the transfer function is dominant.

Fig. 11 and 12 show the frequency-transfer function relationship in the x-axis and y-axis directions. From the waveform, multiple excitations can be confirmed. This is probably because there are several architectures attached to the surveyed area, and the natural frequencies of these architectures were observed simultaneously. It is difficult to grasp the natural frequency of the surveyed area from this waveform alone.

From the graph in the X-axis direction, it can be confirmed that the waveforms of the combinations of N1 and N2 and N3 and N4 are identical. These combinations are located on a common beam in the X-axis direction. Next, from the graph in the Y-axis direction, it can be confirmed that the waveforms are identical for the combinations of N1 and N3, and N2 and N4. This combination is installed on a common beam in the Y-axis direction. The waveforms of the combinations of measuring points in each axis direction are identical, and the waveforms of the combinations of measuring points parallel to each axis are different, indicating that the shear deformation is caused by the low in-plane shear stiffness of the horizontal structure.

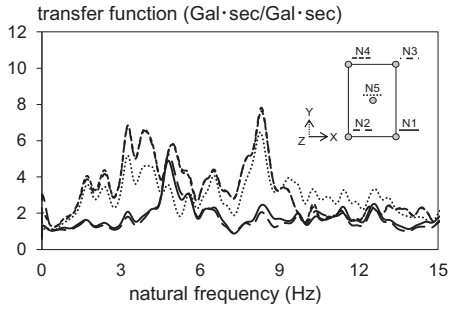

Fig. 11 *X-axis frequency-transfer function relationship*

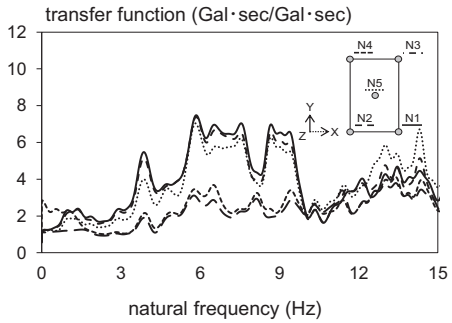

Fig. 12 *Y-axis frequency-transfer function relationship*

3.2 Results of Normal Microtremor Measurement and Manpower Excitation

In this survey, the natural frequency of the surveyed area could not be determined because multiple excitations were observed only by microtremor measurement. Therefore, the natural frequency was determined by combining the results of microtremor measurement with the results of free vibration by human power excitation. Fig. 13 and 14 show the results of constant microtremor measurement and free vibration in the X- and Y-axis directions. From the measurement results, it can be confirmed that there is a frequency that is dominant in the constant microtremor measurement but not in the free

https://doi.org/10.52202/069179-0524

vibration. This frequency is considered to be the natural frequency of the architecture in the range where no vibration is applied (outside the survey area) or the natural frequency of the first mode in the survey area. Therefore, the natural frequency of the second mode of the surveyed area is judged to be the frequency that shows excellence in both microtremor measurement and free vibration. From the measurement results, the natural frequency of the second mode in the investigated range is 3.26 Hz in the X-axis direction and 3.88 Hz in the Y-axis direction.

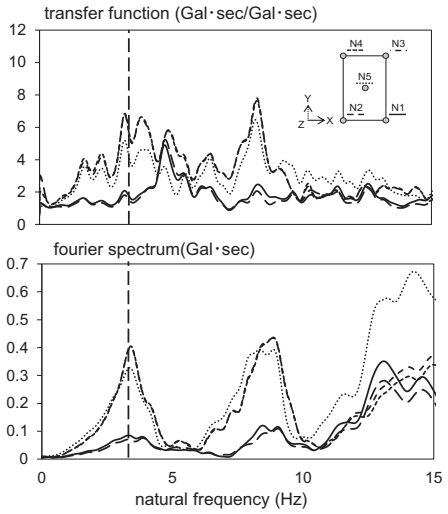

Fig. 13 *X-axis vibration*

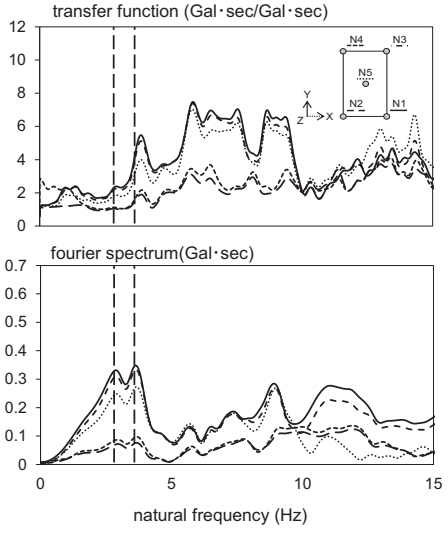

Fig. 14 *Y-axis vibration*

Fig. 15 shows the vibration modes at the dominant natural frequency. The vibration modes at 3.26 Hz and 3.88 Hz are the same, although the frequencies are different. From the vibration modes in the X-axis direction, it can be confirmed that the amplitudes of N1 and N2 are small, and those of N3 and N4 are large because the amplitudes of N1 and N2 are small due to the wall dividing the room. On the other hand, the amplitude of N3 and N4 is larger because they are adjacent to the courtyard and there is nothing to disturb the vibration. The amplitudes of N2 and N4 are small, and those of N1 and N3 are large because the walls of the corridor are placed on the N2 and N4 sides, which restricts the vibration. On the other hand, the amplitude of N1 and N3 is larger because they face the garden and there is no wall to disturb the vibration.

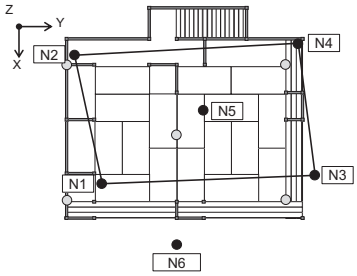

Fig. 15 *Vibration modes (3.26 Hz and 3.88 Hz)*

4 Finite element analysis

Fig. 16 shows an overview of the model. The columns and beams are "beam elements", and the walls are "braced elements". All joints are pin joints because rotational rigidity is not expected. The cross-sectional dimensions of each member were measured in the structural survey, and the column cross-sectional dimensions were approximately 105 mm square. The columns are made of cedar with a bending Young's modulus of 7 kN/mm2 and a density of 380 kg/m3, and the beams are made of cypress with a bending Young's modulus of 9 kN/mm2 and a density of 380 kg/m3 [8,9]. The stiffness of the earthen wall is based on the specific deformation angle of 1/250 rad by the Agency for Cultural Affairs [10]. The in-plane shear stiffness of the wall in the micro-deformation region observed by microtremor measurement is approximately three times the specified deformation angle [6], which is determined by the in-plane shear test. Since the purpose of the present finite element analysis is to determine the natural frequency in the small deformation region, the in-plane shear stiffness of the wall is set to be three times the stiffness at the specified deformation angle of 1/250 rad. The weight of the roof is 1250 N/m2 for a pier-tile roof and 100 N/m2 for a pole-vaulted ceiling [8].

Fig. 16 *Model overview*

4.1 Analysis results

Figs. 17, 19, and 23 show the natural frequencies and vibration modes of the finite element analysis model, and Figs. 18, 20, and 24 show the natural frequencies and vibration modes of the microtremor measurement results corresponding to the analysis model. Figs. 18, 20, and 24 show the natural frequencies of the finite element analysis

https://doi.org/10.52202/069179-0524

results and the microtremor measurement results in parentheses.

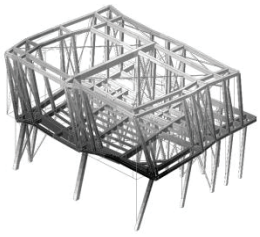

Fig. 17 *Eigen vibration mode (3.64 Hz)*

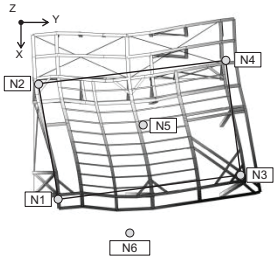

Fig. 18 *Natural modes of vibration (3.64Hz/3.26Hz)*

From the vibration mode of 3.64 Hz in the finite element analysis shown in Fig. 17, it can be confirmed that this is the second mode of architecture because only the floor of the second floor deforms horizontally. From the natural vibration mode shown in Fig. 18, it can be seen that the 3.64 Hz vibration mode of the finite element analysis and the 3.26 Hz vibration mode of the microtremor measurement coincide. This indicates that the dominant natural frequency of 3.26 Hz observed by human power excitation and microtremor measurement is the natural frequency of the second mode of the architecture, and confirms that the analytical model is correctly modeled.

The first modes of the eigenvalue analysis of the same model are shown below.

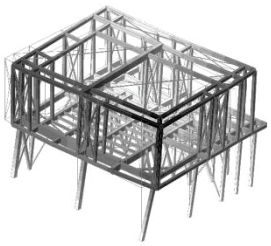

Fig. 19 *Eigenmode (0.91Hz)*

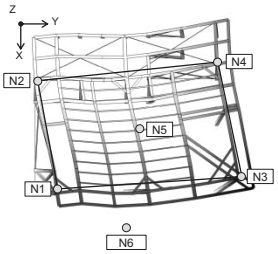

Fig. 20 Eigenmode (0.91Hz/1.05Hz)

From the vibration mode of 0.91 Hz in the finite element analysis shown in Fig. 19, it can be confirmed that 0.91 Hz is the natural frequency indicating the first mode of the architecture because the horizontal deformation of the entire second floor is large. Since the second floor has more walls than the first floor, the deformation of the first floor is dominant in the overall behavior, while the second floor behaves like a rigid body with little deformation. From the natural vibration modes shown in Fig. 20, it can be confirmed that the amplitude of N2 and N4 is small, while that of N1 and N3 is large. This is because the walls of the corridor restrain the vibration of N2 and N4, but there are no walls to restrain the vibration of N1 and N3 facing the edge.

Fig. 21 and 22 show the frequency-transfer function relationship in the X- and Y-axis directions. The natural frequency of the first mode of 0.91 Hz revealed by the eigenvalue analysis corresponds to the measured value of 0.98 Hz in the Y-axis direction, and there is no dominant value close to 0.91 Hz in the X-axis direction. In the finite element analysis, the horizontal displacement in the Y-axis direction is dominant, which confirms the validity of the observed waveforms in the X- and Y-axis directions.

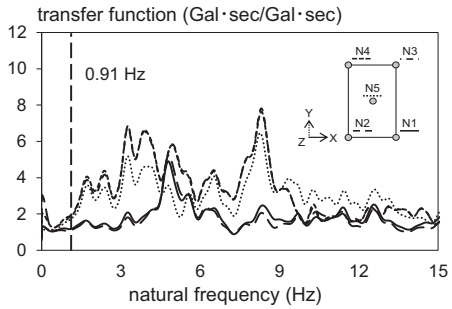

Fig. 21 *Relationship between frequency and transfer function in X-axis direction*

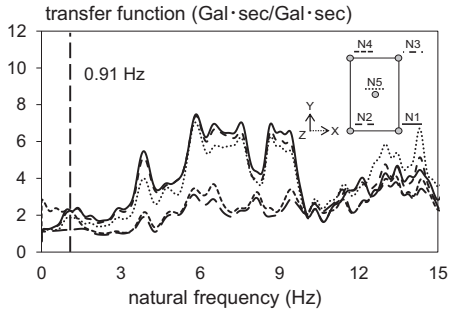

Fig. 22 *Y-axis frequency-transfer function relationship*

Among the results of the microtremor measurement where multiple excitations were observed, the excitation of the natural frequency of the first mode in the Y-axis direction was about 36% larger than that of the other frequencies, which would normally be ignored. In addition, despite the first mode, only N1 and N3 are dominant in the graph due to the difference in the amount of deformation of N1 and N3 and N2 and N4 caused by the uneven distribution of the wall, while N2 and N4 are not dominant. It is difficult to conclude that 0.98Hz is the natural frequency of the first mode under normal circumstances.

Fig. 23 *Eigenmode (1.68Hz)*

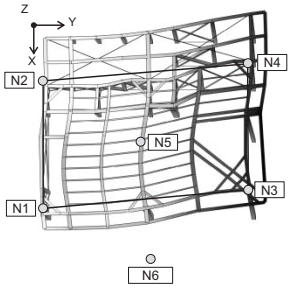

Fig. 24 *Eigenmode (1.68Hz/1.72Hz)*

Fig. 23 shows that the entire second floor deforms horizontally in the X-axis direction in the vibration mode of 1.68 Hz based on finite element analysis, indicating that 1.68 Hz is the natural frequency of the first mode of the architecture. The amplitudes of N1 and N2 are small, and those of N3 and N4 are large, according to the vibration modes in Fig. 24. This is because the vibration of N1 and

https://doi.org/10.52202/069179-0524

N2 is constrained by the wall dividing the room, but there is no wall to constrain the vibration of N3 and N4 facing the courtyard. Figs. 25 and 26 show the frequency-transfer function relationship in the x- and y-axis directions. The natural frequency of the first mode, 1.68 Hz, which was revealed by the eigenvalue analysis, corresponds to 1.72 Hz in the X-axis direction, and there is no dominant value close to 1.68 Hz in the Y-axis direction.

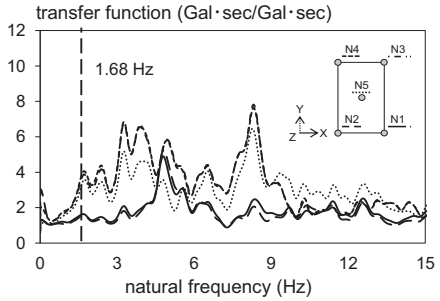

Fig. 25 *X-axis frequency-transfer function relationship*

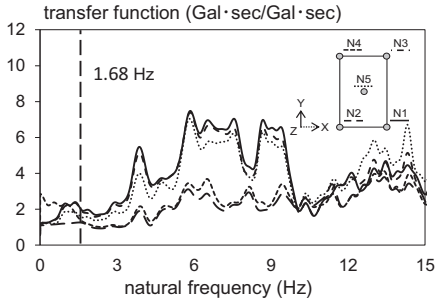

Since the horizontal displacement in the X-axis direction is dominant from the vibration modes of the finite element analysis, the validity of the observed waveforms in the X- and Y-axis directions can be confirmed. Among the results of the microtremor measurement where multiple excitations were observed, multiple excitations were observed near the natural frequency of the first mode in the X-axis direction, and it is difficult to determine the natural frequency only from the results of the microtremor measurement. In addition, only N3 and N4 show the predominance in the graph due to the difference in the amount of deformation of N1 and N2 and N3 and N4 caused by the uneven distribution of the wall, while N1 and N2 do not show any predominance. It is difficult to determine that 1.68 Hz is the natural frequency of the first mode under normal circumstances.

5 CONCLUSIONS

In Japan, the Law for the Protection of Cultural Properties was enacted to preserve the cultural value of historical architecture, and seismic diagnosis for national treasures and important cultural properties has been developed. However, there is no progress in the development of seismic diagnosis methods for registered tangible cultural properties, which are newly subject to preservation under the revised Law for the Protection of Cultural Properties. In this study, the following findings were obtained by conducting a structural survey of historical timber architecture with specifications similar to those of registered tangible cultural properties:

1. By analyzing the data on registered tangible cultural properties published by the Agency for Cultural Affairs, we found that the number of architectures of registered tangible cultural properties is large, and that two-story architecture accounts for half of the total.
2. By conducting microtremor measurement on the existing architecture, we observed multiple excitations of the architectures.
3. The dominant natural frequencies of the second modes were determined by analyzing the resonant frequencies of human power excitation on the first floor of the building.
4. The model was modeled by finite element analysis, and the correctness of the model was confirmed by using the natural frequencies of the second modes observed by microtremor measurement.
5. The natural frequencies of the first modes were determined using the analytical model whose correctness was confirmed, and by comparing them with the measurement results of the microtremor measurement, a slight predominance was confirmed, and the vibration mode was confirmed to be the first mode.

To understand the natural frequency characteristics of existing architecture, it was necessary to consider the results of three methods: microtremor measurement, human power excitation, and finite element analysis.

In this study, we have dealt with only one case of a structural survey, but there are various measurement environments for microtremor measurement, and it is necessary to develop seismic diagnosis methods that can cope with various measurement environments in the future.

ACKNOWLEDGEMENT

This work was supported by Toyo University Top Priority Research Program (2021.4~2024.3).

REFERENCES

[1] Agency for Cultural Affairs: Guidelines for Ensuring the Safety of Cultural Property Architectures during Earthquakes, 1996-01

[2] Tabata, C. Ohashi, Y.: Microtremor Measurement and Possibility of Its Application to Seismic Diagnosis -Study on Seismic Diagnosis for Wooden Structures Part 2-, Journal of Structural and Construction Engineering (Transactions of AIJ), Vol.72 No. 616, 141-147, 2007-06

[3] Takaiwa, Y. and Matsuno, K.: An Experimental Study on Shear Stiffness Evaluation under Large Lateral Deformation of Traditional Wooden Building with Mud Wall, Journal of Structural and Construction Engineering (Transactions of AIJ), Vol.82 No. 738, 1245-1253, 2017-08

[4] Agency for Cultural Affairs: Publication of the Results of the Survey on the Current Status of

https://doi.org/10.52202/069179-0524

Seismic Countermeasures for National Treasures and Important Cultural Properties, 2019.12
[5] Tizo Fujiwara: Summary of damage to timber architectures. 1995 Hyogo-ken Nanbu Earthquake - Damage to Timber Architectures, Kinki Branch of the Architectural Institute of Japan, pp.1-10, 1995. 6.
[6] K. Tsuchimoto: "Seismic Performance of Timber Houses", 1996 Panel Discussion on Timber Structures, Architectural Institute of Japan, pp.57-68, 1996.
[7] Yamada, K.: Study on the Evaluation of Earthquake Resistant Capacity of Traditional Timber Houses in Consideration of the Floor Stiffness and Grid Lines of Bearing Walls, Journal of Structural and Construction Engineering (Transactions of AIJ), Vol.64 No. 525, 79-84, 1999-11
[8] Architectural Institute of Japan: Architecture Load Guidelines and Commentary
[9] Architectural Institute of Japan: Design Criteria and Commentary for Architecture Structures - Allowable Stress and Allowable Strength Design Method
[10] Agency for Cultural Affairs: Guidelines for Aseismic Foundation Diagnosis of Important Cultural Properties (Architectures) (Revised 2012)

World Conference on
Timber Engineering
Oslo 2023

DEVELOPMENT OF SIMPLE REPAIRING HARDWARE FOR DAMAGED ENDS OF WOODEN BEARING WALLS

Wataru Kambe[1]

ABSTRACT: This study investigated the repairing effect for wooden bearing walls (which wall length was 910 or 1820mm) which are repaired by developed hardware. The study found that the repair was effective in increasing the maximum load and energy by more than 100% and 120%, respectively, but not very effective in increasing stiffness, which was often less than half. Additionally, the structural performance of the load-bearing walls with only the repair hardware was found to be equivalent to that with only the joint hardware, suggesting that these performances contribute to the overall structural performance of the repaired specimens.

KEYWORDS: Bearing wall, Repairing hardware for brace-ends, Structural performance

1 INTRODUCTION

This study examines repair methods for braces in wooden bearing walls, specifically in the case of horizontal forces acting on bearing walls due to earthquakes or other causes. Conventional frame construction is the most common type of wooden house construction in Japan and in case of an earthquake, an emergency hazard assessment is made to evaluate the need for repair or reinforcement [1](***Fig. 1***). Repair techniques are used to restore the structural performance of damaged buildings to its pre-damage state, and reinforcement techniques are used to make it higher than the pre-damage state.

This study proposes a new steel hardware repair method, which is simple enough to be installed by DIY hobbyists using tools such as impact wrenches. The study aims to investigate the effect of this repair hardware on the structural performance of 1P and 2P wall-length, bearing walls under monotonic and cyclic loading. The repair hardware will be installed after a horizontal force test, and the structural performance will be compared before and after the repair. Additionally, a separate test will be conducted on a load-bearing wall with only the repair hardware installed to determine the basic structural performance when the repair hardware is used.

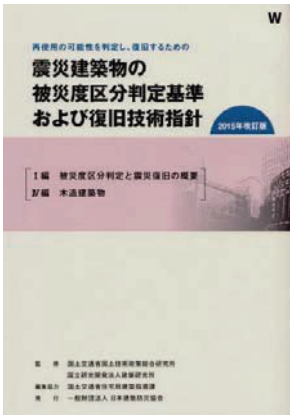

Figure 1: *Documentation*

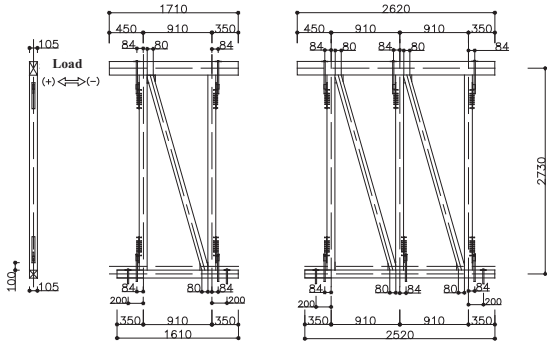

Figure 2: *Geometry of specimens(Unit:mm)*

2 SPECIMENS AND REPAIRING HARDWARE

2.1 SPECIMENS

In this study, horizontal load tests on 1P or 2P wall-length (indicated in ***Fig. 2***) with single-brace which were made of laminated veneer laminate (LVL) were conducted. The species of the LVL members was larch, grade 100E-1 (graded in Japan Agricultural Standard [2]), and the cross-sectional dimensions were 45 x 90 mm. The foundation, columns, and beams were made of laminated timbers of different grade compositions, grade E105-F300 (graded in

[1] Wataru Kambe, Kanto Gakuin Univeristy,Japan, wkambe@kanto-gakuin.ac.jp

https://doi.org/10.52202/069179-0525

Japan Agricultural Standard [3]) with cross-sectional dimensions of 105 x 105 mm for the foundation and columns, and 105 x 180 mm for the beams. The hardware used for the column legs was the screw-fastening type for Hold-down U 35 kN and "Justy Gusset Lite" were used for the joint hardware at the end of the brace. Monotonic and cyclic forces were applied to the specimens before and after repair. A total of 8 bearing walls were prepared, 4 of which were repaired, and 12 force tests were conducted indicated in ***Table 1***.

Table 1: *Specimens and test parameter*

Specimen	Wall length [mm]	Loading types	Type of joint in 1st test	Type of joint in 2nd test
A	910	Monotonic	Ordinally hard ware	Ordinally hardware + repair hardware
A-re				
B		Cyclic		
B-re				
C	1820	Monotonic		
C-re				
D		Cyclic		
D-re				
r-A	910	Monotonic	Only repair hardware	none
r-B		Cyclic		
r-C	1820	Monotonic		
r-D		Cyclic		

2.2 PAIRING HARDWARE

The repair hardware used in this study was a prototype developed in a previous study [4]. The shape of the repair hardware is shown in ***Fig. 3*** and ***4***, and it is larger than the joint hardware used in the study, with approximate dimensions of thickness t=1.6 mm, 200 x 120 x 55 mm. The screw holes are placed outside the edge of the joint hardware, allowing the repair hardware to be placed over the joint hardware and fastened with screws. The thickness of the steel plates of the joint hardware and the repair hardware are the same. The study used CPQ-45 screws to fasten four screws to the foundation and beams, six screws to the columns, and seven screws to the fascia side. Only one type of screw was used for the repair hardware to simplify the repair process.

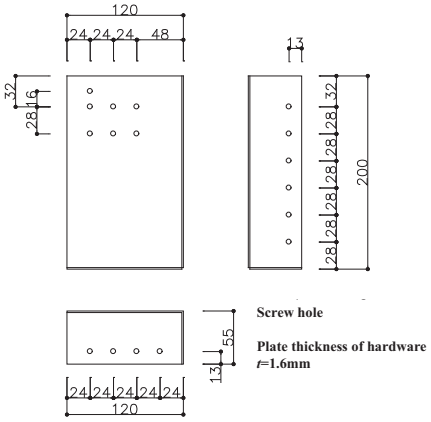

Figure 3: *Repair hardware*

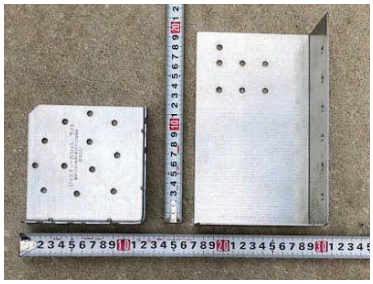

Figure 4: *Repair hardware*

2.3 REPAIR PROCESSING

This statement suggests that the study includes both a description of a test procedure and an installation procedure for reinforcement hardware in load-bearing walls. The test procedure likely describes the method used to evaluate the effectiveness of the reinforcement hardware in load-bearing walls, while the installation procedure describes the steps necessary to properly install the hardware in load-bearing walls. The procedure begins by applying a horizontal force to a specimen that has joint hardware attached. After the test is completed, the specimen is pushed back by the testing machine until the column is at right angles. The fastened hardware is not removed, and repair hardware is fastened over the fastened hardware. The repaired load-bearing wall is then subjected to another horizontal force. The flow of this procedure is illustrated in ***Fig. 5***.

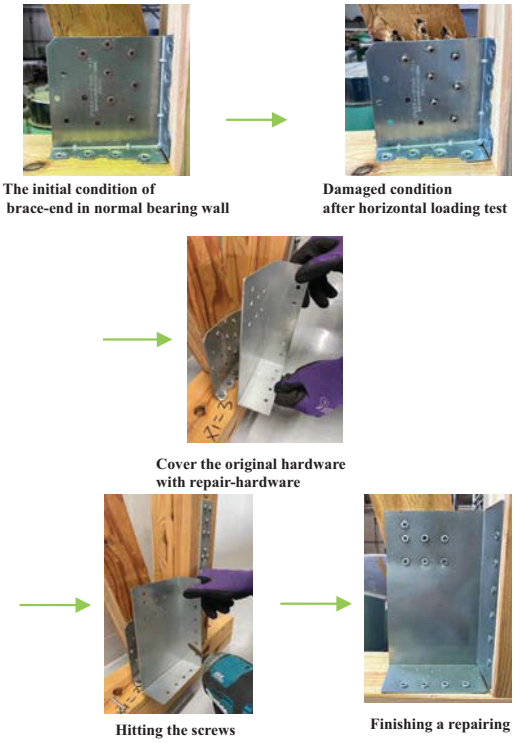

Figure 5: *Processing of tests and reinforcement of brace ends with hardware*

2.4 TEST METHODS

The test method in this study used a manual from the Japan Housing and Wood Technology Centre [5]. The

specimen was anchored to a foundation steel beam with anchor bolts and horizontal forces were applied to the top of the specimen with an oil jack. Loads were applied using load cells and displacement transducers were used to measure the displacement of the test top and foundation. The loads were applied by monotonic tensile and repetitive positive and negative forces and the test results were processed using "pickpoint" [6] to calculate the structural performance.

3 TEST RESULTS

3.1 DAMAGED CONDITIONS

The main failure conditions of the specimens are shown in ***Fig. 6-9*** and listed in ***Table 2***.

The study found that in the 1P and 2P specimens using joint hardware, the main failure type was the pulling-out of screws. This occurred when the screws fastened to the brace penetrated into the brace and subsequently pulled out. The degree of screw pull-out was greater at the outermost end of the brace-edge than at the end of the brace attached to the central column. However, no screws were pulled out at the foundation, beams or columns, and no bending deformation or other damage was observed in the hardware.

In the repaired specimens, deformation was observed in many of the repair hardware in both the 1P and 2P specimens. Additionally, cracks were observed in the fiber direction at the foundation, beams and columns, starting at the screw holes. In the 2P specimens, the degree of screw pull-out was greater on the foundation side where the repair hardware was fastened, particularly on the lower right-hand side of the specimen, compared to the fascia joint in the center of the specimen. The repair hardware fastened to the foundation, beams and columns showed screw pull-out, while the screws fastened to the fascia side did not show any pull-out.

The specimens that used repair hardware only showed deformation of the hardware and cracking similar to the specimens that underwent repair. The 2P specimens showed screw pull-out at the foundation, beams and columns, while the 1P specimens did not show any screw pull-out. The 2P specimens showed no screw pull-out at the foundation, beams and columns. However, the screws on the fascia did not pull out in both specimens. The only exception was the r-C specimen, where the deformation of the repair hardware at the joint in the middle of the specimen was greater than at the joint in the lower right-hand corner of the specimen. At the repair hardware joints, the hardware was deformed first, followed by damage around the screws.

The screws were found to be in good condition and had not undergone any bending deformations during those tests.

The study found that using joint hardware alone resulted in screw pull-out as the main type of damage, while the use of repair hardware resulted in a combination of screw pull-out and other types of damage. This could be misleading as it may suggest that repair hardware is more prone to damage. However, the study also found that when repair hardware was used, the deformation of the bearing walls was greater, resulting in greater deformation at the joints, which also caused other damage. Despite this, the study found that the use of repair hardware did not result in a reduction in bearing capacity, which is considered to be a useful aspect of the repair hardware.

The study found that when only joint hardware was used, the damage was more pronounced in the fascia, but when repair hardware was used, the damage was more pronounced in the foundations, columns and beams. This suggests that the resistance mechanism changed when repair hardware was used. However, it is possible that the repair hardware was not the only factor in this change, and that internal damage to the foundations, columns and beams may have also contributed to the change in the resistance mechanism.

Figure 6: *Damaged condition1*

Figure 7: *Damaged condition2*

Figure 8: *Damaged Condition3*

Figure 9: *Damaged condition4*

Table 2: *Failure conditions*

Condition and specimen		Pulled out of screws			Failure of hardware	Failure of members
		Brace	Foudation	Beam		
Only normal hareware	A	✔				
	B	✔				
	C	✔				
	D	✔				
after repairing (damaged noral hardware and repair hardware)	A-re			✔	✔	✔
	B-re			✔	✔	✔
	C-re		✔	✔	✔	✔
	D-re		✔	✔	✔	✔
Only repairing hardware	r-A				✔	✔
	r-B				✔	✔
	r-C			✔	✔	✔
	r-D			✔	✔	✔

3.2 LOAD-DISPLACEMENT RELATIONSHIPS

The load-deformation angle relationships for specimens with joint hardware and those with repair hardware only are shown in ***Fig. 10-13***.

The study found that when comparing the load-deformation relationship of specimens with joint hardware to those with repair hardware only, the specimens with only repair hardware tend to have a

https://doi.org/10.52202/069179-0525

smaller initial slope and behave differently in the initial phase of the applied force. After a period of stagnation, the load tends to rise again and the maximum load tends to reach the same level as the specimens with joint hardware. This behavior is likely due to plate buckling of the steel plate caused by the large unscrewed surface, and the transition to tensile deformation as the deformation progresses. This two-stage behavior is characteristic of the cases where this repair hardware is installed. The study found that the displacement at maximum load was clearly larger than that of the specimens with joint hardware, confirming that the hardware was designed to be a load-bearing wall with excellent deformation performance.

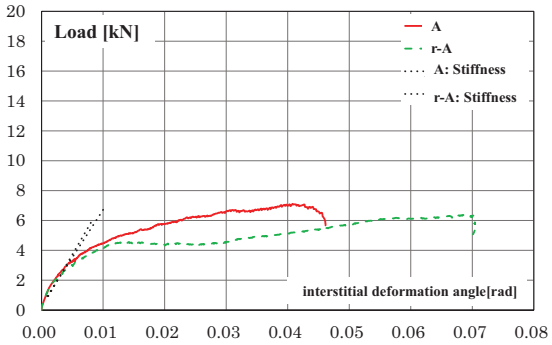

Figure 10: *Comparison with A and r-A(Load-angle)*

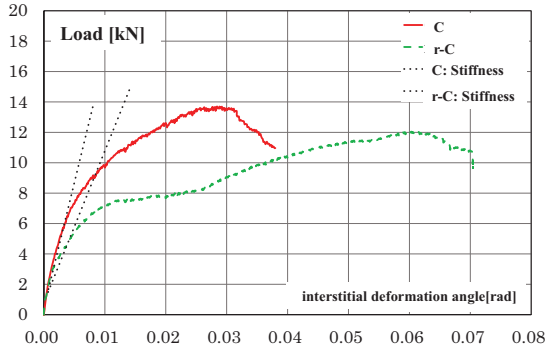

Figure 11: *Comparison with C and r-C(Load-angle)*

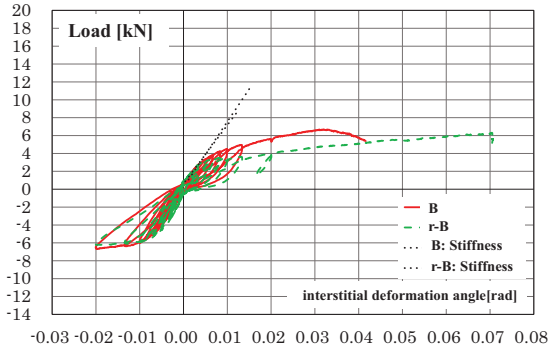

Figure 12: *Comparison with B and r-B(Load-angle)*

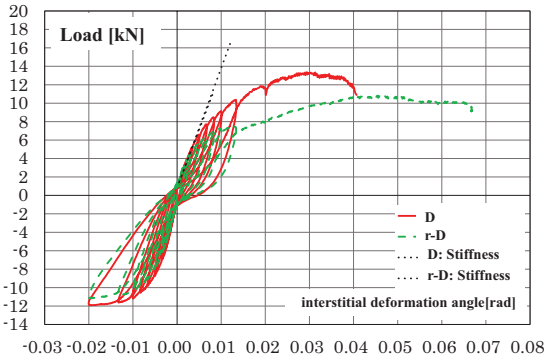

Fiure 13: *Comparison with D and r-D(Load-angle)*

The load-deformation angle relationships of the specimens with the joint hardware and after repair are then shown in ***Fig. 14-17***.

The study found that the initial stiffness of the specimens after repair tends to be smaller than before repair. This is likely due to the slightly smaller stiffness of the wall with only the repair hardware. However, the maximum load and displacement at maximum load of the specimens after repair were clearly larger than before repair. This suggests that the repair is effective in increasing the load-bearing capacity and deformation performance of the wall.

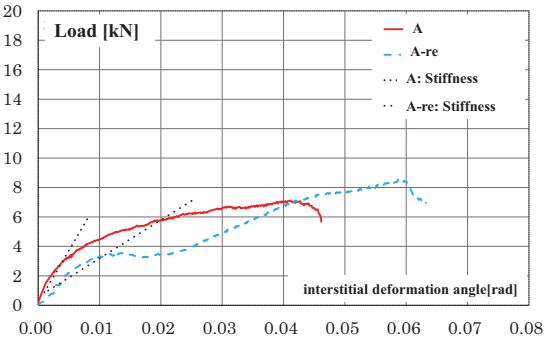

Figure 14: *Comparison with A and A-re(Load-angle)*

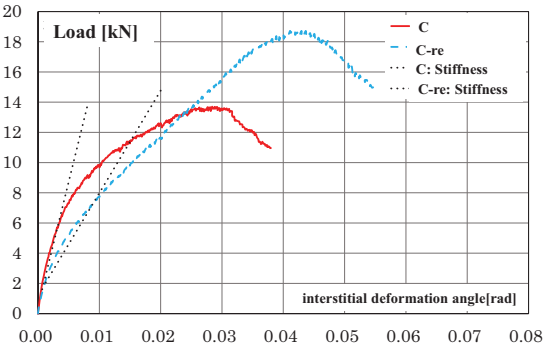

Figure 15: *Comparison with C and C-re(Load-angle)*

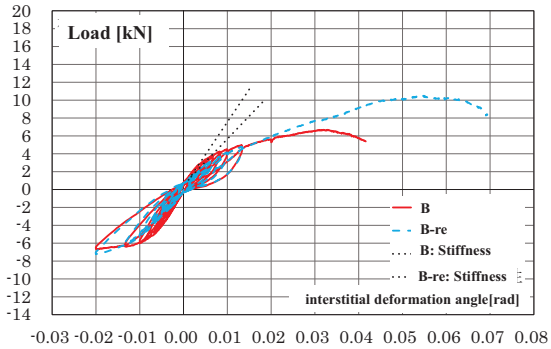

Figure 16: *Comparison with B and B-re(Load-angle)*

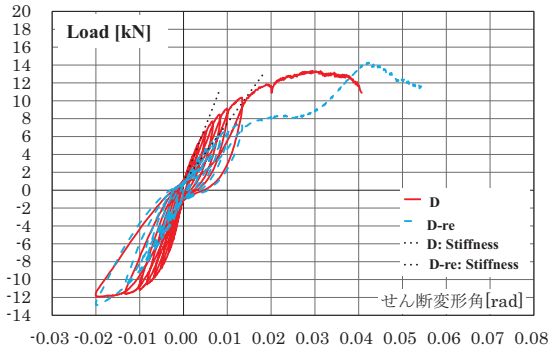

Figure 17: *Comparison with D and D-re(Load-angle)*

3.3 COMPARISON OF JOINTING HARDWARE AND REPAIR HARDWARE

The results using jointing and repair hardware are shown in ***Table 3*** and ***Fig. 18 -19***.

The study found that the maximum load on the specimens with repair hardware only was slightly lower than on the specimens with joint hardware, but the energy absorbed was higher. The ratio of the maximum load value of the repair hardware only divided by the value of the joint hardware was 89% for the r-A specimen, 94% for r-B, 88% for r-C and 80% for r-D. The ratio of energy absorbed was 136% for r-A, 153% for r-B, 158% for r-C and 138% for r-D.

The study found that the ratios of the load-bearing walls with repair hardware to those with joint hardware were more than 80% (88% on average) for maximum load, more than 60% (85% on average) for stiffness and more than 136% (146%) for energy. As shown in Figure 12, all were greater than the joining hardware with regard to energy, confirming that the effect was more akin to reinforcement than repair. Although the maximum load and stiffness values were not 100%, it was confirmed that the structural performance was at a level similar to that of a load-bearing wall with jointed metalwork. Based on these results, the study concludes that the repair hardware is considered to be effective in terms of repair for the joint hardware covered in this study.

Table 3*: Comparison of specimens with joint and repair hardware*

Specimen	Maximum load [kN]	Reparid/ Original	Stiffness [kN/mm]	Reparid/ Original	Energy [kN・mm]	Reparid/ Original
A	7.11	89.9%	0.26	88.5%	692.95	136.1%
r-A	6.39		0.23		943.09	
B	6.69	94.5%	0.27	88.9%	586.57	153.8%
r-B	6.32		0.24		902.28	
C	13.70	88.0%	0.60	61.7%	1121.44	158.5%
r-C	12.06		0.37		1777.71	
D	13.37	80.9%	0.46	104.3%	1172.23	138.4%
r-D	10.82		0.48		1622.71	
Ave.		88.3%		85.8%		146.7%

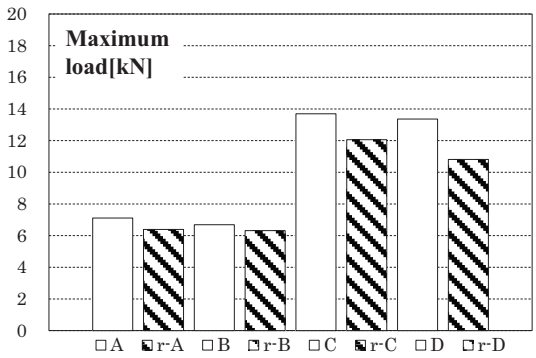

Figure 18: *Comparison of maximum loads on specimens with jointing hardware and reinforcing hardware*

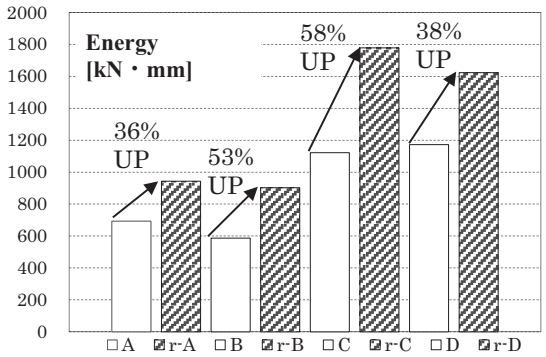

Figure 19: *Comparison of energy on specimens with jointing hardware and reinforcing hardware*

3.4 COMPARISON BEFORE AND AFTER REPAIR

Comparisons before and after repair are shown in ***Table 4***, maximum load comparisons in ***Fig. 20*** and energy comparisons in ***Fig. 21***.

The study found that compared to the specimens before repair, the specimens after repair had lower initial stiffness, but increased maximum load and energy. The ratio of the post-repaired value divided by the pre-repaired value for maximum load was 120% for the A-re specimens, 156% for the B-re, 136% for the C-re and 106% for the D-re. The energy ratios were 131% for the A-re specimens, 240% for the B-re, 173% for the C-re and 123% for the D-re. No trend was found within the scope of this study with respect to these repair effects for different wall lengths.

https://doi.org/10.52202/069179-0525

The study found that the use of repair hardware tends to increase the maximum load by more than 100% and the energy by more than 120%. Based on these results, it can be considered that repair hardware has a repair effect. However, it has been shown that the maximum load of those using only repair hardware is 85% of those using only joint hardware. It is believed that the joint hardware after damage also contributes to some extent, working in a combined manner and resulting in a higher maximum load. With regard to energy, the contribution of the repair hardware is considered to have been significant. In terms of stiffness, on the other hand, the results showed that there was no significant repair effect.

***Table 4**: Comparison of before and after repairing with hardware*

Specimen	Maximum load [kN]	Reparid/ Original	Stiffness [kN/mm]	Reparid/ Original	Energy [kN・mm]	Reparid/ Original
A	7.11	120.1%	0.26	38.5%	692.95	131.4%
A-re	8.54		0.10		910.37	
B	6.69	156.8%	0.27	44.4%	586.57	240.6%
B-re	10.49		0.12		1411.07	
C	13.70	136.6%	0.60	41.7%	1121.44	173.1%
C-re	18.72		0.25		1940.72	
D	13.37	106.8%	0.46	52.2%	1172.23	123.0%
D-re	14.28		0.24		1442.2	
Ave.		130.1%		44.2%		167.0%

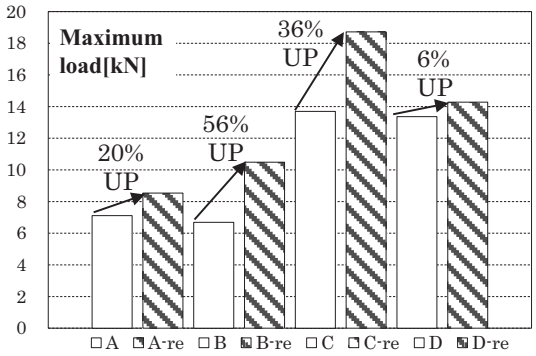

***Figure 20:** Comparison of maximum loads on specimens before and after reinforcement*

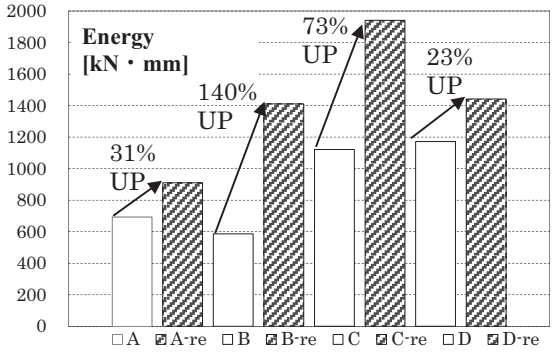

***Figure 21:** Comparison of energy on specimens before and after reinforcement*

4 CONCLUSION

The study investigated the effectiveness of repair hardware in reinforcing load-bearing walls that have undergone damage. The findings of the study are as follows:

1. The ratio of the structural performance of the repaired hardware alone to that of the joined hardware, the repaired hardware had values of around 88% for maximum load, 85% for stiffness and 146% for energy, confirming that the hardware is expected to be effective in repairing the damage.
2. The values obtained by dividing the post-repair by the pre-repair were more than 106% for maximum load and 123% for energy. It was confirmed that the repair was effective with regard to load capacity and deformation performance. However, with regard to stiffness, the repair effect was small. No influence of different wall lengths and application methods was found within the scope of this study with regard to these values.
3. The maximum load was considered to have been restored by the combined action of the damaged joint hardware and the repair hardware. The contribution of the repair hardware was considered to be the main contribution with regard to energy.
4. For stiffness, the effect was small. With regard to screw damage, the damage in the fascia was more pronounced in the case of the joint hardware only, whereas it was more pronounced in the foundation, columns and beams after the repair, suggesting that this difference in resistance mechanisms may have influenced the lack of increased stiffness.

In the current study, cyclic force tests were conducted incrementally. However, in recent years, research using more complex cyclic force tests such as fatigue tests has progressed [7],[8]. It is suggested that future research should examine this specimen using such force tests.

REFERENCES

[1] Japan Building Disaster Prevention Association: Criteria for determining the degree of damage classification of earthquake-damaged buildings and technical guidelines for restoration,2016 (in Japanese).

[2] Japanese Agricultural Standards for Veneer Laminated Timber, Notification No. 475 of the Ministry of Agriculture, Forestry and Fisheries,2019.6.

[3] Japanese Agricultural Standards for Glued Laminated Timber, Notification No. 475, Ministry of Agriculture, Forestry and Fisheries, 2019.6.

[4] W.Kambe, M, Maniwa, T. Yamazaki, A. Umakawa and S. Nakano: Repair effect using hardware on damaged bracing walls, J. of technological researches, Vol.65, pp.63-69, 2022 (in Japanese).

[5] Japan Housing and Wood Technology Center, test method R. Mahnken. A Newton-multigrid algorithm for elasto-plastic/viscoplastic problems. *Comp. Mechs*., 15:408-425, 1995.
[6] M. Karube, M. Harada and T. Hayashi: A proposal of bi-linear modeling tool for assess its method and problems in common tool for load-deformation curves of wooden structures, Trans. AIJ,C-1, pp215-216,2001.
[7] R. Inoue, T. Mori and S. Matsumoto: Effect of numerous small deformations caused by moderate earthquakes on shear performance of wooden walls, Construction and Building Materials, Vol. 364, 2023.
[8] R. Inoue, T. Mori, A. Ariki and S. Matsumoto: Evaluation of single shear performance of nailed joint damaged by cyclic deformation due to moderate earthquakes, Construction and Building Materials, Vol. 342, 2022.

https://doi.org/10.52202/069179-0525

World Conference on Timber Engineering Oslo 2023

STUDY ON THE MECHANICAL PERFORMANCE OF MULTI-LAYERED BRACKET COMPLEX

Kohei Komatsu[1]

ABSTRACT: This document provides the experimental attempts for making sure the mechanical performance of the multi-layered bracket complex used on the upper parts of stone columns in a repaired ancient temple in China. Making model multi-layered test specimens having layer numbers from 1 to 5, a dynamic vibration test for evaluating the natural frequency and the damping factor was done. Further, using the same test specimens, a push-pull static cyclic loading test was done. It was a satisfactory result that the damping factor of the model multi-layered bracket complex was higher than the preliminary anticipation. Tentative nonlinear analyses using a commercial FEM program on the model multi-layered specimen, however, showed unsatisfactory prediction for the skeleton curves. A lot of further improvements are necessary to do a seismic FEM analysis of the real existing structure involving a multi-layered bracket complex.

KEYWORDS: Multi-layered bracket complex, Damping coefficient, Ancient temple in East Asia

1 INTRODUCTION

In a part of the existing *Kaiyuan* Temple *Tenno-den* (established in 979, largely repaired in 1980) in *Chaozhou* City, *Guangdong* Province, China, the upper part of the stone pillar is composed of the multi-layered bracket complex structure (Figure 1). This structure is a very rare structural form that can only be seen here even in China. This structure is quite motivating for such a researcher who is interested in the structural mechanism of ancient wooden architecture in East Asia. Why was such a multi-layered bracket complex structure adopted? The background and purpose of this research are to scientifically investigate even part of the reason.

Figure 1: *Multi-layered bracket complex structure in Kaiyuan Temple Tenno-den* (*Photo*:©*Kohei Komatsu*)

2 EXPERIMENTS

2.1 SPECIMEN DESIGN

To investigate the mechanical performance of the multi-layered bracket complex structure, a simplified model specimen was created to enable the moment distribution of the actual multi-layered structure shown on the left-hand side[1] of Figure 2 simulate.

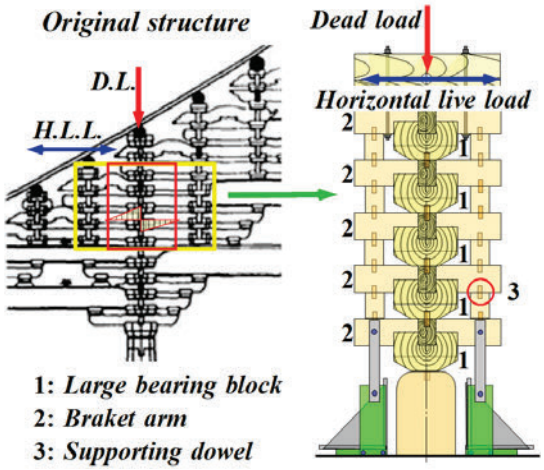

Figure 2: *Simplified model specimen for simulating a part of the actual multi-layered bracket complex structure*[1] *(Refer to Figure16 for the significance of the red-circled #3 dowel when subjected to a tensile force)*

In the yellow square area on the left-hand side of Figure 2, bracket arms are arranged on the large bearing brock

[1] Kohei Komatsu, RISH, Kyoto University, Japan
komatsu.kouhei.55z@st.kyoto-u.ac.jp

https://doi.org/10.52202/069179-0526

of each layer, and the rotation of the bracket arm is prevented by the vertical dead-load acting on the large bearing brock. This situation can be assumed to be a state in which an anti-symmetrical moment is generated in the bracket arm so as to balance the moment at the large bearing brock, and a zero-moment point in the bracket arm seems to exist around the middle of the two nodes. Therefore, a simplified model multi-layered bracket complex test specimen was proposed as shown in the right-hand side of Figure 2. In this model, the point of zero moment was simulated by setting a pin-joint at both ends of the bracket arm using a supporting wooden block fixed by a dowel.

2.2 KINDS OF MODEL SPECIMEN

To make clear the effect of the number of layers on the mechanical performance of the model specimen, five different kinds of specimens having one to five layers of the bracket complex as shown in Figure 3 were prepared.

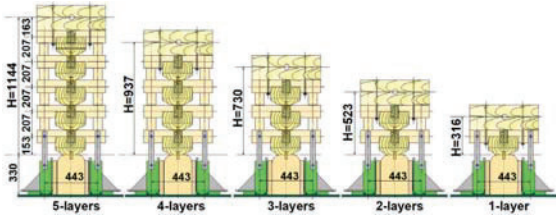

Figure 3: *Five different kinds of model specimens.*

2.3 DYNAMIC TEST SET-UP

To grasp the initial stiffness and damping factor of the model specimens, a sinusoidal sweep vibration test was first conducted by fixing a small exciter on the top of the model specimen as shown in Figure 4.
One accelerometer A_0 was fixed to the steel foundation and another A_1 was fixed to the center of the loading block to measure the response accelerations. At the same time, the horizontal displacement D_1 at the center point of the loading block and the horizontal displacement D_0 at the interface between the bottom of the lowest large bearing block and the column head were measured with displacement measuring devices.

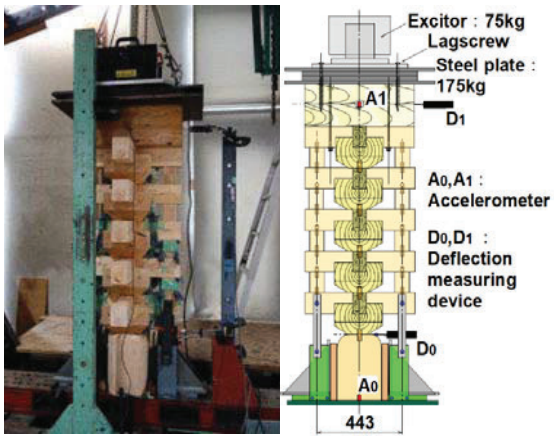

Figure 4: *Test set-up for the dynamic experiment*

The sinusoidal sweep tests were done by giving from 1Hz to 10Hz sin-wave step by step with 1Hz increment to detect the first rough resonance range then the fine sweep-out detections were done with 0.1Hz increment within the range of the first found-out rough region. For this dynamic test, a total of about 2.5 kN weight was loaded, including the weight of the exciter and the steel plates.

2.4 STATIC TEST SET-UP

After finishing the dynamic tests, the static push-pull cyclic horizontal loading tests were conducted using the same test specimens used for the dynamic test.
Figure 5 shows the static test set-up. The vertical dead load was applied on the top of the loading brock using a pulley and wire system which was pulled by an oil jack having 100kN capacity. While the horizontal load was applied at the geometrical center of the loading brock using an oil jack having 250kN capacity.
Horizontal loading protocol was first assigned so as to be set out as the following target values by the shear deformation angle (γ); γ= ±1/300, ±1/200, ±1/150, ±1/100, ±1/75, ±1/60, ±1/50, ±1/40, ±1/30, ±1/20 and ±1/15 rad. Actually, however, in many cases, as the #3 dowel shown in Figure 2 was pulled out when the shear deformation angle was beyond 1/20 rad, thus loading after 1/20 rad was cancelled in such cases. Within each ± target deformation angle, one cycle push-pull loading was given. For the dead load, two loading levels (5kN and 10kN) were adopted.

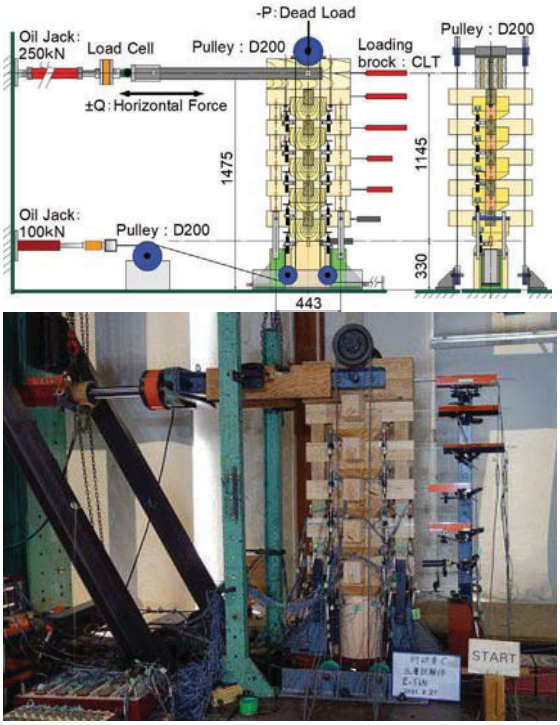

Figure 5: *Test set-up for the static experiment*

https://doi.org/10.52202/069179-0526

2.5 MATERIAL

The test material used was all high-quality solid wood of Japanese cypress (*Chamaecyparis obtusa*) which is preferably used for constructing traditional timber constructions in Japan. The moduli of elasticity of the materials (E0) were measured using an ultrasonic pulse velocity measuring device (PUNDIT-7) as shown in Figure 6. The moisture content was measured using a high-frequency capacitive moisture content meter (Kett HM-520). The result of the mechanical properties of materials is shown in Table 1.

Figure 6: *Measuring E0 using PUNDIT-7*

Table 1:*Mechanical properties of materials used*

	Large bearing brock			Bracket arm		
	ρ*1	MC	E0	ρ*1	MC	E0
	kg/m^3	%	kN/mm^2	kg/m^3	%	kN/mm^2
Mean	471.7	20.9	14.02	472.6	21.9	14.06
STD*2	19.6	1.8	0.95	27.5	3.2	0.83
N	15	15	15	30	30	30

*1:Density
*2:Standard deviation based on the sample number N-1

2.6 ELEMENT TESTS

2.6.1 Dowel shear test

The shear performance of the wooden dowel (d=20mm, L=60mm) joint between the lowest large bearing block and the column head was evaluated by the experiment shown in Figure 7. For the dowel joints belonging to the upper layers than the lowest part, no dowel shear tests were done due to an incorrect judgment of the author.

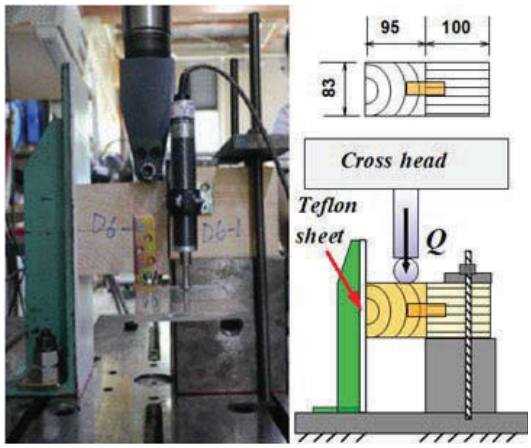

Figure 7: *Shear performance test of wooden dowel joint.*

2.6.2 Moment-resisting test on the large bearing block

To evaluate the quantitative relationship between moment (M) and rotational angle (θ) of the large bearing block, a moment-resisting test shown in Figure 8 was preliminarily done in the elastic stress level using the large bearing blocks which are to be used for the multi-layered bracket complex test specimens.

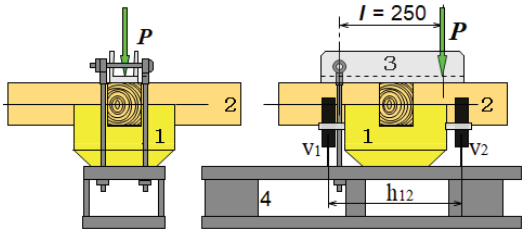

1:Large bearing block (bottom size: 154×154mm)
2:Bracket arm (83×104×571mm)
3:U-shape steel jig
4:Steel base jig

Figure 8: *Moment-resisting test on large bearing block*

In this experiment, moment (M) and rotational angle (θ) were defined by equations (1) and (2).

$$M = P \times 0.25 \quad \text{(kNm)} \tag{1}$$

$$\theta = \frac{v_2 - v_1}{h_{12}} \tag{2}$$

2.6.3 Compressive strength perpendicular to the grain

Compressive strength perpendicular to the grain is an important factor for predicting the yielding performance of the joint between a wooden tie-beam and wooden column according to *Inayama*'s embedment theory [2] and *Kitamori*'s interpretations [3],[4], therefore the compressive strength tests shown in Figure 9 were done using the supporting wood blocks (69×75×102mm) after the main experiments were all finished.

Figure 9 *Compressive strength test of Japanese cypress block perpendicular to the grain.*

3 FINITE ELEMENT MODELING

As a preliminary attempt for predicting the skeleton curve of the multi-layered model specimens provided in this study, FEM analyses using a commercial FEM program were tentatively tried.

https://doi.org/10.52202/069179-0526

3.1 LARGE BEARING BLOCK

The elastic relationship between the moment (M) and the rotational angle (θ) of the large bearing block subjecting to a constant vertical load (P_0) and a moment (M) as shown in Figure 10 was derived based on *Kitamori*'s original proposal [5] as shown in eq. (3).

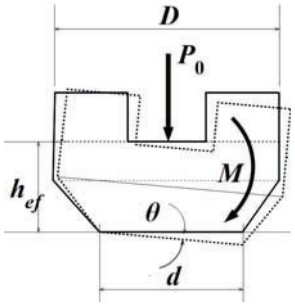

Figure 10: *Definition of the large bearing block subjecting to the moment M and the vertical load P_0*

$$M = \frac{b \cdot d^3 \cdot k_{w90}}{6} \cdot \theta = R_{D1} \cdot \theta \qquad (3)$$

where,

$$k_{w90} = \frac{E_{w90}}{h_{ef}} : \text{ bearing constant (kN/mm}^3) \qquad (4)$$

b: bottom width of the large bearing block (mm)
d: contact length of the large bearing block (mm)
R_{D1}: initial rotational stiffness of the large bearing block
E_{w90}: modulus of elasticity of the large bearing brock perpendicular to the grain estimated as 1/25 of that of the parallel to the grain (E_{w0}) (kN/mm^2)

The first yielding rotational angle was given in equation(5)[5].

$$\theta_{y1} = \frac{2P_0}{b \cdot d^2 \cdot k_{w90}} \qquad (5)$$

The second rotational stiffness was assumed to be smaller than the usual case [2] because the bottom surface of the large bearing block and the upper surface of the bracket arm are both perpendicular to the grain. The second stiffness was assumed as 1/12 of the first stiffness consequently.

$$R_{D2} = R_{D1}/12 \qquad (6)$$

3.2 BRACKET ARM

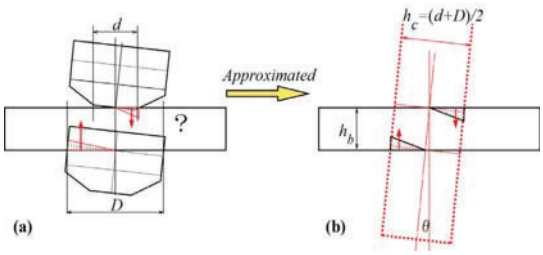

Figure 11: *An approximated mechanical model for the bracket arm contacting with two large bearing blocks.*

Mechanical modelling of the bracket arm seems to be complicated because the equilibrium condition of the vertical resultant forces is unknown as contact areas at the upper and bottom are not the same as shown in Figure 11-(a). Hence, in this study, this situation was approximated by assuming that the pressing condition by the upper and lower large bearing blocks is replaced by that given by a virtual column with an average width $h_c = (d + D)/2$ as shown in Figure 11-(b) and its longitudinal modulus of elasticity is E_{w90}. This assumption implies that the reactions from the virtual column surfaces are far softer than the normal column and tie-beam joint [3] [4] so no spring-back effect nor friction effect will not be considered in this soft contact model.

The moment (M)-rotational angle (θ) relationship for the virtual column-bracket arm joint shown in Figure 11-(b) was derived as equation (7) from *Kitamori* [3].

$$M = \frac{b \cdot {h_c}^3 \cdot k_{w90}}{12} \cdot \theta \qquad (7)$$

where,

b : width of the bracket arm.

$k_{w90} = \frac{E_{w90}}{h_b}$ bearing constant of the bracket arm

The rotational angle at the yielding was given by *Kitamori* [3] [4] as equation (8).

$$\theta_y = \frac{F_m}{h_c k_{w90}\left(1 + \frac{4h_b}{3h_c}\right)} \qquad (8)$$

where,

F_m : bracket arm's partial embedment strength (N/mm^2) =0.8×F_{c90}. In this study, F_{c90} (whole cross-sectional strength) was evaluated by the block compressive test shown in Figure 9.

Figure 12 shows an example of FEM modelling in the case of the three-layered specimen. In this modelling, the large bearing block was simulated by a single spring element having the axial stiffnesses and the rotational stiffness connected with short rigid beams for making the rotational behaviour of the spring element promote.

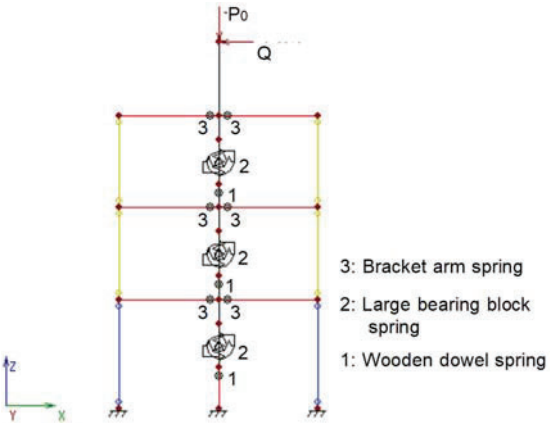

Figure 12: *An example of FEM modelling.*

https://doi.org/10.52202/069179-0526

4 RESULTS AND DISCUSSION

4.1 DOWEL SHEAR TEST RESULTS

Figure 13 shows wood-to-wood doweled shear joint test results. The grain directions of wooden members subject to the shear force were both perpendicular to the grain. While wood-to-wood doweled joints upper than the lowest layer were parallel to perpendicular joints. As no experiments, however, were done for the parallel-to-perpendicular joints, P-Δ curve approximated by a tetra-polygonal line in Figure 13 was applied to all FEM calculations for the multi-layered model specimens.

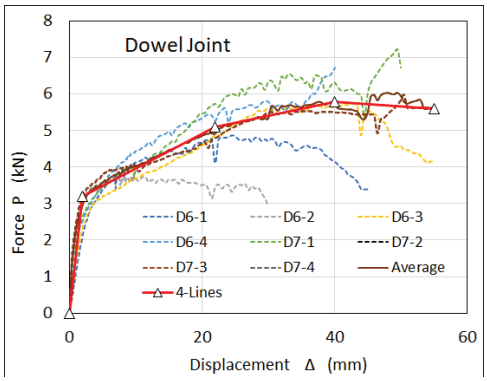

Figure 13: *Dowel joint shear test results and approximation by a tetra-linear polygonal line.*

4.2 VERIFICATION OF THE STIFFNESS OF THE LARGE BEARING BLOCKS

Figure 14 shows comparisons between the observed stiffness and the theoretical one calculated by equation (3) for the large bearing blocks subjecting to the moment shown in Figure 8. Theoretical value seems not to be bad, thus an application of the theoretical stiffness to the FEM models will be appropriate.

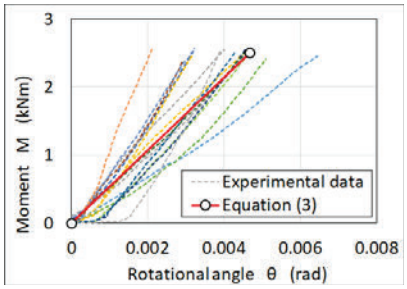

Figure 14: *Comparisons between observed stiffness and theoretical one [eq.(3)] for the large bearing blocks.*

4.3 DYNAMIC TEST RESULTS

In the dynamic test, the natural frequency (*f*) and the damping factor (*h*) of each test specimen were evaluated. The natural frequency (*f*) was evaluated using the Fourie spectral analysis method [e.g. 6]. For the actual calculations, an open computer program SPCANA-Ver4.92 created and provided by Dr. *Teruo Kamada*, an Emeritus Professor at Fukuyama University, was used.

The identification of the damping factor (*h*) was done by the Random Decrement (RD) method [e.g. 7]. For the actual identification, "Random Response Identification Program 3.0.xlsm" created by Dr. *Takehiro Wakita*, former Chubu University, Faculty of Engineering, Department of Architecture, was used.
When using the EXCEL macro, it was important to maintain the condition that the width of the bandpass filter was set so as to include the skirts on either side of the first-order peak of the Fourier spectrum, as described in previous studies [8], [9].

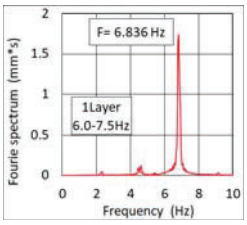

(a)Natural frequency (f)

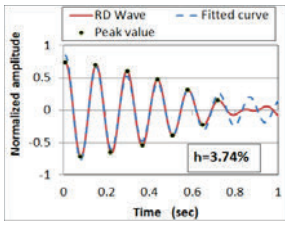

RD method for the 1-layer specimen

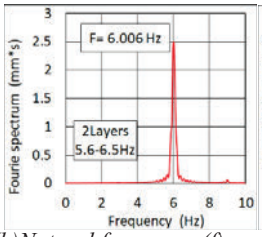

(b)Natural frequency (f)

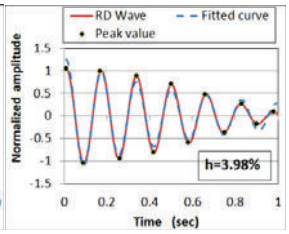

RD method for the 2-layers specimen

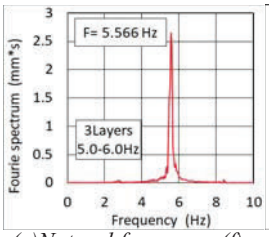

(c)Natural frequency (f)

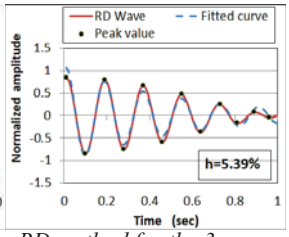

RD method for the 3-layers specimen

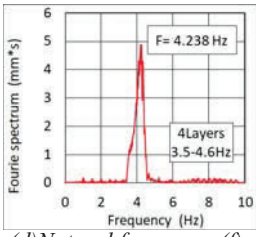

(d)Natural frequency (f)

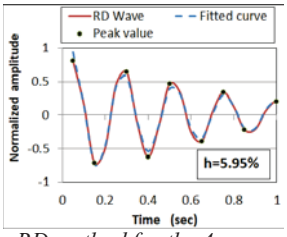

RD method for the 4-layers specimen

https://doi.org/10.52202/069179-0526

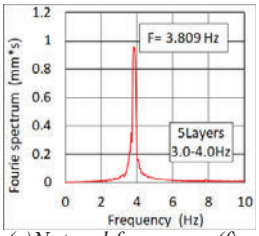

(e)Natural frequency (f)

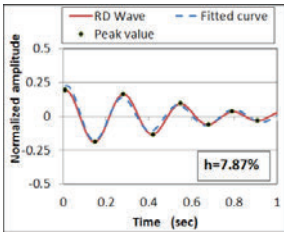

RD method for the 5-layers specimen

Figure 15: *Fourie spectrum and fitting process in the RD method*

Figures 15-(a), (b), (c), (d), and (e) show the identification results of the natural frequency (*f*) by the Fourie spectral analysis method and the fitting process on the selected vibration data of each test specimen for identifying the damping factor (*h*) and the natural frequency (*f*) by the RD method.

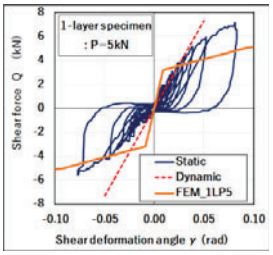

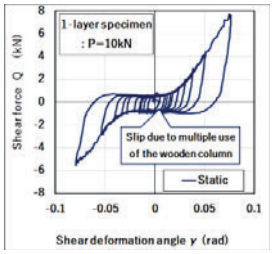

(a)1-Layer Specimen

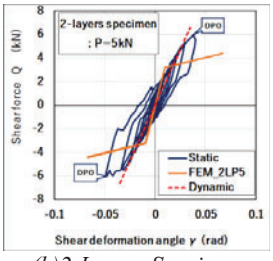

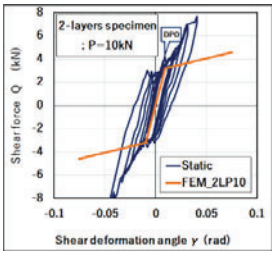

(b)2-Layers Specimen

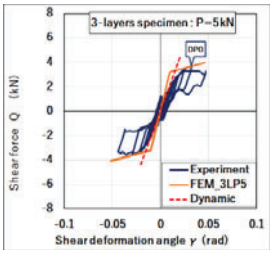

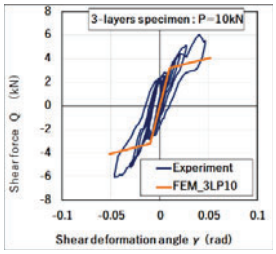

(c)3-Layers Specimen

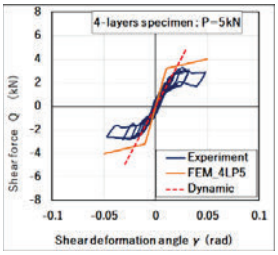

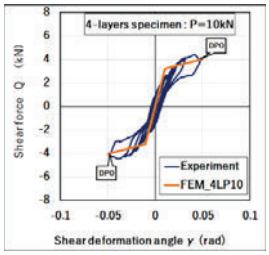

(d)4-Layers Specimen

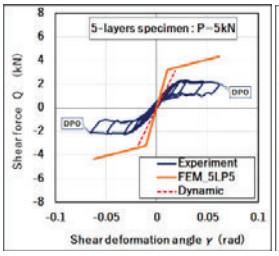

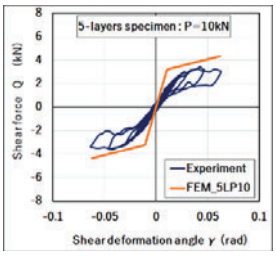

e)5-Layers Specimen

Figure 16: *Shear force Q and shear deformation angle γ relationships of each test specimen.*

**Note: DPO means " pull-out" of #3 dowel shown in Figure 2. This was occurred due to lack of slotted hole at the pin joint in the steel bar for escaping from the tensile force.*

4.4 STATIC TEST RESULTS

The relationships between the shear force Q and the shear deformation angle γ of the test specimens subject to the constant dead load P=5kN and P=10kN are shown in Figure 16-(a), (b), (c), (d) and (e) with FEM analyses results. In the FEM analyses, an optional function for the "*P*Δ-effect" involved in the computer program [10] was used.

The static loading experiments were executed first starting from the 5-layers specimen, next using the same wooden column and a new wooden dowel, 4-layers, 3-layers, 2-layers, and finally 1-layer specimen, therefore in the last specimen (1-layer specimen), large slip occurred as shown in the right-hand side of Figure 16-(a) as the dowel hole became loose due to multiple re-uses of the same column member.

Agreements between the hysteresis curves of the observed Q-γ relationships and predicted skeleton curves by the commercial FEM analysis program were generally bad. One of the reasons for these discrepancies is the unmatured FEM modelling done by the author. Thus, to obtain more satisfactory results, a lot of improvement of the FEM modelling method and reconsiderations on the nonlinear spring constants of each element will be required. While, however, the stiffness (dotted red line) obtained by the dynamic test agreed generally well with the initial slopes of static experimental results.

Figure 17 shows the relationship among the equivalent stiffness (*K*), natural frequency (*f*), damping factor (*h*), and the number of layers of the specimen.

https://doi.org/10.52202/069179-0526

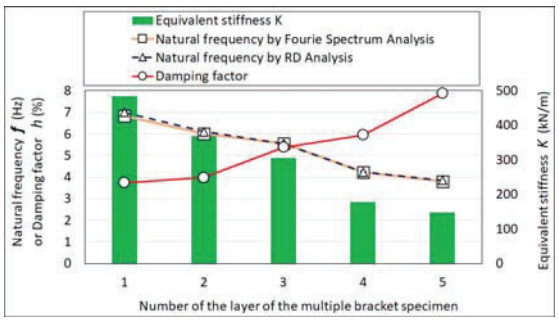

Figure 17: *Relationship among stiffness (K), natural frequency (f), damping factor (h), and number of layers*

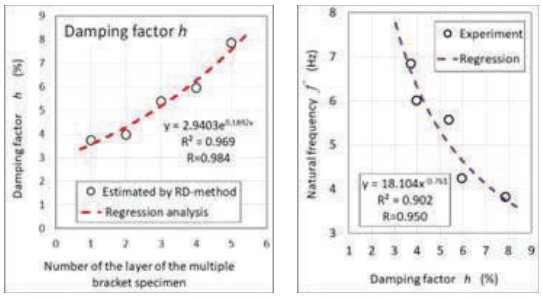

Figure 18: *Relationship among the damping factor (h), number of layers, and the natural frequency (f)*

As can be seen in Figure 17, the evaluated natural frequency (*f*) was considered to be reliable because almost the same values were obtained by both the Fourie Spectral Analysis method and the Random Decrement (RD) method.
There was a tendency for the equivalent stiffness (*K*) that gradually increased as the number of layers of the bracket complex decreased. This tendency seemed to be reasonable judging from the principle of layered structures.
Figure 18 shows the relationship among the damping factor (*h*), the number of layers of the specimen, and the natural frequency (*f*).
As expected preliminary, the damping factor (*h*) increased with the increase of the number of layers as shown in the left-hand side figure of Figure 18. The increasing tendency, however, showed an exponential rather than a linear. In addition, an inversely proportional relationship was observed between the natural frequency (*f*) and the damping factor (*h*) as shown in the right-side hand of Figure 18.

5 CONCLUSION

In this study, a very unique "multi-layered bracket complex structure", which can be seen in *Kaiyuan* Temple *Tenno-den* in *Chaozhou* City, *Guangdong* Province, China, was targeted as the research objective. To clarify at least a small part of the mechanical performance of this unique structure, simplified model layered bracket complex test specimens were created, and dynamic as well as static experimental investigations in conjunction with a tentative FEM modelling composed of beam and spring elements were attempted. Through experimental investigation and numerical analyses, the followings were concluded.

- The model multi-layered test specimens showed an increasing tendency of the damping factor (*h*) as the number of layers increased. This tendency gave an anticipation that this kind of multi-layered structure might have the potential to be a better energy dissipation function.

- Tentative numerical analyses using a commercial FEM program showed unsatisfactory agreements with the hysteresis curves obtained in the static push-pull cyclic loading experiments. Further improvements in the mechanical modelling of each structural element are necessary to obtain more satisfactory results.

- Hysteretic modelling of the multi-layered model specimens has not started yet hence the seismic analyses on the actual temple structure existing in China remained a future research subject.

ACKNOWLEDGEMENTS

This research is funded by the Japan Society for Promoting Science (JSPS) Grant-in-Aid for Scientific Research (C) [No. 21K04352 Principal Investigator: *Kohei Komatsu*].
For executing the experiments, various advice and technical support were given by Mr. *Horimoto Naohiro.* Dr. *Li Zherui*, and Ms. *Zhang Xiaolan* took part in the assistant roles not only for the dynamic and static experiments but also for all the element tests.
The author deeply appreciates not only the financial support from JSPS but also the help and technical support of the above-mentioned three persons.

REFERENCES

[1] *Wu Guozhi*: Architectural Structure of the *Tenno-den* in *Kaiyuan* Temple (1), Ancient Architecture and Garden Technology, 3(16), pp.41-47, 1987. (in Chinese)
[2] *Masahiro Inayama* : Embedment Theory of Timber and Its Application, Ph.D. Thesis Submitted to The University of Tokyo, December, 1991. (in Japanese)
[3] *Akihisa Kitamori*, *Yasuyo Kato*, *Yasuo Kataoka* and *Kohei Komatsu*: "Proposal of mechanical model for beam-column '*nuki*' joint in traditional timber structures", *Mokuzai Gakkaishi* (Journal of the Japan Wood Research Society),49(3), pp.179-186, 2003. (in Japanese)
[4] *Akihisa Kitamori* (Co-author): "4.4 Embedment Theory and *Nuki*-joint", in Fundamental Theory of Timber Engineering, pp.97-103, Architectural Institute of Japan (edited and published), 2010. (in Japanese)
[5] *Akihisa Kitamori, Kiho Jung, Ivon Hassel, Wen-Shao Chang, Kohei Komatsu and Yoshiyuki Suzuki*: Mechanical Analysis of Lateral Loading Behavior on Japanese Traditional Frame Structure Depending

on The Vertical Load, Proceedings of WCTE2010, Italy, 2010.
[6] *Yorihiko Osaki:* New- Introduction to the Spectral Analyses of the Earthquake Motion, *Kajima* Publishing, 1994. (in Japanese)
[7] *John Christian Asmussen*: Modal Analysis Based on the Random Decrement Technique - Application to Civil Engineering Structures, Aalborg: Department of Mechanical Engineering, Aalborg University, 1997. 227 p. (Fracture and Dynamics; No. Paper no. 100). Research output: Book/Report, Ph.D. thesis *https://vbn.aau.dk/en/publications/modal-analysis-based-on-the-random-decrement-technique-applicatio*
[8] *Izuru Okawa, Masanori Iiba, Shin Koyama, Koichi Morita, Shigeki Sakai, Atsushi Fujii, Mitoshi Yasui and Morimasa Watakabe*: Research on Dynamic Characteristics of A Residential Building Based on Micro Tremor Measurement and so on, Building Research Data, No.122, pp.1-51, Building Research Institute, December 2009. (in Japanese)
[9] *Takahiro Toyoda* and *Kiyoshi Takano*: Estimating the Damping Ratio of Buildings Using Weak Seismic Ground Motion: A Case Study on Buildings of the University of Tokyo, Bulletin of the Earthquake Research Institute, The University of Tokyo, Vol.88, pp.1-36, 2013.(in Japanese)
[10] ANON: **S**tructural **N**on-linear **A**nalysis **P**rogram (SNAP) ver.7, Technical Manual, *Kozo* System Inc., 2021. (in Japanese)

https://doi.org/10.52202/069179-0526

World Conference on Timber Engineering Oslo 2023

EXPERIMENTAL STUDY ON LATERAL PERFORMANCE OF A FRAME WITH DEEP BEAMS AND HANGING MUD WALLS IN TRADITIONAL JAPANESE RESIDENTIAL HOUSES

Zherui Li[1], Hiroshi Isoda[2], Akihisa Kitamori[3], Takafumi Nakagawa[4], Yasuhiro Araki[5]

ABSTRACT: This study aimed to investigate the resistance of a frame with deep beams and hanging mud walls, clarify the working mechanisms and contributions of different load-bearing elements in the frame. A series of comparative experiments of the frames with and without hanging mud walls were carried out in the first step, as well as frames with hanging mud walls of different height aspect ratios. The contributions of main load-bearing elements, including mortise-tenon joints, deep beams, and hanging mud walls, were identified. Secondly, the performance of the deep beam and beam-column joints were discussed. Additionally, the parameter analysis of the height aspect ratios of hanging mud walls was also performed combined with component tests.

KEYWORDS: Traditional timber structure, Lateral resistance, Hanging mud wall, deep beam, interior notch

1 INTRODUCTION

Timber frame composites with mud walls constitute the basic structure for resisting lateral forces and are widely employed in both traditional oriental temples and castles in Japan. Specifically, the composition of hanging mud walls and deep beams have been promoted for use in traditional Japanese residential houses since 17th century (Edo-era) [1]. Due to the requirement of space permeability, the proportion of large-scale shear walls is relatively reduced and partially replaced by large-section timber frames with hanging walls in traditional-style houses (Figure 1). However, this practice may cause the risk of insufficient shear capacity according to current seismic design standards.

Figure 1: *Common structural systems in traditional Japanese residential houses.*

From the perspective of reinforcement of existing buildings, an accurate evaluation of the seismic performance of original structures is required for the need to maintain the appearance and minimize the expense in traditional residential houses. While the overall resistance of a frame with hanging wall height less than 750mm is underestimated according to the current seismic assessment method [2, 3], the resistance of mortise-tenon joints and deep beams are also not clearly involved in the evaluation of traditional residences in Japan. Simultaneously, considering that the shear force generated by hanging mud walls and deep beams and the moment of mortise-tenon joints all act on the column body and easily lead to bending deformation, the bending capacity of columns should be reassessed as a limiting factor of the drift-resisting capacity of the frame.

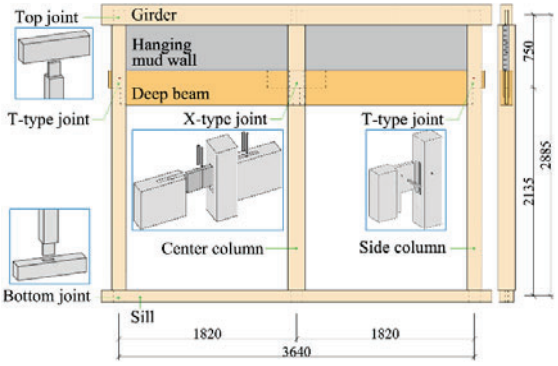

Figure 2: *Object frame with deep beams and hanging mud walls.*

[1] Zherui Li, College of Civil Engineering, Xi'an University of Architecture and Technology, China, lzr_6527@163.com
[2] Hiroshi Isoda, Research Institute for Sustainable Humanosphere, Kyoto University, Japan
[3] Akihisa Kitamori, Faculty of Engineering, Osaka Sangyo University, Japan
[4] Takafumi Nakagawa, Research Institute for Sustainable Humanosphere, Kyoto University, Japan
[5] Yasuhiro Araki, National Institute for Land and Infrastructure Management, Japan

https://doi.org/10.52202/069179-0527

This study took the double-span frame with deep beams and hanging mud walls as the object (Figure 2) and investigated the working mechanisms and contributions of different load-bearing elements, including mortise-tenon joints, deep beams, and hanging mud walls. Then the influence of different wall heights on lateral resistance capacity and damage mode of the frame were discussed based on comparative experiments.

2 EXPERIMENT

2.1 FRAME TESTS

With the purpose of visualizing the load-bearing mechanism and the contribution of the structural elements, in-plane static cyclic tests were conducted on frames with and without hanging mud walls, marked as *FW-M* and *F-M*, respectively. Then, to grasp the resistance of hanging mud walls with different heights, comparative experiments were conducted on frames with hanging mud walls of two height aspect ratios, marked as *FW-S* and *FW-L*, respectively. The dimension of frame specimens and mortise- tenon joints are shown in Figures 3 and 4.

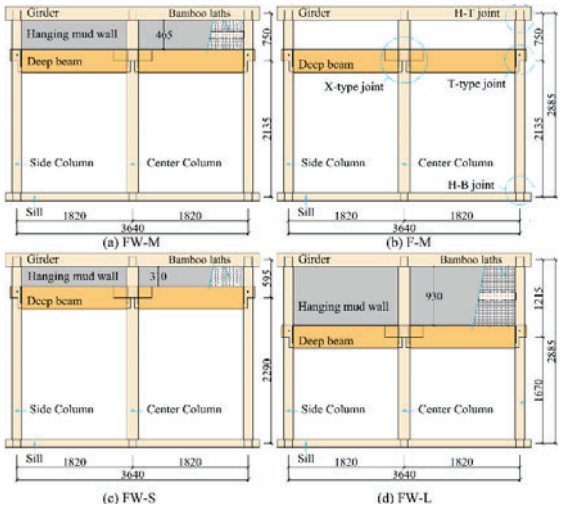

Figure 3: *Frame specimens (Unit: mm).*

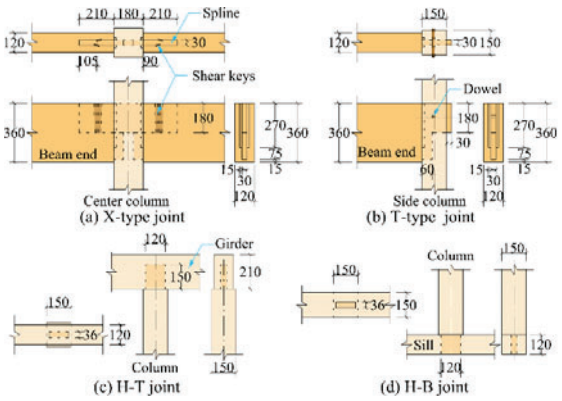

Figure 4: *Mortise-tenon joints in frame specimens (Unit: mm).*

For specimen FW-S, the clear height of the hanging mud wall was 310 mm. For specimens FW-M and FW-L, the wall height increased to 465 mm (1.5 times) and 930 mm (3 times). The aggregate thickness of the hanging mud wall was 70 mm, including the 40 mm thickness of rough-coated mud and 15 mm thickness of intermediate-coated mud. The dimensions, wood species and material properties of timber components in frame specimens are listed in Tables 1and 2.

Loading procedures of two groups of frame specimens were adapted from the standard ISO 16670. Cyclic load was applied along the centreline of the girder. Frame specimens were loaded with nine phases, each containing three fully revised cycles of equal amplitude. Target shear angles are raised from ±1/450, 1/300, 1/200, 1/150, 1/100, 1/75, 1/50, 1/30, to 1/15 rad, and then the load was added until the displacement limit of the hydraulic jack (approximately 1/10 rad) along the pull direction. Tie rods were installed along the side columns to control the vertical displacement and rotation of the frame, and the sill beam was fixed by sliding limit blocks.

Table 4: *Dimensions and wood species of members in frame specimens.*

Member	Dimension (mm)	Wood species
Side column	150×150×2720	Japanese cedar
Center Column	180×180×2720	Japanese cedar
Deep beam	120×360×1655	Douglas fir
Girder	150×210×4000	Japanese cedar
Sill	150×120×4000	Japanese cypress
Dowel	15×15×170	Oak
Shear key	6.5×30×135	Oak

Table 5: *Material properties of members in frame specimens.*

Category	Members	F-M	FW-M	FW-S	FW-L
MOE (kN/mm^2)	Column	8.72	8.75	8.69	8.84
	Deep beam	15.82	14.64	11.17	11.08
	Girder	9.69	8.01	10.30	8.83
	Sill	13.65	13.00	13.64	14.63
ρ (g/cm^3)	Column	0.41	0.40	0.39	0.40
	Deep beam	0.57	0.57	0.51	0.51
	Girder	0.41	0.43	0.41	0.40
	Sill	0.53	0.54	0.58	0.48
MC (%)	Column	19.6	20.0	19.2	20.6
	Deep beam	14.3	13.8	13.5	11.2
	Girder	19.6	20.3	18.2	17.4
	Sill	20.0	22.6	22.4	23.0

2.2 ELEMENTAL TESTS

To clarify the resistance contribution and deformation characteristics of the main components in the frame, including the rotational performance of mortise-tenon joints, shear resistance of deep beams and hanging mud walls, as well as the bending performance of columns with mortise, elemental tests were carried out and compared with frame tests.

https://doi.org/10.52202/069179-0527

Cyclic loading tests on two types of mortise-tenon joints of column and deep beam connections, the column top and bottom joints, the single-span frame containing a deep beam and two side columns, and mud wall elements with different heights corresponding to frame tests (310 mm, 465 mm, 930 mm) were conducted (Figure 5). Loading protocol of all these elemental tests were all consistent with the frame tests. Then 3-point bending tests of columns with mortise were performed.

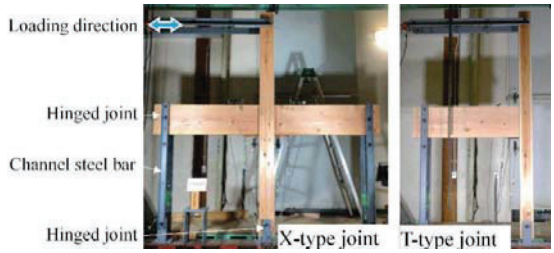

(a) Elemental tests of mortise-tenon joints

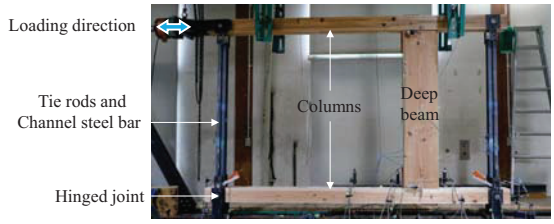

(b) Elemental test of deep beam

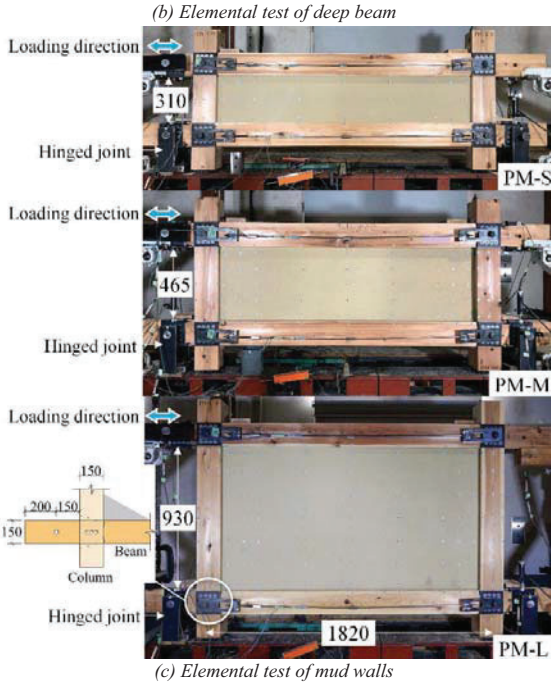

(c) Elemental test of mud walls

(d) Bending test of columns

Figure 5: *Elemental tests of main components in the frame.*

3 RESULTS AND DISCUSSION

3.1 LATERAL FORCE RESISTANCE OF OBJECT FRAMES

3.1.1 Observed damage

When the bare timber frame specimen F-M deformed under lateral force, there was an evident relative rotation between the columns and horizontal members (girder, deep beams, and sill). The effective length of deep beams gradually changed into the diagonal length and squeezed the columns on both sides. Although no obvious damage of joints or main components was observed even under a large displacement angle (1/10 rad), the outwardly bending tendency of both left- and right-side columns was very clearly observed. For specimen FW-M in contrast, the bending deformation of columns was not as significant as specimen F-M because of the restraint effect of hanging mud walls. Correspondingly, crushes of the left and right corners of the mud walls were observed as the displacement angle increased over 1/50 rad. Except for the shear failure that suddenly appeared on the top of the left column at 1/10 rad, there was no significant damage observed at mortise-tenon joints, and there was no clearly shear failure in the middle part of the hanging mud walls. The damage state of both specimens is shown in Figure 6.

(a) Deformation of F-M at 1/10 rad

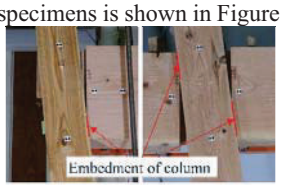

(b) Relative rotation of column-deep beam joints

(c) Deformation of FW-M at 1/10 rad

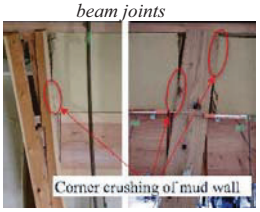

(d) Shear failure of left column and corner crushing of mud wall

Figure 6: *Damage state of F-M and FW-M at 1/10 rad.*

For specimens FW-S and FW-L which contain hanging mud walls of different heights, the most significant differences between the two frames at the displacement angle of 1/10 rad are the failure mode of hanging mud walls (Figure 7). For hanging mud walls with a height aspect ratio of 0.19 in FW-S, no significant shear failure was observed. Except for crushes at the left and right corners, vertical cracking occurred at the upper and lower surfaces of the mud wall at about 1/4 length from the edge. For hanging mud walls with a height aspect ratio of 0.56 in FW-L in contrast, diagonal cracks occurred from the interior area of both mud walls and expanded towards the edge. And because of the more obvious lifting effect of mud walls, the crushing failures of upper and lower surfaces at the wall corners were observed. In addition, bending deformation of the side columns was also more significant than that in FW-S, due to the greater shear

force transmitted by hanging mud walls and closer action position to the mid-span of columns.

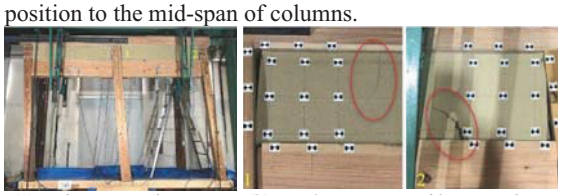

(a) Deformation of FW-S at 1/10 rad *(b) Cracks at upper and lower surface of mud walls*

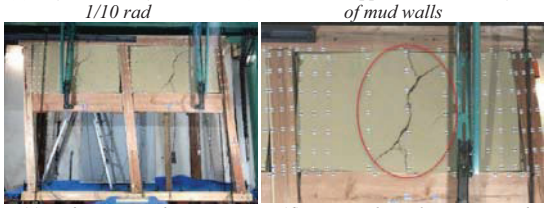

(c) Deformation of FW-L at 1/10 rad *(d) Diagonal cracks at center of mud walls*

Figure 7: *Damage state of FW-S and FW-L at 1/10 rad.*

3.1.2 Restoring characteristics

The restoring force characteristics of four frame specimens, and the main damage with corresponding displacement angles are shown in Figure 8. By comparing the skeleton curves of specimens F-M and FW-M, the contribution of hanging mud walls to the lateral resistance of the frame can be extracted (Figure 9(a)). When the hanging mud walls with a centreline height of 750 mm are included, the initial rigidity is increased by 1.57 times compared to the bare timber frame. After the peak value of lateral force reaches 15.73 kN at 0.06 rad, the load-carrying capacity of the FW-M slowly decreases with the occurrence of corner crushing of mud walls. In contrast, the lateral force added on F-M maintains an upward trend and reaches 13.11 kN at 0.1 rad, which is very close to that of FW-M.

From the perspective of the influence of wall height on the lateral resistance of the frame (Figure 9(b)), the initial rigidity of FW-L is 2.5 times higher than that of FW-S, and the peak load is also 1.34 higher. However, after the shear cracks occurred at 1/15 rad, the bearing capacity of FW-L decreased rapidly. As for FW-S, as the height aspect ratio of hanging mud walls is small and there is no shear failure occurs, the integral frame can maintain a stage lateral resistance even under large deformation. The result indicates that although the shear area of hanging mud walls remained the same, the stiffness as well as bearing capacity of the frame are positively correlated with the height of hanging mud walls.

The structural indices of frame specimens calculated according to the design method of JHWTC [4] as shown in Figure 9, including initial rigidity K, yield load P_y, maximum load P_{max}, ultimate load P_u, ductility factor μ, and short-term allowable lateral force P_a are listed in Table 3. P_a of the frame with different heights of hanging mud walls is derived by Eq. (1).

$$P_a = \alpha \cdot \min \begin{cases} P_y \\ 0.2\sqrt{(2\mu - 1)}P_u \\ 2/3 \cdot P_{max} \\ P_{120} \end{cases} \quad (1)$$

in which P_{120} is the lateral force at displacement angle of 1/120 rad, $\alpha = 1.0$.

Table 3: *Structural indices of frame specimens.*

Frame	K (kN/rad)	P_y (kN)	P_u (kN)	P_{max} (kN)	μ	P_a (kN)
F-M	362.46	7.60	11.79	13.11	3.08	3.83
FW-M	568.05	9.26	14.38	15.73	3.94	5.56
FW-S	408.31	11.11	17.08	19.53	2.32	3.73
FW-L	1026.95	18.47	22.94	26.14	4.57	8.99

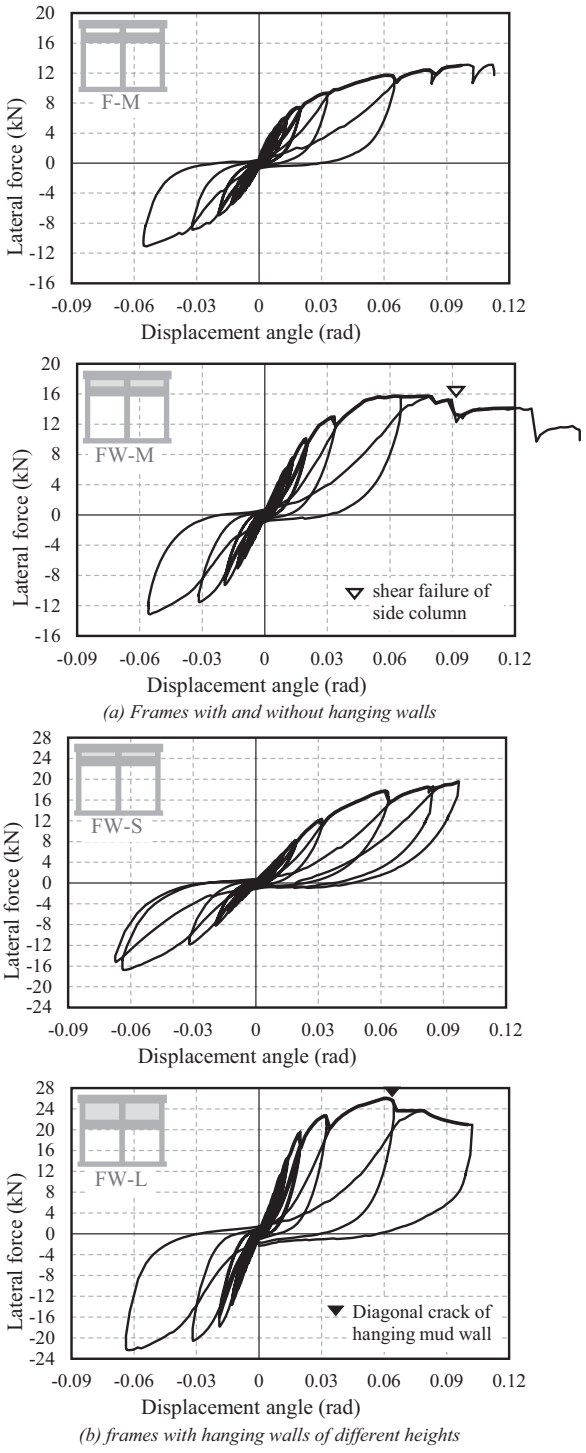

(a) Frames with and without hanging walls

(b) frames with hanging walls of different heights

Figure 8: *Restoring characteristics of frame specimens.*

https://doi.org/10.52202/069179-0527

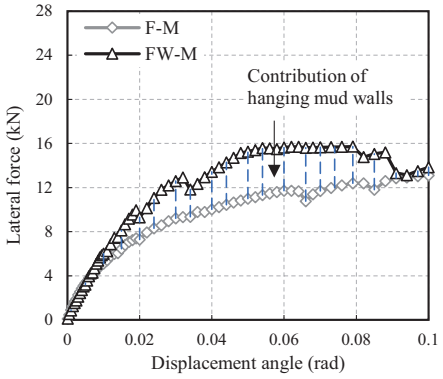

(a) Frames with and without hanging walls

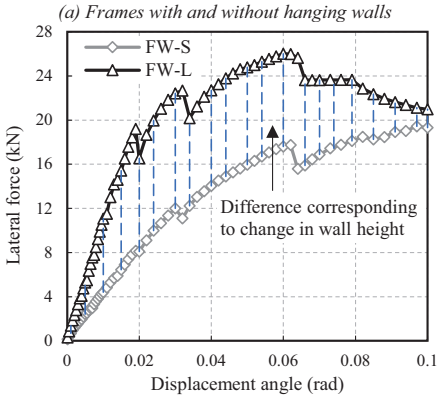

(b) frames with hanging walls of different heights

Figure 9: *Skeleton curves of frame specimens.*

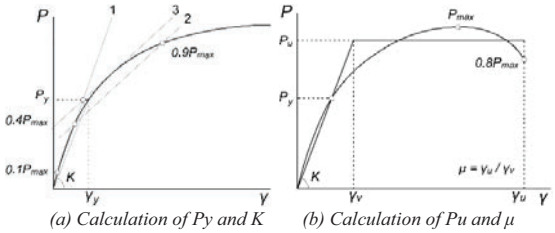

(a) Calculation of Py and K *(b) Calculation of Pu and μ*

Figure 10: *Calculation procedure of structural indices [4].*

3.2 PERFORMANCE OF MAIN COMPONENTS IN THE FRAME

Based on the lateral force-deformation relationship obtained from elemental tests, the contributions of main load-bearing components, including the mortise-tenon joints (Q_{Fj}), deep beams (Q_{Fb}), and hanging mud walls (Q_{Fw}), are extracted from the entire frame. The burden ratio of them is shown in Figure 11. It is observed that the resistance proportion of mortise-tenon joints exceeds 60% when the centerline height of the hanging mud wall is less than 750 mm. For hanging mud walls, the resistance proportion of which is positively correlated to the wall height, the peak occurs at about 0.02 rad and then begins to decline. The resistance proportion of deep beams in the bare timber frame accounts for about 10-15%, while in frames with hanging mud walls, its resistance is manifested when the displacement angle is above 0.02 rad.

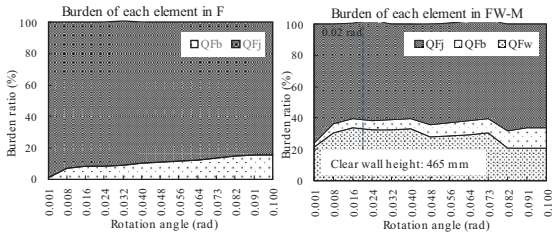

(a) Frames with and without hanging walls

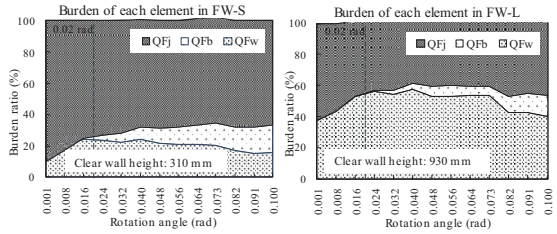

(b) frames with hanging walls of different heights

Figure 11: *Burden ratio of each element in frame specimens.*

3.2.1 Interaction between mortise-tenon joints and deep beams

By comparing the results of the frame and elemental tests, the interaction between beam-column joints and deep beams is identified.

Firstly, from the experimental phenomenon, the displacement angle corresponding to shear damage of the column-deep beam joints in the frame tests is greater (0.1 rad) than that in joint elemental tests (0.06 rad). This is mainly caused by the compression effect generated by the rotation of the deep beam clamped between two columns, which delays the tenon removal. From the moment-displacement angle curve extracted from the frame, it can be seen that the initial rigidity of the column-deep beam joint in the frame is lower than that in elemental tests (Figure 12(a)). And due to the failure delay of mortise-tenon joints, the overall resistance of the frame can maintain an increasing trend at 0.1 rad. Conversely, due to the pressure generated by the rotation of the beam end joint being partially balanced by the tensile force generated by the dowel, the axial force transmitted along the diagonal direction of the deep beam decreases (Figure 12(b)).

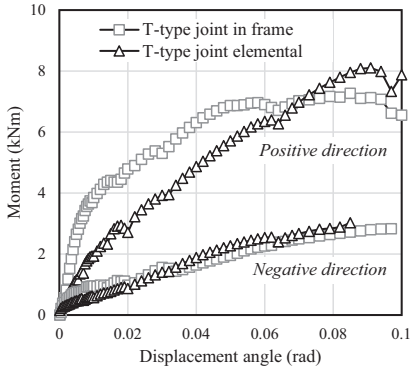

(a) Moment of T-type joint with and without influence of deep beams

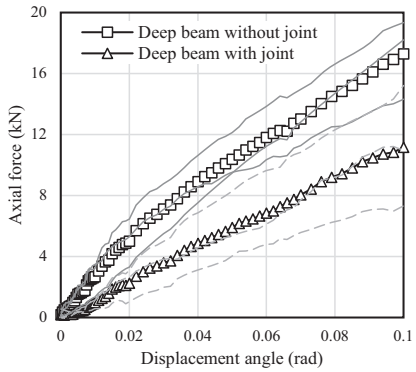

(b) Axial force on deep beams with and without influence of joints

Figure 12: *Interaction between deep beams and joints.*

3.2.2 Performance of hanging mud walls

Based on the elemental tests of squat mud walls, a positive correlation between the resistance of squat mud walls and the height aspect ratio is confirmed when the height aspect ratio is lower than 0.5 (Figure 13). Furthermore, the resistances generated by shear and corner compression are extracted respectively.

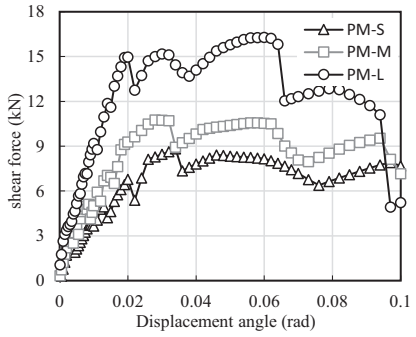

Figure 13: *Shear resistance of squat mud walls.*

3.2.3 Bending performance of columns

Although there was no bending failure occurred on the columns of both FW-S and FW-L specimens, the bending moments measured from the center and the leeward side columns of FW-L significantly increased as the concentrated load transmitted by hanging mud walls increased. Based on the comparative bending tests of columns with and without mortise at the loading point, the reduction coefficient β of bending moment (Eq. (2)), affected by the stress concentration of mortise is calculated. The experimental result shows that when the width lost ratio on the tensile side is lower than 0.4, the mean value of β is obtained as 1.0. Compared with the much lower coefficient (β=0.45~0.6) in the regulations in AIJ standard [5], it can be inferred that the continuous part out of the mortise plays an important role in relieving stress concentration.

$$M_{b-M} = \alpha \cdot \beta \cdot M_{b-0} \quad (2)$$

in which M_{b-0} is the bending moment of columns without mortise, M_{b-M} is the bending moment of columns with mortise, α is the nominal section modulus, calculated by the ratio between the weakest net section of mortise and the entire section.

4 CONCLUSIONS

The presented work focused on the lateral performance of a frame with deep beams and hanging mud walls in traditional Japanese residential houses. With the change of wall height, the initial rigidity, yield load, and ductility of the entire frame, as well as the resistance contribution of moment-resisting joints, deep beams, and hanging mud walls were evaluated.

The experimental results indicate that for the timber frame with deep beams and hanging mud walls, the lateral rigidity and lateral load-bearing capacity are positively correlated with the increase of the height of hanging mud walls. Regardless of whether the shear failure occurs on the hanging mud wall, its burden ratio of lateral force contribution reaches the peak at 0.02 rad. The collaborative working mechanism of mortise-tenon joints and deep beams ensures the good ductility of the entire frame. For the timber frame with the wall centerline height below 750 mm, the contribution of mortise-tenon joints to the lateral resistance accounts for over 60%.

ACKNOWLEDGEMENT

This study is one of the items of the project for the promotion and maintenance for building standards by MLIT.

REFERENCES

[1] Komatsu K., Kitamori A., Jung K., and Mori T.: Prediction of Non-linear Load-deformation Curves of Various Types of Mud Shear Walls Subjected to Lateral Shear Force. In 11th World conference on timber-engineering, 2708-2715, 2010.

[2] Official gazette co-operation of Japan. No. 1100 Notification of Ministry of Land, Transport and Tourism Infrastructure. In *Technical standard of building structure*, 111-121, 2020. (in Japanese)

[3] Japan building disaster prevention association (JBDPA). Guidance for seismic assessment and reinforcement method of timber residences. *Maeda print.co.jp,* 18-50, 2012. (in Japanese)

[4] Japan housing and wood technology center (HWTC). Design of allowable stress of wooden frame construction housing. *Japan housing and wood technology center, Tokyo,* 571-572, 2008. (in Japanese)

[5] Architectural institute of Japan, AIJ standard for Structural Design of Timber structures. *Maruzen publishing Inc*, *Tokyo*, 188-193, 2006. (in Japanese)

https://doi.org/10.52202/069179-0527

World Conference on Timber Engineering Oslo 2023

ASSESSMENT OF NAILED CONNECTIONS IN EXISTING STRUCTURES

Lars Völlmecke[1], Sascha Schwendner[2], Ai Phien Ho[3], Jens Fischer[4], Werner Seim[5]

ABSTRACT: This paper presents the development of an assessment scheme for a visual qualitative evaluation of nailed connections in existing structures, such as board trusses. In terms of further use and preservation, a quick visual inspection will help to evaluate the quality of a structure regarding its load-bearing capacity and deformation behaviour. Tests of old and new nailed joints in combination with a rating scheme point out the correlation between the load-bearing capacity and condition of a joint. Old joints of comparatively good condition tend to exhibit better results than those of poor condition. Moreover, aged joints are generally more load-bearing than newly assembled ones.

KEYWORDS: nailed trusses, nailed constructions, Corrosion, Preservation, Re-use, Structural Post-strengthening

1 INTRODUCTION

Carpentry-based timber construction in the 20th century underwent a strong development towards engineered timber construction, which was driven by the development of new materials (glulam, laminated veneer lumber, wood-based boards), on the one hand, and new connections, on the other. Moreover, steel structures were replaced by timber structures in times of material and resource scarcity, and in this context, nails played a decisive role.
Utilising nail construction, smaller board cross-sections could be economically connected to form efficient trusses with large spans, without having to pay attention to patents, as was the case with the various types of shear connectors, and could also be erected by untrained workers. A nailed truss construction from this time is depicted in Figure 1.

Figure 1: *Bailed truss Type-II*

However, acceptance of the structural use of the nail had to be created first. While dowels and bolts were widely used in many applications at the beginning of the last century, the nail in a load-bearing function was still prohibited. The nail only become part of the standardised codes after extensive basic research in the 1930s [1-3] and, thus, establish itself in the construction industry. Until the introduction of nail plates, countless roof trusses were built with nailed joints. Nailed trusses were still used in countries with a planned economy until about 1990.

The question of continued use and preservation is an important issue for many of these structures, leading to the need for engineering assessment. In this context, strongly varying conditions might be found. The nodes, which are, in many cases, decisive for the load bearing capacity, might especially exhibit deficiencies. A scheme is developed here for a simple, rapid evaluation of the condition of nailed connections in terms of load-bearing capacity and serviceability to generally support a decision about their further use.

With the help of this scheme, the condition of the nail connections is to be determined regarding nailing patters, edge distances and spacing, the presence of small or large cracks or fractures and moisture damage. The effort should be limited to the extent that non-destructive examinations are used almost exclusively. This means that the assessment is carried out mainly by visual inspection. In order to obtain information on the load-bearing behavior of nailed connections, the objectives of this paper are to determine the load-bearing capacities based on experimental tests on aged connections of nailed trusses, and combine these with visual classification based on the scheme presented.

The further use of such connections or load-bearing structures is to be supported by the combination of visual and experimental examinations. In addition to the examination utilising the scheme, the corrosion of the nails is also considered.

[1] Timber Structures and Building Rehabilitation, University of Kassel, Germany, l.voellmecke@uni-kassel.de
[2] Timber Structures and Building Rehabilitation, University of Kassel, Germany, s.schwendner@uni-kassel.de
[3] Timber Structures and Building Rehabilitation, University of Kassel, Germany, phienho@uni-kassel.de
[4] Timber Structures and Building Rehabilitation, University of Kassel, Germany, fischer.jj@t-online.de
[5] Timber Structures and Building Rehabilitation, University of Kassel, Germany, wseim@uni-kassel.de

https://doi.org/10.52202/069179-0528

2 ASSESSMENT OF CONNECTIONS

2.1 CLASSIFICATION SCHEME

A comprehensible rating scheme had to be developed to support a visual qualitative evaluation. In this context, Imamura and Kiguchi [4] presented a scheme based solely on the degree of corrosion of the nails. In this case, the condition of the nail was assigned from completely intact to failure. This approach was extended to the evaluation scheme for nailed joints of roof trusses, which also considers the integrity of the wood. This scheme is shown in Figure 2.

Rating	Standard	Example
1	Scarcely rusted	
2	Partially rusted, no visible defect	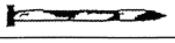
3	Totally rusted, no defect inside	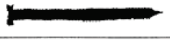
4	Partially defect, with original length	
5	Failure	

Figure 2: *Rating scheme of corrosion of the nails from* [4]

The classification into different categories is based only on the external appearance. Consequently, various conditions were imposed to enable the categorization of the individual nodes. These conditions are depicted in Figure 3. Each category is divided into a side and bottom view.

The reference to the load, depending on the grain direction, is established for this purpose. The assessment is carried out for the diagonal components loaded in the direction of the grain.

Category 1 is reached if the penetration length, the edge distance and the spacing are in accordance with the regulations applicable. In addition, at least 90 % of the nails must be hammered flush with the connecting timber, otherwise the joint falls directly into category 2. Category 1 should not generally show any visual damage.

A joint is classified as category 2 if either the penetration length, the edge distance or the spacing are not in accordance with the regulations applicable. No visible damage should be apparent in category 2 either.

Category 3 is divided into subcategories: 3a and 3b. In 3a, the joint complies with the penetration length, the edge distance and the spacing according to the regulations applicable. The joint is classified as 3b if any condition from 3a is not fulfilled. Basically, a joint is classified as category 3 if it has cracks smaller than 1 mm, less than 90 % of the nails are nailed flush with the connecting timber or there are first signs of deterioration of the wood.

In category 4, a distinction is again made between subcategories: 4a and 4b. The subcategories are the same as for condition 3. The criteria for classification as category 4 are any visible defects, including cracks larger than 1 mm wide, splitting, local moisture damage, wood decay or insect infestation.

Figure 3: *Classification scheme for aged nail joints*

Category		Description		Illustration		
				side view	bottom view	
					Type-I	Type-II
1		➢ Specifications for edge distance, penetration length and spacing are in accordance with the code regulation. ➢ > 90 % of the nails flush with connecting timber ➢ Timber without visible damage / cracks		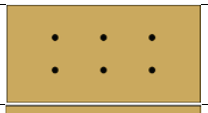		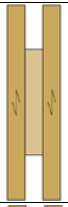
2		➢ Specifications for edge distance, penetration length or spacing are in accordance with the code regulation. ➢ Timber without visible damage / cracks				
3	a	➢ small cracks, width < 1 mm ➢ < 90 % of the nails flush with connecting timber ➢ Indications of moisture impact	Specifications for edge distance, penetration length and spacing are in accordance with the code regulation.	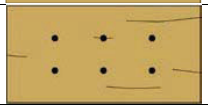		
	b		Specifications for edge distance, penetration length or spacing are not in accordance with the code regulation.	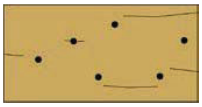		
4	a	➢ crack width > 1 mm ➢ splitting and disconnection ➢ moisture impact ➢ timber decay ➢ insect infestations	Specifications for edge distance, penetration length and spacing are in accordance with the code regulation.	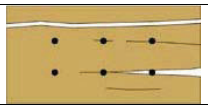		
	b		Specifications for edge distance, penetration length or spacing are not in accordance with the code regulation.			

https://doi.org/10.52202/069179-0528

2.2 APPLICATION OF THE CATEGORIZATION

The scheme was applied to two test series with the same roof shape, which was the mono-pitched roof. Type I consisted of a chord as the middle member and struts and posts as side members, respectively. The construction is shown in Figure 4 and 5. A total of 62 connections were tested. Furthermore, 11 connections of Type II were tested. In the latter, struts and posts are between two bottom chords, as shown in Figure 6 and 7.
The scheme to evaluate the condition was applied to all joints. Only timber members which are loaded in the direction of the grain were analysed. The chord, which is loaded orthogonal to the grain, can be neglected for the categorization.
The designations of the joints AH – "Adorf Hessen" and GH – "Gießen Hessen" refer to the region in Germany, while PD refers to the roof shape. In both cases the roof shape was a pitched roof.

Joint Type I

The connections were made with a different number of nails and two different nail diameters. The posts and struts are on the outside in this type. The chord between the posts and struts is a single beam with the dimensions 8 x 16 cm. The chord has not been categorized due to its full integrity and the loading, which is not parallel to the grain. The assessment of the diagonal side members with a geometry of 2.3 x 10 cm is illustrated by the examples in Figure 4 and 5.

(a)
side view A:
post cat. 2,
strut cat. 2

(b)
side view B:
post cat.: 3b,
strut cat.: 3b

Figure 4: Evaluation of Joint Type I B09

The post for joint B09 in Figure 4a was assigned to Category 2 based on a nonstandard nailing. No cracks could be found. The strut on this side was assigned to category 2 because no cracks were discernible here either and standard nailing was missing. On the other side of the connection, the post was assigned to category 3b due to nonstandard nailing and small cracks up to 1 mm wide.
The strut on side B was classified in category 3b as it also lacked standard nailing and showed small cracks up to 1 mm in the lower part of the board.

(a)
side view A:
post cat.: 4b,
strut cat.: 4b

(b)
side view B:
post cat.: 4b,
strut cat.: 4b

Figure 5: Evaluation of Joint Type I B12

The posts for joint B12 in Figures 5a and 5b were classified as category 4b due to nonstandard nailing and cracks larger than 1 mm. The struts on both sides were classified as category 4b because there were also cracks larger than 1 mm and a standard nailing was missing.

Joint Type II

The connections of Type II were made with a different number of nails. In this type, the posts and struts formed the middle parts. The chords were on the outside, each with dimensions of 2.3 x 10 cm. Since the direction of the force is not in the direction of the grain of the chord, it was assumed to have no influence on the evaluation. The middle members with a geometry of 2.3 x 10 cm have been evaluated using two examples in Figure 6.

bottom view:
cracks
→ post cat.: 4

Figure 6: Evaluation of Joint Type II A01

The post for Joint A01 is decisive for the evaluation of the entire joint. It was classified as category 4b due to the bottom view because there was a crack of more than 1 mm (see Fig. 6).

https://doi.org/10.52202/069179-0528

bottom view:
cracks →
post cat.: 4,
strut cat.: 4

Figure 7: Evaluation of Joint Type II A02

The post and the strut were again taken as significant for the evaluation of joint A02. These were classified as category 4 due to the bottom view, since cracks larger than 1 mm were present there (see Figure 7b).

3 ANALYTICAL CALCULATION

The characteristic lateral resistance for the shear loaded connections was calculated according to EN 1995-1-1:2010 for purposes of comparison [7]. The geometrical and the material parameters used in this calculation are documented in Table 1. The construction of each type with the geometrical parameters is shown in Figure 8.

Table 1: Parameters for the calculation of the two test series

$f_{u,k}$ [N/mm²]	ρ_m [kg/m³]	ρ_k [kg/m³]	f_{ax} [N/mm²]
600	420	350	2.45

Calculation of the load-bearing capacity

The following steps show the calculation of the shear capacity for the two test series.

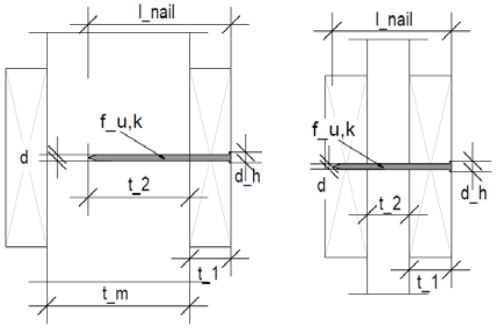

(a) (b)

Figure 8: Geometry of (a) Type I and (b) Type II

It could be shown using pre-calculations that for all diameters of the nails, mechanism d was decisive for Type I, in which a yield hinge was formed in the middle timber, and mechanism c for Type II, with embedment failure in all timbers.

The yield moment $M_{y,Rk}$ is calculated as

$$M_{y,Rk} = 0.30 \cdot f_{u,k} \cdot d^{2.6} \quad (1)$$

where $f_{u,k}$ is the tensile strength and d the diameter of the nails. The embedment strength $f_{h,k}$ is calculated as

$$f_{h,k} = 0.082 \cdot \rho_k \cdot d^{-0.3} \quad (2)$$

where ρ_k is the characteristic density. The withdrawal strength $f_{ax,k}$ is calculated as

$$f_{ax,k} = 20 \cdot 10^{-6} \cdot \rho_k^2 \quad (3)$$

The head pull-through resistance is calculated as

$$f_{head,k} = 70 \cdot 10^{-6} \cdot \rho_k^2 \quad (4)$$

The ratio of embedment strength is calculated as

$$\beta = \frac{f_{h,2,k}}{f_{h,1,k}} = 1 \quad (5)$$

with $f_{h,2,k} = f_{h,1,k}$. The load-bearing capacity for the joints of Type I is calculated as

$$F_{v,Rk} = 1{,}05 \cdot \frac{f_{h,1,k} \cdot t_1 \cdot d}{2+\beta} \left[\sqrt{2 \cdot \beta \cdot (1+\beta) + \frac{4 \cdot \beta \cdot (2+\beta) \cdot M_{y,Rk}}{f_{h,1,k} \cdot t_1^2 \cdot d}} \right] - \beta \quad (6)$$

with the parameters determined previously. The load bearing capacity for Type II is calculated as

$$F_{v,Rk} = \frac{f_{h,1,k} \cdot t_1 \cdot d}{1+\beta} \cdot \left[\sqrt{\beta + 2 \cdot \beta^2 \cdot \left[1 + \frac{t_2}{t_1} + \left(\frac{t_2}{t_1} \right)^2 \right] + \beta \cdot \left(\frac{t_2}{t_1} \right)^2 - \beta \cdot \left(1 + \frac{t_2}{t_1} \right)} \right] \quad (7)$$

To include the rope effect $\Delta F_{ax,Rk}$, the significant withdrawal force is calculated as

$$F_{ax,Rk} = min \begin{cases} f_{ax,k} \cdot d \cdot t_2 \\ f_{ax,k} \cdot d \cdot t_1 + f_{head,k} \cdot d_h^2 \end{cases} \quad (8)$$

where d_h is the nail head diameter. The additional force is calculated as

$$\Delta F_{v,Rk} = min \begin{cases} 0.25 \cdot F_{ax,Rk} \\ 0.15 \cdot F_{v,Rk} \end{cases} \quad (9)$$

The total load capacity of a nail is calculated as

$$F_{v,Rk,total} = F_{v,Rk} + \Delta F_{v,Rk} \quad (10)$$

The dimensions of the nails correspond to those found in the components. The standard dimensions of nails nowadays are different. Nails with diameters of 2.8, 3.1 and 3.4 mm are used in these specimens.

The analytical calculated capacity according to EC5 is documented in Table 2 for each diameter.

https://doi.org/10.52202/069179-0528

Table 2: Load capacity per nail diameter

d [mm]	d_h [mm]	t_m [mm]	t_1 [mm]	t_2 [mm]	$F_{v,k}$ [N]	$F_{ax,k}$ [N]	$F_{v,k,total}$ [N]
2.8	6	80	23	42	588	288	660
3.1	6	23	23	23	604	175	647
3.4	7	80	23	57	727	475	836

4 EXPERIMENTAL TESTING OF JOINTS

The joints evaluated with the scheme developed were finally tested to determine the capacity of the connections. The whole test programme included shear tests on specimens taken from trusses of existing structures and additional tests to determine material parameters. The evaluations of all tests are presented by Schwendner et al. [6].

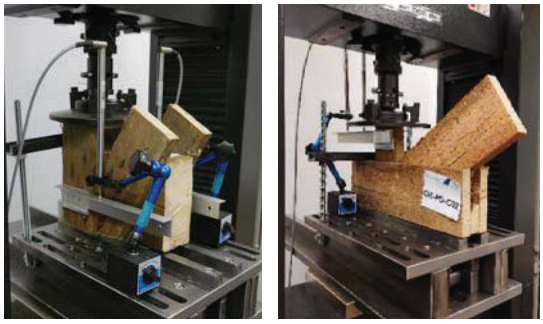

(a) (b)

Figure 9: Test set-up for joints (a) Type I; (b) Type II

Only the experimental tests on joints will be discussed in this paper. The failure of the joints was defined corresponding to a displacement of 15 mm. Figure 9a shows the test set-up for Type I and Figure 9b for Type II. Both configurations can be tested with the set-up developed.

5 TEST RESULTS AND VALIDATION

In this section, the experimental test results are compared with the results of the analytical calculation according to EC5. In a second step, the scheme developed is validated. Therefore, the categories are compared with the ratio between the experimental test results and the strength calculated according to EC5.

5.1 TYPICAL FAILURE MODES

Application examples of the rating scheme show a correlation of the joint and the failure mode. The joints which are depicted in Figure 11a and b, for example, were evaluated in advance with condition 4 and show that not all nails have formed plastic hinges after the execution of the test; the wood was unable to contribute to the embedment strength due to the cracks and, thus, a lower load-bearing capacity of the joint results.

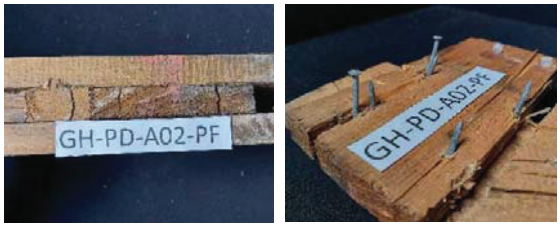

(a) (b)

Figure 10: Type II: joint GH-PD-A02 before and after testing

As a further example, Figure 11a and b show a test specimen of Type II before and after the shear test. Here, the rating 4 also indicates a lower load-bearing behaviour. After testing, it can be seen that the specimen could not reach its full load-bearing capacity in the area of the crack, due to the missing yield hinge. Consequently, not all nails reached their capacity.

(a) (b)

Figure 11: Type I: joint AH-PD-B06 before and after testing

5.2 COMPARISON BETWEEN EXPERIMENTAL TEST RESULTS AND ANALYTICAL CALCULATION

The geometrical components and the assessment category for each joint taken from the aged roof trusses are documented in Table 3 to 6. Additionally, the number of nails, the analytically calculated characteristic strength $F_{v,Rk}$ according to EC5 and the maximum strength F_{max} determined by the experimental tests are given. As a final result, the ratio between F_{max} and $F_{v,Rk}$ is calculated.

Nails with a diameter of $d = 3.4$ mm and $d = 2.8$ mm were used for Type I. The calculated load capacity in relation to the number and diameter of existing nails per joint are shown in Table 3 and 4.

Nails with a diameter of $d = 3.1$ mm were used for Type II. The calculated load capacity in relation to the number of nails per joint are shown in Table 5 and 6.

https://doi.org/10.52202/069179-0528

Table 3: Type I, Serie AH-PD-PF (ST = strut)

Joint	α	Cate-gory	$n_{2.8}$	$n_{3.4}$	$F_{v,Rk}$	F_{max}	$F_{max}/F_{v,Rk}$
	[°]	[-]	[-]	[-]	[kN]	[kN]	[-]
A02-ST	90	3	7	8	11.31	24.62	1.4
A04-ST	90	2	9	6	10.96	26.75	1.9
A05-ST	83	2	9	6	10.96	30.09	1.9
A06-ST	90	2	7	6	9.64	27.72	2.2
A08-ST	90	3.5	0	14	11.70	26.33	2.5
A09-ST	83	3	7	6	9.64	20.20	2.0
A10-ST	90	2.5	11	6	12.28	23.90	1.8
A11-ST	83	4	7	7	10.47	22.71	2.7
mean-A-ST		**2.8**			**10.87**	**25.29**	**2.0**
B04-ST	90	3	0	13	10.87	30.70	2.6
B06-ST	90	3	0	13	10.87	26.93	2.6
B07-ST	83	2.5	0	12	10.03	21.79	1.9
B08-ST	90	2.5	0	13	10.87	29.10	1.9
B09-ST	83	2.5	0	12	10.03	27.21	1.7
B10-ST	90	4	0	14	11.70	20.09	2.5
B11-ST	83	3	0	12	10.03	22.94	1.8
B12-ST	90	4	0	12	10.03	15.70	1.5
mean-B-ST		**3.1**			**10.55**	**24.31**	**2.1**

Table 4: Type I, Serie AH-PD-PF (PF = post)

Joint	α	Cate-gory	$n_{2.8}$	$n_{3.4}$	$F_{v,Rk}$	F_{max}	$F_{max}/F_{v,Rk}$
	[°]	[-]	[-]	[-]	[kN]	[kN]	[-]
A02-PF	90	4	9	6	10.96	15.64	2.2
A04-PF	90	2.5	9	6	10.96	21.09	2.4
A05-PF	83	3	9	6	10.96	20.94	2.7
A06-PF	90	2	4	11	11.84	25.86	2.9
A08-PF	90	3.5	0	12	10.03	25.56	2.2
A09-PF	83	3	9	6	10.96	21.54	2.1
A10-PF	90	3	11	6	12.28	21.70	1.9
A11-PF	83	3	8	6	10.30	27.48	2.2
mean-A-PF		**3.0**			**11.03**	**22.48**	**2.3**
B04-PF	90	2.5	0	12	10.03	26.22	2.8
B06-PF	90	2.5	0	12	10.03	25.77	2.5
B07-PF	83	2.5	0	12	10.03	18.59	2.2
B08-PF	90	2.5	0	12	10.03	19.10	2.7
B09-PF	83	2.5	0	12	10.03	16.77	2.7
B10-PF	90	2.5	0	11	9.20	23.34	1.7
B11-PF	83	3	0	12	10.03	18.43	2.3
B12-PF	90	4	0	11	9.20	13.92	1.6
mean-B-PF		**2.8**			**9.82**	**20.27**	**2.3**

Table 5: Type II, Serie GH-PD-ST (ST = strut)

Joint	α	Cate-gory	$n_{3.1}$	$F_{v,Rk}$	F_{max}	$F_{max}/F_{v,Rk}$
	[°]	[-]	[-]	[N]	[N]	[-]
A02	35	4	13	16.82	22.55	1.3
B02	35	3	7	9.06	13.06	1.4
A03	30	3	14	18.12	29.33	1.6
B03	30	3	16	20.70	34.05	1.6
C02	35	3	14	18.12	30.95	1.7
C03	30	2	14	18.12	49.99	2.8
mean-ST		**3.0**	**13**	**16.82**	**29.99**	**1.8**

Table 6: Type II, Serie GH-PD-PF (PF = post)

Joint	α	Cate-gory	$n_{3.1}$	$F_{v,Rk}$	F_{max}	$F_{max}/F_{v,Rk}$
	[°]	[-]	[-]	[kN]	[kN]	[-]
A01	85	4	8	10.35	20.17	1.9
B01	85	4	8	10.35	5.70	0.6
C01	85	4	8	10.35	16.58	1.6
A02	90	4	8	10.35	15.03	1.5
B02	90	4	8	10.35	15.18	1.5
mean-PF		**4.0**	8	**10.35**	**14.53**	**1.4**

The experimental test results achieved a higher load than the calculation according the EC5 for all joints, with the exception of joint B01.

5.3 VALIDATION OF THE ASSESSMENT SCHEME

The results from experimental testing are used for the validation of the classification system. Thus, the characteristic capacity per nail was assigned to the respective category for each test.

Figure 12a shows the graphs for Type I. Based on the shear tests, it was possible to establish a trend line showing a clear tendency for a decreasing quality to correspond to a lower load-bearing capacity (see Figure 12). On average, a ratio of 2.6 between experimental and analytical results can be obtained for Category 2, 2.2 for Category 3 and 1.7 for Category 4.

Figure 12b shows the graph for Type II. By assigning the load-bearing capacities to the pre-rated categories, a trend line could again be generated here. This supports the hypothesis of the correlation of the assessed category and capacity. The average ratio of category 2 is 2.8, of category 3, 1.6 and of category 4, 1.4.

https://doi.org/10.52202/069179-0528

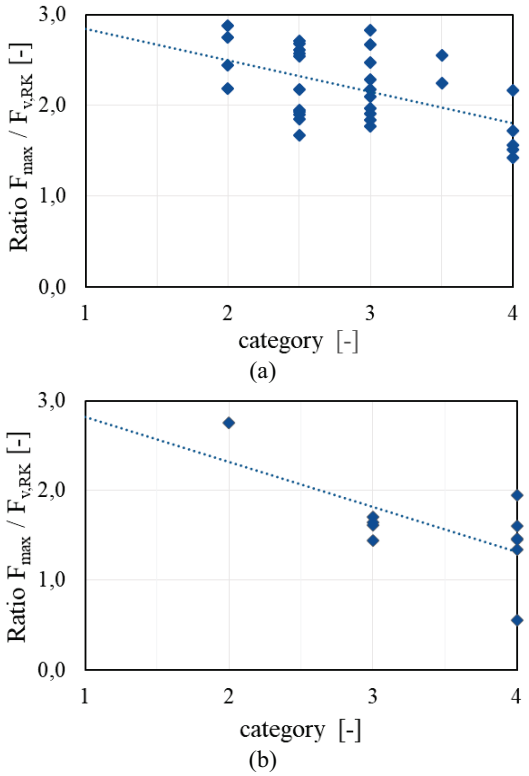

Figure 12: Load-bearing capacity per nail depending on the category, (a) Type I, (b) Type II

6 SUMMARY AND CONCLUSION

A classification scheme which is based on the visual inspection of individual joints was successfully applied and confirmed. It could be shown by investigating joints of aged nail trusses that a lower bearing capacity was reached on average with a decreasing rating.

In addition, the rating can also predict the possible form of failure, such as the preliminary splitting of the wood so that the nails cannot form a yield hinge. Cracks indicate that the nails cannot develop their full load-bearing capacity. The category and assignment correspond to the quality of the joints in terms of their load-bearing capacity.

Regarding further research on aged nail trusses, experiments should be carried out on complete trusses. An assessment of the load-bearing behaviour of the intact trusses is missing because only joints and their parameters have been investigated so far. This could be used to describe further factors, such as bending or buckling.

In addition to other component tests in the future, an exact evaluation of the load-bearing capacities measured so far per condition should be determined. This means that a percentage load-bearing capacity can be assigned per category of the connection according to Eurocode 5. The aim here is that the load-bearing capacity of worse joints may have to be corrected. For this purpose, further investigations are needed, for example, to check repair measures on aged structural members. The aim is to gain more knowledge about the compliance of the connections. Is it sufficient to hammer additional nails into a component to reactivate defective parts? How does a replaced board affect the whole system? Which joints need to be repaired?
Large-scale tests are necessary to answer these questions. In addition to determining the load-bearing capacity, other factors should also be considered. Due to the slenderness of the components, the fire protection class is often significantly lower than F30. A possible fire can have a direct influence on the nails and lead to an abrupt collapse of the construction. Measures should be considered to increase the stability in case of fire.

Another factor is the influence of moisture. Although the thinness of the component results in less swelling, the slenderness of the boards means that the full cross-section is probably saturated and could lead to a faster failure of the component in the long term.

In addition to these open points, an application of the evaluation scheme in existing buildings would be desirable. The target is to evaluate the load-bearing capacity of the roof structure without removing components in order to be able to plan possible replacement measures in an economical and sustainable way.

REFERENCES

[1] Stoy, W.: Über Versuche mit Drahtstiften als Holzverbindungsmittel. *Deutsche Bauzeitung*, 64(19):141–148, 1930.
[2] Gaber, E.: Statische und dynamische Versuche mit Nagelverbindungen. In: *Versuchsanstalt für Holz, Stein und Eisen*, 3:1–36, Karlsruhe, 1935.
[3] Grabbe, H.: Die Festigkeit der zweischnittig genagelten Holzverbindungen bei gleicher und ungleicher Holzstärke. PhD Thesis, Technical University of Braunschweig, Institute for timber engineering, Germany, 1935.
[4] Imamura, H., and Kiguchi, M.: Prediction of wood decay in the exterior wall of wooden houses by the deterioration of nails – Prediction of decay by nails. *Durability of Building Materials and Components*,8:746–755, 1999.
[5] EN 26 891: Timber structures; Joints made with mechanical fasteners; General principles for the determination of strength and deformation characteristics; German version EN 26 891: 1991
[6] Schwendner, S., Seim, W., Völlmecke, L. and Fischer, J., 2023. testing of connections taken from old nailed roof trusses. Proceedings WCTE, 2023.
[7] Eurocode 5: Design of timber structures – Part 1-1: General – Common rules and rules for buildings – German version EN 1995-1-1:2004 + EN 1995-1-1/AC:2006 + EN 1995-1-1/A1:2008

World Conference on Timber Engineering Oslo 2023

TESTING OF CONNECTIONS TAKEN FROM OLD NAILED ROOF TRUSSES

Sascha Schwendner[1], Lars Völlmecke[2], Phien Ho[3], Jens Fischer[4], Werner Seim[5]

ABSTRACT: Experimental testing of nailed connections taken from old roof trusses is presented in this paper. To enable the further use and preservation of nailed roof trusses, it is important to understand how the nail corrosion and aging processes of steel and wood affect the load-bearing capacity and deformation behaviour of such structures. The hypothesis was investigated whether corroded nails allow an increase in load-bearing capacity. Several old and new joints were tested in a first test series, and the results were very promising regarding the initial assumption. However, more tests must be carried out to verify the results.

KEYWORDS: Nailed Connection, Corrosion, Degradation, Preservation, Withdrawal, Shear Loaded

1 INTRODUCTION

Connections with nails experienced a real boom in the middle of the 19th century and often turned out to be the construction method of choice, especially in times of material and resource scarcity. In addition, labour costs were significantly lower than today, which meant that the large amount of time required to create the trusses with many fasteners was still economical. Nevertheless, nails were not allowed for load-bearing purposes at the beginning of the 20th century in Germany until they were established as widely accepted fasteners through extensive basic research in the 1930s [1,2].
The combination of comparatively small timber sections and nails led to the development of trusses, which achieved large spans with a minimal use of materials. Moreover, nails were not subject to patent protection and could also be installed by untrained laborers, two important advantages compared, for example, to connections with dowels.

A large variety of different types of roof trusses were developed over the years. The load-bearing capacity of nailed trusses might be questioned today when it comes to discussing further use and preservation. Takanashi et al. [3] have already suggested an increase of the load-bearing capacity of nailed connections from existing structures based on their pull-out tests on artificially aged nail joints.

The aim of this paper is to investigate the load-bearing capacity of aged timber joints and the influence that corrosion of nails can have on this. Against this background, an investigation into how aging, especially nail corrosion, affects the load-bearing capacity and the deformation behaviour of the nailed joints was undertaken. The basic assumption of a potential increase in the load-bearing capacity due to partially corroded nails was investigated by tests on aged joints from nailed roof trusses taken from existing buildings. The truss nodes were examined with a newly developed testing device. Additional tests were carried out on single components to analyse their specific properties and determine parameters. This can provide conclusions about differences between the aged connections and new construction. Therefore, geometrically identical node connections were produced with new materials and tested (see Figure 1). All test results will be compared and discussed in the following.

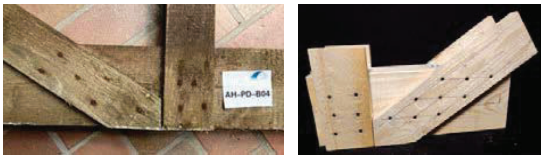

(a) (b)

Figure 1: *(a) Type-I_old: joint B04 and (b) Type-I_new: joint SV-1947-01*

2 EXPERIMENTAL TESTING

In order to be able to investigate the behaviour of aged nodes, trusses were chosen from a structure which had been used primarily for roofing a car wash and later a beverage store. After demolition, the trusses were stored

[1] Timber Structures and Building Rehabilitation, University of Kassel, Germany, s.schwendner@uni-kassel.de
[2] Timber Structures and Building Rehabilitation, University of Kassel, Germany, l.voellmecke@uni-kassel.de
[3] Timber Structures and Building Rehabilitation, University of Kassel, Germany, phienho@uni-kassel.de
[4] Timber Structures and Building Rehabilitation, University of Kassel, Germany, fischer.jj@t-online.de
[5] Timber Structures and Building Rehabilitation, University of Kassel, Germany, wseim@uni-kassel.de

https://doi.org/10.52202/069179-0529

outside under a tarp sheathing for several years (see Figure 2). This structure has been exposed over time to different climatic conditions, which have caused significant corrosion at the joints and local cracks to appear in the timber. On the other hand, some nodes are completely undamaged, so, there was a wide range between intact and considerably damaged nodes.

2.1 TESTING PROGRAMME

The test programme consists basically of two groups. The elements selected for the first group (Type I-old) are taken from the original trusses. These specimens showed cracks in the timber and corrosion of the nails, together with irregularities of the nailing pattern.
The elements selected for the second group (Type I-new) were made with new materials and served as a reference to evaluate the load-deformation behaviour of aged elements (see Figure 1). The specimens in the second group are identical to those taken from the trusses to be comparable to each other.

Figure 2: *Roof trusses*

In a first step, parameter tests were carried out to get an initial impression of the quality of the materials which were used for the joints. The parameters determined were

- the density of the timber,
- the embedment strength of the timber,
- the tensile strength of the steel,
- the yield moment of the nails and
- the withdrawal strength of the nails.

In terms of timber materials, a distinction was made between strut and chord. The position in the truss beam does not play a role in the determination of the parameters for the nails.

An overview of the whole test programme is given in Table 1. The tests to indicate the specific properties and the tests on connections are listed here.

Table 1: *Overview of the test programme*

Number of tests	Old	New
Density ρ_k	27	18
Embedment strength $f_{h,k}$	16	16
Tensile strength $f_{u,k}$	20	8
Yield moment $M_{y,k}$	10	10
Withdrawal strength $f_{ax,k}$	18	10
Connection I-old	8	15
Connection I-new	8	15

2.2 DENSITY AND EMBEDMENT STRENGTH

The density of the timber in both groups was tested according to DIN 52182 [4]. The test specimens were dried until the weight dropped to under 0.1 %.

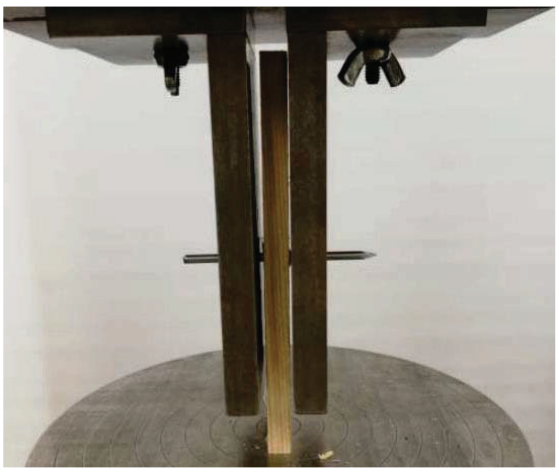

Figure 3: *Test set-up to determine the embedment strength of the timber*

The embedment strength of the timber was tested according to EN 383:2007 [5]. Figure 3 shows the test set-up to determine the embedment strength of the timer elements. The embedment strength is determined at a deformation of the specimen of 5 mm with the maximum force F, the thickness of the timber specimen t and the diameter of the fastener d, according to equation (1). Based on the code for all specimens, the loading was parallel to the grain.

$$f_{h,k} = \frac{F_{\max}}{t \cdot d} \tag{1}$$

2.3 TENSILE STRENGTH AND YIELD MOMENT

The tensile strength of the fasteners was determined according to DIN 2002-001 [6] after the nail heads had been cut, whereby the clamping of the nails had to be reduced due to their length. This had no influence on the fracture pattern of the nails. Testing at a constant speed, the maximum strength is calculated with the maximum force and the cross-section for the original nominal diameter of 3.40 mm of the nail. Figure 4 shows the aged

https://doi.org/10.52202/069179-0529

and new nails and the test set-up to determine the tensile strength of single nails.

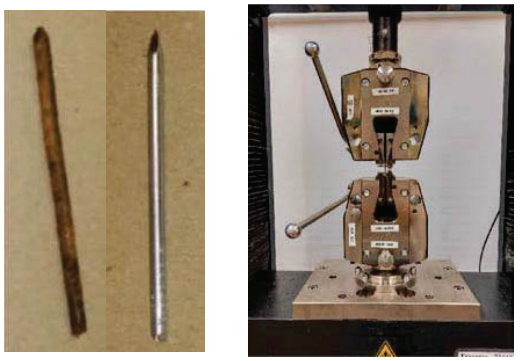

(a) (b)

Figure 4: *(a) Aged and new nail and (b) test set-up to determine the tensile strength of a single nail*

The yield moment of the nail was determined with a test set-up proposed by Werner and Siebert [7]. The construction is depicted in Figure 5. The nail in the frame can be deformed with a long cantilever with the length l_v. A load cell is located at the end of the lever arm. The yield moment of a single nail can be determined with the force F_{max} detected in the load cell and the length of the lever arm, see equation (2).

$$M_{y,Rk} = F_{max} \cdot l_v \tag{2}$$

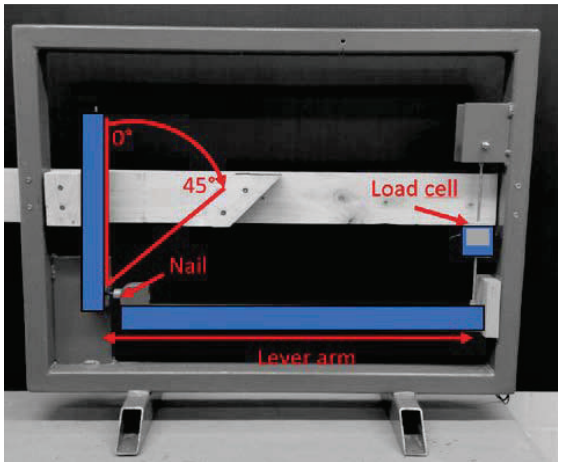

Figure 5: *Test set-up to determine the yield moment of a single nail*

2.4 WITHDRAWAL STRENGTH

The withdrawal strength of the nails was determined according to EN 1382:2016-07 [8]. The test set-up is shown in Figure 6. To determine the withdrawal strength of the aged nails, parts of the truss beams were cut out to obtain realistic results. The test specimens were conditioned under a humidity of 65 ± 2 % at 20 ± 2 °C prior to testing.

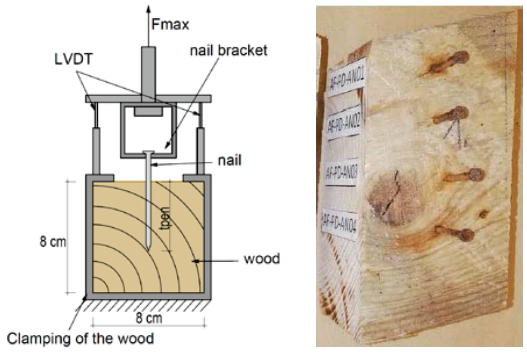

(a) (b)

Figure 6: *(a) Test set-up and (b) specimen for the determination of the withdrawal strength*

2.5 TESTS ON CONNECTIONS

In a second step, tests on joints cut out from the trusses were carried out. A special test set-up was developed for this so that the connection of posts and struts that act in a node can be tested separately, one after the other (see Figure 7). The set-up was designed in such a way that different inclinations of the struts could be tested. The chord of the truss beam ran continuously as one section between the two supports, whereas the posts and the struts were separated into two parts, each connected sideways to the chord. Each pair of posts or struts in the test set-up were loaded and could deform up to 50 mm, which ensured that the maximum load was achieved in the connections when the tests were carried out. The test set-up is depicted in Figure 7 (b). Due to the test set-up developed, it was necessary to test the posts first and then the struts.

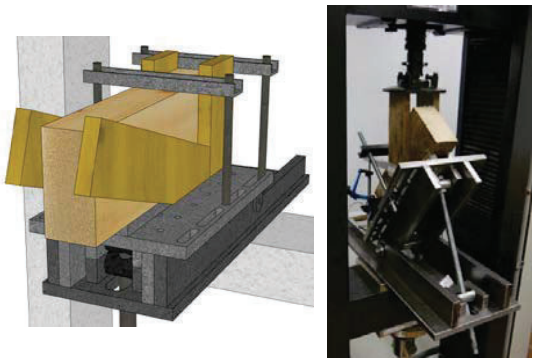

(a) (b)

Figure 7: *Test set-up for joints (a), isometric view and (b) photo*

All tests were performed and evaluated under the monotonic loading protocol according to EN 26891 [9]. Displacement transducers were installed to measure the relative displacement between the chord and the posts and struts, respectively. The load-bearing capacity of the connections was, firstly, estimated at the mean value level to determine the loading rate. This resulted in a loading rate of 41.6 and 62.3 N/sec, depending on how many

https://doi.org/10.52202/069179-0529

fasteners were arranged in the node to be tested. This ensures that failure was achieved in a time span of 120 s ± 30 sec. The test specimens were conditioned under a humidity of 65 ± 2 % at 20 ± 2 °C prior to testing.

3 RESULTS AND DISCUSSION

The results of the experimental investigations are presented and evaluated in this section. Firstly, the experiments for determining the parameters of the single elements of the truss are discussed, followed by a consideration of the nodes. Finally, the 5 % fractile values are derived from experimental results which are then compared with the characteristic values from EC 5 [10]. This makes it possible to compare whether the aged trusses have similar properties to the nodes created with new materials. The values according to EC 5 are calculated as follows:

$$f_{h,k} = 0.082 \cdot \rho_k \cdot d^{-0.3} = 0.082 \cdot 350 \cdot 3.4^{-0.3} = 19.9 N/mm^2 \quad (3)$$

$$M_{y,k} = 0.3 \cdot f_{u,k} \cdot d^{2.6} = 0.3 \cdot 600 \cdot 3.4^{2.6} = 4336 Nmm \quad (4)$$

$$f_{ax,k} = 20 \cdot 10^{-6} \cdot \rho_k^{\,2} = 20 \cdot 10^{-6} \cdot 350^2 = 2.45 N/mm^2 \quad (5)$$

3.1 MATERIAL PARAMETERS

Table 2 summarises the parameters determined for the elements from the trusses and compares them to the specifications according to EC 5. The values are always given as characteristic values. The exact number of samples and the coefficient of variation (COV) are also given.

Despite considerable signs of aging of both nails and wood, the test results meet the specifications of EC 5 regarding density, embedment strength and tensile strength.

(a) (b)

Figure 8: *(a) Tensile failure of old and (b) new nails*

In terms of tensile strength, it is noticeable that the new nails have a significantly higher characteristic value. This is probably due to the standardised production and better steel quality compared to the nails from the old truss. Only the yield moment and withdrawal strength exhibit shortcomings for the specimen taken from the aged truss.

Table 2: *Truss Type I-old: results of parameter testing – characteristic values*

Parameter			Value	n [-]	COV [%]
Density ρ_k [kg/m³]		chord	401	27	1.6
		strut	392	28	11.0
		EC5	350		
Embedment strength $f_{h,k}$ [N/mm²]		chord	22.1	16	4.0
		strut	21.0	16	20.6
		EC5	19.9		
Tensile strength $f_{u,k}$ [N/mm²]	nails ø = 3.4 mm	old	781	20	10.3
		new	1045	8	0.4
		EC5	600		
Yield moment $M_{y,k}$ [Nmm]		old	4102	10	5.4
		new	6212	10	1.1
		EC5	4336		
Withdrawal strength $f_{ax,k}$ [N/mm²]		old	2.22*	18	52.6
		new	2.94	10	13.0
		EC5	2.45		

** minimum value*

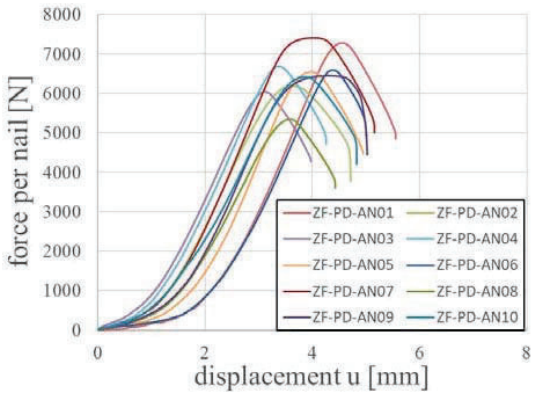

Figure 9: *Tensile strength test results with corroded nails*

Tensile strength

Three different test series were carried out to determine the tensile strength of the nails. Nails with corrosion were taken from the aged roof trusses for the first test series. The second series of tests was also on nails from aged roof trusses but with the difference that the nails were galvanized. This layer protected the nails from corrosion. The third test series was on new nails. When testing the tensile strength of the nails from the first test series, it was interesting to see failure always occurring in a zone of the nails which was originally situated close to the contact surface between the middle and side parts. This can be an indication of slightly higher corrosion in the small gap between the two timber parts. The specimens tested are

depicted in Figure 8. The test results are shown in Figure 9 to 11.

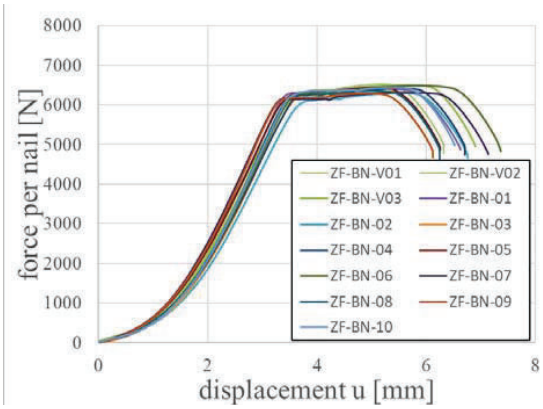

Figure 10: *Tensile strength test results with galvanised, aged nails*

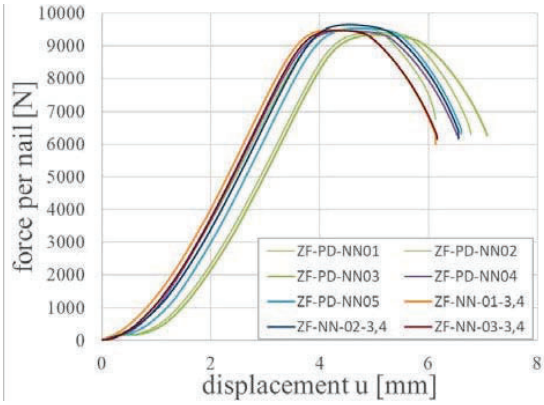

Figure 11: *Tensile strength test results with new nails*

Table 3: *Yield moment $M_{y,k}$ for old and new nails*

d = 3.40 mm, l_v = 655 mm			
old nails		new nails	
	$M_{y,k}$ [Nmm]		$M_{y,k}$ [Nmm]
FM-PD-AN01	3596	FM-PD-NN01	5964
FM-PD-AN02	3701	FM-PD-NN02	6213
FM-PD-AN03	2672	FM-PD-NN03	6220
FM-PD-AN04	2324	FM-PD-NN04	6391
FM-PD-AN05	3948	FM-PD-NN05	6539
FM-PD-AN06	3558	FM-PD-NN06	5894
FM-PD-AN07	2818	FM-PD-NN07	6399
FM-PD-AN08	2838	FM-PD-NN08	6364
FM-PD-AN09	3028	FM-PD-NN09	5945
FM-PD-AN10	3234	FM-PD-NN10	6192

Yield moment

A very homogeneous result with a low COV is observed for the yield moment, both for the old and new nails. It can be seen that the old nails only achieve about 2/3 of the yield moment of the new nails. The value achieved by the old nails corresponds to that calculated according to EC5. New nails, thus, achieve significantly higher yield moments. The result of each test is given in Table 3.

Table 4: *Withdrawal strength test results for old nails*

old nails					
	b [mm]	t [mm]	d [mm]	t_{pen} [mm]	f_{ax} [N/mm]
AF-AN-01	80.0	45.5	3.36	41.5	4.78
AF-AN-02	80.0	80.0	3.55	56.0	2.39
AF-AN-03	80.0	80.0	3.44	56.0	3.02
AF-AN-04	80.0	80.0	3.48	56.0	9.51
AF-AN-05	80.0	80.0	3.55	56.0	8.86
AF-AN-06	80.0	80.0	3.45	56.0	10.8
AF-AN-07	80.0	80.0	3.55	56.0	8.97
AF-AN-09	80.0	80.0	3.55	56.0	4.24
AF-BN-01	75.8	48.0	3.42	40.7	7.65
AF-BN-02	75.8	48.0	3.44	41.4	3.38
AF-BN-03	76.7	46.0	3.45	39.2	2.22
AF-BN-04	76.7	46.0	3.42	40.1	3.09
AF-BN-05	76.5	45.0	3.33	42.2	6.11
AF-BN-06	76.5	45.0	3.46	41.5	4.77
AF-BN-07	75.7	46.0	3.38	42.6	2.51
AF-BN-08	75.7	46.0	3.35	42.0	2.82
AF-BN-09	76.3	46.4	3.33	41.0	4.61
AF-BN-10	76.3	46.4	3.36	42.1	4.40

Withdrawal strength

The withdrawal strength is generally subject to a high degree of scattering, which is why the results are not very robust and, together with the characteristic value, the minimum value determined in the tests is given in Table 2. Consequently, further tests are required. Old nails were assigned their original diameter for the calculation of the withdrawal strength due to the small amount of corroded material. The result of each test for the old nails is given in Table 4. The test results for corroded nails taken from the first test series with the tests AF-AN-01 to -09 are shown in Figure 12. The test results for galvanized nails taken from the second test series with the tests AF-BN-01 to -10 are shown in Figure 13.

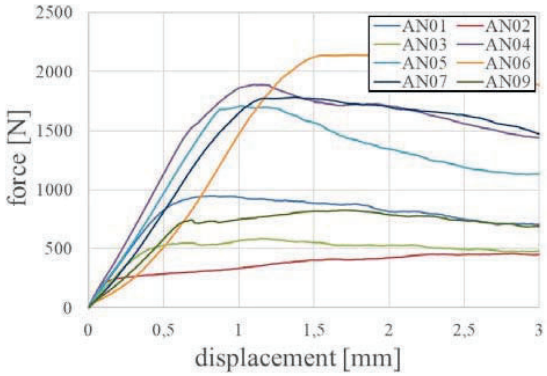

https://doi.org/10.52202/069179-0529

Figure 12: *Withdrawal strength test results with corroded nails*

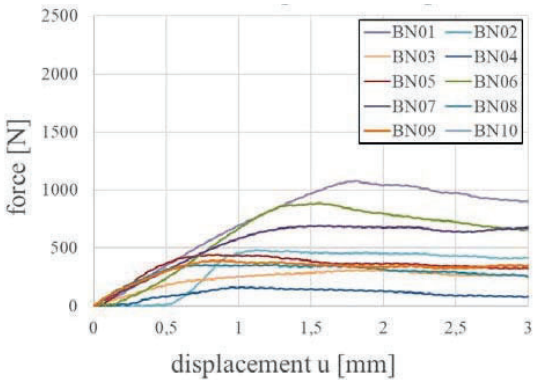

Figure 13: *Withdrawal strength test results with galvanised, aged nails*

The test results made with new materials are given in Table 5 and shown in Figure 14.

Table 5: *Withdrawal strength test result for old nails*

new nails			
b x t = 80 x 80 mm, d = *3.40 mm*, t_{pen} = 56 mm			
Test	f_{ax} [N/mm²]	Test	f_{ax} [N/mm²]
AF-NN-01	5.47	AF-NN-05	4.12
AF-NN-02	12.0	AF-NN-06	3.51
AF-NN-03	6.55	AF-NN-07	5.75

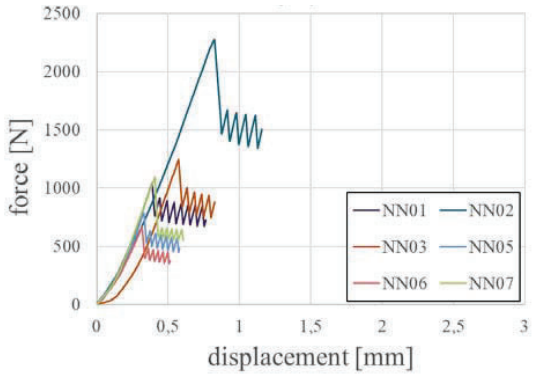

Figure 14: *Withdrawal strength test results with new nails*

Embedment strength

The test specimens for the embedment strength test are shown in Figure 15. As specified in the standard, all tests were performed perpendicular to the grain. The characteristic value of the embedment strength is almost identical for the chord and the strut, but the strut shows a significantly higher scattering. Results are summarised in Table 2.

Figure 15: *Embedment strength: specimens after the test*

3.2 TESTS ON JOINTS

Regarding the experimental tests on the connections, eight different nodes were cut out of two beams (A and B), and the posts and the struts were tested in each case. The results are summarised in Tables 6 to 9.

The connection of the struts could generally take a higher load per nail than the connection of the posts. This was most probably due to the larger contact area and the greater friction associated with it. Additionally, the spacing and the edge-distance of the fasteners were larger compared to the posts. Typical load-displacement curves of connections of struts and posts are depicted in Figure 16.

Table 6: *Test results for Type I-new, Serie SV (PF = post)*

	α [°]	n_{Nail} [-]	F_{max} [N]	F_{max} /n_{Nail} [N]
SV-1947-PF-01	90	12	15010	1251
SV-1947-PF-02	90	12	13152	1096
SV-1947-PF-03	90	12	13447	1121
SV-1947-PF-04	90	12	14956	1246
SV-1947-PF-05	90	12	15248	1271
mean		**12**	**14363**	**1197**
SV-1969-PF-01	90	12	15748	1312
SV-1969-PF-02	90	12	13349	1112
SV-1969-PF-03	90	12	13084	1090
SV-1969-PF-04	90	12	18317	1526
SV-1969-PF-05	90	12	14041	1170
mean		**12**	**14908**	**1242**
SV-EC5-PF-01	90	14	18915	1351
SV-EC5-PF-02	90	14	21198	1514
SV-EC5-PF-03	90	14	19335	1381
SV-EC5-PF-04	90	14	21258	1518
SV-EC5-PF-05	90	14	22648	1618
mean		**14**	**20671**	**1476**

https://doi.org/10.52202/069179-0529

Table 7: *Test results for Type I-old, Serie AH-PD-PF (PF = post)*

	n_{Nail} [-]	F_{max} [N]	F_{max}/n_{Nail} [N]
AH-PD-PF-B04	12.0	26224	2185
AH-PD-PF-B06	12.0	25772	2148
AH-PD-PF-B07	12.0	18586	1549
AH-PD-PF-B08	12.0	19096	1591
AH-PD-PF-B09	12.0	16769	1397
AH-PD-PF-B10	12.0	23337	2122
AH-PD-PF-B11	12.0	18432	1536
AH-PD-PF-B12	12.0	13917	1265
mean-PF-B	**11.8**	**20267**	**1725**

Table 8: *Test results for Type I-new, Serie SV (ST = strut)*

	α [°]	n_{Nail} [-]	F_{max} [N]	F_{max}/n_{Nail} [N]
SV-1947-ST-01	35	18	25274	1404
SV-1947-ST-02	35	18	26754	1486
SV-1947-ST-03	35	18	28799	1600
SV-1947-ST-04	35	18	24068	1337
SV-1947-ST-05	35	18	23161	1287
mean		**18**	**25611**	**1423**
SV-1969-ST-01	35	24	35145	1464
SV-1969-ST-02	35	24	37762	1573
SV-1969-ST-03	35	24	32429	1351
SV-1969-ST-04	35	24	35774	1491
SV-1969-ST-05	35	24	37358	1557
mean		**24**	**35694**	**1487**
SV-EC5-ST-01	35	22	27781	1263
SV-EC5-ST-02	35	22	31744	1443
SV-EC5-ST-03	35	22	31405	1428
SV-EC5-ST-04	35	22	31305	1423
SV-EC5-ST-05	35	22	32058	1457
mean		**12**	**30859**	**1403**

The comparison between the old joints and the new joints are shown in Figure 17. The average load-bearing capacity across all the tests of a series evaluated here can be considered similar for the old and the new connections. Nevertheless, the different deformation behaviour of the individual tests is clearly visible. The new nodes have significantly higher stiffnesses than the old ones. In addition, a hardening can be seen in the old nodes after about 5 mm of deformation. This could be due to a larger hole clearance in the old nodes or corrosion of the nails.

Table 9: *Test results for Type I-old, Serie AH-PD-ST (ST = strut)*

	α [°]	n_{Nail} [-]	F_{max} [N]	F_{max}/n_{Nail} [N]
AH-PD-ST-B04	32	13,0	30703	2362
AH-PD-ST-B06	37	13,0	26925	2071
AH-PD-ST-B07	30	12,0	21789	1816
AH-PD-ST-B08	42	13,0	29097	2238
AH-PD-ST-B09	35	12,0	27206	2267
AH-PD-ST-B10	47	14,0	20094	1435
AH-PD-ST-B11	39	12,0	22935	1911
AH-PD-ST-B12	60	12,0	15701	1308
mean-B-ST		**12.6**	**24306**	**1925**

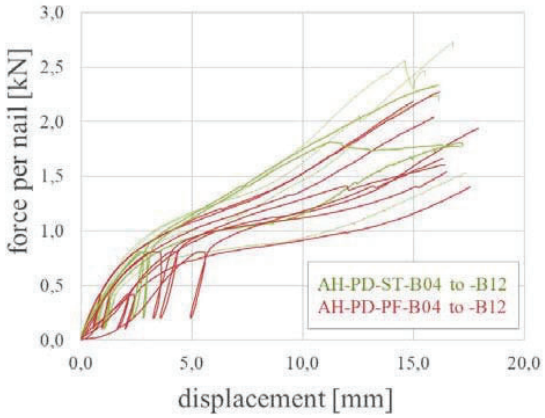

Figure 16: *Load-displacement curve – comparison between old strut and post*

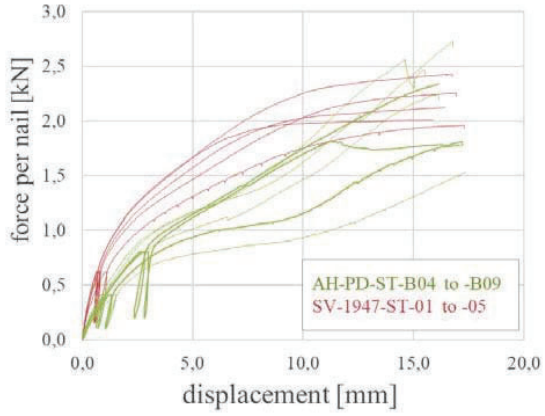

Figure 17: *Load-displacement curve – comparison between old and new joints*

The comparison between the load-bearing capacity per nail for Type I-old and I-new is presented in Table 10. The evaluation shows the higher load-bearing capacity of

https://doi.org/10.52202/069179-0529

Type I-old. Although the values of the old joints are scattered to a greater extent, the capacity of I-old connections exceeds that of the I-new connections slightly. The larger variation of Type I-old can be explained by different degradation conditions. Otherwise, it became apparent that Type I-new performed better in terms of initial stiffness.

The initial assumption that the "ageing" of joints could improve the load-bearing capacity due to nail corrosion seems to be partially confirmed, especially regarding the significantly lower tensile strengths and yield moments of the old nails in the testing of the individual parameters. Despite these lower strengths, higher load-bearing capacities can be achieved than with the new joints. However, it can also be seen that the assumed effect of the load increase does not seem to be significant at all. There is a clear scattering of the results, which refers mainly to the parameter testing. further investigations are still required to be able to assess whether aged constructions with corroded nails always have a higher load-bearing capacity.

Table 10: *Load capacity per nail for Types I-old and I-new with characteristic and mean values*

Type		nails [-]	$F_{u,m}$ [N]	n [-]	COV [%]	$F_{u,k}$ [N]
I-old	post	11.8	1724	8	21.4	920
	strut	12.6	1926	8	20.2	1078
	total	12.2	1825	16	20.1	1109
	EC5					969
I-new	post	12.7	1305	15	6.8	1066
	strut	10.7	1438	15	8.7	1257
	total	11.7	1371	30	7.7	1175
	EC5					836

4 CONCLUSIONS AND OUTLOOK

Test on connections which were taken from old, nailed trusses showed a good agreement between experimental results and characteristic resistance according to EC 5. This also applies to the relevant parameters, which are the tension strength and yield moment of the nails and embedment strength of the timber. Nevertheless, a positive effect of aging, such as an increase of the rope effect due to the slightly corroded nails, could not be confirmed. On the other hand, no negative effect of aging could be detected.

The large scattering of the withdrawal strength for the old connections indicates that this phenomenon should be studied in more detail. Another observation concerns the different condition of the joints in terms of spacing and edge distance, as well as cracks in the timber. An assessment schema to consider different forms and levels of irregularities is presented by Völlmecke et al. [11].

REFERENCES

[1] Stoy, W.: Über Versuche mit Drahtstiften als Holzverbindungsmittel. *Deutsche Bauzeitung*, 64(19):141–148, 1930.

[2] Gaber, E.: Statische und dynamische Versuche mit Nagelverbindungen. In: *Versuchsanstalt für Holz, Stein und Eisen*, 3:1–36, Karlsruhe, 1935.

[3] Takanashi, R,, K. Sawata, K., Sasaki, Y., and Koizumi, A.,: Withdrawal strength of nailed joints with decay degradation of wood and nail corrosion. *J. Wood Sci.*, 63(2):192–198, 2017.

[4] DIN 52182: Testing of wood; determination of density; German version, 1976.

[5] EN 383:2007: Timber Structures – Test methods – Determination of embedment strength and foundation values for dowel type fasteners; German version EN 383:2007

[6] DIN 2002-001: Aerospace series – Metallic materials – Test methods – Part 1: Tensile testing at ambient temperature; German and English version EN 2002-001:2005

[7] Werner, H., and Siebert, W.: Holz als Roh- und Werkstoff – Neue Untersuchungen mit Nägeln für den Holzbau. Springer Publisher, 1991.

[8] EN 1382:2016-07: Timber structures – Test methods – Withdrawal capacity of timber fasteners; German version EN 1382:2016

[9] EN 26 891: Timber structures; Joints made with mechanical fasteners; General principles for the determination of strength and deformation characteristics; German version EN 26 891: 1991.

[10] EN 1995-1-1: Eurocode 5: Design of timber structures – Part 1-1: General – Common rules and rules for buildings; German version EN 1995-1-1:2004 + AC:2006 + A1:2008, 2010-12.

[11] Völlmecke, L., Schwendner, S., Seim, W., and Fischer, J.: Assessment of nailed connections in existing structures. Proceedings WCTE, 2023.

World Conference on Timber Engineering Oslo 2023

INFLUENCE OF MOISTURE CONTENT ON THE ASSESSMENT OF DECAY LEVELS BY MICRO-DRILLING MEASUREMENTS IN WOODEN FOUNDATION PILES

Michele Mirra[1], Giorgio Pagella[2], Wolfgang Gard[3], Geert Ravenshorst[4] , Jan-Willem van de Kuilen[5]

ABSTRACT: In the historic city centre of Amsterdam (NL), the most widespread foundation system consists of wooden piles. With the aim of modelling and predicting remaining service life of these foundations and the piles in particular, one of the possible methods for collecting data and monitoring their condition consists of micro-drilling (MD) measurements. This work evaluates the reliability of MD measurements in identifying decayed portions and specific features of wooden foundation piles, considering different moisture content (MC) values. To this end, 24 segments were selected, sawn from wooden piles extracted from site, and having time in service (TS) of 2 to 294 years (with reference to 2021, the year of extraction). 240 MD measurements were conducted at varying MC values of 7% to 212%. The obtained MD profiles showed for all TS a slight decrease in drilling resistance when increasing MC. However, from the MD signals it is possible to reliably detect the areas affected by biodegradation phenomena (e.g. bacterial decay) along the drilling depth, regardless the MC of the segment or its gradient along the drilling depth. The present study contributes to research aiming at utilizing (in-situ) MD techniques for reliably assessing and quantifying decay and to be used in remaining service life planning of wooden foundation piles.

KEYWORDS: Wooden foundation piles, Micro-drilling, Moisture content, Biodegradation, Service life prediction.

1 INTRODUCTION

The utilization of wooden piles as foundation system of historical or existing buildings has been widespread throughout Europe. In this context, the city of Amsterdam (NL) constitutes one of the reference examples for such foundation structures, since it is estimated that eleven millions wooden piles are present, still supporting existing and historical buildings as well as bridges and quay walls. Given the essential function of these foundations and their spatial extension, the estimation of the remaining service life of the piles is crucial for arranging timely maintenance interventions. Therefore, an extensive experimental campaign has been started in cooperation with the municipality of Amsterdam [1], aimed at characterising the current state of wooden foundation piles [2],[3], as well as providing solid input for service life prediction models [4].

Among the available techniques for monitoring timber piles, micro-drilling (MD) measurements are a promising option, because extensive in-situ sampling of a large number of piles could be realized. Yet, the use of MD signals for decay quantification requires still attention [5], thus a preliminary investigation of the reliability of this method for the specific context of wooden foundation piles in Amsterdam was necessary, including the development of a drill for underwater use.

When performing in-situ MD measurements on the piles, their moisture content (MC) is above fibre saturation point. Thus, it is important to ascertain that, also in submerged conditions, decayed portions of the cross section of the piles are correctly detected from the MD signals.

This work aims to assess whether MD measurements can provide reliable information on the decay levels of wooden foundation piles, independently of their moisture content (MC). These biodegradation phenomena on submerged wooden piles are caused by erosion bacteria [6]. The outer portion of the cross section is usually subjected to bacterial decay, since erosion bacteria can more easily attack the less durable sapwood [7]. Such decayed areas should also be visible from MD signals, independently of the actual MC, as this parameter is in principle unknown for the piles on site.

However, previous research works have shown opposite results on the effect of MC on MD measurements, showing that drilling resistance can both decrease [8] or

[1] Michele Mirra, Delft University of Technology, The Netherlands, m.mirra@tudelft.nl
[2] Giorgio Pagella, Delft University of Technology, The Netherlands, g.pagella@tudelft.nl
[3] Wolfgang Gard, Delft University of Technology, The Netherlands, w.f.gard@tudelft.nl
[4] Geert Ravenshorst, Delft University of Technology, The Netherlands, g.j.p.ravenshorst@tudelft.nl
[5] Jan-Willem van de Kuilen, Technical University of Munich, Germany, and Delft University of Technology, The Netherlands, vandekuilen@hfm.tum.de

https://doi.org/10.52202/069179-0530

increase [9],[10] with increasing MC. This is because the outcomes from MD measurements can be influenced by different parameters besides MC itself, such as drill and feed speed, drilling depth, wood species, all factors influencing the shaft friction along the drill [8]–[10]. In light of these uncertainties, the reliability of MD measurements in correctly identifying decay in wooden foundation piles was evaluated in the present study, considering different MC values.
More specifically, segments from wooden foundation piles with a time in service (TS) ranging from 2 to 294 years (with reference to 2021, when their extraction took place) were selected, and MD measurements were conducted at varying MC values between 7% and 212%. To confirm large decay levels identified with MD measurements, compression tests were also conducted on the pile segments, after submerging them under water.

2 MATERIALS AND METHODS

2.1 MATERIALS

In this work, 8 wooden foundation piles were selected:

- 2 piles from 1727 (TS = 294 years as of 2021);
- 2 piles from 1886 (TS = 135 years as of 2021);
- 2 piles from 1922 (TS = 99 years as of 2021);
- 2 piles from 2019 (TS = 2 years as of 2021).

The piles from 1727, 1886, and 1922 were retrieved from the foundations of the piers of two bridges in the city centre of Amsterdam [3], whereas those from 2019 were extracted from a separate testing field [2] in the Overamstel area (Figure 1).

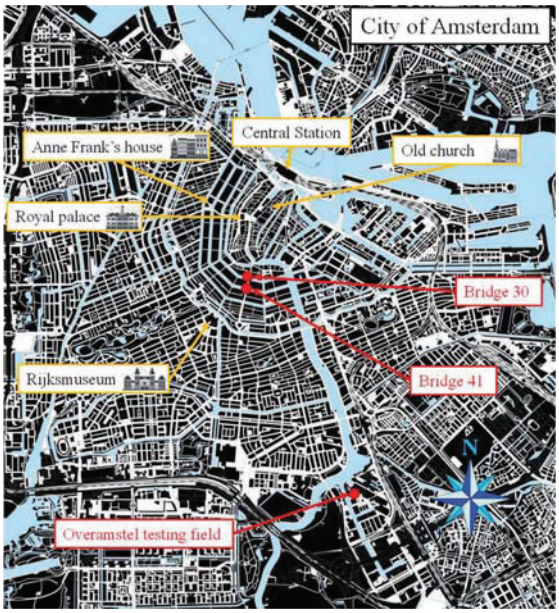

Figure 1: *Map of Amsterdam and locations (in red) from where the piles were extracted: to better highlight their position, some of the main monuments of the historic city centre are also reported as a reference. Adapted from [11].*

The piles had length of approximately 14 m, and diameters ranging from 175 to 290 mm at the head, and from 130 mm to 230 mm at the tip. All piles were made of spruce (*Picea abies*), with the exception of one pile from 1886, made of fir (*Abies alba*), and one from 2019, made of pine (*Pinus sylvestris*).
The retrieved piles were all subdivided in smaller segments, representative for the head, middle, and tip part of the piles (see also Section 2.2), for a total of 24 segments: Table 1 reports a detailed overview of the tested pile segments, their TS and MC range.

2.2 METHODS

2.2.1 General

The extracted full-length piles were cut in three parts (head, middle, tip), and delivered to TU Delft Stevin II Laboratory. From each part, a smaller segment to be tested in compression (Section 2.2.4) was sawn, having length equal to six times its diameter, following EN 14251 [12]. In this way, 24 segments were obtained (6 for each TS, see again Table 1) having lengths of 900, 1350, and 1800 mm, depending on their diameter. All segments were kept under water for two weeks to represent the on-site submerged conditions, and were characterised in terms of wet density [13] and moisture content, determined through the oven-dry method [14]. These compression tests allowed to mechanically characterise the pile segments, and to detect the presence of biodegradation phenomena (especially for the older piles), corresponding to a reduction of compressive strength with respect to fully sound samples.
MD measurements were performed on these segments, evaluating their reliability in capturing the features of the cross section (e.g. sound or decayed sapwood, knots, and so forth) for different MC values. This analysis was conducted considering the following two scenarios:

1. Assessment of the possible influence of different MC values referred to a whole segment on the corresponding drilling resistance (DR), thus an analysis at *global segment level* (see Section 2.2.3);
2. Evaluation, with reference to submerged conditions, of the possible influence of the MC gradient along the drilling depth on the MD signals, thus an analysis at *cross-sectional level* (see Section 2.2.4).

Table 1: *Overview of TS and MC of the tested pile segments.*

Number of segments	TS (years)	MC range (%)
6	294	14–212
6	135	8–57
6	99	12–100
6	2	7–84

2.2.2 Compression tests

Mechanical testing was performed to determine the compressive strength of the pile segments ($f_{c,0}$) in submerged conditions and confirm the information on the level of decay obtained with MD measurements. To this end, a displacement-controlled test setup was used (Figure 2), where the pile segments were subjected to an axial load in direction parallel to the fibres [12],[15].

The displacement between the two steel plates surrounding the pile segment was monitored with four linear potentiometers, placed on the four edges of the top plate and connected to the bottom plate. Four additional linear potentiometers, screwed to the segment, measured its deformation. The sensors were placed along the lateral surface of the piles, at 90° from each other, and had a variable length equal to 2/3 of that of the specimen.

The tests were conducted at a displacement rate of 0.02 mm/s, and the compressive strength was derived from the ratio between the maximum force reached in compression by each specimen and its average cross-sectional area.

2.2.3 Execution of MD measurements at different MC values (analysis at global segment level)

The MD measurements were conducted with an IML-RESI PD400 drill (Figure 3a). This device provides the profiles of drill and feed amplitude against drilling depth as output [8]. All measurements were taken 300 mm below the top of each segment, in two orthogonal directions (A and B in Figure 3b; see also [3]), and at approximately 1 cm distance from each other for every direction. A drill speed of 2500 r/min and a feed speed of 150 cm/min were adopted; the drill bit was 400 mm long, with a thin shaft of 1.5 mm diameter and a 3.1 mm wide triangular cutting part, with hard chrome coating.

The first two MD measurements on a segment were executed in submerged conditions, immediately prior to its compression test (Section 2.2.2), and were also used to evaluate the influence of MC gradient along the drilling depth (see Section 2.2.4). Other four MD measurement-pairs were then taken during the drying process of each segment after the compression test, recording every time the weight of the segment and determining the corresponding global MC. Thus, a total of 240 MD measurements were conducted.

Since the outer decayed areas of the pile segments are linked to lower basic densities compared to sound wood, a correspondingly low drilling resistance is observed at the beginning and at the end of the MD signals, showing the degraded portion. In order to objectively define which part of the MD signal pertains to decayed areas, and which part to sound wood, the procedure already proposed in [3] was adopted. Thus, the average drilling amplitude (DA) of the drilling resistance (DR) profiles along the drilling depth H was firstly determined. Following [5], this is defined as:

$$DA = \frac{\int_0^H DR \, dh}{H} \quad (1)$$

Figure 2: *Setup for compression tests.*

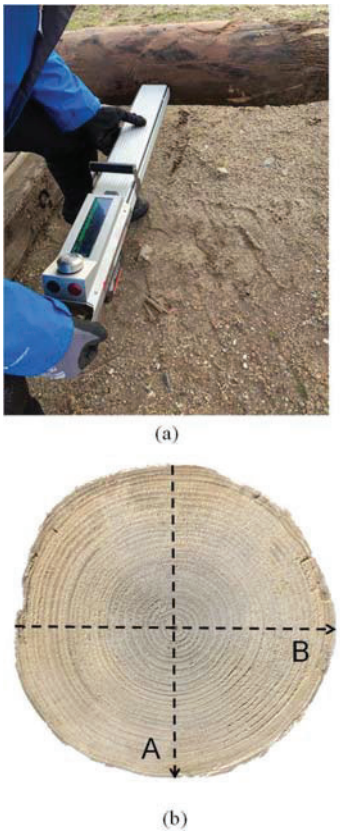

Figure 3: *Adopted MD device (a) and drilling directions (b).*

https://doi.org/10.52202/069179-0530

Then, the starting and ending sections of the signal portions identifying decayed areas were determined as the intersection between the average DA decreased by 30% and the MD profile [3] (Figure 4). This method has the advantage of detecting decayed areas relatively to the specific MD signal, without providing an absolute threshold in terms of DR. Finally, the independence from MC of the detected outer decayed portion was assessed.

2.2.4 Evaluation of MC gradient along the drilling depth (analysis at cross-sectional level)

After testing the segments in submerged conditions, the corresponding MC gradient along the drilling depth was determined as well [14], by retrieving five small prisms of dimensions 20×20×120 mm^3 (Figure 5). Sample 3 was taken in correspondence to the pith, whereas samples 1 and 5 included sapwood. These prisms allowed to detect the MC variations along the drilling depth: in this way, the influence of such variations on DR profiles could be evaluated for both sound and decayed pile segments.
Sound sapwood is associated to a higher density, but also larger MC than heartwood, whereas in presence of decay the basic density is reduced due to bacterial degradation, and the MC locally increases further. Thus, this analysis allowed to check that MD signals retrieved in underwater conditions can still enable the distinction between sound and decayed sapwood, independently of MC gradients.

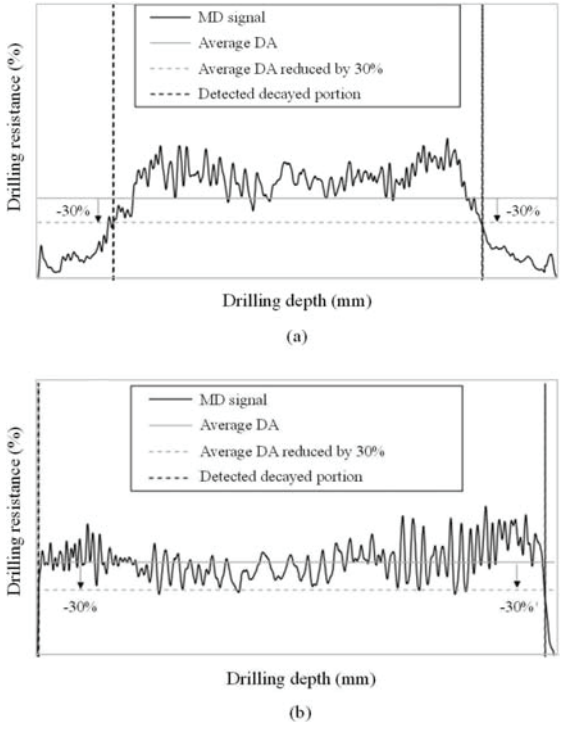

Figure 4: *Procedure adopted for determining the degraded portion of the pile segments from MD signals, corresponding to low drilling amplitudes at the beginning and at the end. Examples are shown in the case of a heavily decayed pile (a) and a sound pile (b). Adapted from [3].*

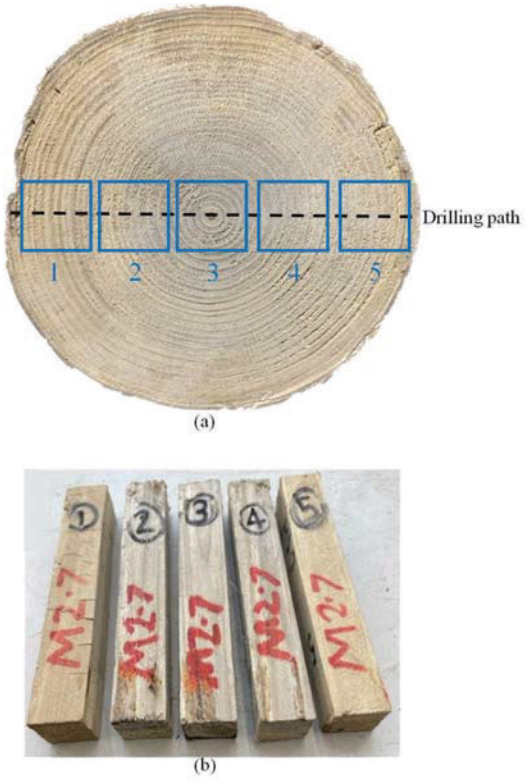

Figure 5: *(a) Location of the samples taken to determine MC variations among sapwood, heartwood, and pith; (b) example of prisms retrieved from a pile segment along the drilling depth.*

3 RESULTS

3.1 COMPRESSION TESTS

The 24 segments tested under compressive loading exhibited the values of compression strength $f_{c,0}$, wet density in submerged conditions ρ_w, and MC reported in Table 2.
A distinct drop in $f_{c,0}$ is observable for all pile segments from 1727, linked to large global MC values as well. Besides, as can be noticed, the wet density of such samples is comparable to that of piles from 2019: in combination with the large global MCs, this indicates a strong reduction of basic density due to bacterial decay for the pile segments from 1727. Such outcomes thus confirm the presence of biodegradation phenomena for the oldest piles, which were also detected with the MD measurements, as shown in the next section.
The other segments showed higher values of $f_{c,0}$, and closer to each other, suggesting that the extracted piles up to 1886 did not undergo significant decay. Only the 1886-2 segments exhibited lower compressive strengths, but these were also associated with low wet density and global MC.

Table 2: *Overview of the compressive strength of the tested pile segments after being submerged in water for two weeks; the corresponding wet density and moisture content is also reported. Samples with decay are reported in italic.*

Sample	$f_{c,0}$ (MPa)	ρ_w (kg/m^3)	MC of the segment (%)
2019-1-head	15.5	779	74
2019-1-middle	13.7	748	80
2019-1-tip	13.7	657	85
2019-2-head	20.1	767	72
2019-2-middle	16.4	675	73
2019-2-tip	17.3	670	81
1922-1-head	15.4	586	66
1922-1-middle	16.2	601	64
1922-1-tip	15.9	663	75
1922-2-head	16.9	750	81
1922-2-middle	16.3	702	77
1922-2-tip	15.4	818	76
1886-1-head	17.2	705	66
1886-1-middle	17.0	730	64
1886-1-tip	15.4	782	82
1886-2-head	11.5	553	77
1886-2-middle	12.3	703	87
1886-2-tip	7.2	625	98
1727-1-head	7.1	778	192
1727-1-middle	5.3	664	170
1727-1-tip	5.1	755	222
1727-2-head	6.1	770	197
1727-2-middle	4.1	648	179
1727-2-tip	5.8	784	139

3.2 MICRO-DRILLING MEASUREMENTS

Representative results from the 240 conducted measurements are shown in Figure 6 in terms of MD signals at different MC levels and TS.

In general, with the adopted drill and feed speed, it appears that a progressively lower drilling resistance is obtained when the moisture content increases. However, this does not influence the detection of specific features of a pile segment, such as denser sapwood for sound samples (Figure 6a-c), presence of an internal knot (Figure 6b), very low drilling amplitude when crossing outer decayed zones for the oldest pile segments (Figure 6d-e).

It is important to notice that this outer layer affected by decay and characterised by much lower drilling resistance could be detected, adopting the methodology described in Section 2.2.3, independently of the MC. This outcome, visible in Figure 6 for samples 1727-1-middle and 1727-2-head, was also obtained for all other segments from 1727, as shown in Table 3, reporting the detected decayed portions (calculated as average from those of each MD measurement-pair) as a function of the global MC of the segments.

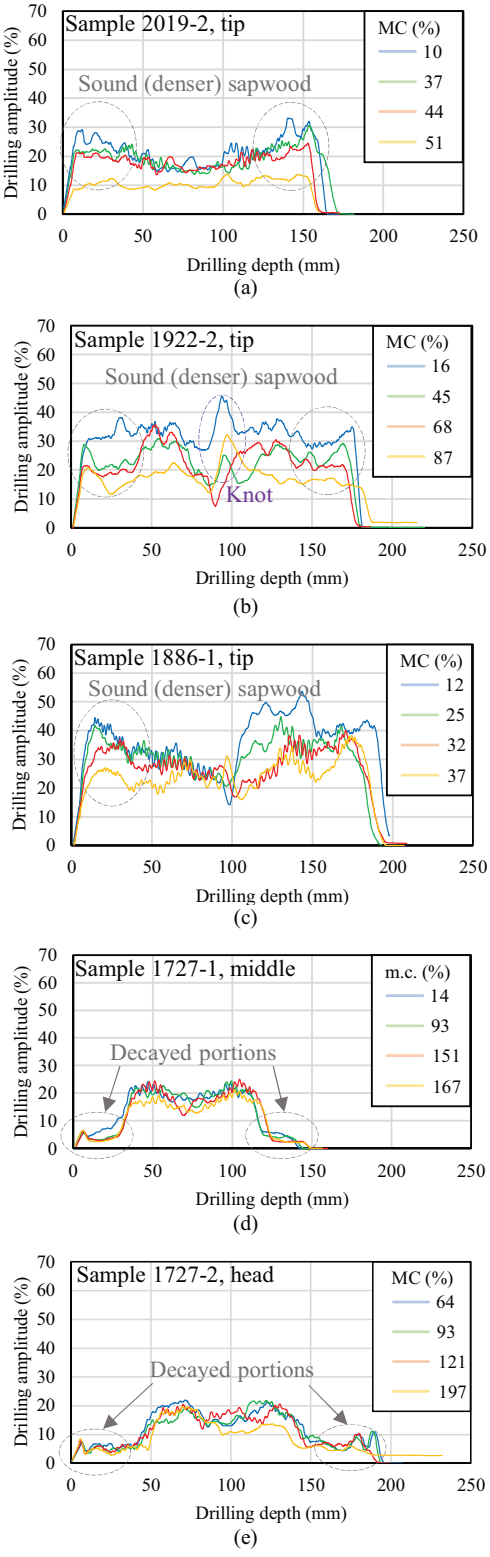

Figure 6: *MD signals (displayed in terms of a 100-mm moving average) ordered from lowest to highest MC for representative pile segments with TS = 2 years (a), 99 years (b), 135 years (c), and 294 years (d-e).*

https://doi.org/10.52202/069179-0530

Table 3: *Overview of the detected decayed portion, determined from the MD measurements according to the methodology presented in Section 2.2.3, as a function of MC for the 1727 samples.*

Samples with decay	Detected decayed portion (average from the two MD signals, mm)	MC of the segment (%)
1727-1-head	12	13
	10	94
	10	129
	9	153
	10	182
1727-1-middle	23	14
	25	93
	24	151
	24	167
	23	170
1727-1-tip	16	13
	17	88
	17	153
	17	188
	16	212
1727-2-head	40	64
	35	93
	36	107
	37	121
	36	197
1727-2-middle	34	105
	33	145
	36	164
	34	179
	35	184
1727-2-tip	24	84
	25	125
	26	139
	22	146
	26	175

As can be noticed, the zones of cross section affected by biodegradation phenomena only show small variations for different MC values (Table 3). This very limited scatter is unavoidable, as the MD measurements were conducted close to each other, but local variations along the drilling depth are very likely to be present.

The previous results referred to the MC of global segments, but they are also confirmed when examining at cross-sectional level the local MC gradients along the drilling depth (Figure 7). These MC gradients, determined with the five prisms retrieved from the cross sections of the segments (Section 2.2.4), show a typical profile, with larger MCs pertaining to the outer prisms (1 and 5 in Figure 5) containing sapwood.

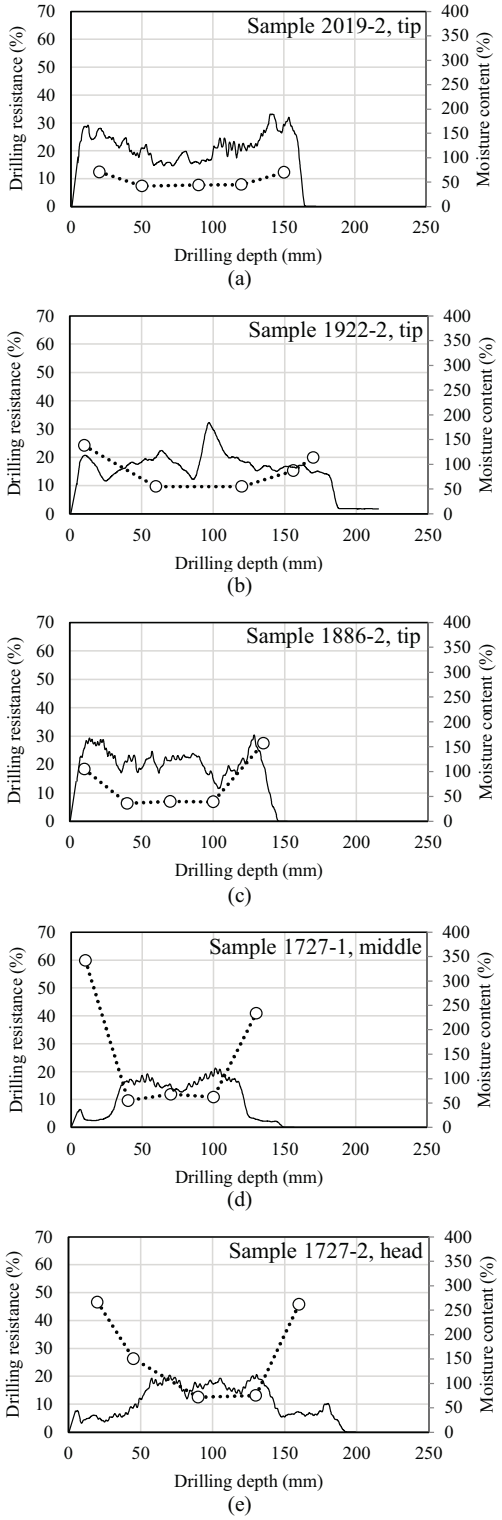

Figure 7: *Example of drilling resistance profile and MC gradient (dashed) for representative pile segments with TS = 2 years (a), 99 years (b), 135 years (c), and 294 years (d-e) in submerged conditions. For d-e, very large MC is observable in the decayed portions, which is not the case in sound samples.*

However, for sound cross sections (Figure 7a-c) the MCs range of prisms containing sapwood was 70–150%, whereas in decayed samples (Figure 7d), values up to 350% were determined.
On the contrary, when considering MCs of the heartwood and juvenile wood portions, these always fall in the range of 40–60%, also in the case of the decayed samples. This outcome is confirmed by the MD signals as well: the drilling resistance in the inner part of the cross section is in all cases close to 20%; for sound sapwood the larger amplitude correctly corresponds to its larger density, whereas in presence of decay a large drop in the drilling resistance is observed.

4 DISCUSSION

Based on the obtained results, it appears that MD signals can reliably identify decayed portions and their extent along the drilling depth independently of the MC (see once more Figure 6d-e). This outcome is relevant, since the determination of the actual MC of a large number of piles on site would not be practically feasible.
Furthermore, the distinction between sound and decayed parts of the cross section is also possible when comparing MD signals with the MC gradients determined in submerged conditions. All sound samples showed MC gradients in line with those expected for green spruce (around 50% in heartwood and 120% in sapwood [16]), confirming the results from MD signals and compression tests. Biodegradation phenomena seemed therefore to be limited to sapwood, since the heartwood and juvenile wood of the decayed pile segments featured MC and DR values comparable to those of the sound specimens (Figure 7).
Thus, the highly decayed portions of the degraded pile segments could be correctly identified with MD measurements, and were coherent with the low compressive strength obtained for these samples (see once more Table 2). Since the signals reported in Figure 7 refer to submerged conditions, it can be concluded that when performing MD measurements underwater, the specific features of the cross sections of the wooden foundation piles can be correctly captured, and independently of the MC gradient.

5 CONCLUSIONS

This work presented an extensive study to evaluate the underwater use of micro-drilling (MD) measurements for assessing the state of wooden foundation piles. In particular, the influence of their moisture content (MC) in the identification of largely decayed portions was evaluated for piles retrieved from the historic city centre of Amsterdam.
Thus, 24 pile segments having time in service (TS) from 2 years to 294 years were subjected to 240 MD measurements at various MC values, ranging from 7% to 212%. Compression tests were also performed on the segments after submerging them under water for two weeks, to determine their load-carrying capacity and compressive strength. These tests also allowed to confirm the decayed pile segments identified with MD measurements, for which a much lower compressive strength and a larger MC were determined.
For the adopted drill and feed speed, a decreasing drilling resistance with increasing MC was detected. Since in practice the on-site MD measurements would be conducted underwater by divers, the MC of the piles is in principle unknown. Yet, it has been proved that the detection of specific features or decayed portions of the cross section through the drilling profiles is not influenced neither by the global MC of a segment, nor by the MC gradient within its cross section. Thus, based on the obtained results, biological degradation phenomena can be reliably identified with MD signals also in underwater conditions, where it is not necessary to know the exact MC.
The results of this study can be further integrated with the data from the in-progress experimental campaign on additional pile segments, and can contribute to the research framework supporting the use of non-destructive testing for estimating decay, (residual) load-carrying capacity, and remaining service life of wooden foundation structures.

ACKNOWLEDGEMENTS

The Authors gratefully acknowledge the Municipality of Amsterdam, for having funded the research study and provided the analysed wooden foundation piles, as well as Michael Lee and Ruben Kunz, for their help in determining the moisture content gradients.

REFERENCES

[1] J.W.G. van de Kuilen, O. Beketova-Hummel, G. Pagella, G.J.P. Ravenshorst, W.F. Gard. An integral approach for the assessment of timber pile foundations. Paper 597, *World Conference on Timber Engineering*, Santiago, Chile, 2021.
[2] G. Pagella, M. Mirra, G.J.P, Ravenshorst, J.W.G. van de Kuilen. Influence of knots and density distribution on compressive strength of wooden foundation piles. In *Current Perspectives and New Directions in Mechanics, Modelling and Design of Structural Systems*, 2022.
[3] G. Pagella, G.J.P. Ravenshorst, W.F. Gard, J.W.G. van de Kuilen. Characterization and assessment of the mechanical properties of spruce foundation piles retrieved from bridges in Amsterdam. *4th International Conference on Timber Bridges*, Biel, Switzerland, 2022.
[4] J.W.G. van de Kuilen. Service life modelling of timber structures. Mater. Struct. 40(1):151-161, 2007.
[5] T.P. Nowak, J. Jasieńko, K. Hamrol-Bielecka. In situ assessment of structural timber using the resistance drilling method – Evaluation of usefulness. *Constr. Build. Mater.* 102:403-415, 2016.
[6] R. Klaassen. Bacterial decay in wooden foundation piles—Patterns and causes: A study of historical pile

 https://doi.org/10.52202/069179-0530

foundations in the Netherlands. *Int. Biodeterior. Biodegradation* 61:45-60, 2008.
[7] A.P. Singh, Y.S. Kim, T. Singh, Chapter 9 - Bacterial Degradation of Wood, *Secondary Xylem Biology*:169-190, 2016. ISBN 9780128021859, https://doi.org/10.1016/B978-0-12-802185-9.00009-7.
[8] E. Sharapov, C. Brischke, H. Militz, E. Smirnova. Combined effect of wood moisture content, drill bit rotational speed and feed rate on drilling resistance measurements in Norway spruce (Picea abies (L.) Karst.). *Wood Mater. Sci. Eng.* 15:198-204, 2018.
[9] C.-J. Lin, S.-Y. Wang, F.-C. Lin, C.-M. Chiu. Effect of moisture content on the drill resistance value in Taiwania plantation wood. *Wood Fiber Sci.* 35:234-238, 2003.
[10] J. Jaskowska-Lemańska, E. Przesmycka. Semi-Destructive and Non-Destructive Tests of Timber Structure of Various Moisture Contents. *Materials* 14, 2021.
[11] https://pixers.nl/fotobehang/zwart-wit-amsterdam-city-map-72351719. URL last accessed on 8th March 2023.
[12] EN 14251. Structural round timber - Test methods, CEN, Brussels, Belgium, 2003.
[13] EN 384. Structural timber – Determination of characteristic values of mechanical properties and density. CEN, Brussels, Belgium, 2016.
[14] EN 13183-1. Moisture content of a piece of sawn timber - Part 1: Determination by oven dry method. CEN, Brussels, Belgium, 2002.
[15] EN 408. Timber structures - Structural timber and glued laminated timber - Determination of some physical and mechanical properties. CEN, Brussels, Belgium, 2010.
[16] S.V. Glass, S.L. Zelinka. Moisture Relations and Physical Properties of Wood. *Wood Handbook – Wood as an Engineering Material*. United States Department of Agriculture, 2010.

World Conference on Timber Engineering Oslo 2023

A STUDY ON COORDINATED EXPRESSION OF THE SEISMIC DIAGNOSIS SCORE AND ITS APPLICATION TO RETROFIT REINFORCEMENT PROJECTS UNDER COST CONTROL FOR JAPANESE TIMBER HOUSES

Daisuke Shimizu[1], Chikako Tabata[2], Yoshito Tomioka[3]

ABSTRACT: The seismic diagnosis score for a conventional timber house in Japan is normally calculated as the ${}_{ed}Q_p/Q_r$ ratio. This study presents its coordinated expression as (Q_r, ${}_{ed}Q_p$), making it possible to depict the individual effect and contribution of each specification employed in a retrofit reinforce project as a whole. This method could be used to knockdown not only the change in the force capacity of the whole building but also the level of independent elements, such as a wall or roof. Combining this method to add cost dimension to the coordination as (Q_r, ${}_{ed}Q_p$, *cost factor*) may be feasible in serving as a rational design tool that can achieve a better cost-performance in retrofit design practice. Four factors exist for each of the individual elements of retrofitting performed in seismic retrofit reinforcement, that is, required strength, potential strength, cost for applied element, and cost for eliminated element. In this study, a theoretical method is used to express each factor in a unified manner. This possibility is confirmed by applying the method to real retrofit reinforce design experiences obtained in Mie Prefecture, Japan.

KEYWORDS: Structural design method, Construction cost, Japanese conventional timber house

1 INTRODUCTION

This study explains the idea of the coordinated expression of the seismic diagnosis score and discusses its possible applications as a rational tool in designing retrofit reinforce projects of Japanese conventional timber houses. Its feasibility is estimated by applying it to real design experiences obtained in Mie Prefecture, Japan.

2 COORDINATED EXPRESSION OF THE SEISMIC DIAGNOSIS SCORE

2.1 BASIC THEORY

The seismic diagnosis score, used for the retrofit reinforcement of timber houses is calculated as follows:

$$S = {}_{ed}Q_p/Q_r \quad (1)$$

where S (non-dimensional) = seismic diagnosis score, ${}_{ed}Q_p$ (kN) = potential strength; lateral force capacity of the structure and Q_r (kN) = required strength; necessary lateral resistance led from the weight of supported building part.

The index = 1.0 means that the structure achieves minimum seismic safety. Although this approach may be good for a simple representation of the safety degree in a single number, it lacks the guidance ability for conducting a design rationally and is not a reinforcement cost consideration method. This study proposes its coordinated expression as [1]:

$$\vec{S} = (Q_r, {}_{ed}Q_p) \quad (2)$$

where $\vec{S}$ (non-dimensional) = coordinated expression of the seismic diagnosis score.

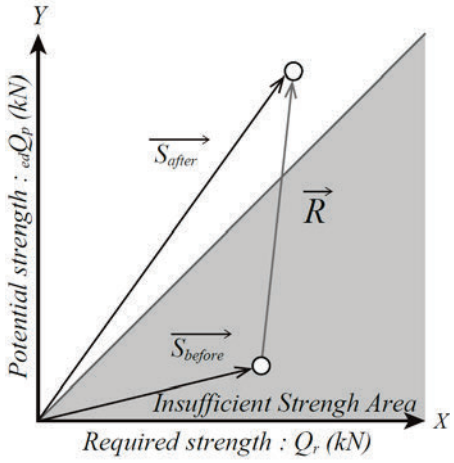

Figure 1: *Performance plot of the required strength vs potential strength*

[1] Daisuke Shimizu, Div. of Archi., Graduate School of Eng., Mie University, Japan, 422m406@m.mie-u.ac.jp
[2] Chikako Tabata, Assoc. Prof., Div. of Archi., Graduate School of Eng., Mie University, Japan, tabata@arch.mie-u.ac.jp
[3] Yoshito Tomioka, Professor, Div. of Archi., Graduate School of Eng., Mie University, Japan, tomioka@arch.mie-u.ac.jp

https://doi.org/10.52202/069179-0531

Figure 1 presents a two-dimensional (2D) theoretical coordination system. On this surface, the seismic performance of the existing building to be reinforced is plotted as "before," while the achieved performance is plotted as "after." Accordingly, the performance improvement due to reinforcement is expressed as a vector connecting both as $\vec{R}$.

$$\vec{R} = \overrightarrow{S_{after}} - \overrightarrow{S_{before}} \quad (3)$$

The minimum safety (i.e., Index = 1.0) is now expressed as a line of $Y = X$. The reinforcement design attempt is recognized to extend the reinforcement vector from "before" to "after," which is beyond the line.

Figure 2 shows breakdown into successive applications of reinforce elements. This case involves two elements, namely $\overrightarrow{E_1}$ and $\overrightarrow{E_2}$, representing two independent reinforcements that constitute the total. Reinforcement (E_1) is normally a combined elimination of a certain existing element (e_1') and an application of another specified element (e_1) that is structurally superior.

$$\vec{R} = \sum \vec{E} \quad (4)$$

$$\vec{E} = \vec{e} - \vec{e'} \quad (5)$$

where $\vec{E}$ = the specification vector representing the score transition due to the reinforcement of each element, $\vec{e}$ = the performance vector of the applied substitute element and $\vec{e'}$ = the performance vector of the eliminated existing element.

Using this expression, we understand the several observations of total reinforcements from all the structural elements employed in the design.
Figure 3 shows the further breakdown and characteristic vector of the element. The performance vector $\vec{e}$ of the structural element is normally cumulative according to its scalar amount (a: length (m) or area (m^2), typically). Therefore, it can be described as

$$\vec{e} = a \times \vec{p} \quad (6)$$

$$\vec{p} = (p_r, p_p) \quad (7)$$

where a (m and m^2) = scalar amount of the element, $\vec{p}$ = characteristic vector, p_r (kN/m, kN/m^2) = required strength of the element per scalar and p_p (kN/m, kN/m^2) = potential strength of the element per scalar.

2.2 COMBINED WITH THE COST DIMENSION

We consider the reinforcement design from a wider perspective by combining this method with a cost factor as an independent dimension. In Figure 4, we express this in a three-dimensional (3D) coordinate system combined with a cost factor. There are costs to apply the element (c_{ap}) and eliminate the element (c_{el}), which are different values.

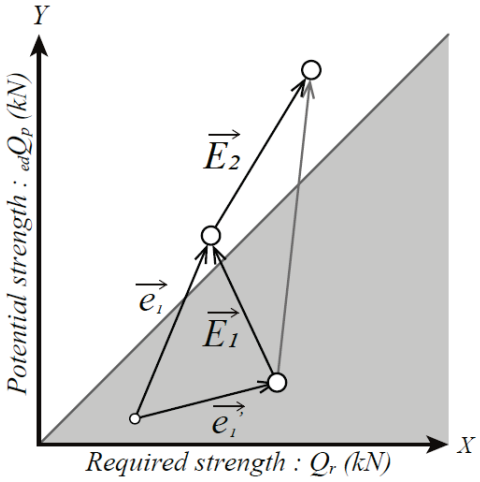

Figure 2: *Breakdown into successive applications of reinforce elements*

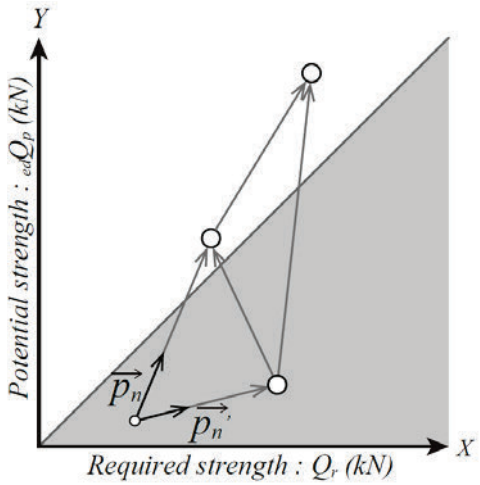

Figure 3: *Characteristic vector of the element*

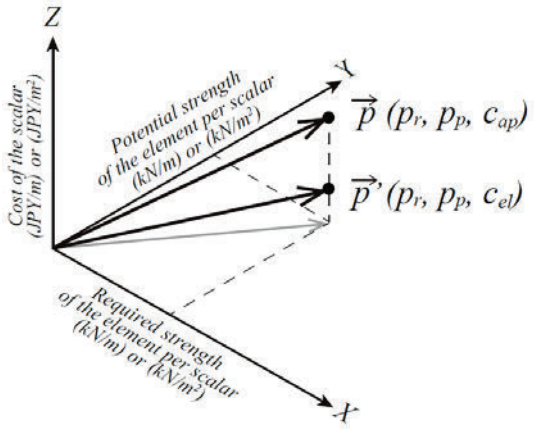

Figure 4: *Characteristic vector of the coordinate system combined with a cost dimension in a three-dimensional coordinate system*

https://doi.org/10.52202/069179-0531

We consider that it would be convenient to unify representation the four factors for the calculation. Therefore, we express the characteristic vector using a four-dimensional column vector as follows:

$$\vec{p} = \begin{pmatrix} p_r \\ p_p \\ c_{ap} \\ c_{el} \end{pmatrix} \quad (8)$$

where c_{ap} (JPY/m or JPY/m^2) = the cost per scalar for the applied element and c_{el} (JPY/m or JPY/m^2) = the cost per scalar for the eliminated element.

The characteristic vector can represent the element characteristics unifacially for both application and elimination. For the elimination, we multiply the characteristic vector by the elimination factor (F_{el}) as follows:

$$\overrightarrow{p'} = F_{el} \times \overrightarrow{p} = \begin{pmatrix} 1 & 0 & 0 & 0 \\ 0 & 1 & 0 & 0 \\ 0 & 0 & 0 & -1 \\ 0 & 0 & -1 & 0 \end{pmatrix} \begin{pmatrix} p_r \\ p_p \\ c_{ap} \\ c_{el} \end{pmatrix} = \begin{pmatrix} p_r \\ p_p \\ -c_{el} \\ -c_{ap} \end{pmatrix} \quad (9)$$

where $\overrightarrow{p'}$ = characteristic vector of the eliminated element and F_{el} = elimination factor.

c_{ap} and c_{el} are transposed by multiplying by the elimination factor. Therefore, we can calculate the required strength in the first row, the potential strength in the second row, and the cost of application or elimination whichever is chosen in the third row.

The total reinforcement is expressed as the synthesis of all the above:

$$\vec{R} = \sum \vec{E} = \sum_n a_n(\overrightarrow{p_n} - \overrightarrow{p_n'}) \quad (10)$$

where a_n (m, m^2) = scalar of the nth characteristic element, $\overrightarrow{p_n}$ = nth characteristic vector of the applied substitute element and $\overrightarrow{p_n'}$ = nth characteristic vector of the eliminated existing element.

3 TRIAL ESTIMATIONS OF THE CHARACTERISTIC VECTOR

We explain herein the method for estimating the characteristic vector. A retrofit reinforcement is normally made by enforcing walls and changing roof materials.
For the walls, the characteristic strength and weight of materials are recognized by dividing the horizontal length (m) while fixing the height as 2.8 m.
For the roofs, the characteristic amounts were considered by dividing the surface (m^2).

A) Wall
The characteristic vectors of walls are calculated as follows:

1) The extra potential strength/length factor was taken from the book entitled "*MOKUZOJYUTAKU NO TAISHINSHINDAN TO HOKYOHOHO* (Seismic Diagnosis and Reinforcement on Timber Houses)" from Ref. [2]. Ref. [2] provides guidelines and explanations on the seismic diagnosis and reinforcement methods for Japanese timber houses.

2) The extra strength per length factor is calculated as follows:

$$p_r = 0.2 \times w \times g \times h \quad (11)$$

where *0.2* (non-dimensional) = theoretical coefficient to make the seismic force consistent at the time of a major earthquake with the evaluated value of the element's bearing capacity, w (kg/m^2) = weight of the specified wall per unit surface [3], g (m/s^2) = gravity acceleration and h (m) = height of the specified wall (i.e., 2.8 m is widely used).

3) The cost factors were taken from the recent report so-called "*BUKKABAN*." In Japan, "*SEKISAN SHIRYO"* [4, 5] and "*SEKISAN POKETTO TETYO"* [6] are the most popular publishers reporting the current construction and material costs of specified construction in each region. We prioritize Ref. [4] here.
We gathered information on the cost estimation from practitioners to fit the raw information of the combination of materials and construction for retrofit projects.

Figure 5 shows example characteristic vectors of the wall estimated by the foregoing.

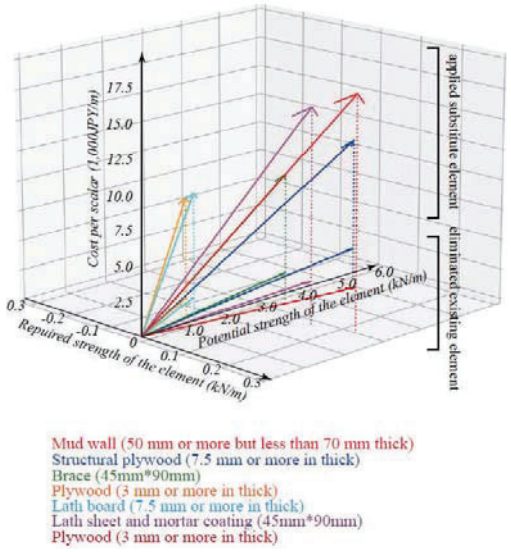

Figure 5: *Example characteristic vectors of the wall*

https://doi.org/10.52202/069179-0531

B) Roof

The characteristic vectors of roofs are calculated as follows:

1) The roof case is much simpler. Roofs normally do not affect strength accumulation but affect the weight reduction through the changing of roof materials. Therefore, the p_p is zero.

2) The extra strength per length factor is calculated as

$$p_r = 0.2 \times w \times g \tag{12}$$

where *0.2* (non-dimensional) = theoretical coefficient that makes the seismic force at the time of a major earthquake with the evaluated value of the element's bearing capacity, w (kg/m^2) = weight of the specified wall per unit surface [3], and g (m/s^2) = gravity acceleration.

3) The cost factors were taken from the recent report, "*BUKKABAN*."

Figure 6 shows example characteristic vectors of the roof estimated by the foregoing.

4 HOW TO USE THE THEORY IN THE STRUCTURAL RETROFIT DESIGN

4.1 COMBINED WITH THE CHARACTERISTIC VECTOR FOR PRACTICAL USE

There are many frequently used reinforcement methods at timber houses. Therefore, synthesizing vectors of application and elimination for each element is convenient (Figure 7). We define herein the element reinforcement vector $\overrightarrow{P_{syn}}$ calculated as follows:

$$\overrightarrow{P_{syn}} = \vec{p} - \overrightarrow{p'} = \begin{pmatrix} p_r \\ p_p \\ c_{ap} \\ c_{el} \end{pmatrix} - \begin{pmatrix} 1 & 0 & 0 & 0 \\ 0 & 1 & 0 & 0 \\ 0 & 0 & 0 & -1 \\ 0 & 0 & -1 & 0 \end{pmatrix} \begin{pmatrix} p_r \\ p_p \\ c_{ap} \\ c_{el} \end{pmatrix} \tag{13}$$

where $\overrightarrow{P_{syn}}$ = element reinforcement vector.

A) Wall

Figure 8 shows an example of the element reinforcement vectors of the wall. These vectors are extracts frequently used in the reinforcement plans gathered from practitioners. We categorize the wall reinforcement work as follows:

1) Insertion: Insert a new wall where no wall exists.
2) Addition: Add an element to the existing wall.
3) Substitution: Substitute a structurally inferior existing wall with a structurally superior new wall.

Insertion uses $\vec{p}$ as is. Addition utilizes $\vec{p}$ of the added element only as is. Substitution is a combination of the characteristic vector of the eliminated existing structurally inferior element ($\overrightarrow{p'}$) and the characteristic vector of the applied structurally superior substitute element ($\vec{p}$).

Even when multiple elements are combined (e.g., a combination of structural plywood and brace), each characteristic vector can be combined and considered as an element reinforcement vector.

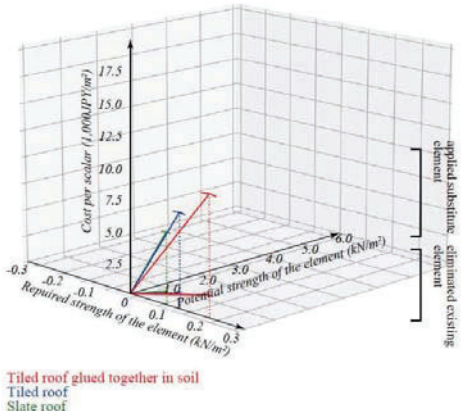

Figure 6: *Example characteristic vectors of the roof*

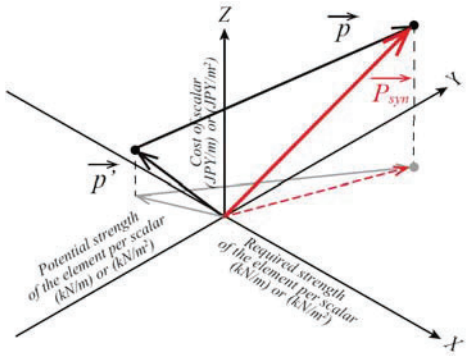

Figure 7: *Synthesizing vectors of application and elimination*

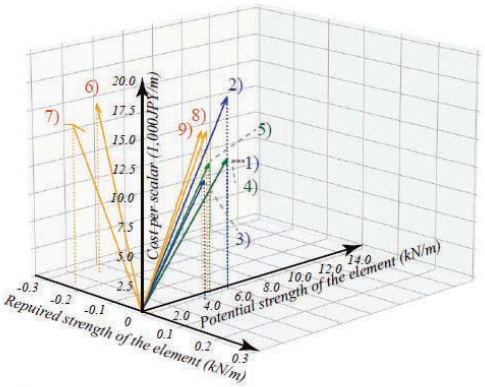

Figure 8: *Example of the element the reinforcement vectors of the wall*

https://doi.org/10.52202/069179-0531

B) Roof
Figure 9 shows an example of the element reinforcement vectors of the roof. For the roof, the heavy material roof is eliminated and substituted with a lighter roof. This can be considered a substitution for the wall case.

4.2 SELECTING THE MOST EFFECTIVE REINFORCEMENT

In seismic reinforcement, the required strength is reduced, for example, by changing the roof materials, while the potential strength is increased, for example, by reinforcing the walls. We consider the case in which the reinforcement method effectiveness is examined only by considering the transition between the required and potential strengths (i.e., using a 2D coordinate system). We can determine that the effective reinforcement is a scalar of inner product projected in the direction to the line $Y = -X$ (Figure 10) because it expresses a great effect on reduces the required strength and increases the potential strength. Therefore, when multiple reinforcement methods are considered, the most effective reinforcement approach is the one that result in the largest inner product, which can be calculated as follows.

$$\left(-\frac{1}{\sqrt{2}}, \frac{1}{\sqrt{2}}\right) \cdot \vec{P} = Max \tag{14}$$

By adopting our explained 3D coordinate system, we can consider the reinforcement cost in addition to the performance improvement (Figure 11). The reinforcement beyond the $Y = X$ perpendicular line must eliminate the existing elements and apply new ones. This means that both elimination and application costs will be required as the reinforcement cost. In some cases, the reinforcement vectors considered as inefficient in a 2D coordinate system (i.e., the reinforcement method that increases p_r and p_p because it does not require eliminate element.) may be optimal from a cost-effective standpoint.

4.3 VISUAL REPRESENTATION OF PERFORMANCE IMPROVEMENT ON CAD SCREEN

We believe that our method can be very useful in practical design works. The software [7] used for seismic reinforcement design is widely used in Japan. By combining our method with this software, the performance improvement caused by the element changes can be displayed on the same screen in real time (Figure 12). We can assume that the 3D theory is maintained here. However, the transition of Q_r and ${}_{ed}Q_p$ are examined in a 2D coordinate system with the change of the method of display. The reinforcement cost is provided as an accumulation on a separate adjacent graph.
The seismic reinforcement design is performed under various constrained conditions, such as the house layout and a limited budget. The ability of designers to watch the optimal cost efficiency in each case can be used as a rational design tool.

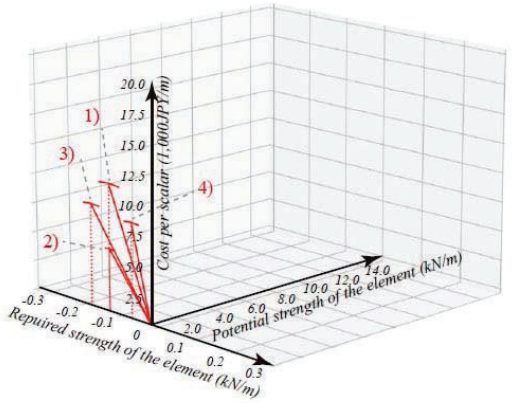

1) 【Substitution】 Tiled roof glued together in soil → Tiled roof
2) 【Substitution】 Tiled roof glued together in soil → Tiled roof (Reuse existing tiles)
3) 【Substitution】 Tiled roof glued together in soil → Slate roof
4) 【Substitution】 Tiled roof → Slate roof

Figure 9: *Example of the element the reinforcement vectors of the roof*

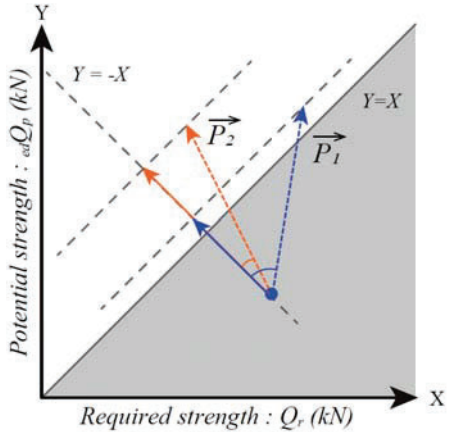

Figure 10: *Consideration for the effective reinforcement method in a 2D coordinate system*

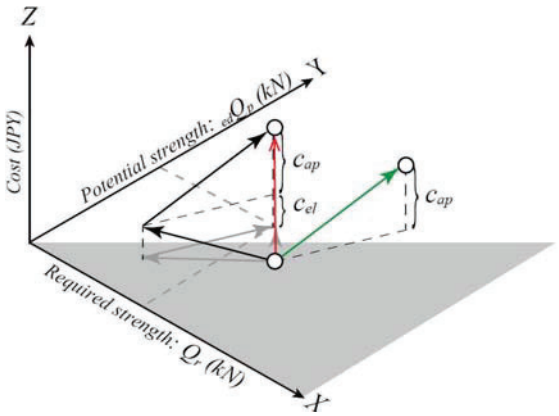

Figure 11: *Consideration for the effective reinforcement method in a 3D coordinate system*

https://doi.org/10.52202/069179-0531

5 CONCLUSIONS

This study explained the method of the coordinated expression of the seismic diagnosis score, derived relevant definitions, and demonstrated how to use the theory in practical design works to enable designers to observe cost efficiency during the design phase.

ACKNOWLEDGMENTS

We are grateful to *KADOWAKI* for theorizing on the early stages of this study, and to *IKEZAWA Associates* for advising us on the current state of seismic retrofit reinforcement design work.

This paper is an outcome of a research project funded by MEXT/JSPS KAKENHI, grant number (C) 21K04588.

We would like to thank Enago (www.enago.jp) for the English language review.

REFERENCES

[1] Hiroko Kadowaki, Chikako Tabata, Yoshito Tomioka: A Proposal and Feasibility of Coordinate Expression of Seismic Resistance Score of Timber House Diagnoses, Proceedings of Tokai Chapter Architectural Research Meeting, AIJ, vol. 58, pp. 137-140, 2020. 2 (in Japanese)

[2] Japan building disaster prevention association: *MOKUZOJUTAKU NO TAISHINSHINDAN TO HOKYOHOHO* (Seismic Diagnosis and Reinforcement on Timber Houses), 2012. (In Japanese)

[3] Architectural Institute of Japan: Recommendations for Loads on Buildings (2015), 2015.

[4] *KENCHIKUKOJIKENKYUKAI*: *SEKISAN SHIRYO pocket edition - Renovation part 2021*, Economic Research Association, 2020. (In Japanese)

[5] *KENCHIKUKOJIKENKYUKAI*: *SEKISAN SHIRYO pocket edition - House construction part 2021*, Economic Research Association, 2020. (In Japanese)

[6] *KENCHIKU SHIRYO KENKYUSHA*: *SEKISAN POKETTO TECHOU architecture part 2021*, *KENCHIKU SHIRYO KENKYUSHA* Co., Ltd., 2020. (In Japanese)

[7] INTEGRAL Corporation: "*HOMUZU KUN TAISHIN SHINDAN* Pro," 2018

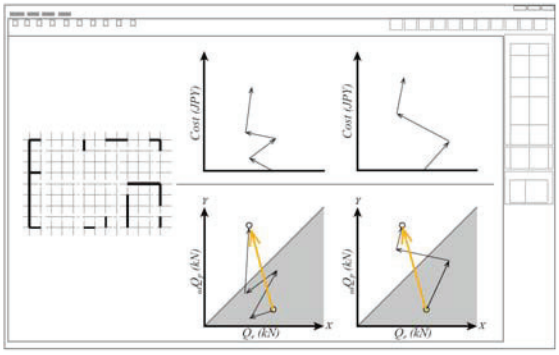

Figure 12: *Real-time display of performance improvement caused by the element changes on the screen*

World Conference on Timber Engineering Oslo 2023

SCALING UP ENGINEERED TIMBER FOR NEIGHBOURHOOD SCALE DEEP RENOVATION: FINDINGS FROM A STUDY IN COIMBRA, PT

Nelson Brito[1], Thomas Thiis[2], Roberto Tomasi[2], Alice Airoldi[2], Andrea Penna[3]

ABSTRACT: European historic city centres embrace a high percentage of masonry buildings with varying materials and configurations, and successive layers of constructive practices. As "deep energy renovations" are progressively imposed in city centres across Europe, structural uncertainty often justifies interior demolitions and the construction of new buildings behind old facades. This linear approach, unsustainable in its´ economical, environmental, and social dimensions, is currently enforced by market players, but also by environmental financing schemes that exclude circular approaches like maintenance and improvement. Departing from a historical masonry building located in the UNESCO-protected area of Coimbra, Portugal, an engineered timber strengthening strategy is shown to solve more than one problem, and proposed as a scalable low-cost solution for entire neighbourhoods' holistic deep renovations. This paper proposes that the high compatibility and "dry" approaches of timber engineering can be scaled up to favour the mass customization, prefabrication and industrialization needed to deliver improved safety and sustainability with lower economic, environmental, and social costs. Taking part in holistic deep renovations will help the sector to solve some of its own difficulties, and to deliver quicker, less expensive, and more sustainable "2050-aligned" deep renovations of European neighbourhoods; and across the world.

KEYWORDS: historic buildings, deep renovation, seismic renovation, masonry buildings retrofit, experimental test

1 INTRODUCTION

Many European historic buildings and neighbourhoods are in-between gentrification and collapse.

These century-old buildings, versatile in attracting new roles and users, are often classified as "energy hogs" by energy efficiency regulations that either exclude them or impose "improvements" mismatched with their design [1]. Prejudice and lack of knowledge about their thermal and structural behaviour often lead to energy-intensive linear processes of demolition and "wet" construction of new buildings inside old facades, with high upfront costs and eviction of their inhabitants for over one year. This process often ends with unaffordable rents for the original inhabitants, leading to gentrification [2].

On the other hand, historic unreinforced masonry buildings—like the one depicted here—are often the least expensive dwellings of European city centres, housing older age/lower income populations vulnerable to (energy) poverty risks. Low rent values mean insufficient income for their maintenance, worsening traditional skilled labour scarcity and rendering them derelict and unstable. As documented in a video filmed nearby, lack of maintenance leads to instability, and collapse. [3]

This dichotomy between gentrification and collapse is not acceptable in a Europe of diversity and knowledge. The relation between structure, energy, materials, finance, architecture, and city planning was tackled in the SAFESUST workshop on "A roadmap for the improvement of earthquake resistance and eco-efficiency of existing buildings and cities", yet the problem is still pending. The cover page image [4], in Figure 1, alerts on the need to guarantee buildings' integrity, and the safety of their users, before "decarbonizing" them.

Figure 1: *Cover page depicting a collapsed "decarbonized" building after a seismic event. [4], Source: Telestense TV, Ferrara Italy - from "TV giornale", 2012 May 21st*

Inclusive deep renovations are at the forefront of European concerns, as stated in a recent call: a low-quality building stock impacts its' residents, "*including poorer health and lower levels of social inclusion. Transforming inefficient housing stock addresses a root cause of energy poverty, however, the topic also has as an objective to tackle the related high upfront costs, lack of information and trust, uncertainty about benefits of the measures, split incentives, and discomfort caused by renovation works, including the potential need to relocate, as barriers to household uptake.*" [5].

[1] University of Coimbra, SES, MIT-Portugal, modular, lda, ADAI-LAETA, ISR-UC. Contact: info@modular.pt

[2] Faculty of Science and Technology, Norwegian University of Life Sciences, Norway

[3] Università degli Studi di Pavia, Italy

https://doi.org/10.52202/069179-0532

This paper proposes that scaling timber-engineered high compatibility and "dry" approaches can deliver quicker, less expensive, and more sustainable deep renovations. Departing from diverse backgrounds and ongoing needs [6] [7] [8] the authors propose engineered timber—a sustainable endogenous material enriched with knowledge—as an emergent solution for 2050 historic neighbourhoods' decarbonization efforts. To bridge the diverse areas this paper aims to engage, this introduction approaches the evolving frameworks and challenges for engineered timber towards the positive and inclusive neighbourhoods needed by 2050, setting the context with academic findings on a historic area under study. Timber in the renovation of existing structures approaches the current (lack of) use of engineered timber, while the discussion questions current legal and constructive practices: scale is needed for holistic views, and to make "deep" diagnosis and design viable before renovation. The conclusion emphasizes the conceptual contradiction of monothematic deep renovations, and the potential of neighbourhood-scale approaches to make interventions more attractive, inexpensive and aligned with 2050 goals.

1.1 ADDED ROLES FOR ENGINEERED TIMBER

Timber is a circular and sustainable alternative gaining momentum, with proven value in compatibility, reversibility, and/or recoverability of interventions.
Several technical timber products are available to improve existing buildings' earthquake safety, increase load solicitation capacity and enhance comfort. Yet the (vernacular) connection with timber lost the scale it once had, and those trained in timber-related arts & crafts can't tackle all the needed daily "repairs", currently performed by unskilled professionals with suboptimal results.
Timber became a technical material that requires highly trained staff—from engineers to onsite workforce—to deliver guaranteed solutions. The timber-based frame with OSB-sheathing panels used in this paper requires studies currently only viable within academic contexts, as trained staff—diagnosis, design, fabrication, construction and maintenance—is still scarce and expensive.
Assuming that historic/existing buildings are mostly similar in neighbourhoods, this paper proposes that engineered timber must take part in wider views, to regain the ubiquity it once had across Europe.

1.2 DEEP RENOVATION

"Deep renovation will boost innovation and investments in the entire construction value chain. Deep(er) renovations imply a need for competence and technical knowledge of high efficiency solutions and processes. Increasing the rate of deep renovation is an opportunity to develop industrialised solutions to renovation and to create even more high-quality jobs and boost the green economy. If deep renovation policies gain appropriate support and become mainstream, the construction sector could experience an important and stable boost comparable to Europe's post-war reconstruction in the 20th century." [9]

This bright future is hanging on "appropriate support" and "mainstream" adoption, yet legislation and practice are targeting linear "demolish" and "rebuild" approaches.
Deep energy renovations are gaining legal prominence and are often presented as an end in themselves. Minimum Energy Performance Standards (MEPS) requirements for existing buildings, already a practice in some European states, are imposed on homeowners that, unaware of alternatives and without negotiation power, opt for what they can afford: gentrification or abandonment/collapse.
Although the term "Deep renovation" is still missing a legally binding definition in Europe, several studies referenced in [9] already point to existing definitions and practices across Europe that support this discussion.
This paper proposes that deep renovations must go beyond energy to "*gain appropriate support and become mainstream"*, to include instead of exclude, to get the scale necessary for mass customization and industrialized prefabrication, and to engage a new generation of highly skilled "green jobs" professionals.

1.3 POSITIVE ENERGY DISTRICTS

As per 2023, the energy performance requirements of new buildings in the EU are in rapid improvement. EU has proposed that from 2030 all new buildings should be built as Zero Emission Buildings (ZEB) and transform the building stock into zero-emission buildings by 2050. This wave of renovation represents an opportunity to improve also other building qualities, such as seismic resilience. However, to take advantage of the characteristics of groups of buildings rather than individual buildings, the literature suggests moving the zero energy objective from the building to the district level [10]. Similar considerations are valid for seismic rehabilitations in historical areas where there are structural effects between buildings that are not accounted for when structural interventions focus on singular buildings only [11].
Moving to a district level implies that the diversity in load profiles, production and storage capabilities can be utilized as well as the possibility of sharing costs and resources in the construction and operational phase of the buildings. The principles have been developed for several years, and already there is an EU-funded program aiming to support the planning, deployment and replication of 100 Positive Energy Districts (PED) by 2025 [12].

1.4 LEARNING FROM A HISTORIC BUILDING

The Montarroio case study, spotted in red in Figure 2, is a three levels masonry building already pictured in 14th-century maps of Coimbra, Portugal. It faces the UNESCO and "Jardim da Manga National Monument" protection areas, closing a row of similar buildings.
This building is composed of load-bearing masonry walls made of undressed stone blocks, thinner towards the top level (Figure 3), with growing internal floor areas: 13.7 m2 at the lowest level; 15.3 m2 at the intermediate level; 20.7 m2 at the upper level. As found in many ancient buildings renovated century after century, openings are not regular in dimension and location, and some windows were closed with a thinner layer of masonry at the upper level, leaving alcoves. This translates into irregular

masonry structural elements and discontinuous transmission of loads to the ground. The roof structure illustrates a 1980s low-quality "repair" of irregularly shaped eucalyptus structure "glued" to the walls using cement, which explains many of the rotten connections.

Figure 2: *Contextual view of Montarroio case study, spotted in red, and neighbouring area (Source: Google Earth)*

This extreme irregularity, illustrated in the sections in Figure 4 imposes so much uncertainty that it ends up as a scientific challenge; yet the lower floors are more than 600 years old, the top floor almost 400; and both survived a foundation settlement from the excavation of south-facing monumental stairs, provoking its tilt around 1980s.

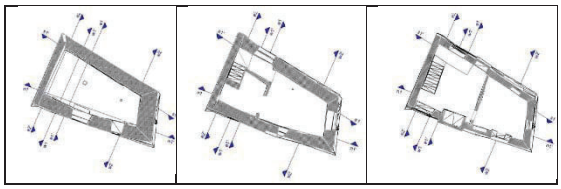

Figure 3: *Plans of the Montarroio case study (source: author)*

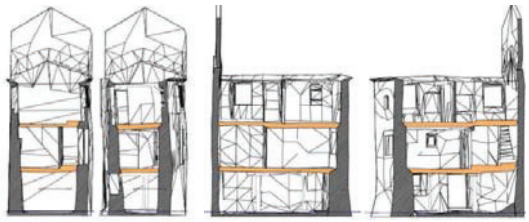

Figure 4: *Transversal and longitudinal sections of Montarroio case study (source: author)*

Visualizing thermal images allows a better grasp of the challenge and the risks of "improvements". Figure 5 shows a Building Information Model (BIM) and a thermal model illustrating the effect of interior insulation.
The original solution (a) displays a balanced "sandwich" of temperatures, cold to hot from the outside to inside, with asymmetries inside. The interior insulation (b) model presents stable indoor temperature, yet thermal stress in the floor connections. Low heat loss in insulated areas contrasts with punctual heated floor connections, enabling differential wet/dry and freeze/thaw cycles, and accelerated wall and timber degradation in those areas.

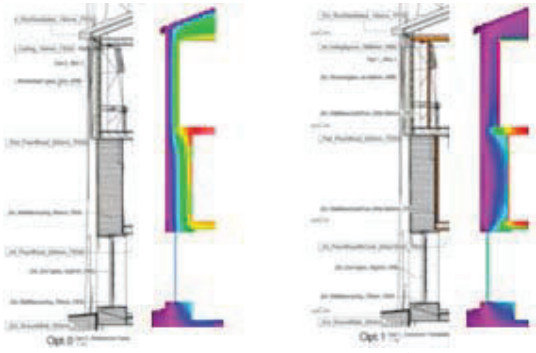

a) b)

Figure 5: *Comparison of the original situation (a) with an interior thermal insulation strategy (b) in a south wall section in a BIM model and thermal behaviour model using THERM* ***[13]****.*

2 TIMBER IN THE RENOVATION OF EXISTING STRUCTURES

This section tackles monothematic approaches to Seismic Renovation and Energy Renovation to demonstrate that the detailed processes they require have much to share.
The case study illustrated must not be seen as a guide, as it results from a limited number of views and assumptions. Nevertheless, the authors use this example to support debate and trigger new views and constructive input.

2.1 SEISMIC RENOVATION

Although Coimbra is not considered a high seismic risk area, this building has evolved through centuries with varied construction techniques, including timber floors and cross-layered timber walls that are probably the explanation for its survival. Nevertheless, it was subjected to significant changes, like the addition of an unbalanced bathroom in concrete, and risky "repairs" that make its´ stability questionable. The following study, documented in [14], tackles problems with assumed simplifications.

2.1.1 Stability refurbishment solution

The studied retrofitting technique consists of a timber-based frame (strong-back) and panels fixed to the internal side of walls using steel connections. The technique has been proposed and tested by Dizhur et al [15]], The result is a hybrid system where the two components, masonry and timber retrofitting, collaborate in resisting earthquake actions. Collaboration is ensured by mechanical bonding obtained through point-to-point connections. Posts act in flexure to transfer wall loads to the adjacent floor diaphragms, subdividing a large planar wall into several vertical buttressed segments. Posts are applied to the masonry wall and connected to it through steel angles (C2 and C3 in Figure 6 and to foundations or slabs through tie-down. In addition to such a system, horizontal nogging elements and OSB boards were added to increase also the in-plane capacity of masonry walls [14]. In-plane cyclic tests on retrofitted walls and shake-table tests on a full-scale retrofitted building demonstrated the validity of the chosen approach [16].

https://doi.org/10.52202/069179-0532

2.1.2 Mechanical model

The conceptual model was developed with the TREMURI computer program [17], an equivalent-frame macro-element model in which the wall structure is represented by an assembly of 2-nodes elements connected by rigid nodes. The macro-element model parameters rely on the experimental characterisation of masonry mechanical properties. If necessary, the use of non-linear beam elements allows the modelling of concrete curbs, wooden elements or reinforced masonry. Further technical detail can be found in [17].

Figure 6: *Example of strong-backs layout (Source:**[14]**)*

The "Equivalent Frame Modelling" approach is based on the identification of deformable structural elements that interact with each other through "rigid portions", connecting the two main macroscopic components. Piers, the main vertical resistant elements, hold both vertical and lateral loads. Spandrels, the secondary horizontal elements, couple the response of adjacent piers and allow or restrain rotations, significantly influencing walls' lateral capacity.

The retrofitted building has been modelled using a dense mesh and adding a non-linear beam as reinforcement. Posts have been located at both lateral ends of piers and with a spacing not higher than 0.9 m. The OSB panel contribution is modelled by increasing mechanical parameters of masonry shear strength.

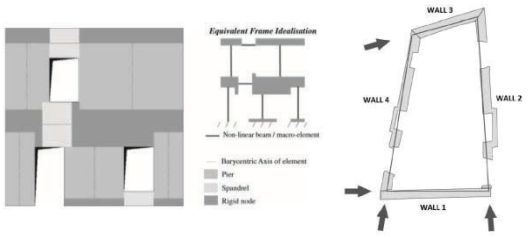

(a) (b)

Figure 7: *Example of equivalent frame idealization for irregularly distributed openings (a)* ***[17]*** *and pushover directions performed (b).*

The seismic verification is carried out using pushover analysis, through the prescriptions suggested by the N2 procedure [18] [19] implemented in several codes [NTC18, EC8]. Pushover analysis is carried out under conditions of constant gravity loads and a horizontal load pattern with fixed distribution and controlled to monotonically increase the displacement of a control node. Four pushover analyses have been performed, parallel to each wall direction.

The verification consists of comparing the displacement capacity of the building with the seismic demand (in Coimbra a PGA of 0,07 g is expected for a return period of 475 years). However, the proposed analyses are valid also for evaluating the global behaviour of the structure before and after the retrofit intervention (local analysis, which should be evaluated with other tools that are out of the scope of this paper).

2.1.3 Results

The comparisons between unreinforced and strengthened masonry provide an idea of the potential of the retrofitting technique proposed.

Damage level in TREMURI software is represented through a graphic convention in which the cross shows the full development of a shear failure mechanism and straight lines at both ends of the element show damage caused by the flexural/rocking mechanism.

The shear damage level on each masonry element is identified through a chromatic scale in which red colour represents the achievement of the maximum shear resistance, while lighter colours identified the development of non-elastic sliding effects (see Table 1).

The result in terms of the capacity curve is reported in Figure 8 for wall 1 and pushover performed in Wall 1 Direction. In this case, the failure is reached for exceeding the flexural drift limit. Capacity curves show a remarkable increase in displacement capacity as well an increment in shear capacity.

Similar results obtained for the other cases in the analysis can lead to the following considerations:

- A significant (250%) increase in displacement capacity, of the whole structure and single walls, in pushover performed parallel to shorter walls
- Minor increments (10-50%) obtained along directions parallel to longer walls
- The retrofit intervention involves changes in the failure mechanism
- Lateral strength capacity increased in all directions in a range of 50-80%.

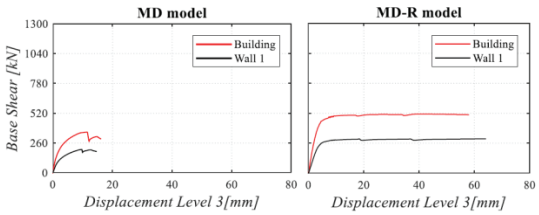

Figure 8: *Comparison of capacity curves between the entire building and Wall 1 of pushover performed in Wall 1 direction for unreinforced model(left) and strengthened model (right).*

To facilitate the comparison of the study [14] results Table 2 illustrates the pushover damage in unreinforced masonry walls, while Table 3 illustrates the added value of an engineered strengthening of these masonry walls.

Table 1: *Percentage variation of maximum shear and displacement of the unreinforced and strengthened models.*

	Base shear variation	***Displacement*** variation
Push_1	+ 72 %	+ 262 %
Push_2	+81 %	+ 10 %
Push_3	+ 53 %	+ 246 %
Push_4	+ 89 %	+ 58 %

Numerical modelling demonstrates that the proposed retrofit solution increases displacement capacity and base shear capacity, with a change of failure mechanism. That means collapse may be reduced due to a brittle mechanism favouring a more ductile behaviour, increasing seismic safety. Later in this text, the importance of a neighbourhood approach to adequately quantify and qualify several parameters will be highlighted.

Table 2: *Pushover damage in* ***Unreinforced*** *masonry walls*

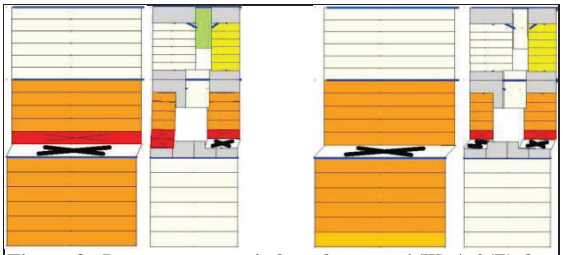

Figure 9: *Damage on* ***unreinforced*** *pairs w1(W) /w3(E) from* ***pushover*** *performed in* ***w1****(left) and* ***w3****(right) directions*

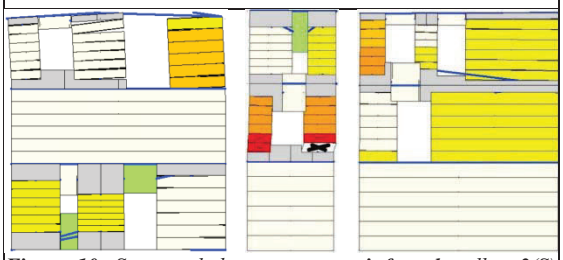

Figure 10: *Structural damage on* ***unreinforced*** *walls w2(S), w3(E) and w4(N)from pushover in w2 direction*

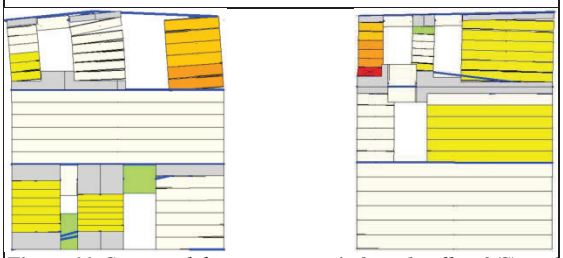

Figure 11: *Structural damage on* ***unreinforced*** *walls w2(S), and w4(N) from pushover in w3 direction*

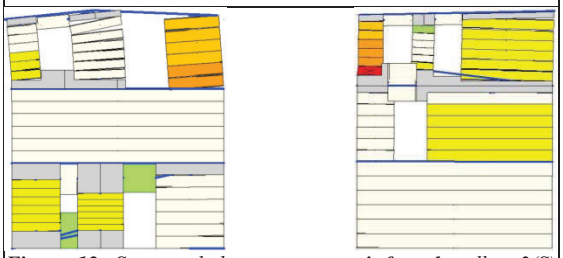

Figure 12: *Structural damage on* ***unreinforced*** *walls w2(S), w3(E) and w4(N) from pushover in w4 direction*

Table 3: *Pushover damage in* ***Strengthened*** *masonry walls*

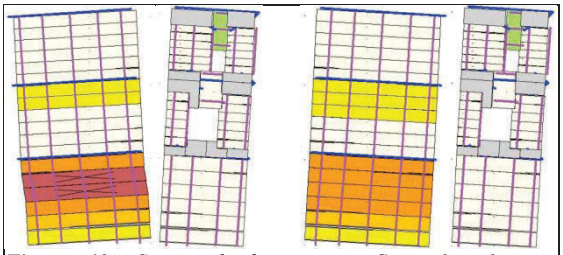

Figure 13: *Structural damage on* ***Strengthened*** *pairs w1(W)/w3(E) from pushover performed in w1 (left)* **and** *w3 (right) directions*

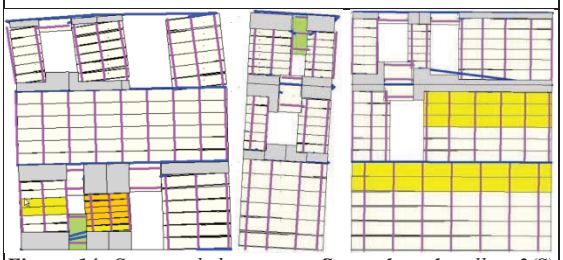

Figure 14: *Structural damage on* ***Strengthened*** *walls w2(S), w3(E) and w4(N) from pushover in w2 direction*

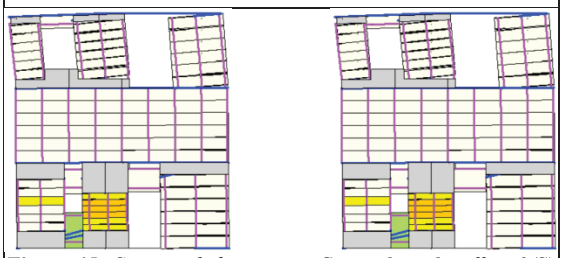

Figure 15: *Structural damage on* ***Strengthened*** *walls w2(S), and w4(N) from pushover in w3 direction*

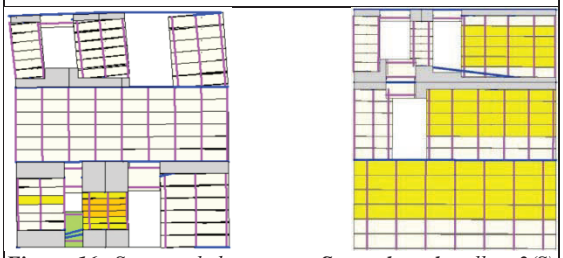

Figure 16: *Structural damage on* ***Strengthened*** *walls w2(S), w3(E) and w4(N) from pushover in w4 direction*

https://doi.org/10.52202/069179-0532

2.2 ENERGY RENOVATION

Figure 17 maps Energy Performance Certificates (EPCs) issued around the case study, spotted in red. Investigation [1] demonstrated that between 2012 and 2022 only one-third (25 out of 76, those with letters overlaid) had EPCs, issued by 13 different experts on different dates and with varied levels of detail. The EPC process often implied two interactions: one EPC requested by the initial selling part—before advertising for sale, so unaware of buyers' or tenants' objectives— and, after renovation, another EPC per legally designated fraction.

The EPC process implies a) an initial service request by the original owner, b) collection of necessary legal data, c) a site visit to diagnose geometry and constructive solutions, d) calculation of a compared "baseline" according to current EPC rules[4], e) diagnosis of the needs and potential of the building, preferably produced together with the client f) identification and calculation of 10 improvement measures viable for this specific fraction, g) consultation of local availability and prices for evaluation of cost/return ratios, h) photos with scaled targets of all divisions and acclimatization equipment with ID tags i) preparation of reports with detailed constructive solutions and thermal bridges discretization, j) insertion of data in the EPC site, k) emission and payment of the EPC and m) explanation to the client.

The improvement measures proposed must follow the EPC portal typification for the whole country, from north to south: demand reduction by adding insulation, replacing single pane wood frame windows for highly efficient double pane glazing; efficient use of energy by electrification using (air-water) heat pumps; and renewable energy production at the end of the priorities.

The split-incentive barrier —requesting an EPC to a seller who pays the costs for benefits that might accrue to the new buyer or tenant—often results in a "lowest cost" market, with excessive simplifications often resulting in EPCs that miss the potential of the building and neighbourhood they sit in.

This mismatch explains a "re-issue" feature in the EPCs portal: only improvement measures listed in each EPC are accepted for financing, forcing candidates to request a new EPC mentioning those desired measures: another cost/difficulty to access prepaid[5] unguaranteed financing.

Figure 17: *In 10 years only 33% of these buildings were certified and most "rehabilitated" do not excel in performance. Source: author sketches over local GIS and Google maps.*

As all buildings in Figure 17 are inside a protection zone, exterior insulation is forbidden, the interior is not realistic for such small areas, and other limitations apply.

2.2.1 Reducing envelope energy demand

The effect of placing expanded cork in the hollow parts of the strengthening timber mesh proposed in 2.1.1 is illustrated in Table 4. A width of 0.05m, inferior to the available space, was chosen to avoid excessive U-values difference between the timber studs and cork, but studies are advised to evaluate the risk of condensation spots.

Table 4: *Effect of inserting 0.06m of expanded cork within the structural mesh proposed for the seismic retrofit.*

Wall width	Original U-value (W/(m².ºC)	U-value with 0.05m insulation (W/(m².ºC)
Level 2 (0,25m)	2.52	0.64
Level 1 (0,6m)	1.4	0,53
Level 0 (0,9m)	1.01	0,46

As for the windows, the estimated U-value defined for single pane windows is 5.1 W/(m².ºC) can be reduced to 3.4 W/(m².ºC) if low airflow external shutters exist. Installing a certified "Classe+" window, the only type financed in Portugal would ensure a U of 1.5 W/(m².ºC). Although these values may seem attractive to "improve" the envelope, an uncontrolled approach would reduce the available useful area and cancel the thermal delay: this would impose regular use of devices for heating and cooling that were previously unnecessary.

The same is true for airtight windows, as stopping infiltrations implies ventilation with extractors or self-regulated grilles: "if you build it tight, ventilate it right". Reducing envelope demand would increase dependence on equipment for heating, cooling, and ventilation, refuting the thermal resilience proven over centuries.

2.2.1 Reducing fossil energy demand

Energy loads such as domestic hot water and acclimatization are sure targets for improved efficiency. Contemporary improvement measures for domestic needs in this building would include improved efficiency water taps (more pressure with less hot water, a dual gain), better efficiency gas boilers and air-water heat pumps, together with similar systems for acclimatization.

In this area, external heat pump evaporators are not allowed, and air-water heat pumps occupy the scarce interior space available. Solar panels are allowed on the roof, but the unknown capacity of these old structures makes installation & maintenance risky in these buildings [1]. Efficient fossil-fueled equipment is both the least expensive/spacious, thus often the chosen solution.

[4] The EPC rules assume that the building is entirely and permanently acclimatized, not reflecting actual Portuguese habits of partial heating in a mostly mild climate [1].

[5] The current support mechanism requires families to invest first, and request funding after the investment is complete.

https://doi.org/10.52202/069179-0532

3 DISCUSSION

Engineered timber's role in deep renovation is dependent on a wider recognition of its arguments. Similarly looking solutions in amount, type and costs can use timber to hold insulation to walls or to deliver engineered improvement, yet only the second can add proven safety to owners/users: there is a value in knowledge. On the other hand, the costs of timber engineering/architecture are hard to charge for a single building, as the efforts for a correct diagnosis, study and design are still expensive, making them rare. The individual approaches to seismic and energetic renovation reported above show space for savings through base model optimizations for these and other future needs.

Yet going further opens new possibilities, as documenting a neighbourhood—often a repetition of construction techniques/materials within a limited area—allows for scaled holistic views, new visions and new strategies.

Departing from a current limitation—individual linear flows underlying energy guidelines/financing schemes—it is proposed that scale, with communities, can deliver what the EU needs: real decarbonization, energy security/poverty prevention, resilience, and a circular economy—with engaged citizens.

3.1 FROM LINEAR TO CIRCULAR ECONOMY

Circular economy combines the reduction, reuse and recycling activities through systemic shifts aligned with sustainable development. A circular intervention must follow the three dimensions of sustainability—economic, environmental and social—to deliver prosperity, environmental quality and social equity [20].

Although proclaiming circularity, many European public financing excludes maintenance/optimization of existent solutions or systems; like the windows referred to above. In Portugal, a window replacement can apply for 70% of public funding if such "improvement" is mentioned in the EPC and the original is replaced by windows classified as "Classe+", with a U-value of 1.5 W/(m^2.ºC). This implies the removal, transportation to a dump site, and all the embodied energy needed to produce/fit the new window into an often-irregular casing: more risks, and added costs. Retrofitting the existing windows can deliver similar results, as shown in Table 5, which depicts scientifically validated values [21] for some window retrofit solutions.

Table 5: *Extract from the "Research into the thermal performance of traditional windows: timber sash windows" comparing the results of several window retrofits [21]*

Details of the test assembly	Glass only: W/(m^2.ºC)	Glass & frame W/(m^2.ºC)
Window as found	5.3	4.3
Heavy curtains	3.3	2.5
Well-fitting shutters	2.0	1.7
Reflective roller blind	1.8	1.9

These values show that circular economy approaches in windows improvement can deliver results while 1) promoting local maintenance and optimization practices, 2) reducing waste and fostering reuse practices, alongside reduced embodied energy, thus 3) fostering sustainable practices—economic, environmental and social— and green jobs able to "spill" to neighbouring buildings.

However, it is more attractive for a private owner with investment capacity to buy a new window for which a grant of 70% may be attributed, instead of spending half of the economic cost retrofitting the existing window. Although having similar levels of performance, these improvements are not homologated by "Classe+" scheme, thus not recognized by the certification entity.

3.2 LINKING ENERGY TO COMMUNITIES

The current urge for electrification— heat pumps, electric cars, and modern electric gadgets—requires either a significant electric network capacity improvement, and/or local renewable production, and/or ICT connections for "virtual power plants" to turn off non-urgent energy needs (water heaters and other postpone-able energy uses) in exchange for retribution for delayed availability.

Instead of requiring homeowners to request an individual EPC, a neighbourhood pre-certification can be offered to overcome split-incentive issues, study scenarios and trigger action. District heating, renewable energy communities and other solutions already funded rarely find the collective necessary to proceed, and to upgrade a neighbourhood into a Positive Energy District.

3.3 ON THE VALUE OF NEIGHBOURHOOD APPROACHES

Scale is often necessary to deliver complete solutions.

The seismic reinforcement strategy presented is limited without out-of-plane (overturning) analysis of common walls. Figure 18 illustrates a study analysing the whole block [11] to characterize the effect of shared walls in the neighbourhood seismic behaviour.

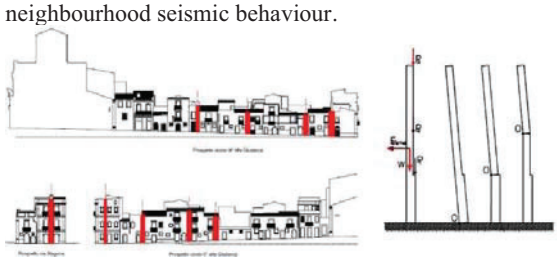

Figure 18: *Image illustrating 9 common walls analysed for overturning in a neighbourhood-scale seismic study [11].*

The energy efficiency neighbourhood scale approaches [1] also facilitate holistic thinking: is it wise to place solar systems in each of these unknown structural capacity roofs—without adequate access to the roof, thus implying cranes for installation and maintenance—when a unified space is available[6] in the blue areas in Figure 17?

Neighbourhoods have the scale and regularity for integrated diagnosis, planning and execution, as defined

[6] This proposal, named "Common Efficacy" was validated by the 2015 VINCI Innovation Awards (4mn video available) [22]

https://doi.org/10.52202/069179-0532

by EN16883 on "Guidelines for improving the energy performance of historic buildings".
Scale attracts new business models, and optimized learning curves while lowering contextual costs, from planning to maintenance, operation and optimization. Making it with local communities closes the circle, fostering new green jobs and the confidence necessary for sharing data in common initiatives.
Renewable Energy Communities are changing the landscape, as some support is already available for the design and implementation of neighbourhood-scale energy systems. Similar supports must be attributed to foster deep renovation strategies, and those will probably be first attributed to lower-income areas.

3.4 HOLISTIC DEEP RENOVATIONS

By 2030 the Renovation Wave aims to double the energy renovation rate and foster deep energy renovation uptake, meaning that "By 2030, 70% of the renovations taking place should be deep" [9].
Multiple benefits, from microeconomic to social, are referenced. From reduced bills/exposure to volatile fossil energy prices to improved Indoor Environmental Quality (IEQ), comfort, well-being and productivity, reduced morbidity and mortality during extreme phenomena, to new green jobs, the advantages are many but not always linked to the proposed metrics.
If deep renovations are to deliver Climate Change mitigation and adaptation—from lower carbon emissions to flexibility on demand, from distributed production to increased resilience and guarantee basic energy services while "*including poorer health and lower levels of social inclusion"* [5]—then the industrialized solutions anticipated require holistic views and a solid legislative background to start moving.

3.5 LINKING ENGINEERED TIMBER TO COLLECTIVE CHALLENGES

It is probably strange to suggest to highly qualified engineered timber professionals that part of their future success may reside in helping the lower levels of society fight (energy) poverty, bad living conditions and safety risks at a time when engineered timber is engaged in high-level design and construction challenges.
Yet the engineered timber sector faces significant challenges—from insurance added costs to concerns on construction and maintenance crews and limited investment for industrialization—to which a European-wide interest would be appreciated.
The advantages of engineered timber are significant: dry and quick onsite responses to energy and safety issues, potential for integral/stagged deep renovation to include natural trigger points, and the use of an endogenous european material enriched by knowledge, among others.
With such edges in this emerging context, will the sector continue waiting for occasional orders, or take the lead, subcontracting the easy parts—infrastructures, systems, renewables—to other partners and stakeholders?

4 CONCLUSIONS

Scaling up timber-engineered supported strategies in neighbourhoods can deliver sustainable, inexpensive, and holistic deep renovations aligned with 2050 goals.
The contemporary individualist monothematic strategies in place to solve collective issues conceptually contradict the Beautiful | Sustainable | Together"[7] European goals.
Holistic deep renovations, at the neighbourhood scale, can deliver more—energy efficiency, (seismic) safety, quality of life, comfort and community well-being—with lower economic, social and environmental costs.
Neighbourhoods, characterized by their repetition, similarity, complementarity and interdependence, have the scale to optimize processes and reduce design, contracting, operation, maintenance and optimization costs; and trust is essential for sharing the resources and information required to achieve Positive Energy Districts.
Future-proofing neighbourhoods with climate adaptation and anticipation—a practice in which the sector has significant experience—can make a difference in most European historic centres, and in many countries that look to Europe as an example. And providing added safety, circularity and sustainability is of no minor importance.
Engineered timber strategies facilitate multistage deep renovations able to match the financial capacity of owners and users with natural trigger points of existing materials and equipment, making the most of historic areas without requiring excessive initial investments. Decarbonizing energy needs, fostering local renewable energy production and peak management generates income for investment payback and other sustainable interventions.
Low embodied energy deep renovations and circular maintenance/optimization procedures must be recognized /funded across Europe. By delivering solutions to wider problems in partnership with other stakeholders, and by defining viable roadmaps, the sector can lead the huge market of deep renovations; and their optimization.
The engineered-timber sector must demonstrate that an endogenous economically, environmentally and socially sustainable material, enriched by knowledge, can redefine the future of deep renovation.

ACKNOWLEDGEMENTS

This research evolved with the support of the "Sustainable Energy Systems" University of Coimbra/MIT Portugal Program (SFRH/BD/51017/2010 FCT grant) and engaged commitment of modular, arq:i+d, lda, Snapmaker & TUCAB (https://snapmaker.com/) (https://www.tucab.pt) for the models to be displayed in the conference. Part of the work presented in the paper was carried out within the framework of the WP5 "Low-impact and integrated rapid execution interventions" of the ReLUIS Research Programmes 2019-21 and 2022-24 funded by the Italian Department of Civil Protection.

[7] New European Bauhaus: https://new-european-bauhaus.europa.eu

REFERENCES

[1] N. S. Brito, "Improving the (energy) performance of (historic) buildings and communities: towards 'neighbourhood Energy Performance Certification' (nEPC)," in *EEHB 2022 Post Prints. The 4th International Conference on Energy Efficiency in Historic Buildings. Benediktbeuern, Germany*, Fraunhofer IRB Verlag., R. Kilian, S. Saba, and C. Gietz, Eds. Stuttgart (Deutschland), 2023, pp. 73–80. Accessed: Feb. 01, 2023. [Online]. Available: https://www.baufachinformation.de/eehb-2022/buecher/255634

[2] "Gentrification," *Wikipedia*. Feb. 09, 2023. Accessed: Feb. 10, 2023. [Online]. Available: https://en.wikipedia.org/w/index.php?title=Gentrification&oldid=1138403255

[3] *Prédio cai em Coimbra (Historic building collapse in Coimbra)*, (Jan. 12, 2006). Accessed: Feb. 01, 2023. [Online Video]. Available: www.youtube.com/watch?v=OVGRkLDhZKQ

[4] A. Caverzan, Lamperti Tornaghi, and P. Negro, Eds., *Proceedings of SAFESUST workshop : a roadmap for the improvement of earthquake resistance and eco-efficiency of existing buildings and cities : Joint Research Centre, Ispra November 26-27, 2015.* 2016. Accessed: Dec. 19, 2017. [Online]. Available: https://publications.europa.eu/en/publication-detail/-/publication/eb954223-b790-11e6-9e3c-01aa75ed71a1/language-en

[5] LIFE-2021-CET-ENERPOV, "Addressing building related interventions for vulnerable districts." https://ec.europa.eu/info/funding-tenders/opportunities/portal/screen/opportunities/topic-details/life-2021-cet-enerpov (accessed Feb. 19, 2023).

[6] LIFE 3.0 - LIFE Project Public Page, "REVERTER: Deep REnovation roadmaps to decrease households VulnERability To Energy poveRty." https://webgate.ec.europa.eu/life/publicWebsite/project/details/101076277 (accessed Feb. 20, 2023).

[7] "e-SAFE." https://esafe-buildings.eu/en/local-platforms/ (accessed Feb. 23, 2023).

[8] "FME ZEN." https://fmezen.no/ (accessed Feb. 23, 2023).

[9] BPIE - Buildings Performance Institute Europe, "Deep Renovation: Shifting from exception to standard practice in EU Policy," BPIE - Buildings Performance Institute Europe, Nov. 2021. Accessed: Jan. 22, 2023. [Online]. Available: https://www.bpie.eu/publication/deep-renovation-shifting-from-exception-to-standard-practice-in-eu-policy/

[10] Y. Saheb, S. Shnapp, and C. Johnson, "The Zero Energy concept: making the whole greater than the sum of the parts to meet the Paris Climate Agreement's objectives," *Curr. Opin. Environ. Sustain.*, vol. 30, pp. 138–150, Feb. 2018, doi: 10.1016/j.cosust.2018.04.014.

[11] F. Braga, G. Monti, D. Liberatore, and G. Scalora, "Survey and Restoration: The Case of the Block Between Vicolo II and Vicolo III at the Giudecca of Ortigia, Sicily," *Struct. Anal. Hist. Constr.*.

[12] "Positive Energy Districts (PED)," *JPI Urban Europe*. https://jpi-urbaneurope.eu/ped/ (accessed Feb. 24, 2023).

[13] N. S. Brito and M. C. Gameiro da Silva, "8.6 Historic residential building upgrade to nZEB Coimbra, Portugal," in *Energy Efficiency in Historic Buildings*, REHVA (Federation of European Heating, Ventilation and Air Conditioning Associations) (www.rehva.eu)., F. Romana d'Ambrosio and L. Mazzarella, Eds. Brussels: REHVA, 2018, pp. 114–119. Accessed: Jun. 28, 2018. [Online]. Available: https://www.rehva.eu/publications-and-resources/eshop/eshop-detail.html?tt_products%5BbackPID%5D=1560&tt_products%5Bproduct%5D=134&tt_products%5Bcat%5D=3&cHash=75b794c7c95f8f1a77cf478d63ee04e0

[14] A. Airoldi, "Numerical modelling of a timber retrofit solution for unreinforced masonry buildings," UNIVERSITA' DEGLI STUDI DI PAVIA, Pavia, 2019.

[15] D. Dizhur, M. Giaretton, I. Giongo, and J. Ingham, "Seismic retrofit of masonry walls using timber strong-backs," vol. 30, pp. 30–44, Jan. 2017.

[16] G. Guerrini, N. Damiani, M. Miglietta, and F. Graziotti, "Cyclic response of masonry piers retrofitted with timber frames and boards," *Struct. Build.*, pp. 1–54, Feb. 2020, doi: 10.1680/jstbu.19.00134.

[17] S. Lagomarsino, A. Penna, A. Galasco, and S. Cattari, "TREMURI program: An equivalent frame model for the nonlinear seismic analysis of masonry buildings," *Eng. Struct.*, vol. 56, pp. 1787–1799, Nov. 2013, doi: 10.1016/j.engstruct.2013.08.002.

[18] P. Fajfar, "Capacity spectrum method based on inelastic demand spectra," *Earthq. Eng. Struct. Dyn.*, vol. 28, no. 9, pp. 979–993, 1999, doi: 10.1002/(SICI)1096-9845(199909)28:9<979::AID-EQE850>3.0.CO;2-1.

[19] P. Fajfar, "A Nonlinear Analysis Method for Performance-Based Seismic Design," *Earthq. Spectra*, vol. 16, no. 3, pp. 573–592, Aug. 2000, doi: 10.1193/1.1586128.

[20] J. Kirchherr, D. Reike, and M. Hekkert, "Conceptualizing the circular economy: an analysis of 114 definitions," *Resour. Conserv. Recycl.*, vol. 127, pp. 221–232, Dec. 2017, doi: https://doi.org/10.1016/j.resconrec.2017.09.005.

[21] H. England, "Research into the Thermal Performance of Traditional Windows: Timber sash windows | Historic England." https://historicengland.org.uk/images-books/publications/thermal-performance-traditional-windows/ (accessed Jun. 13, 2018).

[22] VINCI, N. S. Brito, S. S. Brito, and R. O. Castela, "'Common Efficacy' proposal won the 1st prize in 'Urban Services and the Connected City'.," Sep. 25, 2015. http://www.uc.pt/en/efs/destaques/2016/vinci (accessed Jan. 02, 2016).

https://doi.org/10.52202/069179-0532

World Conference on Timber Engineering Oslo 2023

MODIFICATION OF ROOF STRUCTURE OF THE TRADITIONAL WOOD HOUSES IN THE URBAN AREA OF DAEGU, KOREA DURING MID TWENTIETH CENTURY

Jaemo Cho[1]

ABSTRACT: This study focuses on the roof structure modification of hanok, the traditional Korean timber frame house, in the central urban area of Daegu city, Korea during mid twentieth century. It is based on the 2 years survey of 10,753 cases of hanok architectures in this city. The urban sprawl and population growth gave an impetus to house builders developing new residential areas with modifing traditional plan and structure of hanok.

Instead of traditional way, the wood house builders of this period choose simpler and cheaper roof structure for housing in the dense urban area. They wanted to make the familiar and popular image of tile-roofed traditional wood house using heavy timber frame with cheaper cost and shorter construction time for adapting to housing market. New method using sparsely arranged small square cross-section rafters was in fashion. Other roof type with short and asymmetric eaves was used at small sites. Some special houses have newly designed structure for long span, too.

These modified wood houses shows that there were diverse needs at the housing market. But after this period wood house lost the popularity in the market as modern house building technology, and reinforced concrete construction was widely utilized.

KEYWORDS: Roof structure, thin rafter, Asymmetric eave, Korean timber frame house hanok, housing market

1 INTRODUCTION

This article focuses on the roof structure of hanok in Daegu that is one of the biggest cities in Korea. Hanok is the traditional wood house of Korea made of heavy timber frame structure. The roof structure is usually composed with heavy crossbeam, purlins and circular cross-sectional cantilever rafters supporting eaves covered with roof tiles on the amount of soil.

At the period of mid-twentieth century, there was heavy urban sprawl and population growth at the major cities in Korea. Many citizens wanted cheaper house near central city and the house builders needed to develop new residential areas for them. In the newly developed residential area, the builders made almost same mass houses to reduce construction time with less cost.

This study is based on the 2 years survey of 10,753 cases of hanok architectures in this city. The survey was carried out by Kyungpook National University (2012) and Keimyung University (2013) supported by AURI National Hanok Center. It was the first complete metropolitan council scale enumeration survey for hanok architecture.

The focus of this article is to understand new methodology of roof structure of hanok in Daegu. There were diverse rood structural types for responding market demand. In this article, two major types and one unique case will be presented.

Before this study, there were several researches about hanok architecture of Daegu. J. M. Ha's one was on the typology of the urban traditional housing focused on hanok in Daegu area [1], and J. W. Yoon surveyed the architectural composition of them [2].

2 PREPARATORY STUDY ON KOREAN WOOD HOUSE

2.1 HOUSING MARKET OF MID TWENTIETH CENTURY IN DAEGU

Daegu had been the main administrative city of southeast part of Korea, Gyeongsangdo province, since the beginning of the seventeenth century and is fourth biggest city with about 2.5 million population now.

Since the end of nineteenth century the cities of Korean peninsula has been getting bigger very fast. Busan, Incheon and Wonsan opened ports to foreign trade and the nationwide trunk railway network was built. Among them, Gyeongbuseon railway from Seoul to Busan was one of the main route and Daegu station was the main point for trade. More and more people including both native Korean and the people from other countries mainly Japanese came to this city for industry employment or commercial business during Japanese colonial period of early twentieth century. The central area old town where had been in the city wall before demolish at 1906 was very crowded with population increase. During Korean War,

[1] Jaemo Cho, Kyungpook National University, Rep. of Korea, zozemo@gmail.com

https://doi.org/10.52202/069179-0533

Daegu was in the marginal front of the UN forces, so there was not serious damage at the central area.
More people from north area of peninsula gathered to this city, so the city needed big amount of housing construction for incoming population. For example, the housing problem of Daegu was most serious among big metropolises of Korea at the year of 1970. According to the news on 16 May, 1970 of The Dong-a Ilbo newspaper, while the shortages of house in Seoul was 50.6% and Busan was 56%, Daegu's house shortages was about 60% then.
In the Korean Peninsula, people's house had been only traditional wood structure of hanok, but at the beginning of the twentieth century the new building structures came from foreign countries. Brick wall structure of China or simple and light wood structure of Japan were increasing in the construction field. Also concrete structure was emerging even in the people's housing field. These new structures could make higher and wider building. Moreover the material price of wood building had increased more sharply than other materials.
In this situation, traditional hanok technology met several matter to solve.

(1) For price competitiveness, the construction cost of hanok must be down.
(2) In the urban site condition for housing, the composition of hanok must be more compact in the small site.
(3) To get good marketability, hanok must meet the needs and the sense of beauty of the ordinary people.
(4) Also, for some needs of larger inner living space adapting contemporary life, the traditional method of hanok structure must be changed to make span of column free space longer than before.

For these, the hanok builders had to develop their technology traditionally used for long time.

2.2 TRADITIONAL ROOF STRUCTURE OF KOREAN WOOD HOUSE

The traditional roof of hanok is a kind of cantilever structure. The timber cross beam is put on the columns of front and rear side and shout vertical column (daegong) is supporting purlin on it. If roof need more height, the second beam is used between daegong and top purlin. The purlins located at peak of roof slope and on the front / rear columns make triangle of roof shape and supporting rafters. The rafters make surface for roof slope with soil and rood tiles. This traditional method is similar to other countries like Chinese and Japanese wood structure, so it can be regarded as East Asian ancient wood structure shared in wide area.
In the research field of Chinese ancient architecture, there were 3 major types for making roof structure. For the biggest building, they used big girder and purlins; for smaller buildings such as local residence house, they used more thin columns and purlins without girder, otherwise, horizontally layered timbers are used like log house for small storage; but it is not so commonplace.
The traditional hanok is belong to the first type above even if it is not so big building. So hanok structure is very heavy not only because the girder has usually big cross sectional area but also the roof itself is heavy. The construction cost is also high. If the builders want light structure with cheap cost, they have to make newly modified structure instead of using traditional method.
Additionally, the roof of hanok has about 1 meter's eaves protruding for protect wood timbers and soil wall against rain fall from eaves' end. The cantilever rafters can make it. But in the small site, this outer space under eaves surrounding building mass should be located between the border line of lot and outer wall of building. It is not so effective land use method because there remains narrow and useless space behind the building.

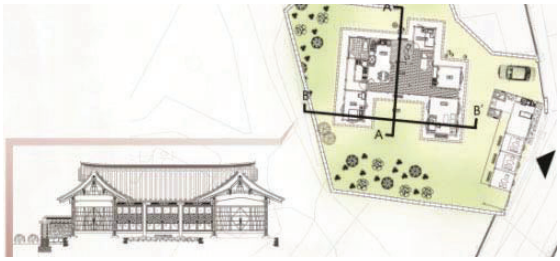

Figure 1: *traditional style hanok in Daegu*

3 GENERAL FEATURE OF WOOD HOUSE IN DAEGU

3.1 INTRODUCTION OF SURVEY

According to the survey, there remained 10,753 hanok architectures in the metropolitan Daegu city. This study is based on the survey the carried out for two years of 2012 and 2013 as mentioned above. Hanok is the typical architecture in Korea so the sizable of wood houses are belong to this type, but there are other types of wood structure such as Japanese or western style wood architecture. [3]
In the building register of Korea, the typology of structure is assorted like masonry structure (brick, block, stone and etc.), concrete, steel, wood, panel and so forth. In the category of wood structure, general timber structure, log house, and others are included; there is not specific tag of hanok or Korean traditional timber structure.
Before this survey there was not the official list of hanok, so the list of whole wood architecture including other types like Japanese, Chinese or western style wood buildings had to be listed up out of the whole building register. So the survey team had to define what makes hanok distinguished from other wood structure. Secondly, the investigators checked on each spot and confirmed 10,753 hanok buildings among 15,344 wood architectures in the list by on-site confirmation.
The ratio of hanok in the whole wood buildings was about 70% average; 35% at the central city (Jung-gu) whereas 87% at outskirt suburban area (Dalseong-gun). Hanok had been normally constructed wherever in the central area or outskirt, but after 1950 most cases were pointed at the

https://doi.org/10.52202/069179-0533

central city. It shows the population growth and urban centralization need more houses in the central city.
By district in detail, Dalseong-gun, the southwest suburban area, has 2,420 hanok and Juon-gu, central urban district, has 1,788 ones. The cases of Dalseong-gun where is the rural area with the largest district and lowest population density are traditional and dilapidated hanok houses while the cases of Jung-gu, the smallest district with high density are newly designed ones built from early to mid-twentieth century. The outskirt area surrounding central district has mass constructed hanok houses against housing requirements with population growth of 1960-1970s period. About 93% hanok (10,015 cases) are used for dwelling and others for commercial, religious, public use and empty houses.

Table 1: *distribution by year and district of hanok in Daegu*

District	~50	50s	60s	70s	80s	90~	null
Jung	552	283	261	208	190	1	256
Dong	491	199	232	313	146	44	35
Seo	235	260	316	191	561	1	4
Nam	46	164	415	300	148	6	27
Buk	165	143	303	278	198	6	4
Suseong	88	189	279	228	161	18	33
Dalseo	58	25	53	107	81	29	2
Dalseong	1,028	608	253	212	118	78	123

3.2 TYPOLOGY OF ARCHITECTRUAL PLAN AND ROOF

The investigating items are as follows; shape of plan and roof, materials of roof, rafters, columns, door & window's frame, outer wall, main gate, fence and the pavement of access alley. The major type of plan is I-shape in rural area and L-shape in central area while hanok with both wings is majority in Seoul. [4]

Table 2: *roof shape of hanok in Daegu*

Type	Number(case)	Ratio(%)
Gambrel roof	7,082	65.9
Hipped roof	1,917	17.8
Gable roof	1,085	10.1
Others	65	0.6
Unidentified	604	5.6
Total	10,753	100.0

In the whole city, L-shape and I-shape's ratio is 45.2% and 43.0% each. Even though L-shape is more difficult to build than linear shape hanok, L-shape of same building area could be built in smaller site. So, it is more efficient in the dense central area.
For the roof shape, 65.9% of hanok used the gambrel roof regarded as quality type. But the roof surface material was not so good. Traditional roof tile made of baked soil had only 5.2% whereas thin cement roof tile occupied 61.7%. Most of surveyed hanok cases were built at mid twentieth century when the fast construction with cheap cost house was needed. Wood house was commensurate with this kind of social need at the first time. But other materials that were supplied to the construction site like bricks, concrete and steel made change to the housing market. So, hanok builders had to develop or modify their traditional technique and construction method.

Figure 2: *examples of urban hanok Residential Areas composed with gambrel roofed L-shape hanok housing (Samdeok-dong 2ga and Namsan-dong 4ga, Jung-gu district)*

4 METHODS OF ROOF STRUCTURE MODIFICATION

4.1 LIFTED SQUARE SECTION RAFTERS

The major roof shape of hanok in Daegu is gambrel type; it means normally people like that roof shape and it has good marketability. But gambrel roof needs more expensive construction cost than other roof types. For both of price competitiveness and marketability, the roof structure had to be changed. Otherwise, the wood architecture of Korea uses timbers not only as structure but also as finishing materials itself. If the structural method is changed, the shape of the house also has the possibility to be changed. So structural modification also should be limited in the range of the similar shape of traditional hanok.
The house builders of that period wanted to make the familiar and popular image of tile-roofed traditional wood house using heavy timber frames with less cost in shorter construction time for adapting to housing market. Some of the builders chose the new simple method using sparsely arranged small square cross-section rafters affected by foreign architectural technology.
In detail, the structural elements from ground level to the purlins on the outer columns supporting rafters are designed like traditional ones while the cross sectional area of members such as columns, cross beams and purlins is smaller than traditional mothed. On the outer purlins, they put short vertical lumbers to lift up extra purlins with square sectional wood bar. On these new purlins, simple lumber rafters are put to make roof surficial structure. Also on the center of cross beam they put the lifter (daegong) to make roof triangle.

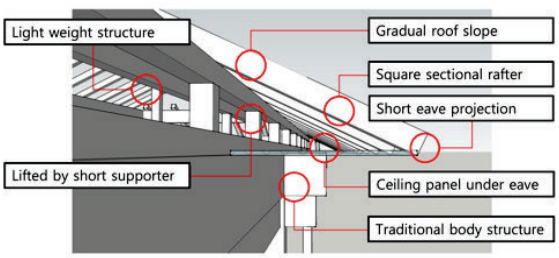

Figure 3: *Lifted square cross section rafters roof structure*

https://doi.org/10.52202/069179-0533

This newly modified roof structure is more simple and light in weight than traditional one, also the construction cost is cheaper.
Especially square sectional rafter is cheaper to make than traditional circular one. But the exterior of the house could not be qualified. So, they added ceiling panel under eave hiding small square sectional rafters lifted with short supporter on the purlin.
Though the roof structure had been changed, the main body and roof of the house has traditional image of hanok only except under eaves partially. So it looks like traditional hanok at the first glance. It can be called as hybrid wood structure. [5]

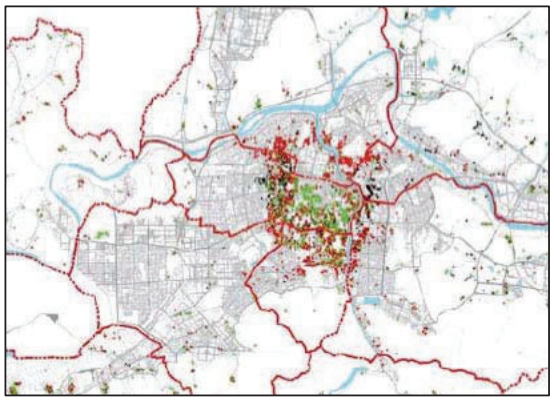

Figure 4: *spatial distribution of 'no rafter type' (red dots)*

In the survey, this kind of hanok is categorized as 'no (traditional) rafter type'. The number of cases is 4,633 and it is about 43.1% cases. These houses are located at the surrounding areas of Jung-gu district and most of them were built during 1960-1970s when the economic condition of the city was not so good. Most of them were built at very small site, so the courtyard is smaller than cases of other decades.

4.2 GAMBREL ROOF OF ASYMMETRIC EAVES

Other method for the urban hanok is making eaves asymmetric. The cases using this kind of eaves were distributed over all urban area of Daegu city, too.
For example, the case of 2504 Namsan-dong, Jung-gu hankok block can be focused where hanok on a similar type were regularly arranged on also typical lots. Actually this urban area was unified one lot of farmland located at the suburban area on the cadastral map of 1911. It belonged to one person named Sihoo Kim and was changed to building site by land readjustment project during 1960s. It was divided into more than 20 small lots of about 136-145 square meters at 1972-1973 and transferred its ownership to each other person right after land dividing. Every 4 or 5 lots were arranged into a line from south to north and 2 meters wide alley was put between each line of lots. This method of land readjustment work was normally applied whole urban area surrounding old central area. But 136-145 square meters' lot is not enough size to build traditional hanok. [6]

Figure 5: *case of urban hanok area of 2504 Namsan-dong, Jung-gu (now destructed)*

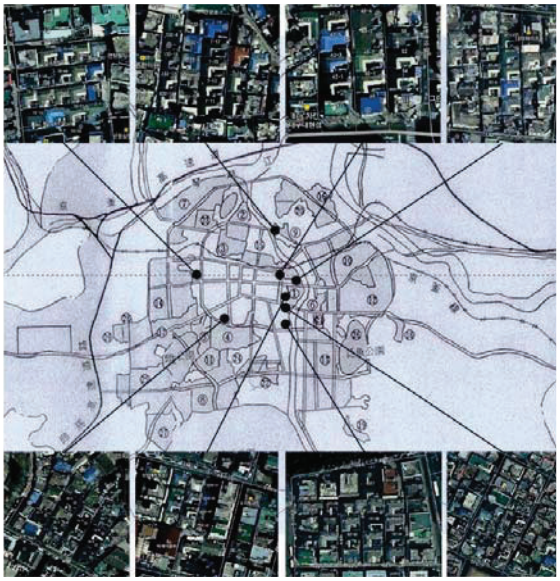

Figure 6: *hanok block made by land readjustment project*

On each lot, the house builder made typical L-shape plan house similar to each other. On the north part there was master bedroom, living room and 2 more bedrooms from west to east and kitchen and 1 more bedroom were at the west wing with courtyard on the southern east part of lot. This type of L-shape hanok was typical shape in Daegu city.
Usually hanok has 1,000~1,200mm projected eaves from outer wall. It is for shading inner space and preventing rain drop into the house. If the roof is gambrel or hipped roof, the eaves are surrounding the main body while gable roof has only 2 side eaves of the house.
People wanted the gambrel roof house, but it needs larger site area. House builders had to modify gambrel roof that could be built in the small area.
The normal eave projection length of more than 1,000mm is used at only 2 concave faces of L-shape plan house toward inner courtyard. Other faces have short eaves of about 400mm projected that is not enough to shading or preventing rain drops. From the structural viewpoint, this asymmetric eave roof is not good for balancing because angle rafter cannot be put on the exact position forming an angle of 45 degrees. But it is more attractive to housing market.

https://doi.org/10.52202/069179-0533

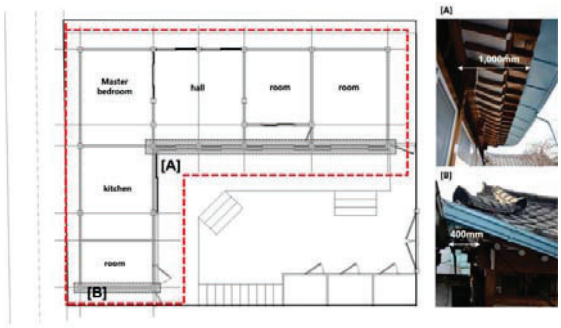

Figure 7: *Gambrel roof with asymmetric eaves*

4.3 NEWLY DEVELOPED ROOF STRUCTURE FOR LONG SPAN HALL

Using the lifted square sectional rafters and asymmetric eaves aims cheaper construction cost of hanok architecture for adaptation housing market's condition. But someone wanted to make bigger hanok with affordable cost. Usually residential hanok's longitudinal span is about 3.6m including 2.4-2.7m's room span and 0.9-1.2m width corridor. If the span is bigger, the cross beam has to more depth for supporting roof weight. But it needs more cost, too.

The case of 66-5, Jong-ro 2ga is the noteworthy one. It is located at the narrow long alley of Jin-golmok where is southern east part of central old quarter used to be inside of Daegu city wall of Joseon Dynasty (1392-1910). Land near Jin-golmok belonged to Dalseong Seo family's ownership. This rich and famous family made diverse style houses such as Western villa (now Dr.Jeong's children hospital), 2-story brick house (now Daegu Korean Chinese Association building) and several hanok houses designed by each architect or house builder. It means 66-5 hanok was also designed not for mass housing even though there is no documental evidence.

Figure 8: *changing of the site of Byeongwon Seo's mansion (1911, 1938, 1949, 1957 and 1977)*

66-5 hanok was the part of Byeongwon Seo's mansion and had been used as restaurant (Jin-golmok Sikdang, now closed) recently. His mansion was composed more than four buildings of family's residential part, reception and living part and 2 more attached buildings of servant's quarters. Buildings of Seo's mansion were built during 1920s. These three parts are used for each commercial function of restaurant on each lot, now. On the first a land registration map of 1911, there was large lot including all buildings of the mansion. It is very deferent from the case of 2504, Namsan-dong. [7]

66-5 hanok was the reception and living part of the mansion. This reception room needed bigger space than traditional hanok so the designer had to make new structural method for it. This 66-5 hanok is also L-shape but the longitudinal span of the north wing is about half as large again as normal hanok.

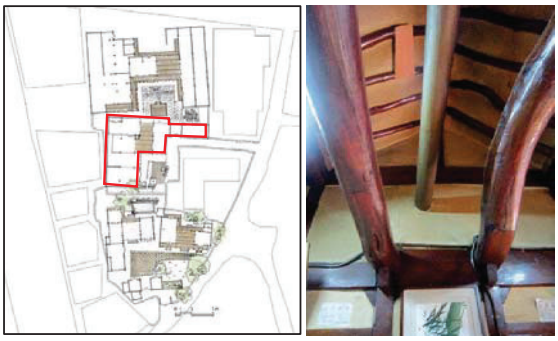

Figure 9: *plan of Byeongwon Seo's mansion and structure of 66-5 hanok*

The 66-5 building is composed with 2 narrow wings of 3-purlins span and they made L-shape structural frame. Additionally wider 2-purlins span is added forward courtyard side for making 5-purlins span. For this wider span, this building has two more cross beams orthogonal direction to the main cross beam. It is so abnormal case among hanok structure. In this way, the builder could make long span with only small sectional timbers.

The rafter is traditional one but thin and sparsely laid. And they didn't put ceiling hiding roof structure. If the builder used the light weight roof structure of lifted square sectional rafters, ceiling had to hide the roof structure and could not make the traditional image of hanok.

Figure 10: *worm's eye view of 66-5, Jong-ro 2ga, Jung-gu*

5 CONCLUSIONS

Daegu's housing market of mid twentieth century was diversified so fast. Hanok builders had to develop their own technique to catch up with the new market trend struggling against other emerging house types. They had to build hanok with low cost in short time. Modified roof

https://doi.org/10.52202/069179-0533

structures such as using lifted square section rafter or asymmetric eaves were their strategy to survive in the market. And the case of 66-5 hanok shows that the traditional technique also could make wider span than before. These modified wood houses shows that there were diverse needs at the housing market.

But after this period wood house lost the popularity in the market as modern house building technology, and reinforced concrete construction was widely utilized.

Traditional carpenters were replaced not only in the housing market but also wood construction field. New wood architecture technology such as lightweight wood frame house was imported and nowadays most of wood houses are built with 2x4 style engineered lumber hided in the wall panel. The traditional carpenter's technology is also used for new hanok with high cost; it is still popular partially. Recently, so called 'neo-hanok' is developed using BIM based automatic design technology, precut with CNC, engineered lumber, metal joint and others.

But it shows possibility and tendency of the evolution of hanok.

REFERENCES

[1] J. M. Ha, S. G. Son, W. H. Yang, C. D. Park and S. K. Park.: A Study on the Plan Types of Urban Traditional Housing. Journal of Architectural Institute of Korea, 12(5):75-84, 1996.

[2] J. W. Yoon. A Study on the Characteristics of the Spatial Composition at the Modern Korean Houses after the Time of Enlightenment in Daegu Province. Journal of the Korean housing association, 14(6):87-93, 2003.

[3] K. M. Lee, C. H. Shin, J. M. Lee and C. W. Ok.: Korean Hanok Survey 2013-Daegu, Jeonju. AURI National Hanok center, Sejong, 2013.

[4] I. H. Song. A study on the types of urban traditional housing in Seoul from 1930 to 1960. Ph. D. Dissertation, Seoul National University, Seoul, 1990.

[5] J. H. Park and J. M. Cho.: A Study on the Light-weight Roof Structure of Urban Hanok - Focused on the Cases in Jung-gu, Daegu. Journal of Architectural History, 22(6):23-34, 2013.

[6] B. K. Kim and J. M. Cho.: A Study of Urban Hanok Clustering in the area of 2504 Namsan-dong, Jung-gu, Daegu. Journal of Architectural Institute of Korea(Planning and Design), 30(12):165-176, 2014.

[7] J. M. Cho. The Typology and Development of Hanok in Daegu During Modern Age. Journal of Korean studies, Academia Koreana 58:57-106, 2015.

https://doi.org/10.52202/069179-0533

World Conference on Timber Engineering Oslo 2023

Hybridization of Western Timber Truss and Traditional Korean Roof Shape in the Early 20th Century

Jeonghyun Kim[1], Jihong Kim[2], BongHee Jeon[3*]

ABSTRACT: During the Japanese colonial period of Korea(1910-1945), the Japanese colonial government built Korean style buildings using Western timber truss. Although these buildings look like traditional Korean pavilions in terms of exterior form, they have significantly different structural frames. The architectural features originated from Korean tradition, such as protruding eaves and curved roof shape, were achieved by different structural system and methods which were developed from late 19th to early 20th centuries in Japan. In this study, we analyzed the hybridized roof structure and how the prototypical methods and their variants were implemented.

KEYWORDS: Japanese colonial period of Korea, tradition, Western truss, eclectic roof structure, roof shape

1 Introduction

Every culture has their way of constructing a building, which is repeatedly used throughout its history. Wooden roof structures, composed of orthogonal columns, beams, purlins and inclined rafters, were one of the most conventional methods used in East Asian architectural tradition. As modernization came to East Asian countries, Western architecture was introduced. Governmental offices, hospitals and courthouses which symbolized new political and social order began to be built in Western styles such as Neoclassicism. Also, traditional-style buildings, whether they are newly built or renovated, were influenced by Western technologies such as truss structures and metal reinforcements.

Adoption of Western truss became the focus of architectural discourse in this time of transition. However, it was not an easy task to adopt Western truss directly to the traditional structural system. East Asian traditional buildings have curved roof profile which is different from linear roof profile generated by trussed structure. In addition, the roof shapes are not only relevant to the roof structures but also closely related to the entire structural system of a building.

While other East Asian countries underwent more complicated transition, Western truss was adopted by Japan during Meiji period after the devastating earthquake of 1891. During the Japanese colonial period of Korea(1910-1945), expositions were held in cities of Japan and Korea by Japanese colonial Authorities. To promote their colonial reign, they built Korean Pavilion, *Cho-seon-kwan*. (Kang, 2004) These buildings look like a Korean traditional pavilions in terms of exterior forms, they have significantly different roof structures. Architectural features from Korean tradition, such as protruding eaves and curved roof shapes, were implemented while Western truss was adopted and hybridized to the roof structures. They have eclectic features which have not been addressed in East Asian Modern architectural studies.

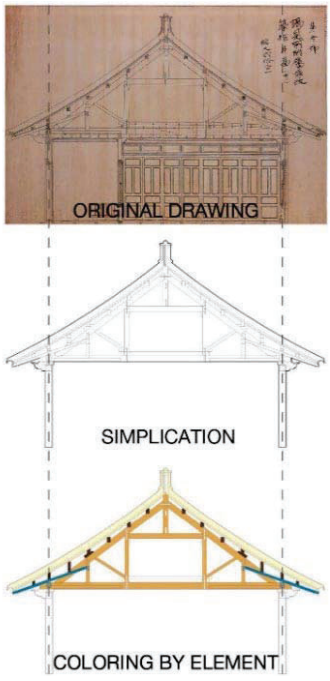

Fig.1. Making of Analytic Diagram

National archives of Korea, the depository of historical records of the country, have recently constructed digital

[1] Jeonghyun Kim, Hongik University, Republic of Korea, jekim@hongik.ac.kr
[2] Jihong Kim, Cultural Heritage Administration, Republic of Korea, jekim@hongik.ac.kr
[3*] Contact Author: BongHee Jeon, Dept. of Architecture and Architectural Engineering · Institute of Construction and Environmental Engineering · Institute of Engineering Research, Seoul National University, Republic of Korea, jeonpark@snu.ac.kr

https://doi.org/10.52202/069179-0534

data base of buildings built in Japanese colonial period. The data base contains schematic plans and detailed drawings of the buildings. It allowed us not only grasp a concept of the design principle, but also understand the structural frames and the concrete methods of construction. (National archives of Korea, 2008) For this study, we selected 22 cases which showed eclectic roof structure and Korean-style roof shape. The drawings include very detailed information so that we need to abstract them into diagrams. (Fig.1)

2 Adoption of Western Truss in Japan and Korea

1861 in Japan, Western wooden truss had been introduced to the Nagasaki steel plant. After a heavy earthquake had struck the Nobi province, the traditional wooden structure was questioned in terms of its safety. Japanese architects and scholars began to pay attention to Western truss and applied it to their projects. (Im, 2011)

Even in repair work for the traditional building, which is national monument, like Todai-ji, Western truss was applied. Daibusuden of Todai-ji had been through precarious situation since 19th century because of the structural defect. It had enormous size of roof which needed structural reinforcement. Although the problem had been addressed since 1880s, the repair work was not started until early 20th century. Architects and scholars who were educated in Western society led the repair work.

The repair work of Daibusuden of Todai-ji, had been continued from 1906 to 1913. According to the construction record, we could find out that the box truss structure had been used to reinforce the roof. (Fig.2) Central structure was replaced by truss and the principle of truss was widely used to replace wooden structural members. Wooden joints were reinforced by bolts and nuts. (Fig.3) Using Western roof tile reduced the roof load by 12%. (Coaldrake, 1994)

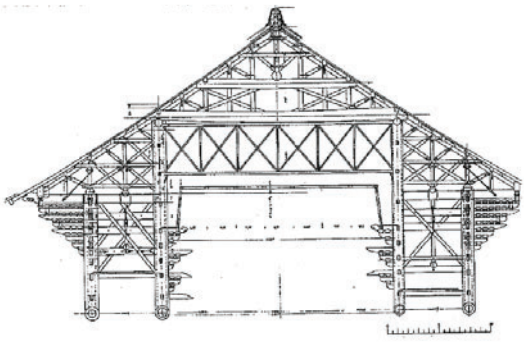

Fig.2. Daibusuden of Todai-ji: sectional detail of restored and rebuilt truss after Meiji restoration project (Coaldrake, 1994)

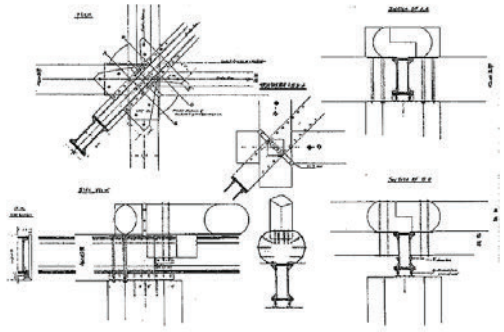

Fig.3. Daibusuden of Todai-ji: Iron pins and plates added to reinforce framing at the time of the Meiji restoration project (Coaldrake, 1994)

In Korea, figuring out the conditions of western influence on roof structure in this era is more complex because the modernization process was led by multiple political groups, the Korean government, Western and Japanese colonialists. In the late 19th century, the first building, *Beon-sa-chang*(1884) (Fig.4) which have a trussed roof was constructed by the Korean government. (Im, 2011)

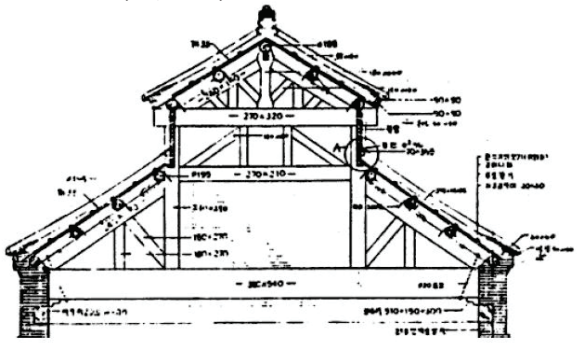

Fig.4. Section Drawing of *Beon-sa-chang* (Im, 2011)

Meanwhile, many other trussed structures were built by western people, mostly for religious purpose. Those buildings had totally western style roof both aesthetically and structurally. In prior studies, these eclectic roofs were classified into three groups, Korean style, Japanese style and eclectic style. Although the classification is clear, it does not represent the eclectic feature embedded. For example, the eclectic style, according to the prior classification, includes too many different types of roofs. It should have been classified much more carefully. In this study, we suggest two points of view to investigate the eclectic roof structure. The first one includes the technic and design integrity of eclectic roof structure and the second one includes the historical origin of the technology. Through this study, we get to expand the scope of discussion about eclectic roof structure in that period.

https://doi.org/10.52202/069179-0534

3 Eclectic Features of Roof Structure

The roof of traditional Korean pavilions is characterized by protruding eaves, curved roof shape and wooden frame composed of rafters and purlins.

Rafters are supported by purlins and categorized into two kinds, short and long rafter. (Fig.5) In order to achieve a desired roof profile, each kind of rafters have different slope. By piling soil on the rafters, a smooth roof profile is achieved. Another noticeable feature of traditional Korean roof is that the long rafter acts like a cantilever to make protruding eaves.

Fig.5. Roof structure of Korean traditional building

Fig.6. Structural diagram of Western truss (Queen truss)

Western Truss, on the other hand, consists of different set of building elements. The most significant difference is the use of diagonal members. (Fig.6) The diagonal part of a trussed roof is not composed of multiple building elements. Rather, the side part of the roof consists of a single long rafter and supporting columns. This structure does not have protruding eaves or curved roof shape.

The complexity in representing the traditional shape of roof emerges here. The typical Western truss itself does not allow for the traditional elements implemented. Several technological references published around 1910s-1930s suggest solutions to this problem. Fig.7 is a drawing from 'Improved Japanese House Structure(改良日本家屋構造)' which was published in 1919. The illustration shows how to adopt a truss structure having protruding eaves and curved roof shape. Based on this reference, we infer that using some additional building elements was a relatively ordinary method to represent a traditional shape of roof with truss structure.

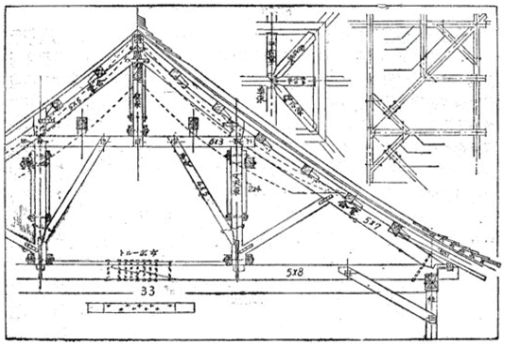

Fig.7. Roof structure of Korean traditional building (Tamotsu, 1919)

4 Structural Characteristics of Hybrid Roof

In this chapter, we will investigate roof structure of eclectic roofs and figure out what methods are specifically implemented. In doing so, we hope to answer the following questions: How are Korean and Japanese traditional timber frame structure and Western truss integrated in hybridized manner? How are the traditional shapes, such as roof curvature, protruding eaves, ornamental elements generated?

As shown in Fig 8, the use of Western truss is a remarkable attribute of the eclectic roofs. While King Truss and Queen Truss structure were widely used, there were several variations of structure which reveal the hybridized characteristic of the eclectic roofs. Case D and Case C show how the King and Queen Truss are implemented.

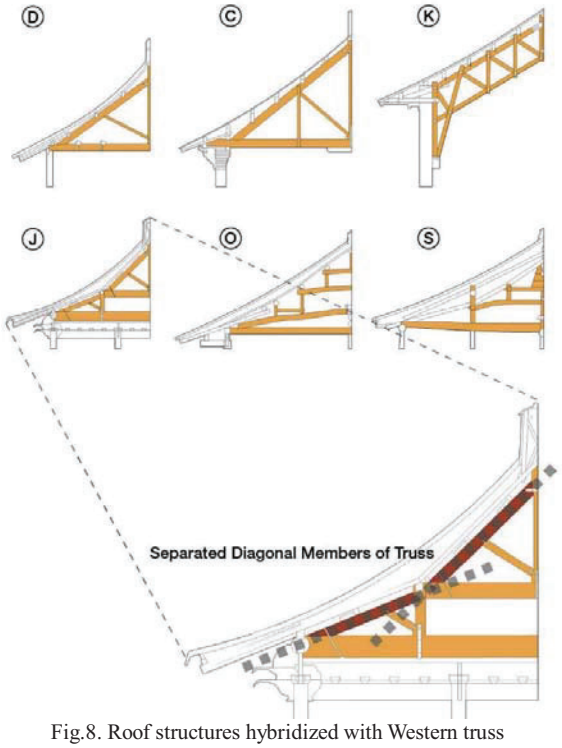

Fig.8. Roof structures hybridized with Western truss

In Case J, we note the separation of a diagonal member of truss structure. The upper and lower

https://doi.org/10.52202/069179-0534

diagonal members have different angles to make the curved roof profile. Case K shows a very unique roof structure which provides higher space for exhibition. In Case O and Case S, the features from traditional Japanese and Korean roof structures were still dominant over truss. However, both of them have double-layered roof structure to avoid piling soil.

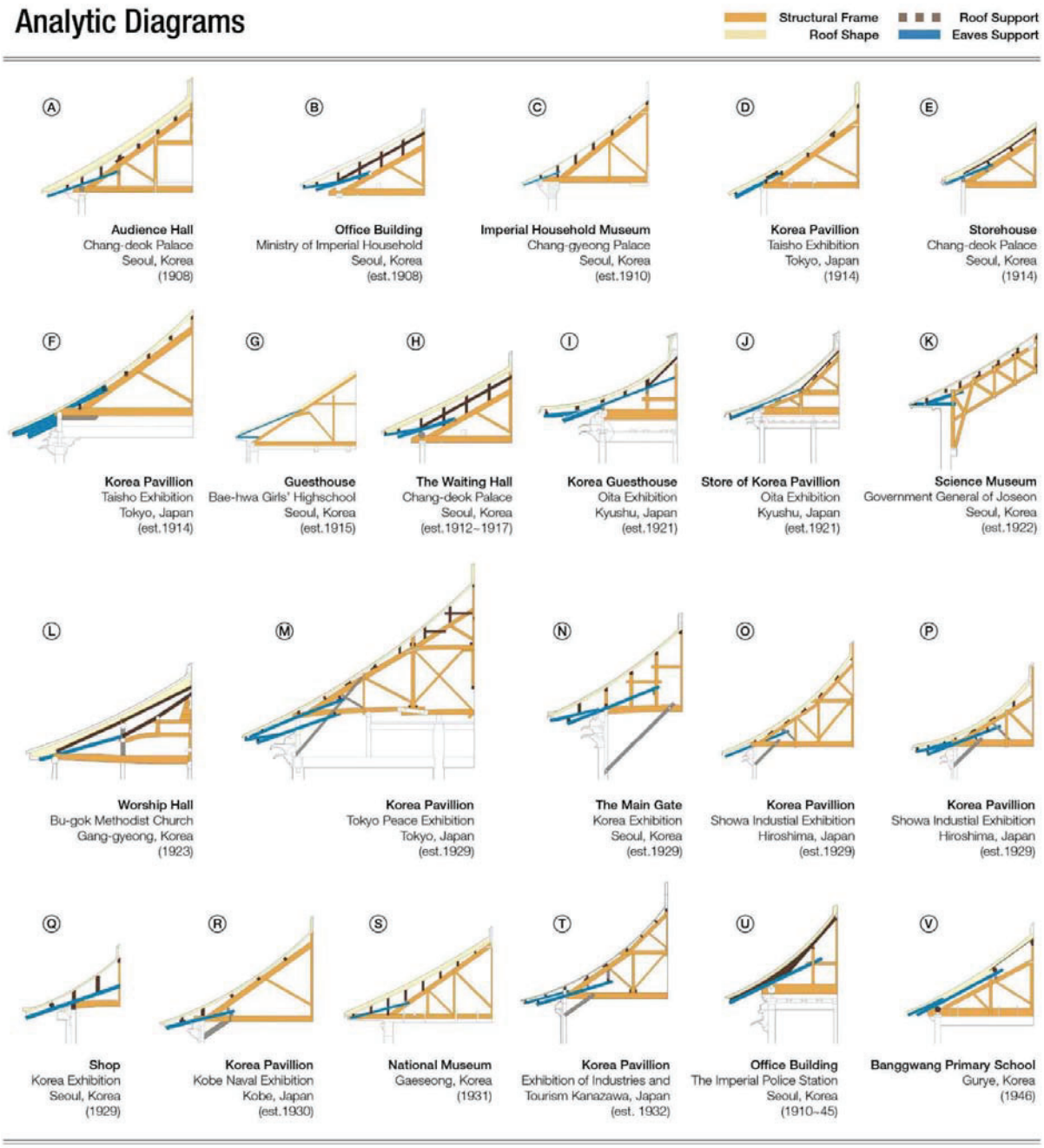

https://doi.org/10.52202/069179-0534

In most cases, the ways of making a curved roof profile are similar. To generate a curved form, vertical supports are added on top of the diagonal member of the truss structure. This seems to be the most common method of making curved roof shape. (Fig.9) The significance of this method is that it reduces the load of the roof considerably by making double-layered roof structure instead of heavy soil.

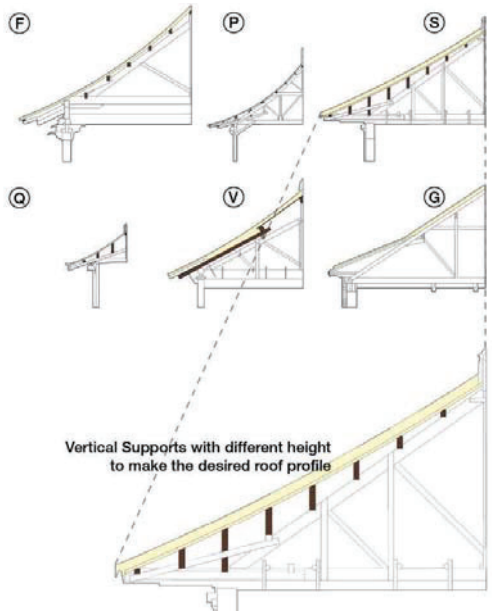

Fig.9. Roof profile generated by vertical supports on truss

Protruding eaves are an essential part for a roof structure because it prevents rain water from entering the enclosure. Unlike traditional protruding eaves, auxiliary rafters are added to the main trussed frame usually on a diagonal member. (Fig.10) Several kinds of auxiliary rafters are used case by case. The connections between auxiliary rafters and the main truss structure are usually located upon a diagonal member of truss structure.

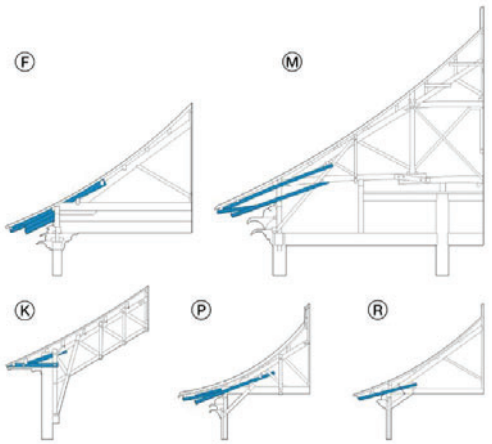

Fig.10. Protruding eaves generated by axillary rafters

We also found similar method of making protruding eaves in 'Improved Japanese House Structure(改良日本家屋構造)' published in 1919. Four methods are illustrated in this book and the second one from the top shows the same method as our cases. (Fig.11) It is a noticeable fact that a particular building element called "桔木"(tied building element) was used. Fig.12 illustrates the positions and the intervals of rafters.

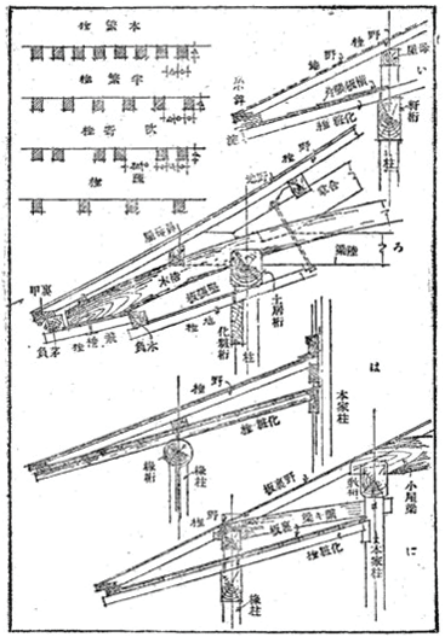

Fig.11. Protruding eaves
(Tamotsu, 1919)

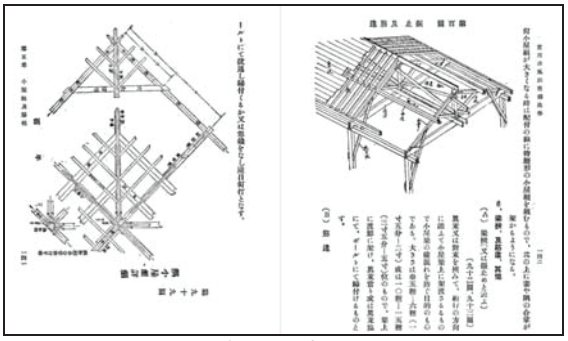

Fig.12. Rafters
(Tamotsu, 1919)

While the main structural frame is replaced by truss, some specific parts of the traditional building elements still remain without structural function. They separated the ornamental part from the building elements and attached to the façade. For example, the end parts of a traditional beam maintain its sculptural shape even though the beam itself does not exist anymore. (Fig.13)

https://doi.org/10.52202/069179-0534

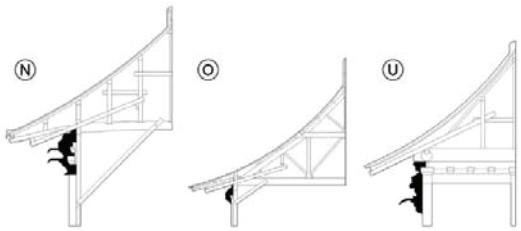

Fig.13. Ornaments from traditional building elements.

5 Conclusion

The cases from the Japanese colonial period of Korea clearly exhibit the eclectic features. Through this study, we found the prototypical method of construction of these buildings and the variations shown in each case. The eclectic features in these cases can be summarized in three points. For the structural frame, adopting the Western truss was a main issue. The cases have different degrees of hybridization as a result of integrating traditional roof structure and Western truss. While most cases clearly represent an embrace of Western truss, certain components and connections of them had been modified to generate traditional roof shapes. Architectural features from traditional Korean pavilion, such as protruding eaves and curved roof shape, were implemented through various new methods instead of traditional way. Roof curvature is implemented by using vertical support on top of truss and the protruding eaves are formed by auxiliary rafters. Ornaments from traditional building elements which lost their original function and lacked authenticity were selectively retained to mimic traditional roof shapes.

Through reviewing the eclectic roofs of the colonial period buildings in Korea, we found an underlying eclecticism between the intention to pursue traditional Korean roof shape and the actual implementation of adopted-technology during cultural exchanges in the earth 20th century.

Acknowledgement

This research was supported by Basic Science Research Program through the National Research Foundation of Korea (NRF) funded by the Mistry of Education (2021R1F1A1062048)

This research was further developed after the abstract submission of WCTE 2023 and published in an academic journal (MDPI: Buildings), titled as 'Korea at the Exhibition: Making the Appearance of Korean Style with 'Hybrid Roof' in Early 20th Century'. This paper shows the initial stage of the research and includes a part of the findings in the published journal paper mentioned above.

REFERENCES

1) Crouch, D. and Johnson, J. (2001) Traditions in Architecture: Oxford
2) Im, J., Kim T. (2006) The receptiveness of Wooden Roof Truss in Modern Age of Korea: Journal of Architectural Institute of Korea v.24 n.8
3) Joo, S. (2010) Characteristics of Building the Modern Facilities administrated by the Japanese Government General in Korea: Seoul National University
4) Kang, S. (2004) Adoption of architectural modernism in modern facilities during Japanese ruling era of Korea : focused on expo buildings, elementary schools and apartments: Seoul National University
5) Lee, K. (2009) The Building Principles and Typology of Roof Structure in the East Asian Wood Architecture: Seoul National University
6) National archives of Korea. (2008) A Bibliographical Introduction of Architectural Drawings in the Japanese Colonial Period vol.1: National archives of Korea
7) National archives of Korea. (2009) A Bibliographical Introduction of Architectural Drawings in the Japanese Colonial Period vol.2: National archives of Korea
8) Park, C., Kim M and Kim T. (2008) A Study on the Type and Characteristics of Wooden Roof Truss in Modern Age of Korea – Focused on the Survey Reports of Modern Architectural Properties: Journal of Architectural Institute of Korea v.24 n.8
9) The Academy of Korean Studies. (2009) Architectural drawing collection in modern period: The Academy of Korean Studies,
10) Coaldrake, W. (1994) Western technology transfer and the Japanese architectural heritage in the late nineteenth century: The Journal of The Society of Architectural Historians, Australia and New Zealand
11) Tamotsu, Y. (1919) Improved Japanese House Structure: Japanese Industrial Society

https://doi.org/10.52202/069179-0534

World Conference on Timber Engineering Oslo 2023

Seismic Performance Evaluation of a Traditional Wooden Townhouse that did not Collapse in the 2016 Kumamoto Earthquake

Yasuhiro Nambu[1], Toshihiko Ninakawa[2], Hiroki Tabata[3] and Akio Kitahara[4]

ABSTRACT: This study presented the results of the structural investigation of a *machiya*, a traditional Japanese wooden townhouse, located in Kumamoto City, which is not significantly damaged during the 2016 Kumamoto earthquake. The seismic performance of the house was evaluated using the limit strength calculations. In addition, the effect of through columns, which were present various parts of the house, was considered using a simplified model. Time history response analyses were conducted using the observed ground motion records, and the differences in the maximum response story drift due to the presence or absence of through columns were investigated. The following findings were obtained. 1) The main house had no full mud walls in the ridge direction on the first story, and most of the columns were through columns. 2) The base shear coefficients for the main house were 0.02 in the ridge direction for a story drift of 1/60 rad. The horizontal resistance was considerably small. However, the house did not collapse during the 2016 Kumamoto earthquake. 3) Time history response analyses were conducted with and without considering through columns, and the results showed that the maximum response story drift in the first story was reduced by 10-45% when the effect of through columns was considered.

KEYWORDS: Traditional wooden building, Japanese townhouse, time history response analysis

1 INTRODUCTION

In 2016, a series of earthquakes struck Kumamoto, a prefecture in Japan's southern island of Kyushu. The first earthquake, with a magnitude of 6.2, occurred on April 14th, followed by a second earthquake, with a magnitude of 7.0, on April 16th. These earthquakes caused widespread damage and loss of lives in the region. Many traditional wooden townhouses called *machiya* in Furumachi, Kumamoto-shi were also damaged by earthquakes (the PGA of the nearest earthquake observation record was 432 gal for the foreshock and 552 gal for the mainshock [1]), and several *machiyas* confirmed to have collapsed [2, 3]. However, not all *machiyas* that do not meet current Japanese seismic regulations suffered serious damage. To gain new insights into improving the seismic performance evaluation method of *machiyas*, we focused on several *machiyas* that were not severely damaged by the earthquakes and still exist in the town. Therefore, we investigated one existing *machiya* in Furumachi to understand the structure and evaluated its seismic performance at the time of the earthquakes. This paper reports the results of the structural investigation and the evaluation of seismic performance through time history response analysis.

2 TARGET HOUSE AND DAMAGE SITUATION

Figure 1 shows the exterior and interior of the target house. The target house was built around 1915–1917.

(a) South (front) exterior

(b) Interior (2nd story, facing north)

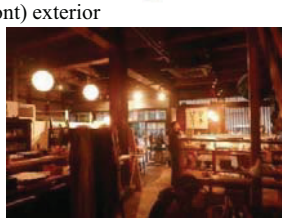

(c) Interior (1st story, facing south)

***Figure 1**: Exterior and interior views (taken on 10/18/2019)*

[1] Yasuhiro Nambu, Dr. Eng., Assist. Prof., Kyushu University, Japan, nambu@arch.kyushu-u.ac.jp
[2] Toshihiko Ninakawa, Dr. Eng., Prof., Kyushu University, Japan, ninakawa@arch.kyushu-u.ac.jp
[3] Hiroki Tabata, M. Eng, Kyushu University (present affiliation is Ministry of Land, Infrastructure, Transport and Tourism), Japan, tabata-h8310@mlit.go.jp
[4] Akio Kitahara, Dr. Eng., Prof., Pref. Univ. Kumamoto, Japan, kitahara@pu-kumamoto.ac.jp

https://doi.org/10.52202/069179-0535

The building was originally a store that handled oil and wheat; thus, brick walls were built on the gable side of the site boundary from the beginning to prevent fire. In 1992 and 2007, renovation work was carried out on the main building, and reinforcing steels were attached to the brick wall on the west side at that time. Then, the damage situation during the 2016 Kumamoto earthquake is described.

Figure 2 shows the damage situation of the main house of the residence (taken on May 14, 2016).

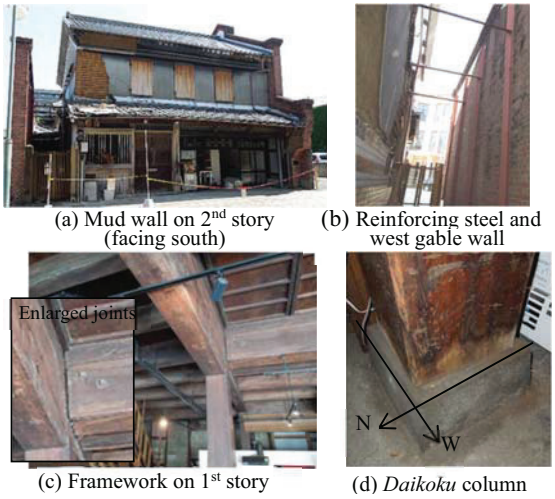

(a) Mud wall on 2nd story (facing south) (b) Reinforcing steel and west gable wall

(c) Framework on 1st story (d) *Daikoku* column

***Figure 2**: Damage after the earthquake (Photo taken 5/14/2016)*

As shown in Figure 2(a), the mud wall on the west side collapsed on the south (front) and north (back) sides of the 2nd story of the house. On the west gable end, as shown in Figure 2(b), the mud wall around the column where the reinforcing steels of the brick wall are connected collapsed. Inside the house, there was some deformation at some of the joints in the framing where wooden pegs were used, and there was some looseness, such as the horizontal timber coming out of the column, as shown in Figure 2(c), but no major damage, such as a broken column, was confirmed. As shown in Figure 2(d), the base of the pillar of the *daikoku* column located near the center of the house had rotated slightly clockwise, based on the marks remaining on the foundation stone, and had moved about 1 cm to the east as a whole. As there was no major damage, the house was repaired by repainting the mud wall and is still in use today [3].

3 STRUCTURAL INVESTIGATION

We conducted a field survey of the house on November 18, 2019. We measured each part of the house as part of a structural investigation, created floor plans and elevation drawings, and identified the structural elements and types of the house. In addition, we conducted microtremor measurements as a vibration survey, but the results are not reported in this paper (refer to [4 for the results]).

The structure of each part is shown in Figure 3, and the framework and floor plan of the house are shown in Figures 4 and 5, respectively.

(a) Cross beam (b) Diagonal strut

***Figure 3**: Structure of each part (taken on the day of the structural investigation)*

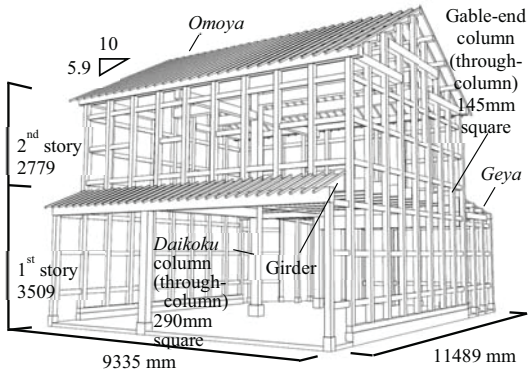

***Figure 4**: Framework of target house (from the south)*

The house consists of a two-story main house called *Omoya* and attached east and west side structures called *Geya*. The height of each story is 3,509 mm (from the ground to the top of the beam) for the first story and 2,799 mm (from the top of the second-floor beam to the top of the purlins) for the second story. The column bases are placed on the top of the foundation stones and not anchored to them. All the gable-end columns are 145 mm square cross-section, and the *daikoku* column (central supporting pillar) is 290 mm square cross-section.

The gable-end columns are spaced at 910-mm intervals and are through columns that reached the purlins, with ridge beams and purlins tenoned into them to form through-column structures. Here, the "cross beams" in Figure 5 represent the beams mortised into the columns. The species of the framework could not be identified. The gable-end exterior walls of the *Omoya* are entirely mud walls, while the non-gable sides have no exterior walls on the first story and are mainly mud walls on the second story. The wall thickness of the exterior walls is approximately 130 mm on both the gable-end and non-gable sides. Additionally, the visible penetrating tenons (called *nukis*) are in the interior side of the exterior walls. The cross-sectional dimensions of the *nuki* includes a width of 30 mm and a depth of 145 mm, with three levels installed on each story's mud walls. There are no interior walls. The first floor is a dirt floor, and the second floor is a board floor. At the level of the roof beam level, diagonal struts measuring 120-mm width and 160-mm depth were installed. The roof is covered in pantile roof for both the *Omoya* and *Geya*. The east-west brick walls are laid in English bond with a thickness of 460 mm. The west brick wall is reinforced with equal-angle steel sections with a width of 100 mm and height of 100 mm (thickness unmeasured) and is connected to the gable-end columns of the *Omoya*, with three reinforcements installed at 910-

https://doi.org/10.52202/069179-0535

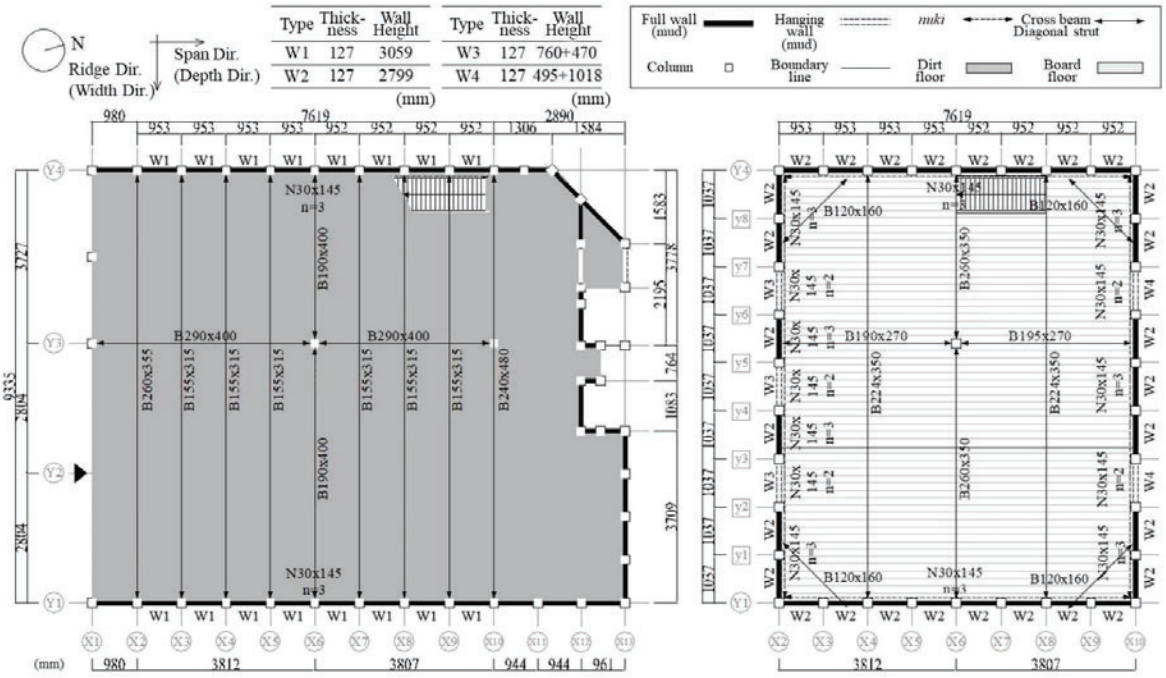

(a) 1st story (Only dirt floor show ground level) (b) 2nd story (Only board floor show 2nd floor level)

***Figure 5**: Floor Plan (mm)*

mm intervals. The east brick wall and the gable-end of the *Omoya* are in contact, but the details of the contact area are not visible. It should be noted that there is a wooden detached house on the north side of the property, separated by a courtyard, but it is not structurally connected to the *Omoya*.

4 SEISMIC PERFORMANCE EVALUATION BY LIMIT STRENGTH CALCULATION

The seismic performance of the target house was evaluated using the limit strength calculation, which is generally used to evaluate the seismic performance of traditional wooden buildings. The calculations were based on [6]. The skeletal curves of the house were calculated from the bearing elements, such as the full mud walls, hanging walls, and column-beam joints, and the response values during earthquakes were obtained using the response spectrum method with equivalent linearization. This report gives an overview of the influence of through columns as a starting point for evaluating the seismic performance of the target house. Therefore, the influence of the *Geya* and brick walls were ignored to simplify the analysis.

4.1 CALCULATION OF WEIGHT

The weight of the first story was calculated as the weight from the upper half of the first story to the lower half of the second story, and the weight of the second story was calculated as the weight from the upper half of the second story to the roof. The weight was calculated by multiplying the area of each part of the house by the fixed and live loads specified in Articles 84 and 85 of Order for Enforcement of the Building Standards Act of Japan, respectively, and the values in [5]. The live load is 600 N/m^2 in residential rooms when calculating seismic forces. The thickness of the mud wall is assumed to be 127 mm (obtained by subtracting the distance of 18 mm between the column surface and the wall surface from the column section dimension of 145 mm), and the roof is assumed to be covered with clay pantiles. The weight of the structural frame was calculated by multiplying the volume of each member by the specific gravity provided in [5] and assuming cedar for the columns and Oregon pine for the beams. Table 1 presents the calculated values of weight and mass, along with the floor area and height of each story.

***Table 1**: Results of weight and mass calculation*

	Weight [kN]	Mass [kg]	Floor area [m^2]	Story height [m]	Weight per unit area [kN/m^2]
2nd story	236.9	24150	71.1	2.799	3.33
1st story	183.8	18740	71.1	3.509	2.58
Total	420.7	42890	142.2	6.308	2.96

4.2 SKELETON CURVES

The skeleton curve of the target house was obtained by summing the skeleton curves of the bearing elements for each story and direction. The bearing elements considered include the full mud wall, hanging wall, *nukis*, and column-beam joints. The skeleton curves for each bearing element were determined based on [6]. It is assumed that all mud walls fail in shear. The skeleton curve of the column-beam joints was obtained by assuming that the bending moment M at the joint (using the dowel-and-

mortise joint "*one-hozo komisen-uchi*") is equally distributed between the upper and lower floor columns. Then, the resulting M was divided by the height of each story to obtain the shear force Q and R curves. The M and θ curves used here for the dowel-and-mortise joint were determined based on [6], and it was assumed that θ was equal to the story drift angle R. The results of the skeleton curve calculation are shown in Figure 3.

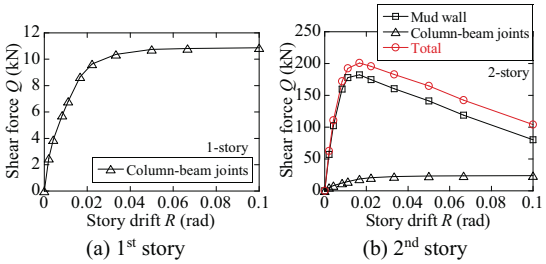

***Figure 6**: Skeleton curves for each story*

In the ridge direction, the lateral resistance of the first story is extremely small compared to that of the second story. It should be noted that the base shear coefficient C_y, which is obtained by dividing the shear force at the first story drift of 1/60 rad by the total weight of the *Omoya*, is 0.40 in the span direction and 0.02 in the ridge direction, indicating that the value in the ridge direction is extremely small.

4.3 MAXIMUM RESPONSE STORY DRIFT

The limit strength calculations were performed using the weight and skeleton curve data. The input data is based on the Japanese design response spectrum, which assumes Type 2 ground classification. The damage limit for rare earthquakes was evaluated using a story drift angle of 1/120 rad, while the safety limit for very rare earthquakes was evaluated using a story drift angle of 1/20 rad [6]. The maximum response story drift angle in each direction is listed in Table 2. Here, "rare earthquakes" and "very rare earthquakes" are input seismic motions used in the structural design in Japan. These earthquakes are classified based on their rarity and represent the maximum seismic force that a building may experience during its lifetime. Specifically, "rare earthquakes" refer to earthquakes that are expected to occur once in approximately 50 years, while "very rare earthquakes" refer to those that are expected to occur once in 500 years.

***Table 2**: Results of weight and mass calculation*

	Target response spectrum	Limit [rad]	Max. response story drift [rad]	
			1st story	2nd story
Span direction	Rare	1/120	1/309	1/518
	Very rare	1/20	1/24	1/242
Ridge direction	Rare	1/120	1/47	1/2731
	Very rare	1/20	No response	

The maximum response story drift in the span direction is within the damage and safety limits for each story. However, the maximum response story drift in the ridge direction is significantly larger on the first story compared to the span direction, and the response value cannot be obtained in the event of a very rare earthquake, resulting in significant seismic performance deficiencies.

As a result, the target house did not collapse during the Kumamoto earthquake even though, based on the limit strength calculations, it would experience a significantly large maximum response story drift in the ridge direction when subjected to seismic motion equivalent to a very rare earthquake. The target house has relatively large through columns, which are not considered in the limit strength calculations. It is speculated that these through columns may affect the seismic performance because the horizontal resistance in the ridge direction at the first story is extremely low. In the following section, we investigate this possibility using time history response analysis.

5 SEISMIC PERFORMANCE EVALUATION BY TIME HISTORY RESPONSE ANALYSIS

In this section, time history response analysis is conducted using a model that considers through columns and a model that does not consider them in the ridge direction of the target house, and the seismic performance of the house is evaluated based on the results.

5.1 ANALYSIS METHOD

We assumed the house to have no torsional motion on a rigid floor and modeled it as a two-mass system. An overview of the analysis model is shown in Figure 7. For the ridge direction, two types of models were used: a model without through columns (referred to as the NTC model; see Figure 7(a)) and a model with through columns (referred to as the TC model; see Figure 7(b)). The through columns were assumed to be linear elastic bodies and modeled with pinned connections to each mass point via rigid beams. Note that the connections between the through columns and the ground were assumed to be pinned.

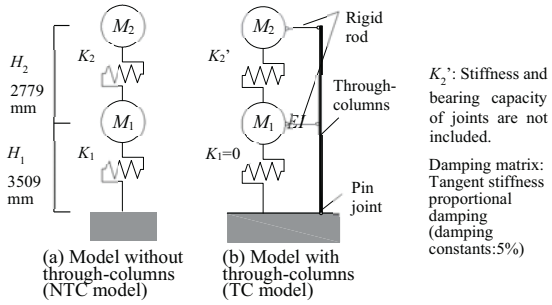

***Figure 7**: Overview of analysis models*

The restoring force characteristics (skeleton curve + history characteristics) of the equivalent shear springs K_1 and K_2 on each story are determined by the bi-linear + slip model, which is the sum of the bi-linear and tri-linear slip

https://doi.org/10.52202/069179-0535

models, representing the history characteristics of the wooden structure (Figure 8).

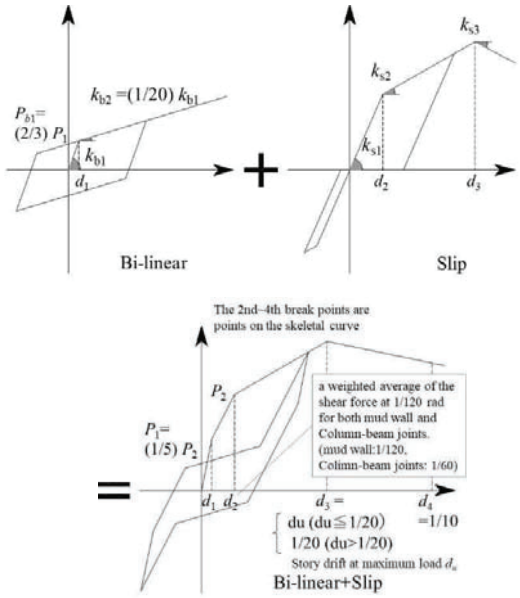

***Figure 8**: Hysteresis model*

The equivalent shear springs K_1, K_2, and K_2' on each model's story are determined as follows: K_1 and K_2 are based on the skeleton curve calculated in the previous section, while K_2' is based on the skeleton curve obtained by subtracting the skeleton curves of the column-beam joints from the skeleton curve of K_2.

The skeleton curves of the equivalent shear springs K_1, K_2, and K_2' for each model are determined as follows:

1) The second breaking point (yield point) was determined as a point on the skeleton curve of each story of the target house, and the story drift at the breaking point was determined based on the inter-story shear force ratio of the mud walls and column-beam joints. Specifically, the story drift of the second breaking point was assumed to be 1/120 rad when only the mud wall was present, and it was assumed to be 1/60 rad when only the column-beam joint was present. When both elements were present, the inter-story shear force at 1/120 rad of both elements was used as a weight to determine the story drift of the second breaking point by weighted averaging.

2) The third breaking point (ultimate point) was taken as a point on the skeleton curve of each story of the target house and set to the value of the story drift R_u at the maximum load. However, if R_u > 1/20, it was taken as the point at 1/20 rad.

3) The degraded stiffness was set to the stiffness connecting the third breaking point and the point on the skeleton curve of the target house at a story drift of 1/10 rad.

The validity of the above settings must be verified in future studies. Figure 9 shows the skeleton curves of the shear springs on each story used in this study, together with the skeleton curves calculated in the previous section. The analysis limit was the intersection of the degraded stiffness of the slip model and the horizontal axis (inter-story shear force = 0), and the analysis was terminated at the point of intersection.

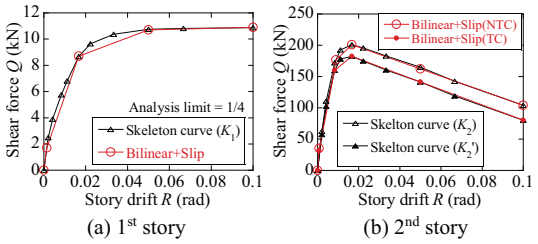

***Figure 9**: Skeleton curves of shear springs for each story*

The history characteristics were assumed to be the same as in [7]. The relationship between the first breaking point load P_1 and the second breaking point load P_2 for the bi-linear + slip skeleton curve is expressed by the following equation [7]:

$$P_1/P_2 = 1/5. \quad (1)$$

The ratio of the bi-linear component at the first breaking point P_{b1}/P_1 is given by the following equation [7]:

$$P_{b1}/P_1 = 2/3. \quad (2)$$

The ratio of the second to first bi-linear component stiffness k_{b2}/k_{b1} is assumed as the following [7]:

$$k_{b2}/k_{b1} = 1/20. \quad (3)$$

The through columns exert horizontal resistance when there is a difference in the story drift between the first and second stories. The relationship between the external force and the deformation acting on through columns is shown in Figure 10 [8].

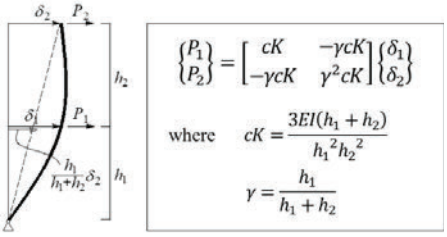

***Figure 10**: Through columns modeling* [8]

Through columns are assumed to be linear elastic. The stiffness matrix of the TC model was obtained by adding the stiffness matrix of the through columns shown in the figure to that of the NTC model. The second moment of area I for the through columns was calculated by adding the second moment of area I_c and I_{cd} for each of the 18 gable-end columns with a cross-section of 145 mm and the central column (*Daikoku* column) with a cross-section of 290 mm. The columns were assumed to be made of

cedar, and the elastic modulus E was used as the basic elastic modulus for an ungraded lumber, E_0 = 7.0 kN/mm^2, from [9].

In addition, for the through columns, the failure due to bending moments M_c and M_{cd} at the first-floor column head of each of the gable-end and *daikokubashira* columns, respectively, is considered based on the difference in story drifts between the first and second stories. M_c and M_{cd} were calculated using the following equations based on the maximum difference in story drifts $|R_2 - R_1|_{max}$ obtained from the time history response analysis:

$$M_c = \frac{3EI_c}{H_1 + H_2}|R_2 - R_1|_{max} + M_\theta, \quad (4)$$

$$M_{cd} = \frac{3EI_{cd}}{H_1 + H_2}|R_2 - R_1|_{max} + 2M_\theta, \quad (5)$$

where M_θ is taken as the maximum bending moment at the column-beam joint (M_θ = 4.0 kNm). H_1 and H_2 indicate the height of each story, respectively.

An additional $2M_\theta$ is added for the *Daikoku* column as two beams are attached in the ridge direction. However, when considering through column failure, it does not consider the maximum bending moment at the column-beam joints M_θ in the TC model. The bending strength of each column $M_{cu}$and M_{cdu} was calculated by multiplying the reference strength F_b of the column by the effective section modulus Z_e, where Z_e is 3/4 of the full section modulus Z of the column considering the section deficiency (M_{cu} = 8.5 kNm and M_{cdu} = 67.7 kNm). The bending strength F_b of the column was taken as the average value of H1, E70 (cedar) in [10], which was 40.9 kN/mm^2. If the bending moment M_c or M_{cd} generated in each column exceeds the bending strength (M_{cu} or M_{cdu}), the column was considered to have failed.

The mass matrix was calculated using the masses of each story, M_1 and M_2, as determined in the previous chapter. The story heights, H_1 and H_2, were determined based on the results of the structural investigation presented in Section 3. The damping was assumed to be proportional to the instantaneous stiffness, and the damping coefficient was set to 5%. The P-Δ effect was not considered in this study.

Figures 11 and 12 show observation points of the input seismic waves and the seismic waveforms and acceleration response spectra, respectively.

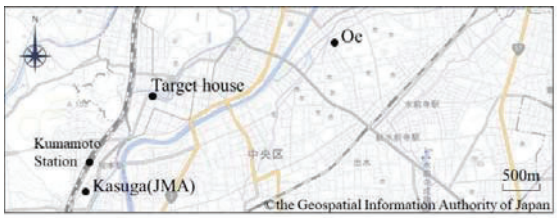

***Figure 11**: Target house and earthquake observation sites*

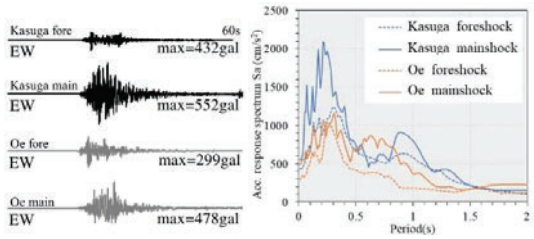

(a) Input earthquake (b) Response Spectrum

***Figure 12**: Target house and earthquake observation sites*

The input seismic waves were based on the observed seismic waves of the 2016 Kumamoto earthquake [11], using the fore and main shock observed seismic waves at the observation points near the target house in Kasuga, Nishi-ku, Kumamoto City and Oe, Chuo-ku, Kumamoto City. The seismic waves used were the EW component corresponding to the ridge direction of the target house. In addition to the input of the mainshock, continuous earthquake ground motions with an interval of 60 s between the fore and main shock were also considered in this study.

5.2 ANALYSIS RESULTS AND EFFECT OF THROUGH COLUMNS

In this study, the relationship between the inter-story shear force and the story drift for each floor obtained from the analysis is shown in Figure 13 using the example of continuous input of observed earthquake waves in Oe. The results of the NTC model are shown in (a) and (b) while those of the TC model are shown in (c) and (d). Furthermore, the time history changes of the story drift for the first story are shown in Figure 14.

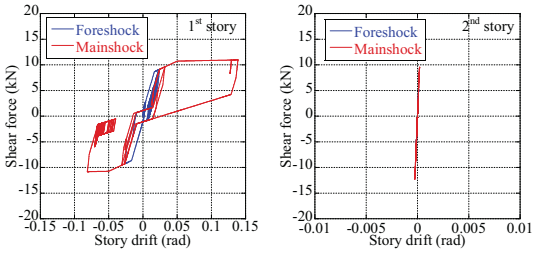

(a) NTC model

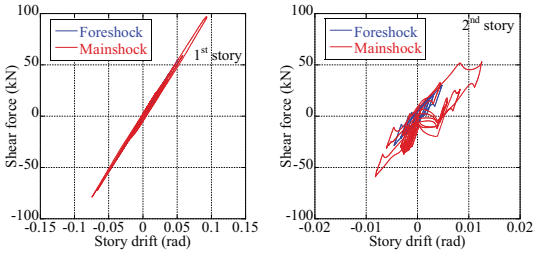

(b) TC model

***Figure 13**: Relationship between the inter-story shear force and the story drift (input: Oe continuity)*

https://doi.org/10.52202/069179-0535

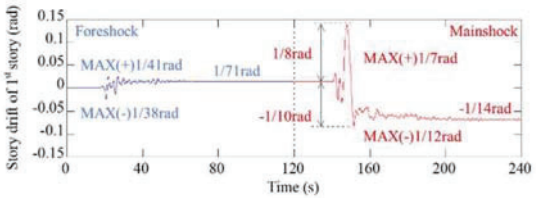

(a) NTC model

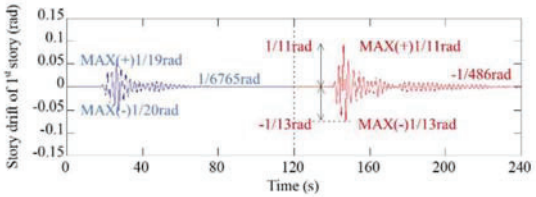

(b) TC model

***Figure 14**: Time history changes of story drift for the first story (input: Oe continuity)*

In the TC model, the second story deforms elastically within its range, while only the first story undergoes significant deformation. In comparison to the NTC model, the maximum response story drift of the first story in the TC model decreases by approximately 36% from 1/7 rad to 1/11 rad. Furthermore, for the second story, the ratio of the maximum response story drift to that of the first story is approximately 0.2% in the NTC model, but it increases to approximately 14% in the TC model, and the second story undergoes plastic deformation in the TC model. These results confirm the effectiveness of through columns in equalizing the story drifts of each story. It is apparent that residual deformation from the foreshock remains in the NTC model based on the observation of the time history response of the story drift of the first story, while it is not observed in the TC model. These tendencies were also observed with the Kasuga seismic input.

Table 3 summarizes the results of time history response analysis for four input ground motions, each analyzed in eight patterns with and without through columns considered. M_c/M_{cu} and M_{cd}/M_{cdu} represent the ratios of the bending moment to the bending strength of the gable-end columns and the Daikoku column, respectively. The ratio of 1.0 or greater indicates that the column is prone to breaking.

***Table 3**: Analysis results*

Earthquake		Model	Max. response story drift (rad)		Residual story drift of 1st story (rad)	Max. bending moment of column (kNm)		M_c/M_{cu}	M_{cd}/M_{cdu}
			1st story	2nd story		M_c	M_{cd}		
Kasuga	main shock	NTC	1/15	1/4122	1/20	12.0	135.5	0.8	1.1
		TC	1/17	1/178	1/4216	6.5	104.3	0.4	0.8
	continuity	NTC	1/9	1/4595	1/44	17.3	220.5	1.1	1.8
		TC	1/17	1/181	1/4900	6.5	104.4	0.4	0.8
Oe	main shock	NTC	1/9	1/3644	1/22	17.9	230.7	1.1	1.9
		TC	1/11	1/79	1/531	10.0	159.6	0.6	1.3
	continuity	NTC	1/7	1/3819	1/14	21.0	280.2	1.3	2.2
		TC	1/11	1/80	1/486	10.0	159.7	0.6	1.3

The results of the time history response analysis for the NTC model show that the maximum response story drift of the first story exceeded the safety limit of 1/20 rad, reaching 1/15 and 1/9 rad for the Kasuga and Oe mainshocks, respectively (Table 3). However, the limit strength calculations indicate that the NTC model collapses in a very rare earthquake, as shown in Table 2. Although the earthquake characteristics and intensities assumed in the time history response analysis and the limit strength calculations are different, the results of both methods are not significantly contradictory.

Figure 15 shows the maximum response story drift of the first story for each model and input.

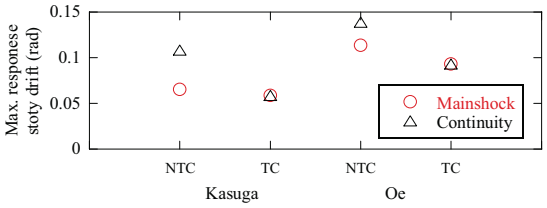

***Figure 15**: Absolute value of the maximum response story drift for the 1st story*

The response story drift of the first story is larger for the continuous input than for the mainshock input. In the TC model, the maximum response story drift of the first story was reduced by approximately 10–20% for the mainshock input and 33–45% for the continuous input compared to the NTC model. Additionally, in the TC model, no residual deformation was observed in the foreshock due to the seismic input used in this study, resulting in similar response values for the continuous input and mainshock input alone. Although the maximum response story drift of the first story exceeded the safety limit of 1/20 rad established in Section 4.3 for both models, the analytical results suggest that the through columns act as bearing elements and suppress the story drift of the first story.

In the target house, according to Table 3, the result of the Kasuga and Oe mainshocks was the breaking of the gable-end column or the Daikoku column in the NTC model, while only the Daikoku column broke due to continuous input from the Oe mainshock in the TC model. It should be noted that there were no through column breakage that was confirmed as damage in the 2016 Kumamoto earthquake for the target house.

Subsequently, the residual story drift for each model and each seismic input for first story is shown in Table 3 and Figure 16.

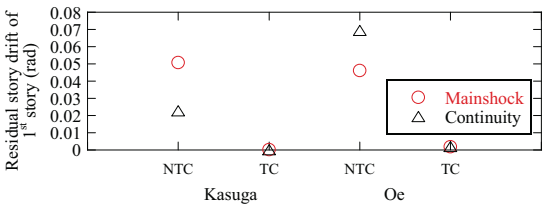

***Figure 16**: Absolute value of the residual story drift for 1st story*

For all cases, the residual story drift for each model was smaller in the TC model than in the NT model, suggesting that the through-column had the effect of reducing the residual story drift. However, in this study, it should be noted that for the TC model, there was no plasticization observed for the second story to generate residual story drift during the foreshock. Moreover, the assumption was made that the through column was a linear elastic body, and that the through column and each mass point were connected by rigid bars (rigid floor assumption), which may have increased the effect of the through column.

6 CONCLUSIONS

This study presented the results of the structural investigation of a machiya, a traditional Japanese wooden townhouse, located in the historic district of Furumachi in Kumamoto City, which is not significantly damaged during the 2016 Kumamoto earthquake. The seismic performance of the house was evaluated using the limit strength calculations commonly used for assessing the seismic performance of traditional wooden townhouses. In addition, the effect of through columns, which were present various parts of the house, was considered using a simplified model. Time history response analyses were conducted using the observed ground motion records from the earthquakes that occurred in Kasuga and Oe in 2016, and the differences in the maximum response story drift due to the presence or absence of through columns were investigated. The following findings were obtained.

1. The main house (Omoya) had no full mud walls in the ridge direction on the first story, and the gable-end columns (145 mm square cross-section) and a Daikoku column (290 mm square cross-section) were reached to the purlins, forming a post-dominant structure.
2. The base shear coefficients for the main house were 0.4 in the span direction and 0.02 in the ridge direction for a story drift of 1/60 rad. The horizontal resistance in the ridge direction was considerably small. If the effect of through columns is not considered in the limit strength calculation, the maximum response story drift in the first story in the ridge direction would be extremely large, but the house did not collapse during the 2016 Kumamoto earthquake.
3. Time history response analyses were conducted with and without considering through columns, and the results showed that the maximum response story drift in the first story was reduced by 10–20% during the mainshock and by 33–45% during continuous input when the effect of through columns was considered.

Therefore, it is suggested that through columns act as bearing elements, potentially reducing the maximum response story drift in the first story. However, it should be noted that the results are subject to assumptions, such as the validity of the rigid floor assumption and the linear elastic behavior of through columns. Furthermore, the stiffness of the second story was much larger than that of the first story. Based on these results, we developed a method for incorporating the effect of through columns into the limit strength calculations.

ACKNOWLEDGEMENT

We would like to express our sincere gratitude to the owners and stakeholders of the target house, Mr. Michikiyo Yamakawa of Kumamoto Association of Architects & Building Engineers, and the students of the Kitahara Laboratory at Prefectural University of Kumamoto and the Ninakawa Laboratory at Kyushu University for their invaluable support in conducting the structural investigation. Without their generous cooperation, this study would not have been possible.

REFERENCES

[1] Japan Meteorological Agency: Seismic Intensity Map, https://www.data.jma.go.jp/

[2] Kurashige K., Kitahara A. and Miyazato A.: Earthquake Damage of Wooden Buildings in the Kumamoto City due to the 2016 Kumamoto Earthquake, AIJ Kyushu Chapter architectural research meeting, No.56, pp605-608, 2017.3. (in Japanese)

[3] Architectural Institute of Japan: Report on the Damage Investigation of the 2016 Kumamoto Earthquakes, pp112-113, 2018.6. (in Japanese)

[4] Nambu Y., Tabata H., Kitahara A. and Ninakawa T.: Structural Performance Evaluation of Townhouses that did not Collapse in the 2016 Kumamoto Earthquake - A Townhouse with Continuous Columns in Furumachi, Kumamoto City - Part2: Microtremor Measurement Result and Limit Strength Calculation, Architectural Institute of Japan Summaries of technical papers of annual meeting, C-1, pp.633-634, 2020.9. (in Japanese)

[5] Architectural Institute of Japan: Recommendations for Loads on Buildings (2015), p132, 2015.2. (in Japanese)

[6] The editorial committee of design manual for traditional wooden buildings: A manual of aseismic design method for traditional wooden buildings including specific techniques for unfixing column bases to foundation stones, Gakugei Shuppansha, 2019.6. (in Japanese)

[7] Isoda H., Kawai N.: HYSTERESIS MODEL OF WALLS ON JAPANESE CONVENTIONAL CONSTRUCTION: Study on seismic behavior of wooden construction, Journal of Structural and Construction Engineering (Transactions of AIJ), Vol.72, No. 616, pp.157-163, 2007. 6. (in Japanese)

[8] Architectural Institute of Japan: Recommendation for Structural Calculation of Traditional Wood Buildings by Calculation of Response and Limit Strength, 2013.2. (in Japanese)

[9] Architectural Institute of Japan: Standard for structural design of timber structures, 2006.

[10] Forestry and Forest Products Research Institute (強度性能研究会 : Strength and Performance Research Group): 「製材品の強度性能に関するデータベース」データ集(Database on Strength and Performance of Lumber Products)

[11] Japan Meteorological Agency: Strong-motion observation data, https://www.data.jma.go.jp/

https://doi.org/10.52202/069179-0535

World Conference on Timber Engineering Oslo 2023

Development of Timber Roof Frames in Korean Modern Architecture

Kangmin Lee[1], Don-Son Woo[2]

ABSTRACT: This study tracks the introduction of foreign timber roof frames into Korean architecture. The foreign timber roof frame introduced in the modern era had not only Western truss but also Japanese conventional timber structure. The traditional roof structure in Korea involves stacking horizontal timber members in a grid shape and placing rafters on top, resulting in thick and heavy horizontal members. To accommodate the introduction of Western trusses, a compromise form was created based on this traditional understanding. However, during the Japanese colonial period, the two foreign roof frames occupied a more dominant position in state-run architecture than that of traditional Korean architecture. Japanese roof frames were applied to small and complex buildings, and Western trusses were applied to large buildings with simple functions. The hidden part of the roof of traditional Korean buildings was also replaced by truss or Japanese roof frame. Both foreign roof frames were designed using *Roof Framing Plan*, and the span and spacing of the structures were determined according to the traditional measuring unit, K. The two types of roof frames shared roles based on their respective strengths and could be used interchangeably. These foreign roof frames were mainstream in modern Korean architecture until reinforced concrete structures became widely distributed.

KEYWORDS: Korean modern architecture, roof frame, timber truss, Japanese roof structure, scale unit

1 INTRODUCTION

Korea has a rich tradition of wood construction, dating back centuries. At the end of the 19th century, two foreign technologies were introduced. This resulted in three types of timber roof frames being used in buildings: the traditional Korean roof frame, the Western truss structure, and the Japanese conventional roof structure. These structures were influenced by one another and coexisted in the majority of buildings until the reinforced concrete structure became more common. This paper aims to summarize the development process of the modern Korean timber roof frames, focusing primarily on the drawings of state-run architecture preserved in the National Archives of Korea.

2 TRADITIONAL TIMBER STRUCTURE AND INTRODUCTION OF FOREIGN ROOF FRAMES

2.1 TRADITION OF KOREAN ROOF CONSRUCTION

One of the defining features of traditional Korean roof structures is the absence of trusses. Instead, horizontal beams are stacked on vertical columns to create right-angled frames, with the beams and short posts supporting the purlins directly. The number of the purlins was limited because they were not only bulky and weighty, but also given Confucian symbolism. [1] It is common for five or seven purlins to be used in formal buildings. The building with the largest number of the purlins in Korea is *Gyeonghoeru* Pavilion in *Gyeongbokgung* Palace, which was rebuilt in 1867, with 11 purlins arranged in a 28.5m span. Therefore, in Korean architecture, the purlin is conceptually more like a longitudinal beam than the purlin used in typical truss structures. Above the purlins, a series of rafters are arranged, and then topped with earth and roof tiles to create a heavy roof.

Figure 1: *The Anglican Church, Ganghwado Island, built in 1900.*

Because the horizontal beams transmit the load to the columns at the intersection with the purlins, the arrangement of the columns creates a square module, which is called *Kan*. *Kan* was the basic unit for combining and dividing spaces. The size of *Kan* determines the horizontal length of the members in the roof structure, which is usually consistent with the dimensions of the

[1] Kangmin Lee, Korea National University of Arts, Republic of Korea, leekaang@karts.ac.kr
[2] Don-Son Woo, Korea National University of Arts, Republic of Korea, woods@karts.ac.kr

https://doi.org/10.52202/069179-0536

Kan or is twice or three times as long. This consistency in structure and space is a shared feature of East Asian wood structures, including China, Korea, and Japan. Prior to the 20th century, one *Kan* was typically about 2.4 meter in houses and more than 3 meter in public buildings in Korean architecture, while it was recognized as about 1.8 meter in Japanese architecture. [2]

Although Western-style architecture had become prevalent in modern large-scale construction, traditional Korean roof frames are still used in some cases. For example, the Anglican Church of Figure 1, built in *Ganghwado* Island in 1900, is an example of how the basilica structure can be completed using Korean traditional building techniques. This reflects the missionaries' desire for self-sustaining church architecture in Korea. [3] From *Janglim* Church in 1892 to *Pyeongbuk Jeongju* Church in 1938, a total of 38 churches with Korean traditional timber structures were identified. These structures evolved to emphasize the facade of the basilica, add bell towers, and widely use brick walls. [4]

2.2 INTRODUCTION OF FOREIGN ROOF FRAMES IN KOREA

In the late 19th century, foreign timber roof frames were introduced along with buildings that served new functions such as factories, government offices, and churches. Since most of these buildings were designed by foreign architects, their space, design, and structure were all different from traditional Korean architecture. However, the brick walls and the two- or three-story buildings with trussed roofs became the representative form of modern Korean architecture. Western-style houses began to be built in the palaces as well as the foreign settlement at the open ports. Starting with *Gwanmungak* Pavilion in *Gyeongbokgung* Palace in 1888, several Western-style buildings were built in *Gyeongunggung* Palace during the Great *Han* Empire (1897-1910). [5] Accordingly, the use of Western truss frames became widespread in high-level architecture. The truss structure was also applied to repair the traditional buildings in 1908 in the project of renovating the *Injeongjeon* Hall of *Changdeokgung* Palace in pursuit of the *Meiji* Palace in Japan, replacing the invisible part of the existing traditional roof frame. [6] Based on the traditional understanding of building techniques, in some cases, structures were compromised with each other. *Beonsachang* Factory of Figure 2, Korea's first timber trussed building, was built in 1884 as a weapon-making factory. Its trusses were fabricated within the traditional concept of placing posts on a thick beam. All members are thick and heavy, and traditional mortise and tenon joints that do not use hardware have been applied. The use of cylinder-shaped round purlins can also be seen as an inheritance of the Korean building tradition. [7] The cross-sectional areas of the top chord, bottom chord, and post of the trusses at *Beonsachang* Factory are 648 ㎠, 2,052 ㎠, and 375 ㎠, respectively. These dimensions are from two to seven times larger than the average cross-sectional area of truss members since the 1920s. [8] This use of larger members can also be observed in the trusses of *Yongsan* Theological School, which was constructed in 1892. It can be interpreted as an adaptation process in the early stages of the truss structure's introduction.

Figure 2: *The Beonsachang Factory, Seoul, built in 1884.*

3 TIMBER ROOF FRAMES UNDER JAPANESE COLONIAL RULE

3.1 CHARACTERISTICS OF JAPANESE CONVENTIONAL TIMBER STRUCTURE

With the introduction of Western structural engineering in the *Meiji* period (1868-1912), traditional Japanese timber structures were criticized for being heavy in their roof design, having isolated columns, significant timber loss for joints, and temporary member fixation [9]. Especially in Japan, where there was a high risk of earthquakes, the traditional timber structure was improved to focus on enhancing seismic performance. This process led to the reinforcement of structures through braces, the use of hardware, and a method for tightening the foundation and column, which is known as *the Conventional Construction Method* in Japan, distinguishing it from the traditional one.

The Japanese conventional construction method favored the *kyouro-gumi* method, which was popular in private houses during the *Edo* period. The *kyouro-gumi* method involves first combining purlins that act as beams on columns to form an outer frame and then placing transverse beams on top of it [10]. This method has the advantage of being easier to add and move roof structures compared to the *orioki-gumi* method, in which transverse beams are joined first on the columns and purlins are placed on them. In addition, the *kyouro-gumi* structure is relatively lightweight. The conventional construction method was widely used not only in the private sector but also in public buildings by governments because it allowed for improved building performance while still preserving traditional building practices.

3.2 COLONIAL RULE AND STANDARDIZATION OF MODERN SPACES

The Joseon Government-General's government facilities were supplied with wood through *Yeongrimchang*, which was established during the Korean Empire. *Yeongrimchang* opened its headquarters in *Sinuiju* in

https://doi.org/10.52202/069179-0536

1907 to develop abundant timber in the two river basins bordering China, and later oversaw the entire Korean forest organization. *Yeongrimchang* began operating a direct sawmill in *Sinuiju* in 1909 and supplied timber for construction in earnest. [11]

In *Yeongrimchang*'s sawmill, logs were cut into lumber using the traditional measurement units S and K used in East Asia. One K translates into six S. Since one S corresponds to 30.303cm, one K corresponds to 1.818m. The lumber produced in the *Yeongrimchang* sawmill had general dimensions of 1S in width and depth and 4K in length, which corresponds to 7.272m. This lumber was superior in quality and size compared to that supplied to the private sector. [12] Additionally, various standardized 2K-long construction timbers were supplied with names indicating where they should be used. In some cases, timber was supplied by separately ordering the type and dimensions of timber according to the design document of the specific construction work.

As a result of Japan's annexation of Korea as a colony in 1910, the urgent need to establish colonial governance facilities quickly and affordably led to the construction of numerous timber structures. In this process, *the Joseon Government-General Building Standards* were enacted in 1916, and standard regulations were applied to buildings such as government offices, schools, hospitals, prisons, and official residences. Standardized designs were repeatedly reproduced through *the Common Drawings*. Among the blueprints of the 1910s, the application examples of *the Common Drawings* were found in the drawings of local courts, weather stations, secondary education facilities, national hospitals, and other facilities. [13] The use of standardized construction members and building plans became widespread and characterized the typical form of roof structures.

3.3 DECLINE OF TRADITIONAL KOREAN ROOF STRUCTURE

During the modernization process, traditional Korean roof frames were marginalized in favor of Western-style truss structures and improved Japanese-style roof structures, which were exclusively used for constructing modern facilities. In the 1910s, many Korean traditional buildings were renovated and repurposed as government offices or schools, but these renovations were limited to changes in floor plan and elevation. Moreover, any new additions were constructed in Western or Japanese styles, rather than in the traditional Korean style. The use of traditional Korean timber structures was limited to community facilities in rural areas with strong national conservatism or houses for Koreans. While the number of such buildings was not insignificant, the potential for expanding and developing traditional Korean architecture was limited.

The decline of traditional Korean timber structures can be attributed to the malicious intent of colonial rule. However, weaknesses in the architectural industry contributed to this decline as well. The large and heavy structures of traditional Korean buildings made construction economically inefficient, and their lack of braces and hardware were considered vulnerable to earthquakes. Specifically, the government sawmill did not provide timber of an appropriate size for Korean-style structures. The cross-sectional width and depth of timber used in modern trusses in Korea ranged about 120-180×120-240mm, with a decreasing trend after 1920. [14] In contrast, traditional Korean structures utilized large, rounded sections for their members. As a consequence, architects were unable to effectively represent the Korean roof structure through efficient design drawings.

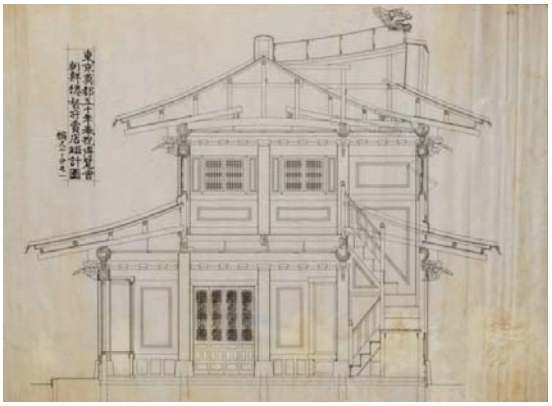

Figure 3: *The section drawing of a Korean-style pavilion with Japanese roof frame at the 50th anniversary Expo of Tokyo's capitalization, 1917, source: National Archives of Korea.*

Even in special situations where Korean-style buildings needed to be reproduced, Western trusses and Japanese roof structures were used as roof structures that were not visible from the outside. Several instances of Korean-style buildings having their roof structures replaced with trusses or Japanese roof structures can be observed in various buildings at *Gyeongbokgung* Palace and *Changdeokgung* Palace. Additionally, many Korean pavilions built at the *Taisho* Expo (1914), the 50th anniversary Expo of *Tokyo*'s capitalization (1917) of Figure 3, the Peace Memorial *Tokyo* Expo (1922), and the *Joseon* Expo (1929) were representative, and there were buildings with strong national colors such as the *Kaesong* Museum (1931) and the *Suungyo* Headquarters memorial service house (1936). [15]

4 CHARACTERISTICS OF TIMBER ROOF FRAMES IN KOREAN MODERN ARCHITECTURE

4.1 COMBINATION OF TRUSS AND JAPANESE ROOF FRAME

Most of Korea's early modern architecture had a western appearance. Until reinforced concrete construction became popular, the most monumental buildings, such as *Seokjojeon* Hall of *Gyeongunggung* Palace, were built of stone, while important government offices, such as the Ministry of the Interior in Figure 4, were made of brick, and the rest were built of wood. In either case, a timber roof frame was an essential requirement for building a

sloped roof. The choice of roof frame was determined by the span of the building. *Shoukou Hikkei*, translated into the Builders Manual, written by *Shishikichi Shibada* in 1886, explained that the king post truss could span up to 30S (9m), the queen post truss could span up to 45S (13.5m), and the compound one could span up to 60S (18m). [9] The truss was able to create a large space that was not easily achievable with traditional roof structures. Therefore, large and important buildings were built with trusses, while smaller buildings were built using Japanese conventional methods.

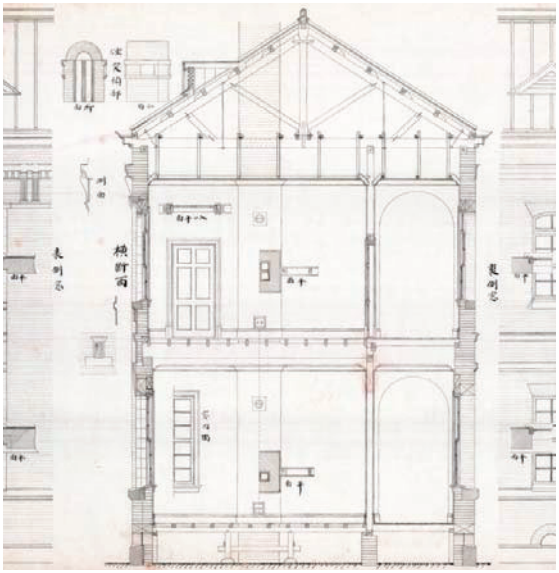

Figure 4: *The section drawing of the Ministry of the Interior, part, built in 1910, source: National Archives of Korea.*

The central government offices in Seoul, customs offices in ports, provincial government offices, police stations, and state-owned factories in each region used trusses in their roof structures, while Japanese official residences, local offices, branch offices, and weather stations used Japanese roof frames. [16] However, some hospitals, schools, courthouses, and prisons, which required rapid construction in the early colonial period, were built using Japanese roof frames regardless of size.

In modern state-run architecture in Korea, it was popular to arrange the main building and annexes in parallel, connecting them with a corridor to form an H-shape or extending wings from both ends of the main building to the rear. At this time, the use of timber structures was allocated specific roles in the architecture. For example, the main building was constructed with trusses, and Japanese roof frames were applied to the wings or other annexes. Even when trusses were applied to the main building, it was common to use a Japanese roof frame for the entrance.

The *Gyeongnam* Provincial Government Office, built in 1924, is an exceptional example of architecture that incorporates both Japanese roof structures and truss structures. Initially designed as a prefectural hospital, the main building was constructed with a Japanese roof frame. [17] Later, both wings were extended to the second floor, and trusses were added to the roofs of the wings. The main building is approximately 13.5 meters wide, with a 2.7-meter-wide (9K) corridor in the middle. The Japanese roof frames were adopted using 280mm thick log beams. In comparison, the left and right wings were approximately 8 meters wide and were built using a king post truss structure. The distance between the king post and the side post of truss is 1.8 meters (6K). The truss timbers were 120mm wide and varied in thickness, and as seen in Figure 5, they differed from the logs used in the main building in terms of size and species of tree.

Figure 5: *Original roof frames from the Gyeongnam Provincial Government Office, built in 1924, expanded in 1931, source: Seokdang Museum of Dong-A University.*

While truss could form large spaces, the advantage of the Japanese roof frame was that it allowed for a greater degree of flexibility in shaping the roof surface. By supporting purlins with standing posts on a stable foundation, a complex or curved roof shape could be achieved more easily. A hybrid structure was also created by combining trusses and Japanese roof structures. The roof volume could be expanded by adding posts on top of the truss and arranging purlins, allowing for the creation of curved domes or arches. This was a simple method even when the building was expanded horizontally. Additionally, the Japanese roof frame could protect the building and its walls made of wood by extending the eaves, and the use of both log and timber as building materials was advantageous.

4.2 STANDARDIZATION TRENDS DEPENDENT ON FLOOR PLAN

In the context of modern state-run architecture in Korea, both Japanese roof structures and Western-style trusses were extensively used, with the latter being considered structurally superior. This was due to the fact that the tradition of wood construction could not be easily abandoned given the circumstances of the building production system of that time. Particularly, in a situation where the construction organization and distribution system were not sufficiently mature, the truss structure did not have an overwhelming comparative advantage in terms of price or mass production. The market share of

https://doi.org/10.52202/069179-0536

trusses depended on the industrialization of lumbering and sawmills, the standardization of timber, the expansion of transportation networks such as railways for delivery from production sites, communication between designers and builders, construction methods on the site, and other factors. From the perspective of consumers, converting long-standing living customs to the Western style was also a challenge for both Korean and Japanese architecture. However, during the era of colonial rule, the Japanese-style timber frame was chosen as an alternative to the truss, while the Korean timber structure became increasingly marginalized.

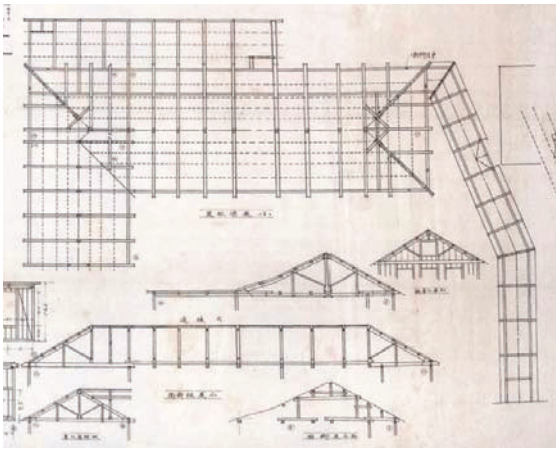

Figure 6: *The Roof Framing Plan of the Pyeongbuk Provincial Government Office, part, built in 1918, source: National Archives of Korea.*

To address the large-scale construction demands, it was imperative to adhere to familiar construction methods that were based on traditional metrology units. In 1921, the Japanese government enforced *the Weights and Measures Act* with the primary aim of mandating the use of the metric system, and in 1926, *the Joseon Government-General* declared *the Joseon Weights and Measures Ordinance*, making it obligatory to use only meters in all tasks. However, due to strong opposition from the industry, a grace period was soon granted. Although the government office buildings were given a grace period of 10 years and others 20 years, the implementation of the law was essentially postponed indefinitely, and it was only after World War II that it was effectively enforced. Hence, the truss structure in the modern era was also inevitably designed based on the traditional unit.

The drawings prepared by the modern government office for construction include various detailed drawings as well as floor plans, elevation drawings, and cross-sectional drawings. One of these drawings is *the Roof Framing Plan* drawing, which displays the horizontal arrangement of the roof structure. *the Roof Framing Plan* helps to determine the location and quantity of timber required for the roof structure by indicating the layout of beams, purlins, hip rafter ridges, and other components. This drawing is comparable to the field drawings traditionally produced by craftsmen on wooden boards. *The Roof Framing Plan* was useful not only for the Japanese-style roof frame but also for the arrangement of trusses. Nonetheless, it is often challenging to differentiate between trusses and Japanese-style roof frame shown in construction plans such as Figure 6. This is because the spacing between the members is similar, and their location is frequently determined by the same traditional dimensional unit.

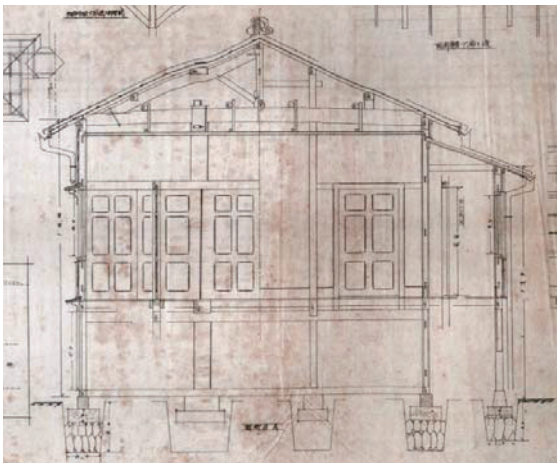

Figure 7: *The Section Drawing of Hwanghae Provincial Government Office, part, built in 1910, source: National Archives of Korea.*

The size and layout of the roof structure became more typical as floor plan was standardized for the rapid dissemination of colonial governance facilities. For example, in school architecture, the width of the school building was fixed at approximately 10m (5.5K) and the width of the students' waiting room and auditorium was fixed at approximately 14.5m (8K), in accordance with the standardization of educational space. [18] Accordingly, the role of each roof structure became clearer, and the possibility of interchangeability between different types of roof structures increased.

For spaces that did not require a large span, the Japanese timber roof frame could replace the truss. About 50% of the existing modern trusses in Korea have a span of less than 10m, and about 80% have a span of less than 12.5m. In addition, the spacing between trusses is often 1.8m, with most of them being less than 3m apart. [8] This means that in many cases, a Japanese-style roof frame, which is not suitable for creating a large space, can be used instead. If columns are inserted indoors to partition the rooms, the possibility of replacing the truss with a Japanese roof frame is further increased.

The spacing between trusses was often determined as a multiple of the traditional metrology unit S or K, which made it similar to that of the Japanese roof frame and suited the standardized floor plan. However, there were exceptions to this pattern, such as the *Myeongdong* Cathedral in *Seoul* (1898), Bell Memorial Chapel of Jennie Speer Memorial School for Girls in *Gwangju*

(1925), *Eonyang* Cathedral in *Ulsan* (1932), where the spacing between trusses was more than 5m. Interestingly, these buildings were all constructed by Western missionaries and did not follow Japanese standardized architectural methods.

5 CONCLUSIONS

In modern Korea, timber roof frames existed alongside Korean, Japanese, and Western styles. However, Korean-style was not used for state-run architecture and was limited to buildings with strong ethnic features such as houses and temples. Public buildings were constructed using Western and Japanese styles. Large-scale buildings were built using trusses, and small-sized buildings were built using Japanese-style roof frames. However, in some cases, the two roof frames were interchangeable as they were designed with the same module that uses traditional metrological dimensions.

After the Great Kanto Earthquake in 1923, the importance of earthquake-resistant structures increased, and reinforced concrete structures rapidly expanded. In addition, the revitalization of private commercial activities and the active involvement of private architects led to the trend of modernism, resulting in the reduction of sloped roofs. The design trend of reinforced concrete structures and modernism began to break away from the long tradition of timber construction.

REFERENCES

[1] K. M. Lee. Purlin Structure and Rafter Structure: The East Asian Civilization and Principles of Structural Design. Spacetime, 2013.

[2] K. M. Lee. A Basic Study on the Standard Scale of Architecture in the Late Joseon Dynasty. Journal of the Architectural Institute of Korea Planning & Design Vol.34 No.6, 2018.

[3] Y. J. Kang. A Study on the Design and Construction of the Ganghwa Anglican Church and the Ss. Mary & Nicholas' Seoul Anglican Cathedral in the Early 20th Century - Focused on the Architectural Activities of Anglican Priest M. N. Trollope. Master's Thesis, Korea National University of Arts, 2017.

[4] S. W. Kim, K. S. Han, and S. K. Song. The Development of Church Architecture in Korean Traditional Style – Based on the Cases of Catholic and Anglican Churches. Journal of the Architectural Institute of Korea Planning & Design Vol.17 No.9, 2001.

[5] D. S. Woo. A Study on Yangkwan or Western Style Buildings in Kyŏng'un Palace during the Great Han Empire. The Journal of Seoul Studies, XL, 2010.

[6] D. S. Woo & S. H. Kee. A Study on the Remodeling of Injeongjeon Area at Changdeokgung Palace in 1908. Journal of Architectural History Vol.23, No.2, 2014.

[7] B. D. Kim & J. S. Cho. A Study on the Feature of Beon-Sa-Chang that was Built in the Open-port Period as a Korean-style House through the Analysis on the Roof Structure. The Journal of Seoul Studies, XLVIII, 2012.

[8] Y. H. Lee, H. R. Yu, and K. H. Kwon. A Study on the Structural and Other Influential Characteristics of Western Timber Roof Truss in Modern Buildings - Focusing the Record of Modern Buildings among the Cultural Assets maintained by Public Institution. Journal of Architectural History Vol.20, No.4, 2011.

[9] Architectural Institute of Japan (Ed.). History of Development of Architecture in Modern Japan. Maruzen, 1972.

[10] Yoshida Masahiro. Improved Japanese House Structures. Industrial Engineering Society of Japan, 1919.

[11] M. K. Lee. The Change of the Timber Industry and the Campaign of Timber Dealer Guild in Sinuiju during Japanese Colonization of Korea (1910~1936). Ph.D. diss., Seoul National University, 2016.

[12] U. J. Park & C. S. Seo. A Study on the Timber Supply of the Government Managed Buildings under Japan's colonial rule of Korea. Proceedings of the Regional Association of Architectural Institute of korea, n.2006, v.01, 2006.

[13] S. H. Joo. The Context of Enactment and the Application to the Design of 'Joseon Government-General Architectural Standard' in 1916. Journal of Architectural History Vol.28, No.6, 2019.

[14] H. C. Jung, S. C. Kwon, and T. Y. Kim. A Study on the Member Size of Wooden Roof Trusses in the Early 20th Century Korea. Journal of the Architectural Institute of Korea Planning & Design Vol.13 No.4, 2011.

[15] J. H. Kim & B. H. Jeon. Acceptance of Truss and Materialization of Korean Style Roof in the Modern Era. Fall Conference Proceedings of Korea Association for Architectural History, 2010.

[16] B. H. Jeon et al.. Architectural Drawings Review of Japanese colonial era, Vol. I-VII. National Archives of Korea, 2007-2014.

[17] Seokdang Museum of Dong-A University (Ed.). Survey and Repair Report on the Government Headquarters of the Temporary Capital in Busan (Former Gyeongnam Provincial Government Office). Dong-A University, 2009.

[18] Y. G. Kang. A Study on the Pupil Waiting Hall, Auditoriums, Gymnasium of Government and Public Secondary Education Facilities in Korea before 1925. Master's Thesis, Korea National University of Arts, 2021.

https://doi.org/10.52202/069179-0536

World Conference on Timber Engineering Oslo 2023

COMBINATION OF NDT AND DESTRUCTIVE TESTS FOR GRADING THE STRENGTH CLASS OF TIMBER TO REHABILITATE STRUCTURES

Marcel Vilches-Casals[1], Eduard Correal-Mòdol[1], Carles Labèrnia Badia[1], M.P Giraldo[1]

ABSTRACT: Non-destructive techniques (NDT) are being implemented in the rehabilitation of the wooden structures of many old and historical buildings trying to assign the strength class of the timber. In Spain, acoustic inspection techniques are commonly used since the wave speed it can be easily predicted the modulus of elasticity. Nevertheless, the correlation with the bending strength usually is not accurate enough. By combining NDTs with destructive tests, the prediction should be significantly improved. To contrast, this hypothesis a study was carried out with the data obtained at the inspection of the timber structure in the refurbishment works done on a late 19th century Barcelona storey building. 724 beams were inspected with acoustic methods onsite and the information was complemented by testing 5 beams according to EN 408: modulus of elasticity, bending strength, density, and moisture. Finally, both sources of information were combined to develop a statistical model to assign the strength class to the beams. This study presents how the data obtained on difficult environments by NDT can be improved with destructive laboratory tests.

KEYWORDS: Non-destructive techniques, rehabilitation, strength class, timber, acoustic methods

1 INTRODUCTION

Timber was the most common material used in load-bearing structures on buildings before the massive introduction of steel and concrete in early 20th century in Catalonia. In consequence, nowadays most refurbishment works that are done on historical buildings have timber structures and old structural elements lack information about their quality or strength class. Therefore, grading all the elements is necessary to know the loadbearing capacity and minimize unexpected structural safety issues. Unfortunately, although the information obtained by the destructive tests according to EN 408 is the most accurate, destroying the elements in service to evaluate them is useless. On the other hand, Non-Destructive Testing (NDT) has a worse correlation but does not damage wood, gives valuable information and is cost-effective. A comprehensive way to evaluate an old structure is to grade visually all the elements, use acoustic waves to complement the inspection and perform destructive tests on some replaced elements. This study focuses on how to optimize the data obtained on the inspection of an existing wood structure.

2 OBJECTIVES

Improve the prediction of the load-bearing capacity of the wooden elements of an old structure in service by developing a cost-effective model based on acoustic techniques and the standardized procedure to determine the MOR, the MOE and the density.

3 METHODS

3.1 FIELDWORK

The case study is the timber structure of a five-storey building placed at 26 Trafalgar Street in Barcelona built in 1878 (Figure 1). Its constructive system was very typical in late 19th and early 20th centuries in the cities of Catalonia: masonry walls, wrought iron pillars and timber beams. The species of the beams was not determined but the gender was Pinus sp. The most common species used by that time in Barcelona was Scots pine (*Pinus sylvestris*) from the Pyrenees, but the authors also found in other contemporary buildings different common local species like Black pine (*Pinus nigra* subsp. *salzmanii*) and poplars (*Populus* sp.). In addition, also the American southern yellow pines from overseas were very common. The timber structure was in a generally good condition

[1] Marcel Vilches-Casals, Forest Science and Technology Centre of Catalonia (CTFC). Catalan Institute of Wood (INCAFUST), marcel.vilches@incafust.cat
[1]Eduard Correal-Mòdol, Forest Science and Technology Centre of Catalonia (CTFC). Catalan Institute of Wood (INCAFUST), eduard.correal@incafust.cat
[1] Carles Labèrnia Badia, Forest Science and Technology Centre of Catalonia (CTFC). Catalan Institute of Wood (INCAFUST), carles@gmail.com
[1] Maria Pilar Giraldo, Forest Science and Technology Centre of Catalonia (CTFC). Catalan Institute of Wood (INCAFUST), pilar.giraldo@incafust.cat

https://doi.org/10.52202/069179-0537

although there were elements that had issues produced by biotic agents.

The study was ordered to evaluate the safety of the new usage of the building. The inspection was done on four wood beam slabs by checking 212 beams on the ground floor, 198 on the first floor, 209 on the second floor and 105 on the third floor (Figure 2). All the 724 wood elements were inspected with a set of analysis techniques and equipment: capacitance handheld moisture meter, microsecond timer, electric drill and hand tools like hammer, awl and measuring tools. The most relevant items checked were the dimensions of the section, the span, the existence of woodworm holes and termites, the relevant splits and cracks, the biggest knots, the hardness and rot, the soundness, the moisture content and the speed of the impact waves.

Figure 1. *Façade of the building on Trafalgar Street*

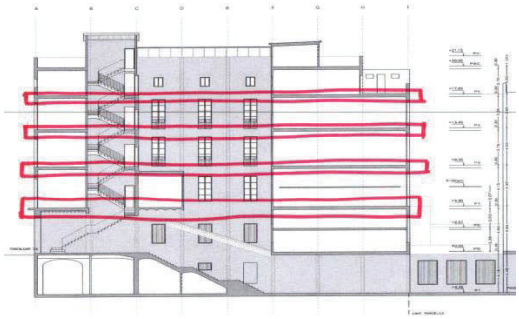

Figure 2. *Section of the building*

The microsecond timer generates impact waves with a frequency of resonance of 23 kHz and measures the time of flight between the transmitter and the receiver sensor (Figure 3). Impact waves are generated by hitting the transmitter with a hammer. Both sensors are metal nail alike transducers, they must be nailed into the wood, and the distance between them must be measured. In this case, the transducers were placed underneath the beams (Figure 4). The principle of this technique is based on the different propagation speeds of the impact waves depending on the soundness of the wood.

Figure 3. *FAKOPP Microsecond timer used in the study*

Figure 4. *Beam inspection with acoustic waves in the building*

3.2 LABORATORY TESTS

The specimens were chosen randomly between those to be removed due to the new distribution of the building. Several minor modifications and a new staircase were planned to connect the ground floor with the first floor. Five timber beams were selected for being tested at the laboratory. Three were from the new staircase on the ground floor, one was from the first floor and the other was from the second floor. The beams of the first and second floors were chosen randomly among those easier to extract. No beam was selected depending on its apparent state of conservation and all were representative of the batch. All the beams were of the same species, there were no abnormal density deviations, and the dimensions were 220×100×4000 mm. MOR, MOE, density, moisture content and stress wave tests were performed. The four-point bending test was done according to UNE EN 408:2011+A1:2012 [4] on a Hoytom bending test Machine. The test samples were symmetrically placed with a span eighteen times the depth (3960 mm) and the two load points were at six times the depth from the support point (1320 mm) (Table 2 and Figure 6).

https://doi.org/10.52202/069179-0537

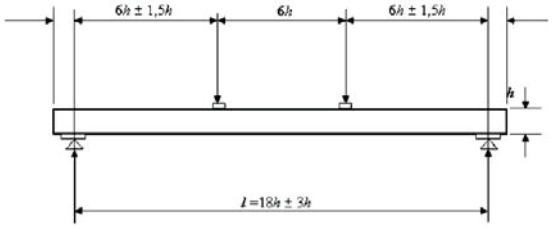

Figure 5. *Bending test geometry according to EN 408 [4]*

Figure 6. *Bending test machine at INCAFUST-CTFC*

The global static modulus of elasticity (MOE) was calculated as follows (See Equation (1):

$$MOE = \frac{3al^2 - 4a^3}{2bh^3\left(2\frac{w_2 - w_1}{F_2 - F_1} - \frac{6a}{5Gbh}\right)} \quad (1)$$

Where MOE = static modulus of elasticity (N/mm^2), l = effective span distance (mm), F = load difference between 10% and 40% of maximum load (N), w = deflection difference at 10% and 40% of maximum load (mm) b = width (mm), h = height (mm), a = distance between loading point and nearest support point (mm).

The Modulus of rupture (MOR) was calculated as follows. See Equation (2) below:

$$MOR = \frac{3Fa}{bh^2} \quad (2)$$

Where MOE = static modulus of rupture (N/mm^2), F = maximum load (N), b = width (mm), h = height (mm), a = distance between loading point and nearest support point (mm).

The density was measured by drying with an oven at 103ºC up to the anhydrous state a full cross-section slice 50 mm thick cut as close as possible from the breakage point. Controlling wood moisture is necessary to correct the MOE as the stiffness varies with the water content. The five beams were checked too with the microsecond timer to correlate the stress wave speed with the MOR and the MOE. The measuring procedure was the same as the one used in the building. Finally, correlation models were developed to predict the MOE and the MOR from the dynamic modulus of elasticity (MOE_{Dyn}) (Table 4).
The dynamic modulus of elasticity (MOE_{Dyn}) was calculated by measuring the wave speed. See Equation (3) below.

$$MOE_{Dyn} = \rho \cdot v^2 \quad (3)$$

Where MOE_{Dyn} = dynamic modulus of elasticity (N/mm^2), ρ = density (kg/m^3), v = wave velocity (m/s).

Finally, the relationship between MOEDyn-MOE and MOEDyn-MOR was analysed through regression models created from the field work data and the laboratory tests results (See Table 4, Figure 9 and Figure 10). The values of the MOE the MOR and the density were corrected according to the standard EN 384 [3]. The MOE was calculated from the global MOE and adjusted by the moisture content. See equation (4) below. The density was also corrected by the moisture content to the reference conditions of 20 °C and 65% of relative humidity. The MOR was adjusted by the depth of the beam.

$$E_0 = E_0(u)\left(1 + 0{,}01\left(u - u_{ref}\right)\right) \quad (4)$$

Where E_0 = modulus of elasticity (N/mm^2), u = moisture content in the moment of the test.

4 RESULTS

Table 1, Figure 7 and Figure 8 show the wave speed on the 724 beams of the building calculated from the time of flight and the distance between transmitters. According to the Shapiro-Wilk test significant results suggest a deviation from normality (p<0,001). The coefficient of variation of the wave speed was 9.1%. Therefore, there was little variability in the data set and the arithmetic mean is a robust parameter for defining the population.

Table 1. *Beams wave speed descriptive statistics*

Descriptive Statistics	Unit	Value
Number of beams	Ut	724
Mean	m/s	5,130.348
Standard deviation	m/s	464,763
Coefficient of variation	%	9.1
Range	m/s	2,689.000
Minimum	m/s	3,543.690
25th percentile	m/s	4,823.560
50th percentile	m/s	5,176.035
75th percentile	m/s	5,483.735
Maximum	m/s	6,232.690

https://doi.org/10.52202/069179-0537

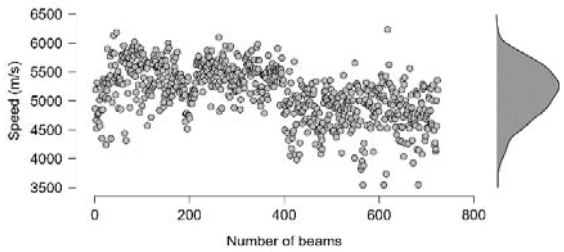

Figure 7: *Scatter plot of all the wave speed measurements (m/s) taken in the building*

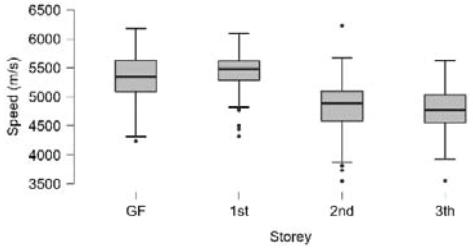

Figure 8: *Wave speed of the 724 beams divided by floors*

The wave speed of the beams split by floors showed statistical differences in accordance with the analysis of variance ($p < 0.001$) (Figure 8). The speed is slower on the upper than on the lower floors, but this difference is considered not to be intentional, and all the building was analysed as one batch.

Table 2 and Table 3 show the results of MOR, MOE, density, moisture content and wave speed of the five beams tested in the laboratory.

Table 2. *Results of the five laboratory tests*

Id. beam	MOE (N/mm^2)	MOR (N/mm^2)	Density (kg/m^3)	%H	Wave speed (m/s)
112	11463.08	39.66	412.99	11.00	5593.22
113	12352.16	31.88	677.17	10.64	4262.10
114	11951.61	40.05	441.43	11.05	5524.74
398	12697.96	33.65	684.49	10.26	4546.62
1st floor	11736.59	33.85	404.57	11.44	5649.35

Table 3. *Descriptive statistics of the five laboratory tests*

Statistics	MOE (N/mm^2)	MOR (N/mm^2)	Density (kg/m^3)	%H	Wave speed (m/s)
Mean	12040.28	35.82	524.13	10.88	5115.21
Deviation	490.68	3.77	143.72	0.44	658.14
CV	4.08	10.52	27.42	4.08	12.87
p_5	11517.78	32.23	406.25	10.34	4319.00

Table 4 shows the results of the models created between MOE_{Dyn}-MOE and MOE_{Dyn}-MOR with the field work data and laboratory test results.

Table 4. *Models that correlate the MOE_{Dyn} (N/mm^2) with the MOR (N/mm^2) and the MOE (N/mm^2)*

Models developed	Correlation (R^2)
$MOE = 13767.63 - 0.15 \cdot MOE_{Dyn}$	0,76
$MOR = 24.99 + 0.00092 \cdot MOE_{Dyn}$	0,51

5 DISCUSSION

The automatic procedure to assign a strength class to a timber element is conceived to be carried out on an industrial production control where density, modulus of elasticity (MOE) and modulus of rupture (MOR) are determined with a set of advanced NDTs. Portable acoustic methods have a good theoretical correlation with the MOE but a low relationship with the MOR and the density. In fact, the correlation between the values of stiffness and strength predicted with this type of NDTs and the actual values may have a deviation between 20% and 50% [1, 2, 6-13].

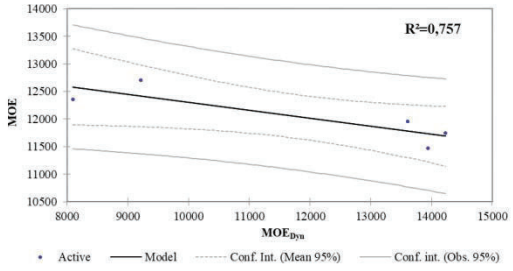

Figure 9: *Graphic of correlation between MOE_{Dyn} (N/mm^2) and MOE (N/mm^2)*

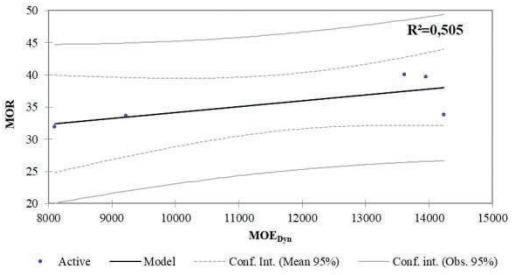

Figure 10: *Graphic of correlation between MOE_{Dyn} (N/mm^2) and MOR (N/mm^2)*

The correlation between the MOE_{Dyn}-MOE and the MOE_{Dyn}-MOR was below 80% (Figure 9 and Figure 10) like in the reviewed references [1, 2, 6-13].

According to the UNE EN 338:2010 [5] the 724 beams had a characteristic MOE of 11,855 N/mm^2, a characteristic MOR of 23 N/mm^2 and a density of 446 kg/m^3. In consequence, the sample should be considered C27 according to the MOE, C22 for the MOR and C50 for the density. Therefore, the strength class of the 724 beams should be around C22 (Table 5).

https://doi.org/10.52202/069179-0537

Table 5. *Characteristic values and strength class of the 724 beams according to the model*

Property	Characteristic Value	Strength class	Final class
Bending strength (N/mm^2)	23	C22	C22
Modulus of elasticity (N/mm^2)	11,855	C27	
Density (kg/m^3)	446	C50	

The models were specifically developed to predict the properties of the beams of the building. It must be considered that all the elements of the structure were of the same kind, and all were in a quite good condition. Therefore, in such a case the accuracy of the model should improve with an increase in the number of destructive tests.

A model with a coefficient of determination of $R^2 = 0.76$ was obtained using the MOE_{Dyn} as an independent variable and MOE as dependent variable. The results are like those discussed in other works. Arriaga *et al*. [1] found coefficients of determination for Scots pine (*Pinus sylvestris*) of 0.76 for linear regressions. Görgün and Dündar [6] obtained coefficients of determination of 0.64 for Turkish black pine (*Pinus nigra*), while Vega *et al*. [13] reported of values up to 0.68 for Sweet chestnut (*Castanea sativa*). Hermoso *et al*. [8] obtained coefficients of determination for logs of Spanish Black Pine (*Pinus nigra*) of up to 0.68. Kovryga *et al*. [10] obtained coefficients of determination of 0.65, 0.39, 0.67, 0.55 for the common ash (*Fraxinus excelsior*), the beech (*Fagus sylvatica*), the maples (*Acer spp*.), and the oaks (*Quercus spp*.) respectively. Both Hermoso *et al.* [8] and Kovryga *et al.* [10] used a Sylvatest.

The coefficients of determination of the MOR were lower and between 0.12 and 0.37. Görgün and Dündar [6] obtained a value of 0.37 for Turkish Black Pine (*Pinus nigra* var *pallasiana*), Vega *et al*. [13] found coefficients of determination of 0.11 for sweet chestnut (*Castanea sativa*) and Kovryga *et al*. [10] 0.12, 0.20, 0.16, 0.31 for the common ash (*Fraxinus excelsior*), the beech (*Fagus sylvatica*), the maples (*Acer spp.*), and the oaks (*Quercus spp.*) respectively.

In addition, the results of the study were also used to run the general model of Arriaga *et al*. [1] (Table 6) but the predicted load capacity resulted lower.

Table 6. *Strength class predicted using the model of Arriaga et al. [1]*

Method	MOR (N/mm^2)	MOE (N/mm^2)	Strength class
MOE_{Dyn} + bibliography*	23.18	9511.46	C18

* $MOE = A + B \cdot MOE_{Dyn} = 579,5 + 0,7548 \cdot MOE_{Dyn}$
* $MOR = A + B \cdot MOE_{Dyn} = -4,84 + 0,0034 \cdot MOE_{Dyn}$

6 CONCLUSIONS

Combining NDTs with destructive tests is useful to reduce the uncertainty of the prediction of the load capacity of the structural timber elements in use.

Assigning a strength class to elements that are out of the requirements of the standards is not normatively possible, but the combination of different techniques might help to make a more precise approach.

NDTs show to be a good source of information. However, proper knowledge of the material and solid experience is essential to correctly manage the data of the NDTs.

ACKNOWLEDGEMENTS

The data of the beams were obtained by the researchers on the previous inspection of the timber structure at the refurbishment works done by Laebon S.A. at number 26 Trafalgar Street in Barcelona.

REFERENCES

[1] Arriaga, F; Íñiguez, G; Esteban, M; Bobadilla, I. Proposal of a Methodology for the Assessment of Existing Timber Structures in Spain. 16th International Symposium on Nondestructive Testing and Evaluation of Wood. 2009.

[2] Esteban Herrero, M., Arriaga Martitegui, F., Bobadilla Maldonado, I., Íñiguez González, G. y García Lantarón, H. Análisis y consolidación de la estructura de madera del edificio antiguo del aserradero de Valsaín, Segovia. Actas V congreso forestal español. 5CFE01[614], 2009.

[3] European Committee for Standardization. Structural timber. Determination of characteristic values of mechanical properties and density. EN 384:2016. Brussels. CEN. 2016.

[4] European Committee for Standardization. Timber structures. Structural timber and glued laminated timber. Determination of some physical and mechanical properties. EN 408:2011+A1:2012. Brussels. CEN. 2012.

[5] European Committee for Standardization. Timber structures. Structural timber. Strength classes. EN 338:2016. Brussels. CEN. 2016.

[6] Görgün, H.V.; Dündar, T. Strength grading of turkish black pine Structural timber by visual evaluation and nondestructive testing. Maderas. Ciencia y tecnología 20(1): 57 – 66. 2018

[7] Grippa, M.R. Structural identification of ancient timber constructions by non-destructive techniques. Tesi di Dottorato. Università degli Studi di Napoli Federico II, 2009.

[8] Hermoso Prieto, E.; Fernández-Golfín Seco, J.I.; Díez Barra, M. R.; Mier Pérez, R. Ultrasound application to evaluation of small round timber mechanic properties. Informes de la Construcción. Vol. 59, 506, 87-95. 2007.

[9] Iñiguez, G. Clasificación mediante técnicas no destructivas y evaluación de las propiedades mecánicas de la madera aserrada de coníferas de gran escuadría para uso estructural. Tesis Doctoral. UPM. Escuela técnica superior de ingenieros de montes, 2007.
[10] Kovryga, A., Chuquin Gamarra, J.O., van de Kuilen, J.W.G. Strength and stiffness predictions with focus on different acoustic measurement methods. European Journal of Wood and Wood Products 78:941–949. 2020.
[11] Ramón, G; Basterra, A; Casado, M; Acuña, L. Analysis of the structural timber diagnosis techniques at the cultural patrimony with an architectural project orientation. I Jornadas de investigación en construcción. Tomo 1, 2005.
[12] Saporiti Machado, J.; Palma, P. Non-destructive evaluation of the bending behaviour of in-service pine timber structural elements. Materials and Structures. 44:901–910. 2011.
[13] Vega, A.; Dieste, A.; Guaita, M.; Majada, J.; Baño, V. Modelling of the mechanical properties of *Castanea sativa* Mill. structural timber by a combination of non-destructive variables and visual grading parameters. Eur. J. Wood Prod. 70:839–844. 2012.

https://doi.org/10.52202/069179-0537

World Conference on Timber Engineering Oslo 2023

THE PRESENT STATE AND ISSUES ON RETROFITTING OF HISTORIC TIMBER-FRAMED BRICK CONSTRUCTION BUILDINGS IN JAPAN

Manabu Fujimoto[1], Naoyuki Matsumoto[2], Mikio Koshihara[3]

ABSTRACT: In the late 19th century, the method of timber-framed brick construction (TFBC, "mokkotsu-rengazo" in Japanese) was introduced to Japan as a western technique. After a while, it became apparent that the TFBC method was vulnerable to earthquakes, and hence, it was not used anymore. However, some TFBC buildings remain in Japan, and several of them require reinforcement. To ensure appropriate and smooth repairs, this paper summarizes the history, past retrofitting works, and current situation and issues regarding the restorations of TFBC buildings in Japan through document survey and building investigations.
We reveal that only a few buildings have been retrofitted seismically, and several buildings still require appropriate restoration. In the current Japanese administration of cultural properties, retrofitting entails highly detailed seismic assessment and reinforcement methods, which results in a limited number of restorations. In addition, lost techniques, including the TFBC method, has not been treated as a significant subject of research. Hence, relevant literature is limited, and detailed knowledge on the topic is lacking. As predicting the occurrence of large earthquakes is not possible, development of reinforcement methods, expansion of systems to support repairs, and study on technical-historical evaluations are necessary.

KEYWORDS: Timber Framing, Brick, Reinforcement, Earthquake, Architectural Conservation, Cultural Property

1. INTRODUCTION

In the late 19th century, the Japanese government hired foreign experts to import the latest technology and systems that modernized and westernized the country. Bricks were the first architectural materials to be implemented as a part of this policy. They were considered cutting-edge materials that had fire resistance and could represent advances. In addition to piling them up, another method for brick construction was timber-framed brick construction (TFBC, "mokkotsu-rengazo [木骨煉瓦造]" in Japanese). The TFBC is a construction method that combines timber frames and brick masonry walls to form walls, primarily exterior walls. However, the use of this method was discontinued after several TFBC buildings were damaged by the earthquakes. However, some TFBC buildings still exist, many of which require restoration.
In this study, we examined the current situation and issues regarding the restoration of TFBC buildings in Japan. The remainder of the paper is organized as follows. Section 2 introduces existing TFBC buildings and their history. Section 3 describes past restoration works. In Section 4, we discuss issues regarding current restoration from the perspective of the system of cultural property protection and historical evaluation in Japan. Section 5 provides the conclusion and future research directions.
The TFBC buildings covered in this study are all national cultural properties.

2. TIMBER-FRAMED BRICK CONSTRUCTION IN JAPAN

2.1 EXISTING BUILDINGS

According to the database of the Agency for Cultural Affairs and the author's research [1], there are 23 TFBC buildings among the national cultural properties in Japan (Figure1, Table 1).

2.2 BRIEF HISTORY [1,2]

2.2.1 The 1860s – the 1880s: Import of TFBC

From the end of the Edo era to the Meiji era, French engineers, such as Edmond Auguste Bastien began the construction of Yokosuka Naval Shipyard in 1865 and Tomioka Silk Mill in 1871. With the start of trade with foreign countries, housing for foreigners, such as the Jugobankan Building in the Former Kobe Foreign Concession (1881) was also built. Similarly, Marc Marie de Rotz, who was a Christian missionary, designed their religious facilities, such as the Former Latin Seminario (1875). Thus, timber-framed masonry was used in relatively large public buildings during this period. The main constructional feature in this period was brick walls filled inside the frame (wall type A, Figure 2).

2.2.2 The 1890s – 1910s: Modification of TFBC

In 1891, the Mino-Owari Earthquake (Nobi Earthquake) caused severe damage to brick buildings. Subsequently, TFBC was used less frequently in public buildings.

[1] Manabu Fujimoto, Ph.D. Student, The University of Tokyo, Japan, jiefoo@iis.u-tokyo.ac.jp
[2] Naoyuki Matsumoto, Assistant Professor, Tohoku University, Japan, nmatsu@rcl.archi.tohoku.ac.jp
[3] Mikio Koshihara, Professor, The University of Tokyo, Japan, kos@iis.u-tokyo.ac.jp

https://doi.org/10.52202/069179-0538

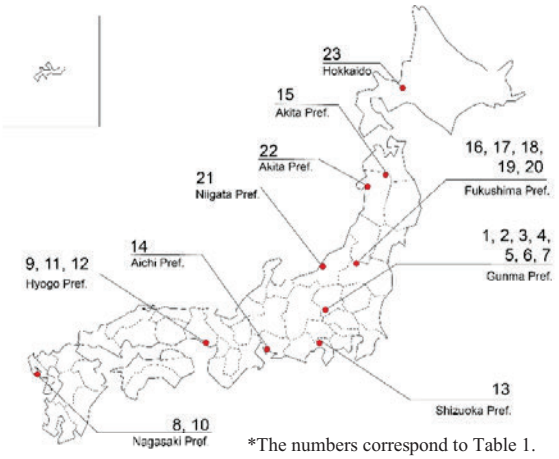

*The numbers correspond to Table 1.

Figure 1: *Location of existing TFBC buildings in Japan*

However, as the domestic production of bricks increased, TFBC was used more in private residences and corporate buildings, such as the Former Kabuto Beer Factory (1898). Some TFBC warehouses built in houses are fused with traditional Japanese construction methods. The main constructional feature in this period was brick walls covering the exterior of the timber frame (wall types B or C, Figure 2).

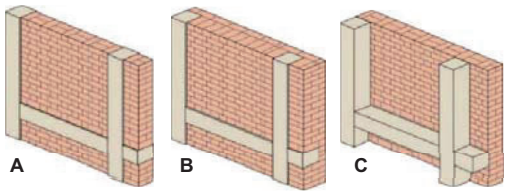

Figure 2: *Wall type of existing TFBC buildings in Japan [1]*

Table 1: *List of existing TFBC buildings in Japan [1]*

No.	Building Name	Grade*	Location (Prefecture)	Construction Year	Wall Type	Seismic Retrofit	Retrofitting Method
1	The West Cocoon Warehouse, Tomioka Silk Mill	NT	Gunma	1872	A	Done	Steel Frames, Glass Ceilings, AFRP Rods
2	The East Cocoon Warehouse, Tomioka Silk Mill	NT	Gunma	1872	A	Partially Done	Steel Frames, Wire Meshes, Gap Filling
3	The Silk-Reeling Plant, Tomioka Silk Mill	NT	Gunma	1872	A	Not Yet	
4	The Cocoon Drying Facility, Tomioka Silk Mill	NT	Gunma	1872	A	Not Yet	
5	The Director's House (Brunat House), Tomioka Silk Mill	NT	Gunma	1873	A	Not Yet	
6	The Dormitory for French Female Instructors, Tomioka Silk Mill	NT	Gunma	1873	A	Not Yet	
7	The Inspector's House, Tomioka Silk Mill	NT	Gunma	1873	A	Not Yet	
8	The Former Latin Seminario	ICP	Nagasaki	1875	A	Not Yet	
9	The Jugobankan Building in the Former Kobe Foreign Concession	ICP	Hyogo	1881	A	Done	Seismic Isolation, SRC Columns, Steel Frames
10	The Seine Factory, Former Shitsu Aid Center	ICP	Nagasaki	1883	A	Not Yet	
11	The Former Hunter House	ICP	Hyogo	1889**	A	Not Yet	
12	The Annex Building of Ijokaku	RTCP	Hyogo	1890**	B	Not Yet	
13	The Brick Warehouse, Yoshizawa House	RTCP	Shizuoka	1891	B	Not Yet	
14	The Former Kabuto Beer Factory	RTCP	Aichi	1898	A	Done	Steel Frames, Steel Buttresses
15	The Former Engine Room of Kosaka Mine Manufacturing Division	ICP	Akita	1904	A	Done	Reinforcing Columns and Beams, RC Foundation
16	The Brick Warehouse, Wakaki Shop	RTCP	Fukushima	1904	B	Not Yet	
17	The Agricultural Work Warehouse, Wakana House	RTCP	Fukushima	1910	B	Not Yet	
18	The Brick Warehouse, Ueno House	RTCP	Fukushima	1911	B	Not Yet	
19	The Kurazashiki, Wakana House	RTCP	Fukushima	1916	B	Not Yet	
20	The Third-floor Warehouse, Wakana House	RTCP	Fukushima	1916	B	Not Yet	
21	The New Warehouse, Takahashi Sake Brewry	RTCP	Fukushima	1922	C	Not Yet	
22	The Rice Warehouse, Kodama House	ICP	Akita	1923	C	Not Yet	
23	The Suginome House	RTCP	Hokkaido	1933	C	Not Yet	

* "NT" = National Treasure, "ICP" = Important Cultural Property, "RTCP" = Registered Tangible Cultural Properties
** Exact year of construction is unknown, so an estimated year is given.

https://doi.org/10.52202/069179-0538

***Table 2**: Exterior view of existing TFBC buildings in Japan*

1. The West Cocoon Warehouse, TSM* (Date of shooting: July 4, 2022)	2. The East Cocoon Warehouse, TSM* (Date of shooting: July 4, 2022)	3. The Silk-Reeling Plant, TSM* (Date of shooting: Oct. 21, 2017)	4. The Cocoon Drying Facility, TSM* (Date of shooting: Oct. 21, 2017)
5. The Director's House (Brunat House), TSM* (Date of shooting: Oct. 21, 2017)	6. The Dormitory for French Female Instructors, TSM * (Date of shooting: July 4, 2022)	7. The Inspector's House, TSM* (Date of shooting: July 4, 2022)	8. The Former Latin Seminario (Date of shooting: July 10, 2022)
9. The Jugobankan Building in the Former Kobe Foreign Concession (Date of shooting: Feb. 25, 2019)	10. The Seine Factory, Former Shitsu Aid Center (Date of shooting: July 8, 2022)	11. The Former Hunter House (Date of shooting: Feb. 25, 2019)	12. The Annex Building of Ijokaku (Date of shooting: Feb. 25, 2019)
13. The Brick Warehouse, Yoshizawa House (Date of shooting: July 21, 2017)	14. The Former Kabuto Beer Factory (Date of shooting: Sep. 26, 2017)	15. The Former Engine Room of Kosaka Mine Manufacturing Division (Date of shooting: Sep. 10, 2019)	16. The Brick Warehouse, Wakaki Shop (Date of shooting: Sep. 3, 2018)
17. The Agricultural Work Warehouse, Wakana House (Date of shooting: Sep. 3, 2018)	18. The Brick Warehouse, Ueno House (Date of shooting: Sep. 3, 2018)	19. The Kurazashiki, Wakana House (Date of shooting: Sep. 3, 2018)	20. The Third-floor Warehouse, Wakana House (Date of shooting: Sep. 3, 2018)
21. The New Warehouse, Takahashi Sake Brewry (Date of shooting: Sep. 13, 2019)	22. The Rice Warehouse, Kodama House (Date of shooting: Sep. 9, 2019)	23. The Suginome House (Date of shooting: Sep. 24, 2019)	

* "TSM" = Tomioka Silk Mill

https://doi.org/10.52202/069179-0538

2.2.3 The 1920s and beyond: Decline of TFBC

In 1923, the Tokyo-Yokohama earthquake (Kanto Earthquake) devastated masonry buildings (Figure 3). The following year, the Urban Building Law (Shigaichi kenchikubutsu hou [市街地建築物法]) (1919) became stricter, which made it difficult to construct masonry buildings in Japan. The use of TFBC was rapidly decreased. This strict standard was implemented into the current the Building Standard Law (Kenchiku kijun hou [建築基準法]) enacted in 1950.

***Figure 3**: Damage to TFBC building during Tokyo-Yokohama Earthquake (1923) [3]*

2.3 VULNERABILITY TO EARTHQUAKES

Timber frames and brick walls are not structurally joined together; therefore, their vibration characteristics are different during earthquakes. Consequently, there is a high risk of failure in the out-of-plane direction. In 1995, the Kobe earthquake destroyed the Jugobankan Building in the Former Kobe Foreign Concession (Figure 4).

***Figure 4**: The Jugobankan Building before (left) and after (right) the Kobe Earthquake (1995) [4]*

3. PAST RESTORATION WORKS

3.1 THE JUGOBANKAN BUILDING IN THE FORMER KOBE FOREIGN CONCESSION

This building is located in Kobe City in the southern part of Hyogo Prefecture, and is designated as an important national cultural property. After its collapse in the Kobe earthquake in 1995, it was reconstructed and reinforced from 1995 to 1998. Two goals were set for seismic retrofitting. First, seismic isolators were installed in the foundation to decrease the seismic forces. Second, to increase the horizontal load-carrying capacity, two steel reinforced concrete (SRC) columns (Figure 6) were set up in place of the original chimneys and connected to steel frames added inside the roof truss and second-floor framing [4].

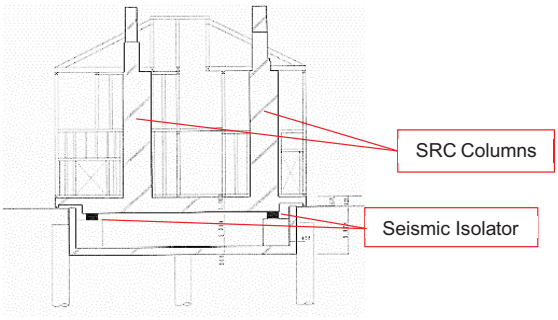

***Figure 5**: Cross-section of Reinforcements (SRC columns and seismic isolators) of the Jugobankan Building [4]*

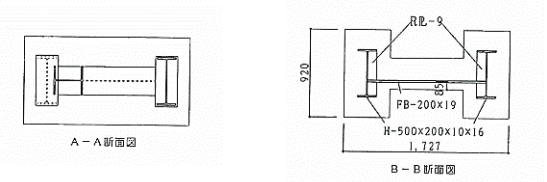

***Figure 6**: Cross-sectional view of SRC columns [4]*

3.2 THE FORMER KABUTO BEER FACTORY

This building is located in Handa City in the southern part of Aichi Prefecture. It is registered as a national tangible cultural property and was restored in 2014. Steel braces and buttresses were installed to increase the horizontal load-carrying capacity, and pillar legs and beams were reinforced with metal fittings.

***Figure 7**: Reinforcements of the Former Kabuto Beer Factory (left: steel frame and brace, right: steel buttresses)*

3.3 THE WEST COCOON WAREHOUSE OF FORMER TOMIOKA SILK MILL

This building is located in Tomioka City in the southern part of Gunma Prefecture and is designated as a national treasure and UNESCO World Heritage Site. It was restored between 2014 and 2020. Two main goals were set for seismic retrofitting. First, to increase the horizontal load-carrying capacity, a variety of reinforcements were installed, such as steel frames, braces, and glass ceilings,

https://doi.org/10.52202/069179-0538

which had less influence on the original interior design. Second, to increase the in-plane strength of brick walls, aramid fibre-reinforced plastic (AFRP) rods were embedded in masonry joints [5].

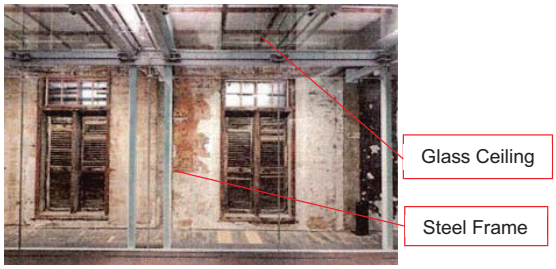

***Figure 8**: Reinforcements at the West Cocoon Warehouse: interior view [5]*

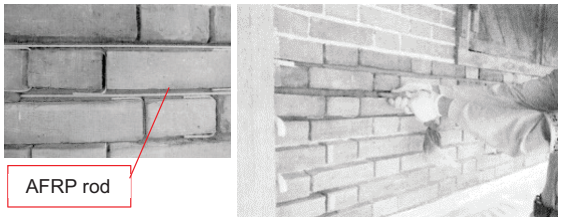

***Figure 9**: Inserting of AFRP rods into brick wall of the West Cocoon Warehouse [5]*

3.4 THE EAST COCOON WAREHOUSE OF FORMER TOMIOKA SILK MILL

This building is a counterpart to the West Cocoon Warehouse, and is also a national treasure and a UNESCO World Heritage Site. Although not yet fully reinforced, transitional reinforcement work was conducted between 2011 and 2012 to reduce the out-of-plane damage from earthquakes. The work includes the following: filling the gaps between the top of the brick wall and wooden girder with mortar, setting up wire meshes, and reinforcing columns and beams on the brick walls facing a busy passageway [6].

***Figure 10**: Reinforcements at the East Cocoon Warehouse (left: zoom out view, right: zoom in view), (Date of shooting: July 4, 2022)*

3.5 FORMER ENGINE ROOM OF KOSAKA MINE MANUFACTURING DIVISION

This building is located in Kosaka Town in the northern part of Akita Prefecture and is registered as a national tangible cultural property. Originally part of a mining facility, it was relocated and restored in 2015, and is now a coffee shop. During relocation, a new reinforced concrete foundation was cast, and reinforcing columns and beams made of laminated wood were added to the interior of the building.

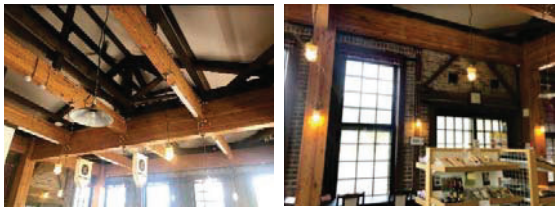

***Figure 11**: Reinforcements at the Former Engine Room of Kosaka Mine Manufacturing Division: interior view (Date of shooting: Sep. 10, 2019)*

4. RETROFITTING ROADBLOCKS

4.1 "AUTHENTICITY" PERSPECTIVE

The concept of "authenticity" in architectural conservation comprises the following sources: design, materials, craftsmanship, setting, use and function, and spirit and feeling. The Nara Document on Authenticity (1994) states that "the respect due to all cultures requires that heritage properties must be considered and judged within the cultural contexts to which they belong [7]." However, the frequent disasters and humid temperate climate make it to be difficult to perfectly preserve the materials and elements which made using the techniques of the time. Therefore, these factors are not equal, and design is often considered the most important factor. For examples, the original joint material was lost when embedding AFRP rods into the joints of brick walls of the West Cocoon Warehouse (Figure 9), and the original foundations were excavated when installing a seismic isolator under the Jugobankan Building (Figure 5).

4.2 JAPANESE ADMINISTRATION OF CULTURAL PROPERTIES

4.2.1 Framework of Cultural Property Building and Subsidy System

In the Japanese Administration of Cultural Properties, national cultural property buildings are classified into two categories. First is important cultural properties (ICP) and national treasures (NT), and the other is registered tangible cultural properties (RTCP). The former is a designation system with strict regulations on their restorations, and ICP of especially high value are designated as NT to safeguard the material, structural system, and building techniques. In these conservation projects, after an assessment by the government, the national treasury pays 50% of the repair costs: repair work costs, disaster prevention work costs, other construction costs, information dissemination costs, design, and construction supervision costs (additional amounts might be added depending on the subsidized organization, project size, region, etc.). In addition, when using government subsidies, the person in charge of the design and construction supervision must be a conservation architect certified by the Agency for Cultural Affairs.

https://doi.org/10.52202/069179-0538

Conversely, the latter is a registration system based on requests from owners and local governments and allows for relatively flexible preservation and utilization, including renovation and conversion. In these conservation projects, after an assessment by the government, the national treasury mainly pays 50% of the design and construction supervision costs. As with ICP and NT, the amount of subsidy can be more in some cases, and the person in charge of design and construction supervision must be a conservation architect certified by the Agency for Cultural Affairs [8-10].
Most TFBC buildings, including non-cultural properties, currently remain unrestored because seismic retrofitting of such vulnerable structures requires a large amount of funding, and the evaluation system for the historical value of TFBC method has not adequately been established.

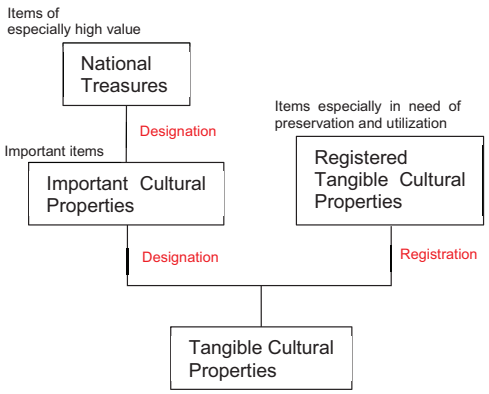

***Figure 12**: Schematic diagram of Japanese cultural properties (structures) [8]*

4.2.2 Steps to Seismic Retrofitting

The repair and management of cultural property buildings is the responsibility of the owner. However, because seismic retrofitting requires a high degree of expertise, technical assistance is provided from the local and national governments during the entire process.
In the case of wooden ICP and NT, under the Law of Protection of Cultural Properties (Bunkazai hogo hou [文化財保護法] in Japanese), before repair work, seismic assessment must be conducted, which is divided into three stages (Figure 13): preliminary seismic assessment (PSA), basic seismic assessment (BSA), and expert seismic assessment (ESA). PSA is sufficiently simple; the owners can perform it by themselves, and it is used to determine the urgency of repair or a more detailed assessment. Both BSA and ESA are used to quantitatively evaluate seismic resistance through structural surveys and structural analysis; however, the difference is that the former is non-destructive, while the latter is more detailed because it includes destructive surveys with dismantling and repair, as required. In the case of non-wooden ICP and NT, PSA might not be conducted and the process may start with BSA or ESA, depending on the characteristics of the building. If this assessment process reveals that the current seismic capacity does not meet the criteria, seismic retrofitting is planned as soon as the budget is available. Conversely, RTCP buildings are restored in accordance with the Building Standard Law, which is the standard for new buildings (however, an exemption from the Building Standard Law might be permitted through a third-party committee assessment) [6].
Thus, there is a strict assessment process to complete the seismic retrofitting of cultural properties; this process might require to a year or occasionally even more. Seismic retrofitting without a correct understanding of the structural characteristics of the building may result in significant earthquake damage and hence must be performed carefully. In particular, seismic assessment of TFBC buildings tends to take long because of large-scale structural experiments and material experiments [5], and the restoration experience is still limited. Therefore, it is necessary to not only conduct a structural survey of individual buildings but also elucidate the general structural characteristics of TFBC.

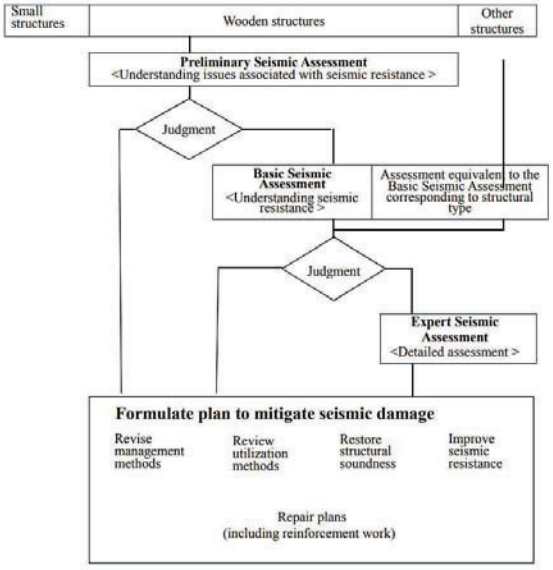

***Figure 13**: Flow chart of seismic assessment and formulation plan [11]*

4.3 TECHNICAL-HISTORICAL EVALUATION OF TFBC

As discussed in Section 2, the TFBC method was introduced and subsequently abandoned. However, the details of TFBC, namely, what type of technology TFBC is, how it is merged with the local methods, and how it is transformed, have not yet been adequately discussed. For example, the database of the Agency of Cultural Affairs lists buildings that are categorized as TFBC but are purely brick masonry or use two construction methods separately in single buildings. Similarly, it contains TFBC buildings, which are categorized as brick masonry buildings. This suggests that the TFBC method is not clearly defined, and that there is no common view of the method among experts, municipalities, and building owners. Specifically, the accumulation of knowledge about the lost technique is insufficient.

https://doi.org/10.52202/069179-0538

In Japan, the few studies on TFBC to date have not obtained its complete view, either because they are case studies [12, 13] or take some of the features of TFBC and place them in technical history [3, 14]. Therefore, in the future, it is necessary to typify the original form and the form that has subsequently changed in Japan, to compare them with the TFBC structures in France and other European countries, to reveal the mechanism of the transition and the decline of foreign construction methods in Japan, and to establish and apply more appropriate survey and historical evaluation methods for existing buildings.

5. CONCLUSIONS

In Japan, the TFBC structure is a Western-derived construction method that was in use for approximately 70 years. There are 23 existing buildings, but only five of them have been reinforced to withstand earthquakes. To repair earthquake-vulnerable cultural property buildings, including TFBC buildings, a precise seismic assessment is required. Currently, because of the significant time and cost involved, adequate earthquake countermeasures have not yet been taken.

Since it is impossible to predict when a large earthquake will occur, it is necessary to develop reinforcement methods, including transitional reinforcement, as shown in the East Cocoon Warehouse of the Tomioka Silk Mill; expand systems to support repairs; study technical-historical evaluations to ensure appropriate and smooth repair work.

ACKNOWLEDGEMENT

This work was supported by JSPS KAKENHI Grant Number JP21J13616. And we would like to thank Editage (www.editage.com) for English language editing.

REFERENCES

[1] Fujimoto, M. [冨士本学], Matsumoto, N. [松本直之], & Koshihara, M. [腰原幹雄]: A Study on the Localization of Imported Construction Methods in Exterior Walls of Timber Brick Composite Buildings in Modern Japan［日本における木骨煉瓦造建造物に見る近代輸入構法の在来性］. In: *Architectural Institute of Japan: Annual Meeting 2020*, 253-254,

[2] Fujimoto, M.［冨士本学], Matsumoto, N. [松本直之], Fujita, K. [藤田香織], & Koshihara, M. [腰原幹雄]: A Study on the Technical History of Construction Methods of Timber Brick Composite Buildings in Japan [日本における木骨煉瓦造建造物の構法に関する技術史的研究]. In *Architectural Institute of Japan Kanto Chapter: Architectural Research Meetings 2018*, 267-270, 2019.

[3] Uchida, Y. [内田祥三]: An Introduction to Building Structure [建築構造汎論], Iwanami Shoten [岩波書店], 1935.

[4] The Japanese Association for Conservation of Architectural Monuments [文化財建造物保存技術協会]: Documentation of the Restoration Work (Disaster Reconstruction Work) at the Jugobankan Building in the Former Foreign Concession in Kobe [重要文化財 旧神戸居留地十五番館 災害復旧工事報告書], NOZAWA Corporation [株式会社ノザワ], 1998.

[5] The Japanese Association for Conservation of Architectural Monuments [文化財建造物保存技術協会] : Documentation of Restoration Work at the WEST COCOON WAREHOUSE of FORMER TOMIOKA SILK MILL [国宝 旧富岡製糸場西置繭所 保存修理工事報告書], Tomioka City Board of Education [富岡市教育委員会], 2020.

[6] Agency for Cultural Affairs [文化庁]: Guideline for Seismic Assessment and Reinforcement of Important Cultural Properties (Buildings) Revised edition [重要文化財(建造物)耐震診断・耐震補強の手引き(改訂版)], 2017.

[7] ICOMOS: The Nara Document on Authenticity, 1994.

[8] Agency for Cultural Affairs: Cultural Properties for Future Generations, 2022.

[9] Agency for Cultural Affairs [文化庁]: Guideline of Government Subsidy for Repair, Disaster Prevention and Utilization of Important Cultural Properties (Buildings, Arts and Crafts) [重要文化財（建造物・美術工芸品）修理、防災、公開活用 事業費国庫補助要項], 2022.

[10] Agency for Cultural Affairs [文化庁]: Guidelines for Government Subusidy for the Repair of Resisterd Tangible Cultural Property Buildings［登録有形文化財建造物修理等事業費国庫補助要項］, 2020.

[11] Agency for Cultural Affairs: Guideline for Assessing Seismic Resistance of Important Cultural Properties (Buildings), 2012.

[12] Muramatsu, T. [村松貞次郎]: Nippon Kagaku Gizyutusi Taikei 17 Architectural Technology [日本科学技術史大系 17 建築技術], Dai-Ichi Houki [第一法規], 1964.

[13] Kikuchi, K. [菊地勝広]: Construction Methods and Materials Used at Yokosuka Naval Shipyard in the French Maritime Journal Published in 1873, A Study on the Introduction of French Technology at Yokosuka Ironworks (Part 1) [1873 年刊行フランス海事雑誌にみる横須賀製鉄所の建築構法と使用材料 横須賀製鉄所におけるフランス系技術の導入に関する研究（その１）], In *Architectural Institute of Japan Kanto Chapter: Architectural Research Meetings 2010*, 209-212, 2011.

[14] Ohashi, Y. [大橋好光], Fukuhama, Y. [福濱嘉宏], Kurita, N. [栗田紀之], Kondo, T. [近藤哲], & Yasumura, K. [安村恵子]: A Study on the Translating Process of “Mokkotsuzo” and its Influence on the Japanese Wooden Structure［洋風軸組・木骨造の導入過程と在来軸組工法に与えた影響について］, *JUSOKEN annual report No.29[住総研 研究年報 No.29]*, 417-427, 2002. https://doi.org/10.20803/jusokennen.29.0_417.

World Conference on Timber Engineering Oslo 2023

REUSE OF WOOD – LEARNING ABOUT THE BENEFITS AND CHALLENGES OF HIGH- AND LOW-TECH DIAGNOSTIC METHODS THROUGH ACTION RESEARCH IN NORWAY

Wendy Wuyts[1], Artur Tomczak[2], Kristine Nore[3], Lizhen Huang[4], Thomas Haavi[5]

ABSTRACT: Digital technologies for the diagnosis of underused timber construction and the reclamation and reuse of wood in timber construction have not been widely deployed. One of the reasons is the need for diagnosis processes with large amounts of data. This paper is a product of the learning process in the Norwegian project SirkTRE, and specifically, the sub-project SirkLåve (Circular Barns), which aims to address the problem of underused and vacant barns and other agricultural buildings in Norway. Moreover, this multiple-case project aims at understanding the feasibility, costs, and benefits of circularity strategies, such as deconstruction and reuse of wood in new projects or renovations. The learning processes draw upon explorative desktop-based research, interviews with key informants, and our own experiments and experiences with various cases of barns. The scope of this paper is the reuse of wood from barns that is deemed ineligible for renovation. This paper describes low- and high-tech methods for surveying redundant buildings to applying extracted components in new designs. This multiple-case study reflects on the preconditions of the context in which these best practices may succeed, as well as on the benefits and the challenges.

KEYWORDS: Digital technologies, Empty barns, Engineering for the circular built environment; Innovation and learning processes; Rural circularity practice

1 INTRODUCTION

Globally, millions of tonnes of wood waste is generated in different phases of the value chain and incinerated after being applied only in one building. The EU-27 produced 60 million tons of wood waste in 2014 (1). There are several categories of wood waste treatment across countries, the most common being energy recovery (incineration) and recycling (panel board industry) (1). European policymakers are adopting circular economy policies and digitalisation strategies that are changing the way we produce and consume timber as well as handle wood waste. The European forests are under stress, and circularity and the cascading use of wood will significantly contribute to reducing the pressure on forests. The cascading use of wood refers to reuse over multiple use cycles, that is, using wood materials more than once, first for the originally intended purpose and then reusing for other purposes, finally recycling it into other wood products before its energy is recovered. Wood cascading delays emitting carbon into the atmosphere by several decades and allows natural resources to be used for a long time in different products instead of mining virgin forests. In countries like Norway, Switzerland, and Belgium, constellations of different actors (e.g. architects, deconstruction companies, local governments, and building owners) are investigating and implementing the reuse of timber in new constructions and renovations. A trend that can foster circularity transitions is digital technologies, such as laser scanning, blockchain, material passports, and artificial intelligence (2,3).

However, digital technologies have not been widely deployed for sustainability goals due to legislative and economic reasons, and investment lock-ins (3, 4). The renewal of new European and national laws and digital transformation strategies are opening new opportunities for circularity (5).

This paper is a product of the learning process in the Norwegian project SirkTRE (6), and specifically, the sub-project SirkLåve (Circular Barns), and aims to address the problem of underused and vacant barns and other agricultural buildings in Norway. This multiple-case project aims at understanding the feasibility, costs and benefits of circularity strategies such as deconstruction and reuse of wood in new projects or renovations. In 2022,

[1] Wendy Wuyts, Omtre AS, Norway, wendy@omtre.no
[2] Artur Tomczak, NTNU Norwegian University of Science and Technology, Norway, artur.b.tomczak@ntnu.no
[3] Kristine Nore, Omtre AS, Norway; kristine.nore@omtre.no
[4] Lizhen Huang, NTNU Norwegian University of Science and Technology, Norway; lizhen.huang@ntnu.no
[5] Thomas Haavi, NTNU Norwegian University of Science and Technology, Norway, thomas.haavi@ntnu.no

https://doi.org/10.52202/069179-0539

around 10 barns were selected within the SirkTRE project. The scope of this manuscript is the reuse of wood from barns deemed ineligible for renovation. Reuse of elements and components is one of the circularity strategies in the built environment, which can create value in different ways: "1) coherent financial structure and viability of the case company, 2) employment and value creation for partners in the value chain network, 3) customer value, 4) environmental impact reductions" (7). However, the reuse of timber is not widely deployed. One reason is that the environmental benefits of reusing timber are not adequately measured under the current carbon metrics (8). Notwithstanding, a low deployment of reuse has not always been the case in the Norwegian AEC sector. Before the Second World War, Norwegian society used to reuse building elements, but after the introduction of new materials and widespread education, accompanied by a new consumption culture, it adopted a linear and throw-away model (9), hence, missing opportunities in creating environmental, financial and social value.

One of the principles behind the SirkTre consortium is supporting the Norwegian industry to become a pioneer in wood reuse while leveraging new digital technologies not available in pre-war times. Back in 2021, the first questions we asked were *what are the best practices of reusing wood,* and *what are the lessons that pilot projects and the growing ecosystems of actors in European countries can provide us* for the Norwegian wood industry to leapfrog to a pioneering position in timber engineering for the circular built environment.

Different scholars investigated the barriers (10, 11, 35), as well as the factors that could enable the reuse of building components (12). Lack of data, as well as the fragmented coordination and exchange of information between key actors in an urban or regional ecosystem or a seamless data pipeline management, where circular systemic solutions could operate, is often pinpointed as one of the big obstacles in digital transformations for circularity (e.g. 14, 15, 16). Digital technologies can help address this perceived barrier of information asymmetry (16). Nordby (9) investigated the barriers and opportunities for reuse in Norway, pointing out technical and organisational, legal restrictions, and information needs. Nordby advocates for an information system that allows the transfer of the right information and data to the right stakeholders at the right moment (9). In literature and practice, there is evidence of an emergence in research, development, and implementation of digital technologies, and in particular information and communication technologies (ICT) enabling circular economy in the architecture, engineering, construction, and demolition sector (17,18). Bellini and Bang (18) did interviews in Norway on data management and also highlighted the lack of data availability and interoperability, lack of competencies, and unwillingness to share data as barriers.

Another concern that we encountered in the first phases of SirkLåve is the lack of a (perceived) fair distribution of costs, benefits, and risks in all the organisations involved in the phase of deconstruction, logistics, relocating, and environmental and economic valuation and reselling. One of the distributional aspects is related to data sharing and trust. Research on the success of Industrial symbiosis projects in the United Kingdom, (19) demonstrated that "the economic benefits should fulfil the desired economic expectation of any actor, and a fair benefit-sharing mechanism is essential to motivate the collaborative behaviours". Different stakeholders can benefit from these inventories, but this requires information facilitation and stakeholder collaboration. There are different stakeholders (users and suppliers of materials and information) who have their different information, personal, collaboration needs and requirements, but also *want* distributional justice and a *perceived* fair distribution of risks, costs and added value/benefits. Hence, we followed the process from the stage of reuse surveys to the actual reuse and map out which actors were involved and why.

2 ACTION RESEARCH

This multiple-case study is action research in engineering and management in the construction sector, addressing practical problems, and creating and extending existing theoretical frameworks (13). This paper should be regarded as an intermediate report of a still ongoing action research within SirkTRE tackling practical problems related to information requirements for reclamation and reuse of wood elements in construction.

2.1 Authors' roles and perspectives

SirkLåve is an applied research project in which learning and innovation are iterative processes. We wish to understand the challenges, costs, and benefits of new digital technologies with the objective of increasing the wider uptake of reclaimed wood. The authors involved in circWOOD and SirkTRE projects (6) had roles ranging from project managers or work package leaders to researchers and solution designers. We had access to internal documents and participated in meetings to discuss, for example, data collection. In 2022, the first author assumed the role of critical researcher, and in early 2023, joined the start-up leading this sub-project in SirkTRE. Thus, this manuscript reflects and describes the learning processes and decisions from a practitioners' perspective. The remainder of this paper includes reflections about mistakes and failures that hindered the authors in calculating the precise impacts at each stage in the life cycle of the different wood elements, as even failures and mistakes can provide valuable insights for the future phases of SirkTRE and SirkLåve, planned for 2023-2024). Consequently, the *learning by doing* was an organic but messy process, which constitutes the foreground in our discussion.

2.2 Desktop-based research and consulting key informants

The first phase involved desktop-based research during 2022. We sought insights on wood reuse workflows and their dataflows on Google Scholar and Scopus. We

reached out to our European networks of circular economy and construction to learn about processes in different life cycle phases and digital solutions which (can) support these practices. We held conversations with key informants and attended international networking events on digital technologies for the built environment and wood reuse. We had talks with key informants and partners in the SirkTRE consortium and read their reports and blogs. We drew from previous research and reflected on circularity in the (timber) construction sector in Norway, Japan, and Belgium. In this sense, we did not do a systematic but rather a critical literature review, relying on academic and industrial circles (20). The risk of this approach is cherry picking potentially missing relevant solutions. On the other hand, as we consider this as an interactive learning process in which we keep our options open, we acknowledge the risk of this approach. The exploratory desktop-based research led to the adoption of an existing framework which helped us to frame and structure the different solutions and information needs we encountered in reclaiming wood from barns to integrate them in new applications.

Fig. 1. Reference building, a traditional Norwegian barn, dismantled in spring 2021. Source: Omtre AS.

2.3 'Follow the Thing'

For transparency, we were not present in every stage in every barn case in SirkLåve. The first author was not often on-site and embraced the role of critical investigator in this case study. On the other hand, as we were also interested in tracing and tracking wood elements, the first author applied the 'Follow the Thing' approach to comprehend the relations between the wood elements and the stakeholders and how digital solutions did or did not help. The 'Follow the Thing' approach is inspired by the work of Appudarai, and developed by Cooke and his colleagues as some sort of 'geographical detective work' (21). In this approach, you start with a product and investigate which people were involved in the creation of this product. Thus, we followed both the material and the data. In some cases, we started with the wood elements in a storage place and asked where it came from and where it might end up. In other barn cases, we started with the barn itself and traced what happened afterwards with the wood elements, which data was created and collected, and used afterwards. This detective-style process became our *modus operandi*.

3 THE FIVE "D"s FRAMEWORK

This conference paper focuses on digital technologies that can assist in the identification of material stock hibernating in vacant constructions that will not serve society anymore (otherwise, it would be more circular to sustain the structure and repurpose them, see (22)) to the relocation of these materials for a new purpose. The structure of this paper follows the 5"D"s-framework by Catherine De Wolf: Data, Detection, Disassembly, Distribution, and Design (23).

3.1 Data (for sourcing)

Data stands for the collection of macro-level data to track which material stocks are or will be available soon which helps planners to prioritise which stocks to reclaim (24). Stock tracking can be done with geographical information systems (GIS) and estimation models of vacancy (see e.g. 25, 26). However, this macro-level data -or estimations- is often not detailed enough for reclaimed wood scouting professionals. Other data that should be collected is which organisations own how much wood waste and in which fractions they are sorted and stacked, for example.

3.2 Detection

Detection refers to the collection of micro-level data and the creation of material, building passports, or building information models. Scholars have investigated designs of digital tools or proposed design criteria for tools to enable reuse of building materials and components. For instance, Durmisevic et al. (48) designed reversible Building Information Model (BIM) to estimate reuse potential, however not with enough data on which function these building components could be reused. Other scholars investigated digital technologies surrounding material banks and platforms where materials get stored and exchanged for value, foregrounding BIM objects as a key intermediary product (27-29). All these technologies need data inputs, and therefore wood reuse surveys or diagnostic tools are required. Starting from available material stocks which can be reclaimed, we can distinguish between different material sources for reuse, which implies several stakeholders. The first group of key actors are the owners of the materials that can sell or donate their timber. In the case of timber in buildings, urban miners, specialised demolition companies, or deconstruction companies, can harvest the materials, often after a reuse survey. In the current state-of-art, these reuse surveys are often done by visual inspection, but sometimes digital scans are also used as a basis for BIM models. Some researchers suggest transcribing such information into Material Passports, which is a tool for value tracking (3).

3.3 Disassembly

Disassembly is a type of non-destructive deconstruction where the objective is to harvest components or materials which are needed for later design. Unlike demolition, where the final product is pure waste, disassembly aims at

https://doi.org/10.52202/069179-0539

waste reduction and mining as many useful elements as possible. In addition, other information that is needed concerns how to disassemble and evaluate safety and feasibility. These reuse surveys can reduce health and safety risk for the deconstruction staff in later phases. OPALIS (30) calls to consider the health and safety risks to be included in the reuse surveys, such as the presence of hazardous substances or if dismantling and subsequent operations would present a safety risk.

3.4 Distribution

Distribution encompasses the logistics: transport and storage. As materials are often not reused directly after mining, the workflow requires a physical circular hub, material banks, and other spaces where the material is collected and pre-treated. They are often at the periphery of cities unless the public authorities provide a space (e.g. Material bank in Trondheim, Norway, RotorDc in Brussels). There, the reclaimed material is often separated according to quality, and which functions they can serve as well as pre-treated. The pre-treatment is a time-intense process, because each reclaimed material is different. For example, in reclaimed wood, nails and hazards have to be removed, while metals (e.g. steel) could be melted. Some of these materials must be treated locally. For example, concrete that has to be recycled locally, not only for environmental reasons, but technical feasibility too (31), while reclaimed wood can be sold to manufacturing companies who integrate them into building components (32).

3.5 Design

Following the above, these building components can return to the supply chain and be sold to those who build new or renovate existing buildings. However, consecutive design requires knowledge, processes, and competencies that are scarce in the current market. Standardisation can help reduce the need for all these "knowledge search costs". A potential enabler is the parametric design approach, where multiple alternatives can be compared in a short time, but it requires proper preparation of the input information, both geometrical and alphanumeric, as well as computational engineering competencies.

4 DIGITAL SOLUTIONS USE CASES

We read the SirkLåve experiments through distributional justice goggles. It is pivotal to ask who benefits, who pays, and who will be accounted for the risk. Some benefits can be perceived as valuable for society, but not for certain stakeholders. For example, interviews on platforms for industrial symbiosis in Norway indicated that managers see sustainability often as a profit-losing business, with benefits for society, but not for the company itself (15). Implicitly, each task requires *specialised* labour with the associated costs for the business itself. In the next section, we focus on costs, benefits, and risks for the *specialised* labour force, using the chosen method, and drawing from live experiences and participatory and marginal observations in SirkLåve.

By winter 2022, we traced wood elements from 6 barns. Table 1 provides an overview of the barns and who got involved in which phases.

Table 1: Experiments and learning experiences on 1. data stage, 2. detection, 3. disassembly, 4. distribution, 5. design, with experimentations done by ◆: NTNU students; ▲: NTNU staff; ●: Omtre AS, ⬢ other SirkTRE demolition and reuse survey organisations, ★: architects and structural engineers, ֍: destructive testing facilities

Barn cases	1	2	3	4	5
C1. Kviteseid, Telemark (Fig. 2)	●	▲◆֍	⬢		
C2. Nes 1, Ådal	●	▲◆֍	⬢		
C3. Nes 2, Ådal	●	▲◆֍	⬢		
C4. Brøttum barn (Fig. 1), with part reused in Slettelokka	●	●	●	●	★◆
C5. Nedre Sem barn, Asker	●⬢	●⬢	⬢	⬢	★⬢
C6. Hønefoss	●	●			

4.1 Data

This stage of collecting data on where and how much reclaimable wood was available, was skipped in the first phase of SirkLåve. Firstly, because the problem of obsolete barns is known, and secondly because the empty barns offered free by their owners were located far, implying a high demolition and waste management costs making it necessary to look into alternatives. The only information that was required for deciding to take this project was the distance costs between the location of the barn and the involved actors of the next D-stages. Noteworthy, barns are widely spread over the countryside which implies longer travel time and transport costs for labour, equipment, and tools; hence, reclaiming the wood might not be economically viable.

4.2 Detection

Different reuse survey methods or diagnostic tools were explored in the Sirklåve project in 2022. Table 2 lists the diagnostic tools and the data analysed by the different stakeholders. In case (6), we observed an expert (with material and building knowledge and surveyance experience), who judged by visual inspection and verified with a crowbar that there was not enough suitable wood for reuse, although no laser scanning was performed. The C6 project ended there; it got demolished in the traditional way. In cooperation with students, partners who are certified to grade materials did destructive testing on elements of cases C2-3. The timber elements were graded as C30 and above (47).

In cases C1-3, a LEICA scanner was used for on-site diagnosis. The scanning took a full day. The 2 students involved in transferring the scans to BIM-objects needed 2-3 weeks, partly because they struggled with material identification and the lack of data of the interior (Fig 2). Please refer to (33) for the technical details. The process was slow, implying high specialised labour costs (i.e. BIM). This issue with scanners has been reported in previous research (4).

Fig. 2. Before and after processing the scan by the two NTNU students. Source (33).

In all these six cases, different basic tools and methods were used to make a data inventory. The reclaimers took mostly photographs and short notes, and made lists of photographs, inserted in templates or cost-benefit reports and invoices. In research projects, the focus is mostly on high-technologies, like scan-to-BIM, and often coupled with automation detection or artificial intelligence (i.e. deep learning methods), which requires large training datasets. We tried different methods, including the use of LEICA scanners, but there was no data availability downstream in the value chain.

Table 2: Overview of diagnostic methods

Data collection method	Technology	Data stored	Barn cases
Destructive quality test	Press test	Reports	C2-3
Non-destructive	X-ray	Compressed images	None.
Scan (of barn onsite)	Laser scanning	Point cloud , processed into BIM object	C1-3
Scan of elements (in sorting centre)	Photogram metry	Mesh, texture	C4
Modelling / estimating	GIS	Graph data, tabular data	None
Visiting the site and measuring with analogue tools	based on hindsight experiences	Photographs (JPEG, PNG); Excel	All
Archive work		PDFs, plans, etc.	C1-C3

4.3 Disassembly

The footprint of one barn (C4; Fig. 1) was ca. 600 m2 and 12–15 m height. There were 158 timber framing elements that ended up in the material bank of Omtre AS, where they were measured and assessed. Then, 66 were selected and further integrated in the new construction, substituting 144 elements from the design of Slettelokka project in Oslo (34). This was made possible by cutting out some elements and assigning them to multiple locations in the model. An important step was labelling (i.e. tagging, adding unique identifiers) for later tracking and tracing wood elements. In most cases, the tagging was performed in the storage places. Numbers, added manually, corresponded with the excel lists that include the inventory, and data about dimensions of these wood elements, next to the descriptions of the faults, such as potholes and carvings. This included those elements that we know are of lower quality (8%) (visual test). Different people measured in two different days (one day in August, and a second day in November 2022) 158 elements with a total volume of 18,4 cubic metres (8,2 cubic metres and 10,2 cubic metres in November). We took photographs of all the elements, including special features, like pockets and carvings. Some scans were captured with a handheld scanner and the Leica scanner, but the process was slow and inefficient.

4.4 Distribution

The distribution and relocation of the wood emits CO2, depending on the means of transport, which is again dependent on the existing logistic infrastructures and systems. There are questions on how much CO2 would be emitted in the deconstruction, manufacture, and transport, especially from the wood products used in the new construction. Most barns are in the periphery of cities like Oslo and Trondheim where they will be integrated, and long travel distances are unavoidable. We needed to critically examine if the CO2 that is avoided and/or captured compensates enough the CO2 emitted in the process.

In case of barn 1, we estimated that the travel distance of one wood element from source (empty barn) to the new construction was 270 km. This is still low compared with the travel distances that virgin wood often travels in the global timber markets. However, we are not certain, as we did not have advanced tags with geolocation data.

Barn C5 was an ideal project from an economic and environmental cost-benefit perspective; the barn and the new project both were and will be located in the same municipality, reducing transport costs in a significant way. Barn C6 was close to the storage space. However, the quality of the reclaimable wood was not deemed as high value.

Additionally, the materials are stored somewhere and for a period. Storage space and time have a cost, which was covered by the SirkTRE project's funding. In the case of these barns, it took at least a year before some building elements were reintegrated. More research is needed on governance and business models to reduce the cost of the storage requirements enabling reuse.

4.5 Design

A fraction of the reclaimed wood from C4 would be integrated in the Sletteloka construction project in Oslo in spring 2023 (34). The designers will use the spreadsheet

https://doi.org/10.52202/069179-0539

list, made after Disassembly and the few images to select the elements for the integration in the Slettelokka design. This led to reflections if scan-to-BIM are needed, and if useful information for design can be used in a more controlled environment, with fast scanners that can label, process, and separate wood elements.

5 DISCUSSION

5.1 Information requirements

In all the D-stages, there are different data requirements, for the different possible users of this information (see e.g. 35). These follow the information requirements in any construction project (see 36); however, there are some new roles and stages that need an expansion in these lists. Sustainability consultants and researchers need data inventories that help them calculate environmental life cycle costs in their Life Cycle Assessment (LCA), and specialised demolition companies need lists with geographic coordinates to harvest reusable components before demolition, etc. We observed indeed the need and emergence of new actors with their own information requirements, as echoed in Table 2. The actors involved in collecting the data and making decisions in the experimentation stages, were the urban miners and specialised demolition companies (●; ⬢) , environmental impact researchers and consultants for the economic and environmental validation (◆; ▲), and designers (★). They have their own information requirements and this D-framework helps mapping the information flows and requirements, which in turn helps collecting data on environmental and economic risks and benefits and assess if this circular economy practice is really sustainable. Figure 3 outlines the workflow for 2022.

Noteworthy, the data collection for diagnosis and data flows are partly subsidised by education institutes (employing students) and research and innovation funds. Not many high-tech digital solutions were used, and this was a (specialised) labour-intensive action research project. On the other hand, this organic and messy learning process and experimentation has led to insights about requirements and specifications for digital solutions (e.g. scanner specifications), which will inform the purchase of equipment in the next phase of SirkTRE. One of the specifications is a result of learning about unintended negative impacts. While learning about all these different tools, we became aware of the growing evidence on the environmental costs of data spaces, programming languages, data formats and their consumption of resources (e.g. 37 about the energy consumption of more than 20 software programming languages).

5.2 Limit in tracking and tracing the wood elements in the case study

We applied the 'Follow-the-Thing' approach to investigate who used which digital solutions during all these phases. However, we did not apply advanced tags to enable tracking and tracing of different wood elements reclaimed from all these six barns, which presented a severe limitation for understanding and collecting data about environmental and economic impacts. Additionally, it was a challenge for the first author to have an overview of the different material and data flows for the different barns: identifying who did what, what did not happen, and the logics behind the different decisions in the material and data flows. In the next phase of SirkTRE, we will investigate different tagging tools to improve traceability and tracking, from QR-codes, bar codes to even wood print solutions (i.e. the constellations of knots can serve as unique identifiers). This would also include deeper studies on data formats, interoperability protocols, and data pipeline management. Currently, our reflections on what happened in 2022 are informing the design of a more standardised workflow for the barns-to-construction projects to be implemented in the following years.

5.3 Tensions with social impact

Barns are part of the cultural heritage of rural landscapes in Norway. There is an observation in the literature (e.g. 38) that cultural heritage and rural circularity practices such as renovation and reuse are interlinked. However, there might also be tensions. In SirkLåve, the barns were offered by the barn owners until now. As long as empty constructions are offered, the circular business model should work, while reducing costs. In Japan, the problem of empty houses is in some cases transformed in opportunities for new purposes creating positive social impacts (39). However, there can also be negative impacts. Altering the rural landscapes in this way might create tensions with sustainability goals of heritage and identity (40). Besides the legal owners, there are neighbours who are culturally the inheritors of these rural landscapes, where barns are considered as inherent landscape scenery, and might feel distressed by changes in the landscape and features that make them feel at home (41). In some places, the constructions will be restored to preserve the identity, but mostly deconstruction, or worse demolition, takes place. By deconstructing the barn, there is the risk that we erode the Norwegian rural identity of that landscape. On the other hand, in interviews with urban miners active in rural southern Norway, we heard about the supporting communication and branding practice for preserving the story of the reclaimed materials. Thus, they can sell the materials if it comes from a building with a historical value. The idea is to collect these stories in the Detection stage (or relabel these steps as part of the Documentation stage). This would contribute to tracing the source of these materials too. However, it was out of the scope to document complaints of neighbours and look into renovation and rural revitalisation strategies. This is one of the potential social value creations—or destructions which can occur in a project such as SirkLåve. Social value creation (or destruction) through circular economy is still under-researched (42).

5.4 Reflecting on the Ds-framework and diverse value creation

The Ds-framework helped us to structure fragmented actions and knowledge creation in different life cycle phases but is focused on data collection and processing for the technical aspects surrounding reuse, namely enabling logistics, design and calculations.

The Detection stage can encompass different diagnoses or detections. One important stage, especially for a material such as wood, is the quality testing and grading. Destructive testing was done by certified stakeholders for elements of barns C2-3. The elements were graded as C30 or above (see 48). However, not all elements can be destructively tested, if we want to reuse them. Then there is also the critique on the current 'virgin wood' grading system. Thus. there is a new standard being developed for reclaimed material. That standardisation work is part of SirkTre consortium (in another work package). The current grading system does hinder a wider uptake because of the uncertainty about ownership of the risks that cannot be covered by the current grading system. The legal research on accountability is outside the scope of this paper, but we mention the legal research to stress out that there is a need for a D-stage of (legal) documentation.

Documentation is the negotiation process where risks are documented through experts or digital technologies. One of the reasons behind documentation and data storage is risk reduction for stakeholders in the construction projects itself, especially in the case of larger projects using reclaimed matters in structures and load-bearing functions. Documentation should include data and information (which implies qualitative data) about social and other values for the different stakeholders, including neighbours and even full landscapes.

Dissemination is the ongoing process that attracts the required suppliers, users of information, and materials. This includes materials for public authorities that want to monitor circularity and the diverse value creations but also materials for training. Universities and other educational institutions are essential for training and educating the required workforce, as well as for monitoring the life cycle costs and advising other key actors about the potential for value creation of the various circularity strategies such as reuse.

5.5 Preconditions for scalability

Early 2023, the reclaiming of wood from abandoned barns is still a small-scale endeavour within the SirkTRE project. One reason is that barns are small-scale sources of materials and require time and effort. Another bottlenecks is the diagnostic tool in reuse surveys. Both high- and low-tech reuse survey methods are time consuming, not only for collecting but also the processing of the complex data (4). Additionally, high-tech methods require large investment and operation costs because of equipment like laser scanning (4). On the other hand, this is a rapidly changing market and we have become more knowledgeable about new diagnostic tools (e.g. 43) which addresses these problems. However, we have noted two concerns.

First, those reuse methods are often tested and applied in high-density areas like cities, while barns are located in remote settings, deep in land and far away from cost effective infrastructure such as river and maritime ways. Therefore, space matters. In the past 1-2 years of the SirkTre experimentations, we have applied a critical lens to the contexts or territories in which these pilot cases and constellations emerge, as different studies already demonstrated how spatial aspects are important for sustainability transitions (44), including for circularity (39). We have to note that actors behind these innovations are situated in economic regions in the periphery with high to moderate levels of cooperation and innovation (e.g. Gjøvik, Asker), but also in less cooperative and innovative regions (e.g. Hønefoss) (45). A more territorial approach on the economic geography of innovations can bring better insights on where urban mining businesses, using diagnostic methods, can thrive.

Second, in other projects in Belgian, Swiss, and Dutch constellations, such as the BAMB project (3), the reuse survey included visits to the building to make a diagnosis of how many and which elements can be reclaimed. This would include tagging and giving all reclaimable elements an unique identifier on-site. However, the tagging of every wood element is only possible after deconstruction. In our experiments, the tagging (and start of tracing) happened in the first temporary storage space, which is often a more controlled and more comfortable environment than a 'chaotic' deconstruction site. In the Nordic timber construction sector, off-site prefab manufacturing is encouraged, and off-site diagnosing, integrated in other off-site processes such as sorting, might be safer and more efficient than on-site diagnosis.

5.6. The risk of linearity at industrial scale

One of the remaining important questions in the iterative learning process is how to scale up to an industrial scale. This activity at industrial scale should compete with the forestry sector and linear waste management practices in a country like Norway. Early 2023, we evaluated the fractions of barns as a possible input for an industrial processing plant. However, the fractions arrive in small volumes, are heterogeneous and not secure, while industrial processing prefers the opposite. This can lead to the risk that reclaimed wood from barns might not be selected for a reuse economy at the industrial scale in the next phase of the consortium. The reuse economy, like the recycling economy, can fall into the profit-oriented logic trap of capitalism. There is considerable critical literature on reuse centres, e.g. in the clothing sector, highlighting how such centres do not address the roots of high consumption, and might even lead to more guilt-free consumption and waste creation of often low-quality items (e.g. 46). Ironically, while the barns in five of these six cases contain enough amounts of high-quality wood, our observations and reflections suggest that the barns might not be considered in a portfolio of industrialised processes. Even more ironically, if this decision of

https://doi.org/10.52202/069179-0539

exclusion would happen, this would render the need for high-cost digital solutions obsolete, instead allowing human creativity and cooperative work, or pushing more circular activities such as repurposing the building and extending the service and lifetime of this construction, or even better, addressing the reasons why such buildings become obsolete in the first place.

6 CONCLUSION

In early 2023, the SirkTRE consortium is still in the first stage of the process of innovation, learning, and unlearning about what circularity means for the wood and timber construction sector, citizens, and public authorities. A fair distribution of costs, benefits, and risks is important, but as long the costs are higher than that in these other industries, and the benefits and other diverse value creations by such activities (e.g. safety, environmental health/toxicity, community cohesion, climate change mitigation and adaptation) do not get monetised or rewarded and valued by policy makers and other decision makers, the problems that circular economy intends to solve will only increase.

Different stakeholders require different data and information, which leads to additional costs. However, in a project like SirkLåve, these data flows are partly subsidised by education institutes (by employing students) and research and innovation funds. Not much high-tech was used, like fast wood scanners, and this was a (specialised) labour intensive action research project. Our final observation is that this model is not competitive on its own. These insights can help formulating the research design for future studies diving into where to draw the line between the cost of collecting and storing the data and information and the benefits of the actors, for different regulatory and economic scenarios. This can be part of a larger systems engineering framework, where this can be integrated in especial technical (e.g. requirement analysis) and agreement processes (e.g. which stakeholder takes responsibility and accountability for which risk and cost). Although the technology readiness level for the proposed methods is high, the market readiness and integration level of these circular systemic solutions in the timber Architecture, engineering, construction and demolition sector is low. Future research should focus more on the actual costs and the identification of sustainable business models and project governance for the required data and information management enabling reuse of materials in new constructions, as well as evaluating the phases in which data is collected and processed and where (e.g. onsite versus offsite) and when to integrate which digital solution.

Fig. 3. Workflow SirkLåve 2022

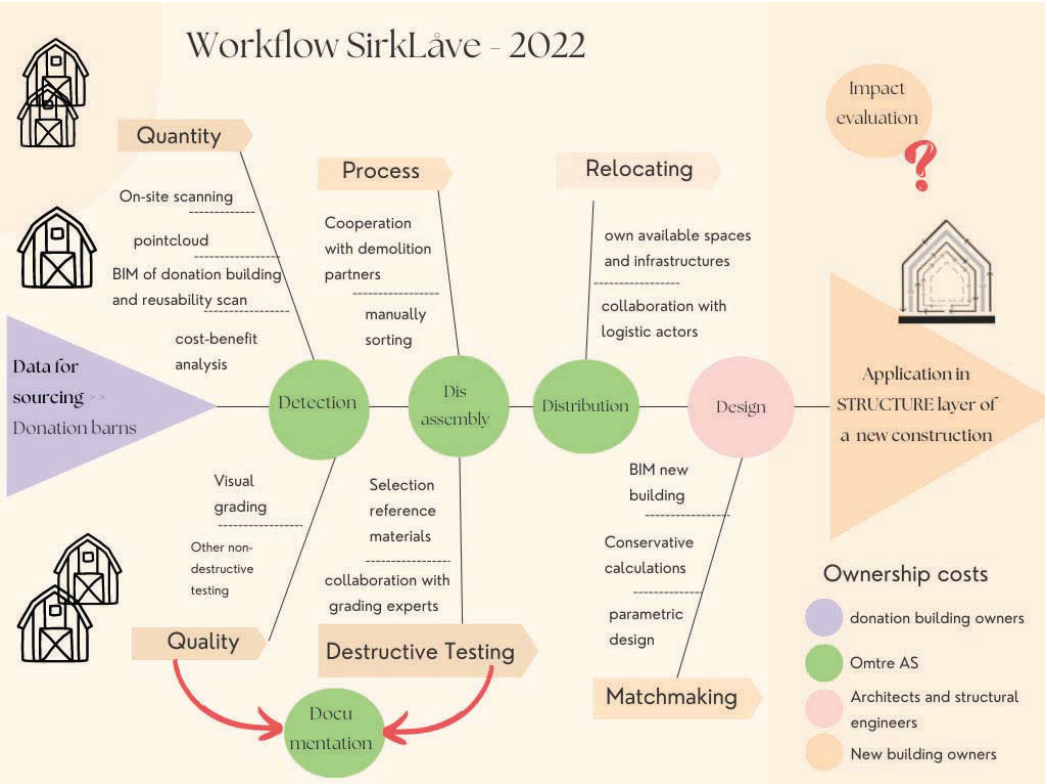

ACKNOWLEDGEMENTS

This conference paper is funded by the projects SirkTRE (project nr 328731) and circWOOD (project nr 328698), funded by the Norwegian Research Council. Secondly, we want to thank the other Omtre AS employees, other SirkTRE partners and NTNU students who contributed in the SirkLåve sub-project.

REFERENCES

[1] Bioreg 2015. 'Absorbing the Potential of Wood Waste in EU Regions and Industrial Bio-based Ecosystems — BioReg' Accessed at https://www.bioreg.eu/assets/delivrables/BIOREG%20D1.1%20EU%20Wood%20Waste%20Statistics%20Report.pdf

[2] Çetin, Sultan, Catherine De Wolf, and Nancy Bocken. 2021. "Circular Digital Built Environment: An Emerging Framework." *Sustainability: Science Practice and Policy* 13 (11): 6348.

[3] Luscuere, 2016, Materials Passports: Optimising value recovery from materials, Waste and Resource Management Volume 170 Issue WR1

[4] Uotila, U., Saari, A., & Junnonen, J. M. (2021). Investigating the barriers to laser scanning implementation in building refurbishment. Journal of Information Technology in Construction, 26, 249–262. https://doi.org/10.36680/j.itcon.2021.014

[5] Staab, P., Pietrón, D. and Hofmann, F., 2022. Sustainable Digital Market Design: A Data-Based Approach to the Circular Economy.

[6] SIRKTRE. 2022. SirkTRE website. Last accessed 31 January 2023. Home | SirkTre

[7] Nußholz, J.L., Rasmussen, F.N., Whalen, K. and Plepys, A., 2020. Material reuse in buildings: Implications of a circular business model for sustainable value creation. Journal of Cleaner Production, 245, p.118546.

[8] Parigi, D., Kanafani, K. and Rasmussen, F.N., 2022. Why current carbon metrics for buildings fail to show the benefits of timber reuse. In Structures and Architecture A Viable Urban Perspective? (pp. 559-566). CRC Press.

[9] Nordby, Anne Sigrid. 2009. "Salvageability of Building Materials: Reasons, Criteria and Consequences Regarding Architectural Design That Facilitate Reuse and Recycling." Norges teknisk-naturvitenskapelige universitet, Fakultet for arkitektur og billedkunst, Institutt for byggekunst, historie og teknologi. https://ntnuopen.ntnu.no/ntnu-xmlui/handle/11250/231092.

[10] Rakhshan, K., Morel, J.C., Alaka, H. and Charef, R., 2020. Components reuse in the building sector–A systematic review. *Waste Management & Research*, *38*(4), pp.347-370.

[11] Charef, R., Morel, J.C. and Rakhshan, K., 2021. Barriers to implementing the circular economy in the construction industry: A critical review. *Sustainability*, *13*(23), p.12989.

[12] Charef, R. and Lu, W., 2021. Factor dynamics to facilitate circular economy adoption in construction. *Journal of cleaner production*, *319*, p.128639.

[13] Salman Azhar; Irtishad Ahmad; and Maung K. Sein, 2009, Action Research as a Proactive Research Method for Construction Engineering and Management, Journal of Construction Engineering and Management
Vol. 136, Issue 1 (January 2010)

[14] Çetin, S., Gruis, V., Rukanova, B., Tan, Y.H. and De Wolf, C., 2022. A Conceptual Framework for a Digital Circular Built Environment: The Data Pipeline, Passport Generator and Passport Pool. In *2nd International Conference on Circular Systems for the Built Environment, ICSBE 2 (Hybrid/Online): Advanced Technological and Social solutions for Transitions* (pp. 97-106). Technische Universiteit Eindhoven.

[15] Krom, P., Piscicelli, L. and Frenken, K., 2022. Digital Platforms for Industrial Symbiosis. *Journal of Innovation Economics & Management*, pp.I124-XXVI.

[16] Knoth, K., Fufa, S.M. and Seilskjær, E., 2022. Barriers, success factors, and perspectives for the reuse of construction products in Norway. *Journal of Cleaner Production*, *337*, p.130494.

[17] Yu, Y., Yazan, D.M., Bhochhibhoya, S. and Volker, L., 2021. Towards Circular Economy through Industrial Symbiosis in the Dutch construction industry: A case of recycled concrete aggregates. *Journal of cleaner production*, *293*, p.126083.

[18] Bellini, A. and Bang, S., 2022, December. Barriers for data management as an enabler of circular economy: an exploratory study of the Norwegian AEC-industry. In *IOP Conference Series: Earth and Environmental Science* (Vol. 1122, No. 1, p. 012047). IOP Publishing

[19] Mirata, M., 2004. Experiences from early stages of a national industrial symbiosis programme in the UK: determinants and coordination challenges. *Journal of Cleaner production*, *12*(8-10), pp.967-983.

[20] Snyder, H., 2019. Literature review as a research methodology: An overview and guidelines. *Journal of business research*, *104*, pp.333-339.

[21] Cook, I. and Harrison, M., 2007. Follow the Thing: "West Indian Hot Pepper Sauce". Space and Culture, 10(1), pp.40-63.

[22] Wuyts, W., Miatto, A., Sedlitzky, R. and Tanikawa, H., 2019. Extending or ending the life of residential buildings in Japan: A social circular economy approach to the problem of short-lived constructions. Journal of Cleaner Production, 231, pp.660-670.

[23] De Wolf C. 2022. Inaugural talk of assistant professorship. Ceci ce n'est pas un pipe. ETH Zurich, Switzerland. 22 March 2022.

[24] Levoso, A.S., Gasol, C.M., Martínez-Blanco, J., Durany, X.G., Lehmann, M. and Gaya, R.F., 2020. Methodological framework for the implementation of

https://doi.org/10.52202/069179-0539

circular economy in urban systems. *Journal of Cleaner Production*, *248*, p.119227.

[25] Wuyts, W., Sedlitzky, R., Morita, M. and Tanikawa, H., 2020. Understanding and managing vacant houses in support of a material stock-type society—The case of Kitakyushu, Japan. *Sustainability*, *12*(13), p.5363.

[26] Wuyts W.; Miatto A.; Khumvongsa K.; Guo J.; Aalto, P: Huang L. 2022. "How can Material Stock Studies Assist the Implementation of the Circular Economy in Cities?" Environmental Science & Technology

[27] Jayasinghe, L.B. and Waldmann, D., 2020. Development of a BIM-based web tool as a material and component bank for a sustainable construction industry. *Sustainability*, *12*(5), p.1766.

[28] Cai, G. and Waldmann, D., 2019. A material and component bank to facilitate material recycling and component reuse for a sustainable construction: Concept and preliminary study. *Clean Technologies and Environmental Policy*, *21*, pp.2015-2032.

[29] Xing, K., Kim, K.P. and Ness, D., 2020. Cloud-BIM enabled cyber-physical data and service platforms for building component reuse. *Sustainability*, *12*(24), p.10329.

[30] OPALIS 2022. FCRBE Reuse toolkit - the reclamation audit. Last accessed 02 February 2023. https://opalis.eu/sites/default/files/2022-02/FCRBE-Reclamation_Audit-v12.pdf

[31] Van den Berghe, K.B. and Verhagen, T.J., 2021. Making it concrete: Analysing the role of concrete plants' locations for circular city policy goals. *Frontiers in Built Environment*, p.136.

[32] Virtanen, M., K. Manskinen, V. Uusitalo, J. Syvänne, and K. Cura. 2019. "Regional Material Flow Tools to Promote Circular Economy." *Journal of Cleaner Production*. https://doi.org/10.1016/j.jclepro.2019.06.326.

[33] Rekdal, J.C. and Billing, J.B.N., 2022. *Scan to BIM av eksisterende bygg* (Bachelor's thesis, NTNU).

[34] Łuczkowski, M., Tomczak, A., Izumi, B. 2023, Proposal Of Interactive Workflow For Circular Timber Structure Design (forthcoming)

[35] Tomczak et al. (2023). Challenges and experiences with the reuse of products in building design. 14th European Conference on Product & Process Modelling. At: Trondheim, Norway

[36] Tomczak, A., v Berlo, L., Krijnen, T., Borrmann, A. and Bolpagni, M., 2022, November. A review of methods to specify information requirements in digital construction projects. In *IOP Conference Series: Earth and Environmental Science* (Vol. 1101, No. 9, p. 092024). IOP Publishing.

[37] Pereira, R., Couto, M., Ribeiro, F., Rua, R., Cunha, J., Fernandes, J.P. and Saraiva, J., 2017, October. Energy efficiency across programming languages: how do energy, time, and memory relate?. In *Proceedings of the 10th ACM SIGPLAN International Conference on Software Language Engineering* (pp. 256-267).

[38] Wuyts, W. and Majidi, A.N., 2022, December. Towards solutions and infrastructure for circular neighbourhoods in rural areas. In *IOP Conference Series: Earth and Environmental Science* (Vol. 1122, No. 1, p. 012023). IOP Publishing.

[39] Wuyts, W. and Marjanović, M., 2022. The Development of Spatial Circularity Discourse in Japan: Ecomodernist, Territorialised, or Both? The Story of Onomichi's Wastescapes. *Circular Economy and Sustainability*, pp.1-27.

[40] Preston, S.D. and Gelman, S.A., 2020. This land is my land: Psychological ownership increases willingness to protect the natural world more than legal ownership. Journal of environmental psychology, 70, p.101443.

[41] Kaltenborn, B.P. and Bjerke, T., 2002. Associations between landscape preferences and place attachment: a study in Røros, Southern Norway. Landscape Research, 27(4), pp.381-396.

[42] Quintelier, K.J., van Bommel, K., van Erkelens, A.M. and Wempe, J., 2023. People at the heart of circularity: A mixed methods study about trade-offs, synergies, and strategies related to circular and social organizing. *Journal of Cleaner Production*, *387*, p.135780.

[43] Raghu, D., Markopoulou, A., Marengo, M., Neri, I., Chronis, A. and De Wolf, C., 2022. Enabling Component Reuse From Existing Buildings Using Machine Learning-Using Google Street View to Enhance Building Databases. In *Proceedings of the 27th International Conference on Computer-Aided Architectural Design Research in Asia (CAADRIA 2022)* (Vol. 2, pp. 577-586). Association for Computer Aided Architectural Design Research in Asia (CAADRIA).

[44] Coenen, L., Benneworth, P. and Truffer, B., 2012. Toward a spatial perspective on sustainability transitions. *Research policy*, *41*(6), pp.968-979.

[45] Giuseppe Calignano, Trond Nilsen, Anne Jørgensen Nordli & Atle Hauge (2022): Beyond 'periphery': a detailed and nuanced taxonomy of the Norwegian regions, Geografiska Annaler: Series B, Human Geography, DOI: 10.1080/04353684.2022.2141654

[46] Berry, B., 2022. Glut: Affective Labor and the Burden of Abundance in Secondhand Economies. *Anthropology of Work Review*, *43*(1), pp.26-37.

[47] Fauske, J.K., Rokke, Å. and Sveen, T.H., 2022. *Ombruk av eldre trevirke* (Bachelor's thesis, NTNU).

[48] Durmisevic, E., Guerriero, A., Boje, C., Domange, B. and Bosch, G., 2021, October. Development of a conceptual digital deconstruction platform with integrated Reversible BIM to aid decision making and facilitate a circular economy. In *Proceedings of the the Joint Conference CIB W78-LDAC, Luxembourg* (pp. 11-15).

World Conference on Timber Engineering Oslo 2023

FERROCEMENT WOODEN HOUSE: LEARNING FROM POST-DISASTER RECONSTRUCTION IN INDONESIA

Andry Widyowijatnoko[1], Dibya Kusyala[2], Fajar Ikhwan Harnomo[3]

ABSTRACT: Earthquakes are the most common natural disasters in Indonesia, frequently causing not just deaths but also considerable damage to buildings and infrastructure. As a result, a quick and effective post-disaster reconstruction infrastructure is required to ensure that recovery operations can begin as soon as feasible. The need for temporary shelters that are adequate and ready to be upgraded to permanent housing in order to reduce the cost involved and reduce construction waste. In response to these constraints, this paper aims to offer an alternative viewpoint on developing a post-disaster architecture reconstruction system leveraging local wood as an affordable material resource that integrates Ferrocement as part of the architectural elements. In addition, the involvement of local workers addresses the shortage of skilled labour and creates employment opportunities for local communities. The paper provides a comprehensive review of the advantages and limitations of the technique and recommends future research and development.

KEYWORDS: Post Disaster, Rehabilitation, Reconstruction, Local Wood

1 INTRODUCTION

Due to its location on the "Pacific Ring of Fire," an active subduction zone area, Indonesia is a country with considerable earthquake activity. Most earthquake disasters in Indonesia have a significant influence on people's life, resulting in deaths, material losses, and severe psychological suffering. Many big earthquakes have occurred in Indonesia in the previous 20 years, according to documented data [1] including the 2004 Aceh earthquake, the 2006 Yogyakarta earthquake, the 2010 Mentawai earthquake, and the 2018 Lombok earthquake. The greatest earthquake to date was the Aceh Earthquake, which measured 9.1 on the Richter scale and produced a massive tsunami wave to impact the coast of Sumatra, including Aceh. Additionally, the most recent earthquake in Indonesia was the Cianjur Earthquake [2], which occurred in 2022 and had a magnitude of 5.6. According to data from the National Disaster Management Agency, 272 persons were killed, 2,046 were wounded, and 62,545 were displaced. There were 56,311 dwellings affected, with 22,267 badly damaged, 11,836 moderately damaged, and 22,208 lightly damaged.

The Indonesian government and elements of society continue to improve preparedness and handling in the face of earthquake disasters. The first step when an earthquake occurs in order of time is to collect information and distribute assistance to institutions and donors to distribute aid. Further steps rebuild damaged infrastructure, one of which is public buildings, and continue with efforts to rebuild housing for affected communities. The earliest emergency effort that needs to be done is the provision of health facilities by building posts and initial buildings so that people can continue their activities and slowly improve their quality of life.

On the other hand, mobility is usually a constraint in the post-disaster restoration procedure on the spot. According to Sinaga [2], the handling of the Mentawai Earthquake rebuilding and rehabilitation in 2010 was constrained by cross-sectoral coordination, which was still difficult to carry properly. Furthermore, the difficulty of post-disaster rebuilding is tied to a wide range of interests and a considerable expenditure. As a result, for two years following the Mentawai Earthquake, victims of the earthquake and tsunami were housed in insufficient temporary shelters.

2 RESIDENTIAL REHABILITATION OF THE COMMUNITY IMPACTED

In responding to the impact of the disaster, the Indonesian government and humanitarian agencies have so far worked together to provide shelter. The Indonesian government usually works with international organizations such as the United Nations (UN) and the International Committee of the Red Cross and Red Crescent (ICRC) to provide shelter assistance for earthquake victims. In addition, many non-governmental organizations are also involved in relief efforts for earthquake victims in Indonesia.
Here are some of the forms of housing reconstruction that are usually provided:

[1] Andry Widyowijatnoko, Institut Teknologi Bandung, Indonesia, andry@itb.ac.id
[2] Dibya Kusyala, Institut Teknologi Bandung, Indonesia, dibja@itb.ac.id
[3] Fajar Ikhwan Harnomo, Institut Teknologi Nasional Bandung (Itenas), Bandung, fajarharnomo@gmail.com

https://doi.org/10.52202/069179-0540

1. Temporary shelter. Once earthquake victims lose their homes, the government and humanitarian organizations offer temporary shelters such as tents, posts, or emergency houses for victims to use while they recover.
2. Home rehabilitation. After the earthquake, the government and humanitarian organizations assist victims in rebuilding or renovating their earthquake-damaged houses. This aid might take the shape of building supplies, financial assistance, or skilled technical advice.
3. Housing programs: Long-term housing programs can be implemented to help earthquake victims obtain liveable homes. These programs can take the form of government assistance to build new houses or provide low-interest housing loans for earthquake victims.

Furthermore, the Institut Teknologi Bandung (ITB), with the assistance of Rumah Amal Salman and the Institute for Research and Community Service, took some action by creating drawings and specifications for refugee shelter. The design and structure were designed to be safe, earthquake resistant, quick to assemble and disassemble, and capable of comfortably accommodating numerous migrants. Moreover, the materials and resources required to construct the refugee barracks must be made accessible during implementation. This includes construction supplies, tools and equipment, and on-the-job labour. In actuality, inexperienced victims are frequently accessible. To guarantee that the refugee barracks are erected appropriately and safely, careful construction and oversight are required.

Standardized designs and standards are necessary, and all of the structure's components must be tested before usage. Additionally, measures to maintain and care for these shared facilities are required to keep refugees safe and comfortable. Other fundamental facility requirements, such as clean water, sanitation, and health care. The government, non-governmental organizations (NGOs), and communities must also collaborate to ensure that evacuees' needs are fulfilled and that they receive the appropriate help during the disaster recovery phase.

3 MATERIAL MATTERS

3.1 INDUSTRIAL MATERIALS vs BIO-BASED MATERIALS

For the speed of on-site construction, the solutions that are now widely used are industrial materials such as concrete and lightweight steel (Figure 1 and Figure 2). While buildings made from concrete and steel materials can provide the stability and strength needed to withstand earthquakes, some drawbacks need to be considered when using these types of buildings for post-earthquake relief, including:

1 Because of the expensive materials and intricate construction procedure, buildings composed of concrete and steel have high expenses.

2 The construction of concrete and steel buildings takes a long time and necessitates a large amount of work as well as specialized equipment. This has the potential to stymie the post-earthquake reconstruction effort.

3 Concrete and steel materials are not ecologically friendly since their production and transportation consume a lot of energy and emit a lot of carbon dioxide.

4 Because of the frequent vibrations induced by earthquakes, concrete and steel constructions are prone to material fatigue. This might result in serious damage to the structure, especially if it is built in an earthquake-prone location.

5 Concrete and steel structures are difficult to demolish and recycle. This might cause environmental and social issues, especially if the building needs to be demolished to return the area to its former state when the post-earthquake relief is finished.

Figure 1: *Shelters built in Petobo, Palu, using light steel, spandex roofs and GRC walls.*

Figure 2: *Model house using risha concrete frame and GRC wall covering.*

On the other hand, bio-based materials are materials derived from natural sources, especially trees that are widely available in nature in Indonesia, and have several advantages as post-earthquake building materials, including:

1 Bio-based materials are manufactured from recyclable natural resources and have a lesser environmental effect than traditional materials like concrete and steel.

2 Certain bio-based materials, such as bamboo and laminated wood, have high strength and durability and may be utilized to construct sturdy and earthquake-resistant structures.

3 Bio-based materials such as bamboo and wood are widely available and reasonably priced in many regions of Indonesia.

4 Because some bio-based materials, such as coconut fibre and straw, disintegrate naturally, they do not cause environmental or social difficulties when the structure is demolished.

5 Since bio-based materials have natural colours and textures, they may improve the appearance of buildings while also enriching local cultural values and traditions.

6 Bio-based materials, such as bamboo, can absorb and minimize seismic vibrations, reducing building damage.

7 Certain bio-based materials offer high thermal qualities, such as heat and sound insulation, which can aid in the creation of comfortable and healthy

3.2 WOOD MATERIAL

Timber has long been utilized in Indonesian buildings and is one of the finest solutions for reducing earthquake damage. It is recommended to utilize high-quality lumber that meets international standards such as SNI or ISO for post-earthquake use. Low-grade timber can cause structural problems and make a building more prone to earthquakes. The following premise is to use the appropriate building system. The proper building system can assist minimize the danger of seismic damage. The wood frame system and the timber beam system resting on poles are two building techniques that are suited for timber materials. The correct construction system should take into account the building's strength, stiffness, and stability. For this reason, it is essential to think about the upkeep and durability features before to use by paying attention to the material's drying process, protection from insects and mildew, and systems that make it protected from weather attacks, particularly rain and high humidity.

There are various varieties of rapid wooden dwellings used for disaster relief in Indonesia. Some of them are:

1. Basic Wooden House (RKS) The RKS is the most often utilized form of a wooden house in Indonesia for disaster relief. The roof is made of zinc and the home is made of wood. RKSs are typically 4x6 meters in size and can accommodate 4-6 persons.
2. Earthquake Resistant House (RTG) An earthquake-resistant house (RTG) is a type of wooden building that is meant to be earthquake resistant and robust enough to withstand natural calamities such as earthquakes. Other constructions, such as steel and thin concrete walls, are generally installed in this dwelling. RTGs vary in size according to the application.
3. Health-House (Rukesa) Rukesa is a type of wooden hut used as a health station in rural or difficult-to-reach places. This residence has medical amenities such as examination rooms, waiting rooms, and sleeping rooms. Rukesa is also often provided with safe drinking water and sanitary services.
4. Ready-to-Use House (RSP) RSP is a sort of wooden home that is meant to be rapidly and readily erected. It generally has basic furniture and home necessities including mattresses, tables, and chairs. RSPs can be utilized as either temporary or permanent buildings.
5. Community House A communal home is a form of wooden structure designed to host numerous families or groups. This house has several bedrooms, living rooms, kitchens, and bathrooms that are shared by several families. Communal houses are usually built in areas affected by natural disasters such as floods or landslides.

4 CASE STUDY

4.1 CASE STUDY I: FERROCEMENT WOODEN CONSTRUCTION IN MAMUJU, SULAWESI

The Mamuju earthquake [3] with a magnitude of M 6.2 that occurred on January 15, 2021, was an aftershock of an earlier earthquake with a magnitude of M 5.9 that occurred on January 14, 2021, where this disaster event occurred when it coincided with a period of activity restrictions due to the Covid 19 Pandemic. Travel restrictions were still in effect in Indonesia at the time. Getting to the field was equally challenging for the ITB team. Disaster management in Mamuju is inextricably linked to the prior program in Palu. The Palu earthquake, which was followed by liquefaction and a tsunami, happened before the Mamuju earthquake. A group of volunteers was trained in timber building there to build communal shelters and a permanent mosque (Figure 3 and Figure 4).

https://doi.org/10.52202/069179-0540

Figure 3: *Vault Structure-based Shelter*

Figure 4: *Nurul Hasanah Wooden Mosque in Palu*

Having developed solid networks with volunteers who had worked together in the previous post-disaster response in Palu, the Mamuju post-disaster response was carried out by activating these volunteers to go to the field with materials and equipment from Palu, which is a 9-hour drive away. Travel restrictions due to the pandemic, especially air travel, made this the most appropriate option. A prefabrication system was employed to keep work on the ground in unfavourable conditions to a minimum. Four shelters similar to the wooden shelters in Figure 3 were built in Mamuju at several evacuation sites plus two wooden Ferrocement houses (see Figure 5).

Figure 5: *Timber + Ferrocement House 24m^2 (above) and 35m^2 (below)*

Ferrocement timber homes are built using a semi-fabricated technology in which hardwood wall frames are combined with chicken wire mesh in a wood workshop in Palu. The manufacture of the wall frame (Figure 6 and Figure 7) took place in areas that were not impacted by the disaster and had accessibility to timber raw materials. This was also done to lower the expense of mobilizing field supervision staff. Another factor to consider was that Mamuju's situation at the time was still affected by the earthquake, thus the availability of labour, materials, and equipment, as well as electricity, was still uncertain. Because of the pandemic circumstances that prohibited travel by plane, supervisor monitoring was conducted by phone, video conference, and Zoom Meetings.

Figure 6: *Prefabrication of timber and chicken wire wall frame modules at the workshop in Palu.*

Figure 7: *Local foundation construction at a house site in Mamuju.*

The basic building method is used to build Ferrocement timber houses, which includes clamping chicken wire between vertical and horizontal logs. The size of the wall frame modules was defined by the measurements of the timber utilized, with as little material as possible left over. Bracing was added to the wall frame, both at the top and at the height of the wall plane on the side of the structure, to give stiffness against horizontal forces such as earthquakes and wind forces, as illustrated in Figure 5. Once the wall frames were finished, they were transported by truck to Palu (Figure 8 and Figure 9). Ferrocement wooden house modules for two dwelling units may be shipped in a single shipment.

Figure 8: *Delivery of Rukaf (Ferrocement wooden house) modules from Palu to Mamuju (left-below) and house construction (right).*

Figure 9: *Ferrocement wooden house before plastering and after plastering*

4.2 CASE STUDY II: FERROCEMENT TIMBER HOUSE CONSTRUCTION IN PASAMAN, WEST SUMATRA

The Ferrocement wood wall method was utilized as well during the construction of a musholla at Pasaman, West Sumatra, following the February 25, 2022 earthquake. The prefabrication system was carried out locally, with the production of the timber wall frame panels and chicken wire mesh taking place in the same area as the building phase. The benefit of this approach is that the

https://doi.org/10.52202/069179-0540

frame panels are made on the ground and beneath the shade of a tarpaulin tent, making the labour considerably easier than standing work. Furthermore, because it does not require vehicle transportation from the workshop to the building site, the wall panel module may be larger.

The application of wood construction integrated with Ferrocement is also carried out as a partition and at the same time provides shear strength in the construction of the Al-Munawarrah Mamuju Musholla (Figure 10). The wood used as the structure of the Musholla is Coconut Wood. Ferrocement-based walls are used as dividers for the imam's room at the front of the Musholla and also on the sides of the Musholla.

Figure 30: *Musholla in Pasaman (left) and Al Munawarrah mosque in Mamuju (right) using ferrocement wood wall construction.*

5 CONCLUSIONS

Based on previous cases, post-disaster rehabilitation in Indonesia has depended more on large industrial materials supplied from outside the region. Steel, GRC, precast concrete, lightweight bricks, and other materials can enable to create of temporary or permanent housing in large quantities fast. Nevertheless, because these industrial inputs are imported from outside the disaster region, the majority of the economic turnover from the aforementioned technique occurs outside the disaster area.

Timber and Ferrocement wall technology are long-established but largely neglected technology. Timber is a renewable building material with huge potential in Indonesia, including coconut wood. Meanwhile, Ferrocement is an old technology that is very efficient to apply due to the relatively minimal use of materials. A wall thickness of 2-3 cm can be achieved with Ferrocement technology. Compared to plastered brick walls on both sides that are up to 15 cm thick, Ferrocement walls are much more cost-effective and much lighter. Combining Ferrocement walls with timber can improve construction performance because they can make up for the shortcomings of each material. Timber framing has the advantages of low carbon footprint, earthquake resistance and speed of construction. The weakness of fire can be covered by Ferrocement, in addition to being a barrier to the exposure of wood to the climate.

REFERENCES

[1] A. Permana, "Understanding Earthquakes, Their Sources and Dangers," 8 February 2021. [Online]. Available: https://www.itb.ac.id/berita/mengenal-gempa-bumi-sumber-dan-bahayanya/57739.

[2] "Damage to buildings caused by the M5.6 Cianjur earthquake," 25 November 2022. [Online]. Available: https://www.bnpb.go.id/berita/kerusakan-bangunan-akibat-gempabumi-m5-6-cianjur.

[3] L. C. Sinaga, "Problematika Rehabilitasi dan Rekonstruksi Studi Kasus Pasca Bencana Tsunami Mentawai 2010," *Jurnal Dialog Penanggulangan Bencana Vol. 4, No. 1,* pp. 23-34, 2013.

[4] "Majene Earthquake Event Study January 2021 Center for Volcanology and Geological Hazard Mitigation," 18 January 2021. [Online]. Available: https://vsi.esdm.go.id/index.php/gempabumi-a-tsunami/kejadian-gempabumi-a-tsunami/3399-kajian-kejadian-gempa-bumi-majene-januari-2021-pusat-vulkanologi-dan-mitigasi-bencana-geologi.

World Conference on Timber Engineering Oslo 2023

HARVESTING THE URBAN FOREST: A CASE STUDY OF THE CIRCULAR BUILDING SEMINAR AT UHASSELT IN BELGIUM

Rafael Novais Passarelli[1], Peggy Winkels[2], Ronald Rovers[3], Elke Knapen[4], Griet Verbeeck[5]

ABSTRACT: The transition to a circular economy (CE) offers an alternative path to the current high-polluting and wasteful practices in construction. However, this transition will require a drastic shift from the way products and services are designed, produced, and used, also in the architecture and construction industry. This paper aims to contribute to the body of knowledge of novel methodologies to integrate CE into architectural design and wood construction education. This paper analyses the 2021-22 edition of the Circular Building Seminar at UHasselt in the Faculty of Architecture and Arts. In this study, we first provide a brief introduction to the course mission and its approach. Then we describe in-depth the 2021-22 winter semester assignment of urban harvesting and the role of wood in it. At the end, we evaluate and discuss the outcomes of the course, its relevance as well as possibilities for improvement in the next editions.

KEYWORDS: Wood Architecture, Timber Education, Circular Economy, Design for Circularity, Bio-based materials

1 INTRODUCTION

The construction sector is responsible for the largest individual share of greenhouse gas (GHG) emissions, accounting for 37% of all emissions [1], due to energy-intensive activities of material extraction, transportation, construction, and energy to operate buildings. Building construction activities alone represent 10% of all emissions [1]. Hence, the high emissions in the sector worsen the continuing heat up of the planet and contribute to the climate crisis. Moreover, the construction industry consumes 40% of the global resources [2] and is one of the leading producers of solid waste generated during the production of materials, construction, and demolition of buildings [3]. That means a large share of emission-intensive building materials produced from precious finite resources end up wasted in landfills at manufacturing, construction, or end-of-life.

The transition to a circular economy (CE) thus offers an alternative path to the current linear high-polluting and wasteful practices in construction [4]. The concept of CE is quickly gaining traction among both scholars and practitioners, indicated by its fast-growing number of peer-reviewed articles [5]. A CE is "restorative and regenerative by design and aims to keep products, components, and materials at their highest utility and value at all times (...)" [6]. By decoupling wealth generation from resource consumption, a CE can simultaneously tackle many pressing challenges of our time, such as climate change, resource depletion, water, and energy scarcity [7]. However, a transition to a CE requires a drastic shift from the conventional way products and services are designed, produced, and used, including construction.

Previous studies emphasized the critical role of education in this transition [8], [9]. More specifically, higher education institutions can be strategic agents supporting a CE due to its dual impact of promoting behavioural change at the personal level and professional implementation in practice [10]. Hence, there is a growing interest in education for a Circular Economy (ECE) as educators from diverse fields start to develop educational approaches to incorporate a CE in their courses [8]. However, a recent literature review on ECE found institutions are still slow to adopt it as a fundamental part of the curriculum [11]. Specifically, in the field of architectural design, there is even less information addressing education from a CE perspective, with only a couple of published cases [12], [13]. Therefore, there is a significant knowledge gap regarding architectural design education in the context of circularity.

Ironically, among the several different fields of application of a CE, design sciences are of particular relevance. The literature on CE consistently identifies design as an enabling activity for the transition from a linear to a circular economy [4], [7], [14]. However, unlike the standard design process, designing for increased circularity requires more complex cognitive skills to approach the design problem from a lifecycle

[1] Rafael Novais Passarelli, UHasselt, Faculty of Architecture and Arts, rafael.novaispassarelli@uhasselt.be
[2] Peggy Winkels, UHasselt, Faculty of Architecture and Arts, Belgium, peggy.winkels@uhasselt.be
[3] Ronald Rovers, RiBuilT, Research Institute Built environment of Tomorrow r.rovers@sustainablebuilding.info
[4] Elke Knapen, UHasselt, Faculty of Architecture and Arts, Belgium, elke.knapen@uhasselt.be
[5] Griet Verbeeck, UHasselt, Faculty of Architecture and Arts, Belgium, griet.verbeeck@uhasselt.be

https://doi.org/10.52202/069179-0541

perspective. That means designers have an expanded work scope and must consider the design process from the origin of materials to multiple appropriate service spans and possible future uses [14].

To address the knowledge gap mentioned above, we must develop new methods to integrate design for circularity into the architectural design curriculum, so it also becomes an implicit part of the practice. This paper aims to contribute to the body of knowledge of novel methodologies to integrate CE into architectural design and education, and training of aspiring architects with new design skills required in the context of circularity.

2 MATERIALS AND METHODS

This study analyses the 2021-22 winter semester edition of the Circular Building Research Seminar at UHasselt in the Faculty of Architecture and Arts. The goal is to contribute to the discussion on education for sustainability and wood construction from the lens of circularity. It is worth noting that although wood was not the primary focus of the course, it consistently emerged as a critical topic in the discussion of circularity throughout the course. In this study, firstly, we provide a brief introduction to the mission of the Circular Building Research Seminar at its inception and its main approach. Then we describe in-depth the 2021-22 winter semester assignment of urban harvesting and the role wood construction had in it. Afterwards, we evaluate the outcomes of the course qualitatively. Finally, we discuss some strengths and weaknesses perceived as well as possibilities for improvement in the next editions.

3 RESULTS

3.1 THE CIRCULAR BUILDING RESEARCH SEMINAR

The Circular Building Research Seminar is a 2-semester course for students in the master program, offered at UHasselt, Faculty of Architecture and Arts, every year since 2017. Originally the semester assignment alternated between an experiment-based and a reality check one. In the former, students were challenged to develop out-of-the-box thinking when considering the design and build assignment, whereas in the latter, students started from standard or established materials and processes in the built environment with the goal to pursue circular innovation. It is worth noting that over the years the relationship between both semesters has become more blurred.

From an educational standpoint, the course aims to uncover the possibilities for circular thinking in architectural design, thus providing an opportunity for students to explore new ways to transform buildings from a liability in terms of environmental impact to positive generators of biodiversity, energy and material resources. The instructional approach consists of a combination of research-based and design exercises. Moreover, at the Circular Building Research Seminar, theory and data operate as the foundation to master circular thinking and action to create innovation. This is further supported by reading assignments and discussion sessions on multifaceted topics that go beyond the mere theme of circularity in the construction sector. The goal is to familiarize students with the wider societal and economic context that is driving the need for more sustainable resource use.

The learning outcomes intended are triple-fold. 1) To contribute to the relatively novel and unexplored theme of circular construction with regenerative materials to inspire colleagues and decision-makers. 2) To stimulate students to engage with circular thinking to become better designers and builders. 3) To provide an opportunity for students to engage with scholarly research as an essential part of the design process.

Over the years, the course experimented with a variety of topics to pursue its goals, namely Circular Building Renovation (2017-18), Circular Building Systems for Cavity Walls (2018-19), use of Regenerative Materials (2019-20), and Prefabricated Building Concepts with Regenerative Materials (2020-21). The 2021-22 run of the Circular Building Research Seminar proposed the topic of Urban Harvesting as a means to advance the discussion of circularity in design and education. Every edition aims at incorporating hands-on experimenting through design-build assignments, as well as conceptual reflections on circularity under the existing frameworks.

In the 2017-18 edition on Circular Building Renovation, students first got familiar with the concept of circularity by exploring the RESOLVE framework [15] (Ellen McArthur Foundation) through different case studies, and then developed six circular renovation scenarios for their main faculty building - a concrete building from the 80s designed according to the principles of Herzberger, perceived as highly flexible, but actually quite rigid. Each scenario started from a perceived challenging issue, such as better water management, making the building fit for a broader use, and using the building as a display for regenerative materials. In the 2018-19 edition, students assembled and disassembled 3 walls (3x3m each) with market-available circular building systems for cavity walls, and evaluated their circular performance with the circularity framework developed by Vandenbroucke [16], also proposing improvements for specific aspects [17] (Figure 1). In the 2019-20 edition, students took part in a 1-day hands-on workshop on 4 bio-regenerative materials (mycelium, willow, earth, lime hemp), and then explored the opportunities of these materials through hands-on experiments (Figure 1). This resulted in the design and execution of a wide range of objects, later exhibited at the construction fair Batibouw 2020 as part of the stand of two organizations promoting sustainable construction. The stand itself was also fully circular and developed by the students and their teachers in collaboration with the organizations. In the 2020-21 students were tasked to rethink and redesign an existing tiny living unit with the

goal to make it fully circular and bio-based. Because of COVID 19, no hands-on activities or experiments were possible in this edition, so the outcome was limited to architectural sketches, drawings, and 3d modelling.

Figure 1: *Outcomes of editions 2018-19 (top) and 2019-20 (bottom) of the Circular Building Research Seminar.*

3.2 THE 2021-22 EDITION OF THE CIRCULAR BUILDING RESEARCH SEMINAR

The 2021-22 edition builds back on the repertoire developed in the previous editions of the Circular Building Research Seminar and tackles the theme of Urban Harvesting, understood as the possibility to leverage existing, readily available material flows in the environment that are currently perceived as waste. The idea opposes the conservative approach of extracting and processing virgin materials, that even if sustainably designed, can contribute up to some extent to resource depletion and environmental impact.

To explore the theme, the course instructors provided a list to the students with four distinct geographic regions to choose from: the municipality of Genk, the city of Hasselt, Hoge Kempen National Park, and UHasselt Campus in Diepenbeek. Each option presented a different context with a fresh batch of challenges to solve, ranging from more consolidated urban areas to a natural reserve. The course flowed through three main phases as follows.

Phase 1: The 2021-22 edition started with an Urban Harvesting workshop. Here lecturers introduced critical concepts of material and energy flows of and in our built environment. The goal is for the students to grasp the challenges and possibilities of combining flows to pursue added value.

Phase 2: Next, the participants mapped, documented, and visualized local flows of raw materials from the surroundings of their chosen areas. (Figure 2) The idea was to brainstorm a diverse range of applications and products based on the mapped resources and flows. For the brainstorm, the positive impact workshop was used, as developed in the Erasmus+ KA Active8 Planet project [18]. In this workshop, four lenses are used to reflect on the opportunities to create positive impact with the local material flows: a local social lens to reflect on the positive impact that can be created locally on social aspects such as jobs, income, community, etc, a local ecological lens to reflect on the positive impact that can be created locally on ecological aspects such as water management, biodiversity, etc. and, likewise, a global social lens and a global ecological lens that induces a reflection on how decisions made locally can have a positive impact globally [19].

Phase 3: The final phase consists of a design exercise in response to the findings from Phase 2. In other words, the design solutions had to answer a realistic challenge or need as detected during the mapping. This phase also encourages a hands-on verification of the design propositions feasibility through prototyping and scale models.

3.3 SCALES OF INTERVENTION AND USE OF WOOD

Students organized themselves into four groups (one per region), with eight participants each on average. Based on the results from the mapping exercise and positive impact brainstorm of Phase 2, students decided the focus of their design proposals between four scales of intervention, namely urban, building, element, and material scale.

https://doi.org/10.52202/069179-0541

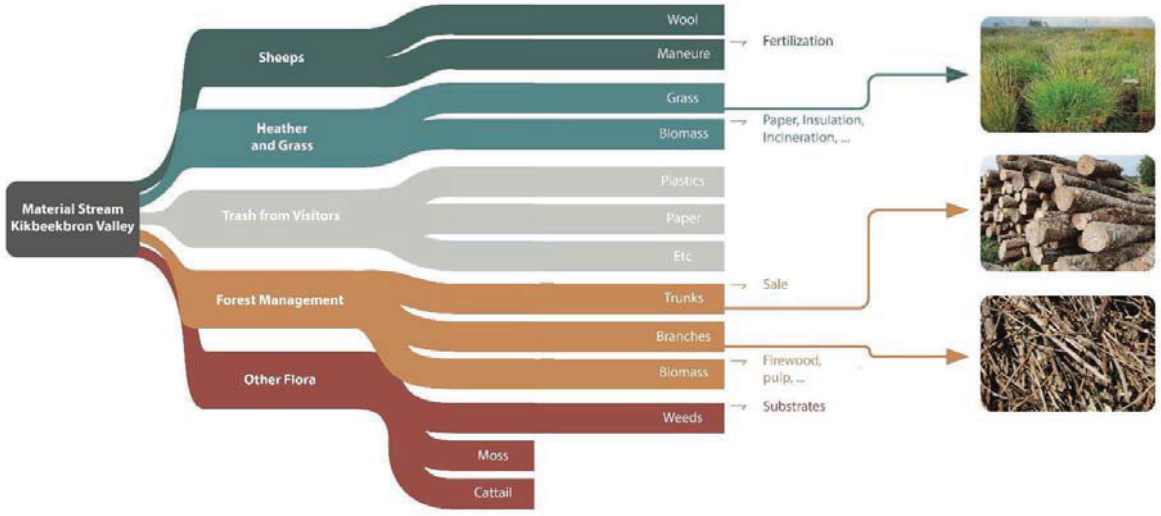

Figure 2: *Material Flow Map of National Park Group*

The UHasselt Campus group focused on the urban scale. In this scale, the challenge was to look for synergies with what is already consolidated and optimize the resource flows to foresee efficient, future-proof land uses. Furthermore, the group linked their research to a real-life ongoing project on the campus related to some perceived mobility issues, such as the limited use of bikes and public transport, and excess of private car use by students and staff, which results in a lack of parking space and plans to build a large allegedly circular parking building. In response to that, the group proposed and developed a multi-modal transportation master plan for the campus, employing locally harvested wood species as engineered wood-based products for the construction of the transportation facilities on campus.

The National Park group focused on the building scale. In this scale, it was critical to couple the development of a given building with its surroundings as to create a virtuous circle during its whole lifecycle. The group looked into ways to use logs obtained from thinning and pruning of forests in the park as the structure for small off-grid holiday units (Figure 3). Their design was a critical reflection and a counter-proposal to a new development of allegedly sustainable, high-end, luxurious holiday units in the National Park.

The city of Hasselt group focused on the element scale. In this scale, versatility, durability, and reuse were key criteria to guarantee an extended lifespan of the materials harvested and used. The group proposed to employ prefabricated panels using reclaimed wood from the demolition of blighted houses for repurposing vacant commercial buildings into temporary student rooms, in response to a real need for extra student rooms offer, due to a growing number of students at UHasselt and nearby university colleges (PXL and UCLL). (Figure 4)

The Genk City group focused on the material scale. In this scale, the investigation of potential materials and methods that prevent further depletion of resources had a prominent role. The group aimed to design affordable DIY furniture kits, reusing wood from discarded pallets from the port. (Figure 5)

Figure 3: *Scale Model of proposed off-grid holiday units*

https://doi.org/10.52202/069179-0541

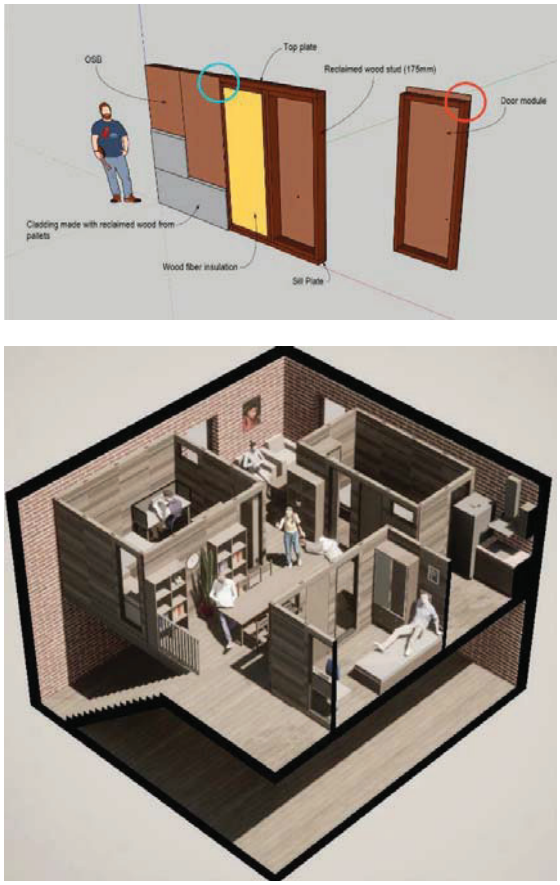

Figure 4: *Visualization of prefabricated panels(top) and retrofit proposal of a vacant commercial building (bottom)*

4 DISCUSSION

Even though the Circular building Research Seminar was not focused on wood construction, the search for materials to harvest in both urban and natural settings, as well as less impactful design solutions led all groups to investigate at least one possible way to utilize wood. In most cases, the information gathered during Phases 1 and 2 pointed to wood as a potential answer for a regenerative and low-impact design. That endorses the critical role that wood as a building material now plays in the broad topic of education for sustainability and design from the lens of circularity. Hence, to generate change through education, it seems relevant that curricula from schools of architecture actively find ways to provide the opportunity for students to engage with the material in both focused and unfocused disciplines.

Furthermore, the Circular Building Research Seminar intended to introduce a new mindset to students related to tackling design problems and finding solutions. More specifically, the seminar works backwards compared to a "traditional" design studio approach. Conventionally, students start pursuing formal and functional aspects by

developing a holistic design concept. Then, students confront the feasibility of their design concepts in terms

Figure 5: *Mock-up of DIY chair using reclaimed wood from pallets*

of materiality, dimensions, and technical performance. The result of this reality check is the design solution. In the Circular Building Research Seminar, students first face a tangible context to understand and interact with, which provides them with only a limited set of resources in terms of materiality, performance, and technology. From the available resources, students must then conceive innovative design solutions that meet a specific need. In this case, the final result is a holistic design concept or approach as an answer to the possibilities and limitations offered by the context.

Likewise, the course also proposes a more scientific approach to the design process, in which theory and data must guide design decisions. Because the course challenges the participants with a fresh new design approach, most likely for the first time in their education, mindset adjustments and new skills development are needed. That, of course, requires time and effort on the part of the participants and instructors. We understand it as a positive part of the learning process and growth of the students as designers, also supporting the expected learning outcomes 2 and 3 (item 3.1). However, the relatively large volume of new information and skills needed also partly hinders the depth of the explorations.

Particularly in the 2021-22 edition of the seminar, it was noticeably difficult to gather the necessary information on material flows, attesting to the still lack of such valuable information publicly available or with enough detail. Additionally, the ambitious goal to achieve innovative

https://doi.org/10.52202/069179-0541

circular design solutions in the period of a single semester (15 weeks) can be hindered by an overall lack of previous experience with basic woodwork skills by the students, leading to a lack of depth and quality of the outcomes both from an aesthetic and circular point of view, such as in the Genk City group.

5 CONCLUSIONS

This paper presented the Circular Building Research Seminar in the Faculty of Architecture & Arts at UHasselt and described its 2021-22 edition in detail. The chosen topic of urban harvesting yielded a diverse scope of design approaches, ranging from the urban to the object scale. In the view of the instructors, it successfully introduced to the students a flipped way of thinking about the design process, developing a holistic design concept from the availability of given resources instead of assigning materiality to a pre-defined design concept. Furthermore, even though wood-based materials were not the particular focus of the course, they had a distinctive role in all four projects, attesting to the relevance of including wood-based design and construction-oriented courses in the traditional curriculum of architecture schools. On the other hand, the overall quality of design solutions was below expectations, partially due to the combination of a lack of primary information on waste flows and unfamiliarity with basic fabrication and construction techniques. It is also noteworthy that the ongoing corona crisis at that time, hindered the possibility of more hands-on activities. Regardless, the two groups that actively integrated physical modelling and prototyping in their workflow achieved slightly better results. That also attests to the relevance of introducing hands-on activities as part of the learning process in balance with more traditional theoretical activities. By sharing and evaluating the experience in the Circular Building Research Seminar, this paper aimed to contribute to the body of knowledge of novel methodologies to integrate CE into architectural design and wood construction education.

ACKNOWLEDGEMENT

The authors gratefully acknowledge the effort and commitment of students enrolled in the multiple editions of the Circular Building Research Seminar.

REFERENCES

[1] United Nations Environment Programme, "Global Status Report for Buildings and Construction: Towards a zero-emissions, efficient and resilient buildings and construction sector," Nairobi, 2021. [Online]. Available: www.globalabc.org.

[2] F. Pacheco-Torgal, "Introduction to the environmental impact of construction and building materials," in *Eco-Efficient Construction and Building Materials: Life Cycle Assessment (LCA), Eco-Labelling and Case Studies*, Elsevier Inc., 2014, pp. 1–10. doi: 10.1533/9780857097729.1.

[3] P. Nuñez-Cacho, J. Górecki, V. Molina-Moreno, and F. A. Corpas-Iglesias, "What gets measured, gets done: Development of a Circular Economy measurement scale for building industry," *Sustainability (Switzerland)*, vol. 10, no. 7, Jul. 2018, doi: 10.3390/su10072340.

[4] D. Andrews, "The circular economy, design thinking and education for sustainability," *Local Econ*, vol. 30, no. 3, pp. 305–315, May 2015, doi: 10.1177/0269094215578226.

[5] J. Kirchherr, D. Reike, and M. Hekkert, "Conceptualizing the circular economy: An analysis of 114 definitions," *Resources, Conservation and Recycling*, vol. 127. Elsevier B.V., pp. 221–232, 2017. doi: 10.1016/j.resconrec.2017.09.005.

[6] Ellen MacArthur Foundation, "Towards a circular economy: Business rationale for an accelerated transition," Nov. 2015.

[7] M. Moreno, C. de los Rios, Z. Rowe, and F. Charnley, "A conceptual framework for circular design," *Sustainability (Switzerland)*, vol. 8, no. 9, Sep. 2016, doi: 10.3390/su8090937.

[8] J. Kirchherr and L. Piscicelli, "Towards an Education for the Circular Economy (ECE): Five Teaching Principles and a Case Study," *Resour Conserv Recycl*, vol. 150, Nov. 2019, doi: 10.1016/j.resconrec.2019.104406.

[9] D. Qu, T. Shevchenko, and X. Yan, "University Curriculum Education Activities Towards Circular Economy Implementation Article in," *International Journal of Scientific & Technology Research*, vol. 9, p. 5, 2020, [Online]. Available: www.ijstr.org

[10] A. Bugallo-Rodríguez and P. Vega-Marcote, "Circular economy, sustainability and teacher training in a higher education institution," *International Journal of Sustainability in Higher Education*, vol. 21, no. 7, pp. 1351–1366, Dec. 2020, doi: 10.1108/IJSHE-02-2020-0049.

[11] H. Kopnina, "Green-washing or best case practices? Using circular economy and Cradle to Cradle case studies in business education," *J Clean Prod*, vol. 219, pp. 613–621, May 2019, doi: 10.1016/j.jclepro.2019.02.005.

[12] A. Wandl, V. Balz, L. Qu, C. Furlan, G. Arciniegas, and U. Hackauf, "The circular economy concept in design education: Enhancing understanding and innovation by means of situated learning," *Urban Plan*, vol. 4, no. 3, pp. 63–75, Sep. 2019, doi: 10.17645/up.v4i3.2147.

[13] G. Dokter, B. W. Jansen, L. Thuvander, U. Rahe, and J. A. Duijghuisen, "Cards for Circularity (CFC): Reflections on the use of a card-based circular design tool in design education," in *IOP Conference Series: Earth and Environmental Science*, 2022, vol. 1078, no. 1. doi: 10.1088/1755-1315/1078/1/012057.

[14] M. Burger, S. Stavropoulos, S. Ramkumar, J. Dufourmont, and F. van Oort, "The

heterogeneous skill-base of circular economy employment," *Res Policy*, vol. 48, no. 1, pp. 248–261, Feb. 2019, doi: 10.1016/j.respol.2018.08.015.

[15] R. Zimmann, H. O'Brien, J. Hargrave, and M. Morrell, "The Circular Economy in the Built Environment," London, 2016.

[16] OVAM, "24 Ontwerprichtlijnen Veranderingsgericht Bouwen," Mechelen, Jun. 2017. [Online]. Available: www.lne.be/bouw-gezond

[17] B. Janssens, E. Knapen, P. Winkels, and G. Verbeeck, "Outcomes of a Student Research Project on Circular Building Systems - Focus on the Educational Aspect," in *IOP Conference Series: Earth and Environmental Science*, Sep. 2019, vol. 323, no. 1. doi: 10.1088/1755-1315/323/1/012138.

[18] G. Cerinšek, V. Fors, G. Verbeeck, E. Puelinckx, and S. van Wijgerden, "Active8 Planet," Mar. 2021. Accessed: Feb. 16, 2023. [Online]. Available: https://active8-planet.eu/deliverables/

[19] K. Raworth, R. Shorter, L. Grcheva, and A. Fanning, "Introducing the four lenses Doughnut Unrolled," Apr. 2022. Accessed: Feb. 15, 2023. [Online]. Available: https://doughnuteconomics.org/tools/142

https://doi.org/10.52202/069179-0541

World Conference on Timber Engineering Oslo 2023

ADHESIVELY BONDED TIMBER-CONCRETE COMPOSITE CONSTRUCTION METHOD (ATCC) – PILOT APPLICATION IN A SCHOOL BUILDING IN GERMANY

Jens Frohnmüller [1], Werner Seim[2], Christian Umbach [3], Johannes Hummel[4]

ABSTRACT: A pilot-application of adhesively bonded timber-concrete composite (ATCC) slab elements with prefabricated concrete parts in a school building in Germany is presented in this paper. Firstly, the concept and the relevant points of the planning process are outlined. The construction and the materials of the ATCC slab are then presented. After the introduction of a suitable calculation model for ATCC beams with discontinuous arrangement of the adhesive bond, a validation in the form of a full-scale bending test follows. Finally, the quality control concept which has been developed for this project is presented.

KEYWORDS: Adhesives, Timber-Concrete-Composite, Pilot Project, Full-Scale Testing, Quality Control, Monitoring

1 INTRODUCTION

The new building of the "Ernst-Leinius Schule" in Kassel, Germany (Figure 1), was planned as a timber construction. Due to the requirements to limit floor vibration, a hybrid timber-concrete composite (TCC) construction with notches as shear connections and cast-in-place concrete is to be used for the slab elements.

Figure 1: *School building "Ernst-Leinius Schule Kassel" (From Baufrösche • Architekten und Stadtplaner GmbH)*

Although TCC constructions with cast-in-place concrete offer great advantages as an end-product and contribute significantly to improving the competitiveness of timber construction in multi-storey construction, there are some disadvantages. The disruption of the construction process particularly plays a decisive role here: the assembly of the timber construction as a classic dry construction with surfaces that are largely ready for use (ceiling soffit, columns, walls) is considerably slowed down by the concrete work: reinforcement has to be laid, joints sealed, surfaces protected, and the concrete has to cure. All this takes time and delays the construction progress. In addition, the risk of water damage increases significantly during the time the reinforcement is being installed and the concrete is poured.

With that in mind, it appears astonishing that there have been comparatively few attempts to eliminate these disadvantages by using dry, prefabricated concrete parts. Apart from a method with plastic sleeves inserted in the precast reinforced concrete elements for subsequent screwing [1], using adhesives is an obvious solution for implementing the composite. The most important advantages of adhesively bonded timber-concrete composites (ATCC) are:

- full bond and optimized mechanical interaction,
- rapid construction progress,
- low moisture penetration into the building due to the use of precast reinforced concrete components and the quick assembly process,
- ready for load-bearing after one day of curing, fully loadable after approximately seven days,
- no contact pressure required when using epoxy resins,
- possibility of producing the floors on-site or in the factory,
- reduction of the influence from concrete shrinkage, and
- comparatively easy separation of components in terms of deconstruction and reuse.

[1] Jens Frohnmüller, University of Kassel, Timber Structures and Building Rehabilitation, 34125 Kassel, Germany, jens.frohnmueller@uni-kassel.de
[2] Werner Seim, University of Kassel, Timber Structures and Building Rehabilitation, 34125 Kassel, Germany
[3] Christian Umbach, University of Kassel, Timber Structures and Building Rehabilitation, 34125 Kassel, Germany
[4] Johannes Hummel, EFG Beratende Ingenieure GmbH, 34277 Fuldabrück, Germany

https://doi.org/10.52202/069179-0542

The client and the specialist planners involved in the project of the school building have created the framework conditions to apply the construction method of ATCC with prefabricated concrete parts for the first time out of the laboratory into the building industry. The pilot application represents the result of many years of development in which several members of the team of the University of Kassel have participated [2]-[8].

2 CONSTRUCTION

2.1 BASIC INFORMATION

The floor is characterised by a span of 7.68 m and design loads ($g_d + q_d$) of about 12.1 kN/m². The pilot project is located in an area of about 30 m², where the static system changes from a two-span to a single-span beam (see Figure 2).

Figure 2: *Top view of the building with marked area for the pilot application*

The composite action is realised by applying the adhesive with a mortar sledge on the timber part and placing the concrete-prefab, which has a weigth of approximately two tons, on top with the help of a crane (see Figure 3 and Figure 4).

Figure 3: *Handling of precast concrete elements*

The adhesive is arranged in stripes perpendicular to the span (Figure 7) which are spaced closer together towards the support according to the shear force distribution. The notches along the edges of the prefabricated concrete parts (Figure 4) do not participate in the shear load transfer due to vertical loading. They are filled with concrete subsequently after bonding to create an in-plane diaphragm action of the slab.

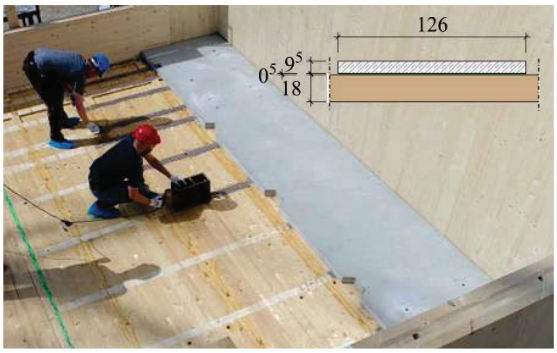

Figure 4: *Application of the adhesive on the timber part*

2.2 MATERIALS

Regarding the timber part, glulam of the quality GL28c with a height of 18 cm has been used throughout the entire slab area. The moisture content was tested at several measuring points on the floor, with values ranging from 13.0 to 15.4 %. Because the shear strength, which can be identified as the most relevant parameter regarding the determination of the bond strength, could not be determined on site, the surface tensile strength of the timber has been determined instead. The parameter was determined according to EN 311 [9] to $f_{ttm,surf} = 2.3$ N/mm² ($n = 6$, $COV = 13$ %).

The concrete parts were ordered with a thickness of 9.5 cm. According to the test certificates of the manufacturer, the concrete parts have a compressive strength $f_{cm,cube}$ of 58.8 N/mm² and can, therefore, be assigned to the strength class C40/50. The underside of the slab has been sandblasted (see Figure 5).

Figure 5: *Sandblasted underside of the prefab concrete part*

The average surface tensile strength $f_{ctm,surf}$ of the concrete has been determined as 3.4 N/mm² ($n = 10$, $COV = 13$ %), according to EN 1542 [10]. The moisture content of the concrete has been determined by weighting and drying (Darr drying-method) to about 0.9 %.

https://doi.org/10.52202/069179-0542

The polymer mortar "Epument 130/2-14_B1" from RAMPF Group was used as an adhesive [11]. This product exhibits an average cylindrical compressive strength $f_{adh,c,mean}$ in the range of 140 N/mm², a flexural tensile strength $f_{adh,t,mean}$ of 28.7 N/mm² (n = 6, COV = 7 %) and an adhesion strength on a sandblasted steel plate of $f_{adh\text{-}steel,t,mean}$ = 13.8 N/mm² (n = 24, COV = 6 %). The mean thickness of the adhesive joint was set to 0.5 cm. The total height of the construction, therefore, was 28.0 cm.

2.3 EVENNESS OF THE SURFACES

The evenness of the surfaces plays a decisive role regarding the success of the bonding, as has been unanimously established in preliminary work on the adhesively bonded joint [5], [12]-[14]. With reference to the construction tolerances for planarity regulated by standards [15], a maximum deviation of ± 1 mm over a length of 0.20 m or ± 3 mm over a length of 1.00 m can be assumed for the flatness of the formwork side of the concrete part, according to DIN 18202 [16]. Regarding the timber, a construction tolerance of ± 4 mm per 2.00 m length can be assumed, according to DIN 18203-3 [17]. This leads to the conclusion that a maximum gap of 7 mm must be assumed in the case that the largest unevenness of timber and concrete are superimposed. In the course of the development of the adhesive system and the application technique, it was found that a gap of 7 mm can be bridged reliably if the adhesive is applied with a toothed spatula, with the height of each tooth of 12 mm (see Figure 6).

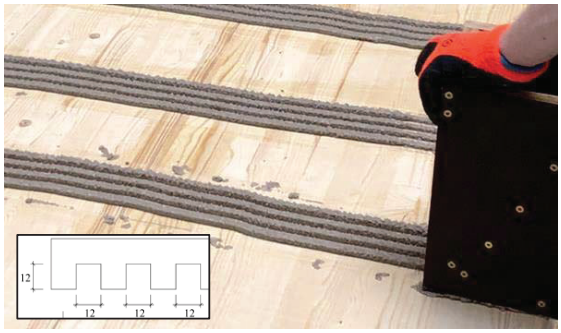

Figure 6: *Application of the adhesive with a toothed spatula, installed in a mortar sledge*

The evenness of the timber elements has been measured on-site with an aluminium batten of 2.0 m length in the range of 0.0 to 3.0 mm. After the concrete part has been placed on top of the timber, the actual gap at the edges of the precast concrete part was measured with a measuring-wedge in the range of 0.0 to 2.0 mm.

3 ANALYTICAL MODEL AND CALCULATION

3.1 PRINCIPLES

Due to the adhesive-bond, the connection between the timber and the concrete can be assumed as rigid, which means that the stresses can be determined analytically with basic, mechanic principles based on the theory of elasticity. This approach is commonly applied in literature [18], [19] and can also be used for TCC constructions with adhesives and cast-in-place concrete [13], as well as for TCC constructions with micro notches, for which, according to Müller and Frangi [20], a rigid bond can be assumed if the notches are arranged continuously over a large area of the span.

The basic relationships that are indispensable for understanding the calculation are briefly listed below. In a first step, the position of the stress zero line z_0 is calculated.

$$z_0 = \frac{\sum_{i=1}^{i} E_i \cdot A_i \cdot z_i}{\sum_{i=1}^{i} E_i \cdot A_i} \tag{1}$$

An effective bending stiffness $(EI)_{cal}$ is then calculated for the composite cross-section, taking into account the different Young's moduli E_i of the partial cross-sections A_i using Steiner's theorem. The geometrical parameter a_i is the distance between the neutral axis of the total cross-section and the neutral axis of the partial cross-sections.

$$(EI)_{cal} = \sum_{i=1}^{i} E_i \cdot I_i + E_i \cdot A_i \cdot a_i^2 \tag{2}$$

Knowing the effective bending stiffness, the bending stresses σ_i at each point of the composite section can be calculated.

$$\sigma_i = M \cdot z \cdot \frac{E_i}{(EI)_{cal}} \tag{3}$$

The maximum stress values at the top and bottom of the composite member are given by substituting the maximum distance between the neutral axis of the composite beam to the outer edges of the cross-section.

With knowledge of the bending stresses σ_i, the relevant criteria for the limit state design of the timber parts and the concrete according to Eurocode 2 [21] and Eurocode 5 [22] have to be fulfilled. For the latter, both bending and tensile strength should be considered.

Further guidelines regarding the long-term behaviour at time t = 3…7 a and t = ∞ are given in CEN TS 19103 [23]. Regarding the verifications in the serviceability limit state, the criteria of deformations and vibrations are of particular relevance, similar to with most other wide-span timber structures for residual use [26]. CEN TS 19103 recommends carrying out the design according to Eurocode 5.

https://doi.org/10.52202/069179-0542

3.2 STRESS CALCULATION FOR ATCC BEAMS WITH DISCONTINUOUS BOND

If the adhesive bond is not continuous along the entire length of the beam but discontinuous (e.g. lateral stripes) as in case of the pilot application, new questions arise with regard to the uniform transmission of shear stresses: How is the shear flow distributed into the adhesive areas and which bond stripe is decisive for the design?

Possible calculation methods to determine the shear flow T_b for a discontinuous bond arrangement are strut-and-tie models, two- or three-dimensional finite element models and analytical models. Because the analytical model offers advantages regarding its simplicity, which has currently only been applied to ATCC composites with a continuous bond, an extension is necessary. The geometric relationships are depicted in Figure 7.

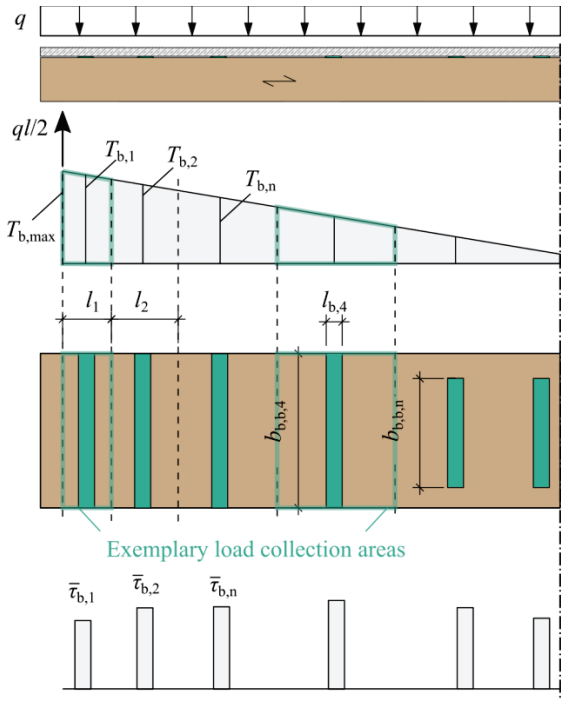

Figure 7: *Composite beam with discontinuous bond – geometric relationships for the analytical calculation model in case of a uniformly distributed load*

Firstly, the shear flow in the bondline $T_{b,i}$ at the stripe i is obtained considering the shear force $V_{n,i}$ at the corresponding stripe and the static moment in the bondline $S_{b,1}$.

$$T_{b,i} = V_{n,i} \cdot \frac{E_1 \cdot S_{b,1}}{(EI)_{cal}} \tag{4}$$

The shear stress in the bondline, which is transmitted at one strip, can then be determined by integration over the partial length. A medium value $\bar{\tau}_b$ can be calculated subsequently by referring the load-collection area to the area of the single strip n.

$$\bar{\tau}_{b,n} = \frac{T_n}{b_{b,n}} \cdot \frac{l_n}{l_{b,n}} \tag{5}$$

3.3 BOND STRENGTH

There are no generally applicable regulations for the verification of the adhesive bond between timber and concrete to date. However, comparable approaches can be found in the literature, whereby the bond failure could usually be attributed to a pure failure in the timber [1], [3]. However, if lower strength concrete, lightweight concrete or hardwood with a high shear strength is used, then the composite failure may be transferred into the top concrete layer [6], [13], [19].

It is generally concluded that the bond failure can be attributed to the substrates timber and concrete if a suitable adhesive is used where adhesion and cohesion failure can be excluded. In the case of the analytical model, where no stresses perpendicular to the joint occur, the bond strength f_b can be set as the minimum of the shear strength of the timber $f_{t,v}$ and the shear strength of the concrete $f_{c,v}$.

$$f_b = \min(f_{t,v}; f_{c,v}) \tag{6}$$

The characteristic value of the shear strength of the timber $f_{t,v,k}$ is defined in the respective product data sheet or the relevant standards of the wood-based material. In addition, according to EN 1995 [22], the modification coefficient k_{cr} should be used to take into account the increased shear stresses due to shrinkage. If k_{cr} is to be considered at the resistance level, the shear strength of GL28c is $f_{t,v,k}$ = 2.50 N/mm².

The determination of the shear strength of the unreinforced concrete surface $f_{c,v,d}$ is less well-supported by systematic studies than it is with timber. Some characteristic values, however, can be found in the literature. They are in the range of $f_{v,c}$ = 3.3 N/mm² for a concrete in the strength class C30/37 (according to the German Committee for Reinforced Concrete [DAfStb] in the guideline for post-reinforcing concrete with glued-on steel plates [25]; where $f_{v,c}$ is a function of the compressive strength and the surface tensile strength) to $f_{v,c}$ = 11,1 N/mm² (according to CEN TS 19103 [23] assuming an angle θ of 45°). Based on own investigations [24], a clear correlation between bond strength and surface tensile strength could be found.

$$f_{c,v} = 2{,}0 \cdot f_{ct,surf} \tag{7}$$

The characteristic surface tensile strength is estimated to be $f_{ctk,surf}$ = 2.20 N/mm², which results in a characteristic shear strength of $f_{c,v,k}$ = 4.40 N/mm².

The design shear strength can be determined if the parameters k_{mod} for the timber and the parameter α_{ct} for the concrete are considered. Furthermore, the safety factor γ_M for the corresponding material is to be included.

https://doi.org/10.52202/069179-0542

The resulting parameters are $f_{t,v,d}$ = 1.54 N/mm² and $f_{c,v,d}$ = 2.49 N/mm², respectively.

A consideration of the factors k_{b1} and k_{b2} is proposed for the last step of the verification of the adhesive bond. These parameters are recommended in accordance with the investigations on steel and CFRP laminates bonded to concrete [25], where comparable factors (e.g. k_{b1}-k_{b4}, k_{sys}) are proposed.

$$\frac{\tau_{b,max}}{k_{b1} \cdot k_{b2} \cdot f_{b,d}} \leq 1 \tag{8}$$

Regarding ATCCs, the coefficient k_{b1} considers possible degradation effects due to swelling and shrinkage depending on the adhesive used for bonding. With the coefficient k_{b2}, it is possible to consider more complex stress situations, for example, due to a varying bond width or stress peaks. Both coefficients are currently under investigation at the University of Kassel.

4 FULL-SCALE TEST

One full-scale test in the laboratory in a four-point bending configuration was carried out to validate the calculation model and the considerations regarding the bond strength. The test was designed as a single-span girder with a span of 7.68 m. The same materials were used as for the construction of the school building; the prefabricated concrete parts were manufactured in the same batch as the concrete parts for the construction site.

The test set-up is depicted in Figure 8. The force was measured with a load cell with a measuring range of up to 500 kN. In addition to the displacement of the hydraulic cylinder (S0), the deflections were measured with six displacement transducers: S1/S2 for the mid-span deflection and S3–S6 for the relative deflection between the concrete and timber. The deflection w at the mid-span of the composite beam was calculated as the average of transducers S1 and S2. Furthermore, the strains in the bondline were measured using fibre-optical sensors.

The specimens were loaded in a quasi-static procedure applying a constant displacement with a rate of 0.2 mm/s. The global failure of the ATCC beam occurred at a load level of $F_{u,exp}$ = 387 kN ($F_{u,exp}$ = sum of the load-bearing construction and machine load, without the self-weight of the specimen) as a combined bond failure in the timber and the concrete (see Figure 9).

Figure 9: *Bond failure in the timber and the concrete substrate, as predicted from the calculation.*

Before loading to failure, the specimen was, firstly, loaded up to 120 kN, which is approximately 30 % of the ultimate failure load, and then unloaded again up to 20 kN in order to visualise the hysteretic effects. The load was held for 30 seconds at each of these loading points. The full-scale test exhibited a quasi linear-elastic behaviour. No hysteresic behaviour was observed visible (see Figure 10).

The calculation of the full-scale specimen was carried out with the calculation model mentioned above. The prediction of the failure load was referred to mean material properties. The shear strength of the concrete $f_{c,v,m}$ was determined with reference to the experimentally determined surface tensile strength of the concrete ($f_{ctm,surf}$ = 3.0) as $f_{c,v,m}$ = 6.0 N/mm².

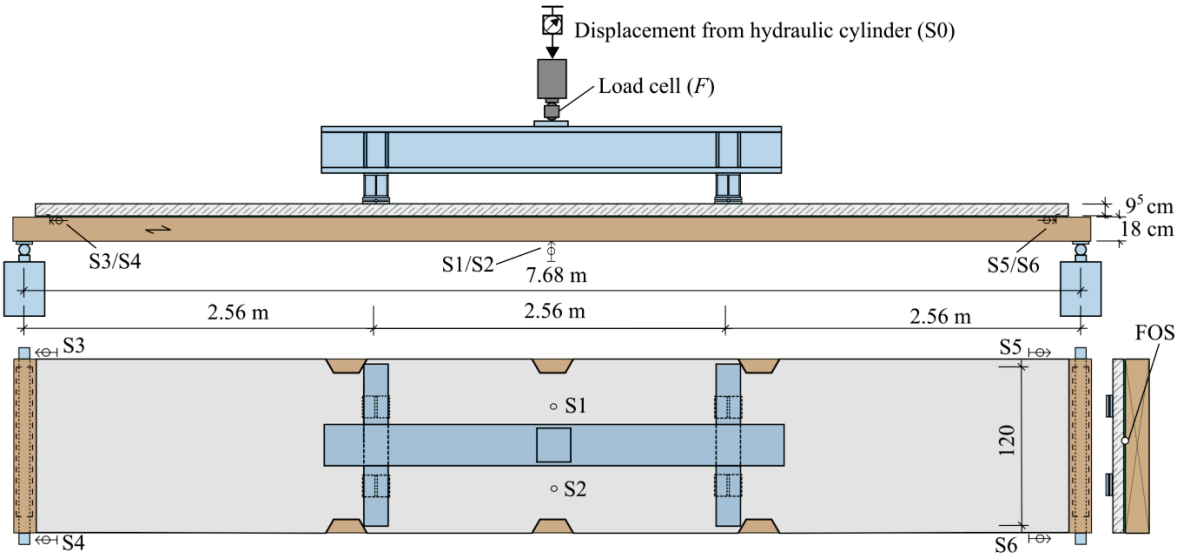

Figure 8: *Test set-up for the full-scale test: four-point bending configuration*

https://doi.org/10.52202/069179-0542

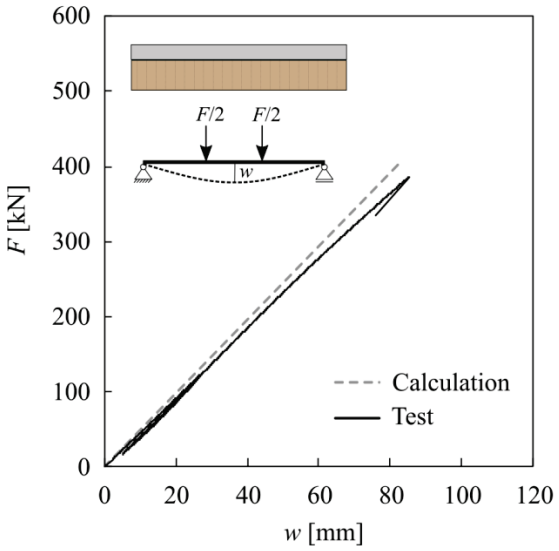

Figure 10: *Load-displacement behaviour of the full-scale test*

The shear strength of the timber was estimated according to Blaß and Krüger [27] as $f_{t,v,m}$(GL28c) = 4.2 N/mm². The resulting bond strength is the minimum of both $f_{b,mean}$ = min($f_{t,v,m,}$; $f_{c,v,m}$) = 4.2 N/mm².

As a result, the failure of the beam is expected to take place in the bondline at a load of $F_{u,cal}$ = 406 kN. The corresponding, predicted failure loads for a bending failure in the timber ($F_{u,cal,m+t}$ = 421 kN) and compression failure in the concrete ($F_{u,cal,c}$ = 438 kN) are higher and, therefore not expected to happen in the test.

The agreement between the test $F_{u,exp}$ = 387 kN and the calculation model is very good, for both the predicted failure mechanism (bond failure) and the failure load ($F_{u,exp}$ = 95 % of $F_{u,cal}$ = 406 kN).

5 QUALITY CONTROL

5.1 CONCEPT

The procedure of the construction work has been planned carefully and diligently to ensure successful bonding. In this context, a reliability concept has been implemented. The aim is to prevent the following potential defects:

- insufficient adhesion formation, or adhesion failure between the adhesive and joined part (due to insufficient surface preparation, too high or too low temperature, humidity or other inappropriate climatic conditions),
- insufficient cohesion strength of the adhesive due to a disturbed curing or an incorrect mixing ratio,
- insufficient load-bearing capacity of the concrete or timber surfaces, and
- contamination of the bonding surfaces.

5.2 PREPARATION

Some universal requirements for the components themselves and the weather and environmental conditions during the first 24 hours of adhesive curing on site were defined and checked before starting the execution process (see Tab. 1).

The requirements have been defined based on EN 14080 [28] and Part 3 of the DAfStb guideline on the bonding of concrete components [25]. Special attention has been paid to the surface tensile strength of the concrete because experience has shown that this particular parameter is a key factor for the success of the bond. Minimum requirements on the surface tensile strength in literature can be found in the range of $f_{ctm,surf}$ > 1.0 N/mm² [25]. A minimum value of 2.0 N/mm² has been defined in this project.

Table 1: *Requirements for the quality control of the pilot application*

Category	Criterion	Requirement
Weather conditions	Outdoor temp.	> 8 °C
	Rel. humidity	< 75 %
Concrete	moisture	< 4 %
	Surface temperature	3 K above the dew point
	Strength class (delivery receipt)	C30/37
	Surface tensile strength $f_{ctm,surf}$	≥ 2.0 N/mm²
Timber	Moisture	< 16 %
	Cleanliness of the surface	Free of dust and loose parts, free of grease
	Planing or grinding the surface	24 hours before starting the bonding
	Strength class (delivery receipt)	GL28c
Tolerance	Evenness timber	± 4 mm (on 2000 mm)
	Evenness concrete	± 1 m (on 200 mm) and ± 3 mm (on 1000 mm)
	Gap between timber and concrete	< 7.0 mm

https://doi.org/10.52202/069179-0542

5.3 GLUING

The environmental conditions (temperature and moisture) can strongly influence the hardening of the adhesive, therefore, bond samples were manufactured in-situ under on-site conditions. After seven days, the samples were tested in the laboratory. The gluing was carried out on 18 May 2022. The weather that day was very sunny and over 25 °C warm. It had rained the previous day, and although the ceiling area was covered, some moisture had entered the timber elements. However, since the moisture content of the timber elements were in the range of 13.0 to 15.4 %, the works could still take place.

The work was carried out in such a manner that the timber elements were lifted by a crane and fixed against displacement. As soon as the surrounding walls were in place, the timber surfaces were checked for evenness using an aluminium batten. The precast concrete elements were then lifted in on a trial basis and the unevenness between the timber and concrete was checked again with a measuring wedge.

In a next step, the position of the subsequent adhesive strips was marked and then freshly planed with a planing depth of about 1 mm. After the gluing surfaces had been planed, careful attention was paid during the work to ensure that no dirt, dust or grease residues got onto the gluing surfaces. This was achieved by wearing disposable gloves and disposable shoe covers. After cleaning with a vacuum cleaner, the adhesive was mixed and applied area by area with a mortar sledge for one precast concrete part at a time.

The pot-life of the adhesive was controlled by a time measurement. The concrete slab was then placed and fixed to the timber part with 12 assembly screws per precast concrete part by means of holes which had been installed in the precast part before pouring.

5.4 SAMPLE MANUFACTURING DURING THE GLUING PROCESS

Accompanying the gluing work, selected test specimens of each adhesive batch were produced directly on-site (see Tab. 2).

Table 2: *Quality assurance – tests during the bonding process*

Category	Criterion	Number of tests
Adhesive	Flexural tensile strength	2 per batch
	Surface tensile strength on a sandblasted steel plate	3 per batch
Bond to concrete	Surface tensile strength of the concrete prefab on-site with polymer mortar as adhesive	3 per batch

The number of specimens produced for the bending tensile prisms were chosen according to the technical approval Z-10.7-282 [29] as a related adhesive construction method is regulated there. At least two specimens should be produced for each adhesive batch according to EN 12350-1 [30] and tested after seven days of curing, according to EN 12390-5 [31]. Since all adhesive containers were manufactured in one batch at the production factory, two test specimens would theoretically have been sufficient due to the relatively small surface area and the resulting small quantity of adhesive. However, it was decided in this case to take samples from each container which was opened and mixed.

A similar procedure was followed for the tensile adhesion tests on a sand-blasted steel plate, and three specimens were taken per mixture. The surface tensile strength of the concrete was also tested again on a separate concrete plate to verify whether the adhesive formed a sufficient bond to the concrete. The surface tensile strength of $f_{ctm,surf}$ = 3.4 N/mm² was above the value of 3.0 N/mm² determined previously in the laboratory and also larger than the value of 2.0 N/mm² required. All further tests which were conducted in-situ also show no loss of strength compared to the reference value taken in the laboratory (Table 3).

Table 3: *Comparison of strength parameters from laboratory and in-situ*

Parameter	Lab.	In-situ
Flexural tensile strength $f_{adh,t,mean}$	28.7	30.0
Surface tensile strength $f_{ctm,surf}$	3.0	3.4

6 CONCLUSIONS

The pilot application of the ATCC construction method under realistic conditions on the construction site has been proved to be successful.

The construction process could be significantly accelerated compared to the conventional construction method with in-situ concrete, as the gluing operations of the prefabricated concrete parts were executed quickly and efficiently. It can be seen that it is possible to integrate ATCC constructions into the planning and construction process with the combination of a validated calculation method, a diligent planning process and a solid quality control concept. The economic use of prefabricated concrete parts for use in TCCs opens up new, promising possibilities for the whole building industry.

https://doi.org/10.52202/069179-0542

ACKNOWLEDGEMENTS

The period between the first tests on adhesively bonded TCCs and the practical implementation in construction as shown in this paper is about 15 years. During this time, extensive experience was gained in an intensive and fruitful collaboration between science and practice. The work would not have been possible without the financial support of:

- IGF research project 17274 N ("BestKleb"), finished 2015
- ZIM research project KF2512006KI4 (Co-operation with Schaffitzel Holzbau GmbH & Co. KG), finished 2017
- IGF research project 19417 N ("SpeedTeCC", Co-operation with WKI Fraunhofer Institute and Technical University Braunschweig), finished 2020
- ZIM research project (Co-operation with BEWO – Betonwerk Oberessendorf GmbH & Co. KG), finished 2022

The authors would like to thank the funding agencies, the colleagues named in the bibliography and, last but not least, the representatives of the companies involved in the projects and the associated project committees for their contributions.

REFERENCES

[1] ETA-13/0029. Würth ASSY plus screws. Self-tapping screws for the use in timber-concrete composite constructions.

[2] Schäfers M., and Seim W.: Investigation on bonding between timber and ultra-high performance concrete (UHPC). *Constr Build Mater*, 25 (7): 3078–3088, 2011. Doi: http://dx.doi.org/10.1016/j.conbuildmat.2010.12.060

[3] Eisenhut L., Seim W., Kühlborn S.: Adhesive-bonded timber-concrete composites – Experimental and numerical investigation of hygrothermal effects. *Eng Struct*, 125: 167–178, 2016. Doi: https://doi.org/10.1016/j.engstruct.2016.05.056

[4] Ginz A., Seim W.: Moisture induced internal stress within adhesive-bonded timber-concrete composites, WCTE 2018, Seoul, South Korea, 2018. https://doi.org/10.1016/j.engstruct.2016.05.056

[5] Frohnmüller J., Fischer J., Seim W.: Full-scale testing of adhesively bonded timber-concrete composite beams. *Mater Struct*, 54(5): 1–21, 2021. Doi: https://doi.org/10.1617/s11527-021-01766-y

[6] Frohnmüller J., Seim W.: Adhesively bonded timber-concrete composites: state-of-the-art (*Geklebter Holz-Beton-Verbund- Stand des Wissens und der Forschung*). *Bauen Holz*, 3: 30–35, 2021. ISSN: 0005-6545

[7] Frohnmüller J., Seim W., Mérono M., Wisner G., Stammen E.: Adhesively bonded timber-concrete composites with smooth concrete surfaces. WCTE 2021, Santiago de Chile, Chile, 2021.

[8] Seim W., Frohnmüller J.: Timber-concrete composites with prefabricated concrete parts: building "dry" consistently (*Holz-Beton Verbund mit verklebten Fertigteilen – konsequenter Trockenbau*). 26. Internationales Holzbau-Forum IHF, 2022.

[9] EN 311. Wood-based panels – surface soundness – test method. EN 311:2002

[10] EN 1542. Products and systems for the protection and repair of concrete structures – Test methods – Measurement of bond strength by pull-off. EN 1542:1999

[11] RAMPF Machine Systems GmbH & Co. KG (2015) EPUMENT 130/3, Technical data sheet

[12] Shrestha R., Mak J., Crews K.: Experimental investigations on epoxy bonded shear connection for timber-concrete composites. WCTE 2012, Auckland, New Zealand, 2012.

[13] Schmid V., Zauft D., Polak M.A.: Bonded timber-concrete composite floors with lightweight concrete. WCTE 2016. Vienna, Austria, 2016.

[14] BenMekki O., Toutlemonde F.: Experimental validation of a 10-m-span composite UHPFRC carbon fibers timber bridge concept. *J Bridge Eng*, 16: 148–157, 2011. Doi: https://doi.org/10.1061/(ASCE)BE.1943-5592.0000114

[15] DIN 18202. Tolerances in building constructions – Buildings, 2019-07

[16] EN 13747. Precast concrete products – Floor plates for floor systems. EN 13747:2005+A2:2010

[17] DIN 18203-3. Tolerances in building constructions – Part 3: Building components of wood and derived timber products, 2008-08

[18] Kästner M., Rautenstrauch K.: Efficient shear transfer in timber concrete-composite bridges by means of grouting with polymer mortar. WCTE 2016, Vienna, Austria, 2016.

[19] Grönquist P.: Load-bearing behaviour of adhesively bonded timber-concrete and timber-polymer-concrete composites with bar-laminated timber made of beech (*Tragverhalten von verklebten Holz-Beton- und Holz-Polymerbeton-Verbunddecken mit Buchen-Stabschichtholz*). S-WIN-Conference, ETH Zurich, 2022.

[20] Müller K., Frangi A.: Micro-notches as a novel connection system for timber-concrete composite slabs. *Eng Struct*, 245: 112688, 2021. Doi: https://doi.org/10.1016/j.engstruct.2021.112688

[21] EN 1992-1-1. Eurocode 2, Design of concrete structures – Part 1-1. EN 1992-1-1:2004 + AC:2010

[22] EN 1995-1-1. Eurocode 5: Design of Timber Structures – Part 1-1. EN 1995-1-1:2004 + AC:2006 + A1:2008: 2010.

[23] CEN TS 19103. Eurocode 5: Design of Timber Structures – Structural design of timber-concrete composite structures – Common rules and rules for buildings; CEN/TS 19103:2021.

[24] Frohnmüller J., Seim W.: Development of a rapid construction method for HBV ceilings by means of bonding prefabricated concrete elements

https://doi.org/10.52202/069179-0542

(*Entwicklung einer Schnellbaumethode für HBV-Decken mittels Verklebung vorgefertigter Betonelemente*). Research report, University of Kassel. 2022.
[25] DAStb-Richtlinie. Post-strenghening of concrete structures with glued-on reinforcement (*Verstärken von Betonbauteilen mit geklebter Bewehrung*), Deutscher Ausschuss für Stahlbeton (DAfStb). Berlin. 2012.
[26] Winter S., Hamm P., Richter A.: Vibration and damping behaviour of timber and timber-concrete composite slabs (*Schwingungs- und Dämpfungsverhalten von Holz- und Holz-Beton-Verbunddecken*). Research report, TU Munich, 2010.
[27] Blaß H.J., Krüger O.: Shear-reinforcement of timber with self-tapping screws and threaded rods (*Schubverstärkung von Holz mit Holzschrauben und Gewindestangen*). In: Karlsruher Berichte zum Ingenieurholzbau. Vol. 15 (in German), technical report, 2010. ISBN 978-3-86644-591-8
[28] EN 14080. Timber structures – Glued laminated timber and glued solid timber – Requirements. EN 14080:2013
[29] Z-10.7-282. Strengthening of timber beams by grouting with polymer concrete (*Polymerverguss zur Verstärkung von Holzbauteilen*). Allgemeine bauaufsichtliche Zulassung, DIBt Berlin; 2021
[30] EN 12350-1. Testing fresh concrete – Part 1: Sampling and common apparatus. EN 12350-1:2019
[31] EN 12390-5. Testing hardened concrete – Part 5: Flexural strength of test specimens. EN 12390-5:2019

World Conference on Timber Engineering Oslo 2023

APPLICATION OF A WOODEN PREFABRICATED SHELL EXOSKELETON FOR THE INTEGRATED AND SUSTAINABLE RETROFIT OF A RESIDENTIAL BUILDING

Jacopo Zanni[1], Chiara Passoni[2], Alessandra Marini[3], Ezio Giuriani[4], Andrea Belleri[5], Simone Labò[6], Giovanni Brumana[7], Simone Castelli[8], Claudio Abrami[9], Stefano Santini[10], Giuliano Venturelli[11], Angelo L. Marchetti[12]

ABSTRACT: The ambitious target of decarbonization requires a deep transformation of the construction sector and a systematic renovation of the existing building stock. Such a transition requires the adoption of new technologies conceived with a Life Cycle Thinking approach and implementing digital tools, maximizing performances, while enabling reduction of impacts and costs along the building life cycle. In the paper, a wooden construction technology for the deep renovation of existing buildings is presented. The solution is prefabricated off-site, made of a renewable bio-based material, and adopts innovative dry, standardized connections, enabling concentrating damage in case of earthquakes. The system is applied from the outside, without relocating inhabitants, that might otherwise hinder the renovation. An additional CLT engineered shell, coupled with an optimized thermal layer and new plants along the building perimeters, allow the combined energy and structural upgrade of the building. Finally, specific sensors are added for the continuous monitoring of structural health and environmental parameters. The proposed solution was developed within an industrial project integrating academic research and industrial leading-edge technologies and was applied to a typical post-WWII masonry building.

KEYWORDS: Wooden exoskeleton, Cross-Laminated Timber (CLT), Life Cycle Thinking (LCT), Holistic renovation.

1 INTRODUCTION

A great effort is required to the construction sector to become more sustainable and to proactively contribute to the European goal of carbon neutrality by 2050 [1]. In this transition, the deep renovation of the existing building stock is critical, as highlighted by the recent European "renovation wave" roadmap [2] and by the "New European Bauhaus", since existing buildings are expected to constitute about 85% of the 2050 European construction heritage [3].

In this scenario, it may be observed that the effort to build a few new sustainable green buildings or to renovate buildings targeting the sole energy efficiency is totally insufficient. To reach the ambitious EU goals, a complete transformation of the construction industry and of the concept of building renovation inspired by the Life Cycle Thinking (LCT) approach is required [4,5]. Adopting a LCT approach in the building renovation process means considering the fulfillment of the building needs and the reduction of potential impacts along its whole life cycle, from renovation to end of life. For example, at the product stage, impacts due to material supply and production should be minimized; at the construction stage, impacts connected to the transport and to the construction process should be limited; in the use stage, the energy consumption should be minimized together with impacts connected to maintenance, to the possible change of destination use, or, even more importantly, to possible hazards such as earthquakes or superstorms; finally, impacts connected to demolition/deconstruction of buildings and to waste management should be addressed since the earlier steps of the design phases. When the LCT approach is considered during the selection of a retrofit strategy, the role of structural engineers become critical in the definition and the detailing of the techniques. Life Cycle Structural Engineering (LCSE) should thus be adopted, including new LCT design principles, such as prefabrication, standardization, off-site production, adoption of eco-efficient materials, etc., to conceive and design truly sustainable retrofit techniques [6].

Economic sustainability of the interventions should also be considered when a LCT approach is pursuit. To overcome the economic and operational barriers that arise

[1] Jacopo Zanni, University of Bergamo, Italy, jacopo.zanni@unibg.it
[2] Chiara Passoni, University of Bergamo, Italy,
[3] Alessandra Marini, University of Bergamo, Italy,
[4] Ezio Giuriani, University of Brescia, Italy,
[5] Andrea Belleri, University of Bergamo, Italy,
[6] Simone Labò, University of Bergamo, Italy,
[7] Giovanni Brumana, University of Bergamo, Italy,
[8] Simone Castelli, University of Bergamo, Italy,
[9] Claudio Abrami, Microdevice, Italy
[10] Stefano Santini, Italia Smart Building, Italy
[11] Giuliano Venturelli, Architect, Italy
[12] Angelo Luigi Marchetti, Marlegno, Italy

https://doi.org/10.52202/069179-0543

for the rehabilitation of buildings in case of restricted budgets, the incremental rehabilitation approach may thus be adopted. This concept, introduced in [7] and further explored in [8], among others, involves planning a comprehensive intervention through a series of steps distributed over time and organized according to structural (minimum intervention), economic (budget limitations) and functional criteria (site sharing with planned maintenance interventions) so as to ensure the feasibility and effectiveness of the intervention.

From these premises comes the idea of employing holistic renovation techniques built from the outside of the building, coupling seismic reinforcement exoskeletons with energy and plant efficiency systems and with customizable architectural finishes, designed to meet the LCT principles and to be realized according to an incremental rehabilitation perspective [9].

Among these solutions, some of the authors recently proposed the AdESA System [10, 11], a wooden shell exoskeleton composed of a structural, energy, and architectural layer, able not just to guarantee maximum structural, energy and comfort performances, but also to minimize environmental, social, and economic impacts along the retrofitted building's life cycle, being conceived including some LCT principles such as material eco-efficiency, prefabrication, standardization, damage control, demountability, and reusability, among others. In this context, the use of wood-based materials allows, on the one hand, to limit the environmental impacts thanks to the use of a material with a positive CO_2 emission rate, and, on the other hand, to take advantage of the great potential offered by wood in structural and technological terms, such as prefabrication, standardization of connections, speed of assembly, ease of work on site and integration with insulation and finishing systems.

With respect to the first concept of the AdESA project, this paper presents an advancement of the solution. The system was here further engineered by improving the foundation connection system to enhance the demountability of the structural system, by introducing new plants from the outside, and by introducing a continuous monitoring of performances to ensure the building safety, efficiency and durability. The paper present the application of the enhanced system to a real case study, developed within the SCC Innovation Hub & Living Lab Network project (financed by Regione Lombardia, Italy), which, thanks to the collaboration between university and industrial partners involved in the construction and telecommunications sectors, has made it possible to conceive and implement an LCT-based integrated rehabilitation intervention on a social housing residential building featuring an additional prefabricated wooden shell exoskeleton.

2 GLOBAL CONCEPT OF THE INTERVENTION

The goal of the project was to design and apply an LCT-based integrated retrofit intervention to a residential social housing building, in order to achieve better performances and reduce the impacts of the building along its life cycle. The main constraints imposed by the project include adherence to planned budget limits and the need to not interfere with the functionality of the building by ensuring inhabitants full access to living spaces during the renovation works.

The proposed solution, developed from previous studies and applications within an ongoing research project carried out by the University of Bergamo and other partners, involves working from the outside through the implementation of an additional skin (the AdESA system [11]), arranged along the perimeter of the building in adherence to the existing walls, and consisting of three functional layers: structural, energetic and architectural.

The inner layer, which is a structural shell exoskeleton, constitutes a new seismic-resistant system that works in parallel with the building to which it is connected, ensuring an increase in overall strength and stiffness. The thickness of this layer can vary depending on the materials used and the structural solution adopted (e.g. single walls, coupled walls, shell). This is overlaid with the energy layer, made of thermal insulating materials capable of reducing the transmittance of opaque walls by limiting heat loss between inside and outside. A variety of thermal insulating materials are available to reach the same final energy performance. The choice of the best material depends on the transmittance and thermal capacity of the existing walls and of the structural layer selected, on the environmental impacts related to the materials, and on the total allowable thickness for the exoskeleton according to local building codes and functional needs. Finally, the architectural layer encloses the finishing of the new envelope and has both an aesthetic and protective value for the underlying layers. Since this layer does not have to perform energy/structural functions, it is highly customizable and can range from traditional solutions with painted plaster to panelized cladding with a variety of geometric and material textures.

From the LCT perspective, the system is studied to implement dry-mounted elements that, on the one hand, limit the use of raw materials and operations for on-site installation, and, on the other hand, ensure easy disassembly for the purpose of inspecting and maintaining the layers behind as well, and to enhance recyclability and reusability of the elements at the end-of-life stage. In addition, the system is also design to minimize the impacts due to earthquakes.

An important innovation introduced by the SCC Innovation Hub & Living Lab Network project concerns the implementation of a new plant distribution system integrated into the energy layer. The system, called Fluxus Ring®, is developed to substitute traditional wall and in-wall water supply pipes and electric wiring with a new type of pre-assembled isolated pipes, with the aim of making them easy to locate, inspect and implement over time thanks to a removable sheet metal cover and the use of special components that allow new utilities to be moved or added within the building without requiring any masonry work. In addition, another advantage is to create,

along the perimeter of each floor, equipotential rings that limit energy losses at the various utilities. The system consists of modules made up of extruded aluminum C-shaped profiles and sheet metal covers with a small footprint (103x265 mm) designed as a multi-service physical infrastructure able to accommodate all the plant ductwork expected for a residential building (hydraulic, electric, multimedia and building & automation control systems, optic fiber) (Figure 1).

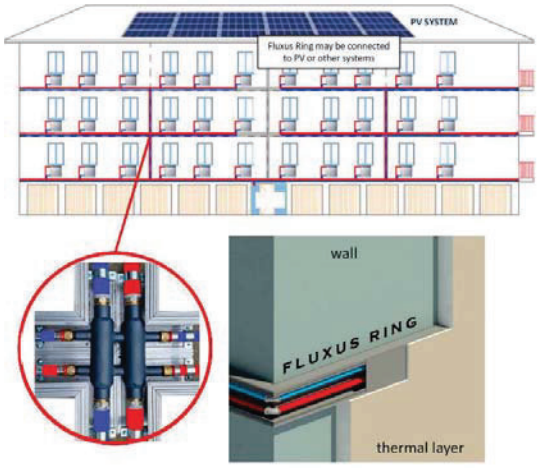

Figure 1: *Fluxus Ring system (©Italia Smart Building)*

In order to guarantee the building performances during its use phase, an aspect of great importance concerns the continuous structural health monitoring (SHM) [12]. This process involves the observation of the structure over time, the extraction of features from measures sensitive to structural damage, and, finally, the statistical analysis for the automatic detection of the state of health.

To this end, SHM systems consisting of tools for acquiring, processing, storing and sharing data on digital platforms were designed (Figure 2). The monitored parameters are the building's vibration frequencies, through the acquisition of accelerations induced by environmental vibrations and seismic events, and the state of preservation of the material constituting the structural exoskeleton, by measuring the moisture content in the CLT panels. These parameters, compared with the targets used in the design and construction phase, can provide important feedback on any damage or deterioration phenomena not directly detectable by visual inspections.

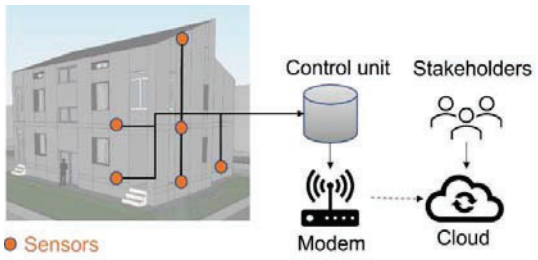

Figure 2: *Structural Health Monitoring concept*

3 DESCRIPTION OF THE REFERENCE BUILDING

In the project, the proposed LCT-based wooden retrofit solution was applied to a residential building. The case study is a social housing building constructed in 1960, located in northern Italy. The building has two floors above-ground, each featuring two apartments, and an attic with roofing on staggered levels having a practicable part, used for storage and cellars, and a non-walkable part under the lower pitch.

The plan organization is regular, with a gross surface of about 131 m^2. The main façade has an extension of 13.6 m, the rear façade has an extension of 12.4 m, and the side façades have an extension of 10 m and an indentation of about 0.60 m in the middle of the length as shown in Figure 3.

The load-bearing structure presents masonry walls made of clay hollow blocks (245x245x120) mm^3, with the holes arranged horizontally, and cement-based mortar. In the corners between orthogonal walls and at the ends of longitudinal walls the masonry is made of solid brick; while the walls of the crawl space between the foundations and the first-floor slab (75 cm above ground level) are made of solid brick and cement mortar, resting on continuous perimetral foundation made of unreinforced concrete mixed with stones. The floor slabs consist of 20 cm-high RC beam and clay block system, with spans of 4.20 and 5.00 m and perimeter curbs above the masonry walls made of poor quality weakly reinforced concrete.

The two-roof pitches, arranged at different heights, consists of reinforced brick joists and hollow-core lacking the extrados screed.

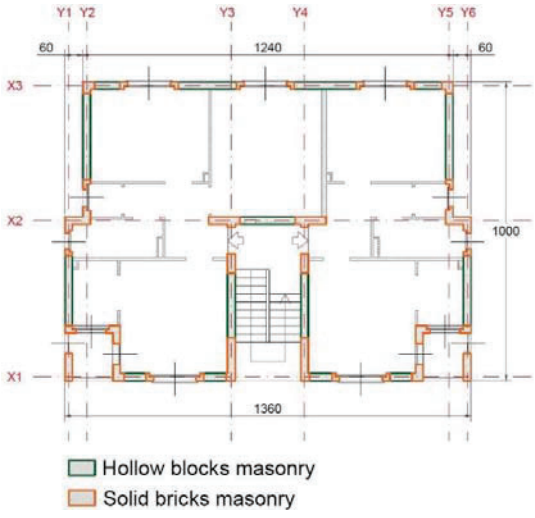

Figure 3: *Floor plan of the building*

Under a structural point of view, masonry walls exhibit vulnerability both with respect to out-of-plane actions, due to the absence of roof diaphragm providing effective constraint against overturning, and with respect to in-plane actions, due to the masonry quality that exhibits

https://doi.org/10.52202/069179-0543

poor mechanical performances and more brittle behavior than traditional masonry type due to the arrangement of hollow blocks [13]. The reference seismic spectrum at LSLS is obtained, according to Italian code [14], from the following parameters: $a_g = 0.158$ g, $F_0 = 2.463$, $T_c^* = 0.266$ s, S = 1.200. The main vulnerability of the building is represented by the local out-of-plane collapse mechanisms of the masonry on the attic floor, associated with a safety index of 0.12. The seismic retrofit is therefore necessary.

Moving to the energy considerations, the selected building represents the classic example of social housing of the '60 and was not improved during the years. The envelope obsolescence is the cause of a poor energy performance, as quite usual of buildings of those years. The walls are covered with plaster and the roof with tiles; all the surfaces lack thermal insulation, and different types of cold bridges can thus be identified. Single glass windows with old frames affect the energy performance and drive a high air infiltration ratio. In addition, the stairwell, which is centrally placed to the main façade, is open to the outer courtyard (Figure 4). The facilities are outdated and inadequate. The combination of these factors leads to a large energy consumption for space heating and a low indoor comfort for the users.

Finally, under an architectural point of view, the building presented poor conditions and a bad state of preservation with widespread deterioration on the façades and low living comfort for the inhabitants, needing renovation both under an aesthetic and a functional point of view.

Figure 4: *Picture of the main façade*

4 DESIGN OF THE RETROFIT INTERVENTION

4.1 STRUCTURAL LAYER OF THE INTERVENTION

The choice to intervene from the outside to avoid inhabitants' relocation implies the introduction of new seismic-resistant systems that cooperate with those of the existing building, called exoskeletons [15,16]. This requires special attention in the evaluation of the actions transferred at the floor and foundation levels and in the definition of the relevant construction details. Furthermore, to enable the transfer of actions between the exoskeleton and the existing building, preliminary verification and possible reinforcement of the existing floor diaphragms is necessary as they represent indispensable elements of the seismic force resistant system [17,18].

Exoskeletons can be divided into two main categories according to their structural organization: bi-dimensional and three-dimensional systems.

Bi-dimensional (or wall) systems are those applied on individual building façades, designed to make a resistant contribution only in the reference direction without interacting with systems arranged on adjacent façades. Three-dimensional systems (or shell structures), on the other hand, are characterized by the widespread presence of structural elements along all façades that cover the entire exterior surface of the building. This has significant advantages from a structural point of view since orthogonal walls, being connected to each other, make it possible to increase overall stiffness and strength by reducing stress on individual elements and in the foundation.

For the definition of the seismic retrofitting intervention, performance targets that are stricter than those required by the Italian national standard [14] have been identified to respect those LCT principles connected with the damage and downtime minimization. According to such principles, in addition to the fundamental criterion of structural safety, it is also important to ensure building resilience through damage control for high intensity earthquakes so as to minimize the economic and social impacts resulting from a seismic event.

Based on these considerations, the Life Safety Limit State (LSLS) was taken as a reference, and it was imposed that: the exoskeleton must be able to transfer the entire seismic action expected for the building; the structure must experience a maximum limit drift of 0.2%, dictated by the poor masonry quality and the need to preserve its strength against vertical loads; residual drift must be limited so as not to compromise disassembly and repairability of components; a ductile collapse mechanism for the building must be ensured.

According to the previous design objectives, the structural exoskeleton applied to the case study building, represented in Figure 5, is composed of a new foundation system, a wooden shell made of 10cm-thick five layers CLT panels connected each other and with existing floors, and an extrados roof diaphragm made with plywood panels.

The foundation system consists of a RC perimetral curb placed in adherence to the existing foundation to support the CLT panels and transfer their actions to 16 small-diameter piles, deeply driven into the ground (15 m), to support the tensile and compressive actions induced by the wooden shell, and an outer RC diaphragm (100x20)cm^2 to collect the seismic load of the entire building and ensure its shear-slip resistance with respect to the ground.

Figure 5: *Layout of the structural intervention*

Given the geometry of the building, the CLT panels are arranged vertically adjacent to the existing wall piers and shaped to contour existing openings (Figure 6). A shear connection is placed between adjacent panels to obtain a coupled wall system with high stiffness, comparable to that of the existing building. The shear connections between panels, shown in Figure 7, were ad-hoc designed to ensure ductile and dissipative behavior by avoiding damage in the CLT panels and keeping the other connections in the elastic range, thus ensuring the minimization of damage and replacement actions in the aftermath of the earthquake. These connections are made with segments of HEA100 welded along the flanges, exhibiting hysteretic behavior due to bending plasticization of web plates, whose ductility was tested through an experimental campaign conducted by University of Bergamo [19]. The connection is prefabricated and mounted to the CLT panels on site by into millings prepared on the edge of the panels and fixed with over-resistant self-drilling dowels.

CLT panels are then connected to the building floors by means of dowels (φ20/30) and tie rods (2φ12/panel) grouted in the RC curbs, designed with elastic and over-resistant behavior.

The continuous connections between adjacent panels and between orthogonal panels were realized by means of cross-connecting screws (φ9x140mm) designed for shear and tensile strength with overstrength behavior.

The panels are restrained to the new foundation by means of unbonded steel ties (Dywidag 18WR) for transferring the high tensile stresses induced by the exoskeleton, and shear keys inserted at the base of the panels (φ50 tubular studs, of 3 mm thickness, welded to the base plate nailed to the panel). The ties are prepared and pre-installed off-site inside the panel and jointed in place with coupler, while the shear keys are housed in special recesses prepared in the cast-in-place foundation curbs (Figure 8) and sealed with high-performance mortar after assembly operations are completed.

The development of this connection system arose from the need to transfer higher shear and tensile actions for which the traditional connections used in new wooden construction (hold-down and angle brackets) are insufficient, but especially to ensure easy assembly and disassembly of the system in the LCT perspective.

The roof diaphragms, built at the extrados of the two pitches of the existing roof, consist of 3-cm-thick plywood panels joined together with nailed strips (Figure 9) and perimeter chords made of steel plates connected to the existing RC curbs by dowels and tie rods and to the CLT walls by nails.

Figure 6: *Prefabricated CLT panels ready to be installed*

Figure 7: *Dissipative connection between CLT panels*

https://doi.org/10.52202/069179-0543

Figure 8: *Panels arranged on the façade and connected with the new foundation*

Figure 9: *Construction of the diaphragm at the extrados of the existing roof*

To evaluate the effectiveness of the structural intervention, two finite element models of the building were developed with Midas Gen and nonlinear static analysis were carried out.

The first model represents the building in the as-is condition in the hypotheses that the local mechanisms were inhibited. Given the regularity and simplicity of the structure, equivalent frame modelling was employed.

The masonry piers were introduced with beam elements with an extension equal to the interstory height, connected by the RC curbs. To both elements were assigned concentrated plastic hinges in shear and bending; in particular, the shear-slip mechanism was evaluated for masonry.

In the second model, shown in Figure 10, the wooden exoskeleton is overlapped to the initial configuration. CLT panels were introduced adopting plate elements and considering the orthotropic properties of the material and the actual geometry and stratigraphy of the adopted panels. Connections were modelled as distributed general links with calibrated stiffness and elastic strength based on the theoretical and experimental behavior of individual connectors. At the base of the panels, compression-only type point spring supports, to simulate the vertical interaction with the reinforced concrete foundation, and rigid shear constraints were introduced.

Figure 10: *Finite Element Model of the retrofitted building*

The building in the as-is condition develops a soft story mechanism in which capacity is dictated by the achievement of the ultimate flexural drift of the slender wall piers arranged on the main façade. The displacement demand at LSLS is therefore not satisfied.

The results, reported as a comparison of pushover curves in Figure 11, show that, with the introduction of the exoskeleton, the structure gains stiffness and strength, and the displacement demand at LSLS is lower than capacity. At this point, plasticization of some dissipative connections is reached while the connections between panels and foundation are all found to remain in the elastic range; internal stresses in CLT panels, evaluated in accordance with [20] and considering the actual panel stratigraphy, are lower than the prescribed limits. In the existing structure some masonry walls reach the plasticization; however, the maximum drift recorded is 0.12%, lower than the maximum imposed limit of 0.20%. The ultimate displacement capacity of the building also increases by moving from a weak storey mechanism to a global mechanism that allows an increase in the ductility of the structure.

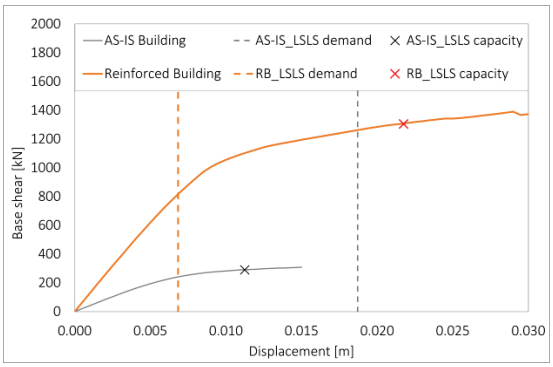

Figure 11: *Comparison between the pushover curve of the As-is building and retrofitted building for the main direction*

https://doi.org/10.52202/069179-0543

4.2 ENERGY AND ARCHITECTURAL LAYERS OF THE INTERVENTION

The final stratigraphy of the integrated intervention, shown in Figure 12, includes a structural layer with 10-cm-thick CLT panels, covered with an energy layer consisting of 12-cm-thick rock wool panels and completed by a finish with painted plaster. Several proposals were developed for the design of the outer architectural layer to explore the expressive potential of the system, an example is shown in Figure 13; however, the final choice was dictated by the budget constraints.
The energy efficiency intervention also includes closing and insulating the stairwell, insulating the attic floor with 16-cm-thick XPS panels and windows replacement.

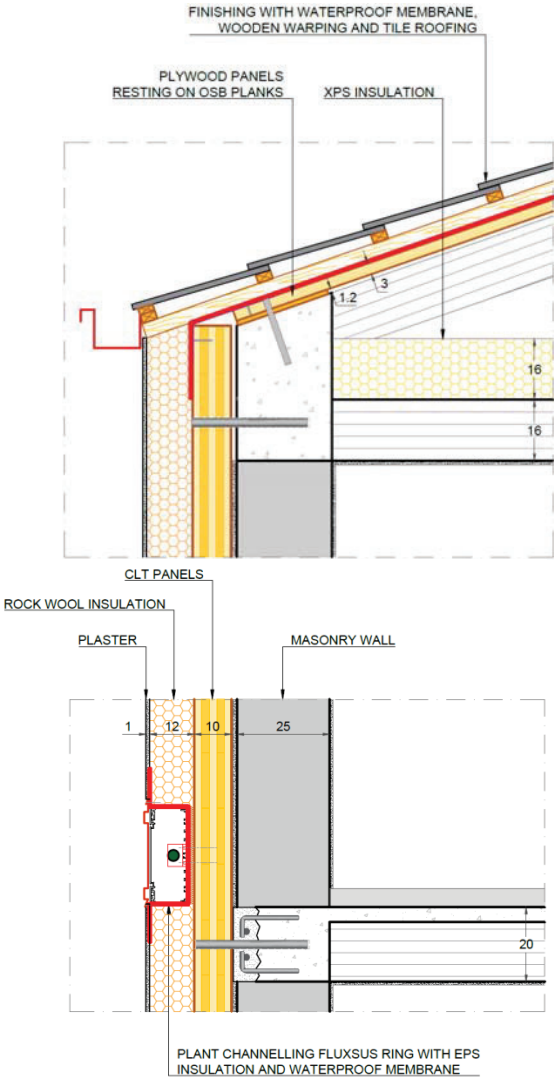

Figure 12: *Stratigraphy of the retrofitted building*

Figure 13: *Rendering of one of the proposed architectural solutions*

From the energy point of view, coupling the structural layer with an energy layer allows to reduce the thermal transmittance of the opaque elements from 0.96 to 0.22 W/(m^{2}K) and avoid cold bridges.
A detailed transient analysis has been carried out adopting a numerical Trnsys simulation. Starting from a 3D geometrical model, the evaluation considers the behavior of the building including the physical properties of walls and the internal gains (occupancy, appliances, and lights) on hourly basis in terms of temporal and spatial distribution. The results showed a reduction of primary energy requirement for the space heating, compared with the as-is conditions. In fact, as shown in Figure 14, the forecasted peak load shifts from 22 kW to 9 kW; whilst, on annual basis, the heating load drops from 54 MWh to 15 MW, with an energy savings of 72%.

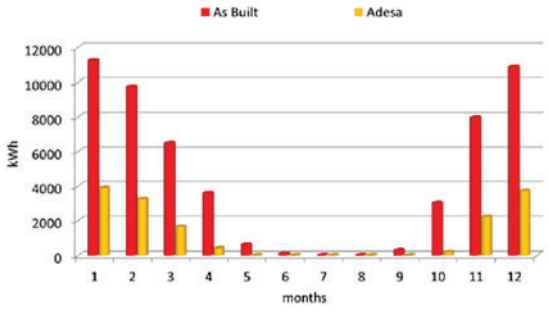

Figure 14: *Comparison between the energy performances of the building in the as-is and retrofitted conditions*

4.3 ADDITIONAL PLANTS FROM THE OUTSIDE AND MONITORING SYSTEM

With respect to the traditional AdESA system, in this project, the integrated renovation solution was further engineered to ensure both the adaptability of the plant system and the monitoring of the building performances along its life cycle. To this aim, the Fluxus Ring ® plant system was installed along the perimeter of the building close to the structural layer, to which it is connected by screws, and, inside it, it was housed the monitoring system (Figure 15) with associated wiring connecting the acquisition instrument to the control unit located in the

https://doi.org/10.52202/069179-0543

attic of the building where the collected data are processed, stored and shared on a cloud platform.
Eight uniaxial accelerometers, oriented in the three main directions, are placed on the structural layer; two hygrometers are placed on the CLT panels of the north and south façades and one inside the plywood panel of the roof diaphragm. Finally, a weather station is placed on the roof of the building to collect environmental parameters such as humidity, temperature, pressure and wind speed.

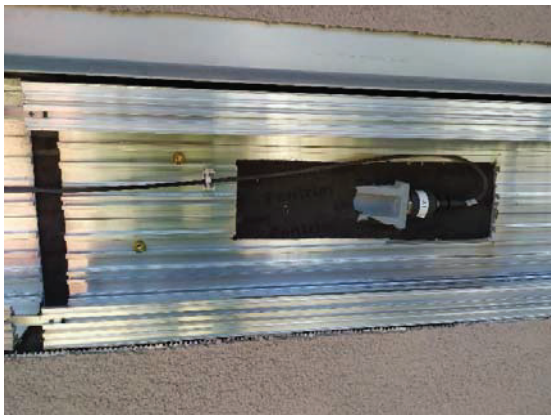

Figure 15: *Placement of an accelerometer within the Fluxus system*

The adoption of Fluxus Ring would allow the substitution and/or future modification of the plants without the relocation of inhabitants, according to the evolving needs of its occupants and in line with the LCT and incremental rehabilitation approaches, thus allowing the building owners to fulfill the requirements of building flexibility and adaptability.

5 CONCLUDING REMARKS

The need to make the building stock more resilient and sustainable requires a deep change of the current practices adopted in the construction sector. In the present paper, a new wooden retrofit technology inspired by the principles of Life Cycle Thinking and Incremental Rehabilitation integrated with innovative digital tools for Structural Health Monitoring is proposed and applied for the holistic and smart renovation of a residential building, which shows important structural, energetic and architectural deficiencies. The solution consists in a prefabricated multi-layered wooden exoskeleton, implementing bio-based materials, standardized elements, and dry and demountable connections. An innovative system to introduce new plants without relocating inhabitants is provided, and sensors are installed for monitoring of the structural health of the building.
The presented solution, which results from the collaboration of academic and industrial partners, represents the evolution of the prototype AdESA system [11], which is here further enhanced by enforcing the application of the LCT principles and by implementing digital technologies to improve building performances and comfort of the inhabitants.
In particular, the choice of a material such as wooden panels for the realization of exoskeletons is favorable for intervening on small regular buildings, due to limitations imposed by the mechanical properties of the material and by production and assembly operations. In addition, wooden exoskeletons may be easily conceived to comply with sustainable LCT criteria; timber is in fact an eco-friendly material, produced in certified factories and employed with dry technologies thanks to the use of standardized mechanical connections that reduce site operations. Moreover, wood is easily workable and adaptable on the construction site for the management of interference and assembly tolerances, and it also offers excellent support for the fixing of additional elements such as windowsills, parapets, ventilated façades, technological installations, etc... Also, from the energy point of view, thanks to its thermal properties, timber offers a contribution in terms of insulation, which has positive effects on the thickness of the insulating layer. On the other hand, special attention should be paid to fire and moisture protection of wood in order to ensure durability.
In this paper, the proposed wooden prefabricated shell system was applied for the renovation of a social housing building. The design of the integrated retrofit intervention was discussed, and the enhancement of the seismic and energy performances of the building after the retrofit were shown by means of numerical analyses.
To complete the retrofit intervention, the construction site took 6 months, including 5 months for the structural works; the most time-consuming operations involved the construction of the new foundations, while the installation of 20 vertical CLT panels, with maximum dimension of (250x790x10)cm^3 and the 8 connecting panels took only one week. Figure 16 shows the new building envelope following the completion of the intervention.
Observations from this pilot application will enable further enhancement of the proposed technology and will improve the replicability of the solution.

Figure 16: *Appearance of the building when the work is completed*

https://doi.org/10.52202/069179-0543

ACKNOWLEDGEMENT

The proposed solution was tested within an industrial project integrating academic research and industrial leading-edge technologies, with the aim of testing new solutions for smart and connected cities, financed by Regione Lombardia (Italy). The authors greatly acknowledge the SCC Innovation Hub & Living Lab Network partners who have supported and collaborated in the development of the project and ALER Brescia-Cremona-Mantova for providing the case study building.

REFERENCES

[1] JRC Report EUR 26497 EN, Marini, A., Passoni, C., Riva, P., Negro, P., Romano, E., et al.: Technology options for earthquake resistant, eco-efficient buildings in Europe: Research needs, Report EUR 26497 EN. JRC87425, 2014.

[2] COM 662 final: A Renovation Wave for Europe - greening our buildings, creating jobs, improving lives. Brussels, 14.10.2020.

[3] BPIE Report. Vitali Roscini A., Rapf O., Kockat J.: On the way to a climate-neutral europe. Contributions from the building sector to a strengthened 2030 climate target, 2020.

[4] Huang B., Gao X., Xu X., Song J., Geng Y., Sarkis J., Fishman T., Kua H., and Nakatani J.: A Life Cycle Thinking Framework to Mitigate the Environmental Impact of Building Materials. One Earth, 3, 564-573, November 20, 2020.

[5] Passoni C., Marini A., Belleri A., Menna C.: Redefining the concept of sustainable renovation of buildings: state of the art and an LCT-based design framework. Sustainable Cities and Society, 64, January 2021.

[6] Passoni C., Palumbo E., Pinho R., Marini A.: The LCT challenge: defining new design objectives to increase the sustainability of building retrofit interventions. Sustainability 14 8860, 2022.

[7] FEMA P-420. Engineering Guideline for Incremental Seismic Rehabilitation. Federal Emergency Management Agency (FEMA) – USA, 2009.

[8] Zanni J., Labò S., Passoni C., Marini A., Belleri A., Menna C.: Incremental integrated holistic rehabilitation: a new concept to boost a deep renovation of the existing building stock. IOP Conf. Ser.: Earth Environ. Sci. 290 012140, 2019.

[9] Marini A., Passoni C., Belleri A., Feroldi F., Preti M., Metelli G., Giuriani E., Riva P., Plizzari G.: Combining seismic retrofit with energy refurbishment for the sustainable renovation of RC buildings: a proof of concept. European Journal of Environmental and Civil Engineering, 2017.

[10] AdESA (Adeguamento Energetico Sismico ed Architettonico). Final Report. Project ID n. 379259; Smart Living Project; Regione Lombardia: Brescia, Italy, 2019

[11] Zanni J., Cademartori S., Marini A., Belleri A., Passoni C., Giuriani E., Riva P., Angi B., Franchini G., Brumana G.: Integrated Deep Renovation of Existing Buildings with Prefabricated Shell Exoskeleton: The AdESA Case Study. Sustainability 13 11287, 2021.

[12] Cury A., Ribeiro D., Ubertini F., Todd M. D.: Structural Health Monitoring Based on Data Science Techniques. Structural Integrity 21. Springer, 2022.

[13] Labò S., Marini A.: In-plane flexural behavior of hollow brick masonry walls with horizontal holes. Engineering Structures 273 115086, 2022.

[14] Decreto Ministeriale del 17/01/2018 – Norme Tecniche per le Costruzioni (NTC18).

[15] Passoni C., Guo J., Christopoulos C., Marini A., Riva P.: Design of dissipative and elastic high-strength exoskeleton solutions for sustainable seismic upgrades of existing RC buildings. Engineering Structures, Volume 221, 15 October 2020.

[16] Di Lorenzo G., Colacurcio E., Di Filippo A., Formisano A., Massimilla A., Landolfo R.: State of art on steel exoskeletons for seismic retrofit of existing RC buildings. International Journal of Earthquake Engineering XXXVII(1):33-49, 2020.

[17] Marini A., Belleri A., Passoni C., Feroldi F., Giuriani E.: In-plane capacity of existing Post-WWII beam-and-clay block floor systems. Bulletin of Earthquake Engineering. 20(3):1655–1683, 2021.

[18] Giuriani E., Marini A., Preti M.: Thin-folded shell for the renewal of existing wooden roofs. International Journal of Architectural Heritage: Conservation, Analysis and Restoration, 2015.

[19] Cademartori S.: Structural issues in exoskeleton solutions for the integrated renovation of existing buildings. PhD Thesis, Supervisor: prof. A. Marini, University of Bergamo, Cyle XXXV.

[20] Bogensperger T., Moosbrugger T., Silly G.: Verification of CLT-plates under loads in plane. In: 10th World Conference on Timber Engineering, 2010.

https://doi.org/10.52202/069179-0543

World Conference on Timber Engineering Oslo 2023

BUILDING WITH WOOD STRUCTURES – SUCCESFULL DESIGN PROCESS

Alain Bradette[1], Geir Glasø[2], Tor Øistein Andresen[3]

ABSTRACT: Building with wood construction (glulam, CLT, LVL etc.) poses challenges compared to conventional buildings in steel and concrete. Load bearing systems, stability, spans (thickness and vibration of floor elements), connections between structural elements, the behaviour in case of fire and sound insulation properties are the main characteristics that must be addressed individually.

These challenges grow in importance when one desires to display the wood construction as much as possible. The reasons for building with timber are many. To name some: low CO_2-emissions, reduced duration of the building phase, low noise on building site, architectural properties as well as use of prefabricated elements and design processes combining virtual design and construction (VDC) with building information modelling (BIM) that reduces risk and cost compared to on-site building systems.

Planning building projects with normal design phase level of development is in our experience not appropriate to successfully plan and execute building projects with visible timber structures. The reason being that the necessary multidisciplinary aspect of the design is not sufficiently considered.

In this paper we will, through case studies, showcase some of the multidisciplinary design challenges with exposed timber structures and show how a multidisciplinary design process can help to achieve project goals and meet design requirements.

KEYWORDS: Collaboration, Sustainability, building design, structural design, acoustics, fire safety, timber structures, Building information model (BIM), project management, large timber buildings, multidisciplinary engineering, WCTE 2023, Oslo, Norway.

1 INTRODUCTION

Using timber as material for structure in buildings is following an exponential growth in recent years as part of the efforts in reducing CO2-emissions from the construction industry.

To build with timber structures poses more challenges compared to conventional buildings with steel and concrete. These challenges grow in importance with the increasing technical complexity resulting from timber material properties, the number of stories or when one aspires to exhibit the timber construction as much as possible.

Use of modern prefabrications and design processes such as virtual design and construction (VDC) and building information modelling (BIM) are very useful tools, but the design process is also very crucial. Indeed, our experience is that planning massive timber project with normal phase maturity in early project phases will not address properly the engineering challenges posed by larger building projects, especially when some of the massive timber structure is apparent. The main reasons being insufficient multidisciplinary design and level of development.

In this paper we will, through case studies, investigate some of the challenges with exposed timber structures and explain how to achieve project goals and meet design requirements through multidisciplinary design. The case studies focus on CLT and Glulam buildings.

2 SHOWING TIMBER STRUCTURES

2.1 REASONS TO SHOW TIMBER STRUCTURE

There are several reasons for showing timber structures compared to embedding the timber material in other materials such as gypsum boards:

[1] Alain Bradette M.Sc., Sweco Norway AS, Norway, alain.bradette@sweco.no
[2] Geir Glasø, Sweco Norway AS, Norway, geir.glaso@sweco.no
[3] Tor Øistein Andresen, Sweco Norway AS, Norway, tor.andresen@sweco.no

https://doi.org/10.52202/069179-0544

- Architectural expression: visible wood is growingly sought after as it gives to the architects a new palette of forms, textures, and colours to exploit in their research of building identity and impression.
- CO2-emission: Fewer linings and false ceilings mean less materials and therefore less emissions.
- Reduced costs: Fewer linings and false ceilings lead to less material and less time spent on execution, both contributing to reduce the costs.
- Reduces execution time: As less operations are required, the execution time is consequently reduced.
- Indoor climate: Exposed massive timber helps to regulate the indoor climate with its ability to absorb and release humidity and its thermal insulating properties.
- Psychological effect: This field is currently the topic of research. Strong evidence and conclusions are still to come, but feedbacks from projects indicate that apparent massive timber is generally beneficial for the "feel good" of users. Wood is perceived as a natural material and the presence of natural elements may have positive psychological effect. The physical touch is also felt soft and warm, which may procure a calming effect. Other feedback is that pupils in schools tend to be quieter and calmer in schools with visible wood. Studies of positive effect on patient's recovery in rooms with visible wood constructions are undergoing.

2.2 CHALLENGES

Structure

Timber structures require a different design approach due to the properties of the material compared to other structural materials such as steel and concrete. The design of timber members, such as beams and columns, depend heavily on the design and load capacity of the connections as the connections give the requirements for the associated elements. This means that connection design needs to start early, at the same time as the structural members.

The integrity of visible connections in case of fire loads is also a design requirement that needs to be attended by a structural engineer.

The aesthetic of the connections is an architectural opportunity. However, as showed above, any aesthetic consideration must be part of the connection design right from the start as an input like loads, associated member dimensions and fire safety requirements.

The fact that timber elements and the connections are not standardized gives place to a large degree of innovation. However, new assemblies require in-depth knowledge of wood properties. Advanced calculation and laboratory tests may be needed to reach sufficient confidence and documentation of the solutions.

Fire safety

Fire safety is a crucial aspect for timber buildings. Timber constructions are combustible and as such will contribute to increase the amount of combustible material and hence, the development of the fire.

Height, use and location of the building are determining factors for fire safety requirements imposed by the local legislation.

Fire codes are commonly based on the use of non-flammable materials and approved construction and details providing a known fire resistance. Since timber is a flammable material, the fix fire resistance logic of the fire codes is not directly applicable for apparent timber constructions. The dynamic fire behavior of the load bearing structure in massive timber is therefore established through calculations of the fire energy over time, taking into account both the contribution from the burning structure and the charring insulating effect. This is an iterative process leading to the balance between the amount of exposed timber structure and the required integrity duration for the structure.

The calculated charring layer must be added to the dimensions of the timber elements and solutions for fireproofing the connections must be designed. These two elements are of great influence for the properties and appearance of the bearing structure, proving necessary to integrate fire safety in the early design of any timber construction with exposed timber.

Acoustics

Massive timber has a density around one-fifth of concrete. Sound insulation and impact noise properties of massive timber are therefore quite different from concrete. For instance, for a given thickness, a massive timber element will typically provide sound insulation 15 – 18 dB lower than a concrete element.

As a basic rule, massive timber walls alone do not provide sufficient sound insulation to meet most of the acoustical requirements between rooms. Concerning floors, the combination of limited airborne insulation and high impact noise makes it impossible to have bare elements without any improving construction such as a floating floor and/or a sound insulating ceiling.

The low mass of timber also makes flanking transmission through wall and floor elements an important issue to address. The simplest solution is to use gypsum board linings and ceilings. The flip side is that more operations and material are needed, with their consequences on time, costs, and the environment.

As described above in section 2.1, there are many reasons for showing massive timber structure. The adequate approach to optimizing visible massive timber while taking care of the Acoustics is as follow:

- Use fire safety measures for sound insulation: Fire safety may require non-flammable material in a corridor. Mounting a gypsum board directly on the CLT-wall will barely improve the sound insulation, 1 - 2 dB. Using the same gypsum board as a lining with an air space can improve the sound insulation by 10 or 15 dB.
- Coordinate fire safety measures with sound insulation: Avoid having situations where

https://doi.org/10.52202/069179-0544

gypsum board is applied on one side of a wall for fire safety reasons and a lining is mounted on the other side because of the sound insulation.

- Use decoupling to reduce flanking transmission: Elastomer strips between wall and floor elements are commonly used for that purpose, but the connections often "short circuit" the elastomer, significantly reducing the effect of the decoupling. Split of floors can also be used, but this measure has important consequences on the load bearing system and the architecture since supplementary beams and columns can be necessary as well as changes of the layout.

Given the important implications of the approach explained above, the acoustical design must absolutely be integrated at an early stage of the design when alternatives for solutions are still there.

Contrary to common expectation, sound absorption properties of massive timber are very low. That means that a building solely made of massive timber will not even get close to fulfilling standard requirements for reverberation time. Additional sound absorbing elements such as false ceiling, free hanging units and wall absorbers are unavoidable.

3 SOLUTIONS

When facing the technical complexity of designing massive timber buildings, it is not uncommon to see architects, builders or property developers asking for a reduction of the requirements.

On a general basis, we do not agree with this approach. For instance, we cannot have less firesafe buildings. Furthermore, people do not want less comfortable buildings than what they are accustomed to. To take an example, electric cars' popularity began the day they became as performant as cars with combustion engine. Likewise, less comfortable timber buildings will lead to reduced buyers' and users' interest.

On the other hand, we believe that better understanding of the material could lead to more harmonized and more adapted requirements for fire safety.

The standard design process is sequential with the architect drawings, then structural design, then fire safety and acoustics. Our experience is that this sequential design is not adapted to massive timber constructions and is the major reason for the perceived added complexity and disappointing results. Changing the design approach rather than the requirements appears then to be the right option.

Based on our experience with successful projects, we strongly believe that early involvement of fire safety and acoustics in the design process and tight coordination between disciplines, especially with structure, are key to success. This approach is explained and exemplified in the paragraphs below.

3.1 DESIGN PROCESS

All building design process goes through different design phases, from the beginning to the end. There are many different definitions and scales of each phase depending on the project size and complexity. Professionals have developed methodologies and tools to handle, standardize and optimize project design processes. In our company Sweco, we do this through our platform *sweco@work* which provides an overview as well as tools and routines for concrete tasks in each phase (Figure 1).

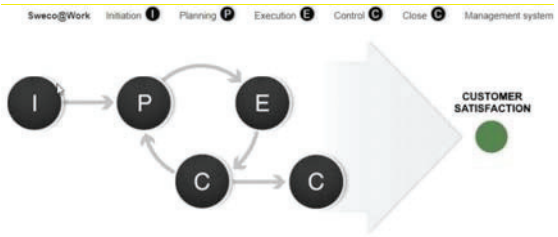

Figure 1: *Sweco@work project planning and execution process overview*

For all project participants, such as decision makers, architects, and consultants, the level of design freedom and influence on project costs evolve during the design and construction process (Figure 2). As the project advances, design changes become increasingly complex and more expensive.

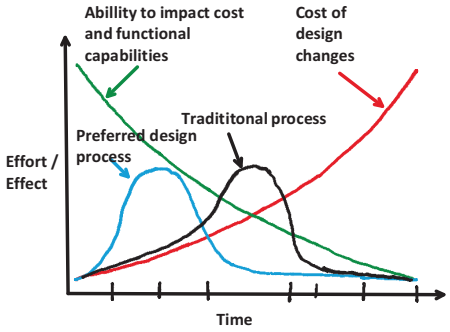

Figure 2*: Illustration of design freedom, cost of changes and design process versus timeline*

Building information modeling, hereafter referred to as "BIM"[1], allows in general building design processes to create digital prototypes during the design process. BIM evolves with increased level of development (or detail) during the design phase.

By sharing BIM during the design process with different disciplines and using design processes like Virtual Design and Construction (VDC)[2] and Integrated Concurrent Engineering (ICE), a greater level of development can be achieved in earlier design phases. This, because design participants share their work before it's finished and by doing so, enables an efficient process where design challenges are identified through a continuous and multidisciplinary process rather than at the end of each deliverable. Design requirements and feedback need to be visualized for all participants to achieve this process. BIM

https://doi.org/10.52202/069179-0544

and VDC methodology are preferred tools for that purpose.

Know-how
Timber construction is for many stakeholders new and the skills and experience in the design teams may vary more than in common building constructions.

An example of this is found in structural engineering. The most common design criteria for the cross section of beams and columns with steel and concrete construction is the moment and shear forces in each member. For timber construction, it is the member connections design that most of the time govern the type of cross section to use.

The same type of alternative engineering is found in fire safety and acoustics as well as the design management and the building team. Without the knowledge of timber properties and of the know-how of building techniques with timber construction, there is a great risk of not achieving the project goals.

4 CASE STUDIES

The projects below showcase some of the multi-disciplinary design challenges and solutions with exposed timber structures.

4.1 SCHOOOL AND KINDERGARTEN

Biri elementary school and kindergarten
Biri elementary school and kindergarten is under construction and is expected to be completed in January 2024. The buildings are erected right by the existing high school. The elementary school is approx. 6 150 m^2 and consists of two stories plus technical room on the roof. The kindergarten is approx. 2 220 m^2 over one story with technical room on the roof.

Figure 5. *Biri elementary school and kindergarten. Illustration courtesy* of *JAF arkitekskontor AS.*

The kindergarten is formed as a circle to best adopt to the existing forest around the building site. The roof had originally a fixed inclination from one end to the other in the schematic design model. In the detail project this inclination, together with the circular form, gave some challenges for production of the prefabricated elements and on building site. The level of development in the schematic design phase could in this case had been prolonged in time and resources to better address these challenges before the detail design process. The solution was to have a fixed level between each load bearing axis and to level up the roof from one load bearing axis to the next.

Both buildings are designed with timber construction in the form of CLT slabs and CLT walls and glulam beams. The roof of the kindergarten is built with CLT elements while the school has prefabricated light weight roof elements.

The load bearing system for the elementary school was changed in the detail design phase. These last-minute changes resulted in more steel beams than in the earlier phase of the project. Further glulam beams had to be changed to steel beams to make space (free height) for the ventilation ducts in the detail phase.

Figure 8. *Biri elementary school – Atrium. Picture by Sweco*

To maintain the progress on building site and to meet the delivery deadline, the design of the CLT elements went through a cross disciplinary engineering process early in the detail phase so that all the necessary detailing could be transferred into the production model. The production model was built by the CLT manufacturer based on the structural BIM model. The production model was then verified by the structural engineer before the production of CLT elements started.

Plan drawings of visible side of CLT elements were established early on based on input from fire engineer and acoustic demands.

4.2 HEALTCARE

Frøya healthcare center and nursing home
Frøya is a project that consists of two buildings, one healthcare center and one nursing home, together approx. 8 800 m^2. The healthcare center is a traditionally prefabricated hollow-core concrete element and steel building while the nursing home is mainly a timber construction. The two buildings are connected with a bridge between them for easy access between the buildings.

https://doi.org/10.52202/069179-0544

Figure 7: *Frøya healthcare center and nursing home. Illustration courtesy of Link Architects.*

The project had ambitious environmental goals. Hence, the use of timber construction together with solar panels on the roof that make the buildings self-sufficient with energy.

The load bearing system for the roof in both buildings consists of prefabricated wood trusses. The timber building consists mainly of CLT panels for walls and slabs. In more open areas, the load bearing system consists of steel beams (HSQ) and glulam columns. Steel beams are used mainly to achieve better access and space for the ventilation ducts going through the building. The exterior walls are built as light frame stud walls.

The stability of the timber building relies on CLT shear walls and CLT shear slabs to withstand the high wind loads in this area located on the Norwegian coastline.

The patients of the center have neuropsychological deficiencies and are often confused. They have limited capacity to escape by themselves during a fire incident. The fire strategy is based on a fire resistance R60 for the load bearing system. The CLT slabs in the ceiling up to the roof are designed for R60 because of low load bearing resistance in case of burning roof trusses. The buildings are fully sprinklered and every CLT wall in resident rooms facing the corridor (and escape route) has EI60 demands.

Sound insulation between resident rooms and between resident rooms and corridors is solved with CLT slabs with concrete topping floating on insulation.

The design team on this project had variable experience with timber buildings. Some had little and some had very long experience. Those with less experience had to learn and/or adapt to the following elements:

- Communicate early multidisciplinary challenges with use of timber and CLT.
- Multidisciplinary design to make sure all the necessary cuts, splits and holes are in the production model of CLT-elements.
- How to achieve and document sound and fire demands with timber solution
- How to achieve rational load bearing solution with ventilation ducts and pipes trough the building.
- Produce a plan of which side of the CLT elements can be visible and which side needs to have a gypsum board lining.

4.3 OFFICE BUILDINGS

Lumber Bygg 4

Lumber Bygg 4 is a massive timber building with a commercial area at the ground floor and office area from the first to fifth floor to be delivered in April 2023. The brief includes BREEAM-NOR 2016 certification, and the ambition was to have as much visible massive timber as possible.

The project started with a multidisciplinary design/build phase with involvement of fire safety and acoustics at each meeting. Hence, every aspect of the different load bearing system alternatives was covered simultaneously. This resulted in an efficient design process and robust principal solutions minimizing changes to be made in the detailed phase.

Figure 3: *Illustration courtesy of VEF Entreprenør AS*

The chosen load bearing system is based on glulam columns and beams. The floors are a hybrid type with CLT combined with concrete slab, both components are mechanically connected. Hence, a larger span was possible, and the number of columns was reduced which led to beneficial consequences for the overall construction layout and the construction costs.

This hybrid solution is also interesting for the point of view of acoustics. Thanks to the good sound insulation properties, it was not necessary to add a floating floor and/or a false ceiling to meet the sound insulation requirements vertically and solve the flanking transmission horizontally.

Strict requirements for reverberation time would normally lead to a sound absorbing false ceiling over the whole office areas. The fire safety engineer has, however, established that an area of around 350 m^2 could be in exposed massive timber in each story. Visible elements in massive timber are the glulam columns and beams as well as part of the CLT-slab underneath. In order to keep that area in visible timber, a great deal of the façade was use for sound absorption using large area of wood wool board instead of wood paneling on the inside of the outer walls.

https://doi.org/10.52202/069179-0544

The fire proofing of the floor required the use of gypsum boards while the acoustics required the addition of a layer of mineral wool and ceiling tiles underneath. Efforts were put to simplify this construction and showed that the gypsum boards could be replaced with a specific type of mineral wool with sufficient thickness. The sound absorptive properties of the product were investigated and proved to be adequate. Fire safety and sound absorption were then combined in this simple solution consisting in a 70 mm mineral wool layer with wood wool ceiling tiles for the finishing aspect.

Close cooperation between the structural engineer and the acoustician was established right at the beginning of the design when different floor construction alternatives were investigated. It resulted in a cost-efficient construction allowing great flexibility for the fit-out layout with a great deal of visible massive timber. Further on, in the design phase, the cooperation between the fire safety engineer and the acoustician led to a reduction of the costs for the ceilings.

Fredrik Selmers vei 5 (Pilar)

The project Pilar consists of renovating and extending an existing concrete and steel building from 1937 and building a new timber building above the existing building.

The new building is planned to have ten stories, approx. 18 000 m² and to house commercial activities such as offices and café, and/or restaurants. The project is in the schematic design phase when this article is written. The project has ambitious environmental goals and aims to be certified BREEAM NOR Excellent and Paris Proof.

Figure 4: *Fredrik Selmers vei (Pilar) Illustration courtesy of Grape Architects*

The load bearing system consists of glulam timber columns and beams. The two internal stairs and elevator shafts consist of cast-in-place concrete that maintain horizontal stability together with steel and glulam bracing in the facade. The superstructure works therefore as a hybrid structure with concrete, steel, and timber elements.

The building and the floor plans are being planned for future flexibility within a defined technical grid that corresponds to the structural grid.

Local regulation limits the building's overall height and thereby also the height of each story. From the very beginning of the project, this issue is addressed by having coordination between structural engineers, MEP engineers, the builder and the architects. The result of this is that the glulam beam system includes cantilevers to make room for MEP installations. This solution reduces the floor height and also allows to expose beams below the ceiling in most areas.

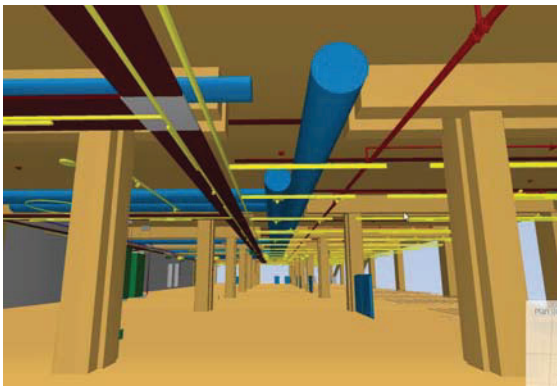

Figure 5: *Cantilever beams designed to reduce floor height due to ventilation ducts.*

Another example of analysis is the calculation of the real fire development curves considering how the fire would evolve rather than to use the pre-accepted fire development curves. The goal being to reduce the timber cross-sections, hence creating more free space between the glulam columns for the technical grids.

The project uses BIM, VDC and ICE sessions to plan and coordinate the design. An example of the visual plan used during the ICE-sessions is shown in Figure 6. By having by-weekly ICE-sessions with work meetings and activities in between, the design participants can plan, share design, coordinate, and provide design information as required to reach the project milestones. The process also measures the completed activities on schedules and keeps track of reasons why activities were not completed as planned.

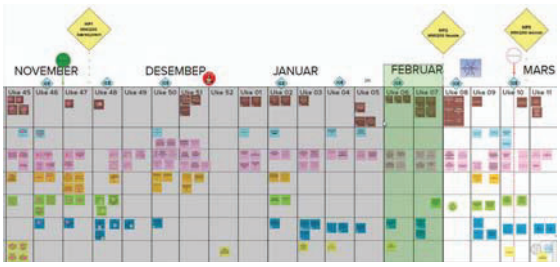

Figure 6*: Visual planning*

One of the first milestones in the planning was for the structural design to achieve a level of development (LOD) of 200. That meant that the sections and members for all the structure had to be designed from very early on. By doing this, the entire cross-disciplinary team of architects,

https://doi.org/10.52202/069179-0544

builder and consultants got an early idea of the required dimensions and the challenges this posed.

The design process also includes an iteration of the amount of visible timber with the first goal to visually expose all timber columns. The number of beams is still under consideration due to space requirements. However, by addressing this issue at this early phase the project can handle the challenges and design the building accordingly.

The whole design team consists of consultants with experience with timber buildings.

5 DISCUSSION

In the following section we highlight some of our findings from the case studies we've presented in this paper and experience with other projects.

Level of development vs. timeline
The *Macleamy curve[3]* is in our experience a good visualization of a preferred process where the effort of design and the level of development LOD[4] is higher in earlier phases as to highlight and solve more issues and reach goals early. By having a high LOD in the early phases, more project risks can be identified and addressed, and changes and optimizations are much easier to implement. This requires building owners and the project managers to involve all the consultants from an early stage and thus invest more in engineering work in early phases.

Timber buildings have always a certain level of complexity, which means that the costs associated with changes made late in the design process will contribute to making the technical and economic consequences even greater. That implies that timber buildings must be designed as such from the beginning. Adapting a concrete and steel building to a timber construction in the detail design phase cannot be done without restarting the design process from the beginning.

Objectives related to timber structures should be set as early as possible and eventually adjusted along the way if needed. A common example of this is the amount and location of visible timber surfaces. Answering this means choosing the type of structures with a strong involvement of fire safety and acoustics to find solutions that meet requirements and are cost-efficient. Having a BIM with a sufficient level of development helps to visualize these design intentions early on.

Timber elements are prefabricated and assembled on site. All the design aspects affecting the elements must therefore be coordinated in advance of manufacturing to achieve time efficient assembly on site.

Adaptation of design management
It is important for project design managers and contractors unfamiliar with timber design process to establish an understanding of the different challenges that timber construction poses, to acknowledge that goals related to visible timber needs to be set early and to establish good processes to solve the details.

Timber buildings often require a larger design team as specialists in timber are hired in supplement to a general design team. The larger team results in more interfaces to coordinate, making the need for efficient coordinating tools and methodology even more important.

Efficient design methods
By frequently sharing preliminary design by means of ICE and VDC processes, the discipline challenges are solved along the way between milestones and deliverables. This is key to achieve an efficient multidisciplinary process. By sharing work-in-progress, more design issues are being addressed and participants have more time to solve them compared to processes that are more linear and top-down.

Design culture
Communication with digital platforms that keeps record of changes together with BIM-software support the multidisciplinary design process. However, these are just tools and add little value if not combined with participants that have the know-how to solve the issues, not just from their own discipline's perspective, but also in incorporating other disciplines' requirements and issues. Indeed, technical issues with timber buildings are very seldom solved adequately when disciplines work independently but rather solved by a multidisciplinary team. delivering one integrated solution that often solves multiple requirements. This is especially important when solving issues related to visible timber structure.

Communication
Solving the multiple issues related to visible timber requires to communicate during early stages of the design process. This communication should be directly between architects, design consultants and specialists. In our cases, the most successful projects had consultants that communicated horizontally and solved issues together first, and then presented solutions to the rest of the team and design management.

Knowledge and experience
In our successful cases, project consultants had experience with timber construction, also often combined with a positive attitude towards problem solving, innovation and applying or improving solutions from previous projects.

Proactive participation from the specialist consultants as fire safety engineer and acoustician is essential as their requirements define a frame for the possible solutions.

No need to compromise
It's worth mentioning that in all the above case studies, no compromises were made on the technical requirements, not even on the acoustics although the Norwegian regulation is quite strict in that field.

The costs had also to be equivalent to a standard construction. Hence, the owners' aim of affordable, environmentally friendly, functional, and esthetical buildings were fulfilled.

6 CONCLUSION

In this paper, we showcased some of the multidisciplinary design challenges with exposed timber structures and explained through case studies how a multidisciplinary design process can help to achieve project goals and meet design requirements. Other essential key factors are design effort in early phase, consultants with experience in massive timber, and efficient design management tools.

REFERENCES

[1] Building Information Modelling (BIM) Digital byggeprosess og BIM | standard.no *[accessed 14 Feb, 2023]*

[2] VDC VDC: Virtual Design & Construction | Autodesk *[accessed 14 Feb, 2023]*

[3] *The MacLeamy Curve Building Information Modeling and Integrated Project Delivery in the Commercial Construction Industry: A Conceptual Study - Scientific Figure on ResearchGate. Available from: https://www.researchgate.net/figure/The-Macleamy-Curve-2004_fig3_266054953 [accessed 14 Feb, 2023]*

[4] Level Of Development (LOD) (Norwegian MMI) https://rif.no/wp-content/uploads/2018/11/mmi-modell-modenhets-indeks.pdf

https://doi.org/10.52202/069179-0544

World Conference on Timber Engineering Oslo 2023

CAN RISING DEMAND FOR TIMBER IN CONSTRUCTION ACCELERATE DEFORESTATION?

AUTHOR

Eduardo Rojas Briales[1], Simon Flinn[2]

ABSTRACT

Timber, and increasingly Mass Engineered Timber (MET), plays a key role in green building programmes around the world. Its use addresses the UN Sustainable Development Goals, especially SDG 11 – Sustainable Cities and Communities, SDG 13-Climate action, SDG 15-Life on Land and many others that are directly or indirectly linked to forests and construction. Many Life Cycle Assessments (LCAs) recognize the environmental benefits of Mass Engineered Timber in comparison to traditional construction materials such as steel and concrete. The importance of timber in the construction industry has led asset specialists to estimate that over the next 30 years, timber consumption could rise by over 140%. In the EU alone, wood consumption is estimated to be 3.5 times higher than the global average.

Sustainable Forest Management has been fundamental in ensuring both forest resource preservation with the highest possible sustainable supply of forest products and environmental services. 233 million ha of forests globally were under management plans in 2000, increasing to 2.05 billion ha in 2020. Nevertheless, between 1990 and 2020, both growing stock and forest carbon stock at the global scale have fallen, though the rate of loss has declined significantly over the same period. In 2020, the forest and carbon stocks reached an even balance due to reduced tropical deforestation and significant forest recovery in Asia-Pacific, Europe, and North America. Research into forest management (FM) practices has shown that producing the same volume of wood in different ways, may result in substantially different performance regarding biodiversity and other environmental services, including carbon sequestration or rural livelihoods. Therefore, while continuous improvement in FM is beneficial to the timber industry, it is also vital for biodiversity, environmental services, and rural livelihoods.

Finding the balance between demand for forest products and preserving forests through FM will ultimately rely on robust Chain of Custody (CoC) data - informing policy; purchasing strategy; and due diligence, especially if aligned with consistent domestic policies in the areas of tenure, land use and forestry. PEFC's role is to ensure, through certification, that built environment professionals can be confident that they are sourcing timber responsibly and avoiding unsustainable and/or illegal timber or wood products. Technology and specifically blockchain (including the PEFC sponsored Wood-chain Project), will have an important role to play in not only facilitating traceability operations, but also in providing visibility, accountability, and the ability to extend to other enhancements such as carbon credit systems or related to other environmental services.

KEY WORDS

Sustainable Forest Management: Responsible Sourcing: Mass Engineered Timber: Built Environment: Carbon Balance

1 INTRODUCTION

Built environment professionals from around the globe increasingly recognise the importance of timber as a low

[1] Eduardo is Chair of the Board of Directors of PEFC International and Chair of the Spanish Board of MSc. Foresters. He has previously been a Director of the Catalan Forest Owners Association, Associate Professor at the University of Lleida, Head of the forest policy area of the Forest Science and Technology Centre of Catalonia and Vice-Dean of the Life Science Faculty of the Polytechnic University of Valencia, where he is presently a professor in forestry. From 2010-2015 he was Assistant Director-General and Head of the Forestry Department at FAO, UN Commissioner General for Expo Milan in 2015 and co-chair of UNREDD.

[2] Simon is Senior Systems Development Officer with the Soil Association Forestry team, working on digital transformation and business improvement projects of their PEFC and FSC certification systems, for Forest Management, Chain of Custody and Carbon Schemes.

https://doi.org/10.52202/069179-0545

carbon, renewable and recyclable building material. But some are concerned that this rush to timber could accelerate deforestation.

Forests are a vital natural resource for the planet. It is important that their multiple functions – environmental, social, and economic – are balanced.

The Sustainable Forest Management (SFM) tool has been developed to help maintain this balance. as demand for timber continues to grow, PEFC (Programme for Endorsement of Forest Certification), regularly engages with built environment professionals - architects, contractors, engineers, and their clients - to increase their understanding of SFM and the importance of responsible sourcing,

Sustainability has become integral to all areas of industry and society, and the built environment has become one of the crucial priorities for sustainable change. As life-cycle assessments (LCAs) highlight energy and carbon intensive building materials, namely steel and concrete, the focus has been placed on developing and using carbon neutral alternatives. Mass or Mass Engineered Timber (MET) has been identified through numerous LCAs to be a viable and sustainable building material. It is increasingly being embraced by architects, builders, and engineers around the globe.

However, if the building industry turns toward mass engineered timber (MET) as a less carbon intensive material, will this create a sustainability paradox? As demand for timber grows, what impact will this have upon the global timber supply or the resource that provides it (forests)? Is this rising global demand for timber compatible with sustainable forest management?

2 SUSTAINABLE FOREST MANAGEMENT

In 1713, Carlowitz defined the *Nachhaltigkeit* principle [1] in a time where wood was the main source both of materials and energy, causing restricted availability and frequent signs of exhaustion - important societal challenges. This concept was later operationalised at the end of that century, establishing the starting point for forest science as one of the legacies of the Enlightenment. If wood was a renewable resource, the way to avoid its exhaustion is to know its renewable rate and optimize where and when to extract it. During the 19th and early 20th Centuries, forest science expanded from Central Europe to the rest of the World. The increased use of fossil and mineral materials and their ready availability through the rail network, reduced the potential impact that the increased population and available income (GDP/per capita) would have had potentially for forests.

When Brundtland [2] (1987) presented the key document for the Río 1992 Conference, her inspiration for sustainability was the Carlowitz forest science paradigm[1]. In fact, in the two predominant languages in Central Europe (German and French), the modern term for sustainability is identical to the forest one (Nachhaltigkeit, durabilité). In fact, misunderstanding around that intellectual linkage was caused by the restricted English translation as “sustained yield” if compared to the French, German or even Spanish (persistencia) terms.

In the process to the Rio Conference 1992, four environmental conventions were negotiated (Climate Change, Biodiversity, Desertification and Forests). While the first three reached broad consensus and entered into force during the decade, the forest convention was not agreed, but negotiations were kept open until they were institutionalised in the form of the UN Forum on Forests, as a time bound setting, extended twice in 2006 and 2015.

In the absence of a convention, many formerly non legally binding documents have been approved since Rio, starting with the Rio Forest Principles (known officially as the Non-Legally Binding Authoritative Statement of Principles for a Global Consensus on the Management, Conservation and Sustainable Development of All Types of Forests), established that while forests are essential to economic progress, sustainable development and management should be the guiding principles that nations should follow.

An intensive process was conducted during the rest of the decade with the International Panel/Forum on Forests agreeing 300 proposals for action in the expectation of a later agreement on a convention that failed to materialise. It became obvious that sustainable forest management could not be further defined at a global scale, because of strong regional and climatic differences, other than the basic principles and the structure of criteria and indicators (C&I). However, nine regional processes started that decade to agree on criteria and indicators for sustainable forest management and were agreed at regional scale.

For the European region, including the countries of the former Soviet Union, the framework of the 1990 Ministerial Conference on Protection of Forests held in Strasburg, was agreed as the basis for the regional Criteria and Indicators. The following Ministerial Conference held in 1993 in Helsinki, first agreed on a regional definition for sustainability in forestry: "The stewardship and use of forests and forest lands in a way, and at a rate, that maintains their biodiversity, productivity, regeneration capacity, vitality and their potential to fulfil, now and in the future, relevant ecological, economic and social functions, at local, national, and global levels, and that does not cause damage to other ecosystems." [3]. On that basis, the Criteria were agreed during the same

https://doi.org/10.52202/069179-0545

conference while the indicators during the following one held in Lisbon in 1998.

At a global scale, the pressure for action, especially around deforestation, grew as the aspiration for a global convention on forests remained unfulfilled as two major players in the OECD and G-7, plus China, USA and Brazil, were clearly opposed to the convention on forests. The demand for alternative solutions in the absence of a convention grew. The eNGO community proposed consideration of the important growth in ISO certification during this period, as a solution to address the failure of states suffering deforestation, to establish sustainable forest management certification mechanisms.

The application of forest certification was first introduced by the Forest Stewardship Council (FSC) in 1994 driven by WWF, as a direct response to the Rio Forest Principles. Certification soon became accepted across the globe, and by 1999, 10 million hectares of forest were certified to FSC standards and the first book was printed on FSC-certified paper [4].

Figure 1: Map of global PEFC certified forest area [13]

PEFC was founded in 1999 by the national forestry organisations of 11 European countries, responding to demand from small and family forest owners who encountered considerable difficulties accessing certification through existing schemes, especially because of audit costs. Later, PEFC expanded beyond Europe to include other regional or national existing certification schemes such as SFI in North America and Responsible Wood, Australia.

PEFC "endorses national forest certifications systems developed through multi-stakeholder processes and tailored to local priorities and conditions."[5] Its standards are oriented to the Criteria & Indicators agreed at regional level by governments in formal processes. PEFC firmly believes that forest certification functions most effectively when the impetus, intent and influence come from local and national organisations, through bottom-up processes.

By December 2022, 288,154,245[6] hectares of Forest area were managed and conformed to PEFC's Internationally accepted sustainability bench marks – 71% of all certified forests globally are certified to PEFC. This has allowed more than 20,000 companies to achieve chain of custody certification in more than 70 countries. PEFC now has 55 national members with 48 endorsed national certification systems.

It should be noted that wood regrows in a reasonable time frame (100 years on average), and that it continues to store carbon when used in long term uses like buildings. Additionally, it requires much less energy to harvest and process than conventional building materials.

Wood used in construction globally is more than 95% coniferous and sourced from boreal and temperate forests, where no deforestation has recently been recorded. FAO has repeatedly confirmed that less than 10% of deforestation is linked to wood use being the primary cause (>80%) agriculture[7]. 50% of the global wood use is for energy, mostly in the countries of the global south and this is the main cause of forest degradation, especially in the dryland forests of Sub-Saharan Africa; a problem exacerbated by unclear land tenure rights.

2.1 BENEFITS OF SUSTAINABLE FOREST MANAGEMENT

The benefits of sustainable forest management are numerous and complex. Marchi et al[8] describe five key performance indicators of SFM – Economics, Ergonomics, Environment, People and Society and Quality optimisation. And these five indicators can be used to understand the complex web of benefits and relationships, including air quality, cost optimisation, energy consumption, health, training, etc. They argue that SFM leads to resource optimisation in forest operations; the promotion of timber as an environmentally renewable and sustainable material; the ability of forest owners to adapt and influence climate change; reducing the impacts of harvesting; and finally promotes workers' rights, thereby improving conditions and safety.

2.1.1 Biodiversity

Forests are the most diverse ecosystems on the planet. 80% of Earth's land animals and plants live in forests. Biodiversity provides natural pollination, fertilisation, and seed pollination. Biodiversity benefits in several ways from SFM. SFM promotes the UNFCCC Warsaw framework REDD+ activities - the reduction in emissions from deforestation and forest degradation plus conservation and enhancement of forest carbon stocks. SFM practices such as reduced impact harvesting, fire management, reforestation and restoration have had a direct effect in halting bio-diversity loss [9]. An example of this impact has been measured in Sabah, Borneo where vertebrate diversity is greater in SFM forests than conventionally managed forests[10]. In fact, several publications have confirmed that locally managed forests, often by indigenous communities in the tropics, show better performance (e.g., on forest fires), than protected areas, state managed or concessions).[11]

2.1.2 Carbon Storage

Forests are also nature's best form of carbon capture and storage. Well managed forests remain carbon sinks while at the same time, contributing to economic development. Figure 2 below shows how SFM maintains a steady carbon sink through harvesting.

Figure 2: Patchwork of Emissions and removals from Forest Harvesting, source Harris et al [12]

The PAFC Congo Basin project is endorsed by PEFC. The Republic of Congo, Cameroon and Gabon have jointly developed a regional forest certification system. The PAFC Congo Basin project is "the first to contain two new requirements linked to current climate issues: the mapping of the carbon stock in a forest, and a greenhouse gas (GHG) emissions assessment linked to forestry operations. Born during the standard development process, the innovative requirements are a response to the new expectations that companies and forests owners are facing." [13]

EU forests alone currently provide a net sink of 300 million tonnes of CO^2, around 10% of the EU's greenhouse gas emissions.[14] It has been estimated that reduced-impact logging in tropical forests, could reduce between 29% and 50% of net carbon emissions from tropical deforestation and land use changes whilst supplying 45% of global roundwood timber demand[15]

2.1.3 Water

Forested catchments supply 75% of fresh water, and millions of people from around the world depend on high-quality, fresh flowing, forest water. Forest trees absorb water through their roots from the ground in a process known as evapo-transpiration – a key element of the global water cycle.

2.1.4 Products & Energy

Sustainable forests deliver sustainable products; from raw materials transformed into books, packaging, and buildings, to pharmaceuticals, textiles, and personal care goods. Forests that are managed sustainably need not be finite but continue to provide sources of income to forest owners, sawmills, factories, and business within the supply chain.

Energy from forests is recognised as the single most important resource, providing 9% of the global total of primary energy supply and above 60% of the total renewable one, especially in Sub Saharan Africa. In fact, it is astonishing to note the marginal recent and present attention paid to forest-based biomass when comparing it to its historical and present contribution to renewable energy supply.

2.1.5 Social

The livelihoods 1.6 billion people worldwide have some impact from forests, including 60 million indigenous people who are fully dependent on them. In developing countries, forest-based enterprises provide about 13–35% of all rural, non-farm employment; equivalent to 17 million formal sector and 30 million informal sector jobs[16].

Sustainable Forest management is focussed on ensuring not only that forest workers' rights and safety are respected, but also those of workers along the supply chain, through chain of custody certification.

It is a core value of SFM, that cultural values and traditions are respected, protecting indigenous people and their cultural, social, and spiritual mores.

2.2 TIMBER CERTIFICATION

Timber certification allows organisations, businesses, and consumers to have a direct link to and impact on SFM. There are a range of reasons for different organisations to certify their forests and/or choose to specify certified material. According to Zubizarreta et al [17] in a case study on forest certification in Spain, the two main certification drivers for forests and companies are accessing new markets and improving corporate image. However, fundamentally, the value of forestry certification only works if it is understood and recognised by consumers and therefore affects consumption behaviour.

Certified products can bring economic benefits as materials can add premiums to prices. Zanchini et al [18] analysed customer behaviour and forestry certification, through a consumer study. They demonstrated that while price was the main attribute affecting consumer choice, the second most important, was the presence of recognised forest certification labels such as PEFC and FSC. Consumers will not only choose to make an ethical purchase, but will also perceive labels to have an added value[18].

Certified products can help companies penetrate new markets. The European and UK Timber Regulations, United States Lacey Act, and the Japanese Clean Wood act, have all placed legislative barriers on the trading of timber. Adopting SFM practices through certification allows companies around the world to find new and valuable customers. The positive effects on biodiversity protection and development, may also be used for

https://doi.org/10.52202/069179-0545

political advantage or to demonstrate corporate values [19].

Owari et al [20] identified that companies adopting forestry certification gained recognition from environmentally sensitive customers; better retention of existing customers; improved public reputation; and increased customer satisfaction.

PEFC through its partners, makes SFM certification available to 750,000 forest owners globally and chain of custody certification to more than 20,000 companies. PEFC SFM certification respects ecological, social, and cultural frameworks, while improving economic values. It supports healthy forest ecosystems, while securing livelihoods for workers and local communities.

Chain of custody certification enables companies and consumers to identify products from responsibly sourced raw material. It provides confidence that products are legal and from a verifiable supply chain. It allows organisations to demonstrate their commitment to, and business leadership on, sustainability.

3 SUSTAINABLE BUILDING MATERIALS

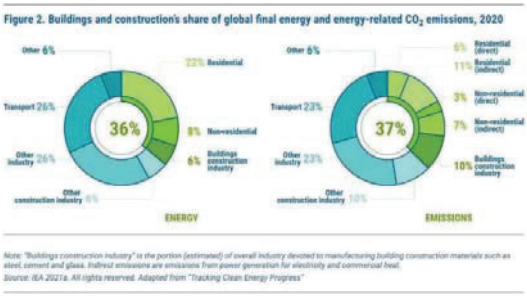

Figure 3: Graph taken from the 2021 UN Global status report for buildings and construction. [21]

Although building operations and construction industry together accounted for up to 37% of the global CO^2 emissions, much of this comes directly or indirectly from fossil fuels. Figure 3, from the UN Global Status Report for Buildings and Construction, shows that this sector used 36% of the global energy resource in 2020. Whilst there has been a shift away from the direct use of coal and oil for energy to electricity, the high dependency of electrical generation on fossil fuels, has contributed to an increase in emissions from the buildings and construction sector. Governments and institutions globally have unsurprisingly turned their attention towards sustainable buildings, construction, and maintenance. Inger Andersen, Executive Director of the UN Environment Programme states "Rising emissions in the buildings and construction sector emphasize the urgent need for a triple strategy to aggressively reduce energy demand in the built environment, decarbonize the power sector and implement materials strategies that reduce lifecycle carbon emissions" [21]. Additionally high insulation performance, earthquake resistance and recyclability should be recalled in this context.

Cross-laminated timber (CLT) and glulam are both examples that provide an exciting glimpse into the possibilies for engineered wood. Commonly made from PEFC-certified spruce, pine, fir and larch from European and North American forests, they can reduce the carbon impact of steel and concrete.

As a lightweight building material, timber can provide time and cost savings due to reduced foundation work as the structural loads required with CLT are small compared to those from concrete and steel.

CLT and glulam are prefabricated within a precision, factory-controlled environment, using accurate data from BIM modelling and CNC processes. Openings can also be pre-cut or routed in the factory for windows, doors, or services, facilitating quick and easy installation. This means that it is easier to timetable the construction critical path and eliminate site delays, while improving working conditions and reducing on-site accidents.

The drive to improve the sustainability of buildings has caused wood to be substituted in place of materials such as steel and cement, which all have higher carbon emissions. The manufacture of concrete and steel each contribute about 5% of global emissions. MET is a material specifically engineered to deliver high strength ratings for the construction industry. It is formed by gluing together strands or panels of wood to create outstanding strength.

The structural properties that MET products offer as a sustainable alternative have been widely recognized, and resulted in the 2021 International Building Code allowing the use of wood in buildings up to 18 storeys[22]. Indeed, Zanchini et al state "several recent studies have shown that substituting MET for steel and concrete in mid-rise buildings can reduce the emissions associated with manufacturing, transporting, and installing building materials by 13%-26.5%."[18]

The Mjøstårnet building in Brumunddal, Norway is a testament to the properties and potential of both CLT and Glulam. Standing at 85.3 metres tall, the 18 storey MET development contains a hotel, restaurants, offices and apartments [23]. As they are substantially lighter, such buildings necessitate specialist engineering to overcome challenges including fire safety, and resistance to the extremities of nature such as earthquakes. However, the entire building meets Eurocode 5 and can withstand extensive fire. It is thought that similar buildings can reduce emissions from material production by up to 85%, while timber absorbs CO^2 from the atmosphere. Additionally, a higher timber use would reduce sand and concrete demand in the construction

sector reducing the impact of river sand drain or open pit limestone mines.

3.1 LIFECYCLE ASSESSMENTS

Many life-cycle assessments of MET have provided evidence of its excellent environmental credentials. Duan [24] et al found that the average embodied energy of MET construction is 23% higher than that of reinforced concrete alternatives, and the average embodied greenhouse gas emissions of reinforced concrete buildings are 42.68% higher than that of MET alternatives. They concluded that "mass timber buildings generally have lower GHG [greenhouse gas] and life cycle primary energy than RC [reinforced concrete] and steel buildings, indicating that the use of mass timber to substitute conventional materials could help mitigate climate change and promote sustainable construction."

Nevertheless, within the circular economy, caution does need to be applied when considering the environmental benefits of MET. Hart and Pomponi reason that while re-use of structural steel is possible, it is "hindered by current regulations and a poor financial case". Structural timber provides a similar challenge including the fact that "engineered structural timber is typically a composite of organic and mineral substances that may be impossible to separate in a controlled way. [25]"

In a study published in 2020, Chen et al used the Athena life-cycle impact assessment for buildings to compare those using concrete and CLT. The team followed the scope, adapted and shown in figure 3, following the EN15978 guidelines but going beyond the building life cycle to look at recycle and recovery of materials.

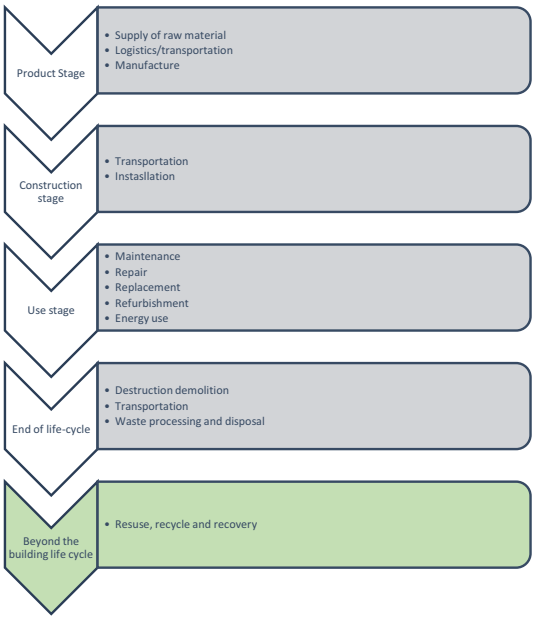

Figure 4: Adapted from an assessment system boundary from Zhongija Chen et al [26]

The study showed that the total of greenhouse gas emissions, shown in figure 5 below, from mass-timber buildings walls and floor were reduced from 50% to 80% between mass timber buildings and reinforced concrete buildings.

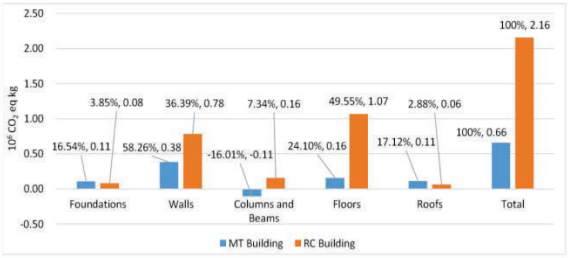

Figure 5: From Chen et al[26]. A comparison of global warming impact.

4 DEMAND FOR TIMBER AND FOREST PROTECTION

In pursuit of cleaner, sustainable building materials, the growth and promotion of MET as a potential solution might seem somewhat incompatible with forestry conservation. This should not be of concern, as Churkina et al state[27] "although global mass timber production has increased rapidly in recent years, it still constitutes a small fraction of total global wood consumption (less than 1% global softwood lumber consumption)". Still, this understates the prediction that by 2034 North American 16.3 million cubic metres of MET panels would be required, meaning that "manufacturers would need to boost their current capacities by a factor of nearly 40 to meet those demand projections." [28]

Academic research has recently focused on unravelling this apparent paradox. The Global Mass Timber Impact Assessment (GMTIA) is a collaborative research programme, commissioned by The Nature Conservancy which focuses on five phases of work[29] which are:

- Whole-building Life Cycle Assessment
- Regional demand assessments
- Global Trade Modelling
- Regional forest modelling
- Integration and communication.

The aim of the project will be to capture those impacts of MET which are not normally captured by traditional life-cycle assessments. This will include examining the effects of MET demand on forest carbon stock; understanding the implications for biodiversity; whether there is an increase or decrease on embodied carbon (transportation, harvest, production); carbon storage in wood products; and end of life cycle of MET.

Higher demand supposes higher prices and incentives to preserve and manage forests according to the best standards. The dynamic nature of forests is frequently

https://doi.org/10.52202/069179-0545

overlooked when the risk of deforestation is considered as a trade off against increasing demand. Through clear tenure and rule of law and with land use planning as a prerequisite, increased demand does not negatively affect forests.

4.1 FORESTRY IMPACT

The critical phases of the GMTIA will officially report in 2023. Still, in a 2021 related study about the effects on global forests as a result of the increased demand for MET, Nepal et al [22] identified four key findings:

- That increase in MET demand will lead to price inflation for products using MET. The price inflation will correlate directly with timber demand.
- Conversely the levels of product prices directly effects "production, consumption and trade of forest products in a country and accordingly alter its timber harvest, forest growth and forest stock level."
- The increased demand for MET will lead to increased competition for softwood, reducing consumption for less valuable present uses.

Moreover,

- They found that with sustainable forest management "most of the projected depletion in aggregate forest stock due to mass timber-induced increases in removals will be replaced by biological forest growth occurring over time, suggesting relatively smaller impacts on forest stock at aggregate national, regional, and global levels."[22]

In their projection, there is negligible effect of increased MET demand in a model which assumes sustainable forest management practices – "that is, mass timber-induced increases in demand for timber and harvest activities do not lead to deforestation." [22]

Therefore, if wood for MET is sourced solely from sustainably certified forests with well managed stock levels, the effects of price inflation and substitution, will ensure that demand has no negative effect upon forest stocks.

In a recent example published in 2022, Comnick et al [30] examined the increasing consumption of MET in the USA against the timber supply. They arrived at the following conclusion:

- The current rate of harvesting and consumption of softwood in the United States is currently 56% that of growth.
- The most aggressive estimate for increase in MET demand by 2035 would amount to a 17% increase in current softwood consumption.
- This most optimistic of MET growth rate would still only represent a consumption of 68% of growth, or 82% of lowest projected growth estimates.

The sustainable benefits of MET cannot be realized in the material alone, it must be accompanied by ensuring the raw products come from certified forests. As Mark Wishnie, Director of Forestry and Wood Products at the Nature Conservancy states, "We must ensure that mass timber drives sustainable forestry management, otherwise all of these benefits are lost"[31]

The study by Chen et al[26] referenced in 3.1 above, demonstrated that if forests continue to be renewed after logging, there will be a continual offset of greenhouse gas emissions. In the study they demonstrated significant impact on carbon out of a MET building, estimating a saving of 150,000 ton of CO^2 when compared to a reinforced concrete equivalent. It is this measurable benefit which will help drive the promotion of SFM and ensure that sustainable MET continues to be preferred.

Ultimately though, the popularity of MET is not only attributable to its durability and versatility as a construction material. One of the primary recognized motivations for adopting MET is its sustainability credentials, and the associated benefits that this brings along the commercial supply chain. Therefore, while sustainability prompts customers to demand this material, it is sustainability which will surely determine how the raw material is sourced. As certification will ensure that MET continues to be recognised as environmentally responsible choice, then sustainable forest management practices demanded by certification will ensure that demand does not exceed sustainable supply.

Increased demand for higher value uses like construction would suppose an additional incentive to increase rotations, to improve degraded stands, to prioritize valuable species, to implement quality driven thinnings or to expand forests by planting and paying more attention to forest management by local actors than was the case in the past when wood prices were lower.

4.2 PEFC AND SUSTAINABLE TIMBER

While PEFC supports the advancement of mass engineered wood as the future of architecture and construction, this can only be positive for ecological progress if underpinned by certification. In the long run, in comparison to concrete, steel, cement and glass, buildings made with engineered wood from sustainably managed forests require less energy and emit less carbon.

"PEFC-certified timber, whether it is solid wood or engineered wood such as CLT and glulam, comes from a

PEFC-certified forest – a forest managed sustainably in line with strict international requirements.

This means that forest owners manage their forest in a way that provides a good supply of timber and other forest products, while at the same time ensuring that the forest will be around for generations to come.

Certification matters. It not only demonstrates that wood used in construction is sourced sustainably, but that a positive choice has been made to design and build with a future for healthy forests in mind." [32]

PEFC-certified timber and engineered wood products for the construction industry are available globally, with a steadily increasing range of global suppliers. Furthermore, construction projects can also obtain PEFC Project Chain of Custody certification to demonstrate excellence in responsible sourcing. The impact of certification is not only crucial for the preservation of our forests, but also demonstrates the integrity and innovation of companies that choose to specify these materials.

While recognizing the benefits of timber in construction, PEFC is committed to supporting its certificate holders. PEFC is currently working with online product platform 2050 Materials [32] to help drive generational change in choosing certified forest-base products at all stages of a construction project. The platform will be a user-friendly way to find PEFC-certified suppliers,

5 THE FUTURE OF SUSTAINABLE FOREST MANAGEMENT AND CHAIN OF CUSTODY

The future of sound forest management and sustainable timber products undoubtedly lie within the effectiveness of chain of custody procedures, monitored by certification bodies. PEFC wants to ensure that customers throughout the chain of custody can have full confidence in the procedures that protect the authenticity and integrity of sustainable products. As highlighted earlier, the growth in use of MET products within the construction industry will result in increased scrutiny of both forest management and chain of custody practices. The benefits of MET as a sustainable, low carbon alternative to traditional building materials can only be assured by demanding certification audits throughout the supply chain.

An efficient chain of custody process relies on a rigorous monitoring of critical control points such as observing processes around segregation of timber and processing of timber products. Ensuring that personnel along the chain understand the importance of PEFC principles is crucial and that possibility of tampering and fraud is minimised; PEFC recognises that efficiency within this process can only come from ongoing innovation in chain of custody processes.

5.1 BLOCKCHAIN AND RFID

The success and efficiency in balancing timber demand with sustainable forest practices is likely to rely on PEFC, certification bodies and certificate holders adapting to new technology. Figorilli et al[33], for example, showed how the use of blockchain technology can be used to record the traceability of a finished product. The use of Radio Frequency Identification RFID might be able to reduce the information gaps in critical control points such as logistics. This could help certificate holders optimize valuable operational factors such as time, materials, and costs.

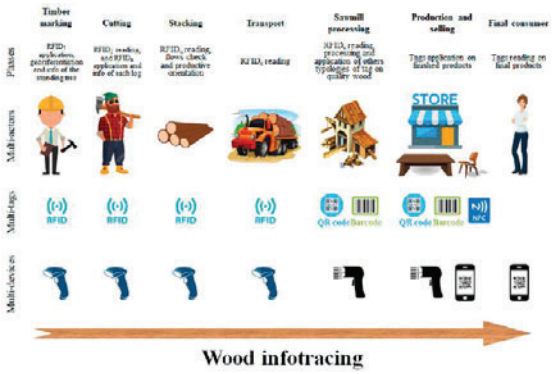

Figure 6: Figorelli et al [33]

Figorelli et al showed the potential of this technology by tagging and monitoring the progress of chestnut trees felled in Cardinale, Italy. After the trees were felled and cut, RFID tags were inserted into each of the logs. The progress of the logs could be monitored through to the sawmill where they were processed into boards and marked with a QR code. They then demonstrated that a final consumer product could be created and tagged allowing the consumer to know exactly where the tree was felled. It is perhaps this final step that might prove the most powerful aspect of blockchain technology, giving information to the consumer such as exactly where the tree was felled and how far the timber has travelled. This would certainly ensure that a premium could be applied to blockchain timber and timber products.

PEFC is committed to exploring the value of technology in improving the strength of traceability within the chain of custody. To this end, PEFC International funded a project with Italian and French partners in 2019, known as the Wood-chain project[34]. The project was designed to test the application of blockchain technology for forestry and wood applications.

https://doi.org/10.52202/069179-0545

The project's specific goal was to explore blockchain in the creation of secure, dependable data chains that could improve the efficiency and accuracy of forest management certification.

5.2 FUTURE GROWTH OF SUSTAINABLE FOREST MANAGEMENT

The future growth of responsible forest management and the security of MET as a sustainable resource relies on careful and adaptable sustainable forestry policy making. Daigneault et al [35], in 2022 released a study on the relationship between the global forest carbon sink and timber demand. They concluded that in areas where SFM is applied "strengthening forest product markets, expanding forest areas and boosting forest productivity can…be successful climate mitigation strategies".

Future growth of SFM can only happen with continued investment in training and certification training. PEFC are committed to investing in innovation and technology to ensure that the growth in SFM continues:

- PEFC UK [36] have developed an online certification application, a forestry tool to assist group managers and small to medium-sized woodland owners participle in forest certification.
- PEFC Italy[37] are working with the Foundation Euro-Mediterranean Center on Climate Change on digital projects that use tree sensors to help forest owners monitor the health of their forests. This will help provide certification bodies with valuable-pre audit data, thereby boosting efficiency.
- PEFC Spain [38] are also involved in a similar project, which will use GIS technology and remote systems to monitor SFMs.

6 CONCLUSIONS

This paper set out to examine the relationship between increased consumption of mass engineered timber and its supply through sustainable forest management, as well as the potential risk of increased deforestation. Some of the latest available studies and research have been reviewed to ascertain whether a positive or negative correlation has been confirmed. Firstly, SFM was summarised from conception at the 1992 Rio Summit, before looking at the rewards it provides, and the tools used to help deliver it, via certification. It also examined the drivers behind the rush to mass engineered timber in the built environment and the evidence supporting its sustainability claims. The potentially paradoxical paradigm behind the growth and values of SFM and MET was then compared, and the available evidence reviewed.

MET promises to provide architects, engineers, towns, cities, and their inhabitants with a building material that could potentially diminish the harmful by-products of steel and concrete and their implicit consequences in the form of mines and increasing sand extraction. In both cases, they can either not be recycled (concrete) or require high energy inputs to be recycled (steel). And while these MET materials are in their relative infancy, the benefits in terms of reduced carbon emissions and LCAs are promising. Ultimately, timber is a natural, renewable, and precious resource that contributes to the livelihoods of an estimated 33 million people employed in the forestry sector globally. Where mining provides income to very limited areas, sustainable forestry provides income to extensive disadvantaged areas of the world that cover 40% of the terrestrial area. This is currently the single most significant income they receive for preserving the global forests and their key contributions in terms of environmental services like climate, erosion, water, or biodiversity.

Evidence reviewed shows that the growth in MET can aid and strengthen the growth of Forests if SFM practices are adhered to and monitored through certification and labelling.

PEFC and other forestry certification bodies have an important role to play in helping to ensure that, MET can deliver global benefits in a sustainable way. By improving and developing access to forestry certification, PEFC can give forest owners, and wood product suppliers, the benefits of certified products, while ensuring that sustainable forestry practices continue.

Through continued investment in innovation and research, PEFC can continue its contribution to SFM practices globally. MET can contribute to the health and growth of forests globally, but only if it is responsibly sourced. It is therefore crucial that certification schemes such as PEFC's, encourage MET manufacturers to source their raw materials from certified forests. If they do, then the full potential LCA and reduced carbon benefits of timber as a construction material can be realised.

REFERENCES

[1] F. J. Schmithüsen, 'Three hundred years of applied sustainability in forestry', 2013, doi: 10.3929/ETHZ-A-009955604.

[2] F. O. for S. D. ARE, '1987: Brundtland Report'. https://www.are.admin.ch/are/en/home/medien-und-publikationen/publikationen/nachhaltige-entwicklung/brundtland-report.html (accessed Feb. 27, 2023).

[3] 'FOREST EUROPE | Publications'. https://foresteurope.org/publications/ (accessed Feb. 05, 2023).

[4] 'Our History', *fsc.org*. https://fsc.org/en/our-history (accessed Feb. 11, 2023).

[5] 'What is PEFC?' https://www.pefc.org/discover-pefc/what-is-pefc (accessed Feb. 05, 2023).

[6] 'Facts and figures'. https://www.pefc.org/discover-pefc/facts-and-figures (accessed Feb. 05, 2023).

[7] 'COP26: Agricultural expansion drives almost 90 percent of global deforestation', *Newsroom*. https://www.fao.org/newsroom/detail/cop26-agricultural-expansion-drives-almost-90-percent-of-global-deforestation/en (accessed Feb. 27, 2023).

[8] E. Marchi *et al.*, 'Sustainable Forest Operations (SFO): A new paradigm in a changing world and climate', *Sci. Total Environ.*, vol. 634, pp. 1385–1397, Sep. 2018, doi: 10.1016/j.scitotenv.2018.04.084.

[9] J. A. Parrotta, C. Wildburger, and S. Mansourian, Eds., *Understanding relationships between biodiversity, carbon, forests and people: the key to achieving REDD+ objectives ; a global assessment report ; prepared by the global forest expert panel on biodiversity, forest management and REDD+*. Vienna: International Union of Forest Research Organizations (IUFRO), 2012.

[10] N. Imai *et al.*, 'Co-Benefits of Sustainable Forest Management in Biodiversity Conservation and Carbon Sequestration', *PloS One*, vol. 4, p. e8267, Dec. 2009, doi: 10.1371/journal.pone.0008267.

[11] Nawari, Rifardi, Nofrizal, E. H. Halim, Suwondo, and T. Warningsih, 'An Indigenous Based Forest Management for Achieving Sustainable Development Goals: Reducing CO_2 Emissions in Pelalawan District, Indonesia', presented at the 3rd Annual Conference of Education and Social Sciences (ACCESS 2021), Dec. 2022, pp. 293–302. doi: 10.2991/978-2-494069-21-3_32.

[12] 'Climate change: Are forests carbon sinks or carbon sources?', *World Economic Forum*, Feb. 12, 2021. https://www.weforum.org/agenda/2021/02/forests-climate-change-carbon-absorb-environment-earth-trees/ (accessed Feb. 06, 2023).

[13] 'Carbon stock and emissions mapping: PAFC leads the way'. https://www.pefc.org/news/carbon-stock-and-emissions-mapping-pafc-leads-the-way (accessed Feb. 06, 2023).

[14] 'How has the forest-based carbon sink and stock evolved in the European Union? | European Forest Institute'. https://efi.int/forestquestions/q16 (accessed Feb. 27, 2023).

[15] N. Sasaki *et al.*, 'Sustainable Management of Tropical Forests Can Reduce Carbon Emissions and Stabilize Timber Production', *Front. Environ. Sci.*, vol. 4, 2016, Accessed: Feb. 06, 2023. [Online]. Available: https://www.frontiersin.org/articles/10.3389/fenvs.2016.00050

[16] 'The state of the World's forests 2022'. https://www.fao.org/3/cb9360en/online/cb9360en.html (accessed Feb. 27, 2023).

[17] M. Zubizarreta, G. Arana-Landín, and J. Cuadrado, 'Forest certification in Spain: Analysis of certification drivers', *J. Clean. Prod.*, vol. 294, p. 126267, Apr. 2021, doi: 10.1016/j.jclepro.2021.126267.

[18] R. Zanchini, S. Blanc, L. Pippinato, F. Poratelli, S. Bruzzese, and F. Brun, 'Enhancing wood products through ENplus, FSC and PEFC certifications: Which attributes do consumers value the most?', *For. Policy Econ.*, vol. 142, p. 102782, 2022.

[19] H. Paluš, M. Krahulcová, and J. Parobek, 'Assessment of forest certification as a tool to support forest ecosystem services', *Forests*, vol. 12, no. 3, p. 300, 2021.

[20] T. Owari, H. Juslin, A. Rummukainen, and T. Yoshimura, 'Strategies, functions and benefits of forest certification in wood products marketing: Perspectives of Finnish suppliers', *For. Policy Econ.*, vol. 9, no. 4, pp. 380–391, Dec. 2006, doi: 10.1016/j.forpol.2005.10.005.

[21] '2021 Global Status Report for Buildings and Construction | Globalabc'. https://globalabc.org/resources/publications/2021-global-status-report-buildings-and-construction (accessed Feb. 11, 2023).

[22] P. Nepal, C. M. T. Johnston, and I. Ganguly, 'Effects on Global Forests and Wood Product Markets of Increased Demand for Mass Timber', *Sustainability*, vol. 13, no. 24, p. 13943, Dec. 2021, doi: 10.3390/su132413943.

[23] 'The World's Tallest Timber-Framed Building Finally Opens Its Doors | Architectural Digest'. https://www.architecturaldigest.com/story/worlds-tallest-timber-framed-building-finally-opens-doors (accessed Feb. 11, 2023).

[24] 'Life cycle assessment of mass timber construction: A review | Elsevier Enhanced Reader'.

[25] J. Hart and F. Pomponi, 'More Timber in Construction: Unanswered Questions and Future Challenges', *Sustainability*, vol. 12, no. 8, p. 3473, Apr. 2020, doi: 10.3390/su12083473.

[26] Z. Chen, H. Gu, R. D. Bergman, and S. Liang, 'Comparative Life-Cycle Assessment of a High-Rise Mass Timber Building with an Equivalent Reinforced Concrete Alternative Using the Athena

https://doi.org/10.52202/069179-0545

Impact Estimator for Buildings', *Sustainability*, vol. 12, no. 11, Art. no. 11, Jan. 2020, doi: 10.3390/su12114708.
[27] G. Churkina and A. Organschi, 'Will a Transition to Timber Construction Cool the Climate?', *Sustainability*, vol. 14, no. 7, Art. no. 7, Jan. 2022, doi: 10.3390/su14074271.
[28] 'A new report predicts significant demand growth for mass timber components', *Building Design + Construction*, Jul. 05, 2020. https://www.bdcnetwork.com/new-report-predicts-significant-demand-growth-mass-timber-components (accessed Feb. 06, 2023).
[29] R. Pasternack *et al.*, 'What Is the Impact of Mass Timber Utilization on Climate and Forests?', *Sustainability*, vol. 14, no. 2, Art. no. 2, Jan. 2022, doi: 10.3390/su14020758.
[30] J. Comnick, L. Rogers, and K. Wheiler, 'Increasing Mass Timber Consumption in the U.S. and Sustainable Timber Supply', *Sustainability*, vol. 14, no. 1, Art. no. 1, Jan. 2022, doi: 10.3390/su14010381.
[31] 'As Mass Timber Takes Off, How Green Is This New Building Material?', *Yale E360*. https://e360.yale.edu/features/as-mass-timber-takes-off-how-green-is-this-new-building-material (accessed Feb. 07, 2023).
[32] 'Designing the future with sustainable timber'. https://www.pefc.org/what-we-do/our-collective-impact/our-campaigns/designing-the-future-with-sustainable-timber (accessed Feb. 06, 2023).
[33] S. Figorilli *et al.*, 'A Blockchain Implementation Prototype for the Electronic Open Source Traceability of Wood along the Whole Supply Chain', *Sensors*, vol. 18, no. 9, Art. no. 9, Sep. 2018, doi: 10.3390/s18093133.
[34] P. Italy, 'Wood-chain: the technology for strengthening traceability and PEFC certification', *MedForest*, Apr. 26, 2019. https://medforest.net/2019/04/26/wood-chain-project-the-technology-for-strengthening-traceability-and-pefc-certification/ (accessed Feb. 04, 2023).
[35] A. Daigneault *et al.*, 'How the future of the global forest sink depends on timber demand, forest management, and carbon policies', *Glob. Environ. Change*, vol. 76, p. 102582, Sep. 2022, doi: 10.1016/j.gloenvcha.2022.102582.
[36] 'PEFC Forest Certification Checklist – PEFC UK Forest Certification Online Tool'. https://forestrytool.pefc.co.uk/ (accessed Feb. 12, 2023).
[37] 'Fostering tree monitoring technologies to support climate adaptation and mitigation'. https://www.pefc.org/what-we-do/our-collective-impact/our-projects/fostering-tree-monitoring-technologies-to-support-climate-adaptation-and-mitigation (accessed Feb. 12, 2023).
[38] 'Using technology to make certification more accessible to smallholders'. https://www.pefc.org/what-we-do/our-collective-impact/our-projects/using-technology-to-make-certification-more-accessible-to-smallholders (accessed Feb. 12, 2023).

World Conference on Timber Engineering Oslo 2023

RIGID JOINTS ON GLUED-IN RODS OF BENDING AND COMPRESSION-BENDING ELEMENTS OF LARGE-SPAN LAMINATED TIMBER STRUCTURES

Alexander Pogoreltsev[1], Stanislav Turkovsky[2], Vladimir Stoyanov[3]

ABSTRACT: Elements of large-span laminated wood structures can have a long length, which causes difficulties for manufacturing and transportation. This is especially true for bent laminated elements of arches, frames, meridional ribs of domes and other structures. There is a need to break down long structures into technological elements with implementation of consolidation rigid joints. Russia has developed a system of node joints of wooden structures on inclined glued-in rods - the "TSNIISK System". The basic principle of rigid joints is to fasten the embedded part to the wooden element by means of obliquely glued rods. Two types of rigid joints are proposed: with unidirectional inclined glued-in rods and with glued-in rods forming V-shaped anchors. A methodology for calculating knots and joints on glued rods has been developed. During the design and construction of long-span buildings and structures with glued wooden frames, control tests are conducted. Examples of control tests of the mineral fertilizer warehouses structures are presented. The results of the control tests confirm the correctness of the calculation methodology. Hundreds of buildings and structures with glued wood frames with glued-in rods used in the nodes have been built in Russia.

KEYWORDS: Bending, compression-bending, glued-in rebar, glued-in rod, large-span, rigid joint, test, V-shaped

1 INTRODUCTION

Elements of large-span glue laminated timber structures can have a long length, which causes difficulties for manufacturing and transportation. This is especially true for bent laminated elements of arches, frames, meridional ribs of domes and other structures. There is a need to devide long structures into technological elements with the arrangement of rigid joints performed on the assembly.

The traditional solution is the dowel joints. The assemblies with steel plates in wood kerfs and steel pads on dowels are widely used.

A modern type of joints are steel rods with metric threads or reinforcing bars glued into the wood.

In Russia, a new type of consolidation joints on obliquely glued rods has become widespread. In the laboratory of wooden structures of the Central Research Institute of Building Structures named after V.A. Kucherenko (CNIISK). The institute has developed a system of node joints of wooden structures on glued-in rebars - "TSNIISK System". The founder of the system is S.B. Turkovsky, who is conducting research since 1974 [1].

Based on the results of studies of knotted joints on inclined glued-in rods, the design principles and calculation methods for such joints have been developed.

[1] Alexander Pogoreltsev, V.A. Koucherenko Central Research Institute of Building Construction, Moscow, Russian Federation, e-mail: pogara@yandex.ru

[2] Stanislav Turkovsky, V.A. Koucherenko Central Research Institute of Building Construction, Moscow, Russian Federation, e-mail: sbt39@yandex.ru

[3] Vladimir Stoyanov, Wood Housing Association, Moscow, Russian Federation, e-mail: stoianov-kdk@yandex.ru

2 KNOT CONNECTIONS ON GLUED-IN RODS

The basic elements of the CNIISK System are rod elements glued into the wood at an angle to the fibers [2]. The 0° and 90° angles are special cases. In Europe, mainly glued-in rods with metric threads are used [3]. In Russia, mostly periodic profile bars A400 or A500 are used, but bars from other materials - different grades of steel, aluminum alloys, composite reinforcement (carbon fiber, fiberglass, basalt-plastic), etc. can also be used. The main requirement is that the rods have irregularities on the surface: periodic profile (steel or composite reinforcement), threads (e.g. metric), special rifling, etc. The bars are glued with epoxy adhesives.

The first satisfactory results were obtained by S. Turkovsky in 1975 when testing a girder joint on a new type of joints - obliquely bonded reinforcing bars (Fig. 1). Despite the fact that the joint was located in the area of maximum bending moment, the failure occurred outside the joint.

The use of inclined glued-in rods makes it possible to obtain rigid joints equivalent in bearing capacity to a solid section. The use of inclined glued-in rods is widespread in joints stressed by bending or compression with bending.

Compression-curved assemblies include support assemblies of columns rigidly connected with the foundation. The first objects with such assemblies on threaded adhesive screwed rods are the 24 m span warehouse (1979) and the panel production shop (1983) built at the Volokolamsk Experimental Building Structures Plant. Scheme of the support assembly of 6 m high columns is shown in Fig. 2a. The bearing structures of the roof were lenticular glued timber trusses, in which the junction of the upper and lower chords was also

https://doi.org/10.52202/069179-0546

made on glued-in screwed rods for the first time for such trusses.

A tennis court was built in 1983 in the Moscow region. Its main load-bearing structures were a double-hinged frame of 18 m span with glued wooden uprights of variable height (6 - 8) m and a bent-roofed girder.

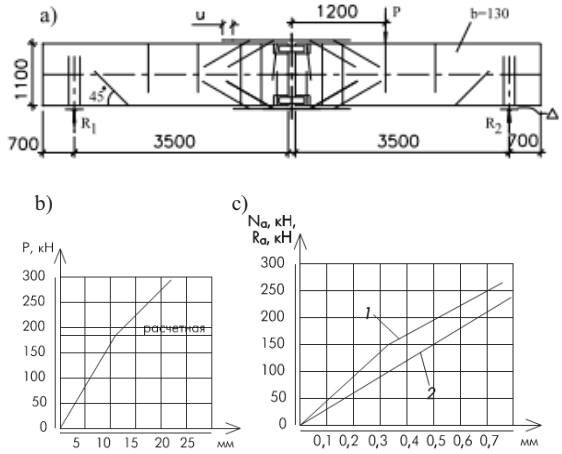

Figure 1: *Bending tests of a beam with a rigid joint: a - test pattern; b - deflections in the middle of the span; c - shear deformations in the joint*

The design of the stiffening of the struts differed from the first two in that the glued-in rebars were used (Fig. 2 b)

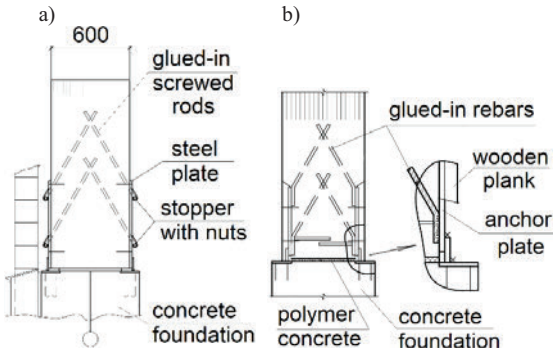

Figure 2: *Stiff pinch-post assemblies in the foundation: a - bonded-rod warehouse assembly (1979); b - bonded-rod tennis court assembly (1983)*

Bendable joints in large-span structures were first used in the construction of the community center of the pioneer camp (now holiday home) "Lipki" in the Moscow region, built in 1985 (Fig. 3).

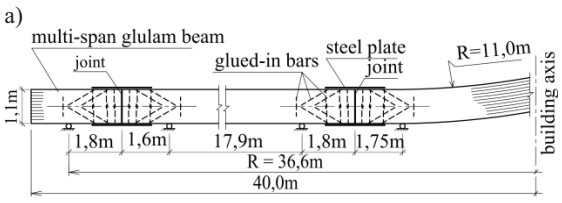

b)

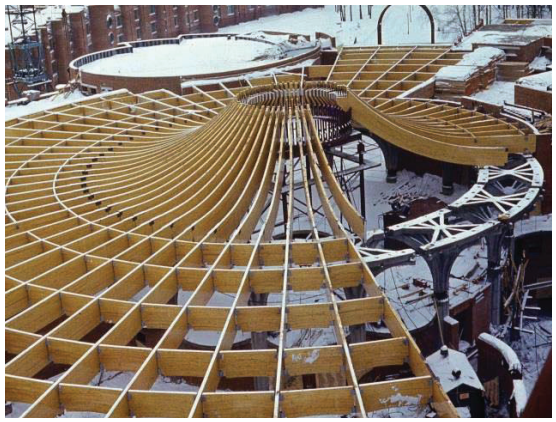

Figure 3: *Radially arranged multi-span beams of the Lipki boarding house roof with rigid joints on inclined glued-in bars (1985): a -structural scheme of the girder; b - installation of roof beams*

3 DESIGN AND CALCULATION OF RIGID JOINTS

3.1 CALCULATION SCHEMES

The basic principle of a rigid joint is to fasten the embedded plate to the wood member by means of obliquely bonded rods. The bending moment and the longitudinal force cause tension and compression in the joint. The tensile force Nt is taken up by the embedding plate, and the compression force Nc is taken up by the stop at the ends of the wooden elements, either by the stop through the centering gasket or by the embedding plate (Fig. 4). The magnitudes of the forces depend on the shoulder of the internal force pair h_0.

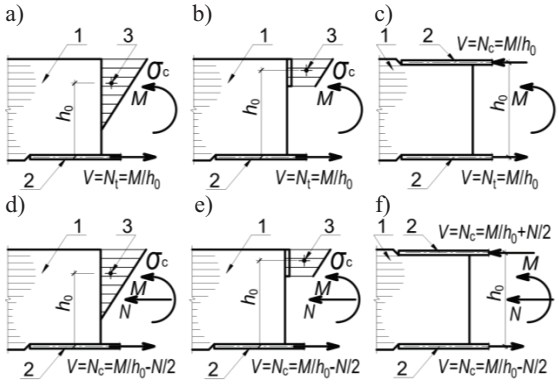

1 - glulam element; 2 - embedded detail; 3 - center of gravity of the compressive stress diagram

Figure 4: *Joint force diagrams: a, b and c - bending members; d, e and f - compression-bending members*

The axial forces in the embedded parts cause shear forces V between the part and the wood, which are taken up by the glued-in rods. In the tensile zone, the

https://doi.org/10.52202/069179-0546

embedded parts are always installed, while in the compressed zone, the structural solutions for the transmission of the compressive forces can be different:
- By the butt-end of wooden elements (Fig.4a and Fig.4d), in this case, if there are no technical possibilities to ensure a tight adjacency, a gap of 30 ± 10 mm is made which is filled with polymer concrete during assembly;
- through the centering gasket (Fig.4b and Fig.4e), which is made of steel or polymer concrete;
- through the embedded part (Fig.4c and Fig.4f).

3.2 JOINTS DESIGN SCHEMES AND THEIR CALCULATION

Two types of structural solutions for rigid joints have been developed (Fig. 5): with unidirectional inclined glued-in rods and with glued-in rods forming V-shaped anchors.

Two types of joint designs have been developed: with unidirectional inclined glued-in rebars and with glued-in rebars forming V-shaped anchors.

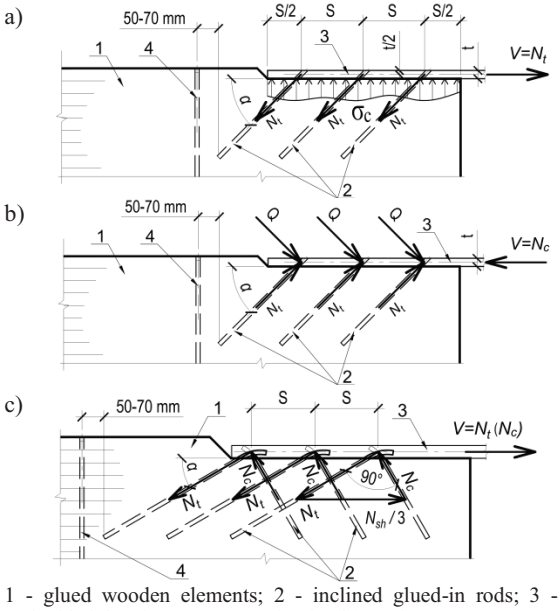

1 - glued wooden elements; 2 - inclined glued-in rods; 3 - embedded detail; 4 - transversely glued-in rods

Figure 5: *Types of structural solutions for rigid joints: a - unidirectional inclined glued-in rods in the tensile zone; b - unidirectional inclined glued-in rods in the compressed zone; c - V-shaped anchors*

3.2.1 Joints with unidirectional inclined glued-in rods in the tensile zone

In the tensile zone of a joint with unidirectionally inclined riveted rods, the bending work of the rods is not considered, assuming the formation of a plastic joint at the point where the rod is attached to the embedded plate, which is usually done by welding.

The displacement force in the embedded plate V is decomposed into the tensile force in the rods N_t and the compressive force on the contact between the embedded plate and the wood σ_c (Fig.5a):

$$N_t = V / (n \cdot k_n \cdot \cos\alpha), \quad (1)$$

where:
N_t - pulling force in the inclined glued-in rod;
V - shear force in the embedded part of the joint;
n - number of inclined glued-in rods;
k_n - non-uniformity factor that takes into account the number of glued-in rods;
α - angle of inclination of a glued-in rod to the direction of force in the embedded plate.

$$\sigma_c = N_t \cdot \sin\alpha / (b_{e.d} \cdot S \cdot k_{n.\sigma}), \quad (2)$$

where:
σ_c - the normal buckling stress under the embedded part;
$b_{e.d}$ - width of the embedded plate;
S - step of inclined glued-in rods;
$k_{n.\sigma}$ - nonuniformity coefficient, taking into account the pitch and angle of glued-in rods and the stiffness of the embedded plate.

Based on the results of many years of research, a methodology for calculating the rigid joints of wooden structures on glued-in rods has been developed. It is based on determining the bearing capacity of glued-in rods during pulling out and punching. The main provisions of the calculation procedure are outlined in the Russian Construction Norms and Rules [4,5].

The calculated value of bearing capacity $R_{ax.\alpha.d}$ for pulling out or punching out of a rod glued-in at an angle to the wood fibers should be determined by the formula:

$$R_{ax,\alpha,d} = f_{v,\alpha,d} \cdot \pi \cdot d_1 \cdot l_{ad} \cdot k_v \cdot k_d \le f_{a.d} \cdot A_a, \quad (3)$$

where:
$f_{v.\alpha,d} = f^A_{v.d} \cdot m_{dl} \cdot \Pi m_i$ – design resistance of wood to pulling or punching of the rod glued-in at an angle to the fibers;
$f^A_{v.d}$ – design resistance of wood to pulling out or pressing the core glued-in at the angle of 90° to the fibers, for the loading mode A by SP 64.13330 [4], characterized by linearly increasing load at standard machine tests;
m_{dl} – coefficient of prolonged strength, corresponding to the combination of loading;
Πm_i – product of the coefficients of working conditions mi, considering the angle of slope of the rod to the direction of wood fibers, temperature and humidity conditions of operation;
d_1 – hole diameter;
l_{ad} – calculated length of the rod;
d – diameter of the glued-in rod;
k_v – coefficient taking into account uneven distribution of shear stresses depending on the calculated length of the rod;
k_d – coefficient taking into account the dependence of design resistance on the rod diameter;
A_a – sectional area of the rod;
$f_{a.d}$ – design resistance of the rod material.

It should be noted that the length of the glued-in rods is not only determined by the required load-bearing

https://doi.org/10.52202/069179-0546

capacity. In the wood at the end of a tensile bonded rod, normal tensile stresses occur across the fibers. The shallower the gluing depth in relation to the section height and the greater the angle of the rod to the direction of shear of the embedded detail, the higher the magnitude of the maximum stresses. Thus, if the inclination angle of the glued-in rod is 45°, the gluing depth should be set on the condition that the vertical projection of the rod is not less than 0.4h - cross-sectional height. If the gluing depth is less, to reduce the tensile stresses across the fibers, the rod should be glued-in across the fibers at a distance (50-70) mm along the fibers from the end of the stretched inclined glued-un rod.

3.2.2 Joints with unidirectional inclined glued-in rods in the tensile zone

If the compression forces in the joint are taken by the embedded plate, the shear force in it V acting on one rod is decomposed into the compressive force in the rod N_c and the shear force Q (Fig.3b):

$$V / (n \cdot k_n) = N_c \cdot \cos\alpha + Q \cdot \sin\alpha, \quad (4)$$

Hence:

$$N_c = V \cdot \cos\alpha / (n \cdot k_n), \quad (5)$$

$$Q = V \cdot \sin\alpha / (n \cdot k_n). \quad (6)$$

The bearing capacity of a rod glued-in at an angle to the wood fibers, working for pulling with bending or punching with bending, should be checked by the formula:

$$(N_c / R_{a.d})^2 + Q / F_{v.R.d} \leq 1, \quad (7)$$

where:

$R_{a.d} = f_{a.d} \cdot A_a$ – design bearing capacity of one rod under the condition of tensile strength of the rod material;

$F_{v.R.d}$ – design bearing capacity of the rod in terms of its operation as a dowel in bending at rigid (welded) connection of the glued-in rod with a steel embedded part, MH, it is taken:

$$F_{v.R.d} = 65d^2 \cdot \sqrt{m_{дл}} \cdot \Pi m_i \text{ – for rebars A300;} \quad (8)$$

$$F_{v.R.d} = 85d^2 \cdot \sqrt{m_{дл}} \cdot \Pi m_i \text{ – for rebars A400;} \quad (9)$$

where d is the nominal diameter of the reinforcing bar.

As far as in the rigid joints of bending and compression-bending structures the bearing capacity of unidirectional inclined glued-in bars in the stretched zone is considerably higher than in the compressed zone, the bars are located in the stretched zone, and compression is taken by the frontal stop or through the centering gasket. In structures with a variable arrangement of the compressed and stretched zones, such as arches, the glued-in rods are placed on both sides.

3.2.3 Joints with V-shaped anchors

One of the glued-in rods of the V-shaped anchor, glued-in at an angle α to the direction of the shear force V, works for pulling out (tensioned rod), the second one, glued-in at an angle β, works for pushing through (compressed rod) (Fig. 5c). The forces in the rods are determined from the expression:

$$V / (n \cdot k_u) = N_t \cdot \cos\alpha + N_c \cdot \cos\beta, \quad (10)$$

where N_t and N_c are the pulling and punching forces in obliquely glued-in rods.

Hence:

$$N_t = V / (n \cdot k_n \cdot \cos\alpha \cdot (1 + \mathrm{tg}\alpha / \sin\beta)), \quad (11)$$

$$N_c = V / (n \cdot k_n \cdot \sin\beta \cdot (1/\mathrm{tg}\alpha + 1/\sin\beta)). \quad (12)$$

When α = β, the forces in the tensile and compressed rods are equal:

$$N_t = N_c = V / (n \cdot k_n \cdot (1 + \cos\alpha)), \quad (13)$$

In practice for V-shaped anchors the angle between the glued-in rods is usually taken to be 90°. Then, with the angle of the rod to be pulled out α:

$$N_t = V \cdot \cos\alpha / (n \cdot k_n), \quad (14)$$

$$N_c = V \cdot \sin\alpha / (n \cdot k_n). \quad (15)$$

The design value of the bearing capacity $R_{ax.\alpha.d}$ for the pulling out or punching through of the rod glued-in at an angle to the wood fibers shall be determined according to the formula (3).

V-shaped anchors can be installed in both tensile and compressed zones. However, it is most effective to install them in the tensile zone, especially for compression-curved elements.

4 JOINT CONTROL TESTS

4.1 PURPOSES OF CONTROL TESTS

For large-span structures, control tests of the main assemblies are often required. The rationale for the need to test the knots of laminated timber structures is that:

- structures of unique structures;
- constructions of structures of the 1st responsibility class according to GOST 27751-2014 [6];
- pilot experimental constructions;
- long-span structures with manufacturing defects;
- large-span structures with assembly defects;
- units of critical structures during the mastering of production.

The purposes of control tests of large span laminated timber structures joints are:

- evaluation of the correctness of the adopted design solutions and calculation assumptions;

- determination of the bearing capacity in the absence of the standard calculation methods;
- verification of manufacturability.
- quality control of manufacturing;
- verification of assemblability and quality control on assembly;
- expert evaluation of the causes of structural failures.

An example of testing to determine the bearing capacity of bendable assemblies of critical experimental structures during production development is the above-mentioned test of the rigid girder joint of the boarding house "Lipki" (Fig. 3).

4.2 TESTS OF JOINTS OF LARGE SPAN STRUCTURES

High chemical resistance to various salts aggressive to steel and concrete makes wood competitive in the construction of structures for the storage of such materials. An example of control tests are tests of rigid joints on glued-in rods of the main elements of glued wood frameworks of mineral fertilizer storage facilities and other similar structures.

4.2.1 Warehouse of anti-icing chemicals in Moscow

During the reconstruction of the Moscow Ring Road in 1999, a de-icing agent warehouse was built in Moscow, the frame of which was made in the form of three-jointed bent-beam frames with a span of 60 m - the first long-span structure with compression-curved rigid joints on glued-in rebars (Fig. 6a) [7].

a)

b)

Figure 6: *De-icing agent storage with a span of 60 m: a - installation; b - rigid joint testing*

In order to assess the correctness of the adopted design solutions and design assumptions, control tests were carried out on a fragment of the structure with a rigid joint in the middle of the length (Fig. 6b). The joint was made symmetrical with a frontal stop through epoxy-based polymer concrete. Since the bearing capacity of the joint is determined by the tensile zone, bending tests were performed, with the tensile forces in the joint corresponding to the forces in the tensile zone of the compression-bending joint of the bent frame.

To assess the stress-strain state of the wood in the joint area, electrical strain gauges were glued and mechanical strain and displacement sensors were installed. During the tests, the opening of the joint in the tensile zone, the shear deformations of the embedded plate relative to the wooden element, and the relative deformations along the fibers in the compressed zone were determined.

The tests confirmed the correctness of the adopted design solutions and design assumptions. The failure was caused by wood rupture in the tensile zone outside the joint.

During the tests, an additional task was set to check the effectiveness of the method developed in CNIISK to strengthen glued wooden elements in which shrinkage cracks and delamination of glue joints can appear in the process of tests [8]. In the supporting zone of one of the joined fragment elements in the middle of the section height, an artificial through crack was created with the length of about half the element length. There was performed an inclined reinforcement by reinforcing bars with diameter of 20 mm of class A400 with length of 1000 mm glued-in at an angle of 45° to the fibers. Along the artificial crack, shear gauges were installed.

At the initial stage of tests, approximately up to the normative load, shear was minimal, the structure did not work as a composite element on compliant bonds, but as a monolithic one. The test results confirmed the effectiveness of inclined reinforcement of zones with high levels of tangential stresses and tensile stresses across fibers for strengthening and restoration of wooden structures, primarily the supporting zones of beams.

4.2.2 Potassium salt deposits in Volgograd Region

In the Volgograd region at the mining and beneficiation plant for the extraction and processing of potassium salts two warehouses with frames of glued wooden structures were built (Fig.7).

a)

b)

c)

Figure 7: *87.2 m span warehouse arches: a - frame assembly; b - joint of collapsed arch; c - joint testing*

https://doi.org/10.52202/069179-0546

Structural scheme represents three hinged glued wooden arches with 87.2 m span and 36.7 m height at the ridge. Each half-arch consists of three elements, which at their ends are fitted with embedded parts fixed on inclined glued-in rebars. During installation, the elements are joined into a semi-arch by rigid joints by connecting the embedded parts with M20 bolts made of A4-80 stainless steel.

In 2014, at the beginning of installation of the frame of the first warehouse, two bent wooden girders collapsed as a result of a hurricane. The bolts in the lower rigid joints had sheared off after the half-arcs collapsed. To determine the cause of the collapse, a decision was made to repair one of the rigid joints and conduct a test to confirm sufficient load-bearing capacity. An 8-metre long section with a rigid joint in the middle was cut out of one of the collapsed arches. Restoration of the joint consisted of installing new bolts.

In the first phase, tests were performed for compressive force and bending moment (Fig. 7c). The H and M ratios corresponded to the forces in the arch for the design load combination. During the tests, the shear deformations of the embedded parts relative to the wood, the joint opening width in the tensile zone, and the compression deformations along the fibers in the compressed zone were determined. When the required level of loading was reached, no fracture occurred, the instrumentation showed that the joint was working in the elastic stage.

Since the load-carrying capacity of the joint is determined by the work of the glued-in rods in the tensile zone, it was decided to conduct further tests only in the bending zone, comparing the forces in the glued-in rod located in the tensile zone with the forces in the compression-bending element joint. The bolts were replaced with stronger bolts of class 10.9. The bolts sheared off under a load much greater than the design load.

In the third phase, the bolts were replaced by welding. The failure of the joint occurred from the rupture of the glued-in rebars.

Tests showed sufficient load-bearing capacity and confirmed that the rigid bonds on the bonded bars were not the cause of the collapse.

4.2.3 Potash warehouses in Perm Territory

The main load-bearing structures of the potash production complex warehouses in Perm Krai, built in 2016-2020, are glued wooden triangular arches with a span of 60 m and a height at the ridge of 38.5 m. The 49.3 m long half arches, based on technological and transport limitations, consist of 2 elements along the length with a rigid joint between them on unidirectional obliquely glued-in rebars. Due to the fact that the warehouses of chemical enterprises belong to the constructions of the 1st responsibility class and two companies selected for the manufacture of glued wooden structures of warehouse frameworks had no experience in the manufacture of critical structures with the nodes on the glued-in rebars, the control tests of the rigid joint were required.

A full-scale fragment with a rigid butt-joint in the middle of the span was tested in compression and bending (Fig. 8). The two elements forming the fragment were manufactured at two QDC manufacturing plants. The tensile forces in the joint are taken up through the embedded detail by unidirectional obliquely glued-in rebars. The compression is transmitted by the frontal stop via polymer concrete alignment pads.

In the area of the joint, the test fragment is equipped with electric strain gauges and mechanical strain and displacement sensors to record the stress-strain state of the wood and steel embedded parts, shear strains of the embedded parts, opening of the joint in the tensile zone, deflections of the sample, etc. (Fig. 8b).

a)

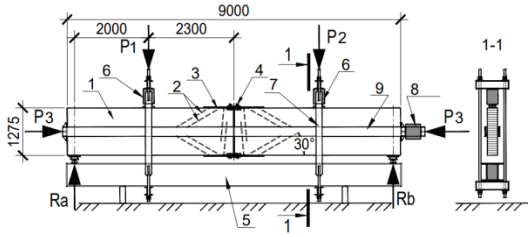

b)

1 – laminated wood test sample; 2 - rebars 22 mm diameter, 1000 mm long, glued-in at an angle of 30° to the grains; 3 - anchor plate; 4 – bolts; 5 - power traverse; 6 - hydraulic jack with capacity 1000 kN; 7 - vertical tie bar; 8 - hydraulic jack with capacity 1500 kN; 9 - horizontal tie bar

Figure 8: *Control tests of a compression-bending rigid joint of an arch with a span of 60 m*

Maximum bending moment in the rigid butt-joint M = 667 kN-m with a longitudinal force N = -532 kN and a shear force Q = 64 kN. The adopted testing scheme allowed to have ratios of internal forces in the butt at any stage of tests, which were proportional to the previously given design values. Loads were applied on the specimen by means of hydraulic jacks in a special stand (Fig.8a). Compressive force N was created by resting it in the end face of a 1500 kN hydraulic jack. The bending moment M was created by two hydraulic jacks of 1000 kN capacity each, with different loads on jacks, resulting in a transverse force Q at the junction.

The tests were conducted in two stages. The first stage of tests was conducted with metal overlays removed in the compressed zone of the joint, which allowed for the exclusion of embedded parts with glued-in rebars in the compressed zone. The second stage was performed with the overlays in place to allow the wood and metal embedded parts with the glued-in rebars to work together in compression.

Each stage consisted of several stages. The first two stages of the tests in both stages were characterized by the work of the specimen in the elastic strain zone. In the first stage, only vertical loads were applied to the specimen, allowing only pure bending to be simulated in the element junction zone. The second stage simulated compression with bending, adding horizontal compressive loads to the vertical loads.

The third stage was conducted only for the second stage of tests and was a continuation of the second stage. At this stage, the specimen was brought to failure.

The maximum loads exceeded the design loads by 1.8 times and the required maximum test loads by 1.18 times. The test results showed that the technical solutions adopted in the design are technological, provide the required load-carrying capacity and confirm the quality of rigid joints in the manufacture of structures.

4.2.4 Mineral fertilizer warehouse of Gomel Chemical Plant

In 2021, a mineral fertilizer warehouse was built at the Gomel chemical plant. The main load-bearing structures were three-armed non-symmetrical triangular arches (Fig. 9a). One half-arch has a slope to the horizon of 45°, the second - 30°. The second half-arch, 33.2 m long, has a rigid joint on inclined glued-in rebars.

The building code of Belarus regulates the compulsory control tests of critical structures. In 2020, in Brest (Belarus), tests were carried out on a fragment of a half-arch with a rigid joint on glued-in rebars (Fig. 9b). The tests were conducted under the scientific supervision of A. Naychuk according to the method developed by A. Pogoreltsev [9]. The tests were conducted in two stages: in compression with bending and in bending. The sample was equipped with measuring instruments (Fig. 9c).

While carrying out the tests, there were determined the regularities of change in the stress-strain state of wood in the area of location of the inclined glued-in rebars, compliance of connection elements, height of the compressed zone (Fig. 9e and 9e), the width of joint opening in the stretched area between the ends of the connected elements (Fig. 9f), depending on the magnitude of applied loads.

It follows from the test results that the height of compression zone of the joint is not a constant value and depends on the suppleness of the embedded parts and the level of tension in the connecting plates. The height of the compressed zone decreases with increasing load.

When testing the specimen under the loading scheme of the compression-bending element the carrying capacity of the joint in vertical direction is Rsup,c,90 = 131.5 kN and in horizontal direction - Rsup,c,0 = 124.9 kN, which is more than values of the required carrying capacity.

When testing the prototype according to the bending element loading scheme, the value of actual bearing capacity Rsup,v = 364.9 kN, which is significantly higher than the value of the required bearing capacity.

At the same time, numerical studies of the joint operation were performed (Fig. 9g). The obtained data were compared with the test results.

a)

b)

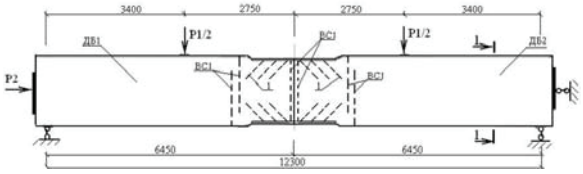

c)

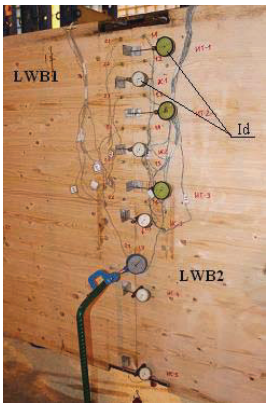

d)

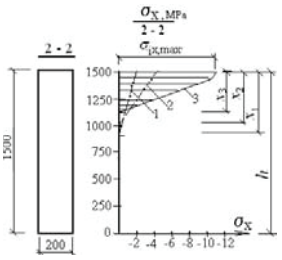

e)

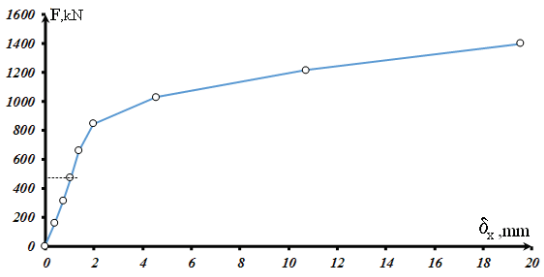

f)

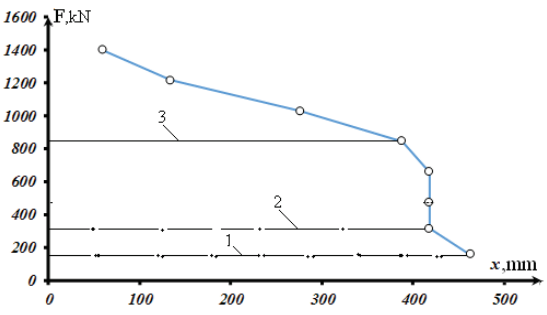

g)

https://doi.org/10.52202/069179-0546

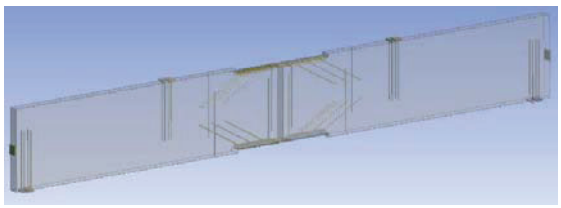

1 - F = 157 kN; 2 - F = 315,3 kN; 3 - F = 843,8 kN

Figure 9: *Fertilizer warehouse: a - installation of arches with a span of 45 m; b - test scheme of a fragment with a rigid joint; c - indicators and strain gauges in the joint zone; e - diagram of normal compressive stresses in section 2-2; f) - dependence of height of compressed zone x on the load value; f) - dependence of width δx of joint opening on the load value; g) - numerical model*

The discrepancy between the data obtained as a result of numerical calculations and tests was most typical for the value of compression zone height, which was 22%. Such a difference is caused by the fact that during the prototype production, a partial adhesive bond between the surfaces of the embedded parts and the wood in the process of gluing of the inclined reinforcing bars took place. This circumstance led to a decrease in the suppleness of the embedded parts and an increase in the height of the compressed zone. In the KE model, the friction coefficient between the surfaces of the embedded parts and the wood was assumed to be zero.

5 CONCLUSIONS

During all the control tests, additional research tasks were solved as part of the glued-in rebar joints research program.

The results of control tests confirm the correctness of the design assumptions laid down in the Russian construction norms and rules [4, 5].

Over the past 25 years in Russia, dozens of buildings with large-span laminated wooden structures using rigid joints on the glued-in rebars have been built: water parks at the Abzakovo ski resort (beams of span 29.8 m), in Ulyanovsk (lenticular trusses of span 32.3 m), in Mytishchi ((lenticular trusses of span 44 m), Rostov-on-Don (lenticular trusses of span 35 m), Saint Petersburg (90 m diameter dome), Novosibirsk (95 m diameter dome); swimming pools in St. Petersburg (lenticular trusses with spans of 45 m and 56 m), Saransk (frames with spans of 40 m and 30 m), Kazan (frames with spans of 54.6 m); sports palaces in Moscow (lenticular trusses with 48 m span and frames with 42 m span), Nefteyugansk (metal and wood lenticular trusses with 42 m span); ice palaces in Moscow (metal and wood lenticular trusses with 50,5 m span), Krasnoyarsk, Irkutsk and Novokuznetsk (sickle-shaped arches with 99,9 m span and many others).

REFERENCES

[1] Turkovsky, S.B. 1989. Designing of glued wood structures joints on glued-in bars. In: Proceedings of CIB-W18 meeting 22, Berlin, Germany, Paper CIBW18A/22-7-3.

[2] Turkowskij S., Lukyanov E. and Pogoreltsev A. Prefebricated joints of timber structures on inclined glued-in bars // Proceedings of the International Timber Engineering Conference, 2-5 September 1991, London, United Kingdom. Pp. 3.212—3.217.

[3] Aicher S., Stapf G.: Eingeklebte Stahlstäbe – state-of-the-art – Einflussparameter, Versuchsergebnisse, Zulassungen, Klebstoffnormung, Bemessungs- und Ausführungsregeln. MPA Universität Stuttgart, Stuttgart, Deutschland Internationales Holzbau-Forum IHF 2017, pp. 193-208, 2017.

[4] SP 64.13330.2017 Timber structures. СНиП II-25-80.

[5] SP 382.1325800.2017 Glued laminated wooden structures on glued-in rods. Calculation methods.

[6] GOST 27751-2014 Reliability for constructions and foundations. General principles.

[7] Turkovsky S.B., Pogoreltsev A.A. Wooden structures with rigid joints in structures with corrosive medium // Industrial and Civil Engineering, № 10, pp. 10-13, 2001

[8] Pogoreltsev A.A. Shear strength of bendable laminated timber structures with transverse reinforcement: dissertation ... D. Thesis. M., CNIISK, 1989, 243 p.

[9] Naichuk A., Pogoreltsev A., Demchuk I., Ivaniuk A. and Roshchina S. Rigid Joint of Bent Glued Laminated Timber Structures Using Inclined Glued-In Rods // Proceedings of MPCPE 2021. Selected Papers - Lecture Notes in Civil Engineering, vol. 182: 501-521, 2022.

[10] Turkovsky S.B., Pogoreltsev A.A., Preobrazhenskaya I. Glued wood structures with nodes on glued-in rods in modern construction (CNIISK system). - Moscow: RIF "Stroymaterialy", 2013. - 300 p.

World Conference on Timber Engineering Oslo 2023

MJØSTÅRNET: THE WORLD'S TALLEST TIMBER BUILDING

Harald Liven[1], Rune Abrahamsen[2]

ABSTRACT: Mjøstårnet is an 18-storey mixed-use timber building in Brumunddal, Norway, built by the shore of the lake Mjøsa. The building was completed in March 2019 and has been ratified by CTBUH as the world's tallest all-timber building. Mjøstårnet consists of offices, 72 hotel rooms, 33 apartments with balconies, a restaurant on the ground floor, conference rooms and a rooftop terrace. The architectural pergola extends the building 85,4 m from the ground level.

KEYWORDS: Multi-storey buildings, high rise, assembly, glulam, fire

1 INTRODUCTION

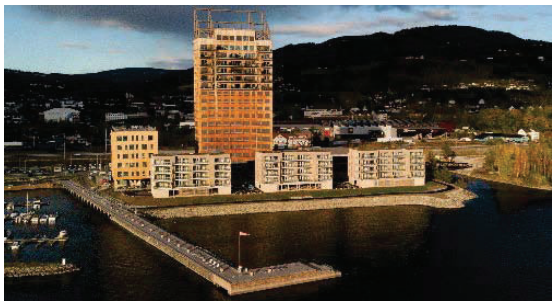

Figure 1: *"Mjøstårnet". View from the lake Mjøsa*

The initiative to build Mjøstårnet comes from investor Arthur Buchardt and the company AB Invest AS. He grew up in Brumunddal and wanted to build the world's tallest timber building placed in his hometown. In that way he wanted to show the world what is possible by using local resources, local suppliers, local competence and sustainable materials. He made the first sketch in February 2015 where he drew the building and its facilities.

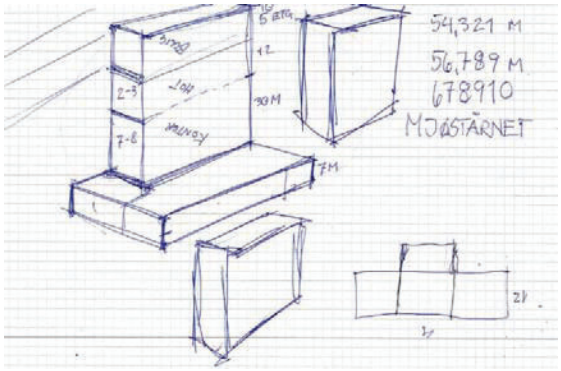

Figure 2*: Sketch from February 2015 © Arthur Buchardt*

Together with Moelven Limtre AS – Norway's largest glulam manufacturer - he continued to develop the project. VOLL architects were engaged as architects and HENT as main contractor. Only four years later, in March 2019, the tallest timber building was completed [6].
Brumunddal is located close to the shore of lake Mjøsa, 140 kilometres north of Norway's capital Oslo.

Figure 3: *Brumunddal located in the central part of Norway*

The completed building has a majority of wooden components originating from nearby sustainable forests. The wooden components comprise glulam structures in the main load bearing, CLT in the elevator and staircase shafts, as well as wooden based floor and façade elements. In total about 4000 m^3 of wooden products were used. To produce this quantity about 16.000 spruce trees were harvested.
The glulam structures as well as floor- and façade elements were produced only 15 kilometres from the site.

[1] Harald Liven, Structural Designer of Moelven Limtre AS, MSc Structural engineering, Moelven Limtre AS , Norway, Email: Harald.Liven@moelven.no

[2] Rune B Abrahamsen, CEO of Moelven Limtre AS, MSc Structural engineering, Moelven Limtre AS , Norway, Email: Rune.Abrahamsen@moelven.no

https://doi.org/10.52202/069179-0547

2 STRUCTURAL SYSTEM

The structural and dynamic design of the tower was carried out by the Norwegian branch of the design company Sweco in collaboration with Moelven Limtre. The design was performed according to Eurocode 5 [1,2].

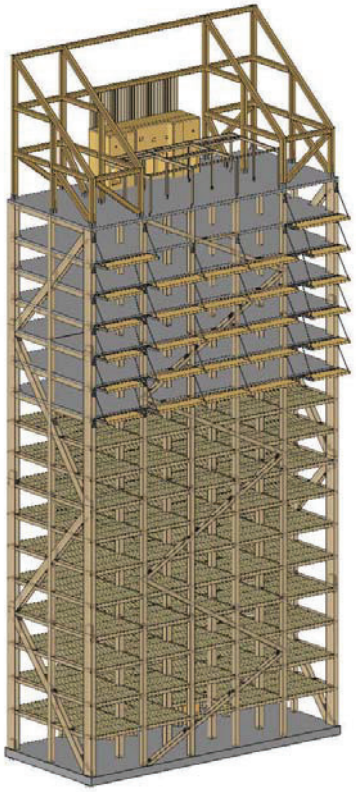

Figure 4: *Structural system*

2.1 The main load bearing

The main load bearing consists of large-scale glulam trusses along the façades as well as internal columns and beams. The footprint of the structure is 16,3 m x 36,9 m measured from the outer corners of the columns.

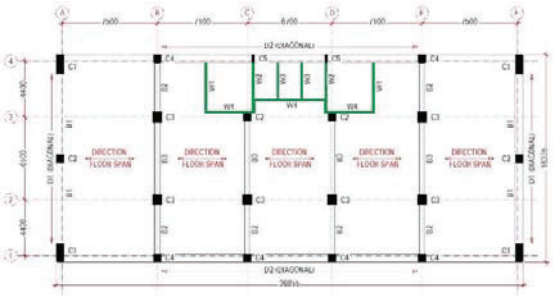

Figure 5*: The axes and main load bearing system*

The 22 columns (C) transfer the vertical load from beams and diagonals to the foundation. The cross-section of the corner columns is 625 mm x 1485 mm. These are the largest elements in the structure. Maximum span for the beams (B) is 6,5 meters and for floor elements 7,1 meters.

The lateral bracing system is quite basic. Four trusses consisting of columns and diagonals (D) are bracing the entire building. There is one truss in each façade and together they give the building the necessary rigidity to handle horizontal deformation and dynamic effects. Focus was placed on keeping the connections as simple as possible. One example is that the diagonals transferring the wind load are connected to separate columns.

Table 1*: Cross-sections of columns, beams, diagonals and walls*

Structure	Width (mm)	Height (mm)
C1	625	1485
C2	625	630
C3 at the bottom C3 at the top	725 625	810 630
C4	625	625
C5	215	625
B1 (wooden floor) B1 (concrete floor)	625 625	439 585
B2 (wooden floor) B2 (concrete floor)	395 625	585 585
B3 (wooden floor) B3 (concrete floor)	395 625	675 720
D1	625	990
D2	625	495
W1	220	-
W2	180	-
W3	160	-
W4	140	-

When designing tall timber buildings, it is important to verify that relevant comfort criteria are met. Timber buildings are light, and horizontal accelerations induced by wind must be carefully considered. For Mjøstårnet this was one of the governing aspects for the design. The structural damping obtained from the Treet building in Bergen was used for Mjøstårnet. The accelerations in the tower were monitored both during installation and after completion. The dynamic design was solved as a combination of structural stiffness and mass distribution. Tuned mass dampers (TMD's) to further reduce accelerations were not required and are not installed in Mjøstårnet. Four years after the opening there have been no reports of people feeling nauseated or uncomfortable.

2.2 Walls

CLT panels are used for secondary load bearing of three elevators and two staircases, but do not contribute to the building's lateral stability. Thicknesses of CLT walls (W) are listed in *Table 1* and the placement is shown in *figure 5*. All the CLT elements are produced by Stora Enso and installed by the local company Woodcon AS.

2.3 Floor elements

Each floor acts as a nearly rigid diaphragm which distributes the horizontal forces into the façade trusses. From levels 2 to 11 wooden floor elements are used. This is a wooden cassette deck adopted from the Swedish glulam manufacturer Moelven Töreboda, and it is called

https://doi.org/10.52202/069179-0547

Trä8. The digit 8 refers to the span of this element which is up to 8 m.
Glulam joists spaced 600 mm make up the main structures in these elements. As top flange a plate of crossbanded veneers (LVL-C) is used, and as bottom flange a board of solid wood is used. By gluing the flanges to the joists, a static composite is achieved with increased bending and stiffness properties. The top flange cantilevers from the edge beam and transfers the vertical load into the supporting glulam beam. In this way the element can be mounted between the glulam beams, and only the thickness of the LVL-C plate is above the beams. This is an efficient way to minimize the structural height. The total height of the floor element is 439 mm.
A local company, RVT, produced the elements for Moelven Limtre.

***Table 2**: Cross-sections of components in the floor element*

Structure	Width (mm)	Height (mm)
Joist	66	360
LVL-C top flange	31	-
C3 at the bottom	148	48

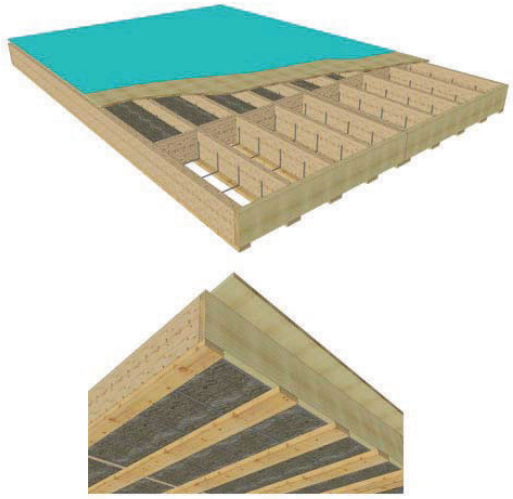

***Figure 6**: Trä8 floor element*

The seven upper floors are 300 mm thick concrete slabs supported by glulam beams. This adds extra weight to the structure which is beneficial for the dynamic behaviour.

2.4 Pergola

The glulam pergola at the very top of the building is not produced with solid rectangular cross-sections. To reduce potential shrinkage cracks on the outer surfaces these glulam parts were produced as hollow sections. The hollow section is composed of four rectangular beams with a width of 90 mm, glued together in each corner. All corners are rounded with a radius of 140 mm to improve aerodynamics.

***Figure 7:** Hollow cross-section in the Pergola*

2.5 Balconies

In the six upper floors, which contain the apartments, balconies are attached to the façade and suspended from the columns with steel bars. CLT panels are used as floor elements. Polyurea coating is used to seal and protect the top of the elements from the weather.

2.6 Connections

Slotted-in steel plates with 12 mm steel dowels are used to transfer the forces between the glulam elements. The distance between the slots is 115 mm and the number of steel plates are two or four. The thickness of the plates is 8 mm or 12 mm. The number and thickness of the steel plates depend on the value of the force transmitted.

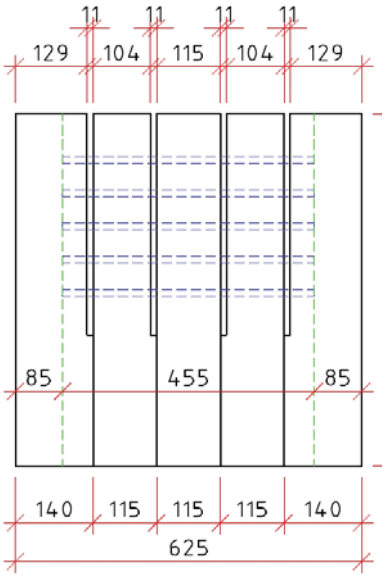

***Figure 8**: Typical cross-section build-up with slotted-in steel plates and dowels.*

Approximately 5000 kN of tension is the highest design force for a connection. It appears in the bottom of each corner when the wind load acts on the longest façade and tries to tilt the building. This requires 4 pcs of 12 mm steel plates and 100 psc of 12 mm steel dowels. All dowels are embedded 85 mm into the wood, which is the same distance as the charring after 120 minutes.

https://doi.org/10.52202/069179-0547

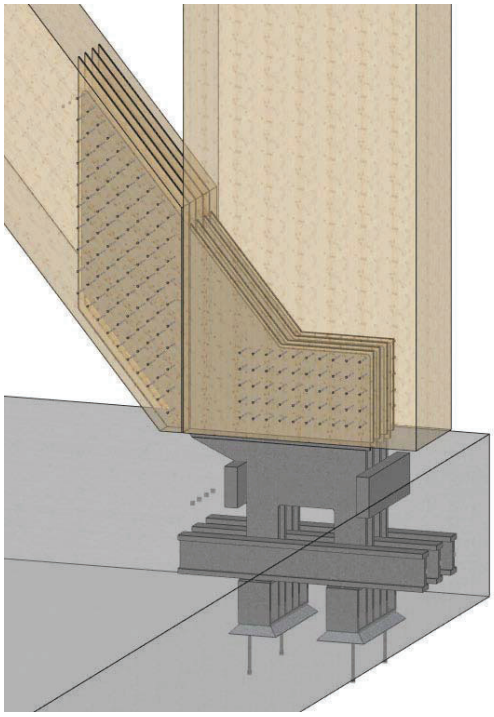

***Figure 9**: Connection at the foundation in each corner.*

3 MATERIALS

A third of the volume of all materials used in the building is wood such as glulam, CLT and solid wood. The percentage of the different materials used to build Mjøstårnet is shown in *Table 3*.

***Table 3**: Volume of materials*

Material	Share %
Wood	34
Insulation	33
Concrete	26
Steel	1
Other materials	6

3.1 The main load bearing

Glulam is used for trusses, beams and columns in the primary load bearing system. For the structural design, glulam strength classes according to EN 14080 [3] are used. Strength class GL30c, combined build-up, is used for all glulam structures accept from the bottom part of the corner columns which is produced as GL30h, homogeneous build-up. Lamellas with strength classes T22 and T15 are used for combined glulam, and only T22 for homogeneous glulam. Spruce is the species used for lamellas.

3.2 Walls

CLT panels is used for elevator shafts and staircases. The strength class of the lamellas is C24 according to EN 338 [4]. Spruce is the species used for these lamellas.

3.3 Floor elements

Timber floor cassettes are used in levels 2-11 and 300 mm thick concrete slabs are used in storeys 12-18. The floor joists are resawn glulam with strength class GL28cs [3]. The characteristic bending strength is 28 MPa and the modulus of elasticity parallel to grain is 12500 MPa. Kerto®-Q panels, produced by Metsä Wood, are used for the top flange and also the edge beam of the elements. Strength class for the bottom flange in solid wood is C24 according to EN 338 [4]. Spruce is the species used for all these components.

3.4 Pergola

GL30c [3] is the strength class used in the pergola structures, and the glulam is Cu-impregnated throughout. Pine is the species used for these lamellas.

3.5 Balconies

CLT is also used as floor elements for the balconies. The strength class of the lamellas used in the panels are C24 according to EN 338 [4]. Spruce is the species used for these lamellas.

3.6 Connections

S355 steel is used in connections together with acid-proof steel dowels with tensile strength f_u=700 MPa.

4 FIRE DESIGN

The fire strategy report for Mjøstårnet states that the main load bearing system must withstand 120 minutes of fire. Secondary load bearing such as floors must withstand 90 minutes. In addition, the structure must withstand a full burnout and prevent a total collapse. This means that after a burnout, the load bearing system will still be in intact and the fire in the structural elements will be put out by itself. The fire design is verified by 90 minutes burnout tests that were performed in 2016 at SP Fire Research AS in Trondheim. The tests prove the fire behaviour of large-scale glulam sections and their connections [5].

***Figure 10**: Burnout test at SP Fire Research AS in Trondheim.*

4.1 Reduction of cross-section

The structural fire design was done by calculating the remaining cross-section after charring according to Eurocode 5 [2]. The charring rate is 0,7 mm/min at every exposed side of the cross-section. This means that 120

https://doi.org/10.52202/069179-0547

minutes of fire gives a charring depth of 84 mm. In addition, a layer of 7 mm with loss of strength must be taken into account. The total reduction of cross-section for every exposed side will be 91 mm for 120 minutes of fire.

4.2 Protection of steel connections

Steel plates and dowels used for connections are embedded deep into the timber. In this way the timber insulates the steel and protects it from fire exposure. All gaps and slots between beams, columns and plates are fitted with an intumescent fire strip. When the heat reaches 150°C this material will start to expand up to twenty times. In this way open gaps and slots will be sealed and the steel inside will be protected. The 90 minutes fire test by SP Fire Research AS [5] proved that the temperature in the steel connections did not reach more than 250°C, which is structurally acceptable.

***Figure 11**: Sealed slots and gaps using intumescent fire strips.*

4.3 Robustness in fire

As for robustness the structure is designed to sustain the loss of the horizontal stiffness of one entire floor. It can also carry the impact load of a timber deck falling down on the floor below.

4.4 Other fire measures

The entire building is sprinklered. In escape stairs, the wall panels are covered with fire gypsum and in all open public areas the wooden surfaces are treated with a fire-retardant paint. The wooden boards used on the façade are heat treated pine, additionally pressure treated with a fire retardant. For every storey in the façade there is also a fire stop device.

5 ASSEMBLY

The assembly of the building was divided into six stages. The main body up to level 18 was built in four steps, were each step comprised four or five storeys. Thereafter came the installation of balconies and in the very end the rooftop pergola.

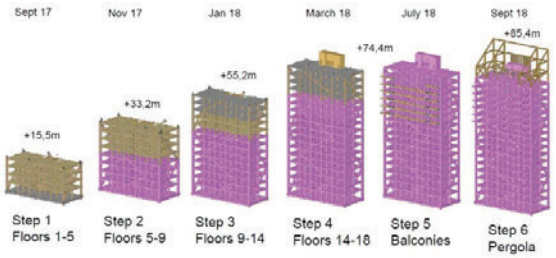

***Figure 12:** Assembly steps*

The first timber element was installed on the 4th of September 2017, and the final beam on the pergola's top was mounted exactly one year later.

***Figure 13:** The last beam installed.*

5.1 Preparation of elements in factory

Every single structural element is processed using Computer Numerical Control (CNC) machines. All cuttings and drillings are done in the factory. It means that the accuracy of the geometry is very high and produced practically with zero tolerances. steel plates were installed into the glulam columns in the factory before being transported to the building site.

***Figure 14**: CNC processing / Block gluing / Installation of steel plates*

5.2 Embedding of base connections

Embedding of the base connections is maybe the most crucial part of the assembly. If the placement of the bases is inaccurate the timber elements will not be possible to assemble correctly, and the geometrical tolerances of the building will be unacceptable. This is particularly important since all the elements arrive the building site precut and predrilled.

https://doi.org/10.52202/069179-0547

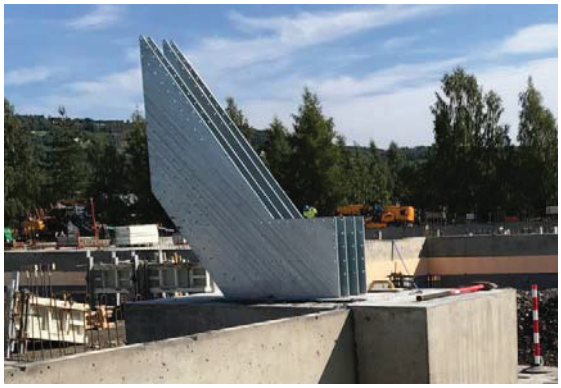

***Figure 15**: Base connection of the corner column and diagonal.*

5.3 Assembly on ground and hoisting of frames

Before the erection started all the glulam structures for the upcoming assembly step were put together into frames on the ground. Then these frames were hoisted into the building and installed. The frame sections were four or five storeys high.

***Figure 16**: Hoisting of frames.*

5.4 Assembly of floor and balcony elements

Both the floor and balcony elements were prefabricated at the factory and hoisted directly on site. There were four lifting hooks on each floor element for lifting the floor elements. A specially designed lifting device was made for the balcony elements. This was done to avoid lifting hooks that potentially would damage the polyurea membrane coating on top of these elements.

***Figure 17**: Hoisting of balconies with tower crane.*

5.5 Assembly in height

The timber skeleton was installed using a tower crane, mobile cranes and lifts. It was not needed to use any kind of scaffolding for the installation of the load bearing structure. The tower crane was operated by the turnkey contractor HENT.

6 CONCLUSIONS

The completed building proves that an 85 meter high glulam building can be built using local competence, local suppliers and local materials. Mjøstårnet is already an iconic landmark in Norway and serves as an inspiration on how to build sustainably in the future. Using the same structural principles, it is possible to double the height.

ACKNOWLEDGEMENTS

The authors would like to thank colleagues and all collaborating parties for their great efforts in this project. Thanks to investor Arthur Buchardt who had the courage, will and opportunity to build Mjøstårnet.

REFERENCES

[1] European Standard
NS-EN 1995-1-1:2004/NA:2010/A1:2013
Eurocode 5: Design of timber structures.
Part 1-1: General. Common rules and rules for buildings.

[2] European Standard
NS-EN 1995:2004/AC:2009/NA:2010
Eurocode 5: Design of timber structures.
Part 1-2: General. Structural fire design.

[3] European Standard
NS-EN 14080:2013/NA:2016
Timber structures
Glued laminated timber and glued solid timber
Requirements.

[4] European Standard
NS-EN 338:2016
Structural timber
Strength classes

[5] P. A. Hansen, SP Fire Research AS: Brannteknisk prøving av limtresøyler basert på NS EN 1363-1, Limtreforeningen v/Moelven Limtre AS, SPFR-rapport 155060-05, Trondheim, Norway, 2016

[6] https://www.ctbuh.org/buildings-of-distinction/mjostarnet

World Conference on Timber Engineering Oslo 2023

THE FIRST MASS TIMBER BUILDING IN BRAZIL

Carlito Calil Neto[1], Alexander Takata[2], Vitor Afonso Neves Silva[3,]

ABSTRACT: The use of new technologies in wood for construction is increasing every year in Brazil. This work aims to demonstrate step by step the entire building system that was used for the construction of the first massive wooden building in Brazil located in one of the main avenues of São Paulo city.

KEYWORDS: First massive timber Brazil, Wood building, Massive Timber, Glued Laminated, Cross Laminated Timber.

1 INTRODUCTION

The mass timber revolution is on the rise, Architects and engineers are working around the world to understand and revolutionize the building industry of how to use wood and create large-scale and sustainable buildings. The move to mass timber is even farther along in North America and Europe. That's because mass timber panels and systems like posts and beams glued under pressure or floor and wall systems nailed together in layers, is not only prized as an innovative building material, superior to steel and concrete in many ways, it is also hoped it will come into its own as a significant part of a climate change solution. In Brazil, this revolution already started with the first mass timber building just have been finished located in the city of São Paulo, Brazil.

Figure 1: *First Timber building in brazil – render*

The four-storey commercial building has a construction system based on the use of CLT (Cross Laminated Timber) panels as floors, walls and slabs. The Glulam (Glued Laminated Timber) panels are used as posts and beams systems. The connections between these elements are made by self-tapping screws developed for this type. application, facilitating and reducing assembly time.

This system has been widely accepted in the European and North American market that besides being able to build single-family residences, it is possible to build multi-floor buildings. Unfortunately, in Brazil this system is not yet as widespread as it could be most of the works are performed in the traditional masonry system with bricks or structured concrete blocks with reinforced concrete columns and beams or steel structures. The choice for the traditional building system is linked to factors such as culture, ease of access to material and especially the wide dissemination of knowledge of the building system that is chosen.

The building owner is DENGO, a Brazilian company that manufacture healthy and sustainable chocolates, and this mass timber building will be a model store for the company. The building has a net area of 1500 m2 and the basement, which holds parking facilities, technical rooms and storage rooms, that has a net area of 564 m2. Rewood is the Brazil's largest glulam manufacturer, and delivers and installs the glulam and CLT. KLH in Austria provides the CLT to Rewood. The architect for the project is the São Paulo based company MFMM. Rewood and Stamade are the responsible for the technical design and design management.

This work aims to demonstrate step by step the entire building system that was used for the construction of the first mass timber building in Brazil located in one of the main avenues of São Paulo.

2 LOCATION

The building site is in an urban and central area of São Paulo, the largest city in Brazil, and is located at Avenida Brigadeiro Faria Lima, one of the main avenues of São Paulo City, see map on Figure 2.

[1] Carlito Calil Neto, Rewood – structural timber solutions, Brazil, calil@rewood.com.br
[2] Alexander Takata, Rewood – structural timber solutions, Brazil, alex@rewood.com.br
[3] Vitor Afonso Neves Silva– structural timber solutions, Brazil, vitor.eng@rewood.com.br

https://doi.org/10.52202/069179-0548

Figure 2: *First wood building in Brazil - outside view*

Figure 2.1: *First wood building in Brazil - outside view*

Brazil has a deficit of 6 million housing units to attend its population, with the projection of a 20 million deficit by 2024. This represents a need for investment of around R$ 76 billion annually to solve the problem. The challenge of sheltering these people clashes with the pressing challenge in addressing in a proper way climate change and the need to reduce greenhouse gas emissions in the recent commitments assumed by the country under its NDC – National determined contributions. Such as many other places around the world, the dominant construction system in Brazilian larger cities is based on two materials: steel and concrete, which are materials thar have been widely used in last century, whose production is based on enormous energy consumption and low concern about GHG emissions.

There are estimates that show that only the production of these two materials accounts for 8% of all humanity's GHG emissions. Also, based on these materials, the construction industry accounts for 47% of the total emissions, the transport sector, 33%, and the primary industry, 19%. Thus, meeting this growing demand for housing, while combating the effects of GHG emissions on climate change, is the challenge posed.

3 WOOD IS THE SOLUTION

Among architects, manufacturers, and environmentalists, many want nothing less than to turn the coming decades of global construction from a giant source of carbon emissions into a giant carbon sink by replacing concrete and steel construction with mass timber. It will avoid the CO2 generated in the production of those building materials and sequester massive amounts of carbon by tying up the wood in buildings.

Wood is the only renewable building material that has grown with sunlight and uses atmospheric CO2 to develop. However, this potential for the use of wood as a smart alternative for GHG emission in the construction industry generally meets the Brazilian tradition in processing timber in the way of keeping the focus on the production of solid high density wood, which has its charm and usefulness. However, to shift the general logic of using wood in the construction industry to upscale its reach and competitiveness for the housing sector it is needed to develop a new industry and a new market for highly processed wood products, such as wood-frame panels or laminated wood panels.

Glulam and or CLT are industrialized products and like any industrialized product the value of its cubic meter is increasingly taken into account the more it is produced. Increasingly wood technology has been well received in the Brazilian market and the engineered wood product has gained shape and knowledge.

The Brazilian market needs to understand that we need a fast and sustainable solution for the next generations and that is why our company Rewood worked hard to build the first timber building in Brazil and to show that it is possible to build large structures with the engineered wood product.

4 STRUCTURAL TIMBER SYSTEM

The main material of the building is wood. Wood is flexible to apply a huge range of building types and applications (structural and aesthetic) and renewable. In addition, engineered wood is innovative, adaptable, and efficient for the uses in construction, therefore, the architects tried to bring out those strengths in design and construction.

https://doi.org/10.52202/069179-0548

The Building has a strong and geometric shape with modern design. The first floor has an opened (wide) rectangular shape and also other floors have rectangular medium spaces. The design objective of the DENGO is to maximize the use of wood in the structural and non-structural application rather than any other material.

The main structural system is made of glued laminated timber (glulam) post and beam grid structure with cross-laminated timber panels (CLT). The CLT is used as slab on glulam beams and glulam columns. The Columns are typically on a 5,4m x 5,4m grid, supporting the CLT floor assemblies. The columns were manufactured continuous with 10 meters length over the three floors with a typical cross-section dimension is 270x270 mm.

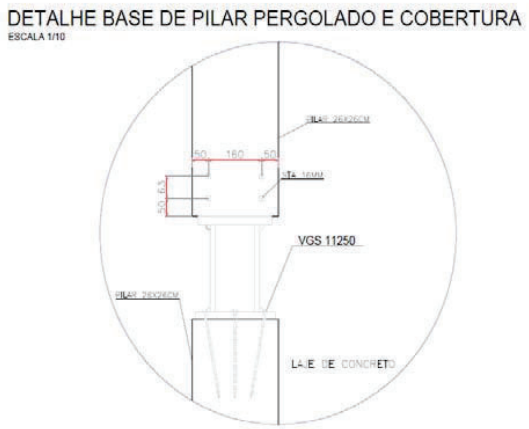

Figure 3: *Connection columns to column*

The 270x320 mm cross-section beams were framed into the column faces using a customized steel connector. The glulam elements are connected by steel plates and dowels. This is a commonly connection used in orther timber structures. Typically, 6 mm steel plates manufactured in Brazil and 12 mm dowels are imported from Rothoblaas in Italy. All the connections were recessed and encapsulated by the surrounding wood material, and is therefore inherently fire resistant.

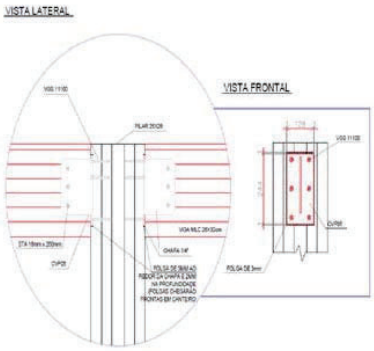

Figure 4: *Detail of connection Columns / Beams steel plate.*

The structural timber is with few exceptions covered behind either glass or metal sheeting. This protects the timber from rain and sun, increases durability and reduces maintenance.

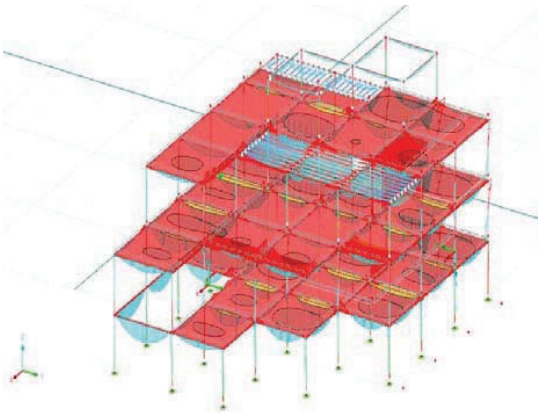

Figure 5: *Global RFEM-model of DENGO*

5 STRUCTURAL FIRE DESIGN

The current Brazilian codes and standards do not adequately address or provide engineering guidance for modern mass timber structures. Base on that, to made the building system we commonly adopt design methods and requirements from regions with well-established mass timber industries, such as those in Europe Eurocode-5.

For a building of this size, Brazilian standards require a 60 min fire-resistance rating on the primary structural frame. This rating is achieved through the charring effect of wood, which provides thermal protection of the competent wood below the char layer. The structural fire design is also performed according to the Eurocode 5. The so-called reduced cross-section method has been used, which determines the effective residual cross-section after charring, A notional charring rate of 38 mm/hr leads to a charring depth of 38 mm after 60 minutes.

Steel connectors are typically designed to rely on wood cover as their protection against fire. A similar concept is used to evaluate the required wood cover thickness to achieve a fire-resistance rating on a steel connector, they are not able to be protected with an adequate wood cover, care must be taken to provide some other means of fire protection. In the typical cases of column base plates and column- to-column connections, the steel is typically protected with a grouted pedestal or by painting the exposed steel surfaces with intumescent paint.

https://doi.org/10.52202/069179-0548

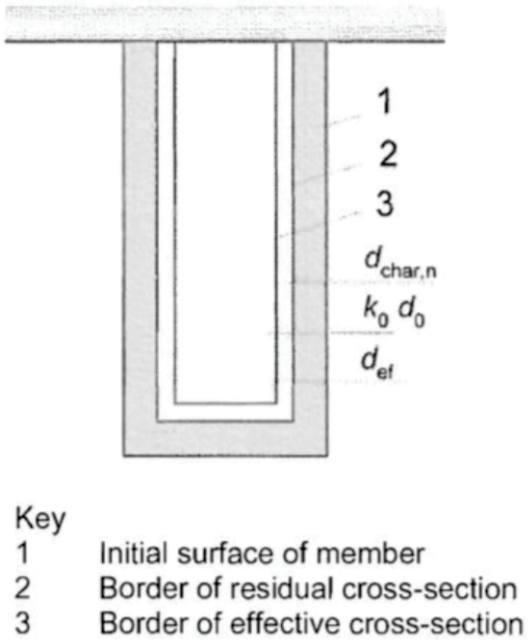

Figure 6: *Definition of residual cross-section and effective cross-section*

6 MATERIALS

All load-bearing structures in the building are wooden. Glulam is used for the columns and beams. Cross-laminated timber (CLT) panels are used for floor/ceiling and internal walls as the wood-frame system.

In the structural model, the properties stated for glulam strength classes GL24h are used. The CLT specifications have bending strength fmk=24 MPa, and properties similar to C24 structural timber. The totally of the glulam is made out Pine of Brazil. Glulam that can be exposed to weathering is made of copper-treated lamellas from Nordic Pine. Structural timber in the building modules and CLT is produced one side from Spruce and the other side is Pine of Brazil.

7 LOADING

The Eurocodes with national annexes for Norway were used to determine the design loads. The wind loading turned out to be the dominating load in the design combinations. The calculated maximum wind speed became V = 45.0 m/s, giving corresponding wind pressure of q = 0,90 kN/m2. The wind load was applied as a transient static load on two sides of the building. The wind load directions considered were 0° e 90°.

Self-weight is set to 5,5 kN/m3 for glulam and CLT, and 25 kN/m3 for the concrete topping. The following loads were applied:

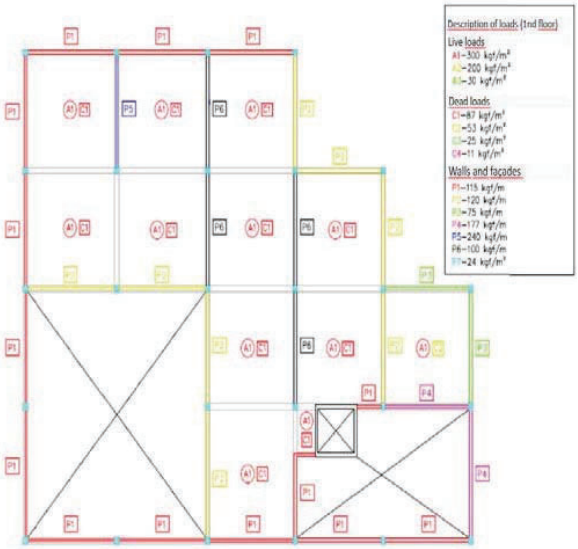

Figure 7: *First floor Loadings*

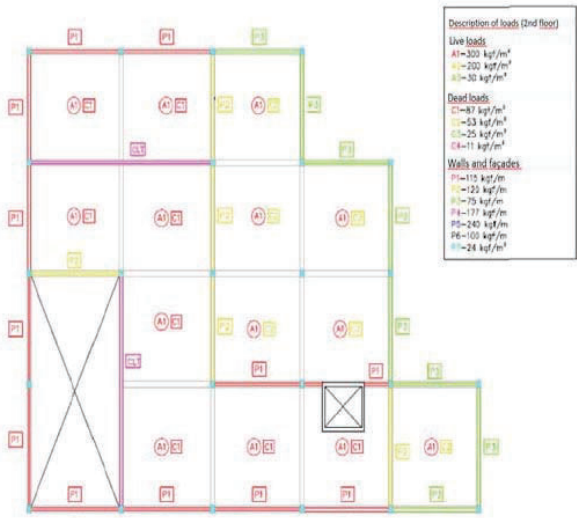

Figure 8: *Second floor Loadings*

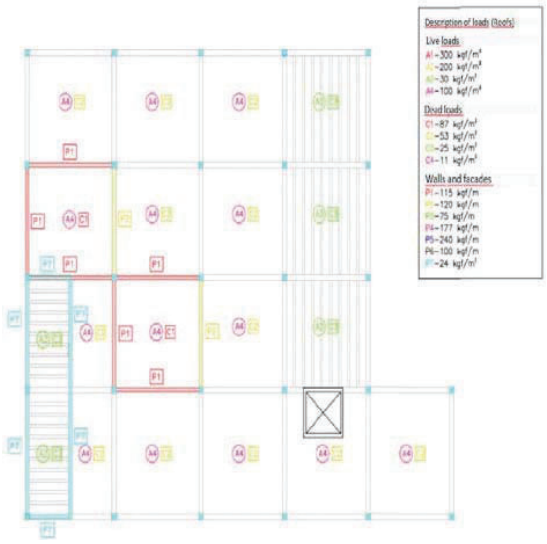

Figure 9: *Third floor Loadings*

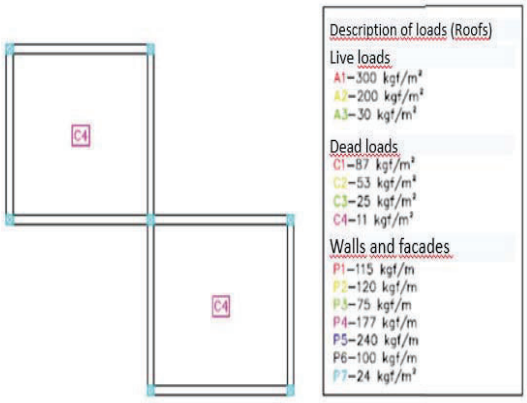

Figure 10: *Roof floor Loadings*

8 ASSEMBLY

The assembly of the building is mostly about installation of prefabricated elements on site. Optimizing the logistics and installation procedures are important to get a smooth building process. Rewood and Pedra Forte use a tower crane as well as a climbing scaffolding system during the building erection.

A step-by-step model ensures that the building can be built correctly. Below is a simplified visualization of the assembly.

The main structure was assembly with 37 days of work. At the moment of this study, the building is already finished September 2020.

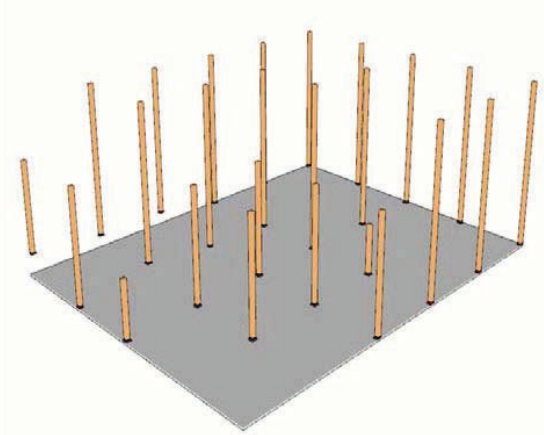

Figure 11: *Step 1*

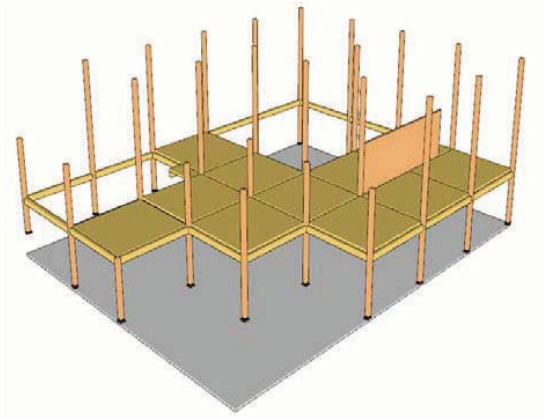

Figure 12: *Step 2*

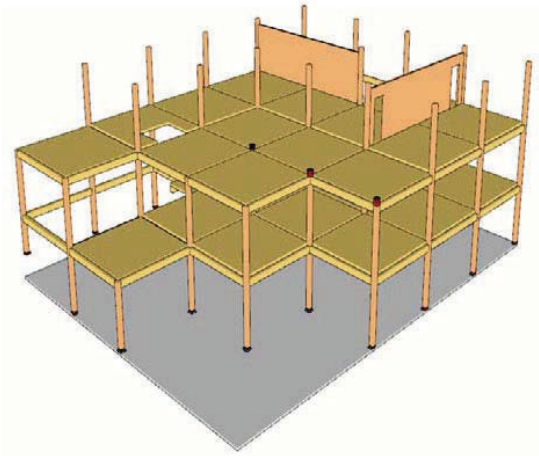

Figure 13: *Step 3.*

https://doi.org/10.52202/069179-0548

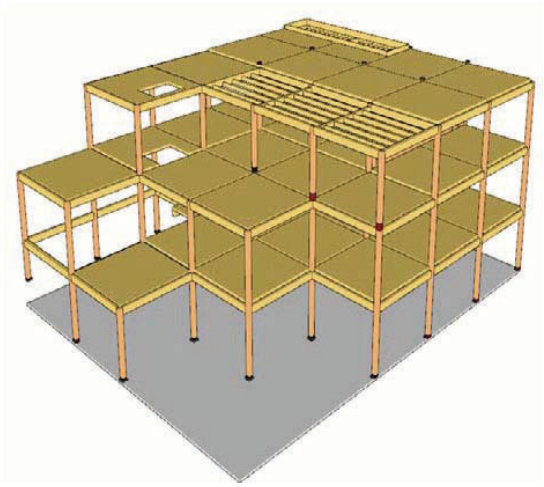

Figure 14: *Step 4.*

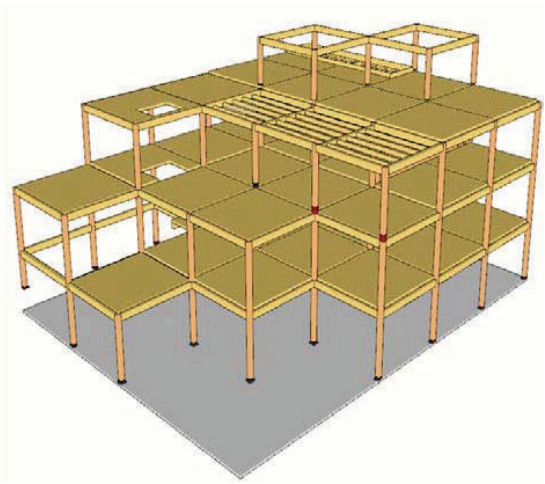

Figure 15: *Step 5.*

Figure 16: *First wood building in Brazil – outside view*

Figure 17: *First wood building in Brazil - outside view*

Figure 18: *First wood building in Brazil – under construction.*

Figure 19: *Completed buildng.*

9 CONCLUSIONS

We can conclude that the use of wood for building structures has high potential in the Brazilian market because besides presenting a fast and clean solution it provides volume in the production of engineered wood products. Consequently lowers the value of the product thus allowing a greater opportunity of competitiveness with other materials - it is a renewable and sustainable solution.

10 ACKNOWLEDGEMENT

The dedication of many researchers, engineers and architects is allowing for the refining of traditional techniques, the adoption of new technology and the deployment in the country of an industry focused on the construction in wood.

REFERENCES

[1] Carlito Calil Junior, Francisco Rocco and Antonio Dias: Dimensionamento de Elementos Estruturais de Madeira. Manole, Barueri, 2003.

[2] Marcos Cesar de Moraes Pereira: Metodologia para estudo da caracterização estrutural de painéis de Madeira Laminada Colada Cruzada. São Carlos, São Paulo, 2014.

https://doi.org/10.52202/069179-0548

World Conference on Timber Engineering Oslo 2023

SPOR X – 10-STOREY TIMBER OFFICE BUILDING, DRAMMEN, NORWAY

Katie Overton[1], Gaute Mo[2], Ivana Katavic[3], Manuel Sánchez-Solís[4]

ABSTRACT: SporX is a ten-storey office building in Drammen, Norway. Timber, as the main structural material, was chosen at the start of the project being a readily available local material and to support the ambition for maximum sustainability to achieve a BREAM-NOR Outstanding certification. Another advantage was to minimise building loads at the riverside location with poor ground conditions. Based on an optimal architectural layout SporX makes use of timber elements, both glued-laminated and cross-laminated, for all load-bearing structure above ground floor. Two large central CLT cores, combined with two façade shear walls, act as bracing elements for the 600m^2 floor plate giving a robust timber structural solution designed for R90 fire resistance. The element removal method is used to resist progressive collapse. Timber connections are made using fully threaded, cylindrically headed, wood screws and proprietary concealed connectors. BIM was used by all disciplines for design coordination and to produce a digital twin controlled throughout the construction process. Timber structural elements were fabricated from a LOD400 BIM model developed by Degree of Freedom. Fabrication with strict tolerances allowed for a rapid construction process. Larger element sizes were chosen as having design advantages both for robustness and for connections design.

KEYWORDS: Timber, CLT, cross-laminated, fire, connections, BIM, fabrication, LOD, BREAM_NOR, digital twin

1 INTRODUCTION

Degree of Freedom were responsible for the structural design of SporX, an innovative, ten-storey, timber-framed office building, built on behalf of the property developer Vestaksen Eiendom AS.

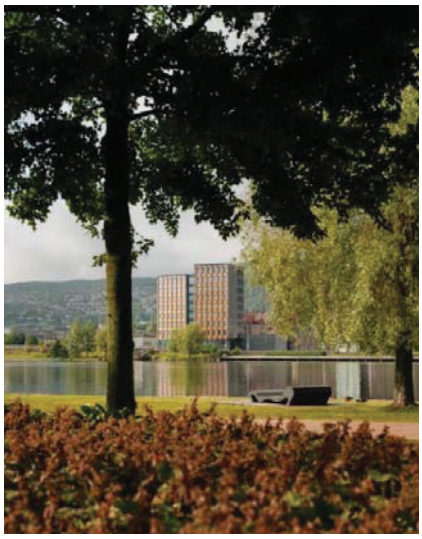

Figure 1: *SporX - Location*

The building, in Drammen, Norway, is adjacent to both the river and the main train station, and was conceived by the architects, Dark, to become the most sustainable office building in the Nordic countries. The use of structural timber as a low-carbon construction material was therefore a fundamental part of the project from the start. This paper describes the advantages of using timber compared to more standard solutions in concrete or steel, for all the main load bearing elements above ground level. Key aspects and challenges related to the design, modelling, fabrication, and construction process are explained. There is a focus on design aspects where special attention was needed including fire design, connection details, horizontal sway, vibrations and progressive collapse.

2 DESIGN PRINCIPLES

2.1 ARCHITECTURAL CONCEPT

The architectural intent was for a sustainable office building and as the building's location has excellent links to public transport only the provision of bicycle parking was needed. Features such as this, combined with the use of timber as the main structural material were key to achieving the BREEAM-NOR Outstanding certification. Harvested responsibly, and in this case locally, timber is arguably one of the best tools both architects and engineers have for reducing greenhouse gas emissions and storing carbon in buildings. Timber, as a construction

[1] Katie Overton, Degree of Freedom SLU, Valencia, Spain, k.overton@dofengineers.com
[2] Gaute Mo, Degree of Freedom AS, Oslo, Norway, g.mo@dofengineers.com
[3] Ivana Katavic, Degree of Freedom AS, Oslo, Norway, i.katavic@dofengineers.com
[4] Manuel Sánchez-Solís, Degree of Freedom SLU, Valencia, Spain, m.sanchez@dofengineers.com

https://doi.org/10.52202/069179-0549

material also has inherent benefits for the health and well-being of the building users, for the environment and for the construction process. Advantages include reducing CO2 emissions and construction time whilst maintaining a competitive overall cost.
Architecturally an aesthetically pleasing interior design can be achieved taking advantage of the exposed structure as seen in Figure 2.

Figure 2: *Interior with exposed timber*

The building is divided into nine-storey and ten-storey parts with a two-storey lateral extension, as shown in the architectural section below, and provides approximately 6800m^2 of office space.

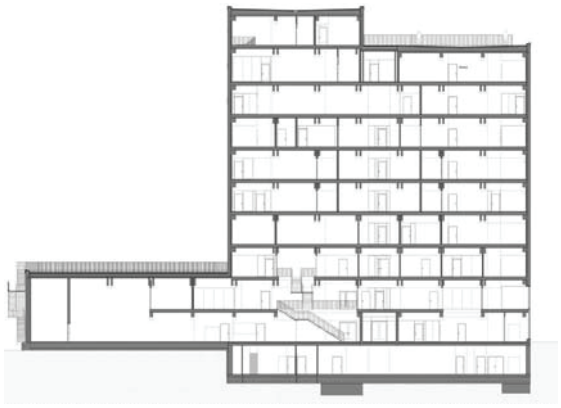

Figure 3: *Architectural section*

2.2 STRUCTURAL CONCEPT

Below the main building is a single storey reinforced concrete basement founded on steel HP piles to bedrock at a depth of approximately 100m. The use of timber was shown to give a 50% cost saving for the foundation design due to the reduced overall building loads.
The architectural requirement for two large cores servicing a relatively small floor plan allowed the original concrete core walls as planned at concept design phase to be substituted by cross laminated timber shear walls. Additional CLT shear walls were introduced on the two side façades to increase the stiffness in the weaker direction. Figure 4 shows a typical floor plan highlighting the location of the shear walls. Glulam timber "columns" are used to reinforce both the corners of the cores and the ends of the shear walls.

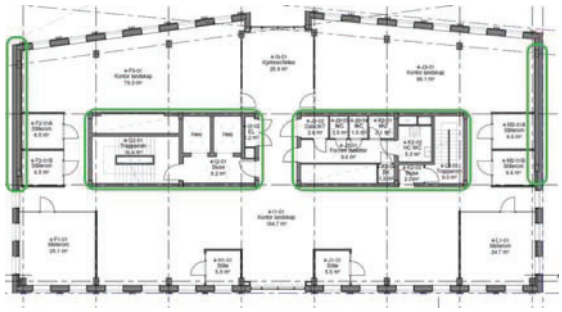

Figure 4: *Architectural floor plan showing shear wall location*

The structural grid is 4.85m with vertical loads transferred via CLT floor slabs to a system of double glulam beams and columns as can be seen during construction in Figure 5. The CLT floor slabs act as diaphragms for the transfer of horizontal actions to the shear walls. At ground level all loads, both horizontal and vertical are transferred to the concrete substructure. This load transfer is one of the key details in timber building design.

Figure 5*: SporX under construction showing the exposed structural frame*

https://doi.org/10.52202/069179-0549

2.3 MATERIALS

2.3.1 Glued laminated timber

GL30c glulam was used for both columns and beams based on standard Nordic production dimensions. Column sizes are typically 355mm by 450mm. In addition, 280mm by 450mm GL30c columns were used to reinforce the ends of the CLT shear walls and facilitate the connection between the timber superstructure and concrete substructure.

Variable depth beams, 190mm wide were adopted to suit both the architectural concept and the integration of openings for services as can be seen in Figure 6.

For the structural design only the beam section over the large openings is considered for calculations, however the timber section adjacent to the holes is reinforced with screws to control possible cracking.

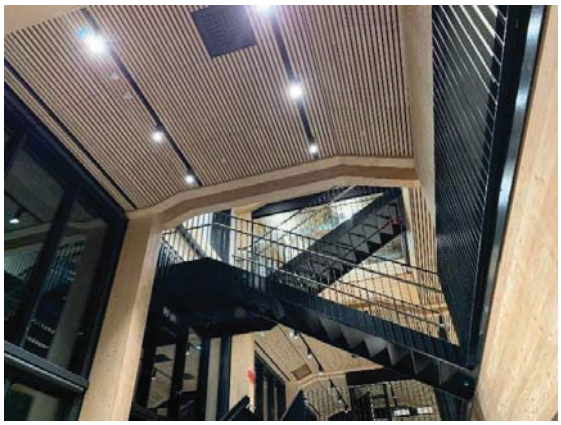

Figure 6: *Double glulam beam & glulam column*

Figure 7: *Opening for services through glulam beam*

2.3.2 Cross laminated timber

Floor slabs are 180mm five-layer cross-laminated timber. Main shear walls are 260mm seven-layer CLT, as shown in Figure 8, with 220mm secondary walls in seven-layer CLT.

Figure 8: *CLT layers in shear walls*

2.3.3 Connectors

The connections between timber elements are by using fully threaded, cylindrically headed timber screws, or by either proprietary or bespoke timber connectors.

2.3.4 Quantities

A summary of the total structural building materials above ground incorporated in the finished building is shown in Table 1.

Table 1: *Material quantities*

Material	Quantity
GL30c glulam	520m3
180(5s) CLT slabs	940m3
260/220(7s) CLT walls	950m3
Timber screws	≈64,000no.
Proprietary brackets	≈64,000no.
Timber nails	≈64,000no.
Steel plates	2,650kg

3 STRUCTURAL DESIGN

3.1 GENERAL

The building is designed in accordance with the relevant Eurocodes to the Norwegian National Annexes [1][2].

No requirement for seismic verifications was established early in the design process by confirming a seismic ground acceleration of 0.2596m/s^2 with NORSAR. The subsequent publication of the 2021 version of the Norwegian National Annex [3] confirmed a value of a_{gR} = 0.25m/s^2 for Drammen Kommune.

For consideration of progressive collapse, the building is classified as consequence class 2b (upper risk group)[4] for an office building less than 15 storeys. The structure allows for the notional removal of columns and beams. Double-storey height columns, triple-storey height CLT walls, continuous façade beams and triple-span CLT floor slabs enhance the structural redundancy and result in a robust overall design. This also minimises the number of connections.

https://doi.org/10.52202/069179-0549

Sway imperfections, based on ϕ equal to 0.005 radians are accounted for by applying Equivalent Horizontal Forces to the structure at each level.

3.2 SERVICEABILITY LIMIT STATE

Timber structures are commonly governed by the Serviceability Limit State, both by vertical and horizontal deflections and vibrations. The design of the 180mm thick CLT floor slabs, spanning 4.85m, was governed by deflection and vibration criteria.

The inclusion of the slip modulus (k_{serv}) for all timber connections was critical for evaluating the overall sway of the structure under horizontal loads. This was particularly relevant for the joints between the panels that formed the CLT shear walls and for the connections between CLT walls and concrete substructure.

The lateral stiffness of the structure is also relevant to checking the effects of the deformed frame geometry and whether a second order linear analysis is needed although EC5 does not give an explicit limit unlike the concrete and steel codes.

3.3 FIRE DESIGN

Well defined and predicable fire behaviour is an intrinsic property of mass timber elements. All the principal structural elements are designed to guarantee a load bearing resistance for 90 minutes in the fire design situation, R90. Generally the structural timber elements are partially or completely exposed to fire as can be seen in Figure 9.

Figure 9: *Timber structure exposed to fire*

Columns have been designed as exposed on all four sides, double beams exposed to fire on one side and all CLT floor slabs exposed to fire on one side only. The CLT shear walls in the cores are designed for fire exposure on both sides, although with a reduced fire duration on the second side based on the separation into fire cells with R60 fire doors.

Timber columns and beams have been designed using the reduced cross section method from NS-EN 1995-1-2 [2]. This method defines a charring depth of 70mm for R90. This char layer insulates the core of the section preventing it heating up. The reduced section maintains its full strength and is verified for the critical fire load combination. In some locations particular elements are considered as redundant in the fire design situation. An example of this is the timber diagonal bracing element in the façade shear wall seen below in the Architectural model.

Figure 10: *Architectural model showing timber diagonal bracing*

Timber-to-timber connections were also verified for R90 fire resistance. Generally this was achieved by providing the calculated depth of timber cover to the concealed connections.

3.4 FINITE ELEMENT MODELLING

A finite element model in SAP2000 of the complete timber structure was used for the verification of both the mass timber elements and for the connections. This model enabled aspects related to the structural design to be considered including:

- Timber as an orthotropic material.

https://doi.org/10.52202/069179-0549

- Orthotropic panel build-up for CLT.
- Connections slip modulus, k_{serv}.
- Nonlinearity.
- Imperfections.
- Fire design situation.

Glulam elements, both beams and columns, were modelled using the frame element of the software. CLT panels, both slabs and walls were modelled using the thick shell element which combines both membrane and plate degrees of freedom.

Timber is an orthotropic material thus modifications of the elastic parameters need to be carried out for both frame and shell elements. To correctly model the shear deformation of the timber frame elements a reduction factor is required for the shear stiffness. For the orthotropic CLT panels, modelled as shell elements, the values for the stiffness matrix were calculated using the software CLT designer created by the Institute for Timber Engineering and Wood Technology of Graz University of Technology (©holz.bau forschungs gmbh).

For the connections between different timber parts links were used with the stiffness for each degree of freedom defined according to the calculated slip modulus for the connection type. For vertical loads, a high stiffness value is defined to ensure that the loads are transferred as expected. Non-linear links were used to model connections in the core walls that are very stiff for compression loads but have a reduced stiffness, or no capacity for the transfer of tension loads.

The concrete substructure is not included in the timber FE model, as shown in Figure 11 and at the base of each column or CLT panel links were used to model the actual connection stiffness and behaviour at the timber-concrete interface.

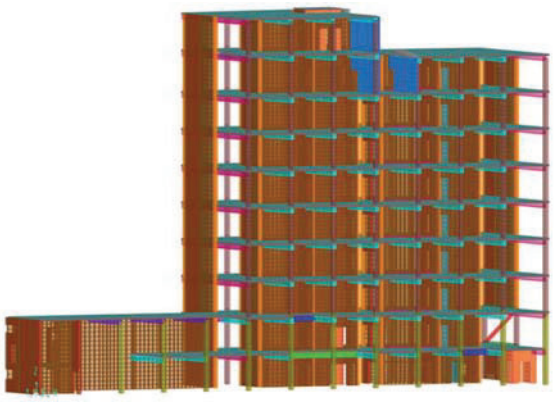

Figure 11: *3D view of FE model*

Degree of Freedom have developed a design tool, compatible with SAP2000, Timber Interactive Modelling and Post-Processing Software (TIMPS) for the purpose of the analysis, design and optimization of timber structures based on the relevant design codes and technical approvals. This tool can provide visual plots of the results for both CLT panel and connection verifications. Selected images are shown below in Figure 12 with the results of both the in-plane shear check and the combined axial load, bending check for a section of the 260mm CLT shear wall.

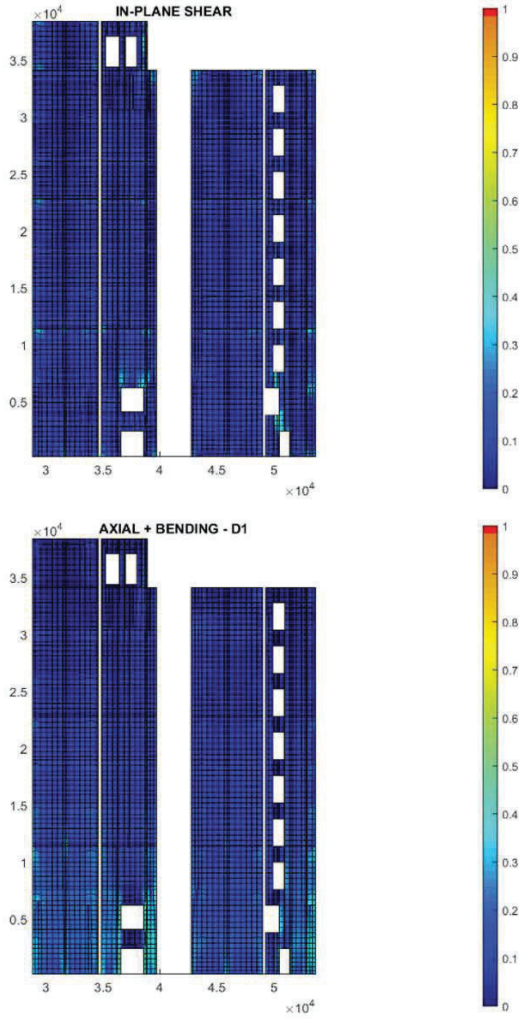

Figure 12: *TIMPS output for CLT verification*

Similarly output for the connections between CLT panels can be plotted. Figure 13 shows the plot for vertical shear forces, an envelope for all ULS load combinations, at the connection between the CLT panel and the glulam column at the corner of the cores.

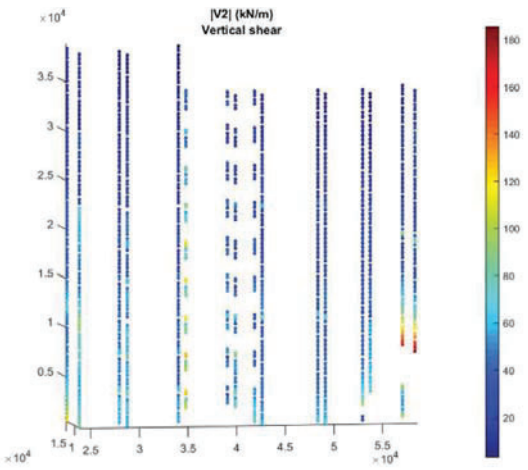

Figure 13: *TIMPS output for connection forces*

3.5 CONNECTIONS

3.5.1 Timber-to-concrete connections

At the base of the CLT shear walls a combination of proprietary steel angle brackets and plates are used to transfer horizontal shear forces to the concrete substructure as seen in Figure 14 and Figure 15.

At the corners of the CLT cores and at the ends of the CLT shear walls a bespoke steel column shoe was designed. This needed to be hidden within the depth of the floor finishes and can be seen in both Figure 14, before floor finishes were installed, and in the construction detail in Figure 16.

Figure 14: *Timber to concrete connection – CLT panel and glulam column*

Figure 15: *Proprietary timber to concrete connector plate*

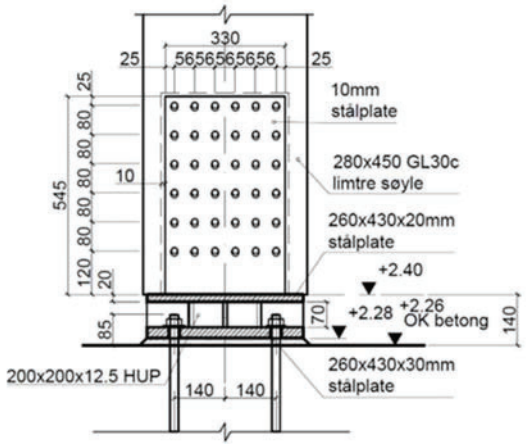

Figure 16: *Construction detail – column shoe*

Careful detailing was required for all timber to concrete connections to allow for different construction tolerances and because of the limited architectural finishes to conceal connections as can be seen in the finished building in

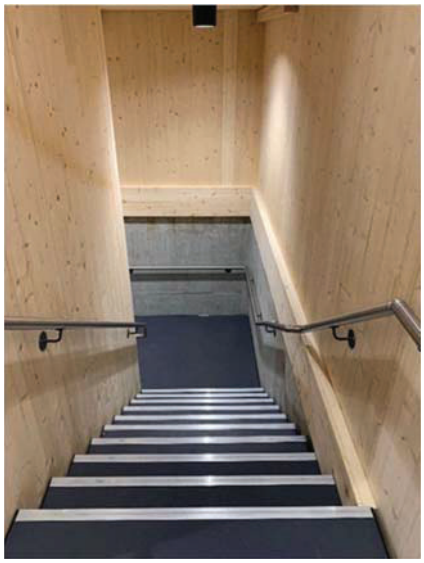

Figure 17: *Timber- concrete interface in finished building*

3.5.1 Timber-to-timber connections

Principal timber-to-timber connections include the double beam to column connections which uses fully threaded timber screws at 45°, WT-T ø8.2x300mm screws from SFS intec. This resulted in a concealed connection with a good load carrying capacity. To facilitate erection the columns are notched to allow for temporary support. The construction detail is shown in Figure 18. Images from both during construction and in the finished building show how timber plugs were used both for aesthetic reasons and to protect the timber screws for the R90 fire design situation.

https://doi.org/10.52202/069179-0549

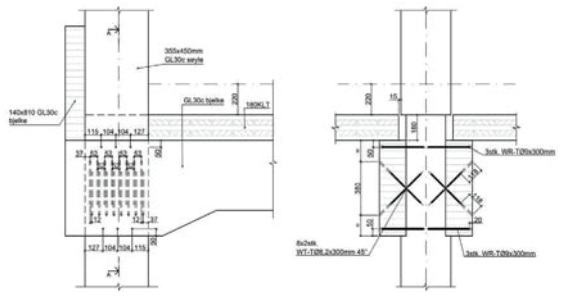

Figure 18: *Timber double beam to column connection*

Figure 19: *Timber beam to column connection – without timber plugs*

Figure 20: *Timber beam to column connection – finished detail*

For timber beam to CLT wall connections both the LOCKT and ALUMAXI concealed connectors from the supplier Rothoblaas were used. This combination of proprietary connector at one end of the beam and screwed connection at the other allowed for erection tolerances.
Between CLT slabs and the CLT core walls proprietary steel angle brackets were detailed to transfer horizontal forces due to wind loads from slab diaphragm to shear walls. Figure 21 shows the typical distribution of angle brackets.

Figure 21: *Steel brackets at CLT slab to CLT shear wall interface*

The connection between CLT panels make use of fully threaded timber screws installed at 45°.

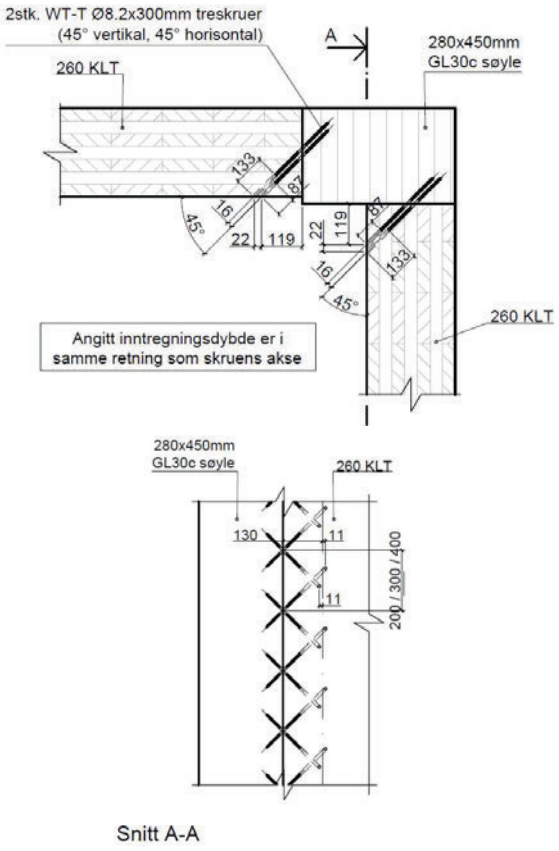

Figure 22: *Timber screws at CLT shear wall to glulam column connection wall interface*

4 BUILDING INFORMATION MODELLING

The project used the most up to date BIM methods during both design and construction. A digital twin was also created and during construction a weekly scan was used to control non-conformances by comparison with the digital twin.

BIM models were developed by all disciplines and coordinated during the design phase. This resulted in a fully integrated LOD350 model at the end of the design phase.

This timber structural model was then advanced to a LOD400 fabrication model on behalf of the contractor. Figure 23 shows the LOD400 timber model as used by the timber supplier for production.

Erection drawings were then produced directly from the BIM model using the software Cadworks.

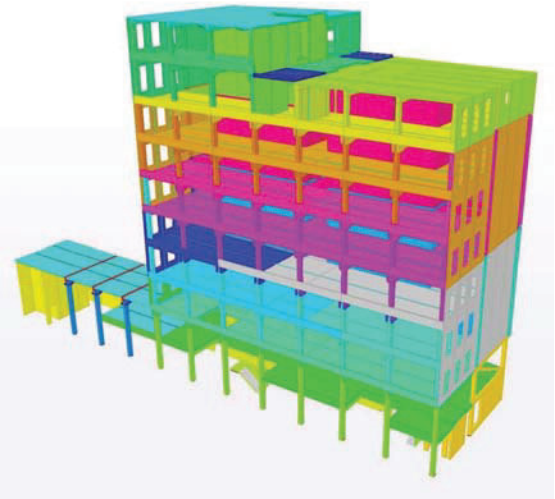

Figure 23: *LOD400 timber production model*

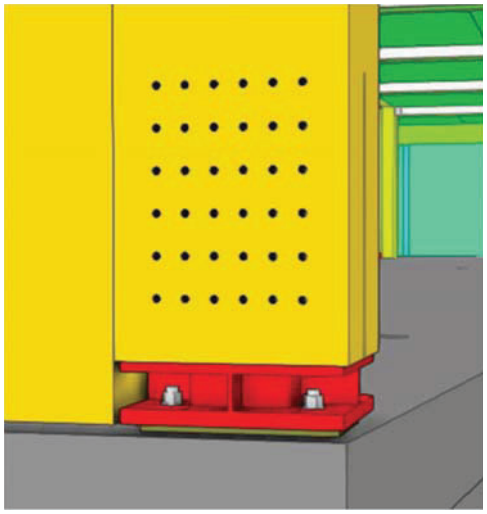

Figure 24: *LOD400 timber production model – connection detail*

Erection drawings were then produced directly from the BIM model using the software Cadworks. An example of the drawings for the 260mm CLT panels that form one of the cores can be seen in Figure 25.

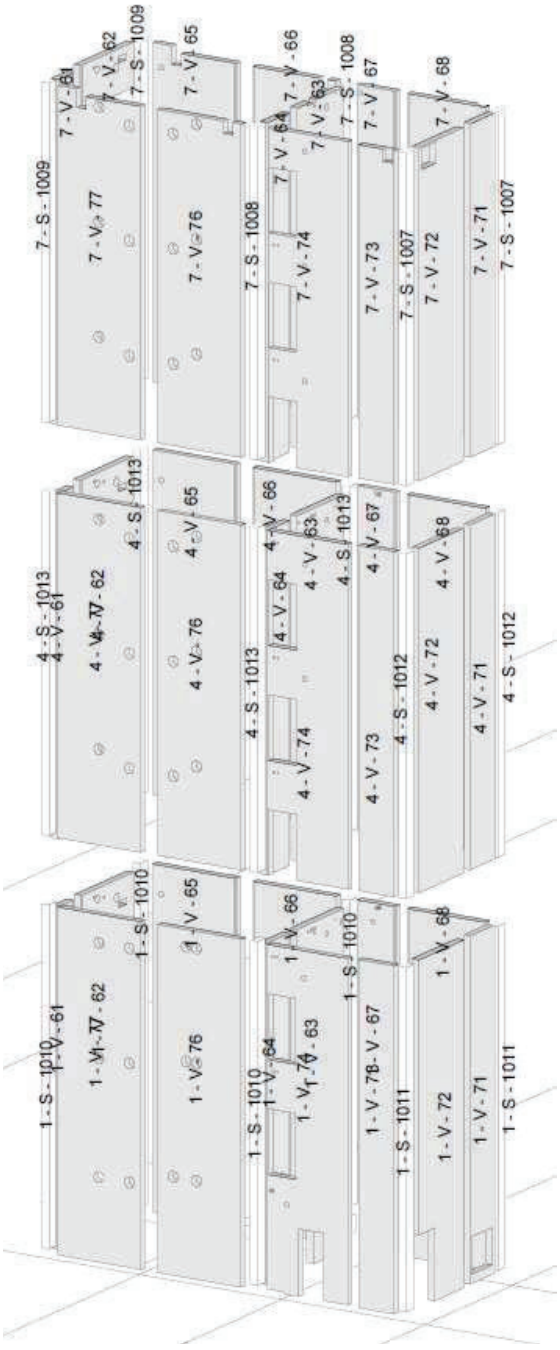

Figure 25: *Timber erection drawing for CLT core*

https://doi.org/10.52202/069179-0549

5 CONSTRUCTION PROCESS

The timber frame was erected over a period of 15 weeks in early 2021 and the building completed in 2022. A key feature of timber construction is the rapid work on site due to the precision of the prefabricated elements. Figure 26 and Figure 27 show the progression of the timber erection from start to finish.

Figure 26: *Start of timber erection*

Figure 27: *Completion of timber erection*

6 CONCLUSIONS

The design of SporX uses a traditional building material, timber, as the load bearing structure for a ten-storey office building. It takes advantage of BIM modelling for the timber elements that can then be prefabricated with strict tolerances for a rapid construction process. The result is an innovative building that makes the best use of a traditional building material with the most up to date construction aids with the use of BIM and precision fabrication.

The result of the architectural and engineering vision of this project can be seen in the images below of the building in its final stages of fit out.

Figure 28: *SporX – finished interior*

Figure 29: *SporX – finished building*

ACKNOWLEDGEMENT

The realisation of this project is thanks to a dedicated design team including the architects, DARK Arkitekter (https://darkarkitekter.no/) The completion of the project has been in collaboration with the main contractor, Betonmast (https://www.betonmast.no/) and the timber fabricator, Splitkon (https://splitkon.no/).

Additional photos by Zinc/Thomas Mellbye

REFERENCES

[1] NS-EN 1995-1-1:2004+A1:2008+NA:2010 Eurocode 5: Design of timber structures - Part 1-1: General - Common rules and rules for buildings.

[2] NS-EN 1995-1-2:2004+NA:2010 Eurocode 5: Design of timber structures - Part 1-2: General - Structural fire design.
[3] NS-EN 1998-1:2004+A1:2013+NA:2021 Eurocode 8 - Design of structures for earthquake resistance - Part 1: General rules, seismic actions and rules for buildings.
[4] NS-EN 1991-1-7:2006+NA:2008 Eurocode 1: Actions on structures - Part 1-7: General actions - Accidental actions

https://doi.org/10.52202/069179-0549

World Conference on Timber Engineering Oslo 2023

Case Study in the Next Generation of Point-Supported CLT Structures

Jamie Pobre Sullivan[1], Carla Dickof[2],Christian Slotboom[3]

ABSTRACT: The new Tall Timber Student Housing tower in Burnaby, British Columbia at the British Columbia Institute of Technology (BCIT) represents a shift forward in tall, hybrid, encapsulated mass timber construction (EMTC). The tower comprises of flat, two-way spanning cross-laminated timber (CLT) floor plates, point-supported on hollow structural steel columns. The structure is encapsulated per the 2018 British Columbia Building Code and uses the latest advances in engineered wood products, prefabrication, and encapsulation strategies for fire resistance. The following case study provides an overview for the next generation of point-supported CLT structures, as encapsulated tall timber buildings, highlighting design challenges and their solutions.

KEYWORDS: Tall Wood Buildings, Mass Timber Encapsulation, Mass Timber, CLT, Point-supported CLT

1 INTRODUCTION

Until recently, timber construction was restricted in height due to limitations in stability and in fire resistance. However, recent advancements in engineered wood products, prefabrication, construction approaches, and codified encapsulation have led to a shift in these restrictions. These advancements include lessons learned in mitigating wood moisture during construction and shipping, and the prevalence of larger high-frequency presses that allow fabrication of wide-format cross laminated timber (CLT) panels beyond the traditional 3.0-metre (10'-0") width. As a result, delivery of mass timber projects has significantly improved. Better understanding of fire resistance in mass timber with use of encapsulation measures, alongside demonstration in precedent projects, has catalysed the use of mass timber in increasingly taller, EMTC-compliant hybrid buildings.

The TallWood House at the University of British Columbia in Vancouver, BC set the precedent for tall timber buildings. With 17 mass timber levels over 1 level of concrete podium above grade, TallWood House achieved a cost competitive alternative to the common concrete student residential tower. The mass timber superstructure comprised of two-way spanning CLT panels supported by glulam timber (GLT) columns; a point-supported CLT system. This flat slab system uses no beams, allowing for unobstructed service distribution. Thus, the need for significant penetrations through supporting structure is minimized, and allows for more compact floor-to-floor heights without sacrificing head room.

Early coordination and construction modelling allowed for an accelerated construction timeline, with the construction of the building completed 2 months ahead of schedule. This success demonstrated what is achievable in tall mass timber structures and that point-supported CLT is cost competitive system for tall-rise, multi-unit residential construction. Stemming from this success, the British Columbia Institute of Technology (BCIT) undertook the development of the Tall Timber Student Housing (BCIT Tall Timber Tower) as the latest tall-timber project incorporating a point-supported CLT floor structure. This project takes advantage of the latest advancements in product fabrication, as well as the new Encapsulated Mass Timber Construction (EMTC) [1] provisions in the National Building Code of Canada (NBCC 2020) [2], which provides a code compliant approach to tall timber using provisions for encapsulated mass timber. Using lessons learned from TallWood House, the BCIT Tall Timber Tower utilizes a wide format panel on hollow structural steel (HSS) columns that aim to further accelerate structural and construction schedule efficiencies. The following case study highlights the Tower's unique design challenges and the proposed solutions implemented to resolve those challenges that aim to make it the next generation in tall, hybrid, ETMC-compliant point-supported CLT structures.

2 CODES AND STANDARDS

BCIT Tall Timber is located in the province of British Columbia in Canada and is governed by the 2018 British Columbia Building Code (BCBC) [3], which was updated in 2019 to include the provisions for EMTC from the 2020 NBCC [2] for tall-rise timber buildings up to 12 storeys.

2.1 Code Compliance and Fire Design

BCBC 2018 Division B [3] classifies encapsulated mass timber construction up to 12 storeys. The Architectural Institute of British Columbia (AIBC) and the Engineers and Geoscientists of British Columbia (EGBC) jointly published the Joint Professional Practice Guidelines for EMTC [1], which include guidelines to the 2019 revisions to the BCBC requirements for minimum member sizes,

[1] Jamie Pobre Sullivan, Associate, Fast+Epp, jpobresullivan@fastepp.com
[2] Carla Dickof, Associate Principal, Fast+Epp, cdickhof@fastepp.com
[3] Christian Slotboom, Graduate Engineer, Fast+Epp, cslotboom@fastepp.com

https://doi.org/10.52202/069179-0550

fire rating requirements (FRR), and minimum thickness and extent of gypsum encapsulation of the wood. Under the 2018 BCBC Division B, EMTC is required to be at least partially encapsulated to ensure fire safety, with the structural system designed to achieve a 2-hour fire resistance rating through any combination of encapsulation and/or char. A typical encapsulated floor assembly that meets this fire resistance rating includes a build up of 38mm (1½") thick concrete topping over a mass timber floor panel and 2 layers of 12.7mm thick Type X gypsum board at the underside, which achieves a maximum 50-minute encapsulation rating; or 60 minutes, if the gypsum layers are directly applied to the CLT per a prescribed spacing according to CSA O86-19 [4]. See Figure 1 below. The remaining 60 or 70 minutes required to achieve a 2-hour fire resistance rating must be achieved through char on the underside of the CLT panel. The concrete topping provides the full 2-hour fire resistance rating at the top side of the floor assembly, as well as providing separation between floors.

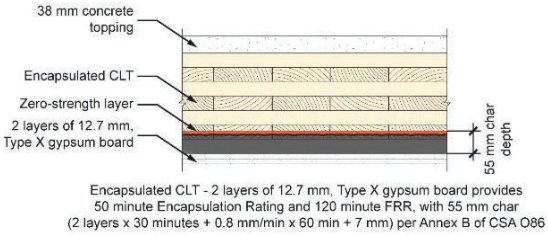

Figure 1: *Encapsulation of CLT from the Joint Professional Practice Guidelines published by AIBC and EGBC [1].*

The HSS columns must also be fire rated or encapsulated, and must meet a mass (M) to perimeter (D) ratio of 75 in conjunction with minimum 31.8mm of Type X gypsum board in order to provide a 2-hour fire resistance rating per Appendix D of the 2018 BCBC Division B. The minimum M/D ratios can control the design of the HSS column, where axial loads may be low.

2.2 Material Standards and Timber Design

The material standards for wood construction in Canada (CSA O86-19) [4] provides prescriptive approaches for the design of timber elements for typical gravity conditions, and for both exposed and encapsulated conditions in fire. Within the CSA wood material standard, guidance is provided on the bending capacity, stiffness, and fire design of CLT panels.

Unlike a post-and-beam system where panels are line-supported, a main consideration for point-supported system design is rolling shear at the column supports, similar to punching shear in a concrete flat slab system. Rolling shear in wood is defined when timber grains "roll over" each other under shear stresses perpendicular to grain. Rolling shear strength is much lower than longitudinal shear strength in timber. Testing shows that panel configuration and confinement at the supports result in added restraint against rolling shear, and thus, effectively increases the assumed rolling shear strength. However, low rolling shear strength values often result in rolling shear being a controlling factor. The punching shear resistance and reinforcing is not addressed in Canadian standards, and thus, research completed in Europe and Canada is used as a baseline for the punching shear evaluation [6,7], similar to the design of TallWood House [5]. Further desktop studies and physical testing [6,7] has also helped to justify values and methods that go beyond the codified CLT design approaches.

To design for resistance against rolling shear, strategies similar to those used for punching shear design in a concrete flat slab are available. This includes using larger supports at column locations to increase shear area, or using inclined fully-threaded screws to reinforce the CLT locally, similar to stud rails in a concrete slab. In general, however, reinforcing is avoided.

3 CASE STUDY OVERVIEW

BCIT Tall Timber Tower is a 22,800 m^2 12-storey building with 11 stories of encapsulated point-supported CLT floors over 1 level of concrete podium above grade and one level of basement below ground. The Tower will house 464 studio units in the upper stories; offices, student lounges, and storage will be contained within the ground and below-grade basement levels. Levels L2 through L6 contains single studio units with a common amenity room at the northwest corner and communal kitchens for residents. Above, at Levels L7 through L12, the same single studio units and common amenity rooms occur as they do in the floors below, but the communal kitchen areas are replaced with accessible studio apartments. See Figure 2 below for a typical architectural layout at the BCIT Tall Timber Tower.

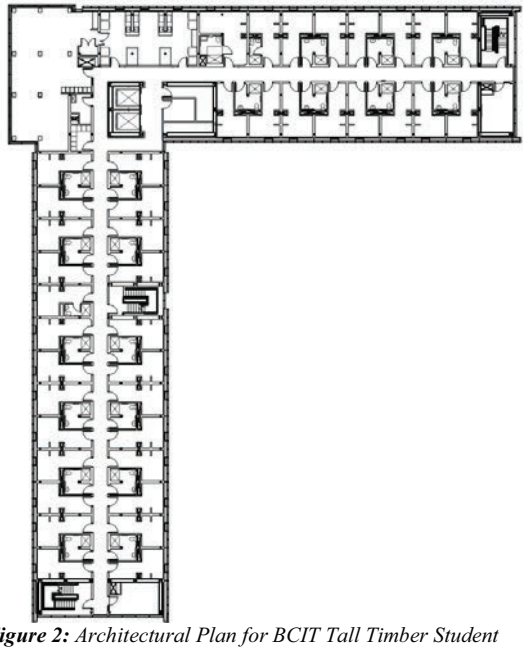

Figure 2: *Architectural Plan for BCIT Tall Timber Student Housing, Courtesy: Perkins&Will*

https://doi.org/10.52202/069179-0550

Given the consistent architectural layout at each floor, the CLT panel sizes are consistent throughout the majority of the typical floor plate. 3.5-metre (11'-6") wide CLT floor panels are supported by HSS columns at the edges and spaced at 4.5 metres across the building width along the length of the panel. The CLT panels are designed for two-way bending with consideration for punching shear, and are designed to develop a 2-hour fire resistance through 1 hour of effective encapsulation and 1-hour char in the panel. The use of steel columns simplifies the column-to-column connection, in comparison to the GLT column-to-column connection used at TallWood House, which minimizes fabrication time and adds speed to steel erection. The smaller HSS sections also allows for columns to occur within suite-to-suite party 152mm (6") deep steel stud walls that align with column grid spacing. This results in the use a of a standard party wall assembly. The lateral resisting system at the BCIT Tall Timber Tower consists of moderately ductile, concentrically braced frames above level L2 and concrete shear walls below level L2 down to the foundation. The braced frames are situated at the egress cores: at the northeast and southwest "bookends", the central elevator and service room core, and the central stair core. Like the typical HSS columns, braced frame columns are encapsulated within the walls, and anchor down into the concrete shear walls that support them with anchor bars continuing down to foundations from level L2. See Figure 3 below for a 3D rendering of the structural framing for the building.

4 KEY DETAILS

The design at BCIT Tall Timber Tower takes advantage of opportunities in wood technology, updated provisions in the building code for encapsulation, and lessons learnt from TallWood House, representing the next generation in point-supported CLT. It optimizes efficient panel design and utilizes added benefits in use of a hybrid design by way of the HSS columns and steel braced frame lateral resisting system. The success of these improvements to TallWood House further underline mass timber's viability in cost and constructability against the more conventional concrete tower residential construction.

4.1 CLT Layup

CLT panels for BCIT Tall Timber Tower consist of 5 total layers of machine stress-rated (MSR) and visually graded lumber interlaced to provide adequate bending resistance and stiffness in two directions. To reduce the number of columns and maximize the CLT span in the strong axis, MSR grade lumber is specified for the primary (outer) layers for increased bending resistance and stiffness. Weak axis bending is significant for point supported CLT, and due to the large panel width, a minimum of No.1/No. 2 visually graded lumber is required in the weak direction. Figure 4 below summarizes the layers used. At the time of design, most North American CLT manufacturers only

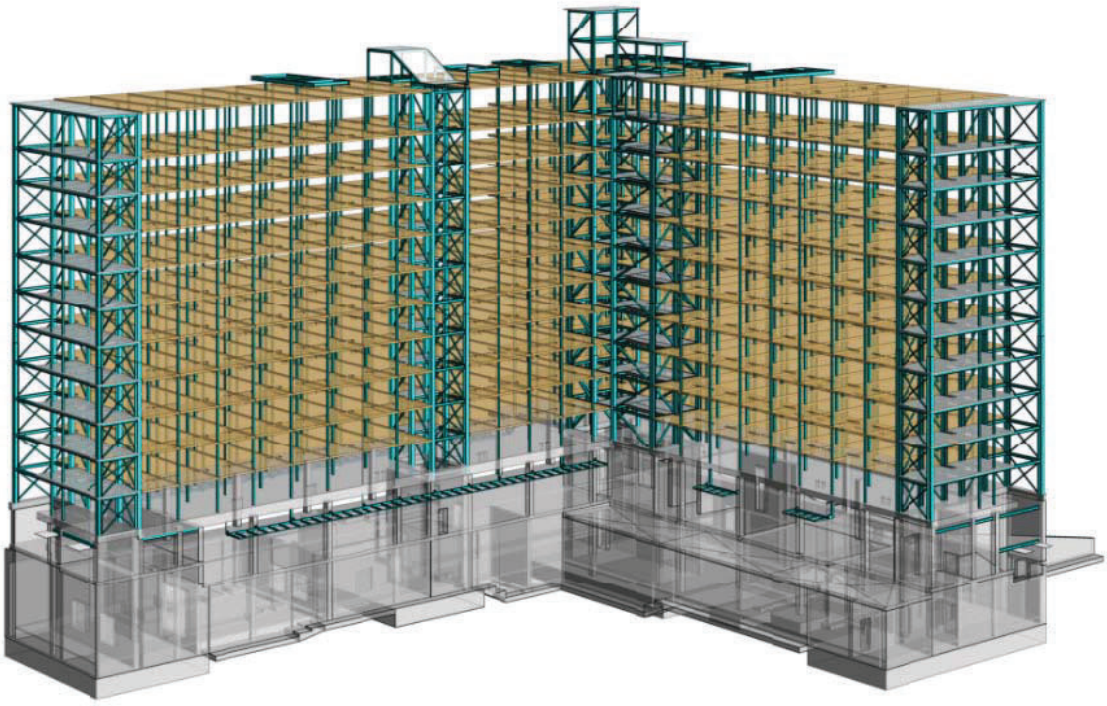

Figure 3: *A 3D rendering of the structural elements for BCIT Tall Timber Student Housing*

https://doi.org/10.52202/069179-0550

provided No.3 laminations in the weak axis, and therefore a custom CLT panel was required.

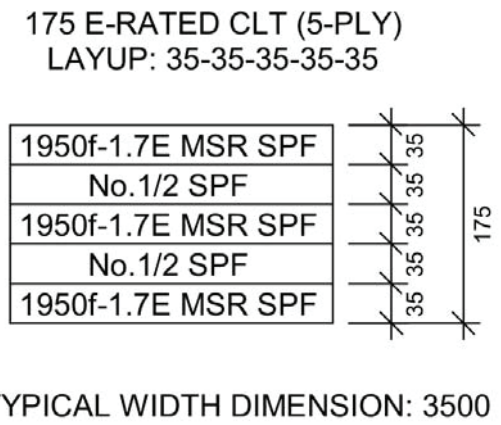

Figure 4: *CLT Panel Layup, BCIT Tall Timber Student Housing*

4.2 CLT Floor Panel Layout

As mentioned previously, the architectural layout lends to an efficient CLT panel layout. Each studio bedroom unit is sized to a maximum 3.5-metre width (see Figure 2), which aligns with the maximum width available for a CLT panel currently available in North America. The depth of the building, governed by the depth of two studio units plus the corridor width, is also sized to be within a maximum CLT panel length. This setup, in which the architectural layout aligns with maximum CLT panel dimensions, means that panel supports can align within suite-to-suite party walls. The CLT panel design is designed to maximize the spacing of HSS supports, in order to further minimize the number of column lines across the building depth. This leads to minimization on overall steel material. The shared washrooms and service risers were located to avoid spatial conflict with columns and reduce openings near column supports. See Figure 5 for the CLT floor panel layout.

More importantly, the architectural layout allows one CLT panel length to be the width of the building, which leads to efficiencies in panel press fabrication and installation. The construction schedule currently shows that each floor level will be erected in one week. At 22,800 m^2, the BCIT Tall Timber Tower is 2x the building area as Tall Wood House, which also erected 1 floor per week during construction. Therefore, BCIT Tall Timber Tower will aim to accelerate construction by a factor of 2 in comparison to that of TallWood House.

Shipping is a primary challenge of utilizing a wide format CLT panel at a maximum length of 12.8 metres. The traditional 2.3- and 3.0-metre wide CLT panel dimensions allow for panels to be shipped within a sea container from Europe or trucked in from outside of the province. Therefore, without a local plant with wide-format press capabilities, the viability of a wide format is limiting. However, the opening of a new CLT plant in the Kootenay Region, an area just east of Metro Vancouver where BCIT Tall Timber Tower is located, made the wide-format CLT panel dimensions viable from a procurement and cost perspective. While this has limited the number of manufacturers that could competitively tender the project, the key stakeholders, specifically BCIT, were willing to take advantage of the benefits of the wide format panels for the project.

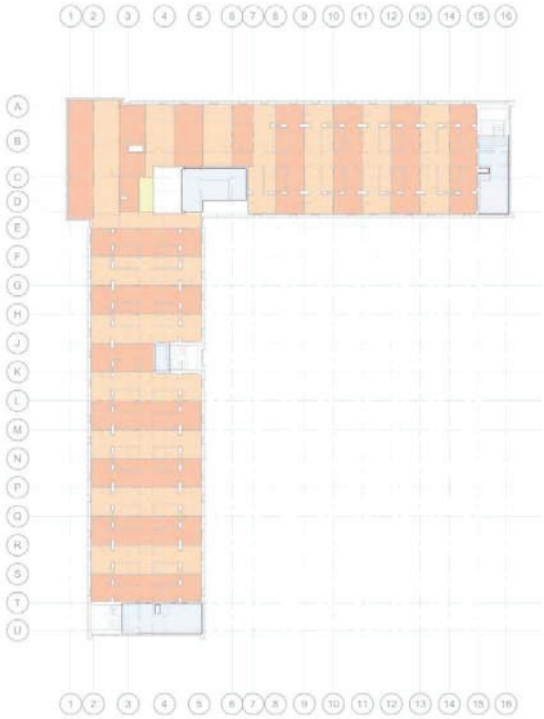

Figure 5: *CLT Panel Layout, BCIT Tall Timber Student Housing*

4.3 HSS Column Supports

HSS columns are sized as 127mm x 127mm square typically, with larger rectangular sizes, as required by increased axial forces at the lower stories. The size limitation is aimed so that the columns can occur within a standard 152mm deep steel stud party wall between units. Columns are then kept to within walls only, at least for the typical residential layouts, and allows for a higher net-to-gross floor space ratio, which is key to maximizing occupiable space, a benefit particularly for developers.

Column lines are then fully encapsulated within the fire-rated demising walls,. and take advantage of the encapsulation already required by BCBC 2018. Added Type X gypsum layers are included to provide the steel column its required fire resistance rating.

Steel columns require a mass to perimeter dimension (M/D) ratio, as required by BCBC 2018 [3], to meet EMTC and fire resistance ratings. Sizing of the HSS column thicknesses, specifically at the smaller plan dimension sizes that were targeted so that the columns can fit within demising walls, is therefore governed by this M/D ratio at the upper stories that contain lower axial

https://doi.org/10.52202/069179-0550

loads. This leads to oversized column weights where not required by structural loading.

To balance this, further analysis and specification of the encapsulation strategy, as shown in Figure 6, were included as part of an alternative solution proposed by GHL Consultants. Within an encapsulated wall, the HSS column perimeter, D, can be considered to only be the sum of column dimensions parallel to the wall length, as long as additional layers of Type X gypsum board are applied to the perpendicular dimensions. This refinement results in a higher M/D ratios for columns, well above the code requirements, which then allows for reduction in column weights, M, where axial loads are low, or at the upper stories.

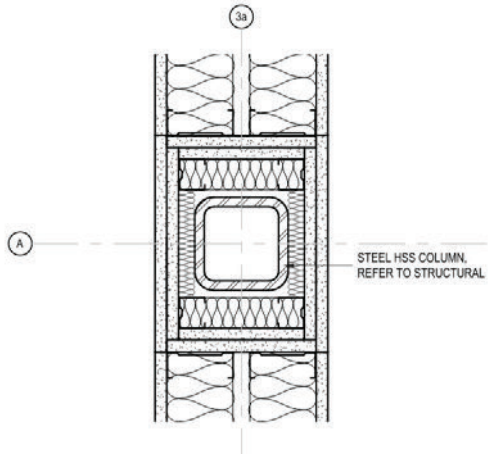

Figure 6: *In-wall Encapsulation of the Steel HSS Columns at BCIT Tall Timber Student Housing, Courtesy: Perkins&Will*

For HSS columns encapsulated outside of walls all four sides of the column are considered for the variable D. These columns are a small percentage of the overall number of columns across the building. Therefore, the cost increase for added weight in these columns is not as significant as the added weight for all of the columns to meet fire resistance requirements.

The lower weight not only reduces material, but also reduces weight and lifting effort required to erect the columns on site. Installation of the glued-laminated columns at TallWood House was celebrated for being so light-weight that 4 installers could lift each column without use of a crane. In the aim to achieve a similar ease of construction, BCIT Tall Timber Tower also anticipates a similar strategy for the column installation by maintaining lighter column weights wherever possible.

4.4 Column-to-Column Connection

The column-to-panel connection comprises of a flat bearing plate that supports the CLT floor and receives the column for the floor above, using a telescopic detail to position and lock in the column above. The 25mm-thick bearing plate is sized to provide vertical stiffness to the connection, as well as sufficient bearing capacity for the CLT panel (See Figure 7). The connection detail accommodates a direct transfer of axial forces between columns and eliminates perpendicular-to-grain bearing issues that might otherwise limit the CLT panel capacity. Shrinkage is a common issue in wood and mass timber buildings, specifically in wood bearing wall and post-and-beam configurations, but this detail also limits the effect of shrinkage and eliminates cumulative shrinkage over the height of the building. Likewise, by using steel column everywhere, including the lateral resisting system, any axial shortening that might be expected in wood columns due to axial load and shrinkage, as well as any differential deformation, is avoided. If wood and steel columns are desired to be used in conjunction on any given floor, shrinkage and any differential deformation is an important consideration.

The detail provides simplicity in design and construction. Once the supporting HSS columns are erected, the CLT panels can be directly dropped in place. Vertical bolts dapped into four corners of the bearing plate are used to position the CLT panel during install with oversized holes through the CLT to allow for tolerance. Then, the HSS column above is lowered into place and bolted to the telescope, and rods through the CLT are then fastened to the CLT with a top plate at the column, providing a nominal panel-to-panel connection. Installation of this detail in the field is simple and provides accuracy, and thus accelerates construction schedule.

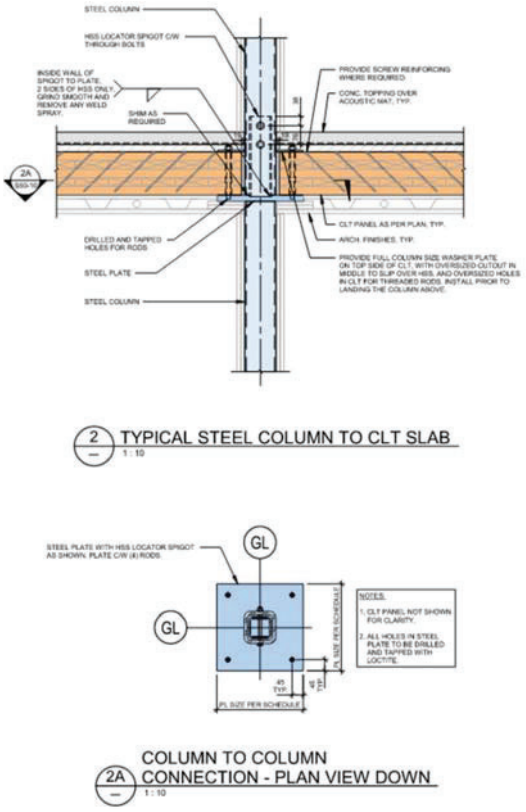

Figure 7: *Structural Column-to-Column Detail for Point-Supported CLT at BCIT Tall Timber Student Housing*

https://doi.org/10.52202/069179-0550

4.5 EMTC Compliant

The CLT floor assembly comprises of a 50mm concrete topping over an acoustic mat, the 175mm thick 5-ply CLT panel, and two layers of 16mm thick Type X gypsum board. The two layers of gypsum are directly attached to the underside of the CLT panel, using provisions listed in CSA 086-19 Annex B [4]. According to the BCBC 2018 Division B [3] provisions and the EMTC Guidelines [1], this assembly is code compliant.

Figure 8 illustrates the gypsum layers where they intersect at the HSS columns and the bearing plate. Careful consideration was given to encapsulation of the steel bearing plate at the HSS columns. Where dapping the bearing plate into the underside of the CLT panels would have eased installation of the encapsulating layers, this would have added considerable time and effort in the shop. Each panel, after pressing, would have been required to be flipped and run through the computer-numerical control (CNC) machine to router the recess for the plate. Additionally, a reduction in CLT panel thickness at the column locations, where shear is highest, would have resulted in added shear reinforcing near the corridors. It was determined that this effort impact plus the addition of screw reinforcing outweighed the install effort of the gypsum layers, and therefore, the following detail was maintained as a result.

Within the single bedroom and studio suites, however, this detail changes slightly to allow for a 25mm deep hat track. This was done to allow for small electrical and communications conduit in a minimal dropped ceiling over the bedroom areas. Despite this slight change, the two layers of 16mm Type X gypsum are still present and are ultimately attached to the CLT, as per CSA O86-19 Annex B. Therefore, the system is still considered to be fully encapsulated under the BCBC 2018 Division B provisions.

Along with the HSS encapsulation strategy as discussed in the previous section, floor assemblies are EMTC compliant

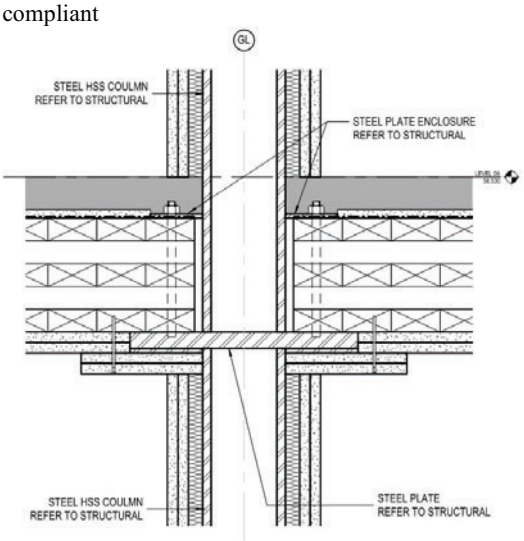

Figure 8: *A Typical CLT floor assembly with encapsulation, Courtesy: Perkins&Will*

4.6 Steel Lateral Resisting System

A moderately ductile, steel concentrically braced frame lateral resisting system is utilized at BCIT Tall Timber Tower, see Figure 9. The steel braced frames occur from the L2 concrete podium slab to the roof level. The is laid out to provide lateral resisting redundancy in both orthogonal directions, while seamlessly integrating the lateral resisting system within cores required for egress.

By placing the braces at the cores, location and frequency of the braced frames limit the mass timber diaphragm span lengths, and therefore diaphragm shear demands. Most importantly, taking advantage of the cores also results in cores that are self-stabilizing during construction, similar to a concrete tower. This significantly reduces the need for temporary bracing of the braced frames during construction.

A steel braced frame lateral resisting system was promoted due to its benefits in construction schedule over a concrete lateral resisting core that extends completely to the roof level. The steel frame is proposed to be completely erected from top of concrete podium at level L2 to the roof before the installation of any CLT floors. The self-stabilizing cores further bolster this strategy. Additionally, up to six levels of the steel frame are proposed to be prefabricated and lifted as one piece, which further limits crane picks and time on site. As a result, this strategy avoids trade overlap and crane sharing, and accelerates construction efficiency.

The concrete shear walls align with the steel braced frames to transfer loads down to foundations below L2. Additional walls added at L1 and at B1 ensure significant added stiffness below the steel braced frame system. The concrete podium lateral resisting shear walls are designed to the capacity of the steel braced frames above. The additional concrete walls further ensure added stiffness below L2 to allow for a two-stage lateral analysis of the structure. Due to the added stiffness of the concrete shear walls in comparison to the steel braced frames above, a two-stage analysis was considered for overall design of the lateral resisting system.

The transition between a concrete shear wall system and a steel braced frame system comes with complications. Balancing a base plate with anchor bolt design that can provide sufficient uplift capacity while still maintaining a reasonable concrete core wall thickness, not greater than 600mm, was a challenge. Another challenge was finding a braced frame layout configuration that allowed for necessary access to the stair and elevator cores. However, the lighter weight of the steel braced frame structure, as well as its capabilities for prefabrication over a concrete jump-forming system to accelerate the construction schedule, far outweigh the benefits of maintaining a consistent concrete core shear wall system from foundation level to roof level.

https://doi.org/10.52202/069179-0550

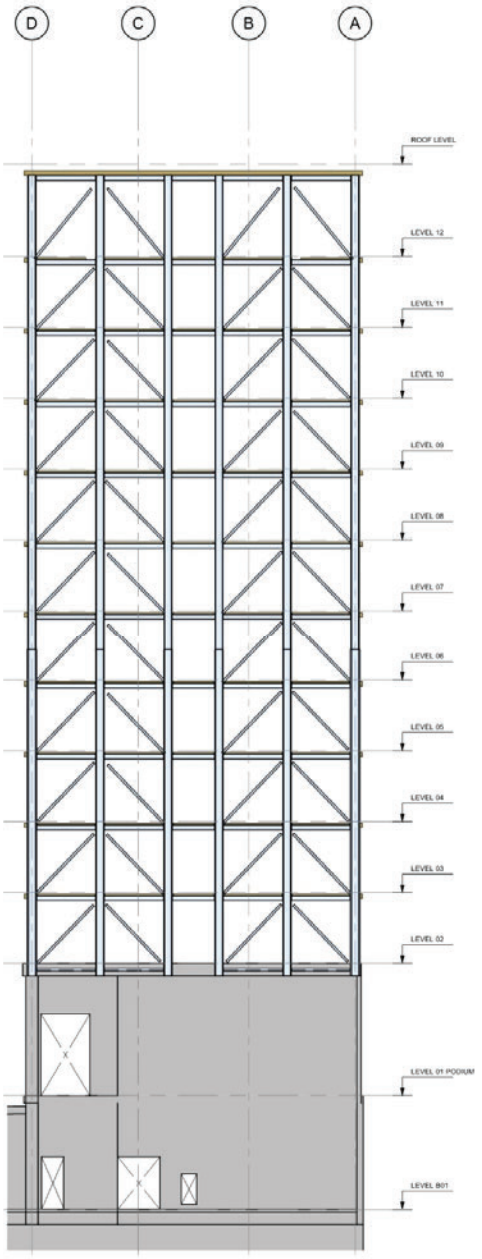

Figure 9: *Steel concentrically braced frames over concrete shear walls, BCIT Tall Timber Student Housing*

5 CONCLUSIONS

The use of point-supported CLT offers benefits to construction, architecture, and building services. The latest point-supported CLT projects, such as the BCIT Tall Timber Tower, showcase updated advances in wood products. The introduction of new mass timber suppliers in BC has resulted in cost and procurement viability for wider panels to allow column grid spacing that aligns with architectural layout. Recent research and lessons learned has further developed the point-supported design approach, pushing for use of wider panel sizes and longer spans that maximize panel layout efficiency and construction. Industry acceptance of encapsulation assemblies to resist fire have also progressed, now codified into both Canadian national and provincial building code provisions. Codification particularly has minimized the need for a peer review, as was done with Tallwood, smoothing the path to acceptance of the project overall, and has allowed for partial encapsulation to reduce the number of Type X gypsum layers to achieve sufficient encapsulation resistance.

The design of the BCIT Tall Timber Tower takes full advantage of the technological advancements in wood and fire design. In particular, mass timber panel and steel braced frame prefabrication is utilized in such a way to minimize construction time. While this might increase costs upfront, by requiring pre-planning and more work in the shop for prefabrication, the benefits outweigh the cost in quality control within a more protected environment, and lower construction tolerances in the field, and thus less construction waste. As was observed at TallWood, this upfront cost for prefabrication and the early coordination that it requires, pays dividends in construction.

More importantly, BCIT Tall Timber and the details at which it employs, underline that encapsulated mass timber construction up to 12 storeys is not only achievable, but a true cost competitor to a more typical concrete tower construction. It should also be noted that by going to mass timber construction, it does not mean that the whole system must be purely comprised of mass timber. BCIT Tall Timber capitalizes on a hybrid structure to maximize the timber product that is most effective by volume and weight; in this case, the CLT floor panels. By using details that are intentional to the EMTC provisions, while employing mass timber to its maximum benefit, BCIT Tall Timber Tower is the next generation of tall, hybrid, CLT point-supported structures.

ACKNOWLEDGEMENT

The Authors would like to thank British Columbia Institute of Technology, whose campus at the City of Burnaby will be home to the Tall Timber Student Housing Tower; to Perkins&Will, the Architect of Record; and to GHL Consultants, the building code consultants and fire design engineers for the project.

REFERENCES

[1] Architectural Institute of British Columbia and Engineers and Geoscientists British Columbia, Joint Professional Practice Guidelines, Encapsulated Mass Timber Construction Up to 12 Storeys (EMTC), Version 1.0, March 30 2021

[2] National Research Council of Canada (NRC), National Building Code of Canada (NBCC 2020), Ottawa, ON, Canada: NRC, 2020.

[3] BC Building and Safety Standards Branch, British Columbia Building Code 2018 (BCBC), Revision 2.01, December 12, 2019

[4] Canadian Standards Association (CSA), Engineering Design in Wood, CSA Standard O86-19, Toronto, ON, Canada: CSA, 2019.
[5] Fast, P, Gafner B., Jackson R., Li J, Case Study: An 18 Storey Tall Mass Timber Hybrid Student Residence At The University Of British Columbia, Vancouver in *14th World Conference on Timber Engineering,* 2016
[6] Mestek P., "Punktgestützte Flächentragwerke aus Brettsperrholz (BSP) – Schubbemessung unter Berücksichtigung von Schubverstärkungen", Ph.D. dissertation, Technische Universität München , 2011
[7] Muster M., "Column-Slab Connection In Timber Flat Slabs", Ph.D. dissertation, ETH Zurich, 2020

https://doi.org/10.52202/069179-0550

World Conference on Timber Engineering Oslo 2023

TALLWOOD 1: LESSONS LEARNED ON COMPLETION OF CANADA'S FIRST 12 STOREY TIMBER-STEEL HYBRID BUILDING

Ornagh Higgins[1], Ilana Danzig[2], Brendan Fitzgerald[3], Jackson Pelling[4], Mehrdad Jahangiri[5]

ABSTRACT: This paper presents the design considerations and construction challenges for the District 56 Tallwood 1 project; a 12 storey mixed-use steel-timber hybrid tower constructed in the South-West region of British Columbia, Canada. The project was completed in 2022 and is located in a region with some of the highest seismic demands in the country. The structural systems made use of pre-fabricated timber and steel components with the goal of decreasing on-site assembly time. This paper describes the structural systems chosen to resist both gravity and lateral loads, design for fire resistance, robustness, and lessons learned during construction.

KEYWORDS: Tall Timber Buildings, Glulam, CLT, Mass Timber, Hybrid, Ductile

1 INTRODUCTION

Tallwood 1 at District 56 is a 12-storey mixed-use residential and commercial mass timber tower located in Langford, BC, Canada. The project is the first of its kind to incorporate the newly adopted British Columbia Building Code (BCBC) [1] provisions for Encapsulated Mass Timber Construction. At the time of completion in 2022, it was also the tallest steel-timber hybrid structure in Canada.

The design takes advantage of prefabricated mass timber panels and pre-assembled steel braced frame components to increase the speed of assembly on site.

Figure 1: *Tallwood 1, completed construction*

This paper will present the solutions chosen for the gravity and lateral systems and discuss the advantages of each. The approach towards fire protection and robustness will be explored as well as challenges faced during construction and lessons learned.

Key Project Info

Location: Langford, Victoria, British Columbia

Height: 41m (12 storeys above ground + 2 levels below ground)

Typical storey height: 3.0 m

Typical floor Area: 1,175 m^2

Total Area: 18,300 m^2

Gravity Super Structure: SPF CLT & Douglas Fir glulam

Lateral structure: Steel Eccentrically Braced Frame (EBF)

Main level & below ground structure: Concrete

Figure 2: *Key project information*

2 STRUCTURAL DESIGN

2.1 GRAVITY FRAMING

The building consists of 11 storeys of mass timber construction with residential occupancy over a one-storey concrete podium with commercial occupancy. There are two levels of underground parking. A concrete transfer structure at L2 accommodates the different column grids between the different structural systems and occupancies.

[1] Ornagh Higgins, ASPECT Structural Engineers, Vancouver, British Columbia, Ornagh@aspectengineers.com
[2] Ilana Danzig, ASPECT Structural Engineers, Vancouver, British Columbia, Ilana@aspectengineers.com
[3] Brendan Fitzgerald, ASPECT Structural Engineers, Vancouver, British Columbia, Brendan@aspectengineers.com
[4] Jackson Pelling, ASPECT Structural Engineers, Vancouver, British Columbia, Jackson@aspectengineers.com
[5] Mehrdad Jahangiri, ASPECT Structural Engineers, Vancouver, British Columbia, Mehrdad@aspectengineers.com

https://doi.org/10.52202/069179-0551

Gravity framing for the typical residential levels consists of point supported cross-laminated timber panels, spanning in two directions, supported on glue-laminated timber columns. The flat-slab structural system was chosen to minimize the overall floor-to-floor height and to reduce the total number of structural elements to be installed.

The typical residential column grid is 2.95m by 3.60m to accommodate maximum panel widths available from local CLT suppliers. The architectural size and layout of the residential units generally allow for columns to be located within partition walls. Additional glulam beams are used in select locations at larger living rooms or around the elevator openings, where the typical column spacing could not be maintained. The floor plates are identical at all levels with the exception of the penthouse, where longer spans were required to meet the architectural intent.

The typical CLT panel used is a 5 ply panel, 175mm in depth, with two way spanning capabilities. The critical panels are located in the corridor areas where the live load design requirement is 4.8kpa, the design is governed by the minor axis bending moment capacity and deflection. In the major axis the panels are either 2 or 3 span continuous; in the minor axis the panels are single span due to the limit on panel width. Design for bending and one way shear was carried out as per the Canadian standard for Engineering Design in Wood, CSA O86:19 [2]. There is currently no guidance in the Canadian standard on how to calculate punching shear capacity of a CLT panel, however one source of relevant research on this topic can be found in the doctorial thesis by Mestek [3]. The research developed equations to calculate the rolling shear analysis which we then used in our design.

Figure 3: *Installation of CLT on Glulam Columns*

The balconies are also designed for 4.8kpa live load and these panels are exposed from the underside. They are designed for 2hr fire rating without encapsulation and thus are 7 ply panels, 245mm thick.

The penthouse structure consists of 3 residential units, each with custom-designed areas, open spans, and impressive vaulted ceilings. The grid spacing of the columns was increased at this level to achieve the architectural intent. It is constructed from glulam post and beam structure forming a gable roof, with CLT panels primarily spanning in one direction. A combination of custom steel hangers with bearing plates, and pre-engineered concealed connectors are used for the glulam beam connections.

Figure 4: *Penthouse Structural Framing*

2.2 COLUMN TO COLUMN CONNECTION

Due to the standardized panel sizes and grid layout, the glulam columns are generally evenly loaded across the floor plate. This regularity allows standardization of columns sizes and connections. The column sizes are uniform across each floorplate and decrease only 3 times moving up the building. Each of the 3 column sizes uses a variant of the standard column-to-column connection detail.

The column connection contains two elements, see Figure 3; the upper element is a horizontal steel plate screwed to the underside of the column welded to a vertical plate with a slotted hole. The lower element is a horizontal plate screwed to the top of the column welded to a HSS stub. The upper and lower elements are each shop-installed into the glulam columns. During install on-site the vertical steel plate is slotted into the HSS, and a single 19mm dia. pin passes through the HSS and plate to secure the connection. The vertical gravity load is transferred through bearing on the horizontal steel plates and the HSS. The connection is also designed for a tensile force to allow for robustness. This tensile force is resisted through screws in withdrawal installed at an angle into the end grain of the column. The load is then transferred

https://doi.org/10.52202/069179-0551

through the steel components of the connection, and the pin acts in shear and bearing to resist the load.

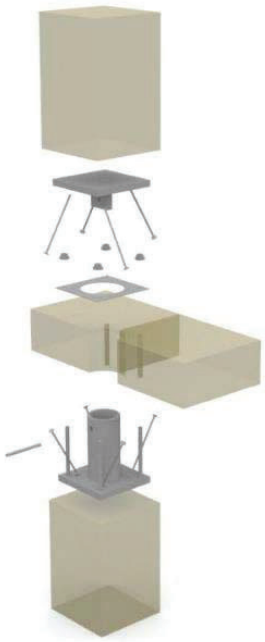

Figure 5: *Column connection detail components*

An important consideration in the detailing of a hybrid mass timber and steel structure is the way in which the different materials behave and playing to the strength of each. One of the benefits of this connection is that it avoids any perpendicular to grain loading of the mass timber elements, which can result in cumulative shrinkage and crushing in excess of what would be manageable from a serviceability limit state. While axial shortening will occur in the glulam columns, with the stress oriented parallel to grain the calculated cumulative deformations are not significant even for 12 storeys. To account for the potential axial shortening, multiple 2mm shim plates were introduced in the glulam column connection. The level of each column could be checked on site and shimmed as appropriate. The result of this approach was an essentially flat floor plate at each level. These shims also helped to reduce the impact of deflections in the concrete transfer slab at Level 2 as it was loaded during erection of the timber structure.

The CLT panels bear directly onto the plates on top of the glulam columns. Threaded anchors provide locating points for the panels during erection and provide temporary lateral support.

Due to the repetitive nature of the floor plate, and the simplicity of the point supported CLT slabs, this column-to-column detail is the primary connector throughout the entire project, with a very limited number of other detail types required. The details that were provided were shop installed where possible, to allow for quick and simple erection on site.

Figure 6: *Glulam column connection – mock up*

2.3 LATERAL FORCE RESISTING SYSTEM

Langford, BC has some of the highest seismic demands in Canada, therefore choosing an appropriate lateral system was one of the key considerations in the design process. Typically for structures of this height in this region we would see ductile concrete shear walls commonly used. These employ a design using a ductility force modification factor, R_d = 3.5, and an overstrength force modification factor R_o = 1.6. The concern with using this system in combination with mass timber was:

1) Concrete construction tolerances are much higher than with mass timber, which could lead to issues with the detailing of connections.
2) Speed of erection on site would be impacted by the time required to construct the concrete core in advance of the timber erection.
3) A single central core would not have been sufficient for the lateral demands, and additional cores or shear walls would be required.

As such, the design team sought out a lateral force resisting system with similar or improved ductility and overstrength, along with a material which allowed for tighter construction tolerances and improved erection times. The system chosen was a highly ductile eccentrically braced steel frame (EBF). This system has similar elastic stiffness when compared to concentrically braced frames, but does not rely on brace buckling to provide ductility. Rather, the stable inelastic response is closer to that of a ductile steel moment frame. The EBF ductility force modification factor, R_d = 4.0, and the overstrength force modification factor R_o = 1.5.

https://doi.org/10.52202/069179-0551

The building's rectangular floor plan necessitated a distribution of frames throughout the building, rather than a single central core, to avoid excessive torsional displacements. This distribution was easily achieved by positioning the frames within walls between units as well around the core.

The steel frames were partially pre-fabricated in multi-storey half-width segments. Each half of the frame was installed and then connected together with a link beam at each level, critical to the performance of the EBF. The goal of this approach to prefabrication was to decrease overall construction time by simplifying on-site assembly, and eliminating most of the site welding.

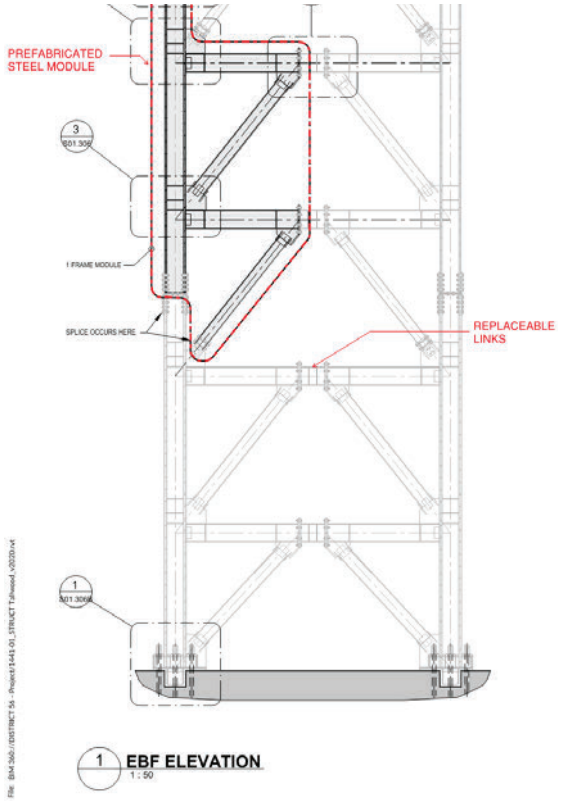

Figure 7: *Lateral force resisting system – EBF*

Capacity design principles in EBF design ensures that inelastic deformations are concentrated in yielding steel links that are capable of repeated cycles of large displacement demand, while remaining stable, and without significant strength degradation. The remaining structural elements are designed to remain elastic at load levels associated with all yielding links having reached their upper limit on capacity.

After a seismic event, yielded links could be replaced to repair the brace frames, increasing the building's resiliency. This repairability has an advantage over more common construction methods such as concrete cores, where the yielded core would likely have to be replaced in its entirety after a major seismic event.

Figure 8: *Installation of EBF modules on site*

Diaphragms consist of CLT panels connected with nailed plywood splines with steel plates and light gauge steel straps providing the chord and collector elements. All timber panels, joint connections, chords, and collectors are capacity protected to ensure they remain elastic. The roof diaphragm's increased complexity due to the geometry resulted in a lengthy design process with a number of bespoke details. A high level of coordination was required between with the CLT supplier and architect during design and construction.

Figure 9: *Roof diaphragm drag strap*

https://doi.org/10.52202/069179-0551

2.4 LATERAL ANALYSIS

Internal forces due to seismic loads were determined from an elastic response spectrum analysis. Three-dimensional dynamic analysis is a requirement of the 2018 BC Building Code due to the building height, seismic hazard, and mass irregularity present with the much heavier L2 level.

Diaphragm storey forces capture higher mode effects and are based on the greatest of: (1) code minimum equivalent static forces based on a percentage of the building's base shear, and (2) forces from the response spectrum analysis scaled up to exceed the probable capacity of the steel braced frames. At all levels, the scaled response spectrum value governs the storey force for this building, and results in an almost constant storey force, and a consistent diaphragm design, over the building height.

Serviceability limit states for drift and accelerations are in accordance with the requirements of the 2018 BC Building Code and 2015 Structural Commentaries [4]. Careful design consideration was given to wind induced accelerations due to the lightweight nature of the building structure relative to concrete buildings of a similar size. Canadian design standards do not provide specific damping values to be used for service level wind analysis in hybrid mass timber buildings, so a lower bound critical damping ratio of 0.01 was assumed, which is consistent with steel framed buildings. Along wind and across wind accelerations are highly influenced by the building's mass, stiffness, and fundamental frequencies in the two principle directions. Tallwood 1, designed for the governing seismic loads, did not require any additional damping or lateral stiffness to minimize response to wind loads.

2.5 FIRE PROTECTION

Changes in the 2020 National Building Code of Canada (NBCC) [5] allow for the construction of timber buildings up to 12 stories tall by introducing a new construction type called Encapsulated Mass Timber Construction (EMTC).

The NBCC is a model code, which is then adopted by the provinces. An amendment to the 2018 BCBC adopted the EMTC provisions in 2020. However, only a select number of local jurisdictions within the province adopted these code provisions. The city of Langford where Tallwood 1 is located was one of 13 local jurisdictions that did.

The EMTC code provisions include details on fire protection requirements during construction, fire rating, minimum member size, allowable occupancies, and square footage limitations. There are also limits on the amount of exposed (unencapsulated) mass timber permitted. Prior to this new construction type, limits on combustible construction of up to 6 stories were permitted, unless an application was made to the Authority Having Jurisdiction (AHJ) proposing an alternative solution demonstrating that the design complies with the objectives of the code, a potentially long and costly process.

Tallwood 1 was the first building in BC to be built to the newly adopted code and the first instance of an EMTC building.

Load bearing columns and floor assemblies are designed for a 2hr fire resistance rating achieved through a combination of encapsulation with 2 layers of 16mm type X gypsum board, which provides 1 hour of fire resistance, and allowance for 1 hour of charring. Char rates, effective cross-sectional properties, and residual member capacities are in accordance with the CSA-O86 standard.

Figure 10: *Mass timber encapsulation progress*

At the penthouse level a significant percentage of the roof structure is exposed so that the timber making up the vaulted ceilings can be visible and celebrated. The design team prepared and submitted an alternative solution application to the AHJ, and the AHJ agreed that a 1-hour fire resistance rating and a higher percentage of exposed wood were acceptable. These exposed elements were designed for 1 hour char as described above.

The steel braces are fire protected through a combination of encapsulation where braces are located within walls, and intumescent paint where braces are exposed across window locations.

2.6 ROBUSTNESS

Structural integrity is a requirement of CSA-O86, stating: *"the general arrangement of the structural system and the interconnection of its members shall provide positive resistance to widespread collapse of the system due to local failure"*

It is important to address integrity when designing high rise mass timber structures since traditional detailing practises do not necessarily provide inherently robust structures. Tallwood 1's integrity design is based on the Eurocode 1 2006 [6]. The tying method is used for the

timber portion of the structure and key element design for the concrete transfer slab. The splines provide the horizontal ties for the CLT floor panels with additional ties provided by the steel diaphragm straps. The columns act as vertical ties with the column-to-column connections being designed for the required tensile force, as previously discussed.

3 CONSTRUCTION

3.1 SHOP DRAWING PROCESS

The shop drawing process for the mass timber elements of the structure was highly detailed and included modelling the slab service penetrations to minimize site drilling. This high level of coordination also allowed the design team to review and comment on all penetrations prior to fabrication.

The timber shop drawings were produced ahead of the steel shop drawings, each using a separate model, preventing proper integration between the timber and steel shop drawings and associated models. Having one complete structural model including both the timber and steel would have helped flag some, if not all, of the tolerance issues we encountered on site between the steel and mass timber components.

3.2 ON SITE ASSEMBLY

Construction of the mass timber structure began in March of 2021 and the structure was topped off in November 2021. The mass timber and structural steel generally came together quite smoothly, in part because steel tolerances tend to be similar to mass timber tolerances. The structure was framed in blocks of 2 to 3 stories, matching the EBF prefabricated module sections. Once the EBF sections were erected and connected together with the links, the mass timber portion of the structure was installed to the same level with no need for temporary lateral support. This sequencing simplified the construction and maximised speed on site, however, due to supply chain challenges related to the wall panels, speed of construction was not as fast as initially anticipated. A code requirement for EMTC states that a maximum of four stories can be constructed without encapsulation, and inability to ship and receive the planned prefabricated external wall panels in time impeded progress on site. Furthermore, there were tolerance issues between the mass timber and steel components, likely due to insufficiently coordinated fabrication models, which required remediation on site and lead to delays. Finally, a highly intricate penthouse structure had a lengthy build, but with stunning results.

Moisture management in timber structures is critical to avoid issues associated with degradation, rot, mould, and visual issues like staining. The bulk of the mass timber construction took place during the drier months, however the climate on Vancouver Island is renowned for its rain and therefore additional measures were required to mitigate the risks associated with moisture. Steps included:

1) Providing protective waterproof covering to glulam beams during construction
2) Sealing joints between the CLT panels once the splines were installed.
3) Removing pooling water from the CLT slabs during heavy rain events
4) Allowing panels that were subject to rain to fully dry before being covered to avoid issues with mould forming.
5) At level 9 the CLT panels had SIGA wetguard applied creating a rainproof layer. An exterior sill plate created a tub effect and 6 drains were installed to manage any surface water. It has become more common to see all CLT floor panels complete with a shop applied membrane. This functions to protect the CLT and provides a dry interior space below so that fit out can progress.
6) At level 12 there were extended delays while the final design of the penthouse was being completed. A torch on waterproof membrane was applied at this level to try mitigate water ingress. There were still localised issues at the column locations where there were openings in the CLT panels. At drag strap locations, where the strap and fasteners stood proud of the slab, repeated impact from walking and moving materials caused the membrane to wear down and allowed moisture to pass through.

3.3 LESSONS LEARNED

Overall, one of mass timber's primary advantages to the cost of a project can be speed of construction, so realizing that speed is critical on a tall wood building. Lessons learned were generally related to items that slowed down construction:

- Although the tolerances of a steel frame are far closer to mass timber than a concrete core, field welds were required at some locations due to misalignments. Introducing more tolerance in the steel to timber details can reduce the need for field welds, along with more stringent coordination between suppliers.
- The importance of simple, repetitive detailing was evident on this project. While the typical panel to column detail was efficient and highly repetitive, the diaphragm connectors were numerous and in the future could be simplified and streamlined to improve fabrication and site installation.
- Due to supply-chain challenges, the non-load bearing external walls were fabricated on-site instead of off-site as originally planned, which slowed down the pace of construction. Offsite prefabricated wall panels are much more ideally

https://doi.org/10.52202/069179-0551

suited to a largely prefabricated mass timber building like this one.

4 CONCLUSIONS

This paper has outlined the main structural design aspects of a completed 12-storey steel-timber hybrid tower. Lessons learned during the design and construction of the project are valuable in advancing more efficient, safe, and cost-effective tall timber buildings in Canada.

ACKNOWLEDGEMENT

The authors would like to acknowledge the consultants and mass timber supplier that worked on Tallwood 1: Design Build Services, Jack James Architect, and Structurlam Mass Timber Corporation.

REFERENCES

[1] British Columbia Building Code, Crown Publications, 2018.
[2] CSA O86:19 Engineering Design in Wood, CSA Group, 2019.
[3] Punktgestützte Flächentragwerke aus Brettsperrholz (BSP) – Schubbemessung unter Berücksichtigung von Schubverstärkungen; Mestek, 2011
[4] Structural Commentaries (User's Guide – NBCC 2015: Part 4 of Division B), Fourth Edition, National Research Council of Canada, 2017.
[5] NBCC 2020: Part 3 of Division B, First Print, National Research Council of Canada, 2020.
[6] BS EN 1991-1-7:2006: Eurocode 1 – Actions on structures, Part 1-7 General actions – Accidental actions

World Conference on Timber Engineering Oslo 2023

Suitability of slim-floor steel-timber composites as intermediate floor constructions - case study based on projects in Finland

Aku Aspila[1], Lauri Lepikonmäki[2], Sami Pajunen[3]

ABSTRACT: The structural engineer provides module divisions and intermediate floor structural thicknesses for the preliminary architectural design. Usually, such data is based on design guidelines provided by manufacturers, national design guides or experiential knowledge from earlier projects. However, there are a few well-known and standardized timber floor systems in Finland, and the knowledge of timber composite structures is still very limited, largely because of the small number of reference cases. Therefore, this study addresses the gap by first presenting general information regarding the slim-floor steel-timber composite (slim-STC) and timber-concrete composite (TCC) systems. Furthermore, this study analyses the implementation of the slim-STC system in the existing office and public buildings in Finland by comparing the vibration behaviour of the slim-STC floor to the selected reference cases. The used six reference cases were selected from Sweco Finland Oy projects and they are representing the typical timber floors and TCC solutions used in office and public buildings in Finland. Based on the analysis, the slim-STC system can provide advantages to the vibration behaviour and the structure could be successfully used in office and public buildings in Finland without complex technical barriers because it has many similarities with the existing floor solutions.

KEYWORDS: Steel-timber composite, Intermediate floor, timber construction

1 INTRODUCTION

New timber-based composite floor structures, such as timber-concrete composite (TCC) and steel-timber composite (STC) floors, have been shown to provide material efficiency and higher load-bearing capabilities by utilizing the best aspects of the used materials (Aspila et al. 2022, Hassanieh et al. 2017a, Heinisuo et al. 2019, Karki and Far 2021, Karki et al. 2021, Loss and Davison 2017, Lukaszewska 2009, Siddika et al. 2021). However, to utilize these new composite structures, information about their capabilities and design methods needs to reach all the stakeholders involved in construction projects. For example, the structural designer should provide module divisions and structural thicknesses for the architects in a relatively early stage of the project to avoid project delays and additional expenses arising from necessary design changes. Usually, such data is based on experience or can be found in design guidelines provided by manufacturers and national regulations. In the project's later phases, the structural design becomes more precise and detailed, and the structural designer needs relevant design rules and calculation tools for validating the selected structural solution. In Finland, the properties of STC and TCC floors are not well-known, and the number of reference cases is still small. Thus, providing information regarding these solutions is more time-consuming and challenging when compared to more traditional floor structures like plain timber or concrete floors.

This study provides information to various parties involved in public and office building projects by first discussing the most important structural design aspects and challenges in intermediate timber or timber composite floor structures when using a beam-column frame system. Secondly, general information about the STC and the TCC systems is presented, based on the literature, so that the advantages and disadvantages of these solutions would be better known. The paper pays special attention to a slim-floor STC floor configuration called the Nordic System. Finally, a comparative analysis is conducted by studying the feasibility of the slim-floor STC solution in selected realized reference cases. The reference cases are provided by Sweco Finland Oy, and they include typical timber floor solutions used in office and public buildings in Finland. The presented information is summarised and the suitability of the slim-floor STC system is discussed for the Finnish public and office building projects.

2 STRUCTURAL DESIGN ASPECTS

2.1 Critical design criteria

The design of timber floor structures consists of two parts - the ultimate limit state (ULS) and the serviceability limit state (SLS) considering structural safety, and user comfortability issues, respectively. The dimensions of timber floors are determined by the SLS design criteria for vibration and maximum deflection especially when using long span (Fink et al. 2018a). The wood material itself has a relatively high stiffness-to-weight ratio, which results in high flexural vibration frequencies. However, the acoustic and fire resistance properties of the wood, as well as the associated regulations require additional structural layers, which in turn inevitably degrade the timber floor vibration properties. Hence, getting the intermediate floor's lowest natural frequency above the threshold value (9 Hz in Finland) sets the most demanding condition for the floor design. Reaching this threshold becomes a harder task if the timber floors are supported by flexural beams affecting the combined vibration.

[1]Aku Aspila, Tampere University, Finland, aku.aspila@tuni.fi
[2]Lauri Lepikonmäki, Sweco Finland Oy, Finland, lauri.lepikonmaki@sweco.fi
[3]Sami Pajunen, Tampere University, Finland, sami.pajunen@tuni.fi

https://doi.org/10.52202/069179-0552

In the ULS design, the most critical design criterion is typically the perpendicular compressive strength in the support or load areas. Additionally, in cross-laminated timber (CLT) floors, the rolling shear strength is another key criterion. These strength criteria are such, that exceeding the associated limit value does not lead to an overall collapse of the floor structure, but instead to local damages. Thus, from the structural design perspective, the SLS design criteria for vibration and deflection are the most significant ones. Consequently, the bending stiffness of the floor can be stated as the most important design parameter as it affects both criteria. Bending stiffness can be affected by modifying the following properties: floor supporting structures and boundary conditions, floor material stiffnesses, and floor cross-section shape and dimensions. As the possibilities to modify the abovementioned features in pure timber floors are rather limited, the STC and TCC become very attractive choices for intermediate floor structures.

The current Eurocode 5 (CEN 2005) provides design guidance only for timber floors that consist of glued or mechanically jointed beams and timber decking whereas similar international guidance is not provided for CLT and STC floors. The lack of guidelines for these structures has been identified as a barrier that hinders the mainstreaming and structural understanding of these solutions (Cheraghi-Shirazi et al. 2022, Fink et al. 2018b, Schenk et al. 2022) According to Schenk et al. (2022) "different tools, based on different background theories and with different levels of accuracy may lead to quite diverging results." Considering the TCC floors, additional guidance to the Eurocode 5 was given in 2021 where the ULS design is presented but no further guidance regarding SLS is given (CEN 2021). The SLS deign for TCC is described by Cuerrier-Auclair (2020), Breneman et al. (2021).

2.2 Determining the key structural responses

As justified above, the vibration and deflection properties are the most significant ones when examining the feasibility of the floors to be applied in different construction projects. In what follows only the vibration properties are considered in more depth in terms of the design equations for the floor's lowest natural frequency. The design criterion for the deflection is more straightforward to calculate requiring mainly relevant methods for considering the partial composite action as presented eg. in (Aspila et al. 2022).

The lowest natural frequency of a one-span timber floor supported by rigid supports, for example by walls, can be modelled as a beam and calculated, according to Eurocode 5 as

$$f_0 = \frac{\pi}{2L^2}\sqrt{\frac{EI_L}{m+m_1}} \quad (1)$$

where L is the span length of the slab, EI_l is the bending stiffness along the span length, m is the structural mass per unit length and m_1 is an additional 30 kg/m mass, that considers the live loads according to the Finland's national Annex. In the upcoming Eurocode 5 the m_1 is 10 % of living load (CEN unpublished (updated 2022-05-30)).

Equation (1) assume that the supports underneath the floor slabs are rigid, which is not true in the case of STC floors. Thus, the combined vibration of the floor slab and the supporting steel beam must be both considered. Typically, such a combined vibration problem for a floor slab supported by two flexible beams can be analysed by using the Dunkerley relation as

$$f_{sys} = \sqrt{\frac{1}{\frac{1}{2*f_{0.beam,1}^2}+\frac{1}{2*f_{0.beam,2}^2}+\frac{1}{f_{slab}^2}}} \quad (2)$$

in which the subscript *slab* stands for the floor slab, the frequency of which can be calculated according to Equation (1). The subscripts *beam,1* and *beam,2* denote the steel beams that are supporting the slab. In the calculation of the term $f_{0,\text{beam}}$ for STC structures, the composite action between the timber slab and the steel beam can be taken into account by using eg. the layered beam theory as shown by Aspila et al. (2022). It should be noted that the upcoming Eurocode 5 proposes changes to equation (2) in a form

$$f_{sys} = \sqrt{\frac{1}{\frac{1}{3*f_{0.beam,1}^2}+\frac{1}{3*f_{0.beam,2}^2}+\frac{1}{f_{slab}^2}}} \quad (3)$$

in which the influence of the supporting beam frequencies is reduced.

3 TIMBER-BASED COMPOSITE FLOORS

3.1 The composite action

Timber-based composite structures can provide lightweight structures, quick installation, and low greenhouse emissions as well as increased structural capacity to carry loads and floor spans. Nowadays there exist two main systems for timber-based composite floors, STC and TCC. In STC the composite action is formed with a steel beam by using bolts and screws as shear connectors. In the case of TCC the composite action is formed with a concrete slab by using not only dowel-type shear connectors but also grooving in the timber slabs. The structural behaviour of composite structures is determined by the degree of the composite action, which can be separated into three different stages as shown in Figure *1*.

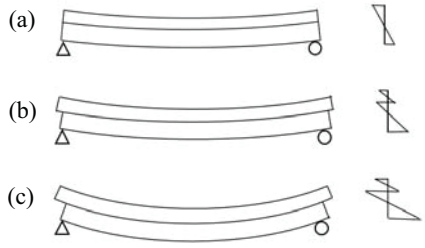

Figure 1. *Deflections and bending stress with different degrees of composite action, (a) full, (b) partial, and (c) no composite action at all.*

The first stage is full composite action where the two parts are acting as one solid block of material and there is no slip between different parts. The second stage is partial composite action in which the flexibility of the

connections causes a slip between the parts. Lastly, if the connection is so weak that it does not carry the shear force at all, the slip is free to occur, and no composite action is formed. Thus, the degree of the composite action is governed by the stiffness and load-carrying capability of the connection.

The effectiveness of the composite action is governed by the distance between the centroids of the beam and slab as depicted in Figure 2. Increasing the distance also increases the effectiveness of the composite action providing that the connectors can carry the increased shear forces between the parts.

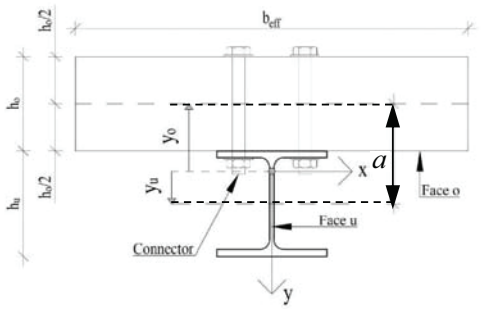

Figure 2. *Cross-section of a traditional STC. The parameter a denotes the distance between part centroids.*

3.2 TIMBER-CONCRETE COMPOSITE FLOORS

The concrete slab has traditionally been used as a reinforcing layer on top of the wooden slab to improve the fire and acoustic properties of the floor. By forming a composite action between timber and concrete parts, structural efficiency, load-bearing capacity, and vibration performance can be substantially increased (Cuerrier-Auclair 2020, Lei Zhang 2022, Siddika et al. 2021). In Finland, TCC structure is typically constructed by using CLT slabs beneath the concrete slab as illustrated in Figure 3. In such a configuration, the CLT slab also provides the casting mould and the support during the construction. The composite action is formed by using screws and grooves.

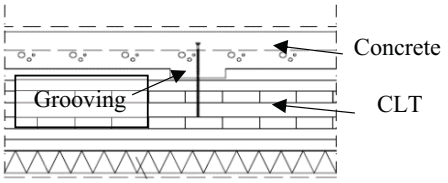

Figure 3. *Typical Finnish CLT-concrete slab has a total height of ca. 200 mm CLT and 100 mm concrete. Due to the fire and the impact of sound insulation regulations, linings might be needed above or below.*

ULS of TCC structures can be analysed by using the Eurocode 5 design guides (CEN 2021). In general, the TCC floors are considered robust structures, in which the only feature requiring further research, is the long-term deflection determination affected by different creep properties of concrete and timber (Breneman et al. 2021).

3.3 STEEL-TIMBER COMPOSITE FLOORS

Steel-timber composite floors differ from the TCC floors substantially since the composite connection is formed now between a slab and a beam, not between two slabs. Depending on the location of the steel beam, the STCs can be divided into two categories. In traditional STC floors the steel beam is located beneath the slab as shown in Figure *2*, whereas, in slim floors, the timber slab is supported by the lower flange of the steel beam as shown in Figure 4. In traditional floors, the efficiency of composite action can be high because the centroids of the beam and the slab are far from each other, as pinpointed in Figure *2*. Typically, such STC structures produce 30%-90% higher load-bearing capacities compared to non-composite constructions (Aspila et al. 2022, Hassanieh et al. 2017b, Karki et al. 2021, Loss and Davison 2017). However, the connections between the steel beam and timber slab must be capable of carrying the developed high shear forces and the connections must be stiff enough to form the desired degree of the composite action. The importance of the connections has led to intense research and development of different connection types such as (Chybinski and Polus 2022, Hassanieh et al. 2017b, Hassanieh et al. 2017c, Loss et al. 2016a, Loss et al. 2016b, Yang et al. 2020).

Field Heinisuo et al. (2019) present the slim-floor STC concept where the possibilities of slim-floor steel-timber composite structures are discussed. The most important benefit of the slim-floor application is the reduced total floor height which in turn creates material savings on the vertical structures and allows the building of more floors with the same building height.

In this paper, the considered slim-floor STC, called as a Nordic system, consists of CLT slabs connected to the welded WQ-beam as presented in Figure 4. In this system, the composite connection is formed by using steel plates on top of the WQ beam and the CLT slab. All the installation regarding the connections can be carried out on top of the platform and the connections can be also easily disassembled. As in all slim-floor configurations, the effectiveness of the composite action is rather small, but based on the results given by Heinisuo et al. (2019), the composite action can reduce the stresses in the steel profile by up to 20%.

https://doi.org/10.52202/069179-0552

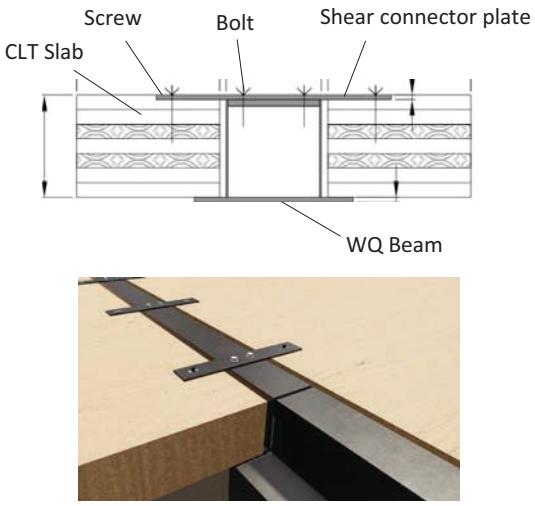

Figure 4. *The considered Nordic system slim-floor. Cross-section (top) and side-view (bottom). The CLT slab and the steel beam are fastened only on top of the profile using the steel plates.*

4 COMPARATIVE ANALYSIS

4.1 Reference cases

The practical feasibility of the Nordic system in the office and public buildings is studied by comparing the key structural responses in realized construction projects. The reference cases are chosen from timber construction projects conducted or participated in by Sweco Finland Oy. A total of two schools and six office building projects with the beam-column system were selected. In the selected reference cases the intermediate floors were built by using TCC, CLT or LVL ribbed-slab systems, see Table 1. Figure 5 illustrates the platforms with modulus divisions.

Table 1. *Reference case data.*

Reference cases						
	Floor			*Primary beam*		
Case	Type	Code	Span (m)	Type	Code	Span (m)
1	TCC	220mm 60-30-40-30-60 100mm C37/45	7,0	GL30c	240x1080	7,0
2	CLT	160mm 40-20-40-20-40	4,0	Delta	D40-500-20	7,0
3	LVL-ripa	H661-5x63x600	8,5	LVL-X	225x590 300x590 (midle)	4,8
4	TCC	220mm 60-30-40-30-60 80mm C30/37	6,0	Delta	D32-400	6,0
5	CLT	280mm 80-40-40-40-80	6,0	LVL-X	2x288x890	6,7
6	TCC	220mm 80-40-40-40-80 80mm C30/37	5,5	WQ22-500	260x20-2x6x200-20x500	5,3

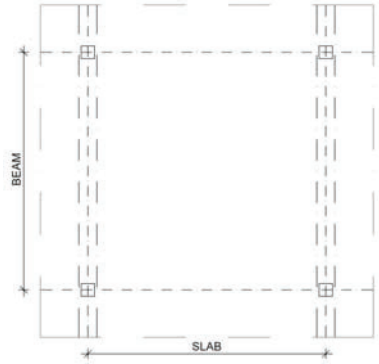

Figure 5. *Platform and modulus divisions of reference cases.*

Table 2 presents the design parameters such as the top and bottom surface masses, self-weight of the structure and living load for the reference cases.

Table 2. *Reference case design parameters.*

Reference cases				
Design parameters				
Case	Top surface mass (kg/m2)	Bottom surface mass (kg/m2)	Selfweight (kN/m2)	Living load (kN/m2)
1	10,0	4,0	3,8	5,0
2	37,0	3,0	0,7	2,5
3	74,0	30,0	0,4	3,0
4	50,0	14,0	3,2	2,5
5	90,0	14,0	1,2	3,8
6	69,0	14,0	3,2	5,0

4.2 Calculation of the Nordic system

The Nordic system is calculated by using the presented data from the reference cases. Span lengths and living loads are taken directly from Table 1 and Table 2. However, for cases 1, 3, 4 and 6 the medium of cases 2 and 5 values were used, see Table 3. For each case, the extra load imposed by the heating, ventilation, and air conditioning (HVAC) was taken also into consideration as a permanent load.

Table 3. *Design loads used to calculate the Nordic system.*

Nordic system				
Design parameters				
Case	Top surface mass (kg/m2)	Bottom surface mass (kg/m2)	HVAC load (kN/m2)	Living load (kN/m2)
1	63,5	8,5	0,5	5,0
2	37,0	3,0	0,5	2,5
3	63,5	8,5	0,5	3,0
4	63,5	8,5	0,5	2,5
5	90,0	14,0	0,5	3,8
6	63,5	8,5	0,5	5,0

The results of the calculation are presented in Table 4 where presented values are obtained by calculating CLT as a beam structure by using Equation (1). In Table 4 the f_1 refers to the lowest natural frequency of the floor

structure that was calculated by using Equation (1) and f_2 refers to the lowest natural frequency of the floor systems that can be calculated by using Equation (2) or (3). Results were obtained by optimizing the CLT and WQ-beam to reach the 9,0 Hz frequency according to the upcoming Eurocode 5.

Table 4. *Nordic system midfloor solution where CLT is calculated as a beam structure.*

Nordic system, CLT as a beam								
	Beam		*floor*		*EC5*		*Upcoming EC5*	
Case	WQ-type	Weight (kg/m)	CLT -type	Weight (kg/m)	f1 (Hz)	f2 (Hz)	f1 (Hz)	f2 (Hz)
1	470x6-360x15-572x13	145,0	320mm 80-40-80-40-80	134,4	9,2	6,7	8,9	7,2
2	330x6-260x15-472x12	106,2	180mm 40-30-40-30-40	75,6	13,8	7,9	14,0	9,1
3	570x8-450x20-662x15	220,2	320mm 80-40-80-40-80	134,4	6,3	6,3	6,3	6,2
4	400x6-370x20-582x15	164,3	300mm 80-40-60-40-80	126,0	10,7	8,4	10,8	9,1
5	570x8-400x20-612x14	201,7	320mm 80-40-80-40-80	134,4	10,6	8,6	10,5	9,0
6	280x6-350x15-562x12	120,5	280mm 80-40-40-40-80	117,6	12,4	8,3	11,9	9,0

4.3 Comparison

The conducted calculation allows comparison between the Nordic system and reference cases as well as between current Eurocode 5 and upcoming Eurocode 5. A comparison between the Nordic system and reference cases is presented in Table 5. Cases 1 and 3 did not reach the boundary limit value of 9 Hz when CLT was calculated as a slab.

Table 5. *Comparing the structural height of the Nordic system to the reference cases when CLT is calculated as a beam structure.*

Comparing Nordic system structural heights to reference cases						
	Reference cases		Nordic system		Comparison	
Case	Floor	Floor+beam	CLT as a beam	CLT+WQ	Floor difference	Floor+slab difference
1	320,0	1400,0	-	-	-	-
2	160,0	400,0	180,0	330,0	-11 %	21 %
3	661,0	1251,0	-	-	-	-
4	300,0	320,0	300,0	400,0	0 %	-20 %
5	280,0	1170,0	320,0	570,0	-13 %	105 %
6	300,0	300,0	280,0	280,0	7 %	7 %

A comparison between the current and the upcoming Eurocode 5 has been shown in Table 6. Upcoming Eurocode 5 provides better values in all cases when examining the lowest natural frequency of the floor system.

Table 6. *Comparing results from Table 4 where the lowest natural frequencies are calculated according to Eurocode 5 and upcoming Eurocode 5.*

Comparing Eurocode 5 and upcoming Eurocode 5		
	CLT as a beam	
Case	f1 (Hz)	f2 (Hz)
1	-3 %	7 %
2	1 %	15 %
3	-2 %	-2 %
4	1 %	8 %
5	-1 %	5 %
6	-4 %	8 %

5 DISCUSSION AND CONCLUSION

This study presents some key design aspects in timber and timber-composite floors in the context of the beam-column structural system. Special attention is paid to a steel-timber composite slim-floor system called the Nordic system. The major objective of the study is to examine the feasibility and effectiveness of the Nordic system in typical practical applications in office and public construction projects in Finland. Based on a selected set of realized construction projects, the results prove that the Nordic system would result in slimmer solutions compared to the adopted current floor types by offering a total build-to-be-disabled floor system. To adopt the full potential of the studied slim-floor system, further research should be carried out to accurately determine the slabs' effective width and formulate an overall structural optimization design task for the whole floor system where the bending stiffness of the CLT in both directions should be taken into consideration.

REFERENCES

Aspila, A., Heinisuo, M., Mela, K., Malaska, M. and Pajunen, S. 2022. Elastic design of steel-timber composite beams. *Wood Material Science & Engineering,* 17(4), 243-252.

Breneman, S., Zimmerman, R., Gerber, A., Epp, L., Dickof, C., Taylor, A., Loasby, W., McDonnell, E., Slotboom, C., McCutcheon, J. and Visscher, R. 2021. U.S. Mass Timber Floor Vibration Design Guide.

CEN, 2005. Eurocode 5. Design of timber structures - Part 1-1: General. Common rules and rules for buildings. *EN-1995-1-1.*

CEN, 2021. Eurocode 5: Design of Timber Structures. Structural design of timber-concrete composite structures. Common rules and rules for buildings. *CEN/TS 19103:2021.*

CEN, unpublished (updated 2022-05-30). Eurocode 5: Design of timber structures — Common rules and rules for buildings — Part 1-1: General. *Vibrations (Clauses 9.3 and annex K).*

Cheraghi-Shirazi, N., Crews, K. and Malek, S. 2022. Review of Vibration Assessment Methods for

https://doi.org/10.52202/069179-0552

Steel-Timber Composite Floors. *Buildings,* 12(12).

Chybinski, M. and Polus, L. 2022. Mechanical Behaviour of Aluminium-Timber Composite Connections with Screws and Toothed Plates. *Materials,* 15(1).

Cuerrier-Auclair, S., 2020. *Design Guide for Timber-Concrete Composite Floors in Canada.* Special Publication SP-540E.

Fink, G., Honfi, D., Köhler, J. and Dietsch, P., 2018a. *Basis of Design Principles for Timber Structures.*

Fink, G., Kohler, J. and Brandner, R. 2018b. Application of European design principles to cross laminated timber. *Engineering Structures,* 171, 934-943.

Hassanieh, A., Valipour, H. R. and Bradford, M. A. 2017a. Composite connections between CLT slab and steel beam: Experiments and empirical models. *Journal of Constructional Steel Research,* 138, 823-836.

Hassanieh, A., Valipour, H. R. and Bradford, M. A. 2017b. Experimental and numerical investigation of short-term behaviour of CLT-steel composite beams. *Engineering Structures,* 144, 43-57.

Hassanieh, A., Valipour, H. R., Bradford, M. A. and Sandhaas, C. 2017c. Modelling of steel-timber composite connections: Validation of finite element model and parametric study. *Engineering Structures,* 138, 35-49.

Heinisuo, M., Mela, K., Pajunen, S. and Malaska, M., 2019. New steel-composite beam, Nordic system. *XII Conference on Steel and Composite Construction.* Coimbra, Portugal: ce/papers, 193-202.

Karki, D. and Far, H. 2021. State of the art on composite cold-formed steel flooring systems. *Steel Construction-Design and Research,* 14(2), 117-127.

Karki, D., Far, H. and Saleh, A. 2021. Numerical studies into factors affecting structural behaviour of composite cold-formed steel and timber flooring systems. *Journal of Building Engineering,* 44.

Lei Zhang, J. Z., Ying Hei Chui, 2022. Development of high-performance timber-concrete composite floors with reinforced notched connections. *Structures,* 39(945-957).

Loss, C. and Davison, B. 2017. Innovative composite steel-timber floors with prefabricated modular components. *Engineering Structures,* 132, 695-713.

Loss, C., Piazza, M. and Zandonini, R. 2016a. Connections for steel-timber hybrid prefabricated buildings. Part I: Experimental tests. *Construction and Building Materials,* 122, 781-795.

Loss, C., Piazza, M. and Zandonini, R. 2016b. Connections for steel-timber hybrid prefabricated buildings. Part II: Innovative modular structures. *Construction and Building Materials,* 122, 796-808.

Lukaszewska, E., 2009. *Development of prefabricated timber-concrete composite floors.* (PhD). Luleå University of Technology.

Schenk, M., Hübner, C. and Cabrero, J. 2022. Cross-Laminated Timber: A Survey on Design Methods and Concepts in Practice. *CivilEng,* 3, 610-629.

Siddika, A., Al Mamun, M. A., Aslani, F., Zhuge, Y., Alyousef, R. and Hajimohammadi, A. 2021. Cross-laminated timber-concrete composite structural floor system: A state-of-the-art review. *Engineering Failure Analysis,* 130.

Yang, R. Y., Li, H. T., Lorenzo, R., Ashraf, M., Sun, Y. F. and Yuan, Q. 2020. Mechanical behaviour of steel timber composite shear connections. *Construction and Building Materials,* 258.

World Conference on Timber Engineering Oslo 2023

THE BV2020 SOLUTION – GOING BIG WITH LIGHT TIMBER STRUCTURES

Knut Magnar Sandland[1], Julia Bosnes Tønne[2], Per Gunnar Nordløkken[3]

ABSTRACT:

A growing population world-wide and a strong increasing trend towards more urbanisation calls for changes in the way we develop urban areas and cities. The building sector will play an important role in this development. Better utilization of land with more multi-storey buildings both for residential and commercial use is an important part of the solution. Climate change requires us to take action and substituting building materials with large CO_2 emissions with wood-based solutions which will make a huge positive contribution. Glue-laminated and cross-laminated timber are good alternatives. However, lightweight load bearing timber frame solutions will make an additional contribution to even more sustainable building construction due to less use of raw materials and the possibility to build on weaker ground. The BV2020 solution has the goal to develop concepts that enable mass customized production of prefabricated light timber frame, load bearing elements for buildings up to eight - 8 - storeys for the volume market.

KEY WORDS: tall lightweight timber buildings; wood-based building systems; mass customized production; prefab

1 INTRODUCTION

1.1 BACKGROUND

The challenge of designing tall and safe timber buildings has been a priority for the wood industry and researchers throughout several studies and projects [1]. Even though timber is one of our oldest and most traditional building materials, building codes have limited wide use in higher buildings due to fire safety concerns, amongst other issues [2].

The introduction of function-based regulations instead of material based regulations has played a key role in the use of wood in multi-story buildings with more than four floors. For instance, in Norway the function-based regulations regarding fire risk were introduced in 1997 [3]. This was important for the use of wood in big buildings, and therefore the development of techniques and systems for multi-story wooden buildings is rather new, and it is still a high potential for further development of effective production systems.

Until recently, the attention has mainly been on unique high rise, solid wood, signal-building projects. In later years, an increasing interest has grown also for lightweight timber frame constructions. All these projects have helped to identify and solve many of the fundamental obstacles that follows with an expanded use of timber in high-rise buildings. Now, time has come to realize returns of these findings and to go big, also with respect to volume.

1.2 OBJECTIVES

To really take advantage of the engineering developments that have been made within the timber building industry, one needs to convert all the good work that has been done into complete building concepts that can compete within the volume markets. This is the main goal of the BV2020 project, which paves the way for mass production of prefabricated lightweight timber frame load bearing elements for use in apartment buildings with up to eight storeys. In Figure 1, a typical example of a lightweight timber frame element is shown.

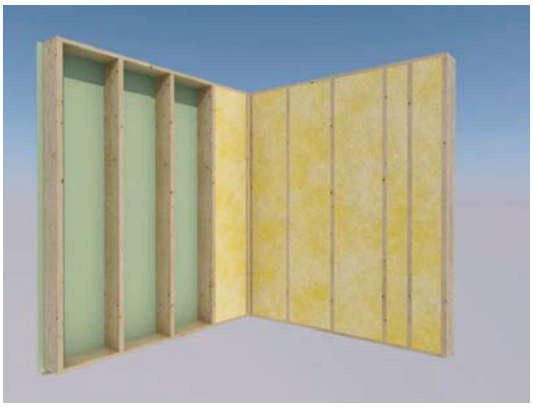

Figure 1: *Example of a typical lightweight timber frame element.*

[1] Knut Magnar Sandland, Project Manager, WoodWorks! Cluster
[2] Julia Bosnes Tønne, Structural Design, Støren Treindustri AS, Norway
[3] Per Gunnar Nordløkken, Technical Manager, Støren Treindustri AS, Norway

https://doi.org/10.52202/069179-0553

The project includes work packages that cover topics such as i) identifying the required material properties for light-weight timber structures, ii) solutions for the overall and detailed design of prefabricated constructions and their connections, iii) optimization and adaptation of the production process, as well as iv) verifying that all relevant aspects of the building as a whole and its solutions meet the required standards.

Støren Treindustri is a member of WoodWorks! Cluster (www.woodworkscluster.no), and the BV2020 project and concept fits well into the main work in the building sector in the cluster, with focus on:

- Transition of Industry 4.0 and Industry 5.0 in the wood based building industry.
- Effective use of digital information in the whole value chain, from raw material to end of life for the buildings.
- Increased industrialization of the building process – more performed in the factory and less at the construction site.
- Sustainability reporting, and the use of it to promote wood as a building material.
- Development of urban building concepts (multi-storey buildings) that are effective to produce, and eliminate the uncertainty among professionals to use wood as a building material for multi-story buildings.

The network in WoodWorks! Cluster exists of R&D organizations and companies covering the whole value chain from forest to building operations, and is used as a resource in the performance of the project work.

2 IMPACT OF BV2020-CONCEPT

The BV2020-concept, by using light framework construction, has potentially several beneficial impacts on the building industry concerning greenhouse gas emissions and cost efficiency. However, this has to be calculated and proven when the concept is fully developed, but in the following sections the most important motives for developing the building concept are discussed.

2.1 Use of wood – the substitution effect concerning greenhouse gas emissions

In the European Union, building construction consumes 40% of materials and 40% of primary energy, and generates 40% of waste annually [4]. The potential to benefit the environment by replacing reinforced concrete structures with timber is illustrated by Skullestad et.al [5], where a 34-84 % reduction in climate change impact has been calculated for 3-21 storey buildings. However, an essential prerequisite when comparing two products is that they can fulfill the same function in a building. In the LCA language, this is referred to as the "functional equivalent of the object". There is a quantification of the technical characteristics and functions required by the object (product). The functional equivalent makes it possible to derive a reference unit used to produce results from calculations (e.g.: per m², per year, per employee, per m² per years).

Comparisons of greenhouse gas calculations should only be made on the basis of the functional characteristics of the objects equivalent. This requires that the functional requirements are described together with the intended use and relevant technical requirements. The functional equivalent of a building or part of a building shall include factors as:

- Building type
- Technical and functional requirements
- Required lifetime
- Total area
- Total heated utility floor space

The BV2020-concept is based on a lightweight construction, and therefore it is not a material intensive construction. This is positive due to greenhouse gas emissions per kg. material. However, the BV2020-construction involves several materials, and in the development of the concept effort to minimize the total greenhouse gas emissions is a priority. Calculations on how the various materials influence the total account of greenhouse gas emissions of the whole building will be important in the BV2020-concept, not limited to parts of the building or single materials.

In [6] it is shown examples of variations in the greenhouse gas emissions dependent on which materials, and the amount of each material, that are used in a wall construction. The difference between the construction systems is rather high, also within the wood construction systems. However, the example of lightweight framework system shows a rather low value in the example. The development to reduce the greenhouse gas emissions is currently very intensive, and therefore it is important to perform dynamic calculations to take this into consideration consecutively. For the BV2020-concept this will be important to optimize the construction due to the total greenhouse gas emission for the whole building.

2.2 Urban nodes

In Norway, residential buildings represent 37 % of the total building mass [7]. Even though multi dwelling buildings constitute a small part of these today, it is evident that the demand for this type of buildings will increase in the years to come. Due to a general population growth, increased urbanisation, and the need to preserve more agricultural area, the call for higher apartment buildings will grow significantly. It is a policy making process in progress in EU to establish urban nodes for effective transport and infrastructure [8]. This development is also reflected in smaller scale, e.g.

establishment of small cities in connection with railway stations.

A compact building mass is cost effective due to infrastructure, and multi-story buildings will be important in this development. It is therefore of great importance that concepts for timber buildings represents a competitive alternative. To exploit the potential of timber as a CO_2-sink, we need to provide the market with competitive timber alternatives within the segments that constitutes the largest volumes. A new normal must be to go big with timber, and the goal for the BV2020-project is to develop a flexible concept and solutions both for construction, fire safety and acoustics that can be manufactured and built in an effective, economical and also environmentally sustainable way, ready to be used. These are on-going activities that will be presented on the WCTE-conference in Oslo 2023.

There will be increasing demands to utilise today's building stock to a much greater extent than has been the case so far. Extensions in the height of existing buildings can therefore be socio-economically advantageous and at the same time contribute to sustainable management of existing buildings. In addition, it will increase the value of existing buildings. In [9] these aspects are described more in detail.

A limitation is what existing buildings can withstand from the extra load from building at top. Some buildings are already planned for this, while most are not. However, due to the relatively low specific gravity, load-bearing structures in light-weight framework constructions of wood will be well suited as a load-bearing system for extensions on existing buildings – and thus it may also be possible on some buildings that were not originally intended for this.

In many existing buildings made of heavier materials such as concrete, masonry and steel, there may be reserve capacity compared to an extension. However, it is an advantage that the extension and load-bearing system do not impose excessive loads on existing buildings. Heavier building systems on extensions may limit the number of additional floors that can be built on. By choosing a "light" extension and lighter load-bearing structures, there are greater opportunities to get more floors and increased usable square meters for the extension.

2.3 Pre-fabrication and industrialisation

For timber constructions to be a truly sustainable and viable alternative, the economic side of it must also be competitive. An effective production process is crucial to attain to be competitive with other building systems. The BV2020-concept is based on prefabrication of elements (Fig. 2), that means fabricate as much as possible in the factory, and then put together on the construction site.

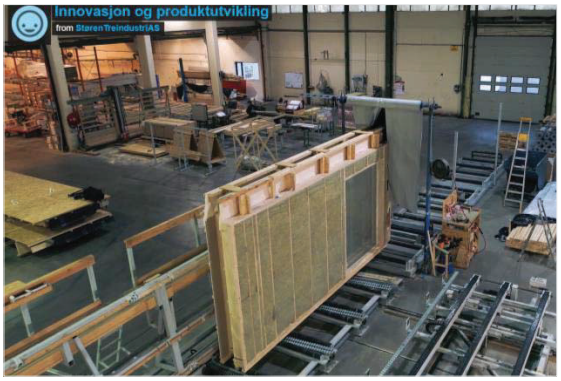

Figure 2: *Production line for elements at Støren Treindustri AS (https://storen-treindustri.no/produkter/).*

There are benefits by performing the building operations in a factory, and are also discussed by [10]:

- Better quality of the wood building product.
- Lower cost compared to performing the operations at the construction site.
- Shorter construction time.
- Independent of weather conditions, which will reduce the risk for humidity in the constructions.
- Reduction of on-site accidents.
- Reduction of waste

A range of variables influence the costs. Even though the direct material costs of wood can be slightly higher than others, the total cost of a finalized mid-rise wood building will often be lower compared to a concrete construction (6 % for eight storey buildings according to [11]). Prefabrication and mass production are key elements to achieve necessary competitiveness of this alternative, and thus even more projects can make the environmentally friendly choice and increase the total use of wood in buildings. This will heavily affect the ability of the building industry to achieve a noticeable reduction in climate change impact, and by doing so, contribute to the crucial global climate goals.

In the life cycle of a building, the operation phase has been dominant concerning energy use and green house gas emissions, but emissions that occur during the operation has declined dramatically over time due to existing substantial energy saving codes or other policies, and thus, the relative contribution of construction stage emissions and impacts becomes more dominant and significant. Therefore, green house gas emissions or impacts in the construction stage must be analysed [12]. The choice of material is the most important at the construction stage concerning green house gas emissions, but also the way of producing the buildings is of importance.

The building industry based on conventional on-site construction approach is by [12] characterized as labor-

https://doi.org/10.52202/069179-0553

intensive, wasteful, and inefficient, and that it is need for more introduction of lean production and prefabrication in the building industry.

In [13] research concerning the development of productivity in industrial wood building sector and conventional building sector has been performed in Sweden. It is the period from 2014-2018 that has been investigated. The results show that the industrial approach has increased the productivity expressed as cost per area of 30 % compared to conventional building processes, and that the lead time for the building process has been reduced by 3,3 months.

Through an Internet survey [14] of hundreds of AEC professionals (Architecture, Engineering, and Construction), data were gathered on the impact of prefabrication and modularization on key industry productivity metrics including project schedules, costs, safety, quality, eliminating waste and creating green buildings. It is reported that some of the most significant productivity findings from prefabrication and modularization users include the following:

- 66 % report that project schedules are decreased – 35 % by four weeks or more.
- 65 % report that project budgets are decreased – 41 % by 6 % or more

Further, [14] report that productivity is the top driver of prefabrication/modularization use among all firms. It is described that time savings and even small cost reductions make a big difference for players in the construction industry, where profit margins are slim due to the labour-intensive and expensive nature of on site construction. In the investigation it is found that 92 % of contractors see productivity as a stronger driver to use prefabrication/modularization, compared to engineers (70 %) and architects (68 %). Competitive advantage (85 %) and generating greater ROI (70 %) (return of investment) are stronger drivers for contractors than they are for architects and engineers [14].

In the research of [12], models and case- studies were performed to calculate the reduction of green house gas emissions when increasing the prefabrication level. It was found that the reduction was 2-5 %, but that it can be even more reduced by higher degree of pre-fabrication.

In the investigation of [14] “green aspects” were not a major driver to prefabrication and modularization adoption. However, when they asked about environmentally aspects, including site waste and amount of materials used, a different story emerged. 76 % of respondents indicated that prefabrication/modular construction reduces site waste – with 44 % indicating that it reduced site waste by 5 % or more. In addition, 62 % of respondents believe that these processes reduce the amount of materials used – with 27 % indicating prefabrication/modularization reduced materials used by 5 % or more [14].

In the development of the BV 2020-concept, and in the WoodWorks! Cluster, the industrialization of the building process has high priority, including the logistic from raw material sources to transport and assembling at the construction site. To optimize the use of raw material and reduction of waste through the whole value chain is important together with high productivity. It is, however, impossible to eliminate the waste totally, but the side streams that the waste represent can be raw material for other types of industry in the region, ant it is on-going activities to study these possibilities.

2.4 Mass customization

To produce buildings effective in an industrial way, it is a challenge to combine it with high variation in the products to meet the customers requirements. Mass customization is, according to [15], a manufacturing paradigm that enables customized and personalized design at a cost near mass production, and that mass customization's ability to lower unit cost, increase quality, and shorten project duration for customized offerings is considered highly relevant for tomorrow's house building industry.

Støren Treindustri has ongoing activities concerning mass customization of the production of buildings up to four floors, and it is possible to adopt it into the BV 2020-concept for buildings up to eight floors.

In [15] it is concluded that a great potential exists for applying mass customization in the house building industry. However, despite its potential, research on mass customization in the house building industry is sparse. In particular, research on developing the solution space and choice navigation tools is limited in this industry.

Several challenges for implementing mass customization in the house building industry have been identified and reported in the literature review of [15]:

- “The requirement for changing the supply chain setup. At the moment, supply chains in the house building industry are structured to fit engineer-to-order building projects and thus lack standards necessary to cope with builders and suppliers of mass-customized offerings.”

- “To align what customers want with the internal capabilities of the company, that is, to define the solution space offered to customers.”

The last bullet point has high priority in the development of the industrial building process in the BV 2020-project and in WoodWorks! Cluster. The variation in the product spectre has to be limited to the limitations in the factories for maintaining high productivity, but at the same time offer more variations where the industrial limitations are lower.

3 FURTHER WORK

To verify the interaction between both technical solutions, fire safety, acoustics, design for efficient manufacturing/ prefabrication, environmentally friendly material use and production and finally a profitable concept for all parts of the value chain, the BV2020 solution must be tested in full scale with a pilot project, preferably an 8 storey residential apartment block.

Furthermore, the concept is also applicable for other building types such as offices, etc., which is also planned for, even though not being part of the initial project description.

For fire safety, the project has developed loadbearing prefabricated floor slab elements of lightweight structural wood with the ability to withstand the complete duration of a fire, including the decay phase, according to Eurocode 1 [16]. This has been possible by taking advantage of products with improved material properties during fire and focus on fire performance in the design of the construction.

With regards to acoustics, the developed concept for the floor elements for spans of approximately 8 meters has shown very good test results both with regards to airborne sound and step sound.

Similar development and tests will be carried out for load bearing walls and transitions. Several other aspects of the concept also need to be managed, ensuring the required flexibility of the entire building.

4 CONCLUSIONS

By substituting building materials with large CO_2 emissions with wood-based solutions, we can make a huge positive contribution to the necessary actions against climate change. The BV2020 solution has the goal to develop concepts that enable mass customized production of prefabricated light timber frame, load bearing elements for buildings up to eight - 8 - storeys for the volume market. The development of the concept is well under way. A concept also for load bearing walls and transitions is under development, and both fire safety and acoustics will be studied this year.

Further development of the design for manufacturing, establishing cost-effective production processes and optimalization of the carbon footprint will be carried out.

Pilot project(s) will hopefully confirm achievement of the projects overall goals and give positive contribution to the reduction of green-house gas emissions.

ACKNOWLEDGEMENT

The BV2020 project is performed together with Veidekke Bygg Trøndelag and InnTre Kjeldstad AS. SINTEF Community is the R&D-partner. The Research Council of Norway and Skogtiltaksfondet have contributed with funding.

REFERENCES

[1] M. Ramage, R. Foster, S. Smith, K. Flanagan and R. Bakker, «Super Tall Timber: design research for the next generation of natural structure». *The Journal of Architecture*, vol. 22, nr. 1, pp. 104-122, 2017.

[2] A. Gosselin, P. Blanchet, N. Lehoux and Y. Cimon, "Main motivations and barriers for using wood in multi-story and non-residential construction projects". *Bioresources*, vol. 1, no. 12, pp. 546-570, 2016.

[3] Bjelland, H. "Fire Safety Concepts for Residential Apartment Buildings – Fire safety measures and risk". M. Sc. Thesis, University in Stavanger, 2009.

[4] Solís-Guzmán J., Martínez-Rocamora A., Marrero M. Assessment of Carbon Footprint in Different Industrial Sectors. Volume 1. Springer; Singapore: 2014. Methodology for determining the carbon footprint of the construction of residential buildings; pp. 49–83.

[5] J. L. Skullestad, R. A. Bohne og J. Lohne, «High-rise timber buildings as a climate change mitigation measure - A comparative LCA of structural system alternatives». *Energy Procedia*, vol. 96, nr. September 2016, pp. 112-123, 2016.

[6] Selvig, E., Enlid, E., Næss, A., Alfredsen, G., L. R. Gobakken, L. R. and K. M. Sandland. Lavutslippsmaterialer i bygg. Barrierer og muligheter. NIBIO RAPPORT vol. 6, nr. 20 2020.

[7] Statistics Norway, «Building stock». [Internet]. Available: https://www.ssb.no/bygg-bolig-og-eiendom/bygg-og-anlegg/statistikk/bygningsmassen. [Accessed 18 March 2022].

[8] European Commission. Trans-European Transport Network (TEN-T) https://transport.ec.europa.eu/transport-themes/infrastructure-and-investment/trans-european-transport-network-ten-t_en

[9] Treindustrien, 2021: Treindustrielle muligheter for oppgradering og påbygg av eksisterende bygningsmasse. https://www.treindustrien.no/resources/filer/20210614-Treindustrielle-muligheter-Prosjektrapport.pdf.

[10] Padilla-Rivera A., Amor B., Blanchet P. Evaluating the Link between Low Carbon Reductions Strategies and Its Performance in the Context of Climate Change: A Carbon Footprint of a Wood-Frame Residential Building in Quebec, Canada. Sustainability. 2018;10:2715. doi: 10.3390/su10082715.

[11] P. D. Kremer and L. Ritchie, «Understanding Costs and Identifying Value in Mass Timber Construction: Calculating the 'Total Cost of Project' (TCP)». *Mass timber construction journal,* vol. 1, pp. 14-18, 2018.

[12] Mao, C.; Shen, Q.; Shen, L.; Tang, L. Comparative Study of Greenhouse Gas Emissions between Off-Site Prefabrication and Conventional Construction

https://doi.org/10.52202/069179-0553

Methods: Two Case Studies of Residential ProjectsEnergy and buildings, 2013, v. 66, p. 165-176.
[13] Stehn, L. and Jimenez, A., Produktivitetsmått för Industriellt träbyggande, slutrapport. Luleå Tekniska Universitet, 2021.
[14] McGraw-Hill, Prefabrication and Modularization: Increasing Productivity in the Construction Industry, in, McGraw-Hill Construction, New York, 2011.
[15] M. S. S. Larsen, S. M. Lindhard, T. D. Brunoe, K. Nielsen and J. K. Larsen, Mass Customization in the House Building Industry: Literature Review and Research Directions. Front. Built Environ., 10 October 2019. Sec. Construction Management, Volume 5 – 2019.
[16] Eurocode 1: Actions on structures – Part 1-2: General actions – Actions on structures exposed to fire, Standard Norge, 2002.

World Conference on Timber Engineering Oslo 2023

THE BENEFITS AND CHALLENGES OF WOOD IN HIGH CORROSIVE SURROUNDINGS

Sigurdur Gunnarsson[1], Tim Skotheimsvik[2]

Summary: The paper addresses the design strategy of designing the joints of large timber structures for corrosive surroundings like swimming hall facilities. It addresses the blind spots of Eurocode 5 and the shows the analytical and practical approach solving both the technical and economical demands of the project both in design- and realization phase.

KEYWORDS: clt, corrosive environments, large structures, WCTE 2023, Oslo, Norway

1 INTRODUCTION

The city of Oslo has a strong environmental policy with an increased use of timber in public buildings as a strategic part to fulfill this policy. The use of timber was therefore a declared the aim of the design for the new main swimming facilities at Tøyen in Oslo.
Swimming halls have high corrosive demands. Timber has obvious advantages regarding corrosive environments in comparison to ferreous materials.
The approach between Eurocode 2 towards reinforcement and Eurocode 5 towards fasteners, have several similarities. Minimal distances between members as well as mechanisms of force-transfer between base material and reinforcement/fastener.

Though the differences are categoric when it comes to corrosions of metals in concrete versus corrosion of metals in timber. The concrete cover is quantitatively defined for the different concrete types and the design of wood only use qualitative terms like ”metal completely covered with wood”. The solution was to contact researchers, producers and institutions in USA, Germany, Italy, and Norway. Applying the fact that corrosion of metals in wood is aqueous [1] and the range of wood moisture content [2] to be expected for the lifetime of the construction, gave the guidelines for both the overall structural design and especially the details.

2 DESIGN PRINCIPLES

The roof structure of the new main swimming facilities at Tøyen in Oslo is designed as hollow wooden beams in a combination of clt and glued laminated timer. The hollow space within the wooded structure in utilized as a technical floor. The basic design idea behind the roof structure, to something more as merely a technical floor, was to use all surfaces as an active part of the structural system. Hence instead of the classical thinking of a lattice structure with a passive cladding and a passive roof slab, inner the lattice was “omitted” and replaced by the visual surfaces as well as the roof slab forming a hollow beam.

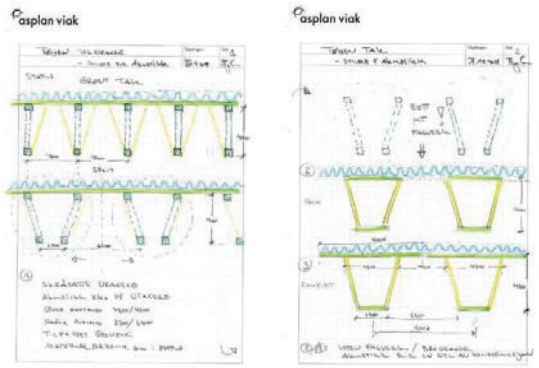

***Figure 1**: Design process – transformation from a spatial additive structure to an integrated solution.*

Additional to the obvious saving in materials by reducing layers also the architectural concept in this way merges completely with the structure.

***Figure 2**: Realisation process: model, mock-up, site.*

The on the top of the structure is a green roof, collecting water which will be used in the bath. The inner surfaces of the structure are for all HVAC and electrical services.

[1] Sigurdur Gunnarsson, Asplan Viak AS, Norway, sigurdur.gunnarsson@asplanviak.no
[2] Tim Skotheimsvik, Asplan Viak AS, Norway, tim.skotheimsvik@asplanviak.no

https://doi.org/10.52202/069179-0554

Holes in the surface serve the acoustics. The form of the structure enhances the use of light.
Combined the task is rather straight forward. A span little over 40 meters with a beam height totaling a little over 4 meters. Put simply, the bearing of the roof is always perpendicular to the direction of swimming, whereas the services inside the roof are parallel to the swimming.

3 SECTION COMPOSITION

The structural target of the design was flexural stiffness, answering both to the economical demands of the client and the available production of the market. A CLT production width of 3.5m was chosen to enable a wider range of bidders even though a few producers can deliver withs of 4 meters and more.
A parametric study was performed to compose the final section. A total of seven different compositions were evaluated regarding amount of material used and the stiffness. To enable a comparison, the values were normalized in the following way: the lightest section was defined as 100% - green line, the softest section was defined as 100% - yellow line. In this way the relative values became visually comparable as shown in the Figure 1.

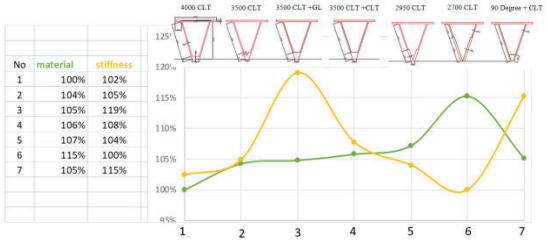

Figure 3: *Comparison of the different compositions for the main beam structure.*

The roof is created of several beam sections spaced out with a cc of 4.5 meters. The roof is completed by placing a smaller plate in between the top of two beam elements where the tolerance of the roof is taken up. The final section for construction is as shown in figure 4.

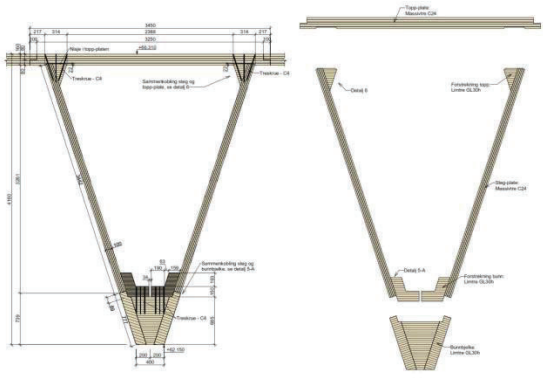

Figure 4: *The final section for construction*

One of the most sensitive points of the functional section "beam + column" is the column foot point. Here an early assessment was made, and a careful material composition and detailing was a successive inter-disciplinary process.

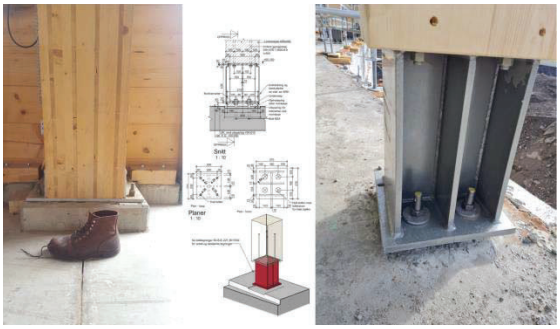

Figure 5: *Column foot point: reference, detailing, site*

4 DESIGNING FOR CORROSIVE ENVIROMENT

It is hard to avoid the use of fully threaded screws when designing large scale spatial timber structures with stiffness as an aim. Unfortunately, the availability fully threaded screws in C5 quality are next to none. Hence the strategy to avoid this problem was twofold: all critical sections being internal and avoiding too high wood humidity. Since the operational humidity and temperature is quite predictable for swimming facilities, it was possible to place the different parts of the construction. This meant designing such that the hygroscopic isotherms had acceptable and non-corrosive values in the zones of maximum forces. This was done in close cooperation with the projects building physic, Fredrik M. Haaland. The following humid zones for order, building and use were defined and placed on the Keylwert-diagram as shown in Figure 2. Thus, it was possible to localize areas non-fitted for connections, but also to verify that other zones had humidity values non-critical in regard to corrosion.

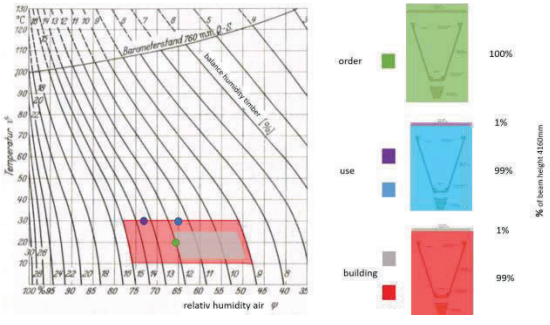

Figure 6: *Humid zones on a Keylwert-diagram.*

https://doi.org/10.52202/069179-0554

In the recent years a strong focus has been set both to assess and to assure the moisture level in wooden constructions. An excellent source used for comparison is “Quality assurance of timber structures” [3] published in Biel 2019. Here different types of buildings, including swimming facilities were evaluated.

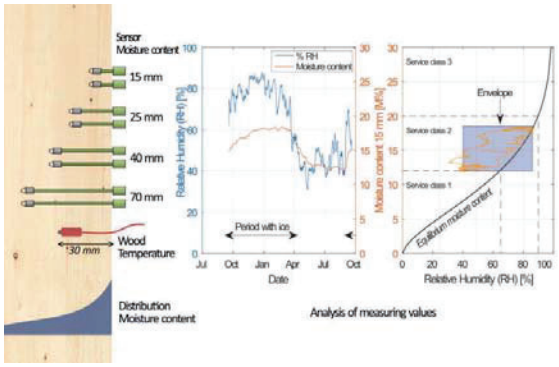

***Figure 7**: Used source for monitoring concept of moisture level [3]*

Due to the large size of the new bath and the different sones of use a monitoring concept reflecting to this was both set out in plan and section of the structure as shown.

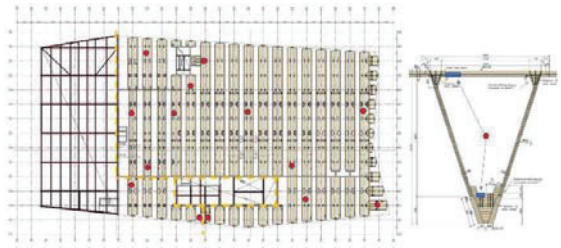

***Figure 8**: Monitoring of moisture in different sones of usage and sectional part of the wood structure.*

5 DESIGNING FOR STIFFNESS

A construction with such large dimensions will always consist of numerous smaller members. Also due to the use for internal services a considerable number of cut-outs must be made. The approach for designing this was straight forward. Starting with a “perfect section” with complete stiffness and no holes gradually increasing flexible boundary conditions and evaluating the influence of material removal. The process of incremented softness is shown in Figure 9 and Figure 10.

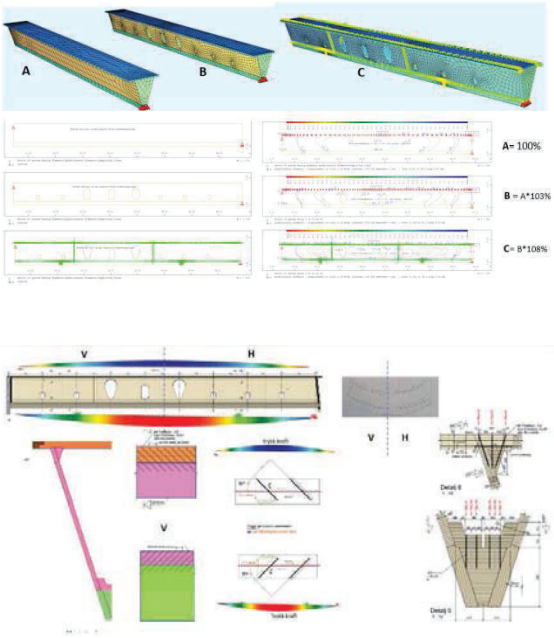

***Figure 9:** The process of incremented softness and link towards detailing in structure*

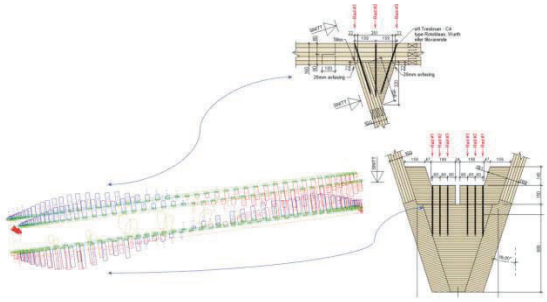

***Figure 10:** Shear flow along the main details of the incremented softness between different elements.*

***Figure 11:** Screws from the top plate ready to be drilled in.*

Resulting spring forces in overall modell as comparative bases for the design of fasteners and checking on deformations.

https://doi.org/10.52202/069179-0554

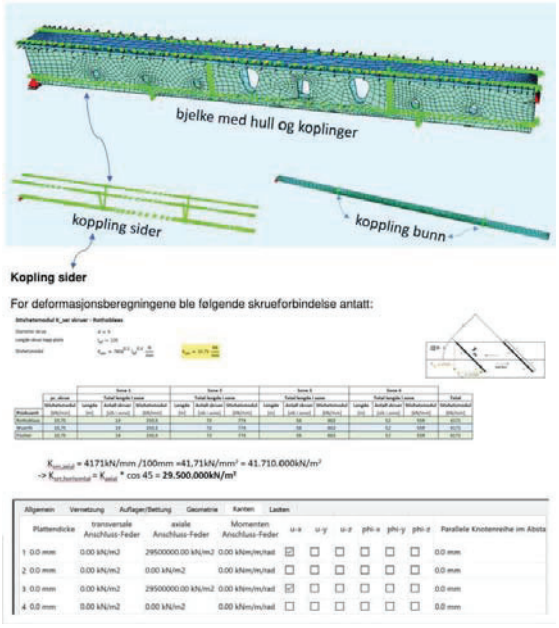

Figure 12: *The process of incremented softness – shell structure modelling principle for a single beam analysis.*

This method of increment made it possible to evaluate the potential of influence quite precisely regarding both forces and deflection. It is important to point out that the use of laminated shell-elements and a complete 3D model of the structure is imperative to assess a reliable result.
One of the most delicate details in the whole project is the connection of the bottom part of the beam. Here a considerable spectrum of solutions was evaluated according to stiffness and feasibility on site.

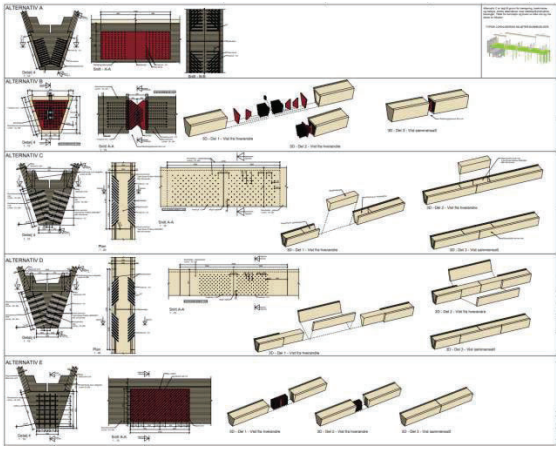

Figure 13: *Variation study of tension detail.*

This was important both due to the high-tension forces, 2.5MN, as well as this is a non-redundant part of a simple-span structure. Before application in the complete model a simple comparative study of stiffness and robustness was executed with the aim to verify the design target.

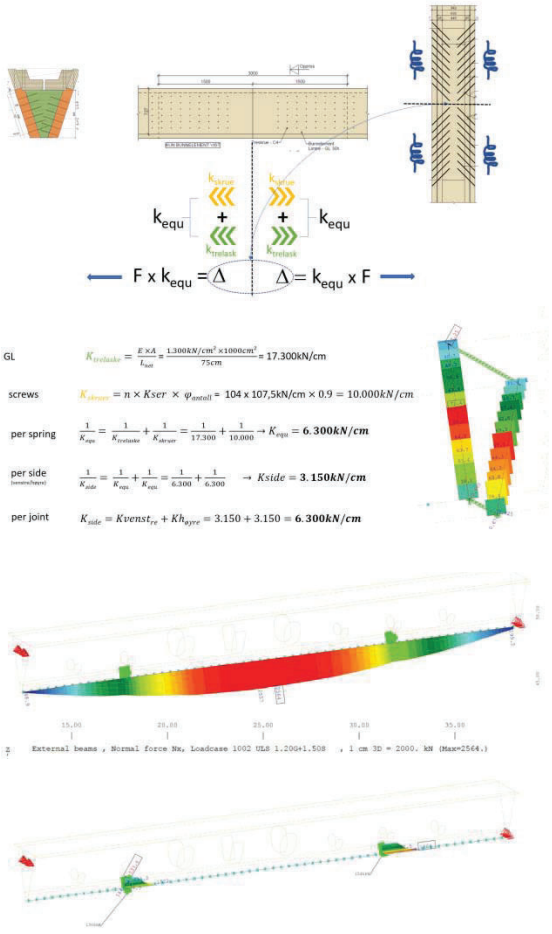

Figure 14: *Tension force distribution – max value 2.5MN, and values at planned site-connections 1.5MN (60%).*

Due to the importance of the on-site tension-connection and the harsh conditions of a swimming hall the following N+1 approach was taken: a combination of a mechanical and glued solution was chosen. In this way both the screws and the glue are independently able to transfer the force at intersection. The design suggested using a 2-component glue solution complying both to the EN 301 as well as low-contact-pressure with allowable thickness around 1.5mm to enable detail-deviations on site. Several rounds were taken with different producers, but the suggested design was clarified in a series of structural-workshops resulting in a 11 step detail description including temperature, humidity, application time shown on the next page in figure 15.

https://doi.org/10.52202/069179-0554

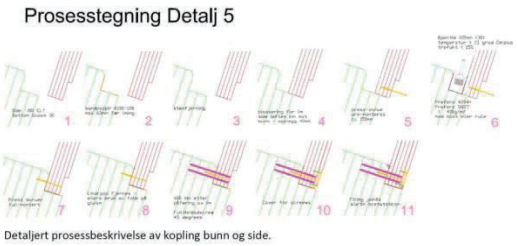

***Figure 15**: 11 step process of an on-site gluing according to EN301 and ETA demands to glue and CLT*

This early working on a high level of detail and practical issues formed the secure basis for a precise description in the tender documents and later a guideline for montage on the site.

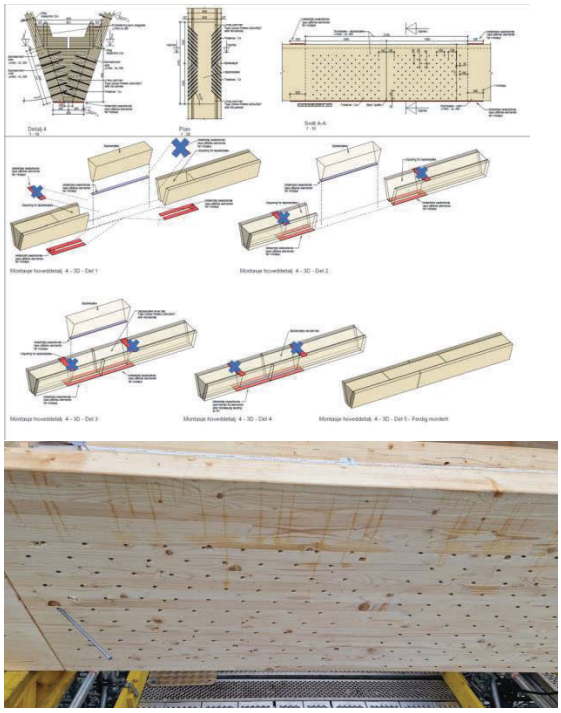

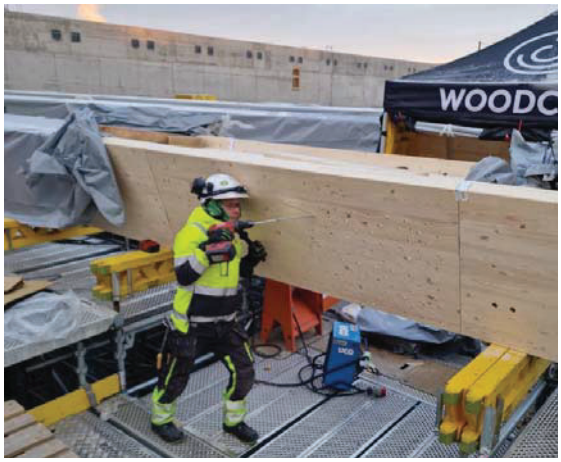

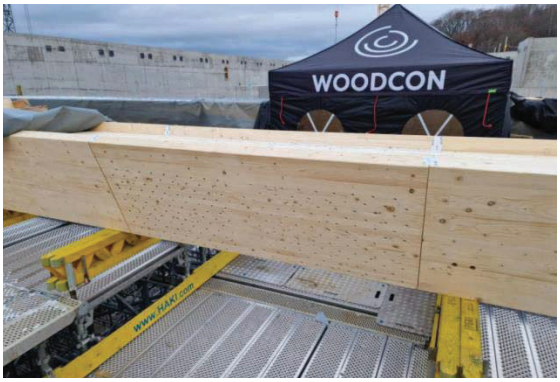

***Figure 16**: Final detailing and realisation on site*

6 CONCLUSION

The New Tøyenbath in Oslo is a project extending boundaries regarding size, functionality and corrosive demands. When compiling such a project this demands the full and continuous focus on details in material, humidity, craftmanship and process of building. While approaching the structural concept and key details of the project a cooperation and open-source approach has been key to developing a contractable and buildable project. Client with a strong vision, early discussions with producers of wood and fasteners. Simple calculations in early phases checking the feasibility of key details and the consequent use of sketches and BIM to navigate between client, producers, and design work. Every project has its delicate points. When realizing a project in C5 environment, success is an incremental process where client, material producers, companies on site and design team will only succeed together.

ACKNOWLEDGEMENT

We would like to thank the client, Oslobygg KF, for their intended aim to push boundaries for larger wood structures in Norway. This project and paper would not be possible without Oslobygg KFs focus on wood structures, continues support and close follow-up throughout the project.

REFERENCES

[1] Zelinka, Samuel L. 2014. Chapter 23: Corrosion of Metals in Wood Products. Samuel L. Zelinka (2014). Corrosion of Metals in Wood Products, Developments in Corrosion Protection, Dr. M. Aliofkhazraei (Ed.), ISBN: 978-953-51-1223-5, InTech. 2014; pp. 567-592

[2] Kollmann, Franz 1951. Technologie des Holzes und der Holzwerkstoffe. Bd.1, 2.Aufl., Berlin/Heidelberg/Göttingen: Springer Verlag 1951

[3] Franke, Bettina, Franke Steffen, Schiere Marcus Müller Andreas 2019. Kapitel 7: Überwachung und Inspektion von Holztragwerken.
Praxisleitfaden - Beurteilung der Holzfeuchte für

https://doi.org/10.52202/069179-0554

Tragwerke und Brücken für die Planung, Errichtung und Nutzung
Biel/Bienne Berner Fachhochschule, 2019, ISBN 978-3-906878-04-1

World Conference on Timber Engineering Oslo 2023

THE NEW CENTRE FOR ADVANCED TIMBER TECHNOLOGY: A LIVING LAB FOR DESIGNERS, INDUSTRY, AND EDUCATION

Gabriele Tamagnone[1], Robert Hairstans[2]

ABSTRACT: To meet the net zero requirements, UK industry will need to change how it operates, relying on more sustainable resources and practices. Within this scheme, the construction industry must move, when possible, from carbon-intensive material to more environmentally-friendly ones (e.g., timber). The general lack of expertise, however, is likely to slow down the transition process. With this in mind, the Centre for Advanced Timber Technology, in Hereford, has been established to form the professionals of the future and to upskill and reskill those willing to learn more about advanced timber practises. Part of this mission is played be the implementation of a living lab approach within the building, through which data will be gathered to inform the curricula and to provide external proof of good or bad practices in timber buildings, which will impact the industry at different levels (e.g., construction practices, design specification or insurance stipulations). This paper analyses the steps taken in this living lab project so far, analysing literature cases, presenting the methodology, and listing the projects involved in the gathering of the data through monitoring of the building.

KEYWORDS: Living lab, Building monitoring, Structural monitoring, Timber education

1 INTRODUCTION

The Centre for Advanced Timber Technology (CATT) at the New Model Institute for Technology and Engineering (NMITE) in Hereford is established to act as Centre of excellence for timber engineering and, more broadly, to deliver high quality teaching in the field of sustainable built environment. In alignment with NMITE's ethos "learning by doing", CATT wants to create learning material underpinned as much as possible by research and first-hand data. This is why the building hosting the Centre is to be a living lab, where features and performances of the building are measured to inform learners, and influence change in the construction industry, raising awareness about timber in constriction and act as test cast to inform how more reliable and durable timber buildings can be built.

1.1 CATT'S MISSION

The declared mission is to establish a centre of timber engineering excellence by:

- Implementing collaborative frameworks;
- Establishing connected ecosystems; and
- Leveraging opportunities.

The first point has been crucial since the beginning, when the Centre was founded in collaboration with Edinburgh Napier University (ENU) as well as external industry stakeholder and representative groups, including Timber Development UK.

The second point has to do with how the research carried out within the Centre can inform and help both inside and outside, and how other experiences of other Centres, Institutions, or research can inform and influence the activities of the CATT. A main asset to this is the implementation of a living lab approach within the building, which will be discussed in later sections.

Figure 1: *Centre for Advanced Timber Technology and Centre for Automated Manufacturing exterior (credits Bond Bryan Architects).*

[1] Gabriele Tamagnone, NMITE New Model Institute for Technology and Engineering, CATT Centre for Advanced Timber Technology, gabriele.tamagnone@nmite.ac.uk
[2] Robert Hairstans, NMITE New Model Institute for Technology and Engineering, CATT Centre for Advanced Timber Technology, robert.hairstans@nmite.ac.uk

https://doi.org/10.52202/069179-0555

The third and final point is all about seizing the day, balancing opportunity with feasibility and financial sustainability, yet always with a proactive approach to external discussions and proposals that align with the strategic intent of the centre.

The intent is for the CATT/CAM (Centre for Automated Manufacturing, co-located) building to act as a Living Lab within a portfolio of Living Lab projects working with industry and external stakeholders. This approach will ensure the educational model is actively engaged with industry and informed by live projects and real-world challenges. The delivery of the CATT/CAM building will derive the methodological approach to this. The emphasis will be to collate and codify information during the building delivery and post occupancy phases (including user occupant behaviours) to enrich a Building Information Model (BIM) and correlate it with predicted performance via a feedback loop in accordance with digital twinning approaches and the "Gemini Principles" [1]. Rolling this concept out to other projects will create an ecosystems of assets capable of demonstrating the virtues of utilising advanced timber technologies for built environment delivery when combined with manufacturing techniques, with an emphasis on regenerative design, circularity, socio-economic impact and health and wellbeing [1]-[3]. The aim is to create the necessary condition for a mass validation exercise of predicted performance relative to actual performance considering a range of metrics including, but not limited to, productivity, time/cost certainty, thermal, structural, acoustic, quality assurance, safety (including fire), and environmental impact. Curriculum content will be curated utilising the case study content captured and learning from each project will be through a particular lens or series of lenses tailored to the correct level of educational attainment and necessary learnings of the derived competency framework. The CATT/CAM building will be the HUB of this ecosystem, acting as the showcase given the opportunity to continually test, learn, iterate, and innovate. Further, the co-location of CAM with CATT will result in a symbiosis of timber engineering and advance timber technologies with automated manufacturing and integrated engineering approaches, generating further learning, including the need to consider, for example, the integration of mechanical, electrical, and renewable technologies, utilisation of robotics and interfacing with alternative materials. The CATT/CAM living lab will therefore instil holistic mindsets and collaborative working approaches through the embedded educational model whilst deriving industry solutions and value return to the sector, challenging traditional construction business model and procurement practices.

2 THE CONTEXT

According to the last data, the built environment, when considered as the union between construction industry and building utilisation, is responsible for the 37% of equivalent CO_2 emissions and 34% of global energy consumption, forming the highest portion of human induced climate change [4]. The way we build in the future and how we improve the built environment will have a huge impact on the net zero policies pursued by governments and communities around the world.

Wood, as a natural material, is seen as one of, if not the, main answers of the construction world to global warming contribution. Trees are excellent carbon storers, with 1.83kg of CO_2 stored in each kilogram of wood, on average. Improving the timber industry can result in a better management of woodlands, as wood would become a more and more valuable resource, raising the level of attention to detect wildfires and diseases. However, this is true as long as structures are built to last and materials are procured sustainably, otherwise the carbon stored in the materials is released after too short a period of time, resulting in a counterproductive effort to implement more natural materials, ending in a situation where the use of less sustainable products, but longer lasting, would have produced a more sustainable outcome.

It is, in fact, at least in the UK, the maintenance and durability of timber one of the main causes of concern when a wider implementation of this material in the built environment is discussed. The majority of warranty provider don't see wood as reliable, and to insure the same structure, but built with a more traditional material, such as concrete or steel, can cost up to eight times less when compared to the same made of timber [5]. This fact, together with other misconception around the material, such as the behaviour in case of fire or its reaction to water, have undermined utilisation.

Although it is true many things around timber are misunderstood, it is also true many are the things we still don't know about this material in constructions and its reaction to external actions naturally occurring during erection or in use. Some of the questions that need an answer are, but not limited to:

- How should a building team behave towards timber elements that get wet on-site during construction and how should they assess that those same elements have dried enough to continue with the subsequent construction phases?
- What is the actual difference in sustainability between a timber structure and a more "common" one when everything, from origin of materials to construction and use, is considered?
- Is there a natural decay of mechanical properties of timber elements outdoor or indoor?
- Do systems need to be tweaked, especially air conditioning and heating, when a timber building is considered?
- Do general rules apply adequately to timber constructions with exposed wood?

Numerous are the doubts still surrounding many aspects of these kind of constructions, and many of them need to be addressed to build more sustainably, more reliably, and at lower cost.

Although, things are changing, and CATT acting as a Living Lab has the aim of creating evidence-based information and educational content to this shift towards a more sustainable way to build.

2.1 OBJECTIVES

Goals for CATT acting as a Living Lab can be grouped in four areas:

2.1.1 Durability and Warranty

Timber is regarded as a natural and sustainable material, but being natural can also be a weakness when it comes to durability, due to different issues that may occur during the lifetime of a structure, mainly due to poor detailing and/or lack of knowledge of these materials and products. Consequently, given the scarcity of first-hand data regarding what goes well and what's done wrong, and longevity of timber structure is low-balled by insurance and warranty providers, the latter overprice policies, which in turn renders prohibitive for many customers to build their new project out of wood.
One of the objectives of CATT is to create and gather information on timber structures, both good and bad practice, and to provide useful information for insurance companies to base their judgement on and give prices in line with other materials for timber buildings too. Furthermore, the objective is not only to provide proof timber can be durable, but also to assess when it isn't and what are the countermeasures to be taken to extend the life of wood-based structural and non-structural members.

2.1.2 Sustainability and User experience

Regardless of being natural, with trees sequestering carbon during their growth, the real degree of sustainability of timber constructions is yet to be evaluated precisely. The whole life carbon assessment of these structures is crucial to compare the embodied carbon of these buildings to that of other building materials constructions. Moreover, the durability issue may play a vital role in assessing these figures, with less sustainable, at least at the beginning, materials resulting more environmentally friendly in the long run due to the necessity to maintain and substitute timber decayed elements in inadequately built timber constructions.
In the utilisation of the building, attention must be paid to its serviceability and check if other materials could be better used instead or provide different characteristics to it, not only for its usage, but also for its possible modification of spaces or quality of the experience of the occupants from any point of view.
To summarise, the building must be sustainable before, during, and after, and liveable and functional during.
In this regard, CATT wants to investigate the supply chain of timber constructions, assessing the impact of all elements involved and looking into what differentiate these buildings from others. The aim is also the evaluate users' experience and indoor quality.

2.1.3 Digitisation and Digitalisation

These two topics are at the base of the development of any industry out there. Construction industry will use digital tools, IoT devices, and monitoring campaigns more and more in the years to come. In order to assess the wellbeing of a structure, sensors must be utilised and measurements taken, which then can be used to simulate different scenarios to prepare and act against possible future events before these happen. In the manufacturing and design phases, computer aided and controlled technologies will make production and construction more and more sustainable, with less waste and optimisation both off-site and on-site.
CATT, together with the Centre for Automated Manufacturing, wants to pilot new technologies and partner with industrial stakeholders to develop new ones in order to progress and push the whole timber industry, from seed to building and reuse/recycle, forward.

2.1.4 Outreach and Education

The lack of knowledge in the UK when it comes to wood and timber engineering is palpable, with very few institutions providing specialistic modules in their curricula covering what industry needs to operate in this sector in the best way possible. Many rely on CPDs after graduation or on the experience passed from employee to employee when inserted in the new company. The minority of college or university educated come out work-ready.
CATT is keen to provide education, at any level, for students and professionals wanting to have a career in the field of timber and wood industry and of sustainable built environment. The objective is to deliver up-to-date learning content in different areas, with materials underpinned by research outputs, helping, this way, not only learners, but the whole industry through outreach and dissemination.
Part of these objectives will be pursued using the CATT/CAM building as a living lab, collecting data in different areas directly from it.

3 LIVING LAB

Even if the term "Living lab" has assumed several meanings and has been used in different contexts [6], it is fair to say that the difference between that and a traditional lab is that a living lab doesn't set up tests using a controlled environment, well established boundary conditions, and predetermined loads, actions, or disturbances to see the influence of various aspects on a certain phenomenon.
A living lab takes advantage of ordinary situations, it gathers information from the actual environment to test real life scenarios and see how different approaches work when applied to a situation with unpredictable variables, which are naturally present and constitute the existent operative conditions.
This means a living lab can test a setup with way more external influences than those of a traditional test: usually, in a lab, conditions are established to analyse a specific behaviour when a particular perturbation is applied to the system. In a living lab, nothing, usually, is externally

https://doi.org/10.52202/069179-0555

applied to the system, but naturally occurring events contribute to the variation of settings.
As any test, living labs makes use of sensors and other tools to measure specific quantities. However, as they are bigger in size, greater is the number of sensors too, if compared to a normal test, to be able to get the correct information from the assessed area, which can be a school, a hospital, a factory, or even an entire city. Depending on the characteristics to be evaluated, the desired degree of precision, and the dimensions of the specimen, the capillarity and number of measuring devices could vary from few units to hundreds.
Basically, everything could be transformed into a living lab, depending on the information one wants to extrapolate and from where. Plus, a living lab runs itself: once sensors are placed and the platform starts to collect data, it is just a matter of analysing that data and extract the right information once the sample is wide enough to draw useful conclusions.

4 CATT AS A LIVING LAB PROJECT

4.1 MOTIVATIONS

The main reason behind the Living Lab implementation is to provide the evidence base to support the need to deliver a better, more sustainable built environment. As previously reported, the construction industry and building operations combined are responsible for the biggest slice of carbon emissions and energy consumption in the world, meaning that reversing the trend passes through more sustainable practices in these areas.
This means to adopt sustainable materials and technologies and to build less energivorous buildings. The former means to use natural materials, that, at least, but not only, from a structural point of view, usually means timber. In the UK, however, given the recent policies to reduce the use of flammable materials in construction, the general lack of expertise in timber engineering, and a broad distrust of wood, especially by insurance companies and warranty providers, the spread of timber structures struggles to take off. The insurance question is the one that would benefit the most from living lab approaches within timber buildings: monitoring the actual performance of the structure, especially the load-bearing elements, will give the actual picture of timber durability, providing real data that could change the perception of this material and simultaneously lower the insurance costs, which is the main reason for reconsideration for many costumers willing to have a timber building. The living lab approach will give the opportunity to learn from possible mistakes, inform policy makers, designers, manufacturers, and building companies, and in general will enable the creation of conditions for better, more reliable, and long-lived buildings of this type in the future.
The second aspect, namely, the less energy demanding building piece, can gain from the living lab approach too: the monitoring of the building can challenge the effectiveness of the design solutions adopted, informing the suitability of materials, correct performance of the details, and in general help, once more, to build better timber buildings, with better materials and better details.

4.2 METHODOLOGY

As mentioned, given the lack of skills in the UK and the necessity to change the construction industry, implementing more and more bio-based products in future and retrofitted buildings, CATT's mission is to bridge the gap, providing educational solutions for both professionals and students.
In doing so, the CATT/CAM building, together with other case studies and projects, will be used to create research-based, up-to-date learning content through a living lab approach.
The methods that will be implemented to address the four objectives outlined in 2.1 will be:

4.2.1 Durability and Warranty

The building will be used to test directly the possible issues a timber building can experience, plus measure several properties over time, such as mechanical properties and insulation performance, to give a more complete picture of the construction and its behaviour year after year.
To do this, sensors will be deployed to measure real-time quantities, both inside and outside the building, to compare internal and external conditions and get the best image of the building performance, especially in terms of humidity and moisture, and temperature. Periodic measurements on structural elements will be made to ascertain their properties remain in a suitable range over time [7]-[10]. Measurements like these, or those involving sensors, will be replicated on other buildings to get statistically relevant results and formulate better theses, with attention to the influence of different boundary conditions [11].
In the workshop, laboratory tests may be carried out to simulate different environmental conditions, and outside natural weather could be used in a "controlled" fashion to assess the behaviour of different timber products outside or to evaluate the protection capabilities of different solutions, especially those not yet covered in literature [12], [13].
The major part, if not all, of the data gathered will be used to inform insurance and warranty providers in order for them to understand better the material and related products, and what actually are the things to look more carefully at when stipulating a policy, instead of focusing solely on the fact that the building to be insured is made of timber, and so will eventually rot or burn. Moreover, the proof will be able to inform designers and constructors on non-working details or concepts, moving towards more reliable and durable solutions.

4.2.2 Sustainability and User experience

Life-Cycle Assessment (LCA) and Whole Life Carbon Analysis (WLCA) have already been used successfully to analyse the effective sustainability of timber structures [14]-[18]. However, a shared strategy is still missing, especially to compare timber figures with other materials. CATT's supply chain mapping will be used to do LCA

and WLCA to assist in the establishment of a methodology to assess the actual impact of timber constructions and judge their actual carbon storage capacity when compared to other forms of construction. This exercise will be repeated for other buildings to find a consistent and reliable method to address the issue.
Given the outputs of the first objective, the ability to deliver a more durable timber-built environment will act as an amplifier for sustainability, with less maintenance and replacement needed for timber elements resulting in longer storage of carbon within the buildings.
In addition, relying on the experience gathered from other researches in literature [19], [20], the user experience and comfort will be monitored to address the optimal use of air conditioning and heating system in an environment with exposed wood elements, being wood a hygroscopic material. This part will be covered with direct involvement of occupants with surveys and workshops [21], but other means might be used in the future to analyse other aspects and/or get rid of the human judgement/perception from the equation [22]-[24].

4.2.3 Digitisation and Digitalisation

Information from measuring the building and from the supply chain mapping will be captured within a BIM model, which will be used in the teaching activities, with the different information being used in different contexts to help teaching different topics.
In the future, the digital strategy could then be broadened to include other goals, such as:

- Understand the building from an operational perspective, enabling consumption optimisation [25];
- Have a 3D image of the measurements allowing the visualisation of the conditions and to interrogate whether different measurements are interrelated;
- Run simulations on the building using non-standard scenarios, stress-testing the system.
-

4.2.4 Outreach and Education

Finally, the above will be used, as already mentioned, to inform the outside, namely, all the areas directly or indirectly involved with the timber industry, to push the material forward, help finding better solutions to old and new problems, build more reliable constructions, and develop new technologies. This will be done in partnership with every layer of the sector, from forest to landfill, for CATT to act like glue joining together all these different entities.
More importantly, the data gathered, research undertaken, and knowledge acquired will be used in all the different programmes CATT will deliver to upskill and reskill today's professionals, or to train the future ones [26]. The educational offer will be strongly based on a learning-by-doing approach, with evidence-based content being the backbone of the teaching activities [27].

4.3 LIVING LAB RELATED PROJECTS

4.3.1 Stora Enso partnership

Stora Enso is world leader in the supplying of mass timber products. The company provided the CLT panels for the building, and started a research partnership with the Centre.
48 Wiiste sensors (Figure 2) have been installed in different locations of the building. These sensors are able to monitor the moisture content of the CLT panels at determinate depths using coated screws that work as the pins of a moisture meter. The uncoated part of the screws, namely, the tip, is the measuring part, so that different length screws can measure different parts of the panel. The sensors are all set to measure the moisture content of the inner and outer layer. Furthermore, the sensors allow also the gathering of temperature and humidity data inside the building.
The information collected will be compared to that gathered by a weather station placed on top of the building to assess the correlation between external weather and internal conditions.

Figure 2: *Moisture measuring Wiiste sensors: side (top) and frontal (bottom) view (credits Wiiste Oy).*

4.3.2 Measuring Mass Timber

Together with the architects' firm dRMM, CATT (via ENU) has submitted a proposal to fund a project that will focus on Whole Life Carbon (WLC) and Quality of Life Methods for mass timber buildings. The CATT will act as one of five case studies, and the project itself will use the information gathered with the Supply Chain Mapping (SCM) to contribute to the creation of data bank to demonstrate whole-life value of timber structures. The outline of the advanced proposal is:

- Whole Life Carbon (WLC) assessment: combining the latest industry best practice guidance for assessing

https://doi.org/10.52202/069179-0555

carbon in general and specifically for timber buildings. Defining core input requirements, challenges in data collation and comparing outcomes against business as usual and best practice datasets/benchmarks (e.g., RIBA 2030, LETI)

- Post-Occupancy Evaluation: monitoring relevant essential activity components of the RIBA's POE & BPE Primer, with an emphasis in terms of assessing Quality of Life and user satisfaction. Additional monitoring of internal air quality & thermal comfort to support any qualitative feedback. Comparing outcomes against national and building POE specific datasets.
- Fundamental project information: essential information for each building, to contextualise each case study project's WLC and POE outcomes in terms of their unique circumstances (e.g., date constructed, project build cost, detail on the building's use and client/occupiers, suppliers of mass timber systems, etc.).

4.4 DIGITAL SOLUTIONS

During the construction phase, the companies shared information through a level 2 BIM model to coordinate activities and check whether any modification to the original plan had an impact on any other already schedule undertaking.

The importance of this digital approach is that everyone is sharing the same design space and can know right away what is going on in the other operations, which optimise productivity and increase safety.

From a Living Lab perspective, the digital model can be used to collate data about different aspects of the building: a BIM model can be used not only to plan, but each element within the model can be populated with information regarding several aspects, such as supply chain (e.g., manufacturer, origin of materials, or ubication of production site), performance (e.g., U-value, sound absorption, or structural grade) sustainability (e.g., CO_2 equivalent). This way, a comprehensive tool can be generated and used as a library containing all the information about the building.

The next step is to use the model to create a digital twin. The new model takes advantage of part of the information stored in the BIM model and augment this with information about mechanical, electrical, and plumbing (MEP) systems, such as consumptions and performance. This approach helps to understand if the designed performance is met by the actual building.

The third, and more interesting, step, from a Living Lab perspective, is to use the digital twin to gather data from sensors. This approach allows for the direct estimation of localised performance of the building, enabling immediate action against any possible problem, or the ability to track the evolution of the construction over time, to check performance is maintained throughout. Another advantage of this is the possibility to use up-to-date information to run simulations, both for different from usual scenarios and for different characteristics of the buildings, namely, different materials or MEP systems, to study the building from any desired perspective and address specific problems.

At the present stage, the array of sensors currently deployed is not allowing us to take full advantage of this tool, but, given the goal we set ourselves, the will is to increase the amount of sensors and to expand the current range of monitored characteristics, making the adoption of this technology very likely, if not necessary, in the future.

Furthermore, as previously mentioned, these solutions are of interest for building maintenance and operations, which means not only research and learning activities can be based on this, but also analyses on costs and consumptions can benefit from the digital twin. Therefore, not only the CATT team, but the NMITE's Estate team is interested in this technology and will collaborate on this project too.

5 CONCLUSIONS AND FUTURE STEPS

In this paper, the current operations regarding the implementation of a living lab within the CATT/CAM building of NMITE are presented. The living lab approach is discussed together with the projects that will take advantage of said approach. Finally, digital solutions to be implemented are depicted.

The methodology illustrated is, for now, just a methodology, apart from the moisture in CLT sensors and the supply chain mapping. Nevertheless, the direction shown is clear and the targets set are well-defined and implementable over time with the correct resources secured.

In the future, further measurements and monitoring should be carried out, such as structural health monitoring or thermal performance assessment of the envelope, to not only augment the base knowledge of the building, but also to provide further information on the actual behaviour of such buildings, with an emphasis on durability. The information collated, together with that already gathered, will inform the educational programme providing first hand evidence. The LCA and supply chain mapping will provide evidence of the sustainable procurement approaches taken toward the derivation of a more standardised methodology to evidence the actual sustainability of timber buildings. Digital solutions are also considered as an approach for transparency and visualisation to convey in a more powerful and incisive way concepts regarding timber constructions, capable of assisting with the gathering of data and its interpretation, particularly as the level of sensors and measurements grows and becomes more complex.

https://doi.org/10.52202/069179-0555

REFERENCES

[1] Bolton, A., Butler, L., Dabson, I., Enzer, M., Evans, M., Fenemore, T., Harradence, F., et al.. Gemini Principles. (CDBB_REP_006), 2018. https://doi.org/10.17863/CAM.32260

[2] Guglielmo C., Nitesh M.. Circular Business Models for the Built Environment. In Arup & BAM, 2017.

[3] Ellen MacArthur Foundation. Intelligent Assets: Unlocking the Circular Economy Potential, 2016. https://emf.thirdlight.com/link/1tb7yclizlea-116tst/@/preview/1?o

[4] United Nations Environment Programme. 2022 Global Status Report for Buildings and Construction: Towards a Zero-emission, Efficient and Resilient Buildings and Construction Sector. Nairobi, 2022.

[5] Giddings J.. Mass Timber: Challenges & Potential Solutions - Summary report of the ASBP's Timber Accelerator Hub. The Alliance for Sustainable Building Products, 2022.

[6] Leminen S. Q&A. What Are Living Labs? Technology Innovation Management Review, Vol. 5(9), pp 29–35, 2015. http://timreview.ca/article/928

[7] Palma P., Steiger R.. Structural health monitoring of timber structures – Review of available methods and case studies. Construction & Building Materials, Vol. 248, 118528, 2020. https://doi.org/10.1016/j.conbuildmat.2020.118528

[8] Alarcón M., Soto P., Hernández F., Guindos P.. Structural health monitoring of South America's first 6-Story experimental light-frame timber-building by using a low-cost RaspberryShake seismic instrumentation. Engineering Structures, Vol. 275, part B, 2023. https://doi.org/10.1016/j.engstruct.2022.115278

[9] Wang J., You H., Qi X., Yang N.. BIM-based structural health monitoring and early warning for heritage timber structures. Automation in Construction, Vol. 144, 2022. https://doi.org/10.1016/j.autcon.2022.104618

[10] Larsson C., Abdeljaber O., Bolmsvik Å., Dorn M.. Long-term analysis of the environmental effects on the global dynamic properties of a hybrid timber-concrete building. Engineering Structures, Vol. 268, 114726, 2022. https://doi.org/10.1016/j.engstruct.2022.114726

[11] Kukk V., Kers J., Kalamees T., Wang L., Ge H.. Impact of built-in moisture on the design of hygrothermally safe cross-laminated timber external walls: A stochastic approach. Building and Environment, 226-109736, 2022. https://doi.org/10.1016/j.buildenv.2022.109736

[12] Evans, P. D., Matsunaga, H., Preston, A. F., Kewish, C. M.. Wood Protection for Carbon Sequestration - a Review of Existing Approaches and Future Directions. Current forestry reports, Vol. 8, pp 181-198, 2022. https://doi.org/10.1007/s40725-022-00166-x

[13] Ayanleye S., Udele K., Nasir V., Zhang X., Militz H.. Durability and protection of mass timber structures: A review. Journal of Building Engineering, 46, 103731, 2022. https://doi.org/10.1016/j.jobe.2021.103731

[14] Pomponi F., D'Amico B.. Holistic study of a timber double skin façade: Whole life carbon emissions and structural optimisation. Building and environment, Vol.124, pp 42-56, 2017. http://dx.doi.org/10.1016/j.buildenv.2017.07.046

[15] Hart J., D'Amico B., Pomponi F.. Whole-life embodied carbon in multistory buildings: Steel, concrete and timber structures. Journal of industrial ecology, Vol.25 (2), pp 403-418, 2021. https://doi.org/10.1111/jiec.13139

[16] Dong Y., Qin T., Zhou S., Huang L., Bo R., Guo H., Yin X.. Comparative Whole Building Life Cycle Assessment of Energy Saving and Carbon Reduction Performance of Reinforced Concrete and Timber Stadiums - A Case Study in China. Sustainability (Basel, Switzerland), 2020, Vol.12 (4), 1566, 2020. https://doi.org/10.3390/su12041566

[17] Morris F., Allen S., Hawkins W.. On the embodied carbon of structural timber versus steel, and the influence of LCA methodology. Building and Environment, Vol. 206, 108285, 2021. https://doi.org/10.1016/j.buildenv.2021.108285

[18] Stocchero, A., Seadona, J. K., Falshaw, R., Edwards, M.. Urban Equilibrium for sustainable cities and the contribution of timber buildings to balance urban carbon emissions: A New Zealand case study. Journal of Cleaner Production, Vol. 143, pp 1001-1010, 2017. https://doi.org/10.1016/j.jclepro.2016.12.020

[19] Mazutti J., Londero Brandli L., Lange Salvia A., Fritzen Gomes B. M., Damke L. I., Tibola da Rocha V., dos Santos Rabello R.. Smart and learning campus as living lab to foster education for sustainable development: an experience with air quality monitoring. International Journal of Sustainability in Higher Education, Vol. 21-7, pp 1311-1330, 2020. http://dx.doi.org/10.1108/IJSHE-01-2020-0016

[20] Ascione F., Borrelli M., De Masi R. F., Vanol G. P.. Nearly zero energy target and indoor comfort in Mediterranean climate: Discussion based on monitoring data for a real case study. Sustainable Cities and Society, Vol. 61, 2020. https://doi.org/10.1016/j.scs.2020.102349

[21] Ebbesson E.. Towards a co-creation framework based on citizens' dreams of future mobility. Transportation Research Interdisciplinary Perspectives, Vol. 16, 2022. https://doi.org/10.1016/j.trip.2022.100686

[22] Dong W., Do E., Lee B. S., Cohn J.. Quantifying worker interactions and characterizing worker performance through ubiquitous IoT. Pervasive and Mobile Computing, Vol. 87, 2022. https://doi.org/10.1016/j.pmcj.2022.101702

[23] Piselli C., Pisello A. L.. Occupant behavior long-term continuous monitoring integrated to prediction models: Impact on office building energy performance. Energy, Vol. 176, pp 667-681, 2019. https://doi.org/10.1016/j.energy.2019.04.005

https://doi.org/10.52202/069179-0555

[24]Eon C., Morrison G. M., Byrne J.. The influence of design and everyday practices on individual heating and cooling behaviour in residential homes. Energy Efficiency, Vol. 11, pp 273–293, 2018. https://doi.org/10.1007/s12053-017-9563-y
[25]Bursill J., O'Brien L., Beausoleil-Morrison I.. Multi-zone field study of rule extraction control to simplify implementation of predictive control to reduce building energy use. Energy and Buildings, Vol. 222, 110056, 2020. https://doi.org/10.1016/j.enbuild.2020.110056
[26]Ridley-Ellis D., Nolte S.. The educational needs of the timber industries – report of an online survey by the centre for timber engineering, 2006. https://www.napier.ac.uk/-/media/worktribe/output-249416/cteedusurveyapr2006pdf.ashx
[27]Mortesen A., Tupenaite L., Naimaviciene J., Kanapeckiene L., Amado M., Hamburg P., Taylor R. H.. Improving transnational education in timber construction by the use of project-based learning approach: as evaluated by teachers and students. Baltic Journal of Real Estate Economics and Construction Management, Vol. 7, 1, pp 228-244, 2019. https://doi.org/10.2478/bjreecm-2019-0014

World Conference on
Timber Engineering
Oslo 2023

QUANTIFYING AND REDUCING EMBODIED CARBON IN THE ACOUSTIC DESIGN OF MASS TIMBER BUILDINGS

James Bligh[1], MIOA, Piltes

ABSTRACT: An adoption of mass timber construction is the construction industry's best shot at reducing its significantly large contribution to global CO_2 emissions and to play its part in slowing down the climate crisis. Acoustic design in mass timber buildings typically relies on mass and facing materials in order to meet design criteria, and can account for a high proportion of the embodied carbon (CO_{2e}) per m² on a build. In order to fit with the ethos of mass timber construction; low embodied carbon, reusable, cradle to cradle materials must be adopted.

This paper presents the findings of a study into the relationship of acoustic performance and CO_{2e}, and proposes alternate approaches that reduce the CO_{2e}/m² of the acoustic design by up to 66% with little to no detriment to acoustic performance. Through single variable analysis in third party laboratory testing, and in situ testing, it has been found to be possible to utilise low CO_2e acoustic systems that reduce the CO_2e/m² in not only the acoustic design, but structural, M&E and architectural disciplines, too.

KEYWORDS: Acoustics, Mass Timber, CLT, Embodied Carbon

1. INTRODUCTION

Mass timber construction (predominantly Cross Laminated Timber [CLT] in Europe), is a method of utilizing sustainably FCS forestry commissioned timber to create building material that is used for structural support, roofs, floors and walls. It has garnered praise from most building design disciplines for its material properties – from structural loading capacity through to its biophilic appeal. Provided reforestation of these FSC supplies keeps up with demand, and in fact accelerates beyond it, the carbon sequestering capability of mass timber construction could lead to a significant reduction in the carbon emissions of the construction industry. To go theoretically further, if adopted on a global scale, mass timber could sequester more carbon than is omitted during the construction program.

Reforestation, increased biodiversity and an increased use of biomass fuels all are secondary beneficial factors to mass timber construction, too. However, the variability in moisture content, density, surface mass and timber species from manufacturer to manufacturer can create uncertainty in the acoustic and structural design of mass timber, leading to overspecification of floor and wall systems. Given these two disciplines have a historical tendency to utilise heavyweight isotropic mass in order to achieve relevant design criteria, the CO_{2e} of acoustic and structural design in mass timber buildings often account for an unnecessarily large proportion of the overall building design.

This paper sets out an observed correlation in acoustic performance and CO_2e/m² in mass timber construction and proposes alternative methods of construction and design approach that greatly reduces the CO_2e/m² of the acoustic design.

2. EMBODIED CARBON AS A METRIC OF SUSTAINABILITY

The lifecycle of a material can be allocated an embodied carbon figure given as CO_{2e}, which is obtained through a review of the CO_2 emissions generated from the entire lifespan of the material. This broadly covers raw material sourcing, manufacturing, transportation and longevity of the material (i.e. does it need replacement/maintenance throughout its life, and can it be demounted, recycled or reused at the end of life). As a result of this, a quantitative metric can and should be placed on any building material being used within a mass timber

[1] James Bligh, Pliteq UK, jbligh@pliteq.com

https://doi.org/10.52202/069179-0556

building – from the structural timber, right the way through to the light switches.

Manufacturers of building materials can opt into obtaining Life Cycle Assessments (LCA) in accordance with ISO 14040:2006 or EPD (Environmental Protection Declaration) in accordance with ISO 14025:2006 in order to provide evidence of the 'sustainability' of their products. However, these assessments are self declarations that are peer reviewed by regulatory bodies, but do not always address secondary ancillary materials required for those products to be used effectively – for example, floating floor isolators requiring heavy mass to obtain sufficient isolation efficiency or ceiling hangers requiring multiple layers of plasterboard. As a result, seemingly low CO_{2e} material products in isolation seem to fit the mass timber ethos, yet require high CO_{2e} materials such as multiple plasterboard linings and wet trades such as concrete and screed in order for them to meet required acoustic performance criteria.

The IPCC 6th Assessment Report offers guidance on how to reduce CO_{2e} emissions in construction, which are broken into 3 leading changes that yield the largest net reduction emission reduction, as **Figure 1** illustrates. The size of the orange circle reflects the size of the contribution of net emission reduction, the intensity of the color within the circle reflects the cost implication of implementing it, assuming material cost, delivery and construction cost:

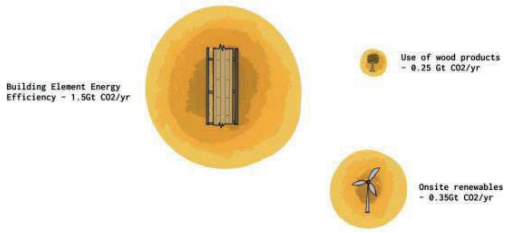

Figure 1: *Contribution to net emission reduction by 2030 (Gt CO_2/yr) – Construction* [1]

The IPCC report goes further, too. It suggests that not only changes to design criteria to aid emission reduction are considered, but also the role building materials play in the net emission reduction of CO_2 are too. **Figure 2** below reflects the data the IPCC report produces, in the same graphical format as Figure 1 follows:

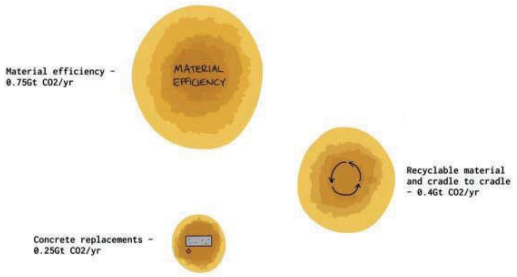

Figure 2: *Contribution to net emission reduction by 2030 (Gt CO_2/yr)- Industry* [2]

As can be seen from **Figure 2**, the efficiency of a building material (whether that be thermal, acoustic, lighting, M&E or other performance based metric) can have a large impact on net emission reduction. This can be interpreted as its ability to perform uniformly across time (low performance creep), as well as its ability to perform with as little secondary ancillary material support as possible, as discussed in the final paragraph of section 2.2**.** If this material was then to be recyclable at the end of its life (or even better demountable and reusable), the net emission reduction of the overall building is vastly improved. Lastly, the use of materials that replace concrete yields a smaller yet still significant impact on reducing emissions. In the context of building materials (i.e. facing layers, poured solutions and foundations), a reduction in the use of concrete still provides a significant chance to reduce net emissions and is largely interchangeable with materials with much lower CO_2 in most building types, but given the manufacturing, shipment and ultimate demolition of concrete accounts for 8% of global CO_2 emissions, a multi-disciplined approach to engineering out concrete where not required and favouring low CO_{2e} material is critical in slowing the climate crisis.

Finally, the benefits of switching to mass timber construction comes with many other quantitative benefits outside of CO_{2e}. Faster construction to meet demand of the housing crisis as urbanization increases worldwide, less site delivery movements, more dynamic thermal reaction, less on-site waste, and its biophilic appeal to name a

few. **Figure 3** illustrates a comparison of two hypothetical 7 storey buildings, one constructed from 100% CLT, the other concrete frame and slab.

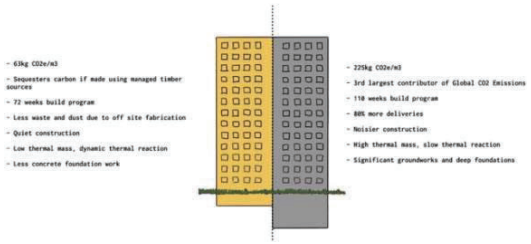

Figure 3: *Comparison of mass timber vs isotopic mass buildings.*

3. RELATIONSHIP OF EMBODIED CARBON AND ACOUSTIC PERFORMANCE

Correlating embodied carbon and acoustic performance is a difficult task to undertake due to the variables associated with design proposals, and the potential positive impacts that seemingly high CO_{2e} building materials may have on the performance of a building. A comparison with the analogy of a plastic wrapped cucumber creating unnecessary plastic waste can be drawn in construction – a plastic wrapped cucumber has a longer shelf life than an unwrapped cucumber, and is resistant to damage in transit. Therefore the plastic significantly reduces food waste - a major contributor of global CO_2 emissions. That said, alternatives to plastic wrap are now available that provide comparative, if not identical wrappage performance.

In the case of mass timber, commonly adopted concrete and screed pours onto the structural mass timber floors, or multiple layers of dense plasterboard wall linings is the plastic. Although these options all provide high thermal mass, good acoustic performance and predictable structural behavior, we must explore low CO_{2e} alternatives to meet comparable or identical performance. **Figures 4** presents an approximate correlation in airborne or impact acoustic performance and embodied carbon of concrete/screeded floor systems that can and are used in mass timber buildings. The estimated CO_{2e} of each system (not including the mass timber) has been obtained through 3rd party LCA.

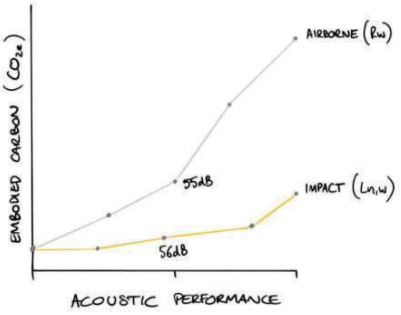

Figure 4: *Correlation of CO2e and acoustic performance in concrete/screeded acoustic floors in mass timber construction.*

Figure 4 provides not only an insight into the relationship between embodied carbon and acoustic performance in the context of floor systems, but also more broadly, the relationship between embodied carbon and general mass loading in mass timber construction. The implications of which have a significant impact on not only structural layouts, but also structural types that having varying CO_{2e} associated with them. **Figure 5** investigates the structural design implications of utilizing high dead loads to obtain high acoustic performance, and the effect on the CO_{2e} associated with that structural type.

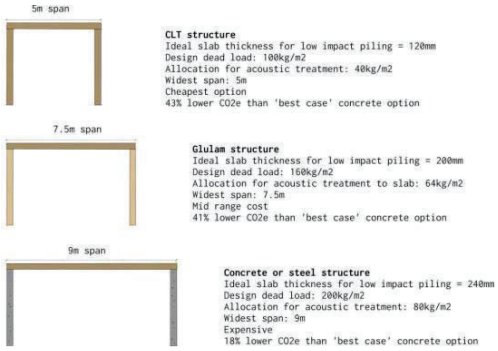

Figure 5: *Structural layout and design dead loads and CO_{2e}*

Figures 4 & 5 demonstrate that the reliance on heavy weight mass to achieve relevant acoustic performance criteria will tend to require heavier duty structural requirements, and subsequently result in higher CO_{2e} of the overall project. Increasing mass timber slab thickness to negate the requirement for heavy weight mass loading yields poor improvements in airborne performance relative to the uptake in cost. The mass law region of mass timber is narrower than

https://doi.org/10.52202/069179-0556

isotopic materials, typically between 125Hz - 2000Hz in mass timber, compared with 63Hz to 2500Hz in isotopic material such as concrete. As a result, doubling the mass of a CLT floor or wall will not provide a 6dB increase in airborne performance. This can be demonstrated through Stora Enso's mass law formula for CLT floor panels as seen below as **Equation 1**, of which estimations compares favorably with almost all laboratory testing of bare CLT panels undertaken to date.

$$Rw = 12.2LOG * (m'CLT) + 15 \qquad (1)$$

where: m,CLT = surface mass of CLT in kg/m^2

Equation 1: *Stora Enso estimation of Rw performance of CLT floor*

4. DESIGN PRINCIPLES TO MAINTAIN ACOUSTIC PERFORMANCE AND REDUCE EMBODIED CARBON

A review of fundamentals of sound insulation design holds the key into looking at reducing embodied carbon in mass timber design. In order to obtain low resonance in a floating floor, and consequently providing good transmission loss values at low frequency on mass timber slabs, mass loading needs to be considered in conjunction with a selected resilient layer, the material properties of which are relative to one another depending on the dynamic stiffness of the resilient layer type, and the density of the mass layer. Resilient materials that have a linear load vs Fn relationship will naturally require more mass per m^2 in order to obtain low Fn, elastomeric materials less so. But both materials requiring mass in order to achieve a Fn that is sufficiently far 'left 'on an airborne sound insulation test, nonetheless. Conversely, ceiling or floor voids provide a much efficient method of lower the Fn of a separating element whilst keeping CO2e low. Airgaps does not cost the earth. The resonance of a floating floor or the resonance of an air stiffness can be calculated as shown below in **Figure 6**.

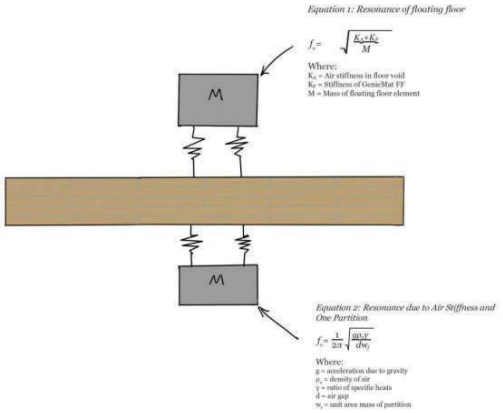

Figure 6: *Resonance calculations of separating elements of a slab.*

Figures 7 & 8 overleaf demonstrate this in effect. A relatively lightweight screed performs similarly to a dry laid, fully demountable boarded system on the same resilient layer, despite drastically different loadings – 82kg/m^2 for the screed, 30kg/m^2 for the dry laid board. It may be theorized that the resonance weakness in sound insulation still lies with the CLT, as the resonance of the floating floor isn't low enough to take this out. An inefficient use of a high CO_{2e} material. If we apply the same thinking to a ceiling void utilizing resilient clips and a sufficiently sized ceiling void (~150mm and above) and a single layer of 15mm plasterboard at 12.8kg/m^2, a much better airborne performance is achieved than the screed, whilst using ~85% less CO_{2e}/m^2.

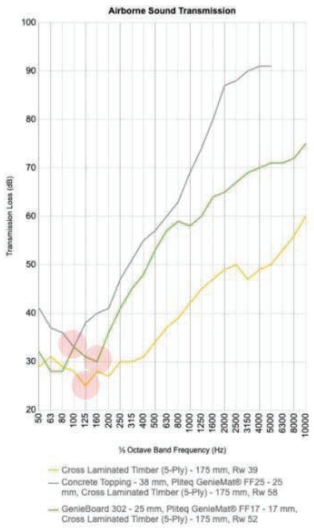

Figure 7: *Airborne and impact performance of differing mass layers on the same resilient layer, on CLT slab*

https://doi.org/10.52202/069179-0556

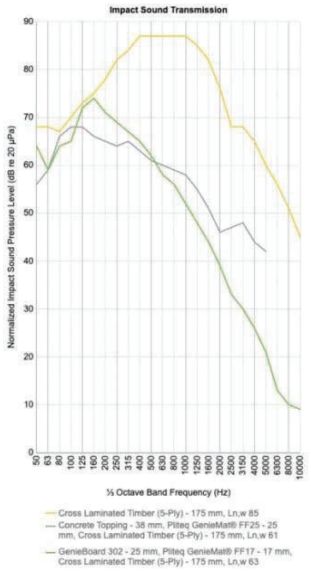

Figure 8: *Airborne and impact performance of differing ceiling void sizes on bare CLT slab*

5. VERIFYING HYPOTHESIS

Building mass timber buildings without using any form of concrete or screed still has many risks outside of acoustics. Insurance for the building is still a significant hurdle for developers as fire regulations are yet to recognize the extensive research into exposed mass timber fire performance. As a result, full encapsulation of the structure with minimum A2:Sfl1 rated material is required in order to obtain insurance for buildings over 7 storeys – materials that are commonly gypsum based. However, this balance of fire performance and the use of high-density material can still work hand in hand with the acoustic design, and obtain high quality acoustic performance. It is possible that we may be at a stage of overdesign of mass timber buildings to compensate for the high fire and acoustic criteria, reflective of current regulatory requirements. A case study of a care home is taken as an example of this. **Figure 9** below illustrates an acoustic system that was devised to provide encapsulation of the structure (direct fix plasterboard) to the soffit, and full class A2:Sfl1 encapsulation of the floors and walls, between each unit. 120 airborne and impact site tests were undertaken on separating floors and walls upon completion to check for compliance with $D_{nT,w} + C_{tr} \geq 45dB$ and $L'_{Tn,w} \leq 62dB$. The average of these site tests are provided, with a data spread of +/- 6dB for airborne performance (largely driven by penetration details or pattressing requirements, and +/- 3dB for impact performance. It is unclear what variables affected the impact performance data spread, but it is theorized that CLT slab spans and room orientations were a contributing factor.

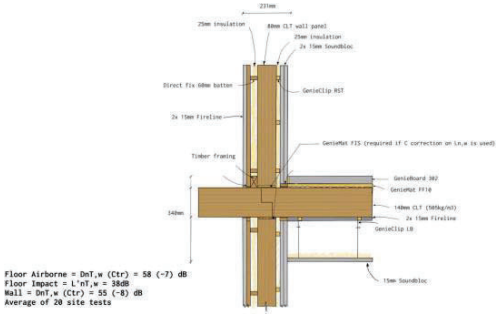

Figure 9: *Full encapsulation CLT detail for residential care home.*

It's estimated that the overdesign of this system led to an 'overspending' of approximately 5.6kg/m^2 of CO_{2e} or, accumulatively, 67.2tons of CO_{2e} across the whole development. If we adopt mass timber for even 20% of the current housing stock requirements, this will lead to an unnecessary 'spend' of approximately 8000 tons of CO_2 per year, at the current housing stock demand construction rate. The residential sector is arguably CLT smallest market currently in the UK, with offices making up most of the demand.

A similar case study was conducted on an office development where 1200m^2 of screed was to be poured on a 140mm CLT slab, with a 5mm virgin polyurethane foam resilient layer separating the two. This system was high in CO_{2e} (approximately 59kg/m^2), non-recyclable and likely to creep in impact performance across the lifespan of the building given the compressibility of the resilient material. An exercise was conducted to review the use of dry laid, demountable and recyclable material in lieu of the poured solution and it was deemed a cost saving system when factoring in the 12 week program saving it provided. **Figure 10** below illustrates the system that was installed.

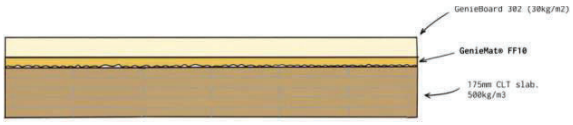

Figure 10: *Dry laid office floor system on CLT to meet BCO Shell and Core (DnT,w 45dB).*

https://doi.org/10.52202/069179-0556

This system provided the structural requisite 0.4kN/m^2 dead load damping to meet minimum floor response factor requirements in conjunction with an installed raised access floor, and achieved an in situ performance of $D_{nT,w}$ 45dB and $L'_{nT,w}$ 50dB before the RAF was installed. The LCA estimated CO_{2e} saving across 1,200m^2 was approximately 34kg/m^2, or 40 tons of CO_{2e} across the development. If this approach would be adopted at current office development construction/refurbishment rates it will save up to 4800 tons of CO_{2e} per year. Providing service/conduit routing within this floor system to negate the requirement for the RAF would provide further significant CO_{2e} savings.

6. CONCLUSIONS

The design of mass timber buildings needs a considerate approach to utilize low embodied carbon materials to achieve relevant criteria for reasons twofold:

- To achieve the 'as little as possible' ethos when considering material use, wastage, cradle to grave material lifecycles in order to reduce embodied carbon in mass timber construction to as low levels as possible.
- To provide high quality mass timber buildings that perform as good or better than currently adopted high CO_{2e} construction (concrete, steel etc) that can be constructed fast, efficiently and to required specification - leading to the furthering of confidence, enthusiasm and trust in mass timber construction and all related engineering disciplines.

Mass Timber construction needs to be considered as a option for most construction projects where viable for the purposes of slowing down the climate crisis, and coordinated engineering approach between all disciplines (but most importantly fire, acoustic and structural) from an as early stage as possible, to ensure the viability of the design from a cost, buildability and cradle to cradle material perspective is ensured. Through third party data and assembly specific testing, this can be done and the elimination of high embodied carbon acoustic materials can be achieved.

7. ACKNOWLEDGEMENT

Thank you to my wife Stefanie for listening to me air my thoughts about mass timber at the dinner table and being disproportionately raging about cement for nearly 2 years, Pliteq for supporting me in my research, and to my immediate Pliteq UK team for laughing at me when I walked into a lamp post whilst enthusiastically talking about CLT, rather than checking if I was ok.

8. REFERENCES

[1] Core Writing Team, IPCC AR6 Synthesis Report, Climate Change 2022, Sixth Edition, 2022.

[2] Core Writing Team, IPCC Climate Change 2022, Mitigation of Climate Change, 2022.

[3] Waugh Thistleton, 100 CLT projects, Softwood Lumber Board & Forestry Innovation Investment, 2018.

[4] Robert Hairstans, Mass Timber - an Introduction to Solid Laminate Timber Systems, *Arcamedia*, 2018

[5] Byrick, Wilson, Laboratory Impact and Airborne Sound Attenuation in Cross-laminated timber Construction Using Resiliently Mounted Ceilings and Poured Concrete Toppings, *Acoustics Week in Canada*, 2016.

[6] Byrick, Wilson, Comparing Laboratory Measured Impact Sound To Calculated Prediction Of Resonance, *ICSV24*, 2017.

[7] Michael Dickson, Sustainable Timber Design, *Routledge*, 2015

[8] Roynon, Jonathan, Embodied Carbon, *Structural Sensitive Study*, April 2020.

[9] Golden, Matthew, Acoustical Treatment Strategies For CLTs Including Underlayment, Resilient Ceilings And The Effect Of Various Floor Finishes, February 2017.

World Conference on Timber Engineering Oslo 2023

NEW HQ COPENHAGEN
A NEW STANDARD FOR SUSTAINABLE BUILDINGS IN AN INTERNATIONAL CORPORATION

Elias Mohr Wilson[1], Dorthe Keis[2], Mai Marcussen Yoon[3]

ABSTRACT: This paper provides an insight into the process of developing the new headquarters for an international client in Copenhagen. The preliminary analysis leading to the decision to go for a timber construction, as well as the direct and derived effects of using a timber construction in the new headquarters.

KEYWORDS: Headquarter, office building, Copenhagen, Denmark, Arkitema, COWI, timber frame, timber building, hybrid structure, glulam, CLT, LCA, exposed timber, upcycling, recycling.

1 TIMBER HYBRID STRUCTURE AS A DRIVER FOR SUSTAINABILITY

1.1 INTRODUCTION

The client is the Danish branch of a global corporation but wishes to stay anonymous. The client is planning a new headquarters in Ballerup on the edge of Copenhagen.

The client has its current headquarters in an existing building from the 70s in Ballerup, near Copenhagen. Over the past years the needs of the corporation have outgrown the existing facilities, so when the client approached Arkitema/COWI in 2019, the question was how to either accommodate future needs in the existing building, or completely rethink the site and create a headquarters that would be state of the art and show the way forward for future facilities in the global corporation.

Figure 1: *Interior and exterior visualizations of the future building, Arkitema/COWI.*

1.2 PRELIMINARY ANALYSIS AND BACKGROUND

The preliminary analysis showed that the existing buildings would be unfit for the functions needed in the future, and therefore the choice was made to start from scratch. In the early phases, the strategy for the building was laid out. The client's wish to create a futureproof and sustainable new headquarters acted as a main driver.

Sustainability can be interpreted very widely. For their new office building in Ballerup, the client chose to set ambitious goals regarding environmental sustainability.

Giving environmental sustainability highest priority makes good sense. The 2016 illustration of Stockholm Resilience Centre shows this precisely: there is no functional economy without a functional society, and there is no functional society without a functional biosphere.

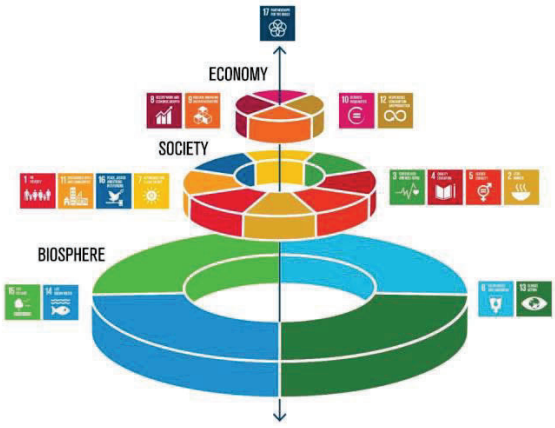

Figure 2*: There is no functional economy without a functional society, and there is no functional society without a functional biosphere. Source: Stockholm Resilience Centre 2016, Contributions to Agenda 2030 - Stockholm Resilience Centre*

Furthermore, this is much in line with the direction of the corporation globally, which aims to conserve natural

[1] Elias Mohr Wilson, Arkitema, elmj@arkitema.com
[2] Dorthe Keis, Arkitema, dke@arkitema.com
[3] Mai Marcussen Yoon, Arkitema, mamyo@arkitema.com

https://doi.org/10.52202/069179-0557

resources and to become CO_2 -neutral by minimizing energy consumption and investing in compensating measures. To the client, minimizing energy consumption is a key element.

Different design strategies for achieving these goals were assessed, and the eventual preferred choice was a timber grid, with timber columns, beams, and slabs, which would allow for maximum flexibility in the future layout while also having a markedly lower CO2 impact on the overall Life Cycle Assessment (LCA) analysis. The lower CO2 impact from the timber structure was a key element in the overall strategy to create the sustainable headquarters for the future.

Due to the early stage of design, a comparative analysis was done on a timber structure vs. a traditional concrete structure, giving the client an overview of the advantages and disadvantages before choosing the method of construction.

The following topics were mentioned as facts regarding timber:

- Timber is a renewable resource.
- Timber is easy to recycle.
- Green energy is used to manufacture the building material, and timber uses considerably less energy than for concrete.
- The timber structure requires no maintenance provided the timber is protected from moisture.
- There is not yet the same tradition in Denmark for using timber as the main structural elements in multi-story office buildings as there is for concrete structures.
- It is not yet routine work for construction companies, architects and engineers in Denmark.
- Using timber as a structural material is in line with the Danish government's recommendation and ambition towards a climate-neutral construction sector.
- It is very good branding for the client to be one of the front runners in Denmark.

Topic	Advantage	Neutral	Dis-advantage
CO_2 emission	+		
Recycling	+		
Energy used on site during construction	+		
Maintenance		-	
Tradition in Denmark, few contractors			÷
Branding	+		
Prefabricated elements		-	
Composite solutions		-	
Shorter grid for columns and higher structural beams and decks			÷
Less foundation required	+		
Time schedule during construction	+		
Construction costs			÷
Planning costs			÷
Limitation of highest floor level			÷

Figure 3: *Advantages/disadvantages for timber construction compared to concrete construction, summarized in note "Timber versus concrete", Arkitema/COWI February 2020*

2 AMBITIONS & FOCUS POINTS

With inspiration from the client's draft for a 'sustainability laboratory', environmental sustainability has the following focus points:

- The GWP (CO_2 -equivalents) should be minimized for the building's whole life cycle by energy efficient design and choice of energy supply.
- LCA should be applied in the early design. No specific limits will be defined before this project. In Bl110 no specific requirements for the use of BIM tools have been defined.
- The clint's "sustainability checklist" applies.

Furthermore, indoor climate is part of the client's project-specific goal about working conditions. No special effort will be made within design regarding "electro smog". For thermal indoor climate and indoor air quality, the requirement is category II according to DS/EN 16798-1:2019.

In alignment with the 'sustainability laboratory'-goals, efforts will be made within the masterplan, building design, renewable energy on site, choice of materials as

https://doi.org/10.52202/069179-0557

well as design of mechanical installations. The stages described correspond to DS/EN 15978:

- Stage 0: The demolition of existing structures (outside system boundary)
- Stage A: Product stage and construction process stage
- Stage B: Use stage (operation and maintenance)
- Stage C: End of Life
- Stage D: Reuse, recovery, and recycling of materials

3 SUSTAINABILITY STRATEGY

A sustainability strategy for the life cycle of the building was decided at the beginning of the outline proposal, and the status was updated at the end of the outline proposal.

3.1 STAGE 0 + A, ENERGY USED ON SITE

This is usually not considered in Danish building projects, even though significant GWP and PE are related to this. The client has decided that within this field no special measures will be carried out.

3.2 STAGE 0 + A, EMBODIED GWP

This is usually not considered in Danish building projects.

Focus is to minimize GWP and PE related to the materials, which are demolished as well as materials used for the new building. Demolished materials should be utilized/recycled in the best possible way.

The GWP and PE of new materials will influence the building design and the choice of materials.

Included: Sensible, qualitative considerations by the general choice of new materials generally and applications of LCA for the selected cases:

- Foundations: Comparison of sand bed or pile foundations
- Construction of floor slabs (3 alternatives)
- External façade cladding (3 alternatives)
- Whole building LCA according to Danish DGNB to provide the client with a benchmark for GWP and PE

3.3 STAGE B, OPERATION AND MAINTENANCE

The building is to meet the (strict) low energy option of the Danish building regulations (for heating, cooling, domestic hot water and auxiliary energy).

The energy demand in operation is to be optimized during design with an eye to the future renewable energy system.

The client will consider all energy demands (GWP and PE) during operation, and not only operation of the building. The client will revise its purchasing policy and implement tough requirements regarding energy demand (GWP and PE) for all equipment.

This is in line with the client's interest for the passive house criteria, which include all equipment, not only the building itself.

The client will apply a commissioning period covering the first 14 months of operation in order to ensure proper operation.

Commissioning covering the first 14 months of operation supplied by COWI/Arkitema.

3.4 STAGE C + D, END OF LIFE AND RECYCLING

The building will basically be designed for long-term usability, in order not to repeat the choices, which led to the planned demolition of the client's buildings dating from 1970-1990.

Included: Design of sensible (in the designer's interpretation) extra space for ducts and in technical rooms. Designing for higher live loads (3.5 rather than 2.5 kN/m²).

But inevitably, possibly for other reasons than its usability, the building will be demolished at some time. This should be accounted for with a "design for disassembly" approach or at least in a way to minimize resources required in demolition and recycling. Demolition is closely connected to the recyclability of the materials and the choice of materials.

Included: minimal, qualitative considerations.

This set of initiatives is in line with the corporation's principles for product development:
"As a matter of principle, we start optimizing products in the development phase, applying the following criteria: energy and material efficiency, emissions education, and repairability.", Client, Sustainability report 2018 spotlights.

4 TIMBER AS ADDED VALUE TO THE OFFICE ENVIRONMENT

4.1 MENTAL HEALTH BENEFITS

Several studies have shown that, as humans, we perceive timber surfaces as more natural and calming compared to other traditional building materials. This added benefit of timber has also become a significant factor in design, and efforts have been taken to ensure as much visible timber in the interior as possible. [1]

4.2 SUSTAINABILITY AS PART OF THE CORPORATE STRATEGY

Utilizing the mental health benefits of timber by exposing the surfaces has several other benefits. The strategy to build and focus on sustainability becomes visible

https://doi.org/10.52202/069179-0557

throughout the building and speaks clearly to the employees and visitors that sustainability is an integrated part the client's identity in the 21st century. This is possible due to the general perception of timber as a natural material.

With the organization of the building around one large multi-story atrium, where all employees and visitors pass through, the strategy is further emphasized by maximizing the amount of exposed wood surfaces in this space. Furthermore, extra steps will be taken by using upcycled wood (offcuts from the wood industry) in the construction of the auditorium podium to save CO2 and improve the overall footprint.

In the vison of the future headquarters, the client had the concept that the use of wood is to be visible and the building material would represent "Nordic Nature".

5 CHALLENGES

5.1 GEOMETRY AND LAYOUT

An appropriate module is 6 x 6 meters. A larger span affects the thickness of the timber required for the constructions, which is not economically viable. A wooden construction requires many pillars, and this can affect floor plans. Therefore, it is important to think about the construction principle from the start.

5.2 BUILDING PARTS

Though timber has been chosen as the main material for the structural frame, concrete still has its place in modern buildings. For example, concrete is required for in foundations, basement and parking facilities and stairwells, since timber is not a viable option.

Another example is if a cantilevering structure is chosen for aesthetic reasons to make the top part of the building ("the cloud") free from the building base. In this area, steel in combination with timber will be necessary to ensure stability and strength.

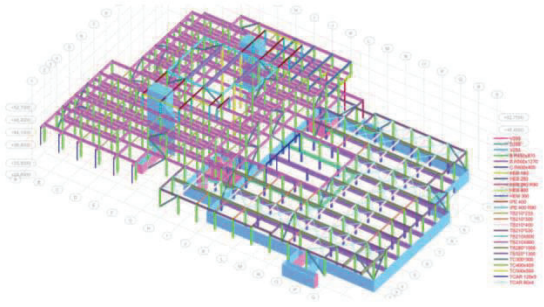

Figure 4: *Structure, Isometry – Building. Outline Proposal, Arkitema/COWI*

Finally, floor-slabs have been designed with a layer of concrete on top of the CLT elements to meet the demands for acoustic dampening between floors in a modern office environment.

At an early stage the client decided not to use wood as the façade cladding, since this would increase maintenance costs, although an exception was made in the courtyard. A panel system of thermo dried FSC-wood lamellas and 100% collected and recycled Green Aluminium offers a distinctive and sustainable façade.

5.3 ACOUSTICS

Wood generally has lower sound insulation than concrete. Therefore, noise and vibrations will spread more easily through the construction. The client's headquarters will be a multifunctional building with office, education and noisy workshops. The noisy functions will be located away from noise-sensitive functions. Some workshops will be "box in a box". Floor partitions made of CLT wood with floating concrete floor will create sound insulation due to the increased weight. Due to few reference projects in Denmark, there is some uncertainty in relation to calculation methods. We must learn through measurements of these new buildings. Until then, Arkitema/COWI have learned from, among others, Norwegian projects through COWI Norway and thus obtained evidence for calculations.

5.4 FIRE SAFETY

The project is favoured by the fact that in Denmark the limit for the maximum height has now been raised for wooden buildings from 9.4 m to 12 m. Less documentation is therefore required.

Requirements for the maximum extent of internal exposed wooden surfaces is 20%, and this must be documented.

Constructions are designed for 60 min. fire. The underside of CLT decks need to be covered with mineral wool or plaster boards for fire protection of the wooden surface.

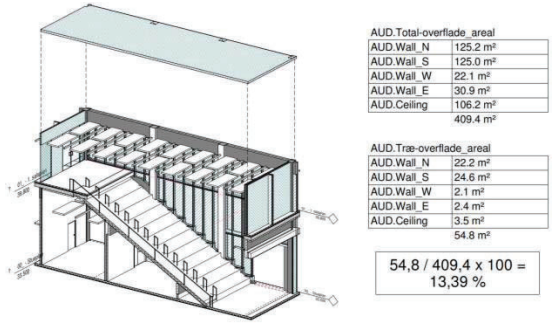

https://doi.org/10.52202/069179-0557

Figure 5: *Quality check/documentation of max 20% exposed wooden surface in the auditorium. Arkitema/COWI*

Great attention must be paid to how installations are routed through a load-bearing wooden construction. It is recommended to plan with longitudinal guides to minimize the number of cross main penetrations. When drilling holes, great attention must be paid to fire sealing and fire joints.

5.5 BUILDING PROCESS

A significant challenge during construction is how to deal with the rain and moisture of the Danish climate. The proposal is to use site-cover weather protection during construction of the building, but this cover comes with the drawback of extra cost compared with traditional construction methods. However, the cover is storm proof and snow proof to Danish standards and offers factory-grade production facilities for the work and therefore gives the possibility to minimize the overall construction time. In the project, it was decided to only cover the taller part of the building. The single-storey part of the building has a steel-trapeze roof, which has interim weather protection.

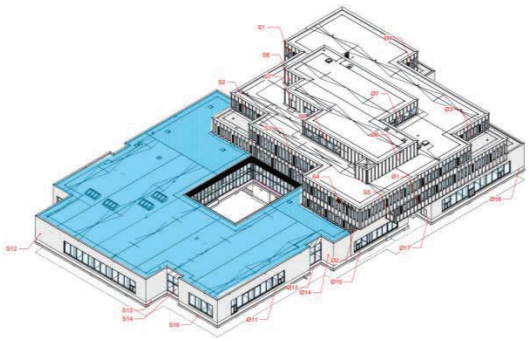

Figure 6: *Lower part of the building with a steel roof solution to minimize use of site-cover. ARKITEMA/COWI*

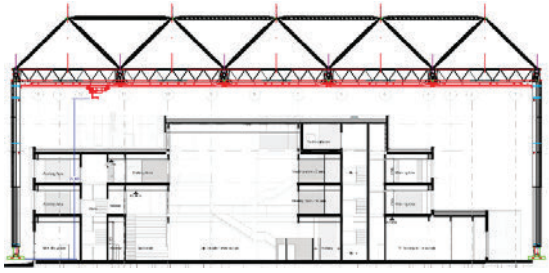

Figure 7: *Site-cover planned as protection for the tallest part of the building. Arkitema/COWI*

6 LIFE CYCLE ASSESSMENT

6.1 ASSESSMENT AS A DESIGN TOOL

Throughout the design process comparative studies have been made on balance aesthetic, functional, financial and sustainability requirements. Life cycle assessment (LCA) was an important design tool in defining building parts and technical solutions:

- The first LCA study compares the GWP and PEtot of a pile foundation and a gravel bed foundation solution. Results of the calculations showed that the gravel bed is the best option in terms of LCA. Based on this, it was decided to use the gravel bed for the project, as there was no significant difference in cost for the two scenarios.

- Lightweight balloon frame exterior walls with slate as façade cladding, was chosen due to good LCA performance.

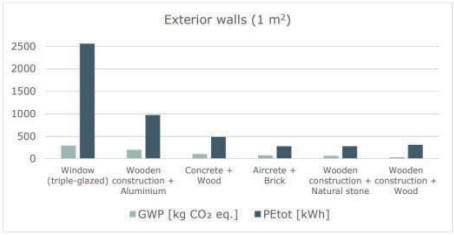

Figure 8: *LCA CALCULATIONS, Outline proposal. Arkitema/COWI, August 2020.*

- Climate sails were chosen in favor of a full-covering climate ceiling, as this solution has significantly lower CO2 emissions

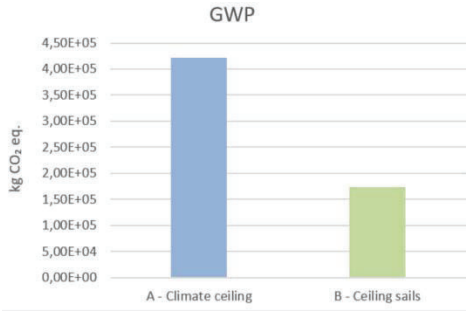

Figure 9: *Integrated design LOG, Arkitema/COWI,*

https://doi.org/10.52202/069179-0557

October 2020.

- 6 relevant types of floor construction were analyzed and the one with the best GWP performance was chosen

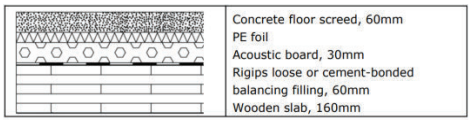

Figure 10: *LCA CALCULATIONS, Outline proposal. Arkitema/COWI, August 2020*

- Acoustic ceilings; Wooden lamellas were chosen due to best GWP performance.

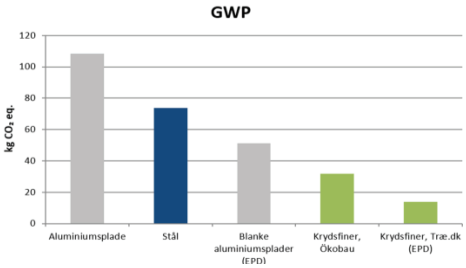

Figure 11: *LCA CALCULATIONS, Outline proposal. Arkitema/COWI, August 2020.*

6.2 ADDITIONAL POTENTIALS

Late in the design process, the client decided to explore additional potentials for sustainability. The following focal points were investigated and incorporated into the final tender project:

- Circular potentials / Reused materials: One aspect, which in the future could be better integrated into the early-stage design process, is the use of recycled/ upcycled building materials. One example is the aforementioned podium stair in the auditorium, which will be built with recycled timber. Other building parts like the choice of carpets have also been chosen with circularity in mind.

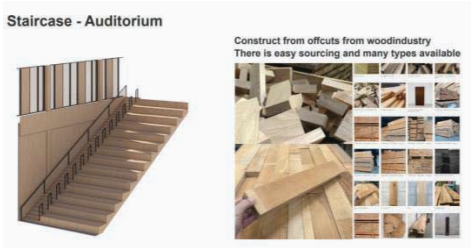

Figure 12: *Circular potentials presentation, Arkitema/COWI, March 2021.*

- Design for disassembly and material loops: Design for disassembly in selected construction details and overview of material loops (facade, floors, interior walls).
- Minimizing harmful substances in building components: Purpose is to protect building workers, building users and the environment in general.
- Reusing rainwater: Rainwater for watering plants, is collected in an underground tank.

6.3 FINAL ASSESSMENT

A life cycle assessment (LCA) was carried out for the full building to have a benchmark for future buildings in the corporation. The assessment describes the full LCA-calculation for the building based on the main project. The results were analyzed with focus on global warming potential (GWP) and total primary energy (PEtot). The additional environmental impact categories were included in the overall results. Generic data were used for all materials except aluminum facades, carpets and wooden floors. Environmental data for wood was also changed to Danish EPD data to represent the Danish market. The method follows the Danish 2020 DGNB manual for new buildings, except for the use of uncertainty factors.

The building has a total GWP of 6,752 tonnes CO_2 eq, which is 9.6 kg CO_2 eq/m²/year over the 50-year calculation period. The results have been compared with the Danish CO_2 requirements from 2023, where the limit is 12 kg CO_2 eq/m²/year. The results show that the slabs, walls, roof, windows/ doors/ curtain walls and solar panels contribute to the largest GWP and PEtot impact. For PEtot especially slabs, beams/ columns and roof have a large impact caused by the wooden constructions. Results have been compared with the Danish DGNB reference office building. Compared with the reference, the client's headquarters in Denmark has a lower environmental impact on all categories. The building would score 56 out of 75 possible DGNB points in the LCA criteria.

https://doi.org/10.52202/069179-0557

6.4 SUSTAINABILITY STRATEGY – STATUS END MAIN PROJECT

By the end of the main project, the following measures will be included in the strategy and design:

- A sustainability manager has been involved in the project since the beginning and will participate in meetings regularly to maintain the focus on sustainable solutions.
- The building will be constructed with timber as a large part of the structure.
- The extent of concrete basement and foundations will be minimized.
- Energy demand for building operation will meet the low energy requirements of the Danish building code.
- Cooling and heating will be supplied by groundwater.
- Demolished materials will be used in the best possible way.
- Sensible, qualitative considerations by the choice of new materials and LCA for selected cases.
- Reused and recycled materials will be used in selected areas (carpets, wooden stair by the auditorium and some lighting fixtures).
- Rainwater will be collected and reused for irrigation of plants and rinsing machines.
- Improved operation and energy efficiency of heating and cooling heat pumps through whole building simulation.
- Indoor climate mostly category II according to DS/EN 16798-1:2019.

The client's project in Ballerup makes a special effort regarding SDG13 by reducing the GWP throughout the life cycle of the building and SDG7 by improving energy efficiency.

REFERENCES

[1] J. Rice, R. Kozak, M. Meitner, D. Cohen - Wood and Fiber Science, 2006

https://doi.org/10.52202/069179-0557

World Conference on Timber Engineering Oslo 2023

A WORKABILITY AND SUSTAINABILITY ASSESSMENT OF MULTI-STOREY EARTHQUAKE-RESISTANT TIMBER BUILDING

Kazuki Tsuda[1], Ahmad Ghazi Aljuhmani[2], Arata Minegishi[3], Yutaka Goto[4], Masaki Maeda[5]

ABSTRACT: Although two-thirds of the area of Japan is covered with forests, the domestic wood resources are not widely used in the construction sector. Due to the complex design process, construction work and high precision needed, most of timber constructions are limited to one or two-storey buildings. This paper aims to clarify the efficiency of a proposed joint system for CLT walls-steel beams hybrid structure. In addition, the workability and the environmental impact of the proposed hybrid system in comparison to other structures were analysed. The proposed joint system showed higher workability and efficiency compared to other conventional joints in Japan. The construction process of a prototype of a module with the proposed system was studied and confirmed its easier and faster work than the conventional system. A 4-storey building was taken as a case study to evaluate the environmental impact of the proposed system. Although the proposed hybrid system showed higher carbon emissions than a conventional CLT alternative, advantage in terms of the environmental impact was confirmed in comparison to a reinforced concrete and a steel structure.

KEYWORDS: Cross-laminated Timber, Hybrid structure, Workability, Life cycle assessment, Sustainability

1 INTRODUCTION

In recent years, a mid-to-high-rise wooden building has been attracting attention from the perspective of a low-carbon building and the effective use of forest resources. In Japan, although 66% of the total land area is covered by forests (Japanese Forestry Agency (JFA)), these renewable resources are not being used to their full potential. Buildings higher than three stories (mid-to-high-rise buildings) are mainly non-wooden structures [1], with a share of only 0.06% for timber buildings.

Cross-laminated Timber (CLT) is considered a promising engineered wood product (EWP) for a structural material of a mid-to-high-rise building with low carbon emissions. CLT has a similar structural performance as reinforced concrete, which means that CLT has the capacity to resist the weight of the building and large earthquakes. Moreover, recent studies [2-5] found the environmental superiority of mid-to-high-rise CLT buildings compared with reinforced concrete buildings.

However, the common structural systems for CLT buildings have challenges regarding reasonable seismic design and workability. For instance, an unreasonable amount of CLT walls (i.e., to compensate for the low strength and stiffness connections) and a large number of complex connections are needed. In order to tackle the structural challenge, CLT-steel hybrid structures can be a possible solution. The effect of the high strength and stiffness of the steel could be effectively used to increase the CLT panel's capacity under lateral loading, thus reducing the number of CLT panels required. The seismic behaviour of the structure using innovative CLT-steel hybrid systems was investigated by several researchers in the past years [6-8]. Fukumoto et al. [9] theoretically investigated the structural performance of steel frames with CLT infill. They found that the use of steel can increase lateral performance by almost 2.0 times compared to the CLT structure.

Nevertheless, such CLT-steel hybrid structures have a difficulty in workability due to a large number of complex connections. Hence, construction companies struggle to deal with the complex construction due to the hybridization. In addition, studies regarding the environmental performance of the hybrid structure are limited.

This paper proposes a novel hybrid structure with CLT and steel beams with steel joints that are designed to have both high efficiency and workability. Moreover, a case

[1] Kazuki Tsuda, Tohoku University, Japan, tsuda@rcl.archi.tohoku.ac.jp
[2] Ahmad Ghazi Aljuhmani, Tohoku University, Japan, aljehmani@rcl.archi.tohoku.ac.jp
[3] Arata Minegishi, Tohoku University, Japan, minegishi@rcl.archi.tohoku.ac.jp
[4] Yutaka Goto, Chalmers University of Technology/Tohoku University, Sweden/Japan, yutaka@chalmers.se
[5] Masaki Maeda, Tohoku University, Japan, maeda@archi.tohoku.ac.jp

https://doi.org/10.52202/069179-0558

study of a building with the proposed system is also introduced (Figure 1) in order to analyse the environmental performance. The targeted building is 4-storey residential building to promote the mid-rise building. The objectives of this paper are 1- Discussing the efficiency and workability of the proposed joint compared to the conventional connections. 2- Demonstrating the workability of the proposed system. 3- Analysing the environmental performance of the hybrid system in comparison to other common structure systems.

Figure 1: *Targeted CLT walls and steel beams hybrid structure.*

2 PROPOSAL OF A HYBRID STRUCTURAL SYSTEM WITH CLT PANEL AND STEEL BEAM

2.1 Problems of conventional structural systems

In Japan, the ductility of a building is essential to resist earthquakes. Therefore, conventional structural systems are designed to have high ductility. Figure 2 shows the conventional structural systems of CLT panels in Japan. They consist of CLT walls and slabs. The use of CLT slabs caused the reduction of the seismic capacity of the building. When the wall is subjected to lateral force, the wall transfers compression force to the CLT slab perpendicular to the grain, which leads to low rocking resistance.

For the connections of conventional systems, two types of joints are required: tensile joints and shear joints. The tensile joints are installed at the corners of the wall. The common tensile joints are a screw joint with a U-shaped metal bracket and a tensile bolt joint. On the other hand, the shear joints are at the top and bottom of the CLT wall. The common shear joints are a U-shaped and a L-shaped metal connector joint with screws.

These conventional connections have structural challenges. The flexural yielding of screws and the yielding of tensile bolt contribute to the ductility performance of a building. However, although the conventional systems have the desired structural ductility, they do not take advantage of CLT performance to its full potential. For instance, the material's lateral strength of the CLT wall made from Japanese cedar with a thickness of 90 mm (3-ply 3-layer) is reported as 2.31 MPa [10]. Nevertheless, when the tensile bolts are applied as the tensile joints, the strength for designing is 0.40 MPa according to the design guideline of CLT structure [11] This means that the current structural systems utilize only 17 % of the CLT panel performance.

Furthermore, the conventional joint systems have difficulties in material processing and construction workability. The three out of four tensile and shear joint types require Computerized Numerical Control (CNC) processing of the panels for rectangle holes and cut-outs. Making the CNC data and the actual processing in a factory for each CLT panel takes time. Hence, processing CLT wall panels with conventional systems entails higher labour and longer process time.

Regarding the workability of the screw joint, in order to have the necessary structural performance, a large number of screws is required to be installed for 6 joint types. This process takes longer time. As for the tensile bolt joint, anchor bolts are already fixed to the base/floor. Then, the wall is fixed by the anchor inside the pre-drilled holes in the walls. Therefore, high precision for the anchor bolts in the installation is required, which leads to higher labour time and cost.

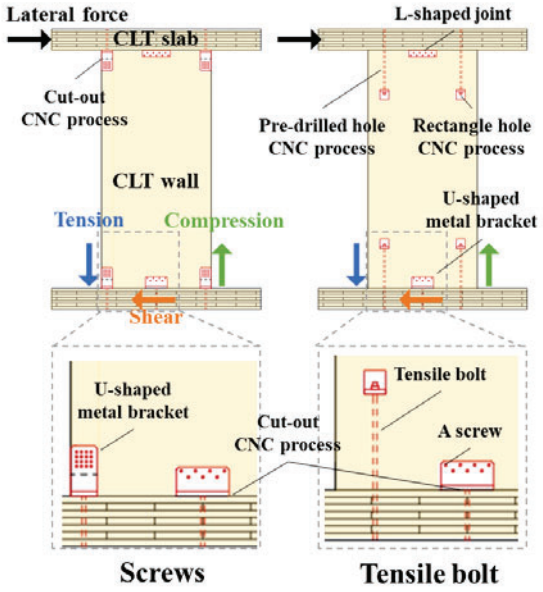

Figure 2: *Conventional structural systems of CLT panels in Japan.*

2.2 Description of a hybrid structural system

To overcome the low efficiency and workability of the conventional systems, a hybrid structure with CLT panels and steel beams is proposed as shown in Figure 3. The use of steel beams increases lateral capacity compared with the use of CLT slabs. Figure 4 shows the differences in the embedment behaviour between the wood slab and the steel beam. The wall transfers compression force parallel to the grain in the main axial layers, which leads to high rocking resistance and better CLT panel performance.

In the joint of the proposed hybrid system configured at the CLT panel corners, steel plates are applied on one side of the CLT panel to connect the panel with steel beams using three bolts in the CLT panel and one bolt in the steel beam. In the proposed structural system, the joint is resisted as the combination of both tension (uplift) and

https://doi.org/10.52202/069179-0558

shear forces which are induced by the lateral force applied on the wall. Therefore, the plate joint requires a smaller number of connectors compared with the conventional joints. Regarding processing, CLT walls can be directly shipped from a production factory to a construction site because carpenters can make bolt holes for the walls on site. Hence, the plate joint system can reduce the cost derived from processing. In addition, the construction of materials by bolts does not require a high construction accuracy as opposed to the tensile bolt connection. This makes the installation of CLT walls easier compared to conventional systems.

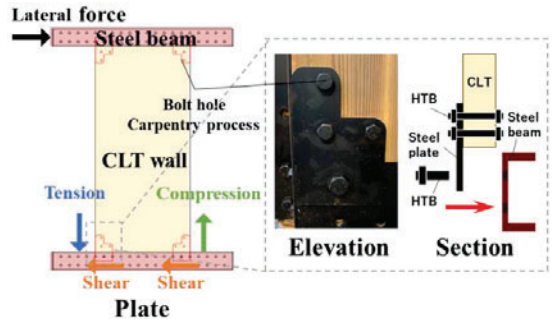

Figure 3: *Details of the hybrid system.*

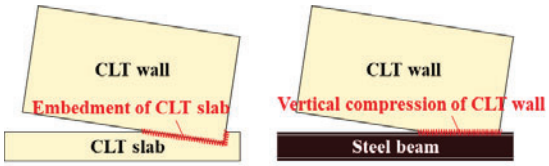

Figure 4: *Embedment difference between a CLT slab and a steel beam.*

3 WORKABILITY PERFORMANCE ANALYSIS

3.1 WORKABILITY COMPARISON

In order to compare the efficiency and workability of the three variations of the joints (two conventional ones and the proposed plate joint), a comparison of the intensity of constructive works of these joints was conducted. The three joints were designed to have the same strength. The design specification and strength of the plate joint were gained from the shear wall tests in a past study [12]. In this study, the joint consisted of three bolts with a diameter of 20 mm (M20), the steel plate with a thickness of 9 mm and the CLT wall with a thickness of 90 mm. The ultimate tensile strength was 66.8 kN. The two conventional joints were designed to have the same strength as the plate joint, based on the design guideline of CLT structure [11]. For the screw joint, the strength of the joint was calculated by multiplying the strength of each screw (5.5 kN) by the number of screws. For the tensile bolt joint, to ensure a ductile failure of the joint, the strength of the joint was calculated based on the yielding capacity of the tensile bolt. In addition to that, the vertical and horizontal edge of the joint (i.e., the distance from the edge of the joint to the edge of the CLT panel) was designed to avoid brittle failure in the CLT wall panel's corner before the tensile bolt yielding.

The specific design and the appearances of the three joints are shown in Figure 5. To have a similar tensile strength with the plate joint, in the case of the screw joint, a U-shaped metal bracket and 12 screws were needed per one corner of the CLT wall, and the thickness of the wall was 90 mm. In the case of the tensile bolt joint, a M20 bolt was needed, and the thickness of the CLT wall was 150 mm to avoid the failure in the CLT wall panel's corner.

As for the screw joint, 48 screws need to be installed per wall for tensile connections, which requires a high workload to drive all necessary screws. The tensile bolt joint required CLT walls whose thickness was 150 mm, which causes a higher production cost. However, in the plate joint, 12 bolts were needed per wall for the connection of the wall and the plate, and the thickness of the wall was 90 mm. In addition, the plate joint required no shear joint. Hence, it was shown that the workability of the plate was better than that of the conventional ones.

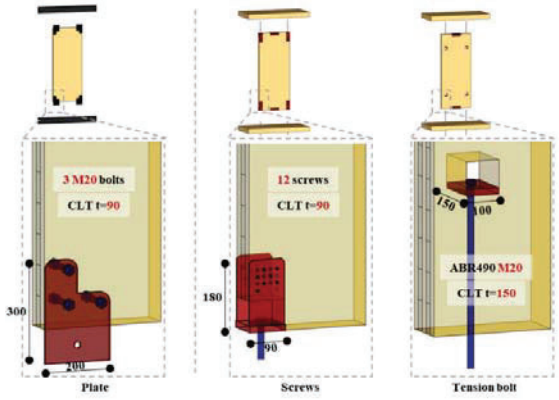

Figure 5: *The specific design and the appearances of each connection that has the same ultimate tensile strength.*

3.2 DEMONSTRATION OF A CLT MODULE WITH THE PROPOSED PLATE JOINT SYSTEM

A module using the proposed structural system with the plate joint was demonstrated to confirm the workability of the proposed joint system. Figure 6 shows a photo and a schematic diagram of the CLT module. The module with a size of 2 m by 4 m in floor plan was constructed for an open-air event in August 2021 in Sendai, Japan. In this event, the module, which housed a small commercial store, contained eight CLT panel walls arranged along the three sides and back of the structure. In Sendai, in the case of the use of local woods, the maximum width of CLT panels is 1.2 m due to the limitation of the production facility of the local manufacturer. Hence, CLT panels with 1 m in width and 2.4 m in length were used as structural walls. The used CLT wall panels were made from Japanese cedar. C-shaped steel section with a 90x200 mm size was used for the beams and the base. For the floor, a wood panel with a thickness of 36 mm was used. For the

https://doi.org/10.52202/069179-0558

roof, a wood panel with a thickness of 200 mm was applied.

Figure 7 shows the process of the construction work with the following steps: (a) Holes with a diameter of 22 mm were drilled through for inserting the M20 bolts. (b) The steel base and beams were assembled on the ground. (c) For the installation of the CLT walls, two CLT wall panels were splined together in advance by convex shear connectors to increase the efficiency of the construction. (d) The CLT walls were put on the steel base and jointed by bolts. (e) The steel beam frame was installed by a crane. (f) The roofs were constructed by the crane. They were fastened with the steel beams by bolts. (g) Carpenters carried wood panels for the floor by hand and put them on the steel base.

As shown in Figure 8, 173 minutes were needed to finish the construction from (b) to (g). The time required to install the eight CLT panels was about 36 minutes. There was an actual CLT building that was built recently with a conventional joint system. According to local construction experts, 18 to 20 panels can be installed in one day (eight hours of construction time). Thus, the demonstration of the single CLT module indicated better workability compared with the conventional joint system.

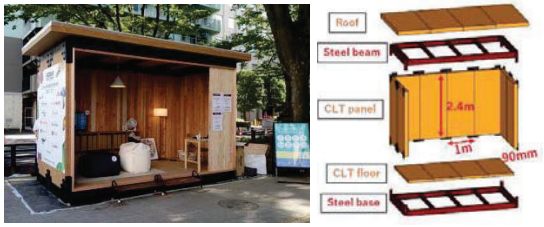

Figure 6: *Photo of the CLT module (left); schematic diagram of the module's structural system (right).*

(a) Opening bolt holes for a CLT wall by a carpenter

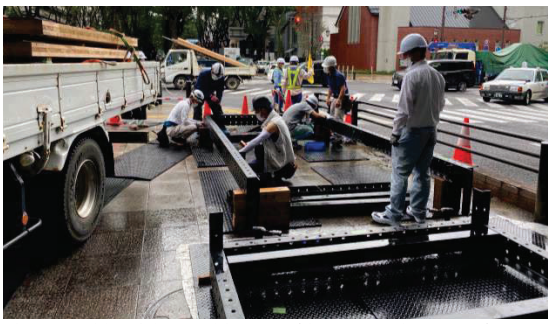

(b) Assembly of the steel base and beams on the ground

(c) Installation of the CLT walls

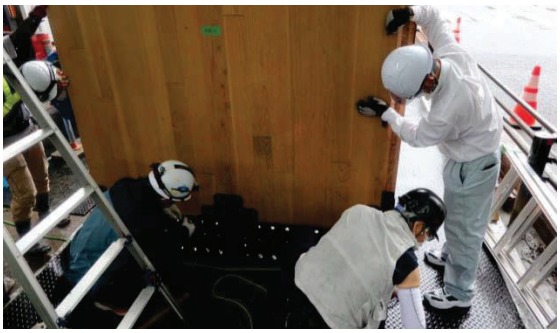

(d) Jointing the walls and the steel base with bolts

(e) Construction of the steel beam frame

https://doi.org/10.52202/069179-0558

(f) Construction of the roofs

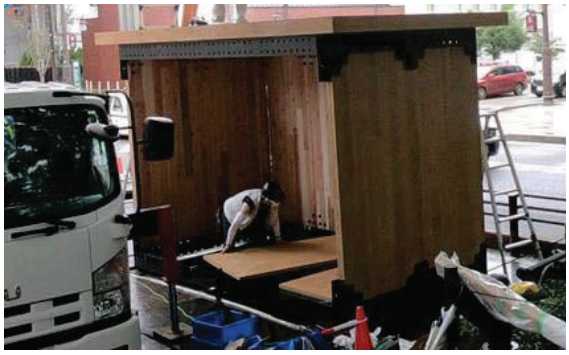

(g) Construction of the floors

Figure 7: *CLT module during construction.*

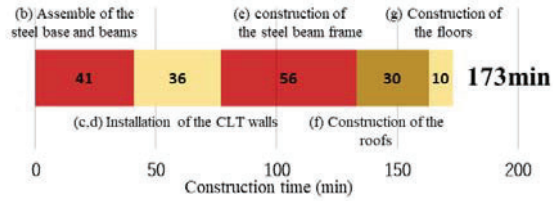

Figure 8: *Each construction time in order.*

4 SUSTAINABILITY PERFORMANCE ANALYSIS

4.1 Target buildings

In order to analyse the sustainability performance of the hybrid structure, a life cycle assessment (LCA) was conducted. The analysis quantitatively compared the environmental impacts among four structural systems, including the proposed hybrid system, conventional CLT, reinforced concrete and steel structures. 4-storey prototype residential buildings with total floor area of 1,000 m^2 were designed in Sendai, Japan. As shown in Figure 9, the structure includes a residential space (8x24 m^2) surrounded by a long corridor and balcony.

4.1.1 Functional unit for structural design

The functional unit was defined as the structural performance margin factor equals to 1. The margin factor of 1 means that the building has the minimum structural safety performance that satisfies the Japanese Building Standards Law (JBSL) regarding structural performance.

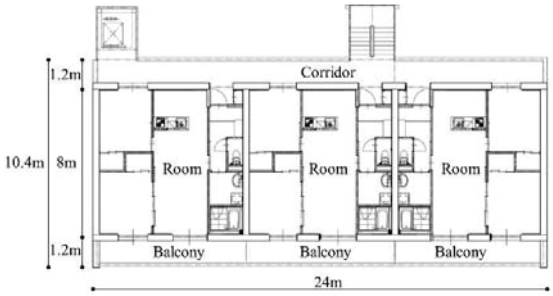

Figure 9: *The image of the floor plan of the 4-storey residential building.*

4.1.2 Building design

In this section, the building design of each scenario is explained. Floor plans and, dimensions and details of structural components were selected to satisfy requirements in JBSL against vertical load and seismic load. Figure 10 shows the floor plans of each building.

The building with the conventional CLT structure (hereinafter CLT building) was designed in the module of 4 m by 8 m. This was because CLT slabs allow spans to be increased up to 4 meters. CLT walls with 1200 mm in width and 210 mm in thickness were used. For the tensile joint, the tensile bolt joint with the diameter of 24 mm was applied. For the floor and the roof, a CLT panel with a thickness of 210 mm was applied according to the design example in the Guidance of Notification of Building Standard Law concerning CLT [13].

Regarding the reinforced concrete structure, two types of structural system are commonly used; moment resisting frame and wall panel structure (hereinafter called "wall type"). In the Japanese design practice, the middle-rise wall type structure is generally selected for residential buildings of reinforced concrete structure. Hence, in this study, the wall type structure was applied for the reinforced concrete structure.

The building with the wall type reinforced concrete structure (hereinafter RC building) was designed in the module of 6 m by 8 m. The floor area is limited up to 60 m^2 in the specification of the JBSL for the wall type structure considering the vibration of slabs. If the module were 8 m by 8 m, an area of one section would have been 64 m^2. Thus, the longitudinal span length was designed as 6 m which gave the same area for four rooms. The RC walls with 1700 mm in width and 250 mm in thickness were used. For the roof and the floor, a reinforced concrete slab with a thickness of 270 mm was applied according to the design example of the guideline for the reinforced concrete [14].

The building with the steel structure (hereinafter S building) was designed in the module of 8 m by 8 m. Steel beams can allow spans to be increased according to the functionality of a building. Therefore, the longitudinal span length was designed as 8 m which gave the same area for three rooms, which can secure larger spaces than the CLT and the RC building. The steel beams with the cross

https://doi.org/10.52202/069179-0558

sections of 440x300 mm and the steel columns with that of 400x400 mm was chosen. For the roof and the floor, a reinforced concrete slab with a thickness of 104 mm was applied according to a catalogue of a deck plate company.

The building with the CLT walls-steel beams hybrid structure (hereinafter CLT+S building) cannot be designed based on the current JBSL. This is because it does not include specifications regarding new hybrid structures. In order to make a reasonable design, the ductility factor was assumed to be between the values of the CLT and S building. As a result, the CLT+S building was designed in the module of 8 m by 8m. Compared to the CLT building, the steel beams allow longer spans. In addition, the needed quantity of CLT walls was decreased from 49 t to 19 t thanks to the hybridization. Compared with the S building, the steel beams could be smaller from the cross sections of 440x300 mm to that of 294x200 mm. This is because the weight of CLT slabs is smaller than that of RC slabs. In addition, putting CLT walls on beams leads to shorter spans that are crucial to bending stress to beams. For the floor and roof, a CLT panel with a thickness of 210 mm was applied according to the design example in the Guidance of Notification of Building Standard Law concerning CLT [13].

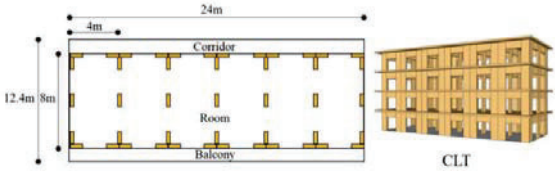

The floor plan and the image of the CLT building.

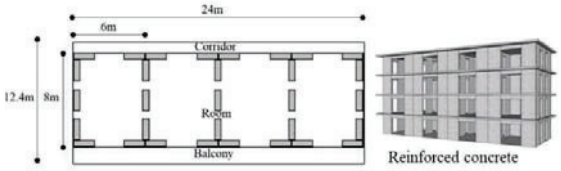

The floor plan and the image of the RC building.

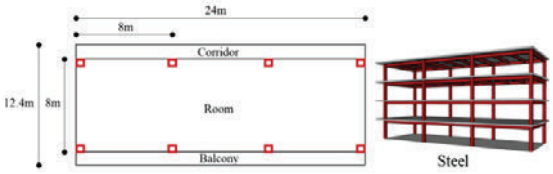

The floor plan and the image of the S building.

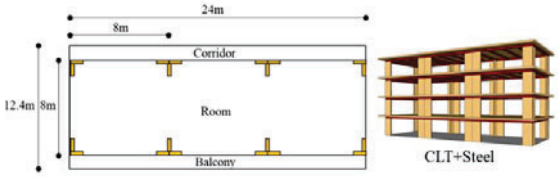

The floor plan and the image of the CLT+S building.

Figure 10: *The floor plan and exteriors of each structure (not considering the foundation).*

The plate joint system of the CLT+S building was improved from the previous one (Figure 3) to correspond with the 4-story buildings as shown in Figure 10. An insertion plate was used to fix two CLT wall panels together using four large diameter high-tensile bolts. A bolt diameter of 30 mm was chosen to have larger embedment strength compared to that of 20 mm. The insertion steel plate with a thickness of 22 mm was designed not to fail. Because C-shaped beams are not available in large sizes in Japan, H-shaped steel beams whose flanges were partially removed were used to accommodate the CLT panel.

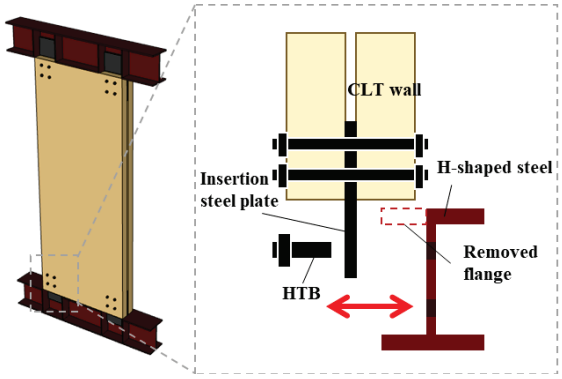

Figure 11: *The specification of CLT walls-steel beams of the hybrid system.*

4.1.3 System boundary in LCA

The life cycle of a building can be divided into material production, transport, construction, use/repair, and demolition/disposal phase. In this study, material production and transport phases were considered in the system boundary to analyse differences by structures. Construction, use/repair, demolition/disposal were excluded for the following reasons. According to [15] and [16], environmental loads during construction are under 1 % of whole emissions. Therefore, ignoring this phase does not make a significant difference. The loads in the use/repair phase are highly dependent on a user of a building. Hence, differences by structures are expected to be small. The data regarding demolition/disposal lacks accuracy because CLT is a new material and most of the buildings with CLT structure are yet to reach their service life.

Wood by-products (wood offcuts and wood shavings) are generated by the pre-cutting of wood laminae and CLT panels. According to an interview with local manufacturing companies, the yield rate from cedar log to wood laminae is almost 50 %. The yield rate from the CLT master panel to the pre-cut panel is approximately 90%. The by-products are used as a heat source for drying cedar lamina, which are the raw material for CLT. It was assumed that the GHG emissions resulting from this drying process are included in the emission intensity value according to Nakano et al. [17].

According to local construction companies, the volume of margin fresh concrete is adjusted to be as small as possible

https://doi.org/10.52202/069179-0558

because the disposal of hardened concrete takes additional money. Hence, the concrete residue was assumed to be negligible.

Steel by-products are generated in a process factory. They are shipped to recycle factory and reuse them into other steel products. In this study, environmental impacts regarding the reuse of the steel by-products were out of the boundary.

4.1.4 Inventory analysis

To evaluate the environmental loads, GHG (Green House Gas) emissions and carbon storage were selected as the impact indicators.

GHG emissions at the material production phase were calculated by multiplying the material weight by the intensities of each material. Table 1 shows the weight of each material. For the intensities of steel and concrete, IDEA version 3.1 (National Institute of Advanced Industrial Science and Technology; Sustainable Management Promotion Organization) [18] was applied. Because it does not contain the intensity data of CLT, it was derived from the work by Nakano et al. [17]. Regarding steel production, the most common manufacturing method in Japan was assumed for each product. Specifically, the blast furnace method was assumed for shaped steel and steel plates, and the electric furnace method was assumed for rebars.

Regarding concrete intensity data, the GHG emissions by production and shipment of cement and aggregate are included in the intensity data of concrete according to IDEA v3.1.

Transport distances of each material were decided by discussing it with local construction companies. The distances of concrete, CLT and steel (including joints, bolts, and rebars) were assumed to be 6.4 km, 50 km, and 192 km respectively. The distances were based on the local market situations around Sendai. The GHG emissions by each return way shipment were calculated by considering the impacts emitted by vehicle with no load from a construction site to a manufacturing factory. Vehicles for concrete, CLT and steel shipment were assumed as the 4-t pomp car, the 10-t track, and the 10-t track respectively. The intensities of the vehicles were applied from IDEA v3.1. Because IDEA v3.1 does not contain the intensity data of the 4-t pomp car, the intensity data of the 4-t track was applied.

Carbon storage was calculated using the following Equation (1) based on "the Guidelines for the Indication of Carbon Storage in Wood Used for Buildings" in Japan [19].

$$C_s = W \times D \times C_f \times \frac{44}{12} \quad (1)$$

where C_s is carbon sequestration of wood used in a building (t), W is the quantity of wood used for building (m^3) (value of air-dried lumber volume), D is the dry density of wood (t/m^3), C_f is carbon content of the wood (-).

Table 1: *Summary of the materials assessed in the study.*

The CLT building

CLT building			
Materials			Quantity [t]
CLT wall		1200x2790x210	4.94x10
CLT lintel		895x2000x210 (X-direction) 895x2290x210 (Y-direction)	2.80x10
Tension bolt		Diameter equals to 24 mm	2.92
U shear plate	L shaped	Thickness equals to 4.5 mm	$3.78x10^{-1}$
	Screw	22 screws per the plate	$8.40x10^{-3}$
L shear plate	L shaped	Thickness equals to 4.5 mm	5.51
	Screw	33 screws per the plate	$2.41x10^{-2}$
Shear plate	Plate	Thickness equals to 6 mm	$5.76x10^{-1}$
	Screw	48 screws per the plate	$6.36x10^{-2}$
CLT slab		Thickness equals to 210 mm	8.68x10

The RC building

Reinforced concrete building			
Materials			Quantity [t]
RC wall	Concrete	1700x2800x250	$3.25x10^2$
	Rebar		$4.83x10^2$
RC beam	Concrete	250x450	3.25x10
	Rebar		4.83
RC slab	Concrete	Thickness equals to 270 mm	$4.76x10^2$
	Rebar		7.07x10

The S building

Steel building			
Materials			Quantity [t]
Column		□-400x400	4.62x10
Girder		H-440x300	3.56x10
Beam		H-350x175	8.54
RC slab	Concrete	Thickness equals to 104 mm	$2.29x10^2$
	Rebar		3.40x10
	Deck plate		1.70x10
Exposed column base			1.54

The CLT+S building

CLT+Steel building		
Materials		Quantity [t]
CLT wall	1200x2706x180	1.93x10
Plate	300x550x22	8.29
HTB	Diameter equals to 30 mm	1.78
Girder	H-294x200	1.75x10
Beam	H-250x125	5.29
CLT slab	Thickness equals to 210 mm	8.67x10

4.2 RESULTS AND DISCUSSION

Figure 12 shows the results of GHG emissions and carbon storage of each building per square meter of the total floor area. GHG emissions of the CLT building, the RC building, the S building and the CLT+S building were 118 kg-CO_{2eq}/m^2, 268 kg-CO_{2eq}/m^2, 308 kg-CO_{2eq}/m^2 and 143 kg-CO_{2eq}/m^2 respectively. Carbon storage of the CLT, CLT+S building were 225 kg-CO_{2eq}/m^2, 156 kg-CO_{2eq}/m^2. The results showed that the CLT+S building emitted higher GHG emissions than the conventional CLT alternative and lower than the RC and S buildings.

Regarding GHG emissions of the CLT+S building and the S building, the emissions by the girder of the CLT+S building (42 kg-CO_{2eq}/m^2) was almost half of that of the S building (83 kg-CO_{2eq}/m^2). The smaller size of steel

beams thanks to putting the CLT walls on the beams significantly reduced GHG emissions.

Regarding the GHG emissions of the CLT+S building and the CLT building, the hybridization reduced the emissions of the CLT wall and the connections (35 kg-CO_{2eq}/m^2) compared with those of the CLT building (64 kg-CO_{2eq}/m^2). However, the additional GHG emission by the steel girders and the beams resulted in larger whole emission of the CLT+S building. From an economical point of view, the current material cost of CLT is very high in Japan. The weight of the CLT walls of the hybrid system (19 t) were one third of that of the CLT building (49 t) thanks to the hybridization. Hence, the reduction of the CLT wall's weight could result in lower production cost.

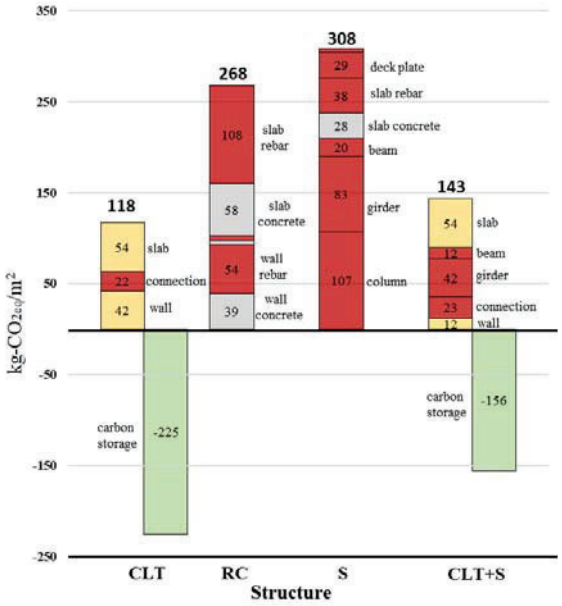

Figure 12: *GHG emissions and carbon storage of each building.*

5 CONCLUSIONS

In this paper, the efficiency and workability of a new hybrid structural system with CLT walls and steel beams with steel plate joints was introduced. Moreover, the environmental impact analysis of 4-storey buildings with four different structural system scenarios was discussed. The conclusions are as follows:

1. To compare the efficiency and workability of the proposed steel plate joint, conventional screw joint and tensile bolt joint, a comparison of the intensity of constructive works of these joints was conducted. It was shown that the workability of the plate joint was better than that of the screw joint and the tensile bolt joint thanks to the reduced construction processes and a lower precision target.
2. A CLT module with the proposed joint system was demonstrated to confirm the workability. The construction of the proposed system was found to be faster and easier than conventional structural systems. This showed the advantage of the workability of the hybrid system and the steel plate joints.
3. To analyse the sustainability performance of the hybrid structure, a LCA study was conducted. The analysis quantitatively compared the environmental impacts of four different structural systems, including the proposed hybrid system, conventional CLT, reinforced concrete and steel structures.
   As a result, the proposed hybrid system showed higher GHG emissions than a conventional CLT alternative and lower than a reinforced concrete and steel alternatives.
4. The weight of the wall panels of the hybrid system were one third of that of the CLT alternative owing to the hybridization. The current material cost of CLT is very high in Japan. Hence, the reduction of the CLT wall's weight could result in lower production cost.

ACKNOWLEDGEMENT

This research was supported by JSPS Kakenhi Grant Number JP19K22001 and JP22H01632, and CLT Building Components Technology Development and Dissemination Project by Japanese Forestry Agency. This fund is gratefully acknowledged. The support of Dr. Naoyuki Matsumoto, Assistant Professor, Tohoku University, and members from Miyagi Prefecture CLT Promotion Council are also appreciated.

REFERENCE

[1] Japanese Forestry Agency, accessed 24 February 2023, <https://www.rinya.maff.go.jp/j/kikaku/hakusyo/r1hakusyo_h/all/chap3_2_2.html>. (In Japanese)

[2] J.H. Andersen, N.L. Rasmussen, M.W. Ryberg, Comparative life cycle assessment of cross laminated timber building and concrete building with special focus on biogenic carbon, Energy Build. 254 (2022), 111604.

[3] G. Felmer, R. Morales-Vera, R. Astroza, I. Gonz´alez, M. Puettmann, M. Wishnie, A lifecycle assessment of a low-energy mass-timber building and mainstream concrete alternative in Central Chile, Sustainability 14 (2022) 1249.

[4] A. Jayalath, S. Navaratnam, T. Ngo, P. Mendis, N. Hewson, L. Aye, Life cycle performance of Cross Laminated Timber mid-rise residential buildings in Australia, Energy Build. 223 (2020), 110091.

[5] Japanese CLT Association: Environmental performance of CLT buildings and announce to end-users, accessed 24 February, <https://clta.jp/wp-content/uploads/2022/04/R2ho_CLTkankyouseinouhyoukaLCA.pdf>. (In Japanese)

[6] Loss C., Rossi S., Tannert T.: In-plane stiffness of hybrid steel–cross-laminated timber floor diaphragms. Journal of Structural Engineering, 144(8):04018128, 2018.

[7] Khajehpour M., Pan Y., Tannert T.: Seismic Analysis of hybrid steel moment frame CLT shear walls structures. Journal of Performance of Constructed Facilities, 35(5):04021059, 2021.

https://doi.org/10.52202/069179-0558

[8] Kanazawa K., Isoda H., Kitamori A., Usami T., Araki Y.: Structural performance of composite structure with CLT wall infilled in steel frames using drift-pin with steel plate. Journal of Structural and Construction Engineering, 86(788):1430-1439, 2021. (In Japanese)
[9] Fukumoto K., Kouda M., Saito M., Okazaki T., Isoda H., Yasui N.; A case study and future subjects of steel frame hybrid structure with CLT infill shear walls, AIJ J. Technol. Des. Vol. 26, No.64, 923-928, 2020. (In Japanese)
[10] Nakasima S., Araki Y., Ohashi Y., Nakajima S., Miyatake A.: Evaluation of in-plane shear strength of CLT based on the real size horizontal loading shear test, The effect of species of laminae on in-plane shear strength, J. Struct. Constr. Eng. AIJ. Vol. 84 No. 760. 843-849., 2019. (In Japanese)
[11] Japan Housing and Wood Technology Centre: CLT Building Design Manual, 2016. (In Japanese)
[12] Minegishi A., Atsuzawa E., Tsuda K., A. G. Aljuhmani, Goto Y. and Maeda M.; Development of a hybrid CLT walls and steel beams structural system Part 3: Experiment results and evaluation of the flexural performance of the steel joint (In Japanese)
[13] Japan Housing and Wood Technology Centre: Guidance of Notification of Building Standard Law concerning CLT, 2016 (In Japanese)
[14] Architectural Institute of Japan: Standard Design of wall reinforced concrete structures, 2015. (In Japanese)
[15] Ichimiya T., Osumi M., Kobayashi Y., Nagasaka K., and Inoue M.: Environmental and Economic Evaluation of Wooden and Reinforced Concrete Non-residential Buildings I. A comparative analysis of GHG emissions by process-based LCA (In Japanese)
[16] Kobayashi K., Ueda K. and Yamada Y.: A study on the possibility of achieving life cycle carbon minus in apartment houses, J. Environ. Eng., AIJ, Vol. 87, No. 792, 169-179, 2022 (In Japanese)
[17] Nakano K., Shibahara N., Nakai T., Shintani K., Komata H., Iwaki M., Hattori N.: Greenhouse gas emissions from round wood production in Japan, Clean Technologies and Environmental Policy (2020) 22:2193–2205 (In Japanese)
[18] National Institute of Advanced Industrial Science and Technology: Sustainable Management Promotion Organization (2016) LCA database IDEA version 3.1 Tukuba and Tokyo, Japan (In Japanese)
[19] Japanese Forestry Agency: the Guidelines for the Indication of Carbon Storage in Wood Used for Buildings, accessed 24 February, < https://www.rinya.maff.go.jp/j/mokusan/attach/pdf/mieruka-1.pdf> (In Japanese)

World Conference on Timber Engineering Oslo 2023

COMPUTATIONAL DESIGN DEVELOPMENT OF A WOODEN FAÇADE SYSTEM

Camilla Schlyter[1], Karin Sandberg[2]

ABSTRACT: The implementation of computer design within the building industry has created new possibilities for creating digital tools for users such as architects. There is however a lack of easy to use, efficient digital tools to aid and explore design alternatives for architects when using products within the wood building industry. This paper demonstrates how a modular facade system in wood can be adapted for facade configurations in different contexts by using computational design.

The goal is to develop a digital design tool that is easy to use and provides the architect with a high degree of freedom to create project-unique facades. The design tool is developed with computational design methods for flexible and adaptive design. In parallel, assessment is made that the design solutions can be manufactured smoothly and quickly via digitalization and industrial production. The result of this research shows that the façade system can be customized by using parametric programming methods, and thus enable architects to design facades for different contexts. The design tool was verified with the architect partners concerning usability and manufacturers concerning production.

KEYWORDS: Façade design, Cladding, Heartwood, Parametric design, Adaptable design, Digital design tool

1 INTRODUCTION

Advances in computational design introduces new possibilities for designers, architects, and the wood building industry to collaborate from the initial idea thru the development process to a product ready to manufacture [1,2,3,4]. Previous research has shown that computational design approaches can be used to support the exploration and optimization of design solutions in the building design process [5]. In this paper computational design means a design method using algorithms and parameters to solve design problems by computer processing. Computational design methods support "file-to-factory" processes and interdisciplinary collaborations; it also enables adaptive design towards different contexts and cost-effective manufacturing.

The implementation of computational design within the building industry has its challenges. There is a need to clarify how and when different computational design approaches can be used to support the building design process [5].

There is a lack of easy to use, efficient digital tools to aid and explore design alternatives for architects using products within the wood building industry.

Since the Swedish wood industry is highly digitalized, it can serve as a good foundation for advances in computational design methods.

Parametric design, a software-based programming method, has proven to enable a creative exploration in design development. Data input can be gathered and organized rendering it usable in automated generation of design alternatives. This can be done manually by a user or for instance, using an automated algorithm [6].

Adaptable design is a design paradigm aiming at creating designs and products that can be adapted for different requirements and be influenced by users. An existing design of a product can be adapted to create a new or modified design based on changed requirements. Adaptive design enables manufactures to produce standardized products that are possible for end users to customize [7].

The goal with this project was to develop a digital design tool easy to use for architects when designing an adaptive wood façade system.

This paper demonstrates the use of computational design methods for developing a design tool to enable the façade system to different configurations. Thereby aiding architects in design decisions combined with a freedom to create project-unique facades and manufacturers by

[1] Camilla Schlyter, RISE Research Institutes of Sweden, Sweden, camilla.schlyter@ri.se
[2] Karin Sandberg, RISE Research Institutes of Sweden, Sweden, karin.sandberg@ri.se

https://doi.org/10.52202/069179-0559

assessing that the generated digital data is prepared for use in production so called “file to factory”.

A group of residential buildings in Lombolo, Kiruna Sweden, owned by Kiruna Bostäder AB are used as case to test the digital design tool. Figure 1 shows one of the façades in Lombolo.

Figure 1*: One of the façades today in Lombolo, Kiruna, Sweden. Photo by Karin Sandberg.*

Two case studies using definitions of case study approaches by Yin [8] are presented.

The façade system discussed in this paper was developed in the project “The facade of the city Swift, Stylish, Smart” [9,10] hereafter called the façade project. It consists of an industrial prefabrication of façade elements, corners and connections to windows and doors.

2 MATERIAL AND METHODS

For development of the design tool and the digital workflow a computational design approach was used, which requires information to be digitalized and organized so that it can be used in the automated generation of design alternatives.

The included parameters in the two studies were based on data collected from the façade project [9]. To test the digital design tool, data from the case in Lombolo was used.

The data collected from the façade project consisted of digital models of the façade element and corners. Data collected from the case was boundary information acquired from the configuration of one of the façades by drawings and site visit. Figure. 2 shows examples of collected data.

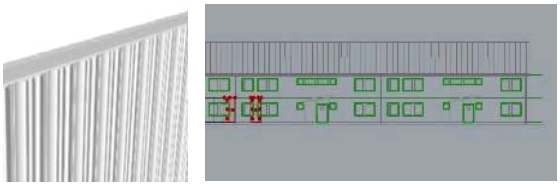

Figure. 2: *To the left - detail of the façade element model, to the right -boundary data from the façade case in Lombolo. Image by Camilla Schlyter.*

The facade system in this case is a facade solution for buildings consisting of a set of components assembled to elements that are fully or partially ready-made and dimensioned regarding adjustment for specific dimensions of buildings, and industrially manufactured. The components of the facade system are joined industrially to facade elements.

The facade system consists of a combination of adaptable elements. The element dimensions are possible to customize for users, such as height, width and surface design but the interfaces between components and assembly components are not possible to customize for users.

2.1 IMPLEMENTATION OF THE TWO STUDIES

2.1.1 Case Study 1

Research question for case study 1: How can an adaptable façade system be explored and optimized using a computational design approach?

The case study was conducted using an explorative approach as described by Yin [8]. The purpose with case study 1 is an exploration of possibilities and functions concerning a digital design tool for enabling design of a and adaptable façade system. Requirements on the digital design tool are: that is easy to use and provides the architect with a high degree of freedom to create project-unique facades within the products design possibilities and limitations. The design tool was developed with computational design methods for ensuring flexible and adaptive design for the user.

In case study 1 a digital design tool was developed to enable the façade system to be easy for the architect to use for different façade configurations. The design tool was developed using parametric design methods. This was done by developing the product´s design rules in parallel with manufacturing processes to assess that the generated data could be used with industrial production techniques. For manufacturers, this means that the façade system can be reused for the development of new designs to save product development time and costs. For architects this means that an adaptable design product gives them the opportunity to design in different ways for different contexts, having the security of using a predefined façade system.

https://doi.org/10.52202/069179-0559

The design tool's function and usability were verified in parallel in workshops together with a reference group of three architects, having different levels of knowledge of computational design from proficient to general user.

2.1.2 Case Study 2

Research question for case study 2: How can a computational design approach be integrated in a digitalized workflow in the value chain of an adaptable façade system?

The case study was conducted using an explorative approach as described by Yin [8]. Case study 2 concerned how the digital information created in case study 1 could travel thru a digital value chain, from design to manufacturing. Ensuring that the design solutions made by the architect can be manufactured smoothly and quickly by industrial production within the boundaries of the façade element design. A prototype of a future digital workflow was developed estimating the required information in the different stages in the design- and manufacturing process. The purpose was gathering knowledge of the requirements of data in the different stages in the value chain so that, in the next step enable a seamless digital workflow without digital information and design intent getting lost thru the value chain.

Moving into fabrication it is important to analyse how to use the "cocktail of software" available. The analysis was managed by using design methods to eliminate data and assess what data is necessary at different points through the whole value chain.

To solve this analysis of available software that allows for information exchange between different systems and tools is required.

For the control files used in industry, transfer of the information is needed from the software architects commonly use such as Autodesk Revit (Revit). In this study Microsoft Excel files (Excel) or Autodesk AutoCad (AutoCad) was used as a middleware between different software. From Excel, for instance, wood cutting lists can be made enabling feeding into the manufacturing machines.

3 RESULTS AND DISCUSSION

3.1 CASE STUDY 1, DEVELOPMENT OF THE DESIGN TOOL

The requirements of the design tool:

- Provide that the facade elements can adapt size wise to different façade contexts.
- Manage different measurements, such as variation of floor level hights and window openings.
- Adapt the size of the façade elements to production, transport and assembly.

Digital models of the facade system were built up using Rhinoceros 3D (Rhino) and Grasshopper software. Thereafter a prototype of the design tool was created using Rhino, Grasshopper, AutoCad and Revit. Revit is commonly used by architects and engineers in Sweden. Dynamo is an extension to Revit and Grasshopper is an extension to Rhino and both Dynamo and Grasshopper enable parametrization. Parametric software such as Rhino thru its extension Grasshopper is seldom used in the wood construction industry, but is interesting since int can provide important digital data concerning customization in the value chain.

What sets computational design approaches apart from more conventional design methods (where the user usually reacts with digital sketches, drawings, or models) is that the user instead interacts with the digital environment and the mechanisms responsible for generating digital representations [10]. The architect can see and interact with the design in real time, adjustments made are visualized immediately.

Using parametric design enabled exploring the structure of relationships between the parameters in the façade system. By using parametric design, it was possible to use algorithms to design boundaries for both, the predefined, standard components (not customizable for users) and the adaptable components (customizable for users).

Case study 1 consisted of four phases:

3.1.1 Phase 1: Inventory of design criteria and design tool

The objective:

- Initial discussion on suitable programming for the design tool prototype.
- Analyse the design criteria, established in previous research, by studying the variability of the components to assess what parts required adaptability towards different contexts and which could remain static.
- Model façade elements and components in Rhino.

Components in the facade system that should be customizable for the user were already established in the previous façade project. After discussions in the project- and reference group it was concluded that the size and adjustment to openings of the facade elements was interesting to explore. The decision was also based on inventory and experience of the façade projects manufacturing processes and aesthetic analyses.

The decision established the boundaries of the case study. Initial analysis of different software was conducted thru a series of meetings within the research group where

https://doi.org/10.52202/069179-0559

possible capacities for automating design procedures, i.e., what the software needed to achieve was discussed. This concerned searching for a method ensuring that the facade elements could be adapted size wise to different façade contexts, including different measurements, floor level heights, and window openings. The initial discussion on suitable programming for the design tool prototype was important, since it created a background for important knowledge for the data collection in the next step. Figure 3 shows ideas for different configurations for the façade elements from the façade project.

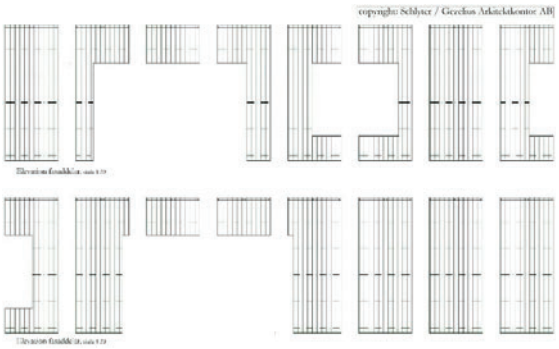

Figure.3: *Exploring the size of the façade elements, from the earlier façade project. Image by Camilla Schlyter.*

The analysis concluded that parametric design was suitable for the façade systems properties, combined with the potential of reducing the amount of time and effort needed to obtain optimized façade solutions for every situation. The hypothesis was that parametrization would enable that the façade system, in a new context, could be created without the need for redesign of the whole system. The façade elements and components were modelled in Rhino to aid in assessing variability, by visualisation. Figure 4 shows evaluation of façade element components that must be considered, such as height, width, thickness, distance to attachment etc.

Figure 4, *Phase 1 resulted in an analyse and overview of the design variability of the components from the project. Image by Camilla Schlyter.*

3.1.2 Phase 2: Systematizing input data

- The objective:
- Study of the components in the facade element in more detail.
- Develop data concerning which components could stay "standard" and which should be able to customize.
- Systemize the input data.

Systematizing the required data resulted in a structured and detailed excel file for identifying data input for digital parameterization. The Excel file was constructed specifically for data input for use in digital parametrisation and aided in establishing a suitable hierarchy, going from system components to data needed for adaptation of the façade elements to the specific case, the building in Lombolo. Summarizing the hierarchy in the Excel file see figure 5.

System level, concerns variables of the components
- Boards, joints, surface, etc.

Existing building
- Façade, plan, width, height, windows etc.
- Floor levels, height etc.

Adaptation of façade element to existing building
- Module, façade system, width, height, littera etc.

Figure 5: *Hierarchy for data input for digital parametrization concerning variables in case, Lombolo. A* ***s****hort summery of the Excel file where information was collected concerning data for digital parameterization.*

The result from managing the large excel file added to the understanding of required additional data input, but also of exactly which data that was essential at a specific level. The data input was discussed with the manufacturer to assess that all required data was accounted for. The Excel file was continually reworked as the study developed.

3.1.3 Phase 3: Test of software

The objective:
- Evaluate programming solutions and software, to ensure that possibilities were not overlooked.
- In Revit the min-max possibilities of the facade element and ways to subdivide the model was tested.

In phase 3 different software and programming solutions to enable the façade system towards different configurations were tested using an iterative approach.

The result from phase 2 was used as background data. Revit, Dynamo, Rhino, Grasshopper and AutoCad software were tested and analyzed see figure 6.

- Revit, with BIM modelling capabilities, is good on documentation and tracking capacities, but lacks parametric features and generation of complex geometry is limited. The Revit structure with families can be a good way of organizing the data in later development when creating an end user interface.
- Dynamo, interesting for next stage in the development in combination with Revit.
- Rhino, lacks BIM modelling capabilities but enables optimization exploration thus making it an ideal platform for design analysis.
- Grasshopper, is an extension of Rhino and has good parametric capacities. Grasshopper enabled the possibility to parametrise the facade system according to the excel sheet and enabled adjustment of the facade system to the case.
- Autocad, contained the component details of the fasade system and was used as a base for modelling in Rhino.

Figure 6: *Test of software with short comments*

Phase 3 resulted in choice of software. The design space of Grasshopper/Rhino proved easy to work with and test solutions valid for the study. Grasshopper/Rhino enabled the possibility to parametrise the facade system according to the excel sheet and adjust the facade system to the case.

3.1.4 Phase 4: Adaptable design

The objective:

- Programming in Grasshopper enabled testing a prototype solution of the design tool. A code for automatic subdivision of facade elements was sketched in Grasshopper, including a "sanity" check.
- Verification of the design tool with a reference group of users, architects.

Phase 4 resulted in a prototype design tool, for adapting the façade elements to different façade configurations using parametrization software. Assessment was made that the façade element details, design criteria, material characteristics, dimensions, material properties can be formulated in program code to provide customized design output, see figure 7, 8.

Figure 7: *Screen shot from Grasshopper, showing boundary lines and a script running on an underlay of a drawing of the residential block in Lombolo. Image by Ola Jaensson and Camilla Schlyter.*

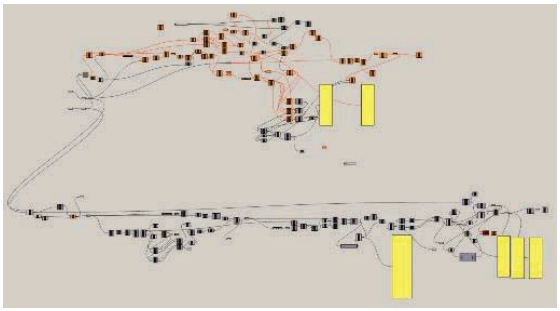

Figure 8: *Screen shot from Grasshopper showing the script. Image by Ola Jaensson and Camilla Schlyter.*

Verification of the design tool with the reference group of architects was done at two occasions. The first meeting was a teams meeting, securing that the chosen variables were valid, in this meeting the manufacturer also attended ensuring that manufacturing data was provided. The second meeting at Equator architects concerned testing the usability of the prototype design tool together with three architects. The architects tested the prototype design tool on the case façade using drawings of a residential building in Lombolo, first applying boundary lines and thereafter creating a façade layout. The result of the test showed that it enabled the architects to create a façade layout quickly once they had set up the boundary lines of the façade. The immediate response was positive and the design of the façade system was much appreciated. The result of the meetings were documented in meeting protocols.

3.1.5 Comments on the results

A master model concept, such as Revit can be used in the future to structure and contain the components and their link inputs, outputs, and processes. BIM software such as Revit can be used as a container to define the façade system, its design variables, constraints, and objectives, and thus support manufacturing.

https://doi.org/10.52202/069179-0559

The software combination of Grasshopper/Rhino worked well in study 1. Revit is suitable for documentation and tracking key information but is not suitable for generating complex geometry nor for analysing real-time simulations, both possible in parametric software. Based on study 1 conclusion was made that further explorations of the "cocktail of software" i.e. middleware is an interesting way to continue the research.

To facilitate information exchange and interoperability for the systems involved in computational design approaches, middleware components can be used as an interface to support information exchange. This could facilitate the integration of existing computer-based methods and tools in BIM-based workflows into computational design approaches.

Important knowledge was gathered concerning how to adjust the programming and data input for the next step. For example, concerning rules on how to cut the individual façade elements when manufacturing the façade system. Figure 9 shows a diagram summarizing the development process of the design tool.

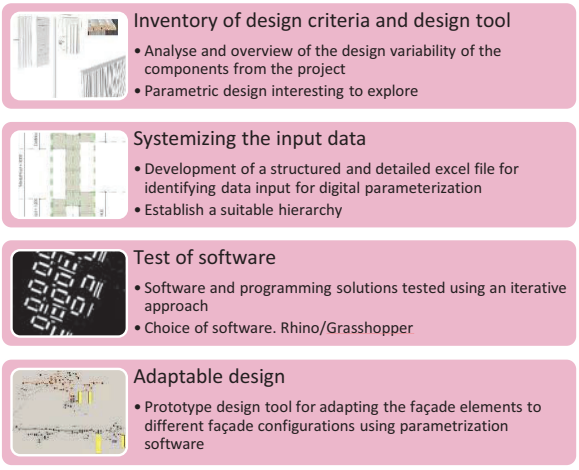

Figure 9: *The digital design tool process*

3.2 CASE STUDY 2, THE FUTURE WORKFLOW

Case study 2 concerns a prototype of a future digital workflow estimating the required information in the different stages in the value chain using the case of adjusting the façade system to a building in Lombolo.

3.2.1 Telling the digital tool what the project is, going from general to specific input

Since the digital tool accepts a generous variety of input, an automatic sanity check was programed enabling the result to be visually communicated to the user. This was done with the purpose of warning when the values or resulting calculated properties seem suboptimal or invalid.

3.2.2 The construction system

Example of system level parameters:

- Wood component dimensions
- Detail dimensions, distances, limits, shapes, and choices
- Standard module width
- Minimum and maximum module height

Proposed next step in the development of the tool: Surface ornamentation type.

3.2.3 The manufacturer

Here, and the properties of the manufacturer's tools, materials and processes are to be defined.

Examples of manufacturer parameters:

- Standard green wood dimensions
- Machines and tools used for a specific construction and design.
- Cost-driving parameters for different machines and treatment methods.
- Preferred output file formats for specific machines such as the g-code, a programming language for CNC (Computer Numerical Control) machines. G-code stands for "Geometric Code". A G-code tells a machine what to do or how to do something for instance, instruct the machine where to move, how fast to move and what path to follow and others etc.

3.2.4 The project parameters

In this level, the specific project is created and defined.
Examples of project parameters:

- Project name
- Geographic location of project (project origin)
- Other administrative data
- Project units
- Number of buildings

3.2.5 The building

In this level specific project data is required.
Examples of building parameters:

- Building names
- Ground contour polylines
- Number of facades
- Number of levels

3.2.6 The buildings façades

Examples of existing facade parameters:

- Elevation contour polylines
- Wall opening contour polylines.

3.2.7 New façade parameters

Examples of new façade parameters:

- Elevation division levels (Z values, the bottom alignment lines of the façade modules)
- Number of modules
- Left and right corner/end module types
- Offset to first façade module.

3.2.8 Dance of adjustments

Dance of adjustments, test of different façade layouts until desired design is achieved. After the design tool has been fed with user input, the façade element generation algorithm calculates necessary directly related parameters and makes a first automatic element division elevation per façade and level.

Figure 10 shows a screenshot from a first automatic element division. This can be adjusted by the user if the division does not comply with the wanted design outcome, but always within the programed boundaries.

Figure 10: *A screenshot from Grasshopper showing a first automatic element division on a façade in Lombolo.*

3.2.9 Outputs

Examples of output and formats:

- Excel module property lists.
- Timber cutting lists.
- Waste prediction
- CO_2 and other resource calculations
- Lists of assembly jig support positions for each module or sub-component.
- Visualization oriented, detailed geometry.
- Metadata-rich BIM geometry.
- Overview elevation drawings with façade modules annotated.
- Annotated construction drawings of individual façade modules.
- Wood shop CNC machinery G-code

4 CONCLUSIONS

The design tool, the result of this research, shows that the façade system can be customized by using parametric programming methods, and enable architects to design facades for different contexts. This has been shown thru analysing the result of the design tool together with architect partners. Assessment has been made that the façade elements details, design criteria, material characteristics, dimensions, materials' properties can be formulated in program code to provide customized design output. Knowledge has been gathered on how to adjust the programming and data input for the next step, the development of a plug in for BIM software such as Revit.

Assessment has been made that the digital information gathered in case study 1 can be used for manufacturing. In case study 2 the digital flow has been hypothetically tested thru the value chain in close collaboration with industry partners. Though the results have to be further confirmed to assure that the façade system will be possible to manufacture smoothly and quickly, best assessed thru physical prototype tests with the industry partners.

An assumption made in the project is that Revit can be interesting for a commercial application in a future by developing an end user interface thru a customized plug in. A plug in is a software component that adds a specific feature to a software that enables customization. The plug in can be infused with diverse input data concerning material properties, keying the specific elements placement in a project and cost et cetera.

Future development can include how numerical data in middleware can be fed into Revit via parametric software to control the parameters of Revit Family components aiming towards a plug in a Revit environment. Thru the Revit family's output, for example, cutting files for the timber industry and control files for manufacturing can be created.

The project shows that the wood building industry can adapt computational design methods when developing adaptable building products. The methodology precented in the paper also provides a possible scaling-up effect applicable to other products. The next step is to further develop the design tool and test it on façade configurations of different design.

ACKNOWLEDGEMENT

Thanks to the strategic program Bioinnovation Construction & Design, IPOS – Innovations in wood-based building materials and products, subproject "The facade of the city Swift, Stylish, Smart". The project is founded equally by Vinnova Sweden's innovation agency, the Swedish Energy Agency, and Formas together with the industry partners. Thanks to E2B2 Swedish Energy Agency concerning the project Climate smart renovation with innovative façade system. A special thanks to Equator Architects in Stockholm for the collaboration with the digital tool, SCA and Hedlunda for industrial input and KBAB.

https://doi.org/10.52202/069179-0559

REFERENCES

[1] Eriksson H., Mukkavaara J., Sandberg M., Assessing Digital Information Management Between Design and Production in Industrialised House-Building : A Case Study, ISARC, 2019.

[2] W.J.C. Verhagen et. al. A method for identification of automation potential through modelling of engineering processes and quantification of information waste. Advanced Engineering Informatics, 29(3), 307-321, 2015.

[3] B. Kim, Y. Lee, Genetic algorithms for balancing multiple variables in design practice. Advances in Computational Design, Vol. 2(3), 225-240, 2017.

[4] A. Menges, T. Schwinn, OD. Krieg. Advancing wood architecture: a computational approach, Routledge, London, UK, 2016.

[5] Mukkavaara J., Exploration and optimization of building design solutions using computational design. Doctoral thesis, Luleå University of Technology. https://www.diva-portal.org/smash/get/diva2:1544058/FULLTEXT02, 2021.

[6] Caetano, I., Santos, L., & Leitão, A. Computational design in architecture: Defining parametric, generative, and algorithmic design. Frontiers of Architectural Research, 9(2), 287-300. https://doi.org/10.1016/j.foar.2019.12.008, 2020.

[7] Joseph Pine II, I. B. "Mass Customization: The New Frontier in Business Competition" Harvard Business School Press, Boston, MA, 1993

[8] Yin, R.K. Case study research: design and methods. (4. ed.) London: SAGE, 2014

[9] Sandberg K., Schlyter C., Arkitektonisk utformning och konstruktiva lösningar – Fasaden i staden Snabb, Snygg, Smart, RISE Rapport 2021:109, 2021

[10] Sandberg K., Serrano E., Sundqvist B., Henriksson F., (2021). IPOS – Innovations in wood-based building materials and products, RISE Report 2021:117, p44-79, http://urn.kb.se/resolve?urn=urn:nbn:se:ri:diva-63140.

[11] Oxman R. Theory and design in the first digital age. Design Studies, Volume 27, Issue 3, May 2006, Pages 229-265, 2006

World Conference on Timber Engineering Oslo 2023

STUDY CASE: REFURBISHMENT OF THE GARE MARITIME IN BRUSSELS

Charline Lefèvre[1]

ABSTRACT: This paper presents the study case of the Gare Maritime, a former train station in Brussels in Belgium that covers an area of 40.000m² and that has been entirely renovated to welcome under its roof the construction of twelve multilevel pavilions in fully timber structure. Those 4500 m² of twelve new buildings are hosting shops, publics functions and offices and creates a new covered quarter inside the city. This paper introduces first the project, its historical context, its situation and its refurbishment.
Then an explanation of the structural design is given and divided in different parts. A focus is first made over the specific features of the project to explain the challenges of the structure. Then the joints developed on the project are explained explaining the main type of assemblies. Thirdly, all the fire engineering process of the project is described; how the dossier was accepted by the authorities, the simulations and calculations that needed to be done. The last section finally gives information about the mounting process and the upstream preparation that it required. In the next chapter, more can be learned over the innovative technologies that have been implemented on the project to make it completely energy neutral and fossil free before finally concluding and giving some important numbers over the project.

KEYWORDS: Cross-laminated-timber, Glulam, Refurbishment, Collaborative ribbed floor; Thermal analysis.

1 INTRODUCTION

The "Gare Maritime", located on the site of Tour & Taxi in Brussels, is a former railway terminal, built in the early 20th century) by architects Constant Bosman and Henri Vandeveld and engineer Frédéric Bruneel.

Figure 1: *Front facade of the Gare Maritime*

It was once Europe's largest railway terminal but the development of road transport and the gradual removal of European customs barriers reduced activities to the point where this 40,000 m² area (276 by 138 m) was completely abandoned. For many years, it has been vacant and deteriorating. In 2014 a real estate developer bought the site Tour & Taxi and began transforming the storage halls and customs buildings around and to transform step by step the neighbour into a greener quarter.

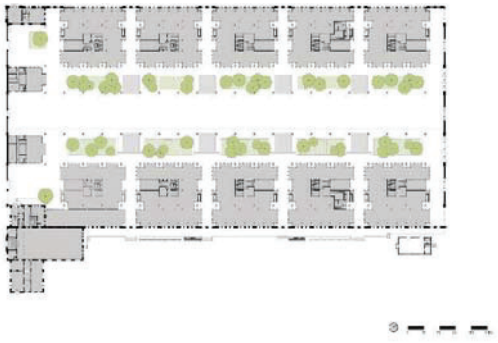

Figure 2: *Ground floor plan*

The former station reaches a maximum height of 23 m. The load bearing structure consists largely of three-hinged frames, made of riveted metallic trusses, covering a 26 meters span. In this magnificent historical hall that has been renovated and reinforced, the Neutelings-Riedijk Architecten's office has inserted twelve four levels pavilions in timber structure with a total of 45.000 m². They will host shops, offices and public functions to make the Gare Maritime a real covered city. The structure of these interior volumes is entirely made of wood. In each of the lateral naves, 5 pavilions fit perfectly into the existing structure, making a total of 10 almost identical pavilions. At the front, 2 additional small pavilions

[1] Charline Lefèvre, Ney & Partners WOW, Belgium, CLE@ney.partners

https://doi.org/10.52202/069179-0560

complete the entrance and the central hall remains an free, covered avenue that can be used for events, sports and arts.

Figure 3: *Elevation*

1.1 RENOVATION PHASE

A first phase of the project was to renovate and reinforce the structure where necessary and to renew the building envelope to contemporary standards. The steel structure was overall in good condition, except for some damaged and corroded elements in the rear façade and under the gutters. One of the important points in the renovation of the structure was to be able to add solar panels on the existing roof. This was possible with a small amount of reinforcement as the structure still had some reserves of strength. Only some elements had to be replaced and there was some strengthening needed on elements that had potential for buckling.

An expertise of the wooden roof frame was also carried out. Some parts were attacked by fungi and had to be completely replaced. However, the expertise and the implementation of a monitoring system to ensure that the wood was properly dried out made it possible to preserve the existing wooden deck as much as possible. The refurbishment focused on a safe structure in accordance with current standards, with maximum respect for the initial project.

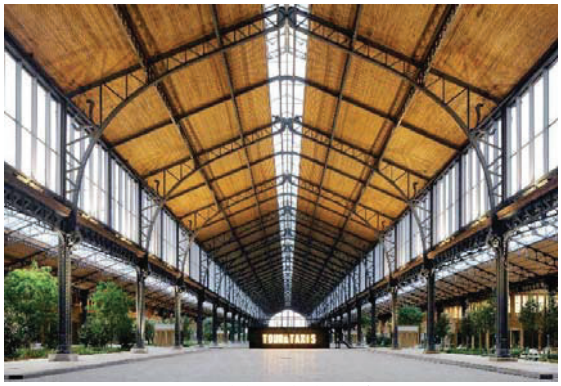

Figure 4: *Interior view of the refurbished naves*

1.2 THE CHOICE OF MATERIAL

At the start of the project, various structural concepts were proposed to the project owner (real-estate developer Extensa) and, for each one, the grid they suit best and their advantages. Those concepts were made of concrete or steel as well as wood.

However, it soon appeared to us that a timber solution was the most adapted proposal in the case of the Gare Maritime and the client was soon convinced too.

First, there was a strong desire from the design team to make the Gare Maritime a pioneering project in line with the existing structure. The aim was therefore to make it an example in terms of sustainability and circularity. The design of a mechanically assembled wooden structure makes it completely removable. Moreover, 1 m^3 of wood on the project represents approximately 1 metric tonne of stored CO2. We can also ensure that the wood is certified and comes from sustainably managed forests. Secondly, the demand was to build these 45,000 m^2 in a really short term. A fully prefabricated structure was the most appropriate way to meet this requirement. Further, it was important to work with relatively light elements. The idea was to limit the impact of the new structure regarding the existing foundation but also to be able to work with small and light machines since the structure is entirely covered, making it impossible to use traditional cranes.
Lastly, since the whole construction site was protected from weather conditions, the situation was ideal for a timber construction.

2 STRUCTURAL DESIGN

One of the challenges for this project was to integrate the 12 new buildings inside the existing historic hall. All the buildings are close to the existing building but remains completely independent of it. The connections between the new and the old building had to consider the thermal expansion of the historic framework. A 7cm gap had to be leaved between the two structures. As a result, there are many cantilevers in each pavilion so that the new structure meets the old one without being fixed to it.

The cores are made of cross laminated timber (CLT) and completed with columns-beams structure and with ribbed floor in glulam and CLT. Walkways and cross stairs connect pavilions to each other's.

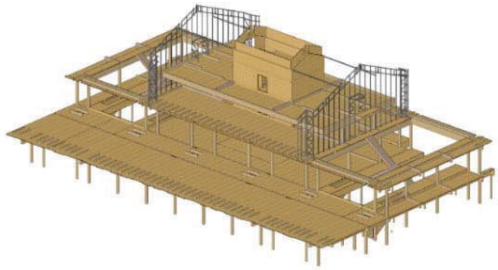

Figure 5: *3D model of one pavilion made with Cadwork [1]*

2.1 SPECIFIC FEATURES

Neutelings Riedijk Architects decided to work with a plan based on a grid of 1.2 by 1.2 m, ideal for the development of offices and perfectly fitting the existing grid of 12 m between the main steel structures. The structure was developed on this concept. All the floors are collaborative screwed ribbed floor composed by a CLT-100 panel that is screwed with glulam ribs every 1.2m. This type of floor

https://doi.org/10.52202/069179-0560

allows to reach bigger spans (up to 8.4 m in this project) while optimizing the volume of wood.

At the beginning, the ribs were supposed to be glued to the CLT panels at the factory but Ney worked with a German timber company (Zublin Timber) on this project and this system would have made transportation from Germany to Brussels very inefficient. The possibility of setting up a workshop to do the gluing on site was considered by the company but the cost was prohibitive. This is why a screwed connection was designed instead.

To solve the cantilevers, the presence of a raised technical floor has been used to implement ribs on the upper side of the CLT. Thanks to this system, users of the buildings have the feeling that only a 10 cm thick CLT slab goes up to the existing structure.

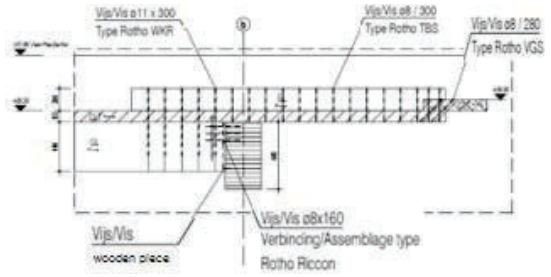

Figure 6: *Reversed collaborative ribbed floor in cantilevers*

To limit the number of holes in the timber elements and to facilitate de mounting, most of the techniques were also integrated under this raised technical floor. But on the ground floor, due to the presence of existing foundation, it was not possible to excavate too much to create a raised floor. An important number of holes had to be made in the ribs to offer flexibility for the future tenants so that they can install techniques in the ceiling. Each hole had to be reinforced by fully threated screws in the ribs.

It was important for the architect to design a structure completely made of wood. To be able to do it, in some areas where we were limited in height and where the stresses were particularly high, spruce LVL (Kerto) and beech LVL (Baubuche) beams have been used for their better mechanical properties. This is the case for the 16.5m long beams that cantilever by 4.8m to support the mezzanine on the third floor and that are made of laminated veneer spruce. The architect chose to clad them to keep the project homogeneous.

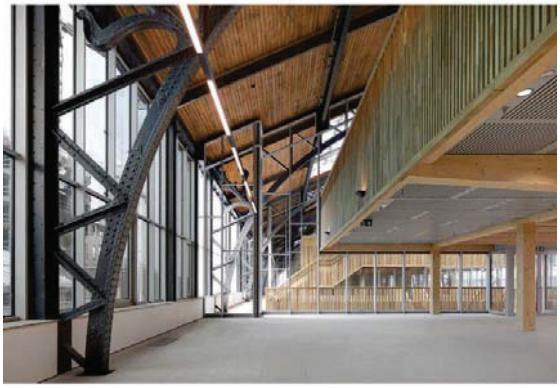

Figure 7: *Mezzanine on cantilevered LVL beams*

2.2 JOINTS

Nearly all joints remain visible on the project. The aesthetics of the connections has therefore been a key point in the design. The ribs on the second and third floors are assembled with concealed connectors using the principle of sliding dovetail joints made with a steel connector.

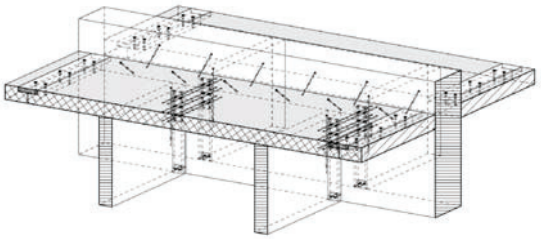

Figure 8: *Ribs connections*

In order to avoid compression problems perpendicular to the grain. Large steel profiles ensure direct load transmission between columns.

For the most heavily loaded beams, an HSK system has been used. These are perforated steel plates (HSK plates) moulded into the wood and glued with epoxy resin ensuring that they remain completely invisible. Those specific joints have also been used the ensure the continuity of the glulam stair stringers.

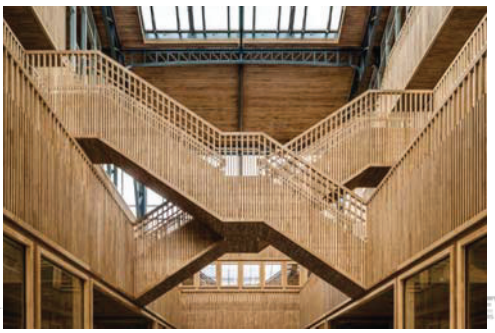

https://doi.org/10.52202/069179-0560

Figure 9: *Crossing stairs between pavilions using HSK joints*

2.3 FIRE

A big topic on this project was fire safety. It was difficult for the renovation project to comply with existing fire safety Belgian standards and a derogation file had to be drawn up. For example, Belgian fire safety laws require evacuation stairs to be enclosed to protect against fire and smoke while the architect's intention was to work with open staircases.

Thus, several compensatory measures and solutions hade to be integrated in order to be able to execute such a project. Adapting thermal heat scanners used by the US military are used to act as fire detection, crossing stairs between pavilions were designed to act as evacuation stairs, 800 ventilation stacks were added along the existing roof ridge to help with air circulation as well as smoke extraction in case of fire. In addition to those solutions, a modelling of various escape scenarios and simulations of temperature and smoke evolution made by a fire engineering office were necessary to convince the authorities to approve the unconventional solution.

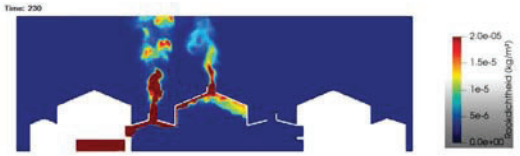

Figure 10: *Simulation of the smoke density*

Concerning the timber structure, an advanced study for fire stability has been performed for this project in collaboration with the University of Liège. Indeed, we were asked to demonstrate that the structure could withstand a longer period of time than originally planned while maintaining the same sections.

When necessary, it was chosen to work with an intumescent transparent paint specially developed for wood. Many products exist on the market to improve the fire reaction of wood but it was not easy to find a paint that improves the fire resistance with technical datas to understand how to calculate the impact of this painting over the timber section during fire. The painting found had valid datas for a floor with a certain load and span. As these assumptions were not met, the project configuration was tested to validate that the values used were still applicable and so a fire test on a real scale mock-up of the floor has been performed in order to validate the complex.

In addition to the fire test, we did further numerical analysis.
A finite element modelling of some joints has been done with the software SAFIR [2] to perform thermal and mechanical analysis and study the behaviour of those joints after a determined time without any protection or with de addition of an intumescent paint.

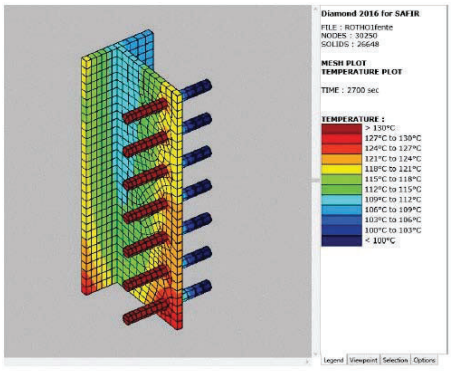

Figure 11: *Thermal analysis of a joint*

In case of fire, the behaviour of the timber depends not only on the temperature of the material but also on the type of solicitation (tension, shear, …). To be able to determine the load bearing capacity of a dowel, we modelled a beam (the dowel) supported by stiffeners whose stiffness varies along the dowel according to the evolution of the mechanical properties of the wood. The stiffener was thus representing the behavior of the wood depending on its temperature.
With the first general model of the joint, we knew the temperature of the wood along the cross section of the beam so we were able to characterize the stiffeners along the dowel. Then we applied at the position of the slotted plate a load that was incremented until the load bearing capacity of the dowel was reached.

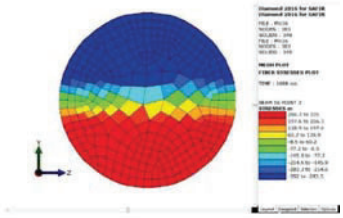

Figure 12: *Mechanical analysis of a dowel in case of fire: stresses in the dowel.*

2.4 MOUNTING

One of the biggest challenge of this project was the great volume of timber alongside the very short programme. The project's extensive scale, the need for precise integration of new elements into the existing structure and the tight deadlines were crucial factors in choosing a BIM process.

Timber construction is undeniably linked to a high degree of prefabrication. The entire structure was then already designed based on a 3D model drawn with software specialized in timber construction. This makes it possible to integrate this BIM process that is conducive to

https://doi.org/10.52202/069179-0560

prefabrication, from the designer to the erector via the supplier, and so on.

The contractors were also required to build a two-storey, full size mock-up on site. This mock-up had to integrate the timber structure, oak siding, steel façade and technical equipment in detail. As part of the project requirements, the contractors were tasked with constructing a full-scale mock-up on site, consisting of a two-storey structure that meticulously incorporated timber elements, steel façade, oak siding and technical equipment.

On one hand, being under cover eliminated any weather dependency during construction. But on the other hands, the new buildings had to be closely integrated into the existing structure – with limited room for manoeuvre. The use of traditional cranes was not possible and the assembly of all the elements and the phasing with the techniques had to be carefully studied.

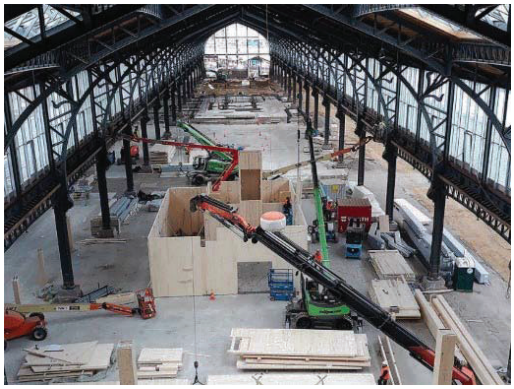

Figure 13: *Construction of the CLT core*

Finally, thanks to the BIM, all the elements were prefabricated, and the construction of the timber structure was extremely fast. It took in average 8 weeks to build 1 pavilion. It means the logistics of delivery and storage of the many pieces had to be tightly managed. The timber structure was fully executed in 10 months, only 14 months after the timber constructor signed the contract.

Figure 14: *Mounting of one pavilion*

3 MODERN AND INNOVATIVE TECHNOLOGIES

The original building has been preserved, including the wood and steel roof, while integrating modern and sustainable technologies for this high energetic performance project. Indeed, the Gare maritime is entirely energy neutral and fossil free.

In addition to CO2 stocked into the volume of wood, sustainability measures have been implemented.

On the roofs a total area of 17 000 m² of solar panels has been installed. The solar technology can also be found in the form of cells integrated into the windows on the south façade of the building. 140-metre deep boreholes were drilled between the pavilions into the bedrock and a subterranean lake system. The then probes are able to provide heating and air conditioning of the space by geothermical energy.and a rainwater recovery system has been installed on the 4 hectares of the roof to maintain the interior gardens and sanitary facilities.

Each pavilion is a highly insulated house underneath the existing envelope. This way, it was not necessary to heat the entire hall. The lateral skylights feature thus triple glazing only in the areas bordering the ten pavilions.
In addition to insulating the offices, Halio's smart tinting glass is used to enhance lighting management of the building. The glass begins tinting within seconds and reaches full tint in less than 3 minutes. It manages not only the intensity of light but also solar heat. Using electrochromic technology, this interactive glazing uses an electrical impulse to switch from total transparency to a dark tint, reducing glare. The glass then transforms into a virtually opaque surface, allowing only 3% of light to pass through. The privacy of the occupants is preserved without cutting them off from the outside environment.

https://doi.org/10.52202/069179-0560

4 CONCLUSIONS

In just three years, the entire 40 000m² of the former railway station underwent a complete renovation, resulting in its transformation into a covered, climate neutral quarter in the heart of Brussels city.

The Gare Maritime now houses a fully wooden structure with a total of 9000 m³ divided into 3000 m³ of glulam and 6000 m³ of CLT. This made the Gare Maritime one of the largest timber projects in Europe when it was inaugurated in September 2020. Since its completion, the project has won several awards, among them in 2020 the Dutch ARC20 Architecture Award, the Belgian Timber Construction Award and the RES Award, and in 2021 the Belgian Building Award, the Europa Nostra Award, the MIPIM Award and the ULI Europe Award for Excellence.

The covered city has now transformed into a bustling hub of various activities, welcoming day workers and visitors. In the evenings and at weekends, the activity continues thanks to its food market and the events held there, such as the world padel tour, which will be held there in 2023 for the second year running.

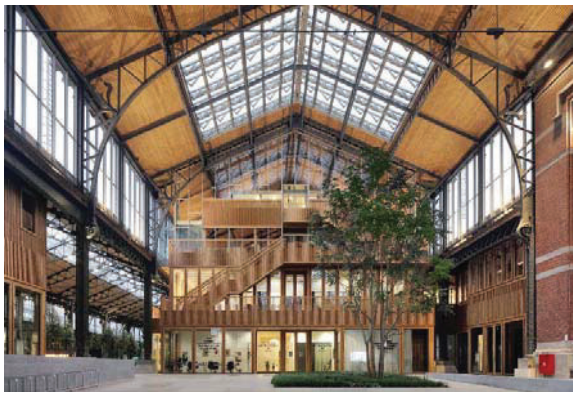

Figure 15: *View of one pavilion inside the existing structure*

REFERENCES

[1] Cadwork v26, solutions logicielles pour la construction, [online], accessed on March 1,2023, https://04.cadwork.com/solutions/construction-bois/

[2] J.M. Franssen, T. Gernay, Modeling structures in fire with SAFIR : Theoretical background and capabilities, Journal of structural fire Engineering, 8(3):300-323, 2017

[3] J. Vander Beken, O. Gallez, M. Jacques de Dixmude, C. Lefèvre, N. Néron, Ney & Partners : Designing Building Structures, 2022

[4] F. Kaltenbach, Detail magazine, 11/2021

[5] Ney and Partners WOW, Gare Maritime, 2019, [online], accessed on March 2, 2023, https://wow.timber-engineering.partners/projects/gare-maritime-brussels/

[6] H. Russel, Building Magazine, [online], accessed on April 11, 2023, https://www.building.co.uk/projects-gare-maritime-brussels/5105333.article

World Conference on Timber Engineering Oslo 2023

WIDE-SPAN LVL ROOF STRUCTURE FOR AN INDOOR SWIMMING POOL

Laurent Giampellegrini[1], Samuel Blumer[2], Hendrik Pfeffinger[3]

ABSTRACT: The wide-span roof structure for a new indoor swimming pool in Luxembourg was built as a prefabricated LVL ribbed slab system. The 23.75m span was achieved with PI-elements consisting of slender (75mm) closely spaced and 1100mm deep webs. With the thickness-to-height ratio outside the current standards and a structural behaviour close to the performance limits, the dimensional stability and torsional stiffness of the Kerto Q material was exploited to realise the desired filigree architectural appearance. Given the chloride-laden air of indoor swimming pools, metallic components were limited to a minimum to guarantee a durable and maintenance free structure. The bearing on the reinforced concrete substructure was developed in timber through widely notched supports in the girder webs, exploiting the tension capacity of the cross-layers in the LVL. The webs are connected to the roof plate via hot-dip galvanized dowels to maximise the corrosion resistance. The high and precise degree of prefabrication of the PI-elements in transportable elements enabled a quick and efficient assembly on site.

KEYWORDS: Wide-span, LVL, ribbed slab, dimensional stability, corrosion

1 INTRODUCTION

As part of the redevelopment of a school in Luxembourg City, Cents, the campus was extended to include a sports centre as well as an indoor swimming pool. Embedded in the sloped topography, the school campus designed by Auer Weber Architects, Germany, Stuttgart, creates a new plaza for the local neighbourhood.

Figure 1: *Exterior view of swimming hall within the school campus*

2 STRUCTURAL SYSTEM

The timber roof structure covers the entire 36mx40m plan dimensions of the swimming hall. The indoor space is partitioned on axis 18', at roughly two thirds of its width, into the pool and the general facilities area. The structural system of the roof follows this separation and consists of two simply supported spans. Vertical supports for the timber roof are provided (a) on an intermediary steel beam and the concrete core walls on axis 18' and (b) a concrete ring beam on the outer periphery. The concrete ring beam rests on regularly spaced slender concrete wall elements while the steel beam is supported on the concrete core walls and by additional intermediary steel columns. The lateral stability of the building is achieved through the concrete core and the peripheral concrete wall elements. The top slabs of the timber roof PI-beams are connected to form a diaphragm. On the short span, the roof diaphragm is interrupted to accommodate a skylight.

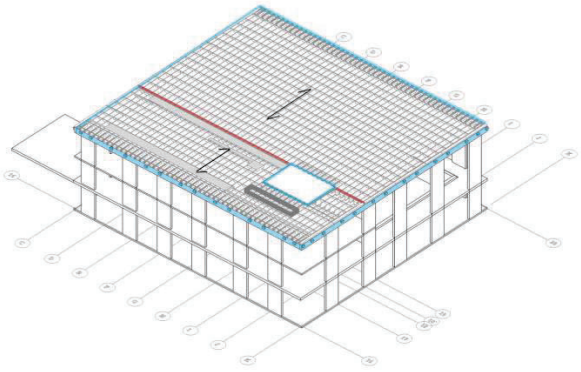

Figure 2: *Axonometry of the indoor swimming hall (blue – concrete ring beam and core, red – steel support)*

[1] Laurent Giampellegrini, PhD, MSc, Director ppa., knippershelbig, Germany, lg@knippershelbig.com
[2] Samuel Blumer, Dipl.-Ing. Dr.techn., sblumer, Austria, samuel.blumer@sblumer.com
[3] Hendrik Pfeffinger, Dipl. Holzbau-Ing. (FH), Projektleitung, Holzbau Amann, Germany, h.pfeffinger@holzbau-amann.de

https://doi.org/10.52202/069179-0561

To achieve the architecturally desired uniform and seamless appearance of the entire roof, the structural elements spanning over the two partitions of the swimming hall roof consist of the same type of PI-beams. The height, spacing and thickness of the ribs and plates is kept the same for both spans, although they differ significantly.

Spanning over a free length of 23.75m over the pool area, the prefabricated PI-beams consist of a pair of slim LVL ribs (Kerto Q) at 800mm centres with a height of 1100mm and a thickness of 75 millimetres. The ribs are structurally connected in shear to the top 69mm LVL slab (Kerto Q) by means of hot-dip galvanised steel dowels. The choice for this type of connector was driven by the required corrosion protection, a topic that is further elaborated in section 4 below. The production limits of the LVL Q-plates were exploited to a maximum as the webs and the top slab are both milled from one continuous plate element. The Q-panels were chosen for their high dimensional and torsional stability considering that the thickness-to-height ratio of the webs exceeds current standards. The webs are additionally restrained by 200mm high transverse bulkheads spaced at 140cm centres along the length of the PI-beams.

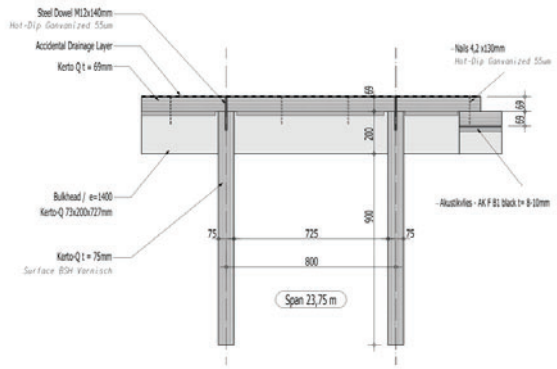

Figure 3: *Section through LVL PI-beams for the 23.75m span*

Figure 4: *Prefabricated PI-beam in the workshop*

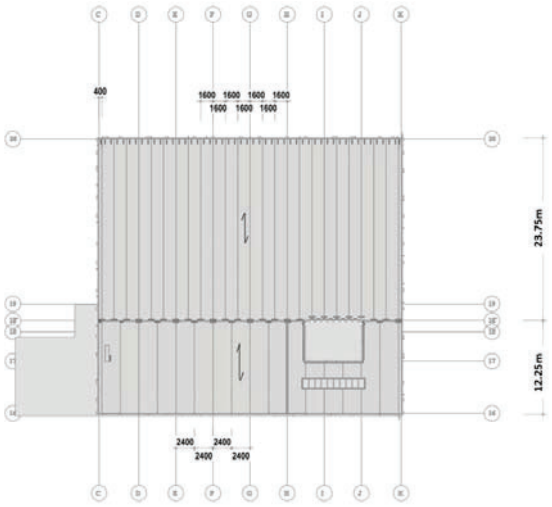

Figure 5: *Plan view of roof*

The LVL ribs are precambered which was achieved via CNC milling of the plates. The precamber was required on the one hand to avoid visual sagging of the beams from the interior view and on the other, to secure the required slope of the roof for drainage. A different precamber was used at the top (180mm) and bottom (120mm) of the ribs.

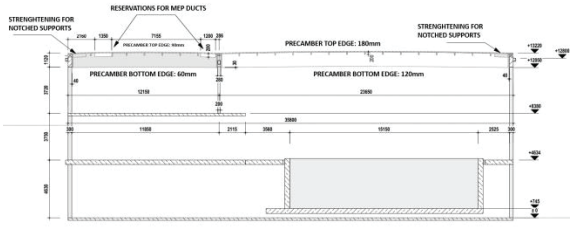

Figure 6: *Section through swimming hall*

The MEP ducts run in the direction of the span so that the number of reservations the roof structure could be kept to a minimum. The lateral distribution of the MEP fixtures was achieved above the general facilities area through reservations made in the smaller span beams at the top of the ribs just below the top plate. An acoustic ceiling with timber lamellas running in the transverse direction closes the space between the ribs. The PI-beams were fully prefabricated in the shop including the accidental drainage layer to allow for a fast and efficient assembly.

https://doi.org/10.52202/069179-0561

3 SPECIAL DETAILS

3.1 SUPPORTS

3.1.1 Introduction

To achieve the desired architectural appearance coupled with the ambition to minimise the use of metallic components, the support of the PI-elements was realised with a deep notch that extends well beyond the usual half-depth limit of the webs. Two main critical points are highlighted in the following figure:

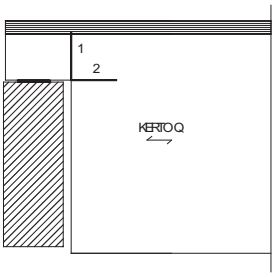

Figure 7: *Support of the single span beam – critical points*

The notches reduce the shear capacity of the beam (1) and raise the risk of tensional failure (2). An alternative solution had been developed by the design engineers.

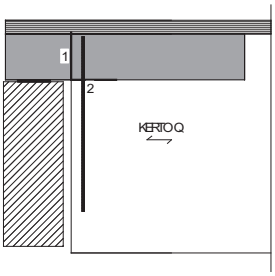

Figure 8: *Thicker beam in upper part (1) and glued in rods (2).*

For this solution, the supports were strengthened on either side of the webs (1) by glued-on LVL plates and strengthened with M14 glued-in rods (2) in the direct vicinity of the support. Additionally, the tensile strength of the cross-layers in the Kerto Q webs was exploited and at the top of the section, the diameter of the glued-in rods was increased via M22/M14 Rampa-sleeves to attain the necessary overall strength.

A verification method of the notch by a reduced shear capacity is given in Eurocode 5 [1].

$$\tau_d = \frac{1.5 \cdot V_d}{h_{notch} \cdot b_{notch}} \leq k_v \cdot f_{v.d} \qquad (1)$$

Whereas k_v represents the reduction factor that considers the geometry of the notch (cf. Formula 6.62 in [1]), the use of formula (1) has to fulfil geometrical parameters according to the Austrian national appendix of Eurocode 5 [3]. The height of the notch has to be bigger than half of the total height of the beam.

$$\frac{h_{notch}}{h_{beam}} \geq 0.5 \qquad (2)$$

In this case, this geometrical requirement is not fulfilled. A finite element model of the entire beam and its support condition has been created to assess the load bearing capacity of the notched support.

3.1.2 Material and methods

One beam with a span of 23.75m has been modelled with the commercial finite element software RFEM 5. The model consists of about 80'000 Triangular surface elements with an edge size of 2.5cm. A detailed stress analysis has been performed on two different models. Model A (MA) consists of a thicker beam in the upper region without glued in rods. Model B (MB) has additionally been reinforced with glued in rods. The linear beam elements of the rods have been connected to the surface elements.

3.1.3 Results

The tension perpendicular to the fibre below the notch is represented in the following table.

Spec.	Reinforcement	σ_y [MPa]
MA	Thicker upper part	4.3 [MPa]
MB	Thicker upper part + rods	2.5 [MPa]

The stress distribution of Model B (MB) is represented in figure 6. The peak vertical stress is located directly below the thicker upper part of the beam. The thickening was pulled down a little on the front side.

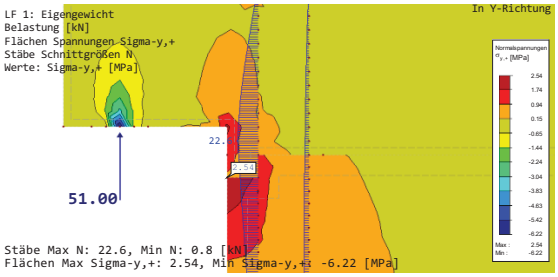

Figure 9: *Traction perpendicular to the fibre σ_y= 2.54 [MPa]*

Due to the higher resistance of Kerto Q, cracking can be prevented.

$$f_{t.90.edge.Rd} = \frac{k_{mod} \cdot f_{t.90.edge.Rk}}{\gamma_M} = 3MPa \qquad (3)$$

Where k_{mod}=0.6 is the reduction factor for permanent loading, $f_{t.90.edge.Rk}$=6 MPa the tensile stress perpendicular to the grain according to the declaration of product of Kerto Q and γ_M=1.2 the material safety factor for LVL timber defined in [1] and [2]. The final solution is presented in the following figure:

https://doi.org/10.52202/069179-0561

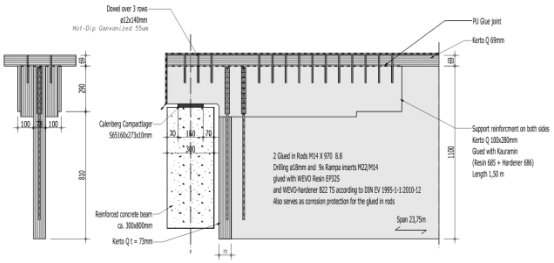

Figure 10: *Final technical solution of the support*

3.1.4 Discussion and conclusion

A detailed stress check was performed for the notched support. The use of Kerto Q reduces the risk of cracking perpendicular to the grain. Additional glued-in bars and thickening of the beams above the bearing area made it possible to solve this geometrically demanding support system. In addition, steel could be avoided. Before such special solutions are worked out, an attempt should be made to achieve direct beam support without notching. However, this is not always possible due to the given boundary conditions.

Figure 11: *Finished notched support of the PI-beams on the concrete ring.*

3.2 PI – Beam

The webs of the PI-girder were statically connected to the slab by steel dowels. The connectors are distributed along the entire beam length and concentrated near the support points (see Figure 12). Without the use of glue, a partially rigid connection is created between the web and the roof panel.

The spring stiffnesses of the anchors can be calculated according to Eurocode 5 [1]. However, they may vary slightly depending on production and tolerances of the holes in the panels. Therefore, the verifications were carried out with half and double spring stiffnesses.

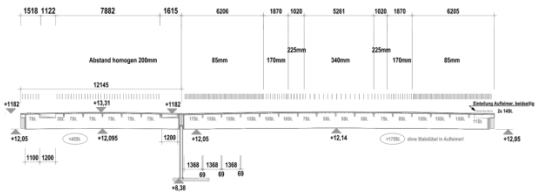

Figure 12: *Arrangement of shear dowels along the beams*

4 CORROSION PROTECTION OF METALLC FASTENERS

A major challenge was the corrosion protection of the metallic fasteners and to get the approval by the local checking authorities.

4.1 SWIMMING POOL ATMOSPHERE

The risk for corrosion of metallic components rises with increasing water vapour in the air. Since the air in an indoor swimming pool is always to some extent humid due to the water evaporation, this environment presents an increased risk for corrosion. Through adequate ventilation and air conditioning measures, a water content of 14g/kg dry air should be an upper bound [5], which for typical indoor pool air temperatures of around 30°C corresponds to approximately 50% relative air humidity. This corresponds to approximately double the amount of humidity present in the atmosphere of typical western European cities. This environment gives rise to a wood equilibrium moisture content between 7-9 M.-% [5] and thus, according to [1], the LVL timber can be classified into the service class 1.

In addition to the air humidity, the presence of salts in the water, in particular chloride salts, contribute to metallic corrosion. The pool is operated with tap water and has a typical average chloride content of around 55mg per litre. Through convection, sodium chloride salts in aerosols are transported through the air and can deposit onto metallic surfaces to amplify the corrosion process. Also, chlorine is usually added to the pool water for disinfection purposes. Free chlorine is typically dosed to a concentration of around 0.3mg per litre and reacts with water to form hydrochloric and hypochlorous acid. The latter, with its high oxidation potential, is the disinfectant active ingredient. Excess chlorine can evaporate as chlorine gas into the ambient air and transform into hydrochloric acid in electrolyte films on metallic surfaces in the presence of water, for example due to condensation.

4.2 CODE REQUIREMENTS

The minimum corrosion protection requirements for metallic fasteners in the Eurocodes [1] is given in Section 4, Table 4.1, reproduced below.

https://doi.org/10.52202/069179-0561

Table 1: *Examples of minimum specifications for material protection against corrosion for fasteners from Table 4.1 in [1]*

Fastener	Service Class[b]		
	1	2	3
Nails and screws with $d \leq 4$ mm	None	Fe/Zn 12c[a]	Fe/Zn 25c[a]
Bolts, dowels, nails and screws with $d > 4$ mm	None	None	Fe/Zn 25c[a]
Staples	Fe/Zn 12c[a]	Fe/Zn 12c[a]	Stainless steel
Punched metal plate fasteners and steel plates up to 3 mm thickness	Fe/Zn 12c[a]	Fe/Zn 12c[a]	Stainless steel
Steel plates from 3 mm up to 5 mm in thickness	None	Fe/Zn 12c[a]	Fe/Zn 25c[a]
Steel plates over 5 mm thickness	None	None	Fe/Zn 25c[a]
[a] If hot dip zinc coating is used, Fe/Zn 12c should be replaced by Z275 and Fe/Zn 25c by Z350 in accordance with EN 10147			
[b] For especially corrosive conditions consideration should be given to heavier hot dip coatings or stainless steel.			

It can be seen from this table, that for service class 1, there are no specific corrosion protection requirements for nails, screw, dowels, and steel plates. However, the nature and severity of the corrosive environment and whether the steel is completely exposed to the atmosphere or within and protected by the timber is not addressed.

The German national annexe [2] states in Section 4, that for moderate, severe, or very severe corrosive environments (corrosion categories C3, C4, C5 according to DIN EN ISO 12944-2:1998-07 [7]), the minimum specifications for material protection against corrosion can be taken from the DIN SPEC 1052-100 [4]. In DIN EN ISO 12944-2:1998-07 [7], swimming pools are classified under the category C4 which is a highly corrosive environment. Consequently, according to the DIN SPEC 1052-100 [4] a minimum average zinc coating of 55µm for screws, nails and steel plates is required. Although in the latter document, the corrosive environment is considered, no distinction is made between fasteners directly exposed to the atmosphere and those within and protected by the timber.

This distinction is made in [6], where the minimum requirements for corrosion protection for metallic fasteners in timber as a function of the equilibrium moisture content are given. The relevant table from [6] is reproduced below.

Table 2: *Classes for corrosion resistant materials and zinc coatings for fasteners in the timber — Minimum requirements. Table 1 from [6]*

Timber class	T1	T2	T3	T4	T5
Moisture content	$\omega < 10\ \%$[a]	$10\ \% \leq \omega \leq 16\ \%$[a]	$16 < \omega \leq 20\ \%$[a]		Permanent $\omega > 20\ \%$
Treatment/acidity of timber	–	–	Untreated and pH > 4	Treated[b] or pH ≤ 4	–
Minimum zinc thickness on carbon steel	–[c]	10 µm	20 µm	55 µm	n/a
Stainless steel grade	–	–	K2	K2 / K3[d]	K3
[a] Short periods with higher moisture content may be disregarded.					
[b] Treatment containing copper or salts (e.g. chlorides) and fire retardants that may influence corrosion rate.					
[c] The appearance may change without a protective coating.					
[d] Class of stainless steel depends on the type of treatment applied to the timber.					

It can be seen that for an equilibrium moisture content below 10%, no particular protection is required. This is very much in line with the conclusions of the specialist approval [5] that was undertaken for this project. In the latter study, it was concluded that the low concentration of chloride aerosols that get into the atmosphere from the tap water operated swimming pool and deposit onto the timber surface would not pose any considerable corrosion risk for the fasteners embedded in the timber elements. This is to be attributed to the low humidity present in the timber (7-9%) on the one hand, and on the other, the phenolic resin used to glue the veneers in the LVL plates that forms an impenetrable barrier.

5 ASSEMBLY

To ensure a quick erection of the visible timber construction on site, the contractor, Holzbau Amann, decided to preassemble the roof into elements in the workshop. To do so, the maximum width for transportation by truck and the maximum preassembly grade were to be considered.

The initial schedule intended a preassembly for both types of elements, with lengths 12,20m and 23,75m, with a width of 2,40m with each element consisting of 3 LVL ribs. Due to production limitations with the supplier of the LVL boards from Finland it was not possible to manufacture the LVL boards with a thickness of 69mm into 23,75m x 2,40m elements. Hence the roof elements were preassembled with dimensions 23,75m x 1,60m, consisting of 2 LVL webs only.

The fabrication of the roof elements in the contractor's workshop started by milling the LVL beams of 23,75m and 12,20m length on a CNC-machine. On the underside of each beam, the precamber according to the results of the structural analysis was milled. Additionally, on top of each beam the roof pitch was milled by the CNC-machine, giving the roof its final shape.

Figure 13*: Production of the PI-elements in the factory*

The threaded rods for the strengthening of the supports were glued in the LVL beams in the workshop under controlled ambient conditions. Lateral strips of LVL were glued to both sides of the beams to absorb the shear forces near the notched supports.

Furthermore, a protective coating was applied to protect the wood from grime and effects of the weather during transportation and assembly.

https://doi.org/10.52202/069179-0561

After connecting the ribs to the LVL roof boards with hot-dip galvanized steel dowels (55µm), 2 preassembled roof elements were loaded on the truck. Each truck, moving from Southern Germany to the site in Luxembourg, was accompanied by an escort vehicle.

***Figure 14**: Two roof elements loaded on the truck*

Arriving on site, the preassembled roof elements, already covered with a sheet acting as a secondary water protection layer, were lifted from the trucks and directly assembled on the concrete structure.

***Figure 15**: Delivery via a side street in Luxembourg*

***Figure 16**: A prefabricated 23,75m roof element on the crane*

To ensure the assembly of the timber roof without constraint forces, the contractor responsible for the concrete structure had been preliminary advised of the required precision and the admissible tolerances of his works. The concrete works were verified by a surveyor and deviations were to be corrected by the concrete contractor if needed. Thus, the timber roof could be assembled quickly without any difficulties.

***Figure 17**: Assembly of the roof with individual LVL PI-Panels*

On one edge of the roof, the LVL beams rest on the concrete ring wall, on the other edge on a fire-proof coated steel profile. Above the steel profile, in between the LVL beams, LVL planks were installed vertically to realize the continuation of the fire barrier.

***Figure 18**: Support points*

To protect the wood elements from the weather the waterproofing was installed in parallel to the assembly of the timber roof. Due to the milled pitch on the upper side of the LVL beams, the final roof pitch was in place right away.

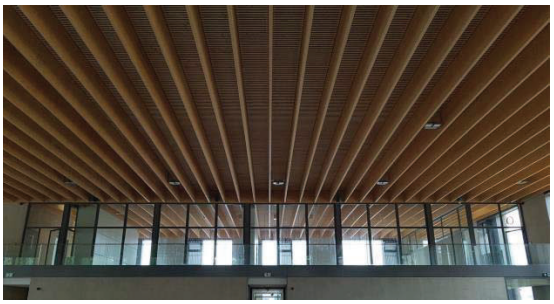

***Figure 19**: Finished Roof underside view*

The ensemble of air ducts and cable lines were projected in the design phase. Cutouts and slots in the LVL beams were realized in the workshop, making sure they were placed in structurally stress-free zones of the beams.

https://doi.org/10.52202/069179-0561

***Figure 20**: Roof underside with acoustic ceiling and LVL-Panels in visual quality*

6 CONCLUSIONS

To meet the architectural requirements and to provide a visually simple and durable structural design, various technical challenges had to be overcome and special solutions had to be developed beyond the limits of the current regulations and standards. The solutions developed exploit the material and size limits of the LVL panels and the details were designed with a minimum of metallic components given the stringent corrosion protection requirements. A high degree of prefabrication allowed for a fast and minimally disruptive assembly on site. The result is a sophisticated ribbed-slab roof structure, milled and assembled in a quality close to joinery.

REFERENCES

[1] Eurocode 5: Design of timber structures - Part 1-1: General - Common rules and rules for buildings; German version EN 1995-1-1:2004 + AC:2006 + A1:2008.

[2] National Annex Germany - Nationally determined parameters - Eurocode 5: Design of timber structures - Part 1-1: General - Common rules and rules for buildings

[3] National Annex Austria - Nationally determined parameters - Eurocode 5: Design of timber structures - Part 1-1: General - Common rules and rules for buildings

[4] DIN SPEC 1052-100:2013-08 Timber structures - Design of timber structures - Part 100: Minimum requirements for the materials or corrosion protection of fasteners

[5] Specialist Approval: Corrosion of metallic timber screws for an indoor swimming pool in Luxembourg city, Prof. Dr.-Ing. Habil. Prof. H.C. Ulf Nürnberger, 10.10.2017, Stuttgart, Germany

[6] Timber Structures – Dowel-Type Fasteners – requirements: German and English Version prEN 14592: 2017.

[7] DIN EN ISO 12944-2:1998-07: Paints and varnishes - Corrosion protection of steel structures by protective paint systems - Part 2: Classification of environments (ISO 12944-2:1998); German version EN ISO 12944-2:1998

https://doi.org/10.52202/069179-0561

World Conference on
Timber Engineering
Oslo 2023

DESIGN OF A TALL MASS TIMBER TOWER FOR OCCUPANT COMFORT UNDER WIND-INDUCED ACCELERATIONS

Laurent Giampellegrini[1], Anthony Rety[2], Guillaume Caussarieu[3], Tim Sleik[4], Lucia Theurer[5], Johannes Pohl[6], Tobias Wacker[7]

ABSTRACT: The current trend of increasing the height limits of timber buildings makes wind-induced accelerations for occupant comfort an important design parameter. This article presents the two-step process used for the design of a 51m tall mass timber tower located in Sweden. The lateral stiffness of the tower is provided through a CLT inner core and a braced glulam post-and-beam system along its outer periphery. The structural scheme, the dynamics of high-rise timber structures, the 3D modelling assumptions to capture the global stiffness with suitable accuracy as well as the analytical state-of-the-art methods used to determine the wind-induced accelerations in the along-wind, across-wind and torsional direction at the top of the tower are presented. Through a parameter study, the sensitivity of the structure to changes in connection stiffnesses and mass distribution is assessed. Given the uncertainty inherent to the analytical methods, the calculations are validated in a second step against the acceleration response obtained from wind tunnel testing. The differences between the analytical and experimental approaches are compared and the key parameters are discussed.

KEYWORDS: Tall Mass Timber Building, Wind-induced Accelerations, Occupant Comfort, Parameter Study, Design process, 3D Modelling, Wind Tunnel Testing

1 INTRODUCTION

For the *Embassy of Sharing* project in Malmö, Sweden, a total of seven buildings are in planning. The *Fyrtornet* is the first of these buildings and with a height of 51m, will be Malmö's first and Sweden's tallest office building in mass timber. This 11-story building, a landmark for progressive and sustainable construction built entirely in timber above ground, consists of offices with public functions on the two lower floors. The wooden structure is visible from the outside through the glazed facades. The structure is expected to be completed in 2023.

Figure 1: *Architectural rendering of the Fyrtornet Tower*

2 STRUCTURAL SYSTEM

2.1 OVERVIEW

The gravity system consists of CLT slabs that span from the timber core across an intermediary and an outer post-and-beam system in glued laminated timber. The only exception is at the 11th floor, where a concrete slab is used to add mass to control the wind-induced vibration levels. The lateral bracing of the building is achieved via the combined action of an inner CLT core and the outermost braced post-and-beam structure. To accommodate the sloped geometry of the two glazed facades facing south and east, a horizontal transfer is introduced at the 6th level. Vertical transfers occur on the 2nd and 8th floor.

2.2 STRUCTURAL LAYOUT

The following sections and plan views from the building show the structural layout of the CLT slabs, the CLT core and the post-and-beam structure in glued laminated timber. The columns are spaced on a regular 4.8m grid in both directions. The main structural elements are located between gridlines A1-A6 and B1-B6. Within these gridlines, all columns and diagonals are directly supported on the reinforced concrete foundations. Between gridlines

[1] Laurent Giampellegrini, Director ppa., knippershelbig, Germany, l.giampellegrini@knippershelbig.com
[2] Anthony Rety, Structural Engineer, Binderholz, France, anthony.rety@binderholz.com
[3] Guillaume Caussarieu, Head of Computational Timber Engineering, knippershelbig, Germany, g.caussarieu@knippershelbig.com
[4] Tim Sleik, Head of Research and Development, Binderholz, Austria, tim.sleik@binderholz.com
[5] Lucia Theurer, Structural Engineer, knippershelbig, Germany, l.theurer@knippershelbig.com
[6] Johannes Pohl, Structural Engineer, Binderholz, Austria, johannes.pohl@binderholz.com
[7] Tobias Wacker, Managing Director, Wacker Ingenieure, Germany, t.wacker@wacker-ingenieure.de

https://doi.org/10.52202/069179-0562

A6-A7 and B6-B7, the vertical loads from the upper levels are brought to the foundation through cantilevering beams on the first floor, supported by inclined columns. This design feature allows for a protected pedestrian area. Due to the sloped geometry of the south and east facades, the floors decrease in surface as higher levels are reached. On every third floor starting from level 2, there is an accessible terrace just behind the glass facade. The next 2 levels are then identical but without any terrace.

Figure 2: *Axonometric overview of timber structure*

The CLT slabs span over two bays, except around the CLT core where they are simply supported. The top faces of the slabs are either flush or laid on top of the glued laminated timber beams. This provides the required space for the main ventilation ducts coming from and running around the CLT core. On the first floor, due to the library usage, 7-ply CLT slabs with a thickness of 240mm are used. The slabs on all the upper floors are 5-ply with a thickness of 180mm. The inner core is built-up from 125cm wide and 280mm to 320mm thick CLT panels.

To accommodate the geometry of the sloped facades, the diagonal bracing, which contributes to the overall lateral stability of the building and provides the necessary torsional stability around the CLT core, is shifted from axes A6/B6 to A5/B5 respectively. To ensure structural continuity of the horizontal load transfer across the height of the building, the horizontal loads are transferred from the bracing on axes A5/B5 above level 6 to the shifted bracing on axes A6/B6 and the CLT core on axes A4/B4 on the lower levels through the CLT slabs, which form a diaphragm at each level. The vertical loads are directly transferred through the columns located on gridlines A2/B5, A4/B5, A5/B2, and A5/B4.

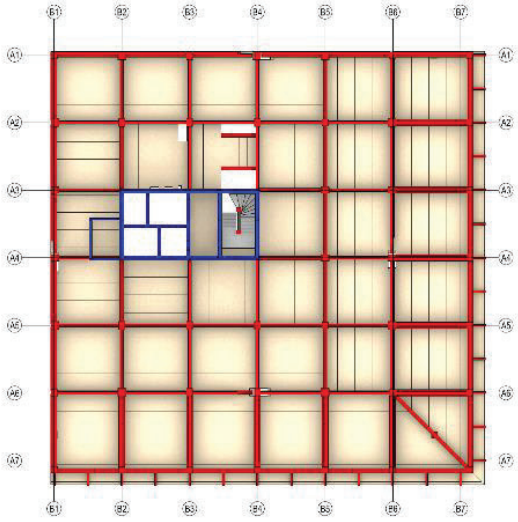

Figure 3: *Level 1 plan view (View from below - Core in blue, beams and columns in red)*

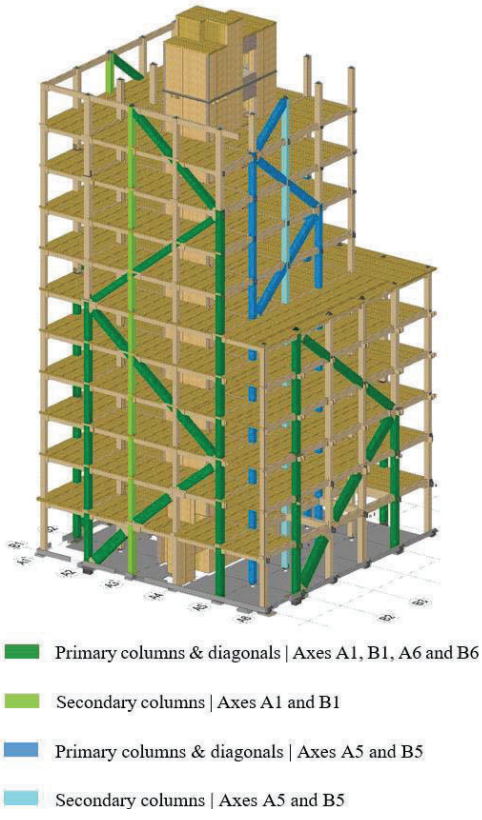

Figure 4: Axonometric view of the glued laminated bracing system

On axes A1 and B1, the glazed facade is vertical so that the bracing system is continuous across the height of the building. To reduce the amount of steel connections, the primary columns are, in general, continuous over 2 to 3

https://doi.org/10.52202/069179-0562

levels. Secondary columns span, in general, from one level to the next.

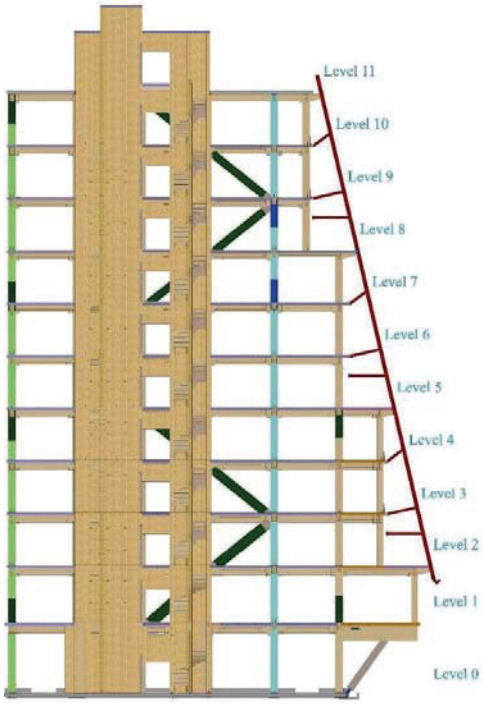

Figure 5: *East-West section of the Fyrtornet Tower*

The cross sections of the bracing diagonals (GL28h) are 560x920mm on the first floor and reduce to 560x600mm on the top floor. The main columns of the bracing system have a constant cross-section of 560x560mm and 440x560mm for the shifted bracing beams from level 6 onwards while the secondary columns are 440x560mm wide. These columns and diagonals are defined as "key elements" according to the Swedish national annex to the Eurocode 1-7 and are therefore designed with an additional safety coefficient of 1.3.

The sloped glazed facades start from the 2nd floor and extend through the entire height of the building. The design of the facade was outside the design scope but a close exchange with the facade designers was necessary to assess the weight distribution on the building and to coordinate the geometry for the assessment of the wind induced loads.

2.3 CONNECTION DESIGN

The bracing diagonals located on the ground floor must sustain a characteristic load of approximately 4000kN. The joints are realized with a dowel-type connection with multiple shear planes. The design of these connections is based on Eurocode 5 [1] and the related Swedish national annex as well as the recommendations given in reference [2]. The connection between the timber elements and the foundation follows the same principle and is achieved through a multiple shear plane connection (4 slotted-in steel plates) with dowel-type fasteners. The large cross-section sizes were achieved by block gluing three beams together.

Figure 6: *Connection design (Cadwork 3D) and bracing glulam beam in the factory.*

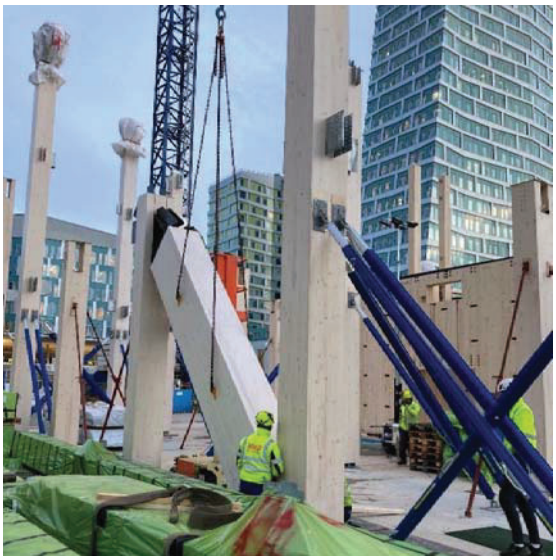

Figure 7: *Bracing beam during installation*

The slab-to-slab connections are realized with a rabbet and a screwed 27mm, 3-ply coverboard. On level 6, these connections are replaced by nailed perforated steel plates to transfer the horizontal loads coming from the shifted bracing diagonals. The 125cm wide CLT core-wall panels are joined with a steel slot connector fixed with inclined auxiliary screws that tighten the panels against each other. This design allows for a very stiff connection and therefore generates a near-monolithic behaviour.

3 DESIGN FOR VIBRATION

3.1 APPROACH

At an early design stage, wind-induced comfort at the top of the tower was recognised as an important design driver. To assess the influence of various design decisions early in the process, a set of analytical tools based on the relevant construction codes and state-of-the-art literature were developed to allow for a quick assessment of the wind-induced accelerations at the top of the tower and to provide feedback to the design team. Once the calculations from these initial calculations showed satisfactory results, the accelerations were subsequently checked in a second step with the input from the data generated from a wind tunnel test. Sufficient time was

https://doi.org/10.52202/069179-0562

allowed to make final adjustments to the structure if needed and to steer the dynamic properties in the right direction in order to meet the required comfort criteria.

3.2 COMFORT CRITERIA

For high-rise buildings, and in particular for tall mass timber buildings such as the Fyrtornet tower, which have a low mass compared to their traditional concrete or steel counterparts, it is important to assess if the horizontal accelerations on the top occupied floors under (turbulent) wind action might be disagreeable or even unacceptable. The perception of acceleration levels is dependent on many factors and is to some extent subjective. Furthermore, the planned usage of the building must be considered. For residential buildings, more restrictive acceleration criteria apply than for office buildings.

Of interest are, in general, the peak accelerations expected to occur only a few times over the lifetime of the building, (for instance during a windstorm) as opposed to the root-mean-square values which are also sometimes used. The common criteria for the perception of acceleration relates the acceleration levels to the frequency of occurrence. Following the generally accepted criteria for high-rise buildings given in [3], the wind-induced horizontal peak accelerations should not exceed the values given in table 1 below.

Table 1: *Generally acceptable 10-year peak accelerations depending on the usage of the building [8]*

Planned usage	Generally acceptable accelerations
Office	2.0 – 2.5 %-g
Hotel	1.5 – 2.0 %-g
Residential	1.0 – 1.5 (to 1.8) %-g

g denotes gravitational acceleration

Extensive examinations indicate that the people's sensitivity to motion becomes less as the frequency of motion (eigenfrequency of the building) decreases. This dependency is not fully reflected in the criteria mentioned above. The criteria in [3] were developed primarily for tall buildings which tend to have natural frequencies in the range of about 0.15 Hz to 0.30 Hz. Following the criterion of the International Organisation Standardization (ISO 10137:2007) [4], the dependence of the frequency is considered in the range of interest between 0.06 Hz and 1 Hz. The published criteria are based on a one-year wind and the peak accelerations of the considered building should not exceed the evaluation curves given in ISO 10137: 2007 – Annex D [4], reproduced below for convenience.

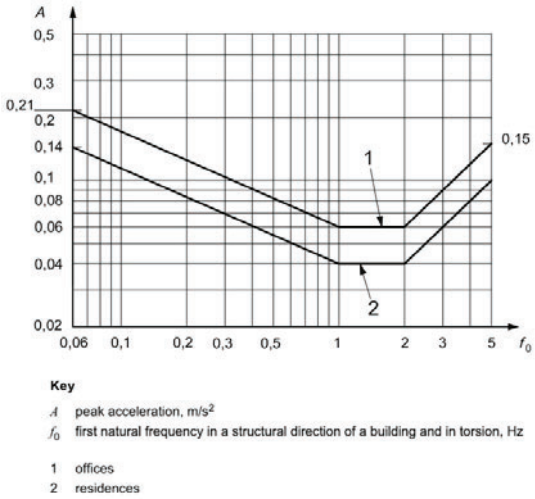

Figure 8: *ISO 10137: 2007 – Annex D: Evaluation curves for wind-induced vibrations in buildings in the horizontal direction for a 1-year return period.*

The acceleration limits in [4] need to be satisfied for peak accelerations resulting from a 1-year return period wind in the along-wind, across-wind, and torsional direction. In many cases, however, the fundamental translational and torsional modes are not independent, and the superposition of these modes will result in higher accelerations than from each mode alone. Although there is little information in the technical literature on how to address the combined acceleration from different modes of vibration, this was considered in both the analytical and wind tunnel assessment. This is described in more detail in subsequent sections.

Finally, it is important to note that the threshold of vibration perception is around 0.5%g. In other words, even if the limiting acceleration criteria above are met, wind induced accelerations will be felt by the occupants under strong winds, but the levels are limited such that with a high likelihood, they do not cause discomfort.

3.3 3D FE MODEL AND KEY PARAMETERS

The creation of a reliable global FE model was critical to properly assess the wind-induced accelerations, which strongly depend on the natural frequencies and mass distribution of the building.

3.3.1 Workflow

Two important criteria for the modelling were the geometrical accuracy and a precise representation of the structural system. For the former, the procedure consisted of extracting the geometry as well as the relevant structural attributes from the 3D Cadwork construction model provided by Binderholz. Centerlines of the structural elements, material grades and cross-sections were retrieved and referenced in the modelling Software Rhinoceros 3D from Robert McNeel & Associates and its visual programming interface Grasshopper. The finite-element model was then created using the Grasshopper

https://doi.org/10.52202/069179-0562

interface to the finite-element software SOFiSTiK AG This workflow allowed for a precise and seamless translation from a "Solid" 3D geometry to the needed line and surface geometry. Furthermore, relying on a semi-automated process greatly improved the speed and flexibility of the information transfer while reducing the risk of errors.

3.3.2 Connection stiffness

To capture the natural frequencies and associated vibration modes of the building with sufficient accuracy, it is important to consider the loss of stiffness generated by the mechanical connections (a) between the 1.25m wide CLT panels in core walls (b) between the CLT panels that make up the floor diaphragms and (c) the diagonals in the peripheral bracing elements. The connections between the post-and-beam elements were considered ideally articulated.

The approach chosen was to generate equivalent material properties with reduced shear stiffnesses (G-modulus) rather than representing the detailed plate discretization in the global model. To estimate the equivalent material properties, sub-models were generated, and the key behavioural parameters extensively studied. For the walls (
Figure 9), the actual panel partition was considered together with the connector stiffness. In addition, the stiffness of the hold-down bracket and the bottom shear connector were also integrated in the model to accurately capture the wall behaviour. An iterative procedure was then undertaken to obtain the same lateral and rotational displacements between the detailed wall model and the simplified one based on equivalent material properties. For the floors (
Figure 10), the full discretization of the constitutive panels and the associated spline connector stiffness was modelled and evaluated to determine the equivalent material properties. A similar strategy was implemented to capture the stiffness behaviour from floor to floor where the hold-down and shear brackets were modelled as continuous springs rather than discrete elements while maintaining the overall wall in-plane rotational behaviour.

This approach had the advantage to greatly simplify the global modelling while maintaining the overall behaviour sufficiently accurate. This proved to be an effective strategy to perform fast and reliable parameter studies.

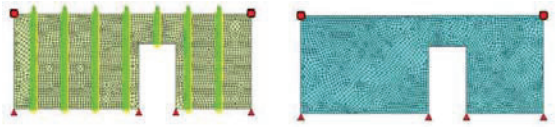

Figure 9: *Walls sub FE-models used to tune the equivalent shear stiffness (G-Modulus)*

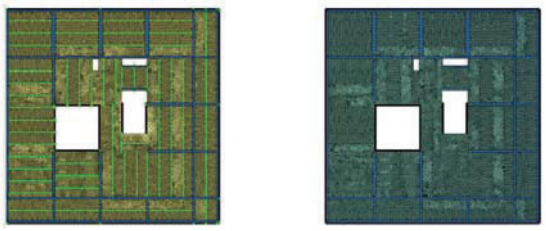

Figure 10: *Floor sub FE-models used to tune the equivalent shear stiffness (G-Modulus)*

To assess the effect of the basement and the foundation on the overall stiffness, the soil and anchorage stiffness provided by the local engineers responsible for the foundation design were considered at an early stage in the model. Considering that the connections had a high stiffness coupled with the fact that the soil stiffness is, in general, significantly higher under dynamic loads (increased by factor of around 4 to 6 compared to its stiffness under static loads [5]), the differences in natural frequencies compared to an idealized rigid support proved to be insignificant.

3.3.3 Analytical assessment of vibrations

The methods given in the Eurocodes and its national annexes are restricted to the calculation of the wind-induced accelerations in the along-wind direction. Furthermore, these methods are approximations that cover only simple geometries, and the effect of the surrounding buildings is not considered leading to uncertainties in, for instance, the force coefficients and peak factors. Moreover, as pointed out in the comparative study in [6], the methods according to the EKS 11, BFS 2019:1 [7] yield a significantly higher accelerations than those presented in EN 1991-1-4 [8]. The Eurocode framework does not provide methods to calculate the across-wind accelerations nor those arising from torsional modes. Furthermore, no guidance is given to account for the superposition of these components. To be able to steer the design into the right direction and assess the effect on the wind-induced vibrations early in the design, the approach described below was adopted.

To calculate the accelerations in the along-wind direction, the method in EN 1991-1-4 [8] was used according to the framework set-out in Annexe B. This method has also been employed in recent studies [6][9][10][11] to assess the wind-induced acceleration of tall mass timber buildings to meet the ISO 10137:2007 [4] comfort standards. In particular, based on the comparative studies in [6], the input parameters according to the EKS 11, BFS 2019:1 [7] were used for the reasons already mentioned above. The wind-induced accelerations in the across-wind direction were calculated according to the Canadian National Code NBCC [12], with the basic wind input data brought back into the Eurocode framework. The accelerations from the torsional modes were calculated according to the principles given in [13]. Also, the superposition of all three components as a square-root-of-sum-of-squares, with an overall reduction factor of 0.8 according to [13] was assessed to account for the fact that

the peaks of all three components are unlikely to occur simultaneously.

3.3.4 Parameter study

To assess the effect of the connection stiffness and mass distribution over the height of the building on the wind-induced vibrations of the tower and use this as an input to inform the structural design, a parameter study was undertaken. For each set of parameters, the wind induced accelerations at the last occupied floor of the tower were computed following the method outlined in the analytical assessment given in the previous section i.e., the accelerations from the first three modes of vibration (along-wind, across-wind and torsion) as well as their superposition. The sensitivity of the vibration response to the various parameters could be determined and changes made where they are the most effective.

The wind-induced accelerations based on the modal parameters obtained from the global finite element model were computed by considering the variation of the following parameters: a) Inter-panel shear connection between wall elements b) Inter-panel shear connection between floor elements c) Tie-down anchors level to level d) Horizontal shear connection level to level e) Tie down anchors level to basement f) Horizontal shear connection level to basement g) Damping and h) Mass distribution over the height of the building.

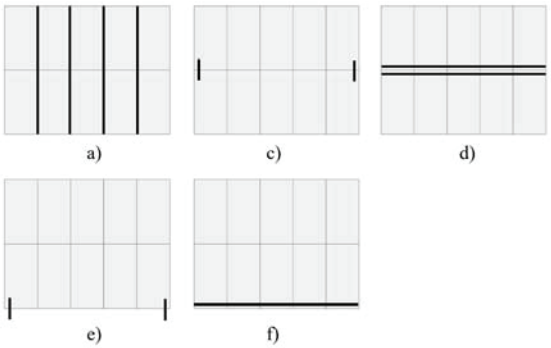

Figure 11: *Schematic illustration of the different parameters at the walls between two levels.*

For a constant damping value, it was found that the mass distribution and the shear connection between the CLT-panels in the core walls (Figure 11 - a) were the driving parameters. The stiffness of the tie-downs (Figure 11 - d, f) and the horizontal shear connection (Figure 11 - e, g) had only a marginal effect on the calculated accelerations. The reason was that under the 1-year and 10-year return period winds, the CLT core walls remained largely in compression. In general, it was found that a variation of the connection stiffnesses of around 20% from the base design values would not lead to a significant increase in acceleration levels. This was also the case for the connection stiffness of the bracing elements. To satisfy the ULS requirements, these connections inherently exhibited a very high stiffness.

While increasing the mass in the top third of the building decreases the natural frequencies, wind-induced peak accelerations could efficiently be decreased by this measure. This effect has been used to influence the floor build-ups in the top floors and to set out the thickness of the concrete slab on the last level to meet the required comfort criteria.

Figure 12 below shows the robustness of the calculated acceleration levels with the changes in stiffness and mass parameters towards the end of the design stage. While the acceleration levels from each individual mode were met with sufficient margin, the superposition tended to exceed the criteria given in ISO 10137:2007 [4]. However, given the uncertainties inherent in this computation and the lack of guidance available, it was chosen to give the modal parameters of the structure (see Figure 13) to the wind engineers and assess the accelerations via wind tunnel testing on this basis.

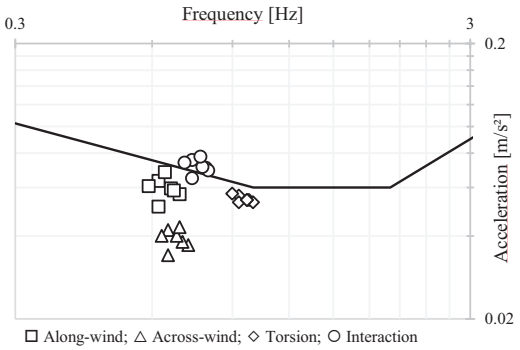

Figure 12: *Summary of the parameter study near design completion showing the first three natural frequencies (translational and torsional modes) and the resulting acceleration as well as the acceleration limit for office buildings according to [4]*

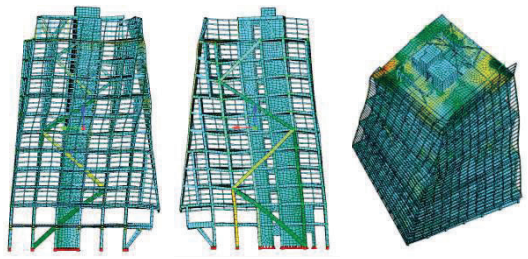

Figure 13: *First lateral mode-shape (0.72Hz), second lateral mode-shape (0.73Hz) and third torsional mode-shape (0.97Hz) from the finite-element model.*

3.3.5 Damping

The damping of a structure, expressed either as the logarithmic decrement δ or as the damping ratio ζ (% of critical damping), is a key parameter in determining the dynamic response of a structure subjected to dynamic loads. Yet, as opposed to stiffness and mass, it cannot be directly calculated, and the designer must rely on values that are code-based or given in state-of-the-art literature for similar types of structures.

https://doi.org/10.52202/069179-0562

EN 1991-1-4 [8] provides a table in appendix F with damping values for various types of structures depending on type, material and connections used. However, the damping values given cover primarily different types of structures made from steel and reinforced concrete. For timber structures, only a single reference is given in this table, namely that for timber bridges with the damping expected to be in the range from δ =0.06 to δ =0.12. The ISO 10137 [4], from the which the acceleration limits are taken for the one-year return period wind, gives damping values of ζ =0.01% for steel frame buildings and ζ =0.02% for concrete frame buildings. Timber buildings are not covered.

The major contributors to overall damping are (i) material damping (ii) structural damping and (iii) damping due to friction from relative movement of non-structural elements (e.g., screed and cladding). In addition, aerodynamic damping i.e., energy dissipation as the building moves through the air may also be considered according to EN 1991-1-4 [8] but was omitted here on the conservative side.

Due to the fact that (a) the Fyrtornet tower consists of a CLT core and slab diaphragms made up from 1.25m wide panels connected with a significant number of dissipative connectors (b) on the periphery, bracing is provided by a braced post-and-beam system, joined with dowel-type connections across multiple shear planes (c) each floor has at least 4cm of floating screed and (d) the building is closed with a timber façade system, it is expected that the overall damping of the tower will be significant. Most studies that address the issue of wind-induced vibrations tend to take damping ratios in the vicinity of 2% of critical, see for instance [6][9][10][11]. Damping ratios from measured examples show a significant scatter: minimum values tend to be around 1.3% while high damping ratios around 3%-4% and values in excess of 5% have been reported [14][15][16]. The large scatter can be attributed to the type of lateral resistance system and its connections, the inclusion of façades and other non-structural elements during measurements as well as the amplitude of the vibration levels. Measurements in [17] showed that for large vibration amplitudes, defined as > 0.05m/s² i.e., in the perceptible range but still below the ISO 10137 limits, the damping ranged from 2.5%-3.5%, depending on the mode. In [15][16], damping values across different structures with different lateral bracing systems are listed, also with measurements after non-structural elements have been included. For post-and-beam systems with a CLT core, the measured damping ranges between 2-3% [16]. In the conclusion of [16], the following recommendations based on the pool of measurements taken are given: for a post-and-beam structure a damping ratio of 1.9% may be used while for a CLT structure, a damping ratio of 2-2.5% may be used. For hybrid structures, damping values are in the range between 2-3% of critical.

Based on the above literature research, while staying within the limits given in EN 1991-1-4, a damping of

1.9% of critical or δ=0.12

was chosen for the 1-year and 10-year wind criterion given that the lateral bracing system of the Fyrtornet consist of both a braced post- and-beam system and a CLT core and diaphragm system.

4 WIND TUNNEL TESTING

To eliminate the uncertainties and unknowns outlined in the analytical assessment, the wind-induced accelerations at the last occupied level of the tower were computed with the wind tunnel generated data.

4.1 WIND TUNNEL SET-UP

For the pressure measurements, a rigid model of the tower in a scale of 1:200 was constructed. The tests were carried out in two configurations: (1) the Fyrtornet tower as a stand-alone solitary building without any additional surrounding buildings and (2) in a configuration including all significant existing and proposed future buildings in the near vicinity within a radius of approximately 200 metres. Surroundings beyond the immediate neighbourhood of the building are simulated by appropriate roughness elements on the tunnel floor in order to provide an accurate simulation of the wind speed profile and turbulence of the approaching wind. The facades of the tower were equipped with about 150 pressure taps and the time-series were recorded simultaneously by means of high-response differential pressure transducers.

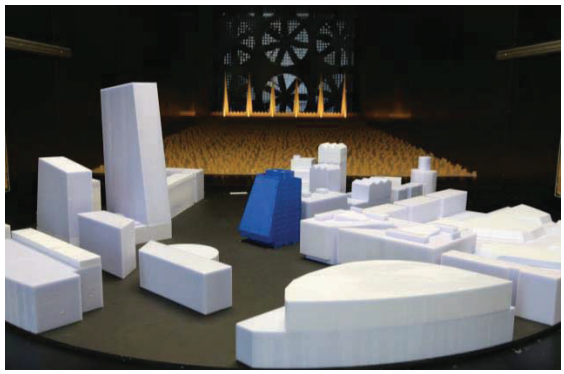

Figure 14: *Wind tunnel test set-up with local environment*

4.2 CALCUATED ACCELERATIONS

As a basis for the wind-induced vibration calculation based on the wind-tunnel measurements on the rigid model, a simplified linear analytical model was established that correctly represents the mass distribution and modal properties of the tower as established in the more complex 3D finite-element model.

The main steps for the computation of the dynamic response of the tower can be summarized as follows: (1) calculation of the generalized force-time series based on the measured pressure time-series and the mode shape information, (2) Fourier transformation of the generalized force-time series and multiplication with the mechanical

admittance function for the respective mode shapes. This results in the complex generalized deformation spectrum. On this basis, the deformation and acceleration time-series are computed. (3) Extreme value analysis of the acceleration time-series.

For the vibration response calculation, a logarithmic damping decrement of $\delta = 0.12$ was assumed to be representative for 10-year and 1-year winds. The predicted peak accelerations in the upper floors of the tower are:

$$a_{10a,peak}\,(\delta=0.12) = 2.40\%\text{- g}$$

for the 10-years-wind and

$$a_{1a,peak}\,(\delta=0.12) = 0.70\%\text{-g}$$

for the 1-year-wind.

These accelerations occur on the outer corner range of the last occupied floor level (Level 20; 39.6 m above ground) and include the contribution of the along wind, crosswind, and radial accelerations. The values represent the maximum peak accelerations of all investigated wind directions and constellations. Considering the natural frequencies of the building, both the 10-year and the 1-year accelerations are within the acceptable limits for an office building according to the comfort criteria described above.

It is important to note that, although the wind tunnel analysis seems to validate the code-based analytical calculations, the reasons for the reasonably good match are not obvious. In fact, the general wind climate on site proved to be less onerous than the wind speeds given in the code. On the other hand, the peak acceleration values given above arise predominantly from one direction in which the presence of one of the tall buildings next to the Fyrtornet plays a significant role.

5 SITE ASSMEBLY

The assembly sequence starts with the CLT core. Walls are pre-assembled on the floor and are then installed as one monolithic element. Once the core over the height of one storey is assembled, the glulam structural elements are installed: first all the columns, which are temporarily propped, then the bracing and finally the horizontal beams.

In the next step, the CLT slabs are installed and act as a temporary water protection. A moisture protective, diffusion open, membrane is already applied to the slabs in the factory and only some minor rework on-site is required. Keeping timber as dry as possible during assembly is one of the key elements to ensure a good quality to the building. This sequence of steps is then repeated for each storey.

The timber structure assembly started in November 2022 and is planned be completed by June 2023.

Figure 15: *On site situation the 6th of December 2022. Picture taken from south-east.*

Figure 16: *On site situation the 21st of February. Picture taken from south-west. Timber structure levels 1 to 4 is completed.*

6 CONCLUSIONS

The two-step approach taken to assess the wind-induced accelerations for comfort on the Fyrtornet tower proved to be a reliable and necessary strategy.

In the first step, the analytical assessment of the acceleration at the last occupied floor of the tower based on methods given in codes and state-of-the-art literature, coupled with a parameter study on the influence of the connections stiffnesses and mass distribution on the accelerations allowed to steer the structural design in the right direction. However, the code-based methods that are available to date do not provide comprehensive guidance on how to compute the wind-induced vibrations for the across-wind and torsional modes and no information is given on how the response from individual modes is superposed. Also, recommendations for damping values applicable for tall mass timber buildings are not existent in the current European codes so that an extensive literature research of the current state-of-the-art must be undertaken. Additional research in this field is needed.

https://doi.org/10.52202/069179-0562

Given that analytical methods ultimately remain idealisations for simple geometries and cannot fully account for the effects of the wind effects from adjacent buildings, it is recommended to assess the wind-induced vibrations in second step through wind-tunnel based methods in order to yield a reliable and yet efficient structural design.

REFERENCES

[1] Eurocode 5: Design of timber structures - Part 1-1: General - Common rules and rules for buildings; French version NF EN 1991-1-5:2005 + A1:2008 + A2:2014

[2] Jean-François Bocquet, Romain Lemaître, Thomas K. Bader (2018). Design recommendations and example calculations for dowel-type connections with multiple shear planes, Design of Connections in Timber Structures, COST.

[3] Council on Tall Buildings and Urban Habitat": International organization in the field of tall buildings and the recognized source of information on tall buildings internationally, Chicago, Illinois Institute of Technology, United States of America.

[4] International Organization for Standardization, 2007. Bases for design of structures – Serviceability of buildings and walkways against vibration, ISO 10137:2007, Geneva, Switzerland.

[5] Wichtmann, T., Triantafyllidis, T.: Über die Korrelation der ödometrischen und der „dynamischen" Steifigkeit nichtbindiger Böden. Bautechnik 83, Heft 7

[6] Landel, P., Johansson, M., & Linderholt, A. (2021). Comparative study of wind-induced accelerations in tall timber buildings according to four methods. WCTE 2021, World Conference on Timber Engineering, Santiago, Chile, 9 - 12 August.

[7] Boverket, 2019. Boverket mandatory provisions amending the board's mandatory provisions and general recommendations on the application of European design standards (Eurocodes), EKS 11, BFS 2019:1, Sweden.

[8] Eurocode 1: Actions on structures - Part 1-4: General actions - Wind actions; German version EN 1991-1-4:2005 + A1:2010 + AC:2010actions – Wind actions, EN 1991-1-4:2005

[9] Johansson, Marie & Linderholt, Andreas & Jarnerö, Kirsi & Landel, Pierre. (2016). Tall Timber Buildings – a preliminary study of wind-induced vibrations of a 22-storey building

[10] R. Abrahamsen, Mjøstårnet - Construction of an 81 m tall timber building, 23. Internationales Holzbau-Forum IHF 2017

[11] Wind-induced vibration of the "Treet" – A 14 Storey Timber residential building in Norway, Magne Aanstad Bjertnaes, Kjell Arne Malo, WTC 2014, Quebec City, Canada

[12] NBCC (National Building Code of Canada). 1995. National building code of Canada (NBCC), Part 4 and Commentary C. Ottawa

[13] Beton-Kalender 2003: Hochhäuser und Geschossbauten, Konrad Bergmeister, Johann-Dietrich Wörner, Ernst und Sohn

[14] Feldmann, Angela & Huang, Haoyu & Chang, Wen-Shao & Harris, Richard & Dietsch, Philipp & Gräfe, Martin & Hein, Carsten. (2016). Dynamic properties of tall Timber Structures under wind-induced Vibration. WCTE 2016, World Conference on Timber, Vienna, Austria, 22-25 August

[15] Edskär, Ida & Lidelöw, Helena. (2017). Wind-Induced Vibrations in Timber Buildings— Parameter Study of Cross-Laminated Timber Residential Structures. Structural Engineering International. 27.

[16] Modal Analysis, Dynamic Properties and Horizontal Stabilisation of Timber Buildings, Ida Edskär, Doctoral Thesis, Luleå University of Technology, 2018

[17] Abrahamsen, Rune & Bjertnæs, Magne & Bouillot, Jacques & Brank, Boštjan & Cabaton, Lionel & Crocetti, Roberto & Flamand, Olivier & Garains, Fabien & Gavrić, Igor & Germain, Olivier & Hahusseau, Ludwig & Hameury, Stéphane & Johansson, Marie & Johansson, Thomas & Ao, Wai Kei & Kurent, Blaz & Landel, Pierre & Linderholt, Andreas & Malo, Kjell & Tulebekova, Salue. (2020). Dynamic response of tall timber Buildings under service load – the DynaTTB research program.

World Conference on
Timber Engineering
Oslo 2023

BUILDING INFORMATION MODELING OF A TIMBER BRIDGE – A CASE STUDY

Alvdis Hardeng[1]

ABSTRACT: The development of using BIM models as the sole documentation in road projects has come a long way, but in Norway the development has come particularly far. A BIM model gives the user a good overall picture with access to any information needed. One of the biggest advantages of BIM is that the design basis is more elaborated and with higher level of details. The reduction in change orders on site is noticeable.

This case study shows how a BIM model can be used, from calculation and modeling to structural review, productions and procurements, assembly and useability after construction. Tande Bridge is chosen as an example of this process as it one of the first timber bridges to be built based solely on BIM models and was a success. A BIM model of a timber bridge includes large glulam beams, concrete abutments and steel joints with essential detail. We can therefore conclude that we have a well-functioning system for BIM models in a bridge life span that can be used on every kind of construction and material. Even greater success will come with more standardization and development of software.

KEYWORDS: Timber Bridge, Building Information Modeling (BIM), Model-based Design, Drawingless Design, Model Maturity Index (MMI).

1 INTRODUCTION

Norway has a long history of timber bridges. The breakthrough came with the Olympics in Lillehammer in 1994. A new method for connections was developed (slotted steel plates with dowels) and creosote impregnation guaranteed a life span of 100 years. This was the beginning of making larger road bridges in glulam. In recent years, many overpasses have been built in glulam, especially in the eastern part of Norway. Medium-sized timber bridges with a pre-stressed timber deck are competitive with other materials, especially when there is limited construction time and deck hight is needed.

The design basis has historically been 2D drawings. The change from 2D drawings to 3D models was done in a few years' time around 2016 in Norway. At first Building Information Modeling (BIM) models were used as the basis for creating 2D drawings, whereas we now use the same BIM models throughout the whole project. The development has come a long way, and in Norway the development of drawingless projects has come the furthest [1]. This paper shows how BIM can be used as sole documentation for the whole life cycle of a timber bridge. From calculation and modeling to structural review, productions and procurements, assembly and ultimately archiving and maintenance.

BIM models offer a much better visualization than 2D drawings, but it is important to find the right platforms to disseminate the knowledge. One of the biggest advantages of BIM is that the design basis is more elaborated with a higher level of detail. A 3D model can also make clash controls easy in the early stages of the bridge design, which leads to a reduction of the number of changes on site.

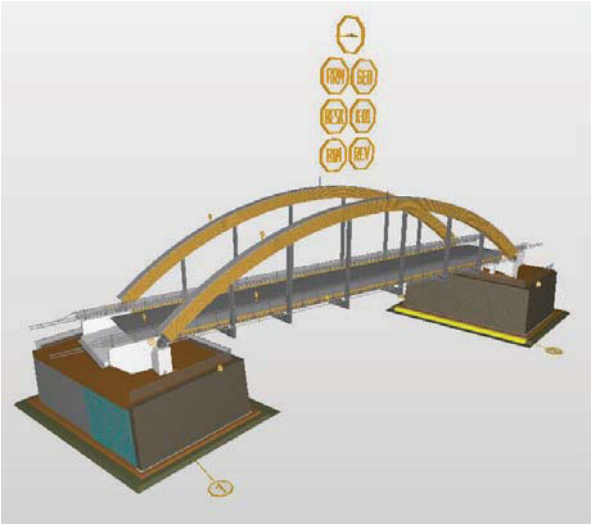

Figure 1: *BIM model of Tande Bridge*

[1] Alvdis Hardeng, Sweco Norge AS, Norway, alvdis.hardeng@sweco.no

https://doi.org/10.52202/069179-0563

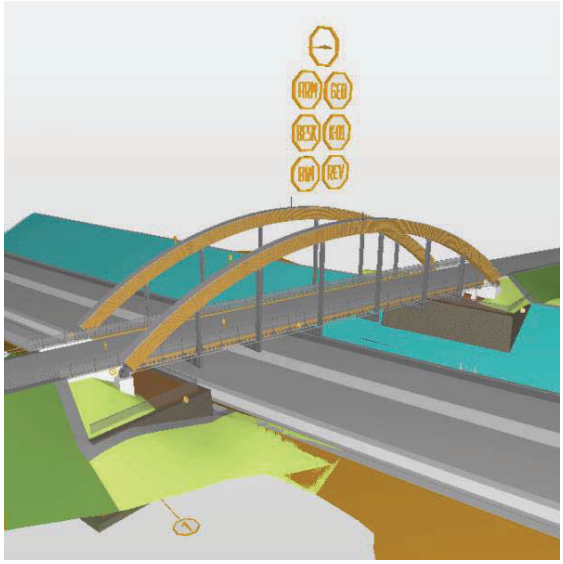

Figure 2: *BIM model of Tande Bridge with road geometry and landscape*

A BIM model consists of several files. Typically, there will be separate files for each discipline, which provides the user with a clear overview and easy access to relevant information. Figure 1 shows the BIM model of Tande Bridge. In Figure 2 road geometry and landscape design have also been added. To ensure that the BIM model file will not be too big, the road geometry and landscape are customized and only showing what's relevant to the specific bridge. The «coins» (shown over the bridge in Figure 1 and Figure 2) have been developed by Sweco as a practical way of gathering links to useful documents such as the "overview drawing", the design report, the geotechnical report etc. Typically, the documents you will need throughout the life span of the bridge.

To make a good BIM model it is necessary to know who will use it and what they will use it for, for example structural review, procurement, or assembly etc. It is also of great importance what kind of information is needed in the various phases. There is a lot of information inside a model and without good filters in the software, it is difficult to sort and utilize the information. Material, dimension, object name and construction part are examples of topics the BIM model should filter on. An accurate and structured BIM model is necessary to avoid that the user will not experience an overflow of information.

As a tool to ensure good information flow, the BIM manual was introduced. This is a document that always follow the BIM model. The BIM manual describes how the model's structured, the level of detailing used in this particular model, how object information is sorted, how to filter in the model, a review of how model maturity index (MMI) is used, and other relevant information are important topics that are reviewed in the BIM manual. The MMI number describes the level of maturity through number codes. It is not possible to determine whether a construction part has been subject to structural review by simply looking at the object in the model. The MMI level is therefore utilized to link the maturity with the object to explain which phase it is in and if you could use the information for preliminary design, clash controls or procurement. The use of MMI is primarily for the design, structural review and construction phases.

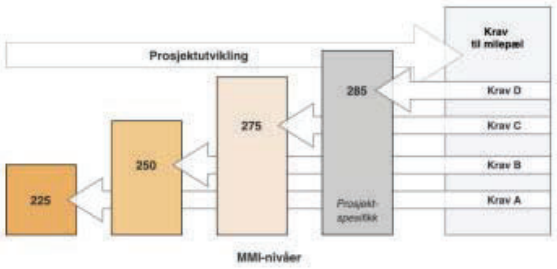

Figure 3: *Conceptual sketch showing the MMI level increasing during the project development and linked to requirements [2].*

Figure 3 shows how the level of MMI increases through the project development and how it is linked to requirements that constitute a milestone. It is possible to have different levels of MMI on different objects in the same model. The total level of MMI for a model always refers to the lowest MMI level. To get a good overview it is possible to sort on the different levels of MMI in every BIM model.

A timber bridge consists of glulam beams, concrete abutments and steel details and generally has a lot of different components from small steel connections to large glulam beams. It is important to choose the right level of detailing on each component. If you can manage the life cycle of a timber bridge solely based on BIM models, you can manage every type of construction and material. Tande Bridge is chosen as an example of this process. Tande Bridge is one of the first timber bridges built solely based on BIM models. Tande Bridge was designed in 2018 and built in 2020. The bridge is a two-way 80km/h road south of Lillehammer, crossing the E6 highway. It has an arch span of 48,5 meters connected with tension bars. The glulam arch is connected at the top with a steel joint.

2 TANDE BRIDGE – FROM DESIGN TO MAINTENANCE

2.1 STRUCTURAL DESIGN

The development of BIM models has come furthest in the planning phase. The priority in this phase is to optimize the structural design and make it even more efficient. In Norway, many of the large road projects are Engineering, Procurement and Construction (EPC) contracts. This has resulted in a reduction of time to complete the structural design, and the need for streamlining and optimizing the design period is noticeable. The introduction of parametric design into modelling is particularly favourable when working with preliminary design. The need for detailing is superior, and the focus is finding a buildable solution for the right price. The use of

https://doi.org/10.52202/069179-0563

parametric design enables quick changes and gives a good overview over the geometry with a detail level sufficient for the design phase. Pre-made script for all the typical bridge solutions makes it easy to choose the right bridge solution fast. As it is easy to add road geometry, landscape, traction pipes etc., showstoppers are quickly discovered, and a solid bridge solution can be established.

It is important to consider what level of detailing a BIM model needs. Objects must have enough details to be useful for a good understanding of the model and in a clash control. At the same time, unnecessary details can make the model hard to use, as the files become too large. An example is screws. Screws come predefined in every modelling program, with everything from head to thread modelled visually. However, you still need to describe the object with information such as material, surface treatment etc. in the model before the object can be used for procurement and construction. This means that a better-looking screw will make the file heavier without providing much benefit. For design purposes you would achieve equal result with a cylinder of the same diameter and description as the screw which would not make the file heavier. Considering the number of screws in a bridge construction, it can be favourable to make a simplified screw duplicate as shown in Figure 4.

Figure 4: *Simplified screw duplicate used at Tande Bridge*

All price-bearing elements must be modelled. The focus on Tande Bridge were the glulam beams with steel details, necessary detailing of the steel details, the abutments and to sort every component into phases. The holes in the steel are especially important and can be difficult to model. It is important to ensure that the hole stays a hole for the whole process from modelling and to procurement.

Object information is added in the design software before the IFC export (a PDF file for BIM models). Object information is called user-defined attribute (UDA). The UDAs are important information that should be easily accessed, such as material quality, placement priority, links to drawings etc. The information should be short and descriptive. A high-quality BIM model includes useful attributes to objects in the model. The key is understanding what information is needed in the different phases.

The detail level needed for the UDA differs from phase to phase. For a preliminary design, there is less need for detailed attributes compared to a building project where the attributes should be adjusted to procurement. The input in the UDA enables the possibility to classification. Figure 5 shows the UDA for the glulam beams on Tande bridge. Everything from dimension to surface treatment and MMI level are described.

INFO

(B) Object.1.196

Identification	Location	Quantities	Material
Egenskaper	*Pset_BuildingElementProxyCommon*		

Property	Value
A.01 Objektnavn	Limtrebue
A.02 Objektkode-tekst	D8
A.03 Objektkode-nummer	86100000
A.04 Beskrivelse	Limtrebue, tverrsnitt 980x1400, limes opp av 3x140, 2x165 og 2
B.01 Parsell	P2
B.02 Område	S18
B.03 Konstruksjon	04-1752_K660_Tande bru
C.01 MMI	400
E.01 Material	GL30c
F.01 Merknad	Bueender ansees som tilstrekkelig klatresikret med rekkverk.
F.02 Merknad	Buer overflatebehandles med ett strøk Jotun Visir pigmentert c
G.01 Vertikalniva	2
H.01 Status	Teknisk godkjent iht. notat 17/9536-36
H.02 Revisjon	B
H.03 Revisjonsdato	10.03.2019
I.01 PNS	P2210

Figure 5: *Extract from the UDA for a glulam beam*

The setup for UDA shown in Figure 5 follows guidelines given by the Norwegian Public Road Administration in addition to the needs of the glulam subcontractor and the contractor. Every set of attributes is linked to an element to ensure that the necessary amount of information for every phase is provided in the model.

Figure 6 and Figure 7 show how it is possible to filter and sort in the BIM model. In Figure 6 all glulam arcs are shown, and in Figure 7 all element with the material "GL30C" are shown.

https://doi.org/10.52202/069179-0563

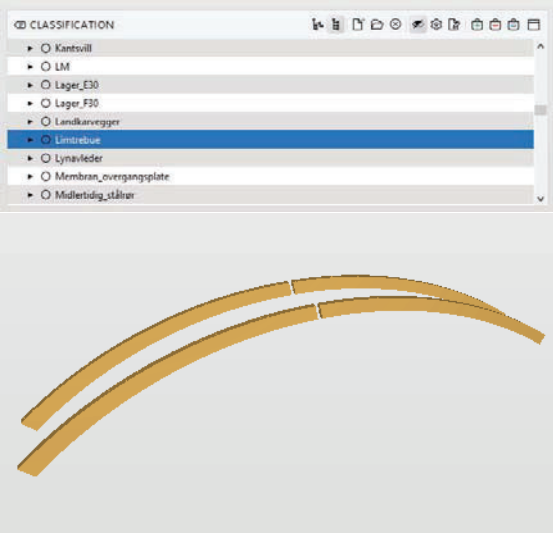

Figure 6: *The BIM model when sorting on glulam arc*

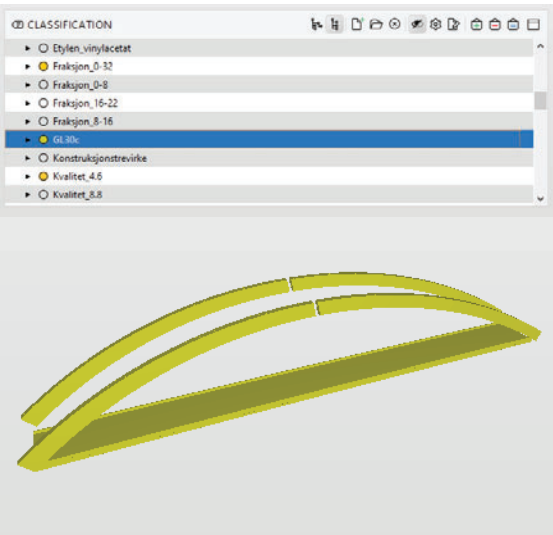

Figure 7: *The BIM model when sorting on "GL30c"*

Even if we have a BIM model, we still make the "overview drawing". The drawing gives an overall view of the construction and should provide the necessary information without having to look up the design report or look at the model. When modelling a bridge, a cost-benefit assessment should be made. How do you show what is needed without doing a needless amount of work that will also make the file unnecessary big? Therefore, drawings showing the principle of backfilling around the bridge and maintenance drawings with tables to be filled out after the bridge opening are still being made.

2.2 STRUCTURAL REVIEW

When working with a 3D model, collisions will immediately be apparent. Discovering collisions at an early stage gives a far more effective opportunity to address the issues than fixing collisions when discovered in the late stage of structural design or on site. This advantage is significant for economic reasons and decreases time delays for the contractor. In the first phase after model completion, the models are used for interdisciplinary control and afterwards for third-party control. With a greater degree of standardization, more checks can also be done automatically and that will help improve quality and save time.

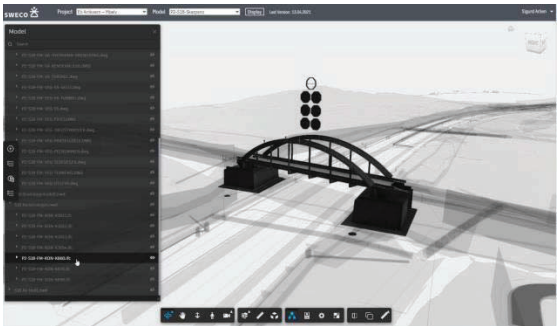

Figure 8: *Tande Bridge in the online model viewer for the road project*

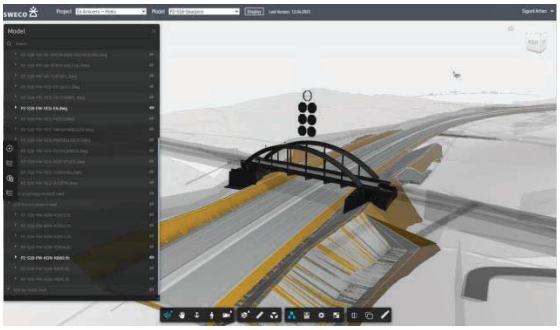

Figure 9: *Tande Bridge with road geometry in the online model viewer for the road project*

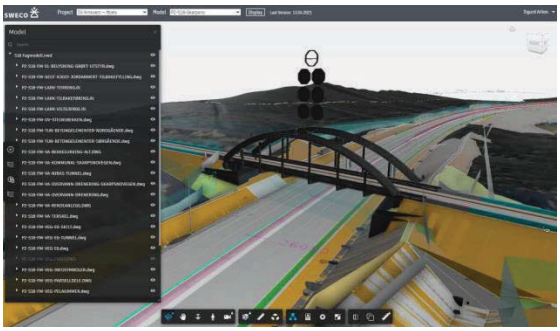

Figure 10: *Tande Bridge with all the different models visible in the online model viewer for the road project*

Having a good solution for showcasing all the different models are important. This is particularly useful when you have several bridges with models not only from the civil engineer, but also from road engineer, landscape architect etc. It should be easy to navigate and to turn on and off

https://doi.org/10.52202/069179-0563

each model. Figure 8, 9 and 10 show Tande Bridge in the online model viewer used in the road project. Figure 8 highlights the bridge alone, while Figure 9 also includes the road geometry is highlighted. In Figure 10 all the different models are visible.

The BIM model is also used for structural review. This is an efficient method where it is possible to perform the structural review and add comments directly in the model. The comments are saved in a separate file where it is possible to add answers. The file is then sent back and forth until every comment is sufficiently addresses. Figure 11 shows a screenshot of the structural review of Tande Bridge. The different comments are listed at the bottom with supplementary comments on the left and a visual display top right.

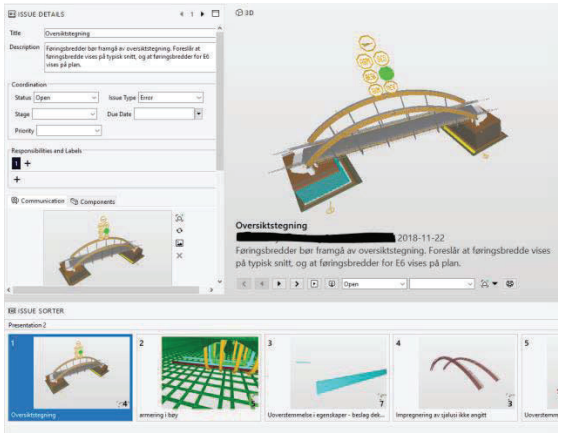

Figure 11: *Screenshot of the structural review of Tande Bridge*

It is recommended to use the BIM manual to inform the person performing the different reviews. A good, standardized model with a good setup of filters, this will ensure that the structural review can be done in an effective way.

2.3 GLULAM SUBCONTRACTOR

The biggest advantage for the glulam subcontractor is how quickly they get a good overview with a BIM model and how easily the model can be updated when changes occur.

INFO

(B) Object.1.235

Identification	Location	Quantities	Material
Egenskaper	Pset_BuildingElementProxyCommon		

Property	Value
A.01 Objektnavn	Brudekke
A.02 Objektkode-tekst	D8
A.03 Objektkode-nummer	86100000
A.04 Beskrivelse	Tverrspent tredekke. 68 stk. 119x433 mm lameller. Kreosotim
B.01 Parsell	P2
B.02 Område	S18
B.03 Konstruksjon	04-1752_K660_Tande bru
C.01 MMI	400
E.01 Material	GL30c
F.01 Merknad	Ytterste lamell på hver side skal ha kvalitet GL30h.
F.02 Merknad	Dekke produseres med konstant radius R =2500 m
G.01 Vertikalniva	2
H.01 Status	Teknisk godkjent iht. notat 17/9536-36
H.02 Revisjon	B
H.03 Revisjonsdato	10.03.2019
I.01 PNS	P2210

Figure 12: *Extract from the UDAs for the glulam deck*

Figure 12 shows how the glulam deck is described in the attributes, sufficient for procurements. The attributes include surface treatment, radius on the deck, material etc. The attributes also show the status of the model and the corresponding date, as well as the level of MMI for the specific element (here: 400 and ready for procurement).

The import of the BIM model into the supplier's software normally works adequately, but there may be some bugs and the import can be time consuming. The glulam subcontractor produces the glulam with a CNC machine. CNC machines are used to computerize production machines in various types of industry. It is particularly the holes in the glulam that make transfer to the CNC machine challenging. When the model is exported to IFC format, it is important to check that each hole remains a hole and does not transform into splines. Work is continuously being done to address this challenge. A good import depends on an accurate and thorough model, since the IFC format is less accurate than the precision of the CNC machine. A very detailed BIM model is not necessarily sufficient for the supplier. It can make the model too heavy without any benefits. Improved software with good filters and a more standardized setup for models, which considers the needs of the suppliers, are important.

2.4 CONSTRUCTION

Looking at hourly consumption, it is on the construction site that the BIM model is used the most. However, this is also where available software is least developed. Software must be optimized to present views and information from BIM models in an easy and efficient way. All information in the BIM model is connected to a component. Thus, a single file can provide all the information needed to build the bridge.

The glulam beams on Tande Bridge were transported to the construction site pre-assembled. Smaller elements

https://doi.org/10.52202/069179-0563

were prepared at the factory and then transported to the construction site by night. The abutments where already built on each side of the highway. The traffic was redirected, and the assembly could take place during a weekend. Figure 13 shows the assembly of the glulam arcs.

Figure 13: *The glulam arches are assembled on the construction site. Picture taken by Sweco*

Using the BIM models sequenced information for the assembly will be an advantage. The contractor can then go through the construction period to check any time-critical elements and perform space-saving measures.

However, the use of tablets and other digital tools can be difficult on site, especially due to weather conditions. An example is the challenges of using touch screens in rainy weather.

Revisions done in the model must be marked and described carefully, as it is not possible to highlight the revisions as it is for drawings. When updating a model, the change must be described sufficiently including the revision mark and date. That way it is possible to filter the model regarding the updates as shown in figure 14.

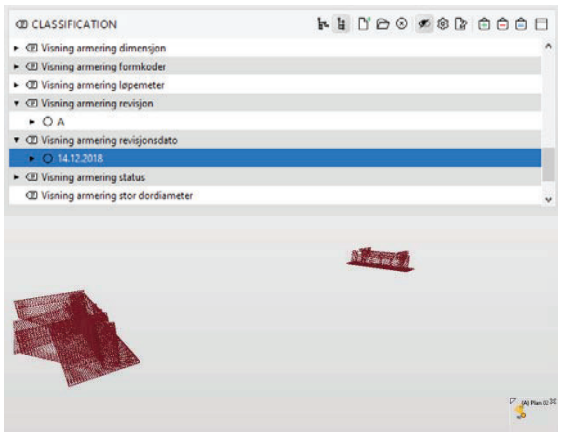

Figure 14: *The BIM model showing a revision made at a certain date*

The history of 3D models on construction sites is not long, so it is important to constantly get feedback from contractors and to incorporate the feedback into the model. A good project includes the contractors' needs from the beginning. Even though there is a requirement that all cost-bearing elements must be included in the model, the needs of the contractors should be given more emphasis.

2.5 USEABILITY OF BIM MODELS AFTER CONSTRUCTION

There is little experience with using BIM models in the operation and maintenance phase. Experience will come with time as main inspections are carried out every five years on bridges in use. As in all other projects, it is important that the BIM model is updated with any changes along the way. The existing national archive system is not adapted for handling BIM models. Currently, everything is just stored together and then it is practical that the BIM model comes in a single file.

On the road project where Tande Bridge is situated, the contractors made a digital display of the entire project which contained all BIM models. All information was connected to a component. It is then possible to extract parts of the database by sorting on object information. This ensures that only the information needed will be provided, thus avoiding information overload.

Figure 15 shows Tande Bridge in the summer of 2022.

Figure 15: *Tande Bridge open and in use. Picture taken by Sweco*

3 CONCLUSION AND FUTURE WORKS

Tande Bridge as a BIM model was a success. This shows that we have a well-functioning system for BIM models that can be used on any type of bridge and any kind of material, and that we can use one BIM model for the whole process. The industry will become more automatized and the need for digital information will increase. The key to even greater success is more standardization in every phase.

As with all projects made with BIM models the collisions are discovered sooner rather than later and often in a phase where it easier and cheaper to correct them. At the moment, the software developed for each phase is not at a stage where we can take full advantage of all opportunities. Since the models are full of information, it must be easy to sort relevant information. We need a

https://doi.org/10.52202/069179-0563

better structure for information and how to sort it into different phases. If not, it is very easy to get information overload.

The advantages of increased quality and a more efficient workflow will give financial gains and increase the impetus for working solely with BIM models. Hopefully, this will also be an incentive for the development of software. Further collaboration on standardization will be time-consuming and involve some trial and error, but it will be necessary to move the process forward. The collection of best practice from every phase to ensure that the needs of different actors are met, should also be considered in future work on standardization.

ACKNOWLEDGEMENT

I would like to thank my colleagues at Sweco and the many contributors in the E6 Arnkvern – Moelv road project for a great and ground-breaking collaboration. I also want to thank Sweco for facilitating work on this paper, as well as the great interlocutors at Sweco who have given me useful feedback on the text.

REFERENCES

[1] Vieira T, Ulvestad Ø, Cabral P, Geicke A. Randselva bridge, Norway: Designing and building solely based on BIM models. Structural Concrete. 2022.

[2] Fløisbonn H. W., Hoel C., Lystad Ø., Markussen B., Rasmussen S., Ræder M. M., Sunesen S., Yggeseth H. MMI-veilederen 2.0. 2022.

https://doi.org/10.52202/069179-0563

World Conference on Timber Engineering Oslo 2023

NLT DEVELOPMENT FOR BRAZILIAN MARKET – TESTS AND USE

Carlito Calil Neto[1], Alexander Takata[2], Vitor Afonso Neves Silva[3]

ABSTRACT: NLT is an old method of construction with a range of modern opportunity to create compelling architecture. Used in many historic applications, it is enjoying renewed interest as we rediscover the many benefits of mass timber and advance wood technology and manufacturing. Lightweight, low-carbon, and very compatible with high-performance buildings, innovation with NLT is inspiring new opportunities for large- and small-scale buildings across sectors and around the world. The use of new technologies in wood for construction is increasing every year in Brazil. This work aims to demonstrate the development and construction of the first NLT structure in São Paulo city.

KEYWORDS: NLT, Brazil,

1 INTRODUCTION

Part of the family of mass timber products, Nail-laminated timber (NLT) is mechanically laminated to create a solid structural element. NLT is created by placing dimension lumber on edge and fastening the individual laminations together with nails. Typically used as floors and roofs, NLT can also be used for walls, elevator shafts, and stair shafts. Plywood/OSB added to one face can provide in-plane shear capacity, allowing the product to be used as a shear wall or diaphragm.

The mass timber product range available in North America includes Glued-laminated Timber (GLT), Cross-laminated Timber (CLT) and Nail-laminated Timber (NLT). While this wide range of products affords many options for specific design applications, each has different design challenges, performance characteristics, and construction advantages.

Among architects, manufacturers, and environmentalists, many want nothing less than to turn the coming decades of global construction from a giant source of carbon emissions into a giant carbon sink by replacing concrete and steel construction with mass timber. It will avoid the CO2 generated in the production of those building materials and sequester massive amounts of carbon by tying up the wood in buildings.

Wood is the only renewable building material that has grown with sunlight and uses atmospheric CO2 to develop. However, this potential for the use of wood as a smart alternative for GHG emission in the construction industry generally meets the Brazilian tradition in processing timber in the way of keeping the focus on the production of solid high density wood, which has its charm and usefulness. However, to shift the general logic of using wood in the construction industry to upscale its reach and competitiveness for the housing sector it is needed to develop a new industry and a new market for highly processed wood products, such as wood-frame panels or laminated wood panels.

NLT is significant in the range of available mass timber options given the relative ease of fabrication and access to material; NLT requires no necessarily unique manufacturing facility and can be fabricated with local dimension lumber for use in applications across sectors and structure types. While products like GLT and CLT have modern publications and resources aimed at assisting designers and builders with specification, detailing, and installation, NLT resources are dated and focus on prescriptive rather than engineered applications.

In this work, test methods and results were performed at LaMEM (Wood and Timber Structures Laboratory), São Carlos Engineering School, São Paulo University, in Brazil. It was delivered 2 different NLT plates with dimensions of 91 x 1500 x 2600 millimeters. The element is made up of 34 lamellae of Pinus taeda, each measuring 44x80x2600 mm, nailed together by two distinct arrangements of ring nails measuring 35 mm in length and 3 mm in diameter. This set is coupled to an OSB APA Structural board 11.1x1200x2600 mm using nails of the same model as the previous one.

[1] Carlito Calil Neto, Rewood – structural timber solutions Brazil, calil@rewood.com.br
[2] Alexander Takata, Rewood – structural timber solutions, Brazil, alex@rewood.com.br
[3] Vitor Afonso Neves Silva – structural timber solutions, Brazil, vitor.eng@rewood.com.br

https://doi.org/10.52202/069179-0564

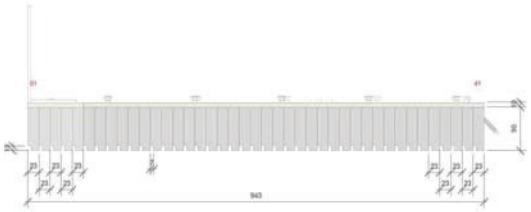

Figure 1: *test scheme NLT plate*

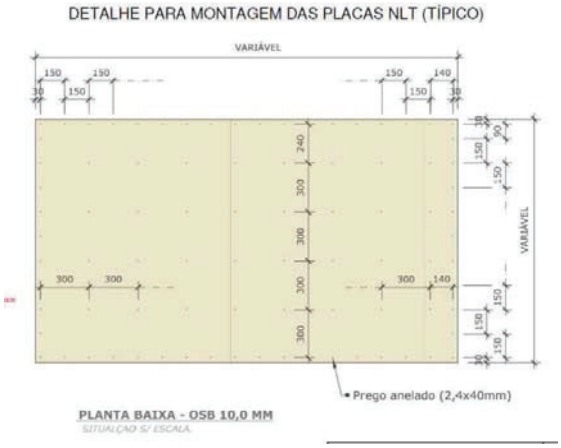

Figure 2: *test scheme NLT plate / OSB*

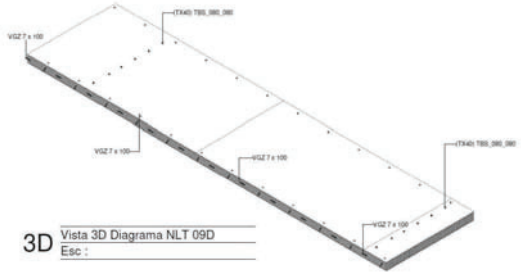

Figure 3: *test scheme NLT plate / OSB*

The NLT 1 board has 1 nail every 270 millimeters that alternates the height with respect to the section, as shown in Figure 1. The NLT 2 board has 2 nails every 270 millimeters, spaced 30 millimeters apart and 25 millimeters apart with in relation to the section limits.

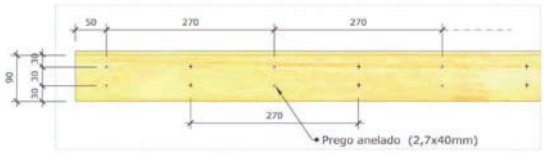

Figure 4: *test scheme Nail - NLT plate*

2 METHODS

The board tests were performed according to PEREIRA (2014) which is based on ASTM PRG 320 and whose scheme is illustrated in Figure 1.

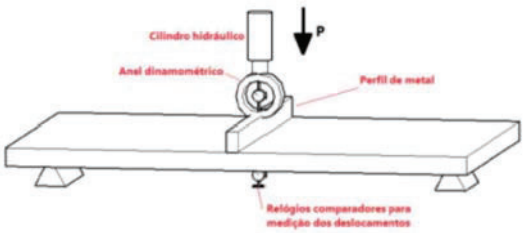

Figure 5: *test scheme*

This procedure was carried out by positioning the NLT plate, with the direction of the pine lamellae oriented towards the span, on two supports composed of metallic tubes positioned 100 mm from the edges of the plate. Then, a steel profile beam I was positioned on the central axis of the plate and the hydraulic cylinder was adjusted so that its center coincides with the center of the face of the NLT element. Finally, 3 strain gauges are positioned on the underside of the plate, along the axis of the metal beam. One of them is aligned with the axis of the hydraulic cylinder and the other two are equidistant in the middle of the distance between the center of the plate and its edge.

Figure 6: *NLT board assembly*

https://doi.org/10.52202/069179-0564

Figure 7: *Detail of the positioning of the strain gauges*

The procedure adopted was to apply the load gradually until the limit of l/300 was reached, with the value of the span being measured by the distance between the supports of the plate. Thus, the load was applied until the limit of 8 millimeters was reached. The load was then relieved and the procedure was repeated two more times, and in each process the applied force and the respective displacements were recorded by the software.

Finally, the load was increased until the NLT element ruptured, and the critical values were recorded. The figures below illustrate the rupture of both NLT plates, which was caused by traction on the lower fibers of the pine lamellae.

Figure 8: *NLT panel rupture details*

3 RESULTS

Based on the results obtained for certain forces and displacements, it was possible to generate 3 stress x strain curves for each plate. It can be observed that as the tests were performed up to a strain of 8 millimeters, there was no material flow in none of the 3 analyzes of each NLT plate, which corroborates the linear arrangement of the graphs presented, having elastic behavior in this interval.

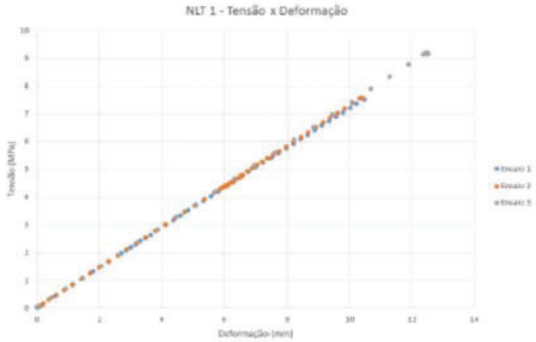

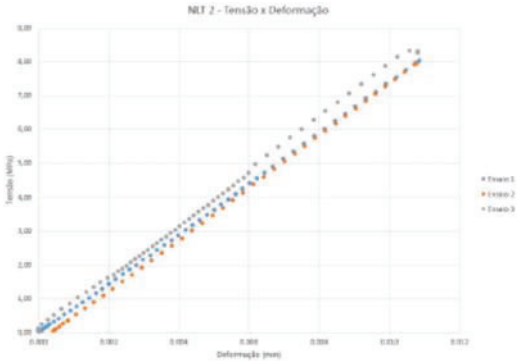

Figure 9: *Tension x Deformation curve of the NLT plate*

Next, the summary table of the performed assay is presented, containing the average of the MOE of the 3 assays performed for each NLT plate.

Table 1: *Margin settings*

NLT plate 1				
Test	Desity	Rupture	MOR (kfg)	MOR (kgf)
1	570,5	9327	8614	34
2			8725	
3			8824	
NLT plate 2				
Test	Desity	Rupture	MOR (kfg)	MOR (kgf)
1	580,1	9081	8839	33
2			9170	
3			9173	

The results obtained were imputed in the RFEM calculation program for the structural calculation of the architectural proposal. The project was designed by the architectural studio MK27.

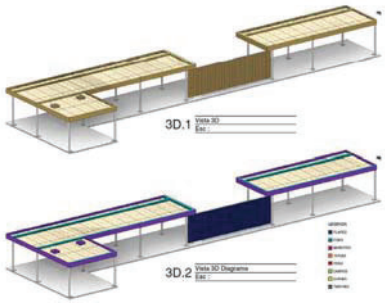

Figure 10: *architectural proposal*

https://doi.org/10.52202/069179-0564

Figure 11: *layout structure*

The big difference in using NLT in this project was that instead of the boards being placed on top of the beams, they were actually used hanging.

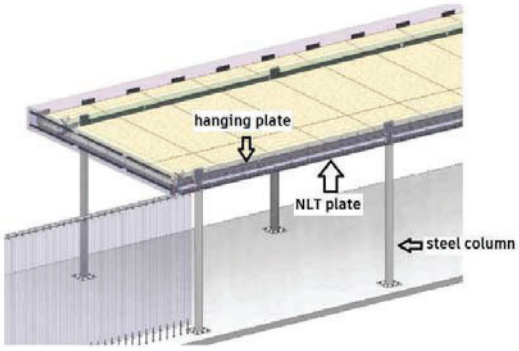

Figure 12: *structural detail*

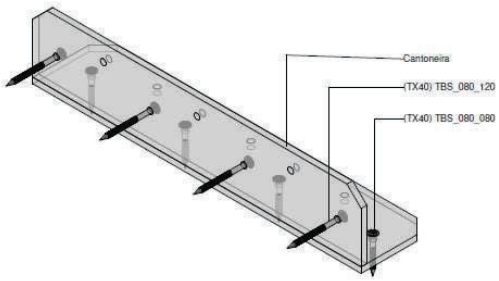

Figure 13: *structural detail*

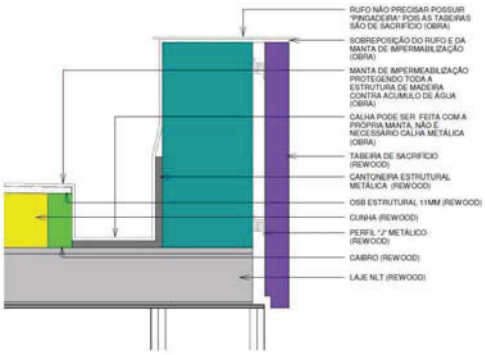

Figure 14: *structural detail*

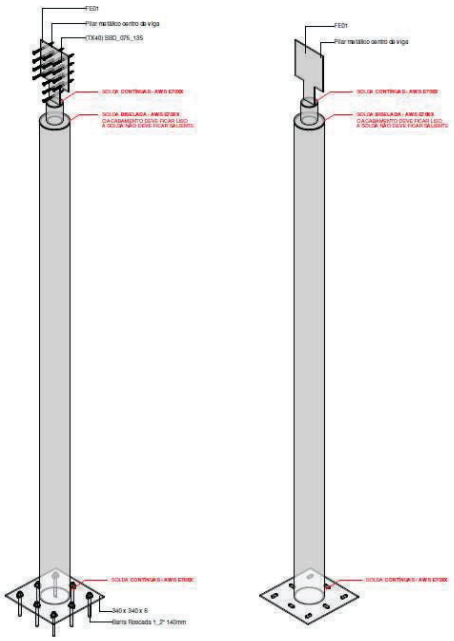

Figure 15: *structural detail*

https://doi.org/10.52202/069179-0564

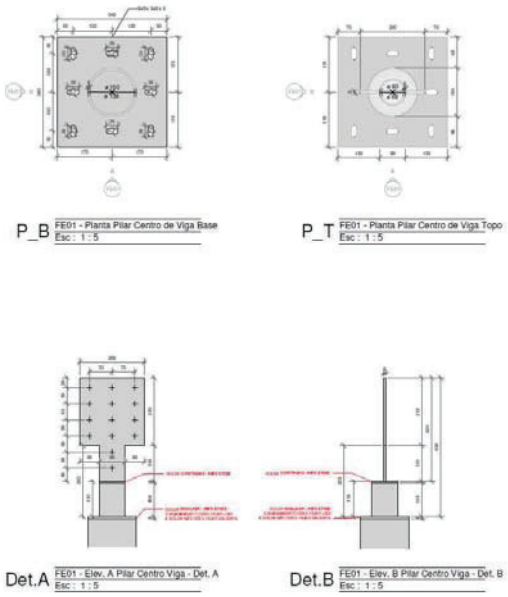

Figure 16: *structural detail*

The entire work, after being manufactured, was assembled in just 15 working days, showing not only its speed but also that wood is still and always will be a symbol of modernity.

Figure 17: *completed work*

Figure 18: *completed work*

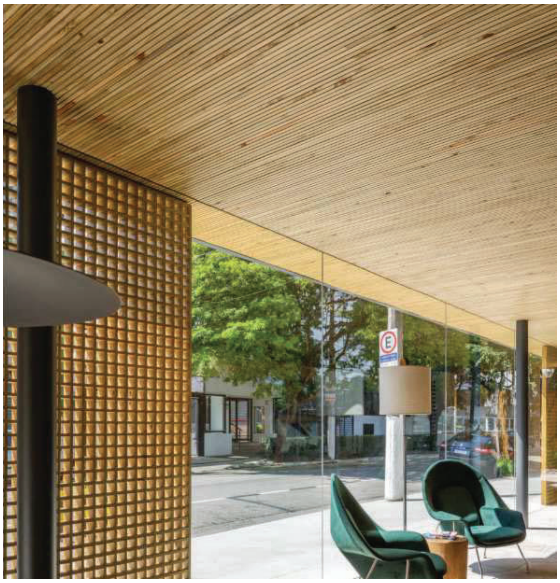

Figure 19: *completed work*

Figure 20: *completed work*

Figure 21: *completed work*

https://doi.org/10.52202/069179-0564

4 CONCLUSIONS

The NLT product, despite being very old technology, still demonstrates very interesting physical and mechanical characteristics for today's projects and when well designed and used, its cost benefit and beauty stands out among the products used today in the Brazilian market.

REFERENCES

[1] International Code Council. 2014. International building code 2015. Country Club Hills, Ill: ICC.

[2] American Society of Civil Engineers. 2010. Minimum design loads for buildings and other structures. Reston, VA: American Society of Civil Engineers.

[3] American Wood Council. 2014. NDS national design specification for wood construction. Leesburg, VA: American Wood Council.

[4] NBR7190: 1997 Design of Timber Structures (draft under revision 2017)

[5] Sales, A. Revision of the Nbr7190/97. Hardwood strength classes. Universidade Federal de São Carlos, SP, 2006.

[6] NBR7190: 1997 Design of Timber Structures –Test Method - Structural timber. Strength classes. (draft under revision 2017)

[7] NBR7190: 1997 Design of Timber Structures - Test Method; Structural timber. Grading. Requirements for visual and mechanical grading standards. (draft under revision 2017)

[8] NBR7190: 1997 Design of Timber Structures – Test Method Structural timber. Grading. Requirements for mechanical connections. (draft under revision 2017)

[9] NBR7190: 1997 Design of Timber Structures – Test Method Structural glulam members. Requirements delamination, shear glue line strength, finger joint strength. (draft under revision 2017)

[10] NBR7190: 1997 Design of Timber Structures – Test Method for clear samples. (draft under revision 2017)

https://doi.org/10.52202/069179-0564

World Conference on Timber Engineering Oslo 2023

A SURVEY OF THE DESIGN OF TIMBER-CONCRETE HYBRID BUILDINGS IN SWEDEN

Carl Larsson[1], Michael Dorn[2]

ABSTRACT: There is a growing interest in timber buildings in Sweden and increased availability of Glulam (GLT) and particularly Cross Laminated Timber (CLT) products. Timber buildings, though, often have difficulties in fulfilling the performance requirements of a building project. The use of concrete elements in addition to timber elements in the load-bearing structure is a widespread solution, introducing timber-concrete hybrid buildings. The study presents responses from interviews regarding ten different timber-concrete hybrid building projects in Sweden with a load-bearing structure above the foundation level in both timber and concrete. Four main types of timber-concrete hybrids were found: a CLT structure on top of a concrete structure, a post-beam system in GLT with CLT slabs and concrete walls, a post-beam system in GLT with concrete hollow core slabs, and a timber structure with some slabs in concrete. The results show that timber-concrete hybrid buildings are flexible and suitable for various construction types. The reasons for using concrete in timber construction were primarily to increase self-weight, obtain longer span lengths, and overcome shear wall capacity issues. There is still a lack of competence in the design of structural timber projects, and at most, five different structural designers were involved in the load-bearing design of a single building. This highlights issues regarding project management of the design process within timber-concrete hybrid buildings.

KEYWORDS: Timber-concrete hybrid, CLT building systems, Timber building systems, Structural management

1 INTRODUCTION

The use of timber in modern, large-scale building projects in Sweden is low compared to concrete. In recent years, though, there has been a growing interest from the construction industry, from architects and from developers to use timber as the primary material in the load-bearing structure of buildings [1]. It is well known that an increased share of timber products like sawn timber, glulam timber (GLT), and cross-laminated timber (CLT) in buildings is beneficial from an environmental perspective. For example, the load-bearing structure is identified to significantly impact the carbon footprint during the construction phase [2].

Timber-concrete hybrid buildings use both materials in the load-bearing system and are a possibility widely used to increase the use of timber overall. Plenty of timber-concrete hybrid structures are operating, including showcase examples like the 18-story Brock Commons in Vancouver, the 24-story HoHo Tower in Vienna, and the 10-story Banyan Warf in London. However, the research in this area is limited compared to other hybrid structures, where several topics have been studied regarding structural systems, connectors, and modeling.

This study aims to give real-life examples of how timber and concrete are combined in hybrid structures today in the Swedish construction industry without going into technical solutions or the performance of these buildings. In addition, the study focuses on the structural design phase, where many decisions are made, e.g., the requirements of the building, how the building will be built, and which structural materials will be used. The study is based on interviews with structural designers, contractors, and developers involved in these projects.

The following research questions are addressed:

1. How are timber and concrete combined in a typical Swedish project? What is the reason for this?
2. How do structural designers work in the late design phase of a timber-concrete hybrid project?

2 METHODS

The study applies a qualitative research methodology based on interviews with primarily structural designers involved in the late design phase in the construction process of building projects in Sweden. In several of the studied projects, complementary interviews were held with other people involved in the respective project, such as developers and contractors. The qualitative method was chosen because it allows the researcher to secure vivid and accurate accounts based on the interviewee's personal experience in building projects [3].

Ten different projects were identified as they were recently completed or under production in early 2020.

[1] Carl Larsson, Linnaeus University, Sweden carl.larsson@lnu.se
[2] Michael Dorn, Linnaeus University, Sweden michael.dorn@lnu.se

https://doi.org/10.52202/069179-0565

Interviews regarding these projects were performed, at least two for each project. In total, 17 people were interviewed, eleven structural designers, one developer, and five contractors. Several respondents have worked on more than one project; in these cases, interviews were held separately for each project. Of the structural designers, there were six timber element designers and five concrete element designers. The concrete element designers acted in some projects also as the main designer. Most of the interviews were held in Swedish, except with two of the timber element designers who were located outside Sweden.

The questionnaire contained nine questions and is presented in Table 1. The test interviews were analyzed to verify that the questionnaire gives responses that fulfill the overall research questions of this study.

Table 1: *Questionnaire of the interviews.*

	Question
1	What are the name and the background of the project?
2	What was the reason for mixing the use of concrete and timber?
3	How has the structural design been divided into different involved contractors or designers?
4	Which designer has been responsible for the collaboration of the structural designers?
5	Which designer was responsible for the total stability of the structure?
6	When did the project agree that the structure had enough stability and which analysis was to be performed?
7	Which project partner was responsible for the robustness criteria of the structure, and which method was used for these criteria?
8	Which structural data were shared between the different structural designers involved, and what software was used?
9	Lessons learned from your point of view in these types of projects?

2.1 Data analysis

Grounded Analysis [4] was performed as a data analysis method for the open-ended questions. It allows the data collection and analysis to proceed simultaneously, allowing the researcher to obtain a complete picture of the respondents' views on their building projects. The Grounded Analysis is commonly used in Management Research [5] and was performed using the suggested methodology by Easterby-Smith & Thorpe [6].

The answers' consistency was controlled by performing interviews with at least two stakeholders for each project. This is also the reason why only ten building projects were included in the final analysis, out of 16 suitable projects identified initially.

3 RESULTS

3.1 Projects

Two Swedish mid-size cities have focused on construction with timber, where political processes were created to foster new developments; Växjö in the Southern and Skellefteå in the Northern part of Sweden, respectively. A relatively large number of the studied project are therefore located in these two towns, see Figure 1. The purpose of the buildings was categorized as schools, residential buildings, offices, and others.

From a structural point of view, four different system types of the timber-concrete hybrid were found in the ten projects identified, shown in Figure 2. The categories and building types do not necessarily coincide.

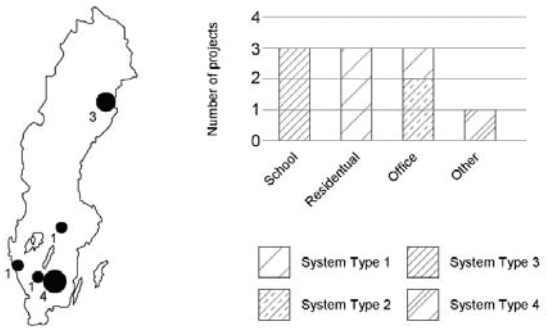

Figure 1: *Project locations and purposes of the buildings in the studied projects*

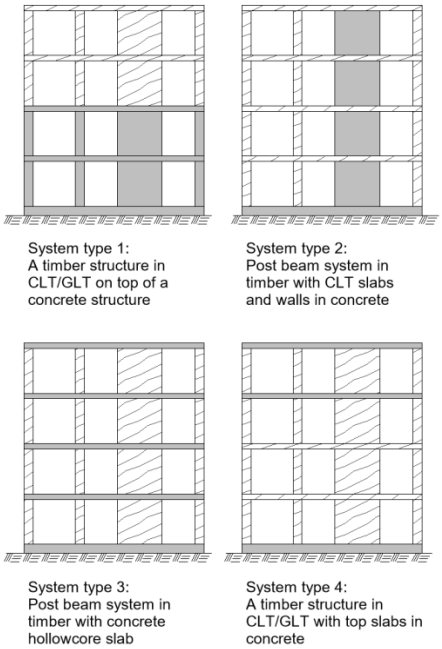

Figure 2: *System types of the load-bearing structure*

https://doi.org/10.52202/069179-0565

3.2 Reasons for choosing a timber-concrete hybrid

The reasons for using timber structural elements in a project are shown in Figure 3. The respondents mentioned the following reasons:

- Architectural competition: The use of timber resulted from an architect competition where timber construction was part of the winning entry.
- Property developer's demands: The property developer required a timber structure.
- Municipality demands: The municipality demanded a timber structure, e.g., enforced in a land allocation process.

The following reasons for using concrete elements over timber elements in the projects were mentioned by the respondents:

- Economy: Timber solutions were too expensive; replacing some structural elements with concrete elements was more economical.
- Experience: Concrete was used on critical structural elements due to a lack of experience and/or knowledge of designing with timber.
- Span width: The use of timber was not feasible due to limited span widths with timber structures. These limitations include dynamics and limited height issues.
- Shear wall capacity: Concrete walls were used due to the increased shear capacity of the wall but also, i.e., for connectors.
- Self-weight: Concrete elements were used to increase self-weight to handle the uplift forces of the structure.

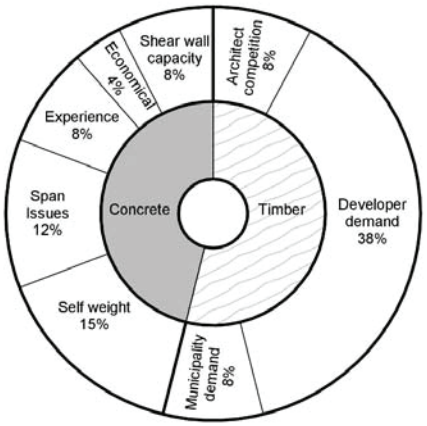

Figure 3: *Reasons for a specific load-bearing structure. One mention by a respondent equals 4% of the figure*

3.3 Project management in structural design

For this study, a *designer* is defined as the company represented as a structural designer within the building project, not the number of individuals working as structural designers.

The total number of structural designers in the projects differs between 2 to 5, with a mean of 3.3 structural designers involved. As seen in Figure 4, no correlation is seen between the number of designers and the contract worth. All respondents highlight that each designer is responsible for their field of expertise and the respective structural elements. Typically, the following structural designers were involved:

- Main designer
- Timber element designer
- Concrete element designer
- Additional designers (e.g., truss, roof, or steel constructions)

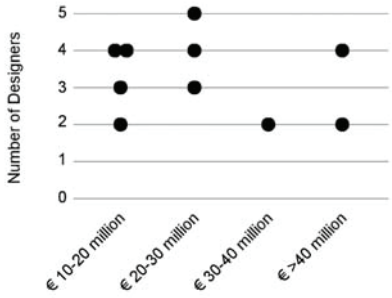

Figure 4: *Contract worth and the number of designers within the projects*

A project's main designer was responsible for collaboration between the partners and the overall coarse calculation checks of other designers' work. In nine of the projects, a specific designer was assigned as the main designer. In one of the projects, there was a contradictive response from the respondents who had this role.

In the nine projects with a designated main designer, the main designer was also responsible for the foundation design. In addition, there is a wide range of tasks related to the role, spanning from the design of precast concrete and steel trusses to details of the building envelope. For a load takedown and stability analysis of the complete building, the main designer had a unified model for calculation in one project. As for the other nine projects, the timber element designer was responsible for these calculations.

Figure 5 shows the type and complexity of calculations performed, mainly 3d Finite Element (FE) analysis and 2-dimensional calculations. The number of included structural elements in the calculational models also varies. The results show that the designers made two different main assumptions for calculations when not including all elements: the first is that the designer simplifies these elements to fictitious beam or shell elements with properties considered suitable, e.g., rigid elements; the second is to view such elements as (fixed) boundary conditions in the calculational model.

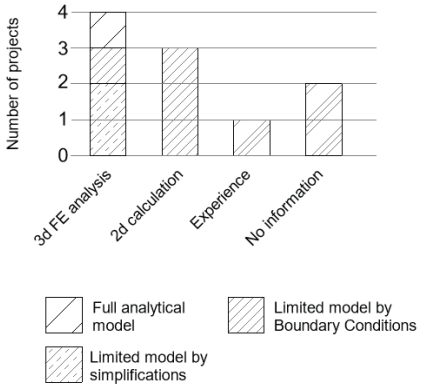

Figure 5: *Type of global calculations performed on timber-concrete hybrid structures*

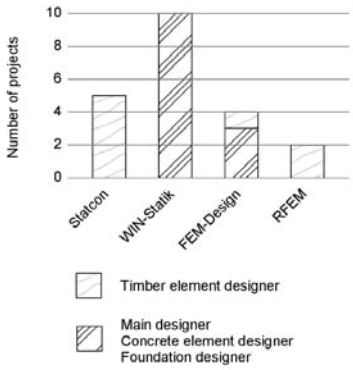

Figure 6: *Type of calculation software used by the designers*

In addition, the findings from the interviews conclude that the criteria of the requirements for horizontal stability differ. Of the ten investigated projects, answers were given for only six. The type of stability criteria within these projects was:

- Maximum load-bearing capacity for a defined truss member.
- Horizontal displacement criteria for the overall building height or story height.
- Comfort criteria such as accelerations due to wind load.
- "Engineering knowledge" (no calculation, stability was considered obvious).

According to all respondents, information on characteristic or design loads, reaction forces, and section forces are exchanged between the designers in the design process. In addition, complementary information in terms of sketches, drawings, or documents was exchanged, explaining these loads. In none of the studied projects, the designers shared their entire structural model for calculation with the other designers. However, three respondents mention that the documentation of calculations is available when their designing task is complete.

All respondents use more than one type of software. The software used in these projects is listed in Figure 6. In general, the timber element designers used the software RFEM by Dlubal [7] for 2D and 3D FE-analysis and design and Statcon by Elecosoft [8] for 2-dimensional element design. The foundation and concrete designers use the WIN-Statik package [9] for 2-dimensional design and FEM-Design [10] for 3-dimensional FE-analysis and design, both by StruSoft.

4 DISCUSSION

4.1 Projects

The study shows four major types of timber-concrete hybrid structures among the studied projects. Previous research primarily discusses timber-concrete hybrids using a post-beam system in GLT with CLT slabs with concrete walls [11] [12] (System type 2 in this study) or systems used for high-rise buildings [13] (System type 4 in this study. This study shows two alternative timber-concrete hybrids, a CLT structure on top of a concrete structure and a post-beam system in GLT with concrete hollow core slabs.

The result shows that it is manageable to replace traditional structural elements with timber structural elements in various ways and still fulfill all requirements of a modern building in Sweden. The findings also show that the use of the building has a significant impact on the structural elements that are in concrete or timber, as seen in Figure 1.

The selection of the projects does not reflect the overall construction industry in Sweden, as the project locations and the number of projects do not match the overall building permits in Sweden [14]. Contact to the project partners was primarily done within the SBUF network, the Development Fund of the Swedish Construction Industry.

However, a voluntary database for timber projects in Sweden, Woodprint Sweden, shows that a majority of these timber projects are located in the cities of Växjö and Skellefteå [15]. This confirms that the selection of projects in this study is representative of seven of the studied projects located in these cities. The municipalities of both these cities have strategies for increasing the number of timber buildings [16] [17], which explains the high number of projects within these cities. It also confirms that the number of timber projects is closely related to political decisions and public actions [18].

https://doi.org/10.52202/069179-0565

4.2 Reasons for a load-bearing structure in both timber and concrete

The main reason for the use of timber in the main structure was the property developer's demand. It is added that in seven projects, municipalities or other public organizations acted as property developers. As confirmed under the project discussion, the rising number of timber projects is due to political decisions and public action. The respondents in this study make the same conclusions, stating that property developers and municipalities are highly represented as key figures for decision-making in favor of a timber structure. Municipalities are both landowners and/or developers in several projects, implying that Sweden's public and political role in timber building is crucial.

Reasons for choosing concrete instead of timber for some elements (apart from the foundation) are mainly due to economic or structural issues. The respondents do not point to other known problems with timber construction, such as acoustic and fire demands. This was also seen in another study where the Swedish architects' perception of using timber as the construction material was investigated [19]. The authors concluded that acoustic and fire demands came in fourth place after issues regarding uncertainties and lack of control over the decision to use timber as the structural material. Altogether, this implies that previously known problems with timber materials in load-bearing constructions are manageable within a modern Swedish building project.

In only one project, the respondents answered that lack of experience in timber design was a reason for choosing concrete. However, one of the interviewed contractors responded that it was difficult to find timber designers in Sweden, and two of the timber designers in this study were located outside Sweden. On the one hand, this suggests that there are structural designers available who are confident in designing CLT components despite the lack of standard regulations such as Eurocodes and the National Annexes. Nevertheless, there still is a lack of experience and knowledge in timber design by Swedish designers, but also by architects and developers who need broader knowledge in the early stage of project development [19].

With most respondents working as structural engineers, developers, and contractors, key personnel in the decision progress, such as architects, are underrepresented in this study. Conclusions, therefore, might not cover the wide range of variables in the decision-making process in a modern construction project due to the limited number of respondents.

4.3 Project management in structural design

As the interviews have shown, designers usually work in well-defined fields within their area of expertise. In particular, the results clearly show that the project's main designer is not the designer responsible for the load takedown and stability analysis of the entire building. The timber element designer mainly performed these calculations.

Although a high number of structural engineers characterizes the investigated projects, no correlation was found between the number of involved designers and the different types of construction, nor the worth of the construction contract for the projects. However, the high number of structural designers is not unique to timber-concrete hybrid buildings. In Sweden, the topic of the number of designers included in construction projects has been discussed at least since the progressive collapse of a three-story building in Ystad in 2012. In a report by The Swedish Accident Investigation Authority [20], the high number of involved structural designers and issues regarding this resulted in revised construction rules. In 2015 [21] and 2018 [22], additional requirements were added, demanding adequate collaboration between different structural designers.

Still, it is noteworthy that in one of the ten projects studied, different answers were given regarding who was the main designer, showing that the different roles of structural designers still can be somewhat unclear and understood differently between various stakeholders within a project. Another topic is the variation of the types of analysis performed for the design calculations in these projects. The results conclude other findings regarding practicing designers where both Fröderberg [23] and Klasson [24] conclude that there is a large variety of design approaches and results.

As for the investigated timber-concrete hybrid projects, several different calculational approaches and design criteria for horizontal stability were used. Combining these results with the findings in this study regarding additional designers in timber-concrete hybrids highlights topics of risk management and project management of the involved designers in these projects.

Results from the interviews are unambiguous in that it is the specifying of load actions on and between separate structural elements that are shared among the designers. No shared models are used between the different designers. It is also clear that the structural designers did not want other designers' structural components within their own structural model for calculation if it was not considered absolutely necessary. Therefore, other designers' elements are either neglected or simplified with stiff elements or by boundary conditions.

Altogether, this leads to a well-working workflow with clear boundaries between the designers. It is also relatively easy to follow which designers are responsible for designing each element. However, one may argue that there is a risk with a fractioned structural model for calculations. The total systems' stiffness and compliance of, e.g., connections, is not considered in such models. Consequently, this will have an effect on the load takedown calculations and the design of the building, and, ultimately, the safety beta index for the structure as a whole.

As computer-aided structural calculations play a vital role for practicing structural engineers, the responses are of

great interest, especially due to the increased number of designers in timber-concrete hybrids. It is noted that the different types of calculation software used by the respondents cannot automatically share their files and models in between.
Other widely used software within the building industry, such as software drawings and modeling, geometric design, or BIM software, have a better basis for collaboration. For example, these fields have several common standards, such as Industry Foundation Classes (IFC) [25], that allow for an automated exchange between designers. This type of standard is missing for structural design software.
The practice of exchanging loads and sectional forces is obviously the most practical way of working. It might explain why the respondents in this study seldom model the complete building for analysis, only the parts that they are responsible for.

5 CONCLUSIONS

This interview study provides a brief and general overview of the state of timber-concrete hybrid buildings in Sweden. While clearly not exhaustive, some overall trends are seen, and the following conclusions are drawn:

- More structural designers are involved in timber-concrete hybrid projects than in regular building projects.
- Collaborative design and project management are identified as key aspects of a successful timber-concrete hybrid project.
- The responsibility for performing statical calculations differs, and it is seldom that the main designer has a statical model for the entire building.

The findings conclude that in the structural design phase of the project, topics regarding collaboration are of great importance. This is prior to topics such as connectors, acoustic, and fire, topics that are usually common in timber buildings. These findings are of great importance for research as they highlight the importance of performing studies on full-scale structures and not only on single components, especially since several regulations are performance-based for the building and not material-specific for a single structural member.
The increased number of involved designers might affect the structural safety of a building. The large variety of design approaches gives different design loads for the single structural element. Fröderberg [23] concluded that the different design approaches done by practicing designers lowered the level of safety of the building significantly. As the safety factors in the current Eurocode framework are calibrated to a specific level of safety in buildings [26], the design approaches and assumptions made by the different designers involved in timber-concrete hybrid projects are of utter importance. Once again, this highlights the collaborative design topics discussed in this study.
In addition, the presented work highlights the importance of knowledge in timber engineering for designers in such projects, even if the main work within a project is within, e.g., prefab concrete elements. The knowledge of the needs and restrictions of other materials' elements must be considered.
In the long run, unified calculation and design models need to be introduced because these models should allow for better results since the building's overall behavior is reflected.
It is in the industry's best interest to quickly establish a well-functioning ecosystem for timber construction. The concrete industry, both in the prefab and the in-situ versions, can be a role model with its standards and how far it has come.

ACKNOWLEDGEMENT

The authors would like to thank all interview partners for their participation. The research is funded by the Swedish construction industry's organization for research and development (SBUF, project number 13721 "Building systems in CLT and other materials") and Skanska Sverige AB. The research work is part of the project "Improving the competitive advantage of CLT-based building systems through engineering design and reduced carbon footprint" with support from the Knowledge Foundation (KKS, project number 20190026).

REFERENCES

[1] E. Markström, M. K. Kuzman, A. Bystedt, D. Sandberg, and M. Fredriksson, "Swedish architects view of engineered wood products in buildings," *J. Clean. Prod.*, vol. 181, pp. 33–41, 2018, doi: 10.1016/j.jclepro.2018.01.216.

[2] A. Younis and A. Dodoo, "Cross-laminated timber for building construction: A life-cycle-assessment overview," *J. Build. Eng.*, vol. 52, no. April, p. 104482, 2022, doi: 10.1016/j.jobe.2022.104482.

[3] R. G. Burgess, *Field Research: a Sourcebook and Field Manual*, vol. 91, no. 5. Routledge Taylor & Francis Group, 1982.

[4] P. Yancey Martin and B. A. Turner, "Grounded Theory and Organizational Research," *J. Appl. Behav. Sci.*, vol. 22, no. 2, pp. 141–157, 1986.

[5] E. Bell, A. Bryman, and B. Harley, *Business Research Methods*, Fifth Edit. Oxford: Oxford University Press, 2019.

[6] M. Easterby-Smith and R. Thorpe, *Management Research*, Second. Sage Publications Ltd, 2002.

[7] DLubal, "RFEM." DLubal, 2019, [Online]. Available: https://www.dlubal.com/en/products/rfem-fea-software/what-is-rfem.

[8] Elecosoft, "Statcon." 2020, [Online]. Available: https://www.elecosoft.se/programvaror/statcon.

[9] Strusoft, "WIN-Statik." 2019, [Online]. Available: https://strusoft.com/products/win-

https://doi.org/10.52202/069179-0565

statik.
[10] Strusoft, “FEM-Design.” 2019, [Online]. Available: https://strusoft.com/products/fem-design.
[11] T. Connolly, C. Loss, A. Iqbal, and T. Tannert, “Feasibility study of mass-timber cores for the UBC tall wood building,” *Buildings*, vol. 8, no. 8, 2018, doi: 10.3390/buildings8080098.
[12] Skidmore Owings & Merrill LLP, “Timber Tower Research Project: Final Report,” Chicago, USA, 2013.
[13] J. Chen, H. Xiong, and C. E. Ventura, “Non-linear simplified models for seismic response estimation of a novel tall timber-concrete hybrid structural system,” *Eng. Struct.*, vol. 229, no. October 2020, p. 111635, 2021, doi: 10.1016/j.engstruct.2020.111635.
[14] J. Johansson, “Bygglov för nybyggnad, antal efter region, hustyp och kvartal [Building Permit of New Buildings, number and region, type and quarter],” *SCB*, 2020. http://www.statistikdatabasen.scb.se/sq/84324 (accessed Mar. 10, 2020).
[15] S. Träbyggnadskansli, “Woodprint Sweden,” 2020. http://woodprintsweden.se/.
[16] Växjö Kommun, “Växjö Träbyggnadsstrategi [Timber Building Strategy in Växjö],” 2018. [Online]. Available: https://vaxjo.se/download/18.cfac4d716951d944dd1a4cb/1551961221853/Växjö kommuns träbyggnadsstrategi - layout version.pdf.
[17] Skellefteå Kommun, “Träbyggnadsstrategi [Timber Building Strategy],” 2014. [Online]. Available: https://www.skelleftea.se/Bygg och miljokontoret/Innehallssidor/Bifogat/Träbyggnaddstrategin skärm.pdf.
[18] J. Lindgren and S. Emmitt, “Diffusion of a systemic innovation A longitudinal case study of a Swedish multi-storey timber housebuilding system,” *Constr. Innov.*, vol. 17, no. 1, pp. 25–44, 2017, doi: 10.1108/CI-11-2015-0061.
[19] K. Hemström, K. Mahapatra, and L. Gustavsson, “Architects’ perception of the innovativeness of the Swedish construction industry,” *Constr. Innov.*, vol. 17, no. 2, pp. 244–260, 2017, doi: 10.1108/CI-06-2015-0038.
[20] M. Karanikas and P. Dahlberg, “Slutrapport RO 2013:03 Husras på Aulingatan i Ystad, Skåne län, den 25 maj 2012 [Report RO 2013:13 Building collapse in Aulingatan i Ystad, Skåne län, 25 of May 2012],” 2013.
[21] Swedish National Board of Housing Building and Planning, “Boverket mandatory provisions amending the board’s mandatory provisions and general recommendations (2011:10) on the application of European design standards (Eurocodes) , EKS10,” 2015.
[22] The Swedish National Board of Housing Building and Planning, “Boverket mandatory provisions amending the board’s mandatory provisions and general recommendations (2011:10) on the application of European design standards (Eurocodes) , EKS11,” 2018.
[23] M. Fröderberg and S. Thelandersson, “Uncertainty caused variability in preliminary structural design of buildings,” *Struct. Saf.*, vol. 52, no. PB, pp. 183–193, 2015, doi: 10.1016/j.strusafe.2014.02.001.
[24] A. Klasson, I. Björnsson, R. Crocetti, and E. F. Hansson, “Slender Roof Structures - Failure Reviews and a Qualitative Survey of Experienced Structural Engineers,” *Structures*, vol. 15, no. June, pp. 174–183, 2018, doi: 10.1016/j.istruc.2018.06.009.
[25] ICS, “ISO 16739-1:2018 Industry Foundation Classes (IFC) for data sharing in the construction and facility management industries,” 2018.
[26] JCSS Joint Committee on Structural Safety, “Probabilistic model code,” 2001.

World Conference on Timber Engineering Oslo 2023

CASE STUDY: A 10-STOREY TIMBER BRACED FRAME AND CLT STRUCTURE IN VANCOUVER, BC

Carla Dickof[1], Robert Jackson[2], Jenna Kim[3], Ashkan Hashemi[4]

ABSTRACT: This paper outlines the structural design approach used for the Keith Drive Office Building project, a 10-storey mass timber building in Vancouver, British Columbia, Canada. The office building includes exposed timber throughout most of the building, including timber brace frames along the perimeter, and cross laminated timber (CLT) shearwalls at the interior near the elevator and stair cores for seismic and wind forces. The project deployed resilient slip friction joint (RSFJ) dampers as energy dissipative devices on both the timber braced frames and CLT shearwalls. Non-linear time history analysis (NLTHA) was completed to evaluate the performance of the building. Detailed modelling and calibration of 2D shell elements was undertaken to ensure a reasonable understanding of the impact of the semi-rigid CLT diaphragm.

KEYWORDS: Mass Timber, Tall Timber, Tectonus, non-linear time history analysis, CLT shear wall, timber brace

1 INTRODUCTION

The Keith Drive Office Building is a 10-storey mass timber structure and construction began in the fall of 2022 in Vancouver, British Columbia, Canada. The 43-meter-tall structure is comprised of nine floors of mass timber construction over a concrete podium and four levels of below-grade concrete parking. The timber gravity structure consists of 9-ply cross laminated timber floor panels supported on dropped perimeter glulam beams and flush interior steel beams. The Seismic Force Resisting System (SRFS) consists of perimeter timber braced frames and interior balloon framed CLT shearwalls. See Figure 1 and 2 for building renderings.

Figure 1: *Keith Drive Rendering*

2 DESIGN

The project intent was to create a mass timber building. The project was awarded significant external funding through the Green Construction in Wood Program from NRCAN allowing it to push the boundaries of timber engineering and design in Canada, the project design quickly headed in a direction of a 'pure' mass timber superstructure complete with a timber lateral system. . Exposing the timber to view wherever possible was a key goal for the architect and owner, providing a unique experience for occupants.

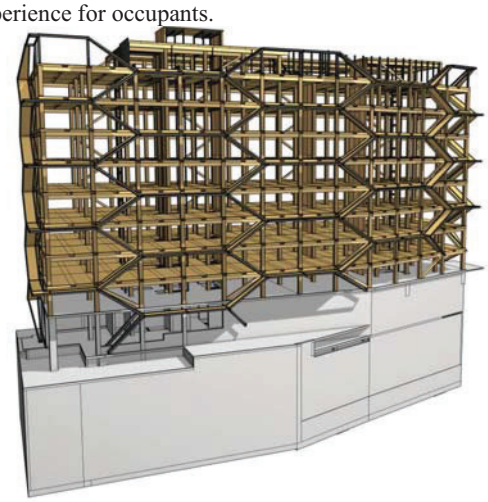

Figure 2: *Structural Framing Model*

[1] Carla Dickof, P.Eng., M.A.Sc., Fast + Epp, Vancouver, BC, Canada, cdickof@fastepp.com
[2] Robert Jackson, P.Eng., Struct.Eng., P.E., S.E., C.Eng., MIStructE., Fast + Epp, Vancouver, BC, Canada, rjackson@fastepp.com
[3] Jenna Kim, P.Eng. P.E. M.A.S.c., Fast + Epp, Vancouver, BC, Canada, jkim@fastepp.com
[4] Ashkan Hashemi, PhD, CPEng, CMEngNZ, IntPE (APEC), University of Auckland, Auckland, NZ, a.hashemi@auckland.ac.nz

https://doi.org/10.52202/069179-0566

The extent of exposed timber in both the gravity and lateral system exceed code prescribed limitations, requiring the project team to work closely with the city to address all concerns. Alternative solutions were provided to address the various issues; the approach for the structural alternate solution included peer review and non-linear time history analysis.

The base of the structural system consists of four levels of below grade concrete parkade and one level of concrete podium to accommodate the sloped site. The timber superstructure springs from the second floor concrete transfer slab as shown in Figure 2. From Level 2 to Level 10 CLT floors are supported on dropped perimeter glulam beams and interior flush steel beams. Interior perimeter timber braced frames and interior balloon framed CLT shearwalls provide the SFRS.

2.1 GRAVITY SYSTEM

The gravity system is comprised of 9-ply, 315mm thick CLT panel with a non-structural concrete topping spanning between glulam perimeter beams and flush steel interior beams. The interior steel beams are comprised of an HSS with an extended bottom plate welded to the underside, acting as a seat for the CLT; this flush framing system allows for unobstructed mechanical distribution and reduces overall building height. Both steel and glulam beams are supported by glulam columns carried down to the concrete podium at Level 2.

The building requires a 2-hour fire rating requirement (FRR) for all structural gravity members. The timber gravity framing achieved its FRR via char design as per the O86-19 Annex B design method [1]. The steel beam achieves the required FRR by way of drywall encapsulation at the underside, matching the aesthetic of other service chases adjacent.

The central area of the building accomodates a dropped ceiling to allow the mechanical, electrical and plumbing (MEP) to be routed as required, with the flush steel supports avoiding any conflicts. Beyond this central zone, the CLT soffit is exposed throughout, with all MEP routing passing within planned spline zones in the CLT floor as shown in Figure 3. 3-ply, 105 mm thick CLT panels act as splines connecting the 9-ply panels.

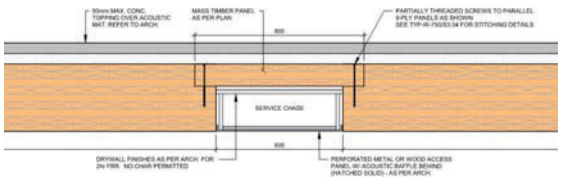

Figure 3: *3-ply CLT spline for MEP routing*

The 9-ply, 315mm panels are fully exposed with double outer layers at the top and bottom to accomdoate a 2-hour FRR over the 8.2m span, while also increasing panel stiffness for deflection and vibration response. Similarly, the supporting glulam columns and perimiter beams are all designed to achieve a 2-hour FRR through char without encapsulation. The 3-ply, 105mm CLT splines are fire protected with type X gypsum board. The flush steel beams are similarly encapsulated to protect the steel withough intumsecent paint or fire spray.

The column-to-column connection, shown in Figure 4, is configured to provide direct load transfer between the vertical elements rather than transfering forces through the beams or the floor plans. The beam-to-column connections at the perimeter make use of Knapp megant form fitted connectors at all locations, embeded to be protected from char, and the interior steel beams bear directly on the column-to-column end connecitons. Glulam columns will arrive on-site with a steel connecting plate and Hollow Square Sections (HSS) stubs fastened to the end-grain with glued-in rods. The glulam column above will have a similar connection with smaller diameter HSS stubs. Stubs are connected using glued in threaded rods bolted to the stub, which allow for simple installation and a tension connection in the extreme event where a column below is eliminated, according to progressive collapse principles. CLT floor panels will be notched around the HSS sections and bear directly on the column below.

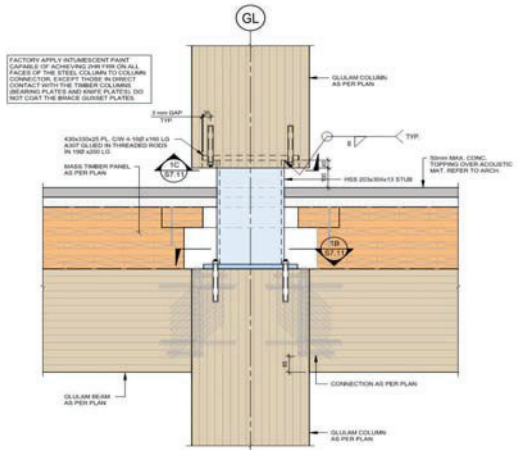

Figure 4: *Column-to-column and beam-to-column connection at perimeter*

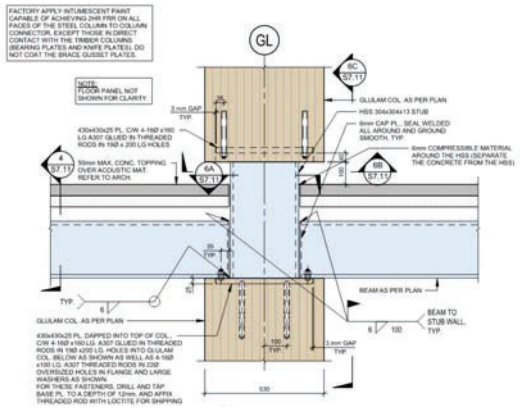

Figure 5: *Column-to-column and beam-to-column connection interior*

https://doi.org/10.52202/069179-0566

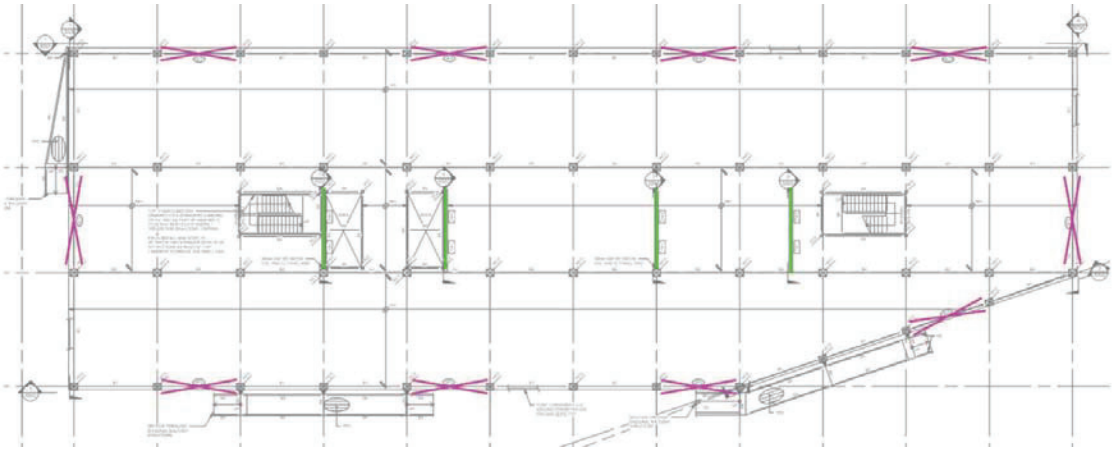

Figure 6: *Plan view of SFRS elements within the timber levels*

2.2 LATERAL SYSTEM

The lateral system consists of perimeter timber braced frames and interior CLT shear walls. The perimeter timber braced frames mimic the architectural expression of the honeycomb on the building's façade. The interior CLT shearwalls are placed near elevator or stair cores to accommodate the large open floor plan desired by the architect and owner to provide flexibility around the egress stair shafts for more interior glazing. Refer to figure 6. To achieve energy dissipation without damaging the structural members or connections, Resilient Slip Friction Joints (RSFJ's) are provided at each brace (one end), and at the ends of the CLT shearwalls, as hold-downs., allowing energy dissipation without damage to the structural system as shown in Figures 7 and 8.

Both timber braced frames and CLT shearwall SFRSs are codified systems in the most recent version of National Building Code of Canada (NBCC 2020), with defined ductility and overstrength values and height limits [2]; however, the prescribed height limits are significantly less than the actual building and the ductility and overstrength values associated with the codified systems are not relevant for a system with RSFJ's.

Therefore, to support the SFRS design, an NLTHA was completed, alongside an onerous third-party peer review in accordance with NBCC Structural Commentary J [2]. Iterative NLTHA was used to optimize the RSFJ design for the 2% in 50-year design earthquake. NLTHA was also implemented at 130%, and 150% of the design earthquake to review the collapse risk for an earthquake exceeding the design earthquake. Linear dynamic analysis was performed at service level earthquake (40% in 50-year) to ensure the RSFJs remain in the initial linear portion of the hysteresis for low level earthquakes.

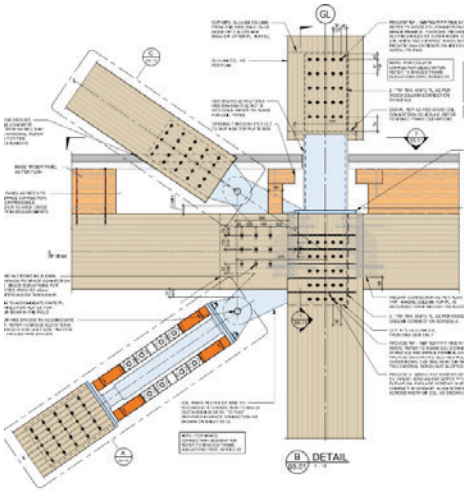

Figure 7: *Timber Braced Frame Connections*

2.3 NLTHA APPROACH

Fifteen ground motion sets, scaled to the design earthquake level (2% in 50-year) were used with each set including two horizontal and one vertical acceleration records. The two horizontal records were implimented in

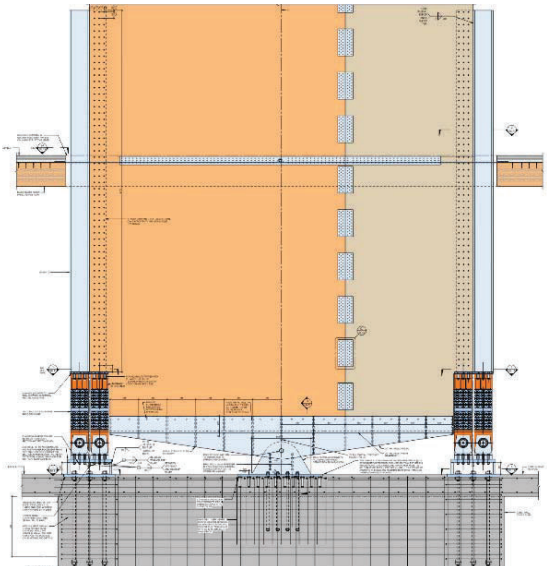

Figure 8: *CLT Shearwall Base Connection*

https://doi.org/10.52202/069179-0566

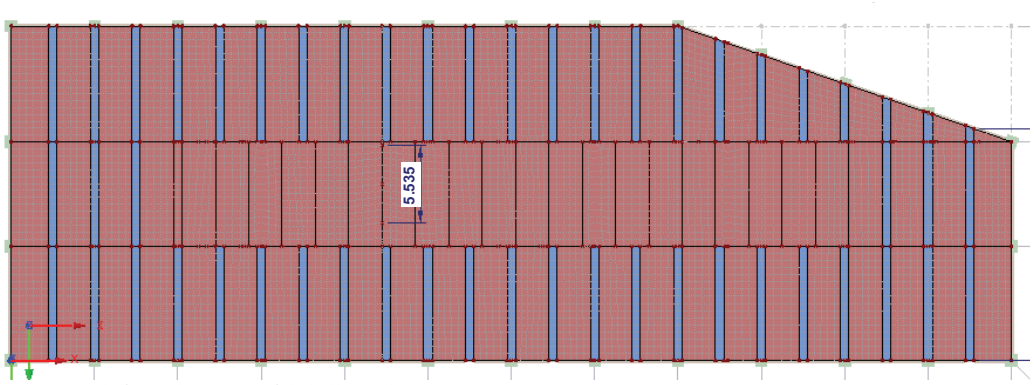

Figure 9: *Detailed Diaphragm Model shell type layout*

two orientations, rotated by 90 degrees, resulting in total of thirty time history load cases. The average responses for the top five records are considered for the acceptance criteria. The maximum response for the top record was also reviewed; while some devices exceeded the ultimate force (F_{ult}) and ultimate displacement (Δ_{ult}) limits, they were within the secondary fuse response, not exceeding the stop force (1.25 F_{ult}) and stop displacement (1.5 Δ_{ult}) limits.

Additional NLTHA was conducted using ground motions scaled to 130% and 150% of the design earthquake level to assess the structure's stability at higher hazard levels. For the 130% of the design earthquake level ground motions, the force and deformation demand of the RSFJ devices remained primarily below the stop force (1.25 F_{ult}) and stop displacement (1.5 Δ_{ult}) for the average of the top five responses. For the 150% of the design earthquake level ground motions, the force demand of the RSFJ devices remained below the stop displacement (1.5 Δ_{ult}) but the force demands were 10% ~ 30% above the stop force (1.25 F_{ult}) for the average of the top five responses. Force demand-to-capacity ratios remained consistent throughout all RSFJ devices in braced frames, suggesting the structure is not likely to develop a soft story failure mechanism or force concentration.

The braced frames were modelled with glulam beam, glulam brace, glulam column and non-linear friction spring damper type links representing RSFJ device. These non-linear springs were active in axial direction and fixed in all other degrees of freedom.

The CLT shearwalls were modelled as 3 panels of 245 mm thick shell elements connected using rigid links representing spline plates. Non-linear friction spring damper type links were modelled at each end of the CLT shearwall bottom on Level 2 representing hold-downs. These non-linear springs were active in axial direction and fixed in all other degrees of freedom. At the centre of the bottom of the CLT shearwall on Level 2, a stiff frame element was modelled representing the shear connection to the concrete structure below. This frame element was released in rotation about the axis perpendicular to the face of the shearwall to represent the true-pin condition. This connection allows the shearwall to rotate about its center and transfer shear forces to concrete wall below.

The CLT shearwall shell element's stiffness properties were calibrated against CLT shearwall modelled in RFEM RF-Laminate.

2.4 DIAPHRGAM CONSIDERATIONS

CLT diaphragms are complex and provide significantly stiffer behaviour than that associated with a flexible diaphragm given the large format stiff billets used throughout. Despite the relatively high stiffness of the panels, the stiffness of the diaphragm is much lower than that of the individual panels due to the flexible nailed or screwed connections between panels. These discrete connection locations between panels result semi-rigid behaviour. Evaluating the rigidity of CLT diaphragms is directly related to the panel sizes, the number of joints, and the stiffness of the joints between panels, as well as the chord and drag connection stiffnesses.

Understanding and representing the diaphragm behaviour in the NLTHA model was a critical component of ensuring a realistic building response in the model. The shared behaviour of the CLT splines, connections to the steel and timber beams and drag connection into the lateral elements is critical due to the comparatively high stiffness of the CLT panels and low stiffness of the connections between elements. Detailed diaphragm models can be developed to include all the elements, but that represent a large computation burden. If implemented in a larger NLTHA they would significantly slow the model processing. To resolve this problem a detailed diaphragm model was developed for a for a single floor to study the diaphragm behaviour and calibrate a simple shell element, which is adjusted to match the load distribution and deformation coincident with the detailed model, via membrane stiffness modifiers. That simple shell element was then implemented in the larger NLTHA model to simplify analysis.

The detailed diaphragm model is composed of a series of shell elements representing each individual panel with properties associated with the panel types described in the structural drawings as shown in figure 9. Drag and chord elements are also incorporated into the detailed diaphragm model. The joints between the panels, drags, and chord elements are represented with linear line springs with stiffnesses representative of the connection

type. Both 3ply 105V panels, and 9ply 315V XL panels with layups based on APA product approvals are implemented in the model. The layout of the individual shell elements and the panel implementation is shown in the light blue panels represent 3 ply CLT panels, and the red panels represent 9 ply CLT panels. The layup for each panel type has been defined using RF-Laminate
The linear springs are designed based on the stiffness properties of the screwed connection between CLT panels and steel drags to CLT panels based on screwed connection stiffness as provided Eurocode 5 (EN 1995-1-1:2004+A1) as described in clause 7.

$$\text{Wood-wood Stiffness} = \rho_m^{1.5} d/23$$

$$\text{steel-wood Stiffness} = 2(\rho_m^{1.5} d/23)$$

The stiffness is generally applied in both the x and y directions are shown in Figure 10. These correspond to the axes in the plane of the CLT floor panel at the spline, drag, and chord connections.

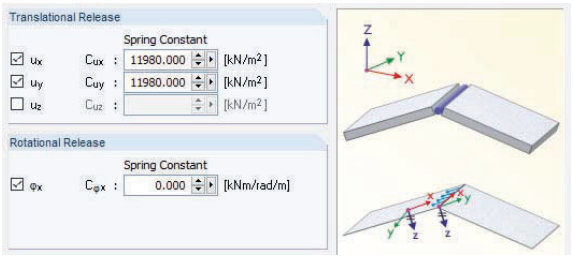

Figure 10: *line spring axes*

The simplified diaphragm model is comprised of a single shell element tuned to represent the combined properties of the complex model as discussed above. The shell element is defined with orthotropic properties modified as needed to allow the load distribution to match that found from the detailed shell element. Additionally, the bending properties in the weak direction of the individual panels (X-direction in the drawings) has been reduced to near zero. This is a conservative simplification to ensure that the shell element does not resist significant weak axis moment, as minimal moment would be transferred across CLT- CLT splines joints. Property modifiers for weak axis bending and torsion for the shell are thus reduced to near zero.
An iterative process was implemented to bring the force distribution for each lateral element to within 5% of the detailed diaphragm model for a unit applied area load. To verify the behaviour, the reactions of each LFRS elements were compared for both the complex and the simplified shell diaphragm model. For all cases the variation in load distribution was within 5% or less. A summary of the variation in LFRS shear is provided in Table 1.

Table 1: *Variation in reaction SFRSs*

	LFRS Location	Variance
Y-dir.	Brace @ GL 2	4.80%
	Brace @ GL 14	3.80%
	Wall @ GL 5	2.00%
	Wall @ GL 6.5	2.05%
	Wall @ GL 9	2.50%
	Wall @ 10.5	0.50%
X-dir.	Braces @ GL D	0.2-0.9%
	Braces @ GL A	0.2-1.0%
	Braces @ GL 15	1.5-2.3%

2.5 BEAM-TO-COLUMN CONNECTIONS

The glulam beam-to-column connections required a 2-hour FRR. To achieve this with exposed members, Knapp Megant form fitting connectors are specified with sufficient timber encapsulation to provide the necessary FRR. Inter-storey drift tolerance of these connections was investigated with testing was undertaken to show the inter-storey drift tolerance and established rotation stiffness and strength of the joint.
Perimeter glulam beams connected using Knapp Megant concealed hangers were the connection of primary study, as the direct bearing connection of the flush steel beams at the columns should not pose a problem. The drift capacity of these hangers was not explicitly available from the supplier or fabricator but it is critical to the behaviour of the system. To better understand the behaviour of the hangers, testing was completed to determine the rotational capacity of the hanger under the design loads of the system and localized drift studies and sensitivity studies were completed to assess the behaviour of the frames [5].

2.6 THE RESILIENT SLIP FRICTION JOINT DEVICES

The Resilient Slip Friction Joint (RSFJ) is a friction device that dissipates the seismic energy through friction while providing re-centring force. Friction dissipation occurs via sliding movement of clamped plates. An RSFJ device consists of 2 outer plates and 2 centre plates with elongated holes, which are grooved and clamped together with high strength bolts and disc springs (refer to Figure 13).

https://doi.org/10.52202/069179-0566

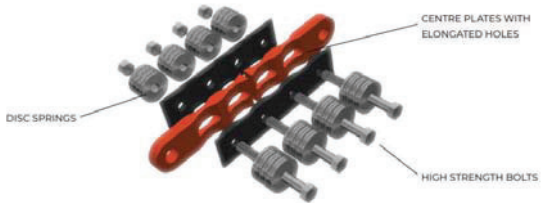

Figure 11: *The RSFJ components*

When the applied force overcomes the frictional resistance between the sloped bearing surfaces, the centre slotted plates start to slide, and energy is dissipated through friction during cycles of sliding. During unloading, the reversing force induced by the elastically compacted disc springs is larger than the friction force acting between the facing surfaces, providing self-centring characteristics

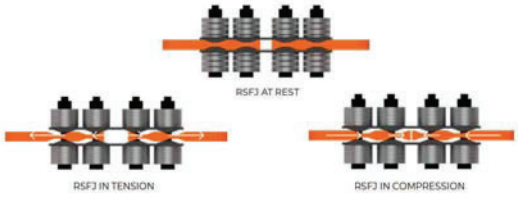

Figure 12: *RSFJ cyclic loading behaviour*

The hysteretic shape of the response of this type of RSFJ device is a flag shape common for friction based dampers. Each point in the hysteresis is a uniquely defined parameters (F_{slip}, F_{ult} , $F_{restoring}$, $F_{residual}$ and Δ_{ult}) as shown in Figure 15. The number of tapered friction planes and associated bolts/spring washers is flexible, allowing for a 'tunable' connection in both force and displacement.

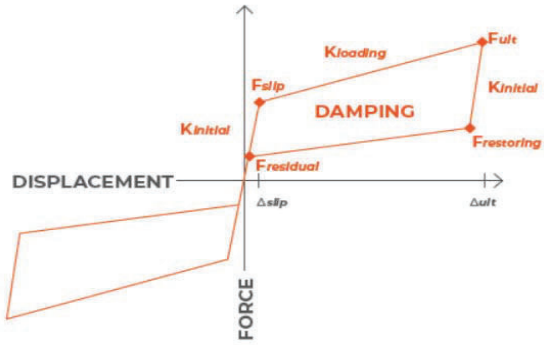

Figure 13: *Typical RSFJ Hysteresis*

The flag shape of the hysteresis can be tuned as needed to meet the design requirements to achieve the desired load-slip response up the F_{slip}, and F_{ult}. This is achieved by changing variables like the number or angled of the ridges in the plate, and/or the number of bolts and disc springs at each bolt. The behaviour and performance of the RSFJ has been extensively evaluated via joint component tests and large-scale experiments. With testing showing that the performance of the RSFJ is stable and that the theoretically predicted hysteretic behaviour (see Fig. 3(a)) matches well with test results [3]. This technology has been studied and tested for different configurations and applications. Experimentally tested full-scale rocking Cross Laminated Timber (CLT) and Laminated Veneer Lumber (LVL) walls with RSFJ hold-own connections. The mass timber lateral systems showed repeatable and damage free performance without any strength or stiffness degradation. The damage observed in the timber elements or connections was insignificant and negligible given that all non-fuse members were capacity-protected [3] [4]

The RSFJs also have 25% additional capacity beyond the F_{ult} provided in resulting from bolt bending in the RSFJ bolts. This additional capacity prevents failure after the ultimate strength is reached but will no longer represent a self-centering system without damage.

The RSFJs strength and deformation capacities were chosen through multiple iterations of Non-Linear Time History Analysis. the final hysteretic flag shapes for each device are shown in Figures 14 for the braces. The hold-downs are consistent across all 4 walls as shown in Figure 15.

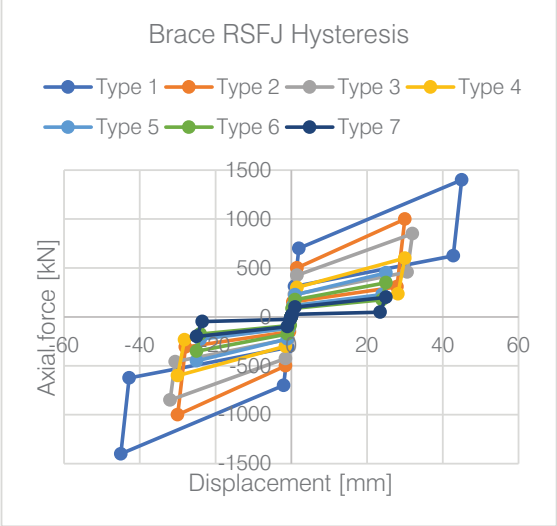

Figure 14: *Hystersis for brace RSFJs at various plan and storey locationas*

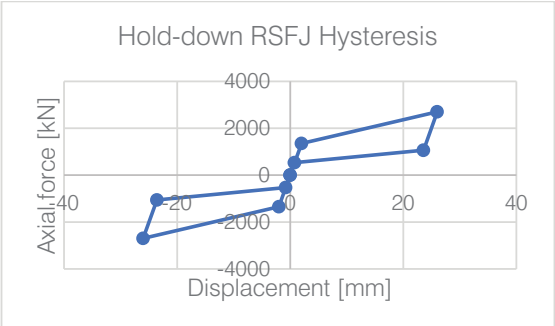

Figure 15: Hysteresis for CLT wall RSFJ hold-downs

Each RSFJ is tested (Figure 16) to ensure that it achieves the specified hysteretic forms as shown in figure 14 and

15. This testing ensures that the ultimate and slip strengths and deformations match the specified values and also is critical in minimizing the overstrength required for capacity protected elements as there is little variability prior to the yield in the bolts.

Figure 16: *Testing of RSFJ for brace at upper level of Keith Drive project*

To achieve the varied ultimate strengths and hysteretic forms shown the RSFJs are tuned with a varying number of spring discs and angle of the saw-tooth plates as previously described. At the CLT walls, the system is stable without the presence of the RSFJ due to the base connection and the connections to the diaphragms at each level, allowing the RSFJs to fastened directly to the CLT panels without additional components for stability as shown in Figure 8. At the braces, the RSFJs interrupt the length of the brace; to avoid issues with instability in the brace member under compression, two RSFJ devices are paired with central elongating tubes called Anti-Buckling Tubes (ABTs) to address this issue, without compromising the hysteretic behaviour (Figure 16).

Figure 17: *Brace RSFJ for upper-level braces at the Keith Drive Office Building*

These assemblies are then bolted to highly coordinated end plates that are either connected in to braces frame nodes at the beam to column connections, or into the ends of timber braces as shown in Figure 18.

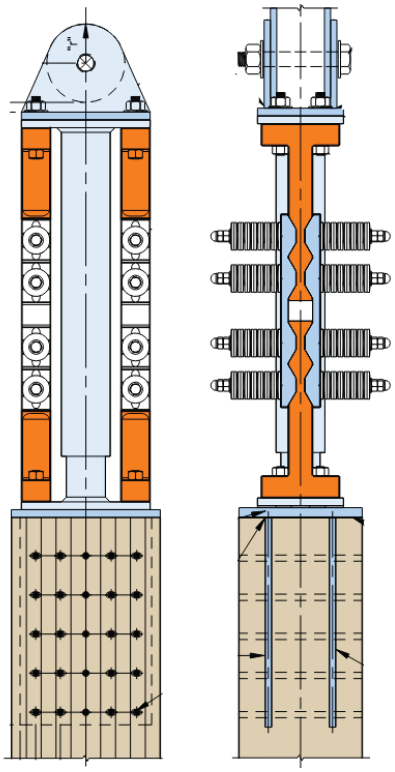

Figure 18: Brace connection of RSFJ and ABTs

2.7 CAPACITY DESIGN

Capacity design principles are applied based on the overstrength of the RSFJ devices, overstrength of the RSFJs is applied to the ultimate strength (F_{ult}) of the RSFJs within the SFRS element in the system. This direct overstrength is applied to: Timber Brace members and their connections to both the RSFJ and the frame, beam members and their connections in braces based, CLT shearwall panels, CLT shearwall base-shear connections, RSFJ hold-down connections the Shearwall, and all other connections between CLT panels in the shearwall. A the CLT shearwalls, because the RSFJs were able to be tuned within a few percent of the ultimate RSFJ strength, the overstrength factor could be applied directly to the NLTHA results.

The glulam column and glulam column-to-column connection design loads have been determined based on the maximum of the probable capacity of the RSFJ devices and the NLTHA results increased by the RSFJ overstrength. As the likelihood of each device within a brace frame simultaneously reaching its probable capacity is low, a Square Root Sum of Square (SRSS) approach is applied to all the columns and column-to-column connections in the brace frames (i.e.. components subject

https://doi.org/10.52202/069179-0566

to determine the tension/compression design forces in the brace frame columns. The column design loads are determined by combining the SSRS overturning earthquake with appropriate dead, live, and snow loads. The diaphragm panels and connections are also capacity protected. The design loads for the diaphragms are based on the capacity of the braced frames and CLT shearwalls, at that level, such that the 'fuse' remains the RSFJ, rather than the diaphragm fasteners themselves.

3 CONCLUSIONS

The innovative timber braced frame and tall CLT shearwall system proposed for this project significantly exceeds prescriptive approaches for timber systems in the NBCC. With the implimentation of self-centering, zero damage dissipative RSFJ devices, this building will achieve a high level of performance and will represent a first-of-its-kind timber lateral system in a seismic zone for a tall timber building in North America. By performing detailed NLTHA modeling including the non-linear link elements to represent the dissipative RSFJs and linear elements to test drift tolerance of the gravity structure, and accurate shell elements representing the true behaviour of the semi-rigid diaphragm, the overal behaviour of the system has been tuned through performance based design

To achieve a realistic distribution of loads between SFRS elements, a detailed diaphragm model was developed with the development of a simplified, calibrated, shell element to simplify the NLTHA model and analysis.

The building is currently under construction, targeting concrete completion up to level 2 by December 2023, and timber superstructure completion by end of summer 2024

ACKNOWLEDGEMENT

The authors gratefully acknowledge the involvement of the architect, DIALOG, as well as Tectonus Resilient Seismic Solutions. The project was supported by Natural Resources Canada (NRCAN) through the Green Construction through Wood (GCWood) Program.

REFERENCES

[1] Canadian Standards Association (CSA), Engineering Design in Wood, CSA Standard O86-19, Toronto, ON, Canada: CSA, 2019.

[2] NBCC (2015). “National Building Code of Canada 2015.” Institute for Research in Construction, National Research Council of Canada, Ottawa, ON.

[3] Hashemi, Ashkan, Pouyan Zarnani, Reza Masoudnia, and Pierre Quenneville. 2017. “Experimental Testing of Rocking Cross Laminated Timber (CLT) Walls with Resilient Slip Friction (RSF) Joints.” Journal of Structural

[4] Hashemi, Ashkan, Hamed Bagheri, Seyed Mohammad Mehdi Yousef-Beik, Farhad Mohammadi Darani, Armin Valadbeigi, Pouyan Zarnani, and Pierre Quenneville. 2020. “Enhanced Seismic Performance of Timber Structures Using Resilient Connections: Full-Scale Testing and Design Procedure.” Journal of Structural Engineering

[5] C. Dickof, R. Jackson P.Eng., J. Kim. 2023. “Case Study: A High-Rise Mass Timber Building in Vancouver, British Columbia.” in *ASCE Structures Congress 2023,* 2023

World Conference on Timber Engineering Oslo 2023

HUT – INDOOR CLIMBING CENTRE, SKIEN, NORWAY

Katie Overton[1], Gaute Mo[2], Fernando Ibañez[3], Sondre Dolsvåg[4]

ABSTRACT: HUT, Høyt Under Taket, is an indoor climbing centre in Skien, Norway designed by Degree of Freedom in collaboration with the architect Snøhetta. The building combines a single-storey climbing hall, with a maximum clear height of 14.6m, and a three-storey annex. The architectural concept is based on a variable series of 12.5m wide timber portals forming the signature element of this building, the climbing hall. All structural members above ground level are timber, principally cross-laminated timber (CLT). CLT is also used both for the climbing hall façades and for the load bearing walls of the three-storey annex building. Glued-laminated timbers are used as framing elements in the glazed façades at either end of the climbing hall, as part of the CLT rib slabs, and as long span beams supporting the annex roof. Structural analysis has been performed using a finite element model that models the CLT panels as shells and uses link elements to model the connection stiffnesses. Timber-to timber connections are principally realized using timber screws. All timber elements have been fabricated using a LOD400 BIM model fully coordinated with all other disciplines during the design process.

KEYWORDS: Timber, cross-laminated, glued-laminated, CLT rib slab, screws, connections, BIM, portal.

1 INTRODUCTION

HUT Skien is a signature building for the indoor activity centre Høyt Under Taket (High under the Roof), located in Skien, Norway. The load bearing structure is 100% timber above ground level. The project was developed in close collaboration with Snøhetta, Betonmast and Degree of Freedom.

Figure 1: *HUT Skien – Finished building*

From the start there was a high level of ambition regarding sustainability and innovation in timber construction.

This paper is a case study describing how the architectural concept has been translated into a structural frame that reflects the original architectural vision.
The timber structure was erected early in 2022 and the building was opened to the public in late 2022. The finished building can be seen in Figure 1.

2 ARCHITECTURAL CONCEPT

The building is designed to be a landmark, of high architectural quality that provides a unique experience whilst being functional, climate smart and cost-effective.
The building, named 'Portal' at its inception, was conceived by the architects as a low threshold entrance portal to provide access to indoor climbing for all skill levels. The result is a 1,500 m^2 climbing centre with a focus on activity and inclusion for the local community.
The aim was to have a recognizable profile, with internal activity visible from the outside through large glass façades. These large glass surfaces bring natural light into the building and provide extra airiness and connection to nature complemented by the extensive use of exposed timber surfaces throughout.
The architectural identity was based on the concept of a cave, similar to the image in Figure 2, a portal to a world which one would want to explore further. In a cave the distinction between wall and ceiling is blurred, replicated here in the timber structural form. Timber was chosen early in the concept design phase as the main material for both structural and architectural purposes.

[1] Katie Overton, Degree of Freedom SLU, Valencia, Spain, k.overton@dofengineers.com
[2] Gaute Mo, Degree of Freedom AS, Oslo, Norway, g.mo@dofengineers.com
[3] Fernando Ibáñez, Degree of Freedom SLU, Valencia, Spain, f.ibanez@dofengineers.com
[4] Sondre Dolsvåg, Degree of Freedom AS, Oslo, Norway, s.dolsvaag@dofengineers.com

https://doi.org/10.52202/069179-0567

Figure 2: *Architectural inspiration*

A key feature of the building are the frames, or portals, with a changing geometry as you move through the space. The starting architectural geometry is shown in Figure 3. At concept design phase the construction of these portals as cross-laminated, CLT, elements was proposed and evaluated to ensure that an adequate lateral stiffness could be achieved.

Figure 3: *Portal concept geometry*

An architectural aim was to leave the structural timber exposed as much as possible as seen in Figure 4.

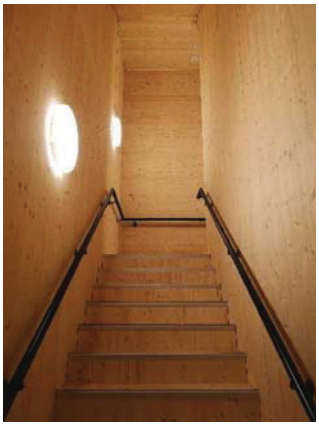

Figure 4: *Exposed timber structure in staircase*

Timber was also chosen as the main cladding material. There is no vapor barrier/plastic used in the external walls, which allows the timber's hygroscopic properties to naturally help regulate humidity, improving the indoor climate. Externally the structure is clad in a dark timber façade as both a protective outer layer and visually to highlight the building's bright interior.

Figure 5: *Building exterior with dark timber cladding*

3 STRUCTURAL SYSTEM

3.1 DESCRIPTION

The building is divided into two parts, the climbing hall and the annex each with a different structural system.
The climbing hall has a series of CLT portals as vertical load bearing elements Portals are spaced at 6m centres generally, and with a single 9m end span. Portal height steps from 11m up to 14.5m. The portals are clad with CLT panels to provide out of plane stability with the portals having an in-plane stiffness to act as moment frames.

Figure 6: *Climbing Hall structure*

The portals support the roof which is a combination of CLT slabs and CLT rib slabs. The rib slab is used for the single span where portals are separated 9m. Figure 6 shows an overview of the climbing frame structure once erected on site.

The climbing hall also includes a mezzanine floor at one end which spans 12.5m across the full width of the hall using CLT rib slabs.

Figure 7: *Soffit view of mezzanine rib slab*

The glazed façades at either end of the climbing hall have vertical and horizontal glulam members for additional restraint as seen in Figure 8.

Figure 8: *View of glazed façade from mezzanine*

The annex building has a combination of CLT walls and glulam columns as vertical load bearing elements. Floor slabs are standard CLT slabs with glulam beams used at roof level where larger open spaces were required. A view of the finished annex structure can be seen in Figure 9.

Figure 9: *View of annex from mezzanine*

The timber superstructure is anchored to the concrete substructure with a combination of both proprietary and bespoke steel brackets.

3.2 MATERIALS

Different thicknesses and build-up of CLT slabs are used in the building ranging from three-layer 100mm CLT panels as part of the roof CLT rib slab to seven-layer 240mm thick CLT panels for the tallest portal frames.
Glulam elements are typically GL24h but with GL28h for the ribs of the CLT rib slab.
The building contains 62m^3 of glulam elements and 627m^3 of CLT panels in total, of which 130m^3 are in the portal frames.

3.3 DESIGN

The building is designed for R30 fire resistance, and all elements have been designed using the reduced cross section method from NS-EN 1995-1-2 [1]. In general all timber elements are exposed with no additional protection provided.
The slip modulus, k_{serv}, for all connections has been considered in the design based on NS-EN 1995-1-1 [2]. The connection stiffness is of particular importance when calculating the overall horizontal sway of the timber portal frames. The slip modulus of both CLT-to-CLT panel connections and CLT to concrete connections was allowed for in the detailed design.
For the long span mezzanine floor the governing criteria for the design of the CLT slab were vibration limits.

3.4 FINITE ELEMENT MODEL

Structural analysis was carried out using a full 3D finite element model in SAP2000, shown in Figure 10. This model allowed for both ULS and SLS design of the CLT panels, and for the design of the connections.

https://doi.org/10.52202/069179-0567

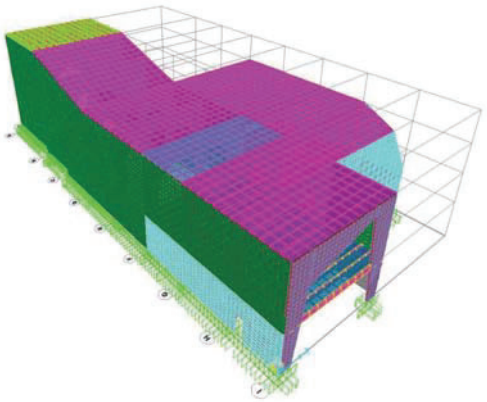

Figure 10: *3D view of FE model*

.

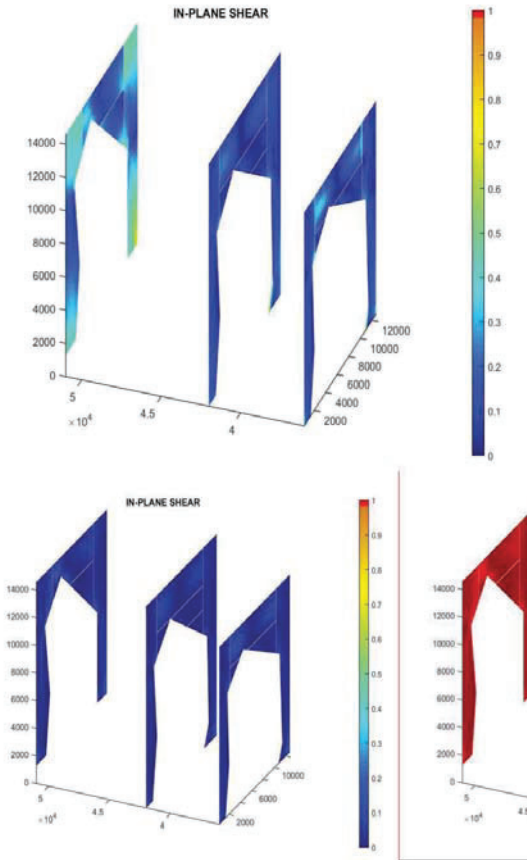

Figure 11: *ULS and Fire design verifications for 240mm CLT portals*

For the orthotropic CLT panels the values for the stiffness matrix were calculated using the software CLT designer created by the Institute for Timber Engineering and Wood Technology of Graz University of Technology (©holz.bau forschungs gmbh). All CLT models were modelled as shell elements with link elements modelling the joints. The stiffness for each degree of freedom was defined based on the calculated slip modulus for the connection type.

Verifications for the CLT panels were carried out for the Ultimate Limit State, the Serviceability Limit State and the fire design situation. An example is shown in Figure 11 for the 240mm thick portal frames demonstrating the check for in-plane shear. For the same 240mm thick CLT portal frames the horizontal displacement for the envelope of characteristic SLS load combinations is shown in Figure 12.

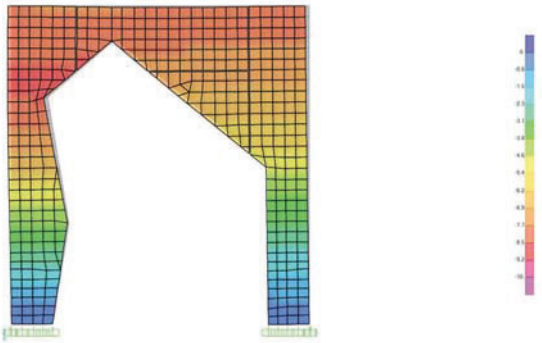

Figure 12: *SLS verifications for 240mm CLT portal*

3.5 CONNECTIONS

The two main types of connections to be resolved for this project were the timber-to-concrete connections and the connections between the different parts of the CLT portal frames.

Timber-to-concrete connections, dependent on location, were required to resist in-plane horizontal loads, out-of-plane horizontal loads, and in some locations uplift. Due to the extent of exposed timber structure in this building alternative solutions had to be found to give a concealed connection. A combination of proprietary angle brackets, see Figure 13, and bespoke, dowelled, steel plate connections were used.

Figure 13: *Proprietary angle bracket to base of portal frame*

https://doi.org/10.52202/069179-0567

Figure 14: View of timber concrete interface details

Where a concealed connection was required architecturally a dowelled connection with an central steel plate was used as shown in the detail in Figure 15. The central steel plate is 8mm thick and the connection has 39no. 12nn diameter steel dowels. For this detail the steel baseplate was cast in-situ with the ground floor slab to a detail by the concrete designer. The central steel plate was subsequently welded in the correct position on site before installing the portal frame.

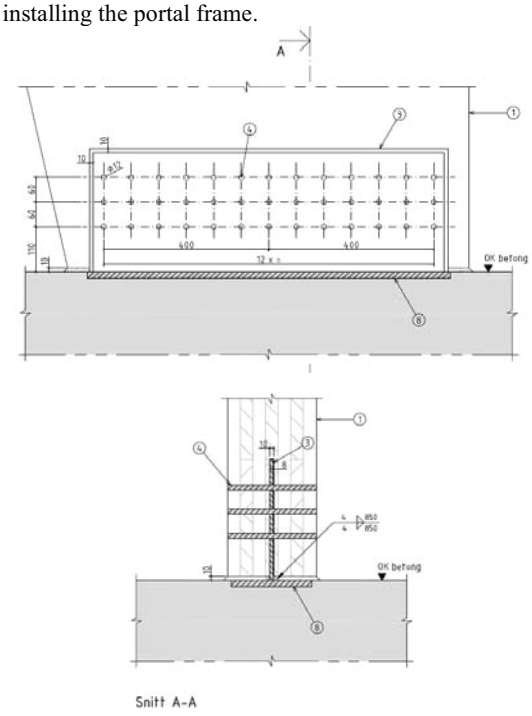

Figure 15: Concealed doweled connection for portal frame

Timber-to-timber connections for the portal frames were realized using fully threaded, cylindrically headed, timber screws installed at 45°, 9mm VGZ screws from Rotho Blaas. The detail is shown in Figure 16. Crossed screw connections, with screws at 45°, give the most robust connection detail for the critical CLT panel to CLT panel connections. The position of these screws can be seen in Figure 17, during construction, prior to the final timber plugs being installed.

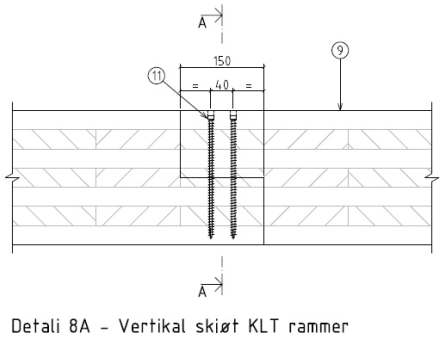

Figure 16: *CLT portal frame connection – screws at 45°*

Figure 17: *Screwed connection between portal frame panels*

In the finished building these divisions between CLT panels are barely visible as seen in Figure 18.

Figure 18: *Portal frame joints*

4 BIM

From the initial concept phase through to the construction phase information was shared and coordinated between disciplines using BIM. Degree of Freedom produced the LOD400 model in Tekla (Figure 19) as the basis for the timber fabrication model.

Included in the BIM model were all the different steel brackets needed at the timber-to-concrete interface. This use of the BIM model allowed for full coordination with the concrete designer, coordination with the Architects to

https://doi.org/10.52202/069179-0567

check visibility, in addition to providing the complete information to the timber supplier for fabrication.

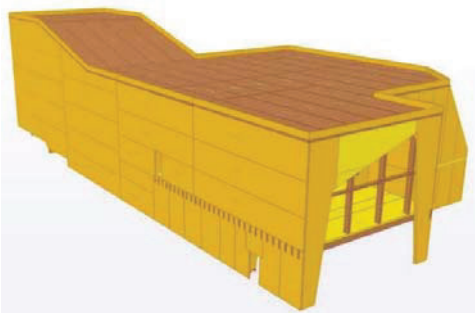

Figure 19: *Overview of BIM model*

An example of the detail of the LOD400 BIM model is shown below in Figure 20 for the 240mm CLT portal with steel brackets at the portal base.

Figure 20: *240mm CLT portal in LOD400 BIM*

The erection drawings were then produced in Tekla directly from the BIM model.

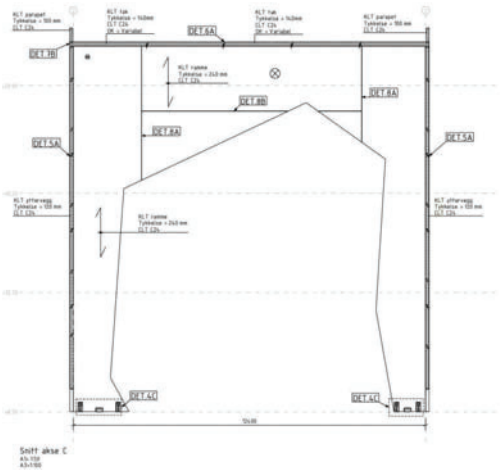

Figure 21: *Portal frame erection drawing*

5 CONSTRUCTION

A combination of LOD400 production models for off-site fabrication, and the site-handling of lighter timber parts, facilitated a rapid erection process on site, despite the adverse weather conditions of the Norwegian winter. Total time for timber erection was five weeks. The use of timber elements also led to less environmental impact on and around the construction site with a reduced number of deliveries and a faster and cleaner construction method with significantly less noise.

Figure 22: *HUT under construction – climbing hall*

Figure 23: *HUT under construction – annex building*

The location of all steel brackets on the erection drawings, produced directly from the BIM model, facilitated their installation on site as shown in Figure 24.

Figure 24: *Installation of steel brackets between timber and concrete*

https://doi.org/10.52202/069179-0567

6 CONCLUSIONS

This project successfully demonstrates how timber has been used to realise the original architectural vision whilst providing both a cost-effective design and a rapid site erection procedure. The load bearing structure has become multi-functional as it also forms part of the building finishes. The use of timber has given a solid, durable, natural and sustainable solution to this singular building as can be seen below in the finished building both without fittings and its final use as a climbing centre.

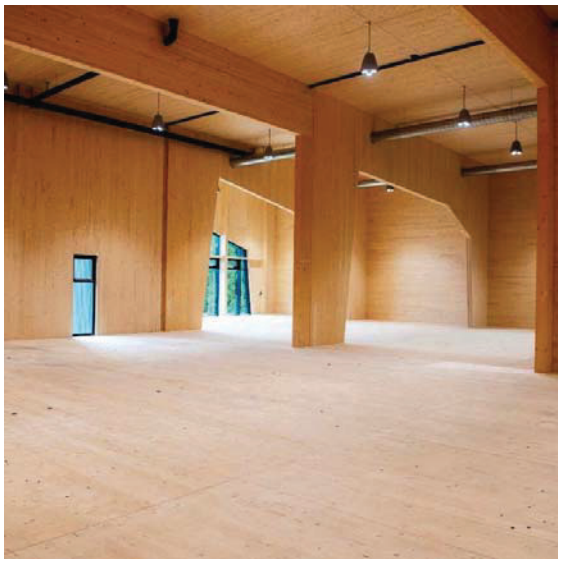

Figure 25: *Finished building before fitting out*

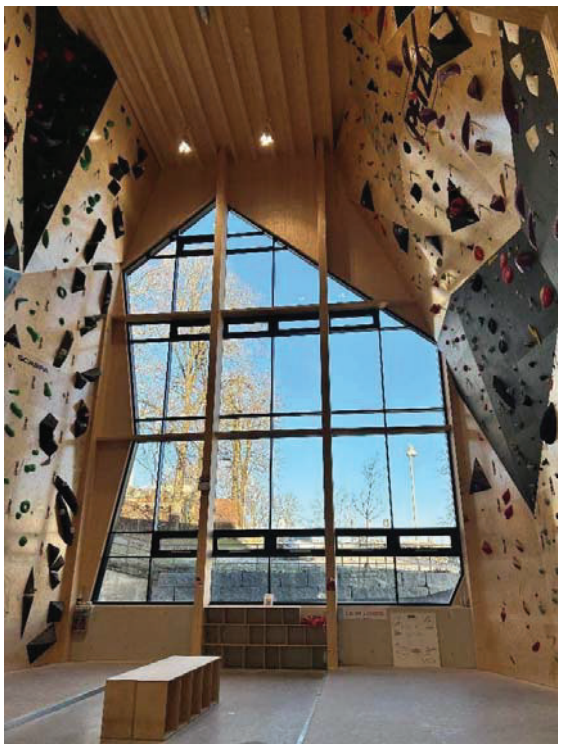

Figure 26: *Finished building as climbing centre*

ACKNOWLEDGEMENT

This project has been realised in collaboration with the client, Høyt Under Taket, the architect, Snøhetta (https://snohetta.com/) and the Contractors, Betonmast (https://www.betonmast.no/).
Additional photographs by Kai-Otta Melau/Høyt & Lavt.

REFERENCES

[1] NS-EN 1995-1-2:2004+NA:2010 Eurocode 5: Design of timber structures - Part 1-2: General - Structural fire design.

[2] NS-EN 1995-1-1:2004+A1:2008+NA:2010 Eurocode 5: Design of timber structures - Part 1-1: General - Common rules and rules for buildings.

https://doi.org/10.52202/069179-0567

World Conference on Timber Engineering Oslo 2023

ECONOMIC COMPARISON OF MASS TIMBER AND CONCRETE CONSTRUCTION IN THE NORDIC REGION

Julie Swartz Andersen[1], Yutaka Goto[2], Michael Englund[3], Henning Johansen[4], Ketil Armann Hansen[5], Alexander Hollberg[6], Daniela Grotenfelt[7]

ABSTRACT: The timber sector has been growing strongly in various regions of the world. Yet, the construction industry is still far from being sustainable. One barrier is the economic concern in planning and construction works of timber constructions. This study aims to provide insights on the cost performance of Cross Laminated Timber (CLT) constructions for stakeholders to make an informed decision. It analysed the production cost of multi-story residential buildings with CLT in comparison to concrete in Norway and Sweden. The production cost data of various construction projects with either CLT or concrete was collected and analysed. Interviews with stakeholders were conducted to complement the interpretation of the cost data. The result showed that each project had its individual conditions in the economic background and requirements by client, and thus it was difficult to formulate a general tendency on the cost performance. The variability of the cost was larger and the average production cost was higher in CLT cases. Yet, there are high incentives of contractors and clients for a more sustainable alternative in general. The incentive is also reinforced by the general experience of contractors that the construction cost is better optimized as the contractor gains more experiences.

KEYWORDS: Construction cost, LCC, mass timber, CLT, Nordic region, residential building, comparison to concrete

1 INTRODUCTION

1.1 Background

The construction sector is the source for approximately 37% of the global greenhouse gas emissions [1]. When considering the application of technologies with greenhouse gas (GHG) emission reduction potentials, one must consider its economic aspect as well in order to practically succeed in reducing the GHG emissions. In the practices of construction projects in the current market, decisions are very often made based on the priority on the economic performance among all viable technical alternatives. This is because construction projects must satisfy numbers of legislative requirements for safety, comfort, energy efficiency, etc., and this incurs already a large cost in general even in the case of solution with the lowest possible cost.

In fact, there is an increasing number of applications of more costly solutions with a higher initial investment in the construction industry. This is especially the case when those technologies directly concern the energy efficiency of the buildings, such as thicker insulation, heat exchanger, better-insulating window, etc. This trend is driven by both environmental and economic views. While the solution may be more environmentally, the saving of energy over a certain period can compensate the higher initial investment. This payback time analysis is key to promote those energy efficiency measure in many cases. However, in the case of embodied carbon emissions of construction materials, there is no tangible payback time for different levels of investment unless some substantial carbon tax rules would be introduced in the market. The current market situation does not economically favour a less carbon intensive material unless it is less costly than other common materials.

In order to reduce the climate impact of the industry, the use of timber is seen to be an efficient alternative to conventional materials [2]. The Nordic construction market has seen a major development of the timber construction sector in the past decades especially in Norway, Sweden and Finland. The major drivers of this significant growth are; (1) there are large areas of productive forest and thus there are sufficient resources for the local market, (2) there are well-experienced wood-processing and timber construction companies since timber construction has been very common for smaller buildings, and (3) there is the growing consciousness of environmental sustainability and timber is seen as a more favourable option for its carbon neutrality, renewability and circularity. This advancement of the timber

[1] Julie Hansted Andersen, Arkitema, Denmark, juhan@arkitema.com
[2] Yutaka Goto, Chalmers University of Technology, Sweden, yutaka@chalmers.se
[3] Michael Englund, Arkitema, Sweden, MIED@arkitema.com
[4] Henning Johansen, COWI, Norway, HJOH@cowi.com
[5] Ketil Armann Hansen, COWI, Norway, KEHE@cowi.com
[6] Alexander Hollberg, Chalmers University of Technology, Sweden, alexander.hollberg@chalmers.se
[7] Daniela Grotenfelt, Arkitema, Sweden, dagro@arkitema.com

https://doi.org/10.52202/069179-0568

construction industry is primarily supported by research and developments in structural and fire safety technologies. Among various technologies, cross laminated timber (CLT) has been a major contributor of the expansion of the technical possibilities especially in structural capacity [3].

Yet, the construction industry is still far from being sustainable in terms of the use of renewable resources among other sustainability concerns. Although there have been innovative solutions for CLT constructions to overcome technical challenges in structure, moisture, fire and acoustics, the economic aspect is still a barrier for the further expansion of the timber industry is the economic uncertainty. There is a common concern that timber structures tend to become more costly in planning and construction works compared to other alternatives such as concrete structures.

1.2 Objective and limitation

This study aimed to analyse construction cost of timber buildings and to discuss the advantages, disadvantages and potential of cost optimization in comparison to concrete alternatives. The objectives of the study were (1) a systemic literature review on the construction cost of timber structures, (2) the quantitative data collection and comparison of production cost of various residential construction projects in CLT and concrete in Norway and Sweden, (3) qualitative data collection on the view of stakeholders on the production cost of CLT/concrete constructions, and (4) analysis of the cost structure in order to highlight the economic advantages and disadvantages of CLT structure.

The investigation was limited to the cost of the design and construction stage (A1-A5 module, according to [4]) until the project is handed over to the occupants. Only the actual construction cost was investigated, and the sales price and other sales- associated factors of the apartments is not included. The rest of the life cycle was disregarded in this study. [5, 6] show that if a timber construction is fully protected against weather, the lifespan of the construction will be the same as for a conventional concrete construction. Thus, it was assumed that the maintenance cost for the load bearing frame was zero in both CLT and concrete cases during a calculation period of 50 years. The operational cost for heating etc., was assumed to be the same between CLT and concrete cases with the same energy performance and appliances installations. The demolition phase was excluded as CLT constructions are still new in the market and there is little practical experience in the demolition of CLT apartments.

2 Methodology

2.1 Literature study

The aim of the literature study was to investigate the state-of-the-art research of the cost of timber projects. By examining previous studies about the topic, their results can serve as reference for the results of present study's case study analyses and interviews. As a literature study uses second- hand data and case studies deliver first-hand data, the study opens for a wider perspective of results for the study.

2.2 Construction cost of case studies

A case study represents the actual problems and benefits which might occur during the design stage and construction stage of a project. By using case study as first-hand data it enables to examine the data more deeply in a specific context, which is for multi-story residential buildings in the Nordic countries for this study. This specifies the results of the study to actors in the construction industry in the Nordic countries and creates a more detailed insight into the subject of interest for these actors.

However, case study research has its limitations. The results based on a case study are only as good as the data is and the method is as well criticized for generalizing results based on limited number of cases. Yet, case study is useful to explain a process and the result of the studied subject by using both the quantitative and qualitative data for real-life projects. Hence, case study is chosen as the primary method for this study. These case studies are examined during qualitative interviews and quantitative data analyses.

Before choosing the case buildings and collecting data, limitations were set in order to obtain data with sufficient quality and comparability.

The types of case studies were limited to multi-story residential buildings constructed in CLT and conventional concrete and steel in Sweden and Norway. The building should have at least three stories in some parts of the building and a maximum of eight stories. For the timber building the primary loadbearing system should be constructed in CLT. Furthermore, it was prioritized to use case buildings which were built by contractors who have built such types of buildings before. This was for minimizing additional cost as a result of developing new construction methods and larger beginner mistakes. It was identified in previous studies that cost might increase when the contractor is doing a CLT project for the first time [7, 8].

All contractors and building owners who responded to the request for the data collection were asked to provide the construction data in the same cost group structure to ensure comparability. The construction cost data was collected in accordance with the cost structure model in the Norwegian Standard (NS) 3451 "Bygningsdelstabell (Building component table)" [9]. Table 1 shows the structure of the cost items and how the data was delivered. If the contractors or building owners were not able to deliver the cost data according to the standard, they were asked to deliver the total cost sum of the project. It was decided to include these projects with limited level of detail in order to increase the amount of case buildings. However, these projects were excluded from the comparison of each cost group and only used for comparison of the total cost.

https://doi.org/10.52202/069179-0568

Table 1: *Cost group structure according to NS 3451*

Cost elements		Cost
01	Common costs	
02	Building	
03	Plumbing andHVAC installations	
04	El-instrations	
05	IT and automation	
06	Other installations	
Building cost (01-06)		
07	Outdoors	
Contractors cost (01-07)		
08	General cost	
Construction cost (01-08)		

2.3 Stakeholder interview

Qualitative analyses have been performed as interviews of developers and entrepreneurs of the case project and of other stakeholders within the building industry. The interviews can collect insights into behaviours and thoughts which quantitative data cannot. It can as well explain the reason for the data to occur in a specific way. The interviews were performed as semi-structured interviews with the ability to be flexible from the planned questions and to be creative with more questions, which come throughout the interview. The planned questions were provided to the interviewees from Denmark, Sweden and Norway in writing in advance. In some cases, response was collected in writing, which was complemented by an oral interview to ask further questions afterwards. This method was useful for the project since the people interviewed were able to speak of their experiences. Table 2 shows the interviewed stakeholders.

Table 2: *The interviewed stakeholders*

Stakeholder group	Position	Country
Contractor	Technical dorector	Denmark
Municipality	Business Developer	Sweden
Municipal developer	Project Manager	Sweden
Municipal developer	Project staff	Sweden
Contractor	Cost/project/purchase manager	Sweden
Developer	Project manager	Sweden
Contractor	Cost manager	Norway
Contractor	Project and property manager	Norway
Contractor	Project manager	Norway

3 CASE STUDY BUILDINGS

This chapter describes the 9 case buildings (6 projects in Norway and 3 projects in Sweden) for the analyses in the study.

3.1 Bergheim bo- og aktivitetssenter (CLT 1)

Bergheim bo- og aktivitetssenter (CLT 1) is a care home for 96 residents located in Halden in the south of Norway. The gross total area (GTA) of the building is 11,700 m^2, with no underground parking. The building is distributed on three storeys. The upper two storeys were constructed in CLT and the ground floor in concrete. The building is shaped in a horseshoe form with a yard in the middle. The rendering and the completed project are shown in Figure 1. The building was constructed in the period from October 2017 to February 2019 by a turnkey contractor, Solid Entreprenør. The building owner is Halden municipality. The municipality specifically demanded a massive timber building for the care home, and thus the project was planned to be a timber building from the beginning. The supplier of the CLT was Binderholz in Austria.

Figure 1: *Bergheim bo- og aktivitetssenter project (CLT 1) constructed with CLT in Hadlen, Norway*

3.2 Solhøy (CLT 2)

Solhøy (CLT 2) is a care home for 67 residents located in Vestby in the south of Norway. Solhøy has four storeys. The basement is constructed in concrete and steel, and the above three storeys are constructed in CLT. The building has a GTA of 11,536 m^2 including parking basement, with an average apartment size of 33.5 m^2. The construction of the building started the January 2021 and is planned to end in December 2022. The project has a turnkey contractor with a fixed price for the total cost of the building. The contractor is Solid Entreprenør, which is the same company for CLT 1. The building owner is Vestby municipality, who demanded a building constructed in massive timber from the beginning. The supplier for the CLT panel is Splitkon, located in Norway. Figure 2 shows the rendering and the status of the construction in March 2022.

Figure 2: *Solhøy project (CLT 2) constructed with CLT in Vestby, Norway*

3.3 St. Olavsvej 18 (CLT 3)

St. Olavsvej 18 (CLT 3) is an apartment building in five storeys including the basement, located in Kristiansand in the south of Norway. The GTA of the building is 1,657 m^2 including 550 m^2 parking basement and 28 apartments of average 45 m^2. The basement is constructed in concrete and the upper storeys are constructed in CLT. The construction started in 2021. Similar to CLT 2 project, this project also has a turnkey contractor, VEF Entreprenør, with a fixed price of the project. Figure 3 shows how the building's rendering and the state under construction.

https://doi.org/10.52202/069179-0568

Figure 3: *St. Olavsvei 18 project (CLT 3) constructed with CLT in Kristiansand, Norway*

3.4 Ski BB1 Magasinparken (Concrete 1)

Ski BB1 Magasinparken (Concrete 1) is an apartment complex, consisting of 7 buildings with 183 apartments in total, and is located in Ski in the south of Norway. The building is owned by Solon Bolig AS Solon Eiendom, and was built by Solid Entreprenør, which as well constructed CLT 1 and 2. The average apartment size is 79 m^2 and the GTA of the project is 24,805 m^2, including 7,800 m^2 parking basement. The number of storeys varies for each building. Three of the buildings have four storeys, three other buildings have five storeys and one building has eight storeys. In addition, each building has a basement. The buildings are constructed in concrete slabs and steel columns. The foundation was made as pile foundation, which often has a higher cost. The project was constructed from March 2019 to September 2020. Figure 4 shows some pictures of the buildings.

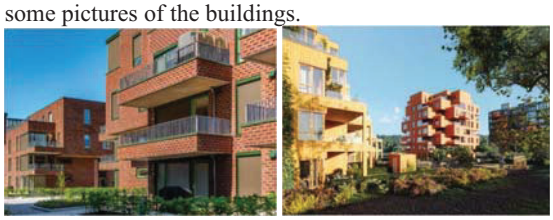

Figure 4: *Ski BB1 Magasinparken project (Concrete 1) built with concrete in Ski, Norway*

3.5 Trelasttomta (Concrete 2)

The project Trelasttomta consists of four apartment buildings varying from four to seven storeys and one shared basement underneath all the four buildings. The project is owned by Ekornud Eindom AS and is located in Myrvoll in the southern part of Norway. Architect of the buildings are Nuno Architects and is constructed by Solid entrepreneurs as the turnkey contractor, from January 2019 to December 2020. The total gross area for all four buildings is 9,950 m^2 including 2,250 m^2 parking basement and consists of 72 apartments with an average size of 63.2 m^2. The buildings are mainly constructed in concrete and steel, with concrete slabs and loadbearing system in steel. Figure 5 shows some renderings.

Figure 5: *Trelasttomta (Concrete 2) constructed in concrete in Myrvoll, Norway*

3.6 Fagertun Panorama (Concrete 3)

Fagertun Panorama consists of four apartment buildings with two or three storeys and a basement, which are made in concrete. The GTA of the project is 3,359 m^2 including 1,216 m^2 parking basement with 21 apartments with an average size of 91 m^2. The owner is Dovreveien 3 AS, and buildings are located in Lillesand in the south of Norway. VEF Entreprenør was the turnkey contractors of the project and constructed the building from November 2019 to October 2021. The buildings were constructed as conventional apartment buildings of Norway with steel columns and concrete slabs. Figure 6 shows the project after construction completion.

Figure 6: *Fagertun Panorama (Concrete 3) constructed in concrete in Lillesand, Norway*

3.7 Fagertun Panorama (CLT 4)

Arken consists of three buildings with total of 85 rental apartments and has a GTA of 8,327 m^2 with above ground parking only. The project was built in Växjö in the southern part of Sweden. From the beginning it was required to be constructed as a wooden construction, with environmentally friendly materials and low energy consumption. In fact, the project was planned as a part of the regional Energy Plan with a requirement of yearly energy consumptions of 55 kWh per unit heated floor area. However, this project has lower U-values for the building envelope with thicker insulation compared with buildings built according to the minimum requirement by the Swedish regulation. The buildings consist of apartments with one to five rooms, with an average apartment size of 65,3 m^2. The buildings were constructed with a CLT frame, with slabs, outer walls, load bearing inner walls, joist, balconies, elevator shafts, beams and columns in CLT and glue laminated timber from Martinssons in the north of Sweden. The buildings were constructed by a local contractor in Växjö, Värends Entreprenad. Figure 7 shows the project after the construction completion.

Figure 7: *Arken (CLT 4) constructed in CLT in Växjö, Sweden*

https://doi.org/10.52202/069179-0568

3.8 Björkdungen 5 (CLT 5)

Björkdungen 5, located in Bengtsfors in the south-west of Sweden, is a four-storey apartment building with a dentist office placed on the ground floor of the building. The basement and the ground floor were made from concrete, including the elevator shaft. The load bearing structure in the two storeys above was made from CLT, including half of the facade walls. The other half of the facades was made from Sven Johansson Bygg (SJB bygg) own light weight system in wood. The inner load bearing walls of the smaller top floor was from CLT. The facade walls were made from their own light weight system. The elevator shaft was made from CLT in the three top levels. The CLT was delivered from the mill of Stora Enso in central Sweden

The building is owned by Bengtsforshus AB, which is the municipal housing company in Bengtsfors. The building was built by SJB bygg as the turnkey contractor with a construction time of 15 months, from March 2020 to August 2021. This project was the first CLT building built by SJB Bygg. The GTA of the project is 1,536 m^2 including 375 m^2 for the dentist office, a basement of 166 m^2 and 11 apartments with a size of 55-76 m^2. Figure 8 shows the building Björkdungen 5 under construction and as a finished building.

Figure 8: *Björkdungen 5 (CLT 5) constructed in CLT in Bengtsfors, Sweden*

3.9 Tingstorget (Concrete 4)

Tingstorget, located in Botkyrka in the south-east of Sweden, consists of 729 apartments distributed in 14 buildings varying from rowhouses in 3 storeys to multi-storey buildings with 6-8 storeys. The GTA of the whole project is 43,007 m^2 including 3,964 m^2 parking basement. Tingstorget has a load-bearing system in concrete, load bearing inner walls, elevator shaft, staircase and joist constructed in steel and massive concrete. The exterior wall is made of concrete sandwich elements. The roofs are constructed with prefabricated timber elements and is covered with steel roofing plates. The contractor team was a combination between a turnkey contractor, Titania, and an executive contractor. The turnkey contractor was responsible for the framework construction and roof, and the executive contractor was responsible for the rest of the work with in- house employees as well as external consultants which might have contributed to a slightly higher cost. The total construction time was 3 years, from August 2016 to 2019. Figure 9 shows the Tingstorget buildings after the construction completion.

Figure 9: *Tingstorget (Concrete 3) constructed in concrete in Botkyrka, Sweden*

4 RESULT

4.1 Literature study

The period for the design and construction stage (project period) has a great impact on the total construction cost of a building, hence it has been examined in different comparative studies of traditional concrete/steel buildings and timber buildings. Table 3 shows the results of project period and cost for five different studies (M.F. Lagurda-Mallo et al. (2016) [10], R.E. Smith et al. (2017) [8], Center for Sustainable Architecture with Wood (2016) [7], Østnor (2018) [11], and Halseth (2019) [12]), comparing concrete/steel and timber buildings.

Table 3: *Comparisons of time and cost of timber building compared to concrete/steel alternative in five different studies.*

Articles	Construction time of timber buildings compared to concrete/steel building [+/- % time]	Project period of timber buildings compared to concrete/steel building [+/- % time]	Cost of timber buildings compared to concrete/steel building [+/- % time]
M.F. Lagurda-Mallo et al. (2016)	-61.1%	N/A	-21.7%
R. E. Smith et al. (2017)	N/A	-20%	-4.2%
Centre for Sustainable Architecture with wood (2016)	+20%	N/A	+4%
Østnor (2018)	-42%	N/A	+60%
Halseth (2019)	-40%	N/A	+13%

The results in Table 3 show a varying result of the project period and cost, but most of the examined studies have a shorter construction time for the timber building. The only study with a longer construction time for the timber building was in [7]. The reason for this study having a longer construction time was that the timber building was constructed as a prefabricated timber frame structure, which was stated to have a longer construction time compared to panel system in concrete. Meanwhile, the other studies, which all showed a shorter construction time in the timber case, compared CLT with concrete. Furthermore, the timber frame construction in [7] was supposed to receive 5 Star grading of the Australian sustainable building certificate, Green Star [13], which was not the case for the compared concrete building. The certification system required more documentation and additional tasks, thus the process extended the construction time additionally.

One of the reasons for higher cost in three of the examined studies was due to the higher material prices for timber compared to concrete [7, 11, 12]. Another reason is that the cases in those studies (with CLT or prefabricated timber frames) were pilot projects, which resulted in more working hours for the design team to create solutions for e.g., acoustic and fire.

The Swedish company, ETC, who develops, finances and built timber buildings, describes how they have developed

construction and design methods and thereby decrease the cost. After building three buildings they have seen that their second building was 9% less expensive in labor costs. The third building was 10% less in labor costs than the second building. They observed this despite of the fact that during this time the labor costs in general had risen substantially [14]. It shows an example of the cost reduction potential in learnings from the experiences for further process optimization.

4.2 Construction cost of case studies

The cost data for the Norwegian and the Swedish case buildings was analysed separately since the market's general economic structure and technical and legislative construction standards are not the same for the two countries.

In order to normalize the influence of the inflation and to show the magnitude of difference in the two markets, the cost data of each project was converted to euro and index regulated to prices of 2021 by the construction cost index regulation for residential buildings [15]. By converting the prices to 2021 euros it enables for comparison between the project and for future similar projects. Furthermore, all prices are presented without VAT (value added tax) and without the cost of land purchase and landscaping.

The results of the analysis of cost data are based on the raw data which was supplied by the contractors and developers. Results are strictly based on those inputs with no subjective correction of those raw data.

4.2.1 Norwegian cases

The cases CLT 1-3 and Concrete 1-3 are Norwegian buildings, and they were analysed and compared to each other in the same analysis. The collected data is divided into the cost group structure according to [9], which is presented in Table 4 and the total construction cost of the Norwegian projects are illustrated in Figure 10. Common cost (Cost element 01 in Table 4) includes dismantling and setup of construction site, cranes, barracks and operation of construction site, insurance, collateral and guarantees. General cost (Cost element 08) includes engineering and the client's administration, project management, constructions management, special consultants (legal, financial, etc). The landscaping cost was excluded in these results since the cost of landscaping is not relevant for the cost of the building in terms of the selection of the construction materials.

Table 4 and Figure 10 shows that all the Norwegian concrete project has a lower construction cost compared with the CLT building. Thereby this is a clear tendency for the analysed Norwegian project, that it is more costly to construct CLT buildings compared with CLT buildings. However, Table 4 shows that the cost of each project can vary for each cost group. When looking into the cost group, common cost, it shows that the cost for CLT 2 was more than twice higher than for the other projects. Furthermore, the general cost is three times higher for CLT 1 and CLT 2 than for Concrete 1, Concrete 2 and Concrete 3. This might show, together with the literature study (Section 4.1) that there is a tendency that the CLT buildings have higher cost in the design stage than concrete buildings. However, the general cost for CLT 3 is not shown explicitly but is included implicitly among the other cost groups. This is a typical example of the cost calculation practice that even though the cost is divided according to the same standard [9], the calculators of each project can objectively allocate the cost figures to different cost groups. Due to this, the figures of each cost group must only carefully be compared directly and cannot be compared without knowing the background of the numbers.

Table 4: *Results of Norwegian case projects divided into the cost group structure according to NS 3451*

Cost elements		CLT 1	CLT 2	CLT 3	Concrete 1	Concrete 2	Concrete 3
		EUR/m^2(GTA) (2021)					
01	Common costs	251	679	232	309	190	161
02	Building	1302	1561	1573	1232	1105	865
021	Site preparation	16	0	0	0	1	0
021	Ground and founda	140	219	384	195	129	119
022	Load-bearing syster	20	34	139	15	-	59
023	External walls	167	335	244	186	152	289
024	Internal walls	424	389	277	281	251	61
025	Slabs	223	284	177	300	393	180
026	Roof	103	116	52	38	43	56
027	Fixed furniture	147	144	97	88	73	36
028	Stairs. balconies.	18	24	167	111	52	60
029	Structural relief work - Plumbing	45	16	8	18	11	2
029	Structural relief work - Electrical	0	0	28	-	-	4
03	Plumbing and HVAC installations	350	360	350	226	211	123
04	El-instrations	182	264	141	139	117	52
05	IT and automatio	-	-	-	-	-	-
06	Other installation	18	27	257	17	24	151
Building cost (01-06)		2104	2891	2553	1922	1646	1353
08	General cost	200	163	-	69	65	22
Construction cost (01-0		**2303**	**3054**	**2553**	**1991**	**1711**	**1374**

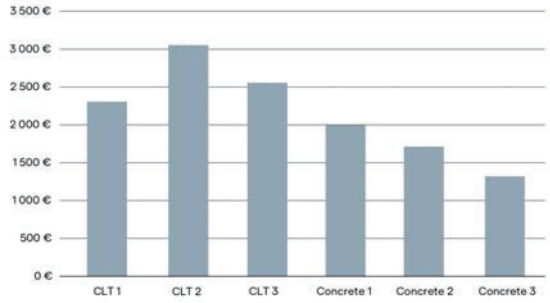

Figure 10: *Total construction cost per GTA for the Norwegian projects*

In the investigation on the cost of CLT buildings compared to concrete buildings, it is necessary to exclude the cost of building parts which are not directly related to building being a CLT or a concrete building. Such building parts are the fixed furniture and installations. The costs of these groups are more dependent on if e.g., the building needs more ventilation according to its particular usage or has many small apartment units (care homes) where each unit has its own bathroom and kitchen. This increases the cost of these groups but is not related to it

https://doi.org/10.52202/069179-0568

being a CLT or concrete building. Therefore, the cost of fixed furniture and other installations are excluded in Figure 11.
The cost of six cases presented in Figure 11 illustrates that the cost of the concrete buildings is still lower than the CLT building. However, the cost difference between all three CLT buildings and the concrete buildings have become lower but cost still varies within the CLT cases and the concrete cases. However, the largest variation was observed for CLT 2. According to the additional questions asked to the contractor of case CLT 2, it was commented that one of the reasons for the case CLT 2 to have a higher cost was that there is a large underground work for the basement constructed in concrete. For this basement, which includes parking areas, technical installation rooms and other functions beneath the whole building, it was required more blasting and other works which were costly. However, this shows that a higher cost of a CLT project do not necessarily need to be a result of the building being constructed in CLT but might be because of other conditions which affects the total cost more.

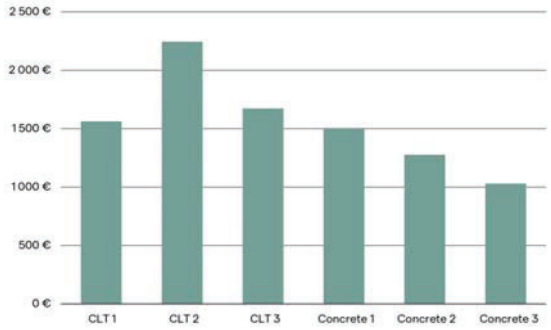

Figure 11: *Cost per GTA for the Norwegian cases, excluding fixed inventory and installations*

Furthermore, it is relevant to investigate the cost of the cases without common cost, and general cost, and thereby only looking at the cost of the materials and labour cost during the construction. This investigation is shown in Figure 12 where the cost of site preparation, ground conditions, load-bearing system, external walls, internal walls, slabs, roofs and stairs and balconies is evaluated separately.

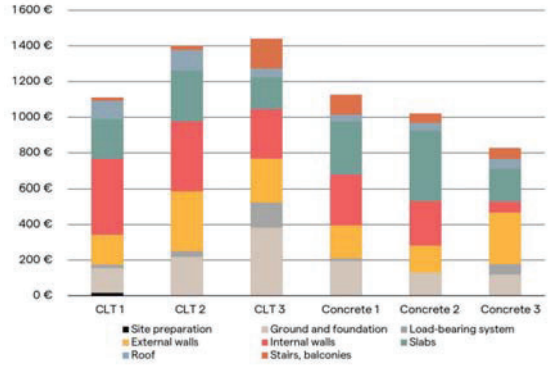

Figure 12: *Cost of the building parts including materials and labour cost of the Norwegian cases*

The results of the cost of the building parts show that the variation within the CLT buildings changed from case CLT 2 having the highest cost to case CLT 3 having a slightly higher cost per GTA. As mentioned earlier, the cost group general cost was not shown explicitly in CLT 3, thus this cost might be included in cost of the building parts shown in Figure 12. Therefore, it cannot be concluded that the building parts are the most expensive for case CLT 3 compared to the other cases.
Through the analysis of the Norwegian cases, it can be concluded that cost varies within the CLT projects and the concrete projects. But there is a tendency that the concrete building has a lower construction cost compared to CLT buildings.

4.2.2 Swedish cases

For the data collection of Swedish case buildings, there was a limited willingness to share cost data from the stakeholders' side. Also, for the ones who contributed with the data, the breakdown of the cost groups was not possible to provide with the level of details as the Norwegian cases. Thus, it was only possible to receive the total cost for three projects, two CLT projects and one concrete project. Table 5 and Figure 13 shows the total cost per GTA for the three Swedish case buildings and the percentage difference from the highest cost per GTA of the three buildings.

Table 5: *Results of total cost per GTA for the Swedish cases*

	CLT 4	CLT 5	Concrete 4
Total cost per GTA (EUR/m^2)	1970	1915	2232
Percentage difference from maximum	-11.7%	-14.2%	0%

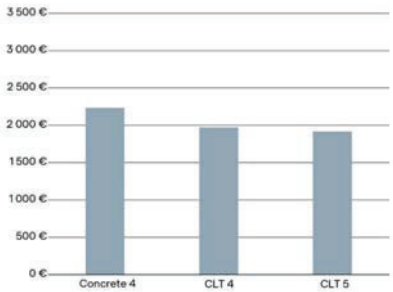

Figure 13: *Total cost per GTA for the Swedish cases*

The results show that the two Swedish CLT case buildings has a respectively 11.7% and 14.2% lower cost than the concrete building. As mentioned above, the results of the Swedish projects are not divided into the same cost group structure. Therefore, it cannot be concluded which cost groups had the highest and lowest cost for each project. However, the contractor of Concrete 4 is different than the projects CLT 4 and CLT 5. Concrete 4 have had a combination of a turnkey contractor and an executive contractor, whereas CLT 4 and CLT 5 only have had a turnkey contractor. This might cause some cost

differences. Furthermore, Concrete 4 consists of 14 building whereas CLT 4 consists of three buildings and CLT 5 only consists of one building. It can be assumed that the cost per GTA for the same total floor area becomes higher with increased length of building envelope (more windows, more insulations etc.). Thus, the cost per GTA for Concrete 4 might show somewhat higher number compared to a regular concrete building with just one volume.

Through the questions to the contractor for Concrete 4, Titania, they described that the cost of the final building ran over budget due to complication with the ground and foundations work. This as well might be one of the reasons for the higher cost for case building Concrete 4. Furthermore, Titania stated that if they had a more optimized logistic solution and a lower construction rate, they would probably have been able to save 5-10% of the total cost.

The case building CLT 5, which has the lowest cost per GTA of the Swedish project, can as well be defined as a hybrid building between concrete and CLT. The ground floor and the slab above the ground floor was constructed in concrete. The 1st and 2nd floor are mostly constructed with CLT. The contractor SJB bygg stated that the entire building would have been cheaper if the building was constructed in only concrete and steel or with a timber frame structure. This statement should however be seen in the context that SJB bygg are used to work with concrete and steel and timber frames, but not with CLT. Furthermore, they stated that if they are doing a similar project again the project time would be approx. 10-20% shorter, which should be reflected as a lower cost for the next time.

Moreover, the results illustrated in Figure 13 show that the CLT projects have a low variety for the Swedish project, whereas the earlier mentioned Norwegian projects has a larger cost variation between the CLT projects. Since we know the cost of only two Swedish CLT projects, it cannot be concluded that this shows a general tendency for Swedish projects, and this can be studied further in an additional study where more case studies are available. Even though the cost data of Swedish projects are limited in this study, the results of the Swedish projects still show that CLT buildings do not necessarily have a higher cost than concrete buildings. For a deeper analysis and investigation more project and cost data divided into a cost group structure are needed.

4.3 Stakeholder interview

The results of the interviews from the building industry and the case studies were analyzed in order to recognize tendencies in the costs and methods to construct in CLT and concrete.

4.3.1 Materia cost

The Danish contractor and the one of the Norwegian contractors (see Table 2), who both have constructed concrete building and CLT buildings, stated that it has been more expensive to build CLT buildings compared to concrete buildings up until June 2022 when the project has concluded. They both pointed out that the material cost has been higher in the CLT project, compared to the material cost for a concrete project. The higher material cost has been a result of fewer suppliers and a long transportation. However, the Danish company stated that more suppliers are coming to the Nordic countries and therefore transportation prices have decreased in the last three years. Furthermore, the Norwegian company pointed out that due to the fire regulations in Norway large amounts of fire gypsum boards are needed and it increases the material cost of CLT buildings. In addition, a building of 8 stories constructed in CLT in Norway would need a sprinkler system, which is not the case for a concrete and steel building in Norway. Thereby the material cost for a CLT building may increase further for a building of this height, by adding additional gypsum boards.

However, the weight of a timber building is lower than a concrete building, thus less material is needed for the foundation. This means that in areas with challenging ground conditions, the cost of the foundation can be reduced because of a lighter building.

The contractors and owners of the CLT cases stated that those case studies were planned as timber constructions from the beginning, and thus there was no solid cost comparison to other alternatives. Yet, as stated in section 4.2.2. according to the contractor, SBJ Bygg, CLT 5 projects would have become less costly if other conventional materials than CLT would have been used.

4.3.2 Time and logistics

Through the interviews with the Swedish municipality, one Norwegian contractor and the Danish contractor, they have all pointed out that construction time of CLT building have potential to be shorter than concrete buildings. The Norwegian company has had experience of shorten the construction time by two months by constructing a CLT building compared to a similar building constructed in cast-in concrete and steel.

It was also pointed out that in order to shorten construction time, then the logistics is important to optimize. For the Norwegian company, it was important that the CLT elements and materials arrived as planned every week, so that all the workers were able to do their job and follow the time schedule.

On the first CLT project that the Danish company carried out, they optimized the cost for deliverance of CLT elements by loading the trucks to the maximum, and thereby decrease the numbers deliveries. However, they found huge logistic challenges by handling all CLT elements before they needed them. It demanded to handle the elements 2, 3 and 4 times and every time with a risk for scratches and marks on the elements. Furthermore, the risk of moisture in the elements as a consequence of unstable Danish weather conditions and no weather protection on the site. From this experience they have learned to demand the CLT elements in the order they needed it for the assembly of the building, and thereby streamline the processes.

In addition, the interviews pointed out that CLT buildings constructed by an architect, engineer and contractor who

https://doi.org/10.52202/069179-0568

experienced a CLT project for the first time, have a higher project cost. The Swedish municipality stated that in the beginning their CLT projects, they had a 20-30% higher project cost than concrete alternatives. As more CLT projects were built in the municipality by various local contractors, the cost difference decreased to 10% between CLT and concrete, where CLT is still higher. During the pandemic period the construction cost was heavily influenced by it.

In addition, the Norwegian contractor stated that the shorter construction time is beneficial for the developer of the project, since the occupancies can move into the apartments earlier and start paying rent, which means that the developer will save interest rate for the earlier incoming money.

In the case of the Swedish municipality, in 2013 they launched the policy that more than 50% of the newly built municipal buildings would be timber construction (including hybrid construction where timber is the primary material) by 2020. Their goal was not only reached but succeeded with an average of 70%. From the city planning viewpoint, the municipality appreciates buildings that are more prefabricated and faster to build as the disruption in the town is shorter. While there are several materials and ways to prefabricate, CLT shows a high advantage for high level of prefabrication.

4.3.3 Weather protection

For the construction work of either a CLT building or a concrete building the weather is an important factor in the construction cost. Concrete must dry before the interior finish work can start, and if the humidity is high, it is more difficult to dry the concrete and might need heating equipment to dry the concrete. Timber constructions is built by an organic material and therefor is important to keep the material dry in order not to be infected by fungus or mold. Therefore, it has been investigated throughout the interviews and in the case studies what have been experienced in relation to weather protections. Through the questions for the case study buildings, it showed that none of the studied cases in Norway and Sweden used a tent to cover the construction for protection against rain. For the case CLT 3 VEF Entreprenør had to dry the construction with heated air, however they only did it for a very limited time. For case Concrete 3, VEF Entreprenør as well used heating to dry the concrete before closing the construction, but in a larger scale compared to case CLT 3.

During the project Maskinparken 3, whose cost data was not a part for this study, its construction company did not use weather protection during the construction. They explained that due to the cold and dry weather in Trondheim they had no need for using a tent or drying, other than natural aeration. According to their experience, when they had snow, they could easily remove it and afterwards let the construction dry. Furthermore, they experienced that if they had snow or rain during a weekend, only a small amount of water had penetrated the construction. The construction was then easy to dry before closing it by gypsum boards and insulation. However, they stated that they had a great awareness of the risk of moisture during the entire construction period.

In addition to the risk of rain, they also had to be aware of the wind. When they had to hoist the large wall and deck elements it was important that the wind was weak. If it was too windy then they were not able to control the large elements with the crane.

In the case of the Danish contractor, they have bad experiences by constructing a CLT building in Denmark without using a tent or other weather protection. They stated that in Denmark they have other weather conditions than Norway, which might occur as a higher risk to build a CLT construction without a tent in Denmark than in Norway.

In the case of the Swedish municipality, two out of ten recent timber buildings were built under a tent, and others were exposed. Meanwhile, they stated that they have experience to save money by using a tent as a result of continuously dry work conditions, which does not incur waste of time by waiting for the construction to dry after accidental wetting.

5 DISCUSSION

5.1 Sensitivity and uncertainties

Throughout the process of data collection, it was clear that the project and results would be limited by the number of cases studies. Many of the companies who were contacted and asked to contribute to the project, did not had time or wanted to participate in the project. The limited number of cases resulted in a limited data base for the project, and therefore creates some uncertainties throughout the project. The uncertainties have been identified and are listed below.

Identified uncertainties:

- Representativeness of the collected data set
- Cost differences which are derived from different types of buildings (care homes, family apartments, apartment buildings with service facilities)
- Influence of the timing of the project in relation to the general economy and labour market
- Influence of different locations within each country
- Influence of different construction methods
- Influence of the variation of the contractor team
- Influence of the pandemic since 2020

The uncertainty of the representativeness of the data can cause a large sensitivity for the assessment since each project constitute to a large impact of average result. Nevertheless, the results of the cases examined in the project still show that a timber building does not necessarily need to be more expensive. In addition, the interviews and literature studies showed that there are other advantages and disadvantages in the construction methods for timber buildings, which cannot directly be seen in the total cost, such as the construction time.

Not all the case projects are built in the same year. Even though the costs have been index regulated for the price development of the construction industry, the numbers can still be affected by the time the building was built. For instance, there could be advancements in the construction

techniques in 2021 compared to those in 2016. Moreover, the prices for different materials develop differently. Thereby, the comparison of projects built during different time periods might cause an uncertainty for such an economic analysis. This must always be considered when project cost is compared.

In our study, the costs were only compared with other project within the same country. This was done in such a way since each country has its own market with different material prices different labour cost, different definitions of floor areas etc. However, there are also different prices within the countries. A project constructed in the northern part of Sweden most likely has a different price in the southern part of Sweden. This is as well an uncertainty in the project.

The global pandemic of corona virus caused a substantial impact on the global economy, and the construction sector have been also heavily affected in many regards such as labour cost, material cost, transportation cost, logistic, real estate price etc. The influence of the pandemic on the construction cost might become more apparent in the near future.

6 CONCLUSIONS

The results found throughout the analysis reflect the cost of cases of CLT buildings and concrete/steel buildings in Sweden and Norway, as well as information from interviews of stakeholders. The results showed tendencies of how the cost have been at the time where the buildings were designed and build. The market develops continuously, especially within more projects with a stronger focus on sustainability. Therefore, it is important not to apply the conclusions of the case studies as an exact forecast for future buildings but must be used as an indicator of the costs and what to be aware of due to cost of timber and concrete buildings in the Nordic countries.

The following are the main findings of the study:

- There is a tendency that the CLT buildings has a higher construction cost compared with the concrete buildings for the Norwegian case buildings.
- The cost of a CLT building does not necessarily need to become higher compared to a concrete building. It depends on the type of project and how it is executed.
- The more experience one has with CLT buildings, from cost calculation to designing and constructing, the more likely the building becomes more cost efficient.
- The material cost is often higher for CLT buildings compared with concrete buildings.
- The prefabrication of CLT modules most often result in a shorter construction time as well as better working conditions in the factory and on site.
- The logistics of a CLT building is different than for a concrete building and most be considered carefully to lower the cost.
- CLT buildings are lighter than concrete ones and in many cases that presents an advantage on foundation costs.
- None of the cases studies used a tent as weather protection, but it is stated that it possible to save money when applying a tent, due to a more continuously workflow.

ACKNOWLEDGEMENT

COWI Foundation is acknowledged for its financing for the project execution. The construction companies and the other stakeholders are greatly acknowledged for their contribution with the data and to the interviews.

REFERENCES

[1] UN Environment Program. 2021 Global Status Report for Buildings and Construction. 2021.

[2] A. Younis, A. Ambrose: Cross-laminated timber for building construction: A life-cycle-assessment overview. Journal of Build. Eng., Vol. 52, 2022.

[3] R. Brandner, G. Flatscher, A. Ringhofer, G. Schickhofer, A. Thiel.: Cross Laminated Timber (CLT): overview and development. European Journal of Wood and Wood Products, vol.74, pp.331–351. 2016.

[4] EN 15978:2011. Sustainability of construction works - Assessment of environmental performance of buildings - Calculation method. 2011.

[5] S. Liang, H. Gu, T. Bilek, R. Bergman: Life-cycle cost analysis of a mass timber building – methodology and hypothetical case study, USDA, 2019.

[6] Waugh Thistleton Architects: 100 Projects UK CLT, Waugh Thistleton Architects, 2018.

[7] D. Bylund: A cost comparison between multi-residential prefabricated timber frame and precast concrete construction, Forest & Wood products Australia, 2016.

[8] R. E Smith, G. Griffin., T. Rice, B. Hagenhofer-Daniell: Mass timber: evaluating construction performance. Architectural engineering and design management, 14:1-2, pp.127-138, 2017.

[9] NS 3451: Bygningsdelstabell. (In Norwegian)

[10] M. Laguarda-Mallo, O. Espinoza: Cross-laminated timber vs. concrete/steel: Cost comparison using a case study. Proceeding of WCTE 2016. Vienna, Austria.

[11] T. Østnor: Massivtre og Plasstøpt betong: en casestudie - forskjeller, erfaringer og forbedringspotensial. NTNU, 2018. (In Norwegian)

[12] P.T. Halseth: Boligbygging i massivtre: Sammenligning av boligblokk i massivtre og betong. NTNU, 2019. (In Norwegian)

[13] https://new.gbca.org.au/green-star/exploring-green-star/ (Accessed on 13.03.2023)

[14] https://etcbygg.se/bygg/ekonomin-for-vara-forsta-hus/ (Accessed on 13.03.2023)

[15] Danmarks statistik, Index of production in construction: https://www.dst.dk/en/Statistik/emner/erhvervsliv/byggeri-og-anlaeg/indeks-for-byggeri-og-anlaeg (Accessed on 13.03.2023)

https://doi.org/10.52202/069179-0568

World Conference on Timber Engineering Oslo 2023

THE RELATIONS IN THE PLANAR AND SECTIONAL SCALES AND KAN COMPOSITION OF TRADITIONAL KOREAN ARCHITECTURE

Sangyeon Park[1], BongHee Jeon[2*]

ABSTRACT: In traditional architecture of East Asia, a distinct feature is the clustering of multiple buildings to form a single-unit. Therefore, the expansion of a single-unit building has not been given as much consideration as in Western architecture. This study aims to examine the planar and sectional scales in the Kan composition of traditional Korean architecture and to identify the limitations of scale expansion. Although previous studies have focused on the characteristics of the plan and section, this study is the first to conduct a comprehensive survey of all nationally designated cultural properties and derive statistical significance. The typical plan configuration consists of three bays for both the front and side, which emphasizes the facade. However, a plan with a side of five bays is relatively uncommon, and there are no examples of buildings in Korea exceeding five bays. This can be attributed to the structural characteristics of East Asian wooden architecture, where expansion to the side is difficult and the desire for depth and height is not prominent. In contrast, China and Japan have buildings with a side length of six and seven bays, respectively, allowing for a more expandable limit of scale.
KEYWORDS: traditional Korean wooden buildings, Kan Composition, scale of Kan, limitations of scale expansion

1 INTRODUCTION

Traditional wooden architecture in East Asia is comprised into three main components: the foundation, body, and roof. These three parts are constructed into a single building through the joining method of the structural members. This study focuses on the planning and scale of the body section. In the process of constructing wooden architecture, the initial consideration is to establish a floor plan, which subsequently informs the creation of a section plan and elevation plan. The floor plan plays a crucial role in determining the overall size of the building. [1]

In traditional East Asian architecture, the floor plan is divided into units called "Kan" (bay). Kan is a term with a wide range of meanings, including length, width, the width between columns, or the unit area where four columns are placed. [2] This is due to the development of East Asian architecture based on the post and lintel structure. The length of one Kan, or the distance between columns, must be determined on the floor plan [1]. A standard Kan is approximately 8ja (about 2.4m), but the size may vary depending on the dimensions of other wooden components such as purlins and the distance between the body and the bracket set (gongpo) that connects the body and the roof. [2]

In traditional wooden architecture, a single building is constructed using a combination of bays. Therefore, the number of Kans is a vital measure in determining the size of the architecture [1]. The single building is composed of the Purlin-Direction, which makes up the façade, and the Beam-Direction, which makes up the side. The arrangement of bays is achieved by combining the number of bays in the Purlin-Direction and the Beam-Direction. This study aims to examine the scale of the façade, side, and height, based on the configuration of the bays, and to understand the characteristics and relationship between the plan and section in Korean traditional wooden-structure buildings. Although some studies have investigated the characteristics of the plan and section in the past, this study is significant as it conducts a comprehensive survey of representative cultural assets throughout the country and statistically processes them, thereby providing a more accurate understanding of the characteristics of Korean traditional architecture.

In traditional architecture across Korea and other parts of East Asia, it is common for individual buildings to be clustered together, leading to less emphasis being placed on the expansion of a single building's scale when compared to Western architecture. The objective of this study is to investigate the extent of the expansion of scale achieved in traditional Korean architecture. The evolution of Korean architecture has moved towards dispersing functions across multiple buildings to form clusters. As a result, the depth of space cannot be fully appreciated from the entry point of a single building or house (chae) alone. Since the chae is composed of several kan and differentiates, [3] the investigation of kan is crucial for understanding traditional Korean space. Similarly, the scale of individual buildings in traditional Chinese architecture is also limited in terms of expansion due to

[1] Sangyeon Park, Seoul National University, Republic of Korea, syhee55@snu.ac.kr
[2*] Contact Author: BongHee Jeon, Dept. of Architecture and Architectural Engineering · Institute of Construction and Environmental Engineering · Institute of Engineering Research, Seoul National University, Republic of Korea, jeonpark@snu.ac.kr

https://doi.org/10.52202/069179-0569

the fact that its units are based on a cluster composed of "number".[4]

2 METHODS

The Korean government manages a total of 489 buildings constructed using the traditional-timber structure that are of historical or archaeological significance. Among these buildings, 238 excluding residential buildings and clusters of multiple buildings have been selected and classified into categories based on their function, which includes Buddhist temples, Confucian schools, royal halls (palace), pavilions, shrines, government-managed buildings, residential buildings, and others. The exclusion of residential buildings was due to their high frequency of practical use, resulting in a wide range of styles that do not preserve traditional forms. This study aims to investigate the characteristics and limitations of the floor plan and height of the 238 buildings, including the number of bays, scale, relationship between the core bay (jeongkan) and side bay (hyeopkan), and external and internal heights, as well as to classify them by their function. In traditional Korean architecture, the function of a building plays a crucial role. During the traditional era, buildings were differentiated based on their formality and scale depending on one's social class, [2] which applied not only to residential buildings but also to public buildings such as temples and schools. Previous studies have suggested that the internal spatial structures were modified according to the building's function, not only in terms of scale but also in terms of the arrangement of internal columns to create appropriate spaces. [5]

Upon classifying the floor plans according to their architectural type, the findings revealed that Buddhist temples comprised approximately 45% of the total number of buildings, followed by Confucian schools at 20%, palaces at 10%, pavilions at 11%, shrines at 7%, government-managed buildings at 6%, and others at 1%. These results suggest that Buddhist-related facilities represent a significant portion of the traditional timber-structured buildings in Korea, comprising almost half of the total number of structures examined

Table 1: Classification of Research Subjects by Composition of Kan/Building Type

Bay		Number of Buildings							
P	B	BT	C	R	P	S	G	E	Total
1	1	2							2
	2	1				2			3
2	2						1		1
3	0	1							1
	1	3	3						6
	2	21	3	5	6	2	3		40
	3	44	7	1	1	2	2		57
	4	4	1				1		6
4	2		2						2
	3	1	1		1				3
	4				1				1
5	1		2			1			3
	2		2	1	1	2	3		9
	3	17	12	2	1		1	1	34
	4	4	3	3	4	2	2		18
	5	2		1	1				4
6	2					1			1
	4						1		1
7	2		1						1
	3	1			1				2
	4	1		1					2
	5	1		1					2
9	1		1						1
	2	1							1
	4			2					2
	5						1		1
10	2		2						2
	4			1				1	2
11	1		1						1
	2		3						3
	5			1					1
12	1		2						2
15	2	1							1
	5						1		1
16	4					1			1
19	4					1			1
		105	46	19	17	14	16	2	219

P: Purlin-direction, B: Beam-direction, BT: Buddhist temple, C: Confucian school, R: Royal hall(Palace), P: Pavillion, S: Shrines, G: government-managed, E: etc

3 SCALE OF KOREAN WOODEN TRADITIONAL ARCHITURE

3.1 Composition of Kan

Upon examination of the layout of 238 buildings, it was determined that 92.0% (219 buildings) of the structures adhered to a rectangular shape with perpendicular columns. In analyzing the size of the kan (bay) within these structures, a 3x3 structure with Purin-Direction 3-bay type (front) and Beam-Direction 3-bay type (side) was identified as the most frequent, accounting for 26.0% (57 buildings) of the surveyed structures. The subsequent most common layout was a 3-bay front and 2-bay side structure, which constituted 18.3% (40 buildings). A layout with a 5-bay front and 3-bay side was found in 15.5% (34 buildings), whereas a 5-bay front and 4-bay side layout was present in 8.2% (17 buildings). Structures with a 5-bay front and 2-bay side were discovered in 4.1% (9 buildings). The remaining bay configurations were scarce, with only 1-3 structures per configuration. In summary, the layout with 3 bays along the front was the most commonly found in the survey. [6]

In a prior study, the predominant occurrence of a 3-unit front width (Purin-Direction 3kan) and 3-unit side width (Beam-Direction 3kan) in traditional Korean architecture was attributed to several factors. First, the front width of 3 units was determined to be the minimum unit capable of achieving centrality and serving as the entrance facade of the building [5]. Thus, having centrality was deemed significant. Second, a survey of buildings in 219-dong found that all structures, with the exception of two, had a front width that was either longer or equal to the side width. In the two buildings with a greater side width, the

https://doi.org/10.52202/069179-0569

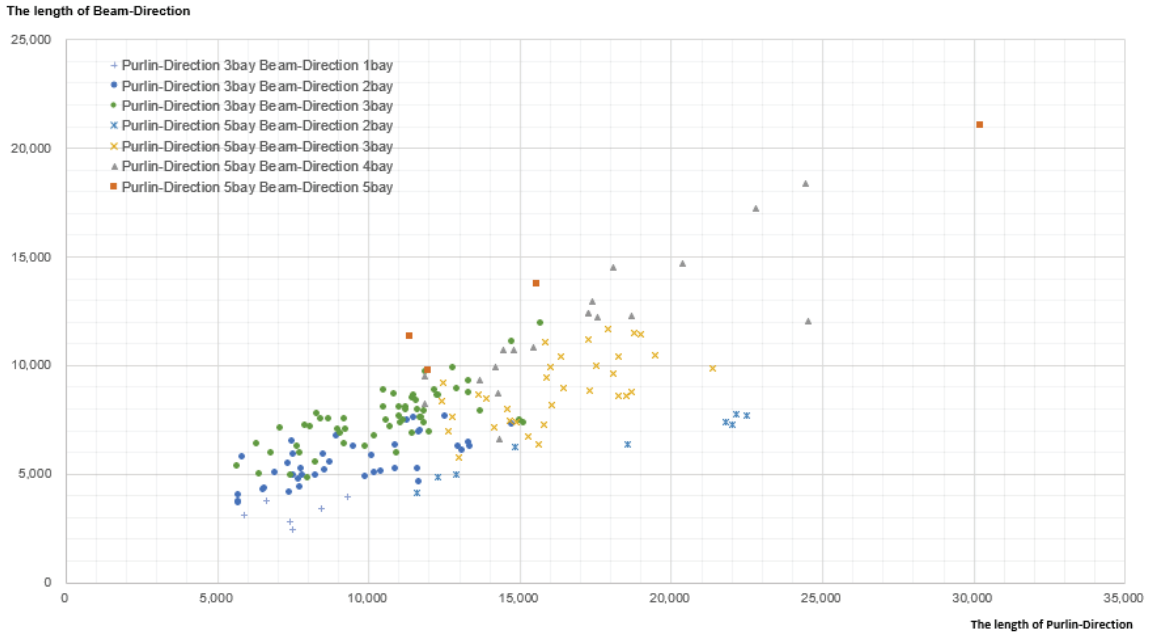

Figure 1 : Kan composition and the length

front-to-side ratio was 0.94 and 0.99, signifying no significant variance in side width. Furthermore, when comparing the widths of the core and side bays in 110 buildings with a front width of 3 units, it was found that the widths of the core and side bay were almost equal in 46% of the cases.[6] In a 3-unit configuration, the core bay (jeongkan) refers to the middle bay, while the side bays (hyeopkan) are located on either side.

In addition, it has been established through previous research that the 3-bay façade represents a fundamental structure in traditional wooden architecture not only in Korea but also across East Asia [5]. The recognition of this structural element has been preserved through generations and continues to be employed in contemporary design. For instance, the Korean pavilion at the Montreal Expo '67 was designed with the intention of linking tradition and modernity through the use of this architectural feature [8]. Notably, this fundamental structure has remained steadfast in its traditional essence.

In Chinese architecture, the importance of frontality has also been widely recognized. This can be observed in the design of the great hall (大殿) at the Foguang Temple (佛光寺) during the Tang Dynasty, where the core bay (當心間) was enlarged by widening the gap between the columns relative to the other bays [4].

In traditional East Asian architecture, the standardized wooden structures require joints that restrict the expansion of space in the beam direction due to the size of the wooden components. As a result, the scale and structure of buildings are limited. The longitudinal direction, on the other hand, represents 44% (94 buildings) of the total, with the majority consisting of three bays. The maximum number of bays found in the longitudinal direction is five, with nine buildings exhibiting five bays on the side. All of these are classified as the highest level of Korea's traditional cultural heritage classification system, as national treasures or treasures, indicating their high hierarchy and scale.

3.2 Scale of Kan

Research was conducted on the relationship between the length of the purin-direction and the beam-direction in various bay configurations, including 3X1 Bay(purin-direction 3bay and the beam- direction 1bay), 3X2 Bay, 3X3 Bay, 5X2 Bay, 5X3 Bay, 5X4 Bay, and 5X5 Bay. The most commonly utilized floor plan, the 3X3 Bay configuration, exhibited a purin-direction length ranging from 5.6m to 15.7m (with a median value of 11.2m) and a beam-direction length ranging from 4.8m to 11.9m (with a median value of 7.5m). It was observed that for small-scale planning, the kan were combined in 3X2 Bay due to the shorter length in both directions compared to the 3X3 Bay configuration. For even smaller-scale planning, while the number of cases was limited, it was found that the 3X1 Bay configuration was combined.

In cases where there was a demand to expand beyond the 3X3 Bay configuration, it was observed that the 5X3 Bay configuration was commonly utilized. For the 5X3 Bay configuration, the purin-direction length ranged from 12.4m to 21.4m (with a median value of 15.9m) and the beam-direction length ranged from 5.8m to 11.7m (with a median value of 8.8m). As the front bays expand in size, it is expected that the overall scale of the structure will increase. However, it is noteworthy that even with only 3 bays in the side, the resulting structure can still possess a significant length.

In matters for significant increase in scale, 5X4 Bay was adopted. Even compared to 5X3 Bay, which had the same 5 cells in the front, it is evident that a rapid expansion of the scale was achieved in both the purin and beam directions. The purin-direction length ranges from 11.9m to 24.5m (with a median of 17.3m) and the beam-direction

https://doi.org/10.52202/069179-0569

length ranges from 8.3m to 18.4m (with a median of 12.1m).

The 5X2 Bay floor plan exhibited a variety of front length distributions, while the 5X5 Bay floor plan had a unique combination of longitudinal and latitudinal lengths similar to the Geunjeongjeon Hall in Gyeongbokgung Palace. However, compared to floor plans with 3 or 4 bays in the side, no significant expansion of the scale was observed.

3.3 Distribution of Heights by Kan Composition and Building Function

The height of buildings has been classified into three categories and measured accordingly. Initially, the height perceived from the outside of the building, which includes both the body and roof, was determined. The measurement criteria were based on the distance from the stylobate (gidan) to the roof ridge (yongmaru). Subsequently, the interior height of the building was measured, taking into account whether a ceiling was present or not. In cases where no ceiling was present, the height was quantified from the floor to the top purlin, which is typically perceived as the maximum height of the building. Conversely, where a ceiling was present, the height was measured from the floor to the ceiling, which is assumed to be the element that people perceive as the maximum height of the building and detect the sense of space. In cases where multiple ceilings are present, the height was determined based on the highest ceiling.

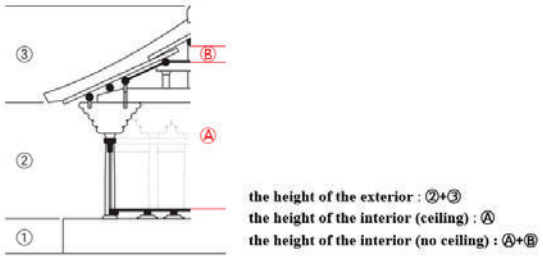

Figure 2. Standard for determining the height of a building.

The relationship between the height of the building and the use of the building was examined. The numerical values were analyzed using the median. For the height outside the building, the values were recorded in the order of shrine, Confucian academies, Buddhist temples, palaces, and governmental buildings. In terms of internal height, in cases where there was no ceiling, ancestral shrine buildings (3,666mm) and school buildings (4,753mm) exhibited a height of approximately 4 meters, while government buildings (5,411mm), Buddhist buildings (6,425mm), and residential buildings for noble families (6,898mm) showed a height of 6m. The palace recorded the highest value of 8 meters. For cases where there was a ceiling, the internal height was recorded as follows in descending order: residential buildings for noble families (3,034mm), school buildings (4,132mm), ancestral shrine buildings (4,452mm), the palace (4,978m), Buddhist buildings (5,635mm), and government buildings (6,788mm).

The median of the palace, which had the highest recorded values for outside height and inside height without a ceiling, was unexpectedly smaller than anticipated. This can be attributed to the significant difference between the minimum (4,413mm) and maximum (8,483mm) values. Among various types, palace buildings recorded the highest value for inside height with a ceiling, with the Deoksugung Junghwajeon (8,483mm) being the maximum recorded value. Conversely, the Sunwonjeon, a shrine building dedicated to ancestral worship located within the Changdeokgung Palace compound, has been recorded to have the minimum interior height. Despite being classified as a palace, its use as a sacrificial space within the palace accounts for its limited vertical elevation. Notably, shrine buildings tend to exhibit comparatively lower height values when classified by function.[9]

The composition of the kan and the distribution of heights by building function suggest that higher-ranked palaces and Buddhist buildings tend to have taller structures. Specifically, in the case of purin-direction 3 kan, Buddhist buildings displayed the highest heights irrespective of the type of beam-direction. For the most prevalent form of 3x3 kan, the heights of Buddhist buildings ranged from 9.2m to 20m, with an average height of 15 meters. Meanwhile, in the case of purin-direction 5 kan, both Buddhist and palace buildings demonstrated higher values for height compared to other building types. For a 5x4 kan, which is typically employed for large-scale expansion, the increase in height was significantly greater compared to a 3x3 kan. The average height of Buddhist buildings was 18.8m, whereas the average height of palaces was 17.7m. This represents an increase of approximately 3-4m in comparison to the 15m average height of a 3x3 Buddhist building.

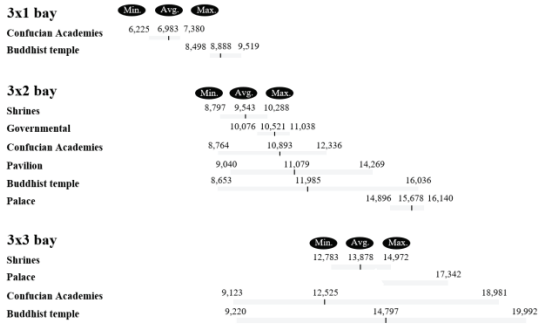

Figure 3: Height Distribution by Building Function with purin-direction 3 kan

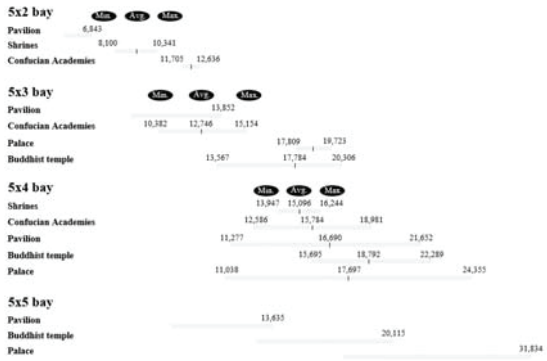

Figure 4. Height Distribution by Building Function with purin-direction 5 kan

https://doi.org/10.52202/069179-0569

We analyzed the relationship between composition and scale of kan and heights as a key element of the floor plan and section plan in traditional wooden architecture.

Considering the characteristic of purin-direction kan with a strong symbolic meaning and the side bay with a strong structural meaning, [5] the relationship between the height and purin-direction kan, height and beam-direction kan were analyzed respectively.

Upon data analysis, in the case of purin-direction kan, when the scale increases from 3 to 5 kans, the median showed a difference of about 3.8-6.6m. However, the difference in height is narrower, ranging from 3.8-4.7m.

In contrast, for beam-direction kan, an increase in size from 2 to 3 kans resulted in a difference of 2.2-3.6m, and when increased from 3 to 4 kans, the numerical difference was recorded to be 1.9-3.3m, indicating that the range of numerical values was not significantly large. Thus, it can be concluded that while purin-direction kan exhibits greater flexibility in scale expansion, there are limitations to the expansion of height and beam-direction kan.

4 Limitations of Planar Structures and Expansion

4.1 Scale and expansion of plan

Traditional East Asian architecture employs standardized wooden structures, which allows for expansion in the purlin direction by connecting wooden pieces. However, expansion in the direction is limited due to the standard size of wooden beams, resulting in limitations on the structure and size of the building. In Korean traditional architecture, expansion in purin-direction(front) can extend up to 19 kan, while expansion in the beam-direction(side) is limited to a maximum of 5 kan.

The existence of large-scale expansion in the front direction in Korean architecture may be attributed to the pursuit of frontality, despite its cluster-like characteristics. Moreover, expansion may occur for functional reasons when a large space is required even for a single building. An example of such expansion can be seen in the Jeongjeon building at the Jongmyo Shrine, a national treasure that exhibits an overwhelming front length of 70m and side length of 14m with 19 kan in the front and 4 kan in the side. This large space was created to accommodate the functional space required for the addition of royal funeral tablets.

Figure 5. the façade of Jongmyo

On the other hand, the expansion of buildings in the side direction is limited to a maximum of 5 kan, resulting in a total of 9 buildings in Korean traditional architecture with such a design feature. Of these, the buildings with five bays on the front are the Bulguksa Temple Daeungjeon Hall in Gyeongju(cultural assets designated as treasures), the Kangnung Gyeongpodae Pavilion (Treasure), and the Geunjeongjeon Hall in Gyeongbok Palace (National Treasure). The buildings with seven bays on the front are the Gyeonghoeru Pavilion in Gyeongbok Palace (National Treasure) and the Gakhwangjeon Hall in Gu-rye Hwaeomsa Temple (National Treasure), both of which are main halls in Buddhist temples. Next, the buildings with five bays on the side and nine bays on the front are the Sebyeonggwan Guest House in Tongyeong (National Treasure), and the buildings with eleven bays on the front are the Huwonjeong Hall in Changdeok Palace (Treasure). Finally, one building has fifteen bays on the front, which is Guest House in Yeosu (National Treasure).

The lateral span of the beams in the beam-direction, consisting of five kan, is characterized by a broad distribution ranging from a minimum of 9.8m at Gangneung Gwanryongnu Pavilion to a maximum of 28.2m at Gyeonghoeru Pavilion in Gyeongbokgung Palace, with an average length of 16m. The column-beam construction method exhibits a structural limitation in terms of extending the length of the beams. Furthermore, the employment of wooden beams is subject to constraints on the maximum length, as even the most massive trees fail to exceed 20m in length. Typically, the beam spans in the beam direction do not surpass 10m, with a majority of structures being limited to lengths of 5-6m. [10]

4.2 Scale and expansion of height

When examining the utilization of large-scale buildings, it can be deduced that practical necessities, such as the requirement to accommodate numerous individuals and the inclusion of guest quarters, prompted the construction of sizable structures rather than a desire for scaling up a singular building. The dimensions and elevation of the lateral bays are contingent upon the number of rafters and the limitations of the beams. The purlin framework, referred to as ryangga, was analyzed to ascertain the height of the edifice based on the dimensions of the ryangga. Concerning the external height of the building, the average height of 3 ryang was 7,955m, 5 ryang was 14,170mm, 7 ryang was 17,907mm, and 9 ryang was 18,675mm, illustrating a correlation between an increasing height and an expanding size of the ryangga. Nevertheless, it was observed that the height discrepancy between 7 ryang and 9 ryang was merely around 0.8m, which is an insignificant difference. In the case of buildings without an interior ceiling, the height also increased proportionate to the dimensions of the ryangga, and the gap in height between 7 ryang (8,439mm) and 9 ryang (9,447mm) was approximately 1m, but the disparity between 5 ryang (6,474mm) and 7 ryang was approximately 2m, signifying an increase in the magnitude of the difference. The height of structures with an internal ceiling followed the same pattern. In conclusion, a substantial association between the size and height of the ryangga is apparent, and the relatively minimal height difference between 7 ryang and 9 ryang suggests that the dimensions of the ryangga were not a

https://doi.org/10.52202/069179-0569

significant consideration when designing the furniture structure.

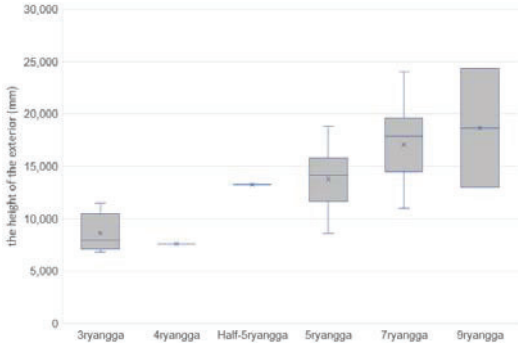

Figure 6. The relationship between the ryangga structure and height

Regarding the limitations of column components, the expansion of building height is also subject to such constraints. When assessing building height across different historical periods, the median height was found to be highest during the late Chosun era, measuring 13,947mm, followed by the Goryeo period at 13,234mm. During the Chosun period, building height tended to increase progressively from the early to the middle to the late period. The difference in height between the middle (13,843mm) and late (13,947mm) periods of the Chosun era was minimal, whereas the transition from the early period (11,008mm) to the middle period resulted in a substantial increase in height. Over time, the column component played a critical role in determining building height, and efforts to raise height through bracket sets (gongpo) became evident. An analysis was conducted on the trend in the height of columns and bracket sets (gongpo) over time. When examining the median height trend of the interior height of buildings without ceilings, there was no notable change in the absolute height of the column. However, the height of bracket sets (gongpo) component exhibited an increasing trend during the late Chosun period.

Concerning the interior height of buildings with ceilings, the column height displayed a declining trend during the late Joseon period, while the height of bracket sets (gongpo) component showed an upward trend as the Chosun era progressed from the early to the middle to the late period. In conclusion, it can be deduced that, as the Chosun period advanced into the later periods, the adjustment of bracket sets (gongpo) for height became a more significant consideration than column height.

5 CONCLUSION

Traditional Korean wooden architecture permits unrestricted expansion along the purlin-direction, enabling buildings to extend up to 19 kan (approximately 32 meters) in length. However, the expansion in the beam-direction is constrained to a maximum of 5 kan (approximately 8.5-23 meters) due to the structural limitations of the side walls. Many traditional Korean cultural properties reflect this maximum length of 5 kan. Similarly, the height is also restricted to around 19 meters due to the length of the column and their connection with the side walls. While attempts were made to increase the height to some extent as time progressed, owing to the addition of columns and bracket sets, it can be surmised that there was limited interest in expansion, as evidenced by the minor differences in height between the 7 and 9 kan structures.

In traditional Korean wooden architecture, similar to Chinese and Japanese architecture, there were clear limitations on the scale of buildings, particularly in terms of lateral expansion, with a maximum length of 5 kan. In China, traditional architecture never expanded beyond a certain point and remained at a consistent level, with the maximum front length in Tang-era architecture being only 11-13 kan and depth limited to 5-6 kan. The Taehwajeon of the Qing palace is the largest surviving single-story wooden structure with a front length of 11 kan and depth of 5 kan [4]. In Japan, there was a period when lateral kan counting was not present, indicating a lack of concept for depth in ancient Japanese architecture [7]. Unlike China and Korea, which recognized maximum lengths of 6 and 5 kan, respectively, Japanese architecture shows many examples of traditional buildings with a maximum lateral length of 7 kan, including the Kondo of Todai-ji Temple. This can be attributed to not only differences in recognition, but also differences in the sophisticated wooden structures required to achieve larger scales and heights in the three East Asian countries. A detailed comparison of these differences requires further research.

ACKNOWLEDGEMENT

This study was supported by the Ministry of Science and ICT of the Korean Government under Grant No. 2020R1A2C2101056) (A Critical Reorganization of historical Stylistics of Korean Architecture – Focusing on Data-Library Development of Architectural Style Through Multifaceted Anaysis).

This research was supported by the BK21 FOUR (Fostering Outstanding Universities for Research)

funded by the Ministry of Education(MOE, Korea) and National Research Foundation of Korea(NRF)

REFERENCES

[1] National Hanok Center : Building Hanok. Architecture & Urban Research Institute, pages 26–27, 1998

[2] Jang, K.: Wood. Boseonggak, page 56, 1993

[3] Joo, N. : Korean traditional wooden architecture. Seoul: Seoul National University Press, page 384, 1999

[4] Li, Yunhe.: Cathay's idea : design theory of Chinese classical architecture(Lee. S et al, Trans). Sigongsa, 167-171, 2000 (Original work published 1984)

[5] Jeon, B. and Lee. K.: 3kan x 3kan: hangung geonchung ui yuhyeonghakjeong jeopgeun. Seoul: Seoul National University Press, page 6-14, 99-104, 2006

[6] Kim, J. et al.: A Comparative Study on the Korean Architectural Style, Korea Association for Architectural History, 2021

[7] Lee, K.: Dori/rafter structure. spacetime, 210, 2013

[8] Seo, M.: Architecture as Mediation: The Korean Pavilion at the Montreal Expo '67, Journal of Asian

https://doi.org/10.52202/069179-0569

Architecture and Building Engineering, 16:2, 271-278, 2017
[9] Park, S. et al.: A Study on the Height of Buildings among the Cross-sectional Elements of Korean Traditional Architecture -Focusing on the State-designated Architectural heritage-, Korea Association for Architectural History, 2022
[10] Kim, D: Korean architecture, Chinese architecture, Japanese architecture. Kimyoungsa, page 37-38, 2015

World Conference on Timber Engineering Oslo 2023

COMPARATIVE RESEARCH OF SINGLE-FAMILY HOUSING CONSTRUCTION SYSTEMS BY CONSTRUCTION COST USING STRUCTURAL WOOD AND OTHER MATERIALITY

Carlos Kahler[1], Janina Gysling[2], Daniel Soto[3], Wilson Mejías[4], Francisco Jiménez[5], Carolina Molina[6]

ABSTRACT:

The wood construction massification in Chile has been considered in the last years as a strategic axis in forestry, and environmental policies, considering that this is a forestry country, the remarkable environmental contribution potential the use of this material has, and the necessity of reducing the housing deficit.

In order to evaluate the development feasibility of a massive housing wood construction, with higher quality standards than the ones traditionally used, a comparative analysis is conducted in terms of construction costs based on 4 constructive systems: wood framing, post and beam construction system, galvanized steel, and confined masonry.

The wood frame system is presented as the most competitive mainly due the wall, and roofing final cost, but also in the carcass work final cost; it is also more competitive in the construction final cost, but here the gasps are reduced. All evaluated systems have budgets that may be eligible for state subsidies.

Among the keys to improve competitivity in wood construction is the diversification of lengths, and dimensions in structural products supply. In relation to the post and beam system, traditionally associated to higher value, and size, it is concluded that is possible to develop delimited footage projects, with low cost, which also allows a greater use of the system advantages in terms of the possibility to modify the house internal distribution.

KEYWORDS: wood construction; construction system costs; lumber dimensions.

1 INTRODUCTION

In Chile, the authorized area of new housing constructions that used wood as a predominant structural material reached only 12.9% of the authorized housing area at national level in 2019 [1]. This participation of wood is in contrast with others wood-producing countries, where the participation of this material exceeds 80%, as in case of United States, Canada, Finland, and others [2].

The wood participation in the Metropolitan region housing construction, which is where the present research is focused on, reached in 2019 only 1.3% of the authorized area in the housing building permits [1].

In recent market researches carried out by INFOR [3], several construction materials demanding actors recognize the value of wood in terms of thermic, and acoustic insulation, seismic performance, and construction, and products costs. But they also claim a low valuation in durability, fire resistance, structural features, and clients' perception.

To promote wood housing construction, especially in those regions far from forest resources, a lack of wood construction culture, and where this kind of houses are perceived as a low-cost option, but with poor quality, it is necessary to promote proper construction systems, based on structural graded timber products. On the other hand, it is necessary to clear up doubts in terms of feasibility of the use of quality structural timber, with accessible construction costs for mass population, which in great proportion make use of state subsidies.

[1] Carlos Kahler, (INFOR), ckahler@infor.cl
[2] Janina Gysling, (INFOR), jgysling@infor.cl
[3] Daniel Soto, (INFOR), dsoto@infor.cl
[4] Wilson Mejías, (INFOR), wmejias@infor.cl
[5] Francisco Jiménez, Arquitecto Consultor
[6] Carolina Molina, Arquitecta Consultora

https://doi.org/10.52202/069179-0570

Currently, an important opportunity is being presented to promote wood construction massively in Chile, since the Ministry of Housing, and Town Planning has applied a Housing Emergency Plan, which aims to resolve during the 2022-2025 period, at least 40% of the current housing deficit, calculated in 643.000 dwellings. This means that the goal of this period is 260.000 dwellings, from which 135.590 corresponds to new works, and 124.410 are under construction [4]. In this plan, is expected that wood starts to play a fundamental roll as a structural material. Due to the short deadlines established, it is suggested that a great part of this wood housing demand to be develop through industrialized construction. However, companies that work with these systems are recently created, and with limited capacity, so the challenge should be approached by working together with traditional construction onsite, and industrialized construction. The present research focus on the background related to the former type of construction, with the aim to incorporate in this process the small, and medium size construction companies, as well as the small, and medium size sawmill industry.

This research is approached with the purpose of evaluate costs structures, feasibility in choosing massive construction alternatives in accordance with Chile being a forestry country, and with the challenges the climate crisis brings.

The analysis is based on recent research carried out by the Area of Information, and Forest Economics' professionals, in coordination with an architecture company with a vast experience in volume calculation, and in average value, single-family housing construction projects, using different materials [5].

2 MATERIALS AND METHODS

The construction costs of four construction systems are evaluated, these systems use different predominant structural materials: wood frame (in two models, with different dimensions), wooden post-beam, steel frame, and confined masonry. These construction systems are defined hereunder.

a) Wood frame system: a frame is a constructive disposition based on the use of linear structural members, combined in different positions to build structural elements [6].

A partition is a vertical frame constituted by two posts located at short distances (between 0.30, and 1.0m) jointed by their edges with horizontal, or inclined members.

The most frequently used framing systems, since they are more cost effective, are characterized by the supporting function of the majority of their partitions that jointed together constitute the whole system, these are simple systems with butt, and nailed joints.

In the present research, two models of this construction system have been considered: framing with 2x4 members, and 2x6 members framing.

b) Post-beam system: it is constituted by horizontal, vertical, and inclined members connected one to another. They transmit the static, and dynamic loads from beams to posts (pillars), and then to foundations. It is characterized by using big dimensional, and/or laminated timber, allowing greater distances between posts.

The constant technologic development in construction materials has allow this construction system to be highlighted by its architectural features, in accordance with the modern architecture concepts. However, it is important to note that this type of solutions is not applicable in dwellings with state subsidy, basically because of its high cost. [7].

c) Steel frame: this construction system follows the same concept as the frame system aforementioned, since for its execution, linear structural members are needed, which are combined in different positions to build structural elements.

This construction system consists in light steel profiles that provide horizontal, and vertical structural solutions, partition walls, and roofing structures.

d) Confined masonry system: This construction system is constituted by reinforced concrete elements, posts, beams, and chains which completely frame brick walls. This may be executed with handmade bricks or industrialized bricks, and different materials like a clay, or aerate concrete blocks, among others. Mortar is used in brick laying.

In the first methodological phase, a general architectural model is defined upon which this research is based on, allowing a cost comparative analysis for all of the construction systems to be developed. The architectural model considers a construction area of 80 m², which represents the average declared values in building permits in 2019 [8]

The base model presents the following architectural planning:

- Living-dining. Useful area: 27 m^2
- Kitchen. Useful area: 8.06 m^2
- Room 1. Useful area: 11.53 m^2
- Room 2. Useful area: 9.05 m^2
- Room 3. Useful area: 8.25 m^2
- Bathroom. Useful area: 4.34 m^2
- Hallway. Useful area: 3.42 m^2

It should be noted that the indicated useful areas, which in total amounts to 71.65 m², are referential, since dimensions can change depending on walls thickness in each construction system.

As a part of the model's design definition, it was decided to consider a spread footing, and concrete ground in all cases. While it is true that the majority of the evaluated systems in this research can be executed with isolated footing, and flooring frame, it is also true that the

foundation system, and the selected concrete base represents the country's predominant preference, basically due to cultural reasons [8]. This decision can go in detriment of systems that do not require them, but the finishing standards make this definition advisable.

As dwelling location, the commune of Santiago, in the Metropolitan region, has been considered. This region is by far the main housing demand center in Chile, representing 43% of the authorized dwellings in 2019, and 45% of the new works area. However, it has a low wood construction participation at national level, representing only 3.6% of number of dwellings, and 4.6% of the authorized housing area that uses wood as a predominant structural material in walls [9]

In a second phase, and counting on the base design, a particular structural, and architectural design was developed for each alternative, considering the features of each construction system, and trying at the same that they all share, where possible, the same useful footage, window dimensioning, and finishing materials. The suggested designs are in compliance with standards required by *La Ordenanza General de Urbanismo y Construcción* (OGUC) in relation to inhabitability, and safety.[10]

In the volume calculation process, the amounts of projected materials for each model in the corresponding unit of measure are quantified. The budgetary process continues with the development of a Unit Price Analysis (APU) for each model, where each item is identified and quantified, considering for that purpose the market value prices, and recognized suppliers in the construction industry. The APU analyses incorporate all the variables included in the execution of every item, like cost of materials put in work, workforce costs, and performance, tools, equipment, operational costs, and contractor's utilities. With APUs results, budget itemized tables were created for each model, whose final sum determines the construction direct cost, which includes general expenses, utilities, and taxes.

3 RESULTS

3.1 TECHNICAL SPECIFICATIONS OF SUGGESTED MODELS

According to the research objectives, the differences in design of the five construction models suggested are concentrated in carcass stage, and in particular, in the structure of exterior, and interior walls. To identify the cost gaps among structural materiality, foundation proposals, quality roofing, and finishings, and equivalent designs were formulated.

a) Carcass specifications

Vertical structures of walls, and partitions proposals

In case of the wood framing models suggested, vertical partition is assembled out of 2x4" sized impregnated pine posts (IPV) for the first model, and 2x6" with C16 structural grading (according to European norm) or similar for the second model. The distance between 2x4" posts is 40 cm, and 60 cm in case of 2x6", in both cases dimensions are the same for inferior, superior, and stick framing sills, and bridging. The members are dried to a moister content of 15%. The members length are 3.2 meters for 2.4" dimensions, and 4.8 meters in case of 2x6".

In the wooden post- beam model, structural posts should be laminated of 115x115 mm in members of 2.7 meters long. The anchoring will be executed with dawer inserts in stem wall, and lateral metallic connectors. It contemplates the use of structural double tee pine beams of 2x6" with C16 structural grading or similar, dried in chambers to a moisture content of 15%. Structural, and non-structural vertical partitioning uses pine IPV 2x4". The anchoring in the concrete ground is executed with expansion bolts, and posts, and beams with drywall screws.

The design suggested to the steel framing profiles model considers the use of vertical partition (perimeter, and structural) conformed by structural studs of 90x38x12x0.85 mm type. In case of inferior, and superior sills, a channel profile of 92x30x0.85 mm is used. Capping beams are considered for partitioning bearing the load from roofing, which are conformed by two studs, and a channel profile of the same type aforementioned. All the structural, and/or perimeter partitioning should be coated in the outer side with OSB panels of 11.1 mm thick.

The model suggested for confined masonry considers the use of reinforced-concrete pillars. The ironwork has 4 ribbed steel bars of 9.2, or 10 mm long, with 4 ribs every 20 cm. It will be used reinforce concrete bridging and beams with the same dimension as stem wall, as well as its ironwork. The partitioning walls will used pine framework IPV of 2x4" in all its elements.

Foundation proposals

For all framing models, a reinforced-concrete spread footing system is proposed in their perimeter axis. The stem walls correspond to reinforced-concrete chains of 15x30 cm. The stick framing beams considers the same dimension, and ironwork.

In case of confined masonry, a reinforced-concrete spread footing foundation is proposed in its perimetral axis, as well as in interior structural axis. This aspect is presented as a significant difference with the aforementioned models. The vertical structure load suggests foundations to transmit the load to the floor in all of its extent. Stem walls corresponds to the same stem wall proposed in the previous reinforced-concrete pillars of 15x30 cm.

For all proposed models, it is considered for concrete ground sub-bases the use of aggregates in different sizes compacted in layers. In the different models, it is proposed

https://doi.org/10.52202/069179-0570

the construction of a reinforced-concrete ground of 9 cm thick.

Roofing structures proposals

For the three models based on wood as a structural material, as well as to confined masonry model, it has been considered a roofing structure formed by 1x4", and 2x4" IPV sized pine trusses. Above them, dry pine rafters of 1x4". It is proposed the use of a base cover in OSB of 11.1 mm, and a steel roofing sheet of the product called "PV6 zincalum"

The model based on galvanized steel profile structures presents a roofing structure conformed by trusses set up with studs of 90x38x12x0.85 mm, in case of superior, and inferior webs, and king post, and stud profiles of 60x38x0.85 mm in case of diagonals. Above them, rafters made with structural omega profiles of 38x35x0.85 mm. In a similar way of the rest of models, a OSB cover base of 11.1 mm thick, and a PV6 zincalum steel sheet covering is suggested.

b) Finishing specifications

As flooring finishings in all models, it is suggested the use of porcelanato floor of 60x60 cm in all surfaces, and baseboards of the same material, in all spaces except for the bathroom. For all models it is proposed the use of PVC (Polyvinil chloride) thermal panels in windows.

As interior walls coating for models based on wood, and steel structures, it has been considered the use of gypsum wall board of 15 mm, and moisture resistant gypsum board for dry, and humid areas respectively. For the confined masonry model, it is contemplated in interior walls the use of stucco, and refining in dry zones, and for bathrooms only stucco as substrate for coating.

For interior walls it is used an insulation product: a mat-like polyester fiber, or technical equivalent in compliance with the corresponding Chilean norm. This type of insulation is suggested for all models.

It is proposed the use of EIFS (Exterior Insulation, and Finishing System) exterior cladding. For its installation, OSB boards from the vertical structure will be provided with waterproof coating, then polyester plates of 30 mm thick are assembled using a special elastomeric sticky paste. For finishing, it is considered the placement of a glass-fiber mesh in continuous strips using the same paste used to assemble polystyrene plates. Special granulated painting will be applied. It should be noted that this solution is presented as a finishing after the coating, erasing thermal bridges that could be present in partitions, and/or walls. [11]

In case of confined masonry model, the EIFS exterior cladding is suggested. The application of this system is similar to previous cases, but the waterproofing of OSB panels is replaced by adhesive bonding previous to polystyrene placement.

3.2 COST ESTIMATION AND GAPS

In the design proposals for different models, it was decided to develop medium-high standard solutions, in finishings, installations, and other carcass work elements such as roofing, and its base. Nevertheless, the budgets obtained can be perfectly eligible for state subsidy.

The results present final budgets ranging from US$636.4/m², to US$672.2/m², for 2x4" wood framing model, and the wooden post-beam model respectively. This represents a gap of 5.6% (Figure 1).

This result was expected since the post-beam system is frequently associated to high-standard solutions. What is remarkable is there is no significant differences in terms of costs, but it does represent important architectural advantages in terms of interior design modification, in respect of distribution, and area dimensions.

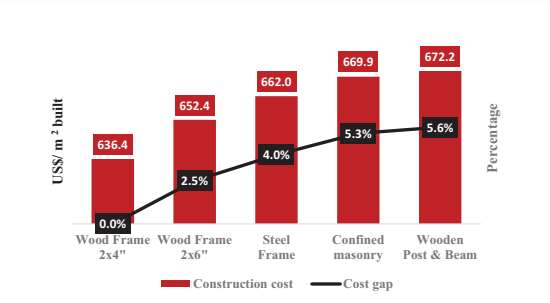

Figure 1: Final cost of construction per square meter built by model, and costs gaps.

Another interesting result is the margin difference of 2.5% between the two frame work alternatives, being the 2x6" framing the most expensive alternative. In 2x6" framing cost, the unit cost of the member used is three times superior to the 2x4" impregnated pine. The dimensions found in the market play an important roll in lowering differences in prices. The length of the 2x6" (4.8 m) allows a better use, generating scraps of only 30 cm, while in case of 2x4" member, (3.2 m) it generates scraps of 95 cm. To the better-use factor of 2x6" members, it is added the lower number of members required, due to its greater dimensions, and more distance within the frame, at the same time improving the performance in construction since there are less unions to be used.

Given the marginal cost difference of the 2x6" framing, in relation to the 2x4" framing, the evaluation of both models can be seen more as an appreciation, and comparison of these structures. Considering that the appreciation corresponds to a subjective valuation, it is assumed that clients tends to prefer more stable, and robust constructive solutions, therefore the 2x6 framing solution becomes more attractive since it presents partitioning of 18cm, which are similar to masonry walls with stucco in both faces.

The galvanized steel alternative also presents advantages in offers in terms of dimensions, with a variety of products in the market of 2.4;2.5;3.0; and 6.0 meters long.

Both wood frame models are presented as the most competitive in budget, in relation to other models using different materiality as in case of steel framing, and confined masonry. The latter is the only one who is not qualified as a dry construction, which increases execution deadlines, and project delivery.

When analyzing the cost structure of main items for each system, it is possible to verify that, due to the high, and homogenous finishings standards proposed for different projects, the cost for this concept is very similar to carcass work's, even surpassing it in case of the three models that use framing whether in wood, as well as in steels profile.

In short, big gaps among models occurs in structural cost related to carcass work. Thus, in construction of wall structures, gaps reach a maximum record of 49.8% between 2x4" wood framing model, and the wooden post-beam model, and a minimum record of 11.6% between the same 2x4" framing model, and the steel framing model. However, the maximum gap drops to 32.1% when considering the wall, and roofing as a whole, and it attenuates in 13.3% when considering the whole carcass phase. It should be highlighted that when comparing the wall structure costs, the steel framing has less costs than the 2x6" wood framing, advantage it loses when adding roofing structures, where reinforce steel has the highest cost from all the other models (Figure 2).

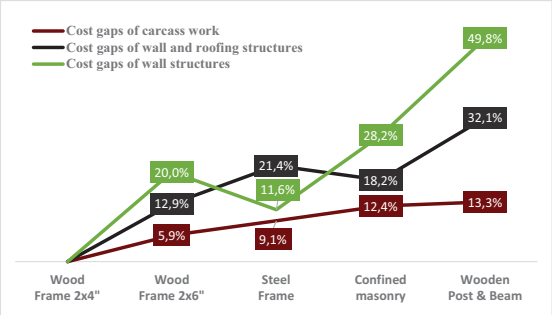

***Figure 2**: Cost gaps by construction system, and project's key phases*

4 CONCLUSIONS

It is concluded that wood framing systems are competitive in relation to the use of systems based on other materials.

The estimated budgets for three wood construction models revels that it is possible to move to better standard housing projects than to the traditional ones, with prices that may be eligible for state subsidy.

This research has proved that the initial impact when comparing the unit values of analyzed wood members (2x4", and 2x6") is mitigated with design, greater use of members in works, and operational performance improvements. It is evident that a more diverse supply of products in terms of length, and dimensions, would increase wood construction competitivity.

On the other hand, the research demonstrates that is perfectly possible to incorporate other wood construction systems that may be eligible for state subsidy, and that provides greater opportunities than conventional systems. This is the case of post-beam construction system, which is traditionally associated to higher value, and size dwellings. It emerges that is feasible to develop a delimited footage project, with low cost, additionally enabling a greater use of the structural, and constructive advantages of the system in terms of interior distribution modification. It is also an attractive system for clients, and is appreciated by architects due to the possibilities it offers in terms of space, natural lighting -since it allows big openings-, and also because of the visible presence of wood in greater dimensions.

ACKNOWLEDGEMENT

The present research have been carry out under the framework of the project entitled: *"Fortalecimiento de las Capacidades Tecnológicas del Instituto Forestal (INFOR), para el desarrollo de la Industria Secundaria de la Madera, a través de bienes públicos, orientados al sector de la construcción"*. The project was funded by *la Corporación de Fomento a la Producción* (CORFO).

REFERENCES

[1] Instituto Forestal. Anuario Forestal 2020. INFOR. Santiago, Chile, 2020.

[2] Gysling J., Kahler, C., Soto, D., et al. Madera y construcción. Hacia una simbiosis estratégica. INFOR. Santiago, Chile, 2021.

[3] Gysling, J., Kahler, C., Soto, D., et al. El mercado de la madera aserrada para uso estructural en Chile. INFOR. Santiago, Chile, 2020.

[4] Ministerio de Vivienda y Urbanismo (MINVU). Plan de Emergencia Habitacional 2022-2025. Santiago Chile, 2022.

[5] Jiménez, F., Soto, D., Gysling J., Kahler, C. Estudio comparativo de costos de construcción de una vivienda unifamiliar, según sistemas constructivos. INFOR. Santiago Chile, 2022.

[6] Hempel Holzapfel,R. Cuadernillos de Edificación en Madera, Entramados Verticales. Universidad del Biobío, Concepción, Chile, 1987.

[7] Gerardi, J. Construcción de Postes y Vigas. https://proest.com/es/construccion/proceso/post-and-beam/ . 2022.

https://doi.org/10.52202/069179-0570

[8] Centro UC. Encuesta Panel Vivienda 2014 – Informe Final. Santiago, Chile, 2015.

[9] Instituto Nacional de Estadísticas. *Bases de datos de permisos de edificación*. In www.ine.cl. 2022

[10] MINVU. Ordenanza General de Urbanismo y Construcciones (OGUC). (D.S. N°1-D.O.29-05-2020), Chile, 2020

[11] Fritz Durán, A.; Ubilla Sanz, M. Manual de diseño, construcción, montaje y aplicación de envolventes para la vivienda de madera. CIDM, CORMA, FONDEF. Santiago, Chile, 2011.

World Conference on Timber Engineering Oslo 2023

CASE STUDY ON A LARGE-SCALE TIMBER ACADEMIC BUILDING DESIGNED TO ADDRESS CURRENT INDUSTRY CHALLENGES

Javier Fierro [1], Herry Chen [2], Tyler Hull[3], Andrea Atkins[4], Daniel Lacroix[5]

ABSTRACT: The need for more sustainable construction has led to the desire to increase the use of wood materials in our buildings. However, challenges in terms of larger column grids, future design flexibility, and fire resistance have occurred in institutional, commercial, and industrial building types that have hindered mass timber's adoption. This study reviews these challenges and provides insight into the design of a mass timber academic building as a viable design solution. The building creates open-concept and future flexible spaces by taking advantage of several novel structural solutions, while achieving fire resistance requirements. The structural solutions include the long span hollowcore mass timber floor panels for large amenity areas, two flat plate "service towers", and a combination of timber braced frames and CLT shear walls for the lateral system, in order to meet the challenges faced.

KEYWORDS: Academic building, hollowcore mass timber, flat plate, design challenges, design precedents

1 INTRODUCTION

1.1 BACKGROUND

The Intergovernmental Panel on Climate Change has emphasized that global warming needs to be limited in order to avoid the worst effects of climate change and prevent long-lasting changes to our planet [1]. One approach to tackle this global issue is the way in which we build our structures. As per the United Nations Global Status Report 2017, the buildings and construction industry accounted for 39% of global energy-related CO_2 emissions, with 11% embodied in the construction processes and materials [2]. This, combined with the wider availability of mass timber products, has led to a desire to use more sustainable materials, such as wood, in our buildings.

Still, challenges remain in some building types that are hindering mass timber's adoption, in particular, in high-end residential as well as institutional, commercial, and industrial (ICI) buildings[3,4]. Key features of these building types that are challenging and limiting the use of mass timber include:

1. Larger column grids – these buildings often require large, open floor plan spaces;
2. Future design flexibility – the use of these spaces often changes over the building's lifetime;
3. Fire resistance – codes often require non-combustible materials and/or increased fire resistance ratings in these spaces.

1.2 LITERATURE REVIEW

Currently, a limited number of mass timber projects have been able to solve the design challenges faced in ICI and high-end residential structures. These solutions have often involved the use of novel structural systems pioneered or innovated to overcome a specific challenge on a project. Despite the additional analysis and engineering required at the time, these novel systems now serve as precedents to those looking to build ICI and high-end residential structures using mass timber as opposed to conventional materials such as concrete or steel. To illustrate the potential and capabilities of mass timber in ICI and high-end residential structures, a handful of these projects and their innovative solutions are presented.

The four-storey Edward J. Ray Hall at Oregon State University uses a post-and-beam system to meet the owners' requirements for adaptability and the large open classroom spaces [5]. To optimize the CLT thickness, while maintaining the required 9m clear span, the main grid has columns spaced at 3.05m, with glulam beams spanning 9.75m over the classrooms. A 3.05m wide grid with shallower beams is run down the middle of the building to act as a service corridor. This allows services to access any of the spaces between the deeper 9.75m-long beams without having to drill holes through beams, or jog beneath them. The underside of the wood slab is left fully exposed while a 100mm concrete topping is used for lateral design and to limit floor vibration [5]. The post-

[1] Javier Fierro, Undergraduate in Architectural Eng., University of Waterloo, Waterloo, Canada, jsfierro@uwaterloo.ca
[2] Herry Chen, Undergraduate in Architectural Eng., University of Waterloo, Waterloo, Canada, herry.chen@uwaterloo.ca
[3] Tyler Hull, PhD Candidate, University of Waterloo, Waterloo, Canada, tyler.hull@uwaterloo.ca
[4] Andrea Atkins, P.Eng., Lecturer, University of Waterloo, Waterloo, Canada, andrea.atkins@uwaterloo.ca
[5] Daniel Lacroix, Assistant Professor, University of Waterloo, Waterloo, Canada, daniel.lacroix@uwaterloo.ca

https://doi.org/10.52202/069179-0571

and-beam system used in the Oregon State project is depicted in Figure 1.

The four-storey John W. Olver Design Building at the University of Massachusetts (UMass) also consists of a post-and-beam glulam system; however, the slab spans are longer (i.e., up to 8m distance over the open spaces) [6]. The latter was achieved by using a timber-concrete composite (TCC) floor supported by shallower beams spanning the shorter distance between columns.

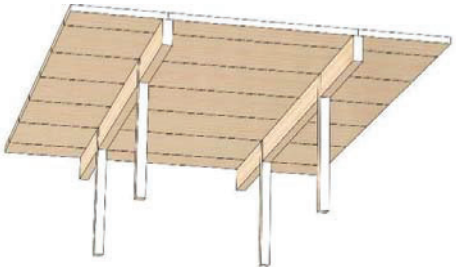

Figure 1. *Post-and-beam system* [7]

Brock Commons, which is located at the University of British Columbia, uses a flat plate system to frame an 18-storey (53m) hybrid mass timber and concrete student residence (Figure 2). The structure includes CLT floor panels that are point-supported on glulam columns; eliminating the use of beams which is highly efficient in framing tall buildings with a smaller, regular grid. The column grid of 4m x 2.85m was chosen to match the maximum available CLT panel size as each panel had to be supported in the corners by columns [8]. Eliminating the dropped beams maximized the future adaptability; however, the column grids are limited by the largest available width of CLT panels, as well as the two-way spanning capabilities of the CLT slabs.

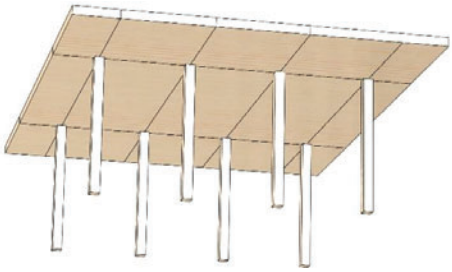

Figure 2. *Flat plate system* [7]

The Limberlost project at George Brown College, also known as The Arbour, uses an advanced structural system aiming to eliminate the use of deep glulam beams. Large flat beams consisting of 2.4m wide TCC slabs are used to support thinner CLT slabs spanning in the opposite direction in a similar fashion to systems employed in concrete parking garages. These wide beams require large "wall-column" supports, of similar width, to prevent the slabs from toppling due to unbalanced loads [9]. This system is shown in Figure 3. Here the wide flat beams consist of a 7-ply (245mm) CLT slab with 150mm of concrete compositely connected to span 9.2m over the open areas to provide flexibility for space planning [9].

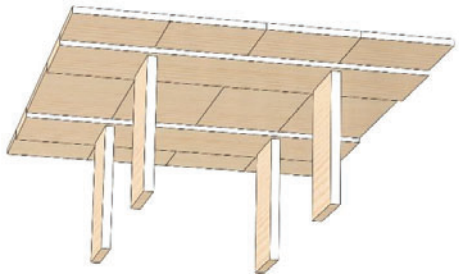

Figure 3. *Wide flat beam system* [7]

With regards to lateral systems, a number of approaches are observed in these projects. Brock Commons and the Oregon State project make use of concrete shear walls for the lateral load resisting system [5,10]. This was attributed to the lack of perimeter beams in the gravity systems, the ongoing development of code guidance on the use of mass timber lateral systems, and the relative familiarity of concrete shear wall systems. The Limberlost project uses steel braced frames, and again, this choice was attributed to the developing code provisions and lack of precedents using mass timber lateral systems as well as the designers' familiarity with steel braced frames. The UMass project was one of the first to make use of a mass timber lateral system. This system incorporates a combination of CLT shear walls and glulam braces [11]. The combination works well together due to their similar relative stiffnesses, and the ability to use shear walls in the vertical circulation core areas while braces are used around the perimeter to allow for openings [11]. In terms of tall structures, the 51m Mjøstårnet building in Norway showcases the use of glulam braced frame trusses along the exterior of the structure to resist wind-dominant lateral loads, thereby eliminating the need for shear walls [12]. With a growing list of building precedents using mass timber lateral systems, as well as ever-growing knowledge and code guidance around these systems, more projects are able to employ mass timber lateral systems including the Origine building in Quebec, Canada, the Candlewood Suites in Alabama, USA, and the Fast and Epp Home Office building in Vancouver, Canada [13–15].

1.3 OBJECTIVES

This case study focuses on a review of the main challenges faced by using mass timber in ICI and high-end residential building types, as well as provides an overview of a large-scale mass timber academic building design in the context of an international design contest. The building design was completed as part of Rothoblaas Build the (Im)possible design challenge, where it was selected as the winner in the academic category [16]. The design approach, along with design solutions to the identified three main challenges, is discussed with the intention of providing architects, engineers, and decision-makers with novel solutions to the design of mass timber ICI and high-end residential buildings, adding to the growing precedent list of these types of buildings.

https://doi.org/10.52202/069179-0571

2 CHALLENGES TO MASS TIMBER IN ICI BUILDINGS

2.1 LARGER COLUMN GRIDS

ICI and high-end residential building types often require large, open floor plan spaces that can challenge the efficient use of mass timber building products. For example, commercial office space frequently demands at least a 9m (~30ft) column grid [17], which is challenging to efficiently achieve using conventional mass timber slab products such as CLT or nail laminated timber (NLT) on glulam beams (e.g., Figure 4). This is primarily due to strict serviceability limits and poor vibration performance limiting the achievable slab spans [3]. To overcome these shortcomings, a common solution consists of using a concrete topping on top of the wood, thereby contributing to a greater slab depth as well as increased total weight of the building. While a beam and purlin system can be implemented to limit the spans of slab products, this leads to deep purlins which can negatively impact the clear floor-to-ceiling height and the ease of running services, as well as causing more "beam shadowing" [7]. For these reasons, a flat slab post and beam system is preferable, if an efficient structural system allows for the long slab spans. Furthermore, in the principal girder span direction, large column grids can also lead to deeper beams that can affect the overall floor-to-floor height and impact the running of building services.

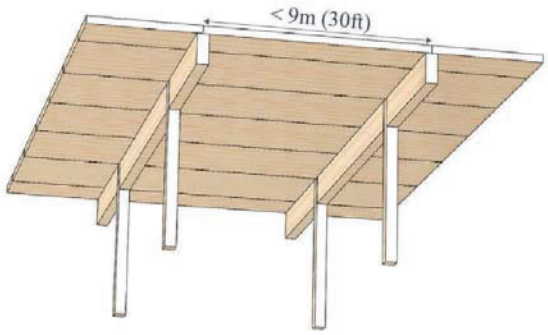

Figure 4. *Flat slab post and beam system [6]*

2.2 FUTURE DESIGN FLEXIBILITY

ICI buildings generally have a longer design life which means that the building, or individual spaces, will likely change occupancy over the lifespan of the building. The need for future-flexible spaces is thus tremendously important in these types of buildings. When combined with larger column grids to create more open-flexible spaces, this often requires limitations on the number of large load-bearing walls and deep beams. An open floor plate thus allows for building services and partition walls to be placed almost anywhere within the space (Figure 5). Therefore, selecting a structural system that allows future flexibility in design plays a key role in the design of ICI buildings.

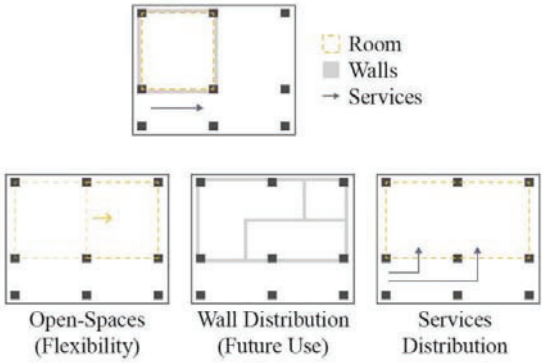

Figure 5. *Design flexibility in ICI buildings*

2.3 FIRE RESISTANCE

Structural members that are exposed to view are not uncommon in ICI buildings, as leaving structural elements exposed often optimizes costs by limiting the number of finishes. Mass timber also has the added aesthetic and biophilic benefits associated with natural materials [18], which often means mass timber building owners want the structure left exposed. However, wood is a combustible material and if desired to be left exposed requires compliance with prescriptive design code provisions, engineering analysis using known charring rates, or more time-consuming "alternative solution" pathways to justify the structure's fire resistance. These extra steps can hinder mass timber's use as prescriptive design codes typically limit how much wood-based materials can be exposed, often varying from jurisdiction to jurisdiction. These exposure restrictions limit the aesthetic and biophilic benefits of using wood-based materials. It is possible to expose nearly all of the mass timber in a structure using the reduced cross-section method (i.e., charring) in the Canadian *Engineering design in wood* standard (CSA 086) [19], as shown in Figure 6. However, this approach can be much more complex and time consuming than simply achieving the required fire resistance through encapsulation of the timber structure in non-combustible materials.

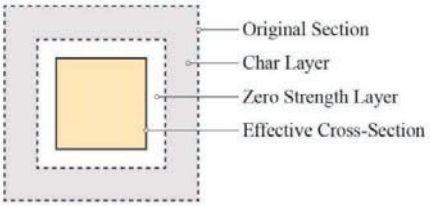

Figure 6. *Effective cross-section for fire design (CSA 086)*

3 CASE STUDY OF ALL-WOOD MASS TIMBER ACADEMIC BUILDING

3.1 OVERVIEW OF DESIGN APPROACH

The proposed design solution is a 7-storey state-of-the-art Mass Timber Engineering Building (MTEB), as shown in Figure 7, that is proposed for the University of Waterloo main campus in Waterloo, Ontario, Canada.

https://doi.org/10.52202/069179-0571

Figure 7. *Exterior render of METB*

The MTEB aims to provide academic and research spaces to nurture research in timber and sustainable construction at the University of Waterloo, promote the adoption of mass timber in ICI buildings and confront the changing climate with innovative new solutions. The building creates 28 000m^2 of multifunctional and future-flexible spaces by taking advantage of several novel structural solutions (Figure 8Figure 7).

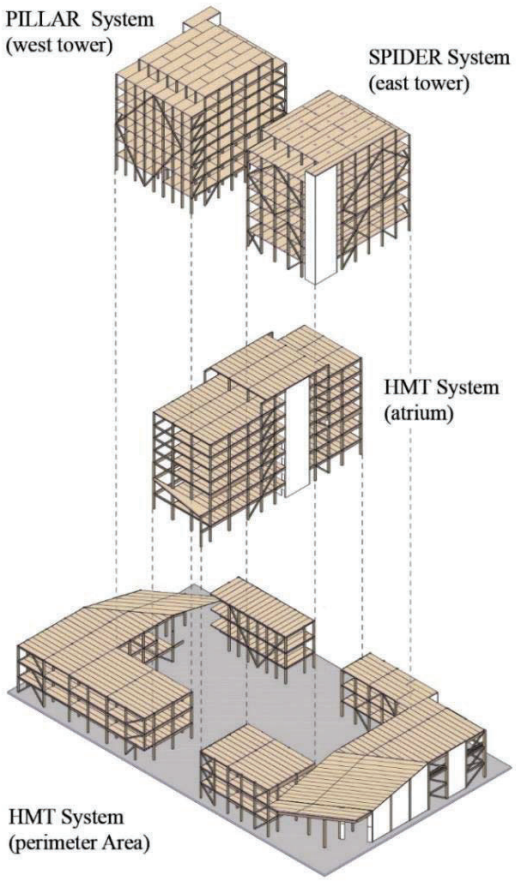

Figure 8. The *MTEB structural system*

Hollowcore mass timber (HMT) panels [20] are used at the perimeter areas and to connect the two towers through a multilevel atrium. Large open space areas, with clear spans ranging from 7-15m are created with the HMT panels. The perimeter structure accommodates lecture halls, workshops, testing laboratories, classrooms, computer laboratories, and a library. The atrium provides a connection between the two towers at each level of the structure and creates gathering areas, event spaces, and access points at the ground level.

Rothoblaas' SPIDER and PILLAR connectors [21] are used to create a flat plate structure in the two towers adjacent to the atrium. The flat plate system, traditionally only achievable with reinforced concrete, takes advantage of the two-way spanning capabilities of CLT to create spaces with tremendous flexibility, where building services do not conflict with beams or load-bearing walls, and partition walls can be placed as desired. For this reason, the towers accommodate spaces that can be distributed in a smaller and consistently repeating grid (5m x 5m and 3.5m x 5m) for small laboratories, meeting rooms, office spaces, etc. The system also allows the two flat plate regions to act as "service towers" bringing services from the centre of the building into the perimeter zone without conflict.

The lateral system uses a combination of braced timber frames, supplemented by CLT shear walls that are used for the elevator and stair cores. The Waterloo lateral design loads are wind-governed, allowing for braced timber frames to be selected for their material efficiency compared to a shear wall system, and to free up the perimeter of the structure of large load-bearing walls, allowing for windows and other openings in the current and future layouts of the space.

The design of the structural system aims to serve the growing demand for space with a flexible design to serve multiple functions, with adaptability considerations for future use. The building form is the result of an optimization of the HMT, flat plate, and bracing systems to obtain an efficient structural design.

3.2 GRAVITY SYSTEM

The structural gravity framing was designed as per the Ontario Building Code (OBC) 2012 [22]. The loading consists of the structure's self weight, superimposed dead loads, live loads, as well as snow and rain loads (Table 1).

Table 1. *Loading summary*

Dead Loads		
HMT Panel (420-740mm)	1.10-1.50	kPa
CLT Panel	0.8	kPa
Live Loads		
Lecture Hall/Mechanical	3.6	kPa
Library*	7.2	kPa
Corridor/Gathering Areas	4.8	kPa
Flexible Space	4.8	kPa
Labs/Other Spaces	2.4	kPa
Snow + Rain Load		
Base	2.0	kPa

*50% considered as long-term loading

Table 2 provides information regarding the material properties for the main structural members from the CSA

https://doi.org/10.52202/069179-0571

086 to provide designers a reference against other international wood design codes.

Table 2. *Material information* [19]

Beams and Slabs			
Material	Grade	F_b (MPa)	E (MPa)
Glulam	SPF 20f-E	25.6	10,300
CLT	E1	28.2	11,700
Columns			
Material	Grade	Fc (MPa)	E (MPa)
Glulam	SPF 12c	25.2	9,700

3.2.1 Hollowcore Mass Timber (HMT) System

The requirements for long-span spaces at the perimeter of the building and atrium area are met using an HMT system. This is a one-way floor system with a fully assembled depth varying from 420mm to 740mm for the 7m to 15m spans achieved. The HMT panel utilizes 3-ply CLT panels for the top and bottom flanges, with glulam beams acting as web members as shown in Figure 9.

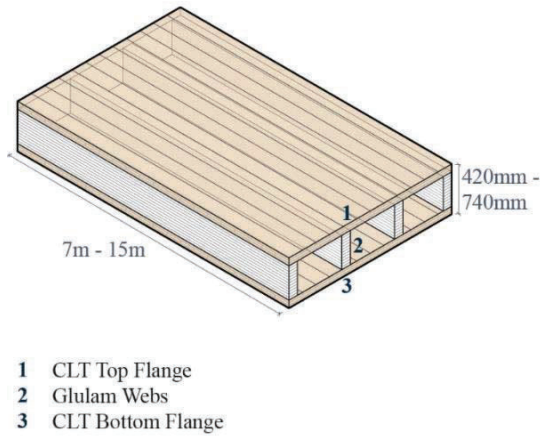

Figure 9. *Hollowcore mass timber panel*

The CLT and glulam can be fastened together using mechanical or adhesive shear connectors in order to provide a partially- or fully-composite section. For this project, the HMT panels utilize shop-glued connections for the bottom flanges and Rothoblaas HD sharp plates for the top flanges (Figure 10a). This allows for the ribbed sections to be interlaced during long-distance shipping, thereby decreasing the amount of "void air" shipped as shown in Figure 10b. The top flanges are attached using sharp plates on site where some services and acoustic treatments can be installed in the void space of the panels (Figure 10c). For shorter shipping distances, the top flanges can also be shop-glued to limit the work required on site. The shear connections play an important role in the degree of composite action achieved between the flanges and the webs. As such, the glued connection and HD sharp plates were deemed optimal as both were able to provide near-fully composite shear transfer.

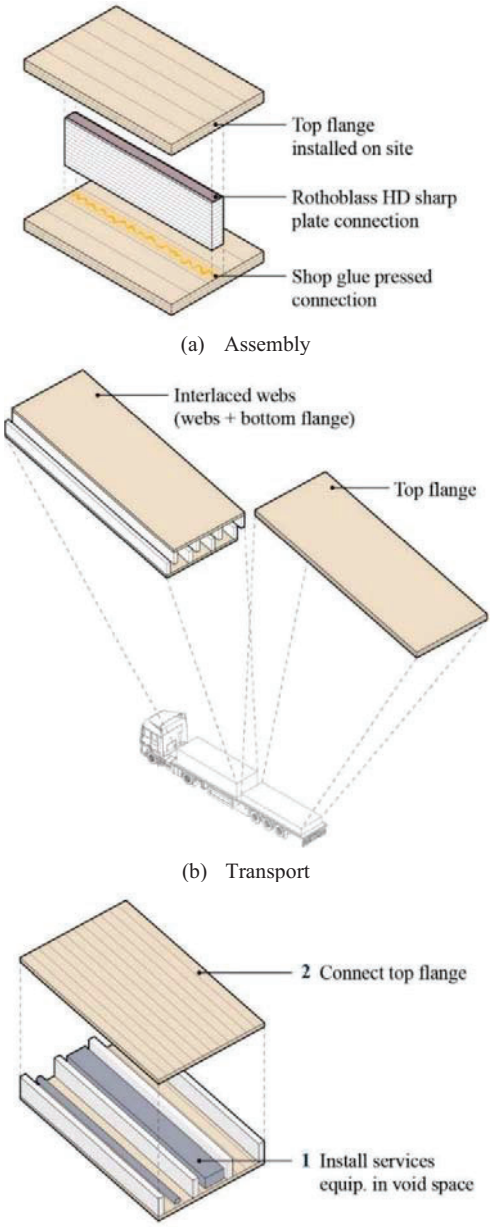

Figure 10. *HMT construction sequence*

The HTM panels are supported by a post-and-beam glulam structure by face-mounting the glulam webs to main beams or columns using flush hangers. Beams typically span seven meters in order to have a depth that is similar to the HMT panel depth, providing relatively continuous headroom clearance. Building services are integrated within a raised access floor system to maximize the overhead visibility of exposed mass timber slabs providing biophilic benefits. A cement board layer is installed between the mass timber slabs and raised floor to meet concealed space requirements and aid with acoustics. The post-and-beam structure using the HMT panels is shown in Figure 11.

https://doi.org/10.52202/069179-0571

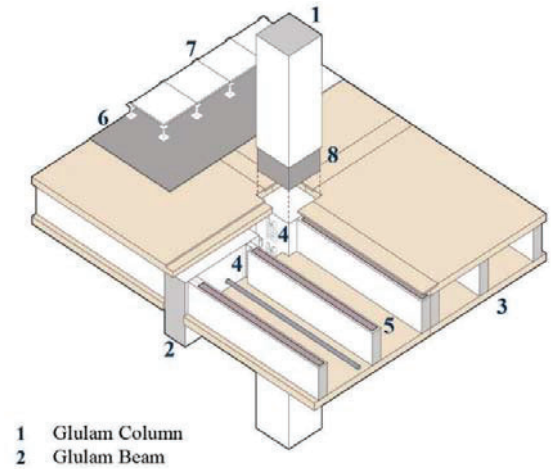

1 Glulam Column
2 Glulam Beam
3 Hollowcore Mass Timber (HMT) Panel
4 Flush Beam Hanger
5 Composite Shear Connection
6 Cement Board Fire Proofing Layer & Acoustic Assembly
7 Raised Floor with Integrated Building Services
8 Gypsum Wall Board Encapsulation
9 Mechanical Services in Void Space

Figure 11. *HMT system*

3.2.2 Mass Timber Flat Plate Floor System

The seven-storey central towers are designed to engage the two-way spanning capabilities of CLT panels by point-supporting them on glulam columns using the Rothoblaas SPIDER and PILLAR connectors [21]. The flat-plate system eliminates beams which reduces the structural depth, thereby creating a clear ceiling space that allows for easy distribution of building services in addition to the possibility of installing large exterior windows. However, flat plate systems create areas of high shear and bending stresses, as well as compression perpendicular-to-grain, at the support locations. This can lead to high rolling shear stresses in the CLT panel [23]; similar to the punching shear behaviour seen in flat plate concrete structures. The east and west towers use the SPIDER and PILLAR connectors, respectively, to provide adequate reinforcement for punching shear stresses and to bypass compression perpendicular-to-grain caused by bearing on the CLT slabs.

Rothoblaas SPIDER System

For the east tower, a 5m x 5m column grid is created using a 220mm 7-ply CLT, with dimensions of 3m x 15m (width x length), for panels centred over the columns, and 2m x 15m for intermediate panels connected to the column bands using a metal plate and epoxy moment connection as seen in Figure 12.

The SPIDER connector consists of three main components: a cylinder and bottom plate fixed to the column below, the top plate attached to the column above, and the coupling disk and cone to engage the six arms connected to the panel to the steel core (Figure 13) [24]. For aesthetic and fire resistance purposes, the bottom plate is concealed by grooving the column below and the segment of the connector above the CLT panel can be covered with the finished floor.

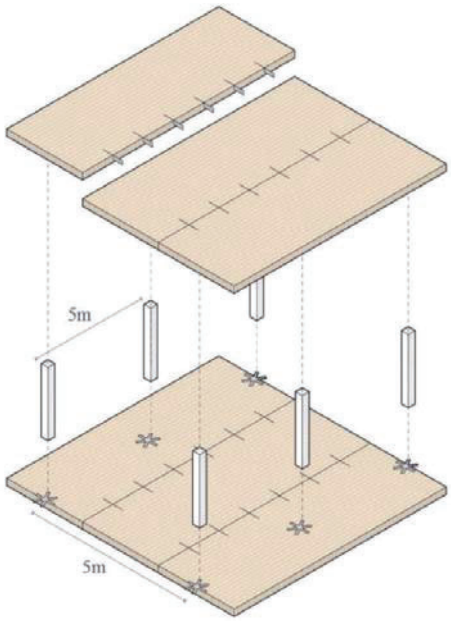

Figure 12. *5m x 5m flat plate grid with spider connector*

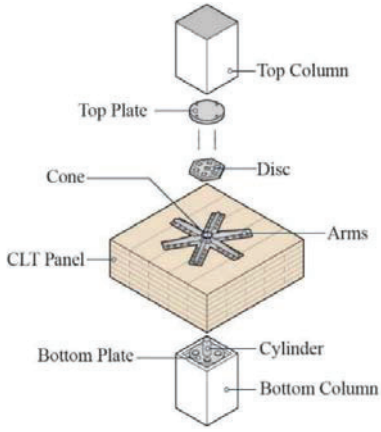

Figure 13. *SPIDER connector components*

To connect the glulam columns to the CLT, the connector (1) transfers the axial load from the column above to the column below through the steel core, (2) resists rolling shear with 45-degree fully-threaded screw reinforcement in its arms, and (3) reduces the concentrated stress at the column below by transferring the slab loads directly to the steel core (Figure 14). Further information can be found in the extensive research performed by Maurer and Maderebner [23] on the mechanical methods and numerical simulations of the SPIDER system to provide engineers with an insightful understanding of the structural response of the connector.

Due to the imposed limit on the width of CLT panels to around 3.5m during transportation, for column grids greater than 3.5m, a moment connection is necessary between CLT panels. In the design, these connections are placed 1.5m from the centre line of the column (Figure 10) to avoid the zones of maximum bending and shear stresses over the column, and the large bending stresses

found at midspan. The manufacturer recommended that the moment connection consist of steel plates that are epoxy-glued into vertical grooves in the top of the CLT panel [24]. The grooves are cut deep enough to ensure positive and negative bending strength while leaving enough wood material beneath to protect the connection from the fire below. Moment connections between panels can also be created using other systems such as TS3's high performance glued butt-joint [25] or metal tension straps.

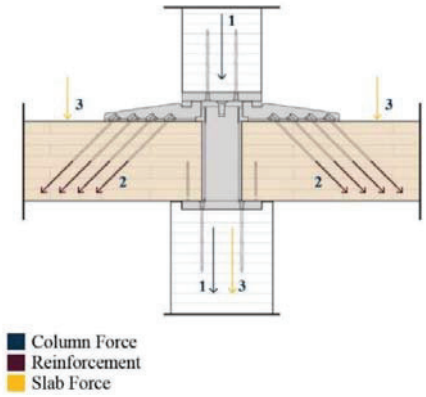

Figure 14. *SPIDER connector mechanics*

Rothoblaas PILLAR System

For the west tower, a 3.5m x 5m column grid is created using a 200mm 7-ply CLT panel with dimensions of 3.5m x 10m (width x length) that are edge- and corner-supported by the PILLAR system (Figure 15).

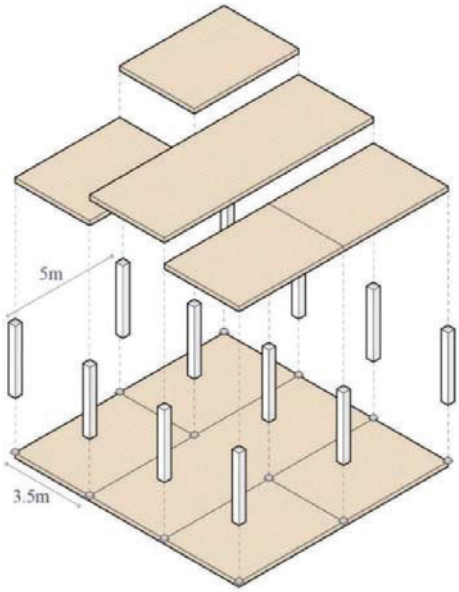

Figure 15. *3.5m x 5m flat plate grid with PILLAR connector*

This connector is a simpler alternative for the smaller column spacing of the west tower, where stresses at the columns are lower. The PILLAR connector also has three main components; the cylinder, bottom plate, and top plate (Figure 16) [24].

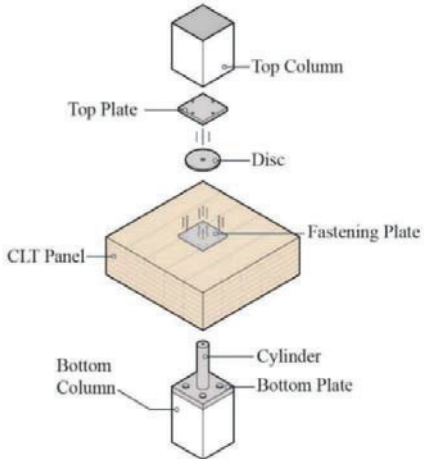

Figure 16. *PILLAR connector components*

The mechanics of the PILLAR connector are similar to that of the SPIDER connector; however, the absence of the arms diminishes the rolling shear and punching shear resistance. The rolling shear and bending resistance, as well as the bearing resistance, are provided by the CLT panel itself, and therefore this limits the maximum column spacing due to the absence of additional reinforcement seen in the SPIDER connector (Figure 17).

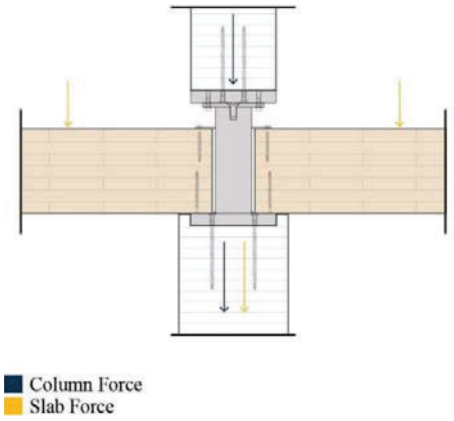

Figure 17. *PILLAR connector mechanics*

3.3 LATERAL SYSTEM

Mass timber buildings are fortunate in having a lower overall weight, and thus reduced seismic demands, but are more susceptible to vibrations induced by wind or occupant loading. Currently, design provisions in the CSA O86 [19] focus solely on the use of CLT as shear walls in platform construction for mass timber lateral load resisting systems (LLRS). Despite not being included in CSA O86 [19], code provisions for braced timber frames (BTFs) are provided for use in low- to mid-rise buildings [26]. The lack of guidance for the design and detailing of BTFs and their connection on the overall system ductility and stiffness has contributed to the limited use on projects. However, ongoing research has contributed to design guides being developed and future iteration of the wood design code to incorporate BTF design [27]. Many

https://doi.org/10.52202/069179-0571

international design codes are similarly limiting with explicit guidance lacking, or novel guidance having recently been added as a result of on-going research efforts [28]. With limited explicit guidance, or designers lacking the most current knowledge base, many opt to fall back to more familiar steel bracing and concrete shear wall LLRS in lieu of pursuing more complex, and possibly 'alternative solution'-based paths with mass timber LLRS. With the goal of demonstrating the viability of mass timber LLRS, the design of the MTEB makes use of CLT shear walls and BTFs. However, these systems can easily be substituted with concrete shear walls (e.g., Brock Commons) or steel braced frames (e.g.., Limberlost).

3.3.1 Braced Timber Frames

Despite including provisions on the design of panel-based LLRS (e.g., CLT and light frame shear walls), the current CSA O86 [19] does not provide explicit guidance for BTFs. However, it is a generally accepted practice that connections can be designed for highly ductile yielding failure modes in order to achieve moderately ductile performance for seismic design [29]. This has allowed BTFs to be successfully deployed in several past projects, such as the Mjorstarnet [12].

In Waterloo, a city located in a low seismic hazard zone, the proposed LLRS for the MTEB consists of braced frames fastened to beams and columns by two internal knife plates and 7.5mm SBD self-drilling dowels (Figure 18). The BTFs are located around the perimeter of the building in order to counteract wind-induced vibration and are left exposed to contribute to the architectural expression of the entire building.

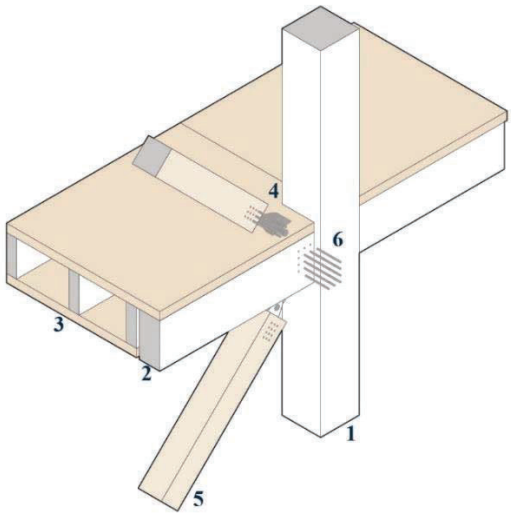

1 Glulam Column
2 Glulam Beam
3 Hollowcore Mass Timber (HMT) Panel
4 Lateral Brace Knife Plate Connection
5 Lateral Brace
6 Steel Dowel Fasteners

Figure 18. *Lateral brace system*

3.3.2 Shear Walls

Similar to BTFs, CLT shear walls heavily rely on the yielding of connections to dissipate energy [29]. The high relative stiffness of CLT can prove to be an efficient LLRS in low- to mid-rise buildings if careful attention is given to achieve the necessary detailing required by code for "rocking" to occur [29]. This mechanism is heavily reliant on a combination of elastic and plastic connectors acting upon wall segments of appropriate aspect ratio, a challenging feat in high-rise timber construction. Given that the MTEB already employs a CLT-based gravity system for the elevator and stair cores, these walls can be effectively utilized as shear walls to counteract the governing wind loads, all while using the same CLT suppliers and trades.

The CSA O86 [19], like many other international standards, includes discussion on the design and detailing of platform-type CLT shear walls. However, design provisions for balloon-framed CLT shear walls (e.g., John W. Olver Building, UMass) are still under development, and often require alternative approval and reference material outside the design codes [29]. The Canadian CLT Handbook is a prominent reference that provides guidance on the design of CLT balloon-framed LLRS [30].

3.4 FIRE DESIGN

An acceptable level of fire performance of mass timber structures can be achieved through the encapsulation of some or all wood elements. While straight-forward in achieving the desired fire performance rating, full encapsulation of the structural elements in fire resistant finishes, such as gypsum drywall, severely discounts the biophilic benefits of using timber. It was desired to expose a large portion of the mass timber structure in the MTEB, including nearly 100% of ceilings to maximize these benefits for the greater university community. This was done through calculations of the charring and residual cross-section of mass timber elements, including around connections. While the acceptable code solutions in many jurisdictions lag behind the level of exposure and design solutions prosed for the MTEB, the goal was to design to the approved requirements for the 2024 International Building Code (IBC) in the United States as an easier justification for the alternative solution being proposed. The 2024 IBC has been approved to allow mass timber buildings up to 12 storeys to fully exposed ceilings and exposed up to 40% of walls and columns based on testing from the Research Institute of Sweden [24].

Overall, the main fire performance solutions of the MTEB include; 1. Beams and columns designed to have residual capacity after 2 hours of charring to support the required loading, 2. The bottom flange of the HMT panels insulate the webs and top flange which have sufficient capacity as a ribbed panel given that the HMT panels are governed by vibration, rather than strength as in a fire scenario, and 3. The concealed space under the raised access floor contains a non-combustible cement board layer to meet code requirements for concealed spaces.

https://doi.org/10.52202/069179-0571

4 ADDITIONAL CONSIDERATIONS

Other considerations regarding the design of the MTEB include the sustainability, building envelope opportunities, and benefits of mass timber structures.

4.1 NON-STRUCTURAL BENEFITS

4.1.1 Sustainability

The MTEB is a sustainable timber building that depicts the possibilities of mass timber innovative systems to serve multipurpose academic buildings. Wood as a building material, when harvested from sustainably managed forests, has a smaller carbon footprint than traditional construction materials. Wood also has the added benefit of absorbing and storing carbon over its life, storing approximately one tonne of carbon per $1m^3$ of wood building product [31]. As a result, mass timber structures can play a crucial role in reducing a building's material and construction environmental impact and in achieving a design team's green building goals. From the carbon analysis of the MTEB it was found that when compared to an equivalent steel or concrete building, the MTEB would contribute an estimated four times less carbon emissions in terms of building materials for the primary structure (Fig. 19). Foundations were not designed for the MTEB case study and therefore were excluded from the analysis. However, it should be noted that mass timber structures are often much lighter, thus requiring smaller foundations than their concrete or steel alternatives thereby resulting in less carbon emissions. Overall, it is estimated the MTEB would also store 9800 tonnes of carbon in the wood structural materials [32]. This analysis further validates the fundamental need for the use of mass timber in net-zero carbon construction of ICI buildings.

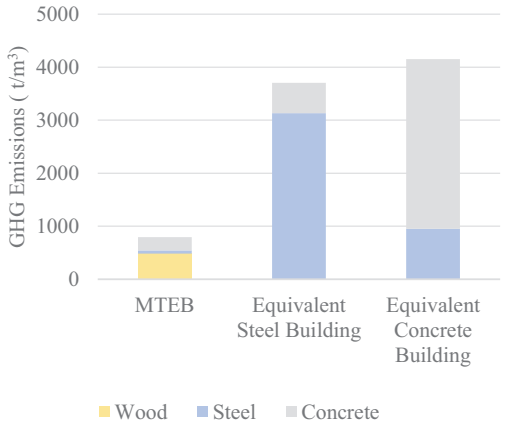

Fig. 19: *Carbon impact of the MTEB and alternative designs*

4.1.2 Occupant Impact

Wood buildings have also shown learning and happiness benefits in their occupants, a phenomenon known as biophilia. Studies have found that students benefit from being surrounded by natural materials. Demattè et al. [18] stated that wooden environments make users feel comfortable, generate a greater level of positive feelings, and even encourage sensory stimuli. Determan et al. [33] found that biophilic learning spaces result in students with higher academic performance and reduced stress levels. The biophilic appeal of wood spaces can also lead to increased design longevity, reducing long-term costs of upgrades, renovations, and re-designs.

4.1.3 Construction Efficiency

Projects that use mass panel systems are completed faster and more efficiently. Brock Commons Tallwood House, an 18-story student residence at the University of British Columbia, took just 2.5 months for timber erection [10] – four months faster than a comparable reinforced concrete building. Prefabrication also leads to fewer site errors, remedial work, and material waste. At one-fifth the density of concrete, wood projects have smaller foundation requirements, thereby decreasing project costs. All this translates to less time on site, fewer disruptions on campus, and long-term beneficial space for the campus community.

5 CONCLUSIONS

This paper outlines challenges facing the adoption of mass timber in institutional, commercial, industrial, and high-end residential buildings including; larger column grids, future design flexibility, and fire resistance. Design strategies previously used to overcome them are presented, along with a detailed description of those implemented in this case study, in order to give designers an additional precedent exhibiting the capabilities of mass timber for types of structures typically reserved for concrete and steel. The project has shown:

- The importance of selecting efficient structural systems based on the needs of the intended building use early in the project;
- Mass timber composite panels, specifically hollowcore mass timber panels, can be an efficient system for achieving the long spans in a simple post-and-beam system;
- Flat plate systems are viable with mass timber products, including column grids larger than the typical maximum panel width of 3.5m;
- With a focus on future design flexibility, mass timber can be designed to accommodate future use changes of these building types;
- In wind-governed lateral system design, the use of CLT shear walls as vertical circulation cores, in combination with glulam braced frames in perimeter walls provides an efficient structural and architectural solution.

REFERENCES

[1] IPCC. IPCC Special Report on the impacts of global warming of 1.5°C above pre-industrial levels and related global greenhouse gas emission pathways, in the context of strengthening the global response to the threat of climate change, sustainable development, an. [V. Masson-Delmotte, P. Zhai, H. O. Pörtner, D. Roberts, J. Skea, P.R. Shukla, A. Pirani, W. Moufouma-Okia, C. Péan, R. Pidcock, S. Connors, J. B. R.

https://doi.org/10.52202/069179-0571

Matthews, Y. Chen, X. Zhou, M. I. Gomis, E. Lonnoy,T. Maycock, M. Tignor, T. Waterfield (Eds.)]: 2018.
[2] Wang Cai T, Wang S, Cozzi L, Motherway B, Turk D. Towards a zero-emission, efficient, and resilient buildings and construction sector. 2017.
[3] Kirsten Lewis Rijun Shrestha, Keith Crews BB. The Use of Cross Laminated Timber for Long Span Flooring in Commerical Buildings. WCTE 2016 - World Conf. Timber Eng., 2016.
[4] Hull T, Lacroix D. Analytical Investigation of the Potential of Hollowcore Mass Timber Panels for Long Span Floor Systems. CSCE 2021 Annu. Conf., Niagara Fall, ON: 2021.
[5] WoodWorks - Wood Product Council. Case Study - Oregon State University Cascades, Edward J. Ray Hall. 2022.
[6] WoodWorks. Case Study: University of Massachusetts Olver Design Building. Massachusetts, USA: 2017.
[7] Bowick JD. Mass Timber Primer. Candian Archit 2019:48–52.
[8] Fast P, Gafner B, Jackson R, Li J. Case study : An 18 storey tall mass timber hybrid student residence at the university of British Columbia , Vancouver. World Conf. Timber Eng., Vienna, Austria: 2016.
[9] Md. S, Robert J, Thomas T. The Arbour: An Innovative Composite Floor System. Struct Congr 2022 2023:251–9. https://doi.org/doi:10.1061/9780784484180.022.
[10] Council CW. Brock Commons Tallwood House, University of British Columbia Vancouver Campus, The advent of tall wood structures in Canada, A Case Study. Vancouver, British Columbia, Canada: 2018.
[11] WoodWorks. UMass Design Building - WoodWorks Case Study. 2017.
[12] Abrahamsen R. Mjøstårnet - Construction of an 81 m tall timber building. Int. Holzbau-Forum, Garmisch Partenkirchen, Germany: 2017.
[13] Cecobois CWC. Case Study: Origine Pointe-Aux-Lièvres Ecocondos, Quebec City. Quebec, Canada: 2018.
[14] WoodWorks - Wood Product Council. Candlewood Suites - Construction Advantages Sell Hotel Developer on CLT. 2016.
[15] naturallywood.com. Fast+Epp Headquarters - Project Profile. 2021.
[16] Rothoblaas. Build the (Im)possible - Winners n.d. https://buildtheimpossible.rothoblaas.com/en/winners.
[17] Powell D. Pillars of Design. UrbanLand 2011.
[18] Demattè ML, Zucco GM, Roncato S, Gatto P, Paulon E, Cavalli R, et al. New insights into the psychological dimension of wood–human interaction. Eur J Wood Wood Prod 2018;76:1093–100. https://doi.org/10.1007/s00107-018-1315-y.
[19] CSA. CSA-O86-19 Engineering Design in Wood. Mississauga, ON: 2019.
[20] Hull T, Lacroix D. Comparative Analysis of the Feasibility of Hollowcore Mass Timber Panels for Long Span Floor Systems. World Conf. Timber Eng., Santiago, Chile: 2021.
[21] Zingerle P, Maderebner R, Flach M. System Solutions for Point-Supported Wooden Flat Slabs. WCTE 2016, Vienna: 2016.
[22] Reg O. Ontario Building Code. 2012.
[23] Maurer B, Maderebner R. Cross Laminated Timber under Concentrated Compression Loads - Methods of Reinforcement. Eng Struct 2021;245:112534. https://doi.org/10.1016/j.engstruct.2021.112534.
[24] Rothonblass. Plates and Connectors for Timber Buildings. 2019.
[25] Zöllig S. TS3 – A New Technology for Efficient Timber Structures. Curr Trends Civ Struct Eng 2020;4. https://doi.org/10.33552/CTCSE.2020.04.000592.
[26] Canadian Commission on Building and Fire Codes. National Building Code of Canada 2020 n.d.
[27] Chen Z, Popovski M. Expanding wood use towards 2025: Seismic performance of braced mass timber frames - Year 2. Ottawa, ON, Canada: 2020.
[28] ANSI/AWC. Special Design Provisions for Wind and Seismic (SDPWS) 2021.
[29] FPInnovations. Technical Guide for the Design and Construction of Tall Wood Buildings in Canada 2022 - Second Edition. Special Pu. 2022.
[30] FPInnovations. Canadian CLT Handbook. 2nd Editio. Pointe-Claire, Quebec: 2019.
[31] Canadian Wood Council. Quick Facts - Sustainable Building Series: Embodied Energy of WOOD Products. 2004.
[32] FondsVert. GHGMAT - Towards Low Carbon Construction 2019. https://www.gestimat.ca/.
[33] Determan J, Craig Gaulden Davis Mary Anne Akers F, Albright T, Browning B, Aia H, Martin-Dunlop C, et al. The impact of biophilic learning spaces on student succes. Archit Plan Inter 2019.

World Conference on Timber Engineering Oslo 2023

EUPHORBIA: MASS TIMBER STADIUM

Alexandros Kitriniaris[1], Sotiris Monachogios[2], Zannis Konteas[3]

ABSTRACT: The key concepts of material efficiency, lifespan, design for manufacture and assembly (DFMA), design for flexibility of use and design for disassembly and reuse, are currently at the forefront of mass timber development. The role that timber must play in decarbonising the construction industry is of vital importance, replacing the more conventional building methods building established in the last century, mainly using concrete and metal; materials and ways of building that are widely blamed for excessive amounts of carbon dioxide emissions. These topics are at the centre of our architecture philosophy, both in research and practice. In this spirit, we present "Euphorbia," a mass timber stadium in Galatsi, Athens, designed by KAAF – Kitriniaris Associates Architecture Firm in collaboration with timber engineers and consultants.

KEYWORDS: Mass Timber, Energy Performance Design, Sustainability, Material Ecology, DfMA, BIM

1 INTRODUCTION

Use of mass timber has been put forward as one solution for the construction industry to address its contribution to climate change. It has the potential to transform the industry, but its potential impact on design remains to be seen. Even though mono-materiality comes to the foreground, mass timber design is still connected with standardized manufacturing processes lacking aesthetic expression as an equivalent form of architecture quality.

On this point, throughout our case study it is essential to interconnect architecture, engineering, science, art, culture, and aesthetics under the umbrella of a holistic transdisciplinary target focused on mass timber design and construction. To this end, the paper analyzes three main topics. The first is related to the mass timber performance research methodology applied to the mass timber stadium; the second, to the mass timber design and fabrication techniques; the third, to the quantitative analysis of the project. This in turn, is related to the calculation of the number of trees to be used for the construction of the project, the total CO2 stored in the building mass, and the number of projects that could be constructed per forest growth in Greece.

2 MASS TIMBER PERFORMANCE

One of the first major efforts to reduce the consumption of energy and consequent emissions in the built environment has been the introduction of energy efficiency through several incentives, policies, and norms. The large release of carbon in recent centuries can, to a great extent, be attributed to urban life. Our cities are growing. Currently urban areas consume some 67 to 76 % of all primary energy and cause 71 to 76 % of greenhouse gas emissions. [1]

Figure 1: *Exterior Perspective from the pedestrian corridor*

2.1 GOVERNMENTAL POLICIES

As awareness increases and governments and regulatory bodies around the world begin to understand the need to regulate embodied carbon, the industry is having to quickly establish consistent methods to measure and quantify the impact of the materials they use to build, and to benchmark what 'low carbon' should mean to meet environmental targets.

With improvements in thermal fabric and operational energy having historically been the target of sustainability agendas, the significance of embodied carbon has increased and is subsequently moving to the forefront of political agendas. Building with wood not only provides embodied carbon benefits through the substitution of familiar, highly carbon intensive conventional building materials such as steel and concrete, but wood also stores biogenic carbon absorbed during the life of the trees.

[1] Alexandros Kitriniaris, MArchEng NTUA, MscRes, PhD Researcher NTUA, MArch IAAC Mass Timber Design, Spain, KAAF - Kitriniaris Associates Architecture Firm, Greece, akitriniaris@kaaf.gr, info@kaaf.gr

[2] Sotiris Monachogios, MArchEng UoP, ARB Registered Architect, MArch The Bartlett UCL Design for Manufacture, UK, KAAF - Kitriniaris Associates Architecture Firm, Greece, smonachogios@kaaf.gr, info@kaaf.gr

[3] Zannis Konteas, MCivEng NTUA, Msc Restorator NTUA, Co-Author of technical notes for Eurocode 5 & the Technical Manual for Wood and Modern Wooden Construction, Former Associate professor at the School of Firefighting of the Athens Fire Academy, Greece, zanniskon@yahoo.com

https://doi.org/10.52202/069179-0572

2.2 CARBON SEQUESTRATION

The use of mass timber construction has the potential to counterbalance short-term declines in the carbon stock of forests [2]. As they regrow, they will renew their place in the carbon cycle, absorbing carbon dioxide. In general terms, as global temperatures rise, increasing the effects of climate change on forests, the relocation of carbon from the forest to the urban environment may counterbalance these effects, along with those caused by dwindling land-based carbon sinks.

The carbon sequestered in a tree has already been absorbed from the atmosphere. The benefit of sustainability and responsible construction is to protect wood so as not to release carbon back into the atmosphere [3]. So, the benefit is that as long as it comes from a sustainable forest, those trees are allowed to regrow. This is one of the reasons for building with wood and not leaving trees unprotected from fire and decay. But this concept has a duration of 60-70 years. The longer the lifespan of the structure, the less risk is involved. The answer to these questions is that the right balance must be found. We really need to focus on upfront carbon to see the implications that may be caused at the end of a project's life.

2.3 LIFE-CYCLE ASSESSMENT

The construction sector is responsible for over 35% of the EU's total waste generation and accounts for about 50% of all extracted resources and an estimated 5-12% of total GHG emissions. Passive design minimized energy demand as well as using energy from renewable sources. Now industries focus on how to balance the embodied carbon within the building either through offsetting – the scheme of being able to plant trees - or by sequestering carbon within the building. Material choices minimize embodied carbon and sequestered carbon as off-setting. So, we should focus on making the building fully sustainable.

Through this process an understanding of the direct relationship between the lifespan of building components and materials and their overall embodied carbon impact has been established, that means we must consider not only the immediate carbon cost, but also the maintenance requirements, how these can be minimised, and the lifespan extended. [4]

2.4 MATERIAL ECOLOGY

For timber components which store carbon, lifespan is even more significant. The longer these components and elements are utilised within a building, where they are protected from damage and decay that would re-release their stored carbon, the greater their contribution to the new 'carbon store' within the built environment, which can act as an urban forest. [5]

Nowadays, traceability of the materials and the embodied energy are critical aspects of the design process to inform the value chains and distribute the material catalogues throughout each project life cycle from certified forests with responsible management of manufacturing, assembly, and reuse. Mass timber components should last longer than 60 years, which is the equivalent of the time needed for a tree to grow, mature and be logged for construction purposes. The lifespan of the timber components is 30-300 years, of the envelope 60 years, of the interior 15 years, and of systems 10 years. In our case study, it is important to examine the following:

Materials

• Choice of materials and their attributes
• The distance between the site of manufacture and the construction site
• Ergonomic application

Their lifespan and plans for recycling them

Construction

• Airtightness of the building shell
• Controlled ventilation with heat reclamation
• Internal air quality

The total energy footprint in relation to the environment
Collection and reuse of rainwater
Use of solar and wind power

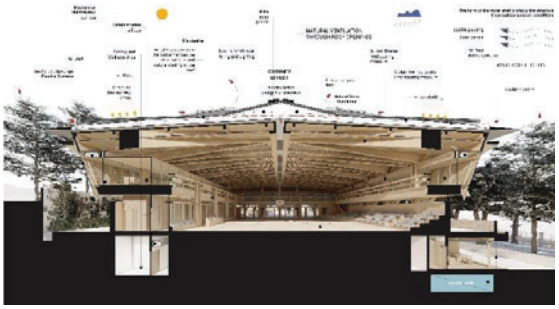

Figure 2: *Perspective Section of the Mass Timber Stadium*

3 MASS TIMBER DESIGN

Design for disassembly (DfD), is related to the component's lifespan so if components last long enough, they are more likely to achieve net-zero KgCO2e/m2. To this end, and given that there are different levels of demountability, it is necessary to translate our concept in relation to the full disassembly or reassembly potential of the structure in a different location, or the partial reuse of parts of the project's components such as glazing, timber panels, CLT decks, GluLam components, and metal connectors. Components must be easily identifiable with quantitative and qualitative data available for future uses (eg. through digital twins) and clear documentation of the method of deconstruction is important. The BIM model gives digital insight of the building to all its stages. In our case, building as a material catalog in this huge dataset is critical to understand which material is used and to review the quality of each component.

After stone, wood is the most ancient reusable construction material of natural origins, yet the shared global concerns of our time are leading to renewed architectural norms. Since the dawn of industrialisation through to today, even though

architecture is constantly becoming more complex, the building industry does not seem to make effective use of contemporary computational fabrication technologies. New questions regarding the manufacturing processes have been addressed, while at the same time a new way of architectural tectonic has emerged by shifting the paradigm from digital design manufacturing to evolutionary robotic manufacturing of natural forms.

3.1 CONCEPT

The main architectural concept of the project is related to a plant called Galatsida, a *Euphorbia* genus. It is believed that Galatsi area in Attica was named for the Galatsida plant which is abundant in the area. The name comes from the milky juice secreted by the shoots and leaves of *euphorbia. Euphorbia* is a large genus of plants in the *Euphorbiaceae* family, represented in Greece by more than 40 species. A special feature of euphorbias is their cup-shaped inflorescence, which is why it is called "kyanthos" from the ancient Greek word for cup. The mass timber stadium is located inside the premises of the "Veikos Grove" in Galatsi and has a total gross buildable area of 3.000 sqm.

The purpose of the design, according to the Municipality initiative, is to create an iconic, sustainable, passive-design stadium made of ecological and biobased materials such as wood, which will promote the principles of recyclability, reusability, energy performance, traceability, and material ecology through athletic values, by accommodating local basketball games, training and gymnastics facilities, and administration offices.

On the ground floor is the sports area and the central entrance for spectators and athletes. Spectator stands are in the northwest wing, numbering 200 seats, and there are separate restrooms for spectators. The stands communicate with the upper level through two linear staircases, allowing more standing spectators. The southeast wing hosts the reception, the athlete and referee changing rooms, and the two central stairways that connect the ground floor with the basement and the upper floor. Also on the upper floor are the administrative offices which overlook the playing field, while the remaining wings on this level can host additional sporting activities. The basement includes additional changing areas, the central space of the gymnasium, storerooms and engineering facilities. In the northwest wing the basement becomes the ground floor as it is at pedestrian street level. This area is reserved for the sports associations. The case study has controlled air flow, is watertight, the internal air quality is excellent, while part of the necessary energy production uses BIPV.

Special attention is given to the correct application of the connection between elements of different materials to avoid thermal bridges, through automated control of air conditioning and temperature in the building interior according to maximum and minimum public use of the space.

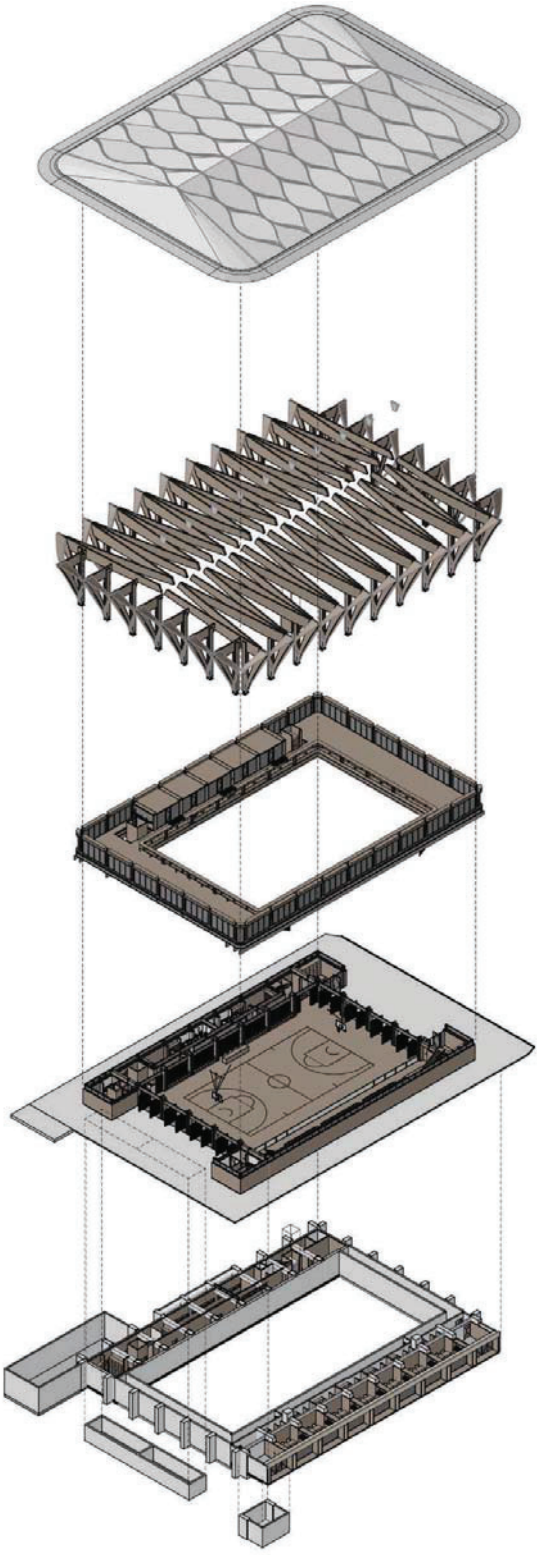

Figure 3: *Axonometric Exploded Analysis Diagram*

https://doi.org/10.52202/069179-0572

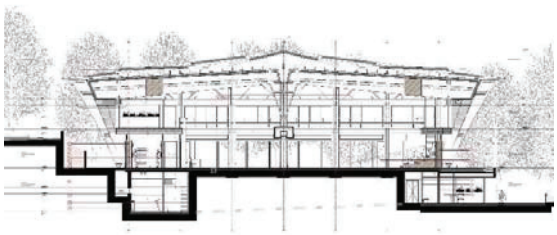

Figure 4: *Cross Section of the Mass Timber Stadium*

Rainwater is collected in a special tank from the tiled surfaces of the surrounding area and the roof. Using special filters and recirculation, it is reused in the changing rooms and restrooms. Part of it is reused for irrigating the surrounding Grove, while there is a second tank for fire safety.

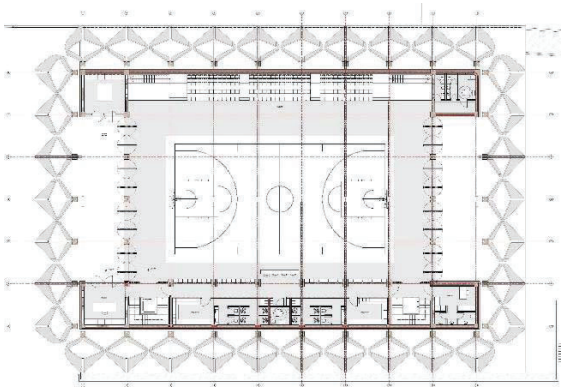

Figure 5: *Main Plan of the Mass Timber Stadium*

3.2 TIMBER LOAD BEARING STRUCTURE

The mass timber stadium is designed so that the Load Bearing Structure consists of:

- Wooden elements for the sections above the final gymnasium level, and specifically, glued timber (GluLam, GL32 category), non-glued timber (plywood) and cross-laminated timber (CLT). Supplementary metal elements are used when judged necessary, mostly as connecting elements but also for rigidity. These elements relate to the ground floor, the upper level, and the roof.
- Reinforced concrete for the sections beneath the ground, and more specifically beneath the final gymnasium level, partially extending into view at the pedestrian street level under the gymnasium. The foundations of the building and all the underground sections are constructed of reinforced concrete. These elements are in the first and second basements.

The load bearing system of the gymnasium is organised on a 5 metre rectangular grid, with seven repetitions on the one axis, and ten on the other, with general dimensions of 45 m in length and 30 m in width.

The foundation is strengthened around the perimeter of the building, since the load bearing elements are arranged around it, while internally a grid is formed from strap beams parallel to the smaller dimension of the building. These beams receive the horizontal loads exerted on the columns supports, while transverse beams are used mostly for the lateral stiffening of the first strap beams. On these beams lies the ground floor slab made of reinforced concrete.

3.2.1 BUILDING SHELL

The **shell** of the structure consists of 10 identical isostatic frames, bridging a 30-metre span. They are symmetrical and consist of beams and columns as shown in the drawings, functioning as a three-pin arch, since they include three joints within their plane: one joint at the support of each column and one at the top, where the two beams are connected. Each three-pin frame consists of the following:

1. **Two twin vertical columns,** 20 by 60 cm cross-section, 8.40 metres high.
2. **Two main beams** between the twin columns, slightly inclined. The main beams are approximately 18 metres long, 20 cm wide, and variable in height from 1.65 metres at the point of connection with the twin column, to 1.05 metres at their other end.
3. **Two deviating beams,** of the same dimensions as the main beams above, only deviating horizontally comparing to them, symmetrically arranged on either side of the twins columns. These beams connect to one another at the middle axis of the gymnasium, at half the distance across the 5-metre grid, at 2.5 metres.
4. **An inclined column** between the two twin ones, sloping outwards. Its external side is curved, resulting a variable cross-section. The base of this column starts from a cross section of 20 by 60 cm and ends at the top, under the roof, at 20 centimeters by 96 cm. A UPN 140 stainless steel element is added alongside this inclined column so as to stand in for the static function and allow easy replacement of the timber member.
5. **Two curvilinear V-shaped members** emanating from either side of the inclined column and extending to the top of it, at face level, with the flare of the geometry occurring approximately at mid-height. The inner stems of two arrays in a row connect in the middle, at half the distance of the 5 meter grid, at 2.5 meters.
   The 3 aforementioned elements (1, 4 and 5) have a common starting point in a metal joint at the base of the building on the ground floor.
6. **Horizontal beams** between the twin columns, extending towards the interior of the gymnasium, on which the CLT plates of the mezzanine rest. Their cross-sections are 20 by 80 centimetres with a length of 7 metres for the

three sides of the gymnasium, except for the beams that support the loft above the spectator stands, which have a cross-section of 20 by 35 centimetres and a length of 3.5 meters.

The use of a large number of beams: 1 main beam and 2 inclined beams, each 5 meters long and with a large cross-section, allows their flexural-torsional buckling to remain non-critical and thus they do not require flexural-torsional security against wind, snow, and earthquake loads. However, it is necessary to ensure against flexural buckling, and for this reason a dense mesh of blinds is placed around the middle of the static height of the beams which also has an architectural function related to the acoustics and lighting of the sports area.

The shell is completed on the upper surfaces with composite frames of wood and plywood with thermal insulation within, which are built into the ground and bolted to the upper seat of the main and diagonal beams.

The small facades of the building are shaped in a similar way to the large ones, with vertical and inclined columns and diagonal elements. More specifically, on the two narrow sides of 30 metres, the load-bearing body consists of 7 groups, each arranged on the 5 metre framework. Each of these groups consists of the elements described previously. More specifically: a twin vertical post (1), an inclined post (4), two curved V-shaped members (5) and horizontal beams with cross-sections of 20 by 80 cm and 7 metres long (6). Instead of the main beam (2) at full length, there are shorter beams that extend until they touch the outer main beams of the long sides, 20 cm wide, about 1.5 metres high and 3.85 metres long.

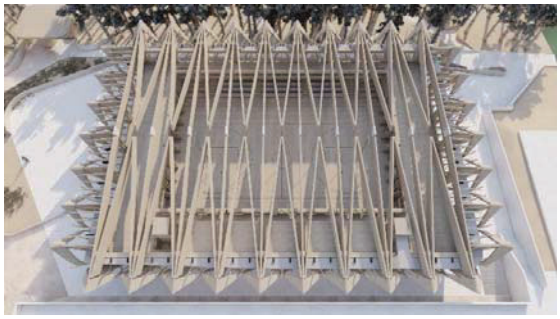

Figure 6: *Main Structural System of the Mass Timber Stadium*

The out-of-plane stiffness of the beams is achieved by the frames formed by the vertical posts and a grid at their upper level. This network is formed at the upper end of the twin vertical posts (member 1), there is a system of double, parallel GluLam wooden beams, and two more inclined ones, which runs throughout the gymnasium and provides rigidity at the face level.

3.2.2 BUILDING CORE

All areas of the internal are made of CLT and GluLam. All floors are made of CLT, and so are the walls, whereas vertical members of GluLam in conjuction with steel members are used as columns between openings.

Higher than the ground floor spectator stand, a 35-meter-long and 3-meter-wide loft is formed. Its floor is again made of CLT, like all other areas, only this floor is partly suspended by the main beams of the roof, and partly supported by the aforementioned 20 by 35 cm GluLam beams.

On the outer side of the corridor in the changing room area there are twin columns 20 by 60 centimetres cross-section and 4.8 metres high, between which the horizontal beams (member 6) of the changing room side terminate. On them lie the CLT plates and office spaces of the upper level. A corresponding function is served by the twin columns on the two narrow sides, with the CLT plate resting on the horizontal beam system on each of these sides. The stairwells on the changing room side, as well as the lift core, are made of CLT slabs and walls respectively.

Figure 7: *Interior Perspective of the Basketball Court*

3.2.3 ROOF

The roof is made of a metal frame and fiberglass panels on curved surfaces which, with an appropriate slope, channel the rainwater into special channels which end in the perimeter gutters. The choice of fiberglass material has a double meaning. On the one hand, it is a material with great resistance to weather conditions, and on the other, it helps to reduce the burden of additional loads on the construction. The metal frame is placed on the underlying wooden cross-beam and plywood cladding, the outer surface of which is protected externally by a vapor barrier and water resistant membrane. The construction consists of numbered pieces which will be fabricated off-site with CNC machines, and will be transported and assembled on-site.

4 FOREST GROWTH

Forests cover 31 percent of the planet. Approximately half of this forest area is reasonably intact, and more than one third is primary forest. The net loss of forest area has decreased significantly since 1990, but deforestation and forest degradation continue at alarming rates resulting in significant loss of biodiversity. The world is not on track to meet the target of the United Nations Strategic Plan for Forests to increase forest area by 3 percent worldwide by 2030 [6]. Urban and built-up areas are equal to 1% of the total land area of the world. As forests are vulnerable to wildfires and decay it is important to secure forests from

https://doi.org/10.52202/069179-0572

releasing carbon back into the atmosphere. Apart from world forest management plans that have already been implemented and increased in the last decade, the other way to secure carbon from being released is to store it in buildings.

4.1 WORLD FOREST AREA

The world forest area is equal to 4 billion hectares. In the last 30 years, world forest losses demonstrate an absolute change of -177 million hectares, or a relative change of -4 percent. The number of trees in the world are equal to 3 trillion trees with an average of 22,500 trees per square kilometer and 422 trees per capita. The report shows that the over the last 30 years, -35 million hectares of primary forest were lost, a relative change of -3 percent. A planted forest gained +105 million hectares, a relative change of +56 percent, while the naturally regenerated forests have lost approximately -200 million hectares, a relative change of -8 percent. [7]

4.2 EUROPEAN FOREST COVER

By considering the increase of forest growth in Europe in the last 30 years, between 1990 (208 million hectares) to 2020 (227 million hectares), we notice that there is an annual change of +0.3 percent, with a forest growth of 19 million hectares, equal to 650 thousand hectares of forest growth per year, while the forest area in Europe per capita equates to 0.33 people. [8]

4.3 FOREST COVER IN GREECE

Forest area in Greece was reported at 30.27 percent in 2020, according to the UN F.AO & the World Bank collection of development indicators, compiled from officially recognized sources. In 2020, forest area for Greece was 39,018 sq. km (3.9 million hectares). Forest area of Greece increased from 36,304 sq. km (3.6 million hectares) in 2001 to 39,018 sq. km in 2020 growing at an average annual rate of +0.38 percent. [9]

4.4 QUANTITATIVE ANALYSIS

With the aim of linking mass timber construction to the forest growth in Greece, we calculate that 1,825 mature trees (by taking into account a mature tree with a height of 30m and a trunk diameter of 0.75m) required for the construction of the mass timber stadium, 2,500 tn of CO2 on building mass (by taking into account that 1 tree absorbs 1tn CO2 and releases 727 kg O2 per cubic meter of growth), while 1.7 projects per hour or 40.7 projects per day or 14,872 projects per year could be constructed per forest growth in Greece. The total wood product calculated for the mass timber stadium equals to 2,500 m3 including off-cuts.

5 CONCLUSIONS

Through the analysis of the case study, the following points have been evaluated:

- understand mass timber structural solutions for larger scale, big span spaces, as well as how these systems deal with the performance aspects and the occupant benefits of exposed timber surfaces within these buildings.
- consider building longevity as well as flexibility for future change of use and adaptation at the design stage.
- focus on key aspects which influence the ability to disassemble a building into components that can be re-used at end of life, as opposed to demolition.
- highlight how the significance of building and component lifespan on the embodied carbon of buildings is critical for consideration of sequestered carbon within LCA analysis of biobased products such as wood.
- calculate the number of trees per project as well as the number of projects per forest growth per year as a quantitative analysis of a mass timber building.

ACKNOWLEDGEMENT

The project management and architectural design are undertaken by KAAF Kitriniaris Associates Architecture Firm. Founder Architect: Alexandros Kitriniaris, Project Architect: Sotiris Monachogios. Structural Engineer: Zannis Konteas. MEP: ITKV. Consultant: Panagiotis Touliatos Prof. NTUA & Frederick University of Cyprus.

REFERENCES

[1] Churkina G. et al., Buildings as Global Carbon Sink. In: Nature Sustainability. Perspective, Springer Nature Limited, 2020.
[2] Putalik, E., and Barber D.A. Forest, Tower, City: Rethinking the Green Machine Aesthetic, in Sigler, J. (ed.). 'Into the Woods', Harvard Design Magazine, No. 45, 2018, pp. 234-243.
[3] Organschi, A. 'The Carbon Transcend,' in Ibañez, D., Hutton, J. and Moe, K. (ed.). Wood Urbanism: From the Molecular to the Territorial. Barcelona: Actar Publishers, 2019, pp.110-127.
[4] Chadwick D. O., et al: Carbon, Fossil Fuel, and Biodiversity Mitigation With Wood and Forests. In: Journal of Sustainable Forestry, 33:3, 248-275, Taylor & Francis, Harvard Library, 2014
[5] Ramage et al.: The wood from the trees: The use of timber in construction. Renewable and Sustainable Energy Reviews, Open Access: Elsevier, Ltd., 2016
[6] UN FAO. Global Forest Resources Assessment 2020 – Main Report 2020. Rome. Available at: https://www.fao.org/3/ca9825en/ca9825en.pdf. (Accessed: July 2022).
[7] Ibid.
[8] Ibid.
[9] UN FAO & World Bank Available at: https://data.worldbank.org/indicator/AG.LND.FRST.ZS?end=2020&locations=GR&start=2020&view=bar & Available at: https://rainforests.mongabay.com/deforestation/2000/Greece.htm (Accessed: February 2023).

World Conference on Timber Engineering Oslo 2023

PLASTIC DESIGN OF BESPOKE INTERLOCKING TIMBER-TO-TIMBER CONNECTIONS FOR ROBOTIC ASSEMBLY

Davide Tanadini[1], Giulia Boller[2], Pok Yin Victor Leung[3], Pierluigi D'Acunto[4]

ABSTRACT: *CantiBox* is a robotically assembled pavilion composed of linear timber elements. The interweaving logic of the structure makes it possible to use exclusively interlocking timber-to-timber connections during the automatic assembly. The design of the connections is based on the static method of limit analysis, which allows adjusting the geometry of each joint according to the internal force distribution.

KEYWORDS: Spatial timber structure, Interlocking timber-to-timber joints, Robotic assembly, Limit analysis

1 INTRODUCTION

In recent years, the timber industry has increasingly promoted the introduction of digital technologies in the manufacturing and construction processes. Thanks to the major developments in Computer Numerical Control (CNC) machines, the production of complex and customized timber geometries is no longer a major challenge. Moreover, much scientific research has been carried out in the field of robotic assembly of timber structures made of plates and linear elements [1] [2] [3].
In this context, the *CantiBox* project demonstrates two novel contributions for jointed timber structures: (a) the application of the static method of limit analysis for designing interlocking timber-to-timber connections, which allows the adjustment of individual joint geometries based on real-time performance assessment; (b) the use of distributed mechanical tools operated by a robotic arm to achieve a fully automatic assembly process. Both contributions complete a critical knowledge gap that enables bespoke design and construction of spatial timber structures. Their flexibility to accommodate custom designs is enabled by the interweaving logic used to create a reciprocal network.

2 LIMIT ANALYSIS

2.1 INTERLOCKING TIMBER-TO-TIMBER CONNECTIONS

An approach based on the static method of limit analysis (e.g. lower bound theorem of the theory of plasticity) is well suited to the analysis and design of any structural timber element. Indeed, it is not restricted to a specific structural typology, scale or material [4] [5]. In the context of this project, the static method is adopted to address the analysis and design of interlocking timber-to-timber connections.

Figure 1: *The Cantibox project leverages innovative approaches to structural design and robotic assembly to enable the development of a customized spatial timber structure (©Ali Zigeli 2022).*

Timber-to-timber connections are particularly favourable for robotic assembly. Compared to other connections that require metal fasteners, an interlocking timber-to-timber connection is advantageous because it is composed of a smaller number of elements (i.e. a minimum of two) and thus requires fewer actions by the robotic arm (i.e. a minimum of one insertion). Therefore, this type of connection is highly suitable to be integrated into a digital automated process.
Digital fabrication makes it possible to achieve great freedom in terms of geometry. Since manufacturing complex interlocking timber-to-timber connections is no longer an obstacle due to recent developments in digital fabrication, their adoption is mainly limited by the difficulties in structural analysis. However, applying the

[1] Davide Tanadini, Chair of Structural Design, ETH Zurich, Switzerland, tanadini@arch.ethz.ch
[2] Giulia Boller, Chair of Structural Design, ETH Zurich, Switzerland, boller@arch.ethz.ch
[3] Pok Yin Victor Leung, Gramazio Kohler Research, ETH Zurich, Switzerland, leung@arch.ethz.ch
[4] Pierluigi D'Acunto, Professorship of Structural Design, School of Engineering and Design, Technical University of Munich, Germany, pierluigi.dacunto@tum.de

https://doi.org/10.52202/069179-0573

static method of limit analysis to timber provides a new possible approach to the analysis and design of interlocking timber-to-timber connections. The illustrative representation of the state of internal forces in the form of strut-and-ties, or stress fields, makes the interactions between force and geometry explicit. It represents, therefore, the basis for the development of efficient connections.

2.2 PLASTIC DESIGN OF CONNECTIONS

The objective of plastic design is to analyze the connection, determine its load-carrying capacity by assessing the collapse load with reasonable accuracy and inform the design by optimizing its geometry. In an interlocking connection, the capacity is expressed as a function of two parameters: the contact surface A_i and its strength $f_{y,i}$. The former controls the flow of forces between timber elements, while the latter controls the flow of forces within an element. Given these two parameters, it is then possible to evaluate and adjust the capacity of the connection. The contact surface indicates the area available for force transfer. The contact surface strength indicates the maximum stress that a surface can withstand. In general, the larger the contact surface and/or the more efficient the internal force flow, the greater the connection capacity.

$$\text{Connection capacity} = f\left(A_i, f_{y,i}\right)$$

$\rightarrow F_{Rd,i} = A_{F,i} \cdot f_{y,i}$

$\rightarrow M_{Rd,i} = A_{M,i} \cdot f_{y,i} \cdot h_i$

A_i : Contact surface
$f_{y,i}$: Contact surface strength
h_i : Lever's arm

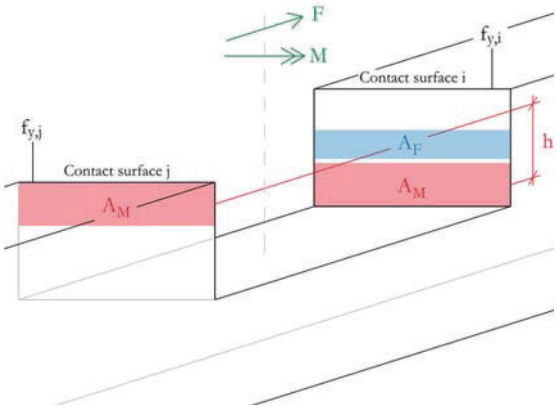

Figure 2: *Schematic representation of the redistribution of forces in an interlocking connection.*

2.2.1 Transfer of forces between timber elements

In the case of interlocking timber-to-timber connections, the forces between elements are transmitted through contact surfaces. Unlike other types of connection, here, only compressive forces are transferred. Being timber anisotropic, the positioning of the connection with respect to the grain's orientation is decisive.

Different strategies can be adopted to meet the material requirements [5]. In this project, three strategies are employed: (a) the tension forces are transmitted by designing connection geometries that transform tension into compression; (b) large contact surfaces enable the transmission of higher forces; (c) the transmission of different kinds of stresses required contact surfaces oriented in multiple directions.

2.2.2 Flow of internal forces in timber elements

The compressive forces transmitted via contact surfaces are considered a starting point for analyzing internal forces. The limit analysis allows the visualization of the internal state of equilibrium, represented in the form of stress fields (continuous case) or strut-and-ties (discrete case). This representation is helpful for the analysis and especially for the design of interlocking timber-to-timber connections. Stress discontinuities may be present in the equilibrium state of the internal forces, in line with the plastic theory.

By comparing connections with different geometries, it can be observed that their structural capacity differs, although the joints have the same dimension of the contact surface over which the force is introduced [5]. In fact, some connections may favour a more efficient internal force flow than others (e.g. less force redirection or more effective exploitation of anisotropy). Therefore, it is necessary to conduct a quantitative analysis of the internal force flow to determine the capacity.

This analysis can be performed by means of stress fields, strut-and-tie models, force diagrams and yield conditions, as shown in Figure 3.

Stress fields and related strut-and-tie models, which show the resultants of the underlying stress field, represent the equilibrium condition of the internal force flow. They also provide visual information on internal forces, which is very useful in qualitative analysis. Given the geometry, the applied external forces and the boundary conditions, the compression force must be redirected towards the support. The force diagram represents the equilibrium of the forces acting in the strut-und-tie models using a closed cycle of vectors (i.e. force polygon) at each node, allowing for computing the magnitude of the forces. The compatibility of the internal stress states with the material properties is verified through yield conditions. In the yield conditions diagram, the individual stress states, one for each element of the strut-and-ties, are displayed. If the stress states lie within the curve of the yield conditions, the latter are respected. The yield conditions are represented by the uniaxial strength formula (i.e. Hankinson [6]) of the Swiss code 265 [7].

The possibility to model the internal forces, combined with the understanding of the material behaviour, allows for identifying possible critical situations and, consequently, improving the efficiency of the connection by manipulating the geometry or the internal forces model.

https://doi.org/10.52202/069179-0573

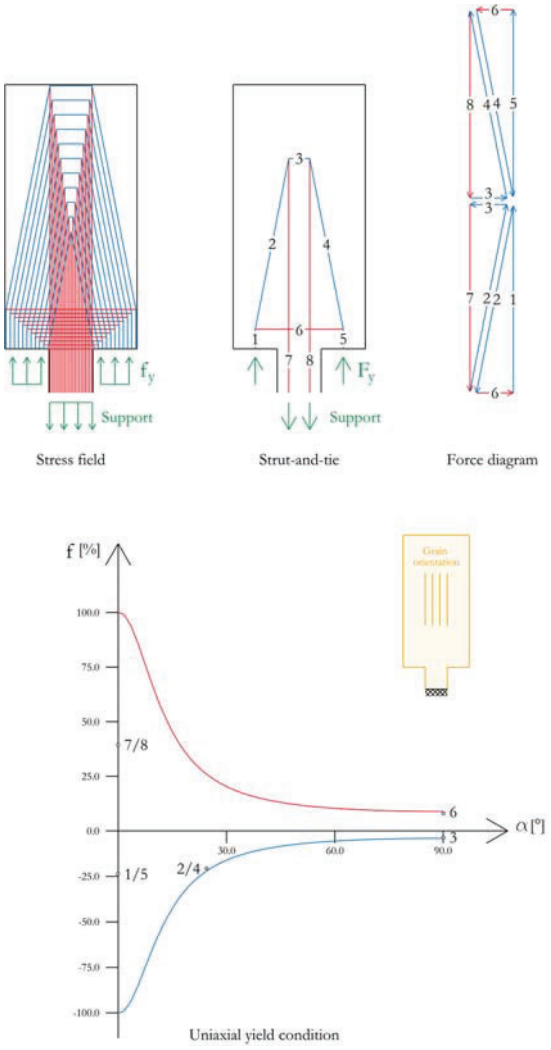

Figure 3: *A parallelepiped timber element is tested. The element presents two notches through which the external load is transferred. Tension forces are shown in red, compression forces in blue and external forces in green. The analysis allows the understanding of the flow of internal forces and the assessment of the collapse load.*

2.2.3 Algorithm for the definition of contact surfaces

An algorithm is responsible for the plastic allocation of contact surfaces. Having defined as input the available contact surfaces A_i and the respective strength $f_{y,i}$, it determines which surface to activate for a given load. This process can also be performed manually, but in the case of combined loads, it becomes quickly tedious. The algorithm follows the principles below:

No overlapping between contact surfaces:

$$A_{Force} \bigcap A_{Bending} = \emptyset$$

Axial forces equilibrium:

$$F + \int_{(+)} f_y \, dA_{Force} - \int_{(-)} f_y \, dA_{Force} = 0$$

Bending forces equilibrium:

$$M + \int_{(+)} f_y \cdot h \, dA_{Bending} - \int_{(-)} f_y \cdot h \, dA_{Bending} = 0$$

(+) positive side (-) negative side

The graphical representation of the result of the algorithm is shown in Figure 4.

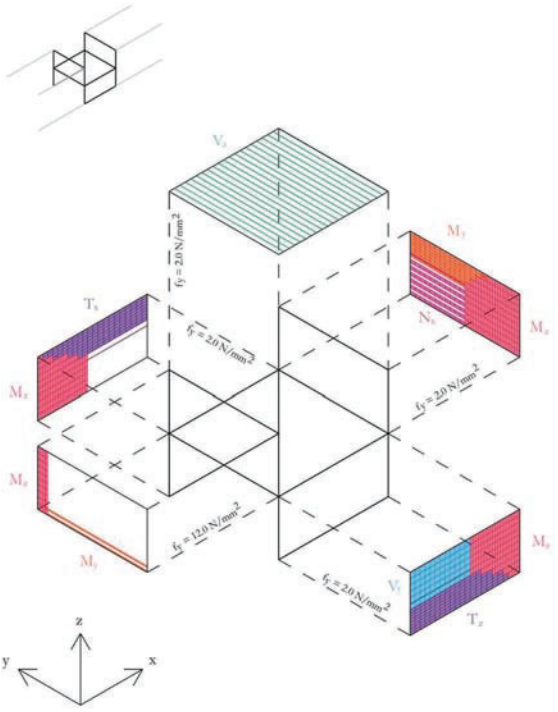

Figure 4: *The algorithm is responsible for distributing the contact surfaces required for efficient force transfer between timber elements.*

3 PAVILION DESIGN

The *CantiBox* pavilion features a complex three-dimensional reciprocal structural system based on geometrically optimized and customized interlocking timber-to-timber connections.

3.1 STRUCTURAL CONCEPT

A reciprocal structure is composed of a minimum of three elements that support each other so that each element is supported either by another element or by the ground [8].

https://doi.org/10.52202/069179-0573

In this structural system, each element is essential, and the failure of a single element leads to a chain reaction that results in the collapse of the entire structure. This structural principle has been known for a long time, and its use is widespread [9].
Besides three-dimensional structures such as vaults or bridges, reciprocal systems are also used to obtain planar geometries. The adoption of reciprocal structures for the formation of ceilings is well known. Villard de Honnecourt, Sebastiano Serlio, and John Wallis provide relevant examples of this technique. In this case, the reciprocal system is called planar grillage [9]. Indeed, the planar structure composed of short timber elements forms the ceiling connecting the vertical structural elements of a building.

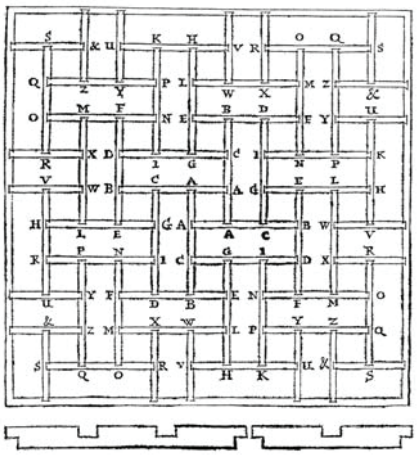

Figure 5: *Sketches of the planar grillage developed by Wallis [10]. The reciprocal structure allows long distances to be covered using multiple short elements that support each other.*

In the *CantiBox*, a planar grillage is used as a basic structural module. From a structural point of view, it acts like a Vierendeel truss. The reciprocal planar grillage module presents three horizontal and three vertical elements, as shown in Figure 6. The elements are interwoven, with connections oriented in opposite directions. Only once the last component is assembled, the reciprocal system is closed, the structure can be considered stable, and the disassembly is prevented. Furthermore, the assembly of the grillage complies with the automatic robotic assembly process developed for this project, which does not allow any triangulation in the structure. Connecting several reciprocal planar grillages together allows the development of spatial structures using only interlocking timber-to-timber half-lap connections.
In the design of the *CantiBox*, strict rules must be considered, which are dictated by the planar nature of the grillage module, by the use of square timber elements, and by the assembly process, which allows only planar connections (i.e. the plane of the reciprocal planar grillage module must be shared by two faces of the beam to which it is to be connected). Therefore, the design presents box-like structures where each face consists of a reciprocal planar grillage module.

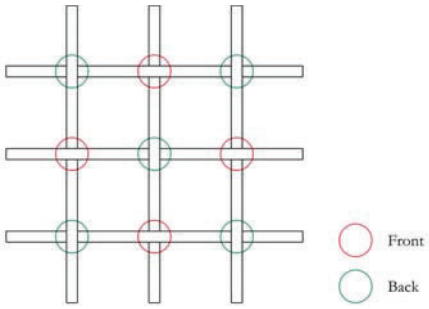

Figure 6: *Schematic representation of a reciprocal planar grillage module used in the CantiBox pavilion. In a real scenario, the assembly of this type of reciprocal structure is impossible without relying on the elastic flexibility of the elements. The interwoven composition prevents disassembly by presenting an alternating orientation of the connections. In the CantiBox pavilion, the last element to be assembled - the key element - exhibits a different orientation of the connections that allow it to be assembled without compromising the reciprocal system.*

3.2 GLOBAL DESIGN

CantiBox consists of three independent units: two lateral boxes connected to the ground and a cantilevering central box supported by the other units, as shown in Figure 7. The boxes are connected via shared horizontal planes. Each unit is composed of 20 linear timber elements of solid spruce with a cross-section of 10 by 10 cm, which are automatically assembled via robotic fabrication. The six linear timber elements of each face of the boxes are interconnected through bespoke half-lap joints arranged in the plane to generate a reciprocal system. Of these six elements, four present connections facing two opposite directions (e.g. two inward and one outward). This characteristic allows assembling each face with an interweaving pattern that ensures the correct automatic positioning of the elements within the face using a robotic arm. The sixth linear element of each face - the key element - has three connections pointing in the same direction to allow assembly by a robot. For this reason, one connection of the key element is ensured by a metal fastener that prevents disassembly [11].
For the evaluation of the global structural behaviour of the *CantiBox*, Finite Element Analysis (FEA) is used. In the analysis, each joint is regarded as a rigid connection. Since the project is built in the open air, the following external forces are considered according to the Swiss codes 260 [12] and 261 [13]: self-weight of the structure and wind load. The wind load acts in different directions. For each element, the most unfavourable direction is considered. In the definition of the support conditions, translational movement is blocked in all directions while rotational movement is allowed. The construction detail of the supports is characterized by a steel blade penetrating a notch in the timber, which is then fixed with a steel pin. The capacity of linear timber elements to resist

https://doi.org/10.52202/069179-0573

axial forces, shear forces and bending moments is determined according to Swiss code 265 [7].

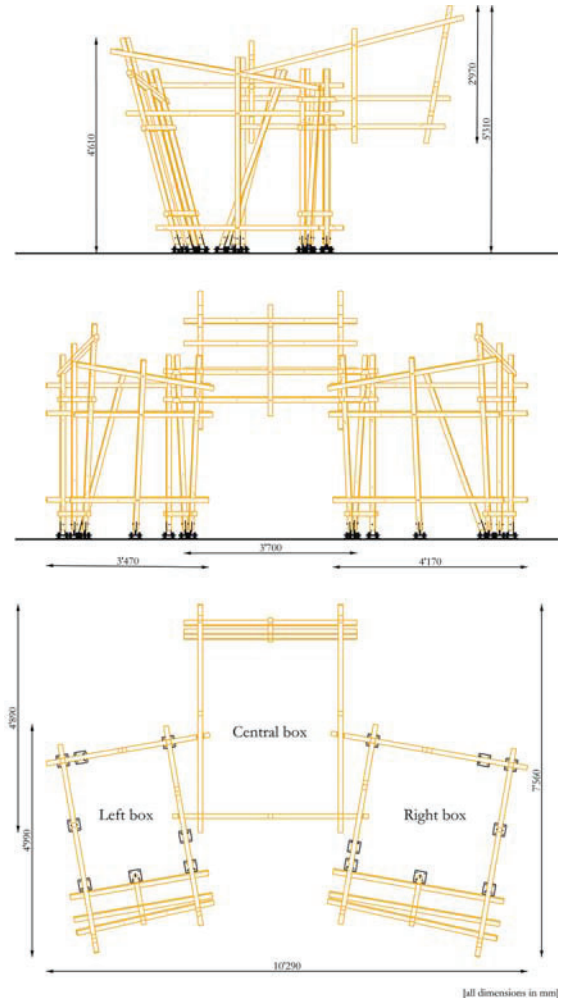

Figure 7: *The structure occupies an area in plan of 10.3 by 7.6 m and reaches a maximum height of 5.3 m.*

3.3 CONNECTION DESIGN

3.3.1 Half-lap connections

Among the many types of interlocking timber-to-timber connections, half-lap connections are adopted since these connections best meet the requirements of automatic robotic assembly. The prototypical half-lap connection is produced through a subtractive process in which half of the cross-section in each of the two elements to be connected is removed. From a static point of view, half-lap connections allow both axial forces and bending moments to be transferred. In addition, this single typology enables great flexibility in the geometry of the structure since a wide range of angles can be achieved on several planes.

3.3.2 Structural capacity of the connections

Based on plastic theory, the static method of limit analysis is adopted to determine the capacity of the interlocking timber-to-timber connections and their design (Section 2.2). The structural capacity of a connection depends on the geometry and the boundary conditions of the connected elements. Here, it is conservatively assumed that the connection has a fixed end on the left side and a free end on the right side.

Contact surfaces

In the half-lap connection, five contact surfaces are identified. These allow axial forces to be transferred in each direction except that of insertion, as shown in Figure 8. The transfer of bending moments occurs by combining in pairs the contact surfaces used for transferring axial forces (Figure 9). A bending moment can be transferred by activating multiple combinations of contact surfaces. From this first analysis, the importance of the extension of the beam beyond the connection that constitutes the free ends becomes apparent. This part activates an extra contact surface to transfer axial forces and bending moments.

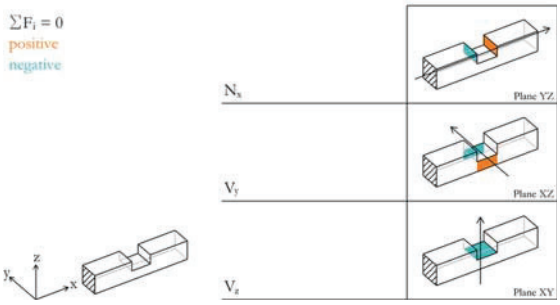

Figure 8: *Contact surfaces activated for the transfer of axial forces. Positive load transfer requires a positive surface.*

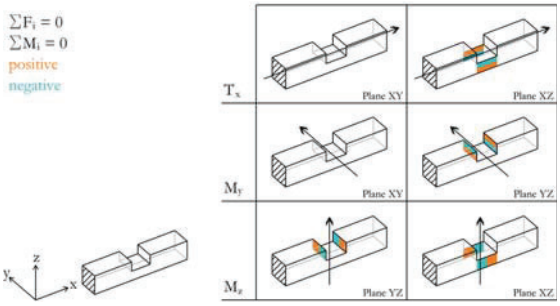

Figure 9: *The coupling of contact surfaces responsible for transferring axial forces ensures the transfer of bending moments.*

Strength of the contact surface

The internal force flow analysis aims to determine the maximum stress applicable to a contact surface. Therefore, this value represents the strength provided by

https://doi.org/10.52202/069179-0573

the internal force flow system. It may be different for each contact surface.
As a reference, Figure 10 shows a more in-depth view of the force flow for several activated contact surfaces. A complete internal force flow analysis based on stress fields, strut-and-tie models, force diagrams and yield conditions is performed according to 2.2.2.

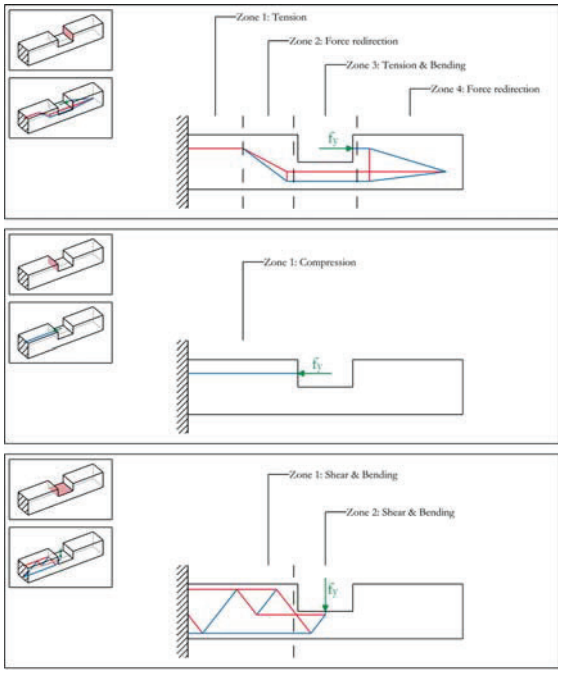

Figure 10: *Several typologies of internal force flow developing in the XZ plane are illustrated. Tension forces are shown in red, compression forces in blue and external forces in green.*

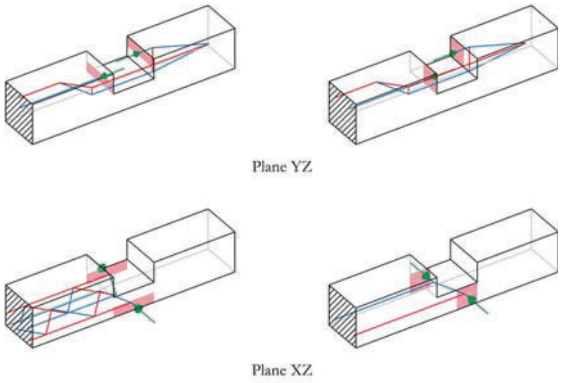

Figure 11: *The transfer of a bending moment occurs by activating two contact surfaces in the same plane. This results in a double flow of internal forces that must be controlled. For example, in the case of contact surfaces activated in the YZ plane, the single flow of forces develops on the XZ plane. Since the flow of forces is double, they can interact. Consequently, an analysis in the XY plane may be necessary as well.*

While in the case of single-activated contact surfaces, the development of internal forces develops in one plane, in the case of simultaneous activation of multiple contact surfaces, multiple flows of internal forces can develop. This happens with bending moment transfer, which occurs by activating a minimum of two contact surfaces, as shown in Figure 11. In this case, the interaction between multiple internal force flows, occurring in planes different from that of the single force flow, can cause changes in the strength of a contact surface.

3.3.3 Parametrization

As each connection is subjected to different loads, it is possible to modify the contact surfaces required for load transfer by varying the geometry of the joints. The prototypical half-lap joint connection is customized whenever necessary to adapt its capacity to internal stresses. In the *CantiBox* project, the prototypical half-lap connection is modified via four parameters (i.e. x, y, z^+, and z^-), as shown in Figure 12 and Figure 13. In this case, the increase in the capacity of the connection is achieved through an increase in the contact surface, while the associated strength is assumed unchanged.

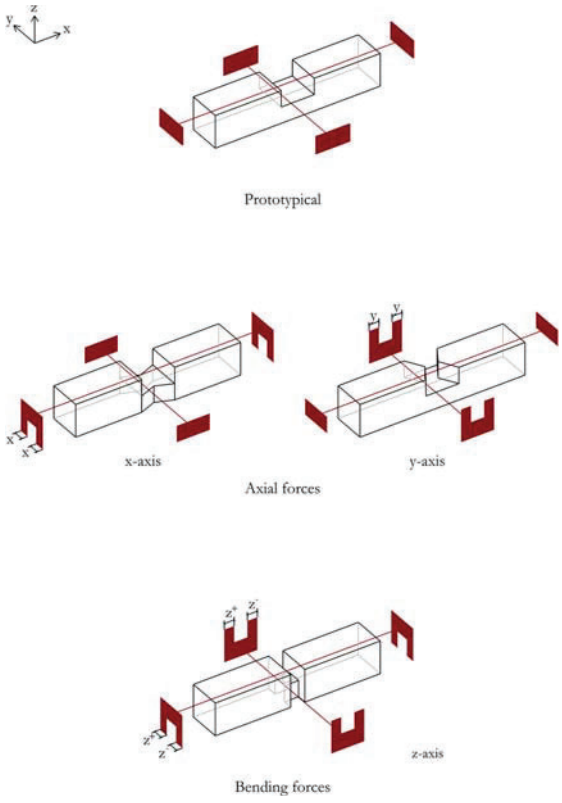

Figure 12: *The geometry modification occurs through four parameters. This allows the capacity of the prototypical half-lap connection to be changed by manipulating the size of the contact surface used to transfer the forces. As contact surface is considered the projection of the connection geometry plane perpendicular to the axes in which the acting loads are determined.*

https://doi.org/10.52202/069179-0573

The capacity to transfer axial forces is governed by the parameters x and y for the respective axes. Parameters z^+ and z^- govern the bending moment capacity in the z-axis for positive and negative moments, respectively. The parameters are considered independent, which means, for example, that the parameter x only influences the transfer of axial forces in the x-axis, not the bending moment in the z-axis.

The connection design process is parameterized and integrated into an algorithm that is automatically able, given the forces to be transferred and the strength of the contact surfaces, to define the geometry of the connection. The algorithm defines the geometry by a control polyline governed by the four parameters described earlier. Geometrical changes take five steps up to a maximum value for a single parameter of 10 mm. The limit is set because geometric changes involve a subtractive process that, if uncontrolled, could change the flow of internal forces and, thus, the strength of individual contact surfaces.

The digital interface developed for this project is shown in Figure 14. It allows the plastic redistribution of forces to be monitored and provides valuable information for fabrication. Concerning fabrication, acute angles are avoided. In addition, there is a real-time three-dimensional visualization of the connection generated by the algorithm. The final design showcases bespoke connections according to the different load conditions, as shown in Figure 15.

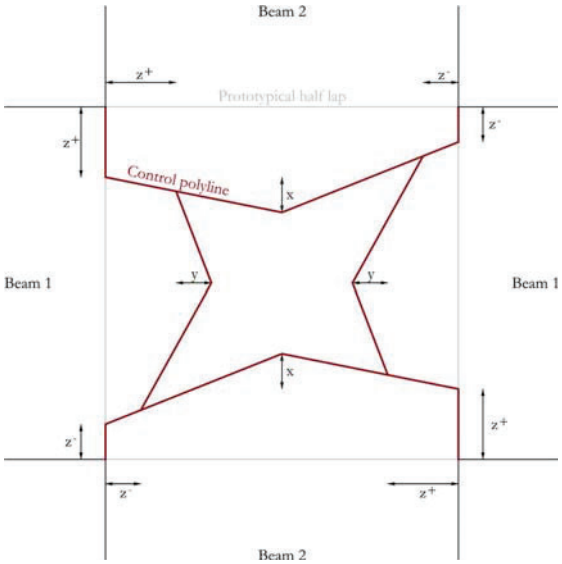

Figure 13: *A polyline defines the three-dimensional geometry of the half-lap connection.*

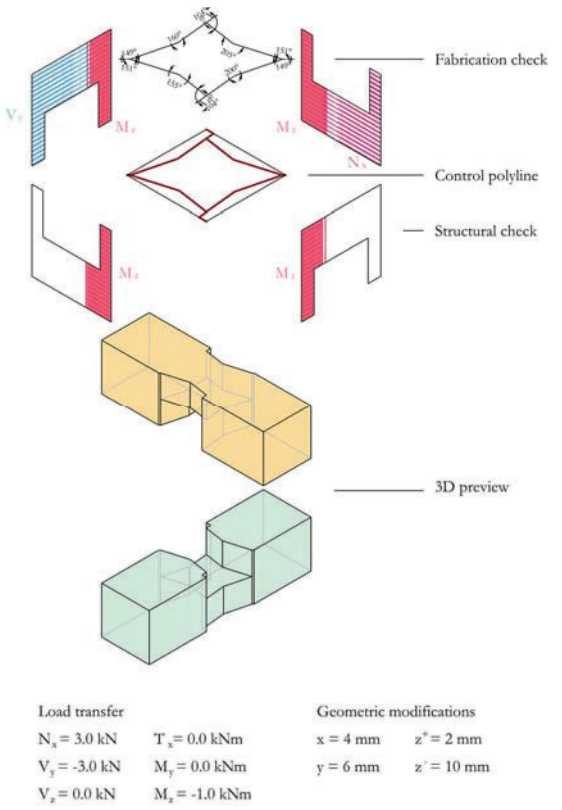

Figure 14: *The digital interface developed for designing and analyzing the connection integrates geometry, fabrication and structural feedback. The parametric space for customization is carefully designed so joints can be machinable by commonly available automatic joinery machines and assembled by our robotic tools.*

Figure 15: *CNC machines foster the design of bespoke geometry for the connections. All the half-lap connections – prototypical and bespoke - are machined with a Hundegger Robot Drive automatic joinery machine (©GKR 2022).*

https://doi.org/10.52202/069179-0573

3.4 ASSEMBLY

The structure is constructed through a fully automatic process [14], which involves using a set of custom-built, remote-controlled, distributed robotic clamps (Figure 16) and screwdrivers (Figure 17). Each of the three units is constructed spatially in an automatic process (Figure 18) instead of planar sub-assemblies. Robotic clamps are used for joints that do not require fasteners. Robotic screwdrivers, which can be loaded with a left-in fastener, are used for the key elements. Those operate in collaboration with an industrial robotic arm to assemble the timber structure spatially. This assembly method is explicitly developed for half-lap connections and allows for overcoming several problems traditionally experienced in the assembly of interlocking timber-to-timber connections, such as:

- The clamp provides a guide that reduces misalignment problems when inserting a new beam into an existing structure.
- Since the clamps are controlled remotely and each clamp is independent, several clamps can be used simultaneously. This allows the simultaneous insertion of a new beam in multiple connections.
- The clamp introduces a large but localized force, which the robotic arm cannot do. This exceeds the resistance given by friction during insertion, as the connections are tight-fit.

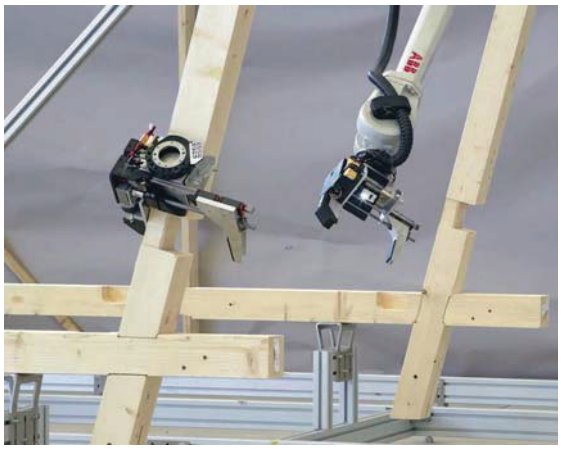

Figure 16: *The robotic arm positions two robotic clamps to insert a new timber element in the structure (©GKR 2022).*

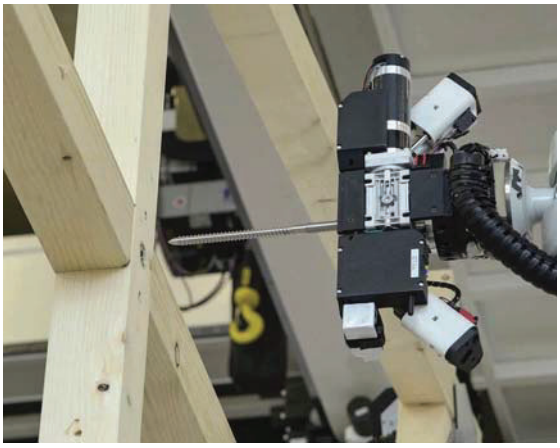

Figure 17: *A key timber element is assembled by a robotic screwdriver loaded with a left-in fastener (©GKR 2022).*

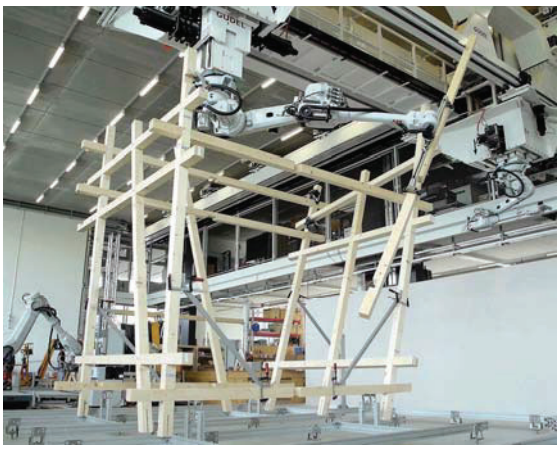

Figure 18: *One of the timber units during construction, with the robotic arm positioning a timber element following the assembly sequence (©GKR 2022).*

The assembly sequence of one face of the box is shown in Figure 19. The interweaving logic of the face allows the use of interlocking timber-to-timber connections during the automatic assembly. Only the last assembled element - the key element - requires a non-structural screw to close the reciprocal system and prevent the system from disassembly.

Figure 19: *The interweaving logic used during the assembly allows the number of metal fasteners to be limited to one per face.*

4 CONCLUSIONS

This paper discusses the design and fabrication of the *CantiBox*, a robotically assembled structure composed of linear timber elements and customized interlocking timber-to-timber connections. The project is made possible by the interweaving logic used in its assembly. Special attention is given to the method developed for analyzing and designing the interlocking timber-to-timber connections, which is based on the lower bound theorem of the theory of plasticity. This novel application of limit analysis to timber allows for informing the design and assessing the collapse load. The proposed static method for limit analysis uses stress fields, strut-and-tie models, force diagrams and yield conditions. Furthermore, it facilitates understanding the relationships between geometry and structural performance, thus allowing to customize each connection according to the specific load conditions. The development of a bespoke assembly set-up allows the structure to be automatically assembled in its final three-dimensional configurations.

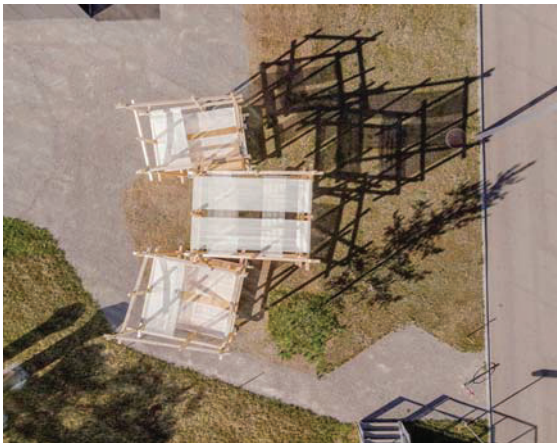

Figure 20: *The CantiBox is partially covered with translucent fabric to provide shading (©Ali Zigeli 2022).*

Figure 21: *The reciprocal configuration allows high geometric complexity using only simple planar joints (©Ali Zigeli 2022).*

https://doi.org/10.52202/069179-0573

CREDITS

Project coordination:
Davide Tanadini (Chair of Structural Design, ETH Zurich), Victor P.Y. Leung (Gramazio Kohler Research, ETH Zurich), Yijiang Huang (Digital Structures, MIT Boston).

Structural design:
Davide Tanadini, Giulia Boller (Chair of Structural Design, ETH Zurich), Pierluigi D'Acunto (Professorship of Structural Design, TU Munich).

Structural analysis:
Davide Tanadini.

Mechatronics & robotic execution:
P.Y. Victor Leung.

Motion planning & robotic task:
Yijiang Huang.

Robotic screwdriver:
Marco Rossi (ILT, OST, Rappeswil).

Algorithm development support:
Ziqi Wang (Geometric Computing Laboratory, EPF Lausanne).

ACKNOWLEDGEMENT

Special thanks for their significant support in the project go to Prof. Dr. J. Schwartz, L.N. Barroso, R.M. Diaz, D. Quaglia, V. Ribi, and L. Strologo (Chair of Structural Design, ETH Zurich); Prof. F. Gramazio, Prof. M. Kohler, Dr. A.A. Apolinarska, Dr. L. Vasey, and G. Casas (Gramazio Kohler Research, ETH Zurich); Prof. Dr. C. Mueller (Digital Structures, MIT Boston); Prof. Dr. A. Koller-Hodac, and L. Steiner (ILT, OST Rapperswil); P. Fleischmann, and M. Lyrenmann (NCCR Digital Fabrication, ETH Zurich).

REFERENCES

[1] C. Robeller, Y. Weinand, V. Helm, A. Thoma, F. Gramazio, and M. Kohler, Robotic integral attachment. In *Fabricate*, London, UCL Press, United Kingdom, 2017.

[2] A. Thoma, A. Adel, M. Helmreich, T. Wehrle, F. Gramazio, and M. Kohler, Robotic Fabrication of Bespoke Timber Frame Modules. In *ROBARCH 2018*, Zurich, Switzerland, 2019.

[3] C. Hua, Z. Guo, H.J. Wagner, T. Stark, A. Menges, and P.F. Yuan, In-Situ Robotic Fabrication of Spatial Glulam Structures. In *CAADRIA 2022*, Sydney, Australia, 2022.

[4] D. Tanadini, O.P. Ohlbrock, M. Kladeftira, M. Leschok, E. Skevaki, B. Dillenburger, and P. D'Acunto, Exploring the potential of equilibrium-based methods in additive manufacturing: the Digital Bamboo pavilion. In *IASS 2022*, Beijing, China, 2022.

[5] D. Tanadini and J. Schwartz, Analysis and design of timber-to-timber connections based on the lower bound theorem of the theory of plasticity. In *WCTE 2020*, Santiago, Chile, 2021.

[6] R.L. Hankinson, Investigation of crushing strength of spruce at varying angles of grain. In *Air service information circular*, Vol. 3(259), Washington D.C., 1921.

[7] Swiss society of engineers and architects, *Timber structures SIA 265*. Zurich, Switzerland, 2021.

[8] U. Thönnissen, A form-finding instrument for reciprocal structures. In *Nexus Network*, Vol. 16(1), 89-107, 2014.

[9] O.P. Larsen, Reciprocal frame architecture. Elsevier, Oxford, United Kingdom, 2008.

[10] J. Wallis, Opera mathematica. E Theatro Sheldoniano, Oxford, United Kingdom, 1695.

[11] D. Tanadini, G. Boller P.Y.V. Leung, Y. Huang, and P. D'Acunto, The CantiBox: Robotic assembly of interweaving timber linear elements using bespoke interlocking timber-to-timber connections. In *ACADIA 2022*, Philadelphia, Pennsylvania, 2022.

[12] Swiss society of engineers and architects, *Basis of structural design SIA 260*. Zurich, Switzerland, 2021.

[13] Swiss society of engineers and architects, *Actions on structures SIA 261*. Zurich, Switzerland, 2021.

[14] P.Y.V Leung, A.A. Apolinarska, D. Tanadini, F. Gramazio, M. Kohler, Automatic assembly of jointed timber structure using distributed robotic clamps. In *CAADRIA 2021*, Honk Kong, 2021.

World Conference on Timber Engineering Oslo 2023

CASE STUDY: TERMINUS – NEW FRONTIERS IN HYBRID MASS TIMBER SEISMIC DESIGN

Brendan Fitzgerald[1], Ilana Danzig[2], Mehrdad Jahangiri[3], Ornagh Higgins[4], Jackson Pelling[5]

ABSTRACT: Terminus is a recently completed 5-storey mass timber commercial building in one of the highest seismic regions in Canada. The seismic demand and the exposed timber drove ASPECT Structural Engineers to undertake a thorough investigation to select a lateral load resisting system that would complement the building's mass timber superstructure, maximize use of timber, and provide a high level of ductility. The selected system involved the novel integration of steel buckling restrained brace frames within a timber post and beam frame. During design and construction ASPECT worked closely with the builder and the mass timber supplier to ensure that all elements of the lateral system were detailed carefully and that all components fit together seamlessly during installation.

KEYWORDS: Mass Timber, Seismic, Innovation, BRB, Hybrid

1 INTRODUCTION

Terminus is a 5-storey mass timber commercial building designed and constructed by a project team consisting of ASPECT Structural Engineers, Jack James Architecture, Design Build Services (DBS), and Structurlam. Located in one of North America's highest seismic regions on Vancouver Island, BC, Terminus' lateral design warranted a lengthy investigation of various systems. Vancouver Island's code-based seismic design parameters are some of the most demanding in North America. According to the Structural Engineers Association of British Columbia, the West Coast of Canada is one of the few locations in the world where all three major categories of tectonic plate boundaries occur: convergent, divergent, and transform. Over the past 70 years these plate boundaries have accounted for more than 100 recorded earthquakes of magnitude 5 or greater [1]. The investigation undertook by the project team involved a selection of different lateral systems that would simultaneously satisfy the onerous seismic loads of the region and meet the client's desire for an aesthetically interesting structure – one that would complement the building's mass timber superstructure.

Terminus' gravity load resisting system is composed of four levels of glulam columns and beams sitting atop a concrete podium and underground parking structure. The diaphragm at each timber level comprises one-way spanning CLT panels, all of which are connected with plywood splines and a matrix of steel plate drag straps fastened to the top of the panels. ASPECT and DBS worked closely in sizing all gravity members and designing all gravity connections to satisfy the building's loading demands and one hour fire rating. The time and effort that went into detailing Terminus' timber components and connections helped motivate the project team in choosing a lateral system that would celebrate the beautiful exposed west coast timber in the building.

Figure 1: *Terminus, Finished Building*

The Buckling Restrained Brace (BRB) timber hybrid system that was ultimately chosen was decidedly best suited to satisfy these requirements, and allowed for a well-integrated, ductile, and highly architectural lateral load resisting system.

[1] Brendan Fitzgerald, ASPECT Structural Engineers, Vancouver, British Columbia, Brendan@aspectengineers.com
[2] Ilana Danzig, ASPECT Structural Engineers, Vancouver, British Columbia, Ilana@aspectengineers.com
[3] Mehrdad Jahangiri, ASPECT Structural Engineers, Vancouver, British Columbia, Mehrdad@aspectengineers.com
[4] Ornagh Higgins, ASPECT Structural Engineers, Vancouver, British Columbia, Ornagh@aspectengineers.com
[5] Jackson Pelling, ASPECT Structural Engineers, Vancouver, British Columbia, Jackson@aspectengineers.com

https://doi.org/10.52202/069179-0574

2 LATERAL SCHEMES AND SELECTED SYSTEM

As developer, designer, builder, and eventually, occupant for the project, DBS was committed to a mass timber structure that was highly architectural, safe, and celebrated the best of what timber can be. Coupled with their desire to furnish themselves and future tenants with a beautiful and robust building, DBS' stake in the project bolstered their willingness to explore various state-of-the-art options for the building's lateral force resisting system. Working together ASPECT and DBS identified cost, aesthetics, ductility, post-earthquake repairability, and precedence as the guiding criteria that would be used to make their selection. ASPECT undertook an investigation of potential candidates for the lateral system, and with DBS' help they shortlisted four options that were determined to best meet the associated parameters. The proposed systems are summarized below, including a list of advantages and disadvantages associated with each option:

2.1 Glulam Brace Frames with Quaketek Friction Dampers

This proprietary system manufactured by Quaketek (a Canadian based seismic protection technology company) is a steel Seismic Friction Damper that is installed at the brace/column interface within a glulam braced frame. The dampers are fuses, dissipating energy induced by the earthquake via friction. The dampers respond symmetrically throughout their cycle (in compression and tension), offering energy dissipation through a range of building motions [2].

The advantages offered by this system include:
-High ductility and offers substantial energy dissipation, which accordingly reduces forces on the other elements in the brace frame.
-Post-earthquake reusability (they can also be easily replaced if necessary).
-Quaketek offers in-house testing to suit a project's specific needs (helps to streamline the design process).

The disadvantages associated with this system include:
-It is not currently codified in Canada (although some research has shown that this system performs similarly to buckling restrained braces, which are an available option in the Canadian Code) [3].
-This product requires additional moment frames for optimal performance, including self-centring, which comes at a high cost in a mass timber building.

2.2 Glulam Brace Frames with Tectonus Resilient Slip Friction Joints (RSFJ)

The RSFJ is manufactured by New Zealand based company Tectonus Resilient Seismic Solutions. This system can be installed at the brace/column interface within a glulam brace frame, and it works by dissipating energy via slip friction as its tightly clamped grooved components move across each other. During a seismic event, the RSFJ will slip and re-centre cyclically before any of the other brace components yield [4].

The advantages offered by this system include:
-High ductility and offers substantial energy dissipation, which accordingly reduces forces on the other elements in the brace frame and other building elements such as the foundations and diaphragms.
-Self-centring capability, which helps to limit residual drifts and associated repair costs post-earthquake.
-Replaceable after an earthquake.
-All RSFJs are tested to suit a project's specific needs.

The disadvantages associated with this system include:
-It is not currently codified in Canada (although to-date there are some recent Canadian projects that have successfully employed this system) [3].
-This system presents higher associated costs relative to the other solutions listed herein.

2.3 Moderately Ductile Glulam Brace Frames (R_D = 2.0, R_O = 1.5)

This codified system features a glulam frame complete with glulam brace members connected to the columns and beams with detailed steel components designed to yield, dissipating energy during an earthquake.

The advantages offered by this system include:
-It is currently codified in Canada (although the code does not provide design guidance) [3].
-Not a proprietary system, so it would be easy to source and detail the component materials and parts. It is also a system that is relatively popular as a mass timber lateral scheme, so there are precedent projects that would offer design guidance.

The disadvantages associated with this system include:
-Lower ductility and energy dissipation than other options, which would increase the cost of the other frame components, and other building elements such as the foundations and diaphragms.
-It is not self-centring, and it is not easily replaced or repaired following an earthquake. This implication could result in substantial post-earthquake costs and could potentially require demolishing the building.

2.4 Steel Buckling Restrained Braces (BRB) in a Timber Frame (R_D = 4.0, R_O = 1.2)

A BRB is a steel section (highlighted in red and blue in Figure 2, below) that is encased in a concrete sleeve (shown in grey in figure 2, below), thus restrained from buckling. The centre of the steel section is slender and designed to yield in both tension and compression during an earthquake [5]. Incorporating a BRB in a timber frame is a unique approach that allows designers the opportunity to preserve the timber structure (incorporating only a limited amount of steel), whilst achieving an impressive level of ductility. Within the BRB braced frame, columns and beams are timber, and the diagonal brace elements are steel encased in concrete.

https://doi.org/10.52202/069179-0574

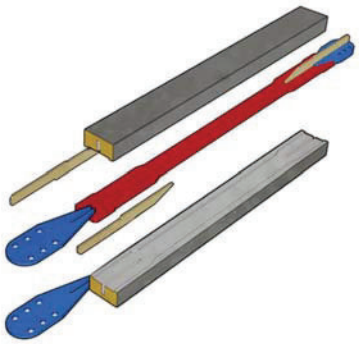

Figure 2: *BRB Cross-Section*

The advantages offered by this system include:
-It is currently codified in Canada (as an all-steel system) [3].
-Comparatively low costs (especially relative to the level of ductility that it achieves).
-High ductility and offers substantial energy dissipation, which accordingly reduces forces on the other elements in the brace frame and other building elements such as the foundations and diaphragms.
-Does not require backup moment resisting frames (as is the case with other lateral systems, such as the Quaketeck dampers).

The disadvantages associated with this system include:
-It is not self-centring. This implication could result in substantial post-earthquake costs and could potentially require demolishing the building.
-There are no precedents for using BRBs in a timber frame.

Following much deliberation between ASPECT, DBS, and Jack James, the timber-BRB hybrid was selected for Terminus' lateral system. Despite the lack of precedence for this type of system (steel BRBs are codified in Canada as an all-steel system, but no other project in North America has featured buckling restrained braces within a timber frame), the project team agreed that the high ductility and the low associated costs would be appropriate for the high seismic loads and the project budget. Furthermore, the opportunity to integrate the steel braces within the timber superstructure meant that DBS' design preference to maximize the amount of timber on the project would be fulfilled.

3 DETAILING OF STEEL/TIMBER CONNECTIONS

Following a linear dynamic analysis of the structure, ASPECT established brace loads, and worked with CoreBrace (the BRB designer and supplier) to finalize the brace dimensions. To optimize geometry and aesthetics, ASPECT and DBS elected to position the braces in a chevron orientation, spanning from floor to ceiling. Framed within glulam columns and beams, the BRBs are the only primary steel elements in the building. Evident in figure 3 below, the integration of the steel braces within the building's timber gravity elements presented the unique opportunity to showcase its mass timber with only minimal additional lateral steel (or concrete) components. CoreBrace's BRB design features a ductile steel plate core enclosed within an outer steel casing, a grout fill, and a proprietary debonding interface material. The ends of the ductile steel plate core are connected to steel lug plates extending out beyond the ends of the outer casing, complete with a bolt hole pattern for connection to the timber columns and beams.

Figure 3: *Newly Installed Braces*

The Canadian engineering steel design standard [3], requires suppliers to perform qualification tests on proprietary buckling restrained braces to demonstrate that design resistances can be developed without buckling the braces under deformations of 2x the design storey drift. CoreBrace performed these tests in-house and used the results to ascertain tensile and compressive strength design factors that were necessary to approximate the design overstrength factors for the brace connections. In compression, the overstrength factor is calculated as the product of three design parameters: ω (a strain hardening adjustment factor equal to approximately 1.4), β (a friction adjustment factor ranging from approximately 1.2 to 1.4), and Ry (the probably yield stress material factor equal to 1.1). In tension the overstrength factor is calculated similarly, without the inclusion of β. The resulting overstrength factors for the braces in compression and tension respectively are 2.1 and 1.6. Accordingly, all the timber connections and timber elements within the frame were designed to the probable capacities of the braces, including the overstrength factors noted above.

As shown in the following figures (4 and 5), ASPECT designed the typical brace connections using steel knife plates projecting from the ends of the braces, complete with multiple rows of stainless steel tight fit pins fastening the plates to the timber frame elements. All these connections were designed in accordance with the Canadian Engineering Wood Design Standard [6].

https://doi.org/10.52202/069179-0574

Figure 4: *Painted Brace Apex Connection*

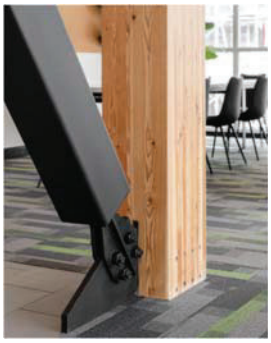

Figure 5: *Painted Brace-Column Connection*

Figures 6 and 7 show typical details for the brace apex and brace column connections. The brace-column connection features a 25mm thick steel knife plates fastened to the column with large groups of 16mm diameter tight fit pins. The plates project from the base of the columns to receive the end of the braces where they are fastened with 28mm diameter heavy hex bolts. The brace apex connection features a V-shaped 25mm thick steel knife plate that projects through a slot in the bottom of the beam and extends up to the top of CLT where it connects with a steel drag element running along the top of the floor. The steel drag strut eliminates the need to utilize the beam as a tie member, which greatly reducing the number and complexity of connections in the system. Whereas conventional chevron brace frames typically require large beams to resolve net vertical forces resulting when one brace buckles in compression and the other yields in tension, BRB's allow designers to avoid this design challenge as the compression capacity and the tension capacity are much closer. Accordingly, the glulam beam was simply designed to resist the comparatively small vertical reaction at the brace apex resulting from the brace action. As shown in figure 6, the beam is top flush with the floor panels. Shifting the beam upwards facilitated higher ductility in the braces by increasing their length, reducing the amount of steel required at the connections. Self-tapping screws installed through the depth of the beam serve to reinforce it against perpendicular to grain splitting, and screws installed through its width effectively clamp the beam and knife plate.

With deformation compatibility in mind, the intersections between the braces and the timber frame elements were detailed to accommodate sufficient rotation such that they could be idealized (as much as possible) as pinned connections. Horizontally slotted holes in the steel knife plates and the use of small diameter stainless steel tight fit pins help to prevent the connections from attracting moment and protect the timber elements from brittle failures. Researchers at the University of Canterbury performed a test program with a glulam frame BRB mock up comprising tight fit pin connections similar to those designed by ASPECT on this project. Their study investigated the cyclic performance of this type of system, and it demonstrated that the tight fit pins connecting the braces to the timber frame elements provided a decent amount of auxiliary ductility to the system while also carrying adequate strength to ensure the primary ductility mechanism would occur in the braces [7]. Additional ductility in a structure that is susceptible to significant earthquake effects is an invaluable benefit that can set the highest performing structures apart in a seismic event.

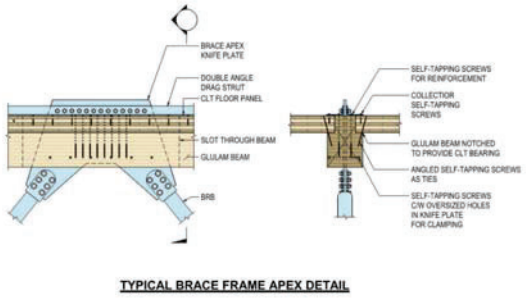

Figure 6: *Brace Apex Detail*

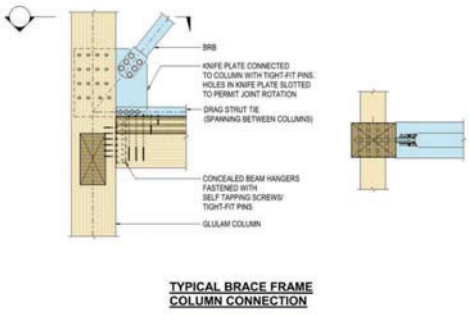

Figure 7: *Brace-Column Detail*

4 FABRICATION AND ERECTION OF TIMBER STRUCTURE

Following the design process, ASPECT worked closely with Structurlam (the timber supplier) for modelling, fabrication, and shop installation of the lateral system components and connections. A steady supply of detail sketches delivered by ASPECT coupled with frequent coordination meetings between the two teams aided Structurlam as they modelled the structure and prepared a

https://doi.org/10.52202/069179-0574

comprehensive shop drawing package. Despite the difficulties associated with having to navigate most of the design process during the early months of the Covid Pandemic, the help of remote meetings and a cohesive coordination schedule assisted the project team in successfully delivering construction drawings on time from their temporary home offices. The coordination between ASPECT and Structurlam aided to ensure accuracy in the fabricated components, and it helped to expedite and ease the installation process.

Structurlam assembled the largest and most critical lateral system connections in their shop. An example of this is observed in figure 8, where the large pre-installed column/brace knife plates located at the tops of the columns can be seen awaiting installation of the braces for the storey above. The pre-installation of the most complex components (notably the tight fit pin column-brace connections) saved a significant amount of onsite installation time and ensured that each of these critical connections was installed in a controlled environment by individuals with abundant mass timber experience.

Figure 8: *Brace Installation*

Tight fit connections demand very strict tolerances in both the steel and timber, and routinely this type of connection has shown to be quite difficult to install in-situ. Being installed in the shop meant that the exposed column faces housing the tight fit pin connections would not be subject to hammer blows by contractors with less experience during installation. To further alleviate the difficulty of installing some of the complex connections onsite, as shown in figure 9 below, the columns were fabricated and installed continuous over the building's first three storeys. Reducing the number of column splices also helped to provide as direct a load-path as possible, which was ultimately a huge benefit due to the high axial forces present in the columns towards the base of the structure.

Figure 9: *Continuous Column Installation*

Despite concerns about inclement weather and moisture management leading into the installation process, DBS's experience in mass timber construction ensured that due care was taken to protect the timber elements and all the crucial lateral system connections from damaging water ingress. Thanks to a carefully planned and executed moisture management strategy (one which included frequent squeegeeing, temporary rainwater leaders, coverings for the vital steel components, and an aggressive installation process) DBS was able to meet their erection goals even though installation occurred during a particularly rainy Pacific Northwest Winter (DBS' team had to deal with a combination of intense rains, snow, and driving winds throughout the mass timber installation process). Terminus' superstructure (including all gravity and lateral system elements) was assembled and erected over a span of roughly 2.5 months (this included 3 occupiable levels of mass timber and the roof, each of which comprise close to 1250m^2).

5 CONCLUSION

Several factors threatened to dampen progress on this building throughout design and construction, including the seismic demands of the region, the complexity of the lateral system connections, low tolerances in the system, a tight construction schedule, and the threat of inclement weather. Despite all these complications, the combination of collaboration, motivation, and experience displayed by the project team ultimately propelled this beautiful mass timber structure and its innovative lateral system to a timely completion. Opened in May 2021, Terminus' beautiful timber structure houses several new tenants, including DBS' entire design office. As the first of its kind in North America, the timber-BRB hybrid lateral system serves as a benchmark for success and innovation in modern mass timber.

https://doi.org/10.52202/069179-0574

Figure 10: *Terminus Interior, DBS Office Space 1*

Figure 11: *Terminus Interior, DBS Office Space 2*

ACKNOWLEDGEMENT

The authors would like to acknowledge the support from the rest of the project team, including Design Build Services, Jack James Architect, Structurlam Mass Timber Corporation, and CoreBrace.

REFERENCES

[1] Structural Engineers Association of British Columbia. British Columbia Earthquake Factsheet. 2013. Online. https://seabc.ca/resources/practice-guidelines. Accessed 2022.

[2] Quaketek. Seismic Dampers - Friction Dampers. 2020. Online. https://www.quaketek.com/seismic-friction-dampers. Accessed 2022.

[3] CSA S16-14 Design of Steel Structures, The CSA Group, 2014.

[4] Tectonus Resilient Seismic Solutions. Tectonus Seismic Technology. 2022. Online. https://www.tectonus.com/structuraltechnology. Accessed 2022.

[5] Corebrace. Corebrace Buckling Restrained Braces. 2022. Online. https://corebrace.com/seismic-brace-systems. Accessed 2022.

[6] CSA O86-19 Engineering Design in Wood, The CSA Group, 2019.

[7] Dong, W., Li, M., Lee, C.-L., MacRae, G., & Abu, A. (2020). Experimental Testing of Full-Scale Glulam Frames with Buckling Restrained Braces. *Engineering Structures.*

World Conference on Timber Engineering Oslo 2023

HARDWOOD GLULAM IN COMPLEX STRUCTURES: DESIGN AND CONSTRUCTION OF THE MACA MUSEUM IN URUGUAY

Vanesa Baño[1], Leandro Domenech[2], Carlos Mazzey[3], Thomas Vieillard[4], Jean-Bernard Journot[4]

ABSTRACT: This work presents the process of structural design, fabrication, and construction of the MACA museum in Uruguay, with a focus on the use of hardwood species. The main room of MACA museum (1600 m^2) is a 3D complex structure made of Red Grandis (*Eucalyptus grandis*) glulam. The structure was designed by 19 bi-hinged frames, made up of inclined columns of 15 m of maximum height and curved beams of variable cross-section up to 27 m long. Given that Uruguay's first forest plantations date in the '90s, there is not yet a structural timber industry. The first timber standards were approved in 2018, and even Europe lacks a harmonized standard for the manufacturing of hardwood glulam. This paper presents the state of the art in hardwoods glulam and focuses on the difficulties and opportunities associated with the use of a hardwood species. In addition, it contemplates the importance of coordinated work between the academy and the industry (architects, structural engineers, and constructors) in the development of the design, manufacturing, and construction of the complex hardwood glulam structure of the MACA museum.

KEYWORDS: *Eucalyptus grandis*, hardwood, glulam, timber industry, structural design, construction, New European Bauhaus

1 INTRODUCTION

1.1 SOLID TIMBER OF HARDWOOD SPECIES WORLDWIDE

By 2030, the global production of coniferous (softwood) sawn wood is expected to increase at an annual rate of 1.8% [1]. Approximately 50% of this timber will be used for construction purposes as a substitute for steel, concrete, and masonry. The other 50% is destined for other uses of solid timber, such as packaging, furniture, or carpentry. In an analysis of the volume production of softwoods and hardwoods worldwide, according to data obtained from FAOSTAT, all the continents, except Asia, produce a higher volume of softwood species (Fig. 1).

This higher use of softwoods can be also observed in Europe, where while the production of coniferous sawn wood maintained an increasing trend over the years, the production of hardwood (non-coniferous) remained constant. Fig. 2 shows the graph of solid wood volume production from 2000 to 2020, generated from the FAOSTAT database.

In addition, the growing interest in sustainable low-carbon biobased materials for construction implies that the trend in demand for mass timber (glued laminated timber -GLT or glulam- and cross-laminated timber -CLT-, among others), continues increasing worldwide, mostly focused on softwood species [1].

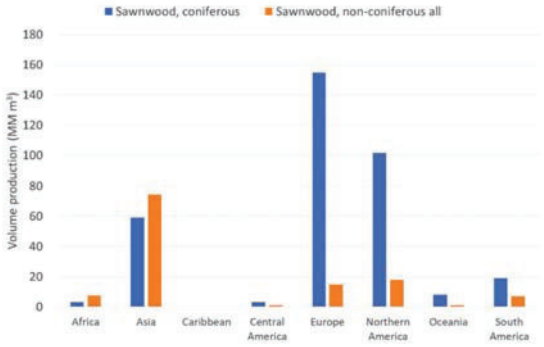

Figure 1: *Sawnwood volume production per continent (data obtained from FAOSTAT, 2022)*

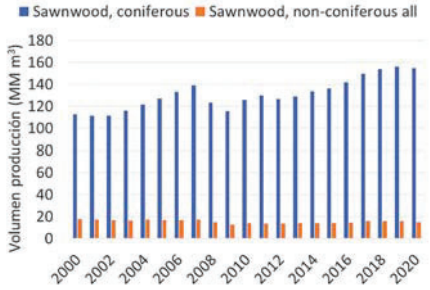

Figure 2: *Sawnwood volume production between 2000 and 2020 in Europe (data obtained from FAOSTAT, 2022)*

[1] Vanesa Baño, Dr. Eng., InnovaWood, Belgium, and Universidad de la República, Uruguay vanesa.bano@innovawood.eu
[2] Leandro Domenech, MEng., Universidad de la República and Oak Ingeniería, Uruguay, ldaguiar@fing.edu.uy
[3] Carlos Mazzey, Civil Eng., Universidad de la República and Oak Ingeniería, Uruguay, cmazzey@fing.edu.uy
[4] Thomas Viellard and Jean-Bernard Journot, Eng., Simonin SAS, France, vieillard@simonin.com

https://doi.org/10.52202/069179-0575

Under this panorama of increasing coniferous´demand for construction, is when the possibility of considering hardwood for structural use arises. Traditionally, hardwood prices were higher than those of softwoods due to, among other factors, the higher energy consumption in drying. However, softwood sawnwood prices have increased considerably in the last few years. As an example, in the US the prices increased more than double from 2010 to 2018, to nearly quadruple by September 2020, decreasing again to values close to those of 2010 at the end of 2020 [2].

1.2 OVERVIEW OF THE HARDWOODS GLULAM IN EUROPE

According to the European standard prEN 1912:2021 [3] data, most European countries have national softwood timber visually graded for structural use, and only five countries (GE, FR, BE, ES, and IT) have graded hardwood sawn wood (ash, beech, poplar, Southern blue gum, shining gum, and sweet chestnut), as shown in Fig. 3. Although this shows the current reduced interest in hardwoods for structural use, the number of species and countries has increased slightly since the previous version of 2012 [4].

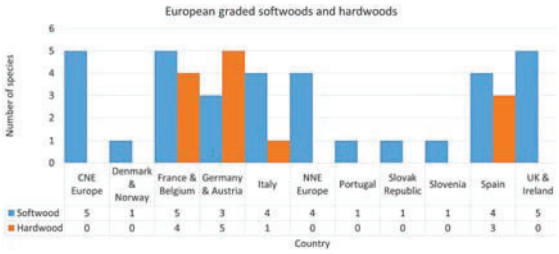

Figure 3: *Softwood and hardwood species visually graded for structural use in Europe (data obtained from* [3]*)*

Current European standards for engineered wood products (EWPs), such as GLT [5], CLT [6], or laminated veneer lumber (LVL) [7] are focused on softwood species, and harmonized European standards for hardwood species are not yet developed. The draft of the European standard about hardwood GLT is under development since 2014 [8], but there is not yet a consensus on the manufacturing requirements which contemplate the variability of the hardwood species. Therefore, it´s not possible to obtain the CE marking via the harmonized European standards, which is mandatory under the Construction Products Regulation (EU 305/2011) [9]. The European Technical Assessment (ETA), which is the basis for a Declaration of Performance (DoP), offers a voluntary route for the manufacturers to obtain the CE marking for hardwood glulam and other novelty products. In the absence of EN standards, European Assessment Documents (EADs) are the technical specifications developed by the European Organisation for Technical Assessment (EOTA) as the basis for the ETA certifications. The ETA for hardwood glulam can be obtained from the EADs for hardwood glulam production number 130010-01-0304 [10] and 130320-00-0304 [10], depending on the species.

Although there are several manufacturers in Europe able to produce hardwood glulam, only four (one in Germany, one in Austria, and two in Spain) obtained the CE marking throughout the ETA certification, according to the EOTA database [11]. Other alternatives are to go to the market using the report of the experimental test results from an external laboratory, and under the responsibility of the manufacturer, as presented in this paper.

1.3 EUCALYPTUS GLULAM IN SOUTH AMERICA

In the South American context, glulam production is mainly concentrated in Chile, with some industries in Argentina and Brazil, and a factory under construction in Uruguay. However, only Brazil has been manufacturing hardwood glulam beams for structural use for years. The company ITA began eucalyptus glulam production in 2008 and built some long-span structures, such as the Haras Polana with a cantilever of 12 m or the Iporanga Convention Center with a span of 14 m [12], Fig 4. However, the lack of standards and marketing strategies has slowed down the development of the glulam industry in the country, although the recent development of standards and the interest of new companies to produce glulam will probably increase the current production capacity by tenfold [13].

Figure 4: *Eucalyptus glulam structures in Brazil* [12]

1.4 FOREST AND TIMBER INDUSTRY IN URUGUAY

During the 90s, Uruguay's forestry sector experienced significant growth and currently, there is 845,000 ha of planted forests. *Eucalyptus spp*. covers 71% of the planted area, with approximately 600.000 ha, from which 42% corresponds to *Eucalyptus grandis* and *Eucalyptus saligna.* and 17% to Southern blue gum (*Eucalyptus globulus)*. *Pine spp*. covers 18% of the planted area, most of them of Loblolly and Slash pine (*Pinus taeda* and *Pinus elliottii)* [14]. The annual production of *E. grandis* is 11.2 million m^3 of roundwood, which is primarily used by the pulp industry and energy sector. The trees used for this purpose are typically between 10 and 12 years old. Approximately 1.2 million m^3 from the annual average supply are intended for mechanical transformation, with trees between 18 and 24 years old [15]. With growth rates of $30 m^3 ha^{-1} yr^-$, *E. grandis* becomes a promising raw material for glulam production in Uruguay.

https://doi.org/10.52202/069179-0575

Since timber is not a traditional construction material in Uruguay, the standards focused on structural timber are very recent. The first standards of timber grading for eucalyptus [16] and pine [17] were approved in 2018, while the standard with the requirements for glulam production [18] was approved in 2019, even though there is not yet a local manufacturing industry for structural products. However, the Uruguayan company *Urufor* has a large tradition in manufacturing laminated Red Grandis (a genetically improved variety of *Eucalyptus grandis*) products for non-structural use, but aesthetics and carpentry use, mainly for exportation. Regarding the national pine industry, the first manufacturing company of glulam and CLT is currently under construction, and it will start to produce in 2023 (*Arboreal*). According to the Uruguayan Technical Standard UNIT 1262 [16], mechanical properties of *E. grandis* sawn wood visually graded are $f_{m,k}$=21.4 N/mm^2, $E_{0,m}$=11960 N/mm^2 and ρ_k=386 Kg/m^3, which could be assigned to a strength class C20 of the European standard EN 338 [19]. Under the lack of a national structural code for designing timber structures in Uruguay, Eurocode 5 [20] [21] has been adopted as the reference code.

1.5 OBJECTIVE

This paper focuses on the importance of coordinated efforts between academia and industry (including architects, structural engineers, and constructors) in the design, manufacturing, and construction of complex and aesthetically pleasing hardwood glulam structures. Specifically, it examines the Atchugarry Museum of Contemporary Art (MACA), which features beams with spans of up to 27 meters and is aligned with the criteria of the New European Bauhaus (NEB).

2 CASE STUDY: MACA

2.1 ARCHITECTURAL DESIGN

MACA museum is situated in Maldonado, Uruguay, and was devised by the sculptor Pablo Atchugarry, throughout the Pablo Atchugarry Foundation. The main building, destined for the sculptures showroom, consists of a 3D curved structure with a floor area of 1600 m^2, designed by Carlos Ott Architect (Fig. 5). It was initially thought to be solved with a steel structure, but it turned to be a timber structure (Fig. 6) after a positive technical feasibility study carried out by some of the authors through the Faculty of Engineering of Universidad de la República.

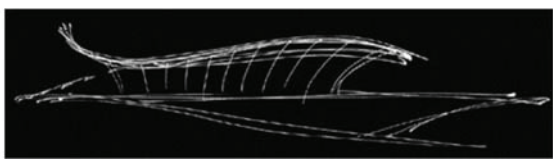

Figure 5: *Architectural sketch of MACA (Source: Carlos Ott)*

Figure 6: *3D rendering of MACA (Source: Carlos Ott)*

This study was focused on the pre-dimensioning of the frames, estimation of wood volume, analysis of the potential glulam suppliers, possibilities of transportation to Uruguay, and construction logistics.

2.2 STRUCTURAL DESIGN

The continuation of the engineering work from the feasibility study developed at the University was made through the creation of a timber engineering study named *Oak Ingeniería*, which was responsible for converting the architectural design into a timber structure, respecting the three-dimensional shape of the envelope.

The initial structural design was solved by 19 bi-hinged frames, made up of inclined columns of 15 m of maximum height and curved beams of variable cross-section up to 27 m long. It was initially designed with softwood glulam of strength class GL24h and the frames were composed of double columns connected to the curved beams by mechanical fasteners (Fig. 7). The design was made looking for a simple solution that could be provided by as many international companies as possible during the tendering process, and which implied a softwood wood volume of 237 m^3. The international tendering was won by the French company *Simonin SAS* with an initial solution using spruce glulam.

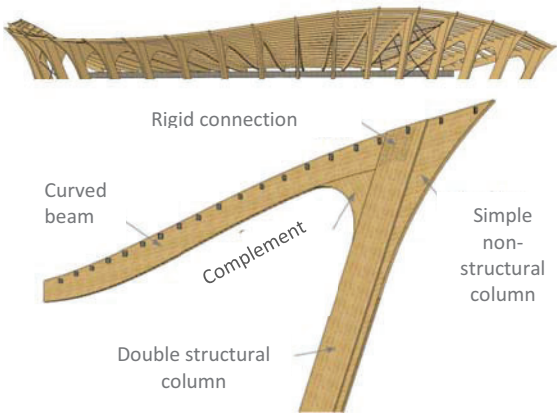

Figure 7: *BIM model of the preliminary softwood structural solution*

https://doi.org/10.52202/069179-0575

2.3 MATERIALS AND GLULAM MANUFACTURING

Since MACA was intended to become an iconic structure and building for the country, the involved actors proposed the option to use local wood for its construction, with the aim to give a local character to the design. Red Grandis was selected for the structure, mainly because of its aesthetics and color, which differ from the most common softwood species used in structures. The tradition and expertise of the company *Urufor* sawing, sorting, and drying this species was key for the selection. 350 m^3 of dried Red Grandis boards (Fig. 7a) of 25/28 mm of thickness were provided by *Urufor* and sent to the *Simonin* facilities in France for glulam manufacturing (Fig. 7b).

(a) (b)

Figure 7: *Red Grandis boards and glulam at Simonin facilities*

The initial environmental cost of this business model was accepted thinking that this iconic building would contribute of promoting the use of local wood for structural purposes. Also, it would allow evaluating of a potential future hardwood-based timber industry, which could provide local structural glulam in a more environmentally friendly solution.

The manufacturing of hardwood glulam implies the reduction in the thickness of the lamellas with the aim to ease the drying process and saving costs. The thickness of the lamellas after the board planning resulted in 20/23 mm in the case of Red Grandis, much lower than the common thickness in softwood, which usually varies between 35 and 45 mm for curved and straight beams, respectively. The increase in drying time of *E. grandis* of 25 mm of thickness versus *Pinus taeda* of 40 mm of thickness corresponds to a factor of 4.25 [22]. In addition, the reduced thickness implies that the number of glue lines increased by 1.6 in the case of lamellas of 25 mm of thickness than that of 40 mm and, therefore, a higher amount of adhesive is required. Both factors have a direct incidence on the hardwood glulam cost.

Under the lack of a specific standard for glulam production, the manufacturing process followed the requirements of standard EN 14080. The initial type testing and the factory production control were made through an agreement with the industrial technical centre *FCBA* to ensure the mechanical properties and the gluing quality. In addition, an internal delamination control according to method C of EN 14080 was made.

The characteristic values of the mechanical properties of the boards and the bending strength of the finger joint ($f_{m,j,k}$) were obtained from experimental tests, resulting in three hardwood strength classes depending of the visual quality: D18 ($f_{m,j,k}$=22 N/mm^2), D20 ($f_{m,j,k}$=36 N/mm^2), and D24 ($f_{m,j,k}$=30 N/mm^2). The values were like those declared for sweet chestnut or Poplar nigra (D24 and D18) and for the lower visual qualities of beech (D18, D24) from France [3]. Glulam beams were manufactured using a Melamine Urea Formaldehyde (MUF) adhesive for hardwood species and results from the initial type testing on full-scale glulam beams resulted in the strength classes named GLD20h (ρ_k= 475 Kg/m^3), GLD24h (ρ_k= 485 Kg/m^3), and GLD28h (ρ_k= 530 Kg/m^3) for the lamellas of strength classes D18, D20, and D24, respectively. The obtained hardwood strength classes were like those of softwood species in terms of bending strength and modulus of elasticity, but with higher values of density.

As a comparison, densities resulted in values 1.3 higher than those of softwood for GL24h and GL28h. These results also showed the increase in the density of Red Grandis, the *Eucalyptus grandis* genetically improved by *Urufor*, with respect to that declared in the Uruguayan standard UNIT 1262 [16].

2.4 STRUCTURAL REDESIGN

The change from a softwood to a hardwood species during the tendering implied a revision of the initial structural design. Not only the cross-section of the members had to be modified, but also the configuration of the frame with the aim to reduce the total wood volume and, in this way, to partially compensate for the higher costs of hardwood versus softwood glulam. The double columns that braced the beams were substituted by simple columns joined by a high resistance connexion of glued bars that support the corresponding bending moment. This connection was solved with the Resix system, patented by *Simonin,* which benefited from the higher timber density of Red Grandis with respect to the softwood species. With the aim to facilitate the transportation of the glulam beams from France to Uruguay, with a total span of up to 27 m, they were manufactured in two parts, joined *in situ* generating a rigid connection with this *Resix* system. Each of the 19 bi-hinged frames consisted of the connection of seven glulam pieces, as shown in Fig. 8, with parts 1, 2, and 3 constituting the main structure of the portal frame. The columns were divided into two parts with the aim to separate the parts located in the interior from those in contact with the weather environment. The objective was that the exterior part of the columns could be repaired or replaced easily in the case of damage due to weather exposure, without affecting the structure of the bi-hinged frame. Fig. 9 shows the final configuration of the frames and the detail of the rigid Resix connection.

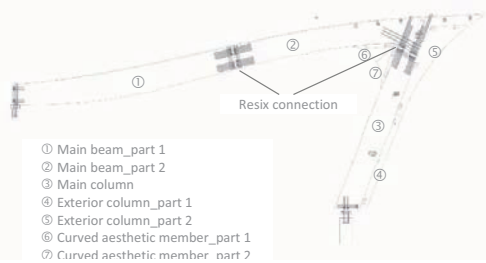

Figure 8: *Scheme of one of the bi-hinged frames*

Figure 9: *Final design of the frames and rigid Resix connection*

The BIM model was modified according to this final design and all the notches were designed to be manufactured by a computer numerical control machine (CNC), which was the key to the successful building process over 10,000 km away from the manufacturing company. Fig. 10 shows the machining of the main beams for the Resix connection and the location of the purlins.

Figure 10: *CNC machining in the beams and purlins*

2.3. CONSTRUCTION PROCESS

The timber structure was erected by *Simonin France* in collaboration with the Uruguayan building company *Atchugarry Arquitectura y Construcción*, which served for the local training in timber construction. With a total of 196 m^3 of Red Grandis glulam (48 m^3 for the purlins, 68 m^3 for the columns, and 80 m^3 for the beams), the construction process started in October 2020 and the MACA Museum was inaugurated in January 2022.

The complex 3D design of the building implied that each glulam piece is different from the other, resulting in a total of 322 purlins, each one with a unique cross-section, length, and angle of insertion on the beams, which also implied the design of unique steel fasteners for each member. Different stages of the construction process are shown in Fig. 11.

Figure 11: *MACA construction process*

https://doi.org/10.52202/069179-0575

During the construction process, black stains were observed on the hardwood timber structure associated with the rains that occurred during the installation of the steel structure for the envelope. It was caused by the contact between the natural wood tannins of the Eucalyptus diluted in water with the oxidized iron contained in steel filings, a problem that doesn´t occurs with softwood species. After different tests developed in the frame of a Master Engineering thesis [23], they were removed by applying oxalic acid, as shown in Fig. 12.

Figure 12. *Steel structure for supporting the envelope and experimental tests with oxalic acid to remove the stains* [23].

Fig. 13 shows images of MACA museum once finished.

Figure 13: *Images during the construction process of MACA*

3 ALIGNMENTS WITH THE NEB VALUES

The design and construction of the sculptures hall of the MACA museum were aligned with some of the New European Bauhaus (NEB) values, launched in 2021 by the European Commission.

1) Together

According to Pablo Atchugarry, owner and developer of the museum, the intention of MACA, located in a 40-hectare greenery field, which is also an international sculpture park, is "to be a bridge for local and international art, an open and free museum where the art can be available all the year". To reach his objective, a collaborative design work process between the owner and the architect in the first stage of the project conception, and then with the academy, engineers, providers, manufacturers, and constructors, made it possible for MACA to become a reality.

2) Sustainable

During the collaborative design work process, the building´s structure was converted from steel to wood. With a total structural wood volume of 197 m^3, the content of biogenic carbon, which was calculated according to EN 16449, was 148 tn. This calculation doesn´t consider the influence of transportation, which would affect the result because the wood made a round trip between Uruguay and France due to the lack of national glulam manufacturers, as had been the case of steel, usually imported from China because of the lack of national steel industry. *Eucalyptus grandis* provided by Urufor comes from sustainable forest management, certified by FSC [24].

3) Beautiful

The 3D building's shape and the aesthetics of Red grandis wood made the MACA museum cited by several international institutions and magazines as a monument to timber architecture or highlighted its aesthetics [25] [26] [27] [28] [29]. In addition, it was selected as one of the best museums of 2022 worldwide by the Conde Nast Traveller magazine [30].

4 CONCLUSIONS

This paper presents the design, fabrication, and construction of the MACA museum's structure, with a focus on the challenges and opportunities that arise when using a hardwood species. The successful implementation of the project was only possible due to the collaborative efforts of all stakeholders from the outset. The architectural and engineering design was developed through an iterative process between the owner, architects, and engineers, with close collaboration with the wood supplier and the manufacturing company. The outcome was a flawless building process, with only one purlin requiring modification due to a human error in the digital order of the CNC machine.

The final redesign with Red Grandis, with values of density 1.3 higher than that of a GL24h from softwoods, resulted in a reduction of 41 m^3 in total wood volume with respect to the initial solution in spruce. However, the

https://doi.org/10.52202/069179-0575

increased cost of this hardwood glulam with respect to a softwood (4.25 times the drying time and 1.6 the amount of adhesive), coupled with transportation costs for manufacturing in another continent, didn´t offset the volume savings. Nonetheless, the choice of Red Grandis, a sustainable and local raw material, resulted in an aesthetically pleasing building, where the wood's natural color and curved building´s structure highlight a unique design in South America, as a result of a collaborating design, complying with the NEB values.

ACKNOWLEDGEMENT

The writing and presentation of this work in the WCTE were made in the frame of the European research project Horizon 2020: BASAJAUN No. 862942, funded by the European Union.
Photography: Agustín Mazzey

REFERENCES

[1]. Nepal, P.; Johnston, C.M.T.; Ganguly, I. Effects on Global Forests and Wood Product Markets of Increased Demand for Mass Timber. *Sustainability (Switzerland)* **2021**, *13*, doi:10.3390/su132413943.

[2]. Verkerk, P.J.; Hassegawa, M.; van Brusselen, J.; Cramm, M.; Chen, X.; Maximo, Y.I.; KoÇ, M.; Lovric, M.; Tegegne, Y.T. *Forest Products in the Global Bioeconomy. Enabling Substitution by Wood-Based Products and Contributing to the Sustainable Development Goals*; FAO, 2022; ISBN 978-92-5-135151-2.

[3]. CEN TC 124 PrEN1912:2002. Structural Timber — Strength Classes — Assignment of Visual Grades and Species. *CEN TC 124* 2021.

[4]. CEN EN 1912:2012. Strength Classes. Assignment of Visual Grades and Species. Brussels, Belgium 2012.

[5]. CEN EN 14080. Timber Structures. Glued Laminated Timber and Glued Solid Timber. Requirements 2013.

[6]. CEN EN 16351:2021. Timber Structures. Cross Laminated Timber. Requirements 2021, 1–7.

[7]. CEN EN 14279:2004+A1:2009. Laminated Veneer Lumber (LVL) - Definitions, Classification and Specifications 2009.

[8]. CEN WD WI 124250. Timber Structures – Glued Laminated Timber Made of Hardwood-Requirements. **2014**, 1–81.

[9]. EU *2011R0305-EN 16.06.2014-001.001-1. Laying down Harmonised Conditions for the Marketing of Construction Products and Repealing Council Directive 89/106/EEC*; 2014;

[10]. EOTA EAD 130320-00-0304. GLUED LAMINATED TIMBER MADE OF SOLID HARDWOOD 2018.

[11]. EOTA ETA Database Available online: https://www.eota.eu/etassessments (accessed on 2 February 2023).

[12]. Olga De Souza Junior, H.; Fernandes, D.S. *WOODEN STRUCTURES IN BRAZIL: PRESENT SITUATION AND PERSPECTIVES*;

[13]. Maximo, Y.I.; Hassegawa, M.; Verkerk, P.J.; Missio, A.L. Forest Bioeconomy in Brazil: Potential Innovative Products from the Forest Sector. *Land (Basel)* 2022, *11*.

[14]. DGF-MGAP *2021_Anuario OPYPA*; Montevideo, 2022;

[15]. DIESTE, A. Posibles Destinos Para Los Productos de Madera Fabricados En Uruguay. *Dirección Nacional de Industrias Ministerio de Industrias, Energía y Minería Consejo Sectorial Forestal-Madera* **2014**, 30.

[16]. UNIT UNIT 1262. Madera Aserrada de Uso Estructural. Clasificación Visual. Madera de Eucalipto (Eucalyptus Grandis) 2018, 18.

[17]. UNIT UNIT 1261.Clasificación Visual de La Madera Aserrada Para Uso Estructural – Madera de Pino Taeda y Pino Ellioti (Pinus Taeda y Pinus Elliottii) 2018.

[18]. UNIT UNIT 1264:2019. Estructuras de Madera. Madera Laminada Encolada. Requisitos de Fabricación 2019.

[19]. CEN EN 338:2016. Structural Timber. Strength Classes. Brussels, Belgium. **2016**.

[20]. CEN TC 250 EN 1995-1-1:2004/A2:2014. Design of Timber Structures - Part 1-1: General - Common Rules and Rules for Buildings 2014.

[21]. CEN TC 250 EN 1995-1-2:2004. Design of Timber Structures - Part 1-2: General - Structural Fire Design 2004.

[22]. Dieste, A. *Plan de Inversiones En Maquinaria y Equipos. (Investment Plan for Machinery and Equipment)*; Montevideo, 2014;

[23]. Domenech, L. Diseño y Construcción Del Museo de Arte Contemporáneo Atchugarry. Desafíos, Soluciones y Oportunidades de Una Estructura Compleja de Madera Laminada Encolada (Design and Construction of the Atchugarry Contemporary Art Museum. Challenges, Solutions and Opportunities of a Complex Glulam Structure. Master Engineering thesis, Universidad de la República: Montevideo, 2022.

[24]. FSC FSC CERTIFICATES PUBLIC DASHBOARD.

[25]. Uruguay_XXI MACA MUSEUM IN URUGUAY, A MONUMENT TO WOODEN ARCHITECTURE.

[26]. Madera_21 MUSEO MACA ASOMBRA POR SU CARÁCTER ESCULTÓRICO LIGADO A LA TECNOLOGÍA EN MADERA LAMINADA (MACA Museum Amazes for Its Sculptural Character Linked to the Laminated Timber Technology).

[27]. Archinet_news Construction Update: An Artist-Designed Museum Takes Shape in Uruguay.

[28]. revista_Construcción MACA, Arte En Construcción (MACA, Art in Construction).

https://doi.org/10.52202/069179-0575

[29]. MALEVA 7 Highlights Del Imponente MACA de Punta Del Este: El Nuevo Museo de Arte Contemporáneo Atchugarry Que Enorgullece a Los Orientales (7 Highlights of the Stunning MACA in Punta Del Este: The New Atchugarry Museum of Contemporary Art That Makes Orientals Proud).
[30]. Conde Nast Traveller Hot List 2022: Los Mejores Nuevos Museos Del Mundo (The Best New Museums Worldwide).

World Conference on Timber Engineering Oslo 2023

CASE STUDY – THE USE OF ROBOTICS IN THE CONSTRUCTION OF TIMBER STRUCTURES USING WESTERN AUSTRALIA'S LARGEST MASS ENGINEERED TIMBER BUILDING AS A TEST BED

Ralph Belperio[1] Pratik Shrestha[2]

ABSTRACT: In 2023, Murdoch University in Australia opened a new teaching facility, called Boola Katitjin. The focal point of this building is the use of Mass Engineered Timber (MET). Boola Katitjin is the largest timber building in Western Australia (WA). Due to their modular and prefabricated nature, MET buildings provide a fertile testing ground for deploying robotics in construction. This paper presents the research that was undertaken to explore the use of robotics in the construction of a MET building to improve the productivity of timber construction. It also presents the findings of the successful deployment of the robot on Boola Katitjin, in a collaboration between Aurecon, University of Technology, Sydney & Murdoch University – bringing an opportunity for academia to collaborate with industry. The findings demonstrated that by using robots to install screw fixings into CLT panels, approximately 15-20% saving in the timber installation construction programme could be realised, compared with using humans to install the screw fixings into CLT. Furthermore, our results show that a robot can install screw fixings at a faster rate (on average) than a human, and with greater accuracies. Finally, this paper presents the challenges faced and assumptions made.

KEYWORDS: Mass Engineered Timber; Robotics; Innovation; Automation, Academia & Industry Collaboration

1 INTRODUCTION

In a world first, Murdoch University (MU), in partnership with Aurecon & University of Technology, Sydney (UTS) deployed robots on a live construction site to construct part of Murdoch's Mass Engineered Timber Building, Boola Katitjin. This tripartite partnership created an academia & industry collaboration to investigate the use of robotics to improve construction productivity.

2 SYNOPSIS

Boola Katitjin is Murdoch University's (MU) new teaching and learning facility, opened in February 2023. Using mass engineered timber (MET), it is the largest mass timber building in Western Australia (WA).

MET buildings can be exemplar in sustainable, circular design by using local renewable materials, designing out waste through modular design and construction, and reducing the carbon footprint of materials using timber, which sequesters carbon. However, due to their relative niche status in Australia, the price of MET buildings often remains a barrier.

In engineering Boola Katitjin, Aurecon challenged traditional mindsets around financial viability through:

• Deep engagement with the timber industry, including a WA Timber Forum to identify risks, challenges and opportunities with timber supply and construction

• Incorporating a world-first robotics technology trial to provide a proof of concept to increase construction efficiency and safety and reduce cost.

The deployment of robotics on Boola Katitjin was led by Aurecon, leveraging an Aurecon Design Academy [1] research thesis on robotics in timber construction, in partnership with the University of Technology, Sydney (UTS). The modular and prefabricated nature of MET buildings provides a fertile testing ground for deploying robotics. Seizing this opportunity, the client, Murdoch University and contractor, Multiplex, were supportive of using the construction of Boola Katitjin as a testbed and exemplar for this emerging innovative technology.

3 INNOVATIONS

3.1 ACADEMIA/INDUSTRY COLLABORATION

The commitment to deploy robotics resulted from a brainstorming session between MU and Aurecon where we explored the challenges the construction industry is currently facing around safety and productivity.

During the workshop, a blue-sky question emerged "Wouldn't it be cool if robots built Boola Katitjin?". This simple question turned into an opportunity to embed academic research into Boola Katitjin around deployment of robotics. This idea gained further traction with the inclusion of UTS, creating a tripartite partnership.

Together, Aurecon, UTS and MU created an academia/industry collaboration project to investigate the use of robotics in construction to advance innovation and improve productivity and safety, through the robotic installation of up to 100 screws (300-400 mm long) into the timber slabs. There are 200,000 – 300,000 screw

[1] Ralph Belperio, Major Projects Director, Aurecon, Australia, ralph.belperio@aurecongroup.com
[2] Pratik Shrestha, Associate, Aurecon, Australia, pratik.shrestha@aurecongroup.com

https://doi.org/10.52202/069179-0576

fixings in total on the Boola Katitjin project. The proof of concept concluded with the successful deployment of the robot – Quenda-bot - on a live construction site in May 2022. This research predicts that it is possible to achieve time savings of 15-20 per cent of the construction schedule once the technology is fully developed and deployed.

3.2 DISRUPTING THE CONSTRUCTION INDUSTRY

This innovation not only has the potential to improve construction productivity and safety on a larger scale, but also contributes to the decarbonisation of the construction industry, with the potential to improve efficiency to embed timber as a preferred material of choice. There are great opportunities for this innovation to be replicated on future timber construction sites and change the way in which we design and construct buildings, to increase speed of construction and reduce embodied carbon. Ultimately, this innovation has the potential to significantly disrupt the construction industry – historically a laggard when it comes to innovation and automation.

Despite being one of the oldest and largest global industries, the sector remains resistant to change, preferring to use historically prevalent materials and construction techniques.

3.3 SUSTAINABILTY AND COST REDUCTION

Building and construction are responsible for 40 per cent of global carbon emissions. Timber building systems can help reduce these emissions. Not only is timber renewable, but it also has a lower embodied carbon footprint than traditional materials, while lending itself to modular design and construction techniques that cut waste and enable reuse of elements, improving the circularity of the construction. When sustainably sourced and manufactured, timber can play an important role in a regenerative economy. Yet it remains more costly in practice. This project aimed to demonstrate cost savings through supply chain collaboration and technological innovation. If cost-effectiveness can be improved to the point where building in timber is cheaper than traditional alternatives, we expect the flood gates to open in terms of uptake of timber as a structural material of choice.

3.4 IMPROVING SAFETY

On Boola Katitjin, there are approximately 200,000 – 300,000 screw fixings. The traditional method of installation is for a construction worker to use a battery-powered impact driver to install these individually, in a crouched position. Being crouched in the same position, while exerting downwards force on the screw, causes back/leg and ergonomic issues.

Aurecon conducted a stakeholder interview with the site team, which uncovered that worker fatigue and morale was a major concern, which the site team had to mitigate by giving the operators more regular breaks every 45 minutes. The introduction of robotics has the potential to largely eliminate these related health and safety concerns. The robot can autonomously install screw fixings throughout the day and night, potentially eliminating robot/human interactions. This will enable construction workers to undertake higher value tasks, assisting with physical and mental health and skill development.

By coupling automation and MET, timber buildings will become safer to build, more efficient, and less costly, enabling the construction industry to move towards a more sustainable and innovative future.

3.5 SUPPLY CHAIN COLLABORATION

As MET is a relatively new material in the Australian context, engagement with the timber industry was conducted via industry workshops, hosted by Aurecon, to identify risks, challenges and opportunities with timber construction and support the timber industry to emerge and scale up.

With exemplar projects such as Boola Katitjin, we remain hopeful that the industry will continue to scale to embrace the opportunities created by the existence and promotion of projects such as Boola Katitjin.

4 PROOF OF CONCEPT TRIAL

4.1 QUENDA-BOT TRIAL

There are 200,000 – 300,000 screw fixings in total on the Boola Katitjin project. The proof of concept concluded with the successful deployment of the robot on a live construction site in May 2022, installing around 100 screws. This research predicts that once the technology is fully developed, it will be possible to save 15-20 per cent of the construction schedule.

The challenges around the robotics technology trial were considerable, which were solved through creating a digital twin and using 3D simulations.

Figure 1: *Quenda-bot on site at Boola Katitjin*

4.1.1 Creating a digital twin

The robot is equipped with a LIDAR (Light Detection and Ranging) navigation system for autonomous travel. However, while the robot could navigate around a place, it needed to still understand where it was globally.

As the civil and structural consultant engineers on the project, Aurecon already had a BIM model (REVIT) of Boola Katitjin. Aurecon and UTS devised a workflow whereby the UTS team exported Aurecon's BIM model and inserted it into their robotics software - Gazebo. This created a digital twin of the building, to allow the robot to understand where in space it was and where it was in the building relative to grid references. Once the robot understands where it is from a global perspective, it then switches to an onboard navigation system to pinpoint where to install the screws.

This workflow has redefined the term 'digital twin'. Historically, we have always considered digital twinning from a construction/built environment/infrastructure perspective. We have now created a new workflow where the digital twin is relatable to robotics, opening a new offering to two industries. Based on this workflow and navigation system methodology, the robot was then able to install the screw fixings to within +/-5mm accuracy, which is acceptable and, in many cases, exceeds the accuracy of manually installed screws.

4.1.2 3D simulations

Pandemic restrictions limited usual lab experimentation practices, hence numerous complex 3D simulations were used to prototype virtually and learn. The robot 3D simulation tests are conducted inside the Gazebo software, which allows the simulation of robots in complex indoor and outdoor environments. This was a fast way to prototype virtually. We were able to trial new and different elements, fail fast in a virtual environment, learn, reset and move on. Following the successful completion of the simulations and virtual prototyping, the robot was then built and tested in a physical lab environment, prior to the successful deployment on site.

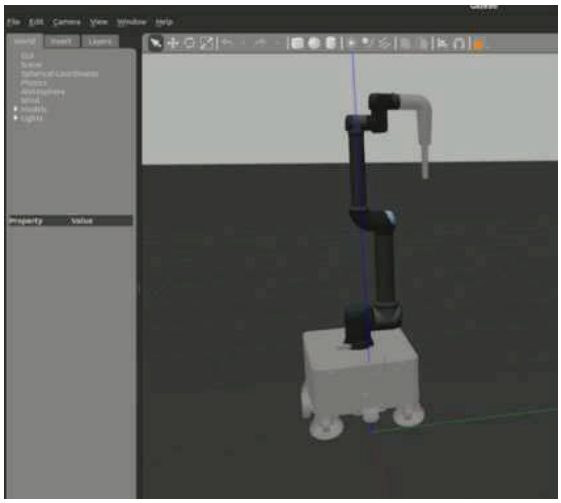

Figure 2: *Robot simulation*

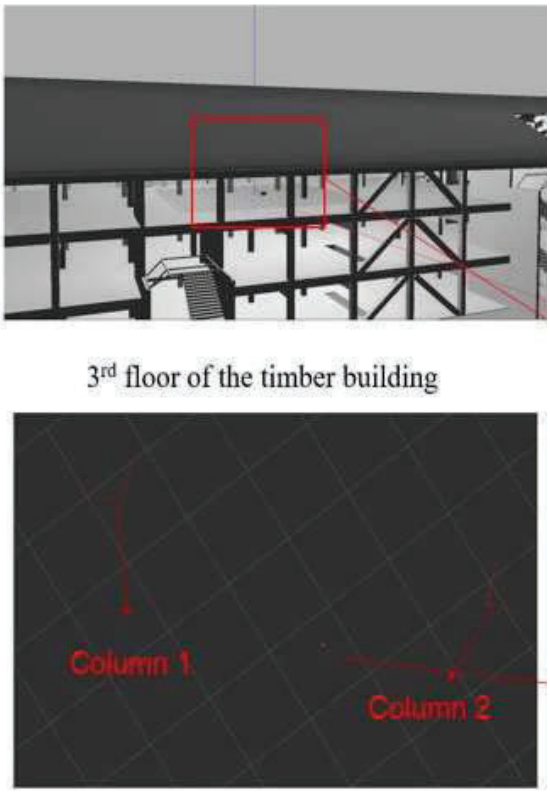

Figure 2: *Estimation of location based on relationship to building columns*

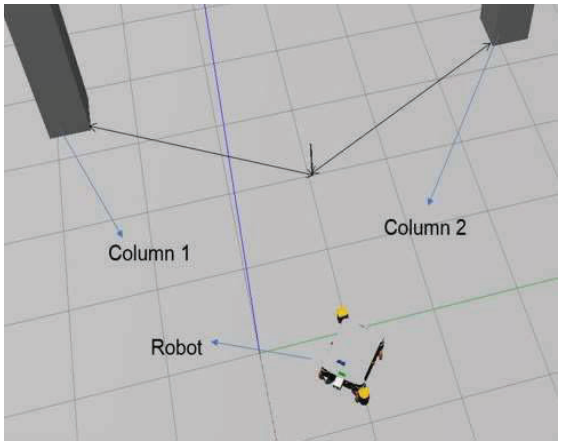

Figure 3: *Virtual model of robot locating process*

https://doi.org/10.52202/069179-0576

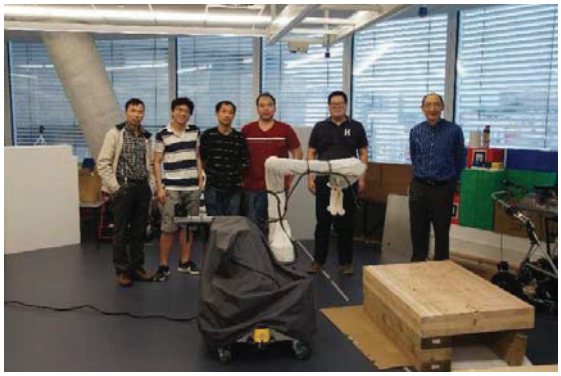

Figure 4: Physical robot testing at UTS labs, Sydney

4.2 Outcomes of the innovative application of the technology

The objectives of this project were to create a sustainable, circular building and to enable projects of this type to flourish across the Asia Pacific region, by demonstrating economic viability, safety, and sustainability.

5 FUTURE OPPORTUNITIES

5.1 THE OPPORTUNITY

MET building systems can help reduce carbon emissions, of which the building and construction sector contributes 40 per cent. It also lends itself to modular design and construction techniques that cut waste and enable reuse of elements in the future. When sustainably sourced and manufactured, timber can play an important role in a regenerative economy. By enabling the efficient and safer construction of timber structures, the aspiration is to make timber the building material of choice. This will contribute to a "step change" in the decarbonisation of the construction industry.

5.2 THE CHALLENGE

MET construction remains costly in practice. This project provided a testbed to research innovations that seek to drive greater efficiencies through supply chain collaboration and technological innovation. If timber construction can achieve greater efficiency to be directly cost competitive to concrete and steel, volumes would increase, further reducing the cost of timber construction. Another challenge will be the ability of the supply chain to meet demand without diminishing supply volumes to traditional markets such as stick built housing. Once cost competitiveness is achieved, then we believe that the focus of the timber industry will shift to meeting the demand in a sustainable way.

6 OUTCOMES

The research commenced with industry engagement to identify risks, challenges and opportunities, and concluded with the successful deployment of the robot – Quenda-bot - on a live construction site, through the collaboration of Aurecon, UTS, Murdoch University and Multiplex. The following outcomes were achieved:

- The robot successfully installed 100 screws as a world-first proof of concept.
- The research predicts a saving of 15-20 per cent off the timber construction schedule if the robotics are suitable developed and deployed fully on site.
- Further gains in productivity and safety could be realised via a 24-hour construction site.
- Worker safety can also be improved through the removal of rote and repetitive tasks, enabling a greater focus on higher value tasks and skills development.
- This research is highly replicable and scalable and is ready to be deployed onto future projects.

6.1 OVERVIEW OF FUTURE APPLICATIONS

Timber remains the only truly sustainable mainstream building material yet has not reached its full potential for commercial applications in the region due to cost and supply chain challenges.

The objective of the Boola Katitjin robotics project was to demonstrate that MET buildings, which also lend themselves to modular design and construction, are economically viable, safe, and sustainable – contributing to a regenerative economy. This in turn reduces waste and increases the potential for future reuse of some elements.

Aurecon has amassed an enviable track record in successful timber design over the past 40 years, including Australia's tallest commercial timber building, 25 King St, one of Australia's tallest residential timber buildings, Monterey Apartments, both located in Brisbane and one of the world's largest timber buildings, Nanyang Technological University Academic Building South in Singapore.

Boola Katitjin is the largest mass timber building in Western Australia. Through the successful design and construction of these and future timber buildings, Aurecon aims to consolidate our reputation as the 'designers of choice' for MET and low carbon buildings of all typologies.

Following the successful deployment of the robot in May 2022, which demonstrated potential savings of 15-20 per cent off the timber construction schedule, the project team have been working on the next stage of robot development. Future developments include improvements to the robot to enable it to install screw fixings more autonomously and at a faster rate.

The project team is currently working on sourcing funding and have identified potential future timber projects on which the robot could be deployed at scale. The aspiration

of the next project is for the robot to do an entire floor plate without any human intervention.
This innovation not only improves construction productivity and safety, but also contributes to the decarbonisation and circularity of the construction industry.
Ultimately, this replicable and scalable research has the potential to disrupt the construction industry for more sustainable outcomes.

6.2 MEDIA COVERAGE

The project generated significant interest from local media outlets, resulting in elevated profile for the project and interest in the emerging technology from various parties:

FINANCIAL REVIEW

Murdoch Uni pilots robot construction

Michael Bleby

The newest worker fixing screws in the framing of Murdoch University's Building 360 is not doing it in hi-vis jackets, or even with eye protection.

Rather, it is on wheels and has a six-axis arm, in a world-first operation to use a robot to install screw fixings – the industrial-sized screws that secure the timber framing to the wooden floor – in a further step down the road to manufacturing-like processes in construction.

It is only a pilot at this stage, testing the safe use of the University of Technology Sydney-designed robot on a live site. It will only place between 50 and 100 out of a total 200,000-300,000 screw fixings on the four-storey structure that will be WA's largest engineered timber building.

But the productivity gains were potentially huge, said Tim Spies, Aurecon's built environment managing director and a consultant to the project.

"On a typical 18-month schedule for a building of this scale and configuration, it would be possible to save between 15-20 per cent of the timber construction schedule," he said. "This could represent a saving of between 4-8 weeks on the overall build."

Further gains could come from the work robots could provide during night work, he said. Humans could "drop in" the timber slabs during the day, and the robot work throughout the night installing screws.

Multiplex is the construction contractor on the building with a $145 million budget. Practical completion is due in November.

UTS Robotics Institute and the project leader, Dikai Liu, said intelligent robots were changing construction.

"Construction sites are varied, complex and changing – and that can be a real challenge for a robot to navigate and conduct operations," Professor Liu said. "What we have been able to design is an intelligent robot that can focus on an important task even amidst this disruptive environment."

Mass Engineered Timber buildings offer a good testing ground for robotics in construction. Installing screw fixings into CLT slabs is typically the most repetitive task in any timber project.

Figure 4: *The Australian Financial Review article*

We were informed that Rory Campbell from 7 News Perth would attend site briefly during the trial. Such was the enthusiasm for Quenda-bot that he and the 7 News team ended up remaining on site for 3 hours during the trial, resulting in coverage on multiple media platforms.

7NEWS Perth
@7NewsPerth

Robots can already cook and clean, now they're turning their attention to construction. A trial happening in Perth right now could be a glimpse into the future for Perth's building industry. #7NEWS @RoryDCampbell 7NEWS.com.au

5:23 pm · 4 May 2022 · Twitter Media Studio

Figure 5: *7 News Perth coverage*

The project also generated significant interest in engineering circles, including an article in the Innovation section of Create, Engineers Australia's magazine and website [2].

Meet the robot helping to build Western Australia's largest mass-engineered timber building

by Jonathan Bradley — July 26, 2022 in Innovation 3 min read 0

Figure 6: *Engineers Australia coverage*

https://doi.org/10.52202/069179-0576

7 CONCLUSIONS

International design, engineering and advisory company Aurecon has introduced robotics technology into the construction of Murdoch University's new Boola Katitjin building in a world-first trial, in collaboration with major partners Murdoch University (MU) and University of Technology, Sydney (UTS).

Boola Katitjin is Western Australia's largest mass-engineered-timber (MET) building. MET buildings can be exemplar in sustainable, circular design by using local renewable materials, designing out waste through modular design and construction, and reducing the carbon footprint of materials using timber, which sequesters carbon. However, due to their relative infancy in Australia and New Zealand (ANZ), the price of MET buildings can be perceived as a barrier.

The objectives of the research project were to create a sustainable, circular building and to enable projects of this type to flourish across Australia and New Zealand, by demonstrating economic viability, safety, and sustainability. Conceptualised by Aurecon as part of an Aurecon Design Academy [1] thesis project and delivered as an industry/academia collaboration between Aurecon, University of Technology, Sydney (UTS) researchers, Murdoch University and Multiplex, the aim was to demonstrate that robots could deliver cumbersome screw fixings - a repetitive and time-consuming task that causes fatigue and injury in workers.

The robot – "Quenda-bot" – was successfully deployed on the 'live' Boola Katitjin construction site in May 2022, demonstrating how automation could improve worker safety and construction efficiency, with potential savings of 15-20 per cent from the timber construction schedule.

There are around 200,000 to 300,000 screw fixings on the Boola Katitjin construction site. The proof-of-concept trial successfully installed around 100 screw fixings.

Following the successful deployment of the robot, the project team have been working on the next stage of development. The future application is for the robot to be refined to enable it to install screw fixings at a faster rate. The project team is currently working on sourcing funding and have identified potential future timber projects on which the robot could be deployed at scale. An aspiration for the next project is for the robot to screw fix an entire floor plate without any human intervention.

Ultimately, this research has the potential to disrupt the construction industry for more sustainable outcomes

ACKNOWLEDGEMENTS

The Authors would like to acknowledge the support and tireless efforts of the following parties in making this work possible:

- Murdoch University – for having the vision to build WA's largest Mass Engineered Timber building, and entrusting Aurecon to conceptualise and deliver that game-changing building for them. Also, to allow Aurecon to assist them in developing a process for achieving a world-first innovation, using their project as a testbed. We will forever be thankful for the support and trust they put in us to deliver.
- University of Technology, Sydney – Robotics Institute, and particularly the leadership of the quintessential gentleman Professor Dikai Liu, and his team led capably on site by Professor Shoudong Huang. Without access to the eminent skills and capability contained in that Institute, and their innate willingness and ability to collaborate, the outcomes presented here would not have been possible.

REFERENCES

[1] Aurecon Design Academy – The paper Authors Ralph Belperio and Pratik Shrestha are both Alumni of Aurecon's internal talent accelerator program. https://www.aurecongroup.com/about/future-ready/eminence/aurecon-design-academy

[2] Create Engineers Australia article – Meet the robot helping to build Western Australia's largest mass-engineered timber building https://createdigital.org.au/the-robot-behind-western-australias-largest-mass-engineered-timber-building/#:~:text=A%20robot%20designed%20by%20Aurecon,very%20smoothly%2C%E2%80%9D%20Shrestha%20says.

World Conference on Timber Engineering Oslo 2023

VALIDATING MOISTURE-SAFE ENERGY EFFICIENT CLT ASSEMBLIES IN HOT AND HUMID CLIMATES USING EXPERIMENTAL TESTING

Marcus Strang[1], Paola Leardini[1], Maryam Shirmohammadi[2]

ABSTRACT: Climate specific cross-laminated timber (CLT) construction detailing to manage moisture risks in subtropical and tropical regions of Australia is validated through experimental testing, statistical analysis, and computational hygrothermal modelling. Three projects in Australia are monitored: a CLT micro-unit built in a subtropical climate, a small CLT structure assembled inside a controlled double climatic chamber simulating a tropical environment, and an existing residential building located in a tropical climate. Several parameters are altered in the experiment design to understand the most reliable assemblies for CLT buildings in hot and humid climates that can sufficiently control the moisture risks. The findings suggest that the hygrothermal modelling guidance from ASHRAE 160 pertaining to construction unprotected from stormwater accurately represents CLT assemblies in hot and humid climates. The importance of adhering weather resistant membranes (WRB) to both the external face and edge grains of the CLT panels is revealed. In tropical climates, the positioning of internal insulation and WRB with increased vapour resistance are also shown to be beneficial, while ventilated cavities and drainage layers behind the cladding is critical for rain protection.

KEYWORDS: CLT, Hot and humid climates, Moisture, Construction wetting, Field monitoring, Energy efficiency.

1 INTRODUCTION

CLT construction and highly energy efficient buildings were originally developed and adopted in temperate and cold climates, where the vapour transfers predominantly from the inside to the outside. Instead, buildings in tropical and subtropical climates face different conditions, where cooling-dominated interior zones exert a vapour pressure in the direction of the interior for much of the year, due to high ambient relative humidity (RH) and temperatures. In addition, buildings constructed with CLT envelopes that are located in tropical climates have enhanced susceptibility to biotic deterioration [1] due to ambient temperatures and RH being within a range that is optimal for biotic growth to occur. As the market for energy efficient CLT buildings expands into these climates, performance testing and subsequent design adaptation is required. This is especially concerning in Australia, where the building industry has been slowly transitioning towards energy efficient buildings with increased levels of airtightness and thermal protection, adopting modern construction materials and practices that may exacerbate moisture risks. [2]. Therefore, this study focuses on experimental testing — including design and results — to validate simulation results and, thus, the proposed moisture safe solutions in subtropical and tropical regions.

[1] Mr Marcus Strang and Dr Paola Leardini, School of Architecture, University of Queensland, Brisbane, Australia m.strang@uqconnect.edu.au & p.leardini@uq.edu.au
[2] Dr Maryam Shirmohammadi, Forest Product Innovation, Department of Agriculture and Fisheries, Brisbane, Australia. maryam.shirmohammadi@daf.qld.gov.au

2 METHODOLOGY

Three projects in Australia were subjected to a monitoring campaign aimed to validate results of previous hygrothermal simulation. A CLT micro-unit has been designed and built at the Salisbury research facility of Queensland Department of Agriculture and Fisheries (DAF) and exposed to the hot and humid subtropical climate of Brisbane, as shown in Figure 1. A small CLT structure, employing the same assemblies of the micro-unit, has been placed inside a controlled double climatic chamber to simulate exposure to a tropical environment, as shown in Figure 2. Lastly, an existing CLT residential building located in tropical Cairns was also instrumented, as shown in Figure 3.

Figure 1: *The CLT micro-unit's shown before cladding is installed (left) and after installation (right)*

https://doi.org/10.52202/069179-0577

Figure 2: *The arrangement of the internal and external insulation of the small structure within the double climatic chambers is shown before the seal is completed between the two climatic chambers*

Figure 3: *Construction of a CLT residential project in Cairns, depicting the steel framing and ground floor CLT panels with scaffolding and the weather resistant membrane visible*

The monitoring campaign of the three projects included the installation of moisture content (MC) sensors within the CLT panels. This was done to demonstrate the impact of different parameters and investigate the moisture performance and hygroscopic characteristics of the CLT structures over two phases. The first phase of the study monitored changes in MC of CLT panels through exposure to hot and humid climates during the 'construction' period, while the second phase investigated the change in vapour flow through the CLT assemblies once construction was complete and the building space was conditioned. The experiments allow the evaluation of specific parameters, including the influence of weather resistant membranes (WRB), location of the insulation layer (internal/external), and exposure of unprotected walls to high humidity and high temperature during construction, to verify moisture-safe assemblies developed in earlier studies using hygrothermal simulation for these same hot and humid climates [3]. The different parameters investigated in this study are shown in Figure 4.

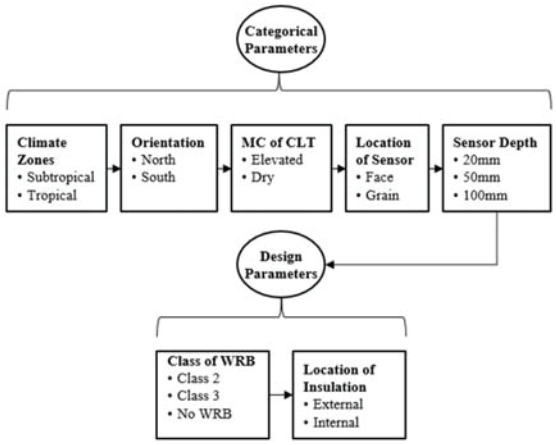

Figure 4: *Parameters evaluated within the two experimental tests*

The MC measurements were processed and inputted into calibrated hygrothermal simulation models to evaluate these parameters over the construction and operational phases. This was done to support the identification of the most appropriate CLT assemblies for hot and humid climates to avoid moisture risks.

2.1 CONSTRUCTION OF THE CLT MONITORING PROJECTS

The purpose of the three experiments was to cover specific climatic conditions for assessing long-term construction risks for CLT assemblies in hot and humid Australian climate.

2.1.1 CLT MICRO-UNIT EXPERIMENT

The CLT micro-unit was constructed to understand the impact of membrane vapour permeability on MC of the CLT panels during construction. For this reason, the two types of WRBs (a Class 2 and Class 3 product) were adhered to the external surface of the CLT panel on the north and south orientations. To assess the worst-case orientations, due to solar-driven inward diffusion effect on the north orientation and wind-driven rain and minimal drying potential effect on the south orientation. While the east and west oriented CLT panels were left exposed as reference cases. The CLT envelope was left exposed for 6 months during Brisbane's hot and humid summer season, as shown in Figure 5. This was expected to provide conservative results in terms of moisture risk, as a typical summer season in Brisbane was associated with the highest precipitation and RH for the year, which was a key consideration for this research. The duration of the experiment was decided to reflect worse-case delays during the construction phase of large-scale CLT buildings, for instance, due to procurement issues of the windows, concrete structure, or steel framing.

https://doi.org/10.52202/069179-0577

Figure 5: *The CLT micro-unit during the 'construction' period. The location of the sensor arrays on the interior CLT surface, the 2 WRB types, as well as the exposed CLT surfaces, edge grains, and rough door opening are visible*

The protected 'operational' phase commenced with the installation of the door, insulation panels, eave over the door, wall cladding, and roofing sheets flashed for rainfall drainage. A small, decentralised ventilation system with heat recovery and a small split system were also installed internally and activated during the 'operational' phase.

2.1.2 CLIMATIC CHAMBER EXPERIMENT

The climatic chamber experiment was developed to understand how CLT assemblies dry-out in tropical climates after construction wetting. This was done by changing certain parameters in the assembly, including the insulation layer location, vapour permeability of the WRB, and initial MC of the CLT panels. The configuration of the internal and external insulation, as well as the 2 types of WRBs with different vapour permeabilities can be seen in Figure 6.

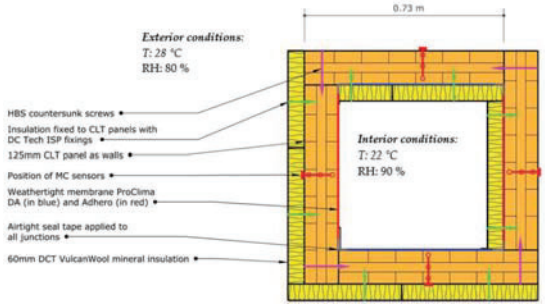

Figure 6: *The position of the insulation, different WRB types, and MC sensors in the double climatic chamber experiment*

To assess the influence of the initial MC of the CLT, 4 CLT panels were installed 'dry', while 4 CLT panels were 'wetted', letting them soak with a 10 mm layer of water sitting on their surface to represent two wetting events on-site, of 4 days and 7 days respectively, with a 10-day gap. All 8 CLT panels were then assembled in the double climatic chamber, as shown in Figure 7. The CLT assemblies were then subjected to 'exterior' condition of 28 °C and RH of 80 % for two months — a typical monsoon season in Cairns or Darwin. Insulation was then added, and the 'interior' condition was set to 22 °C and RH of 90 % for an additional two months, to represent an actively cooled building with a very high internal humidity loads, such as a kitchen or bathroom zone with an inadequate ventilation strategy.

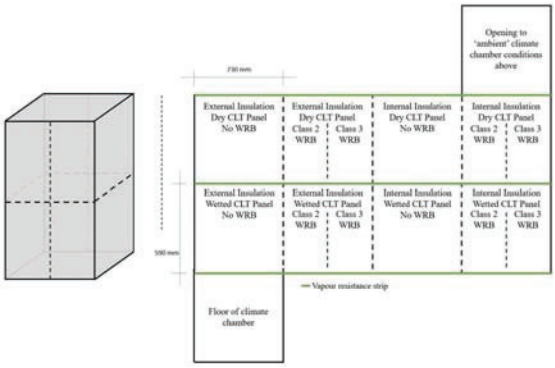

Figure 7: *Unfolded configuration of the CLT panels installed in the double climatic chamber*

2.1.3 RESIDENTIAL CLT BUILDING

A detached three-bedroom residential CLT building located in Cairns, comprising 180 m^2 of conditioned space was monitored over its construction period. No monitoring during occupation of the building took place. The project was instrumented to understand the moisture risks inherent with 'real-world' CLT buildings construction and the challenges of building with CLT in locations exposed to monsoon weather patterns. Only the north and south orientations were instrumented with MC sensors, as shown in Figure 8. As these were the worst-case orientations, due to solar-driven inward diffusion effect on the north orientation and wind-driven rain and minimal drying potential effect on the south orientation.

Figure 8: *Each red dots depicts the locations of two MC sensor arrays for the tropical residential construction (plan view)*

https://doi.org/10.52202/069179-0577

2.2 INSTALLATION OF THE WIRELESS SENSING SYSTEM

The monitoring of the MC within all three projects was achieved with small, wireless, pin-type electric resistance moisture meters from OmniSense LLC (sensor S-11) [4]. The sensors have a sampling frequency of 6 minutes, a temperature error of ±2 °C, and a RH error of ±5 %. Installation of the MC sensors involved covering the MC probes (18-8 stainless steel mounting screws) with heat-shrink tubing to electrically isolate the screw shaft, while the screw head and tip were left exposed by 20 mm, to enable an electrical connection through the timber back to the electric circuit, and then embedded into the CLT panels as shown in Figure 17. The insulated probes were installed as arrays at three depths — 20 mm from the internal CLT panel surface, at the centre of the panel (50 mm from the internal surface), and 20 mm from the external panel surface (100 mm from the internal surface). An array of sensors was installed for each unique combination of assembly design parameters in each experiment, leading to the installation of 45 sensors in the CLT micro unit, 48 sensors in the double climatic chamber, and 18 sensors in the residential CLT project.

Figure 9: *A MC sensor with heat-shrink tubing and 20 mm exposed screw tip (left), then embedded in to the CLT wall (right) in the residential CLT building in Cairns*

2.3 CALIBRATION AND VALIDATION OF HYGROTHERMAL SIMULATIONS

Calibrated hygrothermal simulations require that the initial and boundary conditions represent the real conditions of the experiment as closely as possible. The monitored data of the external and internal boundary conditions, and the initial MC within the CLT panels were used for this purpose. The hygrothermal material properties were assigned from the material library within WUFI, which is the hygrothermal simulation tool utilised within this study. The dataset from the WUFI material library contains all the relevant hygrothermal properties to allow realistic simulation of the assembly layers used in the experiments.

2.3.1 BOUNDARY CONDITIONS FOR CALIBRATION

In the case of the CLT micro-unit and residential CLT building, the exterior boundary conditions were downloaded from a local weather station. While the exterior boundary conditions of the climatic chamber experiment and the interior boundary conditions for all three experiments were generated by RH and temperature sensors located in the plastic housing of the MC sensors. The temperature and RH values for the interior and exterior boundary conditions were processed and then formatted for use in WUFI. The boundary conditions are shown in Figure 10, Figure 11, and Figure 12 for the CLT micro-unit, double climatic chamber, and residential building, respectively.

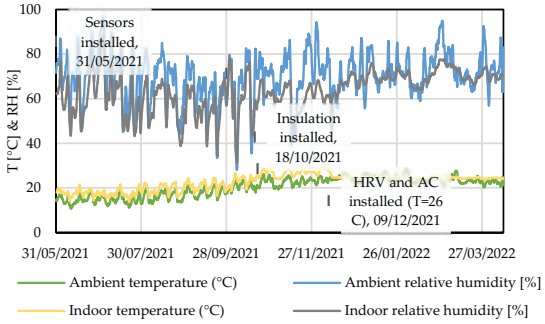

Figure 10: *The internal and ambient conditions from the naturally exposed prototype CLT micro-unit experiment in Salisbury. Data presented in a 24-hour moving average for visual clarity*

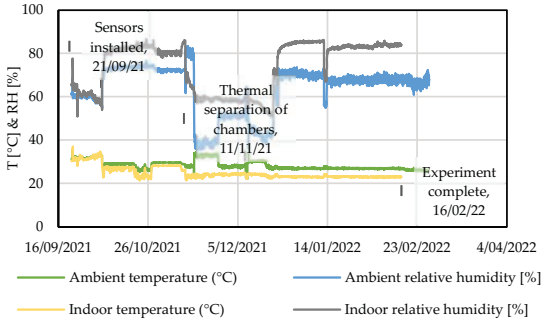

Figure 11: *The internal and ambient conditions from the double climatic chamber experiment simulating tropical conditions*

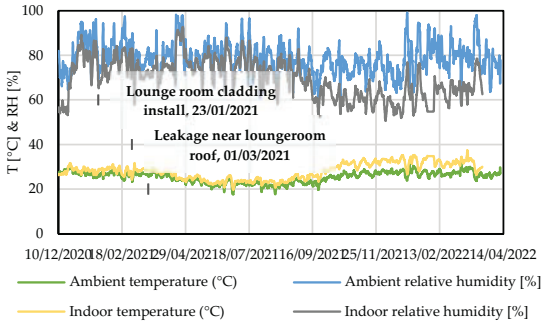

Figure 12: *The internal and ambient conditions from the tropical CLT residential building in Cairns. Data presented in a 24-hour moving average for visual clarity*

For the CLT micro-unit experiment, the air change rate in the 35 mm ventilated air gap behind the cladding was tested using an Almemo 2690 Ahlborn hand-held anemometer device [5]. Recordings were taken multiples times per day, over the course of two days, and the average air change rate was calculated as 54 ac/h. This appears to be a reasonable air change rate for fully ventilated fibre cement cladding, as air change rates of around 50 ac/h have previously been suggested in the literature [6], [7]. This air change rate was used as a boundary condition in both the hygrothermal models representing the CLT micro-unit and CLT residential building.

The initial MC settings used in the calibrated simulations were approximated by taking the average MC from the first 5 hours of MC monitoring for each sensor. This initial MC from each sensor was converted to a water content and assigned across the thickness of the three lamellae respectively. An example of the initial MC assignments can be seen for the CLT micro-unit, where Figure 13 depicts the 'construction' phase and Figure 14 depicts the 'operational' phase. These figures depict the 125 mm thick CLT panels which consist of 3 lamellae of radiata pine adhered together. Where in contrast to European CLT, it should also be noted that the edge gap of Australian CLT is not adhered.

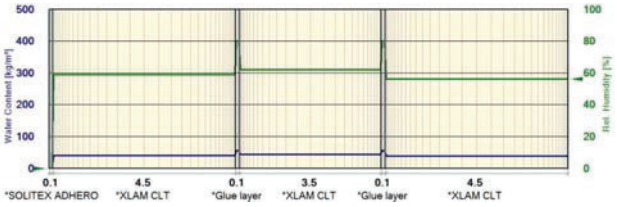

Figure 13: *Screenshot taken from WUFI of the cross-section of the CLT micro-unit wall assembly [cm] representing the 'construction' phase, where the initial MC assigned to the three lamellae is calibrated from the monitored data*

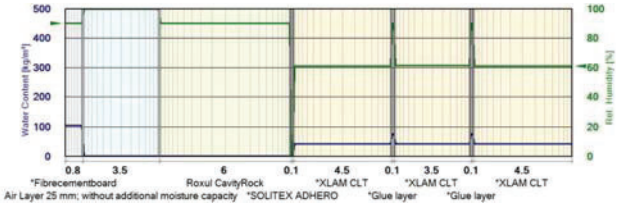

Figure 14: *Screenshot taken from WUFI of the cross-section of the CLT micro-unit wall assembly [cm] representing the 'operation' phase, where the initial MC assigned to the three lamellae are set to be consistent with the MC from the end of the 'construction' phase simulation.*

2.3.2 VALIDATION OF THE CALIBRATED HYGROTHERMAL SIMULATIONS

To validate the calibrated simulation data, hourly MC values were extracted from a 1 mm slice of CLT at the 20 mm, 50 mm, and 100 mm depths from the internal surface of the CLT panel to represent the positions of the MC sensors. The MC data from the sensors was cleaned by removing any null values and values lower than 8 % MC, which represented a loss of connection of the sensor probe with timber. Linear regression statistics packages were utilised in the statistical software R-studio and R to establish if a significant correlation exists between the simulated MC data and the monitored data. This was done by fitting the data to a regression model. The root mean squared error (RMSE) was used to quantify an error of deviation in the predictive quality from the simulations, as shown in Equation 1. While, the Pearson's product-moment correlation method was used to verify if sufficient correlation exists between the calibrated WUFI simulations and the monitored MC readings, as shown in Equation 2.

$$\mathrm{RMSE} = \sqrt{\frac{1}{n}\sum_{i=1}^{n}\left(y_i - f(x_i)\right)^2}$$

Equation 1: *Root mean squared error (RMSE) to measure average residual MC error [8]*

$$r = \frac{\sum(x_i - \bar{x}) \cdot (y_i - \bar{y})}{\sqrt{\sum(x_i - \bar{x}) \cdot (y_i - \bar{y})}}$$

Equation 2: *Pearson's correlation coefficient (r) [9]. Where 0 is equivalent to no relationship and 1.0 is equivalent to a perfect relationship*

If RMSE values were computed to be less than the average error of the OmniSense sensors, then the hygrothermal simulation was deemed to be validated. The variable error of a OmniSense sensor can be calculated by comparing the MC of radiata pine samples using the OmniSense sensors against the oven-drying gravimetric method. The variable error range of the OmniSense sensors can be defined by the equation given in Figure 15, and was thus used for the purpose of validating the WUFI simulations.

https://doi.org/10.52202/069179-0577

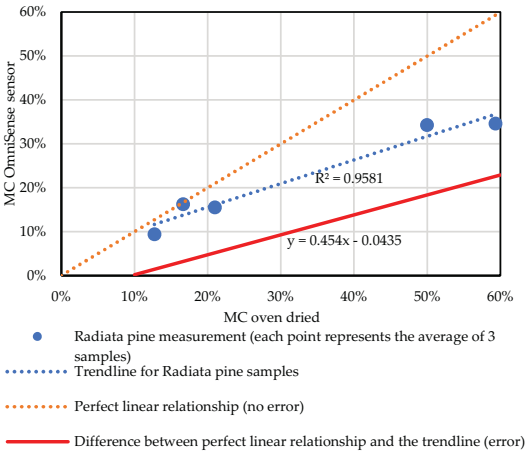

Figure 15: *Variable MC measurement error given for OmniSense sensors [10]. The coefficient of determination (R^2) is shown for the radiata pine samples, while an equation is given for the variable error*

3 RESULTS AND FINDINGS

Results from the monitoring campaigns of the three CLT projects in representative Australian subtropical and tropical climates are used to support notable observations about the monitored data relating to moisture risks within the CLT assemblies.

3.1.1 MONITORING OF THE CLT MICRO-UNIT

The monitoring data from some of the sensors in the CLT micro-unit shows that the sensor embedded in the assembly without a WRB has consistently higher MC, as shown in Figure 16; a maximum of 21.7 %, compared to the assembly with a WRB that records a maximum MC of only 13.1 %. MC of the assembly without a WRB remained higher even after the cladding was installed; showing that the assembly was never able to achieve a dry-out condition by returning to a MC equivalent to that of the assembly with a WRB over the monitored period.

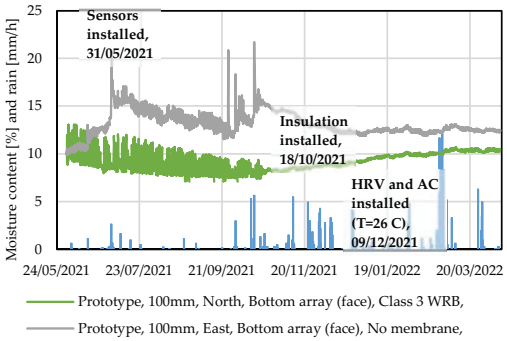

Figure 16: *Comparison between MC of an unprotected and protected CLT panel. Rainfall (mm/h) indicated by the blue vertical lines*

Table 1 statistically compares the CLT micro-unit predictive simulation results against the monitored results. The importance of installing a WRB can, again, been seen, as the assembly without a WRB had excessively high MC. It was also notable that Class 2 assemblies appeared to perform more poorly than Class 3. This was likely because the Class 2 WRB was not a pressure-adhered product; instead, it was stapled to the exterior surface of the CLT and then the staples were sealed with proprietary tape. It was noted that on windy days, air convection passed the Class 2 WRB, as movement of the membrane could be seen. This confirms the importance of using an adhered WRB product to avoid MC peaks during construction wetting. It should also be noted that the calibrated simulations for all assemblies returned maximum mould growth index (MGI) values that did not exceed the critical threshold of 3, which is given by ASHRAE 160 [11]. This means that, although peaks in MC may have occurred during construction, the long-term moisture safety was still ensured in subtropical climates.

Table 1: *D = embedment depth of sensor (mm). O = orientation of assembly. C = class of WRB. MC = maximum monitored MC (%), values greater than 18 % are highlighted in pink to indicate excessive moisture. R = RMSE (%), values highlighted in pink where the value exceeds the arithmetic mean sensor error. E = arithmetic mean sensor error (%). P = Pearson's correlation coefficient, values lower than 0.3 are highlighted in pink to indicate a weak relationship. MGI = maximum simulated MGI for the assembly*

D	O	C	MC	R	E	P	MGI
20	N	3	13.5	0.93	0.33	0.709	
50	N	3	12.4	0.52	0.55	0.446	0.0161
100	N	3	13.1	1.88	0.38	0.553	
20	N	2	16.5	0.60	0.74	0.713	
50	N	2	13.1	0.67	0.75	0.149	0.0164
100	N	2	13.5	3.20	0.56	0.444	
20	E	-	20.5	0.89	0.46	0.472	
50	E	-	24.2	1.41	1.23	0.608	0.0654
100	E	-	21.7	1.53	1.61	0.588	
20	S	3	13.9	0.45	0.67	0.821	
50	S	3	12.0	0.58	0.62	0.763	0.0164
100	S	3	10.4	1.24	0.12	0.713	
20	S	2	13.1	0.62	0.43	0.821	
50	S	2	21.6	1.79	0.90	0.066	0.0163
100	S	2	23.3	1.12	0.41	0.713	

3.1.2 MONITORING OF THE CLIMATIC CHAMBER

The monitoring data from the sensors in the double climatic chamber experiment shows that positioning vapour-open insulation internally is beneficial in maintaining a lower MC in comparison to externally positioned insulation (see Figure 17), departing from the construction method in cold and temperate climates with external insulation. However, Figure 18 demonstrates the importance of avoiding construction wetting for long-term moisture durability, for both external and internal insulation assemblies. As when wetted, the assemblies do not achieve dry-out equilibrium and continue to increase in MC over the duration of the experiment.

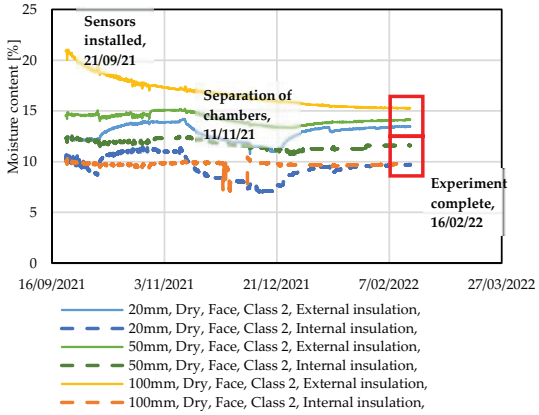

Figure 17: *Red rectangles highlight a comparison between the insulation position, external and internal*

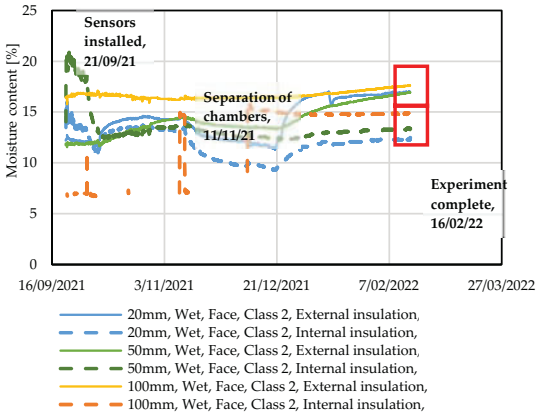

Figure 18: *Red rectangles highlight a comparison between the effect of construction wetting in tropical climate (dry and wetted panels)*

Table 2 summarise the CLT micro-unit monitoring results. It reveals that for dry assemblies, Class 3 WRB was most appropriate for assemblies with external insulation, while a Class 2 WRB was most appropriate for internal insulation. This is because a Class 2 WRB resists vapour from diffusing into the assembly. However, if the CLT panel is wetted, then the Class 3 WRB was most suitable to allow sufficient drying-out capacity. Predictive simulations were statistically compared against a few of the monitored results; this was because the 'ambient' boundary conditions of the climatic chamber experiment could not be correctly defined, as the air in the chamber was inadequately mixed. However, the MGI values for these assemblies did not indicate any mould growth over the duration of the experiment.

Table 2: *D = embedment depth of sensor (mm). L = location of insulation, external (e) or internal (i). C = class of WRB. I = initial state of CLT, wetted (w) or dry (d). MC = maximum monitored MC (%), values greater than 18 % are highlighted in pink to indicate excessive moisture. R = RMSE (%), values highlighted in pink where the value exceeds the arithmetic mean sensor error. E = arithmetic mean sensor error (%). P = Pearson's correlation coefficient, values lower than 0.3 are highlighted in pink to indicate a weak relationship. MGI = maximum simulated MGI for the assembly*

D	L	C	I	MC	R	E	P	MGI
20	d	3	e	12.3	1.75	0.67	0.957	
50	d	3	e	12.4	0.56	1.03	0.168	0.1116
100	d	3	e	11.4	1.21	0.37	0.721	
20	d	2	e	14.2				
50	d	2	e	15.2			-	
100	d	2	e	21.0				
20	d	-	e	19.9	2.03	1.72	0.759	
50	d	-	e	14.4	1.07	1.32	0.532	0.0660
100	d	-	e	15.7	1.53	1.20	0.477	
20	w	3	e	18.4				
50	w	3	e	17.9			-	
100	w	3	e	21.6				
20	w	2	e	17.1				
50	w	2	e	16.9			-	
100	w	2	e	17.6				
20	w	-	e	27.8				
50	w	-	e	21.7			-	
100	w	-	e	26.9				
20	d	3	i	13.4				
50	d	3	i	13.8			-	
100	d	3	i	17.1				
20	d	2	i	11.4	2.44	0.41	0.910	
50	d	2	i	12.5	0.53	0.97	0.205	0.0893
100	d	2	i	10.5	1.05	0.15	0.045	
20	d	-	i	14.0				
50	d	-	i	13.7			-	

https://doi.org/10.52202/069179-0577

100	d	-	i	13.7	
20	w	3	i	15.2	
50	w	3	i	17.1	-
100	w	3	i	17.8	
20	w	2	i	16.0	
50	w	2	i	20.9	-
100	w	2	i	15.9	
20	w	-	i	15.1	
50	w	-	i	14.6	-
100	w	-	i	14.4	

3.1.3 MONITORING OF THE RESIDENTIAL CLT BUILDING

The monitoring data from the sensors in the CLT residential building shows the moisture risks due to leaks in roof cladding over the north-east wall orientation, causing high MC. Figure 19 shows a MC range of 17.5–28.2 % for a sensor in the north-east orientation, compared to the equivalent sensor in the south-west assembly that was not exposed to the roof leak, with a lower MC range of 8.7–17.8 %.Table 3 statistically compares the CLT micro-unit predictive simulation results against the monitored results. This shows a general trend for sensors installed near the CLT floor panel, which had a greater predisposition for higher MC ranges. This was likely due to the window frame rough openings during construction, which allowed stormwater to pass inside of the construction and be absorbed into the CLT floor panel end-grain. However, the MGI values for these assemblies were shown to be less than the critical threshold over the duration of the experiment.

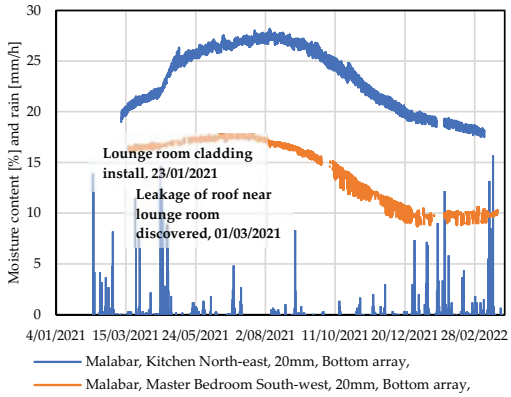

Figure 19: *Comparison between the effects of a roof leak. Rainfall (mm/h) indicated by the blue vertical lines*

Table 3: *D = embedment depth of sensor (mm). O = orientation of assembly. C = class of WRB. L = location of array, upper (u) or lower (l). MC = maximum monitored MC (%), values greater than 18 % are highlighted in pink to indicate excessive moisture. R = RMSE (%), values highlighted in pink where the value exceeds the arithmetic mean sensor error. E = arithmetic mean sensor error (%). P = Pearson's correlation coefficient, values lower than 0.3 are highlighted in pink to indicate a weak relationship. MGI = maximum simulated MGI for the assembly*

D	O	C	L	MC	R	E	P	MGI
20	NE	3	l	28.2	8.14	6.35	0.235	
50	NE	3	l	26.5	2.4	4.30	0.765	0.7159
100	NE	3	l	19.0	1.98	3.38	0.564	
20	NE	3	u	14.8	2.63	0.60	0.798	
50	NE	3	u	18.8	2.14	3.10	0.838	0.1635
100	NE	3	u	21.4	2.39	2.57	0.791	
20	SW	3	l	17.8				
50	SW	3	l	17.0		-		
100	SW	3	l	17.5				
20	SW	3	u	13.8	2.55	1.19	0.787	
50	SW	3	u	13.6	1.54	1.12	0.476	0.1229
100	SW	3	u	12.8	3.31	0.65	0.628	

3.1.4 LIMITATIONS OF THE STATISTICAL RESULTS FOR THE CALIBRATED MODELS

Generally, the statistical results of the monitored data and calibrated simulations indicate a strong measure of closeness from the Pearson's correlation coefficients. However, the RMSE values are generally larger than the mean sensor error, which means that calibration is not validated for the respective sensor. Only 30 % of the calibrated simulations achieved both the accepted values for Pearson's correlation and RMSE values, and thus can be deemed validated. While this shows that calibration is possible, it also shows that more accurate knowledge of boundary conditions and a higher quality representation of the microclimate may align the other simulations with the monitored data. A notable observation was that the sensors embedded closest to the external surface had the worst correlation to the measured MC values. Therefore, the weather data collected at nearby weather stations may insufficiently represent the 'microclimate' around the projects for adequate calibration.

In the case of the CLT residential building, failure to sufficiently calibrate the models was due to leaks occurring during the construction phase. This was because the exact nature of the stormwater's flow, speed, and path could not be adequately represented by a simple ratio of driving rain applied to a position within the assembly. However, this failure to calibration for leaks was also

interesting because they appear to validate guidance from ASHRAE 160, which recommends assigning an initial MC of two times the equilibrium MC at a RH of 80 % across the entire assembly when construction sites were not protected from stormwater. Following this guidance would have led to an initial MC of 30 %, which accurately represents the peak MC due to the leak. This suggests that for projects where defects such as water intrusion past the roofing may occur during construction (practically all projects), this 'unprotected' modelling guidance should be used to assess long-term moisture risks. Additionally, this guidance avoids overly complex procedures, such as 3D hygrothermal modelling or quantifying the exact amount of water leaking through an envelope defect. However, it should be noted that this same modelling approach is not capable of replicating the exact nature of the stormwater's flow and thus, it cannot be used to calibrate simulations.

Calibration of the hygrothermal simulations for the climatic chamber experiment was also problematic because the sources of heating, cooling, and humidification were all localised on one side of the chamber, with insufficient blending of the air volume, which led to non-homogenous conditions within the climatic chambers. To resolve this issue in future experiments, internal fans or diffusers should be installed in each chamber to distribute and disperse the conditioned air evenly around the monitored space.

4 CONCLUSIONS

Results from the monitoring campaigns of three CLT construction projects are used to draw conclusions about moisture risks in hot and humid Australian climates.

A notable observation about the monitored data relating to moisture risks within the CLT assemblies is that, in hot and humid climates, external insulation is appropriate — which is supported by simulation results. However, in tropical climates, positioning of insulation on the internal CLT face, and airtight and vapour resistant membranes positioned behind the cladding are shown to be beneficial. Good interior ventilation strategies as well as ventilated cavities and drainage layers behind the cladding are also highly advantageous for improved moisture safety. These results also show that adhered WRBs are critical for moisture safety.

The simulations revealed a faster drying sequence in the monitored data as compared to WUFI simulations. In addition, regardless of the difficulty in calibrating the hygrothermal simulations with the monitored data, the simulations showed a low MGI, and thus moisture safety in the CLT assemblies. This corresponded with the monitored data, which showed that despite elevated MC during the 'construction' stage, the MC dropped to safe levels during the 'operational' stage. The simulation results also confirm that the guidance about simulation settings and initial conditions given by hygrothermal standard ASHRAE 160 are appropriate for CLT assemblies in hot and humid climates.

Future work would use the simulated MGI values from the calibrated simulated MC values to produce a maximum initial MC to maintain moisture safety for the various CLT assemblies in hot and humid climates. Additional details and discussions about these monitoring campaigns can be found in the PhD thesis by the primary author.

ACKNOWLEDGEMENT

This research was conducted by the Australian Research Council Research Hub for Advanced Solutions to Transform Tall Timber Buildings (project number IH150100030), with funding from the Australian Government and Department of Agriculture and Fisheries.

Donations of construction materials and components were used to build the experiments. A decentralised energy recovery ventilation unit, Lunos NeXXt ERV system donated by LAROS Technologies. Weather resistance barriers, Solitex Adhero and DA airtight vapour check product, tapes, and grommets donated by Pro Clima Australia. PHI-certified 2.4 by 2.4 m French-style double door opening with double glazing and motorised exterior Zipscreen blinds donated by Logikhaus. 2 kW split type Alira air conditioner heat pump donated by Daikin. Zinc coated steel self-tapping wood screws, WB4 90 plate, and acoustic sealants donated by Rothoblaas. 15 sheets of Tectiva 8 mm fibre cement cladding donated by EQUITONE. 6 untreated radiata pine CLT panels of 125 mm thickness donated by XLam. NVELOPE NV9 aluminium sub-frame profiles along, fixing, and joint trims, 60 mm, and 80 mm Vulcanwool rigid mineral wool insulation batts donated by DCTech.

REFERENCES

[1] G. L. Oliveira, F. L. de Oliveira, and S. Brazolin, "Wood preservation for preventing biodeterioration of Cross Laminated Timber (CLT) panels assembled in tropical locations," *Procedia Struct. Integr.*, vol. 11, pp. 242–249, 2018, doi: 10.1016/j.prostr.2018.11.032.

[2] ABCB, "Condensation in Buildings Handbook," *Aust. Gov. States Territ. Aust. 2019*, p. 163, Jul. 2019.

[3] M. Strang, P. Leardini, A. Brambilla, and E. Gasparri, "Mass Timber Envelopes in Passivhaus Buildings: Designing for Moisture Safety in Hot and Humid Australian Climates," *Buildings*, vol. 11, no. 478, Oct. 2021, doi: 10.3390/buildings11100478.

[4] OmniSense, "OmniSense S-900-1 Wireless Sensor Product Brief," 2021. https://www.omnisense.com/help/sensor1_brief.asp (accessed Sep. 06, 2021).

[5] ALMEMO, "ALMEMO® Measuring Instruments." Oct. 2021. [Online]. Available:

 https://doi.org/10.52202/069179-0577

https://www.ahlborn.com/download/pdfs/kap01/eng/2690e.pdf
[6] J. Falk and Lunds universitet, “Rendered rainscreen walls - cavity ventilation, ventilation drying and moisture-induced cladding deformation,” Lund University, 2014. Accessed: May 16, 2022. [Online]. Available: https://portal.research.lu.se/ws/files/3857646/4249703.pdf
[7] J. Straube and G. Finch, “Ventilated Wall Claddings: Review, Field Performance, and Hygrothermal Modeling,” Building Science.com, 0906, 2009.
[8] G. James, D. Witten, T. Hastie, and R. Tibshirani, “An introduction to statistical learning with applications in R,” *Springer Sci. Bus. Media*, vol. 6, no. 1, pp. 87–87, Aug. 2021, doi: 10.1080/24754269.2021.1980261.
[9] A. Schneider, G. Hommel, and M. Blettner, “Linear Regression Analysis,” *Dtsch. Ärztebl. Int.*, vol. 107, no. 44, pp. 776–782, Nov. 2010, doi: 10.3238/arztebl.2010.0776.
[10] M. Shirmohammadi, “Investigating the effects of moisture ingress on the performance and service life of mass timber panels in Australian climates,” *QG Dep. Agric. Fish.*, vol. Unpublished manuscript, 2022.
[11] ASHRAE, “ASHRAE Standard 160 - Criteria for Moisture-Control Design Analysis in Buildings,” p. 24, 2016.

World Conference on Timber Engineering Oslo 2023

LOAD LEVELS AND CRITICAL DESIGN ISSUES IN A MULTI-STOREY RESIDENTIAL TIMBER BUILDING BUILT UP BY PREFABRICATED VOLUMETRIC ELEMENTS

Johan Vessby[1], Tomas Forsberg[2], Marie Johansson[3], Rajan Maharjan[4]

ABSTRACT: The use of structural timber in residential buildings has increased considerably in Sweden during the last decade. Concomitantly, there has been an emphasis on augmenting the level of prefabrication for such structures. A simultaneous need for education imparted in universities exists, and this paper contributes to this need by outlining a design example of a residential timber building with simple geometry using prefabricated volumetric elements. The serviceability limit state as well as the ultimate limit state have been defined and studied for some critical design situations. The results indicate, for example, that the degree of utilisation in the studied building system for compression perpendicular to the bottom rail in the first storey and buckling of the studs are in the same range - 91 % to 97 % - for the walls separating apartments.

KEYWORDS: Design, Education, Prefabrication, Volumetric structure, Module

1 INTRODUCTION

The number of residential buildings with structural timber in their load-bearing frames, has increased considerably in Sweden over time. The primary reason for this is the increase in the population of urban regions in the country, which has led to a rise in demand for housing stock. Another driver, which has been influencing this trend, is the need to truncate the life-cycle greenhouse gas footprint of buildings, and timber-based structures perform well in this regard [1].

A noticeable trend in the last few years is the practice of increasing the level of prefabrication of the building modules. Some advantages of this practice are the increased speed in which the building can be assembled on-site, see Figure 1, the controlled climate in which the modules are produced and not the least the improvement in working environments for labourers at different stages of the construction.

The rapidity with which developments are happening in this sector warrants and motivates the design of new academic course modules in the universities, which both students and professionals opting for competence enhancement opportunities, can avail of [2]. The primary aims of this paper are:

- to present a typical timber structure produced by volumetric modules,
- to calculate a selection of critical design loads acting on the structure and,

Figure 1: *Example of installation of a prefabricated timber module in a four-storey building.*

[1] Johan Vessby, Karlstad University, Sweden, johan.vessby@kau.se
[2] Tomas Forsberg, Karlstad University, Sweden, tomas.forsberg@kau.se
[3] Marie Johansson, RISE Research Institutes of Sweden, Sweden, marie.johansson@ri.se
[4] Rajan Maharjan, Karlstad University, Sweden, rajan.maharjan@kau.se

https://doi.org/10.52202/069179-0578

- to discuss some of the challenging design issues related to such a building according to current harmonized design codes [3-5].

The dual motives are to make these results the foundation on which a new academic course can be designed and to facilitate the evolution of numerical models [6, 7], the results from which can be related to load levels obtained.

2 OBJECT DESCRIPTION

The building studied in the case study is a four-storey building designed using prefabricated volumetric elements, so called "modules", using a light-weigth stud-and-rail system. The building is designed using 10 volumetric elements in width and four volumetric elements in height. The total length, width and height dimensions of the building are 40, 10.5 and 15.5 m respectively and the exterior corridor is 1.5 m wide.
The prefabricated volumetric elements are approximately 4.0 m wide (in the A direction, Figure 2), 9.0 m long (in the B direction, Figure 2) and 3.0 m in height. The long wall elements of the volumetric elements are made of 45 · 95 mm sawn timber with a centre-to-centre distance of typically 600 mm. The bottom rail and top rail is made up of sawn timber with a dimension of 45 · 95 mm. On the inside of the studs, sheets are screwed to the studs giving horizontal stability. The sheet material can be OSB, plywood and/or gypsum wallboards depending on manufacturer. The load bearing part of the gable (short walls) of the volumetric elements is made up of 45 · 170 mm studs with sheet material on the inside screwed to the studs. The floor and ceiling are made up of sawn timber orientated in the short direction of the module with a board glued and screwed to the sawn boards. In the studied version module the floor and ceiling elements are screwed to the inside of the wall elements to minimise the amount of timber loaded perpendicular to the grain.
The northern and eastern facades of the complete building studied are shown in Figure 3 (*a, b*) together with a section of the building (*c*). The direction north, east etc. is used in this paper to ease the understanding of directions.
The roof trusses with a 28° inclination on the top chord to a horizontal axis are oriented with their span in a north-south direction so that self-weight and the snow load, contribute to the total load, only along the edges A_4-B_4 and E_4-F_4, respectively, for each single volume on the top floor respectively, see Figure 4. The northern and southern walls (the shorter walls of the single volume) are exterior walls requiring a greater degree of insulation, vis-à-vis the eastern and western walls (the longer walls of the single volume) for a typical volume inside the building. Owing to the requirement of extra insulation and the fact that the load attributed to the snow will act primarily on those walls, almost a doubling of the height of the cross-sections of their studs, vis-à-vis those in the interior eastern and western walls, is called for. As depicted in Figure 4, the cross-section (width · height) of the latter is typically 45 mm · 95 mm.

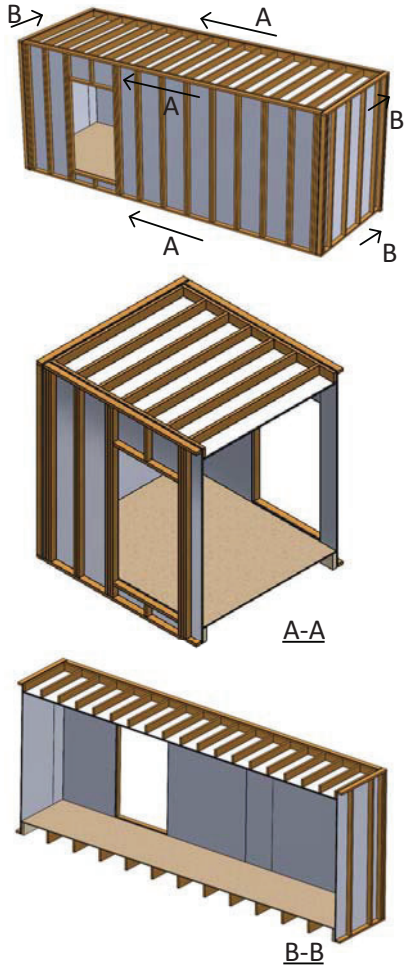

Figure 2: *Illustration of a typical module used for assembling residential buildings.*

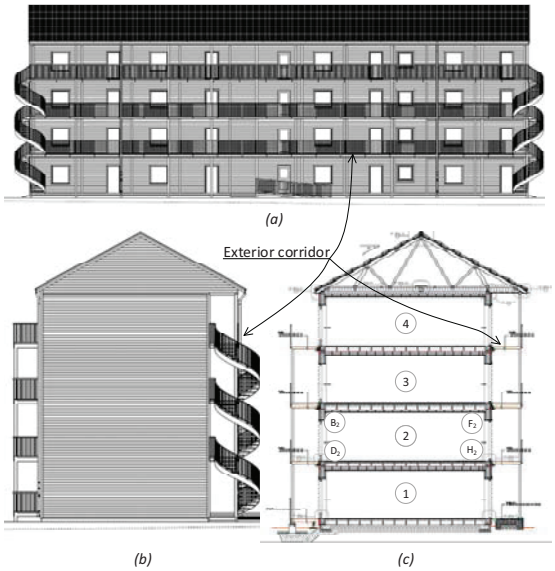

Figure 3: *Illustrations of the studied building: (a) northern façade (b) eastern façade and (c) section of the building.*

https://doi.org/10.52202/069179-0578

The eastern and western walls of the lowest storey are subjected to all the imposed loads in the building by virtue of the orientation of the joists in the flooring for each module. Along the northern façade of the building there is an exterior corridor linking the different apartments on each floor.

How the prefabricated volumetric elements are attached to each other, is a critical design issue, which is complicated by conflicting design requirements. Designing for structural stability calls for strong tie-downs, while designing for good acoustics entails a decrease in number of mechanical connections is desired to reduce the level and transmission of structure-borne noise. In this study, an extreme case devoid of any mechanical connections securing the elements to one another will be considered. The critical issue with load transfer among self-bearing modules will not be discussed.

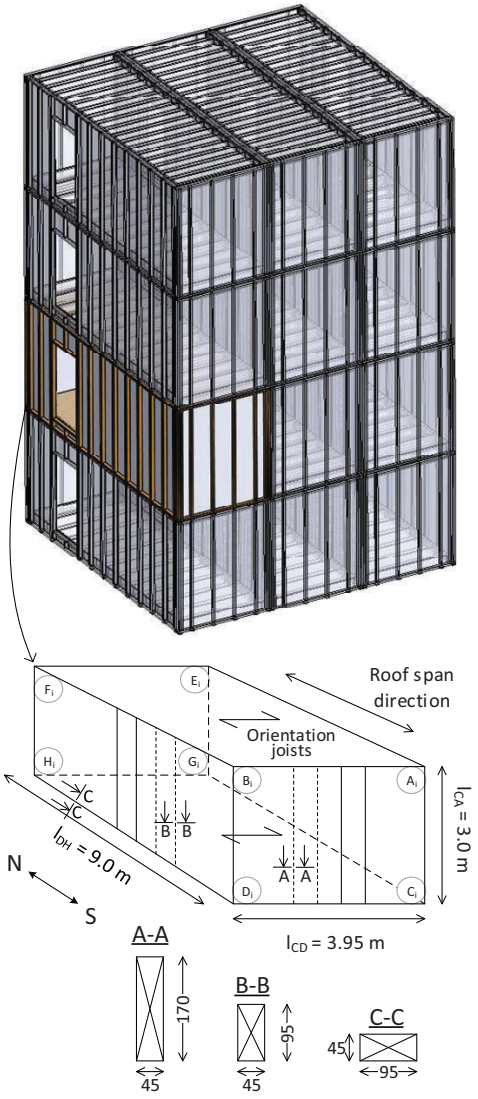

Figure 4: *Example of simplified volumetric element for storey i in the studied structure. Geometrical dimensions as well as the direction of the compass are indicated.*

3 LOAD COMBINATIONS

Design loads acting on a building are calculated in ultimate limit state (ULS) and in serviceability limit state (SLS). For the design cases selected and studied herein the self-weight of the various structural components are unfavourable and thus the load combination for the ULS designed is obtained as

$$E_d = \gamma_d \cdot 0.89 \cdot 1.35 G_k + \gamma_d 1.5 Q_{k,1} + \gamma_d 1.5 \sum_{i>1} \psi_{0,i} Q_{k,i} \quad (1)$$

where E_d is the design load, G_k the self-weight, $Q_{k,1}$ the leading variable action and $Q_{k,i}$ accompanying variable actions acting on the structure being reduced by the reduction factor $\psi_{0,i}$ due to the improbability of simultaneous maximum occurrence of accompanying variable actions. The partial safety factor γ_d is a safety factor defined in the Swedish national annex depending on safety class dependent of the risk of consequences of a failure [5].

In the SLS the characteristic, frequent and quasi-permanent load combinations will be used and they are formulated as

$$E_d = G_k + Q_{k,1} + \sum_{i>1} \psi_{0,i}\, \mathrm{Q_{k,i}} \quad (2)$$

$$E_d = G_k + \psi_{1,1} Q_{k,1} + \sum_{i>1} \psi_{2,i}\, \mathrm{Q_{k,i}} \quad (3)$$

and

$$E_d = G_k + \sum_{i\geq 1} \psi_{2,i} \mathrm{Q_{k,i}} \quad (4)$$

where $\psi_{2,i}\mathrm{Q_{k,i}}$ equates to the average value over a period of time. The characteristic combination (2) is used for calculating the load levels for irreversible permanent actions such as fracture, the frequent combination (3) is used for reversible actions such as vibrations and finally the quasi-permanent combination (4) is used for long term effects, e.g. creep.

The permanent action is considered for the building as a whole. The total self-weight for a single volumetric element of the type used in the studied building ranges between $G_{k,vol}$ = 80 and 90 kN. Permanent loads caused by floor and walls are considered to be distributed loads. The walls range from g_k = 0.35 kN/m^2 for interior load bearing walls to g_k = 0.54 kN/m^2 for exterior load bearing walls and the self-weight of the floor is set to g_k = 1.02 kN/m^2.

Beside the permanent action three variable actions add to the total loading of the building; snow load, wind load and imposed load.

The residential building used as an example is assumed to be located in the city of Karlstad (Sweden), where the characteristic snow load is s_k = 2.5 kN/m^2 for the horizontal projection of the area (less than half of extreme values common in some regions of Sweden, reaching 5.5 kN/m^2). The reference wind speed at height z = 16 m for the studied object is v_b = 23 m/s which in terrain category III corresponds to a wind pressure

https://doi.org/10.52202/069179-0578

q_p = 0.61 kN/m^2 (less than half of the maximum wind load of 1.29 kN/m^2 in terrain category 0, in coastal regions; and 64% more than the minimum value of 0.37 kN/m^2 in terrain category IV).
The third substantial variable load is the imposed load (q_k). For a residential building, where the floor area is used as living space, it is a category A load, and thus q_k = 2.0 kN/m^2. The imposed loads for the exterior corridors for each floor on the northern façade of the building, and the attic, are set to 3.5 kN/m^2 and 0.5 kN/m^2 respectively. The total imposed load can be multiplied by the reduction factor α_n which in turn is calculated as

$$\alpha_n = \frac{2 + (n-2)\psi_0}{n} \quad (5)$$

where n denotes the number of storeys in the same load category (>2) above the loaded structural parts, and ψ_0 is a reduction factor.
The horizontal force caused by the initial inclination of interacting structural parts should be considered in the design of the shear walls within one storey. In the structure analysed in this paper, this has been done by calculating a total inclination of such parts consisting of one systematic part, and one random part, so that the total angle $\alpha_{m.d}$ can be determined as

$$\alpha_{m.d} = 0.003 + \frac{0.012}{\sqrt{n_{part}}} \quad (6)$$

Service class 1 is used for all structural parts within the prefabricated volumetric elements, and structural timber of quality C24 is assumed. The partial safety factor is set to γ_d = 1.0.

4 SELECTED CRITICAL DESIGN CASES

A comprehensive structural design of the building studied, necessitates several calculations. Some of them, being standard and conventional in nature, are not interesting in the context of this paper. Others which are interesting are scrutinized in greater details in this section. The three selected design cases which are related to critical issues the building industry encounters, are illustrated in Figure 4 and discussed thereafter, and degrees of utilisation are determined for them.

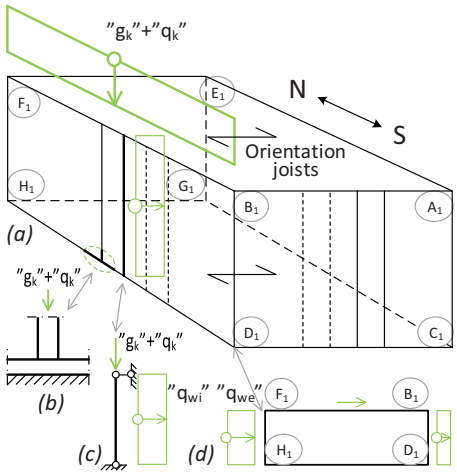

Figure 5: *Illustration of selected design cases a) overview of module in storey 1, b) load perpendicular to the fibres, c) buckling of stud and d) wind load on the structure.*

4.1 Vertical loading in ULS

The design vertical load in the eastern and western walls of the module, see Figure 4, is calculated by including self-weight and the imposed load in the ULS design, equation (1). The combination can be used to calculate the design load for local compression perpendicular to the bottom rail, see Figure 5 (b), and for obtaining the vertical design load in studs in the internal wall which are used in combination with the internal wind load to design for buckling, see Figure 5(c). For the local compression perpendicular to the grains, the design load calculated to N_{Ec90d} = 17.5 kN with the imposed action being the leading action. The centre-to-centre distance (cc) of the studs is assumed to be equal to 400 mm. The most critical load in the analysis of buckling of the stud is the one with imposed load as the leading action, and the internal wind load as the accompanying variable action. For that design case, N_{Ec90d} = 14.1 kN and $q_{w.int}$ = 0.033 kN/m.
In a typical stud in the exterior (northern or southern) wall of the module where a load consisting of snow (leading action), self-weight and imposed loading from the floor- and ceiling elements, and the exterior corridor, is acting, the design load is $N_{Ec90d.N}$ = 31.9 kN but due to the smaller cross section in the eastern and western walls focus is put on those walls in the following.
An important detail in the design of compression perpendicular to the fibres is the addition in the EKS11 [5] that allows for assigning the material coefficients γ_M = 1.0 and k_{mod} = 1.0 under specified circumstances. These circumstances are [5] that the "*sole consequence*" of the pressure perpendicular to the grain is *"increased deformations that have no significant impact on the system´s stability and mechanical resistance"*. Cases where this may be applicable include the *"indentation of joists into a sill beam and waling of low buildings*.". Finally, it is also stated that *"where deformations have significant effect on function (e.g. in tall buildings), the recommended partial factors in"* EC5 should be utilized. This implies a necessity for defining whether the building is a tall building or not, *a priori*, which is often

challenging. Compared to a situation with $\gamma_M = 1.3$ and $k_{mod} = 0.8$, the reduction in the design material parameter is substantial, 62%, when $\gamma_M = k_{mod} = 1.0$.

4.2 Vertical loading in SLS

Vertical loading leads to instantaneous and time dependent vertical displacements [8]. In a design situation this is particularly interesting, if the elevator shaft is made of another material (concrete, for instance), or if the load bearing structure for the exterior corridor is made of steel, for example, see Figure 3. In such cases, relatively large differences in vertical displacements may be seen; and this may lead to a series of undesired effects.

According to EC5, the loads for design of the long-term effects should be calculated using Equation (4). Quasi-permanent value ($\psi_2 Q_k$) is used for the variable loads so that the load levels are reduced to the long-term average. The variable action to be included in the load case derives purely from the imposed load. The design load on a stud in wall D_1-H_1 at the first storey is calculated to $E_d = 7.9$ kN. Methods are presented in EC5 to take account of the short term (elastic) and long term (creep) effects in the timber material. In addition, the reduction of the moisture content of the timber, from around $mc_{init} = 13\%$ on average, to $mc_{avg\_longterm} = 9\%$ in the long-term results in a reduction in the nominal dimensions of the members, and contributes considerably thereby to the total displacement. Note that only "direct" effects of the *mc* decrease is included here. In the calculations performed herein the total vertical displacement is the sum of the contributions from elastic, time dependent effects, and the shrinkage owing to the change in the moisture content. As far as the physical structure is concerned, deviations from the nominal dimensions such as small length deviations or saw-cuts not perfectly perpendicular to the length direction of the timber member are very likely to play a key role, at least during the initial phase after the installation is completed. However, these effects being difficult to quantify, have not been included in this analysis.

The deformation limit is not defined in EC 5 for example, but should be specified at a project level. For a building assembled using prefabricated modules, a suggested total vertical displacement span of 15 mm < $v_{lim} \leq 20$ mm is recommended. This is based on a rule of thumb that the angle for the exterior corridor should be a minimum of 1:100 so that the floor of the corridor is always inclined away from the building facilitating possible flow of rain water (and meltwater) outwards. The typical width of a corridor lies in the range of 1.5 to 2 metres. For the case-study building with an approximate height $h_{tot} = 15$ m this correlates to $v_{lim.longterm} = h_{tot}/(750 \text{ to } 1000) = 15 – 20$ mm.

4.3 Wind load acting on the northern façade (SLS and ULS)

One of the most challenging loads to design for in prefabricated modules with a load bearing timber structure braced with sheathings mechanically attached to the frame members is the lateral load caused by wind. In the current study, only the effects of the load acting on the northern wall (and suction on the southern) will be analysed. Thus, only the shear walls parallel to F_1-B_1- D_1-H_1 see Figure 5(d), will be subjected to the wind load and therefore analysed. Each "tower" of modules is assumed to stand separate. It follows that 50% of the load on the area B-A-C-D enters along the line A-C, and the other half acts along B-D. The horizontal elements in the ceiling and the flooring are assumed to be stiff, continuous and securely attached to the walls.

In addition to the wind load, the initial inclination of the studs, see equation (6), combined with the acting imposed load and self-weight, contribute to the total horizontal load for any given module. Challenges in ULS arise if the modules are designed with large openings in the walls used as shear walls. Such analyses, however, are straight forward and the load effect can easily be compared with resistance (using method A in EC5).

For the current building, the design horizontal load acting on and in parallel with the eastern wall in the first storey, is $H_{d.w.ULS} = 30.9$ kN of which the contribution due to inclined members is only $H_{d.i.ULS} = 1.4$ kN.

In SLS, there are uncertainties related to the task of manually calculating the horizontal displacement for each storey, as well as for the building as a whole. A recommendation has been given [9] and is formulated as

$$u \approx 4.5 \frac{sH_{d.SLS}}{bk} + \frac{H_{d.SLS}h}{G_k bt} \qquad (7)$$

where s is the fastener spacing, $H_{d.SLS}$ is the design force (no account of inclined members), b, h and t are the width, height and thickness of the sheet respectively, and G_k is its shear modulus. The largest uncertainty relates to the slip modulus k. Due to the relatively high horizontal load ($H_{d.SLS.char} = 19.7$ kN) in characteristic combination, see equation (2), the secant slip modulus used is that calculated as $k = K_u = 2/3 \cdot K_{ser}$. For the screw with $d = 3.9$ mm in combination with a plywood sheathing material the secant modulus is calculated to $k = 922$ kN/m which is a relatively high value.

The design criteria for the horizontal displacement is the next issue the designer of the building is faced with. Limitations of that displacement are project-specific, though general recommendations suggest that they must be limited – for the building on the whole, as well as for each storey – to $h/500$ [10,11] where h is the total height of the building (when calculated for the building as a whole) or the height of each storey (when calculated for that purpose).

5 RESULTS AND DISCUSSION

The selected critical design cases were:

1. Vertical loading in ULS,
2. Vertical loading in SLS,
3. Wind load acting on the northern façade (SLS and ULS).

As it turns out, the degree of utilisation is relatively high for all the three cases, and they are accounted for, in the sub-sections which follow.

https://doi.org/10.52202/069179-0578

5.1 Vertical loading in ULS

The degree of utilisation for local compression under each stud along the bottom rail – between points H_1-D_1 and G_1-C_1, is calculated to be 91 %. The corresponding degrees of utilisation for the second, third and fourth storeys are 73 %, 54 % and 32 % respectively. It must be recalled that this applies for the assumed situation with no openings in the long walls on the eastern and western sides of the module.

For the design situation with buckling in the studs around the strong axis, the degree of utilization has been tabulated in Table 1 for two different centre-to-centre distances.

Table 1: *Load levels and degree of utilisation within parenthesis.*

Storey:	1	2	3	4
Local comp., cc 400 mm [kN,(%)]	17.5 (91)	13.9 (73)	10.4 (54)	6.2 (32)
Buckling, cc 400 mm [kN,(%)]	14.1 (97)	10.5 (73)	6.7 (48)	2.5 (20)
Buckling, cc 600 mm [kN,(%)]	21.2 (144)	15.7 (108)	10.1 (70)	3.7 (28)

5.2 Vertical loading in SLS

The storey-wise long-term cumulative vertical displacement is tabulated in Table 2. The total vertical long-term displacement for the top storey thus is calculated to $v_{lim.longterm}$ = 13.7 mm. This corresponds to a value less than the suggested limit of 15 - 20 mm, and thereby the use of $k_{mod} = \gamma_M = 1.0$ for the ULS design of the local compression in section "Vertical loading in ULS" could be adopted here if the suggested methodology is followed. However, since the suggested method is still not common practice the conventional values for k_{mod} and γ_M are used for the design in ULS in the current example. Had the displacement $v_{lim.longterm}$ been greater than the suggested limit, the partial coefficients in the ULS should be set to their actual "ordinary" values.

In Figure 6 the vertical displacements over the building height are illustrated with the long-term component (including immediate elastic displacement), the shrinkage caused by variation in moisture content and the total vertical displacement. Note the considerable contribution of the regions including timber compressed perpendicular to the fibers. It is also worth noticing that the effect of shrinkage due to change in moisture content from 13% to 9% is larger than the effect of the external load acting under long term.

Table 2: *Components contributing to the total vertical long-term displacement for each storey.*

Storey:	1	2	3	4
Elastic [mm]	1.43	1.06	0.68	0.31
Long term [mm]	0.59	0.44	0.30	0.15
Shrinkage [mm]	2.17	2.17	2.17	2.17
Total [mm]	4.19	3.67	3.15	2.63

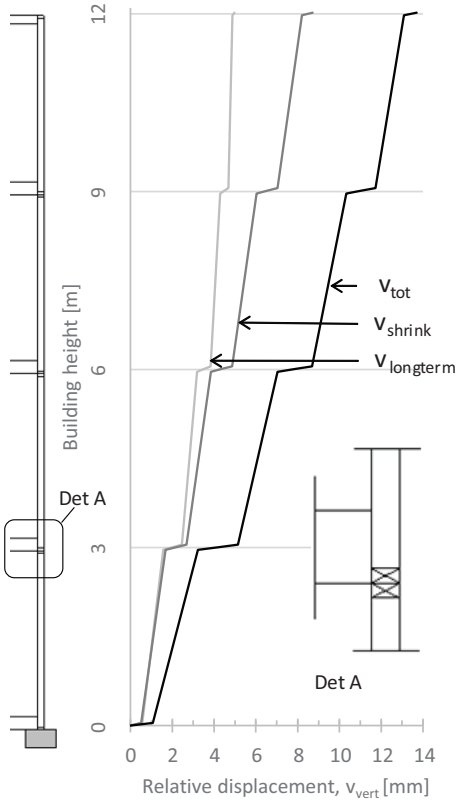

Figure 6: *Relative vertical displacement over the height of the building caused by immediate, long term and shrinkage.*

5.3 Wind load acting on the northern façade (SLS and ULS)

For the first storey, the total horizontal load to be accounted for during the design of the shear walls in ULS, and with wind as the leading action is $H_{d,w}$ = 30.9 kN, which includes both wind load and the horizontal component caused by the initial inclination of the studs, and the vertical load from all the storeys above. Under the assumption of an even load distribution across the top rail, this would correspond to a total load of 3.7 kN/m. The corresponding loads for the 2nd, 3rd and 4th storeys, are tabulated in Table 3. If the SLS is considered, the design loads for characteristic and frequent load combinations are very different from each other. For example, for the first storey, the characteristic combination, Equation (2), gives five times higher load levels compared to the frequent combination, Equation (3). There are reports of repeated cracking of the plasterboard for such buildings, commencing from the interior corners of the doors or window openings. If such cracks are to be regarded as "permanent damage", the horizontal load to be used when calculating the action causing these cracks should be taken from the characteristic load combination. If they instead are regarded as "temporary disturbances" since they normally are not even visible, the load used (frequent combination) for the design is only a fraction of the other. This issue calls for further investigation in future research. For the purpose of this study, conservatively, the

characteristic combination 6.14 is used for calculation of the action in SLS.
The horizontal displacement for each storey is calculated using Equation (7) and used load levels are shown in Table 3, the degree of utilisation shown within parentheses. This gives a total horizontal displacement u_{tot} = 7.0 mm (30%).

Table 3: *Horizontal load ULS and SLS. Degree of utilisation is shown within parentheses.*

Storey:	1	2	3	4
ULS [kN, (%)]	30.9 (100)	23.5 (76)	16.0 (52)	8.5 (27)
SLS, Characteristic [kN, (%)]	19.7 (46)	14.9 (35)	10.2 (24)	5.5 (13)
SLS, Frequent [kN, (%)]	3.9 (9)	3.0 (7)	2.0 (5)	1.1 (3)

6 CONCLUSIONS

In this paper, some critical design issues are identified, selected for further analysis and discussed with respect to load levels and degree of utilisation for a four-storey building using prefabricated volume elements. For the four-storey residential building studied, the degree of utilisation is 97% for the design case with buckling of individual studs in the first storey, and 91% for loading perpendicular to the rail at the same storey, in both cases in the eastern and western walls. It is concluded that this high degree of utilisation indicates the necessity for special attention since minor changes in the design might lead to overutilization.
For the building studied, the calculated maximum long term relative vertical displacement is $v_{lim.longterm}$ = 13.7 mm. In addition to elastic and time-dependent effects the displacement is calculated based on a 4% reduction in moisture content in the timber material. It must be noted that these reductions may be much higher from time to time. Since the design criteria must be project-specific, and very limited guidelines exist, it is, for this building, suggested to limit the displacement based on a minimal inclination of an external corridor with typical width. This results in a limitation being 15 - 20 mm corresponding to h/(750;1000), for the case-study building. It is suggested to assume "no significant impact" for the ULS design as long as this calculated displacement does not exceed h/750 including effects of short- and long term as well as shrinkage. It is concluded that relatively large vertical displacements occur, that limits are set on project basis and that selection of partial coefficients largely influences the analysis in ULS.
The horizontal displacement caused by wind loading for instance, may initiate the formation and propagation of cracks at (and from) the vicinity of the "inner" corners in door openings. Such crack-initiations may occur for low levels of loading, and may not always be visually observed. However, they should be considered as causing permanent damage to the structure. In the current study, the load levels obtained in the characteristic combination (corresponding to permanent damage) is used for obtaining those loads serving as input data for the calculation of horizontal displacement. Also note that there might be other causes for cracks occurring, such as differential vertical displacement.
The use of prefabricated modules in light-weight timber systems is a building system that is common in the Nordic countries as well as in North America. It is, however, a subject rarely covered in the education for structural engineers today. As the building system is frequently utilized it is important that it is also covered in the curriculum for future students and the case study in the current paper is one way to cover the subject. The example include some of the critical aspects when designing buildings using modules such as:

- load paths in both vertical and horizontal directions,
- design calculations for selected elements in ULS and
- critical design calculations for SLS.

7 FURTHER WORK

The current work has proven that there is a high degree of utilisation for some of the selected load cases in the design of residential buildings. Regarding local compression perpendicular to the grain as well as relative vertical displacement, the utilisation may be reduced considerably if the rails are imparted greater stiffness and strength. Waste material from CLT-production is of particular interest in this respect, and will be investigated further in the future.
It will also be interesting to further scrutinise the criteria for long-term vertical displacements and cracking caused by the wind load. These issues are becoming increasingly important due to the tendency to construct taller buildings.
As a closing note, it must be mentioned that in spite of the prevailing tradition in Sweden to design timber buildings, the general design knowledge and the comprehension of the challenges associated with buildings constructed using prefabricated elements, leaves a lot to be desired. Load transfer among modules, effects of accidental loads, uplift due to wind load, and other issues related to modules with large openings have to be studied in greater detail in the future.
The example can also be further developed as a design example in education by including parts as design of the floor elements in ULS and SLS as well as horizontal stability and design of connections e.g. between volumes.

ACKNOWLEDGEMENT

The research is financially supported by several wood construction companies in Sweden and by the strategic innovation programme Smart Built Environment (2020-00224). The authors acknowledge that support with great gratitude.

REFERENCES

[1] Dodoo, A. (2019). Lifecycle impacts of structural frame materials for multi-storey building systems. Journal of Sustainable Architecture and Civil Engineering, 24(1), 17-28.
[2] Johansson, M., Mahapatra, K., Vessby, J., Blom, Å., & Olsson, A. (2014). Expert competence for sustainable timber engineering : a master program in

https://doi.org/10.52202/069179-0578

close cooperation between industry and academia. WCTE 2014 - World Conference on Timber Engineering, Proceedings.
[3] EN-1995-1-1, Eurocode 5: Design of timber structures-part 1-1: General - Common rules and rules for buildings, Brussels (2004).
[4] EN 1991-1-4: (2005). Eurocode 1: Actions on structures - Part 1-4: General actions - Wind actions.
[5] BFS 2011:10 with amendments up to BFS 2019:1 (EKS 11), available at: https://www.boverket.se/globalassets/publikationer/dokument/2019/application-of-the-european-construction-standards---eks-11.pdf
[6] Kuai, L., Ormarsson, S., Vessby, J., & Maharjan, R. (2022). A numerical and experimental investigation of non-linear deformation behaviours in light-frame timber walls. Engineering Structures, 252, 113599.
[7] Ormarsson, S., Vessby, J., Johansson, M., & Kuai, L. (2019). Numerical and experimental study on modular-based timber structures. Modular and Offsite Construction (MOC) Summit Proceedings, 471-478.
[8] Serrano, E., Enquist, B., & Vessby, J. (2014). Long term in-situ measurements of displacement, temperature and relative humidity in a multi storey residential CLT building. In *World Conference on Timber Engineering, Quebuec City, 10-14 August* (pp. 398-405). World Conference on Timber Engineering (WCTE).
[9] Källsner, B., & Girhammar, U. A. (2009). Analysis of fully anchored light-frame timber shear walls—Elastic model. Materials and structures, 42, 301-320.
[10] SBN avd 2A Bärande konstruktioner med kommentarer, Statens Planverks författningssamling 1979:7.
[11] DIN-Taschenbuch 34, Holzbau Normen, Deutsche Institut für Normung e. V., Beuth Verlag GmbH, Deutschland, 1994.

World Conference on Timber Engineering Oslo 2023

ARBORETUM, THE LARGEST EVER WOOD OFFICE CAMPUS IN EUROPE: TECHNICAL, ORGANIZATIONAL, AND SUSTAINABILITY CHALLENGES : AN EXAMPLE OF LOW CARBON PROJECT FAR BEYOND THE ALIGNMENT WITH THE EUROPEAN TAXONOMY

Laurent Petit[1], Renaud Blondeau-Patissier[2]

ABSTRACT: this article describes the design and construction of the Arboretum office campus, near Paris, which represents the largest complex built in CLT solid wood; through this experience, the developer shares their convictions: the resolute hunt for carbon emissions, which needs science based tools to measure the efficiency of the design and monitor possible improvements; the sobriety of design, which consists in getting rid of all materials that are not absolutely essential, and giving some of them a double function, structural and decorative, without any addition of other materials; the aesthetic interest of structural wood, which, if it can be left visible, provides unparalleled comfort. The article also describes specific test campaigns, regarding the efficiency of sprinkler or water mist on constructions entirely made of apparent wood.

KEYWORDS: Arboretum, Visible Mass Timber, Sobriety, Low Carbon Building Initiative, LCBI, European Taxonomy, BBCA

1 INTRODUCTION

Arboretum, the largest wooden structure office complex ever built in Europe, will be completed in autumn 2023.

This project, developed by WO_2 on behalf of the ICAWOOD investment fund, is located on the banks of the Seine river in Nanterre, 15 minutes away from Paris and includes 5 buildings with a wooden structure totalling 118,000 m² as well as two refurbished industrial buildings for 8,000 m².

WO_2 is a developer created in 2014 with the main objective of reducing the carbon footprint of construction. WO_2 is currently developing 370,000 m² of office buildings and mixed-use projects. When the company was created, little attention was paid to controlling emissions related to building materials; Many efforts had been made throughout Europe to reduce energy consumption: the hunt for kWh/m² had already begun, but there was still little interest in the materials themselves, although traditional materials are very emissive. WO_2 naturally turned to biosourced materials by associating them with a very broad approach of sobriety and control of quantities.

The Arboretum project is the best example of this approach: it responds to several challenges:

- A considerable reduction in carbon emissions (-47% compared to traditional construction, namely concrete post and beams, hollow core slabs), measured according to the BBCA ("Bâtiment Bas Carbone") association method [1]. This methodology has been recently revised in order to be used in all European countries. This initiative known as "Low Carbon Building Initiative – LCBI", is further presented in 2.3.
- The use of timber, as the main structural material, at a never seen before scale: This needed very efficient supply logistics, enabling the wooden structure, representing 28,000 m³ of CLT and Glulam, to have been erected in 15 months. The job required delivering around eight 50m³ loads of precision-packed wood materials from Stora Enso mills every week.
- Very high energy sobriety, the buildings consuming only 61 kWh/year /m², in accordance with the new French 2020 regulations, one of the most demanding in the world.

In short, Arboretum demonstrates the very latest in what is possible with industrial processes to reduce the embodied emissions from buildings by utilizing wood. Efficient construction employing prefabricated CLT has never been taken to this scale before. This instills fresh thinking and optimism for a future with a low-carbon architecture for all.

2 THE HUNT FOR CARBON EMISSIONS

2.1 UNDERSTAND, MEASURE, ACT

In many European countries, authorities encourage economic players to reduce their CO_2 emissions. It is up

[1] Laurent Petit, Technical Director, WO_2, l.petit@wo2.com
[2] Renaud Blondeau-Patissier, Stora Enso, Wood Product – Building Solutions Research Manager, renaud.blondeau@storaenso.com

https://doi.org/10.52202/069179-0579

to developers and real estate companies to comply with the new Corporate Sustainability Reporting Directive, by revising their business model with the aim of reducing their emissions and aligning themselves with the objectives of the European Taxonomy.
For corporations, the point is to create a new culture of carbon calculation, which must now even supplant economic criteria alone.
This requires understanding where CO_2 emissions come from and making LCA a major decision criterion. WO_2 has therefore based its emissions reduction strategy on:

- The sobriety of design,
- Low-emitting materials
- The detailed ACV calculation, as exhaustively as possible.

2.2 2015, THE FIRST STEPS OF COMPLETE LCA WITH BBCA LABEL

BBCA pioneered the first carbon calculation method for a complete building; the methodology can be summarized in several stages, which can also be found in the European Level(s) methodology:

- Breakdown of the building into 14 construction lots: the entire building is assessed. It is relatively easy to assess construction materials, the manufacturing processes of which are well described in the EPDs (Environmental Product Declarations), but it is still difficult to precisely measure the embodied carbon of technical equipment (which includes many materials, electronic components, and require complex industrial processes). Despite this difficulty, and the vagaries that still exist in the calculation of the building's technical equipment, it was deemed essential to have a complete assessment. Carbon savings must be made wherever possible, and not only by substituting emissive materials with biobased materials.

  In this, the BBCA Label differs from many environmental labels, which consider carbon emissions as one parameter among others without requiring a performance on complete emissions.
- Definition of a reference surface: to make the projects comparable with each other, the calculation of the ratio of embodied carbon per m² requires great transparency in the choice of the denominator, namely the reference surface.
- Finally, the heart of the evaluation process lies in knowing the impacts of each component: the EPDs are the key to the quality of the evaluation; about 7000 EPDs are available on the INIES (French government initiative) database. This revolutionizes the way projects are designed, since in addition to the technical properties of the materials (fire resistance, mechanical resistance, thermal conductivity, etc.), their aesthetic appearance, their cost, they are selected according to their embodied carbon. This new design approach is just emerging among most architects and design offices. It is therefore the role of the developer to foster this new approach in the design team. Nice challenge!

2.3 FURTHER DEVELOPMENT OF BBCA LABEL : LOW CARBON BUILDING INITIATIVE (LCBI)

The number of buildings assessed in LCA is still very limited in Europe; differences in approach are noted between EU countries, which lead to significant differences in results. Although the LCA is based on European standards (EN 15804+A2 and 15978), some LCA modules are not systematically taken into account in all countries; and the evaluation of buildings is most often uncomplete, limited to the envelope.
This makes a pan-European view of property company portfolios relatively confusing. Different European real estate players have therefore come together to adopt a common methodology [2], which can be applied in several countries. This is based on:

- A breakdown of the buildings by allotments (according to the Level(s) Standard of the EU)
- A complete analysis of the building, if necessary, if the assessment is partial, supplementing it with fixed data
- The use of EPDs for materials and equipment that web platforms are able to recalculate according to the country of use, or production (depending on the energy mix of each country).
- This new LCBI Label, which should be available after a calibration phase at the end of 2023, will make it possible to certify the compliance of a building with the European Taxonomy, and will make available figures that can be used in the SBTi strategies of real estate companies.

2.4 DESIGN SOBRIETY

Sobriety is not penance! But this can be achieved by removing unnecessary architectural features, while paying attention to what is meaningful to users.
In the case of the Arboretum project, wide terraces on each level provide fantastic comfort to people, making the building desirable and therefore sustainable. Each occupant can benefit from direct access to the park, via stairs that combine the dual function of escape routes and pleasure stairs.

Figure 1: *"enjoyable stairs" to replace dull lifts – dec 2022 © Raffin*

Wood (CLT and glulam) was used both for the structure and for the decoration: rather than designing banal structures, of poor aesthetics, which are then hidden by decorative materials, as it is often the case, the designers of the project have chosen to leave the timber structures exposed.

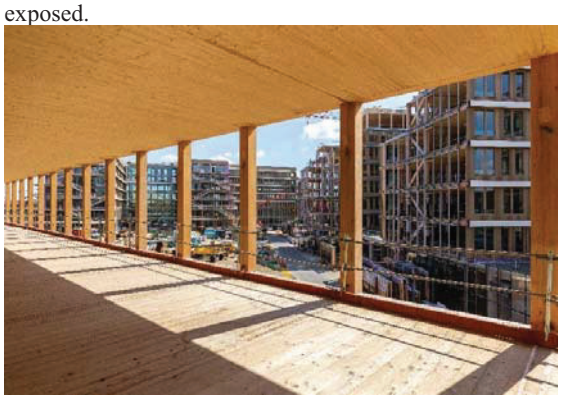

Figure 2: *Erection of CLT slabs meant to remain visible in the project © Raffin*

This is yet another challenge for the design team, which requires excellent collaboration between the engineers who design the structure that must remain visible and the architects.

Figure 3: *Mock-up of the office floor, with visible CLT ceiling © WO_2*

Great attention has been paid to the exposed wood: all the assemblies have been designed so as to remain invisible: in addition to aesthetics, this gives the connecting metal elements a degree of protection against fire. Complete tests had to be carried out to size the sprinkler system. These tests are described in section 4.
Finally, a very meticulous site organization was put in place to ensure flawless installation of the wooden elements that must remain visible.
WO_2 is convinced of the qualities of a wood environment, both for comfort and aesthetics, and quality of life in general.

Figure 4*: View of the construction site (Aug. 2022) – © Raffin*

2.5 LOW EMISSION MATERIALS

Significant reduction of CO_2 emissions has been achieved by replacing most of the concrete with wood and reusing materials from former industrial building. Each part of the building had its own "CO_2 budget", carefully monitored by engineers, in order to challenge the selection and optimise the choice of materials. The project used the INIES database, a government initiative, assessing more than 7000 building components.

2.6 ENERGY SOBRIETY

The project uses heat pumps to heat or cool the building using groundwater as the energy source or sink. Combined with excellent insulation, limited need for

https://doi.org/10.52202/069179-0579

artificial lightning, the project will require only 61 kWh/year /m².
The renewable energy source of geothermal energy is transformed into electricity that powers the heat pumps. The energy-related CO_2 emissions are therefore very low, i.e. 3.9 $kgCO_2eq/m^2$/year; for comparison, the emissions generally observed in European office buildings, according to CRREM data, are 51.4 $kgCO_2eq/m^2$/year (average AT, BE, DK, FR, DE, IT, ES, UK).

2.7 FULL CALCULATION OF LCA

The project was awarded the highest distinction from "Association Bâtiment Bas Carbone" (BBCA). This CO_2 focused certification is the first ever to assess emissions from building materials as well as over the 50 year life cycle for energy. The full LCA amounts to 673 $kgCO_2/m^2$, **ie -47 % compared to a panel of recently designed projects.**
This matches the 2028 cap of CO_2 emissions set by the new French regulation (Environmental Regulations RE 2020): For the first time a cap has been set, requiring to assess emission when filing a building permit. Construction of a building exceeding this cap is not allowed.

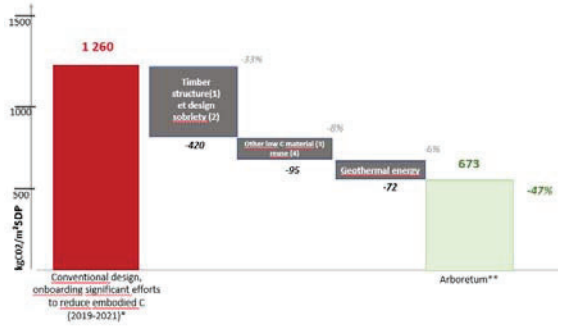

Figure 5: *breakdown of CO_2 savings for Arboretum*

* Benchmark LCA – Artelia 2021 – GHG BBCA v3.1 comparison of 6 concrete buildings located in the Paris region, designed between 2019 and 2021.

** Source: BBCA v3.1 calculation, Artelia 2021

(1) Wooden structure: Storage effect (142 $kgCO_2e/m^2$), superstructure substitution effect (129 $kgCO_2e/m^2$) and wooden facades (33 $kgCO_2e/m^2$)
(2) Sobriety: reduction of car parks, no false ceiling, wooden frame wall on the facade instead of curtain walls (single or double skin) in a conventional design
(3) Low-carbon materials: Recycled carpet, CEM III type concrete
(4) Reuse: Crushed concrete, aggregates

3 BENEFITS OF CLT

3.1 PERFECT LOGISTICS

Thanks to a disciplined and efficient design process the CTL supplier (Stora Enso), was provided with precise manufacturing drawings. The erection of the building superstructure, completed in 15 months, was as fast as expected.

3.2 PRESERVATION OF THE QUALITIES OF THE CLT DURING THE WORKS

It proved impossible to fully protect the 9-hectare site from bad weather as it is sometimes done in Nordic countries. The contractor, French company MATHIS, therefore developed specific tools in order to:
- Guarantee a perfect erection of CLT panels, with extreme care, without any scratches and fully controlled adjustment tolerances;
- Protect the open connexions from moisture
- And if needed, an efficient procedure to clear the stains which might affect the CLT ensuring a perfect finish.

4 FURTHER TESTS: FIRE PROTECTION

The design of Arboretum, whose timber structures are widely visible, required the development of a fire protection system using water spray. WO_2 brought together the various manufacturers to test the two available technologies:

- On one side, the traditional sprinkler (described by the European standard EN 12845)
- On the other hand, the water mist technology (according to the EN 14972 standard): this technology, although less widespread in buildings, has many advantages: the mode of action is different from the traditional sprinkler: rather than drowning the start of a fire by spraying water at a pressure of about 3 bars, it is a matter of instantaneous vaporization of micro-droplets diffused at a pressure of 80 bars, to absorb a large quantity of heat and lower the temperature of the room. The propagation of the fire is then controlled, and it becomes possible for the firemen to intervene. The amount of water sprayed is less than that of a traditional sprinkler system, and it is the preferred technology for all sensitive premises, such as historical buildings, museums, luxury hotels, where water damage can be more important than fire outbreaks.

From the point of view of the building owner, this technology also has the advantage of requiring very small diameter pipes (from 12 to 32 mm), in crimped stainless steel, which is a guarantee of durability.
WO_2 therefore had a test campaign carried out by the EFECTIS laboratory, accompanied by the LISI

https://doi.org/10.52202/069179-0579

engineering office, which allowed each of the concepts to be fine-tuned (choice of nozzles, spacing, flow rate, etc.) in order to verify their effectiveness.

4.1 TEST MODEL

A 300 m² test mock-up was built at the EFECTIS test site in St Yan (FR); it includes CLT and Glulam structures identical to the real building: exposed ceiling (height 3.10 m) along the facades; glulam columns and beams; central part of the mock-up with a false ceiling.

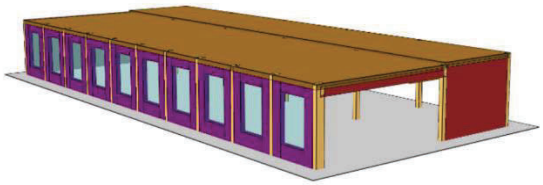

Figure 6: *mock-up*

The model was equipped with side wall nozzles (in green) and hanging nozzles located under the false ceiling (in red) or protecting the space of the technical airducts (in blue).

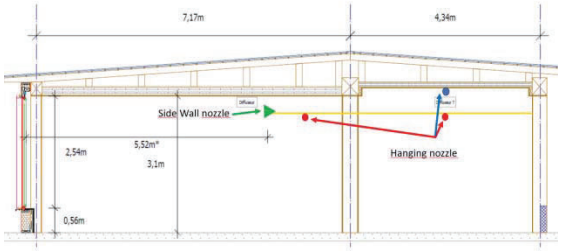

Figure 7: *cross section of the mock-up*

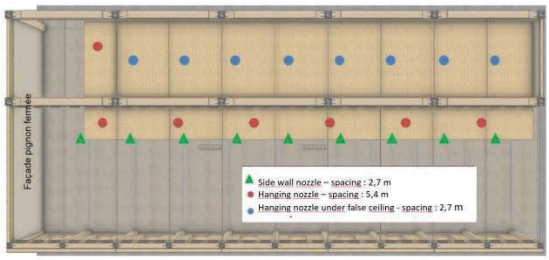

Figure 8: *plan view of the nozzles*

Different locations of fire starts were tested: at the foot of a facade post (figure 9), and at the end of an office floor (figure 10): each fire start being located at the farthest location from the nozzles and at the foot of a glulam post. The purpose of the test was to verify that the rapidity of action of the sprinkler system or water mist allowed to counter the ignition of the wooden structures. Indeed, there are many test reports in the technical literature attesting to the effectiveness of these systems for furniture fires in non-combustible rooms, but few demonstrating their effectiveness in the event of flashover of a solid wood structure, particularly the ceiling.

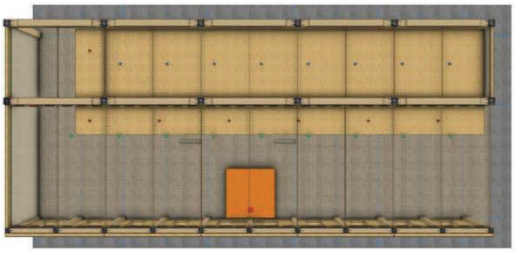

Figure 9: *the orange square shows the fire start, at the foot of a post*

Figure 10: *fire start at the end of the office floor*

4.2 CONDUCT OF THE TESTS

The fire starts were carried out with relatively high start-up kinetics (1 MW in 5 minutes), in order to stress the structures even before the nozzles were triggered.
4 fire start locations were tested for each extinguishing technology. In all configurations, fire control was observed, demonstrating the effectiveness of the extinguishing systems in the case of exposed timber structures, including the ceiling.

Figure 11*: fire start at the end of the office floor*

Photo 12 shows the activation of the nozzles, after the fire has started; photo 13 shows very limited damage to the ceiling after activation of the water mist system.
In conclusion, the tests carried out have allowed the design of the systems to be finalized, and offer a wide choice of technologies (traditional sprinkler, high or low pressure water mist) likely to meet the need for protection of a largely exposed timber structure.

https://doi.org/10.52202/069179-0579

***Figure 12**: activation of water mist*

***Figure 13**: limited damage to the ceiling structure*

5 CONCLUSIONS

The critical need for decarbonisation increases the value of biobased materials.

The Arboretum project demonstrates the ability to significantly decrease carbon emissions. As the largest development of its type, it has been a laboratory of solutions which have shown their relevance.

ACKNOWLEDGEMENT

Architects: LECLERCQ ASSOCIES, NICOLAS LAISNE, DREAM.
Engineers: TERRELL, BARBANEL, AIDA Acoustics, ARTELIA
Contractors: MATHIS, GCC
Fire Lab & Engineers : EFECTIS, LISI
CLT Supplier: STORA ENSO

REFERENCES

[1] Association BBCA: Référentiel Neuf V4.0, 2022. Published on the website „batimentbascarbone.org“.
[2] Association BBCA: LCBI methodology, 2023, published on the website „lowcarbonbuilding.com“.

World Conference on Timber Engineering Oslo 2023

CLEAR THE STAGE FOR TIMBER CONSTRUCTIONS

Jonas Schmidt[1]

ABSTRACT: The Globe Theater is currently under construction in Coburg, an ensemble of four buildings connected by intermediate structures. The center of the building complex is formed by a striking round building in timber hybrid construction. The three adjoining buildings are designed as two-story timber buildings in skeleton construction. Initially, the Globe Theater will serve as an interim venue for the Landestheater, which is undergoing fundamental renovation. In the long term, the new building will be used for various purposes. The circular theater structure, which is predominantly made of wood as a building material, involves many engineering challenges. In structural design, these included the "subtensioned system" of the ceiling over the open area, the "compression-tension ring system" that mutually supports the roof structure, the cantilevered wood-concrete composite ceiling, and the trusses that span the stage. In the fire protection planning, the challenge lay in the detailed design as well as the integration of the technical systems into the building structure. In the process, details were developed that are outside the rules and regulations. This article explains these special features. However, the Globe Theater is not only special in its construction. Among other things, the design also has the special feature that it was created by two students from Coburg University of Applied Sciences. The implementation of a student design into reality is something very special.

KEYWORDS: Structural timber engineering, hybrid structures, structural fire protection, vibrations

1 INTRODUCTION

The idea for the circular shape of the theater building came from Coburg architecture students Isabel Stengel and Anders Macht. The design is based on the Elizabethan Globe Theatre in London. This picked up on Coburg's connection to the British royal family, which came originated from the marriage of Prince Albert to Queen Victoria in 1840.

The main building has a diameter of 36 m and a height of 18 m. The basement is designed as a water-impermeable reinforced concrete structure. The high-value building component is assigned to service class A and additionally protected against groundwater by means of fresh concrete composite foil.

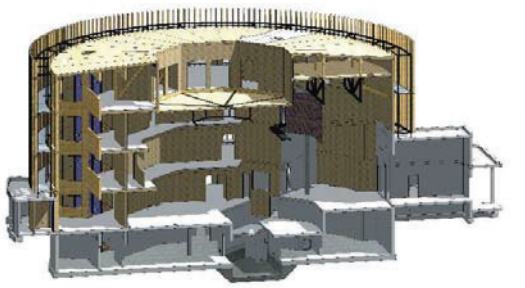

Figure 1: *Cross section through the main building*

The 18 m high wooden building consists of four floors and has a gross floor area of about 5,100 m^2. The first floor houses the revolving stage and the auditorium as well as the height-adjustable orchestra pit. In the entrance area is the foyer, which is open across all floors up to the roof. The foyer is flanked on both sides by representative staircases made of solid wood.

Figure 2: *Foyer area*

The first and second floors contain the galleries. The third floor contains preparation rooms and an interior open-air area (Figs. 1 and 3).

[1] Jonas Schmidt, Dr.-Ing., Ingenieurgruppe Knörnschild & Kollegen, Germany, js@ig-knoernschild.de

https://doi.org/10.52202/069179-0580

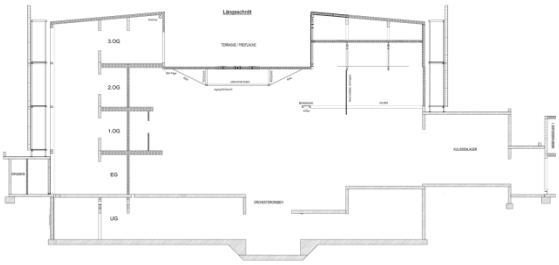

Figure 3: *Cross section through the main building*

In addition to the main building, there are three subsidiary buildings as a wooden structure (Fig. 4) with a total gross floor area of about 1,750 m^2. These buildings are connected to the main building via the stage storage area and are also connected with each other via an open arcade.

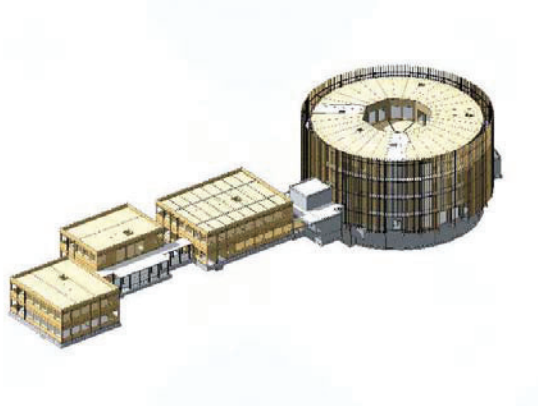

Figure 4:*: Main building with outbuildings and connecting corridor*

Figure 5:*: Aerial photo with main building in foreground*

2 STRUCTURE

2.1 Overview of the structure

The basement and two stairwells as well as the scenery storage are made of reinforced concrete. The four-story main building is largely made of wood from the first floor to the attic. The exterior and interior walls as well as the roof are made of cross-laminated timber and the slabs are a wood-concrete composite construction. Above the auditorium, there is an accessible open space on the 3rd floor (Figs. 3 and 7). This is designed as a subtensioned system. The polygonal structure of the top floor is mutually supported on the inner side by a steel compression-tension ring system. Above the stage are three steel trusses that support the floor above and the lacing floor. The structure is braced by the two reinforced concrete stairwells and the cross-laminated timber walls.

Figure 6: *State of construction of the main building*

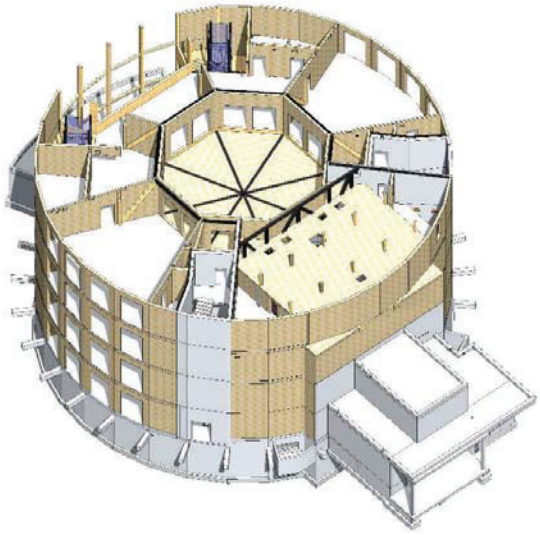

Figure 7: *Illustration upper floor*

2.2 Subtensioned system

The roof structure above the auditorium is designed as an subtensioned system (Fig. 9). For this purpose, eight steel girders are arranged in a star shape and infilled with triangular cross-laminated timber elements. The steel girders are supported by eight air columns, which are connected by a tension ring (octagon) and attached to the steel girders by inclined tension rods. Thus the tensile forces are short-circuited in the steel girder (compression element). In order to dispense with shoring, the star-shaped roof structure was pre-assembled on the construction side and lifted into place. To reduce the weight, not all the cross-laminated timber elements were installed, only the amount necessary for holding the steel girders with respect to bending torsional buckling. The

https://doi.org/10.52202/069179-0580

remaining cross laminated timber (CLT) elements were subsequently lifted into place.

***Figure 8:**: Lifting of the subtensioned system*

Since the subtensioned ceiling is fixed below the compression ring structure of the roof, a mounting joint of the steel girders close to the support had to be provided for reasons of space. The subtensioned system is supported by the large truss spanning the gap between the stairwells and, in the remaining area, by vertical steel tension elements attached to the compression ring.

***Figure 9:**: Suspended System above the spectators*

2.3 Compression-tension ring system

The vertical load is mainly carried by the outer walls (outer ring) and the parallel inner walls (inner ring) (Fig. 3). The inwardly cantilevered ceilings serve as spectator galleries on the first and second floors and as usable space for preparation rooms on the third floor. Further, on the third floor, the subtensioned ceiling above the auditorium is suspended from the compression ring and further derived into the wooden compression struts.

Since the polygonal three-story wooden structure on the 3rd floor cantilevers inward and receives additional loads from the suspended, subtensioned ceiling, the structure requires horizontal support from the compression ring. The steel compression ring runs underneath the roof and supports the roof structure. The compressive forces are transmitted via the compression struts from the roof level to the ceiling level and there to the tension ring (Fig. 10). The tension ring consists of a steel plate that is milled into the CLT slab and installed below the concrete slab of the wood-concrete composite floor. The vertical component of the compression strut is transferred into the interior wall below. A steel detail was developed for the footing (Fig. 17) to transfer the loads through the slab. When the tension or compression ring is closed, the horizontal forces in the ring cancel each other out. In the Globe, however, these are interrupted in the area of the platforms, so that the forces are transferred into the reinforced concrete stairwells.

***Figure 10:**: compression ring and compression strut at the 3rd floor*

https://doi.org/10.52202/069179-0580

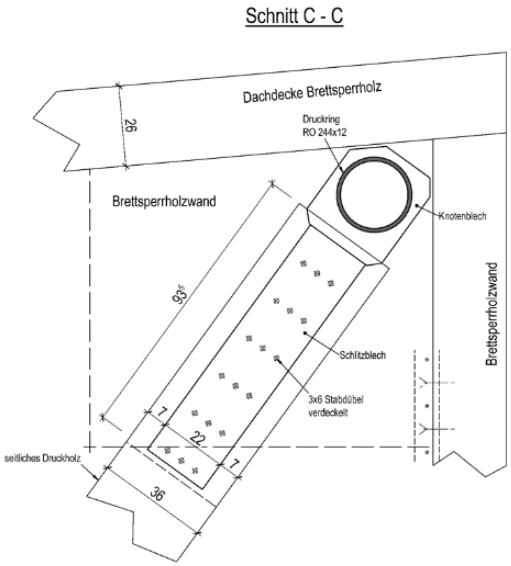

***Figure 11:**: Detail tension-compression ring: compression strut*

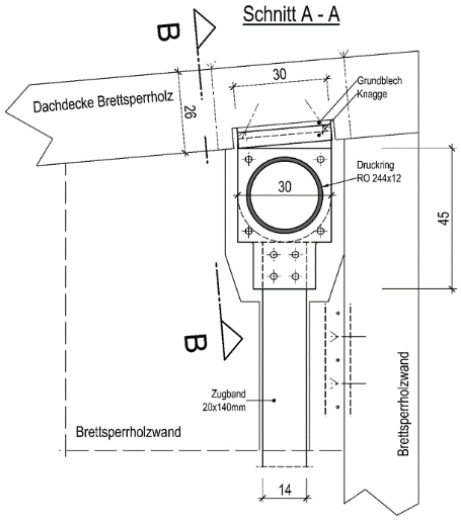

***Figure 12:** Detail tension-compression ring: tension rod that hangs up the open-air area to the compression ring*

2.4 Wood-concrete composite deck

Another special feature is the wood-concrete composite floor. Since this has cantilevered areas, the simplified assumption that the tensile forces are absorbed in the wood and the compressive forces in the concrete is deviated from. In the area of the supporting moment, it is the other way round. The tensile forces occur in the concrete, which must be reinforced accordingly. The wood-concrete composite floor was modeled as a framework model according to Kneidl/Hartmann. The cross laminated timber element was considered as the lower chord, the concrete slab as the upper chord and the connecting elements for coupling the two chords. The connecting elements was modeled with compliant bond to obtain the internal forces and deformations as close to reality as possible. For economic design, the slab was divided into sections to adjust the spacing of the connecting elements to the shear force line. In particular, the length of the upper tension zone had to be taken into account depending on the load combinations. The cracked concrete in the support area was taken into account by modifying the stiffnesses. The concrete slabs are precast elements and were bolted to the cross-laminated timber slabs on site.

***Figure 13:** Cantilevered ceiling elements in the as-built condition*

Thus, the penetration of moisture into the wood was reduced, the ceiling was immediately loadable and the construction process could be continued steadily.

***Figure 14:** Screwing the concrete slab at the construction site*

2.5 Truss girder

Above the stage, steel lattice girders were used to span the stage area without supports. In addition to the technical equipment above the stage, the lattice girders also support part of the open-air area on the 3rd floor.

https://doi.org/10.52202/069179-0580

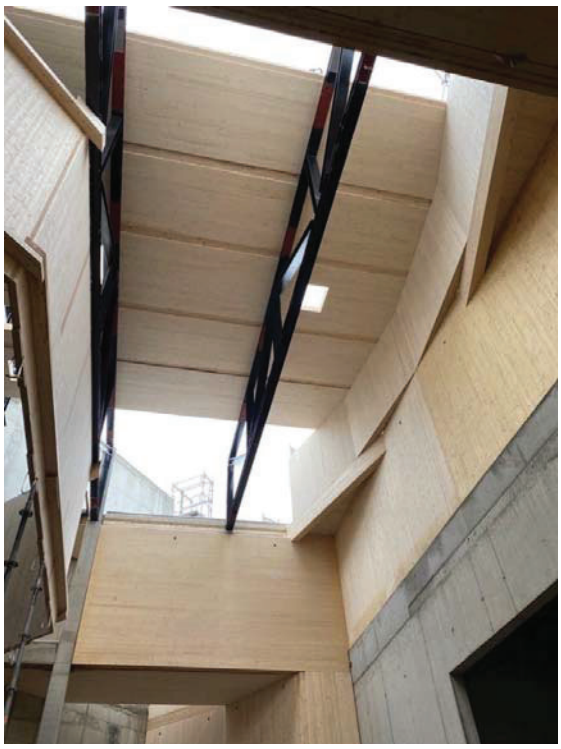

Figure 15: *Truss girder above the stage*

Figure 16: *Trusses in the area of the lacing floor*

3 CONSTRUCTION AND DETAILS

3.1 Connection of compression strut to tension ring

The compression strut, which transmits the compressive forces from the compression ring, meets the tension ring and the wall below in the area of the ceiling above the 2nd floor. The horizontal component of the compressive force must be transferred to the tension ring. There is a steel part developed for this purpose, which is the base of the compression strut and at the same time connected to the tension ring (Fig. 18). The connection must allow horizontal slip parallel to the compression strut so that the tension ring is activated and the horizontal force is not transferred into the ceiling. At the same time, however, the joint must transfer horizontal differential forces into the ceiling. These arise in the tension ring due to asymmetrical loading of the sub-tensioned ceiling structure.

Figure 17: *Detail of the base of the compression strut on the tension ring – tension ring and steel connector*

Figure 18: *Detail of the base of the compression strut on the tension ring – including wooden column*

3.2 Connection of foyer column to concrete ceiling

The foyer column must absorb tensile and compressive forces. To be able to absorb the tensile forces, threaded rods were glued into the wooden column. The threaded rods were attached to a steel profile that was designed and dimensioned for this joint. The anchoring in the reinforced concrete slab was done by welded reinforcement.

https://doi.org/10.52202/069179-0580

Figure 19: *Detail of the base of the foyer column with special steel part and glued-in threaded rods*

3.3 Joint of beam to foyer support

The beam that spans along the foyer serves as a support for the ceilings. Since the ceilings in the auditorium cantilever, lifting forces also occur here. To be more effective in terms of assembly, the beam was connected to the foyer support using fully threaded bolts. For this purpose, protection against the effects of fire had to be provided by covering. In order to avoid increasing the cross-sections as much as possible, gypsum fiberboards were milled into the joint area and these in turn were joined with wood materials.

Figure 20: *Interceptor beam with cut-out for capping on the left side*

4 CONSTRUCTIVE FIRE PROTECTION

Fire protection was a particular challenge for this special wooden building. While the model timber construction guideline was used for the ancillary buildings, most of the details had to be developed individually for the round main building with regard to the fire resistance criteria. Most of the structural components are rated for a fire resistance duration of 90 minutes. The wooden components are dimensioned by taking into account the fire. The steel components as well as connecting elements of the joint are also largely manufactured with sufficient timber covering or capping.
In order to keep the component cross-sections as slim as possible, some connections are provided with cut-outs, installed in the gypsum boards and then covered again with three-layer wooden-boards. Exposed steel parts are provided with a fire protection coating.

5 VIBRATIONS

Since visitors to theater performances also sit quietly in the stands and thus on the cantilever, low-intensity vibrations can also be felt. People react differently to the vibration behavior of structures. When used as a theater, special attention was paid to this. Human-induced vibrations caused by foot traffic were reduced to a minimum by the wood-concrete composite ceiling, so that during quiet performances there is no risk of visitors feeling uncomfortable due to building vibrations. Furthermore, the vibration behavior due to the excitation "bouncing" was also investigated. This load situation can also be absorbed by the selected slab system. For evaluation, the natural frequency and the deformation under static load were considered on both the two-dimensional system and the three-dimensional system. The natural frequency of the ceiling is about 9.4 Hertz, which is above the human excitable range and above the Eurocode 1 limit of 8 Hertz. In addition, the limit deformations under a load of 2 kN on the cantilever were also considered, and the limit values are complied with.

6 FACADE

The circular theater building received a closed formwork of vertical boards as a facade cladding. To "hide" the maintenance aisles in front of it, the building is enclosed by a second facade in the form of glulam slats with varying spacing. Where there are foyer areas and thus large window areas, the distances are larger, in the area of closed walls they are smaller. Sheet metal covers on the slat heads and air-flushed connections ensure that water cannot penetrate anywhere or dry out again properly. The wood was given a pre-greying coating. The wooden slats have been designed in a way that damaged wood can be replaced.

Figure 21: *Facade*

7 CONCLUSIONS

The round Globe Theater, built predominantly in wood, consists of a sophisticated timber construction. The building material wood was focused on from the beginning for reasons of sustainability. The approach to only use wood from the region was not implemented in the value chain due to the logistical effort. Nevertheless, the implementation in wood is a success for timber construction.

For the ceilings, a wood-concrete composite ceiling was used, particularly because of the vibration requirements. Prefabricated reinforced concrete elements were used, which were screwed onto the cross-laminated timber panels at the construction site. Although the precast reinforced concrete elements consisted of a tapered geometry, the assembly on the construction site worked very well. This is also a very good variant for the future in the prefabrication of hybrid structures.

Fire protection is always a major challenge in timber structures. The planners of the fire protection, the structural design, the technical building equipment as well as the inspectors have to work together very well.

In fire protection planning, the challenge lay in the detailed design of the demanding supporting structure and the integration of the technical systems into the building structure. In the process, details were developed that are outside of the rules and regulations.

REFERENCES

Text and images are by the author.

https://doi.org/10.52202/069179-0580

World Conference on Timber Engineering Oslo 2023

TRANSFORMATION OF RECLAIMED MATERIALS FROM BARN BUILDINGS – DESIGN OF A NEW TIMBER BUILDING FRAME

Terje Planke[1], Kristine Nore[2], Victoria Rygh Nordhagen[3], André Bockelie[4], Dimitrios Kraniotis[5]

ABSTRACT: Norsk Folkemuseum, the Norwegian Museum of Cultural History, plans to build a centre for traditional wood crafts and building customs, *TradLab TRE*. TradLab will be built as a modern and traditional building with the reuse of the materials of old barns. A desire to use these materials for the load-bearing system and in the new buildings demands careful dismantling of the barn building. The Norwegian Museum of Cultural History requires the design and execution of special solutions by the design team and executors. The goal is to integrate as much old timber as possible in the new building and to add new timber where it is needed. The project also wants to reuse cladding and find more ways to use the material in the new buildings, such as in the floor surface or climate walls. By using the craftmanship skills to integrate the traditional knowledge into the design of the building, the overall goal is to investigate the actual efficiency of tradition.

KEYWORDS: Reuse of timber, Problems of legality, barn, digital mapping, demonstration project, standardisation.

1 INTRODUCTION

TradLab will increase interest in and strengthen the practice of traditional crafts inside and outside the museum. Through exploration and training, the museum will attract both established expert environments at (international) level and new, broad target groups in the museum's catchment area [1]. TradLab will be the preferred place to cultivate the sustainability of tradition.
In the sub-project TradLab TRE, the focus will be on continuing and disseminating knowledge about material quality and wood crafts related to handicrafts, building customs and building protection. The primary goal is to erect a new building at *Østlandstunet* in the centre of the openair museum, which is well adapted to conduct training in manual wood crafts and building customs. The reuse of (reclaimed materials of) barns is a mission of the SirkLåve project within the bigger SirkTRE-project [2]. In a resource-efficient circular economy perspective, the ideal practice of reuse is to keep the structure of building in the existing location. The next level, when the barn's use life is ended, is the reuse of the area, preferably with the materials from the old barn. This was the main execution of new barns during the raise of the "unit-barn" which led to almost 10 000 barns raised between 1820 and 1920 in Norway. In this period, the reclaimed wood from earlier logged barn buildings was used to build the new, larger structure, leading to more built area. However, the functionality of these barns has been reduced because of the introduction of threshers and tractors in general.

2 METHOD

Norsk Folkemuseum was able to receive materials from old barns which did not serve society anymore and would be demolished, see Fig. 1 and 2. The goal is to use as much as possible of the materials for the load-bearing system and climate wall in the new buildings. This demands a sufficiently careful, and efficient dismantling of the barn building. The museum also wants to reuse cladding and find more ways to use the material in the new buildings.

Figure 1. The first old barn from Sande.

2.1 EXISTING BUILDING – OLD BARNS

The project started with documenting an old wooden barn located in Vestfold, Norway, see Fig.1. This old construction has been housing multiple functions throughout the last hundred years and has gone through several structural changes in that time. The barn is supported by a wooden structure consisting roughly of

[1] Terje Planke, NTNU Norwegian University of Science and Technology, Norway & Norsk Folkemuseum, ORCID 0000-0001-9561-5419
[2] Kristine Nore, NTNU Norwegian University of Science and Technology, Norway Omtre AS, Norway, kristine.nore@omtre.no ORCID 0000-0003-0008-9853
[3] Victoria Rygh Nordhagen, Omtre AS, Norway, victoria@omtre.no
[4] André Bockelie, Resirqel AS, andre@resirqel.no
[5] Dimitris Kraniotis, Oslo Metropolitan University (OsloMet), Oslo, Norway, dimkra@oslomet.no

https://doi.org/10.52202/069179-0581

155 × 155 mm timber (columns, beams, truss). There is a simple truss design supporting the roof. As for many traditional buildings, it is the total building system, with the dependency between different building parts that gives the full load capacity of the barn structure. The building represents a tradition of great strength with a minimum of wooden structure. In addition, only a small amount of iron parts was used, which supports easy reuse. The existing building has been documented through traditional means and by a full scan.

The chosen building for reuse was suddenly not available, due to external causes. The museum chose to look for other possible objects and was offered the spare parts from the large barn from the Nedre Sem farm in Asker that was to be taken down. This project is a "FutureBuilt" project where they are reusing much of the old construction [3], see Fig. 2.

Figure 2. The second old barn from Nedre Sem in Asker.

2.2 BUILDINGS IN TRADLAB

The new construction project consists mainly of two buildings, see Fig. 3. TradLab TRE is placed in a building environment consisting of many old wooden buildings. The two buildings are placed next to each other. The first building is given a traditional construction based on reuse of the 155 × 155 mm^2 beams, see Fig. 4.

Figure 3. Traditional structure to be built for a new purpose. Drawing by Olav Vidvei.

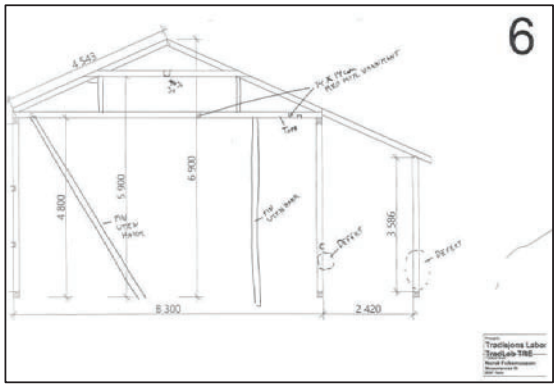

Figure 4. The documentation of section #6 of the old barn. Drawing by Magnus Wammen and Olav Vidvei, Norsk Folkemuseum.

Traditional building

This building will house a workshop for researching and teaching traditional wood techniques. It also includes public areas for exhibitions of woodworking technologies. The museum wants the building to express craftsmanship and display traditional ways of making wooden constructions. At the same time, it must fulfil modern demands required by a new building, as a workplace for traditional craftsmen.

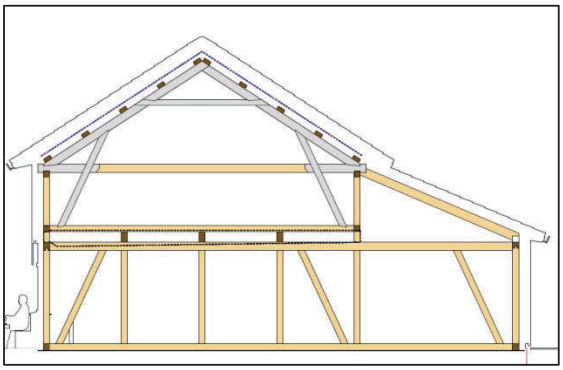

Figure 5. Traditional structure to be built for a new purpose. Drawing by Olav Vidvei, Norsk Folkemuseum.

The open building

The other building will be a two-storey building for outdoor work and outdoor exhibitions about "Norwegian Wood". This building also functions as a means for general availability to the main building by connecting the first floor to the terrain. This building construction is named "grindbygg", which could be translated with timber framing with "post and beam", see Fig. 5. This open structure is extremely material-efficient, made from local wood, with a minimal effort for manufacturing the logs into beams.

2.3 CONCEPTS CONSIDERED

Two main concepts have been considered in the startup of the project: *reuse in the same way* and *reuse in a new way.* The objective was regardless to find the best use of the

https://doi.org/10.52202/069179-0581

existing barn, thereby ending up in between the two ideal types.

Reuse in the same way

This method of reuse is about taking down the existing building and use the reclaimed timber in nearly or the same way it stood before, see Fig. 6. This has been used extensively in Norway with wooden/timber buildings traditionally. The museum has moved and reused many buildings "as is". The museum has recorded that many of the log buildings and the "post and beam" buildings have been moved, also before the museum collected them. The challenge in doing it now lies in new demands and regulations. The fact that it will have a different use (a public building and a two-storey building) also entails challenges.

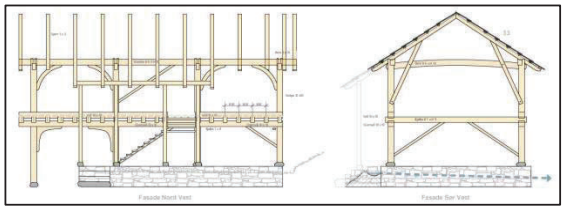

Figure 6. The grindbygg, as an open building without insulation nor wall-cladding.

Reuse in a new way

Reuse in a new way is at the other end of the scale of reuse. This method is about finding new ways of using the reclaimed old building parts in new buildings. This can be as simple as using a beam as a column. Finding new uses for what has been load bearing constructions in the climate wall, interior, non-load bearing constructions (internal walls e.g., or combine elements to form a load-bearing element. The need for design must follow Eurocode 5 [4].

Combination new and old

This envelops finding new ways to use old building elements and adding parts of new structures where necessary. Using old wood for a cordwood masonry wall or stack wall will ensure a near to 100% use of the old timber frame elements.

2.4 SCANNING AND MODELLING OF THE OLD BARN

One important step is the diagnosis, which means collecting data and information for careful dismantling and design choices [5]. The scanning of the barn in Vestfold was done with a Leica BLK360 imaging laser scanner, resulting in dome pictures. The point cloud (Fig. 7) was used as reference to create a BIM model. The point cloud of the barn contains of 480 820 205 points from 22 scans linked together. The scans have all been done on about the same level 1,3 meter above the ground. The overall error of the point cloud was 3mm and have an average overlap of 58%. The model is based on the point cloud where the framework is modelled with an accuracy of ±2,5mm. Information about position, damage, load impact and variation in dimension are included in the BIM model.

The barn was also measured manually, taking out the relevant dimensions of reusable elements.

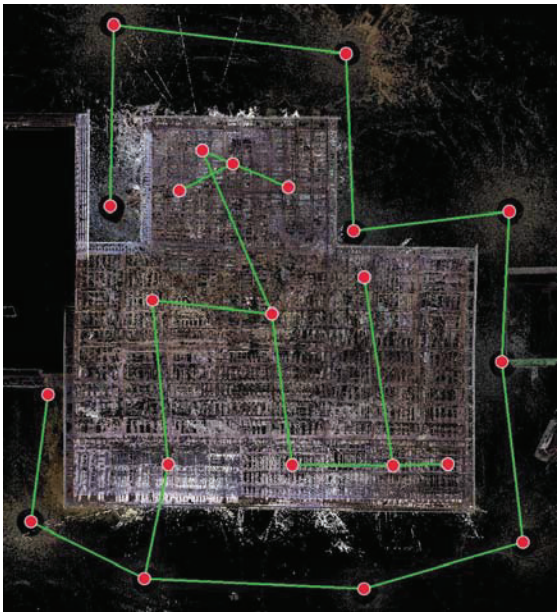

Figure 7. Sitemap of the scans.

Figure 8. 3D representation of point cloud.

3 RESULTS

In this project we ended up using the principles and dimensions of the old barns and reshaping it for our new purposes. The design of the new building was thereby closely related to the dimensions and quality of the old, reusable parts. The old posts (155×155 mm) and beams are sorted out for reuse as posts and ground sills. The quality of each post must be assessed. This is done when dismantling the old barn, and further in the process of pre-cut all the parts before shaping the joints.

The craftspeople who will do the joinery and raise the building, are certified for controlling and sorting constructive timbers into classes like C20, C30 by visual means [6], and are now establishing a procedure to certify constructive timber for C40 for traditional constructions.

The main challenge in the design process is to make the building according to tradition, while supporting the building technical requirements in the Norwegian

building regulations TEK17 [7], since the project is moving besides or outside the pre-accepted solutions within the standard. The goal is to use as little constructive timber as possible to reduce the footprint.
The solution chosen in this project, for reusing as much as possible of the original timber is to use the old parts in the vertical standing and horizontal elements with little forces, for the parts with most tension. To maximize the reuse, all the shorter fragments of the posts is to be used as *kubb*, or bricks in between the posts. This way, all parts longer than the thickness of the construction, will be used as the inner part of the outer climate structure.

3.1 MAPPING OF DAMAGES

Figure 9 is also a screenshot from a dome picture showing damage, drying cracks, and cut-outs. The dome pictures make it easier to identify the quality of the timber. Figure 10 shows the same area but as a point cloud from about the same spot.

Figure 9. Screenshot from a dome picture of the barn showing damage.

Figure 10. Screenshot from the point cloud of the barn showing damage.

Fig. 11 and 12 display a screenshot of TruSlicer in Cyclone REGISTER 360 BLK edition of the point cloud from above showing point around columns, walls, and some items. In the TruSlicer mode it is possible to slide through the point cloud and find damage and measure them like in Figure 13.

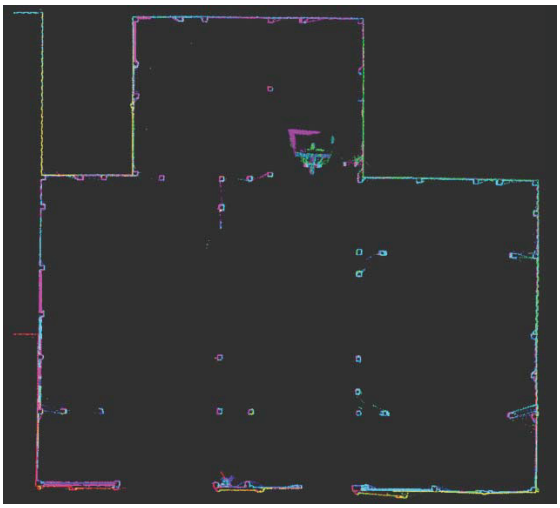

Figure 11. Screenshot of floor plan view of the barn.

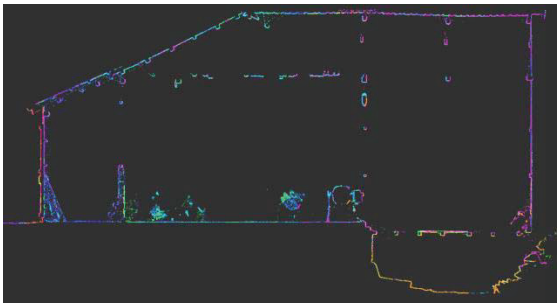

Figure 12. Screenshot of a section of the point cloud.

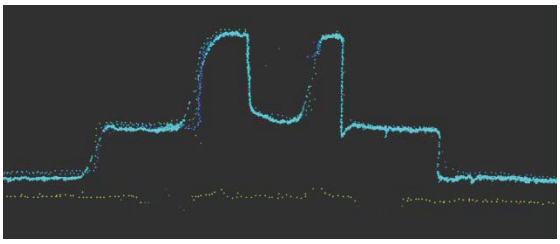

Figure 13. Damage shown in TruSlicer.

3.2 Natural materials - beneficial for ventilation

When it is not painted, the wood has a great hygroscopic quality to support a wanted indoor climate. The wooden bricks will be mortared with local clay. Wood and clay are hygroscopic. The beneficial effect is called hygrothermal mass, a moisture buffer effect which increase human comfort and reduce the need of energy for comfort reasons, and thus energy needs of the building. Hence, the properties of clay and wood fit well with passive

https://doi.org/10.52202/069179-0581

ventilation. The effect of these choices will be studied after the building is raised. A minimum and natural source of ventilation will be chosen in the first period, when starting the use of the building.

4 DISCUSSION AND CONCLUDING REMARKS

Reduce – the need for a new building?
This project already had a good decision for the barn mapped in Sande. When the farmer saw the value of his old building, he decided not to replace it with a new building. From a circular economy perspective, not building and prolonging the service time of the construction can be the best option. However, an additional critical question must be raised [8]. Is the service time extension beneficial, healthy, and safe for the user and/or society?

Reuse of material - in the same way
How much of an existing construction is fit for reuse in the same way? Since it was not possible to copy the shape of the old building, it was impossible to reuse the parts just as they were. In Norway, existing standards for testing or assessing the load bearing capabilities are available. By visual assessment of the class or quality, the loadbearing parts are sorted out. This documentation enables further use.
Architectural challenges exist. The architecture is closely designed based on the dimensions of the old parts. The architect is basing the structure on dialogue with the craftspeople and the solutions are further discussed with the engineers to have sufficient capacity.
Which jointing techniques are preferred? Old notches in the reused materials are placed in the places with least stress and static problems. The joints are "bladed" with 1/3 and 2/3 felling and wooden pegs, to ensure easier disassembly and reuse in the future.

Reuse in a new way
The new use of the timber structure is different from the use in the old barns. During the design, three questions arose which are related to the diagnosis methods, and the domains of architecture and building physics:

1. How much of the existing construction is fit for reuse in a new way?
2. How can we adapt and match the architectural needs, structural demands, and material properties of reclaimed wood?
3. Do traditional timber structures (when using old building parts in walls, or using traditional techniques) used in new constructions provide satisfactory building physical properties?

For the TradLab TRE project, it turned out that the main delivery of structural reclaimed timber will come from Sem Gård in Asker. The TradLab will need more timber parts, preferably reclaimed wood of constructions that do not serve society anymore.

Combination new and old
By using the craftmanship skills to integrate the traditional knowledge into the design of the building, the overall goal was to investigate the actual efficiency of tradition. The prospected way of using old beams combined with new ones and in addition using the small parts for *kubb* led to a very high degree of reuse. The building system is also linked to a former technique. A desire for the future is that the TradLab TRE will inspire future generations to use old building techniques, customised for the future needs. Cooperation with traditional craftsmen in circular construction projects brings in inherited properties and intangible cultural heritage that can create multiple value for society. Mapping of the basis is the way to learn old structural techniques and to provide a material bank for planning the next use of this valuable resource. The potential use of reclaimed wood is emerging in the construction sector and should be explored more in future practice and research.

ACKNOWLEDGEMENT

The authors acknowledge the Norwegian Research Council, Innovation Norway and Siva, the actors behind the program Green Platform and the public financing of SirkTRE (project nr. 328731).

REFERENCES

[1] Norsk Folkemuseum - collection management plan, 2022. Website. Last accessed 14. Mars 2023 https://eidsvoll1814.no/samlingsforvaltningsplan-20222026#SFP-Norsk-Folkemuseum
[2] SirkTRE. 2022. SirkTRE website. Last accessed 14. March 2023. www.sirktre.no
[3] https://www.futurebuilt.no/Forbildeprosjekter#!/Forbildeprosjekter/Nedre-Sem-gaard
[4] EN-NS1995-1-1:2004+A1:2008+NA:2009 Eurocode 5: Design of timber structures - Part 1-1: General - Common rules and rules for buildings, Standards Norway, 2009.
[5] Wuyts, W., Tomczak A., Nore K., Haavi T., Huang L., 2023. Reuse of wood - learning about the benefits and challenges of high- and low-tech diagnostic methods through action research in Norway. World Conference on Timber Engineering 2023, Oslo, June 19-22.
[6] NS-INSTA 142:2009. Nordic visual strength grading rules for timber Standard Norway, Oslo
[7] TEK 17 https://dibk.no/regelverk/byggteknisk-forskrift-tek17 Last accessed 14. Mars 2023
[8] Wuyts, W., Miatto, A., Sedlitzky, R. and Tanikawa, H., 2019. Extending or ending the life of residential buildings in Japan: A social circular economy approach to the problem of short-lived constructions. *Journal of Cleaner Production*, *231*, pp.660-670.

World Conference on Timber Engineering Oslo 2023

DESIGN OF THE ROADMAP FOR THE CONSTRUCTION OF WOODEN SOCIAL HOUSING IN URUGUAY.

Juan José Ugarte[1], Andres Sierra[2], Keren Codriansky[3], Marcia Croci[4], Carolina Pérez-Gomar[5], Virginia Campodónico[6]

ABSTRACT: The government of Uruguay, aware of the new forest heritage present in its territory, has decided to promote the production of social housing in wood [1]. From a strategic planning process based on the "Delta Model" methodology [2] and the participation of all the different actors, represented by: the academic sector, government agencies, the productive and industrial sector, professional organizations, and users, it was possible to agree on a set of 10 actions that allow a qualitative and quantitative leap in this matter [3].

Thus, progress was made in the definition of priorities and actions for the development of pertinent public policies, such as: improvement of regulations, standards, and characterization of national wood; design of training programs for technical and professional skills; compliance with challenges of technological progress of small companies; and the implementation of a dissemination program at the national level. In addition, a crucial aspect has been the activation of the demand, from the execution by the public sector of calls for the construction of social housing in wood (in extension and height) and the creation of economic or fiscal incentives to develop this type of houses.

KEYWORDS: Strategic planning, public policies, promotion programs, wooden houses.

1 INTRODUCTION

1.1 DIAGNOSIS AND CONSULTING

Various studies diagnosed the gaps and challenges that the wood products sector faces today in Uruguay [4], as well as the regulations to increase the participation of this type of building in its public policies and the construction industry [5].

Figure 1: *Forest plantation in Uruguay. Source: SPF.*

Within the framework of this Administration, the Uruguayan Ministry of Housing and Territorial Planning (MVOT) has established various programs that make it possible to achieve a housing solution for large sectors of the population. Within them, it has been proposed to promote the use of wood of national origin in constructive solutions tending to increase the supply of public housing, reducing execution times and construction costs.

To carry out this challenge, the MVOT, with the support of the Inter-American Development Bank (IDB), decided to manage an international consultancy to support the preparation of this "Roadmap" which would allow prioritizing and coordinating the actions necessary to achieve this goal.

1.2 WOODEN CONSTRUCTION AROUND THE WORLD

According to the World Bank, there will be a need for 300 million housing units by 2030 [6], and how different countries address this deficit will be fundamental to guaranteeing global sustainable development.

[1] Juan José Ugarte G., Tallwood, Pontifical Catholic University of Chile, jugarte@tallwood.cl
[2] Andrés Sierra, Tallwood, Pontifical Catholic University of Chile, asierra@tallwood.cl
[3] Keren Codriansky, Tallwood, kcodriansky@tallwood.cl
[4] Marcia Croci, Ministry of Housing and Territorial Planning of Uruguay, mcroci@mvot.gub.uy
[5] Carolina Pérez-Gomar, Ministry of Housing and Territorial Planning of Uruguay, cperez@mvot.gub.uy
[6] Virginia Campodónico, Ministry of Housing and Territorial Planning of Uruguay, vcampodonico@mvot.gub.uy

https://doi.org/10.52202/069179-0582

In this sense, two factors have positioned wood as the optimal construction material for the 21st century: productivity and environmental impact.

Regarding productivity, during the last decades, the wood industry has evolved thanks to the development of the industrialization of the production of engineered wood elements, the creation of more efficient construction systems, and the prefabrication of parts and components, which have resulted in the massification of its use in construction.

Regarding the environmental impact, wood "sequesters carbon," a process that takes place from the afforestation stage when the trees absorb carbon dioxide in their photosynthesis process and stores it inside for years. When trees are treated to produce wood, carbon remains stored inside for the entire useful life of the element.

1.3 WOODEN CONSTRUCTION IN URUGUAY

Although Uruguay is not a country with a long history of wood construction, the forestry industry has great national relevance, contributing to 4% of the national GDP, translating into more than 2,100 million dollars; this arises from the implementation of the Forestry Law in Uruguay in 1987, at which time the production of the national forestry industry began to grow exponentially, registering an increase from about 200 thousand hectares in the 1990s to about 1 million hectares in 2020, encouraging the use of wood for both construction and carpentry. In addition, the sector generates around 18,000 jobs, which rises to more than 25,000 jobs when considering the indirect and induced effects [7].

Figure 2: *Morgavi Woods sawmill. Source: Morgavi Woods.*

Regarding the construction industry in Uruguay, there is a record of at least 14 low-income housing projects in wood, totaling more than 260 units built in the last decades. These are framed in individual initiatives of specific departmental governments, some in agreements with other state agencies or institutions.

In this line, the Government of Uruguay, through the MVOT, ensures in its Five-Year Housing Plan 2020-2024 that in this period, it must offer 105,545 housing solutions, which include construction of new homes, relocations, repairs, neighborhood improvement, among others. Furthermore, in the same document, the MVOT states as one of its objectives is "To promote the use of wood of national origin in constructive solutions aimed at increasing the supply of public housing, reducing execution times and construction costs" [8].

In this line, the government has implemented a series of initiatives to promote the use of wood in construction, among them, the creation of the Honorary Wood Commission (CHM) according to the National Budget Law 2020-2024; a collaborative table, made up of actors from the private, public, academic and professional sectors that seeks to develop a plan to promote the use of Uruguayan forest resources.

2 CO-CONSTRUCTION OF THE ROADMAP

2.1 METHODOLOGY

For the definition of the "baseline" and the identification of barriers and challenges to achieving this objective, those surveyed by the Honorary Wood Commission were considered:

Table 1: *Challenges defined by the Honorary Wood Commission*.

Nº	Challenge
1	Updating of laws, rules, and regulations.
2	Building capacity of professionals, technicians, and workers.
3	Research and development of construction elements and systems.
4	Technology transfer to the MSME sector.
5	Supply of structural Wood.
6	Overcoming cultural and market barriers.
7	Structure multi-stakeholder governance models.

As a methodology to carry out this strategic planning work, this project was inspired by the "Delta Model" conceived by MIT professor Arnoldo Hax and already used during other projects, together with one of the authors of this article [9] [10], and establishes the following five strategic tasks:

Table 2: *Five strategic tasks*.

Nº	Task
1	Constituent segmentation and value proposition.
2	Existing and desired capabilities.
3	Define Mission-Vision for Roadmap.
4	Roadmap Agenda: Axes, actions, and goals.
5	Management of the agenda: Indicators and metrics.

Following this model, a critical step was the segmentation of the different "constituents or stakeholders," for which we worked based on five large reference groups, all of them linked in some way to the theme of building wooden houses:

The public sector, represented by the ministries of Housing (MVOT), Agriculture (MGAP), Industries (MIEM), Environment (MA), and Economy (MEF), together with the respective agencies and directorates; the private sector, represented by the world of forestry, wood processing, and industrialized construction; the academic sector, coming from the university faculties of architecture, engineering, chemistry, among others, the technical careers and the LATU and LATITUD laboratories; the technical-professional sector, represented by the associations of architects, engineers, developers, and technicians; and the civil society sector, represented by social workers who have participated in this type of project and neighbors who live in wooden houses.

During the process, the following activities were carried out:

Table 3: *Process Activities*

Nº	Activity
1	Review and comparison of documentation
2	Systematic documentation and benchmark
3	Collaboration with Technical Committees
4	Structured interviews with stakeholders
5	Departmental visits
6	Advisory to the MVOT
7	Cooperation in the definition of public policies.
8	Development of a Roadmap or Map of Actions
9	Review and dissemination

Some of the most relevant processes are described below.

2.2 LOCAL DIAGNOSIS

In Uruguay, to promote the wood industry in general, and thus enabling the use of the material for both construction and carpentry, among other actions, the MVOT creates the Office of Construction Advice, Planning, and Development in wood, whose objectives are:

Table 4: *Objectives of the Wood Office*

Nº	Objective
1	Promote the use of Uruguayan wood for construction.
2	Promote research and standardization of construction systems and technologies in wood to define quality standards.
3	Prepare technical documents for the use and acceptance of wood in construction.
4	Participate in the process of granting the “CIR” (registration certificate) for construction technologies in wood.

Uruguay's national housing policies are implemented by the Public Housing System (SPV), an organization headed by the National Housing Directorate (DINAVI) of the MVOT, which is made up of various institutions, such as the Honorary Commission for the Eradication of Unhealthy Rural Housing (MEVIR), the National Housing Agency (ANV), the Social Welfare Bank (BPS) and the Mortgage Bank of Uruguay (BHU), from where various housing programs are developed to provide access to housing promoted by the Ministry.

There are currently some social housing projects in wood, such as Barrio Progreso (nine houses) and Barrio Manduví (forty-five houses), located in Rivera; the T15 project (twenty-three homes), situated in Tacuarembó.

Figure 3: *Barrio Manduví Houses (forty-five houses), located in Rivera.*

In addition, there are other detonating works, in engineered wood, such as the Wanderlust Hotel (1805m2 in GLULAM and CLT) in José Ignacio, the Anastacio Inn (1200m2 in CLT), and the Atchugarry Museum of Contemporary Art (5000m2 in Eucalyptus Grandis GLULAM).

Figure 4: *Wanderlust Hotel (1805m2 in GLULAM and CLT) located in José Ignacio.*

https://doi.org/10.52202/069179-0582

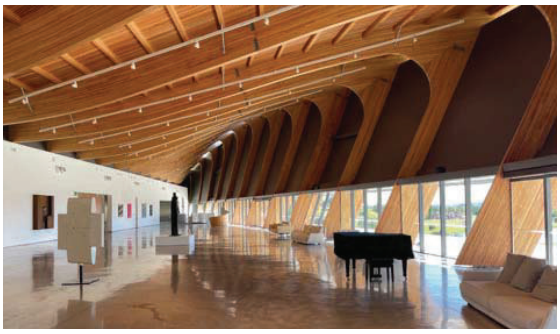

Figure 5: *Atchugarry Museum of Contemporary Art (5000m2 in Eucalyptus Grandis GLULAM).*

A series of organizations and associations that bring together companies and institutions with similar objectives related to the forestry sector in Uruguay were also identified, the most critical being: The Honorary Wood Commission (CHM: made up of representatives of the MGAP, MIEM, MVOT, MA, Congress of Mayors, LATU, UdelaR, and Private Universities); The Timber Development Network (REDEMA: in charge of the project to Strengthen the Timber Industry in the Northern Region, with Emphasis on the Competitiveness of MSMEs); The Association of Entrepreneurs of Wood and Related Products (ADEMA: which represents all its associates in defense of the interests of MSMEs, both in sawmilling and carpentry) and the Association of Wood and Related Industrialists of Uruguay (ADIMAU, which brings together furniture manufacturers).

Some limitations and needs revealed were the following:

Table 5: *Limitations and needs revealed*

Nº	Limitations and needs
1	Regulatory limitations related to the Horizontal Property regime.
2	Limitations to incorporating non-traditional construction solutions.
3	Restrictions related to the action of fire loads and fire regulations.
4	Need for infrastructure and equipment for laboratory tests and to verify the performance of construction systems with wood.
5	Necessity to develop a conformity assessment and certification system for wooden houses.

2.3 INTERNATIONAL BENCHMARK

In addition to the local diagnosis, an International Benchmark study was carried out, which allowed drawing a baseline on the "state of the art" in areas related to wood construction through the experiences of other countries which have a history of using wood for the construction of collective housing, but they are different in their level of progress, internal characteristics, and development.

Chile: Where the Wood Agenda of the Ministry of Housing and Urbanism (MINVU) was created in 2012 around five strategic axes: regulations, quality, constructive solutions, training and dissemination, and triggering projects. Axes have been critical to developing a roadmap that has advanced in terms of wood construction thanks to continuous collaborative work.

Figure 6: *Ecosustainable neighbourhood in Chañaral, Chile.*

Figure 7: *Experimental Tower with 6 floors. Peñuelas, Chile.*

Canada: With a public agenda for wooden construction (2010 - 2030) led by Natural Resources Canada (NRCan), where since 2010, the programs have sought to develop two different axes of wooden construction: construction at height and construction at massive wood. They proposed a multivariate challenge, including developing new materials, new manufacturing and assembly processes, new building codes, and new design approaches, among others.

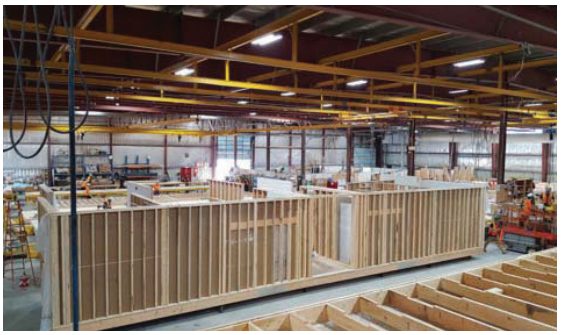

Figure 8: *Prefabricated plant for wooden structures: Metric Modular. Source: www.naturallywood.com*

Finland: where there is the Wood Construction Program (2016-2025), a joint venture of the Finnish government coordinated by the Ministry of the Environment, aimed at increasing the use of wood in urban development, public buildings, and large constructions such as bridges or sheds. The program also aims to diversify and expand the different applications of wood by developing the most significant possible added value to this material.

Figure 9: *Houses in Sipoo. Source: https://www.a-kruunu.fi*

Thus, the result was a comparative documentation of three countries that have faced similar challenges at different times, considering their particular institutions and existing capacities. It was also possible to know each country's historical line of development and the ambitious goals for the coming years aimed at increasing the construction of social housing in wood in those latitudes.

2.4 DEPARTMENTAL VISITS

The political-territorial ordering of Uruguay follows a regional logic, being organized into 19 departments. In this way, the administrative functions are distributed in two levels: The National Government and the Departmental Government. Furthermore, the Municipalities of each department are organized differently from each other to meet the needs and particularities of each of them.

The participation of departmental governments in general, and of forestry departments in particular, was considered essential for creating and developing the Roadmap.

In this line, more in-depth departmental work was carried out with the municipalities with the highest incidence of forestry, which are Tacuarembó and Rivera, considering them possible pilot departments for the development of the construction of social housing in wood. In addition, field visits and face-to-face interviews were conducted with authorities, professionals, business academics, workers, and users, and facilities, industries, and projects were visited. Thus, it sought to obtain a vision from the territories on the opportunities, barriers, and challenges that implementing an agenda for promoting low-income housing in Maderas would present, in addition to inviting them to participate actively in its performance.

Figure 10: *Guided tour by the owner of the Nortimber sawmill, located in Rivera.*

Figure 11: *Visit to the Arboreal plant, located in Tacuarembó.*

Figure 12: *Conversation with the owner of one of the houses in the T15 project, located in Tacuarembó.*

2.5 INTERVIEWS WITH STAKEHOLDERS

A series of structured interviews were carried out online via the Zoom platform, which allowed for conversations with 75 stakeholders in the sector, organized into five reference groups:

Table 6: *Five reference groups*

Nº	Reference groups
1	Public sector.
2	Business sector.
3	Academic sector.
4	Professional colleges.
5	Users.

https://doi.org/10.52202/069179-0582

The objective of these meetings was to understand the position of the actor interviewed in the production chain of the forestry sector and/or in the construction processes, considering the existing barriers to development in the current context, the possible lines of action for the future of the interviewed, and the appropriate external actions that would influence these lines of action.

It was considered that the "one-on-one" meeting methodology would be more suitable for the participants compared to more massive modalities such as the focus group, so that they have the space to express their points of view without restrictions, and thus gather the greatest amount of information possible and reliable.

Figure 13: *Diagram (cloud) of sectors and constituent actors of the Roadmap.*

For each interview, a detailed minute of the conversation was made, leaving a formal record. Firstly, one hundred and eight actions proposed by the seventy-five participating leading actors from the forestry and construction sectors were obtained. Many of these actions were repeated and/or aimed at similar themes, for which reason an analysis and processing of the proposals was carried out, after which the number was reduced to a total of sixty-two actions that were classified systematically in seven thematic axes.

2.6 PRIORITIES OF THE WORKING COMMITTEE

The sixty-two proposals for action obtained from the structured interview process were ordered around the following seven axes:

1. Laws, norms, and regulations for building in wood: Actions linked to innovating in the legal, normative, and regulatory bodies for building with wood, both nationally and departmentally, such as fire protection, horizontal property, structural performance, hygrothermal comfort, protection, and durability, among others.

2. Capacity building of professionals, technicians, and workers for the evaluation, design, and execution of wood projects: Actions aimed at strengthening professional and technical capacities, both in the public and private spheres, for building with wood in areas such as engineering, architecture, construction, economy, industries, administration, and assemblies.

3. Research and development in elements and construction systems in wood: Actions aimed at strengthening the scientific and innovation bases linked to building with wood (materials and techniques) concerning advanced human capital, laboratory infrastructure, and other resources.

4. Transfer of technological capabilities to the SME sector of industrialized building with wood: Actions aimed at strengthening the scientific and innovation bases linked to building with wood (materials and systems) concerning advanced human capital, laboratory infrastructure, and other resources.

5. Supply of structural wood to the industrial processing chain, emphasizing SMEs: Actions aimed at strengthening the supply chain of certified structural wood, of national origin, to wood SMEs, guaranteeing a wide range of products sustainably over time.

6. Overcoming cultural and market barriers for wooden buildings: Actions aimed at overcoming the cultural and market gaps around wooden structures, which allow prejudices to be reduced and to recognize their environmental, economic, and quality advantages.

7. Governance structure for the promotion of low-income housing with wood: Actions aimed at strengthening the participation of multi-stakeholders in the development of the roadmap, integrating the network of initiatives currently under development (national and departmental), involving international experience in its management to accelerate in a guaranteed way the obtaining of good results.

3 ANALYSIS OF THE RESULTS

3.1 INTERNATIONAL BENCHMARK WORKSHOP

For the design of the Roadmap, it was considered of great value to share the information collected in the study with the actors involved and other interested parties. To this end, the International Benchmark Workshop was held on April 6, 2022, in a hybrid format, with a face-to-face attendance of 70 people, in addition to 499 connections in an online form.

The workshop had the participation of 9 Uruguayan speakers, who delved into the different topics in the base case of Uruguay, and five international speakers who presented the cases of Chile, Canada, and Finland.

The day was organized around five thematic blocks within which three experts presented, to then move on to a

question space led by a moderator. They talked about Uruguayan programs and regulations, the benchmark with Chile, Finland, and Canada, the wood industry in Uruguay, and academic capacities and national laboratories. With this, it was possible to draw a baseline and identify the leading local challenges to overcome the gaps to effectively promote social housing in wood.

Figure 14: *Exhibitors of the Block nº1 of the International Benchmark Workshop.*

Figure 15: *Participation of the Minister of Housing and Territorial Planning of Uruguay, during the International Benchmark Workshop.*

3.2 10 (+1) PRIORITIZED ACTIONS

As a result of the previously described structured interviews with the different actors involved in the forestry and construction industry, a series of actions grouped into seven thematic axes were defined, then discussed and prioritized by a select Working Committee to prioritize them. in order of importance and urgency.

A selection of the actors previously interviewed worked in a committee around three tables, placing different representatives of the five reference groups in each, thus achieving a broad and non-sectoral vision of the proposals for action.

Figure 16: *Working Committee Tables.*

Figure 17: *Presentation by one Working Committee Table.*

Figure 18: *Space for questions during Workshop.*

Each table discussed and voted on at least 2 of the seven axes, defining each of their assistants which actions were first (3 points), second (2 points), or third priority (1 point) for the development of this Roadmap.

This collaborative process resulted in a list of 10 priority actions to promote the construction of affordable housing in wood, which were defined as primary lines of action for the development of the Roadmap. These actions had a high transversal adherence averaging 87.9%, varying between 100% and 74%.

Thus, the ten prioritized actions (plus one that which was considered a necessary cross-section), accompanied by a communication process and a governance plan, were the following:

https://doi.org/10.52202/069179-0582

Table 7: *Prioritized actions after voting and % of consensus.*

Nº	Prioritized action	%
1	Create or update the national and local regulations for wood construction, such as: the national fire decree, the horizontal property law, wood durability and others.	100%
2	Develop and carry-out several wood projects: high- rise and block housing units and public buildings to stimulate demand.	96%
3	Complete the description of local wood to support the updating of the legislation and the certification of production standards (including resistance and protection, among others).	94%
4	Generate and implement collaborative training program at all levels (professionals, technical staff and workers) in the private and public sectors.	93%
5	Encourage the development of building solution suitable for the local wood and its required performance standards (structures, fire, acoustic, thermal, etc.) through access to public CIR (registration certificate), or similar.	91%
6	Develop an investment and support program for woodworking SMEs to improve the competitiveness and productivity, including training activities and partnership.	89%
7	Create and implement an effective communication strategy for the different audiences: users, developers, professionals, general public (at national and departmental level).	85%
8	Generate incentives for private developers so that they choose wood for their buildings (exemptions, contributions, financial or insurance costs).	81%
9	Promote trade in forestry products, ensuring a constant quality supply for SMEs, sawmills and component production.	76%
10	Generate guidelines for the design, specifications, construction, and use (maintenance) of timber buildings (wood framing and engineering) for the different target audiences.	74%
C.	CROSS-SECTION. Generate a governance structure involving all Roadmap stakeholders, working together with other proposals currently under development.	N/A

Each of these actions is associated with the priority axes of the working committee described above and has specific tasks, internal groups, external advisers, complementary initiatives, and a metric with particular goals for six months, two years, and four years. For example, among the most relevant:

Table 8: *Examples of specific actions and metrics.*

Action	Specific task	Term
Action 1	Approval of new fire resistance laws and regulations.	Two years
Action 2	Architecture competitions and the start of works.	Two years
Action 2	Constructed works of isolated housing complexes, a collective housing building, and a social equipment building.	Four years
Action 4	Training and specialization program.	Four years
Action 7	Communication Strategy.	Two years
Action 8	Economic Incentive Instruments.	Four years
Action 10	Publication of Wood Design Guides.	Two years

3.3 INTERNAL GROUPS AND EXTERNAL ADVISORS

For the correct development of the Roadmap and each of the ten prioritized actions, internal groups were defined in charge of meeting the specific objectives that each of them poses. These groups were determined based on their relationship with the topic to be dealt with and the existing capacities they can offer to face the challenges.

The five reference groups were included, maintaining the intersectoral methodology of the project. In addition, it was considered, for specific lines of action, to work with external advisors specialized in the issues to be dealt with, but simultaneously, with a broader perspective than internal groups directly related to these.

Each group has members committed to a dedication of 4 hours per week (nucleus), 1.5 hours per week (committee), and 1.5 hours per month (assembly).

4 CONCLUSIONS

4.1 MULTI-SECTOR PARTICIPATION

The success of the Roadmap for promoting low-income wooden housing in Uruguay is subject to joint multisectoral participation in its creation, development, and implementation. For this reason, including the experiences and points of view of actors from all areas of the forestry and the construction sector was essential for analyzing the current national context prior to its co-construction.

Figure 19: *Release of the "Roadmap for the construction of wooden social housing in Uruguay".*

4.2 ONGOING ACTIVITIES

Technical Cooperation with Japan is currently under development through the efforts of the Inter-American Development Bank (IDB), which offers an investment of USD 750,000 to support the MVOT and other relevant actors in developing wooden construction nationwide. The previous emphasizes the evaluation of the regulations and the existing regulatory framework, identifying existing obstacles and gaps; public policies to encourage sustainable construction; research and development on relevant topics for the development of the value chain and the positioning of wood products in the national and international market; technology transfer between the public sector and the private sector; and positioning of the national market at a regional and global level, among others.

There is a continuity of the "Petit Committee" made up of the consultants who carry out the Roadmap, representatives of the MVOT, and the IDB, where the progress of the tasks is monitored, as well as new initiatives and forms of financing are proposed.

Two technical secretaries were hired, who organized and monitored the meetings and the progress of the different technical groups. After adjustment, the Technical Groups are already constituted, meeting periodically.

Three international competitions are underway: one for the design and construction of a high-rise social housing building in the city of Durazno, which the ANV will develop; another, for the design and construction of new types of housing in extension with wood technology of 20 units in the town of Tranqueras, department of Rivera, which MEVIR will develop; and, finally, a third competition for the design and construction of a health Polyclinic, which the PMB will produce.

Figure 20: *Call for architectural competition for mid-rise residential buildings and extended housing, respectively.*

Finally, two international consultants are working to generate economic incentive instruments for construction in wood and design and implement a training strategy for building in wood in Uruguay.

4.3 DOCUMENTS OF THE PROCESS

The co-creation process of the Roadmap for the Construction of Social Housing in Wood in Uruguay was documented through a triptych for mass distribution and a book, both available since May 2022 at the Ministry of Housing and Territorial Planning (MVOT) and the Inter-American Development Bank (IDB).

Figure 21: *Book "Roadmap for the construction of wooden social housing in Uruguay".*

https://doi.org/10.52202/069179-0582

ACKNOWLEDGEMENTS

To all the actors from the public, business, academic, professional, and user sectors, who participated with extraordinary enthusiasm during this process.

REFERENCES

[1] Oriental Republic of Uruguay Ministry of Economy and Finance: Draft Law: National Budget 2020 – 2024. Montevideo, Uruguay, 2019.
[2] Hax, A., Wilde, D.: The Delta Model: Reinventing Your Business Strategy. Springer, 2010.
[3] Ugarte G., J, Sierra, A., Codriansky, K: Roadmap for the Construction of Social Housing in Wood. Montevideo, Uruguay, 2022.
[4] Godoy, D., Baño, V., Romay,C., Moya, l.: Barriers for timber construction development in Uruguay. *World Conference on Timber Engineering WCTE 2021*. Santiago de Chile, 2021.
[5] Dieste, A., Baño, V., Cabrera, M.N., Clavijo, L., Palombo, V., Moltini, G., Cassella, F.: The potential of Uruguay within the global expansion of wood construction. *World Conference on Timber Engineering WCTE 2021*. Santiago de Chile, 2021.
[6] World Bank: Housing for All. 2016.
[7] Society of Forest Producers (SPF): The Contribution of the Forestry Complex to the Uruguayan Economy: The growth of the forestry sector in recent decades, Montevideo, Uruguay, 2020.
[8] Ministry of Housing and Territorial Planning of Uruguay: Five-Year Housing Plan 2020-2024. Montevideo, Uruguay, 2019.
[9] Hax, A., Ugarte G.: Towards the great Chilean university: a model of strategic transformation. UC Editions, Santiago de Chile, 2014.
[10] J. Ugarte, Using the Delta Model to transform Chilean timber construction industry. *World Conference on Timber Engineering*. Vienna, Austria, 2016.

World Conference on Timber Engineering Oslo 2023

USING ARIMA MODELS TO PROJECT SAWLOGS, AND SAWN WOOD PRICES IN THE CHILEAN CONSTRUCTION MATERIALS MARKET

Wilson Mejías[1], Janina Gysling[2], Carlos Kahler [3], Daniel Soto[4] Evaristo Pardo[5]

ABSTRACT:

One of the most remarkable factors when defining the materiality of a construction is the material cost. In this context, by having the tools to help reduce the uncertainty of wood cost will contribute to carry out projects with this material. The ARIMA models are management tools that have the potential to support projections in the short, and medium term. In the present research, the implementation of local ARIMA models were carried out in Biobío, La Araucanía, and Los Lagos regions, using as supplies the time series of radiata pine (*Pinus radiata*) sawn wood, and sawlogs prices, which have been collected periodically by the Forestry Institute (INFOR). The estimations on the implemented models had positive results in respect of validation data, with the exception of sawn wood prices from the four quarter of 2020, and part of 2021, which presented an unusual increase during the COVID-19 pandemic.

KEYWORDS: Sawn wood, sawlogs, construction with wood, ARIMA models, time series.

1 INTRODUCTION

The Chilean forestry industry produces near to 15 million m³ of radiata pine sawlogs, which are production supplies of approximately 7.9 million m³ of sawn wood, these figures make Chile one of the 15 largest producers of this material in the world [1]. Despite this, the national statistical institute (INE) indicates that approximately 13% of the area which is built annually in the country uses wood as a predominant structural material, which implicates a low consumption of wood estimated in approximately 500.000 m³ [2].

According to INFOR's figures, in 2021, the Biobío, La Araucanía, and Los Lagos regions produced approximately 4.5 million m³ of sawn wood, equivalent to 52% of what Chile produced that year [3]. On the other side, from 2020, a strong increase in sawn wood price has been observed, due to the increase of demand of this material during the COVID-19 pandemic. This increase in consumption was the result of several government policies that allowed a partial withdraw of workers' pension funds, which generated an increase in repairs, and extensions of housing.

According to construction companies, one the most determining factors when deciding on the use of wood is the price [2], therefore, by having models with the ability to generate robust estimations, it would help to have more clarity, and to project costs in a better way for the forestry industry, as well as for the construction industry, and for planification of public investment in this matter.

A time series is a set of data recorded in a monthly, quarterly, or annual period [4]. Its analysis is useful for decision making in the present time, and to generate projection on information, on the assumption that the past behavior patterns will continue in the future. The time series consist in three components:

a) Trend: It can be defined as a change in the long term that it is produced in relation to the average, or the long-term change in the mean. The trend is identified as a smooth movement of series in the long-term period.

b) Seasonal variation: Several time series have certain periodicity, or, in other words, variation of a certain period (monthly, quarterly, etc.).

c) Irregular variation (random): This component does not respond to any behavior pattern, since it is the result of fortuitus, or random factors having a remote impact in a time series.

[1] Wilson Mejías, (INFOR) Instituto Forestal, wmejias@infor.cl
[2] Janina Gysling, (INFOR) Instituto Forestal, jgysling@infor.cl
[3] Carlos Kahler, (INFOR) Instituto Forestal, ckahler@infor.cl
[4] Daniel Soto, (INFOR) Instituto Forestal, dsoto@infor.cl
[5] Evaristo Pardo, (INFOR) Instituto Forestal, epardo@infor.cl

https://doi.org/10.52202/069179-0583

Depending on time-series behavior, they can be classified as:

i) Seasonal: the series are seasonal when it is stable in time, that is to say, when the mean, and variation are constant over time. This is graphically reflected on the fact that the values of series tend to range around a constant mean, and that the variance in respect of that mean also remain constant over time.

ii) Non-seasonal: These are series in which the trend, and/or variability change over time. The changes in the mean determine a long-term increasing, or decreasing trend, so the series do not vary around a constant value

In the biography, several time series models are described [5-7], however, the ARIMA model is noted due to its simplicity, and practicality in modeling, and forecasting [8]. This model consists in a combination of an autoregressive term (AR), and a moving average term (MA) with a differencing element given by the letter I, based on research conducted by Yaglom [9]. In overall, these models are represented with the word ARIMA (p,d,q)(P,D,Q)[s], where the first parenthesis –(p,d,q)-, refers to the regular part of the series, the second parenthesis –(P,D,Q)- refers to the seasonal variations, and [s] corresponds to the seasonality order, which is 12 in annual series, 4 in quarterly series, and 2 in monthly series.

There are many studies where the ARIMA models have been used to analyze, and predict the behavior in short, and medium-term of prices of forestry industry products [10-12], obtaining good results in this regard.

ARIMA models can be generalized as:

$$Y_t = -(\Delta^d Y_t - Y_t) + \phi_0 + \sum_{i=1}^{p} \phi_i \Delta^d Y_{t-i} - \sum_{i=1}^{q} \theta_i \varepsilon_{t-i} + \varepsilon_t$$

Where Y_t corresponds to the current value of a series; Δ^d are the differences needed to remove the trend from the series; $\phi_1, \ldots, \phi_p$ are the corresponding parameters of the autoregressive part of the model (AR); $\theta_1, \ldots, \theta_q$ corresponds to the parameters of the moving-average part of the model (MA); ϕ_0 is a constant, and ε_t is the error term.

With this background, in the present research the ARIMA models were fitted to the time series of Chilean forestry product prices to prove the utility of this tool in terms of sawlogs, and sawn wood prices within the selected regions of the country.

2 MATERIALS AND METHODS

In the present research it was analyzed the behavior of nominal values of forestry products: sawlogs, and sawn wood of radiata pine (in Chilean pesos/m³). Based on the information available in INFOR's Forestry Statistical Platform (PEF), time series of selected product prices were created, considering the regions of Biobío, La Araucanía, and Los Lagos, fitting local time-series models. The time series of prices available in the PEF are of quarterly nature, and comprehends year 1980 until now. The prices used to create the series consider the average of quarterly measures recorded in a region for each product, including different provinces, and delivery locations (sawmills, sales plant, or purchase plant).

In the analysis of time series, the Box, and Jenkins protocol [13] was used, which indicates a divided process in the following stages:

a) Identification: the time series are presented graphically indicating if the series are seasonal or not. If the series have a trend, the differencing method is applied until making it seasonal, proving this through the ADF Dickey, and Fuller test [14]. The difference consists in an operation where each of the series values are subtracted from the previous one in order to remove any trend accumulated. Once the transformations on series are carried out, a simple autocorrelation function (ACF), and partial correlation function (PACF) are determined, which allows to determine the series structure, that is to say, if it has mobile average, or autoregressive components.

b) Estimation, and verification: by observing the two ACF, and PACF graphics of the transformed series, the ARIMA (p,d,q)(P,D,Q)[s] candidate models are raised. The models randomly distributed, or in a white noise pattern were selected by using the Ljung-Box test [15]. The statistic associated to this statistical evaluation is defined as:

$$Q = n(n+2) \sum_{k=1}^{h} \frac{\hat{\rho}_k{}^2}{n-k}$$

Where $\hat{\rho}_k$: autocorrelation of the sample in the delay, k y h are lag numbers being proved, and n is the size of the sample. The significance level associated to the critical region to reject the hypothesis of randomness is:

$$Q > \chi^2_{1-\alpha,h}$$

As a second criterion of the evaluation, those models presenting better performance metrics were selected by calculating the values of "Akaike Information Criterion" (AIC) [16], and the "Bayesian Information Criterion" (BIC) [17], which are defined as:

$$AIC = 2k - 2\ln(\hat{L})$$

$$BIC = kln(n) - 2\ln(\hat{L})$$

Where k is the number of estimated parameters, and $\hat{L}$ is the maximum value of the model's likelihood function.

These information criteria help to differentiate the efficiency that the models gain when adding new parameters, therefore benefiting the simplicity, and flexibility of models.

c) Prediction: Once the model has been selected, predictions were made for the values of the series. To evaluate the accuracy of the model predictions, the "Root Mean Square of Error" (RMSE), and "Mean Absolut Error" (MAE) indicators were determined, which would also help in differencing according to the predictive capacity of the models. The formulas of these indicators are:

$$RMSE = \sqrt{\frac{\sum_{t=1}^{n}(\hat{y}_t - y_t)^2}{n}}$$

$$MAE = \frac{|\hat{y}_t - y_t|}{n}$$

Where: $\hat{y}_t$ is the value estimated by the model, y_t is the observed value, and n is the number of observations.

The last 5 records of time series were used to validate the model forecasts, and to determine the percentage difference between the recorded, and estimated values.

In addition to what it is stated in the methodology suggested by Box, and Jenkins, for each one of the time series, an automatic model was fitted which is suggested by "auto-ARIMA" function of the statistical software R [18].

Beside of the Box, and Jenkins methodology, for each one of the time series, an automatic model was fitted, which is suggested by the auto-ARIMA function of the statistical software R: tseries [19], forecast [20], ggplot2 [21], and gridExtra [22].

3 RESULTS

3.1 SAWLOGS

a) Biobío region

For the analysis of this region, it was considered the available information of sawlog prices in the platform of forestry industry (PEF) since 2007, to the last quarter of 2022, since in that period it showed more uniform records. The missing measure for the third quarter of 2011 was completed through linear interpolation. The data was transformed through a logarithmic function in order to improve the model forecasting.

When applying the ADT test to the time series of log prices in Biobío region, it indicated that differencing was needed to remove the trend from the series, for this to be a seasonal type of series. However, models with two differences were fitted, since these presented better metrics.

The PACF, and ACF associated to the differenced series of sawlogs prices in Biobío region presented significant values in the third lag (Figure 1). Besides, the PACF records a significant lag in the second year, which is similar to the ACF behavior.

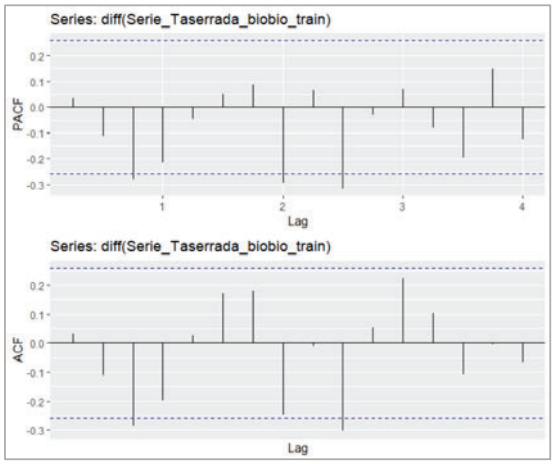

Figure 1: *The ACF, and PACF of differenced time series of sawlogs prices in Biobío region*

From the ARIMA models fitted to the series of sawlog prices in Biobío region (Table 1), the M_4 model showed better performance metrics at validation data level. This model also had no problems with the distribution of its residuals, since the Ljung-Box test did not deliver significant values.

Table 1: *Fitted models, and performance metrics of time-series prices of sawlogs in Biobío region.*

	ARIMA Models	AIC	BIC	Train		Test	
				RMSE	MAE	RMSE	MAE
M_1	(0,1,0)(0,0,2)[4]	**-181.69**	**-173.45**	0.0464	0.0354	0.1839	0.1761
M_2	(0,2,0)(0,0,2)[4]	-148.93	-141.79	0.0590	0.0427	0.1103	0.0927
M_3	(1,2,0)(0,0,2)[4]	-152.03	-143.86	0.0567	0.0431	0.0663	0.0515
M_4	(2,2,0)(0,0,2)[4]	-153.40	-143.19	0.0548	0.0410	**0.0459**	**0.0403**
M_5	(3,2,1)(0,0,2)[4]	-173.37	-161.11	**0.0386**	**0.0295**	0.2194	0.2116

Once the model is chosen, a validation of the forecast was carried out with the data slice that was not used in the model fitting, determining the percentage variation between the model prediction, and the observed values.

In Table 2, it can be observed that the error level of the model for the series values without logarithmic fitting varied between 1.58%, and 7.82%.

https://doi.org/10.52202/069179-0583

Table 2: *Variation of sawlog prices in Biobío region estimated with the M_4 model, and the values observed.*

Año	Trimestre	Observado ($/m3)	Predicción ($/m3)	Variación (%)
2021	Q4	40.271	37.122	7,82%
2022	Q1	39.759	39.129	1,58%
2022	Q2	43.057	41.323	4,03%
2022	Q3	45.501	44.043	3,20%
2022	Q4	45.251	46.653	-3,10%

In Figure 2 it can be seen the original data of time series, and the values that the m4 model fits, and predicts. It also can be observed that the validation data is included, almost entirely, within the defined range of the prediction generated by the model, following the trend that this data presents.

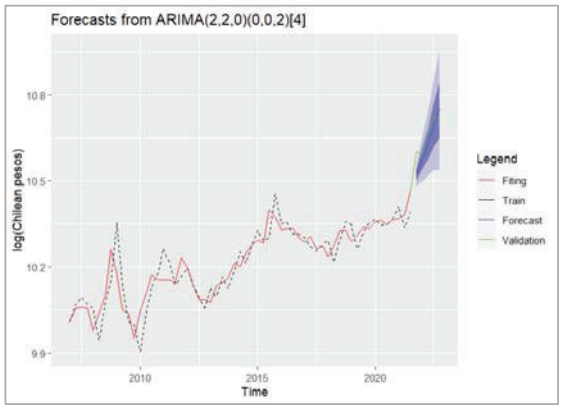

Figure 2: *Logarithmic time series of radiata pine sawlogs prices in Biobío region, forecast, and fitting made with the M_4 model.*

b) La Araucanía Region

For La Araucanía region, the prices recorded in the PEF since 2007, until the last quarter of 2022 were used, since this period has more uniform records. The missing measure in the third quarter of 2011 was linearly interpolated. The data was transformed through a logarithmic function in order to increase the forecast efficiency of the models to be fitted. The ADT test indicated that the prices series of sawlogs in La Araucanía region needed differencing to remove the trend from the data. With this information, models that consider a maximum of two differences were raised.

On the other hand, The PACF, and ACF associated to this time series (Figure 3) show that there is no significant time lag, which indicates a lack, or very low impact of the autoregressive term (AR), and the mobile average term (MA). The models presented in Table 3 were fitted by using the information of this analysis.

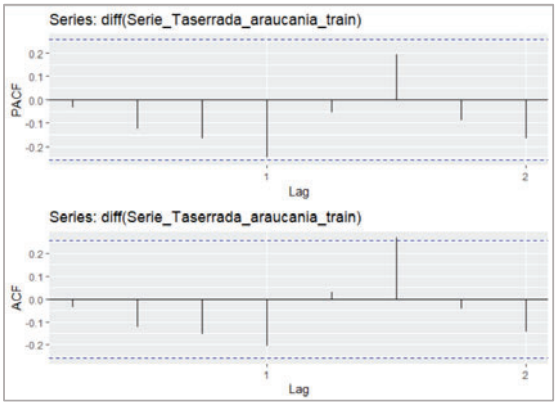

Figure 3: *ACF Y PACF de serie de tiempo diferenciada de precios de trozas aserrables en la Región de la Araucanía.*

From the model fitted for the sawlog series in La Araucanía region (Table 3), it was observed that the M_2 model shows the best validation metrics, which indicates that it generates better projections in relation to the last period data.

Table 3: *Fitted models, and performance metrics of time series of sawlog prices in Biobío region*

ARIMA Models		AIC	BIC	Train		Test	
				RMSE	MAE	RMSE	MAE
M_1	(0,1,0)(0,0,1)[4]	**-167.63**	**-173.45**	**0.0464**	**0.0354**	0.1839	0.1761
M_2	(1,2,0)(0,0,1)[4]	-137.30	-131.17	0.0672	0.0497	**0.0328**	**0.0273**
M_3	(0,2,1)(0,0,1)[4]	-159.01	-152.88	0.0535	0.0394	0.1742	0.1679
M_4	(1,2,1)(0,0,2)[4]	-157.25	-149.08	0.0533	0.0394	0.1796	0.1733
M_5	(0,2,0)(0,0,1)[4]	-123.67	-119.58	0.0774	0.0555	0.0533	0.0437

The residuals of this model were reviewed through the Ljung-Box test, which obtained non-significant values, concluding that the residual distribution corresponds to white noise. By validating the M_2 Model projections with data that was not used in the fitting (Table 4), it is observed that there is a percentage variation which range between 0.26%, to 5.71%.

Table 4: *Variations of sawlog prices in La Araucanía region estimated with the M_2 model, and the observed values.*

Year	Quarter	Observed ($/m3)	Forecast ($/m3)	Variation (%)
2021	Q4	41.032	38.689	5,71%
2022	Q1	42.587	41.431	2,71%
2022	Q2	43.582	43.468	0,26%
2022	Q3	46.179	45.202	2,12%
2022	Q4	45.976	47.216	-2,70%

In Figure 4 it can be seen the original data of time series, and the values that model fits, and forecast for the validation period.

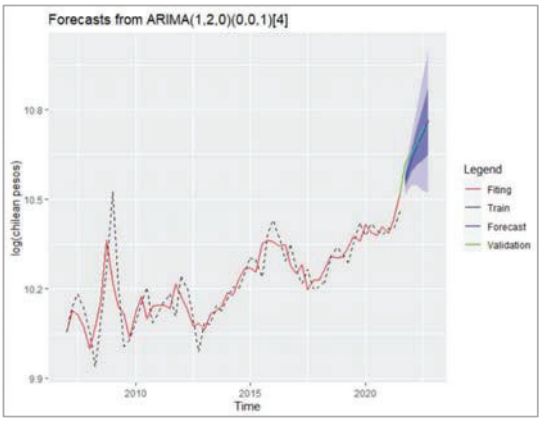

Figure 4: *Logarithmic time series of radiata pine sawlog prices in La Araucanía region, fitting, and forecast carried out with the M_2 model.*

c) Los Lagos region

For Los Lagos region, prices recorded in the PEF since the last quarter of 2012 until the first quarter of 2020 were used, since this period has more uniform records.

The ADT test shows that two differences are needed for the series of Los Lagos region's sawlog prices to be seasonal.

Figure 5: *The ACF, and PACF of differenced time series of sawlog prices in Los Lagos region*

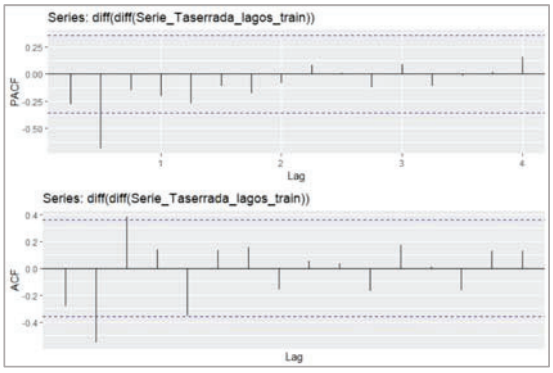

The M_4 Model presents the best validation, and train metrics in comparison with the rest that were fitted. While M_1 Model has better AIC, and BIC, this one has RMSE, and MAE validation values more than double that the ones presented in M_4 Model.

Under this analysis, the M_4 Model is the one with the best forecast from all the fitted ones. The M_4 residuals were reviewed through the Ljung-Box, which indicated that the residual distribution corresponds to white noise.

Table 5: *Fitted models, and performance metrics of time series of sawlog prices in Los Lagos region.*

ARIMA Models		AIC	BIC	Train		Test	
				RMSE	MAE	RMSE	MAE
M_1	(0,1,0)	**-101.86**	**-98.99**	0.0432	0.0331	0.1081	0.1046
M_2	(0,2,0)	-79.60	-78.19	0.0601	0.0455	0.1046	0.0836
M_3	(1,2,1)	-92.60	-88.39	0.0441	0.0300	0.0708	0.0698
M_4	(2,2,1)	-98.80	-93.20	**0.0383**	**0.0283**	**0.0277**	**0.0206**
M_5	(2,2,2)	-98.51	-91.51	0.0371	0.0281	0.0357	0.0296

When comparing the forecasts obtained with the M_4 Model, and the recorded values (Table 6), it was calculated that the variation between the values delivered by the model with respect to the real data was lower than 7%. Moreover, in Figure 6 it is observed the model fitting, and variations between the forecast, and the validation data set.

Table 6: *Variation of sawlog prices in Los Lagos region estimated with the M_4 model, and the observed values*

Year	Quarter	Observed ($/m3)	Forecast ($/m3)	Variation (%)
2021	Q4	43.911	43.782	0,29%
2022	Q1	46.333	44.343	4,30%
2022	Q2	47.444	44.478	6,25%
2022	Q3	48.778	46.772	4,11%
2022	Q4	50.223	48.476	3,48%

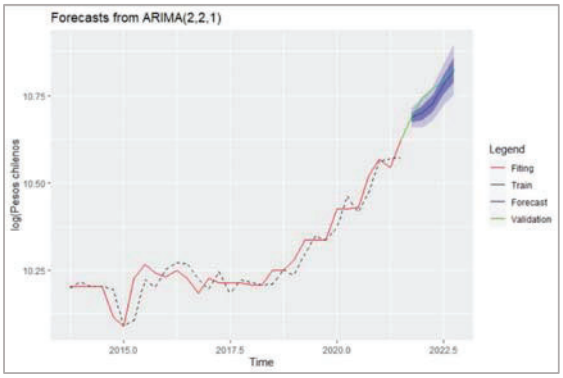

Figure 6: *Logarithmic time series of radiata pine sawlog prices in Los Lagos region, forecast, and fitting carried out with the M_2 model*

3.2 SAW WOOD

a) Biobío region

The series of sawn wood prices in Biobío region has complete information since the first quarter of 2007 until the last quarter of 2022, with the exception of the corresponding record in the third quarter of 2011, which was linearly interpolated.

https://doi.org/10.52202/069179-0583

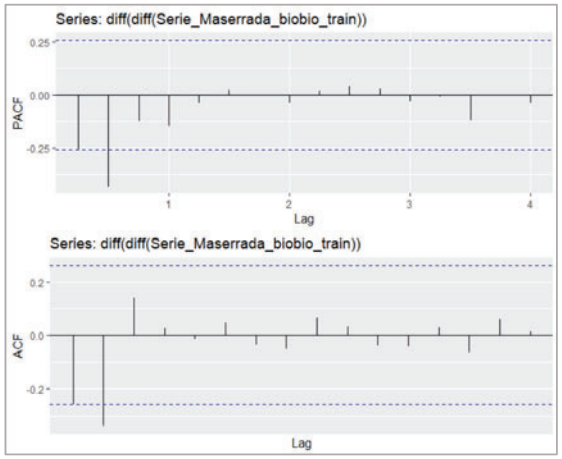

Figure 7: *The ACF, and PACF of differenced time series of sawn wood prices in Biobío region.*

Through the ADT test it was determined that differencing was needed to remove the trend from the series. Once the series are differenced, their PACF, and ACF were determined, which are shown in Figure 7, and they indicate that there is a significant lag associated to the autoregressive component, and another in the mobile average.

Table 7: *Fitted models, and performance metrics of the sawn wood prices time series in Biobío region.*

ARIMA Models		AIC	BIC	Train		Test	
				RMSE	MAE	RMSE	MAE
M_1	(0,2,3)	-209.90	-201.73	0.0350	0.0197	0.3144	0.2680
M_2	(1,1,1)	**-210.73**	**-204.55**	0.0369	0.0192	**0.0348**	**0.0291**
M_3	(1,2,2)	-208.42	-200.25	0.0350	0.0198	0.2115	0.1738
M_4	(2,2,2)	-208.75	-198.54	**0.0347**	**0.0203**	0.3202	0.2792
M_5	(2,2,3)	-206.79	-194.53	0.0347	0.0204	0.3495	0.3067

From the models fitted to the sawn wood prices series in Biobío region (Table 7), the M2 Model is the one with the best AIC, BIC, and validation metrics, forecasting in a better way the values of series beyond the range it was fitted with. The residuals associated to the M2 model were validated through the Ljung-Box test, indicating that it is distributed in a random pattern or as white noise.

Table 8: *Variation of sawn wood prices in Biobío region estimated with M_2 model, and the observed values.*

Year	Quarter	Observed ($/m3)	Forecast ($/m3)	Variation (%)
2021	Q4	134.830	128.604	4,62%
2022	Q1	136.771	136.425	0,25%
2022	Q2	140.650	142.917	-1,61%
2022	Q3	144.530	148.245	-2,57%
2022	Q4	144.530	152.579	-5,57%

When comparing the extrapolations that the M_2 Model produces (Table 8), it is observed that the variation between what is observed, and what is projected by this model is lower than 6%, where the minimum difference was 0.25% in the first quarter of 2022.

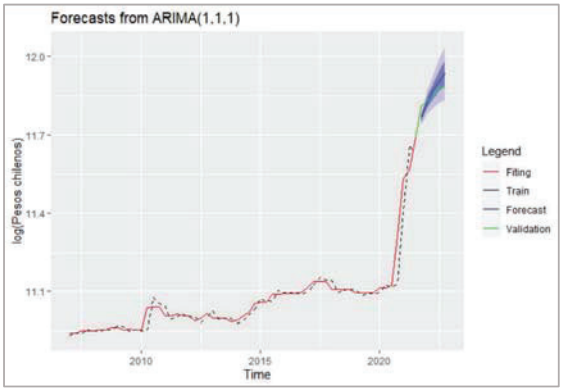

Figure 8: *Logarithmic time series of radiata pine sawn wood prices in Biobío Region, forecasts, and fitting carried out with the M_2 model.*

b) La Araucanía region

The series of sawn wood prices in La Araucanía region has information from the first quarter of 2007, until the last quarter of 2022, which is a period with more complete information, except for the records from the third quarter of 2011, which were linearly interpolated.

When applying the ADT test, it was determined that two differences were needed to remove the trend in the series of sawn wood price in La Araucanía region. Once the differencing was carried out, its PACF, and ACF were determined, which are shown in Figure 8, and they indicate that there is a significant lag associated to the autoregressive component, and another in the mobile average.

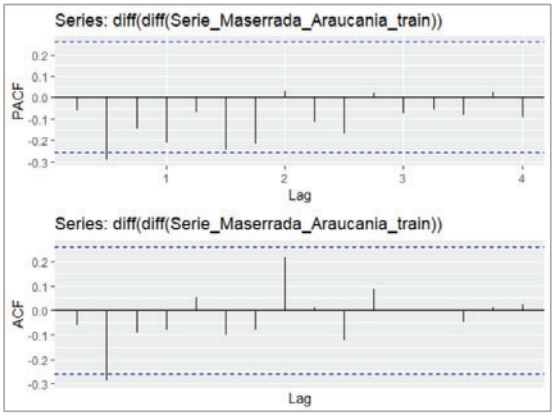

Figure 8: *The ACF, and PACF of differenced time series of sawn wood prices in La Araucanía region.*

From the models raised for the series of prices of radiata pine sawn wood in La Araucanía region (Table 9), the one with the best results in validation metrics fitting is the M_5 Model, at the same it has no significant lower indicators in train metrics, and its residuals are associated to white noise according to the Ljung-Box test.

Table 9: *Fitted models, and performance metrics of time series of sawn wood prices in La Araucanía region.*

ARIMA Models		AIC	BIC	Train		Test	
				RMSE	MAE	RMSE	MAE
M_1	(2,2,1)(2,0,0)[4]	**-224.73**	**-212.47**	**0.0289**	0.0181	0.1522	0.1374
M_2	(1,2,2)	-219.92	-211.75	0.0319	0.0170	0.0756	0.0636
M_3	(2,2,1)	-220.40	-212.23	0.0318	**0.0166**	**0.0679**	0.0562
M_4	(2,2,3)	-216.60	-204.35	0.0314	0.0177	0.0757	0.0642
M_5	(3,2,2)	-217.31	-205.05	0.0312	0.0177	**0.0679**	**0.0557**

When assessing the percentage differences between values provided by the model, and the ones used in validation (Table 10), it is observed that the difference in respect of the first two quarters is higher than 7%, while from this point it starts to decrease, reaching even 0.22%.

Table 10: *Variation of sawn wood prices in La Araucanía region estimated with the M_2 model, and the observed values.*

Year	Quarter	Observed ($/m3)	Forecast ($/m3)	Variation (%)
2021	Q4	133.645	124.421	6,90%
2022	Q1	146.308	129.809	11,28%
2022	Q2	142.267	136.781	3,86%
2022	Q3	144.423	144.110	0,22%
2022	Q4	144.423	151.212	-4,70%

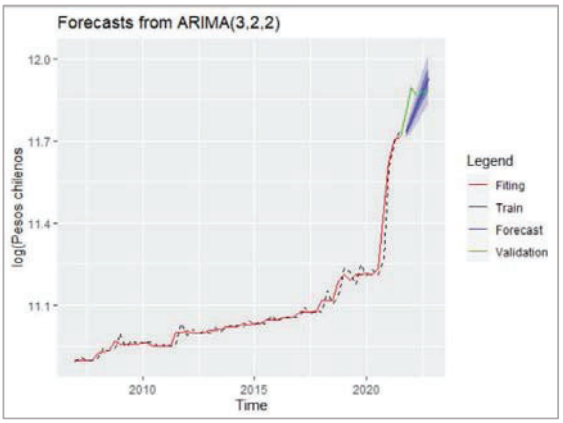

Figure 9: *Logarithmic time series of radiata pine sawn wood prices in La Araucanía region, forecasts, and fitting carried out with the M_2 model, and the observed values.*

Due to the lack of information on different periods, it was not possible to build a time series for the sawn wood prices in Los Lagos region with the necessary consistency to properly apply the methodology presented in this study.

4 CONCLUSIONS

The information collected, and managed by INFOR has an important potential that goes beyond of being a historical record of prices of several forestry products; it also can be used to generate new management tools allowing to promote construction with wood in Chile.

The models fitted for radiata pine sawlogs forecasted in a good way the prices of this product. In overall terms, the variations obtained were lower than 8%, which was validated with five quarter measures. The best results were obtained in La Araucanía region, where variations did not exceed 6%.

In case of time series of sawn wood prices, the models presented differences of up to 11.28%. In La Araucanía region, there were major differences between the last quarter of 2021, and the first quarter of 2022, which is due to unusual price increase of this material during the COVID 19 pandemic.

If the result obtained in this study are compared with other authors, it is observed that results are similar to Broz, and Viego [10], who obtained percentage differences lower than 10% by estimating the values of prices of forestry products in a 9-months period.

The ARIMA models are a good tool to carry out short, and medium-term projections of the forestry product prices, with a low level of uncertainty. Nevertheless, they cannot work efficiently with sudden market fluctuations, as the ones derived from the government policies for economic support in time of a pandemic.

ACKNOWLEDGEMENT

The present research have been carry out under the framework of the project entitled: *"Fortalecimiento de las Capacidades Tecnológicas del Instituto Forestal (INFOR), para el desarrollo de la Industria Secundaria de la Madera, a través de bienes públicos, orientados al sector de la construcción"*. The project was funded by *la Corporación de Fomento a la Producción* (CORFO).

REFERENCES

[1] Alvarez González, V., Poblete Hernández, P., Soto Aguirre, D., et al. La Industria del Aserrío 2021. Instituto Forestal, Santiago, Chile, 2021

[2] Gysling Caselli, J., Kahler González, C., Soto Aguirre, D., et al. El Mercado de la Madera Aserrada para uso estructural en Chile. Instituto Forestal, Santiago, Chile, 2020.

[3] Alvarez González, V., Poblete Hernández, P., Soto Aguirre, D., et al. Anuario forestal 2022. Santiago, Chile. Instituto Forrestal (INFOR). 276p. 2022.

[4] Lind, D., Marchal, W. y Wathen, S. Estadística aplicada a los negocios y la economía. McGraw-Hill, DF, México, 2015.

https://doi.org/10.52202/069179-0583

[5] Chatfield, C. The Analysis of Time Series, An Introduction. 352p. Chapman and Hall/CRC, United States of America, 2003.
[6] Guerrero, V. Análisis estadístico de series de tiempo económicas. 395p Thomson, D.F, México, 2003.
[7] Bowerman, N. Pronósticos, series de tiempo y regresión: un enfoque aplicado. 720p. International Thomson Editores D.F., México, 2009.
[8] Amarís, G.; Ávila, H. & Guerrero, T. Aplicación de modelo ARIMA para el análisis de series de volúmenes anuales en el río Magdalena. *Revista Tecnura*.2017.2. a07, 2017
[9] Yaglom, A. Correlation theory of processes with random stationary nth increments. In Matematicheskii Sbornik (N. S.), volume 37(79), number 1, pages 141–196. 1955.
[10] Yin, R. Forecasting short-term timber prices with univariate ARIMA models. *South Journal of Applied Forestry* 23(1):53-58, 1999.
[11] Broz, D. & Viego, V. Predicción de precios de productos de *Pinnus spp.* con modelos ARIMA. *Madera y Bosques* 20 (1): 37-46, 2014.
[12] Mei, B., Clutter, M. & Harris, T. Modeling and forecasting pine sawtimber stumpage prices in the US South by various time series models. *Canadian Journal of Forest Research*, 40(8), 1506-1516, 2010.
[13] Box, G. & Jenkins, G. Time Series Analysis: Forecasting and Control. Series in Probability and Statistics. Holden-Day, U.S.A, 1970
[14] Dickey, D. & Fuller, W. Distribution of the Estimators for Autoregressive Time Series with a unit root. *Journal of the American Statistical Association* 74(366):427-431, 1979
[15] Ljung, G. M., & Box, G. E. On a measure of lack of fit in time series models. *Biometrika*, 65(2), 297-303, 1978
[16] Akaike, H. A new look at the statistical model identification. *IEEE transactions on automatic control*, 19(6), 716-723, 1974
[17] Schwarz, E. Estimating the dimension of a model». *Annals of Statistics* 6 (2): 461-464, 1978
[18] R Core Team. R: A language and environment for statistical computing. R Foundation for Statistical Computing, Vienna, Austria. URL https://www.R-project.org/, 2021
[19] Trapletti A. y Hornik K. tseries: Time Series Analysis and Computational Finance. R package version 0.10-48, 2020
[20] Hyndman, R.J., y Khandakar, Y. Automatic time series forecasting: the forecast package for R. *Journal of Statistical Software*, 26(3), 1-22, 2008
[21] Wickham H. ggplot2: Elegant Graphics for Data Analysis. Springer-Verlag New York, 2016
[22] Aguirre, B. gridExtra: Miscellaneous Functions for "Grid" Graphics. R package version 2.3, 2017

World Conference on Timber Engineering Oslo 2023

CHARACTERIZATION OF GLUED-LAMINATED TIMBER SUPPLY IN CHILE

Janina Gysling[1], Carlos Kahler [2], Daniel Soto[3], Wilson Mejías[4], Pamela Poblete[5]

ABSTRACT: The rise of construction with wood in the world has its presence at local level, where there is great activity on this matter. The forestry institute (INFOR) actively participates in research projects carried out for the purpose of generate, and transfer economic, and technical information, which allow actors to make informed decisions to improve the development, and consolidation of construction with wood in Chile. In terms of economic information, for the first time the industry of wood engineering products is addressed, which is represented mainly by glulam (Glued laminated timber), whose supply is characterized in the present research. Thus, this study contributes to the decision-making process of private, and public actors involved in construction with wood; delivering an informed, and detailed analysis of the glulam in Chile; at the same time, the presentation of glulam industry profile aims to share this reality with the international interested community, and experts to gather opinions, and experiences about this industry's contribution in wood construction.

KEYWORDS: Engineered Wood Products, Glued laminated timber, Supply, Statistics.

1 INTRODUCTION

The Engineered Wood Products (EWP) corresponds to a series of construction structural products, made from beams, veneers, and other wood fibers mixed with adhesives, obtaining a larger dimensional unit, with superior resistance features than wood. It has a predictable performance, therefore reliable, additionally, it uses forests resources more efficiently [1].

The importance of these wood engineered products in construction it is demonstrated by the great development this industry has had in many countries where wood is a predominant material in this activity. While its use started, and reach notoriety in the non-housing construction sector, in the las few years, the use of engineered wood products has significantly increase in the housing sector, with important innovations in products, and applications, along with innovations in the architectural design.

Currently, Nordic countries are leading in wood construction projects, where the wide use of CTL (Cross Laminated Lumber) in high-rise housing building construction should be highlighted. Other countries that should be mentioned in this regard are: Japan, Italy, and Canada, among others. A lot of these developments are related directly to the need of countries of reaching in 2030 the UN's Sustainable Development Goals, due to the fundamental role the wood construction has played in matters of reducing the emissions of greenhouse gases. [2]

The number of companies in this sector is relatively small: 15 glulam facilities, one of I-joist beams, and six of industrialized truss. In CTL production there are two big companies in the Chilean forestry sector: Arauco, and CMPC (Niuform), and some sporadic actors.

The evolution of this sector has been relatively slow, in line with the evolution of construction with this material. However, in the last few years, the construction with wood has generated much interest, where the engineered products industry is becoming part of. For this reason, INFOR has added to its Forestry Statistic Platform this important sector of wood products, carrying out annual cadasters since 2020, which has allowed to understand the main parameters, and features, and the way the industry is evolving [1].

The main EWP elaborated in Chile is Glulam (Glued laminated timber). There are around a dozen facilities producing glulam, while other types of EWP for structural use, as in case of I-joist beams, and reticulated beams, have a limited participation. It should be noted that the first trails of glulam use in Chile are from 1960, when the forestry institute, supported by CORFO, brought Finnish experts with whom projects were developed as in case of the Universidad del Biobío sawmill in 1964; the industrial warehouse of the Sociedad Agrícola Forestal Copihue also in 1964, and the former Forestry Institute headquarters in Santiago, built in 1969 [3]. As a prove of

[1] Janina Gysling, (INFOR), jgysling@infor.cl
[2] Carlos Kahler, (INFOR), ckahler@infor.cl
[3] Daniel Soto, (INFOR), dsoto@infor.cl
[4] Wilson Mejías, (INFOR), wmejias@infor.cl
[5] Pamela Poblete, (INFOR), ppoblete@infor.cl

https://doi.org/10.52202/069179-0584

the job done in 1960 by the Finnish experts is the Forestry Institute's 18 Technical Report [4]. Regarding the CLT, there are a few Chilean companies with project to produce CLT in large volumes. For example, the case of the Niuform company, a joint venture between CMPC, and Cortelima companies, which have carried out several construction projects with CLT, and glulam.

In this context, this research aims to contribute in decision-making processes made by public, and private actors involved in the wood construction sector, delivering an informed, and detailed analysis of glulam supply in Chile, industry with history in the country, and with highly relevant products for the wood construction development perspectives.

The 2151 NCh norm defines the glulam as "a resulting product of the assemble of structural graded lumber using adhesives, through their faces, ends, and edges, to finally create elements not limited by squareness nor length in which fibers must remain longitudinally parallel with each other, working as whole structural unit". The pieces of wood are longitudinally assembled through finger joints.

INFOR has series of glulam statistical information generated in three consecutive years of measurement. From these it can be seen that glulam production in Chile revolves around the 23.000 m³, far behind from records from other countries with long history like Germany, and Austria, whose production figures are near to 2 million m³ [6].

At world level, the wood species generally used in glulam production are coniferous, and in Chile, it is mainly manufactured with one of these species: radiata pine. The main use of this engineered product in Chile is as structural beams in non-housing works [3], while in United States, it is used massively as columns, beams, and headers in residential construction [7].

The glulam allows to design structures with different structural, and aesthetic qualities. There are industrial quality pieces (for those without aesthetic requirements), normal visual quality (for pieces to be use in construction in general), or selection quality (for pieces with high aesthetic requirements), the latter being treated to erase knots, and details of the material [8]. Another glulam feature is that it allows to work with variable, and lower squareness, and lengths, so when bonded together, it reaches the required structural quality, providing the project with an image of lightness, especially in works with big lights. Another advantage of glulam in respect of sawn wood it that it has 80% more resistance, and up to 40% more stiffness, which also contributes to the construction of big lights buildings with slender pieces [3]. The variety of forms, and dimensions that glulam allows is certainly its main attraction, therefore it is a material that has been used in several architectural projects, for housing, and non- housing purposes.

The norm related to glulam, where the procedures for its manufacture, and use are established, is included in the following Chilean norms:

- NCh 2148: *Madera laminada encolada estructural – requisitos e inspección* [8]. (Glued-laminated structural lumber – requirements, and inspection)
- NCh 2149: *Madera – Madera aserrada – determinación del módulo de elasticidad en flexión – método de ensayo no destructivo* [9]. (Wood – sawn wood, bending modulus of elasticity determination – non-destructive testing method)
- NCh 2150: *Madera laminada encolada – Clasificación mecánica y visual de madera aserrada de pino radiata* [10]. (Glued-laminated timber – Radiata pine sawn wood visual, and mechanical grading)
- NCh 2165: Madera laminada encolada – Tensiones máximas admisibles para la madera laminada encolada estructural de pino radiata [11]. (Glued-laminated wood – tension grades for radiata pine structural glulam)

2 MATERIALS AND METHODS

The information on glulam presented in this research comes from three cadasters carried out by INFOR on this product's manufacturer companies.

The cadasters of the glulam industry, carried out in 2020, 2021, and 2022, is an activity that INFOR will continue to do annually in order to provide the country with statistical series of this secondary industry remarkable segment, whether for the definition of public policies, as well as for the development of investment that contributes to increase this product supply.

Following the methodology INFOR uses when generating forestry statistics for the country, a total of 15 glulam manufacturer companies were identified. These companies were surveyed by INFOR's professionals through a survey form design for this matter. The information collected was added to the Forestry Statistical Platform, this is a tool to generate series, and statistical reports, which are available for the interested public. The information processing in the present research was carried out using EXCEL database.

To know the problems, and goals the producers are facing, they were asked to choose from 10 options, the three most important by priority. Their responses were valued according to this prioritization, thus creating a value index for each option.

3 RESULTS

The glulam industry in Chile is constituted by 15 manufacturer companies, from which 12 were producing in 2021, and 3 were paralyzed, or without glulam projects. The glulam plants have presence in five regions around the country, but they are mainly concentrated in Metropolitan Region (7), and to a lesser extent, in Biobío region (4). Another 2 plants are located in La Araucanía Region, 1 in Ñuble Region, and 1 in Los Ríos Region.

3.1 PRODUCTION

In 2021, glulam production in Chile reached 24.478 m³ (Figure 1), which represented an increase of 10.8% in respect of the previous year. With these figures, the evolution of the 2019-2021 period shows an upward trend, in accordance with the forecast for the industry conducted in 2022, which indicates a growth of 9.3% in relation to 2021. The drop recorded in 2020 is attributed to the long periods where people could not go to work, with a consequent drop in the economic activity.

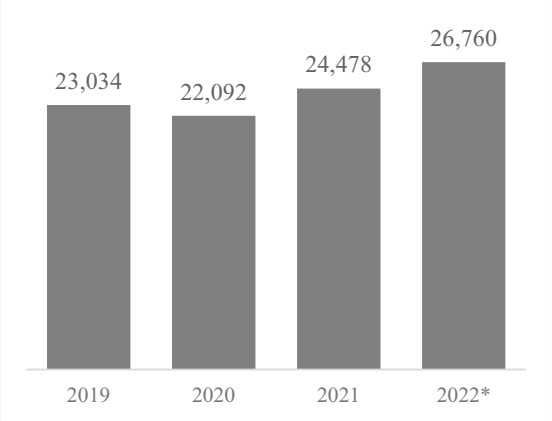

*: Industry estimation

Figure 1: *Evolution of glulam production in Chile*

The 2019 production was originated in 14 manufacturer plants, while in 2020 the number of plants dropped to 13, and in 2021 a new company was added, but three of the companies already added stop operations, therefore that year, the total of manufacturer companies was 12.

More than 90% of production is generated in regularly working plants, while some other plants only work occasionally or sporadically, this situation slightly increased due to the pandemic.

The glulam industry products are beams, and columns, impregnated or not (Figure 2). In the first two years of the analyzed period, beams, and then columns concentrated around 90% of production. However, in the last year of that period, the production of impregnated beams increased significantly, even exceeding non- impregnated beams, which is definitely in accordance with the requirements of specific projects where these products were used.

Production is determined mainly based on companies' orders. A proportion lower than 10% is made on the basis of last year production, and in 2021 also near 10% was produced to have a supply volume available. It should be noted that in the first two years, some companies did not provide information on this matter; however, the statistical procedure by itself, and the universal utility of the data it provides, contributes considerably to generate trust in all actors.

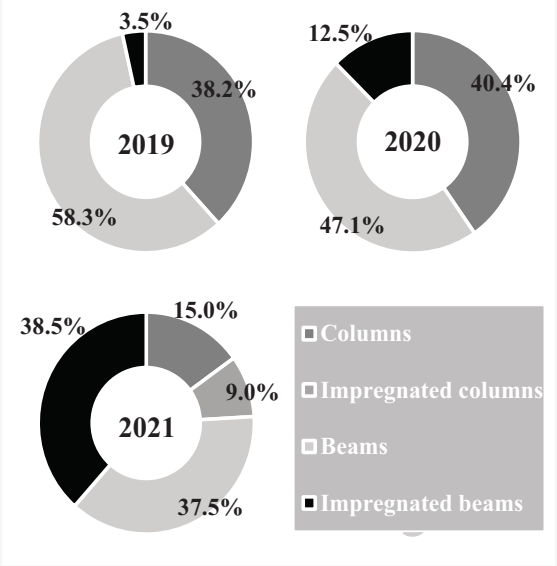

Figure 2: *Glulam production by type of product*

According to the information provided by the companies, approximately 83% of production was made based on orders (Figure 3). This means that it is a production generated in response to a known demand, through diverse construction projects in which the glulam industry participates as a structural elements provider.

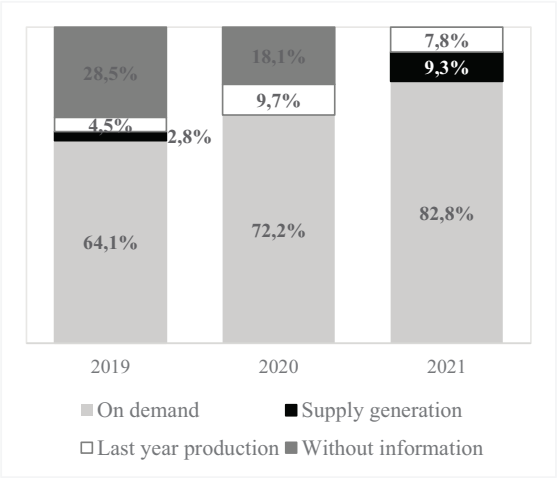

Figure 3: *How it determines the production of glulam in the*

https://doi.org/10.52202/069179-0584

industry?

In glulam manufacturing, radiata pine is by far the most dominant species, as well as in the whole forestry, and wood industry. However, the Douglas fir is highlighted with a relatively significant participation, even though this experimented a strong fall in 2021, as a result of the sawn wood prices increase, and a lower relative availability of Douglas fir (Figure 4).

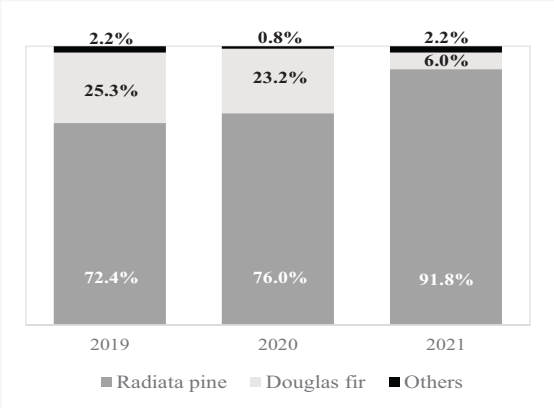

Figure 4: *Distribution of glulam production by species*

According to production volumes, there are three different groups of plants: with production >to 3.000 m³/year; with production between 1.000 – 3.000 m³/year, and plants with production < to 1.000 m³/year. It should be taken into account that, based on differencing according to annual production ranges, a plant can change of range from one year to another.

Glulam plants in superior ranges currently participate with more than 60% of production, while the ones in intermediate ranges produce 30%, and the one in inferior ranges participates with something more than 7%. Although proportions have varied between one and other ranges in the analyzed period, it can be affirmed that 2021 figures, with mitigated pandemic effects, are closer to the local industry reality (Figure 5).

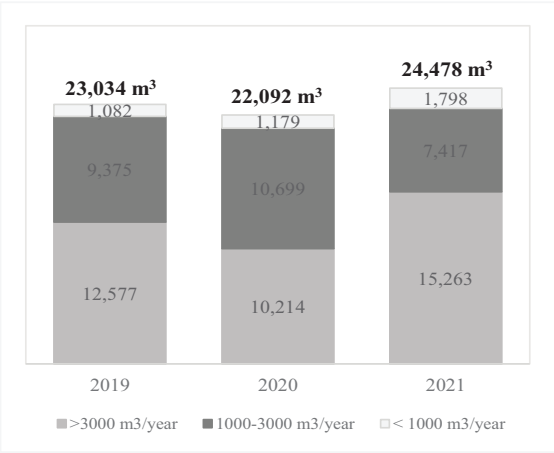

Figure 5: *Evolution of glulam production by annual production ranges*

On the other hand, the main variable cost of production is raw material, with a share of 42% in the first two years within the period, that grew in 53% in 2021. This growth reflects the significant increase in construction materials prices, like sawn wood, as a result of a demand activated by several state programs in support of families affected by the pandemic. Secondly, the workforce is included, that together with raw material represents more than two thirds of glulam's total production cost (Figure 6).

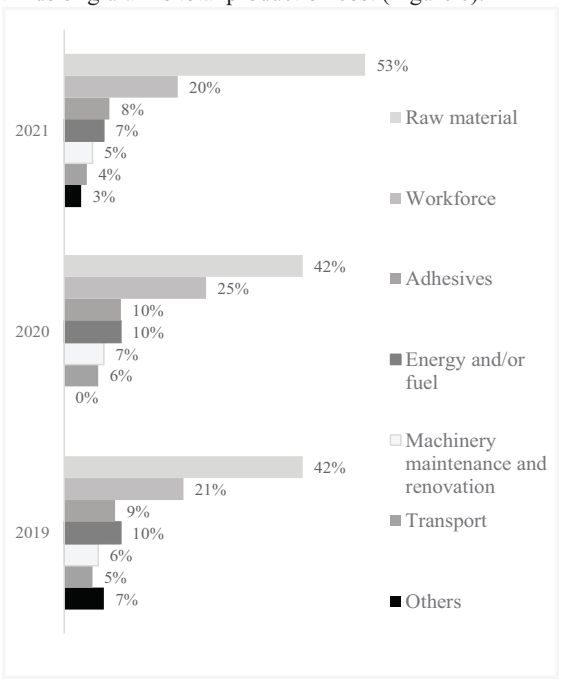

Figure 6: *Distribution of production variable cost by main items*

The occupation in glulam industry is relatively low, with 616 employed people in 2020, and 640 in 2021. Nearly 90% of occupation corresponds to permanent type of workers, mainly operators since the number of people working at the administration represent less than 10%. Moreover, more than 93% are men.

3.2 MARKETING

Glulam production is mainly destined to the internal market, but there is also a volume for exports, being Australia by far the main, and more stable market of destination.

During 2019 and 2020, the relation between the internal, and external market remained relatively stable, however, in 2021 exports increased until exceeding 40% of production (Figure 7). It could thus be supposed that the stimulus to increase production was the external market demand, more than the local market recovery.

https://doi.org/10.52202/069179-0584

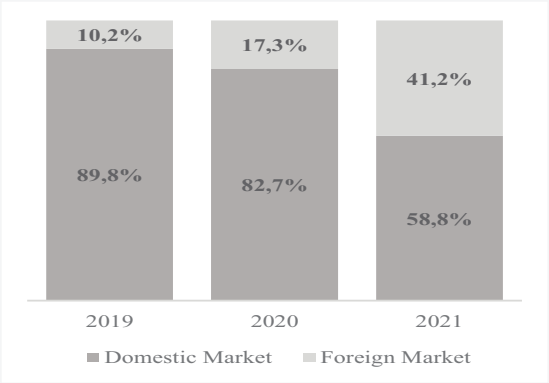

Figure 7: *Distribution of glulam production by market*

The main marketing channels for production that remain in the internal market are six, and their participation is relatively regular when compared with 2019, and 2021, however, in 2020, glulam producer sales in the internal market changed a lot in terms of destination, making marketing chains way more relevant, at expenses of the non-housing construction companies' participation (Figure 8).

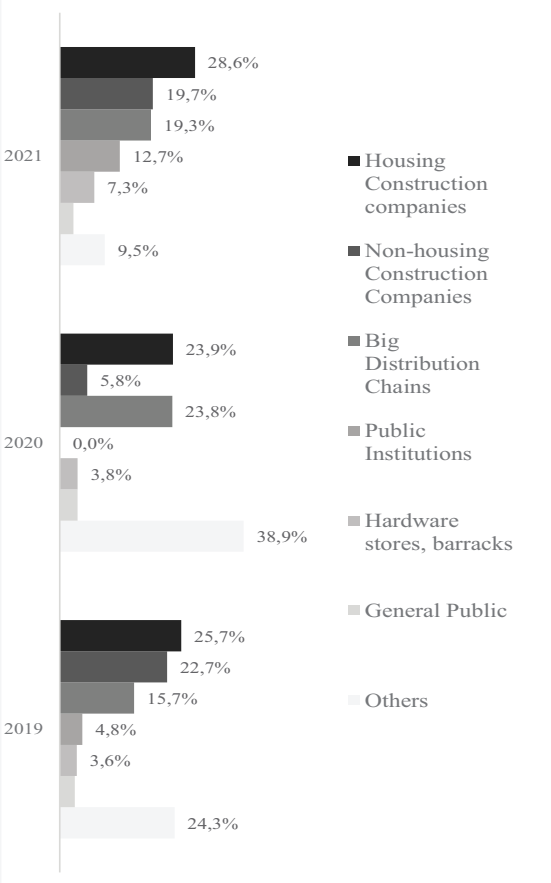

Figure 8: *Marketing channels in the domestic market*

In relation to the Chilean market perspectives in the next five years, glulam producers are solidly optimistic. In 3 annual consultations carried out, around 70% anticipates a growth in the market, while 10% thinks that the market will remain unchanged. The remaining 20% did not give a response, but none of the producers think that it will drop.

3.3 RAW MATERIAL

As mentioned before, the main raw material in glulam manufacturing is sawn wood, reaching in 2021 a total consumption of 34.010 m³, which reflects a decrease of 12.8% in respect of 2020. In Table 1, it can be seen that the most frequently way to obtain sawn wood is in dry state, although some plants purchase part of it in green state, and they dried it onsite. In other cases, sawn wood arrives impregnated or planned at the glulam plant. Only 9.4% of supply in 2020 was determined by the producers as structural sawn wood, meaning a classified wood with structural grade according to NCh 1198 norm, with moisture content lower than 20% according to NCh 1207 norm, dimensions, and tolerances according to NCh 2824, and preserved according to NCh 819 norm [12].

Table 1: *Sawn wood supply by state*

Type	2019	2020	2021
Green sawn wood	42	42	5,828
Impregnated sawn wood	313		104
Dry sawn wood	33,479	30,909	27,072
Impregnated sawn wood dried in chamber	1,116	1,519	509
Dry planned wood			497
Structural Sawn wood		3,682	
No information	3,469	2,867	
Total supply of sawn wood	38,419	39,019	34,010

On the other hand, glulam plants are supplied with sawn wood mainly from their own sawmills, this modality shows a growing tendency in the analyzed period, reaching a participation of 54% of supply in 2021 (Figure 9). On the contrary, the supply from sawmills with production lower than 1.000 m³/year is not significant, since in 2021 none of the glulam plant were provided from these productive units. The superior, and intermediate ranges participation does not show a clear tendency in the analyzed period, but they are very important when considering that together they provide something more than 40% of supply.

https://doi.org/10.52202/069179-0584

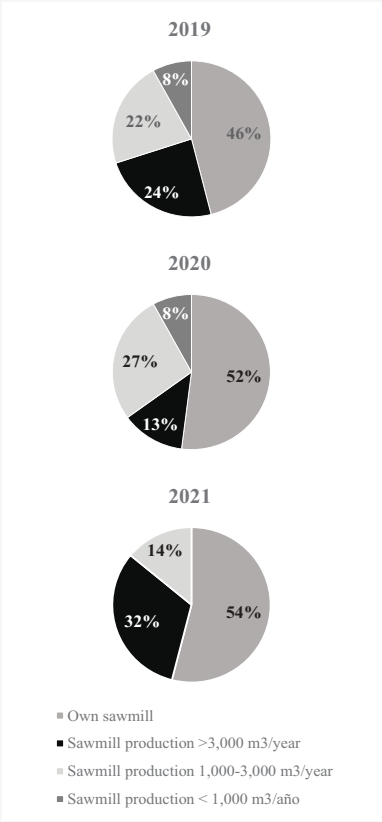

Figure 9: *Sawn wood supply distribution by type of sawmill of origin.*

3.4 PROBLEMS AND GOALS

The glulam producers were consulted about the main problems this activity faces, and the main goals they have planned. In respect of problems, the producer's prioritizations show differences year to year, but the one with higher valuation rate in the period is the low demand on glulam, and low availability of sawn wood for its manufacture. Way more behind is the lack of qualified workforce, sawn wood high cost, and its low quality. The valuation index for prioritized problems in 2021 are presented in Figure 10.

In the valuation of goals, the strong, and permanent disposition to increase production, and improve productivity is highlighted. In a second level, the produce's goals show the investment in technologic production, and diversification of products, and markets. It is worth to mention that even though one the biggest problems mentioned by the industry is the lack of trained workforce, there is no prioritization assigned in training the personnel in 3 years of consultation, which represents a contradiction. The valuation index for prioritized goals in 2021 are presented in Figure 11.

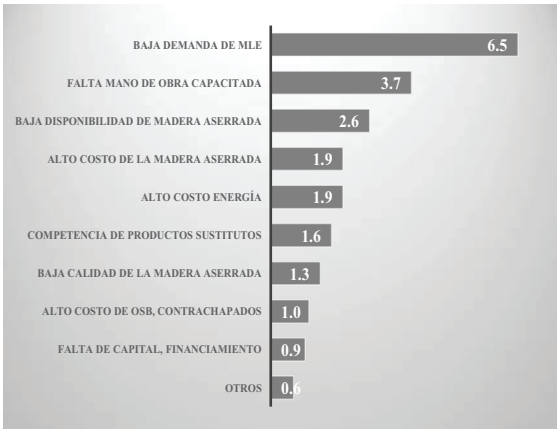

Figure 10: *Valuation index of problems in glulam industry, year 2021*

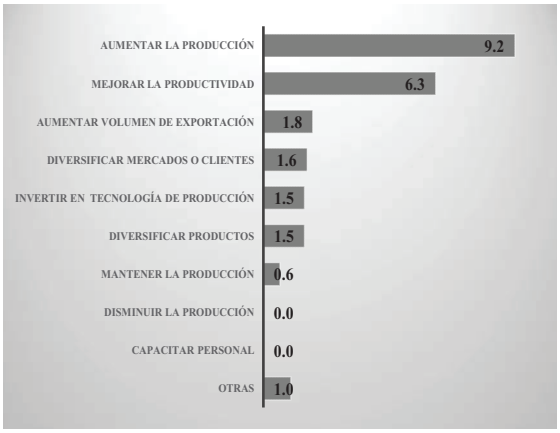

Figure 11: *Valuation index of glulam industry goals in 2021.*

3.5 PRODUCTION PROCESS

According to information collected through survey application, glulam plants are supplied almost entirely with dry sawn wood, but when they are supplied with green sawn wood, first it is dried, and then graded. Eventually, sawn wood is impregnated, depending on the component's requirements for it to be manufactured.

The first process in production of sawn wood laminations is obtaining this product with the allowed defects according to the structural grade required by the lamination (A, or B grades, according to NCh 2148). Then, the lumber is bounded together through finger joints to form laminations. When the length allows it, some companies are partially or totally supplied with laminations. After that, laminations are planed for they to reach desire dimensions. Subsequently, they are glued together and pressing to form laminated timber, before the curing of adhesives starts, whose thickness must remain as a thin layer. The most used adhesives in manufacture are melamine-urea-formaldehyde (MUF), and liquid polyurethane plastic (PUR). Lastly, the glued-laminated

timber piece is planed to reach its final dimension. Optionally, beams can include painting, or varnish finishings, which are applied depending on the client's requirements. The complete process of glulam production takes 4 days, being pressing the process that takes the longest time, between 4, and 12 hours, depending on the adhesive used.

Figure 12: *General Layout of glulam productive process*

Regarding the machinery used in the productive process, all consulted companies declare to have drying chambers, and impregnation to prepare the raw material. Then, in the lamination process, there are features to be highlighted, cutting tools like band saw blades, and sliding table saw, while two companies have CNC machines. The clamping process is carried out in a hydraulic, and mechanical press, and to a lesser extent, by hand press.

4 CONCLUSIONS

The most important EWP product in Chile, due to the number of companies involved, but overall due to its long history in the country, is glulam. However, the industry level of production is low, and has not been able to improve to superior levels of development, mainly due to limitation related to wood use, and its products in construction, resulting in, just as stated by producers, a low glulam demand.

Another limitation that producers have highlighted is the low availability of sawn wood, referring mainly to the structural sawn wood, which is the type of sawn wood that glulam requires to its production. This limitation comes from the sawmill industry, which produces low volumes of structural sawn wood, but this also originates from in the quality of lumber supply as a result of the predominant modalities in forest plantation management.

Even though the great activity existing in wood construction Chile has stimulated the interest, and expectations of wood products companies, the low production of structural elements allows to conclude that this is not enough to reach significant increases in the activity, in the short, and medium term, and what is probably needed is a more determined, and focalized boost from public policies.

ACKNOWLEDGEMENT

The present research has been carried out under the framework of the project entitled: *"Fortalecimiento de las Capacidades Tecnológicas del Instituto Forestal (INFOR), para el desarrollo de la Industria Secundaria de la Madera, a través de bienes públicos, orientados al sector de la construcción"*. The project was funded by *Corporación de Fomento a la Producción* (CORFO) and INFOR.

REFERENCES

[1] Gysling, J., Kahler, C., Soto, D., Mejías, W., et al. 2021. El mercado de productos de ingeniería en madera en Chile. Madera laminada encolada y cerchas industrializadas. INFOR. https://doi.org/10.52904/20.500.12220/31356

[2] Gysling, J., Kahler, C., Soto, D., Mejías, W., Poblete, P., Alvarez, V., Bañados, J.C., Baeza, R. & Pardo, E., 2021a**.** Madera y construcción. Hacia una simbiosis estratégica. INFOR. https://doi.org/10.52904/20.500.12220/31291

[3] CORMA, 2011. Madera Laminada: Arquitectura, Ingeniería y Construcción. Corporación de la Madera. Editorial Centro de Transferencia Tecnológica de la Madera. 239p.

[4] Niskanen, E., Mäkeläinen, R., 1965. Informe Técnico 18: Estructuras de madera laminada. Estudio preliminar. Santiago, Chile: INFOR. https://doi.org/10.52904/20.500.12220/6509

[5] INN, 1989a. Madera laminada encolada estructural: Vocabulario: Norma chilena oficial NCh 2151.OF89, Instituto Nacional de Normalización . Chile.

[6] Holzkurier, 2020. Die größten BSH-Hersteller 2019. [En línea] Disponible en https://www.holzkurier.com/holzprodukte/2020/09/brettschichtholz-produktion-2019.html. [Consulta 12 de diciembre 2022]

[7] FEA, 2017. Global Outlook for Engineered Lumber Products. Forest Economic Advisors. LLC.

https://doi.org/10.52202/069179-0584

[8] INN, 2013. Madera laminada encolada estructural - Requisitos, métodos de muestreo e inspección (NCh N° 2148). Instituto Nacional de Normalización Santiago, Chile. 17p.

[9] INN, 1989b. Madera – Madera aserrada – determinación del módulo de elasticidad en flexión – método de ensayo no destructivo (NCh N° 2149). Instituto Nacional de Normalización Santiago, Chile. 7p. INN, 1989

[10] INN, 1991a. Madera laminada encolada - Clasificación mecánica y visual de madera aserrada de pino radiata. (NCh N° 2150). Instituto Nacional de Normalización Santiago, Chile. 11p.

[11] INN, 1991b. Tensiones admisibles para la madera laminada encolada estructural de pino radiata. (NCh N° 2165). Instituto Nacional de Normalización Santiago, Chile. 31p.

[12] Gysling, J. et al., 2019. El mercado de la madera aserrada para uso estructural en Chile. INFOR. https://doi.org/10.52904/20.500.12220/29220

World Conference on Timber Engineering Oslo 2023

ESTIMATING THE GLUED-LAMINATED TIMBER DEMAND IN NON-RESIDENTIAL BUILDINGS IN CHILE

Daniel Soto Aguirre[1], **Janina Gysling Caselli**[2], **Carlos Kahler González**[3]

ABSTRACT: Glued laminated timber has taken center stage in recent years in Chile. The non-residential building sector is attracting the attention of local architects and builders, possibly due to the multiplicity of types of buildings, in which the attributes and advantages of this product are expressed. There is no record of the amount of glued laminated timber that is consumed annually in the country. The present study is a contribution to the knowledge of the demand, from the point of view of the potential that the non-residential construction market would offer. The main result indicates that, if all the potential non-residential area use glued laminated timber as a structural element, the associated demand would be in the range of 192 to 220 thousand cubic meters. This volume accounts for the enormous space that exists in the construction market to position this product, since production does not exceed 25,000 m3.

KEYWORDS: glued laminated timber, potential demand, non-residential building.

1 INTRODUCTION

In developed countries as Germany, Austria, and Japan, glued laminated timber (GLULAM) it is produced in large volumes, which is used in different types of residential, and non-residential building, usually found where large spans members are required [1].

In Chile, glulam has a vast history of usage since 1960's in the last century. The production is mainly oriented to internal market in architectural works with big spans, as warehouses, industrial plants, gyms, roofed sport centers, indoor swimming pools, pedestrian bridges, and other public infrastructure works. In Chile, there are different types of non-residential buildings which are highlighted by the use of glulam in wall, and roof structures. In general, this product operates as other materials complement which are more frequently found as concrete, or bricks. However, there are buildings whose wall, and roof structures are only composed by glulam. From some years now, glulam is drawing the attention of constructors, and architects to be used in non-residential building in the country [2].

In the present research, it was carried out an estimation of glulam cubic meter consumption that non-residential construction may reach in Chile, by means of potential demand.

In marketing, the potential demand is the maximum volume a product, or service can reach in a stablished time horizon. The marketing potential demand is calculated from an estimation of potential buyers' number, which are assign with an individual consumption rate. The potential demand represents the superior limit reached by the sum of sales of all companies participating in the market for a determined product or service [3].

2 MATERIAL AND METHODS

In order to develop this research, the main input in the analysis was the information contained in the building database recorded by the National Statistics Institute (INE). This information contains, among other fields, the following: region, and commune where works will be located, the type of building permit (new works permit, or extension permit), the purpose of building (public building, commercial premises, kindergartens, hospitals, among many others), the total authorized area to build (in square meters), and total area distribution according to predominant material in wall structure. The purpose of building was based on a table of purposes INE has elaborated to fill the Single Building Form (FUE), adding a broader definition. On the other hand, the list of predominant materials in wall structure, also elaborated by INE for the same purpose, was used without any changes [4].

[1] Daniel Soto, (INFOR), dsoto@infor.cl
[2] Janina Gysling, (INFOR), jgysling@infor.cl
[3] Carlos Kahler, (INFOR), ckahler@infor.cl

https://doi.org/10.52202/069179-0585

Table 1: *Purposes of non-residential buildings based on INE's table to fill the FUE*

Purposes	Purposes
Customs (offices, and other similar constructions).	Leisure and amusement (sports centers, indoor pools, sports fields and other similar)
Agricultural (aviaries, yards, greenhouses, nurseries, fodder storage facilities, among others)	Financial institutions (banks, stockbrokers, and similar ones)
Storage (warehouses) y Transport (bus stations, air terminals, and similar ones)	Sheds (maintenance of several products)
Social assistance	Hotels, residences, cottages
Bars, restaurants, and coffe shops	Industry
Jails	Courts
Market (commercial premises, pharmacies, bakeries, others)	Mines and quarries
Communications, mail	Markets, and fairs
Cultural (theaters, cinemas, public libraries, and similar ones)	Offices
Public building (municipalities, ministries, and similar ones)	Religious organizations (churches, chapels, others)
Kindergartens	Fishing (roofed agricultural crops, and similar)
Basic education	Health (hospitals, clinics, and other healthcare facilities)
Secondary education	Public services
Professional institutes	Supermarkets
Universities	Technical agencies, Laboratories
Electricity, gas	Other non-residential buildings N.E.I not elsewhere identified

Source: Own elaboration, based on the INE, 2021
N.E.I not elsewhere identified

Table 2: *Predominant materials in walls used by INE to fill the FUE*

Wall material
Mud brick
Concrete block
Concrete
Brick
Wood
Preformed metal panel
Ferro-concrete panel
Expanded polystyrene reinforced Panel enabled for stucco
Stone

Source: INE, 2021

The database of building from INE do not allow to determine directly the cubic meters of predominant materials contained in wall structure, since, as stated before, it is only available the information on area built in each one of them. Another difficulty in regards of obtaining the volume of materials in a direct way, and, particularly in timber category, is that there is no specification on type of wood, or to which wood product it is referred.

The individual consumption is given by the glulam volume needed in a built area unit, that is to say, the usage factor. The non-residential authorized area in a certain year is the potential area. Thus, with the quantities of predominant materials in walls, and roofing the potential demand is estimated. The amount of glulam in potential area is the expression of the volume that may be consumed by construction of non-residential works if this structural material was used ("potential demand").

To obtain the maximum demand, in first place it was carried out an estimation of potential non-residential area using INE's database, and subsequently, a documentary inquiry of non-residential works tendered by the State, to obtain the usage factor (m^3 glulam/m^2 built).

3 RESULTS

3.1 ESTIMATING THE NON-RESIDENTIAL POTENTIAL AREA

The total of new non-residential works area, according to data published by INE, was 4.216.362 m^2 in 2019. INE obtained this area considering the total of building permits authorized by the different municipalities in the country during one year.

In order to express in a better way, the "potential" feature of area to the used of glulam, in this research, it was considered appropriate to make some adjustments (reduction) on INE's figure:

- It was eliminated non-residential buildings from the database that could be interpreted as of small spans. This criterion is supported in that glulam emerges as a construction material mainly to cover large distances between building supports. Clearly, the relation between square meters of a determined building, and the size proception of it (large, or small) will depend on what it is being analyzed. In this research it was fixed arbitrarily a limit of 140 m^2 to establish non-residential building with large spans.

- From the remaining area, it was excluded works related to a mixed project, that is to say, building with more than one purpose. Among the most frequently found mixed constructions in urban areas are buildings with commercial premises in the first floor, and housing purpose from the second floor and up. According to INE's database, the majority of this mixed projects are characterized because of the predominant material in walls is concrete, and to a lesser extent, bricks, and metal, without the participation of wood in wall structures.

Figure 1: *Buildings with mixed purposes, Housing, and Market (Located in Avenida Irarrázaval avenue, Ñuñoa commune, Chile)*

- It was excluded the number of non-residential corresponding to large area works recorded under the purpose of storage, and transport, and industry purpose. The first one corresponds to large goods storage warehouses, which are commonly rented by retail companies by means of storage, and product delivery. In industry purpose, it is common that the extensions of roof coating under product processing plants, as well as the structural walls that support them, are made with predominant materials different from wood [5]. While the structures, and roof of both types of buildings (Storage, and transport, and industry) are a potential market for glulam use, so far it is thought that this may not bring positive results, due to that the alternative materials already being used, as steel, and concrete, have more competitive costs [6].

Figure 2: *Non-residential building, Industry purposes (Wood pellet plant, Biobío region, Chile)*

Figure 3: *Non-residential building, Industry purposes (Sawmill, Biobío region, Chile)*

The resulting area, after applying the previous three points, it was reduced due to not executed buildings. The municipal permit grant to build lasts for three years; in practice, this permit represents an intention of building on behalf of the architect, since the construction may not be finally carried out for various reasons. Given it was no found an official data on numbers of not executed building permits, nor the area involved, in this research it was considered that 5% of the building permits are not finally executed.

Table 3: *Total and potential area by purpose, for the estimation of glulam potential demand*

Categories of Construction purposes	Total area (m^2)*		Potential area (m^2)**	
	2019	2020	2019	2020
Agriculture and fishing (aviaries, yards, animal fodder storage facilities)	134,74	244,94	126,8	210,523
Storage and transport (product storage warehouses, bus stations, others)	570,033	462,544	164,67	140,348
Market (coomercial premises, supermarkets, pharmacies, bakeries, others)	901,042	562,889	653,081	446,412
Public buildings (custom, courts, mail, cultural centers, others)	102,081	42,177	92,162	37,336
Education (kindergartens, basic, and secondary education, professional institutes, universities, others)	162,231	107,028	152,55	100,677
Leisure and amusement (sports centers, roofed yards, indoor pools, museums, theaters, cinemas, others)	151,52	114,093	108,256	80,266
Hotels, residences, cottages and others	322,583	96,694	162,208	73,902
Religious organizations (churches, chapels, others)	24,701	13,049	20,755	11,726
Industry	706,549	411,06	179,979	179,117
Offices	250,333	391,532	181,07	306,907
Health (hospitals, clinics, family healthcare centers, others)	300,744	225,574	283,148	211,11
Other non-residential buildings N.E.I	589,805	443,748	380,92	377,466
TOTAL	4,216,362	3,115,328	2,505,599	2,175,790

Source: (*) INE, 2022; (**): Own elaboration,
N.E.I not elsewhere identified.

https://doi.org/10.52202/069179-0585

3.2 GLULAM USAGE FACTOR

Once the potential area is defined, the usage factors were calculated for different purposes categories of non-residential buildings. In order to do this, it was used information available in different public tenders of the state in the website www.mercadopublico.cl [7] systemizing the documentation presented by tenderers adjudicated. It was analyzed nearly 80 public tenders to several works' constructions, among these: kindergartens, sports centers, public indoor pools, schools, universities, hospitals, family healthcare centers, primary health clinics, fire stations, civil registration offices, police stations, town halls, and others. From these, 20 that use glulam as a structural material were selected.

Table 4: *Public tender selection for calculation of glulam usage factor.*

Year	: 2020
Project Name	: Héroes de la Concepción high school
Purpose Assigned	: Secondary education
Region	: Biobío
Commune	: Laja
Tender N	: 3735-57-LR20
Authorized Area	: 3,570 m^2
Glulam Volume	: 45 m^3
Factor	: 0.013 m^3 MLE / m^2
Year	: 2016
Project Name	: Huechuraba Semi-Olympic Swimming Pool
Purpose Assigned	: Leisure and amusement
Region	: Metropolitan
Commune	: Huechuraba
Tender N	: 2793-113-LR16
Authorized Area	: 2.120 m^2
Glulam Volume	: 167 m^3
Factor	: 0.079 m^3 MLE / m^2
Year	: 2018
Project Name	: Consistorial Llanquihue Building
Purpose Assigned	: Public Buildings
Region	: Los Ríos
Commune	: Llanquihue
Tender N	: 1437-9-LR18
Authorized Area	: 2,243 m^2
Glulam Volume	: 81 m^3
Factor	: 0.036 m^3 MLE / m^2
Year	: 2019
Project Name	: Municipal Market Temuco
Purpose Assigned	: Markets and Fairs
Region	: La Araucanía
Commune	: Temuco
Tender N	: 1658-321-LR19
Authorized Area	: 12,000 m^2
Glulam Volume	: 1,010 m^3
Factor	: 0.084 m^3 MLE / m^2
Year	: 2020
Project Name	: Muñequitos Kindergarten
Purpose Assigned	: Kindergarten
Region	: Maule
Commune	: Cauquenes
Tender N	: 848-94-LR20
Authorized Area	: 946 m^2
Glulam Volume	: 17 m^3
Factor	: 0.018 m^3 MLE / m2

The selected tenders that use glulam were assigned to one of the construction purpose categories from the table of purposes. Those containing information on the use of glulam as a structural material in walls, and roofs were revised in more detail, particularly the itemized budget, the unitary price analyses (APU), elevation planes, and building technical specifications. Thus, it was obtained the volume (in m^3) of glulam used. With this data, in addition to the area built recorded in the building permit, it was obtained the usage factor for each construction work expressed in m^3 of glulam per unit of area built.

For each resulting purpose category, it was averaged the usage factors of assigned tenders in each one of them. The average factor was multiplied by the potential area of each construction typology. In table N°4 it is presented 5 of the 20 projects where glulam was used as a structural material, the project area, glulam volume, and usage factor.

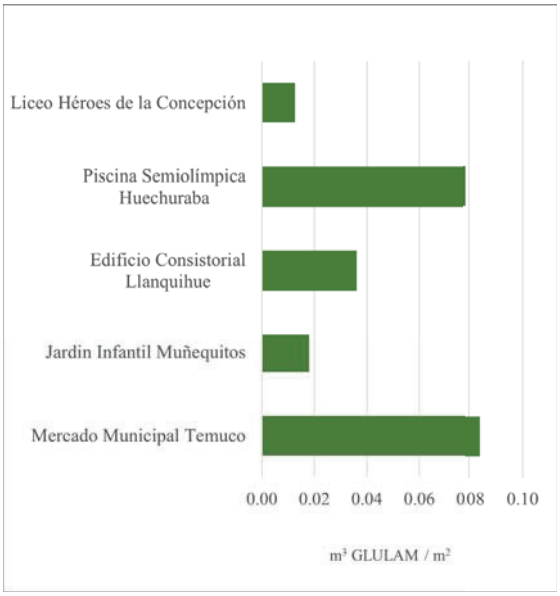

Figure 4: *Glulam usage factors expressed in cubic meters by square meter built*

Table 5: *Glulam usage factor by construction purpose*

Categories of Construction purposes	Volume (m^3)
Agriculture and fishing (aviaries, yards, animal fodder storage facilities)	0.107
Storage and transport (product storage warehouses, bus stations, others)	0.101
Market (coomercial premises, supermarkets, pharmacies, bakeries, others)	0.102
Public buildings (custom, courts, mail, cultural centers, others)	0.063
Education (kindergartens, basic, and secondary education, professional institutes, universities, others)	0.104
Leisure and amusement (sports centers, roofed yards, indoor pools, museums, theaters, cinemas, others)	0.074
Hotels, residences, cottages and others	0.074
Religious organizations (churches, chapels, others)	0.088
Industry	0.051
Offices	0.088
Health (hospitals, clinics, family healthcare centers, others)	0.074
Other non-residential buildings N.E.I	0.088
TOTAL	0.085

Source: Own elaboration

The resulting potential volume of glulam demand of the estimation it is presented in Table N°5. At country level, this estimation presents a potential glulam demand of 219,839 m³, and 192,552 m³ for 2019, and 2020, respectively.

Table 6: *Demand volume of glulam in Chile*

Categories of	Volume (m^3)	
Construction purposes	2019	2020
Agriculture and fishing (aviaries, yards, animal fodder storage facilities)	13,542	22,483
Storage and transport (product storage warehouses, bus stations, others)	16,605	14,153
Market (coomercial premises, supermarkets, pharmacies, bakeries, others)	66,288	45,311
Public buildings (custom, courts, mail, cultural centers, others)	5,783	2,343
Education (kindergartens, basic, and secondary education, professional institutes, universities, others)	15,884	10,483
Leisure and amusement (sports centers, roofed yards, indoor pools , museums, theaters, cinemas, others)	7,991	5,925
Hotels, residences, cottages and others	12,015	5,474
Religious organizations (churches, chapels, others)	1,837	1,038
Industry	9,19	9,146
Offices	16,022	27,157
Health (hospitals, clinics, family healthcare centers, others)	20,974	15,638
Other non-residential buildings N.E.I	33,706	33,401
TOTAL	219,837	192,552

Source: Own elaboration

4. CONCLUSIONS

The production of Glulam in Chile in 2019 reached 23,034 m³. This figure is only 10.5% of the potential volume of laminated timber that could be demanded in the country, therefore existing wide range to increase the use of this material in the national market.

A possible explanation of this gaps between supply, and demand of glulam, is the timber industry limited perception in terms of the remarkable market potential this product has. Certainly, the availability of the raw material to increase glulam production can be limiting; in this sense, sawmills play a very important role as suppliers of structural sawn wood (MAE) of companies producing glulam.

Regarding 2020, this estimation exercise shows that the potential area calculated decreased in 15.2%, and the potential demand volume in 12.4% in respect of the previous year. This drop it is attributed to less construction activity in 2020 due to COVID-19 pandemic effects.

While the research considered only the non-residential building segment, the gap between supply, and demand presented in this research may be higher, that is to say, the percentage of potential volume covered by the current supply could be lower than 10.5%, since the housing sector has not been included.

Moreover, there is a glulam demand volume which has not been evaluated in this research, that it would be determined by the structural reparations market in the existing buildings, that may contemplate a partial, or total reposition of glulam volume currently in operation.

REFERENCES

[1] Ingelam. Proyectos de grandes luces en madera laminada. URL https://ingelam.cl/grandes-luces-proyectos-deportivos-con-madera-laminada. 2021.

[2] Gómez Llantén, J. Madera Laminada, Fabricación y Montaje de Sistemas Estructurales. Internationales Holzbau-Forum 2012. 13p. 2012.

[3] Cárdenas Figueroa, L. Modelo de estimación de demanda agregada de productos de infraestructura eléctrica en proyectos de edificación residenciales, memoria para optar al título de Ingeniero Civil Industrial. Facultad de Ciencias Físicas y Matemáticas, Universidad de Chile. 116p. 2021.

[4] Instituto Nacional de Estadísticas. Base de datos Permisos de edificación. URL https://www.ine.gob.cl/estadisticas/economia/edificacion-y-construccion/permisos-de-edificacion. 2021.

[5] Souza, E. ¿Es hora de pensar en edificios industriales de madera?. ArchDaily. URL https://www.archdaily.cl/cl/957662/es-hora-de-pensar-en-edificios-industriales-de-madera. 2021.

[6] Wagner, M. Comunicación personal mediante correo electrónico,21 de septiembre 2021.

[7] Mercado Público, ChileCompra. Licitaciones. Ministerio de Hacienda, Gobierno de Chile. URL https://www.mercadopublico.cl/Home. 2023.

https://doi.org/10.52202/069179-0585

World Conference on Timber Engineering Oslo 2023

DIGITAL TWIN FRAMEWORK FOR VISUAL EXPLORATION OF MATERIAL FLOWS AND CARBON IMPACTS OF ENGINEERED WOOD SUPPLY CHAINS FROM FOREST TO BUILDINGS

Stephan Ott[1], Andreas Rudena[2], Uwe Kies[3], Anna Wagner[4], Oliver Jancke[5]

ABSTRACT: Engineered wood products (EWP) can achieve a better environmental performance i.e. a lower carbon footprint than most conventional building materials, mostly due to the high carbon storage potential of such products and production processes with lower carbon emissions. Increasing the use of EWP in new built and renovation can thus play a major role for the transformation of the built environment into a large-scale carbon sink. The necessity to make the impact of this use both as a whole and in detail measurable and to directly make the optimization impact visible, the Forest2Building Digital Twin Framework (F2BDF) has been developed. The F2BDF aims at a holistic view of the entire wood construction supply chain and the whole life cycle, including all steps from forest biological production and supply of raw materials, to processing and engineering of products, their installation and use in buildings, and their recovery during deconstruction. The open framework provides a backbone for interconnecting digital twins and harvesting of data across different steps and scales of the supply chain for analytical and predictive purposes. Visual data exploration tools provide insight into material flows, traceability, pinpointing hotspots for optimizing industrial processes, and enable information-based decision making.

KEYWORDS: system, visualization, mapping, supply chain, substitution, environmental impact, resource consumption, circularity, recycling, change management

1 INTRODUCTION

Every consumption has consequences and "[we] are leaving a trail of devastation across the earth with our daily lives, and we don't care […]" [1]. This quote from the German Federal Minister of Economic Affairs and Climate Action was addressed to all consumers in general, but it applies just as much to the economic activities of companies: every action they take has consequences for the environment and especially for the global climate. Unfortunately, many businesses fail to recognize their own trail of devastation by their economic activities. This trail is connected to the entire upstream of resources and generates a significant impact on the global climate, especially in the construction industry. Here the need for lowering emissions through decarbonization actions is very urgent, because resource streams are massive. Due to Greenhouse Gas (GHG) emissions during the use stage and a high share of embodied carbon in products, developing strategies and tools to supervise the way to reach the 1.5 °C climate target is necessary. To meet the climate protection goals of the Paris Climate Agreement, the European Union (EU) has defined targets and measures. Within the scope of the Green Deal, which aims for a climate-neutral Europe by 2050, the EU's Fit for 55 legislative package is now being implemented [2].

Emission reduction or decarbonization as a way towards carbon neutrality in the industry is driven by carbon saving (sufficiency path), carbon reduction through low carbon resources (efficiency), and carbon substitution of fossil-based resources (consistency) by neutral carbon resources, such as bio-based raw materials sequestering CO_2 during growth. Research and development in all three dimensions can enable reduction in real construction projects, new products and innovative and transformative processes on local, regional or even international level. The urgent fields and most powerful levers for the construction industry to implement carbon neutrality are described as follows. Rockström et al. recommend that "[t]he construction industry must either use emissions-free concrete and steel or replace those materials with zero- or negative-emissions substances such as wood, stone, and carbon fibre" [3]. Achieving climate-neutral buildings requires the production of building materials and products that are themselves climate-neutral. This is a significant challenge because resources, transport, and processing require auxiliary substances and energy,

[1] Stephan Ott, Technical University Munich, Germany, ott@tum.de
[2] Andreas Rudenå, Paramountric, Sweden, andreas@paramountric.com
[3] Dr. Uwe Kies, InnovaWood, Belgium, uwe.kies@innovawood.eu
[4] Anna Wagner, Technical University Munich, Germany, anna.wagner@tum.de
[5] Dr. Oliver Jancke, InnovaWood, Belgium, oliver.jancke@innovawood.eu

https://doi.org/10.52202/069179-0586

resulting in environmental impacts from emissions to air, water and soil, which must be avoided [4].

There are several ways to reduce emissions, including avoidance strategies such as using alternative materials and technologies that produce little to no emissions or compensating for excess emissions through appropriate carbon neutral technologies or raw materials themselves. Additionally, building components and materials must be processed after dismantling, then be reused or recycled for secondary use, which again requires energy, technologies and auxiliary substances. Therefore, achieving a climate-neutral building in its entire life cycle requires two main tasks: i) optimizing the building to zero-emission operation itself over its useful life and ii) producing and dismantling the building and its materials in a way that generates no emissions or even sequesters CO_2 [6]. Making the supply chain more sustainable has very positive implications: companies and other actors will begin toavoid the path of destruction and take effective action towards protecting the climate through decarbonization and emissions reduction [7].

This exploratory essay studies how a digital framework can be created which can address and reduce environmental impacts and help to implement these strategies in the scope of the *BASAJAUN* project. We focus on decarbonized raw material transformation and logistics of EWP and bio-based materials in modular and hybrid building solutions, sequestration and long-time storage of biogenic carbon in bio-based construction products, and substitution of fossil carbon use, and innovative circular concepts, such as side streams, reuse, and recycling. *BASAJAUN* is a major European innovation action about sustainable building with wood. The main objective is to demonstrate with wooden demo buildings, how wood construction chains can be optimized to foster both rural development and urban transformation whilst being connected with sustainable forest management in Europe.

Our goal is to better understand the mechanisms behind the trail of devastation caused by economic activities and gain deeper insights into the eco-industrial system which at its core consists of supply chain networks. Through better information of connections and data from places of transformation in all networks, and by tracing end products back to their origins and examining raw material extraction, resource flows and processing, we can better understand the impact of supply chains on GHG emissions and value creation.

2 BACKGROUND

2.1 Product integration in sustainable construction

Integrators, such as timber construction companies, face multiple challenges, such as incorporating various eco-friendly precursors into their integrated end products. To manage the supply chain according to sustainability goals, data on technical product specifications, resource consumption, environmental impact, health, origin, manufacturing, and corporate governance must be collected and analyzed from the entire supply chain.

To achieve optimal product performance, integrators require an overview of a complex and multi-layered supply chain, along with the ability to collaborate with suppliers throughout the development process. The overall supply chain system is the bioeconomy, and its sub-systems addressed are originating from renewable resources cultivated in agriculture and forestry. The supply chain comprises various transformation stages of the raw material from first to second and following Transformation Production Systems (TPS), comprising their main product streams but also side streams. Tier Suppliers (TIER) is a method of organizing different suppliers into categories in order to delineate which materials are most important in your supply chain. Organizing suppliers into TIERS can stimulate better, necessary communication between a company and its suppliers. Understanding the system and its sub-systems with their interwoven production and supply chain hierarchy helps to trigger necessary transformation processes of the entire TPS to manage it more sustainably. *Industry 4.0* with its connected production systems that are designed to monitor, predict, and interact with the physical world, to enable decisions that support production in real- or right time, offers a technology approach to map the (micro) sub-systems of the wood supply chain as a macro eco-industrial system, visualize their interrelationships, and extract specific, characteristic data from almost all points in the system. With this characteristic data, the state and behavior of the system can be identified in the event of changes and managed in a targeted manner. However, keeping the data simultaneously up-to-date, consistent with the final product and adaptive to changes during the design, tendering, order, delivery, and construction process of each project is a significant challenge for the digital system design.

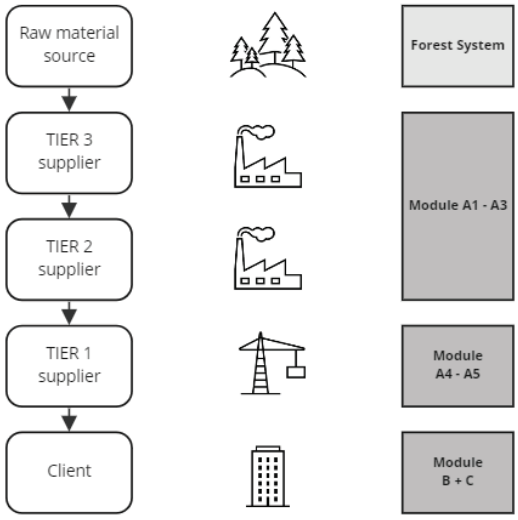

Figure 1: *Integrators deliver complex products or components by integrating lower-level suppliers' products*

The primary goals are to reduce GHG emissions and to close resource loops in supply chains. It is essential to

https://doi.org/10.52202/069179-0586

reduce primary resources, increase the use of secondary raw materials, increase durability, use renewable raw materials, and expand the CO_2 storage potential, which is especially high for renewable resources. However, the comprehensive knowledge needed to make informed decisions is often not available and sufficiently transparent, which makes it difficult to change established patterns of action and select products that are suited to build in a climate-, resource-, and recycling-friendly way. The main points of interest are the system build-up by means of the digital backbone F2BDF, which offers capabilities for mapping and visualization of resource flows within the chain, trace back raw materials to their upstream origin, follow their split into diverse products downstream, and target the resources and emissions along all processing steps.

2.2 SCM challenges in construction industry

In the construction industry, the supply chain faces several challenges, including complex and changing requirements of building projects, limited visibility and poor communication, limited supplier options and long lead times, and a lack of standardization on many levels. Effective supply chain management can improve efficiency, reduce costs, and increase customer satisfaction. Key strategies include efficient inventory management, transportation optimization, and effective communication and collaboration among supply chain partners.

Supply chain management (SCM) is a critical aspect of any industry. In the construction industry, managing the supply chain is especially challenging due to several unique factors. In this section, we will examine the challenges that SCM faces in the construction industry.

The construction supply chain involves a network of organizations and individuals that work together to design, produce, and deliver products and services to customers. This process includes sourcing raw materials, manufacturing, transportation, and distribution of products. Effective SCM can improve any businesses performance. To achieve these benefits, key strategies must follow each step and decisions along the supply chain and check and verify its compatibility with lowered impact on resource consumption combined with environmental impact as well as social and governance objectives.

Despite these benefits, the construction industry's supply chain faces several challenges. One of the most significant issues is the complex and changing project requirements. Construction projects are often large and complex, with changing requirements and tight deadlines. This can make it difficult for supply chain partners to plan and coordinate effectively, leading to delays, increased costs, and potential quality issues.

Another challenge is limited visibility and poor communication. Construction supply chains often involve multiple parties, such as architects, engineers, contractors, and subcontractors. Poor communication and a lack of visibility into the actions and decisions of other supply chain partners can lead to delays, errors, and increased costs.

Furthermore, some materials and equipment used in construction, such as steel and concrete, have long lead times and limited supplier options. This can make it difficult for supply chain managers to ensure that materials are available when they are needed, leading to delays and increased costs.

The lack of standardization is also a challenge in the construction industry's supply chain. This sector often involves a wide range of materials, equipment, and systems, with limited standardization. This can make it difficult for supply chain managers to ensure that materials and equipment are compatible and that quality standards are met.

Site-specific logistics is another issue that supply chain management must consider in construction. The construction site can be remote and difficult to access, requiring specialized logistics and transportation. This can include using heavy equipment and cranes to transport materials, as well as managing the logistics of waste disposal and recycling.

Safety and quality control are also critical considerations in construction supply chain management. Construction projects have a lot of risks, such as accidents and quality control issues. SCM must ensure that all materials and equipment meet safety and quality standards, and that adequate safety measures are in place to protect workers.

Finally, construction industry supply chain management must ensure compliance with regulations and standards on environmental protection, waste management, and recycling. This involves ensuring that all materials and equipment are environmentally friendly, and that adequate measures are in place to protect the environment.

2.3 Sustainable transformation of supply chains

Supply chains play a significant role in sustainable development. Sustainable transformation of construction supply chains is a complex and challenging process that requires the creation of new supply chains and their integration into existing business processes. In the bioeconomy, sustainable supply chain transformation is necessary to produce environmentally friendly products. The timber construction industry, as integrators, faces multiple challenges, including the incorporation of improved and eco-friendly precursors into integrated end products. Collaborating with suppliers throughout the development process can achieve optimal product performance. Data on various technical specifications, resource consumption, environmental impact, health, origin, manufacturing, and corporate governance must be collected from the supply chain to trigger necessary transformation processes of the system to manage it more sustainably.

The overall goal is to reduce greenhouse gas emissions and close resource loops in supply chains. The challenge is how to make informed decisions and select products that are climate-, resource-, and recycling-friendly.

2.4 Environmental challenges in construction SCM

The construction industry faces various environmental challenges that impact SCM. These challenges arise from environmental regulations and standards that demand strict compliance, sustainability considerations, carbon footprint reduction, and penalties for non-compliance. Additionally, the industry's reputation can suffer when it fails to meet environmental standards, leading to lost business opportunities.

Compliance with environmental regulations is vital in the construction industry, given its potential for negative impacts on the environment. These regulations may cover air and water pollution, hazardous waste disposal, and the use of certain materials and chemicals. To meet these regulations, supply chain managers must ensure that all materials and equipment used in construction comply with the required standards. Moreover, they must implement measures to protect the environment adequately.

Sustainability considerations are crucial in construction projects, which can have significant impacts on the environment. Supply chain managers must take steps to ensure that materials and equipment used are environmentally friendly. This includes sourcing from suppliers with sustainable certifications and promoting sustainable practices such as recycling, reducing energy consumption, and water usage.

Reducing the carbon footprint is another critical aspect of environmental SCM in construction. Supply chain managers must evaluate GHG emissions produced throughout the product life cycle and develop strategies to reduce them. This evaluation ranges from sourcing raw materials to final product disposal.

Non-compliance with environmental regulations can lead to significant penalties and fines, impacting companies' finances and reputations. In some cases, non-compliance can lead to legal action and suspension of construction projects. Additionally, companies that fail to meet environmental regulations and standards may struggle to win new business opportunities, impacting their reputations.

In conclusion, environmental challenges are significant for the construction industry and require a proactive approach in SCM. Effective strategies include compliance with regulations, sustainability considerations, carbon footprint reduction, and avoiding penalties and reputational damage. By addressing these challenges proactively, companies in the construction industry can gain a competitive edge while contributing positively to the environment.

2.5 Problem of GHG emissions reduction and closed resource loops in supply chains

As companies strive to reduce their environmental impact, they must consider how they can make decisions both as individuals and as representatives of the industry to reduce their use of primary, fresh resources and increase the use of secondary raw materials. This includes increasing product durability, using renewable raw materials, and expanding the potential for CO_2 storage, which is high for renewable resources. However, it often lacks comprehensive knowledge and transparency about the resources they use and the impact they have, making it challenging to make informed decisions and change established patterns of action.

To address this issue, companies need to narrow down the objects and subjects of knowledge and decision-making problems, focusing on the origin and production of materials and their effects in the industrial context. By doing so, they can formulate ways to build in a climate-, resource-, and recycling-friendly way.

To achieve this goal, we propose a digital backbone called the Forest-to-Building Digital Twin Framework (F2BDF) to companies, which uses mapping and visualization to analyze resource flows within the system. With F2BDF, they can trace the origin of raw materials upstream and their transformation into various downstream products. This allows them to target resources and emissions along processing steps and identify areas for improvement.

By implementing this framework, businesses can build a more sustainable and environmentally friendly industrial system by reducing GHG emissions and creating closed resource loops in supply chains.

2.6 Disrupting the supply chain

The wood construction industry is undergoing a digital transformation, with a clear vision presented by thinkers, innovators, and makers on the frontline. One aspect of disruption is the rising effort in integration of preliminary products into a prefabricated and integrated end-product. This integration is increasingly important for both large and small projects, as clients expect the end-product to fulfill superior properties, such as load-bearing, fire resistance, and other functions related to weather protection and resource-saving. The integration is expected to result in higher quality, improved manufacturing quality, on-time delivery, waste reduction, and faster construction activities.

However, to achieve this level of integration and quality, a detailed understanding of the supply chain is key. This includes the flows, stocks, processes, and upstream data that are characteristic for each product. This data is critical to enable sustainable, integrated, prefabricated, quality-controlled, durable, and on-time building projects. The concept of *Industry 4.0* and the *Internet of Things* (IoT) can help us see the big picture and system connections of Sustainability Supply Chain Management (SSCM) [8].

To achieve this goal, we propose a Digital Twin Framework for visual exploration of material flows and carbon impacts of engineered wood supply chains from Forest to Buildings. Digital twins can provide a virtual representation of a product or system, which can be used to optimize its performance and sustainability. In addition, the use of sensor data, real-time data, big data, machine learning, data mining, data analytics, simulation, and optimization can help to leverage the supply chain into a more sustainable direction.

The F2BDF will allow to analyze the entire supply chain from forest to buildings and identify areas where

https://doi.org/10.52202/069179-0586

improvements can be made. The framework will incorporate all data related to the supply chains of products and building materials, their origins, transparency, and impact on GHG emissions and value creation, allowing for a more sustainable and environmentally friendly system.

By using these concepts and technologies, the wood construction industry can transform its supply chain and create more sustainable and efficient projects. It can help to reduce waste, improve quality, and create more sustainable products that meet the needs of clients and consumers. With a focus on advanced SSCM and digital transformation, the wood construction industry can lead the way in creating a more sustainable economy.

3 METHODS AND DATA

3.1 Generic system representation and visualization

Development of the description of a generic system representation and the need of F2BDF backbone and other digital tools in combination with visualization tools, material flow tools as Sankey, LCA tools. Plus, the "resource" data from the digital twins, i.e. glulam factory, building design, and others.

The overall system of supply chain is the bio-economy and its sub-systems addressed are based on nature and renewable resources cultivated in agriculture and forestry and harvested from nature. The focus is dedicated to the timber supply chain from the forest over sawmills and downstream until urban timber buildings. The supply chain comprises various transformation stages of the raw material from first to second and following TPS with their main product streams but also side streams (logs, beams, wood cut-offs or particles, timber construction products, timber buildings).

We need this understanding of the system and sub-systems with their interwoven production and supply chain hierarchy to recognize single entities, dependencies, and routes between each of them. In an advancing digitalization through *Industry 4.0* concept, it is possible to map the (micro) sub-systems of the wood supply chain itself as macro eco-industrial system, visualize them in their interrelationships, and more importantly, extract specific, characteristic data from almost all points of the system. With this characteristic data, the behavior of the system can be read off in the event of changes and managed in a targeted manner.

We started to give a first overview on the necessary data pertaining to technical product specifications, resource consumption (including material, energy, and water usage), environmental data (including emissions), health data, origin data, manufacturing data (including social aspects), and corporate data (including governance). All this data changes continuously updated, and needs to be kept up-to-date, consistent with the final product and with changes during the design, tendering, order, delivery and construction process of each project.

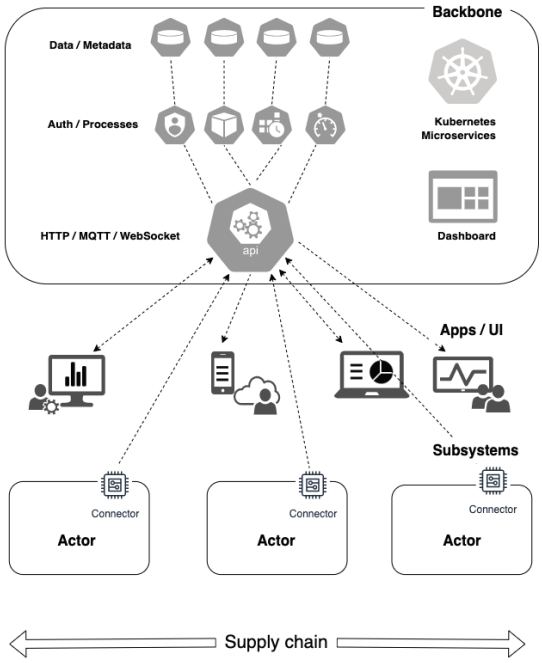

Figure 2: *System architecture of F2BDF*

3.2 Description of the F2BDF and Backbone

In the light of the *Industry 4.0* digitalization and automation transition a lot of work has been done in the area of systems interoperability. The F2BDF is specifically inspired by the *OPC UA* standard where information models can be used to define this interoperability layer with schema representation.

One challenge with the timber construction wood value supply chain is that it spans several industries and data domains making it difficult to rely on existing information models and schemas for data interoperability. A common and complete information model for the forest-to-building supply chain across Europe does not exist. Work could potentially be spent trying to define such data format for the full supply chain. However, taking into account the diversity of actors and traditions between countries this would not be feasible in relation to time and resources available in the *BASAJAUN* project. This work would also likely need to be connected to work in standardization and alignment in and between many domains that composes the wood material to building construction and life cycle supply chains. Instead, a more dynamic "data first" approach is proposed here based on bottom-up principles, where company data is collected and analyzed using flow visualization, and then mapped to indicators built through common understanding.

The studied approach for flexible data collection looks into work with digital twin city implementations where interoperability between actors and their data, products and artefacts, a similar major challenge can be identified as the diverse interconnections are quickly expanding. The change management in such a system with hundreds or thousands of actors is a challenge, and full

interoperability is still only theoretically imaginable. This is also connected to a wish to get started with sustainability work immediately and not wait for an industrial agreement or standard committees to finalize their work potentially still not reaching industrial consensus due to systemic boundaries and abstractions that in the end still does not fit some of the actors.

3.3 Mapping and Visualization of the Supply Chain

First, the F2BDF backbone is the representation of the entities; in the next step, the entities are connected, and their interrelationships and interaction options are represented. Here, the data can already be entered into the entities or transferred from sensors into the backbone. Through the representation as Sankey chart, it is possible to visualize the material flows between the entities and the size of the flows is represented proportionally. Main flows and gaps in the flow become visible. Side streams can leave the flow for other manufacturing processes and new side streams can be added, for example from secondary sources, if linearly thought in up- and downstream. The representation clarifies which quantities are on the way where in the system at point in time *x*.

4 RESULTS AND DISCUSSION

4.1 Analytics of the Supply Chain

The analytics of supply chains are an essential aspect of managing and optimizing the flow of goods and services from raw materials to finished products. One methodological approach to analyzing the supply chain involves the use of the forest-to-building digital framework introduced above. This framework collects data on raw materials, intermediary products, and end products as they move through various production systems, allowing for a comprehensive view of the entire supply chain.

Scientific and operational analysis of structured data from a production network involves various techniques such as network analysis, flow analysis, machine learning, prediction, scenario building, and concept verification.

Machine learning techniques can be used to analyze structured data from a production network to identify patterns and predict future trends. For example, machine learning algorithms can be used to predict demand for specific products, identify maintenance needs for machinery, or optimize production schedules. Scenario building involves using data from the production network to simulate different scenarios and identify potential outcomes. This can be used to evaluate the impact of different decisions or changes to the production network. Concept verification involves using data analytics to verify the effectiveness of new concepts or ideas in the production network. For example, a new production process can be simulated using data analytics to evaluate its feasibility and potential impact on the network. Other examples of data analytics for structured data from a supply chain and production network include:

- Quality control analysis to identify patterns of defects and improve product quality,
- Inventory management analysis to optimize inventory levels and reduce waste,
- Sustainability analysis to evaluate the environmental impact, circularity of the production network and identify areas for improvement,
- Risk analysis to identify potential risks and develop mitigation strategies.

4.2 Supply chain management and LCA

Digitalization has the potential to greatly enhance the integration of SCM and Life Cycle Assessment (LCA) [7]. Digital technologies can support the collection, analysis, and communication of data throughout the entire life cycle of a product, from the sourcing of raw materials to the disposal of the final product. Data collection and analysis: Digital technologies such as sensors, Internet of Things (IoT) devices, and cloud-based platforms can be used to collect data on the environmental impact of products and materials throughout their entire life cycle. This data can then be analyzed to identify areas of improvement and support decision making [7].

Collaboration and communication: Digital technologies such as Electronic Data Interchange (EDI) and Enterprise Resource Planning (ERP) systems can be used to improve collaboration and communication among supply chain partners [10]. This can include sharing information and tracking orders in real-time, improving coordination and reducing errors and delays [11]. In addition, applications such as social-LCA can be carried out with transparent supply chain documentation [13].

4.3 Data collection possibilities and needs

4.3.1 Tracking data and network analysis

Tracking data is an essential tool for identifying the origin of the materials used in construction, particularly the glulam used in the demo structure. By tracing the journey of wood through all the different locations and means of transportation, it is possible to pinpoint the forest stand from which the raw material originated. This process involves a location-based scenario that helps track the origin of wood backward from its source. Network analysis is a crucial aspect of this process, as it allows for optimization of the production network by identifying key nodes, bottlenecks, and dependencies, which can lead to improved efficiency and resilience.

Furthermore, linking the backtracked data to external certification label databases, such as the FSC/PEFC label database, can provide clients with additional information about the origin of the wood, such as logging type used in the forest and the sustainability and environmental friendliness of the materials used. This additional information can enhance transparency and improve client understanding of the materials used in the construction process. Apart from the logistics chain application, the backtracked data also help in quality control by detecting and querying wrong or damaged supplies in the chain, leading to better-quality products. The process of backtracking data and analyzing the production network

https://doi.org/10.52202/069179-0586

topology, together with linking to external certification label databases, can provide useful data for clients, including machine learning, prediction, scenario building, and concept verification.

Figure 3: *Tracking locations of production from raw materials extraction to construction sites of Northern (Finland) and Southern (France) demos*

In summary, backtracking data are a valuable tool for tracing the origin of materials used in construction, and network analysis can optimize the production network and improve efficiency and resilience. Linking to external certification label databases can provide clients with more detailed information about the sustainability and environmental impact of the materials used, while other forest-related information, such as logging type, can improve transparency and client understanding. Overall, the use of backtracking data and network analysis provides critical insights for the quality control and optimization of production networks in construction.

4.3.2 Environmental and sustainability data

The responsible use of resources and minimization of the impact of industrial processes on the environment are critical aspects of sustainable development. This can be achieved through collection and analysis of environmental and sustainability data. One important aspect is tracking the quantity of raw material flow and assessing the loss of wooden raw material throughout the supply chain. To accomplish this, producer- and quantity-based scenarios can be implemented. By tracking the flow of raw materials from the forest to the final product, it is possible to measure the net mass and volume at each stage of transformation and determine the amount of timber lost during processing.

At the sawmill, the gross volume of wood can be measured along with the output of the cut boards and their net volume, weight, and moisture content. Side streams, such as bark, sawdust, and low-quality wood, sorted during processing should also be documented. Intermediate wholesalers or refiners can also be included in the tracking process to measure the gross in and net out of wooden material, as well as any side-streams produced. At the glulam factory, the gross in of the boards can be measured along with the net out of the glulam beams and their volume. Side streams, such as quality sorting waste, cut-offs from finger jointing, and wood shavings from planing should also be documented. Finally, at the

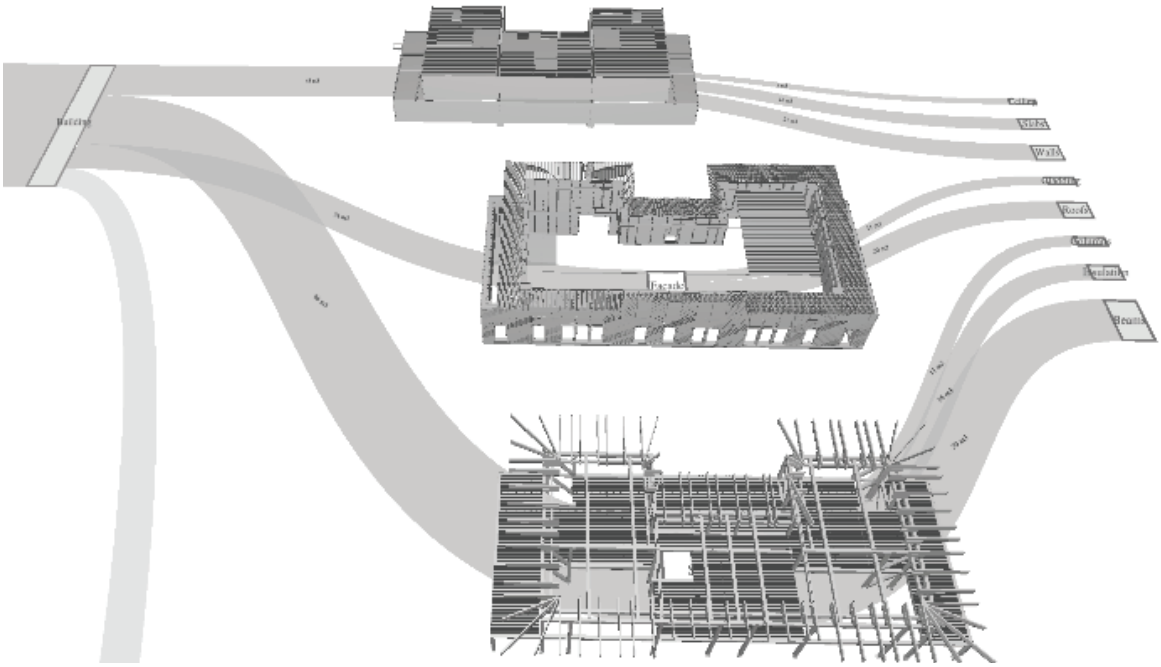

Figure 4: *IFC model of demonstrator connected to glulam Sankey chart of F2BDF backbone*

https://doi.org/10.52202/069179-0586

construction site, the gross in of the wooden material can be measured along with the net amount used in the structure.

By tracking all stages of production and linking with environmental impact data, it is possible to obtain a comprehensive picture of the supply chain's environmental impact. This information can be used to identify areas where improvements can be made, such as reducing the loss of raw materials or finding more sustainable methods of production. Additionally, BIM (Building Information Modelling) can be used in construction projects to ensure that materials and equipment are compatible with BIM systems and that BIM data are shared and integrated with all stakeholders, see [12]. The data collected can be linked to the BIM model, enabling stakeholders to visualize the environmental impact of the construction process and identify opportunities for optimization. Environmental performance tracking with digital tools such as digital dashboards, data visualization, and analytics can be used to track and monitor the environmental performance of products and materials throughout their life cycle. This can help supply chain managers to identify areas for improvement and to make data-driven decisions.

In summary, the collection and analysis of environmental and sustainability data are crucial for responsible resource use and minimizing the impact of industrial processes on the environment. Tracking the quantity of raw material flow and assessing the loss of raw wooden material throughout the supply chain can be achieved by measuring the net mass and volume of each stage of transformation. This information can be used to identify areas where improvements can be made, and BIM can be used to integrate the data and optimize the construction process.

4.3.3 Auxiliary streams and co-products

Flow analysis focuses on the movement of materials and products through the production network. By analyzing

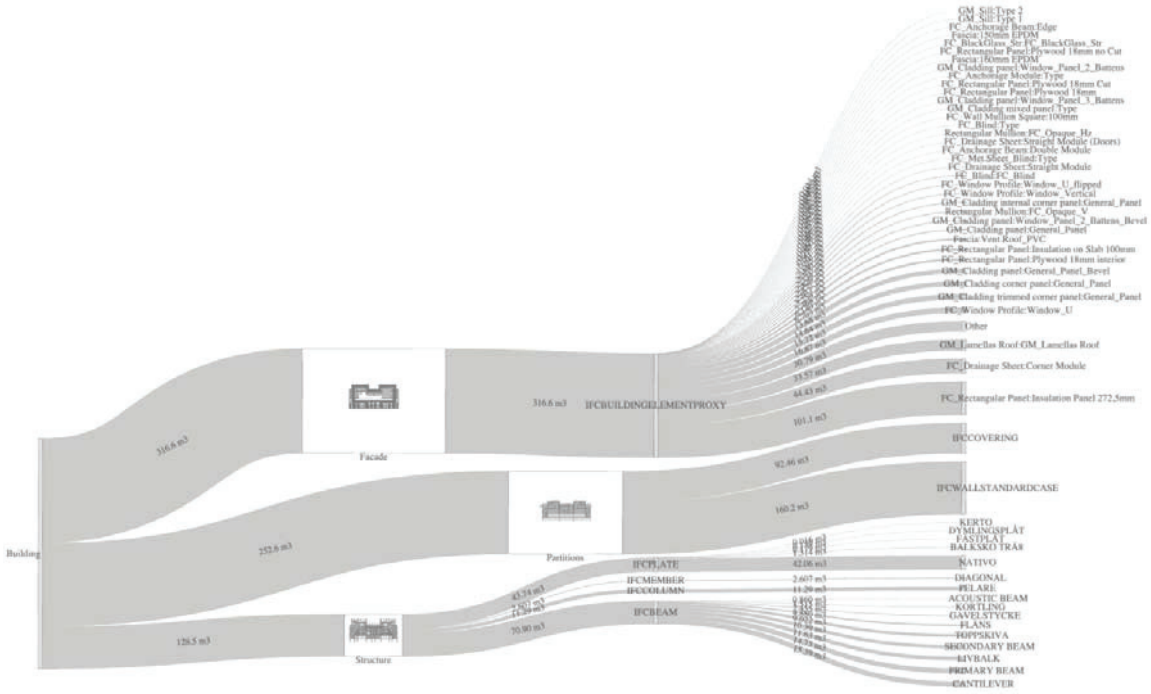

Figure 5: *Full Sankey chart of material flow from forest to building visualized from F2BDF backbone*

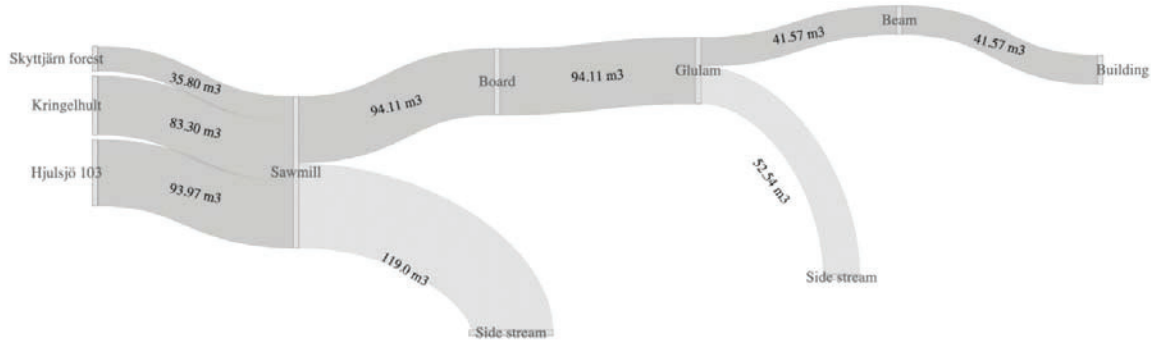

Figure 6: *Exemplary auxiliary streams of co-products taking place during the production of glulam from forest raw materials*

https://doi.org/10.52202/069179-0586

the flow of materials and products, bottlenecks and inefficiencies can be identified and addressed.

To better understand the flows in production of glulam, it's important to look not only at the main raw materials used but also at the auxiliary flows that are needed in the production process. This includes energy, glue, and other supplies. It's important to track these flows in each main production stage/phase and determine the quantity, supplier, and location of these supplies.

A flows-based scenario would be useful in analyzing other interesting flows in each main production stage/phase. For example, tracking energy flows for harvesting, sawmill operations, and drying of the wood would provide insight into the energy usage of the production process. Additionally, tracking the energy and emissions generated during transport would provide valuable data. Side streams, such as glue and packaging materials, should also be considered. It's important to track these materials at each step of the transformation process and determine their origin, quantity, and disposal method. Understanding the auxiliary flows and side streams of glulam production is crucial for identifying areas where sustainability and efficiency improvements can be made.

5 CONCLUSIONS

In conclusion, achieving climate-neutral buildings is an urgent goal that requires significant changes in the way we produce, use, and dispose of building materials and products. By applying the principles of efficient raw material transformation, long-time storage of biogenic carbon, innovative circular concepts, and using a Digital Twin Framework for Visual Exploration of Material Flows and Carbon Impacts of Engineered Wood Supply Chains from Forest to Buildings, we can make a difference and support the urgent goals of exceptional amounts of carbon reduction, up to carbon neutrality and positivity. We want to make the resource consumption that takes place in complex, interwoven systems visible and comprehensible, so that we are not overwhelmed by the complexity and confusion. We will need digital tools and *Industry 4.0* technology that helps to extract siloed data to allow us to map the current systems, especially the raw material and energy flows within them, to identify their quality, quantity and potential problems. From this, the next step is to think about change and to anticipate and understand the effects of change to be able to take corrective action if necessary or to control the change process.

As shown in the *BASAJAUN* project digital tools can be used to collect data about sustainable sourcing, identifying and tracking the environmental impact of products and materials throughout their life cycle. This can include using F2BDF digital tools to track the environmental impact of suppliers, identify sustainable materials and products, and monitor the environmental performance of logistics providers. Once these data are collected, there are various possibilities for their analysis which have to be done in follow up studies.

ACKNOWLEDGEMENT

BASAJAUN project 2019-2023 | BASAJAUN-horizon.eu. The project has received funding from the European Union's Horizon 2020 research and innovation program under grant agreement no. 862942.

REFERENCES

[1] R. Habeck: In *Talk Show Lanz*, ZDF, 31.03.2022.

[2] European Commission: 'Fit for 55': delivering the EU's 2030 Climate Target on the way to climate neutrality, 2021.

[3] J. Rockström, et al.: A roadmap for rapid decarbonization. *Science*, 355(6331), 1269-1271, 2017.

[4] M. Kuittinen, A. Organschi, A. Ruff.: Carbon: A Field Manual for Building Designers. Wiley, 2022.

[5] European Parliament: What is carbon neutrality and how can it be achieved by 2050. Online https://www.europarl.europa.eu/news/en/headlines/society/20190926STO62270/what-is-carbon-neutrality-and-how-can-it-be-achieved-by-2050, 2020.

[6] G. Churkina, et al.: Buildings as a global carbon sink. Nat Sustain 3: 269–276, 2020.

[7] Dadhich, P., Genovese, A., Kumar, N., Acquaye, A.: Developing sustainable supply chains in the UK construction industry: A case study. In *International Journal of Production Economics* 164, 271–284, 2015. DOI: 10.1016/j.ijpe.2014.12.012.

[8] T. Saurabh: Supply chain integration and Industry 4.0: a systematic literature review. In *Benchmarking: An International Journal* 28 (3), 990–1030.,2021.

[9] OPC FOUNDATION: OPC UA online reference: https://reference.opcfoundation.org/, 2023.

[10] Seuring, S., Müller, M.: From a literature review to a conceptual framework for sustainable supply chain management. In *Journal of Cleaner Production* 16 (15), 1699–1710. 2008. DOI: 10.1016/j.jclepro.2008.04.020.

[11] Tuni, A., Rentizelas, A., Chinese, D.: An integrative approach to assess environmental and economic sustainability in multi-tier supply chains. In *Production Planning & Control* 31 (11-12), p. 861–882. 2020. DOI: 10.1080/09537287.2019.1695922.

[12] Xue, K.; Hossain, M. U.; Liu, M.; et al.: BIM integrated LCA for promoting circular economy towards sustainable construction: an analytical review. In *Sustainability* 13 (3), 1310-1331. 2021. DOI: 10.3390/su13031310.

[13] Benoit-Norris, C.; Cavan, D. A.; Norris, G.: Identifying social impacts in product supply chains: overview and application of the social hotspot database. In *Sustainability* 4 (9), S. 1946–1965, 2012. DOI: 10.3390/su4091946

World Conference on Timber Engineering Oslo 2023

MATERIAL DISRUPTION: CROSS-LAMINATED TIMBER IN TEXAS

Ulrich Dangel[1]

ABSTRACT: The rise of mass timber construction in the U.S. can be traced to the introduction of one building product: cross-laminated timber, or CLT. Originally developed in Europe, CLT panels have revealed the potential for mid- and high-rise buildings with primary structural systems that are made almost entirely of timber. By combining these panels with glulam beams and columns, this novel approach competes with conventional steel and concrete building systems for structural performance. While many European countries have used CLT products for almost 20 years, the U.S. has been slow to adapt. Early pioneer projects relied on European manufacturers for their panels, and CLT fabrication in North America did not commence until 2011.

As one of the fastest-growing regions in the country, Texas continues to experience a substantial increase in its population. Most of this growth is concentrated in urban areas, and sustainable urban development will need to focus on affordable, healthy environments for living and working while also reducing carbon emissions. However, concrete and steel continue to be the building materials of choice. This paper will present case studies and recent developments in mass timber construction in a part of the world that is not known for its sustainability efforts.

KEYWORDS: Mass Timber, Texas, Cross-Laminated Timber, Multi-Story Timber Construction, International Building Code

1 INTRODUCTION

The rise of mass timber construction in the United States can be traced to the introduction of one particular building product: cross-laminated timber, or CLT. Originally developed in Europe in the 1990s, cross-laminated timber consists of several layers of lumber board that are stacked at right angles to one another and glued face-to-face to form large-format structural panels up to 3 meters (10 feet) wide, 18 meters (60 feet) long, and 30 centimeters (12 inches) thick. This cross-lamination yields exceptionally strong and dimensionally stable products with bi-directional load-bearing capacity, particularly suitable for floors, walls, and roofs in multi-story applications [1].

CLT panels have revealed the potential for residential and commercial mid- and high-rise buildings with primary structural systems that are made almost entirely of timber. By combining these planar panels with glulam beams and columns, this novel approach competes with conventional building systems for structural performance. Most important, building with mass timber takes advantage of one of the most significant benefits of wood: its ability to store, or sequester, significant amounts of atmospheric carbon. Substituting wood for energy- and carbon-intensive materials such as steel and concrete can therefore result in substantial carbon savings over time. Although wood is not necessarily the appropriate choice for all construction applications, there are clear environmental advantages to using it when possible. Contrary to popular belief, using wood does not contribute to deforestation as long it is obtained from responsible sources, making it a truly renewable building material. Each log harvested from a sustainably managed forest and processed into lumber makes room for new trees to grow, with the ability to absorb more carbon dioxide from the atmosphere. That's why well-managed forests can provide more significant climate change mitigation than unmanaged forests while also preserving wildlife habitats, increasing biodiversity, and improving water and soil quality. The widespread deforestation occurring in the tropics is rarely related to harvesting wood for construction but instead is caused by clearing land primarily for agriculture, particularly commodity crops and cattle ranching.

While many European countries have used cross-laminated timber products for almost 20 years, the U.S. has been slow to adapt. Pioneer projects here relied on European manufacturers for their panels. CLT fabrication in North America started in 2011 when Canadian companies Structurlam in British Columbia and Nordic in Quebec began operations. The U.S. trailed its northern neighbor by four years, with DR Johnson in Oregon and SmartLam in Montana starting commercial production in 2015. Since then, International Beams (now SmartLam in Alabama) and Katerra (now Mercer Mass Timber) in Washington have begun production. But in Texas, one of the fastest-growing states in the United States, concrete and steel continue to be the building materials of choice. Although dimensional lumber is used extensively for

[1] Ulrich Dangel, The University of Texas at Austin, USA, dangel@utexas.edu

https://doi.org/10.52202/069179-0587

residential and small commercial light wood framing, timber construction has played only a minor role in the state's construction industry. That is partly because trees big enough to supply large-scale commercial production do not grow in much of Texas. Regardless, architects, engineers, developers, and clients today, recognizing the environmental challenges of our times, are looking for new ways to improve the performance of the built environment. As the operational energy consumption of buildings has been vastly reduced, the need to lower their embodied energy becomes more apparent since it makes up a considerable portion of a building's life-cycle energy use. This is where mass timber and its potential for carbon sequestration comes in.

2 EARLY ADOPTERS OF MASS TIMBER

Eager to undertake aspirational building projects, enlightened clients have proven instrumental in teaming with Texas architecture firms to employ these novel technologies.

The architecture firm Lake|Flato of San Antonio has been at the forefront of bringing engineered wood products to the state. In 2018, the firm's rooftop addition to the Museum of Fine Arts in Houston — the Sarah Campbell Blaffer Foundation Center for Conservation — featured the first installation of dowel-laminated timber (DLT) panels in North America. Two more of Lake|Flato's DLT projects, the Hotel Magdalena in Austin and the 13,000-square-meter Soto Building in San Antonio, were completed in 2021.

Figure 1: *Hotel Magdalena, Austin, Texas; Architect: Lake|Flato; Engineer: StructureCraft*

The 4,500-square-meter complex of Hotel Magdalena consists of three buildings and is the first mass-timber boutique hotel constructed in North America (Figure 1). The primary structure for the hotel rooms is made of DLT panels, which are supported on light wood frame bearing walls. Exposed exterior DLT walkways connect the rooms and are supported by a glulam substructure. The interior panels are exposed at the ceiling, while the exterior panels are exposed on both sides, floor and ceiling. Other custom mass timber elements include DLT stair and elevator shafts, hanging balconies, hybrid timber-steel staircases, and a stand-alone porte-cochere [2,3]. The 13,000-square-meter Soto Building, a collaboration with BOKA Powell, consists of a glulam post and beam frame supporting dowel-laminated timber floor panels and is the first six-story, mixed-use mass timber building in Texas (Figure 2). Its well-thought-out systems integration strategy features a raised floor plenum with underfloor air distribution. The result not only maximizes flexibility for tenants but also removes the visual impact of suspended air ducts while highlighting the beauty of the exposed structural components [3,4].

Figure 2: *The Soto Building, San Antonio, Texas; Architect: Lake|Flato and BOKA Powell; Engineer: StructureCraft*

In Austin, TB/DS, a joint venture between Thoughtbarn and Delineate Studio, worked with ambitious client Endeavor Real Estate Group to reimagine a turn-of-the-century warehouse aesthetic for a contemporary five-story office building in its eclectic East Side context (Figure 3). Completed in 2019, 901 East Sixth is the first Texas project to use cross-laminated timber as part of a composite structural system. Steel beams and columns with bolted connections provide flexible, column-free spaces with an industrial feel, while mass timber floor decks add warmth and form the finished ceiling. The 12,000-square-meter, five-story hybrid structure went through a yearlong alternate materials and methods approvals process with the city, paving the way for future CLT projects [3, 5].

Figure 3: *901 East Sixth, Austin, Texas; Architect: Thoughtbarn and Delineate Studio; Engineer: Leap Structures*

https://doi.org/10.52202/069179-0587

3 MASS TIMBER ESTABLISHES A PRESENCE

For the First United Bank branch in Fredericksburg, Gensler's Dallas office completed the state's first full mass timber structure in 2019 (Figure 4). The forward-thinking client wanted a building that not only reflected the bank's strong presence in rural communities but also aligned with their sustainability goals. The 800-square-meter building is also the first mass timber structure in the United States to use CLT panels made from Southern Yellow Pine. Using this species native to Texas, the architects delivered a net-zero energy design with a vernacular yet modern look, showcasing that any building can be a steward for the environment [3, 6].

Figure 4: *First United Bank, Fredericksburg, Texas; Architect: Gensler; Engineer: DCI Engineers*

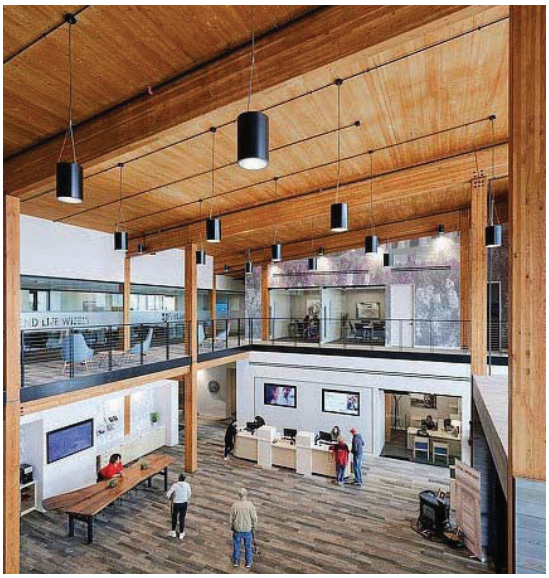

Figure 5: *First United Bank Regional Headquarters, Sherman, Texas; Architect: Gensler; Engineer: DCI Engineers*

Gensler is also behind the company's other mass timber building in Texas: the two-story First United Bank Regional Headquarters in Sherman, which opened in 2021 (Figure 5). The bank commissioned the architects to design the 3,500-square-meter building with the goal of attracting and retaining top talent, uniting its teams in one connected hub, and serving the wider community. The design creates an environment representative of the local area while placing a heavy emphasis on sustainable materials and practices using mass timber construction. In addition to using mass timber, the bank's regional headquarter meets net-zero energy objectives by having the ability to provide the entire building's power requirements with solar panels located on the roof. A collection system also harvests all rainwater runoff from the roof and condensation from the HVAC system to service the site's irrigation. The building fulfills the client's vision for a community-centric location that remains inclusive and sustainable [3, 7].

With Fifth + Tillery in Austin, Gensler recently completed an adaptive reuse project by reimagining a post-industrial site as a vibrant, wellness-focused office complex with indoor/outdoor connections (Figure 6). The repurposing of a large and dark existing warehouse was an opportunity to create a multi-tenant office space with the purpose of attracting creative businesses and talent. The client also wanted the design to minimize the environmental impact and positively contribute to the surrounding neighborhood, resulting in a high-performance building that embraces sustainable practices. Exposed wood, ample daylight, access to fresh air, and the integration of abundant landscaping were key elements of the project's biophilic design strategy. The 17,550-square-meter utilizes a hybrid steel and timber structural system to reduce embodied carbon while also introducing the natural beauty of wood into the spaces. Drilled piers support steel columns that are paired with long-span Douglas Fir glulam beams and a long-span metal deck with concrete topping. Even though this project does not specifically utilize CLT, it demonstrates the viability of using mass timber in the revitalization of existing structures in Texas [3, 8].

Figure 6*: Fifth + Tillery, Austin, Texas; Architect: Gensler; Engineer: MJ Structures*

Gensler is also collaborating with Duda|Paine Architects on the Offices at Southstone Yards, the first mass-timber office development in the Dallas-Fort Worth Metroplex (Figures 7+8). The seven-story, 22,000-square-meter building will anchor an 18-hectare visionary mixed-use development in Frisco, Texas, with the goal of creating well-located offices that accommodate the requirements

https://doi.org/10.52202/069179-0587

of future workers. The client is seeking to develop an office environment that caters to the increased expectations of employers and their teams in a post-pandemic world by delivering a dynamic experience that enriches their daily lives and is supported with virtues of wellness, flexibility, and enhanced amenities. With completion expected in the third quarter of 2023, the building is projected to become the largest mass-timber office building in the United States [9].

***Figure 7**: Offices at Southstone Yards, Frisco, Texas; Architect: Gensler and Duda|Paine; Engineer: Thornton Tomasetti and BDD*

***Figure 8**: Offices at Southstone Yards, Frisco, Texas; Architect: Gensler and Duda|Paine; Engineer: Thornton Tomasetti and BDD*

Kirksey Architecture in Houston is leading the way in the higher education sector with several mass timber university projects in East Texas. The three-story, 11,000-square-meter Anderson-Ball Classroom Building is a mass timber structure on the Central Campus of San Jacinto College (Figures 9+10). The structural system is made entirely out of mass timber, except for steel bracing used for lateral support, making it one of the first in the Greater Houston Area. Featuring a glulam post and beam frame, CLT floor plates, and CLT staircase enclosures, it was the nation's largest academic building constructed from mass timber when it opened for the 2022-23 academic year [10].

The firm is also collaborating with American/German architectural practice Barkow Leibinger on a five-story, 165-bed dormitory for Rice University (Figure 11). The 5,200-square-meter Hanszen College New Wing will replace an aging building with the goal of making on-campus living more attractive for upper-level students. The university hopes that the innovative design of the building will benefit the well-being of its inhabitants since early studies show that mass timber buildings can positively affect physical and mental health. In addition, Kirksey Architecture has recently begun working on a four-story, 338-bed dormitory on the Stephen F. Austin State University campus. The scheme is in its early planning stages and will include a new dining hall, welcome center, and an addition, as well as renovation of the school's fine arts facilities [11].

***Figure 9**: Anderson-Ball Classroom Building, San Jacinto College, Pasadena, Texas; Architect: Kirksey; Engineer: Armstrong-Douglass Partners*

***Figure 10**: Anderson-Ball Classroom Building, San Jacinto College, Pasadena, Texas; Architect: Kirksey; Engineer: Armstrong-Douglass Partners*

***Figure 11**: Hanszen College New Wing, Rice University, Houston, Texas; Architect: Kirksey; Engineer: knippershelbig*

All three higher education projects are supported by federal funding from the Mass Timber University Grant Program, a cooperative partnership established by the U.S. Department of Agriculture Forest Service and the U.S. Endowment for Forestry Communities. This

initiative aims to break barriers related to the design and construction of cost-competitive, code-compliant mass timber buildings while showcasing the architectural and commercial viability of these materials in sustainable construction. It also seeks to clearly demonstrate the direct relationship between the use of mass timber products, the health and resilience of American forests, and the potential for economic development in rural communities [12].

Hines, an international real estate developer, is collaborating with architecture firm DLR Group to bring its mass timber concept T3 (timber, transit, and technology) to Austin ((Figures 12+13). Deemed T3 Eastside, the project is poised to redefine the standard for modern, creative office space. The building will feature 8,500 square meters of Class-A office space and 850 square meters of residences, with the goal of inspiring creativity, attracting talent, promoting productivity, and honoring the unique spirit of Austin's Eastside neighborhood [13, 14].

***Figure 12**: T3 Eastside, Austin, Texas; Architect: DLR Group; Engineer: MKA*

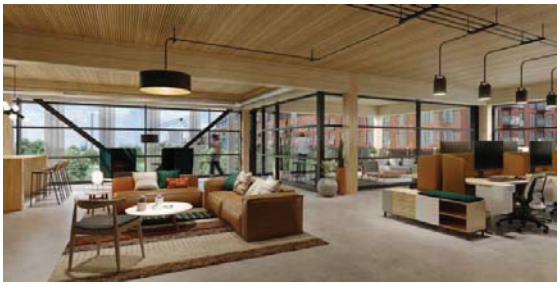

***Figure 13**: T3 Eastside, Austin, Texas; Architect: DLR Group; Engineer: MKA*

Mass timber is also replacing building materials in North American construction methods that have historically relied on concrete.

The Southfield Park 35 warehouse by architecture firm PDMS Group in Dallas uses CLT in place of the concrete tilt-wall panels of a typical industrial warehouse, with the goal of supporting the client's ambition to reduce the environmental impact of their developments (Figure 14). The decision to use CLT over traditional concrete tilt-up construction helped reduce the carbon footprint of the 15,000-square-meter building by more than 45% [3].

Architecture firm DesignTrait recently completed the mixed-use project The Duke in Austin's Webberville neighborhood (Figure 15). The 3,700-square-meter building consists of three stories of light wood framing over a ground floor podium. Instead of a commonly used concrete podium structure, the designers opted for glulam beams and columns with CLT floor slabs to create a more sustainable urban design project [3, 15].

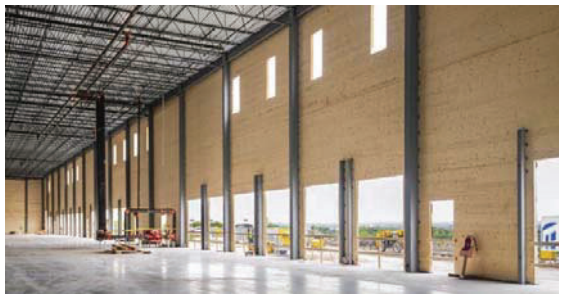

***Figure 14**: Southfield Park 35 warehouse, Dallas, Texas; Architect: PDMS Group; Engineer: Timberlab*

***Figure 15**: The Duke, Austin, Texas; Architect: DesignTrait; Engineer: WGI*

Other significant mass timber projects currently in development or under construction in Texas include the new San Antonio Spurs training facility, designed by architecture firm ZGF and Arup engineering. Twenty 40-meter-long glulam beams will support the roof structure, providing uninterrupted space for basketball training courts (Figure 16). When the 12,300-square-meter building opens in August 2023, it will be the largest practice facility made of mass timber in U.S. professional sports and the largest mass timber construction in Texas [16].

Architecture firm Bohlin Cywinski Jackson is bringing mass timber into the educational realm in Addison, Texas, with the Valdes STEM + Innovation Center for Greenhill School, an independent school serving the greater Dallas community (Figure 17). The 4,800-square-meter project will house flexible classrooms and labs for the school's math and science departments. A modular approach to

https://doi.org/10.52202/069179-0587

classroom design will ensure spaces can adapt to changing use and technologies over time while creating an open and collaborative environment that empowers students to incorporate STEM learning in all facets of their education. The building will provide opportunities for students to learn about integrated sustainable design through its exposed mass timber structure, daylight autonomy, rainwater harvesting, and visible energy conservation strategies, allowing them to draw connections between their work and the physical environment [17].

***Figure 16**: San Antonio Spurs Training Facility, San Antonio, Texas; Architect: ZGF; Engineer: Arup*

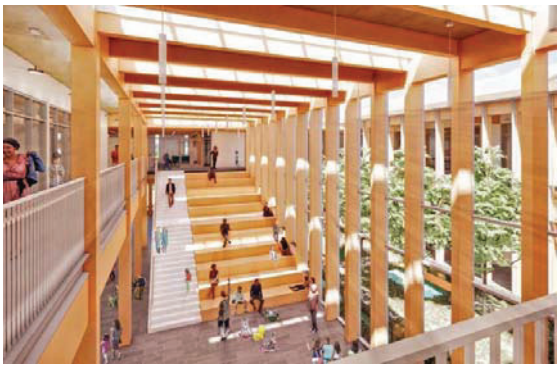

***Figure 17**: Valdes STEM + Innovation Center, Addison, Texas; Architect: Bohlin Cywinski Jackson; Engineer: DBR*

4 REGIONAL PRODUCTION

Many mass timber buildings in Texas have been completed with cross-laminated timber from European suppliers. Despite the disadvantage of long transportation distances and panel sizes limited by the dimensions of international shipping containers, these products have been very cost-competitive, thanks to the manufacturers' high production volumes and significant market shares.

North America's most established CLT production facilities are concentrated in Canada and the northern U.S., which can still present procurement challenges to early adopter projects in more distant states, including Texas. For example, there are no CLT production lines yet in Texas that manufacture for building applications, but several suppliers are in nearby states. SmartLam's Dothan, Alabama, plant, operating since 2018, is the first to offer certified CLT products made of Southern Yellow Pine. Located in Magnolia, Arkansas, Texas CLT gets its raw materials within a 160-kilometer (100-mile) radius of its facility. In addition, the company has plans to set up a second plant in Jasper in East Texas.

Canadian company Structurlam has expanded its operations to Conway, Arkansas, for its first U.S. CLT and glulam plant, which opened in 2021. About 40% of the facility's entire manufacturing output will be solely for Walmart for the first three years. The world's largest retailer has pledged to build its home office campus in Bentonville out of mass timber, and Structurlam will serve as its exclusive supplier.

Illinois-based Sterling has been manufacturing CLT mats for temporary access roads and working platforms in Lufkin, East Texas, since 2019. In 2022, the company received a Wood Innovation Grant from the U.S. Department of Agriculture to accelerate mass timber adoption with standard-format CLT panels. Its cross-laminated timber product line recently received PRG 320 certification, which is required in North America for CLT panels used in structural building applications. With its 700,000-cubic-meter annual production capacity, Sterling is poised to contribute to the mass timber construction market in Texas significantly.

Anyone interested in building with wood in Texas will surely welcome a ramp-up of production capacities. Broader availability of mass timber products throughout the Southern states will facilitate material procurement, reduce transportation costs, and foster healthy competition between manufacturers. Moreover, as the number of built projects made possible through regional production grows, the increased visibility is likely to lead to broader acceptance of timber buildings by the public and rising demand for their construction by future clients.

BUILDING TALLER IN WOOD

Most mass timber buildings completed in Texas have been permitted as Type III and Type IV construction under current applicable building codes. For these construction types, the 2018 International Building Code, or IBC, allows building heights of up to 26 meters (85 feet) with a maximum of five stories for residential and six stories for office occupancy.

While both types are similar in allowable height and the number of stories, there are some notable differences. Unlike Type IV, Type III requires char rate calculations for member sizes to determine residual cross sections for load capacity calculations, which can lead to oversizing of structural members to achieve the necessary fire rating. Exposed steel connections also are not permitted under Type III and require protection. Just these two examples highlight the potential impact of code limitations on architectural expression.

Therefore, it is advisable to engage the local Authority Having Jurisdiction early in the design process since it can serve as a valuable partner in selecting the most appropriate construction type. Mass timber structures taller than 26 meters (85 feet) and exceeding six stories are currently only possible in many parts of Texas if they undergo an Alternative Materials and Methods Request, a provision in the IBC. This gives local building officials the flexibility to address new concepts, innovations, and developments that the current code may not formally recognize yet. Depending on the extent of the request, this can be a lengthy, costly process that might require structural tests as well as fire resistance testing.

In response to the growing interest in tall timber construction, the International Code Council approved a set of proposals in 2019 to allow tall wood buildings as part of the regular code changes cycle. Based on the previous Heavy Timber construction type, which has been renamed Type IV-HT, the 2021 International Building Code (IBC) now includes three new construction types: Types IV-A, IV-B, and IV-C, arranged from the highest fire resistance and safety requirements to the lowest.

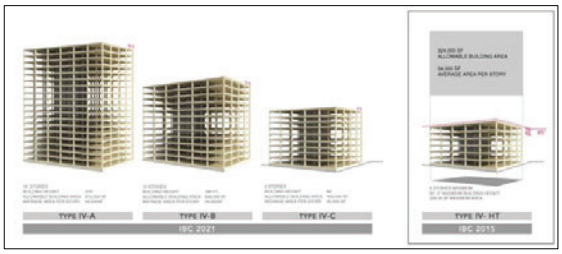

***Figure XX**: IBC new construction types: IV-A, IV-B, and IV-C; courtesy of atelierjones*

For business occupancy, Type IV-A allows buildings with 18 stories up to 82 meters (270 feet) tall with no exposed mass timber components. Type IV-B allows 12 stories up to 55 meters (180 feet) with some exposed mass timber elements, and Type IV-C allows nine stories up to 26 meters (85 feet) with almost all interior mass timber exposed.

Several jurisdictions in Texas have already adopted the tall mass timber provisions of the 2021 IBC, either in their entirety or with local amendments. This includes the cities of Allen, Austin, Bryan, Carrollton, Plano, Grand Prairie, and Fort Worth. In addition, the City of Dallas has incorporated some tall mass timber allowances of the 2021 IBC and the upcoming 2024 IBC [18, 19].

5 CONCLUSIONS

As one of the fastest-growing states in the nation, Texas will continue to experience a substantial increase in its population. Most of this growth will be concentrated in urban areas, and the increasing density of its cities will play a critical role in reducing the state's impact on climate change. Sustainable urban development will need to focus on affordable, healthy living and working environments while reducing carbon emissions.

Building with responsibly sourced timber can decrease the state's reliance on fossil fuels and turn its buildings and cities into carbon sinks rather than sources of CO_2 emissions. With wood deemed unsuitable for dense urban environments for so long, the recent development of engineered wood products and amendments to building codes have allowed its return to the city.

Innovative strategies for structural design and fire protection have enabled the construction of multi-story buildings that satisfy the most stringent standards, offering opportunities for the emergence of a new type of urban architecture. Increasing demand for timber buildings in cities will not only ensure that forests remain sustainably managed but also drive economic development in Texas' rural areas through new jobs from the manufacturing of wood products. Building with mass timber has the potential to positively impact the state's environment, local economies, and building culture.

ACKNOWLEDGEMENT

The author would like to thank Mark Bartlett, regional director of WoodWorks, for providing the latest information on current mass timber developments in Texas.

REFERENCES

[1] Dangel, Ulrich: Turning Point in Timber Construction – A New Economy. Birkhäuser Basel, 2017.
[2] Lake|Flato, www.lakeflato.com/hospitality/hotel-magdalena
[3] Woodworks Innovation Network, www.woodworksinnovationnetwork.org
[4] Lake|Flato, www.lakeflato.com/developmentcommerical/soto-building
[5] Thoughtbarn, www.thoughtbarn.com/projects/901-east-6th-street/
[6] Gensler, www.gensler.com/projects/first-united-bank
[7] Gensler, www.gensler.com/projects/first-united-bank-sherman-regional-headquarters
[8] Gensler, www.gensler.com/projects/fifth-and-tillery
[9] Crown Holdings, www.crowholdings.com/insights/crow-holdings-development-announces-plans-for-the-offices-at-southstone-yards-a-first-of-its-kind-mass-timber-construction-in-north-texas/
[10] Kirksey Architecture, www.kirksey.com/portfolio/projects/san-jacinto-college,-central-campus-classroom-building
[11] Kirksey Architecture, www.kirksey.com/portfolio/projects/rice-university-hanszen-college-new-wing

https://doi.org/10.52202/069179-0587

[12] Forest Service, U.S. Department of Agriculture, www.fs.usda.gov/news/releases/mass-timber-university-grant-program-projects-support-forest-health-and-vibrant
[13] Hines, www.hines.com/news/hines-announces-next-generation-timber-office-in-austins-eclectic-eastside-neighborhood
[14] T3 Eastside, https://www.t3eastside.com/
[15] WGI, wginc.com/projects/the-duke/
[16] Timberlyne, www.timberlyne.com/gallery/commercial/san-antonio-mass-timber
[17] Bohlin Cywinski Jackson, www.bcj.com/projects/academic/greenhill-school-valdes-stem-innovation-center/
[18] WoodWorks, www.woodworks.org/resources/tall-wood-buildings-in-the-2021-ibc-up-to-18-stories-of-mass-timber/
[19] WoodWorks, www.woodworks.org/resources/status-of-building-code-allowances-for-tall-mass-timber-in-the-ibc/

World Conference on Timber Engineering Oslo 2023

ACCELERATION OF UNITED STATES MARKETS FOR WOOD

Bill Parsons[1], Brian Brashaw[2]

ABSTRACT: While the United States (U.S.) market for wood products is well-established for single-family housing, there has also been a consistent and sustained effort over the past decade to significantly increase wood's share of the multi-family, commercial, and institutional segments. This paper examines the current state of wood construction in these markets, emerging trends post-COVID, opportunities, and obstacles to continued growth. It will utilize data and built projects to highlight key areas of momentum and provide examples where resources have had a direct market impact.

KEYWORDS: Wood-frame construction, Podium construction, Mass timber, Tall wood, Markets

1. INTRODUCTION

Over the last fifteen years, there has been growing interest in the use of wood in structures beyond single-family homes. This has coincided with a sustained effort to communicate wood's value for a wider range of building types, and to educate and assist design teams who have typically defaulted to other materials. WoodWorks – Wood Products Council plays a leadership role in partnership with the USDA Forest Service, Softwood Lumber Board, and others, on behalf of the North American wood industry.

In particular, larger structures and the use of innovative new systems pose challenges for building designers and construction professionals who seek to expand their use of wood. Modern projects also continually push the boundaries of wood engineering. In addition to encouraging the *desire* to use wood, the U.S. industry, through WoodWorks, provides expertise and resources that lead to quality wood buildings. Embodied carbon entering the conversation has further expanded the need for credible information around Whole Building Life Cycle Assessments (WBLCA).

2. DEFINING THE OPPORTUNITY

Although the COVID-19 pandemic has depressed construction markets in 2020 [1], there continue to be opportunities for increased wood use. As supply chain disruptions continue, cost will become an even greater concern. The most economically viable projects will come to fruition, and wood will be well-positioned as a low-cost/high-performance structural solution.

There is no shortage of economic predictions related to the future of construction markets. WoodWorks has been assessing data from a number of sources but is also in the unique position of working directly with developers and design/construction teams to assist on projects, which provides an additional layer of insight. Dodge Data & Analytics has provided some of the best information in terms that are helpful to the WoodWorks program. Dodge is projecting total construction starts will be flat in 2023.

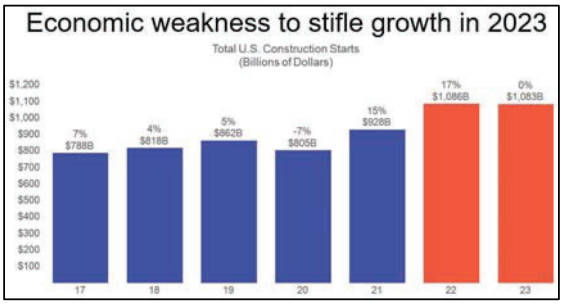

***Figure 1**: U.S. construction starts. Source: Dodge Data & Analytics*

In 2021, almost a billion square feet of new construction are accessible to wood each year in the U.S. About half of that area (over 17,000 structures) could be wood by code but are not utilizing wood today. Wood currently has a significant opportunity for increased market share.

***Figure 2**: US Markets for Wood Buildings (Source: Dodge Data & Analytics 2020, WoodWorks analysis)*

[1] Bill Parsons, PE, WoodWorks – Wood Products Council, Boise, ID, USA, bill.parsons@woodworks.org
[2] Brian Brashaw, USDA Forest Service, Cooperative Forestry, Wood Innovations, MN, USA brian.k.brashaw@usda.gov

https://doi.org/10.52202/069179-0588

3. MULTI-FAMILY

Since the last Great Recession (2007-2009), the multi-family market has grown significantly as a percentage of all homes constructed. The trend toward greater densification and urbanization in all major metropolitan areas has led both to an increase in multi-family projects and more design variation. Buildings with five or more stories of wood-frame construction are becoming more common, as are podium structures, which further increase the value of buildings that are primarily wood-frame. There are now nearly 600 five-, six-, or seven-story wood-frame buildings constructed in the U.S. each year [2].

While the trend is positive, many designers are still unaware that wood can be used in buildings greater than four stories or that podiums can be more than one level. This underscores the need for continued education and outreach to help people understand where wood is allowed by code, and to assist designers with the more demanding requirements of larger wood projects.

Under most U.S. codes, a multi-family wood building can be up to five stories (Type III construction), and the wood structure can then be placed on top of a podium (typically concrete). So far, most podiums are a single story, but multi-level podiums were included in the 2018 International Building Code (IBC) and are growing in use. Overall, the total multi-family market is 687 million square feet built annually, or a total of 23,400 projects.

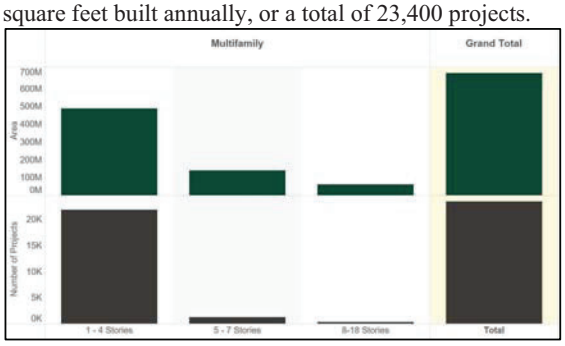

***Figure 2**: Total multi-family market in the U.S.; 687 million square feet annually, or 23,400 projects. Source: Dodge Data & Analytics 2021*

There are many examples of podium structures built throughout the U.S. Two are featured in case studies on the WoodWorks website, Crescent Terminus in Atlanta, GA and Stella in Marina del Rey, CA. The latest case study on a podium multifamily structure is Thomas Logan Apartments.

***Figure 3**: Thomas Logan case study Source: WoodWorks*

4. COMMERCIAL/INSTITUTIONAL

Initial gains in commercial and institutional market segments involved buildings that were similar in design to multi-family projects—e.g., hotels, motels and student housing. However, the performance capabilities of mass timber, and growing interest in products such as cross-laminated timber (CLT) as a carbon-friendly alternative to steel and concrete, have led to a much more diverse range. Mass timber has also become a significant draw for developers who want to attract quality, long-term tenants, and design teams eager to explore its creative potential.

WoodWorks tracks active mass timber projects and publishes an updated map each quarter [3]. (See Figure 4.)

https://doi.org/10.52202/069179-0588

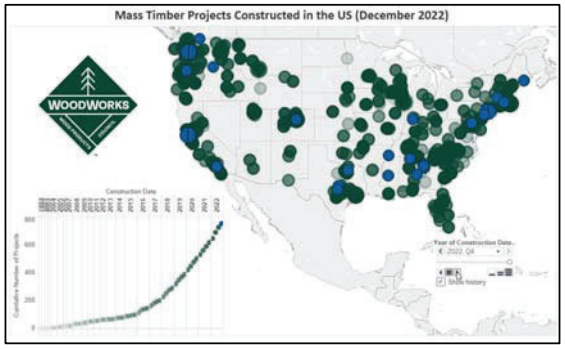

Figure 4: *Map of U.S. mass timber projects. Source: WoodWorks – Wood Products Council*

As of December 2022, 767 multi-family, commercial or institutional projects had been constructed out of mass timber in the U.S., and 910 were in design. (This includes mass timber and post-and-beam structures built since 2013.) The acceleration of mass timber is easily seen in Figure 4 — this growth is out pacing the growth seen with other wood systems.

WoodWorks is a leading provider of mass timber education, and assisted on more than 75% of the built projects noted in Figure 4. However, staff identified a significant barrier to continued growth. General contractors who had yet to build a mass timber project were adding risk premiums that priced wood out of the running, and projects were being converted to other materials. Recently, WoodWorks launched a program to address the issue through mass timber construction management and installation training.

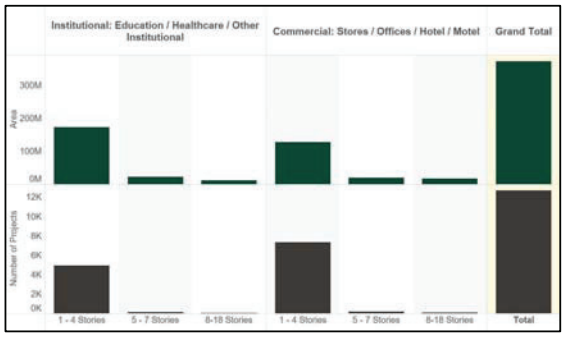

Figure 5: *Commercial and institutional market in the U.S. Source: Dodge Data & Analytics 2021*

The majority of commercial and institutional projects built in the U.S. are one to four stories. (See Figure 5.) In both of these categories, wood is only lightly penetrated and there are literally thousands of projects where wood can be used as the structural frame. Mass timber is gaining particular traction in these segments.

This is where the U.S. market narrative starts to diverge from other countries that have seen a trend toward the use of mass timber. After only a few years of product availability, the U.S. has 143 substantial multi-story mass timber business occupancy buildings (primarily offices) under construction or built. (See Figure 6.) These structures represent about 12.5 million square feet of cumulative construction. As far as WoodWorks is aware, this level of commercial building activity has not been seen in other countries—especially this early in the adoption phase. With 84 million square feet of annual construction opportunity in offices alone, the U.S. market has a great deal of room to expand this emerging technology.

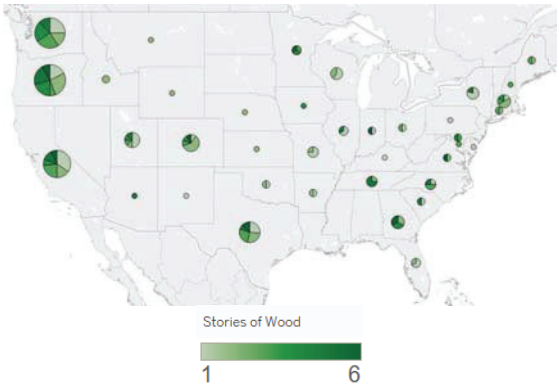

Figure 6: *Mass timber projects with business occupancies built or under construction (200 as of December 2022). Source: WoodWorks – Wood Products Council*

Exposed wood structure in office buildings is becoming a point of market distinction, both for the aesthetic and connection to nature. Post-COVID developers continue to look for ways to differentiate their products.

The WoodWorks case study, *Breaking Convention with Wood Offices*, outlines the benefits of wood for business occupancies and highlights examples of built projects. This resource has been very helpful in demonstrating the viability of wood in this segment. (See Figure 7.)

https://doi.org/10.52202/069179-0588

Figure 7: *Case study featuring multiple mass timber office buildings. Source: WoodWorks – Wood Products Council*

The educational and student housing segments have also shown an early uptick in the use of mass timber, with 31 projects under construction or built. (See Figure 8.) However, the financial impacts of COVID-19 may slow the growth in these markets, especially for university-owned buildings.

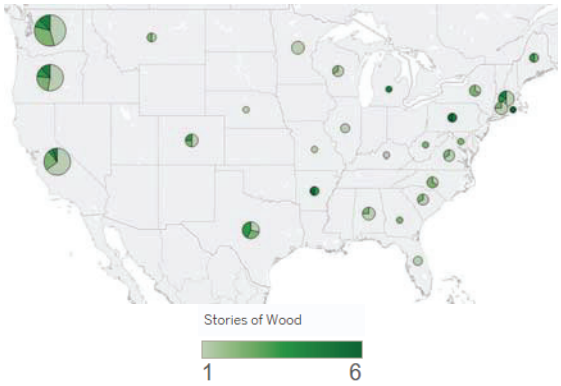

Figure 8: *Mass timber projects with education and student housing occupancies built or under construction (123 as of December 2022). Source: WoodWorks – Wood Products Council*

The 123 buildings noted above represent 5.4 million square feet of construction, which is very small in the context of over 106 million square feet built annually in this segment. In addition to aesthetics and connection to nature, drivers for these projects have included wood's sustainability and light carbon footprint.

A groundbreaking example in this category is the John W. Olver Design Building at the University of Massachusetts – Amherst. This project is featured in the WoodWorks case study, *Inspiration through Innovation*. (See Figure 9.) This includes a WBLCA analysis – which is a very hot emerging topic. We are active on several other case studies.

Figure 9: *Case study featuring the John W. Olver Design Building at the University of Massachusetts – Amherst. Source: WoodWorks – Wood Products Council.*

5. TALL WOOD (7+ STORIES)

Innovative wood products and building technologies are taking wood beyond new building types and opening markets that have been entirely out of reach for wood solutions. Changes approved for the 2021 IBC will allow wood buildings up to 18 stories, which creates the 90 million square feet of opportunity noted in Figure 2.

Figure 10 captures the opportunity by building height; Type IV-A has a maximum of 18 stories, Type IV-B has a maximum of 12, and Type IV-C has a maximum of nine. WoodWorks is currently assisting on nearly 200 projects over seven stories.

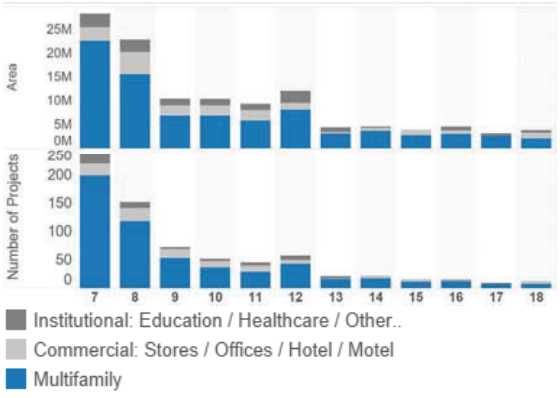

Figure 10: *Opportunity for tall wood (Source: Dodge Data & Analytics 2020, WoodWorks analysis)*

Many jurisdictions are adopting the 2021 IBC, which became the model code on January 1, 2021. At the end of

https://doi.org/10.52202/069179-0588

2022 there were nine tall projects built or under construction in the U.S.:

- Carbon12 – Portland, OR – Eight stories of mass timber.
- INTRO – Cleveland, OH – Eight stories of mass timber over a concrete podium.
- Ascent – Milwaukee, WI – Nineteen stories of mass timber over six stories of concrete.
- 80M – Washington, DC – Two new mass timber floors + habitable penthouse over an existing seven-story structure.
- Apex Clean Energy – Charlottesville, VA – Six stories of mass timber over two stories of concrete.
- 11 E Lenox – Boston, MA – Seven stories ofmass timber.
- Heartwood – Seattle, WA – Eight stories of mass timber
- 1510 Webster – Oakland, CA – 18 stories of mass timber over a concrete podium
- Minnesota Places – Portland, OR – Seven stories of mass timber over a concrete podium

Ascent is currently be the tallest mass timber building in the world.

Over 700 projects with seven or more stories are built in the U.S. each year. Early interest indicates that mass timber is poised for significant advancement in this market segment.

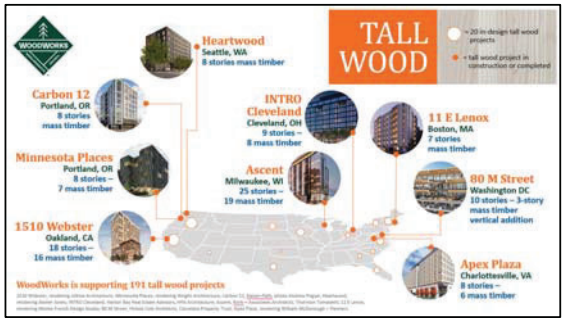

Figure 11: *Tall Wood Projects built or under construction at the end of 2022. Nearly 200 are in-design throughout the U.S. Source: WoodWorks – Wood Products Council*

WoodWorks has a number of resources and dedicated staff to assist with tall wood projects. (See Figure 12.) A common landing page for these topics can be found at: https://www.woodworks.org/learn/mass-timber-clt/tall-mass-timber.

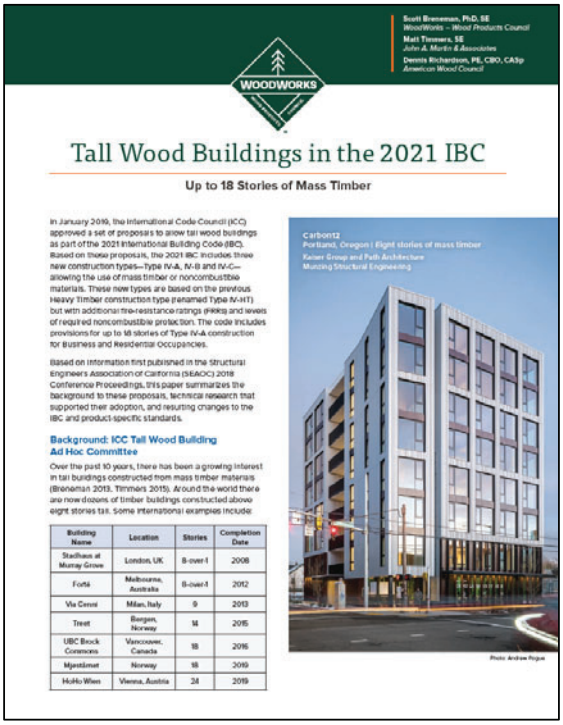

Figure 12: *One of many resources published by WoodWorks to assist with the design of tall wood buildings. Source: WoodWorks – Wood Products Council*

6. CONCLUSION

Historically, the U.S. single-family housing market has represented one of the most robust markets for wood in the world. With design teams turning to larger wood-frame and mass timber buildings, supported by the strategic combination of education and project assistance, the U.S. is poised to develop equally robust markets for these products in the multi-family, commercial and institutional sectors

REFERENCES

[1] Dodge Outlook 2022 Q3. Dodge Data & Analytics. November, 2022.

[2] Dodge Data and Analytics, 2021. WoodWorks – Wood Products Council (analysis).

[3] Building Trends: Mass Timber. WoodWorks – Wood Products Council, 2023. Retrieved from https://www.woodworks.org/publications-media/building-trends-mass-timber/

https://doi.org/10.52202/069179-0588

World Conference on Timber Engineering Oslo 2023

RECENT ADVANCEMENTS IN MASS TIMBER CONSTRUCTION TECHNOLOGIES IN CANADA

Mohammad Mohammad[1], Julie Tourrilhes[2], Richard Coxford[3], Miranda Williamson[4]

ABSTRACT: Interest in mass timber is growing among designers, builders, developers and other stakeholders worldwide due to its environmental benefits as a low-carbon and sustainable building material. In Canada, several recent initiatives by industry and governments to expand the use of wood in construction have led to an increased number of mass timber buildings across the country and enhanced existing manufacturing capability. Supported by progressive building codes, a growing supply chain, and a rising number of designers and builders with mass timber expertise, mass timber construction is poised to continue to take off in Canada. To support this momentum, the Government of Canada launched the Green Construction through Wood (GCWood) program to expedite market acceptance and foster commercial uptake of mass timber products and systems in Canada.

This paper provides an overview of the GCWood program activities, showcasing the design and construction of several demonstration projects and the ongoing efforts to implement a national wood education roadmap. This is in addition to funding critical technical research to support the adoption of tall wood buildings in the Canadian building code and transitioning the code to become more performance based.

KEYWORDS: Tall wood buildings, demonstration projects, mass timber, building codes, advanced wood education

1 INTRODUCTION

The emergence of mass timber, and the use of engineered wood products in construction as a green building material, continues to gain traction in Canada and abroad. The Government of Canada recognized that in order to decarbonize the built environment and increase the acceptance of wood products and systems domestically, it is critical to showcase the use of wood in non-traditional applications. This led to several initiatives and programs being launched over the last 12 years. Funding demonstration projects, advancing wood education and training, and revising building codes to allow taller and larger wood buildings in Canada are the cornerstones of such initiatives.

2 DEMONSTRATION PROJECTS

In 2013, the Government of Canada launched the Tall Wood Building Demonstration Initiative (TWBDI), which supported the construction of two tall wood buildings in Canada (Figure 1). The first is an 18-storey hybrid mass timber student residence (Brock Commons - Tallwood House) located in Vancouver, which was the world's tallest hybrid wood building at the time of its completion. The second is a 13-storey residential building in Québec City (Origine). NRCan funded the critical incremental R&D activities required to design, approve, and construct the two demonstration buildings. This included fire, structural, and acoustics testing [1]. The success of the TWBDI led to new initiatives by the Government of Canada that further encouraged the design and construction of timber structures in non-traditional construction applications.

Figure 1: *Brock Commons on the left, and Origine on the right (Courtesy of Stéphane Groleau)*

[1]Mohammad Mohammad, NRCan, Canada, mohammad.mohammad@nrcan-rncan.gc.ca
[2]Julie Tourrilhes, NRCan, Canada, julie.tourrilhes@nrcan-rncan.gc.ca
[3]Richard Coxford, NRCan, Canada, richard.coxford@nrcan-rncan.gc.ca
[4]Miranda Williamson, NRCan, Canada, miranda.williamson@nrcan-rncan.gc.ca

https://doi.org/10.52202/069179-0589

The Green Construction through Wood (GCWood) program was launched in October 2017 with the objective of increasing the use of mass timber as a green construction material in infrastructure projects. This included not just high-rise applications, but also low-rise non-residential and bridge construction. The Canadian federal government's budget in 2017 provided funding of $55 million over 5 years for GCWood under the *Pan-Canadian Framework on Clean Growth and Climate Change* to support the various GCWood program activities. GCWood program has three key components:

1) Mass timber and hybrid demonstration projects (e.g., high-rise, low-rise non-residential and bridges)
2) Building code revisions and supporting research (i.e., targeting 12-storey tall wood buildings by 2020 and performance-based in 2025 and 2030)
3) Technology transfer and advanced wood education (i.e., training courses, design and costing tools for architects, engineers and builders, and Life Cycle Assessment data and tools)

To expedite market acceptance of mass timber products and systems in Canada, three calls for proposals (CfP) were launched for innovative wood-based buildings and bridges between 2017 and 2018. To support the construction of these proposed projects, the GCWood program funded up to 100% of eligible incremental project costs associated with the design, approval, construction, and post construction activities of the selected demonstration projects.

Sixteen high-rise, low-rise non-residential wood buildings and timber bridges across Canada were funded under the GCWood program. These projects were selected based on specific criteria focused on design innovation, the expertise of the design and project team, replicability of the proposed wood-based systems, and the strength of the project business case, among a number of other criteria. All selected demonstration projects showcased advanced use of engineered wood-based products and systems in their design and construction. Several of the buildings are now completed, currently under construction, or at an advanced stage of design and approval across Canada.

2.1 TALL WOOD BUILDINGS

The first CfP was for tall wood buildings (minimum of 10 storeys) which targeted innovative use of advanced wood products and systems in high-rise applications. The choice for the number of storeys was based on a close consultation with the industry and based on market intelligence data. With the help of an expert evaluation panel, a handful of highly innovative projects that showcase advanced wood-based technologies in their design and construction were shortlisted for funding. The following are some examples of several tall wood buildings funded by the GCWood program.

2.1.1. George Brown College's Limberlost Place

One of these shortlisted projects was "Limberlost Place" (formally The Arbour), a 10-storey innovative tall wood building located at George Brown College's waterfront campus in downtown Toronto, Ontario (Figure 2). This academic building will serve as a learning space and a living laboratory for students. It will likewise house a mass timber research and testing facility to study renewable energy systems, fire performance, and durability.

The relatively thin structural system requires no use of conventional drop beams, which reduces the building height, volume, and material costs. The lateral load resisting system is composed of concentric steel braced frame core, which is being erected in tandem with the mass timber superstructure. The structural systems employ an innovative 7-ply timber-concrete-composite "slab band" to achieve the 9.2 m span (Figure 3). Extensive structural testing of the composite floor system was conducted at the University of Northeren British Coumbia (UNBC) to support the design. Huge glulam columns of 1,725 x 630 mm spanning three storeys tall will be used to support the gravity loads. Renewable energy systems, such as rooftop photovoltaic arrays, heat pumps, and rainwater recycling mechanisms are incorporated in the building design. The building is currently under construction and is scheduled for completion by the end of 2024. It will be Ontario's first tall wood, low-carbon institutional building with assembly occupancy.

Figure 2: *Limberlost Place (Courtesy of Moriyama & Teshima Architects)*

https://doi.org/10.52202/069179-0589

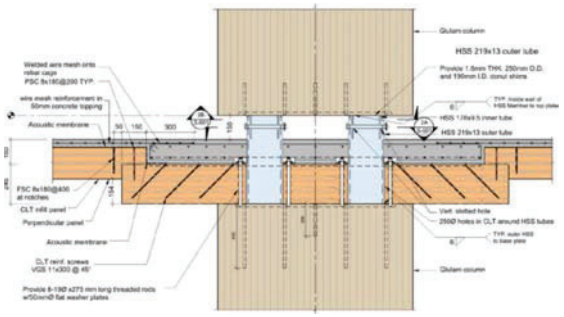

Figure 3: *Composite CLT/concrete slab and glulam floor system and connection (Courtesy of Fast+Epp)*

2.1.2. 2150 Keith Drive Tall Wood Building

Another shortlisted tall wood building was the 2150 Keith Drive project (Figure 4), a 10-storey mass timber tall wood building in Vancouver, British Columbia. This mass timber office building will be home to multiple office tenants from the technical and creative sectors. The design involves fully exposed mass timber elements, relying on charring to achieve a 2-hour fire-resistance rating.

The innovative design uses massive braced timber frame on the exterior as the main lateral load resisting system, complete with state of the art seismic dampers to improve the building's seismic resiliency. It likewise eliminates the need for a stiff interior concrete core by using four CLT shear walls in the interior which provide a design flexibility.

Figure 4: *2150 Keith Drive Office Building (Courtesy of DIALOG)*

2.1.3. University of Toronto's Academic Tower

Another project the GCWood program is providing funding to is the University of Toronto's Academic Tower (Figure 5). This 14-storey tower will be the tallest mass timber building in Ontario once completed, and will serve as an academic and research facility, as well as a living laboratory for the university.

The project is at the advanced design and approval stage with construction planned to begin in 2023. The top 10 storeys of this hybrid building will be made of glulam and engineered mass timber panels, with the four bottom storeys constructed of both timber and steel. One-way GLT slabs will be used for the deck to offer ample floor space, and to meet the required two-hour fire-resistance rating. The structural design uses wood super bracing as the lateral force resisting system against wind and seismic loads. Innovative connections engineered for off-site assembly will facilitate faster construction. The design involves partially exposed mass timber structural elements. Extensive engineering analysis and modelling including wind engineering studies has been conducted to support the design and approval of the building.

Figure 5: *Academic Tower (Courtesy of the University of Toronto)*

2.2 LOW-RISE NON-RESIDENTIAL BUILDINGS

The GCWood's second CfP targeted low-rise non-residential buildings including commercial, industrial, office, and institutional buildings of 4 storeys or less which demonstrate the innovative use of wood products or systems that could be easily replicated. Thirty applications were received and ten projects were short-listed for funding.

2.2.1. Toronto and Region Conservation Authority's (TRCA) New Administrative Office Building

One of the successful projects was Toronto and Region Conservation Authority's (TRCA) new Administrative Office Building. This is a 4-storey mass timber office building located in Toronto, Ontario and is part of the Canada Green Building Council's *Zero Carbon Building Pilot Program* (Figure 6*)*. The building is designed to achieve a low-carbon footprint through all lifecycle phases, with model simulations predicting a 50% reduction in operating emissions and over 75% reduction in embodied carbon compared to the average office building in Toronto. The mass timber structure is complete, and the remaining building construction will be completed by the end of 2023.

The structural system is composed of CLT mass timber floor panels supported on glulam beams and columns and uses a structural grid of approximately 6 m x 6 m. Metal steel strapping is installed on the top surface of the CLT floor/diaphragm where drag forces are concentrated to transfer the forces from the diaphragm to the shear walls. The lateral force resisting system for the office building utilizes a combination of stair and elevator cores

constructed of CLT wit lateral glulam bracing. There is no structural concrete utilized above the main floor concrete slab. The LCA study that was originally submitted was completed before the open loop modelling, so the results reflect operating emissions based on the closed loop system. It is expected the open loop system to improve energy efficiency by an additional 10-15%, which will lower operating emissions accordingly. The final updated model will be completed in 2023 with an updated LCA report.

Figure 6: *Toronto and Region Conservation Authority Administrative Office (Courtesy of TRCA)*

2.2.2. KF Aerospace Centre for Excellence

KF Aerospace Centre for Excellence is a highly visible commercial 2-storey project that serves as a working and display hangars, a centre of expertise, an aviation history museum, and community gathering place at the Kelowna International Airport in British Columbia (Figure 7).

The project uses long span roofs, floors and tall walls, which is a unique application of wood for this type of building application. The primary and secondary structural elements are glulam beams and glulam and DLT trusses. Pre-fabrication of large integrated components helped minimize on-site erection time. Building assemblies for the projects' central hub and two working hangars incorporate long span roofs, floors, and tall walls components and assemblies. The project was completed in the summer of 2022, and the building is now occupied.

Figure 7: *Centre for Excellence (Courtesy of KF Aerospace Centre for Excellence)*

2.2.3. Yukon Street Office Building

The Yukon Street Office Building is a 4-storey hybrid mass timber and steel commercial office building built tightly on the property line as an infill project and serves as a living laboratory to gather data to evaluate the performance of the hybrid mass timber design (Figure 8).

The project used prefabricated mass timber components, offering strength and structural simplicity, while helping decrease construction time. The system allows for long spans without interior columns. Composite panels accommodate the large spans, providing exposed soffits, and hide required services for the building. The CLT shear walls, as well as elevator and stair core, are specially designed to resist earthquake forces using an advanced seismic resistance hold-down system from New Zealand (Tectonus). CLT walls were prefabricated with the exterior envelope and cladding to minimize access and construction along the tight property line. A 2-hour structural fire-resistance rating for the exterior wall is achieved through the application of non-combustible insulation.

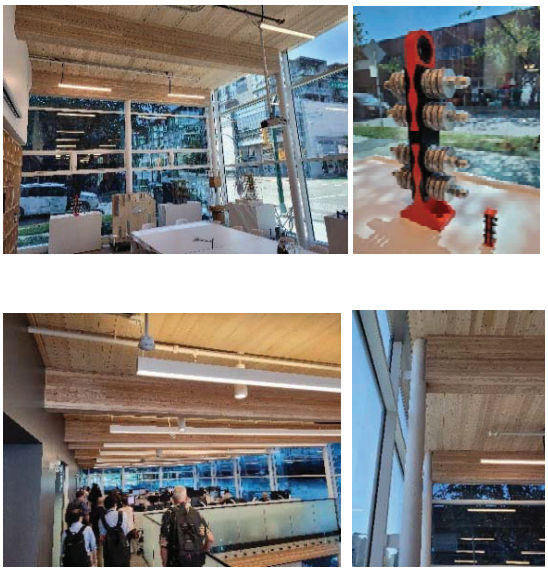

Figure 8: *Yukon Street Office Building with the Tectonus seismic hold-down system*

2.2.4. Bayview Elementary School

Bayview Elementary School is a 2-storey school in a high visibility location (Figure 9). It is one of the first schools to act on British Columbia's school seismic retrofit program. The design presents a large clear span roof using CLT panels and glulam webs, creating a "double T" design. The CLT shearwalls are installed throughout the building with multi-storey continuous shearwalls at the exterior to provide more efficient connections. There is CLT gravity walls at the upper level comprised of hybrid steel-CLT beams located at the second floor cantilevers over the ground level.

https://doi.org/10.52202/069179-0589

Figure 9: *Bayview Elementary School (Courtesy of Bayview Elementary School)*

2.2.5. wəkʷaʔnəs tə syaqʷəm Elementary School

The wəkʷaʔnəs tə syaqʷəm Elementary School, which in English means "the sun rising over the horizon", is completed and has a very similar design to the Bayview school described above, and aims to achieve the same environmental targets such as LEED Gold certified (Figure 10). Extensive structural testing on the hybrid floor system and shear walls took place at the University of Northern British Columbia (UNBC) to support the balloon type shearwalls design used in this project (Figure 11).

Figure 10: *wəkʷaʔnəs tə syaqʷəm Elementary School*

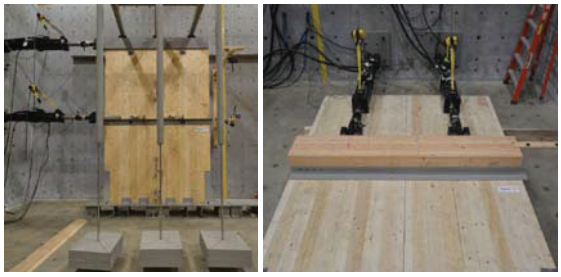

Figure 11: *Balloon Shearwall test setup (Courtesy of UNBC Wood Innovation Research Laboratory)*

2.2.6. Canadian Nuclear Laboratories

A series of three mass timber buildings and one with partial mass timber is being constructed as part of a first of its kind project in Canada at the Canadian Nuclear Laboratories (CNL) in Chalk River, Ontario. The site is owned by Atomic Energy of Canada Limited (AECL), a Canadian Crown corporation, and operated by CNL. The mass timber buildings showcase the use of advanced design and construction technologies, both structurally and aesthetically, at a nuclear science and technology campus. The mass timber buildings include a site entrance building, support and maintenance facility, administrative building (Science Collaboration Centre), and a large nuclear research facility, the Advanced Nuclear Materials Research Centre (ANMRC). NRCan provided funding through the GCWood Program for the Support and Maintenance Facility, the Science Collaboration Centre and the ANMRC. All four of these buildings are being constructed to revitalize the campus, thanks to a $1.2 billion investment by AECL.

The Science Collaboration Centre is a hybrid building that will serve as a collaboration complex to house a new data centre with S&T computing capabilities, a university-style auditorium, a welcoming library space, a roof-top terrace, and office space and meeting rooms for approximately 450 employees (Figure 12). The design incorporates CLT slabs with glulam columns, beams, and purlins as the main gravity structural system. The structure consists of a reinforced concrete lower level, elevator, and stair core. Mechanical, electrical, fibre optics, and life safety distribution system are all concealed within mass timber elements. The lateral bracing system against earthquakes and wind is a hybrid system of concrete shear walls and timber braced frames, with CLT slabs acting as diaphragms to transfer lateral loads to shear walls. The building is currently under construction.

Figure 12: *Science Collaboration Centre (Courtesy of CNL)*

The Support and Maintenance Facility is a 2-storey industrial use building which is home to various trades, transportation, and roads and grounds crews (Figure 13). The design includes a CLT elevator shaft, floors, and roof panels, which also act as diaphragms that are supported by glulam timber purlins, beams, and columns as the main structural system. The CLT mezzanine floors are suspended and supported by glulam beams. Glulam cross bracing is also provided to resist lateral loading. The construction of this building is complete.

Figure 13: *CNL's Support and Maintenance Facility mass timber project (Courtesy of CNL)*

The Advanced Nuclear Materials Research Centre (ANMRC) is a hybrid wood/concrete design, which includes a two-storey mass timber office wing, a two-storey laboratory wing, and a two-storey concrete hot cells wing (Figure 14). The prefabricated CLT and glulam components will include columns, posts and beams, floor panels, diaphragm, bracing, and exterior walls. The building will have exposed soffits, eliminating the need for an alternative ceiling system. CNL will be taking a modular prefabricated approach for the construction of both the laboratory wing and the office wing. The building is at advanced stage of design. The building is at advanced stage of design/development.

An Integrated Project Delivery approach was broadly adopted in the design and construction of all of mass timber projects at CNL. The process brings together the manufacturers of the mass timber products, the full design team, trades, and the construction manager to work collaboratively to optimize the design, increase value to the owner, and maximize efficiency through all phases of design, fabrication, and construction.

Figure 14: *Advanced Nuclear Material Research Centre (Courtesy of CNL)*

2.2.7. oN5 Office Building

oN5, a new 4-storey office building in downtown Vancouver was completed in 2022 and is being occupied by several engineering and architectural firms (Figure 15). The building uses CLT panels to demonstrate the potential for commercial mass timber. The structure utilizes a highly innovative self centering Lateral Force Resistance System (Tectonus) for resisting seismic loads. Prefabricated CLT panels were used in the design, from shearwalls to roof, and were produced by BC Passive House. The design aims to produce a replicable infill mass timber design for the construction industry. Exposed CLT panels offer great fire resistance and act as vertical supports, eliminating glulam or steel column requirements. Constructed at the property line, creative techniques were used to address the tight lot lines. The lightweight mass timber building elements were prefabricated and lifted into place quickly and efficiently (40-50% faster than typical construction).

Figure 15: *oN5 4-storey office building*

2.3 TIMBER BRIDGES

Industry and provincial and federal governments in Canada initiated several market and research efforts over the last 10 years to promote the use of timber in bridge applications. As a result, several modern innovative timber bridges have been built recently. The majority have been constructed in the provinces of Quebec, Ontario, and British Columbia. The Mistissini Bridge, built in 2014 and located at Uupaachikus Pass in Mistissini, Québec, is 160 m long and features four spans of straight girders supported by semi-continuous glulam arches (Figure 16). This is one of the longest modern timber bridges in Canada and was one of the first bridges to use CLT in the country.

The GCWood call for proposal for bridges (launched in the spring of 2018) builds on the success of previous efforts and projects, and ensures continued market momentum for timber bridges. The CfP received 13 applications for both vehicle traffic and pedestrian bridges that had a minimum clear span of 20 m. With the guidance of an expert evaluation panel, NRCan shortlisted several mass timber and wood-hybrid bridge demonstration projects for funding. Almost all selected demonstration bridges belong to provinces or municipalities, with many being a proposed replacement of an existing bridge. These bridges had been either closed to traffic, or their load carrying capacity reduced as they are showing signs of deterioration and require major maintenance.

The shortlisted timber bridges varied in length and complexity, but all demonstrated a high level of innovation in the engineering design, treatment, and the use of engineered mass timber products and systems. In

https://doi.org/10.52202/069179-0589

the end, only two timber bridges advanced to the design and construction stage with funding from NRCan.

Figure 16: *Mistissini Bridge (Courtesy of Stantec)*

2.3.1. Duchesnay Creek Bridge

One of shortlisted projects is the Duchesnay Creek Bridge in North Bay, Ontario (Figure 17). The new bridge replaces the original which was closed by the Ministry of Transportation (MTO) in 2019 for safety reasons due to its poor condition. The original bridge had a timber deck truss and was constructed in 1937. Replacement of this 74 m long heritage deck truss bridge on the existing alignment imposed challenges. To avoid multiple timber pile bents in the approach spans, it was decided to select a bridge type sympathetic to the cultural heritage value of the original structure and a timber design that is efficient and reflects the key attributes of the original timber structure in modern form [2]. The redesign of the bridge was done with the intention to maintain the original timber aesthetic. The bridge design is an innovative three-span hybrid glulam girder bridge with precast concrete deck and arched glulam braces at the piers. The utilization of the glulam braces at the piers helps with the reduction of the shear loads experienced by the structure. The deck is attached to the main glulam girders using shear connectors to allow for the transfer of diaphragm forces. The bridge is 83 m long and 13 m wide with three spans and was opened for traffic in August 2021.

Figure 17: *Duchesnay Creek Bridge (Courtesy of MTO)*

3 EDUCATION AND DESIGN TOOLS

3.1 NATIONAL EDUCATION ROADMAP

Until recently, only a few Canadian engineering and architectural schools offered wood design courses at the undergraduate level. To address this gap, the GCWood program funded the implementation of a Canadian wood education roadmap, led by the Canadian Wood Council (CWC). The goal is to expand wood education at Canadian universities and colleges, and consequently, contribute to the development of the future timber design capacity in Canada.

The architectural and engineering community is always changing, and professionals need access to state-of-the-art tools, resources, and continuing education to ensure the wood products industry remains competitive. Innovation doesn't always start on the construction site, but often through the students and recent graduates who shape the next wave of design and construction. Therefore, expanding the wood education curriculum in Canada requires supporting an engaged network of enthusiastic educators, as they are essential to equip future professionals with a solid foundation of education and skillsets. The focus of the education Roadmap is to:

1. Build a network to support educators and institutions to increase availability of curricula and encourage students to study wood design and construction.
2. Develop up-to-date curriculum/manuals/ materials, presentations, lectures, learning modules, design exercises, sample calculations and more.
3. Develop several teaching modules, interactive case studies, hold site visits and tours, and host student competitions to engage students and trigger their interest in wood structures.

Three new sets of teaching manuals are being developed: Wood Design for Architects, a Wood Handbook for Builders, and an Advanced Wood Engineering Manual. So far, project activities have led to the addition of wood design and construction curricula at 11 accredited civil engineering, architectural and construction management programs across Canada which is a huge success.

3.2 STATE OF MASS TIMBER IN CANADA

Until recently, there was no comprehensive database of modern mass timber projects or production capacity in Canada. In order to fill this gap, NRCan worked closely with industry partners to develop a "The State of Mass Timber in Canada" (SMTC) report, which was the first of its kind (Figure 18). The SMTC report was released in May 2021, and established a baseline of data with the intent to measure future growth against and help inform decision making associated with he future of mass timber construction in Canada [3].

Figure 18: *State of Mass Timber in Canada 2021 report*

The report presented a baseline dataset that included over 480 projects completed or currently under construction since 2007 and represented nearly 1.5 million m^2 (or 16 million sf) of gross floor area. This is in addition to data on 20 mass timber manufacturing facilities in Canada (Figure 19). A web-based interactive map was also developed and is updated quarterly to provide users with information on the locations of all the mass timber projects and producers from across the country [4]. The following figure outlines the number of manufacturers for each type of mass timber elements in Canada.

Figure 19: *Number of Canadian manufacturing facilities by product*

Several updates to the SMTC dataset and map since its publication have now brought the total project number to over 750 projects. The web-based dashboard shows the location of the mass timber projects and manufacturing facilities across Canada. Users can zoom in and select individual projects, or filter by categories such as project type and use, year of completion, size, region, and other criteria (Figure 20). The SMTC map dashboard was recently included in the Living Atlas, the biggest collection of maps and geographical based data and information in the world! The Living Atlas offers a variety of contextual tools to visualize and analyze data, and now users will be able to access the SMTC map and dashboard on both the Mass Timber Construction in Canada Page and the Living Atlas.

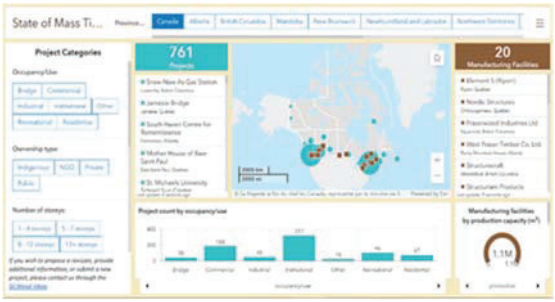

Figure 20: *SMTC map dashboard*

3.3 DESIGN TOOLS

To support the deployment of mass timber construction in Canada, the GCWood program has been funding the development and deployment of several advanced design tools to assist designers, builders, and decision makers. Overall, the program supported the development of over 10 new design guides, tools, and datasets. This includes advanced wood design handbooks for engineers, architects and builders, carbon calculators, and Life Cycle Assessment (LCA) tools to help demonstrate the environmental benefits of building with wood. To further the governments' carbon accounting goals, GCWood provided funding to a major 4-year initiative called *Low-Carbon Assets through Life Cycle Assessment* (LCA^2) led by the National Research Council of Canada (NRC). This initiative focused on developing a national Life Cycle Inventory (LCI) database and whole building LCA guidelines.

The LCI data and LCA guidelines will be used to facilitate procurement policies at the federal and provincial levels, and by the design and construction industry. This work will expand opportunities to build with wood, open new markets for manufacturers and provide stimulus to the broader forest sector.

4 UPDATES TO CANADIAN BUILDING CODES

The 2015 edition of the National Building Code of Canada (NBCC) included some significant changes with respect to wood design as it permitted 5 and 6 storey tall wood frame buildings [5]. Building on the revolutionary acceptance of 12-storey mass timber buildings as a "pre-approved" Alternative Solution by the province of Québec in 2015 [6], a code change proposal for Encapsulated Mass Timber Construction (EMTC) was submitted in 2016 by the Canadian Wood Council to the NBCC Code Committee for their consideration targeting the 2020 edition of NBCC.

A Task Group and several Working Groups were established by the Standing Committee on Fire Protection (SC-FP) to discuss the proposed EMTC code change and identify potential issues and research needs to be

https://doi.org/10.52202/069179-0589

addressed. Several research projects (mainly on fire and seismic performance) were conducted at the National Research Council (NRC), with funding from GCWood, to support the proposed code change provisions. The fire testing focused on the allowable percentage of exposed mass timber that should be permitted in EMTC buildings, and the effectiveness of water mist systems compared to conventional sprinkler systems that are commonly used in tall buildings.

The 2020 edition of the National Building Code of Canada (NBCC) was published in the Spring of 2022 and allows for EMTC up to 12 storeys. Several jurisdictions including British Columbia, Ontario, and Alberta have adopted the EMTC provisions in their respective codes. In addition, extensive efforts are being invested in transitioning the NBCC to become more performance-based in the future.

Additional research is ongoing to develop seismic design guidelines for mass shearwalls for tall wood buildings applications. A technical guide was developed recently by the Canadian Construction Materials Centre (CCMC) which will be used to support future code change provisions for tall wood buildings in the 2025 building code [7]. A series of design examples were also developed to validate and clarify how those guidelines will be used by engineers involved in the design and construction of tall wood buildings. The guidelines presented in the CCMC Technical Guide are being used to refine the current seismic design provisions in the 2024 edition of the Canadian Timber Design Standard CSA O86 [8].

NRCan has been funding critical research and development activities to support the NBCC code change process since 2010 and will continue to support future developments of the NBCC targeting a more performance-based code by 2030. Extensive efforts are currently underway to introduce performance-based design as one of the priorities for the current code cycle at the Canadian Commission for Buildings and Fire Codes (CCBFC) and its various standing committees.

4.1 MASS TIMBER FIRE DEMONSTRATION TEST

A national research program focused on demonstrating the fire performance of mass timber products in tall wood buildings was conducted in Canada over the past two years. The project was led by the Canadian Wood Council (CWC) and was jointly funded by the federal and provincial governments, including Natural Resources Canada, the provinces of Ontario, Quebec, British Columbia, and Alberta. The project's key objective was to encourage the acceptance of tall wood buildings in Canada and help inform the Authorities Having Jurisdictions (AHJs) about the performance of mass timber construction under various fire conditions. The fire tests were performed by the National Research Council of Canada.

The program comprised of two phases: Phase 1 involved conducting a series of pilot-scale fire demonstrations, which were carried out successfully in Vancouver in June 2021 (Figure 21). The tests represented typical construction fire scenarios. Phase 2 focused on testing a full scale 2-storey, 350 m^2, mass timber structure (Figure 22). Findings from Phase 1 pilot demonstration project were used to refine the design and testing approaches of the full-scale mass timber structure and supported the approval of several tall wood buildings in British Columbia.

In Phase 2, five different fire test scenarios were conducted on the full scale 2-storey mass timber structure designed and built at the Canadian Explosives Research Laboratory (CERL) in Ottawa. The tests investigated among other things, the fire performance of protected & unprotected mass timber, fire dynamics, and the behaviour of construction and garbage bin fires. The initial test conducted in Phase 2 was the world's largest mass timber demonstration fire presented to date. Preliminary observations have indicated that the fire performance of the mass timber structure was similar to that of non-combustible construction and have confirmed that mass timber performs well under the rare fire scenarios in which the sprinkler system fails, and the fire department is unable to respond.

One of the key objectives of the fire tests was to demonstrate to a host of decision makers (e.g., fire services, municipal building officials and regulatory authorities, insurance and finance industries, and other key construction stakeholders) that the fire performance of mass timber construction can meet, or even exceed, the performance achieved by non-combustible construction as permitted in the building code. Over 200 experts from across Canada, including fire officials, building regulators, insurance industry representatives, engineers, and architects (including some from governments), witnessed the tests to learn about the behaviour of mass timber construction under fire conditions.

Analysis and reporting of data collected from the tests will be used to support future code change proposals, including performance-based codes and the development of alternative solutions and new fire suppression systems.

Figure 21: *Vancouver Pilot Demonstration Test (Courtesy of GHL Consultants Ltd.)*

https://doi.org/10.52202/069179-0589

Figure 22: *Ottawa Mass Timber Fire Demonstration Test during and after the test as the fire died down*

5 CONCLUSIONS

The Government of Canada is making significant investments in expanding the use of wood as a low-carbon building material in Canadian building and infrastructure projects. Through demonstration projects and strategic activities focused on advancing wood design education and supporting science-based code revisions, the GCWood program is supporting greater market and regulatory acceptance of wood in non-traditional construction applications across Canada.

REFERENCES

[1] Mohammad, M.; Robert Jones, Maureen Whelan, Richard Coxford. Canada's Tall Wood Buildings Demonstration projects. Proceedings of the 2018 World Conference on Timber Engineering (WCTE), Seoul, Korea, 2018.

[2] Richard Krutzler, Mohammed Rashed, Sergiy Morozevych. Highway 17B Duchesnay Creek Timber Bridge. 11th International Conference on Short and Medium Span Bridges, Toronto, Canada, 2022.

[3] NRCan. The State of Mass Timber in Canada. Natural Resources Canada, Ottawa, Ontario, 2021. https://cfs.nrcan.gc.ca/publications?id=40364

[4] NRCan. State of the Mass Timber in Canada Interactive Map. Natural Resources Canada, Ottawa, Ontario, 2022. https://experience.arcgis.com/experience/58e313c4ac0247138ba5057d655ed1d4

[5] National Research Council. National Building Code of Canada (NBCC). National Research Council of Canada, Ottawa, Ontario, 2015

[6] Government of Québec. Mass timber buildings up to 12 Storeys: Directives and Explanatory Guide. Régie du bâtiment du Québec, Québec, 2015.

[7] DeVall R, Popovski M, McFadden JBW., Yang TY, 2021. Technical guide for evaluation of seismic force resisting systems and their force modification factors for use in the national building code of Canada with concepts illustrated using a cantilevered wood CLT shear wall example. CLT shear wall example, National Research Council of Canada, Ottawa, ON.

[8] Canadian Standard Association (CSA). Engineering Design in Wood (CSA O86), Rexdale (Toronto), ON

https://doi.org/10.52202/069179-0589

World Conference on Timber Engineering Oslo 2023

INVESTING IN MASS TIMBER CONSTRUCTION IN AUSTRALIA: THE CLEAN ENERGY FINANCE CORPORATION TIMBER BUILDING PROGRAM

Christina Wijeratne[1] and Paolo Lavisci[2]

ABSTRACT: The built environment must play a significant role in achieving Australia's decarbonisation objectives. Whilst energy efficiency measures and renewable energy sources helping to address the operating emissions of Australia's built environment have gained significant traction, the embodied carbon in the materials used in construction is becoming an increasingly important component of the built environment's carbon emissions profile. Where application is appropriate, mass timber provides a lower embodied carbon alternative to conventional construction materials. The Clean Energy Finance Corporation (CEFC) Timber Building Program, launched in February 2022, offers AUD 300 million in debt financing to encourage greater use of mass timber in construction. The CEFC Timber Building Program looks to increase the use of mass timber in Australia, to achieve direct carbon savings through individual projects and drive demand for mass timber products in Australia. It also aims to enable increased exposure and capacity building for construction professionals and help to influence the broader market through providing demonstration value. The Timber Building Program highlights the unique and broad impact potential of targeted, purpose-driven financing.

KEYWORDS: Debt program, timber funding, embodied carbon, financing

1 INTRODUCTION

The Clean Energy Finance Corporation (CEFC) is Australia's 'green bank' with a 10-year track record of investing to reduce emissions across the economy, working with co-investors, business, industry, and government to deliver on Australia's ambitions to reach net zero emissions by 2050. In February 2022, the CEFC launched an AUD 300 million Timber Building Program, aimed at accelerating the use of mass timber construction in Australia, with the provision of tailored debt finance to eligible projects.

2 THE AUSTRALIAN CONTEXT

Australia produces approximately four-and-a-half times the world average per-capita CO_2 emissions, at over 14 tonnes in 2021 [1]. This is on par with the United States, and more than double that of the European Union [2]. With the building and construction sector accounting for 39 per cent of global emissions, [3] the built environment has a significant role to play in reaching net zero targets in Australia and globally.

2.1 THE EMBODIED CARBON CHALLENGE

Efforts to decarbonise the built environment have traditionally focused on operating emissions. As improvements to operational energy become common industry practice and net zero commitments become more mainstream, the market's attention is turning to the embodied carbon of materials used to build. According to the Green Building Council of Australia (GBCA), in 2019 operating emissions contributed 84 per cent of Australia's built environment emissions, with the remaining 16 per cent contributed through embodied carbon. Without intervention, and as the electricity grid continues to decarbonise, by 2050, this is expected to shift, with embodied carbon projected to contribute 85 per cent of Australia's built environment emissions [4].

The embodied carbon emissions of the materials used in Australia is 30–50 million tonnes of CO_2 emissions per year, which is approximately five to 10 per cent of national greenhouse gas emissions [5]. The economic value of the construction materials sector is approximately AUD 65 billion, contributing roughly three per cent of Australia's GDP [6]. The CEFC industry report *'Australian buildings and infrastructure: Opportunities for cutting embodied carbon'* (herein referred to as the '*Embodied Carbon Report'*) found that, depending on the initiatives and low carbon products utilised, it is possible to achieve embodied carbon savings of between three and 18 per cent whilst reducing materials costs by between 0.3 and three per cent [7].

2.2 THE ROLE OF MASS TIMBER

Conventional building materials such as concrete and steel are traditionally made by highly carbon intensive processes. Comparatively, the carbon emitted during the processes of making mass timber is much lower [8]

[1] Christina Wijeratne, Clean Energy Finance Corporation, Australia, christina.wijeratne@cefc.com.au
[2] Paolo Lavisci, FWPA, Australia, paolo.lavisci@woodsolutions.com.au

https://doi.org/10.52202/069179-0590

Furthermore, with sustainable timber production and improved building dis-assembly practices, mass timber has the ability to maintain substantial amounts of sequestered carbon [9]. The *Embodied Carbon Report* found that the embodied carbon emissions of a mass timber building can be up to approximately 75 per cent less compared to a conventional concrete and/or steel counterpart on a per square meter basis [10].

2.3 THE MASS TIMBER INDUSTRY

The use of mass timber construction materials in Australia lags that of more mature markets such as North America and Europe. Whilst Australian forests and plantations sequester, and wood products store, approximately 57 million tonnes of CO_2, equal to approximately 10 per cent of the total greenhouse gases emitted in Australia [11], Australia has a limited domestic supply chain, with only a handful of onshore mass timber manufacturers.

Australia's commercial building sector is highly competitive and has adopted efficiencies such as the use of precast concrete and steel. However, the market has not widely adopted the use of mass timber, with one important impediment being structural and fire engineering standards which, until the NCC 2016 revision, did not allow the use of mass timber in structures above three storeys within a 'Deemed-to-Satisfy' provision. This necessitated a 'performance solutions' approach requiring additional design time, costs, and greater approval risk.

The residential building sector is highly fragmented, largely comprised of many smaller scale builders. Australian residential buildings up to three storeys in height are typically built with reference to the largely prescriptive AS1684 standard, rather than seeking greater performance outcomes through the performance-based AS1720 (noting this provisions for GLT and LVL, but not for CLT) or through the reference to other standards such as the Eurocode 5. Thus, the residential building sector typically lags the commercial building sector in sustainability outcomes and progress.

The use of mass timber in medium-to-large scale construction is further limited due to the cost savings of reduced labour and build times often not being factored into project feasibility analyses, thus not considered to offset the often higher upfront costs of mass timber (on a 'bill of quantities' basis) compared with traditional construction materials in Australia. Further, limited builder experience constructing with mass timber, and resistance from lenders and insurers to support off-site prefabrication, pose additional hurdles to broader uptake.

While constructing with mass timber offers many benefits compared with traditional construction approaches, including the ability to achieve embodied carbon savings, increased productivity through shorter construction times, lower physical impacts to site surrounds from the construction process, and improved site safety, the adoption and growth in use of mass timber construction approaches seen in North America and Europe have not yet been achieved in Australia.

2.4 ENABLERS OF CHANGE

Driving change in the Australian mass timber market requires a broad and collaborative cross-sectorial approach. There are several initiatives currently underway which seek to address the barriers to the uptake of mass timber in Australia, including:

- Regulation: building standards have a significant impact on material selection and construction techniques. The National Construction Code (NCC) has been progressively updated in 2016 and 2019 to include positive changes in support of the use of mass timber in mid-rise construction (up to 25 meters in height) [12]
- Disclosure: the measurement of embodied carbon and collection of such data unlocks the ability to benchmark and drive higher standards. Rating tools play an important role in providing consistency and fostering positive behavioural changes in the market. The GBCA has launched a *Responsible Products Framework* which sets embodied carbon targets for buildings seeking high ratings [13], and the National Australian Built Environment Rating System (NABERS) is creating a framework for measuring, benchmarking, and certifying emissions from construction and building materials [14]. Some Australian states are using policy levers to introduce embodied emissions measurement and reporting requirements across residential and commercial developments [15].
- Industry partnership: industry collaboration between relevant stakeholders can enable a consistent understanding of economy-wide hurdles and provide a feedback loop to policy and regulation. The Materials and Embodied Carbon Leaders' Alliance (MECLA) is a collaborative thinktank which has attracted over 100 industry partners with a collective decarbonisation vision, including the CEFC [16].
- Education: technical knowledge building is required to increase building professionals' comfort and confidence in using novel construction materials and techniques. Forest & Wood Products Australia Limited (FWPA) is a not-for-profit company that, through its WoodSolutions program, provides integrated services to the Australian forest and wood products industry, the construction industry, and the broader community.
- Supportive capital: capital is necessary to influence progress across the economy. Supporting projects demonstrating the benefits of mass timber construction can support the development of the domestic market in a myriad of ways. The CEFC is providing financing in support of the use of mass timber through its targeted Timber Building Program.

2.5 FOREST AND WOOD PRODUCTS AUSTRALIA

FWPA has the mission of investing in effective and relevant research and development designed to grow the

https://doi.org/10.52202/069179-0590

market for forest and wood products, increase productivity and profitability across the value chain and ensure positive environmental and social outcomes. An example of FWPA's work in this area is its investment in fire testing and collection of engineering evidence to support the evolution of the NCC. The NCC 2016 revision introduced Deemed-to-Satisfy provisions for using timber structures in buildings up to 25 meters effective height.

In 2010, FWPA launched WoodSolutions, an industry initiative designed to provide independent, non-proprietary information about timber and wood products to professionals and companies involved in project development, design and construction in the built environment.

In 2011, the Grattan Institute, an independent Australia public policy organisation, quantified the growing gap between housing supply and demand and suggested that multi-residential timber framed construction was an innovative technique that would contribute favourably to the supply of housing [17]. In response to the new and growing demand for support in relation to multi-storey timber framed construction, WoodSolutions launched the Midrise Advisory Program (MAP), involving 22 industry and institutional partners.

MAP helped to build the mass timber knowledge base of developers, builders, architects, engineers, building surveyors, and quantity surveyors, supporting building professionals and decision makers in their designs, procurement, and construction activities. MAP demonstrated the benefits of wood-based construction using multiple free-access tools such as case studies, seminars, project-specific meetings and feasibility analyses, site visits, a demonstration building, a help desk, engineering software and design guides. An example of this is the *Cost Engineering of Mid-rise Timber Buildings* technical design guide which uses data from several mid-rise timber projects in Australia and overseas to quantify the cost savings associated with the use of timber structures, and provides guidance on how to appropriately capture their value proposition in activities related to the design, procurement and installation of mid-rise wood structures in Australia [18].

The primary target of the MAP was to support the use of timber in 'significant' projects. This was accomplished by supporting key decision-makers in developing their understanding of mass timber products and their complementarity within an optimised design. The 30 projects which were completed, started, or fully confirmed within the MAP's activity term (2016-2022) used approximately 53,000 cubic meters of structural wood products, as well as additional ancillary products and services. This represents approximately three per cent of the projects considered to have the potential of being developed using timber. Most of the projects supported by the MAP featured a significant design quality combining aesthetics, performance, cost efficiency, and quick delivery, reflecting the benefits of timber and enabling the successful introduction of the materials to major players in the market.

WoodSolutions has become well known and trusted as a provider of reliable educational tools for timber design and construction, supporting the development of new professional and technical competencies, with the organisation's website being one of the world's most visited in the field of timber information and education (with 1.9 million overall visits in 2022, as measured by Google Analytics). WoodSolutions' Technical Design Guides and Environmental Product Declarations, which are all free for public download from their website are frequently used as the de-facto industry standard, being referenced in design specifications and tender documents. As the number of contacts and projects grows, awareness of the benefits of timber is increasing in Australia. Many professional associations involved in construction (including developers, builders, architects, engineers, building surveyors, and quantity surveyors) have collaborated with WoodSolutions to develop their associates' awareness of the value proposition of timber structures in the market.

3 CEFC TIMBER BUILDING PROGRAM

An AUD 300 million Timber Building Program was established by the CEFC and launched in 2022 as part of its broader strategic focus on reducing embodied carbon as an essential component of a low emissions economy. The Timber Building Program is a novel approach to addressing the issue of upfront embodied carbon in the commercial construction context, using tailored finance solutions to support the increased adoption of mass timber in construction.

3.1 CLEAN ENERGY FINANCE CORPORATION

The CEFC is a specialist investor at the centre of efforts to help deliver on Australia's ambitions for a thriving, low emissions future. With a strong investment track record, it is committed to accelerating Australia's transition to net zero emissions by 2050. In addressing some of Australia's toughest emissions challenges, the CEFC invests to fill market gaps, collaborating with investors, innovators and industry leaders to spur substantial new investment where it will have the greatest impact.

CEFC lifetime investment commitments to 31 December 2022 were AUD 11.7 billion. Together with institutional investors, business, industry and cleantech innovators, the CEFC catalysed AUD 42.8 billion in investment in Australia's low emissions economy, with each dollar of CEFC capital leveraging an additional $2.62 from the private sector. In investing on behalf of the Australian Government, the CEFC has a strong commitment to deliver a positive return for taxpayers across its portfolio. The CEFC has a flexible approach to investment, which recognises the needs of an evolving market. CEFC financial products and structures, including debt and equity, are shaped to help drive private sector investment across a diverse range of activities.

In recognising the urgent nature of the emissions challenge, the CEFC has focused investment origination

activities, prioritising emissions challenges across the wider Australian economy. These include backing the clean energy system of the future, where Australia requires significant new investment to support a substantial uplift in renewable energy generation, storage and grid transmission project. The CEFC also invests in in low emissions solutions in property, infrastructure, industry, natural capital and resources, which can deliver benefits across the economy, from lower energy consumption to alternative approaches to production, reducing demand on the energy network and abating carbon emissions. In tapping into new investment models and opportunities the CEFC develops new financial markets and products, builds investor confidence and crafts tailored and innovative investment solutions for new and emerging industries.

3.2 THE ROLE OF CEFC FINANCE

Capital is a powerful tool able to influence technology, innovation, and growth across the economy. Finance can impact all aspects of the transition to net zero emissions, including through supporting utility-scale renewable energy, major infrastructure and real estate projects, innovative climate technologies, and broader debt capital market approaches.

By operating across all sectors of the economy, the CEFC mobilises capital to support both the supply of, and demand for, renewable energy, energy efficiency, and low emissions technologies. A strong governance approach helps ensure intended commercial and emissions outcomes are achieved across the portfolio. As well as direct carbon abatement impacts, investments have demonstration value, showcasing commercially viable solutions with key learnings leveraged and shared to influence and educate the broader market.

The CEFC is an active investor across the property sector. This extends from commercial office, retail and industrial segments through to alternative and emerging asset classes, including student housing, retirement living and residential markets. The CEFC also invests across the capital stack, using debt and equity instruments. CEFC cornerstone investments in new property funds continue to demonstrate the positive link between financial returns and Environmental, Social, and Governance outcomes. In order to optimise emissions performance and achieve long-term sustainability targets, the CEFC operates as a 'patient' investor, recognising there are opportunities to reduce emissions across the investment lifecycle, from the development approval process to design, procurement and construction, then finally into operations, as well as the need to address the emission of existing building stock and support circular economy principles. At 31 December 2022, the CEFC have made lifetime investment commitments of AUD 2.1 billion across the property sector.

In Australia, building with mass timber generally proves more expensive than conventional concrete and steel approaches, especially as the cost savings of reduced labour requirements and build times are often not factored into project feasibility analyses. An additional barrier relates to lack of awareness, with many contractors and developers not familiar with mass timber, and a perception of increased risk in relation to durability, fire resistance, and building code compliance. These factors present challenges to developers committing to the use of mass timber and being able to source investment and finance for mass timber projects.

The CEFC Timber Building Program has been designed to support an increase in mass timber projects in Australia, to provide direct exposure and capacity building for construction professionals involved in individual projects, as well as influencing the broader market through providing demonstration value and concerted knowledge sharing. As more projects utilise mass timber in construction, more data will be generated to combat myths around durability, fire resistance, and costs. Such data can also help guide policy, building standards, and rating tools to recognise the full benefits of mass timber, including its role in addressing the embodied carbon challenge. Supporting demand for mass timber products may also aid in the development of local supply chains. The Timber Building Program aims to drive demand to support these integral market enabling approaches.

3.3 CEFC PROGRAM PARAMETERS

The CEFC Timber Building Program is a tailored debt program designed to attract projects that are incorporating the material use of mass timber to achieve significant embodied carbon outcomes. Finance is bespoke and tailored to best suit each individual transaction and borrower. Funding can be project-specific senior secured property finance, or portfolio-level corporate debt secured by a pool of assets. The CEFC can offer fixed or floating interest rates, and can lend as sole financier, or alongside co-financiers in syndicated or club structures. Investments are made at commercial returns and financing packages are structured to optimise sustainability outcomes on a risk-adjusted basis. Governance is guided by the *Clean Energy Finance Corporation Act 2012* (the CEFC Act) and CEFC policies and guidelines.

Opportunities are evaluated on a case-by-case basis and with consideration of the overall commercial and carbon outcomes and initiatives. The program is sector agnostic, open to developments including commercial offices, retail, industrial, healthcare, education, multi-residential apartments, retirement living, aged care, hotel, and student accommodation, as mass timber can have a role to play across all asset types. The Timber Building Program is seeking to support scalable projects that drive strong demonstration value, and where possible, draw in third-party capital to optimise the program reach. The Timber Building Program has an Australian focus as per the objectives of the CEFC Act.

All projects must use low carbon mass timber products during the construction phase to achieve material embodied carbon outcomes and use appropriately sourced and accredited timber materials.

https://doi.org/10.52202/069179-0590

3.4 CEFC PROGRAM IMPACT

The CEFC Timber Building Program is anticipated to be a multi-year scheme, acknowledging that through-cycle investment certainty is necessary to drive the momentum required to achieve broader adoption of mass timber construction approaches in the Australian market. This also reflects the CEFC early engagement model required to ensure sponsor and project alignment with required carbon and impact outcomes; the necessary project and financial due diligence, approval, and documentation processes; and ultimately the financing and project construction timelines.

The CEFC February, 2022 launch of the Timber Building Program was positively received by the market, attracting a significant level of responses from property companies and developers, positive support from industry groups and the Australian government, and considerable attention from the respected and specialist media outlets.

3.5 FIRST PROGRAM INVESTMENT

The CEFC successfully executed on its first finance package under the Timber Building Program in September 2022, with its involvement in T3 Collingwood. T3 Collingwood is the first Australian addition to the Hines 'T3' global portfolio, a Timber, Transit, and Technology-oriented development methodology which is centred upon sustainable design, efficiency, and profitability, supporting the delivery of credible decarbonisation pathways. T3 Collingwood, a 15-storey prime-grade office tower in the inner-city Melbourne suburb of Collingwood, aims to deliver a dual emissions reduction impact – cutting embodied carbon levels by as much as 40 per cent during the construction phase and, once operational, targeting market-leading net zero emissions.

The hybrid construction approach used to build what will be one of Melbourne's tallest hybrid timber buildings will feature a glue laminated timber (GLT) post and beam structure with cross-laminated timber (CLT) flooring starting from the sixth level, on top of five reinforced concrete podium levels. Timber will be sustainably sourced from two specialist local mass timber manufacturers, with Xlam Australia supplying the CLT and Australian Sustainable Hardwoods supplying the GLT. T3 Collingwood will use approximately 4,000 cubic metres of mass timber components for the structural frame, storing approximately 3,000 tonnes of CO_2.

Hines Australia Managing Director Simon Nasa noted:

> 'Mass-timber construction is an important step in driving a sustainable future for the built environment we live and work in. Not only is timber a completely renewable resource, but timber offices are also biophilic in creating a more natural working environment for tenants and their staff. This results in increased productivity and better mental health outcomes, helping to create the people-friendly live-work-play communities that Hines is known for' [19].

Figure 1: *External façade architectural rendering of T3 Collingwood*

Figure 2: *Cross section architectural rendering of T3 Collingwood*

Figure 3: *Internal architectural rendering of T3 Collingwood*

https://doi.org/10.52202/069179-0590

T3 Collingwood was supported from its early concept stage by the WoodSolutions MAP through an established collaboration with the architects, engineers, program manager, and builder.

As one of the world's largest privately held real estate investors and managers [20], and with a global T3 portfolio, the Hines development of T3 Collingwood signals the readiness and investable nature of Australia's mass timber construction market.

T3 Collingwood aims to achieve significant carbon abatement outcomes, as well as create demand for Australian domestic mass timber, and encourage owners, developers, architects, engineers, and builders to use mass timber where appropriate as an alternative to conventional construction materials such as concrete and steel.

Learnings in relation to fire resistance and code compliance are expected to help inform regulatory approaches; embodied carbon measurement and outcomes can contribute to rating tool developments; and the project will help demonstrate the investable nature of mass timber buildings to the broader finance market, driving the adoption of larger-scale capital programs.

Through the Timber Building Program, the CEFC is encouraged to see interest from parties across the spectrum, from significant developers such as Hines, through to mid-market and private market participants, signifying the scale of the investable mass timber market, and the opportunity to educate and influence building professionals across the economy. The Timber Building Program aims to support more projects achieving strong emissions savings and broader positive market impacts.

4 CONCLUSIONS

The CEFC plays a unqiue role in supporting Australia's economy-wide decarbonisation ambitions. Embodied carbon is becoming an increasingly important challenge in the decarbonisation of the built environment, and as a low carbon alternative to traditional construction materials, where applicable, mass timber has a key role to play in addressing the challenge. The adoption of mass timber construction approaches in Australia faces multiple impediments, including from a lack of awareness across construction, development, investment, and finance industries, leading to perceptions of increased risk and cost. The CEFC has found that in the Australian context, working with early adopters can create significant behavioural change and shift key market drivers. The CEFC Timber Building Program looks to achieve direct carbon savings from investee projects, drive demand and increase the use of mass timber in Australia to provide direct exposure and capacity building for construction professionals, and to influence the broader market through demonstration value. Learnings from an increased number of projects can help to combat myths; guide policy, building standards, and rating tools; and aid in the development of local supply chains, highlighting the unique and broad impact of purpose-driven financing in accelerating emissions reduction.

REFERENCES

[1] Ritchie H., Roser M., Rosado P.: CO_2 and Greenhouse Gas Emissions. Our World in Data, 2020.

[2] Ritchie H., Roser M., Rosado P.: CO_2 and Greenhouse Gas Emissions. Our World in Data, 2020.

[3] IEA: Global Status Report for Buildings and Construction 2019. IEA, Paris, 2019.

[4] GBCA, thinkstep-anz: Embodied Carbon and Embodied Energy in Australia's Buildings. Green Building Council Australia and thinkstep-anz, 2021.

[5] Clean Energy Finance Corporation: Australian buildings and infrastructure: Opportunities for cutting embodied carbon. Clean Energy Finance Corporation, 2021.

[6] Clean Energy Finance Corporation: Australian buildings and infrastructure: Opportunities for cutting embodied carbon. Clean Energy Finance Corporation, 2021.

[7] Clean Energy Finance Corporation: Australian buildings and infrastructure: Opportunities for cutting embodied carbon. Clean Energy Finance Corporation, 2021.

[8] Hough, R.: Rethinking Timber Buildings Seven Perspectives on the Use of Timber in Building Design and Construction. ARUP, London, 2019.

[9] Clean Energy Finance Corporation: Australian buildings and infrastructure: Opportunities for cutting embodied carbon. Clean Energy Finance Corporation, 2021.

[10] Clean Energy Finance Corporation: Australian buildings and infrastructure: Opportunities for cutting embodied carbon. Clean Energy Finance Corporation, 2021.

[11] Department of Industry, Science, Energy and Resources: National Greenhouse Gas Inventory Quarterly Update: March 2021. Department of Industry, Science, Energy and Resources, 2021.

[12] England, P., Bennetts, I.: Fire Safety Design of Mid-rise Timber Buildings. WoodSolutions, Melbourne 2016.

[13] Chapa, J., Cornell, T., Barbov, N., Bezzina, E., Wouters, T.: Driving responsible products in the built environment – Changes to Green Star Buildings and our strategy for the future. Green Building Council of Australia, 2021.

[14] Vickers, J., Sullivan, N., Davies, A., Kogileru, T., Wouters, T.: Embodied Emissions Technical Report. NABERS, 2022.

[15] NSW Department of Planning and Environment: Sustainable Buildings SEPP Overview. NSW Department of Planning and Environment, 2022.

[16] Materials and Embodied Carbon Leaders Alliance: MECLA Partners, https://mecla.org.au/partners, accessed Feb. 2023.

[17] Kelly, J-F., Breadon, P., Reichl, J. Getting the housing we want. Grattan Institute, Melbourne, 2011.

https://doi.org/10.52202/069179-0590

[18] Ritche, L., Lavisci, P., Carter, N., Kennedy, T.: Cost Engineering of Mid-rise Timber Buildings. WoodSolutions, Melbourne, 2019.
[19] Clean Energy Finance Corporation: Landmark T3 Collingwood kickstarts CEFC Timber Building Program. https://www.cefc.com.au/media/media-release/landmark-t3-collingwood-kickstarts-cefc-timber-building-program/, accessed Feb. 2023.
[20] Hines: About Hines, https://www.hines.com, accessed Feb. 2023.

World Conference on Timber Engineering Oslo 2023

TOWARDS A BROADER USE OF WOODEN CONSTRUCTION MATERIALS: INTERMEDIARY ORGANISATIONS IN THE SUSTAINABILITY TRANSITION OF THE CONSTRUCTION SECTOR

Antje Klitkou[1], Lina Ingeborgrud [2]

ABSTRACT:

Aim: This paper presents an ongoing study on sustainability transitions in the Norwegian construction sector, with a focus on increasing the use of wood. The construction sector is very conservative and path dependent. Existing path-dependencies and lock-mechanisms are interrelated and reinforce each other, contributing to an unsustainable development within the sector and preventing a sustainable transformation. These interacting lock-ins create social problems, such as the lack of affordable city dwellings, a high cost for energy efficiency and renovation measures, and less flexibility for adapting dwelling spaces to new needs. A crucial question is therefore how to change path-dependencies and overcome these interacting lock-ins by developing new pathways – what types of actors and efforts are required for such a change? In this paper, we pay attention to the specific role of different types of intermediary organisations in the transition to a more sustainable construction sector in Norway. We investigate how such intermediaries contribute to more sustainable pathways in the construction sector, with a focus on the use of wood.

Method: We apply a mixed methods approach, combining media analysis, interviews, and document analysis.

Findings: We find that intermediary organisations have been very active in the development of new pathways. This applies especially to cluster organisations, which have a clear aim of increasing the use of wood in the construction sector, but also intermediaries taking a more 'neutral' role concerning choice of materials, provide innovation arenas for experimenting with sustainable material use and architectures. We identified technological, institutional, and behavioural path dependencies and barriers for sustainable development. Correspondingly, we discuss new pathways for more sustainable and wood-based constructions and the role of intermediaries in shaping these new pathways.

Conclusions: Development and deployment of new technologies for wood construction need to be accompanied by changes in institutional conditions and in social practices of dwelling. Intermediaries need to broaden their horizon and networks when lobbying for new wood-based solutions addressing such social problems. Intermediaries evolve over time and get new roles, while older roles are taken over by other actors. Different types of intermediaries need to cooperate, have different roles, and interact with other actors in the innovation system.

KEYWORDS: Wooden construction, Intermediary organisations, Norway, Sustainability transition, Path creation, Path dependence

1 INTRODUCTION

This paper presents a study on the innovative use of wood in the Norwegian construction sector to facilitate a sustainable transition of the sector. The construction sector has a considerable economic and social importance, as well as major environmental impacts. Furthermore, it is very conservative and path-dependent, but also rather diverse, encompassing not only the entrepreneurs who are constructing buildings, but also those actors who order the construction, as well as architects, consultants, producers of construction materials, etc. Sustainability transitions must overcome path-dependencies.

Existing path-dependencies contribute to unsustainable development within the construction sector and prevent a sustainable transformation of the sector. A crucial question is therefore how we can change path-dependencies and barriers to enable sustainable development in the construction sector: what kind of new pathways have emerged and what types of actors are required for such a change? In this paper, we pay attention to the specific role of different types of intermediary

[1] Antje Klitkou, NIFU, Norway, antje.klitkou@nifu.no
[2] Lina Ingeborgrud, NIFU, Norway, lina.ingeborgrud@nifu.no

https://doi.org/10.52202/069179-0591

organisations in the transition to a more sustainable construction sector in Norway. We investigate how such actors work to facilitate the increased use of wood-based materials within the sector.

The research questions for this paper are therefore:

- Which new pathways have emerged for a more sustainable construction and building sector based on the use of wood?
- What is the role of different types of intermediary organisations in shaping these new pathways?
- How do intermediary organisations generate new users and markets for wood-based construction materials?

2 BACKGROUND

The construction sector has a considerable economic and social importance, as well as major environmental impacts. If we include the whole lifecycle of buildings, the global construction and building sector stands for 42% of total energy consumption, 35% of total greenhouse gas emissions, 50% of extracted materials and 30% of water consumption [1, 2]. Therefore, improving the resource efficiency and sustainability in the building sector has become an important climate policy goal in the EU and in the Nordic countries [3-7].

As one possible solution it has been suggested to use more wooden construction materials. Wood is a renewable material and has a considerably lower carbon footprint compared to steel and concrete. Studies on the mitigation potential of wood use in buildings and furnishing have shown that wood products have lower greenhouse gas emissions than alternatives over the complete life cycle of the product [8]. There is plenty of evidence supporting the substitution effects [9, 10], but this is still a niche market. Another problem is the large amount of waste generated in the construction and building sector. This includes the construction of new houses, the rehabilitation of buildings and the demolition of existing buildings and other constructions. Construction and demolition waste (CDW) accounts for more than a third of all waste generated in the European Union (Source: Eurostat)[6] and for 29 per cent in Norway (Source: SSB)[7]. Over the last 17 years, there has been a steady increase of waste generated in this sector in Norway: from 1.2 million ton in 2004, to 2.1 million ton in 2020 (data: SSB). Here, demolition waste stands for 46 per cent, rehabilitation of buildings for 24 per cent and new constructions for 30 per cent [11].[8] The highest shares belong to bricks and concrete: 0.6 million ton in 2004 and 0.87 million ton in 2020 (SSB).[9] Wood waste has increased as well: from 0.22 million ton in 2004 to 0.27 million ton in 2020 (ibid.). In addition, there are contaminated resources, which have increased as well.

In Norway, the use of wood as a construction material has dominated the marked for cottages in the countryside and, only to some extent, for houses with no more than two storeys. Normally, houses in the cities are multi-storied and mostly built in concrete and steel. This means that the challenges regarding high energy consumption, GHG emissions, use of extracted materials, water consumption, and waste generation, dominate in this sector.

In the literature, researchers have distinguished between six types of barriers for the extensive use of timber as a structural material for multifamily and non-residential buildings: "code implementation, technology transfer, costs, material durability and other technical aspects, culture of the industry and material availability" [12].

While the literature about the sustainability transition of the construction sector in general is targeting low-energy or passive houses [13], the literature on the wood construction industry has been mainly technical, focusing on quality of construction materials and assembling techniques [i.e., 10, 14, 15] or on specific projects and there used materials and assembling techniques [16]. Recently, there has been more research on the functions of technological innovation systems for wood-frame multi-storey construction [17].

3 THEORETICAL FRAMEWORK

The theoretical framework for this paper consists of three main conceptual building blocks: 1) path-dependence and lock-ins, 2) path creation for sustainability transitions, and 3) the role of intermediaries in sustainability transitions.

Path dependencies can be described as the ways in which a sector, here the construction sector, is 'locked-into' certain patterns due to historical developments [18]. Path dependency is not inherently negative, but when the chosen path turns out to be a hinder for new, more effective, and environmentally friendly solutions, those lock-ins function as a barrier for sustainable transitions. Such developments are, therefore, path dependent. Path dependencies are realised through lock-in mechanisms. The discussion of lock-in mechanisms in this paper is motivated by our interest in transition processes and their key barriers. We focus especially on transitions towards a more sustainable construction sector.

We can distinguish between *three groups of lock-in mechanisms:*

- Technological and infrastructural lock-ins,
- institutional lock-is, and
- behavioural patterns and shared social practices of everyday life.

All three types coevolve and are interdependent [19].

[6] https://ec.europa.eu/environment/topics/waste-and-recycling/construction-and-demolition-waste_en
[7] https://www.ssb.no/natur-og-miljo/avfall/statistikk/avfallsregnskapet
[8] https://www.ssb.no/natur-og-miljo/avfall/statistikk/avfall-fra-byggeaktivitet
[9] https://www.ssb.no/statbank/table/09247/tableViewLayout1/

https://doi.org/10.52202/069179-0591

The scientific discourse about lock-ins was originally mostly about technology-related lock-ins, and first later, institutional and behavioural lock-ins came on the agenda.

Technological lock-ins can be defined as positive feedbacks or increasing returns to the adoption of a selected technology [20-22]. Positive feedback mechanisms decrease production costs and create additional benefits for users. The costs and performance of a new technology are more uncertain compared to incumbent technologies [23].

High costs of supporting infrastructure can also contribute to a technological lock-in because it is a barrier to change. Infrastructure is often used for encompassing the communicative system, including transport or distributive systems, like the systems for producing and distributing heat, water, and electricity. Infrastructure systems are special types of societal systems that include the physical artefacts and the institutions, which regulate and manage these systems [24]. With Freeman, we argue that any larger built environments are long-lived fixed assets that can constrain investments in the deployment of new solutions [25].

A stable incumbent regime is the outcome of various lock-in processes, and it favours incremental as opposed to radical innovation. As a result, incumbent technologies have a distinct advantage over new entrants, not because they are necessarily better, but because they are more widely used and diffused. The concept of lock-ins has been extensively used to explain the persistence of fossil fuel-based technological systems, even though their well-known environmental externalities contribute to climate change. Moreover, this 'carbon lock-in' inhibits the diffusion and adoption of carbon-saving technologies [21, 24]. In this regard, initially "minor changes and marginal developments may evolve into massive structural configurations that then restrict the variety of directions to future changes" [26:13].

What are the differences between *institutional and technological lock-ins*? Seto et al. [19] have discussed these differences: (1) Institutional lock-ins are intended and coordinated efforts. They are *not* early chance events like technological lock-ins. (2) Those who enforce these institutional lock-ins profit from them, while others do not. (3) Institutional lock-ins "occur more often and with greater intensity than technological lock-in[s]" (p. 433). However, both institutional lock-ins and technological lock-ins contribute to a trajectory that is resistant to change and that creates increasingly costly and challenging barriers to switching to any alternative trajectory.

Social practices of everyday life can be understood as configurations of meanings, skills, and material objects [27]. Meanings are here referred to as shared understandings and purposes guiding a practice. Skills are forms of routinised, embodied know-how and competence. The material dimension highlights the importance of material objects and infrastructures, which significantly shape the possibilities of practices to change over time [28]. These three elements of social practice can act as lock-ins for change. The social practice of dwelling, for instance, encompasses the material dimension of dwelling, including houses, flats, streets, towns, etc. Meanings include social norms for what is understood as a good and preferred form of dwelling, for example a single house with an individual garden, a shared house, or a flat in a multi-storey building. Skills can encompass maintenance skills, competence for energy efficient living etc. The different social practice fields, such as dwelling, mobility, eating and working, interact and form bundles of practices which can also act as lock-ins [28].

So, how can we overcome path dependence and lock-ins? The concept of *path creation* has gained special relevance in analyses of sustainability transitions [29]. Path creation has been used as a concept to examine how new and more sustainable niches may overcome incumbent systems, and in this way contribute to a sustainability transition [30]. With Simmie [30], we distinguish between the initial conditions of path dependence and ongoing path-creation experiments by different niche actors, planned actions and new path establishment processes to achieve critical mass, key path creation barriers, and envisioned outcomes.

Research on path-creation processes highlights that engaged and entrepreneurial actors are central to technological and societal change [31]. Typically, through long-lasting efforts and interaction between many actors, new paths of development are created which move beyond existing path dependencies. One type of such engaged actors operating in niches are intermediary organisations. The role of different *intermediary organisations* in sustainability transitions has been in focus recently [32-36], and has been proposed as central in accelerating sustainability transitions [32]. A key issue relating to the activities of intermediaries is their survivability and the source and long-term stability of their funding [36]. Kivimaa, Boon [32] define transition intermediaries as:

> "…actors and platforms that positively influence sustainability transition processes by linking actors and activities, and their related skills and resources, or by connecting transition visions and demands of networks of actors with existing regimes in order to create momentum for socio-technical system change, to create new collaborations within and across niche technologies, ideas and markets, and to disrupt dominant unsustainable socio-technical configurations" [32].

Intermediaries can be classified according to their visions, sources of funding, scope of activities, and intended targets (short-term vs. long-term, actor level or system-level outcomes) [37]. We can also distinguish between systemic-, regime-based-, niche-, process-, and user intermediaries [32]. Systemic intermediaries have different functions, such as using and interacting, network building, brokerage, consensus building, long-term strategy development, and creating conditions for learning by doing [38-40].

https://doi.org/10.52202/069179-0591

In this paper we apply the classification developed by Kivimaa, Boon [32], and applied by Vihemäki, Toppinen [41] who investigated the role of intermediaries in the diffusion of wooden construction of multi-storey buildings. They point out that intermediaries are able

> "to work across the often-impermeable boundaries between different actor groups, arenas of action, or geographical scales. Intermediaries are seen to play an important role in connecting actors in situations in which direct interaction is challenging because of high transaction costs, communication challenges and information asymmetries" [41].

4 METHOD AND DATA

We apply a mixed methods approach, combining media analysis, interviews, and document analysis. The media analysis is based on the retrieval of all printed newspaper and magazine articles (national, regional, local, trade press and magazines) published in Norway on wooden construction between 2011 and 2021. The data source is Retriever, the leading media monitoring company in Northern Europe. We applied a keyword approach and downloaded all the articles. Following keywords were used in the search: *(wood-based OR wooden) AND (buildings OR construction*)*
This covers both wooden buildings and constructions, but also wooden construction materials.

We read all the articles retrieved from the search. Furthermore, all the relevant articles were registered in an event database, containing all the necessary bibliographic information and the thematic focus of the articles. We distinguished between unique events to avoid double counting: some articles have been published in several newspapers, either with the same or similar titles. They were identified and in the final analysis they were only considered once, to avoid artificially high numbers. We registered 179 unique articles out of 235 articles. The media analysis also informed the other steps of the analysis, such as the selection of interviewees and the selection of commissioned reports and policy documents. The next step was to gain a broader insight through interviews with different actors identified in the media analysis and via the snowballing technique among interviewees. We created an interview guide and conducted 20 interviews (see Table 1).

Table 1: *Interviews (N=20)*

Type of organisation	Number of interviews
Private intermediaries	7
Cluster organisations	4
Systemic intermediaries	2
Niche project	1
Public agencies, ministries	6

The interviews lasted for about an hour, were conducted online and were recorded and transcribed afterwards. The interviews were analysed with NVivo, a qualitative data analysis software. Document analyses of important commissioned reports and policy documents, highlighted in the media analysis and during the interviews, completed the empirical background of the study. These documents were included in the NVivo analysis as well. As a result, we created a narrative addressing the research questions. Here, we concentrated on path dependencies and major obstacles for new developments, new pathways for more sustainable and wood-based construction, and not least the role played by intermediaries in shaping these pathways.

5 FINDINGS

Based on the media analysis, a timeline was constructed to point out the main developments in the sector. This timeline includes the following elements:

- main companies, important projects, municipalities, and intermediary organisations,
- political events and policy strategies,
- and barriers and challenges.

The development of media coverage since 2001 can be grouped into three periods:

1. 2011–2012: Introduction of policy instruments, but rather limited awareness.
2. 2013–2016: Political lobbying for public procurement of wooden buildings, strategy development, and the start of the first forest-based cluster organisation.
3. 2017–2021: Industrial capacity building, pilot projects and new intermediary organisations.

When analysing the new pathways for a more sustainable construction and building sector based on the use of wood, we need to first identify the existing path dependencies and lock-ins.

5.1 PATH DEPENDENCIES

Path-dependencies in the construction sector concern technology and material infrastructure, including learning effects, use of technology and materials, existing physical building infrastructures, high costs and a lot of waste; as well as institutional lock-ins, such as policy instruments and quality standards for construction; and social practices, such as preferences for living in single houses, lacking flexibility in dwelling solutions and lacking competences about effects of building materials on residents' wellbeing.
We mainly identified the following path dependencies, which function as barriers for new path creation:

Technology and material infrastructure:
The building and construction sector is traditionally dominated by solutions based on concrete, bricks, and steel, and the related skills. The existing physical building infrastructure in larger cities is dominated by multi-storey houses in steel, concrete and bricks, while smaller towns have more 1–2 storey-houses in wood. Many larger dwelling complexes in larger cities need energy efficiency upgrading, such as better insulation of walls, which is rather costly.

The *circular economy* is still not well established in the construction sector in general. Reuse and material recycling of wooden construction material is not well established in normal practice yet. Wood-based waste has mostly been used for energy production. Skills regarding the maintenance and improved energy efficiency of dwellings are outdated. Waste production at the construction site has been the usual practice, also in wood-based construction. Demolition of buildings, instead of maintenance and upgrading, have contributed to more waste. The EU's waste directive, to which Norway is affiliated through the EEA agreement, had as a goal that 70 per cent of the waste from both building and construction activities should be materially recycled by 2020. However, in 2020, only 44 per cent of the waste from construction activity was delivered for material recycling.

Costs of wooden construction materials are not stable, and changes are less predictable: A strong growth in costs for all construction materials as energy has become more expensive due to the war in Ukraine, the Corona pandemic, and supply shortages in Canada and other countries. Access to processed wooden construction material from Norway is limited. The import of the material creates higher transport costs and therefore less sustainable projects.

Documentation: The sustainability effects of modern wooden construction are not well enough documented, and this knowledge is not systematized. Technical solutions for fire, sound, rot prevention, wall coverings etc. need to get prequalified, approved, tested, and documented.

Code implementation: Wood-based construction must engage more in developing industrial standards (see institutional path dependencies). Wooden construction projects often require a longer design phase.

Lack of digitalisation happens often due to limited digital competency in the sector. Here, digitalisation is related to information flow, application of data, input parameters in production, and how one can make use of it. A lack of digitalisation leads to higher operation and maintenance costs because the construction process is less effective, things have to be changed constantly, and learning over time is limited. Today, there are far too many opportunities for the digital chain to be broken and inaccuracies to occur. Building Information Modelling (BIM) is the foundation of digital transformation in the architecture, engineering, and construction industry. The signals that most BIM systems create are too inaccurate for a Computerized Numerical Control machine in a factory to understand and to produce the right goods based on them. Therefore, full digitalisation must start with architects and planners.

Institutions:
Existing policy instruments are not adapted to the need for more sustainable construction, and they do not facilitate the use of wood in construction. Too narrow building regulations favour minimal demands regarding environment and climate. They also focus more on energy requirements and less on GHG emissions of materials. Furthermore, they do not include the operation of a building, as well as all the stages of construction. There are many actors in the wooden construction industry who argue for stricter requirements: The environmental product declaration should include the entire value chain, from the production of raw materials and transport of the raw materials to the actual construction site, the construction process, operation and maintenance, and finally how the building materials can be reused at the end of a building's life.

The *governance of the construction sector* in general and of wooden construction specifically is distributed over many ministries and public agencies, which leads to fragmentation of the political steering. This political fragmentation hampers coordinated strategies and better regulations. All these ministries and agencies issue directives and support schemes, which go in different directions and are often just restricted to a short period. Because there are so many policy actors, this is perceived as very bureaucratic and less impenetrable. Thus(?), policy learning across those different actors is quite impossible.

Public procurement regulations are misinterpreted, and often local administrations do no not favour wooden solutions in their tenders. Competencies in public administration is not updated, and there exist tighter connections with concrete and steel construction.

The *lack of ordering competencies* in municipalities contributes to maintaining established path dependencies. Municipalities are obliged to publish tenders for constructing schools, childcare, or elderly care. There are several municipalities who have developed ambitious climate strategies and link such tenders to these strategies. However, very many municipalities still ignore the new possibilities for sustainable construction because they lack competencies about how to include sustainability requirements for the choice of material in their tenders. Wooden construction solutions were traditionally restricted to 1 or 2 storey-buildings due to fire regulations, with little architectonic innovation.

Behaviour and social practice:
The building and construction sector is very *conservative* and there exist many conflicts. New wood-based solutions must compete with well-established practices in the steel and concrete industry, which also has improved their carbon footprint, instead of combining the most innovative and sustainable solutions from wood, steel, and concrete. Established entrepreneurs mostly favour proved solutions, where they already have collaboration partners and supply chains, and know the costs and the risks.

There are big challenges regarding *construction waste:* Wooden construction waste is commonly used as an energy source – so-called energy recovery – but this is not

https://doi.org/10.52202/069179-0591

material recycling. Large amounts of waste come from the established practice of tearing down existing buildings, and building new ones, instead of maintaining, retrofitting, and upgrading existing buildings.

Small and medium-sized enterprises (SMEs) have less of a focus on developing new competencies, collaborate little with higher education and research institutions, do not hire many new candidates with new ideas and competencies, and are not at the forefront regarding the deployment of innovation. The collaboration between SMEs is not well developed because the SMEs are afraid of losing a competitive advantage. Some of the *larger companies* are more active. Often, they do not want to carry the costs of being a fast mover in wooden construction but would rather sit and wait until the costs decline further. The willingness and ability of the Norwegian state and other public builders to *pay the high prices* of construction firms is a part of why these firms are not being forced into become more effective and innovative.
There is a lack of living space in larger cities due to restricted space and due to inflexible dwelling solutions. Large dwellings are not used effectively because elderly people don't want to leave their social environment and alternatives are not offered.

These path dependencies and lock-ins are of course interlinked and reinforce each other: The consequences are high energy and water consumption, high waste generation, GHG emissions, and extended use of extracted materials.

5.2 NEW PATHWAYS

We identified four types of new pathways for more sustainable and wood-based constructions. We distinguish between pathways that are centred on organising sustainable construction processes differently, pathways that lead to more sustainable and innovative wood-based construction technology, pathways for broader market developments, and pathways that are supported by changes in institutions and policy.

New pathways for organising a more *sustainable* construction process:

- *Cooperation of the value chains in the construction process:* The construction process is traditionally divided into three main stages: an early stage which includes planning and designing, the main construction stage, and the operation and maintenance of the building. However, we must also include the other value chains, which ensure the access to the wooden building materials. A closer cooperation between different parts of the value chain is required. This includes the industrial production of wooden construction elements. Moreover, modules from local resources allow much faster and more effective production, with less wooden residues.
- *Transportation:* The reduction of costs concerning transport of construction materials is one of the priorities for the industry. This implies shorter distances from the sawmills to the producers and the factories, but also improved transportation infrastructure, such as forest roads and bridges that allow transportation of larger volumes and access to containers.
- *Sustainability criteria:* The introduction of GHG accounting and Life Cycle Assessments allows builders to identify the key areas for necessary improvements: necessary efficiency gains, transport costs and emissions, waste reduction, as well as reuse and recycling.

New pathways for more sustainable and wood-based construction *technology*:

- *New technologies for timber constructions:* Cross-laminated timber (CLT), often combined with Glued laminated wood (Gulam) is used for building larger wooden constructions which replace steel and concrete solutions. The use of CLT was initially more common through import of material and competence from Austria. Later, own production capacity has been developed, which allows the use of local or regional timber resources, which has also lower GHG emissions.
- *Timber stud partition:* Norway has traditionally used timber stud partition for buildings up to 4 storeys, but now there is a new development: a pilot for using timber stud partition for 8 storeys buildings.
- *Hybrid materials:* Wooden construction elements are combined with other low-carbon construction materials, such as low carbon concrete or steel, recycled aluminium or glass, to deploy wood where it has the most advantageous characteristics, such as low weight and easy add-ons.
- *Retrofitting & superstructures:* Besides constructing new buildings in wood, a new market segment has received attention: (1) retrofitting of existing buildings with the help of prefabricated wooden façade elements, which allows a faster and less costly retrofitting process; (2) construction of wooden superstructures on top of existing apartment buildings and adding a lift house which better utilises the building ground and existing infrastructure in cities.
- *Prefabrication:* By automating the prefabrication processes, the construction process at the building site can be much shorter. Moreover, the working environment at the building site, especially regarding noise and dust, will improve dramatically. Wooden residues minimise, and costs go down.
- *Digitalisation:* A stronger focus on documentation of characteristics of each construction element is essential to facilitate the reuse of construction elements in future disassembly of buildings, which also will allow the reuse of these materials. Moreover, it will benefit from the digitalisation of the whole value chain, from forestry to sawmills, to producers of

construction materials, to the planning and design stage, to the construction process, and finally to the operation and maintenance stage. The use of digital twins allows a much better coordination in these processes.

New pathways for *broader market development:*

- *Niche development from show cases to individual one-off buildings:* In the first years, wooden construction concentrated on interesting show cases, such as the famous buildings for the Winter Olympic games in Lillehammer 1997 or the Gardermoen Airport in Oslo. However, it is difficult to move from huge show cases to a broad deployment of wooden construction, to achieve an upscaling of this niche. Therefore, an important step in that direction was the construction of individual one-off buildings, such as schools, kindergartens, and health care homes, commissioned by municipalities. This allowed entrepreneurs to learn and build collaboration networks. Many of these projects, such as schools etc., had repetitive characteristics, which allowed economic gains and reusing existing solutions.
- *Niche upscaling towards a mass market:* An important pathway has been the construction of residential buildings for students. These were not just one-off buildings, and were based on collaboration with student welfare organisations, which commissioned many buildings, such as in Ås, Trondheim, Fredrikstad and Oslo. A further step has been to move into the private market for industrial buildings in wood, being it office buildings or factories.
- *Cooperation with housing associations:* While the cooperation with municipalities targets the construction of individual one-off buildings, the cooperation with housing associations opens a market for larger volumes. Housing associations often have many buildings which need to be renovated and retrofitted (new facades). Many of the newer buildings have flat roofs, which allow extensions on the roof in light-weight wooden construction. Combined with added lift houses, this allows for building more flats that the elderly people can stay in (due to the new lifts). Moreover, this lowers the costs for the residents.
- *Export market:* The sale of Norwegian wooden construction materials is still concentrated in the domestic market, and the possibilities of the international market are not in focus.

New pathways for more sustainable and wood-based construction regarding *institutions and policy*:

- *Policy instruments:* Three dedicated policy instruments have provided public support for the use of wood in construction: Innovation Norway had a wood innovation programme, which also included co-funding, together with regional authorities of a national network of intermediary experts – so-called *tredrivere* – to facilitate the use of wood. The Ministry of Agriculture and Food has financed subsidies for the construction of wooden farm barns, and the Directorate for Environment has a funding instrument, Klimasats, that is supporting municipal projects in different areas of sustainability transitions. In one period there was a focus on municipal projects using CLT for schools, daily childcare, nursing homes, etc.
- *Public procurement:* The development of competence on public procurement rules in municipalities is essential to facilitate more sustainable solutions.
- *Initiatives for reuse and material recycling:* In 2021, the development of a Circular Resource Centre was started, which operates a National Knowledge Arena for reuse in the construction industry and a warehouse centre for used building materials. While this centre is for the construction industry in general, it has also been necessary to address reuse and material recycling in wood-based building and construction.
- *Regulation and standards:* The regulatory framework conditions for building with wood changed around the year 2000. According to the Planning and Building Act and technical regulations, it was allowed to build higher than three storeys. The technical regulations on the construction side have been focused on steel and concrete construction, both how they are formulated and how they are exercised. What we are seeing now is that sustainability criteria, such a LCA and CO_2 footprints, will be included into technical regulations and standards for construction materials. The European revised construction products regulation will also be effective in Norway when it is approved. This will include an assessment of construction materials regarding sustainability and documentation requirements for reused materials. This will be a driver for using wood as it has a lower footprint than other materials.

5.3 INTERMEDIARY ORGANISATIONS

Intermediary organisations have been very active in the development of these new pathways and in addressing the path dependencies and barriers discussed above. In the following we discuss the roles of different types of intermediaries in shaping the new pathways and how they generate new users and markets for wood-based construction materials. We take the new pathways, discussed above, as a starting point.

New pathways for organising a more sustainable construction process: Here we included issues related to the cooperation of the value chains in the construction process, transportation of materials, and sustainability criteria in the construction sector.
For these issues, two types of intermediaries were very active: systemic intermediaries and industry associations, a type of niche intermediary.

https://doi.org/10.52202/069179-0591

Systemic intermediaries pursue sustainability goals on a systemic level, but they do not belong to the wood construction niche. We could identify systemic intermediaries which take a more 'neutral' role concerning choice of materials, but they provide innovation arenas for experimenting with sustainable material use and architectures. Examples are the Norwegian Green Building Council, a member organisation of the building sector, and the Future Built Programme, owned by municipalities, ministries, and public agencies.
Industry associations: Treindustrien (The wood industry) for example, is an industry association for manufacturers of lumber and other wood-based building materials. This association works towards the national government, regional authorities, municipalities, and other public actors, through lobbyism regarding better framework conditions for wooden construction, improvements of transportation possibilities, and stricter sustainability criteria in technical regulations, standards, etc.

New pathways for more sustainable and wood-based construction technology. Here, we cover new technologies for timber construction, timber stud partition, the use of hybrid materials, retrofitting and superstructures, and automated prefabrication and digitalisation.
Regarding technological pathways, there were especially two types of niche intermediaries that were very active: cluster organisations and private niche intermediaries, in addition to the Wood innovation programme under the regime-actor Innovation Norway.
Niche intermediaries mediate between local projects, and/or at a higher level of aggregation. They are part of, and advance, the wood construction niche. *Cluster organisations*, like WoodWorks!, Norwegian Wood Cluster, and Tre på Agder (Wood in Agder), set clear goals to increase the use of wood in the construction sector and to facilitate the development and deployment of new technologies in their member firms. The cluster organisations also include research institutes, universities, and providers of vocational education and training, which develop new knowledge and a competent work force.
Private niche intermediaries are small companies, such as TreFokus, Trebruk, and Tretorget, who distribute knowledge and competence about new technology to municipalities and entrepreneurs.

New pathways for broader market development: This encompassed niche development from show cases to individual one-off buildings, niche upscaling towards a mass market and cooperation with housing associations.
Here, different types of intermediaries were very active. *Systemic intermediaries*, like Future Built, have made innovative projects more visible so that they can function as show cases.
Many *regime-based intermediaries* contributed to this market development, such as Innovation Norway, the Wood innovation programme and subsidies for the construction of farm barns under the Ministry of Agriculture and Food, and Klimasats under the Directorate for Environment. Public procurement by municipalities and other regional authorities, led to funding of sustainability projects at the municipal or county level. Two types of niche intermediaries have to be highlighted: A network of knowledge mediators financed by Innovation Norway and county authorities who support lobbying activities of an expert in each county for deploying wood, a so-called *Tredriver*. Moreover, the private niche intermediaries were decisive for starting entrepreneurial activities together with student- and housing associations.
The efforts made by these intermediaries have contributed to a better collaboration within and across the wood-based industry, such as between the forestry sector and the wooden construction sector. For example, intermediaries create learning arenas and connect actors by hosting seminars, site visits, field trips—nationally and abroad (e.g., to the Netherlands and Germany) —. as well as dissemination and communication work. They also connect companies with research groups and act as translators by assisting companies in applying for research grants.

New pathways for more sustainable and wood-based construction, regarding institutions and policy: This includes the development of dedicated policy instruments, competence for public procurement, policy for a circular economy, and regulations and standards.
Industry associations like Treindustrien have been active in lobbying for better political framework conditions, including regulations, standards, and support schemes. The network of knowledge mediators and the small private niche intermediaries were mostly active regarding the development of ordering competencies in municipalities for facilitating public procurement of wooden construction projects. Moreover, they contributed to attracting new users to create a demand for wooden construction solutions, and to support competence development—among others by working to change education institutions towards a greater focus on wood-based constructions.
For addressing the circular economy of wooden construction, there has been established a new large green platform project, SirkTre, which targets reuse and recycling of wooden construction materials. In this niche project, the Circular Resource Centre is a member, beside many other players in the sector. One of the goals is to function as a "reverse sawmill" and produce lumber again, from material-recycled wood. Lobbying for supportive policies for reuse and material recycling is a priority.

It is important to point out that, very often, the intermediaries work together: the cluster organisations cooperate with the small private niche intermediaries, the network of experts and the industry associations. Moreover, the intermediaries have close connections to the different actors in the technological innovation system around wooden construction: to knowledge providers, such as research organisations and architecture and engineering consultancies; to education institutions at different levels; to entrepreneurs, who have gained a lot of experience in wooden construction; and to

municipalities and other public builders, who have commissioned wooden buildings and can serve as a source of inspiration and competence about how to organise such processes.

6 CONCLUSIONS

The development of wooden construction depends on an interplay between technological innovation and the different actors in the innovation system, contributing to new path creation and overcoming existing path dependencies and lock-ins.

Development and deployment of new technologies for wooden construction needs to be accompanied by changed institutional conditions, regulations which require more sustainable solutions in the construction sector leading to reduced GHG emissions, reduction of waste and energy consumption, and changes in social practices of constructing. This requires competence development in all parts of the innovation system.

We mainly identified the following path dependencies, which function as barriers for new path creation: technology and material infrastructure, institutions, as well as behaviour and social practices. They are interrelated and reinforce each other, and they create social problems, such as lack of affordable dwellings in cities, high costs for energy efficiency and renovation measures, low shares of material reuse and recycling, and less flexibility to adapt dwelling spaces to new needs (for young families or for elderly people).

Intermediaries must address and break up these interlinked path dependencies and barriers for new path development.

Intermediaries evolve over time and get new roles, while older roles are taken over by other actors. Intermediaries need to broaden their horizon when lobbying for new, wood-based solutions, addressing such social problems.

When organising a *more sustainable construction process*, there were especially two types of intermediaries which were very active: systemic intermediaries and industry associations, a type of niche intermediary.

For the development of *more sustainable and wood-based construction technology*, there were especially two types of niche intermediaries which were very active: specialised cluster organisations and private niche intermediaries, in addition to the innovation programme under the regime-actor Innovation Norway.

New pathways for broader market development have been facilitated by systemic intermediaries like Future Built. Regime-based intermediaries nevertheless also contributed to this market development, such as Innovation Norway, the Wood innovation programme, and other programmes, as well as two types of niche intermediaries: a network of experts in each county, a so-called *Tredriver*, and the private niche intermediaries, who have been decisive for starting entrepreneurial activities.

The efforts made by these intermediaries have contributed to a better collaboration within and across the wood-based industry, such as between the forestry sector and the wooden construction sector. It is important to point out that very often the intermediaries work together and that the intermediaries have close connections to the different actors in the technological innovation system around wooden construction.

ACKNOWLEDGEMENT

We acknowledge funding by the Research Council of Norway for the project “Addressing climate change with innovation in the forest-based industry (Inno4Tree)” (Project number: 324167).

REFERENCES

[1] Hurmekoski, E., *How can wood construction reduce environmental degradation?* 2017, Helsinki: European Forest Institute. 11.

[2] Hurmekoski, E., R. Jonsson, and T. Nord, *Context, drivers, and future potential for wood-frame multi-story construction in Europe.* Technological Forecasting and Social Change, 2015. **99**: p. 181-196.

[3] Antikainen, R., et al., *Renewal of forest based manufacturing towards a sustainable circular bioeconomy*. Reports of the Finnish Environment Institute 2017, Helsinki: Finnish Environment Institute. 124.

[4] European Commission, *Roadmap to a Resource Efficient Europe*. 2011, European Commission: Brussels.

[5] European Commission, *Strategy for the sustainable competitiveness of the construction sector and its enterprisesStrategy for the sustainable competitiveness of the construction sector and its enterprises*. 2012, European Commission: Brussels.

[6] European Commission, *On resource efficiency opportunities in the building sector*. 2014, European Commission: Brussels.

[7] European Commission, *A sustainable Bioeconomy for Europe*. 2018, European Commission: Brussels.

[8] FAO, *Forestry for a low-carbon future: Integrating forests and wood products in climate change strategies*. FAO Forestry Paper. 2016, Rome: Food and Agriculture Organization of the United Nations.

[9] Leskinen, P., et al., *Substitution effects of wood-based products in climate change mitigation*. From Science to Policy. 2018: European Forest Institute. 27.

[10] Ramage, M.H., et al., *The wood from the trees: The use of timber in construction.* Renewable and Sustainable Energy Reviews, 2017. **68**: p. 333-359.

[11] Chaudhary, M. *Størst økning i avfall fra riving i 2020*. 2021.

[12] Gosselin, A., et al., *Collaboration Enables Innovative Timber Structure Adoption in Construction.* Buildings, 2018. **8**(12): p. 183.

[13] Nykamp, H., *A transition to green buildings in Norway.* Environmental Innovation and Societal Transitions, 2017. **24**: p. 83-93.

https://doi.org/10.52202/069179-0591

[14] Buck, D., et al., *Comparison of Different Assembling Techniques Regarding Cost, Durability, and Ecology - A Survey of Multi-layer Wooden Panel Assembly Load-Bearing Construction Elements.* BioResources, 2015. **10**(4): p. 19.

[15] Rose, C., et al., *Cross-Laminated Secondary Timber: Experimental Testing and Modelling the Effect of Defects and Reduced Feedstock Properties.* Sustainability, 2018. **10**.

[16] Abrahamsen, R., *Mjøstårnet - Construction of an 81 m tall timber building*, in *23. Internationales Holzbau-Forum IHF 2017*. 2017. p. 13.

[17] Lazarevic, D., P. Kautto, and R. Antikainen, *Finland's wood-frame multi-storey construction innovation system: Analysing motors of creative destruction.* Forest Policy and Economics, 2020. **110**: p. 101861.

[18] Klitkou, A., et al., *The role of lock-in mechanisms in transition processes: The case of energy for road transport.* Environmental Innovation and Societal Transitions, 2015. **16**: p. 22-37.

[19] Seto, K.C., et al., *Carbon Lock-In: Types, Causes, and Policy Implications.* Annual Review of Environment and Resources, 2016. **41**(1): p. 425-452.

[20] Arthur, W.B., *Increasing returns and path dependence in the economy*. 1994, Ann Arbor, Mich.: University of Michigan Press. XX, 201 s. : ill.

[21] Unruh, G.C., *Understanding Carbon Lock-in.* Energy Policy, 2000. **28**: p. 817-830.

[22] Unruh, G.C., *Escaping carbon lock-in.* Energy Policy, 2002. **30**(4): p. 317-325.

[23] Sandén, B.A. and C. Azar, *Near-term technology policies for long-term climate targets economy wide versus technology specific approaches.* Energy Policy, 2005. **33**(12): p. 1557-1576.

[24] Frantzeskaki, N. and D. Loorbach, *Towards governing infrasystem transitions: reinforcing lock-in or facilitating change?* Technological Forecasting and Social Change, 2010. **77**(8): p. 1292-1301.

[25] Freeman, C., *Innovation, Changes of Techno-Economic Paradigm and Biological Analogies in Economics.* Revue économique, 1991. **42**(2): p. 211-231.

[26] Voß, J.-P. and R. Kemp, *Sustainability and reflexive governance: introduction*, in *Reflexive Governance for Sustainable Development*, J.-P. Voß, D. Bauknecht, and R. Kemp, Editors. 2006, Edward Elgar: Cheltenham. p. 3-28.

[27] Shove, E., M. Pantzar, and M. Watson, *The dynamics of social practice: everyday life and how it changes*. Social practice. 2012, Los Angeles: Sage. vii, 191.

[28] Klitkou, A., et al., *The interconnected dynamics of social practices and their implications for transformative change: A review.* Sustainable Production and Consumption, 2022. **31**(May): p. 603-614.

[29] Kemp, R. and A. Rip, *Constructing transitions paths through the management of niches*, in *Path dependence and path creation*, R. Garud and P. Karnøe, Editors. 2001, Lawrence Erlbaum Associates: Mahwah, New Jersey. p. 269-299.

[30] Simmie, J., *Path Dependence and New Technological Path Creation in the Danish Wind Power Industry.* European Planning Studies, 2012. **20**(5): p. 753-772.

[31] Garud, R. and P. Karnøe, *Path creation as a process of mindful deviation*, in *Path dependence and path creation*, R. Garud and P. Karnøe, Editors. 2001, Lawrence Erlbaum Associates: Mahwah, New Jersey. p. 1-38.

[32] Kivimaa, P., et al., *Towards a typology of intermediaries in sustainability transitions: A systematic review and a research agenda.* Research Policy, 2019. **48**(4): p. 1062-1075.

[33] Kivimaa, P., et al., *Experiments in climate governance – A systematic review of research on energy and built environment transitions.* Journal of Cleaner Production, 2017. **169**: p. 17-29.

[34] Kivimaa, P., et al., *Passing the baton: How intermediaries advance sustainability transitions in different phases.* Environmental Innovation and Societal Transitions, 2019. **31**: p. 110-125.

[35] Kanda, W., et al., *A technological innovation systems approach to analyse the roles of intermediaries in eco-innovation.* Journal of Cleaner Production, 2019. **227**: p. 1136-1148.

[36] Kant, M. and W. Kanda, *Innovation intermediaries: What does it take to survive over time?* Journal of Cleaner Production, 2019. **229**: p. 911-930.

[37] Mignon, I. and W. Kanda, *A typology of intermediary organizations and their impact on sustainability transition policies.* Environmental Innovation and Societal Transitions, 2018. **29**: p. 100-113.

[38] Van Lente, H., et al., *Roles of systemic intermediaries in tranisition processes.* International Journal of Innovation Management, 2003. **7**(3): p. 1-33.

[39] van Lente, H., W.P.C. Boon, and L. Klerkx, *Positioning of systemic intermediaries in sustainability transitions: Between storylines and speech acts.* Environmental Innovation and Societal Transitions, 2020. **36**: p. 485-497.

[40] Kanda, W., et al., *Conceptualising the systemic activities of intermediaries in sustainability transitions.* Environmental Innovation and Societal Transitions, 2020. **36**: p. 449-465.

[41] Vihemäki, H., A. Toppinen, and R. Toivonen, *Intermediaries to accelerate the diffusion of wooden multi-storey construction in Finland.* Environmental Innovation and Societal Transitions, 2020. **36**: p. 433-448.

World Conference on Timber Engineering Oslo 2023

STATUS QUO OF AUSTRIAN TIMBER CONSTRUCTION SECTOR

Aída Santana-Sosa[1,2], Martin Aichholzer[1], Elena Mitrenova[1], Iva Kovacic[2]

ABSTRACT: The application of industrialized timber in large-volume buildings is considered as one main strategy promoting sustainability in the construction sector. Austrian timber construction ecosystem is mainly conformed by small and medium sized enterprises (SMEs) that are mostly limited to single and multiple housing projects and it is rarely represented in multi-storey buildings. Within a five days' workshop, 19 experts from research and practice including SMEs, discussed the challenges and potentials, and specially the implication of SMEs, by the completion of those, exchanging experiences and expertise. The workshop was inductive coded looking for factors affecting the design and construction process, in which seven categories were defined containing 33 overall concepts with 105 factors embedded. Further, a SWOT analysis was conducted, in which over half of all factors are conflicts, mostly related to the coordination of the team along the process, mainly caused by the lack of an integrated design approach. Highly positive rated are those aspects related to greater levels of prefabrication, while general rising awareness together with political support represent relevant opportunities, and common prejudices a threat. This overview of the sector may help further research to develop strategies focused on handling internal factors to exploit opportunities and minimize threats.

KEYWORDS: Multi-storey timber buildings, off-site construction, design and construction process, SWOT Analysis

1 INTRODUCTION

Construction sector has been performing widely unsatisfactorily along decades. While productivity [1], digitalization, profitability and customer satisfaction remain low, risks, claims, fragmentation, insolvencies, and budget, and time overruns arise [2]. Its ecological and environmental impact has become also an issue, as it is responsible for 32% of the waste generated annually [3] and the largest producer of CO_2 emissions worldwide [4], being a large part of these a result of cement production [5]. A shift in construction sector, including processes and working methods, is expected in an early future, in which the introduction of new materials and the promotion of the digitization, the industrialisation and the automation will play a major role as a response to combination of higher sustainability requirements, increased cost pressure and a general shortage of skilled workers [2]. Industrialized timber construction is seen as an attractive ecological, economic and social solution to reshape the sector and assess its significant impact, especially in terms of resource efficiency, comfort and carbon emissions together with their atmospheric concentration [6–10]. This disruptive solution is gaining interest from various stakeholders, meaning great chances to take the lead in upcoming years, but also large concerns related to the lack of experience of new entrants. Due to its multi-layered character and own value and supply chain, planning and building with timber involves different actors, approaches and expertise [11, 12], and yet there exists no common understanding about interdependences what leads to inefficient collaboration and large conflicts meaning higher costs, time overruns, tension and dissatisfaction [13]. Previous studies have shown higher concerns in the production and assembly phase of a industrialized timber construction than in the acquisition and design phase [14]. Timber construction companies in Austria are small and scattered, and the structure of the industry is very fragmented and locally organized [15]. Its traditional approaches and its average sizes lead to mostly small projects. For example in 2019, 65% of all new buildings were residential and with one or two apartments, while just 11% had three or more apartments [16]. Nevertheless, a growing trend towards multi-storey timber construction can be appreciated within the last years [17], where the involvement of small and medium-sized enterprises

[1] Aída Santana-Sosa, Competence Center for Building and Design, University of Applied Sciences Campus Wien-FH Campus Wien, 1100 Vienna, Austria, aida.santana_sosa@fh-campuswien.ac.at
Martin Aichholzer, Department for Building and Design, University of Applied Sciences Campus Wien-FH Campus Wien, 1100 Vienna, Austria, martin.aichholzer@fh-campuswien.ac.at
Elena Mitrenova, Competence Center for Building and Design, University of Applied Sciences Campus Wien-FH Campus Wien, 1100 Vienna, Austria, elena.mitrenova@fh-campuswien.ac.at

[2] Aída Santana-Sosa, Doctoral candidate in Engineering Sciences: Civil Engineering, TU Wien, 1040 Wien, Austria, e11734193@student.tuwien.ac.at
Iva Kovacic, Department of Integrated Planning and Industrial Building, TU Wien, 1040 Wien, Austria, iva.kovacic@tuwien.ac.at

https://doi.org/10.52202/069179-0592

(SMEs) is very challenging. On the one hand, this small size reduces the competitiveness of those companies in the completion of large-volume residential constructions in comparison to their larger competitors on the market. On the other hand, through this regional supply chain and fragmented structure, local value is added and resilience in crises is ensured. In addition, the global monopoly positions of large companies should be reduced to the detriment of local companies in order to facilitate a social balance. This study deals with the identification and analysis of factors affecting the completion of multi-storey timber buildings, specifically from the point of view of SMEs.

2 METHODOLOGY

This explorative study was developed based on two previous projects, a series of round tables organised by *MAGK Architekten* and *ecoplus Bau.Energie.Umwelt Cluster NÖ* named *Holz.System.Bau* [18], and a multi-case qualitative analysis based on experts' interviews [14], where the main barriers against timber use in large-volume constructions were analysed and strategies were discussed. This specific workshop called *Holzbau 4.0* was developed and run by the Vienna University of Applied Sciences in cooperation with *ecoplus Bau.Energie. Umwelt Cluster NÖ,* and funded by the Austrian Agency for the promotion of research *FFG* (*Österreichische Forschungsförderungsgesellschaft*). The five days' workshop was recorded, documented and inductive coded within several iterative rounds. Additionally, a SWOT analysis was run, in which the defined codes were classified as Strengths, Weaknesses, Opportunities and Threats. Figure 1 represents the overall process of this study with its steps from data collection to analysis and findings.

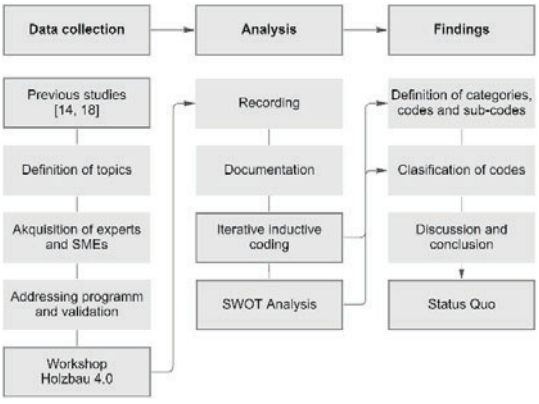

Figure 1: *Overview of the project*

2.1 DESCRIPTION OF THE WORKSHOP

The five days-workshop aimed to offer an exchange platform where to discuss the status quo of the industry with its barriers and opportunities. Once the overall topics were defined, participants were purposive sampled. Experts from science and practice including SMEs were selected to participate actively in the workshop. Several previous cooperative rounds were organized to address specific topics, goals and working methods, in alignment with the needs of all 19 participants, conformed by three researchers and seven planners with an average experience of 20 years, and nine professionals with key roles from six SMEs, including carpentry and timber components, glass construction, pluming, roofing, and lean management (Table 1).

Table 1: *Summary of participants within the workshop*

Area of expertise	N° participants
Research	3
Architectural design	5
Specialist consultants	2
SMEs employees	9

The workshop combined theoretical inputs and practical application in form of a cooperative project exercise with group discussions and reflexions, and was organized around the following five thematic blocks:

1. Team and process
2. Business models and cooperation processes
3. Systemisation and digital tools
4. Prefabrication and logistics
5. Equal opportunities

The first unit addressed a common understanding of an expected change in construction sector and its processes due to digitization and automation, exploring new ways of thinking, and establishing a common vision about the innovativeness, resilience and competitiveness of SMEs. Within the second unit, various business models and cooperation processes were explored, including legal framework and specific logistical, technical and digital aspects and requirements for large-volume timber buildings. The focus of the third unit was on systemisation, standardisation and digital tools for collaborative work. Design and production planning were compared in terms of level of information, development and detail, while several digital tools for design and production were explored, including their interfaces, working processes and information exchange. Building services and their standardization were extensively explored, together with prefabricated wall-elements and volumetric modules. The fourth unit was dedicated to production, prefabrication and logistics, where best practice examples were discussed, and methods based on Lean Management and efficient logistics were explored, together with their application to design, production and assembly. Topic of the last unit was equality and fair opportunities encompassing different social and political aspects, like funding, anti-discrimination, and laws. To conclude, feedback was collected, and a networking round offered to ease possible future cooperation.

To practically assess the acquired knowledge, participants were divided in two teams for an interdisciplinary and

cross-company teamwork to analyse two different existing multi-storey residential buildings and collaboratively develop a new planning and construction process, aligning trades, identifying interfaces and players, and optimising tasks with milestones and deliverables. Both projects were alike in terms of volume, construction and height, but different in the financing type, being one private and the other one public with their corresponding focus, process model and tendering as shown in Table 2.

***Table 2**: Description of both projects*

	Project A	**Project B**
Approach	Private	Public
Focus	Individuality	Fixed budget
Quality	High-Tech	Low-Tech
Process model	Cooperative	Traditional
Time of tendering	Irrelevant	Fixed

Besides exploring suitable cooperative planning and building systems and its intrinsic high competence level, other soft aspects like trust, willingness to work together and innovative ways of thinking were discussed.

3 FINDINGS

3.1 QUALITATIVE ANALYSIS

The five days' workshop was analysed qualitatively through an iterative process of coding and categorizing. Excerpts representing relevant factors affecting the correct and efficient design and construction of multi-storey timber buildings were referred into sub-codes and further organized into codes and overall categories. A total amount of 105 sub-codes were identified and structured into 33 codes and seven categories according to their content and relations. The distribution of categories and their codes is shown in Figure 2.

The category *team and process* is the one with the highest amount of codes with seven, followed by the categories of *product and performance*, *mind-set of the industry* and *competence and expertise* with six codes each (Figure 3). *State of the industry* has five codes and the categories with the fewest numbers of codes are *awareness* with two, and *politics and funding* with one. Attending to the sub-codes embedded in each code the relevance of the categories remains the same, being the only difference the higher amount of sub-codes by the category *state of the industry* with 15 in relation to the ones by *competence and expertise* with 13. Therefore, the same structure remains, being *team and process* the one with the highest amount of sub-codes with 25, followed by *product and performance* with 19, and *mid-set of the industry* with 17. The categories *awareness* and *politics and funding* encompass 11 and five each.

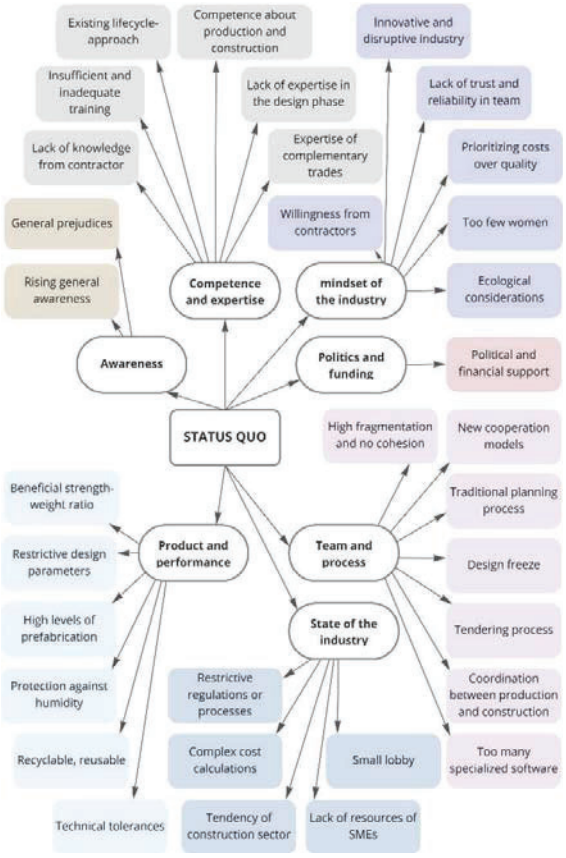

***Figure 2:** Relation of codes and categories*

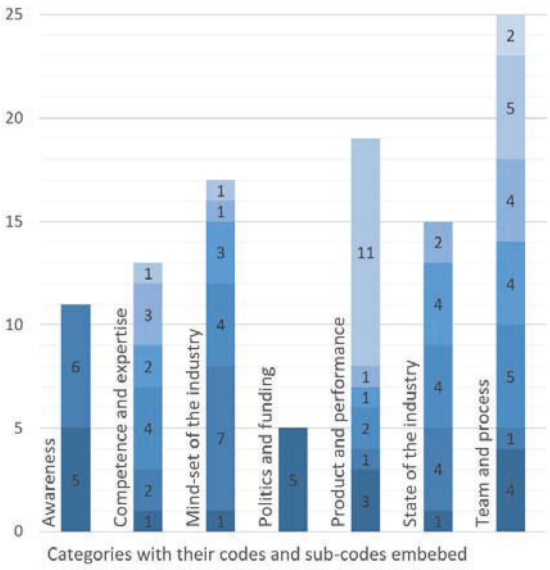

***Figure 3:** Categories with their embedded codes and sub-codes*

https://doi.org/10.52202/069179-0592

3.1.1 Awareness

This category refers to the consciousness of general society related to the capabilities and properties of timber applied to large volume construction and encompasses two codes with overall 11 sub-codes as represented in Table 3.

In common terms there exists a great deal of mistrust and scepticism towards industrialized timber constructions, based mainly on general prejudices of inadequate performance related to cost efficiency, fire protection, noise insulation, structural response and durability. Nevertheless, a changing attitude and a rising general awareness about more sustainable procedures have been recognized. The ecological and healthy properties of timber supports this shift as a response to the rising resource scarcity, the higher carbon emissions and the new social and economic requirements of the sector and society.

Table 3: *Sub-codes and codes in the category "Awareness".*

Awareness (2) (11)	
General prejudices (5)	**Aw1**
· Too expensive	
· Fast combustion	
· Not enough noise insulation	
· Lack of durability	
· Little structural resistance	
Rising general awareness (6)	**Aw2**
· End of fossil energy and materials	
· Ecological properties of timber	
· Aesthetics and comfort	
· New generation, new requirements	
· Resources scarcity	
· Shared economy incl. platforms	

3.1.2 Competence and expertise

Due to its multi-layered character, its material properties and its different value and supply chain, planning and building with timber implies specific approach and competence, which are different from those widely used within mineral constructions. Related to this issue, six codes with 13 associated sub-codes were defined and are represented in Table 4.

A common lack of knowledge and expertise was found from the side of the contractor, complementary trades and planners. Due to their little experience, contractors refuse to build with timber, while the lack of expertise of complementary trades implies higher mistakes rate on site and therefore higher coordination efforts to avoid them or minimize their impact. General architects and engineers also lack competence related to the higher complexity of large industrialized timber constructions, mainly due to insufficient and inadequate training, where little know-how is found as well in common architectural and engineering trainings, as in specialized. On the contrary, there exists a recognisable competence of manufacturers and construction companies about production and construction, and a beneficial lifecycle-oriented approach.

Table 4: *Sub-codes and codes in "Competence and expertise".*

Competence and expertise (6) (13)	
Competence about prod. and constr. (1)	**Co1**
· High competence of manufacturers and constr. companies	
Insufficient and inadequate training (2)	**Co2**
· Lack of know-how in conventional training	
· Lack of specialized trainings	
Lack of expertise in the design phase (4)	**Co3**
· Related to common planers	
· High complexity of specific software	
· Overestimation of own competence	
· Underestimation of complexity	
Existing lifecycle-approach (2)	**Co4**
· Interdisciplinary multi-layered character	
· Lifecycle costs approach	
Expertise of complementary trades (3)	**Co5**
· High mistakes rate related	
· Higher coordination effort on site	
· Lack of competence or expertise	
Lack of knowledge from contractor (1)	**Co6**
· Little knowledge and experience	

3.1.3 Mind-set of the industry

In this category, those aspects related to the attitude or way of thinking of the construction sector are referred, encompassing six codes and 17 sub-codes (Table 5).

Table 5: *Sub-codes and codes in "Mind-set of the industry".*

Mind-set of the industry (6) (17)	
Green washing (1)	**Mi1**
· Use of timber as marketing	
Innovative and disruptive industry (7)	**Mi2**
· Towards open mind-set, ready for new	
· Open-source databases (projects / network)	
· Rising number of small start-ups	
· Rising number of young experts	
· Little speculation	
· Transfer of Lean concepts	
· Rising number of independent planning eng.	
Lack of trust and reliability in team (4)	**Mi3**
· No transparency / communication	
· Lack of trust and reliability in design team	
· Lack of trust between SMEs	
· Silo thinking and lack of cooperation of SMEs	
Prioritizing costs over quality (3)	**Mi4**
· Criteria within arch. competitions	
· Criteria within tendering processes	
· Conventional investments' criteria	
Too few women (1)	**Mi5**
· Too few and with no key roles	
Willingness from contractors (1)	**Mi6**
· Rising willingness	

Although the rising willingness of contractors to build with timber is remarkable, conventional investment criteria based primarily on prioritising cost over environmental or health benefits make its actual implementation difficult, as it occurs within architectural competitions and tendering processes. At the same time, the misuse of timber as "green washing" represents a threat that must be kept under control. Focusing directly on the timber industry, its innovative character was highlighted, with the transfer of concepts from other industries as well as disruptive start-ups, open-source platforms, young experts and independent planning engineers playing a role, but in which women are too rare and with no key positions, and a general lack of reliability between players is found.

3.1.4 Politics and funding

Only one code with five sub-codes comprehends this category, where current topics related to political and financial support were addressed (Table 6).

The great environmental impact of construction sector has led to the development of several political initiatives to promote and accelerate a shift from a mineral-based and resource-intensive sector towards a bio-based and resource-saving one, including circular economy and re-densification as a reaction of current shortage of urban space and resources, with timber playing an important role. Existing European initiatives to promote sustainable building methods were discussed as examples for their application in further countries, including the French government's requirement to use at least 50% wood and other bio-based materials in all new public buildings [19]. Additionally, carbon fees and financial support for circular bio-based constructions help to minimise the use of carbon intensive materials.

Table 6: *Sub-codes and codes in "Politics and funding".*

Politics and funding (1) (5)	
Political and financial support (5)	**Po1**
· Carbon (CO_2) fees	
· Financing of bio-based construction	
· Reinforcement of re-densification	
· Fix % of timber in public financed projects	
· Rising awareness towards circular economy	

3.1.5 Product and performance

This category contains the higher amount of codes with six and sub-codes with 19 (Table 7) after the category *team and process*, and refers to the characteristics of timber as construction material.

Recyclability was highlighted as highly advantageous, as was the strength-to-weight ratio, which allows great degrees of prefabrication and therefore higher material efficiency and quality due to industrialised production processes, reliable stock-keeping, cost and time calculation, as well as shorter overall project time due to optimised assembly work on site with less coordination efforts and parallel work in the factory. Further benefits of prefabrication include the construction of mock-ups to run different tests and the possibility of tracking the whole supply and production chain. At the same time, specific parameters related to production, transport, assembly and structural performance influence the design. Particular attention must be paid to tolerances to other materials and moisture protection, especially on the construction site and for building elements, but also when planning the building services and the façade.

Table 7: *Sub-codes and codes in "Product and performance".*

Product and performance (6) (19)	
Protection against humidity (3)	**Pr1**
· Complex planning of building services	
· Protection of the façade	
· Protection of building elements and site	
Recyclable, reusable (1)	**Pr2**
· Recyclable, reusable	
Restrictive design parameters (2)	**Pr3**
· Raster (uneconomical free forms)	
· Transport requirements	
Technical tolerances (1)	**Pr4**
· Between concrete and timber	
Beneficial strength-weight ratio (1)	**Pr5**
· Beneficial strength-weight ratio	
High levels of prefabrication (11)	**Pr6**
· Higher production quality	
· High industrialized production	
· Material efficiency (excl. CLT)	
· Mock-up (simulation and technical proof)	
· Reliable cost estimations after tendering	
· Reliable stock planning	
· Reliable time estimation	
· Parallel work on-site and in the factory	
· Tracking (RFID / QR-Code)	
· Assembly site (shorter construction time)	
· Less trades on site (less coordination)	

3.1.6 State of the industry

Aspects related to the current situation of the industry, including its capacities and developments, are assigned to this category, which encompasses five codes and 15 sub-codes as represented in Table 8.

In general, there are restrictive or inadequate regulations or procedures that make the use of timber difficult, especially with regard to fire protection or maximal height, and their different local specifications, but also the material-neutral character of most architectural competitions and the required technical proofs for specific construction elements and connections, before and after tendering. One way to force the needed adjustment of those is seen in the move of the construction sector towards a digitally connected, product-based approach, in which timber can play a main role due to its increasingly digital and industrialised manufacturing. Nevertheless,

https://doi.org/10.52202/069179-0592

the timber sector has a small lobby with little influence on policies and a general low willingness of decision-makers to build with timber, partly due to the higher complex cost estimation before tendering and a lack of planners and reference projects, as well as an own timber oriented network. Also at the construction side, very few companies can act as general or total constructors and accomplish large timber constructions, as the ecosystem consists mainly of labour-overloaded SMEs with inadequate infrastructure and low financial strength and bank confidence.

Table 8: *Sub-codes and codes in "State of the industry".*

State of the industry (5) (15)	
Complex cost calculations (1)	**St1**
· Complex and not standardized	
Restrictive regulations or processes (4)	**St2**
· Material neutral arch. competitions · Technical proof of each solution · Restrictive regulations (fire, height…) · Lack of common standards (fire, noise…)	
Small lobby (4)	**St3**
· Acquisition of projects through own network · Small pool of partners · Lack of influence in policies · Little predisposition of decision-makers	
Lack of resources of SMEs (4)	**St4**
· Lack of financial capacity · Lack of infrastructure · Too few companies as general or total constr. · Resistance to adaptation (overloaded)	
Tendency of construction sector (2)	**St5**
· Towards product-based construction · Towards industry 4.0 (Smart/Virtual Factory)	

3.1.7 Team and process

This category has the highest number of both, codes with seven and sub-codes with 25 (Table 9), and includes aspects related to the coordination of stakeholders within design and construction along the course of a project.

The small and fragmented structure of SMEs limits cohesion due to locally organised logistics and own internal systems, resulting in an overwhelming repertoire of solutions that cannot be combined, and makes cooperation difficult, for which they often have to work as sub-constructor. The traditional linear planning process separates design and construction and therefore limits the inclusion of timber expertise in early design stages, including designers, manufacturers and suppliers. This results in complex and elaborate tendering processes with few bids, where details and joints have to be adapted, leading to an unnecessarily higher design workload forehand and extra redesign efforts after the tender. This planning process also complicates an interdisciplinary approach and the involvement of other disciplines such as building services, which reduces the required greater definition for the correct application of prefabrication. Several international cooperation models were discussed as examples of how to overcome this separation, which should be digitally supported, for what there are still too many incompatible specific software on the market. Another aspect to take into account is the need for a design freeze, where no late decisions or accompanying planning are possible, and therefore, an early inclusion of users' wishes is necessary. After the design freeze and tenders, the production line and construction site with their specific suppliers, capacities and delivery times must be coordinated including the combination of different elements, their transport and store logistics.

Table 9: *Sub-codes and codes in "Team and process".*

Team and process (7) (25)	
High fragmentation and no cohesion (4)	**Te1**
· Close systems and platforms (logistics) · Too many possible solutions · Lack of combination of 2D and 3D prefabrication · Traditional construction process (sub-constructor)	
New cooperation models (1)	**Te2**
· Alliances (UK, USA and Canada)	
Traditional planning process (5)	**Te3**
· No interdisciplinary approach · High influence of financing type to the process · Late inclusion of timber competence in design · Lack of prefabrication of building services · No inclusion of manufacturers and suppliers in the design (detailing)	
Design freeze (4)	**Te4**
· Early involvement of end-user (wishes, goals) · Late decisions (end-users, contractor, planners…) · Earlier higher definition · No accompanying planning possible	
Tendering process (4)	**Te5**
· Complex and elaborate tendering · Redesign after tendering (in-house systems) · Over-processing (interface between arch. to prod.) · Reduced bids, higher resources (redesign)	
Coord. between prod. and constr. (5)	**Te6**
· Higher logistics related to transport · Store capacity and time (logistics) · Different delivery times · Coordination between timber and concrete constr. · Coordination between prod. and constr. capacity	
Too many specialized software (2)	**Te7**
· Incompatibility between software · Open BIM still works like file transfers	

3.2 SWOT ANALYSIS

After coding and categorizing all identified factors, a SWOT analysis was carried out, checking that the sub-codes were also related to the character of the labelled code and ensuring coherence. Figure 4 represents all factors characterized as strengths, weaknesses, opportunities and threats, including codes and sub-codes.

Strengths and weaknesses refer to positive and negative internal aspects respectively. In contrast, opportunities and threats picture external factors that affect positively and negatively each. The amount of global internal aspects (strengths and weaknesses) is four times higher than the external ones (opportunities and threats). Analysing the proportion of positive and negative factors, the sector is represented with a two times higher amount of negative aspects (including weaknesses and threats), than overall positive factors (strengths and opportunities). Figure 4 represents the distribution of all codes and embedded sub-codes according to their character. Weaknesses embody over half of all factors, while strengths only around 1/5 of all factors, and opportunities and threats 1/6 and 1/17 each. That means that the sector is highly aware about its own issues and should develop strategies and set objectives to exploit own strengths and address own weaknesses with its current resources and capabilities, since its control over internal factors is higher than over external ones. These last ones can be influenced or at least anticipated, in order to avoid or minimize their impact, or to take advantage from them, but not fully controlled. All strengths, weaknesses, opportunities and threats are described in detail in the following sections.

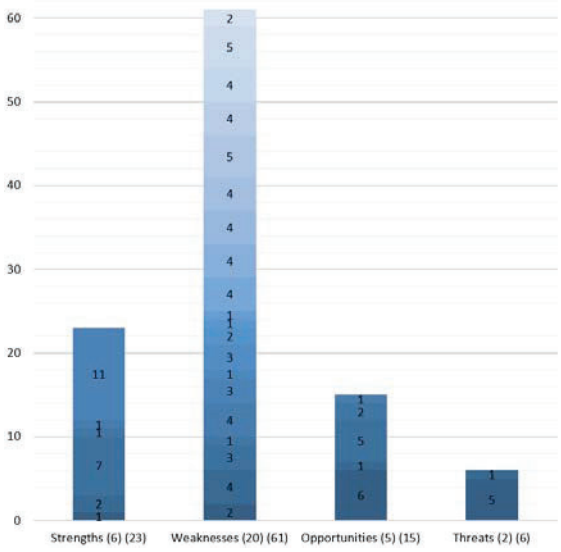

Figure 4: *Summary of all codes and their embedded sub-codes classified according to the SWOT analysis.*

3.2.1 Strengths

Table 10 shows a summary of all strengths, including their sub-codes, ranging from one to 11, with an average of 3.8, and representing around 1/5 of all factors with six codes and 23 sub-codes.

The high expertise about production and construction from manufacturers and construction companies together with the existing lifecycle-approach of the industry represent two strengths regarding *competence and expertise*, what ensure an efficient and effective erection of large timber constructions. Related to the *mind-set of the industry*, its innovative and disruptive character is a positive and significant factor with seven sub-codes that supports relevant improvement potential, while the recyclability and beneficial strength-to-weight ratio of timber represent two strengths related to the *product and performance*. Its consequent higher workability and greater prefabrication levels have the highest number of sub-codes with 11, being therefore the most discussed factor and the best-rated strength.

Table 10: *Codes identified as Strengths.*

Strengths (6) (23)	
Co1	Competence about prod. and const. (1)
Co4	Existing lifecycle-approach of the industry (2)
Mi2	Innovative and disruptive industry (7)
Pr2	Recyclable, reusable (1)
Pr5	Beneficial strength-weight ratio (1)
Pr6	High levels of prefabrication (11)

3.2.2 Weaknesses

Weaknesses encompass over half of all identified factors with 20 codes and 61 sub-codes ranging between one and five with an average of 3.3 (Table 11).

One of the most relevant weaknesses is the traditional linear planning process, which together with the lack of expertise in the design phase and reliability within the team, caused by inadequate specific training, constrain the right definition of industrialized constructions and their required design freeze. By separating design and construction, an integrated design is impracticable, where the amount of incompatible specialized software is also a problem. Mineral-oriented regulations, which have not been adapted to industrialised constructions mainly due to the small lobby of the sector, limit an earlier and correct assessment of timber buildings. Further, the high fragmentation and lack of cohesion of the industry make tendering processes complicated with complex cost calculations, fewer offers and re-design efforts, where also the prioritizing of cheapest offers over quality plays a negative role. Another major conflict is the coordination between production and construction, needing higher logistics, which may be caused by the lack of resources and infrastructure of SMEs. Although prefabrication was the most highly rated strength, the specific design parameters related to material properties and production and transport measures, and the consideration of technical tolerances to other materials are disadvantageous. Protection of the elements and the site from rain and moisture, together with increased coordination efforts on site due to the lack of experience of the complementary trades, represent further disadvantages.

https://doi.org/10.52202/069179-0592

Table 11: *Codes identified as Weaknesses.*

Weaknesses (20) (61)	
Co2	Insufficient and inadequate training (2)
Co3	Lack of expertise in the design phase (4)
Co5	Expertise of complementary trades (3)
Co6	Lack of knowledge from contractor (1)
Mi3	Lack of trust and reliability in team (4)
Mi4	Prioritizing costs over quality (3)
Mi5	Too few women (1)
Pr1	Protection against humidity (3)
Pr3	Restrictive design parameters (2)
Pr4	Technical tolerances (1)
St1	Complex cost calculations (1)
St2	Restrictive regulations or processes (4)
St3	Small lobby (4)
St4	Lack of resources of SMEs (4)
Te1	High fragmentation and lack of cohesion (4)
Te3	Traditional planning process (5)
Te4	Design freeze (4)
Te5	Tendering process (4)
Te6	Coordination between prod. and constr. (5)
Te7	Too many specialized software (2)

3.2.3 Opportunities

The five opportunities with their 15 sub-codes are shown in Table 12 with an average of 3.0., and representing 1/6 of all factors.

The main opportunity is the general increase in awareness, which can expand the collective pressure to accelerate the sector's shift towards more sustainable strategies that reduce embodied carbon and store carbon in buildings while forests sequester it. Political and financial support is seen as a major opportunity to support this transformation by promoting bio-based solutions. The tendency of construction sector from design-oriented to product-oriented is also considered as a chance to promote prefabrication, what together with a perceived higher willingness of contractors and the implementation of new cooperation models represent relevant opportunities for the right design and construction assessment of large timber constructions.

Table 12: *Codes identified as Opportunities.*

Opportunities (5) (15)	
Aw2	Rising general awareness (6)
Mi6	Willingness from contractors (1)
Po1	Political and financial support (5)
St5	Tendency of construction sector (2)
Te2	New cooperation models (1)

3.2.4 Threats

Threats summarize the fewest amount of factors with only two codes and six sub-codes, as shown in Table 13, and representing around 1/17 of the total discussion.

Common prejudices like insufficient fire protection or noise insulation represent the most threatening aspect that affect the wider implementation of timber in large constructions with five embedded sub-codes, where a better communication of its benefits could help. At the same time, its misuse as the so-called green washing could be enormously disadvantageous, and therefore should be avoided and coherently implemented.

Table 13: *Codes identified as Threats.*

Threats (2) (6)	
Aw1	General prejudices (5)
Mi1	Green washing (1)

4 DISCUSSION

Locating all strengths, weaknesses, opportunities and threats in their corresponding categories, an overview of the status quo of the timber sector with its positive and negative factors is shown in Figure 5.

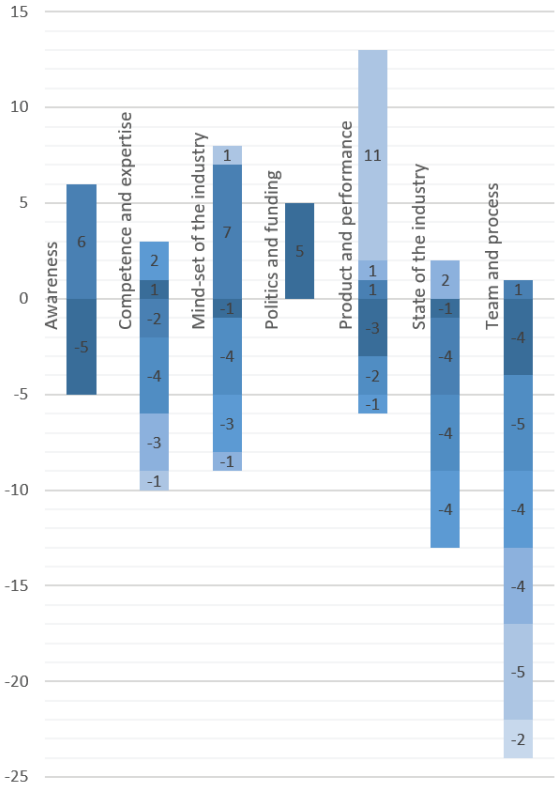

Figure 5: *Positive and negative aspects related to their categories*

Team and process, *product and performance* and *mind-set of the industry* were the most discussed categories with the highest number of codes and sub-codes as shown in Figure 3. *Team and process* account the greatest number of both codes and sub-codes with seven and 25, being all

of them except one classified as weaknesses what makes it the most conflictive category. Only the application of new cooperation models is seen as an opportunity to overcome all the weaknesses in this category, which are mainly caused by the traditional lineal and fragmented planning process with its separation of disciplines constraining a coordinated and cooperative working method with a design freeze and making tendering processes complicated.

Contrary, the second most discussed category, *product and performance*, is the one with the highest amount of strengths with three codes and 13 sub-codes which encompass aspects related to the recyclability and workability of timber and its associated higher levels of prefabrication. At the same time, three codes with six sub-codes were classified as weaknesses, which relate to the restrictive design parameters due to off-site construction and their correlated technical tolerances to other materials and the necessity of rain and moisture protection of the elements and the site.

Mind-set of the industry may be the most controversial category, being the third most discussed and sharing equally positive and negative sub-codes. Its innovative and disruptive character is seen as a great strength with seven sub-codes that could help against weaknesses by increasing trust in the team, and fostering gender equality, as well as rewards based on quality rather than on the cheapest offer. Further, a perceived increase in the willingness of contractors to build with timber is seen as a great opportunity to implement its use, but in a coherent way and no as green washing, what is considered a threat.

State of the industry is the second most conflictive category after *team and process*, where only one code with two sub-codes are classified as opportunities, and four codes with 13 sub-codes as weaknesses. Many regulations are not aligned with industrialized construction, which limit common standards and increase complexity, making the sector unattractive, which therefore consists on few overburdened experts lacking resources and infrastructure. The tendency of the sector from a design-based and labour-intensive construction site towards a product-based assembly site is seen as a chance to force the required adjustments and ease the completion of industrialized large timber constructions.

The third most conflictive category is *competence and expertise*, where two codes with three sub-codes are rated as strengths, while four codes with 10 sub-codes as weaknesses. There exists a lack of adequate specific training in architectural and engineering degrees, leading to very few competent designers or rather little expertise in design, and conflicts at the interface with construction. Parallel, complementary trades lack of experience causing greater coordination efforts on site due to higher risks. On the contrary, construction companies and manufacturers have remarkable knowledge regarding production and construction that should be exploited and transferred, together with the holistic design approach of experts covering the lifecycle of buildings and materials.

The category *awareness* encompasses equal number of codes and sub-codes classified as opportunities and threats. The rising general awareness about reducing carbon emissions and using more sustainable materials should be exploited, while general prejudices minimized.

The least discussed but most highly rated category is *politic and funding*, since its single code with five sub-codes are classified as opportunities. This category covers policy and financial support to move from lineal constructions with carbon-intensive materials to circular buildings with bio-based materials.

5 CONCLUSIONS

A wider use of timber within large-volume construction is seen as a disruptive ecological, economic and social solution to mitigate the great environmental impact of construction sector, while increasing wellbeing, productivity and promoting circular economy. On the one hand, its bio-based nature reduces carbon emissions, absorbs it from the atmosphere and stores it in the long term, while on the other hand, its renewable character and beneficial strength-to-weight ratio alleviates the scarcity of resources and the lack of urban space respectively. It also promotes higher productivity and resource efficiency thanks to its greater levels of prefabrication and advanced industrial production logistics. These characteristics imply different actors, processes and expertise than for mineral constructions, leading to a multitude of errors, inefficiencies and misunderstandings. This study takes a close look to the factors affecting the right definition and completion of large-volume timber constructions with a special focus on the production and construction side by implying SMEs with their expertise and experience. A five days' workshop was organized with 19 experts from science and practice including SMEs employees with key roles, where challenges and chances of their implication in the completion of multi-story timber buildings were discussed. The explorative study was inductive coded, where 105 factors were identified and labelled into 33 more generic concepts and organized into seven categories. Further, a SWOT analysis was run, in which the recognized strengths, weaknesses, opportunities and threats were located in their corresponding categories. The coordination of the team along the process to achieve an integrated design, which supports the right assessment of prefabrication, represents a major conflict, while prefabrication itself with their corresponding benefits is considered the greatest strength of the sector. Cooperation models supported by the tendency of construction sector towards a product-based approach are seen as opportunities to overcome this prominent barrier and exploit this strength. A general rising awareness together

https://doi.org/10.52202/069179-0592

with political support to move away from carbon intensive materials represent another relevant opportunity, while common prejudices related to insufficient fire protection constitute a main threat. Further research may use this overview of the status quo of the sector to develop strategies and set objectives, in which internal strengths can be used to exploit external opportunities (SO strategies), as well as to avoid or minimize the impact of external threats (ST strategies). At the same time, internal weaknesses can be overcome by exploiting external opportunities (WO strategies) while minimizing external threats (WT strategies).

ACKNOWLEDGEMENT

Authors want to express their gratitude to all contributors for their encouragement in seeking for sustainability. Special thanks to the Austrian Agency for the promotion of research "FFG" (*Österreichische Forschungs-förderungsgesellschaft*) for funding this project (Project number 884233).

REFERENCES

[1] E. Allmon, C. T. Haas, J. D. Borcherding, and P. M. Goodrum, "U.S. Construction Labor Productivity Trends, 1970–1998," *J. Constr. Eng. Manage.*, vol. 126, no. 2, pp. 97–104, 2000, doi: 10.1061/(ASCE)0733-9364(2000)126:2(97).

[2] M. J. Ribeirinho *et al., The next normal in construction: How disruption is reshaping the world's largest ecosystem*, 2020. [Online]. Available: https://www.mckinsey.com/~/media/McKinsey/Industries/Capital%20Projects%20and%20Infrastructure/Our%20Insights/The%20next%20normal%20in%20construction/The-next-normal-in-construction.pdf

[3] E. E. European Environment Agency, *The European environment: State and outlook 2010 (SOER 2010) : material resources and waste*. Luxembourg: EUR-OP, 2011.

[4] T. Abergel, B. Dean, J. Dulac, I. Hamilton, and T. Wheeler, "GLOBAL STATUS REPORT: Towards a zero-emission, efficient, and resilient buildings and construction sector," *Global Alliance for Buildings and Construction*, 2018.

[5] M. Herczeg *et al.,* "Resource efficiency in the building sector: Final Report," May. 2014. [Online]. Available: https://environment.ec.europa.eu/system/files/2020-12/Resource%20efficiency%20in%20the%20building%20sector_0.pdf

[6] P. Cheret, Ed., *Urbaner Holzbau: Handbuch und Planungshilfe,* 1st ed. Berlin: DOM Publishers, 2013.

[7] M. Green and J. Taggart, "Introduction: Wood, sustainability and climate change," in *Tall wood buildings: Design, construction and performance*, M. Green and J. Taggart, Eds., Basel: Birkhäuser, 2017, pp. 12–19.

[8] J. Hildebrandt, N. Hagemann, and D. Thrän, "The contribution of wood-based construction materials for leveraging a low carbon building sector in europe," *Sustainable cities and society*, pp. 405–428, 2017.

[9] T. Ibn-Mohammed, R. Greenough, S. Taylor, L. Ozawa-Meida, and A. Acquaye, "Operational vs. embodied emissions in buildings—A review of current trends," *Energy and Buildings*, vol. 66, pp. 232–245, 2013, doi: 10.1016/j.enbuild.2013.07.026.

[10] F. Pomponi, J. Hart, J. H. Arehart, and B. D'Amico, "Buildings as a global carbon sink? A reality check on feasibility limits," *One Earth*, vol. 3, no. 2, pp. 157–161, 2020.

[11] B. Höfferl, *Mehrgeschossiger Wohnbau: Planen und Bauen*. Wien: proHolz Austria, 2021.

[12] W. Huss, S. Geier, F. Lattke, and M. Stieglmeier, "Planning," in *Edition Detail, Manual of multi-storey timber construction*, H. Kaufmann, S. Krötsch, and S. Winter, Eds., Munich: Detail Business Information, 2018, pp. 130–137.

[13] W. Huß and M. Stieglmeier, "leanWOOD: Buch 1, Teil A—LeanWOOD. In Herausforderungen & Motivation," München, Germany, 2017.

[14] A. Santana-Sosa and I. Kovacic, "Barriers, Opportunities and Recommendations to Enhance the Adoption of Timber within Multi-Storey Buildings in Austria," *Buildings*, vol. 12, no. 9, p. 1416, 2022, doi: 10.3390/buildings12091416.

[15] U. Oschischnig, "Holzbau: Branchendaten," WKO Statistik Österreich., Sep. 2022. [Online]. Available: http://wko.at/statistik/BranchenFV/B_107.pdf

[16] K. Schöber, H. Hama, R. Heuberger, S. Hofbauer, K. Vollmann, and M. Weinauer, *Wohnen: Zahlen, Daten und Indikatoren der Wohnstatistik*. Wien: Statistik Austria - Bundesanstalt Statistik Österreich, 2021.

[17] R. Stingl, M. L. Zukal, and A. Teischinger, *Holzbauanteil in Österreich: Statistische Erhebung von Hochbauvorhaben,* 1st ed. Wien: ProHolz Austria, Arbeitsgemeinschaft der Österreichischen Holzwirtschaft zur Förderung der Anwendung von Holz, 2011. [Online]. Available: https://permalink.obvsg.at/AC08769292

[18] A. Santana-Sosa and A. Fadai, "A holistic approach for industrializing timber construction," *IOP Conf. Ser.: Earth Environ. Sci.*, vol. 323, p. 12015, 2019, doi: 10.1088/1755-1315/323/1/012015.

[19] LADEPECHE, *Tous les bâtiments publics devront être construits à plus de 50% en bois d'ici à 2022*. France, 2020. [Online]. Available: https://www.ladepeche.fr/2020/02/05/tous-les-batiments-publics-devront-etre-construits-a-plus-de-50-en-bois-dici-a-2022,8712149.php

World Conference on Timber Engineering Oslo 2023

THE ROLE OF BOARD INTERLOCKS IN INCREASING THE USE OF WOOD IN CONSTRUCTION

Silje Marie Svartefoss[1]

ABSTRACT: This paper studies the existence of board interlocks between wood-based firms in the construction supply chain and firms in other industries and their role in enabling increased use of wood in construction. Despite recent technological developments in wood-based construction, it is still a niche within the construction market. The literature highlights two main barriers to wood-based construction: (1) lack of material expertise and (2) lack of coordination and collaboration across the supply chain. Interfirm governance structures, such as board interlocks, may constitute a path towards innovation in construction by establishing strategic partnerships. By combining resource dependence theory and dynamic capabilities, we formulate expected findings and analyse these through social network analysis and interviews with board of director's members of wood-based firms in Norway. The dataset consists of 549,449 firms. We find that most wood-based firms have board interlocks with other firms. Furthermore, these other firms are spread across industries, but most belong to industries within the construction supply chain. Additionally, the role of these board interlocks is not to secure access to material resources but to access immaterial resources, such as knowledge, expertise and skill, which contribute to the firms' dynamic capabilities and consequently their competitive advantage.

KEYWORDS: Wood, construction, board interlocks, resource dependence theory, dynamic capabilities

1 INTRODUCTION

This paper studies a specific type of interfirm governance structure, namely board interlocks or directorate interlocks, which occurs when the same person is a member of the board of directors (BoD) in two different firms [1]. More specifically we study if there exists board interlocks between wood-based firms in the construction supply chain and firms in other industries, and their role in enabling increased use of wood in construction.

There is plenty of evidence supporting the substitution effects of replacing the most common building materials with wood-based products [2–4]. New solutions have also developed, such as wood multi-storey constructions [5–7], and the focus on digitalization of the supply chain has increased [8, 9]. Still, wood-based construction is a niche in the European and global construction market [10, 11]. The literature highlights two main barriers to the increasing use of wood in construction: (1) the lack of material expertise [5, 12, 13], and (2) the lack of coordination and collaboration across the construction supply chain [10, 14, 15]. Miozzo and Dewick [16] argue that interfirm governance structures may constitute a path towards innovations in construction by establishing strategic partnerships. One specific type of interfirm governance structure is board interlocks. Previous studies of board interlocks have shown that they secure access to resources of other firms, such as materials, technology and expertise [17–19], and that they enable coordination and collaboration across the supply chain [20, 21].

Moreover, we study board interlocks through the lens of resource dependence theory and the notion of dynamic capabilities. Resource dependence theory allows us to understand why and how organisations, such as wood-based firms, may establish relations to their external environment and, to some extent, the role of such relations. The notion of dynamic capabilities allows us to further elaborate the role of such relations, especially it's role within specific organisations, such as a wood-based firms. These allow us to formulate expectations for an empirical analysis of registry data, using social network analysis (SNA) and analysis of interview data.

2 LITERATURE REVIEW

In this section we review the literature on the use of wood in construction and main barriers to increasing the use of in construction, which forms the basis for our research question. The construction sector has a considerable economic and social importance and is a sector with major environmental impact. If we include the whole lifecycle of buildings, the global construction and building sector stands for 42% of total energy consumption, 35% of total greenhouse gas emissions, 50% of extracted materials and 30% of water consumption [2]. Improving the resource efficiency and sustainability in the building sector has thus become an important climate policy goal in the EU and in the Nordic countries [22–24]. In this context, an increased use of wood is seen as having large potential as a substitute for more energy intensive and non-renewable

[1] Silje Marie Svartefoss, Nordic Institute for studies of Innovation, Research and Education, silje.marie.svartefoss@nifu.no.

https://doi.org/10.52202/069179-0593

materials [25]. There is plenty of evidence supporting the substitution effects of replacing the most common building materials with wood-based products [2–4]. Studies on the mitigation potential of wood use in buildings and furnishing have shown that wood products have lower greenhouse gas emissions than the alternatives, considering the complete life cycle of the product [26]. It is also superior to common construction materials, such as concrete and steel, when considering all performance indicators [27]. Increasing the use of wood in construction is also important because it enables a transition to the circular economy through recycling [28].

Previous literature about the sustainability transition of the construction sector in general has targeted low-energy houses or passive houses [29], while the literature on the wooden construction industry has been mainly technical and focused on qualities of materials and assembling techniques [25, 30–32] or on specific projects [33, 34]. However, in recent years, a body of literature has developed concerning the role of wood multi-storey constructions (WMCs) in the sustainability transition of the construction sector, as the need for such a transition has become increasingly apparent. Research on new solutions, such as designs using cross laminated timber (CLT) or glulam, has developed [5–7]. In addition, there has been an increased focus on digitalization of the supply chain [8]. Even though wood-based construction is gaining momentum [35], it is still a niche in the European and global construction markets and so there is a potential for expansion beyond the niche [10, 11].

The literature highlights several barriers to the increased use of wood in construction and lack of material expertise among actors in the supply chain (e.g. consultants, architects, construction engineers and contractors) has previously been highlighted as one of the main barriers [36]. Gosselin et al. [12] further confirmed this finding in a review of scientific literature and major construction projects that used wood. More recently, an interview study in Finland concluded that the lack of construction expertise was considered one of the major obstacles [5]. Santana-Sosa and Kovacic [13], in their study based on a literature review and expert interviews, also highlighted the lack of material expertise as a barrier.

However, this is not the only barrier. Mlecnik [37] showed how the project-based approach may hinder innovation within the construction sector, and how enhanced coordinated collaboration may enable better conditions for innovation. Gosselin et al. [38] studied fifteen wooden construction projects in nine different countries, using a mixed methods approach. They showed how the increased use of wood is obstructed by the complexity of the supply chain relationship, and that partnerships along construction supply chains rarely reach outside the project level. A more recent study by Gosselin et al. [15] further supports the need for collaboration and tighter relations along the supply chain. Furthermore, Santana-Sosa and Kovacic [13] recommend that experts on wood construction should be included in the early stages of the design phase to avoid re-design, cost, and time overruns. Gharaibeh et al. [14] present a similar finding when studying the implementation of Building Information Modelling (BIM) in wood construction projects. Finally, the review by Jussila et al. [10] on WMCs market development calls for more research on forms of collaboration within the construction supply chain.

The outlined barriers to the increased use of wood in construction call for further research on this issue. Miozzo and Dewick [16] argue that interfirm governance structures can constitute a path towards innovations in construction, such as applying new materials or products based on new materials, by establishing strategic partnerships. A specific type of interfirm governance structures are board interlocks or directorate interlocks, which occurs when the same person is a member of the board of directors (BoD) of two different firms [1]. Studies have shown that board interlocks secure access to resources from other firms, such as materials, technology, expertise and information [17–19, 39]. Palmer [21] has also shown that multiple board interlocks increase the likelihood of collaboration through joint ventures. Gulati and Westphal [20] also found that board interlocks may be influential in forming strategic alliances, which enables collaboration, depending on the context of the board interlocks. Board interlock may also positively influence firms' innovation performance [40–42].

Drawing on this literature we formulate the following research question: *To what extent do board interlocks exist between wood-based firms and firms in other industries, and what role do they have in enabling increased use of wood in construction?*

3 THEORETICAL FRAMEWORK

The theoretical framework for this paper is draws on resource dependence theory and the notion of dynamic capabilities. Resource dependence theory allows us to understand why and how organisations, such as wood-based firms, may establish relations with their external environment and, to some extent, the role of such relations. The notion of dynamic capabilities allows us to elaborate the role of such relations further, especially their role within a specific organisation.

The premise of resource dependence theory states that the environment surrounding organisations is uncertain, and that the organisations try to gain control over this uncertain environment, and avoid dependence, because they need a persistent and reliable flow of resources [1]. The source of uncertainty is the existence of interdependencies, which describes a situation where "one actor does not entirely control all of the conditions necessary for the achievement of an action or for obtaining the outcome desired from the action" [43, p. 40]. Furthermore, a central assumption of resource dependence theory, which separates it from ecological

and institutional perspectives, is that managers within an organisation have discretion, which entails the ability to actively manage the uncertainties of the external environment [44]. Another important distinction is that resources are not just material, but may also be immaterial resources such as expertise or specific skills [45].

Malatesta and Smith [46] present three main strategies for reducing uncertainty and dependence: (1) Mergers, (2) alliances and (3) co-opting or board interlocking (hereafter board interlocking). The choice of strategy depends on how much control over resources the focal organisation views as necessary [47]. The strategies can be viewed as a part of a continuum because they require varying degrees of coordination and loss of autonomy [46]. Furthermore, the control gained by applying these strategies is highly dependent on the characteristics of the organisation's environment. The literature suggests that board interlocking is the most likely strategy for gaining control in environments characterised by low concentration and high levels of competition [43, 46]. A study by Boyd [48] showed that the number of board interlocks is greater in such environments. The assumption is that through board interlocks, the focal organisation trades sovereignty to an organisation in which the focal organisation is dependent on, which in turn establishes self-interest in the focal organisation's development and survival [49]. The construction sector is characterised as a highly competitive sector with low concentration [50–53]. Therefore, we expect wood-based firms to use board interlocks as a strategy for gaining control and reducing their dependency on the environment.

Expectation 1: A majority of the wood-based firms will have board interlocks with other firms.

Another relevant characteristic of the construction sector is the complexity of the supply chain relationship [15, 37, 38]. A construction supply chain encompasses architects, engineers, builders and suppliers [15, 54]. Papadopoulos et al. [55] describe how the construction supply chain differs from the manufacturing supply chain because of the frequent changes in product, production, and location. Board interlocks may enable better coordination with the environment because it establishes a channel for communication between firms [46, 56, 57]. Given the need for coordination, we expect the wood-based firms to have board interlocks with actors across the construction supply chain.

Expectation 2: The wood-based firms have board interlocks with actors across the construction supply chain.

We rely on both resource dependence theory and the notion of dynamic capabilities to understand the role of board interlocks. Within resource dependence theory, board interlocks are viewed as a way to secure access to material and immaterial resources [46, 56]. Wood-based firms are particularly dependent on access to wood and wood-based materials. This dependency suggests that wood-based firms will be more likely to have board interlocks with firms that may supply the necessary material, due to the potential to secure a persistent and reliable flow of resources [1].

Expectation 3: Wood-based firms use board interlocks to secure access to material resources.

Board interlocks also have the potential to function as transfer channels for immaterial resources such as knowledge, expertise and skills between organisations [43, 45, 58]. However, the role of immaterial resources within an organisation is less clear within resource dependence theory. Teece [59, p. 516] developed the notion of dynamic capabilities, which he defines as: "the firm's ability to integrate, build, and reconfigure internal and external competences to address rapidly changing environments". Furthermore, he suggests that the extent to which a firm has this ability forms the basis of a firm's competitive advantage. More recently, Teece [60] disaggregated dynamic capabilities into three processes: sensing, seizing and reconfiguration. Sensing entails identifying opportunities in the environment which requires market understanding, seizing entails addressing the identified opportunity which often require new knowledge and skills. Finally, reconfiguration entails restructuring assets and organisational structures to environmental changes which demands business and management skills.

Expectation 4: Wood-based firms use board interlocks to secure access to immaterial resources such as knowledge, expertise, and skills.

4 METHODS

This paper builds on two types of data: registry data and interview data. The two types of data are used in combination because while the registry data allows for investigation into if, and to what extent, there exists board interlocks between wood-based firms and firms in other industries, it does not contribute to the understanding of the role of these potential board interlocks.

4.1 REGISTRY DATA

We collected the data for this study in February 2022 from the Central Coordinating Register for Legal Entities (CCR), a registry of all firms in Norway. To collect the data, we used the R software and web scraping. Each firm registered in Norway is given a unique identifier. We used this unique identifier to access and collect information about each firm. The information we collected for each firm was the NACE (Nomenclature of Economic Activity) code, the number of employees and the BoD members, if the firm had a BoD. 549 449 firms were registered with a BoD at the time of data collection.

https://doi.org/10.52202/069179-0593

To collect data on firms in the construction supply chain that use wood-based materials in their products, we gathered information on firms that were members of the primary industry organisations in Norway[2] for the promotion of wood-based products. In addition, we collected information on firms that are partners in initiatives working on solutions that promote the use of wood-based products. Based on the collected information, we had a list of 357 firms. Given that we have information about the NACE-code of each firm, it is possible to argue that it is better to use these to identify groups of wood-based firms. This method is problematic because the basis for the classification of firms is activity rather than material used which may lead to inclusion of many non-wood-based firms. A potential limitation with our approach is the reliance on our knowledge of the industry, we may have inadvertently excluded wood-based firms.

For the analyses we created a two-mode network, using the data collected from CCR and the list of wood-based firms. A two-mode network connects firms through persons. The two-mode network allowed us to create a projection of a one-mode network of firms connected to firms from the two-mode network. To get an overview of how connected wood-based firms are to other firms in the network, we calculated the distance from the wood-based firms to all other firms in the network. By only considering directly connected firms (distance = 1) and their NACE-codes, we get an overview of to what extent wood-based firms are interlocked with firms in other industries. An additional measure used in the analysis is degree centrality. Degree centrality measures the number of links (interlocks) a node (a firm or board member) has to other nodes (a firm or board member) in the network. The basis for this measurement is that nodes with many links have a more prominent position in the network [61].

It should also be noted that one firm may be registered with several NACE-codes, which may question the reliability of our analyses based on NACE-codes. We consistently used the first NACE-codes of each firm, but most firms are only registered with one NACE-code [62]. In the remainder of this paper, we will use the term "industry" when we refer to the NACE sections and the term "industry subdivision" to refer to NACE divisions.

4.2 INTERVIEW DATA

Our interview data was collected in the period from June 2022 until October 2022. Our initial sampling strategy entailed creating a one-mode network of persons connected to persons from our two-mode network. From this one-mode network, we calculated the degree centrality. We then selected potential informants among those BoD members of wood-based firms who were well connected to firms in other industries. Furthermore, we added a requirement, that among the firms, the potential informant who was connected to at least one firm should have a couple of employees, as we wanted to avoid sending requests to board members of very small firms. Subsequently, we collected information about the informant's email address and phone number and sent them requests, by email and phone calls, for an interview. However, it was difficult to get any response, after 40 requests with no response we changed strategy. We changed our strategy to something more similar to the snowballing method. This entailed that we reached out to persons we knew or collaborated with in the industry and asked them to recommend informants. In some instances, they made the first request, and we followed up with a more formal request. We made sure that most of these informants were board members of wood-based firms and that they had connections, through board interlocks, to firms in other relevant industries. This strategy led to interviews with seven informants that were well distributed across industries in the construction supply chain. We also conducted two additional interviews: one interview with someone who was not a board member of a firm on our list of wood-based firms, but several firms involved in real estate development, and one with another informant who was a board member of several firms. This informant also had in depth knowledge about the legal and operational aspects the work of BoD.

The interviews were semi-structured, and we used an interview guide as the starting point for each interview. We also adapted our questions depending on the background of the informant and topics that came up during the interview. In the interview guide, we listed several probes that we used if a topic we were interested in was not raised or discussed by the informants themselves. The interviews were all recorded and transcribed. To analyse the interviews, we developed a codebook and used NVivo to code the interviews. The interviews were coded by one person, which can question the reliability of the coding. However, the interviews were conducted as part of a larger project and two persons jointly conducted all of the interviews and discussed the coding and findings, which increases the reliability.

5 RESULTS

The results from the analysis of the different types of data are presented separately. The results from the quantitative analysis of the registry data are presented first, and second the results of the qualitative analysis of the interview data.

5.1 RESULTS – REGISTRY DATA

The results from the analysis of registry data are primarily related to the first two expectations. These state that a majority of the wood-based firms will have board interlocks with other firms, and that the wood-based firms have board interlocks with actors across the construction supply chain. Our analysis showed that of the 357 firms in our list of wood-based firms 81% (N = 289) were

[2] These are: Treindustrien, Norske Trevarer, Byggevareindustrien and Treforedlingsindustrien.

connected to other firms through board interlocks. The wood-based firms were interlocked to 3,113 other firms. Of these 3,113 firms 84 % (N = 2629) are unique firms.

Our analyses show that the wood-based firms are interlocked with firms in all industries across the construction supply chain. However, there is a great deal of variation regarding the degree of interlocks to each of these industries. A majority of the firms, that the wood-based firms are interlocked with are found within the following industries: real estate (24%), construction (13%), manufacturing (7%), and professional, science and technical activities (7%). Only 3% of the firms that the wood-based firms are interlocked with are within the industry of agriculture, forestry of fishing.

The division into industries can be even more detailed by applying industry subdivisions which is a more fine-grained classification. Table 1 shows the most common industry subdivisions, within the most common industries that the wood-based firms are interlocked with. It is interesting that 73% of the construction firms that the wood-based firms are interlocked with are found within the industry subdivision "construction of buildings". This industry subdivision consists of firms involved in development of building projects and construction of residential and non-residential buildings. This indicates that few of the construction firms, that the wood-based firms are interlocked with, are involved in other types of construction, such as construction of bridges. It is also interesting to note that the most common industry subdivision within professional, science and technical activities is related to head-office activities, business, and management activities, and not architectural and engineering activities. However, the second most common industry subdivision within this industry, is architectural and engineering activities, with 30%.

Table 1: *Most common industry subdivision within each industry.*

Industry	Industry subdivisions	Percentage of firms
L Real estate activities	Real Estate activities	100% (734)
F Construction	Construction of buildings	73% (297)
C Manufacturing	Manufacture of wood and products of wood and cork, except furniture; manufacture of articles or straw and plaiting materials	42% (91)
M Professional, science and technical activities	Activities of head offices; management consultancy activities	46% (100)
A Agriculture, forestry, and fishing	Forestry and logging	55% (47)

The firms that the wood-based firms are interlocked with also seem to have a higher mean number of employees, compared to all firms in the same industries. These firms also have a higher mean score on degree centrality, compared to all firms in the same industries, which indicates that the firms that the wood-based firms are interlocked with may have a more prominent position in each industry.

5.2 RESULTS – INTERVIEW DATA

The results from the analysis of interview data primarily relate to the last two expectations which state that wood-based firms use board interlocks to secure access to material resources and immaterial resources such as knowledge, expertise and skills.

5.2.1 Access to material resources

We interviewed several informants with various connections to other firms in other industries through board interlocks. However, when we asked them about how these interlocks might enable a steady supply of material resources, such as wood or more advanced wood-based products, few seemed to think of or use interlocks to secure access to a steady supply of such resources. One informant (2), who was on the board of a carpenter firm and a firm supplying forest plants for planting after trees have been cut down, alerted us to the large difference between the business each firm was in. The products of the forest plant firm would not become usable lumber for the carpenter firm until several decades have passed. Another informant (5) suggested that firms might use interlocks in this way, but added that, in most cases, firms would select the material most suited for a specific purpose, and that this consideration would be given a substantial weight in the decision on material selection. However, the same informant (5) also suggests that an interlock might give some influence in the interlocked firms future developed. This informant is on the board of a firm that often functions as a contractor in larger construction projects and of a smaller firm that builds private houses and prefabricated elements. The informant (5) explains how the additional element of a costumer relation between the contractor firm and the smaller firm enables the firm to give input on future development.

Furthermore, a board interlock might not be a strong enough connection between firms for it to function as a way to secure access to material resources. One informant (1), who was interlocked with several firms across the supply chain because of ownership through a parent company, describes the interlocks something reassuring, in light of the uncertainty caused by the recent pandemic, in the supply of material resources. At the same time, it is also noted by the informant that they are mindful not to make this a too big advantage.

Even so, our interviews show that this should not be interpreted as the only motivation for parent companies to have interlocks with firms they have ownership shares in. Several informants (1, 6, 7 and 8) noted that ownership shares were one of the main motivations for interlocks. One of the informants (6) explain that this is not because

https://doi.org/10.52202/069179-0593

of the parent companies' interest in securing access to material resources, but because of having made investments and wanting to influence and have information about the development of the firm. This finding lends more support to our expectation about immaterial resources, which we now turn to.

5.2.2 Access to immaterial resources

It seems that board interlocks function as a way to secure access to immaterial resources such as knowledge, expertise, and skills. We asked the informants about why they were appointed to the BoD of the various firms. Several (2, 6 and 8) noted that knowledge and experience from wood-based firms was important. One informant (1) also noted that they were actively seeking potential board members with such knowledge and experience, but that they are hard to come by. Many of the informants (2, 3, 4, 6 and 9) also had previous work experience from firms that worked with wood as a material.

Several informants (1, 2, 3, 4, 5, 7 and 9) stressed knowledge and experience from business management, and the ability to engage and understand how the market develops, as important for their appointment as a board member. One informant (3) described how the informant was recruited to the board of a wood-based firm because the firm was facing economic struggles, and that they were subsequently recruited to other firms when the economic situation was improved. Another informant (4) described the importance of having board members that understand the firm's business model and elements that influence the firm's failure or success.

The importance of experience from business management and market understand seems to be related to how the informants perceive the role of the BoD. Many of the informants (2, 3, 5, 6, 7 and 9) view the role of the board BoD as particularly responsible for the long-term development of the firm. They describe how the BoD should be a partner for the CEO in thinking about the future development of the firm. Moreover, they should try to have a more long-term perspective, than the operative management, focusing on future development opportunities, but at the same time, be a supporting actor for the short-term development. Most of the informants (1, 2, 3, 4, 6, 7 and 8) also said that they had experience form previously being on a firm's BoD.

5.2.3 Disqualification, procedures, and competition

Throughout the interviews, the informants also mentioned some issues related to the role and use of board interlocks. The first issue relates to qualification of the board members in making decisions which may benefit the firm of the board member. Some informants (8 and 9) mentioned that in these situations the board member in question would be disqualified from taking part in the decision. The task of the board member is to act in the best interest of the firm in question. This is also in accordance with the legal regulations [64].

This is seemingly not only a legal issue, but it may also be seen as an unfair advantage by the outside world. One informant (1), who had owned several wood-based wholesale firms previously, mentioned this issue. They described how builders became sceptical towards their business and suspected that the sawmill might sell their materials at a cheaper price to their own wholesale firms. According to the informant, ownership increases the need to conduct business in a transparent manner. Another informant (3), who moved from interest organisations to industry, had to cut ties with the former to avoid suspicions around a dual role.

Another aspect which might make it difficult to use boards in a strategic manner is that there may be election procedures in place for selection of board members, especially in larger firms. One informant (3) suggested that the possibility of appointing a strategically important member to the BoD might be difficult, since the election committee might not think of or be aware of the possibility. Another informant (7) suggested that the committees might resort to selecting the person who is next in line, because it is the most convenient, instead of considering the firm's needs.

The final issue relates to competition among firms. One informant (1) mentioned that they tried to collaborate with other firms, but that it was difficult because of the competition. Moreover, collaboration often lead to conversations about acquisition or mergers. This informant also mentioned that the price is of course an important factor for deciding which material to use. This was also repeated by another informant (5). This suggests that it might be difficult to select materials or products that a firm is interlocked with if the price is not competitive.

6 DISCUSSION

According to resource dependence theory, board interlocks allow the focal firm, in case of interdependencies to other firms in the environment, to trade sovereignty for self-interest in the focal firm's development and survival [43, 49]. In contrast to other methods for reducing interdependencies and thereby uncertainty of the focal firm, such as mergers and alliances, establishing board interlocks involves less coordination and loss of autonomy, it is also viewed as the most likely strategy in environments with low concentration and high levels of competition [43, 46]. In the literature, the construction sector is characterised as a highly competitive sector with low concentration [50–53]. We therefore expected that a majority of the wood-based firms would have board interlocks with firms in other industries. Our results, based on the analysis of registry data, show that of the 357 wood-based firms 81% (N = 289) are interlocked with other firms, which supports our expectations. However, our data does not cover the prevalence of mergers and alliances among wood-based firms. This means that we are not able to conclude that

board interlocking is the most likely strategy for the wood-based firms.

The second expectation relates to another characteristic of the construction sector which is the complex supply chain. A construction supply chain encompasses architects, engineers, builders, and suppliers [15, 54]. The complexity of the supply chain also increases because of the frequent changes in product, production, and location [55]. We expected that this complexity of the supply chain would lead to wood-based firms having board interlocks with actors across the construction supply chain, based on the potential for needed coordination board interlocks provide by establishing communication channels between firms [46, 56, 57]. Our results show that the wood-based firms have board interlocks with industries across the construction supply chain. A majority of the firms that the wood-based firms are interlocked with is found within the following industries: real estate (24%), construction (13%); manufacturing (7%), professional, science, and technical activities (7%). However, only 3% of the firms that the wood-based firms are interlocked are found within industry of agriculture, forestry, and fishing which is an important due to their role as the supplier of wood and wood-based materials. Our results also show that most of the interlocked firms within construction are related to the construction of buildings, while few of the interlocked firms are involved in other construction activities, such as construction of bridges. If we consider the interlocked firms within the industry of "professional, science and technical activities", which is where engineering and architectural firms belong, the most common industry subdivision was the one related to head-office activities, business, and management activities (46%). Moreover, the industry subdivision related to engineering and architectural activities was the second most common (30%). Even so, we find support for the expectation that wood-based firms will have interlocks with actors across the construction supply chain. The firms that the wood-based firms are interlocked with also seem larger, in terms of number of employees, compared to all the firms within each industry. They seem to have a more prominent position in the industry network.

The third expectation stated that wood-based firms use board interlocks to secure access to material resources. Wood-based firms are especially dependent on one type of material. We expected them to be more likely to have board interlocks with firms that may supply the necessary materials, due to board interlocks having the potential to secure a persistent and reliable flow of resources [1]. However, our results show that this does not seem to be the case. This is supported by the fact that the main supplier industry, agriculture, forestry, and fishing, is among the industries which few of the firms that the wood-based firms are interlocked are found within, compared to the industries mentioned above. In the interviews, one informant highlighted the fact that there may be a large difference between the materials and products a firm produces and the materials and products a firm needs, even if there exists a board interlock between the two firms. It also became clear that material selection must be based on a consideration of what the best material is for a specific purpose. This suggests that even if there exists a board interlock between a wood-based firm and a construction firm, wood might not be viewed as the best material for a specific purpose, and so another material is used. One implication of this is that it may be difficult to use board interlocks in this way because it creates an expectation between firms that may be difficult to fulfil. Another important aspect is that board interlocks may be too weak of a connection. Based on the interviews, it seems like stronger connections, such as ownership, is needed to secure access to material resources. However, this should not be interpreted as the only motivation for parent companies to have interlocks with firms they have ownership shares in. The interviews highlighted that an important motivation for board interlocks, in the case of ownership, is to have control over the parent companies' investments, receive information, and have influence over the future development of the firm. Additionally, the informants described how using board interlocks in this way may be difficult because of the issue related to disqualification and things may appear to the outside. As a result, is does not seem like board interlocks function the way we expected. In terms of securing access to material resources, there seems to be too weak of a link. Furthermore, the legal and appearance aspects make it difficult for board interlocks to have this role.

The fourth and final expectation was related to the use of board interlocks as a method for securing access to immaterial resources, such as knowledge and skills. In the literature, it is suggested that board interlocks have the potential to function as transfer channels for immaterial resources [43, 45, 58]. Teece [60] describes how such immaterial resources are important for the dynamic capabilities of a firm which involve sensing, seizing and reconfiguration. Our informants highlighted knowledge and experience for wood-based firms as a reason for becoming a board member, and several of them had work experience from firms that uses wood as a material. Moreover, they stressed the need for experience and knowledge about business management and market understanding, which seem to relate to the role of the board as having a special responsibility for the long-term development and future opportunities for the firm. Thus, our expectation about the use of board interlocks as a method for securing access to immaterial resources seems to be supported. It also seems like they contribute to all aspects of Teece's [60] notion of dynamic capabilities: sensing, through their understanding of the market; seizing, through their knowledge and experience concerning new opportunities; and reconfiguration, through their business and management skills.

7 CONCLUSION

This paper contributes to the understanding of the role of board interlocks in increasing the use of wood in

https://doi.org/10.52202/069179-0593

construction. Trough analyses of registry data we show that board interlocks exist between wood-based firms in the construction supply chain and other firms. Furthermore, the firms that the wood-based firms are interlocked with belong to industries across the construction supply chain. Most importantly, the additional analyses of the interview data allow us to nuance our understanding of the role of such board interlocks. We find no support for our expectation that they function as a way to secure access to material resources. However, they do have an important role in securing access to immaterial resources, such as knowledge, expertise and skills. Knowledge and experience from using wood as a material, business and management skills, and market understanding are all important and contribute to important aspects of Teece's [60] notion of dynamic capabilities, which forms the basis of a firm's competitive advantage.

There are certain limitations to this study. The comprehensive registry data allows for a very broad analysis, but it also limits our ability to study the data in a detailed manner. The selection of wood-based firms in the construction supply chain is probably not complete. There may be wood-based firms that have not been included. However, other methods may have been too broad in terms of inclusion or required an extensive amount of time and resources. Historic data was not available, which does limits us to study data collected at one point in time. This means that we were not able to discuss development over time. Regarding the interview data, more interviews would have been preferrable, but given the difficulties of recruitment, this was not possible in the time available.

Future research should focus on further exploring the role of board interlocks in increasing the use of wood in construction. We specifically suggest case studies of BoD to further the understanding of internal dynamics within firms. Future studies may also consider board interlocks and their relation to alliances and mergers. Finally, we suggest that studying firms who have made or are in a transition towards use of more wood-based materials may be an important avenue for future research.

ACKNOWLEDGEMENT

I would like to express my gratitude to Antje Klitkou and Marco Capasso. Antje Klitkou for providing valuable feedback and support throughout the process of writing this paper. Marco Capasso for sharing his knowledge about social network analysis and for valuable contributions to the early draft of this paper.

REFERENCES

[1] M. S. Mizruchi, 'What Do Interlocks Do? An Analysis, Critique, and Assessment of Research on Interlocking Directorates', *Annual Review of Sociology*, vol. 22, pp. 271–298, 1996.

[2] E. Hurmekoski, 'How can wood construction reduce environmental degradation?', European Forest Institute, Joensuu, Finland, 2017.

[3] P. Leskinen *et al.*, *Substitution effects of wood-based products in climate change mitigation*. Joensuu: EFI, 2018.

[4] V. Poljatschenko and L. Valsta, 'Carbon emissions displacement effect of Finnish mechanical wood products by dominant tree species in a set of wood use scenarios', *Silva Fenn.*, vol. 55, no. 1, 2021, doi: 10.14214/sf.10391.

[5] M. Karjalainen, H. E. Ilgın, and L. Tulonen, 'Main Design Considerations and Prospects of Contemporary Tall Timber Apartment Buildings: Views of Key Professionals from Finland', *Sustainability*, vol. 13, no. 12, p. 6593, Jun. 2021, doi: 10.3390/su13126593.

[6] D. Lazarevic, P. Kautto, and R. Antikainen, 'Finland's wood-frame multi-storey construction innovation system: Analysing motors of creative destruction', *Forest Policy and Economics*, vol. 110, p. 101861, Jan. 2020, doi: 10.1016/j.forpol.2019.01.006.

[7] N. Viholainen, E. Kylkilahti, M. Autio, J. Pöyhönen, and A. Toppinen, 'Bringing ecosystem thinking to sustainability-driven wooden construction business', *Journal of Cleaner Production*, vol. 292, p. 126029, Apr. 2021, doi: 10.1016/j.jclepro.2021.126029.

[8] L. Gharaibeh, K. M. Eriksson, B. Lantz, S. Matarneh, and F. Elghaish, 'Toward digital construction supply chain-based Industry 4.0 solutions: scientometric-thematic analysis', *SASBE*, Mar. 2022, doi: 10.1108/SASBE-12-2021-0224.

[9] T. O. Olawumi and D. W. M. Chan, 'Concomitant impediments to the implementation of smart sustainable practices in the built environment', *Sustainable Production and Consumption*, vol. 21, pp. 239–251, Jan. 2020, doi: 10.1016/j.spc.2019.09.001.

[10] J. Jussila *et al.*, 'Wooden multi-storey construction market development – systematic literature review within a global scope with insights on the Nordic region', *Silva Fenn.*, vol. 56, no. 1, 2022, doi: 10.14214/sf.10609.

[11] R. Toivonen, A. Lilja, H. Vihemäki, and A. Toppinen, 'Future export markets of industrial wood construction – A qualitative backcasting study', *Forest Policy and Economics*, vol. 128, p. 102480, Jul. 2021, doi: 10.1016/j.forpol.2021.102480.

[12] A. Gosselin, P. Blanchet, N. Lehoux, and Y. Cimon, 'Main Motivations and Barriers for Using Wood in Multi-Story and Non-Residential Construction Projects', *BioResources; Vol 12, No 1 (2017)*, 2016, [Online]. Available: https://ojs.cnr.ncsu.edu/index.php/BioRes/article/view/BioRes_12_1_546_Gosselin_Main_Motivations_Barriers_Wood_Use/4963

[13] A. Santana-Sosa and I. Kovacic, 'Barriers, Opportunities and Recommendations to Enhance the Adoption of Timber within Multi-Storey

Buildings in Austria', *Buildings*, vol. 12, no. 9, p. 1416, Sep. 2022, doi: 10.3390/buildings12091416.

[14] L. Gharaibeh, S. T. Matarneh, K. Eriksson, and B. Lantz, 'An Empirical Analysis of Barriers to Building Information Modelling (BIM) Implementation in Wood Construction Projects: Evidence from the Swedish Context', *Buildings*, vol. 12, no. 8, p. 1067, Jul. 2022, doi: 10.3390/buildings12081067.

[15] A. Gosselin, Y. Cimon, N. Lehoux, and P. Blanchet, 'Main Features of the Timber Structure Building Industry Business Models', *Buildings*, vol. 11, no. 4, p. 170, Apr. 2021, doi: 10.3390/buildings11040170.

[16] M. Miozzo and P. Dewick, 'Building competitive advantage: innovation and corporate governance in European construction', *Research Policy*, vol. 31, no. 6, pp. 989–1008, Aug. 2002, doi: 10.1016/S0048-7333(01)00173-1.

[17] B. Brullebaut, I. Allemand, E. Prinz, and F. Thépot, 'Persistence in corporate networks through boards of directors? A longitudinal study of interlocks in France, Germany, and the United Kingdom', *Rev Manag Sci*, vol. 16, no. 6, pp. 1743–1782, Aug. 2022, doi: 10.1007/s11846-021-00490-9.

[18] M. D. Howard, M. C. Withers, and L. Tihanyi, 'Knowledge Dependence and the Formation of Director Interlocks', *AMJ*, vol. 60, no. 5, pp. 1986–2013, Oct. 2017, doi: 10.5465/amj.2015.0499.

[19] J. Lu, F. Mahmoudian, D. Yu, J. A. Nazari, and I. M. Herremans, 'Board interlocks, absorptive capacity, and environmental performance', *Bus Strat Env*, vol. 30, no. 8, pp. 3425–3443, Dec. 2021, doi: 10.1002/bse.2811.

[20] R. Gulati and J. D. Westphal, 'Cooperative or Controlling? The Effects of CEO-Board Relations and the Content of Interlocks on the Formation of Joint Ventures', *Administrative Science Quarterly*, vol. 44, no. 3, pp. 473–506, 1999, doi: 10.2307/2666959.

[21] D. Palmer, 'Broken Ties: Interlocking Directorates and Intercorporate Coordination', *Administrative Science Quarterly*, vol. 28, no. 1, pp. 40–55, 1983, doi: 10.2307/2392384.

[22] R. D. Antikainen *et al.*, 'Renewal of forest based manufacturing towards a sustainable circular bioeconomy', Finnish Environment Institute, Helsinki, 2017.

[23] European Commission, 'On resource efficiency opportunities in the building sector', European Commission, Brussels, 2014.

[24] European Commission, 'A sustainable Bioeconomy for Europe: strenthening the connection between economy, society and the environment Updated Bioeconomy Strategy', European Commission, Brussels, 2018.

[25] M. H. Ramage *et al.*, 'The wood from the trees: The use of timber in construction', *Renewable and Sustainable Energy Reviews*, vol. 68, pp. 333–359, Feb. 2017, doi: 10.1016/j.rser.2016.09.107.

[26] Organisation des Nations Unies pour l'alimentation et l'agriculture, Ed., *Forestry for a low-carbon future: integrating forests and wood products in climate change strategies*. Rome: FAO, 2016.

[27] J. Abed, S. Rayburg, J. Rodwell, and M. Neave, 'A Review of the Performance and Benefits of Mass Timber as an Alternative to Concrete and Steel for Improving the Sustainability of Structures', *Sustainability*, vol. 14, no. 9, p. 5570, May 2022, doi: 10.3390/su14095570.

[28] K. Rakhshan, J.-C. Morel, and A. Daneshkhah, 'A probabilistic predictive model for assessing the economic reusability of load-bearing building components: Developing a Circular Economy framework', *Sustainable Production and Consumption*, vol. 27, pp. 630–642, Jul. 2021, doi: 10.1016/j.spc.2021.01.031.

[29] H. Nykamp, 'A transition to green buildings in Norway', *Environmental Innovation and Societal Transitions*, vol. 24, pp. 83–93, Sep. 2017, doi: 10.1016/j.eist.2016.10.006.

[30] D. Buck, X. Wang, O. Hagman, and A. Gustafsson, 'Comparison of Different Assembling Techniques Regarding Cost, Durability and Ecology - A survey of Multi-layer Wooden Panel Assembly Load-Bearing Construction Elements', *BioResources*, vol. 10, no. 4, pp. 8378–8396, 2015.

[31] S. Grynning, S. K. Asphaug, L. Gullbrekken, and B. Time, 'Moisture robustness of eaves solutions for ventilated roofs: Experimental studies', *Science and Technology for the Built Environment*, vol. 25, no. 9, pp. 1121–1131, Oct. 2019, doi: 10.1080/23744731.2019.1660113.

[32] C. Rose *et al.*, 'Cross-Laminated Secondary Timber: Experimental Testing and Modelling the Effect of Defects and Reduced Feedstock Properties', *Sustainability*, vol. 10, no. 11, p. 4118, Nov. 2018, doi: 10.3390/su10114118.

[33] R. Abrahamsen, 'Mjøstårnet - Construction of an 81 m tall timber building', presented at the 23. Internationales Holzbau-Forum IHF 2017, Garmisch-Partenkirchen, Germany, 2017.

[34] A. Koronaki, A. Bukauskas, A. Jalia, D. U. Shah, and M. H. Ramage, 'Prefabricated Engineered Timber Schools in the United Kingdom: Challenges and Opportunities', *Sustainability*, vol. 13, no. 22, p. 12864, Nov. 2021, doi: 10.3390/su132212864.

[35] M. Maniak-Huesser, L. G. F. Tellnes, and E. Zea Escamilla, 'Mind the Gap: A Policy Gap Analysis of Programmes Promoting Timber Construction in Nordic Countries', *Sustainability*, vol. 13, no. 21, p. 11876, Oct. 2021, doi: 10.3390/su132111876.

[36] K. Mahapatra and L. Gustavsson, *General conditions for construction of multi-storey wooden buildings in Western Europe*. School of Technology and Design, Växjö University Växjö, Sweden, 2009.

[37] E. Mlecnik, 'Opportunities for supplier-led systemic innovation in highly energy-efficient

https://doi.org/10.52202/069179-0593

housing', *Journal of Cleaner Production*, vol. 56, pp. 103–111, Oct. 2013, doi: 10.1016/j.jclepro.2012.03.009.
[38] A. Gosselin, P. Blanchet, N. Lehoux, and Y. Cimon, 'Collaboration Enables Innovative Timber Structure Adoption in Construction', *Buildings*, vol. 8, no. 12, p. 183, Dec. 2018, doi: 10.3390/buildings8120183.
[39] C. Shropshire, 'THE ROLE OF THE INTERLOCKING DIRECTOR AND BOARD RECEPTIVITY IN THE DIFFUSION OF PRACTICES', *The Academy of Management Review*, vol. 35, no. 2, pp. 246–264, 2010.
[40] G. Ahuja, 'Collaboration networks, structural holes, and innovation: A longitudinal study', *Administrative science quarterly*, vol. 45, no. 3, pp. 425–455, 2000.
[41] C. Helmers, M. Patnam, and P. R. Rau, 'Do board interlocks increase innovation? Evidence from a corporate governance reform in India', *Journal of Banking & Finance*, vol. 80, pp. 51–70, 2017.
[42] Y. Teng, E. Gimmon, and W. Lu, 'Do Interlocks Lead to the Convergence of Interfirm Innovation Performance? Evidence From China', *SAGE Open*, vol. 11, no. 2, p. 215824402110071, Apr. 2021, doi: 10.1177/21582440211007132.
[43] J. Pfeffer and G. R. Salancik, *The external control of organizations: a resource dependence perspective*. Stanford, Calif: Stanford Business Books, 2003.
[44] C. Oliver, 'Strategic responses to institutional processes', *Academy of management review*, vol. 16, no. 1, pp. 145–179, 1991.
[45] B. R. Barringer and J. S. Harrison, 'Walking a tightrope: Creating value through interorganizational relationships', *Journal of management*, vol. 26, no. 3, pp. 367–403, 2000.
[46] D. Malatesta and C. R. Smith, 'Lessons from resource dependence theory for contemporary public and nonprofit management', *Public Administration Review*, vol. 74, no. 1, pp. 14–25, 2014.
[47] S. Finkelstein, 'Interindustry merger patterns and resource dependence: A replication and extension of Pfeffer (1972)', *Strategic Management Journal*, vol. 18, no. 10, pp. 787–810, 1997.
[48] B. Boyd, 'Corporate linkages and organizational environment: A test of the resource dependence model', *Strat. Mgmt. J.*, vol. 11, no. 6, pp. 419–430, Oct. 1990, doi: 10.1002/smj.4250110602.
[49] G. F. Davis and J. Adam Cobb, 'Chapter 2 Resource dependence theory: Past and future', in *Research in the Sociology of Organizations*, vol. 28, C. Bird Schoonhoven and F. Dobbin, Eds. Emerald Group Publishing Limited, 2010, pp. 21–42. doi: 10.1108/S0733-558X(2010)0000028006.
[50] M. Ball, M. Farshchi, and M. Grilli, 'Competition and the persistence of profits in the UK construction industry', *Construction Management and Economics*, vol. 18, no. 7, pp. 733–745, 2000.
[51] W. Bremer and K. Kok, 'The Dutch construction industry: a combination of competition and corporatism', *Building Research & Information*, vol. 28, no. 2, pp. 98–108, Mar. 2000, doi: 10.1080/096132100369000.
[52] J. Lowe, 'Concentration in the UK construction sector', *Journal of Financial Management of Property and Construction*, vol. 16, no. 3, pp. 232–248, Nov. 2011, doi: 10.1108/13664381111179215.
[53] M. W. Staniewski, R. Nowacki, and K. Awruk, 'Entrepreneurship and innovativeness of small and medium-sized construction enterprises', *Int Entrep Manag J*, vol. 12, no. 3, pp. 861–877, Sep. 2016, doi: 10.1007/s11365-016-0385-8.
[54] R. Vrijhoef and L. Koskela, 'The four roles of supply chain management in construction', *European journal of purchasing & supply management*, vol. 6, no. 3–4, pp. 169–178, 2000.
[55] G. A. Papadopoulos, N. Zamer, S. P. Gayialis, and I. P. Tatsiopoulos, 'Supply chain improvement in construction industry', *Universal Journal of Management*, vol. 4, no. 10, pp. 528–534, 2016.
[56] A. J. Hillman, 'Politicians on the board of directors: Do connections affect the bottom line?', *Journal of management*, vol. 31, no. 3, pp. 464–481, 2005.
[57] F. D. Schoorman, M. H. Bazerman, and R. S. Atkin, 'Interlocking Directorates: A Strategy for Reducing Environmental Uncertainty', *AMR*, vol. 6, no. 2, pp. 243–251, Apr. 1981, doi: 10.5465/amr.1981.4287813.
[58] P. R. Haunschild and C. M. Beckman, 'When Do Interlocks Matter?: Alternate Sources of Information and Interlock Influence', *Administrative Science Quarterly*, vol. 43, no. 4, p. 815, Dec. 1998, doi: 10.2307/2393617.
[59] D. J. Teece, G. Pisano, and A. Shuen, 'Dynamic Capabilities and Strategic Management', *Strategic Management Journal*, vol. 18, no. 7, pp. 509–533, 1997.
[60] D. J. Teece, 'Explicating dynamic capabilities: the nature and microfoundations of (sustainable) enterprise performance', *Strat. Mgmt. J.*, vol. 28, no. 13, pp. 1319–1350, Dec. 2007, doi: 10.1002/smj.640.
[61] D. Luke, *A User's Guide to Network Analysis in R*, 1st ed. 2015. Cham: Springer International Publishing : Imprint: Springer, 2015. doi: 10.1007/978-3-319-23883-8.
[62] Brønnøysundsregistrene, 'Næringskoder', Aug. 26, 2022. https://www.brreg.no/bedrift/naeringskoder/ (accessed Nov. 22, 2022).
[63] A. Bryman, *Social research methods*, Fifth Edition. Oxford ; New York: Oxford University Press, 2016.
[64] ASL, 'Lov om aksjeselskaper', LOV-2021-06-18-122, 2022. [Online]. Available: https://lovdata.no/dokument/NL/lov/1997-06-13-44

World Conference on Timber Engineering Oslo 2023

HARMONISATION OF THE ENVIRONMENTAL PRODUCT DECLARATIONS FOR WOOD PRODUCTS

Lauri Linkosalmi[1], Harald Schwarzschachner[2], Tuovi Valtonen[3]

ABSTRACT: Environmental Product Declarations (EPD) are developed to compare materials and solutions in building level to achieve sustainable choices for the built environment. European standardisation body, CEN/TC 350 Sustainable Construction, have developed harmonised standard EN 15804 to create EPD's for the building products. Although harmonised standards exist, different methodologies and scenarios are used under different EPD operators and countries, which is not supporting sustainability assessment in building level. Identified challenges are e.g. generic background datasets, allocation in modules A1–A3, use of guarantees of origin for purchased energy, scenarios for transportation and installation, and end-of-life scenarios. Different assessment approaches challenge the assessment in the building level to achieve targets for sustainable buildings.

KEYWORDS: Wood products, Life cycle assessment, Environmental product declaration, Harmonisation

1 INTRODUCTION

In this study Environmental Product Declarations (EPDs) of wood products were examinate, looking differences in assessment methods and how those are affecting to the reporting of the results in EPDs. Study was done by using selected EPDs of wood products published by EN 15804 standard. All studied EPDs were third-party verified and published by an EPD operator.
Earlier studies shows the importance of the harmonisation of the EPDs [1–6]. EPDs helps decision making in building level assessment to ensure sustainable choices for the building design and construction. In this perspective, comparison of the products and solution in building level should base on harmonised and verified data [7]. Where assessment methods are aligned and based on same scenarios.

At the moment, differences between data are challenging use of EPDs by designers and decision makers. As result might vary based on selected method to imply in assessment.

2 MATERIALS AND METHODS

In the Environmental product declaration - Core rules for the product category of construction products standard (EN 15804) [8] the life cycle phases are divided in four stages; production stage (A1–A3), construction stage (A4–A5), use stage (B1–B7) and end-of-life stage (C1–4). Also, additional information beyond the product system can be stated in the module D, information module. In this study assessment is following life cycle principle presented in Fig. 1.

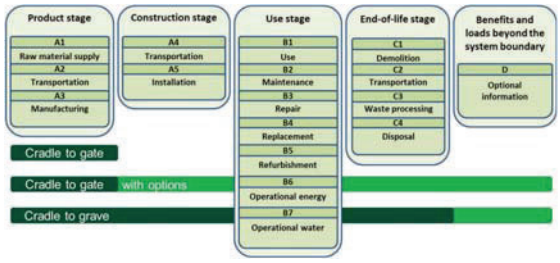

Figure 1: *Life cycle stages and environmental product declaration coverage according EN 15804 standard.*

In this study specific methods for different life cycle stages were studied. From product manufacturing perspective A1–A3 stage is most accuracy, based on annual inventory of raw material supply and production. Following life cycle stages are based on specific scenarios or scenarios recommended by the publishing platform (EPD Operator). For each life cycle module or stage, can be identified typical assessment/methodological options which will have effect on results.

In EN 16485 standard [9], Product Categories Rules are defined for wood-based products. Standard gives

[1] Lauri Linkosalmi, Stora Enso & Aalto University, Finland, lauri.linkosalmi@storaenso.com
[2] Harald Schwarzschachner, Stora Enso, Austria, harald.schwarzschachner@storaenso.com
[3] Tuovi Valtonen, Stora Enso, Finland, tuovi.valtonen@storaenso.com

https://doi.org/10.52202/069179-0594

guidance's how to implement some assessment method specifically for wood products.

For this study data were collected from the published EPDs of wood-based products. All available EPDs or datasets following EN 15804+A1, EN 15804+A2 and ISO 21930 were included to the assessment. Table 1 shows EPDs used for the assessment. CLT data is separated by EPDs and French FDES, as FDES have some specific rules to follow. Study focused to review reported CO_2 eq. emissions from product stage (A1–A3) and the biogenic carbon content of the product. Also, other methodological differences reported in EPDs where assess.

Table 1: *EPDs used for the assessment*

Product	Manufacturer EPDs
Sawn dried timber - EPD	Egger
	Moelven
	SCA Wood
	Swedish Wood
	Trae DK
	Stora Enso
	UPM
Cross Laminated Timber (CLT) - EPD	Artuso Legnami
	Binder
	Cross Timber systems
	Derix (2020)
	Derix (2022)
	Egoin
	Hasslacher
	Holzius
	KLH
	Kuhmo
	L.A. COST
	Nordic X-Lam
	Rubner
	Schilliger
	Setra
	Södra
	Splitkon
	Stabilame glued
	Stabilame nailed
	Stora Enso (2017)
	Stora Enso (2020)
	Studiengemeinschaft
	Trae DK
	Red Stag
	X-LAM Australia
	SmartLam Columbia Falls
	SmartLam Dothan, Alabama
	Terralam
Cross Laminated Timber (CLT) - FDES	Binder
	KLH
	Nordic X-Lam
	Panneau
	Piveteaubois
	Schilliger
	Stabilame glued
	Stabilame nailed
Laminated Veneer Lumber (LVL) - EPD	Stora Enso (2017)
	Stora Enso (2022)
	Kerto LVL
	Nelson Pine Industries
	North American LVL
	Roseburg
	STEICO LVL
	Stora Enso LVL
	Stora Enso LVL G
	Wood for Good LVL

3 RESULTS

Firstly, production stage data were assessed for Sawn dried timber, CLT and LVL. Results of global warming potential and biogenic carbon content in modules A1–A3 are shown separately for each product. In Figure 2, sawn dried timber results are shown. Major findings for classic sawn goods are:

- Only generic forestry data available – own research field to create more precise data for different regions where logs are felled.
- In some cases, no mentioning of biogenic carbon content. Biogenic carbon content is calculated based on product density by authors.
- Wrong calculation of biogenic carbon content, not following principle of "material inherent properties" - CO_2 biogenic carbon is referred to whole log entering the mill.
- Possible different assumption for utilization rate in A2 transportation and differences in back-and-forth transportation is considered.
- Difference requirements from EPD operators, like "shall declare the emissions for energy mix" kg CO_2/kWh in EPD Norge.

Results of CLT - EPD, CLT - FDES and LVL are shown in Figures 3–5. Major findings for further processed CLT and LVL are:

- Difference between integrated operations (basic and further production in same site) and mills who have purchased timber from external suppliers.
- Primary vs generic data for glues. Modelling of glue data based on supplier information can vary.
- Correct consideration of dry content of glues.

https://doi.org/10.52202/069179-0594

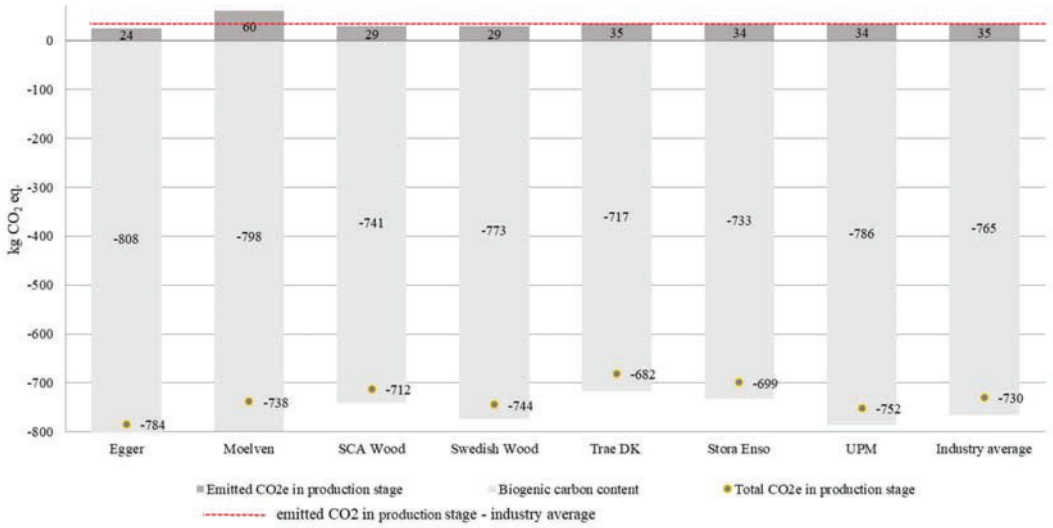

Figure 2: *Global warming potential (GWP) [kg CO_2-eq/m³] of sawn dried timber in modules A1–A3 according EPDs.*

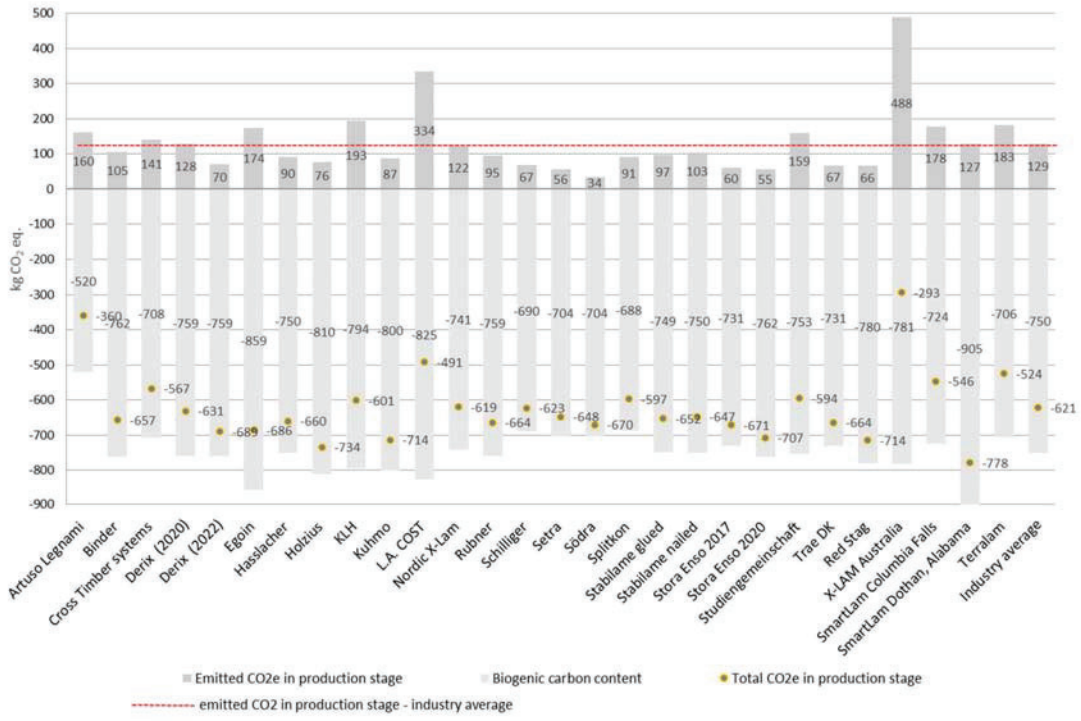

Figure 3: *Global warming potential (GWP) [kg CO_2-eq/m³] of CLT in modules A1–A3 according EPDs.*

https://doi.org/10.52202/069179-0594

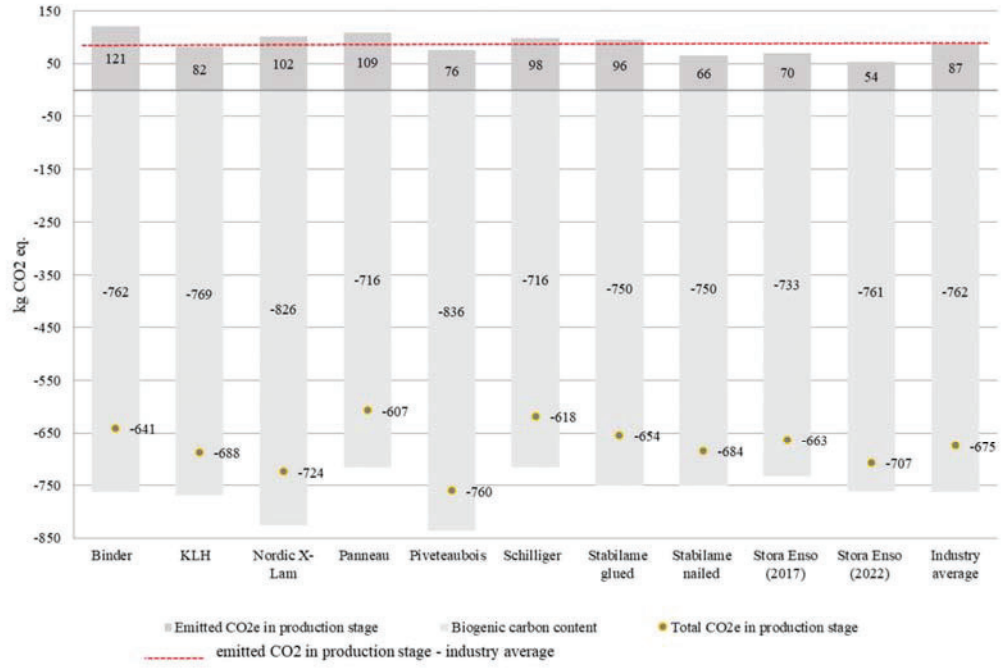

Figure 4: *Global warming potential (GWP) [kg CO_2-eq/m³] of CLT in modules A1–A3 according FDESs.*

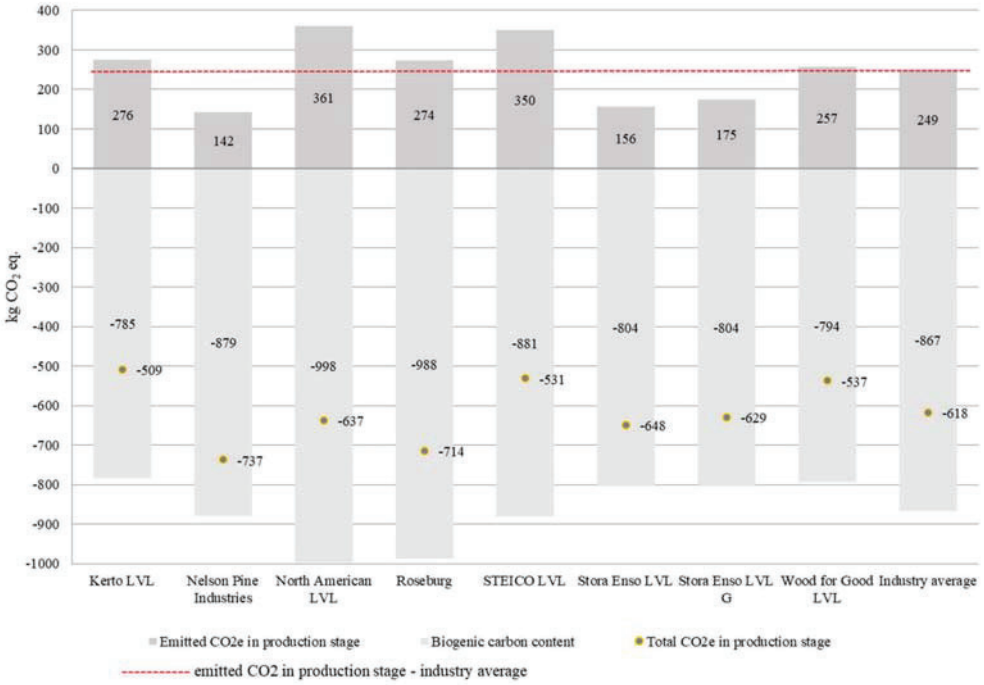

Figure 5: *Global warming potential (GWP) [kg CO_2-eq/m³] of LVL in modules A1–A3 according EPDs.*

Other identified findings based on EPD reporting data are:

- Energy consumption in A1 (EN 15804) vs. A3 (ISO 21930). Is guarantees of origin of purchased energy allowed to be used.
- By-product's allocation and interpretation:
    - Everything is allocated to sawmill residues and products according economic values without considering different level of processing ("Blackbox").
    - Allocation acc. Economic values separated by different product stages.
- Volatility of prices and effect on results, depending on reference year of data [10].
- Product transportation and installation (modules A4–A5):
    - Back-and-forth transportation.
    - Installation can vary depending on final application. Functional unit vs. declared unit.
    - Lack of specific installation data or estimate.
- End-of-life scenarios (modules C1–C4 and D):
    - Reference scenario for the end-of-life.
    - Lower Heating Values for wood and glue end-of-life scenarios.
    - Thermal and electrical burning efficiencies.
    - Database version used for assessment (e.g. ecoinvent version).
    - Used data for the substituted fuel in module D.

4 CONCLUSION

Based on the data collection more and more EPDs on wood-based products are available. This is highlighting the importance to have an EPD to claim the environmental impacts of a construction products. Many European countries have established regulation for embodied carbon or whole life carbon of building [10]. Building level assessments are depending on product level data.

Results indicate that EPDs are more harmonised in reporting and data quality than earlier. Non-harmonised methods are leading lack of comparability of EPDs in building level assessment. Many questions are arising by EPD users when there are major differences in the results of EPDs. Some differences are explained by the background datasets (generic data) and different energy mixes by countries. But some differences exist by the different assessment approaches, like by-products allocation influenced by volatility of prices [10].

To be able to calculate construction products environmental impacts harmonised approach is needed. As the complexity of the life cycle assessment modelling and different standard existing guiding the modelling in European (EN standards) and international (ISO standards) levels.

As shown in this study, choice of the assessment method can have a significant effect to the CO_2 emissions of the wood-based products. It is recommended in EPD standard [8] to use harmonised assessment methods, but it gives some freedom to do the assessment. Also, verification process of the EPDs differ by EPD Operators and individual verifiers.

A practical solution is that Product Category Rules of wood-based products [9] are revised to support common assessment method. This would harmonise environmental impacts assessments in woodworking industry field and provide more comparative datasets of wood-based building products.

REFERENCES

[1] Passer A., Lasvaux S., Allacker K. et al. Environmental product declarations entering the building sector: critical reflections based on 5 to 10 years experience in different European countries. *International Journal on Life Cycle Assessment,* 20:1199–1212, 2015.

[2] Rasmussen, F.N., Andersen, C.E., Wittchen, A., Hansen, R.N., Birgisdóttir, H. Environmental Product Declarations of Structural Wood: A Review of Impacts and Potential Pitfalls for Practice. *Buildings*, 11:362, 2021.

[3] AzariJafari H., Guest G., Kirchain R., Gregory J., Amora B. Towards comparable environmental product declarations of construction materials: Insights from a probabilistic comparative LCA approach. *Building and Environment*, 190:107542, 2021.

[4] Takano A., Winter S., Hughes M., Linkosalmi L. Comparison of life cycle assessment databases: A case study on building assessment. *Building and Environment*, 79:20–30, 2014.

[5] Linkosalmi L., Husgafvel R., Takano A., Valtonen T., Dahl O.. Environmental product declaration of timber products: The impact of allocation method to the impact categories. *Journal of Cleaner Production*, 256:120386, 2020.

[6] Tellnes L.G.F., Rønning A.R. Modelling options for module C and D: Experiences from 50 EPD for wood-based products in Norway. *IOP Conf. Ser.: Earth Environ. Sci.* 323:012052, 2019

[7] Johnsen F.M., Tellnes L.G.F. Verification of Environmental Product Declarations (EPDs) – how strict should it be? *E3S Web of Conferences 349*:08002, 2022

[8] EN 15804+A2 Environmental product declarations - Core rules for the product category of construction products. *European Committee for Standardization, Technical Committee 350, Sustainability of construction works*, 2019.

[9] EN 16485 Environmental Product Declarations - Product category rules for wood and wood-based products for use in construction. *European Committee for Standardization, Technical Committee 175, Round and sawn timber*, 2014.

https://doi.org/10.52202/069179-0594

[10] One Click LCA. Construction Carbon Regulations In Europe - Review & Best Practises. 2022.
[11] The GWS. Strong increase in timber prices due to rising global demand, supply bottlenecks and trade embargoes. https://www.gws-os.com/en/the-gws/news/detail/our-figure-of-the-month-05-2022-strong-increase-in-timber-prices, accessed 05.01.2023.

World Conference on Timber Engineering Oslo 2023

6x6x6: INTRODUCING THE CONCEPT OF REUSE OF TIMBER MATERIALS IN THE 1ST YEAR OF ARCHITECTURAL EDUCATION

Colm O'Brien[1], Anna Røtnes[2], Mads Øiern[3], Petter Kveseth[4], Lone Sjøli[5], Sindre Wam[6], Katherina Putzer[7], Kristoffer Røgeberg[8]

ABSTRACT: 6x6x6 is a student design project in 1st year Architecture that takes place during the spring semester.

In 2022 the students designed a house in timber measuring a maximum of 6m x 6m x 6m. The project focused on teaching students how to use different timber construction principles and how to actively, and creatively, re-use structural timber components. The project had 3 parameters: a timber construction method, a hypothetical site, and a client.

The 6 timber construction methods were columns, beams, plates, trusses, shell, and solid log building (laft). For each construction principle the students were given a specific number of materials to be reused, for example 60 recycled columns 30 cm in diameter. The students produced a timber model of their project in the scale of 1:20 as well as a cross section drawing in the scale of 1:50

This project is the first-time students are introduced to timber as a construction material. They are instructed to look at their principle as more than just a technical requirement but something that inspires design. The result of the project for the students is a better understanding of timber as a construction method, how to incorporate reused materials into their projects, as well as dealing with how a client and a site influence a design.

KEYWORDS: Timber, reuse, education, construction principles

1 INTRODUCTION

In the UN's most recent climate report from March 2023 it was shown that the aim of reducing the global temperature increase to less than 1,5 degrees has become more unrealistic and that more drastic changes in society are needed to tackle the climate crisis [1]. Everyone needs to contribute but architects have an especially important role and responsibility. The building industry contributes up to 40% of the global C02 emissions through building, energy use and the demolition of existing buildings [2].

The climate crisis is immediate and gloomy, but it is important to remember that a crisis also offers new opportunities. The current situation allows us to rethink our way of designing architecture and educating future architects.

One of the clear consequences of the climate crisis and the building boom in Europe the last 10 years is that we need to build less new buildings. It's been suggested that 80% of the buildings that we will be using in 2050 are already built. So, transforming and re-using existing buildings will be a larger and larger part of how architects work.

There is a huge sustainable potential in reusing existing building materials and resources. Research shows that transforming existing buildings can reduce the amount of C02 emissions by 50% in contract to building new. This is mainly associated with the production of building materials and elements [3].

Tine Hegli, professor at AHO, emphasizes that we must have circular economic principles in the building sector: - to reuse resources that are already used would be the most radical approach in terms of reducing emissions [4].

Introducing ideas about reuse early in the education of architecture students is vitally important for the future of the profession. Reuse must be seen as an essential part of the design and building process and the earlier we can introduce this to students the better. The teaching team in

[1] Colm O'Brien, The Oslo School of Architecture and Design (AHO), Colm.Jeremiah.Obrien@aho.no
[2] Anna Røtnes, The Oslo School Architecture and Design, Norway (AHO), anna.rotnes@aho.no
[3] Mads Øiern, The Oslo School of Architecture and Design (AHO), mads.oiern@aho.no
[4] Petter Kveseth, The Oslo School of Architecture and Design (AHO), petter.kveseth@aho.no
[5] Lone Sjøli, The Oslo School of Architecture and Design (AHO), lone.sjoli@aho.no
[6] Sindre Wam, The Oslo School of Architecture and Design, (AHO), sindre.wam@aho.no
[7] Katherina Putzer, The Oslo School of Architecture and Design (AHO), katherina.putzer@aho.no
[8] Kristoffer Røgeberg, The Oslo School of Architecture and Design (AHO), kristoffer.rogeberg@aho.no

https://doi.org/10.52202/069179-0595

first year architecture at AHO have been exploring different ways to thematise reuse in the projects the students work with.

2 REUSE AS A THEME IN ARCHITECTURAL EDUCATION

2.1 FUNDAMENTALS OF THE PROJECT

Students in first year architecture at AHO work on five main design projects throughout the first year of their studies. The projects become increasingly complex as students gain more experience. New parameters and more complex issues like context or construction are introduced with each new project. The fourth project in the year, which starts at the beginning of the spring semester is called 6 x 6 x 6 and has been a part of the course plan since 2020.

6x6x6 project is inspired by the house *Huset i Mellbyedalen* on Bygdøy designed by Terje Moe, completed in 1970. The house is a timber construction with a volume of 6m x 6m x 6m. Moe designed the space for himself and his family. The house contains a living / dining space, 2 bedrooms and an office. Moe designed and built most of the house himself. He had a retractable bench in the living room and a standard tool set which he used to make almost all the elements in the building. [5] This has led to an architecture which is easily understood and readable. It makes for an excellent case study for students to study because of the focus on constructions and creating space being completely interdependent.

The students design a project in timber measuring a maximum of 6m x 6m x 6m. The project focused on teaching students how to use different timber construction principles The project had 3 parameters: a timber construction method, a hypothetical site, and a client/ function. The 6 timber construction methods were columns, beams, plates, trusses, shell, and solid log building (laft).

In 2021 we introduced how to actively, and creatively, re-use structural timber components as part of the construction method.

2.2 MATRIX

6 x 6 x 6 refers to the size of the project the students will work on but also to a matrix we have set up to create enough variations between the three parameters to guarantee that no students end up with the same combination of factors.

The students receive a brief with all the required information for the project at the beginning of the spring semester. Students are introduced the project and the 6 construction methods. In the brief we include the matrix with the three parameters (construction method, client, site) and all sixty students. By staggering the 6 options in each parameter it is possible to create 216 unique combinations. This means that none of the 60 students will have the same project. If for example two students have the same client, they will have a different site or a different construction principle.

The matrix is really the DNA of the entire project- it guarantees that all the students work on similar but not the same project, it creates a dynamic class environment, inspiring students to discuss their project with each other without being protective of their own solution. The total work in the project enlightens all the students, it is not 1 project repeated 60 times but 60 individual projects.

The matrix also generates strange and contradictory combinations, for example a solid log building on pier edge, which instead of being problematic create interesting starting points for a project and tests the extents of the construction principle they have been given.

2.3 REUSE

In the 2021 project we included an element of reuse in the construction principle. This was to introduce students to the idea of re use of materials as an essential part of architecture in the future. Students were given a set number of materials to reuse so for example if a student was working with columns, they received 60 reused columns of a set dimension to be incorporated into their project. The students were free to rework the materials in any way they saw fit, for example dividing them or combining them. The students were not limited to only using the reused materials but were encouraged to incorporate them into their design as an integral part of the project.

2.4 SECTION

In the fall semester of their first year in architecture the students work mostly with models and plan drawings. The 6 x 6x 6 project time the first-time students being to work with section drawings as a method of representing a project but also developing the design of a project. The nature of the 6 x 6 x6 project forces students to work in section as the full brief is not possible on one floor plan, this makes the students work with more than one level and vertical connections in their project. Section drawings allow students to fully explore the projects in height as well as in plan.

Section drawings are also a fundamental way of understanding the construction method the students have been given as it encourages them to investigate the floor, roof, and wall construction. Finding out for example the largest span, which direction is the most efficient to span in, standard sizes for construction elements etc.

https://doi.org/10.52202/069179-0595

Matrise

Student	Tomt	Konstruksjons-prinsipp	Beboere	Sparrings-partner
Hennie	mellom to gavler	Søyle	Paul og Eva	1
Maja	skog	Søyle	Julie	4
Mary	stup	Søyle	Louis	6
Cora Linn	skråning	Søyle	Simon	15
Hedda	skog	Skive	Paul og Eva	22
Hanna	elvebredd	Skive	Louis	12
Amalie K.C.	skog	Skive	Simon	4
Sigurd	stup	Skive	Aisha	6
Eine	skråning	Skive	Tom	15
Henrik	mellom to gavler	Skive	Simon	23
Jeppe	forblåst vidde	Skive	Aisha	26
Malin S.F.	mellom to gavler	Skive	Tom	1
Lars Tore	skråning	Skive	Paul og Eva	9
Jiro	mellom to gavler	Bjelke	Simon	2
Lina	elvebredd	Bjelke	Tom	27
Guro	forblåst vidde	Bjelke	Paul og Eva	26
Franziska	stup	Bjelke	Julie	18
Kariann	mellom to gavler	Bjelke	Aisha	2
Julie	stup	Bjelke	Tom	7
Brage	skog	Bjelke	Paul og Eva	5
Gutav	skråning	Bjelke	Aisha	16
Haakon	mellom to gavler	Bjelke	Simon	23
Magda	skog	Bjelke	Louis	22
Sofie	stup	Skall	Paul og Eva	7
William	skråning	Skall	Julie	10
Jenny F.H.	forblåst vidde	Skall	Louis	11
Marie	elvebredd	Skall	Simon	27
Joakim	skog	Skall	Julie	19
Martin	mellom to gavler	Skall	Paul og Eva	24
Martin J.	mellom to gavler	Skall	Simon	3
Teo	skog	Skall	Tom	14
Emanuel	elvebredd	Skall	Aisha	12
Sanna	skråning	Skall	Louis	16

Figure 1_ matrix

https://doi.org/10.52202/069179-0595

Figure 2

Figure 3

Figure 4

https://doi.org/10.52202/069179-0595

3 RESULTS OF STUDENTS' WORK

By the end of the project the students had produced an exciting and wide range of solutions to the parameters they were given. The students had a much deeper understanding of working with timber construction principles by the end of the project. Also, a whole the students learned more about each other's construction's principles leading an increase in the overall knowledge of the class.

Students produced a large 1:20 model of their project and detailed 1:50 drawings. The models in Fig. 2 and Fig. 3 act almost as structural prototypes, allowing students to text spans and thicknesses which relate closely to the real-world dimensions.

The influence of reuse varied from project to project. Some students willingly engaged with reuse as a theme, developing their own briefs and parameters beyond what was set out in the original project description. Some students found existing buildings which were for sale and actively reused these real buildings in their design. This gave their project an extra dimension of reality and tactility.

Other students struggled with differentiating between reused materials or regular materials, The authors believe this problem mostly relates to the hypothetical nature of the project. If students are dealing with a hypothetical material, it is difficult to differentiate or relate to it being new or re used.

4 DISCUSSION AND CONCLUSION

The authors found introducing an element of reuse in a student project in first year to be successful. Students engaged with the theme and were inspired by it. Some students actively incorporated it into their project as a key design driver. However, as it is the first year of their studies the students were limited by how far into detail they could go with reusing materials. More experience developing projects and working with detail drawings would be needed for the theme of re use to be more central in a student's project.
But as the first step towards moving architectural education to embrace the world of reusing timber elements we feel the project was a success.
.
If 2023, we have also included re use of architectural materials and elements into a design project. However, this time the authors have found an existing building in Oslo which will be demolished in the coming year. Students have visited the building, map the existing materials there and have begun making both analogue and digital models of the elements which they will then use in their own project. The project will be finished by May 2023 and the authors believe this strategy of using an existing building to be even more effective as the students will have a tactile relationship to the material, they are re using. It is also a part of their final project, which is twice the length of the 6 x 6 x6 project. This will give the students more time to study the existing materials and explore how they can be used in different ways.

As final note, the authors find the including on reuse to be an inspiring and unpredictable aspect to add into students' design project in first year. The authors are still testing how best to do this but are committed to making reuse a permanent and essential part of the curriculum in first year architecture studio at AHO.

ACKNOWLEDGEMENT

The authors thank the students of GK2 2022, and colleagues at the Institute of Architecture AHO for their support producing this paper.

REFERENCES

[1] Online Report https://www.ipcc.ch/report/ar6/syr/ Last accessed March 23, 2023
[2] The International Energy Agency. https://www.iea.org/topics/buildings
[3] Research Report Sintef 2020: Grønt er ikke bare en farge – bærekraftige bygninger eksisterer allerede
[4] Arkitektnytt 12. august 2021: https://www.arkitektnytt.no/nyheter/kode-r%C3%B8d-for-arkitektene

https://doi.org/10.52202/069179-0595

World Conference on Timber Engineering Oslo 2023

FINDINGS FROM THE 2022 NORTH AMERICAN MASS TIMBER RESEARCH NEEDS ASSESSMENT WORKSHOP

Samuel L. Zelinka[1] Richard Bergman[2], Marco Lo Ricco[3], William A. Martin[4], Bill Parsons[5], Iain Macdonald[6], Jennifer Cover[7]

ABSTRACT: The 3rd North American Mass Timber Research Needs Assessment Workshop sponsored by the US Forest Service, Forest Products Laboratory was held September 20-22, 2022. The purpose of the workshop was to convene experts on mass timber and cross laminated timber to develop a prioritized list of research needs for the North American mass timber industry. Invited workshop participants included design professionals, academics, industry leaders, and government employees. The workshop built upon prior mass timber research needs workshops that were conducted in 2015 and 2018.

KEYWORDS: mass timber, cross laminated timber, building codes, structural design, fire design, life cycle analysis, economics

1 INTRODUCTION

Mass timber typically refers to engineered wood composites such as cross laminated timber, glulam, and structural composite lumber that have been laminated into large members with unique fire and structural properties. Of the composites that comprise mass timber, cross laminated timber (CLT) has received the most attention in recent research [1-3].

CLT is unique among mass timber composites in that it consists of large panels (up to 18 m long) that can be shipped to the job site with precut fenestrations and easily erected as wall or floor systems [4,5]. CLT was first recognized in the International Building Code (IBC) in 2015 [6]. Following this recognition within the IBC, interest in mass timber, especially CLT has rapidly increased within the United States and Canada. As of December 2022, the number of projects using modern MT and post-and-beam construction in multifamily, commercial, and institutional buildings had grown to 1,677 across all 50 states in the United States, an increase of approximately 40% in just 18 months [7].

In 2015, the US Forest Service, Forest Products Laboratory held a workshop to characterize what was needed to move the mass timber industry in North America forward [8]. A subsequent meeting was held in 2018 [9]. These research needs workshops helped to focus research activities and funding towards high impact research projects within the field of mass timber. Since the original workshop in 2015, research findings have justified code changes that have resulted in increases to the height and area requirements for mass timber buildings recognized within the 2021 and 204 version of the IBC [10].

2 2022 NORTH AMERICAN MASS TIMBER RESEARCH NEEDS WORKSHOP DEMOGRAPHICS

The workshop organizers solicited participation from members of industry, academia, government, and other research institutions. In total there were 132 workshop participants.

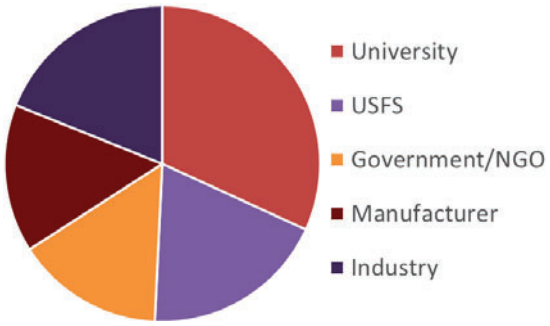

***Figure 1**: Professional composition of the 2022 North American Mass Timber Research Needs Workshop.*

[1] Samuel L. Zelinka, Forest Products Laboratory, United States, Samuel.L.Zelinka@usda.gov
[2] Richard Bergman, Forest Products Laboratory, United States, Richard.D.Bergman@usda.gov
[3] Marco Lo Ricco, Forest Products Laboratory, United States, Marco.LoRicco@usda.gov
[4] William A. Martin, Forest Products Laboratory, United States, William.Martin2@@usda.gov
[5] Bill Parsons, WoodWorks, United States, bill.parsons@woodworks.org
[6] Iain Macdonald, TallWood Design Institute, United States, iain.macdonald@oregonstate.edu
[7] Jennifer S. Cover, WoodWorks, United States, jennifer.cover@woodworks.org

https://doi.org/10.52202/069179-0596

Figure 1 illustrates the composition of the workshop attendees. The largest group was University participants, with 42 members. The US Government had 32 attendees. The remaining 58 participants represented the industry, including non-governmental organizations that represent the wood industry. The geographical locations of the attendees are shown in (Figure 2), and is highly correlated with North American forest products manufacturing production in the Southeast US, Northeast US and Eastern Canada, and the West Coast of the US and Canada.

Figure 2: *Geographical location of the participants.*

Interestingly, nearly two-thirds of workshop participants had not participated in any of the previous mass timber research-needs workshops. Twenty percent of participants had participated in both previous workshops (Figure 3).

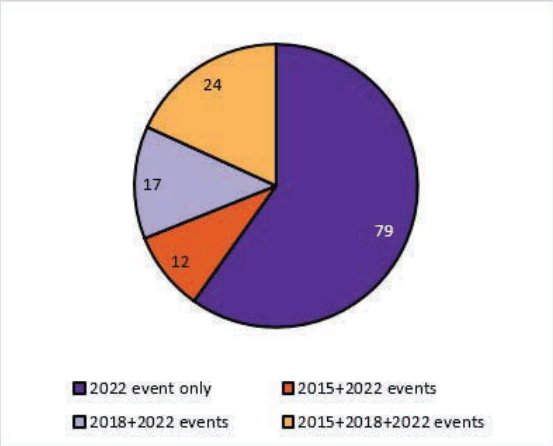

Figure 3: *Number of workshop attendees that had attended either the first or second Research Needs Workshops.*

3 PRIORITIZING RESEARCH NEEDS

Workshop participants were asked to give numerical scores to each research topic (Table 1) in both "effort" and "impact". The results were then plotted in real time on an impact-effort graph (Figure 4). The zero to one hundred scale of *effort* was calibrated by equating fifty percent effort with a 2-year $500,000 total investment of research time and money. This mark was chosen as it corresponds with a single Wood Innovation Grant. No other scaling was offered, so participants had to discuss and judge lower and higher impact efforts as a multiple of the time and budget assigned to the fifty percent effort. Scaling for *impact* was much less certain, because workshop participants were instructed to consider a variety of criteria. High impact could be judged by moving large volumes of wood, making commercial construction more sustainable, or developing a technology that fulfils a niche that competing materials cannot satisfy.

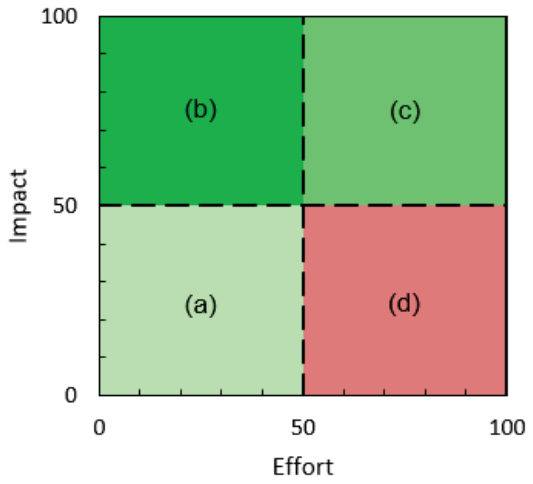

Figure 4: *Example of the impact effort matrix used to plot the results of the research needs symposium.*

Proponents of the impact-effort matrix recommend this type of group evaluation, because the results may be plotted and divided into four quadrants that may assist prioritization [11]. According to the vernacular terms, the bottom left (a), top left (b), top right (c), and lower right (d) quadrants respectively represent *incremental* gains, *easy wins*, *big bets*, and *money pits* [12]. Gilad critiques the standard effort-impact ranking system because people often underestimate effort and overestimate impact. To account for this bias, Gilad suggests using confidence values to redraw proportions of the chart quadrants, which typically renders the regions unequal in size. In addition, Gilad argues that negative impacts should be considered to identify potential *loss generators* in a fifth region of the plot.

https://doi.org/10.52202/069179-0596

3.1 BREAKOUT SESSION TOPICS

The workshop contained seven breakout sessions for the prioritization of research needs. Workshop participants were divided into four rooms for the prioritization of research needs. Each room contained a moderator and a notetaker. An effort was made to shuffle the composition of the breakout rooms throughout the workshop while keeping the overall demographics similar to the workshop demographics (Figure 1).

Each of the seven breakout sessions covered a different topic (Table 1). Most breakout sessions were two hours long. However, the breakout sessions for "Architectural Research and Construction" and "Sustainability and Economic Analysis" were each only 1 hour long.

Table 1: *Breakout session topic areas*

Order	Subject
1	Fire performance
2	Durability and building physics
3	Architectural and construction research
4	Structural system design and performance
5	Materials and manufacturing processes,
6	Sustainability and economic analysis
7	Infrastructure and nonbuilding applications

The moderators began each session by collecting scores on ten topics that were identified as research needs by the meeting organizers. These topics were typically developed by identifying high priority topics from the previous workshop [9] that had not been addressed.

The 10 research topics suggested for prioritization in the *fire performance* breakout session are included below.

Table 2: *Topics prioritized in the fire performance breakout session*

Order	Subject
1	Non gypsum methods of encapsulation/fire protection
2	Penetrations in CLT for fire protection
3	Char rates for CLT (linear/non-linear models)- extending out to 3 hours
4	Safe amounts of exposed CLT
5	Hybrid connections (Steel + CLT)
6	Adhesives, lamella thicknesses, and delamination risk
7	Minimum separation distances for exposed mass timber surfaces (column to wall/floor or corner)
8	Fire spread in cavities and concealed spaces
9	Construction fires in mass timber buildings
10	Traveling fires in open floorplans

In addition to these research topics, moderators and notetakers were encouraged to collect "write-in" topics from the audience. These write-in topics were also scored within rooms.

3.2 DATA ANALYSIS

Following the workshop, the scores for research topics were then compared across rooms. Each room had a different method for determining a consensus score for the research topic. The polling method in one room asked participant to raise hands at the beginning of each polling period and lower them, when the level of effort that was called out seemed too high. Some hands were lowered early, while others remained up for the entirety of the topic scoring. The moderator, having the best perspective of the entire room had to judge the consensus score, based on values when most participants lowered hands. In other rooms, vocal participants proposed an initial score and revised it higher and lower via debate. Because individual and anonymized input was not recorded during the live polling sessions, the consensus score may be significantly influenced by moderator discretion and peer interactions within each room.

To account for these differences across rooms, it is important to examine both the mean value of the score along with the variation in the score across rooms. To illustrate this variation in the impact-effort matrices, a diagonal line was included for each data point. The length and slope of the error bars provides more insight. Short error bars indicate good consensus, in contrast to long error bars that indicate dissension among the consensus scoring of each room. Error bars with a shallow slope,

nearly horizontal, indicate variations in assessing effort while there is general agreement on impact. Error bars with a steep, nearly vertical slope, indicate variations in assessing impact while there is general agreement on effort. Diagonal error bars of approximately one-to-one slope indicate differences in judging both impact and effort. The absence of an error bar typically indicates that a *write-in* topic was mentioned and scored only in one of the discussion rooms.

4 RESULTS

4.1 FIRE PERFORMANCE

The impact-effort graph for the fire performance breakout session is shown in Figure 5. The pre-determined topics for the group are illustrated as numbered topics shown in Table 2 and the write-in topics are listed in Table 3.

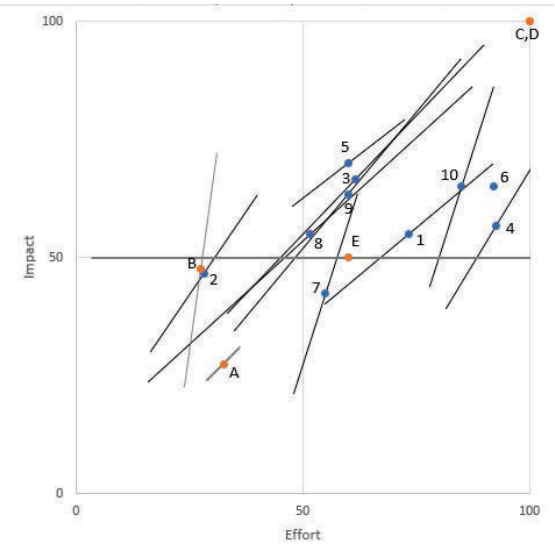

Figure 5:*Impact-Effort matrix for the fire performance breakout session. Numbered points refer to prepared research topics. Lettered points refer to a write-in topic. The topics associated with the numbers and letters are given in Table 2 and Table 3.*

Numerical values of the effort and impact along with the coefficients of variation are given in
Table 4. No topics in the fire research were ranked as "easy wins", that is, lying in the top left quadrant. However, Item B was nearly ranked as an easy win, falling just below the 50% impact. This item involved developing a database of fire tests that could be used for code approvals.

The fire research breakout session had only one item that could be characterized as fell in the lower right quadrant of the graph. This research topic involved determining the minimum safe separation distances for exposed wood members in mass timber structures. It should be noted that different rooms had a widely different view of the impact of this research item; the coefficient of variation was 50%. Most items fell in the upper-right quadrant (which Gilad [12] calls "*big bets"*). This speaks to the cost, and potential impacts of additional fire testing on mass timber.

Table 3: *List of write-in topics for the fire performance breakout session.*

	Subject
A	Post fire impacts: insurance loss models and post-fire repair.
B	Database development for approvals (prescriptive and performance-based design)
C	Fire retardant treated CLT
D	Exterior fire protection systems for mass timber buildings/infrastructure/structures
E	Development of guidelines or tools for performance-based design

Table 4: *Average effort and impact of the topics discussed in the fire performance breakout session along with their coefficients of variation (COV). A description of the items is given in Table 2 and Table 3. There was no COV for Item 6 as only one session provided results.*

	Average		**COV**	
	Effort	**Impact**	**Effort**	**Impact**
Item 1	73	55	25%	27%
Item 2	28	47	42%	36%
Item 3	62	67	46%	43%
Item 4	93	57	12%	31%
Item 5	60	70	20%	13%
Item 6	92	65	-	-
Item 7	55	43	13%	50%
Item 8	52	55	69%	57%
Item 9	60	63	42%	45%
Item 10	85	65	8%	33%
A	33	28	11%	13%
B	28	48	13%	52%
C	100	100	-	-
D	100	100	-	-
E	60	50	94%	0%

https://doi.org/10.52202/069179-0596

4.2 STRUCTURAL SYSTEM DESIGN AND PERFORMANCE

The impact-effort graph for the structural system design and performance breakout session is shown in Figure 6. The prepared topics for the group are illustrated as numbered topics (1-10) and the numbers correspond with the topics in Table 2 and the write-in topics are listed in .6 and are represented by numbers 11-25.

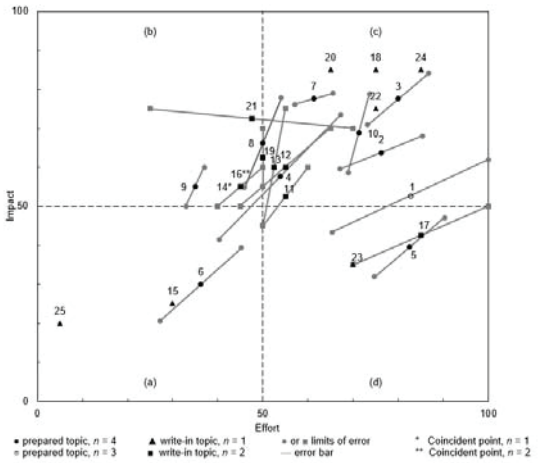

Figure 6: *Impact effort matrix for the structural system design and performance breakout session. Numbered points refer to prepared research topics. Lettered points refer to a write-in topic. The topics associated with the numbers are given in Table 5 and 6 .*

Table 5: *Topics prioritized in the structural system design and performance breakout session*

Order	Subject
1	Full-scale validation testing of structural assemblies (seismic, wind, blast, or progressive collapse simulations)
2	Braced frame development of various configurations (BRBs, specially detailed, concentric, range of ductility R = 3 to R = 6, etc.)
3	Shear wall development of various configurations (rocking post-tensioned or passive, conventional, hybrid, stiff R= 1.5 vs. ductile R= 6, etc.)
4	Diaphragm development of various configurations (simple span, cantilever, service, failure, load and displacement capacity, chord and fastener details)
5	Moment-frame development of beam-to-column connections (post-tensioned or passive systems)
6	Protective performance for multi-hazard resilience (wind-launched debris, blast and ballistics, disproportionate/progressive collapse)
7	Two-way slab development (post-tensioning, punching shear, load distribution, etc.)
8	Glued-in and cast-in connection development for improved force transfer in panelized and hybrid assemblies
9	Perp to grain bearing capacity and characterization of deformations under uniform and varying loads
10	Mass timber slab development for composite action, enhanced stiffness and vibrational characteristics

https://doi.org/10.52202/069179-0596

Table 6: *Write-in topics for the structural systems design and performance session*

	Subject
11	Standardization of mass timber rocking walls
12	Compare panelized SCL alternatives to CLT (e.g. GLT, NLT, DLT, LVL, MPP)
13	Mass timber moment connections
14	Screw reinforcement of mass timber
15	Edgewise bending of CLT beams
16	Penetrations and holes through mass timber panels and beams
17	Full-scale progressive collapse testing
18	Connection details for seismic displacement compatibility
19	Period estimation via vibrations monitoring for seismic and wind design
20	Intermediate shear wall - ordinary with ductile hold downs
21	Reinforcing at notches/openings of mass timber panels and beams
22	Timber-to-timber composites and built-up structural members
23	Full scale blast testing- windows, connector system
24	Seismic tests of 4-8 story buildings with fully wood systems
25	CLT tornado saferooms

The structural design section contained one item that fell into the lower right quadrant of the graph, Item 5, "Moment-frame development of beam-to-column connections (post tensioned or passive systems). The session also contained one "*easy wins*" in the top right quadrant, Item 9, "Perp to grain bearing capacity and characterization of deformations under uniform and varying loads." A summary of the scores along with the coefficients of variation are given in Tables 7 and 8.

Table 7: *Average effort and impact of the topics discussed in the structural system design and performance breakout session along with their coefficients of variation (COV). A description of the items is given in Table 5.*

Topic	Average		COV	
Number	Effort	Impact	Effort	Impact
1	83	53	36%	31%
2	76	64	24%	13%
3	80	78	17%	17%
4	54	58	50%	55%
5	83	40	19%	38%
6	36	30	50%	62%
7	61	78	14%	4%
8	50	66	16%	35%
9	35	55	12%	18%
10	71	69	7%	29%

Table 8: *Average effort and impact of the topics discussed in the structural system design and performance breakout session along with their coefficients of variation (COV). A description of the items is given in*

Topic	Average		COV	
Number	Effort	Impact	Effort	Impact
11	55	53	13%	20%
12	53	60	26%	24%
13	53	60	7%	35%
14	45	55	-	-
15	30	25	-	-
16	45	55	16%	13%
17	85	43	25%	25%
18	75	85	-	-
19	50	63	0%	17%
20	65	85	-	-
21	48	73	67%	5%
22	75	75	-	-
23	70	35	-	-
24	85	85	-	-
25	5	20	-	-

Note: COV = Coefficient of variation
No COV reported if $n = 1$
$n = 2$ unless noted otherwise

4.3 OTHER BREAKOUT SESSIONS

Given the space constraints of the proceedings paper, it is not possible to present all the data collected at the 2022 Mass Timber Research Needs Workshop. However, the full proceedings from the workshop will be available from the Forest Products Laboratory and WoodWorks.

5 FUTURE WORK

The research needs collected during the 2022 Mass Timber Research Needs Workshop will be used to guide mass timber research over the next few years. Coordinated efforts on mass timber research can continue to help the adoption of CLT and other engineered wood composites in building sectors of the United States and Canada.

6 ACKNOWLEDGEMENT

The workshop was partially funded through a joint venture agreement, 21-JV-11111137-026 between the US. Forest Products Laboratory and WoodWorks – Wood Product Council. The findings and conclusions in this report are those of the author(s) and should not be construed to represent any official USDA or U.S. Government determination or policy.

7 REFERENCES

1. Stegner, H.; Fotheringham, N. Research and Testing Lead to Historic Code Change: The History of Getting a Sustainable Tall Building

https://doi.org/10.52202/069179-0596

Option—Mass Timber—Approved in the U.S. Building Codes. *Forest Products Journal* **2022**, *72*, 226-234, doi:10.13073/2376-9637-72.4.226.
2. Dawson, E.; Anderson, R.; Muszynski, L. *International Mass Timber Report*; Forest Business Network: Missoula, MT, 2022.
3. Ding, Y.; Pang, Z.; Lan, K.; Yao, Y.; Panzarasa, G.; Xu, L.; Lo Ricco, M.; Rammer, D.R.; Zhu, J.Y.; Hu, M., et al. Emerging Engineered Wood for Building Applications. *Chemical Reviews* **2022**, 10.1021/acs.chemrev.2c00450, doi:10.1021/acs.chemrev.2c00450.
4. Mohammad, M.; Gagnon, S.; Douglas, B.K.; Podesto, L. Introduction to Cross Laminated Timber. *Wood Design Focus* **2012**, *22*, 3-12.
5. Jakes, J.E.; Arzola, X.; Bergman, R.; Ciesielski, P.; Hunt, C.G.; Rahbar, N.; Tshabalala, M.; Wiedenhoeft, A.C.; Zelinka, S.L. Not Just Lumber—Using Wood in the Sustainable Future of Materials, Chemicals, and Fuels. *JOM* **2016**, *68*, 2395-2404.
6. Parajuli, R.; Gale, C.; Vlosky, R.; Martin, R. An Overview of Cross-Laminated Timber in North America. In Proceedings of Increasing The Use Of Wood In The Global Bio-Economy. 12th International Scientific Conference WoodEMA 2018, Belgrade, Sebia, September 23rd-28, 2018.
7. WoodWorks. Building trends: mass timber. Available at https://www.woodworks.org/publications-media/building-trends-mass-timber/. WoodWorks: Washington, DC, 2021.
8. Williamson, T.; Ross, R.J. *Proceedings: Mass Timber Research Workshop 2015. General Technical Report FPL-GTR-247*; U.S. Department of Agriculture, Forest Service, Forest Products Laboratory: Madison, WI, 2016; pp. 364.
9. Zelinka, S.L.; Williamson, T.; Martinson, K.L.; Ritter, M.A. *Research Needs Assesment for the Mass Timber Industry: Proceedings of the 2nd North American Mass Timber Research Needs Workshop. General Technical Report FPL-GTR-273*; U.S. Department of Agriculture, Forest Service, Forest Products Laboratory: Madison, WI, 2019; pp. 43.
10. Anon. *International Building Code*; Delmar Cengage Learning: Florence, KY, 2021.
11. Helmke, S. WHERE DO YOU START WHEN EVERYTHING FEELS URGENT? Use an effort-to-impact matrix. *The Learning Professional* **2022**, *43*, 72-74.
12. Gilad, I. Why The Impact Effort Prioritization Matrix Doesn't Work. Availabe online: https://itamargilad.com/why-impact-effort-prioritization-doesnt-work/ (accessed on Nov. 3).

World Conference on Timber Engineering Oslo 2023

HYBRIDTIM, DESIGN AND CONSTRUCTION OF ENVIRONMENTAL HIGH PERFORMANCE HYBRID ENGINEERED TIMBER BUILDINGS

Kamyar Tavoussi[1], Alireza Fadai[1], Laia Haurie[2]

ABSTRACT: Immediate actions need to be taken to reach the sustainability target for 2050 of the European Commission for reduction of greenhouse gas emissions and net zero carbon (CO_2) emissions. Architects and engineering companies have already started designing hybrid timber buildings. In order to satisfy the needs of the labor market, it is necessary to prepare students with innovative applied skills in the area of design, construction and onsite construction management of hybrid timber buildings. The HybridTim project promotes sustainable, environmentally friendly design and construction of hybrid timber buildings.

KEYWORDS: Multi-story buildings, hybrid structures, study module, Erasmus+ program

1 INTRODUCTION

To educate a new generation of students, it is necessary to develop and integrate an innovative multi-disciplinary BSc/BA study module. Main target groups are higher education institutions (HEIs), in particular teachers/trainers and BSc/BA students.
Project HybridTim [1] aims to fulfil the future demands in higher education of students in design and construction of high environmental performance hybrid engineered timber buildings by trans-disciplinary innovative student-centered learning approaches. The objectives are:
1) To develop and deliver new trans-disciplinary module on design and construction of engineered hybrid timber buildings, which meets the needs of the HEIs and labor market representatives.
2) To improve competencies of students and teachers in problem solving and teamwork, innovative thinking, motivation, awareness of cross-professional project input and project management by using project-based learning, learning by doing and blended learning approaches.
3) To educate all participants (students, teachers, entrepreneurs) in the field of the engineered hybrid timber construction.
4) To ensure open awareness of the project results to local, national, European Union (EU) level and international target groups. The project is implemented by five higher education institutions from Denmark (Via University College, VIA UC), Lithuania (Vilniaus Gedimino Technikos Universitetas, VGTU), Spain (Universitat Politècnica de Catalunya, UPC), Latvia (Rigas Tehniska Universitate, RTU) and Austria (Technische Universitaet Wien, TU WIEN), assisted by Study and Consulting Center in Lithuania and Spanish association Gremi Fusta i Moble.

The aim is the development of a module of 9 ECTS (**E**uropean **C**redit **T**ransfer and Accumulation **S**ystem) for bachelor. The module will be dedicated to architectural design, architectural technology, construction technology, civil engineering, real estate management and related BSc/BA specializations. Working on one project in an intensive course seems to be the most effective way to transfer the knowledge to students. A module of 9 ECTS in one semester is recommended. Each HEI will adapt this module to local requirements. It means that also 3 times 3 ECTS courses in 3 following semesters are possible and optional. In this case it would be necessary to get sure, that the students are going through all courses.

2 MODULE PHASES

The new module will be tested during the project in three intensive learning/teaching courses. The first part of the module was held in Vienna, Austria in September 2021. The second part took place in Spain (September 2022) and the third one will take place in Latvia (April 2023). International building and construction project phases, which are used in most EU countries, have been adapted in the HybridTim project as a main template, namely brief phase, outline proposal, scheme design, detail 1 and detail 2 phases.

[1] Kamyar Tavoussi, Institute of Architectural Sciences, Structural Design and Timber Engineering Vienna University of Technology, Austria, tavoussi@iti.tuwien.ac.at

[1] Alireza Fadai, Institute of Architectural Sciences, Structural Design and Timber Engineering, Vienna University of Technology, Austria, fadai@iti.tuwien.ac.at

[2] Laia Haurie, Department of Architectural Technology, Universitat Politècnica de Catalunya, EPSEB, Barcelona, Spain; laia.haurie@upc.edu

https://doi.org/10.52202/069179-0597

In total, 75 BSc/BA students will be educated. Students will gain innovative trans-disciplinary knowledge in hybrid timber construction; using innovative learning approaches they will develop their research, teamwork, communication, and cooperation, creative thinking, problem-solving skills required in modern daily work environment. Stakeholders whose activities are related to construction and, in particular, timber construction, e.g. associations and private enterprises, will be involved in development of new module, therefore they will have an opportunity to share their expertise and include the topics that will help to acquire competences, required in labor market. In this way collaboration between academic and business sector will be strengthened.

3 FIRST MODULE IN VIENNA

The first module was held successfully in Vienna in September 2021, 25 students and a dozen lecturers from 5 participating universities took part.
The task was the development of a multi-story hybrid timber building for a given property in the area of "aspern Seestadt" in Vienna's fast-growing 22nd district in the north-east of the city - one of Europe's largest urban development projects. (Figure 1, 2, 3).

Figure 1: *Location of "Seestadt" inside Vienna (@google Earth)*

Figure 2: *Location of building site in "Seestadt" (@google Earth)*

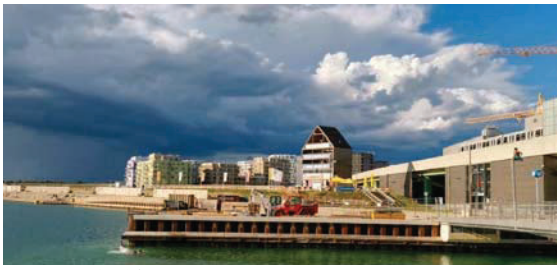

Figure 3: *building site*

The predefined task can be briefly summarized as follows:
"The developer wants to build a 10-story high multi-story house where timber is the dominating material. The plinth level 1-3 (first 3 stories) must be built with concrete as load bearing material. On top of this plinth a terrace must be created/designed, where there is common access for the inhabitants of the building, and also public access for people from the area. From level 1-3 the building must be designed as business-related functions (shops, restaurants, offices etc.) included common access areas is 985m² gross area in 3 floors.
From Level 4-6, there must be designed 8 apartments of different sizes where the apartments included common access areas is 810m² gross area. The rest of the roof for level 3 must be arranged as green area for common use.
From Level 7-10, there must be designed 4 apartments where the apartments included common access areas is 545m² gross area. The rest of the roof for level 6 must be arranged as green area for common use. (Figures 4 and 5).
Generally, the project must not contribute to adverse effects on the surrounding environment. The aim should be for the project to contribute to the improvement of the environment in the area, and to create an attractive building that simultaneously affects users for environmentally responsible behavior."

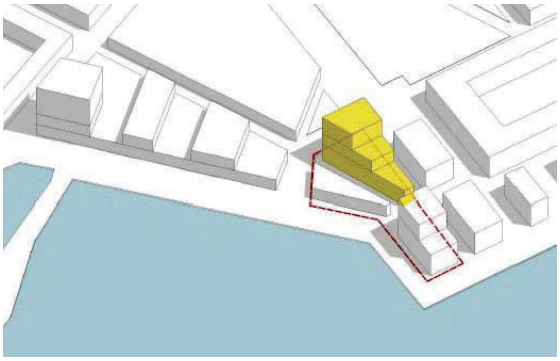

Figure 4: *Predefined building volume*

https://doi.org/10.52202/069179-0597

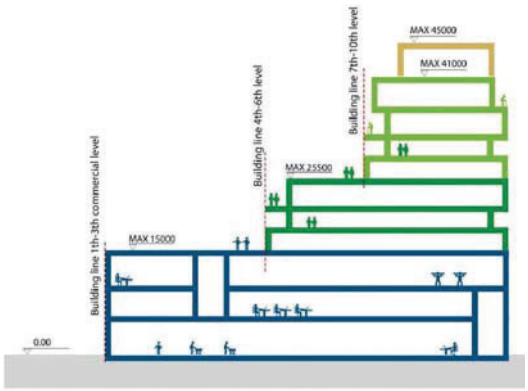

Figure 5: *Predefined section of the building*

Some face-to-face and online lectures have been held in the morning of the first week in the historical building of TU WIEN (Figure 6). The topics were about teaching methodology **p**roblem-**b**ased **l**earning (PBL), Architectural concepts, technical aspects of timber buildings, building management, building systems, statics and dynamics, sustainability, façades and building physics.

Figure 6: *Lectures*

In the afternoon, student groups developed and presented their project ideas (Figure 7).

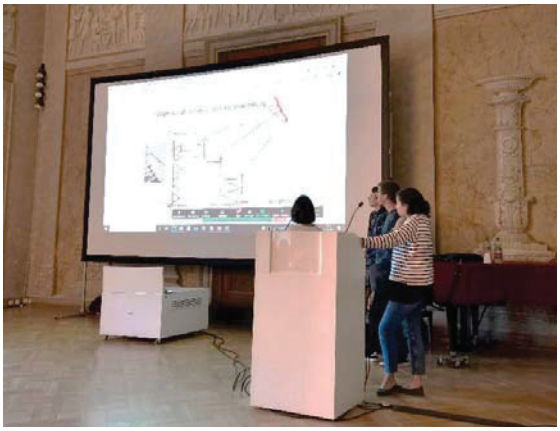

Figure 7: *Student presentation*

In the second week, site visits (Figure 8) and the workshop next to the project property were on the agenda (Figure 9).

Figure 8: *Site visit*

Figure 9: *Workshop*

Five projects were presented at the end.
In the following, one figure per group shall represent the results. The names of the group members are indicated.

https://doi.org/10.52202/069179-0597

Figure 10: *Image by Javier Arés, Christian Regelmann, Reinis Zars, Kipras Dankevicius, Henrikke Lockert-Hansen*

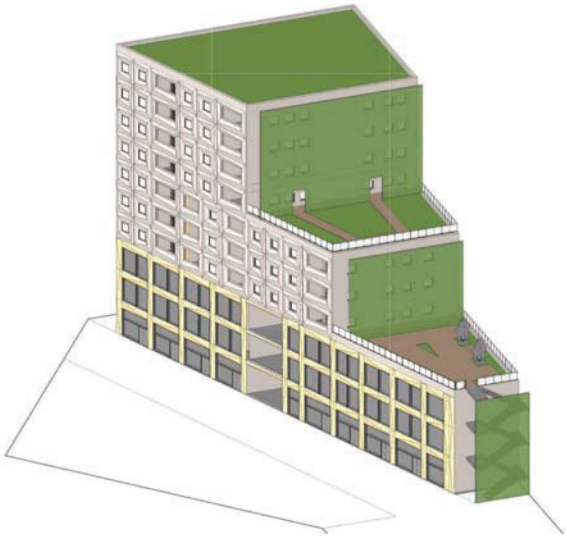

Figure 11: *Image by Asger Overgaard Ottesen, Cesar Pena Ostos, Oksana Generalova, Anna Haijima*

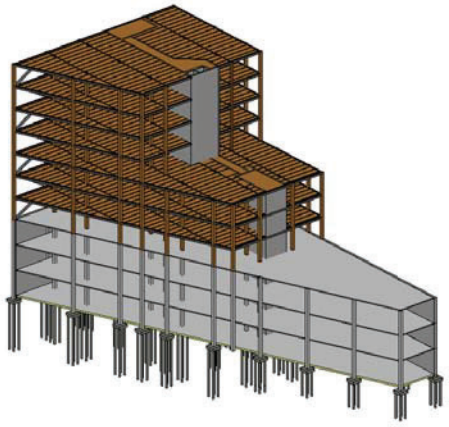

Figure 12: *Image by Aija Pusepa, Theis Trolle, Nada Ahmed, Oscar Galera Lara, Azuolas Skucas*

Figure 13: *Image by María Fernanda Zehl Pardo Valle, Artūrs Dzenis, Karagozaiym Turganbek, Darijus Jankauskas, Thomas Bonde Knudsen*

Figure 14: *Image by Lluc Ruiz Esteve, Peteris Petersons, Søren Gustav Lindstrøm Gleerup, Romualdas Jurgilevicius, Sebastian Eckert*

After the final presentation, the module was finished. (Figure 15)

Figure 15: *Closing day*

https://doi.org/10.52202/069179-0597

4 SECOND MODULE IN BARCELONA

The second module was held in the Barcelona School of Building Construction of the UPC, during two weeks in September 2022. The number of participants was similar to the Vienna course, 25 students from the 5 participant universities and around a dozen lecturers. This intensive course had the aim to cover the scheme design phase of a multi-story hybrid timber building. In order to have enough information about the outline proposal phase it was selected an existing social housing complex located in Barcelona made with reinforced concrete structure and the students had the task to implement a structural system that maximizes the use of timber. The architects of the original project provided us with information and drawings that the students received as starting working material. Figure 16 shows an image of the existing building.

Figure 16: *Social Housing in Trinitat Nova. Source: Ruisánchez Arquitectes*

In the same way as in Vienna, the assignment for the students was contextualized with the area in which they were going to develop the project. In the case of Barcelona, the location was the neighborhood of Trinitat Nova in the district of Nou Barris (figure 17). This district located in the outskirts of Barcelona has one of the lowest household incomes of Barcelona and it is part of a program of urban regeneration from the Barcelona council. Among other actions the council has promoted social housing buildings, recovery of green spaces and increase of public services.

Figure 17: *Map of the districts of Barcelona*

The students were divided in five groups with participants from each university in each group. The task that they had to solve was as follows:

On 2005 the council of Barcelona set a public competition to build 189 units of social housing. The selected project consisted of a main building of ground floor plus 7 floors with a structure of reinforced concrete. The experience has been successful and the residents are happy with the outcome of the project. Now the city council wants to build a new social housing in the neighborhood, but they want to minimize the environmental impact of the building. Therefore, the use of timber structures is highly encouraged. On the other hand, for this project the maximum height restrictions allow to increase the number of floors to ground floor plus 9 floors.

Your studio has decided to modify the project of 2005 and adapt it to the new requirements. Therefore, your work team has to:

- *Implement a timber structural system.*
- *Define a ground plan at 1:50 to define the modularity and the integration of the structural elements in the spatial distribution.*
- *Pre-dimension of the constructive elements. Give one example of the structure and the façade.*
- *Description of the horizontal and vertical efforts and deformations.*
- *Description of the strategies to comply with the fire resistance requirements.*
- *Description of the joint system.*
- *Proposal to guarantee acoustic insulation and to reduce acoustic impact transmittance.*
- *Examples of constructive façade details.*
- *CO_2 footprint of the structural system.*
- *Compliance with the thermal transmittance of the envelope.*

As it can be seen in figure 18, during the course the students received some lectures related with relevant topics to develop the assignment, such as hybrid timber systems, statics and dynamics of timber constructions, acoustics and fire protection strategies. There were also organized technical visits to timber buildings in Barcelona city, including the Nou Barris area (figure 19) and to some timber constructions outside from Barcelona (figure 20).

Figure 18: *One of the lectures of the course*

https://doi.org/10.52202/069179-0597

Figure 19: *Technical visit to a building site near Nou Barris*

Figure 20: *Visit to a Passive House timber building*

The working groups also had time and space to work in their proposal, which they presented on the last day of the course. Figures 21 to 25 display an example of the outputs obtained by each group.

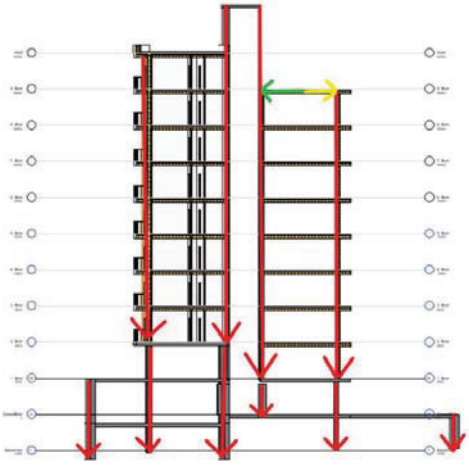

Figure 21: *Description of the effect of vertical and horizontal loads. Image by: Aija Pusepa, Leva Gendvilate, Rasmus Fredskilde, Erika Viviana Beltrat*

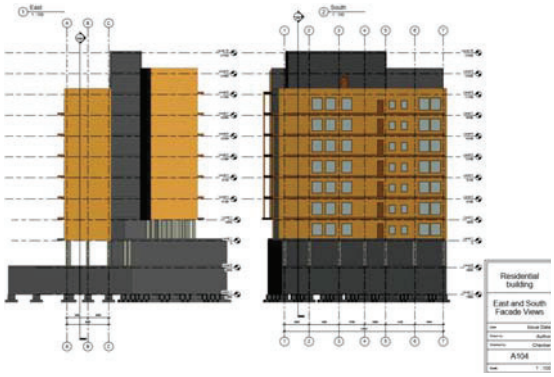

Figure 22: *View of east and south façade. Image by: Hawks Turtles: Emanuel Balaj, Gabriele Remeikaite, Artus Dzenis*

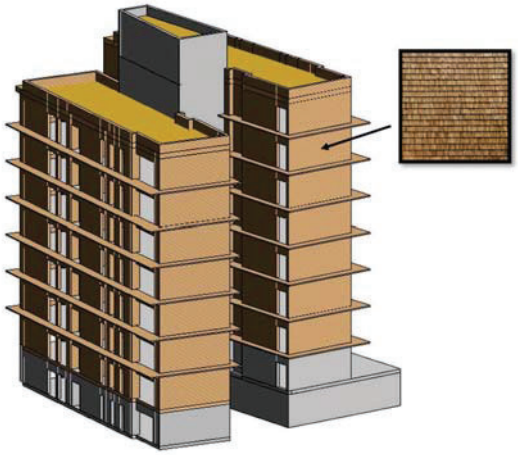

Figure 23: *Proposal of the façade timber cladding. Image by: Christian Regelmann, Lykke Skjerbaek, Ruta Gricenaite, Reinis Zars, Anna Haijima.*

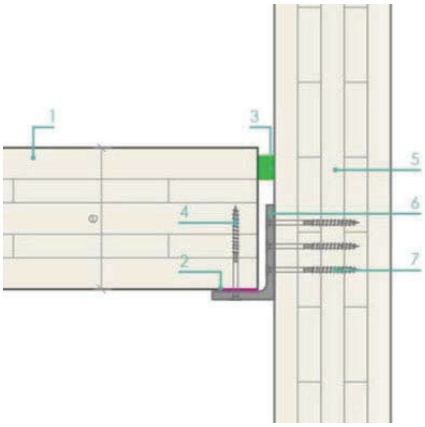

Figure 24: *Detail of a timber-steel joint. Image by Lars Ravn, Mantas Petronis, Usama Malik, Peteris Petersons, Martina Dolic*

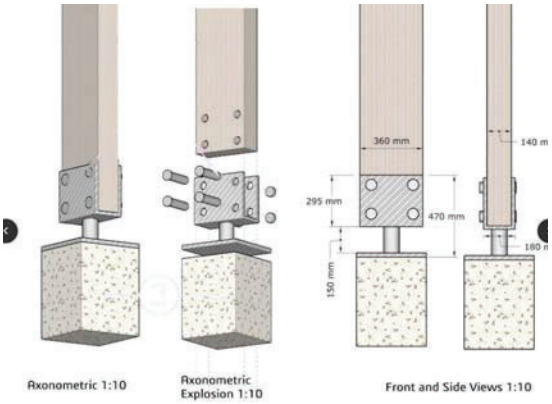

Figure 25: *Detail of the connections of the timber pillars with the concrete floor. Image by Danie HØjlund, Paulius Gadeikis, Andrejs Kavlaks, Karagozaiym Turganbek, MªFernanda Zehl*

https://doi.org/10.52202/069179-0597

5 CONCLUSION AND OUTLOOK

The third module will take place in Riga in April 2023.
In the near future timber buildings will form a much bigger part of the European and international built environment. The future sustainable hybrid timber buildings will be designed and constructed with sustainable-engineered timber components.
The project aims are to fulfil the future demands in higher education of students in design and construction of high environmental high-performance hybrid engineered timber buildings by trans-disciplinary innovative student - centered learning approaches. Along Europe there is still a significant difference in the level of development of timber construction of different countries. This project has allowed the participant institutions to share experiences that could be later implemented in different bachelor degrees at a local level. Participation of professional associations help to increase the collaboration with stakeholders of the building sector

ACKNOWLEDGEMENT

This project, HybridTim 2020-1-DK01-KA203-075045 [1], is funded as an Erasmus+ program for education, training, youth and sport by the European Union.
The authors gratefully acknowledge the support of the UPC, Spain and the TU Wien, Austria.
Special Thanks to project leader Vijoleta Sulciene and all other colleagues for their excellent work: Roger Howard Taylor, Steen Fynbo, Agata Golab-Nielsen, Keld Bossow Nielsen, Frank Bertel, Martin Aicholzer, Daniel Stephan, Laura Tupenaite, Tomas Gecys, Mariana Palumbo, Pilar Giraldo, Edgar Segués, Alina Avellaneda, Ana Lacasta, Janis Zvrigzdins, Girts Zarins, Marta Loza.

REFERENCES

[1] HybridTim, Design and Construction of Environmental High Performance Hybrid Engineered Timber Buildings; https://hybridtim.eu/ (accessed March 5, 2023)

https://doi.org/10.52202/069179-0597

World Conference on Timber Engineering Oslo 2023

HIBIWOOD – DIDACTIC APPROACHES FOR ACADEMIC EDUCATION ON MULTI-STOREY TIMBER BUILDINGS

Elena Mitrenova[1], Martin Aichholzer[2], Aída Santana-Sosa[3]

ABSTRACT: Due to climate change, political and societal demands for the greening of the building sector are increasing. The use of regionally renewable building materials, such as wood, is recognised as one of the main strategies whose potential cannot be fully exploited due to the lack of specialised know-how in the building sector. The present project responds to this challenge through a cross-border cooperation between five European universities. The partnership aims to conduct strategic research on the conditions necessary for the design and construction of multi-storey timber buildings, and to develop guidelines and principles to align the demands of the building sector with current academic education. The transdisciplinary elective module, developed through three international workshops and combined with innovative teaching and learning methods such as problem-based learning (PBL) and integral planning, provides students with specialized training in timber design methods and prepares them for the global requirements and changing demands in the construction industry.

KEYWORDS: cross-border academic cooperation, multi-storey timber buildings, transdisciplinarity, problem-based learning, integral planning, didactic approaches, academic education

1 INTRODUCTION

The EU Green Deal, the EU Taxonomy and the New European Bauhaus are initiatives of the EU Commission that aim at leading Europe into a climate-neutral future by 2050. The construction sector is currently responsible for an immense contribution to global warming, where about 8% of anthropogenic CO2 emissions worldwide come from the manufacturing process of cement [1]. To meet the EU climate targets for the reduction of greenhouse gas emissions, a rethink in the construction industry is unavoidable. One of the greatest opportunities for reducing emissions in the building industry lies in the increased use of regionally, renewable building materials. Timber has excellent constructive properties and is also ideal to bind CO2 in the long term due to its carbon storing effect. In addition, it offers high levels of prefabrication, which means that construction time spent on site can be remarkably reduced compared to conventional methods [2]. Timber is increasingly being used globally, but it requires specific expertise as well as a general rethinking of current planning and construction processes [3]. For fully exploiting its potentials, the current training of civil engineers and architects is still insufficient, especially in highly prefabricated construction, where extensive knowledge is already required during preliminary design due to fire protection, building physics and panelization of building components. The industry needs specially trained experts who understand the technical and economic interrelationships with other trades and building materials, which makes the embedding of timber specific design methods in the civil engineering and architecture curricula necessary [4]. Due to the complexity of the matter, the traditional academic transmission of knowledge is not sufficient. An integrated approach that brings together several disciplines and the acquisition of real-life skills are necessary.

2 HIBIWOOD – PROJECT DESCRIPTION AND OBJECTIVES

The project HiBiWood is implemented within the framework of ERASMUS+ Strategic Partnerships for Higher Education. It aims to satisfy the future demands of European higher education in the field of design and construction of sustainable, high performance building solutions in timber. It explores the following questions: how to integrate the latest timber-specific knowledge in the classic university curricula and how to guide students during the learning process by applying innovative didactic approaches. The cross-border partnership of five European universities (FH Campus Vienna, Austria; HAMK Finland; RBC Latvia; Cracow University of Technology, Poland and KVK Lithuania) ensures the international exchange of knowledge on sustainable building practices and increases the competences of all project participants (students, teachers, but also construction companies). The main target groups are European higher education institutions, especially teachers/trainers and BSc/BA students of architecture, civil engineering and building site management.

[1] Elena Mitrenova, Vienna University of Applied Science Campus Wien, Austria, elena.mitrenova@fh-campuswien.ac.at
[2] Martin Aichholzer, University of Applied Science Campus Wien, Austria, martin.aichholzer@fh-campuswien.ac.at
[3] Aída Santana-Sosa, Vienna University of Applied Science Campus Wien, Austria, aida.santana_sosa@fh-campuswien.ac.at

https://doi.org/10.52202/069179-0598

Focus of the project is the assessment of the framework conditions and requirements for planning and implementation of multi-storey timber buildings in the partner countries. A comprehensive survey was conducted among over 100 companies and experts within the timber construction industry, using a combination of questionnaires and expert interviews as the data collection methods. The results of the survey indicated a critical need for skilled workers within the timber construction sector. Over 70% of the respondents indicated that recent graduates lack the fundamental knowledge and expertise in timber construction. An analysis of the data revealed that a lack of familiarity with the matter among architects is crucial for the timber construction industry, as architects who were not well-versed with the material were unlikely to design wooden buildings due to time and respectively financial constraints. Furthermore, architects who are specialized in the subject often face challenges in finding contractors to execute their buildings.

A comparison of the markets in Austria and Finland with those in Poland, Latvia, and Lithuania showed that the former had a significant advantage due to the presence of companies producing high-quality timber building products. In contrast, the need to import them in the latter countries results in increased costs for erecting timber buildings and consequentially in a significantly smaller percent of constructed multi-storey timber buildings nationwide. Although all the analysed countries have traditional wooden constructions, projects of modern high-performance timber buildings are still mainly limited to the scale of single-family houses. Multi-storey residential buildings and larger-scale structures using wood construction are scarce in the case of Poland, Latvia, and Lithuania, and underrepresented in the case of Austria and Finland. However, due to political interest and related strategic programs promoting timber construction in Austria and Finland, there has been a growing trend of constructing multi-storey wooden buildings in these countries.

This tendency is also reflected in the education and training programs for timber construction specialists. Strategic research on available timber-related education in the respective countries is conducted with the aim to identify gabs and inconclusiveness with the requirements of the construction industry. In Poland, Latvia, and Lithuania, timber construction topics are minimally included in educational programs, while in Finland and Austria, they are widely offered as part of the bachelor's and master's programs in architecture and civil engineering at various universities and universities of applied sciences. In some cases, the topic is becoming increasingly essential to construction studies due to the high demand for multi-story timber buildings.

However, educational analysis and company surveys indicate an inconsistency between the programs offered and the graduates' perceived lack of real knowledge and know-how by the companies. The complex nature of timber construction may explain these results, as the design and implementation of timber buildings require a comprehensive understanding of various legal, planning, technical, economic, and logistical aspects. Knowledge transfer of these aspects should occur gradually and simultaneously, as close to reality as possible and in an interdisciplinary way, to create a tangible and long-term understanding of the matter.

Based on the analysis, guidelines and principles are developed jointly by the universities. The identified challenges are addressed through a transdisciplinary elective module with nine ECTS, that will be embedded in the academic programmes of the partner universities. The module is designed to provide a comprehensive coverage of the key aspects related to multi-story timber construction – architectural design, structural systems, timber technology, building physics, building site management. The approach taken is interdisciplinary and holistic, integrating these various aspects in all module phases, with varying levels of depth to address students with different levels of knowledge. Simultaneously, it complements conventional academic teaching by implementing innovative approaches, as integral planning, problem-based learning, problem solving, learning by doing and blended learning.

3 DIDACTIC APPROACH AND METHODOLOGY

At the core of the didactic concept of the module is the PBL method (problem-based learning) [5] [6] – students from different European countries and fields of study (architecture, civil engineering and building site management) plan a multi-storey building in timber in small groups, carrying out all real-life project phases (from preliminary design to detailed planning and building site management) and implementing sustainable principles. Three workshops are held as part of the project (Vienna 2021, Cracow 2022, and Riga 2023), which serve as test runs for the development of the module curriculum. Each workshop focuses on different real-life project phase (architectural design, construction solutions and building site management), while dealing simultaneously and holistically with the complexity of planning a multi-story timber building. The workshops require the collaboration and mutual understanding of the different disciplines involved, while visits to timber construction companies provide a realistic picture of acute challenges in the timber construction industry. The following subchapters will give an overview of the concrete didactic approaches and the tasks of the individual workshops.

3.1 WORKSHOP VIENNA 2021 – ARCHITECTURAL DESIGN AND “THINKING” IN TIMBER

Bachelor students of architecture, building site management and civil engineering enrolled in the 2nd and 3rd year of their respective programs were brought together within an international and integral design workshop. Having a team of different disciplines involved and working together from the conceptual phase is essential for optimizing the design process and increasing prefabrication level of timber buildings. A well-coordinated team encourages creativity while simplifying the design. This approach minimizes confusion and misunderstandings between team members, resulting in a more streamlined planning process. The diverse

https://doi.org/10.52202/069179-0598

perspectives of an interdisciplinary team allow for early identification of interdependent planning decisions and their consequences, providing a solid foundation for making informed decisions in the early stages of the project.

Nevertheless, the project faced some challenges regarding this approach. A comprehensive knowledge across various disciplines simultaneously, including structural systems, building physics, and timber technology is required for the design phase of wooden buildings. The lack of education in timber construction offered in the partner universities resulted in limited prior knowledge among the participants. To adequately apply the PBL-method in the design of a timber building, students must be brought up to an appropriate level of knowledge and taught how to "think in timber" – conceptualize construction using timber as a primary material. The issue was addressed through a preparatory exercise in which students were organized into groups of 5 and assigned the task of analysing an existing timber building using specified criteria. The parameters for analysis were: 1) architecture: concept, typology, plans, urban integration, flexibility; 2) structural system: vertical and horizontal load transfer, bracing; 3) building construction: timber technology, details, assembly site and construction process, tendering process, joining technology; 4) building physics: sound, head and moisture management, fire protection; 5) sustainability concept: social, ecological (life cycle assessment), and economical; dismantling strategies. The comprehensive theoretical and technical research and analysis served as a foundation for future elaboration of the workshop assignment.

The two-week workshop was conducted in September 2021 at the University of Applied Sciences Campus Vienna. The thirty students from the five universities who participated in the project were organized into six multidisciplinary teams. Each team was composed of three architects and two representatives from the fields of civil engineering and/or building site management.

The primary objective of the project was to create high-quality residential units with flexible planning and direct access to outdoor spaces. To achieve this, the focus of the project development was to explore and exploit the potential of industrial prefabrication, including an organized configuration grid with high architectural quality that allows modular-based construction with the possibility of small modifications for customisation. The workshop tasked the students to design a multi-storey timber building with 3 to 4 storeys tailored to the needs of young people and young families. The design should include individual flats with sizes of 30 to 45 m2 and larger ones of approx. 60 to 90 m2, with the possibility that two small flats could be merged into one bigger flat. Additional common areas, community rooms, gardens and a bicycle storage room should be included for better usability of the residential area and staircase. The construction should meet the criteria of an Austrian construction class III and the maximum building height should not exceed 11 meters. Furthermore, the design had to be quick and cost-effective, with innovative serial or modular construction, high architectural quality, and the greatest possible conservation of resources in production, construction, operation, and dismantling. In terms of sustainable conceptualisation, the life cycle aspect, and the question of reuse (resource-saving, dismantling, and recycling) were also highlighted.

The project partners provided continuous guidance and supervision to the students throughout the duration of the assignment, as well as face-to-face lectures that covered the essential planning aspects of timber buildings. These lectures were introductory in nature and aimed to provide a comprehensive understanding of the various criteria needed for the design process of timber constructions, such as architectural planning and specific requirements for the design process; forestry and sustainable aspects; structural systems and static requirements; timber technology and products; tendering, structural systems and elements; building physics - sound, moisture, heat, fire protection.

To ensure a real-life learning experience, two field trips were organised. The students visited the timber production hall of the Austrian company "Handler Group" and were given an inside-view of the prefabrication process of building elements. Additionally, a visit was paid to the timber construction site of "Forum Am Seebogen" in Seestadt Aspern, Vienna, which was designed by the architectural studio "heri @ salli" and executed by the construction company "Strobl Bau GmbH". This gave the students a first-hand experience of a timber and modular construction site.

As the final output of the workshop, the students prepared a presentation of their projects, along with a poster containing all plans, basic calculations, and a physical model. This was then presented and defended in front of a jury.

The constructability of the project was evaluated through a structural analysis and design, which identified the vertical and horizontal load transfers and estimated the dimensions of the main elements. As a result of the workshop, the students gained an excellent understanding of timber constructions systems, their load bearing properties, and its effect on the design requirement. This understanding enabled them to creatively incorporate the analysis into the design process, resulting in the design of multi-storey timber buildings with high architectural quality.

3.2 WORKSHOP CRACOW 2022 – CONSTRUCTION SOLUTIONS AND DETAILING IN TIMBER

The second instalment of the HiBiWood workshops took place over a period of two weeks, commencing in May of 2022, at the Cracow University of Technology (CUT). It was attended by thirty-six participants, two-thirds of whom were architects. The task of the workshop was to build on the projects designed in Vienna and develop details of building elements (superstructure catalogue) considering the physical and technical properties of timber. Of the participants, eight had also attended the workshop in Vienna and were able to explain the peculiarities and development of the projects to the additional participants.

During the workshop, the lecturers encountered again the issue of heterogeneous knowledge levels among the

students regarding timber buildings. To mitigate this discrepancy, a preparatory exercise was conducted. The students were divided into pairs and assigned to write a two-page short paper in response to a question focused on either building physics or structural aspects of timber constructions. The aim of these questions was to equip the participants with a foundational understanding of the aspects, prior to engaging in the main workshop task. The questions covered the topics of vertical and horizontal load transfer and bracing; cantilever structures; roof, ceiling, and wall systems; airborne and impact insulation; decoupling; summer suitability in timber buildings; moisture protection; air tightness; systematization and prefabrication. The students who effectively addressed these questions were designated as subject matter experts and were available to provide guidance and support to their peers besides the supervisors during the workshop activities.

The initial phase of the main workshop assignment involved a comprehensive static analysis of the projects. This analysis comprised of the explanation of the structural grid, the transfer of vertical and horizontal loads through the primary and secondary constructions and bracing concept, and the examination of the foundation and roof system spanning. Based on the results of this assessment, the selected timber technology was re-evaluated, and necessary modifications were made to the architectural plans and building element dimensions.

Subsequently, informed decisions regarding the building systems were made, including the selection of roof systems (warm roof vs. cold roof) and the explanation of ventilated structures, the selection of wall systems (bar-shaped, flat components, mixed forms) and their bracing, prefabricated elements and modules, and constructive moisture protection. The facade design was also evaluated with regards to its energy efficiency, and the construction system of cantilevers was considered. These decisions were based on a sustainability concept that emphasized the temporary approach, combinability, and dismantling potential of the building.

The final objective of the task was to develop a superstructure catalogue that detailed the connections of exterior wall-roof, exterior wall-ceiling, interior wall-ceiling, plinth (exterior wall), interior wall-roof, and cantilever components. These details were created in a scale of 1:10 or 1:5 considering important aspects such as the thermal insulation (u-value) and thermal envelope, seals and thermal breaks, impact and airborne sound insulation (Rw, Lnw), and moisture protection.

The task was executed through comprehensive, in-depth face-to-face lectures that built on the knowledge acquired during the first workshop. They had a profound emphasis on construction engineering and building physics, encompassing topics such as structural systems and mechanics, Eurocodes, thermal insulation, soundproofing, and moisture management. Additionally, they were specifically geared towards the elaboration of constructive details. The deepened examination of roof, ceiling, wall systems, openings, facade finishes, interior finishes, and cantilevers was emphasized in the context of prefabrication and utilization of digital tools. Furthermore, a practical exercise was provided to the participants aiming to reinforce their understanding of how to develop appropriate details that meet project specifications and technical requirements.

The examination of building physics with regards to longevity, durability, and sustainability was performed. An assessment of appropriate regional and low-carbon materials was carried out and fire protection, noise insulation, and moisture control were analysed. In addition, initial considerations were made regarding the assembly sequence of the construction elements. Skills related to communication and project management were developed, including the ability to plan collaboratively, make informed decisions, and integrate interdisciplinary knowledge.

As a result, the students demonstrated an in-depth understanding of timber's physical and technical properties. They were capable of effectively incorporating sound, heat, fire, and moisture protection concepts into the projects, which were successfully integrated into the elaborated constructive details.

3.3 WORKSHOP RIGA 2023 – BUILDING SITE MANAGEMENT AND BUILDING PROCESS WITH TIMBER

The final HiBiWood workshop, the third in a series of two-week workshops, will be held at the Riga Building College (RBC) in March 2023. It will concentrate on the aspects of required planning processes and building site management in the construction of timber buildings. Thirty-three bachelor students of architecture, building site management and civil engineering from the five partner universities will continue the work on the projects in small international and interdisciplinary groups, following the didactic approaches (integral planning and problem-based learning) of the previous two workshops. For the successful elaboration of the tasks is to be ensured that at least one participant per group is enrolled in a program of building site management.

To establish a shared knowledge base among the participants, the topics/ fact sheets developed during the second workshop are peer-reviewed by the project partners and utilized as teaching materials. Participants should familiarize themselves with the materials as preparation for the third workshop. During the workshop a random assignment process is to be employed to allocate a topic to each student. Subsequently, the students will be expected to collaboratively present the main points of the assigned topic, alongside some of their peers. This method will provide a solid knowledge foundation, which will be built upon by the lectures and workshop activities.

The assignment during the workshop involves the development of preliminary building site management concepts for the projects. Students are expected to consider various factors such as: costs, logistics, moisture protection on the building site, transportation and dimensions of building elements, prefabrication, digital processes, life cycle assessment, and management of all involved trades. By incorporating these aspects, students will be able to transition from planning to implementation and erection phase of the buildings. This know-how will have several benefits for the building process, including reduced time and costs, improved quality and life-cycle

https://doi.org/10.52202/069179-0598

optimization, and enhanced communication and transparency.

At the conclusion of the workshop, students will be able to understand the workflow of construction processes in timber, assess the advantages and disadvantages of various structural systems and building components, understand the impacts of changes, and make informed decisions. They will submit and present a report to a jury, including the topics of: 1) construction: level of prefabrication, modularity, selected products, applied digital processes; 2) logistics: dimensions of building components, transportation, assembling, timeline and coordination of trades, moisture protection and management of the building site; 3) assembly sequence from the foundation to the roof in chronological order; 4) rough cost estimation; 5) sustainability concept: temporary approach and combinability, dismantling concept, life cycle considerations; 6) reflection on the design mistakes from the first workshop that could be identified as roots of the encountered challenges and rectified in light of the acquired knowledge.

In addition to the report, students are expected to select one of the projects and construct a physical model in 1:20 scale, representing all storeys of the building, from the foundation to the roof, including the individual layers of the building elements. The model should be capable of being disassembled into the individual components, visualizing the chronological order of erection, building element dimensions by the transportation, prefabrication level, assembly process, and dismantling concept.

These assignments aim to create a tangible understanding of the process of erecting a timber building and require effective coordination, time management, and teamwork. Through implementation of this approach, the participating students can acquire and enhance their abilities in communication, project management, and interdisciplinary planning.

The elaboration of the assignments will be supported by in-depth face-to-face lectures on cost estimation, digital approaches, prefabrication, transportation, logistics, and dismantling. Leading timber construction companies are invited to present their building site processes, as well as best-practice examples of successful large-scale international projects in timber, with the aim to provide students with real-world insights. A comprehensive training session will be held at the beginning of the workshop with the aim to illustrate the corelation between the parameters: physical properties, costs, and sustainability of building materials. This approach will equip students with the crucial abilities to make well-informed choices regarding building material selection during the implementation phase of the projects. Continuous oversight by the supervisors aids in the elaboration of the assignments and guarantees the high quality of the completed projects.

As a result of the workshop, students will have a holistic and tangible understanding of the planning and execution process of multi-storey timber buildings. They will be able to make informed decisions and changes considering costs, logistics, and sustainable requirements, and incorporate them into a rough building site management concept.

4 RESULTS

The present publication reports on the outcomes of the first two international workshops that were completed at the time of writing.

Following the completion of the workshop in Cracow, six design projects were developed with a high level of detail. The didactic approaches implemented in the workshops demonstrated significant advantages in the elaboration of these projects. The use of wood as a building material motivated the students to incorporate sustainable aspects in their designs and to minimize the impact of the buildings on the environment. Sustainability concepts, such as green roofs, unsealing and leaving green areas free, screws instead of glue for joining components, sustainable insulation materials, and self-generated energy systems (including solar panels, heat pumps, district heating, and rainwater collection ponds) were integrated into the projects.

The students' elaborated plans, characterized by a compact design and simple shape, won the jury's approval. This simplicity encouraged cheaper and more creative solutions, and the projects included flexible internal walls that allowed for adaptation to the residents' needs and living situations. Furthermore, smaller units were designed to optimize cost and space efficiency.

Cross-laminated timber (CLT) was chosen as the primary construction material for most of the projects due to its durability, sustainability, and personal contact with Stora Enso employees during the first workshop in Vienna. During the second workshop, the students identified some oversized components in their designs, which were corrected to save material according to the corresponding load calculation. Some of the projects had also used CLT in the partition walls, which were replaced with lightweight frame structures in the second workshop.

The projects were characterized by a clear configuration grid with high architectural quality that facilitates the repetition of building elements for a modular-based construction, with small adaptations for customization. The students also prepared detailed planning of the repeating building elements (number, size, and endings for transport purposes), which had a prefabrication degree of over 80%. They selected local production companies to minimize transport costs and relied on a few suppliers. The selection of materials was based on an assessment of the correlation between durability of the materials during the life cycle and their costs. Façades and balconies were designed to be easily degradable and exchangeable due to the different life cycles of the individual building components.

Initial concept for the construction process was also developed that employed cost and time optimization strategies while minimizing the local area's exposure to traffic, noise, and dust due to the high level of prefabrication. The sustainability of the buildings was evaluated throughout their lifecycle, including resource-efficient production, construction, and operation, dismantling, reuse and recycling.

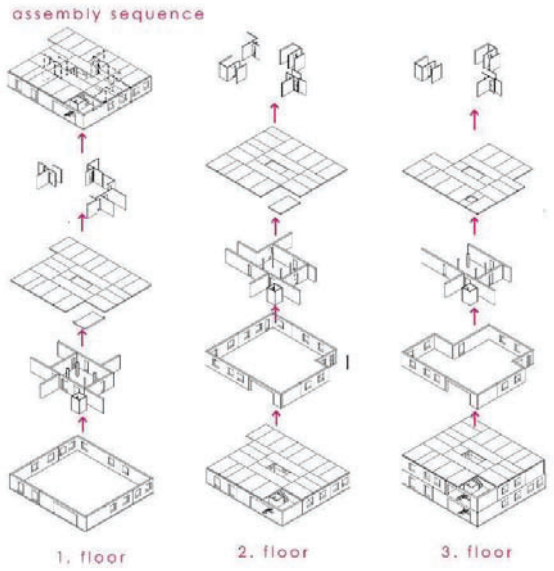

Figure 1: *Assembly sequence of project 4.*

The workshop implemented a didactic methodology where each discipline had predetermined tasks and deliverables that provided structure to the team's work. However, due to the different thematic focuses of the workshops (architecture, construction, site management), collaboration was sometimes challenging, as each discipline had different workloads at different stages of project development. This was particularly evident during the first workshop with focus on architectural design, where civil engineers and building site managers initially contributed less to the project and acted in more of an advisory or observational role. As the workshop progressed, these disciplines became more involved and completed their sub-tasks. Despite these challenges, students from both architecture and civil engineering disciplines gained a mutual understanding of each other's roles and challenges, which was given as feedback by several students at the end of the workshop. Early involvement of the different disciplines during the conceptualization phase prevented collisions and misunderstandings at the technical interfaces and significantly benefited the projects by allowing informed design decisions that facilitated the planning process in further phases. This approach resulted in fewer changes during the advanced phases of the planning process, leading to reduced time and costs, minimized errors, and higher quality and lifecycle optimization. Furthermore, better communication and transparency among the students increased shared knowledge, leading to a more collaborative and productive planning process.

The role allocation of the teams greatly influenced the successful completion of the projects. In projects where students lacked leadership positions, coordination of group task distribution and time management suffered noticeably. Significant progress in project development occurred after individual supervisor talks. These talks were conducted informally, at least twice per workshop per group, with lecturers providing direct feedback and answering questions.

The applied nature of the assignments and targeted in-depth input from the project partners had an impressive effect on the speed and the depth at which students acquired knowledge and know-how. This was particularly evident in students with little to no prior knowledge of timber construction, who were able to catch up on gaps in knowledge and get on the same level as their peers with prior know-how by the end of the workshops.

Overall, the workshops were evaluated positively by the students. The applied didactic approaches provided several benefits, including improved and applied knowledge and know-how about timber constructions, quality of designed timber buildings, international exchange, and the ability to act in a global context.

5 DISCUSSION: APPLYING THE DIDACTIC APPROCH TO EXISTING EDUCATIONAL PROGRAMES

The HiBiWood project employed experimental learning techniques in a series of international workshops. They demonstrated significant improvements in learning outcomes and designed timber projects, and thus outlined the need for alternative didactic approaches due to the complexity and diversity of the subject matter. The project's main objective is to implement sustainably the applied didactic approaches in partner universities' educational programs after the end of the project and make them available as open source to the broader scientific and academic community.

This challenge is addressed by the development of a BSc/BA module with 9 ECTs (240 academic hours), which has the overall objective to be both flexible and adaptable to meet the varying needs and levels of expertise of the target audience. It aims to provide a comprehensive understanding of timber construction, encompassing both foundational knowledge for those with no prior exposure, as well as more advanced topics for those with existing knowledge on the matter.

This is achieved by structuring the module into two stages, with the first half focusing on introductory concepts, such as architectural conceptualization, sustainable aspects, timber building products, building physics and technical properties, modular thinking, decomposability, and structural systems. The second half deals with the content in much greater detail, and includes additional topics of detail development, logistics, cost estimation, and the consideration of LCA in product selection. The module can be completed in one or two semesters, allowing universities to choose specific parts based on their needs (study program and/or previous knowledge of the students).

The educational module is composed of three distinct components. The first component consists of 25% of the total module duration (equivalent to 60 educational hours), delivered via four lecture courses with different deepening of the content, which provide fundamental theoretical inputs. The second component, also representing 25% of the module, is designed for individual self-directed learning, and comprises provided

https://doi.org/10.52202/069179-0598

learning materials and interactive problem-solving tasks such as in-depth analysis of best-practice timber construction projects or elaboration of timber-specific topics. The remaining 50% of the module follows the problem-based learning (PBL) methodology presented in this paper, centred on the design, and detailed planning of a multi-storey wooden building, covering all (or as needed, individual parts of) real-life project phases.

Ensuring interdisciplinarity and involving students from different disciplines is a key aspect of the module, albeit its implementation may be challenging for certain universities and technical colleges that offer programs only in architecture or engineering disciplines.

FH Campus Wien aims to introduce the second phase of the module in the regular curriculum, with the aim to provide an in-depth understanding of timber construction, building upon the fundamental knowledge and introductory concepts covered in the offered study programs. The module is intended as an optional advanced design exercise for architecture and civil engineering students, which can replace a pre-defined regular course. To maintain the international character of the program, the module is planned to be conducted as a summer school and open to international students from other universities. In the summer semester, students are expected to acquire the necessary background knowledge about timber constructions through blended lecture courses and preparatory assignments. In summer, students from diverse academic and national backgrounds will collaborate for several weeks to complete the practical construction task. The proposed summer academy will take place at the University of Applied Sciences Campus Vienna with the possibility of being hosted by partner universities in the future. It emphasizes practical experience, testing of different building approaches, and the inclusion of additional bio-based materials in the learning content, i.e., straw, clay in combination with timber. The summer school aims at active participation and mutual exchange of students and experts from different international universities, companies, and research institutions. The ultimate goal of this project is to establish an academic and scientific community that promotes the use of timber and other bio-based building materials and sustainable construction practices via interdisciplinary learning approaches.

6 CONCLUSIONS

HiBiWood responds to the increasing demands for greening the building sector by disseminating expert knowledge of multi-storey timber buildings. It promotes international networking, valuable exchange of knowledge and experience, and thus leads to an increased quality in teaching and research. The development and implementation of a module on timber construction in the academic programs of the partner universities ensures sustainable and lasting training of alumni with the required timber construction skills and expertise, which consequentially leads to sustainable promotion of multi-storey timber buildings. The teaching process is supported through innovative teaching methods that allow the students to work internationally and interdisciplinary, elaborate all actual project phases of a timber construction holistically and find solutions to real-life problems. The international teamwork deepens the intercultural competence of the participants and leads to open-mindedness towards others, cross-cultural thinking, and responsible action in a global context. The students are prepared for the future global requirements and changing demands in the construction industry.

Through strategic research, development of guidelines and principles and implementation of an innovative academic module, different actors at local, national, EU and international level are sensitised to sustainable building processes. The project bridges the gap between workforce and education on timber construction by meeting the needs of the building sector, providing university apprentices with actual real-life expertise, and guiding them through the learning process. It empowers the students to take sustainable action and contribute to achieving the climate goals.

ACKNOWLEDGEMENT

The project is funded by the European Union within the framework of ERASMUS+ Strategic Partnerships for Higher Education.

The authors express their gratitude to all students for their active participation in the project and their enthusiasm towards implementing the didactic methods outlined.

Appreciation is extended to MAGK Architektur Aichholzer Klein for facilitating the architectural assignment and construction site documentation.

The authors express sincere gratitude to all lecturers and construction companies who guided the students during the workshops and provided them with a real-life understanding of the subject matter.

REFERENCES

[1] European Commission, „A European Green Deal – Striving to be the first climate-neutral continent“, https://ec.europa.eu/info/strategy/priorities-2019-2024/european-green-deal_en [28.02.2023]

[2] H. Kaufmann, R. Strauch, „Ressourcenschonung durch Synergie – Hochbauten in Holz-Hybridbauweise“, Best of DETAIL – Holz, Institut für internationale Architektur-Dokumentation GmbH & Co. KG, München, 2014

[3] F. Lattke, M. Stieglmeier, „Holzbaugerechter Planungsprozess“, in: Zuschnitt – Zeitschrift über Holz als Werkstoff und Werke in Holz, Nr. 70, proHolz, Wien, 2018

[4] J. Koppelhuber, K. Schafferer, „Ein Gesprch über den Holzbau und die Bedeutung der Ausbildung (…)“, in: Zuschnitt – Zeitschrift über Holz als Werkstoff und Werke in Holz, Nr. 78, proHolz, Wien, 2020

[5] Kim, H., & Lee, J. (2014). An investigation into the effectiveness of problem-based learning in architectural design education. Journal of Architectural Education, 68(3), 233-244.

[6] Al-Hussaini, A., & Al-Jibouri, S. (2016). The implementation of problem-based learning in civil engineering education: A case study. Journal of Education and Practice, 7(13), 105-114.

World Conference on Timber Engineering Oslo 2023

HORIZONTAL AND VERTICAL KNOWLEDGE MANAGEMENT IN MULTIDISCIPLINARY RESEARCH AND DESIGN-BUILD TEACHING: A TIMBER-ONLY TRAIL

Günther H. Filz[1], Gengmu Ruan[2]

ABSTRACT: "The Kouvola Trail" is part of our timber-only research project and consists of 2 realized parts, (i) the prefabricated, "Modular Trail" and the customized "Plaza" modules. On the example of the trail project, this paper describes its combined systemic horizontal and vertical processes, network, knowledge management and multidisciplinary collaboration. Based on systemic knowledge management and the concept of the vertical design studio, we have simultaneously implemented and exposed our research in timber-only structures and architecture to teaching, real world application and manufacturing to enable both, horizontal and vertical alignments. We provide insights into how our academic research on using locally salvaged timber and wooden nail connections vertically links both, disciplines within Aalto, to the Kouvola region vocational college and to industrial partners and manufacturers. This vertical alignment and collaboration not only facilitated academic and practice-oriented knowledge transfer but also increased project-complexity by exchanging ways of thinking. Consequently, we recognized a significant increase of students´ technical expertise, functional development of knowledge, skills, and also motivation, as demonstrated by the "Street Furniture" prototype. Additionally, horizontal learning and collaboration as an inter-organizational system-relationship was fostered by setting up multidisciplinary design teams including the disciplines of civil engineering, architecture, arts and design, plus practical approaches to construction by the vocational school. Expanding this approach e.g. to business schools may open new perspectives and opportunities for industrial partners in future.

KEYWORDS: knowledge management, horizontal and vertical teaching, vertical studio, timber-only structure, wooden nails, architecture, timber engineering, multidisciplinarity.

1 SYSTEMIC KNOWLEDGE MANAGEMENT

Today, we can increasingly recognize the importance of knowledge and expertise as the basis for successful products and services. Not only companies have to adapt to this change, but also organizations of all kinds with respect to the transformation to a knowledge society [1]. In addressing the specific question of systemic knowledge management, according to [1], the task is to consider "knowledge management as an element of a context of social, organizational, technological and individual factors". However, one essential aspect of knowledge management is differentiating personal knowledge from organizational knowledge. In the context of knowledge-based societies and organizations, "knowledge work" has become a crucial factor for success, and in distinction from purely scientific work it involves the application of knowledge to practical tasks [2]. The interplay between individuals and organizations is essential in knowledge work, with an emphasis on how the expertise of the individual is continuously revised and refined in this context. Expertise has become a control element in knowledge-based societies, and this highlights the significance of personal and organizational knowledge. One of the critical insights in knowledge management is the need to organize both personal and organizational knowledge effectively including a departure from an exclusive focus on the individual. The challenge of managing increasing amounts of knowledge is often seen as a threat rather than an opportunity. Systemic knowledge management offers valuable and effective support wherever increasing amounts of knowledge have to be managed or the intention is to generate this increase [3]. In this regard various disciplines and branches from the supply chain management of companies to the curriculum planning of universities take into consideration both, vertical and horizontal alignments, when it comes to achieving specific strategic goals [3].

2 HORIZONTAL AND VERTICAL TEACHING, LEARNING AND COLLABORATION

The UNESCO International Bureau of Education (IBE) describes the organization of contents according to the sequence and continuity of learning within a given knowledge domain or subject over time as vertical articulation to improve coherence, and the scope and integration of curricular contents from different knowledge domains within a particular grade level as

[1] Günther H. Filz, Aalto University, ENG | Department of Civil Engineering ° ARTS | Department of Architecture, Finland, guenther.filz@aalto.fi & LSU Lightweight Structures Unit, Universität Innsbruck, Austria, guenther.filz@uibk.ac.at

[2] Gengmu Ruan, Aalto University, ENG | Department of Civil Engineering, Finland, Gengmu.ruan@aalto.fi

https://doi.org/10.52202/069179-0599

horizontal articulation or balance to develop integration between subjects, disciplines or knowledge domains [4]. In other words, alignment in teaching can be vertical when a specific subject or topic is taught to various grades, or horizontal when those in the same grade level teach different subjects. The steps that can be taken to make sure every student is receiving the same level of quality instruction is curriculum alignment that brings teams of teachers together to plan instructions. Therefore, vertical alignment is when teachers who teach the same content area meet across grade level bands, while horizontal alignment is when teachers at the same grade level meet to coordinate learning activities. Educators who use vertical alignment to support cohesive instruction find it helps them save instructional minutes by reducing repetition. On the other hand, horizontal alignment provides a higher probability that the majority students will be brought to a certain level, which can consequently be built upon.

Some architecture, design and arts schools have introduced for example so-called "vertical design studios", where students from multiple cohorts are taught together to provide holistic and contextual thinking skills essential to architectural design education [5–8]. Basically, [8] describes the vertical studio as a single-class combination of students at different levels in a given program of study, and [9] argues that the “Vertical Studio” system challenges traditional, sequenced design studio organization by allowing students of various developmental and skill levels to interact and compete with one another in a topical, thesis–based studio. To [10] the key feature of a vertical studio model is the collaboration of students across all years to address specific themes without overriding the traditional curriculum, but to both add, as well as, amplify design skills, and to create peer-to-peer learning opportunities.

In the context of systems design, [11] identifies three learning approaches that can be applied to vertical studio learning; learning through confusion, single versus double loop learning, and social learning through the "Master-Apprenticeship" model. The process of learning often involves confusion and uncertainty, and learning through this experience can help students develop a deeper understanding of the subject matter. Single versus double loop learning involves taking for granted versus questioning the assumptions and frameworks that inform goals and strategies. Social learning through the "Master-Apprenticeship" model involves project-based learning and critiques, allowing students to learn from experienced designers and develop the social competence and personal experience needed for collaborative design projects. The motivation behind most of these approaches is not only to train students to solve complex design problems or even research questions [12], but also to familiarize them with teamwork in which individual group members depend on each other's performance.

From the students´ perspective horizontal learning is about developing competencies such as communication, active listening skills, and responding effectively and constructively to conflict [13]. In addition to these general aspects, they also expand their technical and artistic knowledge and skills through collaboration with other disciplines [14]. They also gain expertise and an awareness of the potential and practical challenges that arise from interactions. So, the main focus of horizontal learning is the functional development of knowledge, skills, and behaviours that strengthen key competencies. Vertical learning from the students´ perspective, is about changing the way they think [15], feel, and make sense of the world; it is about increasing the complexity of how one sees and relates to the world and what one knows.

The authors of this paper conducted a review of literature pertaining to systems approaches, teaching and learning in vertical and horizontal articulation. The majority of the literature reviewed, which is related to vertical and horizontal articulation, highlights approaches and case studies from the design and arts disciplines, with a particular focus on architecture, industrial design, and the arts.

While the International Bureau of Education (IBE) describes horizontal and vertical curricular contents from various knowledge domains, it appears that even in architecture or design schools, these approaches are not systematically or explicitly implemented in the curricula. While we found single course descriptions that explain the contents and methodology to students, it is not reflected or incorporated into the overall curriculum. Interestingly, it appears that these approaches are not commonly followed or even known in engineering and business disciplines, as the authors could not find indication of vertical studio practices in those curricula or related publications. And even though we found extensive literature about multi- and transdisciplinary teaching and learning, to the authors knowledge there is marginal to no literature on combined multidisciplinary vertical teaching and learning articulations. In addition to our observations, we found that also only few companies and organizations seem to use an organizational development process that acknowledges the power of vertical learning conflict [13, 16].

3 VERTICAL AND HORIZONTAL, MULTIDISCIPLINARY RESEARCH AND DESIGN-BUILD TEACHING OF TIMBER-ONLY STRUCTURES AND ARCHITECTURE

In the context of the co-author´s research on timber-only structures and architecture, we investigate the topic both, from an engineering [17–19] as well as from an architectural and artistic point of view [20–22].

On the example of “The Kouvola Trail”, a timber-only trail project [17], this paper describes its systemic

horizontal and vertical processes, network, knowledge management and multidisciplinary collaboration.

Kouvola is a city and municipality in southeastern Finland. It is located along the Kymijoki River in the region of Kymenlaakso. “The Kouvola Trail” is part of a development initiative by the city of Kouvola and Kouvola Innovation Oy (Kinno) a business development company, which supports local companies and boosts the overall business environment.

Figure 1 provides an overview of the network of involved entities. As mentioned the PhD project “Timber-only Structures and Architecture” is located at the threshold of architecture and structural timber engineering, at the Department of Architecture, School of Arts, Design and Architecture and the Department of Civil Engineering, School of Engineering, Aalto University, Finland.

dimensions, orientations, and arrangements to determine their performance in timber-to-timber connections. Results showed that inclined wooden nails exposed to shear and tensile forces had a higher shear resistance due to their activated tensile capacity, with failure predominantly observed in nails loaded in tension rather than at the interface with the timber. An analytical model, later validated with experimental test, was developed using the results from shear tests to predict the load bearing capacity of timber-to-timber connections exposed to bending stresses.

At Aalto University, both of the above studies were presented to an almost equally distributed numbers of Master´s students from architecture and from civil engineering, whereas roughly 30-40% of students had international background including Spain, Belgium Austria, Italy and Latvia (Figure 1). All students took part

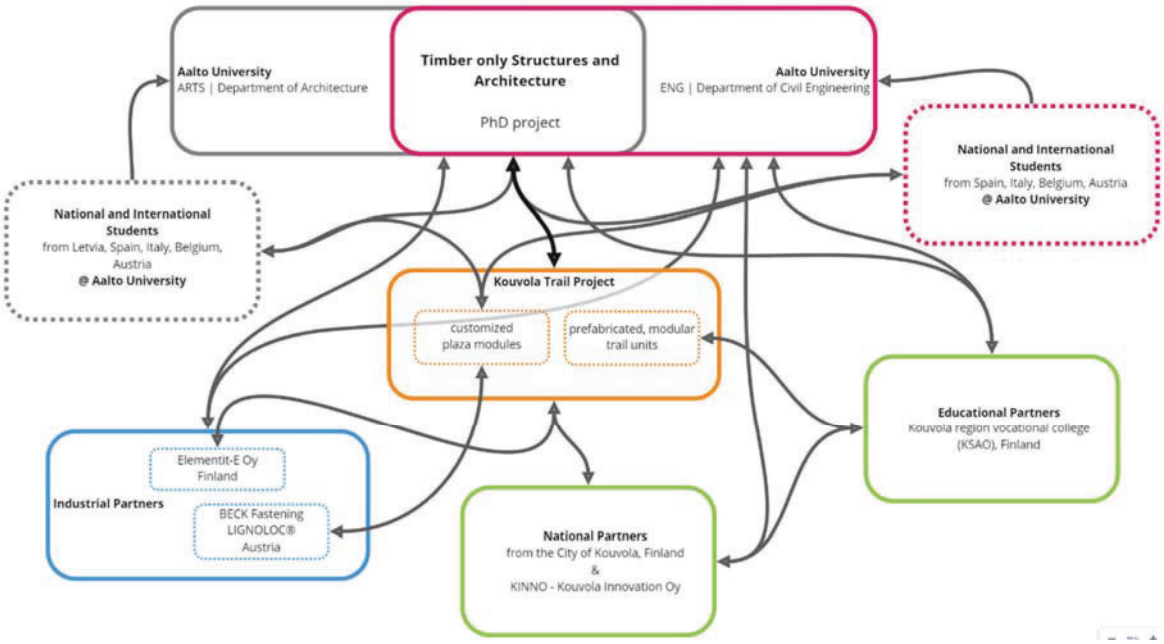

Figure 1: *Network of entities involved in the research and design-build teaching of the Kouvola trail with an emphasize on its systemic horizontal and vertical processes, network, knowledge management and multidisciplinary collaboration.*

The study [17] introduces a new low-tech design concept for short span structures using salvaged timber products and hardwood nails. Different design proposals for batches of salvaged materials with varying dimensions are guided by three aspects: timber board patterns, assembly process, and nail arrangement. The design concept is first conceptually applied short span bridges on a natural trail path in Finland. As a follow-up, in [18] we report about a series of 90 shear tests to explore the shear capacity and slip modulus of timber-to-timber connections with wooden nails. As densified wooden nails might become an alternative to metallic fasteners, this study examined different specimens of wooden nails in varying

in the same courses and classes. Leaving the exclusive focus on the individual the shared knowledge and expertise formed the basis for multidisciplinary groupwork, initially in pairs of architects and engineers and later as a larger group. After an introduction to the technological aspects and full-scale testing, the students rapidly got into the subject and were then challenged to creatively design structures and spaces based on the knowledge they had previously gained. From a course-of-study perspective, the approach may seem horizontal, but in reality, it is a more vertical articulation, as the level of knowledge about each other's disciplines put all participants on both an expert and novice level at the same time. The disadvantage of this approach is sometimes the slower development speed of projects, as the "expert input" is sometimes perceived as a limitation, but in the authors' experience, this delay is later more than made up for and the results are comparatively superior in quality.

https://doi.org/10.52202/069179-0599

However, the horizontal teaching and learning component could be most recognized by the increased technical expertise, functional development of knowledge, material understanding [23] and skills for all involved parties by disciplinary exchange between the individuals and groups. Additionally, an underestimated horizontal learning and collaboration effect as an interorganizational system relationship was fostered by the fact that the participating students came from different nationalities and (design) cultures.

Our academic research at Aalto University on using locally salvaged timber and wooden nail connections only vertically linked with the Kouvola region vocational college (KSAO), now Eduko (Kouvola Vocational Institute Ltd.) and industrial partners and manufacturers. Compared to academic research, teaching and learning, Eduko follows other principles. Eduko, an Erasmus+ accredited organization, is a vocational training institute involving annually approximately 6500 students in various training activities, and employs more than 300 experts on education, counselling, administration and other services. Training programmes focus on enhancing skills and expertise that are essential in the working life, including basic, advanced, or specialized qualification. On-the-job learning is a vital part of the learning process.

Similar to the previous experience within multidisciplinary courses at Aalto, the vertical alignment and vertical collaboration between Eduko and Aalto not only facilitated academic and practice-oriented knowledge transfer [20] but also an increase of complexity by exchanging ways of thinking [24]. The horizontal collaboration of same level or stage but different studies allowed greater ease of work and cooperation towards achieving common objectives, while emerging additional design and manufacturing options.

4 THE SIMPLEXITY OF A MODULAR TIMBER-ONLY TRAIL

"The Kouvola Trail" is part of above-mentioned timber-only research project and consists of 2 parts, (i) the prefabricated, "Modular Trail" units and (ii) the customized "Plaza" modules. Not least because of its low-tech [25, 26] and low processing approach, the Kouvola trail project can also be seen as a case of simplexity [27, 28], an emerging theory that proposes a possible complementary relationship between complexity and simplicity. Presently, both types of physical outputs have been realized, the more industrialized modular set of prefabricated trail units realized by Eduko, and a set of customized, bespoke but also modular elements for a plaza area of the trail by Aalto University.

4.1 PREFABRICATED "MODULAR TRAIL"

Due to practicality reasons, the fabrication of the "Modular Trail" was organized as a workshop at the facilities of Eduko in Kouvola. The expectations were to communicate the design intend and the approach to fabrication of modules from salvaged wood and wooden nails, with the aim to assembly a few prototypes.

6 Eduko-students were involved (3 female and 3 male), all of them vocational school students in construction. At the time of the workshop, their age was in the range of 25 to 60 years. The supervising team was formed by the co-author and one teacher from Eduko.

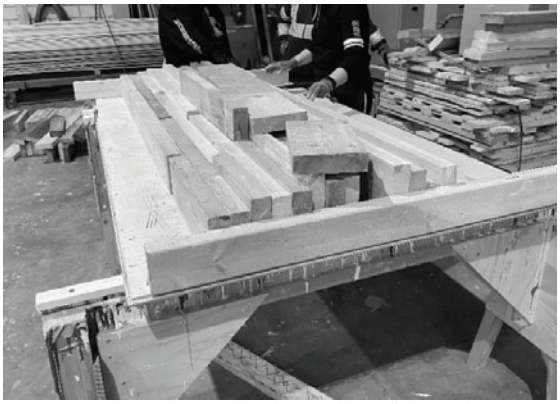

Figure 2: *The working table, designed by Eduko students to ease and expedite the precise fabrication of the modular trail elements*

Figure 3: *First finished modular elements*

Based on previously gained knowledge and expertise in the assembly of specimen for testing purposes, the supervisor provided an input lecture regarding the trail project, which covered the design concept, the intended salvaged material, and the connection details. Following this, a 5-day hands-on workshop was conducted, during which the first two elements were constructed under the guidance of the supervisor, serving as examples for the students to comprehend the process and the nailing gun with wooden nails. Due to their practical education and backgrounds, which provided them with a strong foundation in construction techniques and materials, the students were trained to act and improvise within specific boundaries and restrictions. They brainstormed ideas to streamline and simplify the work process, including considerations for working height, ergonomics, and efficiency. Consequently, they designed specific tools

such as the working table and nailing marker, to expedite the process. This practical approach enabled them to maximize their efficiency and fabricate an unexpected additional number of 10 elements, a total of more than 30m of trail, during the workshop days.

4.2 CUSTOMIZED "PLAZA" MODULES

In the context of the "Plaza" within the design build phase of "The Kouvola Trail", 7 university students were involved (5 female and 2 male), 6 of them Master students (3 in Engineering, 2 in Architecture and 1 in Architectural Engineering) plus 1 bachelor student in Engineering. Their age is in the range of 19 to 25 years. The supervising team was formed by the authors.

Figure 4: *Working process using templates and guides for precise fabrication of bespoke plaza elements*

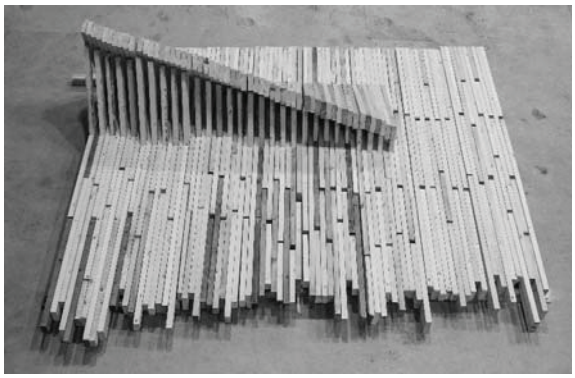

Figure 5: *Finished plaza part as exhibited at the exhibition SALVAƎƎ – sustainable use of salvaged wood [29]*

The fabrication of the "Plaza" clearly took advantage from the experience with Eduko students and their processes. Additionally, the fabrication process followed the above-mentioned course, its theoretical inputs and students´ work on their design proposals. Again a 5-day workshop was organized, but Aalto students prepared both digital drawings and working tools such as the working platform and nailing marker, based on the lessons learned from the fabrication of modular elements. During the first of a 5-day workshop, the students received instruction on the use of the tools and the arrangement of the timber boards from the supervisors, resulting in the completion of one element as a showcase on the first day. Then, the students were assigned different roles, such as nailing, arranging the timber boards and marking nailing locations, and cutting, in order to finalize the remaining elements. Interestingly, the role assignment was perceived in a very positive way by the students, since they were equally informed and updated on the processes, aims and results. As a consequence of this collaborative effort, seven elements were successfully completed over the course of the following four workshop-days.

5 STREET FURNITURE: A FOLOW-UP PROJECT

As a follow-up two students, one Master student in Engineering and one Master student in Architecture, who continuously followed the design as well as the design-build course and the workshop, gained experience on many levels. Besides expanding their skills and knowledge in each other´s discipline, they familiarized themselves with sustainability aspects such as the use of salvaged timber, with structural testing and architectural design or with using nailing guns.

Figure 6: *Preassembled units for a novel slide-in connected, planar reciprocal frame structure. The units are assembled from salvaged wood by the use of wooden nails.*

Figure 7: *Students on the assembled Street Furniture on campus of Aalto University, Finland [19]*

Consequently, they applied for involvement in the design of reciprocal frame structures from salvaged timber, another project within the research in timber-only structures and architecture. Based on our investigations in this field and their collected skills, the students successfully built and assembled a small-scale prototype of "Street Furniture" in just one day.

https://doi.org/10.52202/069179-0599

6 DISCUSSION AND CONCLUSIONS

Even though vertical studio practices are known and used in architecture, design and arts education, they are not reflected or incorporated into many curricula, and it appears that these approaches are not commonly followed or even known in the engineering and business disciplines. Combined multidisciplinary vertical teaching and learning articulations seem almost non-existent.

The attempt of combined multidisciplinary vertical teaching and learning articulations in the presented approaches and setting took advantage from involving at least one discipline, architecture, that is more familiar with the concept. Architectural students are also more used to problem-framing [14] and learning through confusion as described by [11]. Combined with problem-solving [14] skills and analytical work style, as they are very much taught at engineering schools, as well as practical down-to-earth and even improvising approaches, can significantly enhance the final quality of a project.

Obviously, the student groups of 15 in earlier design courses and 6 to 7 in the design-build phase have been of small size. With larger groups the risk of losing overview drastically increases for both sides, the students and teachers. In earlier courses with up to 290 students we perused similar vertical studio and multidisciplinary approaches. Although we could prove a significantly positive effect on students' creativity through creativity tests, such as Alternate Uses Tests (AUT) and ShapeStorm (SS) Exercises [30, 31] but together with challenging pedagogical and logistic tasks a relatively high number of students complained about lack of clarity and meaningfulness.

However, any system that allows free choice does so at the expense of rigorous control. The vertical studio provides considerable freedom of choice but with this freedom come some distinct limitations and new responsibilities for both faculty and students. For the success of the presented workshops and the project consequently, it was crucial to be well organized, with clear milestones and a very clearly communicated aim. In best case, the vertical studio advances the idea of collaborative design pedagogies. Not only does it promote and encourages a close working relationship between students of all years, across disciplines and the teaching staff but demonstrates an overall improvement of student's general development and self-responsibility as they identify their individual roles and contribution to the project. The confidence in decision-making is a side-effect of what [11] describes as social learning through the "Master-Apprenticeship" model. The follow-up project of the "Street Furniture" is an excellent example for the empowerment of students by this approach. The "Master" is both peer-to-peer learning and learning from teachers, that serve as a backup in case.

Accordingly, we have simultaneously implemented and exposed our research in timber-only structures and architecture to teaching, learning, manufacturing and real-world application by utilizing both, horizontal and vertical approaches, offering unparalleled opportunities for teaching, learning research and potential projects.

As the business value is hidden, only few companies and organizations seem to use an organizational development process that acknowledges the power of vertical learning [10, 12]. The collaboration with Eduko may be seen as a step in this direction and may open new perspectives and opportunities for companies but also academic partners from business schools in future.

ACKNOWLEDGEMENT

Thanks to the involved schools, departments and students across Aalto University, to Eduko (former KSAO) for their active participation in the manufacturing process of the modules, to the city of Kouvola and Kinno for their project support and for providing the opportunity for a first prototypical timber-only trail, to the industrial partners for providing the materials and tools, and to Gerhard Fink for the suggestion to write this paper.

REFERENCES

[1] *Systemisches Wissensmanagement,* 2nd ed. Stuttgart: Lucius und Lucius, 2001.
[2] A. Bögle and E. Popova, Eds., *BuildDigiCraft : New Mindset for High-quality Baukultur in Europe: Bridging Craft and Digital*: HafenCity Universität Hamburg, 2023.
[3] H. Willke, *Einführung in das systemische Wissensmanagement*. Heidelberg: Carl-Auer, 2018.
[4] International Bureau of Education, *Curriculum alignment.* [Online]. (accessed: May 3 2022).
[5] James Barnes, "A Case for the Vertical Studio," *Journal of Interior Design*, vol. 19, pp. 34–38, 1993.
[6] A. Liem, "Planning and early implementation of Vertical Studio Teaching based on a systems design approach," pp. 143–149, 2010.
[7] D. Adıgüzel Özbek, A. S. Melikoğlu Eke, E. Yücesan, and B. Ozar, "Vertical Design Studio Experience in Interior Architecture Education," 2018.
[8] M. Peterson and B. Tober, *Institutionalizing the Vertical Studio: Curriculum, Pedagogy, and the Logistics of Core Classes with Mixed-Level Students*, 2014.
[9] J. Barnes, "A Case for the Vertical Studio," *Journal of Interior Design*, vol. 19, no. 1, pp. 34–38, 1993, doi: 10.1111/j.1939-1668.1993.tb00150.x.
[10] A. Giencke, "Vertical Studio," *cubic*, no. 4, pp. 100–107, 2021, doi: 10.31182/cubic.2021.4.041.
[11] A. Liem, "Planning and early implementation of vertical studio teaching based on a systems design approach," in *DS / Design Society*, vol. 62, *When design education and design research meet:*

Proceedings of the 12th International Conference on Engineering and Product Design Education, Norwegian University of Science and Technology (NTNU) Trondheim, Norway, 2nd - 3rd September 2010, C. Boks, C. McMahon, W. Ion, and B. Parkinson, Eds., Glasgow: Design Society, 2010, pp. 143–149.

[12] K. Varnelis, "Is There Research in the Studio?," *Journal of Architectural Education*, vol. 61, no. 1, pp. 11–14, 2007, doi: 10.1111/j.1531-314X.2007.00121.x.

[13] Diamond Management Consulting, *Horizontal & Vertical Learning - Diamond Management Consulting.* (accessed: May 3 2022).

[14] S. Ylirisku and G. H. Filz, "Resolving 7 Tensions in-between Design and Engineering Education : Cases for Reflective Studio Practice," in *IV INTERNATIONAL CONFERENCE ON STRUCTURAL ENGINEERING EDUCATION: STRUCTURAL ENGINEERING EDUCATION WITHOUT BORDERS*, Eduardo Torroja Institute for Construction Science, Madrid, 2018, pp. 618–627.

[15] E. Parry, "Design thinking: the studio as a laboratory of architectural design research," *Arq*, vol. 1, no. 2, pp. 16–21, 1995, doi: 10.1017/S1359135500002712.

[16] Fadzidah Abdullah, Asiah Abdul Rahim, and Saodah Wok, "A Comparative Study of Horizontal and Vertical Architectural Design Studio Management," 2010.

[17] G. Fink, G. Ruan, and G. H. Filz, "Sustainable design concepts for short span, timber-only structures," in *IASS 2019 Annual Symposium of the International Association for Shell and Spatial Structures & Structural Membranes 2019: IASS 60th Anniversary: Form and Force*, Barcelona, 2019.

[18] G. Ruan, G. H. Filz, and G. Fink, "Shear capacity of timber-to-timber connections using wooden nails," *Wood Material Science and Engineering*, vol. 17, no. 1, pp. 20–29, 2022, doi: 10.1080/17480272.2021.1964595.

[19] G. Ruan, G. H. Filz, and G. Fink, "Planar rectangular, slide-in reciprocal frame structures using salvaged timber and wooden nails," in *IASS 2022 Annual Symposium of the International Association for Shell and Spatial Structures and 13th Asian-Pacific Conference on Shell and Spatial Structures: IASS/APCS 2022: Innovation, Sustainability and Legacy*, Peijing, China, 2022.

[20] G. Ruan, G. H. Filz, and G. Fink, "Master Builders revisited - The importance of feedback loops: a case study using salvaged timber and wooden nails only," in *Architectural Research in Finland: ARF 2022*, G. H. Filz, P. Savolainen, and J. Lilius, Eds., 2022.

[21] G. Ruan, G. H. Filz, and G. Fink, *SALVAƏƎ*. Espoo: Aalto University; Aalto-yliopisto, 2022.

[22] G. Ruan, G. H. Filz, and G. Fink, *Timber-Only Structures and Architecture*. Online: BuildDigiCraft, 2022.

[23] O. Popovic Larsen and G. H. Filz, "The Meaning of Material, Materiality and the Digital for Baukultur," in *BuildDigiCraft : New Mindset for High-quality Baukultur in Europe: Bridging Craft and Digital*, A. Bögle and E. Popova, Eds.: HafenCity Universität Hambrurg, 2023, pp. 260–293.

[24] G. Ruan, G. H. Filz, and G. Fink, "An integrated architectural and structural design concept by using local, salvaged timber," in *IASS 2020/21 Annual Symposium of the International Association for Shell and Spatial Structures and the 7th International Conference on Spatial Structures: Inspiring the Next Generation Proceedings of the International Conference on Spatial Structures 2020/21 (IASS2020/21-Surrey7)*, Guilford, UK, 2021.

[25] G. H. Filz, "Low-tech or High-tech? "cut.enoid.tower" - three times two facets of irregularity," in *VI International Conference on Textile Composites and Inflatable Structures (Structural Membranes 2013)*, Barcelona, 9-11 October, 2013, pp. 250–257.

[26] G. H. Filz, "cut.enoid.tower [kʌt.ənɔɪd.taʊər]," in *Tensinet Symposium 2013 [RE]THINKING Lightweight Structures*, May, 2013, May. 2013.

[27] J. Kluger, *Simplexity: Why Simple Things Become Complex (and How Complex Things Can Be Made Simple)*. New York: Hachette Books, 2008.

[28] A. Berthoz and G. Weiss, "Simplexity: Simplifying principles for a complex world," *Simplexity: Simplifying Principles for a Complex World*, pp. 1–265, 2012.

[29] G. Ruan, G. H. Filz, and G. Fink, *SALVAƏƎ – sustainable use of salvaged wood.* (accessed: Jun. 9 2022).

[30] S. Deo, K. Hölttä-Otto, and G. H. Filz, "Creativity and Engineering Education: Assessing the Impact of a Multidisciplinary Project Course on Engineering Students' Creativity," in *Proceedings of the ASME International Design Engineering Technical Conferences & Computers and Information in Engineering Conference - 2020: Volume 3: 17th International Conference on Design Education (DEC)*, 2020.

[31] G. H. Filz, S. Elmas, A. A. Markou, K. Hölttä-Otto, and S. Deo, "Zero Gravity: radical creativity by multidisciplinary collaboration," in *IASS 2020/21 Annual Symposium of the International Association for Shell and Spatial Structures and the 7th International Conference on Spatial Structures: Inspiring the Next Generation Proceedings of the International Conference on Spatial Structures 2020/21 (IASS2020/21-Surrey7)*, Guilford, UK, 2021, pp. 2873–2885.

https://doi.org/10.52202/069179-0599

World Conference on Timber Engineering Oslo 2023

RESOURCE-EFFICIENT MATERIALIZATION | SUSTAINABILITY FUTURE TRENDS

Alireza Fadai[1], Daniel Stephan[2]

ABSTRACT: The growing enormous number of mid-rise timber buildings in European metropolitan areas leads to the investigation of a possible optimization potential in the use of timber in combination with other building materials.
Within the framework of the Master's Course "Resource-efficient materialization" the Department of Structural Design and Timber Engineering at the Vienna University of Technology developed a multidisciplinary course including design concepts, feasibility studies and performance assessments of the timber components in order to improve the overall performance.
Due to this process, the focus in the development of a Master's Course lies on the feasibility and optimization of the structures on overall component level on the one hand, as well as on the normative realization aspects of innovative timber-based composite structures on the other hand. The Master's Course "Resource-efficient materialization" has formulated the integration of the natural building material timber to the current requirements of the construction industry as a parent research objective.
This paper shows the results of the studies and the conceptional design. The objective of the studies is to develop application-optimized timber systems with a special focus on the sustainability. A construction-optimized design with increased resource efficiency can be achieved.

KEYWORDS: Education, Sustainable building, Wood-based building systems, Life cycle assessment, Quality control

1 INTRODUCTION

In the past twenty-five years, an increasing number of timber-based buildings have been constructed in Europe. In fact, nearly all European countries allow at least six-story buildings in timber as regular solutions and pilot projects had been built up to twenty-four-stories.
In Austria, timber construction has increasingly gained market share over the last 20 years. Currently around one quarter of the construction volume in building construction is made of timber [1]. In the study [1], it is assumed that buildings with a timber content of 50 percent or more are classified as timber constructions. Here, only the statically supporting parts (wall, floor, roof) are used to assess this classification. Based on the total constructed usable space in the building sector, it has increased from 14 up to 24% between 1998 and 2018. Further increases are to be expected, especially for large-volume buildings (residential and public buildings). The timber-based proportion in housing construction is distributed to 53% (newly built single and multi-family houses as well as extensions and conversions) and 47% in non-residential construction (public, commercial and industrial buildings as well as agricultural buildings). At the residential segment, the proportion of timber-based construction has risen particularly strong with an increase from 10 up to 23% in the mentioned period [1].
The analysis in [2] show that the share of multi-story residential buildings between 2008 and 2019 was below 2% in Vienna, slightly above 3% in the other federal provinces and around 10% in federal province Styria (because there is a politically enforced timber construction quota).
Parallel to this, the number of start-ups of companies in timber construction is growing. On the whole, they are small: on average, five employees work in the companies. 83% of the companies have nine or fewer employees [3].
Not only the depicted timber-based building sector is under continuous change, but also the related building codes are in constant revision. Due to this process, the focus in the development of a Master's Course lies on the feasibility and optimization of the structures on overall component level on the one hand, as well as on the normative realization aspects of innovative timber-based composite structures on the other hand.

[1] Alireza Fadai, TU Wien, Research Unit of Structural Design and Timber Engineering, Austria, alireza.fadai@tuwien.ac.at
[2] Daniel Stephan, TU Wien, Austria, daniel.stephan@tuwien.ac.at

https://doi.org/10.52202/069179-0600

1.1 TEACHING A COMPREHENSIVE SET OF SKILLS

The Vienna University of Technology (TU Wien) is Austria's largest research and educational institution in the field of technology and natural sciences. More than 4,000 scientists are researching "technology for people" in five main research areas at eight faculties. The content of the studies offered is derived from the excellent research. More than 27,000 students in fifty-five degree-programs benefit from this. As a driver of innovation, TU Wien strengthens the business location, facilitates cooperation and contributes to the prosperity of society [4].
At the TU Wien, teaching and research are closely intertwined: excellent teaching depends on excellent research, and only leading researchers in their field are able to take the students forward to the next levels of science and technology [5].
TU Wien has been conducting research, teaching and learning under the motto 'Technology for people' for over 200 years. TU Wien has evolved into an open academic institution where discussions can happen, opinions can be voiced and arguments will be heard. Although everyone may have different individual philosophies and approaches to life, the staff, management personnel and students at TU Wien all promote open-mindedness and tolerance [4].
Aiming for relevance to practical applications is an essential component of teaching at the TU Wien, giving students a rich learning experience. The university also gives its students a great degree of freedom in choosing their curricula to promote a sense of personal responsibility for learning at the university and throughout life. This method-oriented solid foundation gives students the tools required for lifelong learning. Involving students in ongoing research programs at the TU Wien is key to train young scientists and to prepare them for future challenges in academia, industry, or business [5].

For several years, the Department of Structural Design and Timber Engineering (ITI) at the TU Wien has been offering neutral expert advice on the planning of multi-story timber construction projects. In the course of this expert advice and numerous discussions with developers and project managers, it has become apparent that no compactly summarized answers are available for the most common questions. In most cases, decisions with far-reaching consequences have to be made in a short time during planning and execution. Therefore, that proven processes, materials and methods are often relied upon, leaving little time and scope for new ideas.

Within the framework of the Master's Course “Resource-efficient materialization” the ITI at the TU Wien developed a multidisciplinary course including design concepts, feasibility studies and performance assessments of the timber components in order to improve the overall performance.

2 TEACHING METHODS

Timber construction requires a different planning and construction process than mineral construction. Due to the high degree of prefabrication, decisions have to be made in the planning phase in order to benefit from all the advantages of timber construction.
The approach in timber construction differs from the conventional construction processes in mineral-based solid construction. In mineral solid construction, it is economical to erect the shell of building in first step and then to install the windows and façade, as well as the building services and interior fittings.
In timber construction, on the other hand walls are produced in the workshop, irrespective of the weather. Windows, façades and interior cladding can be already ready for installation. This guarantees a high quality of workmanship and reduces installation time on site.
Prefabrication requires a different approach from design to construction. Many decisions have to be made at the beginning, in the planning phase. Prefabrication brings a high degree of planning, scheduling and cost reliability. It reduces the transport of materials to the construction site, the coordination of the trades on the construction site and the space required for construction site equipment (construction containers, material storage, debris troughs ...) [6].

Therefore, the Master's Course “Resource-efficient materialization” deals with the materialization of supporting structures and building envelopes in dense urban construction; special attention being paid to the use of resource-saving building materials, especially natural building materials.
The focus is on the interaction between choice and use of materials and the architectural, technical and ecological requirements to be met in the design and implementation.

The course offers a selection of solutions for implementing technically and economically successful projects and shows a way into the world of timber housing as well as helps to break down entry barriers due to a lack of knowledge among students. Investigated topics thereby are related to a wide range of structural and building physical indicators, such as strength and weight properties, thermal and noise insulation properties, as well as fire protection properties, always under a simultaneous focus on an optimized sustainability of the developed systems.

After having successfully completed the course, students are able to

1. define and apply criteria for sustainability and energy efficiency, acquire a technical way of thinking with the criteria of sustainability and energy efficiency, which have a direct impact on the design in an interdisciplinary exchange.
2. to acquire architectural and design possibilities of hybrid construction in the context of the requirements for flexible and adaptable building;

https://doi.org/10.52202/069179-0600

3. to learn the possibilities for the production and assembly of large-volume hybrid structures and to use methods for quality control Rationalization is addressed as well as the question of costs.
4. to deepen oneself in background and in design and calculation methods of hybrid construction (static, physical, ecological and economic aspects).

2.1 CONCEPTUAL STUDIES

The course teaches the basic skills of architectural design. It pursues an integrative approach that introduces students to all the central practical fields of architecture - from building design, structural and detailed planning to urban planning and landscape design.

The basis of the course is formed around the project-based learning, learning by doing and blended learning education methodologies. This will lead to the transfer of new innovative educational practices, where critical thinking, problem solving and flexibility will be implemented in multicultural group work.

Working in multidisciplinary groups students increases their knowledge and will obtain a wider overview in present and future challenges of design and construction of timber buildings. The intensive learning course consists of two main parts: theoretical face-to-face lectures (25% of all hours), practical teamwork on project (75% of all hours). Project work of students are guided by prepared assignment book, site visits and instructors.

In close succession of presentations and demonstrations of practice-oriented solutions, a flexible feedback culture is established in order to consolidate the student's ideas. While the student's group is working different ways of solving problems, special emphasis is placed on providing them with impulses in the right direction through practical inputs given by experts from business, industry and research at the appropriate time. In doing so, the students are encouraged to pursue the challenges independently instead of simply accepting prefabricated systems.

3 LEARNING OUTCOMES

The course conveys an understanding of the tasks of architecture in society, of its aesthetic, technical, economic and ecological foundations, and of the interaction of various disciplines in planning and construction processes. The focus is on the training of technical, aesthetic and intellectual competencies that enable the successful handling of complex design tasks. Methodological clarity and conceptual thinking are just as much a part of this as the ability to communicate and cooperate in a team.
Learning outcomes describe the knowledge, skills or competences students acquire until the end of the course. The skills acquired provide the best prerequisites for starting a successful professional career after graduation.

The students work on real hybrid timber building projects and share different skills according to their specialization and prepare proposals that will include project program, location and floor plans, façades and sections, room and wet room layouts, structural design, fire precautions, floor and wall partitions, acoustic airborne and impact sound, moisture and cold bridge prevention, building services pathways, choice of materials and building components, important key assembly details (sketches to scale), façade cladding, roof construction, balcony design and construction, external building components insulation and stair enclosure and stairways etc. [6].

An optimized ratio of investment costs to utilization costs should be reached by means of construction and technical measures.
In the design concept the manufacturing, operating and maintenance costs are to be taken into account by the appropriateness of the construction measures (especially area efficiency, building form, supporting structure, façade, etc.).

Additionally, working on real hybrid timber projects results in a number of synergies, such as the exchange with the people involved in outstanding projects or the opportunity to take part in national and international competitions.

3.1 ENERGY AND ENVIRONMENT

The ever-increasing demand for energy affects both the extraction of resources and the climate and environment. Alternative energy sources must be further developed, reliable solutions to climate issues must be found, and there are still some serious problems relating to harmful substances that have not yet been solved. Although significant progress has already been made in these areas, there are still many outstanding questions that are almost impossible to answer using traditional technological approaches.
Currently, the required energy standard for buildings in Austria according to the Building Standards Act is at the low-energy residential level. With the introduction of the Energy Performance of Buildings Directive, the European Council has created the basis for a harmonized assessment. These directives state that buildings must be sustainable, the building materials and components used must be recyclable and the use of environmentally friendly resources and secondary materials is desirable [7].
The high level of thermal insulation in timber construction saves on investments in heating, ventilation and air conditioning (HVAC) as well as operating costs. This means that the necessary technology can be implemented much more simply, is less prone to errors and takes up less space. The fewer water-carrying pipes in the building, the lower the risk.

https://doi.org/10.52202/069179-0600

High thermal insulation, even a thermal transmittance (U-value) of about 0.1W/m²K, is easy to achieve in timber construction with little additional expense. With suitable insulation, less heating is required in the winter and less cooling in summer. This also affects the HVAC. The amounts of energy required for heating and cooling are significantly lower than in a conventional building. In high-efficiency buildings, because of the low power the proportional distribution and circulation losses are particularly high. In the case of central water heating, these amount to up to 85% of the energy demand. Therefore, decentralized water heating can be can be more efficient [6].

In order to address not only the ecological and resource-efficient aspects of sustainable construction, but also to contribute to the discussion on climate-resilient construction, studies and analyses have been carried out. Simulations already carried out in [8, 9] discusses the main factors influencing the overheating of buildings in summer.
The zone overview in Figure 1 shows that the average temperature values vary greatly in relation to individual zones (rooms). The temperature difference between the coolest and warmest room is approx. 2.5 °C. Nevertheless, when comparing the individual room temperatures due to different construction methods, the difference is hardly noticeable.

In all simulated scenarios, these show a maximum difference of only 0.2 degrees Celsius between the individual building types. On the other hand, as the scenarios studied show, increased shading and effective air exchange can reduce the average summer temperatures by several degrees Celsius.
As an effective storage mass, the centimeter inside the building component is particularly important. Deeper layers do not participate significantly in the 24-hour buffering. Building simulations show that the masses act symmetrically. Heavy buildings react slower, light buildings react faster. Both have their advantages.

3.1.1 Investigation of influencing parameters

The case studies on existing buildings in the course include various thermal simulations in the cities Vienna and Wels (Austria), Bochum (Germany) and London using the 3D online simulation tool Thesim 3D [10]. Thesim 3D simulates the thermal behavior of a room in a steady-state, periodic condition (period length: 1 day). It is therefore particularly suitable for standardized summer overheating tests according to EN ISO 13791 [11] or ÖNORM B 8110-3 [12].

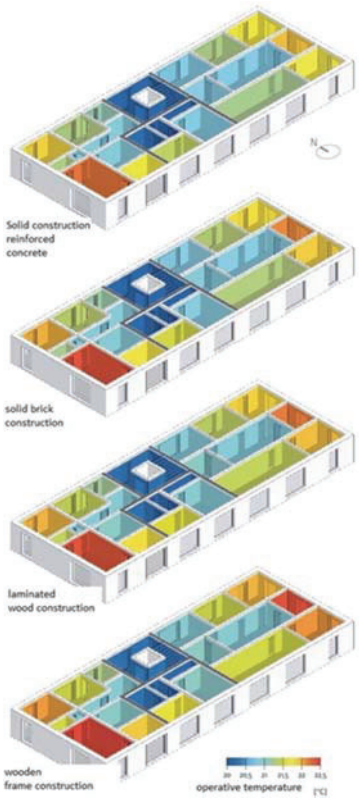

Figure 1: *Analysis model Temperature averages of the individual zones for the four construction methods (© proHolz Austria and the authors* ***[8]****)*

The framework conditions in several European cities are unquestionably different. The simulations in the cities Vienna and Wels, Bochum and London with regard to different constructions made of timber, reinforced concrete and brick as well as their summer overheating variants are intended to cover a wider range of climatic conditions and lead to more differentiated solutions. The following factors are identified as influencing a proper investigation: orientation and size of windows, g-values of window panes and awnings.
Therefore, differentiated measures are developed to avoid summer overheating and to save energy while maintaining sufficient natural light.
The building design contributes significantly to the desired indoor climate in summer. Thermal-dynamic building simulations investigate the placement of exterior windows, the reduction of window area and the effects of balconies and canopies. The zones with the highest solar radiation are mainly located in the southwest.

https://doi.org/10.52202/069179-0600

In simulations carried out on passive house standard buildings in reinforced concrete skeleton construction combined with wooden panel shells (U-value = 0.7W/m^{2}K; g-value = 0.48 coated 3S insulating glass) in Bochum (Germany), the temperature remains comfortable as long as night ventilation (20:00 to 8:00) and sun protection provided by a sun shade system (the shading factor Fc-value = 0.27) are assumed.
The average summer temperatures in Bochum are cooler than in Vienna. However, when the building is placed in Vienna, it can be observed that the indoor temperature is hot but still does not reach the limit of 27 degrees (cf. Figure 2). This shows that the surface elements and window sizes are well designed even in hotter conditions. In Vienna's outdoor climate, efficient night ventilation also proved to be an effective measure against summer overheating of indoor spaces.

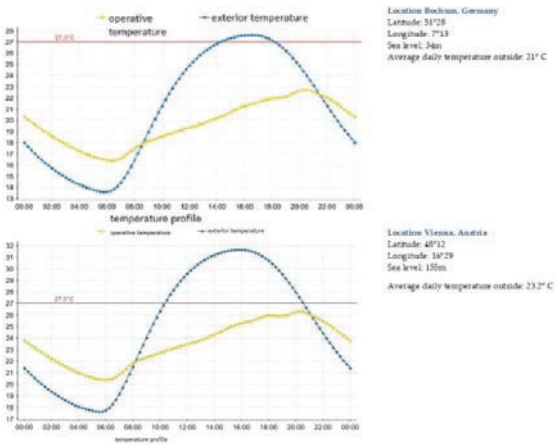

Figure 2: *Thermal dynamic building simulation in Bochum (left) and Vienna (right) (© ITI/TU Wien)*

Thermal simulations on existing buildings show that the construction method has no significant effect with a good U-value. Orientation, night ventilation and sun protection have been shown to have significantly higher effects and have been investigated.

In Wels (Austria), solar radiation is almost constant throughout the year due to the low horizon elevation. In the simulations, no shadows from surrounding buildings influenced the study area, as the surrounding houses are built relatively low.
All common rooms in the building have high daylight quotients. This is at least 2% for all common rooms. In Austria, a daylight quotient of at least 1.9% should be achieved [13]. Basically, this means a pleasant quality of life even in a north-facing room. There are no pure north-facing flats, essentially as a result of the good placement of the flats in the overall floor plan.
The bedroom in the attic, which is to be regarded as a problem room in this calculation, is characterized by two external walls (south-west) and south-facing windows. The room size is relatively small at around 11m² and can quickly overheat. However, due to the smaller room volume, it can cool down more quickly during the night. At first, different combinations of night ventilation (20:00-8:00) and blind use with direct sunlight (Fc value = 0.27) are compared in the current state of the building. A comfortable indoor climate is only possible if ventilation is provided during the night and the blinds are automatically closed when the sun is shining. Consequently, it is preferable to keep the blinds closed if the flat is not visited for a longer period of time (e.g. when travelling). However, the room heats up to 37°C even when the blinds are closed (cf. Figure 3).

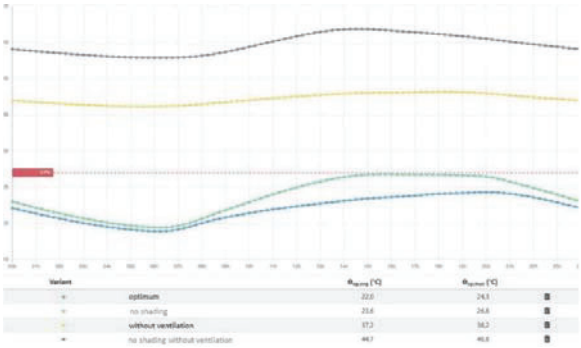

Figure 3: *Thermal dynamic building simulations of the building in Wels; comparison of optimization measures (© ITI/TU Wien)*

The next step is to compare the different constructions for optimal ventilation and blind use. Lightweight timber constructions are hottest during the day, but coolest at night due to their low storage capacity. Reinforced concrete structures provide the less heating during the day but more heat accumulation at night. This is due to its high heat storage capacity.

3.2 LIFE CYCLE ASSESSMENT

The ecological and resource-efficient aspects of sustainable construction are analyzed during the course. To ensure comparability, all values refer to 1m² of components and they have similar thermal transmittance values (U-values) and load-bearing capacities in each category.
The life cycle of buildings is analyzed according to EN 15978 "Sustainability of buildings - Assessment of the environmental performance of buildings - Calculation methods" [14], considering recyclability. The ecological properties of the building materials compared are taken from the databases "IBU-EPD" [15] and "ÖKOBAUDAT" [16]. Both are standardized databases for ecological assessment of the German Federal Ministry of Housing, Urban Development and Building (BMWSB) [16]. The considered criteria are the use of non-renewable primary energy (PEIne), the use of renewable primary energy (PEIe), the global warming potential (GWP) during a time horizon of 100 years based on the German Sustainable Building Council (DGNB) [17].

https://doi.org/10.52202/069179-0600

As an example, the analyses and optimization are presented on an existing building in France.
The corrugated sheet metal façade with the fastening steel angles, as well as the rock wool have the most impact in the production stage. The wood, on the other hand, has much less impact (Figure 4 und Figure 5).

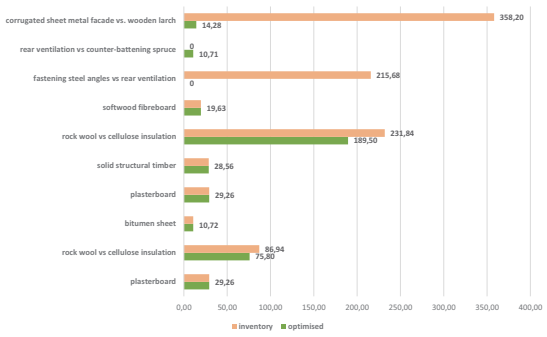

Figure 4: *Non-renewable primary energy (PEIne) [MJ] in production stage; comparison of inventory and optimization (© ITI/TU Wien)*

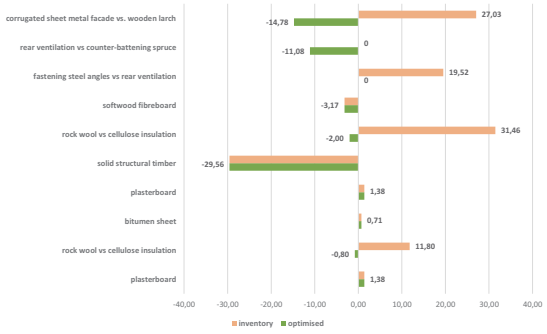

Figure 5: *Global warming potential (GWP) [kgCO_2 equ.] in production stage; comparison of inventory and optimization (© ITI/TU Wien)*

To achieve an improvement in the production stage, the outer wall is optimized. The corrugated metal façade is replaced by a wooden façade with counter battens and the rock wool is replaced cellulose insulation. Through these measures the values significantly smaller and improved (Figure 4 und Figure 5). Therefore, it is important to pay attention to the decisive materials to be considered and also to make appropriate economic decision.

4 CONCLUSIONS

Timber construction requires a different planning and construction process than mineral construction. Due to the high degree of prefabrication, important decisions have to be made already in the planning phase in order to benefit from all advantages of timber construction. For this purpose, more value and time must be put into the planning process itself in order to achieve improvements in the construction phase. This preliminary planning is elementary in wood-based architecture.

The Master's Course “Resource-efficient materialization” has formulated the integration of the natural building material timber to the current requirements of the construction industry. In terms of architectural and engineering questions, the focal point is the cooperation between all professions while integrating sustainability aspects. The intention of the course is to increase student's awareness of holistic lifecycle-oriented approaches. Interdisciplinarity is crucial to the success of the course. This means that master students will be in a position to implement the principles of sustainability, inter alia, economic and ecological aspects in project development and design as well as realization, especially in the operation stage and demolition of building structures.

Through a sustainable materials concept, avoidance of high-maintenance building technology and low energy costs through reduced energy demand as well as optimized energy demand coverage sustainable solutions can be achieved.

ACKNOWLEDGEMENT

The course is a collaborative effort of the ITI/TU Wien and the working group of the Austrian timber industry proHolz Austria. The authors gratefully acknowledge the support of the TU Wien and the proHolz Austria.

REFERENCES

[1] Teischinger, Alfred ; Sting, Robert; Praxmarer, Gabriel Oliver, "pro:Holz Holzbauanteil: Ein Viertel des Hochbau-Aufkommens bereits aus Holz," 15 07 2019. [Online]. Available: http://www.proholz.at/news/news/detail/holzbauanteil-in-oesterreich-ein-viertel-des-hochbau-aufkommens-bereits-aus-holz/. [Accessed 26 10 2019].

[2] Koppelhuber, Jörg, Detlef Heck, and Georg Hillinger, "Immobilienbewertung im mehrgeschoßigen Holzwohnbau: Spezifika und holzbauliche Einflüsse in der Immobilienbewertung gegenüber mineralischen Bauweisen," Technische Universität Graz, Graz, 2020.

[3] Wirtschaftskammer Österreich , Holzbau Branchendaten, WKO, Abteilung für Statistik, [Online]. Available:

https://doi.org/10.52202/069179-0600

https://wko.at/statistik/BranchenFV/B_107.pdf. [Accessed 2 5 2022].

[4] TU Wien, "Technology for People," [Online]. Available: https://www.tuwien.at/en/tu-wien/about-tu-wien. [Accessed 07 02 2023].

[5] TU Wien, "Mission Statement," [Online]. Available: https://www.tuwien.at/en/tu-wien/about-tu-wien/mission-statement. [Accessed 07 02 2023].

[6] B. Höfferl, "Mehrgeschossiger Wohnbau Planen und Bauen," pro:Holz Austria, Wien, 2021.

[7] P. J. Sölkner, A. Oberhuber, S. Spaun, R. Preininger, F. Dolezal, H. Mötzl, A. Passer and G. Fischer, "Innovative Gebäudekonzepte im ökologischen und ökonomischen Vergleich über den Lebenszyklus," Austrian Ministry for Transport, Innovation and Technology, Vienna, 2014.

[8] Ferk, H., Rüdisser, D., Riederer, G., & Majdanac, E., Sommerlicher Wärmeschutz im Klimawandel Einfluss der Bauweise und weiterer Faktoren, isbn 978-3-902926-16-6: Zuschnitt Attachment– Sonderthemen im Bereich Holz, Holzwerkstoff und Holzbau, 1-22, 2016.

[9] Bachinger, J., Wolffhardt, R., Nusser; B., "Sommer, Sonne, Hitze – Wohin geht die Reise? Klimawandel und sommerliche Überwärmung im Wohnbau," *Holzbau,* pp. 45-48, Januar 2021.

[10] J. Nackler, "Thesim," 2022. [Online]. Available: www.thesim.at. [Accessed 15 Juli 2022].

[11] EN ISO 13791, *Wärmetechnisches Verhalten von Gebäuden - Sommerliche Raumtemperaturen bei Gebäuden ohne Anlagentechnik - Allgemeine Kriterien und Validierungsverfahren,* 2010.

[12] *ÖNORM B 8110-3, Wärmeschutz im Hochbau - Teil 3: Ermittlung der operativen Temperatur im Sommerfall (Parameter zur Vermeidung sommerlicher Überwärmung),* 2020-06-01.

[13] EN 17037, *Tageslicht in Gebäuden,* 2019.

[14] *ÖNORM EN 15978: Sustainability of construction works - Assessment of environmental performance of buildings - Calculation method,* Vienna: Austrian Standards Institute, 2012-10-01.

[15] "Institut Bauen und Umwelt e.V., "IBU-EPD" Institute of Building and Environment e.V., 2019.," [Online]. Available: https://ibu-epd.com. [Accessed 15 02 2019].

[16] "ÖKOBAUDAT platform," Federal Ministry of Housing, Urban Development and Building , [Online]. Available: https://www.oekobaudat.de/en.html. [Accessed 26 August 2022].

[17] DGNB Deutsche Gesellschaft für Nachhaltiges Bauen e.V., "DGNB," German Sustainable Building Council e.V., 2018. [Online]. Available: https://www.dgnb.de/en/. [Accessed 08 02 2023].

World Conference on Timber Engineering Oslo 2023

PROFESSIONAL WORKSHOP IN WOOD: STRUCTURAL EFFICIENCY INDEX, FOR ARCHITECTURE STUDENTS.

Martín Hurtado C.,[1] Andrés Sierra M.[2]

ABSTRACT: The Professional Wood Workshop, developed within the School of Architecture of the Pontifical Catholic University of Chile, proposes to students in the final stage of their careers the analysis of different case studies with various architectural programs, such as houses, buildings, schools, and factories, auditoriums, gyms, and warehouses, before the design of their projects, through a quantitative index of the efficiency of the structures that compares the volume (m3) of wood used per surface (m2) of construction.

With the objective that architecture students can identify and understand what criteria and strategies are behind a wooden design, it is that, through tools such as 3D modeling of the referents, they obtain exact parameters of the volume of the foundations, of the primary structure and the secondary structure, managing to comparatively systematize several historical and contemporary examples of good wooden architecture, before beginning to design their projects. The results obtained, quantitative (index) and qualitative (what and how the designer thinks), motivate permanent realization of the workshop, participation in national competitions for students, and a book as a permanent contribution to knowledge in this area.

KEYWORDS: Wooden Architecture, Teaching of Wood Technologies, Educational Theory, Architectural Education.

1 INTRODUCTION

During the professional performance of architects (especially those specialized in wooden constructions), each project is determined by efficiency parameters since the needs are too many, while the resources are limited.

Typically, the design process establishes a maximum expected cost per floor area (USD/m2). This parameter determines many of the decisions of the project, even before deciding its physical form and its materiality since it is a "reality criterion" that conditions the development of the form. We are interested in including and transmitting this concept in the academic context of the last year of undergraduate architecture.

For this, it is necessary to understand the origin and history of these principles, shape a methodology that fits the curriculum for the training of architects in Chile (which comes from the world of Fine Arts) and transmit those results from a quantitative and qualitative.

1.1 THE CRAFT

The craft is an accumulation of knowledge created in a slow process of trial and error: what will I do, how will I do it, and who it will be for.

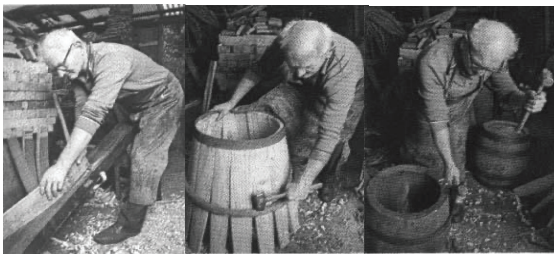

Figure 1: *Wine barrel cooper.*

Every construction system is based on a trade, which usually brings together three elements: (a) The availability of resources or "site material"; (b) The uses and customs associated with the climate, topography, and landscape, which result in what we know as "local culture" as a material good; (c) A heritage that we want to preserve, which we call "culture of origin."

Seen this way, the way of building each place says a lot about the nature of the site; their customs, ways of life, food, clothing, festivals, rituals, and shelter needs that force local builders to seek simple and common solutions so that anyone can carry them out, what we call "Vernacular Culture."

[1] Martín Hurtado Covarrubias, Pontifical Catholic University of Chile, mhurtada@uc.cl
[2] Andrés Sierra Martínez, Pontifical Catholic University of Chile, agsierra@uc.cl.

https://doi.org/10.52202/069179-0601

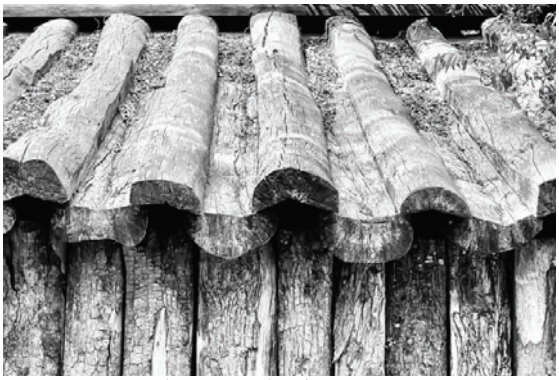

Figure 2: *Pewenche Ancestral Refuge.*

In recent years, wood construction has once again positioned itself as a valid option to respond to the many building needs due, among other factors, to good environmental indices, being a renewable, recyclable, low-cost, and flexible, added to its exemplary environmental behavior and lower carbon footprint, the possibility of being industrialized, and its flexibility and warmth properties in the finishes.

1.2 THE TRAINING OF THE ARCHITECT

Architects learn, above all, by studying reference projects, which serve as a guide to see how others have solved a project in similar conditions. Although technical construction manuals are helpful in many cases, helping to clarify how a detail is designed, they do not solve the fundamental questions of any project, which are related to the totality of the problem: What to do and how to do it.

As the Chilean architect Cristian Valdés says, "more important than thinking about the 'form' that I am going to give to a project, the central thing is to think about the 'attitude' that I am going to take towards it" [1]. Thus, for example, if it is determined that the main thing will be to build with local materials and technology, the range of possibilities is limited, probably rescuing a trade related to the degree of technical precision that can be chosen.

Figure 3: *J. Vignola and his translation on Chiloe wood.*

This apprenticeship method does not prevent the necessary questioning that architects must undertake to "move the border of the possible." Still, it makes the difference between the virtuosity of someone who, mastering a trade, explores new possibilities. Conversely, someone seduced by novelty risks the resources of others by trying untested solutions that usually result in construction defects that jeopardize the stability and durability of the building.

We study, for example, the "Churches of Chiloé," a series of Catholic temples built in the archipelago of that name, located in the wooded area of southern Chile, where, since the 17th century, more than 20 prominent temples were built in wood. Declared a World Heritage Site by Unesco, based on the manual by Jacopo Vignola brought by the Jesuits, are examples of the adaptation of classical architecture thought of stone to a language built of wood. The local carpentry trade, highly developed for constructing wooden houses and boats, allowed us to produce these marvelous temples. It seemed to us a critical case study since it let us know the amount of wood used based only on knowledge of the trade of the local carpenters and compare these data with buildings of similar characteristics currently developed, with all the support of the current structural modeling and calculation. That is to say, to contrast carpenters' and engineers' logic.

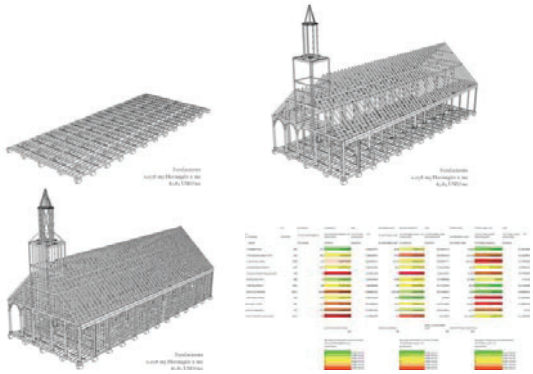

Figure 4: *"Achao Church" index of efficiency of structures.*

We did the same with a series of 25 historical and current works in wood to contract the data that quantifies its structure with the constructed surface area and thereby provide quantitative reference information associated with specific projects that students can know and ponder based on whether or not they can serve as reference models for your project.

Knowing this information at the beginning of the development of a project, even before its formal composition, makes a difference since, in wooden buildings, the adequate modulation of the structure is the fundamental basis to ensure optimal performance.

The trade of good wood construction involves the associated technical solutions and, very exceptionally, considers the architectural variables that are usually not named and therefore forgotten. The questions discussed during the course are: What happens with the concepts in large part of architecture treatises, such as proportion, scale, rhythm, order, and, ultimately, the harmony of the whole? How can you safeguard the constructive wisdom

https://doi.org/10.52202/069179-0601

and, at the same time, the beauty of any well-designed wooden structure?

We call this “The aesthetics of logic” or, in other words, the wise way of arranging the pieces and parts that make up the supporting structure of a built body that always result in a harmonious and beautiful skeleton.

Figure 5: *San Francisco Javier School, in Puerto Montt.*

An example of the above is the natural structure that makes up the skeletons of vertebrate animals. So fair, precise, and efficient to support the demanding loads and, at the same time, respond during its life.

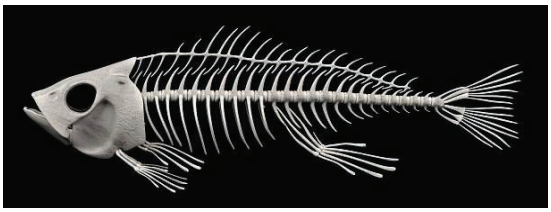

Figure 6: *Animal structure*

1.3 EXPECTED RESULTS

The course intends to discuss the questions posed by rescuing examples of the construction trade present in different wooden buildings, taking both historical and current cases, and measuring them under the same parameter, a structural efficiency index, which quantifies the volume (m3) of wood used in the supporting structure of the building and relates it to the surface (m2) built, allowing reflection and knowing in a single data, in a figure, the amount of wood required for its structure.

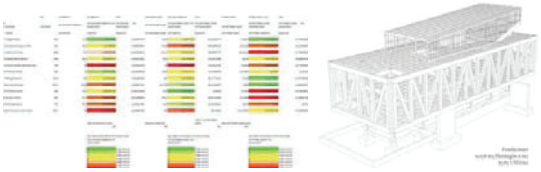

Figure 7: *IEE Comparative table 25 cases.*

This index makes it possible to understand the process behind designing a wood system and allows obtaining a parameter that can be used as a comparison and help make decisions about how the most efficient supporting skeleton of a new building in this material should be.

2 EFFICIENT WOODEN STRUCTURES

In this academic activity, the criteria used to measure and compare the efficiency of the structure of the different wooden buildings were cost, proportion, and language.

2.1 COST

The "cost" is always a priority in any actual project, not only the monetary cost but also the cost of technical and physical resources.

For example, to build the Sewell mining camp - a group of light-framed wooden buildings located in the high mountains of central Chile - at the beginning of the 20th century, North American engineers from the Braden Cooper company determined that all the construction material had to be loaded by "oxen yoke," given the problematic accessibility on steep slopes. This condition decided that the primary construction material for the structures and finishes would be wood due to its characteristics, such as being light, resistant, malleable, and workable by hand.

Figure 8: *Sewell housing building, Chile, 1920.*

Hundreds of carpenters could build large warehouses, bridges, pipelines, levees, retaining walls, offices, restaurants, and accommodations for all staff. The low cost and the availability of abundant wood brought by ships as ballast on their return voyages from North America were the starting point for determining that everything built-in mining operations would be made with this wood.

https://doi.org/10.52202/069179-0601

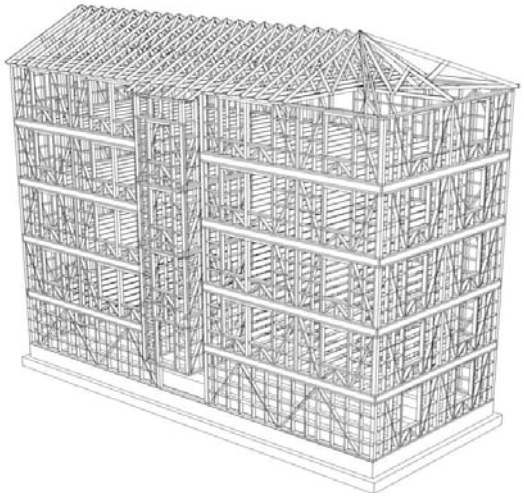

Figure 9: *Sewell bedrooms light-frame structure, Chile, 1920.*

The low weight of wood implied low transportation costs and the possibility of building with only hand tools, taking advantage of hermetic enclosures in extreme climates, and even constructing ponds and wooden pipes to store and transport water with high corrosion resistance.

Students are taught that every project is determined by the conditions of the environment where it will be built. Thus, deciding what material to build with always derives from a chain of implicit consequences, which go beyond the physical form of the project. It is not just an aesthetic problem; it is integral.

In summary, the cost of a structure is a variable that involves the value per m3 of the material plus the cost of the resources necessary to build with the chosen material and sizes in a specific place.

2.2 PROPORTION

Any building built based on a reticular structural system must combine these variables: "Architectural Module" and "Structural Module."

The architectural modulation provides the minimum dimensions necessary to house the activities required by a project, depending on the acts it hosts, which results in different sizes of enclosures.

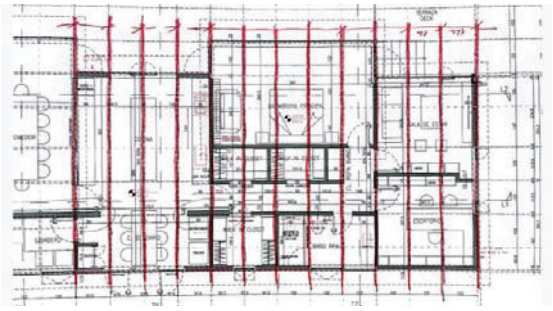

Figure 10: Architectural Module vs. Structural Module.

Structural modulation provides a system of columns, beams, or walls to cover the minimum free spans necessary to house the program's activities, generally determined by the dimensions of the construction materials used.

The students are taught that the first thing is to make a detailed analysis of the program and verify the dimensions of the "free span" necessary for the room with the most significant demand in size, and with this, decide the system of pillars and beams to use, in the "simple, most economical and best way".

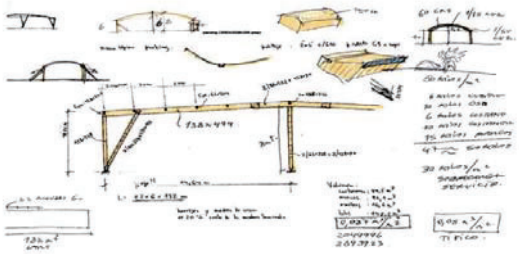

Figure 11: *Calculations of the Greenvic Packing structure.*

Then, we ask the students to analyze from evaluating the different materials to use the modulation or primary grid of dimensions that best suits the program's requirements.

In these cases, a grid's initial design allows the program's different parts to be organized in a simple matrix. However, care must be taken that this matrix is accessible enough for the base module to adapt to the size of the rooms necessary for the program. The smaller the dimension of the modules, the more freedom to adjust the program to the exact needs and not oversize or undersize an enclosure.

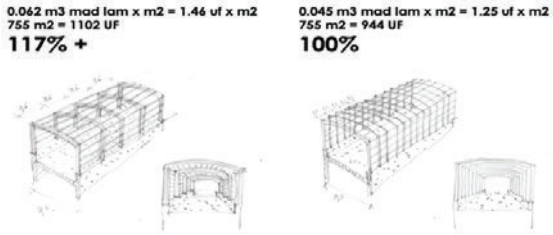

Figure 12: *Venue-Scale Rhythm and Efficient Modulation.*

After that, the "rhythm" determines the expression of the constructive skeleton matrix. In general, the timing of the grid is appropriate to the size of the project and is based on the dimensions of the materials in your commercial site measurements, such as columns, beams, plates, and cladding to be used.

In our country, it is customary to use a 1.22 x 2.44-meter grid, or its derivatives, from the size in which many construction materials are marketed. You can use the module divided into 3, 2, or 1, 40.5, 61.0, or 122 centimeters for smaller buildings, 244 centimeters for

https://doi.org/10.52202/069179-0601

medium buildings, and 366 4.88, 6.00, or 7.32 centimeters, or more, for large (extra large) structures.

2.3 LANGUAGE

In the words of Peter Zumthor, "construction is the art of configuring a whole with meaning from many particularities" [2]. Wooden architecture brings with its discontinuity. To build a wooden building, it is necessary to join pieces and parts, assembling and joining different components to achieve a unitary body. For this reason, the carpentry trade is essentially the trade of joining and assembling.

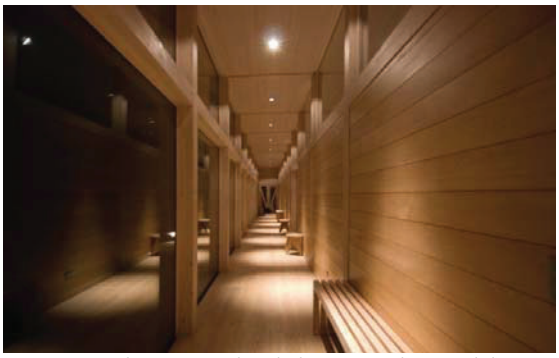

Figure 13: *The parts vs. the whole. Casa Colico 2, Chile.*

Once the decision is made on the most appropriate modulation for the program that will be housed, the detail emerges as an assembly point, a solidary union to build a continuous envelope, where the gaze does not stop at the discontinuity of the detail but rather the totality traps that.

"The details, when they come out well, are not decoration. They do not distract, do not entertain, but lead to the understanding of the whole, to whose essence they necessarily belong." [3].

Figure 14 : *Craft Structure Galpon Osorno.*

Architecture has always needed to find a language that supports the physical image of the project. The buildings developed with reticular structures have exposed the supporting structure as the accurate skeleton that underlies the form, expressed through the vectors that conduct the static and dynamic loads derived from the structural weight.

Modernism, supported by mathematical calculation as an indisputable truth, which uses the aesthetics of constructive logic in a spirit of stripping away everything that is not strictly necessary to sustain the building, resulted in an abstract aesthetic of elements that conduct the forces of gravity. Still, they do not necessarily resolve the physical expression of the building envelope, which is mediated by other needs of the architectural form.

Figure 15: *Main structure and secondary structure.*

Mies Van der Rohe, perhaps one of the fathers of constructive puritanism, in his well-known Seagram Building project in Chicago, uses two structures for the façade: (a) load-bearing steel covered with concrete, which remains "hidden" as the main load-bearing structure; (b) a second façade structure, built with slimmer steel profiles that give rhythm and proportion to the building's walls.

This freedom in design possibly allows for play, assigning to the main supporting structure the static and dynamic requirements of the system, plus the required fire resistance requirements, and freeing the secondary structure of the façade to build with it the visual language of the building.

3 THE INDEX

The index is a figure which summarizes, in a number, a complex web of factors that determine a reality. The carbon footprint is a good example. Let's compare it with the automobile industry, and we have to design, for example, a very affordable city car. We use as a parameter that its fuel consumption should be between 25 and 30 km/lt.

This index involves several parameters at the beginning of a design to achieve the objective. For example, size, weight, and relative dimensions will be present before starting to study the form of the model to be developed.

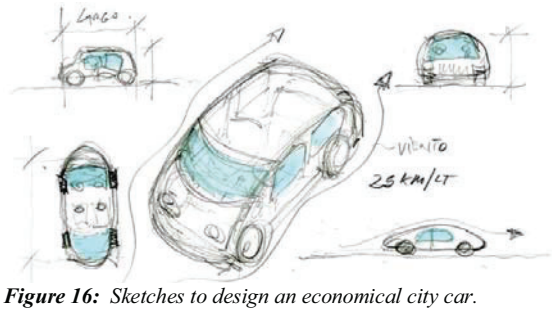

Figure 16: *Sketches to design an economical city car.*

https://doi.org/10.52202/069179-0601

In our case, applied to wood construction, the index should be a helpful tool for architecture students to identify a primitive order before defining a shape based on a premise: the best structure is the one that uses the least quantity. Of wood to achieve the same results required.

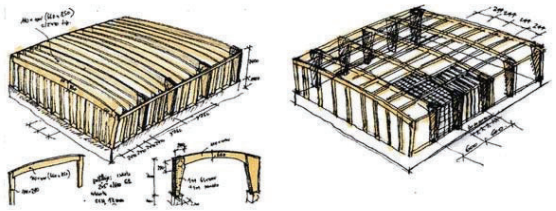

Figure 17: *Sketches of an example of an economic structure.*

3.1 A TOOL FOR ARCHITECTURE STUDENTS

In the same way, the design of a building begins specified by qualitative parameters, also determined by the enclosure program, but also by specific quantitative metrics usually determined by the expected cost per m2. The first parameter has been studied for various types of buildings, even forming part of construction laws and ordinances that set minimum standards according to the activity to be carried out, which determines lighting and ventilation conditions, average comfort temperature, acoustic reverberation, etc.

The cost of the structure of a wooden building in Chile is determined by the concurrence of three factors: seismic stability, fire resistance, and wind resistance. Given its low weight, it is not the problem of seismic stability that mainly determines the sections of the elements. Even so, studying it is essential to develop the system of joints and hinges necessary to resist earthquakes. At the same time, the most critical conditions for a wooden structure are its stability against the wind and its resistance to fire. Quantifying these variables allows the study of different combinations of parts and components, which imply different costs.

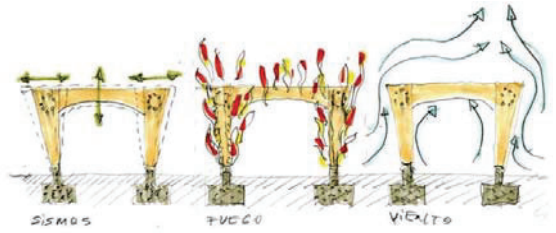

Figure 18: *Sketches of seismic stability, fire resistance and wind resistance.*

Understanding the above, through 3D modeling of different projects, students quantify and compare the volume of concrete in cubic meters and the steel foundation; sawn timber structures; glued laminated wood structures; the fittings and connection components, and the square meters of coatings and skins for each project.

The initial results in a structure efficiency index or IEE, associated with the cost per m3 of material, determine a quantitative parameter of design efficiency concerning the built area.

This index can also be associated with a recycling rate for the building -generally associated with the wooden elements it uses- to show its sustainability and the estimated carbon footprint index.

3.2 MORE THAN A FORM, AN STRUCTURE.

As Alberto Campo Baeza points out, “gravity builds the space (…) the load-bearing structure, rather than transmitting loads of the building to the ground, what it transmits is the order of the space, it builds the space. As a result, the structure supports not only endures but is well resolved, tuned, waiting to be pierced by light” [4].

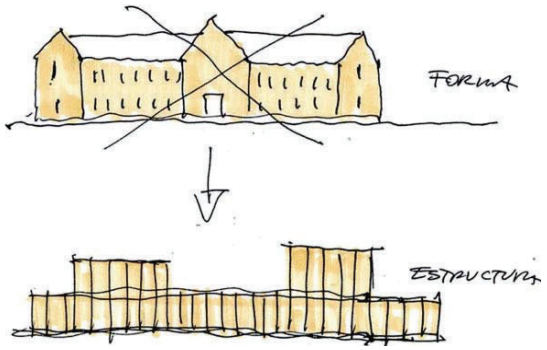

Figure 19: *Sketches of the “More than a shape, an structure” concept.*

To develop a wood project, the first thing that students do in the course, after carefully studying the conditions of the place, the program in charge, and the available resources, is to discover the deep organization that will order it. More than finding a plastic form, which depends on the design of a "skillful hand" of the person who makes it, an order is sought, a deep structure that organizes the program and the construction in a straightforward matrix, which builds the entire project.

Once this internal order is discovered, the project flows into a sequence of reasonable, appropriate, and consistent decisions between what, to quote Louis Kahn, a building "wants to be" [5] and the material that will be used to make it.

In this previously described way, innumerable data, intuitions, tastes, and sensibilities converge to know "what" and "what" should be what we are doing. The form is thus a consequence and not a goal.

https://doi.org/10.52202/069179-0601

3.3 A METHOD FOR AUSTERITY

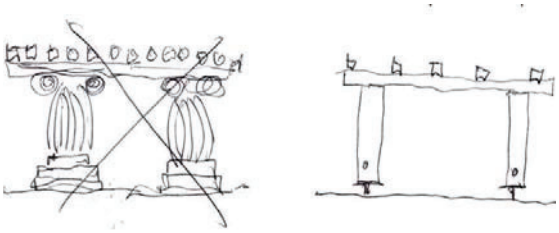

Figure 20: *"A method for austerity" scheme.*

For various reasons, most of the carpentry in Chile has been developed under the premise of an essential economy of resources.

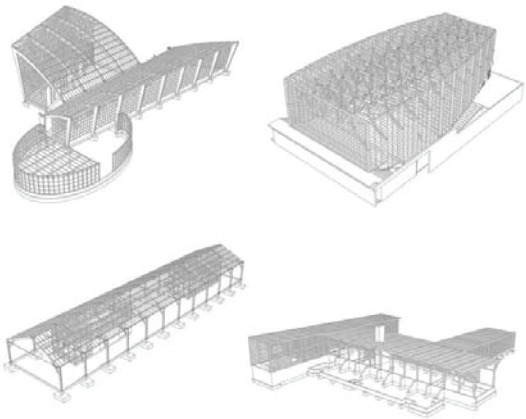

Figure 21: *Mim Museum, Matucana Theater 100, Haras Las Camelias and House 2 wooden structure models.*

Chile is a country that hardly looks at the benefits of development, where most people live at subsistence levels. Therefore, preparing a student to work under strict austerity measures seems ethically prudent. This self-discipline has meant that when tackling each project, we are very strict in leaving what is essential or the minimally necessary to accommodate the requested program, and with this finding the most suitable material for the available budget.

In this way, based on years of experience in the design of a significant number of wooden buildings and university teaching on building with this material, the need arose to have quantitative judgment elements when making decisions arose. Decisions regarding the supporting structure of a building are a way to optimize and create more efficient use of resources.

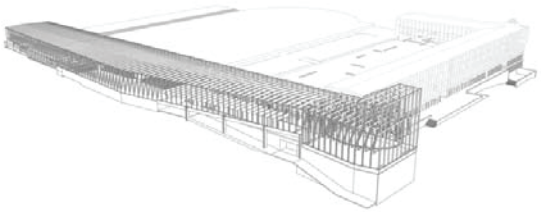

Figure 22: *Wooden structure model of the San Francisco Javier School Puerto Montt.*

4 CONCLUSIONS

After different editions of the course, studying and measuring the m3 of wood per m2 of the building became a way of helping to decide and project the structure of a building without this being a mere result of the structural calculation at the end the process.

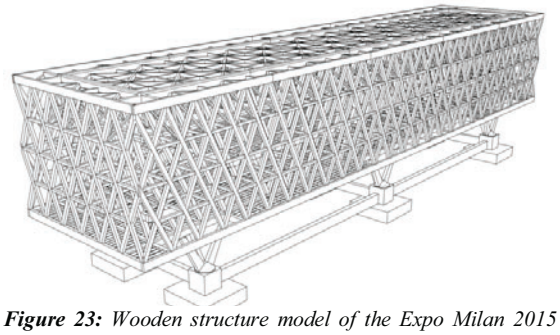

Figure 23: *Wooden structure model of the Expo Milan 2015 Chilean Pavilion. Undurraga Deves Architects.*

The students, by modeling and drawing the details of each building studied, the product of a careful selection of significant works of architecture in wood, allowed us to understand why the author decided on one or another modulation of the structure, to know how he solved the details, to question his plastic expression and increase their architectural culture.

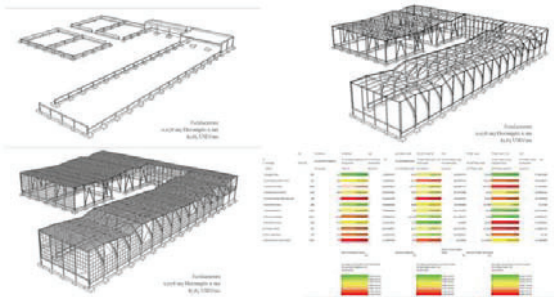

Figure 24: *Foundations, main structure and secondary structure of the Greenvic Packing.*

4.1 THE PROBLEM

Regarding the concepts present in large part of the architecture treatises, such as proportion, scale, rhythm, order, and, ultimately, the harmony of the whole, the idea of parameterizing cases and extracting valuable lessons for future projects, He delivered a method of systematization in decision-making based on the consideration of seismic, fire and wind conditions, which make evident what determines the dimensions of the structure of a building. Being able to identify the craft and constructive wisdom, later managing to design with criteria of beauty by taking into account costs, but also the proportion and language of the structures as plastic resources to provide "architectural identity" to the buildings.

https://doi.org/10.52202/069179-0601

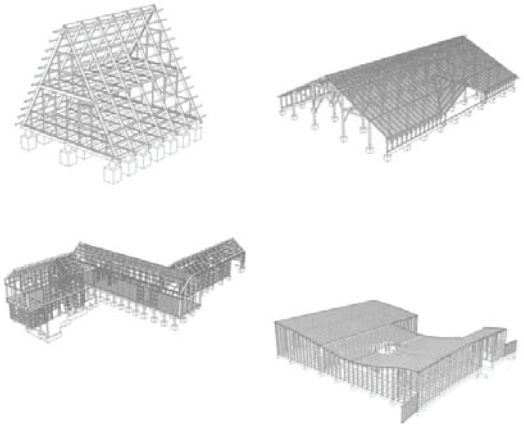

Figure 25: *A-Frame House, Osorno Warehouse, Molinahue House and Nadalie Barrel Factory wooden structure models.*

4.2 MAIN FINDINGS AND RESULTS.

From a methodological point of view, the results obtained, both quantitative (index) and qualitative (what and how the designer thinks), have motivated: the permanent realization of the workshop, the participation and obtaining of prizes in different national competitions for students and the creation of a book as a permanent contribution to knowledge in this area.

4.3 CONTRIBUTION TO LITERATURE AND KNOWLEDGE IN THE AREA: THE MANUAL

After two years, the study managed to comparatively systematize several historical and contemporary examples of good wooden architecture, finding efficiency parameters in terms of discovering the wisdom of the trade present in the amount of material necessary to build a wooden building, similar to the index used by engineers in reinforced concrete constructions, which measures the weight (kg) of steel per volume (m3) of concrete, knowing a priori when a structure is within reasonable efficiency margins.

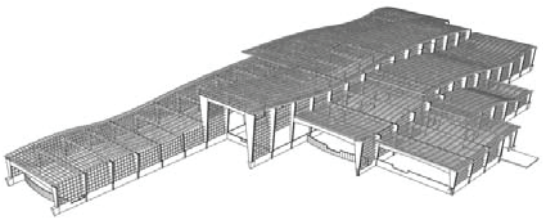

Figure 26: *Viña Almaviva Winery wooden structure model.*

This result will become a Manual for architects, builders, and students, to verify the amount of wood in the structure during the design process, involving in this edition, thirteen projects developed in our architecture office, four historical projects and three contemporary wooden buildings.

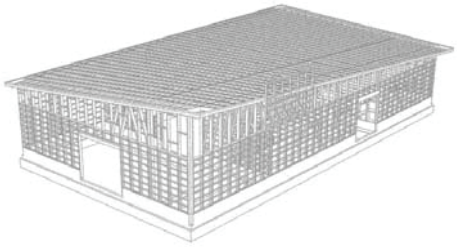

Figure 27: *Wooden structure model of the INFOR Laboratories.*

IEE INDEX OF EFICIENCY OF STRUCTURES							
m3 concret fundations/ m2 constructio n		m3 laminated wood / m2 constructio n		m3 Timber wood / m2 constructio n		Cost Euros / m2	
A	0.020 m3/m2	A	0.030 m3/m2	A	0.010 m3/m2	A	0-55 Euros/m2
B	0.036 m3/m2	B	0.048 m3/m2	B	0.016 m3/m2	B	56-71 Euros/m2
C	0.052 m3/m2	C	0.066 m3/m2	C	0.023 m3/m2	C	72-87 Euros/m2
D	0,068 m3/m2	D	0,084 m3/m2	D	0,030 m3/m2	D	88-104 Euros/m2
E	0,084 m3/m2	E	0,102 m3/m2	E	0,037 m3/m2	E	105-121 Euros/m2
F	0,100 m3/m2	F	0,124 m3/m2	F	0,043 m3/m2	F	122-138 Euros/m2
G	0,116 m3/m2	G	0,146 m3/m2	G	0,050 m3/m2	G	139-155 Euros/m2

Figure 28: *IEE Index of Eficiency of Structures..*

Nr	buildings	m2 construction	m3 laminated wood / m2 construction
	INDICE		m3 mad/m2
1	Peugeot Shop	582	0,049
2	Workshop Museum MIM	524	0,103
3	Almaviva Winery	3688	0,063
4	Nadalie Barrel Factory	1190	0,057
5	Cultural Center Matucana 100	765	0,124
6	Morande winery	660	0,075
7	Paking Greenvic	4303	0,068
8	Stud Las Camelias	625,3	0,065
9	Pirihueico House	380	0,022
10	House 2 Colico	481	0,054
11	ECIM Laboratory	755	0,046
12	San Francisco Javier school	6322	0,108
13	Achao Church	490	0,000
14	House A	56	0,081
15	Chile Pavilion Expo Milan	2121	0,321
16	Architecture School PUC	1428	0,196
17	CMPC Headquaters Los Angeles	6946	0,207
18	Las Quemas Barn Osorno	687	0,054
19	Building 42 Sewell	657	0,083
20	Infor Concepción	1216	0,081

Figure 29: *20 cases compared by the IEE index.*

ACKNOWLEDGEMENTS

To the students of the "Directed Research" course: Cristóbal Claro; María Jesús González; Benjamín Herrera and Camila Rivera.

REFERENCES

[1] Iturriaga, S.: Cristián Valdés: La Medida de la Arquitectura. Ediciones ARQ. Santiago, Chile, 2008.
[2] Zumthor, Peter. Thinking Architecture. Birkhäuser, Basel, 2010.
[3] Íbid.
[4] Campo Baeza, A.: La estructura de la estructura. Nobuko, Buenos Aires, 2010.
[5] Kahn, L.: Order and Form. Perspecta 3: The Yale Architectural Journal, 1957.

World Conference on Timber Engineering Oslo 2023

THEORISING A NEW EDUCATIONAL AGENDA FOR SUSTAINABLE BUILT ENVIRONMENT PROFESSIONALS: TIMBER TECHNOLOGY, ENGINEERING, AND DESIGN PROGRAMME

Aghlab Al-Attili[1], Robert Hairstans[2], Tim Belden[3], Gabriele Tamagnone[4], Sarah Hitt[5], Tabitha Binding[6], Joseph Walters[7]

ABSTRACT: (200) The paper reports on the most recent activities undertaken on the local and national levels to create a competency framework for timber engineering in an effort to change the traditional construction methods into more sustainable and environment friendly methods based on the use of biogenic materials. The paper further details the various pilot projects and educational programme developed to upskill professionals of the built environment. More details are provided on the capstone educational programme including its structure, strategy, delivery and content.

KEYWORDS: Timber Design Education, Sustainability, Architecture

1 INTRODUCTION

The construction sector, including building materials, is at the centre of a climate change and global warming since it represents 33% of global final energy use, generates nearly 40% of global energy-related Green House Gases emissions and consumes 40% of global raw materials [1]. In the UK, Co_2 emissions from construction industry reached 13.5 million metric tons in 2019 [2]. The direct cause for emissions might be the elements mentioned above, but in reality, there is an underlying cause which contributes and converges to form the results above. One might argue that the main contributors are lack of research into sustainable building materials, the education which is not based on sustainability, and the economic drivers that favours financially short-term cost-effective measures over long-term sustainability.

The desire to use sustainable materials needs to be coupled with active research into sustainable biogenic materials that effectively competes with the currently available non-sustainable traditional construction materials.

On the other hand, the formative educational outputs from higher education institutions and training centres around the globe revolve around old and traditional knowledge that has the economic costing feasibility at its centre, whereas sustainability and environmental friendly materials come as an afterthought when compared to project design, construction and economic costing considerations.

Moreover, the current practices in-place within the construction industry are direct responses to the market demand which sees construction and built environment professionals under-trained and ill-equipped with the knowledge to tackle sustainability considerations for two reasons: a) they do not have the knowledge required for sustainable construction, and b) the context in terms of practices and materials does not necessarily aid the endeavour to achieve sustainability. In other words, a construction manager, or an architect, or even an architectural technologist will not necessarily have the experience of running sustainable projects, and their knowledge of designing, detailing or running projects includes traditional materials that are not necessarily sustainable.

Triple factors above; namely practice, education, and knowledge are not up to date with sustainable options. Each of the factors need to be addressed on a global scale. The paper and its outcome describe an attempt on a national scale in the UK to address the issue by proposing a new triple helix action to address the emergency. Our efforts and reaction are demonstrated using Biogenic materials as an example of sustainable construction materials, and in specific, we are using timber as an

[1]Aghlab Al-Attili, NMITE New Model Institute for Technology and Engineering, CATT Centre for Advanced Timber Technology, aghlab.al-attili@nmite.ac.uk
[2] Robert Hairstans, NMITE New Model Institute for Technology and Engineering, CATT Centre for Advanced Timber Technology, robert.hairstans@nmite.ac.uk
[3] Tim Belden, NMITE New Model Institute for Technology and Engineering, tim.belden@nmite.ac.uk
[4] Gabriele Tamagnone, NMITE New Model Institute for Technology and Engineering, CATT Centre for Advanced Timber Technology, gabriele.tamagnone@nmite.ac.uk
[5] Sarah Hitt, NMITE New Model Institute for Technology and Engineering, sarah.hitt@nmite.ac.uk
[6] Tabitha Binding, TDUK Timber Development UK, tbinding@ttf.co.uk
[7] Joseph Walters, NMITE New Model Institute for Technology and Engineering, joseph.walters@nmite.ac.uk

https://doi.org/10.52202/069179-0602

example of such sustainable materials. So, what follows will be addressing timber.

It is evident that the sector's contribution is an issue that requires addressing. This paper reports on the unique approach developed and implemented by the Centre for Advanced Timber Technology within The New Model Institute for Technology and Engineering that predicates over multiple axioms linking professionals of the built environment, operations in construction industry and its supply chain, and finally materials used in construction. Through this multiple approach, analysis is carried out in the sector to outline a new agenda for sustainable built environment education that redefine the built environment professional, equips him/her with new knowledge, skills and tools to address the climate crisis through net zero carbon design, and finally offers alternative sustainable construction materials (biogenic) with specific focus on Timber as an example. This forms our future action triple helix of research into sustainable materials, education of sustainability in construction using sustainable materials, and finally informing the new standards of professional practice that is based on sustainable education and sustainable materials.

2 THE COMPETENCY FRAMEWORK

The first step in creating an agenda, is understand the professional practice environment, which in turn requires a survey that covers the construction and built environment needs as derived from various professional roles within it. To be able to conduct such survey and link it to all levels of the problem on the one hand, and feed it to all levels of solution, on the other, it is important to have an overarching strategy that regulates the relationship between different elements and parties. The development of such strategy was the first step in our endeavour, and the outcome, (figure 1), and identifies the delivery partners (namely NMITE, Edinburgh Napier University and Timber Development UK) and the steering group committee which consists of various key players in the market.

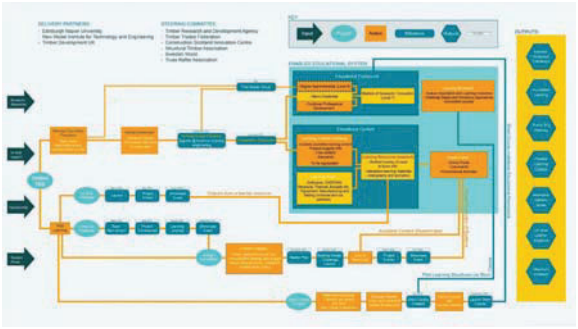

Figure 1: *The overarching strategy*

The strategy identifies areas of investigation that links the market assessment, and the resulting working group, to market needs leading to a series of projects, actions and outputs. From the outset, the educational output was a major key player in that it required a survey of requirements, and a framework that regulates the knowledge to help identify the gap.

The result is an educational framework that acts as a guide to any trail-blazer group that reacts to the requirements above. The reactions required were in the form of continuing professional development short courses, undergraduate and postgraduate degrees. The content of the degrees will respond to the market assessment which included analysis of roles and duties of each built environment profession, and assessment of the knowledge gap.

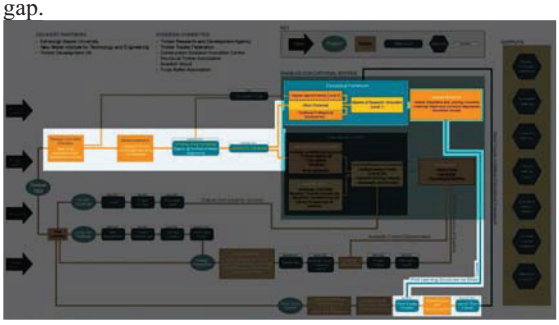

Figure 2: *Development process*

Figure 2 above highlights the educational process stemming from the strategy. It progresses from the survey of the market needs into the development of an educational framework that outlines the content and type of knowledge required for the educational intervention. What follows below is a description of the process of developing the educational framework.

2.1 FRAMEWORK DEVELOPMENT

The competency framework is developed to document the knowledge, meta skills, and industry experience the next generation of timber professionals in construction need in order to drive the change in the construction industry towards biogenic offsite manufacture.

Figure 3: *Steps to be taken produce a feamwork*

The process starts by analysing available resources to the project in the form of logistics, then establishing action frameworks for each individual component listed in figure 3, and then moving to an interview phase where key stakeholders were asked to share their reflections and views in order to draw the themes that frame the intended outcome. Several revisions saw the final framework through. The process also saw the creation of a working group of different contributing parties and a steering group to oversee the implementation.

https://doi.org/10.52202/069179-0602

2.2 COMPETENCIES

The competency framework sought to answer the question of what are the competencies underpinned in the practice for sustainable construction and therefore education? To which, the answer came from the surveys and partners and after an extensive analysis of different built environment roles in contrast with activities and processes linked to sustainable practices taking timber as the main construction material. The result was divided into two categories: core technical competencies (figure 4), and cross-disciplinary competencies (figure 5).

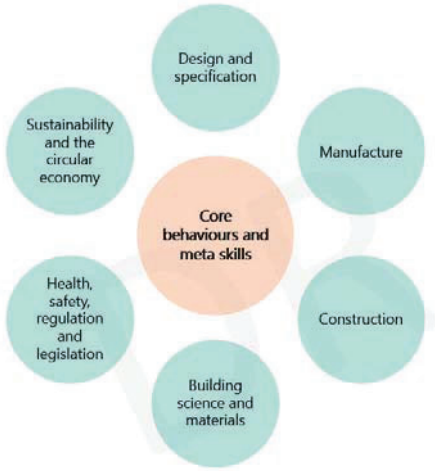

Figure 4: *Core technical competencies*

The former cover aspects like sustainability, manufacture, health and safety, construction, building science, and design and specification, while the latter include the topics of communication, business and commercial, quality, management and digital data.

Figure 5: *Cross-disciplinary competencies*

At the heart of the cross disciplinary competencies, we have certain core behaviours and meta skills (table 1), that revolve around qualities like teamwork, critical thinking, innovation, organisation, professionalism, and ethics.

Table 1: *Core behaviours and meta skills*

Behaviour
Collaboration and teamwork
Critical thinking and problem solving
Innovation
Organisation
Professionalism and career development
Ethics

Each of the competencies contain several knowledge topics, which will be tested in several learning experiences or activities in order to ensure its effectivity in addressing the challenge that is the climate emergency. In what follows, we will have a brief description of learning experiences.

3 PILOT LEARNING EXPERIENCES

The learning experiences suggested predicate on three axioms:

a) the concept of deconstructing existing professional knowledge and its method of attainment into various constituting components and then augmenting the knowledge with our competencies, with the focus being on the technical competences.

b) the action of gauging existing learning styles in the market, with the professional reception of activities being a measure of success through demonstrated demand, and

c) the multiplicity of pedagogic approaches utilised and demonstrated in the learning experiences act as a method of assessment for the efficacy of the approaches.

The learning experiences are described in what follows.

3.1 SUSTAINABILITY ENRICHMENT WEEK

The Sustainability Enrichment Week is series of events involving postgraduate university students within the field of the sustainability in the built environment, who will assemble at our living lab centre in Hereford to engage in several activities, such as workshops focusing on topics like sustainability in construction, environmental ethics, or organisational change management; field trips; and seminars. This is treated as an opportunity to assess their existing knowledge of the topic and find out any potential gaps in this knowledge in order to allow us to trial different techniques to top up the knowledge and experience and take it into the level required by the competency framework. While the participating students are at university level, the intention is to have learners from different parts of the built environment sector. The choice of sample for this activity (postgraduate students) reflects the midpoint in the spectrum of professionals in the field which has undergraduate students on one end of the spectrum, and experienced professionals on the other end. Within the spectrum postgraduate students tend to have the underpinning experience in addition to some professional experience.

https://doi.org/10.52202/069179-0602

3.2 ICE BOX CHALLENGE

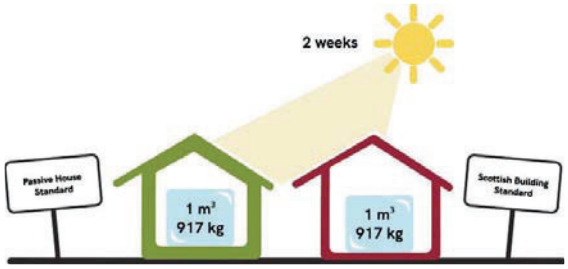

Figure 6: *Ice Box Challenge concept*

The Ice Box Challenge was presented as part of the COP26 event held in Glasgow. The learning experience is designed to allow participants to interrogate existing energy-efficiency building design standards and codes when it comes to sustainability within the built environment. This is carried out through showcasing the potential of an energy-efficient, Passivehaus standard design against a Scottish building standard design.
Two groups are tasked with designing, manufacturing and building two different box structures and applying the insulation as coded by the two different standards. Not only did the outcome favour the Passivehaus standards, but the two structures which were designed, manufactured and assembled, are acting as demonstration for both critical and comparative thinking all while allowing learners the opportunity to examine the result of applying the codes into practice.

Figure 7: *Actual ice boxes designed and manufactured by participants.*

The two boxes have been shipped to Hereford and will be used to carry out further research and as a learning tool for students to learn about thermal efficiency and to be used as a model to learn about manufacture software.

3.3 TDUK DESIGN COMPETITION

TDUK, in association with the Passivehaus Trust, NMITE, and ENU, have launched a university design challenge for built environment students and 2021 graduates from across the UK.
The design competition is learning experience based on forming groups of built environment students to undergo a Passivehaus design in reaction to a real design brief. The group of students need to design and make all the calculations to ensure their work is a NetZero design, or even negative. In its most recent iteration, the aim of the competition is to design a new building to be built in Hereford that will serve as a sports, food, and skills community focal point for the people of South Wye, UK. As part of the programme, students had the chance to learn from webinar series hosting several experts of the sector.
The pedagogic approach behind the learning experience is to allow graduating students to have first-hand experience of working on a project with a real targets. This is one of the cases where work-place challenge is proposed to participants with the outcome to be built. The groups are supported with design and production software and tutoring sessions to guide their design.

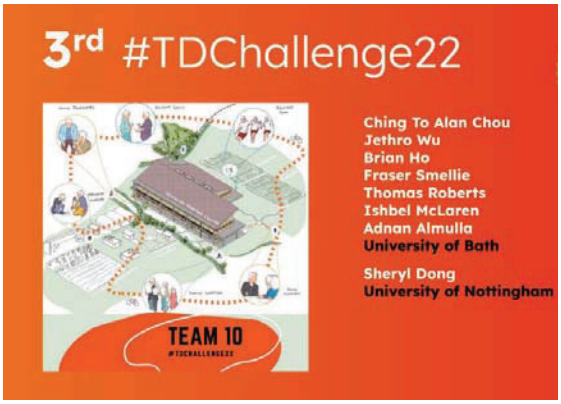

Figure 8: *The winning entry and team members' names and affiliations*

4 THE PROGRAMME

4.1 TIMBER TED SHORT COURSES

The Timber Technology, Engineering, and Design (Timber TED) short courses create comprehensive and flexible upskilling and reskilling training on modern methods of timber construction. Micro-credentials approach is utilised to aid learners in gaining specialist timber construction knowledge and skills for built environment 'better, faster and greener' delivery, addressing the climate emergency and affordable housing crisis. Underpinned by the competency framework described in section 2, identifying the evidence-based technical knowledge and meta-skills required, the short courses are grounded in immersive 'learning by doing' activities, stimulating critical thinking and instilling new knowledge and skills for net zero carbon.
The courses are also based on all of the previously trialled learning experiences, and that leads up to the main experience which is embedded in (Timber TED) series. Combining various competencies from the framework to compile short 12-week courses with different learning and teaching strategies, embeds resilience into the content and delivery mode of the course. All courses are based on workplace challenges that sees students take on activities that mimic their workplace activities and apply different areas of knowledge and application to create learning outcomes (figure 9).

https://doi.org/10.52202/069179-0602

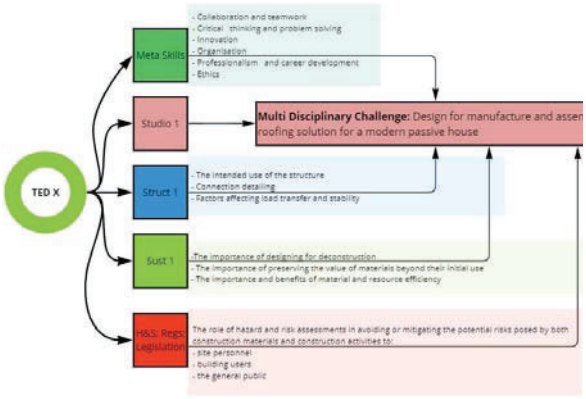

Figure 9: *Example of different areas of knowledge and areas of application compiled to form learning outcomes.*

Once areas of knowledge are compiled, the themes of the TED short course are decided and are ready for development. The diagrams in figure 10 and figure 11 show TED1 and TED2 themes respectively. It is worth noting that the Design and specifications demonstrated in Figure 4 is translated into 'studio' element in the figures below as in our view, the studio element is the place where learners have the chance to design and apply the technical knowledge they attain other modules. This is a crucial element as it prepares the learners to experiment and make mistakes as opposed to learning only how to repeat ready-made of the shelf solutions.

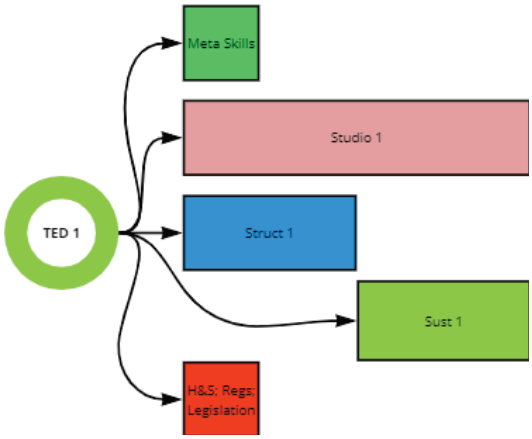

Figure 10: *Different thematic technical competencies are mixed with cross disciplinary skills to form TED1*

TED 2 in figure 11 shows yet another different themes in the technical competencies, namely 'construction' and 'technology'. Both areas are applied in the studio element to allow learners to put their gained knowledge to test.

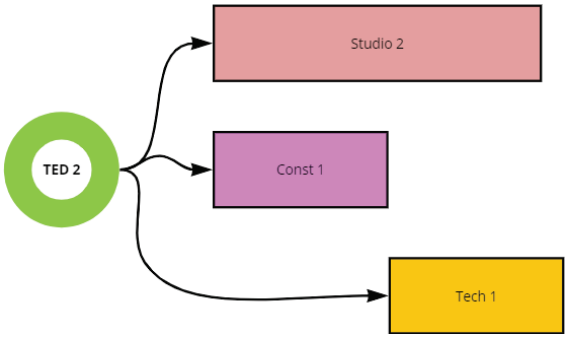

Figure 21: *Different thematic technical competencies are mixed with cross disciplinary skills to form TED2*

The main *aim* of Timber Technology, Engineering and Design (Timber TED) courses is to cover the 'core technical competencies' in the framework (figure 4). From now, on, we will be using Timber TED1 as a subset and an example.

Figure 32: *TED1 core technical competencies*

In the figure 12, competencies are derived from the Timber competency framework which was developed based on a market survey involving Timber engineering and design stakeholders. In addition, an extra layer that covers the 'cross-disciplinary competencies' is introduced to each element of the technical competencies. The three areas covered are: a) Timber Design, b) Timber Material Science, and c) Sustainability. The way they are lined up is visually demonstrated in the diagram below where the first part of the 'Design' module runs concurrently with the 'Materials' module for six weeks. The second part of the 'Design' module runs concurrently with the 'Sustainability' module for the following six weeks. The total is 12 weeks. During the twelve weeks, learners will have residential weeks in the first, sixth and twelfth week

https://doi.org/10.52202/069179-0602

at our campus in Skylon Park. The rest of the activities are delivered online.

4.1.1 Teaching and Learning Environment

The teaching and learning environment of Timber TED1 is divided into real environment and virtual environment. The latter is hosted on our VLE, whereas the former is divided into 3 major parts: a) the CATT building in Skylon Park, b) workplace environment of our course learners, and finally c) the selected locations that the course will drive learners to in the form of fieldtrips.

4.1.2 Teaching and Learning Strategy

The strategy is, therefore, divided into various techniques and methods, but all revolve around NMITE ethos and principles of learning by doing, and utilising workplace challenges as a method to achieve hands-on experience.

The 'Material Science' module is delivered online with some interactive elements that are examined on campus. Learners are required to review the resources provided online (read, listen, watch and sometime answer questions to frame their gained knowledge. Learners are also invited to obtain sample timber pieces during their first week on campus, and to take it back with them to their homes and keep it exposed to their local weather conditions for twelve weeks and bring it back during their last residential week in order to allow all to have a look at the weathering effect on each sample from different geographic location. During their first residential week, learners are taken in a field trip to a forest, sawmill and an under-construction timber building. This is to take them through the different stages of timber lifecycle.

The direct interaction with the expediated timeline lends itself to the metaphor of time-travel, where learners meet the experts in each field and watch a synoptic 'time-slice' of the intended lifecycle.

Similarly, the 'Timber Design' part of the course is delivered partially online. The main metaphor behind the delivery of the module is to mimic the professional environment in firms. Learners from different professional backgrounds and career paths engage in the following activities:

a) Week 1 begins by revealing the first design challenge they need to respond to. They are presented with a design brief asking them to individually carry out a design and build exercise (design a timber joint). From that point they are taken through a journey of learning:

b) Sketch design exercise where they express their initial raw ideas and demonstrate their current level of knowledge and skills. It also allows the tutors to supervise the activity and provide guidance on how to brain storm concepts and sometimes contradicting demands to reach an outcome in a short space of time.

c) Week 2 presents another challenge where learners are tasked with producing a technical report. Again the idea is to present the knowledge gained in Material Science module about timber and deploy it in the Timber Design module to justify their choice of timber that they are going to use in their design and build exercise. Writing the report also mimics professional activities in the workplace and can be produced within each learner's work environment. Learners will also present further sketches/technical drawings of their idea to demonstrate the research and development work they carried out.

d) Week 3 sees learners delivering their CAD drawings to finalise their ideas.

e) Week 4 is the first chance for learners to discuss manufacture techniques. They consult the learning facilitators to find out what working drawings they need to produce and what activities and tools they will consider in the process of manufacture. The advantage of this activity is that it ties together the information gained in weeks one and the work that will be carried out in week 6

f) Week 5 will be reserved for presentation work.

g) Week 6 will see learners arrive on campus and use our facilities in the CATT workshop to:

I. Produce their design. This is a hands-on exercise where they work under the supervision of the learning facilitator, to produce their design using manual carpenter's tools.

II. Present their work to a critique panel and their colleagues and answer questions

Week 7 to 12 will run a similar design and build activity with two major distinctions:

- The design project will increase in complexity.
- The learners will be divided into groups.

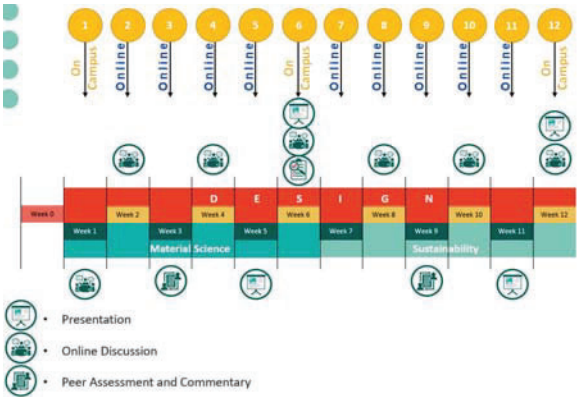

Figure 43: *Distribution of different activities over the period of 12 weeks.*

The second design brief is a group work exercise. Learners bring all their backgrounds and experiences and work together to design and build a relatively complex outdoor structure. They navigate group-work dynamics to achieve their target. They replicate the steps in weeks 1 to 6 and they produce a group technical report, group drawings presentation and work collectively in the workshop to produce their design. Throughout week 7 to 12, they will take special consideration of sustainability concepts in their design.

The 'Sustainability' module runs from week 7 to week 12 and will see learners carry out the following activities:

a) They will appraise the key reading and provide a short critical commentary and reflective account on their ideal definition for sustainability. This is a chance to digest the readings and decide the view that they align with, then try and apply it to their professional area. The exercise will be submitted on the VLE.

b) Following the initial submission, Learners will be asked to provide comments on one of their colleagues' posts. The exercise serves two purposes:

I. It mimics classroom discussions that take place in tutorials by asking each learners to express their ideas and then ask colleagues to respond and discuss.

II. It also provides an element of peer assessment where the feedback is diverse and reflects the background of the different learners, which would enrich the discussion.

The posts described above, and the instructions related to them are all made available on the VLE

c) Learners are asked to identify some of the key information from the readings and share it with their colleagues on the VLE as a way of framing their knowledge on the subject.

d) Some self-assessment exercises are also available on the VLE.

5 TEACHING RESOURCES

Multiplicity of resources are developed and made available and those created for the delivery of the programme are presented together with the intended kind of activities learners will engage with.

5.1 THE CATT BUILDING – THE STUDIOS

The building is part timber, part steel. The timber part is where the studios and communal areas are. This part will be used as a case study to offer a variety of examples, ranging from structural design to building performance, thanks to the implemented living lab approach. Further, the supply chain involved in the delivery of the building, with a special focus on timber elements (CLT, GLT, and insulated panels), will be mapped to offer additional insights on what's needed to calculate the embodied carbon and energy consumption of a building.

5.2 THE CATT BUILDING – THE WORKSHOP

The steel frame part of the building house a factory-like workshop and its intended use is presented in this section. The activities students will be likely to be involved in are described and the philosophy followed in the equipment of the space is explained. The activities may be different every year depending on the industrial partner, but will be of the type that can allow for the same level of assessment, requiring various pieces of knowledge and several skills.

5.3 INDUSTRY ENGAGEMENT

The link with industry, current partnerships and future possibilities, is described and the involvement of the sector in the professional development is depicted in this section. Industrial partners will be involved in the challenge-based learning system, presenting real life problems students will need to work on, and possibly solve, and collaborating in the preparation of scaled and full-scale models for the assessments, sharing their experience and knowledge or manufacturing specific elements that can't be made in the workshop. The CATT is already cooperating with several association, e.g., Timber Development UK or the Association of Sustainable Alliance for Sustainable Building Products (ASBP), and will expand its net of collaborations to increase this academic-industry cross-fertilization.

5.4 OTHER RESOURCES

Other teaching material available, such as case studies reports, or research outcomes, and related activities are presented in this section. Edinburgh Napier University (ENU), which is partner of NMITE in the establishment of the CATT, has been asked to help rewrite and update the knowledge library of the Timber Research and Development Association (TRADA), part of Timber Development UK (TDUK), key collaborator of the CATT. This material will be available for students and will help teachers shaping the different modules.

6 CONCLUSIONS

It is evident that the climate emergency is urging an action against the odds of survival and this paper reports on the approach taken by the NMITE in collaboration with national parties to account for some of the changes that need to be made in order to reach our targets for the climate change. The learning experiences reported in this paper culminated in the Short Timber TED courses that theorise a new agenda for education in the built environment, and each element of the courses is being trialled and enhanced.

The proposed short courses come with many types of challenges. For example, it is evident from the outset, that different learners come from different backgrounds (architects, technologists, structural engineers, timber production operatives, technical sales, project managers or even those switching to a built environment profession and seeking to expand knowledge). Therefore, learners have varying knowledge backgrounds and skill levels. This forms a continuum where on one side we have no knowledge and no skills, and on the other we have highly knowledgeable and highly skilled and everything else in between.

The challenge posed by this variety is mainly:

- Ensuring that the resources and knowledge offered in the course caters for the variety.
- Ensuring that the- learners all have the minimum Built Environment Knowledge and skills not only to attain the knowledge offered in the content, but actually to progress through it at the same pace and be able to get through it.
- Since the course is partially based on learning by doing, it was important to ensure that learners are able to progress through the practical tasks at a similar pace, given that they have different levels of skills.

This introduces a strategic challenge when it comes to teaching and learning because catering for all learners

https://doi.org/10.52202/069179-0602

would require applying one of two strategies: a) use minimum baseline, where we provide the information from the baseline of the lowest point, but this could potentially make the more advanced learners feel they are not learning anything new, or b) use customised personal learning approach, where we help each individual improve according to their level.

The team uses a combination of both, where the online materials are baseline for all participants with the opportunity to advance using optional readings. Sometimes the texts selected, and topics are more generic to allow for a common grounds between different professional backgrounds.

In the 'Timber Design' module, learners are allowed to advance according to their skills and passion. Group work allows for a different dynamic where different learners use different skills and therefore complement the shortcomings of others.

This is a work in progress and is developing over expanding scale in terms of knowledge and geographic expansion. While the work started in our centre in Hereford, we are currently in the process of entering into agreement with another centre in Scotland to act as a regional hub to mirror and further our efforts within the UK.

ACKNOWLEDGEMENT

We would like to acknowledge the support of the New Model Institute for Technology and Engineering, (NMITE), Edinburgh Napier University (ENU), which is partner of NMITE in the establishment of the CATT, has been asked to help rewrite and update the knowledge library of the Timber Research and Development Association (TRADA), part of Timber Development UK (TDUK), key collaborator of the CATT.

REFERENCES

[1] Bathe K.-J.: Finite-Elemente-Methoden. Springer-Verlag Berlin Heidelberg New York, 2002.

[2] R. Mahnken. A Newton-multigrid algorithm for elasto-plastic/viscoplastic problems. *Comp. Mechs*., 15:408-425, 1995.

[3] Zener C., Hollomon J. H.: Effect of strain rate upon plastic flow of steel. Journal of Applied Physics, 15(1):22-32, 1944.

[4] Johnson G. R., Cook W. H.: A constitutive model and data for metals subjected to large strains, high strain rates and high temperatures. In: 7th International Symposium on Ballistics, 514-546, 1983

[5] H. Vegter, Y. An, H. H. Pijlman, B. D. Carleer, and J. Huétink. Advanced material models in simulation of sheet forming processes and prediction of forming limits. In *First ESAFORM Conference on Material Forming*, pages 499–502, 1998.

[6] J. K. Lee, G. L. Kinzel, and R. H. Wagoner, editors. *Proceedings of the 3rd International Conference: Numisheet '96*, 1996. The Ohio State University.

[7] M. H. A. Bonte, A. H. van den Boogaard, and J. Huétink. A metamodel based optimisation algorithm for metal forming processes. In D. Banabic, editor, A*dvanced Methods in Material Forming*, pages 55–72. Springer Verlag, Heidelberg, Germany, 2007.

World Conference on Timber Engineering Oslo 2023

FIRE SAFE USE OF WOOD IN BUILDINGS -GLOBAL DESIGN GUIDE

Christian Dagenais[1], Andy Buchanan[2], Birgit Östman[3], Michael Klippel[4], David Barber[5], Ed Claridge[6], Andrew Dunn[7], Paul England[8], Marc Janssens[9], Alar Just[10], Esko Mikkola[11], Colleen Wade[12], Norman Werther[13]

ABSTRACT: Building codes around the globe dictate the design and construction of buildings. For most buildings, designers will follow prescriptive code provisions to demonstrate code compliance. However, some building codes allow the use of performance-based design to demonstrate code compliance. Performance-based design is usually more complex but allows for greater flexibility in the selection of materials and systems. Regardless of the code compliance methods, the combustibility of timber structures and wood products needs to be well-understood and properly accounted for in building designs. This paper describes the development of a new international guidance document on fire safety in timber buildings within the Fire Safe Use of Wood (FSUW) network, written by 13 lead authors assisted by more than 20 experts in over a dozen different countries.

KEYWORDS: Fire safety, mass timber, light timber frame, fire spread, encapsulation, structural fire design, active fire protection, performance-based design, robustness, building control, firefighting.

1 INTRODUCTION

Building codes around the globe dictate the design and construction of buildings. In a prescriptive building code, the type of building occupancy, the building floor area, the building height, and the presence of an automatic sprinkler system often dictates whether a timber structure is permitted and if timber surfaces can be exposed. For most buildings, designers follow prescriptive code provisions to demonstrate code compliance. Prescriptive design allows for a straightforward design and approval and reflects the academic training of most designers. However, some building codes allow the use of performance-based design (PBD) to demonstrate code compliance. PBD is usually more complex but allows for greater flexibility in the selection of materials and systems.

Regardless of the code compliance methods, the combustibility of timber structures and wood products needs to be well-understood and properly accounted for in building designs. This is of utmost importance when a PBD is being developed and where other aspects of fire science need to be considered, such as fire dynamics, reaction-to-fire, fire-resistance, and design to prevent the spread of fire within a building and to adjacent buildings.

2 OBJECTIVE

The objective of this international guideline, shown in Figure 1, is to present information for wood products in a wide range of new buildings [1]. It provides state-of-the-art scientific knowledge on a global level for practical applications. The guideline includes extended use of design codes and standards, practical guidance and examples of fire-safe design methods and principles of PBD. It is published both as a hard-bound book and as an

[1] FPInnovations, Canada, christian.dagenais@fpinnovations.ca
[2] PTL Structural Consultants, New Zealand, a.buchanan@ptlnz.com, Editor.
[3] Linnaeus University, Sweden, birgit.ostman@lnu.se, Editor.
[4] ETH Zürich, Switzerland, klippel@ibk.baug.ethz.ch, Chair of Steering Committee.
[5] Arup, Australia, david.barber@arup.com
[6] Auckland Council, New Zealand, ed.claridge@aucklandcouncil.govt.nz
[7] Timber Development Association, New Zealand, andrewdunn@tdansw.asn.au
[8] EFT Consulting, Australia, paul.england@eftconsult.net
[9] Southwest Research Institute, USA, marc.janssens@swri.org
[10] TalTech, Estonia, alar.just@taltech.ee
[11] KK-Fireconsult, Finland, Esko.Mikkola@kk-palokonsultti.com
[12] Fire Research Group, New Zealand, colleen.wade@fireresearchgroup.com
[13] Technical University of Munich, Germany, n.werther@tum.de

https://doi.org/10.52202/069179-0603

open access version available for free PDF download via the Fire Safe Use of Wood website (www.fsuw.com).

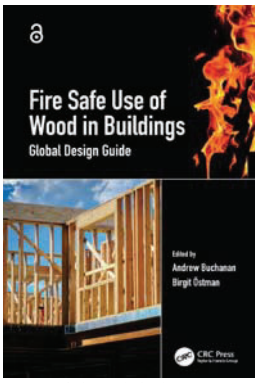

Figure 1: *Cover page of the Global Design Guide*

The guideline is based on the 2010 European guideline, Fire Safety in Timber Buildings – Technical Guidelines for Europe [2], enhanced with the latest outcomes from the recently completed COST Action FP1404 - Fire Safe Use of Bio-Based Building Products [3], to which many of the authors have actively contributed. This COST Action was intended to create a platform for networking, exchange and collection of research results and design skills, including performance data, design expertise, and many other factors which affect the design of bio-based building materials for fire safety.

This new international guideline was produced in the framework of the Fire Safe Use of Wood (FSUW) network. It is also inspired by recent code changes to allow taller and larger timber buildings in Australia, Canada, the US and elsewhere. The guide is supported by various eminent research centres and universities conducting research in this area.

The core audience is all those involved in the fire safety of timber buildings, including architects, engineers, firefighters, educators, regulatory authorities, insurance companies and others in the building industry.

2.1 INTERNATIONAL RELEVANCE

Many well-known fire scientists and engineers worldwide wrote the different chapters to ensure its quality and relevance for use in all countries, see Table 1. More than 20 expert co-authors supported the lead authors. The emphasis is on describing basic principles of fire science and fire engineering for buildings using timber as a structural or lining material, leading to practical solutions, rather than specific details of building regulations in any one country.

Future research topics in relation to fire safety in timber buildings are also proposed on an international level.

National and international building codes in different regions of the world are compared, but not explained in detail. The guideline is of benefit to design engineers in any country and will be of special interest to code writers in countries where timber buildings are not established and the use of modern structural timber elements are only just being considered.

2.2 TECHNICAL CONTENT

The guideline consists of 14 chapters, starting with a description of the various timber products, types of structures and their use in buildings, to a more in-depth chapter dealing with PBD, as shown in Table 1.

The guideline addresses structural fire engineering by providing the latest detailed guidance on structural design of separating and load-bearing elements of timber structures. It also contains guidance on design for surface flammability and limiting fire spread. The importance of proper detailing in building design is stressed with examples of practical solutions to limit the spread of fire or smoke. Active fire protection and building execution and control are presented as important means of fulfilling fire safety objectives. In the following, the key elements of each chapter are summarised.

2.2.1 Chapter 1: Timber structures and wood products

This chapter 1 introduces timber structures and wood products. The types of construction presented in this chapter may have different names in different countries, but the fundamentals and design principles remain essentially the same. Some building codes may limit the use of timber and wood products, either for structural elements or interior finish materials, but these materials are being used throughout the world in many types of buildings and occupancies. With the increasing demand for sustainable buildings and performance-based design, it is expected that timber will gain even more popularity in the near future. Fire performance of timber structures and wood products can be evaluated by the guidance and design methods detailed in the following chapters.

Figure 2: *Residential building made of light timber frame (photo: cecobois)*

Table 1: *List of chapters, lead* authors and co-authors (in alphabetical order)*

Chapters	Author (Affiliation, Country)
1. Timber structures and wood products	*Christian Dagenais (FPInnovations, Canada) Alar Just, Birgit Östman
2. Fire safety in timber buildings	*Andrew Buchanan (University of Canterbury, PTL Consultants, New Zealand) Andrew Dunn, Alar Just, Michael Klippel, Cristian Maluk, Birgit Östman, Colleen Wade
3. Fire dynamics	*Colleen Wade (Fire Research Group, New Zealand) Christian Dagenais, Michael Klippel, Esko Mikkola, Norman Werther
4. Fire safety in different regions	*Birgit Östman (Linnaeus University, Sweden) David Barber, Christian Dagenais, Andrew Dunn, Koji Kagiya, Eugenly Kruglov, Esko Mikkola, Peifang Qiu, Boris Serkov, Colleen Wade
5. Reaction to fire performance	*Marc Janssens (Southwest Research Institute, USA) Birgit Östman
6. Fire separating assemblies	*Norman Werther (Technical University of Munich, Germany) Christian Dagenais, Alar Just, Colleen Wade
7. Load bearing timber	*Alar Just (TalTech, Estonia) Anthony Abu, David Barber, Christian Dagenais, Michael Klippel, Martin Milner
8. Timber connections	*David Barber (Arup Fire, Australia) Anthony Abu, Andrew Buchanan, Christian Dagenais, Michael Klippel
9. Prevention of fire spread	*Esko Mikkola (KK-Fireconsult, Finland) Andrew Buchanan, Birgit Östman, Dennis Pau, Lindsay Ranger, Norman Werther
10. Active fire protection by sprinklers	*Birgit Östman (Linnaeus University, Sweden) David Barber, Christian Dagenais, Andrew Dunn, Kevin Frank, Michael Klippel, Esko Mikkola
11. Performance-based design	*Paul England (EFT Consulting, Australia) David Barber, Daniel Brandon, Christian Dagenais, Gianluca De Sanctis, Michael Klippel, Dennis Pau, Colleen Wade
12. Robustness in fire	*Michael Klippel (ETH Zürich, Switzerland) Andrea Frangi, Robert Jockwer, Joachim Schmid, Konstantinos Voulpiotis, Colleen Wade
13. Building execution and control	*Andrew Dunn (Timber Development Association, Australia) Ed Claridge, Esko Mikkola, Martin Milner, Birgit Östman
14. Firefighting considerations	*Ed Claridge (Auckland Council, New Zealand) Christian Dagenais, Andrew Dunn, Claudius Hammann, Kamila Kempna, Martin Milner, Jan Smolka

One of the main advantages of timber structures is the variety of systems that can be designed and constructed to suit almost any need and to provide the level of fire performance required in building codes. Traditional light timber frame construction are widely used in low-rise and mid-rise buildings (Figure 2). As shown in Figure 3, innovative systems such as modern post-and-beam construction, mass timber construction, long-span and hybrid structures allow for expanding the use of timber in impressive and innovative structures, such as taller buildings. Prefabrication of timber elements and modules is also gaining popularity, due to the speed of construction, increased building control and waste reduction at the job site.

Another factor facilitating the use of timber in buildings is the variety of products available to designers. A broad range of structural engineered wood products has been developed over recent years to provide high-valued timber products through more efficient use of the raw material. For most countries, timber and engineered wood products are required to be manufactured, tested and evaluated by applicable standards. Quality control procedures are usually required to ensure high-quality end products and buildings with acceptable fire safety. Given the large variety of timber products around the globe, some of the engineered wood products presented herein may not be available in all countries.

This chapter is not intended to provide an exhaustive historical review of timber constructions and wood products but rather aims to provide sufficient information for designers, builders, building officials/authorities and fire services to better understand and differentiate the various wood products and timber building systems available.

https://doi.org/10.52202/069179-0603

Figure 3: *Curved beams and decking at a commercial centre in Canada (photo: Western Archrib)*

2.2.2 Chapter 2: Fire safety in timber buildings

Chapter 2 provides an overall description of the strategy for delivering fire safety in timber buildings (Figure 4). As in the design of all buildings, the goals are to provide life safety for occupants, safe access for firefighters and protection of affected property. It is essential to control the severity and duration of any accidental fire and prevent it from spreading elsewhere in the building. An important design objective for timber buildings is to control the burning or charring of exposed timber or protected timber, because this can add to the fuel load, and it will reduce the load capacity of structural timber members due to loss of cross section. Many of the topics introduced here are expanded on in the following chapters.

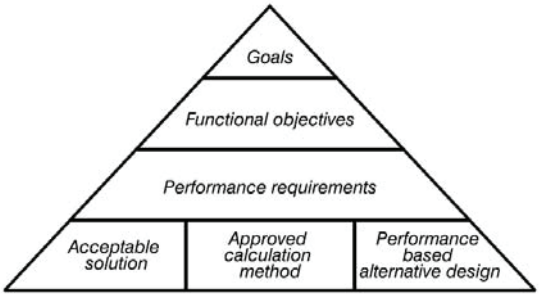

Figure 4: *Typical hierarchical relationship for fire safety design*

Fire safety during construction is a hazard for all timber buildings. Light timber frame buildings under construction are especially vulnerable before protective linings and other fire safety design features have been installed. Severe fires during construction have caused large financial losses in several countries. The construction fire hazard may be less severe in mass timber structures than in light timber frame buildings, but comprehensive fire precautions are essential. Management to control fires during construction is covered in Chapter 13.

2.2.3 Chapter 3: Fire dynamics

The third chapter provides information on fire dynamics in timber buildings. It summarises the fire behaviour in compartments with a focus on buildings with exposed timber structures and wood linings. It includes basic information on the pyrolysis and charring of wood, along with fire dynamics in compartments and the impact of having exposed timber surfaces. A description of common approaches to characterising post-flashover fires with parametric time–temperature curves is provided with guidance on a simplified design method to account for exposed timber surfaces based on parametric fire curves (Figure 5). Limitations in current knowledge are highlighted.

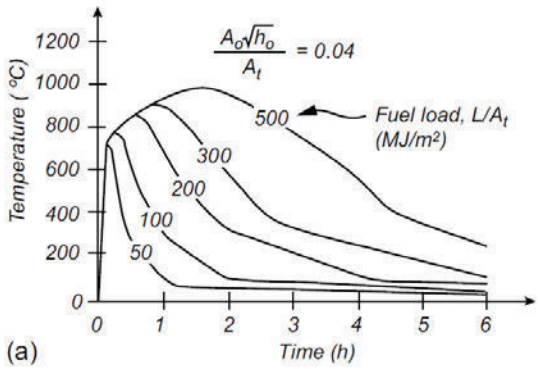

Figure 5: *Time-temperature curve for varying fuel load and constant ventilation factor*

2.2.4 Chapter 4: Fire safety in different regions

The regulatory control systems for fire safety design of buildings differ between regions around the globe, but it is based on the same principles of saving life and property and specifying requirements for structural and non-structural applications. This chapter 4 summarises the regulatory control systems for the fire safety design of buildings in different regions around the globe.

The possibilities for building in wood have gradually increased in recent decades in many countries, mainly due to the environmental benefits of using wood. But there are still restrictions in terms of fire regulations in many countries, especially for taller buildings. The situation has therefore been mapped in 40 countries on four continents as an update to a survey in 2002 (Figure 6). The main issues are how high buildings with load-bearing wooden frames may be built and how much visible wood may be used both inside and as façade claddings.

The requirements shown in this chapter apply primarily to prescriptive fire design according to so-called simplified design with detailed rules, which are mainly used for residential buildings and offices. For more complicated construction e.g. public buildings, shopping centres, arenas and assembly halls, performance-based design can be used by fire safety engineers using, for example,

https://doi.org/10.52202/069179-0603

engineering methods for predicting evacuation and smoke filling, which increases the possibilities of using wood in buildings.

In most countries, the possibilities of using wood in buildings increase if sprinklers are installed. More information on sprinklers is presented in Chapter 10.

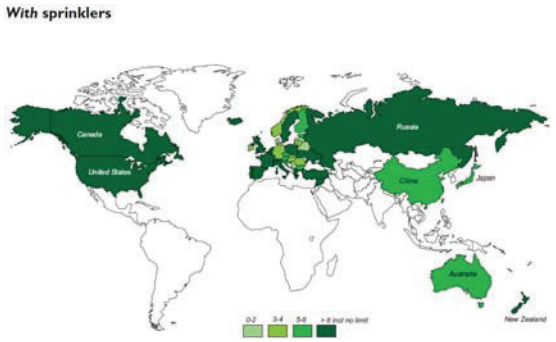

Figure 6: *Maximum number of storeys allowed for structural timber elements in prescriptive residential buildings (with sprinklers)*

Major differences between countries have been identified, both in terms of the number of storeys permitted in wood structures and of the amounts of visible wood surfaces in interior and exterior applications. Several countries have no specific regulations or do not limit the number of storeys in wooden buildings, mainly due to limited experience and lack of interest in using wood in taller buildings. The differences between countries are still large, and many countries have not yet started to use larger wood buildings despite supplies of forest resources.

Performance-based design may be used in several countries to verify further applications of wood (as presented in Chapter 11).

2.2.5 Chapter 5: Reaction to fire performance

This chapter 5 presents the reaction to fire performance of wood products used in buildings as internal surface finishes, exterior wall claddings, roof coverings and façade claddings. For façade claddings, the several different ways of assessing and regulating the fire performance of exterior wall systems are included. The chapter also describes the systems used for compliance with prescriptive regulations in different regions (Table 2), and the characteristics of wood products for performance-based design and methods for improving the reaction to fire performance of wood products.

2.2.6 Chapter 6: Fire separating assemblies

This chapter 6 describes the important role of fire-separating assemblies for passive fire protection in any type of building. Fire-separating assemblies provide essential compartmentation, which limits fire spread, contributing to both life safety and property protection. It gives design recommendations for providing fire resistance to timber- and wood-based separating assemblies, including walls, floors and roofs.

Table 2: *Comparison of reaction to fire classification in different countries*

Product	United States	Australia / New Zealand	Europe	Japan
DF[(1)] plywood	C	Gr. 3	D	[(4)]
FRT[(2)] DF plywood	A	Gr. 1 or 2	C	[(4)]
OSB 1	C	Gr. 3	D	[(4)]
PSB 2	C	Gr. 3	D	[(4)]
White pine[(3)]	C	Gr. 3	D	[(4)]
White oak[(3)]	C	Gr. 3	D	[(4)]

[(1)] DF: Douglas fir
[(2)] FRT: Fire-retardant treated
[(3)] Timber planks
[(4)] Unclassified

In addition to maintaining the load-carrying capacity of the structure during a fire, the concept of compartmentation is one of the most effective passive measures for providing fire protection for life safety and property protection. Without firefighting or automatic fire suppression, the concept of compartmentation is the only way of preventing a fire from spreading beyond its room of origin. This concept has become an essential requirement in both prescriptive and performance-based building codes all over the world.

The main objective of applying fire-resistance rated separating assemblies is to limit the probability that fire or smoke will spread from the compartment of fire origin to other compartments at the same or other storeys in a building, or to neighbouring buildings, within a defined time. By an optimum arrangement of separating assemblies (Figure 7), the development and spread of fire is slowed down, property damage is reduced, fire exposure to multiple sites is limited, safety of occupants is improved, and firefighting and rescue operations will be more effective.

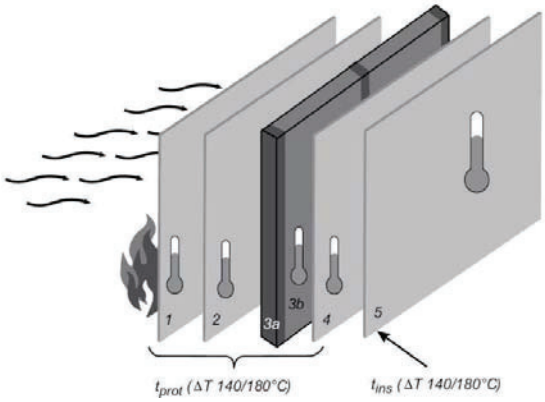

Figure 7: *Design approach of the European Separating Function Method (SFM)*

https://doi.org/10.52202/069179-0603

2.2.7 Chapter 7: Load bearing timber

Chapter 7 gives guidance for design of load-bearing timber members exposed to a standard fire. An overview of the principles needed to predict the effect of charring and heating is presented. Simplified design models around the world are described, including design models from the second generation of Eurocode 5.

The design objective in the event of a fire is determined by regulatory requirements and the fire safety strategy for the building. Most fire safety strategies are for load-bearing timber structures to resist the design loads for a specified fire exposure time. In this chapter, only the standard fire exposure is considered, according to e.g. ISO 834-1. Design of timber members in a standard fire situation requires an assessment of the reduction of cross-section caused by charring and the effect of heat on strength and stiffness of the residual cross-section. Charring may be influenced by protective linings and cavity insulation. For engineered timber members the glueline integrity in fire can also affect the rate of charring and load bearing capacity.

Unlike steel and concrete, thermal expansion of timber does not need to be taken into account because it is negligible. Timber members can be analysed individually without considering possible thermal actions from other timber members.

Fire resistance of structures can be assessed by fire testing or by simplified and advanced calculation methods. Calculation methods, as illustrated in Figure 8, typically give conservative results compared to fire testing. The design parameters for timber and protective materials are needed for calculation methods. If these parameters are unavailable or unknown, fire testing will be the only option for verifying the fire resistance.

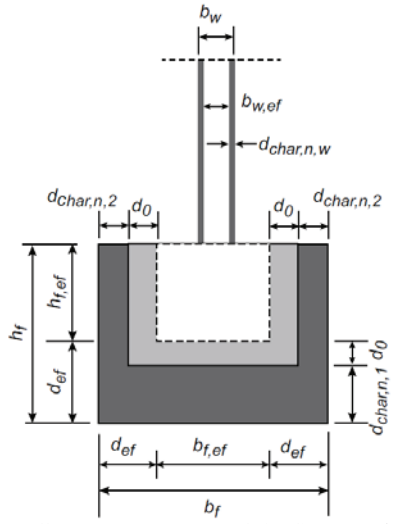

Figure 8: *Effective cross-section of the flange and web with cavity insulation*

Applicable fire exposures are stated in national building codes. For example, in Canada exterior walls are to be exposed on the interior side, interior walls on either side and floors are only exposed to fire on the underside. In Europe, Australia and New Zealand, walls delimiting a fire compartment are to be designed for fire exposure from one side, walls located within a fire compartment are to be designed for fire exposure from two sides, floors and roofs are usually to be designed for fire exposure from underneath. In some countries there are requirements to design floors for fire exposure from above (e.g. attics). In the UK and other countries there may be building types and storey heights where the stability of the structure is to be maintained in the event of a fire that is not controlled by firefighters, resulting in design of the load bearing timber structure to maintain its load-bearing function throughout fire decay until burnout.

Calculation examples of timber members are also presented. The examples demonstrate that for a timber product of similar strength and stiffness, the design for fire resistance will provide similar results whether the European, Canadian or US approach is used. However, design assumptions and load combinations must be consistent with the appropriate building codes and design standards.

2.2.8 Chapter 8: Timber connections

Chapter 8 introduces structural timber connections and provides information on potential failure modes and methods to provide fire resistance to connections exposed to a standard fire. Timber structures and their connections must be designed to have strength to resist all anticipated loads during the required fire resistance period and where required, to prevent the passage of heat and flames. Figure 9 shows an example of modern mass timber concealed connections.

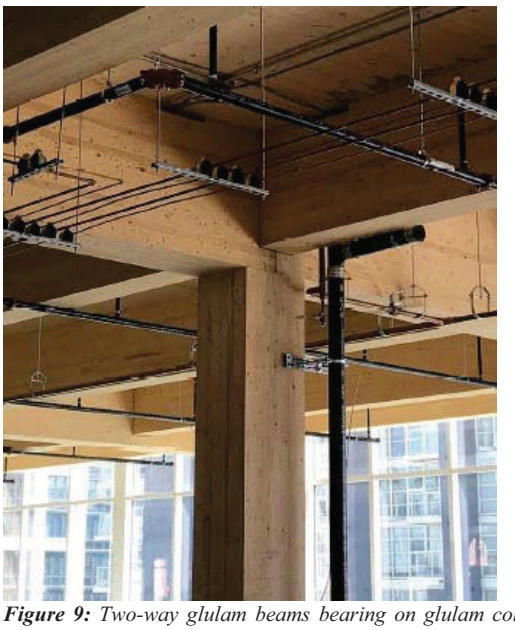

Figure 9: *Two-way glulam beams bearing on glulam column (photo: David Barber)*

https://doi.org/10.52202/069179-0603

2.2.9 Chapter 9: Prevention of fire spread

Fire spread within the structure is one of the main challenges for the fire safety of timber buildings. This chapter describes means of preventing spread of fire and smoke between compartments in timber buildings. Much of this applies to all buildings independent of materials used, but some topics are especially relevant for timber buildings. The chapter highlights critical paths of possible spread of fire into, within and through timber structures including solutions and detailing to prevent uncontrolled spread of fire and smoke (Figure 10).

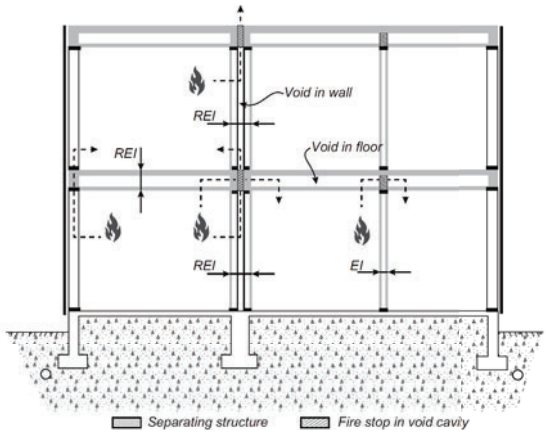

Figure 10: *Fire-stopping in voids – REI is for load-bearing and separating assemblies, EI is for separating assemblies*

It is important that the designers of all timber buildings consider prevention of fire and smoke spread through joints in and between building elements/assemblies, and through penetrations of building services and openings, including external walls. Chapter 9 is complementary to Chapter 6 which describes fire-separating elements and assemblies.

2.2.10 Chapter 10: Active fire protection by sprinklers

A wide variety of active fire protection systems are available to fire safety practitioners. In addition to passive fire protection measures, some level of active fire protection is normally required to meet the expected minimum level of fire safety in modern buildings. Active fire protection can also be used to increase the fire safety in order to achieve a more flexible fire safety design and an acceptable level of fire safety in buildings, especially in tall timber buildings. There are many types of active fire protection systems, but this chapter deals mainly with automatic fire sprinkler systems, since they are often used to facilitate the use of timber as structure, internal linings and external facades in large or complex buildings (Figure 12). Sprinklers, such as those shown in Figure 11, are required in some countries for taller timber buildings, as described in Chapter 4.

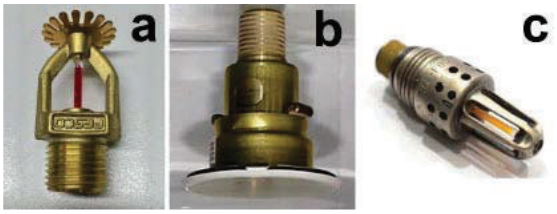

Figure 11: *Typical sprinkler heads for a) pendent, b) concealed pendent and c) water mist sprinklers*

An automatic fire sprinkler system can play an important role in the fire safety design of timber buildings. Provided that they are installed correctly and operate effectively, sprinklers will control or extinguish a fire at an early stage and prevent flashover. An increased use of sprinklers in residential buildings would considerably decrease the number of fire victims, independent of the construction materials used in those buildings. Building designs to incorporate sprinkler systems may facilitate increased use of timber, to be used as the structural material, the internal linings or the external facade. Reliable sprinkler systems are essential in tall buildings of any material, and especially so for tall timber buildings.

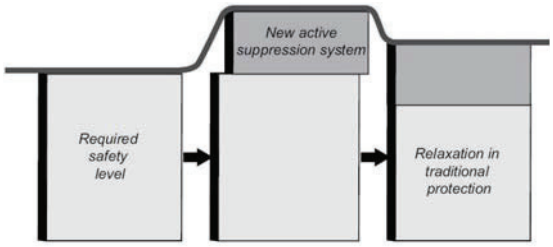

Figure 12: *Principle for fire safety design by sprinklers*

2.2.11 Chapter 11: Performance-based design

An overview of the application of performance-based approaches to the fire safety design of timber buildings is provided in Chapter 11. Performance-based designs, as illustrated in Figure 13, are relevant for the design of tall timber buildings and other timber buildings that vary from accepted prescriptive solutions. Performance-based design approaches are commonly categorised as deterministic or probabilistic and should be applied in accordance with the applicable regulations, building codes and standards. This chapter provides references to detailed information that should be consulted when undertaking performance-based designs or risk assessments.

https://doi.org/10.52202/069179-0603

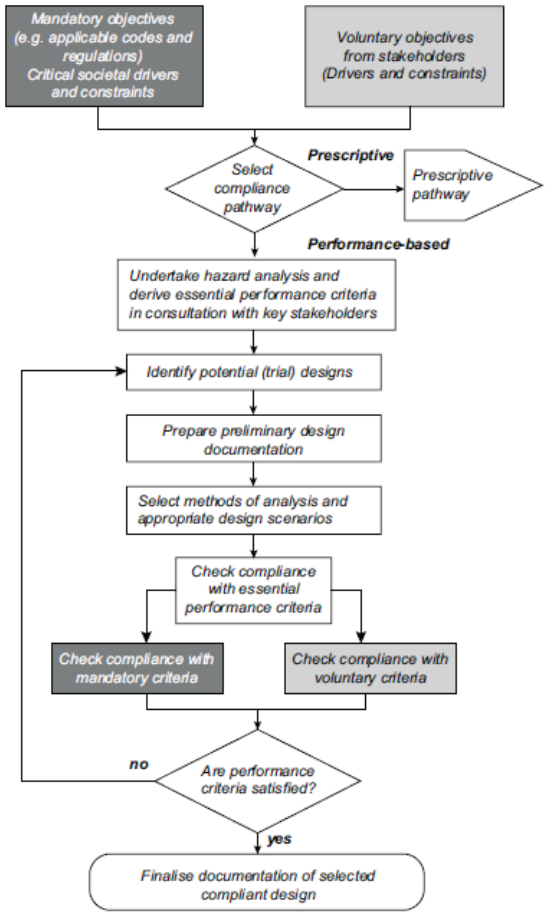

Figure 13: *Overview of a performance-based design process*

2.2.12 Chapter 12: Robustness in fire

With the increasing number of complex and tall timber buildings with a significant area of unprotected timber surfaces, questions arise about the robustness of these buildings in fire. In recent building projects, measures for robustness have been implemented on an ad hoc basis in agreement between the designers and the authorities. This chapter 12 discusses general approaches to achieve a robust fire safety concept which includes providing structural redundancy to prevent the failure of critical load-bearing elements such as isolated columns. Further, guidance is provided on how robustness of a fire safety concept can be enhanced for buildings using timber as a structural member.

2.2.13 Chapter 13: Building execution and control

Chapter 13 covers standards of workmanship and quality control of fire safety precautions during design and construction of timber buildings. Quality and inspection of workmanship are vital for high-quality buildings, whether of timber or other construction materials. Timber buildings require certain precautions due to the risk for greater exposure of combustible materials, namely hot works (Figure 14). Furthermore, not all fire safety measures for the final building will be in place throughout the construction period, so adequate processes are required to maintain the fire safety of building sites until the building is completed. All construction sites require formalised fire safety management systems, including auditing of contractors and subcontractors.

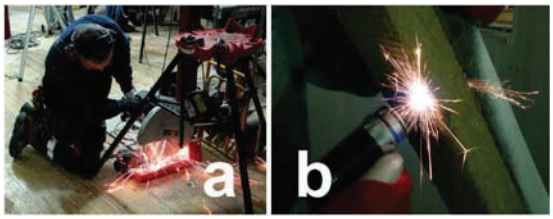

Figure 14: *Examples of hot works on a construction site (photos: Rohlén, Brandskyddslaget)*

2.2.14 Chapter 14: Firefighting considerations

Firefighting practices may be different in timber buildings compared with non-combustible construction. Internationally, fire services have raised concerns regarding the increased use of wood within buildings and specifically the use of timber structural elements of tall buildings. These concerns often stem from lack of knowledge of timber performance in fire, and firefighter experience from fires in non-combustible steel and concrete construction and traditional low-rise timber buildings. This chapter discusses relevant concerns of firefighters regarding large and tall timber buildings.

There is a significant lack of knowledge and practical experience with firefighting in tall timber buildings. The fire environment associated with exposed timber surfaces is different to non-combustible construction and may present new hazards and risks for occupants as well as for firefighters. There is a need for collection of data, knowledge and case studies from firefighting events, in order to develop a better understanding and new strategies and approaches for firefighting in tall timber buildings (Figure 15).

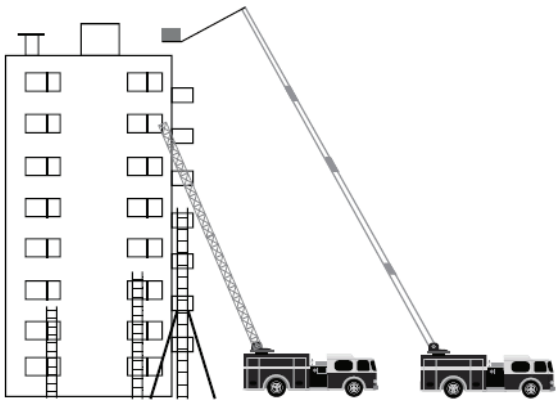

Figure 15: *Firefighting appliances for buildings up to about 8 storeys*

As combustible structures become larger, taller and more complex, the robustness and resilience of the buildings

and their fire safety features also need to increase. This will require appropriate changes to national and international building codes.

There is a critical need for more understanding of the smouldering combustion of large timber elements after fire exposure. As structural concepts progress and move away from the traditional assumption of burnout, a greater reliance will inevitably be placed on firefighters to extinguish fires and ensure that continued smouldering of the timber structure does not occur.

Lastly, it is essential that all emergency responders be knowledgeable and have an understanding of how combustible structures and tall timber buildings perform in severe fires. Without sufficient fire-ground experience of mass timber buildings, the emergency response must be informed by education and research that considers the needs of the responders (Figure 16). As buildings evolve, so must the firefighter response, with new strategies to ensure the most favourable outcomes for all stakeholders.

Figure 16: *Firefighter team during a timber fire test scenario at the Technical University of Munich in 2021*

3 CONCLUSION

Further to the success of the 2010 European guideline, combined to the latest outcomes from the recently completed COST Action FP1404 - Fire Safe Use of Bio-Based Building Products, a new collaborative international effort was made to produce a Global Design Guide on Fire Safe Use of Wood in Buildings, with the main objective to provide state-of-the-art scientific knowledge on a global level for practical applications. More than 20 expert co-authors supported the l3 lead authors.

This new Global Design Guide is expected to be of use to a wide range of stakeholders involved in designing fire safety in timber buildings, including architects, engineers, educators, regulatory authorities, building industry personnel, the timber industry and building code writers.

The Global Design Guide is published both as a hard-bound book and as an open access version available for free PDF download via the Fire Safe Use of Wood website (www.fsuw.com).

ACKNOWLEDGEMENTS

The lead authors wish to thank all their co-authors and a large number of colleagues and reviewers in many countries who provided much assistance in the preparation of this guide. Melody Callahan produced the line drawings and managed the delivery of text and images to the publisher.

We also acknowledge the large number of consulting firms, research institutions, universities and professional organisations around the world who supported this project through in-kind support of authors and reviewers. Generous financial contributions were made by FPInnovations, Natural Resources Canada (Canadian Forest Service), Softwood Lumber Board, BRANZ, SFPE New Zealand, Federation of the Finnish Woodworking Industries and Linnaeus University, Sweden.

REFERENCES

[1] Fire Safe Use of Wood in Buildings - Global Design Guide. Andrew Buchanan and Birgit Ostman, editors. CRC Press, 2022. https://doi.org/10.1201/9781003190318

[2] Fire Safety in Timber Buildings - Technical Guidelines for Europe, Stockholm (Sweden), SP Technical Research Institute of Sweden, 2010.

[3] COST Action FP 1404, Documents available at: https://costfp1404.ethz.ch/ and www.fsuw.com.

https://doi.org/10.52202/069179-0603

AUTHOR INDEX

Aalto, Pasi....1056
Aarsbog, Lina....1044
Abdeljaber, Osama....421
Abecker, Andreas....4010
Abrahamsen, Rune....2907, 4209
Abrami, Claudio....4173
Abu, Anthony K.....1526
Acquah, Richard....549
Acuña, Gustavo....2627
Adachi, Koji....1365
Aeran, Ashish....3979
Ahn, Kyung-Sun....188, 232, 989
Ahn, Namhyuck....3581
Aicher, Simon....688, 1261, 1443, 2978, 3264
Aichholzer, Martin....4545, 4590
Ailaitijiang, Kapulanbayi....3753
Aioi, Yohei....3551
Airoldi, Alice....4093
Åkerström, Carl-Johan....2118
Akiyama, Nobuhiko....1481, 2968, 2987
Akutagawa, Tsuyoshi....1383
Al Rahim, Adham....3342
Al Sabouni-Zawadzka, Anna....2426
Alakukku, Laura....3896
Alam, Marc....3007
Alamdari, Mehrisadat Makki....794
Alanen, Mika....238
Al-Attili, Aghlab....4619
Albino, Carlos....3121
Albright, Dustin....3518
Alegría, Gustavo Acuña....2642
Aljuhmani, Ahmad Ghazi....1183, 3309, 4286
Almazán, José Luis....2134
Aloisio, Angelo....1244, 1988, 2179, 2327, 2695, 3015, 3154, 3229
Álvarez, Verónica....683
Alwashali, Hamood....3309
Amaddeo, Carmen....2898
Amin, Rikesh....1667, 1758
Amini, M. Omar....3033, 3069
Amtsberg, Felix....688
Andersen, Julie Swartz....4360
Andic, David....4029
Andresen, Tor Øistein....4182
Ao, Wai Kei....2892, 2907
Aoki, Kenji....251, 259, 2150, 3398
Aoki, Shogo....2406
Aoki, Takashi....2104
Aoki, Yukari....2350
Appavuravther, Elif....3148, 3161
Aquino, Caroline D.....3685
Aquino, Caroline Dapieve....3667
Araki, Yasuhiro....4058
Araújo, Gustavo A.....2562
Aravena, Alberto....2717
Armanet, Gerardo....3963
Arnold, Matthias....2432, 3718
Asgari, Mehrdad....941
Ashraf, Mahmud....153
Aspila, Aku....4247
Assadi, Soheil....2556
Asshoff, Carsten....629
Atkins, Andrea....4383
Atsuzawa, Eito....1183
Auclair, Samuel Cuerrier....2356, 2922
Augustin, Manfred....2365, 2442
Augusto, Renato....3121
Aurand, Simon....3256
Auslender, François....443
Autengruber, Maximilian....398
Avellaneda, Alina....564
Avesani, Stefano....3816
Avikainen, Timo....449
Azemi, Tokuma....1283
Azinovic, Boris....1231, 2432
Baas, Esther....2244
Bacher, Philipp....1855
Bader, Thomas K.....1146, 3101
Badia, Carles Labèrnia....4128
Bailleres, Henri....3177
Baird, Zoe....1176
Bajzecerová, Viktória....3221
Bakke, Ingrid....1044
Ballarin, Adriano Wagner....3084
Bamonte, Patrick....1848
Baño, Vanesa....1342, 4415
Barbaresi, Luca....1914
Barber, David....1545, 1627, 1644, 1667, 1701, 1758, 1768, 1778, 1798, 4627
Barbosa, Andre R.....1009, 1034, 2156, 2244, 2562, 2669, 3896
Barclay, Sarah....1821
Bard, Delphine....1863
Bascuñan, Felipe....927
Beatriz, Sheila....3747, 3769
Beauchêne, Jacques....2820

Becker, Edward 3775
Bedon, Chiara 1001, 2761
Belden, Tim 4619
Bell, David 41
Belleri, Andrea 4173
Belperio, Ralph 4423
Benedetti, Franco 512, 1953, 2342
Berg, Sven 1216
Bergman, Richard 4576
Berman, Jeffrey 2084
Bert, Anna Maria Basso 358
Bertelsen, Stine Lønbro 225, 3835
Besançon, Franck 3608, 3708
Bestler, Maximilian 1322
Bhandari, Sujit 2185
Bhardwaj, Bibek 2792
Bianchi, Natália Andrade 729
Binck, Charles 2958
Binder, Eva 3101
Binding, Tabitha 4619
Birkholz, Antonia 948
Bisby, Luke 1536, 1788, 1839
Bissig, Dominik 2600
Bita, Hercend Mpidi 1160
Bitsuamlak, Girma 2922
Bjarvin, Christina 3581
Bjertnæs, Magne A. 2907
Blanchet, Pierre 1583
Bléron, Laurent 3708
Bligh, James 4273
Blom, Åsa Rydell 3829
Blomgren, Hans-Erik 1627, 1798, 2000
Blomqvist, Lars 1154
Blondeau, Renaud 1831
Blondeau-Patissier, Renaud 4447
Blumer, Samuel 3625, 4309
Bockelie, André 4460
Bøe, Andreas Sæter 1576
Boggian, Francesco 1988, 3154, 3229
Boli, Gotre Bi Djeli Bienvenu 3184
Boller, Giulia 4399
Boloux, Alexandra 1536
Bolte, Edward D. 493
Bolte, Edward 1
Bontemps, Arthur 542
Boretzki, Jakob 3256
Borghese, Vittoria 957
Bothra, Harsh 914
Boudaud, Clement 1943
Bouffard, Félix 2030
Bouillot, Jacques 2907
Bourne, Keith J. 1559
Bourne, Keith 1545
Bouzada, Ana Maria Santos 976
Bradette, Alain 4182
Branco, Jorge M. 276, 285, 1960, 2253, 3667, 3685
Branco, Jorge 2173
Brandner, Reinhard 1289
Brandon, Daniel 1001
Brandstätter, Florian 398
Brank, Boštjan 2892, 2907
Brashaw, Brian 4513
Braun, Matthias 1409
Braun, Max 89, 3485
Braun, Werner 3649
Breijinck, Thomas 1110
Bremer, Martina 698
Briales, Eduardo Rojas 4190
Brieden, Matthias 89, 3485
Briggert, Andreas 740
Brischke, Christian 549
Brito, Leandro Dussarrat 3048, 3062
Brito, Nelson 4093
Brogli, Julian 571
Brooke, Harrison 3417
Brotschi, Thomas 1269
Brown, Nathan C. 858, 1009
Broyles, Jonathan M. 858
Brüchert, Franka 119, 711, 766
Brugnara, Paola 1330, 1914, 3816
Brumana, Giovanni 4173
Brunauer, Marie Theres 3357
Bruneau, Denis 3924
Brunetti, Michele 723
Brunkhorst, Sven 1848
Brütting, Jan 3588
Buchanan, Andy 4627
Buchholz, Lea 1168
Bui, Tuan-Anh 2609
Bunzel, Frauke 629
Burgert, Ingo 3241
Burkart, Hauke 3001
Busch, Aleesha 2084, 2633
Buschmann, Birger 629
Bustamante, Waldo 927
Byrick, Wilson 1983
Cabrera, Gonzalo 1342
Cabrero, J. M. 2768
Cabrero, José Manuel 2432, 2678, 2798
Cador, Luc 2820
Caicedo-Llano, Natalia 3917
Callaghan, Aedan 1983
Callegari, Ernesto 1305, 1330, 2497, 2517
Camnasio, Elena 3167

Campodónico, Virgina 4465
Canetti, Davide 1416
Cao, Alex Sixie 6, 2268
Cárcamo, Sebastián 3963, 3973
Carrascal, Jeronimo 1644
Casagrande, Daniele 1001, 1224, 1305, 2227, 2376, 2497, 2783, 3492
Cascante, Diego Valdivieso 383, 2717
Casey, Flynn 1034, 2669
Casiraro, Ignazio 3423
Castelli, Simone 4173
Castro, Juan 98
Catapano, Anita 455
Cattelino, Jason 65, 75
Caussarieu, Guillaume 4316
Cavoli, Denise Li 3423
Cenci, Giuseppe 2227
Cepelka, Martin 3979
Chaboki, Hamidreza 3235
Chacón, Matías F. 2851
Chang, Wen-Shao 168, 1873
Chaplain, Myriam 209
Chapman, Daniel 3091
Charney, Finley A. 2776
Chen, Fei 3318
Chen, Herry 202, 4383
Chen, Lin 1123
Chen, Meizhen 521
Chen, Yuchen 435, 3845
Chen, Zhiyong 1610, 2234, 2288, 2479
Cheng, Zhuo 521
Cheraghi-Shirazi, Najmeh 1936
Chevalier, Romain 455
Cho, Jaemo 4102
Chorlton, Bronwyn 1592
Christensen, Eirik G. 1758, 1778
Christensen, Eirik 1701, 1768
Christoforo, André 31
Chui, Ying Hei 1117, 1873, 2063, 2464, 2479, 2523, 3127
Chúláin, Caitríona Uí 875, 888
Cisternas, Jorge Uribe 383
Cizmar, Dean 2090, 2834
Claesson, August 1154
Claridge, Ed 4627
Codriansky, Keren 4465
Colic, Antonela 1788, 1839
Collins, Steven 428, 671
Cominelli, Stefania 358
Conta, Simone 1908
Corpataux, Laurent 3851
Correal-Mòdol, Eduard 4128
Costa, Antonio 909
Costa, Joaquim 909
Costa, Letícia 920
Couceiro, José 759
Coureau, Jean-Luc 209
Coutellier, Daniel 3184
Cover, Jennifer 4576
Cowled, Craig J. L. 3177
Cowled, Craig 3417
Coxford, Richard 4518
Cramer, Marlene 3558
Creagh, Ariel 1936
Crews, Keith 1936, 3417
Crocetti, Roberto 1154, 1453, 2907
Croci, Marcia 4465
Crovella, Paul L. 376
Cui, Jianrong 24
D'Acunto, Pierluigi 4399
D'Amato, Giulia 1330
D'Arenzo, Giuseppe 1001, 2070, 2454, 2489, 3423
Da Silva, Antonio 909, 920
Dagenais, Christian 1583, 1592, 1610, 2356, 2922, 4627
Dahl, Kristian B. 3995
Dahlberg, Justin M. 244
Daneshvar, Hossein 2063, 2464, 2479, 3127
Dangel, Ulrich 4505
Danielsson, Henrik 2396, 2432
Danzig, Ilana 4240, 4409
Darby, Antony 3475
De Arteaga, I. 2768
De Cillia, Luca 586
De Joigny, Blanche Blondel 24
De Oliveira, Fabiana Lopes 175
De Santis, Yuri 1244, 2695, 2761
De Souza, Márcio Sartorelli Venâncio 3076
Debnath, Ramit 903
Dechent, Peter 1953
Degée, Hervé 3568
Demarchi, Efrem 3507
Demonte, Florian 139
Demschner, Thomas 2416
Derikvand, Mohammad 677, 3575
Desantis, Aaron 333
Dhonju, Roshan 41
Diao, Yue 3439
Dias, Alfredo 31, 3121, 3364
Dias, Antonio Alves 196
Dickof, Carla 352, 2063, 2384, 2660, 2861, 4232, 4345
Dietsch, Philipp 366, 1322, 1900, 2432, 2678, 3054, 3256, 3718
Dinehart, David W. 493
Dinehart, David 1, 14

Ding, Yewei 1123
Diógenes, Hidelbrando J. F. 276
Dodoo, Ambrose 3581
Dolan, Daniel 2627
Dolan, J. Daniel 2642
Dolan, James D. 2084
Dölerud, Erik 1336, 2118
Dolsvåg, Sondre 4353
Domenach, Leandro 4415
Dorn, Michael 1930, 2898, 3829, 4338
Dos Santos, Lorenzo Lube 3084
Doudak, Ghasan 1176, 1224, 2261, 2298, 2376, 2783, 3141
Drexler, Hans 3944
Duchanois, Gilles 3708
Dunn, Andrew 4627
Dusicka, Peter 1350
Eckert, Alexandra 1289
Eddin, Mohamad B. 858
Eddin, Mohamad Bader 1863
Eder, Robert 2537
Edgar, Russell 65
Ehrhart, Thomas 315
Engelbrecht, Gerhard 3874
England, Paul 1721, 4627
Englund, Michael 4360
Eriksson, Jacob 139
Ervine, Adam 1738
Esaka, Yoshisato 1283
Eslami, Hooman 982
Esser, Lukas 2268
Estévez-Cimadevila, Javier 3296, 3303
Estrella, Xavier 3430, 3588, 3600
Evers, Tobias 339
Eversmann, Philipp 3485
Fadai, Alireza 868, 3357, 4583, 4604
Faggiano, Beatrice 2173, 2995
Faircloth, Adam 1873
Fakhrzarei, Mahboobeh 2464
Fanti, Riccardo 1305, 1416, 3492, 3507
Fares, Sameer 14
Faria, José Amorim 4001
Farias, Ana 920
Fast, Tobias 2861
Fawcett, Daniel 1312
Fawzia, Sabrina 3177
Feng, Wen 1200
Feroldi, Francesca 358
Ferreira, Cláudio 3121
Fierro, Javier 4383
Filz, Günther H. 4597
Fink, Gerhard 428, 671, 677, 1001, 3575
Fischer, Erica C. 2650
Fischer, Erica 2185
Fischer, Jens 4064, 4071
Fischer, Oliver 967
Fitzgerald, Brendan 4240, 4409
Fivet, Corentin 3588, 3600
Fjellström, Per-Anders 3979
Flamand, Olivier 2907
Flindall, Ona 1491
Flinn, Simon 4190
Flores, Diego 1583
Flores, Francisco 2776, 3069
Florisson, Sara 759
Follesa, Maurizio 2227, 3492
Forsberg, Tomas 4439
Förster, Ralf 3694
Forsthuber, Boris 3874
Fortino, Stefania 449, 536
Fossetti, Marinella 2454, 3423
Foster, Robert M. 2841
Founti, Maria A. 1748
Fournely, Eric 542, 2820
Fragiacomo, Massimo 1244, 1988, 2179, 2200, 2227, 2761
Frangi, Andrea 6, 315, 571, 1728, 2268, 2416, 2600, 2686, 2915, 2958, 3241
Franke, Bettina 268, 1081, 1512, 1894
Franke, Steffen 268, 1001, 1081, 1299, 1512, 1894
Franssen, Jean-Marc 1839, 1848
Franssila, Juha 1095
Fréchard, Victor 3708
Fretz, Mark 1034, 2669, 3728
Friquin, Kathinka Leikanger 1576, 1637
Frohnmüller, Jens 750, 4164
Fruehwald-Koenig, Katja 638
Fu, Rongji 3410
Fuchs, Alain 3608
Füchslin, Matthias 3241
Fujii, Daisuke 1050
Fujimoto, Manabu 4134
Fujita, Kaori 2207
Fukumoto, Kouji 3281
Fukuta, Satoshi 1104
Fülöp, Ludovic 449
Furley, Jace 1009
Furtmüller, Thomas 1900
Furuta, Tomoki 2731, 2739
Füssl, Josef 391, 398, 465, 2432
Gagnon, Sylvain 2356
Gan, Zhaozhuo 105
Ganjali, Houman 352
Ganß, Martin 3888

Gao, Ying 3201
Gao, Zizhen 112
Garains, Fabien 2907
García-Navarro, Justo 3594
Gard, Wolfgang 4079
Gata, Kevin Moreno 705
Gattas, Joseph M. 51
Gavric, Igor 1244, 2200, 2907
Gehri, Ernst 132, 315
Geiser, Martin 2686
Geng, Minghao 3201
Gernay, Thomas 1848
Gerold, Matthias 3001
Gershfeld, Mikhail 3728
Gesh, Jacob 2244
Gharaibeh, Laith 3141
Giampellegrini, Laurent 4309, 4316
Gikonyo, Joan W. 3101
Gilbert, Benoit P. 474, 1873, 2811
Gil-Moreno, David 773, 780, 875
Giraldo, M. P. 4128
Giraldo, María Pilar 564
Girardi, Roberto 2517
Giron, Nicolas 3860
Giuriani, Ezio 358, 4173
Glarner, Ben 2268
Glas, Bo 1062
Glasner, David 1289, 3649
Glasø, Geir 4182
Glew, Adam 1701
Glišovic, Ivan 407
Godi, Gaël 542, 2820
Gomes, Nádia Barros 729
Gong, Meng 112, 521, 1129, 2523
Goni, Tahiat 2479
González-Alegre, Violeta 3594
González-Serna, Pablo 2678, 2798
Goodarzi, Azadeh 2724
Goto, Yutaka 1183, 1497, 4286, 4360
Gotou, Humihiko 2350
Gottardi, Luca 2517
Götz, Tobias 1855
Goudarzi, Hamid Valipour 794
Granello, Gabriele 2244
Graziotti, Francesco 2510
Gril, Joseph 443, 542, 2820
Grizmann, Denis 705
Groba, Moritz 1491
Groba, Ute 1067, 3625
Grönquist, Philippe 3241
Gross, Shawn 14
Grotenfelt, Daniela 4360
Grüll, Gerhard 3874
Gstettner, Michael 3660
Guan, Hong 1873, 2811
Guay, Ryan 1350
Gubana, Alessandra 586, 2471
Guindos, Pablo 2125, 2134, 2851, 3430
Gullbreken, Lars 3823
Gunalan, Shanmuganathan 2811
Gunasekaran, Prashanth 794
Gunnarsson, Sigurdur 4259
Guo, Chenyue 1129, 1921, 1968
Gysling, Janina 683, 4377, 4475, 4483, 4491
Haakonsen, Sverre M. 3644
Haase, Peter 3256
Haavi, Thomas 4141
Hackel, Martin 647
Hafeez, Ghazanfarah 84
Hafner, Annette 842, 935, 4010
Hagen, Martin 1660
Haggart, Kirsten 903
Hagle, David 3868
Hahusseau, Ludwig 2907
Hairstans, Robert 4265, 4619
Halin, Gilles 3608
Haller, Peer 621, 698, 3111
Hamm, Patricia 1855
Hammad, Mahmoud Wajdi 57
Han, Lei 666
Hanaoka, Hiroya 1383
Hånde, Eldbjørg Aaraas 3015
Haneda, Naohiro 2870
Hansen, Jesper Kierkegaard 1252
Hansen, Ketil Armann 4360
Hansen, Søren Gustenhoff 1252
Hansson, Lars 759, 1519
Hanus, François 3568
Hara, Tadashi 829, 882
Hardeng, Alvdis 4325
Harnomo, Fajar Ikhwan 4151
Harte, Annette M. 216, 773, 780, 875, 888, 2594, 3618
Hartig, Jens 621
Hartmann, Carina 842
Hasburgh, Laura E. 1559
Hasburgh, Laura 1545
Hasemi, Yuji 1551, 1620, 1653
Hashemi, Ashkan 1389, 2556, 4345
Hataj, Martin 162
Haupt, Jona 345, 804, 812
Häuptle, Franziska 2577
Haurie, Laia 564, 4583
Hawasly, Firas 1365
Hawkins, Will 3475

Hayashi, Yasuhiro 3410
Hayata, Keisuke 3191
Hazzard, Peter 903
He, Minjuan 105, 3318
Hedlund, Patrik 1453
Heffernan, Patrick 299
Hegeir, Osama Abdelfattah 1206
Hegeir, Osama 2940
Heidari, Mohammad 1667, 1758, 1768
Hein, Carsten 1017
Hellman, Alan 2717
Hellmayr, Raphaela 3535
Heltorp, Kaja 1067
Heng, Piseth 3333, 3342
Henjum, Jim 65, 75
Henke, Klaudius 629
Henriques, José 3148, 3161
Heyvaerts, Robbe 413
Hidalgo, Juan P. 1673
Higgins, Ornagh 4240, 4409
Higuchi, Adma M. D. 196
Higuchi, Niro 196
Hilditch, Ryan 1738
Hillberger, Thomas 1900
Hinata, Daiki 2870
Hisada, Masanori 2870
Hitts, Sarah 4619
Ho, Ai Phien 4064
Ho, Phien 4071
Ho, Tu X. 1009, 2156, 2562
Hochreiner, Georg 465
Hoffman, Rebecca 14
Hoffmeister, Benno 2335
Hofmann, Nicolas 119, 711
Hofmeyer, Hèrm 529
Hogan, Paul 875, 888
Hokibara, Tomoyo 1620, 1653
Hollberg, Alexander 4360
Homb, Anders 1908
Hopkin, Danny 1831
Horne, Paul D. 1526
Hörnel-Metzger, Beate 119, 711
Hosseini, Seyyed Hasan 3808
Hossell, Shane 3475
Houck, Leif D. 995
Hough, Richard 849
Hradil, Petr 449, 536
Hrovatin, Niki 3896
Hsu, Cheng-Chieh 895
Hu, Lin 1873, 2885
Hu, Qibin 3201
Huang, Bowen 1888
Huang, Da 2633
Huang, Hao 2098
Huang, Harrison 3753
Huang, Lizhen 4141
Huang, Puxi 3937
Huang, Wanru 941
Huang, Yunbo 1216
Huber, Christoph 2537
Huber, Johannes A. J. 766
Huber, Johannes 421, 1216, 1519
Hubmann, Gerhard 3649
Hufnagel, Paul 2570
Hui, Zhan 3753
Hull, Tyler 3455, 4383
Hummel, Johannes 4164
Hundhausen, Ulrich 413
Hunter, Matthew 3033
Hurtado, C. Martín 4611
Husel, Anja 2678
Ibáñez, Fernando 2531, 3989, 4353
Ibell, Tim 3475
Icimoto, Felipe Hideyoshi 3062, 3084
Iizawa, Naoya 836
Iju, Takahiro 2046
Ilgin, Hüseyin Emre 238
Iljkic, Ivana 2090
Imai, Makoto 882
Imamoto, Kei-Ichi 836
Imanpour, Ali 3127
Inayama, Masahiro 251
Incerti, Andrea 2517
Ingeborgrud, Lina 4535
Íñiguez-González, Guillermo 3594
Inoue, Ryo 126, 2008
Inutsuka, Chisato 323
Iovane, Giacomo 2173, 2995
Iqbal, Asif 1397, 1403, 2143, 2179
Iraola, B. 2768
Isaksen, Leif Tore 1660
Ishihara, Wataru 498
Ishikawa, Atsuko 505
Ishiyama, Hiroki 2617
Ishizaki, Tatsuki 1283
Iskra, Boris 1721
Isoda, Hiroshi 2504, 2584, 3281, 3499, 4058
Itagaki, Naoyuko 1075
Ito, Satoru 2278
Iwamoto, Daiki 3134
Iwuoha, Stanley Emeka 717
Izumi, Bunji 3644
Jaaranen, Joonas 428
Jackson, Robert 352, 2660, 3272, 4345

Jahangiri, Mehrdad 4240, 4409
Jahreis, Markus 3041
Jalil, Alan 2907
Jancke, Oliver 4496
Janssens, Marc 4627
Jara-Cisterna, Alan 512, 1953, 2342
Jaramillo, Juan Sebastian Zambrano 2650
Javoríková, Miroslava 3221
Jayasekara, Labuwatte M. M. B. 2841
Jayasinghe, Laddu Bhagya 982
Jeitler, Georg 615
Jensen, Tore Myrland 3823
Jeon, Bonghee 3794, 4108, 4370
Jia, Huijuan 1712
Jiménez, Francisco 4377
Jockwer, Robert 251, 1001, 1358, 1497, 2118, 3675
Johansen, Henning 4360
Johansson, Marie 740, 1154, 2877, 2907, 4439
Johansson, Thomas 2907
Johnson, Lorna 1788
Jorge, Luís 3364
Jorissen, André 529
Journot, Jean-Bernard 4415
Jucutan, Arman 1117
Judd, Johnn 2111
Junda, Eknara 2214
Junior, Carlito Calil 3048, 3062, 3084
Just, Alar 4627
Kaboorani, Alireza 3845
Kado, Yuji 2504
Kadono, Daisuke 2077
Kahler, Carlos 683, 4377, 4475, 4483, 4491
Kaitaniemi, Pekka 3896
Kakehashi, Naoki 1088
Kälin, Benoît 3600
Kallenborn, Roland 1044
Kamata, Toko 2278
Kamatoko, Miyako 1088
Kambe, Wataru 4043
Kamikawa, Daisuke 505, 1620
Kampenes, Camilla By 2577
Kanazawa, Kazumi 3499
Kang, Thomas 1506
Kanócz, Jan 3221
Karacabeyli, Erol 2288
Karampour, Hassan 474, 1873, 2811
Karannagodage, Chamith 1728
Karjalainen, Markku 238, 3526
Karla, Viktor 3221
Karlsons, Maris 3351
Karolin, Joel 1894
Kashyap, Rimjhim 2594, 3618
Kästner, Martin 3888
Katavic, Ivana 4222
Kato, Hidao 829
Kawahara, Hiro 3134, 3398
Kawai, Naohito 2406, 2548, 3449
Kawasaki, Riko 3465
Kawasoe, Atsuya 3465
Keis, Dorthe 4279
Kelch, Steffen 3241
Kellgren, Laura Vestergaard 3868
Kemda, Blériot Vincent Feujofack 1275
Khajehpour, Mehdi 941
Khokhar, Aamir 41
Khoo, Benjamin 1778
Khoshkbari, Parham 1936, 2724
Kies, Uwe 4496
Kilpatrick, Tony 1712
Kim, Chul-Ki 3513
Kim, Dongwook 3794
Kim, Gee Heon 3794
Kim, Jenna 4345
Kim, Jeonghyun 4108
Kim, Jihong 4108
Kim, Jiyong 232
Kim, Keonho 1238
Kim, Min-Jeong 188, 232
Kimura, Hirokatsu 1653
Kitahara, Akio 4114
Kitamori, Akihisa 4058
Kitriniaris, Alexandros 4393
Kiyohara, Chizuru 836
Kjolsing, Eric 65
Kleinhenz, Miriam 2416
Klippel, Michael 4627
Klitkou, Antje 4535
Kloiber, Michal 162, 787
Knapen, Elke 4157
Knippers, Jan 3905
Knöpfle, Valentin 1855
Knutsen, Sivert 1216
Kobayashi, Hironobu 882
Kobayashi, Kenji 1104, 1437
Koch, Johannes 3041, 3888
Koch, Lori 3033
Koda, Marina 3281
Koesling, Stephanie 804, 812
Koetsier, Mathieu 407
Koklas, Andrianos E. 1748
Kolaitis, Dionysios 1748
Kolbe, Jana 804, 812
Komatsu, Kohei 4050
Konteas, Zannis 4393

Kontra, Steven 1009
Koronaki, Antiopi 903
Koshihara, Mikio 1365, 2548, 4134
Koski, Keijo 449
Kosuge, Yua 3392
Kotmel, Miroslav 787
Kotsovinos, Panagiotis 1667, 1701, 1758, 1778
Kotsovinos, Panos 1768
Kouyoumji, Jean-Luc 1863
Kovacic, Iva 4545
Kraler, Anton 3880
Kramer, Anthonie 1269
Kramer, Lukas 2686
Kraniotis, Dimitrios 413, 3835, 4460
Krenn, Harald 1831
Kresz, Miklos 3896
Kromoser, Benjamin 599, 1409, 3535
Krtschil, Anna 3905
Kržan, Meta 1231, 3667, 3685
Kuai, Le 1261, 2709
Kubo, Koji 2390
Kubojima, Yoshitaka 829
Kubota, Jun 2870
Kubotera, Hiroaki 3551
Kuhlmann, Ulrike 1168
Kulha, Pavel 3874
Kumar, Chandan 474, 1873
Kunecký, Jirí 162, 558, 787
Kunic, Anja 1252
Kurent, Blaž 2892, 2907
Kurzinski, Shaghayegh 376
Kusyala, Dibya 4151
Kutnar, Andreja 666
Kveseth, Petter 4571
Kwiecien, Arkadiusz 1231
Labò, Simone 4173
Lacasta, Ana M. 564
Lacis, Raitis 3351
Lacroix, Daniel 202, 2261, 3455, 4383
Lager, Markus 3761
Lahr, Francisco 909, 920
Lam, Waikong 3134
Lamadon, Thierry 2820
Lanata, Francesca 1943
Landel, Pierre 1336, 2118, 2877, 2907
Landolfo, Raffaele 2995
Lang, Peter 1305
Langer, Sarka 1062
Langevin, Marc-André 1592
Lapointe, Étienne 1269
Lara, C. 2768
Lardeur, Pascal 2609
Larsson, Carl 1930, 4338
Lasala, Bridget 1
Lavisci, Paolo 723, 4528
Layton, Patricia 914
Leardini, Paola 1497, 4429
Lebossé, Maxence 3608
Lecomte, Roberto 3747, 3769
Lee, Gwang-Ryul 188, 232
Lee, In-Hwan 1238
Lee, Kangmin 4122
Lee, Min 3513
Lee, Seung Heon 1506
Lefèvre, Charline 4303
Leggate, William 2811
Leitch, Matthew 3382
Lemaître, Romain 1146
Lemke, Ulf 740
Leonard, Jayson 3518
Leonard, Samantha J. 858
Lepikonmäki, Lauri 4247
Lepourry, Clemence 3342
Létourneau-Gagnon, Mathieu 1592
Leung, Pok Yin Victor 4399
Lewicki, David E. 493
Li, Bin 435, 3845
Li, Dehong 435, 3845
Li, Ling 112
Li, Minghao 2014, 2020, 3318
Li, Weitian 2306
Li, Zheng 105, 3318, 3667, 3685
Li, Zhengyao 1192
Li, Zherui 4058
Liao, Weichong 2221
Lie, Sivert 3542
Liljelind, Ingrid 1062
Lima, Daniel F. 285
Lin, Jingyuan 1358
Lindblad, Thomas 488
Linderholt, Andreas 2877, 2907
Line, Philip 2633, 2776, 3069
Lines, Nicola 3475
Linkosalmi, Lauri 4565
Lins, Dio 1299, 1894
Linzer, Finn 599
Lira, Geraldo 196
Lisboa, Felipe Dutra 729
Liu, Jiwei 2745
Liu, Zhiyuan 1712
Liven, Harald 3015, 4209
Llana, Daniel F. 875, 888
Llana, Daniel Fernandez 3594
Lliso, Màxim 2531

Lockner, Emil 657
Loebjinski, Maria 3023
Longman, Ryan 2244
Lopez-Garcia, Diego 2125, 2134
Loss, Cristiano 1275, 1880, 3248, 3439
Loth, Andreas 3694
Lourenço, Paulo B. 276, 2253
Løvstad, Anders 1975
Lu, Peiqing 474
Lu, Yong 307
Lu, Yurong 1123
Lucherini, Andrea 1681
Luczkowski, Marcin 3644
Lukacevic, Markus 391, 398, 465, 2432
Lumpkin, Bryce 2930
Lyu, Chunhao 2811
Macdonald, Iain 4576
Macdougall, Colin 1110
Macilwraith, Andrew 1691
Madden, Joshua 1738
Maderebner, Roland 366, 1322, 1900
Madland, Haley 2185
Maeda, Masaki 1183, 4286
Maegawa, Toshio 1481, 2968
Magenes, Guido 2510
Maharjan, Rajan 2709, 4439
Mahjoub, Musaab Ahmed 1261
Mahnert, Karl-Christian 225, 482, 2695
Malaga-Chuquitaype, Christian 2214
Malagic, Alen 2442
Malaska, Mikko 238
Malek, Sardar 1936, 2724
Malekabadi, Reza Abbasi 84
Malo, Kjell Arne 1136, 1206, 2318, 2907, 2940, 2950
Maluk, Cristian 51, 1644
Mamie, Tim 3241
Manser, Nadja 2686
Manthey, Manuel 2892, 2907
Marcel, Muster 1160
Marchetti, Angelo L. 4173
Marchi, Luca 1431, 2194
Marini, Alessandra 358, 4173
Marino, Dario 903
Martin, William A. 4576
Martín-Gutiérrez, Emilio 3296, 3303
Martins, Carlos 3121
Martyniuk-Sienkiewicz, Kamila 2426
Mascarenhas, Fernando 31
Masoudnia, Reza 1389
Masroor, Mohammad 1224
Massaro, Francesco Mirko 1136, 2318
Masuda, Akira 323
Matsuda, Kazuhiro 323
Matsumoto, Kouta 3404
Matsumoto, Naoyuki 1365, 2207, 4134
Matsumoto, Shinya 2008
Matsuoka, Nao 3211
Matsushita, Shizuka 1566, 1602
Maurer, Bernhard 1322
Mazelli, Alessandro 586, 2471
Mazzey, Carlos 4415
Mazzolani, Federico M. 2995
Mazzotti, Claudio 2517
McDonnell, Erica 2633
McGavin, Robbie L. 474
McGetrick, Patrick J. 216
McGetrick, Patrick 888, 2594, 3618
McLain, Richard 2930
McNamee, Robert 1839, 1848
McPhee, Rodney 3007
McRobie, Allan 3091
Mehdipour, Zabih 2253
Mejías, Wilson 683, 4377, 4475, 4483
Melotto, Massimo 586
Ménard, Sylvain 858, 1863
Mendez, Daniela 927
Meng, Xinmiao 3201
Meng, Yiping 903, 3937
Menges, Achim 688, 2978, 3905
Mensah, Rhoda Afriyie 1519
Merryday, Hugh 3373
Metelli, Giovanni 358
Meulmann, Sebastian Svensson 3829
Meyer, Julien 3708
Mikael, Ali 2783
Mikkolo, Esko 4627
Minami, Ryota 1481, 2968
Mindeguia, Jean-Christophe 1839
Minegishi, Arata 1183, 4286
Minoura, Run 1075
Miranda, Joaquín 2717
Mirdad, Md. Abdul Hamid 1117, 2479
Mirra, Michele 4079
Mitchell, Harry 1667, 1758
Mitrenova, Elena 4545, 4590
Miyake, Akihiko 3325
Miyake, Tatsuya 2584
Miyamoto, Kohta 147
Miyazu, Yuji 2056, 2104, 2312
Mo, Gaute 3989, 4222, 4353
Modaresi, Roja 976
Modderman, Jeff 529
Moeller, Carsten 849
Moerman, Benjamin 2014

Mohaine, Siyimane 1839
Mohammad, Mohammad 4518
Mohammadi, Mohsen 112
Mohammadyzadeh, Samira 2885
Molina, Carolina 4377
Molina, Julio Cesar 729
Molinari, Marco 723
Møller, Johan Kr. 1637
Moltini, Gonzalo 1342
Momose, Haruki 1050
Momose, So 2584
Monachogios, Sotiris 4393
Monard, Nils 804, 812
Montaño, Jairo 2125, 2134, 2851
Montemurro, Marco 455
Montgomery, Graham 1798
Moreno-Zapata, Ezequiel 2768
Mori, Kazuya 2046
Mori, Takuro 126, 2008
Moritani, Fabiana Yukiko 3084, 3364
Mork, John Haddal 3801
Morrell, Jeffrey 1673
Morrisset, David 1788, 1839
Mowafy, Ahmed 3127
Mózer, Vladimír 1681
Mrissa, Michael 3896
Mugabo, Ignace 1350
Muin, Sifat 2143
Mukai, Motohiro 3191
Müller, Andreas 1081
Müller, Maximilian L. 711
Müller, Maximilian Leonhard 119
Müllner, Alex 3357
Munch-Andersen, Jørgen 1422, 3054
Munden, Joakim P. 2510
Münzer, Aaron 688
Murakami, Katsuhide 2077
Murakami, Masahide 2077
Murata, Ryoma 3325
Muresan, Alex 3588
Musselman, Eric 1
Muster, Marcel 2600
Muszynski, Lech 2244, 3581
Myna, Roman 3535
Myronycheva, Olena 1062
Naboni, Roberto 1252
Naceur, Hakim 3184
Næss, Johann Kristian 976
Nagano, Masayuki 2104, 2312
Nagaoka, Tsutomu 1620
Nagashima, Taisuke 1481, 2968
Nagy, Edwin 65
Nakagawa, Takafumi 2406, 2504, 2584, 4058
Nakajima, Shiro 609
Nakakuki, Joichi 3134
Nakamichi, Kohei 2548
Nakao, Masato 2731, 2739
Nakashima, Hiroki 1481, 2968
Namari, Siavash Mahjourian 3111
Namba, Tokikatsu 2504
Nambu, Yasuhiro 2312, 4114
Narancic, Payton 1034, 2669, 3738
Nasu, Hideyuki 292, 836, 3392, 3398, 3404, 3860
Natterer, Johannes 3600
Naveda, Leo Anderson 2118
Nåvik, Petter 2907, 2950
Nemoto, Shuya 2350
Néron, Laurane 3701
Nesheim, Sveinung Ørjan 3801
Nestmann, Anna 967
Neto, Carlito Calil 4215, 4332
Neubauer, Gregor 3905
Neumüller, Andreas 735
Neuner, Hans-Berndt 599
Ni, Chun 2752
Nicolussi, Valentino 2805
Niederwestberg, Jan 1117
Nielsen, Mads Friborg 1252
Nieri, Guido 1017
Niikuma, Kazuo 3551
Niklewski, Jonas 549, 3808
Nikoo, Mehdi 84
Ninakawa, Toshihiko 4114
Nizarali, Rafik 1536
Nogueira, Rodrigo De Souza 3084
Norbäck, Viktor 1336, 2118
Nord, Tomas 1062
Nordby, Kjetil 3954
Nordhagen, Victoria Rygh 4460
Nordin, Björn 1062
Nordløkken, Per Gunnar 4253
Nore, Kristine 4141, 4460
Norman, James 1375
Northcutt, Dale 1034
Noviello, Celeste 2995
Nsumbu, Horly Luzolo 3924
Nunes, Lina 285
Nurdiah, Esti 168
Nygaard, Marius 3954
Nyrud, Anders Q. 1067
Nyrud, Anders 1044
O'Brien, Colm 4571
O'Ceallaigh, Conan 216, 1691, 2594, 3618
O'Halloran, Simone 3728

O'Loughlin, Eoin 1701
Öberg, Vera 1497
Obernosterer, David 615
Oda, Shogo 3290
Odenbreit, Christoph 3568
Ogawa, Keita 1104, 1437
Oh, Jae-Won 188, 989
Oh, Jaewon 232
Oh, Jung-Kwon 188, 232, 989
Ohashi, Yoshinori 498
Ohta, Takao 2046
Ohtsuka, Akiko 1075
Øiern, Mads 4571
Oikawa, Daisuke 2350
Oja, Johan 421
Okamoto, Shigefumi 2617
Okuda, Shinya 3851
Oliveira, Damian 2298, 2783
Oliveira, Gabriela Lotufo 175
Olsen, Cory 3782
Olsson, Anders 421
Omi, Shogo 98
Onishi, Satoshi 836, 3392
Opazo-Vega, Alexander 1953, 2342
Ormarsson, Sigurdur 1261
Orozco O., Gustavo F. 2156
Orozco, Gustavo F. 1009, 2562
Orozco, Gustavo Fernando O. 1034
Orozco, Gustavo 2669
Orozco, Luis 3905
Osmane, Zakaria Ben 1154
Ostapska, Katarzyna 3823
Östman, Birgit 4627
Ota, Yuki 2617
Otero-Chans, Dolores 3296, 3303
Ott, Stephan 967, 4496
Ottenhaus, Lisa-Mareike 1200, 1358, 1497
Ou, Sovanroth 182
Ouch, Vanthet 3333
Oudjene, Marc 3184
Oudjene, Marcel 2609
Overton, Katie 4222, 4353
Øvregård, John 3868
Owolabi, David 1880
Özdemir, Özlem 842, 935
Paananen, Valtteri 3526
Pacchioli, Stefano 2805
Pagella, Giorgio 4079
Pajunen, Sami 4247
Palas, Franck 3342
Palermo, Alessandro G. 1526
Palma, Pedro 132, 315, 1001, 3054, 3675
Pan, Yuxin 2040, 2384
Pang, Sung-Jun 188, 232, 989
Pang, Weichiang 182, 333, 914, 2792, 3518
Pantak, Marek 1930
Pantelides, Chris 2000
Pantscharowitsch, Marc 599
Paoloni, Francesca 1416
Papastavrou, Panayiotis 3091
Pardo, Evaristo 683, 4475
Park, Sangyeon 4370
Paroissien, Jeanne 2609
Parra, Roger 1936, 2724
Parsons, Bill 4513, 4576
Partl, Gabriel 3874
Pasca, Dag Pasquale 1244
Pasca, Dag 2695
Pascal, Fernanda 512
Passarelli, Rafael Novais 4157
Passoni, Chiara 4173
Pasternak, Hartmut 3023
Pauliny, Dusan 666
Pavic, Aleksandar 2892
Pavic, Alex 2907
Pavkovic, Krunoslav 2090, 2834
Pavlovic, Marko 407
Payne, Wyatt 2111
Pazlar, Tomaž 2432
Pech, Sebastian 391
Pecnik, Jaka Gašper 1231
Pei, Shiling 2084, 2633
Pelczynski, Jan 2426
Pelling, Jackson 4240, 4409
Peltonen, Simo 3167
Penna, Andrea 4093
Pereira, Marcos Cesar 196
Perez, Cedric 209
Perez, Fernando 2907
Pérez-Gomar, Carolina 4465
Perria, Elena 1472
Persson, Pontus 1453
Perstorper, Mikael 139, 657
Pestana, Catarina 3581
Petersen, Arnkell J. 995
Petit, Laurent 4447
Petrycki, Adam 1814, 3382
Pfeffinger, Hendrik 4309
Phan, Nhat-Tung 443
Phung, Hung Quang 3618
Pini, João Tavares 3076
Pinotti, Riccardo 3816
Piran, Farid 1873
Pitelková, Daniela Šejnová 1681

Pitt, Christopher 1350
Pitti, Rostand Moutou 443, 542, 1519, 2820
Planke, Terje 4460
Pletz, Everaldo 3048
Plos, Mitja 875
Plüss, Yannick 1462
Poblete, Pamela 683, 4483
Pogoreltsev, Alexander 4201
Pohl, Johannes 4316
Pojatina, Juraj 4029
Polastri, Andrea 1305, 1416, 2497, 2805, 3492, 3507
Poletti, Elisa 2253
Pomaroli, Andreas 3880
Pommier, Régis 455, 3924
Pondelak, Andreja 1231
Popovski, Marjan 352, 2234, 2479
Portela, María 3594
Pospiš, Nina 2834
Potuzak, Megan 3373
Poulsen, Frederik Møller 1701
Poupet, Boris 759
Poutanen, Tuomo 3526
Pozza, Luca 1330, 1431, 2194, 2517, 2805
Prandini, Renan 3076
Prichard, Morgan K. 858
Proulx, Jean 2030
Pryor, Steve 2084, 2792
Przystup, Alicja 307, 1216
Puettmann, Maureen 3581
Putzer, Katherina 4571
Qi, Brian 2479
Qi, Yunyang 2098
Qiang, Ruite 2752
Quenneville, Pierre 1389, 2556
Quinteros-Mayne, R. 2768
Quistin, Paul 2820
Qureshi, Irshad 2627, 2642
Racine, Josephine 2930
Rahman, Shaikh Atikur 153
Ramage, Michael H. 903
Ramazzini, Alvise 1305, 2497
Rammer, Doug 3069
Rammer, Douglas R. 244
Rammer, Douglas 2000, 2792
Rasmussen, Jeppe 3868
Rasmussen, Kristian Mæland 3995
Rauber, Lukas 2335
Ravenshorst, Geert 4079
Rebhi, Amal 209
Rebolledo, Pedro 512
Rebouças, Arthur S. 276, 3675
Redealli, Dario 3588
Redmond, Laura 914
Reichenbach, Sara 3535
Rein, Guillermo 1667, 1758
Reinholz, Bernhard 3535
Renard, Silvio 1848
Rety, Anthony 4316
Reulecke, Cordula 1472
Reynolds, Thomas 307
Ricco, Marco Lo 65, 75, 4576
Ridley-Ellis, Dan 735, 773, 780
Riggi, Ezio 3492
Riggio, Mariapaola 666, 2244, 3581, 3896
Rigo, Pietro 2497, 3507
Rinaldi, Vincenzo 2200, 2227
Ringhofer, Andreas 1358, 3649, 3660
Rinke, Mario 3634
Robert, Fabienne 1839, 1848
Rodemeier, Sebastian 2517
Rodrigue, Denis 435, 3845
Rodrigues, Leonardo G. 3667
Rodrigues, Leonardo 2173
Rodrigues, Quentin 1519
Rodriguez, Gustavo A. Araujo 1009
Rodriguez, Gustavo Adolfo Araujo 2156
Røgeberg, Kristoffer 4571
Rohde, Emma E. 1027
Romana, Laurence 2820
Romero, Alfredo 3568
Rønnquist, Anders 2907, 2950
Rosales, Víctor 512, 2342
Rössler, Albert 3874
Røtnes, Anna 4571
Roueche, David B. 1027
Roueche, David 3373
Rovers, Ronald 4157
Ruan, Gengmu 4597
Ruane, Kieran 1691
Rudenå, Andreas 4496
Ruf, Johannes 1855
Rug, Wolfgang 3023
Ruggeri, Elisabetta Maria 2454, 3423
Ruther, Petra 3823
Ryan, Keri 2084
Sahata, Tomoya 3449
Saile, Bettina 629
Sakai, Yuta 2150
Sakata, Katsuhiko 1050
Sakurai, Nobuji 2390, 4020
Salamah, Hafshah 1506
Salem, Sam 1807, 1814, 1821, 3382
Salenikovich, Alexander 1269, 1512, 3675
Sánchez-Solís, Manuel 2531, 3989, 4222

Sandak, Anna 549, 666, 3896
Sandak, Jakub 549, 666, 3896
Sandberg, Dick 666, 759
Sandberg, Karin 3558, 3931, 4295
Sandin, Ylva 3558
Sandland, Knut Magnar 488, 4253
Sandor, Boris 766
Santini, Silvia 957
Santini, Stefano 4173
Santos, Pedro 3364
Sasatani, Masamichi 1383, 3134
Sato, Toshiaki 2312, 3551
Satou, Nozomi 1075
Sauter, Udo H. 119, 711
Schär, Styfen 2915
Scheibenreiter, Johann 3357
Schenk, Martin 2432, 2678
Scherf, Maximilian 3874
Schickhofer, Gerhard 615, 2365, 2442
Schiere, Marcus 268, 1081
Schimleck, Laurence 3581
Schirén, Whokko 1930
Schlyter, Camilla 3931, 4295
Schmid, Joachim 1728
Schmidt, Jonas 4453
Schmidt, Laura 1738
Schober, Kay-Uwe 119, 711
Schramm, Kristina 3485
Schulz, Judith 1701, 1758, 1768, 1778
Schwarzmann, Wolfgang 3788
Schwarzschachner, Harald 4565
Schweigler, Michael 1146, 3101, 3667, 3685
Schwendner, Sascha 4064, 4071
Schwertfeger, Ramona 3761
Sciomenta, Martina 2761, 2826
Scotta, Roberto 1431, 2194
Sebera, Václav 1231
Seeberg, Astrid Charlotte 3868
Segeur-Villanueva, Suzanne 3917
Seguchi, Tsubasa 1283
Seim, Werner 89, 717, 750, 2070, 2454, 2489, 3485, 4064, 4071, 4164
Seiter, Alex 705
Sejkot, Petr 1397, 1403
Sempey, Alain 3924
Senalik, C. Adam 65, 75
Sener, Kadir C. 1027
Sener, Kadir 3373
Serna, Pablo Gonzalez 2432
Serrano, Erik 2396, 2432, 2442
Sestigiani, Luca 1305, 1330, 1914, 2497, 2517
Setti, Alessandro 1416, 3492
Sguerri, Lorena 957
Shah, Darshil U. 903
Shahin, Alireza 3177
Shahnewaz, Md 352, 2384, 3272
Shehadeh, Zijad 1146
Sheine, Judith 1034, 2669, 3728
Shengdong, Zhang 24
Shi, Benkai 1888, 2745
Shim, Kugbo 3513
Shima, Takashi 1050, 2870
Shimizu, Daisuke 4087
Shimoirisa, Yuuto 2046
Shioya, Shinichi 1566, 1602, 2046, 3191, 3211, 3465
Shirmohammadi, Maryam 578, 4429
Shirmohammadli, Younes 1389
Shrestha, Pratik 4423
Shrimpton, Catherine 202
Siciliano, Serena 202
Sieder, Mike 1462, 1472
Siegert, Svenja 1472
Sierra, Andrés 3963, 4465
Sierra, M. Andrés 4611
Silva, Franco 2717
Silva, Sandra M. 1960
Silva, Vitor Afonso Neves 4215, 4332
Silvo, Jonna 593
Simlinger, Thomas 766
Simões, Rogério 31
Simon, Antje 3041, 3888
Simon, Kai 1443, 3264
Simpson, Barbara G. 1009, 2156
Simpson, Barbara 2562
Sinha, Arijit 1009, 2156, 2185, 2562
Sjøli, Lone 4571
Skartveit, Alfredo 3995
Skotheimsvik, Tim 4259
Slattery, Tom 3417
Sleik, Tim 1831, 4316
Slotboom, Christian 352, 2166, 2660, 2861, 4232
Smith, Ian 2805
Smith, Simon 903, 3091
Smith, Stuart 1017
Somja, Hugues 3333, 3342
Sonoda, Satomi 829
Soquet, Thierry 3333
Sosa, Aída Santana 4545, 4590
Soto, Daniel 683, 4377, 4475, 4483, 4491
Spangenberg, Ann-Charlotte 750
Spearpoint, Michael 1831
Speranza, Alice 1914
Spitaler, Irene 3874
Spörri, Sabrina 1728

Spyridakis, Stavros 1644
Sroka, Katharina 315
Stæhr, Efthymia R. 995
Stamatopoulos, Haris 1136, 1206, 2940
Stapf, Gordian 1831
Stavric, Milena 465
Steiger, René 132, 315, 2686
Steinert, Martin 1056
Stenson, Jason 1034, 2669, 3728
Stenstad, Andreas 482, 2695
Stephan, Daniel 868, 4604
Stepinac, Mislav 1001, 2834, 4029
Stieb, Thomas 1322
Stolpe, Harro 4010
Stoner, Michael 182, 333, 914, 2792, 3518
Stoyanov, Vladimir 4201
Stracke, Matthias 2570, 2577
Strahm, Thomas 132, 315
Strang, Marcus 4429
Stucki, Sandro 3241
Suárez-Riestra, Félix 3296, 3303
Subhani, Mahbube 153
Sudo, Ryutaro 259
Suesada, Hiroto 147
Sugino, Mina 3410
Sullivan, Jamie Pobre 4232
Sun, Xiaofeng 105
Sunakozawa, Sora 292
Sundkvist, Bror 1062
Šušteršic, Iztok 1001, 1244, 2907
Suyama, Takumi 3465
Suzuki, Soma 1653
Suzuki, Tatsuro 1551, 1653
Svartefoss, Silje Marie 4555
Svatoš-Ražnjevic, Hana 3905
Tabata, Chikako 3290, 4087
Tabata, Hiroki 4114
Tachibana, Kazuki 1481, 2968
Takaiwa, Yuya 2278, 2390, 4020, 4035
Takanashi, Ryuya 498
Takano, Atsushi 819
Takase, Ryo 505, 1653
Takata, Alexander 4215, 4332
Takatani, Shinji 2870
Takino, Atsuo 2504
Takizawa, Hina 4020
Talke, Daniel 629
Talledo, Diego A. 2805
Tam, Mandy 352
Tamagnone, Gabriele 4265, 4619
Tamburini, Fabrizio 1416
Tanadini, Davide 4399
Tanner, P. 2768
Tannert, Thomas 307, 352, 941, 1160, 1216, 2040, 2063, 2306, 2384, 3235
Tanskanen, Jouko 3526
Tao, Haotian 1888
Tapia, Cristóbal 688, 2978
Tashakori, Javad 1807
Tavoussi, Kamyar 4583
Teflissi, Thomas 2040
Tekleab, Medhanye Biedebrhan 2365
Tenório, Marina 1960
Terasaki, Shinichi 1075
Terui, Kiyotaka 292, 3404
Tetlak, Tomas Bravo 51
Theurer, Lucia 4316
Thiis, Thomas K. 995
Thiis, Thomas 4093
Thomson, Daniel 1667
Thunber, Kari Ryen 3015
Todorovic, Marija 407
Toftemo, Eli 1975
Toivonen, Ritva 3896
Tojo, Takaki 2104
Tomasi, Roberto 1988, 2327, 2510, 3015, 3154, 3229, 4093
Tomczak, Artur 3644, 4141
Tomioka, Yoshito 3290, 4087
Tomita, Ai 2104
Tommasini, Mirko 2517
Toncic, Marija Babic 2090
Tong, Fei 2885
Tønne, Julia Bosnes 4253
Too, Richard Yip Je 3499
Totsuka, Marina 251
Toumpanaki, Eleni 1312, 1375
Tourrilhes, Julie 4518
Trautz, Martin 705
Treml, Simon 2978
Treu, Andreas 488
Tronnier, Moritz 1462
Truskaller, Michael 3874
Trutalli, Davide 1431, 2194
Tsai, Meng-Ting 895
Tsalkatidis, Themistoklis 3542
Tsavdaridis, Konstantinos Daniel 1192
Tsuchimoto, Takahiro 498, 1481, 2968, 2987
Tsuda, Kazuki 1183, 4286
Tsukazaki, Hideyo 3449
Tsunetsugu, Yuko 1050
Tsuwa, Iuko 2548
Tulebekova, Saule 1136, 2907, 2950
Tung, Dorian 2288

Turk, Goran 875
Turkovsky, Stanislav 4201
Turnbull, Rory 1701
Tycho, Jørgen 1491
Uarac, Patricio 1009, 2562
Ueno, Tsukasa 3211
Uesugi, Shuhei 2077
Ugarte, Á. Juan José 3963
Ugarte, G. Juan José 3963
Ugarte, Juan José 4465
Ullah, Samee 3835
Ullah, Sameer 413
Umbach, Christian 4164
Ummenhofer, Thomas 3256
Ussher, Ebenezer 2327, 3015
Vafadar, Farid 671
Valdivieso, Diego 2125, 2134, 3963, 3973
Valenzuela, Tomás 2342
Valipour, Hamid R 57
Vallée, Till 339, 345, 804, 812
Valtonen, Tuovi 4565
Van De Kuilen, Jan-Willem 4079
Van De Lindt, John W. 1009, 2084, 2143, 3069
Van Den Wymelenberg, Kevin 1034, 2669
Van Niekerk, Philip Bester 549, 3808
Van Rie, Johnny 529
Vandamme, Esther 3634
Vandoren, Bram 3148, 3161
Varga, Zsofia 948
Vargas, Mauricio 512
Vázquez-Rodríguez, José A. 3296, 3303
Vcelak, Jan 3896
Vehrenberg, Philipp 2570
Véliz, Fernando 3430
Venturelli, Giuliano 4173
Verbeeck, Griet 4157
Vessby, Johan 139, 657, 2709, 4439
Vetter, Yannick 202
Via, Brian K. 1027
Viau, Christian 299, 1001, 1176, 2261, 2298
Victorero, Felipe 927
Vida, Christoffer 465
Vieillard, Thomas 4415
Viertel, Martin 2416
Vik, Kristine 482
Vilches, Marcel 564
Vilches-Casals, Marcel 4128
Vögele, Katrin 1462
Vojnovic, Luka 1375
Völlmecke, Lars 4064, 4071
Voss, Morten 339, 345
Voulpiotis, Konstantinos 2915
Vuillod, Bruno 455
Wacker, James P. 244
Wacker, Tobias 4316
Wade, Colleen 4627
Wagner, Anna 948, 967, 4496
Wagner, Hans Jakob 2978
Wakita, Takehiro 2104
Waldmann, Daniele 982
Wålinder, Magnus 1453
Walters, Joseph 4619
Wam, Sindre 4571
Wang, Dawei 521
Wang, Hongjun 819
Wang, Tianxiang 1453
Wang, Tsung-Hsien 168
Wang, Xiaodong Alice 435, 3845
Wang, Yue 1453
Wang, Zhiqiang 1129
Warmuth, Jonas 3588, 3600
Weaver, Mark 65, 75
Weber, Roger 1894
Wegrzynski, Wojciech 1831
Wehsener, Jörg 698
Wei, Kua Harn 3851
Weidenhiller, Andreas 735, 766
Wen, Bo 1888
Werther, Norman 4627
West, Salla-Mari 3167
Westerholm, Ninni 1095
Wichman, Sarah 2084
Wickström, Anders 1336
Widyowijatnoko, Andry 4151
Wiesner, Felix 1644, 1673
Wight, Nicole 299
Wijeratne, Christina 4528
Wiliamson, Emily 2000
Williamson, Miranda 4518
Wilson, Elias Mohr 4279
Wimmer, Heinz 2537
Wimmer, Rupert 3535
Winder, Sam 3091
Winkels, Peggy 4157
Winter, Klara 366, 967
Winter, Stefan 948, 967, 2432, 2678, 3718
Winward, Alex 2111
Wong, Kin Sang Michael 2221
Woo, Don-Son 4122
Woods, Joshua 1110, 1176
Wright, Thomas 2020
Wu, Shao-Chi 895
Wu, Wenxuan 1673
Wuyts, Wendy 4141

Xing, Dalu 2376
Xiong, Haibei..... 1123
Xu, Feiyang 3201
Xu, Rui 2098
Xuan, Lu 2306
Yaghma, Alireza..... 982
Yairi, Motoki..... 1050
Yamada, Koji 1994
Yamagata, Kaito..... 126
Yamawaki, Katsuhiko 2207
Yamazaki, Yoshihiro 1481, 2968, 2987
Yan, Zidi 1200, 1358
Yang, Huifeng..... 1888, 2745
Yang, Jie 3568
Yasir, Muhammad..... 1691
Yedinak, Kara 1559
Yermán, Luis..... 1200, 1673
Yin, Tianxiao 1129
Yli-Jyrä, Anssi 3896
Yoon, Mai Marcussen 4279
Yoshinuma, Hiroki..... 4035
Yoshioka, Tomokazu..... 3465
Yost, Joseph 14
Yuan, Cheng..... 1123
Yurrita, Miguel..... 2798
Zani, Mathilde 455
Zanni, Jacopo..... 4173
Zargar, Seyed Hossein 1009
Zehfuss, Jochen..... 1839
Zehfuß, Jochen..... 1848
Zelinka, Samuel L..... 1559, 4576
Zernicke, Caya..... 4010
Zhang, Binsheng..... 1712
Zhang, Chaoyue..... 3248
Zhang, David 1873
Zhang, Lei..... 1160, 3235
Zhang, Sigong..... 2523
Zhang, Xiaoyue..... 941, 2306
Zhao, Zijian 1968
Zheng, Lin 2523
Zheng, Wei..... 1129
Zhou, Jianhui 1129, 1921, 1968, 2885, 3235
Zhou, Lina 2752
Ziethén, Rune..... 740, 1154, 2118
Zimmer, Linda 3782
Zimmerman, Reid B. 1350, 2633
Zimmerman, Reid 2084
Zumbrunn-Maurer, Bruno..... 1269

SKIPET

Sone
30
Sone 23
P
in town!

The organisers of the WCTE 2023 want to thank our sponsors and exhibitors for your generous support on the World Conference on Timber Engineering 2023. We appreciate your commitment.

Innovation Norway

SWECO

PAPER PROVINCE

Region Värmland

Platinum Sponsors

Moelven

Aanesland Treindustri

Gold Sponsors

DEGREE OF FREEDOM

NY STRUKTUR Bærekraftige Konstruksjoner

white

BERGENE HOLM AS

PEFC PEFC/03-01-01

Silver Sponsors

rothoblaas Solutions for Building Technology

KLH

SPLITKON

OMRE

Bronze Sponsors

Exhibitors & Supporters

a part of
VÄRMLAND
Innovations from the forest
Scan me!
Region Värmland

Scan me!
PAPER PROVINCE

Architecture for a Sustainable Life

White Arkitekter is one of Scandinavia's leading architectural practices. We work with sustainable architecture, urban design, landscape architecture and interior design for current and future generations. Our mission is to enable sustainable life through the art of architecture. Our vision is that by 2030 all our architecture will be carbon neutral, through design excellence. We are an employee-owned architect collective with just over 700 employees and a presence in Sweden, Norway, the UK, Germany, Canada and East Africa.

IMAGE: VISIT SKELLEFTEÅ

SARA KULTURHUS, SKELLEFTEÅ

TALK TO US!
whitearkitekter.com
@whitearkitekter

white

dofengineers.com

architecture oriented,
flexible, and international
structural engineers

DEGREE OF FREEDOM

OSLO / VALENCIA / ATHENS

Bridges
Building Structures
BIM and Fabrication Models
Site Management and Technical Assistance
Maintenance and Inspection
Rehabilitation

NY STRUKTUR
Bærekraftige Konstruksjoner

Sustainable Timber Engineering

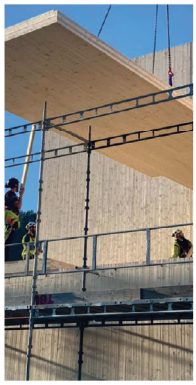

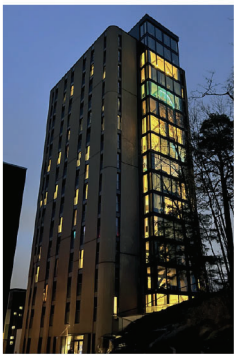
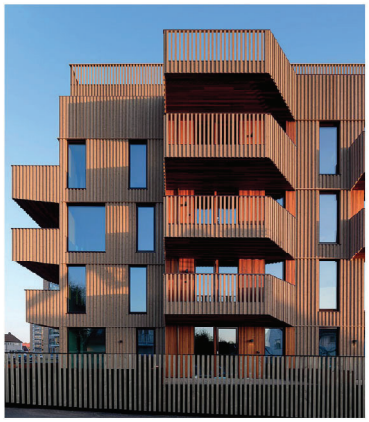

We are an independent consulting engineering office with focus on efficiency and sustainability.

www.nystruktur.no

NÅR DU SKAL BYGGE MED TRE

Med inspirasjon fra norsk natur og nordiske byggetrender, har vi utviklet unike kolleksjoner innen fasader, interiør og uterom til hus, hytter og leilighetsprosjekter.

SATURE Uterom – Miljø- og vedlikeholdsvennlige terrassebord

SATURE Fasade – Miljø- og vedlikeholdsvennlige kledninger

NORD Eksteriørkolleksjon - Kledning og tilbehør til barske fasader

TRYR Eksteriørkolleksjon - Kledning til all slags vær

NORD Interiørkolleksjon - Tidløse paneler og listverk

TELE Interiørkolleksjon - Storslåtte paneler og listverk

BERGENE HOLM AS

- Beste valg når du skal bygge med tre -

LES MER HER!

For mer inspirasjon og kunnskap om våre kolleksjoner les mer på **www.bergeneholm.no** eller benytt **QR koden** for mer informasjon.

FØLG OSS PÅ NETT!

@bergeneholm | #bergeneholm

WWW.BERGENEHOLM.NO

KLH®

VISIT US AT BOOTH 10

ASCENT C.D. Smith Construction

- PIONEER IN THE PRODUCTION OF CLT
- OVER 20 YEARS OF EXPERIENCE
- 38,000+ PROJECTS GLOBALLY
- EXPERTISE IN INTERNATIONAL PROJECT MANAGEMENT
- SOLUTION-ORIENTED PROJECT PARTNER
- WIDE RANGE OF SOFTWARE SOLUTIONS

KLH MASSIVHOLZ GMBH
Tel +43 (0)3588 8835 | office@klh.at | www.klh.at

PEFC: Your assurance of responsibly sourced timber

PEFC are silver sponsors of WCTE 2023

Designing the Future with Sustainable Timber

World Conference on Timber Engineering Oslo 2023

Discover more at **bit.ly/3pCME2d**

PEFC
PEFC/01-00-01

PEFC – Programme for the Endorsement of Forest Certification

PRODUSERT I NORGE

Massivtre – lagrer CO2 i enorme mengder

Treet suger til seg CO2 når det vokser og lagres som karbon i trestrukturen.

Splitkon leverer komplette byggesystemer i massivtre og limtre.

Moderne og miljøvennlige trebygg er fremtiden. Fra en av verdens største massivtrefabrikker, forsyner vi den norske byggebransjen med bærekraftigeløsninger.

Massivtre fra Splitkon lages kun med PEFC-sertifisert trelast fra norsk skog. Dette gir den høyeste kvaliteten – tilpasset nordiske forhold.

Avansert CNC-teknologi gir oss uendelige muligheter, og en presisjon på millimeternivå selv på elementer som er opptil 3,5 x 16 m.

Tre er både sterkt, lett i forhold til styrke og kan formes i alle fasonger. Tre er det mest miljøvennlige byggematerialet vi har.

Fakta: Miljøgevinsten/ besparelsen ved bruk av massivtre vs betong er 1 tonn CO2 per m³.

Les mer på **splitkon.no**

Se video om massivtre

Spor X – et av verdens mest miljøvennlige kontorbygg

Spor X i Drammen er et tietasjers kontorbygg med kortreist massivtre fra Splitkon. Prosjektet består av over 200 tilpassede limtrebjelker og 2500 m3 massivtre. Helt uten betong og stål fra grunnmur og opp.

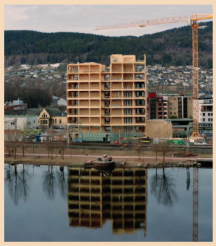

ILLUSTRASJON: DARK ARKITEKTER

SPLITKON

LEVEL UP
WITH OUR
SOLUTIONS
IS THIS WHERE WE'LL END UP?
It doesn't matter what heights we'll reach in the future. Tomorrow will have shapes and sizes imagined by today's designers, and solutions from those, like us, who believe in timber construction. Let's build the future together, let's climb higher.
OUR IDEAS TO REACH NEW HEIGHTS ARE HERE
rothoblaas
Solutions for Building Technology
rothoblaas.com

WORLD CONFERENCE ON TIMBER ENGINEERING 2025

BRISBANE, AUSTRALIA

IT'S LIVE! in Queensland

WCTE 2025 THEMES:

- Material Performance & Durability
- Sustainability and Timber in a Circular Economy
- Timber Engineering & Structural Performance
- Timber Architecture & Biophilic Design
- Education, Innovation & Challenges
- Exemplars & Construction Case Studies

Brisbane, Tourism Queensland

Murdoch University Boola Katitjin Building: Aurecon Group

25 King St, Brisbane: Lend

Advancing Timber for the Future Built Environment

It is with great pleasure, that the Australian Organising Committee invite delegates from around the world to join us in Brisbane to attend the next WCTE, from 22nd to 26th June 2025.

Our host organisation for the conference is The University of Queensland, home of the recently established Australian Research Council Industrial Transformation Research Hub to Advance Timber for Australia's Future Built Environment (ARC Advance Timber Hub).

The use of timber in building construction is growing at a rapid pace in Australia and the government continues to provide incentives for the utilisation of engineered timber products in construction, including a commitment of $100 million for the creation of a national institute for Forest Products Innovation, designed to position the Australian Timber Industry to make huge contributions to Australia's carbon positive bio-future.

Australia is bringing innovative timber solutions to the tall buildings market, developing uniquely performance-based design solutions to make timber viable for building of height and complexity equal to that of any other country in the world.

There is a rise in engineering and architectural firms, developers and investors, now emphasizing timber engineering as a preferred solution for many projects, providing further relevance and importance to the research carried out by the timber design and construction community.

A number of exemplar buildings and structures are located within Brisbane, providing an ideal opportunity for site visits as part of WCTE 2025; whilst some stunning examples of modern timber buildings can also be seen in Sydney, Melbourne and Perth.

Our host city of Brisbane, is the capital of the State of Queensland; Australia's favourite tourist region and host of the 2032 Olympic Games. It is an ideal location for both the WCTE conference and extending your trip to visit some of the natural wonders of this part of Australia.

WCTE 2025 is supported by the Queensland Government through Tourism and Events Queensland and features on the It's Live! in Queensland events calendar.

For more information on WCTE 2025, please visit **www.wcte2025.org**

SUPPORTED BY

Tourism & Events Queensland

Australian Government Australian Research Council

ADVANCE TIMBERHUB

The University Of Queensland AUSTRALIA

brisbane ECONOMIC DEVELOPMENT AGENCY